



## Galvanic Cells Containing Cathodes of Iron-Doped Beta-Alumina

John H. Kennedy\* and Anthony F. Sammells\*\*

Department of Chemistry, University of California, Santa Barbara, California 93106

### ABSTRACT

Galvanic cells of the form Na/ $\beta$ -alumina/ $\text{Na}_2\text{O}\cdot 11(\text{Fe}_x\text{Al}_{2-x}\text{O}_3)$  where  $x$  varied between 0.9 and 1.2 were operated at 120°C, and currents of 50 mA/cm<sup>2</sup> could be drawn. The cells were electrochemically regenerative, and the cathodes could be thermally regenerated. Initial open-circuit voltages varied between 2.37 and 2.45V. Cells were discharged at constant current, and two distinct voltage regions were observed. The reduction process was investigated by Mössbauer spectroscopy. The lower voltage region was shown to involve the reduction of Fe<sup>3+</sup> to Fe<sup>2+</sup>. The higher voltage region is possibly explained by the filling of holes in the valence band of the iron-doped spinel-type structure, created during the sintering process.

Sodium  $\beta$ -alumina  $\text{Na}_2\text{O}\cdot 11 \text{Al}_2\text{O}_3$  has become increasingly attractive as an electrolyte in recent years due to its relatively high conductivity and its applicability to alkali metals (sodium in particular) as potential anode materials. Beta-alumina single crystals have been shown to exhibit rapid sodium ion diffusion in the plane perpendicular to the  $c$ -axis (1), and the sodium ions can be almost completely exchanged in molten salts for Ag, K, Li, Rb, and to a lesser extent Cs ions. This ion exchange property infers ion conductivity and makes  $\beta$ -alumina an electrolyte also worthy of consideration in any battery systems that incorporate K or Li as anode materials. Sodium ions, however, exhibit the largest diffusion coefficient, the mechanism of which has been shown to be interstitial. Interest in  $\beta$ -alumina as a sodium ion conducting electrolyte has revolved around its use in the sodium/sulfur battery first reported by Kummer and Weber (2). This battery operates in excess of 300°C due to the high melting point of the sodium polysulfide cathode material used. Many of the early investigations with  $\beta$ -alumina as a sintered polycrystalline material were concerned not only with the achievement of high conductivity but also with the deterioration of the electrolyte at such temperatures. The development of batteries operative at temperatures considerably below 300°C has been limited by low conductivities of the sintered electrolyte material and the availability of suitable cathode materials. Recent investigations (3-5) have shown that sodium ion conductivity in sintered  $\beta$ -alumina can be sufficiently increased by the incorporation of MgO to make  $\beta$ -alumina feasible as an electrolyte at temperatures considerably below 300°C.

Cathode materials for  $\beta$ -alumina galvanic cells present more formidable problems. The substitution of M<sup>3+</sup> transition metals for Al<sup>3+</sup> sites in  $\beta$ -alumina was first suggested for cathode material by Hever (6) who synthesized cathode materials of the stoichiometry (a)  $\text{Na}_2\text{O}\cdot 5(\text{Fe}_{0.95}\text{Ti}_{0.05}\text{AlO}_3)$ , and (b)  $1.3 \text{K}_2\text{O}\cdot 0.2\text{Na}_2\text{O}\cdot 10$

( $\text{Fe}_{1.9}\text{Ti}_{0.1}\text{O}_3$ ). Cell (a) used the electrolyte M-brick (Harbison-Carborundum) which consists of an  $\alpha$ -alumina/ $\beta$ -alumina eutectic in which the presumed mobile species was Na<sup>+</sup>. The electrolyte used in cell (b) was  $1.3 \text{K}_2\text{O}\cdot 0.2 \text{Li}_2\text{O}\cdot 10 \text{Al}_2\text{O}_3$  in which K<sup>+</sup> was assumed to be the mobile species. In these cells both of the electrodes consisted of the same material, and the cell was charged after fabrication. The transition metal ions were considered to be immobile, and the electrochemical process taking place in the cathode did not involve a phase change. It was postulated that the measured voltage came from the reduction of M<sup>3+</sup> to M<sup>2+</sup> accompanied by the migration of Na<sup>+</sup> through the electrolyte to maintain electroneutrality. Titanium dioxide was added to the cathode material to increase the electronic conductivity by providing Fe<sup>2+</sup> donor ions. These cells ran at 300°-500°C under vacuum (10<sup>-4</sup> Torr) and exhibited potentials of < 1V. The cells had identical electrodes in which one acted as an anode while the other acted as a cathode. The charge capacity was limited by the availability of Na<sup>+</sup> in the electrolyte material. In order to devise a cell using sodium  $\beta$ -alumina electrolyte which is not limited by the amount of electrolyte material, the anode must supply the needed sodium ions. The natural choice for such an anode is sodium metal. We report here electrochemical cells which were operated at temperatures just above the melting point of sodium and contained sintered cathodes in which some of the Al<sup>3+</sup> sites were replaced by Fe<sup>3+</sup> in the  $\beta$ -alumina structure.

### Experimental

*Preparation of  $\beta$ -alumina cups prior to sintering.*—Beta-alumina (Alcoa 325 mesh) was ground to particle size 0.5-1 $\mu$  in an alumina grinding mill using alumina balls. Ethylene glycol was used as a grinding aid, and the final particle size was determined with a Unitron 11 microscope. The 2% MgO and 1.7% Na<sub>2</sub>CO<sub>3</sub> of similar particle size were mixed with the ground  $\beta$ -alumina in a mechanical Fisher alumina mortar and pestle. To this material was then added a binder (2% carbowax 1000 as a 10% aqueous solution). Thick pellets (0.85 cm) were made in a KBr-type press using pressures of

\* Electrochemical Society Active Member.

\*\* Electrochemical Society Student Associate.

Key words: battery cell, beta-alumina, iron spinels, Mössbauer spectroscopy, sodium electrode.

80,000 psi, and the binder was removed by slowly heating to 400°C and leaving 24 hr. The pellets were then pre-fired at 1100°C for 1 hr so that a cup could be drilled with a 11/32 in. flat bottom drill bit, while holding the pellet in a wooden jig.

**Sintering conditions.**—The pre-fired  $\beta$ -alumina cups were sintered in an Astro ultra-high temperature graphite resistance furnace Model No. 1000A-2560 under oxidizing conditions with the use of an alumina muffle tube assembly. The graphite heating elements surrounding the alumina muffle tube were protected by a nitrogen atmosphere. The cups were placed face down and covered with coarse 325 mesh  $\beta$ -alumina during the sintering so as to provide an alkaline atmosphere and hence reduce the loss of sodium. The cups together with the  $\beta$ -alumina packing were kept covered in an alumina crucible during the sintering. Heating rates of 250°C/hr were employed so as to prolong the muffle tube life. Temperatures of 1750°–1860°C were controlled with a boron-graphite thermocouple and maintained for extended periods of time up to 8 hr. Recorded temperatures were measured directly by use of a Micro-Optical pyrometer (Pyrometer Instrument Company) through a viewing port in the side of the furnace.

**Cathode materials and cell fabrication.**—In the  $\beta$ -alumina care was given to the particle size and homogeneity of the 2% MgO added. Excess sodium was incorporated by the addition of 1.7%  $\text{Na}_2\text{CO}_3$  before sintering the electrolyte. The thick pellets (ca. 1g) were made at 80,000 psi and did not give laminations as have been found with thinner pellets (ca. 0.3g, 0.25 cm thick). Attempts to drill the pellet immediately after pressing were unsuccessful, and a pre-firing at 1100°C after binder removal gave the pellet sufficient cohesion to allow the use of a flat bottom drill-bit.

Cathode materials were synthesized by heating stoichiometric amounts of  $\text{Al}_2\text{O}_3$ ,  $\text{Fe}_2\text{O}_3$ ,  $\text{TiO}_2$ , and  $\text{Na}_2\text{CO}_3$  at 1100°C for between 1 and 24 hr until an x-ray pattern was observed, indicating the presence of the  $\beta$ -structure. The cells were fabricated by placing a sintered cup face down in  $\beta$ -alumina packing and resting a pressed pellet of cathode material on the cup base. Care was taken that the packing was not in contact with the cathode material. This pair was then sintered at between 1520° and 1620°C in a closed alumina crucible for between 5 min and 1 hr, after which the cathode fused to the electrolyte.

**The sodium electrode.**—All procedures with molten sodium were carried out in an Overly Model B-100 dry box equipped with a nitrogen recirculating system, consisting of heated catalysator-pellets (BASF) to reduce  $\text{O}_2$  to  $\text{H}_2\text{O}$ . Molecular sieves were used to trap water. The molten sodium was transferred rapidly from a heated beaker by means of a small dropping pipette into the recess of the heated cell. After the sodium had been added to the cell, it was found necessary to press the sodium down into the cup to ensure contact with the electrolyte. The cell was then transferred rapidly with the molten sodium (the sodium was not allowed to solidify) to the heated conductivity jig.

**Cell measurements.**—A Bissett-Berman Corporation E-cell digital coulometer was used for constant current discharge and charge of cells. A Harrison 6112A d-c power supply across suitable resistances was used as a constant current source when small changes in current were required.

**Application of thin films.**—Gold evaporations were performed in a Veeco 776 automatic high vacuum evaporator and an Edwards Model E12E3 thin film evaporator.

**Mössbauer spectroscopy.**—A 256 multichannel analyzer (Northern Scientific Company) was used in the multiscaler mode. The constant acceleration mode was used with a triangular wave form. For detecting the

14.4 keV Mössbauer line a proportional counter was used. The source was a 20 mcurie  $\text{Co}^{57}/\text{Pd}$ .

**X-ray diffraction.**—X-ray diffraction of cathode materials was performed with Philips Electronics Instruments x-ray diffraction equipment using  $\text{CuK}\alpha$  radiation, a Philips Type 52572 scintillation counter, and a chart recorder.

## Results

Before the development of cathode materials could be pursued, the nature of sodium as an anode material was investigated. A cell of the form  $\text{Na}/\beta\text{-alumina}/\text{Au}$  was fabricated by using a pool of sodium in the cup and evaporated gold on the cup base. The 1 kHz resistance values were measured at different temperatures above and below the melting point of sodium. Figure 1 shows that at temperatures above the melting point of sodium (98°C), the resistance of the cell was about 20 ohms or less. When the high temperature line was extrapolated back to 25°C, the resistivity (300 ohm-cm) was about the same as that observed during our previous conductivity studies for  $\beta\text{-Al}_2\text{O}_3$  compositions containing 2% MgO and using two inert metal electrodes (4). Below 98°C the cell resistance rose rapidly and was not stable with time. The two lines intersected at the melting point of sodium indicating that molten sodium formed a satisfactory electrode/electrolyte interface while solid sodium did not. It appeared that the loss of contact between solid sodium and  $\beta$ -alumina was probably caused by a lack of wetting by molten sodium allowing it to pull away when cooled. Wetting could be improved by heating the cell to > 300°C for 16 hr before cooling, but the contact was still not satisfactory. Therefore, all subsequent investigations with cells containing pure sodium were performed at temperatures above its melting point.

Cathode materials were synthesized directly from  $\text{Al}_2\text{O}_3$ ,  $\text{Fe}_2\text{O}_3$ ,  $\text{Na}_2\text{CO}_3$ , and  $\text{TiO}_2$ , with the initial stoichiometries  $\text{Na}_2\text{O}\cdot 5(\text{Fe}_{0.95}\text{Ti}_{0.05}\text{AlO}_3)$  and  $\text{Na}_2\text{O}\cdot 11(\text{Fe}_x\text{Al}_{2-x}\text{O}_3)$  where  $x$  ranged from 0.9 to 1.2. The incorporation of  $\text{TiO}_2$  in some of the samples was intended to increase the electronic conductivity by giving rise to Fe donor ions as reported by Hever (6). However, we found no significant reduction in our cell resistances for material containing  $\text{TiO}_2$ . X-ray diffraction data indicated the presence of a small amount of  $\alpha\text{-Al}_2\text{O}_3$  in all samples.

During sintering the cathode material rested on top of the electrolyte and conditions had to be determined which would sinter the cathode both to itself and the electrolyte. Too high a temperature allowed the cathode material to diffuse all the way through the electrolyte, whereas too low a temperature resulted in

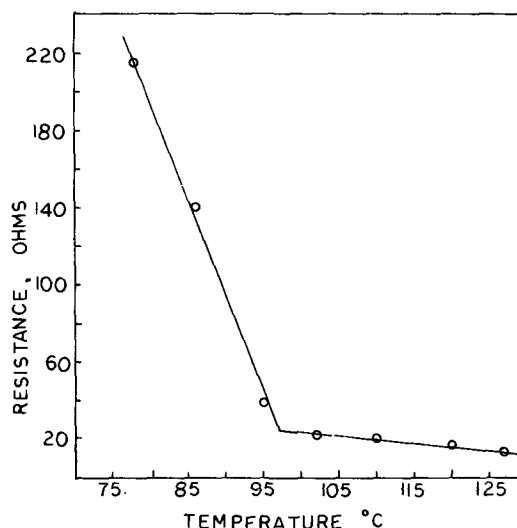


Fig. 1. Variation of pellet resistance at 1 kHz with temperature for the cell  $\text{Na}/\beta\text{-Al}_2\text{O}_3/\text{Au}$ .



poor contact between the electrolyte and cathode and thus gave high cell resistances. Different sintering procedures were necessary for each cathode material used. Generally temperatures in the range 1520°-1600°C for 5 min to 1 hr were adequate. For material of stoichiometry  $\text{Na}_2\text{O}\cdot 11(\text{Fe}_x\text{Al}_{2-x}\text{O}_3)$  all attempts to sinter this cathode material with  $x$  values of 0.3 and 0.6 to the electrolyte were unsuccessful. With higher iron content the cell fabrication became easier. Above  $x$  values of 1.2 x-ray patterns indicating the  $\beta$ -structure were not observed. All the iron-containing cathode materials indicated the presence of some  $\text{Fe}_2\text{O}_3$ . Mössbauer spectroscopy also showed the presence of  $\text{Fe}^{2+}$  (even in the absence of  $\text{TiO}_2$ ).

All cells were discharged and charged in a dry box. The experimental setup of the cells is shown in Fig. 2. The cells were operated at 120°C to avoid the sodium/electrolyte interface problem described above. Open-circuit voltage for these cells was 2.37-2.45V, and currents as high as 40-50 mA/cm<sup>2</sup> could be drawn from them. A typical load curve is shown in Fig. 3. Up to about 30 mA/cm<sup>2</sup> the slope indicated a d-c cell resistance of 40 ohms compared to the a-c value of 26 ohms.

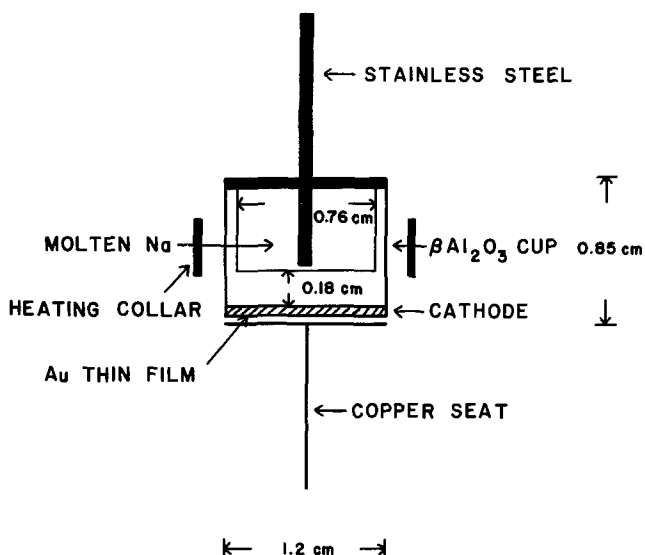


Fig. 2. Experimental set-up of cell. Electrode area: 0.45 cm<sup>2</sup>

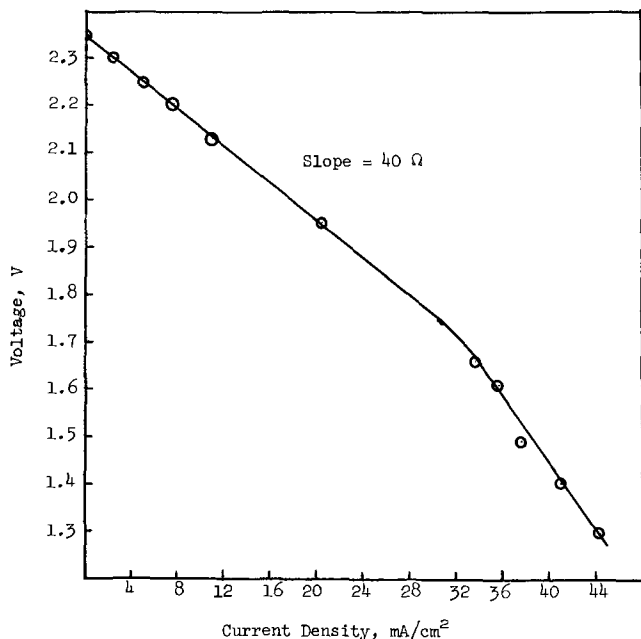


Fig. 3. Load curve for  $\text{Na}/\beta\text{-Al}_2\text{O}_3/\text{Na}_2\text{O}\cdot 11(\text{Fe}_{0.95}\text{Ti}_{0.05}\text{AlO}_3)$  cell at 120°C.

Above 30 mA/cm<sup>2</sup> the voltage dropped more rapidly indicating the presence of significant polarization effects. Most cells were discharged under constant current conditions although constant load was used in some cases. An open-circuit potential of 2.37V has been maintained by a cell for 12 months at 120°C without any apparent variation due to electronic shorting or chemical effects leading to self-discharge.

Cells discharged either by constant current (ca. 0.7 mA/cm<sup>2</sup>) or constant load (10 kohms) exhibited two distinct voltage regions as shown in Fig. 4. Approximately one-third of the total discharge was in the high voltage region in which the cell voltage fell almost linearly with depth of discharge. The second voltage region was observed around 0.9V and exhibited a slower voltage decay until 20-40% of the iron atoms had been reduced an average of one electron/iron atom. The total amount of charge which could be drawn was dependent on the current density used in the discharge. Cells discharged at 350  $\mu\text{A}$  delivered ca. 25% of theoretical for one electron/iron atom, Fig. 4, whereas cells discharged at 36  $\mu\text{A}$  delivered in excess of 40% of theoretical, Fig. 5. In each case the cell could be recharged to the starting potential by the passage of an equivalent amount of charge at a similar current density. The cell voltage during charge at 350  $\mu\text{A}$  tracked the voltage during discharge quite closely, Fig. 6. Cells have undergone as many as ten charge-

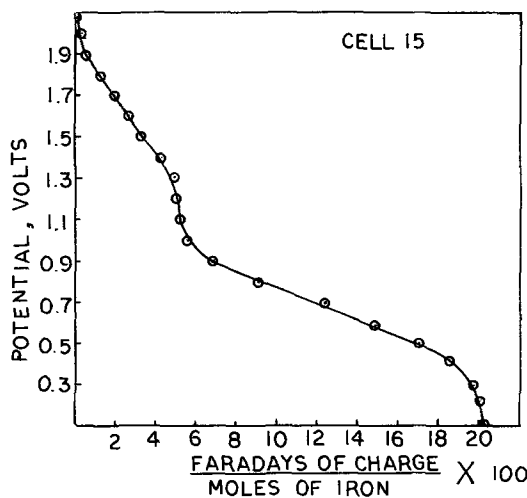


Fig. 4. Discharge curve for  $\text{Na}/\beta\text{-Al}_2\text{O}_3/\text{Na}_2\text{O}\cdot 11(\text{FeAlO}_3)$  cell at 120°C, 0.75 mA/cm<sup>2</sup>.

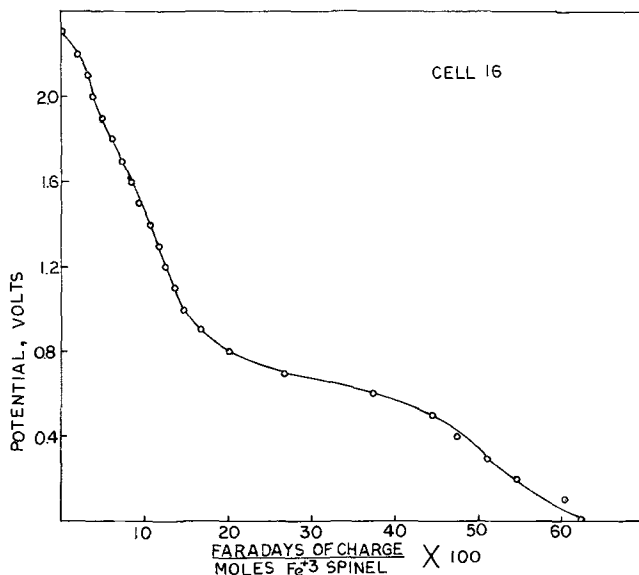


Fig. 5. Discharge curve for  $\text{Na}/\beta\text{-Al}_2\text{O}_3/\text{Na}_2\text{O}\cdot 11(\text{FeAlO}_3)$  cell at 120°C, 0.077 mA/cm<sup>2</sup>.

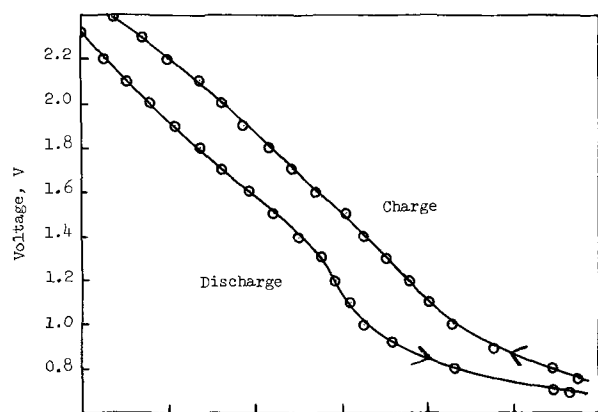


Fig. 6. Charge-discharge cycle for  $\text{Na}/\beta\text{-Al}_2\text{O}_3/\text{Na}_2\text{O}\cdot 11(\text{Fe}_{0.95}\text{Ti}_{0.05}\text{AlO}_3)$  cell at  $120^\circ\text{C}$ ,  $0.75\text{ mA/cm}^2$ .

discharge cycles with no apparent damage and coulombic efficiency close to 100% (Table I). Cells could also be charged to a higher voltage than the original value up to 2.7V (Fig. 7). At this point the charging voltage at constant current rose rapidly while the open-circuit voltage reached a plateau value.

The possible thermal regeneration of the cathode material was investigated after the complete discharge of cell No. 18 (Fig. 8, curve B) containing the cathode material  $\text{Na}_2\text{O}\cdot 11(\text{Fe}_{0.9}\text{Al}_{1.1}\text{O}_3)$  on the second discharge. The sodium was carefully removed in the dry box, the cell was heated to  $1500^\circ\text{C}$  for 10 min in an oxidizing atmosphere, and a fresh gold thin film electrode was deposited on the cathode. Upon addition of a molten sodium anode at  $120^\circ\text{C}$  the cell again gave an open-circuit potential of 2.3V and was discharged at  $315\ \mu\text{A}$  as shown in Fig. 8, curve A.

A Mössbauer spectrum (Fig. 9) was run on a cell prior to its discharge to determine the electrochemical process taking place in the cathode material  $\text{Na}_2\text{O}\cdot 11(\text{FeAlO}_3)$ . A gold electrode was then evaporated onto the cathode, sodium was added to the cup in the dry box, and the cell was then discharged at  $36\ \mu\text{A}$  (Fig. 5) to zero voltage. It was necessary for a successful Mössbauer experiment to have approximately 0.05g of cathode material which contained about 0.02g of iron. This cell was discharged 43.5% of theoretical assuming one electron/iron atom. After complete discharge of the cell the sodium was removed from the cup by a pipette while still molten, any residual sodium being scraped off in the dry box. A second Mössbauer spectrum shown in Fig. 10 was run in an analogous manner to the initial one. From the spectra, four of the six magnetically split lines due to  $\text{Fe}_2\text{O}_3$  can be seen which did not go into the spinel block during the cathode synthesis. These lines occur at velocities of  $-0.805$ ,  $-0.43$ ,  $+0.54$ , and  $+0.87\text{ cm/sec}$ . The other two peaks of  $\text{Fe}_2\text{O}_3$  occur at  $-0.08$  and  $+0.2\text{ cm/sec}$  and were not observable because of one of the  $\text{Fe}^{2+}$  quadrupole

Table I. Cell No. 4 discharge-charge cycles at  $350\ \mu\text{A}$ ,  $120^\circ\text{C}$

Discharge			Charge		
Cycle	Coulombs	Final voltage, V	Cycle	Coulombs	Final voltage, V
No. 1 Start	30.1	0.7	No. 1	27	2.35
No. 2	31.2	0.65	No. 2	28.4	2.36
No. 3	28.6	0.69	No. 3	26.5	2.34
No. 4	26.6	0.67	No. 4	26.5	2.32
No. 5	24.7	0.7	No. 5	24.7	2.42
No. 6	29.2	0.62	No. 6	35.1	2.7
No. 7	31.4	0.60	No. 7	32.9	2.6
No. 8	32.9	0.53	No. 8	27.9	2.58
No. 9	28.2	0.53	No. 9	26.8	2.45
No. 10	36.5	0			
Total discharge 262.9 coulombs, No. 1-9			Total charge 255.8 coulombs		
Total discharge 299.4 coulombs					

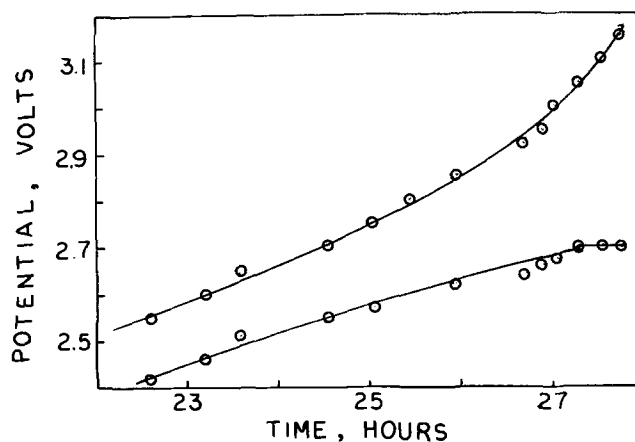


Fig. 7. Charging voltage for  $\text{Na}/\beta\text{-Al}_2\text{O}_3/\text{Na}_2\text{O}\cdot 11(\text{Fe}_{0.95}\text{Ti}_{0.05}\text{AlO}_3)$  cell at  $120^\circ\text{C}$ . Top curve: charging voltage at  $0.75\text{ mA/cm}^2$ . Lower curve: cell open-circuit potential.

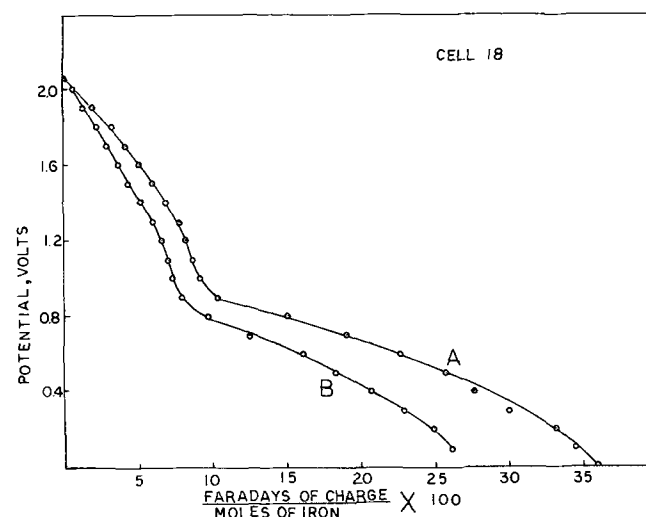


Fig. 8. Discharge curves for cell  $\text{Na}/\beta\text{-Al}_2\text{O}_3/\text{Na}_2\text{O}\cdot 11(\text{Fe}_{0.9}\text{Al}_{1.1}\text{O}_3)$  before (B) and after (A) thermal regeneration. Discharge current  $0.68\text{ mA/cm}^2$ .

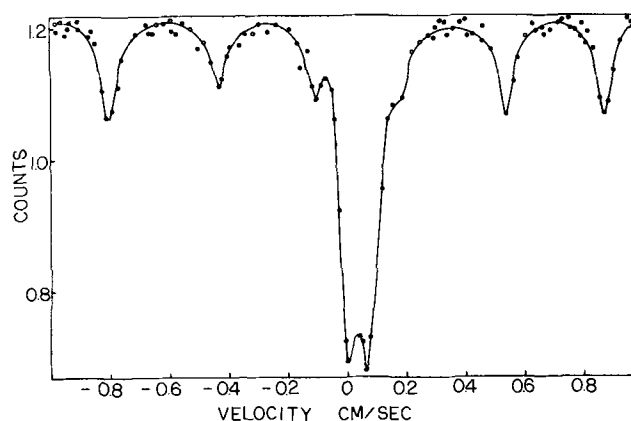


Fig. 9. Mössbauer spectrum of  $\text{Na}_2\text{O}\cdot 11(\text{FeAlO}_3)$  cathode material before discharge.

splittings at  $-0.105\text{ cm/sec}$  and the intense  $\text{Fe}^{3+}$  quadrupole splittings at  $+0.013$  and  $+0.065\text{ cm/sec}$ . It is immediately clear from the spectra that there was an increase in the  $\text{Fe}^{2+}$  peak at  $-0.105\text{ cm/sec}$  and a reduction in the  $\text{Fe}^{3+}$  lines at  $+0.013$  and  $+0.065\text{ cm/sec}$  after discharge of the cell. The  $\text{Fe}^{2+}$  peak at  $-0.105\text{ cm/sec}$  had a contribution from the magnetically split  $\text{Fe}_2\text{O}_3$  line at  $-0.08\text{ cm/sec}$ . A reasonable estimate for this contribution would be one-third the area of the peak at  $-0.805\text{ cm/sec}$  since the magnetically split lines are in the approximate area ratio of 3:2:1. The

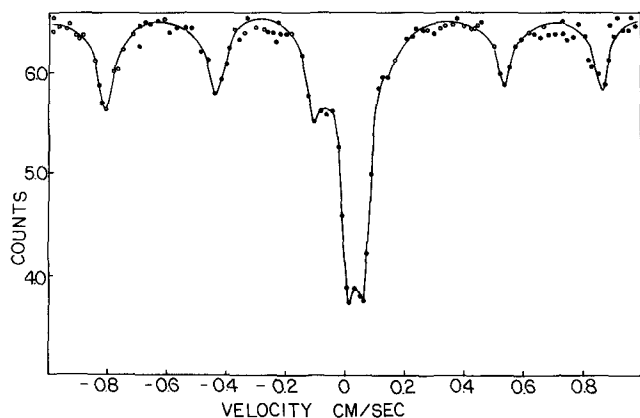


Fig. 10. Mössbauer spectrum of  $\text{Na}_2\text{O}\cdot 11(\text{FeAlO}_3)$  cathode material after discharge to zero volts at  $0.077 \text{ mA/cm}^2$ .

relative areas of the  $\text{Fe}_2\text{O}_3$  peak at  $-0.805 \text{ cm/sec}$  before and after discharge were 5.55 and 6.8, respectively, (arbitrary units used) and therefore the areas of the  $\text{Fe}_2\text{O}_3$  peak at  $-0.08 \text{ cm/sec}$  were estimated at 1.85 before and 2.27 after discharge. Different count rates were used in each Mössbauer experiment.

The area changes taking place in the Mössbauer spectrum before and after discharge can be seen in Table II. These data give a qualitative picture for the reduction process taking place in the cathode. Only 70% of the iron is in the spinel sites of the cathode before discharge. For 70% of the iron atoms active we would expect a maximum charge capacity of 23.3 coulombs assuming a one electron reduction per iron atom. The 14.6 coulombs of charge actually delivered therefore represented 62.5% of theoretical. Over 70% of the total charge was in the low voltage region below 0.9V.

The fact that the increase in the  $\text{Fe}^{2+}$  peak (4% of 31.6 coulombs = 1.3 coulombs) did not correspond to the expected change on the basis of charge passed (14.6 coulombs total charge of which 4.3 coulombs were in high voltage region and 10.3 coulombs in low voltage region) can be explained by air oxidation of the cathode material during recording of the Mössbauer spectrum. The cell voltage was found to be sensitive to impurities such as oxygen in the dry box and when air was purposely introduced, the cell voltage was found to rise even while being discharged under constant current. This enhanced cathode performance was observed in both the high and low voltage regions.

Cell No. 16 was thermally reactivated by heating to  $1500^\circ\text{C}$ , and a further Mössbauer spectrum was taken (Fig. 11). This indicated not only a reduction in the  $\text{Fe}^{2+}$  peak at  $-0.105 \text{ cm/sec}$  but the incorporation of the majority of the remaining  $\text{Fe}_2\text{O}_3$  into the  $\text{Fe}^{3+}$  spinel block sites. The cell was subsequently discharged

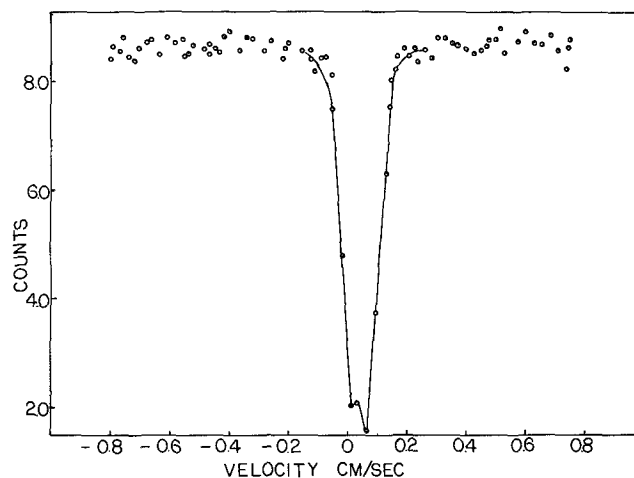


Fig. 11. Mössbauer spectrum of  $\text{Na}_2\text{O}\cdot 11(\text{FeAlO}_3)$  cathode material after thermal regeneration at  $1500^\circ\text{C}$ .

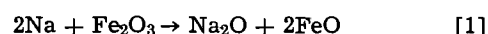
at  $36 \mu\text{A}$  to 1.0V so as to determine whether the reduction of  $\text{Fe}^{3+}$  to  $\text{Fe}^{2+}$  occurred in the high or low voltage region or both. The Mössbauer spectrum after discharge indicated that no apparent reduction of the  $\text{Fe}^{3+}$  had taken place in the high voltage region. The reduction of the  $\text{Fe}^{3+}$  must therefore occur only in the low voltage region, and some other electrochemical process must be responsible for the high voltage region.

High electronic and ionic conduction are essential to any efficient cathode system. The presence of electronic conductivity in the cathode material  $\text{Na}_2\text{O}\cdot 11(\text{FeAlO}_3)$  was determined by fabricating the cell  $\text{Au}/\text{Na}_2\text{O}\cdot 11(\text{FeAlO}_3)/\text{Au}$  and placing a constant d-c voltage across it. Under such conditions, the Au thin film electrodes acted as blocking electrodes to the migration of ionic current through the cell. The current measured through the circuit should therefore be due to the electronic conductivity within the cell. The d-c resistance was 890 ohms at  $120^\circ\text{C}$  and did not vary appreciably over a period of several days. From the d-c resistance and the pellet dimensions (1 cm diameter  $\times$  0.45 cm thick) the electronic conductivity was estimated to be  $6.7 \times 10^{-4} (\text{ohm}\cdot\text{cm})^{-1}$ . When a-c measurements were made on the same cell frequency dependency was found indicating that some ionic conduction was also present in the cathode.

### Discussion

In this approach we have attempted to substitute  $\text{Fe}^{3+}$  ions for  $\text{Al}^{3+}$  ions in the spinel block and use this material as a cathode in which there would be no physical phase boundary between cathode and electrolyte and no phase change in the reduction process. The  $\text{Fe}^{3+}$  in the spinel block would be reduced to  $\text{Fe}^{2+}$  and a  $\text{Na}^+$  ion would move into the layer-type structure to maintain charge balance. From the Mössbauer spectrum of cell No. 16 it appeared that 70% of the iron resided in the  $\text{Al}^{3+}$  sites of the spinel block after the synthesis sintering with the rest of the iron being in the reduced  $\text{Fe}^{2+}$  form or as unincorporated  $\text{Fe}_2\text{O}_3$ . From x-ray diffraction analysis these cathode materials had a spinel-type structure analogous to  $\beta$ -alumina, and the presence of unreacted  $\text{Fe}_2\text{O}_3$  was detected.

From the discharge curves two voltage regions were observed. The lower one around 0.7V can be explained on the basis of the reaction

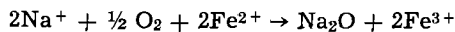


for which the theoretical voltage is 0.71V based on free energies of formation. Further evidence for this process in the low voltage region comes from the Mössbauer spectra. The cell after discharge to zero volts showed a significant increase in the  $\text{Fe}^{2+}$  peak together with a corresponding decrease in the  $\text{Fe}^{3+}$  peak, whereas after being thermally regenerated and then discharged down

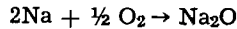
Table II. Cell No. 16 Mössbauer spectra peak areas

Line position, cm/sec		Area (arbitrary units) before discharge	Area (arbitrary units) after discharge	
$\text{Fe}_2\text{O}_3$	-0.805	5.55	6.8	
	-0.43	3.55	5.22	
	-0.08	1.85 (est.)	2.27 (est.)	
	+0.20	1.85 (est.)	2.27 (est.)	
	+0.54	4.08	3.75	
	+0.87	5.4	5.92	
$\text{Fe}^{3+}$ (spinel block)	+0.013	31	27.6	
	+0.065	32.7	27.5	
$\text{Fe}^{2+}$ (spinel block)	-0.105	5.6 (est.)	9.9 (est.)	
Area changes				
Fe species	Before		After	
	Area	Rel. area, %	Area	Rel. area, %
$\text{Fe}^{3+}$ (spinel block)	63.7	70	55.1	61
$\text{Fe}^{2+}$ (spinel block)	5.6	6	9.9	10
$\text{Fe}_2\text{O}_3$	22.3	24	26.2	29
Total area	91.6		90.2	

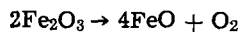
to 1.0V no apparent reduction had taken place. The following oxidative process is proposed to take place at the cathode in the presence of air simultaneously with the electrochemical reduction process



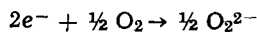
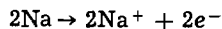
with the  $\text{Na}_2\text{O}$  being formed on the outer surface of the cathode. A white film was observed to form on the surface of the cathode after extensive discharge. Thus, the cell appeared to show some characteristics of a fuel cell in which the over-all reaction is



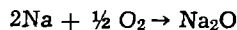
Here the reductant is Na and the oxidant is  $\text{O}_2$  from the atmosphere via the  $\text{Fe}^{3+}/\text{Fe}^{2+}$  couple. This would also explain the thermal regenerative capability of the cathode. The high voltage region is more difficult to explain but there appear to be three possibilities, (a) trapped  $\text{O}_2$  gas, (b) iron in oxidation states greater than plus three, and (c) vacancies in the valence band created by excess  $\text{O}^{2-}$ . The fact that the cells were sensitive to  $\text{O}_2$  leads to the hypothesis that the presence of  $\text{O}_2$  gas trapped in the sintered cathode material would exhibit high voltages. This could be present from two sources. The first is the trapping caused during the sintering process of the cathode. High porosity would be expected since the particle sizes before sintering were much larger ( $> 50\mu$ ) than those used in the sintering of the electrolyte ( $1\mu$ ) and shorter sintering times were used with the cathode. The second source of  $\text{O}_2$  could come from  $\text{Fe}^{2+}$  produced during the sintering from the reaction



The presence of  $\text{O}_2$  gas would give rise to the electrochemical process



over-all reaction

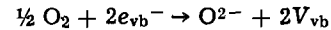


The theoretical voltage for this process is 2.17V based on free energy of formation for  $\text{Na}_2\text{O}$ . With the cathode density of about 3.0 and from a consideration of the volume of  $\text{O}_2$  required for this high voltage region, we calculate an oxygen pressure in excess of 200 atm (assuming a 10% porosity). When we consider the conditions under which the cathode was synthesized such pressures are not realistic. There is also the related mechanism of slow  $\text{O}_2$  migration into the cathode from the traces present in the dry box. However, for this mechanism one would expect the high voltage region charge capacity to be current density dependent. Very little, if any, such dependence was found unlike the low voltage region which was discussed above.

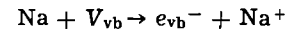
If the oxygen were chemisorbed its pressure need not be 200 atm. A monolayer of chemisorbed oxygen on particles of  $10\mu$  radius would constitute a charge of 0.2 coulomb for the 400 mg cathodes used. This is only a fraction of the 5 coulombs observed, but chemisorbed layers are often thicker than one monolayer. On the other hand, after sintering, the particles are no longer  $10\mu$  radius, and thus this estimate of charge is probably much too high. Also, if the high voltage region were due only to chemisorbed oxygen the discharge curve should be Nernstian (not the nearly linear decay observed) and should not be iron-dependent as was observed. Chemisorption though may play a part and be the first step in the third hypothesis discussed below.

The possibility of iron in an oxidation state of greater than three although reasonable in view of possible ferrate formation was not indicated in the negative velocity range of the Mössbauer spectra where such an oxidation state would be expected (7). Also, sintered  $\beta$ -alumina cups with no iron-doped cathode and just a thin film metal electrode at the base exhibited potentials in the 2V range. Such cells however

had little charge capacity and the potential quickly decayed during a resistance measurement. This suggested that the high voltage region was not due directly to the doped iron but the charge capacity was an indirect function of the iron content or the sintering characteristics of the cathode material or both. The third hypothesis assumes that at the grain boundaries of the polycrystalline material,  $\text{O}^{2-}$  ions are formed from reduction of chemisorbed  $\text{O}_2$  during the sintering process creating simultaneously electron holes in the valence band of the iron-substituted spinel by the following process



where  $e_{\text{vb}}^-$  is an electron in the valence band and  $V_{\text{vb}}$  is a vacancy in the valence band. That is, highly electronegative oxygen atoms draw electron density from the crystal. For the passage of 4 coulombs in the high voltage region of cell 16,  $4/1.6 \times 10^{-19}$  charge carriers, i.e.,  $1.25 \times 10^{19}$   $\text{O}^{2-}$  species, are required which represents 0.33 mg of  $\text{O}_2$  for 50 mg of cathode. The high voltage region can then be explained on the basis of the reaction



A schematic energy level is shown in Fig. 12. As the valence band becomes filled to point B reduction of  $\text{Fe}^{3+}$  to  $\text{Fe}^{2+}$  will become the favored process in the low voltage region.

Discharge curves showed almost linear decreases in the higher voltage region (Fig. 4-6, 8) which is consistent with the proposed mechanism. In addition, there is no reason to expect the density of states to be constant throughout the voltage range of 2.5-0.7V. A low density of states above 2V and below 1.3V would result in a discharge curve as exhibited by cell No. 15 (Fig. 4). The density of states could be slightly different for each cathode leading to the subtle differences observed for the various cells. On the other hand, the plateau at 0.7V is much more Nernstian in behavior and is explained more simply by the reduction of iron +3. Iron doping is necessary to create the electron energy level proposed, but since no iron is reduced in the high voltage region, no changes in the Mössbauer spectrum were observed for cells discharged to 1V.

The regeneration of the cathode in the high voltage region in the presence of  $\text{O}_2$  can be explained by the following process



In this way, the cell is once again able to accept electrons from the anode with potential differences  $> 2V$ .

The question now remains, can this type of cathode material be incorporated into a practical battery system? The great advantage of this system is its relatively low operating temperature compared to the sodium/sulfur battery in which corrosion and insulation considerations are of major concern.

The current densities that can be drawn from the cell are encouraging, as well as its thermal regenerative capability. The electrochemical reversibility of the cell should be intrinsically long-lived because no phase change takes place in the cathode.

The successful operation of these cells makes  $\beta$ -alumina worthy of serious consideration not only as the electrolyte, but, in the doped form, as the cathode material in electrochemical systems operative much

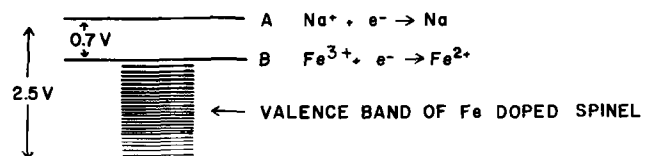


Fig. 12. Suggested electronic energy level diagram for iron-doped spinel.

closer to ambient temperatures than is possible in the sodium/sulfur system.

#### Acknowledgment

The authors acknowledge partial financial support from PHS Research Grant No. 1 RO1 APO 1527-01, Office of Air Programs of EPA and from NSF Grant No. GH-37144. The authors also express thanks to Dr. P. Barrett and his research group for helpful advice and obtaining the Mössbauer spectra.

Manuscript submitted Jan. 19, 1973; revised manuscript received July 6, 1973.

Any discussion of this paper will appear in a Discussion Section to be published in the December 1974 JOURNAL.

#### REFERENCES

1. Y. Y. Yao and J. T. Kummer, *J. Inorg. Nucl. Chem.*, **29**, 2453 (1967).
2. J. T. Kummer and H. Weber, U.S. Pat. 3,404,035, Oct. 1, 1968.
3. I. Wynn Jones and L. J. Miles, *Proc. Brit. Ceramic Soc.*, 161 (1971).
4. J. H. Kennedy and A. F. Sammells, *This Journal*, **119**, 1609 (1972).
5. J. T. Kummer and H. Weber, U.S. Pat. 3,488,271, Jan. 6, 1970.
6. K. O. Hever, *This Journal*, **115**, 830 (1968).
7. T. Shinjo, T. Ichida, and T. Takada, *J. Phys. Soc. Japan*, **29**, 111 (1970).

## Polarization Characteristics and Anodic Disintegration of Beryllium in Nonaqueous Solutions

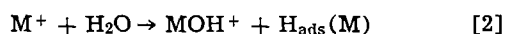
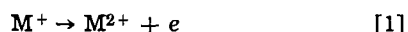
H. Vaidyanathan,\* M. E. Straumanis,\*\* and W. J. James\*

Graduate Center for Materials Research, University of Missouri-Rolla, Rolla, Missouri 65401

#### ABSTRACT

Anodic polarization of Be in both aqueous and nonaqueous media leads to a spalling or disintegration of the anode. The disintegration product is composed of shiny, metallic, crystalline particles embedded in a white brittle mass [BeO and/or Be(OH)<sub>2</sub>] as viewed under an optical microscope. Microstructural studies using scanning electron microscopy provide further proof for the nature and identity of the Be particles. Valency determinations from weight loss measurements give values between 0.34 and 1.75. These anomalous values are attributed to the production of Be by anodic disintegration rather than to a disproportionation reaction of monovalent Be. The "apparent" valency appears to be more a function of the nature of the anion than of the solvent. The apparent valency approaches 1.0 in LiClO<sub>4</sub>/EtOH and KCl/aq and is fractional in LiCl/MeOH. Beryllium is passivated both in aqueous and nonaqueous media containing NO<sub>3</sub><sup>-</sup> ions. Beryllium passivated in NaNO<sub>3</sub>/MeOH has no electronic conduction; the surface when examined optically appears dark with shiny Be crystals on it. Thus anodic disintegration occurs even at potentials where passive oxides predominate on the surface.

The seeming inapplicability of Faraday's law for the anodic dissolution of Be, Zn, Mg, Al, etc. has led to several inquiries into the fundamental aspects of uncommon valency (1-4). The formation of univalent cations as the first stage during anodic dissolution is partly accepted in the case of Al, In, etc. (5, 6). However, the univalent cations react much faster according to



than they are formed and as such there is no evidence for the existence of Zn<sup>+</sup>, Fe<sup>+</sup>, Be<sup>+</sup>, Mg<sup>+</sup>, etc. in solution. The inapplicability of Faraday's law can also be accounted for without considering the formation of stable univalent cations. Straumanis (7) has proposed the phenomenon of anodic disintegration as responsible for this deviation in several instances where anodic spalling is known to occur. This proposition provides a reasonable rationale for the abnormal valences of Be, Zn, Mg, Ag, etc. and the formation of metallic particles in the anolyte solutions. Anodic disintegration, however, is not limited to aqueous solutions alone. This paper presents a case for Be dissolution and the mechanism of anodic disintegration in such anhydrous media as MeOH, EtOH, and dimethyl formamide

(DMF). Anodic disintegration studies in this laboratory were supplemented with microstructural studies using an optical microscope in the past. The present study utilizes a scanning electron microscope also, which has a high resolution and large depth of focus.

#### Experimental

The Be anodes had a purity greater than 99.00%. Circular disks of Be were machined, polished with emery paper, cleansed in an ultrasonic cleaner, degreased with CCl<sub>4</sub> and acetone, and dried in a desiccator. A specially constructed Teflon holder was used to hold these leak-proof Be disks in the electrolyte. The nonaqueous solvents methanol, ethanol, and dimethyl formamide were 99.9% pure. They were purified further by using Davison Type 4A molecular sieves. Valency determinations were carried out as described earlier (8). Prepurified N<sub>2</sub> provided an inert atmosphere in the electrolysis cell. The water content of the electrolyte was determined at the end of each valency study by Karl-Fisher titrations.

Several potential sweep experiments were carried out. Though a steady-state galvanostatic study is extremely simple the potential sweep method enables the evaluation of current density at all potentials within the range of interest and hence the pursuit of passivation stages in the reaction. A Wenking potentiostat externally modulated by an Elron function generator was used. The cyclic current (*i*) vs. potential (*E*) curves obtained at different sweep rates were recorded using

\* Electrochemical Society Active Member.

\*\* Electrochemical Society Active Member, deceased.

Key words: anodic dissolution, anodic disintegration, anomalous valency, scanning electron microscopy, kinetics, nonaqueous electrolytes.

Table I. Apparent valency of beryllium in aqueous solutions\*

Solution and concentration, moles/liter	Current density, mA/cm <sup>2</sup>	Apparent valency, $V_1$
1M KCl	3.8	1.07
	15.4	1.19
	38.5	1.22
1M KI	20	1.41
0.33M K <sub>2</sub> SO <sub>4</sub>	20	1.82
0.01M LiCl + 0.33M K <sub>2</sub> SO <sub>4</sub>	20	1.21

\* Data from ref. (18).

Note: In all electrolytes anodic disintegration occurred.

Table II. Apparent valency of polycrystalline Be in some nonaqueous solutions

Solution and concentration, g-mol/liter	Current density, mA/cm <sup>2</sup>	Apparent valency, $V_1$
0.2M LiCl in MeOH	1.71	0.35
	3.15	0.34
	17.1	0.44
0.2M KI in DMF	3.06	1.75
0.2M NaNO <sub>3</sub> in MeOH	—	*
0.2M LiClO <sub>4</sub> in EtOH	0.613	0.91
	3.06	1.15
	7.66	1.09
	12.25	1.00
	18.40	0.94
	24.5	1.00
30.6	0.98	

\* Valency is indeterminable since the electrode becomes nonconducting due to the formation of a black film on the surface.

Note: Anodic disintegration occurred in all electrolytes. Average water content at the end of each valency determination is in LiCl/MeOH = 0.68%, KI/DMF = 0.30%, NaNO<sub>3</sub>/MeOH = 0.68%, and LiClO<sub>4</sub>/MeOH = 0.4%.

a Mosley 135 AM X-Y recorder. The function generator was adjusted to deliver a single sweep starting at the rest potential. The reference electrode was a freshly prepared Hg/Hg<sub>2</sub>SO<sub>4</sub>/methyl alcohol electrode with a potential of 0.56V vs. NHE in agreement with the literature value (9).

After each valency study, the polarized electrodes were washed with methanol and dried. These were then used for optical and scanning electron microscopic (SEM) studies. In certain cases the electrodes were metalized with Au and then used for the SEM studies.

All experiments were performed at 24° ± 1°C in an all Pyrex "H" cell the two arms of the cell being used to contain the working Be and auxiliary Pt electrodes.

## Results

**Valency studies.**—The apparent valency of Be is a function of several variables. Tables I and II list the values obtained in different electrolytes. The apparent valency approaches one in LiClO<sub>4</sub>/EtOH and KCl/aq. In KI/DMF the value is greater than one and in LiCl/MeOH it is much less than one. In NaNO<sub>3</sub>/MeOH the valency is indeterminable since the electrode loses electronic conductance as the dissolution proceeds. Figure 1 shows the variation of the apparent valency with current density (C.D.). There is a leveling off of the valency at high C.D. Similar behavior was reported earlier by Aida *et al.* (10). Anodic spalling occurs in all cases.

**Current-potential relation.**—Cyclic potential sweep experiments were performed to study the dissolution at varying sweep rates. Potential sweeps from 10-400 mV/sec made no difference in the over-all nature of the *i*-*E* curves. Reproducibility of the curves was best only at sweep rates of 100-200 mV/sec in certain electrolytes. Figures 2-5 show the *i*-*E* behavior in various electrolytes. There is a hysteresis between the anodic (forward) and cathodic (reverse) sweeps in all the curves. Dissolution rates in terms of C.D. are maximum in KCl/aq and least in NaNO<sub>3</sub>/MeOH.

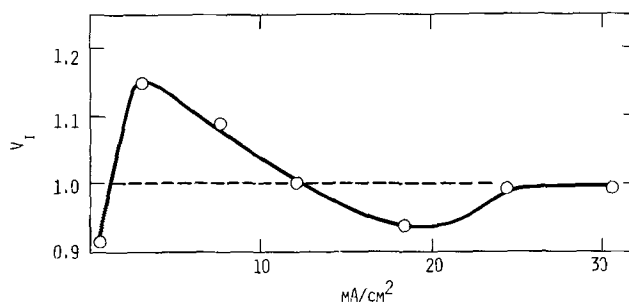


Fig. 1. Apparent valency of Be dissolving anodically in 0.2M LiClO<sub>4</sub>/EtOH. Water content 0.4% by weight at the end of the experiment.

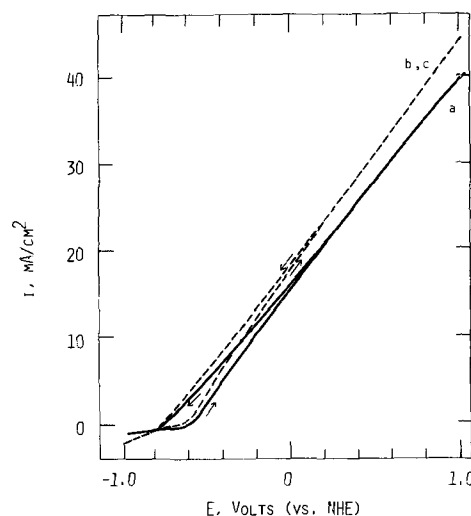


Fig. 2. Cyclic current-potential relations obtained for Be in 0.2M KCl/aq when scanned at 200 mV/sec. Curve a = 1st cycle, curve b = 30th cycle, curve c = 60th cycle.

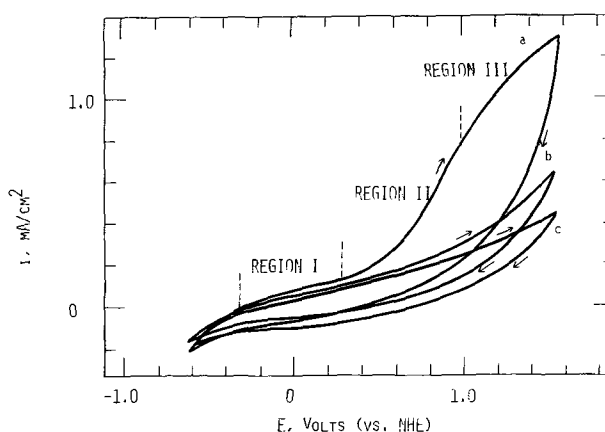


Fig. 3. Cyclic current-potential relation obtained for Be in 0.2M NaNO<sub>3</sub>/aq when scanned at 200 mV/sec. Curve a = 1st cycle, curve b = 3rd cycle, curve c = 8th cycle.

In KCl(aq) and LiCl/MeOH the *i*-*E* relation is very similar, C.D. values being greater during the cathodic sweep and appreciable Be dissolution commencing at approximately the same overvoltage. In KCl(aq) the general shape of the *i*-*E* behavior is unchanged even when scanned 60 times at 200 mV/sec as shown by curves b and c in Fig. 2.

In NaNO<sub>3</sub>/aq the *i*-*E* relation has two transition points dividing the curve into three regions. The rate of Be dissolution is very low up to 0.28V (first transition point) beyond which the rate increases very rapidly up to 0.98V (second transition point). Curves b and c show the effect of repetitive cycling and the magnitude of the C.D. decreases with each subsequent scan.

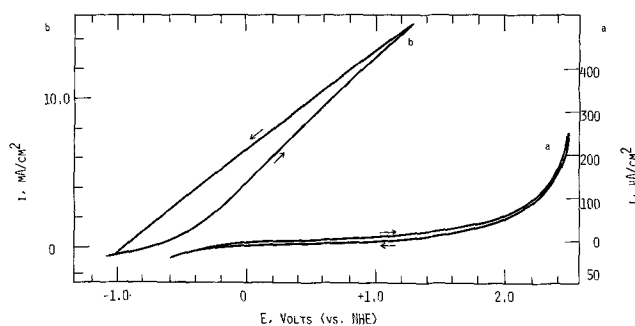


Fig. 4. Cyclic current-potential curves obtained for Be in MeOH when scanned at 200 mV/sec. Curve a = 0.2M NaNO<sub>3</sub>/MeOH, curve b = 0.2M LiCl/MeOH. H<sub>2</sub>O = 0.68% in NaNO<sub>3</sub>/MeOH and 0.76% in LiCl/MeOH.

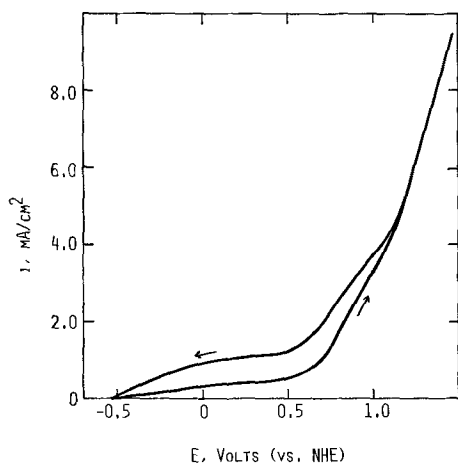


Fig. 5. *i*-*E* relation obtained for Be in 0.2M KI/DMF at a sweep rate of 10 mV/sec. H<sub>2</sub>O = 0.43%.

In NaNO<sub>3</sub>/MeOH the rate of dissolution is very low even at a potential of 2.0V. Methanol oxidation contributes to the C.D. values beyond 2.0V. The electrode surface turns black on repetitive cycling just as it does on prolonged galvanostatic polarization.

The *i*-*E* curve in KI/DMF also shows a transition point. Current density values are very low up to ≈0.7V, beyond which they increase at a greater rate. The electrolyte in the immediate vicinity of the Be anode turns reddish brown during the course of a potential cycle beyond *E* > 0.6V. Since I<sup>-</sup> ions are believed to be oxidized at these overvoltages, there is contribution to the total C.D. from the anode oxidation of I<sup>-</sup> to I<sub>2</sub> and I<sub>3</sub><sup>-</sup>. This is reflected in the C.D. values beyond 0.7V. Anodic disintegration occurs regardless of the I<sub>2</sub> reaction.

The *i*-*E* curves obtained in this study can be used for a comparison of the dissolution rates in the respective media. Current density values at three selected potentials were derived from the *i*-*E* curves obtained at a fixed sweep rate of 200 mV/sec and were used to compose Table III. The variations of C.D. with repetitive potential sweeps were also determined from the *i*-*E* curves. The variations are presented in Table IV.

**Surface studies.**—In all electrolytes studied, large aggregates of black particles appeared in the anolyte. They were filtered, washed, dried, and used for the SEM study. The anode in each experiment was also used for the SEM study. The anodes were heavily pitted. In several instances the anodes were covered with a slime which could be removed only by ultrasonic cleaning. Figure 6 shows the surface structure of a Be anode which has been polarized for 6 hr in 0.2M NaNO<sub>3</sub>/MeOH. Under an optical microscope the surface appears dark with shiny metallic particles on it. Some of the particles are crystalline when viewed by SEM.

Table III. Electrochemical rates of beryllium dissolution in passivating and nonpassivating media

Solution and concentration	H <sub>2</sub> O content as analyzed by KF titration at the end of the expt., %	Reaction rate, i 0.30V	(mA/cm <sup>2</sup> ) at potentials	
			0.68V	1.28V
0.2M NaNO <sub>3</sub> /MeOH	0.68	0.045	0.12	0.304
0.2M NaNO <sub>3</sub> /H <sub>2</sub> O	—	0.131	0.360	1.1
0.2M KI/DMF	0.43	0.88	1.94*	5.3*
0.2M LiCl/MeOH	0.76	8.7	10.3	14.8
0.2M KCl/H <sub>2</sub> O	—	23.8	33.6	—

\* These two data do not truly represent the rates of Be dissolution, since electrochemical oxidation of I<sup>-</sup> occurs under these potentials.

Table IV. Effect of repetitive potential sweeps at 200 mV/sec on the rate of dissolution of Be at 1.0V (NHE)

Electrolyte (0.2M)	Ordinal number of cycles	C.D., mA/cm <sup>2</sup>
KCl/aq	1	41.4
	15	42.1
	30	45.8
	60	46.5
NaNO <sub>3</sub> /aq	1	0.82
	3	0.31
	8	0.24

Figures 7 and 8 show the Be electrode and the anolyte residue when Be is polarized in 0.2M KCl. At the electrode surface, needle-shaped crystals of Be can be recognized readily. Several of the black particles which are in the anolyte appear as hexagonal crystals by SEM.

Figure 9 shows the SEM picture of a Be electrode which has been polarized in 0.2M LiClO<sub>4</sub>/EtOH at 24.5 mA/cm<sup>2</sup>. The surface of the electrode is covered with black particles approximately hexagonal in shape which can be removed only by ultrasonic cleaning.

Figure 10 shows the SEM picture of the anolyte residue obtained when Be is polarized in 0.2M LiCl/MeOH. Some of the particles in the residue have a distinct hexagonal structure.

Figure 11 shows a Be electrode polarized in 0.2M KI/DMF. The surface is covered with particles which have metallic luster. Grain boundaries on the Be surface are also visible.

Anodically disintegrated Be particles embedded in the oxide film can be clearly seen in Fig. 12, which shows a Be anode polarized in LiCl/MeOH. The oxide does not cover the surface totally.

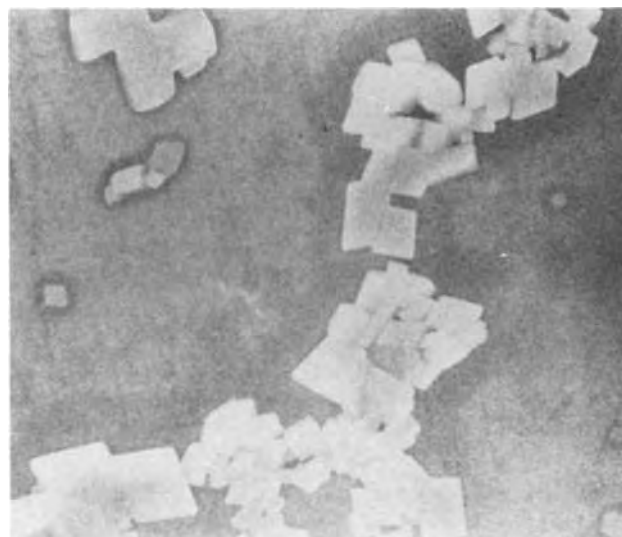


Fig. 6. Be electrode polarized in NaNO<sub>3</sub>/MeOH, H<sub>2</sub>O = 0.68%. Magnification 800X.





Fig. 7. Be electrode surface after polarization in 0.2M KCl/aq. Magnification 800X.

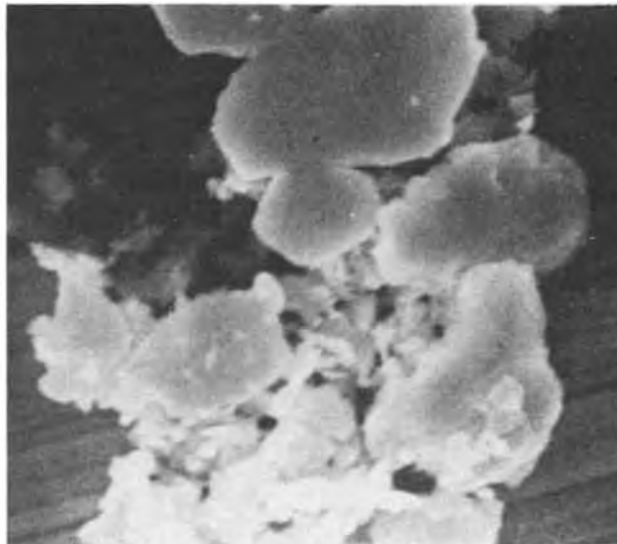


Fig. 10. Anolyte residue obtained when Be is polarized in 0.2M LiCl/MeOH,  $H_2O = 0.60\%$ ,  $V_i = 0.34$ . Magnification 2400X.

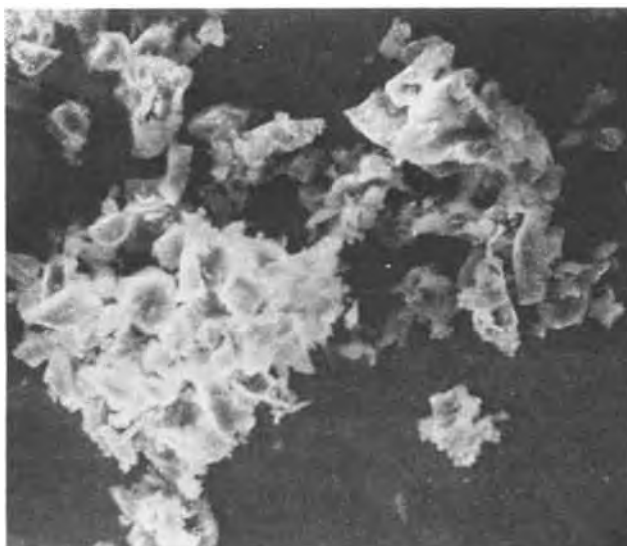


Fig. 8. Anolyte residue obtained when Be is polarized in 0.2M KCl/aq. Magnification 2400X.



Fig. 11. Be electrode surface after polarization in 0.2M KI/DMF,  $H_2O = 0.3\%$ ,  $V_i = 1.75$ . Magnification 800X.



Fig. 9. Be anode polarized in 0.2M  $LiClO_4/EtOH$  at  $24.5 \text{ mA/cm}^2$ ,  $H_2O = 0.4\%$ ,  $V_i = 1.00$ . Magnification 2400X.

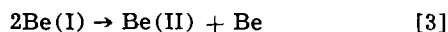


Fig. 12. Be anode polarized in 0.2M LiCl/MeOH,  $V_i = 0.34$ ,  $H_2O = 0.61\%$ . Magnification 2400X.

Large black holes very often occur on the surface. These are not etch pits. They probably arise as a result of detachment of metallic Be leaving a cavity.

### Discussion

The experimental values for the valency of Be (Tables I and II) are interpreted by some as evidence for the formation and existence of both Be(I) and Be(II) in solution (10). One indication of the possible formation of Be(I) is the increased current efficiency for the process as well as the difference between the first and second ionization potentials (11). However, the concept of monovalent ions cannot account for the formation of Be particles in the anolyte unless a disproportionation reaction like



is postulated (10, 12, 13). The source of Be particles, however, in the anolyte has been established clearly as arising from spalling of the electrode as evidenced by the presence of deformation twins on the anode as well as in the anolyte residue (7, 14). In nonaqueous solutions such as methyl alcohol, ethyl alcohol, and dimethyl formamide, the existence of  $\text{Be}^+$  is favored since reaction [2] is believed to take place at a negligible rate. Reaction [2] cannot be totally eliminated since a water content of zero was never obtained at the end of an experiment. If a disproportionation of the type shown in reaction [3] occurs at all, its probability may be the same in aqueous as well as in nonaqueous solution. However, the existence of a long-lived  $\text{Be}^+$ , even in nonaqueous electrolytes, is questionable due to the following facts:

1. Effective valency ( $V_i$ ) as a rule should increase with increase of anodic potential and attain the normal value ( $V$ ) 2.0 (15). Indium and In(Hg) show such behavior and the existence of  $\text{In}^+$  under certain conditions is accepted (6) and in certain others not (16). In the case of Be, however, the valency value levels off at 1.0 at high anodic currents and a value of 2.0 is never obtained.

2. If  $\text{Be}^+$  ions are formed at greater rates than they are consumed by reactions [1] or [3] (considering reactions in nonaqueous solutions), they should diffuse into the bulk of the electrolyte. Thus detection of the univalent ion by polarography and/or ESR should be possible as is the case of Bi (15) by the former method. In the present study the cyclic voltammograms obtained for Be in  $\text{LiCl/MeOH}$  and  $\text{NaNO}_3/\text{MeOH}$  do not show peaks corresponding to two oxidation states (Fig. 4).

3. An apparent valency of less than 1.0, e.g., 0.34 obtained for Be in  $\text{LiCl/MeOH}$  in this study and 0.27 for Mg in  $\text{NaI/pyridine-nitrobenzene}$  (17), can be explained only by assuming a predominant influence of anodic disintegration and/or local corrosion. In no way can the unusual valency or transitory ion concept account for valences less than unity.

4. The anions seem to have a greater effect on  $V_i$  than the medium  $\text{H}_2\text{O}$ ,  $\text{EtOH}$ ,  $\text{MeOH}$ , or  $\text{DMF}$ . The  $\text{Cl}^-$  ions produce a lower value for  $V_i$  in both  $\text{H}_2\text{O}$  and  $\text{MeOH}$  (Tables I and II). The  $\text{I}^-$  ions do not yield as low a value for  $V_i$  as  $\text{Cl}^-$  ions and their values are comparable in  $\text{H}_2\text{O}$  and  $\text{DMF}$ . In aqueous solutions a small anion, e.g.,  $\text{Cl}^-$ , results in a greater lowering of  $V_i$  than does a large anion,  $\text{SO}_4^{2-}$ ,  $\text{PO}_4^{3-}$ , etc. (18). This trend is maintained also in alcoholic solutions:  $\text{Cl}^-$  results in a much lower  $V_i$ , 0.34 compared to 1.0 for  $\text{ClO}_4^-$ . The extent of deviation from  $V = 2$ , approximately corresponds to the degree of disintegration, the lower the  $V_i$  the greater the extent of disintegration. Then, the anion effect during disintegration in increasing order is:  $\text{I}^-$  (DMF),  $\text{I}^-/\text{aq}$ ,  $\text{ClO}_4^-/\text{EtOH}$ ,  $\text{Cl}^-/\text{aq}$ ,  $\text{Cl}^-/\text{MeOH}$ . Experimental values (Table III) for the rate of Be dissolution increase in the order of  $\text{NO}_3^-/\text{MeOH} < \text{NO}_3^-/\text{aq} < \text{I}^-/\text{DMF} < \text{Cl}^-/\text{MeOH} < \text{Cl}^-/\text{aq}$ . This gradation in the reactivity of anions for anodic

dissolution and disintegration follows the same order as the aggressiveness of the said anions in rupturing a protective film. The comparative effect of various anions on  $V_i$  has been discussed earlier (18). It has been postulated (10) that a total elimination of water from the electrolysis system can stabilize Be(I) thus accounting for values of  $V_i$  close to unity. The results described above show that  $V_i \sim 1.0$  can be obtained even in aqueous solutions where Be(I) is supposedly unstable, by choosing the proper anion and C.D. Furthermore, in a nonaqueous media, where Be(I) is believed to be more stable, an anion like  $\text{I}^-$  gives rise to a  $V_i$  close to two (Table II).

It is clear from the potential-current profile shown in Fig. 3a and Fig. 5 that the anodic polarization of Be takes place in three stages in  $\text{NaNO}_3(\text{aq})$  and  $\text{KI/DMF}$ . Transition regions in the polarization curve of a metal are generally noticed in active-passive transitions and electropolishing. As is evident from the curves, Be does not show active-passive behavior under the present experimental conditions. The  $i$ - $E$  curve does not show the kind of polarization stages-anodic dissolution region at low overvoltages followed by a limiting current region at intermediate overvoltages and an  $\text{O}_2$  evolution region at high overvoltages corresponding to electropolishing. This is further substantiated by visual observation of the polarized electrodes which did not show any polishing effect. The transition point 0.28V, apparently indicates a change in the mechanism of dissolution of Be. Beryllium dissolution may occur with the participation of  $\text{NO}_3^-$  ion up to 0.28V, a type of reaction we proposed earlier for Zn (19), and beyond 0.28V with formation of an oxide or hydroxylated species of Be. Normally such oxide formations lead to a passive region in the  $i$ - $E$  curve. This is not the case with Be, since Be salt solutions are known to dissolve several molecules of oxide or hydroxide per mole of Be ion present in aqueous solutions (20). The transition point at 0.98 may denote the mass transfer effects in oxide formation.

The passivation of Be is accomplished more easily in  $\text{NO}_3^-/\text{MeOH}$ . The electrode turns black and loses its conduction as a result of a porous oxide film formation. A microstructural study using SEM (Fig. 6) reveals particles of Be embedded in this film. This observation of anodically disintegrated metallic particles has some parallelism to the occurrence of Zn and Mg particles in the passive film on a Zn or Mg anode (19, 21, 22).

Breaks in the  $i$ - $E$  curves for Be in  $\text{LiClO}_4/\text{EtOH}$  have been reported by Aida *et al.* (23). They observed a change in the slope at 1.0V vs.  $\text{Ag/Ag}^+$  (0.2M) and associated it with the border separating the potential range within which  $V_i = 1$  and the surface is bright from the range within which  $V_i$  differs from unity and the surface is rough due to spalling and/or local corrosion. Such a view is tantamount to stating that the  $i$ - $E$  curve can be divided into regions where anodic disintegration occurs and where it does not occur. This is not the case as proved by our experimental observation of spalling at all potentials. Local corrosion, faradaic dissolution, and anodic disintegration occur simultaneously for Be and an assessment of the degree of each process cannot be made from  $i$ - $E$  curves.

Data in Table III illustrate the decrease in the rate of Be dissolution when  $\text{NO}_3^-$  ions are present in aqueous and nonaqueous media. For the same concentration of  $\text{NO}_3^-$  and  $\text{Cl}^-$ , the rate is much lower in  $\text{MeOH}$  than in water at all potentials. Thus water molecules do not seem to have a predominant influence in the formation of a passive film on the metallic surface. This is in contrast to the behavior of Ti in  $\text{MeOH/HCl}$  (24) but similar to Fe and Cu in  $\text{MeOH/H}_2\text{SO}_4$  (25).

Another aspect of the  $i$ - $E$  behavior (Fig. 2-5) is that the current values are different for the anodic and cathodic sweeps. Such a behavior is very common for metals like Pt, Pb, etc. (26, 27), and could be due to a mass transfer effect, a film formation reaction or

due to two different types of films, an adsorbed oxide or a hydroxylated species. Repetitive potential scans between  $-0.62$  to  $1.56$  V in  $\text{NO}_3^-/\text{aq}$  (Fig. 2) lead to deactivation of the electrode due to film growth. Repetitive cycling in  $\text{KCl}/\text{aq}$  has no deactivation effect, instead there is a slight acceleration effect (Fig. 2 and Table IV). Repetitive cycling is known to bring about changes in the electrode surface structure leading to greater reactivity (28, 29). In the present case, the slight increase in C.D.'s may be due to removal of electro-oxidative impurities from the surface or to an area effect as a result of disintegration.

Anodic disintegration has been associated at times with a grain boundary type of attack (10, 30). However, in the case of Be this is ruled out on the basis of previous studies using Be single crystals which showed spalling (31). It is also proposed (10) that a uniform and homogeneous dissolution occurs whenever the measured valency is 1.0 and  $\text{Be(I)}$  formation is favored. This is disputable since the nature of the attack and the appearance of the Be surface depend more on the nature and concentration of the anions than on the measured valency. For example, when Be is polarized in  $\text{NO}_3^-/\text{H}_2\text{O}$  or  $\text{NO}_3^-/\text{MeOH}$ , a smooth black surface is obtained. The black coloration is unmistakably due to the presence of minute Be particles. On repolishing it is found that the region underneath has been severely pitted in the case of  $\text{NO}_3^-/\text{MeOH}$  and  $\text{NO}_3^-/\text{aq}$ . In  $\text{KI}/\text{DMF}$  the spalling is not as great as in  $\text{KCl}/\text{aq}$  (compare the valency of 1.75 in DMF to 1.07 in  $\text{KCl}/\text{aq}$ ). The surface is not as severely attacked though curiously grain boundaries are still visible. In both cases aggregates of Be particles sticking to the surface can be seen in a microscope (see Fig. 8 and 11). The nature and type of attack of a Be electrode and the appearance of its surface have been reported for various electrolytes (18).

In summary, the results of this study provide direct evidence (optical) for the existence of anodic disintegration during polarization of Be in aqueous and non-aqueous media in accord with Aida *et al.* (10). Cyclic voltammograms obtained for Be in  $\text{LiCl}/\text{MeOH}$  and  $\text{NaNO}_3/\text{MeOH}$  do not show peaks corresponding to two oxidation states, although this observation does not rule out the presence of a short-lived univalent ion. Nevertheless while the findings of our study provide no direct evidence for or against the univalent ion mechanism, the apparent valency of less than one obtained for anodic polarization of Be in  $\text{LiCl}/\text{MeOH}$  and the accompanying spalling of the electrode rule out the univalent ion concept in this instance. The work of Aida *et al.* (23) wherein specific potential regions are attributed to the occurrence of disintegration is not borne out by our experimental studies of  $i$ - $E$  behavior as we observe disintegration at all potentials. Furthermore the variation of valency with potential and the nonattainment of the normal value of two at any potential or C.D. can only underscore our contention that the assumption of the transient univalent state in postulating a mechanism for the anodic dissolution of Be is superfluous.

Manuscript submitted Jan. 23, 1973; revised manuscript received June 22, 1973.

Any discussion of this paper will appear in a Discussion Section to be published in the December 1974 JOURNAL.

#### REFERENCES

1. W. J. James, M. E. Straumanis, and J. W. Johnson, *Corrosion*, **24**, 15 (1967).
2. J. H. Greenblatt, *ibid.*, **18**, 123t (1962).
3. D. T. Sorenson, A. W. Davidson, and J. Kleinberg, *J. Am. Chem. Soc.*, **85**, 1354 (1963).
4. K. E. Heusler, *Z. Elektrochem.*, **65**, 192 (1961).
5. H. H. Uhlig, Editor, "Corrosion and Corrosion Control," p. 334, John Wiley & Sons, Inc., New York (1963).
6. B. Miller and R. E. Visco, *This Journal*, **115**, 251 (1968).
7. M. E. Straumanis, *ibid.*, **108**, 1087 (1961).
8. J. W. Johnson, C. K. Chi, and W. J. James, *Corrosion*, **23**, 204 (1967).
9. D. J. G. Ives and G. J. Janz, Editors, "Reference Electrodes," p. 406, Academic Press, Inc., London (1961).
10. H. Aida, I. Epelboin, and M. Garreau, *This Journal*, **118**, 243 (1971).
11. V. V. Losev, *Electrochim. Acta*, **15**, 1095 (1970).
12. B. D. Laughlin, J. Kleinberg, and A. W. Davidson, *J. Am. Chem. Soc.*, **78**, 559 (1956).
13. W. M. Smirnov and N. J. Tschukrejev, *J. Anorg. Chem. (URSS)*, **4**, 2536 (1957).
14. M. E. Straumanis and D. L. Mathis, *J. Less-Common Metals*, **4**, 213 (1957).
15. V. V. Losev, *Electrochim. Acta*, **15**, 1107 (1970).
16. M. E. Straumanis and R. L. Martin, *Z. Anorg. Allgem. Chem.*, **334**, 321 (1965).
17. M. D. Rausch, W. E. McEwen, and J. Kleinberg, *J. Am. Chem. Soc.*, **77**, 2093 (1955).
18. K. G. Sheth, J. W. Johnson, and W. J. James, *Corrosion Sci.*, **9**, 135 (1969).
19. M. E. Straumanis, J. L. Reed, and W. J. James, *This Journal*, **114**, 885 (1967).
20. F. A. Cotton and G. Wilkinson, Editors, "Advanced Inorganic Chemistry," p. 245, Interscience Publishers Inc., New York (1966).
21. G. S. Vozdvizhenskii and E. D. Kochman, *Zh. Fiz. Khim.*, **39**, 657 (1965); *Russ. J. Phys. Chem.*, **39**, 347 (1965).
22. M. E. Straumanis and B. K. Bhatia, *This Journal*, **110**, 357 (1963).
23. H. Aida, I. Epelboin, and M. Garreau, *ibid.*, **118**, 1961 (1971).
24. F. Mansfeld, *ibid.*, **118**, 1412 (1971).
25. F. Mansfeld, *ibid.*, **120**, 188 (1973).
26. M. W. Breiter, *Electrochim. Acta*, **8**, 447 (1963).
27. H. Vaidyanathan, R. A. Narasagoudar, J. W. Johnson, and T. J. O'Keefe, To be published.
28. M. W. Breiter, *J. Electroanal. Chem.*, **10**, 191 (1965).
29. J. S. Mayell and W. A. Barber, *This Journal*, **116**, 1333 (1969).
30. I. A. Menzies and A. F. Averill, *Electrochim. Acta*, **13**, 807 (1968).
31. K. G. Sheth, H. Vaidyanathan, and W. J. James, In the course of publication.

# Some Aspects of Gas Recombination in Lead-Acid Systems

B. K. Mahato,\* E. Y. Weissman,\* and E. C. Laird\*

Globe-Union Inc., Corporate Applied Research Group, Milwaukee, Wisconsin 53201

## ABSTRACT

It is shown that in a structurally controlled lead-acid cell the electrodes, in addition to their electrochemical function, also provide evolved gas recombination sites. The reaction kinetics and the transport properties in the acid electrolyte solution are making the process possible at practical rates. Typical recombination rates for oxygen are of the order of 15 mA/cm<sup>2</sup> (C/10). For hydrogen, the observed starting rate of recombination exceeds self-discharge evolution in a lead-calcium system by a factor of at least 30. A review of various operational characteristics is given including half-cell potentials, cell voltages, internal pressures, and hydrogen partial pressures.

Although hermetically sealed alkaline battery systems, such as the nickel-oxide-cadmium variety, have been studied and used extensively (1, 2), the same does not hold true for lead-acid batteries. The literature (mostly patents) deals with a variety of approaches: catalytic recombination of evolved hydrogen and oxygen inside the battery or external to it; oxygen, voltage, or pressure sensors used as overcharge limiting devices; hydrogen permeable materials for the battery case; "third electrodes" for oxygen recombination; bifunctional electrodes used as electrochemical and gas recombination components. It is this last approach which forms the subject of the present paper.

From a thermodynamic standpoint, the internal recombination of battery evolved gases is possible (3). In a lead-acid battery, oxygen could be reduced at the lead electrode and hydrogen oxidized at the lead dioxide electrode. From a rate standpoint, the chemical affinity of oxygen for lead in the presence of moisture is well known (4) while the reactivity of hydrogen with lead dioxide has been considered to be of no consequence.

Structural factors will play an important role, particularly: the state of charge of the electrodes and the nature of the electrode-electrolyte solution and gas-electrolyte solution interfaces. If the recombination rate, primarily of oxygen, is diffusion-limited in the liquid phase, which is very likely, the amount of active nonflooded lead sites will play a determining role in the process. An initial study was reported in this general area, dealing with partially exposed and electrochemically active lead electrodes (5), but otherwise there is no significant literature on the subject.

One notes that, compared to the alkaline KOH systems, the lead-acid battery is at an advantage from the standpoint of the pertinent transport properties. Table I summarizes some solubility and liquid diffusivity data of interest.

On the other hand, there is a fundamental difference between the operation of an alkaline and a lead-acid battery and it affects their performance as sealed systems. In an alkaline system such as the sealed nickel oxide-cadmium battery the aqueous KOH electrolyte is essentially an ion transfer medium, whereas in the

lead-acid battery sulfuric acid participates directly in the anode and cathode reactions. In the latter case the minimum amount of electrolyte required for adequate operation, usually results in flooded electrodes, i.e., a system exhibiting high resistance to any kind of dissolved oxygen transfer step. Furthermore, hydrogen is spontaneously evolved in the lead-acid battery, even at open-circuit conditions, and hydrogen and oxygen are evolved during charge and overcharge in non-stoichiometric ratios determined by the design characteristics of the system. This, in turn, makes the use of recombination catalysts (8) and auxiliary recombination electrodes (9) less than effective with the added disadvantage, in the case of catalyst use, of lead electrode contamination followed by increased self-discharge and hydrogen evolution.

## Development of an Internal Recombination Lead-Acid System

If the reactivity of lead with oxygen and, to a certain extent, of lead dioxide with hydrogen could be effectively put to use, a reliable and economic sealed lead-acid battery would result. The use of a high hydrogen overvoltage system such as electrodes with lead-calcium current collectors is, of course, a step in the right direction. If the oxygen recombination cycle can be made to prevail in such a battery, the only hydrogen recombination capacity required would be that corresponding to the existing rates of lead electrode self-discharge.

Figure 1 is a schematic representation of the oxygen cycle in a lead-acid battery. The cycle is symbolized in the upper right-hand corner while the rest of the figure is a more detailed representation where each of the chemical species involved in the process appears as both a source and a sink at steady state. We note that, under these conditions, the lead dioxide electrode is fully charged and evolving oxygen. The lead electrode, on the other hand, is at a constant state of partial discharge below the operating potential corresponding to significant hydrogen evolution.

## Experimental

In order to evaluate the internal gas recombination capability of a hermetically sealed lead-acid system, use was made of a leak-proof pressure chamber (Fig. 2) containing a variety of test cells. Some hermetically

Table I. Comparison of transport properties in KOH and H<sub>2</sub>SO<sub>4</sub> battery electrolyte solutions

Transferring component (p.p. = 1 atm)	Solubility at 25°C*		Diffusivity at 25°C, cm <sup>2</sup> /sec	
	30 w/o KOH	36.8 w/o H <sub>2</sub> SO <sub>4</sub>	30 w/o KOH	36.8 w/o H <sub>2</sub> SO <sub>4</sub>
O <sub>2</sub> (6)	0.1 × 10 <sup>-3</sup>	0.65 × 10 <sup>-3</sup>	0.6 × 15 <sup>-5</sup>	—
H <sub>2</sub> (7)	2.1	8.4	0.7 × 10 <sup>-5</sup>	2.5 × 10 <sup>-5</sup>

\* O<sub>2</sub> solubility data in g-moles/liter; H<sub>2</sub> in cubic centimeters (STP)/liter.

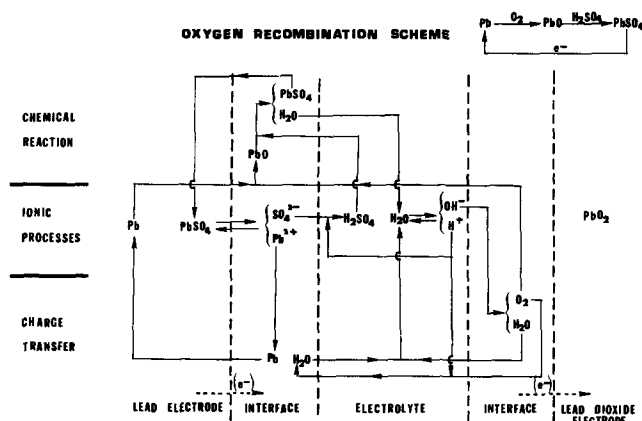


Fig. 1. Schematic representation of the oxygen cycle in a lead-acid battery; chemical species appear as both sources and sinks at steady state.

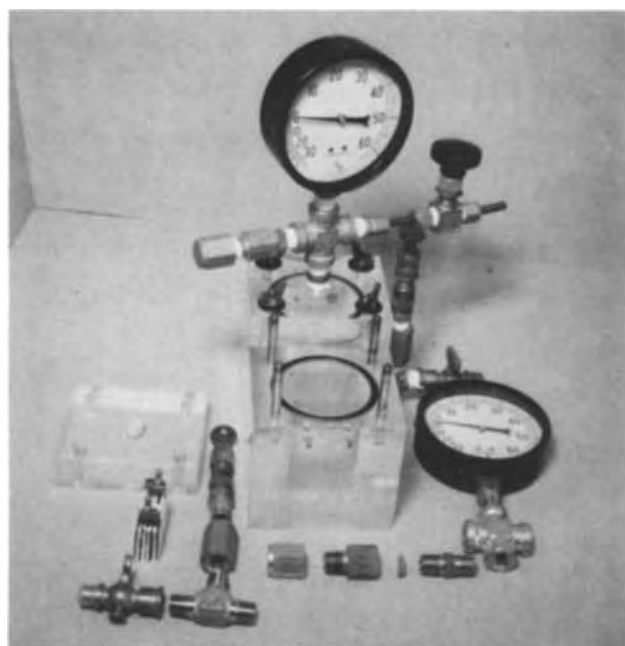


Fig. 2. Photograph of the test vehicle; multiplate test element can be seen at lower left corner of the picture, adjacent to the exploded view of a pressure relief valve.

sealed test cells were subsequently evaluated outside the pressure chamber. The chamber was equipped with pressure and voltage sensors and had ports for gas insertion or evacuation and sampling.

The test cells were normally prepared from selected dry-charged electrodes utilizing lead-calcium grids. Dimensions were generally  $3.5 \times 3.0 \times 0.10$  cm for the lead electrodes and  $3.5 \times 3.0 \times 0.15$  cm for the lead dioxide electrodes and the total amounts of corresponding lead and lead dioxide active material were roughly equal. The electrolyte was approximately 37 w/o (weight per cent) sulfuric acid containing 22 g/liter of 85 w/o phosphoric acid, and it was maintained in an immobilized state by additions of silica gel or by containment in a porous matrix. In the latter case the matrix was electrolyte-saturated to the extent of 85-90% as determined by established procedures (10) and the electrodes were covered with a liquid film having a calculated average thickness of approximately  $10\mu$ . In all cases the cell capacity was electrolyte-limited.

Pressure measurements were carried out with a compound pressure gauge having an accuracy of  $\pm 0.2$  psi or  $\pm 0.2$  in. Hg (for vacuum measurements). The pressure gauge was also used for control of the initial cell activation procedure which consisted of creating a re-

serve of partially discharged lead electrodes by the introduction of predetermined amounts of oxygen.

A precision differential manometer, having an accuracy of  $\pm 0.05$  mm Hg, was used for determining the hydrogen oxidation capacity of the system. For that purpose, the test cell-containing chamber was evacuated and then filled with hydrogen at 1 atm absolute. Pressure changes, corresponding to hydrogen consumption at the partially wet lead dioxide electrodes, were then monitored and corrected for changes in the ambient conditions and for hydrogen permeation losses by comparison with a control pressure chamber not containing electrode elements.

Gas analyses were carried out with an F&M Research Chromatograph and half-cell potential measurements were taken with a Keithley Electrometer No. 610C with respect to a Hg/Hg<sub>2</sub>SO<sub>4</sub> reference electrode.

Results and Discussion

**Oxygen recombination.**—The internal oxygen recombination in a fully charged cell, as reflected in the corresponding pressure vs. time decay curve, is represented in Fig. 3. The initial recombination rate derived therefrom is about 3 cm<sup>3</sup> (STP)/hr/cm<sup>2</sup> of geometric lead electrode area. This is equivalent to a current density of 15 mA/cm<sup>2</sup> which corresponded to approximately 11 times the 20-hr (overcharge) rate for the test cell under evaluation.

Half-cell potential characteristics are represented in Fig. 4 as a function of the extent of charge and discharge, with the rate of charge or discharge as the parameter. So long as the rate is not high enough to cause gas evolution on overcharge also at the lead electrodes, a steady negative potential is achievable. In the particular case under examination the highest tolerable current is somewhere between the 5- and the 10-hr rate.

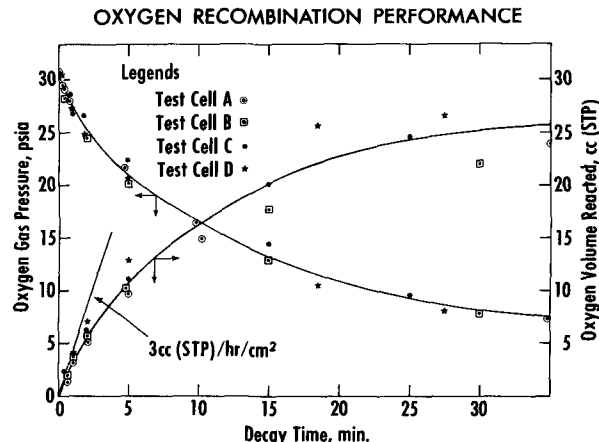


Fig. 3. Oxygen recombination in a hermetically sealed lead-acid cell.

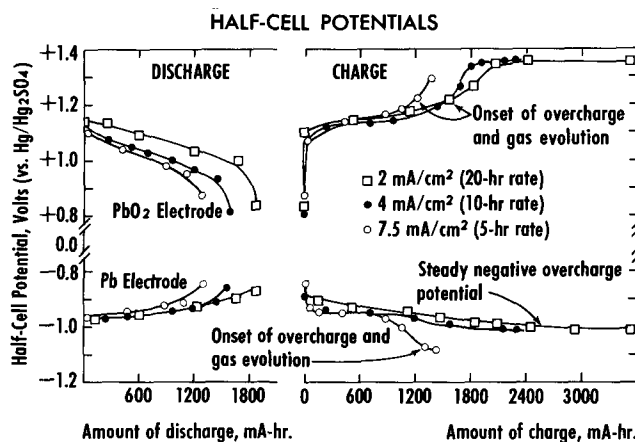


Fig. 4. Half-cell potentials in a hermetically sealed lead-acid cell operating in an oxygen recombination mode.

**Hydrogen recombination.**—Figure 5 is a representation of internal hydrogen recombination, or hydrogen pressure decay, as a function of time compared to a nonrecombining control test unit. The starting recombination rate amounts in this case to  $1.74 \times 10^{-2}$  cm<sup>3</sup> of H<sub>2</sub> (STP)/hr/cm<sup>2</sup> of lead dioxide electrode geometric area. For the test cell under evaluation this corresponds to approximately 30 times the measured self-discharge rate.

Generally speaking, hydrogen recombination in a sealed storage battery has been of limited practical significance. It proceeds to a negligible extent in alkaline systems, such as the nickel oxide-cadmium battery (1, 11), but should do better in the lead-acid system owing to the higher equilibrium hydrogen concentration in the liquid phase (Table I). Hydrogen oxidation in a lead-acid cell has previously been reported as insignificant (12) but the cases under study apparently involved only flooded lead dioxide electrodes where the liquid phase hydrogen diffusion path would be impractically long.

The exponential shape of the gas recombination curves (Fig. 3 and 5) suggests the possibility of active site inhibition by sulfate ion adsorption (12). Looking at the hydrogen data in particular, the measured oxidation rate would seem to be adequate to handle limited self-discharge in a system such as one using lead-calcium alloys for the grids. Operation based on a hydrogen cycle remains, for the time being, out of the question though it would be interesting to determine the nature of the hydrogen oxidation mechanism (e.g., active oxygen in the PbO<sub>2-x</sub> structure).

Another way to demonstrate the capacity for limited hydrogen recombination is presented in Fig. 6 where

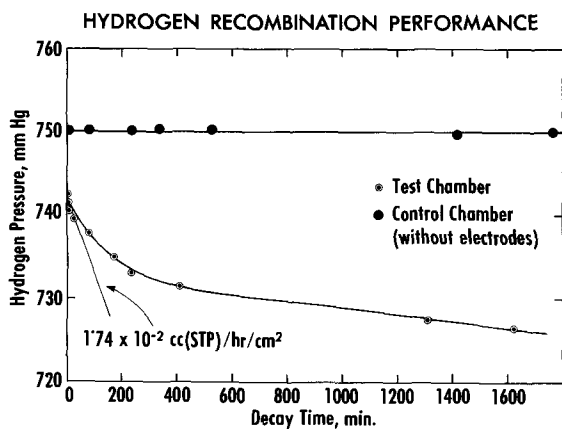


Fig. 5. Hydrogen recombination in a hermetically sealed lead-acid cell.

HYDROGEN RECOMBINATION — COMPARATIVE STUDY

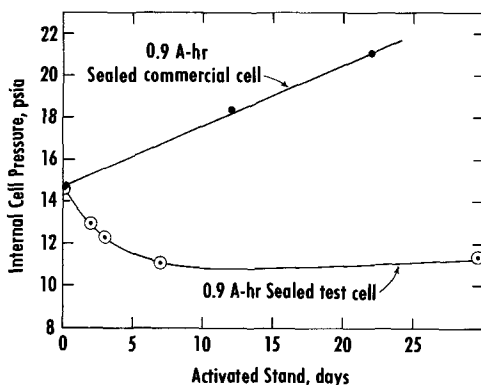


Fig. 6. Comparison between a hermetically sealed commercial and a hydrogen recombining lead-acid cell under conditions of self-discharge (hydrogen accumulation).

the test cell is compared with a hermetically sealed commercial unit of similar size and structure but operating in a "conventional" mode, i.e., with a higher degree of electrode flooding (the electrolyte is of a paste-type consistency owing to SiO<sub>2</sub> additions).

**Operational results: cycling and extensive overcharge.**—Figure 7 represents the internal pressure characteristics and hydrogen concentration in the gas space of test units during initial cycling. Gradual attainment of practical steady-state operating conditions is apparent. The effect of overcharge and the subsequent equilibration as the oxygen cycle takes effect are graphically represented in Fig. 8 for two different operation modes. It is to be noted that the 8-hr "discharge" period indicated in the figure always includes a certain time interval of open-circuit stand following attainment of the 1.7V cut-off point. As the system ages the open-circuit intervals become progressively longer.

At the onset of overcharge the lead dioxide electrode attains a constant oxygen evolution potential. Thus the cell voltage excursions measured in this case are representative of changes occurring at the lead electrode. The cathodic shift is probably indicative of adsorbed hydrogen film formation preceding the conditions for hydrogen evolution. The subsequent anodic shift would seem to represent the depolarizing action, probably at least partially electrochemical in nature

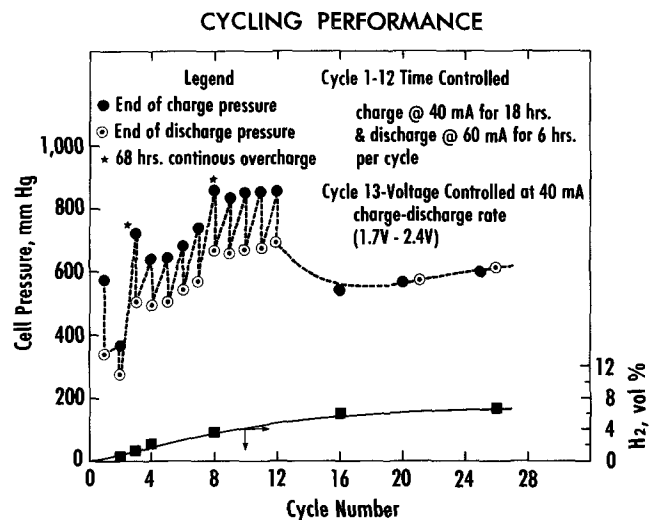


Fig. 7. Gas-recombining lead-acid cell under charge-discharge cycling.

OVERCHARGE CHARACTERISTICS

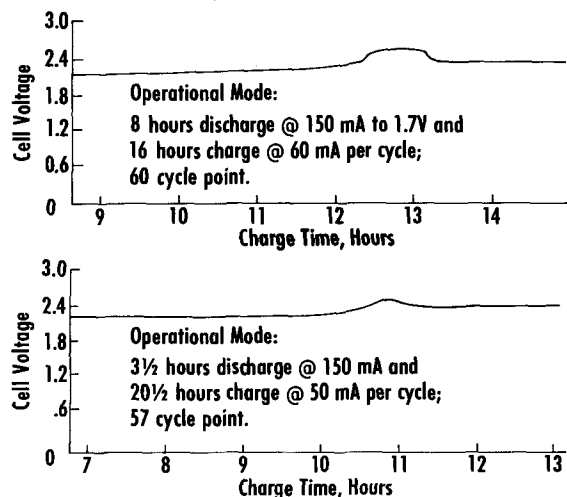
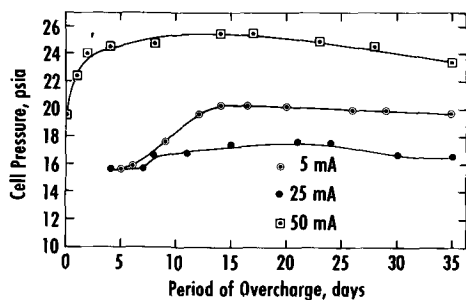


Fig. 8. Voltage excursions in a gas recombination lead-acid cell during charge and overcharge.

## CONTINUOUS CONSTANT CURRENT OVERCHARGE



## CONTINUOUS CONSTANT CURRENT OVERCHARGE

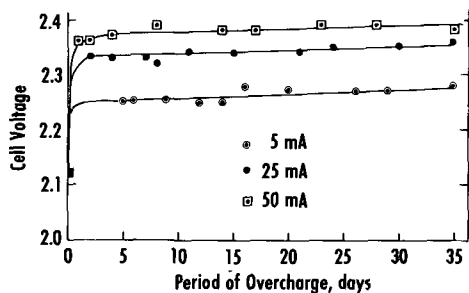


Fig. 9 (upper) and Fig. 10 (lower). Gas-recombining lead-acid cell under continuous constant current overcharge; pressure vs. time representation (50 mA corresponds to a current density of 2 mA/cm<sup>2</sup> and the 20-hr rate).

(5, 9), of the reacting oxygen. Since these voltage excursions are not accompanied by noticeable changes in internal cell pressure it would appear that the net effects of hydrogen generation and subsequent oxidation are relatively insignificant at the rates of charge used.

Steady state at practical equilibrium pressures is also possible under conditions of continuous constant current overcharge applied over long periods of time. This is evident in Fig. 9 and 10, at various equilibrium cell voltages as a function of the charge rate. The equilibrium pressures and voltages depend on such internal structure parameters as the lead plate morphology, the electrolyte soaked separator-matrix assembly and its interface with the plates. No direct relationship between the steady-state pressure and the overcharge rate is evident. Indeed, at 5 mA a higher pressure has been measured than at 25 mA.

### Conclusions

The use of a bifunctional lead electrode in a hermetically sealed lead-acid battery operating in an oxy-

gen cycle mode appears to be possible. The maintaining of a controlled electrode-electrolyte solution interface and a careful selection of the structural parameters are yielding practical oxygen recombination rates. Limited hydrogen recombination at the lead dioxide electrode, at least to the extent required by the self-discharge characteristics of a battery using lead-calcium alloy grids, also appears feasible.

Work in this area is needed for a thorough definition of the structure-dependent rate-limiting steps for both oxygen and hydrogen recombination. An understanding of the chemical and electrochemical mechanisms responsible for the observed behavior of the gas-tight lead-acid system at steady state (e.g., active oxygen sites, sulfate ion inhibition) is a desirable long-range objective.

### Acknowledgment

The authors would like to express their thanks to Globe-Union Inc. for permission to publish this paper.

Manuscript submitted April 2, 1973; revised manuscript received July 23, 1973. This was Paper 33 presented at the Miami Beach, Florida, Meeting of the Society, Oct. 8-13, 1972.

Any discussion of this paper will appear in a Discussion Section to be published in the December 1974 JOURNAL.

### REFERENCES

1. P. C. Milner and U. B. Thomas, "Advances in Electrochemistry and Electrochemical Engineering," P. Delahay and C. W. Tobias, Editors, Vol. 5, pp. 1-86, John Wiley & Sons, Inc., New York (1969).
2. S. U. Falk and A. J. Salkind, "Alkaline Storage Batteries," John Wiley & Sons, Inc., New York (1969).
3. Heat of formation data in: "Handbook of Chemistry and Physics," 46th ed., pp. D22-D27, Chemical Rubber Co., Cleveland, Ohio; Bulletin 542, U. S. Bureau of Mines (1954).
4. G. W. Vinal, "Storage Batteries," 4th ed., p. 41, John Wiley & Sons, Inc., New York (1966).
5. S. Hills and D. K. L. Chu, *This Journal*, **116**, 1155 (1969).
6. K. E. Gubbins and R. D. Walker, *ibid.*, **112**, 469 (1965).
7. P. Ruetschi, *ibid.*, **114**, 301 (1967).
8. S. Sekido, M. Yamashita, and M. Matsumoto, U.S. Pat. 3,622,398 (1971) (Note: This is just an example of a variety of patents in this field).
9. P. Ruetschi and J. B. Ockerman, *Electrochem. Technol.*, **4**, 383 (1966).
10. S. U. Falk and A. J. Salkind, "Alkaline Storage Batteries," pp. 271-273, John Wiley & Sons, Inc., New York (1969).
11. A. Fleischer, Proceedings of the 13th Annual Power Sources Conference, p. 78 (1959).
12. P. Ruetschi and R. T. Angstadt, *This Journal*, **105**, 555 (1958).



# Oxidation of Silver Electrodes in CsOH Solutions

Charles P. Wales\*

*Electrochemistry Branch, Naval Research Laboratory, Washington, D. C. 20375*

## ABSTRACT

Sintered Ag electrodes were cycled under several conditions in aqueous CsOH or KOH solutions. Over a wide range of charge rates the capacity accepted at the Ag/Ag<sub>2</sub>O potential plateau increased as electrolyte concentration decreased, but charge acceptance at the Ag<sub>2</sub>O/AgO plateau increased as concentration increased and was larger in CsOH than in KOH. Polarization was greater in CsOH than in KOH of the same concentration. Cross sections through electrodes were examined by optical microscopy. The structures that formed in CsOH tended to be similar to those that formed in a more concentrated KOH. After several cycles the average Ag particle size became larger in KOH than was typical in CsOH. Results indicated that concentration gradients were higher in CsOH.

The charge and discharge reactions are well known for the Ag electrode in alkaline solutions. First, Ag is oxidized to Ag<sub>2</sub>O and then to AgO during charge. The opposite reactions take place during discharge. The work reported in the literature has been done most often in aqueous KOH solutions and less often in NaOH solutions. The products of charge and discharge are the same in both electrolytes. Nevertheless, electrolyte concentration has a definite effect on the characteristics of Ag electrodes (1-5).

Variations between results in different KOH concentrations may be effects of changes in ionic mobility or in the amount of free water. Dirkse has pointed out the importance of the mobility of OH<sup>-</sup> ions and of hydration of the various ions in the electrolyte (2). Comparison of results in different KOH concentrations can indicate the influence of water concentration.

Another factor that may have an influence on the characteristics of Ag electrodes is the particular alkaline metal cation involved. The cation can have a noticeable effect even though it does not enter into an electrode reaction. For example, the capacity obtained when sheet Zn was oxidized in KOH was a little larger than in CsOH or RbOH, an effect probably related to solubility of Zn oxidation products (6).

The use of CsOH instead of KOH should indicate if the cation of the electrolyte has a strong effect on the Ag electrode. The atomic weight of Cs is 3.4 times that of K. CsOH and KOH solutions having the same molar concentration of cation will contain different amounts of water. The ionic radius of Cs (as measured in crystals) is about 1.26 times as large as K, but hydration of the ions decreases this size difference. A recent review points out the considerable disagreement among various workers as to the actual solvation numbers of most ions (7). It seems reasonable, however, to consider the ionic radius of hydrated Cs to be approximately 1.19 times as large as hydrated K. Thus, it is of interest to determine some of the characteristics of Ag electrodes in aqueous CsOH solutions because results may differ significantly from those obtained in KOH solutions of the same concentration. A better understanding of the behavior of Ag electrodes in alkaline solutions can result in improvements in high energy batteries that use this electrode.

## Experimental

**Electrolyte.**—The aqueous CsOH solutions contained OH<sup>-</sup> ion concentrations of about 8.4 and 3.6M. This gave solutions that were 61 and 36.6% CsOH by weight. The value 8.4M was chosen for comparison with earlier work in 8.4M (35%) KOH. Spectroscopy of the stock CsOH solution indicated that concentration of the main impurity, Rb<sup>+</sup>, was on the order of ten times that of

Na<sup>+</sup> or K<sup>+</sup>. Concentrations of Rb<sup>+</sup>, OH<sup>-</sup>, and CO<sub>3</sub><sup>2-</sup> were determined by chemical analysis. Table I gives the results calculated for the two CsOH solutions and includes the magnitude of Na<sup>+</sup>, K<sup>+</sup>, and Li<sup>+</sup> as estimated by spectroscopy.

**Cells.**—Average dimensions of the sintered Ag electrodes were 43.7 ± 0.1 mm wide, 36.0 ± 0.1 mm high, and 0.87 ± 0.01 mm thick. Electrodes contained a grid of expanded sheet Ag. The average weight of sintered Ag in an electrode corresponded to a theoretical capacity of 2.8 A-hr. Electrodes could be removed from the cell in order to cut samples for microscopic examination. Two other sintered Ag electrodes were placed on each side of a test electrode, and served as counter-electrodes. All three electrodes were wrapped with five layers of separator material. Two of the test electrodes that were cycled in CsOH used a cellulosic separator, while the other 12 in CsOH and all electrodes in KOH used a cross-linked polyethylene. Results for the two separators are combined, because electrode characteristics did not differ. Counterelectrodes had the same separator material as the test electrodes. Cells contained an excess of electrolyte. Electrode potentials were measured with respect to a Ag/Ag<sub>2</sub>O reference electrode.

**Cycling procedure.**—Test electrodes were charged (anodic oxidation) at constant current until oxygen evolution occurred. Except where otherwise stated, charge rates were chosen so that a complete charge of a test electrode required 20 hr. Some electrodes were always discharged (reduced) using the 20-hr rate of constant current, and others were always discharged at the 1-hr rate. Discharges at the 20-hr rate were ended when potential reached -300 mV vs. the reference electrode. This potential was about 250 mV below the observed Ag/Ag<sub>2</sub>O potential plateau during discharge. Discharges at the 1-hr rate took place at a lower potential and were usually continued until potential dropped 200 mV below the observed Ag/Ag<sub>2</sub>O potential plateau. (Results obtained during reduction of charged electrodes will be reported in a separate paper.) Temperature was 24° ± 1°C. Samples were

Table I. Analysis of CsOH solutions\*

Constituent	Concentration (moles/liter)	
OH <sup>-</sup>	3.56	8.39
CO <sub>3</sub> <sup>2-</sup>	0.068	0.16
Cs <sup>+</sup>	3.41	8.05
Rb <sup>+</sup>	0.15	0.35
Na <sup>+</sup>	<0.05	<0.1
K <sup>+</sup>	<0.05	<0.1
Li <sup>+</sup>	<0.0005	<0.001

\* Electrochemical Society Active Member.

Key words: silver oxides, electrolyte, electrode structure, anodization.

\* Analysis and spectroscopy were done by the Analytical Chemistry Branch of Naval Research Laboratory.

cut from most of the electrodes and were prepared for optical microscopic examination as described earlier (8).

When the effect of charge rate was being studied, a new electrode was first given about five charge-discharge cycles at the 20-hr charge rate, until electrode capacity became steady. After these initial cycles an electrode was charged at another rate for three cycles, with each group of three cycles followed by two to four cycles at the 20-hr charge rate to check for shifts in capacity. The 20-hr discharge rate was always used when the effect of charge rate was being studied.

### Results

**Effect of charge rate on capacity.**—Charge acceptance of the Ag electrodes decreased as charge current increased. The capacity of slow discharges was a good measure of charge acceptance. Charge current and capacity are plotted on relative scales in Fig. 1 taking the 20-hr rate as the standard. Relative scales are preferable to actual current and capacity because the actual current that required a particular length of time for a complete charge varied from electrode to electrode, and changed as an electrode was cycled or when a sample was cut from the electrodes.

The relationship between capacity and charge current was linear on a log-log scale for Ag electrodes in KOH solutions over the current range studied (bottom of Fig. 1). The line for 8.4M KOH is also given on the top section of Fig. 1 for comparison with results in CsOH. A linear relationship was only observed at the higher current densities in CsOH solutions. Individual measured values in 8.4M CsOH had no more than a 3% average deviation from the points shown in Fig. 1, but values in 3.6M CsOH varied by about 10%.

**Effect of charge rate on electrode potentials.**—Potentials of the Ag electrodes during charges at three rates are given in Fig. 2. The charges lasting approximately 0.8, 4, and 43 hr were done at currents given in Fig. 1 as 16, 4, and 0.5 times the 20-hr rate, respectively. All potentials reported in this paper are given with respect to the Ag/Ag<sub>2</sub>O reference electrode in the same electrolyte as the test electrodes.

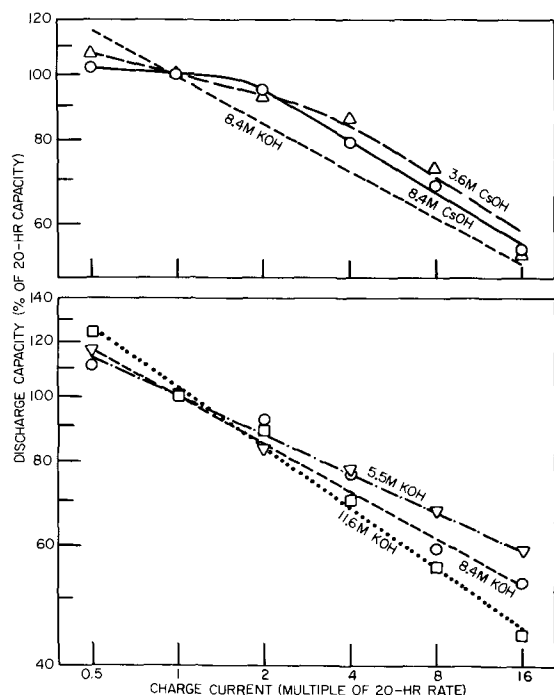


Fig. 1. Log-log relationship between charge current and discharge capacity. Each point is the average of at least three charge-discharge cycles. Straight lines for KOH were fitted by the least squares method.

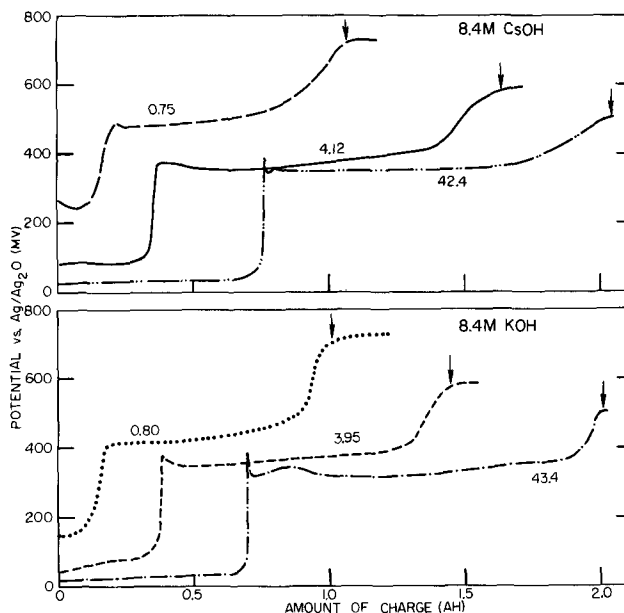


Fig. 2. Charge potentials at various rates of current. Numbers on curves give length of charge in hours. Arrows indicate capacity of following discharge, which was done at the 20-hr rate.

**Effect of charge rate on charge acceptance at Ag/Ag<sub>2</sub>O potential.**—Silver is oxidized to Ag<sub>2</sub>O during the first part of a charge, before potential becomes sufficiently high that AgO can also form. It can be seen in Fig. 2 that the first potential plateau shortened as charge time decreased; that is, as current density increased. In addition, this initial potential plateau constituted a smaller proportion of the total charge at the higher current densities. The proportion of a charge that took place at this Ag/Ag<sub>2</sub>O potential plateau decreased linearly as log of charge current increased over the range of currents studied (Fig. 3). The line fitted to the points in 8.4M KOH in the lower section of Fig. 3 is repeated in the upper section for ease in comparing KOH with CsOH. Although both Fig. 1 and 3 show linear relationships, note that discharge capacity is plotted on a log scale (Fig. 1) but proportion of charge at the Ag/Ag<sub>2</sub>O level is on a linear scale (Fig. 3).

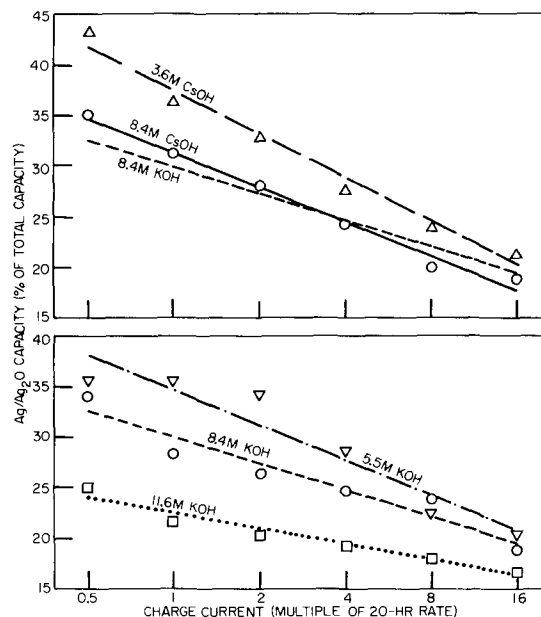


Fig. 3. Dependence of charge acceptance at Ag/Ag<sub>2</sub>O potential plateau on the log of charge current. These straight lines were fitted by the least squares method.

**Effect of discharge rate on charge potentials.**—During the first charge at the 20-hr rate a new sintered Ag electrode always accepted more capacity in 3.6M CsOH solution than in 8.4M CsOH. Charge acceptance of new electrodes at cycle 1 ranged from 2.45 to 2.53 A-hr for four electrodes in 3.6M CsOH, and from 2.10 to 2.44 A-hr for nine electrodes in 8.4M CsOH. Figure 4 includes potentials for the first charges of four previously unused sintered Ag electrodes.

The rate of discharge (reduction) had a strong effect on capacity and on potentials of the following charge. Discharge capacities at the 20-hr discharge rate (arrows in upper section of Fig. 4) were equal to capacity given an electrode up to the point that charge potential became sufficiently high that oxygen evolution occurred. Discharge capacity was smaller at cycle 1 when Ag electrodes were discharged at the 1-hr rate (lower section of Fig. 4). Cycle 1 discharge at the 1-hr rate delivered only 85-90% of the capacity given to an electrode during the charge. Close to 100% capacity was obtained from subsequent cycles at the 1-hr rate.

Potential of the Ag/Ag<sub>2</sub>O charge plateau was not affected by the particular electrolyte used. Potential of the Ag<sub>2</sub>O/AgO plateau tended to rise during the first three to five cycles. The level rose 5-10 mV when the 20-hr discharge rate had been used in 8.4M CsOH, and twice as much when the 1-hr discharge rate had been used. This plateau was usually an additional 5-20 mV higher in 3.6M CsOH than in 8.4M CsOH.

The amount of charge accepted at the Ag<sub>2</sub>O/AgO plateau decreased during the first few cycles (Fig. 4). This decrease corresponded fairly closely to the decrease in discharge capacity between cycle 1 and 3 observed at both rates of discharge. Capacity changes became more gradual beginning about cycle 3, and charge curves at cycle 15 were close to those shown for cycle 4.

The rise to the oxygen evolution potential was more rapid in 3.6M CsOH than in 8.4M CsOH, with 8.4M KOH giving a rise intermediate between the two CsOH concentrations (Fig. 4). At the end of the first charge the potentials at the oxygen evolution plateau averaged 80 mV higher in 3.6M CsOH than in the other electrolytes. The difference between final charge potentials decreased greatly at cycle 2 and had disappeared by cycle 3 or 4.

**Effect of discharge rate on charge acceptance at Ag/Ag<sub>2</sub>O potential.**—It is evident from both sections of Fig. 4 that cycle 1 charge in 8.4M CsOH gave the least charge acceptance at the first potential plateau.

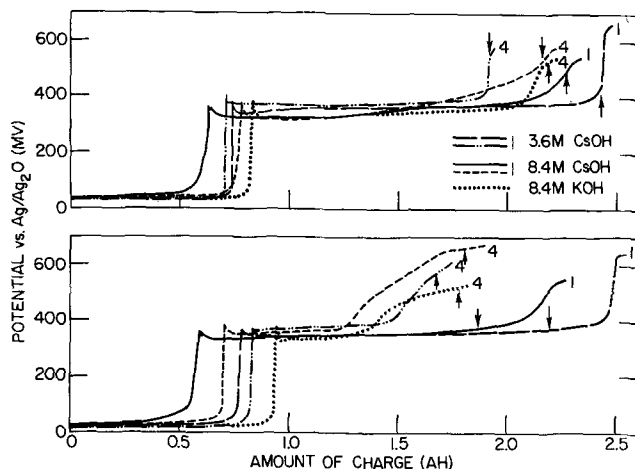


Fig. 4. Charge potentials at the 20-hr rate. Upper half of figure shows the initial charges in two CsOH concentrations, and cycle 4 charges when all discharges had been done at the 20-hr rate. Cycle number is given beside the curves. Lower half shows the results when using the 1-hr discharge rate. Typical cycle 4 charges in 8.4M KOH are included for comparison. Arrows indicate capacity of the following discharges.

The length of this Ag/Ag<sub>2</sub>O potential plateau increased during the first few cycles (Fig. 5). For any particular Ag electrode the charge acceptance at the Ag/Ag<sub>2</sub>O plateau fluctuated from cycle to cycle, but had the general trend shown in Fig. 5. When the 1-hr discharge rate was used, the length of the Ag/Ag<sub>2</sub>O charge plateau was usually less following a stand of two or more days discharged than it was when recharge began a few hours after ending a discharge. Each of the curves given in Fig. 5 is a smoothed composite of measurements from two or three electrodes, except only one electrode was cycled at the 1-hr rate in 3.4M CsOH.

**Structural changes during a charge.**—Typical changes as Ag was oxidized can be illustrated by a series of samples taken from an electrode during cycle 6 charge in 8.4M CsOH. Figure 6 shows a sample taken from an electrode that was 19% charged, judging by capacity accepted later in the charge. All photographs in this work are of cross sections through the electrode and, therefore, show cross sections through individual particles and crystals. During a discharge at the 1-hr

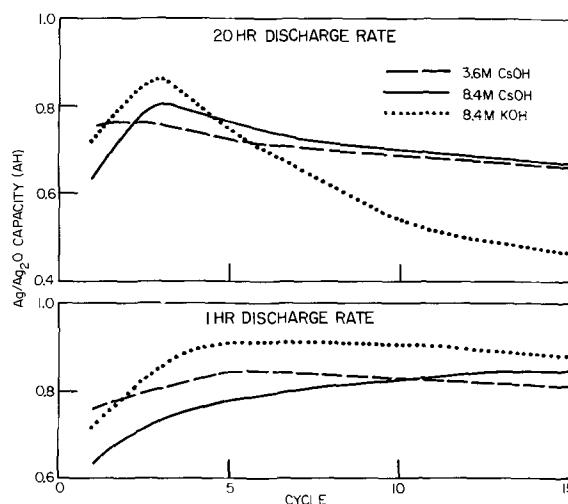


Fig. 5. Charge acceptance at the Ag/Ag<sub>2</sub>O potential plateau. All charges were done at the 20-hr rate.

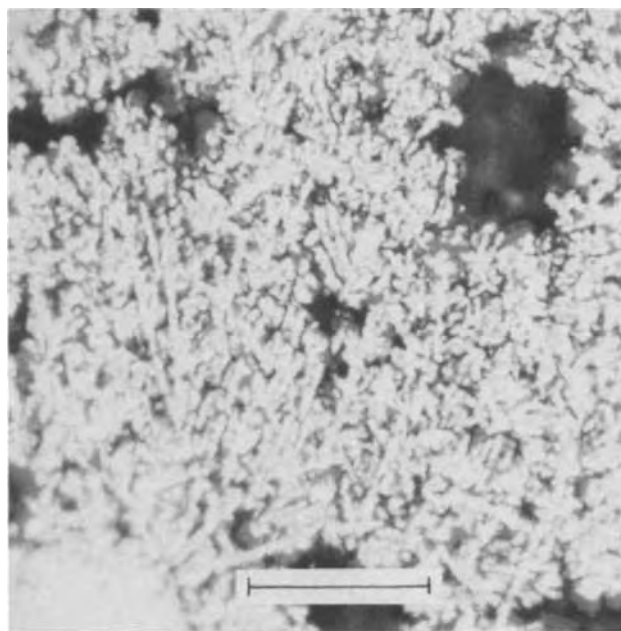


Fig. 6. Silver electrode charged halfway across the Ag/Ag<sub>2</sub>O potential plateau at cycle 6 in 8.4M CsOH. In this cross section metallic Ag is white, Ag<sub>2</sub>O that formed during the charge is gray, and empty areas (formerly filled with electrolyte) are black. Charge was done at the 20-hr rate. All previous discharges were done at the 1-hr rate. Marker indicates 15  $\mu$ m.

rate, Ag formed as small particles, often with dendritic shapes and sometimes with planar components. When these flat or planar components were cut by a cross section they looked like skeleton crystals, or like partially oriented needles. Oxidation of the electrode shown in Fig. 6 had not proceeded far enough to obscure the linear shapes of the Ag particles. Another common form of Ag was nonoriented granular particles. The interior of an electrode tended to have more  $\text{Ag}_2\text{O}$  present than had formed near the surface of an electrode.

A sample was also taken from this electrode when potential rose to the peak that separates the Ag/ $\text{Ag}_2\text{O}$  plateau from the  $\text{Ag}_2\text{O}/\text{AgO}$  plateau (Fig. 7). At this point the electrode was 38% charged. Comparison of Fig. 6 to Fig. 7 shows that Ag particles had become much smaller. Particles that appeared linear were rare in electrodes charged to the end of the Ag/ $\text{Ag}_2\text{O}$  potential plateau, but suggestions of these particles remained if one looked carefully. In some places the region near the surface of the electrode still had less  $\text{Ag}_2\text{O}$  than the rest of the electrode.

The electrode surface had an off-white color when charged as in Fig. 6, indicating Ag with small amounts of  $\text{Ag}_2\text{O}$ . When the electrode was charged to the end of the Ag/ $\text{Ag}_2\text{O}$  potential plateau the surface color was irregular shades of light gray, indicating Ag with varying amounts of  $\text{Ag}_2\text{O}$ . The outline of the expanded Ag grid showed as black ( $\text{Ag}_2\text{O}$ ) at the electrode surface closest to the grid, with only a few signs of the grid visible at the other surface.

An additional sample was cut from this electrode after the charge was 49% complete. Clumps of AgO crystals had formed at many sites (Fig. 8). These AgO sites were usually located within 1 or 2 mm of the grid. Formation of AgO had also taken place near most of the large Ag particles that were present in the active material. Very little AgO had formed near the surface of the electrode. The appearance of the external surface of the electrode had not changed since the potential peak.

The clumps of AgO crystals grew in size as adjacent  $\text{Ag}_2\text{O}$  and small Ag particles were oxidized to AgO. Small Ag particles were much rarer in the AgO clumps than in  $\text{Ag}_2\text{O}$  (Fig. 8). In areas of this sample where AgO had not formed the structure was unchanged from that at the potential peak (Fig. 7). This indicated that

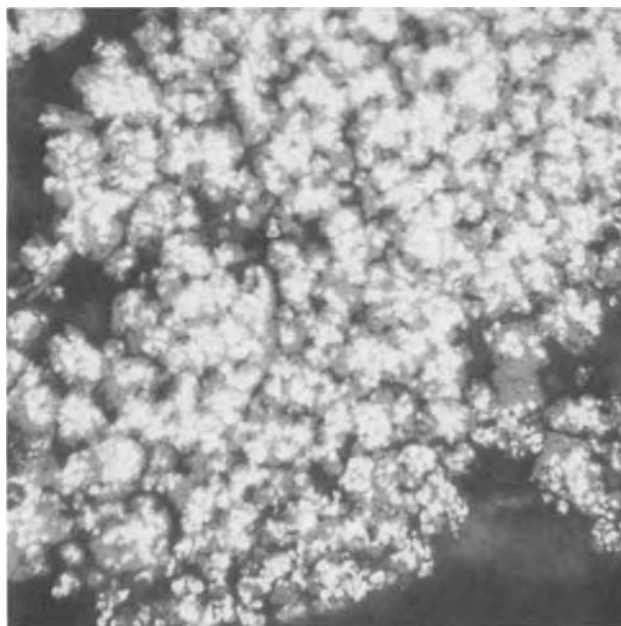


Fig. 7. Another area of the electrode shown in Fig. 6 after being charged until potential rose at the end of the Ag/ $\text{Ag}_2\text{O}$  potential plateau. Both Ag and  $\text{Ag}_2\text{O}$  were present. Same magnification as Fig. 6.

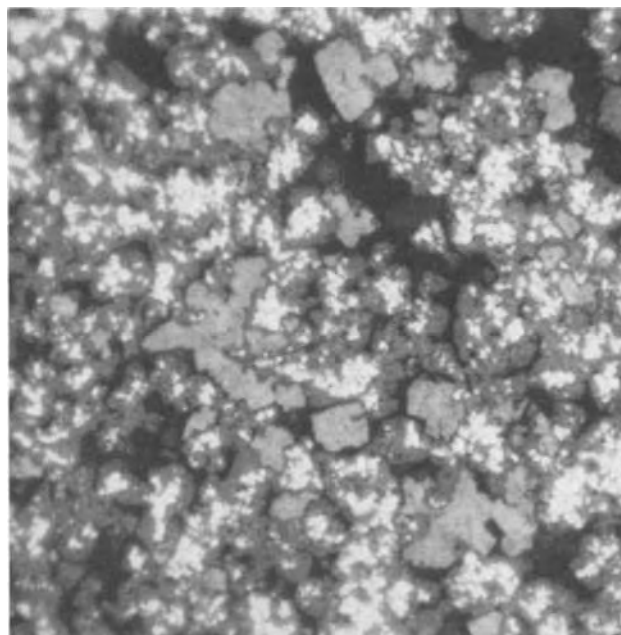


Fig. 8. Typical formation of AgO when the electrode shown in Fig. 6 and 7 was partly charged at  $\text{Ag}_2\text{O}/\text{AgO}$  potential. Metallic Ag is white, AgO is light gray,  $\text{Ag}_2\text{O}$  is darker gray, and voids are black. Same magnification as Fig. 6 and 7.

little or no oxidation of Ag had taken place after potential reached the  $\text{Ag}_2\text{O}/\text{AgO}$  plateau, except in areas where AgO was forming.

By the end of a charge to oxygen evolution many clumps of AgO had grown together into large masses (Fig. 9). All clumps of AgO were not as large as those in Fig. 9. The active material within approximately 1.2 mm of a grid had mostly been oxidized to AgO but little AgO had formed at a distance greater than 2 mm from the grid. The areas that were largely composed of  $\text{Ag}_2\text{O}$  and Ag were unchanged from their appearance at the potential peak (Fig. 7). A charged electrode contained large amounts of  $\text{Ag}_2\text{O}$  under these

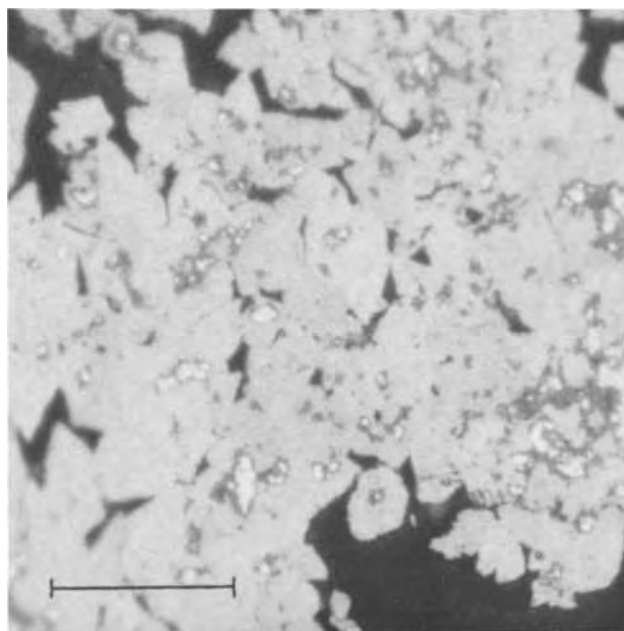


Fig. 9. Silver electrode charged at the 20-hr rate to oxygen evolution in 8.4M CsOH at cycle 6. Most of the Ag had been oxidized to AgO. Remaining Ag was separated from AgO by a thin layer of  $\text{Ag}_2\text{O}$ . Earlier stages of this charge were shown in Fig. 6-8 at the same magnification. Electrode had always been discharged at the 1-hr rate. Marker indicates 15  $\mu\text{m}$ .

conditions. There were fewer voids in the AgO than in areas of Ag<sub>2</sub>O and Ag (compare Fig. 9 with Fig. 7). At lower magnification than was used for Fig. 6-9 it was evident that a progressive filling of small voids took place during a charge.

**Effect of Ag particle size.**—The above description of structural changes refers to an electrode always discharged at the 1-hr rate, a condition that resulted in formation of small Ag particles. Silver formed into larger particles when an electrode was discharged at the slow, 20-hr rate. When electrodes containing large Ag particles were charged until potential rose at the end of the Ag/Ag<sub>2</sub>O potential plateau, the most common structure had the form shown in Fig. 10. Again it was found that some regions closest to the surface had thinner Ag<sub>2</sub>O layers than were normal for the rest of a partly charged electrode. Electrode surface color was darker when the slower discharges had been used, indicating a greater average thickness of Ag<sub>2</sub>O.

Although most Ag had formed as large particles during discharges at the 20-hr rate, groups of small Ag particles had formed in some areas. A greater proportion of the active material had oxidized to Ag<sub>2</sub>O in areas where Ag was in small particles. This resulted in structure being irregular when an electrode was charged at the Ag/Ag<sub>2</sub>O potential after slow discharges had been used, with some areas like Fig. 7 but most of the electrode like Fig. 10.

The large Ag particles that formed during a slow discharge did not oxidize completely during a charge (Fig. 11). Comparison of Fig. 11 to Fig. 9 (at twice the magnification) gives an idea of the sizes of Ag particles that remained at the end of a charge under the two conditions. In contrast to results when small Ag particles had formed, structure was relatively uniform in the electrodes with larger Ag particles. Most of the active material had oxidized to AgO at the end of a charge. The surface of these electrodes had the gray color of AgO.

**Structural changes that occur with cycling.**—During the first charge of sintered Ag electrodes the pore distribution was more regular than in later cycles. Figure 12 shows an electrode at the end of cycle 1

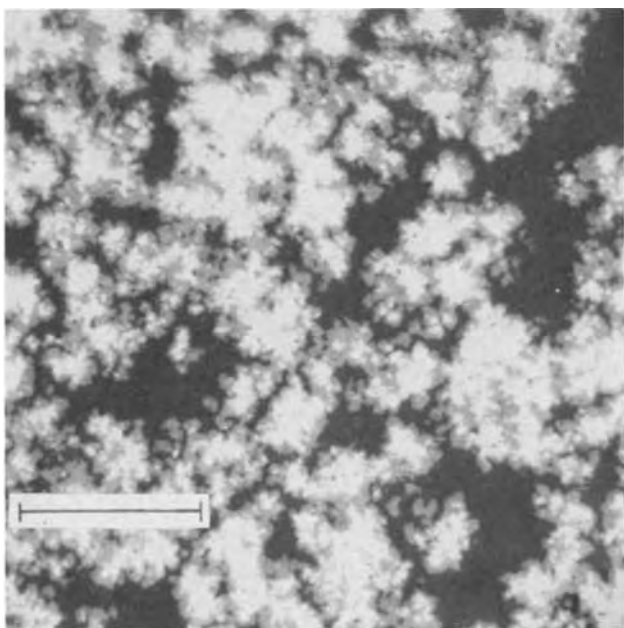


Fig. 10. Electrode charged at the 20-hr rate until potential rose at the end of the Ag/Ag<sub>2</sub>O plateau. Both Ag and Ag<sub>2</sub>O were present. This sample was taken during cycle 15 charge in 8.4M CsOH of an electrode that always was discharged at the 20-hr rate. Compare this cross section with Fig. 7 (at twice the magnification) to see the effect of discharge rate on particle size. Marker indicates 30  $\mu$ m.

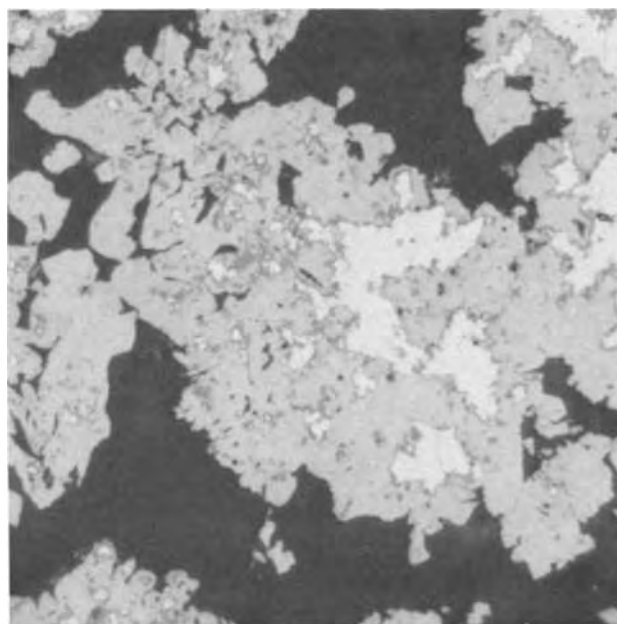


Fig. 11. Electrode charged at the 20-hr rate in 8.4M CsOH until oxygen evolution took place. This is the end of cycle 15 charge of the electrode always discharged at the 20-hr rate shown in Fig. 10. Same magnification as Fig. 10.

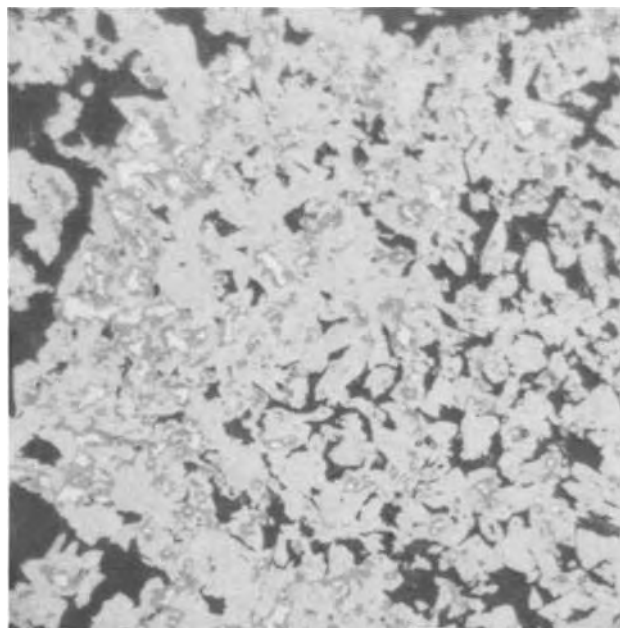


Fig. 12. Appearance of active material at cycle 1 when previously unused sintered Ag electrode was charged to oxygen evolution at the 20-hr rate in 8.4M CsOH. Comparison with Fig. 9 and 11 indicates that active material clumped during the cycling. Same magnification as Fig. 10 and 11.

charge. At cycle 1, AgO was relatively porous but formed into larger masses with fewer pores at later cycles (Fig. 9, 11). Active material gradually clumped into larger masses with cycling. Small voids became less common in these clumps, and large voids gradually formed between clumps. These changes were best seen at low magnification.

An electrode contained a random distribution of small and large particles at cycle 1, but an uneven distribution developed during the next few cycles in CsOH. Silver particles tended to increase in size during the first few cycles when an electrode was given slow discharges, apparently because adjacent particles had grown together. The greatest change took place in the first five cycles, with little additional change between



cycle 6 and 30. Large Ag particles formed in most areas and small particles in a few areas, while intermediate sizes became scarce. Most of the small Ag particles were oxidized completely to AgO during a charge.

The structure of an electrode always discharged at the 1-hr rate changed considerably during cycle 1 discharge, as Ag particles formed that were much smaller than the Ag originally present. A lesser change occurred in the next few cycles. In the first part of a charge, Ag<sub>2</sub>O formed throughout these electrodes, but oxidation to AgO was limited to a distance extending 1-2 mm from each grid member. A low magnification view of the border between areas where AgO predominated and areas largely Ag<sub>2</sub>O and Ag is given in Fig. 13. The nearest grid was about 1.5 mm from this border. A higher magnification view of the same type of structure in another electrode is shown in Fig. 14. Approximately half of a charged electrode contained little or no AgO under these conditions, despite the fact that oxygen evolution had already taken place. Note that the lower part of Fig. 14 has the same structure as Fig. 7, indicating that oxidation had not taken place here after potential reached the Ag<sub>2</sub>O/AgO plateau.

The pattern of the grid was visible as lines of AgO color that were 1.2-2 mm wide on the external surface of these charged electrodes that had formed a high proportion of small Ag particles. The rest of the surface had the colors of Ag<sub>2</sub>O and Ag mixtures. Thus, the surface appearance agreed with internal structure. The two types of charged structure shown in Fig. 13 and 14 formed during the first few cycles when using the 1-hr discharge rate. No additional major changes were noted from cycle 6 to 30 except for clumping of active material into larger masses.

The Ag grid in an electrode was slowly attacked. Some pits developed on the surface of a grid during the first charge. Grids in electrodes given fast discharges gradually became thinner with cycling. The grids sometimes lost as much as 25-30% of their original thickness after 30 cycles (Fig. 15). In the charged electrode shown in Fig. 15 the grid was surrounded by a coating of small AgO particles consisting mainly of

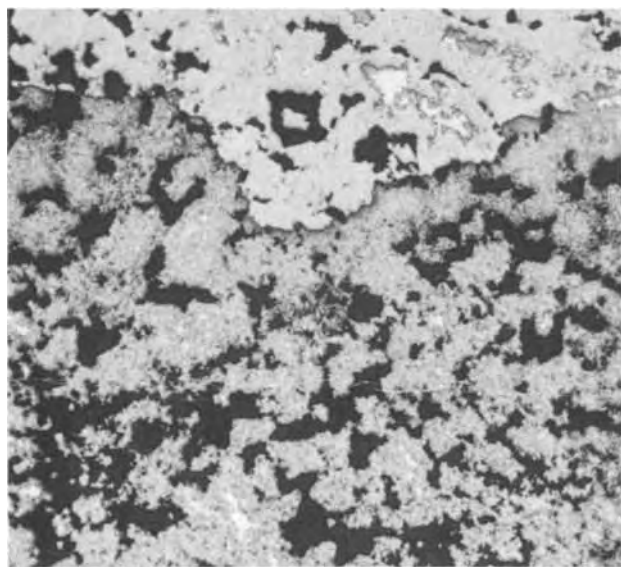


Fig. 13. Cross section through an electrode at the end of cycle 30 charge to oxygen evolution in 8.4M CsOH. All discharges had been done at the 1-hr rate. Areas near the grid were largely oxidized to AgO (top), while more distant areas consisted mainly of Ag<sub>2</sub>O and Ag (bottom). Electrode thickness (from left to right in photograph) was 0.87 mm.

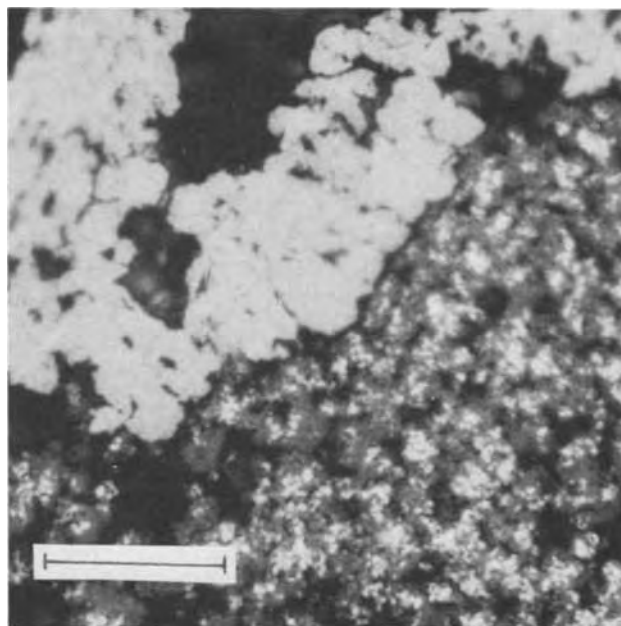


Fig. 14. Electrode charged to oxygen evolution at cycle 16 in 8.4M CsOH. All discharges were done at the 1-hr rate. High magnification view of the type of structure shown in Fig. 13. The AgO is at the top, and the Ag<sub>2</sub>O surrounds small Ag particles at the bottom. Marker indicates 15  $\mu$ m.

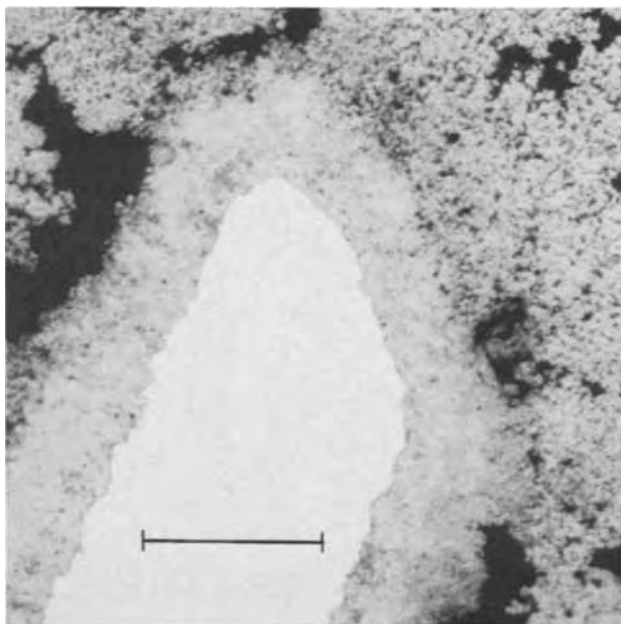


Fig. 15. Structure of AgO at the grid of a charged electrode at cycle 30 in 8.4M CsOH, when all discharges had been done at the 1-hr rate. Cross section through part of the Ag grid shows as white, AgO is light gray, and empty spaces are black. Same charged electrode as Fig. 13. Marker indicates 60  $\mu$ m.

material that had originally been part of the grid. Coatings around a grid gradually became thicker as cycling progressed. Grids of electrodes given slow discharges had more of a penetrating, irregular attack, with pits gradually reaching deeper into the grid as cycling proceeded. Grids of electrodes given 30 cycles with all discharges at the 20-hr rate had not lost as much of their original thickness as did the grid shown in Fig. 15, and had less of an oxide coating.

*Effect of electrolyte on electrode structure.*—Electrodes cycled in 3.6M CsOH differed from those in 8.4M CsOH in several ways. A cross section through a fully

charged electrode that had been cycled in 3.6M CsOH is shown in Fig. 16 in an area where much of the AgO had formed as elongated or thin shapes. Figure 16 can be compared to Fig. 11, an electrode cycled similarly except for CsOH concentration, but note the higher magnification of Fig. 11. Elongated AgO crystals were less common in 8.4M CsOH but were sometimes found, particularly at the surface of an electrode. Many areas of the electrode shown in Fig. 16 lacked elongated AgO. The AgO crystals were in smaller, more porous clumps in 3.6M CsOH. Limited weight measurements indicated that loss of active material was greatest in 3.6M CsOH.

The grid was attacked a little less in 3.6M CsOH than in 8.4M CsOH, and oxide layers on the grid were quite a bit thinner and more porous. Another difference was that less Ag<sub>2</sub>O was present in fully charged electrodes cycled in 3.6M CsOH. Regions that were largely Ag<sub>2</sub>O did not remain at the end of a charge in 3.6M CsOH when electrodes had always been discharged at the 1-hr rate as they did in 8.6M CsOH. Larger Ag particles had formed at the surface of electrodes discharged at the 20-hr rate in 3.6M CsOH than elsewhere, and were still evident at the end of a charge.

The only difference noted between structures in 8.4M CsOH and 8.4M KOH during cycle 1 charge of unused sintered Ag electrodes was that a small amount of thin AgO crystals had formed at some places on the surface of the electrode charged in CsOH solution. These thin or elongated AgO crystals were much rarer in 8.4M KOH. Since thin AgO crystals were found more often in 5.5M KOH than in 8.4M KOH and were also more common in 3.6M CsOH than in 8.4M CsOH, it was concluded that formation of thin AgO was inhibited in concentrated hydroxides.

The average particle size of Ag became at least twice as large in KOH as was typical in CsOH, when electrodes were cycled using the 20-hr discharge rate. The Ag particles had grown together in many places. The fact that larger Ag particles had formed in KOH was evident in all stages of a charge following the slow discharges. Differences between results in KOH and CsOH were less when the 1-hr discharge rate had been used, but in the first part of a charge the Ag particle size was noticeably larger in KOH.

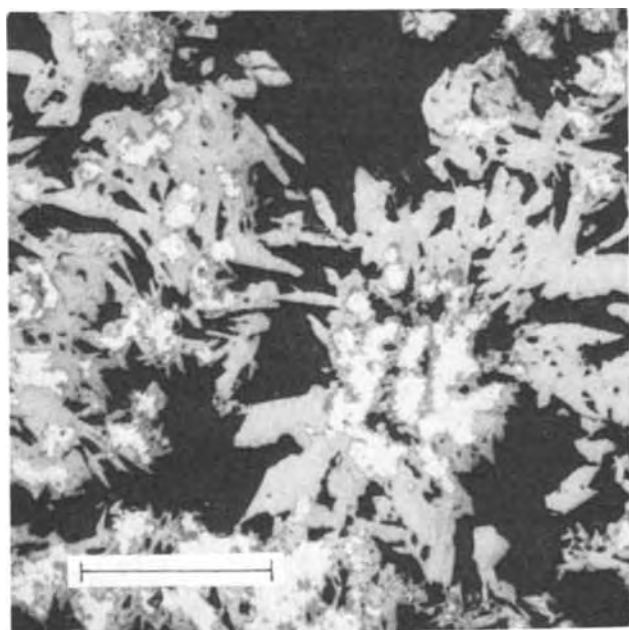


Fig. 16. Active material at the end of cycle 16 charge to oxygen evolution in 3.6M CsOH. All charges and discharges had been done at the 20-hr rate. The AgO had a greater tendency to form as elongated crystals in 3.6M CsOH than in 8.4M CsOH. Marker indicates 50  $\mu\text{m}$ .

## Discussion

*Oxidation of Ag to Ag<sub>2</sub>O.*—During the initial part of a charge the Ag<sub>2</sub>O forms from a dissolved Ag(I) species. A KOH solution becomes supersaturated with dissolved Ag as Ag<sub>2</sub>O is forming (9, 10). The soluble species is usually considered to be Ag(OH)<sub>2</sub><sup>-</sup>. Dissolution is followed by the precipitation of Ag<sub>2</sub>O. Equation [1] gives the over-all reaction for Ag<sub>2</sub>O formation by either the dissolution-precipitation mechanism in the initial part of a charge, or the solid-solid transition after Ag is coated with Ag<sub>2</sub>O



The solvation number for the OH<sup>-</sup> ion is given as *x* in this equation. The amount of solvation decreases in concentrated solutions. According to Eq. [1] pH tended to increase in the interior of the electrode during a charge because of the consumption of OH<sup>-</sup> ions and the formation of water. High rates of charge gave the greatest concentration gradients.

During the first charge in fresh electrolyte an unusually large part of the Ag(OH)<sub>2</sub><sup>-</sup> that formed near the surface of an electrode diffused into the bulk of the electrolyte instead of precipitating within the electrode as Ag<sub>2</sub>O, and thus less Ag<sub>2</sub>O formed near the surface. An electrode charged at cycle 1 until potential rose to the peak that ends the Ag/Ag<sub>2</sub>O plateau had much thinner Ag<sub>2</sub>O on Ag particles in the 50-100  $\mu\text{m}$  closest to the surface. The border was fairly sharp between this region where Ag<sub>2</sub>O was thin and the rest of the electrode at cycle 1, but less noticeable in later cycles. Less Ag(OH)<sub>2</sub><sup>-</sup> diffused from the electrode in subsequent cycles because the electrolyte in a cycled cell contained dissolved Ag. Even if Ag(OH)<sub>2</sub><sup>-</sup> had been depleted during a discharge, some oxide usually remained in the electrode to replenish dissolved Ag.

Electrodes cycled in CsOH did not develop as large an average particle size of Ag as developed in KOH. Particle size will be discussed in more detail in a separate paper on reduction of charged electrodes in CsOH. The smaller size of particles gave a larger surface area and this resulted in a larger quantity of Ag<sub>2</sub>O forming during a charge in CsOH than in KOH.

The decrease in charge acceptance at the Ag/Ag<sub>2</sub>O plateau shown in the upper part of Fig. 5 was the result of a gradual increase in particle size as electrodes were cycled. The largest average particle size had formed in KOH when discharges were always done at the 20-hr rate, and these conditions gave the lowest Ag/Ag<sub>2</sub>O charge acceptance before potential increased to the Ag<sub>2</sub>O/AgO plateau. Under a given set of conditions passivation occurred after Ag<sub>2</sub>O reached a particular thickness, and then potential increased until AgO began to form. The rise to the potential peak that ends the Ag/Ag<sub>2</sub>O plateau was slower in 8.4M CsOH than in 8.4M KOH when other conditions were similar (Fig. 2, 4) indicating that oxidation in KOH took place under conditions that were closer to equilibrium.

*Oxidation of Ag<sub>2</sub>O to AgO.*—The reaction for the formation of AgO



involves the same loss of hydrated OH<sup>-</sup> ions and gain of water as was given in Eq. [1]. Thus concentration gradients continued to be present in the electrolyte, particularly at high rates of charge. An indication of a concentration difference between the surface and the interior of an electrode while charging at the Ag<sub>2</sub>O/AgO potential was the fact that thin or elongated AgO crystals formed on the surface of electrodes in 8.4M CsOH. As AgO formed from Ag<sub>2</sub>O in 8.4M CsOH (Fig. 8) the active material as a whole looked identical to what had been found earlier in 8.4M KOH (11).

The capacity accepted at the Ag<sub>2</sub>O/AgO potential plateau was larger in more concentrated solutions than in dilute solutions over the range of charge currents



that were used. This was opposite to the effect of electrolyte concentration on charge acceptance at the Ag/Ag<sub>2</sub>O potential plateau. The thick Ag<sub>2</sub>O coatings that formed in dilute solutions hindered oxidation of the remaining active material, probably because Ag<sub>2</sub>O has a low conductivity. Total charge acceptance was larger in the more concentrated CsOH or KOH solutions, since the capacity increase at the AgO level was larger than was needed to compensate for the decrease at the Ag/Ag<sub>2</sub>O level. Both the capacity accepted at the Ag<sub>2</sub>O/AgO plateau and the total charge acceptance were larger in CsOH than in the same concentration of KOH. The smaller particle size of Ag that was present in CsOH when slow discharges were always used allowed a more complete oxidation of Ag.

Development of one type of structure within 1-2 mm of the grid members and another type elsewhere, as shown in Fig. 13 and 14, was found when using the most concentrated solutions of CsOH or KOH, but only when the original sintered Ag electrodes contained a low proportion of large Ag particles. The development of two structures in these electrodes that had relatively few large Ag particles can be attributed to a lowered internal conductivity after a discharge at the 1-hr rate had produced a decrease in average particle size (5). Electrode structure was much more uniform when the original sintered Ag electrodes had a higher proportion of large Ag particles, or when use of slow discharges had produced larger Ag particles.

An increasing internal resistance in the active material can be the cause of higher potentials while charging at the Ag<sub>2</sub>O/AgO plateau after using discharges at the 1-hr rate (lower part of Fig. 4) and of a gradual potential increase at the end of this plateau under these conditions. Although potentials were high in the last part of a charge at the Ag<sub>2</sub>O/AgO plateau, most of the current was being used to form silver oxides and not in oxygen evolution. Charge-discharge efficiency was high, as indicated by the arrows in the lower part of Fig. 4, except at cycle 1. A fairly constant amount of oxide remained in an electrode at the end of a discharge at the 1-hr rate, so efficiency was close to 100% after the first charge-discharge cycle.

*Comparison of CsOH to KOH.*—It is of interest to know the water concentration in the solutions used in this work (Table II) since the amount of water present can be an important factor in determining electrode behavior in concentrated electrolytes. The concentrated solutions used in this work did not contain sufficient water to allow the full amount of hydration found in dilute solutions. Measurements of the properties of concentrated CsOH, such as ionic mobility and hydration, are not available. For more dilute solutions various measurements given for the solvation number of the Cs<sup>+</sup> ion range from 0 to 6, and the solvation number of K<sup>+</sup> is generally given as 0.5-2 more positive than Cs<sup>+</sup> (7). The solvation number for the OH<sup>-</sup> ion has been given values ranging from 0 to 8, with 3-6 reported most often. Solvation numbers tend to decrease in concentrated solutions when the amount of free water becomes low, and were likely near or equal to 0 in 8.4M CsOH. Concentrated KOH may exist mainly in the form of water-bridged ion pairs (12). If Cs<sup>+</sup> is not hydrated, as some reports of the solvation number indicate, then the Cs<sup>+</sup> ion may be associated directly with the hydroxyl ion. Formation of either

type of ion pair decreases ionic mobility and, therefore, decreases conductivity in concentrated solutions.

The specific conductances of 3.7-6.5M CsOH and of 3.2-10M KOH solutions were measured by Rubin and Baboian (13). At 25°C the specific conductances reached a maximum in approximately 5.5M CsOH and 6.7M KOH. An extrapolation from 6.5 to 8.4M CsOH is very uncertain, but conductance of 8.4M CsOH might only be two-thirds as much as conductance of 8.4M KOH, although not as low as 8.4M NaOH. The viscosities of 3.7-6.2M CsOH and KOH solutions are close to each other (13). Extrapolation of the values given in (13) suggests that 8.4M CsOH would have a viscosity higher than that of KOH but much less than the viscosity of NaOH.

The lower conductivity of 8.4M CsOH resulted in potentials increasing a greater amount in CsOH than in KOH when charge current was increased (Fig. 2). The higher viscosity of 8.4M CsOH may also be a factor in the higher potentials. These higher charge potentials did not affect capacity more adversely in CsOH than in KOH (Fig. 1). If measurements had been extended to lower charge currents than were used for Fig. 1, the linear relationship on the log-log scale should eventually fail in KOH as it had already done in CsOH. Electrode capacity obviously could not increase indefinitely as charge current decreased.

When discharges were always performed at the 1-hr rate the structures that developed in 8.4M CsOH (Fig. 13 and 14) were like those found in 11.6M KOH (5). At the 20-hr rate of discharge the average size of Ag particle that formed in 8.4M CsOH was only half the size of Ag in 8.4M KOH. Thus, the structures that formed in CsOH tended to be like those found in a more concentrated KOH, or that would be expected in KOH at the same concentration if a higher C.D. had been used.

The differences in potential and structure indicate that concentration gradients were higher in CsOH than in KOH, when electrodes were cycled under the same conditions in electrolytes of the same molar concentration. The different behaviors probably result from mobilities being lower in CsOH because Cs<sup>+</sup> ions are larger than hydrated K<sup>+</sup> ions, and because OH<sup>-</sup> ions are directly associated with the Cs<sup>+</sup> ions and somewhat less mobile than are OH<sup>-</sup> ions in a KOH solution. It is not known whether there is a difference between the solubility of dissolved Ag in CsOH and KOH, or in the degree of supersaturation that forms. Appreciable differences would be important because the formation of Ag during discharge and part of the Ag<sub>2</sub>O formation during charge take place by a dissolution-precipitation mechanism.

When high current densities are used an electrolyte should be chosen that has high conductivity, because ionic mobility can become limiting and polarization will be high. Therefore the most concentrated solutions should be avoided and KOH used if a cell containing Ag electrodes is to be cycled at high rates of charge or discharge. At low currents, however, the somewhat limited ionic mobility found in concentrated electrolytes or in CsOH is desirable because it inhibits growth of large Ag particles during reduction and, therefore, slows or prevents the loss of capacity that occurs with repeated cycling. At decreased temperatures the electrolyte freezing point needs to be considered also, and the low eutectic of CsOH solutions is a desirable feature.

## Conclusions

The products of anodic oxidation were the same in aqueous CsOH solutions as in aqueous KOH solutions. First Ag was oxidized to Ag<sub>2</sub>O and then to AgO. Charge potentials increased a greater amount in 8.4M CsOH than in 8.4M KOH when charge was done at a higher current, because of the lower conductivity of the CsOH solution. Perhaps the higher viscosity of CsOH was also a factor. Oxidation took place under conditions farther from equilibrium in CsOH than in KOH.

Table II. Water present in electrolyte

Solution	Moles H <sub>2</sub> O/liter	Moles H <sub>2</sub> O/mole of CsOH or KOH
3.6M CsOH	51.4	14.4
8.4M CsOH	44.3	5.3
5.5M KOH	51.4	9.3
8.4M KOH	48.3	5.8
11.6M KOH	44.3	3.8

A concentrated CsOH solution was the preferred electrolyte for maximum capacity when using slow discharges, because Ag particle size increased the least in this electrolyte. The rate of discharge (reduction) had a strong effect on electrode structure and, therefore, on capacity and potentials of the following charge in both electrolytes. The capacity decrease observed during the first few cycles corresponded fairly closely to a decrease in charge acceptance at the  $\text{Ag}_2\text{O}/\text{AgO}$  potential plateau.

The structures that developed in CsOH resembled those found in a more concentrated KOH at the same current density, or were like those expected in KOH of the same concentration if a higher current density had been used. These results indicated that concentration gradients were higher in CsOH than in KOH of the same molar concentration. The different behaviors probably resulted from ionic mobilities being lower in CsOH than in a KOH solution. Differences in ion hydration were more important than differences in the total amount of water present.

Sintered Ag electrodes should contain small particles so that the electrodes can be charged to a large per cent of theoretical capacity. The electrodes should also contain some large Ag particles for conductivity if discharges are always to be done at a high current density in a concentrated electrolyte, since small Ag particles develop under these conditions and then conductivity becomes poor during a charge.

Manuscript submitted May 14, 1973; revised manuscript received July 31, 1973. This was Paper 30 presented at the Boston, Massachusetts, Meeting of the Society, Oct. 7-11, 1973.

Any discussion of this paper will appear in a Discussion Section to be published in the December 1974 JOURNAL.

#### REFERENCES

1. C. P. Wales, *This Journal*, **109**, 1119 (1962).
2. T. P. Dirkse, D. DeWitt, and R. Shoemaker, *ibid.*, **114**, 1196 (1967).
3. M. Fleischmann, D. J. Lax, and H. R. Thirsk, *Trans. Faraday Soc.*, **64**, 3128 (1968).
4. M. Fleischmann, D. J. Lax, and H. R. Thirsk, *ibid.*, **64**, 3137 (1968).
5. C. P. Wales, "Power Sources," Vol. 4, p. 163, D. H. Collins, Editor, Oriol Press Ltd., Newcastle-upon-Tyne (1973).
6. C. M. Shepherd and H. C. Langelan, Naval Research Laboratory Report 5635, July 25, 1961.
7. J. F. Hinton and E. S. Amis, *Chem. Rev.*, **71**, 627 (1971).
8. C. P. Wales, *This Journal*, **116**, 729 (1969).
9. B. Miller, *ibid.*, **117**, 491 (1970).
10. V. Tilak, R. S. Perkins, H. A. Kozłowska, and B. E. Conway, *Electrochim. Acta*, **17**, 1447 (1972).
11. C. P. Wales, *This Journal*, **118**, 1021 (1971).
12. G. Yagil and M. Anbar, *J. Am. Chem. Soc.*, **85**, 2376 (1963).
13. E. J. Rubin and R. Baboian, *This Journal*, **118**, 428 (1971).

## The Standard Potential of the Single-Crystal Copper Electrode in Aqueous Solutions

Finn Grønlund and Søren Noer

Chemical Laboratory IV, H. C. Ørsted Institute, University of Copenhagen, 2100 Copenhagen Ø, Denmark

#### ABSTRACT

A cell is described for measuring the equilibrium potential of the  $\text{Cu}|\text{Cu}^{2+}, \text{H}_2\text{O}$  electrode. The cell was vacuum-tight and the water vacuum-distilled in order to eliminate oxygen; the solution was equilibrated with metallic copper before immersion of the electrodes. These were disk-shaped, oriented single crystals made from 99.999% copper and vacuum annealed before use. Pairs of differently oriented crystals showed potential differences smaller than 0.02 mV. The standard potential of such electrodes was determined by measuring the emf of cells of the type  $\text{Ag}, \text{AgCl}|\text{CuCl}_2(m_0), \text{H}_2\text{O}|\text{Cu}$  with  $m_0$  in the range from  $4.8 \cdot 10^{-4}$  to  $2.5 \cdot 10^{-3}\text{M}$ . The resulting value,  $e^\circ_{\text{Cu}|\text{Cu}^{2+}} = 335.2 \pm 0.4$  mV at  $25^\circ\text{C}$ , is significantly lower than those generally accepted, probably because the accepted values were all obtained from measurements in relatively concentrated cupric sulfate solutions.

Measurements of the  $\text{Cu}|\text{Cu}^{2+}$  electrode potential in aqueous solutions have led to a number of values for the standard potential, some of which are listed in Table I. The scatter of these results is so large as to mask the differences between the various types of electrodes. It is probably due to the neglect of one or more of the following conditions, which we found essential in determining the copper single-crystal electrode potential:

1. The electrode should be made from high purity, strain-free copper single crystals, presenting an oriented, clean, and unperturbed surface.
2. Oxygen must be rigorously excluded.
3. The solution must be equilibrated with metallic copper before the electrode is immersed, and pH should be low enough to prevent formation of  $\text{Cu}_2\text{O}$ .

Key words: equilibrium, crystallographic planes, vacuum cells, chloride medium.

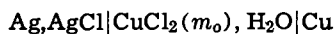
4. The reference electrode should be suitably chosen. In all studies cited above, the reference electrode was  $\text{Hg}, \text{Hg}_2\text{SO}_4|\text{SO}_4^{2-}$ , and the electrolyte  $\text{CuSO}_4$ . As  $\text{Hg}_2\text{SO}_4$  is relatively soluble, it is not feasible to work at concentrations below  $5 \cdot 10^{-3}\text{M}$ . At this level, the Debye-Hückel law is only beginning to assume validity; what is more, an appreciable fraction of the cupric

Table I. Standard potential measurements of  $\text{Cu}|\text{Cu}^{2+}$  electrode

Electrode	Standard potential, V
Copper sponge, grown electrolytically (1)	0.3469
Copper sponge, grown electrolytically (2)	0.3457
Two-phase copper amalgam (3)	0.3502
Two-phase copper amalgam (4)	0.3454
Amalgamated polycrystalline copper (5)	0.3498
Amalgamated copper single crystal (6)	0.3419
Copper single crystal (5)	0.3475

ions is complexed as  $\text{CuSO}_4$  (7). This fact, which adds a considerable systematic error, has apparently been overlooked by most investigators.

The measurements described below were made with an evacuated cell with movable electrodes and a solution previously equilibrated with metallic copper. In a preliminary series, potential differences were measured between copper single crystals; when these worked reproducibly, as indicated by values sufficiently close to zero, the potential difference of the cell



was measured as a function of  $m_0$  down to  $5 \cdot 10^{-4}\text{M}$ .

### Experimental

**Electrodes.**—The copper single-crystal electrodes were made from cylindrical (17 mm diameter) single crystals, grown in vacuum from 99.999% ASARCO copper by the standard Bridgman method (8) in a high purity graphite mold. The crystal was oriented to within  $1^\circ$  using the Laue back-reflection method, and disk-shaped slices 1 mm thick were cut with an acid saw to avoid introducing strains. The disks were electropolished in a 50–60% phosphoric acid bath for at least 20 mn at a current density of about 0.05 A/cm<sup>2</sup>. So prepared, they gave somewhat fluctuating values; satisfactory results were obtained only after a subsequent anneal at 1000°C at  $10^{-6}$  Torr for at least 1 hr.

Silver-silver chloride reference electrodes were prepared as described by Ives and Janz (9): silver oxide deposited on platinum wire is decomposed thermally, and the silver formed is partly chlorinated by electrolysis. To reduce diffusion, the wire was sealed into one end of a glass tube, the other end of which was a capillary 4 mm long and having an internal diameter of 1 mm. More than twenty such electrodes were made, most of which differed by less than 0.1 mV when immersed in cupric chloride solutions more concentrated than  $5 \cdot 10^{-4}\text{M}$ , and remained constant for many days.

Auxiliary copper electrodes were adopted with the purpose of equilibrating the solution before the single-crystal copper electrodes were immersed, as explained below. They were made from 99.999% pure, polycrystalline Johnson-Matthey copper sheet, 0.5 mm thick, cylindrically shaped so as to fit the inside of the glass cell, and with an immersed area of 30–40 cm<sup>2</sup>. They were electropolished and vacuum annealed before use as described above.

**Chemicals.**—In all applications, water was demineralized and twice distilled in a quartz apparatus before use.

$\text{CuSO}_4 \cdot 5\text{H}_2\text{O}$  was Merck, analytical purity; the  $\text{CuCl}_2$  was Riedel-de Haën, analytical purity; and the  $\text{Cu}(\text{ClO}_4)_2 \cdot 6\text{H}_2\text{O}$  was prepared from  $\text{CuO}$  (Riedel-de Haën, pure) and  $\text{HClO}_4$  (Riedel-de Haën, analytical purity).

All salts were recrystallized twice from aqueous solutions before use.

**Electrical equipment.**—In all measurements involving new electrodes, a Keithley Model 610 B electrometer (input resistance  $10^{13}$  ohms, input offset current  $10^{-14}\text{A}$ ) was used. Subsequently a Solartron LM 1420.2 digital voltmeter (input resistance  $10^9$  ohms, sensitivity 2.5  $\mu\text{V}$ ) was connected. In all instances the same reading was obtained, and the DVM with a logging unit was then used to measure and record potential differences.

**Cell.**—Experiments with a simple cell, flushed with purified nitrogen, showed that the potential difference varied with the bubbling rate and time, and that the copper tarnished. To reduce the amount of oxygen present, a vacuum-tight cell (Fig. 1) was constructed which could be evacuated and which permitted vacuum distillation of the water.

The cell, which is made from Pyrex glass, may be evacuated through a large tap T by means of a rotary

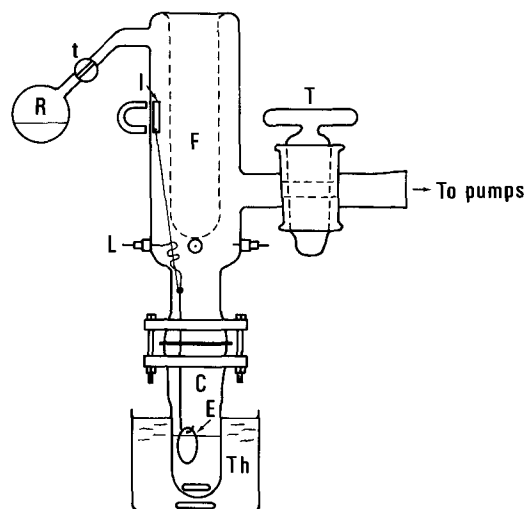


Fig. 1. Cell for emf measurements. E, electrode (only one of four is shown); C, measuring compartment; Th, thermostat; L, electrical lead-through; I, soft iron piece; F, cold finger; R, water reservoir; T and t, taps.

pump or an oil diffusion pump. A liquid nitrogen trap is inserted between the cell and the diffusion pump in order to prevent oil contamination. The limiting pressure is well below  $10^{-5}$  Torr, and the air leak rate is less than  $10^{-8}$  Torr-liter-sec<sup>-1</sup>, or about  $5 \cdot 10^{-13}$  moles of air per second. Water vapor may be admitted from the reservoir R through tap t. A cold finger F which may be filled with liquid nitrogen is placed above the demountable measuring cell C. A small water thermostat Th, controlled to within 0.01°C, may be raised so as to surround C; both are equipped with magnetic stirrers. The cell accommodates a total of four electrodes, only one of which (E) is shown. Each is suspended from a guided copper rod, attached by a thin nylon thread to a piece of nickel-plated soft iron I inside the top part of the apparatus; the iron is maintained in place by a strong external magnet, so that the electrode may be raised or lowered independently of the others. A thin, insulated copper wire connects it to one of the four electrical lead-throughs L.

**Procedure.**—When the electrodes have been prepared, they are suspended in the apparatus, connected electrically, and raised to a high position. A suitable amount of cupric salt is deposited in the bottom of C by pipetting off a small volume of solution of known concentration in the salt; and roughly 25 ml of pure water are introduced into R. The apparatus is assembled and evacuated with a rotary pump, both taps T and t being open in order to remove most of the residual gases, including those dissolved in the water. After a while, the contents of C and R are frozen by cooling from the outside. The diffusion pump is next switched on, and when the pressure is about  $10^{-5}$  Torr, F is filled with liquid nitrogen, while C and R are heated gently. This causes the water frozen in C and R to sublime onto the cold surface of F, whereas residual air in the ice, liberated in the sublimation process, is removed by the pump. When all the water has been carried over, the cell is isolated by closing both taps; and as the liquid nitrogen in F boils off, the ice melts and drips down into C. Stirring and thermostating (to slightly below room temperature, in order to keep all the water down in C) is started, and the electrolyte is now ready to receive the electrodes which may be immersed when convenient. At the end of the experiment, the liquid content of C is determined by weighing the electrolyte so as to permit calculation of the electrolyte concentration with an accuracy of about 0.3%.

### Results

**Preliminary experiments.**—With the cell described, the potential difference was measured between two

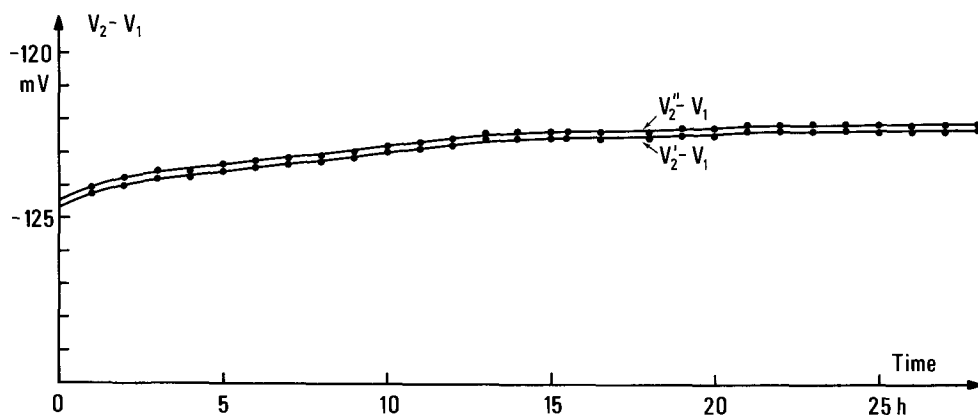
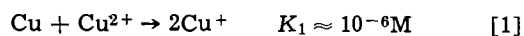
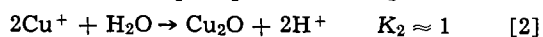


Fig. 2. Behavior of the potential differences between each of two copper single-crystal electrodes and one silver-silver chloride electrode with time.  $t = 0$  at the moment of immersion of the former, and  $m_0 = 1.747 \cdot 10^{-3}M$ .

identical unannealed copper single crystals in aqueous, oxygen-free solutions of  $CuSO_4$  or  $Cu(ClO_4)_2$  in the range  $5 \cdot 10^{-3}$  to  $5 \cdot 10^{-2}M$ . It fluctuated and often changed sign, with peak values decreasing from about 10 to 1 mV over a period of 24 hr; furthermore it was sensitive to light. The electrode surfaces were visibly modified. As pointed out by Jenkins and Bertocci (10), even in the absence of oxygen two reactions may be expected: dissolution of the electrode upon immersion



until equilibrium, and precipitation of  $Cu_2O$



for pH values sufficiently high.

Therefore, the auxiliary copper electrode described above was immersed into the solution in order to equilibrate it with respect to  $Cu^+$  and  $H^+$  prior to measurement. After at least 10 hr it was withdrawn, and only then were the single-crystal electrodes lowered into the solution. Immediately after, the potential difference was about 1 mV, and in 4 hr it decreased to about 0.02 mV where it stayed for days. The electrode surfaces remained perfectly bright throughout this period, and no photosensitivity was detected.

When the copper single crystals were annealed before use, the voltage was found to decrease from an initial value of 0.5 mV to 0.02 mV or less in 1 hr, where it remained for days or even weeks.

The same low value was obtained both when the two single-crystal electrodes were oriented alike and when different orientations were combined from the set of (100), (110), (111), and (311). This result is in complete agreement with the observations of Jenkins and Bertocci (10).

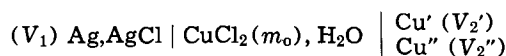
Investigation of the electrode surface with reflection high energy electron diffraction after completion of the measurements showed the presence of a few monolayers of  $Cu_2O$  on the copper crystals. Similar patterns were obtained after the experiments described below. The oxide may, however, have formed during transfer of the specimens from one apparatus to the other.

**Copper-silver chloride potential difference.**—A silver-silver chloride electrode was chosen as a reference for several reasons. It has been thoroughly investigated and is reported to work satisfactorily. The low solubility of silver chloride permits electrolyte concentrations down to  $10^{-4}M$ , a considerable improvement with respect to the mercury-mercurous sulfate electrode. Both  $Cu^{2+}$  and  $Cu^+$  form complexes with  $Cl^-$ , but calculations based on the available complex formation constants (11) show that the amount of chloro-ligated copper is insignificant for  $CuCl_2$  concentrations below  $3 \cdot 10^{-3}M$ . This value is, incidentally, a limit not to be exceeded if precipitation of  $CuCl$  is to be avoided.

The experimental procedure is as described above, with slight modifications: after 3-4 hr of equilibration with the auxiliary electrode, the silver chloride electrode is lowered into the liquid so as to be filled

through the capillary (the system is evacuated). After another 6-7 hr of equilibration, the reference electrode is emptied and refilled with electrolyte; the auxiliary electrode is raised; and two copper single-crystal electrodes are immersed.

The cell may be summarized as follows



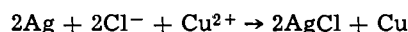
where  $m_0$  is the original molality in  $CuCl_2$  of the solution before equilibration and the  $V$ 's designate the potentials of the three electrodes relative to some common reference potential.

The behavior of the potential differences  $V_2' - V_1$  and  $V_2'' - V_1$  with time from the moment of immersion is shown for a typical experiment in Fig. 2;  $m_0 = 1.747 \cdot 10^{-3}M$ , and  $t = 20.30^\circ C$ . The ordinate difference between the curves  $V_2'' - V_2'$  gives the potential difference between the two single-crystal electrodes. Its constancy and magnitude, of the order of 0.2 mV, indicates that the copper electrodes work reliably. Both curves approach a limiting value which is maintained for many days, and their average,  $(V_2' + V_2'')/2 - V_1$ , is taken to be the emf of the cell,  $E$ .

Nine experiments were performed, in which  $E$  was measured at temperatures close to  $20^\circ C$ . The values of  $m_0$  were chosen in the range from  $4.8 \cdot 10^{-4}$  to  $2.5 \cdot 10^{-3}M$ , the upper concentration limit being imposed by the solubility of  $CuCl$  and complex formation, the lower limit by reaction [1]. In Table II, the first three columns list values of  $m_0$ ,  $t$ , and  $E$ , respectively, while the fourth and fifth give the quantities  $E^o(t)$  and  $E^o(20^\circ C)$  to be defined below.

### Discussion

The cell reaction is



and the emf of the cell

$$E = E^o + \frac{RT}{2F} \ln(a_{Cu^{2+}} a_{Cl^-}^{-2}) \\ = e_2 - e_1 + \frac{RT}{2F} \ln(m_{Cu^{2+}} + m_{Cl^-}^{-2} f_{Cu^{2+}} + f_{Cl^-}^{-2})$$

where  $e_2$  is the standard potential of the  $Cu^{2+}|Cu$  electrode, and  $e_1$  that of the  $Cl^-|AgCl, Ag$  electrode.

Table II. EMF values of the cell  $Ag, AgCl | CuCl_2(m_0) | Cu$  for various values of  $m_0$

$10^4 m_0$ , mol kg <sup>-1</sup>	$t$ , °C	$E$ , mV meas.	$E^o(t)$ , mV calc.	$E^o(20^\circ C)$ , mV calc.
4.820	20.05	-167.0	108.7	108.7
6.214	20.10	-157.3	109.2	109.3
6.241	20.10	-157.5	108.9	108.9
7.029	20.10	-153.1	109.0	109.1
9.145	20.20	-143.9	108.9	109.0
9.292	20.20	-144.0	108.2	108.3
15.22	20.05	-127.0	107.7	107.7
17.47	20.30	-122.5	107.6	107.8
25.62	20.30	-110.2	106.7	106.9

Some of the  $\text{Cu}^{2+}$  ions originally present are transformed into  $\text{Cu}^+$  ions by reaction [1] so that  $m_{\text{Cu}^{2+}} \approx m_0(1 - (\frac{1}{2})\sqrt{K_1/m_0})$  where  $K_1$  is the equilibrium constant of [1]. Reaction [2] has been suppressed by using a  $10^{-5}\text{M}$  solution of  $\text{HCl}$  in water for filling the reservoir R. The amount of complexed  $\text{Cl}^-$  is negligibly small in the concentration range investigated, as already mentioned, so that  $m_{\text{Cl}^-} \approx 2m_0$ .

The activity coefficients may be assumed to follow the modified Debye-Hückel expression  $\log_{10}f_i = Az_i^2\sqrt{I} - B_iI$ , where  $A = 2618T^{-3/2}$ ,  $I \approx 3m_0$ , and  $B_i$  is an individual constant. When this is introduced, the emf expression becomes

$$E = E^0 + \frac{RT}{2F} \left\{ \ln \left( 4m_0^3 \left( 1 - \frac{1}{2} \sqrt{\frac{K_1}{m_0}} \right) \right) - \ln 10 (6A\sqrt{3m_0} + 3Bm_0) \right\}$$

$$\approx E^0 + \frac{RT}{2F} \left\{ \ln (4m_0^3) - \frac{1}{2} \sqrt{\frac{K_1}{m_0}} - 6\sqrt{3} \ln 10A\sqrt{m_0} - 3 \ln 10 Bm_0 \right\}$$

Following the standard procedure, a quantity  $E^{\circ}(t)$  may be defined by

$$E^{\circ}(t) \equiv E - \frac{RT}{2F} \left\{ \ln (4m_0^3) - \frac{1}{2} \sqrt{\frac{K_1}{m_0}} - 6\sqrt{3} \ln 10A\sqrt{m_0} \right\}$$

$$\approx E^{\circ}(t) - \frac{3 \ln 10 RTB}{2F} m_0$$

Values of  $E^{\circ}(t)$ , calculated for the temperature of each experiment, are given in the fourth column of Table II. The corresponding values of  $E^{\circ}$  at  $20^{\circ}\text{C}$  are found in the fifth column; they were obtained by means of the temperature coefficient of the standard potential of the cell

$$\frac{dE^{\circ}}{dt} \approx \frac{dE^{\circ}}{dt} = 0.66 \text{ mV K}^{-1} \quad \text{at } 25^{\circ}\text{C} \quad (12)$$

In Fig. 3,  $E^{\circ}(20^{\circ}\text{C})$  is plotted against  $m_0$ . Assuming a linear relationship to hold, a straight line was drawn by the method of least squares, with equal statistical weight to all points. Its intercept with the ordinate axis was calculated to be

$$E^{\circ}(20^{\circ}\text{C}) = (109.6 \pm 0.2) \text{ mV}$$

At  $20^{\circ}\text{C}$ ,  $e_{\text{O}_2} = 225.6 \text{ mV}$  (11). Therefore, the standard potential of the  $\text{Cu}^{2+}|\text{Cu}$  electrode

$$e_{\text{O}_2} = (335.2 \pm 0.2) \text{ mV at } 20^{\circ}\text{C}$$

The corresponding values at  $25^{\circ}\text{C}$  may be found using the temperature coefficient of the standard  $\text{Cu}^{2+}|\text{Cu}$  electrode,  $de_{\text{O}_2}/dT = 8 \cdot 10^{-3} \text{ mV K}^{-1}$  at  $25^{\circ}\text{C}$  (12)

$$e_{\text{O}_2} = (335.2 \pm 0.4) \text{ mV at } 25^{\circ}\text{C}$$

A few remarks may be in place concerning possible errors. The potential difference between two copper electrodes in solutions of  $\text{Cu}_2\text{SO}_4$  or  $\text{Cu}(\text{ClO}_4)_2$  was repeatedly found to be  $0.02 \text{ mV}$  or less irrespective of orientation, a factor of 5 to 10 smaller than the values obtained by Jenkins and Bertocci (10) in similar experiments. This is probably due to differences in the technique of oxygen exclusion, since annealing was shown to have no effect on the rest potential, and since the solutions were equilibrated in both cases. In solutions of  $\text{CuCl}_2$  and in presence of an  $\text{AgCl,Ag}$  electrode, however, the potential difference between two copper electrodes was found to assume a constant value of about  $0.2 \text{ mV}$  (see Fig. 2). The reason for this increase is not clear. Tests have shown that it is neither caused by the measuring equipment, nor by temperature nor concentration gradients in the cell. It could be due to silver ions from the reference electrode or impurities from the electrolyte, reacting with or adsorbing on the two copper crystals to different extents, thereby causing either a change in the emf value or an increase in the overvoltage produced by some side reaction, e.g., oxidation from a residual leak.

Taking this possible error in consideration we have stated the accuracy of the value found to be  $\pm 0.4 \text{ mV}$ .

The value of  $E^{\circ}$  is based on the effective concentration of free  $\text{Cu}^{2+}$  ions which equals  $m_0$ , determined as mentioned above, and corrected for changes due to chemical reactions. The most important of these is reaction [1], the equilibrium constant  $K_1$  of which is not known accurately. Its value was taken to be  $10^{-6}$ , but it is not critical as calculations show that to  $\Delta K_1 = \pm 10^{-6}$  correspond  $\Delta E^{\circ}(20^{\circ}\text{C}) = \pm 0.2 \text{ mV}$  only. Further, the  $\text{Cu}^{2+}$  ion concentration might be changed significantly if copper compounds precipitated, but electron diffraction has shown that this does not happen on the electrodes, possibly except for insignificant amounts of  $\text{Cu}_2\text{O}$ . Finally, copper ions may complex with chloride ions, in the solution, but a glance at the rectilinear relationship of Fig. 3, which covers a range of 1:5 in  $m_0$ , confirms that  $\text{Cu}^{2+}$  ions are not bound to any measurable extent in a concentration-dependent way.

It will be noted that the value of the copper electrode standard potential found is considerably lower than those determined from previous emf measurements. In our opinion the reason is that in the latter cases,  $\text{Cu}_2\text{SO}_4$  solutions 10 to 100 times more concentrated than ours were used because of the choice of reference electrode. In such conditions, the Debye-Hückel approximation is not sufficiently good, and association between cupric and sulfate ions reduces the content of free (though of course solvated) cupric ions quite considerably. The latter effect was discussed by

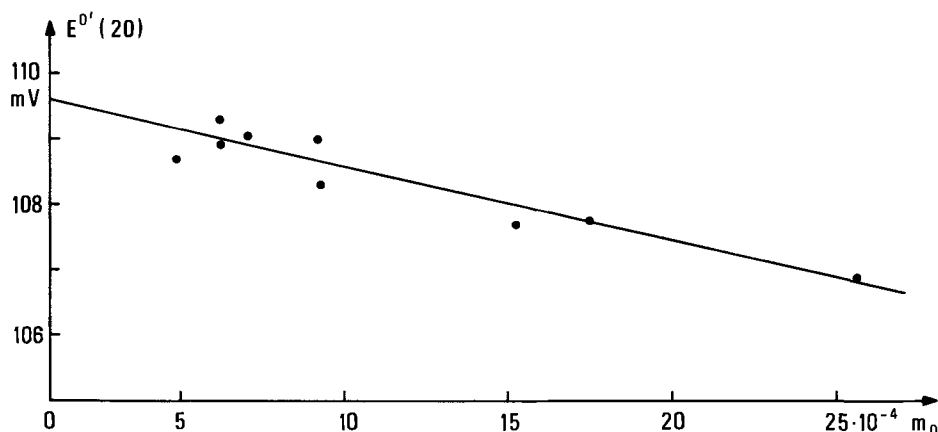


Fig. 3. Plot of  $E^{\circ}$  at  $20^{\circ}\text{C}$  against  $m_0$ , the original concentration of  $\text{CuCl}_2$ . The standard potential  $E^{\circ}(20^{\circ}\text{C})$  of the cell  $\text{Ag,AgCl}|\text{CuCl}_2(m_0)|\text{Cu}$  is found by extrapolating to  $m_0 = 0$ .

Guggenheim years ago (13); we intend to publish in due course a study examining its influence on results reported previously for the  $\text{Hg, Hg}_2\text{SO}_4|\text{CuSO}_4|\text{Cu}$  cell.

### Conclusions

The present study has shown that if all precautions listed at the beginning of this paper are taken, it is possible to obtain potential differences of 0.02 mV or less between two copper single crystals in the same electrolyte.

Second, potential differences between crystals exposing different faces are zero within the limits cited above.

Third, by adopting the silver-silver chloride electrode as a reference, permitting concentrations 10-100 times lower than those used previously, the standard potential of the copper single crystal|cupric ion electrode is found to be  $335.2 \pm 0.4$  mV at 25°C.

Manuscript submitted Feb. 12, 1973; revised manuscript received July 6, 1973.

Any discussion of this paper will appear in a Discussion Section to be published in the December 1974 JOURNAL.

### REFERENCES

1. G. N. Lewis and W. N. Lacey, *J. Am. Chem. Soc.*, **36**, 804 (1914).
2. A. R. Tourkey and S. E. S. El Wakkad, *J. Chem. Soc.*, **1948**, 740.
3. R. F. Nielsen and D. J. Brown, *J. Am. Chem. Soc.*, **49**, 2423 (1927).
4. F. Müller and H. Reuther, *Z. Elektrochem.*, **47**, 640 (1941).
5. F. H. Getman, *J. Phys. Chem.*, **34**, 1454 (1930).
6. W. E. Tragert and W. D. Robertson, *This Journal*, **102**, 86 (1955).
7. W. G. Davies, R. J. Otter, and J. E. Prue, *Discussions, Faraday Soc.*, **24**, 103 (1957).
8. F. W. Young, Jr. and J. R. Savage, *J. Appl. Phys.*, **35**, 1917 (1964).
9. D. J. G. Ives and G. J. Janz, "Reference Electrodes, Theory and Practice," Academic Press, New York (1961).
10. L. H. Jenkins and U. Bertocci, *This Journal*, **112**, 517 (1965).
11. "Stability Constants of Metal-Ion Complexes," Special Publication No. 17. The Chemical Society, London (1964).
12. A. J. de Bèthune, T. S. Licht, and N. Swendeman, *This Journal*, **106**, 616 (1959).
13. E. A. Guggenheim, *Discussions, Faraday Soc.*, **24**, 53 (1957).

## The Undercutting of Organic Lacquers on Steel

O. D. Gonzalez,<sup>1</sup> P. H. Josephic, and R. A. Oriani\*

United States Steel Corporation, Research Laboratory, Monroeville, Pennsylvania 15146

### ABSTRACT

A mechanism for the undercutting of scratched lacquers on black plate (uncoated low-carbon steel sheet) is proposed. Experimental evidence leading to its postulation and some tests carried out to confirm it are summarized. It is believed that the undercutting at breaks in coatings on black plate is initiated by the electrochemical reduction of the air-formed iron oxide film between metal and lacquer effectively to enlarge the break in the film. The subsequent corrosion of exposed steel results in the final undercutting. The stability to reduction of the chromium oxide in the chrome coating of TFS and the absence of iron oxide therein, are the reasons for the resistance of TFS to undercutting.

One of the usual performance tests for coating systems on food and beverage containers is the immersion of container material with scratched coatings in citric acid-sodium chloride solutions. After some tens of hours of immersion at room temperature, organic lacquers deposited on black plate (uncoated, low-carbon steel sheet) exhibit an undercutting which is characterized by extensive corrosion under the lacquer film extending laterally from the scratch. A similar immersion leaves lacquered TFS (*i.e.*, steel plated with chromium-chromium oxide) unharmed. The objective of the work reported here was to elucidate the mechanism of this undercutting, or, from another viewpoint, to understand how the chrome plate affords protection to TFS.

It is evident from Fig. 1 that of the several layers and interfaces which a scratch exposes to the aqueous medium, any one of them can represent the weak link of the assembly, and thus several physical or chemical processes can be postulated as the primary cause for the undercutting. However, for a mechanism to be acceptable it must take account of three aspects of the undercutting: specifically, the extreme difference of behavior of TFS and black plate toward undercutting,

the fact that undercutting always proceeds laterally from the scratch, and the observed rate of spreading. This paper summarizes the experimental evidence leading to the postulation of the autoreduction of iron oxide as the responsible mechanism and describes some tests carried out to check its validity.

In practice a specimen is considered to pass the salt-citrate test when the undercutting shown by the scratched coating after a 5-day immersion extends no more than 0.05 mm from the scratch. Lacquered black

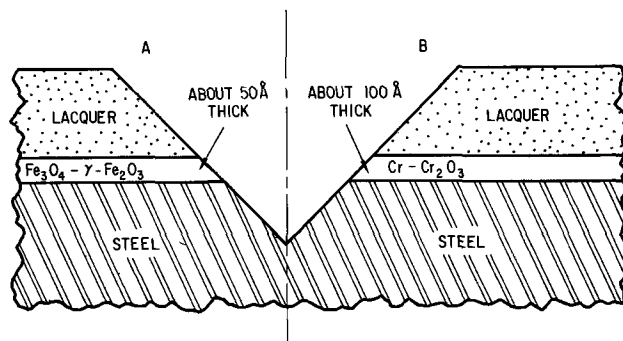


Fig. 1. Schematic diagram of scratch morphology in black plate (A) and TFS (B).

\* Electrochemical Society Active Member.

<sup>1</sup> Present address: Mercer County Community College, Trenton, New Jersey 08619.

Key words: delamination, lacquer films, chrome coatings, auto-reduction.

plate in this time interval shows undercutting of several millimeters. However, the initial evidence of damage to the lacquer on black plate can be detected much earlier than this, in about 15 to 30 min after immersion, as a faint uniform bleaching of the lacquer developing as a band adjacent and parallel to the scratch. This change in color of the lacquer can be seen only under moderate and oblique illumination and at magnifications less than 100X. Except for the slight change in color, the lacquer appears otherwise undamaged. Figure 2, a photograph taken of a specimen after an immersion test, illustrates the effect. We have chosen to call this early change delamination, to differentiate it from the final over-all undercutting which is associated with extensive corrosion and a visible separation of the lacquer from the metal. Detection of the delamination reduces the time for assessment of a particular specimen and/or test solution, and allows for practical rate studies. In this investigation we have limited ourselves to the observation of delamination.

### Experimental

The routine salt-citric acid test consists of dipping a scratched lacquered specimen into an aqueous solution of 15 g/liter each of citric acid and of sodium chloride, corresponding to 0.07M citric acid and 0.26M NaCl. The pH of this solution is 2.1. The lacquer is scratched at right angles to the rolling direction of the underlying metal and sufficiently deeply to penetrate into the steel. The scratch is kept vertical during immersion. We retained essentially the same methodology in this investigation except for variations in bath composition. Where anaerobic conditions were desired, the test was performed in a cell provided with a fritted gas inlet and a water bubbler outlet. Pure argon gas, bubbled first through a chromous sulfate-Zn amalgam solution, and then through a water trap, was used as the gaseous medium. All solutions were similarly deaerated for 1 hr prior to use in the anaerobic tests. The lacquer employed in most of our studies was a phenol formaldehyde heat-cured resin, but some studies were also carried out with two brush-on or dip-type, air-dried lacquers. No significant difference in delamination behavior was observed among the three lacquers.

Close to a hundred delamination tests were performed in different baths with different acids and in two principal pH ranges. In these tests the concentration of the particular acid was kept at 0.07M and NaCl was always added to keep the ionic concentration at 0.26M. The tests were performed both aerobically (*i.e.*, in the ambient laboratory atmosphere) and anaerobi-

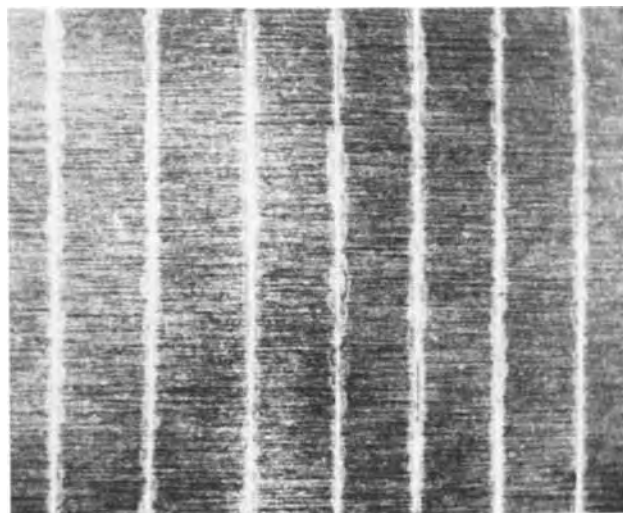


Fig. 2. Photograph of delamination in scratched lacquered black plate after 2 hr in salt-citric acid bath (3.5X). The center white line of the vertical patterns represents the scratch. The contrast has been enhanced in the development of the photograph.

Table I. Delamination of scratched black plate, stability constants of ferrous complexes, and ionization constants of the acids

Acid system*	Result†		Log $K_s$ (Fe(II)L)	$pK_a$
	pH 2	pH 4		
Citric	+	+	2.6, 4.4	3.0, 4.4, 5.7
Tartaric	+	—	2.2	2.8, 4.0
Lactic	+	+	[1.5]	3.9
Oxalic	—	—	4.7, 3.0	1.2, 4.2
Acetic	+	—	1.4	4.6
EDTA	+	+	14.4	2.8, 6.2, 10.3
HCL	+	—	0.4 (2 M)	—
H <sub>2</sub> SO <sub>4</sub>	+	—	0.2 (1 M)	1.4
HNO <sub>3</sub>	—	—	—	—
H <sub>3</sub> PO <sub>4</sub>	+	—	Forms complexes	2.1, 7.2, 12.4
HClO <sub>3</sub>	+	—	—	—

\* All acid concentrations 0.07M; ionic strength kept constant at 0.26M with NaCl except for inorganic acids where the salt of the common anion was used. All values of  $K_s$  were taken from Ref. (1) except for those for citric and tartaric acids, taken from Ref. (8). The value for the lactate complex was estimated from the values for other divalent cations.

† + indicates occurrence of delamination; — indicates no delamination.

cally as described above. The results obtained can be grouped together and summarized simply in tabular form, Table I. In this table a positive sign (+) indicates that delamination was observed for the particular system; a negative result (—) indicates that no delamination was detected at 40X magnification after at least 24 hr (the detection limit in this case was 0.02 mm). No significant differences were observed in behavior under aerobic or anaerobic conditions, except in one experiment with sodium citrate at pH 8 in which delamination was obtained only under aerobic conditions. The pH values used were 2.0 and 4.0 (corresponding to those of soft drinks and beer), except where listed otherwise. The principal information to be drawn from Table I is the difference in delamination behavior between systems containing organic acids and those with inorganic acids: delamination was not observed in any inorganic system at or above pH 4.0. Column 3 of Table I lists stability constants,  $K_s$ , (or over-all equilibrium constants) for the complexes of ferrous ions<sup>2</sup> with the anions of the particular acid; column 4 lists the ionization constants for the acids. The values of the equilibrium constants for complexation indicate that a correlation can be made between appearance of delamination and the complex-forming ability of the particular system. The case of oxalic acid appears anomalous, but an explanation for this will be given later.

The information in Table I indicates only whether a particular system resulted in delamination or not. In Fig. 3a and b we characterize the delamination further by showing its magnitude and time dependence and also the effect of organic acid concentration and pH for a salt-citrate bath. (In these plots the delamination has been measured from the center of the scratch, so that the zero time value includes half the width of the scratch.) Rates of delamination were measured quantitatively only for the systems given in Fig. 3a and b. However, the rates for the other systems producing delamination were of the same order of magnitude.

The effect of changing metal substrate (apart from the use of TFS) was studied by checking the performance of lacquered specimens of stainless steel, low-Cr-Ni alloy (COR-TEN steel), and Cr-phosphated black plate. Of these, only the stainless-steel specimen did not exhibit delamination. The delamination rate for Cr-phosphated steel is shown in Fig. 3b. The difference in behavior between stainless steel and the low-Cr alloy steel would seem to indicate that a minimum

<sup>2</sup> The values for the ferric ion complexes are not included in this table for the sake of simplicity. Ferric ion forms very strong complexes with all these organic anions, with values of stability constants great enough to cause large complexation even at pH 2.0. For inorganic anions the values of the stability constants for the ferric complexes are also larger than for the ferrous complexes, and the same general difference in magnitude between the values for organic and inorganic anions is also displayed.



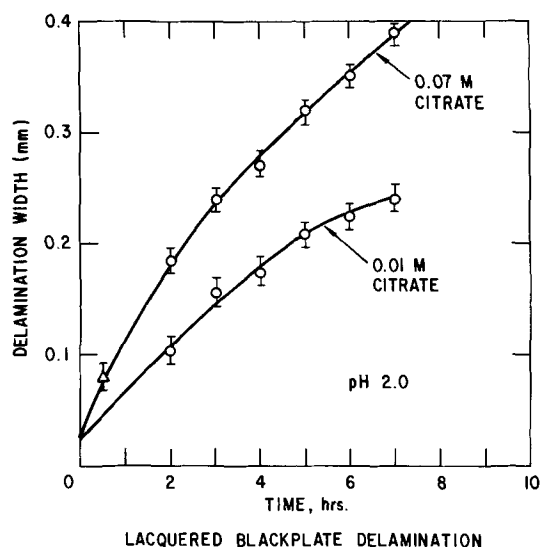


Fig. 3a. Delamination rate of scratched lacquered black plate at two citric acid concentrations.  $\circ$ , Aerobic conditions;  $\Delta$ , anaerobic conditions.

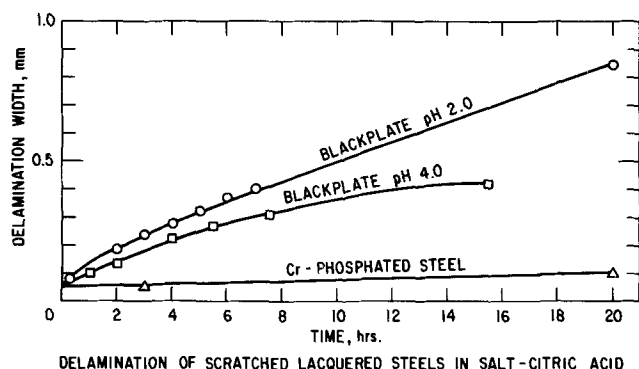


Fig. 3b. Delamination rate of scratched lacquered black plate at longer times. Effect of pH. Delamination rate of Cr-phosphated steel is also shown.

content of Cr in the alloy is necessary to afford protection against delamination.

The use of various etching solutions on black plate prior to lacquering did not significantly change subsequent delamination behavior.

### Discussion

The correlation found between the delamination and the complex-forming ability of the acids immediately suggests that delamination could represent the chemical dissolution of the iron oxide film between the lacquer and steel, but enhanced in rate, since the formation of soluble complexes in the aqueous phase will reduce the activity of metal ions and increase the driving force for dissolution, and consequently the rate. Since the rate of formation of  $\text{Cr}^{3+}$  complexes is known<sup>3</sup> to be several orders of magnitude smaller than for  $\text{Fe}^{3+}$ , this would explain the lack of delamination in TFS. However, a simple measurement of dissolution rates of the appropriate oxides clearly negates the hypothesis of chemical dissolution. In Table II we list the initial dissolution rates of three forms of oxides determined by us in a solution with and without citric acid. The measurement consisted simply of analyzing for Fe in the aqueous phase of a system of known volume and with a known weight of oxide at appropriate times, and converting the iron concentration to gram-atoms of Fe ions dissolved per square centimeter of surface. (The specific surface area was measured by the BET method.) Although the results show that presence of complexing agents does increase the rate of dissolution by a large

<sup>3</sup> See, for example, Table I of Ref. (2).

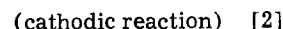
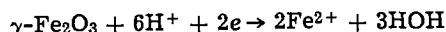
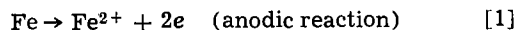
Table II. Dissolution of massive oxides (Initial pH 3.00, concentration 0.01M)

Substrate	Medium	Dissolution rates, g-atoms/cm <sup>2</sup> /day	Ratio of rates citrate: nitrate
1. a. $\text{Cr}(\text{OH})_3$ (amorphous)	Citrate	$4.4 \times 10^{-11}$	15
b. $\text{Cr}(\text{OH})_3$ (amorphous)	Nitrate	$3.0 \times 10^{-12}$	
2. a. $\text{Fe}(\text{OH})_3$ (amorphous)	Citrate	$1.2 \times 10^{-12}$	6000
b. $\text{Fe}(\text{OH})_3$ (amorphous)	Nitrate	$2.1 \times 10^{-12}$	
3. a. $\alpha\text{-Fe}_2\text{O}_3$ (crystalline)	Citrate	$3.0 \times 10^{-11}$	25
b. $\alpha\text{-Fe}_2\text{O}_3$ (crystalline)	Nitrate	$1.2 \times 10^{-12}$	

\* Corresponds to about 0.7 layer of Fe atoms removed per day, or 3A/day.

factor, when the results are converted to a linear basis, the number so obtained (viz., 0.7 atomic layer of Fe ions removed per day) cannot explain the rate of delamination of black plate, which corresponds to about  $3 \times 10^5$  atomic layers of 50Å-thick oxide removed per day.

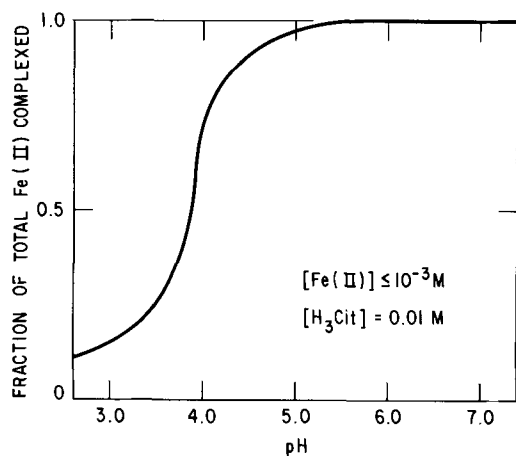
The simplest mechanism that explains the delamination and is consistent with all the facts is the following: when scratched lacquered black plate is immersed in acidified water, an electrochemical reaction between the metal substrate and the air-formed ferric oxide film occurs which may be written as



This process was first invoked by Evans (3), to explain the rapid disappearance of interference colors of oxidized iron surface (a matter of seconds) upon immersion in acid solutions of pH less than 4.0. In contrast, a very slow dissolution occurs (a matter of days) when the same oxide films (removed from the iron substrate by bromine-methanol) are immersed in the same acid solutions. The validity of this mechanism was established by Pryor and Evans in a series of papers (4-6). Pryor and Evans named the reductive dissolution of the iron oxide in contact with iron "autoreduction" to distinguish it from cathodic reduction produced by an external emf. Oswin and Cohen (7) later observed that autoreduction persists up to pH 7.6 if a buffer is present, that is, if an adequate supply of  $\text{H}^+$  ions is maintained to allow the cathodic reaction to continue. In delamination, because of the nearly two-dimensional character of the air-formed film, being at most 50Å thick, the consumption of hydrogen ions by the cathodic reaction is not easily made up by diffusion, so that a rise of pH occurs. At the right conditions the rise in pH produces the precipitation of ferrous hydroxide locally, strongly inhibiting the cathodic reaction and halting the autoreduction. In the presence of anions which can form soluble complexes with the ferrous ions, the formation of ferrous hydroxide is precluded and the autoreduction persists. It should be noted that in the special case of oxalic acid, the complexing of ferrous ion quickly leads to insoluble ferrous oxalate which also effectively inhibits the cathodic reaction. In fact, ferrous oxalate can be seen deposited at the scratch when scratched lacquered black plate is allowed to remain in contact with oxalic acid solution for periods of 24 hr.

Insight into why delamination in organic acid persists beyond a pH of 4 (whereas it does not in inorganic acids) may be obtained by a calculation of the variation with pH of the fraction of total iron complexed by organic acids. This calculation is summarized in Fig. 4a for the  $\text{Fe}^{2+}$ -citric acid system. The complexes formed by ferrous ion are  $(\text{FeHCit}^+)$  and  $(\text{FeCit}^-)$  (8); Fig. 4a shows

$$\frac{([\text{FeHCit}^+] + [\text{FeCit}^-])}{([\text{Fe}^{2+}] + [\text{FeHCit}^+] + [\text{FeCit}^-])}$$



FERROUS ION COMPLEXATION IN CITRATE SOLUTIONS

Fig. 4a. Fraction of total iron complexed in ferrous ion-citrate system as a function of pH; values computed from constants determined by Timberlake (8). Note  $[\text{Fe(II)}] \equiv [\text{Fe}^{++}] + [\text{FeHCit}^+] + [\text{FeCit}^-]$ .

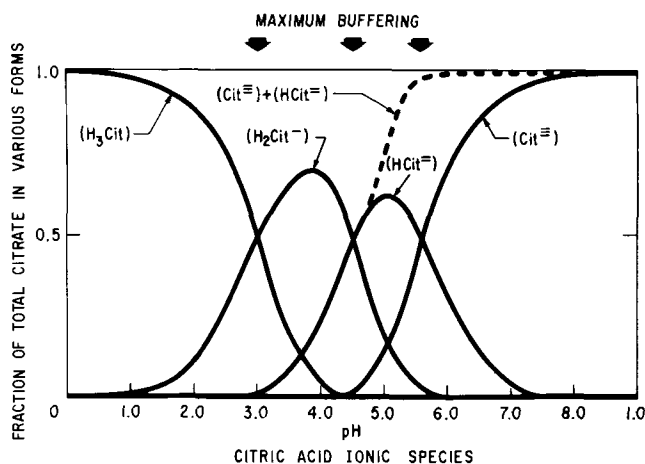


Fig. 4b. Fraction of anionic species present in citric acid as a function of pH. Ionization constants taken from Timberlake (8).

against pH, and one sees that the amount of complexation, and hence of the solubilization of ferrous hydroxide, increases sharply about the pH of 4. In Fig. 4b the fraction of the various anionic species in citric acid is plotted against pH, and the reason for the rapid rise of complexation around pH 4.0 seen in Fig. 4a becomes evident. An inspection of the values for the ionization constants  $[pK_a \equiv (-\log K_a)]$  for the organic acids listed in Table I, shows that the same behavior with pH can be expected for all these acids. It should also be noted that for all these acids, the listed values of  $pK_a$  also indicate that maximum buffering action can be expected around pH 4.0, a fact which contributes to the persistence of delamination. Moreover, the formation of soluble ferrous complexes at the same time reduces the activity of ferrous ion, and hence increases the driving force of both cathodic and anodic reactions, another contributing factor.

On a thermodynamic basis for the system considered,  $\text{Cr}_2\text{O}_3$  is not expected to reduce in the presence of  $\text{H}^+$  ions at the existing potential. The Nernst potential for the reduction of  $\text{Cr}_2\text{O}_3$  to  $\text{Cr}^{++}$  at pH 4.0, and at an activity of  $\text{Cr}^{++}$  ion of  $10^{-6}$ , is about 0.3V more negative than for the reduction of  $\text{H}^+$ . This may be checked by referring to the appropriate Pourbaix diagram (9). Caplan and Cohen (10) have proved this to be true kinetically as well, by observing  $\text{H}_2$  evolution rather than the reduction of  $\text{Cr}_2\text{O}_3$  during cathodic reduction under an impressed current at pH 7.6. Thus, the protection against delamination provided by the chrome

coating on TFS is imparted by the inherent stability of  $\text{Cr}_2\text{O}_3$ .

The proposed mechanism has been examined by three very simple electrochemical techniques devised to answer three questions:

1. Does the air-formed oxide film in black plate in fact dissolve through a cathodic reduction, and at what rate? This was answered by noting the current obtained upon immersing a specimen of unlaquered black plate into a standard salt-citrate bath electrically connected through a known resistance to a large-area specimen of unlaquered black plate placed in the bath some minutes before. The experimental arrangement is shown schematically in Fig. 5a. The currents observed in this fashion are reproduced in Fig. 6 for two specimens of black plate. The polarity of the currents observed indicated that the electron flow was from the large-area black plate to the specimen, as required by the reduction process (Eq. [2]) of the oxide upon it. The results indicate that the oxide is reduced in about 4 min. The initial current rise can be converted to the number of Fe atoms dissolved per square centimeter per hour, thence to the number of atomic Fe layers removed per hour from the iron oxide, assuming  $10^{15}$  Fe atoms per square centimeter. This number, applied to the lateral dissolution of the 50Å oxide film, gives for a calculated rate of delamination a value of 0.03 mm/hr, which is within the order of magnitude of the delamination actually observed, 0.1 mm/hr. Figure 6 indicates also the very small transient current observed when a specimen of TFS is immersed into the bath, confirming the fact that the oxide film of TFS is not reduced by simple contact with Fe.

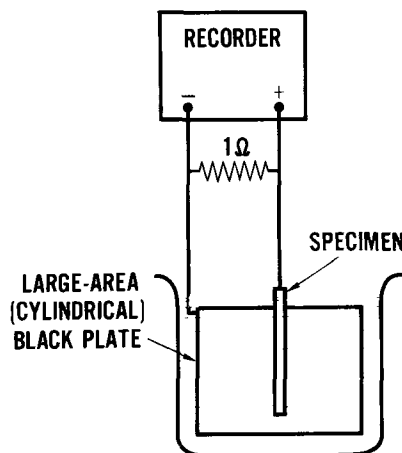


Fig. 5a. Schematic diagram of experimental arrangement for detection of current transients in reductive dissolutions of oxide films on steel.

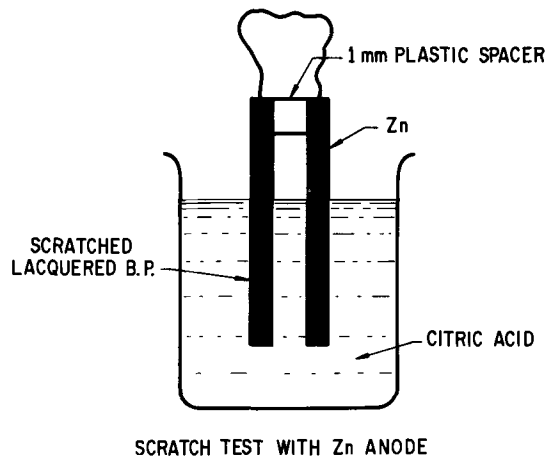
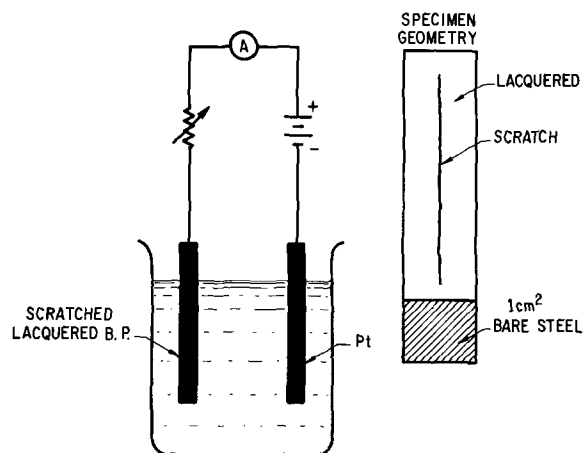


Fig. 5b. Schematic diagram of experimental arrangement for delamination study with Zn anode.



SCRATCH TEST WITH IMPRESSED CURRENT

Fig. 5c. Schematic diagram of experimental arrangement used to apply an anodic current to scratched lacquered black-plate specimen.

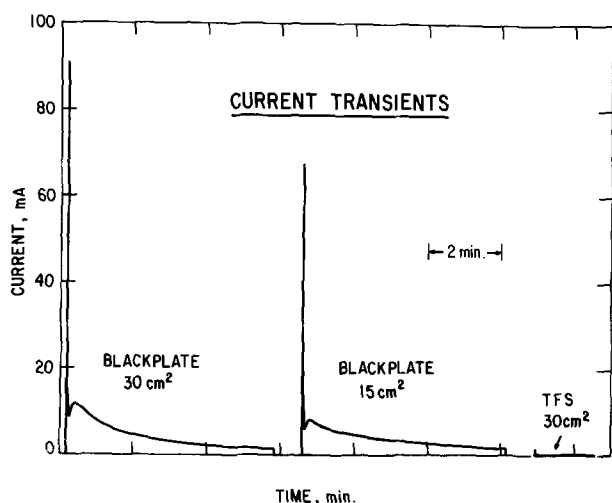


Fig. 6. Current transients observed with black plate and with TFS. The area figures refer to the centrally hung specimen (see Fig. 5a), which is much smaller in area than the surrounding large-area electrode.

2. How will the presence of a more efficient anode affect the delamination? For this test (Fig. 5b) a large-area Zn sheet was short-circuited to a specimen of scratched lacquered black plate, and the two specimens positioned so that the scratch was only 1 mm away from the Zn; the assembly was then immersed in a standard salt-citrate bath. The delamination measured after 2 hr was found to be twice that given by Fig. 3b. (A standard salt-citrate test on a scratched black-plate specimen was simultaneously performed as a control.) Since our experimental scatter in measuring delamination rates was always better than 10%, this result is significant and indicates that delamination is anodically controlled.

3. Can the application of a current to a scratched black-plate specimen stop the delamination? In other words, can the oxide film be made passive? The experimental arrangement used here is shown in Fig. 5c. A current density of 50 mA/cm<sup>2</sup> was used, this value having been selected from the conversion of the delamination rates observed (Fig. 3a) to a current density, assuming the delamination to occur in a slab of thickness 50Å. (The density of the oxide was assumed to be 4.0 g/cm<sup>3</sup>.) This large current density, of course, leads to considerable anodic dissolution of the black plate, so that the time of experiment was confined to 1 hr. The current had the effect of widening and deepening the scratch, as was expected, but no evidence of delamina-

tion was observed. However, this test is not conclusive since all that can be said is that if delamination occurred it did not stay ahead of the corrosive widening of the scratch.

These tests leave no question as to the electrochemical nature of the delamination and indicate that the proposed mechanism is internally self-consistent.

The proposed mechanism implies that the absence of delamination on TFS means that a layer of iron oxide does not exist between lacquer and metal in TFS. This is not unreasonable, considering the electrochemical method of application of the chrome plate; however, this was independently verified (11) by examining the surface of TFS for Fe<sup>2+</sup> and Fe<sup>3+</sup> ions using soft x-ray spectroscopy. Negligible amounts of iron ions were detected on TFS. However, iron ions were found on the surface of Cr-phosphated steel which also exhibits delamination although its outer surface is also chromium oxide.

### Conclusions

The proposed undercutting mechanism may be summarized as follows with the aid of Fig. 7.

1. a. Upon contact of iron and iron oxide with the aqueous medium through a defect such as a scratch in the lacquer film, the oxide dissolves rapidly by the process of reduction (A), exposing more iron surface and, in effect, enlarging the original defect.

b. The exposed iron surface will corrode as usual (B), introducing iron into the aqueous medium. We have found that only a minor fraction of the iron ions in the aqueous phase are attributable to the corrosion of the iron surface of the original scratch.

2. In the presence of complexing buffering agents, e.g., organic acids, the reduction of the oxide film continues because of the formation of soluble ferrous ion complexes and the maintenance of an adequate H<sup>+</sup> concentration.

3. In the absence of complexing buffering agents, the pH at the oxide cathode goes up rapidly because of the depletion of H<sup>+</sup> ions, and Fe(OH)<sub>2</sub> precipitates locally, inhibiting the electrochemical process, and effectively stopping the dissolution of the oxide film.

4. TFS resists undercutting because a ferric oxide layer does not exist between the steel and the chromic oxide layer, and the latter is too stable to be reduced by the oxidation of metallic iron.

### Acknowledgments

The authors acknowledge with appreciation helpful discussion with P. R. Carter, E. J. Helwig, and H. H. Podgurski, of this laboratory and with R. P. Frankenthal, formerly of this laboratory. To J. E. Holliday we are indebted for the soft x-ray data, and to J. B. Prestegiacomo for the BET surface area determinations, both formerly of this laboratory.

Manuscript submitted May 31, 1973; revised manuscript received July 31, 1973. This was Paper 69 pre-

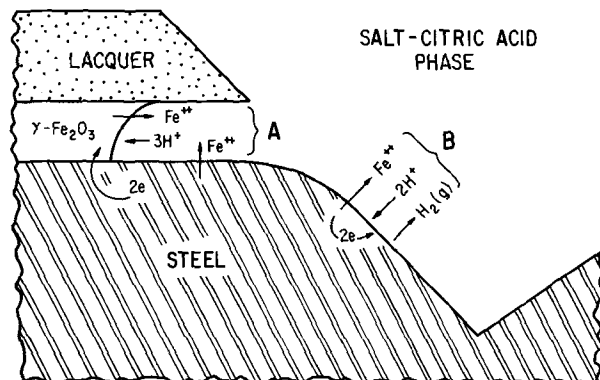


Fig. 7. Schematic diagram showing postulated steps involved in undercutting of scratched lacquered black plate.

sented at the Boston Meeting of the Society, Oct. 7-11, 1973.

Any discussion of this paper will appear in a Discussion Section to be published in the December 1974 JOURNAL.

#### REFERENCES

1. L. G. Sillen and A. E. Martell, *Special Publication No. 17*, The Chemical Soc., London (1964).
2. M. Eigen and R. G. Wilkins, *Advan. Chem. Series*, **49**, 55 (1965).
3. U. R. Evans, *J. Chem. Soc.*, **1930**, 478.
4. M. J. Pryor and U. R. Evans, *ibid.*, **1950**, 1259.
5. M. J. Pryor and U. R. Evans, *ibid.*, **1950**, 1266.
6. M. J. Pryor, *ibid.*, **1950**, 1274.
7. H. G. Oswin and M. Cohen, *This Journal*, **104**, 9 (1957).
8. C. F. Timberlake, *J. Chem. Soc.*, **1964**, 5078.
9. M. Pourbaix, "Atlas of Electrochemical Equilibria," p. 262, Pergamon Press, New York (1966).
10. D. Caplan and M. Cohen, *This Journal*, **108**, 1005 (1961).
11. J. E. Holliday, Research Laboratory, McDonnell Douglas Corp., St. Louis, Mo., Unpublished work.

## Composition of Pt Anode Surfaces by Auger Spectroscopy

W. C. Johnson and L. A. Heldt

Department of Metallurgical Engineering, Michigan Technological University, Houghton, Michigan 49931

#### ABSTRACT

Auger spectroscopy was employed to study platinum surfaces anodized either in 1N H<sub>2</sub>SO<sub>4</sub> with evolution of oxygen, or in 2N NaCl with evolution of chlorine. For the Pt anodized in H<sub>2</sub>SO<sub>4</sub>, Pt and oxygen interact to form a stable film of PtO stoichiometry. Anodization in NaCl resulted in a less stable film; although relatively large concentrations of oxygen and chlorine are present after anodization, these are removed by electron beam bombardment in the Auger apparatus.

Numerous studies have been concerned with the nature of the surfaces of Pt anodes in electrolytic cells, particularly the oxygen electrode (1). It has been demonstrated conclusively that Pt is not inert but does interact with oxygen in some manner to produce an altered surface. Direct evidence concerning the state of the oxygen associated with the Pt anode has been difficult to obtain because the affected layer on the Pt is no more than a few atomic layers thick.

Indirect evidence for this interaction has been gained through detailed studies of the electrochemical behavior of Pt electrodes during anodizing and during subsequent cathodic stripping of the resultant anodic films. For example, Thacker and Hoare (2) in a recent study concluded that for Pt anodes in H<sub>2</sub>SO<sub>4</sub> solutions, no sorption of oxygen occurred below a potential of 800 mV; from 800-1000 mV oxygen was adsorbed (relatively weakly) on the Pt surface; and that above 1000 mV oxygen was adsorbed (dermasorbed) in the first one or two layers of Pt. Evidence for the existence of the dermasorbed oxygen is the difficulty with which this anodic layer is removed during cathodic stripping. At higher potentials (>2000 mV) the behavior of the anode is interpreted in terms of the formation of a PtO<sub>2</sub> monolayer which decomposes to a monolayer of adsorbed oxygen (Pt-O) under open-circuit conditions or at potentials below 1.55V. Further evidence was also obtained for the absorption or dissolution of relatively large quantities of oxygen within the bulk of the Pt; this oxygen is then available for replenishing any adsorbed oxygen lost from the surface.

Interpretations of the several electrochemical studies have given rise to considerable controversy, particularly concerning the question of whether bona fide oxides, PtO and PtO<sub>2</sub>, form under various conditions.

It is well known that chloride ions inhibit the formation of oxygen or oxide anodic films. Kuhn and Wright (3) studied the anodization of bright Pt under conditions simulating those of a chlor-alkali electrolytic cell with concentrated NaCl solutions of pH approximately 3. The electrochemical characteristics of Pt during anodization and cathodic stripping in these environ-

ments were interpreted in terms of the following phenomena occurring with increasing potential: (i) adsorption of Cl<sup>-</sup> ions on bare Pt, (ii) subsequent adsorption of Cl atoms on adsorbed Cl<sup>-</sup> ions, (iii) successive replacement of chloride ions by adsorbed oxygen atoms, and (iv) full coverage achieved with two oxygen atoms per Pt atom.

In view of the thin nature of the anodic layers formed, an extremely sensitive technique is needed to study the surface chemistry. To date the only direct evidence concerning the state of oxygen on Pt anode surfaces is an ESCA study by Kim, Winograd, and Davis (4); this study revealed an electron configuration for the Pt consistent with the formation of chemisorbed oxygen at a potential of 1200 mV in 1M HClO<sub>4</sub>. Above 1600 mV increasing amounts of PtO<sub>2</sub> are formed and it becomes the predominant specie at 2000 mV. These results are in general agreement with the interpretation of recent electrochemical results (2). Auger electron spectroscopy (AES) is a relatively new technique which has been proven effective for chemical determination of small amounts of impurities on a solid surface (5-7). It was decided, therefore, that a study of Pt surfaces after anodizing, using AES for surface chemical analysis, could be used to determine directly if oxygen is present and if present provide information about its chemical state. Since AES is a relatively new technique, a short description is given below.

**AES.**—When an electron is removed from an inner level in an atom by an incident electron (or photon), the atom can fill the vacancy with an outer shell (less tightly bound) electron. The excess energy released can be carried away by an x-ray photon or by ejection from the atom of another outer shell electron, an Auger electron.

Figure 1 gives a schematic example of an Auger emission from a hypothetical solid. In this example a K-level electron is removed by the incident electron beam. When an M-level electron fills the vacancy, the excess energy is carried away by an N-level electron. The kinetic energy of this Auger electron is approximately  $E_K - E_M - E_N$  and is characteristic of the electron levels that took part in that emission, hence

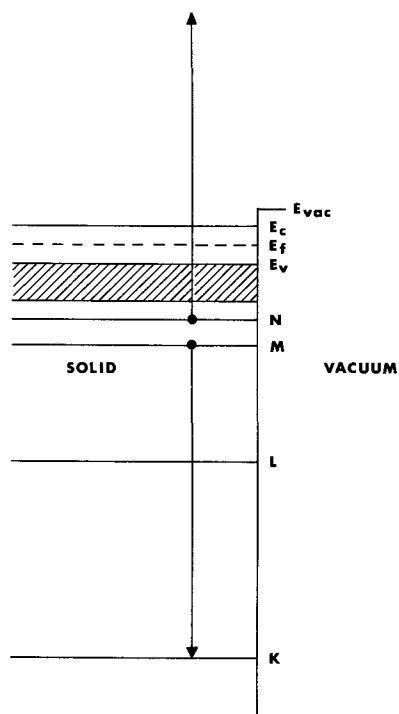


Fig. 1. Schematic energy diagram of an Auger electron emission

of the atom that gives rise to the electron (6). The mechanisms of detection are discussed elsewhere (8-11), but it is important to note that since 50-2000 eV Auger electrons are used for chemical analysis, only the first few atomic layers (3-10Å) can contribute electrons which have not lost energy through scattering. Hence the chemical information obtained using AES applies to the first 1-3 atomic layers of a surface. All AES analysis is done in an ultrahigh vacuum (UHV) system ( $10^{-9}$ - $10^{-10}$  Torr).

### Experimental

Platinum was cut into 5 mm square foil electrodes for use in the anodizing study. Since analysis of the sample surfaces with AES revealed the presence of carbon, oxygen, sulfur, and other impurity species, a further cleaning technique was required to assure that the anodizing began on a microscopically clean Pt surface. Inert-ion sputtering was used to etch into the Pt samples until the clean Pt surface was exposed. The samples were then removed from the vacuum system and given the anodizing treatment. A control specimen was used to monitor atmospheric effects on the Pt surface chemistry. No contamination due to the atmosphere was noticed on the control specimens; only Pt peaks were observed in the Auger spectrum.

**Anodizing procedures.**—Two different anodizing treatments were employed to determine the feasibility of applying AES to advantage in studying Pt anode surfaces. Sufficient voltage was provided in both cases to achieve gas evolution.

1. Anodization (16 hr) in 1N  $H_2SO_4$  solution with evolution of oxygen. Current density 500 mA/in<sup>2</sup>.  $T = 26^\circ C$ .

2. Anodization (12 hr) in 2N NaCl solution, pH 3, with evolution of chlorine. Current density 500 mA/in<sup>2</sup>.  $T = 26^\circ C$ .

After the Pt anodes were removed from the solutions, they were dipped in distilled water to remove any electrolyte adhering to the surfaces and blasted with dry He gas to remove the residual water film. The samples were then transferred quickly to the UHV system and examined with AES after a vacuum in the  $10^{-9}$  Torr range was obtained (10-12 hr). As a qualita-

tive indication of species stability, the electron beam was allowed to bombard the same spot on the samples for various lengths of time and any change in Auger peak height (corresponding to concentration of the given species) noted.

### Results

The results of Auger analysis of a surface are usually presented in a spectrum similar to Fig. 2. The peaks superimposed on the relatively smooth background are due to different elements in the first 1-3 atom layers of the surface and are labeled as to species. To obtain a quantitative estimate of the per cent coverage of a particular element, the observed peak is compared to a peak due to a known concentration of that element on a calibrated standard specimen. The calibration for oxygen was obtained from an  $Al_2O_3$  sample; this, in turn, was found to be consistent with results from an MgO sample. In Fig. 2, which represents the Auger spectrum from the surface of the Pt anodized in  $H_2SO_4$ , only platinum and oxygen peaks are present. The surface concentration (i.e., atomic per cent coverage in the first few atomic layers) of oxygen on this specimen was approximately 45 a/o (atomic per cent). Figure 3 presents the oxygen concentration as a function of time under electron beam bombardment. It was observed that the oxygen concentration remained constant, with the slight variation due to error in measurement of the O peak.

The spectrum of the Pt anodized in NaCl is presented in Fig. 4. In this case, Cl was observed as well as Pt and O. However, after 20 min of electron beam bombardment, both the O and Cl peaks had decayed to a small

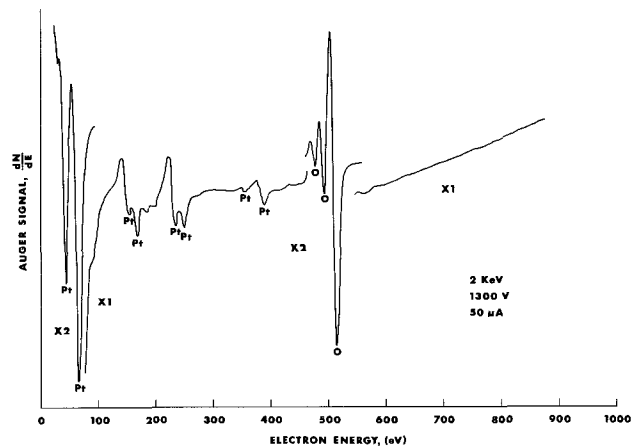


Fig. 2. Auger spectrum of Pt surface anodized in  $H_2SO_4$

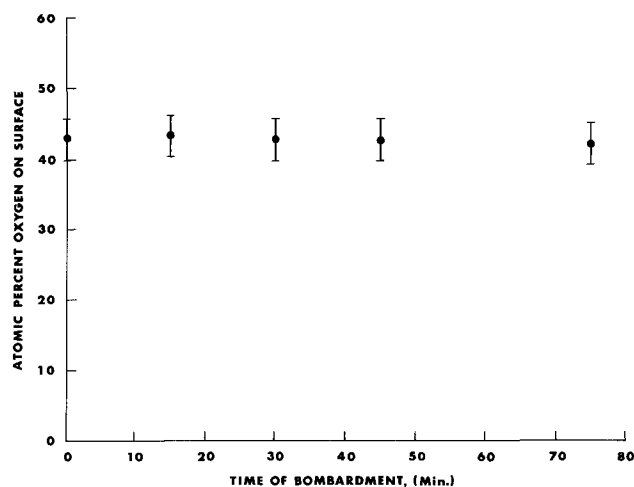


Fig. 3. Effects of electron bombardment on the oxygen concentration of  $H_2SO_4$  anodized Pt surface.

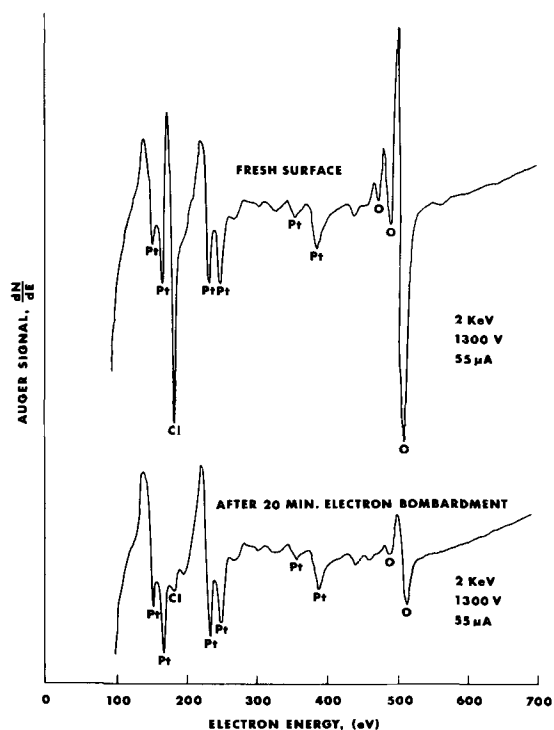


Fig. 4. Auger spectrum of Pt surface anodized in NaCl

fraction of their original size. Since the oxygen and chlorine peaks decayed continuously with time, the initial coverages could not be measured.

#### Discussion

*H<sub>2</sub>SO<sub>4</sub> electrode.*—Analyses of the Pt anode surfaces by AES have revealed directly the presence of oxygen in an extremely stable state of combination or sorption capable of persisting under electron bombardment at pressures of less than  $10^{-9}$  Torr. The surface contains about 50% oxygen, corresponding to a composition of PtO. The high stability is consistent with the fact that the anodic film is difficult to remove during cathodic stripping (1).

The stoichiometry of the anodic layer does correspond to the oxide, PtO, reported to be stable in vacuum (13). This stoichiometry also corresponds with the interpretation of Thacker and Hoare (2) of their electrochemical data. It is possible that oxygen is adsorbed or dermasorbed strongly enough to be present in this concentration and in this stable a state; if this is

the case, the characteristics (stoichiometry and stability) would be difficult to distinguish from an oxide (3).

*NaCl electrode.*—The AES results in this case indicate the presence of both chlorine and oxygen at the Pt surface. Both persist in the hard vacuum but are removed with time by the electron bombardment. This appears to correspond with the third stage of polarization described by Kuhn and Wright (3), namely, partial replacement of a part of the adsorbed chlorine by adsorbed oxygen. It is apparent that the oxygen is not bound as strongly under these conditions as for the H<sub>2</sub>SO<sub>4</sub> electrode.

#### Conclusion

In summary, AES is capable of detecting anodization products present in thin layers on anodized Pt. Additional studies are warranted in which adsorption and/or combination is measured in conjunction with potentiostatic measurements of potential-current characteristics over a range of potentials.

#### Acknowledgments

We wish to thank Dr. B. C. Peters for helpful discussions and Dr. D. F. Stein for continued interest and encouragement. This work was sponsored by the United States Atomic Energy Commission.

Manuscript submitted March 26, 1973; revised manuscript received June 15, 1973.

Any discussion of this paper will appear in a Discussion Section to be published in the December 1974 JOURNAL.

#### REFERENCES

1. J. P. Hoare, in "Advances in Electrochemistry and Electrochemical Engineering," Vol. 6, P. Delahay and C. W. Tobias, Editors, Interscience Publishers, New York (1967).
2. R. Thacker and J. P. Hoare, *J. Electroanal. Chem.*, **30**, 1 (1971).
3. A. T. Kuhn and P. M. Wright, *ibid.*, **38**, 291 (1972).
4. K. S. Kim, N. Winograd, and R. E. Davis, *J. Am. Chem. Soc.*, **93**, 6296 (1971).
5. R. E. Weber and A. L. Johnson, *J. Appl. Phys.*, **40**, 314 (1969).
6. W. C. Johnson, A. Joshi, and D. F. Stein, *Can. J. Spectr.*, **17**, 88 (1972).
7. C. C. Chang, *Surface Sci.*, **25**, 53 (1971).
8. J. J. Lander, *Phys. Rev.*, **91**, 1282 (1953).
9. L. A. Harris, *J. Appl. Phys.*, **39**, 1419 (1968).
10. R. E. Weber and W. T. Peria, *ibid.*, **38**, 4355 (1967).
11. P. W. Palmberg, G. K. Bohn, and J. C. Tracy, *Appl. Phys. Letters*, **15**, 254 (1969).
12. R. V. Stuart and G. K. Wehner, *J. Appl. Phys.*, **33**, 2345 (1962).
13. G. Rädlein, *Z. Elektrochem.*, **61**, 727 (1957).

# Anodic Deposition of Ferric Oxy-Hydroxide Films on Platinum from Perchlorate Solutions

Koji Hashimoto<sup>1</sup> and Morris Cohen\*

Division of Chemistry, National Research Council, Ottawa, Ontario, Canada

## ABSTRACT

The effect of pH and added anions such as phosphate, acetate, chloride, or sulfate in perchlorate solutions on the anodic deposition of ferric oxy-hydroxide films on platinum was studied. In all cases deposition took place by the oxidation of a ferrous species to a ferric film with 100% current efficiency. The growth rate of the film was dependent on the concentration of  $\text{FeOH}^+$  ion which was the depositing species in a ferrous perchlorate solution and in the solutions containing acetate, chloride, or sulfate. In the solution containing phosphate, the anodic deposition proceeded by the simultaneous oxidation of  $\text{FeOH}^+$  and  $\text{FeH}_2\text{PO}_4^+$  ions to  $\gamma\text{-FeOOH}$  and  $\text{FePO}_4 \cdot 2\text{H}_2\text{O}$ .

In previous investigations it was shown that "protective oxide films" could be formed on iron by either direct anodic oxidation of iron (1) or by deposition from aqueous solutions containing dissolved ferrous ion (2, 3). It was also shown that similar films could be deposited on platinum (4). The mechanism of deposition is independent of the substrate metal, but measurements of current efficiency and analysis of the films are less complex using a platinum substrate.

The composition of the films was found to be partially dependent on the anions present in the solution so that films formed in borate (4) or sulfate (5) solutions contain boron or sulfur, respectively. This would indicate that at least part of the film is formed by anodic oxidation of ferrous ion complexes.

In the study reported below the electrolyte was mainly ammonium perchlorate solution containing ferrous ion. The perchlorate ion is usually considered not to form complexes with cations. The effect of other anions on the anodic deposition mechanism and the composition of the film was studied by the addition of phosphate, acetate, chloride, and sulfate to the perchlorate solution. The effect of these results on considerations of the formation and properties of passive film on iron is discussed.

## Experimental

The apparatus for the anodic deposition was the same as that reported elsewhere (4). Smooth platinum sheets  $5 \times 1$  cm with small handles were used as specimens. The purification of the platinum surface was carried out as follows. After oxidation of platinum specimens at  $900^\circ\text{C}$  and 1 Torr of oxygen for 24 hr, impurities on the surfaces were dissolved in boiling 1N-HCl. The specimens were then annealed under high vacuum ( $<10^{-7}$  Torr) at  $800^\circ\text{C}$  for 24 hr and were reduced by hydrogen at 1 Torr and  $800^\circ\text{C}$  for 8 hr.

An aqueous solution of 0.15N- $\text{NH}_4\text{ClO}_4$  with different concentrations of  $\text{Fe}(\text{ClO}_4)_2$  was used as an electrolyte whose pH was adjusted by the addition of 0.15N- $\text{NH}_4\text{OH}$  solution. In some experiments,  $\text{NH}_4\text{H}_2\text{PO}_4$ ,  $\text{CH}_3\text{COONH}_4$ ,  $\text{NH}_4\text{Cl}$ , or  $(\text{NH}_4)_2\text{SO}_4$  was added to the solution in the concentration range of 0.2 to  $20 \times 10^{-6}$  mole/liter. The solution was deaerated by bubbling a stream of oxygen-free argon for more than 20 hr. The oxygen-free argon was prepared by passing commercial argon (99.996%) through a column of finely dispersed copper on Kieselguhr, heated at  $180^\circ\text{C}$ .

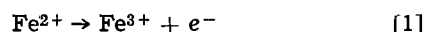
The anodic deposition was carried out by means of a potentiostat at a constant potential of +300 mV (*v.s.* SCE) and constant temperature of  $25^\circ \pm 1^\circ\text{C}$ . The solution was deaerated and stirred by a stream of purified

argon at a constant flow. The limiting current measurements were carried out by streaming purified argon over the solution instead of stirring. The weight change of the specimen,  $G_w$ , was measured by weighing before and after anodic deposition using a microbalance with an accuracy of  $\pm 2 \mu\text{g}$ . The concentration change of ferrous ion during deposition,  $G_c$ , was determined by colorimetric analysis using the o-phenanthroline method (6). The quantity of iron deposited,  $G_a$ , was calculated from the total amount of charge determined by the graphic integration of the experimental curve of current density *vs.* time. After the anodic deposition the film was dissolved,  $G_c'$ , and the weight loss of specimen,  $G_w'$  was determined. The initial concentration of ferrous ion was colorimetrically determined because it could not be obtained from the weight of hygroscopic ferrous perchlorate. The phosphate content of the film was measured from the concentration change of phosphate during deposition by means of colorimetric determination as molybdenum blue (7).

The deposited film was identified by means of reflection electron diffraction. In some cases the film was cathodically reduced in steps and reflection electron diffraction patterns were taken to identify the composition of the inside of the film.

## Results and Discussion

**Perchlorate solution.**—Platinum specimens were anodically polarized at a constant potential of +300 mV with various concentrations of ferrous ion at different pH's. Examples of the change in the anodic current density with time are shown in Fig. 1. The shape of the curves is almost identical with that obtained by the deposition on platinum in borate (4) and sulfate (5) solutions. The changes in quantity of iron deposited as effected by concentration of ferrous ion and pH are shown in Table I. All parts of the film, from the outer side to the inner, which were examined after partial cathodic reduction of the film, corresponded to  $\gamma\text{-FeOOH}$  as determined by reflection electron diffraction. In Table I, values of  $G_w$  and  $G_w'$  were obtained from weight changes after anodic deposition and dissolution of the film, respectively, assuming that the film consisted of  $\gamma\text{-FeOOH}$ . The value of  $G_a$  was calculated by the following Eq. [2] assuming that the total amount of charge passed during deposition was used for reaction [1]



$$G_a = \frac{1}{F} \int_0^t i_a dt \quad [2]$$

where  $i_a$  is the anodic current density,  $t$  the time of deposition, and  $F$  the Faraday. The value of  $G_c$  corre-

\* Electrochemical Society Active Member.

<sup>1</sup> Present address: The Research Institute for Iron, Steel and Other Metals, Tohoku University, Sendai, Japan.

Key words: iron oxide films, deposition, passivity.

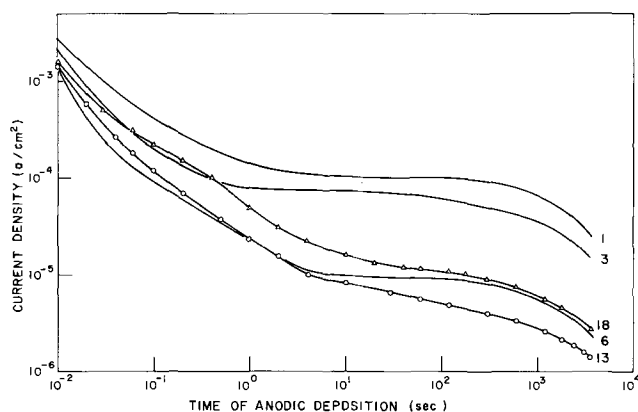


Fig. 1. The change in current density during the anodic deposition in 0.15N-NH<sub>4</sub>ClO<sub>4</sub> solutions. Curve 1, pH 7.62-7.49, Fe<sup>2+</sup> + 82.4 × 10<sup>-5</sup> mole/liter; curve 3, pH 7.12-6.87, Fe<sup>2+</sup> + 79.6 × 10<sup>-5</sup> mole/liter; curve 6, pH 7.01-6.82, Fe<sup>2+</sup> + 8.61 × 10<sup>-5</sup> mole/liter; curve 13, pH 7.00-6.87, Fe<sup>2+</sup> + 8.14 × 10<sup>-5</sup> mole/liter, PO<sub>4</sub><sup>3-</sup> + 21 × 10<sup>-6</sup> mole/liter; curve 18, pH 6.98-6.88, Fe<sup>2+</sup> + 9.06 × 10<sup>-5</sup> mole/liter, CH<sub>3</sub>COO<sup>-</sup> + 21 × 10<sup>-6</sup> mole/liter.

sponds to the concentration change of ferrous ion during anodic deposition, and the value of  $G_c'$  was obtained by dissolving the film in dilute hydrochloric acid. The thickness of the film was calculated from the value of  $G_a$  assuming a solid film of  $\gamma$ -FeOOH with a density of 4.07 (8).

As can be seen, the value of  $G_a$  is in good agreement with that of  $G_c$ , which indicates that the anodic deposition proceeds by the oxidation of the ferrous state to the ferric state with a current efficiency of nearly 100%. The quantity of iron deposited and the thickness of the film should be proportional to the amount of charge passed. Values of  $G_w$  and  $G_w'$  are always larger than  $G_a$  or  $G_c$  and changed from day to day because  $G_w$  and  $G_w'$  were calculated from the weight of film assuming a  $\gamma$ -FeOOH film without water although it did contain some adsorbed water. The water was loosely adsorbed and could be removed by evacuation to 10<sup>-7</sup> Torr, since vacuum x-ray microanalysis of the film in 10<sup>-7</sup> Torr showed the atomic ratio of iron and oxygen to be 1/2 (9).

The concentration of ferrous ion in the solution at any time during the anodic deposition could be calculated from the initial concentration and the total number of coulombs passed up to that time. The relationships between anodic current density and ferrous ion concentration at various pH's are shown plotted on a log-log scale in Fig. 2. At all pH's there is a linear relationship between [Fe<sup>2+</sup>] and current. At high pH's and intermediate or low concentrations of ferrous ion

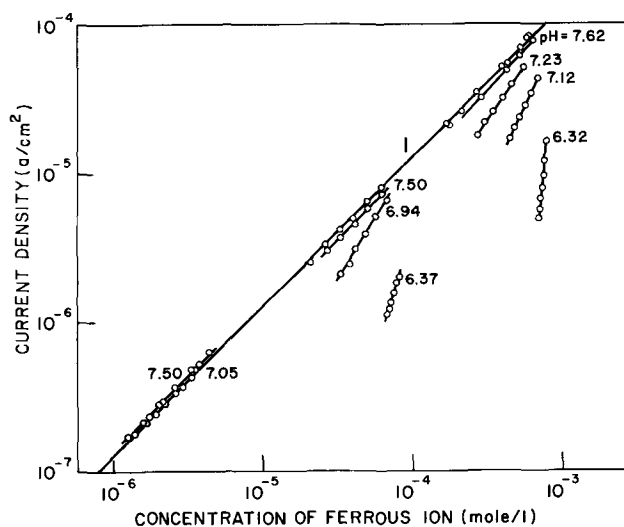
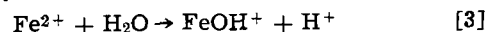


Fig. 2. Relationship between anodic current density and concentration of ferrous ion in 0.15N-NH<sub>4</sub>ClO<sub>4</sub> solution.

all the results fit a single straight line. At lower pH's the deposition rate (current density) at the same ferrous ion concentration is lower. This would indicate that the depositing species is not simply ferrous ion but is a complex ion the concentration of which is pH dependent and increases with increasing pH. At sufficiently high pH (e.g., 7.5) all of the iron is probably in the complex form.

In that the depositing species is stable at high pH's it is probably FeOH<sup>+</sup> formed by the following reaction



and anodic deposition in the perchlorate solutions occurs exclusively by the reaction



Line 1 in Fig. 6 has a slope of 45° and the data would also give a linear plot on linear coordinates. This indicates that the rate of deposition is probably diffusion controlled and that either the iron in these solutions is mainly present as FeOH<sup>+</sup> or that the hydration reaction [3] is very rapid. The fact that the slopes of the other curves shown in Fig. 2 deviate markedly from that of line 1 would indicate that the assumption of an initial high proportion FeOH<sup>+</sup> is the more acceptable assumption, although some hydration must obviously take place during the run. However, the initial rate in the steady-state region of deposition (after the sharp initial drop in current due to the formation of the first 30Å of film) is lower at low pH's than high and this is due to a lower FeOH<sup>+</sup> concentration.

Table I. The quantity of iron deposited as effected by pH and [Fe<sup>2+</sup>] in 0.15N-NH<sub>4</sub>ClO<sub>4</sub> solutions

Experiment No.	pH	Concentration of Fe <sup>2+</sup> (10 <sup>-5</sup> mole/liter)	G <sub>w</sub>	Quantity of iron deposited (10 <sup>-7</sup> g-atom/cm <sup>2</sup> )			G <sub>c'</sub>	Film thickness (Å)
				G <sub>a</sub>	G <sub>c</sub>	G <sub>w'</sub>		
1	7.62-7.42	82.4	22.575	20.279	20.624	22.452	20.053	4427
2	7.23-6.92	83.5	16.476	15.005	14.908	16.285	15.577	3276
3	7.12-6.87	79.6	12.627	11.438	11.048	12.537	12.031	2497
4	6.32-6.15	84.8	5.109	4.239	5.257	5.109	4.532	925
5	7.50-7.38	8.05	2.386	2.001	2.001	2.386	2.005	437
6	7.01-6.82	8.61	2.138	1.889	1.901	2.251	1.897	412
7	6.37-6.12	8.61	0.687	0.599	0.670	0.687	0.615	131
8	5.82-5.74	9.04	0.203	0.186	0.235	0.169	0.145	41
9	7.50-7.49	0.675	0.248	0.192	0.195	0.293	0.144	42
10*	7.05-6.90	0.678	0.338	0.211	0.214	0.236	0.233	46
11	6.40-6.23	0.779	0.259	0.165	0.140	0.270	0.146	36
12	5.80-5.80	0.792	0.135	0.062	0.035	0.158	0.050	14

G<sub>w</sub>, from the film weight after deposition.

G<sub>a</sub>, from the total amount of charge passed during deposition.

G<sub>c</sub>, from the concentration change during deposition.

G<sub>w'</sub>, from the weight loss of specimen by dissolution of the film.

G<sub>c'</sub>, from the concentration of iron in the solution in which the film was dissolved.

Thickness of film calculated from the value of G<sub>a</sub> assuming that the film consists of  $\gamma$ -FeOOH with density of 4.07.

Concentration of ferrous ions calculated from the colorimetric analysis of the solution before anodic deposition.

pH of solution, measured before and after anodic deposition.

\* All depositions were carried out for 60 min except for experiment No. 10 which was done for 90 min.



Table II. Stability constant of FeOH<sup>+</sup>

Concentration of anion (mole/liter)	Initial concentration of Fe <sup>2+</sup> ion (mole/liter)	Initial pH	log K	Average value of log K
—	8.25 × 10 <sup>-4</sup>	7.62	-6.34	-6.63
—	6.67 × 10 <sup>-4</sup>	7.23	-6.69	
—	7.96 × 10 <sup>-4</sup>	7.12	-7.01	
—	8.48 × 10 <sup>-4</sup>	6.32	-6.94	
—	8.05 × 10 <sup>-5</sup>	7.50	-6.27	
—	8.59 × 10 <sup>-5</sup>	6.94	-6.35	
—	8.61 × 10 <sup>-5</sup>	6.37	-6.79	
CH <sub>3</sub> COO <sup>-</sup>				
1 × 10 <sup>-2</sup>	8.53 × 10 <sup>-5</sup>	6.97	-6.14	-6.23
2 × 10 <sup>-3</sup>	9.09 × 10 <sup>-5</sup>	6.98	-6.21	
2 × 10 <sup>-6</sup>	8.75 × 10 <sup>-5</sup>	7.00	-6.27	
2 × 10 <sup>-7</sup>	8.48 × 10 <sup>-5</sup>	6.98	-6.28	
Cl <sup>-</sup>				
2 × 10 <sup>-5</sup>	8.38 × 10 <sup>-5</sup>	7.02	-6.26	-6.23
2 × 10 <sup>-6</sup>	8.14 × 10 <sup>-5</sup>	7.00	-6.29	
2 × 10 <sup>-7</sup>	8.42 × 10 <sup>-5</sup>	7.00	-6.12	
SO <sub>4</sub> <sup>2-</sup>				
2 × 10 <sup>-5</sup>	8.25 × 10 <sup>-5</sup>	7.02	-6.28	-6.28
2 × 10 <sup>-6</sup>	8.14 × 10 <sup>-5</sup>	7.00	-6.23	
2 × 10 <sup>-7</sup>	8.31 × 10 <sup>-5</sup>	7.04	-6.23	

Bolzan and Arvia (10) had an average value of log K of -6.74.

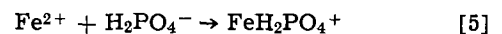
Assuming that the current density is directly proportional to the FeOH<sup>+</sup> concentration and that the Fe<sup>2+</sup> ion in those solutions following line 1 is mainly present as FeOH<sup>+</sup>, one can calculate the FeOH<sup>+</sup> concentration in those solutions which do not give deposition lines on line 1. This gives the FeOH<sup>+</sup> concentration for a range of pH and total Fe<sup>2+</sup> and allows the calculation of a stability constant. The numbers are given in Table II. The average value in the perchlorate solutions is -6.63, which is in good agreement with the value of -6.74 obtained by Bolzan and Arvis (10) using a potential-titration technique. This indicates that the assumption of almost complete hydration to FeOH<sup>+</sup> assumed for line 1 is essentially correct. If one takes the value of 6.6 as correct for the stability constant the ratio of FeOH<sup>+</sup>/Fe<sup>2+</sup> varies from 25 at pH 8 to 0.25 at pH 6.

The deviation of the slopes of the curves at lower pH's or low Fe<sup>2+</sup> concentration from the slope of line 1 would indicate that the concentration of the depositing species FeOH<sup>+</sup> decreases more rapidly than the total concentration of iron in the solution and would indicate that the hydration rate is less than the deposition rate at low pH's and/or Fe<sup>2+</sup> ion concentration.

*Perchlorate solution with phosphate.*—The platinum specimens were anodically polarized at +300 mV at different pH's in perchlorate solutions containing 8 × 10<sup>-5</sup> mole/liter ferrous ion and different quantities of phosphate. An example of the change in anodic current density with time is shown in curve 13, Fig. 1. In Table III are shown the quantities of iron deposited and the

phosphate content of the film at various concentrations of phosphate ion and pH after 1 hr deposition. The quantity of iron deposited increased with an increase of pH of the solution at the same concentration of phosphate ion. In solutions with a high concentration of phosphate ion (curve 13, Fig. 1) the quantity of iron deposited was remarkably lower in comparison with that obtained in solutions with a low concentration of phosphate ion and a significantly larger quantity of phosphate ion was contained in the film. Clear electron diffraction patterns corresponding to γ-FeOOH were obtained from the anodic deposition films except for the film in the experiment portrayed by curve 13. A very diffuse diffraction pattern was obtained from the film formed in a solution with 21 × 10<sup>-6</sup> mole/liter phosphate ion (curve 13) due to the formation of a fine crystalline or amorphous film. The iron phosphate compound of fine crystalline or amorphous state has been reported to be FePO<sub>4</sub> · 2H<sub>2</sub>O (11). If the compound containing phosphate was FePO<sub>4</sub> · 2H<sub>2</sub>O, the quantity of iron deposited, G<sub>a</sub>, can be divided into two portions: one of them corresponds to γ-FeOOH, G<sub>aFeOOH</sub>, and the other to FePO<sub>4</sub> · 2H<sub>2</sub>O, G<sub>aFePO<sub>4</sub></sub>. The latter was estimated from the phosphate content of the film. The thickness of the film was calculated from values of G<sub>aFeOOH</sub> and G<sub>aFePO<sub>4</sub></sub> assuming the film to consist of a mixture of γ-FeOOH with a density of 4.07 (10) and of FePO<sub>4</sub> · 2H<sub>2</sub>O with a density of 2.87 (12).

As shown in Fig. 3, there were linear relationships between the logs of the anodic current density and ferrous ion concentration. It is, therefore, probable that the rate of deposition in perchlorate-ferrous ion solution with phosphate also depended on the concentration of depositing species. The anodic current density, i<sub>a</sub>, can be divided into two parts, that is, current density of γ-FeOOH formation, i<sub>aFeOOH</sub>, and that of FePO<sub>4</sub> · 2H<sub>2</sub>O formation, i<sub>aFePO<sub>4</sub></sub>. Because the phosphate content of the film increased with decrease of pH (Table III), we assume that the depositing species responsible for the formation of FePO<sub>4</sub> · 2H<sub>2</sub>O was FeH<sub>2</sub>PO<sub>4</sub><sup>+</sup> ion formed by the reaction



and that FePO<sub>4</sub> · 2H<sub>2</sub>O was formed by the electrode reaction



If we assume that when the concentration of H<sub>2</sub>PO<sub>4</sub><sup>-</sup> ion was lower than that of ferrous ion, as in the present work, and that the majority of H<sub>2</sub>PO<sub>4</sub><sup>-</sup> species had formed FeH<sub>2</sub>PO<sub>4</sub><sup>+</sup> ion before anodic deposition was carried out (i.e., that the reaction [5] is relatively slow), then the concentration of FeH<sub>2</sub>PO<sub>4</sub><sup>+</sup> ion during anodic deposition can be estimated by subtracting G<sub>aFePO<sub>4</sub></sub> from the initial concentration of H<sub>2</sub>PO<sub>4</sub><sup>-</sup> ion. The latter can be estimated at a given pH and using the equilibrium constant of the reaction

Table III. The change in film composition with pH and concentration of phosphate in 0.15N-NH<sub>4</sub>ClO<sub>4</sub> solutions

Experiment No.	pH	Concentration of PO <sub>4</sub> <sup>3-</sup> ion (10 <sup>-6</sup> mole/liter)	Concentration of Fe <sup>2+</sup> ion (10 <sup>-5</sup> mole/liter)	Quantity of PO <sub>4</sub> <sup>3-</sup> in film (μg/cm <sup>2</sup> )	G <sub>w</sub>	Quantity of iron deposited (10 <sup>-7</sup> g-atom/cm <sup>2</sup> )			Film thickness (Å)	
						G <sub>a</sub>	G <sub>aFeOOH</sub>	G <sub>aFePO<sub>4</sub></sub>	T <sub>FeOOH</sub>	T <sub>FePO<sub>4</sub></sub>
13	7.00-6.87	21	8.14	3.10	1.643	0.927	0.601	0.326	131	219
14	7.49-7.38	2.1	7.90	0.271	2.465	1.959	1.930	0.029	418	19
15	6.97-6.90	2.1	8.12	0.348	1.868	1.607	1.570	0.037	340	25
16	6.36-6.23	2.1	8.33	0.497	0.754	0.637	0.585	0.052	128	35
17	6.97-6.90	0.21	8.42	—	2.228	1.810	—	—	—	—

G<sub>w</sub>, from the film weight after deposition.

G<sub>a</sub>, from the total amount of charge passed during deposition.

G<sub>aFeOOH</sub>, G<sub>a</sub> - G<sub>aFePO<sub>4</sub></sub>.

G<sub>aFePO<sub>4</sub></sub>, from quantity of PO<sub>4</sub><sup>3-</sup> in film assuming that PO<sub>4</sub><sup>3-</sup> is present as FePO<sub>4</sub> · 2H<sub>2</sub>O.

T<sub>FeOOH</sub>, estimated from the value G<sub>aFeOOH</sub> assuming a density of γ-FeOOH of 4.07.

T<sub>FePO<sub>4</sub></sub>, estimated from the value of G<sub>aFePO<sub>4</sub></sub> assuming a density of FePO<sub>4</sub> · 2H<sub>2</sub>O of 2.87.

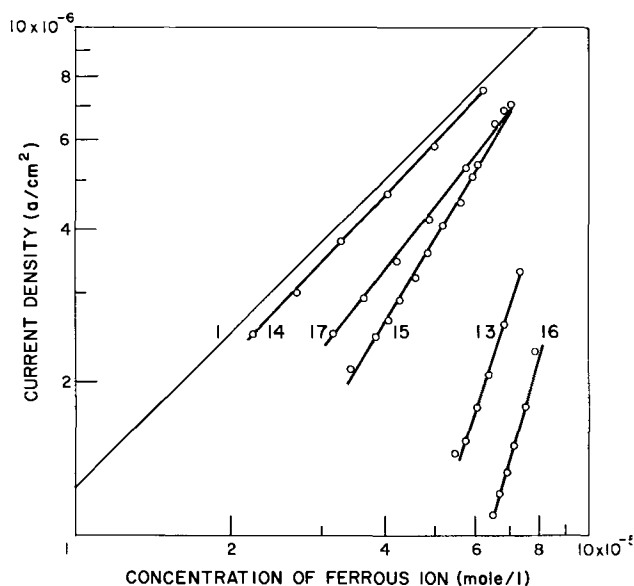
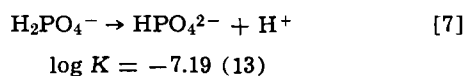


Fig. 3. Effect of phosphate ion concentration and pH on slope of curves of log anodic current density vs. log ferrous ion concentration. Initial concentration of ferrous ion  $\approx 8 \times 10^{-5}$  mole/liter.

pH	Concentration of phosphate ion
13 7.00-6.87	21 $\times 10^{-6}$ mole/liter
14 7.49-7.38	2.1
15 6.97-6.90	2.1
16 6.36-6.23	2.1
17 6.97-6.90	0.21



In Fig. 4 is shown the change of anodic current density of  $\text{FePO}_4$  formation,  $i_{\text{aFePO}_4}$ , as a function of the concentration of  $\text{H}_2\text{PO}_4^-$  ion. If the rate of deposition of  $\text{FePO}_4 \cdot 2\text{H}_2\text{O}$  depended only on the concentration of  $\text{FeH}_2\text{PO}_4^+$  ion, the linear relationship should be seen on the figure of  $i_{\text{aFePO}_4}$  vs. concentration of  $\text{H}_2\text{PO}_4^-$  ion. A fairly good linear relationship between anodic current of  $\text{FePO}_4$  formation and concentration of  $\text{H}_2\text{PO}_4^-$  ion was obtained,<sup>2</sup> although some slight deviation from the ideal gradient of 45° can be seen. It is, therefore, probable that the anodic deposition in perchlorate-ferrous ion solution with phosphate formed the film of  $\gamma\text{-FeOOH}$  and  $\text{FePO}_4 \cdot 2\text{H}_2\text{O}$  by reactions [4] and [6], and that the rate of deposition depended on the concentration of  $\text{FeOH}^+$  and  $\text{FeH}_2\text{PO}_4^+$  ions. The lower thickness may be related to the phosphate containing

<sup>2</sup> This current,  $i_{\text{aFePO}_4}$ , was calculated by subtracting the current due to deposition from the residual iron present as  $\text{FeOH}^+$  from the total deposition current.

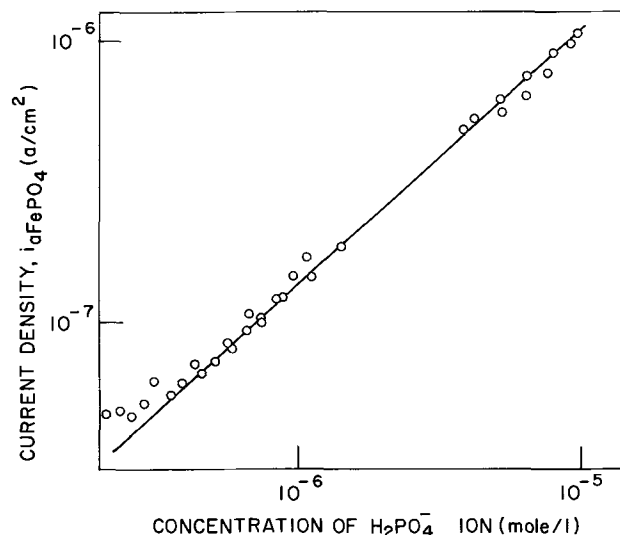


Fig. 4. Change in anodic current density of  $\text{FePO}_4 \cdot 2\text{H}_2\text{O}$  formation,  $i_{\text{aFePO}_4}$ , with concentration of  $\text{H}_2\text{PO}_4^-$  ion.

film having a much higher resistance than  $\gamma\text{-FeOOH}$ , thus causing a greater initial current decrease in the first few seconds.

*Perchlorate solution with other anions.*—The platinum specimens were anodically polarized at +300 mV at pH 7 in perchlorate solutions containing  $8 \times 10^{-5}$  mole/liter of ferrous ion plus various concentrations of acetate, chloride, or sulfate ion. An example of the change in current density with time is shown in Fig. 1 (curve 18). The shape of other curves was similar to that of curve 18 although the current density changed slightly with slight changes of initial pH and initial concentration of ferrous ion. All films formed in these solutions were identified as  $\gamma\text{-FeOOH}$  and compounds containing acetate, chloride, or sulfate ion were not found in the film by means of electron diffraction or chemical analysis.

The relationship between the quantity of iron deposited and concentration of anions in solutions is shown in Table IV. The value of  $G_a$  is again in good agreement with that of  $G_c$ , so that the Eq. [1] and [2] are applicable to the anodic deposition in these solutions. The quantity of iron deposited is not remarkably affected by concentration changes of these anions. All the experimental points are very close to one straight line in the relationship between anodic current density and ferrous ion concentration as shown in Fig. 5. The stability constant of the  $\text{FeOH}^+$  ion in these solutions was estimated as shown in Table II assuming that the anodic deposition proceeded exclusively by the reaction [4]. Although the stability constants showed some variations from those obtained in perchlorate-ferrous

Table IV. The relationship between the quantity of iron deposited and concentration of anions on the anodic deposition for 1 hr in 0.15N- $\text{NH}_4\text{ClO}_4$  solutions with  $\text{CH}_3\text{COONH}_4$ ,  $\text{NH}_4\text{Cl}$ , or  $(\text{NH}_4)_2\text{SO}_4$

Experiment No.	pH	Concentration of $\text{Fe}^{2+}$ ( $10^{-5}$ mole/liter)	Concentration of anion ( $10^{-6}$ mole/liter)	$G_w$	Quantity of iron deposited ( $10^{-7}$ g-atom/cm <sup>2</sup> )			$G_e'$	Film Thickness (Å)
					$G_a$	$G_c$	$G_w'$		
18	6.98-6.88	9.06	$\text{CH}_3\text{COO}^-$ 21	2.420	2.007	2.046	2.341	2.021	438
19	7.00-6.90	8.75	2.1	2.206	1.901	1.882	2.195	1.892	415
20	6.98-6.90	8.48	0.21	2.251	1.801	1.831	2.217	1.887	393
21	7.02-6.90	8.38	$\text{Cl}^-$ 21	2.206	1.834	1.840	2.172	1.844	400
22	7.03-6.93	8.42	2.1	2.138	1.872	1.885	2.127	1.871	409
23	7.00-6.90	8.42	0.21	2.217	1.903	1.903	2.352	1.920	415
24	7.02-6.97	8.25	$\text{SO}_4^{2-}$ 21	2.206	1.789	1.787	2.206	1.789	391
25	6.99-6.89	8.14	2.1	2.239	1.785	1.754	2.149	1.783	390
26	7.04-6.94	8.31	0.21	2.048	1.786	1.781	2.104	1.783	390

Methods by which values listed above were obtained are described in Table I. The film thickness was calculated from the value of  $G_a$  assuming that the film consists of  $\gamma\text{-FeOOH}$ .

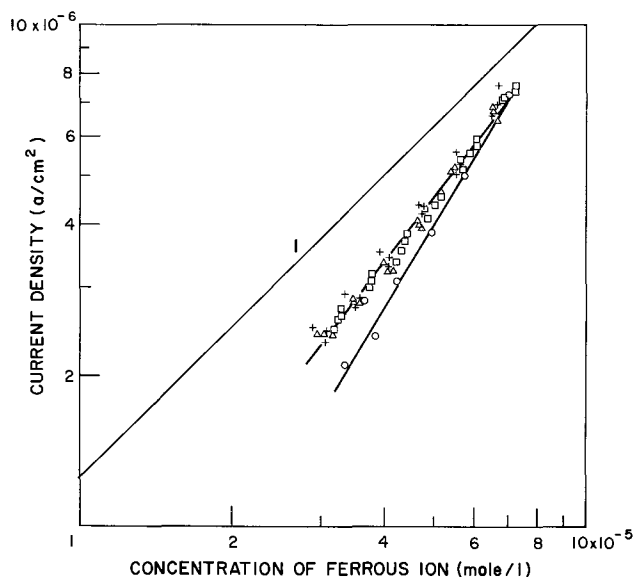


Fig. 5. Relationship between anodic current density and concentration of ferrous ion in 0.15N-NH<sub>4</sub>ClO<sub>4</sub> solution with CH<sub>3</sub>COO<sup>-</sup>, Cl<sup>-</sup>, or SO<sub>4</sub><sup>2-</sup> ion. pH ≈ 7.0-6.9. ○, No addition of other anions; □, CH<sub>3</sub>COO<sup>-</sup> 20.02 × 10<sup>-6</sup> mole/liter; +, Cl<sup>-</sup> 20.02 × 10<sup>-6</sup> mole/liter; △, SO<sub>4</sub><sup>2-</sup> 20.02 × 10<sup>-6</sup> mole/liter.

ion solution without other anions, it can be said that the anodic deposition in perchlorate-ferrous ion solutions with the addition of acetate, chloride, or sulfate ion proceeded mostly by the reaction [4]. According to Leibenguth and Cohen (5) sulfate was contained in the anodic deposition film formed from Fe<sup>2+</sup> in 0.15N-(NH<sub>4</sub>)<sub>2</sub>SO<sub>4</sub> solution and the sulfate content of the film increased with decrease of pH. Thus FeHSO<sub>4</sub><sup>+</sup> ion may play a minor role as one of the depositing species in sulfate-ferrous ion solution.

**Diffusion coefficients of depositing species.**—In order to obtain the limiting current of oxidation of FeOH<sup>+</sup> ion the anodic deposition was carried out in deaerated stagnant perchlorate-ferrous ion solutions without other anions. The results are shown as line 1' in Fig. 6. In stirred solutions the limiting current as a function of FeOH<sup>+</sup> ion concentration was obtained as line 1 in Fig. 2. In solutions with phosphate a linear relationship

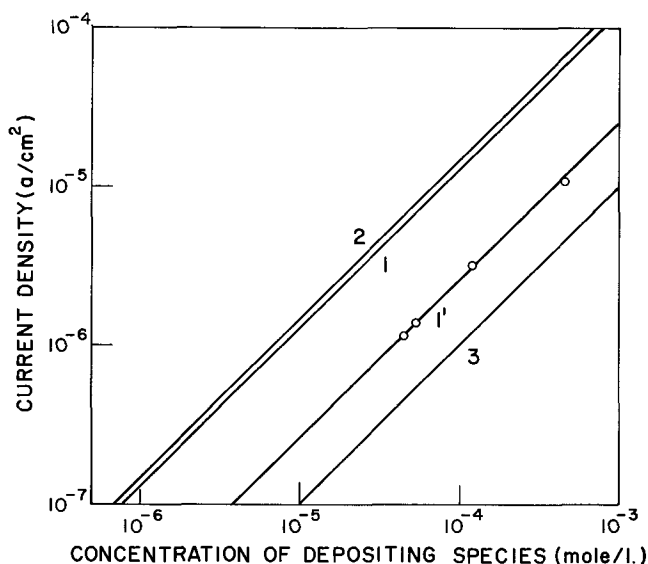


Fig. 6. Effect of concentration of depositing species on the limiting diffusion current of anodic deposition. Curve 1, FeOH<sup>+</sup> in ClO<sub>4</sub><sup>-</sup> solution with constant stirring; curve 1', FeOH<sup>+</sup> in ClO<sub>4</sub><sup>-</sup> solution without stirring; curve 2, FeH<sub>2</sub>PO<sub>4</sub><sup>+</sup> in ClO<sub>4</sub><sup>-</sup> solution with constant stirring; curve 3, in borate-boric acid solution (Nagayama and Cohen).

between anodic current for FePO<sub>4</sub> · 2H<sub>2</sub>O formation and concentration of H<sub>2</sub>PO<sub>4</sub><sup>-</sup> ion was obtained, as seen in Fig. 3, although the gradient of the line is slightly lower than 45°. This has arisen because no account of FeH<sub>2</sub>PO<sub>4</sub><sup>+</sup> ion formation by reactions [7] and [5] during anodic deposition was taken in calculating the FeH<sub>2</sub>PO<sub>4</sub><sup>+</sup> ion concentration. If the correction is made to the concentration of FeH<sub>2</sub>PO<sub>4</sub><sup>+</sup> ion, line 2 in Fig. 6 may be drawn for the anodic current density of FePO<sub>4</sub> · 2H<sub>2</sub>O formation vs. FeH<sub>2</sub>PO<sub>4</sub><sup>+</sup> ion concentration in stirred solution. Nagayama and Cohen (2) had obtained line 3 from neutral borate-boric acid solution.

From Fig. 6, diffusion coefficients of depositing species can be estimated by the simple diffusion equation

$$i_a = nFDc/d \quad [8]$$

where  $i_a$  is the limiting current (A/cm<sup>2</sup>) at a concentration of depositing species of  $C$  (mole/cm<sup>3</sup>),  $F$  the Faraday, and  $d$  the effective thickness of the diffusion layer which was assumed to be  $5 \times 10^{-2}$  cm in stagnant solution. The diffusion coefficient of FeOH<sup>+</sup> ion was approximately  $1.3 \times 10^{-5}$  cm<sup>2</sup> sec<sup>-1</sup> from the line 1' in Fig. 6. The effective thickness of the diffusion layer in stirred solution was estimated to be  $1 \times 10^{-2}$  cm assuming the same diffusion coefficient for FeOH<sup>+</sup> ion in stagnant solution (line 1') and stirred solution (line 1). The flow rate of argon for stirring was the same in solutions without phosphate (line 1) and with phosphate (line 2). Therefore, using  $d = 1 \times 10^{-2}$  cm in stirred solutions, the diffusion coefficient of FeH<sub>2</sub>PO<sub>4</sub><sup>+</sup> ion was estimated from line 2 and was approximately  $1.5 \times 10^{-5}$  cm<sup>2</sup> sec<sup>-1</sup>. The diffusion coefficients seem to be reasonable. The diffusion coefficient of the depositing species in neutral borate-boric acid solution had been reported as  $5 \times 10^{-6}$  cm<sup>2</sup> sec<sup>-1</sup> (2). This confirms a previous observation (4) that deposition in borate solution is partly via a ferrous borate complex.

### Summary

1. The anodic deposition of films on platinum from ferrous ion in perchlorate solutions with and without addition of phosphate, acetate, chloride, and sulfate was studied.
2. In the ferrous solutions containing only perchlorate ion the film was  $\gamma$ -FeOOH and was formed by anodic oxidation of FeOH<sup>+</sup> ion. The rate of deposition depended only on the concentration of FeOH<sup>+</sup> ion. The stability constant  $K$  of the FeOH<sup>+</sup> was estimated as  $\log K = -6.63$ .
3. In ferrous-perchlorate solutions containing phosphate ion the film was a mixture of  $\gamma$ -FeOOH and FePO<sub>4</sub> · H<sub>2</sub>O and was formed by the simultaneous oxidation of FeOH<sup>+</sup> and FeH<sub>2</sub>PO<sub>4</sub><sup>+</sup> ions. The resistance of the phosphate-containing film is probably higher than that of the other films.
4. In perchlorate-ferrous ion solution with acetate, chloride, or sulfate the anodic deposition proceeded mostly by oxidation of FeOH<sup>+</sup> ion to  $\gamma$ -FeOOH film.
5. Diffusion coefficients of FeOH<sup>+</sup> and FeH<sub>2</sub>PO<sub>4</sub><sup>+</sup> ions were estimated as  $D_{\text{FeOH}^+} = 1.3 \times 10^{-5}$  cm<sup>2</sup> sec<sup>-1</sup> and  $D_{\text{FeH}_2\text{PO}_4^+} = 1.5 \times 10^{-5}$  cm<sup>2</sup> sec<sup>-1</sup>.

Manuscript submitted May 14, 1973; revised manuscript received Aug. 10, 1973.

Any discussion of this paper will appear in a Discussion Section to be published in the December 1974 JOURNAL.

### REFERENCES

1. M. Nagayama and M. Cohen, *This Journal*, **109**, 781 (1962).
2. M. Nagayama and M. Cohen, *ibid.*, **110**, 670 (1963).
3. V. Markovac and M. Cohen, *ibid.*, **114**, 674 (1967).
4. V. Markovac and M. Cohen, *ibid.*, **114**, 678 (1967).
5. J.-L. Leibenguth and M. Cohen, *ibid.*, **119**, 987 (1972).

6. F. D. Snell and C. T. Snell, "Colorimetric Methods of Analysis," p. 314, Van Nostrand Reinhold Co., New York (1949).
7. S. R. Dickman and R. H. Bray, *Ind. Eng. Chem. (Anal. Edition)*, **12**, 665 (1940).
8. E. Posnjak and H. E. Merwin, *Am. J. Sci.*, **47**, 311 (1919).
9. D. F. Mitchell, K. Hashimoto, and M. Cohen, To be published.
10. J. A. Bolzan and A. J. Arvia, *Electrochim. Acta*, **8**, 375 (1963).
11. E. P. Egan, Jr., Z. T. Wakfield, and B. B. Luff, *J. Phys. Chem.*, **65**, 1265 (1961).
12. ASTM Powder Diffraction File, Card 15-513, 1969.
13. M. Pourbaix, "Atlas of Electrochemical Equilibria in Aqueous Solutions," p. 504, Pergamon Press, Inc., Elmsford, N. Y. (1966).

## The Cathodic Reduction of Gamma-FeOOH, Gamma-Fe<sub>2</sub>O<sub>3</sub>, and Oxide Films on Iron

Morris Cohen\* and Koji Hashimoto<sup>1</sup>

National Research Council of Canada, Ottawa, Ontario, Canada

### ABSTRACT

A comparison has been made of the galvanostatic reduction of iron oxide films formed by deposition on platinum and by anodic or air oxidation of iron. The major reduction process is that of Fe<sup>+++</sup> ion to Fe<sup>++</sup> ion in solution. Some ferrous ion is adsorbed on the unreduced oxide. There is no evidence for reduction to an intermediate solid phase. The results indicate that the two waves observed in the cathodic reduction of anodically formed (or air-formed) films are due to the presence of the two "phases" Fe<sub>3</sub>O<sub>4</sub> and  $\gamma$ -Fe<sub>2</sub>O<sub>3</sub> in the as-formed films.

Thin iron oxide films of various compositions can be formed in a variety of ways, such as by dry oxidation of iron, direct anodic oxidation of iron, and deposition on either iron or platinum from ferrous ion in solution. In previous work it was shown that films formed in iron by either anodic oxidation (1) or dry oxidation at low temperatures (2) have quite similar cathodic behavior. Cathodic reduction curves in neutral borate solutions showed two waves, one corresponding to the reduction of ferric ion in the outer layer of  $\gamma$ -Fe<sub>2</sub>O<sub>3</sub> to give Fe<sup>++</sup> in solution and the other to the reduction of underlying Fe<sub>3</sub>O<sub>4</sub> to give a combination of Fe<sup>++</sup> in solution and reduced iron. Although two waves are observed, it is not implied that there are two distinct phases with a sharp grain boundary in between in these thin films. The films have a composition varying from Fe<sub>3</sub>O<sub>4</sub> near the metal to  $\gamma$ -Fe<sub>2</sub>O<sub>3</sub> or even Fe<sub>2-x</sub>O<sub>3</sub> at the outer surface.

In the work reported here this previous cathodic reduction behavior is compared to the cathodic reduction of films deposited on platinum. As was shown in the earlier work, the films deposited from Fe<sup>++</sup> ion in borate solutions (3) are amorphous and contain borate, while those deposited from Fe<sup>+++</sup> in sulfate (4) or perchlorate (5) solutions are crystalline and gave the electron diffraction pattern of  $\gamma$ -FeOOH. In both cases the iron in the films was almost completely in the ferric state. It was also previously shown (4) that the  $\gamma$ -FeOOH films could be converted to  $\gamma$ -Fe<sub>2</sub>O<sub>3</sub> by vacuum heating and exposure to air. This type of  $\gamma$ -Fe<sub>2</sub>O<sub>3</sub> was also cathodically reduced and the results compared to those obtained from reduction of both the deposited films and films on anodically oxidized iron.

### Experimental

The anodic deposition on previously cleaned platinum was carried out in a borate buffer solution of pH 8.4 (made by mixing equal volumes of 0.3 mole/liter H<sub>3</sub>BO<sub>3</sub> and 0.075 mole/liter Na<sub>2</sub>B<sub>4</sub>O<sub>7</sub> · 10 H<sub>2</sub>O) or 0.15N-NH<sub>4</sub>ClO<sub>4</sub>, both containing FeSO<sub>4</sub>(NH<sub>4</sub>)<sub>2</sub>SO<sub>4</sub> · 6H<sub>2</sub>O. The solution used for cathodic reduction was the

slightly basic borate solution (pH = 8.4) without ferrous ion. A 1N-HCl-0.55N-H<sub>3</sub>PO<sub>4</sub> solution was used for the dissolution of residual films on platinum after cathodic reduction. H<sub>3</sub>PO<sub>4</sub> was added to stabilize the ratio of ferrous ion to ferric ion in solution (6). Solutions used for anodic deposition, cathodic reduction, and dissolution of films were deaerated by bubbling oxygen-free argon through the solution via a sintered disk for over 40 hr.

Anodic deposition was carried out on platinum specimens of a total area of 10 cm<sup>2</sup> at a constant potential<sup>2</sup> of +300 mV and a constant temperature of 25° ± 1°C in a solution stirred by bubbling argon at a constant flow. Immediately after anodic deposition, the cell with the specimen was rinsed 3 times by the borate-boric acid solution and then cathodic reduction was carried out at a constant current density of 10  $\mu$ A/cm<sup>2</sup> at a constant temperature of 25° ± 1°C in stagnant borate-boric acid solution under argon flow. After an appropriate time, cathodic reduction was interrupted and the solution was stirred by bubbling the argon for 1 min and was then drained from the cell to determine the weight of dissolved iron by the o-phenanthroline method. The cell with specimen was then rinsed 3 times with the borate-boric acid solution and deaerated hydrochloric acid-o-phosphoric acid solution transferred into the cell to dissolve the residual film on the platinum. The solutions formed by the dissolution of the residual film were analyzed using the o-phenanthroline (7) for total iron and  $\alpha\alpha'$ -dipyridyl for ferrous ion.

Anodic deposition takes place with a current efficiency of 100% (2) from ferrous ion to ferric oxide film. Consequently the thickness of the deposited film can be obtained from the graphic integration of current density-time curves of anodic deposition. The deposited film from the perchlorate solution was identified as  $\gamma$ -FeOOH by electron diffraction (5). The deposited film from the borate-boric acid solution was estimated to be Fe · B<sub>0.32-0.35</sub>O<sub>2.0-2.2</sub> · H<sub>x</sub> using the technique of vacuum x-ray microanalysis (8). Some of the  $\gamma$ -FeOOH films were annealed under vacuum at about 10<sup>-8</sup> Torr at 180°C until no release of water from the specimens was observed by a mass spectrometer. Then the films

\* Electrochemical Society Active Member.

<sup>1</sup> Present address: The Research Institute for Iron, Steel and Other Metals, Tohoku University, Sendai, Japan.

Key words: iron oxide films, thin films, passivity.

<sup>2</sup> All potentials in the paper are relative to the saturated calomel electrode.

were exposed to air for 5 days and electron diffraction patterns which corresponded to  $\gamma$ -Fe<sub>2</sub>O<sub>3</sub> were taken. These films were used for cathodic reduction as specimens of  $\gamma$ -Fe<sub>2</sub>O<sub>3</sub>.

### Results

As had been observed previously with films formed in sulfate solutions (4), the  $\gamma$ -FeOOH films on platinum could not be reduced by a single cathodic reduction step. In Fig. 1 are shown a series of cathodic reduction curves for a specimen originally covered with a film containing 9.55  $\mu$ g Fe/cm<sup>2</sup> ( $\approx$  400Å). Curve 1 is the initial cathodic reduction curve and shows a long plateau during which iron is being reduced to give Fe<sup>++</sup> in solution with quite a high current efficiency. However at point A (Fig. 1), at which the second plateau is reached, there is still about 15% of the original iron (1.0  $\mu$ g Fe/cm<sup>2</sup>) left on the platinum. Renewing the deaerated borate buffer solution and re-applying the cathodic current gives a potential curve without a reduction plateau and no further iron is put into solution. If, however, the specimen is first exposed to air before further cathodic treatment, a second reduction wave is observed, as shown in curve 2, Fig. 1, and more iron is put into solution. This can be continued until at about the fourth cycle no further iron goes into solution although a reduction wave is observed. This may indicate that at that point the metal is completely reduced to deposited metallic iron, which oxidized on exposure to moist air. After each cathodic reduction and exposure to air the specimen gave an electron diffraction pattern of  $\gamma$ -FeOOH. No other oxide was identified.

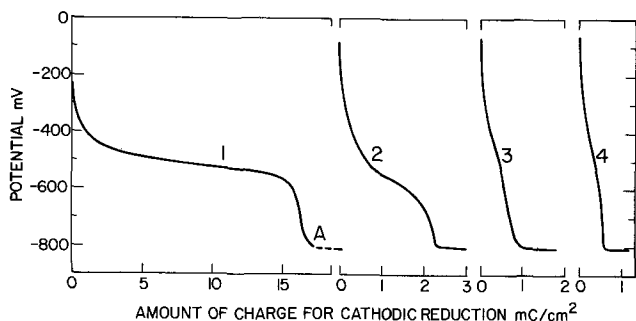


Fig. 1. Successive cathodic reduction curves for  $\gamma$ -FeOOH on platinum. Specimen exposed to air after each reduction cycle. At point A over 80% of the film was reduced.

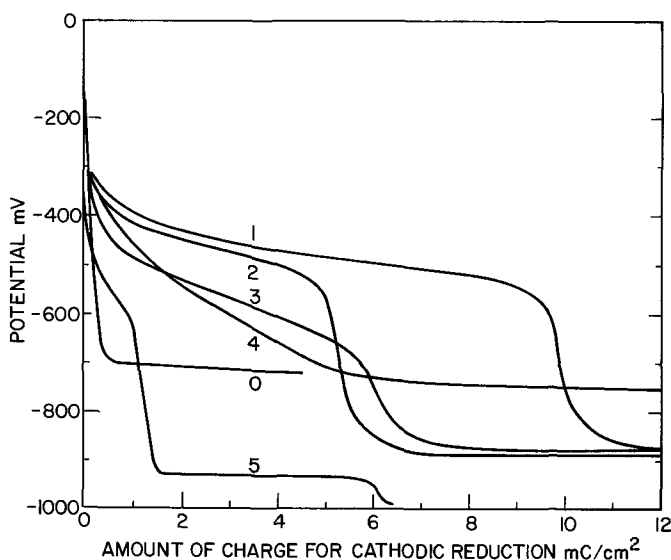


Fig. 2. Cathodic reduction curves for various films. 0—clean platinum. 1. Thick film deposited from borate. 2. Thinner film ( $\approx$ 200Å) from borate. 3.  $\gamma$ -FeOOH film deposited from sulfate. 4.  $\gamma$ -Fe<sub>2</sub>O<sub>3</sub> on platinum. 5. Anodically formed oxide film on iron.

The cathodic reduction curves for the various films are shown in Fig. 2. Curves 1-4 are for various deposited films while curve 0 is for platinum and curve 5 for anodically oxidized iron. Tables I-IV contain a summary of the data for each of the deposited specimens with regard to both anodic and cathodic charges in coulombs and the weights of total, ferric and ferrous iron. Analyses of the films were made for total iron and ferrous ion. Ferric ion was obtained by difference. Only ferrous ion was found in solution after cathodic reduction. The weight of residual ferric ion in the deposited

Table I. Results of cathodic reduction of thicker film formed in borate-boric acid solution

Amount of charge, mcoulombs/cm <sup>2</sup> Q <sub>c</sub>	Weight of iron, $\mu$ g/cm <sup>2</sup>						W <sub>Fe<sup>3+</sup></sub>
	W <sub>d</sub>	W <sub>r</sub>	$\Sigma$ W	W <sub>a</sub>	W <sub>Fe<sup>2+</sup></sub>	W <sub>Fe<sup>3+</sup></sub>	W <sub>Fe<sup>3+</sup></sub>
0	0	6.96	6.96	6.97	0.28	6.68	0.04
0.6	0.03	6.99	7.02	6.98	0.56	6.43	0.09
1.8	0.26	6.72	6.98	6.98	0.71	6.01	0.12
3.6	0.96	5.98	6.94	6.93	1.07	4.91	0.22
6.0	2.19	4.77	6.96	6.97	1.13	3.64	0.31
7.8	3.43	3.57	7.00	6.99	1.02	2.55	0.40
9.6	4.56	2.43	6.99	6.98	0.76	1.67	0.46
10.8	4.77	2.21	6.98	6.99	0.79	1.42	0.51
12.0	4.63	2.48	7.11	7.11	0.99	1.49	0.67

W<sub>d</sub>, weight dissolved.

W<sub>r</sub>, weight remaining in film.

W<sub>a</sub>, weight deposited during anodic deposition.

Table II. Results of cathodic reduction of thinner film formed in borate-boric acid solution

Amount of charge, mcoulombs/cm <sup>2</sup> Q <sub>c</sub>	Weight of iron, $\mu$ g/cm <sup>2</sup>						W <sub>Fe<sup>3+</sup></sub>
	W <sub>d</sub>	W <sub>r</sub>	$\Sigma$ W	W <sub>a</sub>	W <sub>Fe<sup>2+</sup></sub>	W <sub>Fe<sup>3+</sup></sub>	W <sub>Fe<sup>3+</sup></sub>
0	0	3.73	3.73	3.73	0.14	3.59	0.04
0.6	0.08	3.66	3.74	3.72	0.28	3.38	0.08
1.2	0.20	3.53	3.73	3.69	0.42	3.11	0.14
1.8	0.53	3.15	3.68	3.68	0.48	2.67	0.18
3.0	1.05	2.67	3.72	3.73	0.54	2.13	0.27
4.2	1.83	1.91	3.74	3.71	0.48	1.43	0.34
4.8	2.21	1.52	3.73	3.72	0.42	1.10	0.38
5.4	2.63	1.10	3.73	3.69	0.34	0.77	0.45
7.2	2.62	1.12	3.74	3.71	0.37	0.75	0.48
9.0	2.63	1.10	3.73	3.71	0.37	0.73	0.50
12.0	2.63	1.10	3.73	3.73	0.37	0.73	0.50

Table III. Results of cathodic reduction of  $\gamma$ -FeOOH film

Amount of charge, mcoulombs/cm <sup>2</sup> Q <sub>c</sub>	Weight of iron, $\mu$ g/cm <sup>2</sup>						W <sub>Fe<sup>3+</sup></sub>
	W <sub>d</sub>	W <sub>r</sub>	$\Sigma$ W	W <sub>a</sub>	W <sub>Fe<sup>2+</sup></sub>	W <sub>Fe<sup>3+</sup></sub>	W <sub>Fe<sup>3+</sup></sub>
0	0	3.50	3.50	3.51	0.09	3.41	0.03
1.2	0.30	3.18	3.48	3.49	0.28	2.90	0.10
2.4	0.77	2.74	3.51	3.50	0.44	2.30	0.19
3.6	1.41	2.06	3.47	3.47	0.42	1.62	0.26
4.8	2.17	1.31	3.48	3.56	0.34	0.97	0.35
6.0	2.86	0.66	3.52	3.52	0.20	0.46	0.43
7.2	3.00	0.55	3.55	3.55	0.20	0.35	0.56
9.0	2.87	0.64	3.51	3.48	0.28	0.36	0.80

Table IV. Results of cathodic reduction of  $\gamma$ -Fe<sub>2</sub>O<sub>3</sub> film

Amount of charge, mcoulombs/cm <sup>2</sup> Q <sub>c</sub>	Weight of iron, $\mu$ g/cm <sup>2</sup>						W <sub>Fe<sup>3+</sup></sub>
	W <sub>d</sub>	W <sub>r</sub>	$\Sigma$ W	W <sub>a</sub>	W <sub>Fe<sup>2+</sup></sub>	W <sub>Fe<sup>3+</sup></sub>	W <sub>Fe<sup>3+</sup></sub>
0	0	3.48	3.48	3.49	0.03	3.45	0.01
1.2	0.16	3.42	3.58	3.60	0.28	3.14	0.09
2.4	0.56	3.09	3.65	3.68	0.44	2.65	0.17
3.6	1.15	2.54	3.69	3.71	0.54	2.00	0.27
4.2	1.50	2.15	3.65	3.68	0.51	1.64	0.31
4.8	1.89	1.82	3.71	3.71	0.31	1.51	0.21
6.0	2.41	1.31	3.72	3.75	0.23	1.08	0.21
7.2	2.62	0.85	3.47	3.47	0.16	0.69	0.22
9.0	3.22	0.59	3.81	3.78	0.11	0.48	0.23
12.0	3.19	0.55	3.74	3.74	0.10	0.45	0.22
36.0	3.57	0.02	3.59	3.63	0.02	0	—

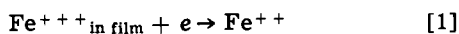
films decreased linearly with time. The calculated current efficiency, based on the current going to the reduction of ferric ion to ferrous ion, was 90+ % for the  $\gamma$ -FeOOH films and about 80% for the  $\gamma$ -Fe<sub>2</sub>O<sub>3</sub> film on platinum.

Plots of the Fe<sup>++</sup> in solution after cathodic reduction vs. coulombs for films of the same ferric ion content formed in three different ways are shown in Fig. 3. The results for films deposited from borate or perchlorate are almost identical. The apparent current efficiency in the linear portion of the curve is almost 100% for appearance of Fe<sup>++</sup> in solution. The current efficiency for the film converted to  $\gamma$ -Fe<sub>2</sub>O<sub>3</sub> is slightly less than 100%. However, the  $\gamma$ -Fe<sub>2</sub>O<sub>3</sub> can be completely reduced to Fe<sup>++</sup> in solution by one long cathodic reduction treatment. The  $\gamma$ -FeOOH film stops reducing after only about 80% of the Fe<sup>+++</sup> ion is reduced. At that point the film also contains some ferrous ion, and as pointed out earlier, further reduction is only possible if the specimen is first exposed to air.

### Discussion

The cathodic reduction behavior of the films on platinum are quite different depending on whether they are reduced as deposited or after heating in vacuum to convert to  $\gamma$ -Fe<sub>2</sub>O<sub>3</sub>. They also differ from anodically formed or air-formed oxide films on iron. This over-all difference in behavior is related to both the initial film composition and to the disposition of the ferrous ion formed during the reduction of the ferric oxide film. A sensible interpretation of the cathodic behavior is only possible by a comparison between the various films in relation to both their method of formation and their reduction products.

The basic cathodic reduction reaction is



The ferrous iron can either go into solution or remain in the film as an adsorbed or occluded species. The solubility of Fe(OH)<sub>2</sub> in these solutions is sufficient to allow all the ferrous ion to go into solution. Sato *et al.* (9) have suggested that the Fe<sub>2</sub>O<sub>3</sub> or FeOOH might reduce to Fe<sub>3</sub>O<sub>4</sub>. In the experiments reported here some ferrous iron is found in the deposited films both as deposited and as converted to  $\gamma$ -Fe<sub>2</sub>O<sub>3</sub> after various stages of cathodic reduction. The amount first goes up and then decreases as the film is further thinned. At the end of the cathodic reduction of the pure  $\gamma$ -FeOOH films formed in perchlorate solution, the Fe<sup>++</sup>/Fe<sup>+++</sup> ratio (0.8) is quite far from that for Fe<sub>3</sub>O<sub>4</sub> (0.5). An Fe<sub>3</sub>O<sub>4</sub> pattern is never observed by diffraction after cathodic reduction. The  $\gamma$ -Fe<sub>2</sub>O<sub>3</sub> film is completely reduced and the Fe<sup>+++</sup>/Fe<sup>++</sup> ratio of Fe<sub>3</sub>O<sub>4</sub> is never observed.

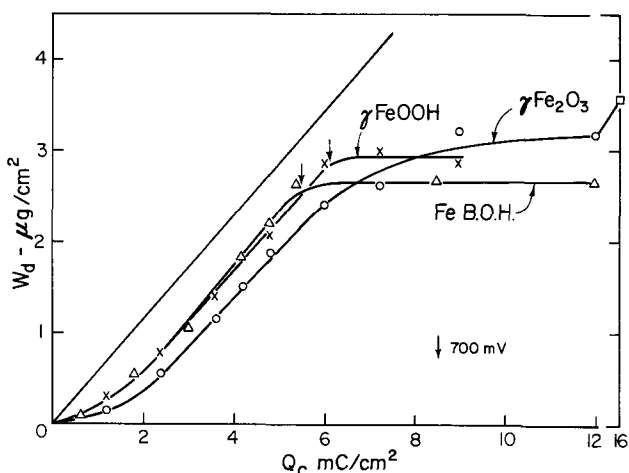


Fig. 3. Amount of ferrous ion ( $W_d$ ) in solution at various stages ( $Q_c$ ) of cathodic reduction. The solid line is the theoretical at 100% current efficiency.

These facts indicate that Fe<sub>3</sub>O<sub>4</sub> is not formed as an intermediate reduction product for either  $\gamma$ -Fe<sub>2</sub>O<sub>3</sub> or FeOOH.

The current efficiency for the cathodic reduction of  $\gamma$ -FeOOH is dependent on how the calculation is made. If we use the amount of Fe<sup>+++</sup> left in the film the current efficiency based on Eq. [1] for about 80% of the reduction (to a potential of -700 mV) is over 90%. The current efficiency then drops and apparently some of the current is used in the production of both hydrogen and metallic iron. Based on previous work, which showed a very low current efficiency for the reduction of Fe<sub>3</sub>O<sub>4</sub>, the high current efficiency suggests that Fe<sub>3</sub>O<sub>4</sub> is not a major intermediate product. The current efficiency for the reduction of the  $\gamma$ -Fe<sub>2</sub>O<sub>3</sub> over the major portion of the curve is somewhat less than this at about 80% (again based on residual Fe<sup>+++</sup> ion in films), and may be due to the early partial baring of platinum and hence earlier evolution of hydrogen.

If the current efficiency is calculated on the basis of an analysis of Fe<sup>++</sup> in solution, a different result is obtained. In all cases the current efficiency is initially small and then approaches 1 over the intermediate range. In the case of the deposited films, both from borate and perchlorate, at about -700 mV no further increase of ferrous iron in solution is observed. With  $\gamma$ -Fe<sub>2</sub>O<sub>3</sub>, although the current efficiency drops after about 80% if the film is dissolved, the Fe<sup>++</sup> iron concentration continues to increase until the whole film is reduced. With the FeOOH type films further reduction is only possible if the specimen is first exposed to air. These results indicate that the major portion of the film is reduced directly to Fe<sup>++</sup> in solution with high current efficiency. Some of the Fe<sup>++</sup> remains in the film as an occluded or adsorbed species. The amount remaining in the film gradually decreases as the film thins, again suggesting an adsorbed species which decreases in amount as the film area and volume decrease. The reduction of the  $\gamma$ -FeOOH ceases before it is completely reduced because it is shielded from the solution by the adsorbed Fe<sup>++</sup> species, and the alternative reactions to evolve hydrogen and reduce the ferrous species to iron can take place. On exposure to air both the ferrous species and iron are oxidized and allow further cathodic reduction.

The potentials at which the various processes take place are of some interest. The potential for the cathodic reduction of  $\gamma$ -FeOOH on platinum appears to be a little higher than that for  $\gamma$ -Fe<sub>2</sub>O<sub>3</sub> on iron. This higher potential for the reduction of  $\gamma$ -FeOOH was also observed by Nagayama (10) for  $\gamma$ -FeOOH formed on top of passive iron. The waves for the reduction of  $\gamma$ -Fe<sub>2</sub>O<sub>3</sub> on platinum or iron occur at essentially the same potential. The  $\gamma$ -Fe<sub>2</sub>O<sub>3</sub> on platinum shows only a single wave, i.e., a single stage reduction, and the final potential is only slightly less than that for hydrogen evolution on platinum (-710 mV). In contrast to this the final potential for the reduction of  $\gamma$ -FeOOH is much lower than this (-875 mV) and probably corresponds to that for hydrogen evolution on a contaminated (with film and possibly iron) platinum surface. The potentials for the cathodic reduction of magnetite on iron and hydrogen evolution on iron both take place at lower potentials than any of those observed during cathodic reduction of the films on platinum.

The two stage cathodic reduction of oxide films on iron has also been observed with films formed by dry oxidation at both low and medium temperature and always corresponded to the reduction of Fe<sub>2</sub>O<sub>3</sub> and then Fe<sub>3</sub>O<sub>4</sub>. The potential arrests for the reduction of the  $\gamma$ -Fe<sub>2</sub>O<sub>3</sub> and Fe<sub>3</sub>O<sub>4</sub> were the same as those observed during the reduction of the anodically formed oxide film on iron. If the iron is oxidized at a temperature sufficiently high to form a film composed of  $\alpha$ -Fe<sub>2</sub>O<sub>3</sub> and Fe<sub>3</sub>O<sub>4</sub>, two reduction waves are again observed. The wave for the reduction of  $\alpha$ -Fe<sub>2</sub>O<sub>3</sub> takes place at a more negative potential than that for  $\gamma$ -Fe<sub>2</sub>O<sub>3</sub>.

### Conclusions

The current efficiencies for the reduction to  $\text{Fe}^{++}$  ion are high for the major portion of all the films which were studied.

Thick films of  $\gamma\text{-FeOOH}$  cannot be completely cathodically reduced to  $\text{Fe}^{++}$  in solution in a single step. This is due to a combination of adsorption of the ferrous species and some complete reduction to metallic iron. There is no evidence for the formation of  $\text{Fe}_3\text{O}_4$  as an intermediate reduction phase.

Gamma- $\text{Fe}_2\text{O}_3$  film can be completely reduced to  $\text{Fe}^{++}$  ion in solution in a single step.

The two waves observed in the cathodic-reduction of both air-formed and anodically formed films on iron correspond to layers of  $\gamma\text{-Fe}_2\text{O}_3$  and  $\text{Fe}_3\text{O}_4$  in the as-formed films.

Manuscript submitted May 14, 1973; revised manuscript received Aug. 10, 1973.

Any discussion of this paper will appear in a Discussion Section to be published in the December 1974 JOURNAL.

### REFERENCES

1. M. Nagayama and M. Cohen, *This Journal*, **109**, 783 (1962).
2. C. D. Stockbridge, P. B. Sewell, and M. Cohen, *ibid.*, **108**, 928 (1961).
3. N. Markovac and M. Cohen, *ibid.*, **114**, 678 (1967).
4. J.-L. Leibenguth and M. Cohen, *ibid.*, **119**, 987 (1972).
5. K. Hashimoto and M. Cohen, *ibid.*, **121**, 37 (1974).
6. F. D. Snell and C. T. Snell, "Colorimetric Methods of Analysis," p. 316, Van Nostrand Reinhold Co., New York (1949).
7. F. D. Snell and C. T. Snell, *ibid.*, p. 314.
8. P. B. Sewell, D. Mitchell, and M. Cohen, *Develop. Appl. Spectr.*, **7A**, 61 (1969).
9. N. Sato, K. Kudo, and T. Noda, *Corrosion Sci.*, **10**, 785 (1970).
10. N. Nagayama and M. Cohen, *This Journal*, **110**, 670 (1963).

## Range Profiles for Ions Implanted into Anodic Tantalum Oxide

J. P. S. Pringle\*

Chalk River Nuclear Laboratories, Atomic Energy of Canada Limited, Chalk River, Ontario, Canada

### ABSTRACT

Radioactive  $^{24}\text{Na}^+$ ,  $^{42}\text{K}^+$ ,  $^{85}\text{Kr}^+$ ,  $^{86}\text{Rb}^+$ ,  $^{125}\text{Xe}^+$ ,  $^{134}\text{Cs}^+$ ,  $^{204}\text{Tl}^+$ , and  $^{222}\text{Rn}^+$  were implanted at 0.5, 1, 2, 5, 10, 20, 40, 80, and 160 keV into anodic tantalum oxide. A sectioning technique, based on slow dissolution of the oxide in concentrated HF almost saturated with  $\text{NH}_4\text{F}$ , was used to obtain integrated range profiles, and these were analyzed for range parameters by means of a least squares fitting procedure. Range profiles at 5 keV and above could be described, within experimental error, as being normally distributed; the modal ranges and standard deviations increased with energy, and with decreasing mass of the implanting ion. The ratio between modal range and standard deviation was such that a portion of the normal distribution extended beyond the oxide surface; evidence showing that a similar fraction of the ions would fail to implant was discussed. Range profiles below 5 keV were much influenced by the nature of the oxide surface, and could be distinguished experimentally in three parts. The first part was located in the contaminant layer adsorbed on the oxide surface, the second in the immediate surface layer itself, and the third at greater depths in the oxide; this last corresponds to the range profiles observed at higher energy. At 0.5 keV, the profile in the third part could be fitted with an exponential; the change to a normal distribution at 5 keV has been interpreted in terms of Poisson statistics.

In the process of ion implantation, a beam of ions accelerated to high energy impinges on the surface of a solid. Most come to rest a short distance into the solid, but a few fail to implant at all. Two concepts describe the situation: the range profile, which measures the concentration as a function of depth beneath the surface, and the sticking factor, which is that fraction of the incident ions that actually remains, or sticks, in the solid. The present paper describes the use of a highly precise sectioning technique (1, 2) to measure range profiles in anodic tantalum oxide; some measurements on the corresponding sticking factors are also reported. The results are used elsewhere (3, 4) in studying the migration process during the anodic oxidation itself.

Range profiles were first reported from this laboratory by Davies *et al.* (5) for radioactive  $^{24}\text{Na}^+$ ,  $^{86}\text{Rb}^+$ , and  $^{137}\text{Cs}^+$  implanted in polycrystalline aluminum. These profiles were markedly skew, for they consisted of a peak near the surface, followed by an approxi-

mately exponential tail extending deep into the metal. In subsequent work, Davies *et al.* (6) showed that the exponential tail was due to channeling of the implanted atoms along preferred directions in the crystal lattice. To eliminate the channeling effect, Domeij *et al.* (7) studied range profiles in amorphous solids such as anodic  $\text{Al}_2\text{O}_3$  and anodic  $\text{WO}_3$ , and found that the range profiles were "rather symmetric;" Jespersgard and Davies (8) subsequently described them as being "Gaussian in form." Anodic  $\text{Ta}_2\text{O}_5$  is also believed to be amorphous (9), and so the range profiles should be similar.

These range profiles had all been measured with the aid of sectioning techniques developed by Davies and his co-workers. Aluminum (10) or tungsten (11) was anodized to produce an oxide film, and the latter dissolved in a reagent that would not attack the underlying metal. By repeating this sequence of operations, thin uniform layers could be removed from the surface of the metal, and the range profile for an implanted species determined; by altering the procedure slightly, it was possible to measure range profiles in the anodic oxides as well (7, 8). The resolution of a sectioning

\* Electrochemical Society Active Member.

Key words: tantalum, anodic oxide, ion implantation, range profiles.



technique depends on the limiting thinness with which the layers can be removed (1), and the latter was about 40Å for both oxides.

By contrast, the sectioning technique described in a previous paper (1) of this series allowed the removal of layers as thin as 5Å from the surface of anodic tantalum oxide. The significance for range profile measurements is that whereas half the ions implanted at 5 keV are removed with a 40Å layer, half the ions implanted at 0.5 keV are removed with a 5Å layer; range profiles can therefore be measured to much lower energies than before.

### Experimental Measurements

**Method.**—Tantalum coupons,  $3.5 \times 1.0 \times 0.037$  cm, were cut from 0.015 in. sheets supplied by the Fansteel Metallurgical Corporation, and polished electrochemically (1). All anodizations were performed at room temperature and 1 mA/cm<sup>2</sup> with the apparatus devised by Walker (12), using 0.1M H<sub>2</sub>SO<sub>4</sub> as the electrolyte. The anodized coupons were wrapped in household aluminum foil leaving the middle  $2.0 \times 0.4$  cm of one face exposed; radioactive ions were implanted into the exposed area by means of the Chalk River isotope separator, whose use for this purpose has been described elsewhere (13). The implantation fluences ranged up to 10<sup>15</sup> ions/cm<sup>2</sup>, but were generally less than 10<sup>13</sup> ions/cm<sup>2</sup>. Except for <sup>85</sup>Kr, obtained from Oak Ridge, and <sup>222</sup>Rn, obtained from the Radium Chemical Company of New York, the radioactive species were all prepared in the NRX and NRU reactors at Chalk River by (n, γ) reactions on the stable precursors.

Range profiles for the implanted ions were obtained by dissolving a series of thin uniform layers in succession from the oxide surface (1) and counting the activity left after the removal of each layer. The dissolution was accomplished using concentrated HF almost saturated with NH<sub>4</sub>F, and the thickness of the remaining oxide was measured spectrophotometrically, with a standard error of 1.8Å (1). All counting was performed with a 2π proportional methane counter, the <sup>222</sup>Rn being estimated from the β-activity of its decay products by the method of Bergstrom *et al.* (14). Counts and their statistical errors were corrected for counter dead time, background, and radioactive decay by means of a program written for a PDP-5 computer, and expressed as percentages of the initial count. The resulting experimental data, in the form of percentage counts remaining *vs.* oxide thickness remaining, described the integrated range profile, from which the range parameters could be extracted by means of the mathematical analyses of the next section.

The implanting conditions were always adjusted so that the peak of the range profile occurred about 1760Å from the metal/oxide interface; the higher the energy, therefore, the thicker the oxide into which the ions were implanted. This thickness was chosen as standard because it has an interference minimum in third order near 350 nm, right in the middle of the favored 300-400 nm region for the operation of the spectrophotometer (1); thicknesses up to 350Å on either side of 1760Å could be measured without changing orders. Furthermore, the interference color changes very rapidly about 1760Å, from blue at slightly greater thicknesses to red at slightly smaller thicknesses; this feature was very useful for monitoring the uniformity of the implanted area, and hence the uniformity of the oxide dissolution (2).

**General description of results.**—The characteristics of the integrated range profiles are illustrated in Fig. 1 for 1 keV <sup>134</sup>Cs<sup>+</sup> and 40 keV <sup>134</sup>Cs<sup>+</sup>. Each profile consisted of several parts, namely: (i) A portion of the activity that could be washed off the surface without any change in oxide thickness. At low energies, this portion could be substantial, and this is why the 1 keV <sup>134</sup>Cs<sup>+</sup> range profile does not start at 100% in Fig. 1. (ii) A range profile characteristic of ions implanted at

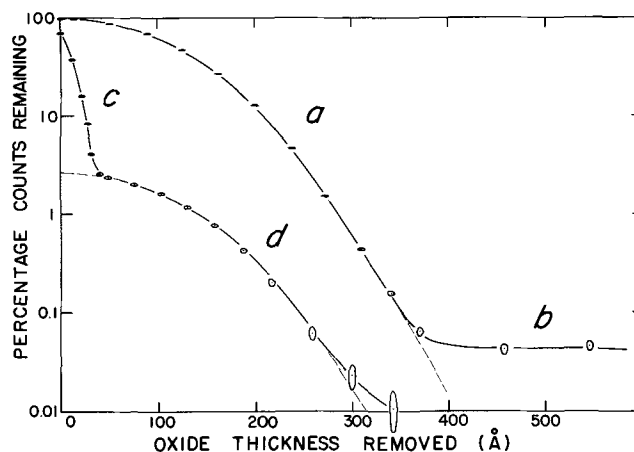


Fig. 1. Integrated range profiles for <sup>134</sup>Cs<sup>+</sup> at 40 keV (a) and 1 keV (c). The fraction of the activity that persists on continued stripping is labeled b, while d represents the neutral tail. Ovals drawn round each point at a radius of twice the standard error indicate the 95% confidence limits; these are ovals rather than ellipses because the plot is semilogarithmic. The abscissa is expressed in terms of oxide thickness removed rather than film thickness remaining to allow comparison of the two samples on a single figure.

the specified energy; these are labeled a and c in Fig. 1. (iii) At low energies, such as 1 keV, this profile was succeeded by another, labeled d in Fig. 1. (iv) Finally, there was sometimes a very small portion of the activity, labeled b in Fig. 1, that could not be removed even on prolonged stripping.

**Removal of activity from the oxide surface.**—The status of the oxide surface after implantation will be different from that left after stripping and washing, and so the first point on the range profile will be anomalous. To reduce the anomaly, coupons implanted in the mass separator were washed for 30 sec in distilled water and 15 sec in acetone, according to the procedure described in a previous paper (1). This initial washing had no detectable (0.5%) effect on the counting rate for any noble gas implant, but it did reduce the counting rates for alkali metal implants, as shown in Table I.

Figure 2 shows the effect of repeated washings, 30 sec in distilled water followed by 15 sec in acetone, on foils containing <sup>134</sup>Cs<sup>+</sup> implanted at 0.5 and 1 keV. The activity remaining decreases to the constant values listed in the figure, and the decrease is approximately exponential. To distinguish the effect of acetone from water, the experiment illustrated in Fig. 3 was performed; foils containing 0.5 and 1 keV <sup>86</sup>Rb<sup>+</sup> were

Table I. Fraction of initial activity left after washing with water (alkali metals) or 10% acetic acid (thallium). The standard error in the determination of each figure was 0.002-0.006, but reproducibility measurements (see text) suggest that the real variation could be perhaps ten times as much at the lowest energies.

Projectile energy (keV)	<sup>24</sup> Na <sup>+</sup>	<sup>42</sup> K <sup>+</sup>	<sup>86</sup> Rb <sup>+</sup>	<sup>134</sup> Cs <sup>+</sup>	<sup>204</sup> Tl <sup>+</sup>
0.5	0.418	0.509	0.517	0.562 0.518	—
1.0	0.765 0.844	0.566	0.746	0.714	0.837
2.0	0.877	0.881	0.844	0.846	0.950
5.0	0.962	0.953	0.908	0.949	0.976
10	0.978	0.965	0.963	0.953 0.969 0.969	0.969
20	N.R.	0.980	0.987	0.982	0.985
40	N.R.	0.983	1.005	0.987 0.998	0.998
80	N.R.	0.991	0.993	0.995	0.989

N.R. = Not recorded. The necessity for washing had not been appreciated at the time these specimens were analyzed.

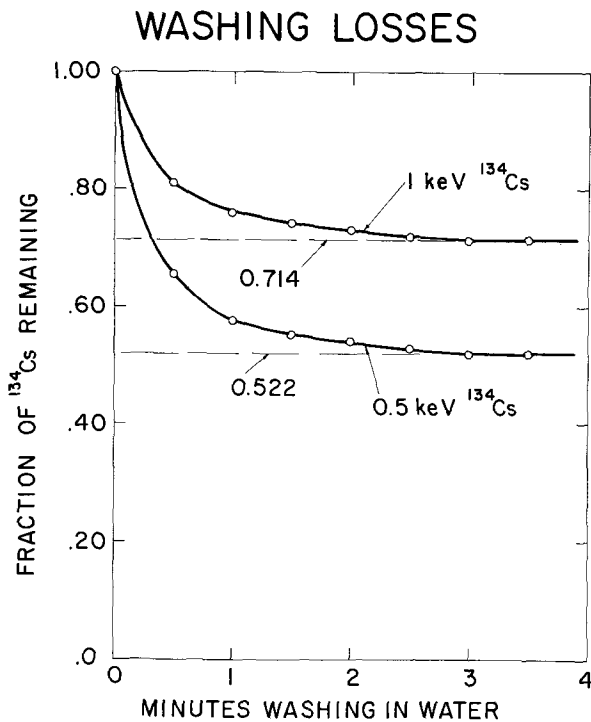


Fig. 2. Loss of <sup>134</sup>Cs from implanted targets on washing with water.

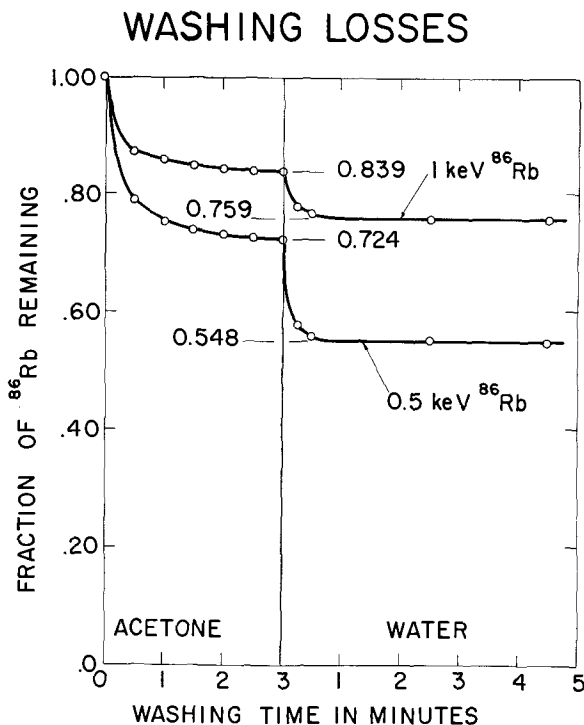


Fig. 3. Loss of <sup>86</sup>Rb from implanted targets on washing first with acetone, and then with water.

washed for several 30-sec periods in acetone, and then for varying periods in water followed by 15 sec in acetone. It is apparent that acetone behaves in much the same way as water; the activity decreases in an approximately exponential fashion as before, but to a slowly decreasing rather than a constant value. Washing with water after the acetone reduces the activity very quickly to a new and constant value, characteristic of the water wash alone (c.f. Fig. 2).

The removal of surface activity from the <sup>204</sup>Tl<sup>+</sup> specimens presented some difficulty. Less than 10% of the activity was removed on washing the 0.5 keV sam-

ple with water, yet by comparison with 0.5 keV <sup>134</sup>Cs<sup>+</sup>, a 50% loss was expected. The sample was therefore washed with saturated NH<sub>4</sub>HF<sub>2</sub>, which reduced the activity substantially, but also dissolved the tantalum oxide at the rate of about 1 A/min. In consequence, the distinction between surface and bulk activity was not well defined for this sample. All the other <sup>204</sup>Tl<sup>+</sup> samples, except 1 keV, were washed for 1 min in 10% acetic acid, as thallium acetate is very soluble (15); this reagent did reduce the activity by about the expected amount, and, from thickness measurements, did not dissolve the oxide. The 1 keV sample was washed for 30 sec in saturated NH<sub>4</sub>HF<sub>2</sub>, which removed about 16% of the activity, followed by 30 sec in acetic acid, which removed another 2%.

The results described so far were obtained in the course of the range profile measurements. To establish the reproducibility of the washing losses, eight anodized foils were implanted with 1 keV <sup>24</sup>Na<sup>+</sup>, and on a second occasion, another four were implanted similarly; all twelve were used for experiments of the kind illustrated in Fig. 2 and 3. On washing first in a reagent grade organic liquid and then in distilled water, both for 9 min, it was found that 2/3 to 5/6 of the total washing loss could be removed in acetone, methyl alcohol, or ethyl alcohol; in all cases the rate of loss was much as depicted in Fig. 3. Curiously enough, no detectable activity was lost in the course of 9-min washing in benzene. After the water wash, the fraction of the activity remaining on the first set of eight foils varied from 0.59 to 0.70, while on the second set it varied from 0.75 to 0.79. There thus appears to be a significant difference between the two sets, and between both of them and the results quoted in Table I, even though the implantation conditions were nominally the same in all cases. Subsequent washing in aqua regia or 1N NaOH caused almost no additional loss of activity.

**Range profiles.**—Range profiles were measured for a variety of atomic projectiles from <sup>24</sup>Na<sup>+</sup> to <sup>222</sup>Rn<sup>+</sup>, and at energies from 0.5 to 160 keV. The experimental data have been analyzed as described in the next section, with the results listed in Tables II-VI.

**Range profiles due to neutral atoms in the implanting beam.**—As has long been known (13, 16), the second profile obtained at low energy is an artifact resulting from the operation of the mass separator. Ions generated in the ion source are accelerated to 40 keV, and then separated into isotopic components by means of a magnetic field. The focusing requirements after separation are such that the ions travel another meter or so before striking the anodized tantalum coupons. Separation is best at energies near 40 keV; the other energies were obtained by applying accelerating or retarding voltages to the coupons. Thus an implantation energy of 1 keV was obtained by applying a 39 keV positive (retarding) potential. These accelerating or retarding potentials will only be effective, however, if the atoms are still ionized as they approach the coupons. If they have been neutralized since leaving the magnetic field, they will implant with the full 40 keV.

Figure 1 shows that the range profile for 1 keV <sup>134</sup>Cs<sup>+</sup> is the sum of two separate range profiles. Analysis of the second profile, by the method described in the next section, shows quite clearly that it corresponds to implantation at 40 keV, and similar effects have been observed with all the other ions implanted. This "neutral tail" is distinct only for energies below about 10 keV; at 20 keV it is reduced to a small inflection. The fraction of the incident beam appearing as neutral tail could be substantial, ranging from about 0.5 to 10%; the 3% shown in Fig. 1 appears to be about average. A liquid nitrogen trap in the target chamber would have reduced the neutral tail considerably (13).

**Effect of impurities.**—As demonstrated in Fig. 1, a very small fraction of the initial activity would some-

times persist even on prolonged stripping. This feature was not always present in the range profiles, but was well defined when it was. The detection limit, set by the ratio of initial to background counting rates, was normally about 0.005%. Persisting fractions were rarely observed in tantalum anodized for the first time, but the same specimens were used repeatedly in the present experiments, being reanodized after each range measurement. After three or four reanodizations, the persisting fraction had risen to about 0.05%, though individual specimens fluctuated considerably about this value. The biggest fraction ever observed was 0.36%.

The effect can be attributed to the presence of inclusions in the oxide film. These could be Ta<sub>2</sub>C particles originating in the parent metal (17) or, more probably, fragments of crystalline Ta<sub>2</sub>O<sub>5</sub> produced by field crystallization during the anodic oxidation process itself (18, 19). Neither is soluble in hydrofluoric acid, and so the inclusions are not removed by the stripping process. Vermilyea (9) found that the inclusions would persist through several cycles of anodizing and stripping; indeed, the amount even tended to increase as more crystalline oxide was formed in the successive anodizations.

Radioactive ions implant at random on the oxide surface, and so some will come to rest in the inclusions, from which they will not readily be removed by stripping. The persisting fraction was found to increase on reanodization, and attempts to clean the foils showed that the activity could not be removed by successive cycles of anodizing and stripping. In all respects, therefore, the properties of the persisting fraction are consistent with the reported behavior of the crystalline oxide fragments.

**Sticking factors.**—Relative sticking factors at very low energies were obtained using a method of Brown and Davies (20). Anodized tantalum foils were implanted to the same fluence at various energies, and the activity present in each foil counted. By fixing the sticking factor for one energy at a particular value, sticking factors for all the other energies could be calculated relative to this standard. The basis for choosing the standards and the presentation of the results are discussed later.

### Mathematical Analysis of the Profile Data

**Least squares fitting procedure.**—The purpose of the mathematical analysis was three-fold: (a) to find a mathematical function that would adequately describe the experimental profiles, (b) to obtain best estimates for the parameters of the function, and (c) to calculate standard errors in these estimates.

A least squares fitting procedure was therefore required, but those available proved unsuitable. Their most important defect was that they would account for errors in the dependent variable only, yet experimentally there were errors in both dependent and independent variables; that is, in both the percentage counts remaining and the oxide thickness measurements. Since the errors were of the same relative magnitude, neither could be ignored. The problem of making least squares fits when there are errors in both variables has been little studied, and so the matter was investigated further.

The experimental data consisted of a series  $I = 1, 2 \dots N$  of percentage counts remaining,  $Y(I)$ , vs. thickness remaining,  $X(I)$ ;  $EX(I)$  and  $EY(I)$  were the observed standard errors in  $X(I)$  and  $Y(I)$ , respectively. A suitable function,  $F$ , defined by

$$YFIT(I) = F(C(J); XFIT(I)) \quad [1]$$

and containing  $M$  parameters  $C(J)$ ,  $J = 1, 2 \dots M$ , was fitted to the  $X(I)$ ,  $Y(I)$  array, in such a way that the sum of the squares

$$S^2 = \sum_I [(X(I) - XFIT(I))/EX(I)]^2 + \sum_I [(Y(I) - YFIT(I))/EY(I)]^2 \quad [2]$$

was minimized; this criterion is due to Deming (21). The minimization of  $S^2$  was accomplished by modifying the standard Newton-Raphson method in such a way that the quantities  $XFIT(I)$  are treated as adjustable parameters of the fit. The resulting program was run on a CDC G-20 computer and provided best estimates for the parameters,  $C(J)$ , together with their standard errors  $EC(J)$  thus meeting requirements (b) and (c) above. To meet (a), the  $\chi^2$  goodness-of-fit test was applied;  $S^2$  was calculated from Eq [2] and compared with the probability,  $p(\chi^2)_{N-M}$ , of obtaining a value as large or larger from a  $\chi^2$  distribution with  $N-M$  degrees of freedom. A special routine was written to calculate these probabilities with an accuracy of one part in a thousand.

**Application to range profiles.**—Following Jespersgard and Davies (8), the range profiles were assumed to be normal distributions, so that they could be described by a function of the form

$$Y_n = (C(1)/\sqrt{(2\pi) \cdot C(3)}) \cdot \exp[-(X - C(2))/\sqrt{2 \cdot C(3)}]^2 \quad [3]$$

as illustrated in the bottom portion of Fig. 4. The experimental points, however, referred to the integral of this function; that is, to

$$Y = (C(1)/2) \cdot \operatorname{erfc}[-(X - C(2))/\sqrt{2 \cdot C(3)}] + C(4) \quad [4]$$

as illustrated in the top portion of Fig. 4. Accordingly, the function actually fitted was

$$YFIT(I) = (C(1)/2) \cdot \operatorname{erfc}[-(XFIT(I) - C(2))/\sqrt{2 \cdot C(3)}] + C(4) \quad [5]$$

where  $XFIT(I)$  is a best approximation to  $X(I)$ , the observed oxide thickness remaining after the removal of  $(I - 1)$  layers, and  $YFIT(I)$  is a best approximation to  $Y(I)$ , the percentage counts remaining after the removal of  $(I - 1)$  layers.

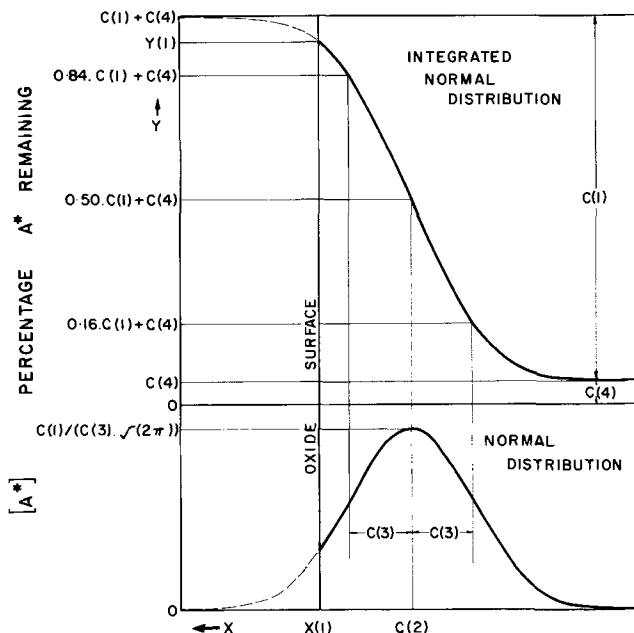


Fig. 4. Relationship between the normal distribution

$$Y = (C(1)/\sqrt{(2\pi) \cdot C(3)}) \cdot \exp[-(X - C(2))/\sqrt{2 \cdot C(3)}]^2$$

and its integral

$$Y = (C(1)/2) \cdot \operatorname{erfc}[-(X - C(2))/\sqrt{2 \cdot C(3)}] + C(4)$$

to illustrate the significance of the various parameters used in the least squares fitting.  $A^*$  represents the implanted radioactive species.

The significance of the parameters in Eq. [5] is illustrated in Fig. 4, where: C(1) is a normalizing factor, expressed in per cent, proportional to the area under the complete normal distribution fitted; C(2) is the mode of the normal distribution, measured, like X(I), in terms of its distance in angstroms from the metal/oxide interface; C(3) is the standard deviation of the normal distribution, also measured in angstroms; and C(4) is a constant of integration, measured in per cent, which accounts for the fraction of the activity that persists on continued stripping.

The parameter C(3) was of direct interest, but C(2) and C(1) had to be converted to more useful forms. To obtain the modal range, C(2) was subtracted from X(1); the error in the range was then a combination of the separate errors in C(2) and X(1), as indicated in Table II. The proportionality between range and standard deviation was such that the normal distribu-

Table II. Fit of an integrated normal distribution to the 40 keV <sup>134</sup>Cs<sup>+</sup> sample illustrated in Fig. 1

A. The Experimental Data

Point number I	Oxide thickness remaining (Å) X(I)	Percentage counts remaining (%) Y(I)	Error in thickness (Å) EX(I)	Error in counts (%) EY(I)
1	1866.8	100.00	1.8	0.20
2	1852.9	97.08	1.8	0.20
3	1816.1	86.77	1.8	0.19
4	1778.1	69.49	1.8	0.17
5	1741.7	47.59	1.8	0.14
6	1704.6	27.27	1.8	0.10
7	1666.9	13.023	1.8	0.072
8	1628.1	4.740	1.8	0.044
9	1593.5	1.542	1.8	0.025
10	1557.3	0.441	1.8	0.013
11	1528.3	0.1582	1.8	0.0080
12	1496.5	0.0637	1.8	0.0051
13	1358.8	0.0425	1.8	0.0041
14	1321.3	0.0456	1.8	0.0043

Number of points fitted, N = 14.

B. The Fitted Data

Point number I	Oxide thickness remaining (Å) X(I)	Percentage counts remaining (%) Y(I)	Relative error in fits	
			X(I)-XFIT(I) EX(I)	Y(I)-YFIT(I) EY(I)
1	1867.1	99.97	-0.18	0.13
2	1851.8	97.14	-0.58	-0.29
3	1816.8	86.75	-0.42	0.11
4	1779.7	69.47	-0.85	0.15
5	1741.4	47.59	0.17	-0.02
6	1703.5	27.28	0.60	-0.07
7	1666.7	13.025	0.13	-0.02
8	1627.7	4.742	0.21	-0.04
9	1592.4	1.546	0.63	0.16
10	1557.6	0.440	-0.17	0.07
11	1528.0	0.1519	-0.91	0.80
12	1496.1	0.0663	0.21	-0.51
13	1358.8	0.0440	0.00	-0.36
14	1321.3	0.0440	0.00	0.39

Function fitted:

$$YFIT(I) = [C(1)/2] \cdot \operatorname{erfc}[-(XFIT(I) - C(2))/\sqrt{2} \cdot C(3)] + C(4)$$

C. Fitted Parameters and Their Standard Errors

C(1) = 105.5%      EC(1) = 0.4%  
 C(2) = 1750.3Å    EC(2) = 0.8Å  
 C(3) = 72.1Å      EC(3) = 0.4Å  
 C(4) = 0.044%; value fixed at the average of the last two points  
 Number of parameters fitted, M = 3.

D. Results

Σ (Relative error in fits)<sup>2</sup>      S<sup>2</sup> = 4.37  
 Number of degrees of freedom    N-M = 11  
 Chi-square probability            p(χ<sup>2</sup>)<sub>11</sub> = 0.958  
 Modal range                        X(1) - C(2) = 116.5Å  
 Standard error in range          [(EX(1))<sup>2</sup> + (EC(2))<sup>2</sup>]<sup>1/2</sup> = 2.0Å  
 Standard deviation                C(3) = 72.1Å  
 Standard error in standard deviation    EC(3) = 0.4Å  
 Fitted sticking factor            (Y(1) - C(4))/C(1) = 0.947  
 Error in fitted sticking factor    [(Y(1) - C(4))/C(1)]<sup>2</sup> + [(EC(1)/C(1))<sup>2</sup> + (EY(1)/C(1))<sup>2</sup>]<sup>1/2</sup> = 0.004

tion extended significantly beyond the boundaries of the oxide film, as illustrated in Fig. 4, so that the observed range profile is more correctly described as a truncated normal distribution. To find out what fraction of a normal distribution was present, the parameter C(1) was divided into the initial percentage count, Y(1), less the correction, C(4), for the persisting fraction; the result is described as the fitted sticking factor.

The analysis was a little more complicated in the presence of a neutral tail. An integrated normal distribution was first fitted through the points in the tail only, to establish that this was due to a 40 keV implant. Thus a fit to the tail portion, d, of the 1 keV <sup>134</sup>Cs<sup>+</sup> profile in Fig. 1, excluding the last two points, gave a modal range of 114.2 ± 2.8Å, and a standard deviation of 70.7 ± 1.2Å, parameters in good agreement with those found for 40 keV <sup>134</sup>Cs<sup>+</sup> in Table II. Once the neutral tail had been confirmed as a 40 keV implant, there was no need to reconfirm it in every range study; only enough points, therefore, were taken to establish its intensity, C<sub>40</sub>(1). Three points sufficed, the fit being made with X(1)-C<sub>40</sub>(2) and C<sub>40</sub>(3) fixed at the appropriate 40 keV values, and C<sub>40</sub>(4) as 0.05%, which was a good average value for the intensity of the persisting fraction of the activity. With the nature and intensity of the neutral tail known, and the intensity of the persisting fraction defined, both effects could be subtracted from the low energy range profile, and a normal distribution fitted to the remainder.

Few range profiles were analyzed in as great detail or as far as 40 keV <sup>134</sup>Cs<sup>+</sup> and so, for comparative purposes, the range profiles were analyzed in a slightly different fashion from that illustrated in Table II. Profiles without a neutral tail were analyzed with C(4) set at 0.05%, and all points with Y(I) less than 2% were eliminated from the fitting, since many of the analyses were not continued below this figure; the limit was set at 1% after the removal of a neutral tail. With these restrictions, the average number of points fitted was approximately ten, ranging from a maximum of sixteen to a minimum, in several 0.5 keV profiles, of four.

*Adequacy of the fitting by the integrated normal distribution.*—The prime requirement in the least squares fitting was that the chosen distribution give an adequate fit to the experimental points. An "adequate" fit must therefore be defined, and this involves an arbitrary decision as to the level of significance required. Application of the χ<sup>2</sup> test at the 5% level means that fits with 0.975 > p(χ<sup>2</sup>)<sub>N-M</sub> > 0.025 are considered adequate; those with 1.000 > p(χ<sup>2</sup>)<sub>N-M</sub> > 0.975 are considered too good, and those with 0.025 > p(χ<sup>2</sup>)<sub>N-M</sub> > 0.000 too bad. These remarks apply to individual samples; when fitting to a large number of different samples, it is to be expected that, on the average, one in forty will have p(χ<sup>2</sup>)<sub>N-M</sub> > 0.975 and another one in forty p(χ<sup>2</sup>)<sub>N-M</sub> < 0.025.

On applying the χ<sup>2</sup> test to the ninety-six samples listed in Tables III, IV, and V, then, there should be two or three samples with p(χ<sup>2</sup>)<sub>N-M</sub> > 0.975 and another two or three with p(χ<sup>2</sup>)<sub>N-M</sub> < 0.025. In fact, it was found that 10 samples had p(χ<sup>2</sup>)<sub>N-M</sub> > 0.975 and 12 more had p(χ<sup>2</sup>)<sub>N-M</sub> < 0.025. The additional variation that this expresses can almost certainly be attributed to EX(I), for which an average value of 1.8Å (1) has been assumed; EX(I) would vary from sample to sample, and even from point to point. Accordingly, the general nature of these fitting probabilities may be taken as indicating that 1.8Å is a good average for EX(I), and that an integrated normal distribution does give an adequate fit to the range profiles. However, it must be noted that the very good fits cluster at low energy, and the very poor fits at high energy; possibly, therefore, the range profiles depart somewhat from a normal distribution at the higher energies, but no significant conclusion can be drawn.

Table III. Modal values of the range profiles as determined from the least squares fit of a normal distribution. All values can be corrected for the depletion depth by adding  $5 \pm 1 \text{ \AA}$ . Results, together with standard error in the fitting, quoted to nearest 0.5 \AA

Ion energy (keV)	$^{24}\text{Na}^+$	$^{42}\text{K}^+$	$^{86}\text{Kr}^+$	$^{86}\text{Rb}^+$	$^{125}\text{Xe}^+$	$^{184}\text{Cs}^+$	$^{204}\text{Tl}^+$	$^{222}\text{Rn}^+$
0.5	$-9 \pm 5.5$	$0.5 \pm 6$	$-4.5 \pm 11$	$8 \pm 2$	$2 \pm 2.5$	$4 \pm 5.5$	$4.5 \pm 10$	$10.5 \pm 2$
1.0	$14.5 \pm 2^\dagger$ $3.5 \pm 4$	$8 \pm 3$	$11 \pm 2.5$ $7 \pm 2$	$6 \pm 10$	$9.5 \pm 3$	$11 \pm 2.5$	$11.5 \pm 2^\dagger$	$14 \pm 2$ $11.5 \pm 2$
2.0	$24.5 \pm 4.5$	$15 \pm 3$	$10 \pm 2.5^\dagger$ $23 \pm 2^a$	$15 \pm 2^\dagger$	$9.5 \pm 3.5$	$15.5 \pm 2.5$	$18 \pm 2^\dagger$	$20 \pm 2$ $16.5 \pm 2$ $36.5 \pm 2$ $36.5 \pm 2^\dagger$
5.0	$57 \pm 3$	$40 \pm 2.5$	$29 \pm 3.5$ $41.5 \pm 2.5^a$	$35 \pm 2.5^*$	$30 \pm 2^b$	$33.5 \pm 2$	$33 \pm 2$	$33 \pm 2$ $52 \pm 2$ $51 \pm 2$ $82.5 \pm 2$ $79 \pm 2$
10	$94.5 \pm 4.5^*$	$62.5 \pm 3$	$46 \pm 2.5$ $57.5 \pm 2.5^a$	$58.5 \pm 2^\dagger$	$47.5 \pm 2$	$45.5 \pm 2$	$41 \pm 2^\dagger$	$41 \pm 2^\dagger$ $51 \pm 2$ $82.5 \pm 2$ $79 \pm 2$
20	$204 \pm 3$	$118.5 \pm 3.5^*$	$83 \pm 3$ $87.5 \pm 3^*, a$	$86 \pm 2$	$72.5 \pm 2$ $75.5 \pm 2$	$75 \pm 2$	$73 \pm 2$	$73 \pm 2$ $129.5 \pm 2^c$ $120 \pm 2$ $122.5 \pm 2$ $185.5 \pm 2.5$ $188 \pm 2$ $188 \pm 3^*$ $203 \pm 2$ $203 \pm 2.5^*$ $296.5 \pm 4^*$
40	$383 \pm 2.5$	$222.5 \pm 4^*$	$141.5 \pm 2.5^a$ $157.5 \pm 2.5^a$ $258.5 \pm 3.5$ $266.5 \pm 2.5^a$	$151 \pm 2$	$129.5 \pm 2^c$	$120 \pm 2$	$109.5 \pm 2$	$129.5 \pm 3.5^*$ $128 \pm 2$ $188 \pm 3^*$ $203 \pm 2.5^*$ $296.5 \pm 4^*$
80	$784.5 \pm 7.5^*$	$424.5 \pm 3$	$474 \pm 4.5^*$	$252.5 \pm 3$	$200.5 \pm 2$	$203.5 \pm 2$	$185.5 \pm 2.5$	$203 \pm 2.5^*$ $296.5 \pm 4^*$
160	—	—	—	—	$351 \pm 3$	—	—	—

$^\dagger$  Unusually good fit; fitting probability greater than 0.975.

$^*$  Unusually bad fit; fitting probability less than 0.025.

$^a$  High intensity  $^{86}\text{Kr}$  bombardments.

$^b$  Average of the six profiles quoted in Table VI, one of which was  $^\dagger$ .

$^c$  Average of five profiles, one of which was  $^*$ .

Table IV. Standard deviation for range profiles as determined from the least squares fit to a normal distribution. Quoted with standard errors of fit to nearest 0.5 \AA

Ion energy (keV)	$^{24}\text{Na}^+$	$^{42}\text{K}^+$	$^{86}\text{Kr}^+$	$^{86}\text{Rb}^+$	$^{125}\text{Xe}^+$	$^{184}\text{Cs}^+$	$^{204}\text{Tl}^+$	$^{222}\text{Rn}^+$
0.5	$14.5 \pm 1.5$	$12 \pm 2$	$11 \pm 3$	$7 \pm 0.5$	$7.5 \pm 0.5$ $7 \pm 0.5$	$10 \pm 2$ $10 \pm 3$	$14.5 \pm 3.5$	$5.5 \pm 0.1$
1.0	$18.5 \pm 0.2^\dagger$ $19.5 \pm 1.0$	$13 \pm 1$	$10 \pm 1$ $10.5 \pm 0.5$	$11 \pm 4$	$13.5 \pm 1$ $15 \pm 2.5$	$11 \pm 1$	$10 \pm 0.5^\dagger$	$9.5 \pm 0.5$ $10.5 \pm 1$ $11.5 \pm 0.5$
2.0	$29 \pm 2.5$	$20 \pm 1.5$	$16 \pm 0.5^\dagger$ $17 \pm 0.5^a$	$15 \pm 0.5^\dagger$	$13.5 \pm 1.5$	$15 \pm 1$	$13 \pm 0.5^\dagger$	$12 \pm 1$ $18 \pm 0.5$ $18 \pm 0.5^\dagger$
5.0	$51.5 \pm 2$	$32.5 \pm 1$	$25 \pm 2$ $22.5 \pm 1.5^a$	$23 \pm 1.5^*$	$20 \pm 0.5^b$	$19.5 \pm 0.5$	$19 \pm 1$	$18 \pm 0.5$ $18 \pm 0.5^\dagger$ $27.5 \pm 1$ $27.5 \pm 1$
10	$84 \pm 2.5^*$	$55.5 \pm 1.5$	$35 \pm 1$ $34 \pm 1^a$	$37 \pm 0.5^\dagger$	$28.5 \pm 0.5$	$27.5 \pm 0.5$ $31 \pm 0.5^\dagger$	$24 \pm 0.5^\dagger$	$38 \pm 1$ $37.5 \pm 1$ $54.5 \pm 2.5^*$ $55.5 \pm 1$
20	$145 \pm 1.5$	$91.5 \pm 1^*$	$57.5 \pm 1.5$ $53.5 \pm 1.5^*, a$	$55.5 \pm 0.5$	$43.5 \pm 1$ $46 \pm 1$	$43.5 \pm 0.5$	$40 \pm 1$	$38 \pm 1$ $37.5 \pm 1$ $54.5 \pm 2.5^*$ $55.5 \pm 1$
40	$245 \pm 1$	$147.5 \pm 2.5^*$	$89.5 \pm 1$ $89.5 \pm 1^a$	$89.5 \pm 1$	$69 \pm 1^c$	$72 \pm 0.5$ $70 \pm 1$	$59.5 \pm 1$	$89 \pm 2^*$ $86 \pm 1.5^*$ $162 \pm 3.5^*$
80	$420 \pm 5.5^*$	$247 \pm 1.5$	$180.5 \pm 2$ $152 \pm 1^a$	$152.5 \pm 1.5$	$114 \pm 1$	$112.5 \pm 1$	$89.5 \pm 1$	$89 \pm 2^*$ $86 \pm 1.5^*$ $162 \pm 3.5^*$
160	—	—	$275.5 \pm 3^*$	—	$191.5 \pm 2$	—	—	$162 \pm 3.5^*$

$^\dagger$  Unusually good fit; fitting probability greater than 0.975.

$^*$  Unusually bad fit; fitting probability less than 0.025.

$^a$  High intensity  $^{86}\text{Kr}$  bombardments.

$^b$  Average of the six profiles quoted in Table IV, one of which was  $^\dagger$ .

$^c$  Average of five profiles, one of which was  $^*$ .

Table V. Fitted sticking factor; the fraction of a normal distribution present as the range profile. Quoted to first significant figure in standard error of fit. Same specimens as in Table I.

Ion energy (keV)	$^{24}\text{Na}^+$	$^{42}\text{K}^+$	$^{86}\text{Kr}^+$	$^{86}\text{Rb}^+$	$^{125}\text{Xe}^+$	$^{184}\text{Cs}^+$	$^{204}\text{Tl}^+$	$^{222}\text{Rn}^+$
0.5	$0.27 \pm 0.09$	$0.5 \pm 0.2$	$0.3 \pm 3$	$0.88 \pm 0.04$	$0.61 \pm 0.09$ $0.76 \pm 0.05$	$0.7 \pm 0.2$ $0.7 \pm 0.3$	$0.6 \pm 0.4$	$0.973 \pm 0.003$
1.0	$0.8 \pm 0.1^\dagger$ $0.58 \pm 0.09$	$0.7 \pm 0.1$	$0.86 \pm 0.07$ $0.74 \pm 0.06$	$0.7 \pm 0.4$	$0.75 \pm 0.08$ $0.6 \pm 0.2$	$0.84 \pm 0.07$	$0.85 \pm 0.04^\dagger$	$0.93 \pm 0.03$ $0.87 \pm 0.05$ $0.95 \pm 0.02$ $0.91 \pm 0.04$
2.0	$0.78 \pm 0.07$	$0.76 \pm 0.07$	$0.73 \pm 0.04^\dagger$ $0.91 \pm 0.02^a$	$0.83 \pm 0.04^\dagger$	$0.7 \pm 0.1$	$0.85 \pm 0.06$	$0.92 \pm 0.02^\dagger$	$0.979 \pm 0.007$ $0.978 \pm 0.003^\dagger$
5.0	$0.86 \pm 0.02$	$0.88 \pm 0.02$	$0.86 \pm 0.6$ $0.96 \pm 0.2^a$	$0.93 \pm 0.03^*$	$0.93 \pm 0.02^b$	$0.957 \pm 0.009$	$0.94 \pm 0.02$	$0.979 \pm 0.007$ $0.978 \pm 0.003^\dagger$
10	$0.86 \pm 0.02^*$	$0.86 \pm 0.02$	$0.90 \pm 0.02$ $0.94 \pm 0.02^a$	$0.945 \pm 0.006^\dagger$	$0.945 \pm 0.009$	$0.952 \pm 0.008$ $0.929 \pm 0.006^\dagger$	$0.956 \pm 0.007^\dagger$	$0.97 \pm 0.01$ $0.97 \pm 0.01$
20	$0.922 \pm 0.008$	$0.90 \pm 0.01^*$	$0.92 \pm 0.02$ $0.94 \pm 0.01^*, a$	$0.935 \pm 0.007$	$0.952 \pm 0.008$ $0.948 \pm 0.009$	$0.959 \pm 0.004$	$0.960 \pm 0.008$	$0.983 \pm 0.003$ $0.980 \pm 0.006$
40	$0.941 \pm 0.004$	$0.93 \pm 0.01^*$	$0.941 \pm 0.006$ $0.958 \pm 0.006^a$	$0.953 \pm 0.005$	$0.969 \pm 0.004^c$	$0.954 \pm 0.004$ $0.959 \pm 0.004$	$0.964 \pm 0.006$	$0.986 \pm 0.008^*$ $0.988 \pm 0.003$ $0.980 \pm 0.005^*$ $0.989 \pm 0.003^*$ $0.946 \pm 0.007^*$
80	$0.974 \pm 0.008^*$	$0.944 \pm 0.009$	$0.944 \pm 0.009$ $0.958 \pm 0.004^a$	$0.950 \pm 0.006$	$0.960 \pm 0.004$	$0.967 \pm 0.004$	$0.974 \pm 0.007$	$0.980 \pm 0.005^*$ $0.989 \pm 0.003^*$ $0.946 \pm 0.007^*$
160	—	—	$0.948 \pm 0.008^*$	—	$0.968 \pm 0.008$	—	—	$0.946 \pm 0.007^*$

$^\dagger$  Unusually good fit; fitting probability greater than 0.975.

$^*$  Unusually bad fit; fitting probability less than 0.025.

$^a$  High intensity  $^{86}\text{Kr}$  bombardments.

$^b$  Average of the six profiles quoted in Table VI, one of which was  $^\dagger$ .

$^c$  Average of five profiles, one of which was  $^*$ .

*Reproducibility of the results.*—The six 5 keV  $^{125}\text{Xe}^+$  profiles in Table VI illustrate the reproducibility obtained. The standard deviation, 2.4 \AA, about the average modal range, 30.0 \AA, agrees with the average error

2.0 \AA in the fitting within the combined statistical error of  $\sqrt{(0.8^2 + 0.1^2)}$  \AA, and indicates that the error of fit is a reasonable estimate for the variability of individual measurements. The same holds true for both the stan-

Table VI. Reproducibility of 5 keV <sup>125</sup>Xe<sup>+</sup> profiles

Number of experimental points	Modal range (Å) X(1) - C(2)	Standard error of fit (Å) (EC(2)) <sup>2</sup> + (EX(1)) <sup>2</sup> <sup>1/2</sup>	Standard deviation (Å) C(3)	Standard error of fit (Å) EC(3)	Fitted sticking factor Y(1) - C(4)		Standard error of fit
					C(1)		
10	27.0	2.1	19.7	0.8	0.907		0.023
11	32.3	2.2	21.6	1.0	0.927		0.023
10	28.4	2.0	19.0	0.6	0.933		0.015
10	30.8	1.9	19.5	0.4	0.944		0.010
10	32.8	1.9	20.3	0.6	0.946		0.012
10	28.5	2.1	21.0	0.8	0.907		0.023
Averages	30.0	2.0	20.2	0.7	0.927		0.018
Std. dev. about average	2.4	0.1	0.9	0.2	0.014		0.006
Std. error in std. dev.	0.8		0.3		0.004		

dard deviation and the fitted sticking factor. Six samples, however, do not provide a very stringent test because the statistical errors are relatively large, as indicated in the bottom line of Table VI.

Further evidence on the reproducibility is provided by the duplicate experiments listed in Tables III, IV, and V and by comparing the results for projectiles of similar atomic weight; i.e., the <sup>85</sup>Kr<sup>+</sup>, <sup>86</sup>Rb<sup>+</sup> and <sup>125</sup>Xe<sup>+</sup>, <sup>134</sup>Cs<sup>+</sup> pairs. In general, the agreement is well within the combined experimental errors, particularly for the standard deviations. There are, however, some notable discrepancies, such as the difference between the modal ranges for 40 keV <sup>125</sup>Xe<sup>+</sup> and <sup>134</sup>Cs<sup>+</sup>.

The <sup>222</sup>Rn<sup>+</sup> results were somewhat peculiar. The first set of <sup>222</sup>Rn<sup>+</sup> profiles, listed on the upper line in the tables, showed that while the standard deviations were, as expected, slightly less than those for <sup>125</sup>Xe<sup>+</sup> at the same energy, the modal ranges were the same or even greater, whereas they should have been less. This observation was so surprising that the measurements were repeated, but with exactly the same result. Subsequent measurements with <sup>204</sup>Tl<sup>+</sup> gave values more in keeping with those expected, and so <sup>222</sup>Rn<sup>+</sup> appears to be anomalous. The reason for the anomaly is not known, and this, coupled with the generally poor fits at higher energy, means that the <sup>222</sup>Rn<sup>+</sup> results must be regarded as being less reliable than the others.

#### Implantation Phenomena at Energies above 5 keV

An implanting ion loses energy by both electronic and nuclear collisions with the target atoms, the latter predominating at energies below about 100 keV. Nuclear collisions can be arbitrarily divided into two types, according to the angular deflection they impart to the ion's trajectory. Small angle nuclear collisions occur every time the ion penetrates an atomic layer in the solid, but little energy is lost in each; large angle nuclear collisions are much less frequent, but are responsible for most of the energy loss. Ions normally penetrate several atom layers before undergoing their first large angle collision, and since the cross section for these collisions increases with decreasing energy, the mean free path to the next such collision decreases. Subsequent large angle collisions follow the same pattern, the process ending either with the ion at rest in the solid (implanted), or recrossing the surface with sufficient energy to escape (reflected).

*Adequacy of the normal distribution as a description of the range profiles.*—The complexity of this energy loss process is such that it is very difficult to predict the size and shape of the range profile. Detailed theoretical calculations by Winterbon, Sigmund, and Sanders (22) suggest that range profiles in amorphous monatomic solids should be close to normal distributions, and very recently Winterbon (23) has given reasons why range profiles in amorphous polyatomic

solids should be even closer. Since the greatest departures from normality are expected in the profile tails, the satisfactory fit of the range profiles in Tables III, IV, and V is readily explained. Both tails were cut off; one by the oxide surface, and the other by arbitrarily limiting the fit to points with greater than 2% of the initial count.

Table II, however, shows that an excellent fit can be obtained even when this limitation is lifted. The modal range of the 40 keV <sup>134</sup>Cs<sup>+</sup> was 120 ± 2 Å (Table III) with the 2% limit applied, and the standard deviation 72 ± 0.5 Å (Table IV); the corresponding figures from Table II are 116.5 ± 2 and 72 ± 0.5 Å, respectively, after rounding to the nearest 0.5 Å. Since the quoted errors are standard errors, they must be doubled to obtain the 95% confidence limits about each value; it is then obvious that the two sets of parameters do not differ significantly. The present results, therefore, provide no evidence against a normal distribution. Indeed it may be impossible to obtain such evidence from range profile measurements alone, for the thickness errors in the present range measurements are already of the order of one atom layer (1); it is hard to see how they could be reduced significantly in the interests of more exact fitting.

*Comparison with previous studies on amorphous oxides.*—It will be shown elsewhere (24) that these range profiles in anodic tantalum oxide are effectively identical to those obtained by Domeij *et al.* (7) in anodic tungsten oxide, as might be anticipated from the similar mix of very light and very heavy atoms present. Schjøtt (25) has compared both sets of experimental data with ranges calculated from the theory of atomic collisions and found that the agreement was within about 10%. This is reasonable considering the difficulty of the calculations. He noted that the experimental <sup>222</sup>Rn<sup>+</sup> ranges obtained here seemed consistently higher than those calculated, but, as explained earlier, this appears to be due to some systematic but unknown experimental error. The calculated ranges for <sup>204</sup>Tl<sup>+</sup> would be almost identical to those for <sup>222</sup>Rn<sup>+</sup>, and so the agreement between theory and experiment would be much better with this ion. Baroody (26) has calculated the straggling of <sup>125</sup>Xe<sup>+</sup> about its projected range in WO<sub>3</sub> and obtained fair agreement with the experimental results of Domeij *et al.* (7).

*Sticking factors.*—To be reflected, an ion must acquire a momentum component normal to and away from the oxide surface, and this can occur only after one or more large angle nuclear collisions with target atoms. The probability for reflection depends, therefore, on the angular deflection in each collision; reflection is obviously much more probable if the deflections are likely to be large. From the conservation of momentum, the average angular deflection of a heavy ion colliding with a light atom is less than that of a light ion colliding with a heavy atom, and so a smaller fraction of

the former should be reflected. The sticking factor will therefore be larger.

Brown and Davies (20) have illustrated this point experimentally. They implanted different materials with the same fluence of radioactive noble gas ions, and then, by counting the activity present, determined the relative fraction of the ions that "stuck" in each material. To obtain absolute values, it was necessary to know the absolute sticking factor for one particular combination of ion, target, and energy; special measurement showed that the absolute sticking factor for 40 keV  $^{85}\text{Kr}^+$  (heavy ion) in  $^{27}\text{Al}$  (light atom) was "unity within  $\pm 2\%$ ." With this as base, Brown and Davies were able to measure absolute sticking factors for 40 keV  $^{125}\text{Xe}^+$  and  $^{133}\text{Xe}^+$  (light ions) in  $^{181}\text{Ta}$  (heavy atom); five determinations gave  $0.95 \pm 0.02$  (standard error), which is significantly less than unity.

The obvious correlation between a sticking factor and a range profile is that the fraction of the ions failing to implant corresponds to the fraction of the normal distribution extending beyond the oxide surface; indeed, this correlation is implicit in the name, fitted sticking factor, given to the quantity listed in Table V. Absolute sticking factors have not been measured for aluminum and tantalum oxides, but it seems reasonable to suppose that the presence of the light oxygen atoms would tend to increase the values over those for the corresponding metals. Range measurements by Domeij *et al.* (7) in anodic  $^{27}\text{Al}_2^{16}\text{O}_3$  have been reanalyzed by the least squares fitting procedure described here, and the fitted sticking factor for 40 keV  $^{85}\text{Kr}^+$  was found to be  $0.998$  in excellent agreement with the  $1.00 \pm 0.01$  (standard error) actually observed for  $^{27}\text{Al}$  metal. Similarly, the five 40 keV  $^{125}\text{Xe}^+$  profiles measured here gave  $0.969 \pm 0.004$  (standard error), again in good agreement with the  $0.95 \pm 0.02$  (standard error) observed in  $^{181}\text{Ta}$  metal.

Additional support for this correlation is provided by the experiment of Böttiger *et al.* (27). They measured the fraction of the ions reflected when  $^{42}\text{K}^+$  was implanted at 60 keV into anodic tungsten oxide and found it was approximately 0.04-0.05; the corresponding sticking factor was therefore 0.96-0.95. Interpolation from Table V will show that the fitted sticking factor for 60 keV  $^{42}\text{K}^+$  implanting in anodic tantalum oxide would be about  $0.94 \pm 0.01$ , so that the two results are in excellent agreement. All in all, therefore, the normal distribution provides an excellent description for the range profiles at implantation energies above 5 keV.

### Implantation Phenomena at Energies below 5 keV

As the implantation energy decreases, the ions penetrate the oxide less and less, until eventually they fail to penetrate even the first atomic layer. At very low energies, then, the nature of the oxide surface is of great importance. One question that immediately arises is: how far must the ions penetrate before they stick? Presumably there must be a minimum of one atom layer above the ions to hold them in place, and so they must penetrate a distance of at least 3Å. A second question concerns the cleanliness of the oxide surface, and the possible presence of adsorbed gases. Since the adsorption process is of great importance for subsequent arguments, it is considered next.

*Adsorption at thermal energies (<0.1 eV).*—A gaseous atom approaching the surface of a solid is accelerated by the surface binding force in such a way that its kinetic energy perpendicular to the surface is increased, and its trajectory is bent toward the normal. On colliding with the surface, the atom loses energy and is reflected. As it leaves the surface, the binding force acts in reverse, so that the kinetic energy perpendicular to the surface is reduced, and the trajectory is bent away from the normal (28). If the kinetic energy is reduced to zero in the course of this process,

the atom will not escape from the surface at all, but will return and be adsorbed. The minimum kinetic energy needed to overcome the binding force is known as the heat of adsorption.

The probability for adsorption therefore depends on the energy of the incoming atom, and on its heat of adsorption. If the incoming energy is small enough, as in the case of low temperature gas, all the atoms must adsorb. When the heat of adsorption is also small, however, the adsorbed atoms may subsequently acquire sufficient thermal energy to overcome it, and they then desorb. Noble gas atoms, for example, are in fact mostly adsorbed on solid surfaces at room temperature, but their heats of adsorption are so low, at about 0.2 eV, that they desorb again in less than a millisecond (29). By contrast, the heat of adsorption for alkali metal atoms is, at about 2 eV (30), so much higher that their residence time on the surface is of the order of centuries (29). Most atomic and molecular species fall somewhere between these two extremes, but some hydrocarbons have very high heats of adsorption (29) so that they too remain firmly adsorbed.

*Surface contamination.*—This phenomenon of adsorption applies to any gas on any surface, and so the residual gas in the vacuum system of the mass separator will tend to adsorb on the surface of the anodic oxide. The presence of such adsorbed layers can lead to significant effects, as McHugh and Sheffield (31) discovered in experiments very similar to those reported here.

These authors implanted noble gas ions into tantalum at energies from 0.3 to 14 keV and studied the positive ions ejected from the surface with the aid of a mass spectrometer. Positive ions of measurable intensity were detected for "practically all masses through 100" when the tantalum was at room temperature, but these ions were "nonexistent at higher temperatures." Since the residence time for an adsorbed species decreases markedly with temperature (29), this behavior confirms the presence of contaminants at room temperature. The numerous mass peaks suggest the fragmentation of large molecules such as hydrocarbons. The latter would certainly have been present, in the form of vapor from the pump oils used to maintain the vacuum.

Conditions in the mass separator would be very similar, and the presence of adsorbed hydrocarbons is confirmed by the carbonaceous deposits formed during the implantation of hydrogen (2). All implantations performed here, therefore, were implantations into contaminated surfaces, so that the target would consist of a thin layer of very light atoms (mostly carbon and hydrogen), superimposed on a much thicker layer of light atoms (oxygen) and very heavy atoms (tantalum).

*Sticking factors for alkali metals.*—Most of the measurements reported at very low energies refer to the reflection coefficient, which is the complement of the sticking factor. These measurements show that the considerations determining sticking factors at high energy continue to apply at low energy also. Thus Arifov and Khadzhimukhamedov (32) measured the reflection coefficient for  $^{133}\text{Cs}^+$  (heavy ion) from a  $^{59}\text{Ni}$  surface (light target atom) and found it was practically zero at 0.2 keV; the corresponding sticking factor was therefore unity. By contrast, Brunnee (33) measured the reflection coefficient for  $^{39}\text{K}^+$  from a  $^{96}\text{avMo}$  surface and found that it was about 0.23 at 0.6 keV; the sticking factor was therefore considerably below unity, as expected for a light ion implanting into a heavy target. Both experiments were performed on surfaces which were believed to be clean.

Brunnee, however, repeated his experiment with a molybdenum surface that had not been cleaned, and then found that the  $^{39}\text{K}^+$  reflection coefficient dropped to rather less than 0.01 at the same 0.6 keV energy. The obvious interpretation is that the uncleaned mo-



lybdenum was covered with light atom contaminants, so that the  $^{39}\text{K}^+$  was then behaving as a heavy ion implanting into a light target. Significantly enough, Brunnee cleaned his surfaces by flashing them to high temperature, a process calculated to desorb any contaminants that might be present.

The  $^{39}\text{K}^+$  ions were implanted into the uncleaned surface at normal incidence, so that they would cross the contaminant layer at right angles and at relatively high energy. Upon reflection from the underlying molybdenum, they would traverse it at all angles and at much lower energy. Since the cross section for large angle nuclear collisions increases with decreasing energy, the probability for colliding with the contaminant atoms and losing still more energy is much increased when the ions are on their way out; furthermore, the trajectory bending discussed in connection with adsorption would tend to hold the  $^{39}\text{K}^+$  ions within the contaminant layer as they slowed down. The lower the implantation energy, therefore, the less likely are the reflected  $^{39}\text{K}^+$  ions to break back through the contaminant layer, and hence the reflection coefficient should decrease. Brunnee observed that the reflection coefficient did in fact decrease from about 0.02 at 2 keV to about 0.005 at 0.5 keV.

The sticking factor for an alkali metal implanting at very low energy into a contaminated surface is therefore expected to be almost unity. Since the tantalum oxide surfaces used here certainly were contaminated, the sticking factor for 0.5 keV  $^{24}\text{Na}^+$  was taken as unity, thus providing a standard against which the sticking factors at 1, 2, and 5 keV could be determined. Within the experimental standard error of about 0.03, the latter are unity as well (Table VII), a result anticipated from the preceding discussion.

**Sticking factors for noble gases.**—Ions arriving at the contaminated surface suffer one of four fates. (i) They can be reflected. If the ions do escape from the surface and its contaminants, they are most unlikely to return, since their mean free path at the pressure,  $10^{-6}$  Torr, inside the mass separator is of the order of a meter. (ii) They can come to rest in the outermost layer of the target, which is the contaminant layer. (iii) They can come to rest at such shallow depth in the oxide that they are not firmly trapped; i.e. within an atom layer or so of the oxide surface. (iv) They can come to rest sufficiently far into the oxide that they are firmly trapped; that is, they implant in the usual way.

When the implanting species is an alkali metal, ions suffering fate (ii) become strongly adsorbed on the oxide surface, while those suffering fate (iii) are adsorbed in the surface. The only ions lost to the system, then, are those suffering fate (i), and these form a very small proportion. Noble gas ions are almost certainly neutralized on coming to rest, and their heats of adsorption are so low that ions suffering fates (ii) and (iii) would rapidly desorb; the only ions that would actually stick in the oxide, then, would be those suffering fate (iv). As the implantation energy decreased, the proportion of the ions that penetrated far enough

to suffer fate (iv) would also decrease, thus accounting for the observed diminution in the sticking factor (Table VII). The xenon sticking factors were therefore standardized by assuming that the fitted sticking factor at 5 keV (Table V) was a good approximation to the experimental value; justification for the equivalence of observed and fitted values at high energy has been given already.

**Washing losses.**—The reason for the loss of activity on washing is now readily apparent. Alkali metal ions adsorbed on the oxide surface (ii) are washed off with organic liquids, while those adsorbed in the surface (iii) are washed out only with water (Fig. 3). Noble gas ions coming to rest in or on the oxide surface have already been desorbed, and so no washing losses are observed with these elements. Since the range profile is determined only by the mass and energy of the incident ions, the fraction of an alkali metal implant left after washing (iv) should be the same as the fraction of the corresponding noble gas that sticks (iv). The comparison between  $^{134}\text{Cs}^+$  and  $^{125}\text{Xe}^+$  in Table VII indicates that this is indeed the case.

The superior efficiency of the water wash can be interpreted in several ways. Alkali metal ions are more soluble in polar solvents, and the oxide surface might well hydrate when exposed to water. In this connection, the exchange reaction between the oxygen of the water molecules and that in the immediate surface layer of the oxide (34) is interesting; presumably no such exchange occurs with organic liquids, since these do not act as oxygen sources during anodization (35). The variation in washing loss from experiment to experiment can then be accounted for as differences in the nature and thickness of the contaminant layer.

**Form of the range observed profiles.**—At low energies, the implanting ions necessarily come to rest after very few collisions with the target atoms. Because the number of collisions is so few, Gaussian statistics cannot apply; the range profiles should not, therefore, be normally distributed. Nevertheless, the range profiles have been adequately described by normal distributions in Tables III and IV, and the fitted sticking factors in Table V are at least in rough agreement with those observed in Table VII. This paradox can be resolved by noting that the least squares fitting procedure lacks power at these low energies to distinguish between alternate descriptions for the profiles; the lack of power is due to the small number of experimental points, and the relatively large error in each.

In view of the small number of collisions, a first assumption would be that some form of Poisson statistics apply, and that the range profiles should therefore resemble a Poisson distribution. When the average number of collisions is very small, the Poisson distribution consists of a peak followed by an exponential tail; as the average number increases, this transforms gradually to a normal distribution, as shown schematically in Fig. 5.

If the energy is low enough, therefore, the peak would occur either in the contaminant layer or in the surface layer of the oxide, so that the measured profile would consist solely of the exponential tail. This suggested that it might be possible to fit an exponential function to the range data at 0.5 keV. If the range profile is described by

$$Y_e = C(1) \cdot \exp[\ln(\frac{1}{2}) \cdot (X(1) - X)/C(2)] \quad [6]$$

the function that must actually be fitted through the experimental points is its integral, namely

$$YFIT(I) = -C(1) \cdot C(2) / \ln(\frac{1}{2}) \cdot \exp[\ln(\frac{1}{2}) \cdot (XFIT(1) - XFIT(I))/C(2)] \quad [7]$$

where, apart from  $C(2)$ , the symbols have the same significance as in Eq. [3], [4], and [5]. The parameter  $C(2)$  is now the distance in angstroms over which the concentration of the implanted ions falls by half. Least

Table VII. The fraction of an alkali metal implant left after washing compared with the observed sticking factors. Data for  $^{134}\text{Cs}$  repeated from Table I; the two columns on  $^{24}\text{Na}$  describe results obtained with the same samples. The standard error in each figure is of the order of 0.03

Energy in keV	Fraction of $^{134}\text{Cs}^+$ activity remaining after washing with H <sub>2</sub> O	Observed relative sticking factors for $^{125}\text{Xe}^+$ (base 5 keV = 0.93)	Observed relative sticking factors for $^{24}\text{Na}^+$ (base 0.5 keV = 1.00)	Fraction of $^{24}\text{Na}^+$ activity remaining after washing with H <sub>2</sub> O
5	0.95	[0.93]	0.97	0.96
2	0.85	0.79	1.02	0.89
1	0.71	0.66	1.02	0.72
0.5	0.56, 0.52	0.44	[1.00]	0.69

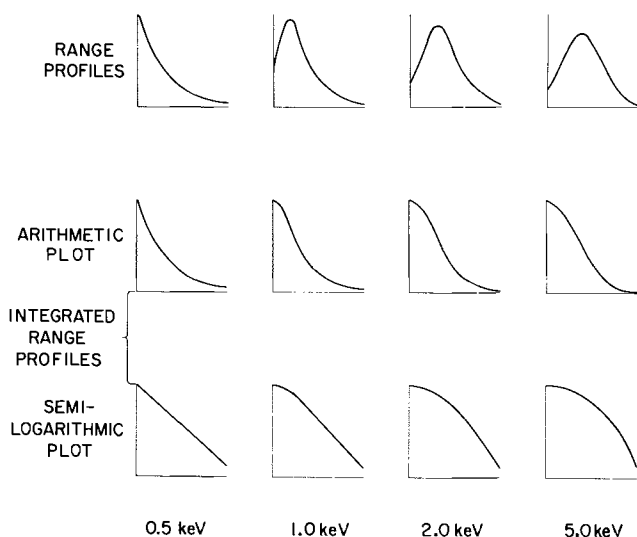


Fig. 5. Schematic diagram to show how the range profiles change from an exponential at 0.5 keV to a normal distribution at 5 keV. Scales arbitrary to emphasize the changes in form; for any particular energy, however, horizontal scales are the same for all three diagrams.

squares fit of the function [7] to the 0.5 keV samples listed in Table III, IV, and V resulted in  $p(\chi^2)_{N-2}$  greater than 0.025 for all except  $^{222}\text{Rn}^+$ ;  $C(2)$  varied from  $5.4 \pm 0.3\text{\AA}$  for  $^{24}\text{Na}^+$  to  $3.4 \pm 0.8\text{\AA}$  for  $^{222}\text{Rn}^+$ , with an average of about  $4.5\text{\AA}$ .

The fit of the exponential is therefore just as good as that of the normal distribution, and rather more convincing, since it involves only two adjustable parameters instead of three. Attempts to fit the exponential to the range data at 1 keV were not successful; only one of the twelve samples listed in Tables III, IV, and V gave an acceptable fit, and that one ( $^{85}\text{Kr}^+$ ) was barely acceptable ( $p(\chi^2)_3 = 0.057$ ). Examination showed that the largest discrepancy between observed and fitted values was almost invariably associated with the first point, the fitted values being too high; when the first points were eliminated, an exponential could be fitted satisfactorily through the remainder. Range profiles at 1 keV are therefore consistent with a peak followed by an exponential tail (Fig. 5); compared to the 0.5 keV profile, therefore, the peak has moved further into the oxide. As the implantation energy continues to increase, the peak moves still further into the oxide until at 5 keV the range profile is unmistakably close to a normal distribution.

It follows from this analysis that any similarity between the fitted sticking factors in Table V and the observed sticking factors in Table VII is largely fortuitous.

**Resolution of the sectioning technique.**—As discussed in a previous paper (1), the accuracy with which the range profiles can be measured is limited by the precision of the sectioning technique, and this depends on a number of factors. In particular, the resolution of the technique is governed by the uniformity with which the layers can be removed, since any nonuniformity will tend to increase the width of the observed profiles. This broadening can be interpreted as the folding of a mathematical distribution describing the nonuniformities into another mathematical distribution describing the true range profile. In terms of root mean square deviations,  $\sigma$ , about their respective means, these distributions are related by

$$\sigma_o^2 = \sigma_c^2 + \sigma_h^2 \quad [8]$$

where the subscripts refer to the observed range profiles, the correct range profile, and the nonuniformities left in the oxide thickness,  $h$ , remaining after the removal of each layer. The quantity  $\sigma_h$  is liable to vary

with the removal of each successive layer; in what follows an average value will be assumed.

Because of the squared dependence,  $\sigma_o$  will be determined mostly by the greater of  $\sigma_c$  or  $\sigma_h$ . At high energies, where  $\sigma_c \gg \sigma_h$ ,  $\sigma_o$  will be effectively equal to  $\sigma_c$ ; as the implantation energy is decreased,  $\sigma_c$  will also decrease, until eventually it becomes less than  $\sigma_h$ . The observed deviation then approximates to  $\sigma_h$  and will not decrease significantly with further decrease in the implantation energy. Since the root mean square deviation for a normal distribution is just the standard deviation, reference to Table IV will show that  $\sigma_o$  becomes sensibly constant once the implantation energy has fallen below 2 keV. Assuming that the nonuniformities are normally distributed, therefore,  $\sigma_h$  is approximately  $10\text{\AA}$ , a figure in excellent agreement with those, 8 and  $9\text{\AA}$ , obtained previously using the re-anodization technique (1). Furthermore, all of these figures must be regarded as maximum estimates.

It is rather unlikely, however, that the nonuniformities would be normally distributed. Quantitative analysis (36) of the accelerated stripping effect (2) suggests that the oxide in the immediate vicinity of each implanted ion dissolves faster than usual, and so the removal of such atoms would tend to leave depressions in the oxide surface. Such nonuniformities would approximate the single-tailed exponential better than the double-tailed normal distribution, and this may account for both the nature and similarity of the range profiles at 0.5 keV. Against this, however, it must be noted that differences in mass become less important as the implantation energy decreases. Thus the ratio of the modal ranges for  $^{24}\text{Na}^+ : ^{204}\text{Tl}^+$  decreases from about 4:1 at 80 keV to about 1.7:1 at 5 keV (Table III). The similarity of the profiles, and hence ranges, at 0.5 keV is then but a continuation of this trend. The exact nature of the profiles at 0.5 keV is therefore somewhat uncertain.

**Magnitude of penetration.**—The dissolution of a thin oxide layer in the  $\text{HF-NH}_4\text{F}$  reagent gives rise to the formation of a new oxide surface. Ions implanted sufficiently close to this new surface will be desorbed (noble gases), or washed out (alkali metals), or even dissolved out by the accelerated stripping effect discussed in the previous paragraph. Whatever the process, the oxide layer immediately beneath the new surface will be depleted in implanted ions, and the remaining profile will therefore begin, not at the oxide surface, but a short distance below it. This phenomenon will not influence the measured form of the range profiles, as long as the depletion distance remains constant; the latter seems probable, in view of the washing experiments. It will, however, affect the measurements of range, since these should be corrected for the depletion distance.

An estimate for this distance may be obtained by assuming that the alkali metal ions washed out only with water are those located in the depletion zone, and that the exponentiality of the range profile at 0.5 keV extends back to the oxide surface. Reference to Fig. 3 will show that 18% of the  $^{86}\text{Rb}^+$  implanted at 0.5 keV is washed out only with water. Taking the exponential half-distance as  $4.5\text{\AA}$ , this corresponds to a depletion depth of  $2.5\text{\AA}$  or about one atom layer (1). As noted earlier, it seems very reasonable that there should be at least one atom layer between an implanted ion and the surface.

The half distance of the exponential is a different parameter from either the mode or standard deviation of a normal distribution, and so an appropriate quantity with which to compare different range profiles is the mean range. For an exponential distribution, the mean range is simply the mean free path, given by  $C(2)/\ln 2$ . It is therefore about  $6.5\text{\AA}$  for 0.5 keV  $^{125}\text{Xe}^+$ . Mean ranges for 1 and 2 keV  $^{125}\text{Xe}^+$  can be estimated as being about 11 and  $20\text{\AA}$ , respectively, including corrections for the depletion distance. At energies of 5

keV or more, where the range profiles can be regarded as normal distributions truncated at the oxide surface, the mean range is computed to be about 3Å greater than the observed modal range. When the depletion distance is included as well, it is 5.5Å greater.

Best estimates for the observed mean ranges of the 0.5, 1, 2, 5, 10, 20, 40, 80, and 160 keV <sup>125</sup>Xe<sup>+</sup> in anodic tantalum oxide are therefore about 6.5, 11, 20, 36, 53, 78, 136, 206, and 357Å, respectively. Strictly speaking, these ranges refer to implantation energies slightly lower than those indicated, since the xenon atoms lose energy in traversing the contaminant layer on the oxide surface. Nevertheless, the results can be summarized by noting that when the implantation energy doubles, the mean range increases by a factor of approximately 1.6. Other implants behave similarly, but the factor increases with decreasing mass, becoming nearly 2.0 with <sup>24</sup>Na<sup>+</sup>.

### Conclusions

At energies of 5 keV and above:

1. The range profiles can be described within experimental error as normal distributions truncated at the oxide surface.
2. The observed sticking factor agrees within experimental error with the fraction of the normal distribution present as the range profile.
3. The results are in accord with previous measurements and with theory, in so far as the latter has been developed.

At energies below 5 keV:

4. The ranges are so short that the nature of the oxide surface becomes important. In particular, a layer of adsorbed contaminants, including hydrocarbons, is present when the surface is exposed to an oil pumped vacuum system.
5. The range profiles have been divided, largely on the basis of washing experiments with alkali metal implants, into three parts. The first part is located in the contaminant layer, the second in the immediate surface layer of the oxide, and the third, equivalent to normal implantation, at greater depth in the oxide.
6. The range profile of an ion implanted at 0.5 keV can be fitted to an exponential function, and the gradual change to a normal distribution at 5 keV has been interpreted in terms of Poisson statistics.

### Acknowledgments

The author would like to express his gratitude to D. Hall, C. Sitter, J. Tole, and O. Westcott for implantations with the mass separator, to D. Phillips for assistance with the experiments, and to J. A. Davies and K. B. Winterbon for comments on the manuscript.

Manuscript submitted March 19, 1973; revised manuscript received July 23, 1973.

Any discussion of this paper will appear in a Discussion Section to be published in the December 1974 JOURNAL.

### REFERENCES

1. J. P. S. Pringle, *This Journal*, **119**, 482 (1972).
2. J. P. S. Pringle, *ibid.* To be published.
3. J. P. S. Pringle, *ibid.*, **120**, 398 (1973).
4. J. P. S. Pringle, *ibid.*, **120**, 1391 (1973).
5. J. A. Davies, J. D. McIntyre, R. L. Cushing, and M. Lounsbury, *Can. J. Chem.*, **38**, 1535 (1960).
6. G. R. Piercy, F. Brown, J. A. Davies, and M. McCargo, *Phys. Rev. Letters*, **10**, 399 (1963).
7. B. Domeij, F. Brown, J. A. Davies, and M. McCargo, *Can. J. Phys.*, **42**, 1624 (1964).
8. P. Jespersgard and J. A. Davies, *ibid.*, **45**, 2983 (1967).
9. D. A. Vermilyea, *This Journal*, **104**, 485 (1957).
10. J. A. Davies, J. Friesen, and J. D. McIntyre, *Can. J. Chem.*, **38**, 1526 (1960).
11. M. McCargo, J. A. Davies, and F. Brown, *Can. J. Phys.*, **41**, 1231 (1963).
12. D. A. Walker, Atomic Energy of Canada Limited Report AECL-2502, Chalk River, 1965.
13. J. A. Davies, F. Brown, and M. McCargo, *Can. J. Phys.*, **41**, 829 (1963).
14. I. Bergstrom, J. A. Davies, B. Domeij, and J. Uhler, *Arkiv Fysik*, **24**, 389 (1963).
15. "Handbook of Chemistry and Physics," 40th edition, Chemical Rubber Publishing Co., Cleveland (1959).
16. I. Bergstrom, F. Brown, J. A. Davies, J. S. Geiger, R. L. Graham, and R. Kelly, *Nucl. Instr. Methods*, **21**, 249 (1963).
17. K. Huber, *This Journal*, **110**, 1286 (1963).
18. D. A. Vermilyea, *ibid.*, **102**, 207 (1955).
19. D. A. Vermilyea, *ibid.*, **110**, 250 (1963).
20. F. Brown and J. A. Davies, *Can. J. Phys.*, **41**, 844 (1963).
21. W. E. Deming, "Statistical Adjustment of Data," John Wiley & Sons, Inc., New York (1943).
22. K. B. Winterbon, P. Sigmund, and J. B. Sanders, *Mat. Fys. Medd. K. Dan. Vid. Selsk.*, **37**, No. 14 (1970).
23. K. B. Winterbon, *Radiation Effects*, **13**, 215 (1972).
24. J. P. S. Pringle, To be submitted.
25. H. Schiøtt, *Can. J. Phys.*, **46**, 449 (1968).
26. E. M. Baroody, *J. Appl. Phys.*, **40**, 2555 (1969).
27. J. Bøttiger, H. Wolder Jørgensen, and K. B. Winterbon, *Radiation Effects*, **11**, 133 (1971).
28. M. W. Thompson, *Phil. Mag.*, **viii**, **18**, 377 (1968).
29. P. A. Redhead, J. P. Hobson, and E. V. Kornelsen, *Advanc. Electron. Electron Phys.*, **17**, 323 (1962).
30. M. Kaminsky, "Atomic and Ionic Impact Phenomena on Metal Surfaces," Academic Press, New York (1965).
31. J. A. McHugh and J. C. Sheffield, *J. Appl. Phys.*, **35**, 512 (1964).
32. U. A. Arifov and K. K. Khadzhimukhamedov, *Bull. Acad. Sci. USSR Physical Series*, **26**, 1450 (1962).
33. C. Brunnee, *Z. Physik*, **147**, 161 (1957); English Translation ORNL-tr-467.
34. J. Siejka, J. P. Nadai, and G. Amsel, *This Journal*, **118**, 727 (1971).
35. M. Croset, E. Petreanu, D. Samuel, G. Amsel, and J. P. Nadai, *ibid.*, **118**, 717 (1971).
36. J. P. S. Pringle, Submitted to *This Journal*.

# Some Practical Aspects of Electroless Gold Plating

Y. Okinaka,\* R. Sard,\*\* C. Wolowodiuk, W. H. Craft, and T. F. Retajczyk

Bell Laboratories, Murray Hill, New Jersey 07974

## ABSTRACT

The electroless gold plating process using potassium borohydride as the reducing agent has been investigated for impurity effects, material compatibility, bath agitation effects, and thickness uniformity and line resolution in selective plating of patterned substrates. Impurities may cause a decrease in plating rate [Ni(II)], bath instability [Ni(II), Co(II), Fe(II)], thickness nonuniformity (polyethylene, organics in deionized water), and nodule formation (some surfactants). Bath agitation is beneficial: it increases plating rate, minimizes porosity of thin deposits, and eliminates nodule formation. Edge build-up generally occurs in selective pattern plating but, with proper selection of bath compositions and agitation conditions, it can be maintained below 10% in the thickness range of 1-12  $\mu\text{m}$ . The rate of lateral growth of electroless gold deposits is about 60% of that of perpendicular growth under optimum plating conditions. Also considered in this paper are certain aspects of the scale-up and waste disposal problems associated with electroless gold plating.

Electroless gold plating has been found to be useful in a variety of applications, especially for selective plating on patterned substrates for electronics applications. Such applications generally require pure soft gold with a thickness in the range of 1-15  $\mu\text{m}$ . A bath developed in this laboratory (1) has been found to be quite suitable for forming such deposits. Previous papers described the general bath characteristics (1), physical properties of deposits (2), bath operation with replenishment (3), reaction mechanism (4), and the nucleation and growth of deposits (5). The purpose of this paper is to describe several other aspects of the process which are important from the practical viewpoint and which have hitherto not been discussed. The topics covered include impurity effects, material compatibility, bath agitation effects, deposit thickness uniformity, and line resolution in selective plating of fine line patterned substrates. General recommendations are made as a guide for users of this process. Specific applications will be described in separate communications.

## Solution Preparation and Plating Procedure

Compositions of three electroless gold plating baths used are listed in Table I. Bath A was used often in our earlier studies (1-3) including those of impurity effects and porosity described in this paper. More recently, baths B and C have been used exclusively. These two baths contain less KCN and  $\text{KBH}_4$  and, therefore, are more preferable than bath A for practical reasons. Bath B gives the highest deposition rate (5-7  $\mu\text{m/hr}$  at 70°-75°C with vigorous agitation), but deposits with acceptable physical properties can be obtained only when plated with agitation. Bath C is slower plating (2  $\mu\text{m/hr}$  at 70°C with agitation) but gives better thickness uniformity on thin deposits in fine line plating. Details will be described in subsequent sections. It is convenient to prepare the baths by dilution of 5 $\times$  concentrated stock solutions. These solutions can be stored at room temperature for at least three months without noticeable decrease in plating rate. Since a very small amount of hydrogen gas

\* Electrochemical Society Life Member.

\*\* Electrochemical Society Active Member.

Key words: electroless plating, gold plating, borohydride.

Table I. Composition of electroless gold plating baths used

	Bath A	Bath B	Bath C
$\text{KAu}(\text{CN})_2$	0.02M	0.003M	0.02M
KCN	0.2M	0.1M	0.1M
KOH	0.2M	0.2M	0.2M
$\text{KBH}_4$	0.4M	0.2M	0.2M

continues to evolve from the solution due to the hydrolysis of  $\text{BH}_4^-$ , it is suggested that the cap of the storage bottle have a pressure vent or be only loosely tightened for safety purposes.

Details of various plating procedures used will be described in each section. Generally it is necessary to carry out the plating with controlled agitation in order to obtain deposits with uniform thickness at a fast rate. A plating temperature of 70°-75°C is recommended.

## Impurity Effects and Material Compatibility

*Inorganics.*—As described earlier (1), the electroless gold deposition takes place on noble metals such as Pd, Pt, Rh, and Au itself as well as on active metals such as Cu, Ni, Co, Fe, and their alloys. The initial reactions, however, are different on these two classes of metals. On noble metals the reaction is catalytic from the very beginning, whereas the gold deposition on the other active metals is initiated by a galvanic displacement reaction. For example, it was found (6) that when a copper substrate is placed in bath A at 70°C, about 100Å of copper dissolves into the solution before the surface is completely coated with pore-free gold deposits. Since such displacement reactions result in accumulation of ions of the substrate metals, it is important to know whether such ions exert any deleterious effects and, if they do, how much of them can be tolerated in the plating solution.

Figure 1 illustrates the effects of Cu(II), Ni(II), Co(II), and Fe(II) ions on plating rate. These ions were added in the form of a sulfate salt. Substrates

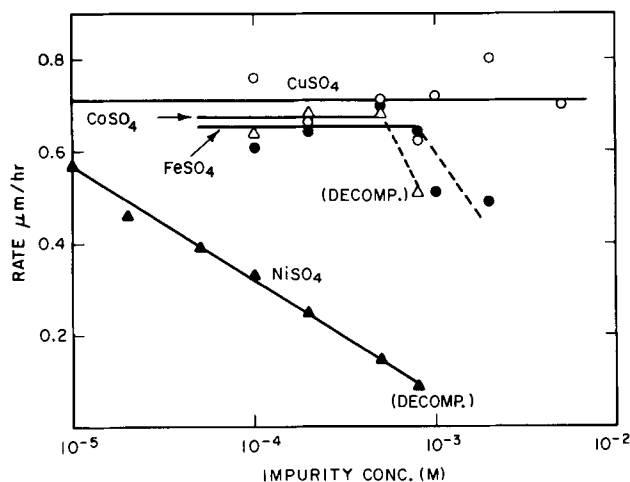


Fig. 1. Effects of metallic ion impurities on plating rate and bath stability. (Bath A, 75°C, no agitation.)

were  $\frac{1}{2}$  in.  $\times$  1 in. glass plates with evaporated Ti(500Å) and Au(1000Å). The plating was performed in 25 ml of bath A at 75°C without external agitation. It is seen in Fig. 1 that the presence of Cu(II) at least up to 0.01M does not affect the plating rate. The bath remained stable, and there was no effect on the deposit appearance as observed with an optical microscope. It is believed that the borohydride reduces Cu(II) to a Cu(I)-cyanide complex, which owing to its high stability remains unreacted in solution. On the other hand,  $10^{-3}$ M Co(II) or Fe(II) was found to decompose the bath, although at lower concentrations the bath remained stable and the plating rate was unaffected. It was noted, however, that the presence of these ions tended to make the deposit rough and nodular. The effect of Ni(II) is different in that it greatly decreases the plating rate at concentrations lower than  $10^{-3}$ M. The deposit obtained in the presence of Ni(II) is nodular, and at  $10^{-3}$ M or greater bath decomposition takes place. It has been shown (4) that the cause of the decrease in plating rate is the poisoning effect of  $\text{Ni}(\text{CN})_4^{--}$  on the electrocatalytic activity of gold, which is due to the inhibition of the anodic partial reaction (oxidation of  $\text{BH}_3\text{OH}^-$ )<sup>1</sup> by adsorbed  $\text{Ni}(\text{CN})_4^{--}$ . The observed bath instability may be due to the formation and precipitation of the heavy metal borides (7) and subsequent catalytic deposition of gold on the precipitates. It is evident from these results that substrates with nickel, cobalt, iron, or their alloys are not generally compatible with the electroless gold system. Such substrates should be precoated with a thin layer of a suitable noble metal catalyst [e.g., displacement ("immersion") gold] before electroless gold plating.

Silicon undergoes a displacement reaction in the bath, which deposits loosely adherent gold with simultaneous dissolution of silicon. Consequently, in plating on silicon wafers, the backs and edges must be effectively protected from exposure to solution (8).

Aluminum is vigorously attacked by the solution because of the high alkalinity.

The following metals are stable in the bath and do not initiate gold deposition: Cr, Mo, W, Ta, Ti, Zr.

**Organics.**—Organic materials and compounds which are stable in the bath include "Teflon," polypropylene, negative photoresists such as KMER and KTFR (Eastman Kodak Company), and perfluoro surfactants.

Polyethylene is not stable in this system because it is attacked by KOH at elevated temperatures. It was found that the exposure of a large area of this material causes a suppression of plating due to its inhibiting effect on the anodic oxidation of  $\text{BH}_3\text{OH}^-$ . The latter effect, which is similar to the effect of  $\text{Ni}(\text{CN})_4^{--}$ , is illustrated by the current-potential curves shown in Fig. 2. These curves were obtained by a potential scan technique using a rotating platinum disk electrode (area 0.465 cm<sup>2</sup>, 1600 rpm) precoated with about 25  $\mu\text{m}$  of electrolytically deposited gold from an alkaline cyanide bath. Curve 1 is due to the anodic oxidation of  $\text{BH}_3\text{OH}^-$  at 75°C in a mixture of 0.2M KOH, 0.1M KCN, and 0.1M  $\text{KBH}_4$  before the addition of polyethylene. Curves 2 and 3 were obtained, respectively, 10 and 30 min after addition of 1g pulverized polyethylene (Allied Chemical Company, No. AC-680). The relatively slow decrease in current is attributed to the slow dissolution of polyethylene powder. While these curves show the inhibiting effect of polyethylene (or its degradation product) on the anodic partial reaction, the cathodic partial reaction [reduction of  $\text{Au}(\text{CN})_2^-$ ] is not affected by polyethylene (curve 4). The poisoning effect of polyethylene manifests itself in the anomalous thickness uniformity of deposits formed on patterned substrates. Figure 3 shows SEM views and profiles of portions of gold deposits [formed on evaporated Ti(750Å)/Pd(1000Å) patterns on oxidized silicon

<sup>1</sup>  $\text{BH}_3\text{OH}^-$  is an intermediate species formed during the hydrolysis of  $\text{BH}_4^-$ , and has been identified as the reducing agent in the electroless gold deposition reaction (4).

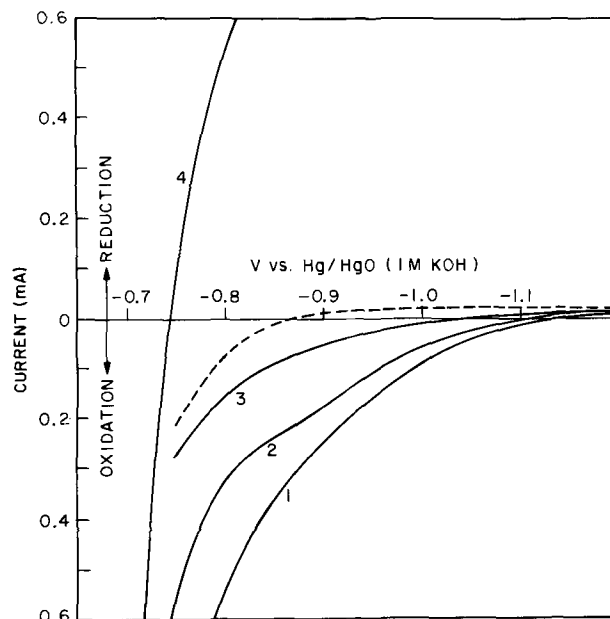


Fig. 2. Effect of polyethylene on anodic oxidation of  $\text{BH}_3\text{OH}^-$  and cathodic reduction of  $\text{Au}(\text{CN})_2^-$  at rotating platinum disk electrode precoated with gold. (75°C, 1600 rpm, 5.56 mV/sec.) Dashed curve, Base electrolyte containing 0.1M KCN and 0.2M KOH. Curve 1, 0.1M  $\text{KBH}_4$  plus base electrolyte before addition of polyethylene. Curves 2 and 3, 10 min and 30 min after addition of 1g polyethylene. Curve 4, 0.001M  $\text{KAu}(\text{CN})_2$  plus base electrolyte (no  $\text{KBH}_4$ ) before and after addition of polyethylene.

wafers] in solutions uncontaminated (top) and heavily contaminated with polyethylene (bottom). The plating was carried out in bath B (Table I) at 70°C for 110 min using the agitation and rotation method described in the subsequent section. The thickness profiles were obtained using a stylus instrument (Dektak, Sloan Instruments Corporation). It is seen that the thickness uniformity of the deposit formed in the uncontaminated solution is excellent, whereas extreme thickness nonuniformity is apparent on the deposit formed in the contaminated solution. The reason why the deposition is less inhibited at edges than at the center is not obvious, but this phenomenon indicates that there is a mechanism whereby the adsorption of polyethylene (or its degradation product) occurs less at the edges.

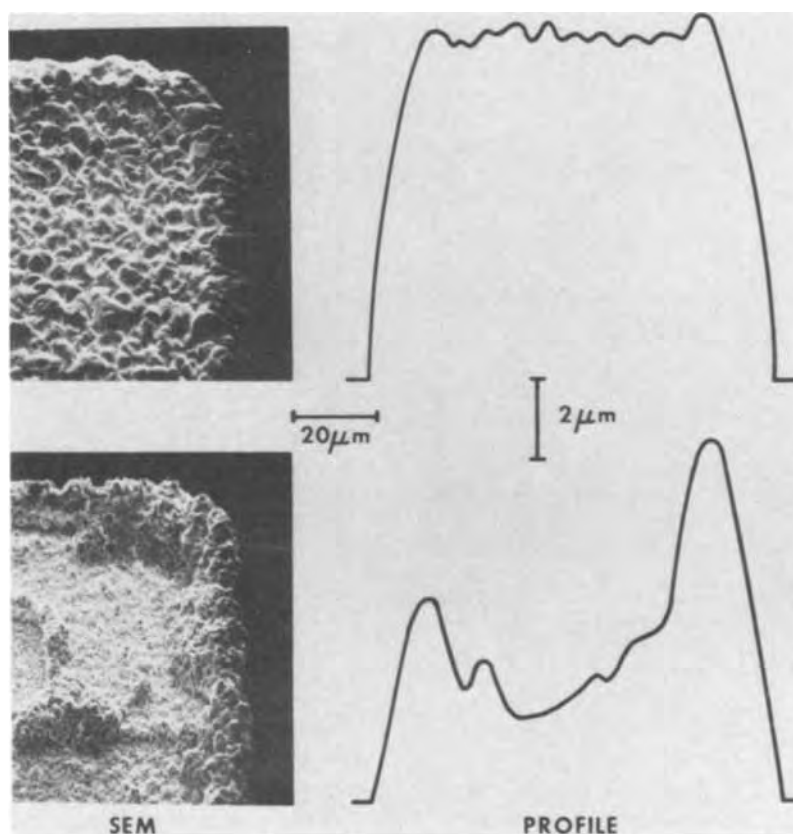
Our experience in plating a large number of patterned substrates shows that a similar center suppression effect occurs, though to a much lesser extent, when water used to prepare the plating solution is contaminated with traces of organics. For example, deionized water not treated with active charcoal was found to bring about center suppression amounting to 20-30%, whereas distilled water or charcoal-treated deionized water invariably gave rise to only  $\leq 10\%$  thickness nonuniformity.

Positive AZ photoresists (Shipley Company) are unstable in alkaline media and therefore not compatible with the electroless gold process. Other organic compounds tested and found to be incompatible are Triton X-100 (Rohm and Haas Company, a nonionic surfactant) and n-dodecylamine. The addition of these compounds formed nodular, discolored deposits.

#### Agitation Effects

In addition to the enhanced plating rate which has already been described (1), bath agitation brings about two important beneficial effects: (i) it entirely eliminates the tendency for nodule formation, and (ii) it facilitates the formation of deposits with lateral growth structure and uniform grain size, which brings about a decrease in porosity. Three typical structures of 2  $\mu\text{m}$  thick electroless gold deposits are illustrated in Fig. 4 by scanning electron micrographs. Figure 4a

Fig. 3. Scanning electron micrographs and thickness profiles showing effects of contamination with polyethylene. Top, uncontaminated; bottom, heavily contaminated. (Bath B, 70°C, rotational plating.)



shows the morphology of deposits formed without agitation in a solution similar in composition to bath A (Table I) except the concentration of  $\text{KAu}(\text{CN})_2$  was decreased to 0.0025M. The plating temperature was 75°C. This deposit was brown in color, consisting of particles approximately micron size, and protruding outwards from the surface. Figure 4b shows the deposit formed in bath A [ $0.02\text{M KAu}(\text{CN})_2$ ] also with no external stirring. The deposit was smooth and yellow, with a fine structure consisting of a network of web-like features. Figure 4c shows a deposit obtained in the same bath but with vigorous agitation. The dilute bath which yielded photograph (a) gave deposits similar to photograph (c) when operated with agitation. These deposits are characterized by well-developed crystalline facets.

As may be expected from the morphological observations, the deposit formed in the dilute  $\text{KAu}(\text{CN})_2$  bath without agitation (Fig. 4a) was found to be most porous. The least porous deposit was formed in vigorously agitated baths (Fig. 4c). Porosities of deposits corresponding to Fig. 4b and c are compared in Fig. 5 as a function of the average deposit thickness. The deposits for the porosity determination were formed on ceramic alumina substrates precoated with evaporated titanium and copper. The porosity was determined by the method described previously (2): namely, each plated sample was immersed in 20%  $\text{HNO}_3$  and ultrasonically agitated for 5 min at 30°C, and the dissolved copper was determined using atomic absorption spectroscopy. The ratio of the copper concentration determined for each plated substrate to that found with an unplated blank substrate was taken to represent per cent porosity. It is seen from Fig. 5 that the effect of agitation on porosity is especially significant for deposits thinner than 0.5  $\mu\text{m}$ . For thicker deposits the effect is insignificant, and essentially zero porosity is achieved at thicknesses greater than 1  $\mu\text{m}$ .

The electrical resistivity and hardness of deposits were also investigated with and without bath agitation. The results obtained with agitation were identical to

those reported previously (2) for deposits obtained without agitation.

From the known dependence of deposition rate on the speed of bath agitation (1), it is clear that the deposition rate is partly controlled by the rate of transport of reacting species from the bulk of solution to the substrate surface. Therefore, conditions of agitation play an important role in determining the uniformity of deposit thickness on a given substrate. This subject is discussed in the next section.

#### Uniformity of Deposit Thickness

It was found that the use of a simple magnetic stirrer or a stirring blade generally gives unsatisfactory results in regard to thickness uniformity across the substrate surface. For example, when a glass substrate ( $2.54 \times 1.75 \text{ cm}$ ) precoated with evaporated Ti/Au was plated for 1 hr with motorized stirring rod agitation, a thickness variation of  $\pm 15\%$  was observed. Using either of the two methods described below, the thickness variation can be maintained within  $\pm 3\%$ .

The first method for providing uniform convection conditions uses a substrate holder of carousel type as shown in Fig. 6. The particular holder shown was constructed for plating silicon wafer substrates 1¼ in. to 1½ in. in diameter. It consists of two Teflon wheels and a Teflon shaft with stainless steel core. Grooves were cut in both wheels to hold the substrates vertically as shown in the figure. Silicon wafers were mounted on suitable supporting plates such as high density alumina or quartz using polypropylene as the mounting material. Blank supporting plates were placed in empty positions in the holder to obtain identical agitation conditions regardless of the number of substrates being plated. The assembled holder was connected to a motor and rotated with periodic reversal to obtain uniform thickness distribution.

The second method is more suitable for plating a larger number of substrates (up to 60) in one run. In this method, substrates are placed vertically in a holder in a radial array, and the holder is connected to a motor

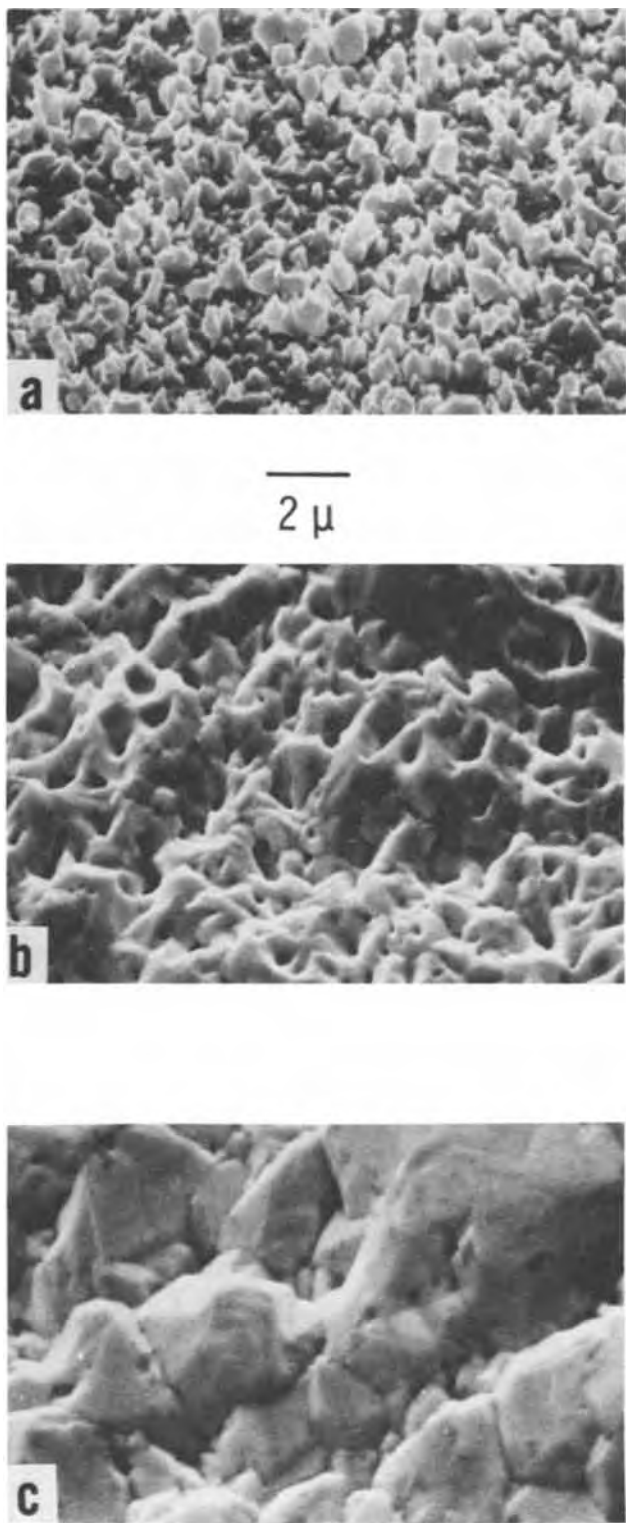


Fig. 4. Morphology of 2  $\mu$ m thick electroless gold deposits. (Substrate, evaporated Au/Ti/glass.) a, Bath A except 0.0025M  $\text{KAu}(\text{CN})_2$ , no agitation, 75°C. b, Bath A (0.02M  $\text{KAu}(\text{CN})_2$ ), no agitation, 75°C. c, Bath A (0.02M  $\text{KAu}(\text{CN})_2$ ), vigorous agitation, 75°C.

through a flywheel in such a way that it moves up and down during plating.<sup>2</sup> A photograph of the equipment constructed for plating silicon wafers with diameter up to 2 in. is shown in Fig.7. The substrate holder used in this particular apparatus was a commercially available Fluoroware wafer carrier fitted with a specially constructed Teflon shaft with steel core.

<sup>2</sup>It should be noted that the principle of vertical oscillatory plating is more readily adaptable to the scale-up for plating large area substrates such as ceramics (3 $\frac{3}{4}$  in. x 4 $\frac{1}{2}$  in.).

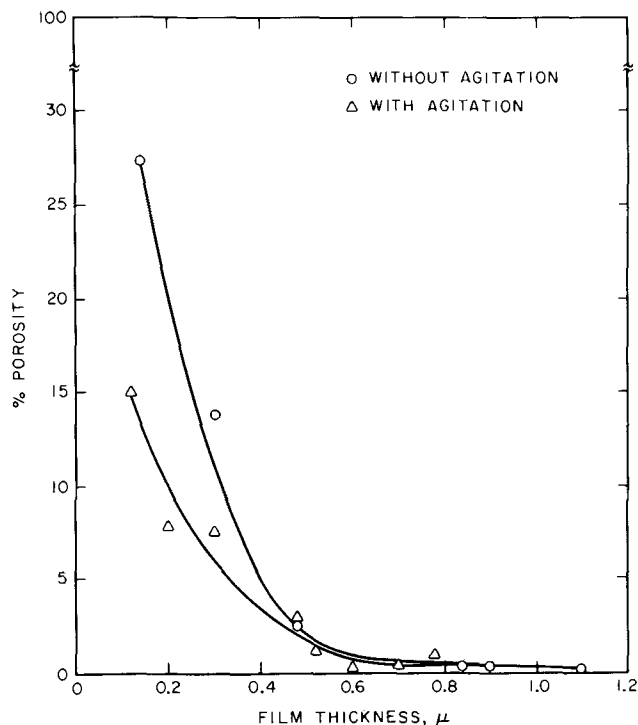


Fig. 5. Effect of agitation on deposit porosity. (Bath A, 75°C, Cu/Ti/alumina substrate).

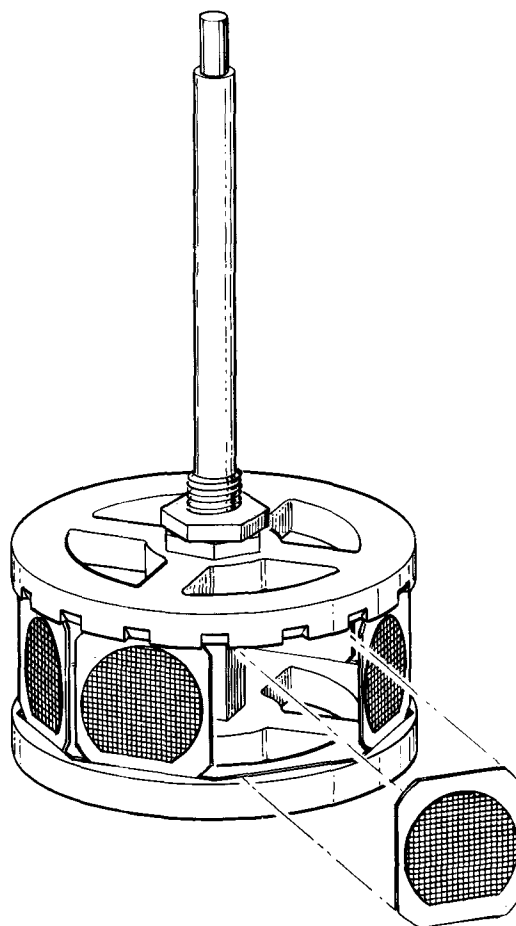


Fig. 6. "Teflon" rotating substrate holder for silicon wafer plating.

Both methods are equally satisfactory for obtaining thick deposits (*i.e.*, >10  $\mu$ m thick) with no significant thickness variation at different locations on a substrate. However, there is a tendency for some thickness non-uniformity to occur on fine line patterned substrates



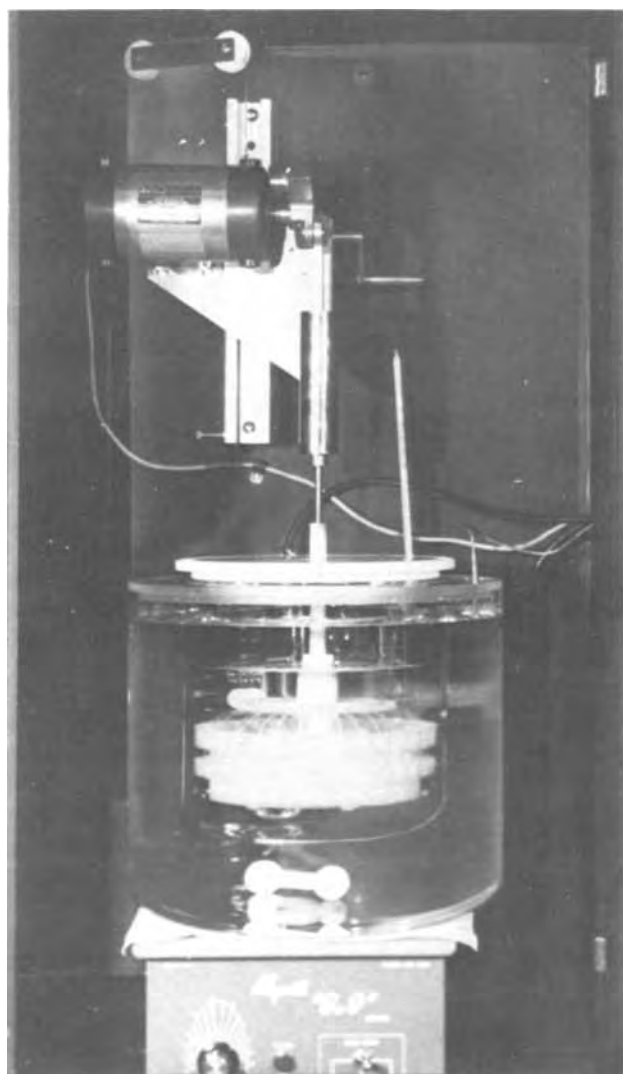


Fig. 7. Front view of vertical oscillatory plating apparatus for silicon wafer plating.

when the plating is carried out to only a few microns in thickness. The substrates used to study this effect were oxidized silicon wafers with suitable patterns of evaporated Ti(750Å)/Pd(1000Å) which were formed either by deposition through a metal shadow mask or by photolithography and etching. The plating was performed in bath B (Table I) at 70°C. Figure 8 shows a plot of deposit thicknesses at the edge and center of 75  $\mu\text{m}$  wide lines against plating time for the vertical oscillatory plating. It is seen that deposits with a center thickness of 10.5–11.5  $\mu\text{m}$  with less than 1  $\mu\text{m}$  high edges are formed in 2 hr. Also noted in this figure is the fact that the edges form in the very early stages of plating, and their height increases only slightly with plating time. Therefore, the edge build-up is relatively more significant for thinner deposits. For example, the edge of 2  $\mu\text{m}$  deposits is 25% higher than the center, whereas this number becomes only 7% for 11  $\mu\text{m}$  deposits. Similar results are obtained with the rotational equipment.

It was found that the thickness uniformity of thin deposits can be greatly improved by plating at a slower rate in a bath containing a larger concentration of  $\text{KAu}(\text{CN})_2$ . The thickness uniformity of deposits plated in bath C (Table I) at 70°C using the rotational equipment is illustrated in Fig. 9. It is seen that at the 2  $\mu\text{m}$  level the edge nonuniformity remains within 10%. It is quite clear also from this figure that the edge build-up to a certain height occurs in the very early stages of deposit growth, and that this height does not change much with plating time. The cause of this

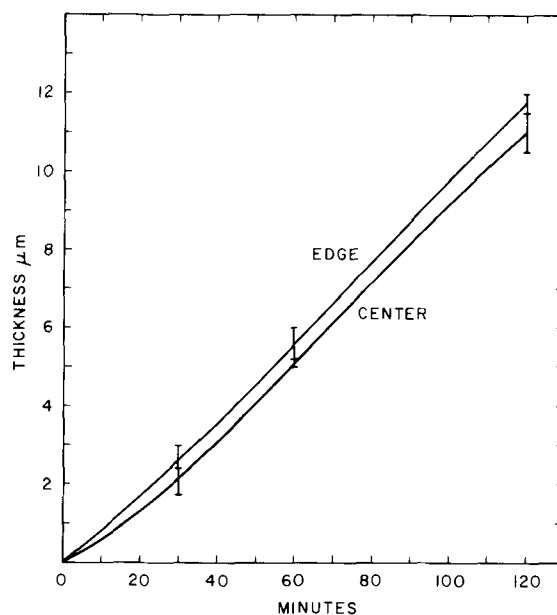


Fig. 8. Deposit thicknesses at edge and center of 75  $\mu\text{m}$  wide lines vs. plating time. (Bath B, 70°C, vertical oscillatory plating.)

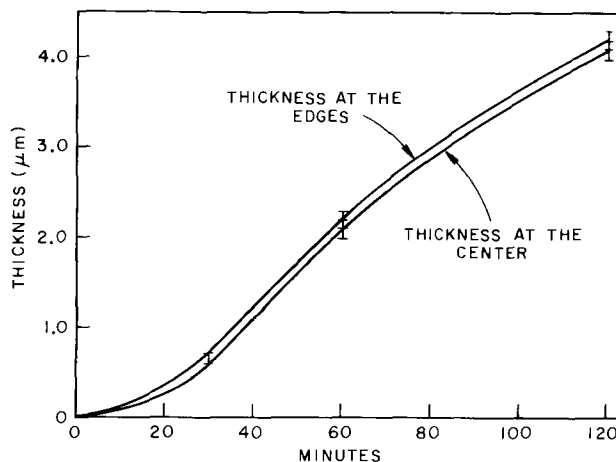


Fig. 9. Deposit thicknesses at edge and center of 75  $\mu\text{m}$  wide lines vs. plating time. (Bath C, 70°C, rotational plating.)

phenomenon is not fully understood at the present time, but conceivably it may be related to the effect of geometry on the initial adsorption of reacting species or the recently discovered effect of crystallographic orientation on plating rate (9). The fact that the edge height changes little as the plating proceeds indicates that the mass transport condition is, on the average, quite uniform.

#### Line Resolution

Information on line resolution is essential in plating substrates with fine line patterns. As long as deposits are not constrained to grow vertically, i.e., by photoresist, they also grow laterally to widen the original lines and narrow the spacing between them. The line resolution was determined using oxidized silicon substrates with Ti/Pd Ealing high resolution test patterns. Bath B and the rotational equipment were used. Plating was carried out for various lengths of time, the deposit thickness was measured with a Dektak instrument, and the set of smallest lines resolved was determined by optical and scanning electron microscopy. The results are tabulated in Table II. A scanning electron micrograph showing the resolution attained at 25 min is shown in Fig. 10. From the resolution data it can be calculated that the lateral growth was only about 60% of the perpendicular growth.

Table II. Line resolution

Plating time (min)	Thickness <sup>(a)</sup> ( $\mu\text{m}$ )	Width and spacing of smallest set of bars resolved ( $\mu\text{m}$ )
100-110	11-13	12.6 <sup>(b)</sup>
50	5.2-5.6	6.3 <sup>(c)</sup>
25	1.8-2.2	2.5

<sup>(a)</sup> Measured at center of 25  $\mu\text{m}$  bars.

<sup>(b)</sup> 10  $\mu\text{m}$  bars resolved except at ends.

<sup>(c)</sup> 5  $\mu\text{m}$  bars resolved except at ends.

The slower lateral growth is beneficial in the application of the electroless gold process on substrates with patterns containing narrow spacings. In one application (10) a transistor structure with initial line spacing of 1.3  $\mu\text{m}$  was successfully plated with 7000Å of electroless gold. It should be emphasized, however, that the success of such critical applications is greatly dependent on the cleanliness of substrate surface. For example, if the initial pattern of catalytic metal is generated by photolithography and etching, the areas where the metal is etched off must be completely free of metal and organic residues.

### Some Considerations Relevant to Scale-Up and Waste Disposal

The vertical oscillatory plating apparatus described in a previous section (Fig. 7) is capable of handling thirty 2 in. silicon wafers in 2 liters of solution if one wafer is placed into each slot. This capacity can be doubled, of course, by placing two substrates back to back in a slot. With such a large number of substrates a significant decrease in the concentration of bath constituents occurs during plating. For example, a typical 2 in. silicon wafer plated in this laboratory had a plating area of about 1  $\text{cm}^2$  and required a gold thickness of 12  $\mu\text{m}$ . Deposition onto 30 of these wafers requires a total of 0.7g of gold. On the other hand, 2 liters of plating solution (bath B) contains 1.18g gold. Thus, the amount of gold depleted at the end of the plating run is 59%. In order to learn whether such depletion causes any significant change in plating rate, experiments were run with a suitable number of wafers blanket coated with Ti/Pd in addition to one patterned wafer. The depletion percentage was calculated from the weight gain of the wafers and the initial quantity

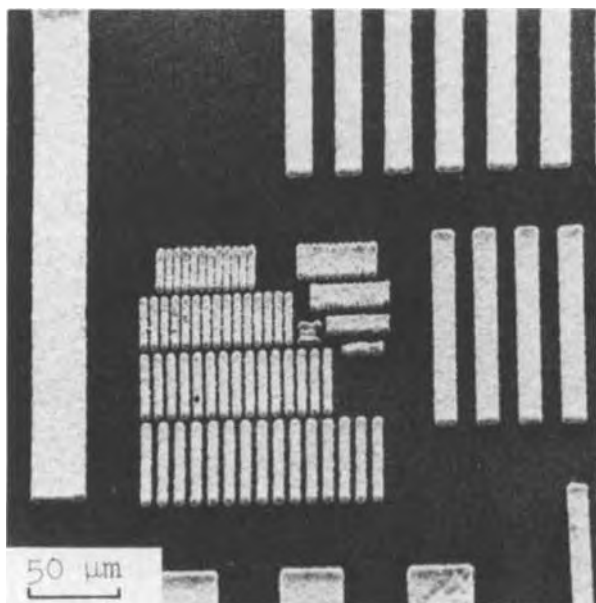


Fig. 10. Scanning electron micrograph showing line resolution after 25 min of plating. (Bath B, 75°C, rotational plating, gold thickness 2  $\mu\text{m}$ .)

of gold present in the solution. Figure 11 shows a plot of plating rate in  $\mu\text{m}/\text{hr}$  calculated from the gold thickness achieved in 2 hr on 75  $\mu\text{m}$  wide lines, vs. the percentage depletion of gold at the end of the plating time. It is seen that the plating rate at 83% gold depletion is only about 10% less than that at 1.5% depletion. In a separate series of experiments using copper sheet substrates, a sharp drop in plating rate was observed only after 95% of gold had been depleted. The dashed portion of the curve in Fig. 11 was drawn based on this information. The result indicates that under the conditions assumed for this evaluation, it would be possible to plate up to 45 wafers without a significant decrease in plating rate. For plating a larger number of substrates or a larger plating area, it would be necessary to increase the gold concentration or solution volume in order to avoid the depletion effects. An alternative method would be to replenish the bath with  $\text{KAu}(\text{CN})_2$  solution either continuously or periodically during plating.

As far as the depletion of borohydride is concerned, it has already been shown (3) that the amount of borohydride consumed for the plating reaction is negligible as compared to the large excess borohydride present in the bath, and that the loss of borohydride can be regarded as being entirely due to hydrolysis (4). The possibility of operating the bath with periodic replenishment of  $\text{KBH}_4$  has been discussed in the previous paper (3).

Waste disposal of spent solutions must be considered before the process is used on a large production scale. Gold can be recovered readily as metal by one of the three methods: (i) precipitation of spongy gold powder by heating to a temperature above 90°C followed by filtration; (ii) continuing electroless deposition on a large area substrate until all gold is plated out; (iii) electroplating gold. Addition of  $\text{KBH}_4$  may be required to carry out method (i) or (ii). Method (ii) is recommended for treating solutions containing relatively small concentrations of gold. Method (iii) (electrolytic method) is suitable for recovering gold from more concentrated solutions because the deposition rate can be increased to a much higher level. The solution left after gold recovery can be treated by the standard alkaline chlorination process for destruction of cyanide ions to  $\text{CO}_2$  and  $\text{N}_2$ . This process also oxidizes  $\text{BH}_4^-$  to borates. In order to keep the boron content of the final waste sufficiently low, dilution will be necessary before disposal.

### Summary and Conclusions

1. Two bath formulations are recommended for obtaining deposits with optimal properties: bath B (Table I) for fast plating of thick ( $>5 \mu\text{m}$ ) deposits, and bath C for forming thin (1-3  $\mu\text{m}$ ), uniform deposits. Both baths can be stored as 5 $\times$  concentrated stock solutions at room temperature. These baths yield pure gold deposits at rates of 5 and 2  $\mu\text{m}/\text{hr}$ , respectively, at 70°C with agitation.

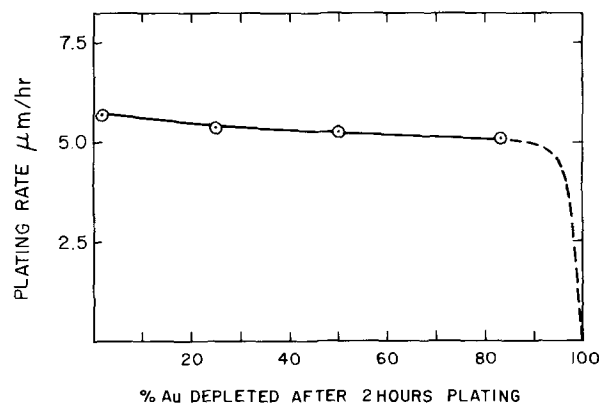


Fig. 11. Effect of gold depletion on plating rate. (Bath B, 70°C, vertical oscillatory plating.)

2. Nickel, cobalt, and ferrous ions cause bath instability and/or a decrease in plating rate; therefore, they should not be present. Copper does not show such effects.

3. Polyethylene is not compatible with the bath due to a chemical instability and can impair the quality of the deposit, whereas polypropylene is stable.

4. Water used to prepare the plating solution should be free of organic impurities when thickness uniformity is important on fine line patterns.

5. Bath agitation is beneficial. It increases plating rate, decreases porosity of deposits  $<1 \mu\text{m}$  thick, and eliminates nodule formation. Hardness and electrical resistivity are not affected by agitation.

6. Two methods of agitation suitable for obtaining uniform deposits are: rotational method with periodic reversal and vertical oscillatory method. Both methods give equally uniform deposits at essentially the same rate, but the vertical oscillatory method is more suitable for large scale operations. Under optimal conditions the thickness nonuniformity across a substrate can be maintained within 3%. On patterned substrates these conditions will maintain any edge build-up on fine lines within 10% over the thickness range of 1-12  $\mu\text{m}$ .

7. The rate of lateral growth of electroless gold deposit is about 60% of the rate of perpendicular growth.

8. Gold recovery and disposal of spent solution are simple and straightforward.

Various practical and fundamental aspects of the electroless gold plating process are now believed to be sufficiently characterized and understood. The process

has found a number of applications in this laboratory, and they will be described elsewhere.

#### Acknowledgment

The authors are grateful to T. A. Shankoff for etching Ti/Pd patterns, T. N. Stauber for evaporation of Ti/Pd, and R. Lieberman for information on effects of water contamination.

Manuscript submitted May 24, 1973; revised manuscript received Aug. 15, 1973. This was Paper 206 presented at the Miami Beach, Florida, Meeting of the Society, Oct. 8-13, 1972.

Any discussion of this paper will appear in a Discussion Section to be published in the December 1974 JOURNAL.

#### REFERENCES

1. Y. Okinaka, *Plating*, **57**, 914 (1970).
2. R. Sard, Y. Okinaka, and J. R. Rushton, *ibid.*, **58**, 893 (1971).
3. Y. Okinaka and C. Wolowodiuk, *ibid.*, **58**, 1080 (1971).
4. Y. Okinaka, *This Journal*, **120**, 739 (1973).
5. R. Sard, Abstract 134, p. 342, Electrochemical Society Extended Abstracts, Fall Meeting, Cleveland, Ohio, October 3-7, 1971.
6. R. Sard, *This Journal*, **117**, 1156 (1970).
7. H. I. Schlesinger, H. C. Brown, A. E. Finholt, J. R. Gilbreath, H. R. Hoekstra, and E. K. Hyde, *J. Am. Chem. Soc.*, **75**, 215 (1953).
8. R. Sard, Y. Okinaka, and H. A. Waggener, *This Journal*, **121**, 62 (1974).
9. R. Sard and B. C. Wonsiewicz, Unpublished results.
10. Y. Okinaka and R. Sard, To be published.

## Electroless Gold Beam Lead Plating

R. Sard,\* Y. Okinaka,\*\* and H. A. Waggener

Bell Laboratories, Murray Hill, New Jersey 07974

#### ABSTRACT

The electroless gold plating process developed in this laboratory has been successfully applied to the fabrication of beam leads on silicon integrated circuits. This unique plating process selectively plates gold onto discrete patterned regions of a substrate at  $6 \mu\text{m/hr}$  with  $\leq 10\%$  thickness nonuniformity for thicknesses of 10-12  $\mu\text{m}$ . Beam lead patterns were formed either by vacuum evaporation of titanium followed by palladium through a metal shadow mask or by photolithography and etching. The compatibility of this processing with a number of other materials present on Si devices has been established. Beam lead structures have been characterized with respect to mechanical properties and found to meet or exceed system requirements. This process is shown to be capable of high yields and is an attractive alternative to conventional methods of fabricating beam leads.

Gold beam leads (1) on silicon integrated circuits are conventionally formed by electroplating through a photoresist pattern onto a base metal such as Ti/Pd or Ti/Pt. As shown schematically in Fig. 1A, a minimum of six basic processing steps are involved: (i) titanium and palladium (or platinum) evaporation, (ii) photoresist application, exposure and development, (iii) gold plating, (iv) photoresist removal, (v) palladium etching, and (vi) titanium etching. Many variations of this processing have evolved, such as etching the palladium before plating then using a second photoresist application to define the beams, or by using back sputtering techniques in place of etching to remove the unwanted metals. All such variations are inevitably more complex than the scheme depicted in Fig. 1A, although they have in some instances (2) been shown to yield improved results.

\* Electrochemical Society Active Member.

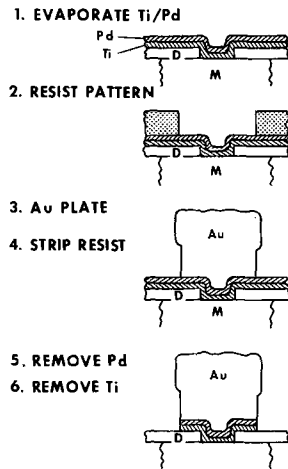
\*\* Electrochemical Society Life Member.

Key words: electroless gold plating, beam lead, silicon integrated circuit.

A program was undertaken to develop a simpler procedure based on the electroless gold process developed in this laboratory (3). This process is known to produce gold deposits with satisfactory properties (4) (i.e., conductivity, hardness, structure and thermo-compression bondability) for device applications. Moreover, this process will only deposit gold on catalytic regions of a substrate and is therefore compatible with all-additive processing (i.e., no metal etching is required). In its simplest form, such a beam lead process consists of the following steps (which are illustrated schematically in Fig. 1B): (i) alignment of a metal shadow mask with apertures corresponding to the regions where beam leads are desired, (ii) Ti/Pd (or Ti/Pt) evaporation, and (iii) electroless gold plating.

In addition to the obvious reduction in the number of processing steps, the electroless gold process entirely eliminates the possibility of gold "underplating" or other complications associated with plating through a

## A. CONVENTIONAL ELECTROPLATING



## B. ELECTROLESS GOLD

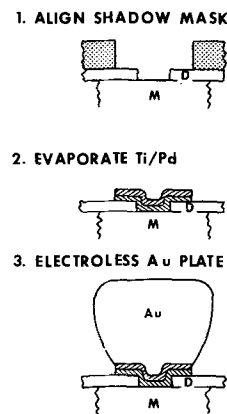


Fig. 1. Schematic representation of beam lead processing sequences. Regions M and D represent contact metallization and top dielectric, respectively. A, electrolytic gold plating; B, electroless gold plating.

patterned photoresist. It does, however, require that the regions of the substrate which are not to be plated, i.e., the intrachip area and the regions between the beams, be covered with a suitable material such as a dielectric.<sup>1</sup>

Fabrication of electroless gold beam leads by this procedure is well suited to the structure shown schematically in Fig. 2. In a sealed structure of this type, the contact metallization, M, is covered by a top dielectric, D, and is accessed through via windows. Test structures of this type were fabricated using oxidized (4000Å SiO<sub>2</sub>) wafers that received two main processing steps prior to beam leads: (i) contact metal deposition (sputtered tungsten was used primarily in this work) and patterning by photolithography and etching and (ii) dielectric deposition and pattern definition of contact windows. The choice of this fabrication method follows directly from the properties of the metals, tungsten and gold. Tungsten cannot be gold plated directly and, from a corrosion standpoint, this combination is relatively poor (5). Hence these metals are not exposed to the same environment (Fig. 2).

After a brief description of the plating method used, the compatibility of various materials (dielectrics and metals) with this processing will be discussed. The final sections of this paper will present specific results relating to beam lead geometry and the physical and mechanical properties of electroless gold beam leads, both for the test vehicle described above and for ran-

<sup>1</sup> An alternative to this procedure, which more closely resembles Fig. 1A, is to deposit Ti/Pd everywhere then pattern and etch Pd only, leaving the Ti as a mask since it is inert in the plating solution. Two important requirements for high yield processing in this case will be (i) residue-free Pd etching and (ii) pinhole free Ti. This approach is feasible but will not be discussed further in this paper.

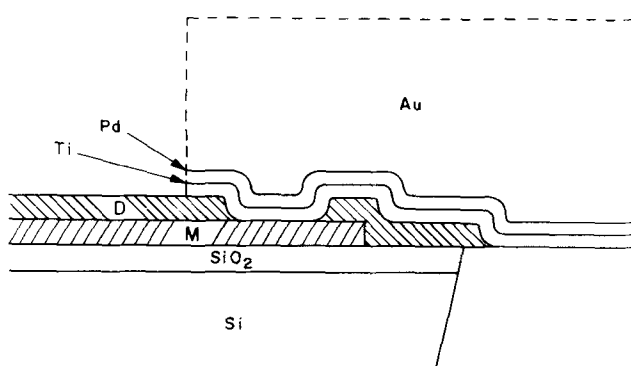


Fig. 2. Schematic representation of beam lead cross section

dom access memory devices (6) to which this processing has been applied.

## Beam Lead Processing

The first step of the beam lead processing scheme outlined in Fig. 1B is the evaporation of titanium and palladium through a metal shadow mask which was previously mounted in a fixture (Fig. 3), aligned, and held in place against the wafer.<sup>2</sup> The mask material used, most often, was molybdenum, fabricated from 0.0005 in. or 0.001 in. thick material. This assembly (Fig. 3) was placed in a conventional vacuum station, either e-gun or filament, pumped  $<10^{-6}$  Torr and then coated with 750Å Ti and 1000Å Pd. After removing from the holders, the patterned wafers were mounted on quartz carrier plates with polypropylene and placed in a carousel-type apparatus using the procedures outlined in Ref. (7).

The electroless gold solution formulation was as follows:

KAu(CN) <sub>2</sub>	0.003M
KCN	0.1M
KOH	0.2M
KBH <sub>4</sub>	0.2M

The plating rate of this solution is 6 μm/hr at 70°C with forced convection provided by rotating the carousel at 150 rpm with a periodic reversal every 10 sec (7). All plating runs were of the batch type. The amount of gold which would be plated out due to beam lead processing of eight wafers is estimated to be less than 40% of that in solution. Separate experiments have shown that the plating rate and deposit structure are unaffected by this amount of depletion for the conditions reported.

## Compatibility of Materials

A number of materials, both metals and dielectrics, that might be used in SIC's were investigated from the standpoint of their compatibility with electroless gold processing.

**Metals.**—Previous studies (3, 7) have reported on the three qualitatively different types of behavior exhibited by metals in electroless gold solution: (i) the directly catalytic noble metals, (ii) the marginal transition metals which begin plating by displacement, and (iii) the inert refractory metals. The reason for using a binary combination (e.g., Ti/Pd) is because the directly catalytic noble metals have rather poor adhesion to dielectric surfaces, whereas the inert metals in category (iii) adhere strongly to such substrates.

**Dielectrics.**—The stability of various dielectrics was determined by making thickness measurements on

<sup>2</sup> Alternatively, beam lead patterns were defined by blanket evaporation of Ti/Pd followed by standard photolithography and etching procedures. This approach gave similar results, but was not used as often because of its greater complexity.



Fig. 3. Photograph of shadow mask and holder

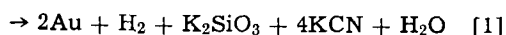
Table I. Stability of dielectrics

Dielectric	Dissolution rate, A/hr
Si <sub>3</sub> N <sub>4</sub> , deposited at 875°C	<30
Si <sub>3</sub> N <sub>4</sub> , deposited at 685°C	100
SiO <sub>2</sub> , deposited at 875°C	100
SiO <sub>2</sub> , thermal 1050°C	250
SiO <sub>2</sub> , sputtered RT	550
SiO <sub>2</sub> + 4% P <sub>2</sub> O <sub>5</sub> , 350°C	2000
SiO <sub>2</sub> + 4% P <sub>2</sub> O <sub>5</sub> , sintered at 700°C/Ar	900
Al <sub>2</sub> O <sub>3</sub>	<50

patterned wafers with a stylus instrument (Dektak, Sloan Instrument Company) before and after exposure to the electroless gold plating conditions. The films used and results obtained are listed in Table I. It is evident from these data that the dissolution rate of the films investigated ranges from a negligible value of <50 A/hr for Si<sub>3</sub>N<sub>4</sub> deposited at 875°C and Al<sub>2</sub>O<sub>3</sub>, to a considerable value of 2000 A/hr for a low temperature P-glass (SiO<sub>2</sub> + 4% P<sub>2</sub>O<sub>5</sub> glass deposited at 350°C).

The optimum choice of dielectric depends mainly on the specific structure being fabricated. Refractory contact metallizations such as tungsten can withstand high temperature processing. Silicon nitride was used primarily in this work. The Si<sub>3</sub>N<sub>4</sub> was patterned using the oxide etch mask technique (8), and, more often than not, the SiO<sub>2</sub> cap was left in place during the subsequent beam lead plating operations.

**Silicon.**—Exposure of bare Si to an alkaline solution containing KAu(CN)<sub>2</sub> is known (9) to result in the deposition of gold by displacement



This fact requires proper masking of Si on the backs of wafers by an appropriate mounting technique (7), otherwise, the high negative potential of the displacement reaction will cause an abnormally fast deposition rate on those beams electrically connected to the silicon bulk. The effects of potential on electroless gold plating are discussed in more detail below.

### Beam Lead Geometry

Neither electroless gold nor any other autocatalytic system for metal deposition has yet been used for an application comparable to the present one which requires uniform plating (within  $\pm 0.0001$  in. or 2.5  $\mu\text{m}$ ) on all of the  $\sim 6000$  discrete regions which must be plated on each substrate. Consequently, it was believed necessary to thoroughly evaluate the final geometry of electroless gold beam leads. The techniques used in this evaluation were optical and scanning electron microscopy and thickness profile measurements.

**Lateral spreading.**—The proper design of beam leads should make allowance for lateral spreading in order to prevent shorts between adjacent beams. It was previously shown with patterned substrates formed by photolithography that lateral growth is about two-thirds of the thickness (7). This result was confirmed in the present study.

**Thickness uniformity.**—The thickness uniformity of electroless gold beam leads was found to be typically, within  $\pm 10\%$  for all variations, i.e., for edge build-up on a given beam, beam-to-beam and wafer-to-wafer variations. To obtain this degree of uniformity, it is necessary to eliminate those organic impurities from the system which can adversely affect plating uniformity as discussed in Ref. (7).

**Potential effects.**—If sources of biasing potentials exist on a substrate being plated, then the thickness uniformity quoted above will not be obtained. The reason for this is that the electroless gold deposition reaction occurs at a mixed potential governed by the

cathodic reduction of Au(CN)<sub>2</sub><sup>-</sup> and the anodic oxidation of BH<sub>3</sub>OH<sup>-</sup> (an intermediate species formed during hydrolysis of KBH<sub>4</sub>) (10). Thus, anything that alters the potential of the surface is expected to affect the rate of deposition. The dependence of deposition rate on potential can be estimated from the current-potential curves shown in Fig. 4. These curves were obtained with a rotating platinum disk electrode plated with electroless gold using a solution of slightly different composition to the one described above. The result, however, is quite general. Curve 1 was obtained by slowly scanning the potential (0.56 mV/sec) in the anodic direction while the current was being recorded. The electrode was rotated at 1600 rpm. This speed was chosen because previous results indicated that under these plating conditions a deposition rate of about 6  $\mu\text{m/hr}$  is observed which is equal to the rate obtained for beam lead plating in the carousel apparatus. In Fig. 4 the electroless deposition occurs at the potential where curve 1 intersects the abscissa (-0.80V). The rate of electroless deposition corresponds to the current measured at this potential on curve 2, which was obtained in the absence of borohydride (broken line). If the potential of the surface at which gold deposition is taking place is altered for some reason, the deposition rate should vary according to curve 2. The current-potential relationship in the range shown is essentially linear with a slope  $0.0258 \text{ mA} \cdot \text{cm}^{-2} \cdot \text{mV}^{-1}$ , which corresponds to a rate variation of 0.97  $\mu\text{m/hr}$  for a potential change of 10 mV.

As mentioned earlier, significant potential shift can be brought about if bare silicon is exposed to the solution and the region being plated is connected to the silicon bulk. A large thickness variation attributable to this cause was observed in one instance. On this test wafer most of the beams were 10-11  $\mu\text{m}$  thick, but there were several very thick ( $\sim 25 \mu\text{m}$ ) beams. Such thick beams always occurred in pairs; namely, they were interconnected by conductor metallization. An electrical probe test revealed that the thick beams were all in direct electrical contact with the silicon, indicating that the dielectric material had suffered breakdown under the thick beams or interconnecting tungsten films. It was further found that portions of the back of this wafer were covered with loosely adherent gold deposits which appeared to have formed by the displacement reaction between exposed silicon and

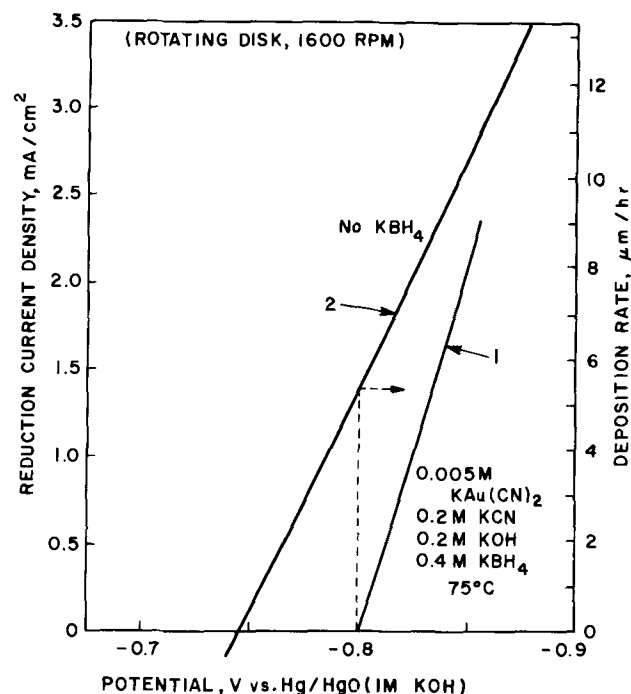


Fig. 4. Current-potential relationship for electroless gold system, obtained at rotating disk electrode.

$\text{Au}(\text{CN})_2^-$  (reaction [1]). In view of the high reactivity of Si in alkali [ $\text{SiO}_3^{--} + 3\text{H}_2\text{O} + 4e^- = \text{Si} + 6\text{OH}^-$ ,  $E^\circ = -1.7\text{V}$  (11),  $\text{H}_2 + \text{SiO}_3^{--} + \text{H}_2\text{O} + 2e^- = \text{Si} + 4\text{OH}^-$ ,  $E^\circ = -2.6\text{V}$ ] and the deposition potential of electroless gold ( $-0.6$  to  $-0.9\text{V}$  vs. NHE) (10), it follows that if beams are in direct contact with silicon and the back side of the wafer has silicon directly exposed to the solution, the deposition potential of such beams must be more negative than that on beams electrically isolated from the silicon. From Fig. 4 it can be deduced that a 72 mV negative shift is sufficient to cause the anomalously high deposition rate observed. It should be noted that beams in actual integrated circuits are not electrically isolated from silicon; therefore, it is important that the back of the wafer be protected from the direct exposure of silicon to the plating solution. This also applies to edges of the silicon. As mentioned previously, and discussed more fully in Ref. (7), the method used to mount the wafers is adequate for this purpose.

As another source of potential, which is extremely important on S.I.C.'s is the photovoltaic effect across a p-n junction. The effect of photovoltage on gold deposition by displacement on silicon has already been described by Silverman and Benn (12). The difference in plating rate of electroless nickel on p- and n-type surfaces of silicon at p-n junctions under strong illumination is also known (13). The magnitude of photovoltage is, of course, dependent upon the conversion efficiency of the particular p-n junction and lighting conditions. The potential across a p-n junction during plating can be much less than the open-circuit value because of the low impedance of the electrochemical process. On the basis of the current-potential curves of Fig. 4, it can generally be stated that if the photovoltage causes a potential shift at the Ti/Pd pads in solution of about 6 mV, the difference in plating rate across the p-n junction will be about 10%. An illustration of how this effect can influence device results is shown in Fig. 5 where the white leads (No. 4, 5) make contact to regions of an IGFET test structure that were positively biased during plating in ordinary room light. Additional evidence for this effect is the fact that the negatively biased beam (No. 8) was plated at a rate of about  $12 \mu\text{m}/\text{hr}$ , which is twice as fast as the normal rate for beams not biased by the substrate (No. 1-3, 6, 7). The effect can, of course, be eliminated should it occur for a particular device simply by plating in the dark.

### Process Yields

A pilot line operation has been set up to implement the processing of electroless gold beam leads on silicon integrated circuits such as a random access memory (6). The factors discussed above which can affect processing yield have been brought under control. It can be stated that this process gives reproducible results

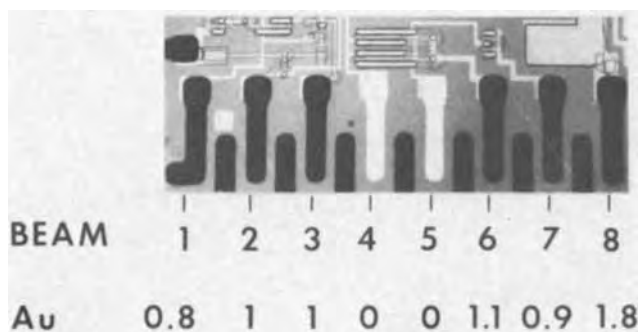


Fig. 5. Photomicrograph of electroless gold beam leads on one side of an IGFET test chip. Beams 4 and 5 are unplated due to positive bias from light incident on p-n junctions. The thickness data shown were normalized based on the standard plating rate. Beam 8 was negatively biased and plated twice as thick as unbiased beams.

with essentially no yield loss except for that due to the shadow mask which is nearly zero. Experience with this process has shown that typical mask defect densities are about  $0.1 \text{ cm}^{-2}$ . An example showing a portion of the beam leads on a finished memory chip is shown in Fig. 6.

### Physical Characteristics of Electroless Gold Beam Leads

*Deposit appearance and morphology.*—The appearance of electroless gold deposits has previously been shown (4, 13) to depend on the morphology of surface features on the scale of approximately  $1 \mu\text{m}$ . The nature of these features is determined by the deposition conditions and they have been classified on the basis of scanning electron microscopic studies as follows: (i) outward growth type; (ii) lateral growth type with weblike features, or (iii) lateral growth type with faceted structure. The beam leads plated under the conditions described above have the characteristic faceted structure illustrated in Fig. 7. This scanning electron micrograph indicates that the deposit surface has a roughness of approximately  $1 \mu\text{m}$  due to the grain structure. This result is in agreement with the fine detail in the profile traces used to obtain thickness data.

*Thermocompression bonding, hardness, and related properties.*—Thin electroless gold deposits are known to be highly suitable for thermocompression (T/C) bonding (4) and relatively high in purity (3) ( $>99.9\%$  Au). Furthermore, they exhibit bulk conductivity and have been classified as being "soft gold" deposits (3, 4).

Although none of these properties is expected to change under the conditions used to plate beam leads,

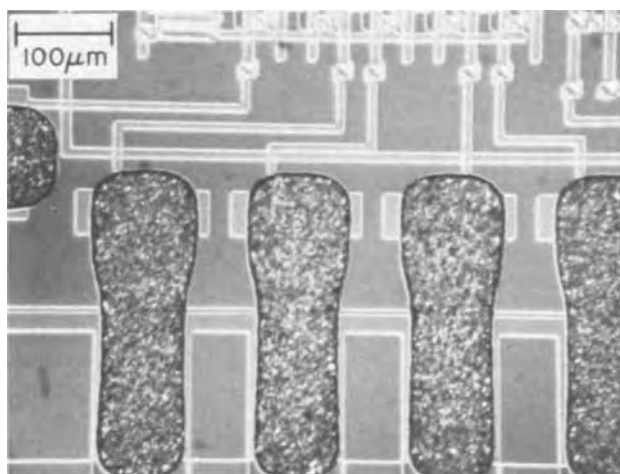


Fig. 6. Photomicrograph of electroless gold beam leads on random access memory chip.

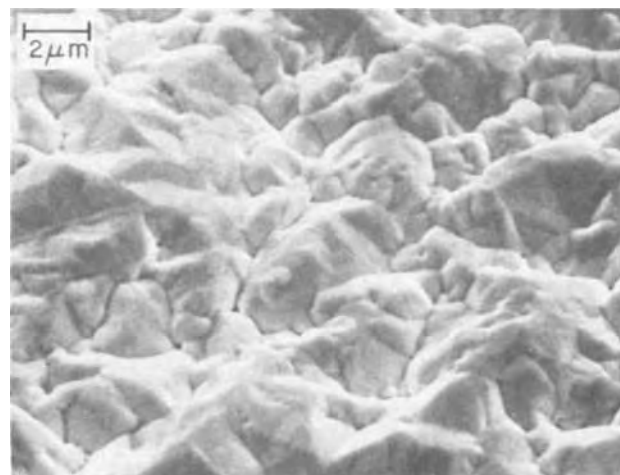


Fig. 7. Scanning electron micrograph showing surface topography of electroless gold beam lead.

it was possible to evaluate the most important ones from a device standpoint simply by processing the slices through a chip separation procedure consisting of mounting the wafer face down, thinning the silicon, back aligning a photoresist pattern, and Si etching to open up the grid areas between chips and expose the ends of the beam leads. Separated chips were T/C bonded to patterned ceramics for electrical, mechanical, and environmental tests. To date, no bonding failures have been observed for these chips. Furthermore, blow tests, which subject bonded chips to pulsed air blasts have shown that these chips can withstand a large number of cycles, typically 50-100 without failure. Standard beam lead devices are required to pass 3 cycles without failure in this test.

Indentation hardness measurements were carried out on the underside of beams (i.e., in the grid area) of etched apart chips that were still supported by sapphire and imbedded in mounting material. Such measurements approximate the techniques used previously for thinner, larger area deposits (4). Typical Knoop hardness values of 50-60 were obtained at 5g load, which agrees well with earlier results and is consistent with the good ductility implied by the T/C bonding and blow test results.

*Peel tests of electroless gold beam leads.*—A detailed study is now underway (15) to characterize the mechanical behavior of beam lead structures of the type shown in Fig. 2 using the 90° peel test. In this test the beams are bent up and pulled, one at a time, at 90° to the chip. It has been found that beams which fail this test, i.e., those with fail values below 2-3g, may cause device failures during subsequent packaging, life testing, or in service. Some preliminary results with electroless gold beam leads on memory chips are shown in Fig. 8. These data, which are plotted as a fail strength distribution, indicate that the mechanical integrity of the structure is satisfactory for device purposes. A more comprehensive report dealing with the effects of processing and design variables on the mechanical properties of this structure is presently being completed.

### Summary

Electroless gold plating can be used to selectively plate discrete geometries to any thickness required for device processing. This unique capability has led to the development of a new method for fabricating beam leads. The main advantage of this method is its relative simplicity which results from the elimination of the photoresist and etching operations used in conventional processing.

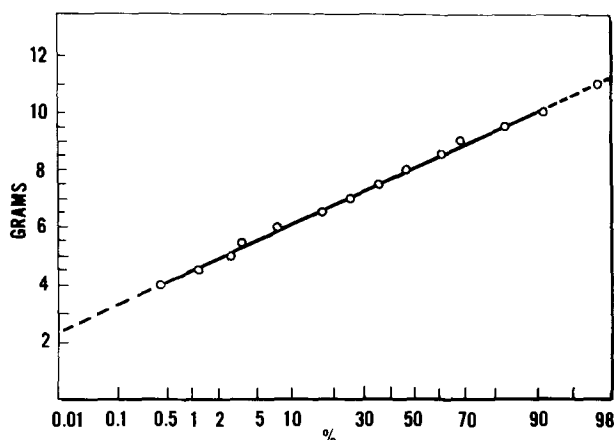


Fig. 8. Fail strength distribution plot for electroless gold beam leads on memory chips subjected to 90° peel tests.

The vehicle used to demonstrate this new approach was a dielectric encapsulated, tungsten metalized tester chip with beam lead patterns formed by vacuum evaporation of Ti/Pd through a shadow mask. These procedures have also been applied to the plating of beam leads on random access memory chips in a pilot line operation.

Some specific results of this work are as follows:

1. Beam leads are plated at 6  $\mu\text{m/hr}$  with a thickness uniformity of  $\pm 1 \mu\text{m}$  at the 12  $\mu\text{m}$  level.
2. The yield of the beam lead processing is mask limited with typical defect densities  $\sim 0.1 \text{ cm}^{-2}$ . Ti/Pd metalization evaporated through a shadow mask proved to be a highly satisfactory technique for beam pattern definition on S.I.C.'s.
3. The compatibility of this processing with a number of metals and dielectrics has been established.
4. The effect of biasing potential on deposition rate is given. Two sources of potential which can lead to nonuniform plating of beams, namely, the photovoltaic effect and Si displacement are shown not to cause problems provided plating is carried out in the dark and the substrate does not have Si exposed to the solution.
5. The mechanical properties and T/C bonding of beam lead chips are satisfactory for device applications.

### Acknowledgment

The authors wish to express their gratitude to the following colleagues who either directly or indirectly, contributed to the success of this program: P. J. Boddy, W. H. Craft, L. D. Gardner, C. J. Graf, D. E. Koontz, R. Lieberman, A. E. Miller, T. S. Miller, W. D. Powell, T. F. Retajczyk, T. N. Stauber, D. R. Turner, and C. Wolowodiuk.

Manuscript submitted May 24, 1973; revised manuscript received Aug. 15, 1973. This was Paper 207 presented at the Miami Beach, Florida, Meeting of the Society, Oct. 8-13, 1972.

Any discussion of this paper will appear in a Discussion Section to be published in the December 1974 JOURNAL.

### REFERENCES

1. M. P. Lepselter, *Bell Syst. Tech. J.*, **XLV**, 233 (1966).
2. R. C. Miller, Abstract 228, p. 558, Electrochemical Society Extended Abstracts, Fall Meeting, Miami Beach, Florida, Oct. 8-13, 1972.
3. Y. Okinaka, *Plating*, **57**, 914 (1970).
4. R. Sard, Y. Okinaka, and J. R. Rushton, *ibid.*, **58**, 893 (1971).
5. J. A. Cunningham, C. R. Fuller, and C. T. Haywood, *IEEE Trans. Reliability*, **R19**, 182 (1970).
6. H. J. Boll and W. T. Lynch, Abstract 7.1, International Electronic Devices Meeting, Washington, D.C., Dec. 1972.
7. Y. Okinaka, R. Sard, W. H. Craft, C. Wolowodiuk and T. F. Retajczyk, *This Journal*, **121**, 56 (1974).
8. W. VanGelder and V. E. Hauser, *ibid.*, **114**, 869 (1967).
9. J. F. Pudvin and F. J. Biondi, in "Transistor Technology," F. J. Biondi, Editor, Vol. III, p. 103, D. Van Nostrand, Princeton, N. J. (1958).
10. Y. Okinaka, *This Journal*, **120**, 739 (1973).
11. W. M. Latimer, "Oxidation Potentials," 2nd ed., Prentice-Hall, Inc., Englewood Cliffs, N. J. (1952).
12. S. J. Silverman and D. R. Benn, *This Journal*, **105**, 170 (1958).
13. H. Iwasa, M. Yokozawa, and I. Teramoto, *ibid.*, **115**, 485 (1968).
14. R. Sard, Abstract 134, p. 342, Electrochemical Society Extended Abstracts, Fall Meeting, Cleveland, Ohio, Oct. 3-7, 1971.
15. R. Sard, L. D. Gardner, and W. S. Lindenberger, Unpublished results.



# Method for Forming a Printed Circuit by Photolysis of Silver Salt of Organic Acid

Hisao Tabei, Shigeo Nara, and Kentaro Matsuyama

Ibaraki Electrical Communication Laboratory,  
Nippon Telegram and Telephone Public Corporation, Tokai, Ibaraki, Japan

## ABSTRACT

A method for forming a printed circuit was carried out. The method comprises coating the surface of an insulating substrate with a solution of silver salts of organic acids in a mixed solvent consisting of alcohol, water, and ammonia to form a photosensitive layer thereon, exposing the layer to uv-light so as to deposit the metal silver on a pattern of a desired circuit, and carrying out the electroless plating on the pattern, whereby the deposited metal silver functions as the nuclei for the plating.

Printed circuit boards, heretofore, have been made by the so-called photoetching process which comprises forming a photoresist layer mainly comprising photosensitive resin on the surface of an insulating substrate with a copper foil top, laying a negative of a desired circuit pattern thereon, exposing the layer by the negative to light, processing the photoresist layer to develop the pattern and to remove the unexposed regions, and etching the copper foil so as to remove the regions of the copper foil corresponding to the unexposed regions. For this, the material loss is great since most of the copper foil is removed by dissolution, only required circuit regions being left. Also this method involves extremely complicated steps such as through-hole plating which effects connection of the circuit patterns on both surfaces, that is, the sensitizing, activating, and plating treatments of the through-hole wall are required for connecting. Therefore, this method requires much time and many processes and incurs low yield and high cost.

We investigated an entirely new method for forming a printed circuit utilizing a photochemical reaction, which is intended to eliminate the above-explained disadvantages of the prior art method.

Certain metal salts of organic acids liberate metal ions when irradiated with uv-light, and liberated metal ions turn to metal atoms as the result of reduction, and the formed metal atoms agglomerate (1-3). This result suggested to us a new method for forming the electrically conductive pattern on insulating substrates.

We investigated the new method which comprises coating the surface of an insulating substrate with silver salts of organic acids, exposing the layer to uv-light so as to deposit silver metal on a pattern of the desired circuit, and carrying out the electroless plating on the pattern, whereby the deposited silver metal functions as the nuclei for plating.

Most of our experiments have been made with the compound silver glutamate. In addition, a more limited experiment of the compound silver acrylate is discussed.

## Experimental

**Materials and effect of uv-light exposure.**—Silver glutamate and silver acrylate were prepared by the usual procedures. Each solution containing 25 ml of 0.02M monosodium L-glutamate or sodium acrylate was mixed with 25 ml of 0.02M AgNO<sub>3</sub> solution. The precipitates were filtered and air-dried at room temperature in the dark. Then 1.5g of silver glutamate was dissolved in 30 ml ammonia-ethanol solution (concentrated ammonia water: ethanol: water = 1:6:3 volume). Similarly 1g of silver acrylate was dissolved in 30 ml ammonia-ethanol solution. These solutions were preserved in polyethylene bottles in a refrigerator.

**Key words:** Silver salt of organic acid, photolysis, printed circuit pattern, electroless plating, silver glutamate.

Coatings on quartz slides were made by the following method. A few drops of the solution containing silver salt were placed on the quartz. After drying at 60°C, the solid adhered to the quartz strongly enough for the quartz to be handled without loss of solid. The coatings contained about 3 mg/cm<sup>2</sup> of silver glutamate and 2 mg/cm<sup>2</sup> of silver acrylate.

The uv spectra were obtained with a Hitachi spectrophotometer Type 124, and the Sakura densitometer Type PDA-60 was used for measuring transmission densities. The amount of silver metal was analyzed by the EDTA chelate titration technique (4). One milliliter of solution containing silver glutamate was pipetted in a dish with flat bottom and dried at 60°C. After exposure to uv-light with 251 nm wavelength, exposed silver glutamate was dissolved in aqueous ammonia (about 3% solution) and filtered. Then K<sub>2</sub>Ni(CN)<sub>4</sub> and MX indicator (Murexide) were added to the filtrate and titrated with 0.01M EDTA solution. Furthermore, 1 ml of solution containing silver glutamate was titrated without the procedures of drying, exposing, and dissolving. The ratio of both amounts of EDTA solution is the proportion of photolysis silver glutamate.

The irradiation source employed was the Nihon Bunko CRM-FA spectro irradiator.

The dark reaction of silver glutamate was examined using a vacuum oven.

**Forming the printed circuit.**—The steps in forming the printed circuit pattern are explained with reference to Fig. 1.

(A) Substrate preparation: The surface of an insulating substrate was cleaned and roughened as required to produce a clean and wettable surface.

(B) Sensitization: A solution layer containing silver salt of organic acid was painted on the surface and the substrate was dried at 60°C. A photosensitive layer was formed on the insulating substrate.

(C) Print (photo-image reaction): A circuit pattern negative was laid in contact with the substrate and it was uv-light exposed in air. Exposed regions of the photosensitive layer were blackened by photolysis, while the unexposed regions remained unchanged.

(D) Fix: On immersion into a mixed solution of sodium hydroxide and ammonium hydroxide (NaOH 40g. conc NH<sub>4</sub>OH 50 ml, water 950 ml), the unexposed regions of the photosensitive layer were dissolved and in the exposed regions, agglomerate silver metal remained insoluble.

(E) Metalization: The exposed regions were metalized by immersion in an appropriate electroless plating bath.

The irradiation source employed was a 250W high pressure mercury lamp (Ushio Uniark 250D). The distance between the sensitive layer and irradiation source was 15 cm.

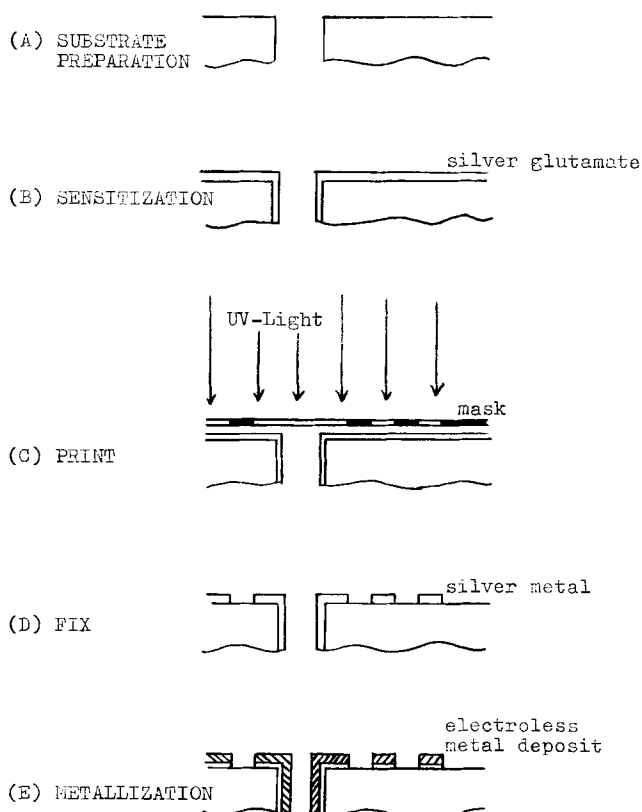


Fig. 1. Steps of method for forming printed circuit

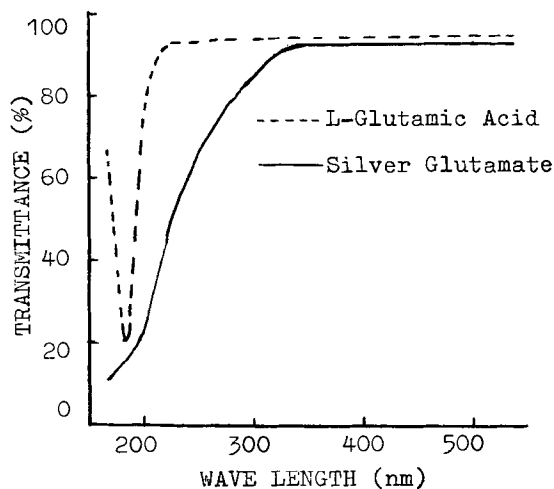


Fig. 2. UV-V spectra of L-glutamic acid and its silver salt

### Results and Discussion

**Materials.**—In Fig. 2 is shown uv spectra of L-glutamic acid and its silver salt ( $\text{HOOCCH}(\text{NH}_2)(\text{CH}_2)_2\text{COOAg}$ ). The L-glutamic acid shows peaking at about 190 nm, while its silver salt shows the absorption band at about 220 nm. Further, the spectra of acrylic acid and its silver salt were similar to that described above, that is, the absorption bands of silver salts are shifted to long wavelength. In general carboxylic acids show peaking at about 200 nm and it is considered that the absorption corresponds to carbonyl group. It can therefore be presumed that  $-\text{COOH}$  turns to  $-\text{COOAg}$ .

In Fig. 3 are shown the relations among exposure energy, transmission densities, and the amount of silver metal liberated by photolysis. Liberated silver metal increases according to the increase of exposure energy and transmission density increases too.

The sensitivity curves of silver salts are shown in Fig. 4. When exposed with light of wavelength longer than 300 nm, transmission densities are small, and

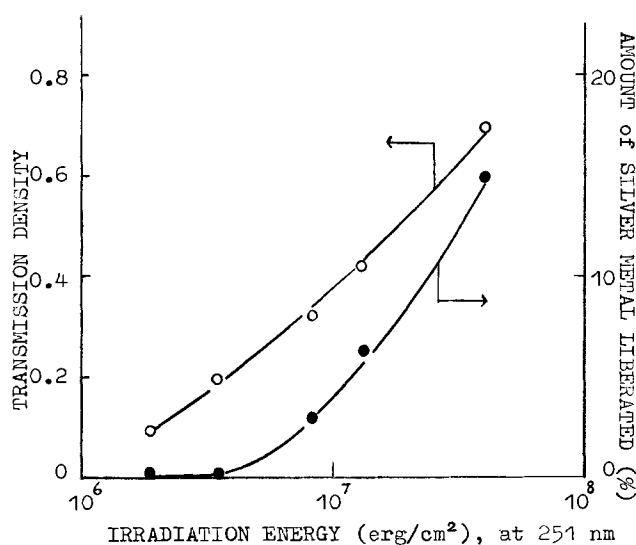


Fig. 3. Relations among exposure energy, transmission density, and amount of silver metal liberated.

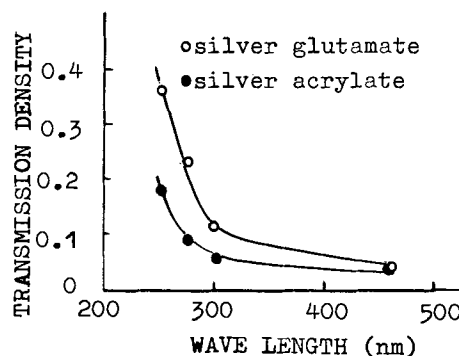


Fig. 4. Sensitivity curves of silver salts

therefore, photolytic deposition of silver metal is poor. The concentrations of silver salts in each film are equal in mole per cent and therefore, in comparison of transmission densities, it is considered that the sensitivity of silver glutamate is greater than that of silver acrylate.

In Fig. 5 is shown the dark reaction of silver glutamate. The decomposition of silver glutamate scarcely proceeds below 80°C within 15 min.

**Forming a printed circuit.**—The surface of the insulating substrates are cleaned and roughened. These

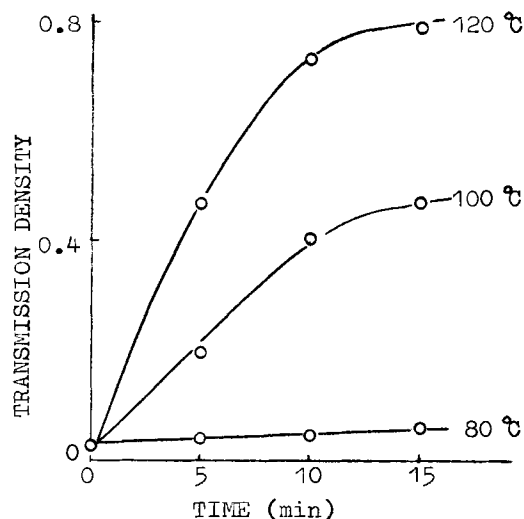


Fig. 5. Dark reaction of silver glutamate

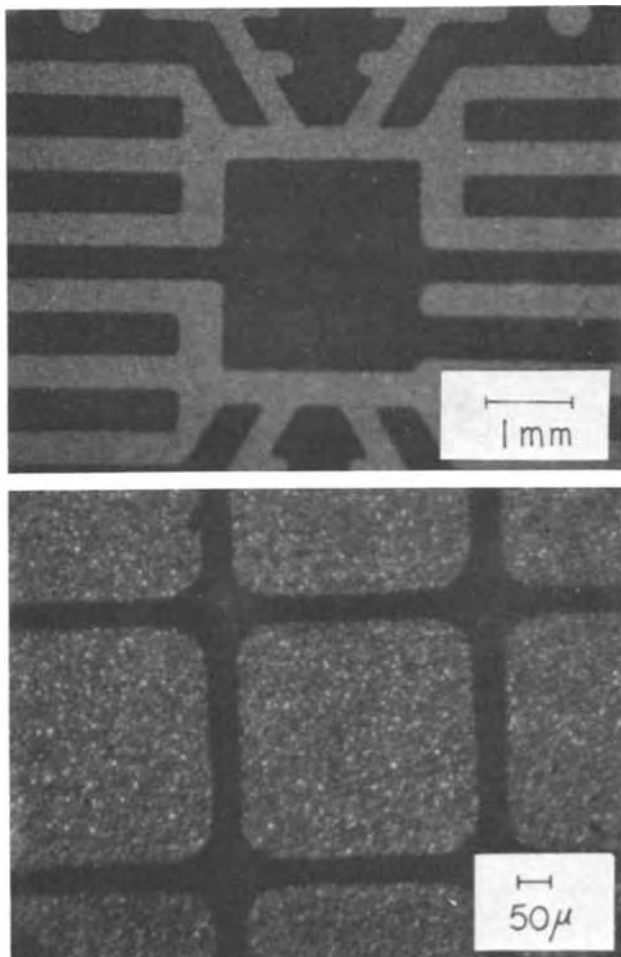


Fig. 6. Examples of circuit patterns obtained

procedures are required to obtain homogeneous sensitive layers and good adhesion between substrates and silver atoms liberated by photolysis. In order to obtain epoxy resin laminates with an active surface, we performed liquid honing with aluminum oxide powder and chemical etching with a solution of potassium dichromate and sulfuric acid ( $K_2Cr_2O_7$  150g, conc  $H_2SO_4$  1000 ml, water 500 ml) at  $60^\circ C$  for 5 min. The surface of the ceramic substrates was polished with diamond powder, and the surface was roughened. As a flexible substrate, polyester tracing film was used.

When the substrates coated with silver salts are exposed to uv-light in air through a mask, exposed regions blacken and deposit colloidal silver atoms. A high pressure mercury lamp is used as a uv-light source and silver glutamate is employed for its high sensitivity. The sensitive layers need to be exposed for 10 min to form stable nuclei for electroless plating. In the fix step, the role of sodium hydroxide is to fix colloidal silver atoms. When sodium hydroxide is not contained in the fix solution, the colloidal silver atoms are liable to be dissolved. That means the decrease of nuclei for electroless plating, and adhesion for electroless plating is labilized. The unexposed regions can be washed away easily with the  $NaOH + NH_4OH$  solution.

The substrate having the pattern of silver particles is then immersed in an ordinary electroless copper plating solution (5), comprising 14.6g copper sulfate ( $CuSO_4 \cdot 5H_2O$ ), 7.5g sodium hydroxide, 7.5g Rochelle salt, and 43.8g, 37% aqueous formaldehyde solution in water to make 1 liter, without employing any activating pretreatment. In 15-20 min, a copper circuit pattern 1-2 $\mu$  in thickness is formed.

Examples of the obtained patterns are shown in Fig. 6. From this figure, it is observed that fine patterns can be obtained by deposition of metal particles.

### Conclusion

We have shown that printed circuits can be formed on insulating substrates utilizing the photolysis of silver salts of organic acids. This is a simple process to form printed circuits and the process can be applied to other fields such as photographic material, inlaid work, and photomask.

At present, basic studies of the important process steps are being carried out and will be reported in the near future.

Manuscript submitted April 2, 1973; revised manuscript received July 9, 1973.

Any discussion of this paper will appear in a Discussion Section to be published in the December 1974 JOURNAL.

### REFERENCES

1. V. W. Gerhard Pohl and H. J. Kuhn, *Kolloid Z. Z. Polymere*, **212**, 1 (1966).
2. A. Finch, P. W. M. Jacobs, and F. C. Tompkins, *J. Chem. Soc.*, **1954**, 2053.
3. K. Sugita and S. Suzuki, *Polymer J.*, **2**, 283 (1971).
4. H. Flaschka and F. Huditz, *Z. Anal. Chem.*, **137**, 104 (1952).
5. F. W. Schneble et al., Japanese Pat. 316,927 or U.S. Pat. 3,033,703 (1961).

# Mutual Effect of Current Density, pH, Temperature, and Hydrodynamic Factors on Current Efficiency in the Chlorate Cell Process

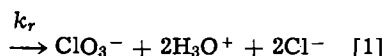
Milan M. Jaksic\*

*Electrochemistry Department, Institute for Chemistry, Technology, and Metallurgy, Belgrade, Yugoslavia*

## ABSTRACT

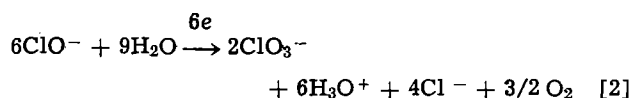
The simultaneous mutual effect of pH, temperature, current density, and hydrodynamic factors on current efficiency in the chlorate cell process has been investigated and considered. Certain practical considerations of the process optimization are also given. Some contributions to the scale-up of chlorate cells have also been introduced. It has been pointed out that by adjusting all other parameters at their optimal values (temperature, pH, and the linear velocity of flow), the current density is then the main factor providing high current yields.

The basic electrode process in electrochemical chlorate production is anodic chloride ion oxidation, accompanied by immediate hydrolysis of the resulting elemental chlorine, that yields as a further intermediate product hypochlorous species or available chlorine.<sup>1</sup> Two simultaneous parallel ways remain for active chlorine to reach the final state of chlorate formation. The first and the useful one ( $t_1$ ) would be its direct chemical conversion



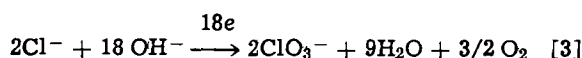
well known as the Foerster reaction of chemical chlorate formation (1).

The second and unavoidable path represents another Foerster reaction of further anodic hypochlorite oxidation to the final state



also known as the reaction of electrochemical chlorate formation (1), which represents an unnecessary loss of current ( $t_2$ ).

For the sake of Faradaic balance treatment, it is much more convenient to present the reaction of electrochemical chlorate formation in a form of total anodic oxidation process from chloride ion to the final species



In the chlorate cell process one practically neglects anodic chlorine evolution and defines as efficient ( $t_1$ ) the electrode path in which the electrochemical oxidation goes to the hypochlorous species only, with chlorate as further final product of the pure chemical conversion. Considering the total anodic chloride oxidation to the final state (reaction [3]) as unavoidable anodic current losses ( $t_2$ ), it can easily be shown that the over-all current efficiency ( $t$ ) of the whole electrolytic process is the same as that of the first stage chloride anion oxidation ( $t_1$ ), or in another words, that  $t_1 + t_2 = 1$ .

\* Electrochemical Society Active Member.

Key words: active chlorine, hypochlorous species, steady-state current yields, back-mix-flow reactor, plug-flow reactor, instantaneous current efficiency.

<sup>1</sup> "Available chlorine" comprises the sum of concentrations of hypochlorous acid, hypochlorite ion, and dissolved elemental chlorine. However, at the pH of usual electrolytic chlorate production the latter can be neglected, so that the more convenient term active chlorine will be used henceforth for hypochlorous entities only.

Both reactions (Eq. [1] and [3]) are dependent on each other and hence both depend on pH, temperature, current density, electrolyte volume ratios, and their active chlorine contents, as well as on the hydrodynamic conditions inside the cells.

A chlorate production system mainly consists of the cells and the holding volume usually in a closed loop. The cell has often been considered primarily as a generator of active chlorine, and the holding volume as a reactor for its further conversion to the final product. (2).

Faradaic stoichiometry and material balance consideration have been leading to the derivation of an equation which relates the over-all current efficiency ( $t_1$ ) of chlorate production to the operational parameters of the process including all partial volume contributions of active chlorine conversion (see Appendix I) throughout the system (2)

$$t_1 = \frac{2}{3} + \frac{2f_c^2 \cdot k_{r,c} \cdot V_c \cdot F}{I} \cdot \frac{K^* \cdot c \cdot (a_{\text{H}_3\text{O}^+})_c^2 \cdot C_{sc}^3}{[K^* \cdot c + (a_{\text{H}_3\text{O}^+})_c]^3} + \frac{2}{3} F \left( \frac{q}{I} \right) \cdot (C_{sc} - C_{sh}) - \frac{2}{3} (t_3 + t_4) \quad [4]$$

or otherwise (2)

$$t_1 = \frac{2}{3} + \frac{2f_c^2 \cdot k_{r,c} \cdot V_c \cdot F}{I} \cdot \frac{K^* \cdot c \cdot (a_{\text{H}_3\text{O}^+})_c^2 \cdot C_{sc}^3}{[K^* \cdot c + (a_{\text{H}_3\text{O}^+})_c]^3} + \frac{2f_h^2 \cdot k_{r,h} \cdot V_h \cdot F}{I} \cdot \frac{K^* \cdot h \cdot (a_{\text{H}_3\text{O}^+})_h^2 \cdot C_{sh}^3}{[K^* \cdot h + (a_{\text{H}_3\text{O}^+})_h]^3} - \frac{2}{3} (t_3 + t_4) \quad [5]$$

where  $I$  denotes the total current or the cell load;  $k_r$  is the rate constant for the reaction [1];  $q$ , the flow rate;  $V$ , the electrolyte volume;  $F$ , the Faraday constant;  $f$ , the activity coefficient of hypochlorous acid;  $K^*$ , the rearranged dissociation constant of hypochlorous acid (see below);  $a_{\text{H}_3\text{O}^+}$ , the hydronium ion activity;  $C_s$ , the active chlorine concentration; and  $t_3$  and  $t_4$ , possible current losses for chlorine evaporation and cathodic hypochlorite reduction, respectively. The last two terms could be neglected in common practice of the chlorate production, that means  $t_1 + t_2 + t_3 + t_4 \approx t_1 + t_2 = 1$ . Subscripts  $c$  and  $h$  shall refer, throughout, to the quantities corresponding to the cells and to the holding volume, respectively. In the above equations  $f^2$  approximately represents the Brönsted's kinetic coefficient (3, 4) for the reaction of chemical chlorate formation (Eq. [1]).

The first term in Eq. [4] and [5] defines current yields under conditions such that all electrolytically produced active chlorine simultaneously undergoes the further electrochemical oxidation to chlorate according to Eq. [3]. The next two terms represent contributions to the over-all current efficiency of the chemical conversion of hypochlorous species taking place inside the cells and the holding volume, respectively.

### The pH Effect of the Whole Chlorate System

One could immediately draw some general conclusions considering Eq. [4] and [5] by quite a simple analysis. Firstly, in very acid solutions, when hypochlorous species decompose and tend to negligible concentration, chlorine evolution approaches its maximal current yields ( $t_3 \rightarrow 1$ ), chlorate current efficiency takes small values, and the whole cell operates as a chlorine producing unit. On the contrary, in alkaline solutions ( $a_{\text{H}_3\text{O}^+} \rightarrow 0$ ), hypochlorous acid approaches zero concentration, and all active chlorine builds up its concentration and exists in the form of hypochlorite ions. This reduces chemical conversion of available chlorine to negligible rates, so that the final effect represents chlorate production taking place from total anodic oxidation only (Eq. [3]). Therefore, one has to seek an intermediate pH range providing the optimal operating conditions and yielding the maximal current efficiencies. In the two limiting cases, just discussed, neither the temperatures and the current density, nor any other operating variable and parameter could bring about any improvement of the chlorate cell efficiency. Hence, a certain mutual effect of variable optimization must exist somewhere in between these two limiting cases.

### The pH Effect of the Holding Volume

Partial differentiation with respect to ( $a_{\text{H}_3\text{O}^+}$ ) of both terms relating over-all current efficiency in Eq. [5] to the contributions of hypochlorous species conversion inside the two volumes,  $V_c$  and  $V_h$ , reveals the optimal pH region providing maximal current yields to be

$$\text{pH}_M = \text{pK}^* - \log 2 \quad [6]$$

The rearranged dissociation constant (5), as well as its corresponding thermodynamic value, represents a quantity dependent on temperature.

It has previously been shown elsewhere (5) that the relevant equilibrium constant for calculating the actual hypochlorous species contents at the ionic strengths of the chlorate cell brine and for evaluating the over-all current efficiency according to Eq. [5], is

$$K^* = \frac{a_{\text{H}_3\text{O}^+} \cdot C_{\text{ClO}^-}}{C_{\text{HClO}}} = K_a \frac{f \cdot a_{\text{H}_2\text{O}}}{f_{\text{ClO}^-}} \approx 10 \cdot K_a \quad [7]$$

where  $K_a$  stands for its thermodynamic value, and other signs have the usual meaning.

Caramazza (6) revealed the functional temperature dependence of the thermodynamic dissociation constant of the hypochlorous acid to obey the equation

$$\text{pK}_a = \frac{800}{T} + 4.892 \quad [8]$$

However, Morris (7) has recently presented somewhat more reliable data expressed by the following relation

$$\text{pK}_a = \frac{3000.00}{T} - 10.0686 + 0.0253 \cdot T \quad [9]$$

which was asserted to be valid up to 45°C (7).

Thus, combining Eq. [8] and [9] with [6] and [7], one obtains the temperature dependence of the optimal pH range ( $\text{pH}_M$ ) for the chlorate cell process. Some experimental and calculated values are shown in Fig. 1. One easily observes that the higher the temperature, the lower is the optimal pH value which provides maximal current yields in the electrolytic chlorate production [cf. (5)]. This matter has been discussed in more detail elsewhere (5).

### The pH Effect of the Chlorate Cell

The pH effect of the chlorate cell itself on the overall current yield was investigated as a function of the holding volume temperature at constant current density (Fig. 2). It has again been experimentally confirmed that the optimal pH range given above provides maximal current efficiencies. However, one could accept as much more important the optimal pH value to be maintained inside the holding volume, whose content and retention time are of incomparably higher values. Due to the chemical conversion of available chlorine, as well as the reaction proceeding (Eq. [1]) the electrolyte tends to be more acid. Hence, one needs a somewhat higher pH value of the brine leaving the cell and entering the holding volume, in order to maintain optimal acidity inside the latter. Of course, this also depends on the buffer content (hydrochloric acid) in the brine. At the same time one tends to reduce and maintain an optimal dichromate concentration for many important reasons. First, of all, the latter is partially lost during the crystallization of the final product. Also, although dichromate enables the cathodic hypochlorite reduction to be effectively suppressed, and

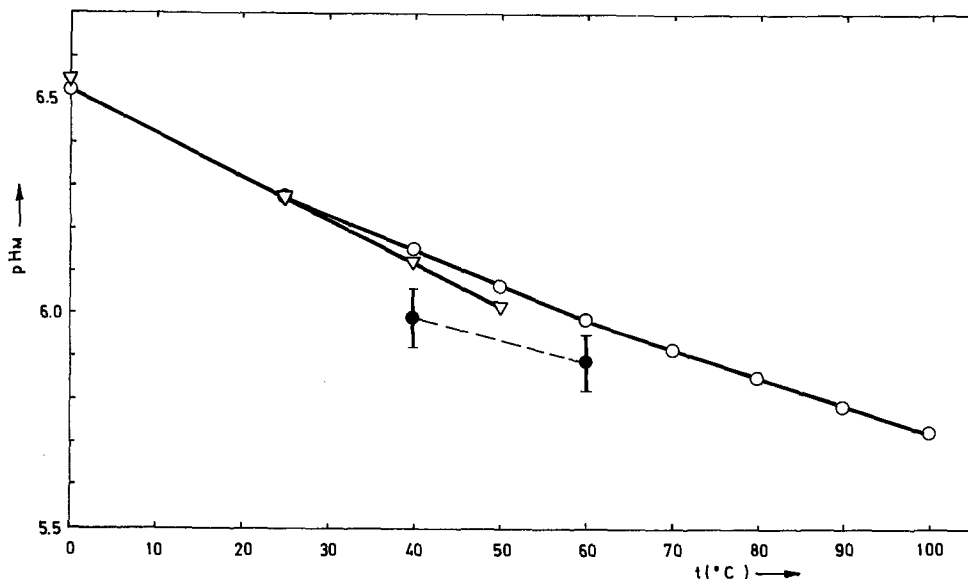


Fig. 1. Theoretical ( $\circ$ ,  $\nabla$ ) and experimental ( $\bullet$ ) temperature dependence of the optimal pH value ( $\text{pH}_M$ ) providing maximal active chlorine conversion rates into chlorate inside the holding volume [ $\circ$  and  $\nabla$  according to Caramazza (6) and Morris (7), respectively].

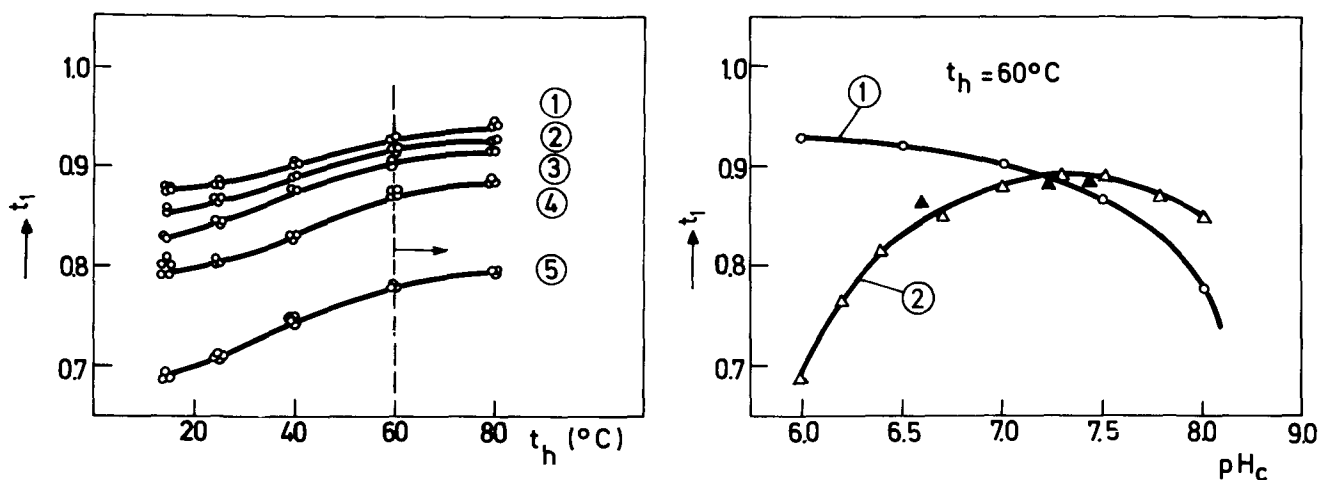


Fig. 2. Mutual effect of the cell pH ( $pH_c$ ) and the holding vessel temperature ( $t_h$ ) on the current efficiency ( $t_1$ ) in the electrolytic chlorate process.  $\circ$ , experimental data ( $pH_c$ : 1—6.0; 2—6.5; 3—7.0; 4—7.5, and 5—8.0); other operating parameters being maintained constant,  $I$ ,  $i$ ,  $q$ ,  $V_{cr}$ ,  $V_{hr}$ , and  $t_c$ ;  $\triangle$  and  $\blacktriangle$ , theoretical and experimental values, respectively, according to Claus (12) [cf. (33)].

enables useful buffering of the brine, chromate ions simultaneously exhibit an undue effect on the anodic cell process (8). On the other hand, however, chromate ions represent an efficient inhibitor of corrosion for precious metals deposited on titanium anodes and hence, one may need to increase their brine content (9) for this reason.

#### The Over-All Temperature Effect of the Chlorate System

The temperature effect of the chlorate producing system is confined by a certain number of kinetic parameters encompassed by the relationships for current efficiency given above, i.e.,  $k_r$ ,  $K^*$  and, as will be seen below, over the rate constant for chlorine hydrolysis. In addition the simultaneous effect of increasing temperature on cell voltage decrease is well known, thus providing for power consumption to be efficiently decreased as well. One tends, therefore, to increase the temperature throughout the whole system. However, the temperature exhibits a negative effect on anode consumption. Thus, economical considerations define a rather limited level of temperature inside the chlorate cells.

One of the most important temperature effects for the process would be to increase the rate of the chemical conversion of active chlorine (Eq. [1]), which otherwise represents a slow reaction. Hence, an economical compromise is found for cells with graphite anodes in temperature range of about 40°C. Nevertheless, to increase chemical chlorate formation inside the whole system, it has been suggested that the retention volume of the reactor should be elevated to a relatively higher temperature level (2).

Due to platinum metal coating corrosion, one also chooses, as well suited from an economical point of view, a rather compromised temperature range of about 60°C for chlorate cells with titanium (DSA) anodes (9). This higher temperature increases current yield and reduces the over-all power consumption.

There exists another important reason for limiting the temperature of the chlorate producing system. It appears because of the thermal decomposition of the hypochlorous species resulting in oxygen evolution and reverting active chlorine to its initial state of chloride ions (10, 11). Therefore, an exact derivation of the relationships given before the over-all current efficiency (Eq. [4] and [5]) requires that the thermal decomposition rate of active chlorine should also be included in the whole material balance treatment of the system [cf. (12)].

All the above considered reasons have resulted in a temperature range for actual chlorate systems of about 60°C.

This region has also been confirmed experimentally and assessed as the optimal and efficient one (Fig. 2 and 3). Namely, mainly due to the relatively low active chlorine concentration inside the optimal pH region for chlorate production, a rather asymptotic leveling effect of temperature on the current efficiency appears above 60°C. This is much more pronounced at lower current densities as could be noted in Fig. 4. Therefore, it could be concluded that the heating effect of the holding volume (2) is efficient enough indeed, and of practical importance only for chlorate cells running at low current densities (unipolar cells with graphite anodes).

The over-all current efficiency ( $t_1$ ) dependence on the holding vessel temperature is evidently not a straightforward one. One should consider that, in addition to kinetic parameters  $k_{r,h}$  and  $K^*_h$ , the effect of active chlorine content ( $C_{sh}$ ) in Eq. [4] and [5] is also temperature dependent in a quite complex manner. This could be comprehended as follows. Both relationships (Eq. [4] and [5]) reflect primarily the Faradaic stoichiometry which states that, the larger the current efficiency, the higher should be the accumulation of the active chlorine inside the cell ( $C_{sc} - C_{sh}$ ) or the lower the hypochlorous species content leaving the holding volume ( $C_{sh} \rightarrow 0$ ). However, a quite converse require-

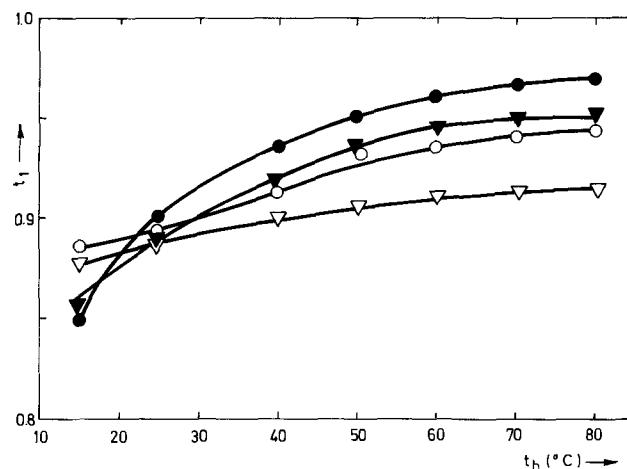


Fig. 3. Mutual effect of the temperature ( $t_h$ ) and the pH inside the holding volume ( $pH_h$ ) on the current efficiency ( $t_1$ ) in the chlorate cell process:  $\bullet$  and  $\blacktriangledown$  experimental data at  $pH_h$  6.0 and 6.5, respectively; other operating parameters being maintained constant:  $I$ ,  $i$ ,  $q$ ,  $V_{cr}$ ,  $V_{hr}$ , and  $t_c$ .  $\circ$  and  $\triangledown$  denote calculated values according to Eq. [10] for experimental values of the  $C_{sc}$  at the  $pH_h$  6.0 and 6.5, respectively.

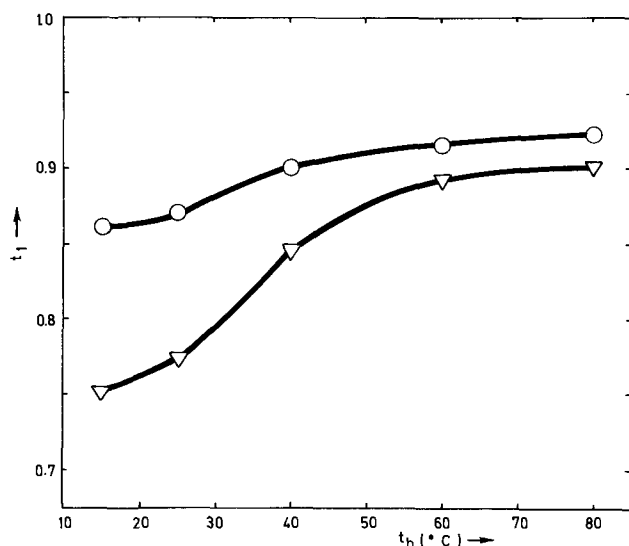


Fig. 4. Mutual effect of the current density ( $i$ ) and the holding vessel temperature ( $t_h$ ) on the current efficiency ( $t_1$ ) at a constant pH of the cell (pH<sub>c</sub>—6.0). ○ and ▽ denote experimental data at current densities 6.67 and 1.8 A/sq. dm., respectively. Other operating parameters of the system being maintained constant are  $q$ ,  $V_c$ ,  $V_h$ , and  $t_c$ .

ment arises from hydrodynamic considerations (see below), because the increase of the  $C_{sc}$  leads consequently to proportional current losses due to increased direct anodic oxidation.

Therefore, although the concentration difference ( $C_{sc} - C_{sh}$ ) is needed as large as possible, one should at the same time also try to maintain the  $C_{sc}$  as low as possible. This fact is in itself a practical reason causing the existence of an optimal holding vessel to cell volume ratio ( $V_c$  and  $V_h$ ), previously often considered in terms of current concentration. This is also the reason why active chlorine concentration ( $C_{sh}$ ) entering the cell is never negligible compared to the one leaving it or why the former does not tend to zero or negligible values at all, as required by Eq. [4], to approach the maximal current efficiencies. Therefore, the increase in the rate of active chlorine conversion into chlorate with temperature must exhibit an asymptotic tendency to a certain maximal value, in spite of the fact that the rate constant is increasing, because the concentration factor in the rate expression (Eq. [5]) decreases with the third power (Fig. 3). Hence, both values of active chlorine content, entering and leaving the cell, under practical operating conditions of chlorate production are usually of the same order.

Considering Eq. [4], it could be easily found that the higher the flow rate ( $q$ ), the smaller the difference of the two active chlorine contents ( $C_{sc} \rightarrow C_{sh}$ ) and the whole term reflecting the holding volume contribution to the over-all current efficiency of the system asymptotically tends to its limiting value.

Quite a simple analysis would lead to the conclusion that, just due to the small active chlorine contents throughout the system, the plug-flow type of reactor ( $V_h$ ), for the same volume, provides higher degrees of conversion to chlorate and higher current yields, than does the back-mix flow one (26).

#### The Contributions of Hydrodynamic Factors to Over-All Current Yield

There has been an old general acceptance in the chlorate cell process that the motion of the electrolyte inside the cell should be reduced in order to provide concentration polarization for the anodic oxidation of the active chlorine. However, Ibl and Landolt (13) were the ones to show an interesting and complex

nature of its anodic diffusion layer. Namely, due to the subsequent chlorine hydrolysis, which prevalently takes place within the diffusion layer, hypochlorous species diffuse in both directions from and toward the generating electrode, thus creating a certain concentration maximum inside the diffusion layer (13).

Hence, in order to really provide the concentration polarization, the diffusion layer should be cut down from the solution side by increasing the linear velocity of brine flow increasing thereby the fraction of hypochlorous species, which then avoids a further anodic oxidation.

The concentration profile, the resulting active chlorine flux and the concentration gradient at the anode surface, were also analytically given by Ibl and Landolt (13). Equating the Ibl-Landolt equation for the flux with the fraction of the current used for further active chlorine anodic oxidation, Despic et al. (14) were able to derive a quantitative expression relating the over-all current efficiency to the hydrodynamic, operational, and kinetic parameters of the process

$$t_1 = \frac{1 - \frac{D_2 \cdot F}{i \cdot \delta} \cdot f_{sc} \cdot C_{sc}}{\frac{3}{2} - \frac{1 - \exp(-\delta \sqrt{k_1/D_1})}{2\delta \cdot \sqrt{k_1/D_1}}} \quad [10]$$

where  $\delta$  is the anodic diffusion layer thickness;  $k_1$ , the rate constant for the reaction of chlorine hydrolysis;  $i$ , the current density;  $D_1$  and  $D_2$  are the diffusion coefficients of the elemental chlorine and the active chlorine, respectively; while  $f_{sc}$  represents the formal activity coefficient of both hypochlorous species taken together as active chlorine. This relationship differs from the original flux equation [cf. (13)] by the correction introduced to extend its application to concentrated solutions. In other words, instead of the concentration, one relates the flux and thereby the current efficiency to the activity of active chlorine (14). Namely, one could easily find it much more convenient to use the chemical potential as the driving force of diffusion in concentrated solutions and, hence, to relate fluxes of the considered species to their individual activities in the first approximation. In general this is a better approximation anyway compared to the application of their concentrations in the Fick's equation (18). Some ions, however (and particularly the hydronium ion is usually the most important among them in aqueous solutions) undergo considerable, but regular activity changes in concentrated solutions of some neutral salts (19). The same conclusion is found to be valid for the hypochlorite ion, and in concentrated solutions of neutral salts also for both hypochlorous species taken formally together in the form of active chlorine (18).

Certain individual activities have recently appeared as experimentally attainable values in the first approximation at least (19, 20). It will be shown at another instance that these activities obey the diffusion relationships much better than their corresponding concentrations (18).

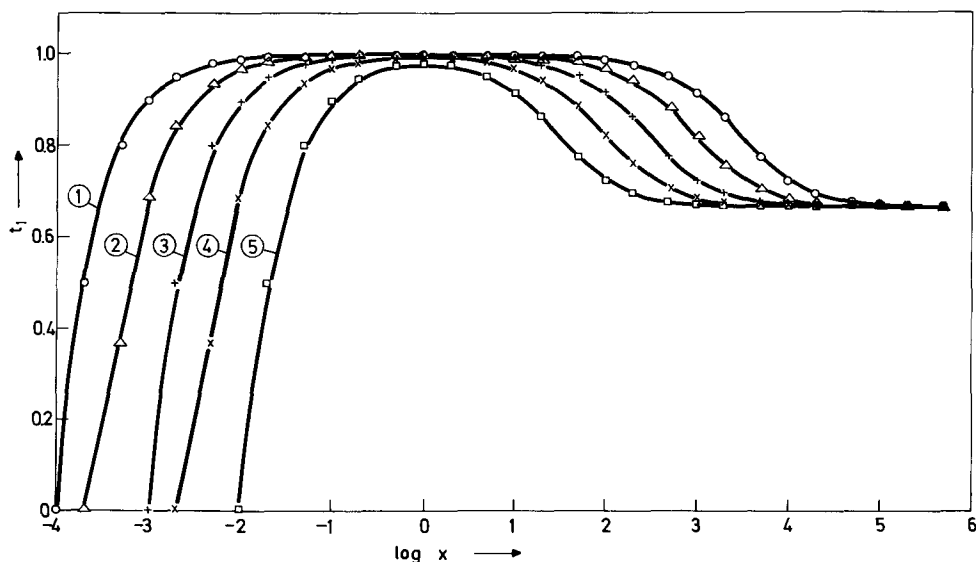
One should not overlook the fact that the concentration of active chlorine,  $C_{sc}$ , does not represent an independent value, but a variable of a very complex nature. Therefore, Eq. [10] is valid for its steady-state values only (2, 14).

Of course, Eq. [10] could be combined with relations [4] and [5], as well as with the one expressing material balance of the holding vessel, in order to eliminate or to introduce the steady-state  $C_{sc}$  and  $C_{sh}$  values in resulting relationship [cf. (14) and (21)].

According to Eq. [10], the over-all current efficiency exhibits a region of maximal values as function of the anode diffusion layer thickness (Fig. 5). This range is defined by the following transcendental function



Fig. 5. The current efficiency ( $t_1$ ) of the chlorate cell as a function of the anode diffusion layer thickness ( $\delta$ ) for various  $C_{sc}/i$  ratios taken as parameter at 25°C (see Appendix II). Calculated values according to Eq. [10].



$$i - D_2 F \cdot f_{sc} \cdot C_{sc} \sqrt{\frac{k_1}{D_1}} + i \sqrt{\frac{k_1}{D_1}} \cdot \delta_M$$

$$= \left( i - 3D_2 F f_{sc} \cdot C_{sc} \cdot \sqrt{\frac{k_1}{D_1}} \right) \cdot \exp \left( \delta_M \sqrt{\frac{k_1}{D_1}} \right) \quad [11]$$

or approximately by the relation

$$\delta_M \approx 2 \sqrt{\frac{D_2 \cdot F \cdot f_{sc} \cdot C_{sc}}{i}} \cdot \sqrt{\frac{D_1}{k_1}} \quad [12]$$

It would be worthwhile to point out that the current yields always reach their maximal values for  $\delta_M > 0$ . Such a conclusion results from the consideration of Eq. [11]. Namely, its left-hand side represents a straight line, while its right-hand side defines an exponential function of the diffusion layer thickness. Both lines, however, always cross each other for  $\delta_M > 0$ . Moreover, under practical operating conditions this represents an easily attainable required condition.

It is also worthwhile to note that the current efficiency, according to Eq. [10] could reach values lower than 2/3 only for unsteady-state active chlorine contents. In such a case,  $t_1$  does not represent the steady-state yield, but the instantaneous one, which changes successively with time and with the active chlorine consumption. It asymptotically approaches both  $C_{sc}$  and  $t_1$ , the final steady values. Moreover, the chlorate cell anode represents in itself a self-adjusting system. That means, the larger the diffusion layer thickness the lower is the instantaneous current efficiency (see Eq. [10]), but it also means the more intensive is oxygen evolution. On the other hand, gas evolution represents an efficient short-circuiting of the diffusion layer [cf. (15, 16, and 31)] and hence, the latter begins to decrease in accordance with oxygen evolution rate, resulting in a gradual increase of the current efficiency with time.

As one could easily note, current losses ( $1 - t_1$ ) now do not represent a direct, but a very complex function of the active chlorine concentration [cf. (3)]. This results from quite an unusual diffusion layer structure and the very complex active chlorine profile, the latter being quite different from the Nernst linear distribution.

Equation [10] has been experimentally found well suited in the chlorate cell process (14) (Fig. 3). In conclusion, it could also be emphasized that the hydrodynamic operating parameters and conditions of the cell represent essential factors (Fig. 5) for the process inside the latter because of the occurrence of quite unusual and specific events taking place inside the anode diffusion layer.

### The Effect of Current Density

The main characteristic of the two parallel anodic reactions taking place simultaneously in the chlorate cells represents the fact that, in common industrial practice at least, chloride oxidation abounds in the ions present (usually the steady-state concentration is about 2 moles/liter), while the reaction of hypochlorous species, being rather concentration polarized, is suppressed ( $C_{sc}$  is usually of the order  $3 - 5 \cdot 10^{-2}$  moles/liter). Therefore, the most efficient and intrinsic parameter of the chlorate cell process providing higher current efficiencies is the current density itself (cf. below Fig. 9). However, in order to effectively use these common conclusions regarding concentration polarization and to adjust the anodic process, a suitable anode material is needed.

Figure 6 shows the current efficiency dependence on the current density. Experimental data are compared with data predicted by Eq. [10] as well as with other values appearing from another theory (12) for environmental (25°C) temperatures and common active chlorine concentrations.

For more than eighty years graphite has been the unique anode material in electrolytic chlorate production. Mainly due to its relatively poor polarization characteristics for the anode reaction of chlorine evolution, and also because of its relatively high resistance, one has had to reduce the current density to between 2.5 and 5.0 A/dm<sup>2</sup> for the industrial cell process.

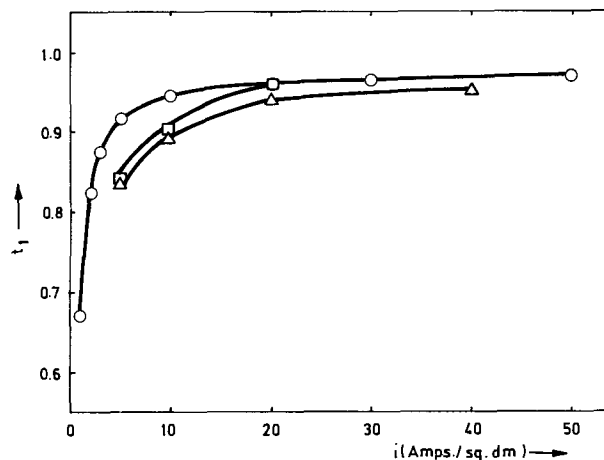


Fig. 6. The current efficiency ( $t_1$ ) of the chlorate cell as a function of the current density ( $i$ ).  $\circ$ , theoretical values according to Eq. [10] for the common active chlorine concentration ( $C_{sc} = 4.0 \cdot 10^{-2}$  mol/liter);  $\delta$ ,  $8.2 \cdot 10^{-4}$  cm;  $f_{sc}$ , 0.1; and  $t_c$ , 25°C;  $\square$ , experimental data; and  $\triangle$ , values according to Claus (12).

At the same time, one had to reduce the cell temperature to maintain the graphite wear to economical conditions of consumption. The graphite wear, however, also represents, besides other factors, an anodic property depending on its potential and thereby on the current density (22). Therefore, both the concentration polarization for the active chlorine oxidation at the anode and its chemical conversion to the final state, have been inconveniently restricted. The resulting current efficiencies, for chlorate cells with unipolar graphite electrodes, at least, are thereby in practice usually rather limited to values of about 0.8 (see Fig. 6). In accordance with relationships [4] and [5], in order to increase the current efficiency, even in the case of cells using graphite anodes, some suggestions have been given (2) consisting of an independent increase of the holding volume temperature, while maintaining the reasonably low temperature of the cell. This provides further intensification of chemical conversion inside the former and, thereby its further contribution to the over-all current yields (30).

Recently, however, metallic electrodes of dimensionally stable behavior and with greatly advanced polarization characteristics (DSA-electrodes) (23) finally appeared.

The higher the current density, the more economical is the consumption of precious metals. However, the IR-drop severely increases linearly with the current density and, moreover, very soon the limiting current is reached for the anode oxidation of chloride ions. Therefore, besides the quite advanced polarization properties of DSA-electrodes which results in a higher asymptotic effect of the current density on the current efficiency (Fig. 6), a range of about 30 A/dm<sup>2</sup> has been chosen as a compromise and accepted as the most convenient. Of course, this requires an optimal pH region of the brine to be maintained, too, because out of it, not only the current density, but also all other process parameters are practically of no effect. The cell operates either as a chlorine producer in the acid region, or produces chlorate as the final product of total electrochemical oxidation in the alkaline region thus yielding the lower steady-state value of the current efficiency ( $t_1 \rightarrow 2/3$ ).

### Some Scale-Up Considerations of the Chlorate Cells

Equation [10] relates the current efficiency to the average value of the actual steady-state active chlorine concentration ( $C_{sc}$ ) for chlorate cells operating as back-mix-flow reactors. A different situation arises in the more frequent case of plug-flow cells. In the latter case one must first integrate a material balance equation (2, 17, 24) for an element of the cell volume along the anode (Fig. 7)

$$\frac{dC_{sc}}{dl} = \frac{i}{2Fq} (3t_{1(l)} - 2) \quad [13]$$

where  $t_{1(l)}$  denotes the local current yield depending on the anode length (l). The  $t_{1(l)}$  from Eq. [10] may be substituted in relationship [13], on the assumption that the former relates the local current efficiency for any element of the anode length to its particular active chlorine concentration ( $C_{s(l)}$ ). Integrating from entering hypochlorous species content of the cell ( $C_{sh}$ ,  $l =$

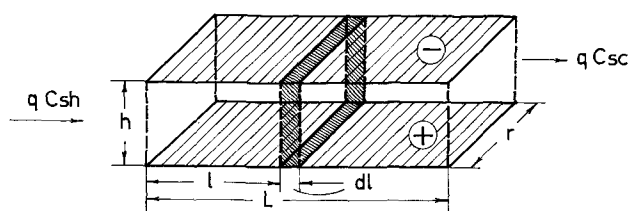


Fig. 7. Elemental cross section of the chlorate cell plug-flow running.

0), to the leaving one ( $C_{sc}$ ,  $l = L$ ), one easily comes to the distribution relation for the active chlorine concentration along the anode (17). Now, again, the over-all current efficiency of chlorate cells running in plug-flow is obtained as an average of the local current yields (17), i.e.

$$t_1 = \frac{1}{L} \int_0^L t_{1(l)} dl \quad [14]$$

or, finally

$$t_1 = \frac{2}{3} + \frac{2}{3} \cdot \frac{Fq}{irL} \left[ \frac{i(1 - \exp(-\delta\sqrt{k_1/D_1}))}{3D_2Ff_{sc}\sqrt{k_1/D_1}} - C_{sh} \right] \cdot \left\{ 1 - \exp \left\{ -\frac{3}{2} \cdot \frac{irL}{Fq} \cdot \frac{D_2Ff_{sc}}{i\delta} \right\} \right\} \cdot \left\{ \frac{3}{2} - \frac{1 - \exp(-\delta\sqrt{k_1/D_1})}{2\delta\sqrt{k_1/D_1}} \right\} \quad [15]$$

where  $\tau$  denotes the anode width. This relationship, as well as the intermediate ones, have also been experimentally tested in a ribbon type of cell and found to well obey the process (17, 24).

The final equation [15] was examined by analogue computer analysis in order to relate the current yields to the anode diffusion layer thickness and cell dimensions (Fig. 8). It could easily be found that the relationship [15] reflects in essence the previous relation (Eq. [10]), which already has been discussed, and which is also implicitly encompassed by the former. In other words, by increasing the linear brine velocity of flow along the anode, the current yields first also increase, and after some maximum, decrease again. At relatively fast flow rates, the anode length exhibits a more pronounced effect, but in its optimal range, the longitudinal cell dimension has practically no further effect on the yields within very wide limits. However, because of an intrinsic effect of gas bubble collection at the upper part of the cell (25), the anode length should be reduced. At the same time the flow rate along it optimized, thus providing the diffusion layer thickness maintained within the optimal range. The latter requirement is, of course, easily attainable by the cell's own gas-lifting effect, known under the term of the natural brine recirculation (32).

Equation [15] was tested experimentally and found well suited (17) (Fig. 9). As one could expect from the theory (cf. Eq. [10]), the current efficiency exhibits its maximum range as a function of the diffusion layer thickness or of the linear flow velocity along the anode.

It should also be noted that all the presented equations relating the current efficiency to the hydrodynamic parameters ( $\delta$ ) are based on the Ibl and Landolt (13) relation for the active chlorine gradient at the anode. However, the authors neglected the chemical conversion of hypochlorous species within the anode diffusion layer. This is correct only for their operating conditions of high pH values and low temperatures. Hence, a more complete diffusion relation would be [cf. (13) and (24)]

$$D_2 \left( \frac{d^2 a_s}{dx^2} \right) + k_1 \cdot a_{Cl_2(x)} - 3f_c^2 \cdot k_{r,c} \cdot \frac{K^* (a_{H_3O^+})^2(x)}{[K^* + (a_{H_3O^+})_x]^3} \cdot C_{s(x)}^3 = 0 \quad [16]$$

The latter, however, could not be easily analytically solved. It would not lead to a simple analytic form of

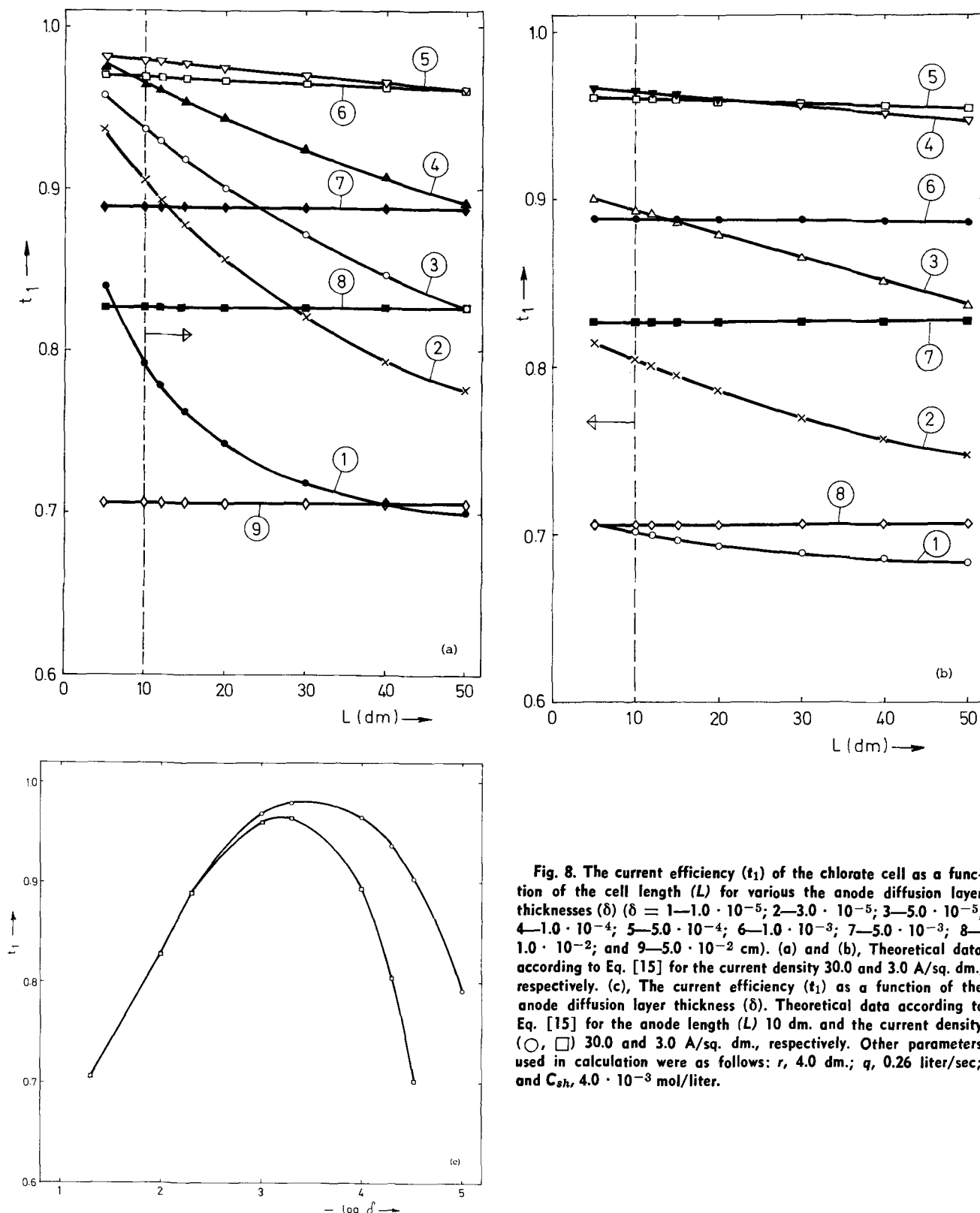


Fig. 8. The current efficiency ( $t_1$ ) of the chlorate cell as a function of the cell length ( $L$ ) for various the anode diffusion layer thicknesses ( $\delta$ ) ( $\delta = 1-1.0 \cdot 10^{-5}$ ;  $2-3.0 \cdot 10^{-5}$ ;  $3-5.0 \cdot 10^{-5}$ ;  $4-1.0 \cdot 10^{-4}$ ;  $5-5.0 \cdot 10^{-4}$ ;  $6-1.0 \cdot 10^{-3}$ ;  $7-5.0 \cdot 10^{-3}$ ;  $8-1.0 \cdot 10^{-2}$ ; and  $9-5.0 \cdot 10^{-2}$  cm). (a) and (b), Theoretical data according to Eq. [15] for the current density 30.0 and 3.0 A/sq. dm., respectively. (c), The current efficiency ( $t_1$ ) as a function of the anode diffusion layer thickness ( $\delta$ ). Theoretical data according to Eq. [15] for the anode length ( $L$ ) 10 dm. and the current density ( $\circ$ ,  $\square$ ) 30.0 and 3.0 A/sq. dm., respectively. Other parameters used in calculation were as follows:  $r$ , 4.0 dm.;  $q$ , 0.26 liter/sec; and  $C_{sh}$ ,  $4.0 \cdot 10^{-3}$  mol/liter.

equation, due to the third power of concentration dependence. Also, the hydrogen ion distribution within the diffusion layer is of rather a complex nature. Thus, it is necessary to solve simultaneously several rather complicated differential equations, encompassing all equilibria, all diffusion fluxes, and also all the electrode reactions at the anode. This advanced and more complex matter will be reported at a latter instance (27).

It should also be noted that, in a view of the fact that active chlorine exhibits the appearance of a maximum concentration within the diffusion layer, which exceeds that in the bulk (13), its further chemical con-

version must not be neglected for higher operating temperatures at least. However, such temperatures just lately characterize up-to-date chlorate cell industrial practice.

The above treatment might be usefully applied as the one leading to the limiting optimal conditions. This implies that, just as the thermodynamic method usually gives the lower limits for the considered processes to be able to proceed at all, the present treatment also provides operational and dimensional limiting conditions for optimal cell current yields. Namely, providing the above-defined optimal cell parameters and main-

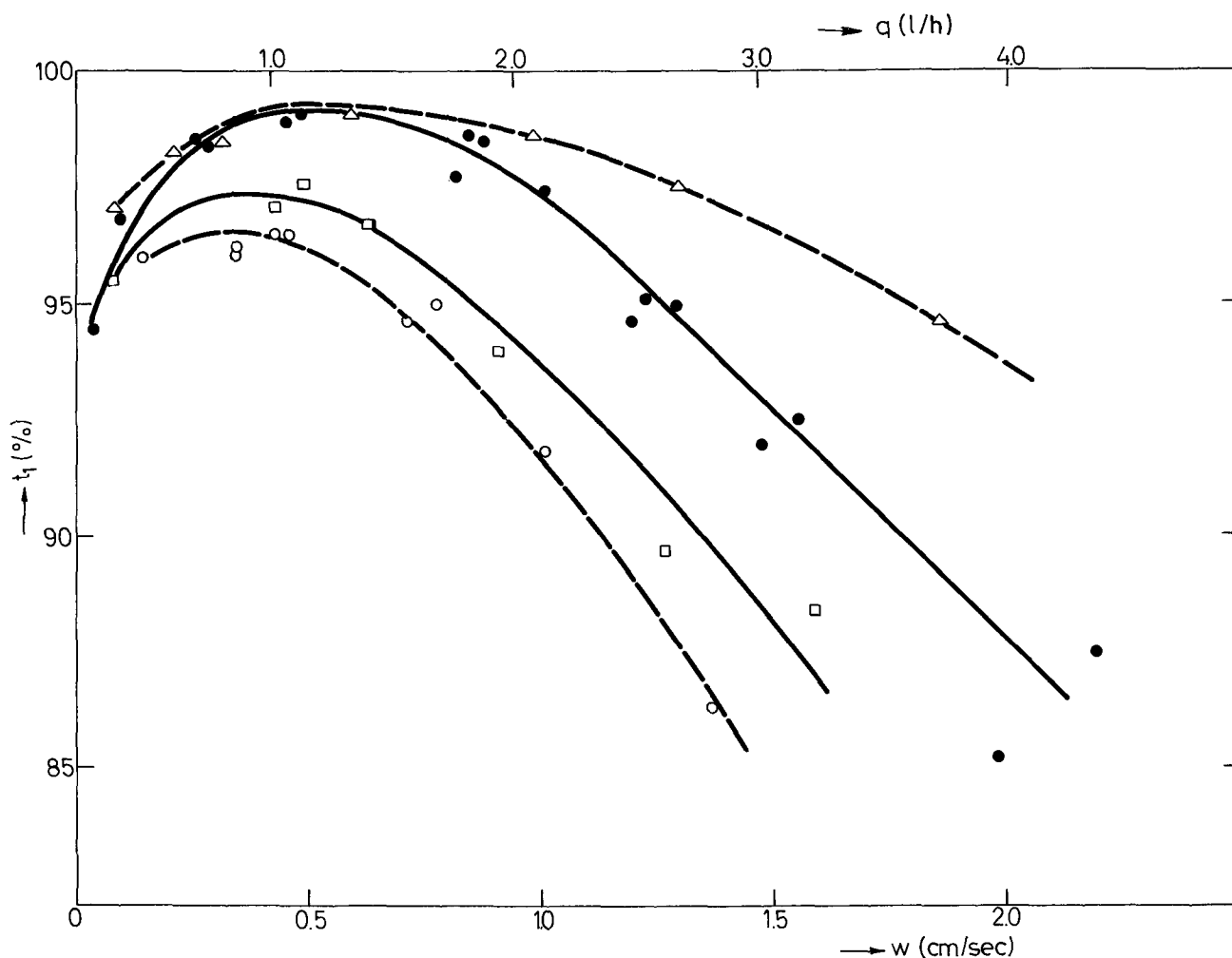


Fig. 9. The effect of the linear velocity of the brine flow on the over-all current efficiency in the chlorate cell plug-flow running. Experimental data for the ribbon type of the cell. ●, □, and ○, values for  $\text{pH}_c$ —6.5, 7.6, and 8.1, respectively, and at the current density 1.97 A/sq. dm.; △, values for  $\text{pH}_c$ —6.5 and  $i = 3.61$  A/sq. dm.

taining their mutual effect, i.e., the linear velocity of the brine flow, current density, pH, and temperature (just because of the effect of the latter on the decrease of the  $C_{sc}$  through its further chemical conversion to chlorate which was neglected in all the equations based on diffusion layer analysis); one could doubtlessly expect better results only, than those predicted by the above equations and consideration (cf. Fig. 5). It should also be noted that both relations which comprise the hydrodynamic factors (Eq. [10] and [15]), exhibit a very pronounced sensitivity on the active chlorine concentration ( $C_s$ ). Hence, the higher the temperature, the lower should be the active chlorine content, and thereby the higher the current efficiency.

The above consideration represents a certain scale-up and optimization guide for the chlorate cell process based on the Faradaic efficiency. Another side of the medal is represented by its voltage and power optimization. The latter has recently been developed and thoroughly carried out by Rousar *et al.* (25), particularly in examination of the cell dimensions and the gas bubble cell effects. Both methods, the mentioned one (25) and the one presented here, of course, lead to the mutual optimal point at which two independent schemes cross each other and thus define the most suitable operating conditions for the whole electrolytic process.

#### Experimental Guide

The experimental data presented in this paper were prevalently obtained by means of the same apparatus as that described elsewhere (2). The setup consisted of

an electrolytic cell 0.6 liter in volume and a holding vessel of 2.2 liters connected in a loop so as to provide a constant recirculation of brine at a given flow rate ( $q = 8.2 \times 10^{-4}$  liters/sec). The pH in the cell was maintained constant to within  $\pm 0.1$  pH unit by means of a pH-stat. The electrolyte was stirred both in the cell and in the holding volume so that they operated as back-mix-flow reactors. The stirring in the cell was intensified by the cathodic evolution of hydrogen and homogenized by an appropriate positioning of both the platinum gauze anode and the wire cathode.

The cell load was maintained at 4.5A, and with the electrode surface area  $A = 67.5$  cm<sup>2</sup>, this implied an anodic current density of 6.67 A/dm<sup>2</sup>.

The cell temperature was maintained at 25°C, while that of the holding volume varied between 15° and 80°C.

In the described setup and under the given hydrodynamic conditions, the diffusion layer thickness was experimentally estimated to be  $8.2 \times 10^{-4}$  cm by measuring the steady-state limiting diffusion current of the ferrous-cyanide oxidation from a usual and appropriate electrolyte composition [cf. (13)].

Other details of the apparatus and of the determination of the current efficiency may be found elsewhere (2).

The value of the rate constant of chlorine hydrolysis ( $k_1 = 0.17$  sec<sup>-1</sup>) was obtained by extrapolation of Spalding's data (28) for the actually existing ionic strength of the chlorate cell brine [cf. (14) and (18)].

The diffusion constants of elemental ( $D_1 = 6.7 \times 10^{-6}$  cm<sup>2</sup>/sec) and active chlorine ( $D_2 = 1.2 \times 10^{-5}$

cm<sup>2</sup>/sec) represents Chao's data (29) corrected for viscosity of solution at the given ionic strength of chlorate production [cf. (14)].

The activity coefficient of hypochlorous acid was taken from data of Imagawa (4) to be about 2.0. The corresponding value for hypochlorite ion, and for active chlorine as well, was estimated to be about 0.1 [cf. (14) and (18)]. Activity of water was approximately taken to be 0.8 (3). The rate constants for the active chlorine chemical conversion to chlorate as function of temperature were taken from data of De Valera (3).

The electrolyte consisted of 300 g/liter of NaCl and about 4.0 g/liter of sodium dichromate. The electrolysis was carried out to 30 g/liter of sodium chlorate, whereupon the electrolyte was renewed.

The apparatus with a ribbon type of cell and the plug-flow circulation was also described elsewhere (17, 24). The entire setup was very similar to the one described elsewhere (2) and partly here, the only difference being that all the dimensions of the apparatus were enlarged. The anode was DSA-electrode supplied by Oronzio de Nora, Milano, Italy ( $L = 70$  dm,  $r = 4.5$  cm). The current densities were  $i = 3.61$  and  $1.97$  A/sq.dm., and temperature ( $t_c$ ) was at  $14^\circ\text{C}$ .

#### Acknowledgments

Thanks are due to Dr. S. Bingulac for numerical computations. The author gratefully acknowledges the important personal help of Dr. Oronzio De Nora, Milano, Italy and his Company in supplying DSA electrodes for investigations and application in the Institute's cell and its chlorate process.

Manuscript submitted Sept. 8, 1972; revised manuscript received ca. July 30, 1973. This paper was presented at the Houston, Texas, Meeting of the Society, May 7-11, 1972.

Any discussion of this paper will appear in a Discussion Section to be published in the December 1974 JOURNAL.

#### APPENDIX I

It should be noted that, in deriving Faradaic stoichiometry and mass balance equations, one has been considering (2) both hypochlorous species as potentially equal entities able to take part in both Foerster's reactions of the chemical conversion and the anode oxidation. Hence, both species are together summationally expressed in a certain mutual and more suitable unique form of the active chlorine ( $C_s$ ). Therefore, for Eq. [1], it could be written

$$-\frac{d[\text{ClO}^-]}{dt} = -\frac{1}{2} \cdot \frac{d[\text{HClO}]}{dt} = \frac{d[\text{ClO}_3^-]}{dt} \quad [\text{A-1}]$$

or, otherwise

$$-\frac{dC_s}{dt} = -\frac{d([\text{HClO}] + [\text{ClO}^-])}{dt} = -3 \frac{d[\text{ClO}^-]}{dt} \quad [\text{A-2}]$$

Further, introducing Foerster's kinetic law for the chemical conversion in concentrated solutions or, in other words, recognizing Brönsted's kinetic theory (1, 4), it could be written

$$-\frac{dC_s}{dt} = 3 \cdot f^2 \cdot k_r [\text{HClO}]^2 \cdot [\text{ClO}^-] \quad [\text{A-3}]$$

As it is already descriptively said, one implies that the active chlorine represents the sum of both hypochlorous species, or otherwise

$$C_s = [\text{HClO}] + [\text{ClO}^-] \quad [\text{A-4}]$$

Two last relations could finally be combined with Eq. [7] that leads to the more suitable form of the kinetic law for the chemical chlorate formation (2, 5)

$$-\frac{dC_s}{dt} = 3 \cdot f^2 \cdot k_r \cdot \frac{K^* \cdot (a_{\text{H}_3\text{O}^+})^2}{[K^* + (a_{\text{H}_3\text{O}^+})]^3} \cdot C_s^3 \quad [\text{A-5}]$$

Namely, considering that both species reversibly interchange their states between each other over an extremely fast reaction of proton exchange [cf. (13)], the active chlorine might be imagined as an instantaneous mutual hybride form similar to an active complex in the transition state. Such a conclusion seems probable for the transition pH range at least, where both hypochlorous species exist in comparable contents.

#### APPENDIX II

##### Explanation of Fig. 5

Equation [10] could be presented in a somewhat more convenient form for further computer analysis. Hence, one firstly introduces another parameter ( $A$ ) being

$$A = D_2 \cdot F \cdot f_{sc} \cdot \frac{C_{sc}}{i \cdot \delta_M} \quad [\text{B-1}]$$

or in combination with Eq. [12] the latter leads to the relation

$$A = \frac{1}{2} \sqrt{\frac{D_2 \cdot F \cdot f_{sc} \cdot C_{sc}}{i}} \sqrt{\frac{k_1}{D_1}} \quad [\text{B-2}]$$

Finally, one more parameter ( $X$ ) can be introduced

$$X = \frac{\delta}{\delta_M} \quad [\text{B-3}]$$

Replacing Eq. [B-2] and [B-3] into Eq. [10], one obtains its other form

$$t_1 = \frac{1 - A/X}{\frac{3}{2} - \frac{1}{2} \frac{1 - \exp(-4AX)}{4AX}} \quad [\text{B-4}]$$

Thus, the parameter  $X$  in Fig. 5 represents in essence the variable  $\delta$  in a somewhat different and more suitable form. Hence, the various curves in Fig. 5 represent the basic relationship (Eq. [10]), expressed in a more convenient form (Eq. [B-4]), for different ratios  $C_{sc}/i$  used as parameter. This is reflected here over different  $A$  values ( $1 \cdot 10^{-4}$ ,  $2 \cdot 3.3 \cdot 10^{-4}$ ,  $3 \cdot 10^{-3}$ ,  $4 \cdot 3.3 \cdot 10^{-3}$ , and  $5 \cdot 10^{-2}$ ).

#### REFERENCES

1. F. Foerster and E. Müller, *Z. Elektrochem.*, **9**, 171 (1903); F. Foerster, *Trans. Electrochem. Soc.*, **46**, 23 (1924).
2. M. M. Jaksic, A. R. Despic, I. M. Csonka, and B. Z. Nikolic, *This Journal*, **116**, 1316 (1969); *ibid.*, **117**, 414 (1970).
3. V. de Valera, *Trans. Faraday Soc.*, **49**, 1338 (1953).
4. H. Imagawa, *Denki Kagaku*, **18**, 382 (1950); *ibid.*, **19**, 271 (1951); *ibid.*, **20**, 571 (1952); *ibid.*, **21**, 520 (1953); *ibid.*, **25**, 607 (1957); *Bull. Fac. Eng. Yamaguchy Univ.*, Spec. Print., Series 10, No. 1, p. 147 (1956).
5. M. M. Jaksic, B. Z. Nikolic, I. M. Csonka, and A. B. Djordjevic, *This Journal*, **116**, 684 (1969).
6. R. Caramazza, *Gazz. Chim. Ital.*, **87**, 1507 (1957).
7. J. C. Morris, *J. Phys. Chem.*, **70**, 3798 (1966).
8. M. M. Jaksic, A. R. Despic, B. Z. Nikolic, and S. M. Maksic, *Croat. Chem. Acta*, **44**, 61 (1972).
9. R. T. Atanasoski, A. Filip, B. Z. Nikolic, M. M. Jaksic, and A. R. Despic, Paper presented at ISE Meeting, Stockholm, August 1972.
10. M. W. Lister, *Can. J. Chem.*, **34**, 465 (1956); *ibid.*, **30**, 879 (1952); *ibid.*, **40**, 729 (1962).
11. G. H. Ayres and M. H. Booth, *J. Am. Chem. Soc.*, **77**, 825, 828 (1955).
12. J. Claus, Paper 256 presented at Electrochemical Society Meeting, Boston, May 5-9, 1968.
13. N. Ibl and D. Landolt, *This Journal*, **115**, 713 (1968); N. Ibl, *Chem. Ing. Techn.*, **39**, 706 (1967); D. Landolt, Ph.D. Thesis, Eidgenössischen Technischen Hochschule, Zurich, Prom. Nr. 3673, Juris-Verlag, Zurich (1965).
14. A. R. Despic, M. M. Jaksic, and B. Z. Nikolic, *J. Appl. Electrochem.*, **2**, 337 (1972).
15. N. Ibl and J. Venczel, *Metalloberflaeche*, **24**, 365 (1970).

16. M. G. Fouad and G. H. Sedahmed, *Electrochim. Acta*, **17**, 665 (1972).
17. A. R. Despic, M. M. Jaksic, and M. D. Spasojevic, *J. Appl. Electrochem.*, To be published; M. D. Spasojevic, Chem. Eng. Thesis, Faculty of Technology and Metallurgy, University of Belgrade, Belgrade (1971).
18. M. M. Jaksic, *J. Appl. Electrochem.*, Submitted for publication.
19. K. Schwabe, *Electrochim. Acta*, **12**, 67 (1967).
20. G. Milazzo and R. Defay, *J. Electroanal. Chem.*, **2**, 419 (1961); G. Milazzo and M. Sotto, *Z. Physik. Chem., Neue Folge*, **52**, 293 (1967); G. Milazzo, M. Sotto, and C. Devillez, *ibid.*, **54**, 1, 13 (1967); G. Milazzo, *ibid.*, **54**, 27 (1967); G. Milazzo, *ibid.*, **62**, 47 (1968); G. Milazzo and J. Chanu, *ibid.*, **68**, 250 (1969); G. Milazzo, *J. Res. Inst. Catalysis, Hokkaido Univ.*, **16**, 387 (1968).
21. M. M. Jaksic, A. R. Despic, and B. Z. Nikolic, *Elektrokhimiya*, **8**, 1573 (1972).
22. V. I. Eberil', D. V. Kokoulina, L. I. Krishtalik, and L. M. Elina, *ibid.*, **5**, 336 (1969); V. I. Eberil' and F. V. Kupovich, *ibid.*, **6**, 332 (1970); V. I. Eberil' and L. M. Elina, *ibid.*, **6**, 782 (1970); V. I. Eberil' and L. M. Elina, *ibid.*, **6**, 1010 (1970).
23. Dimensionally Stable Anodes, Permelec, Milano (1969).
24. M. M. Jaksic, Doctor's Dissertation, Faculty of Technology and Metallurgy, University of Belgrade, Belgrade (1970).
25. I. Rousar, V. Cezner, and A. Regner, *Coll. Czech. Chem. Commun.*, **31**, 4193 (1966); I. Rousar, V. Cezner, and J. Hostomsky, *ibid.*, **33**, 808 (1968); I. Rousar and V. Cerner, *ibid.*, **32**, 1137 (1967); I. Rousar, *This Journal*, **116**, 676 (1969); I. Rousar, V. Cezner, J. Hostomsky, M. M. Jaksic, M. D. Spasojevic, and B. Z. Nikolic, Paper presented at the ISE Meeting, Stockholm, September 1972.
26. O. Levenspiel, "Chemical Reaction Engineering, An Introduction to the Design of Chemical Reactors," John Wiley & Sons, Inc., New York (1962).
27. M. M. Jaksic, Paper 231 presented at Electrochemical Society Meeting, Chicago, Illinois, May 13-18, 1973.
28. C. W. Spalding, Ph.D. Thesis, Lawrence College, Appleton, Wisconsin (1961); C. W. Spalding, *AIChE J.*, **8**, 685 (1962).
29. M. S. Chao, *This Journal*, **115**, 1172 (1968).
30. M. M. Jaksic, Can. Pat. 851,695 (Sept. 15, 1970).
31. L. J. J. Janssen and J. G. Hoogland, *Electrochim. Acta*, **15**, 1013 (1970).
32. Krebs and Cie, Paris, French Pat., 1,502,793 (October 16, 1967).
33. T. Matsumura, R. Itai, M. Shibuya, and G. Ishi, *Electrochem. Technol.*, **6**, 402 (1968).

## Standard Electrode Potential Measurements of Pb/PbCl<sub>2</sub>/HCl and Tl/TlCl/HCl Half Cells in Dimethylformamide at 30°C

Frank Leslie Bates<sup>1</sup> and Yeu Tsang Nee<sup>2</sup>

Department of Chemistry, The University of Detroit, Detroit, Michigan 48221

### ABSTRACT

The potentials of electrodes consisting of metal, solid metal chloride, and a solution of a soluble chloride (anhydrous HCl) in dimethylformamide (DMF) have been measured *vs.* a hydrogen electrode as the reference electrode. Half cells Pb/PbCl<sub>2</sub>/HCl and Tl/TlCl/HCl were prepared by contacting pure metal with its associated chloride after forming the solid phase in a glass tube. Elaborate and scrupulous procedure is important for preparing the hydrogen electrode to attain reliable and reproducible measurements in DMF. Standard electrode potentials of  $-0.3368$  and  $-0.5994V$  *vs.* SHE in DMF, at 30°C, were attained in DMF for the lead chloride and thallium chloride electrodes, respectively, at 30°C.

Measurements of electrode potentials in nonaqueous solvents have shown complications since 1909, even though some of them were found to be a natural and straightforward extension of the corresponding measurements in aqueous solutions. Pavlopoulos and Strehlow (1) measured the standard potentials of some heavy metals in the solvent formamide, but were unsuccessful in using the Ag/AgCl electrode in the same solvent. The Ag/AgCl electrode in formamide was used for measurements without much difficulty by Mandel and Decroly (2).

Since the unsubstituted amides (with the exception of formamide) are all crystalline solids at room temperature, N,N-dimethylformamide was chosen, which is a powerful solvent for both polar and nonpolar compounds. It has not been investigated as a nonaqueous solvent (3) for the measurement of electrode potentials. It was employed in this paper for the measurement of the standard potential of electrodes of the metal-insoluble salt type *vs.* the hydrogen electrode.

### Discussion

In Pavlopoulos and Strehlow's paper (1) the hydrogen electrode was used without adequate descrip-

tion of operational detail. The literature indicates that the level of accuracy of most potentiometric measurements in anhydrous solutions has been insufficient to warrant any distinct choice between alternative methods of preparing the hydrogen electrode. The attainment of a truly reproducible hydrogen electrode actually holds the key to the successful performance in its role as the reference electrode (4) in anhydrous DMF solutions.

A typical laboratory procedure for preparing the platinized hydrogen electrode in aqueous solutions includes cleaning the Pt plate with aqua regia, testing the cleanliness in a 10% solution of H<sub>2</sub>SO<sub>4</sub>, then electrolyzing it as the cathode in dilute NaOH and H<sub>2</sub>SO<sub>4</sub> solutions after electrolyzing it as the cathode for 5 min in a 3% solution of chloroplatinic acid containing 0.5 ml of 0.1N lead acetate in 100 ml solution.

The portion of the procedure most likely to cause a difference in behavior of the hydrogen electrode in aqueous and nonaqueous solutions is the process of platinization. Lead acetate is added to the platinizing solution as an impurity. Purified chloroplatinic acid solutions give only bright Pt deposits upon the platinum plate, which as an electrode can be initially active but decays in activity rather rapidly. Hence the lead acetate has to be retained in the platinizing solution (5). The second factor with prominent importance

<sup>1</sup> Deceased.

<sup>2</sup> Present address: No. 58, Tung Hai Road, Tung Hai University, Tai-Chung, Taiwan, The Republic of China.

Key words: electrode potentials, metals in DMF.

is the thickness of the coating of the Pt black hiding the sheen of the metal base. The actual thickness of the Pt black does not matter at all in water solutions. The thicker the film, the more likely will the electrode give constant results. In 1922, Clark (6) made use of a thin deposit of Pt black to avoid reduction of the metal ion upon the hydrogen electrode. Confirmed by Draves and Tartar (7) in 1925, the reduction on the surface of the Pt plate was due to the use of a thickly coated electrode in nonaqueous solutions. Walter (8) in 1926 renewed platinized hydrogen electrodes after three or four measurements. Kanning and Bowman (9) in 1946 attempted to lengthen the usual short life of hydrogen electrodes in methanol beyond 60 min. Moore and Felsing (10) pointed out that the electrodes which were least platinized gave the highest potential values and approached a near steady state most rapidly. Then in 1956 Oiwa (11) mentioned in a paper dealing with activity coefficients of HCl in methanol-water mixtures that the hydrogen electrodes used were plated with Pt black as thin as possible. It is evident that Pt black is necessary, but only the minimum thickness required to obscure the surface luster should be used.

In view of all the difficulties with the hydrogen electrode in anhydrous solvents, all of which indicating some irreversible change in the condition of the electrode, the only hope of finding the reversible potential is to get it before the irreversible change in the hydrogen electrode occurs, namely at zero time. The spontaneous, irreversible electrochemical process reduces the potential from the hypothetical reversible value given by the cell as it is initially constituted. Mandel and Decroly (2) extrapolated the drifting potential back to zero time, that is to the time the cell was assembled as a complete unit. By soaking the metal electrode in the cell solution for some time and washing the hydrogen electrode with the cell solution before use, all the possible, purely chemical (as distinct from electrochemical) changes are allowed to occur before the circuit is actually completed.

### Experimental Preparation

**Cell.**—The cell is an H-cell with two limbs. The first limb had a diameter of about 1 cm. There was a neck (constriction) made close to the lower end with the purpose of keeping the metal chloride from being stirred up. The second limb had a diameter of 4 cm. Into this limb the hydrogen electrode was placed. Clean glass wool was used in the connecting arm to minimize the diffusion of metal salt onto the platinum plate resulting in the poisoning of the hydrogen electrode.

**Metals electrodes.**—Pure metal in its molten state was sucked into a glass tube through a small nozzle (Fig. 1). The molten metal gradually solidified from the side to the center of the tube.

**Hydrogen electrode.**—The Pt plate was thinly platinized with Pt black so as just to hide the sheen. The electrodes were cleaned before each platinization by electrolyzing in concentrated HCl day and night; sometimes a week or more was required. The hydrogen gas was maintained at 1 atm pressure.

**Metal chlorides.**—Metal chlorides were dried for a sufficient period of time at an appropriate temperature to remove the water of crystallization.

**Hydrogen gas.**—Commercial tank hydrogen purified by passing through a train consisting of basic pyrogallol, sulfuric acid, and anhydrous calcium chloride was used.

**Formamide.**—The formamide used was prepared by Eastman Organic Chemicals, and had a refractive index 1.4457 at 26°C.

**N,N-dimethylformamide.**—The reagent grade DMF purchased from Fischer Scientific Company was purified by shaking it with BaO powder (technical grade, Code 1422), decanted, and distilled at 15–20 mm Hg

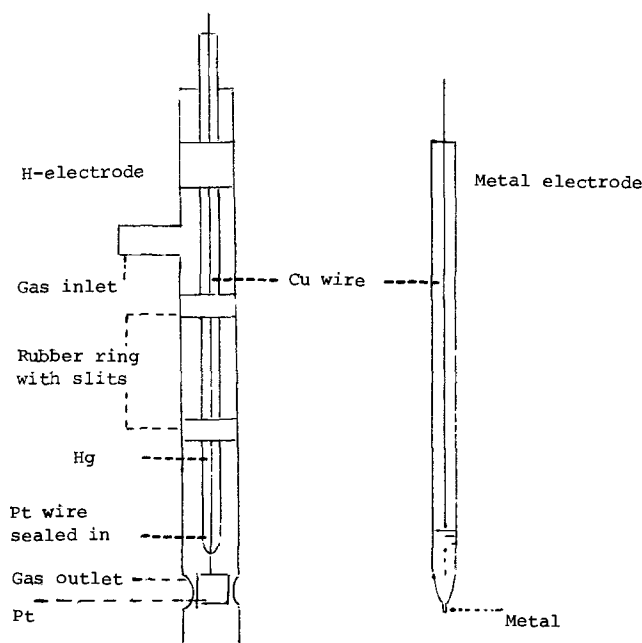


Fig. 1. Form of the electrodes

pressure and the middle fraction of the distillate retained. The distillate had a refractive index of 1.4280 at 26°C.

**HCl-amide solution.**—Dry gaseous tank HCl was passed into the amide one day before measuring. This process could be carried out in a 125 ml Erlenmeyer flask. Care must be exercised to keep the solution dry and away from getting contact with the rubber stopper. It would be much safer to use a glass stopper to fit the flask. The solution was then poured into the cell in which the dry metal salt and clean glass wool were placed beforehand. Subsequently, the metal electrode was introduced into the left cell and allowed to stand with the salt in the HCl-amide solution. After the metal and the metal salt stood in contact with the solution for 10–12 hr indicating that the metal had become coated with metal chloride, the half cell was able to reach a steady and reproducible voltage when coupled with the hydrogen electrode.

The sample of the HCl-amide solution to be analyzed for chloride ion concentration was withdrawn from the bulk of the solution before it was poured into the cell. It was not permissible to prepare a stock volume of HCl-amide solution, enough to be used over a longer period of time, because of the suspected decomposition resulting from hydrolysis of amide by very small traces of water and catalyzed by HCl.

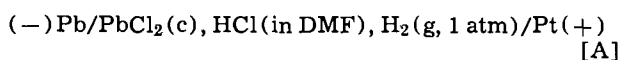
**The determination of the HCl concentration in the solvent amide.**—A 2 or 5 ml sample was treated with enough NaOH to make it basic plus a little excess and evaporated until the residue was only slightly damp. The amide in the form of a light yellow residue was decomposed on the addition of about 1 ml of 15N NaOH and a few milliliters of 3% H<sub>2</sub>O<sub>2</sub>, just enough to react with all the amide. After the foaming ceased, water was then added to dissolve the reaction mixture and to make the total volume about 50 ml. The solution was acidified with HClO<sub>4</sub> and titrated with 0.1N AgNO<sub>3</sub> using potassium chromate as the indicator. Two porcelain crucibles were used in order to catch the end point accurately, since the addition of chromate would give the solution to be titrated a color between orange and light red in a presence of organic amine. As the end point was approached, which can be easily detected in the process of titration, the precipitate was allowed to settle. The liquid was decanted into the second crucible. The color of the precipitate would stay white or nearly so before the end point. At the end point there would be a red precipitate appearing in the



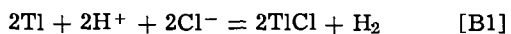
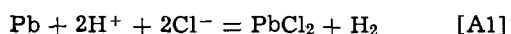
AgCl precipitate like a mass of cottage cheese studded with red crystals. Once the end point was overpassed the whole body of precipitate would turn to clearer red tint. Some of the results from titration were further tested by gravimetric precipitation of silver chloride.

**EMF measurements.**—After the metal electrode stood in the cell with the metal chloride and HCl-amide solution for about 10-20 hr, H<sub>2</sub> gas was bubbled through the cell solution in the larger compartment for 2 hr. Simultaneously, the temperature of the thermostat was adjusted to the desired value. The upper part of the tube containing the hydrogen electrode was dried by passing dry N<sub>2</sub> or H<sub>2</sub> gas through the tube for 2 hr. At the end of the 2 hr, the hydrogen electrode was rinsed several times with the cell solution before it was introduced into the cell. A Leeds and Northrup Type K-2 potentiometer was used to measure the cell potentials at intervals over a period of time. The potential values which changed slightly (not more than a few mV) with time were extrapolated to zero time to obtain the initial value of the cell potential *E*.

**Treatment of data.**—The cells studied were



at 30°C. For the conventional cell reactions



the standard cell potential *E*<sup>0</sup> is related to the actual cell potential *E* and to the activity of the acid electrolyte by the Nernst equation

$$E = E^0 + (RT/F) \ln(a_{\text{H}^+} + a_{\text{Cl}^-}) \quad [1]$$

At a given molar concentration of acid, the approximate value of *E*<sup>0</sup>, indicated by *E'*, can be calculated from the concentration and the experimental *E* by the equations

$$E' = E - 0.1183 \log C_{\text{HCl}}, \text{ at } 25^\circ\text{C} \quad [2a]$$

$$E' + E - 0.1203 \log C_{\text{HCl}}, \text{ at } 30^\circ\text{C} \quad [2b]$$

Equation [1] is valid at unit fugacity (1 atm) of hydrogen gas.

The measured potential values were followed as a function of time. The drift from the "true" cell emf (at zero time) does not appear to exceed a few thousandths of a volt in any case after 30 min.

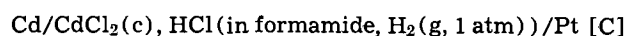
The correct value of *E*<sup>0</sup> for cells [A] and [B] can be found by plotting the *E'* values obtained with various concentrations of HCl via Eq. [2b] against  $\sqrt{C}$ . By the method of least squares, the standard potential *E*<sup>0</sup> of cells [A] and [B] is obtained as the intercept of the *E'* -  $\sqrt{C}$  curve, extrapolated to the limit  $\sqrt{C} \rightarrow 0$ .

The numerical data for cells [A] and [B] with two different hydrogen electrodes are summarized in Tables I and II, respectively. These tables list the observed cell potentials *E* in volts, the values of *E'* calculated via Eq. [2b], and the concentrations *C* in moles of HCl per liter of solution in dimethylformamide. The tables also give the least squares equations for *E'* vs.  $\sqrt{C}$  for two separate hydrogen electrodes with each cell, and give an estimate of *E*<sup>0</sup> with its standard deviation for each of the four sets of data. For each cell, the two values of *E*<sup>0</sup> are consistent within the experimental error, despite the discrepancy in the observed slopes for the two separate hydrogen electrodes (see below).

The cell *E*<sup>0</sup> values reported in Tables I and II for cells [A] and [B] can be equated to what Latimer (13) called the oxidation potentials of the Pb/PbCl<sub>2</sub> and Tl/TlCl redox couples in DMF at 30°C, respectively. Following the conventions adopted by the International Union of Pure and Applied Chemistry (12) at Stockholm in 1953, cell potentials with the SHE at the right-hand terminal should not be called electrode potentials. Rather, the standard potentials of the Pb/PbCl<sub>2</sub> and Tl/TlCl electrodes in DMF may be equated to the cell *E*<sup>0</sup> values of the reversed forms of cells [A] and [B]. Therefore, the electrode potentials reported here are equal in value but opposite in sign to the cell *E*<sup>0</sup> values. The standard electrode potentials *E*<sup>0</sup> are negative for both electrodes, corresponding to the (-) d-c polarity exhibited experimentally by both electrodes in cells [A] and [B] (Tables I and II, bottom line).

### Conclusion

The procedure for the determination of the standard potentials of anion responsive electrodes of the Ag/AgCl type in nonaqueous solvents was checked by measuring the potential of the cell



at 25°C. The equation for *E'* was obtained as  $E' = -0.0308 \sqrt{C} + 0.6158$  giving the standard potential of the electrode: Cd/CdCl<sub>2</sub>/HCl(in formamide),  $E^0 = -0.6158 \pm 0.0068\text{V}$  at 25°C [as compared to the value of  $-0.617 \pm 0.004$  given by Pavlopoulos and Strehlow (1)].

Table I. Potential data for cell [A] at 30°C

Data observed with:	1st hydrogen electrode				2nd hydrogen electrode			
Cell potential <i>E</i> , V (extrapolated to zero time)	0.3689	0.3630	0.3038	0.2365	0.2389	0.2788	0.3075	0.1982
<i>E'</i> , V	0.3748	0.3743	0.3595	0.3518	0.3289	0.3263	0.3271	0.3327
<i>C</i> , moles/liter	0.8926	0.8060	0.3437	0.1101	0.1785	0.4030	0.6785	0.0760
Equation of the <i>E'</i> vs. $\sqrt{C}$ line	$E' = 0.03953 \sqrt{C} + 0.3378$				$E' = -0.01091 \sqrt{C} + 0.3358$			
Standard potential of cell [A]	$E^0 = 0.3378 \pm 0.0011$				$E^0 = 0.3358 \pm 0.0020$			

Standard potential of Pb/PbCl<sub>2</sub>/HCl electrode in DMF, vs. SME in DMF, at 30°C.  
 $E^0(\text{Pb/PbCl}_2 \text{ in DMF}) = -0.3368 \pm 0.0015\text{V}$

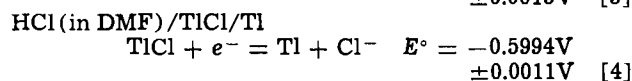
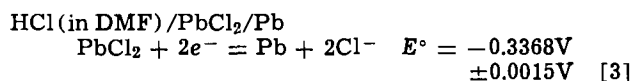
Table II. Potential data for cell [B] at 30°C

Data observed with:	1st hydrogen electrode				2nd hydrogen electrode			
Cell potential <i>E</i> , V (extrapolated to zero time)	0.6018	0.7153	0.5900	0.7000	0.5874	0.5776	0.6760	0.5430
<i>E'</i> , V	0.6761	0.7323	0.6703	0.7230	0.6617	0.6579	0.6990	0.6467
<i>C</i> , moles/liter	0.2410	0.7220	0.2148	0.6443	0.2410	0.2148	0.6443	0.1374
Equation of the <i>E'</i> vs. $\sqrt{C}$ line	$E' = 0.1554 \sqrt{C} + 0.5994$				$E' = 0.1241 \sqrt{C} + 0.5994$			
Standard potential of cell [B]	$E^0 = 0.5994 \pm 0.0010$				$E^0 = 0.5994 \pm 0.0012$			

Standard potential of Tl/TlCl/HCl electrode in DMF, vs. SHE in DMF, at 30°C.  
 $E^0(\text{Tl/TlCl in DMF}) = -0.5994 \pm 0.0011\text{V}$

Upon consideration of the solubility of metal chlorides in dimethylformamide, the standard potentials of the Pb/PbCl<sub>2</sub>/HCl and Tl/TlCl/HCl electrodes have been determined in this study in DMF. The  $E'$  values revealed an interesting point. From the two hydrogen electrodes, two sets of  $E'$  values for different concentrations of HCl in the solvent DMF converge to an identical standard potential  $E^\circ$  value. This phenomenon probably results from the difference in thickness of the Pt black plated upon the two hydrogen electrodes. It supports the hypothesis that Pt black made as thin as possible is effective in improving the reproducibility of voltages obtained in anhydrous DMF.

The standard electrode potentials in DMF at 30°C are obtained from the present study as follows



The individual standard electrode potentials are referred to that of the standard hydrogen electrode in the same solvent, and the algebraic sign conforms to that adopted by the International Union of Pure and Applied Chemistry (12) in expressing the electrode potential.

It appears that not only does the hydrogen electrode respond differently in nonaqueous solvents than it does in water, but also problems are encountered peculiar to the particular solvent employed. The conception we have had for the electrochemical response of the hydrogen electrode in water is not equally applicable to anhydrous nonaqueous solvents. The prolonged usage of the platinized hydrogen electrode in nonaqueous solvents continually for two or more hours is harmful to its proper functioning. Between measurements a procedure of soaking the hydrogen electrode in concentrated HNO<sub>3</sub> for about 3 hr, followed by subsequent electrolysis in NaOH and H<sub>2</sub>SO<sub>4</sub> is a satisfactory way to prevent the deposition of metal ions on the surface of the electrode and to prolong its life. Where the possibility of reduction of metal ion is negligible, the HNO<sub>3</sub> treatment could be omitted. The poisoning of the electrode is indicated by a decrease in potential which may even result in a reversal of polarity. It is conceivable that there is a corresponding span of catalytic life for each thickness of Pt black for its usage

in a particular solvent, although it was not possible to determine any real difference between the two solvents used.

The experimental results indicate that the hydrogen electrodes were functioning satisfactorily during most of the runs generally showing only slow drifts in potential with no erratic behavior. The proper thickness of the platinum black proved to be the critical factor in the use of the platinized hydrogen electrode in the anhydrous nonaqueous solvents: formamide and dimethylformamide.

Manuscript submitted July 24, 1972; revised manuscript received July 11, 1973.

Any discussion of this paper will appear in a Discussion Section to be published in the December 1974 JOURNAL.

#### LIST OF SYMBOLS

$E$	cell potential extrapolated at zero time from the measured potentials, V
$E^\circ$	standard cell potential, V. Also, the electrode potential (IUPAC)
$E'$	approximate value of $E^\circ$ at a given concentration of acid electrolyte, V
$R$	ideal gas constant
$T$	absolute temperature, Kelvins
$F$	Faraday constant, 96487 coulombs/equiv
$C$	molar concentration, moles/liter of solution

#### REFERENCES

1. T. Pavlopoulos and H. Strehlow, *Z. Phys. Chem. (Frankfurt)*, **2**, 89 (1954).
2. M. Mandel and P. Decroly, *Nature*, **182**, 794 (1958).
3. J. F. O'Donnell and C. K. Mann, *J. Electroanal. Chem.*, **13**, 163 (1967).
4. D. J. G. Ives and J. G. Janz, "Reference Electrodes," Academic Press, New York and London (1961).
5. A. M. Feltham and M. Spiro, *Chem. Rev.*, **71**, 177 (1971).
6. W. M. Clark, *J. Am. Chem. Soc.*, **44**, 1072 (1922).
7. C. Z. Draves and H. V. Tartar, *ibid.*, **47**, 1226 (1925).
8. W. L. Walter, *Z. Phys. Chem.*, **121**, 254 (1926).
9. E. W. Kanning and M. G. Bowman, *J. Am. Chem. Soc.*, **68**, 2042 (1946).
10. R. L. Moore and W. A. Felsing, *ibid.*, **69**, 1076 (1947).
11. I. T. Oiwa, *J. Phys. Chem.*, **60**, 754 (1956).
12. IUPAC—Stockholm Conventions, *J. Am. Chem. Soc.*, **82**, 5517 (1960); *J. Chem. Educ.*, **34**, 435 (1957).
13. W. M. Latimer, "Oxidation Potentials," Prentice-Hall, Englewood Cliffs, N. J. (1952).

# On the Transference Number for Li<sup>+</sup> Ion in Propylene Carbonate Solutions from EMF Measurements

James P. Hoare\* and Charles R. Wiese

Electrochemistry Department, Research Laboratories, General Motors Corporation, Warren, Michigan 48090

## ABSTRACT

The rest potential of a Li/Li<sup>+</sup> electrode was determined with respect to a Li/Li<sup>+</sup>, 1M reference electrode in propylene carbonate solutions of LiClO<sub>4</sub> as a function of the Li<sup>+</sup> ion concentration and of the H<sub>2</sub>O concentration. The transference number for Li<sup>+</sup> ion was determined from these data and found to be 0.32. This value is virtually independent of the amount of H<sub>2</sub>O present in the PC solution. For low water content, the electrode is one of the first kind and the potential is determined by the Li/Li<sup>+</sup> reaction. At high water content, the electrode becomes one of the second kind and the potential is determined by the Li/LiOH reaction. The transition from one reaction to the other takes place where, on the average, one H<sub>2</sub>O molecule replaces one PC molecule in the solvation sheath of each Li<sup>+</sup> ion.

To investigate the electrochemical properties of the light, highly reactive metal electrode systems, it is desirable to use an aprotic nonaqueous electrolyte. In the search for a suitable reference electrode for the study of such a system, the possibility of employing the Li/Li<sup>+</sup> couple in propylene carbonate (PC) was considered since this couple has been reported (1) to be reversible and well behaved. From chronopotentiometric and cyclic voltammetric studies (2, 3), it appears that the presence of water in this system may play (3) a complex role. Keller and associates (4) report that the mobility of the Li<sup>+</sup> ion in PC is very low ( $t_+ \sim 0.25$ ) as determined from conductance measurements. Solvation of the Li<sup>+</sup> ion may account for the low value of the transference number,  $t_+$ .

Using a reference electrode composed of a Li rod in 1M LiClO<sub>4</sub> in PC, the potential of a concentration cell, Li/LiClO<sub>4</sub> ( $C = x$ ), PC | PC, LiClO<sub>4</sub> (1M)/Li, was investigated as a function of the Li<sup>+</sup> ion and H<sub>2</sub>O concentration. Some information about the effect of H<sub>2</sub>O on the ionic mobilities and on the potential-determining reactions at the Li electrode can be obtained from these studies. This report describes the results of such an investigation since to these authors' knowledge this information is not available in the reviewed literature.

## Experimental

All experiments were carried out in a glove box in an argon atmosphere in which the oxygen, nitrogen, and water content are maintained below 1 ppm. The PC was vacuum (2 Torr) distilled in a still with a Podbilniak column and the first 30% of the still pot charge was discarded. The next 60% of the pot charge was used in the experiments. Ultrapure LiClO<sub>4</sub> certified to contain less than 20 ppm H<sub>2</sub>O was used to make up a stock solution of 1M LiClO<sub>4</sub> in PC. Further traces of H<sub>2</sub>O were removed from these solutions by gettinger with scraped Li foil until no water was detected by a Karl Fischer titration (<5 ppm H<sub>2</sub>O). Such treated solutions will be referred to as dry solutions.

After investigating a number of designs for the envelope of our reference electrode including cracked glass, wetted ground glass, and asbestos fiber junctions, the best performance was obtained with glass frits. A glass tube (13.5 cm long sealed at one end by a glass frit 1 cm thick and 0.5 cm in diameter with a pore diameter of 4-8 μm) was filled with the dry 1M LiClO<sub>4</sub>-PC reference solution. After a Li wire (0.3 cm in diameter) was placed in the solution, the top of the tube was sealed with an epoxy plug so that electrical connection

to the protruding Li wire could be made. When not in use, these electrodes were immersed in the dry 1M LiClO<sub>4</sub>-PC solution in an auxiliary vessel.

The test electrodes were made from pure Li wire (0.3 cm in diameter) and from a cast rod (1.5 cm in diameter). These electrodes were cast in an epoxy resin and the ends of the electrodes were polished flush with the epoxy cast. From long term compatibility studies, it was found that the epoxy resin did not interact with the electrolyte nor with the Li metal. These electrodes were clamped by a holder in the cell (a glass crystallizing dish 6 cm in diameter and 3 cm deep) filled with the electrolyte to be studied. The reference electrode was clamped in position in the cell only when measurements were being made. Before each run, the faces of the electrode were scraped with a stainless steel spatula.

In a typical run the rest potential of the Li electrode was recorded with a Keithley 600A electrometer after the potential vs. the Li/Li<sup>+</sup> (1M LiClO<sub>4</sub>-PC) reference electrode had come to a steady value (usually within 30 min). The solution was stirred continuously with bubbling argon. Afterwards, a sample of the electrolyte was removed for the determination of its H<sub>2</sub>O content by a Karl Fischer titration. The temperature of these experiments was 24° ± 1°C. Water was added to the electrolyte with a microsyringe and the concentration of Li<sup>+</sup> ion was changed by dilution with pure dry PC.

## Results and Discussion

In Fig. 1 is plotted the rest potential of a Li/Li<sup>+</sup> electrode vs. Li/Li<sup>+</sup>, (1M) for six solutions of LiClO<sub>4</sub> ranging from 1 to 0.001M as a function of the water content of the solution. Each point on these curves is the average value of nine independent readings using three different reference electrodes and three different test electrodes with two different areas (0.28 and 7.1 cm<sup>2</sup>). For those data points where the potential decreases with increasing H<sub>2</sub>O content, the data were reproducible within ±1 mV (for low H<sub>2</sub>O content and high Li<sup>+</sup> ion content, within ±0.5 mV). In the cases where the water content is high and the Li<sup>+</sup> ion content is low, the rest potential increases rapidly with water content and there is a spread of potential values between electrodes of different areas ranging as much as 20 mV. At very high H<sub>2</sub>O content (above 6000 ppm H<sub>2</sub>O in the 0.01M LiClO<sub>4</sub>-PC solution), this area effect disappears and the data can be reproduced within ± 1.5 mV.

The test electrode and reference electrode constitute a concentration cell whose potential is

$$E = E_1 - E_2 + E_j = \frac{RT}{nF} \ln \left( \frac{a_1}{a_2} \right) + E_j \quad [1]$$

\* Electrochemical Society Active Member.

Key words: lithium, propylene carbonate, transference number.

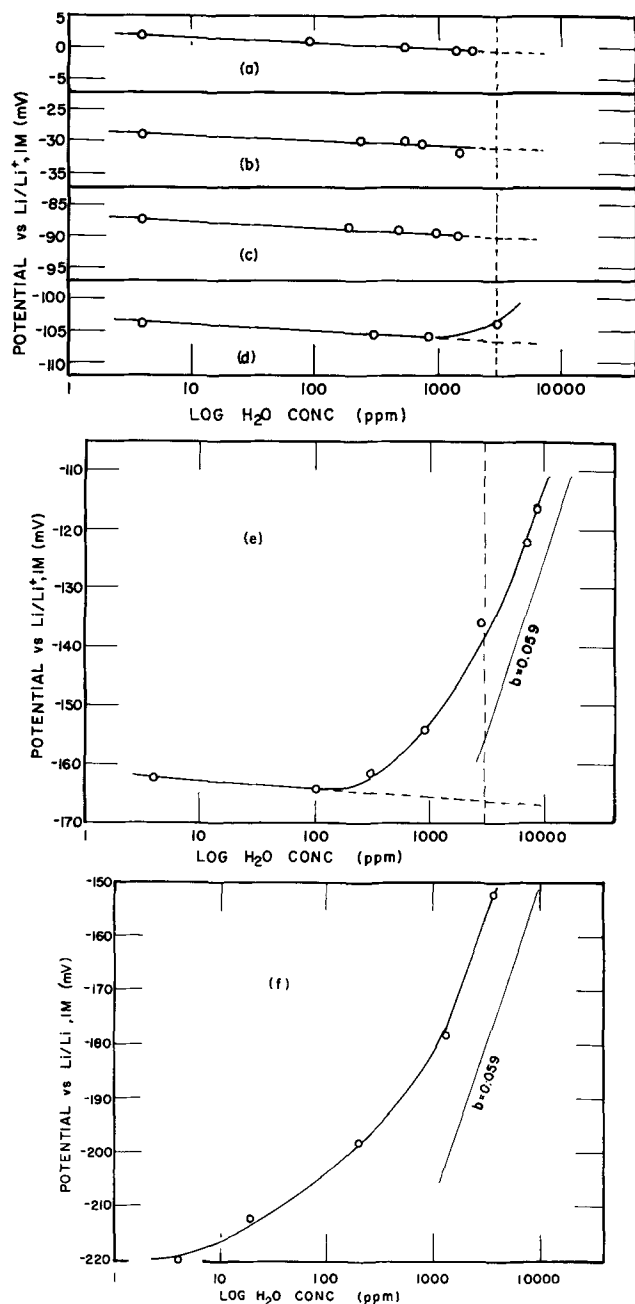


Fig. 1. Plots of the rest potential of a Li/Li<sup>+</sup> electrode as a function of the H<sub>2</sub>O content of the PC solutions of 1M (a), 0.5M (b), 0.1M (c), 0.05M (d), 0.01M (e), and 0.001M (f) LiClO<sub>4</sub>. The vertical dashed line appears at 3000 ppm H<sub>2</sub>O and the lines are extrapolated to this point in (a-e) to obtain the data (triangles) in Fig. 2. A line with a slope of 0.059 is given in (e, f) for the sake of comparison.

where  $a_1$  and  $a_2$  are the activities of the reversible ion on each side of the liquid junction and  $E_j$  is the junction potential which is a function of the activities and transference numbers of all the ions present. It can be shown [e.g., (5)] that for a one-one salt

$$E = \frac{2RT}{F} (t_-) \ln \frac{(a_+)_1}{(a_+)_2} \quad [2]$$

Note that the transference number,  $t_-$ , involved in Eq. [2] refers to the ion (in this case, the anion) which is not the reversible ion (in this case the cation).

A plot of the rest potential as a function of the log of the Li<sup>+</sup> ion concentration is given in Fig. 2 (circles) for dry solutions of LiClO<sub>4</sub> in PC. Here  $a_2$  is always 1M and it is assumed that the activity coefficients are the same for both the test and the reference solution.

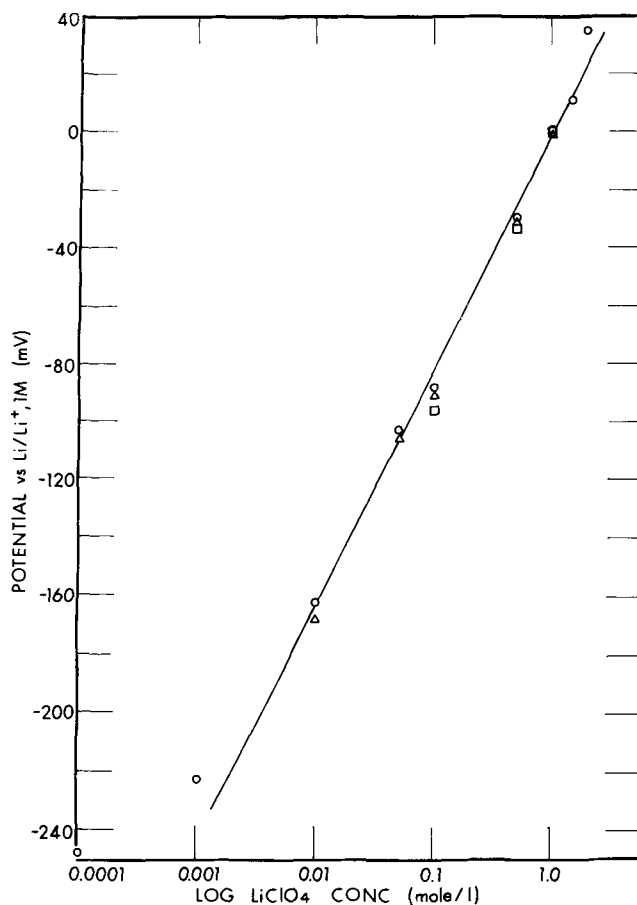


Fig. 2. A plot of the rest potential of a Li/Li<sup>+</sup> electrode with respect to a Li/Li<sup>+</sup>, 1M reference electrode as a function of the LiClO<sub>4</sub> concentration for dry (O) and wet (containing 3000 ppm H<sub>2</sub>O) PC solutions. Data from Meibuhr (6) is also plotted (□). Deviation from straight line at low LiClO<sub>4</sub> concentrations is an activity coefficient effect.

From the slope of this line, a value of  $t_-$  can be obtained and a least squares analysis of the data provides a value of 0.68 for the transport number of ClO<sub>4</sub><sup>-</sup> ion,  $t_-$  from which one calculates for Li<sup>+</sup> ion a value of 0.32 for  $t_+$ . Keller and co-workers (4) report a value of 0.28 for  $t_+$  in PC at 25°C which was determined from conductivity measurements. If the few measurements reported by Meibuhr (6) on a concentration cell are treated (7) similarly (see squares in Fig. 2) at  $t_+$  value of 0.21 is obtained.<sup>1</sup>

This low value for the  $t_+$  of Li<sup>+</sup> ion can be accounted for by solvation of the Li<sup>+</sup> ion. Using conductivity data, the ionic radius  $r$  of the Li<sup>+</sup> ion was determined by Keller *et al.* (4) from Stokes law and was compared with the crystal ionic radius,  $r_c$ . Since  $r \gg r_c$ , the number of solvent molecules,  $n$ , associated at a given instant with a Li<sup>+</sup> ion in the solvation sheath can be determined from the volume of the sheath and the volume of the solvent molecules. They record a value of 2.8 PC molecules per Li<sup>+</sup> ion for  $n$ . For Li<sup>+</sup> ions in DMSO, Yao and Bennion (8) reported a value of 4.8 for  $n$  using conductivity data and an empirically modified Stokes equation (9) which in effect takes into account (10, 11) dielectric relaxation effects. It is generally known (12) that lithium has a coordination number of 4. With these results in mind, it is reasonable to assume that each Li<sup>+</sup> ion at any instant is coordinated with four PC molecules. Because of the hindering effect of these coordinated PC molecules, the solvated Li<sup>+</sup>

<sup>1</sup> One of the reviewers brought the work of Mukherjee *et al.* (14) to our attention where  $t_+$  for Li<sup>+</sup> ion in PC was determined in a concentration cell using Li-amalgam electrodes. Their  $t_+$  values not only vary from 0.18 to 0.24 with the Li<sup>+</sup> ion concentration but also do not agree with this work nor with the conductivity results (4).

ions carry only about 30% of the current while the ClO<sub>4</sub><sup>-</sup> ions which are virtually unsolvated (4, 8) carry about 70% of the current.

When water is added to a PC solution of LiClO<sub>4</sub>, the rest potential of the Li electrode (*vs.* Li/Li<sup>+</sup>, 1M) decreases slowly with the log of the H<sub>2</sub>O concentration as noted in Fig. 1. If these straight lines are extrapolated to a water concentration of 3000 ppm, a plot of the extrapolated potential as a function of the log of the Li<sup>+</sup> ion concentration for solutions containing 3000 ppm H<sub>2</sub>O is shown in Fig. 2 (triangles). A least squares analysis of these data gives a value of 0.31 for *t*<sub>+</sub>. The data of Fig. 2 indicate that the presence of H<sub>2</sub>O in PC does not affect the mobility of the Li<sup>+</sup> ion appreciably. Such an observation is understandable if a water molecule replaces only one PC in the solvation sheath



Because of the large size of the PC molecule, the mobility of the [Li(PC)<sub>3</sub>·H<sub>2</sub>O]<sup>+</sup> ion would be about the same as the [Li(PC)<sub>4</sub>]<sup>+</sup> ion.

Since the transference number is not affected by the presence of H<sub>2</sub>O in the PC solution, the low slope of the *E*-log H<sub>2</sub>O concentration plots in Fig. 1 may be accounted for by a small change in the value of the junction potential, *E*<sub>*j*</sub>, of Eq. [1]. The H<sub>2</sub>O concentration of the reference electrode compartment is maintained at a very low level. It is not possible to calculate the *E*<sub>*j*</sub> for the different values of the H<sub>2</sub>O concentration across the junction because the H<sub>2</sub>O molecule is not an ion. The effect is not large, however, since the *E*<sub>*j*</sub> in a 1M solution of LiClO<sub>4</sub> in PC containing 3000 ppm H<sub>2</sub>O is only 2.5 mV less noble than that in the dry solution according to the data in Fig. 1.

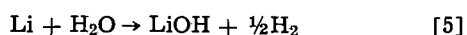
As noted in Fig. 1 when the concentration ratio, *K*, in ppm of Li<sup>+</sup> ions to H<sub>2</sub>O molecules reaches a value of about 5 (0.01M Li ~ 1000 ppm), the potential no longer decreases with the log of the concentration of H<sub>2</sub>O but rises rapidly to more noble potentials with further additions of H<sub>2</sub>O. In the region where *K* < 1 the plot approaches a slope of 0.059. This behavior indicates that the electrode reaction has changed from one in which H<sub>2</sub>O is not a potential-determining species to one in which it is.

In the range where *K* is large (>5), water is tied up in the solvation sheath of the Li<sup>+</sup> ions as [Li(PC)<sub>4</sub>·H<sub>2</sub>O]<sup>+</sup> ions. Here, the potential-determining reaction is



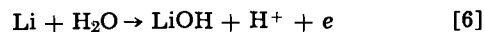
as noted in Fig. 2 where the straight line plot of *E vs.* the log of the Li<sup>+</sup> ion concentration passes through zero for 1M Li<sup>+</sup> ion, and the presence of water does not seriously affect the electrode potential. When *K* reaches a value of 5, the mole ratio of LiClO<sub>4</sub> to H<sub>2</sub>O is unity (1000/106/200/18 ~ 1). At this point there is, on the average, one molecule of H<sub>2</sub>O associated in the solvation sheath with each Li<sup>+</sup> ion present in solution and the system may be saturated with respect to its ability for tying up water.

When water is first added to a dry solution of LiClO<sub>4</sub> in PC, the water molecules are quickly tied up in the solvation sheath of the Li<sup>+</sup> ions. In this region where *K* is large, H<sub>2</sub>O does not react with the Li metal and the electrode surface remains bright. After enough water is added so that 5 > *K* > 2, H<sub>2</sub>O can react with Li metal according to



and one observes a slow tarnishing of the electrode surface as a film of LiOH is built up. It is in this region that the Li electrode potential becomes strongly dependent on the H<sub>2</sub>O concentration (Fig. 1) and large area effects are detected between electrodes of small and large areas. In the presence of a large amount of H<sub>2</sub>O where *K* < 1, the Li surface becomes dark with a thick film of LiOH, the area effects disappear, and ∂*E*/∂ log H<sub>2</sub>O = 0.059. The data in Fig. 1 indicate that

the potential-determining reaction must be a one-electron process involving H<sub>2</sub>O. A reaction consistent with these data is Eq. [6] since LiOH is very insoluble in PC (3)



If the activity of Li and LiOH is taken as unity, then

$$E = E_0 - 0.059 \log C_{\text{H}^+} + 0.059 \log C_{\text{H}_2\text{O}} \quad [7]$$

From this viewpoint, the Li electrode immersed in a PC solution of LiClO<sub>4</sub> changes from an electrode of the first kind (Eq. [4]) to one of the second kind (Eq. [6]) as the H<sub>2</sub>O content of the solution increases. The transition takes place where the mole ratio of H<sub>2</sub>O to LiClO<sub>4</sub> is unity.

It is known (13) that PC is unstable in the presence of small amounts of acids or bases, and a discoloration of the PC takes place. When H<sub>2</sub>O or LiClO<sub>4</sub> or both are added to the distilled PC, the solution remains clear and colorless; but when small amounts of HClO<sub>4</sub> are added (solution 10<sup>-4</sup>M in H<sup>+</sup>), the solution becomes yellowish. This coloration deepens to a dark brown as the H<sup>+</sup> concentration is increased. If Li metal is placed in contact with wet (*K* < 5) PC solutions of LiClO<sub>4</sub>, the solution also develops a light yellow coloration. This coloration develops more quickly and becomes deeper as the H<sub>2</sub>O content of the solution is increased. According to Eq. [6], H<sup>+</sup> ions would be generated and some decomposition of PC could take place. It has been reported by others that wet PC solutions become yellow when coming in contact with alkali metals (13).

When enough HClO<sub>4</sub> (72%) was added to a PC solution of 0.01M LiClO<sub>4</sub> containing about 7400 ppm H<sub>2</sub>O to make it 0.001M in H<sup>+</sup> ions, the potential of the Li electrode (*vs.* Li/Li<sup>+</sup>, 1M) became less noble initially as required by Eq. [7]. However, the potential drifted to more noble values, as the solution became yellow with time.

These data support the conclusion that the potential of a Li electrode in wet PC solutions of LiClO<sub>4</sub> is determined by the Li/LiOH reaction (Eq. [6]).

It appears that the presence of H<sup>+</sup> ions brings about the decomposition of PC with a formation of CO<sub>3</sub><sup>=</sup> ions and propylene residues which probably polymerize to form the colored material. This colored compound was not identified in the literature (13) nor in this work. In the very wet PC solutions, the film on the Li electrode was copious and black. This film was scraped off for analysis and became white when dried. The presence of Li<sub>2</sub>CO<sub>3</sub> was detected in this material as determined from a wet chemical microanalysis of the film scrapings.

### Acknowledgments

The authors are indebted to Professor E. B. Yeager of Case Western Reserve University for his helpful discussion and to the Analytical Chemistry Department of General Motors Research for analysis of the surface film. They also wish to express their gratitude to Dr. J. S. Dunning of Electrochemistry Department of General Motors Research Laboratories for many stimulating conversations.

Manuscript submitted April 16, 1973; revised manuscript received July 16, 1973. This was Paper 62 presented at the Boston, Massachusetts, Meeting of the Society, Oct. 7-11, 1973.

Any discussion of this paper will appear in a Discussion Section to be published in the December 1974 JOURNAL.

### REFERENCES

1. B. Burrows and R. Jasinski, *This Journal*, **115**, 365 (1968).
2. B. Burrows and S. Kirkland, *ibid.*, **115**, 1164 (1968).

3. A. N. Dey, *ibid.*, **114**, 823 (1967).
4. R. Keller *et al.*, NASA Rept. CR-1425, p. 187, Washington, D. C. (1969).
5. S. Glasstone, "The Electrochemistry of Solutions," p. 267, D. Van Nostrand Co., Inc., New York (1939).
6. S. G. Meibuhr, *This Journal*, **117**, 56 (1970).
7. W. H. Tiedemann, Thesis, University of California at Los Angeles, 1971.
8. N.-P. Yao and D. N. Bennion, *This Journal*, **118**, 45 (1971).
9. R. A. Robinson and R. H. Stokes, "Electrolyte Solutions," 2nd ed., p. 126, Butterworths Scientific Publication, London (1959).
10. R. H. Boyd, *J. Chem. Phys.*, **35**, 1281 (1961).
11. R. Zwanzig, *ibid.*, **38**, 1603, 1605 (1963).
12. N. V. Sidgwick, "The Chemical Elements and Their Compounds," p. 97, Oxford Press, London (1950).
13. J. Jansta, F. P. Dousek, and J. Riha, *J. Electroanal. Chem.*, **38**, 445 (1972).
14. L. M. Mukherjee, D. P. Boden, and R. Lindauer, *J. Phys. Chem.*, **74**, 1942 (1970).

## Electrochemical Studies of Uranium and Thorium in Molten LiF-NaF-KF at 500°C

F. R. Clayton and G. Mamantov\*

*Department of Chemistry, University of Tennessee, Knoxville, Tennessee 37916*

and D. L. Manning

*Analytical Chemistry Division, Oak Ridge National Laboratory, Oak Ridge, Tennessee 37830*

### ABSTRACT

Electrochemical studies of U(IV) in molten LiF-NaF-KF (46.5-11.5-42.0 mole per cent) at 500°C reveal a two-step reduction process at a platinum electrode. The first step is complicated by disproportionation of U(III) to regenerate U(IV); the second step involves formation of uranium metal. Standard electrode potentials with respect to a unit mole fraction Ni(II)/Ni electrode are estimated for the U(IV)/U(III) and U(III)/U couples as -1.41 and -1.81V, respectively. These values must be considered tentative because of complications in the electrode processes. The voltammetric oxidation of U(IV) at platinum and pyrolytic graphite electrodes in LiF-NaF-KF occurs at  $\sim +1.3V$  vs. a Ni(II) (saturated)/Ni reference electrode. The results point to the disproportionation of electrochemically generated U(V). In voltammetric studies of Th(IV) in molten LiF-NaF-KF at 500°C, a reduction wave is obtained at nickel and tungsten electrodes, with a peak potential of -2.02V (vs. a Ni(II) (saturated)/Ni reference electrode). Analysis indicated that Th(IV) is reversibly reduced to the metal with alloy formation between the deposited thorium and the nickel. A standard electrode potential for the Th(IV)/Th couple in this melt is calculated to be -2.13V vs. a unit mole fraction Ni(II)/Ni electrode.

In this paper we describe electrochemical studies of uranium(IV) and thorium(IV) in a basic fluoride solvent LiF-NaF-KF [46.5-11.5-42.0 m/o (mole per cent)] at 500°C. Electrochemical studies of uranium in other molten fluorides have been described (1-4) and the results of these investigations have been summarized by one of us (5). The U(IV) reduction in the more acidic LiF-BeF<sub>2</sub>-ZrF<sub>4</sub> (65.6-29.4-5.0 m/o) at 500°C was shown (1,2) to be a reversible, one-electron process occurring at  $\sim -1.5V$  (vs. the unit mole fraction Ni(II)/Ni couple). No voltammetric reduction wave for U(III) was observed at platinum prior to the cathodic limit of the melt. Electrochemical oxidation of U(IV) produced unstable U(V) (4).

The only emf data available for the Th(IV)/Th couple in molten fluorides are the values of standard electrode potential calculated from thermodynamic data for pure thorium fluoride (6) and for ThF<sub>4</sub> solutions in molten LiF-BeF<sub>2</sub> (67-33 m/o) (7). The  $E^\circ$  value (-2.332V vs. a unit mole fraction Ni(II)/Ni electrode) in LiF-BeF<sub>2</sub> at 500°C (7) is indicative of the great thermodynamic stability of the fluoro complexes of thorium(IV).

### Experimental

The eutectic mixture of LiF-NaF-KF (46.5-11.5-42.0 m/o) used as the solvent and the solutes of LiF-UF<sub>4</sub>

(73-27 m/o) and LiF-ThF<sub>4</sub> (73-27 m/o) were obtained from the Reactor Chemistry Division of the Oak Ridge National Laboratory. They were prepared from analytical reagent grade salts and purified by treatment of the molten mixtures with anhydrous HF and hydrogen (8).

The electrolytic cell assembly and the instrumentation employed for this work was the same as that used in a previous study (9). The Ni(II)/Ni reference electrode contained in a lanthanum trifluoride compartment has been described (10,11). The background voltammograms for the melt employed in this work have been reported previously (9).

The details of the experimental procedures are presented elsewhere (12).

### Results and Discussion

**Voltammetric and chronopotentiometric reduction of U(IV).**—The voltammetric reduction of U(IV) was investigated in molten LiF-NaF-KF contained in a platinum crucible at 500°C. Platinum indicator and counter-electrodes were employed, and potentials were measured with respect to a nickel(II) (saturated)/nickel reference electrode (LaF<sub>3</sub> membrane-type). The solute material was LiF-UF<sub>4</sub>.

A typical linear sweep voltammogram for the reduction of U(IV) in molten LiF-NaF-KF at platinum is shown in Fig. 1. The broken-line curve in this figure is the reverse half-cycle obtained on switching the direction of potential scan at a given point between the two

\* Electrochemical Society Active Member.

Key words: molten fluorides, uranium, thorium, linear sweep voltammetry, chronopotentiometry.

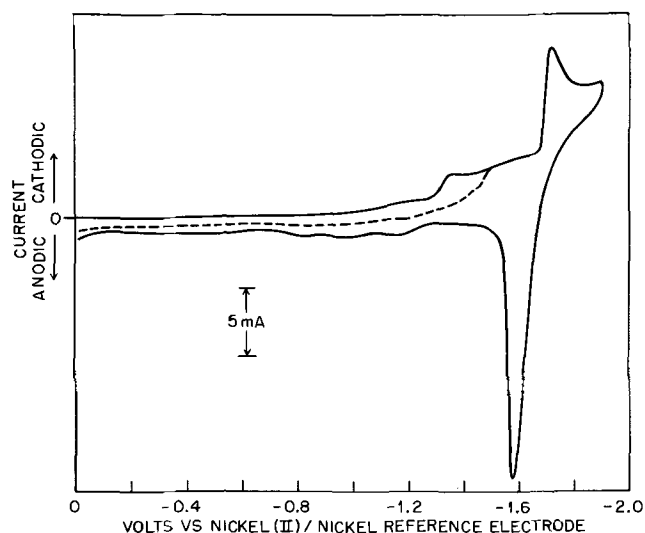


Fig. 1. Linear sweep voltammogram for the reduction of U(IV) in molten LiF-NaF-KF at 500°C at platinum electrode. Scan rate, 0.1 V/sec; U(IV) concentration, 0.220M; electrode area, 0.10 cm<sup>2</sup>.

reduction waves. The first reduction wave at  $\sim -1.3$  V vs. the Ni(II) (saturated)/Ni reference electrode (LaF<sub>3</sub> membrane-type) apparently corresponds to U(IV) + e  $\rightarrow$  U(III). Reduction of U(IV) to U(III) in LiF-BeF<sub>2</sub>-ZrF<sub>4</sub> at 500°C occurs at about  $-1.5$  V vs. a unit mole fraction Ni(II)/Ni reference electrode (2). On the basis of emf data relating the potential of the saturated Ni(II)/Ni electrode in LiF-NaF-KF to a unit mole fraction Ni(II)/Ni electrode (10), the reduction of U(IV) in LiF-NaF-KF occurs at  $\sim -1.4$  V vs. a unit mole fraction Ni(II)/Ni reference electrode.

In contrast with the behavior of the U(IV)  $\rightarrow$  U(III) reduction in LiF-BeF<sub>2</sub>-ZrF<sub>4</sub>, this first reduction wave for U(IV) in LiF-NaF-KF does not behave as a simple one-electron reversible wave. This is demonstrated by the data of Table I. The half-peak to peak potential separation (13) for the wave corresponds to noninteger  $n$  values of 1.5 to 1.6 and is relatively independent of scan rate up to 10 V/sec. In addition, plots of  $\log(i_p - i)/i$  vs. potential (14) resulted in slopes corresponding to  $n$  values between 1.4 and 1.7. The variation of  $i_p/v^{1/2}$  with scan rate for the reduction of U(IV) at a platinum electrode is shown in Fig. 2. This variation is not indicative of simple reversible charge transfer but resembles that predicted for a reversible charge transfer followed by a catalytic regeneration of the reactant (13).

Table I. Peak potentials, half-peak to peak potential separation (theoretical values<sup>(a)</sup> in parentheses), and  $i_p/C$  for the processes U(IV) + e  $\rightarrow$  U(III) and U(III) + 3e  $\rightarrow$  U at platinum electrode in molten LiF-NaF-KF at 500°C; scan rate: 1.0 V/sec

U(IV) concentration (moles/liter)	U(IV) + e $\rightarrow$ U(III)		$i_p/C$ ratio (mA · liter/mole)
	$E_p$ (V)	$\Delta E = E_{p/2} - E_p$ (mV)	
$5.16 \times 10^{-2}$	$-1.33 \pm 0.01$	100 (147)	23.2
$1.11 \times 10^{-1}$	$-1.36 \pm 0.01$	90 (147)	23.0
$2.20 \times 10^{-1}$	$-1.25 \pm 0.01$	90 (147)	23.6
U(III) + 3e $\rightarrow$ U			
	$E_p$ (V)	$\Delta E = E_{p/2} - E_p$ (mV)	$i_p/C$ ratio (mA · liter/mole)
$1.11 \times 10^{-1}M$	$-1.74 \pm 0.01$	20 (17 <sup>(c)</sup> , 49 <sup>(d)</sup> )	85.2
$2.20 \times 10^{-1}M$	$-1.72 \pm 0.01$	25 (17 <sup>(c)</sup> , 49 <sup>(d)</sup> )	86.4

<sup>(a)</sup> Theoretical values for a simple reversible electrode process.

<sup>(b)</sup> Versus Ni(II)(saturated)/Ni reference electrode (LaF<sub>3</sub> membrane type).

<sup>(c)</sup> For reversible deposition of an insoluble product.

<sup>(d)</sup> For reversible reduction yielding a soluble product.

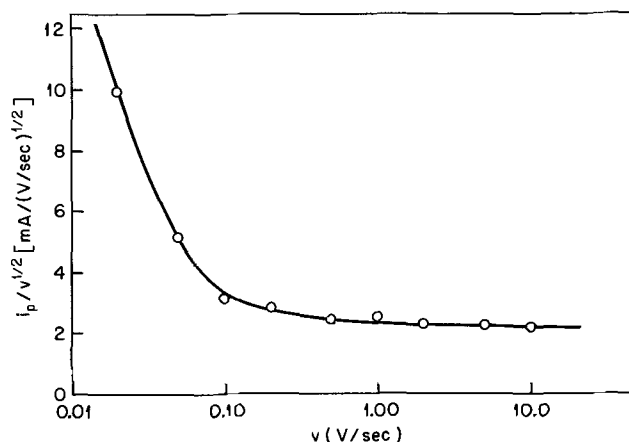
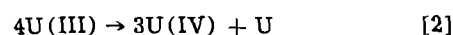
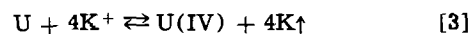


Fig. 2. Variation of  $i_p/v^{1/2}$  with scan rate  $v$  for the U(IV)  $\rightarrow$  U(III) reduction wave in molten LiF-NaF-KF at 500°C. U(IV) concentration, 0.111M; Pt electrode area, 0.10 cm<sup>2</sup>.

A possible reaction scheme which could explain the experimental observations is



The disproportionation of U(III) is at least a second-order chemical reaction which should be favored by the removal of one of the reaction products, uranium metal, by the reaction with potassium ions of the solvent in the following manner



The volatilization of potassium (vapor pressure  $\sim 40$  Torr at 500°C) (15) from the melt to the cooler region of the cell would be a driving force shifting the above equilibrium to the right even though the reverse reaction would be slightly favored on a thermochemical basis (6).

The theory of linear sweep voltammetry for an electrochemical reaction followed by a second-order disproportionation reaction has been worked out for linear (16) and spherical (17) diffusion. The theory provides certain diagnostic criteria for testing an unknown system, such as the effect of concentration and scan rate on peak current and peak potential. The influence on peak current is more significant than on peak potential in the case of disproportionation of the electron-transfer product (16). For such a reaction, the peak current is no longer directly proportional to the concentration; instead, a markedly larger increase occurs. Also the parameter  $i_p/v^{1/2}$  is much larger at slow scan rates than the value corresponding to the transfer of  $n$  electrons under pure diffusion control but decreases with increasing scan rate, approaching a constant value at higher scan rates. This type of variation of  $i_p/v^{1/2}$  with scan rate was observed for the U(IV) reduction in LiF-NaF-KF (Fig. 2). The peak current variation with concentration of U(IV) at the scan rate of 0.1 V/sec is shown in Table II. It is seen that the  $i_p/C$  ratio increases with concentration of U(IV), providing additional evidence that disproportionation of U(III) takes place under our experimental conditions.

Table II. Variation of peak current with concentration for the reduction of U(IV) to U(III) in LiF-NaF-KF at 500°C; platinum electrode area: 0.10 cm<sup>2</sup>; scan rate: 0.10 V/sec

U(IV) concentration (moles/liter)	Peak current, $i_p$ (mA)	$i_p/C$ ratio (mA · liter/mole)
$5.16 \times 10^{-2}$	0.49	9.5
$1.11 \times 10^{-1}$	1.15	10.4
$2.20 \times 10^{-1}$	2.50	11.4



Further support for U(III) disproportionation is provided by another diagnostic criterion, namely, the variation of the peak potential  $E_p$  with scan rate. For an uncomplicated charge transfer process,  $E_p$  should be independent of scan rate but should shift in the cathodic direction with increasing scan rate in the case of disproportionation of the electron-transfer product (16). For the first U(IV) reduction wave,  $E_p$  shifts in the cathodic direction by 100 mV as the scan rate is increased from 0.1 to 5 V/sec.

It is also interesting to note that  $E_p$  for the first wave shifts in the anodic direction by 110 mV when the concentration of U(IV) is increased from 0.11 to 0.22M; such a shift is to be expected from the theoretical treatment of Saveant and co-workers [see Fig. 14 in Ref. (16)]. This shift is accompanied by a small increase in the function  $i_p/C$  (see Table I).

Attempts were made to study the reduction of U(IV) by means of chronopotentiometry and chronoamperometry. The chronopotentiograms at platinum for the reduction of U(IV) to U(III) were poorly defined, particularly at lower current densities (long transition times). Reasonably well-defined chronopotentiograms were obtained at high current densities (transition times of 0.08-0.26 sec) yielding  $i\tau^{1/2}$  values ranging from 2.00 to 2.16 mA·(sec)<sup>1/2</sup>. Using the average  $i\tau^{1/2}$  value of 2.06 mA·(sec)<sup>1/2</sup> and an  $i_p/v^{1/2}$  value of 5.20 mA·(sec)<sup>1/2</sup>·V<sup>-1/2</sup> obtained from voltammetry ( $v = 1.0$  V/sec) under exactly the same experimental conditions ( $A = 0.10$  cm<sup>2</sup>;  $C = 0.220$ M), an  $n$  value of 1.13 was determined from the ratio of  $i_p/v^{1/2}$  to  $i\tau^{1/2}$ . Theoretically, this ratio is equivalent to  $1.96 n^{1/2} V^{-1/2}$  at 500°C, assuming a diffusion-controlled, reversible charge transfer yielding a soluble product (18).

Application of a potential step that corresponded to the peak potential of the U(IV) reduction to U(III) [ $\sim -1.35$ V vs. the Ni(II) (saturated)/Ni reference electrode] resulted in a current that decreased only very slowly with time. The current obtained after a given time was erratic from one experiment to another.

The second reduction wave corresponding to uranium metal deposition was a steep, well-defined curve showing far greater reproducibility than the preceding wave. On reverse scans, the stripping curve revealed no inflection upon passing through the point of zero current; this behavior suggests that the deposited metal is reversibly oxidized.

Evidence for reversible metal deposition is provided by the half-peak to peak potential separation for the wave (see Table I) and by the results obtained from a  $\log(i_p - i)$  vs. potential plot (14) which is shown in Fig. 3. The data for Fig. 3 were obtained from a voltammogram at 0.1 V/sec and a U(IV) concentration of 0.220M. The theoretical slopes ( $2.2 nF/RT$ ) (14) for  $n = 3$  and  $n = 4$  differ by only about 33 V<sup>-1</sup>. Lines corresponding to both slopes were drawn through the data points of Fig. 3. Since the theoretical slope (14) is applicable in the current range 0.5-0.9  $i_p$  as indicated by the dashed lines of Fig. 3, an  $n$  value of 3 is favored from this type of log plot. A plot of  $\log(i_p - i)/i$  vs. potential using the same data as in Fig. 3 gave an unrealistic  $n \approx 6$ . The inapplicability of this type of log plot suggests that a soluble product is not involved in the uranium deposition at platinum, in agreement with other experimental observations. A small shift in the anodic direction for  $E_p$  of the second step was also observed as predicted for a diffusion-controlled reversible deposition of an insoluble product (18) (see Table I). Although U-Pt alloys are known (19), diffusion of uranium into the electrode may be so slow that uranium metal at essentially unit activity remains as a monolayer to be oxidized on the reverse scan. A plot of  $i_p$  vs.  $v^{1/2}$  for the uranium deposition wave is linear for the scan rates 0.1-2 V/sec.

**Voltammetric studies of the oxidation of uranium(IV).**—A voltammetric study was made on the

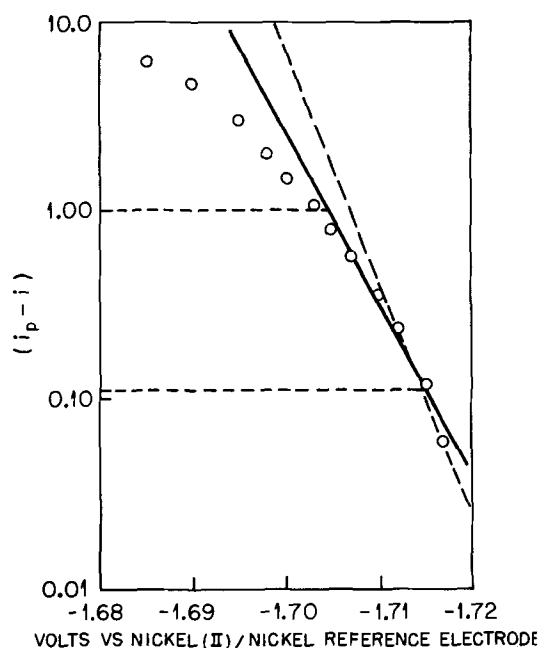


Fig. 3. Plot of  $\log(i_p - i)$  vs. potential for the reduction of U(III) to U at platinum electrode in molten LiF-NaF-KF at 500°C. Solid line, theoretical slope corresponding to  $n = 3$ ; dashed line, slope for  $n = 4$ .

oxidation of U(IV) at unsheathed platinum and PG electrodes in molten LiF-NaF-KF at 500°C. A series of voltammograms at different scan rates for the oxidation of U(IV) at platinum is shown in Fig. 4. Essentially identical voltammograms were obtained at a PG electrode. The oxidation of U(IV) occurs at  $\sim +1.3$ V vs. a Ni(II) (saturated)/Ni reference electrode. The following points should be noted with regard to these voltammograms: (i) no current is observed for the re-reduction process at the slower scan rates (0.2 V/sec and less), (ii) the current for the oxidation of U(IV) at high scan rates ( $\geq 1.0$  V/sec) is about the same as that for the reduction of U(IV) to U(III); the  $i_p/C$  value of 25.0 at 1.0 V/sec compares well with the  $i_p/C$  values for U(IV) reduction given in Table I, and (iii)  $i_p/v^{1/2}$  vs.  $v$  plot is very similar to that shown in Fig. 2. These results are essentially the same as those obtained for the oxidation of U(IV) in molten LiF-BeF<sub>2</sub>-ZrF<sub>4</sub> where a catalytic regeneration of U(IV) from U(V) was suggested based on the following reactions

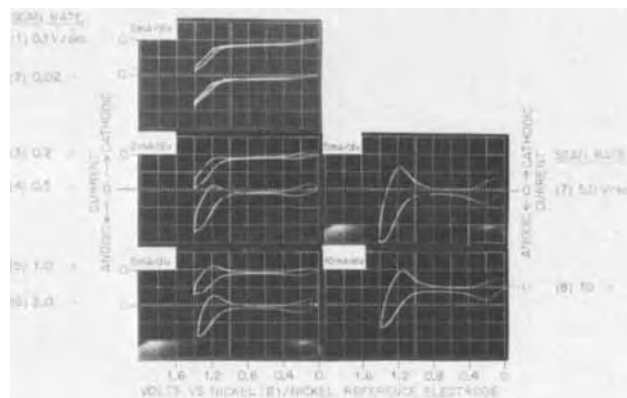
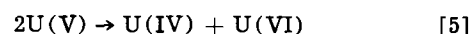
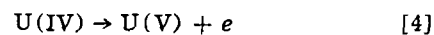


Fig. 4. Linear sweep voltammograms for the oxidation of U(IV) at platinum electrode in molten LiF-NaF-KF at 500°C. U(IV) concentration, 0.220M; electrode area, 0.10 cm<sup>2</sup>.

The small wave near +0.2V in Fig. 4 is believed to be due to the presence of adsorbed H<sub>2</sub> produced electrochemically from traces of H<sub>2</sub>O or HF.

In the previous work (4) chronopotentiometric and chronoamperometric results were obtained which also pointed to the disproportionation of the electrochemically produced U(V). An attempt to study the oxidation of U(IV) in LiF-NaF-KF by chronopotentiometry proved futile due to very poor definition and reproducibility of the chronopotentiograms at both Pt and PG electrodes. These adverse effects are presumably caused by the attack of the working electrode by UF<sub>6</sub> produced in the disproportionation reaction. The attack might be expected to be more severe in molten LiF-NaF-KF than in LiF-BeF<sub>2</sub>-ZrF<sub>4</sub> since the highly volatile UF<sub>6</sub> can be more readily complexed in the former melt and thus may be retained in that melt longer.

**Electrode potentials of the uranium(IV)/uranium(III) and uranium(III)/uranium couples.**—The half-wave potential  $E_{1/2}$  for the process  $U(IV) + e \rightleftharpoons U(III)$  in LiF-NaF-KF at 500°C was used to estimate the standard electrode potential of the U(IV)/U(III) couple in this melt. Assuming an uncomplicated charge transfer, the half-wave potential for the  $U(IV) + e \rightarrow U(III)$  process was determined from the 0.85  $i_p$  point on the wave (13). An average of  $E_{1/2}$  values obtained at three different U(IV) concentrations (scan rate = 1.0 V/sec) gave an  $E_{1/2}$  of -1.27V vs. a Ni(II) (saturated)/Ni reference electrode. Since the potential of the Ni(II) (saturated)/Ni reference electrode is about 0.14V more cathodic than the potential of the unit mole fraction Ni(II)/Ni couple (10),  $E^\circ$  for the U(IV)/U(III) couple in LiF-NaF-KF is estimated as -1.41V vs. a unit mole fraction Ni(II)/Ni reference electrode. This value is less negative than the value obtained in LiF-BeF<sub>2</sub>-ZrF<sub>4</sub> (2). Since an opposite trend was expected from qualitative acid-base considerations (9), the  $E^\circ$  value obtained remains suspect. This is not surprising since the estimate of  $E^\circ$  was based on the assumption that the  $U(IV) + e = U(III)$  reaction is a simple reversible process, which is certainly not the case at lower scan rates and higher concentrations of U(IV).

The electrode potential of the U(III)/U couple will depend on the concentration of U(III). Since the reduction of U(III) at platinum has been tentatively shown to be a reversible deposition of uranium metal at essentially unit activity, the voltammetric  $E_p$  will depend on concentration as given by the following expression (18)

$$E_p = E^\circ + \frac{RT}{nF} \ln fC - 0.854 \frac{RT}{nF} \quad [6]$$

An approximate value for  $E^\circ$  was calculated from Eq. [6] using the experimental  $E_p$  of -1.74V at a concentration of 0.111M and assuming the activity coefficient of U(III) to be unity. The value for  $E^\circ$  determined in this manner is -1.67V vs. the Ni(II) (saturated)/Ni reference electrode. Applying the correction given above, the standard potential for the U(III)/U couple is estimated as -1.81V vs. a unit mole fraction Ni(II)/Ni reference electrode. This value may be compared with the  $E^\circ$  of -1.838V for the U(III)/U couple determined by Baes (7) in LiF-BeF<sub>2</sub> (67-33 m/o) at 500°C.

**Voltammetric studies of Th(IV) in molten LiF-NaF-KF at 500°C.**—The voltammograms obtained at platinum for Th(IV) solutions in molten LiF-NaF-KF at 500°C showed a barely distinguishable shoulder just preceding the onset of the cathodic melt limit at -2.00V vs. a Ni(II) (saturated)/Ni reference electrode. On the reverse scan, only a single large stripping wave was observed which was obviously due to reoxidation of deposited alkali metal; no separate stripping peak for the thorium metal was detected. A nickel working electrode was then employed in an effort to better resolve the thorium(IV) wave. In this case, the cathodic

melt limit shifted in the cathodic direction by about 50 mV, and a much better defined reduction wave due to Th(IV) was obtained. A typical voltammogram for Th(IV) at a nickel electrode is shown in Fig. 5. The peak potential was estimated as -2.02V. On the reverse scan, the corresponding stripping wave displays a sharp peak at -1.83V. Upon scanning to -2.05V, the Th(IV) reduction was followed by the onset of the cathodic limit, and two separate stripping peaks were observed on the reverse scan at -2.00 and -1.83V, corresponding to reoxidation of alkali metal and thorium metal, respectively. Similar voltammograms were obtained at a tungsten working electrode, but the definition was better at the nickel electrode. The differences in behavior between the platinum and nickel electrodes (tungsten, as well) are likely due to different tendencies toward alloy formation. The ready formation of alkali metal-platinum alloys near 500°C (19) is probably responsible for the occurrence of a less cathodic melt limit at platinum than at either nickel or tungsten; nickel and tungsten are more resistant than platinum to alloy formation with the alkali metals at 500°C (19).

A plot of the square root of the scan rate was linear for the rates studied; this is evidence for a simple diffusion-controlled process. A plot of  $\log(i_p - i)/i$  vs. potential for the Th(IV) reduction wave is shown in Fig. 6. The data points display a good fit to a straight line of theoretical slope (14) corresponding to an  $n$  of 4. In comparison, a  $\log(i_p - i)$  vs. potential plot was linear in the region 0.5-0.9  $i_p$  but yielded a slope corresponding to an  $n$  of 1. The results obtained from the slopes of the log plots point to the formation of a soluble product in the case of Th(IV) reduction at nickel. This would require the dissolution of thorium metal in the nickel electrode; the existence of five compounds in the Ni-Th system has been shown (19). The behavior of the anodic stripping curve (Fig. 5) also supports alloy formation since the curve shows an inflection on passing through zero current not expected for reversible stripping of metal at unit activity; also the stripping peak is separated from the reduction peak by about 0.2V, which is greater than that expected for reversible deposition of metal at unit activity.

The half-peak to peak potential separation  $\Delta E$  for the Th(IV) reduction wave shown in Fig. 5 is  $40 \pm 5$  mV, in good agreement with the predicted value (37 mV) for a reversible charge transfer process yielding

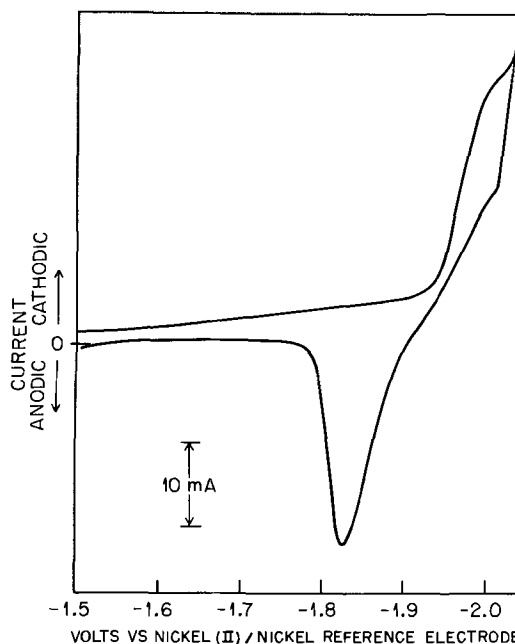


Fig. 5. Linear sweep voltammogram for the reduction of Th(IV) at nickel electrode in LiF-NaF-KF at 500°C. Scan rate, 0.20 V/sec; electrode area, 0.10 cm<sup>2</sup>; Th(IV) concentration, 0.254M.

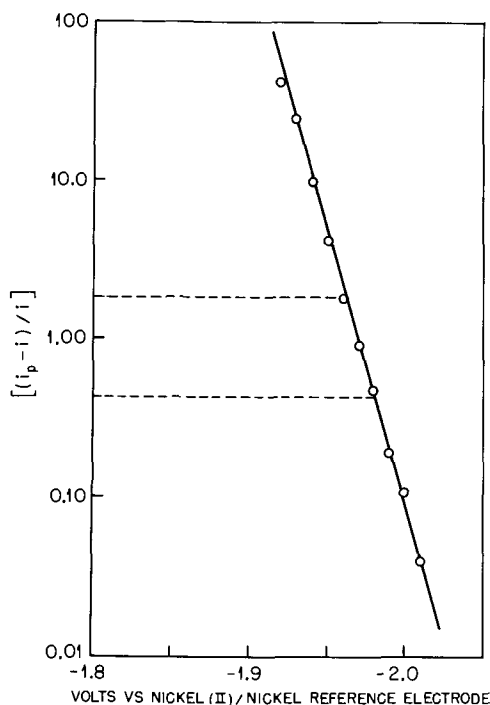


Fig. 6. Plot of  $\log [(i_p - i)/i]$  vs. potential for the reduction of Th(IV) in molten LiF-NaF-KF at 500°C.

a soluble product (13). A much lower value (13 mV) is expected in the case of reversible deposition of an insoluble product (14). A diffusion coefficient of  $1.8 \pm 0.3 \times 10^{-6}$  cm<sup>2</sup>/sec was calculated from the Randles-Sevcik equation (18) using the slope of the  $i_p$  vs.  $v^{1/2}$  plot.

*Standard electrode potential of the thorium(IV)/thorium couple in molten LiF-NaF-KF.*—The standard electrode potential for the Th(IV)/Th couple in molten LiF-NaF-KF at 500°C can be estimated from the half-wave potential  $E_{1/2}$  for the Th(IV) reduction wave assuming solubility of thorium metal in the nickel electrode. In this case,  $E_{1/2}$  for a reversible process is equivalent to the standard electrode potential  $E^\circ$ , assuming that the activity coefficients and diffusion coefficients for the reactants and products are equal (13). Also  $E_{1/2}$  is related to the half-peak potential  $E_{p/2}$  by the following equation (13)

$$E_{p/2} = E_{1/2} + 1.09 \frac{RT}{nF} \quad [7]$$

Using the more conveniently measured  $E_{p/2}$  of  $-1.975$  V,  $E_{1/2}$  for the Th(IV) reduction wave was calculated to be  $-1.993$  V vs. the Ni(II) (saturated)/Ni reference electrode. This particular reference was previously shown to be 0.138 V more cathodic than a unit mole fraction Ni(II)/Ni couple (10). Thus, the standard electrode potential  $E^\circ$  for the Th(IV)/Th couple

in molten LiF-KF-NaF at 500°C is estimated as  $-2.13$  V vs. a unit mole fraction Ni(II)/Ni reference electrode.

#### Acknowledgments

The authors wish to thank the General Analysis Laboratories of the Analytical Chemistry Division of ORNL for analysis of samples. This work was supported by the Atomic Energy Commission under contract with the Union Carbide Corporation and Contract AT-(40-1)-3518. The work was in partial fulfillment of requirements for the Ph.D. degree from the University of Tennessee by F. R. Clayton.

Manuscript submitted April 23, 1973; revised manuscript received Aug. 13, 1973.

Any discussion of this paper will appear in a Discussion Section to be published in the December 1974 JOURNAL.

#### REFERENCES

1. G. Mamantov and D. L. Manning, *Anal. Chem.*, **38**, 1494 (1966).
2. H. W. Jenkins, G. Mamantov, D. L. Manning, and J. P. Young, *This Journal*, **116**, 1712 (1969).
3. D. L. Manning and G. Mamantov, *J. Electroanal. Chem.*, **17**, 137 (1968).
4. G. Mamantov and D. L. Manning, *ibid.*, **18**, 309 (1968).
5. G. Mamantov in "Molten Salts: Characterization and Analysis," pp. 529-561, G. Mamantov, Editor, Marcel Dekker, New York (1969).
6. W. J. Hamer, M. S. Malmberg, and B. Rubin, *This Journal*, **112**, 750 (1965).
7. C. F. Baes, Jr., in "Reprocessing of Nuclear Fuels; Nuclear Metallurgy," Vol. 15, pp. 615-644, P. Chiotti, Editor, AEC Division of Technical Information (1969).
8. W. R. Grimes, D. R. Cuneo, F. F. Blankenship, G. W. Keilholtz, H. F. Poppendiek, and M. T. Robinson, in "Fluid Fuel Reactors," p. 584, J. A. Lane, H. G. MacPherson, and F. Moslan, Editors, Addison-Wesley, Reading, Mass. (1958).
9. F. R. Clayton, G. Mamantov, and D. L. Manning, *This Journal*, **120**, 1193 (1973).
10. F. R. Clayton, G. Mamantov, and D. L. Manning, *High Temp. Sci.* (In press)
11. H. Bronstein and D. L. Manning, *This Journal*, **119**, 125 (1972).
12. F. R. Clayton, Ph.D. Dissertation, The University of Tennessee, Knoxville, Tennessee, 1972.
13. R. S. Nicholson and I. Shain, *Anal. Chem.*, **36**, 706 (1964).
14. G. Mamantov, D. L. Manning, and J. M. Dale, *J. Electroanal. Chem.*, **9**, 253 (1965).
15. "Handbook of Chemistry and Physics," p. D-112, The Chemical Rubber Publishing Co., Cleveland, Ohio (1966).
16. M. Mastragostino, L. Nadjo, and J. M. Saveant, *Electrochim. Acta*, **13**, 721 (1968).
17. M. L. Olmstead and R. S. Nicholson, *Anal. Chem.*, **41**, 862, 851 (1969).
18. P. Delahay, "New Instrumental Methods in Electrochemistry," pp. 119, 124, 184, Interscience Publishers, New York (1954).
19. R. P. Elliott, "Constitution of Binary Alloys, First Supplement," pp. 751-752, 586, 649, 584, 648, 676, McGraw-Hill Book Co., New York (1965).

# Conductances of Protonic and Lewis Acids in N,N-Dimethylformamide (DMF)

A. K. Mishra and K. N. Tandon

Department of Chemistry, University of Rajasthan, Jaipur-4, India

## ABSTRACT

Paul and Sreenathan reported abnormally high values of limiting equivalent conductances for several protonic and Lewis acids in DMF and suggested a proton-jump mechanism (similar to that which is known to exist in water) to explain these data. However, it has been found that these abnormally high values are grossly in error. The error, apparently is made by a uniformly constant factor and seems to have manifested itself in one set of their measurements; it cannot be attributed to be due to a difference in the extrapolation of  $\Lambda$  vs.  $\sqrt{c}$  plots. A careful repetition of their work has revealed values which support the earlier work of Thomas and Rochow and Sears *et al.*, and excludes abnormal proton conductance in DMF. The conductance data have been treated with Shedlovsky's equation and the values of  $K$  have been calculated from the slopes of the plots of  $1/\Lambda_s$  vs.  $C\Delta s f_{\pm}^2$ .

The conductances of a number of organic and inorganic electrolytes have been determined in DMF (1-21). Contradictory and controversial conductometric data exist in the literature for acids in DMF. Dawson and co-workers reported the limiting equivalent conductance ( $\Lambda_0$ ) of hydrogen chloride to be  $70 \text{ ohm}^{-1} \text{ cm}^2 \text{ eq}^{-1}$  at  $25^\circ\text{C}$ . Thomas and Rochow (4) determined the value in a highly purified solvent to be  $79.3 \text{ ohm}^{-1} \text{ cm}^2 \text{ eq}^{-1}$  at  $20^\circ\text{C}$ . The lower conductance value reported by Dawson was explained due to the presence of impurities especially water in his solvent. Since the triethylammonium chloride was found to be more conducting than hydrogen chloride, it was presumed (18) that the abnormal proton conductance was absent in this solvent. This was, further supported by the work of Sears *et al.* (5) who found hydrogen bromide to be relatively strong acid in DMF ( $K_{\text{HBr}} = 1.7 \times 10^{-2}$  at  $25^\circ\text{C}$ ) with a  $\Lambda_0$  value of  $88.7 \text{ ohm}^{-1} \text{ cm}^2 \text{ eq}^{-1}$  at  $25^\circ\text{C}$ , which excludes abnormal proton conductance. In contrast to these results, Paul and co-workers (14-16) have reported  $\Lambda_0$  values for hydrogen chloride of 290 (14) and 280 (16)  $\text{ohm}^{-1} \text{ cm}^2 \text{ eq}^{-1}$  at  $25^\circ\text{C}$ , and similarly high values for several other protonic and Lewis acids (Table I). Our experimental results reported here show that the abnormally high  $\Lambda_0$  values reported by Paul and Sreenathan are grossly in error, and thus the major conclusions drawn by them on the basis of these erroneous data need reconsideration. An attempt has been made to ascertain the nature of the error in the reported data of Paul and Sreenathan.

## Experimental

**Purification of solvent.**—Dimethylformamide (BDH) was fractionally distilled at reduced pressure, the distillate was mixed with about 12% by volume of dry benzene (dried over sodium wire) and the benzene distilled at atmospheric pressure at about  $80^\circ$ . After removing the benzene-water azeotrope, the DMF was again distilled at reduced pressure and benzene free DMF was obtained. The benzene-free DMF was then shaken with pre-ignited, anhydrous alumina powder (BDH chromatographic grade). The solvent was decanted off, distilled, and the middle fraction boiling at  $55^\circ \pm 1^\circ\text{C}$  and 35 Torr pressure was collected and stored in blackened, stoppered Pyrex flasks. The specific conductivity of the solvent was found to be  $0.5\text{-}1.5 \times 10^{-7} \text{ ohm}^{-1} \text{ cm}^{-1}$  at  $25^\circ\text{C}$ .

**Preparation and purification of protonic and Lewis acids.**—One hundred per cent sulfuric acid was prepared by adding the calculated quantity of sulfur tri-

oxide to sulfuric acid (AR). *p*-Toluene sulfonic acid (Riedel) was crystallized from acetic acid and dried in vacuum desiccator. It melted at  $159.5^\circ \pm 1^\circ$ . Fluoro-sulfuric acid was prepared by adding required quantity of potassium bifluoride in small lots at a time, into ice-cold, fuming sulfuric acid. It was then distilled and the fraction boiling at  $160^\circ\text{-}61^\circ$  was collected. The fraction was redistilled in an atmosphere of dry nitrogen. Hydrogen chloride was prepared by dropping sulfuric acid (AR) on solid ammonium chloride (AR) and dried by passing through phosphorus pentoxide towers; it was then immediately absorbed in the purified DMF.

Anhydrous acetic acid was obtained by the process described by Bruckenstein (24). Monochloroacetic acid was purified by simple fractional distillation (bp  $182.5^\circ$ ). Dichloroacetic acid was distilled under reduced pressure, and the fraction boiling at  $102^\circ/20 \text{ mm}$  was collected (bp  $193^\circ \pm 1^\circ$ ). Trichloroacetic acid was recrystallized from hot benzene and dried under reduced pressure.

Tin tetrachloride (BDH) was distilled in an atmosphere of dry nitrogen. The middle fraction was collected which boiled at  $113.5^\circ \pm 1^\circ$ . Tin tetrabromide was prepared by slowly mixing liquid bromine with tin metal (AR). It was purified by redistillation. The middle fraction was collected which boiled at  $201.5^\circ \pm 1^\circ$ . Sulfur trioxide was prepared by distillation of a mixture of phosphorus pentoxide and sulfuric acid (AR) and was led directly into the solvent to avoid moisture. Antimony trichloride was purified by distillation under reduced pressure (bp  $220^\circ$ ). Bismuth trichloride (Riedel) was purified by sublimation under reduced pressure. Antimony pentachloride (BDH) was used as received. Pyrosulfuric acid was prepared by adding one calculated quantity of sulfur trioxide to 100% sulfuric acid.

**Solutions of protonic and Lewis acids in DMF.**—Solutions of protonic and Lewis acids in DMF were prepared by dissolving the requisite quantity of the acids in DMF and made up to 50 ml. The solutions of protonic acids were standardized by titrating with 0.1M sodium methoxide in benzene-methanol mixture using thymol blue as indicator (26, 27). The solutions of Lewis acids were standardized by gravimetric estimation of the metal and the nonmetal in a known volume of the solution. Allowance for the density of DMF ( $D = 0.944 \text{ g/ml}$ ) was made for calculating the molarities of the solutions. Solutions of the desired molarities were then obtained by suitably diluting the above solutions with DMF. Freshly prepared solutions were always used.

**Key words:** acids, conductivity, dissociation, formamide, N,N-dimethyl.

Table I. Conductances in DMF

(A comparison of the values of  $\Lambda$  measured by the present authors with those of Paul and Sreenathan)

Compounds		$\Lambda_M$ (Molar conductances at different concentrations)									
		Concentrations	$10.0 \times 10^{-3}M$	$6.4 \times 10^{-3}M$	$4.9 \times 10^{-3}M$	$3.6 \times 10^{-3}M$	$2.5 \times 10^{-3}M$	$1.6 \times 10^{-3}M$	$0.9 \times 10^{-3}M$	$0.4 \times 10^{-3}M$	$0.1 \times 10^{-3}M$
Fluorosulfuric acid	(a)	—	109	111	114	121.5	129	141.5	—	—	267.0
	(b)	30.6	31.8	32.4	33.5	35.6	37.9	41.5	46.5	57.0	78.5
	(a/b)	—	3.4	3.4	3.4	3.4	3.4	3.4	—	—	3.4
p-Toluene sulfonic acid	(a)	—	—	79	82	91	100	112	—	—	242.0
	(b)	20.6	22.1	22.7	24.4	26.5	29.5	32.9	39.1	54.5	71.2
	(a/b)	—	—	3.5	3.4	3.4	3.4	3.4	—	—	3.4
Hydrochloric acid	(a)	—	46	52	56	66	80	—	—	—	290.0
	(b)	12.9	14.1	15.6	17.1	19.7	23.3	28.8	43.0	60.3	84.0
	(a/b)	—	3.3	3.3	3.3	3.3	3.4	—	—	—	3.5
Pyrosulfuric acid	(a)	92	114	133	156	195	236	—	—	—	490.0
	(b)	26.0	34.3	39.8	46.3	55.2	66.6	80.6	98.5	116.3	142.5
	(a/b)	3.5	3.3	3.3	3.4	3.5	3.5	—	—	—	3.4
Sulfuric acid	(a)	30	40.5	47	56	66	78.5	—	—	—	465.0
	(b)	8.6	12.3	14.1	16.4	18.3	22.2	24.3	30.5	44.4	137.0
	(a/b)	3.5	3.3	3.4	3.4	3.6	3.5	—	—	—	3.4

Compounds		$\Lambda_M$ (Molar conductances at different concentrations)									
		Concentrations	$2.5 \times 10^{-3}M$	$1.6 \times 10^{-3}M$	$1.23 \times 10^{-3}M$	$0.9 \times 10^{-3}M$	$0.63 \times 10^{-3}M$	$0.4 \times 10^{-3}M$	$0.23 \times 10^{-3}M$	$0.1 \times 10^{-3}M$	$0.25 \times 10^{-4}M$
Antimony pentachloride	(a)	—	52.5	55	63	78	100	—	—	—	223.0
	(b)	13.8	15.3	16.7	18.5	23.2	29.4	38.8	46.5	55.7	65.6
	(a/b)	—	3.4	3.3	3.4	3.4	3.4	—	—	—	3.4
Tin tetrabromide	(a)	—	70	83	100	133	180	—	—	—	480.0
	(b)	16.2	20.2	23.7	28.5	38.6	52.0	70.3	88.1	116.2	148.1
	(a/b)	—	3.5	3.5	3.5	3.5	3.5	—	—	—	3.3
Tin tetrachloride	(a)	—	17	20	22	23	25	—	—	—	467.0
	(b)	3.0	5.0	5.7	6.3	6.8	7.4	12.1	30.3	80.5	137.4
	(a/b)	—	3.4	3.5	3.5	3.4	3.4	—	—	—	3.4
Sulfuric-trioxide	(a)	—	—	103	110	117.5	125	136	—	—	245.0
	(b)	26.0	28.0	30.2	32.6	34.4	36.5	40.4	44.5	58.0	71.2
	(a/b)	—	—	3.4	3.4	3.4	3.4	3.4	—	—	3.4

(a) Values of  $\Lambda$  deduced from the curves of  $\Lambda$  vs.  $\sqrt{c}$  plots published by Paul and Sreenathan.(b) Measured values of  $\Lambda$  by the present authors.

**Conductivity measurements.**—The conductivity bridge and cell were the same as used in the earlier investigation (22). Conductivity measurements were carried out at a constant temperature of  $25^\circ \pm 0.5^\circ$  using an oil bath. Twenty grams of DMF was taken in the conductance cell and then installment of the acid solution was added, stirred, and kept for 10 min before measuring the conductance. About 10-12 readings were taken for each acid.<sup>1</sup>

### Results and Discussion

The molar conductivities at infinite dilution ( $\Lambda_{M0}$ ) at  $25^\circ$  of a number of protonic and Lewis acids in DMF have been determined by the extrapolation of  $\Lambda_M$  vs.  $\sqrt{c}$  curves (Fig. 1). Abnormally high values of the conductances of hydrogen chloride, fluorosulfuric acid, p-toluene sulfonic acid, sulfuric and pyrosulfuric acids, and antimony pentachloride, tin tetrabromide, tin tetrachloride, and sulfurtrioxide in DMF as reported by Paul and Sreenathan (14-16) could not be verified by us, even after repeated experiments and utmost care and due precautions during experimental procedures. Their data of equivalent conductances in tabular form are not available, but they have published the curves of  $\Lambda$  vs.  $\sqrt{c}$ . We have deduced their values of equivalent conductances at some arbitrarily chosen concentrations, from the plots of  $\Lambda$  vs.  $\sqrt{c}$  published by them and compared them with those determined experimentally by us (Table I). Their values of equivalent conductances (a) do not agree with those of ours (b), but differ in such a way that the ratio (a/b) is almost a constant factor ( $a/b \approx 3.4$ ). Their values of the limiting equivalent conductances also differ with those of ours (determined by a common method, i.e.,

extrapolation of  $\Lambda$  vs.  $\sqrt{c}$ ) by almost the same constant factor. This indicates that the variation in our values from those of theirs is not due to the variation in the extrapolation of the curves. Clearly, the error in their data lies in the determination of the equivalent conductances and the mistake is uniform by a constant factor. This error appears to be present in one set of their measurements. The values of  $\Lambda_0$  for various protonic acids reported by them in their paper (16) can be sharply divided into two sets viz. (i) high values 125-490 and (ii) low values 2.5-42.0. The values in the first set are in error, whereas the values of the second set agree with our determined values within the range of the experimental error. For instance they have quoted  $\Lambda_0$  values for monochloroacetic acid and acetic acid as 28.6 and 20.0  $\text{ohm}^{-1} \text{cm}^{-1}$ , respectively, which are in agreement with the values determined by us, i.e., 28.0 and 20.0  $\text{ohm}^{-1} \text{cm}^2 \text{eq}^{-1}$ , respectively.

The errors in the values determined by Paul and Sreenathan are also reflected in the following:

1. The limiting equivalent conductance data of acetic acid ( $\Lambda_0 = 20.0$ ) and monochloroacetic acid ( $\Lambda_0 = 28.6$ ) and dichloroacetic acid ( $\Lambda_0 = 125.0$ ) at  $25^\circ$  reported by them do not fit in logically with the well-known principle of gradation. The difference between the values of  $\Lambda_0$  of acetic acid and monochloroacetic acid is only 8.6  $\text{ohm}^{-1} \text{cm}^2 \text{eq}^{-1}$  whereas between mono- and dichloroacetic acid it is 96.4.

2. The pK ( $-\log_{10}K$ ) values of several organic and inorganic acids calculated from conductance data by Paul and Sreenathan (16) do not correlate the limiting conductance data of these acids in DMF determined by the same workers. For example, it can be easily seen from their data that dichloroacetic acid is stronger acid (smaller pK) than sulfuric acid but the value of dichloroacetic acid is much smaller. Similarly, monochloroacetic acid is slightly stronger than pyrosulfuric acid in DMF, whereas the limiting conductance of

<sup>1</sup> An estimate of the errors in our data of the values of molar conductances has been made with the help of four independent measurements carried out in several replicate sets. These measurements were found to agree within  $\pm 1\%$ .

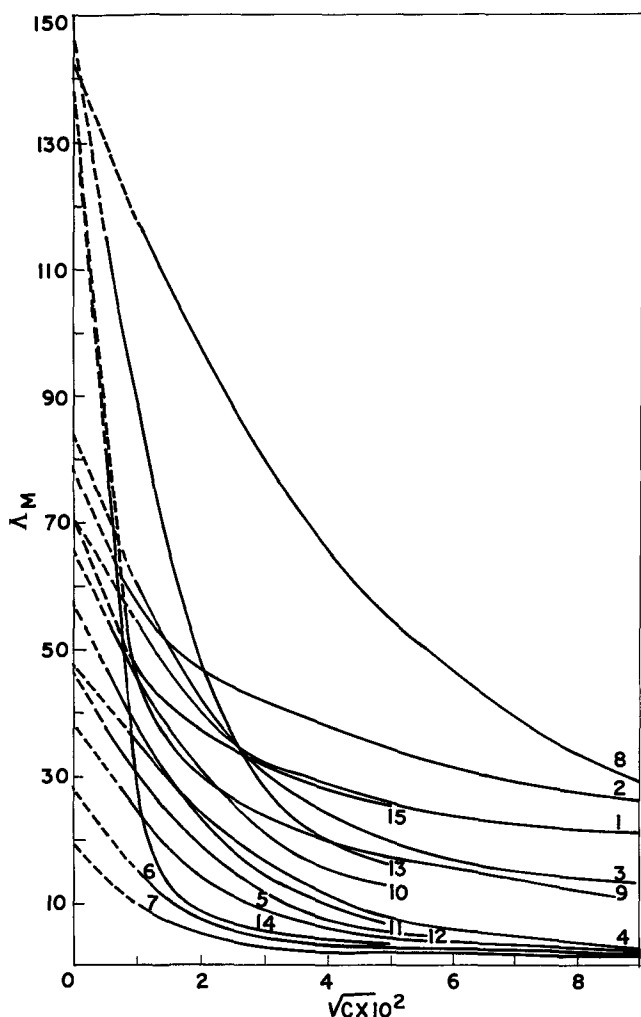


Fig. 1. Plots of  $\Lambda_M$  vs.  $\sqrt{c}$ . 1, p-Toluene sulfonic acid; 2, fluoro-sulfuric acid; 3, hydrochloric acid; 4, trichloroacetic acid; 5, dichloroacetic acid; 6, monochloroacetic acid; 7, acetic acid; 8, pyrosulfuric acid; 9, sulfuric acid; 10, antimony pentachloride; 11, bismuth trichloride; 12, antimony trichloride; 13, tin tetrabromide; 14, tin tetrachloride; and 15, sulfur trioxide. All in DMF.

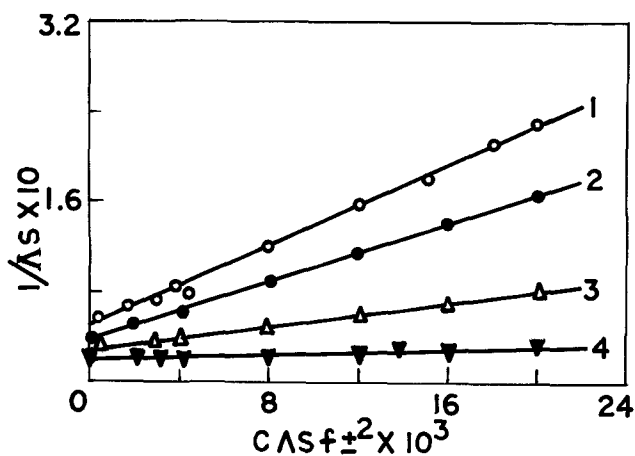


Fig. 2. Plots of  $1/\Lambda_s$  vs.  $c\Lambda_s f \pm 2$ . 1,  $\text{CH}_3\text{COOH}$ ; 2,  $\text{CH}_2\text{ClCOOH}$ ; 3,  $\text{CHCl}_2\text{COOH}$ ; 4,  $\text{CCl}_3\text{COOH}$ .

pyrosulfuric acid ( $\Lambda_0 = 490.0$ ) is very much larger than that of monochloroacetic acid ( $\Lambda_0 = 28.6$ ).

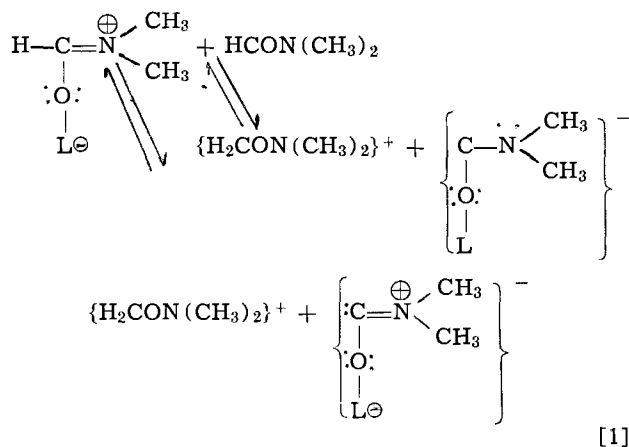
3. In their paper (14) Paul *et al.* have mentioned "The values of equivalent conductivity at infinite dilution for sulfuric acid and pyrosulfuric acid respectively are much higher than those of fluoro-sulfuric acid, p-toluene sulfonic acid, and hydrochloric acid. Sul-

furic acid and pyrosulfuric acid are dibasic acids and at the very low concentrations involved capable of releasing both the protons while the rest of the acids are monobasic and can release only one proton. . . ."

This explanation would be valid if one considers molar conductivity rather than equivalent conductivity but to analyze the data of equivalent conductivity in the above light is fundamentally wrong.

4. In order to explain the abnormally high values of conductances of protonic and Lewis acids in DMF, they suggested abnormal proton conductance in DMF and "proton jump" or "charge transfer" mechanism for the high mobility of proton similar to that suggested for water. However, a fundamental difference exists in the mechanisms suggested for water and DMF. In the case of water system, the actual migration of proton does not occur but the solvated proton may be obtained on the other side of the chain (see Fig. 3), when an electric field is applied, due to the internal rearrangement of electrons inside the chain causing the hydrogen bonds to change into covalent bonds and vice versa, *i.e.*, through tunneling effect. During this process, no change in the structure of water molecules results. But, in the case of DMF system, if the internal rearrangement of electrons be made and the hydrogen bonds be changed to covalent bonds and the required covalent bonds be changed to hydrogen bonds, the structure of DMF molecules are drastically changed. If on the other hand, the solvated proton be obtained on the other side of the chain without causing a change in the structure of the DMF molecules, the migration of proton from position (a) to (b) (see Fig. 3) becomes inevitable which would amount to actual migration and not through the tunneling effect. Consequently, a normal (non-Grothus type) proton conductance would be expected.

5. In order to explain the abnormally high values of the conductances of Lewis acids such as antimony pentachloride, tin tetrachloride, and bromide, in DMF they suggested the protonic nature of the complexes of Lewis acids and DMF. The mechanism suggested by them involves the following ionization process



The above ionization process will occur only when the Lewis acid-DMF complex is dissolved in DMF, but this mechanism does not afford any explanation for the conductance of the complexes in the molten state where no extra DMF molecule is available to facilitate the above ionization.

Further, according to the above mechanism, antimony pentachloride should form 1:2 complex and tin tetrahalides 1:4 complexes with DMF, but the actual formation of 1:1 complex with antimony pentachloride and 1:2 complexes with tin tetrahalides can hardly be explained.

On the other hand, the values of conductances determined by us support the earlier work of Thomas and Rochow (4) and Sears *et al.* (5) and exclude abnormal proton conductance in DMF. Our values appear to be coherent and in correlation with the values of  $K$  (Table

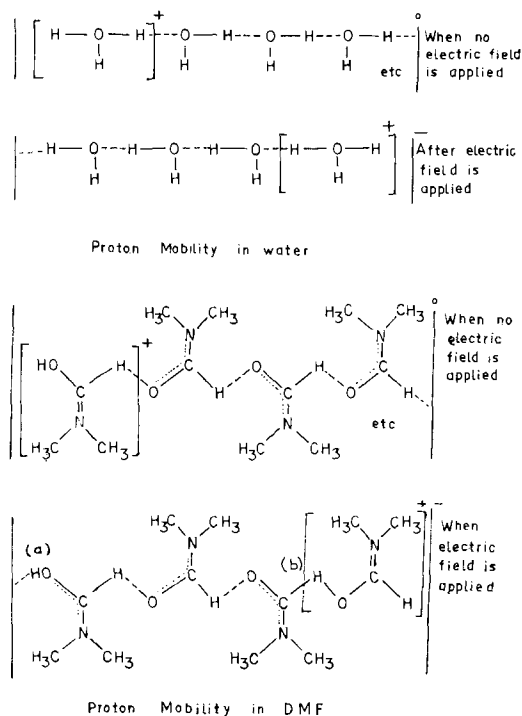
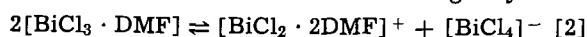
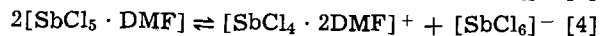
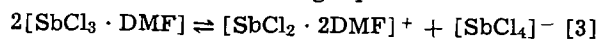


Fig. 3. Proton mobility in DMF

II) determined by the extrapolation of the Shedlovsky plots (Fig. 2). The rationality of our values is reflected in the gradation which exists among acetic, monochloroacetic, dichloroacetic, and trichloroacetic acids, i.e., 20.0, 28.0, 38.0, and 48.0, respectively. The polar nature of the Lewis acid-DMF complexes may be explained better by the ideas suggested by Drago and Purcell (28) who evolved a coordination model for the nonaqueous solvent behavior, rather than the mechanism suggested by Paul and Sreenathan (15). In a recent communication (22) it was shown that bismuth trichloride in DMF ionizes in the following way



Analogous work on antimony trichloride and antimony pentachloride (23) in DMF medium have supported the existence of the following equilibria



The plots of  $\Lambda_M$  vs.  $\sqrt{c}$  are not linear and the experimental Onsager slopes calculated from the limiting slopes of the curves are found to be more negative than the theoretically calculated Onsager slopes computed from the following equation

$$\alpha = (A + B\Lambda_0) = \frac{82}{\eta(DT)^{1/2}} + \frac{8.2 \times 10^5}{(DT)^{3/2}} \Lambda_0 \quad [5]$$

Table II. Conductance parameters of protonic and Lewis acids at 25°C

Acids (protonic and Lewis)	$\Lambda_{M0}$ ohm <sup>-1</sup> cm <sup>2</sup> mole <sup>-1</sup> extrapolation of the curve $\Lambda$ vs. $\sqrt{c}$	Slope $\alpha$ -theoretical	Slope $\alpha$ -experimental	$\Lambda_{M0}$ ohm <sup>-1</sup> cm <sup>2</sup> mole <sup>-1</sup> intercept of curve $1/\Lambda_s$ vs. $c \Lambda s f_{\pm}^2$	K (dissociation constant)
Fluosulfuric acid	78.5	-155	-2313	77.0	$7.51 \times 10^{-3}$
p-Toluene sulfonic acid	71.2	-148	-1971	69.0	$2.80 \times 10^{-3}$
Hydrochloric acid	84.0	-159	-2370	83.3	$9.60 \times 10^{-4}$
Trichloroacetic acid	48.0	-133	-1200	50.0	$3.20 \times 10^{-4}$
Dichloroacetic acid	38.0	-126	-1188	35.7	$2.56 \times 10^{-4}$
Monochloroacetic acid	28.0	-119	-1180	28.8	$1.93 \times 10^{-4}$
Acetic acid	20.0	-113	-1175	22.2	$1.62 \times 10^{-4}$
Pyrosulfuric acid	142.5	—	—	—	—
Sulfuric acid	137.0	—	—	—	—
Antimony pentachloride	65.6	-145	-1970	66.7	$4.40 \times 10^{-5}$
Bismuth trichloride	57.0	-139	-1900	58.8	$7.27 \times 10^{-6}$
Antimony trichloride	47.3	-132	-1650	43.2	$6.87 \times 10^{-6}$
Tin tetrabromide	148.1	—	—	—	—
Tin tetrachloride	137.4	—	—	—	—
Sulfur trioxide	71.2	—	—	—	—

where  $D$  is the dielectric constant,  $\eta$  is the viscosity of the solvent,  $T$  is the absolute temperature, and  $A$  and  $B$  are Onsager constants. The experimental and theoretical Onsager slopes are given in Table II. The deviations of the experimental slopes from the theoretical slopes indicate incomplete dissociation or ion pair formation of the solutes in solution. (The value of  $A$  for DMF is 98.5 at 25° and, therefore, the computed value of  $\alpha$  would always be greater than 98.5. It is, however, not understandable, how Paul and Sreenathan (16) have mentioned the theoretical Onsager slopes of acetic, propionic, monochloroacetic, dichloroacetic, acids and phenol to be 24.05, 21.7, 30.17, 98.81, and 11.6, respectively, in Table III of their paper.)

The conductance data have been further treated by Shedlovsky's equation (25) which may be written as

$$\frac{1}{\Lambda_s} = \frac{1}{\Lambda_0} + \frac{C\Lambda s f_{\pm}^2}{K\Lambda_0^2} \quad [6]$$

where  $\Lambda$  is equivalent conductivity at concentration  $C$ ,<sup>2</sup>  $\Lambda_0$  is equivalent conductivity at zero concentration,<sup>2</sup>  $f_{\pm}$  is mean activity coefficient,  $K$  is thermodynamic dissociation constant, and  $s$  is a function of  $z$  and is equal to

$$s = \left[ z/2 + \sqrt{1 + (z/2)^2} \right]^2 \quad [7]$$

and  $z$  is defined by

$$z = \alpha\Lambda_0^{-3/2} \sqrt{c\Lambda} \quad [8]$$

where  $\alpha$  is the Onsager coefficient determined by the limiting slopes from the  $\Lambda_M$  vs.  $\sqrt{c}$  plots.

The mean activity coefficient  $f_{\pm}$  is computed from

$$-\log f_{\pm} = \beta \sqrt{cs\Lambda/\Lambda_0} \quad [9]$$

where  $\beta$  is the Debye Huckel's  $A$  constant whose value for DMF is equal to

$$\frac{1.812 \times 10^6}{(DT)^{3/2}} = 1.573$$

A plot of  $1/\Lambda_s$  vs.  $c\Lambda s f_{\pm}^2$  is a straight line at low concentrations which on extrapolation gives an intercept of  $1/\Lambda_0$  and slope of  $1/K\Lambda_0^2$  (Fig. 2) (only some samples are given). With the help of such plots the values of  $\Lambda_0$  and  $K$  of monobasic protonic acids have been calculated. These are also described in Table II.

In the equilibria represented by Eq. [2], [3], and [4], two univalent ions are produced from two molecules of the Lewis acid-DMF complex and in this form, the Shedlovsky equation cannot be applied. However, if the two molecules on the left-hand side in these equations are reckoned as one molecule (this can be done by treating the concentration equal to half the molar

<sup>2</sup> For 1-1 electrolyte the equivalent conductivity is the same as the molar conductivity and since the Shedlovsky equation is applicable in the case of 1-1 electrolytes only, no attempt has been made to distinguish molar conductivity from equivalent conductivity here and separate symbols for representing the two conductivities have not been used.



concentration of Lewis acid-DMF adduct), then the Shedlovsky equation would be applicable to these systems. Such an assumption would make little difference as the neutral molecules of the Lewis acid-DMF complex do not contribute towards the conductance of the solution. The Shedlovsky equation has been applied utilizing the above assumption in these systems and the values of  $K$  have been calculated (Table II). The values of  $K$  would correspond to the following mass law equation

$$K = \frac{[(\text{BiCl}_2 \cdot 2\text{DMF})^+][(\text{BiCl}_4)^-]}{[\text{Bi}_2\text{Cl}_6 \cdot 2\text{DMF}]} \quad [10]$$

The actual value of  $K$  (say  $K'$ ) should correspond to

$$K' = \frac{[(\text{BiCl}_2 \cdot 2\text{DMF})^+][(\text{BiCl}_4)^-]}{[\text{BiCl}_3 \cdot \text{DMF}]^2} \quad [11]$$

so that

$$\frac{K'}{K} = K'' = \frac{[\text{Bi}_2\text{Cl}_6 \cdot 2\text{DMF}]}{[\text{BiCl}_3 \cdot \text{DMF}]^2} \quad [12]$$

However, it is difficult to calculate the exact value of  $K$  from the existing data.

#### Acknowledgment

The authors thank Professor R. C. Mehrotra, Head of the Department of Chemistry, University of Rajasthan, Jaipur, for providing laboratory facilities and encouragement and the C.S.I.R. New Delhi for providing a research grant.

Manuscript submitted Jan. 25, 1972; revised manuscript received June 18, 1973.

Any discussion of this paper will appear in a Discussion Section to be published in the December 1974 JOURNAL.

#### REFERENCES

- D. P. Ames and P. G. Sears, *J. Phys. Chem.*, **59**, 16 (1965).
- C. M. French and K. H. Glover, *Trans. Faraday Soc.*, **51**, 1418 (1955).
- L. R. Dawson, M. Golben, G. R. Leader, and H. K. Zimmerman, Jr., *This Journal*, **99**, 28 (1952).
- A. B. Thomas and E. G. Rochow, *J. Am. Chem. Soc.*, **79**, 1843 (1957).
- P. G. Sears, R. K. Wolford, and L. R. Dawson, *This Journal*, **103**, 633 (1956).
- P. G. Sears, E. D. Wilhoit, and L. R. Dawson, *J. Phys. Chem.*, **59**, 373, 375 (1955).
- H. Chateau and M. C. Moncet, *Compt. Rend.*, **61**, 10 (1960).
- J. E. Prue and P. J. Sherrington, *Trans. Faraday Soc.*, **57**, 1795, 1806 (1961).
- V. Prey and W. Unger, *Oesterr. Chemiker-Ztg.*, **61**, 10 (1960).
- L. R. Dawson, M. Golben, G. R. Leader, and H. K. Zimmerman, Jr., *Trans. Kentucky Acad. Sci.*, **13**, 221 (1952).
- L. R. Dawson, G. R. Leader, and H. K. Zimmerman, Jr., *J. Phys. Chem.*, **55**, 447 (1951).
- K. Gingold, E. G. Rochow, D. Seyferth, A. C. Smith, Jr., and R. West, *J. Am. Chem. Soc.*, **74**, 6306 (1952).
- W. F. Luder and L. S. Hamilton, *J. Phys. Chem.*, **60**, 1470 (1956).
- R. C. Paul, P. S. Guraya, and B. R. Sreenathan, *Indian J. Chem.*, **1**, 335 (1963).
- R. C. Paul, S. Sharda, and B. R. Sreenathan, *ibid.*, **2**, 97 (1964).
- R. C. Paul and B. R. Sreenathan, *ibid.*, **4**, 348, 382 (1966).
- L. R. Dawson and W. W. Wharton, *This Journal*, **107**, 710 (1960).
- P. G. Sears, E. D. Wilhoit, and L. R. Dawson, *J. Chem. Phys.*, **23**, 1274 (1955).
- R. C. Paul in "New Pathways in Inorganic Chemistry," E. A. V. Ebsworth, A. G. Maddock, and A. G. Sharpe, Editors, pp. 233-261, Cambridge University Press (1968).
- S. J. Kuhn and J. S. McIntyre, *Can. J. Chem.*, **43**(2), 275, 995 (1965).
- R. C. Paul, B. R. Sreenathan, and S. L. Chadha, *J. Inorg. Nucl. Chem.*, **28**, 1225 (1966).
- A. K. Mishra and K. N. Tandon, *Inorg. Chem.*, **10**, 1896 (1971).
- A. K. Mishra, Unpublished work.
- S. Bruckenstein, *Anal. Chem.*, **31**, 1757 (1959).
- R. M. Fuoss and T. Shedlovsky, *J. Am. Chem. Soc.*, **71**, 1496 (1949).
- J. S. Fritz and R. T. Keen, *Anal. Chem.*, **24**, 306 (1952).
- R. H. Cundiff and P. C. Marknes, *ibid.*, **30**, 1447 (1958).
- R. S. Drago and K. F. Purcell, in "Progress in Inorganic Chemistry," Vol. VI, F. A. Cotton, Editor, pp. 271-329, Wiley Interscience, New York (1964).

## Two-Dimensional Current Distribution Within a Packed-Bed Electrochemical Flow Reactor

Richard Alkire\* and Patrick K. Ng\*\*

Department of Chemical Engineering, University of Illinois, Urbana, Illinois 61801

#### ABSTRACT

An analysis is presented for describing behavior of a packed-bed electrode confined within a thin cylindrical porous separator and surrounded by a concentric counterelectrode. Electrolytic solution, containing reactive species, flows axially in plug flow through the packed-bed electrode while the peripheral surface of the packed bed is held under a constant applied potential. Results are obtained for two types of porous separators, (i) permeable to all solute species and (ii) impermeable to the reactive solute species. For each case, the two-dimensional (radial and axial) concentration, potential, and current distributions are calculated by a finite difference method. The results clarify over-all reactor performance and, in particular, predict the relation between the volumetric reaction rate and the residence time for a wide range of system parameters.

The appealing advantage of electrochemical synthesis processes is that electrical current is inexpensive in

\* Electrochemical Society Active Member.

\*\* Electrochemical Society Student Associate.

Key words: current distribution, porous electrode, copper removal, reactor design.

comparison with the price of chemical oxidizing or reducing agents. Carrying out electrochemical synthesis operations at high rates, however, can be difficult owing to the heterogeneous nature of electrochemical reactions. The volumetric reaction rates of typical elec-

tolysis cells are low in comparison with volumetric reaction rates of chemical reactors, especially those for homogeneous chemical reactions. In order to compete favorably, electrochemical reactors can often be designed with porous electrodes which exhibit very large surface areas for reaction.

The voltage applied to an electrolysis cell is consumed by various means which include ohmic resistance of the electrolyte, diffusional resistance, and hindrance associated with the reactions occurring at the electrode surface. Whereas porous electrodes can substantially relieve charge-transfer hindrances by their very large surface area, they introduce still additional ohmic and diffusional resistances in the electrolyte within the porous region. One way to relieve diffusional resistance is to force electrolyte through the porous electrode. Although flow-through porous electrodes can exhibit moderately high volumetric reaction rates, their design is complex because the potential, reaction rate, and concentration of reacting species will vary with position within the electrode. Knowledge of the reaction rate distribution, however, is exceedingly helpful for a rational analysis, preliminary design, and economic evaluation of the reactor.

Among various possible reactor configurations, two offer particular advantages of simplicity as indicated in Fig. 1. In Geometry A, the counterelectrode is positioned upstream or downstream of the porous reactor electrode. In this configuration, flow of electrolyte and of electrical current take place essentially along the same spatial direction. In order to avoid appreciable mixing of anolyte and catholyte, a porous separator is usually placed between the respective cell compartments. In Geometry B, the porous separator consists of a cylindrical tube within which the porous electrode is placed. In Geometry B, the counterelectrode surrounds the packed-bed electrode with the result that flow of electrolyte and of electrical current take place in different directions. On the basis of a unit volume of packed bed, Geometry B exposes a larger surface area to the counterelectrode than Geometry A.

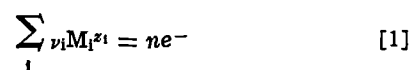
No theoretical analyses are known to be available for Geometry B. A small number of experimental studies of Geometry B are available; these employed the elec-

trode as a potentiostatic chromatograph (1), for elution voltammetry (2), and for removal of heavy metal ions and radioisotope separation (3). On the other hand, a substantial number of experimental investigations have also been conducted in Geometry A (4-6) owing, in part, to the relatively simpler (one-dimensional) basis for theoretical calculations (4, 7-9). Based on model predictions, economic feasibility studies have been carried out for one reactor designed to remove copper from very dilute solutions (10). Other common industrial problems include reclaiming of metals, treatment of chromic acid, cyanide, and acid-mine wastes, and detoxification of refractory organics (11). However, the large-scale usage of such electrochemical methods for waste treatment and synthesis awaits the development of carefully engineered cells. One important task is to predict how current-voltage behavior of a cell depends, for example, on conductivity, flow rates, concentrations, cell geometry, and reaction rate constants. The following study has been undertaken in order to, on the one hand, clarify behavior of an important class of reactors and, on the other hand, to illustrate how predictions of behavior may be compiled for use in cell design.

### Theoretical Aspects

The packed-bed reactor under consideration is of radius  $r_0$ , and is of uniform porosity and specific surface area throughout. Electrolyte of uniform composition enters at the upstream end of the reactor ( $z = 0$ ) and proceeds axially downstream along its length. Several restrictions have been adopted in order to simplify calculations: (i) isothermal operation occurs in the steady-state; (ii) a single, reversible electrode reaction occurs; (iii) the potential along the exterior surface of the reactor (at  $r = r_0$ ) is constant; (iv) the motion of solute species in the electrolyte is described by transport equations for dilute solutions with constant coefficients; (v) electrolyte motion occurs within the reactor in plug flow, and the porous separator is impermeable to flow, although diffusion may occur across it; and (vi) axial diffusion and migration are negligible in comparison with radial diffusion and migration. Some of the foregoing assumptions are necessary for conduct of analysis by the methods employed, while other assumptions are chosen somewhat arbitrarily and could easily be replaced by other choices for particular situations.

The electrochemical reaction under study is represented by the general form



The reaction rate expression for reaction [1] could have a wide variety of forms depending on the system; the present study directs attention toward "reversible" electrodeposition of a metal ion in accord with the Butler-Volmer equation

$$j = i_0 \left[ e^{-\frac{\alpha n F}{R T} (\phi - \phi_e)} - \frac{c_i}{c_i^b} e^{\frac{(1 - \alpha) n F}{R T} (\phi - \phi_e)} \right] \quad [2]$$

Movement of solute species in the electrolyte occurs by diffusion, migration, and convection; in addition, electroactive species are consumed or generated by reaction. Under steady-state operating conditions, an equation for the conservation of species  $i$  therefore has the form

$$D_i \nabla^2 c_i + \frac{z_i D_i F}{R T} \nabla \cdot (c_i \nabla \phi) - \nabla \cdot (v c_i) = \frac{a \nu_i}{n F} j \quad [3]$$

In accord with the assumptions listed previously, Eq. [3] may be written in circular cylindrical coordinates

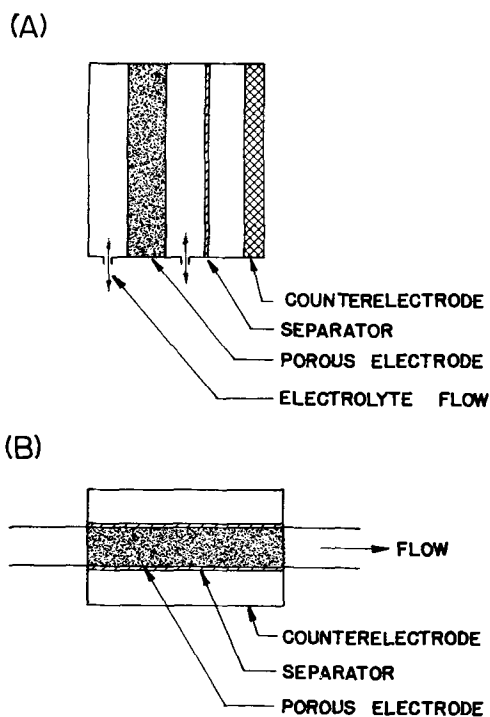


Fig. 1. Schematic diagrams of two flow-through porous electrode configurations: (A) electrolyte flows essentially parallel to current flow, (B) electrolyte flows essentially perpendicular to current flow.

$$v_0 \frac{\partial c_1}{\partial z} = D_1 \frac{\partial^2 c_1}{\partial r^2} + \frac{D_1}{r} \frac{\partial c_1}{\partial r} + \frac{z_1 D_1 F}{RT} \left( c_1 \frac{\partial^2 \phi}{\partial r^2} + \frac{c_1}{r} \frac{\partial \phi}{\partial r} + \frac{\partial \phi}{\partial r} \frac{\partial c_1}{\partial r} \right) - \frac{a v_1 i_0}{nF} \left[ e^{-\frac{\alpha nF}{RT}(\phi - \phi_0)} - \frac{c_1}{c_1^b} e^{\frac{(1-\alpha)nF}{RT}(\phi - \phi_0)} \right] \quad [4]$$

Equation [4] has  $(i + 1)$  unknowns: the  $i$  concentrations and the potential. Relations having the form of Eq. [4] may be written for each of the  $i$  solute species in solution; the remaining relationship is provided by the equation of electrical neutrality

$$\sum_1 z_i c_i = 0 \quad [5]$$

Two sets of boundary and initial conditions have been chosen for study which correspond to two different types of porous separator membranes. The first set characterizes sieve-type membranes which obstruct passage of reactant species but which allow free passage of smaller species. For the acidified copper sulfate system chosen for study, outlined below, the boundary conditions are

$$\begin{aligned} z = 0 & \quad c_1 = c_1^b \\ r = 0 & \quad \frac{\partial c_1}{\partial r} = 0 \\ & \quad \frac{\partial \phi}{\partial r} = 0 \\ r = r_0 & \quad \phi = \phi_a \\ & \quad c_{H^+} = c_{H^+}^b \\ & \quad \frac{\partial c_{Cu^{+2}}}{\partial r} = 0 \end{aligned} \quad [6]$$

The second set of conditions characterizes membranes which permit free passage of all solute species

$$\begin{aligned} z = 0 & \quad c_1 = c_1^b \\ r = 0 & \quad \frac{\partial c_1}{\partial r} = 0 \\ & \quad \frac{\partial \phi}{\partial r} = 0 \\ r = r_0 & \quad \phi = \phi_a \\ & \quad c_1 = c_1^b \end{aligned} \quad [7]$$

Equations [4] and [5] along with side conditions [6] or [7] permit calculation of the concentration and potential distribution throughout the packed-bed reactor. The local reaction rate distribution throughout the reactor can subsequently be determined from Eq. [2]. In turn, the current density distribution along the porous separator, denoted  $i^*(z)$ , is found by integration of Eq. [2]

$$i^* = \frac{a}{r_0} \int_0^{r_0} j r dr \quad [8]$$

Finally, Eq. [8] may be integrated along the length of the reactor to yield the volumetric reaction rate,  $i_v$ , having units amperes per cubic centimeter of reactor volume

$$i_v = \frac{2}{r_0 z} \int_0^z i^* dz \quad [9]$$

In order to reduce the number of independent parameters which influence the system, it is convenient to introduce dimensionless variables

$$\begin{aligned} R &= \frac{r}{r_0} & \theta &= \frac{D_r z}{r_0^2 v_0} & C_1 &= \frac{c_1}{c_r} \\ \Phi &= \frac{F}{RT} (\phi - \phi_0) & J &= \frac{a r_0}{i^*} j \end{aligned} \quad [10]$$

The equations and side conditions which conform to the model then have the form

$$\sum_1 z_i C_i = 0 \quad [11]$$

and

$$\begin{aligned} \frac{1}{\pi_i} \frac{\partial C_1}{\partial \theta} &= \frac{\partial^2 C_1}{\partial R^2} + \frac{1}{R} \frac{\partial C_1}{\partial R} \\ &+ z_i \left[ \frac{\partial}{\partial R} \left( C_i \frac{\partial \Phi}{\partial R} \right) + \frac{C_i}{R} \frac{\partial \Phi}{\partial R} \right] \\ &- \frac{\xi v_1}{\pi_i} \left[ e^{-\alpha n \Phi} - \frac{C_1}{\gamma_i} e^{-(\alpha-1)n\Phi} \right] \end{aligned} \quad [12]$$

with either

$$\begin{aligned} \theta = 0 & \quad C_1 = \gamma_1 \\ R = 0 & \quad \frac{\partial C_1}{\partial R} = \frac{\partial \Phi}{\partial R} = 0 \\ R = 1 & \quad C_{H^+} = \gamma_{H^+} \\ & \quad \frac{\partial C_{Cu^{+2}}}{\partial R} = 0 \\ & \quad \Phi = \Phi_a \end{aligned} \quad [13]$$

or

$$\begin{aligned} \theta = 0 & \quad C_1 = \gamma_1 \\ R = 0 & \quad \frac{\partial C_1}{\partial R} = \frac{\partial \Phi}{\partial R} = 0 \\ R = 1 & \quad C_1 = \gamma_1 \\ & \quad \Phi = \Phi_a \end{aligned} \quad [14]$$

The dimensionless parameters which appear in the foregoing model are

$$\pi_i = \frac{D_1}{D_r} \quad \gamma_i = \frac{c_1^b}{c_r} \quad \xi = \frac{a r_0^2 i_0}{n F c_r D_r} \quad [15]$$

The dimensionless forms of Eq. [2] and [8] which are subsequently employed are, respectively

$$\beta J = \xi \left[ e^{-\alpha n \Phi} - \frac{C_1}{\gamma_i} e^{(1-\alpha)n\Phi} \right] \quad [16]$$

$$\beta = \xi \int_0^1 \left[ e^{-\alpha n \Phi} - \frac{C_1}{\gamma_i} e^{(1-\alpha)n\Phi} \right] R dR \quad [17]$$

where

$$\beta = \frac{i^* r_0}{n F c_r D_r} \quad [18]$$

Equations [16] and [17] imply that

$$\int_0^1 J R dR = 1 \quad [19]$$

Finally Eq. [9] will be used to determine the average volumetric reaction rate between reactor inlet and position  $\theta$  in accord with the integral

$$I = \frac{\int_0^\theta \beta d\theta}{\theta} \quad [20]$$

Before passing to a discussion of the model, it would be useful to pause for a moment to gain a better physical feeling for the dimensionless groupings which

have arisen. The quantity  $\theta$  is a dimensionless distance and may also be interpreted as the dimensionless time period during which a fluid packet has been in contact with the packed bed. That is, since the fluid moves in plug flow, all fluid packets having contact time  $\theta_1$ , would be located at the same distance from the reactor entrance. The quantity  $J$  is the local reaction rate which varies with both radial and axial position within the electrode. For a given value of  $\theta$ , the current density flowing through the porous separator is  $\beta$ , given by Eq. [17]. The current distribution, embodied in  $J$  and  $\beta$ , is related to the potential and concentration distributions by the parameter  $\xi$ , as indicated by Eq. [16]. According to its definition,  $\xi$  is a ratio of diffusion resistance to charge-transfer resistance insofar as it contains the ratio  $i_0/D_r$ . A detailed treatment of these quantities is given below.

### Method of Solution

The solution of the set of equations and side conditions derived above was accomplished by a numerical procedure which employed finite difference equations. Equation [11] is parabolic in the sense that the only  $\theta$ -dependence which enters into the equation is in the derivative on the left side. Therefore integration over the two-dimensional volume can proceed in a step-wise manner beginning at the upstream end of the reactor, at  $\theta = 0$ . At each subsequent step in the axial direction, the  $\theta$ -derivative was placed into finite difference representation in accord with the Crank-Nicolson symmetric form (12). Owing to the plug flow assumption, the quantity  $\theta$  corresponds to the residence time of electrolyte within the reactor; the solution of the model is similar to the analysis of unsteady-state behavior in porous battery electrodes (13).

At each step along the  $\theta$ -direction, the radial dependence of potential and concentrations was determined by linearizing Eq. [10] and [11] about a trial solution and then setting them into finite difference form. The trial matrix was then inverted (14), and the solution of the nonlinear equation was gained by iteration with successive correction of the trial solution. The criterion chosen for convergence was that the potential anywhere within the electrode should change by less than 0.01% upon successive iterations. A typical individual  $\theta$ -step calculation was found to take 2 sec and involved three iterations.

The results presented below were calculated with use of 100  $R$ -increments; the initial size of the  $\theta$ -increment was so chosen that the maximum solute concentration change was 2% of the bulk value. Smaller increments did not improve the numerical results to any appreciable degree. Between successive  $\theta$ -steps, the  $\theta$ -increment was increased by a factor of 1.1 in order to conserve computer time.

### Results and Discussion

The theoretical model developed above was employed to predict behavior during electrodeposition of copper from acidified sulfate solution. This system has been chosen since it lends itself nicely to an experimental program of investigation; values of the system parameters are given in Table I. The results chosen for presentation below are intended both to elucidate details of electrode behavior and to provide a compilation of results. Before proceeding to details of two-

Table I. Properties of the acid copper sulfate system chosen for calculations

Species	$z_i$	$\gamma_i$	$\pi_i$	$\nu_i$
H <sup>+</sup>	+1	4.0	9.312	0
SO <sub>4</sub> <sup>=</sup>	-2	2.1	1.065	0
Cu <sup>++</sup>	+2	0.1	0.7188	-1

$$n = 2,$$

$$\alpha = 0.5.$$

dimensional behavior, the results for two limiting cases are presented.

*Behavior upon initial contact.*—If electrolyte passes through the reactor without appreciable mass transfer limitations, then the solute concentrations will be constant everywhere and the set of Eq. [10] and [11] may be simplified to a single ordinary differential equation

$$\frac{d^2\Phi}{dR^2} + \frac{1}{R} \frac{d\Phi}{dR} = \frac{n\xi}{\sum_i z_i^2 \nu_i \gamma_i} [e^{-\alpha n\Phi} - e^{(1-\alpha)n\Phi}] \quad [21]$$

For a given applied potential, Eq. [21] can be used to determine the uppermost current which may be achieved for a system of known exchange current density, conductivity, and electrode geometry. The potential distribution gained by solving Eq. [21] for a given applied potential may be substituted into Eq. [17] to generate the corresponding total current flowing to the electrode. Figure 2A provides the current-potential curves predicted for various values of the parameter  $\xi$ . It is reasonable to anticipate that the results depicted in Fig. 2A would also apply in the upstream regions of the packed-bed reactor, during initial contact, whether or not concentration variations eventually develop downstream.

*Behavior far downstream.*—Far downstream from the reactor entrance, behavior will depend on which of the aforementioned boundary conditions prevail. When the porous separator is impermeable to reactive species (Eq. [13]), electrochemical reaction will eventually deplete reactants insofar as the applied potential permits. In this situation, the region far downstream is not reactive with the consequence that an optimum reactor length will exist which balances fabrication and maintenance costs against volumetric productivity.

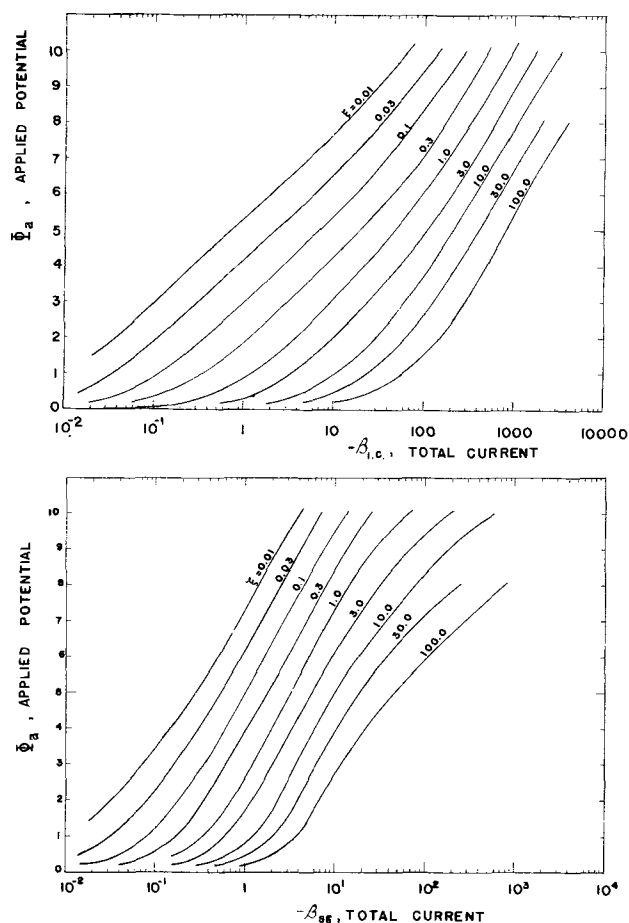


Fig. 2. Current/potential diagrams for two limiting cases of reactor behavior: (A) initial contact, i.e., uniform concentration, (B) well-developed region far downstream.

On the other hand, when the porous separator is permeable to all species (Eq. [14]), the reactor will exhibit quite different behavior far downstream from the entrance. In this case, after a sufficient distance downstream, the reactor will achieve a "well-developed" configuration in which the concentration and potential distributions within the packed-bed will vary with radial, but not axial, position. Since there are no concentration variations along the  $\theta$ -direction in this well-developed region, the left side of Eq. [12] becomes zero and one obtains an ordinary differential equation for each solute species  $i$ . For the copper system under study, integration of the set of equations provides the current/potential curves shown in Fig. 2B. Comparison of Fig. 2A and B indicates that the concentration overpotential inherent in the "well-developed" region serves to reduce the reactivity of the electrode in comparison with the initial contact value. For systems having low values of  $\xi$ , differences in behavior are noticeable only at larger values of applied potential. For systems of large  $\xi$ , however, significant differences between initial contact and far downstream are evident even at low applied potentials. In many instances, interdiffusion of reactive anolyte and catholyte species can lower the current efficiency and be disadvantageous. Therefore permeable separator reactors of excessive length are not attractive with the result that an optimum reactor length needs to be determined.

*Intermediate behavior.*—Between the two limiting cases outlined above lies the region in which reactor behavior is more complex to predict owing to the existence of both axial and radial variations of concentration and potential. Knowledge of this region, however, is of special value for the understanding of reactor behavior.

Figure 3a shows the distribution of copper ion concentration along the radial direction for several locations downstream from the reactor entrance when the porous separator is impermeable to reactants. It is seen that the concentration of cupric ions is initially uniform but decreases with distance downstream. The rate of decrease is initially most rapid near the periphery where the reaction rate is highest. The radial concentration gradient at the periphery is zero throughout the reactor in accord with the boundary conditions [13]. Once reactants near the periphery become substantially depleted, radial diffusion of reactants takes place from regions of higher concentration, along the axis of the reactor, toward peripheral regions. Eventually, the reactants become depleted throughout the reactor and the copper ion concentration approaches the minimum possible value given by the Nernst equation.

Continuing with the impermeable separator case, Fig. 3b shows the radial distribution of reaction rate for various axial positions downstream from the entrance. It is seen that the initial contact current distribution is nonuniform owing to the large values of  $\Phi_a$  and  $\xi$  chosen for the example. The reaction rate is highest at the periphery, near the counterelectrode. The reactivity of the periphery, however, decreases rapidly with distance downstream owing to the depletion of reactive species as already indicated in Fig. 3a. At intermediate positions along the reactor, the most reactive portion of the reactor is far enough from the periphery that reactants are available, but not so far that the ohmic resistance of the electrolyte consumes the applied potential. With sufficient distance downstream, even the central portion of the packed-bed becomes reactive.

In contrast to Fig. 3, Fig. 4 shows concentration and reaction rate distributions predicted for permeable porous separators. From Fig. 4a, it is seen that the concentration of cupric ions remains constant at the periphery of the reactor along its entire length, in accord with the boundary conditions. For large values of  $\xi$ , for which the current distribution upon initial

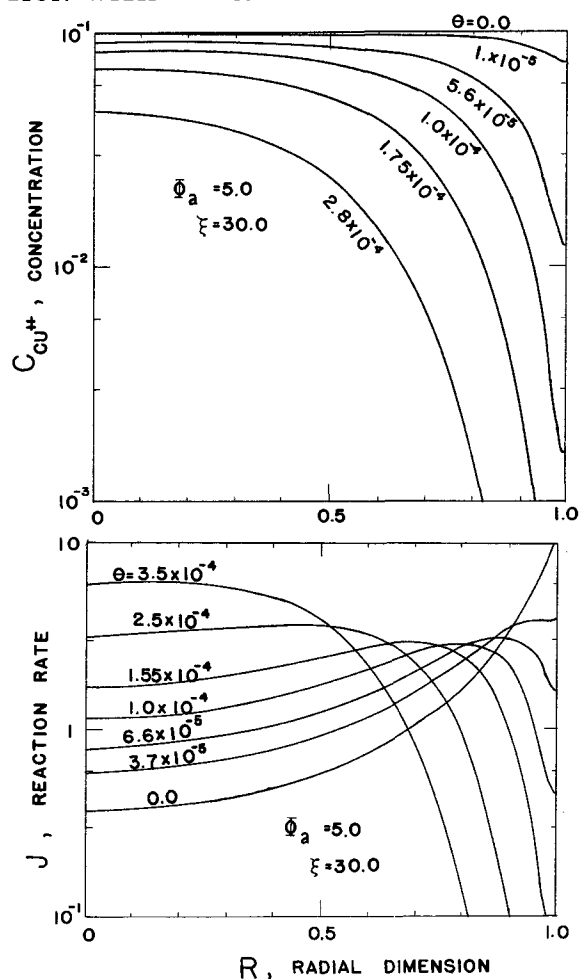


Fig. 3. Dependence of radial distributions on residence time within plug-flow reactor with porous separator impermeable to copper ions ( $\Phi_a = 5$ ,  $\xi = 30$ ): (a, upper) copper ion concentration during cathodic deposition, (b, lower) local reaction rate.

contact is highly nonuniform, the results shown in Fig. 4 are typical. Reactants near the central region are not consumed near the reactor entrance owing to low reactivity of these regions. Although the periphery is highly reactive, the copper ions are easily replenished by diffusion through the permeable separator. The depletion of reactants therefore proceeds most rapidly at intermediate locations, and a minimum in the reactant concentration appears. As the electrolyte flows through the reactor, the minimum shifts toward the center of the reactor; when the minimum reaches the centerline, the reactor is said to be "well-developed."

Figure 4b provides the radial current distributions at various axial distances downstream for the same conditions as in Fig. 4a. It is seen that the reactivity of the peripheral region remains high along the length of the reactor, but that a minimum in reactivity may be located at the regions which are depleted of reactive species. The interior of the reactor (near  $R = 0$ ) becomes relatively more and more reactive with distance downstream until reactant depletion near the axis occurs to a sufficient extent. Far downstream, a well-developed reaction distribution is found for which the peripheral regions alone are reactive by virtue of reactant supply through the porous separator.

Calculations have also been performed in order to determine the current density passing through the porous separator. The radial potential distribution was integrated at each  $\theta$ -increment in accord with Eq. [17]. Because of depletion of reactive species, the current passing the separator decreases with distance downstream from the inlet. For an impermeable separator, Fig. 5 indicates the axial distribution of current for  $\xi = 0.1$  and several values of applied potential. The

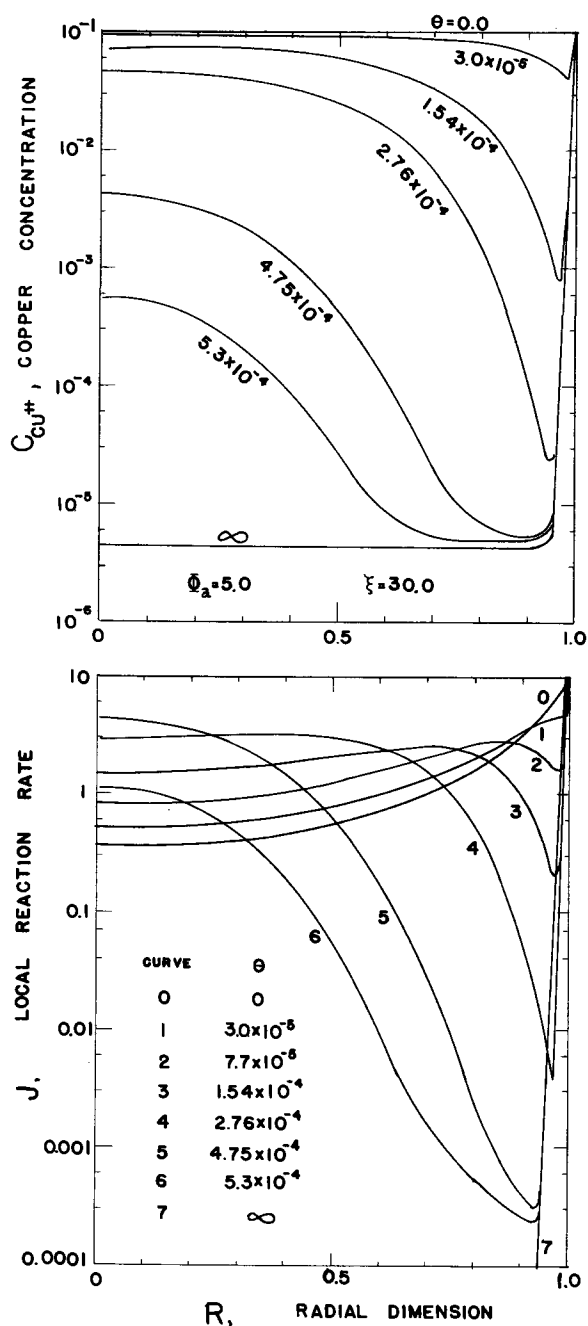


Fig. 4. Dependence of radial distributions on residence time within plug-flow reactor for a porous separator permeable to all solute species ( $\Phi_a = 5$ ,  $\xi = 30$ ): (a, upper) copper ion concentration during cathodic deposition, (b, lower) local reaction rate.

ordinate is normalized by the current density which flows upon initial contact (see Fig. 2a). Although the shapes of the curves are similar, the residence times for onset of depletion at  $\Phi_a = 2.0$  and  $7.0$  differ by a factor of 100. The residence time at which the local current density has decreased to within 5% of the initial contact value is denoted  $\theta_{95\%}$ . Figure 6 illustrates how  $\theta_{95\%}$  varies with  $\xi$  for several values of applied potential. It is seen that the residence time for attainment of  $\theta_{95\%}$  decreases with an increase in either  $\xi$  or  $\Phi_a$ . For a given value of  $\xi$  and  $\Phi_a$ , Fig. 6 indicates the maximum useful ratio of reactor length to flow velocity; reactors having residence times in excess of  $\theta_{95\%}$  will have downstream regions which are essentially unreactive. The 95% criterion is of course an arbitrary choice which may not be well suited for some applications.

The axial current distribution depicted in Fig. 5 has been integrated in accord with Eq. [20] to yield the average current density passing between the packed-

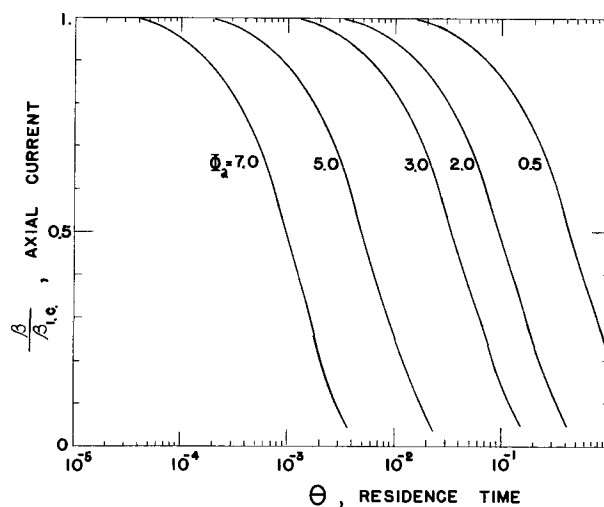


Fig. 5. Axial variation of current flowing through porous separator for various applied potentials and  $\xi = 0.1$  (separator impermeable to copper ions).

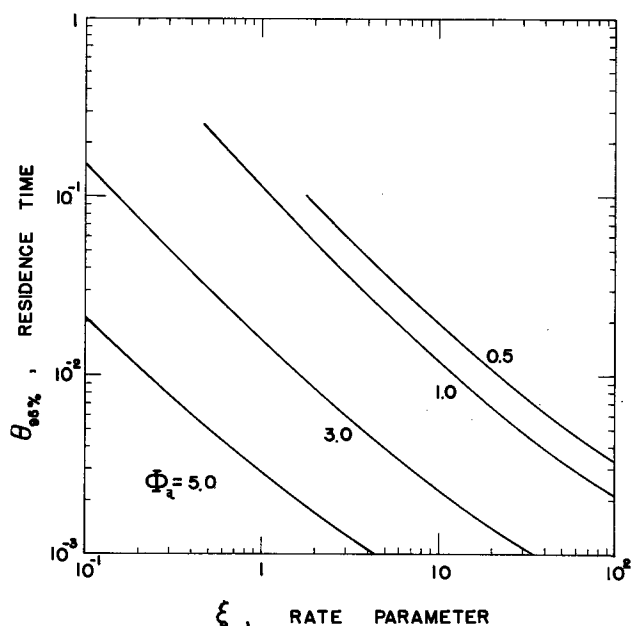


Fig. 6. Dependence of residence time (95% criteria) on system parameters (separator impermeable to copper ions).

bed reactor and counterelectrode, shown in Fig. 7. It is seen that the average volumetric reaction rate increases with both  $\xi$  and  $\Phi_a$ . The results shown in Fig. 7 correspond to reaction rates averaged over the reactor between the entrance and  $\theta = \theta_{95\%}$ . Since the 95% criterion may be ill-suited for certain applications, Table II provides additional information for other criteria and for various values of  $\xi$  and  $\Phi_a$ . Two numbers appear for each row and column entry in the table. The upper number gives the average volumetric reaction rate while the lower number indicates the corresponding residence time,  $\theta_x$ . The residence time  $\theta_x$  is defined as the residence time at which the local current density,  $\beta(\theta)$ , has decreased by  $x\%$  of the initial contact current density (Fig. 2a). It is seen that the average reaction rate increases strongly upon an increase of either  $\xi$  or  $\Phi_a$ , regardless of the value of  $x$  chosen as criteria. For given values of  $\xi$  and  $\Phi_a$ , the average volumetric reaction rate can vary by severalfold according to the choice of  $x$ .

Similar calculations have been conducted for the situation where the porous separator is permeable to all solute species. The current which passes through the separator varies with axial position and is largest at

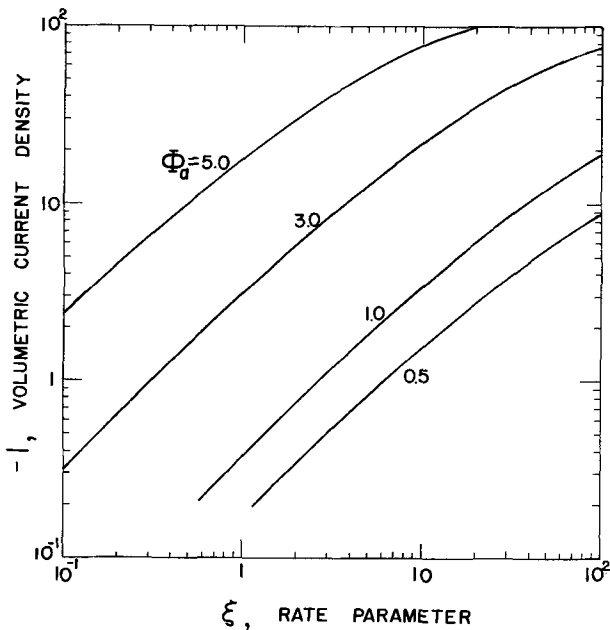


Fig. 7. Dependence of volumetric reaction rate (95% criteria) on system parameters (separator impermeable to copper ions).

the reactor entrance region. Figure 8 indicates how the current varies between the initial contact value and the well-developed (or steady-state) value achieved far downstream for  $\Phi_a = 5.0$  and several values of  $\xi$ . As was already seen from Fig. 2, small values of  $\xi$  lead to negligible concentration differences so that the initial contact and well-developed reaction rates are nearly the same. Larger values of  $\xi$  indicate that significant concentration effects will develop during residence so that the reactivity of the reactor will vary a great deal along its length. Since the initial local reactivity is proportional to  $\xi$ , the residence time (or reactor length) necessary for attainment of the well-developed configuration decreases with an increase of  $\xi$  as shown in Fig. 9.

The residence time at which the local reactivity has decreased by 95% of the difference ( $\beta_{i.c.} - \beta_{s.s.}$ ) is denoted  $\theta_{95\%}$  in Fig. 9. Comparison of Fig. 9 with Fig. 6 indicates that they are nearly identical. That is, even though the nature of the porous separator leads to significant differences in localized behavior, the over-all behavior (as normalized on the basis of Fig. 6 and 9) is not appreciably different.

The total current passing between reactor and counterelectrode is provided in Table III for various criteria. As in Table II, each row and column entry provides two numbers: the upper value gives the average volumetric reaction rate while the lower indicates the corresponding residence time,  $\theta_x$ . The quantity  $\theta_x$  is defined as the residence time at which the local current density,  $\beta(\theta)$ , has decreased by  $x\%$  of the difference ( $\beta_{i.c.} - \beta_{s.s.}$ ) as determined from Fig. 2. Comparison of Tables II and III indicates that corresponding entries

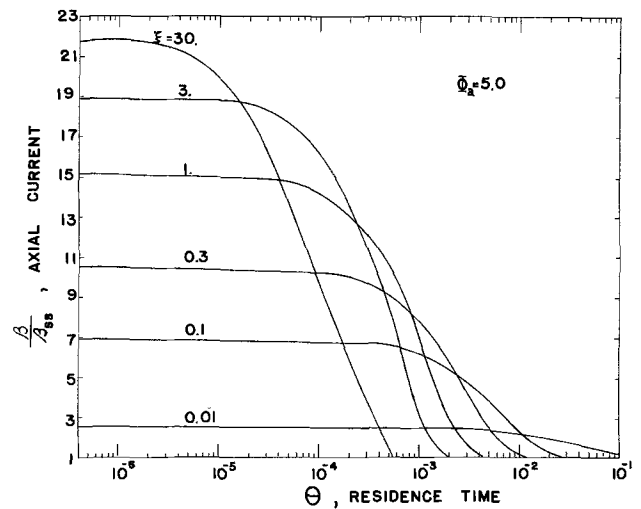


Fig. 8. Axial variation of current flowing through porous separator for  $\Phi_a = 5.0$  and various values of  $\xi$  (separator permeable to all species).

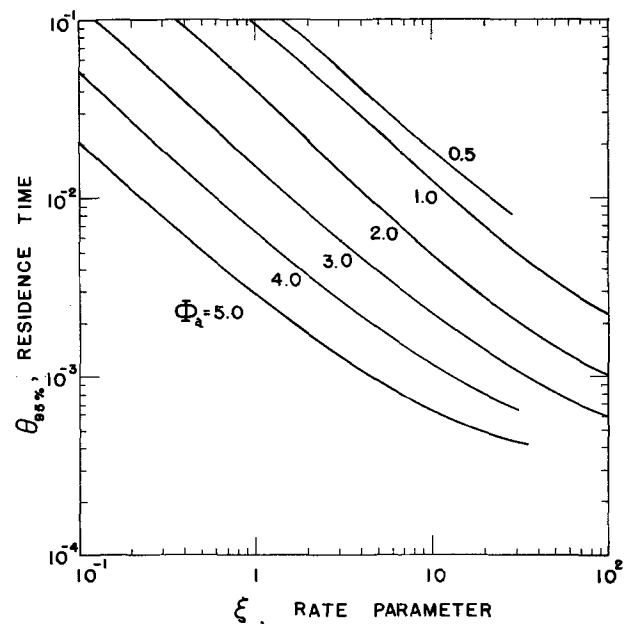


Fig. 9. Dependence of residence time (95% criteria) on system parameters (separator permeable to all species).

have very nearly the same values throughout most of the tables. It is important to recognize, however, that the information contained in the two tables is normalized in very different ways owing to the influence of the porous separator. Figure 10 displays the volumetric reaction rate data for the 95% criterion.

Table II. Reactor performance under boundary conditions (13), separator impermeable to copper ions

$x$	$\frac{\int_0^{x\%} \beta d\theta}{\theta_x}$ at $\Phi_a = 1.0$			$\frac{\int_0^{x\%} \beta d\theta}{\theta_x}$ at $\Phi_a = 5.0$		
	$\xi = 0.1$	1.0	10.0	$\xi = 0.1$	1.0	10.0
0	0.1171	1.155	10.21	6.870	48.56	212.0
	0.0000	0.000	0.00	0.000	0.00	0.0
10	0.1118	1.102	9.79	6.583	46.79	210.5
	0.0489	0.0050	0.00056	0.000964	0.000136	0.0000246
20	0.1060	1.045	9.33	6.259	43.92	199.7
	0.0902	0.0091	0.0010	0.00178	0.000285	0.0000488
40	0.0927	0.910	8.13	5.470	38.72	174.3
	0.200	0.0200	0.0023	0.0040	0.000608	0.000114
60	0.0766	0.770	6.74	4.530	33.50	142.5
	0.362	0.0344	0.0042	0.00714	0.00100	0.000223
95	0.0366	0.373	3.47	2.339	17.68	76.92
	1.175	0.113	0.0121	0.0208	0.0028	0.00065



Table III. Reactor performance under boundary conditions (14), separator permeable to all species

$x$	$-\frac{\int_0^{\theta_x} \beta d\theta}{\theta_x}$ at $\Phi_a = 1.0$			$-\frac{\int_0^{\theta_x} \beta d\theta}{\theta_x}$ at $\Phi_a = 5.0$		
	$\xi = 0.1$	1.0	10.0	$\xi = 0.1$	1.0	10.0
0	0.1171	1.155	10.21	6.871	48.6	212.0
	0.0000	0.000	0.00	0.000	0.00	0.0
10	0.1157	1.121	9.88	6.622	46.3	210.8
	0.0140	0.0035	0.00050	0.00083	0.00016	0.0000297
20	0.1135	1.084	9.25	6.268	43.9	198.0
	0.0327	0.0064	0.00105	0.00174	0.00030	0.0000548
40	0.1100	0.984	8.25	5.606	39.0	175.2
	0.0675	0.0154	0.00224	0.00371	0.00063	0.000122
60	0.1053	0.881	7.07	4.839	33.7	148.8
	0.127	0.0274	0.00398	0.00617	0.00100	0.000220
95	0.0943	0.606	4.13	2.938	19.6	82.7
	0.417	0.0923	0.0120	0.0200	0.0028	0.000676

Let us conclude discussion with a numerical example to illustrate usage of the foregoing results. Consider cathodic deposition of copper from 0.1M  $\text{CuSO}_4$  and 2.0M  $\text{H}_2\text{SO}_4$  having the properties already listed in Table I. The reaction is assumed to proceed with  $i_0 = 10^{-3}$ , in a reactor 1 cm in diameter packed with spherical particles of diameter 0.5 mm; for closest packing of spheres,  $a = 220 \text{ cm}^2/\text{cm}^3$  void volume. For the foregoing values,  $\xi$  has the value 27.5. Operation at 130 mV corresponds to  $\Phi_a = 5$ . To illustrate results with the permeable separator and the 95% criterion, one obtains from Fig. 9 and 10 the values  $\theta_{95\%} = 0.00044$  and  $I = 120$ , respectively. According to the definition of  $I$ , given in the notation, the average volumetric reaction rate is found to be  $i_v = 2nFic_r D_r / r_0^2 = 1.92 \text{ A/cm}^3$ . According to the definition of  $\theta$ , the reactor length is related to the fluid velocity by  $L = \theta r_0^2 v_0 / D_r = 11 v_0$ . In order to determine the reactor length, one may choose a flow velocity which will avoid both high pumping costs and excessive radial flow through the porous separator membrane. For the present example, a pressure drop of 0.1 atm along the reactor length is chosen. The superficial velocity of fluid outside the reactor is obtained in the laminar region from the Blake-Kozeny equation (15)

$$v_0 = \frac{\Delta p}{L} \frac{D_p^2}{150\mu} \frac{\epsilon^3}{(1-\epsilon)^2} \quad [22]$$

With a void fraction of  $\epsilon = 0.3$ ,  $D_p = 0.05 \text{ cm}$ , and  $\mu = 0.01 \text{ g/cm-sec}$ , one finds the relation  $v_0 L = 9.2$ . By combining the above two relations between  $v_0$  and  $L$ , one obtains the results  $L = 10.1 \text{ cm}$  and  $v_0 = 0.92 \text{ cm/sec}$ .

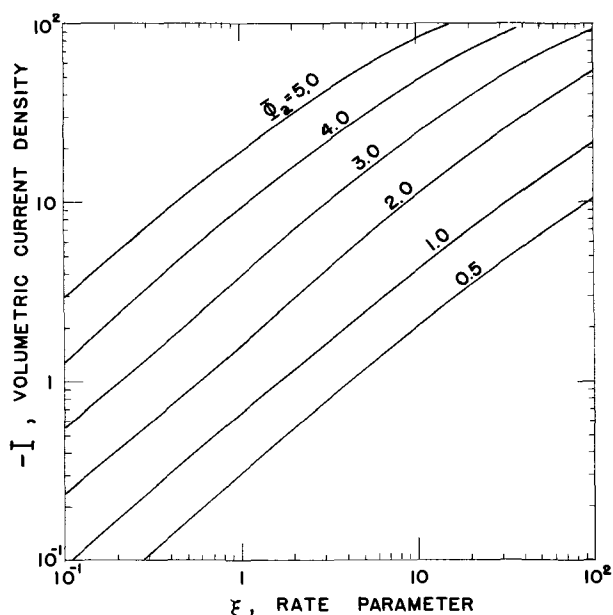


Fig. 10. Dependence of volumetric reaction rate (95% criteria) on system parameters (separator permeable to all species).

## Conclusions

The steady-state operation of electrochemical reactors at high volumetric production rates is difficult to sustain owing, in part, to competing requirements of large surface area, rapid mass transfer, low ohmic resistance, and ready accessibility to the counterelectrode. Porous flow-through reactors can offer high volumetric rates, but are difficult to design without knowledge of the current distribution. The foregoing simple theoretical model may be used in conducting preliminary design steps for one type of flow reactor. The theoretical analysis indicates how the relationship between volumetric reaction rate and residence time depends on the kinetic, mass transfer, ohmic, and geometric parameters of the system. On the basis of these results, economic design and operation of flow reactors with porous electrodes can be accomplished with added confidence.

The predicted results of the model are based on several assumptions which ease computational difficulties. Although extensive use of the plug flow simplification has been made in previous studies, the assumption is known to be invalid in some flow systems having the geometry indicated by Fig. 1A; in the system under study, Fig. 1B, the fluid flows in a perpendicular direction to the electrical current so that the effect of dispersion would be less pronounced. The assumption that axial diffusion and migration are negligible in comparison with radial diffusion and migration may be evaluated by examining the computed results. In general, the assumption is very good near the periphery of the reactor and in the downstream regions; for example, with  $\xi = 1.0$  and  $\Phi_a = 0.5$ , the radial diffusion and migration are  $10^3$  times larger than axial components near the periphery. At large values of  $\xi$ , however, the assumption breaks down in the upstream interior regions of the reactor; on the other hand, the upstream interior region of the reactor does not contribute to electrochemical conversion, as indicated clearly in Fig. 3 and 4, so that breakdown of the assumption is not expected to affect significantly the predicted results. The two assumptions indicated here are, as noted, of limited validity; on the other hand, they are essential for simplifying mathematical treatment of reactor behavior. A more correct two-dimensional analysis would be exceedingly difficult.

The other assumptions placed on the calculations could be relieved in favor of equivalent conditions. In particular, several aspects of the model could be extended in order to investigate more complex systems. Analyses of multiple electrode reactions, or of electrode reactions coupled with homogeneous chemical (scavenger) reactions would be of value. In addition, study of double-porosity reactor structures would be profitable.

Other boundary conditions could be chosen for study. For example, Eq. [14] for the permeable separator indicates that the reactant concentration along the separator is the same as the reactant concentration in the catholyte flowing into the reactor. Entirely different behavior would be encountered if the concentration

along the separator were zero. For large values of  $\xi$ , however, it may be expected that the proposed boundary conditions would lead to behavior very similar to that encountered with reactant-impermeable separators.

The foregoing results may be applied to nonflow porous electrode systems by interpreting the residence time as the time following application of a constant applied potential. The results may therefore be applied directly to the unsteady-state behavior of cylindrical porous electrode systems as, for example, encountered in batteries.

Even the simple model presented above, however, contains several parameters so that portraying results can be awkward. Nevertheless, over-all reactor behavior for one type of electrode reaction has been portrayed on the basis of a limited number of graphs which were based on a large number of calculations. Behavior involving other reaction sequences may perhaps differ in detailed aspects, but would be expected to exhibit similar over-all trends upon variation of system parameters.

### Acknowledgments

Portions of this study constituted partial fulfillment of requirements for a Master of Science degree in the Department of Chemical Engineering, University of Illinois, Urbana-Champaign. Acknowledgment is made to the donors of The Petroleum Research Fund, administered by the American Chemical Society, for partial support of this research. The University of Illinois Research Board sustained the computer costs associated with this study.

Manuscript submitted Jan. 3, 1973; revised manuscript received July 9, 1973.

Any discussion of this paper will appear in a Discussion Section to be published in the December 1974 JOURNAL.

### SYMBOLS

#### English characters

- $a$  specific surface area of reactor,  $\text{cm}^{-1}$
- $c_i$  concentration of solute species  $i$ ,  $\text{g-mole}/\text{cm}^3$
- $c_i^b$  bulk concentration of species  $i$ ,  $\text{g-mole}/\text{cm}^3$
- $C_i$  concentration of species  $i$ ,  $c_i/c_r$ , dimensionless
- $c_r$  reference concentration,  $\text{g-mole}/\text{cm}^3$
- $D_i$  diffusion coefficient of species  $i$ ,  $\text{cm}^2/\text{sec}$
- $D_p$  diameter of reactor packing material,  $\text{cm}$
- $D_r$  reference diffusion coefficient,  $\text{cm}^2/\text{sec}$
- $F$  Faraday's constant, 96,500 coulombs/g-equivalent
- $i_o$  exchange current density,  $\text{A}/\text{cm}^2$
- $i^*$  current density passing through porous separator,  $\text{A}/\text{cm}^2$
- $i_v$  volumetric current density,  $\text{A}/\text{cm}^3$
- $I$  volumetric reaction rate,  $i_v r_o^2 / 2nF c_r D_r$ , dimensionless
- $j$  local reaction rate density,  $\text{A}/\text{cm}^2$
- $J$  local reaction rate density,  $j a r_o / i^*$ , dimensionless

- $L$  reactor length,  $\text{cm}$
- $M_i$  chemical symbol for species  $i$
- $n$  number of electrons taking part in electrode reaction
- $\Delta p$  pressure drop across reactor,  $\text{atm}$
- $r$  radial direction coordinate,  $\text{cm}$
- $r_o$  radius of cylindrical packed-bed reactor,  $\text{cm}$
- $R$  radial direction coordinate,  $r/r_o$ , dimensionless
- $\mathcal{R}$  gas constant, 8.31 joule/g-mole  $^\circ\text{K}$
- $T$  temperature,  $^\circ\text{K}$
- $v_o$  average hydrodynamic velocity in interstices,  $\text{cm}/\text{sec}$
- $z$  axial direction coordinate,  $\text{cm}$
- $z_i$  valence of species  $i$
- Greek characters
  - $\alpha$  transfer coefficient in reaction rate equation
  - $\beta$  local current density in porous separator,  $i^* r_o / nF c_r D_r$ , dimensionless
  - $\gamma_i$  bulk concentration of species,  $i$ ,  $c_i^b / c_r$ , dimensionless
  - $\epsilon$  porosity of packed-bed reactor
  - $\theta$  residence time,  $z D_r / v_o r_o^2$ , dimensionless
  - $\mu$  viscosity of electrolyte,  $\text{g}/\text{cm-sec}$
  - $\nu_i$  stoichiometric coefficient for species  $i$
  - $\xi$  electrode kinetic factor,  $i_o a r_o^2 / nF c_r D_r$ , dimensionless
  - $\pi_i$  diffusion coefficient of species  $i$ ,  $D_i / D_r$ , dimensionless
  - $\phi$  potential in solution,  $V$
  - $\phi_a$  potential applied to reactor,  $V$
  - $\phi_e$  equilibrium potential,  $V$
  - $\Phi$  potential,  $F(\phi - \phi_e) / \mathcal{R}T$ , dimensionless

### REFERENCES

1. W. J. Blaedel and J. H. Strohl, *Anal. Chem.*, **36**, 1245 (1964).
2. D. K. Roe, *ibid.*, **36**, 2371 (1964).
3. J. Molnar, *Magy. Kem. Folyóirat*, **68**, 504 (1962).
4. L. G. Austin, P. Palasi, and R. R. Klimpel, *Advan. Chem. Ser.*, **47**, 35 (1965).
5. R. E. Sioda, *Electrochim. Acta*, **13**, 375, 1559 (1968); **15**, 783 (1970).
6. I. G. Gurevich, Yu. F. Budeka, and V. S. Bagotskii, *Soviet Electrochem.*, **4**, 790, 1134 (1968).
7. I. Zaideman and R. M. Perskaya, *Zh. Fiz. Khim.*, **33**, 50, 437 (1959).
8. I. G. Gurevich and V. S. Bagotsky, *Electrochim. Acta*, **9**, 1151 (1964); I. G. Gurevich, V. S. Bagotskii, and Yu. F. Budeka, *Soviet Electrochem.*, **4**, 286 (1968).
9. N. V. Korovin and A. S. Chudinov, *Soviet Electrochem.*, **3**, 635 (1967).
10. D. Bennion and J. Newman, *J. Appl. Electrochem.*, **2**, 113 (1972).
11. A. T. Kuhn, in "Electrochemistry of Cleaner Environments," J. Bockris, Editor, Plenum Press, New York (1972).
12. D. von Rosenberg, "Methods for the Numerical Solution of Partial Differential Equations," American Elsevier, New York (1969).
13. E. A. Grens and C. W. Tobias, *Ber. Bunseng. Physik. Chem.*, **68**, 236 (1964).
14. J. S. Newman, *Ind. Eng. Chem. Fundamentals*, **7**, 514 (1969).
15. R. B. Bird, W. E. Stewart, and E. N. Lightfoot, "Transport Phenomena," John Wiley & Sons, Inc., New York (1960).

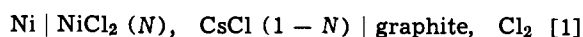


## Thermodynamic Properties of Molten Mixtures of Nickel Chloride with Cesium Chloride at 700° and 800°C

Drannan C. Hamby and A. Roger Hohimer

Linfield Research Institute, Linfield College, McMinnville, Oregon 97128

Reversible emf's of the cell



where  $N$ , the mole fraction of solute, is

$$N = \text{moles NiCl}_2 / (\text{moles NiCl}_2 + \text{moles CsCl}) [2]$$

have been measured over a range of concentration from  $N \cong 10^{-3}$  to  $4 \times 10^{-1}$  for temperatures ranging from 650°-875°C. Supplementary thermochemical data from the literature have been utilized to calculate the activity coefficient and the partial molar Gibbs energy, enthalpy, and entropy of mixing for the solute  $\text{NiCl}_2$  in the solvent  $\text{CsCl}$ . In an earlier paper similar data and calculated functions were presented for  $\text{NiCl}_2$  in the solvents  $\text{KCl}$ ,  $\text{NaCl}$ , 1:1  $\text{NaCl-KCl}$ , and  $\text{LiCl}$  (1).

### Experimental

**Chemicals.—Gases.**—The chlorine, argon, and  $\text{HCl}$  gases were Matheson Company "high purity." The  $\text{HCl}$  and chlorine gases were passed over  $\text{Mg}(\text{ClO}_4)_2$  and hot (500°C) porous graphite (National Carbon Company, grade 60) before entering the cell. The argon was passed over  $\text{Mg}(\text{ClO}_4)_2$  and then over hot  $\text{Cu}$  at 500°C; the  $\text{Cu}$  was in the form of pellets formed by reduction of  $\text{CuO}$  with  $\text{H}_2$ . The gas delivery system was glass except for a few inches of rubber tubing near the cell top.

Reagent grade  $\text{NiCl}_2 \cdot 6\text{H}_2\text{O}$  was dried under flowing argon at reduced pressure in a vacuum oven at 140°C for two days. The salt was then ground to a fine powder in a porcelain mortar, placed in a Pyrex tube, and dried at least 4 hr under anhydrous  $\text{HCl}$  at 400°C. Transfer of the salt to weighing bottles was carried out in a dry box under argon and the bottles were then stored in a desiccator until used. Transfer to the cell involved brief exposure to the atmosphere.

$\text{CsCl}$ , 99.90%, was obtained from Cooper Chemical Company. The salt was dried in the cell crucible under flowing argon at reduced pressure in a vacuum oven at 100°C for 24 hr. The crucible was then placed inside the cell envelope and drying was continued under flowing anhydrous  $\text{HCl}$  over a 24 hr period while the cell temperature was gradually brought to the melting point. After solvent fusion, the chlorine electrodes were inserted and chlorination of the melt in the presence of carbon provided further guarantee of melt dehydration (3).

$\text{AgCl-CsCl}$  mixtures for use in a  $\text{Ag} | \text{AgCl}, \text{CsCl} | |$  reference electrode were prepared from reagent grade  $\text{AgCl}$  and the Cooper Chemical Company  $\text{CsCl}$ . The salts were weighed out in the desired proportions, fused under  $\text{HCl}$ , and chlorinated in the presence of carbon for 1 hr. The solutions were dilute in  $\text{AgCl}$ ,

Key words: nickel chloride, cesium chloride, molten salts (fused salts), formation cells, nickel electrode, thermodynamics.

approximately  $10^{-2}$  mole fraction, and were melted and chlorinated near the melting point of  $\text{CsCl}$ , 646°C. After chlorination the salt was drawn into and sealed in clean, dry, Vycor tubes until used to make up the reference electrode.

**Apparatus and procedure.**—Several experimental details have been described previously (1, 2). These include temperature measurement; measurement of thermoelectric emf's developed by electrode pairs; analytical methods for nickel mole fraction determination; polarization tests for establishment of electrode reversibility; methods of solute,  $\text{NiCl}_2$ , addition; pretreatment of chlorine electrodes; method of preparation of the  $\text{Ag} | \text{AgCl}, \text{CsCl} | |$  reference electrode; source and treatment of metal electrodes; metal electrode housing design; and method of melt sampling. The cell envelope was similar in design to that described previously (2) but was larger in diameter, 78 mm, which permitted insertion of an additional nickel electrode. Thus, when assembled, the cell contained two chlorine electrodes, one  $\text{Ag} | \text{AgCl}, \text{CsCl} | |$  reference, two nickel electrodes, and a Vycor sheathed Chromel-Alumel thermocouple; an additional opening was available in the cell top for melt sampling. Adequate salt was initially placed in the cell crucible to insure a melt depth of at least 4 cm.

Chlorine electrode design is illustrated in Fig. 1. The graphite rod was 1/4 in. diameter Ultra Carbon Company grade UF-4-S. In earlier studies several chlorine electrode designs were tested and found to perform equally well; therefore, the simplest, most easily constructed electrode was chosen for this work (1, 4). Chlorine gas pressure was ambient atmospheric pressure. Uncertainty in cell emf's due to uncertainty in chlorine pressure have been discussed previously (2).

The  $\text{Ag} | \text{AgCl}, \text{CsCl} | |$  reference electrode was used in this work as before to provide a continuous record of chlorine electrode behavior with time (1, 2).

The furnace was a noninductively wound Marshall Company, Model 1057, tube furnace, 3-1/2 in. diameter, 24 in. long. Power and temperature control for the furnace were furnished by a Marshall Model 4042 current proportioning control.

Emf measurements were made with a Keithley 660A differential voltmeter. This instrument was checked against a laboratory standard Eppley cell.

Cell emf's were measured as a function of temperature at eleven mole fractions of the solute,  $\text{NiCl}_2$ ; usually four or five emf measurements and at least three melt samples were taken at each mole fraction.

### Results

The data for cell [1] are illustrated in Fig. 2 where cell emf's  $E$ , are plotted as a function of temperature. All emf's have been corrected for thermoelectric effects. At each mole fraction, the relationship of cell

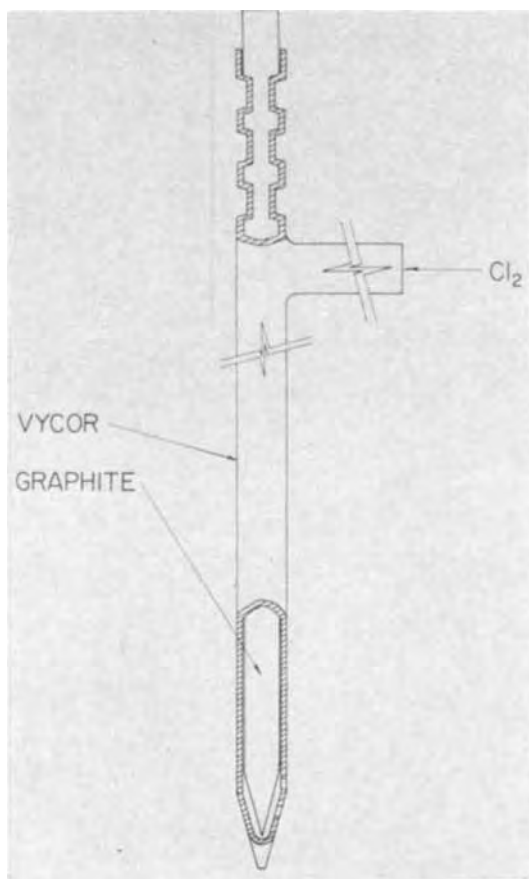


Fig. 1. Chlorine electrode design

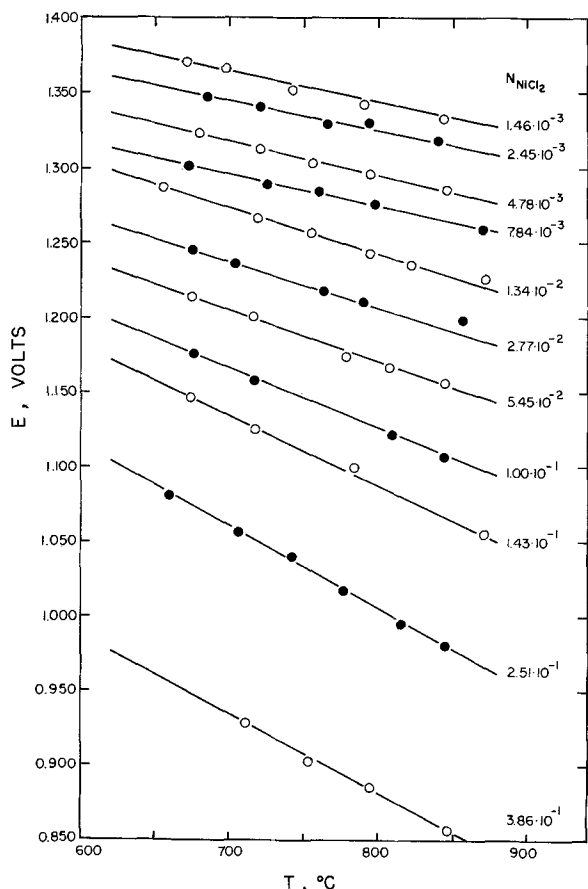


Fig. 2. Primary cell data. CsCl solvent; NiCl<sub>2</sub> solute. Cell emf's, *E*, are plotted as a function of temperature for eleven concentrations. NiCl<sub>2</sub> mole fractions are indicated beside the corresponding emf data.

emf to temperature was assumed to be linear. From Fig. 2 cell emf's were read at 700° and 800°C and plotted as functions of log  $N_{NiCl_2}$  in CsCl in Fig. 3. Also shown in Fig. 3 for comparison are emf vs. log  $N$  curves for other solvents as reported previously (1).

Below  $N = 2 \times 10^{-2}$ ,  $E$  at constant temperature for the solvent CsCl may be represented by

$$E = d - b \log N \quad [3]$$

where

$$b = 2.303 RT/2F \quad [4]$$

The lines in Fig. 3 for CsCl were drawn with the Nernst slopes  $b$  below  $N = 2 \times 10^{-2}$ . The intercept  $d$  was chosen to give the best fit with the data points for  $N < 2 \times 10^{-2}$ ; at 700°C  $d = 1.094V$ , at 800°C  $d =$

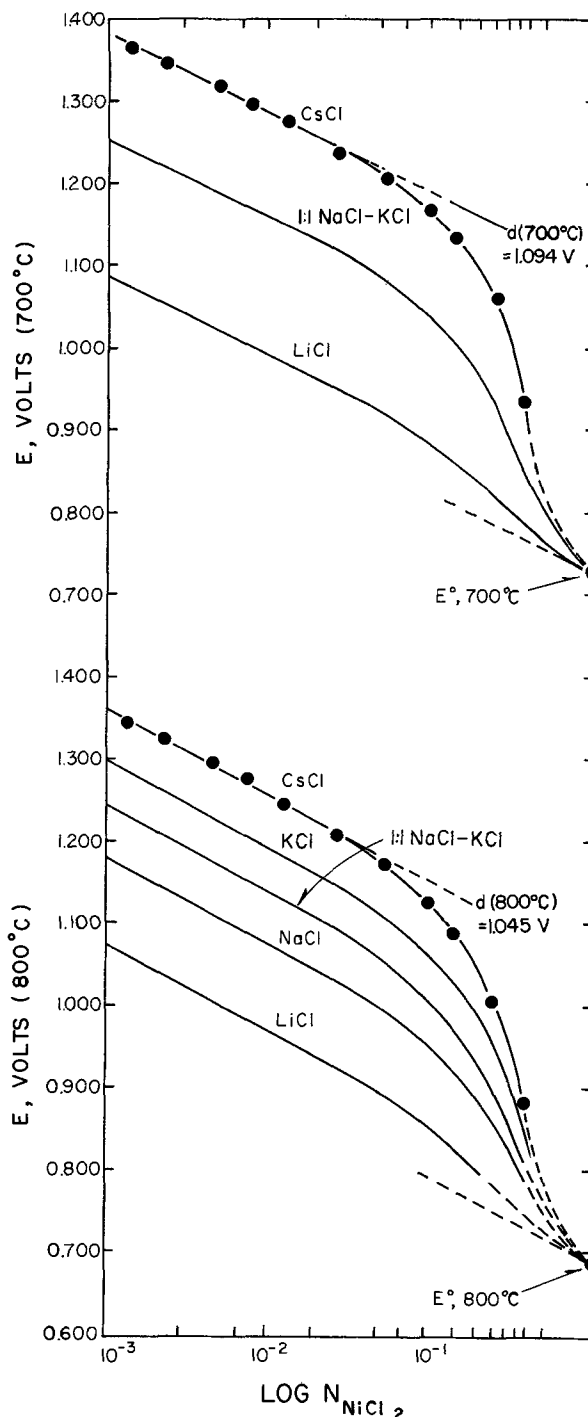
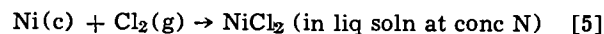


Fig. 3. Cell emf, *E*, vs. log  $N_{NiCl_2}$  at 700° and 800°C. Solvents are indicated beside the corresponding data (1). ● Data for CsCl solvent reported in this paper. Values of  $E^\circ$  are calculated values as described in the text.

1.045V. The calculated least-squares slopes for the five low concentration data points are  $-0.096$  at  $700^\circ\text{C}$  and  $-0.104$  at  $800^\circ\text{C}$  which may be compared with the corresponding Nernst values of  $b$ ,  $0.097$  and  $0.106$ . Average deviations of the six low concentration data points from the lines as drawn in Fig. 3 are  $2.3$  mV and  $3.5$  mV at  $700^\circ$  and  $800^\circ\text{C}$ , respectively.

The thermodynamic functions for the cell reaction



have been calculated on the basis of the Nernst equation and the following definitions and equations

$$\lim_{N \rightarrow 1} a/N = 1 \quad [6]$$

$$a = N\gamma \quad [7]$$

where  $a$  and  $\gamma$  refer to the activity and activity coefficient of the solute,  $\text{NiCl}_2$ . The standard and reference states of the solute are the pure liquid with the properties of the pure liquid at the temperature of the experiment. The partial molar Gibbs energy of mixing and the partial molar enthalpy and entropy of mixing are given by

$$\bar{G} = -nFE - \Delta G^\circ \quad [8]$$

$$\bar{H} = \Delta H - \Delta H^\circ \quad [9]$$

$$\bar{S} = nF(\partial E/\partial T)_p - \Delta S^\circ \quad [10]$$

where  $\Delta G^\circ$ ,  $\Delta H^\circ$ , and  $\Delta S^\circ$  are the standard changes for reaction [5]. The excess Gibbs energy of mixing,  $\bar{G}^E$ , is given by

$$\bar{G}^E = \bar{G} - RT \ln N = RT \ln \gamma \quad [11]$$

Equations describing the temperature dependence of  $\Delta G^\circ$ ,  $\Delta H^\circ$ , and  $\Delta S^\circ$ , calculated from the tables of Wicks and Block (6) and Kubaschewsky and Evans (7) were reported previously (1) and have been used here.

The curves of Fig. 3 have been extrapolated to  $N = 1$ , to give a value of  $E^\circ$ , by using the calculated values of  $\Delta G^\circ$  at  $700^\circ$  and  $800^\circ\text{C}$ ,  $-33.6$  kcal and  $-31.6$  kcal, respectively, and by utilizing Raoult's law to predict a limiting slope as  $N \rightarrow 1$ . Values for  $\Delta S = nF(\partial E/\partial T)_p$  for reaction [5] were calculated from the slopes of the lines shown in Fig. 2 and, therefore, represent average values over the temperature range from  $650^\circ$  to  $850^\circ\text{C}$ . The uncertainty involved in the determination of the slopes is estimated to be  $5 \times 10^{-5}$  V/K.

Emf values were read at selected concentrations from the curves for CsCl solvent, Fig. 3, and used to calculate the functions given in Table I. Values of  $\bar{S}$  and  $\bar{H}$  in the table were calculated from smoothed values of  $\Delta S$  based on graphs of  $\Delta S$  vs.  $\log N$  and the values of  $\Delta S^\circ$  and  $\Delta H^\circ$  mentioned above; scatter of the data for  $\Delta S$  indicating an uncertainty of at least  $\pm 2$  cal/K in this quantity is in agreement with the estimated uncertainty in the values of the slopes  $(\partial E/\partial T)_p$  from Fig. 1. Values of  $\bar{S}$  and  $\bar{H}$  were not included in the table for concentrations above  $N = 0.15$  because the

experimental values of  $\Delta S$  as determined from the slopes of the lines of Fig. 2 were larger in magnitude than  $\Delta S^\circ$ .

## Discussion

Because  $\gamma$  is observed to be independent of  $N$  at low  $N$  over a range of temperatures it follows from the Nernst equation that the partial molar entropy of mixing,  $\bar{S}$ , will follow

$$\bar{S} = \Delta S - \Delta S^\circ = -R \ln N + \text{constant} \quad [12]$$

at low values of  $N$ . At higher values of  $N$  the variation of  $\bar{S}$  with concentration may be predicted on the basis of various microstate models of the liquid (1, 2); however, the present data are insufficiently accurate to make useful comparisons between observed and calculated values.

Combining Eq. [8] and [11], one obtains

$$\bar{G}^E = -nFE - \Delta G^\circ - RT \ln N \quad [13]$$

from which one may calculate  $\bar{G}^E$ . Utilizing Eq. [13] one may deduce the order of variation of the magnitude of  $\bar{G}^E$  for  $\text{NiCl}_2$  with solvent cation at constant  $N$  from Fig. 3. The observed order  $\text{CsCl} > \text{KCl} > \text{NaCl} > \text{LiCl}$  follows the well-established pattern which is commonly explained on the basis of competition for anions between solute and solvent cations (8). However, the observed magnitude of the change in  $\bar{G}^E$  in going from KCl to CsCl is smaller than one might have predicted on the basis of the linear relationship which exists in the Henry's law region between  $\bar{G}^E$  and the hexacoordinate radii (5) of solvent cations in LiCl, NaCl, and KCl.

It is interesting to note that the color of the solid resulting from solidification of the  $\text{CsCl-NiCl}_2$  melt is quite different from that observed for  $\text{NiCl}_2$  in the other alkali halides. At  $N \cong 0.1$  the solidified mixtures with LiCl, NaCl, and KCl are brown to reddish brown whereas with CsCl the solid is a light blue.

## Acknowledgment

The authors wish to thank Research Corporation for its support of this work.

Manuscript submitted Oct. 2, 1972; revised manuscript received June 25, 1973.

Any discussion of this paper will appear in a Discussion Section to be published in the December 1974 JOURNAL.

## LIST OF SYMBOLS

$N$	defined by Eq. [1]
$E$	electromotive force
$d$	defined by Eq. [3]
$b$	defined by Eq. [4]
$R$	gas constant
$T$	temperature in degrees Kelvin
$F$	Faraday's constant
$a$	activity of $\text{NiCl}_2$
$\gamma$	activity coefficient of $\text{NiCl}_2$

Table I. Cell emf's and derived data for cell [1]

$N_{\text{NiCl}_2}$	$E$ (volts)		$-\bar{G}$ (kcal)		$-\bar{G}^E$ (kcal)		$10^{-4}\gamma$		$\bar{S}$ (eu)	$\bar{H}$ (kcal)
	$700^\circ\text{C}$	$800^\circ\text{C}$	$700^\circ\text{C}$	$800^\circ\text{C}$	$700^\circ\text{C}$	$800^\circ\text{C}$	$700^\circ\text{C}$	$800^\circ\text{C}$	$800^\circ\text{C}$	$800^\circ\text{C}$
0.00100	1.383	1.363	30.2	31.3	16.8	16.6	1.66	4.16	+13	-17
0.00300	1.337	1.313	28.1	29.0	16.9	16.8	1.66	4.16	+11	-17
0.00700	1.301	1.274	26.4	27.2	16.8	16.6	1.66	4.16	+9	-17
0.0200	1.258	1.225	24.4	24.9	16.8	16.6	1.66	4.16	+6	-18
0.0500	1.215	1.174	22.4	22.6	16.6	16.2	1.66	5.01	+4	-18
0.0700	1.193	1.153	21.4	21.6	16.3	15.9	2.19	5.75	+4	-17
0.100	1.166	1.125	20.2	20.3	15.7	15.4	2.95	7.24	+2	-18
0.150	1.135	1.084	18.8	18.4	15.1	14.4	4.07	11.7	+2	-16
0.200	1.096	1.047	17.0	16.7	13.9	13.3	7.58	19.5		
0.250	1.061	1.005	15.3	14.8	12.6	11.8	14.8	39.8		
0.300	1.020	0.966	13.5	13.0	11.2	10.4	30.2	75.8		
0.350	0.972	0.920	11.2	10.8	9.2	8.6	85.2	177		
0.400	0.905	0.860	8.1	8.1	6.3	6.2	380	549		

$n$	number of Faradays passed per unit advancement of cell reaction
$G$	Gibbs energy, Gibbs function, Gibbs free energy, free enthalpy (I.U.P.A.C.)
$S$	entropy
$H$	enthalpy
$\overline{G}$	defined by Eq. [8]
$\overline{H}$	defined by Eq. [9]
$\overline{S}$	defined by Eq. [10]
$\overline{G}^E$	defined by Eq. [11]
eu	entropy unit, cal/K
K	Kelvin

## REFERENCES

1. D. C. Hamby and A. B. Scott, *This Journal*, **115**, 704 (1968).
2. D. C. Hamby and A. B. Scott, *ibid.*, **117**, 319 (1970).
3. D. L. Maricle and D. N. Hume, *Anal. Chem.*, **33**, 1189 (1964).
4. D. C. Hamby, Ph.D. Thesis, Oregon State University (1968).
5. L. H. Ahrens, *Geochim. Cosmochim. Acta*, **2**, 155 (1952).
6. C. Wicks and F. Block, *U.S. Bur. Mines, Bull.*, **605**, 85 (1963).
7. O. Kubaschewski and E. L. Evans, "Metallurgical Thermochemistry," 2nd. ed., John Wiley and Sons, Inc., New York (1956).
8. O. J. Kleppa, *Ann. Rev. Phys. Chem.*, **16**, 187 (1965).

## Molten Alkali Treatment of Alumina Surfaces for Bonding to Electroless Copper

G. V. Elmore\* and R. F. Hershberger

System Products Division, IBM Corporation, Endicott, New York 13760

The plating of copper upon a sintered  $\text{Al}_2\text{O}_3$  ceramic substrate is a process of considerable usefulness to the printed circuit industry. Copper plating can be accomplished by covering the  $\text{Al}_2\text{O}_3$  with electroless copper and electroplating to the desired thickness. However, the resulting bond of the copper to the untreated  $\text{Al}_2\text{O}_3$  is weak. The use of boiling acids, such as orthophosphoric has been advocated by Stalneck (1) to improve the bond. Hydrofluoric acid has also been used in ceramics containing silica for improved adhesion (2). This investigation was undertaken to develop a satisfactory method of achieving an improved bond over that previously attained. A comparison of the molten alkali treatment with various other treatments has been made by Ameen, McBride, and Philips (3).

### Test Procedures

A pull test was used as a method of measuring the bond between the copper and alumina. The treated alumina was sensitized with  $\text{SnCl}_2$  solution, activated with  $\text{PdCl}_2$  solution, plated with electroless copper, and plated to 1.3 mils of copper with copper pyrophosphate plating solution. A 150 mil-diameter copper dot was etched upon the surface using photoresist techniques. To this dot was soldered a 150 mil-diameter brass stud. The stud was first immersed in molten solder and placed upon the fluxed Cu dot while the  $\text{Al}_2\text{O}_3$  substrate was heated above the solder melting point. After cooling, this was then placed in a special fixture designed to assure a direct vertical pull. The setup was placed in an Instron tester, and the stud was pulled until a fracture occurred.

### Experimental Procedure

The alumina used for most of the experiments was a 96%  $\text{Al}_2\text{O}_3$  with 4% glass binder, commercially obtained. The treatment process consists of etching the  $\text{Al}_2\text{O}_3$  surface with molten alkali which attacks the glass binder and the  $\text{Al}_2\text{O}_3$ . Of the three common alkali hydroxides (KOH, NaOH, and LiOH), NaOH has the lowest melting point (328°C) and was chosen for investigation. The  $\text{Al}_2\text{O}_3$  modules were first cleaned by treatment in an alkaline solution, rinsed, and then dipped in a concentrated solution of NaOH in water. The modules were placed on a stainless steel screen, and dried. Then, the alkali was melted by placing the

modules, while on a stainless steel screen, in an oven at 450°C for 15 min. After cooling, the modules were rinsed with water, dipped in sulfuric acid solution, rinsed, and dried. The modules were placed on a screen during melting to prevent modules from sticking together. The modules were then sensitized, activated, plated, and a 150 mil diameter dot etched on the surface.

### Results

Pull tests were performed on 17 modules treated according to the above procedure. The pull on the 150 mil dots etched in the copper, varied from 43 to 88 lb with an average value of 68 lb. These results can be compared with pull values of 20 to 25 lb on an untreated module.

In addition, other tests were performed at lower temperatures. For these experiments a eutectic mixture of 60% KOH and 40% NaOH was used; this mixture melts at 167°C. Nine modules were precleaned then dipped in a solution consisting of 330g KOH, 200g NaOH, and 400 ml of water. The modules were heated at 170°C for 15 min, rinsed treated with sulfuric acid solution, rinsed, and dried. Pull test on 150 mil dots varied from 23 to 57 lb, with an average value of 38 lb.

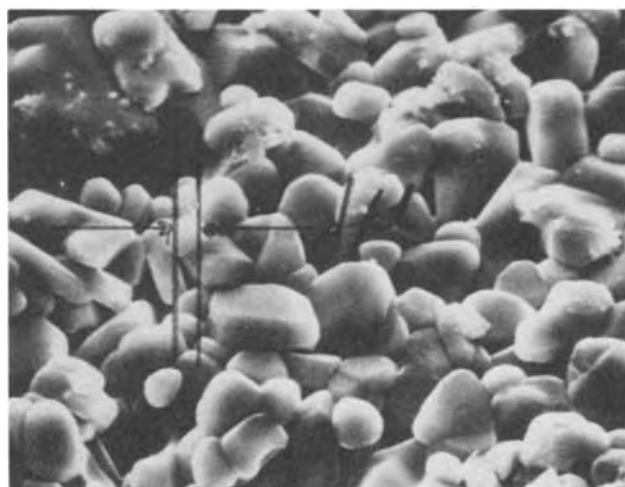


Fig. 1. Untreated surface of sintered  $\text{Al}_2\text{O}_3$  (2400X)

\* Electrochemical Society Active Member.  
Key words: alumina, metallization, bond.

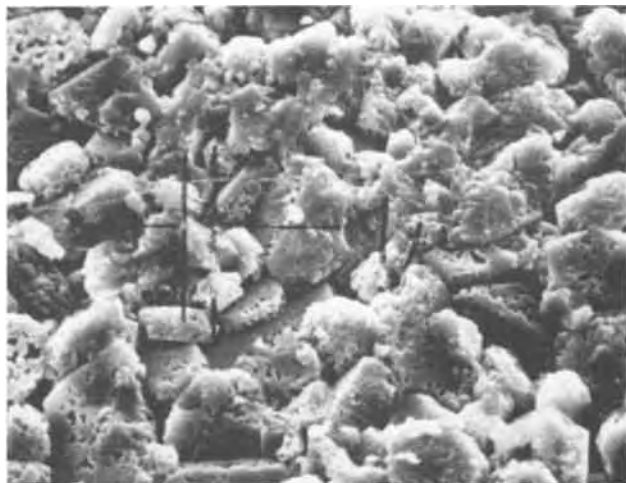


Fig. 2. Treated surface of sintered  $\text{Al}_2\text{O}_3$  (2400X)

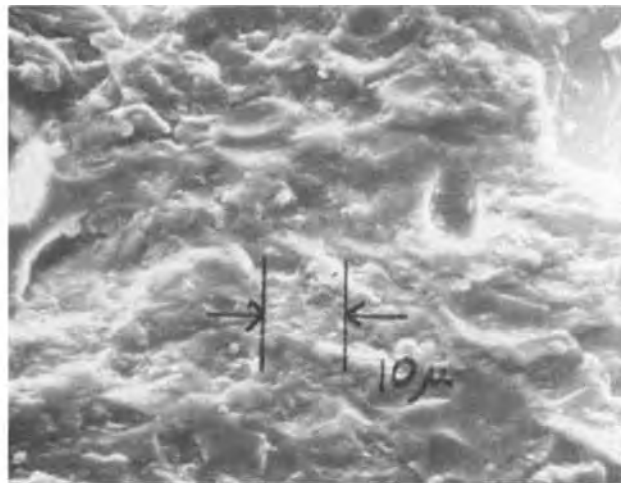


Fig. 5. Untreated surface of polycrystalline  $\text{Al}_2\text{O}_3$  (1200X)

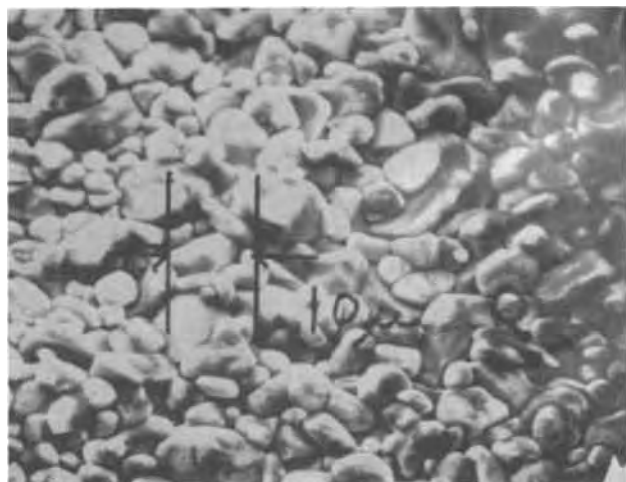


Fig. 3. Untreated surface of another sintered  $\text{Al}_2\text{O}_3$  (1200X)

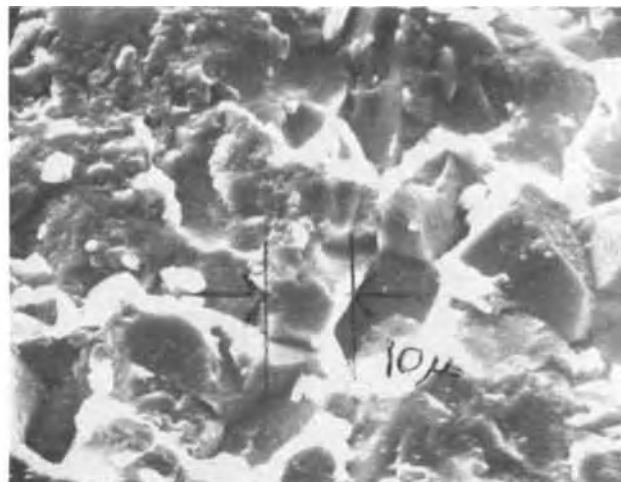


Fig. 6. Treated surface of polycrystalline  $\text{Al}_2\text{O}_3$  (1200X)

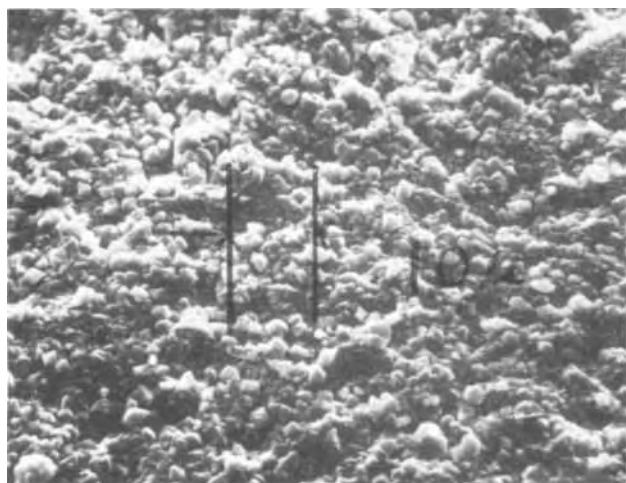


Fig. 4. Treated surface of the sintered  $\text{Al}_2\text{O}_3$  (1200X)

Scanning electron microscope (SEM) photographs were taken of the  $\text{Al}_2\text{O}_3$  surfaces before and after treatment at  $450^\circ\text{C}$ . Figure 1 shows the untreated surface at 2400X while Fig. 2 shows the treated surface at 2400X. The micropits caused by the molten NaOH are quite evident in Fig. 2. Figure 3 shows the untreated surface of 96%  $\text{Al}_2\text{O}_3$ , 4% binder from a dif-

ferent source at 1200X, and the treated surface at 1200X is shown in Fig. 4. A sample of polycrystalline  $\text{Al}_2\text{O}_3$  is shown before treatment in Fig. 5 at 1200X and the treated surface at 1200X is shown in Fig. 6. The attack on the polycrystalline material indicates that the  $\text{Al}_2\text{O}_3$  itself is the material whose etching causes the bondable surface formation.

### Conclusions

All the  $\text{Al}_2\text{O}_3$  samples indicate the molten NaOH at  $450^\circ\text{C}$  attacks the  $\text{Al}_2\text{O}_3$  surface creating a pitted surface which greatly improves the mechanical interlocking of the electroless copper to the  $\text{Al}_2\text{O}_3$  surface. The treatment at  $450^\circ\text{C}$  using NaOH proved to be better than treatment at lower temperatures using a eutectic mixture of NaOH and KOH.

### Acknowledgments

The authors wish to acknowledge the invaluable assistance of W. R. Merwarth for the SEM photographs.

Manuscript submitted July 9, 1973; revised manuscript received Aug. 13, 1973. This was Paper 213 presented at the Miami Beach, Florida, Meeting of the Society, Oct. 8-13, 1972.

Any discussion of this paper will appear in a Discussion Section to be published in the December 1974 JOURNAL.

### REFERENCES

1. S. G. Stalneck, Jr., U.S. Pat. 3,296,012 (1967).
2. J. M. Mochel, U.S. Pat. 2,968,578 (1961).
3. J. S. Ameen, D. S. McBride, and G. C. Philips, *This Journal*, **120**, 1518 (1973).





## Green Direct Current Electroluminescence from Lead-Doped Zinc Sulfide Powder Phosphors

M. S. Waite and A. Vecht\*

School of Materials Science and Physics, Thames Polytechnic, London, England

### ABSTRACT

Green emission (500 nm) under d-c field excitation has been observed with lead-doped ZnS powder phosphor layers, about 100 microns thick, at external applied voltages of 100V and current densities up to 10 mA cm<sup>-2</sup>. The conditions found to favor this emission are a high residual lead concentration, preferably greater than 10<sup>-4</sup> g-atoms per mole ZnS, and absence of copper and chlorine from the bulk of the crystal. The maximum power efficiency obtained so far is about 10<sup>-5</sup> at room temperature, increasing to 10<sup>-3</sup> at 77°K, the room temperature efficiency of ZnS:Mn,Cu phosphors. The origin of the green emission was sought from the luminescent spectra of undoped, copper-doped, and lead-doped zinc sulfide under d-c, a-c, and 365 nm (Hg) excitation at both room temperature and 77°K. Although copper centers may be introduced during the "forming" process the spectral evidence suggests that the DCEL emission at 500 nm is from divalent lead adjacent to substitutional oxygen in the ZnS lattice.

The practical applications of direct current electroluminescence (DCEL) in II-VI powder phosphors are at present restricted to the properties of ZnS:Mn, Cu phosphors, which emit broad band yellow light with a power efficiency up to 10<sup>-3</sup> (1,2). In an attempt to extend the range of emission colors substitution for Mn by various dopants is being investigated, and in connection with this program the effect of incorporating rare earth ions has already been reported (2,3). It was found that blue, green, and orange emission could be obtained from the appropriate rare earth ion dopant but with a low efficiency under d-c excitation of 10<sup>-6</sup>-10<sup>-5</sup>. This means that under practical operating conditions the brightness of each of these devices would be less than 5 ft-L. The lower efficiency of rare earth-doped phosphors compared with manganese-doped phosphors may be partly due to the limited solubility of rare earth ions in zinc sulfide (4). Consequently other classes of dopants have been tested, including some elements which have been used in a-c electroluminescent phosphors. In particular we have re-examined lead-doped phosphors, preparing d-c electroluminescent phosphors and devices by the methods previously established for manganese and rare earth-doped phosphors.

Lead, with copper and chlorine, has been used in the preparation of blue and green a-c phosphors, where it was added in small amounts to improve the emission from the copper centers (5,6). However, the quantity of lead remaining after firing was reported to be less than 10<sup>-4</sup> g-atoms per mole ZnS, and it does not seem to have been used as the principal or sole activator in practical electroluminescent systems although it is known to give green photoluminescence in zinc sulfide (7-11). The green emission is centered at 490-505 nm, dependent on the crystal structure, and has been interpreted by Uehara as due to a localized transition between excited and ground states of divalent lead at

zinc lattice sites. By analogy with excitation processes in ZnS:Mn phosphors there is a possibility that green-emitting DCEL phosphors can be made from lead-doped zinc sulfide since in the methods developed for Mn-doped phosphors deliberate addition of copper is not essential, unlike the case for a-c electroluminescence.

Phosphors have therefore been prepared with a wide range of lead concentrations, and at the higher concentrations, greater than 10<sup>-4</sup> g-atoms per mole ZnS, green DCEL emission was found. Both the spectral distribution and efficiency of the emission are dependent on the lead concentration as will be shown below and the nature of the emission process is discussed as far as the present results allow.

### Experimental

**Phosphor preparation.**—Halogen free zinc sulfide was used to prepare the phosphors, which were doped with lead by firing with lead carbonate in air or nitrogen at 850°-1000°C. Copper and chlorine were incorporated where needed by slurring with cupric and sodium chloride solutions, respectively. After firing surface oxides were removed by treatment with hot, concentrated acetic acid. Table I indicates the formu-

Table I. Formulation and firing conditions of lead-doped phosphors

Phosphor	Preparative conditions	Lead concentration (g-atoms per mole ZnS)
ZnS:Pb (10 <sup>-3</sup> )	Fired in N <sub>2</sub> at 850°C, 12%, w/w, NaCl	10 <sup>-5</sup>
ZnS:Pb (5 × 10 <sup>-3</sup> )	Fired in N <sub>2</sub> at 850°C, 12%, w/w, NaCl	8 × 10 <sup>-5</sup>
ZnS:Pb (1.5 × 10 <sup>-2</sup> )	Fired in N <sub>2</sub> at 850°C, no flux	1.3 × 10 <sup>-5</sup>
ZnS:Pb (4 × 10 <sup>-2</sup> )	Fired in N <sub>2</sub> at 850°C, no flux	4.7 × 10 <sup>-8</sup>
ZnS:Pb (4 × 10 <sup>-2</sup> )	Fired in N <sub>2</sub> at 850°C, 3%, w/w, NaCl	8 × 10 <sup>-4</sup>
ZnS:Pb (6 × 10 <sup>-2</sup> )	Fired in N <sub>2</sub> at 900°C, no flux	2 × 10 <sup>-4</sup>
ZnS:Pb (6 × 10 <sup>-2</sup> )	Fired in air at 950°C, no flux	10 <sup>-2</sup>

\* Electrochemical Society Active Member.

Key words: direct current electroluminescence, lead doped ZnS, powder cells.

1974

lation and typical firing conditions used for the principal phosphors examined.

The residual lead concentration of several phosphors with different initial lead levels was estimated by dissolving the powder in 6M HCl and measuring the absorbance of the chloro-lead complex at 270 nm (12). A reproducibility generally better than 5% was found with this simple method and although interference from cuprous ions is possible there was no spectroscopic evidence for the presence of these ions (Table I).

**Preparation of electroluminescent panels.**—The phosphors were made into electroluminescent devices ("panels") by the methods already evolved for Mn-doped phosphors. This procedure has already been described in detail (1,2) and involves the following stages. Firstly, the phosphor particles are coated with a conducting copper-rich phase, and then, with the aid of an organic binder, spread as a thin layer (approximately  $100\mu$  thick) on a conducting glass surface. This surface provides the positive electrode, while the negative electrode is obtained by evaporating an aluminum film onto the phosphor layer. The cells are then encapsulated with a desiccant. In the final stage, the "forming" process, a gradually increasing d-c field is applied. The current through the cell rises with the voltage until, at about 20 to 30V, the current drops sharply and light emission begins. Earlier work established that diffusion of copper from the copper-rich surface to the bulk of the phosphor particle takes place during forming and operation, and therefore copper centers may be present even in those phosphors prepared without deliberate addition of copper (2).

Copper-coated ZnS:Pb phosphors show a similar forming behavior to that of ZnS:Mn phosphors, but when silver sulfide was tried as a surface coating no forming process and no light emission could be obtained. Consequently it was not possible to eliminate copper centers arising from the copper coating.

**Evaluation of spectra and brightness.**—Photo and electroluminescent spectra were analyzed with a Hilger and Watts D330 monochromator, equipped with a Bausch and Lomb 600 lines per mm grating operated in second order, and a EMI 9558 photomultiplier. A similar photomultiplier was used for the photometric determinations.

### Results and Discussion

Visible emission was obtained from all the phosphors listed in Table I but with considerable variation in spectral distribution and brightness, a variation that is related to the lead concentration.

**Spectra.**—The spectra and brightness both show a definite, if irregular, trend towards increased green emission with increase in lead concentration. This can be seen on comparing Fig. 1 and 2 and Tables I and III.

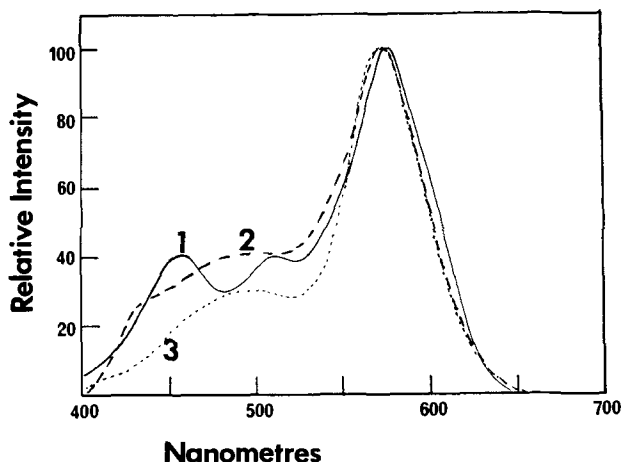


Fig. 1. DCEL spectra at room temperature. Curve 1, ZnS:Pb ( $10^{-3}$ ), 12%, w/w, NaCl flux; curve 2, ZnS:Pb ( $5 \times 10^{-3}$ ), 12%, w/w, NaCl flux; curve 3, ZnS:Pb ( $1.5 \times 10^{-2}$ ).

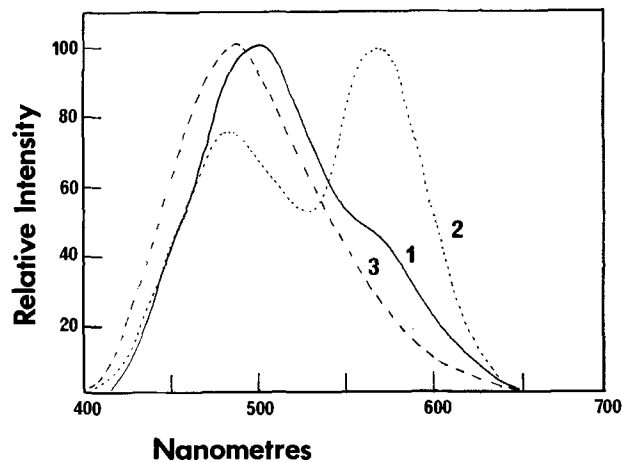


Fig. 2. DCEL spectra at room temperature. Curve 1, ZnS:Pb ( $4 \times 10^{-2}$ ); curve 2, ZnS:Pb ( $4 \times 10^{-2}$ ), 3%, w/w, NaCl flux; curve 3, ZnS:Pb ( $6 \times 10^{-2}$ ).

The electroluminescent spectra of phosphors with low concentrations of lead are illustrated in Fig. 1 and the spectra of heavily doped phosphors in Fig. 2. When the lead concentration is low, the most prominent emission band is at 575 nm with minor, indistinct bands in the blue-green region. The over-all emission is weak and in several cases a voltage greater than 150V had to be applied to obtain spectra. It was noticed that the blue-green bands showed a greater increase in intensity with voltage than did the band at 575 nm. Thus over the range 80-180V at least the spectral emission is slightly voltage dependent. Since the level of lead in these phosphors is very low it is interesting to compare the electroluminescent spectra with those of undoped but copper-coated zinc sulfide and zinc sulfide doped with copper (Fig. 3 and 4). At room temperature the DCEL emission of undoped zinc sulfide (Fig. 3) is very similar to the spectra in Fig. 1. This suggests that at low lead concentrations, below approximately  $10^{-4}$  g-atoms per mole ZnS, the presence of lead does not affect the spectral distribution of the emission which may be associated with copper, oxygen, or defect centers (13) in the material or may be due to Mn contamination. If undoped ZnS is fired in an atmosphere of  $H_2S$ , the resulting DCEL spectrum is identical to that of ZnS fired in  $N_2$  or air, i.e., the major emission band is at 575 nm, although one would expect either a difference in the relative intensities of the different bands or a change in total intensity if oxygen centers are involved. Doping zinc sulfide with copper ( $5 \times 10^{-4}$  to  $10^{-3}$  g-atoms per mole) or copper and chlorine yields phosphors with the main DCEL emission bands in the blue-green region (Fig. 4), not

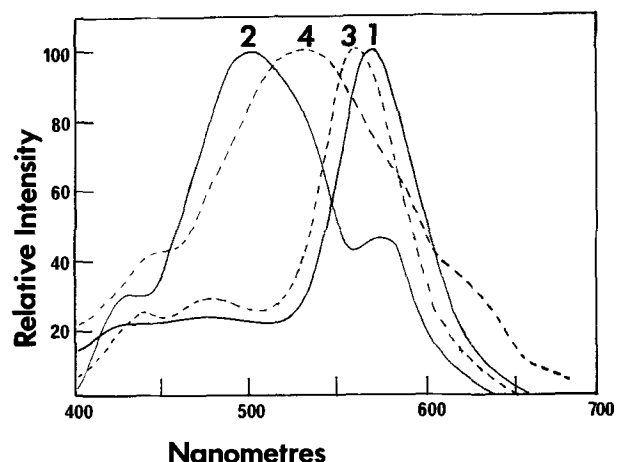


Fig. 3. ZnS, copper coated but undoped. Curve 1, DCEL spectra at room temperature; curve 2, DCEL spectra at 77°K; curve 3, ACEL spectra at room temperature; curve 4, ACEL spectra at 77°K.

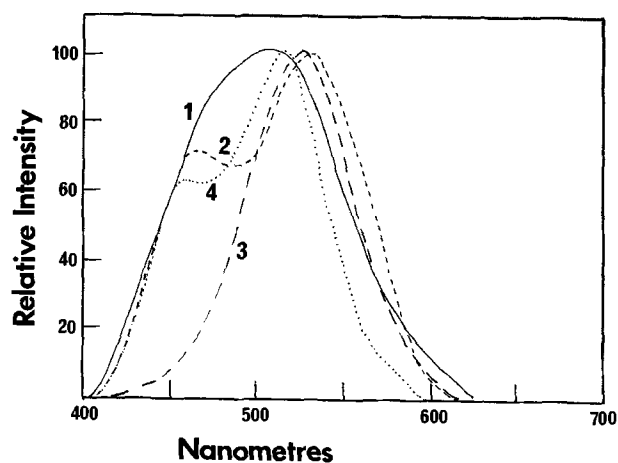


Fig. 4. ZnS: Cu( $10^{-3}$ ). Curve 1, DCEL spectra at room temperature; curve 2, DCEL spectra at  $77^{\circ}\text{K}$ ; curve 3, ACEL spectra at room temperature; curve 4, ACEL spectra at  $77^{\circ}\text{K}$ .

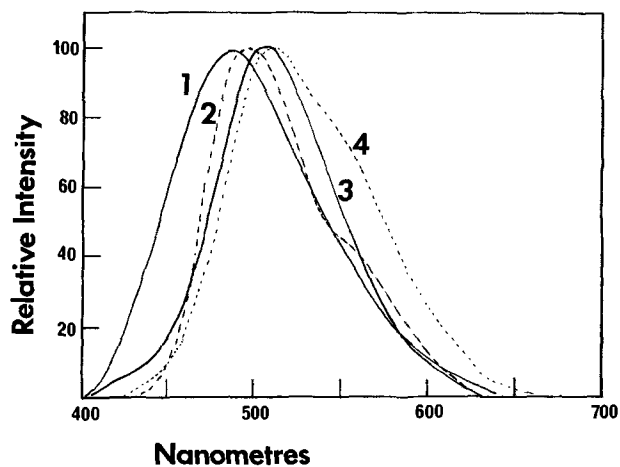


Fig. 5. ZnS:Pb ( $6 \times 10^{-2}$ ). Curve 1, DCEL spectra at room temperature; curve 2, DCEL spectra at  $77^{\circ}\text{K}$ ; curve 3, ACEL spectra at room temperature; curve 4, ACEL spectra at  $77^{\circ}\text{K}$ .

at 575 nm, suggesting that the blue-green bands seen in Fig. 1 are due to copper diffusing from the copper coating or to that copper deliberately added with lead. The 575 nm band appears consistently in phosphors with a low dopant level but is reduced in absolute and relative intensity by the presence of copper and if Mn contamination was responsible for this peak one would expect it even in the presence of copper. The band at 575 nm cannot therefore be readily explained on the present evidence but the origin may lie with a suggestion made recently by one of us (13) that this band is due to a transition involving one or more defect centers.

As the proportion of lead is increased a band at about 500 nm becomes the major feature in the electroluminescent spectra, (Fig. 2). It is reduced in intensity compared to the 575 nm band by the addition of sodium chloride flux which was therefore avoided during the preparation of the more heavily doped phosphors in order to produce a predominantly green emission. These phosphors, with an initial Pb concentration of  $6 \times 10^{-2}$  g-atoms per mole ZnS, gave relatively bright green electroluminescence with only a minor band at 575 nm, if at all. Firing in air seemed to give better results, i.e., higher brightness, than firing in  $\text{N}_2$  and this was adopted as standard practice.

There is an apparent similarity between the electroluminescent spectra of the heavily doped lead-doped phosphors and those of ZnS:Cu phosphors. At room temperature the latter have emission bands at 490-520 nm and this obviously raises the possibility that the green emission from the ZnS:Pb phosphors is due to the copper centers introduced from the copper coating and that this process is somehow facilitated by the presence of lead. However the addition of copper to green-emitting ZnS:Pb phosphors reduces the EL output and raises the current density to the point where the panel may burn out, about  $80\text{-}100 \text{ mA cm}^{-2}$ . A further test of the similarity between lead- and copper-doped phosphors was made by obtaining DCEL spectra at  $77^{\circ}\text{K}$  and the ACEL and photoluminescent spectra at both room temperature and  $77^{\circ}\text{K}$  (Fig. 3-6). The similarity shown by the room temperature DCEL spectra of ZnS:Pb and ZnS:Cu disappears at  $77^{\circ}\text{K}$ . For lead-doped phosphors the spectrum changes little between room temperature and  $77^{\circ}\text{K}$ , but in the case of ZnS:Cu phosphors the single peak seen at 510 nm at  $300^{\circ}\text{K}$  is resolved into two bands, at 455 nm and 510 nm. For both types of phosphor the ACEL spectra resemble the DCEL spectra, showing similar changes with temperature (Fig. 4 and 5). Finally the photoluminescent spectra of ZnS:Pb phosphors have been obtained under 365 nm Hg excitation and can be compared to the DCEL spectra. The peak maxima under uv excitation are close to the range of those found under d-c excitation and those found by pre-

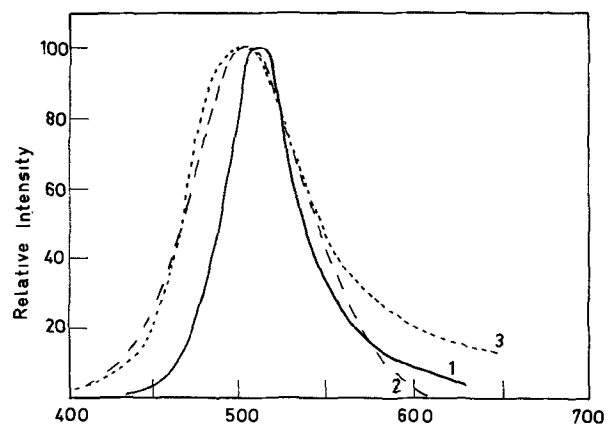


Fig. 6. 365 nm excitation. Curve 1, ZnS:Pb ( $6 \times 10^{-2}$ ), at  $77^{\circ}\text{K}$ ; curve 2, ZnS:Pb ( $6 \times 10^{-2}$ ), at room temperature; curve 3, ZnS:Pb ( $5 \times 10^{-2}$ ), at room temperature, Uehara (11).

vious investigations of the ZnS:Pb system (7-11). In Table II the mean wavelengths of the peak maxima are listed for the various methods of excitation.

**Brightness and efficiency.**—The brightness of the band at 500 nm has been estimated for the lead-doped phosphors from the net photometric response and the spectral distribution, and can be found in Table III. At room temperature the brightness of the most efficient phosphor does not exceed 4 ft-L and the power efficiency is less than  $10^{-5}$ . This is less by two orders of magnitude than the brightness of ZnS:Mn,Cu phosphors. However while measurements were being taken of the variation of brightness with voltage and current it was found that some of the lead-doped phosphors showed efficiencies at  $77^{\circ}\text{K}$  equal to that of the ZnS:Mn,Cu system at room temperature.

**Variation of brightness with voltage and current.**—The relationship between brightness and voltage for cells made as described above have been found to be of the following form for Mn-doped phosphors (2)

Table II. Peak maxima of luminescence for ZnS:Pb ( $6 \times 10^{-2}$ ) phosphors under various excitations

Excitation	Peak maxima, nm	
	Room temperature	$77^{\circ}\text{K}$
d-c field	$497 \pm 7$	$497 \pm 2$
a-c field	$497 \pm 13$	$507 \pm 3$
365 nm (Hg)	$501 \pm 2$	$504 \pm 6$
	494 [Uehara (11) for ZnS:Pb ( $5 \times 10^{-2}$ ) phosphor]	
	490 [Fonda (7) ZnS:Pb,Cu]	
	485 (8)	

Table III.

Phosphor	Total brightness at 100V (ft-L)	Brightness of green band (ft-L)	Energy efficiency for green emission
ZnS:Pb ( $10^{-3}$ )	$4 \times 10^{-3}$	$5 \times 10^{-3}$	$10^{-6}$
ZnS:Pb ( $5 \times 10^{-3}$ )	$5 \times 10^{-2}$	$10^{-2}$	$2 \times 10^{-6}$
ZnS:Pb ( $1.5 \times 10^{-2}$ )	$10^{-2}$	$10^{-3}$	$10^{-7}$
ZnS:Pb ( $4 \times 10^{-2}$ )	$8 \times 10^{-1}$	$7.5 \times 10^{-1}$	$3 \times 10^{-6}$
ZnS:Pb ( $4 \times 10^{-2}$ ) 3% w/w, NaCl	$2.5 \times 10^{-1}$	$6 \times 10^{-2}$	$4 \times 10^{-7}$
ZnS:Pb ( $6 \times 10^{-2}$ ) fired in N <sub>2</sub>	1.5 to 2	1.5 to 2	$8 \times 10^{-6}$
ZnS:Pb ( $6 \times 10^{-2}$ ) fired in air	1 to 4	1 to 4	$6$ to $8 \times 10^{-6}$

$$B = A \exp(-bV^{-1/2})$$

where  $B$  is the luminance,  $V$  is the applied voltage, and  $A$  and  $b$  are constants.

A similar relationship has been looked for in Fig. 7 for green-emitting ZnS:Pb phosphors where the brightness is plotted on a logarithmic scale against  $V^{-1/2}$ . A fairly linear plot can be seen in the samples shown in Fig. 7 which were all encapsulated panels operated at room temperature. For comparison manganese- and rare earth-doped phosphors are also plotted. Linear plots are also found for the 575 nm band of undoped zinc sulfide (not included on the figure). The slope of such plots has, in the case of a-c electroluminescence, been related to the energy of excitation of the center responsible for the emission in various phosphors (14) and it is interesting to note therefore that although the slope is different for each type of phosphor in Fig. 7, it does not seem to be related to the emission energy, Table IVa. In the case of Mn-doped phosphors two intersecting straight lines could be drawn, in agreement with as yet unpublished observations on many examples of this type of phosphor (15).

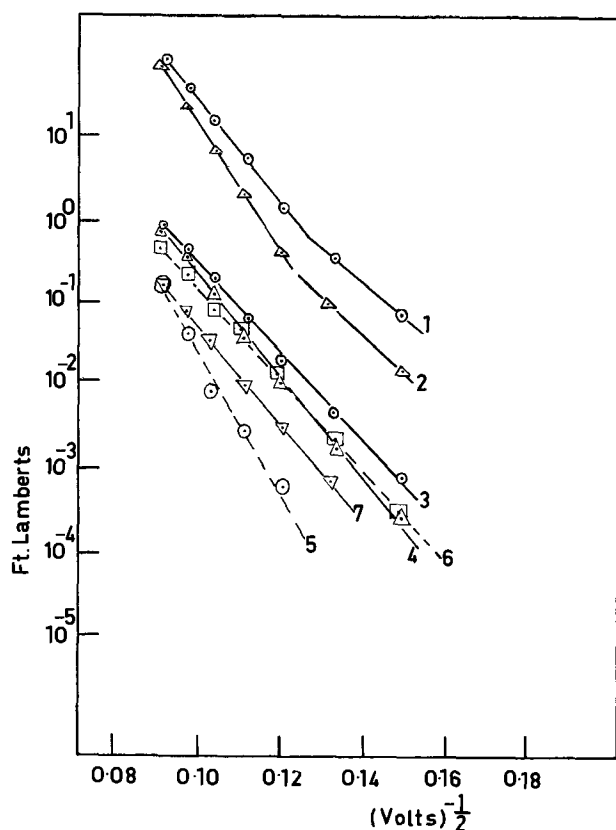


Fig. 7. Brightness vs. voltage of encapsulated panels at room temperature. Curve 1, ZnS:Mn,Cu; curve 2, ZnS:Mn; curve 3, ZnS:Pb, ( $6 \times 10^{-2}$ ), fired in air; curve 4, ZnS:Pb, ( $6 \times 10^{-2}$ ), fired in N<sub>2</sub>; curve 5, ZnS:Cu; curve 6, ZnS:Er,Li; curve 7, ZnS:Nd,Na.

Table IV. Numerical values of brightness/voltage constants,  $b$ 

a. Encapsulated panels at room temperature			
Phosphor	$b$ (Volts <sup>1/2</sup> )	eV corresponding to emission band	
ZnS:Mn,Cu (1)*	$145 \pm 5$ (55V)	2.16	
ZnS:Mn (2)	$175 \pm 5$ (60V)	2.16	
ZnS:Cu (5)	$177 \pm 5$	$2.45 \pm 0.05$	
ZnS:Pb ( $6 \times 10^{-2}$ ) (3)	$137 \pm 10$	$2.5 \pm 0.1$	
ZnS:Er,Li (6)	$134 \pm 10$	2.32	
ZnS:Nd,Na (7)	$130 \pm 10$	2.0	
b. Unencapsulated panels			
Phosphor	$b$ (Volts <sup>1/2</sup> )		Ratio of efficiencies
	300°K	70°K	
ZnS:Mn,Cu	89	$118 \pm 10$	1 to 10
ZnS:Mn	$107 \pm 7$	$150 \pm 10$	
ZnS:Cu	182	$177 \pm 10$	1.5
ZnS:Pb ( $6 \times 10^{-2}$ )	$104 \pm 10$	$185 \pm 30$	10 to 500

\* Number in parentheses refers to the numbered plot in Fig. 7.

The brightness was also measured for unencapsulated panels before and after immersion in liquid nitrogen, and  $b$  values are given in Table IVb. Unencapsulated panels seem to have different  $b$  values from encapsulated panels but the most significant feature is the change in brightness and efficiency of the different phosphors with change in temperature. Whilst the brightness was lower at 77°K in the case of Mn-doped phosphors an increase was found for several lead panels made from ZnS:Pb ( $6 \times 10^{-2}$ ) phosphors. The difference in behavior of the two types of phosphor was even more marked on measuring the power efficiencies at room temperature and 77°K. The ratio of efficiencies at 77°K and room temperature (290°-300°K) is given in Table IVb and although a wide range of values was found, there is a clear difference between manganese- and lead-doped panels. The efficiency of several lead panels increased by two orders of magnitude on reducing the ambient temperature to 77°K and they became comparable in efficiency and brightness to ZnS:Mn,Cu phosphors at that temperature, and one sample of a ZnS:Pb phosphor was as efficient at 77°K as the manganese-doped phosphors at room temperature ( $10^{-3}$ ).

Current densities at room temperature for the lead-doped panels are very similar to those of Mn-doped panels made by the same technique, that is of the order  $10^{-1}$  to  $10$  mA cm<sup>-2</sup> at 100V. The current density falls to the range  $10^{-4}$  to  $10^{-2}$  mA cm<sup>-2</sup> at 77°K and a similar decrease was also noted for Mn-doped phosphors. Thus the difference in the temperature dependence of the efficiencies of Mn- and Pb-doped phosphors may be due to greater thermal quenching of the active centers in the latter case.

*Origin of the green emission.*—In order to improve the room temperature efficiency of the green emission of the lead phosphors it would be useful to identify the active radiating centers involved. A connection between these centers and the amount of lead present is clear from the dependence of the brightness on the level of residual lead (Table III). Furthermore the spectral evidence suggests that the centers responsible for both a-c and d-c electroluminescence are also responsible for the photoluminescence, so that the conclusions of previous investigations on the photoluminescence of lead-doped zinc sulfide are pertinent.

The most comprehensive investigation to date is that of Uehara (11) which followed the earlier work of, particularly, Fonda (7), Smit and Kroger (8), and Voev (9). The relevant conclusions are that: (i) green emission is found for lead phosphors prepared in the presence of oxygen or halogen, (ii) the solubility of Pb in ZnS is  $5 \times 10^{-5}$  g-atoms per mole (9), and (iii) the emission band is centered at 490 nm in wurtzite and 500 nm in zinc blende and is attributed by Uehara

to the transition  $^3P_2-^1S_0$  of  $Pb^{2+}$  at zinc sites with oxygen or chlorine substituting for sulfur in adjacent sites.

Thus the EL brightness of ZnS:Pb phosphors should be increased by increasing the effective concentration of these centers, but a limit may have been reached already with an initial lead concentration of  $6 \times 10^{-2}$  g-atoms per mole ZnS since this was found to correspond to a residual lead concentration of about  $10^{-2}$  under the firing conditions used and this level is far greater than the limit of dissolved Pb in ZnS as found by Voev (9). Separate PbS and PbO phases must therefore be present and it was found that increasing the initial lead concentration beyond the level stated above results in a dark colored and rather sintered powder with low DCEL efficiency.

In ZnS:Mn,Cu phosphors an efficiency of  $10^{-3}$  has proved adequate for practical use in electroluminescent displays, and this level can be reached by ZnS:Pb phosphors at 77°K. Since the behavior of the current density at low temperatures is, qualitatively, similar in both types of phosphor then either the excitation efficiency of the Pb center is more temperature sensitive or the radiationless transitions are greater in the case of the lead-doped phosphors. The evidence gathered does not yet indicate which is the temperature sensitive step or steps.

#### Acknowledgments

We would like to thank all our colleagues for their help, particularly R. Ellis and Miss R. Hayes in the preparative work and N.J. Werring for making available equipment for photometric and electrical measurements. We acknowledge the support of the Ministry of Defence and are grateful for their permission to publish this work.

Manuscript submitted June 4, 1973; revised manuscript received July 23, 1973.

Any discussion of this paper will appear in a Discussion Section to be published in the December 1974 JOURNAL.

#### REFERENCES

1. A. Vecht and N. J. Werring, *J. Phys.(D)*, **3**, 105, (1970).
  2. A. Vecht, N. J. Werring, R. Ellis, and P. J. F. Smith, *ibid.*, **2**, 953 (1969); *ibid.*, **3**, L65 (1970).
  3. M. S. Waite and A. Vecht, *Appl. Phys. Letters*, **19**, 471 (1971).
  4. M. P. Brown and W. A. Shand, *J. Mater. Sci.*, **5**, 790 (1970).
  5. H. F. Ivey, *IRE Trans. Electron. Devices*, **6**, 203, (1959); *This Journal*, **108**, 590 (1961); *Electrochem. Technol.*, **1**, 42 (1965).
- These reviews contain references to patents and papers describing the addition of lead to copper-activated ZnS phosphors to improve electroluminescence (a.c.), possibly by control of the chloride content.
6. H. H. Homer, R. M. Rulon, and K. H. Butler, *This Journal*, **100**, 566 (1953).
  7. G. R. Fonda, *J. Opt. Soc. Am.*, **36**, 382 (1946).
  8. N. W. Smit and F. A. Kroger, *ibid.*, **39**, 661 (1949).
  9. E. I. Voev, A. A. Mikalev, and G. D. Guseva, *Opt. Spectr.*, **22**, 360 (1967).
  10. Y. Mita, *J. Phys. Soc. Jap.*, **20**, 1822 (1963).
  11. Y. Uehara, *J. Chem. Phys.*, **51**, 4385, 4401 (1969).
  12. C. Merrit, Jr., H. M. Hershenson, and L. B. Rogers, *Anal. Chem.*, **25**, 572 (1953).
  13. A. Vecht, *J. Luminescence*, **7**, 213 (1973).
  14. D. Curie, *Prog. Semiconductors*, **2**, 249 (1957).
  15. A. Vecht, N. J. Werring, R. Ellis, and P. J. F. Smith, To be published.

## Oxidation of $GaAs_{1-x}P_x$ Surface by Oxygen Plasma and Properties of Oxide Film

Takuo Sugano and Yoshifumi Mori

Department of Electronic Engineering, University of Tokyo, 7-3-1 Hongo, Bunkyo-ku, Tokyo 113, Japan

#### ABSTRACT

This paper presents a new technology for oxidizing a  $GaAs_{1-x}P_x$  ( $x = 0 \sim 1$ ) surface by oxygen plasma, produced by high-frequency discharge in oxygen, whose pressure is of the order of about 0.1 ~ 1.0 Torr. Growth rate of the oxide film is remarkably high, and can be controlled by the oxygen gas pressure and the high-frequency field over a range of 50 A/sec to 1  $\mu$ /sec. The plasma-oxidized films have complex composition, including polycrystalline  $\beta$ - $Ga_2O_3$ ,  $GaAsO_4$ , and  $GaPO_4$ . The refractive index of these films measured by ellipsometry reveals a dependence on the substrate material and on film thickness, and also distribution in the film, so that the refractive index changes from a value, corresponding to  $\beta$ - $Ga_2O_3$  at the top surface, to the value approximately equal to that of the substrate material at the oxide-substrate interface. Such distribution of the refractive index is useful for attaining optical isolation in monolithic optical integrated circuits. Furthermore, this technique has various applications, such as the surface passivation of  $GaAs_{1-x}P_x$  devices and dielectric isolation in GaAs integrated circuits, fabricated on a semi-insulating substrate.

To attain surface passivation of compound semiconductor devices and fabrication of insulated gate field effect transistors using a compound semiconductor, insulator-compound semiconductor systems offer practical interest. However III-V compound semiconductors such as GaAs have a high equilibrium vapor pressure and are easily decomposed at high temperature, which is common to thermal oxidation or chemical vapor dep-

osition, rendering poor results (1-4) and recognizing the necessity for low-temperature processes. Low-temperature chemical vapor deposition, deposition by glow discharge, and sputtering are examples of anticipated low-temperature processes; however, successful results have not yet been obtained. This paper presents a new technique for forming an insulating film on  $GaAs_{1-x}P_x$  ( $x = 0 \sim 1$ ) wafers. That is, oxidation by plasma, produced by high-frequency discharge in low-pressure oxygen gas. Characteristics of this tech-

Key words: oxide, gallium arsenide phosphide, plasma, surface passivation.

nique, properties of oxide films, and application are described herein.

### Oxidation

**Plasma oxidation apparatus.**—Oxygen plasma was generated in the apparatus shown in Fig. 1, a commercial pumping station with slight modifications. A fused quartz cap (diameter 6.0 cm and length 30.0 cm) is placed on the top of a bell jar (diameter 30.0 cm). Oxygen was supplied through a needle valve from a bottle. A 420 kHz, high-frequency field was applied through the 9-turn coil, surrounding the cap. GaAs<sub>1-x</sub>P<sub>x</sub> substrate, supported by an alumina or fused quartz rod, was inserted into the middle of the plasma, electrically isolating the substrate from the earth.

**Oxidation rate.**—The oxidation rate was strongly dependent on the plasma condition. Figure 2 indicates the relation of output of an Alumel-Chromel thermocouple inserted into the plasma at the pressure of oxygen gas, measured by a Pirani gauge and the anode voltage of the high-frequency oscillator, whose maximum output was rated at 15 kW. By raising the anode voltage, glow discharge (whose temperature measured by the thermocouple was between 150° and 200°C) started initially. The glow discharge produced no appreciable oxide film on the substrates. However, in the bright discharge which we called oxygen plasma, very rapid oxidation occurred. Examples of the oxida-

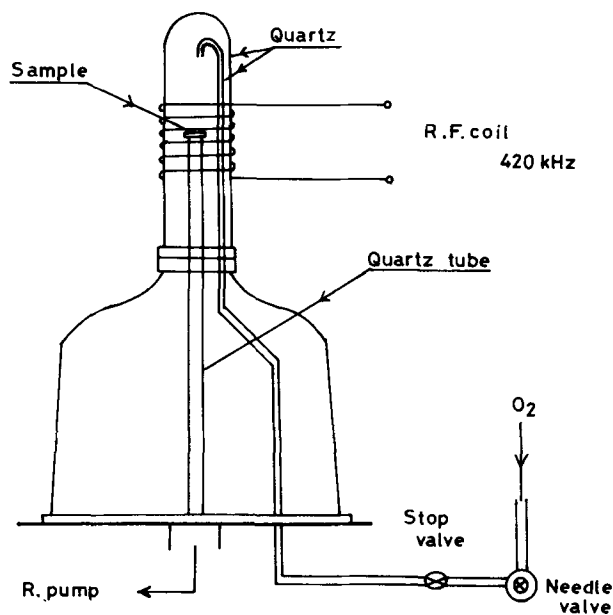


Fig. 1. Apparatus

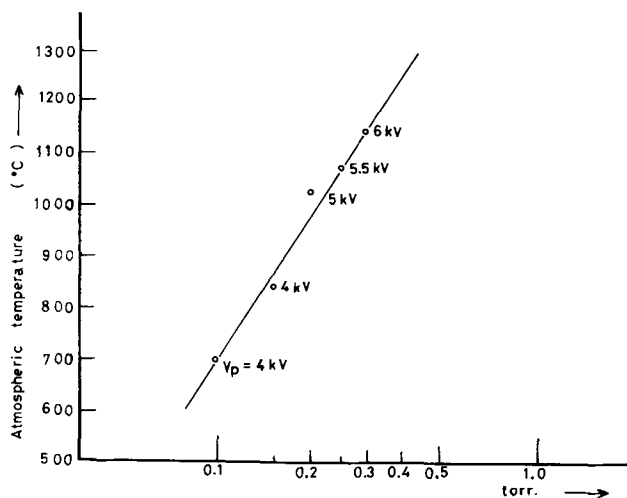


Fig. 2. Atmospheric temperature by thermocouple measurement

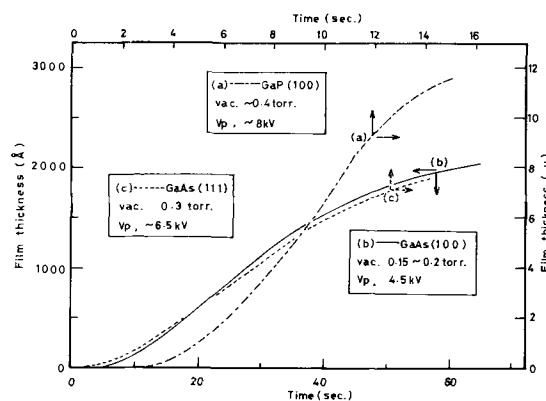


Fig. 3. Oxidation rate

tion rate are shown in Fig. 3 (a), (b), and (c), showing the initial delay of oxidation, perhaps due to delay of the substrate temperature, and the saturation tendency with time. In rather high-pressure plasma, the oxidation rate is extremely high, reaching 1  $\mu$ /sec, but in low-pressure plasma, it is moderate, at 50  $\text{\AA}$ /sec. It was determined from these results that the oxidation rate can be controlled by adjusting the oxygen gas pressure and the anode voltage of the high-frequency oscillator. For dependence of the oxidation rate on surface orientation of the substrates, no appreciable difference is evident except for an extremely thin film.

**Masking by Al film.**—Evaporated Al film thicker than 5000 $\text{\AA}$  was effective in preventing oxidation, rendering it useful as a mask for selective oxidation. Effect of the window opening of the Al mask on oxide thickness is illustrated in Fig. 4. For a window whose opening is 10 $\mu$ , the oxide thickness is decreased by about 10%.

### Properties of Oxide Films

**Chemical properties.**—Oxide films grown on GaAs substrates are quite stable and practically insoluble in various acids and alkalis. Boiling in HCl acid etched them at the rate of 50 ~ 80  $\text{\AA}$ /min. On the other hand, oxide films grown on GaAs<sub>0.6</sub>P<sub>0.4</sub> and GaP were easily soluble in acids and alkalis. The etch rate in 5% HF was 500 ~ 1000  $\text{\AA}$ /min.

**Electrical properties.**—Electrical properties of oxide films were evaluated by the current-voltage characteristics of MOS structures. A typical I-V characteristic of a GaAs MOS diode possessing oxide film (3.5 $\mu$  thick) and an Al electrode (1 mm diameter) is shown in Fig. 5. Region (1) in Fig. 5 can be explained by the Poole-Frenkel mechanism, assuming the dielectric constant of the oxide as 4; region (2) can be attributed to Schottky emission, assuming the dielectric constant as 5.2.

Roughly speaking, resistivity of the oxides ranged from 10<sup>8</sup> to 10<sup>10</sup> ohm-cm.

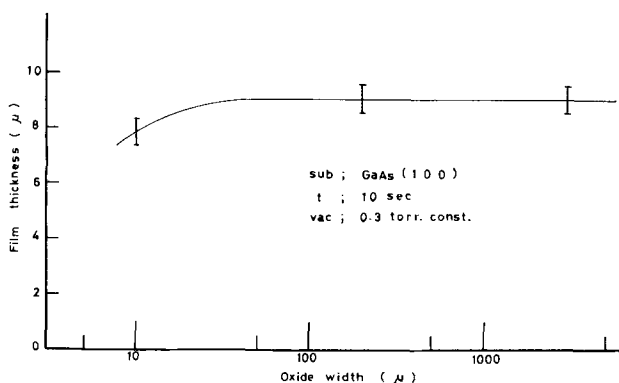


Fig. 4. Effect of window opening of Al mask on oxide thickness

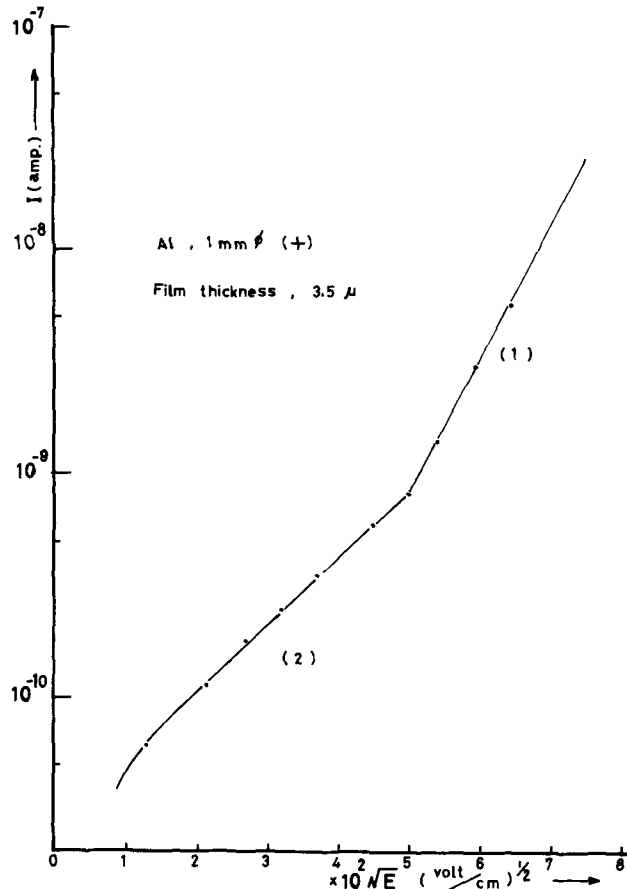


Fig. 5. Typical I-V characteristics of GaAs MOS diode

**Optical properties.**—The average refractive index of the oxide films was measured by split-beam ellipsometry, using a monochromatic light source of 5461Å wavelength with the angle of incidence maintained constant at 70°. Optical constants of GaAs,  $\text{GaAs}_{0.6}\text{P}_{0.4}$ , and GaP at  $\lambda = 5461\text{Å}$ , assumed for calculation of the ellipsometric chart, are (5) (6)

$$\begin{aligned} n_{\text{GaAs}} &= 3.923 & k_{\text{GaAs}} &= 0.304 \\ n_{\text{GaAs}_{0.6}\text{P}_{0.4}} &= 3.840 & k_{\text{GaAs}_{0.6}\text{P}_{0.4}} &= 0.100 \\ n_{\text{GaP}} &= 3.565 & k_{\text{GaP}} &= 0.000069 \end{aligned}$$

As shown in Fig. 6, oxide films with different thicknesses have a different average refractive index. Curve A in Fig. 6 shows the refractive index for the films on GaAs. Curve B shows that of  $\text{GaAs}_{0.6}\text{P}_{0.4}$ , and curve C shows that of GaP. The average refractive index of oxide films on GaAs and  $\text{GaAs}_{0.6}\text{P}_{0.4}$ , indicated by the

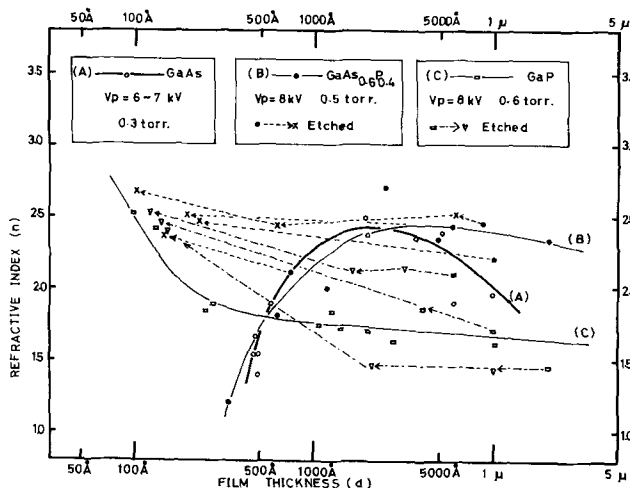


Fig. 6. Ellipsometric investigation of oxide films on  $\text{GaAs}_{1-x}\text{P}_x$

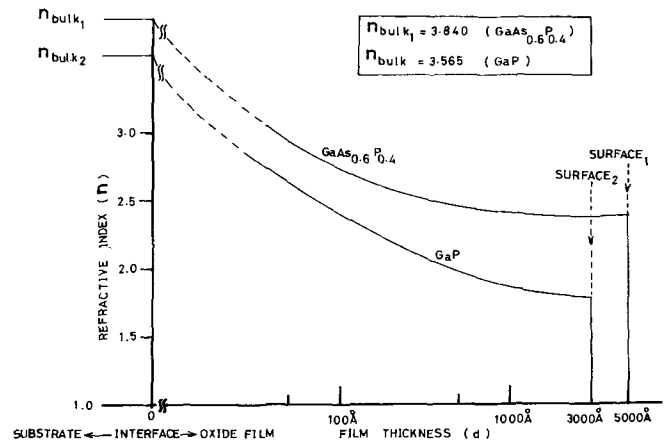


Fig. 7. Estimated distribution of refractive index through oxide films.

thick, solid-line curve, has a peak value of about 2.5, whereas that of GaP does not.

These results imply that the oxide films lack uniform composition, and the difference of these relations of the substrate material seems to be due to the varying vapor pressure of arsenic and phosphor. To determine distribution of the refractive index perpendicular to the surface of films on  $\text{GaAs}_{0.6}\text{P}_{0.4}$  and on GaP, the oxide was step-etched by 5% HF acid. After each etching, the average refractive index of the remaining film was measured by ellipsometry. The results are indicated by the broken-line curves in Fig. 6.

Based on the above results, distribution of refractive index through the oxide films on  $\text{GaAs}_{0.6}\text{P}_{0.4}$  and GaP can be estimated as shown in Fig. 7.

**Structural properties.**—Electron beam diffraction patterns also reveal the complex structure of those oxide films.

A few of the electron diffraction patterns are shown in Fig. 8.

Table I summarizes the results obtained for some of the oxide films, which can be related to the optical properties.

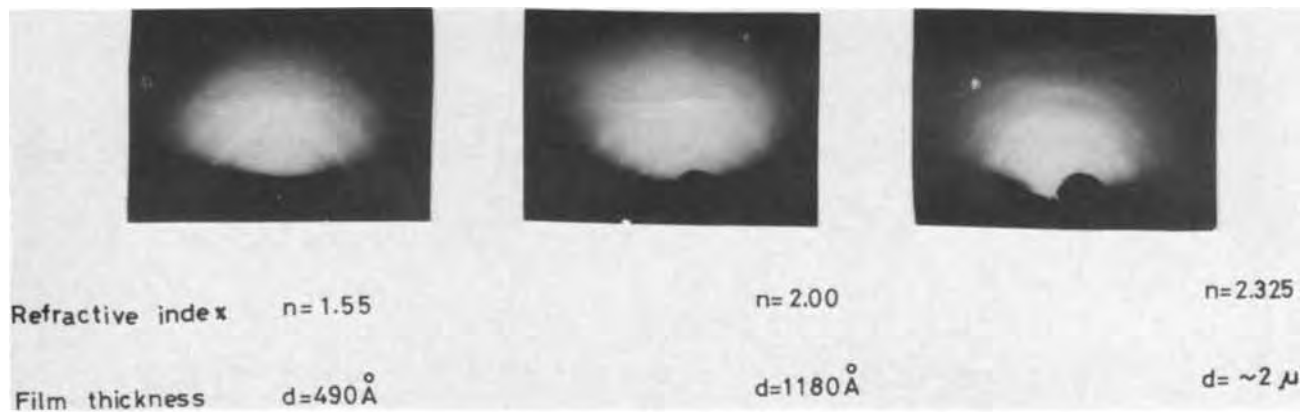
In the first stage of oxidation corresponding to a film thickness less than about 1000Å, the oxide films on GaAs and  $\text{GaAs}_{0.6}\text{P}_{0.4}$  are mostly composed of polycrystalline  $\beta\text{-Ga}_2\text{O}_3$ . This suggests that arsenic is almost completely vaporized from the GaAs and  $\text{GaAs}_{0.6}\text{P}_{0.4}$  surface during oxidation.

The thicker the oxide film becomes, the less the arsenic becomes vaporized. This results in an increase of the average refractive index with the oxide thickness. The thin oxide film on GaP is mostly composed of polycrystalline  $\beta\text{-Ga}_2\text{O}_3$ ; however, the 1000Å-thick film on GaP includes more  $\text{GaPO}_4$  than  $\text{GaAsO}_4$  included on GaAs. The refractive index decreases with oxide thickness. This implies that an accumulation of phosphor occurs at the interface, even during the early stage of oxidation, caused by the vapor pressure of phosphor being lower than that of arsenic.

For the second stage of oxidation, corresponding to a film thickness ranging from about 1000Å to 1μ, composition of the oxide films on GaAs and  $\text{GaAs}_{0.6}\text{P}_{0.4}$  are a mixture of polycrystalline  $\beta\text{-Ga}_2\text{O}_3$  and  $\text{GaAsO}_4$  or  $\text{GaPO}_4$ . The average refractive index becomes maximum at a thickness in this region. This suggests that less arsenic is vaporized in this oxidation stage, caused by a masking effect of the previously formed  $\beta\text{-Ga}_2\text{O}_3$  film. The oxide film on GaP thicker than 2000Å is composed of polycrystalline  $\text{GaPO}_4$ , and the average refractive index also approaches the value of bulk  $\text{GaPO}_4$ .

For the final stage of oxidation, corresponding to film thickness beyond 1μ, composition of the oxide on



Fig. 8. Electron diffraction patterns of  $\text{GaAs}_{0.6}\text{P}_{0.4}$ 

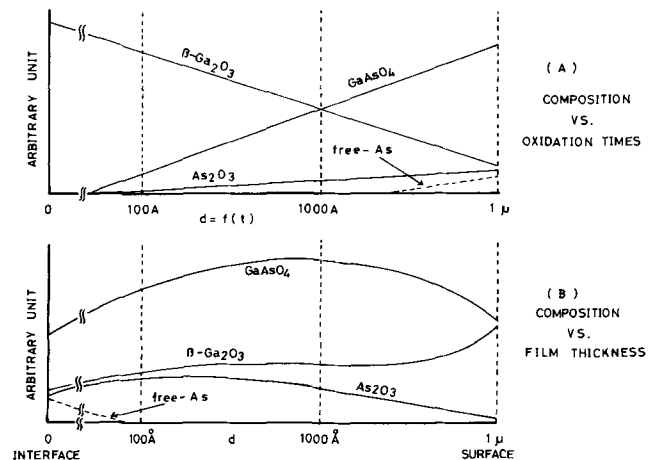
$\text{GaAs}$  and  $\text{GaAs}_{0.6}\text{P}_{0.4}$  is orientated polycrystalline  $\text{GaAsO}_4$  and a mixture of  $\text{GaAsO}_4$  and  $\text{GaPO}_4$ , respectively. In the case of  $\text{GaAs}$  oxidation, a change of composition of the oxide as a function of time and a distribution of composition as a function of depth is schematically indicated in Fig. 9. Chemical stability of the oxide films on  $\text{GaAs}$  is much better than that of  $\text{GaAs}_{0.6}\text{P}_{0.4}$  and  $\text{GaP}$ . This is also related to the structural properties of each oxide film, based on the fact that oxide on  $\text{GaAs}$  includes much  $\beta\text{-Ga}_2\text{O}_3$  which is chemically stable.

In any case, annealing at  $300^\circ\text{C}$  for 60 min in oxygen renders the oxide structure amorphous, decreases the film thickness by about 5%, and increases the average refractive index by about 0.1.

### Applications

**Dielectric isolation in GaAs monolithic integrated circuits.**—Cross-sectional views of the  $\text{GaAs}$  wafers in each process of dielectric isolation in a  $\text{GaAs}$  monolithic integrated circuit are schematically shown in Fig. 10. An active  $\text{GaAs}$  layer is epitaxially grown on a semi-insulating  $\text{GaAs}$  substrate, and  $\text{Al}$  film is evaporated on it and photolithographically etched to form a mask for selective oxidation. Then the wafer is oxidized by oxygen plasma. The oxide penetrates through the epitaxial layer, reaches the semi-insulating substrate, and forms islands of epitaxial  $\text{GaAs}$ , isolated by the oxide and the semi-insulating substrate. The  $\text{Al}$  mask is etched away by  $\text{HF}$  acid finally.

The isolation property was evaluated by the current-voltage characteristics between two islands, as shown in Fig. 11. In much the same way as in the above isolation process, prefabricated pn junctions were isolated as shown in Fig. 12. The pn junction was slightly damaged during the oxidation process as indicated by the broken curves in Fig. 12 in comparison with the solid-line curves, which indicated I-V characteristics of the pn junction obtained by mesa-etching for monitoring. However, in both cases, the epitaxial layer and pn

Fig. 9. Model of plasma oxidation process and profiles of  $\text{GaAs}$  substrate.

junction were not seriously damaged during the oxidation process.

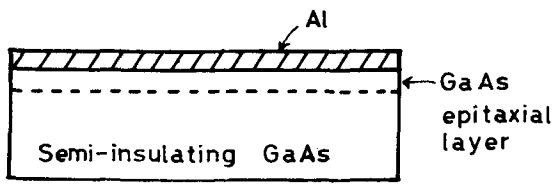
**Surface passivation of light-emitting diodes.**—Surface passivation of light-emitting diodes by this technique is accompanied by an improvement of their external efficiency of light emission. Extensive studies on the reliability of passivated devices by this oxide film have not yet been completed, although a small degree of improvement in the external efficiency of  $\text{GaAs}_{0.6}\text{P}_{0.4}$  light-emitting diodes was evident. Distribution of the refractive index through the film can be conceived as that shown in Fig. 7; consequently, improved optical matching between the light-emitting medium and the oxide film is expected.

**Optical isolation in optical integrated circuits.**— $\text{GaAs}_{0.6}\text{P}_{0.4}$  with a pn junction on  $\text{GaAs}$  substrate was used as a wafer. The wafer was oxidized selectively until the oxide reached the  $\text{GaAs}$  substrate, forming a strip of  $\text{GaAs}_{0.6}\text{P}_{0.4}$  layer that was isolated electrically.

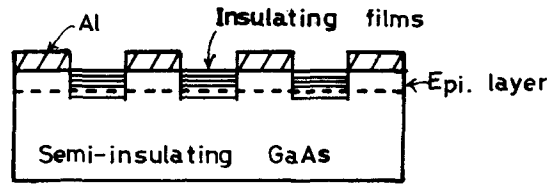
Table I. Structure of oxide films

Substrate	Film thickness	Refractive index	Structure	Composition
Undoped $\text{GaAs}$ (100)	590Å	1.87	Polycrystalline	$\beta\text{-Ga}_2\text{O}_3$
	1100Å	2.49	Polycrystalline	$\beta\text{-Ga}_2\text{O}_3 + \text{GaAsO}_4$
	$\sim 1\mu$	1.97	Oriented polycrystalline	$\text{GaAsO}_4$
	Annealed, 1890Å	2.60	Amorphous	
$\text{Te}(1.45 \times 10^{17} \text{ cm}^{-3})$ doped $\text{GaAs}_{0.6}\text{P}_{0.4}$ (100)	490Å	1.55	Polycrystalline	$\beta\text{-Ga}_2\text{O}_3$
	1180Å	1.62	Oriented polycrystalline	$\beta\text{-Ga}_2\text{O}_3$
	$2\mu$	2.325	Oriented polycrystalline	$\text{GaPO}_4 + \beta\text{-Ga}_2\text{O}_3$
	Annealed, 970Å	2.27	Amorphous	
Undoped $\text{GaP}$ (100)	490Å	1.57	Polycrystalline	$\beta\text{-Ga}_2\text{O}_3$
	1060Å	1.76	Oriented polycrystalline	$\beta\text{-Ga}_2\text{O}_3 + \text{GaPO}_4$
	2710Å	1.63	Polycrystalline	$\text{GaPO}_4$
	Annealed, 1180Å	1.92	Amorphous	

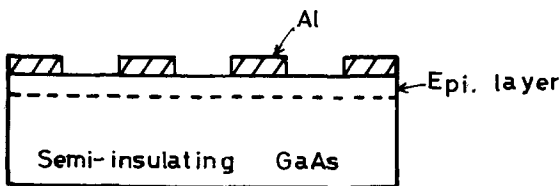
(1) Al evaporation



(3) Discharge



(2) Photo etching



(4) Al mask etch.

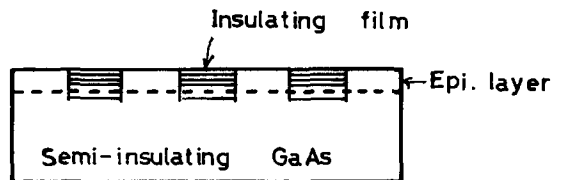


Fig. 10. Cross-sectional views

When light is emitted from a part of the strip, the light passes through the  $\text{GaAs}_{0.6}\text{P}_{0.4}$  layer, which possesses a self-focusing characteristic because of distribution of the refractive index in the oxide film, as shown in Fig. 7. A preliminary experiment revealed a 3 db improvement of the attenuation constant of a  $\text{GaAs}_{0.6}\text{P}_{0.4}$  strip about  $550\mu$  wide in comparison with the air-isolated  $\text{GaAs}_{0.6}\text{P}_{0.4}$  strip.

**Conclusion**

It has been found that plasma oxidation has an extremely high oxidation rate on the surface of

$\text{GaAs}_{1-x}\text{P}_x$  substrate, and the rate can be controlled from  $50 \text{ \AA}/\text{sec}$  to  $1 \mu/\text{sec}$  by oxygen gas pressure and anode voltage of the oscillator.  $0.5\mu$  thick Al film functions well as a mask for selective oxidation and assists this technique in becoming compatible with the photolithic process.

Structural and optical properties of the oxides are not uniform throughout the film. The oxides include  $\beta\text{-Ga}_2\text{O}_3$ ,  $\text{GaAsO}_4$ , and  $\text{GaPO}_4$ , and the composition ratio varies in depth. The average refractive index measured by split-beam ellipsometry also changes with film thickness, and it is estimated that the refractive index is distributed from the oxide-substrate interface (where it has a value very close to that of the substrate) to the surface of the oxide (where it has the value corresponding to that of  $\beta\text{-Ga}_2\text{O}_3$ ).

Such distribution of the refractive index is expected to be useful in the optical integrated circuits of light-emitting diodes, an improvement of the optical characteristics of those devices, and for surface passivation. A flow of Schottky emission current and Poole-Frenkel current through the oxide film has been observed, whereby resistivity of the oxide ranged from  $10^8 \text{ ohm-cm}$  to  $10^{10} \text{ ohm-cm}$ , sufficient to cause dielectric isolation in GaAs monolithic integrated circuits. Physical mechanisms of the rapid oxidation of  $\text{GaAs}_{1-x}\text{P}_x$  by oxygen plasma are not yet known, neither have exten-

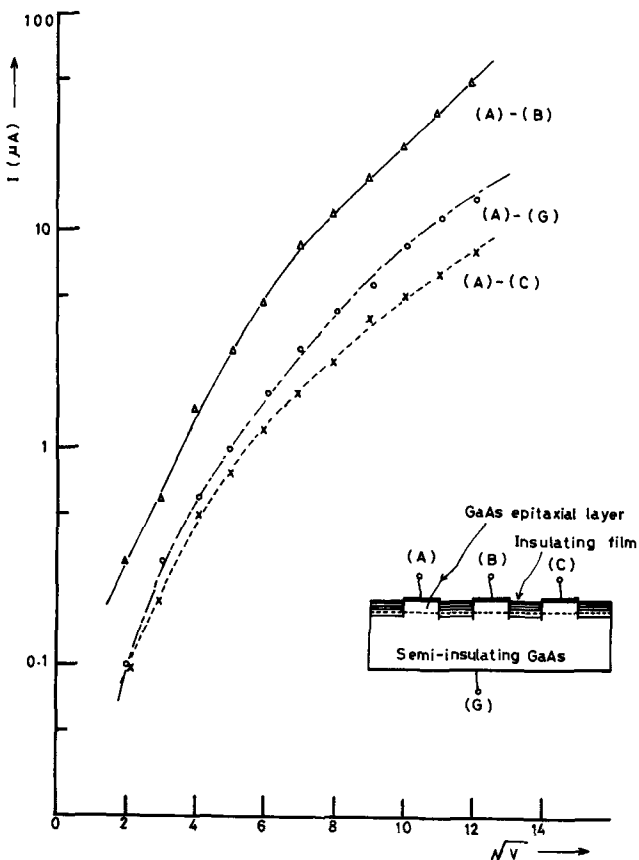


Fig. 11. Current-voltage characteristics between two islands

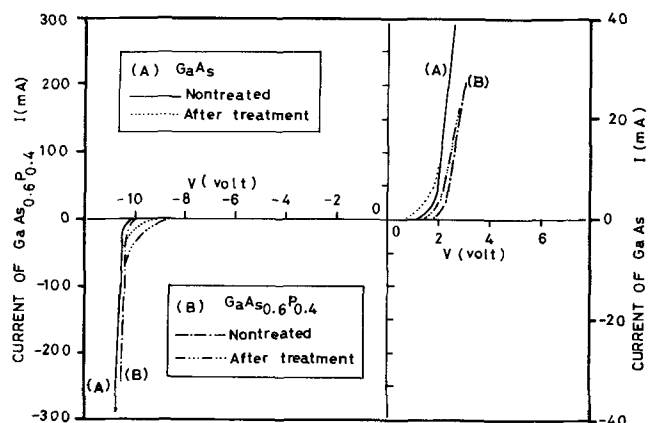


Fig. 12. I-V characteristics of  $\text{GaAs}_{1-x}\text{P}_x$  p-n junction

sive studies on applications of this technique been conducted. Such problems will be pursued subsequently.

### Acknowledgment

We express our sincere thanks to Dr. Y. Tarui, Y. Komiya, and S. Sakamoto, Electrotechnical Laboratory, for their cooperation in ellipsometry measurements. We also acknowledge the kind assistance of S. Abe in measurements and computer programming. This project is partially supported by Grant-in Aid for Developmental Scientific Research from the Ministry of Education (Japan), for which we are deeply grateful. Most GaAs<sub>1-x</sub>P<sub>x</sub> substrates were supplied from the OKI Electric Company, also hereby acknowledged by us.

Manuscript submitted May 16, 1973; revised manuscript received Aug. 21, 1973.

Any discussion of this paper will appear in a Discussion Section to be published in the December 1974 JOURNAL.

### REFERENCES

1. K. H. Zaininger and A. G. Reverz, *J. Phys.*, **25**, 208 (1964).
2. J. Arthur, *J. Phys. Chem. Solids*, **28**, 2257 (1967).
3. J. E. Foster and J. M. Swartz, *This Journal*, **117**, 1410 (1970).
4. J. Gyulai, J. W. Mayer, and I. V. Mitchell, *Appl. Phys. Letters*, **17**, 332 (1970).
5. D. O. Seraphin and H. E. Bennett, "Semiconductor and Semimetals," Vol. 3, Chap. 12, Academic Press, New York (1967).
6. G. D. Clark Jr. and N. Holonyak, Jr., *Phys. Rev.*, **156**, 3 (1967).

## Oxidation Characteristics of Some Nickel Alloy Films in Air and Water Vapor

K. Gupta, J. P. Marton, and J. Shewchun

Department of Engineering Physics and Institute for Materials Research,  
McMaster University, Hamilton, Ontario, Canada

### ABSTRACT

Ellipsometric techniques were used to study the oxidation of Ni, Ni-Cr, and Ni-P deposits. Oxidation was carried out at temperatures ranging from 100° to 500°C in different ambients including air, saturated water vapor, and gas mixtures containing oxygen at 0.05 and 0.5 atm, respectively. The optical constants  $n$  and  $k$  of fresh deposits were found to undergo change on heating. Typically,  $n$  decreased and  $k$  increased, both saturating at longer times. The oxidation of Ni, Ni-Cr, and Ni-P was found to be a three stage process. At temperatures below 300°C, mainly oxygen is absorbed; while above this temperature a surface oxide layer is formed. The third stage occurs at 400°C, and for long times where the films become anisotropic or inhomogeneous. The optical constants of the oxide layers formed on all three metals were found to be nearly the same, and their values to be close to those of NiO. The oxidation in different oxygen pressures indicated that water vapor plays a role in the oxidation process. The oxidation in water vapor could not be accounted for by the oxygen normally present in water as a dissolved gas.

The structure of freshly deposited Ni-P films has been reported (1) to be of a polycrystalline island type. On heating it undergoes a chemical phase transition, the final products (2) being Ni and Ni<sub>3</sub>P. Marton and Chan (3) have determined the optical constants of Ni-P films annealed in hydrogen to be  $n = 2.15$ ,  $k = 2.75$ . The oxidation of Ni-P films has also been studied (3, 4). It was found that an oxide film grows only above 280°C and that it is a two phase mixture of NiO and P<sub>2</sub>O<sub>5</sub>. The optical constants of the oxide were found to depend on thickness of oxide film and the saturated values were determined to be  $n = 1.3$ ,  $k = 0.15$ . The effect of water vapor on the oxidation process and on the oxide layer has not been studied before.

The oxidation of bulk Ni (5-7) and Ni-Cr at high temperatures (8-10) has been shown to follow Wagner's parabolic law. Very little is known, however, about the behavior of films of these metals at temperatures below 500°C. Oxidation of Ni in water vapor has been studied by some investigators (11, 12). Although the mechanism of oxidation in water vapor is not clearly understood, it is known (10) that the rate of oxidation in water vapor is lower than that in air by a factor of three. Rhamel (13) studied the oxidation of Ni at 1000°C in oxygen alone and with 43%

water vapor. His results indicated that the presence of water vapor does not alter the rate of oxidation. Roberts (14) and Meyerson (15) have determined the optical constants of bulk Ni from reflectance studies to be  $n = 1.66$ ,  $k = 3.39$ . Roberts (14) also found these constants to change with temperature. Optical constants of Ni-Cr have not been reported in the literature.

In the present investigation, we have determined optical constants for films of Ni, Ni-Cr, and Ni-P in the thickness range of 1000-1500Å and studied their variation with temperature. We also studied the oxidation of these films in the temperature range of 100°-400°C in different ambients including air, water vapor, and gas mixtures in which the partial pressure of oxygen was 0.05 and 0.5 atm, respectively. The thickness of the oxide film and its optical constants were calculated in each case. Finally, we investigated the effect of water vapor on the oxide layer formed on Ni, Ni-Cr, and Ni-P films. The information found enabled us to construct working models of the oxidation process of these metals. The results also indicated that the oxide film on the three types of film studied consists mainly of NiO.

### Experimental

*Sample preparation.*—Nickel and nichrome films were made by thermal evaporation of these metals in

Key words: ellipsometry, nickel alloy films, oxidation, effect of moisture.

vacuum ( $\sim 4 \times 10^{-6}$  Torr) on Pyrex glass substrates, 1 in. square and  $\frac{1}{4}$  in. thick. An NRC 3116 vacuum coater, with an alumina-coated tungsten boat as source, was used for evaporation. Deposition was carried out at room temperature at the rate of about 200Å/min. The thickness of the deposit was continuously monitored by a Sloan-Omni II deposit control master. Films were grown to 1200-1500Å thickness. Nickel phosphorous films were made by electroless deposition of the metal on Pyrex glass substrates. For cleaning and activation of the substrates and deposition of the metal, we followed accepted procedures (1). Thickness of the deposit as measured by the Angstrommeter was in the range of 1200-1500Å and the composition was maintained at 16 atomic per cent (a/o) phosphorous. The Ni-P was removed from one side of the glass substrate by rubbing the surface with aqua regia. This was necessary in order to enable ellipsometric measurements to be made at the glass metal interface by second surface reflection.

**Thermal oxidation of samples.**—The specimens were subjected to heat-treatment at temperatures ranging from 100° to 500°C for times ranging from 10 to 1000 min. This was done in different ambients including air, saturated water vapor, and two oxygen-nitrogen mixtures containing oxygen at 0.05 and 0.5 atm, respectively. The experimental arrangement consisted of a quartz tube, 3 in. in diameter, placed in a three-zone low-temperature furnace. A quartz boat was used to introduce the sample. The temperature gradient along the length of the boat was determined to be less than 1°. After the sample had been heated in the desired atmosphere for the required period, it was withdrawn from the furnace and allowed to cool in air at room temperature.

**Ellipsometric measurements.**—Measurements were made on freshly deposited samples and after each period of heating. All measurements were carried out in air at room temperature using a Rudolph thin film ellipsometer Model 43603-200E in a conventional manner. The parameters  $\Delta$  and  $\Psi$  were measured at both the air and the glass surface of the metal. The latter were used to calculate optical constants,  $n$  and  $k$  of the metal by second surface reflection (16). Optical constants of the metal were also determined by the multiple-angle of incidence method (17). The results obtained from the two methods agreed only when the oxide was nonabsorbing or very slightly absorbing ( $k \approx 0.05$ ). When the oxide was more absorbing the results varied by 20-25%. In such cases, the optical constants obtained from second surface measurements were taken.

The second surface ellipsometric measurements were carried out at two different angles of incidence between 65° and 75° in all four zones. One of the criteria used for computer iteration was that the oxide film thickness be independent of angle of incidence. The results discussed below are averages of 8 readings for each sample in each state of oxidation. In all measurements the ellipsometer was operated at  $\lambda = 5461\text{Å}$ .

### Analysis of the Data

The interpretation of ellipsometric data in terms of the optical constants and thickness of the oxide film is based on the Fresnel and Drude equations. An iterative computer program, similar to McCrackin and Colson (18) was used for the actual calculations. This program is designed to calculate optical constants of the oxide film and its thickness if the optical constants of the substrate are known. An expected range is specified for the optical constants of the oxide film. The final values for optical constants and film thickness are obtained by iterating the program for best possible convergence.

Interpretation of the ellipsometric data in terms of a surface oxide film is possible only if the oxide film is of uniform thickness, isotropic, and homogeneous. It was found that ellipsometric data on samples heated at lower temperatures, i.e., 100°-250°C did not yield a

satisfactory and acceptable solution in terms of a surface oxide film. This could be due either to the absence of a surface oxide or to extreme inhomogeneities in the initial stages of oxide growth. Since the measurements were not made *in situ* under ultra high vacuum conditions, it is also possible that a thin oxide layer could have been masked by the adsorbed gas on the surface. As the oxide thickness would grow, the effect of the adsorbed gases would be less pronounced. Engell, Hauffe, and Ilschner have reported (19) oxide film thickness of the order of 700Å at 400°C for bulk nickel. They have measured volumetrically the amount of oxygen consumed. However, there is no direct measurement of the thickness of the oxide layer either on bulk nickel or on deposited Ni film.

Although the data for low temperatures of heating could not be interpreted in terms of a homogeneous oxide layer, meaningful results were obtained with the help of Maxwell-Garnett theory (20). The changes in the optical properties of the surface were interpreted as caused by absorption or desorption of gases. For temperatures of heat-treatment at and above 300°C, the observed  $\Delta$  and  $\Psi$  could be interpreted in terms of a surface oxide film. Again when nickel and nickel phosphorous were heated in air at 400°C for longer periods ( $\sim 200$  min or more) or at higher temperatures, the observed data failed to give a satisfactory solution in terms of thickness of oxide film.

### Results and Discussion

Ellipsometer readings  $\Delta$  and  $\Psi$  measured at 70° angle of incidence for some samples of Ni, Ni-Cr, and Ni-P are plotted in Fig. 1. The samples were heated in air at temperatures of 300° and 400°C for various times. In the figure, the oxidation time progresses from right to left. Results of the various interpretations of the ellipsometric data are presented below.

**Optical constants of the metals.**—Optical constants of freshly deposited Ni films were determined to be  $n = 1.9 \pm 0.1$  and  $k = 3.5 \pm 0.1$ . When they were heated in air and water vapor, both  $n$  and  $k$  showed a decrease, saturating at  $n \approx 1.7$  and  $k \approx 3.4$ . For Ni-P films, the optical constants were found to be  $n = 2.6 \pm 0.1$ ,  $k = 2.6 \pm 0.1$ . On heating,  $n$  decreased and  $k$  increased, both saturating at long times. The saturation values of the optical constants ( $n = 2.15$ ,  $k = 2.78$ ) are also in close agreement with those reported by Marton and Chan (3) for Ni-P films annealed in hydrogen.

Optical constants of Ni-Cr (Ni 80%, Cr 20%) have not been reported in the literature before. For freshly deposited nichrome films (1000-1500Å), we determined the optical constants to be  $n = 2.5 \pm 0.1$ ,  $k = 3.4 \pm 0.1$ . The changes in the optical constants on heating were similar to those for Ni-P. The saturation values of the optical constants were found to be  $n \approx 2.25$ ,  $k \approx 3.48$ .

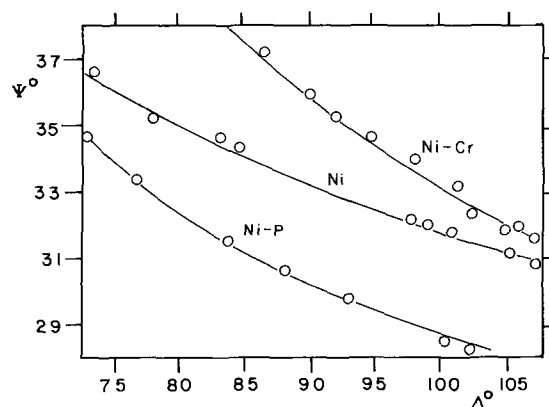


Fig. 1. Plot of  $\Delta$  and  $\Psi$  measured at 70° angle of incidence on Ni, Ni-Cr, and Ni-P samples oxidized in air at 300° and 400°C. Time progresses from right to left.

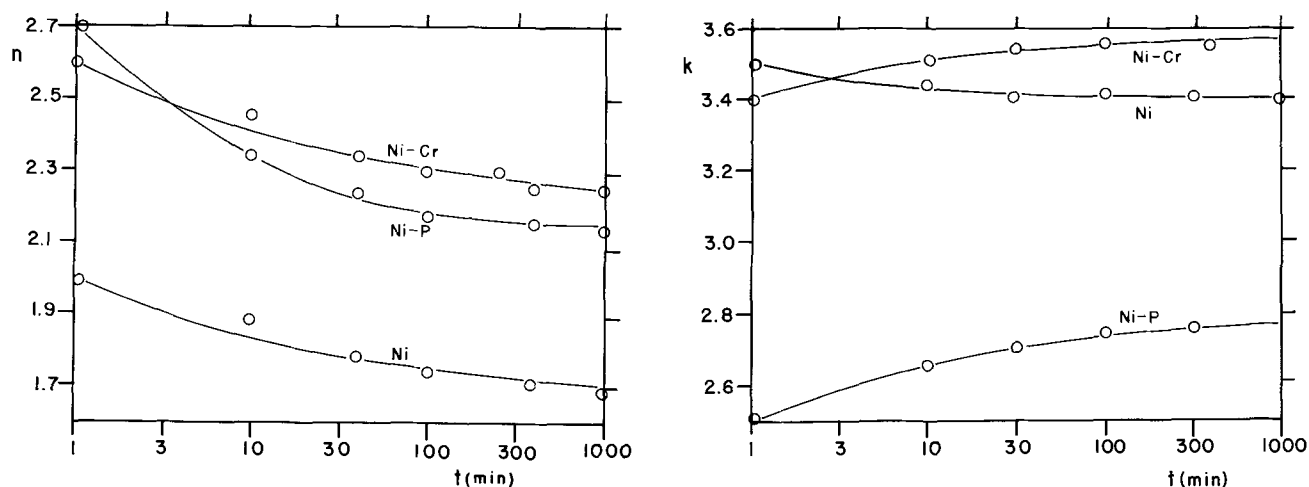


Fig. 2. Variations of  $n$  and  $k$  of metal films of Ni, Ni-Cr, and Ni-P with time of heating at 400°C. (a, left) Changes of  $n$ , (b, right) changes of  $k$ .

Figures 2a and 2b show the variation of  $n$  and  $k$  for Ni, Ni-Cr, and Ni-P at 400°C.

Ni-P films are known to undergo compositional and crystalline changes during heating. Pai and Marton (4) have found that initially the Ni-P film is a fine grain polycrystalline material. Upon heating, the film is transformed into a two phase mixture of Ni and  $\text{Ni}_3\text{P}$ . These changes may also account for the observed variation in optical constants. Roberts (14) and Nag (21) also have reported a temperature dependence of optical properties of nickel. Adams and Rao (22) have suggested that part of the changes in the optical constants of thin films on heating may be due to annealing of defects. It is reasonable to assume that the changes in the optical constants of our films are caused by some of the above processes.

**Growth of oxide in air and water vapor.**—Parameters  $\Delta$  and  $\Psi$  measured on samples that were heated between 300° and 400°C were interpretable in terms of a surface oxide film. Analysis of  $\Delta$  and  $\Psi$  yielded the thickness of the oxide film and optical constants of the oxide. The growth of oxide film appears to be monotonous for temperatures above 300°C. When the samples were heated in water vapor, the rate of oxide growth was found to be considerably less than that in air. The optical constants of the oxide are found to be thickness dependent in all the three materials. Figure 3 illustrates the growth of oxide film on Ni, Ni-Cr, and Ni-P in air and water vapor at 400°C. Figures 4a and 4b show the variation of optical constants of oxide films with thickness in these materials.

On inspection of Fig. 3 and 4 we see that the rate of oxidation in the time interval observed, is highest for Ni and lowest for Ni-Cr, and that the saturation values

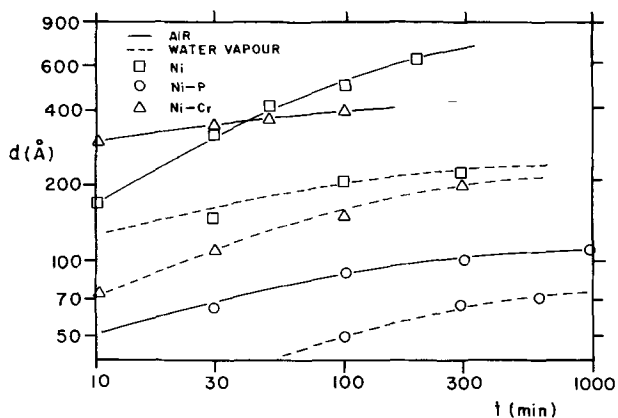


Fig. 3. The thickness of oxide films on Ni, Ni-Cr, and Ni-P at 400°C with time, grown in air and water vapor.

of  $n$  of the oxide formed in all three cases are very close. The common value is approximately 1.4. The  $k$  values do not show the same trend, but for all three oxides they have a low value. The comparison of these values with those of bulk NiO ( $n = 2.36$ ,  $k = 0.05$ ) reported by Powell and Spicer (23) is not favorable. Recently, however, Blondeau *et al.* (24) determined the optical constants of NiO in thin-film form, which compare well with our results. They used ellipsometric techniques for an *in situ* study of anodic oxidation of nickel, and found the optical constants to be  $n = 1.34$ ,  $k = 0.04$ .

**Oxidation at different oxygen pressures.**—It is apparent from Fig. 3 that the rate of oxidation for all three metals in water vapor is less than that in air. To gain a better understanding of the mechanism of oxidation in water vapor, we carried out oxidation of the three metals at two different oxygen pressures. We mixed oxygen and nitrogen at different pressures to achieve 0.05 and 0.5 atm pressures of oxygen. Samples of Ni, Ni-Cr, and Ni-P were heated at 300° and 400°C in these two gas mixtures separately for various lengths of time. The thickness of the oxide film was calculated from  $\Delta$  and  $\Psi$  for each period of heating. The result of these measurements for Ni are shown in Fig. 5 where the thickness of oxide film has been plotted *vs.* oxygen partial pressure. The oxide film thicknesses at 300°C are shown for 100 and 200 min of heating time. Thickness values corresponding to 0.05, 0.21, and 0.5 atm are found to lie on a straight line. The thickness of the oxide which forms in water vapor does not lie on this line. This deviation cannot be accounted for by experimental errors. These results seem to indicate that the observed rate of oxidation in water vapor is higher than is to be expected on the basis of oxygen dissolved in water. The mechanism of oxidation in water vapor is not clearly understood. It is possible that water vapor might act as a catalyst in this process. Figure 6 shows the results of measurements for Ni, Ni-Cr, and Ni-P. The samples were heated at 400°C for 100 min at various oxygen pressures. From Fig. 6 we see that the conclusions drawn for nickel from Fig. 5 also apply to Ni-Cr and Ni-P.

**Effect of water vapor on the oxide layer.**—We also studied the effect of water vapor on the oxide formed on the three metals. Samples of Ni, Ni-Cr, and Ni-P with a sufficiently thick oxide layer ( $\approx 500\text{\AA}$ ) were subjected to heating in water vapor at 100° and 200°C for periods up to 1000 min. In the case of the Ni-P samples, we found the oxide thickness to decrease by 13-15%. The decrease in the thickness of oxide film is of the same order as the phosphorous content of the Ni-P film. This suggests that the decrease is caused by removal of phosphorous from the surface by the water vapor. Pai and Marton (4) have

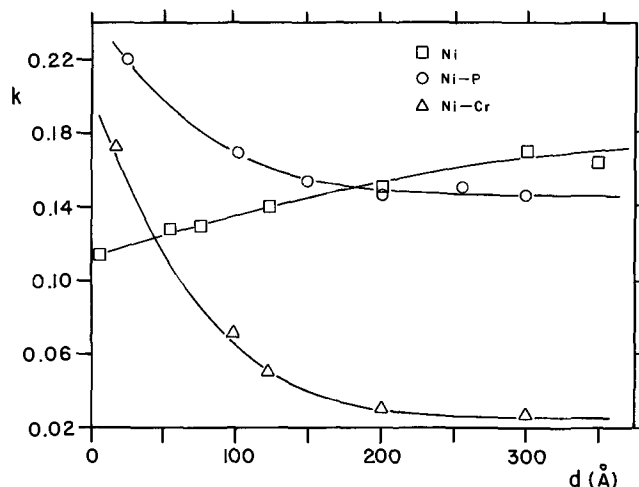
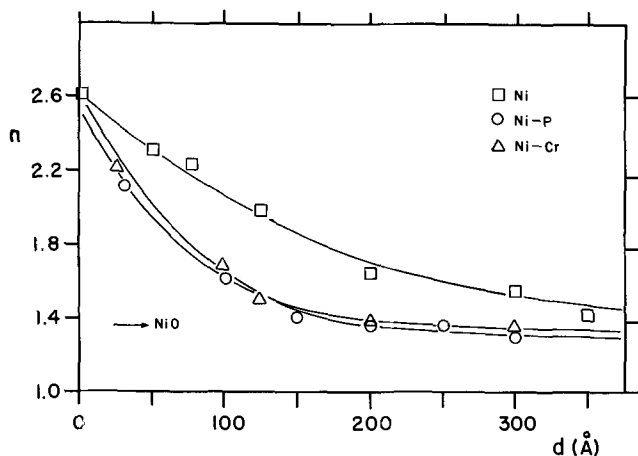


Fig. 4. Variation of  $n$  and  $k$  of the oxide films on Ni, Ni-Cr, and Ni-P with film thickness. (a, left) Variation of  $n$ , (b, right) variation of  $k$ . Note that  $n$  approaches the NiO value for large thicknesses.

found that NiO and  $P_2O_5$  are present in the oxide layer on Ni-P film, thus it may be  $P_2O_5$  that is dissolved and is removed from the surface. In the case of Ni and Ni-Cr, no significant change in the thickness of oxide film was observed.

**Maxwell-Garnett interpretation.**—It was mentioned above that the ellipsometric data on samples heated below  $300^\circ\text{C}$  and the data on samples heated at  $400^\circ\text{C}$  for long periods could not be interpreted in terms of a surface oxide film. The failure to interpret the low temperature data may be understood if we adopt the ideas of Lederick and Bellina (25), Marton and Chan (3), and Pai and Marton (4) who visualized the low temperature oxidation process as a selective oxygen

absorption on the surface, rather than the formation of a uniform oxide layer. The optical properties would then be described in terms of the Maxwell-Garnett (20) theory. The theory gives a connection between the complex index of the metal  $\tilde{N}$  and the effective, measured index  $\tilde{N}_e$  in terms of the volume fraction  $q$  of the metal in the surface as

$$\frac{\tilde{N}_e^2 - 1}{\tilde{N}_e^2 + 2} = q \frac{\tilde{N}^2 - 1}{\tilde{N}^2 + 2}$$

We attempted to interpret the ellipsometric data obtained on the free surfaces in terms of  $\tilde{N}_e$  and those from the back surfaces (metal-glass interface) in terms of  $\tilde{N}$ . The value of  $q$  was calculated for each measurement and was plotted as function of heating time. An example for Ni-P is given in Fig. 7. An increase in  $q$  is interpreted as gas desorption from the surface, and a decrease is interpreted as gas absorption. Both trends are apparent from the figure. The increase at  $100^\circ\text{C}$  is thought to be due to the desorption of  $H_2$  from the film ( $H$  is a by-product in the deposition of Ni-P films) and the decreasing portion of the  $q$  curve at  $300^\circ\text{C}$  is thought to be due to oxygen absorption.

The failure to interpret the high-temperature data obtained at long times cannot be explained satisfactorily. It is possible that the oxide film develops anisotropies and inhomogeneities, in the form of blemishes or cracks. In such situations the assumptions of homogeneity and isotropy of the surface, used in the deriva-

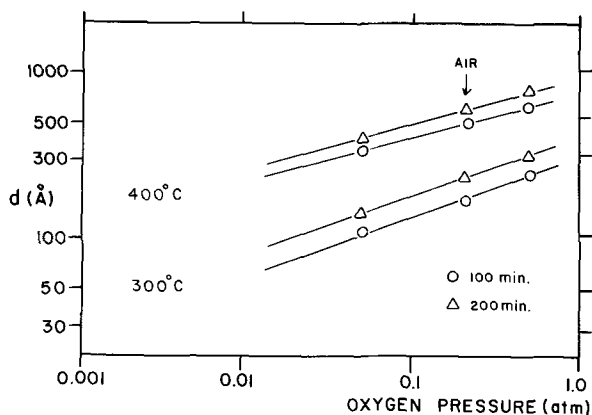


Fig. 5. The thickness of oxide film on Ni, heated at  $300^\circ$  and  $400^\circ\text{C}$  as function of oxygen pressure.

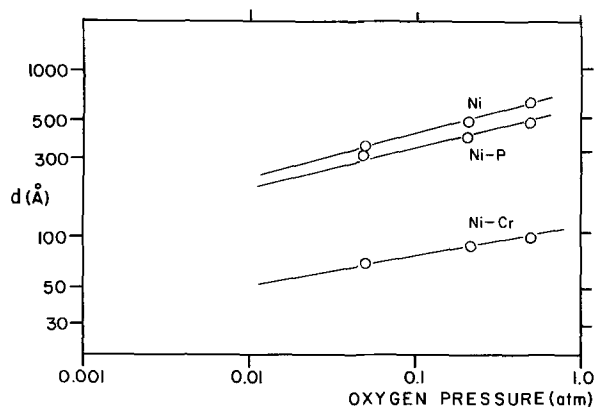


Fig. 6. Thickness of oxide films on Ni, Ni-Cr, and Ni-P heated at  $400^\circ\text{C}$  for 100 min, as function of oxygen pressure.

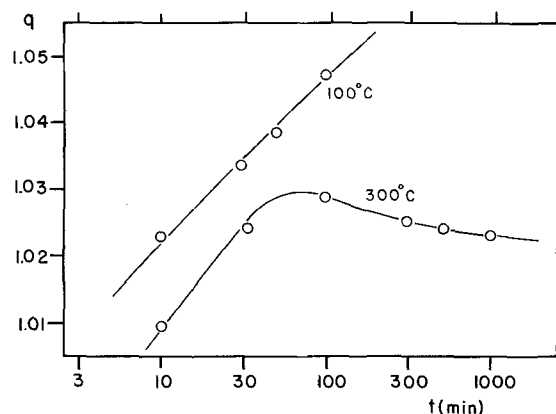


Fig. 7. Maxwell-Garnett interpretation of the optical data on Ni-P samples heated at low temperatures. The parameter  $q$  is a measure of gas absorption (decreasing  $q$ ) in the surface of the metal.

tion of the ellipsometric equations would not apply. Interpretations would yield film thicknesses with either complex values, or angle of incidence dependent real values, which are not accepted as solutions by our computer program.

### Conclusions

The oxidation of Ni, Ni-Cr, and Ni-P films appears to be a three stage process. First, at low temperatures gaseous impurities desorb and oxygen is absorbed in the surface. At temperatures at and above 300°C a surface oxide forms, which at temperatures above 400°C develops optically anisotropic or inhomogeneous features. Quantitative interpretation of ellipsometric data was found possible only in the middle temperature range.

The optical properties of oxide films grown on all three metals in the middle temperature range were found to be similar to those of pure NiO films. This is an indication that the product of oxidation in our case is predominantly NiO. In the case of Ni-P deposits, the experiments also indicated that the oxide contained approximately the same P content as the metal. The P may have been in the form of P<sub>2</sub>O<sub>5</sub> as reported by others.

The study of oxidation rates at various oxygen pressures, though interesting, turned out to be inconclusive. The measured rate of oxidation was found to be higher than that which would be expected on the basis of partial pressure of oxygen in water vapor. Water vapor could be acting as a catalyst in the process.

### Acknowledgment

This work was supported by the National Research Council and by Welwyn Canada Limited, London, Canada.

Manuscript submitted Feb. 28, 1973; revised manuscript received Aug. 21, 1973.

Any discussion of this paper will appear in a Discussion Section to be published in the December 1974 JOURNAL.

### REFERENCES

1. J. P. Marton and M. Schlesinger, *This Journal*, **115**, 16 (1968).
2. S. T. Pai, J. P. Marton, and J. D. Brown, *J. Appl. Phys.*, **43**, 282 (1972).
3. J. P. Marton and E. C. Chan, *ibid.*, **43**, 1681 (1972).
4. S. T. Pai and J. P. Marton, *ibid.*, **43**, 4972 (1972).
5. E. A. Gulbranson and K. F. Andrews, *This Journal*, **101**, 128 (1954); *ibid.*, **104**, 451 (1957).
6. G. C. Wood, I. G. Wright, and J. M. Ferguson, *Corrosion Sci.*, **5**, 645 (1965).
7. K. Hauffe, L. Pethe, R. Schmidt, and Roy S. Morrison, *This Journal*, **115**, 456 (1968).
8. N. Birks and H. Rickert, *J. Inst. Metals* **91**, 308 (1933).
9. D. L. Douglass, *Corrosion Sci.*, **8**, 665 (1968).
10. O. Kubaschewski and B. E. Hopkins, "Oxidation of Metals and Alloys," pp. 135-36, 271, Butterworths, London (1967).
11. G. Bandel, *Arch. Eisenhüttenw.*, **15**, 271 (1941).
12. W. Baukloh and P. Funke, *Korros Metallsch.*, **18**, 126 (1942).
13. A. Rahmel, *Corrosion Sci.*, **5**(12), 815 (1959).
14. S. Roberts, *Phys. Rev.*, **114**, 104 (1959).
15. M. R. Meyerson, *Nat. Bur. Std. Circular*, 485 (1950).
16. E. C. Chan and J. P. Marton, *J. Appl. Phys.*, **43**, 4027 (1972).
17. J. Shewchun and E. C. Rowe, *ibid.*, **41**, 4128 (1970).
18. F. L. McCrackin and J. Colson, *Nat. Bur. Std. Tech. Note*, 242 (1964).
19. H. J. Engell, K. Hauffe, and B. Ilchner, *Z. Electrochem.*, **58**, 578 (1954).
20. J. C. Maxwell Garnett, *Phil. Trans.*, **203**, 325 (1904); *ibid.*, **205A**, 237 (1906).
21. A. Nag and L. Ward, *J. Phys. D*, **4**, 829 (1971).
22. J. R. Adams and K. K. Rao, *Surface Sci.*, **16**, 382 (1969).
23. R. J. Powell and W. E. Spicer, *Phys. Rev.*, **2**, 2182 (1970).
24. G. Blondeau, M. Froment, and M. Froelichov, *Compt. Rend. Acad. Sci.*, **274**, 365 (1972).
25. R. J. Lederich and J. J. Bellina, *J. Opt. Soc. Am.*, **60**, 1697 (1970).

## High-Temperature Dielectric Behavior of Ca-Doped CeO<sub>2</sub>

M. A. Seitz and T. B. Holliday

*Metallurgy and Materials Science, College of Engineering, Marquette University, Milwaukee, Wisconsin 53233*

### ABSTRACT

The dielectric behavior of cerium dioxide with calcium concentrations ranging up to 8 mole per cent (m/o) were investigated as a function of frequency, from 50 Hz to 600 kHz, and temperature, over the interval from room temperature to 1000°C. At temperatures less than 500°C and calcium concentrations less than 1.0 m/o, barrier layer polarization seemed responsible for the observed dielectric behavior. At larger calcium concentrations and higher temperatures, where ionic conduction predominated, the dielectric behavior was rationalized on the basis of a space charge polarization model involving mobile ionic point defects, which were blocked or partially blocked at the specimen electrodes, and electronic carriers, which were able to freely pass through the electrodes. The effective dielectric constant was found to increase exponentially with temperature with an activation energy of approximately 0.74 eV.

The electrical behavior of CaO-doped nonstoichiometric cerium dioxide has been the topic of a number of investigations in recent years (1-5). X-ray diffraction studies indicate that CeO<sub>2</sub> has a cubic fluorite crystal structure and the solubility of CaO in CeO<sub>2</sub> ranges to 15 mole per cent (6). The calcium impurity substitutes for cerium atoms in the structure leading to the formation of oxygen ion vacancies. This results in a sig-

nificant increase in the ionic conduction occurring in this material.

Electrochemical cell experiments in the temperature range 600°-1000°C have shown that the ionic transport number for CaO-doped CeO<sub>2</sub> ranges between 0.8 and 1.0 for calcium concentrations greater than about 2 m/o (7). For reducing atmospheres, P<sub>O<sub>2</sub></sub> < 10<sup>-5</sup> atm, or temperature less than 600°C, the conduction was



predominately electronic in nature. Tracer diffusion studies indicate that the energy for motion of O<sup>18</sup> in yttria-doped CeO<sub>2</sub> is 0.87 eV (8). Energies of motion for oxygen vacancies ranging between 0.71 and 0.76 eV have been obtained by combining conductivity and transport number data (7). Lay and Whitmore, measuring dielectric and mechanical losses in the temperature range 25°-200°C, have found an energy for reorientation of an oxygen vacancy-Ca<sup>+2</sup> dipole of 0.86 eV for calcium concentrations up to 2.5 m/o (9).

In this study, dielectric measurements were performed on CaO-doped CeO<sub>2</sub> over the frequency interval 50 Hz to 6 × 10<sup>5</sup> Hz and at temperatures ranging from room temperature to 1000°C, using a previously developed technique (10). Specimens having calcium concentrations from 0.5 to 8.0 m/o were investigated in order to determine the influence of calcium doping on the dielectric behavior of ceria.

### Experimental Procedure

In early attempts to measure the high-temperature dielectric behavior of calcia-doped CeO<sub>2</sub>, it was noted that the specimen conductance,  $G_{sp}$ , was often greater than the capacitive susceptance,  $\omega C_{sp}$ . This results in dissipation factors which were fairly large,  $0.1 < \tan \delta < 10^2$ . Therefore, a special technique had to be used to perform dielectric measurements. A substitution technique, where corrections are made for parasitic capacitances and inductances associated with the system, was the subject of a previous paper (10). With this technique the capacitance of specimen having a total resistance of greater than 100 ohms and a dissipation factor less than 10<sup>4</sup> can be measured to within ± 15%. For mid-range frequencies (1-50 kHz) the error is less than ± 5%.

Polycrystalline specimens were prepared using pressing and sintering techniques with 99.999% pure CeO<sub>2</sub> obtained from American Potash and Chemical Company and "Specpure" CaCO<sub>3</sub> obtained from Johnson-Matthey Chemicals Limited. The final disk-shaped specimens had a thickness of 0.5 cm and plane parallel surface areas of 2 cm<sup>2</sup>. Doped polycrystalline specimens were produced by mixing the appropriate amounts of CaCO<sub>3</sub> with powdered CeO<sub>2</sub>. The powdered material was heated to 1000°C for 3 hr, to drive off the CO<sub>2</sub> gas resulting from the decomposition of CaCO<sub>3</sub>. The material was then homogenized at 1500°C for 3 hr. After these procedures the material was ground and pressed in the form of a disk at 20,000 psi. Sintering, at 1500°C for 3-6 hr, resulted in specimens having a density approximately 75-80% of the theoretical density. All lines on x-ray powder diffraction patterns could be assigned to the fluorite crystal structure, confirming the completeness of the CaO-CeO<sub>2</sub> reaction. Electrical contact to the specimens was made on their plane parallel surfaces, using Engelhard No. 05 platinum paste. Thick platinum coatings were obtained by repeated applications of platinum paste.

The specimens were loaded into the measurement system. Before performing a measurement, the specimens were allowed to equilibrate at temperature and in various partial pressures of oxygen provided by oxygen-argon tank mixtures. Equilibrium was assumed when the capacitance and resistance changes over a several hour period were less than those due to the variation in temperature. Measurements of capacitance and resistance were made at selected frequencies in the range 50 Hz to 600 kHz. The specimen temperature was increased or decreased at approximately 100°C intervals and the above procedures repeated. The effective dielectric constants were calculated from the data using a parallel equivalent circuit representation of the specimen.

### Results and Discussion

The dielectric behavior of calcium-doped cerium dioxide has been investigated from 10<sup>2</sup> to 6 × 10<sup>5</sup> Hz and over the temperature range from room temperature to

1000°C. In these studies, inert and impervious platinum electrodes were used. The variations of the apparent dielectric constant,  $K'$ , with frequency; the a-c and d-c conductivities with temperature; and  $\tan \delta$  with frequency are shown in Fig. 1 for CeO<sub>2</sub> doped with 0.5 m/o calcium. The variation of the effective dielectric

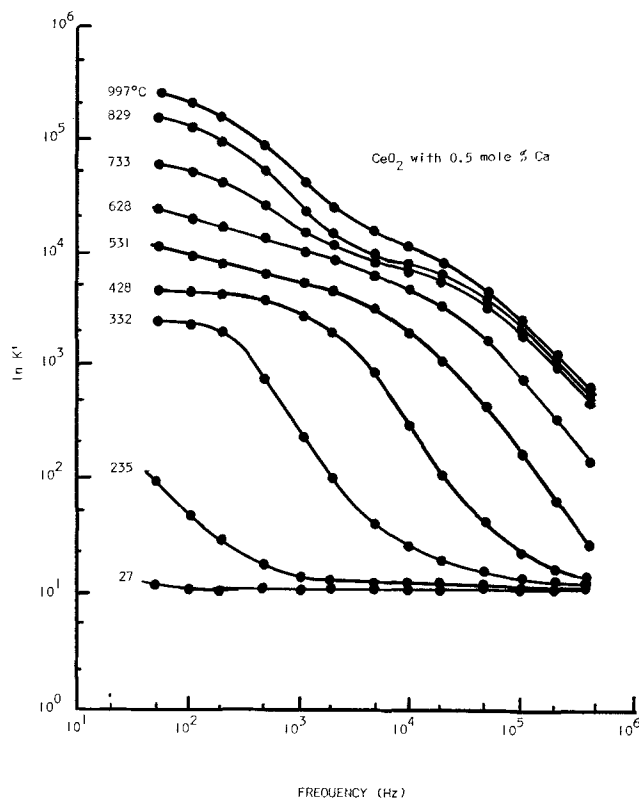


Fig. 1a.  $K'$  vs. frequency for CeO<sub>2</sub> doped with 0.5 m/o Ca over the range 27°-997°C at  $P_{O_2} = 1$  atm.

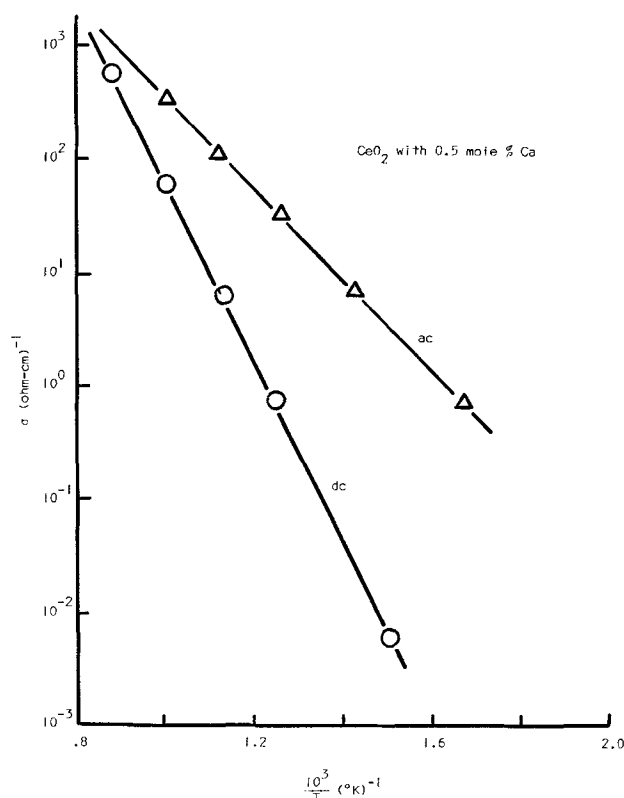


Fig. 1b. Two-probe a-c and d-c conductivity vs.  $1/T$  for CeO<sub>2</sub> doped with 0.5 m/o Ca at  $P_{O_2} = 1$  atm.

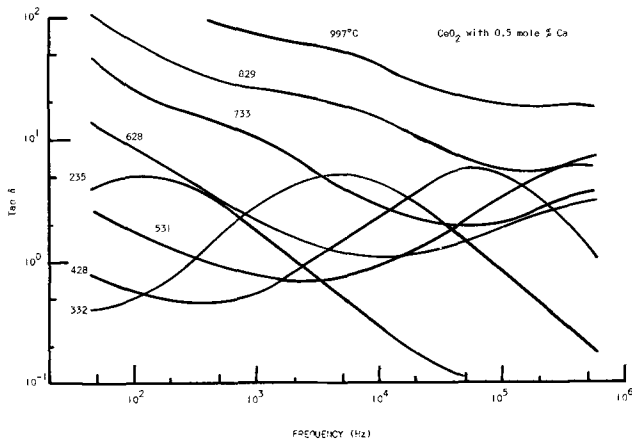


Fig. 1c.  $\tan \delta$  vs. frequency for  $\text{CeO}_2$  doped with 0.5 m/o Ca over the range 235°-997°C at  $P_{\text{O}_2} = 1$  atm.

constant,  $K'$ , with frequency for a specimen doped with 8.0 m/o calcium is shown in Fig. 2, while the temperature variation at 1 kHz for specimens having 1.0, 2.0, and 8.0 m/o calcium dopings is shown in Fig. 3.

The low-frequency dielectric behavior of  $\text{CeO}_2$  doped with 0.5 m/o calcium in the temperature range from 500°-800°K is best explained by a model involving a static space charge or barrier layer within the specimen. These thin barrier layers have a resistivity greater than that of the bulk material. In this range of temperature and composition principally electronic conduction has been shown to exist in  $\text{CeO}_2$  (7). Volger (11) has shown for such a situation where the conductivity,  $\sigma_1$ , of the barrier layer or layers is much less than that of the bulk material,  $\sigma_2$ , the effective low frequency relative dielectric constant,  $K'_s$ , is given by

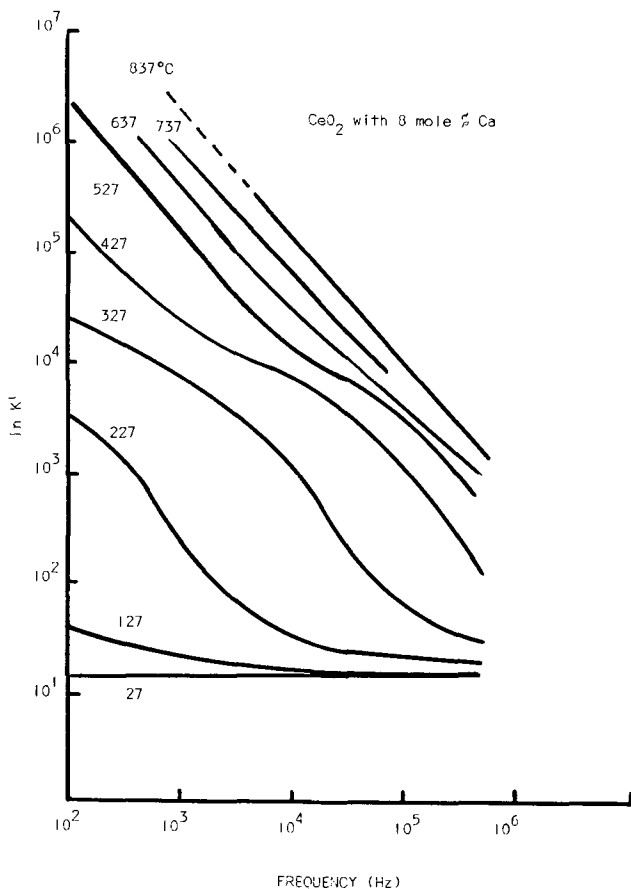


Fig. 2.  $K'$  vs. frequency for  $\text{CeO}_2$  doped with 8.0 m/o Ca over the range 27°-837°C at  $P_{\text{O}_2} = 1$  atm.

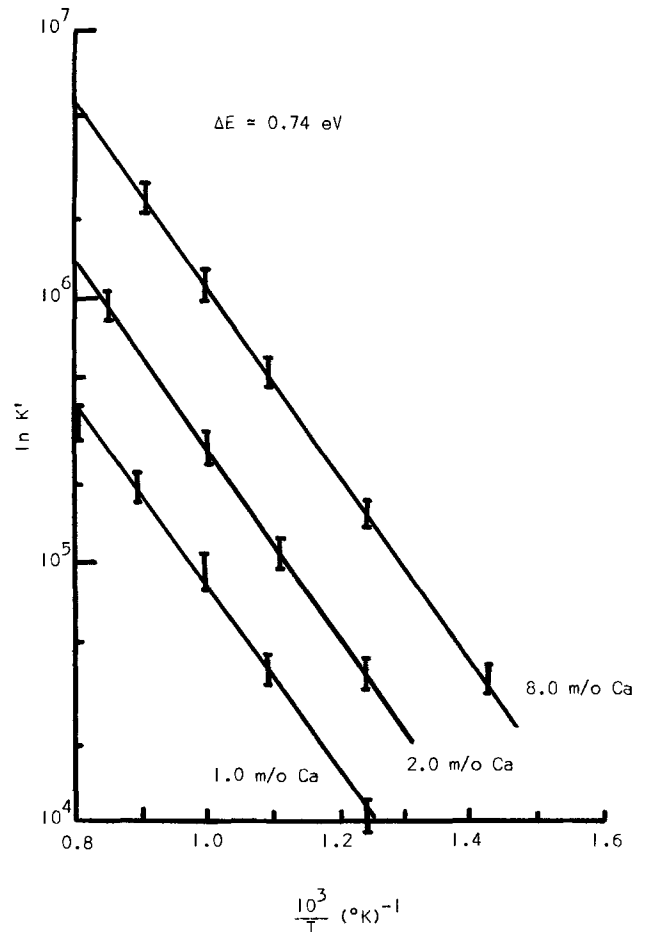


Fig. 3. The logarithm of  $K'$  vs.  $1/T$  for  $\text{CeO}_2$  doped with 1.0, 2.0, and 8.0 m/o Ca and at  $P_{\text{O}_2} = 1$  atm.

$$K'_s = \frac{d_2}{d_1} K'_\infty \quad [1]$$

Here,  $K'_\infty$  is the high frequency value of the relative dielectric constant, while  $d_1$  and  $d_2$  are the total thicknesses of the barrier layer or layers and the bulk material, respectively. The effective low frequency conductivity,  $\sigma_s$ , was shown to be

$$\sigma_s = \frac{d_1}{d_2} \sigma_1 \quad [2]$$

while the high frequency value,  $\sigma_\infty$ , was given as

$$\sigma_\infty = \sigma_2 \quad [3]$$

Between the low- and high-frequency limits,  $K'$  and  $\sigma_{\text{AC}}$  follow the relationships

$$K' = \frac{K'_s + K'_\infty \tau^2 \omega^2}{1 + \tau^2 \omega^2} \quad [4]$$

and

$$\sigma_{\text{AC}} = \frac{\sigma_s + \sigma_\infty \tau^2 \omega^2}{1 + \tau^2 \omega^2} \quad [5]$$

In these expressions,  $\tau$  is a dielectric relaxation time and  $\omega$  is the frequency in radians per second. The dissipation factor,  $\tan \delta$ , was also designated as

$$\tan \delta = \sqrt{\frac{d_2}{d_1}} \frac{\tau \omega}{1 + \tau^2 \omega^2} \quad [6]$$

The dielectric behavior observed in Fig. 1 for  $\text{CeO}_2$  doped with 0.5 m/o calcium reasonably fulfills the prediction of Eq. [1]-[6] at temperatures less than 500°C. The values of  $K'$  follow a Debye type dispersion as predicted by Eq. [4]. From Eq. [1] the ratio of  $K'_s$  to

$K'_z$  indicates that the thickness of the barrier layer is about 1% of the thickness of the specimen. This is further substantiated by the variation of  $\tan \delta$  in Fig. 1c which follows the prediction of Eq. [6] up to about 500°C. Equation [6] further predicts that the maximum

value of  $\tan \delta$  is given by  $\frac{1}{2} \sqrt{\frac{d_2}{d_1}}$ , which again indicates that barrier layers occupy about 1% of the specimen thickness. The nature of the barrier layers or where they exist, although not known at this time, might be the results of air gaps (12), or Schottky barriers (13, 14).

At temperatures greater than about 500°C, the predictions set forth by Eq. [1]–[6] for the aforementioned barrier layer model are not fulfilled as well as they were at lower temperatures. The a-c and d-c conductivities approach one another and there appears to be a further anomalous increase of  $K'$  at low frequencies as the temperature is increased. It is noted that although the general behavior observed for CeO<sub>2</sub> with 0.5 m/o calcium was also observed for pure ceria, the anomalous increase of  $K'$  at low frequency and high temperature ( $T > 500^\circ\text{C}$ ) was not seen. This suggests that the calcium doping was in some way responsible for the low-frequency high-temperature dielectric behavior observed for calcium-doped CeO<sub>2</sub>. Upon increasing the concentration of calcium, the anomalous increase of  $K'$  at high temperatures also increased in magnitude (see Fig. 2 and 3).

It is known that the addition of calcium to CeO<sub>2</sub> results in the formation of oxygen ion vacancies in the ceria lattice (1-9). These vacancies, which become mobile or semimobile at elevated temperatures, can lead to space charge polarization at elevated temperatures. The high-temperature dielectric behavior of CeO<sub>2</sub> doped with calcium is best rationalized on the basis of a two carrier space charge polarization model involving mobile oxygen vacancies, which are blocked at the specimen electrodes, and electrons, which are free to pass through the specimen electrodes (15-17).

Several authors have dealt with two carrier space charge polarization models, where charge carriers of one polarity are completely blocked while those of the opposite polarity are able to freely pass through the electrodes (15-17). These authors, however, generally assume that the positively and negatively charged species are in equal concentration, e.g., Schottky or Frenkel defects. These models indicate that the capacitance and/or apparent dielectric constant would vary with frequency as  $\omega^{-n}$  and would show an exponential dependence on temperature. The value of  $n$  is found to be about 3/2. The exponential temperature dependence arises from the variation of the concentration and diffusion coefficient of the mobile species with temperature.

For calcium-doped polycrystalline ceria the negative charge carrying species would be electrons, while the positive charge carrying species would be oxygen ion vacancies. It should be noted that these would not necessarily be of equal concentrations as is set forth by the aforementioned space charge polarization models. An electroneutrality condition of the type  $n + [\text{Ca}''_{\text{Ce}}] \rightleftharpoons 2[\text{V}_\text{o}^{\cdot\cdot}]^{\text{NS}} + [\text{V}_\text{o}^{\cdot\cdot}]^{\text{Ca}}$  would exist for this material (18, 19). Here, electrons result from the ionization of oxygen ion vacancies that are due to non-stoichiometry,  $[\text{V}_\text{o}^{\cdot\cdot}]^{\text{NS}}$ . The positive mobile ionic species would be oxygen ion vacancies, which predominantly arise from the calcium doping, i.e.,  $[\text{V}_\text{o}^{\cdot\cdot}] \sim [\text{Ca}''_{\text{Ce}}]$ . For  $P_{\text{O}_2} \simeq 1$  atm it would be expected that  $n \ll [\text{V}_\text{o}^{\cdot\cdot}]$ .

If the platinum contacts were reasonably ohmic at elevated temperature, the electrons would be free to pass through them. Thus, the electrons, which are highly mobile when compared to oxygen ion vacancies, would contribute significantly to the conduction current (8, 20). The inert and impervious platinum elec-

trodes would not be expected to chemically react with oxygen ion vacancies or allow the transport of oxygen through them (21, 22). Oxygen ion vacancies, which cannot be annihilated at the Pt/CeO<sub>2</sub> interface, would be blocked at the Pt/CeO<sub>2</sub> interface and lead to a polarization.

The data of Fig. 2 and 3 follow many of the qualitative predictions of the aforementioned two carrier space charge polarization models at temperatures greater than 400°C. The value of  $K'$  at constant temperature decreases as  $\omega^{-n}$ , although the value of  $n$  is between 1.1 and 1.2 rather than being equal to 1.5 as predicted by existing models. The temperature dependence of  $K'$  at constant frequency should be mainly related to variation in the concentration and diffusion coefficient of the blocked species. In this study the concentration of defects was set by the calcium doping and, thus, would not contribute to the temperature dependence of  $K'$ .

The high-temperature dielectric behavior of  $K'$ , as shown in Fig. 3, should essentially contain information regarding the energy of motion of mobile ionic point defects in calcium-doped ceria. Blumenthal and Panlener, combining electrical conductivity and thermogravimetric data, have shown that the electron mobility in ceria increases exponentially with temperature with an activation energy of about 0.13 eV (19). Steele and Floyd (8) have reported an energy of motion of about 0.87 eV for O<sup>18</sup> self-diffusion in yttria-doped ceria in the temperature range 850°–1150°C. Van Handel (7), combining conductivity and transport number data, in the temperature range 700°–1000°C, has observed an activation energy for oxygen vacancy diffusion in calcium-doped ceria of 0.71 and 0.76 eV for 2 and 5 m/o calcium, respectively. The activation energy of approximately 0.74 eV observed for the exponential increase of  $K'$  with temperature in Fig. 3 seems to be consistent with the previously reported energies of motion for oxygen in Ca-doped CeO<sub>2</sub>.

Several other factors support a model involving space charge polarization due to the motion of oxygen ion vacancies in ceria. First, measurements have indicated that the ionic transport number is of the order of 0.9 or greater in the temperature range where space charge polarization is observed (7, 19). Where the ionic transport number was less than 0.5, the previously discussed barrier layer polarization dominated the dielectric behavior. Secondly, the magnitude of  $K'$  in this temperature and frequency range is directly proportional to the calcium concentration for concentrations greater than about 1 m/o. Van Handel found that the ionic conductivity was directly proportional to the concentration of calcium in CeO<sub>2</sub> up to approximately 8 m/o (7).

A more quantitative interpretation of the data must await the development of two carrier space charge polarization models where the concentration of oppositely charged species may differ. Macdonald (23) is presently involved in setting up such a model which will be available at some future date. Added complications arise in the interpretation due to the porosity of the material resulting from its polycrystalline nature, and the fact that an oxygen ion vacancy has a charge of  $2|e|$  rather than  $1|e|$  as assumed in previous modeling.

### Conclusion

In summary it would seem that barrier layer polarization was responsible for the observed dielectric behavior of Ca-doped CeO<sub>2</sub> at lower temperatures and small calcium concentrations, where electronic conduction was predominate. At higher calcium concentrations and temperature, where ionic conduction is significant, space charge polarization was thought to result. These data were rationalized on the basis of a space charge polarization model involving mobile ionic point defects, which were blocked or partially blocked at the specimen electrodes, and electronic carriers, which were able to pass through the electrodes. The

effective dielectric constant,  $K'$ , increased exponentially with temperature with an activation energy of approximately 0.74 eV. This activation energy, which was principally associated with the motion of oxygen vacancies, seemed to be consistent with previously reported energies of motion of oxygen in Ca-doped  $\text{CeO}_2$ .

#### Acknowledgment

The authors gratefully acknowledge the support of the National Science Foundation, Grant No. GK-16284.

Manuscript submitted March 12, 1973; revised manuscript received Aug. 6, 1973. This was Paper 115 presented at the Detroit, Michigan, Meeting of the Society, Oct. 5-9, 1969.

Any discussion of this paper will appear in a Discussion Section to be published in the December 1974 JOURNAL.

#### REFERENCES

1. E. L. Holverson, Ph.D. Dissertation, Arizona State University, Tempe, Arizona (1964).
2. G. J. Kevan, E. L. Holverson, and J. B. Armstrong, Paper presented at the Fifth Rare Earth Research Conference, Ames, Iowa, Aug. 1965.
3. R. N. Blumenthal and B. A. Pinz, *J. Appl. Phys.*, **38**, 2376 (1967).
4. E. Meyer and B. Marincek, *Schweiz. Archiv.*, **36**, 194 (1970).
5. R. N. Blumenthal, F. S. Brugner, and J. E. Garnier, *This Journal*, To be published.
6. E. K. Keler, N. A. Godina, and A. M. Kalinina, *Zurnol Neorganisheshoi Khemii* (Moscow), **1**, 2557 (1956).
7. G. J. Van Handel, Ph.D. Dissertation, Marquette University, Milwaukee, Wisconsin (1972).
8. B. C. H. Steele and J. M. Floyd, *Proc. Brit. Ceram. Soc.*, **19**, 55 (1971).
9. K. W. Lay and D. H. Whitmore, Paper presented at Fifth Rare Earth Research Conference, Ames, Iowa, 1965.
10. M. A. Seitz, R. T. McSweeney, and W. M. Hirthe, *Rev. Sci. Instr.*, **40**, 826 (1969).
11. J. Volger, in "Progress in Semiconductors," Vol. 4, A. F. Gibson, Editor, pp. 206-263, John Wiley & Sons, New York (1960).
12. D. Miliotis and D. N. Yoon, *J. Phys. Chem. Solids*, **30**, 1241 (1969).
13. J. G. Simmons, G. S. Nadkarni, and M. C. Lancaster, *J. Appl. Phys.*, **41**, 538 (1970).
14. J. Maserjion and C. A. Mead, *J. Phys. Chem. Solids*, **28**, 1971 (1967).
15. R. J. Friauf, *J. Chem. Phys.*, **22**, 1329 (1954).
16. J. R. Macdonald, *Phys. Rev.*, **92**, 4 (1953).
17. J. R. Macdonald, *J. Chem. Phys.*, **54**, 2026 (1971).
18. J. Garnier, R. J. Panlener, and R. N. Blumenthal, Conf. on Peculiar Properties of Oxides, Argonne National Laboratory, May 18 & 19, 1973.
19. R. N. Blumenthal, F. S. Brugner, and J. E. Garnier, *This Journal*, **120**, 1230 (1973).
20. R. N. Blumenthal and R. J. Panlener, *J. Phys. Chem. Solids*, **31**, 1190 (1970).
21. H. Yanagida, R. J. Brook, and F. A. Kroger, *This Journal*, **117**, 593 (1970).
22. R. J. Brook, W. L. Pelzmann, and F. A. Kroger, *ibid.*, **118**, 185 (1971).
23. J. R. Macdonald, Private communication.

## The Temperature and Compositional Dependence of the Electrical Conductivity of Nonstoichiometric $\text{CeO}_{2-x}$

R. N. Blumenthal and R. L. Hofmaier

*Metallurgy and Materials Science, College of Engineering, Marquette University, Milwaukee, Wisconsin 53223*

#### ABSTRACT

The electrical conductivity of sintered specimens of nonstoichiometric  $\text{CeO}_{2-x}$  was measured as a function of temperature from 1000°-300°C and composition from  $0.00424 \leq x \leq 0.178$ . These results are described in terms of a high temperature and low temperature region. In both temperature regions the conductivity for fixed values of  $x$  exhibits an exponential dependence on temperature,  $\sigma = \sigma_0 e^{-Q/kT}$ .

The temperature of the intersection between the high and low temperature regions for each composition agrees closely with the composition-temperature dependence of the miscibility gap reported by Brauer and Gingerich. The compositional and temperature dependence of the conductivity in the high temperature region, which corresponds to a single-phase region, may be represented by the expression  $\sigma \propto x e^{-Q/kT}$  where  $Q$  is a function of  $x$ . This expression is rationalized in terms of simple relations for the electron carrier concentration,  $[\text{Ce}'_{\text{Ce}}] \propto x$ , and the electron mobility,  $\mu = \mu_0 e^{-Q/kT}$ , where  $\mu_0$  is independent of  $x$ . For  $\log x$  between -3.0 and -1.8,  $Q$  is constant at 0.22 eV, but increases to 0.37 eV at  $\log x = -0.7$ . In the low temperature region the activation energy,  $0.61 \pm 0.03$  eV, was found to be independent of  $x$ .

Nonstoichiometric cerium dioxide,  $\text{CeO}_{2-x}$ , has been the subject of several x-ray (1-3), thermodynamic (4-6), and electrical conductivity investigations (7-13). Based on these experimental observations,  $\text{CeO}_{2-x}$  may be classified as a metal-excess, n-type semiconductor.

Brauer and Gingerich (3, 4) studied the influence of temperature on the phase relations in the cerium-oxygen system by measuring the oxygen dissociation pressure in the region  $\text{CeO}_2$ - $\text{CeO}_{1.5}$ , from 600° to 1000°C, and by x-ray powder-diffraction analysis in the region  $\text{CeO}_2$ - $\text{CeO}_{1.78}$  over the temperature range 20°-1050°C. They reported a miscibility gap which has the bound-

aries  $\text{CeO}_2$  and  $\text{CeO}_{1.81}$  at room temperature, contracts with rising temperatures, and closes with a composition of approximately  $\text{CeO}_{1.92}$  at 685°C. Above 800°C they report that a homogeneous single-phase region extends from  $\text{CeO}_2$  to about  $\text{CeO}_{1.67}$ .

Bevan and Kordis (6) also studied the oxygen dissociation pressures of the cerium-oxygen system from 636° to 1169°C. Based on their results they constructed a cerium-oxygen phase diagram at these temperatures between the composition  $\text{CeO}_2$  and  $\text{CeO}_{1.5}$ . The results of their study were similar to those of Brauer and Gingerich except that they report a two-phase region between  $\text{CeO}_{1.72}$  and  $\text{CeO}_{1.70}$ . They also report a miscibility gap which appears to have a similar composi-

**Key words:** electrical conductivity, cerium dioxide, electron mobility, nonstoichiometry.

tional dependence on temperature as reported by Brauer and Gingerich (3, 4).

The defect structure responsible for the metal excess behavior of CeO<sub>2-x</sub> has been inferred from the analysis of thermodynamic electrical conductivity, and oxygen self-diffusion studies (7-18). Although defect models involving either oxygen vacancies or cerium interstitials have been proposed, the recent investigations of oxygen self-diffusion (15-17) in nonstoichiometric CeO<sub>2</sub> and Ce<sub>1-2y</sub>Y<sub>2y</sub>O<sub>2-y</sub> and the electrical conductivity (18) of CaO-doped CeO<sub>2</sub> over a wide range of temperature, oxygen pressures, and CaO content appear to be consistent with an oxygen vacancy model.

The electron mobility in nonstoichiometric CeO<sub>2-x</sub> was also calculated as a function of temperature by combining electrical conductivity and thermogravimetric data for the temperature and oxygen pressure region where the atomic defect predominates in one state of ionization (19). The mobility was characterized by an expression of the form.

$$\mu = \mu_0 e^{-E/kT} \quad [1]$$

where the activation energy,  $E$ , was equal to 0.14 eV. These results are consistent with a hopping-type conduction mechanism where the electrons localized at normal cerium sites move to adjacent cerium sites.

The purpose of the present study was to measure the electrical conductivity of cerium dioxide as a function of temperature and nonstoichiometry and to relate these data to the temperature and compositional dependence of the electronic mobility in the single-phase region above the miscibility gap and to investigate the behavior of the conductivity of the cerium-oxygen system below the miscibility gap.

### Theory

Information about the defect structure and electronic mobility of CeO<sub>2-x</sub> can be obtained from measurements of the electrical conductivity as a function of temperature at constant oxygen composition (i.e., fixed values of  $x$  in CeO<sub>2-x</sub>). For example, since  $x = f(T, P_{O_2})$ , the composition of a specimen may be controlled by fixing the temperature and oxygen partial pressure. If a reduced specimen of CeO<sub>2-x</sub> is then placed in an inert atmosphere, which allows the oxygen composition to be maintained, the observed temperature dependence of the electrical conductivity may then be attributed to changes in the concentration of charge carriers and/or a change in the carrier mobility with temperature.

Electron transport in nonstoichiometric CeO<sub>2</sub> has been interpreted in terms of a hopping-type process, whereby the electrons localized on a cerium ion, Ce'<sub>Ce</sub>, may be exchanged with adjacent normal cerium ions Ce<sup>x</sup><sub>Ce</sub> (19). For simple, limiting, case defect models the concentration of electron carriers, [Ce'<sub>Ce</sub>], may be simply related to the departure from stoichiometry in cerium dioxide provided the concentration of defects arising from impurities is negligibly small compared to those produced by the nonstoichiometric defects. For example, if each nonstoichiometric atomic defect contributes the same number of electronic carriers over the whole temperature range, then

$$x \propto [\text{Ce}'_{\text{Ce}}] \quad [2]$$

and the temperature dependence of  $\sigma$  for conditions of constant  $x$  must be the same as for the electronic mobility  $\mu$ .

However, for the case where the nonstoichiometric defects exhibit multiple states of ionization, [Ce'<sub>Ce</sub>] is a more complicated nonlinear function of  $x$  and  $\sigma$  will exhibit a nonlinear dependence on  $x$ , even if  $\mu = f(T)$  only (13).

### Experimental

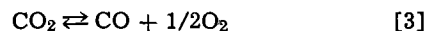
The conductivity specimens were prepared by cold pressing and sintering CeO<sub>2</sub> powder obtained from the American Potash and Chemical Company (12, 13). The

Table I. Mass spectrographic analysis of a typical sintered specimen of CeO<sub>2</sub> (ppmw)

Element	Element
Li	0.3
Be	<0.01
B	≦7.0
F	20.0
Na	15.0
Mg	2.0
Al	15.0
Si	20.0
P	2.0
S	7.0
Cl	10.0
K	15.0
Ca	300.0
Sc	<0.1
Ti	2.0
V	≦0.03
Cr	0.2
Mn	0.2
Fe	6.0
Co	0.4
Ni	20.0
Cu	0.2
Zn	1.0
Ga	—
Ge	<0.2
As	<0.02
Se	<0.4
Br	<0.3
Rb	<1.0
Sr	0.2
Y	0.5
Zr	10.0
Nb	<0.02
Mo	<0.07
Ru	<0.1
Rh	<0.02
Pd	<0.2
Ag	≦0.2
Cd	<0.2
In	<0.1
Sn	0.2
Sb	<0.2
Te	<0.3
I	<0.1
Cs	<0.06
Ba	<1.0
La	<0.5
Ce	—
Pr	10.0
Nd	10.0
Sm	<1.0
Eu	10.0
Gd	<5.0
Tb	2.0
Dy	1.0
Ho	≦0.3
Er	≦0.5
Tm	<0.1
Yb	≦1.0
Lu	≦0.3
Hf	2.0
Ta	≦3.0
W	<0.2
Re	<0.3
Os	<1.0
Ir	<0.2
Pt	<0.4
Au	<0.4
Hg	<0.4
Tl	<0.2
Pb	1.0
Bi	<0.1
Th	50.0
U	<0.06

results of a mass spectrographic analysis of a sintered specimen are shown in Table I.

A standard four-probe d-c technique was employed for the electrical conductivity measurements. An Altair Model C2 constant current source with a continuously variable range from 1  $\mu$ A to 50 mA was used to supply the current. The voltage across the potential probes was recorded on a Sargent Model DSR two-channel recorder. The second channel was used to record the thermocouple emf. Measurements of the temperature dependence of the electrical conductivity under conditions of constant oxygen composition were made using the following procedure. A specimen of ceria was reduced in a known CO-CO<sub>2</sub> mixture at 1000°C. The oxygen partial pressure was calculated as a function of temperature from the well-known reaction



When equilibrium was obtained, the specimen had a fixed oxygen composition which was determined from data on the composition of CeO<sub>2-x</sub> as a function of  $P_{O_2}$  obtained in this laboratory (21). The CO-CO<sub>2</sub> mixture was then purged with purified helium. As explained in the next section, this effectively prevents the loss or gain of oxygen from the specimen over the time intervals necessary to make the conductivity measurements. The helium was purified by passing it over a mixture of TiO<sub>2</sub>-Ti<sub>2</sub>O<sub>3</sub> powder at approximately 950°C (20). This procedure reduced the oxygen partial pressure in the helium to approximately 10<sup>-16</sup> atm as measured by an oxygen gauge. Usually 10 min were used to purge the system of CO-CO<sub>2</sub>. The conductivity remained essentially constant during this time for the nonstoichiometric compositions investigated (i.e., 0.00424  $\leq x \leq$  0.178). The temperature was then lowered to about 300°C at a rate decreasing from about 150° to 50°C per minute and then reheated at a much lower heating rate while recording the temperature and voltage across the potential leads.

### Results and Discussion

The electrical conductivity of sintered specimens of nonstoichiometric CeO<sub>2-x</sub> was measured as a function of temperature from 300° to 1000°C, as well as a function of composition over the range 0.00424  $\leq x \leq$  0.178. The upper limit of  $x$  was fixed by the largest CO/CO<sub>2</sub>

ratio, 97.3%, used in this investigation. As discussed below, the lower limit of  $x$  was determined by the experimental technique since for compositions close to stoichiometry a fixed oxygen composition could not be maintained in the specimen.

Typical results of the electrical conductivity measured as a function of temperature for two different oxygen compositions,  $x = 0.00424$  and  $x = 0.040$ , are shown in Fig. 1 as a plot of  $\log \sigma$  vs.  $1/T$ . As illustrated in Fig. 1, the conductivity for the cooling and heating curves are in good agreement for the case where  $x = 0.040$ . However, for the case  $x = 0.00424$  the conductivity for the heating cycle is slightly lower than the cooling cycle. Thus in this composition range, and for the conditions of the experiment, it is established that any loss or gain of oxygen from the specimens is small enough as to exert a negligible effect on the conductivity. Strictly speaking, in order to maintain a constant value of  $x$  under equilibrium conditions the chemical potential of oxygen in the gas phase would have to be equal to that of the reduced ceria sample. Since  $x = f(T, P_{O_2})$ , (e.g., with  $x = 10^{-3}$ ,  $P_{O_2} \cong 10^{-8}$  atm at  $1000^\circ\text{C}$ , and  $P_{O_2} \cong 10^{-20}$  atm at  $700^\circ\text{C}$ ) (21) the composition of the gas phase would have to be altered at every temperature in order to maintain a fixed temperature-independent composition. From an experimental point of view these conditions would be practically impossible to obtain. As discussed above, the procedure used in this study, however, was to minimize the exchange of oxygen between the conductivity sample and the ambient gas phase by (i) employing a purified helium atmosphere and (ii) by limiting the amount of time that the sample is in contact with the "inert" atmosphere during the conductivity measurements. The success of this technique can be understood on the basis of the following simple considerations. If the partial pressure of the impurities containing oxygen (such as  $\text{CO}_2$ ,  $\text{H}_2\text{O}$ , etc.) are of the order of  $10^{-6}$  atm, then for a flow rate of  $400 \text{ cm}^3/\text{min}$  the maximum amount of oxygen which can be furnished to the sample in a period of 1 hr is about  $32 \mu\text{g}$  which for a 1g sample would correspond to a negligible decrease in  $x$  of about  $3 \times 10^{-4}$ . Similarly, if the equi-

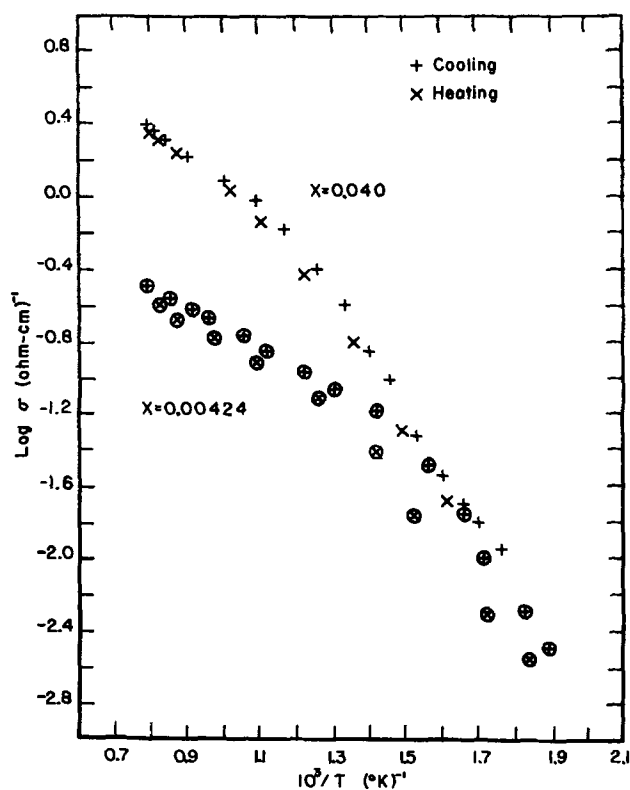


Fig. 1. A plot of  $\log \sigma$  vs.  $1/T$  for cooling and heating under conditions designed to maintain constant values of  $x$  in  $\text{CeO}_{2-x}$ .

librium  $P_{O_2}$  of the reduced ceria specimen is taken as  $10^{-6}$  atm, well above the actual equilibrium pressure for the compositions studied, and the inert gas is absolutely pure, then the maximum amount of oxygen which could be lost from the specimen for the same flow rate and time as above would result in a negligible increase in the value of  $x$  of approximately  $3 \times 10^{-4}$ .

Since the effective  $P_{O_2}$  of the purified helium gas was approximately  $10^{-16}$  atm as determined by an oxygen gauge at  $1000^\circ\text{C}$ , the  $P_{O_2}$  of the gas is probably controlled by the water gas reaction and the amount of  $\text{CO}$ ,  $\text{CO}_2$ ,  $\text{H}_2$ , and  $\text{H}_2\text{O}$  present as impurities. Because the concentration of these impurities is of the order of parts per millions the "buffering" capacity (i.e., the amount of oxygen that can be exchanged with the gas without changing  $P_{O_2}$ ) is extremely small. Thus the actual amount of oxygen exchanged with the sample would be less than the amount given in the above calculations because it would be limited to a great extent by the "buffering capacity" of the gas. On the basis of the above considerations it would be expected that the change in the oxygen composition of the specimen during a conductivity run will be negligibly small except for samples with compositions near stoichiometry (i.e.,  $x < 10^{-3}$ ). In this study the conductivity data obtained on cooling was considered to be more accurate because the amount of time the specimen was in contact with the inert atmosphere at elevated temperatures (e.g.,  $1000^\circ\text{C}$ - $600^\circ\text{C}$ ) was much less than the corresponding time required for heating.

The conductivity data obtained on cooling from  $1000^\circ\text{C}$  is shown in Fig. 2a and 2b as a composite plot of the log of the electrical conductivity as a function of the reciprocal temperature for several different values of  $x$ . The straight lines shown in Fig. 2a and 2b are obtained from a least square curve fit of the conductivity data for sintered specimens which were normalized for porosity using the expression (22)

$$\sigma_{\text{norm}} = \sigma_{\text{meas}} \frac{\rho_{\text{theor}}}{\rho_{\text{meas}}} \quad [4]$$

where  $\rho_{\text{meas}}$  is the density of the sintered specimen. These results may be described conveniently in terms of a high temperature and a low temperature region. Since in both of these temperature regions the conductivity exhibits an exponential dependence on temperature, the conductivity in each region may be characterized by an Arrhenius type expression

$$\sigma = \sigma_0 e^{-Q/kT} \quad [5]$$

The parameters  $\sigma_0$  and  $Q$  which characterize the lines shown in Fig. 2a and 2b and the corresponding compositions are tabulated in Table II. In the high temperature region the activation energy,  $Q$ , increases with increasing departure from stoichiometry. The magnitude of the electrical conductivity is also very dependent on the value of  $x$  between  $x = 0.00424$  and  $x = 0.0855$ . For values of  $x > 0.0855$  the conductivity is less dependent on  $x$ . However, in the low temperature region, with the exception of the largest value of  $x$ , the activation energy does not appear to be a function of  $x$  and the magnitude of  $\sigma$  increases only slightly with increasing  $x$ . Another interesting observation is that the temperature at which the lines in the high and

Table II. The parameters  $\sigma_0$  and  $Q$  from  $\sigma = \sigma_0 e^{-Q/kT}$  which characterize the high temperature and low temperature behavior of the electrical conductivity of  $\text{CeO}_{2-x}$  for fixed values of  $x$

$x$	High temperature		Low temperature	
	$\sigma_0$ (ohm-cm) $^{-1}$	$Q$ (eV)	$\sigma_0$ (ohm-cm) $^{-1}$	$Q$ (eV)
0.00424	2.4	$0.22 \pm 0.01$	1400	$0.59 \pm 0.05$
0.0121	6.4	$0.23 \pm 0.01$	3500	$0.64 \pm 0.02$
0.0400	32.1	$0.28 \pm 0.02$	2810	$0.62 \pm 0.04$
0.0855	52.7	$0.31 \pm 0.02$	3600	$0.64 \pm 0.02$
0.139	81.6	$0.35 \pm 0.01$	4280	$0.62 \pm 0.07$
0.178	96.6	$0.37 \pm 0.01$	462	$0.47 \pm 0.04$

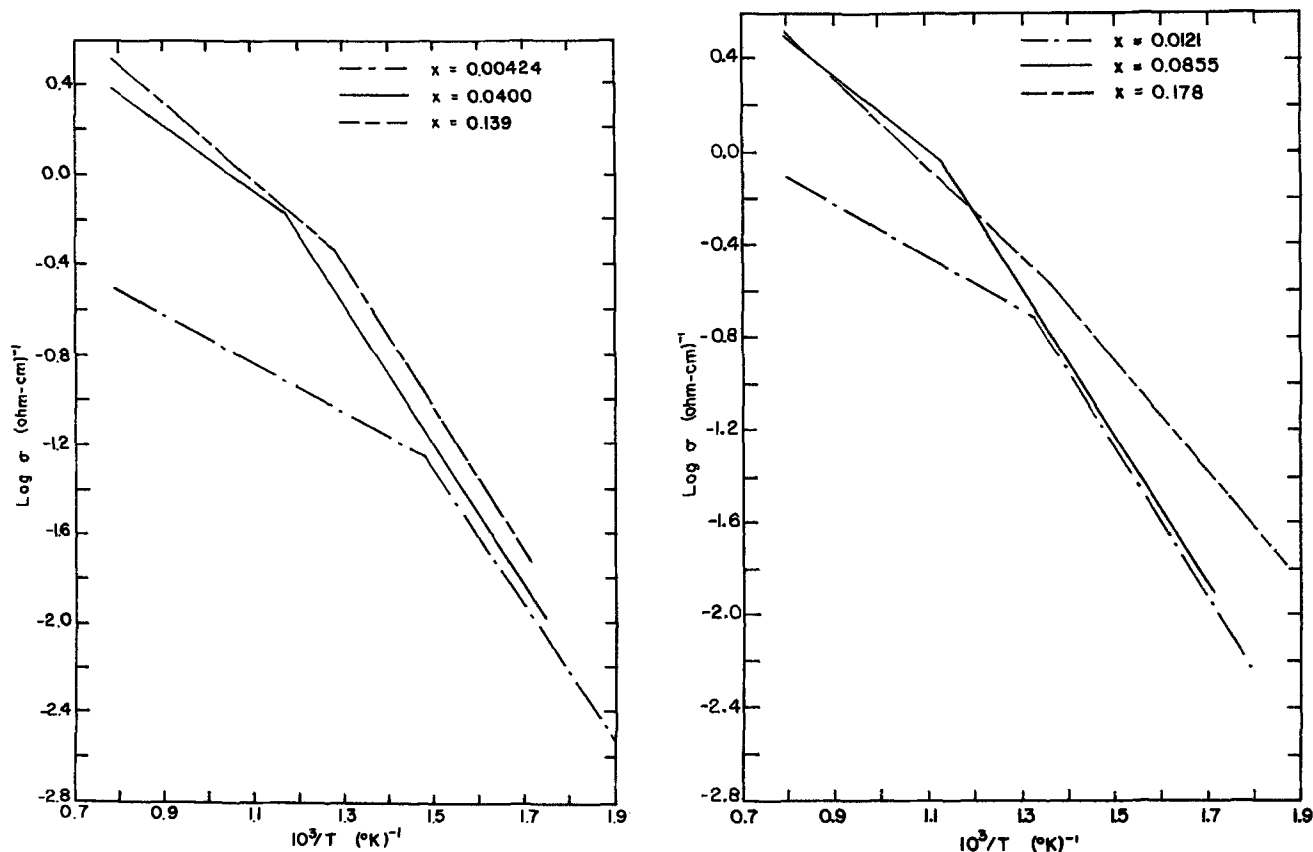


Fig. 2a (left) A composite plot of the logarithm of electrical conductivity and 2b (right) of nonstoichiometric CeO<sub>2-x</sub> as a function of the reciprocal temperature for several nonstoichiometric compositions.

low temperature region intersect, increases with increasing values of  $x$  up to about  $x = 0.0855$ . For larger values of  $x$  the temperature at which the intersection occurs decreases with increasing  $x$ .

The temperature of the intersection for each composition and the composition-temperature dependence of the miscibility gap reported by Brauer and Gingerich are shown in Fig. 3 for purposes of comparison. The error bars shown for the x-ray study were estimated on the basis of the precision of their lattice parameter measurements and the dependence of the lattice parameter on composition which they report. The error bars shown for the data determined in this study were calculated from a least square analysis assuming a 95% confidence limit and from the reproducibility of the data. With the exception of two points all of the data from this study are within the experimental error of the results obtained by Brauer and Gingerich (4). It should be noted, however, that most of the data points obtained in this study lie slightly below the reported miscibility gap.

It thus appears that the sharp break in the slope of  $\log \sigma$  as the temperature is decreased is due to the transition from a single phase to a low temperature, two-phase mixture. The conductivity in the low-temperature region is only weakly dependent, and the activation energy,  $Q$ , independent of  $x$ . Thus one conduction mechanism appears to predominate but the conductivity cannot be accounted for on the basis of a simple phase mixture rule. An interesting question that cannot be explained from the conductivity data in this study is the following. Why is the activation energy for the low temperature conductivity larger than for the high temperature conductivity? Is it because the mobility exhibits a larger temperature dependence or because the concentration of charge carrier varies more rapidly, or both? Hall mobility measurements in this temperature region would help provide an explanation for this question.

In the high temperature region of this study, the compositions of the CeO<sub>2-x</sub> specimens correspond to a single-phase region. As discussed in the theory section, the nonstoichiometric atomic defects may be found

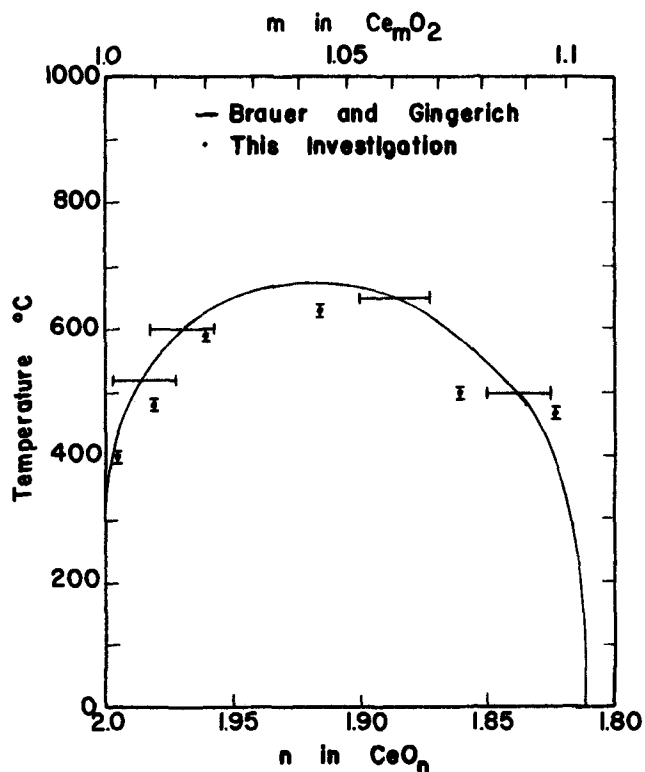


Fig. 3. Phase diagram of the cerium oxide system in the composition region CeO<sub>2</sub>-CeO<sub>1.8</sub>.



predominantly in one state of ionization or they may exhibit multiple states of ionization. In order to test which of these cases is more likely to occur in  $\text{CeO}_{2-x}$ , an isothermal plot of  $\log \sigma$  vs.  $\log x$  was made as shown by the solid line in Fig. 4. This plot was constructed using data from two recent equilibrium studies in this laboratory (21, 23). In one study  $\log \sigma$  vs.  $\log P_{\text{O}_2}$  at  $1000^\circ\text{C}$  was determined; in the other thermogravimetric study  $\log x$  vs.  $\log P_{\text{O}_2}$  at  $1000^\circ\text{C}$  was determined. Smooth curves through the data points of each study were used to obtain the desired  $\log \sigma$ - $\log x$  relationship. For purposes of convenience, the dependence of  $\sigma$  on  $x$  will be described below in terms of two composition regions.

In the composition region,  $-3.0 < \log x < -1.8$ , the slope of  $\log \sigma$  vs.  $\log x$  is equal to 1. Since  $\sigma \propto x$ , it appears that the limiting case given by Eq. [2] is valid (i.e.,  $[\text{Ce}'\text{Ce}] \propto x$ ). For this case, (i) the nonstoichiometric atomic defect exists in one predominant state of ionization and (ii) the temperature dependence of  $\sigma$ , for the fixed values of  $x$  is equal to the temperature dependence of the electron mobility (i.e.,  $Q$  obtained from the relation  $\sigma = \sigma_0 e^{-Q/kT}$  is equal to  $E$  from the expression  $\mu = \mu_0 e^{-E/kT}$ ). To illustrate how  $Q$  varies with  $x$ , a plot of  $Q$  vs.  $\log x$  was made as shown in Fig. 5. From this plot it appears that  $Q$  is relatively insensitive to  $x$  in this composition region. The following expression

$$\mu = \mu_0 e^{-0.22/kT} \quad (-3.0 < \log x < -1.8) \quad [6]$$

for the electron mobility was calculated from Eq. [1], [2], and [5] and the above conductivity data. The previously reported activation energy for the electron mobility was 0.14 eV (19). This value was obtained by combining composition (i.e.,  $x = f(T, P_{\text{O}_2})$ ) and conductivity (i.e.,  $\sigma = f(T, P_{\text{O}_2})$ ) data in the composition region near stoichiometry (i.e.,  $x \approx 10^{-3}$ ) where the nonstoichiometric defect was assumed to exist in predominantly one state of ionization. It is interesting to note that Panlener (21) has recently repeated this analysis using more accurate thermodynamic data. He calculated an activation energy of 0.23 eV for the composition  $\text{CeO}_{1.998}$  and the temperature range  $700^\circ\text{--}1300^\circ\text{C}$ . This value is in excellent agreement with the results of this study.

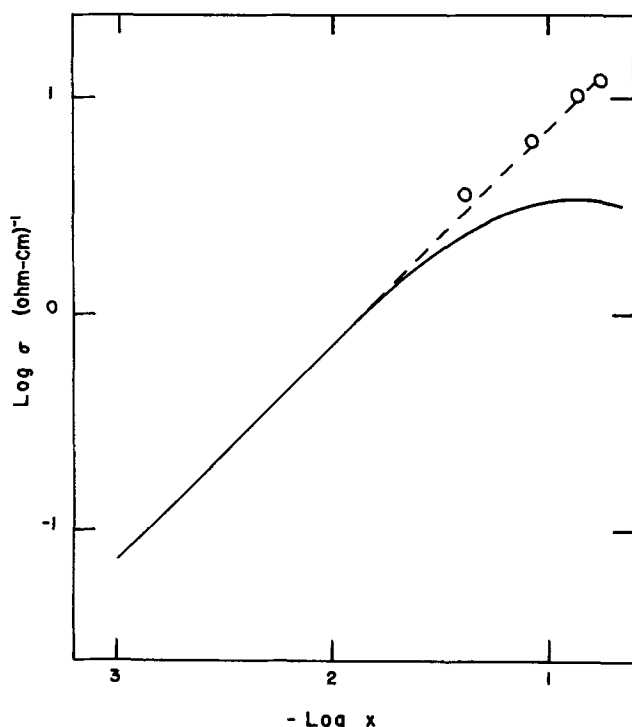


Fig. 4. An isothermal plot of  $\log \sigma$  vs.  $\log x$  at  $1000^\circ\text{C}$  for  $\text{CeO}_{2-x}$  obtained by combining the data from a conductivity and thermodynamic study.

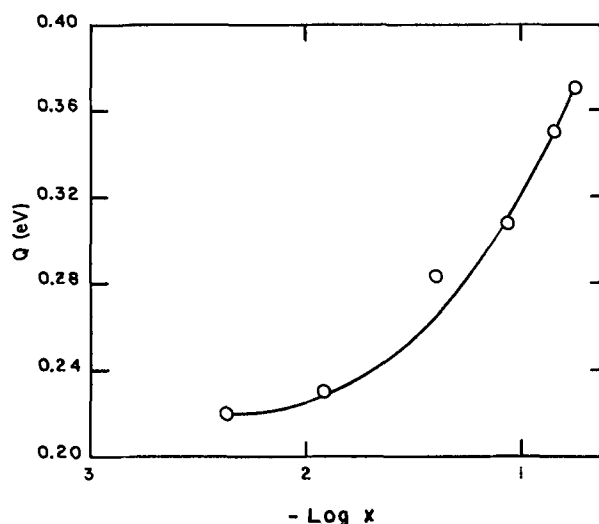


Fig. 5. A plot of the experimental activation energy,  $Q$ , obtained from the relation  $\sigma = \sigma_0 e^{-Q/kT}$ , under conditions of constant composition, as a function of  $\log x$ .

At larger departures from stoichiometry,  $-1.8 < \log x < -0.7$ , the experimental activation energy,  $Q$ , increases with increasing  $x$ . In this composition region  $\sigma$  is no longer proportional to  $x$ . As shown in Fig. 4 the dependence of  $\sigma$  on  $x$  decreases with increasing  $x$ , until  $\log x \approx -0.8$  where a maximum in  $\sigma$  is obtained. For larger values of  $x$ ,  $\sigma$  decreases with increasing  $x$ . The nonlinear dependence of  $\sigma$  on  $x$  in this composition region may be attributed to either of the following limiting case situations: (i) the dependence of the electron mobility on  $x$ ; or (ii) the dependence of the  $[\text{Ce}'\text{Ce}]$  on  $x$ . In case (i) the electron carrier concentration is assumed to be proportional to  $x$ , whereas, in case (ii) the electron mobility is assumed to be independent of  $x$ .

Assuming case (i) predominates, then the experimental activation energy,  $Q$ , is equal to  $E$  and the electron mobility may be represented by the expression

$$\mu = \mu_0 e^{-Q/kT} \quad [7]$$

In addition, if  $\mu_0$  is assumed to be independent of  $x$ , then the ratio of the mobility,  $\mu$ , in the region where  $\sigma$  is nonlinear in  $x$  to the mobility,  $\mu'$ , in the composition region  $\sigma \propto x$ , is given by the following expression

$$\ln \frac{\mu}{\mu'} = - \left[ \frac{Q - 0.22}{kT} \right] \quad [8]$$

The ratios of  $\mu/\mu'$  for different values of  $x$  were calculated from the corresponding values of  $Q$  given in Table II. The results of this calculation at  $1000^\circ\text{C}$  are shown in Fig. 6 where  $\log \mu/\mu'$  is plotted as a function of  $\log x$ . The interesting result to observe from Fig. 6 is that the nonlinear behavior of  $\log \mu/\mu'$  with  $\log x$  is similar to the nonlinear behavior of  $\log \sigma$  vs.  $\log x$ . In order to determine if the nonlinear behavior in Fig. 4 and 6 is caused by the mobility, the calculated dependence of the mobility on  $x$  was adjusted for by adding the corresponding value of  $|\log \mu/\mu'|$  to  $\log \sigma$  for a given value of  $x$ . These "normalized" values of  $\sigma$  are shown in Fig. 4. The most striking observation in this figure is that a single line with a slope of one may be drawn through both the actual values of  $\sigma$  (i.e.,  $-3.0 < \log x < -1.8$ ) and the "normalized" values of  $\sigma$  (i.e.,  $-1.8 < \log x < -0.7$ ).

The following conclusions may be drawn from the above results:

1. The compositional and temperature dependence of the electrical conductivity of nonstoichiometric  $\text{CeO}_{2-x}$  may be represented by the following expression

$$\sigma \propto x e^{-Q/kT}$$

where  $Q$  is a function of  $x$ .

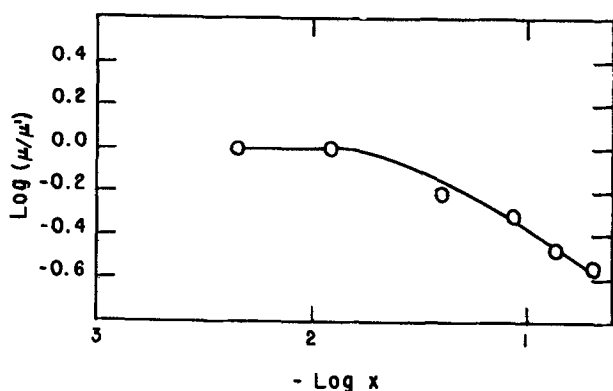


Fig. 6. An isothermal plot of  $\log \mu/\mu'$  vs.  $\log x$  at 1000°C where  $\mu$  is the electron mobility in the composition region, where  $\sigma$  is nonlinear in  $x$ , and where  $\mu'$  corresponds to the region where  $\sigma \propto x$ .

2. This expression may be rationalized in terms of the following simple relations for the electron carrier concentration

$$[\text{Ce}'_{\text{Ce}}] \propto x$$

and the electron mobility

$$\mu = \mu_0 e^{-Q/kT}$$

where  $\mu_0$  is independent of  $x$ ;  $Q$  is independent of  $x$  in the region  $-3.0 < \log x < -1.8$ ; and  $Q$  is a function of  $x$  between  $-1.8 < \log x < -0.7$ .

3. The relation  $[\text{Ce}'_{\text{Ce}}] \propto x$  implies the same nonstoichiometric atomic defect exists in predominately one state of ionization over the entire composition region (i.e.,  $-3.0 < \log x < -0.7$ ).

It should be noted that the results of an earlier study (13) of the electrical conductivity of CeO<sub>2-x</sub> as a function of  $P_{\text{O}_2}$  and  $T$  were rationalized utilizing the law of mass action in terms of a defect model involving cerium interstitials in two states of ionization. The relation  $[\text{Ce}'_{\text{Ce}}] \propto x$  obtained from the analysis of the conductivity data in this study is inconsistent with the earlier interpretation (13) involving a nonstoichiometric atomic defect with multiple states of ionization. The most likely explanation for this discrepancy is that the earlier analyses (13) are probably incorrect because the law of mass action was used in regions where the departure from stoichiometry is large.

It should also be noted that although the analysis used in this study circumvents the problem of consideration of the type of the nonstoichiometric defect and its distribution in the fluorite lattice, it does provide a very important characteristic of the nonstoichiometric defect (i.e.,  $[\text{Ce}'_{\text{Ce}}] \propto x$ ) which should be considered in any detailed analysis of the defect structure of CeO<sub>2-x</sub>. The nature of the nonstoichiometric defect and its state of ionization will be discussed later in a paper based on a thermodynamic study of CeO<sub>2-x</sub> (21, 24).

The following question also arises from this study. Why is  $Q$  a function of  $x$ ? A current study in this laboratory (25) of the dependence of the lattice parameter as a function of nonstoichiometry at elevated temperatures (800°-1000°C) shows that the lattice parameter increases with increasing  $x$ . Since the "hopping-type process" for electron conduction involves an activation

energy, it appears likely that the increase in  $E$  with  $x$  is associated with the increase in the size of the unit cell.

#### Acknowledgment

The authors wish to thank Dr. R. J. Panlener for providing the thermodynamic data for the analysis and Dr. R. F. Brebrick for useful comments. The authors gratefully acknowledge the financial support provided by the U. S. Atomic Energy Commission, Division of Research. This is AEC Report COO-1441-17.

This paper is based in part on a thesis submitted by one of the authors (R. L. H.) in partial fulfillment of the requirements for the M.S. degree, Marquette University, Milwaukee, Wisconsin, December 1971.

Manuscript submitted Oct. 12, 1972; revised manuscript received Aug. 3, 1973.

Any discussion of this paper will appear in a Discussion Section to be published in the December 1974 JOURNAL.

#### REFERENCES

1. G. Brauer and H. Gradinger, *Z. Anorg. Allgem. Chem.*, **277**, 89 (1954).
2. D. J. M. Bevan, *J. Inorg. Nucl. Chem.*, **1**, 49 (1955).
3. G. Brauer, K. A. Gingerich, and U. Holtzschmidt, *ibid.*, **16**, 77 (1960).
4. G. Brauer and K. A. Gingerich, *ibid.*, **16**, 87 (1960).
5. F. A. Kuznetsov, V. I. Belyi, and T. N. Rezukhina, *Dokl. Akad. Nauk SSR, Fiz-Khim.*, **139**, 1405 (1961).
6. D. J. M. Bevan and J. Kordis, *J. Inorg. Nucl. Chem.*, **26**, 1509 (1964).
7. J. Rudolph, *Z. Naturforsch.*, **14**, 727 (1959).
8. E. H. Greener, J. M. Wimmer, and W. M. Hirthe, in "Rare Earth Research II," Karl S. Vorres, Editor, p. 539, Gordon and Breach Science Publishers, Inc., New York (1964).
9. C. J. Kevane, *Phys. Rev.*, **133**, A1431 (1964).
10. C. J. Kevane, E. L. Holverson, and James B. Armstrong, Paper presented at the Fifth Rare Earth Research Conference, Ames, Iowa, Aug. 1965.
11. I. V. Vinokurov, Z. N. Zonn, and V. A. Ioffe, *Soviet Phys.-Solid State (English Transl.)*, **9**, 2659 (1968).
12. R. N. Blumenthal and J. E. Laubach, "Anisotropy in Single-Crystal Refractory Compounds," Vol. 2, p. 137, Plenum Press, New York (1968).
13. R. N. Blumenthal, P. W. Lee, and R. J. Panlener, *This Journal*, **118**, 123 (1971).
14. P. Kofstad and A. Z. Hed, *J. Am. Ceram. Soc.*, **50**, 681 (1967).
15. B. C. H. Steele and J. M. Floyd, *Proc. Brit. Ceram. Soc.*, **19**, 55 (1971).
16. I. V. Vinokurov, *Neorganicheskie Material (English Transl.)*, **6**, 31 (1970).
17. I. V. Vinokurov and V. A. Ioffe, *Soviet Phys. Solid State*, **11**, 207 (1969).
18. F. S. Brugner, R. N. Blumenthal, and J. E. Garnier, *This Journal*, To be published.
19. R. N. Blumenthal and R. J. Panlener, *J. Phys. Chem. Solids*, **31**, 1190 (1970).
20. R. N. Blumenthal, J. B. Moser, and D. H. Whitmore, *J. Am. Ceram. Soc.*, **48**, 617 (1965).
21. R. J. Panlener, Ph. D. Dissertation, Marquette University, Milwaukee, Wisconsin, 1972.
22. F. S. Brugner and R. N. Blumenthal, *J. Am. Ceram. Soc.*, **54**, 57 (1971).
23. R. Sharma, M.S. Thesis, Marquette University, Milwaukee, Wisconsin, 1973.
24. R. J. Panlener and R. N. Blumenthal, To be submitted to *J. Phys. Chem. Solids*.
25. J. R. Sims, Ph.D. Dissertation, Marquette University, Milwaukee, Wisconsin, 1973.

# Low Phosphorus Concentrations in Si by Diffusion from Doped Oxide Layers

J. Middelhoek and J. Holleman

Twente University of Technology, Enschede, The Netherlands

## ABSTRACT

The diffusion of phosphorus into silicon from doped oxide layers, deposited at low temperatures, has been studied in order to achieve reproducible impurity distributions with surface concentrations varying from  $5 \times 10^{15}$  to  $10^{18}$  atoms/cm<sup>3</sup>. Special attention has been given to the differences arising from indiffusion in an N<sub>2</sub> or in an O<sub>2</sub> ambient. The dependence on the temperature of the diffusion coefficients of phosphorus in silicon and in silicon dioxide is determined at a surface concentration of  $5 \times 10^{16}$  atoms/cm<sup>3</sup>.

Doped and undoped oxide layers, which are formed by the oxidation with O<sub>2</sub> of the hydrides of Si, P, B, and other elements at the surface of a slice of monocrystalline silicon at a characteristic temperature of 400°C have valuable applications in the manufacture of integrated circuits (1-4).

The application as a diffusion source is particularly interesting, because an independent control of the surface concentration over several orders of magnitude is made possible.

The purpose of this research is to find the practical lower limit of the phosphorus concentration, which can be obtained by indiffusion. Our research forms an extension of the work of Barry *et al.* (5-7). He reported surface concentrations of phosphorus varying from  $6 \times 10^{17}$  to  $2 \times 10^{20}$  atoms/cm<sup>3</sup>. Moreover we also studied the differences which arise when the indiffusion takes place either in an N<sub>2</sub> or in an O<sub>2</sub> ambient. In particular the indiffusion in an O<sub>2</sub> atmosphere has important applications in integrated circuit technology.

Usually a thin layer of undoped oxide is already present on the surface of the substrate before deposition of the oxide. This is caused by air oxidation or due to a cleaning step in nitric acid. The influence of this barrier layer on the result of the diffusion has been carefully observed.

The temperature dependence of the diffusion coefficients of P on Si and SiO<sub>2</sub> has been studied in view of process control. Activation energy values of importance from a theoretical point of view might be expected due to the method of diffusion and on account of the low concentrations.

## Theory

Barry and Olofsen (5) have given a detailed mathematical description of a model for the evaluation of the diffusion from a doped oxide layer. We shall use the same model and notation. Figure 1 shows a schematic representation of the different layers together with the diffusion parameters.

The expected impurity distribution after indiffusion from an infinitely thick source layer and without a barrier layer present, is

$$C_2(x,t) = C_0 [m\sqrt{D_1}/(m\sqrt{D_2} + \sqrt{D_1})] \operatorname{erfc} x/2\sqrt{D_2t} \quad [1]$$

The segregation constant  $m$  is defined by the equation  $m = C_2(0,t)/C_1(0,t)$ . Throughout this paper we will use the approximation

$$m\sqrt{D_1}/(m\sqrt{D_2} + \sqrt{D_1}) = \sqrt{D_1}/\sqrt{D_2} \quad [2]$$

because in the case of phosphorus, the data from literature (7, 9) indicate that  $\sqrt{D_2} \gg \sqrt{D_1}$  and  $m \gg 1$ .

When a first correction term for a finite thickness of the source layer  $x_0$  is added we arrive at

Key words: impurity distribution, low surface concentration, chemical vapor deposition, MOS channels, IC fabrication.

$$C_2(x,t) = C_0\sqrt{D_1}/\sqrt{D_2} [\operatorname{erfc} x/2\sqrt{D_2t} - 2 \operatorname{erfc} (x/2\sqrt{D_2t} + x_0/2\sqrt{D_1t})] \quad [3]$$

The decrease of the total amount of indiffused atoms due to a finite thickness is less than 1% if  $x_0 > 4\sqrt{D_1t}$ . It is useful to express  $x_0$  in this inequality as a fraction of the desired junction depth  $x_j$ . Using the approximation  $x_j \approx 4\sqrt{D_2t}$ , we find as a general rule

$$x_0 > x_j\sqrt{D_1/D_2} \quad [4]$$

Using Barry's results (7), we find that in the case of phosphorus no decrease is apparent when

$$x_0 > 0.05x_j \quad [5]$$

When a thin, undoped oxide layer is present between the silicon slice and the doped source layer, caused, for instance, by a cleaning procedure, the distribution in the silicon may still be described as a complementary error-function.

$$C_2(x,t) = C_0\sqrt{D_1/D_2} \operatorname{erfc} (x + x_B\sqrt{D_2/D_1})/(2\sqrt{D_2t}) \quad [6]$$

Contrary to expression [1] the surface concentration is now time-dependent

$$C_2(0,t) = C_0\sqrt{D_1/D_2} \operatorname{erfc} x_B/2\sqrt{D_1t} \quad [7]$$

The distribution in the silicon is equal to the profile arrived at when, from a pure complementary error-function profile, a top layer with a thickness of  $x_B\sqrt{D_2/D_1}$  has been removed by a sectioning technique. Irvin (8) has composed a set of graphs which can be used for the evaluation of profiles obtained by sectioning. These graphs are also applicable in the case of the presence of an undoped barrier layer, provided that  $x_B\sqrt{D_2/D_1}$  is known.

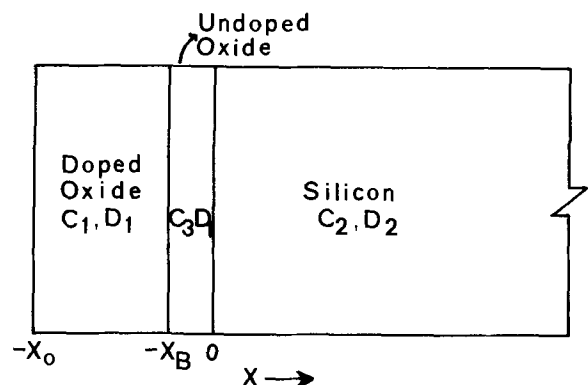


Fig. 1. Diffusion from a deposited doped oxide through a barrier oxide into a semiconductor substrate.

The above solutions are applicable for diffusion in the presence of constant barrier thickness. However, in an oxidizing ambient, an undoped oxide layer grows between the deposited layer of doped oxide and the silicon slice. What occurs can be physically clarified without a thorough mathematical explanation.

The rate of the barrier growth can be derived from the well-known parabolic law for thermal oxidation (9) when the thickness  $x_0$  of the deposited layer is also taken into account

$$(x_0 + x_B)^2 = B(t_i + t), \text{ where } (x_0 + x_{B0})^2 = Bt_i$$

The parabolic rate constant  $B$  is proportional to the diffusion constant of the oxidizing species. By approximation

$$x_B = x_{B0} + Bt/2x_0 \quad [8]$$

The progress of the diffusion in the  $\text{SiO}_2$  barrier is difficult to characterize precisely. We take  $2\sqrt{D_1t}$  as the distance covered, which is a reasonable assumption as  $x_B > \sqrt{D_1t}$ . In Fig. 2 we plotted  $x_B$  and  $2\sqrt{D_1t}$  in one graph as function of the time. What occurs can be clearly seen. Initially the diffusion progresses more quickly than the barrier increases, but after some time the barrier growth overtakes the diffusion of the dopant. At the moment that the processes have the same velocity, the indiffusion into the silicon ceases. The total amount of indiffused impurity remains constant and by further high temperature treatment the distribution begins to approach a Gaussian profile.

### Experimental Details

Standard Monsanto silicon slices, doped with boron to a specific resistivity of about 10 ohm-cm plane direction (100), with one side polished and the other side lapped, were used in this research. The specific resistivity of each slice was determined before the experiments and the dopant concentration was derived from literature data (9).

The pretreatment of the slices comprised treatments in fuming nitric acid and in boiling nitric acid (65%), rinsing and centrifuging until dry. Directly afterwards, the deposition in the reactor was carried out.

The depositions were performed in a home-made, one-slice reactor at a slice temperature of  $325^\circ \pm 2^\circ\text{C}$ . The reactor was cylindrical with a height of 20 cm and a diameter of 8 cm. Before the deposition the reactor was purged with  $\text{N}_2$  and the slice preheated for 2 min. The gas flows were argon: 7 liter/min;  $\text{O}_2$ : 35 ml/min;  $\text{SiH}_4$  (net): 7 ml/min. The gas flow of  $\text{PH}_3$  varied. The dilution in the cylinder used was 6 ppm. The dilution of  $\text{SiH}_4$  in A was 1%.

At first a uniform phosphorus-doped oxide layer of 4000Å was deposited at a rate of 1000 Å/min. Thereafter a densification step (10) followed during 10 min at  $650^\circ\text{C}$  in  $\text{N}_2$ , wetted by leading the gas flow through

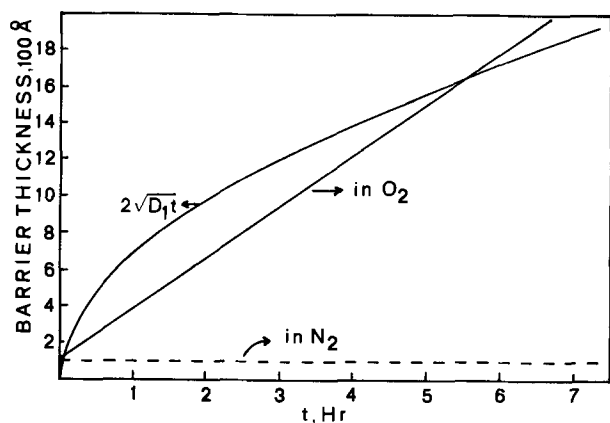


Fig. 2. The increase of the barrier thickness and of the diffusion length of phosphorus in oxide vs. time.

a washing-bottle containing water at room temperature. This step has been proved to be essential for achieving good diode characteristics in the fabrication of MOS transistors.

Finally, the phosphorus-doped layer was covered by another deposited layer of 4000Å. This layer configuration is also applied in the fabrication of MOS transistors.

After diffusion the oxide was etched away and the sheet resistance was determined with a four point probe. The junction was made visible (12) by grinding a circular groove with a steel ball and by staining one of the layers with  $\text{AgNO}_3$  or Fuller and Ditzberger's etching fluid (12). The junction depth was determined with the measuring ocular of a light-microscope.

### Evaluation Method

The theoretical conditions for an evaluation of the indiffusion based on the combined measurement of junction depths and sheet conductivities, assuming an erfc distribution, are excellent. The background as well as the diffusant concentrations are in this research always much smaller than the intrinsic carrier concentrations (14-16) due to an internal field and variation of the vacancy concentration do not occur.

For the justification of the diffusion model it is not only necessary to investigate the variation of  $x_j$  and  $R_s^{-1}$  with diffusion time, but also the variation with the concentration of dopant in the oxide. It is essential that the surface concentration is proportional to the initial dopant concentration in the source layer (1).

The expression for the junction depth, as derived from [6], is

$$x_j = -x_B\sqrt{D_2/D_1} + 2\sqrt{D_2t} \operatorname{argerfc} C_B\sqrt{D_2}/C_0\sqrt{D_1} \quad [9]$$

The value,  $x_B$ , of the thickness of the thin oxide barrier in this research is not determined separately. It has an estimated value (2, 5) between 15 and 50Å. The expected intercept with the ordinate of the curve  $x_j$  vs.  $\sqrt{t}$  is, according to the diffusivity values reported by Barry (7), very small, about 1000Å. The determination of this intercept cannot be done accurately because systematic errors in the junction depth measurement are of the same order of magnitude. However the determination of  $x_B\sqrt{D_2/D_1}$  is made possible by comparing the systematic difference of two series of measurements of  $x_j$  vs.  $C_0$ . The wafers of one series were dipped in a  $\text{SiO}_2$  etchant just before the deposition of the doped oxide layer. The wafers of the other series are covered with the thin oxide layer normally found after a cleaning step with  $\text{HNO}_3$ .

The total amount (6, 9) of indiffused atoms  $Q$  is in the case of a complementary error function distribution

$$Q(t, C_0) = 2\pi^{-1/2}C_s\sqrt{D_2t} = 2\pi^{-1/2}C_0\sqrt{D_1t} \quad [10]$$

For very low concentrations compared with the background concentration, three corrections have to be made. First the integral may not be extended to infinity. For finite thickness of  $x_j$  the expression for  $Q$  can be completed with a factor (11) (Fig. 3)

$$F = (1 - \sqrt{\pi} \operatorname{ierfc} x_j/2\sqrt{D_2t}) \quad [11]$$

Secondly an amount  $x_jC_B$  must be subtracted for the compensation of the background concentration. Thirdly when an undoped barrier layer is present, an amount  $x_B C_0$  must also be subtracted because this thin undoped barrier layer acts to a first approximation as a source for a Gaussian distribution, but then in a negative sense.

Thus, the amount of indiffused atoms, which can be determined by sheet conductivity measurements is

$$Q = 2\pi^{-1/2}C_0F\sqrt{D_1t} - x_jC_B - x_B C_0 \quad [12]$$

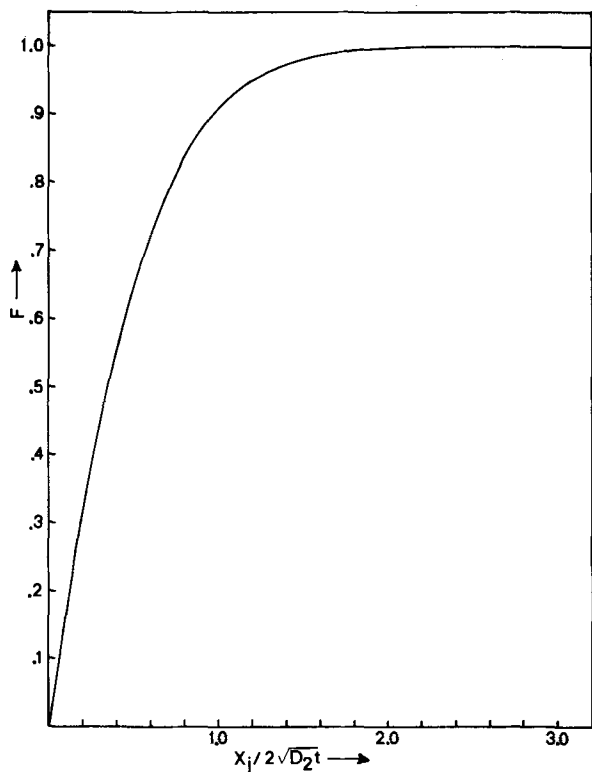


Fig. 3. The factor  $F$ , which accounts for the indiffused atoms beyond the metallurgical junction, vs.  $x_j/2\sqrt{D_2t}$ .

The sheet conductivity  $R_s^{-1}$  would be a linear function of  $Q$ , if the mobility of the charge carriers, in this case electrons, was independent of the concentration. This problem is usually circumvented by using Irvin's graphs (8) for the evaluation in which this mobility variation is taken into account. But it is however, interesting to check how this mobility variation influences the evaluation. The sheet conductivity as well as the surface concentration determined with Irvin's graphs will therefore be plotted vs. the dopant concentration in the oxide. Thereby we shall assume that in our reactor system the following relation is valid for small  $PH_3/SiH_4$  ratios

$$C_o = (PH_3/SiH_4) K_2 \cdot 3 \times 10^{22} \text{ atoms/cm}^3 \quad [13]$$

$K$  is a reactor constant. Therefore we evaluate according to

$$R_s^{-1} = K \cdot \sqrt{D_1 t} (PH_3/SiH_4) \quad [14]$$

**Results and Discussion**

In Fig. 4 and 5 the experimentally found junction depth  $x_j$  and the sheet conductivity  $(R_s)^{-1}$  are both represented as functions of the square root of the time. The graphs show straight lines for diffusion in  $N_2$  as expected according to Eq. [9] and [14] for diffusions in an inert atmosphere.

The intercept of the curve  $x_j$  vs.  $\sqrt{t}$  is smaller than 1000Å and can not be accurately determined from these experiments.

When the diffusion was performed in an oxygen ambient, the junction depths for longer times are somewhat smaller than the values found in  $N_2$ . This is obviously an indication that the amount of indiffused phosphorus atoms is smaller. This is even more evident from the sheet conductivity plot (Fig. 5). By diffusion after a certain time in  $O_2$  the sheet conductivity remains constant. This is a result of the cut-off of further influx caused by the growth of an undoped barrier as explained in the theoretical section (Fig. 2).

The sheet conductivity after indiffusion in  $N_2$  for longer times also remains below the value predicted

by theory. This may be due partly to exhaustion of the source layer, because  $x_o = 4000\text{Å}$  and  $x_j = 10\mu$  and, according to [5], exhaustion should lead to a small decrease of the sheet conductivity.

The average specific conductivity of the layers  $(R_s x_j)^{-1}$  is equal to the quotient of the slopes of the

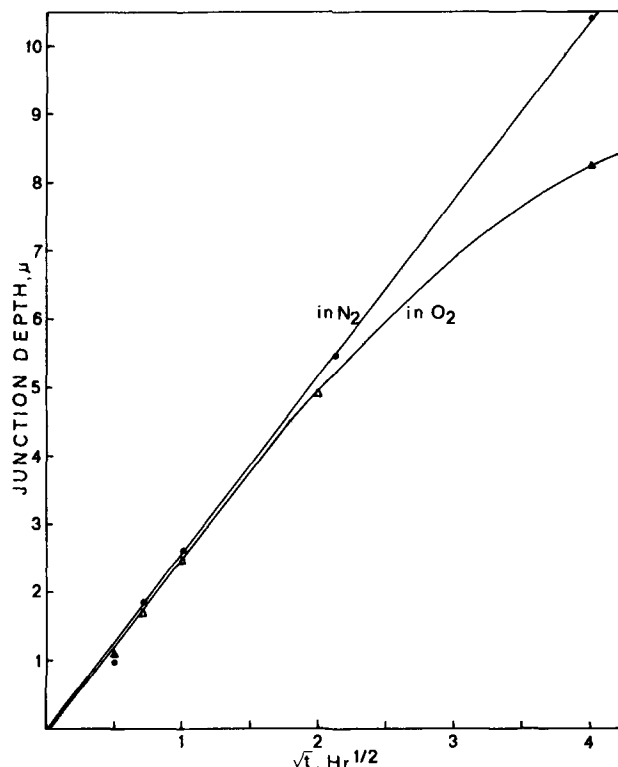


Fig. 4. Junction depths resulting from P diffusion into Si from deposited oxides at 1200°C in an  $N_2$  or in an  $O_2$  ambient, vs. time.  $PH_3/SiH_4 = 2.34 \times 10^{-4}$ .  $C_s = 4.8 \times 10^{17} \text{ atoms/cm}^3$ .

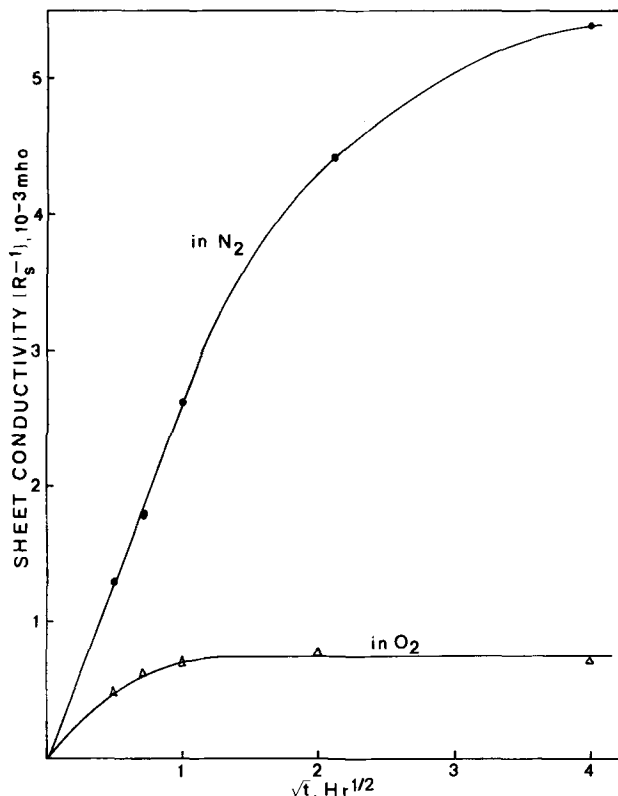


Fig. 5. Sheet conductivities resulting from P diffusion into Si from deposited oxides at 1200°C in an  $N_2$  or in an  $O_2$  ambient, vs. time.  $PH_3/SiH_4 = 2.34 \times 10^{-4}$ .  $C_s = 4.8 \times 10^{17} \text{ atoms/cm}^3$ .

respective curves. It is a constant for the layers diffused in N<sub>2</sub> as would be expected for a complementary error-function profile. With the help of Irvin's graphs (8) the surface concentration for the diffusion experiments in N<sub>2</sub>, represented in Fig. 4 and 5, is found to be  $4.8 \times 10^{17}$  atoms/cm<sup>3</sup>. The diffusivity of phosphorus in silicon at  $1200^\circ \pm 1^\circ\text{C}$  was calculated from the slope of the plot  $x_j$  vs.  $t$  and the found surface concentration.  $\sqrt{D_2} = 0.60 \mu/\text{hr}^{1/2}$ .

Figures 6 and 7 show the result of comparable experiments, but with a much smaller phosphorus concentration C<sub>0</sub> in the oxide. A pronounced difference occurs, when the slice before deposition, is either dipped or not dipped in an SiO<sub>2</sub> etchant. This was not the case with the above discussed concentration of  $4.8 \times 10^{17}$  atoms/cm<sup>3</sup>. Evaluation of the surface concentration gives  $3.0 \times 10^{16}$  atoms/cm<sup>3</sup> when dipping is included and  $8.5 \times 10^{15}$  atoms/cm<sup>3</sup> without dipping. The diffusivities were respectively 0.52 and  $0.56 \mu/\text{hr}^{1/2}$ . The concentration of PH<sub>3</sub> in the deposition gas was 8 times smaller for the experiments of Fig. 6 and 7, than for the experiments of Fig. 4 and 5. The resulting surface concentration was however 16 times smaller with dipping and 57 times smaller without dipping. This means that for this low concentration more than half of the amount of phosphorus is lost during the operation in the reactor system.

Diffusion in an oxygen ambient leads to irreproducible results at this low concentration.

The results of the experiments concerning the temperature dependence of the diffusivities are represented in Fig. 8 and Table I. From the slope of the curve  $\ln D_2^{1/2}$  vs.  $T^{-1}$  an activation energy of  $5.00 \pm 0.10$  eV was calculated at a surface concentration of  $5 \times 10^{16}$  atoms/cm<sup>3</sup>. Compared with other values from the literature (7, 13) such as 2.45 eV ( $2 \times 10^{20}/\text{cm}^3$ ); 3.78 eV ( $5 \times 10^{18}/\text{cm}^3$ ); 2.4 eV ( $9.5 \times 10^{20}/\text{cm}^3$ ); and 3.4 eV ( $3 \times 10^{18}/\text{cm}^3$ ) the value now found is much larger. The calculation of the activation energy depends mainly on the values found for the junction depth. The assumption of a systematic error in the junction depth of  $0.45 \mu$  is necessary to bring the value for the activation energy into agreement with the values reported thus far in the literature for phosphorus diffusion.

The graph of  $\ln R_s^{-1}$  vs.  $T^{-1}$  makes it possible, according to [14], to calculate the activation energy of the diffusion coefficient of phosphorus in the oxide. We found  $2.04 \pm 0.20$  eV. It was assumed that the effective average mobility at  $5 \times 10^{16}$  atoms/cm<sup>3</sup> did not change very much. Literature data indicate a variation of less than 10% and the results, represented in Fig. 10, give reason to believe that the variation is even less. Barry (7) found 4 eV, but this value is not very accurate, as

he states in his article, because it is calculated with the help of the barrier thickness  $x_B$ .

Barry (7) also found by independent measurements of C<sub>0</sub> and C<sub>s</sub> that the ratio  $C_0/C_s = \sqrt{D_2/D_1}$  is independent of the temperature, but dependent on the concentration of the diffusant. This result is incompatible with his diffusion model. We found, however, in Table I that C<sub>s</sub> decreases at a constant C<sub>0</sub> and an increasing temperature, because D<sub>2</sub> has a greater increase with a rise in temperature than D<sub>1</sub>.

Figures 9, 10, and 11 show the results of diffusion experiments at a constant diffusion time and temperature with varying concentrations of PH<sub>3</sub> in the deposi-

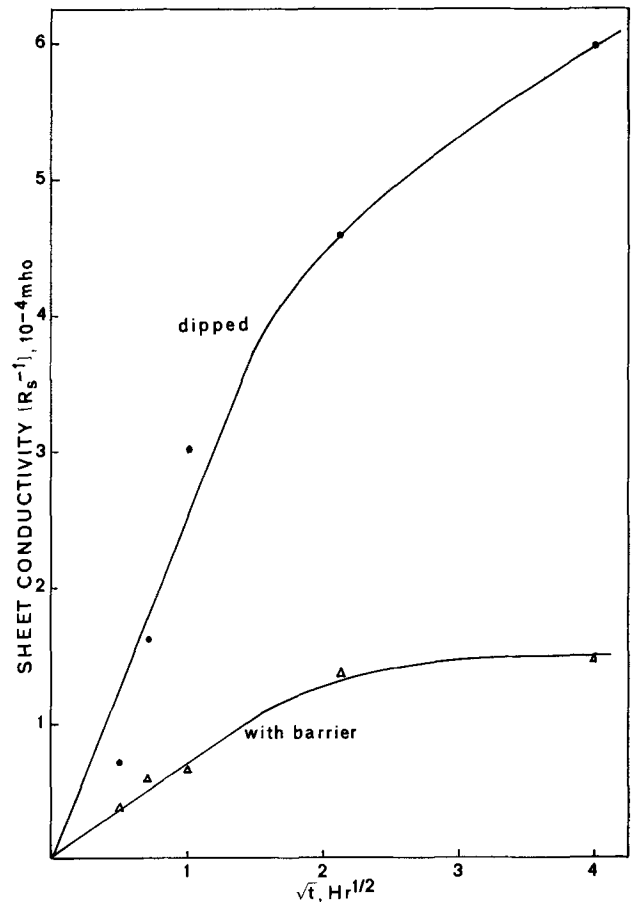


Fig. 7. Sheet conductivities resulting from P diffusion into Si from deposited oxide at  $1200^\circ\text{C}$  in an N<sub>2</sub> ambient, vs. time  $\text{PH}_3/\text{SiH}_4 = 3 \times 10^{-5}$ . After a cleaning step in HNO<sub>3</sub> the wafers of one series are dipped in an HF solution before the deposition of the doped oxide.

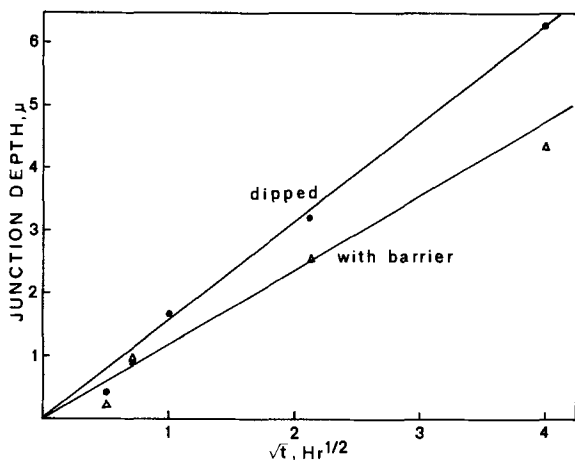


Fig. 6. Junction depths resulting from P diffusion into Si from deposited oxides at  $1200^\circ\text{C}$  in an N<sub>2</sub> ambient, vs. time.  $\text{PH}_3/\text{SiH}_4 = 3 \times 10^{-5}$ . After a cleaning step in HNO<sub>3</sub> the wafers of one series are dipped in an HF solution before the deposition of the doped oxide.

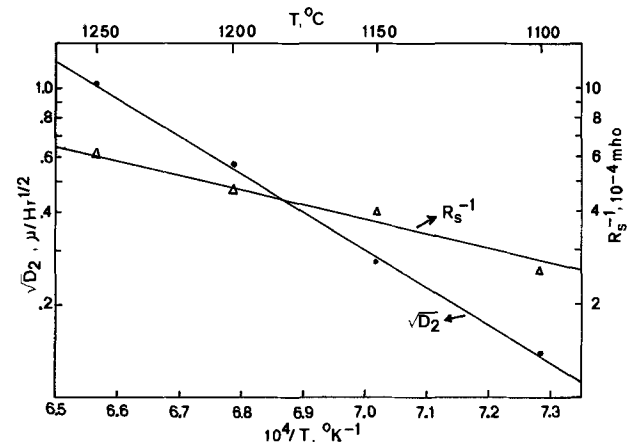


Fig. 8. Temperature variation of the P diffusivity in Si and of the sheet conductivity resulting from P diffusion into Si from deposited oxides during 125 min in an N<sub>2</sub> ambient.  $\text{PH}_3/\text{SiH}_4 = 6.4 \times 10^{-5}$ .

Table I. Temperature variation of the diffusion quantities resulting from P diffusion into Si from deposited oxides in an N<sub>2</sub> ambient. PH<sub>3</sub>/SiH<sub>4</sub> = 0.64 x 10<sup>-4</sup>. Diffusion time is 125 min

Temp, °C	x <sub>j</sub> , μ	R <sub>s</sub> <sup>-1</sup> , 10 <sup>-4</sup> mho	(R <sub>s</sub> x <sub>j</sub> ) <sup>-1</sup> , mho/cm	C <sub>s</sub> , 10 <sup>18</sup> atoms/cm <sup>3</sup>	√D <sub>2</sub> , μ/hr <sup>1/2</sup>
1100	0.71	2.57	3.48	9.0	0.137
1152	1.35	4.00	2.96	6.8	0.272
1200	2.40	4.65	1.94	3.6	0.562
1250	4.34	6.18	1.42	2.5	1.037

tion gas. It was supposed that the concentration C<sub>0</sub> was a linear function of the ratio PH<sub>3</sub>/SiH<sub>4</sub> in the deposition gas (13). That this supposition was correct, is demonstrated in Fig. 10. According to the theory a linear relation is predicted between (R<sub>s</sub>)<sup>-1</sup> and C<sub>0</sub>, and a linear relation between (R<sub>s</sub>)<sup>-1</sup> and (PH<sub>3</sub>/SiH<sub>4</sub>) is found.

At the highest concentrations a deviation occurs. This may be due to a smaller mobility at these concentrations. But this is not probable, because a similar deviation occurs by diffusion in an oxygen ambient, while the concentration is in a range, where no deviation occurs in the results obtained in an N<sub>2</sub> atmosphere. An error in the control of the PH<sub>3</sub> flow is more probable. The graph of the surface concentration vs. (PH<sub>3</sub>/SiH<sub>4</sub>) (Fig. 11) is not as straight as the graph (R<sub>s</sub>)<sup>-1</sup> vs. (PH<sub>3</sub>/SiH<sub>4</sub>) (Fig. 10). It would appear that the dependence of the mobility on the concentration, such as taken into account by Irvin in his graphs (8) is exaggerated in the range of 10<sup>17</sup>-10<sup>18</sup> atoms/cm<sup>3</sup>.

The systematic difference in junction depth between slices with etching and those without etching is obvious. This difference must correspond with x<sub>B</sub>√D<sub>2</sub>/D<sub>1</sub> (9). The series in N<sub>2</sub> show a difference of about 800Å

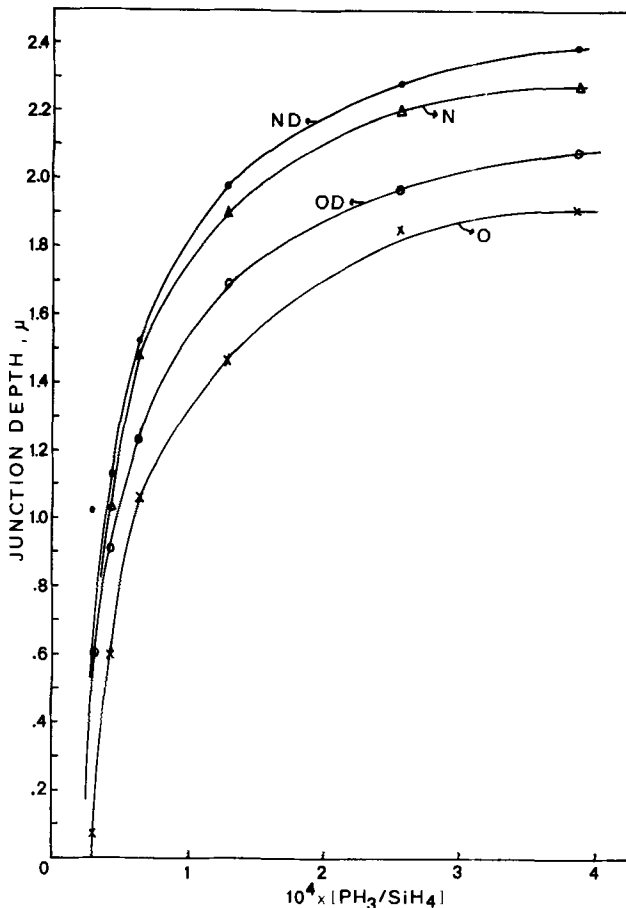


Fig. 9. Junction depths, resulting from P diffusion into Si from deposited oxides during 43 min at 1200°C, vs. the PH<sub>3</sub>/SiH<sub>4</sub> ratio in the deposited gas. N: diffusion in an N<sub>2</sub> ambient. O: diffusion in an O<sub>2</sub> ambient. D: dipped in an HF solution before deposition.

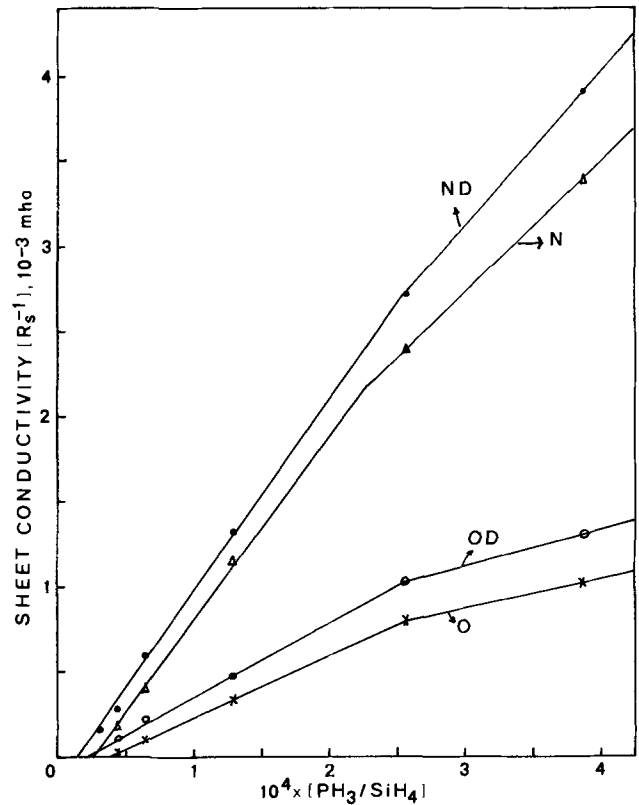


Fig. 10. Sheet conductivities, resulting from P diffusion into Si from deposited oxides during 43 min at 1200°C, vs. the PH<sub>3</sub>/SiH<sub>4</sub> ratio in the deposition gas. For symbol definition see Fig. 9.

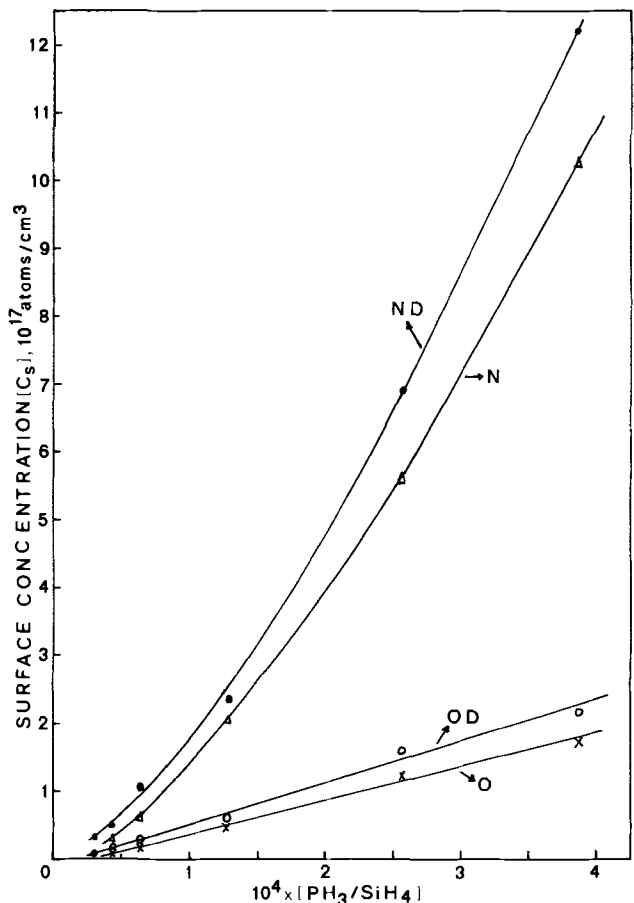


Fig. 11. Surface concentration, derived by means of Irvin's graphs from junction depth and sheet conductivity data, vs. the PH<sub>3</sub>/SiH<sub>4</sub> ratio in the deposition gas. See Fig. 9 and 10.

and those in  $O_2$  of about 1700Å. If we assume that the ratio P/Si in the oxide is the same as in the deposition gas, then  $C_o/C_s = \sqrt{D_2/D_1}$  at 1200°C can be calculated. A value between 11 and 13 is found. Then in the case of  $N_2$ ,  $x_B$  would be 67Å. This value is fairly large, as we expected (2, 5) a value of about 30Å. It may therefore be concluded that at 325°C relatively more P is deposited than according to the ratio  $PH_3/SiH_4$ .

We expected to find a larger value of the effective  $x_B$  in the case of an  $O_2$  ambient during the drive-in but the theory is lacking for further analysis.

The difference between  $(R_s)^{-1}$  in  $N_2$  with or without a barrier corresponds, according to the theory, with  $q\mu C_s x_B \sqrt{D_2/D_1}$ . From this result we also derived a value for  $x_B \sqrt{D_2/D_1}$ . It was 900Å. This value agrees with the 800Å derived from the junction depth measurements. These values show that the theory gives a consistent description of the diffusion process. An application of these diffusion sources with low dopant concentration is shown in Fig. 12. To prevent (13) parasitic channels in p-channel MOS integrated circuits the active regions are surrounded by an area where the surface concentration of the substrate is increased by a diffusion from a phosphorus-doped layer.

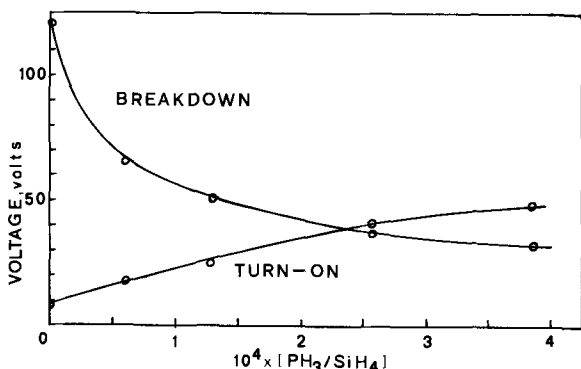


Fig. 12. Breakdown voltage of the drain of a MOS transistor and the parasitic turn-on voltage vs. the  $PH_3/SiH_4$  ratio in the deposition gas for the doped oxide from which a diffusion takes place during the thermal growth of the gate oxide at 1200°C. Field oxide thickness: 8000Å.

The result is that the parasitic turn-on voltage increases. An adverse effect is that the breakdown voltage of the diffused areas decreases. A compromise is found when according to Fig. 12, the turn-on voltage and the breakdown voltage are both 40V. It is interesting to note that measurements of the turn-on voltage or C-V plots give an independent method of determining the surface concentrations. The values may be compared with those obtained by means of Irvin's graphs (8). In our experience the agreement is satisfactory but we do not consider these methods more accurate than Irvin's evaluation.

Manuscript submitted March 5, 1973; revised manuscript received Sept. 18, 1973.

Any discussion of this paper will appear in a Discussion Section to be published in the December 1974 JOURNAL.

#### REFERENCES

1. W. Kern and A. W. Fisher, *RCA Rev.*, **31**, 715 (1970).
2. M. L. Barry and P. Olofsen, *Solid State Technology*, **11**, 39 (1968).
3. A. W. Fisher, J. A. Amick, H. Hyman, and J. H. Scott, *RCA Rev.*, **29**, 533 (1968).
4. M. M. Schlacter *et al.*, *IEEE Trans.*, **ED 17**, 1077 (1970).
5. M. L. Barry and P. Olofsen, *This Journal*, **116**, 859 (1969).
6. M. L. Barry and J. Manoliu, *ibid.*, **117**, 258 (1970).
7. M. L. Barry, *ibid.*, **117**, 1405 (1970).
8. J. C. Irvin, *Bell System Tech. J.*, **41**, 387 (1962).
9. A. S. Grove, "Physics and Technology of Semiconductor Devices," John Wiley & Sons, Inc., New York (1967).
10. W. Kern and R. C. Heim, *This Journal*, **117**, 568 (1970).
11. H. S. Carslaw and J. C. Jaeger, "The Conduction of Heat in Solids," 2nd ed., p. 485, Oxford Press (1959).
12. R. M. Burger and R. P. Donovan, "Fundamentals of Silicon Integrated Device Technology," Vol. 1, pp. 319, 311, 209, Prentice Hall, Englewood Cliffs, N. J. (1967).
13. W. M. Penny and L. Lau, "Mos Integrated Circuits," p. 173, Van Nostrand Reinhold Company, New York (1972).
14. S. M. Hu and S. Schmidt, *J. Appl. Phys.*, **39**, 4272 (1968).
15. S. M. Hu, *ibid.*, **42**, 4102 (1971).
16. D. Shaw, "Atomic Diffusion in Semiconductors," Plenum Press, London (1973).

## The Synthesis and Photoluminescence of $M^{II}M_2^{III}(S,Se)_4$

P. C. Donohue and J. E. Hanlon<sup>1</sup>

Central Research Department, E. I. du Pont de Nemours and Company,  
Experimental Station, Wilmington, Delaware 19898

#### ABSTRACT

The compositions  $M^{II}M_2^{III}(S,Se)_4$  where  $M^{II} = Eu, Yb, Ca, Sr, Ba$  and  $M^{III} = Al, Ga, In$  were prepared by reaction of the elements in evacuated silica tubes with iodine as a mineralizer. All members except  $Ba(Ga,Al)_2S_4$ , which is cubic, exhibit the pseudo-orthorhombic  $PbGa_2Se_4$  type structure. They are high resistivity p-type semiconductors; they exhibit  $Eu^{+2}$ -activated fluorescence which varies from red to blue as the electropositive character of the cations increase. Fluorescence activated by  $Yb^{+2}$  is seen at low temperature. Studies were made of the fluorescence decay lifetimes, temperature dependence, excitation spectra, and optical adsorption of  $SrGa_2S_4:Eu$  in order to relate the  $Eu^{+2}$ -activated fluorescence to the host bandgap. It is concluded that the most efficient phosphors are those in which the  $Eu^{+2}$  excited states lie farthest from the fundamental edge.

Sulfides and selenides of general formula  $M^{II}M_2^{III}(S,Se)_4$  where  $M^{II}$  and  $M^{III}$  are divalent and trivalent

<sup>1</sup>Deceased.  
Key words:  $Eu^{+2}$  and  $Yb^{+2}$  activated photoluminescence of  $M^{II}(Al, Ga, In)_2(S, Se)_4$ .

cations, respectively, form a variety of structures (1,2). The most common are the  $Ag_2HgI_4$  type, spinel type,  $Th_3P_4$  type, and  $CaFe_2O_4$  type. The spinel type is favored by smaller cations while the  $Th_3P_4$  and  $CaFe_2O_4$



types are favored by larger electropositive cations such as the rare earths. The  $\text{Ag}_2\text{HgI}_4$  type, in which all cations are tetrahedrally coordinated, is favored by the more covalent cations, e.g., the  $\text{HgGa}_2\text{S}_4$ -type series (3).

Until recently, with the exception of  $\text{MgGa}_2\text{S}_4$  (4) and  $\text{BaIn}_2\text{S}_4$  and  $\text{SrIn}_2\text{S}_4$  (5), very little work had been reported on compounds combining the larger ionic divalent cations with the more covalent trivalent cations. Eholie and co-workers reported  $\text{PbGa}_2\text{Se}_4$  (6) to exhibit a new orthorhombic structure. In a later paper (7) they reported lattice constants and paramagnetism of  $\text{EuM}_2^{\text{III}}(\text{S,Se})_4$ ,  $\text{SrM}_2^{\text{III}}(\text{S,Se})_4$ , and  $\text{PbAl}_2(\text{S,Se})_4$  where  $\text{M}^{\text{III}} = \text{Al, Ga}$ . The phases exhibit an orthorhombic sublattice with the simultaneous presence of twinning and superlattice.

The luminescence and structural properties of  $\text{Ce}^{+3}$  and  $\text{Eu}^{+2}$  activated  $\text{M}^{\text{II}}\text{Ga}_2\text{S}_4$  where  $\text{M}^{\text{II}} = \text{Ca, Sr, Ba, Pb, Eu (Na, La)}$ , and  $(\text{Na, Ce})$  were reported by Peter and Baglio (8). Their structural data are in agreement with Eholie *et al.*, and they report  $\text{BaGa}_2\text{S}_4$  to be cubic. The alkali earth thiogallates were shown to be efficient hosts for  $\text{Eu}^{+2}$  luminescence. The peak emission was shown to vary from the blue-green to yellow depending on the host.

We here report the extension of the series to include  $\text{Yb}(\text{Ga,Al})_2(\text{S,Se})_4$ ,  $\text{M}^{\text{II}}\text{In}_2(\text{S,Se})_4$ ,  $\text{BaAl}_2\text{S}_4$ , and  $(\text{Ca,Ba})\text{Ga}_2\text{Se}_4$ . We also measured the  $\text{Eu}^{+2}$  and  $\text{Yb}^{+2}$  activated luminescence, electrical resistivity, and optical absorption on several compositions.

**Sample preparation.**—Compositions were prepared by reactions in evacuated silica tubes using a small quantity of iodine as a mineralizing agent.  $\text{EuS}$  and  $\text{EuSe}$  were prepared by starting with ingots of 99.9 pure  $\text{Eu}$  obtained from Kerr McGee Company, and 99.999 pure  $\text{S}$  and  $\text{Se}$  obtained from ROC/RIC. All other reactants were used in elemental form; 99.9999 pure  $\text{Ga}$  obtained from Alcoa, 99.999+ pure  $\text{In}$  obtained from Asarco, and 99.999 pure  $\text{Al}$  wire obtained from ESPI.  $\text{Ca, Sr,}$  and  $\text{Ba}$  were obtained 99.5% pure from ROC/RIC.  $\text{Sr}$  and  $\text{Ba}$  were cut from bars and weighed in a  $\text{N}_2$ -filled dry box. The reactants, in stoichiometric proportions, were placed in dried silica tubes. About  $5 \text{ mg I}_2/\text{cm}^3$  was added and the tubes were evacuated and sealed at a length of about 6 in.

Reactions were carried out in natural gradient tube furnaces with the ends of the tubes containing the metals in the hot center and the chalcogen at the cooler outer edges of the furnaces. The temperature of the centers was raised to about  $500^\circ\text{C}$  and held for 24–48 hr. The cooler ends of the tubes were at  $\sim 300^\circ\text{C}$  to keep the vapor pressure of the chalcogen low. During this

treatment,  $\text{M}^{\text{II}}\text{S,Se}$  formed without reaction of the  $\text{M}^{\text{II}}$  metal with the silica. The temperature of the center was then raised to about  $800^\circ\text{C}$  and after about 24 hr most of the chalcogen was taken up. The tubes were removed and shaken to better mix the reagents or opened, the products reground, resealed in silica. They were reheated at between  $800^\circ$  and  $1000^\circ\text{C}$  for 24–48 hr. When using  $\text{Al}$  wire, several shakings were required since a hard sulfide crust forms preventing further reaction.

Solid solutions and doped compositions were prepared by starting with the desired ratio of reactants and proceeding as described or grinding together pre-prepared material, sealing in evacuated silica tubing, and heating at between  $800^\circ$  and  $1000^\circ\text{C}$ .

The products generally formed in the hotter ends of the tubes as sintered crystalline masses. In some cases crystals were transported to the cool zone.

Boules of several compositions were grown in either graphite or  $\text{Al}_2\text{O}_3$  crucibles, sealed under vacuum in silica tubes, and cooled from about  $50^\circ\text{C}$  above the melting point at  $5^\circ\text{C/hr}$ . The crystalline habit was typically lamellar, and bubbles were seen in the sulfides indicating a high  $\text{S}$  vapor pressure at the melting point.

The melting points of  $\text{EuGa}_2\text{S}_4$ ,  $\text{EuGa}_2\text{Se}_4$ ,  $\text{EuIn}_2\text{Se}_4$ ,  $\text{BaGa}_2\text{S}_4$ , and  $\text{SrGa}_2\text{S}_4$  were determined by DTA and are given in Table I. All appear to melt congruently and freeze with supercooling of between  $50^\circ$  and  $100^\circ\text{C}$ .  $\text{BaGa}_2\text{S}_4$  formed a glass.

## Results and Discussion

**Crystal chemistry.**—Table I summarizes the results of the syntheses, cell refinements, and resistivity measurements. Debye-Scherrer x-ray powder patterns were refined by a computerized least squares technique and standard deviations in the cell parameters are typically  $0.003\text{\AA}$ .

Two structure types are exhibited by this series, the  $\text{PbGa}_2\text{Se}_4$  type and the cubic  $\text{BaGa}_2\text{S}_4$  type. The orthorhombic cell, although it could not account for all diffraction lines, was used to compare relative cell sizes of the  $\text{PbGa}_2\text{Se}_4$  type compounds and for phase identification.

Several crystals of various samples of the  $\text{PbGa}_2\text{S}_4$  type were examined by Buerger precession camera techniques and our results are consistent with those reported (7, 8). In all cases a large orthorhombic superlattice was indicated; however, extinctions inconsistent with any orthorhombic space group were observed suggesting the presence of twinning and that the true symmetry is lower than orthorhombic.

Table I. X-ray data and properties of compounds in the system  $\text{M}^{\text{II}}\text{M}_2^{\text{III}}(\text{S, Se})_4$

Compound	Pseudo-orthorhombic cell (Å)			Body color	Melting point ( $^\circ\text{C}$ )	Resistivity $298^\circ\text{K}$ (ohm-cm)
	a	b	c			
$\text{EuAl}_2\text{S}_4$	10.193	6.060	10.374	Light yellow		
$\text{EuGa}_2\text{S}_4$	10.223	6.108	10.354	Yellow	1215	$\approx 10^8$
* $\text{EuIn}_2\text{S}_4$	10.490	6.497	10.360	Yellow		$\approx 10^{11}$
$\text{EuGa}_2\text{Se}_4$	10.666	6.375	10.795	Yellow-orange	1093-1114	$7 \times 10^6$
* $\text{EuIn}_2\text{Se}_4$	11.104	6.704	10.879	Orange	1012	$\approx 10^{12}$
$\text{SrAl}_2\text{S}_4$	10.227	6.065	10.429	White		
$\text{SrGa}_2\text{S}_4$	10.255	6.107	10.424	White	1215	
* $\text{SrIn}_2\text{S}_4$	10.548	6.510	10.439	Pink		
$\text{SrGa}_2\text{Se}_4$	10.711	6.385	10.864	White		$7 \times 10^4$
* $\text{SrIn}_2\text{Se}_4$	10.938	6.728	11.017	Orange		$7 \times 10^7$
$\text{CaGa}_2\text{S}_4$	10.026	6.06	10.053	White		$\approx 10^{10}$
* $\text{CaGa}_2\text{Se}_4$	10.506	6.319	10.662	Pink		$\approx 10^{10}$
* $\text{YbAl}_2\text{S}_4$	10.045	6.020	10.029	Yellow		
* $\text{YbGa}_2\text{S}_4$	10.041	6.066	10.056	Red-orange		$10^8$
* $\text{YbGa}_2\text{Se}_4$	10.185	6.338	10.501	Red		$4 \times 10^5$
* $\text{BaGa}_2\text{Se}_4$	10.605	6.408	11.321	Light orange		$\approx 10^{10}$
* $\text{BaIn}_2\text{S}_4$	10.840	6.556	10.885	Pink		
* $\text{BaIn}_2\text{Se}_4$	11.262	6.785	11.335	Light orange		$3 \times 10^6$
$\text{BaGa}_2\text{S}_4$	Cubic cells a in Å					
	12.610			White	1055	$\approx 10^{10}$
* $\text{BaAl}_2\text{S}_4$	12.588			White		

Cubic cells a in Å.  
\* New compositions.

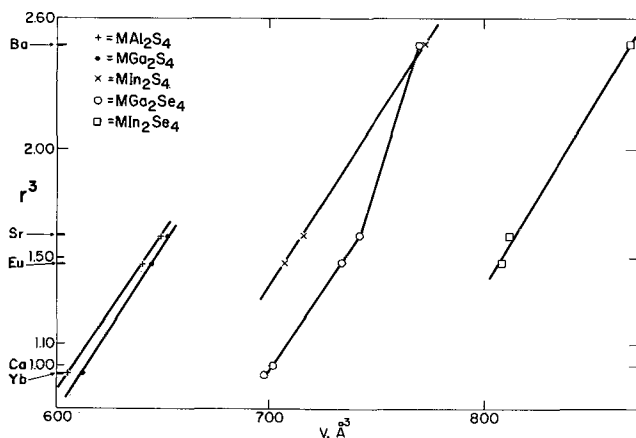


Fig. 1. Size relationships of the orthorhombic  $PbGa_2Se_4$  type cells

In a study of a crystal of  $EuIn_2Se_4$ , a triclinic cell was derived by sorting out untwinned reflections. The dimensions are  $a = 6.42\text{\AA}$ ,  $b = 12.840\text{\AA}$ ,  $c = 15.424\text{\AA}$ ,  $\alpha = 127^\circ$ ,  $\beta = 52.8^\circ$ ,  $\gamma = 116.6^\circ$ .

Figure 1 shows the size relationships. It is a plot of the radii cubed ( $r^3$ ) of the divalent cations vs. the volume of the orthorhombic cells. The radii of the divalent cations were obtained by taking half the cell edge of the rock salt sulfides  $M^{II}S$  and subtracting the ionic radius of S (1.84Å).

The figure suggests that relative cation size is an important factor in the formation of the  $PbGa_2Se_4$ -type structure. When  $M^{II} = Ca$  or  $Yb$ , only combinations with  $M^{III} = Al, Ga$  show this structure. When  $M^{II}$  is  $Ba$ , the structure forms only in combination with the large  $M^{III}$  cation,  $In$ ; with  $M^{III} = Al, Ga$ , a cubic structure forms for the sulfides.

$BaGa_2Se_4$  exhibits the orthorhombic  $PbGa_2Se_4$ -type powder pattern but with an anomalous cell volume. A study of the system  $BaGa_2S_{4-x}Se_x$  showed the  $BaGa_2S_4$  type present for  $x = 3.6$  but a rhombohedral distortion was seen.

**Electrical properties.**—Room temperature resistivities (Table I) and Seebeck coefficients measured on single crystals indicate high resistance, p-type semiconduction. Many attempts were made to dope these materials but resistivities could not be appreciably lowered.

$EuIn_2Se_4$  exhibited photoconductivity with  $\rho$  dark  $> 10^{14}$  ohm-cm; when exposed to light (4000-6000Å),  $\rho = 2 \times 10^9$  ohm-cm.

**Photoluminescence:  $Eu^{+2}$ .**—The  $Eu^{+2}$  photoluminescence emission spectra of  $M^{II}M_2^{III}(S,Se)_4$  phosphors excited by 253.7 nm Hg light were measured on powders between 300 and 750 nm using a 1/2 meter Bausch and Lomb monochromator fitted with an EMI extended S-20 response photomultiplier tube detector.

The monochromator-detector system was calibrated against an Eppley quartz-iodine standard lamp. As a further check, the spectra obtained on NBS reference phosphors were compared with those obtained by Shelton (9).

Consistent with the findings of Peters and Baglio (8), we found the emission of  $Eu^{+2}$  in  $M^{II}M_2^{III}Se_4:Eu$  to consist of narrow bands which peaked, depending on the host, in the blue through red region of the spectrum. We extended studies of the fluorescent properties of  $Eu^{+2}$  in these materials to include cases where  $M^{III} = Al, In$ , selenides and  $EuM_2^{III}(S,Se)_4$ .

The emission band peak positions, peak half widths, and quantum efficiencies are given in Table II.

The photoluminescence quantum efficiencies were estimated by comparing the integrated emission intensities of the  $M^{II}M_2^{III}(S,Se)_4:Eu, Yb$  samples with the integrated intensities of the National Bureau of Standards reference phosphors NBS 1026, 1027, and 1028. The 254 nm excited photoluminescent quantum efficiencies of the reference phosphors were measured by Brill and Hoekstra (10), Kingsley and Ludwig (11), and Shelton (9). For most work, NBS 1026 was the comparison phosphor and was assumed to have a quantum efficiency of 77% under 254 nm excitation.

The  $M^{II}In_2(S,Se)_4:Eu$  compositions are not luminescent at room temperature; 80°K luminescence properties are given in Table II.

From Table II it can be seen that the emission peak position is shifted to the blue region of the spectrum for  $Ba_{0.999}Al_2S_4:0.006 Eu$ . It may be stated that, as the electropositive character of the cations of the host increases, the emission shifts in color from red to blue. In the same way the optical bandgap would be expected to increase since the ionic character of the host would increase.

It can also be seen in Table II that the emissions from  $EuGa_2S_4$  and  $EuAl_2S_4$  are quite strong.

In order to understand the fluorescences of  $Eu^{+2}$  in these materials as a function of host bandgap, we studied the lifetimes, thermal properties, optical absorption, and excitation spectra of selected compositions. We hoped to gain an understanding of the relationship of the band levels of the fluorescent levels for the possibility of achieving injection electroluminescence.

**Decay lifetimes.**—The fluorescence decay lifetimes of several  $Eu^{+2}$  activated  $M^{II}M_2^{III}(S,Se)_4$  phosphors are listed in Table III. The decay lifetimes fall into three groups: (i)  $EuM_2^{III}S_4 \approx 0.2 \mu\text{sec}$ , (ii)  $M^{II}M_2^{III}S_4$ : (dilute  $Eu$ )  $\approx 0.3-0.5 \mu\text{sec}$ , and (iii)  $M^{II}M_2^{III}Se_4$ : (dilute  $Eu$ )  $\approx 1-2 \mu\text{sec}$ . The 0.3-0.5  $\mu\text{sec}$  range is believed to be representative of  $Eu^{+2}$  in the  $M^{II}M_2^{III}S_4$  environment. The oscillator strength estimated from the 0.42  $\mu\text{sec}$  lifetime of  $SrGa_2S_4:Eu$  is  $5 \times 10^{-3}$ , consistent in order of magnitude with previously reported values

Table II. Photoluminescence of  $Eu^{+2}$  and  $Yb^{+2}$  activated  $M^{II}M_2^{III}(S,Se)_4$  phosphors

Composition	Wavelength of maximum photoluminescence emission (nm)		Emission peak half-width (nm)	Luminescence quantum efficiency (254 nm excitation) %	Temperature (°K)
$Ba_{0.999}Al_2S_4:0.006Eu$	475	Blue	57	6	300
$Ba_{0.999}Ga_2S_4:0.005Eu$	495	Blue-green	58	12	300
$Ba_{0.99}In_2S_4:0.01Eu$	680	Red	100	~0.1	80
$Sr_{0.99}Al_2S_4:0.01Eu$	496	Blue-green	42	4	300
$SrGa_2S_4:10 \text{ ppm } Eu$	538	Yellow-green	52	7	300
$Sr_{0.9}Ga_2S_4:0.1Eu$	540	Yellow-green	45	11	300
$Sr_{0.9}Ga_2S_4:0.1Eu$	547	Yellow-green	55	0.2	300
$Sr_{0.99}In_2S_4:0.01Eu$	640	Red	60	0.05	80
$Ca_{0.9}Ga_2S_4:0.2Eu$	560	Yellow	57	9	300
$Ca_{0.9}Ga_2Se_4:0.1Eu$	562	Yellow	53	~0.1	300
$EuAl_2S_4$	508	Yellow-green	32	2	300
$EuGa_2S_4$	546	Yellow	34	5	300
$EuGa_2Se_4$	528				
$Ca_{0.99}Ga_2S_4:0.01Yb$	580	Orange	65	3	80
$YbGa_2S_4$	805	Orange	60	~0.1	80

\* At 80°K.

Table III. Photoluminescence decay lifetimes

Composition	Decay life-time ( $\mu\text{sec}$ )
$\text{EuGa}_2\text{S}_4$	0.16
$\text{EuAl}_2\text{S}_4$	0.19
$\text{Ca}_{0.95}\text{Ga}_2\text{S}_4:0.05\text{Eu}$	0.48
$\text{Ca}_{0.8}\text{Ga}_2\text{S}_4:0.2\text{Eu}$	0.49
$\text{SrGa}_2\text{S}_4:10\text{ ppm Eu}$	0.42
$\text{BaGa}_2\text{S}_4:0.005\text{Eu}$	0.30
$\text{Ba}_{0.95}\text{Ga}_2\text{S}_4:0.05\text{Eu}$	0.31
$\text{BaAl}_2\text{S}_4:0.006\text{Eu}$	0.35
$\text{Ba}_{0.9}\text{Al}_2\text{S}_4:0.05\text{Eu}$	0.45
$\text{Ca}_{0.9}\text{Ga}_2\text{Se}_4:0.1\text{Eu}$	1.8
$\text{Sr}_{0.9}\text{Ga}_2\text{Se}_4:0.1\text{Eu}$	1.4

(12). The shorter lifetimes of the  $\text{EuM}_2\text{III}\text{S}_4$  sample is believed to be a manifestation of concentration quenching: the observed lifetimes are shortened by nonradiative depopulation of the  $\text{Eu}^{+2}$  excited states.

The longer emission lifetimes of the selenides compared to the sulfides may be caused by greater mixing of the  $4f^{65d}$  or  $4f^{66s}$   $\text{Eu}^{+2}$  excited states with  $\text{Se}^{-2}$  excited states than occurs with the  $\text{S}^{-2}$  excited states. In other words, the  $\text{Eu}^{+2}$  excited states may be delocalized in the selenides and lie within or above the conduction band. This is consistent with the emission data (Table II) which shows the selenides  $\text{EuGa}_2\text{Se}_4$  and  $\text{Ca}_{0.9}\text{Ga}_2\text{Se}_4:0.1\text{Eu}$  to emit at energies higher than or nearly the same as the analogous sulfides. Since the bandgaps of the selenides would be expected to be narrower than the sulfides, the  $\text{Eu}^{+2}$  excited states may be within the conduction band. The selenides have very low photoluminescent efficiencies only slightly increased by cooling to  $80^\circ\text{K}$ .

Although most of the photoluminescence of Eu-activated  $\text{M}^{\text{II}}\text{M}_2\text{III}(\text{S},\text{Se})_4$  decays very rapidly, in a few  $\mu\text{sec}$  or less, a small amount of the photoluminescence, typically 1-5% of the total intensity, decays much more slowly, over intervals of 10 msec or longer. The long decay duration emission or phosphorescence is most prominent in the  $\text{BaM}_2\text{III}\text{S}_4$  compositions, for which as much as 10% of the photoluminescence is phosphorescence. Under electron excitation, the phosphorescence of the  $\text{BaM}_2\text{III}\text{S}_4$  phosphors lasts several seconds for samples with the lowest Eu concentrations ( $\sim 100\text{ ppm}$ ). The phosphorescence and fluorescence emission spectra are the same. The more phosphorescent  $\text{M}^{\text{II}}\text{M}_2\text{III}(\text{S},\text{Se})_4:\text{Eu}$  compositions can also be excited by IR light after exposure to uv. We conclude that the phosphorescence is caused by trapped electrons which are thermally ionized over a period of time.

#### Temperature dependence of the photoluminescence.—

The temperature dependence of  $\text{M}^{\text{II}}\text{M}_2\text{III}\text{S}_4:\text{Eu}$  phosphors is sensitive to Eu concentration. The temperature dependence of  $\text{EuGa}_2\text{S}_4$  and  $\text{SrGa}_2\text{S}_4:\text{Eu}$  is shown in Fig. 2. The photoluminescence efficiency of  $\text{Eu}^{+2}$  in  $\text{EuGa}_2\text{S}_4$  decreases with temperature and is a factor of 100 greater at  $100^\circ\text{K}$  than at  $500^\circ\text{K}$ . On the other hand, the photoluminescence of  $\text{SrGa}_2\text{S}_4$  doped with 100 ppm Eu or less is almost temperature independent.

**Excitation spectra and optical absorption.—**The photoluminescence excitation and emission spectra of  $\text{EuGa}_2\text{S}_4$  are shown in Fig. 3: 254 nm light is 60% as efficient in exciting luminescence as is 450 nm light. However, according to the data of Peters and Baglio (8), 254 nm light is only  $\sim 10\%$  as efficient as 450 nm light in exciting luminescence in  $\text{Sr}_{0.98}\text{Ga}_2\text{S}_4:0.02\text{Eu}$ . Thus as the Eu concentration increases in the system  $\text{SrGa}_2\text{S}_4:\text{Eu}$ , the increased relative utility of 254 nm light partially cancels the deleterious effect of concentration quenching.

The optical absorption of  $\text{SrGa}_2\text{S}_4$  and  $\text{Sr}_{0.98}\text{Ga}_2\text{S}_4:0.02\text{Eu}$  crystals are shown in Fig. 4. The absorption was determined by measuring the transmission of  $\sim 2 \times 10^{-3}\text{ cm}$  thick samples in a Cary 14.  $\text{SrGa}_2\text{S}_4$  has an absorption edge at 380 nm and little or no absorption between this edge and the infrared.  $\text{Sr}_{0.98}\text{Ga}_2\text{S}_4:0.02\text{Eu}$

has additional absorption between 360 and 510 nm which we associate with  $\text{Eu}^{+2} 4f^7 \rightarrow 4f^65d$  or  $4f^66s$  transitions. The oscillator strength determined by integrating the  $\text{Eu}^{+2}$  part of the absorption in  $\text{Sr}_{0.98}\text{Ga}_2\text{S}_4:0.02\text{Eu}$  is  $4 \times 10^{-3}$ , in satisfactory agreement with the  $5 \times 10^{-3}$  value derived from fluorescence decay lifetime data and quite reasonable for a parity allowed transition in a multielectron transition metal ion. The  $\text{Eu}^{+2}$  absorption has also been measured in  $\text{Sr}_{0.995}\text{Al}_2\text{S}_4:0.005\text{Eu}$ . In this compound the Eu absorption peaks at 380 nm compared with 393 nm in  $\text{Sr}_{0.98}\text{Ga}_2\text{S}_4:0.02\text{Eu}$ .

**Discussion.—**The Eu luminescence is excited relatively efficiently in the wavelength region where  $\text{Eu}^{+2}$  absorption is dominant. At excitation wavelengths shorter than the host fundamental edge, the  $\text{Eu}^{+2}$

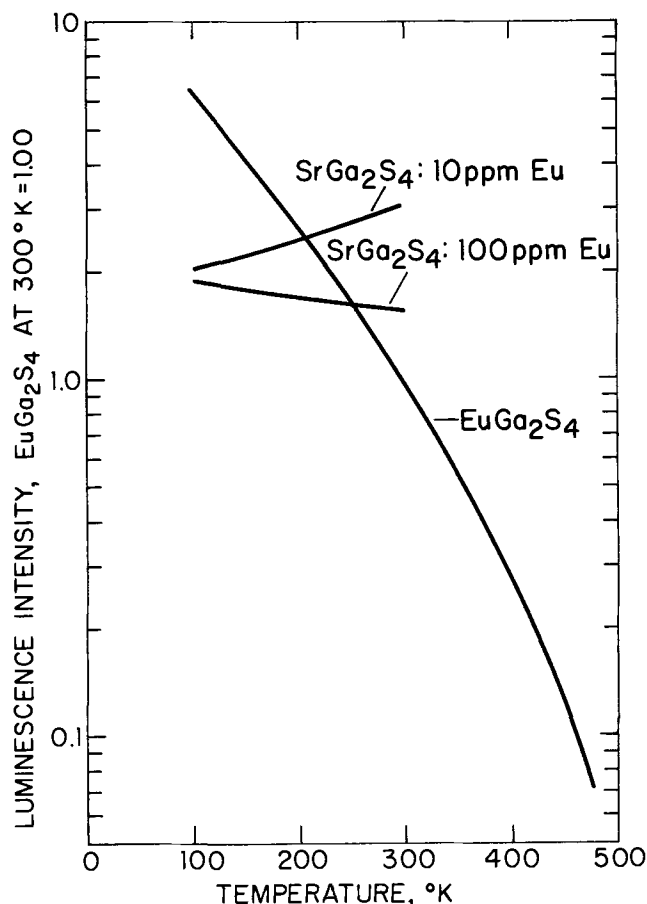


Fig. 2. Temperature dependence of the photoluminescence of  $\text{EuGa}_2\text{S}_4$  and  $\text{SrGa}_2\text{S}_4:\text{Eu}$ .

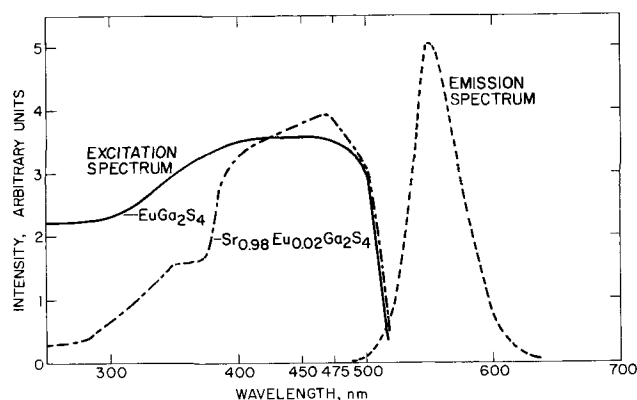


Fig. 3. Photoluminescence excitation and emission spectra of  $\text{EuGa}_2\text{S}_4$  and  $\text{Sr}_{0.98}\text{Eu}_{0.02}\text{Ga}_2\text{S}_4$ . The data on  $\text{Sr}_{0.98}\text{Eu}_{0.02}\text{Ga}_2\text{S}_4$  were taken from Peters and Baglio (8).

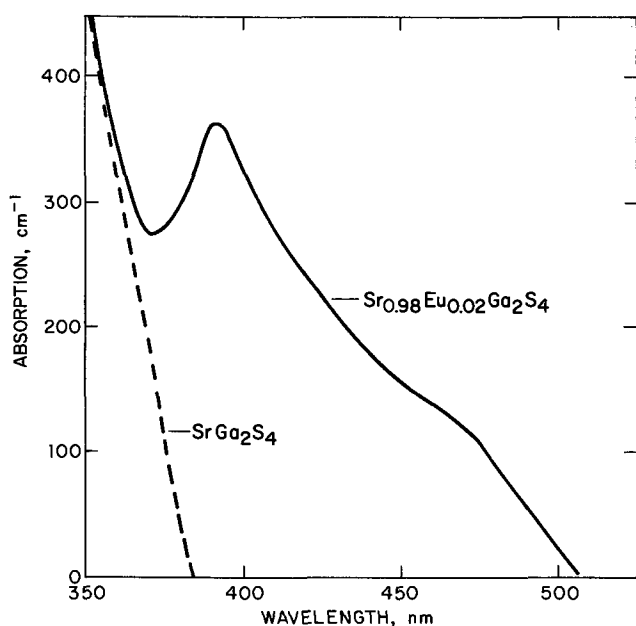


Fig. 4. Optical absorption of  $SrGa_2S_4$  and  $Sr_{0.98}Eu_{0.02}Ga_2S_4$

luminescence efficiency drops sharply in dilutely doped samples (compare Fig. 3 and 4). We conclude that the host absorption mechanism is able to excite the  $Eu^{+2}$  luminescence only weakly or not at all. Consequently the relative  $Eu^{+2}$  photoluminescence efficiency at any exciting wavelength scales with the ratio of the  $Eu$  absorption to the host absorption.

The values of the efficiencies quoted in Table II are therefore insufficient measures of the true efficiencies because the 254 nm excitation is very poor for stimulating fluorescence.

Many of the features noted in these studies may be correlated in terms of the observation that fluorescence is produced more efficiently by excitation directly into the  $Eu^{+2}$  excited states.

When the bandgap or host absorption energy levels are only slightly higher than the  $Eu^{+2}$  excited states, energy may be lost from the  $Eu^{+2}$  excited states to the host where nonradiative processes predominate by thermal excitation. The much greater efficiency of the luminescence of  $EuGa_2S_4$  at low temperature may be interpreted as due to less of this type of thermal excitation. The more isolated  $Eu^{+2}$  levels in the very dilute  $SrGa_2S_4:Eu$  compositions may not receive thermal energy from the host in the same way as in the more concentrated composition. Their different behavior may be related to such an effect.

The low fluorescence efficiency of the selenides and In composition is probably also due to mixing of the  $Eu^{+2}$  levels with the fundamental edge since the bandgaps of these compounds would be expected to be narrower than the sulfides and GaAl compositions. The most efficient phosphors should then be those with the widest bandgaps where interaction between the  $Eu^{+2}$  excited states and fundamental edge is minimal, e.g.,  $BaAl_2S_4:Eu$ .

**Photoluminescence:  $Yb^{+2}$ .**—The photoluminescence of  $Yb^{+2}$  has been observed and measured in a few  $M^{II}M_2^{III}S_4$  hosts, but is bright only at low temperatures (Table II). The color of the  $Yb^{+2}$  emission is yellow or orange. At 80°K, the quantum efficiencies of  $YbGa_2S_4$  and  $Ca_{0.98}Ga_2S_4:0.1 Yb$  are 0.1 and 3%, respectively. The  $Yb^{+2}$  emission intensity is completely quenched at ~200°K. It is not known why the  $Yb^{+2}$  emission is quenched at room temperature, but we speculate that the excitation energy may be degraded by the presence of a small concentration of  $Yb^{+3}$ . In  $YbGa_2S_4$ , the intensity of the 0.97 $\mu$   $Yb^{+3}$  absorption band suggests that about 5% of the  $Yb$  in the sample is trivalent.

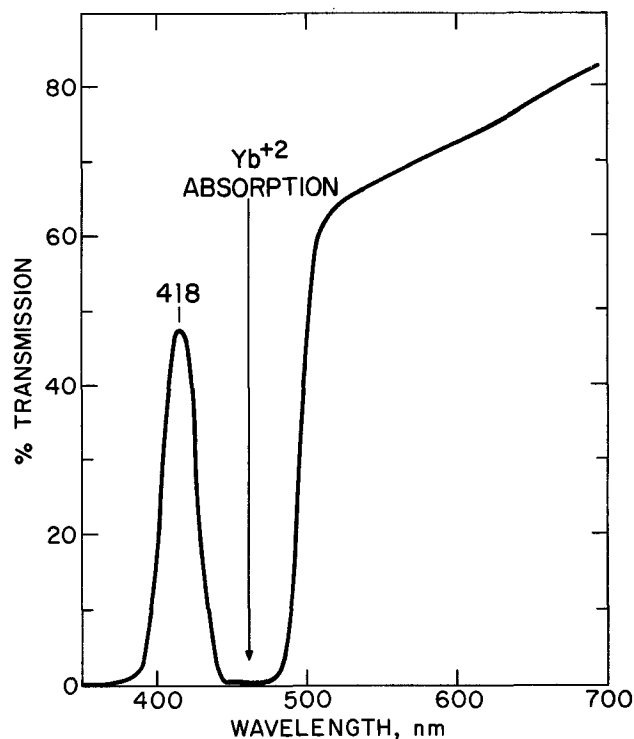


Fig. 5. Optical transmission of  $YbAl_2S_4$

**Optical absorption,  $Yb^{+2}$ .**—The optical absorption of  $M^{II}M_2^{III}S_4:Yb$  is qualitatively similar to  $M^{II}M_2^{III}S_4:Eu$ . There is a long wavelength  $Yb$  absorption band which overlaps the fundamental edge of the host to some extent. The overlap is smaller for  $Yb$  than for  $Eu$ . For example in  $YbAl_2S_4$ , there is a window between the  $Yb$  absorption band and the fundamental edge. This may be seen in the optical transmission data for a  $2 \times 10^{-3}$  cm thick crystal illustrated in Fig. 5.

#### Acknowledgment

Dr. J. D. Bierlein is especially thanked for helpful suggestions and discovering the infrared stimuable fluorescence. Drs. H. S. Jarrett and D. B. Rogers contributed helpful discussion. Dr. W. Jeitschko contributed to the x-ray work. Dr. P. E. Bierstedt and Mr. J. L. Gillson performed electrical measurements. The equipment for measurement of fluorescent lifetime was designed and built by Mr. P. C. Hoell. Many of the photoluminescence emission spectra were measured on equipment developed by Mr. R. P. Schwenker. Mr. D. J. Jones and Mr. D. W. Reutter assisted in sample preparation and testing.

Manuscript submitted June 18, 1973; revised manuscript received Aug. 3, 1973.

Any discussion of this paper will appear in a Discussion Section to be published in the December 1974 JOURNAL.

#### REFERENCES

1. K. Krigimiga and H. Steinfink, *Inorg. Chem.*, **7**, 1762 (1968).
2. J. E. Igiiasias and H. Steinfink, *Solid State Chem.*, **6**, 119 (1973).
3. H. Hahn, G. Frank, W. Klingler, A. Störger, and G. Störger, *Z. Anorg. u. Allgem. Chem.*, **279**, 241 (1955).
4. C. Romers, B. A. Blaisse, and D. W. Ijdo, *Acta. Cryst.*, **23**, 634 (1967).
5. H. Hahn and W. Klingler, *Z. Anorg. Allgem. Chem.*, **263**, 177 (1950).
6. R. Eholie, J. K. Kom, and J. Flahaut, *C. R. Acad. Sci. Paris, Ser. C.*, **268**, 700 (1969).
7. R. Eholie, O. Gorochoy, M. Guittard, A. Mazurier, and J. Flahaut, *Bull. Soc. Chim. Fr.*, **3**, 747-50 (1971).

8. T. E. Peters and J. A. Baglio, *This Journal*, **119**, 230 (1972).
9. C. F. Shelton, Nat. Bur. Std., Tech. Note 417 (1968).
10. A. Brill and W. Hoekstra, *Philips Res. Rept.*, **16**, 356 (1961).
11. J. D. Kingsley and G. W. Ludwig, *This Journal*, **117**, 348 (1970).
12. W. Low, *Nuovo Cimento*, **17**, 607 (1960).

## Candoluminescence in Transition-Ion-Activated Oxide Phosphors

John W. Hess, Jr.,<sup>1</sup> John R. Sweet, and William B. White\*<sup>1</sup>

*Materials Research Laboratory, The Pennsylvania State University, University Park, Pennsylvania 16802*

### ABSTRACT

Flame-excited luminescence (candoluminescence) has been measured for transition-ion-activated phosphors  $Zn_2SiO_4:Mn$ ,  $LaAlO_3:Cr$ , and  $Zn_3(PO_4)_2:Mn$ . Willemite and the Cr-activated phosphors exhibit candoluminescent spectra similar to emission spectra obtained by other excitations. The emission spectra of  $Zn_3(PO_4)_2$  is profoundly different. Certain other common phosphors  $Sr_2P_2O_7:Sn$ ,  $CaCO_3:Mn$ ,  $Pb$ , and  $CaWO_4$  do not luminesce under flame excitation. All emitting phosphors require a temperature of several hundred degrees centigrade for most efficient emission.

Candoluminescence is defined as a process of light emission from solids under flame excitation, in excess of thermal radiation. The phenomenon was once a subject of great interest in connection with the operation of gas mantles and received extensive, although mainly qualitative, investigation in the first quarter of this century (1). There has been a minor but continuing interest in the Russian literature, for example a series of papers by Sokolov (2-5). There have been a number of investigations of the radical recombination mechanism that excites the luminescence (6-9) and at least one attempt to apply candoluminescence to a practical device (10). A report by Mason (11) summarized an investigation of many of the rare earth oxides and numerous commercial phosphors.

The candoluminescent phosphors can be divided into two categories of materials: low- and high-temperature emitters. The latter type luminesce at or near red heat, while the former emit from room temperature up to a few hundred degrees C. The low-temperature emitters can be further subdivided into rare-earth doped phosphors which give a spectrum of many narrow lines, and transition-ion doped phosphors which show a very broad-band spectral energy distribution. Our concern in this paper is with low-temperature emitters activated by transition metal ions.

### Experimental

Rare-earth doped candoluminescent phosphors have been investigated in some detail (12, 13), and the experimental apparatus and procedures used in the present work are identical with those described previously. Briefly, candoluminescence measurements were made by playing a hydrogen diffusion flame on a layer of powder phosphor coated on a Kanthal rod. Spectra were measured with a 3/4-meter grating spectrograph and are shown here as densitometer traces from the photographic plates. Temperature-dependence measurements were made using a Cary 14 spectrophotometer held at a fixed wavelength, while the sample temperature was cycled up and down.

Some phosphors examined were commercial products contributed by Sylvania Electric Company, others were synthesized by dry firing the corresponding oxides or carbonates at 1200°C in an air atmosphere. Table I

summarizes the phosphors examined and the activator concentration. The structure and phase purity of all synthetic phosphors were determined by x-ray diffraction.

### Spectral Measurements and Discussion

*Mn<sup>2+</sup>-activated phosphors.*— $Mn^{2+}$ -doped willemite,  $Zn_2SiO_4:Mn^{2+}$ , is a commercial green-emitting photophosphor obtained in several  $Mn^{2+}$  concentrations from Sylvania Electric Products, Incorporated. Figure 1 shows spectra typical of this material, measured from Type 103-F plates without compensation for spectral sensitivity. Both the candoluminescence spectrum (solid line) and the 254 nm Hg-excited photoluminescence spectrum (dashed line) were taken at about 170°C. The emphasis in this figure is on the similarities, rather than the differences between the spectra. The candoluminescence spectrum was a slightly lower exposure, resulting in a lower peak height, and has a slightly denser background due to the flame. Note that the bandwidth and peak frequency are essentially the same for both excitations. The true bandwidth at half-peak height cannot be directly determined, since the intensity scale is non-linear. The small peak at 625 nm is probably not significant.

Candoluminescent phosphors generally exhibit a temperature dependence of maximum emission intensity characteristic of the activator-host combination. For most of the rare-earth phosphors, the intensity-temperature curve is reproducible over several cycles of heating and cooling (13). A typical response for willemite is shown in Fig. 2. As long as the temperature was held below 200°-250°C the uppermost curve was reproduced. Once the temperature was raised to 360°C, the intensity followed the middle curve, which was again reproducible as long as the temperature was held below 200°-250°C. When the temperature was again raised to 360°C and allowed to cool, the lowest curve was obtained. Once the intensity was degraded by the flame, it did not recover its former value. The phosphor was quite stable to flame heating at low temperature but is rapidly rendered nonemitting by repeated heating at higher temperatures.

The candoluminescence spectrum of willemite, therefore, is not measurably different from the photoluminescence. Gorban' *et al.* (5) reported different decay

\* Electrochemical Society Active Member.

<sup>1</sup> Also affiliated with the Department of Geosciences.

Key words: candoluminescence, phosphors, willemite, zinc phosphate, lanthanum aluminate.

Table I. Summary of phosphors examined

Host	Activator	Luminescence		Source
		254 nm Photo-	Cando-	
Zn <sub>2</sub> SiO <sub>4</sub>	0.022 Mn <sup>2+</sup>	Bright green	Bright green	Sylvania 161
Zn <sub>2</sub> SiO <sub>4</sub>	0.048 Mn <sup>2+</sup>	Bright green	Bright green	Sylvania (?)
Zn <sub>2</sub> SiO <sub>4</sub>	0.093 Mn <sup>2+</sup>	Bright green	Bright green	Sylvania 2282
Zn <sub>3</sub> (PO <sub>4</sub> ) <sub>2</sub>	(?) Mn <sup>2+</sup>	Very weak red	Bright yellow-orange	Sylvania 151
LaAlO <sub>3</sub>	0.0048 Cr <sup>3+</sup>	None	Weak red	National Lead Co.
Al <sub>2</sub> O <sub>3</sub>	0.002 Cr <sup>3+</sup>	None	Weak red	Synthesized
	0.01 Cr <sup>3+</sup>	None	Weak red	Synthesized
	0.02 Cr <sup>3+</sup>	None	Weak red	Synthesized
MgAl <sub>2</sub> O <sub>4</sub>	0.01 Cr <sup>3+</sup>	None	Weak red	Synthesized
	0.01 Cr <sup>3+</sup>	None	Weak red	Synthesized
MgGa <sub>2</sub> O <sub>4</sub>	(?) Sn <sup>2+</sup>	Bright blue	None	Sylvania 243
Sr <sub>2</sub> P <sub>2</sub> O <sub>7</sub>	0.01 Mn <sup>2+</sup>	Bright pink	None	Synthesized
CaCO <sub>3</sub>	0.01 Pb <sup>2+</sup>	None	None	Synthesized
CaWO <sub>4</sub>	None	Medium blue	None	Reagent grade

times for the two excitation mechanisms. The critical temperature for optimum brightness in Fig. 2 ranges from 220° to 190°C and is distinctly lower than the ~260°C reported by Thorington (10).

Zn<sub>3</sub>(PO<sub>4</sub>)<sub>2</sub>:Mn<sup>2+</sup> Sylvania Type 151, is listed as a red cathode-ray-tube phosphor with peak wavelength at 639 nm and bandwidth at half-peak height of 90 nm. It was found to weakly photoluminesce at the same wavelength under 254 nm excitation. Its flame-excited emission, however, was a very intense yellow-orange, which is shown in Fig. 3, as measured from a Type 103-F plate. There appear to be two peaks which are barely resolved, one at ~640 nm, the same as cathodo- and photoexcitation, and another at 600 nm which is not observed with other excitation mechanisms. The candoluminescent emission of Zn<sub>3</sub>(PO<sub>4</sub>)<sub>2</sub> is different from cathodo-excited emission. X-ray diffraction shows this commercial phosphor to consist of β-Zn<sub>3</sub>(PO<sub>4</sub>)<sub>2</sub> which emits in the red at 638 nm (14). One could imagine a phase change to the low temperature α-Zn<sub>3</sub>(PO<sub>4</sub>)<sub>2</sub> in the hydrogen flame, but α-Zn<sub>3</sub>(PO<sub>4</sub>)<sub>2</sub> is known to emit in the green at 551 nm (14), in clear disagreement with Fig. 3. This is an important result that will be discussed in more detail later.

The emission intensity of zinc phosphate exhibits a temperature dependence similar to that of willemite. The optimum efficiency occurs at 225°C (Fig. 4). This

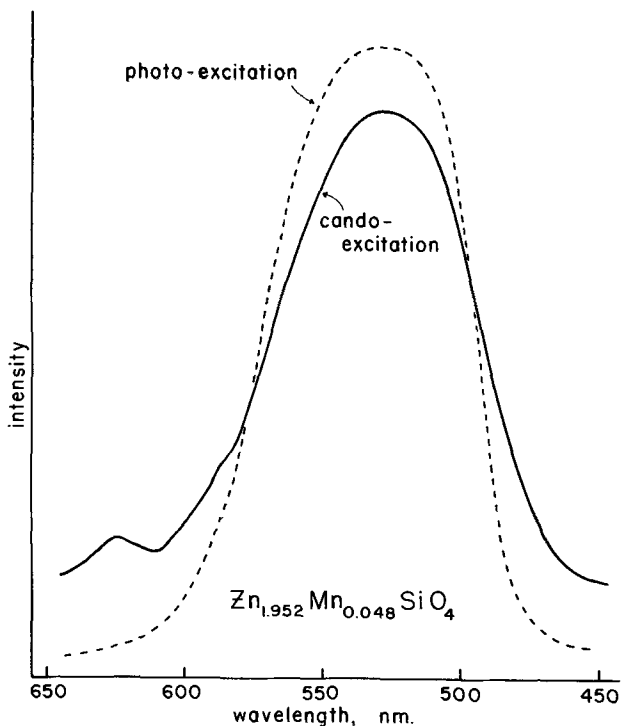


Fig. 1. Candoluminescence and photoluminescence of Mn<sup>2+</sup>-doped willemite, Zn<sub>1.952</sub>Mn<sub>0.048</sub>SiO<sub>4</sub>.

phosphor can be heated to at least 350°C and can be cycled up and down in temperature indefinitely without loss of brightness.

*Cr<sup>3+</sup>-activated phosphors.*—Phosphors activated by Cr<sup>3+</sup> typically exhibit an emission in the far red near 690 nm from the <sup>2</sup>E, <sup>2</sup>T<sub>2</sub> → <sup>4</sup>A<sub>2</sub> transition. It is a narrow band emission at low temperatures, gradually broadening as the temperature is increased. Four different oxide hosts activated by Cr<sup>3+</sup> were examined for flame-activated emission.

A sample of LaAl<sub>0.9952</sub>Cr<sub>0.0048</sub>O<sub>3</sub> obtained from National Lead Company was found to candoluminesce with a very broad band emission in the red (Fig. 5). The emission is quite weak relative to the other phosphors such that very long exposures were needed to produce even the faintest usable images on a plate. The spectrum shown was taken from an ~8 hr exposure on a Type IV-N plate, the sensitivity of which extends to almost 900 nm. The temperature of maximum intensity for this phosphor is higher than for others studied, being approximately 375°C on the first cooling-heating cycle, shown in Fig. 6. A behavior similar to that for Zn<sub>2</sub>SiO<sub>4</sub>:Mn<sup>2+</sup> (Fig. 2) was observed with repeated cycles. These measurements were made at 600 nm on the short wavelength shoulder of the emission peak, rather than on the peak itself, due to the rapidly failing sensitivity of the 1P28 photomultiplier with increasing wavelength and the low intensity of the emission. This wavelength provided optimum instrumental parameters. The broad emission with

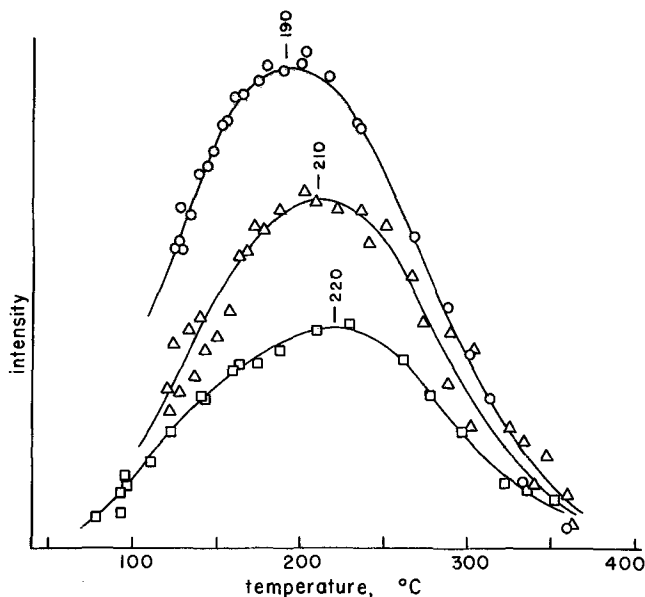


Fig. 2. Temperature dependence of the candoluminescent intensity of Zn<sub>2</sub>SiO<sub>4</sub>:Mn<sup>2+</sup> measured at 530 nm with a 2 mm slit width (spectral band width ~7 nm). First cooling-heating cycle ○, second cycle △, third cycle □.

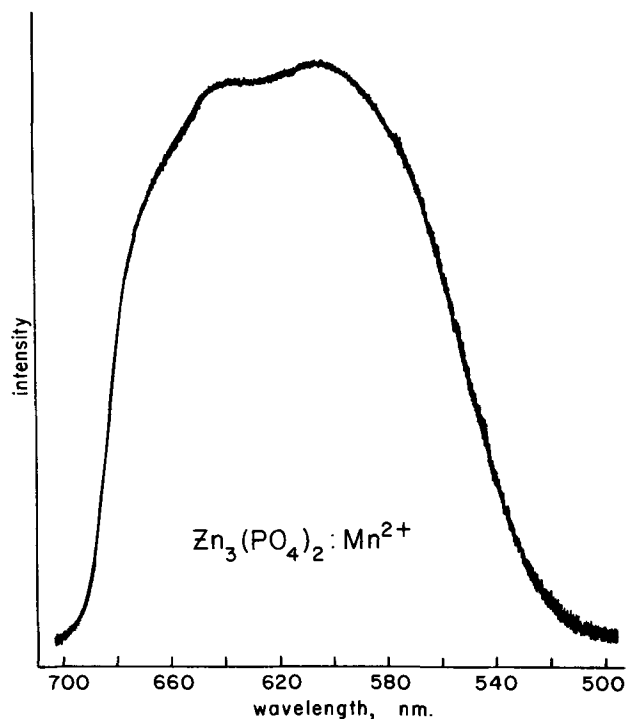


Fig. 3. Candoluminescence spectrum of  $\text{Zn}_3(\text{PO}_4)_2:\text{Mn}^{2+}$ , Sylvania phosphor Type 151. The rapid plunge in intensity above 680 nm is attributable in part to the spectral sensitivity of the 103-F plate, which begins to fall sharply at this wavelength.

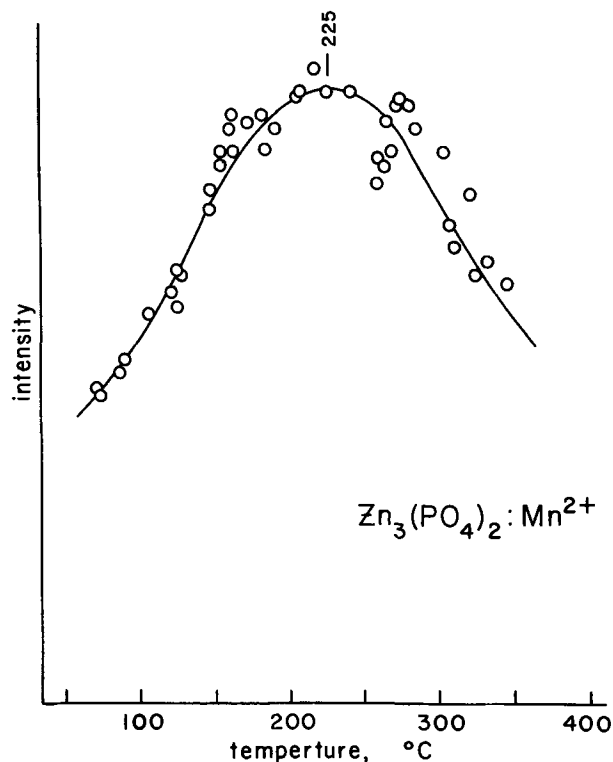


Fig. 4. Temperature dependence of the candoluminescent intensity of  $\text{Zn}_3(\text{PO}_4)_2:\text{Mn}^{2+}$  measured at 600 nm with a 3 mm slit width (spectral bandwidth  $\sim 10$  nm).

poorly resolved features obtained from  $\text{LaAlO}_3:\text{Cr}^{3+}$  is about as expected at the temperature of measurement, 300°C.  $\text{Cr}^{3+}$  is a line-emitter at low temperatures but at higher temperatures and moderate chromium concentrations phonon processes and Cr-pair interactions generate a great complexity of spectral bands which gradually fuse into a single broad emission (15). The spectrum shown in Fig. 5, taken at

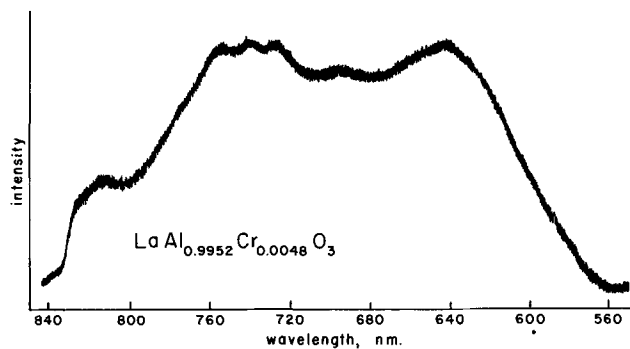


Fig. 5. Candoluminescence spectrum of  $\text{LaAlO}_3:\text{Cr}^{3+}$  measured at roughly 300°C.

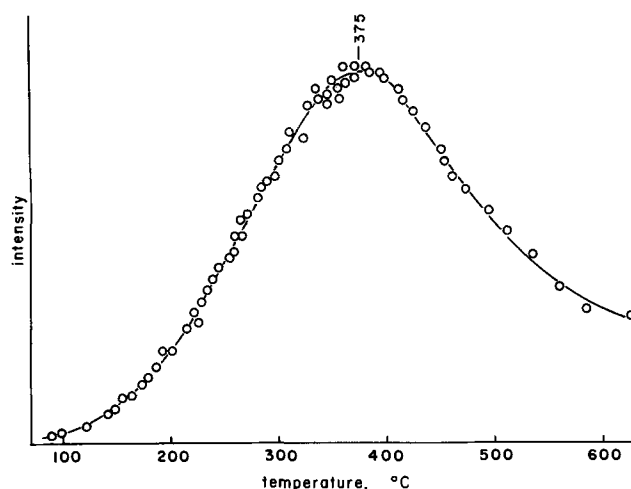


Fig. 6. Temperature dependence of the candoluminescent intensity of  $\text{LaAlO}_3:\text{Cr}^{3+}$  measured at 600 nm with a 3 mm slit width (spectral bandwidth  $\sim 10$  nm).

roughly 570°K, is similar to published  $\text{Al}_2\text{O}_3:\text{Cr}^{3+}$  spectra obtained at similar temperatures (15).

Several other chromium-doped materials were investigated, among them  $\text{Al}_{2-x}\text{Cr}_x\text{O}_3$  with  $x = 0.002, 0.01, 0.02$ ;  $\text{MgAl}_{1.99}\text{Cr}_{0.01}\text{O}_4$ ; and  $\text{MgGa}_{1.99}\text{Cr}_{0.01}\text{O}_4$ . All were observed to emit a faint red candoluminescence at temperatures of a few hundred degrees C. In addition, a faint yellowish-green emission appears as a transient phenomenon at lower temperatures. Neither emission was strong enough for satisfactory spectral measurements. Visual observations seem to indicate a slightly higher efficiency for the  $\text{Al}_{1.99}\text{Cr}_{0.01}\text{O}_3$  than for either the higher or lower chromium fraction. None of the samples was strongly photoluminescent (254 nm excitation), but all emit in the red under cathodo-excitation.

**Other phosphors.**—The commercial phosphor  $\text{Sr}_2\text{P}_2\text{O}_7:\text{Sn}^{2+}$  is a strong blue emitter under 254 nm excitation. This phosphor shows no fluorescence at all under hydrogen flame excitation. The phosphor exposed to the flame retains its strong photo-emission so degradation of the phosphor by reaction in the flame does not seem to be the explanation for the absence of candoluminescence.

$\text{CaWO}_4$ , the usual example of a self-activated phosphor with a strong cathodo-emission in the blue, is inert under the hydrogen flame. No emission was observed at temperatures up to red heat.

$\text{CaCO}_3$  coactivated with 0.01  $\text{Mn}^{2+}$  and 0.01  $\text{Pb}^{2+}$  was prepared by coprecipitation from solution. The dried phosphor emits a bright pink under 254 nm excitation. This material likewise did not luminesce in the hydrogen flame.

Experimentation with several  $\text{Mn}^{4+}$ -activated phosphors,  $\beta\text{-Al}_2\text{O}_3$ ,  $\text{SrAl}_{12}\text{O}_{19}$ , and  $\text{CaAl}_{12}\text{O}_{19}$  produced no

luminescence. No special significance can be assigned to this result because  $Mn^{4+}$  may have been reduced in the hydrogen flame.

### General Discussion and Conclusions

In a recent summary of the extensive Soviet effort on radical recombination luminescence, Volkenstein *et al.* (16) make a very firm statement that, "It should be observed that the same centers give rise to both photo- and candoluminescence . . . the position of the luminescence bands in the spectrum is independent of the nature of the excitation of the crystallophosphor." In spite of a very considerable effort on the part of workers cited previously, relatively few phosphor activator:host combinations have been examined in detail. As a result of the brief survey reported here, we can show that the candoluminescence process must be more complicated than the statement quoted above would imply.

The survey of the spectral emission characteristics of a set of transition-metal-ion-activated phosphors can be summarized as follows: (i) Two phosphors, willemite, and  $Cr^{3+}$ -activated oxides do indeed exhibit the same spectrum under flame excitation as under u.v. or electron excitation. (ii) Three phosphors,  $Sr_2P_2O_7$ :  $Sn^{2+}$ ,  $CaWO_4$ , and  $CaCO_3$ :Mn, Pb are not candoluminescent although they emit brightly under u.v. excitation and show no evidence for damage in the flame. (iii) One phosphor,  $\beta$ - $Zn_3(PO_4)_2$  exhibits a flame-excited emission spectrum of two overlapping broad bands giving a yellow-orange color, whereas the same phosphor under u.v. or cathode-ray excitation emits only in the red band.

Result (iii) is deemed of most importance because it is a form of candoluminescent behavior apparently not observed by any of the previous workers. Since this work was completed, a second such case has been found in  $CaSO_4$ :Mn in which the usual green emission gives way to a deep yellow as the temperature is increased (17). The crystal structure of  $\beta$ - $Zn_3(PO_4)_2$  contains three distinct cation sites on which the  $Mn^{2+}$  activator could substitute (18). Zn(I) is four-fold coordinated and Zn(II) and Zn(III) are five-fold coordinated with nearly the same mean Zn-O bond lengths. However, Zn(2) has an additional long Zn-O distance which changes the local geometry and almost certainly the local crystal field. Although EPR results show that the  $Mn^{2+}$  activator is distributed over all three sites, it is not known which site is responsible for the characteristic red emission. It does not seem impossible, however, that the flame may excite the activator on both 5-coordinated sites and the u.v. and electron induced red emission may be due to only one of them. A similar situation seems to prevail in the  $CaSO_4$ :Mn phosphor noted above.

Two additional lines of evidence have evolved from the examination of other phosphor systems (12, 13) that indicate that candoluminescence is more complicated than just a novel method of excitation. The most characteristic feature of candoluminescence is the strongly peaked response of the intensity to temperature. The explanation offered by Hanle and Niermann (8) is that the rising wing represents the evaporation of adsorbed gases exposing more phosphor surface to the recombination process. The decaying wing represents the thermal quenching of the luminescence. Although this explanation might be appropriate to the phosphors described in this paper, the maxima for the rare earth-activated phosphors occur in the range of

50°-250°C, over which range the thermal quenching is not detectable. Secondly, the lack of much enthusiasm for possible application of candoluminescence in devices is due in large part to Sommermeyer's (6) estimation of the quantum efficiency at  $10^{-5}$ . These calculations were based on measurements of the radical recombination process in nitrogen gas. However, experiments with a microwave discharge cavity (12) showed that activated species from nitrogen or hydrogen gas only, used by many previous investigators, were very ineffective in exciting luminescence whereas radicals obtained from the microwave dissociation of water vapor produced bright luminescence. The efficiency, it appears, is very sensitive to particular excited species and there is no reason to believe that Sommermeyer's  $10^{-5}$  quantum efficiency represents any sort of upper limit.

We conclude from this and our previous studies that the energy transfer process in flame-excited luminescence is by no means fully elucidated and that new mechanisms must be devised.

### Acknowledgment

This work was supported by the Pennsylvania Science and Engineering Foundation under agreement No. 9. We are indebted to Mr. David F. Fortney of Sylvania Electric Products, Inc. for donating the samples of commercial phosphors.

Manuscript submitted July 25, 1972; revised manuscript received Sept. 14, 1973.

Any discussion of this paper will appear in a Discussion Section to be published in the December 1974 JOURNAL.

### REFERENCES

1. E. L. Nichols, H. L. Howes, and D. T. Wilber, Carnegie Institution of Washington, Publication No. 384 (1928).
2. V. A. Sokolov, *Izv. Akad. Nauk SSSR, Ser. Fiz.*, **21**, 528 (1957); **26**, 514 (1962).
3. V. V. Styrov, V. A. Sokolov, F. F. Vol'kenshtein, A. I. Bazhin, and Yu. A. Sivov, *ibid.*, **33**, 915 (1969).
4. A. I. Bazhin, V. A. Sokolov, and V. V. Styrov, *ibid.*, **33**, 919 (1969).
5. A. N. Goban', V. G. Kornich, L. P. Kornich, and A. V. Bogatkov, *ibid.*, **33**, 922 (1969).
6. K. Sommermeyer, *Z. Physik Chem (Leipzig)*, **B41**, 433 (1938).
7. J. R. Arthur and D. T. A. Townend, *U.S. Nat. Bur. Std. Circ.* **523**, 99 (1954).
8. W. Hanle and H. Niermann, *Z. Naturforsch.*, **11a**, 395 (1956).
9. K. M. Sancier, W. J. Fredericks, and H. Wise, *J. Chem. Phys.*, **30**, 1355 (1959); **37**, 854; 860; 865 (1962).
10. L. Thorington, U.S. Pat. 2,920,222 (1960).
11. D. M. Mason, *Am. Chem. Soc. Div. Fuel Chem. Preprints*, **11**, Part 2, 540 (1967).
12. J. R. Sweet, W. B. White, H. K. Henisch, and R. Roy, *Phys. Letters*, **33A**, 195 (1970).
13. J. R. Sweet and W. B. White, *J. Chem. Phys.*, To be published.
14. F. A. Hummel and F. L. Katnack, *This Journal*, **105**, 528 (1958).
15. R. C. Powell, B. DiBartolo, B. Birang, and C. S. Naiman, *Phys. Rev.*, **155**, 296 (1967).
16. T. Volkenstein, V. A. Sokolov, A. N. Gorban', and V. G. Kornich, "Proc. Internatl. Conf. on Luminescence," Budapest p. 1433 (1966).
17. J. R. Sweet, J. W. Hess, and W. B. White, To be published.
18. J. S. Stephens and C. Calvo, *Can. J. Chem.*, **45**, 2303 (1967).



# Investigations of Carbon Residues on Surfaces of Silicon Integrated Circuits

P. V. Fontana

Swiss Federal Institute of Technology, Department of Technical Chemistry, Zurich, Switzerland

J. P. Decosterd<sup>1</sup>

Faselec AG, Semiconductors, Zurich, Switzerland

and L. Wegmann

Balzers AG, für Hochvakuumtechnik und Dünne Schichten, Balzers, Fürstentum Liechtenstein

## ABSTRACT

Material contrasts which were dependent on the doping were seen on integrated circuits during examination with the photoemission electron microscope (PEEM). Surface studies using the PEEM, Auger electron spectroscopy (AES), and secondary ion mass spectroscopy (SIMS) showed that these material contrasts can be traced to doping dependent coverage of the silicon surface by hydrocarbons.

Strong material and relief contrasts were observed during photoemission electron microscopic (PEEM) examinations of integrated circuits from different manufacturers after removal of aluminum and silicon dioxide from the samples (Fig. 1). After a short etch with argon ions the relief contrasts only were seen (Fig. 4). Wegmann (1) proposed that such material contrasts were at least partly produced by contamination layers. This paper is a study on this hypothesis and the possible correlations between material contrasts and the doping of diffused areas in integrated circuits.

One of the possibilities for direct imaging of surfaces is given by the use of photo electrons in an electron microscope (2). It can be assumed that information is gathered up to a depth of a few monolayers in a PEEM picture (3, 4). Ultraviolet radiation ( $2968 \pm 100\text{\AA}$ ) is directed on the object to be observed from which the electrons, released by the photo effect, are accelerated by an electric field between sample and anode and guided via the anode diaphragm into a three stage electromagnetic electron microscope. The magnified emission pattern can be viewed on a screen or can be used to expose a photo plate.

The three types of contrasts are: (i) relief contrast, formed somewhat similarly to contrasts in the scanning electron microscope (1); (ii) material contrast, due to different values of the work function for different substances present within the sample surface; and (iii) orientational contrast, due to different crystallographic orientations of grains of one and the same substance.

Since our investigated integrated circuits are made using 111 single crystal silicon wafers, no orientational contrasts can be expected.

Surface analysis with auger electron spectroscopy (AES) (5) reveals which elements are present in surface layers by means of measuring the energies of Auger electrons emitted from the sample during electron bombardment.

Information on the type of chemical bonding can be gained by secondary ion mass spectrometry (SIMS). In this method, argon ions bombard the sample and secondary ions emitted from the uppermost monolayer of the sample are analyzed by a mass spectrometer (6).

<sup>1</sup> Present address: Balzers AG, für Hochvakuumtechnik und Dünne Schichten, Balzers, Fürstentum Liechtenstein.

Key words: surface contamination, investigation techniques of surface, influence of doping on surface contamination, emission electron microscopy, Auger electron spectroscopy, secondary ion mass spectroscopy.

## Sample Preparation

The following is a description of the manufacturing procedure of the integrated circuits studied in these investigations.

Starting from dislocation-free silicon single crystal wafers which had surfaces on the 111 plane, 38 mm diameter,  $250\mu$  thickness and doping of  $10^{15}$  atoms/cm<sup>3</sup> of boron, phosphorous-doped epitaxial layers with resistivities of 1-10 ohm·cm were grown at 1200°C using SiCl<sub>4</sub>. Oxidations were carried out at 1200°C using oxygen saturated with water at 90°C. Boron was deposited at 975°C using a BBr<sub>3</sub> source. Phosphorus was deposited at 1000°C using a POCl<sub>3</sub> source. Aluminum was deposited at  $10^{-6}$  Torr using electron bombardment heating and 5N aluminum.

Cleaning of the wafers was done in a 1:1 mixture of sulfuric acid and nitric acid at 90°C. The wafers were then rinsed in deionized water with resistivity greater

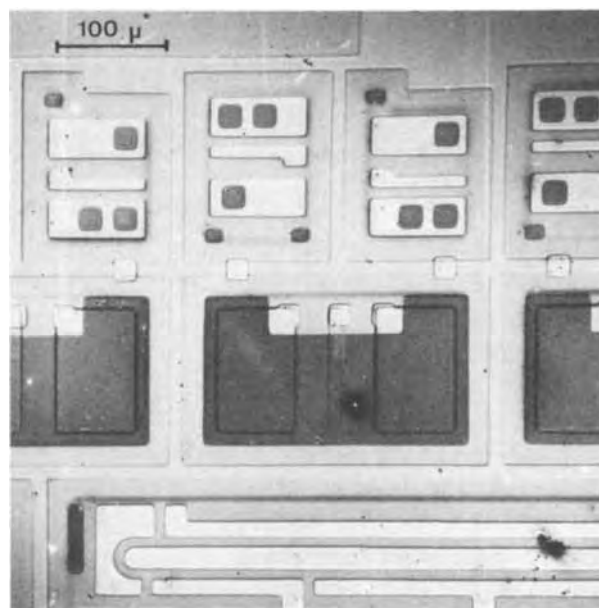
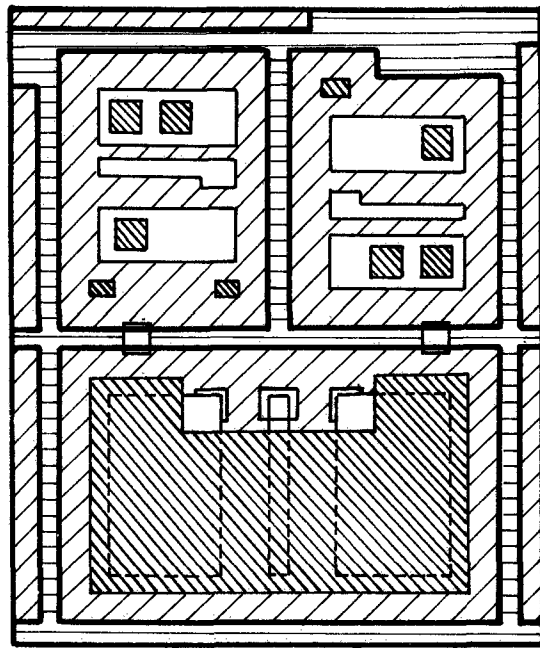


Fig. 1. Picture of an integrated circuit after chemical etching off Al and SiO<sub>2</sub> as seen in the photoemission electron microscope (before argon etching).



100  $\mu$

- ISOLATION-DIFFUSION (P)  
 $C_s \approx 7 \cdot 10^{17} \text{at.cm}^{-3}$ ,  $x_j \approx 12 \mu$
- BASE - DIFFUSION ( $P^+$ )  
 $C_s \approx 3 \cdot 10^{18} \text{at.cm}^{-3}$ ,  $x_j \approx 4 \mu$
- EPITAXY-LAYER (N)  
 $C_s \approx 10^{15} \text{at.cm}^{-3}$ ,  $d_e \approx 10 \mu$
- EMITTER-DIFFUSION ( $N^{++}$ )  
 $C_s \approx 5 \cdot 10^{20} \text{at.cm}^{-3}$ ,  $x_j \approx 3 \mu$

Fig. 2. Characterization of the integrated circuit shown in Fig. 1

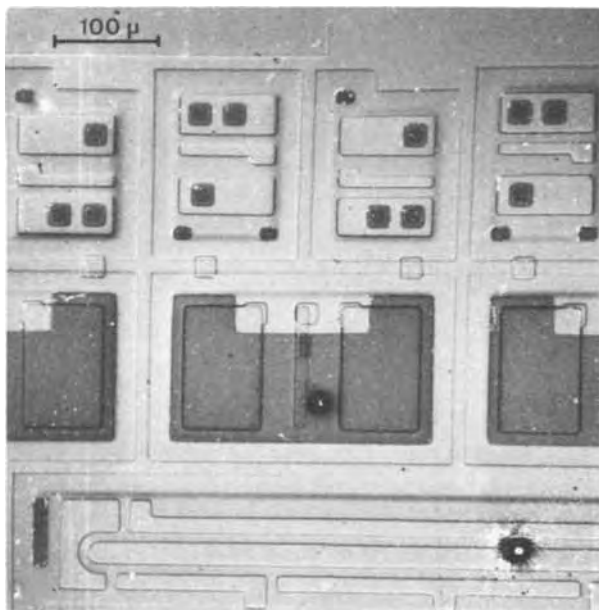


Fig. 3. Picture of the same integrated circuit after a 5 sec argon ion etch ( $I_{\text{Beam}} = 10^{-10} \text{A}$ , 4 kV).

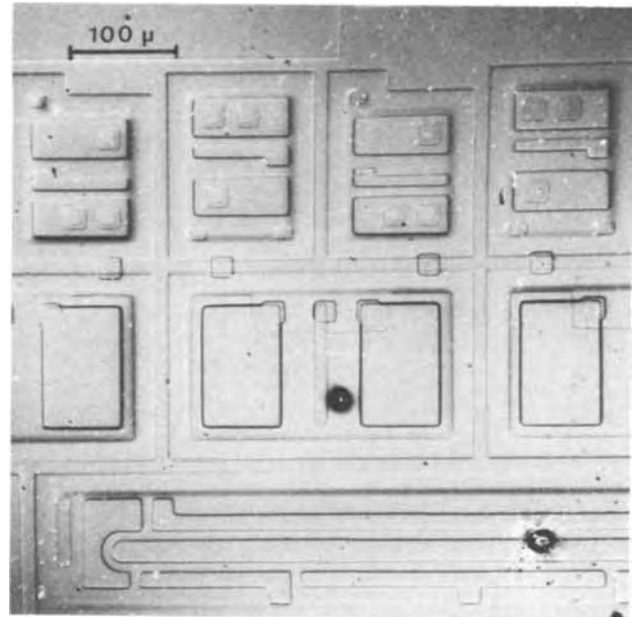


Fig. 4. Picture of the same integrated circuit after a 10 second argon ion etch ( $I_{\text{Beam}} = 10^{-10} \text{A}$ , 4 kV).

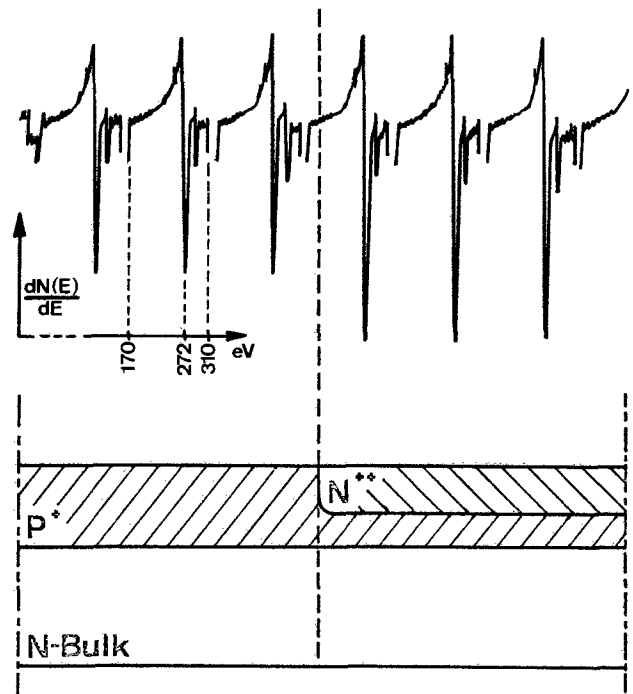


Fig. 5. Auger electron spectroscopic analysis of a P-N junction. (a, upper) Repetitive carbon signal over the surface (b, lower) Cross section of the analyzed P-N junction.

than 14 megohm and spun dry. Photoresist processing was done using negative resist from Hunt or Kodak, the recommended developers, and isopropanol for rinsing. Chemical etching of oxides was done in HF buffered with  $\text{NH}_4\text{F}$  except when oxides were removed just before being studied. In this case concentrated HF was used. Etching of aluminum was done in a mixture of phosphoric, nitric, and acetic acids. Removal of photoresist was done in fuming nitric acid.

All of the above-mentioned chemicals, with the exception of the photoresists and resist developers, were electronic grade chemicals.

### Experimental Results

Figure 1 shows the material contrast of an integrated circuit observed in the PEEM. The diffused

regions and their respective surface concentrations are specified in Fig. 2. As shown in Fig. 3 and 4, the material contrast disappeared after short argon ion etching. (I beam =  $10^{-10}$  A, 4 kV, beam area at the target = 3 mm<sup>2</sup>, etching time 5 respective 10 sec.) During etching the argon ions not only cause material to be sputtered away, but are also implanted into the silicon, thus destroying the crystal structure in the surface region.

In order to show that the material contrast was due to some sort of contamination layer, and that the etching off of this layer and not the creation of an amorphous layer was responsible for removing the contrast, an integrated circuit was heated at  $10^{-6}$  Torr to 1000°C in the PEEM. A residual gas analysis showed that no significant amount of hydrocarbons originating from the vacuum system was present at this pressure. As a cross experiment another circuit was heated in a furnace with oxygen atmosphere to 1000°C. After both treatments, only relief contrast could be observed during examination in the PEEM. It can therefore be assumed that a volatile contamination layer was present which could evaporate at a temperature below 1000°C, or be etched off.

A further circuit was analyzed by AES. The only contaminants that were found were oxygen and carbon, and the concentration of these contaminants was drastically reduced after a similar short argon ion etch.

Since the diameter of the primary electron beam was 25  $\mu$  it was not possible to analyze single homogeneous areas of the circuit which showed minimal dimensions of about 10  $\mu$ . For this reason we manufactured a single junction in silicon wafer which allowed AES studies of each region separately without interference by the others. The primary beam spot was continuously moved from the P to the N side.

As shown in Fig. 5, the concentration of carbon is higher on the N-doped than on the P-doped surface. Measurements showed no difference in oxygen content.

The small peak beside the carbon signal in Fig. 5 was never observed in the complete spectrum of the surface but only in the repetitive sweep mode. Therefore we will attach no importance to it.

Simultaneous PEEM observations of separated P respectively N homogeneously doped samples with widely varying doping levels were made.

No material contrasts were seen. Also the concentration of carbon determined by Auger spectroscopy was the same in the two separated P-doped and N-doped surfaces.

In order to determine the forms of the carbon contamination on the surface we have used the SIMS method.

Figure 6 shows the spectrum of the first monolayer of an integrated circuit. For such an analysis we used a primary ion beam of  $10^{-10}$  A under a partial argon pressure of about  $10^{-7}$  Torr. This spectrum presents the characteristic  $C_nH_m^+$  groups. After removing the first monolayer all the hydrocarbons disappeared.

Table I shows, besides the previously mentioned compounds, the other elements present on the surface. The presence of aluminum can be explained by the fact that previously the circuits had conducting paths, which were etched off according to the described procedure.

### Discussion

The presence of a volatile contamination layer on the surface of silicon was also demonstrated by Chang (7). He found that adsorbed hydrocarbons are desorbed from the silicon surface at temperatures lower than 1000°C. It has also been shown (8, 9) that oxygen is removed from the surface as silicon monoxide (SiO) at 900°-1000°C, while hydrocarbons disappear from the surface in the same temperature range by oxidation through CO or CO<sub>2</sub> or by diffusing into the silicon (>1100°C).

As shown in the experiments the contamination layer on the surface consists of hydrocarbon compounds which are localized in one monolayer. The

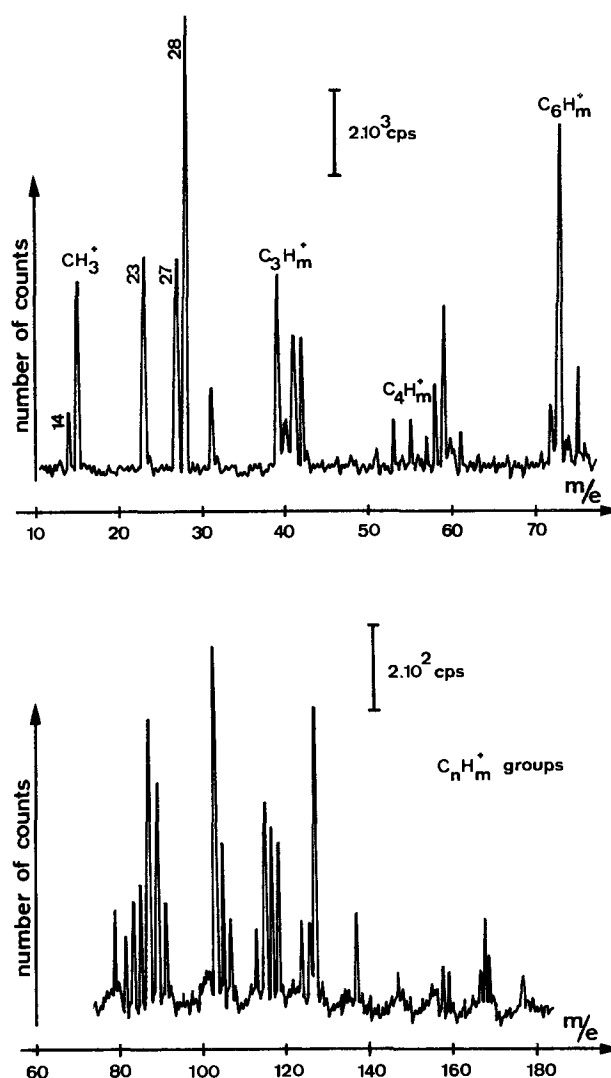


Fig. 6. Positive secondary ion mass spectrum of the first monolayer of the integrated circuit.

coverage of the surface with adsorbates can be quantitatively described by a degree of coverage  $\theta$ , where  $\theta = 1$  represents the case when all possible adsorption sites on the surface are filled, that is to say a complete monolayer is formed. An adsorbed impurity atom generally changes the charge distribution on the surface.

For smaller degrees of coverage, the change in the work function  $\Delta W$  is a linear function of  $\theta$ . With larger degrees of coverage, the interaction between adsorbed particles causes a decrease in the variation of  $\Delta W$  (Fig. 7). The fact that no contrast difference and variation of carbon concentration in AES were seen from the two separated N-doped and P-doped silicon wafers indicates that the same degree of coverage is present on their surface, that means  $\theta_N = \theta_P$ . Hendersen *et al.* (11) observed that the adsorbed carbon concentration on the surface of homogeneous silicon wafers was independent of the type and amount of doping, crystal orientation, dislocation density, and method of crystal

Table I. List of the characteristic energies, beside the typical  $C_nH_m$  groups, of the secondary ions emitted from the first monolayer of the integrated circuit analyzed in Fig. 6

m/e	Secondary ions
14	Si <sup>++</sup> -CH <sub>3</sub> <sup>+</sup>
23	Na <sup>+</sup>
27	Al <sup>+</sup>
28	Si <sup>+</sup>

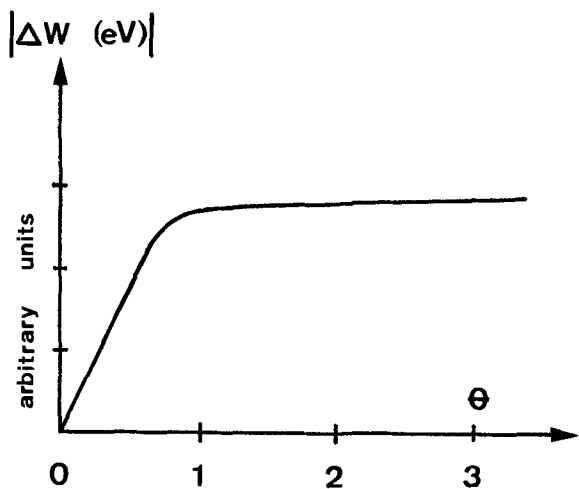


Fig. 7. Change in the work function as a function of the degree of coverage.

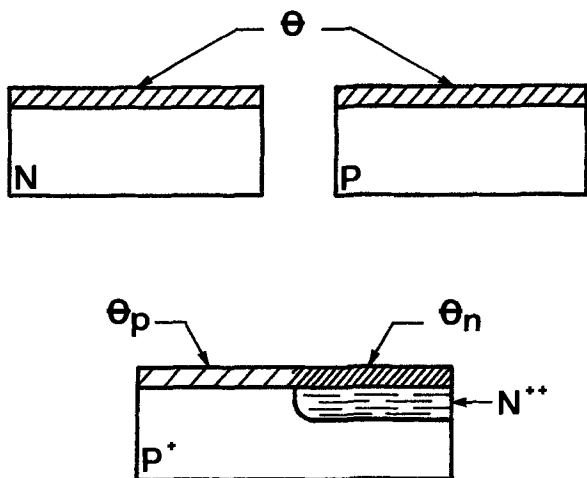


Fig. 8. Schematic presentation of the variation of the degree of coverage with contaminants with and without diffused junction.

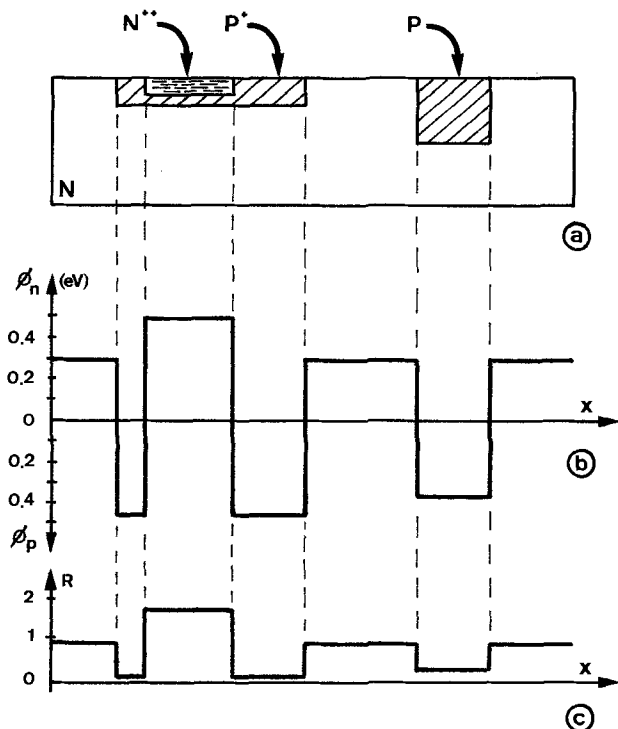


Fig. 9. (a) Cross section of a diffused integrated circuit. (b) Schematic presentation of the Fermi level. (c) Schematic presentation of the reflection density.

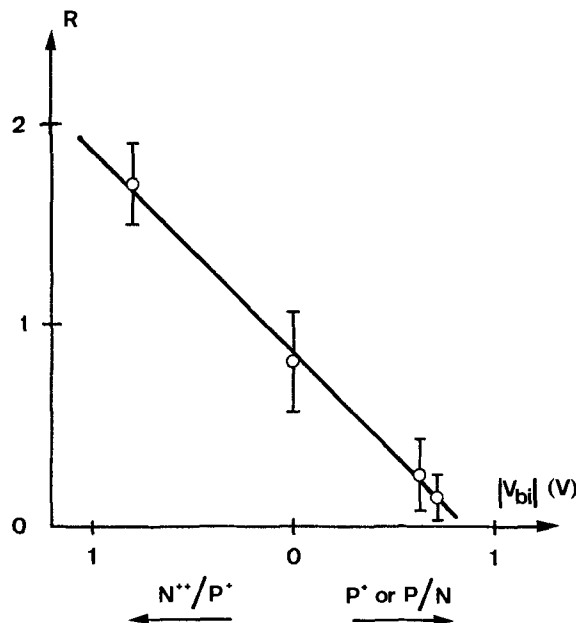


Fig. 10. Relationship between the built-in voltage and the reflection density.

growth. These results are consistent with our observations.

The peak-to-peak amplitudes from the Auger transition are a linear function of the amounts of material present in the first monolayer (10). Since in Fig. 5 we observe a variation of the peak-to-peak amplitude of the carbon, the degree of coverage of each diffused region must be different. All experiments proved that

$$\theta_N > \theta_P$$

Figure 8 demonstrates the found situation.

This last inequation leads to the fact that the work function ( $W$ ) of each diffused region must also be different

$$W_N > W_P$$

This explains the observed contrast of integrated circuits in the PEEM.

From our experiments we can therefore affirm that a diffused junction has an influence on the degree of coverage by hydrocarbons. Figure 9 shows a schematic cross section through an integrated circuit as well as the position of the Fermi level and the variation of the reflection density based on the Kodak gray tones scale.

By recording the reflection density as a function of the built-in voltage of the junction, a monotonous relation (Fig. 10) is obtained. This means that the degree of the contamination layer directly depends on the surface potential. The change of the potential on the surface takes place only in the depletion layer. These have widths of  $0.01-0.5\mu$ , so that, compared with the geometry of the diffused regions, sharp contrasts are shown in a PEEM picture.

After removing the contamination layer ( $\theta = 0$ ), no contrast remained and therefore we can conclude that the work function is practically independent of the doping of silicon. Different authors found the same (12).

### Conclusions

It has been shown that the material contrasts, as seen in the PEEM, are dependent on the built-in voltages of the doped regions, and are produced by hydrocarbon contaminations. The degree of coverage of hydrocarbons is practically constant for regions which have the same doping, but varies as a function of the built-in voltage when regions with different doping are present. No dependence of the work function on the doping was found after removal of the contamination layer.

In the course of our experiments it was not possible to find the sources of contamination, but such contamination was also found on circuits made by other manufacturers. It is probable that they come from the manufacturing and the cleaning processes.

#### Acknowledgments

The authors are grateful to Professor A. Benninghoven and his co-workers, S. Storp and W. Sichtermann, of the University of Cologne and Dr. Löbach of Balzers AG for AES measurements; to Miss E. Grauer-Carstensen for making the PEEM pictures; to Mr. J. Solo de Zaldivar of Faselec AG Semiconductors for diffusing the samples studied.

Manuscript submitted March 13, 1973; revised manuscript received Sept. 10, 1973.

Any discussion of this paper will appear in a Discussion Section to be published in the December 1974 JOURNAL.

#### REFERENCES

1. L. Wegmann, *J. Microscopy*, **96**, 1 (1972).
2. L. Wegmann, *Mikroskopie*, **26**, 99 (1970).
3. G. W. Gobeli and F. G. Allen, *Phys. Rev.*, **127**, 141 (1962).
4. G. W. Gobeli and F. G. Allen, *ibid.*, **137**, A 245 (1965).
5. L. A. Harris, *J. Appl. Phys.*, **39**, 1419 (1968).
6. A. Benninghoven, *Surface Sci.*, **28**, 541 (1971).
7. Chuan C. Chang, *ibid.*, **23**, 283 (1970).
8. B. A. Joyce, *ibid.*, **15**, 1 (1969).
9. R. C. Henderson, W. Polito, and J. Simpson, *Appl. Phys. Letters*, **16**, 15 (1970).
10. R. E. Weber and A. L. Johnson, *J. Appl. Phys.*, **38**, 4355 (1967).
11. R. C. Henderson, R. Marcus, and W. Polito, *ibid.*, **42**, 1208 (1971).
12. F. G. Allen and G. W. Gobeli, *Phys. Rev.*, **127**, 150 (1962).

## The Influence of the Phase Shift on Thickness Measurements of Silicon Epitaxial Layers with a Fourier Transform Spectrometer

P. J. Severin

Philips Research Laboratories, Eindhoven, Netherlands

#### ABSTRACT

The thickness of a silicon epitaxial layer can most easily be measured with Fourier transform spectroscopy. The influence of the phase shift at the substrate-epitaxial layer interface has not been taken into account in earlier treatments and in the available instruments. Under simplified conditions the effect of the phase shift on the interferogram is derived, yielding an instrumental correction to be applied to the position of the side burst maximum. To this result then also a physical correction should be applied as derived earlier from multiple interference measurements in order to finally yield the metallurgical thickness.

Recently Flournoy *et al.* (1) described a thin-layer thickness measuring instrument based on the use of Fourier transform spectroscopy. Referring to the thickness  $d$  of a transparent coating of refractive index  $n$  on an opaque or transparent substrate they state that the distance between two side bursts equals  $2dn$ , ignoring any phase shift. Such an instrument is commercially available and marketed for the main purpose of measuring silicon epitaxial layer thickness by Digilab, Incorporated.<sup>1</sup>

For several years the phase shift  $\delta$  at the substrate-epitaxial layer interface has been subject of discussion. Neglecting this phase shift in the interpretation of the data would cause an error and two different approaches have been followed to obtain the correct results. Schumann *et al.* (2, 3) calculated with classical theory the phase shift  $\delta$  as a function of wave number  $k$  and substrate resistivity  $\rho$  from a model based on an abrupt junction, both for dope and charge carriers, free of stress, characterized by bulk properties. It was found that  $\delta(k)$  decreases with substrate resistivity  $\rho$ , equals  $\pi$  at  $k = 0$  and vanishes at large  $k$  for all  $\rho$ . These data were introduced into a standard procedure (4) for the analysis of an infrared multiple interference (IMI) spectrum. The author (5) followed a different approach, based on experimental evidence. The phase

shift  $\delta$  was deduced directly from IMI data, and it was found that the spectra could be described by a constant phase shift  $\delta_0$ . It was shown then (6) that over the limited wave number range used a function  $\delta(k)$  can be approximated by a linear expression in which  $\delta_0$  only plays a formal role. It has no relation whatsoever to the part of Schumann's curves where  $\delta$  is a constant. In Schumann's evaluation procedure the orders of the extrema are corrected with the appropriate  $\delta(k)$  and the ensuing values of the thickness are averaged. In our approach the uncorrected data yield  $d_s$  and  $\delta_0$ . Eversteyn and van den Heuvel (7) recently described a method by which from the thickness of the layer actually deposited, the metallurgical thickness  $d_m$ , can be determined. Using these methods on a large number of epitaxial N on N<sup>+</sup> and N on N<sup>++</sup> structures  $\delta_0$ ,  $d_s$ , and  $d_m$  were determined and definite correlation was found (8) between  $\Delta d = d_s - d_m$  and  $\delta_0$  for both kinds of structures. Using these data as a calibration for a given production process,  $\delta_0$  determines the value of  $\Delta d$  to be subtracted from  $d_s$  to obtain  $d_m$ . The correction  $\Delta d$  is called a physical correction here because it should be applied wherever  $2dnk - \delta(k)$  occurs, *i.e.*, both to the conventional IMI spectrophotometer results and to the data obtained with Fourier transform spectroscopy.

In the following sections the Fourier spectrum is calculated assuming a phase shift at the substrate-layer interface, carefully stating the assumptions without

Key words: silicon, epitaxial layer thickness, Fourier transform spectroscopy, interferogram, phase shift.

<sup>1</sup> Digilab, Incorporated, subsidiary of Block Engineering Incorporated, Cambridge, Massachusetts 02139.

going into any technical detail. It will be shown that when the phase shifts at the top layer and at the interface are neglected, the distance between the two side burst maxima equals  $2 dn$ , but that due to the phase shift the position and shape of the side bursts are modified. Because all samples show phase shifts in one way or another, the distance between the two side burst maxima which the instrument reads simply as  $2 dn$ , should be corrected. This correction, which should be applied in addition to the physical correction discussed above, is typical of the Fourier spectrometer and therefore called an instrumental correction. Dielectric structures should also be corrected in this way.

Both corrections are indispensable for accurate results and increasingly important with decreasing thickness and increasing need for accuracy for advanced applications of epitaxial layers. With an epitaxial layer grown on an  $N^{++}$  substrate the error due to the neglect of the physical phase shift correction may amount up to  $0.5 \mu\text{m}$  (8). The error due to the neglect of the instrumental correction can be of the same order as will be shown in the last section.

### Instrumental Correction Due to Top Layer and Interface Phase Shift

The interferometer layout is shown in Fig. 1. The phase of ray Y due to topside reflection equals  $\pi$  and that of ray X due to interface reflection equals  $\delta + 4\pi nd/\lambda$ , both apart from an arbitrary but equal constant, upon entering the interferometer.

Calling the position of the movable mirror at which the central burst occurs  $z = 0$  and the departure from that position  $z$ , positive or negative, the signals impinging on the detector are

$$\begin{aligned} E_{y1} &= E_{y1}^0 \cos(\omega t + \pi) \\ E_{y2} &= E_{y2}^0 \cos(\omega t - 2kz + \pi) \\ E_{x1} &= E_{x1}^0 \cos(\omega t - 2kdn + \delta) \\ E_{x2} &= E_{x2}^0 \cos(\omega t - 2kz - 2kdn + \delta) \end{aligned} \quad [1]$$

with  $\omega$ , the frequency and  $k = 2\pi/\lambda$ , the wave number.

The detected signal  $V = AE^2$  equals, with  $A$  unity, after averaging over  $t$  and dropping the constant terms

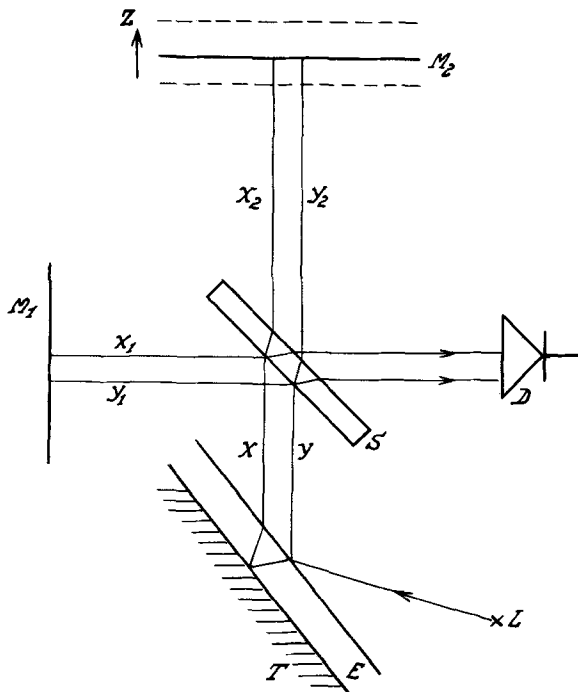


Fig. 1. The principle of operation, with light source L, mirrors  $M_1$  and  $M_2$ , detector D, semitransparent plate S, epitaxial layer E, and substrate T.

$$\begin{aligned} V &= (E_{y1}^0 E_{y2}^0 + E_{x1}^0 E_{x2}^0) \cos 2kz \\ &+ E_{y1}^0 E_{x2}^0 \cos[2k(dn + z) + \pi - \delta] \\ &+ E_{x1}^0 E_{y2}^0 \cos[2k(dn - z) + \pi - \delta] \end{aligned} \quad [2]$$

Assuming a white spectrum between zero and  $k_1$ , of unit total intensity, these noncoherent waves should be added quadratically. This, after integration, yields a  $k$ -dependent part

$$\begin{aligned} V &= (E_{y1}^0 E_{y2}^0 + E_{x1}^0 E_{x2}^0) \frac{\sin 2k_1 z}{2z} \\ &+ E_{y1}^0 E_{x2}^0 \frac{\sin [k_1 2(dn + z) + \pi - \delta] - \sin(\pi - \delta)}{2(dn + z)} \\ &+ E_{y2}^0 E_{x1}^0 \frac{\sin [k_1 2(dn - z) + \pi - \delta] - \sin(\pi - \delta)}{2(dn - z)} \end{aligned} \quad [3]$$

provided  $\delta$ ,  $n$ , and the amplitudes  $E^0$  do not depend on  $k$ . It is a key point of this paper that this condition can be relaxed with respect to  $\delta$ . Writing  $\delta$  in Eq. [2] as a linear relation to  $k$  and the last term as

$$E_{x1}^0 E_{y2}^0 k_1 \frac{\sin \alpha}{\alpha} \cos(\alpha + \pi - \delta) \quad [4]$$

with  $\alpha = k_1(dn - z)$ , it is clear that  $\delta$  can also be linearly related to  $k$  without complicating the mathematics. This will be discussed in the next section. The second and third terms are related by simply changing the sign of  $z$  and Eq. [3] is functionally symmetric with respect to  $z \approx 0$ . The first term is called the center burst, the second and third terms are the side bursts. In Fig. 2 the shape of the  $z > 0$  side burst is presented with  $\delta/2\pi$  as a parameter, varying between 0 and 0.5. The shape of the center burst is identical to the curve labeled  $\delta = \pi$ , that is to say with vanishing top layer and interface phase shifts, with the  $z$ -axis shifted by  $dn$ .

It is clear from Fig. 2 that the distance read between the two extreme values of the two side bursts depends on the value of  $\delta/2\pi$ . At  $\delta/2\pi = 0.25$  the extreme values of both side bursts change sign. In Fig. 3 the positive and negative deviations  $\alpha_p$  and  $\alpha_n$  from the position  $\alpha = 0$  are shown for the nearest positive and negative extrema as a function of  $\delta/2\pi$ . The correction to be applied to the distance read between the two peaks follows from this calculated error, the details being dependent on the peak determination procedure chosen.

In real life, of course,  $\delta$  is not known and should be processed from the Fourier spectrum. From Fig. 2 it is evident that the ratio  $r$  between the heights  $V_p$  and  $V_n$  of the positive and negative peaks nearest to  $\alpha = 0$  could provide a good criterion. This ratio  $r$  has also been shown in Fig. 3 as a function of  $\delta/2\pi$ . The sequence: measurement of  $r$ , determination of  $\delta/2\pi$ , and correction to side bursts distance can easily be built into the instruments. The amplitude of the positive peak which is either the maximum itself of the side burst or the positive maximum most near the negative maximum can also serve this purpose.

### Physical Correction Due to Interface Phase Shift

It has been shown earlier (6) and repeated briefly in the introductory remarks that from IMI spectra follows a  $k$ -dependent phase shift, with  $k = 2\pi/\lambda$ , according to

$$\delta = \delta_0 - 2nk\Delta d \quad [5]$$

Any higher order approximation to the  $\delta(k)$  curve is beyond experimental precision for an infrared spectrophotometer. Also the ASTM corrections (4) admit this approximation in a limited wave number range, but the author did not find the correlation between the values of  $\delta_0$ ,  $\Delta d$ , and  $\rho$  implied in these curves. An empirical relation has been discovered (8) relating  $\delta_0$  and  $\Delta d = d_s - d_m$  by comparing the thickness  $d_s$

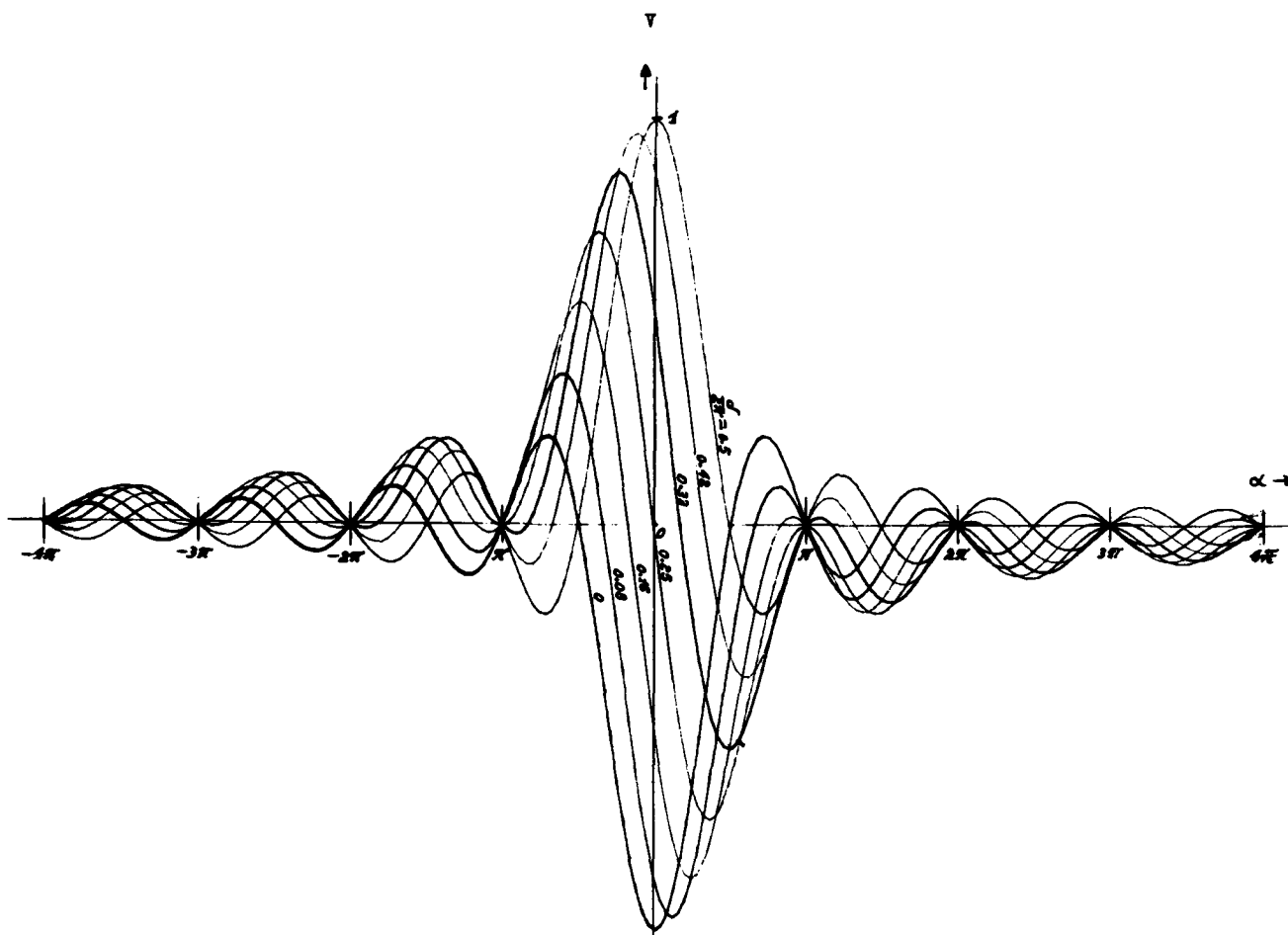


Fig. 2. Interferogram of the side maximum due to interference of rays X and Y plotted with normalized  $V$  as a function of  $\alpha$  and  $\delta/2\pi$  as a parameter.

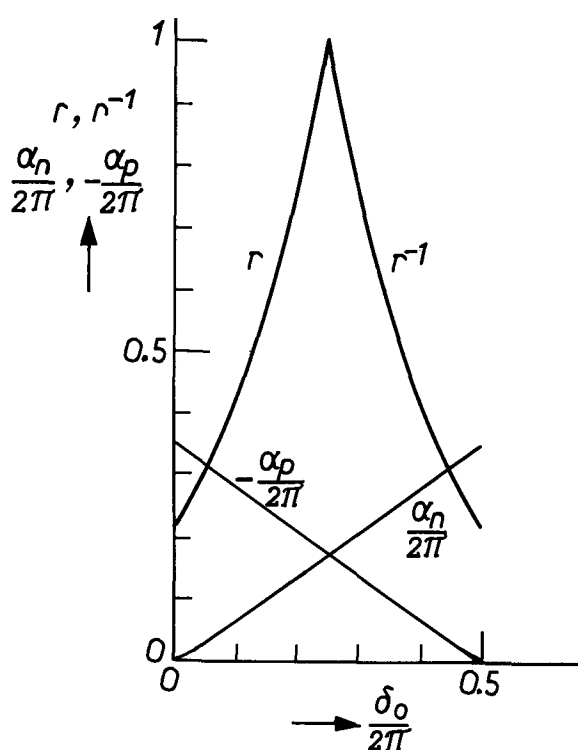


Fig. 3. The phase shift  $\delta/2\pi$  as a function of the ratio  $r$  of the heights of the positive and negative peaks nearest to  $\alpha = 0$  and the ensuing distances  $\alpha_p$  and  $\alpha_n$  of the positive and negative extrema from the point  $\alpha = 0$ .

found from the IMI spectrum (5) and the metallurgical thickness  $d_m$  measured otherwise (7). Introducing Eq. [5] into Eq. [2] it is clear that in Eq. [3] and [4]  $d + \Delta d$  figures instead of  $d$ , and  $\delta_o$  instead of  $\delta$ . This means that the instrumental correction described previously should be followed by a physical correction consisting of subtraction of an amount  $\Delta d$ , determined by  $\delta_o/2\pi$ . The second, physical part of the correction procedure is identical to the procedure to be followed with an IMI spectrum.

When the instrument is used in connection with a single production process of epitaxial slices, the relations  $\Delta d(\delta_o/2\pi)$ , different for  $N^+$  and  $N^{++}$  substrates, can also be built into the instrument.

#### Discussion

The thickness of the epitaxial layer has been measured on a Digilab FTGR-12 and the thickness  $d_D$  found with two sets of thirty slices satisfies the following relationships to  $d_m$ , measured as described by Everstejn and van der Heuvel (7)

$$d_D = 0.983 d_m - 0.06 \mu\text{m} \text{ for } N^{++} \text{ substrates [6a]}$$

and

$$d_D = 0.983 d_m + 0.52 \mu\text{m} \text{ for } N^+ \text{ substrates [6b]}$$

with correlation coefficients equal to 0.99991 and 0.99978, respectively. The data points are shown in Fig. 4 and the difference between the two sets is obvious.

Neither the instrumental nor any physical correction has been made to these data. However, the manufacturer (9) has indicated that a correction mechanism has been built into the instrument, empirically determined to match the data obtained otherwise, that is

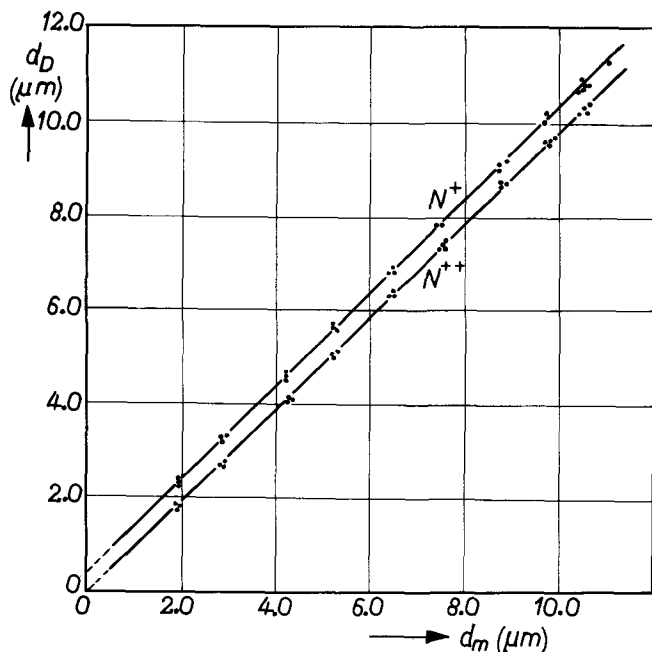


Fig. 4. The Digilab measured thickness  $d_D$  vs. metallurgical thickness  $d_m$ . The layers with resistivities of about 1 ohm-cm were grown in silane at 1050°C corrected temperature, on Sb-doped  $N^+$  substrates and on As-doped  $N^{++}$  substrates.

to say the ASTM-corrected IMI spectra results. Hence no conclusions on the theory and necessary corrections can be drawn from the actual results.

The description given above applied to an idealized version of the instrument which may be realistic only to a limited extent. The spectrum emitted from the

light source is not white, and  $E^0$  will always be a function of  $k$  due to wavelength dependence of optical components. Furthermore, the integral (Eq. [3]) will have to be limited between  $k_1$  and  $k_2$  and the detector efficiency  $A(k)$  should be taken into account. This would imply performing the integration Eq. [3] with a weight function for the  $k$ -dependent light intensity and detector efficiency yielding curves different from those shown in Fig. 2 and 3. Then the correction  $\Delta\alpha$  can be read, if  $\delta_0/2\pi$  is known from  $\tau$  or from an IMI spectrum, and the correction  $\Delta\alpha$  can be translated into a correction  $\Delta d$ . At this stage, however, this cannot safely be done.

In summary, the Digilab FTG produces precise and reproducible results rapidly in an easy way, but the accuracy can be obtained only by calibration, as shown in Eq. [6a] and [6b].

Manuscript submitted Feb. 20, 1973; revised manuscript received Sept. 12, 1973.

Any discussion of this paper will appear in a Discussion Section to be published in the December 1974 JOURNAL.

#### REFERENCES

1. P. A. Flournoy, R. W. McClure, and G. Wijntjes, *Appl. Opt.*, **11**, 1907 (1972).
2. P. A. Schumann, R. P. Phillips, and P. J. Olshefki, *This Journal*, **113**, 368 (1966).
3. P. A. Schumann, *Silicon Device Processing*, NBS Special Publication 337, p. 234 (1970).
4. American Society for Testing and Materials, F95-68T.
5. P. J. Severin, *Appl. Opt.*, **9**, 2381 (1970).
6. P. J. Severin, *ibid.*, **11**, 691 (1972).
7. F. C. Eversteyn and G. J. van den Heuvel, *This Journal*, **120**, 699 (1973).
8. P. J. Severin and F. C. Eversteyn, *ibid.*, Submitted for publication.
9. J. I. Steele, Private communication.

## Determination of the Solidus and Gallium and Phosphorus Vacancy Concentrations in GaP

A. S. Jordan, A. R. Von Neida, R. Caruso, and C. K. Kim

Bell Laboratories, Murray Hill, New Jersey 07974

#### ABSTRACT

The Ga concentration in GaP crystals prepared by a variety of techniques (pulled by the liquid encapsulation Czochralski technique from stoichiometric or nonstoichiometric melts, solution grown, and annealed) has been determined by precision coulometric titration, yielding the experimental solidus boundary which exhibits an excess of Ga along the Ga-rich liquidus. Based on a thermodynamic model, assuming that neutral Ga and P vacancies are the predominant native defects, the analysis of the solidus data permitted the evaluation of the vacancy concentrations over a wide temperature range. At the melting point of GaP (1465°C) there are  $8 \times 10^{18}$  and  $1.3 \times 10^{19} \text{ cm}^{-3}$  Ga and P vacancies, respectively, in the crystal. The calculated solidus curve well represents the totality of experimental data and shows retrograde temperatures at 1375° and 1400°C on the Ga- and P-rich sides, respectively. The enthalpies and entropies associated with vacancy formation are given and discussed. It is shown that the data provide strong additional support to the previous identification of Ga vacancies with killer centers in GaP.

The successful commercial realization of GaP red and green light-emitting diodes (LED's) is based on the extensive scientific and technological accomplishments of the past decade. In order to obtain device quality material of improved and controlled optical properties a considerable effort has been devoted to the study of the physicochemical aspects of the growth and charac-

Key words: defect chemistry, crystal growth, light-emitting diodes, thermodynamics.

terization of undoped and doped GaP crystals. In particular, the thermodynamic properties, liquidus curve, and pressure-temperature boundary of GaP have been critically evaluated (1). In addition, by means of experimental and/or theoretical investigations of the ternary liquidus surface (2-5) and solid solubilities (6-10), a satisfactory understanding of impurity incorporation in GaP has been achieved for such electrically important impurities as Zn (6, 7), Te (8), O



(5, 8, 9), and N (10). However, on account of experimental difficulties, the departure from stoichiometry of GaP represented by the solidus curve and the closely related absolute phosphorus and gallium vacancy ( $V_P$  and  $V_{Ga}$ ) concentrations have not yet been determined. Nevertheless, there is increasing interest in a knowledge of absolute vacancy concentrations in GaP motivated by the accumulating evidence from optical measurements that Ga vacancies or associated complexes may strongly influence the photoluminescence and electroluminescence properties.

A rapid increase in the red photoluminescent efficiency (accompanied by a rise in the shunt path or "killer center" lifetime,  $\tau_n$ ) with decreasing growth temperature has been observed in Zn, O-doped GaP pulled by the liquid-encapsulation Czochralski (LEC) technique from stoichiometric and nonstoichiometric melts and grown from solution (SG) (11). At the same time, a linear correlation was shown to exist between  $1/\tau_n$  and the relative  $V_{Ga}$  concentration for these different crystals. Further studies have also shown that by annealing at 1280° and 1350°C the originally large  $\tau_n$  of SG platelets was drastically decreased to values in good accord with this correlation (12). In contrast, with annealing at 1200°C the small  $\tau_n$  of stoichiometric LEC crystals was significantly increased (13).

Very recently Ladany and Kressel (14) have suggested that  $V_{Ga}$  and/or related complexes are important centers in reducing the green luminescent efficiency of n-type GaP. Furthermore, some evidence for the existence of the  $V_{Ga}-O_P$  complex (orange luminescence at 2.125 eV) has been given by Dean (15) and Bhargava *et al.* (16). Obviously, a more complete understanding of nonradiative or radiative processes attributed to vacancies or associated complexes is impossible in the absence of absolute vacancy concentrations.

The major objective of this paper is to determine the solidus and  $V_P$  and  $V_{Ga}$  concentrations in GaP over a wide temperature range. First, we describe the experimental data obtained by high precision coulometric titration of Ga in undoped and doped GaP crystals prepared by a variety of techniques (pulled by LEC from stoichiometric and nonstoichiometric melts, SG, annealed LEC). Second, the atom fraction of Ga,  $x_{Ga}^s$ , in these samples is deduced to yield the experimental solidus points. Third, by means of a thermodynamic model applied to the data on undoped seed-end crystals, assuming the presence of single neutral vacancies only, the concentrations of  $V_P$  and  $V_{Ga}$  are evaluated. Finally, the full solidus curve is calculated and the results are discussed and compared with those for some other semiconducting compounds.

### Experimental Procedure and the Evaluation of the Solidus Points

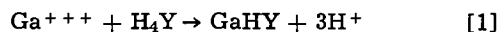
Thermodynamic considerations for a binary system at a constant temperature and pressure lead to the conclusion that in equilibrium, the composition of the liquid (Ga + P liquid solution) and solid (crystalline

GaP) phases is fixed. Usually the published phase diagrams for Group III-V and II-VI compounds (17) only present the variation of the liquid composition with temperature, *i.e.*, the liquidus curve. Meanwhile, the corresponding solidus curve, describing the variation of solid composition with temperature, is given by a vertical temperature invariant line at the stoichiometric composition ( $x_{Ga}^s = 0.50$ ) because the departures from stoichiometry for the solid phase, although generally not known, are expected to be very much smaller than for the liquid phase. Any experimental determination of the solidus boundary requires crystalline samples either grown or annealed in equilibrium with the liquid phase at a set temperature and a high precision analytical technique to determine minute compositional variations in the solid.

*Crystal growth.*—In Table I, the samples analyzed in this study are characterized with respect to origin, growth or preparatory technique, growth or heat-treatment temperature, and doping level. Most crystals were pulled by LEC from stoichiometric melts (atom fraction of phosphorus in the melt,  $x_P^l = 0.5$ ) at 1465°C or from nonstoichiometric melts ( $0.20 \leq x_P^l \leq 0.42$ ) at appropriate liquidus temperatures (1). As in previous work (11, 18), pulled crystals from nonstoichiometric melts provided the crucial bridge, intermediate in growth temperatures and solution compositions, between crystals obtained by standard stoichiometric LEC pulling and SG. Both doped and undoped crystals were available and the net carrier concentrations,  $|N_D - N_A|$ , were determined either by the Schottky barrier capacitance technique (MH crystals) or by Hall measurements (RD crystals).

The SG platelets were prepared in the usual manner by the slow cooling from ~1150° to 900°C of a ~ 6 atomic per cent (a/o) P solution in Ga. In addition, the tail end of a stoichiometric LEC crystal was annealed for 19 hr at 1300°C and held for 120 hr at 1200°C while immersed in  $B_2O_3$  liquid. Minute droplets of Ga were observed on the annealed slice assuring solid-liquid equilibrium.

*Analytical procedure.*—The GaP samples, weighing between ~0.3 and 2.0g, were analyzed for Ga by high precision coulometric titration, a technique described in detail elsewhere (19) and only briefly reviewed here. The samples were etched in  $HNO_3$  to remove traces of free Ga, weighed on a microbalance, dissolved in aqua regia and, after adjusting the pH to 3, an exactly weighed amount of EDTA ( $H_4Y =$  ethylene diamine tetracetic acid) was added to the solution in excess to consume all the Ga by reacting stoichiometrically according to



The excess EDTA was complexed with coulometrically generated  $Hg^{++}$  and the end point of this reaction (appearance of free  $Hg^{++}$  ions) was accurately detected by a potentiometric method. Although EDTA of very

Table I. Experimental data

Sample designation	Growth or prep. technique	Melt comp. $x_P^l$ (a/o)	Growth temp (°C)	Dopant	$ N_D - N_A $ (cm <sup>-3</sup> )	$x_{Ga}^s$ (atom fraction)
RD-238	LEC-seed	50	1465	Zn, Ga <sub>2</sub> O <sub>3</sub>	$5.7 \times 10^{17}$	0.50005 <sub>0</sub>
RD-164	LEC-tail	50	~1465	Zn, Ga <sub>2</sub> O <sub>3</sub>	$8.5 \times 10^{17}$	0.50010 <sub>4</sub>
MH-143	LEC-seed (powdered)	50	1465	None	$3 \times 10^{16}$	0.50005 <sub>1</sub>
MH-143	LEC-seed	50	1465	None	$3 \times 10^{16}$	0.50007 <sub>0</sub>
MH-143	LEC-tail	50	~1465	None	$3 \times 10^{16}$	0.50008 <sub>3</sub>
MH-134	LEC-seed	42	1457	None	$3 \times 10^{16}$	0.50013 <sub>9</sub>
MH-51	LEC-seed	36	1438	Zn(PO <sub>3</sub> ) <sub>2</sub>	$3.5 \times 10^{17}$	0.50016 <sub>7</sub>
MH-101	LEC-seed	36	1438	Ga <sub>2</sub> Te <sub>3</sub>	$4 \times 10^{17}$	0.50019 <sub>0</sub>
MH-120	LEC-seed	30	1407	Ga <sub>2</sub> Te <sub>3</sub> , Ga <sub>2</sub> O <sub>3</sub>	$7 \times 10^{17}$	0.50026 <sub>4</sub>
MH-70	LEC-seed (powdered)	20	1327	None	$3 \times 10^{16}$	0.50023 <sub>0</sub>
RD-164	LEC-tail (annealed)		1200*			0.50016 <sub>3</sub>
	SG (powdered)	6	1160-900	None		0.50015 <sub>3</sub>
	SG (powdered)	6	1160-900	None		0.50015 <sub>5</sub>

\* Annealing temperature.

high nominal purity<sup>2</sup> was used, several calibration experiments were also performed on the basis of 99.9999+ % Ga metal as the primary standard to establish the actual purity of EDTA and thus to obtain analytical results independent of contamination. The high precision of the data is further assured by the fact that at the pH employed, the magnitude of the stability constant for Eq. [1] (20.3) allows only a completely negligible fraction of the Ga complexes to dissociate even in the presence of  $Hg^{++}$  ions.

The analytical data provided a direct measurement of the number of moles of Ga,  $n_{Ga}$ , contained in each sample as the difference between the total number of moles of EDTA added to the solution and the number of moles of  $Hg^{++}$  complexed with the excess EDTA. The total estimated uncertainty by this coulometric technique is 10 ppm, as found by the usual combination of errors.

To remove Ga occlusions, crystals grown at lower temperatures ( $x_P^1 < 0.3$ ) were powdered to a maximum particle size of about 100 mesh under an argon atmosphere to avoid the formation of  $PH_3$  from moisture in the air, and then treated as described above. The mesh size used was sufficient to obtain reproducible results without causing undue handling problems.

Powdering has only a minute effect on the Ga analysis of crystals grown at a higher growth temperature as shown by an experiment in which the seed end of a boule grown at 1465°C (MH-143) was divided and subsequently processed as both a powder and a single piece.

**Evaluation of the solidus points.**—Since presently there is no reliable technique to perform an independent phosphorus analysis of our samples,  $x_{Ga}^s$  was calculated from  $n_{Ga}$  and the weight of GaP,  $w$ . The definition of  $x_{Ga}^s$  gives

$$x_{Ga}^s = n_{Ga} / (n_{Ga} + n_P) \quad [2]$$

where  $n_P$  is the number of moles of P.

Assuming that the sample is pure GaP, we find

$$n_P = \frac{w - n_{Ga}A_{Ga}}{A_P} \quad [3]$$

where  $A_i$  is the atomic weight of the subscripted species. Substituting Eq. [3] into Eq. [2] yields<sup>3</sup>

$$x_{Ga}^s = \frac{1}{1 + (w - n_{Ga}A_{Ga}) / A_P n_{Ga}} \quad [4]$$

Since  $A_{Ga}$  is only known to four significant figures, (69.72) and  $A_P$  to six (30.9738) (22), additional significant figures, consistent with the chemical analysis, were determined by the coulometric titration of 99.99999% Ga, yielding  $A_{Ga} = 69.7219$ . Values of  $x_{Ga}^s$  for each sample were calculated from Eq. [4] and are tabulated in Table I. In Fig. 1 we present the experimental solidus data plotted as growth<sup>4</sup> or annealing temperature vs.  $x_{Ga}^s$ .

The experimental solidus data exhibit the following important features:

(i) There is a systematic functional relationship between temperature and  $x_{Ga}^s$  and all the crystals prepared along the Ga-rich liquidus contain an excess of Ga.

(ii) Different LEC growth systems (MH and RD crystals were grown using Arthur D. Little and Mate-

<sup>2</sup> J. T. Baker, "ULTREX" grade, all determinations from same batch of 99.99+ % purity.

<sup>3</sup> A complete analysis of Eq. [2] through [4], taking into account contributions to  $w$  from impurities, would show a small contribution to the  $x_{Ga}^s$ . As our samples were not analyzed for residual impurities, their influence could only be indirectly ascertained. However, for typical undoped GaP, using measured impurity levels (20, 21) the calculation yields a maximum possible correction of  $+8 \times 10^{-6}$  (atom fraction) to the computed value of  $x_{Ga}^s$ . For mid  $-10^{17}$  cm<sup>-3</sup> of Zn or Te, the corrections are likewise small, being  $-6 \times 10^{-6}$  and  $+20 \times 10^{-6}$ , respectively.

<sup>4</sup> A minor adjustment of  $-2^\circ C$  was applied to the growth temperature of the tail end of LEC pulled crystals, to take into account the decrease in melting point accompanying the slight phosphorus loss in the melt during the growth cycle.

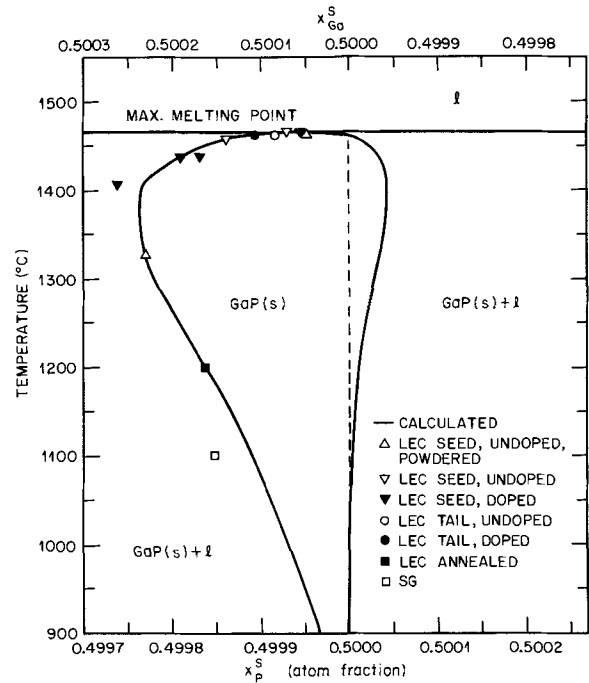


Fig. 1. The solidus of GaP. The data represent the growth or annealing temperature of GaP crystals vs. the Ga concentration (Eq. [4]) found by coulometric analysis. Note that 1100°C was taken as the average growth temperature of SG crystals.

rials Research Corporation pullers, respectively) lead to similar results.

(iii) Near the melting point of GaP the solidus is relatively flat and the tail end of boules always shows a greater departure from stoichiometry than the seed end.

(iv) The solidus is retrograde, as is the case for many other semiconductor systems (23-25), with a maximum departure from stoichiometry near 1400°C.

(v) There is no strong influence on the data resulting from the variation in doping levels; indeed, no combination of inadvertent or intentional impurities can be responsible for the large retrograde maximum in  $x_{Ga}^s$ .

(vi) By annealing an LEC tail-end crystal (RD-164), a change in the stoichiometry is induced.

These observations support the view that the values of  $x_{Ga}^s$  directly evaluated from the chemical analysis accurately represent the solidus boundary. In the next sections below we give a detailed thermodynamic analysis of the solidus data.

### Thermodynamic Analysis and Discussion

**Relationship between the solidus and vacancy concentrations.**—We shall assume that the predominant point defects in the pure GaP lattice are single neutral Ga and P vacancies and consider the concentrations of charged vacancies and vacancy clusters to be negligible. It is convenient to express the concentrations of  $V_{Ga}$  and  $V_P$  in terms of the site fractions, with  $v_{Ga}$  and  $v_P$ , respectively, defined by

$$v_{Ga} = \frac{[V_{Ga}]}{[Ga_{Ga}] + [V_{Ga}]} \quad [5]$$

and

$$v_P = \frac{[V_P]}{[P_P] + [V_P]} \quad [6]$$

where the bracket  $[A_i]$  denotes the total number of lattice constituent A on i-type sites.

Likewise,  $x_{Ga}^s$  and  $x_P^s$  can be expressed in terms of the atomic lattice constituent P as

$$x_{\text{Ga}}^{\text{s}} = \frac{[\text{Ga}_{\text{Ga}}]}{[\text{Ga}_{\text{Ga}}] + [\text{P}_{\text{P}}]} \quad [7]$$

and

$$x_{\text{P}}^{\text{s}} = \frac{[\text{P}_{\text{P}}]}{[\text{Ga}_{\text{Ga}}] + [\text{P}_{\text{P}}]} \quad [8]$$

To express  $x_{\text{Ga}}^{\text{s}}$  in terms of  $v_{\text{Ga}}$  and  $v_{\text{P}}$  let us add  $[V_{\text{Ga}}] - [V_{\text{Ga}}]$  to the numerator and denominator of Eq. [7] and divide both by  $[\text{Ga}_{\text{Ga}}] + [V_{\text{Ga}}]$ . Then, we find with the aid of Eq. [5] that

$$x_{\text{Ga}}^{\text{s}} = \frac{1 - v_{\text{Ga}}}{1 - v_{\text{Ga}} + [\text{P}_{\text{P}}]/\{[\text{Ga}_{\text{Ga}}] + [V_{\text{Ga}}]\}} \quad [9]$$

But by the equality of Ga and P sites,  $[\text{P}_{\text{P}}] = [\text{Ga}_{\text{Ga}}] + [V_{\text{Ga}}] - [V_{\text{P}}]$  which in combination with Eq. [6] transforms Eq. [9] into

$$x_{\text{Ga}}^{\text{s}} = \frac{1 - v_{\text{Ga}}}{2 - v_{\text{Ga}} - v_{\text{P}}} \quad [10]$$

By a similar procedure we also have

$$x_{\text{P}}^{\text{s}} = \frac{1 - v_{\text{P}}}{2 - v_{\text{Ga}} - v_{\text{P}}} \quad [11]$$

For further calculations the use of the difference,  $\delta$ , between Eq. [10] and [11] is very convenient because it reduces to

$$\delta = x_{\text{Ga}}^{\text{s}} - x_{\text{P}}^{\text{s}} = 2x_{\text{Ga}}^{\text{s}} - 1 = \frac{v_{\text{P}} - v_{\text{Ga}}}{2 - v_{\text{P}} - v_{\text{Ga}}}$$

Since  $|v_{\text{P}} - v_{\text{Ga}}| \ll 2$ , the expression sought to relate the experimental  $x_{\text{Ga}}^{\text{s}}$  or  $\delta$  to  $v_{\text{P}}$  and  $v_{\text{Ga}}$  becomes

$$\delta = 2x_{\text{Ga}}^{\text{s}} - 1 = \frac{v_{\text{P}} - v_{\text{Ga}}}{2} \quad [12]$$

*Thermodynamic equations for the vacancy concentrations.*—At any temperature,  $T$ , where solid GaP is in equilibrium with the Ga-P liquid solution,  $v_{\text{P}}$  and  $v_{\text{Ga}}$  are fixed. The incorporation of  $V_{\text{Ga}}$  and  $V_{\text{P}}$  at  $T$  along the liquidus curve can be expressed by the following chemical defect equilibria<sup>5</sup>

$$\text{Ga}(1) = \text{Ga}_{\text{Ga}} + V_{\text{P}} \quad K_{\text{P}} = \frac{v_{\text{P}}}{a_{\text{Ga}}} \times \frac{[\text{Ga}_{\text{Ga}}]}{[\text{Ga}_{\text{Ga}}] + [V_{\text{Ga}}]} \quad [13]$$

and

$$\text{P}(1) = \text{P}_{\text{P}} + V_{\text{Ga}} \quad K_{\text{Ga}} = \frac{v_{\text{Ga}}}{a_{\text{P}}} \times \frac{[\text{P}_{\text{P}}]}{[\text{P}_{\text{P}}] + [V_{\text{P}}]} \quad [14]$$

In Eq. [13] and [14] the site fractions of Ga and P atoms on their own sites ( $\approx 1$ ) can be incorporated in the respective equilibrium constants  $K_{\text{P}}$  and  $K_{\text{Ga}}$  without error. The functions  $a_{\text{P}}$  and  $a_{\text{Ga}}$  are the conventional thermodynamic activities of the subscripted species along the liquidus curve.<sup>6</sup>

As usual, we resolve  $K_{\text{P}}$  and  $K_{\text{Ga}}$  in terms of the enthalpies ( $\Delta H_{\text{P}}$  and  $\Delta H_{\text{Ga}}$ ) and entropies ( $\Delta S_{\text{P}}$  and  $\Delta S_{\text{Ga}}$ ) of incorporation, assuming that these quantities are independent of  $T$  in the range of interest. Then, we find from Eq. [13] and [14] for  $v_{\text{P}}$  and  $v_{\text{Ga}}$  that

$$v_{\text{P}} = e^{\Delta S_{\text{P}}/R} e^{-\Delta H_{\text{P}}/RT} a_{\text{Ga}} \quad [15]$$

and

$$v_{\text{Ga}} = e^{\Delta S_{\text{Ga}}/R} e^{-\Delta H_{\text{Ga}}/RT} a_{\text{P}} \quad [16]$$

It should be noted that  $\Delta H_{\text{Ga}}$  is related to  $\Delta H_{\text{P}}$  through the heat of formation of GaP,  $\Delta H^{\circ}_{\text{f}}$ , according to the reaction



<sup>5</sup> Note that the concentrations of the lattice constituents in subsequent equations appear as site fractions.

<sup>6</sup> By definition  $a_i = x_i \gamma_i$ , where  $x_i$  and  $\gamma_i$  are the atom fraction and activity coefficient of component  $i$  in the liquid phase, respectively.

and the Schottky enthalpy,  $H_{\text{S}}$ , for the defect reaction

$$0 = V_{\text{P}} + V_{\text{Ga}} \quad [18]$$

For it can be seen that by adding Eq. [17] and [18] and subtracting Eq. [13], we obtain Eq. [14]. Hence

$$\Delta H_{\text{Ga}} = \Delta H^{\circ}_{\text{f}} + H_{\text{S}} - \Delta H_{\text{P}} \quad [19]$$

Finally, substituting Eq. [19] into Eq. [16] and subsequently introducing Eq. [15] and [16] into Eq. [12] yields

$$2\delta = e^{\Delta S_{\text{P}}/R} e^{-\Delta H_{\text{P}}/RT} a_{\text{Ga}} - e^{\Delta S_{\text{Ga}}/R} e^{-(\Delta H^{\circ}_{\text{f}} + H_{\text{S}} - \Delta H_{\text{P}})/RT} a_{\text{P}} \quad [20]$$

*Enthalpies and entropies of vacancy formation.*—According to Eq. [20], at any  $T$  the experimental  $x_{\text{Ga}}^{\text{s}}$  or  $\delta (= 2x_{\text{Ga}}^{\text{s}} - 1)$  is related to well-defined thermodynamic quantities. All required values in Eq. [20] except  $\Delta S_{\text{P}}$ ,  $\Delta S_{\text{Ga}}$ , and  $\Delta H_{\text{P}}$  can be obtained from previous work. Therefore, a knowledge of  $\delta$  at three temperatures is necessary to determine these entropies and enthalpy. These quantities were evaluated from a set of three simultaneous transcendental equations which were generated by writing Eq. [20] for three different temperatures with the appropriate values of the activities and experimental  $\delta$ .

The experimental data selected for this calculation were taken from the analysis of undoped seed-end crystals, grown at 1465° (MH-143-powdered), 1457° (MH-134), and 1327°C (MH-70-powdered). The activities  $a_{\text{P}}$  and  $a_{\text{Ga}}$  at these temperatures were derived from the published liquidus and activity coefficient curves (1). A value of  $\Delta H^{\circ}_{\text{f}} = -30.9$  kcal at 1400°C (the average growth temperature of samples used in the calculation) was derived from a combination of the heat of formation of GaP from the solid elements at 25°C (1) with the enthalpy changes (including the heats of fusion of Ga and P) associated with heating Ga (26), P (27), and GaP (1) to 1400°C. The Schottky enthalpy was previously estimated (7) to be 88.6 kcal (3.84 eV) which was based on Kroger's rule (28) stating that the ratios of the heat of atomization to  $H_{\text{S}}$  are relatively constant values for covalent semiconductors.

Due to the complexity of solving the transcendental equations for  $\Delta S_{\text{P}}$ ,  $\Delta S_{\text{Ga}}$ , and  $\Delta H_{\text{P}}$ , a brief outline of the computational procedure is in order. As the equations are linear in  $e^{\Delta S_{\text{P}}/R}$  and  $e^{\Delta S_{\text{Ga}}/R}$ , these quantities were expressed explicitly in terms of  $\Delta H_{\text{P}}$  by applying Kramer's rule to a pair of equations. Then, substituting  $e^{\Delta S_{\text{P}}/R}$  and  $e^{\Delta S_{\text{Ga}}/R}$  as a function of  $\Delta H_{\text{P}}$  into the third equation, an implicit transcendental equation in one unknown was obtained which was solved for  $\Delta H_{\text{P}}$  by a numerical method. Finally, knowing  $\Delta H_{\text{P}}$ ,  $e^{\Delta S_{\text{P}}/R}$  and  $e^{\Delta S_{\text{Ga}}/R}$  were calculated by Kramer's rule.

The results can be summarized in the following manner. For Eq. [13]

$$\Delta H_{\text{P}} = 16.5 \text{ kcal (0.71 eV)}, \quad \Delta S_{\text{P}} = -3.38 \text{ cal/deg}$$

For Eq. [14] (using Eq. [19])

$$\Delta H_{\text{Ga}} = 41.2 \text{ kcal (1.79 eV)}, \quad \Delta S_{\text{Ga}} = 9.11 \text{ cal/deg}$$

*Calculations of the vacancy concentrations and of the solidus.*—Using the above values of the entropies and enthalpies in combination with  $a_{\text{Ga}}$  and  $a_{\text{P}}$ , the site fractions  $v_{\text{P}}$  and  $v_{\text{Ga}}$  were readily calculated over a wide temperature range from Eq. [15] and [16], respectively. Multiplication of the fractional concentrations by  $2.47 \times 10^{22}$  yields the absolute vacancy concentrations in the customary vacancies/cm<sup>3</sup> units; these are presented in Fig. 2 as a function of reciprocal temperature.

It follows from the observation that  $x_{\text{Ga}}^{\text{s}} > 0.5$  in Table I that along the Ga-rich liquidus  $v_{\text{P}}$  is always greater than  $v_{\text{Ga}}$ , as shown in Fig. 2. In particular, at the melting point of GaP there are, respectively,  $8 \times 10^{18}$  and  $1.3 \times 10^{19}$  cm<sup>-3</sup> Ga and P vacancies in the

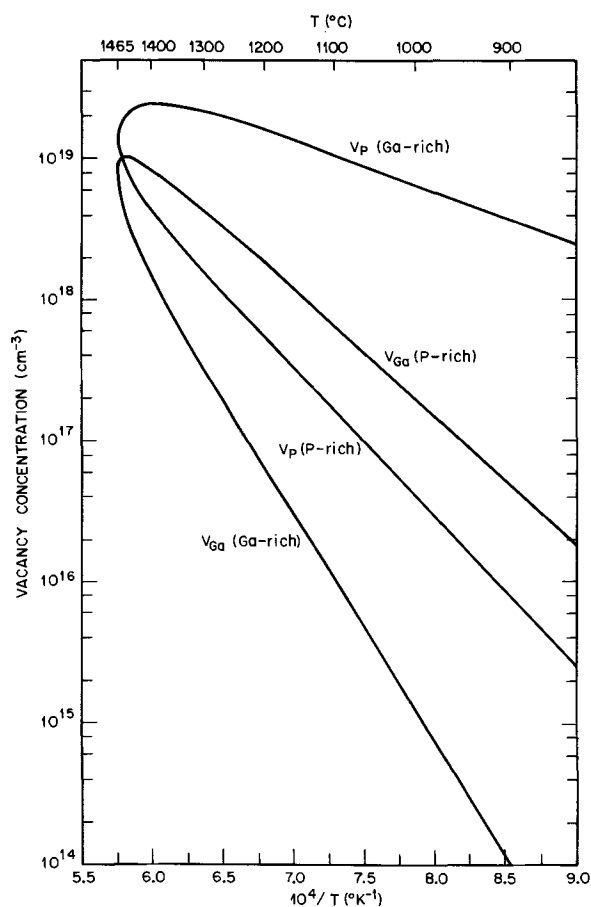


Fig. 2. The calculated Ga and P vacancy concentrations for GaP crystals in equilibrium with liquid solutions along the Ga- and P-rich branches of the liquidus curve.

crystal. However, along the P-rich liquidus,  $v_{Ga}$  is always greater than  $v_P$ .

Having evaluated  $v_P$  and  $v_{Ga}$ , the entire solidus boundary was calculated from Eq. [12] and superimposed over the experimental solidus data in Fig. 1. The calculated solidus is retrograde with a large excess of Ga in equilibrium with the Ga-rich liquid solution and with a much smaller excess of P along the P-rich liquidus. The retrograde maximums are at  $\sim 1375^\circ$  (in the vicinity of the  $v_P$  maximum) and  $\sim 1400^\circ\text{C}$  on the Ga and P-rich sides, respectively.

**Discussion.**—It can be seen in Fig. 2 that along the Ga-rich branch of the liquidus curve,  $v_{Ga}$  drops much more drastically with decreasing temperature than  $v_P$ . Consequently, in view of the maximum along the  $v_P$  curve,  $v_P$  is within a factor of 2 for crystals pulled by LEC at  $1465^\circ\text{C}$  and grown from solution (assuming that the average growth temperature of SG is  $\sim 1100^\circ\text{C}$ ); whereas,  $v_{Ga}$  decreases by a factor of  $\sim 1000$ . This observation bears significantly on the interpretation of electrical and optical measurements. If crystals are grown or heat-treated at different temperatures near or at the Ga-rich liquidus, then subsequent electrical or optical measurements are much more likely to reveal effects associated with the changes in  $v_{Ga}$  rather than  $v_P$ .

Previously, a linear correlation was established between  $1/\tau_n$  and relative Ga vacancy concentration for SG crystals and crystals pulled by LEC from stoichiometric and nonstoichiometric melts (11). The relative insensitivity of  $v_P$  to crystal growth or heat-treating temperature provides additional evidence supporting the interpretation that the dominant nonradiative centers are related to  $V_{Ga}$  and not to  $V_P$ . Moreover, an independent value of  $\Delta H_{Ga}$  was obtained by a reanalysis

of the  $1/\tau_n$  data (11). If  $1/\tau_n = C_1 v_{Ga}$ , where  $C_1$  is a constant of proportionality, then according to Eq. [16]

$$\log 1/\tau_n = \log C_1 + \Delta S_{Ga}/R - \Delta H_{Ga}/RT + \log a_P$$

Combining the temperature-independent terms in a new constant,  $C_2$ , we find that

$$\log 1/(\tau_n a_P) = \log C_2 - \Delta H_{Ga}/RT$$

Since this equation is linear in  $1/T$  and the left-hand side consists of known quantities, the method of least-squares yields  $\Delta H_{Ga} = 1.73 \pm 0.36 \text{ eV}$ .<sup>7</sup> The good agreement found between the above  $\Delta H_{Ga}$ , derived from optical measurements, and that obtained from the thermodynamic analysis of the solidus data (1.79 eV) gives additional strong support to the identification of Ga vacancies with killer centers.

The effect of varying  $H_S$  on  $\Delta H_P$  and  $\Delta H_{Ga}$  was determined by repeating the initial calculation based on Eq. [20]. It was found that  $\Delta H_P$  is relatively insensitive to changes in  $H_S$ . In particular, varying  $H_S$  by  $\pm 10\%$ ,<sup>8</sup> effects  $\Delta H_P$  by less than  $\sim \pm 0.5\%$ , while  $\Delta H_{Ga}$  changes by  $\sim \pm 20\%$  (as seen from Eq. [19]) which is comparable in magnitude to the error in the optical  $\Delta H_{Ga}$ .

The calculated solidus curve, shown in Fig. 1, is in good accord with all the experimental solidus data. Indeed, the solidus data obtained for SG, doped LEC pulled, and annealed crystals, none of which were used in the calculations, by their agreement with the solidus curve, corroborates the consistency of the thermodynamic treatment. In view of the relatively large observed deviations from stoichiometry, precision x-ray and density measurements on nonstoichiometric LEC pulled crystals could provide further confirmation of the analysis.

Recently, Logan and Hurle (23) estimated the solidus curve of GaAs by a detailed analysis of the annealing results of Potts and Pearson (29), Munoz *et al.* (31), and others. The shape of the solidus curve for GaAs is similar to the one obtained for GaP. In essence, the solidus is retrograde and the departures from stoichiometry are much more pronounced along the Ga-rich branch of the solidus than along the As-rich one.

In addition, it is interesting to compare the values of the Schottky entropy and enthalpy ( $H_S$  and  $S_S$ ) for GaAs and GaP. According to Logan and Hurle (23),  $H_S = 4 \text{ eV}$  for GaAs which should be compared with the value of 3.84 eV used in this study. For GaP,  $S_S$  was found by adding the derived values of  $\Delta S_P$  and  $\Delta S_{Ga}$  for Eq. [13] and [14], respectively, and subtracting the  $1400^\circ\text{C}$  value of  $\Delta S_f^\circ$  for Eq. [17]. An application of the third law method to the thermodynamic data for Ga(l) (26), P(l) (27), and GaP (1) yielded  $\Delta S_f^\circ = 14.24 \text{ cal/deg}$ . Thus  $S_S \approx 20 \text{ cal/deg}$  for GaP which is similar in magnitude to the value (18.6 cal/deg) determined by Logan and Hurle (23) for GaAs. The important enthalpy and entropy values for GaP are summarized in Table II.

According to the principles of defect chemistry (28)  $S_S$  is a measurable thermodynamic property not ex-

<sup>7</sup> In the previous work (11) which showed the linear correlation,  $\Delta H_{Ga} = 1.71 \text{ eV}$  was estimated for Eq. [14] from the sum of  $H_S$  (3.84 eV) and the enthalpy for the reaction  $P(l) + V_P = P_P$ ,  $\Delta H_V$ , obtained (7) by a simple generalization of the results of Potts and Pearson for GaAs (29). However, since recently Logan and Hurle (23) showed that the annealing data of Potts and Pearson (29) were not along the liquidus, the estimated  $\Delta H_V$  was not used here.

<sup>8</sup> Note that the selected upper limit for  $H_S$  approaches the sum of the recently estimated values (30) for the vacancy formation energies of Ge (1.9 eV) and Si (2.38 eV).

Table II. Defect entropies and enthalpies for GaP

Reaction	Entropy (cal/deg)	Enthalpy (eV)
$\text{Ga}(l) = \text{Ga}_{Ga} + V_P$	-3.38	0.71
$\text{P}(l) = P_P + V_{Ga}$	9.11	$1.79, \dagger 1.73 \pm 0.36^*$
$\text{Ga}(l) + \text{P}(l) = \text{Ga}_{Ga} + P_P$	-14.24	-1.34
$0 = V_P + V_{Ga}$	19.97	3.84

† From solidus data.

\* From optical data.

perimentally separable into the entropies of individual defects  $s(V_P)$  and  $s(V_{Ga})$ , interrelated by  $S_S = s(V_P) + s(V_{Ga})$ . But a rough estimate of these virtual thermodynamic quantities from the data was possible. Writing out in detail the entropy changes implied by Eq. [13] and [14], we find for  $s(V_P)$  and  $s(V_{Ga})$ , respectively

$$s(V_P) = \Delta S_P + S^\circ(\text{Ga}(l)) - s(\text{Ga}_{Ga}) \quad [21]$$

and

$$s(V_{Ga}) = \Delta S_{Ga} + S^\circ(\text{P}(l)) - s(\text{P}_P) \quad [22]$$

Assuming that

$$s(\text{Ga}_{Ga}) = S^\circ(\text{Ge}(c))$$

and

$$s(\text{P}_P) = S^\circ(\text{Si}(c))$$

and using tabulated thermodynamic data for crystalline Ge (26), Si (27), Ga(l) (26), and P(l) (27), at 1400°C in combination with  $\Delta S_P$  and  $\Delta S_{Ga}$  from Table II, Eq. [21] and [22] yield the virtual vacancy entropies with respect to the atomic sublattice constituents Ga and P as  $s(V_P) \approx 4$  cal/deg and  $s(V_{Ga}) \approx 16$  cal/deg.

Finally, we can estimate the effect of  $V_P$  on the local vibrational frequency of the adjacent Ga atoms and  $V_{Ga}$  on that of the P atoms. If the crystal as a whole has a frequency  $\nu$  and the number of nearest neighbors is 4 then (28)

$$s(V_{Ga}) = k \ln \left( \frac{\nu}{\nu'_P} \right)^4 \quad [23]$$

and

$$s(V_P) = k \ln \left( \frac{\nu}{\nu'_{Ga}} \right)^4 \quad [24]$$

where  $\nu'_P$  and  $\nu'_{Ga}$  are the average vibrational frequencies near  $V_{Ga}$  and  $V_P$ , respectively. Solving for  $\nu/\nu'_P$  and  $\nu/\nu'_{Ga}$  we find

$$\nu/\nu'_{Ga} = 1.65, \quad \nu/\nu'_P = 7.48, \quad \text{and} \quad \nu'_{Ga}/\nu'_P = 4.5$$

Thus the wavelengths of local vibrational modes due to vacancies lie above the lattice modes. This suggests that local mode identification in the far infrared may be aided by these thermodynamic results.

#### Acknowledgments

The authors are grateful to R. H. Saul, J. W. Nielsen, S. Knight, and H. D. Keith for their continued interest in this work.

Manuscript submitted May 8, 1973; revised manuscript received Aug. 2, 1973.

Any discussion of this paper will appear in a Discussion Section to be published in the December 1974 JOURNAL.

#### REFERENCES

1. C. D. Thurmond, *J. Phys. Chem. Solids*, **26**, 785 (1965).
2. M. B. Panish, *This Journal*, **113**, 224 (1966).
3. M. B. Panish, *ibid.*, **114**, 1161 (1967).
4. A. S. Jordan, *Met. Trans.*, **2**, 1959 (1971); *ibid.*, **2**, 1965 (1971).
5. M. Kowalchik, A. S. Jordan, and Mildred H. Read, *This Journal*, **119**, 756 (1972).
6. M. B. Panish and H. C. Casey, *J. Phys. Chem. Solids*, **29**, 1719 (1968).
7. A. S. Jordan, *This Journal*, **118**, 781 (1971).
8. A. S. Jordan, F. A. Trumbore, K. B. Wolfstirn, M. Kowalchik, and D. D. Roccasecca, *ibid.*, **120**, 791 (1973).
9. R. H. Saul and W. H. Hackett, Jr., *ibid.*, **119**, 542 (1972).
10. G. E. Stringfellow, *ibid.*, **119**, 1780 (1972).
11. A. S. Jordan, A. R. Von Neida, R. Caruso, and M. DiDomenico, Jr., *Appl. Phys. Letters*, **19**, 394 (1971).
12. R. Caruso, J. M. Dishman, and D. D. Manchon, Jr., Unpublished data.
13. R. Caruso and A. R. Von Neida, *This Journal*, To be published.
14. I. Ladany and H. Kressel, *RCA Rev.*, **33**, 517 (1972).
15. P. J. Dean, *Phys. Rev.*, **B4** 2596 (1971).
16. R. N. Bhargava, S. K. Kurtz, A. T. Vink, and R. C. Peters, *Phys. Rev. Letters*, **27**, 183 (1971).
17. See, for example, M. Hansen, "Constitution of Binary Alloys," McGraw-Hill Book Co., New York (1958) and supplementary volumes edited by R. P. Elliott (1965) and F. A. Shunk (1969).
18. A. R. Von Neida, L. J. Oster, and J. W. Nielsen, *J. Crystal Growth*, **13/14**, 647 (1972).
19. C. K. Kim, Submitted to *This Journal*.
20. S. F. Nygren, C. M. Ringel, and H. W. Verleur, *This Journal*, **118**, 306 (1971).
21. E. C. Lightowers, *J. Electron. Mater.*, **1**, 39 (1972).
22. "Handbook of Chemistry and Physics," 49th ed., R. C. Weast, Editor, The Chemical Rubber Co., Cleveland, Ohio (1968).
23. R. M. Logan and D. T. J. Hurle, *J. Phys. Chem. Solids*, **32**, 1739 (1971).
24. A. S. Jordan and R. R. Zupp, *This Journal*, **116**, 1264 (1969).
25. F. A. Trumbore, *Bell System Tech. J.*, **39**, 205 (1960).
26. D. R. Stull and G. C. Sinke, "Thermodynamic Properties of the Elements," Advances in Chemistry Series, No. 18, A.C.S., Washington, D.C. (1956).
27. JANAF, Interim Thermochemical Tables, Dow Chemical Company.
28. F. A. Kröger, "Chemistry of Imperfect Crystals," Interscience Publishers, New York (1964).
29. H. R. Potts and G. L. Pearson, *J. Appl. Phys.*, **37**, 2098 (1966).
30. J. C. Phillips and J. A. Van Vechten, *Phys. Rev. Letters*, **30**, 220 (1973).
31. E. Munoz, W. L. Snyder, and J. L. Moll, *Appl. Phys. Letters*, **16**, 262 (1970).

# Crystal Growth and Characterization of Gallium Nitride

T. L. Chu,\* K. Ito, R. K. Smeltzer,\*<sup>1</sup> and Shirley S. C. Chu

Electronic Sciences Center, Southern Methodist University, Dallas, Texas 75275

## ABSTRACT

The crystal growth of gallium nitride has been investigated by using the ammonolysis of gallium suboxide, the sublimation of gallium nitride or gallium oxide in an ammonia atmosphere, and the ammonolysis of gallium monochloride at  $1150^\circ \pm 20^\circ\text{C}$  in gas flow systems. The first two techniques have produced only low resistivity gallium nitride crystals of millimeter size. The ammonolysis of gallium monochloride is most promising; single crystals of gallium nitride as large as  $25 \times 15 \times 5$  mm, heretofore unknown, have been obtained by using sapphire platelets with main faces of (1102) orientation as substrates. The single crystallinity of these crystals was verified by chemical etching and optical microscopy and x-ray diffraction techniques. These crystals, with an electron concentration of about  $10^{19} \text{ cm}^{-3}$  and Hall mobilities of about  $150 \text{ cm}^2 \text{ V}^{-1} \text{ sec}^{-1}$  at room temperature, have been used as substrates for the growth of large gallium nitride crystals of improved structural perfection.

Gallium nitride crystallizes in the wurtzite structure and has a direct energy gap of about 3.5 eV at 2°K (1). It is, therefore, a potentially important optoelectronic material. However, gallium nitride has a high melting point, above  $1600^\circ\text{C}$  (2), and is thermally unstable with respect to decomposition into its elements. Early work has reported that gallium nitride undergoes slow dissociation at temperatures as low as  $600^\circ\text{C}$  (3). The available vapor pressure data on gallium nitride have recently been reviewed and found to be consistent with the equilibrium pressure of nitrogen over gallium nitride and liquid gallium calculated from thermodynamic functions (4). For example, the vapor pressure of nitrogen is in the range of 1-100 atm at  $1000^\circ\text{C}$  and 700-40,000 atm at  $1600^\circ\text{C}$ . These results indicate the severe problems involved in the preparation of large gallium nitride crystals. Also, gallium nitride is essentially insoluble in gallium at temperatures below  $1100^\circ\text{C}$ . Thus, a vapor growth technique with a growth rate of gallium nitride considerably higher than its decomposition rate is best suited for the crystal growth of gallium nitride.

Single crystals of gallium nitride have been prepared in the form of needles with hexagonal symmetry by heating gallium nitride at  $1150^\circ$  to  $1200^\circ\text{C}$  in an ammonia flow (5). However, major efforts have been directed to the epitaxial growth of thin layers of gallium nitride on foreign substrates by physical and chemical vapor growth techniques. The former included the evaporation of gallium in a nitrogen discharge (6) and the rf sputtering of gallium nitride (7), and the latter included the ammonolysis of gallium monochloride (8-10), the thermal decomposition of a gallium tribromide-ammonia complex (11), and the ammonolysis of trimethylgallium (12). The ammonolysis of gallium monochloride on sapphire substrates has been most widely used. In most cases, however, the grown layer exhibited high donor concentrations, due presumably to a native defect such as nitrogen vacancies, and p-type layers have not been produced. Also, sapphire is structurally not an ideal substrate for the epitaxial growth of gallium nitride because of their differences in lattice parameters ( $a = 4.76\text{\AA}$  and  $c = 12.99\text{\AA}$  for sapphire;  $a = 3.18\text{\AA}$  and  $c = 5.16\text{\AA}$  for gallium nitride) and thermal expansion coefficients ( $9.2 \times 10^{-6} \text{ }^\circ\text{K}^{-1}$  for sapphire in the  $a$  and  $c$  directions, range  $0^\circ$ - $1200^\circ\text{C}$ ;  $5.6 \times 10^{-6} \text{ }^\circ\text{K}^{-1}$  and  $7.75 \times 10^{-6} \text{ }^\circ\text{K}^{-1}$  for gallium nitride in the  $a$  and  $c$  directions,  $700^\circ$ - $900^\circ\text{K}$ ). Homoepitaxial growth of gallium nitride, which is inherently capable of yielding better quality layers, has not been

investigated because of the lack of bulk crystals of gallium nitride.

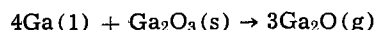
In the present work, three chemical vapor growth techniques were investigated for the growth of bulk gallium nitride crystals. They included the ammonolysis of gallium suboxide, the sublimation of gallium nitride or gallium trioxide in an ammonia atmosphere, and the ammonolysis of gallium monochloride in gas flow systems. The third technique has produced gallium nitride single crystals up to  $25 \times 15 \times 5$  mm in size, heretofore unknown. The experimental procedures of the vapor growth processes and the characterization of grown crystals are discussed in this paper.

## Ammonolysis of Gallium Suboxide

Gallium nitride can, in general, be prepared by the reaction between ammonia and a gaseous gallium compound. Gallium suboxide,  $\text{Ga}_2\text{O}$ , with an appreciable vapor pressure at temperatures near  $1000^\circ\text{C}$ , is suitable for the preparation of gallium nitride as indicated by the thermochemistry of the reaction



Using the free energies of formation of gallium suboxide (13), ammonia (14), gallium nitride (4), and water (14), the standard free energy changes of this reaction have been calculated to be  $-35.7$ ,  $-35.2$ ,  $-27.5$ , and  $-15.1$  kcal/mole at  $1100^\circ$ ,  $1200^\circ$ ,  $1300^\circ$ , and  $1400^\circ\text{K}$ , respectively, indicating that the reaction is thermochemically feasible in the temperature range under consideration. Gallium suboxide can be readily prepared by the reaction of gallium and gallium trioxide according to the reaction



The equilibrium vapor pressure of gallium suboxide over a 4:1 molar mixture of gallium and gallium trioxide has been reported to be approximately 0.2 Torr at  $800^\circ\text{C}$  and 10 Torr at  $1000^\circ\text{C}$  (15).

The ammonolysis of gallium suboxide was carried out with the apparatus shown in Fig. 1. Gallium suboxide was produced in the quartz boat containing a mixture of gallium and gallium trioxide, and the nitrogen flow was used to carry the suboxide vapor into the reaction

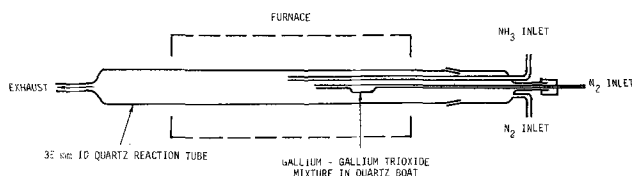


Fig. 1. Schematic diagram of the apparatus for the growth of gallium nitride crystals by the reaction of gallium suboxide with ammonia.

\* Electrochemical Society Active Member.

<sup>1</sup> Present address: Texas Instruments Incorporated, Dallas, Texas 75222.

Key words: ammonolysis, gallium monochloride, sapphire, semiconductor.

tube. The suboxide then reacted with the ammonia to produce gallium nitride. The experiments were carried out with the quartz boat in the temperature range 900°-1050°C and the reaction zone in the temperature range 1000°-1200°C. The flow rate of ammonia was 400 ml/min. The suboxide formation temperature was found to be not critical; however, gallium nitride crystals were obtained only for a reaction zone temperature of 1150° ± 10°C. Needle-like crystals, dark green in color and up to 1 mm in size, were found near the ammonia outlet. Dendritic crystals with dimensions up to 3 mm were sometimes found also. X-ray techniques showed the crystals to be single crystalline gallium nitride with the long axis in the c direction. The limited success of this method for the crystal growth of gallium nitride may be due to the disproportionation of gallium suboxide in the reaction zone, as indicated by the free gallium and powdery material found near the reaction zone.

### Sublimation of Gallium Nitride or Gallium Oxide in Ammonia

It has been reported that small needle-like nitride crystals were obtained by heating powdered gallium nitride in ammonia at 1150°-1200°C (5). Attempts were made to improve upon this result by using different source materials. The apparatus for the sublimation method consisted of a single-zone furnace with an alumina or a fused silica reaction tube. The source material was placed in an alumina boat in the maximum temperature region of the reaction tube, and ammonia or an ammonia-nitrogen mixture was introduced at various flow rates. The reaction tube could be maintained at pressures up to 5 atm. Six types of source material were used: (i) gallium trioxide powder, (ii) gallium nitride powder, (iii) a mixture of gallium and gallium trioxide, (iv) a mixture of gallium and gallium nitride, (v) pressed pellets of gallium and gallium trioxide, and (vi) pressed pellets of gallium and gallium nitride. The pellets weighed about 1g and were made with a Parr Model 2811 pellet press.

The initial experiments were carried out with loosely packed powder of gallium trioxide or gallium nitride. A source temperature of 1170° ± 10°C was necessary to achieve growth of gallium nitride crystals. Typically, after three days of reaction time, very small crystals of gallium nitride were found in the boat. With a fifteen day growth period, crystals were found at two locations. Dark green, slightly transparent, n-type, needle-shaped crystals up to 2 mm long by 0.2 mm thick were found on the wall downstream from the source material; the dark color is due apparently to the thermal decomposition of gallium nitride. Light green transparent crystals of about 0.4 × 0.04 mm dimensions were found in the boat. These results were not affected by changing the flow rate of ammonia, by diluting the ammonia with nitrogen, or by using ammonia pressures up to 5 atm. Similar results were obtained by using loose mixtures of gallium-gallium trioxide and gallium-gallium nitride as the source material except that there was a tendency for larger gallium nitride crystals to form in the boat.

When the pressed pellets of gallium-gallium trioxide and gallium-gallium nitride were used as the source material, source temperatures in the range 1160°-1180°C and ammonia flow rates in the range 50-500 ml/min were used. The experiments were carried out for periods up to 20 days. Two types of needle-like crystals, both with dimensions up to 3 mm long by 0.5 mm thick, were obtained. Light colored crystals were found growing inward from what was the surface of the pellets, and dark green crystals were found on the wall of the reaction tube downstream from the pellets. Usually one type or the other predominated in a particular experiments, but the exact reason for this was not established. Figure 2 shows examples of the two types of gallium nitride crystals; these crystals have a hexagonal cross section and were shown to be single crystalline by the x-ray diffraction

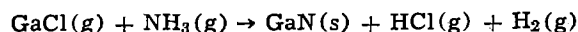
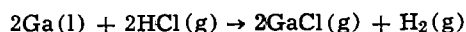


Fig. 2. Gallium nitride crystals grown on the wall of the silica tube (upper) and in the alumina boat (lower) by the sublimation technique.

technique. Chemical etching of these crystals with a 40% sodium hydroxide solution for 30 min revealed no significant structural defects. Using indium as ohmic contacts, the electrical resistivity of these n-type crystals were measured to be essentially independent of temperature in the range 160°-330°K. The darker crystals have a resistivity of about  $3 \times 10^{-3}$  ohm-cm, and the lighter ones about  $3 \times 10^{-2}$  ohm-cm.

### Ammonolysis of Gallium Monochloride

The ammonolysis of gallium monochloride has been used for the epitaxial growth of gallium nitride on the basal plane of sapphire at 850°-1050°C, and the growth rates were up to about 1 μm/min (8-10). This process involves two steps: the formation of gallium monochloride by the reaction of gallium with hydrogen chloride, and the reaction of gallium monochloride with ammonia to form gallium nitride. The chemical reactions are (16)



The ammonolysis of gallium monochloride was also used in this work, and gallium nitride was deposited on sapphire substrates of (1102) orientation at high rates, 10 μm/min for example. The high deposition rate was achieved by the use of high hydrogen chloride concentrations in the reactant mixture, a particular substrate orientation, and a closely spaced geometrical arrangement in the reaction tube. Single crystals of gallium nitride as large as 25 × 15 × 5 mm have been obtained.

The apparatus used in this work is shown schematically in Fig. 3. It consists of a fused silica reaction

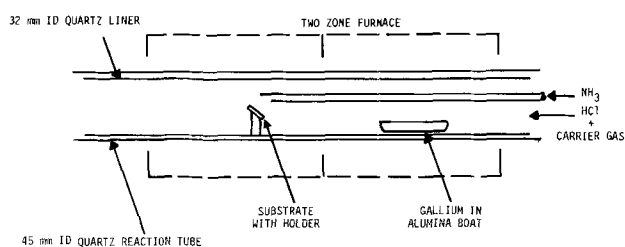


Fig. 3. Schematic of the apparatus for the growth of bulk gallium nitride crystals by the ammonolysis of gallium monochloride.



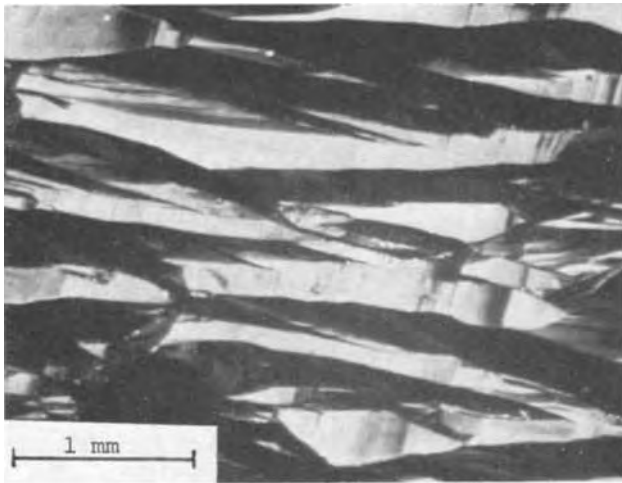


Fig. 4. The as-grown surface of a gallium nitride crystal on a sapphire substrate of  $(1\bar{1}02)$  orientation.

tube, 45 mm ID with a 32 mm ID liner and 90 cm long, situated in a two-zone resistance-heated furnace. The ends of the reaction tube are provided with standard taper joints. The end cap on the gas inlet side has provisions for introducing hydrogen chloride mixed with a diluent, helium or hydrogen, and for introducing ammonia to the reaction zone. Gallium was placed in an alumina boat and heated in one zone of the furnace, and sapphire substrates were located in the second zone of the furnace. The parameters in this process include the composition and flow rate of the reactant mixture, the temperatures of the gallium source and the substrate, and the position of the substrate with respect to the ammonia outlet tube. A large  $\text{NH}_3/\text{HCl}$  molar ratio is necessary to minimize the formation of free gallium. The concentration and flow rate of hydrogen chloride in the reactant mixture determine the rate of formation of gallium monochloride and therefore that of gallium nitride. Also, the reaction between gallium monochloride and ammonia should take place predominately on the substrate surface to minimize homogeneous nucleation through gas phase reactions. The gas phase reaction is more pronounced at high substrate temperatures and can be minimized by using a small separation between the substrate and the ammonia outlet tube.

Both hydrogen and helium were used as the diluent gas. Under optimum temperature and flow rate conditions, the use of helium was found to produce about a 20% higher yield than that of hydrogen, qualitatively

in agreement with a previous report (16). Typical flow rates of helium, hydrogen chloride, and ammonia were 2, 0.02, and 1 liter/min, respectively. The gallium source was held at about  $900^\circ\text{C}$ , and the substrate was maintained at about  $1050^\circ\text{C}$ . The substrate, 5 mm  $\times$  25 mm in area, was located within 1 cm from the ammonia outlet and was tilted at about  $30^\circ$ . After a 6 hr experiment, the single crystal deposit on a  $(1\bar{1}02)$  oriented sapphire substrate was usually 2-5 mm thick, weighing up to 4g. The deposition of gallium nitride on the basal plane of sapphire yielded crystals more than one order of magnitude smaller in volume than the crystals on  $(1\bar{1}02)$  substrates.

The grown crystals range from colorless to dark green in color, and their surfaces always exhibit many growth ridges, as shown in Fig. 4. The faces consist of three orientations at approximately  $120^\circ$  angles to each other. Back-reflection Laue x-ray technique indicated that these faces, each of which has a twofold symmetry, are of  $(\bar{2}110)$ ,  $(1\bar{2}10)$ , and  $(11\bar{2}0)$  orientations. These orientations are symmetry related, and the orientation relation  $(\bar{2}110)_{\text{GaN}} \parallel (1\bar{1}02)_{\text{Al}_2\text{O}_3}$  is in agreement with an early work (12). In addition to a reasonable match in lattice parameters, the development of the  $\{\bar{2}110\}$  faces presumably arises from the fact that the  $\{\bar{2}110\}$  planes are the most densely packed, and therefore the lowest energy planes in gallium nitride. Planes of other crystallographic orientations developed during the growth process will eventually grow out.

Gallium nitride crystals grown on sapphire substrates have high concentrations of structural defects. Defects in gallium nitride may be revealed by etching with a 40% sodium hydroxide solution at about  $100^\circ\text{C}$  for 30 min. Figure 5 shows typical defects observed in gallium nitride crystals. The etch figures on a mechanically polished surface (Fig. 5a) consist of many parallel lines and are stacking fault traces, i.e., the intersections of stacking fault planes with the surface of the crystal. The transmission micrograph of the same area (Fig. 5b) shows the projection of stacking fault planes on the surface of the crystal, mostly in the form of isosceles triangles of the same orientation, indicating that all faulting planes are parallel and make the same angle with the grown surface. The stacking fault plane is presumably a  $\{\bar{2}110\}$  plane, the most densely packed plane, which makes an angle of  $60^\circ$  with the grown surface, intersecting along a  $\langle 0001 \rangle$  direction. Thus, the stacking faults usually commence at certain points and develop along a  $\{\bar{2}110\}$  plane with a rapid increase in area, similar to the formation of stacking faults in epitaxial silicon (17, 18).

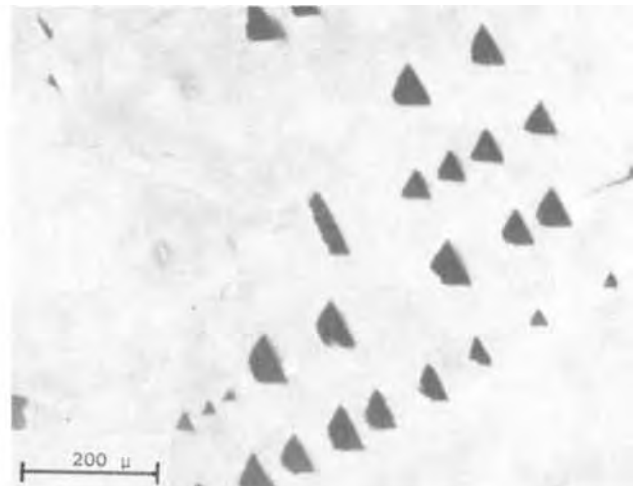
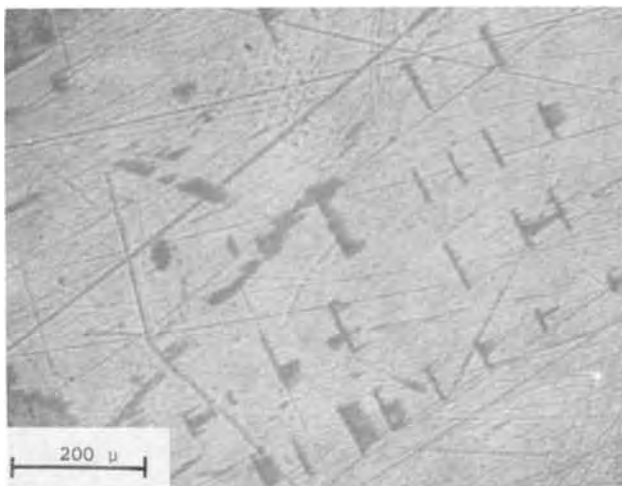


Fig. 5. Stacking faults in vapor-grown gallium nitride crystals. (a, left) Etch figures on a polished grown surface. (b, right) Transmission micrograph of the same area shown in (a).



The sapphire substrate on the grown crystal can be readily removed by mechanical lapping. Hall measurements were made on the bulk gallium nitride crystals at 77° and 300°K by the van der Pauw technique (19). At room temperature, the bulk crystals were n-type, and had an electron concentration of approximately  $10^{19} \text{ cm}^{-3}$  and carrier mobilities in the range of  $120\text{--}180 \text{ cm}^2 \text{ V}^{-1} \text{ sec}^{-1}$ . The carrier concentration was essentially the same at 77°K; however, the mobilities decreased by about 25%, due presumably to the ionized impurity scattering.

The large gallium nitride crystals have also been used as substrates for crystal growth. They were first mechanically polished with an alumina abrasive and etched *in situ* with a hydrogen-hydrogen chloride mixture at 850°C just prior to the deposition process. Single crystals of gallium nitride on gallium nitride substrates with dimensions similar to those on sapphire substrates were obtained. Figure 6 shows two typical gallium nitride crystals grown on a sapphire substrate of (1102) orientation and a gallium nitride



Fig. 6. Gallium nitride crystals obtained by the ammonolysis of gallium monochloride. The upper crystal was grown on a sapphire substrate of (1102) orientation, and the lower crystal was grown on a gallium nitride substrate.

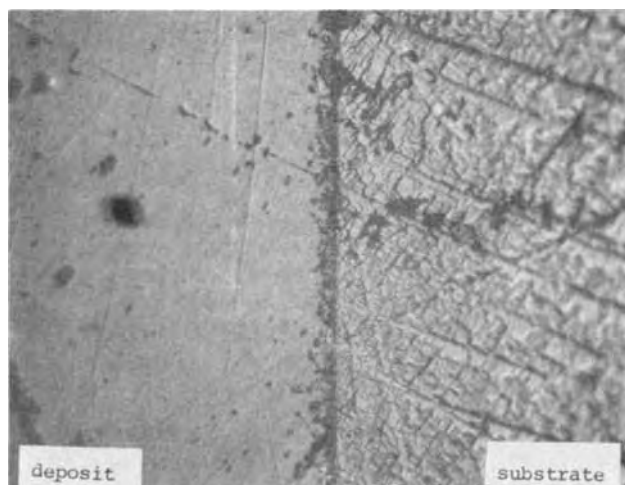


Fig. 7. The angle-lapped and chemically etched surface of a gallium nitride crystal deposited on a gallium nitride substrate. Etchant: 40% sodium hydroxide solution at 100°C for 30 min.

substrate. Figure 7 shows the angle-lapped and chemically etched surface of a gallium nitride crystal deposited on a gallium nitride substrate. As expected, the grown crystal has considerably better structural perfection than the substrate as indicated by the relatively heavy attack of the substrate by the sodium hydroxide solution.

### Summary and Conclusions

Three chemical vapor growth techniques have been used for the preparation of gallium nitride crystals at  $1150^\circ \pm 20^\circ\text{C}$ . The ammonolysis of gallium suboxide and the sublimation of gallium nitride or gallium trioxide in an ammonia atmosphere have produced only gallium nitride crystals of millimeter size. They were n-type and had low electrical resistivities. The ammonolysis of gallium monochloride on sapphire substrates of (1102) orientation at 1050°C has produced single crystals of gallium nitride with dimensions up to  $25 \times 15 \times 5 \text{ mm}$ . Gallium nitride crystals grown in this manner had electron concentrations on the order of  $10^{19} \text{ cm}^{-3}$  and electron mobilities of about  $150 \text{ cm}^2 \text{ V}^{-1} \text{ sec}^{-1}$  at room temperature. Using these crystals as substrates, large gallium nitride crystals with better structural perfection have also been obtained. The growth of large gallium nitride crystals reported in this work, due largely to the use of a relatively high flow rate of hydrogen chloride, the closely spaced reaction tube geometry, and the (1102) oriented substrates, represents a significant contribution to the state of the art technology.

### Acknowledgment

This research was supported by the Langley Research Center of the National Aeronautics and Space Administration under Grant NGR 44-007-052.

Manuscript submitted Dec. 5, 1972; revised manuscript received Aug. 26, 1973.

Any discussion of this paper will appear in a Discussion Section to be published in the December 1974 JOURNAL.

### REFERENCES

1. R. Dingle, D. D. Sell, S. E. Stokowski, and M. Illegems, *Phys. Rev.*, **B4**, 1211 (1971).
2. J. B. MacChesney, P. M. Bridenbaugh, and P. B. O'Conner, *Mater. Res. Bull.*, **5**, 783 (1970).
3. M. R. Lorenz and B. B. Binkowski, *This Journal*, **109**, 24 (1962).
4. C. D. Thurmond and R. A. Logan, *ibid.*, **119**, 622 (1972).
5. R. B. Zetterstrom, *J. Mater. Sci.*, **5**, 1102 (1970).
6. B. B. Kosicki and D. Khang, *J. Vacuum Sci. Technol.*, **6**, 593 (1969).
7. H. J. Hovel and J. J. Cuomo, *Appl. Phys. Letters*, **20**, 71 (1972).
8. H. P. Maruska and J. J. Tietjen, *ibid.*, **15**, 327 (1969).
9. D. K. Wickenden, K. R. Faulkner, R. W. Brander, B. J. Isherwood, *J. Crystal Growth*, **9**, 158 (1971).
10. M. Illegems, *ibid.*, **13/14**, 360 (1972).
11. T. L. Chu, *This Journal*, **118**, 1200 (1971).
12. H. M. Manasevit, F. M. Erdmann, and W. I. Simpson, *ibid.*, **118**, 1864 (1971).
13. C. D. Thurmond and C. J. Frosch, *ibid.*, **111**, 184 (1964).
14. D. R. Stull and H. Prophet, JANAF Thermochemical Tables, Second Edition, National Bureau of Standards, NSRDS-NBS 37, Washington, D. C. (1971).
15. C. J. Frosch and C. D. Thurmond, *J. Phys. Chem.*, **66**, 877 (1962).
16. V. S. Ban, *This Journal*, **119**, 761 (1972).
17. T. L. Chu and J. R. Gavaler, *ibid.*, **110**, 338 (1963).
18. G. R. Booker and R. Stickler, *J. Appl. Phys.*, **33**, 3281 (1962).
19. L. J. van der Pauw, *Philips Res. Rept.*, **13**, 1 (1958).

# High-Temperature Dielectric Behavior of Polycrystalline ZnO

M. A. Seitz and T. O. Sokoly

*Metallurgy and Materials Science, College of Engineering, Marquette University, Milwaukee, Wisconsin 53233*

## ABSTRACT

The dielectric behavior of undoped, lithium-doped, and sodium-doped polycrystalline ZnO was investigated as a function of frequency, from 100 Hz to 600 kHz, and temperature, over the interval from room temperature to 900°K. Barrier layer polarization seemed responsible for capacitance dispersion for undoped polycrystalline ZnO. These barrier layers appeared to occur at the surfaces of the individual polycrystalline grains and seemed to be the result of the chemisorption of oxygen. The data for lithium- and sodium-doped ZnO was rationalized on the basis of a space charge polarization model involving mobile ionic point defects, which were blocked or partially blocked at the specimen electrodes, and electronic carriers, which were able to freely pass through the electrodes. The effective dielectric constant for the doped specimens varied exponentially with temperature. The activation energies of 0.6 eV for Li-doped ZnO and 1.1 eV for Na-doped ZnO were attributed to the energy of motion of the interstitial defect.

In the last two decades zinc oxide has been the subject of numerous investigations. Excellent reviews of much of this work have been presented by several authors (1-3). Zinc oxide has been found attractive for a diversity of applications which include dental cements, catalysts, photoconductive devices, luminescent phosphors, ultrasonic amplifiers, varistors, and field-effect transistors.

Zinc oxide crystallizes in the hexagonal wurtzite crystal structure and has lattice constants  $a = 3.24\text{\AA}$  and  $c = 5.19\text{\AA}$ . Due to the great difference in size of the zinc and oxygen ions, the atomic packing factor is only 0.44. Relatively large (0.95Å radius) open spaces exist in the lattice and play an important role in the electrical, physical, and chemical behavior of this material. Azaroff has demonstrated the role of crystal structure on atomistic diffusion in ZnO (4, 5). The results of other diffusion studies on this material are also to be found in the literature (6-12).

Optical absorption studies have shown that the band-gap energy of ZnO ranges from 3.4 eV at liquid helium temperature to 2.4 eV at 1360°K. The commonly accepted room temperature value is 3.2 eV. The electrical conductivity of ZnO has been found to be n-type and to vary from  $10^{-18}$  to  $10^3$  (ohm-cm) $^{-1}$  depending on the temperature of measurement and the materials previous history (6-12). Hall effect studies have confirmed the n-type behavior of ZnO (13, 14).

A number of investigations of the dielectric behavior of ZnO have been conducted (15-23). These studies, however, have been conducted at relatively low temperatures (room temperature and below) and high frequencies (100 kHz and above). The high frequency relative dielectric constant in the  $a$  direction was found to be  $8.5 \pm 0.2$ , while that in the  $c$  direction was found to be  $10.0 \pm 0.2$ .

Heretofore, the high conductivity of nonstoichiometric ZnO has made it difficult to perform dielectric measurements at lower frequencies and/or higher temperatures. In this study, measurements were performed over the frequency interval  $10^2$  to  $6 \times 10^5$  Hz and at temperatures ranging from room temperature to 900°K, using a previously developed technique (24).

## Experimental Procedure

In our early attempts to measure the high-temperature dielectric behavior of ZnO, it was noted that the specimen conductance,  $G_{sp}$ , was always greater than the capacitive susceptance,  $\omega C_{sp}$ . This results in dissipation factors which were quite large,  $1.0 < \tan \delta$

$< 10^5$ . Therefore, a special technique had to be used to perform dielectric measurements. A substitution technique, where corrections are made for parasitic capacitances and inductances associated with the system, was the subject of a previous paper (24). With this technique the capacitance of specimens having a total resistance of greater than 100 ohms and a dissipation factor less than  $10^4$  can be measured to  $\pm 15\%$ . For mid-range frequencies (1-50 kHz) the error is less than  $\pm 5\%$ .

Polycrystalline specimens were prepared using pressing and sintering techniques with Johnson Matthey "specpure" ZnO powder (99.999% pure), which had an average grain size of about  $5\mu$ . The final disk-shaped specimens had a thickness of 0.5 cm and plane parallel surface areas of 2 cm<sup>2</sup>. Doped polycrystalline specimens were produced by mixing the appropriate amounts of the hydroxides, LiOH or NaOH, with powdered ZnO (8, 14). The powdered material was then heated to 600°C for 12 hr, during which time the hydroxides were converted to the oxide and homogenization occurred by interstitial diffusion. The powdered material was then pressed and sintered at 650°C for a second 12 hr period of time. The relatively low temperature heat-treatments were chosen in an attempt to have most of the added impurity remain in interstitial lattice positions. Electrical contact to the specimens were made, on their plane parallel surfaces, using either fluxed platinum paste (Engelhard No. 05), fluxed gold paste (Engelhard 601-FM), or silver paint (GC Electronics Silver Print). Approximately three coatings were used in each case. Between each application the sample was baked at 600°C for about 6-8 hr. When the resistance between any pair of points across the electrode contact had been reduced to less than 0.1 ohm, the procedure was terminated. In all cases investigated it was attempted to have a slight amount of diffusion of the electrode material into the sample surface to insure an intimate contact with the specimen. Although intergranular diffusion, to a depth of approximately 0.5-1 mil, could be observed under microscopic examination, no convenient technique was available to determine the degree of penetration into the grains themselves.

The specimens were loaded into the measurement system. Before performing a measurement, the specimens were allowed to equilibrate at temperature and in various partial pressures of oxygen provided by oxygen-argon tank mixtures. Equilibrium was assumed when the capacitance and resistance changes over a several hour period were less than those due to

Key words: zinc oxide, chemisorption, dielectric, diffusion.

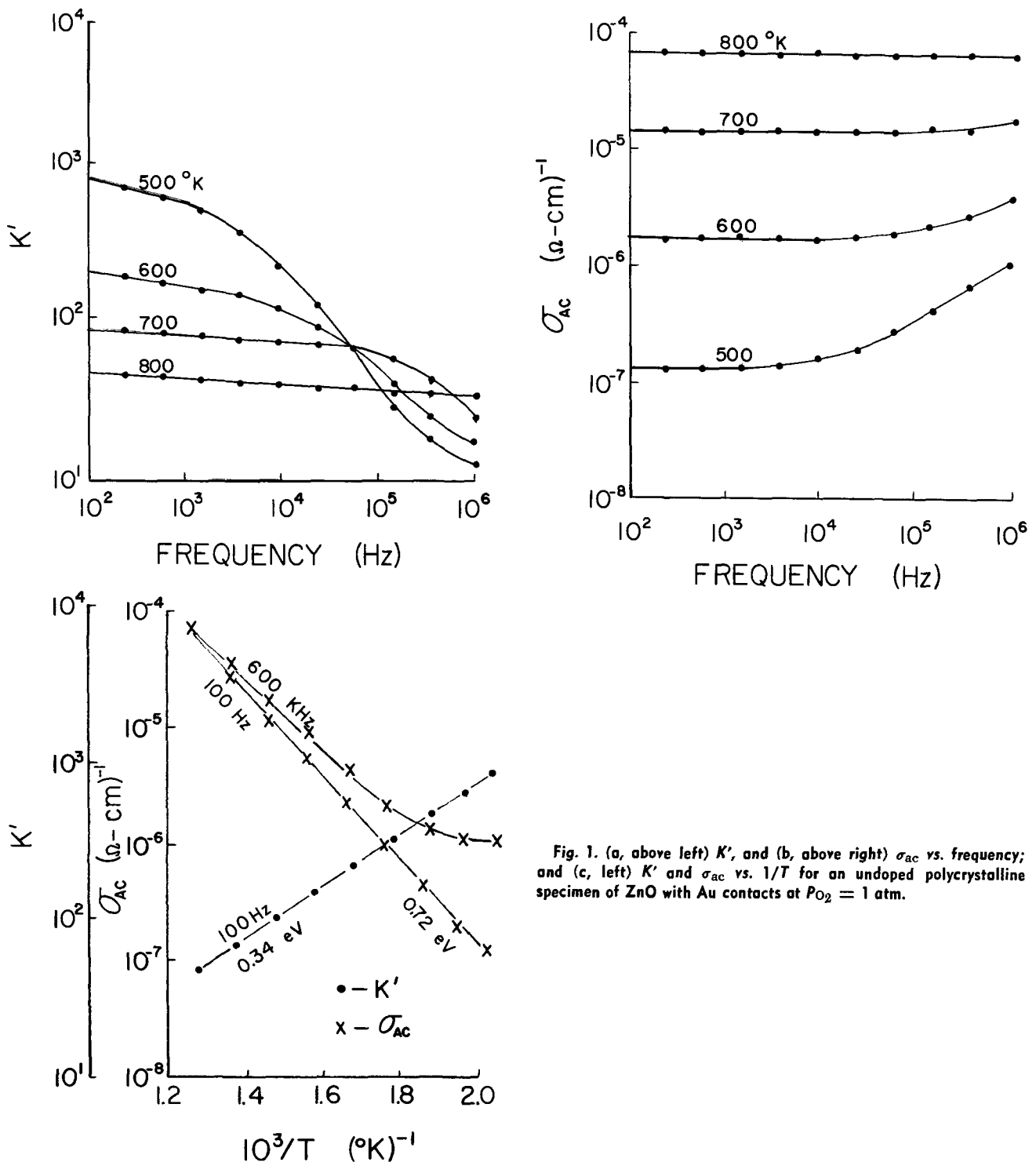


Fig. 1. (a, above left)  $K'$ , and (b, above right)  $\sigma_{ac}$  vs. frequency; and (c, left)  $K'$  and  $\sigma_{ac}$  vs.  $1/T$  for an undoped polycrystalline specimen of ZnO with Au contacts at  $P_{O_2} = 1$  atm.

the variation in temperature. Measurements of capacitance and resistance were made at selected frequencies in the range 100 Hz to 600 kHz. The specimen temperature was increased or decreased at approximately 100°C intervals and the above procedure repeated. Experiments were carried out on pure, Li-doped, and Na-doped ZnO.

### Results and Discussion

**Dielectric behavior of undoped polycrystalline ZnO.**—The dielectric behavior of undoped (99.999% pure) polycrystalline ZnO with gold electrodes has been investigated from 10<sup>2</sup> Hz to 6 × 10<sup>5</sup> Hz and over the temperature range from room temperature to 800°K. The variations of the apparent dielectric constant,  $K'$ , and a-c conductivity,  $\sigma_{ac}$ , are shown as functions of frequency and reciprocal temperature for an oxygen partial pressure of 1 atm in Fig. 1. The dispersion of  $K'$

and  $\sigma_{ac}$  with frequency disappear as the temperature is increased. Upon decreasing the partial pressure of oxygen to less than about 10<sup>-5</sup> atm it was found that the low frequency values of  $K'$  decreased and  $\sigma_{ac}$  increased until no dispersions with frequency were noted for either  $K'$  or  $\sigma_{ac}$ . This behavior was found to be relatively independent of the electrode materials used, *i.e.*, Pt, Au, or Ag.

The aforementioned behavior was distinctly different from that observed for undoped (99.999% pure) single crystal specimens of ZnO that were obtained from the 3M Company. Here, the dispersions in  $K'$  and  $\sigma_{ac}$  increased with increasing temperature. This behavior was strongly dependent on the electrode material being used and was relatively independent of the partial pressure of oxygen surrounding the sample. This seems to suggest that dielectric behavior observed for single crystal specimens was controlled by nonohmic be-

havior of the metal-semiconductor contact, i.e., high-resistance space charge layers at the specimen-electrode interface (25-26).

The low frequency-low temperature behavior of  $K'$  observed for undoped polycrystalline ZnO also suggests the existence of space-charge layers within the sample. These data, however, were independent of the electrode material used, which might indicate that these space-charge layers exist at the surfaces of the grains rather than the electrode interface (27-32). This was further evidenced by the fact that little difference was noted in 2 and 4 probe d-c conductivity of similar samples. The large effective surface area of the metal-semiconductor contact probably yielded a better ohmic contact than the single crystal specimens (33). The space-charge layers seemed to disappear with decreasing partial pressure of oxygen or increasing temperature. This suggests that the space layers are the result of the chemisorption of oxygen at the grain surfaces.

A number of investigations have suggested that when oxygen is chemisorbed on the surface of ZnO it leads to surface acceptors (1, 34-38). These acceptors, which capture conduction electrons from the surface region of ZnO, yield a space-charge or depleted layer having a high resistance. A reduction of surface conductivity has been observed in single crystal and thin layer specimens of ZnO due to oxygen chemisorption (34-36). Powdered samples of ZnO consisting of very small particles have become excellent insulators as the result of the chemisorption of oxygen [ $\sigma \approx 10^{-17}$  (ohm-cm) $^{-1}$ ] (37). The above observations are consistent with the adsorption studies of oxygen on ZnO by Morrison and Miller (38).

Volger has considered the influence of space charge or barrier layers on the dielectric behavior of materials (27). The situations he considered of interest here are those where the conductivity of the surface layer,  $\sigma_1$ , is much less than that of the bulk material,  $\sigma_2$ . Two cases can result, in the first case the thickness of the barrier layer,  $d_1$ , is of sufficient magnitude compared to that of the bulk material,  $d_2$ , such that the resistance of the surface layer is greater than that of the bulk material. The low frequency effective dielectric constant,  $K'_s$ , would be given by

$$K'_s = \frac{d_1}{d_2} K'_\infty \quad [1]$$

where  $K'_\infty$  is the high-frequency value of the dielectric constant. The effective low-frequency conductivity,  $\sigma_s$ , would be

$$\sigma_s = \frac{d_2}{d_1} \sigma_1 \quad [2]$$

while the high-frequency values,  $\sigma_\infty$ , would be

$$\sigma_\infty = \sigma_2 \quad [3]$$

In the second case the barrier layer thickness,  $d_1$ , is sufficiently small compared to that of the bulk material,  $d_2$ , such that the resistance of the surface layer is less than that of the bulk material. Here,  $K'_s$  is given by

$$K'_s = \frac{d_1}{d_2} \left[ \frac{\sigma_2}{\sigma_1} \right] K_\infty \quad [4]$$

while

$$\sigma_s = \sigma_\infty = \sigma_2 \quad [5]$$

Between the high- and low-frequency limits,  $K'$  and  $\sigma_{ac}$  follow a Debye type dispersion, i.e.

$$K' = \frac{K'_s + K'_\infty \tau^2 \omega^2}{1 + \tau^2 \omega^2} \quad [6]$$

and

$$\sigma = \frac{\sigma_s + \sigma_\infty \tau^2 \omega^2}{1 + \tau^2 \omega^2} \quad [7]$$

Here,  $\tau$  is a dielectric relaxation time and  $\omega$  the frequency in radians per second.

The variation of the energy band picture across a grain of ZnO on which oxygen is chemisorbed can be depicted as shown in Fig. 2 (2, 38-40). Here, chemisorbed oxygen molecules take up an electron from the surface and lead to a space charge double layer. The potential,  $\Delta\phi$ , developed at the surface has been proposed to vary exponentially with distance from the surface with a characteristic length,  $L_D$ , i.e., (39)

$$\Delta\phi = \zeta \exp\left(\frac{-x}{L_D}\right) \quad [8]$$

where  $\zeta$  is a characteristic value for the diffuse double layer. The values of  $\zeta$  and  $L_D$  would decrease as the surface concentration of chemisorbed species,  $Q_s$ , decreases and/or as the density of free electrons in the bulk material increases. The space charge at the surface would lead to a barrier layer which has an effective thickness,  $d_1$ , proportional to  $L_D$ . The resistivity, which would vary with distance from the surface, and effective resistance of this barrier layer would also vary with the concentration of chemisorbed species and free electrons in the bulk material.

The competitive processes of adsorption-desorption should cause the concentration of chemisorbed species,  $Q_s$ , to decrease exponentially with increasing temperature (39, 40). If the chemisorbed species were oxygen, then the concentration,  $Q_s$ , would also be expected to decrease with decreasing partial pressure of oxygen.

The lowest temperature data of Fig. 1 is best explained on the basis of a thin space-charge layer or barrier layer whose resistivity and resistance are greater than the bulk material. In this case both  $K'$  and  $\sigma$  should show a dispersion with frequency (see Eq. [1]-[3]). However, as the temperature is increased the dispersions in  $\sigma_{ac}$  disappear and  $K'$  decreases exponentially with increasing temperature according to a relationship of the type:  $K' = K'_\infty \exp\left(\frac{0.34\text{eV}}{kT}\right)$ .

This behavior best fulfills the predictions of a model based on a space charge layer which has a resistivity greater than, but a resistance less than the bulk material (see Eq. [4] and [5]). Here the value of  $d_1 \propto L_D$  would decrease exponentially with temperature as the surface charge,  $Q_s$ , decreases and/or as the concentration of free electrons in the bulk material increases. The effective value of the conductivity of the surface layer,  $\sigma_1$ , would also increase exponentially with temperature more rapidly than the conductivity of the bulk material,  $\sigma_2$ . Thus, the 0.34 eV activation energy observed for the decrease of  $K'$  with increasing temperature would be related to both the decrease in the surface concentration of chemisorbed oxygen,  $Q_s$ , and the increase in the concentration of free electrons in the bulk material of the ZnO grain. The change of  $\sigma_{ac}$  with temperature, similarly, contains information related to both the decrease of surface charge,  $Q_s$ , and the

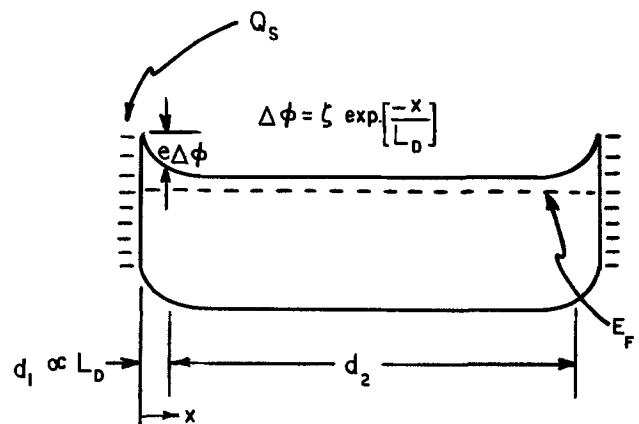


Fig. 2. Band picture representation of a particle of ZnO with surface chemisorbed oxygen.

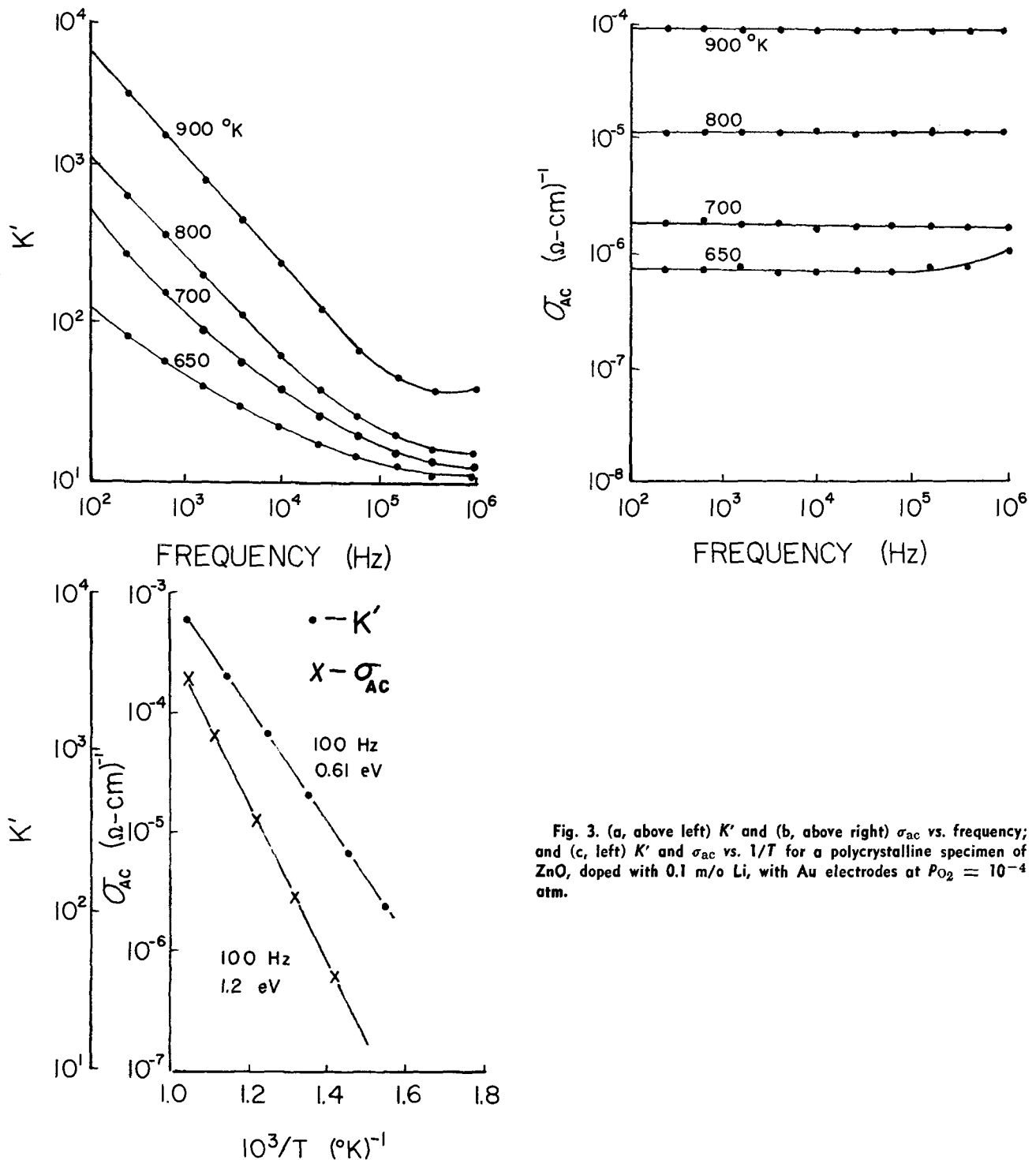


Fig. 3. (a, above left)  $K'$  and (b, above right)  $\sigma_{ac}$  vs. frequency; and (c, left)  $K'$  and  $\sigma_{ac}$  vs.  $1/T$  for a polycrystalline specimen of ZnO, doped with 0.1 m/o Li, with Au electrodes at  $P_{O_2} = 10^{-4}$  atm.

increase in the free electron concentration within the bulk of the grain. Further studies are required to quantitatively define the relative roles played by the chemisorption process as compared to the increase in free electron concentration in determining the dielectric behavior of this material.

**Dielectric behavior of Li- and Na-doped ZnO.**—It was observed for polycrystalline ZnO that the influence of the barrier layer on the values of  $K'$  disappeared as the temperature increased. Therefore, if a polycrystalline sample were doped with an appropriate impurity of small atomic radius, one might observe space-charge polarization due to interstitial diffusion and/or grain-boundary diffusion of the impurity. Interstices in the lattice of ZnO are as large as 0.95 Å. Thus,  $\text{Li}^+$ , which has an ionic radius of 0.6 Å, and  $\text{Na}^+$ , which has an ionic radius of 0.95 Å, were chosen as dopants in the hope that they might be able to diffuse interstitially in the ZnO lattice (41, 42).

Samples of polycrystalline ZnO were prepared having Li concentrations of 0.1 and 0.3 mole per cent (m/o), and a Na concentration of 0.3 m/o. In each case the hydroxide of the alkali metal was converted to the oxide when mixed with ZnO powder. These impurities were introduced by low temperature diffusion ( $T < 950^\circ\text{K}$ ) for relatively long periods of time ( $\sim 1$  day) to keep the majority of the impurity atoms in interstitial sites. The dielectric behavior observed for these specimens with inert gold electrodes is shown in Fig. 3-5.

These data do not seem to fulfill the conditions set forth by Volger for barrier layer polarization, in that the major dispersion in  $K'$  appears at a temperature above that for which the dispersion occurs in  $\sigma$ . The value of  $K'$  increased with increasing temperature, which is also opposite from what one would expect from Eq. [4] where, from the previously discussed behavior, one would expect  $K'_s$  to decrease with increas-

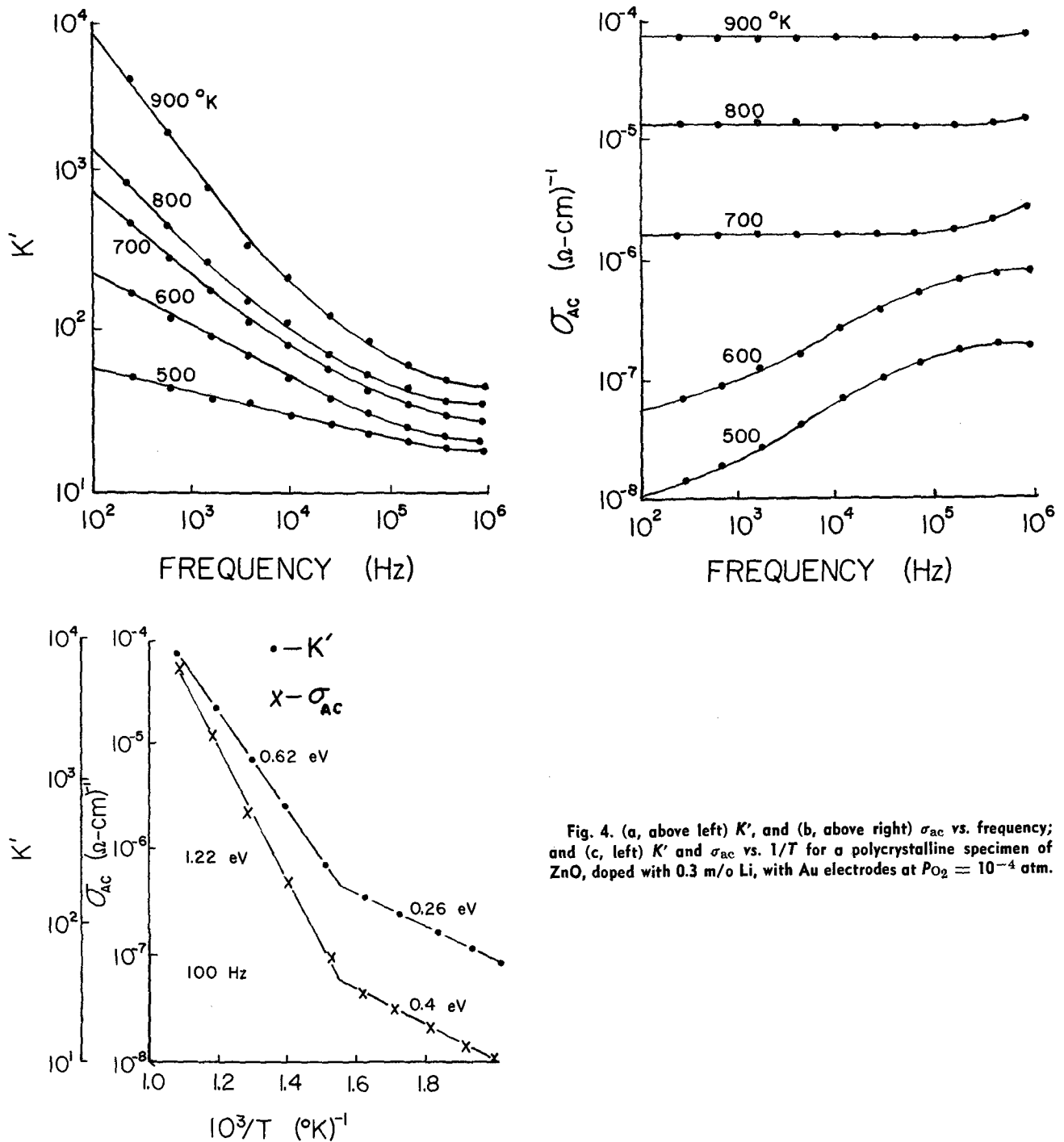


Fig. 4. (a, above left)  $K'$ , and (b, above right)  $\sigma_{AC}$  vs. frequency; and (c, left)  $K'$  and  $\sigma_{AC}$  vs.  $1/T$  for a polycrystalline specimen of ZnO, doped with 0.3 m/o Li, with Au electrodes at  $P_{O_2} = 10^{-4}$  atm.

ing temperature. A space charge polarization model, where mobile electrons are able to freely pass through the electrodes, while mobile ions are blocked at the electrodes seems to best fulfill the conditions observed at elevated temperature (43-45).

Several authors have dealt with two-carrier space-charge polarization models, where charge carriers of one sign are completely blocked while those of the opposite sign are able to freely pass through the electrodes (43-45). These authors, however, generally assume that the positively and negatively charged species are in equal concentration, e.g., Schottky and Frenkel defects. Existing models indicate that the capacitance or effective dielectric constant would vary with frequency as  $\omega^{-n}$  and would show an exponential dependence on temperature. The value of  $n$  is found to be about 3/2. The exponential temperature dependence arises from the variations of the concentration and diffusion coefficient of the mobile species with temperature.

For lithium- or sodium-doped ZnO the negative charge carrying species would be electrons, while the positive charge carrying species would be the ionized interstitial dopant. It is noted that these would not necessarily be of equal concentration as set forth by the aforementioned space charge polarization models. Electroneutrality conditions of the type  $[\text{Zn}^{+i}] + [\text{Li}^{+i}] = [\text{Li}_s^-] + n$ , or  $[\text{Zn}^{+i}] + [\text{Na}^{+i}] = [\text{Na}_s^-] + n$  would be expected for the materials investigated. Thus, electrons result from the ionization of interstitial zinc and impurity atoms. A portion of these would, however, be trapped by impurities occupying substitutional cation positions in the lattice.

If the gold contacts were reasonably ohmic, the electrons would be free to pass through the electrodes. Thus, electrons, which are highly mobile when compared to the ionized interstitial impurity, would contribute significantly to the conduction current. The inert and impervious gold electrodes would, however, block impurity ions from passing through them and lead to a space charge polarization.

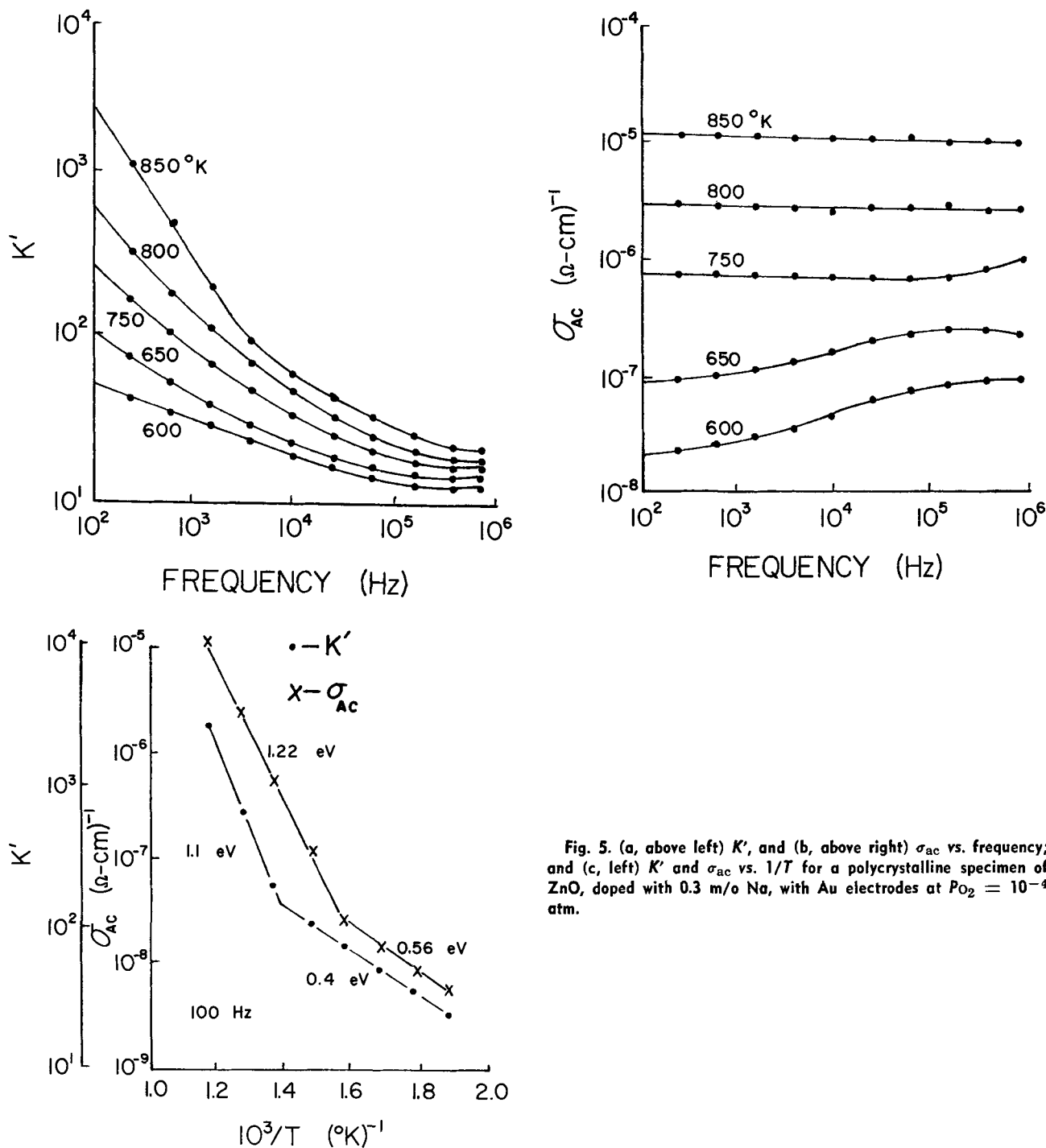


Fig. 5. (a, above left)  $K'$ , and (b, above right)  $\sigma_{ac}$  vs. frequency; and (c, left)  $K'$  and  $\sigma_{ac}$  vs.  $1/T$  for a polycrystalline specimen of ZnO, doped with 0.3 m/o Na, with Au electrodes at  $P_{O_2} = 10^{-4}$  atm.

The effective dielectric constant data of Fig. 3-5 follow many of the qualitative predictions of the aforementioned two carrier space charge polarization models in the higher temperature region. The values of  $K'$  at constant temperature decrease as  $\omega^{-n}$ , although the value of  $n$  is between 0.7 and 0.8 for the Li-doped material and about 1.0 for the Na-doped material, rather than being equal to 1.5 as predicted by existing models. The temperature dependence of  $K'$ , at constant frequency, should be mainly related to the variation in the concentration and diffusion coefficient of the blocked species. In this study, the concentration of interstitial impurities was set by doping and, thus, concentration variations would not be expected to contribute to the temperature dependence of  $K'$ . Thus, the activation energy of approximately 0.6 eV from Fig. 3c and 4c, and 1.1 eV from Fig. 5, should essentially contain information regarding the energy of motion of the mobile ionic point defects. The higher value found for  $\text{Na}^+$  as compared to  $\text{Li}^+$  would seem reasonable in

light of its larger ionic radius. Lander (8) has found that the energy of motion of substitutional  $\text{Li}^+$  was of the order of 0.98 eV, but he states that the energy of motion would be less for the interstitial impurity. The fact that the doping levels 0.1 and 0.3 m/o  $\text{Li}^{+1}$  lead to essentially the same magnitude of  $K'$  and  $\sigma$  suggests that some of the  $\text{Li}^{+1}$  is going into substitutional positions at the higher doping level. The experiment, however, would still only be sensitive to the motions of interstitial  $\text{Li}^{+1}$ .

At lower temperatures, where there is a dispersion in  $\sigma$ , a barrier-layer mechanism might be responsible for the variations of  $K'$  with frequency and temperature. The above is further evidenced by the  $\ln \sigma$  vs.  $1/T$  plots, where for both impurity dopings, the activation energy for conduction is always about 1.2 eV at high temperature where space-charge processes are operative, but varies from sample to sample at lower temperatures where barrier-layer processes are suspected.

A more quantitative interpretation of the data must await the development of two carrier space charge polarization models where the concentration of oppositely charged species may differ. Macdonald is presently involved in setting up such a model which will be available at some future date (46). Added complications arise in the interpretation due to the porosity of the material resulting from its polycrystalline nature.

### Conclusion

In summary it would seem that the single crystalline samples of ZnO led to barrier layer polarization, where the barrier layer was formed at the electrode-specimen interface. For the undoped polycrystalline samples, barrier-layer polarization was again observed. However, in this situation the barrier layer was found to occur at the surface of the individual grains and is thought to be the result of the surface chemisorption of oxygen. The influence of this barrier layer on the dielectric behavior became negligible with increasing temperature.

Upon doping polycrystalline samples with Li<sup>+</sup> or Na<sup>+</sup>, space-charge polarization was thought to result due to the interstitial or grain-boundary motion of various point defects. These data were rationalized on the basis of a space-charge polarization model involving mobile ionic point defects, which were blocked or partially blocked at the electrodes, and electronic carriers, which were able to pass through the electrodes. The activation energies for the exponential temperature dependence of the effective dielectric constant were believed to be associated with the energy of motion of the interstitial impurities. An energy of about 0.6 eV was found for the Li-doped ZnO while that for the Na-doped material was about 1.1 eV. The relative magnitudes of the activation energies are consistent with the size differences of the Li<sup>+</sup> and Na<sup>+</sup> ions.

### Acknowledgment

The authors gratefully acknowledge the support of the National Science Foundation, Grant No. GK-16284.

Manuscript submitted Jan. 31, 1973; revised manuscript received Aug. 30, 1973.

Any discussion of this paper will appear in a Discussion Section to be published in the December 1974 JOURNAL.

### REFERENCES

- G. Heiland, E. Mollwo, and F. Stockmann, *Solid State Phys.*, **8**, 191 (1959).
- H. E. Brown, "Zinc Oxide Rediscovered," The New Jersey Zinc Co., New York (1957).
- F. A. Kroger, "Chemistry of Imperfect Crystals," North-Holland Publishing Co., Amsterdam (1964).
- L. V. Azaroff, *J. Appl. Phys.*, **32**, 1658 (1961).
- L. V. Azaroff, *ibid.*, **32**, 1663 (1961).
- D. G. Thomas, *J. Phys. Chem. Solids*, **3**, 229 (1957).
- W. J. Moore and E. L. Williams, *Discussions Faraday Soc.*, **28**, 86 (1959).
- J. J. Lander, *J. Phys. Chem. Solids*, **15**, 324 (1960).
- E. A. Secco, *Can. J. Chem.*, **39**, 1544 (1961).
- R. Linder, *Acta Chem. Scand.*, **6**, 457 (1952).
- E. A. Secco and W. J. Moore, *J. Chem. Phys.*, **26**, 942 (1957).
- D. G. Thomas, *J. Phys. Chem. Solids*, **9**, 31 (1958).
- A. R. Hutson, *Phys. Rev.*, **108**, 222 (1957).
- M. A. Seitz and D. H. Whitmore, *J. Phys. Chem. Solids*, **29**, 1033 (1968).
- D. F. Crisler, J. J. Cupal, and A. R. Moore, *IEEE Proc.*, **56**, 225 (1968).
- O. Glemser, *Z. Elektrochem.*, **45**, 865 (1959).
- A. N. Soos, *Doklady Akad. Nauk. SSSR*, **33**, 210 (1941).
- K. Kamiyoshi, *Sci. Rept. Res. Inst. Tohoku Univ.*, **42**, 180 (1950).
- E. Hahn, *J. Appl. Phys.*, **22**, 855 (1951).
- R. J. Collins and D. A. Kleinman, *J. Phys. Chem. Solids*, **11**, 190 (1959).
- D. C. Hoesterey, *J. Appl. Phys.*, **33**, 992 (1962).
- E. D. Kolb and R. A. Laudise, *J. Am. Ceram. Soc.*, **48**, 342 (1965).
- R. A. Delaney and H. D. Kaiser, *This Journal*, **114**, 833 (1967).
- M. A. Seitz, R. T. McSweeney, and W. M. Hirthe, *Rev. Sci. Instr.*, **40**, 826 (1969).
- J. G. Simmons, G. S. Nadkarni, and M. C. Lancaster, *J. Appl. Phys.*, **41**, 538 (1970).
- J. Maserjian and C. A. Mead, *J. Phys. Chem. Solids*, **28**, 1971 (1967).
- J. Volger, in "Progress in Semiconductors," Vol. 4, A. F. Gibson, Editor, pp. 206-263, John Wiley & Sons, New York (1960).
- D. F. Gibbs and B. W. Jones, *J. Phys. D: Appl. Phys.*, **3**, 157 (1970).
- R. W. Sillars, *J. Inst. Elec. Eng. (London)*, **80**, 378 (1937).
- C. G. Koop, *Phys. Rev.*, **83**, 121 (1951).
- E. M. Trukhan, *Soviet Phys.-Solid State*, **4**, 2560 (1963).
- M. M. Z. Kharadly and W. Jackson, *Proc. Inst. Elec. Engrs.*, **100**, 199 (1953).
- R. H. Bube, "Photoconductivity of Solids," John Wiley & Sons, New York (1968).
- G. Heiland, *Z. Physik.*, **148**, 15 (1957).
- H. Fritsch, *ibid.*, **133**, 422 (1952).
- G. Heiland, *ibid.*, **142**, 415 (1955).
- W. Ruppel, H. J. Gerritsen, and A. Rose, *Helv. Phys. Acta*, **30**, 495 (1957).
- S. R. Morrison and P. H. Miller, *J. Chem. Phys.*, **25**, 1064 (1956).
- K. J. Vetter, "Electrochemical Kinetics," pp. 73-79, Academic Press, New York (1967).
- A. Clark, "The Theory of Adsorption and Catalysis," Academic Press, New York (1970).
- V. M. Goldschmidt, *Chem. Berichte*, **60**, 1263 (1927); L. Pauling, *J. Am. Chem. Soc.*, **49**, 765 (1927).
- "Handbook of Chemistry and Physics," 49 ed., R. C. Weast, Editor, The Chemical Rubber Co., Cleveland, Ohio (1948); "Table of Periodic Properties of the Elements," Sargent Welch Scientific Co., Chicago, Illinois.
- R. J. Friauf, *J. Chem. Phys.*, **22**, 1329 (1954).
- J. R. Macdonald, *Phys. Rev.*, **92**, 4 (1953).
- J. R. Macdonald, *J. Chem. Phys.*, **54**, 2026 (1971).
- J. R. Macdonald, Private communication.





## Crystallographic Assignment of the Domains in Single Crystals of Gadolinium Molybdate (GMO)

A. S. Bhalla<sup>1</sup>

Materials Research Laboratory, The Pennsylvania State University, University Park, Pennsylvania 16802

The structure of gadolinium molybdate (GMO), which exhibits strongly coupled ferroelectric and ferroelastic behavior (1, 2) has been studied in detail in recent papers (3, 4). In the ferroelectric phase below 159°C the point symmetry is 2 mm with the polar axis parallel to c. The existence of a polar axis in a structure may affect the etching behavior of the surfaces perpendicular to the polar direction (5, 6). Also one should assign these surfaces crystallographically in relation to the nature of the chemical attack. In the present paper the behavior of some chemical etchants is studied on the surfaces of the single domain crystals of GMO. Subsequently the surfaces were assigned crystallographically by the pyroelectric measurements and the x-ray studies.

Crystals were cut in the shape of a rectangular prism and with the edges parallel to the orthorhombic a, b, c axes. The faces were polished with 0.3 $\mu$  alumina powder. The two c-faces (after removing the damaged layer by warm diluted NaOH) of this prism were coated with evaporated silver film (rectangular shape with edges parallel to [110]). Crystals were poled by applying d-c field along the c-axis. A number of etchants (Table I) were tried (after removing Ag-film) to

<sup>1</sup> Present address: Space Sciences Laboratory, Marshall Space Flight Center, Huntsville, Alabama 35812.

Key words: chemical etching, crystal defects, ferroelectric materials.

Table I. Chemical etchants, etching time and other features observed in the chemical etching of GMO

Etchant	Etching time	Remarks
A. HNO <sub>3</sub>	40-60 sec	HNO <sub>3</sub> (reagent grade) and H <sub>2</sub> O solution in 2:3 proportion. (001) face etched faster than (001). Pits were produced on {100} (Fig. 5), {010}, and {001} faces (Fig. 1a and 1b). Pits on (001) face were oriented by 90° about the c-axis from the pits on the (001) face, i.e., on (001) the longer edge was parallel to 'a' whereas on (001) it was parallel to 'b' direction. {010} and {100} did not show these features.
B. HCl	10-20 sec	25% water solution of reagent grade HCl. (5-30% solution produced the well-defined pits.) Other features were similar as in case A. (001) showed the point-bottomed pits (Fig. 3).
C. HF	5-10 sec	20% HF (48%) solution in water. (001) showed the conical pits (Fig. 2). No sharp features on (001) face.
D. H <sub>2</sub> SO <sub>4</sub>	4-7 min	Mixture of reagent grade H <sub>2</sub> SO <sub>4</sub> and H <sub>2</sub> O (1:3). Pits on {001} faces were elongated along the domain direction. (001) showed deep and sharp-bottomed pits (Fig. 4). The pits on the two opposite c-faces were rotated from each other by 90° about the c-axis.

study the etch-pit behavior of the two surfaces at room temperature. One surface showed the well-defined, point-bottomed pits whereas the other showed the



Fig. 1 (a). Etch pits produced on the (001) face of the Gd<sub>2</sub>(MoO<sub>4</sub>)<sub>3</sub> by 40% HNO<sub>3</sub> (45 sec of etching time). This face developed the positive electrostatic charge on heating ( $\times 400$ ).

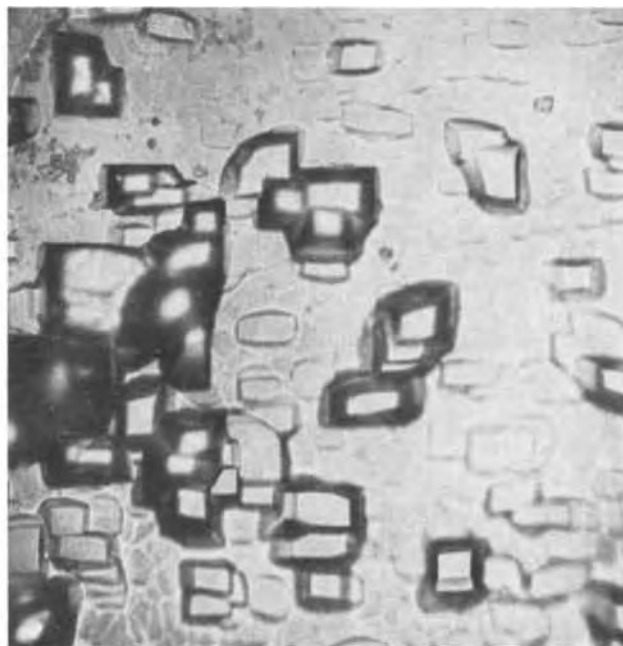


Fig. 1 (b). Etch pits produced on the (001) face of the same crystal. Pits are oriented by 90° from the pits in Fig. 1(a). This face developed the negative electrostatic charge on heating ( $\times 400$ ).

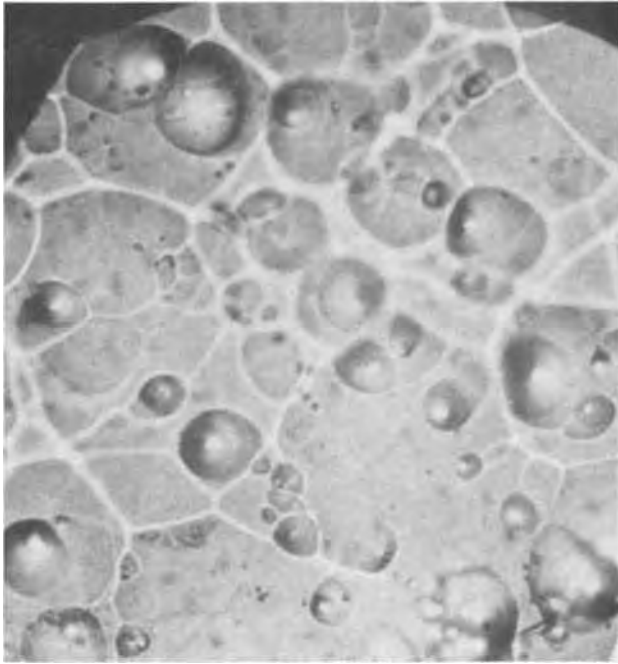


Fig. 2. Conical pits produced by HF:H<sub>2</sub>O (1:3) on (001) face; etching time 7 sec ( $\times 400$ ).



Fig. 4. Point-bottomed and deep pits produced along [110] direction on (001) face by mixture of H<sub>2</sub>SO<sub>4</sub> and H<sub>2</sub>O (1:3); etched for 5 min.



Fig. 3. Pits produced on (001) c-face by 25% water solution of HCl, with 15 sec of etching time ( $\times 400$ ).

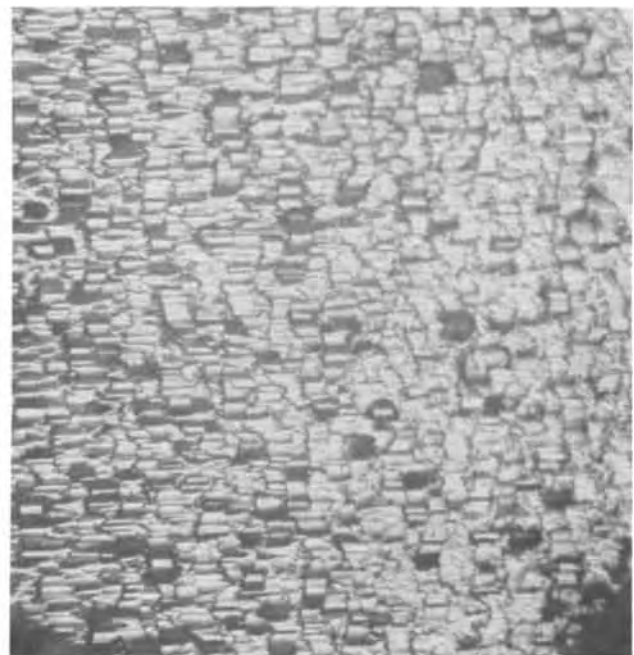


Fig. 5. Pits produced on a-face of the same crystal of Fig. 1 ( $\times 400$ ).

flat-bottomed pits. Various dilutions of the etchants were tried for obtaining the well-defined features. The proper range of concentration, the etching time, and the other features are described in Table I.

In order to identify the (001) and (001) surfaces the pyroelectric measurements were made on the samples after chemical etching. The set up used for the study has been described earlier by Fable and Henisch (7). Two c-faces of the crystal were silver electroded, and the sample was heated through 100°C (much below the Curie temperature). The pyroelectric voltage was measured. It was noticed that the surface with the point-bottomed pits had developed the positive charge whereas the surface with the flat-bottomed pits showed the negative charge in all the cases. In GMO the sense of

the pyroelectric axis is just opposite to the positive crystallographic axis (3). Thus the surface which etched slower, showed point-bottomed pits and developed positive charge on heating was assigned crystallographically, in the present studies, as (001) and the one which etched faster, showed flat-bottomed pits and developed the negative charge on heating as the (001).

Unfortunately, the exact nature of the dislocations in GMO is not known, so that the detailed mechanism of the chemical attack and etching is also questionable. The present studies do, however, reveal the importance of changing anions in the sequence of acids used and identify the positive and negative ends of the single domain crystals.

### Acknowledgments

The author is grateful to Professor Ajit Ram Verma, Director, National Physical Laboratory of India, Delhi, for providing the facilities to work and the encouragement during the work; to Professors L. E. Cross and R. E. Newnham of Materials Research Laboratory for the helpful discussions. Thanks are also due to G. Fable for his help in making pyroelectric measurements. The author also appreciates the reviewers for their helpful suggestions.

Part of this work was done in the National Physical Laboratory of India, while the author was working there as a Scientific officer of CSIR, India.

Manuscript submitted Oct. 24, 1972; revised manuscript received Aug. 6, 1973.

Any discussion of this paper will appear in a Discussion Section to be published in the December 1974 JOURNAL.

### REFERENCES

1. S. C. Abrahams and J. L. Bernstein, Abs. No. 1, p. 58, American Crystallographic Association Winter Meeting Program & Abstracts, February 1966.
2. L. E. Cross, A. Fouskova, and S. E. Cummins, *Phys. Rev. Letters*, **21**, 812 (1968).
3. E. T. Keve, S. C. Abrahams, and J. L. Bernstein, *J. Chem. Phys.*, **54**, 3185 (1971).
4. W. Jeitschko, *Naturwissenschaften*, **57**, 544 (1970); *Acta Cryst.*, **B28**, 60 (1972).
5. H. C. Gatos, "The Surface Chemistry of Metals and Semiconductors," John Wiley & Sons, New York (1960); H. C. Gatos and M. C. Lavin, *This Journal*, **107**, 427 (1960).
6. J. W. Faust, Jr., Scientific Paper 425-C000-P1, (August 1961) Westinghouse Research Lab (Pennsylvania); *J. Appl. Phys.*, **32**, 331 (1960).
7. G. W. Fable and H. K. Henisch, *Solid-State Electron.*, **14**, 1281 (1971).

## Brief Communication



### High Sensitivity Detection of Solution Contaminants by MeV Ion Scattering

Ronald L. Meek\*

Bell Laboratories, Murray Hill, New Jersey 07974

Rutherford ion backscattering (1-3) of MeV He ions has been established as a very sensitive technique for detecting surface impurities heavier than the atoms of the substrate. A typical sensitivity (3) for the intermediate to heavy mass surface atoms is  $10^{12}$  atoms  $\text{cm}^{-2}$ . Suppose that one places  $0.1 \text{ cm}^3$  of a solution on an otherwise clean substrate, allows it to spread to cover  $\sim 1 \text{ cm}^2$  of the substrate and evaporate to dryness. Since one-tenth  $\text{cm}^3$  of water contains about  $10^{22}$  atoms, the detection of  $10^{12}$  atoms  $\text{cm}^{-2}$  on the surface of the solid is equivalent to detecting impurities at levels of 1 part in  $10^{10}$ , atomic. It is emphasized that the ion scattering technique both qualitatively identifies the species present, by the energy of the backscattered ions, and quantitatively determines their number, through the number of scattered ions. Thus standards or references of known impurity concentration are not needed. Usually the detection solid angle is not actually measured, but rather the sensitivity factor is determined through the scattering yield from the substrate, in this case silicon, of known atomic density, and of course the Rutherford cross section.

It has been shown elsewhere (3) that it is possible to obtain silicon surfaces free of surface impurities heavier than chlorine. Such clean silicon substrates have been used for the work reported here. Clearly, clean carbon substrates would allow for analysis of some interesting lower mass contaminants. In order to demonstrate this method, approximately  $0.1 \text{ cm}^3$  of a number of reagents commonly used in semiconductor device processing were transferred directly from a previously unopened bottle onto the surface of a clean silicon wafer. The area of the wafer over which the

solution spreads is about  $1 \text{ cm}^2$ . The volume was determined by comparing the droplet size to that of a droplet of a known volume of water transferred to the wafer with a micropipet. Clearly more exact procedures could be developed to determine the volume and area accurately, but here the primary concern has been to avoid contamination during the transfer. After the reagent had evaporated in a clean hood at room temperature, the surface was examined by ion scattering. The details of the scattering experiments have been described elsewhere (3). It is emphasized that the pile-up system used, combined with channeling, can reduce pile up counts to a point where only  $\sim 10$  counts are found in the  $\sim 100$  channels beyond the silicon edge after He ion fluence  $\sim 10^{16} \text{ cm}^{-2}$ . The energy or mass resolution, however, is limited. For example  $^{39}\text{K}$  and  $^{40}\text{Ca}$  are separated by 14 keV which is about the resolution of the detector so that they can be distinguished; Br and Se, on the other hand, are separated by only 4 keV so that they cannot be unambiguously identified by this technique.

Figure 1 is the spectrum (scattered ion yield as counts per channel vs. scattered ion energy) from a surface on which concentrated HCl had been placed. On the clean wafer only a few isolated counts are present at energies greater than that corresponding to ions scattered from surface Cl after the same incident ion fluence. On the clean surface chlorine was present at  $10^{13} \text{ cm}^{-2}$ ; here we see it has increased to  $4(10)^{13} \text{ cm}^{-2}$ . Also Ca, Fe and Br or Se are present. Concentrations were determined by scanning across the wafer area on which the reagent had been placed. Typical variations of a factor of two were found and the area not contacted by liquid was found to remain free of contamination.

\* Electrochemical Society Active Member.

Key words: semiconductor processing, ion scattering, surface analysis.

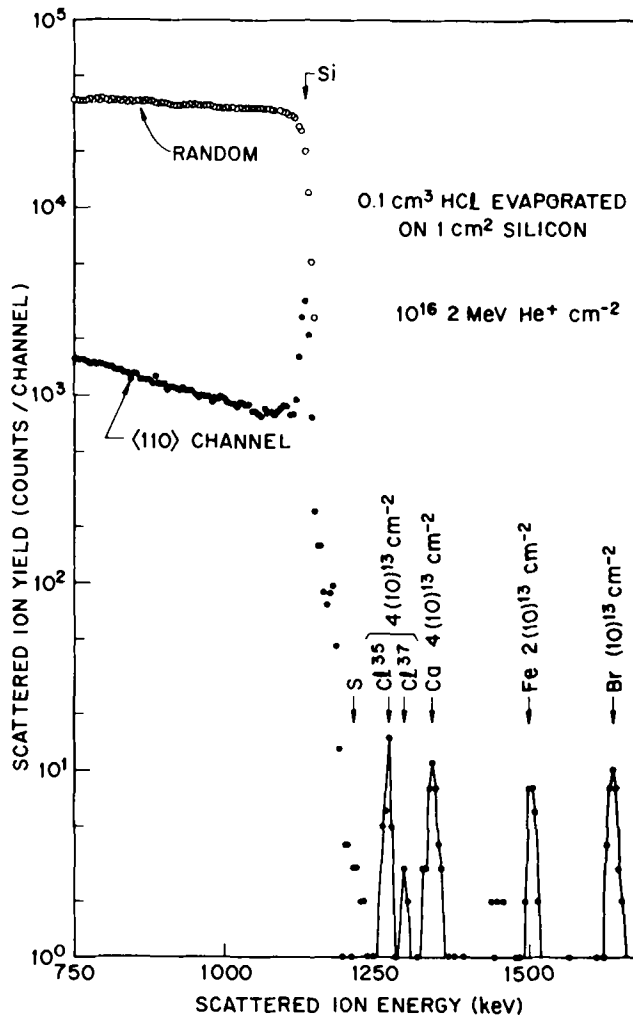


Fig. 1. Scattered ion spectrum from a Si surface on which HCl had been placed.

The surface contaminants found, converted to parts per billion ( $10^9$ ) atomic in the original solution, for HCl and other reagents examined are tabulated in Table I. It is interesting to note that the HCl is contaminated with Fe (2 ppba) which perhaps explains the previous observation (3) that a HCl dip of a wafer previously showing no Fe gave  $10^{12} \text{ cm}^{-2}$  ( $10^{-3}$  monolayer) of Fe. Others (4-6) have shown that for transition metals in acid solutions  $n \sim C$  where  $n$  is the adsorbed surface contamination in monolayers from a solution contain-

Table I. Principal contaminants in some semiconductor processing reagents

Reagents	Contaminant	Contaminant level (ppba)
HCl	Ca	4
	Fe	2
	Br or Se	1
HNO <sub>3</sub>	Ca	30
	Ti	50
	Fe	5
	Zn	6
	I or Te	2
	Pt to Pb	1
HAc	Fe	20
	Cu	20
HF	None detected	—
NH <sub>4</sub> OH	Ca	10
	Zn	10
H <sub>2</sub> O <sub>2</sub>	Sn or Sb	2
	None detected	—
Methanol	None detected	—
Acetone	None detected	—
Trichloroethylene	Fe	2

ing the species at concentration  $C$  in parts per million. Thus, parts per billion in solution should lead to  $\sim 10^{-3}$  adsorbed monolayers as observed in the previous work (3).

Nitric acid proved to be the most contaminated reagent containing Ca, Ti, Fe, Zn, I, or Te and some member of the group Pt, Au, Hg, Tl, or Pb. The observation that HNO<sub>3</sub> is contaminated with a Pt-Pb species (1 ppba) is interesting in light of previous work (3) which showed that cleaning procedures using HNO<sub>3</sub> and HF appeared to introduce a surface impurity ( $10^{-3}$ - $10^{-4}$  monolayer) in the Pt-Pb mass range. Acetic acid was found to contain 20 ppba of the fast diffusing (in silicon) transition metals Fe and Cu. Results for several other reagents are listed in Table I. No impurities were detected in the commonly used organic solvents methanol and acetone nor in HF, while a small amount of Fe was found in trichloroethylene.

Manuscript submitted June 1, 1973; revised manuscript received Sept. 14, 1973.

Any discussion of this paper will appear in a Discussion Section to be published in the December 1974 JOURNAL.

#### REFERENCES

1. M. A. Nicolet, J. W. Mayer, and I. V. Mitchell, *Science*, **177**, 841 (1972).
2. T. M. Buck, J. M. Poate, K. A. Pickar, and C. M. Hsieh, *Surface Sci.*, **35**, 362 (1973).
3. R. L. Meek, T. M. Buck, and C. F. Gibbon, *This Journal*, **120**, 1241 (1973).
4. V. S. Sotnikov and A. S. Belanovskii, *Russ. J. Phys. Chem.*, **34**, 1001 (1960).
5. G. B. Larrabee, *This Journal*, **108**, 1130 (1961).
6. D. A. Thompson, H. D. Barber, and W. D. Mackintosh, *Appl. Phys. Letters*, **14**, 102 (1969).



## Computer-Controlled Battery Pulse Charging

John P. Elder<sup>\*,1</sup>

ESB Incorporated, C. F. Norberg Technology Center, Yardley, Pennsylvania 19067

### ABSTRACT

A Fortran language program system has been developed for computer-controlled, square wave, constant current battery pulse charging. It provides complete experimental control and rapid, accurate data acquisition for a set of test cells with or without *in situ* reference electrodes. It incorporates automatic charge termination and individual cell cut-out features, which may be brought into play for a variety of reasons. Multicell operational data is readily available for cell to cell comparison and interpretation. Examples of the use of the program for charging secondary alkaline battery systems are presented. Information regarding the charging behavior of the limiting mercury-silver substrate positive electrode in the secondary mercury-cadmium cell, not readily available when using conventional pulse charging techniques, has been obtained.

A variety of techniques have been employed to charge secondary cells, particularly for the several alkaline systems (1). Essentially, all attempt by various means to maximize the charge acceptance efficiency. Many applications also require that the charging time be minimized. In attempting to achieve these purposes, certain hazards may be encountered. Some may lead to a potentially physically dangerous situation for the battery user, while others only deleteriously affect the subsequent discharge characteristics of the cell, and the over-all cycle life of the system. For example, while certain battery systems are routinely overcharged, excessive overcharging can be potentially dangerous. Thus, the pressure build-up, observed when nickel-cadmium cells are overcharged (2), can increase rapidly when the cells are charged at a high rate. Furthermore, the oxygen recombination at the negative plate, which acts as an internal pressure relief valve, is dependent upon the state-of-charge of this electrode (3). Heat generation can also be a problem in this system when undergoing high rate charging (2). This is an even more appreciable problem in nickel-zinc batteries (4). If zinc electrodes are too highly polarized on charge, dendritic growth can result with subsequent catastrophic failure, due to internal short circuiting, in cells containing such electrodes.

Secondary mercury cells often incorporate a more noble metal, usually silver, in the mercuric oxide positive, acting as an immobilizing substrate for the discharged state of this electrode. Such electrodes can exhibit large polarization on charge. When charged at moderate to low rates, the electrode potential rises to a value indicative of silver oxidation well before all the available mercury has been oxidized. Catherino and Carson (5) indicate that, in order to achieve full charge acceptance in mercury-cadmium cells, it is necessary to charge well beyond the onset of silver substrate oxidation. If this is pursued on a continuing basis, it could prove detrimental to the system, leading to mechanical degradation of the positive plate and a

concomitant deterioration in its charge acceptance efficiency and cycle life. It has been found possible to approach 100% charge acceptance efficiency of the mercury-silver electrode prior to the onset of silver oxidation by constant current charging at very low rates (6).

In recent years, a limited number of workers have investigated the use of pulse charging techniques to improve charging efficiency. Boyd (7) has recently indicated that the cycle life of nickel-cadmium batteries is increased when they are pulse charged. Wales (8) has found that an a-c pulse superimposed on d-c charging markedly enhances the positive electrode charge acceptance efficiency in silver-zinc cells. Toni (9) has indicated that the response of a mercury electrode to a current pulse is dependent upon its state-of-charge, and has reported briefly on the possible efficacy of square wave, galvanostatic pulse charging in cell systems using this electrode. Recent work in this laboratory on mercury-cadmium cells has shown that charging times may be significantly reduced, without any large detrimental effect on charge acceptance efficiency by using a millisecond regime, square wave, constant current pulse technique (10).

Kordesch has long espoused the viewpoint that one should terminate charging any cell when the equilibrium voltage or potential of the limiting electrode, with respect to a suitable reference, attains a prescribed value. He and his co-workers have successfully accomplished this end by using both square (11a) and sine (11b) wave pulse techniques incorporating the interrupter concept, whereby the IR-free cell voltage or electrode potential may be monitored oscilloscopically during the interruption period.

If multicell pulse charge testing of secondary cells is envisaged, one is limited, when using conventional laboratory instrumentation, in the amount of pertinent data which can be recorded. This is particularly so when rapid perturbations in the millisecond range are employed, and if reference electrodes are incorporated into the cells. Zinder (12) has discussed circuitry which allows the monitoring of the cell response during the off-current phase in a 60 Hz sine wave charger used for the sealed nickel-cadmium system. If one is interested in following variations in both the

\* Electrochemical Society Active Member.

<sup>1</sup> Present address: Mettler Instrument Corporation, Princeton-Hightstown Road, Hightstown, New Jersey 08520.

Key words: computer-controlled experiments, pulse charging, charge acceptance, Ni-Cd cell, Hg-Cd cell.

EST

cell internal resistance, and the open-circuit voltage at the end of the off-current phase, one should attempt to monitor responses as close as possible to the interruption points (13, 14). When the monitored parameter attains a prescribed value, it should be used to activate the appropriate cell cut-out relay. In the absence of a specific device to effect these purposes, oscilloscopic monitoring of the total response of the system to the perturbation serves as a valuable guide. However, the test requires constant attention and is very tedious. Furthermore, the separation of the average voltage data for a group of cells over the entire charging period, monitored on a multipoint recorder, is a time-consuming task.

The disadvantages and limitations of the conventional method may be obviated by using an on-line digital computer. When used in conjunction with a programmable galvanostat, high speed D/A and A/D converters, and the requisite relays, a completely automatic, real-time, experimental control and data acquisition system is possible. Frazer (15) has indicated that it is preferable to employ machine language programming for real-time control and data acquisition in closed loop experiments. A number of computer-controlled electrochemical studies, primarily in the analytical field, have utilized this form of programming throughout (16-19). However, there is no *a priori* reason why a higher level language should not be used, and in many instances it may prove the easier route.

A program system has been developed which fulfills all the requirements for rapid pulse charging of secondary batteries, and the necessary data acquisition. With the exception of five assembly language coded subroutines, which control the operation of the D/A and A/D converters and the cell relays, and the recording of data on magnetic tape, the entire system has been written in Fortran IV. The operation of the program system is discussed in outline, with further details in the Appendix,<sup>2</sup> and some examples of its use with nickel-cadmium and mercury-cadmium cells are presented.

### System Hardware

An E.A.I. 640 computer (Electronics Associates, Incorporated, West Long Branch, New Jersey, 07764) was used in developing and running this program. It is a 16 bit machine with a 1.65  $\mu$ sec memory access cycle time and 16K words of core memory. The SRC Astroverter 3900, rated at 100 kHz, was used for both D/A and A/D converters (Moxon Incorporated, SRC Division, Newport Beach, California). They utilize an eleven plus sign bit pattern, and have a maximum voltage capability of  $\pm 10.024$ V. A binary number bit pattern is transferred from the central processing unit to the D/A converter, and converted into a voltage level, which is held continuously until another bit pattern is transferred. Transfer and conversion is complete within less than 5  $\mu$ sec. The output of the D/A converter is connected to the programmable galvanostat. The A/D converter together with a number of preamplifiers and a multiplexer comprises the analog measuring system, with a total input impedance of 10 megohm. The A/D converter samples an incoming voltage signal and holds till conversion is complete. The sample and hold "window" is open for less than 1  $\mu$ sec, but the total sampling and conversion time is 10  $\mu$ sec.

The programmable galvanostat employed was the LCT 16-365.<sup>3</sup> This module is powered by a 36V regulated power supply. Up to sixteen cells may be connected in series to this unit. Each cell connection is paralleled with a bypass relay, which may be actuated manually or remotely by computer command. The relay switching time is 40 msec. The input impedance of the galvanostat is 167 kohm, and the operational loop rise time, no load to full load, is less than 10  $\mu$ sec. This

module produces a constant current output, range 15 mA to 5A, proportional to the voltage level output of the D/A converter. The test cells, located in the laboratory, were connected to both the galvanostat and the analog measuring system with shielded, twisted pair cabling. No effects, due to cable reactance, were observed. Continual noise problems were not encountered while acquiring data. Occasionally, when the output level of the D/A converter changed, a spike voltage passed through the narrow window in the A/D converter. The program recognizes the spurious voltage and takes appropriate action.

Time was continually monitored with an EECO 915A digital clock (Electronics Engineering Company of California, Santa Ana, California). It incorporates a 1 MHz crystal-controlled oscillator timing system, with a  $3 \times 10^{-8}$  sec/day stability. Four output pulses, of frequency 1 kHz, 100, 10, and 1 Hz, were continually counted in four memory locations in the central processing unit. These "internal clocks" were used for pulse and time synchronization during program operation. Each could be independently reset to zero at any time by the appropriate software command.

All pertinent cell information and data was recorded on magnetic tape in such a manner (see below) that the amount and rate of data acquisition was independent of the speed of the tape unit.

### Main Program

The main, on-line, real-time program controls the square wave, galvanostatic pulse charging of secondary battery systems. It provides an accurate and precise control of the pulse regime, irrespective of whether data is being acquired, modified, compared with previously acquired data, or being recorded on tape. This control is maintained even when a cell cut-out relay is being actuated and its status checked. At prescribed charge input level increments, the cell voltage is monitored at certain time intervals within the pulse period and, if desired, recorded permanently. When reference electrodes are incorporated in the cells, the positive electrode potential is also monitored. All cells remaining on charge are monitored in sequence. Negative electrode potential data are computed by difference.

Charge termination may be effected if: (i) The cell voltage or either electrode potential at the end of the off-current phase of the pulse regime attains or exceeds a predefined limit. (ii) There is a continual significant increase in either the internal resistance or the polarization exclusive of the resistive contribution; or in the contribution of either electrode system to the total parameter. It has been arbitrarily stipulated that if ten consecutive significant increases are observed in any of these parameters, then this is sufficient cause to initiate the cell cut-out command. A build-up in the internal resistance within a cell could prove detrimental to its continuing operation. An increase in polarization could indicate a possibly malfunctioning electrode. (iii) The charge input level attains a prescribed limiting value.

When charge termination for any cell is requested for reasons (i) or (ii), the appropriate relay is deactivated, causing current flow to bypass the cell. When all cells have been cut out, or the charge input level limit is attained, an end-of-file mark is recorded on the magnetic tape, the D/A converter output level set to zero, and the program stops.

In Fig. 1, is shown a simplified flow diagram of the program system which, due to the functions it performs, is nonsequential. A detailed outline of the operation of the program is given in the Appendix. During the running of the experiment, the charge input level,  $Q$ , in mA-hr, is continually incremented by an amount  $Q_{inc}$  per pulse period, where  $Q_{inc} = PA \times PL/3.6$  mA-hr. PA and PL are the pulse amplitude (amperes) and length (seconds), respectively. Data is acquired at predefined mA-hr increments of the charge input level. Two types of data are monitored at speci-

<sup>2</sup> Detailed flow diagrams and program listings are available to interested parties.

<sup>3</sup> ESB Incorporated, Technology Center Bulletin 70-81-02.

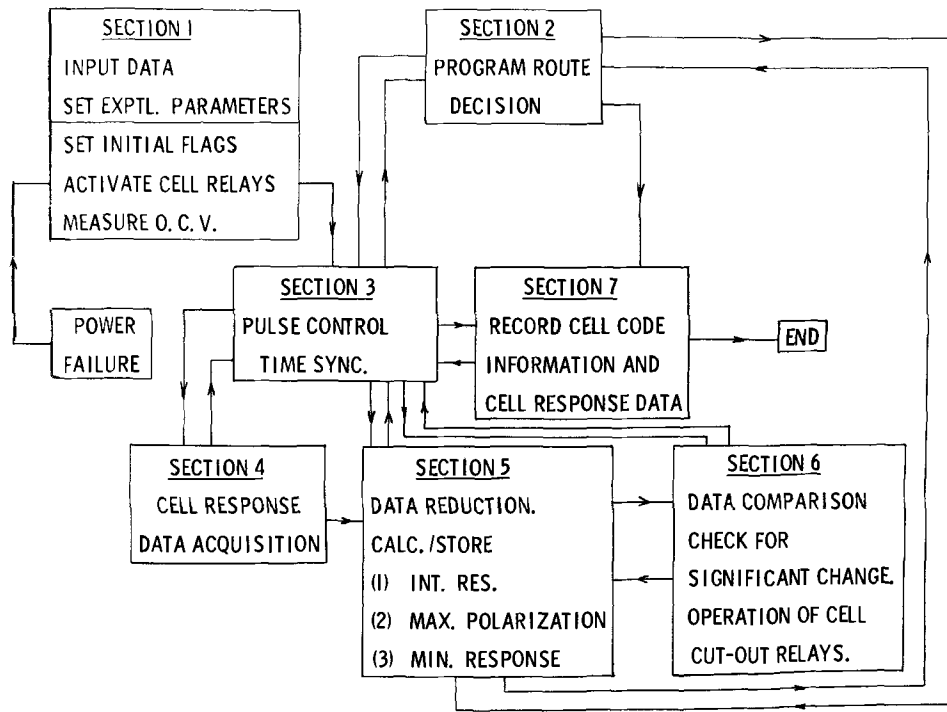


Fig. 1. Simplified flow diagram, main program.

fied intervals throughout the pulse regime, the so-called "complete response" and "partial response" data.

*Maximum and minimum levels.*—It is impossible to maintain correct pulse regime time synchronization during the data acquisition sequences if one attempts to monitor the actual maximum and minimum data points immediately prior to turning the pulse off and on, respectively. The pulse regime is so chosen that the cell voltage and electrode potential values 1 msec prior to turning the pulse off and on show a minimal deviation from the actual maximum and minimum values, as viewed oscilloscopically. Data taken at these time intervals are considered the maximum and minimum values, and are used as such in all decision making.

*Time profile.*—This term refers to the time intervals, in multiples of 1 msec, during the entire pulse regime, at which cell voltage and positive electrode potential data are to be monitored.

*Complete response.*—A request for a "complete response" indicates that data is to be monitored at every interval specified in the time profile. When such a request is made, the data are always recorded permanently.

*Partial response.*—This term indicates that data is to be monitored only at the maximum and minimum levels, as defined above. When "partial response" data is requested, it is recorded permanently, only if a significant change from the previous sequence, whether "complete or partial," is observed.

The charge input levels, at which the two types of "response" are to be monitored, are computed in section 2 of the Appendix from initial and incremental values given as test parameter information. "Complete response" data is usually requested at certain large increments in the charge input level, e.g., at levels corresponding to 10% increments of the theoretical capacity of the cell. At much closer intervals, e.g., corresponding to 1% increments, "partial response" data is requested.

*Information and data storage.*—Throughout the running of the program, information relating to the condition of each cell is stored in coded form in the NCODE array, the structure of which is shown in Table I. When cell data are to be recorded permanently, it is always preceded by an up-to-date record of this array. The

secondary program (see below) utilizes this information in separating and decoding the succeeding block of data. Three sets of data are stored in the IDATA array in the following order: (i) Cell voltage or positive electrode potential or calculated negative electrode potential data for each interval requested in the time profile. (ii) The "IR drop" data or contribution from each electrode-separator interface. (iii) The characteristic and mantissa of the charge input level at which data was monitored for the particular cell.

For each cell,  $N + 3$  locations in the IDATA array are required. For "complete response,"  $N$  is given by the number of intervals in the time profile. For "partial response,"  $N = 2$ . If the cells incorporate reference electrodes, three blocks of the appropriate size are required to accommodate all the data, i.e., the monitored cell voltage and positive electrode potential, and the calculated negative electrode potential. All pertinent data for each cell remaining on charge in sequence is thereby packed into one contiguous block of the IDATA array.

*Data processing time.*—A measure of the total time required to process the numerous program instructions

Table I. Cell condition code—NCODE(M)

M	Information	Value
1	Data record number	Variable
2	"Complete response" data monitored	1
2	"Partial Response" data monitored	2
2	Final information	0
3	Number of cells remaining on charge	Variable
4	"Partial response" data not recorded permanently	1
4	"Partial response" data recorded permanently	2
4	Charge input level limit attained—end program	3
4	Individual cell cut-out	4
4	All cells cut-out—end program	5
I	Cell number $I = 3 \times (\text{Cell No.} - 1) + 5$	1-16
I + 1	Significant increase in minimum cell voltage	1
I + 1	Significant increase in minimum positive electrode potential	4
I + 1	Significant increase in minimum negative electrode potential	7
I + 1	Significant increase in internal resistance	
	Total cell	2
	Positive electrode contribution	5
	Negative electrode contribution	8
I + 1	Significant increase in IR-free polarization	
	Total cell	3
	Positive electrode	6
	Negative electrode	9
I + 2	Cell NCODE(4) value	Variable



in sections 2-6 of the Appendix may be obtained by monitoring the difference in the charge input levels at which the data acquisition sequence is initiated for the first and last cells in a series. By monitoring this value throughout the entire experiment, an average value per cell may be calculated. For example, a number of cells without incorporated reference electrodes were subjected to a 240 mA amplitude pulse of length 5 msec and period 15 msec. "Complete response" data was taken at 1 msec intervals throughout the pulse regime. The average value for the charge input level difference per cell was 1.6  $\mu$ A-hr. At this current level, this difference corresponds to a time of 72 msec, i.e., approximately 5 pulse periods. For pulse regimes of this order of magnitude, for sixteen cells without reference electrodes, the total data acquisition, processing, and recording time was between 1 and 2 sec. When reference electrodes are incorporated into the cells, this time is approximately doubled. For the particular pulse regime referred to above, 1 mA-hr of charge is injected into each cell in 45 sec. Thus, one can acquire data for each cell in a series at the desired charge input levels with reasonable precision, and thus compare cell to cell and cycle to cycle behavior.

**Experimental procedure.**—The cells to be tested are connected in series to the galvanostat. Following section 1 initiation, the starting time of day is noted and pulse charging initiated. Immediately, i.e., at zero charge input level a "complete response" data acquisition sequence is initiated. The program flow then continues as outlined in the Appendix until termination is indicated. Throughout the running of the program, the length of tape used to record permanent information and data is noted. At the conclusion of the test, the time of day is again monitored, and the total experiment run time calculated. For convenience, since most of the tests were scheduled for overnight running, these two pieces of information together with a record of the final open-circuit cell voltages, and positive electrode potentials, if available, were typed out on the teletype. The cells are now disconnected from the galvanostat. They are then discharged at constant current with conventional laboratory instrumentation, in order to measure the charge acceptance efficiency, and in preparation for the next pulse charging cycle.

### Secondary Program

This program is run off-line at the conclusion of the pulse charging experiment, using the main program tape output as input information. The program is much shorter and more simple than the main program, and will not be discussed in any detail. The fixed length NCODE record is first scanned and decoded. The resulting information describes the type, "complete or partial response," and the amount of data, and to which cells they pertain, in the ensuing IDATA record. The requisite calculations are performed and the output, in suitable tabulated format, is printed on the line printer. This procedure is repeated until the final information record is recognized. A copy of some typical records, in the original output format, are shown in Table IV.

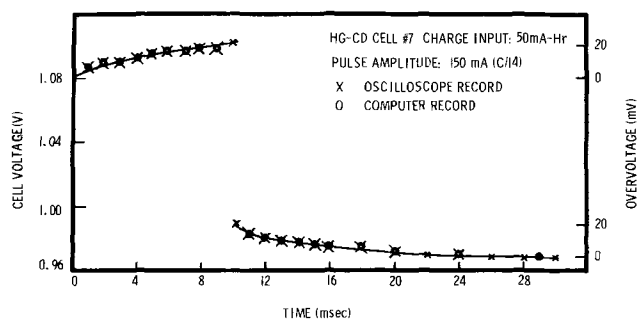


Fig. 2. Comparison of computer and oscilloscopic record of mercury-cadmium cell voltage response to pulse charging.

For the most part it should be self-explanatory. Records 13 and 108 refer to "partial response" data, and indicate that although the data was recorded because of an observed significant change in the positive and negative electrode potentials, respectively, (see Table I) the cells still remain IN circuit.

### Results

**General program operation.**—During the development of the main program, the accuracy of the pulse regime time synchronization and rapid data acquisition was tested in the following manner. A waveform generator (Microdot, Incorporated, Model F230B) was connected to the input of the analog measuring system. A 10 msec period, 0-2V triangular voltage function was triggered by the change in level of the D/A converter. The resulting voltage was monitored at 1 msec intervals and compared with the correct waveform values. With the successful development of the time synchronization, agreement to within less than 1 mV was obtained on continued cycling. In Fig. 2 is shown a comparison of the oscilloscopic and computer record of the cell voltage of a 600 mA-hr mercury-cadmium button cell responding to a 150 mA pulse of 30 msec period and 10 msec length at room temperature. As can be seen, the agreement is excellent.

**Application to a nickel-cadmium multicell system.**—As part of a general pacemaker battery study operative at the Technology Center, six Varta 225 DKH nickel-cadmium button cells were pulse charged at 37°C at the nominal 5 hr rate, viz., 144 mA amplitude, 30 msec period, and 10 msec length. Since these cells do not contain reference electrodes, it was arbitrarily decided to effect cell cut-out when the off-current phase minimum cell voltage attained the value 1.500V. In Fig. 3A and 3B are shown cell No. 6 voltages at 1 msec intervals at charge input levels of 20 and 220 mA-hr, respectively. These curves are typical of the entire set. As charging proceeds, the character of the curves changes gradually from that shown in A to that in B. The pertinent parameters, indicative of the over-all behavior of these cells, are summarized in Table II. Generally, the maximum polarization and the internal resistance remain fairly constant during charging, tending to increase when the cells attain the fully charged state.

Table II.

CHG. input (mA-hr)	VARTA 225 DKH Ni-Cd button cells 37°C						Pulse amplitude, 144 mA; period, 30 msec; length, 10 msec											
	Minimum response (V)						Maximum polarization (mV) $\pm 1$						Internal resistance (mohm) $\pm 7$					
	1	2	3	4	5	6	1	2	3	4	5	6	1	2	3	4	5	6
2	1.426	1.429	1.427	1.426	1.427	1.421	20	23	22	20	19	22	256	250	270	229	256	277
20	1.426	1.432	1.427	1.426	1.429	1.423	15	17	18	16	15	16	250	222	250	215	222	250
40	1.433	1.438	1.434	1.430	1.433	1.427	15	15	16	16	14	13	243	215	236	222	222	256
60	1.439	1.449	1.444	1.437	1.438	1.434	14	13	16	17	13	13	263	215	229	222	243	263
80	1.451	1.459	1.453	1.448	1.448	1.444	16	15	14	16	15	14	236	222	243	201	222	250
100	1.461	1.473	1.466	1.457	1.459	1.454	17	15	16	14	15	16	243	229	229	215	222	256
120	1.476	1.486	1.477	1.469	1.469	1.466	13	13	16	14	14	13	250	236	222	208	222	270
140	1.486	1.498	1.485	1.480	1.481	1.477	21	19	16	12	13	15	250	222	222	222	215	256
160	1.496		1.493	1.489	1.490	1.485	19		20	13	20	18	256		222	222	215	263
180			1.498	1.496	1.499	1.492			23	17	17	17			215	236	215	277
200						1.495												298
220						1.499												291
Cut-out at	176	148	182	192	184	240	mA-hr											



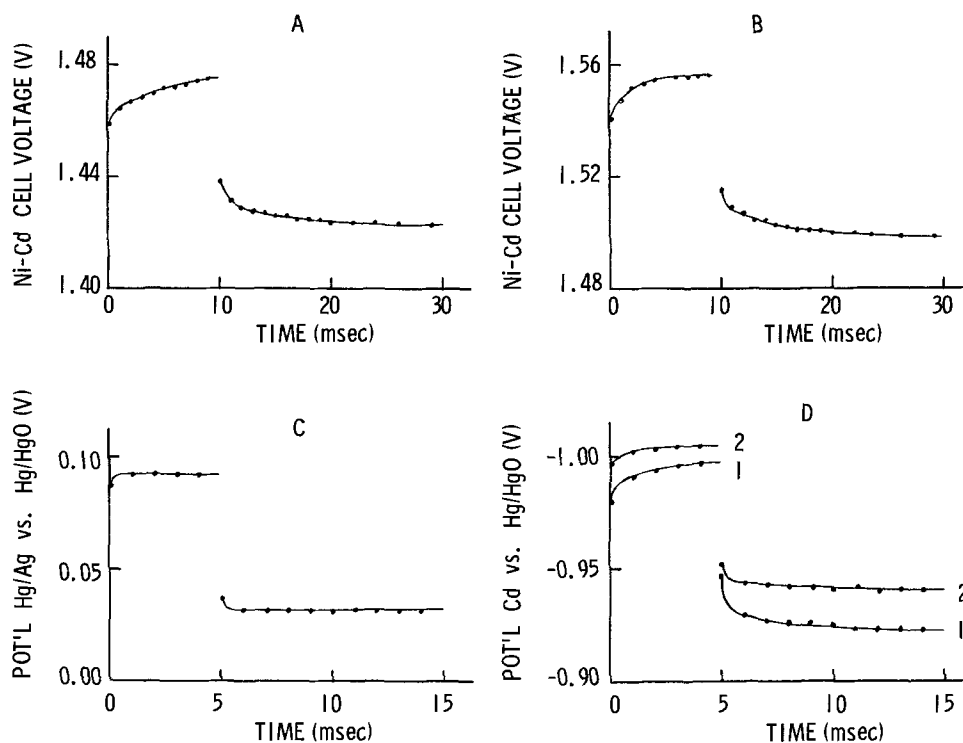


Fig. 3. Computer recorded cell response data to pulse charging. (A, B) Ni-Cd cell, 37°C, 0.144A, 30 msec period, 10 msec length. (A) 20 mA-hr, (B) 220 mA-hr. (C, D) Hg-Cd cell, room temperature, 0.480A, 15 msec period, 5 msec length. (C) 70% Hg-30% Ag electrode potential response. (D) Cd electrode potential response, curve 1, 0.1 A-hr; curve 2, 0.88 A-hr.

**Operational behavior of the mercury-cadmium cell.**—Previous experimental investigations in this laboratory (6) indicated that efficient d-c charging of two-electrode mercury-cadmium button cells can only be attained at very low rates, in excess of the 100 hr rate, if oxidation of the positive electrode silver substrate is to be avoided. It has also been shown that a 70% mercury-30% silver pressed powder positive may be pulse charged with high-charge acceptance efficiency at effectively the 15 hr rate or less without excessive silver oxidation (10). An optimization study indicated that, for this particular cell system and geometry, the preferred regime was a pulse of length in the range 5-10 msec, with an on/off ratio of at least 1:2.

In order to study the charging behavior of this cell system more completely, a cell containing an *in situ* reference electrode was employed. It consisted of a 70% mercury-30% silver pressed powder, rectangular positive plate, 1.5 in.  $\times$  1.4 in.  $\times$  0.037 in., placed between two pressed powder cadmium negative plates, 1.5 in.  $\times$  1.4 in.  $\times$  0.047 in. A smaller positive plate, acting as a mercury-mercuric oxide reference electrode, was positioned orthogonally to the sandwich. Both positive plates were wrapped in untreated Permin 2291, an irradiated, cross-linked polyethylene with an acrylic graft (R.A.I. Research Corporation) acting as a barrier. They were then contained in a sleeve of nonwoven polypropylene, FT 2140 (Pellon Corporation), acting as an electrolyte absorber. The electrodes were placed in a rectangular Lucite container, and filled with 31% potassium hydroxide. The cell, of 1 A-hr nominal capacity, was positive limited on both charge and discharge. All tests were performed at room temperature. Following the initial discharge of the as-formed charged cell, and prior to performing pulse charge-d-c discharge cycling, the positive electrode was conditioned. The negative electrode behaved normally throughout. Conditioning involved a sequence of short charge-overdischarge cycles, and was completed when, on charging, the positive electrode potential initially did not rise above ca. 0.035V, i.e., for this system the cell voltage did not rise above 1.0V. It should be noted that for this type of cell, up to ten conditioning cycles may be required before normal cell operation ensues.

The cell was subjected to a series of high rate, 33.3% duty cycle pulse charge tests, *viz.*, 0.48A amplitude, 15 msec period, and 5 msec length. Charge termination was

to be implemented if the minimum potential of the electrodes with respect to the reference at the end of the off-current phase attained or exceeded the values, indicative of the onset of silver oxidation at the positive and hydrogen evolution at the negative, *viz.*, 0.244V (20) and -1.100V, respectively. "Complete and partial response" data was monitored at charge input level increments of 20 and 2 mA-hr, respectively. "Partial response" data was recorded permanently if any of the following conditions were met:

1. The minimum potential at the end of the off-current phase of the positive and negative electrodes changed by 5 and 10 mV, respectively, from any immediately prior value.
2. The maximum polarization, exclusive of the resistive contribution, increased by 5 mV over the previously monitored value.
3. The contribution of either working electrode-electrolyte interface to the internal resistance changed by 25 milliohms or greater.

Initially, the charging curve of the cell and the positive electrode exhibited two distinct regions, as indicated by Catherino and Carson (5). On continued cycling the following effects were observed:

1. The initial, low plateau, positive electrode rest potential and cell voltage (minimum at the end of the off-current phase) tended to decrease, ultimately leveling at the values 0.035 and 0.955V, respectively.
2. The charge acceptance in this first plateau region increased, finally attaining a steady value of 43% of the total charge accepted, as shown in Table III.

Table III. Charge acceptance behavior of the mercury-cadmium cell

Cycle No.*	Charge input level (A-hr)	
	Low potential plateau	Total**
11	0.272	0.544
12	0.256	0.544
13	0.224	0.448
14	0.268	0.624
15	0.352	0.652
16	0.336	0.880
17	0.320	0.944
18	0.370	0.942
19	0.400	0.940
20	0.405	0.942
21	0.410	0.940
22	0.410	0.940

\* First ten cycles were for positive electrode conditioning.  
 \*\* >95% charge delivered at the C/6 d-c discharge rate.

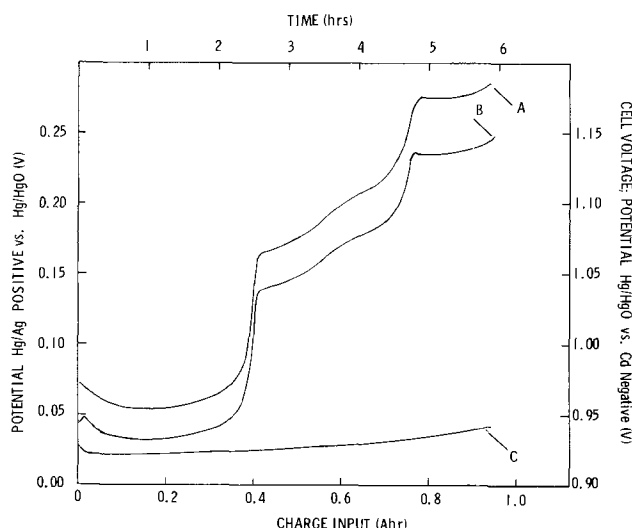


Fig. 4. Mercury-cadmium cell, off-current phase minimum response vs. charge input, room temperature, 0.48A, 15 msec period, 5 msec length. Curve A, cell voltage; curve B, positive electrode potential; curve C, negative electrode potential.

3. The positive electrode potential and cell voltage in the second region commenced to develop a more definite four-step character.

4. Total charge acceptance increased, finally leveling at a value of 0.94 A-hr.

The sequence of cycling tests was terminated after cycle 22. The fully developed minimum data values at the end of the off-current phase for cycle 21 are shown in Fig. 4. There is every reason to believe that this system can exhibit an extensive cycle life. The constancy of the charging data over the final six cycles (see Table III) confirms that it is possible to develop a well-behaved, nondeteriorating mercury-cadmium cell capable of being fully charged without the possible debilitating effect of silver substrate oxidation in the positive electrode. Furthermore, Permion 2291 is seen to be an effective barrier to the transport of mercury to the cadmium cathode during charging, a known cause of capacity losses in this cell system (21). The "complete response" potentials of the mercury-silver positive at a charge input level of 100 mA-hr are shown in Fig. 3C. The character of this curve remained the same throughout the entire charging period. The indicated minimal polarization is not in agreement with the findings of Toni (9). In Fig. 5 is shown an oscilloscopic record of the "complete response" voltage of the mercury-cadmium cell prior to and after the onset of silver substrate oxidation. The curve slowly changes in character from the lower to the upper trace as the off-current phase minimum potential of the positive commences to rise from the fourth plateau at 0.235V (see Fig. 4). In Fig. 3D are shown the "complete response" potential data for the cadmium negative at charge input levels of 100 and 880 mA-hr, curves 1 and 2, respectively. Small polarization effects are in evidence, the magnitude diminishing with increase in charge input. Some examples of the computer output of the secondary program are shown in Table IV. As can be seen, the resistive drop through the cell is equally divided between the positive and negative electrodes, remaining essentially constant at  $256 \pm 6$  milliohms throughout the entire experiment. The "partial response" data shown indicating that the cell is still in circuit, was recorded permanently because a significant change in the positive and negative electrode potentials respectively at the end of the off-current phase was observed.

Although further extensive work is necessary to characterize the behavior of the mercury-silver electrode unequivocally, a tentative explanation is pro-

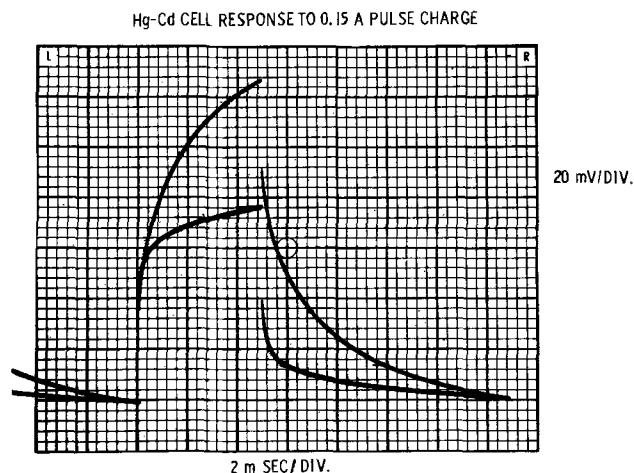


Fig. 5. Comparison of response of a mercury-cadmium cell to pulse prior to and after the onset of silver oxidation. Room temperature, 0.15A, 15 msec period, 5 msec length.

posed for the characteristic curve B in Fig. 4. From a consideration of the phase diagram reported for the mercury-silver system (22), in agreement with Catharino and Carson (5), it appears that the low potential, initial plateau is characteristic of the oxidation of a solid solution of mercury in silver. The fourth, well-defined wave at 0.235V appear to be indicative of the oxidation of mercury from the silver-rich  $\alpha$ -phase. Regarding the two shallow, but distinct waves in the 0.163-0.235V potential region, it is hypothesized that these characterize the oxidation of small quantities of mercury present in the  $\beta(\epsilon)$  and  $\gamma$  intermediate phases, which may develop on continued cycling.

### Summary

Computer-controlled, square wave, galvanostatic battery pulse charging is a successful, viable technique, which affords many advantages over the conventional method, with its limitations, especially when multicell studies are required. It affords an accurate means of monitoring the response of the cell or individual electrodes to the perturbing signal, and separating the contributions due to polarization, the resistive drop and the equilibrium voltage or potentials. Charge termination may be effected for any individual cell in a multicell stack, for a variety of reasons, an extremely difficult task with the conventional method. Multicell data is readily available for cell to cell, and cycle to cycle comparison and interpretation. The application of the technique to the study of the operational behavior of the mercury-cadmium cell has proved very successful, resulting in information not readily available when using conventional charging techniques. Information gleaned in this manner can be of great utility in formulating optimum charging conditions, and as a guideline for designing simple, field operated pulse charging equipment.

### Acknowledgments

The author wishes to thank Dr. R. B. Roe and Mr. D. L. Beals for their invaluable assistance in developing the program system.

Manuscript submitted July 31, 1972; revised manuscript received Aug. 28, 1973. This was Paper 37 presented at the Cleveland, Ohio, Meeting of the Society, Oct. 3-7, 1971.

Any discussion of this paper will appear in a Discussion Section to be published in the December 1974 JOURNAL.

### APPENDIX

*Main program operation.*—Time synchronization was the governing factor in designing the program structure. For the purpose of speed and efficiency, the de-

Table IV. Pulse charging of ESB Hg-Cd rectangular cell with Hg/HgO reference electrode

J. P. Elder Pulse regime File No. EL Cell Time (msec)		1 Cells 0.480A amplitude Record No. 9 Cycle 21 Overvoltage (mV)			Date 11/16/71 0.015 sec period Complete response Voltage (V)			Temp. 25°C 005 sec length 1 Cells remain on charge Internal resistance (milliohms)			Charge input (mA-hr)				
Cell	P-R.	N-R.	Cell	P-R.	N-R.	Cell	P-R.	N-R.	Cell	P-R.	N-R.	Cell	P-R.	Average	
1	1	5	1	-4	1.088	0.097	-0.991		262	127	135	80.000	80.002	80.000	
	2	6	0	-6	1.089	0.096	-0.993								
	3	7	1	-6	1.090	0.097	-0.993								
	4	8	1	-7	1.091	0.097	-0.994	Maximum							
	6	5	0	-5	0.962	0.035	-0.927								
	7	4	0	-4	0.961	0.035	-0.926								
	8	3	1	-2	0.960	0.036	-0.924								
	9	3	0	-3	0.960	0.035	-0.925								
	10	3	0	-3	0.960	0.035	-0.925								
	11	2	-1	-3	0.959	0.034	-0.925								
	12	0	-1	-1	0.957	0.034	-0.923								
	13	0	0	0	0.957	0.035	-0.922								
	14	0	0	0	0.957	0.035	-0.922	Minimum							
File No. EL	1 Record No. 13			Max./min. response			1 Cells remain on charge			Internal resistance		Charge input		Code	
Cell	Maximum overvoltage (mV)			Minimum voltage (V)			Internal resistance (milliohms)			Charge input (mA-hr)		Average			
1	Cell	P-R.	N-R.	Cell	P-R.	N-R.	Cell	P-R.	N-R.	Cell	P-R.	N-R.	Cell	P-R.	Average
1	8	0	-8	0.959	0.030	-0.929	256	129	127	98.000	98.001	98.000	98.000	in 4	
File No. EL	1 Record No. 69			Complete response			1 Cells remain on charge			Internal resistance		Charge input			
Cell	Overvoltage (mV)			Voltage (V)			Internal resistance (milliohms)			Charge input (mA-hr)		Average			
1	Cell	P-R.	N-R.	Cell	P-R.	N-R.	Cell	P-R.	N-R.	Cell	P-R.	N-R.	Cell	P-R.	Average
1	1	2	2	0	1.203	0.215	-0.988	252	127	125	520.000	520.002	520.000		
	2	3	0	-3	1.204	0.213	-0.991								
	3	3	0	-3	1.204	0.213	-0.991								
	4	4	2	-2	1.205	0.215	-0.990	Maximum							
	5	2	1	-1	1.082	0.153	-0.929								
	7	2	1	-1	1.082	0.153	-0.929								
	8	1	1	0	1.081	0.153	-0.928								
	9	0	0	0	1.080	0.152	-0.928								
	10	1	0	-1	1.081	0.152	-0.929								
	11	0	0	0	1.080	0.152	-0.928								
	12	0	0	0	1.080	0.152	-0.928								
	13	-1	0	1	1.079	0.152	-0.927								
	14	0	0	0	1.080	0.152	-0.928	Minimum							
File No. EL	1 Record No. 108			Max./min. response			1 Cells remain on charge			Internal resistance		Charge input		Code	
Cell	Maximum overvoltage (mV)			Minimum voltage (V)			Internal resistance (milliohms)			Charge input (mA-hr)		Average			
1	Cell	P-R.	N-R.	Cell	P-R.	N-R.	Cell	P-R.	N-R.	Cell	P-R.	N-R.	Cell	P-R.	Average
1	6	3	-3	1179	0.240	-0.939	252	127	125	852.000	852.001	852.000	852.000	in 7	

sign adhered to the following rules: (i) Wherever possible, integer arithmetic was used throughout. (ii) All cell condition information, in coded format, and voltage data were stored in integer form in linear arrays. (iii) Wherever possible, logical variables and logical decision making were used (i.e., the logical "if" was preferred over the arithmetic "if"). (iv) All nonsequential routing through the various sections was under the control of the "assigned go to" rather than the slower operating "computed go to" statement.

Section 1.—This section deals with program initiation and is separated into five subdivisions.

(i) Reading of necessary input information, which falls into four categories.

- A. General experimental information according to the requirements of the investigator, e.g., cell description, charging cycle number, environmental test conditions, number of cells on test, presence or absence of reference electrodes in test cells.
- B. Specific test information, i.e., pulse amplitude, period and length; charge input limit, if required; off-current phase cell voltage or electrode potential cut-out limits; magnitude of the increase which will be considered significant in: (a) cell voltage or electrode potentials at the end of the off-current phase of the pulse regime. (b) internal resistance. (c) polarization less resistive contribution.
- C. Time profile information.
- D. The increments in the charge input level at which "complete response" and "partial response" data are to be monitored.

(ii) Setting the values of a number of permanent program parameters.

(iii) Initialization of a number of program counters, the NCODE array, and a number of "significant increase" counting arrays used in section 6.

(iv) Assignment of the initial values of program route flags used in sections 2 and 3.

(v) Activation and status checking of the cell relays, monitoring of the initial open-circuit cell voltages and positive electrode potentials as a final check on all hardware connections.

Section 2.—In the program routing section, the decision is made as to the next charge input level at which a data acquisition sequence is to be initiated, and whether "complete or partial response" data is to be monitored. In order to effect this decision, three charge input level counters are employed. Two of the counters, QC pertaining to "complete response" and QP, pertaining to "partial response," whose initial values are set in section 1, are increased by the increments given as input information. The third counter, QI, initially set equal to -1, is continually incremented by 1 mA-hr, and compared with both QC and QP until an equality is observed. The equality indicates the type of response, and the value of QI sets the charge input level at which the next data acquisition sequence will be initiated. (If  $QI = QC = QP$ , "complete response" data will be monitored.) The appropriate routing flags for the necessary program flow through sections 4-6 are set. The specific locations in the IDATA array are selected. The number indicative of the type of response is placed in NCODE(2) (see Table I), and the entry point into the data acquisition section 4 is assigned.

The experimental charge input level, Q, is continually compared with QI, with frequent interruptive excursions to and return from section 3 for the necessary pulse control. When equality is observed, the characteristic and mantissa of Q are inserted into the assigned locations in the IDATA array, and the selected data acquisition sequence for those cells remaining on charge will commence after the initiation of the next pulse regime.

Section 3.—This section is concerned with pulse control, which is effected by means of the following time synchronization sequence. The location in core memory, which is continually counting the 1 kHz output pulses from the digital clock, is used as a millisecond clock. This count is continually compared with the pulse on and off times, calculated in section 1 from the desired pulse period and length. Approximately 1 msec prior to the time at which the pulse is to be turned on or off the count is set equal to zero. When this count is incremented by unity by an incoming pulse from the digital clock, the count is again set equal to zero and immediately the command to change the output level of the D/A converter is given. In approximately 10 μsec the output of the galvanostat

changes. The parameters for the next D/A converter output are set. Once per pulse regime, the charge input level is incremented. The program then proceeds to the assigned entry point in the appropriate section. Each of these sections is so designed that there is a continual return to section 3 in order to check on the necessity to resynchronize the millisecond clock and process the next pulse on or off command. In this manner, it is possible to maintain sharply defined, constant current pulse charging.

**Section 4.**—In this the data acquisition section, the millisecond clock time is continually compared with the selected data acquisition times according to the type of response requested. The A/D converter monitors the data as an integer number of millivolts at the appropriate intervals throughout the pulse regime, and stores them in the specific locations in the IDATA array. Following the acquisition of the maximum and minimum data points, 1 msec prior to the pulse on and off times, the program returns to section 3 for pulse control. If the cells contain reference electrodes, a second pass through this section is required to monitor the positive electrode potential data. Following the acquisition of data, whether complete or partial, the "IR-drop" in the cell or the contribution from the positive plate-separator interface, is monitored in the following manner. One millisecond after acquiring the minimum voltage level data point in the off-current phase of the pulse regime, the pulse is turned on. Immediately, the cell voltage or electrode potential level is monitored. The difference between this value and the just acquired minimum value is later used as a measure of the "IR-drop." Theoretically, the "IR-drop" should be monitored as soon as the perturbation is applied. Practically, there is a finite interval, whose value is governed by the operational speed of the A/D converter, and the time required for the requisite program instructions to be processed. In this system the interval is about 80  $\mu$ sec. Although by no means correct, it does give a measure of the "IR-drop" as exact as that obtained oscilloscopically.

**Section 5.**—The purpose of this section is (i) to calculate and store in the appropriate locations in the IDATA array the negative electrode potential data, if required; (ii) to calculate the internal resistance and maximum polarization less the resistive contribution, which, together with the minimum data point, are stored in comparison arrays for later use in section 6. When "complete response" data has been acquired, the program returns to that part of section 2 where the IDATA array locations are selected. The updated value of the experimental charge input level is stored and the entire program flow through sections 3, 4, and 5 is repeated for the next cell in the series. This continues until all the cells remaining on charge have been scanned. The program now enters section 7. When "partial response" data has been acquired, the program first enters section 6 prior to returning to section 2.

**Section 6.**—In this section, which is only employed when "partial response" data has been requested, the parameters calculated in section 5 and stored in the comparison arrays are compared with those measured in the previous data acquisition sequence. If significant differences are encountered in any one of the three parameters listed in section 1, [see (i)-B-(a), (b), or (c)], then the data just acquired will be permanently recorded. The reason is noted in the NCODE array by assigning the appropriate code number (see Table I). For each cell, a count is made for each parameter of the number of times it has shown a consecutive significant increase. If any of the counts attain the value 10 or if the minimum cell voltage or either electrode potential has attained or exceeded the prescribed limit, the cell is cut out of the galvanostat by actuating the appropriate relay. The status of the relay position is checked before continuing. The number of cells remaining on charge is decremented by unity. These facts are noted in the appropriate locations in the NCODE array. The program now returns to section 2 and proceeds as described in section 5 above.

**Section 7.**—This section is concerned with the permanent recording of information and data on magnetic tape. This is performed by means of a special core dump routine, which requires that the size of the block of contiguous data to be transferred be specified exactly. Although the size of the NCODE array is fixed, that of the IDATA array varies according to the number of cells remaining on charge, whether electrode potential as well as cell voltage data has been acquired, and whether "complete or partial response" data has been monitored. Furthermore, the speed of the tape unit is limited. Thus, the total data transfer time can be relatively long in comparison with the period and length of the pulse regimes which may be used. The data transfer subroutine incorporates a controllable interrupt and operates in the following manner. Upon being called, data transfer commences. When an excursion to section 3 for pulse control is necessitated, the transfer is interrupted. It continues at the point it left off when the program returns from section 3. This process of interrupted data transfer continues until the specified block of data has been dumped from core. The NCODE array is first recorded followed by the IDATA array. When experiment termination is indicated, either when all cells have been cut out or when the charge input level limit has been attained, the necessary indicative information in the NCODE array is recorded in the final core dump.

#### REFERENCES

1. S. U. Falk and A. J. Salkind, "Alkaline Storage Batteries," John Wiley and Sons, Inc., New York (1969).
2. P. C. Milner and U. B. Thomas, in "Advances in Electrochemistry and Electrochemical Engineering," Vol. 5, C. W. Tobias, Editor, Interscience, New York (1966).
3. D. R. Turner, *Electrochem. Technol.*, **2**, 5 (1964).
4. P. V. Popat, E. J. Rubin, and R. B. Flanders, Proc. 21st Ann. Power Sources Conf., p. 76 (May 1967).
5. H. Catherino and W. N. Carson, Jr., Final Report, Low Temperature Ballon Battery, Phase II, Contract NAS 5-11556, Jan. 1970.
6. N. Margalit and S. J. Thornell, Private communication.
7. W. A. Boyd, Paper 35 presented at Electrochemical Society Meeting, Cleveland, Ohio, Oct. 3-7 1971.
8. C. P. Wales, *This Journal*, **111**, 131 (1964); *ibid.*, **113**, 757 (1966).
9. J. E. Toni, R & D Final Tech. Report, ECOM-0056-F, p. 31 et. seq., Dec. 1969.
10. J. P. Elder, Internal Research Reports, Oct 1970, Jan. 1971, Dec. 1971.
11. K. V. Kordesch and A. Marko, U.S. Pat. 2,622,211 (Dec. 8, 1953); *This Journal*, **107**, 480 (1960).
12. D. A. Zinder, Application Note No. AN-447, Motorola Semiconductor Products, Inc.
13. K. V. Kordesch, Paper 36 presented at Electrochemical Society Meeting, Cleveland, Ohio, Oct. 3-7, 1971.
14. H. W. Liebhafsky and E. J. Cairns, "Fuel Cells and Fuel Cell Batteries," Chap. 8.6, Ref. 17 and 18, John Wiley and Sons, Inc., New York (1968).
15. J. W. Frazer, *Anal. Chem.*, **40**, 26A (1968).
16. G. Lauer, R. Abel, and F. C. Anson, *ibid.*, **39**, 765 (1967).
17. G. Lauer and R. A. Osteryoung, *ibid.*, **40** 30A (1968).
18. S. P. Perone, J. E. Harrar, F. B. Stephens, and R. E. Anderson, *ibid.*, **40**, 899 (1968).
19. H. E. Keller and R. A. Osteryoung, *ibid.*, **43**, 342 (1971).
20. W. J. Hamer and D. N. Craig, *This Journal*, **104**, 206 (1957).
21. N. Margalit and S. J. Thornell, Paper 8 presented at Electrochemical Society Meeting, Cleveland, Ohio, Oct. 3-7, 1971.
22. M. Hansen, "Constitution of Binary Alloys," 2nd ed., pp. 24-26, McGraw-Hill Book Co. (1958).

# Differential Aeration Corrosion of a Passivating Metal under a Moist Film of Locally Variable Thickness

Richard Alkire\* and George Nicolaidis\*\*

Department of Chemical Engineering, University of Illinois, Urbana, Illinois 61801

## ABSTRACT

A theoretical model is developed to predict the current distribution along a metal surface which exhibits passivity during differential aeration corrosion. The process is modeled by assuming that oxygen diffuses through a moist film of variable thickness to the corroding surface whereupon cathodic reaction proceeds in accordance with a Tafel rate expression which includes oxygen concentration dependence. The anodic dissolution rate depends solely upon the potential difference across the electrolyte-metal interface, behavior characteristic of active-passive metals. The model consists of a second-order nonlinear ordinary differential equation which was solved numerically. The influence of the system parameters upon the corrosion process was investigated. The results indicate that multiple steady-state solutions may exist for a single set of system parameters. It is usually found that current is conducted along the moist film between net anodic and net cathodic regions of the corroding surface. It is shown that in certain regions of parameter space the anodic dissolution rate can become highly localized.

Whereas electrochemical corrosion involves two distinct reactions which occur simultaneously, it is not necessary that the two reactions proceed at identical rates everywhere along the corroding surface. The problem of determining the local rate of corrosion reactions corresponds, in part, to determining the details of the current flow between localized anodic and cathodic regions. That is, one needs to know the current distribution. The present study illustrates one method of calculating the current distribution in a simple system which has many features which are characteristic of an active-passive metal undergoing differential aeration corrosion.

Under conditions of uniform attack, corrosion rates may be estimated with use of mixed-potential theory (1) as indicated in Fig. 1 for a situation of aeration corrosion (2). The anodic curve is typical of metals which undergo passivity, while the three cathodic curves correspond to three different oxygen limiting currents. For high rates of oxygen transport (curve A), passivity is attained. For lower rates of oxygen transport (curves B and C), active corrosion may occur to one extent or another.

When two corrodable metal pieces of identical composition are placed in connected solutions of different oxygen concentration, the metals proceed to corrode at different rates. When the two metal pieces are connected by a wire, it is observed that electrons move toward the corroding metal in the more oxygenated compartment (3). That is, the more oxygenated metal becomes cathodic with respect to the other piece. However, merely observing the direction of current flow does not give any information about which metal piece is corroding more rapidly. Kaesche showed (4) that if both metal pieces corrode in the active region (curves B and C in Fig. 1), then the "cathodic" metal corrodes more rapidly. On the other hand, if the "cathodic" compartment contains sufficient oxygen that the metal becomes passivated (curves A and C in Fig. 1), then the "anodic" metal corrodes more rapidly.

A similar situation arises during differential aeration corrosion of a metal surface. While one might expect the local corrosion rate to be higher where the oxygen concentration is higher, the possibility of metal passivation in the more aerated region makes the problem more complex since passivation of the entire surface may not necessarily occur. For example, one

possible type of behavior would be for the metal to be passive in highly aerated regions, inactive in the oxygen deficient regions, and highly reactive in the intermediate regions. Naturally, the question arises as to the specific conditions under which the anodic reaction rate distribution might be highly localized. The problem is complex because the oxygen concentration along the surface, the anodic and cathodic reaction rates, the net current, and the potential in the solution along the surface are all interdependent. Furthermore, in contrast to uniform attack, these quantities can all vary with position along the corroding surface. As a consequence of differential aeration corrosion, one may thus expect certain conditions under which some regions of the metal surface will be anodic while adjacent regions of the same surface will be cathodic. In order to investigate the conditions under which local current flows lead to localized corrosion, it is therefore necessary to combine mixed-potential theory with the concepts of current distribution phenomena.

Electrochemical current distribution problems originated in attempts to predict the over-all current-voltage behavior of electrolysis cells (5). Several such

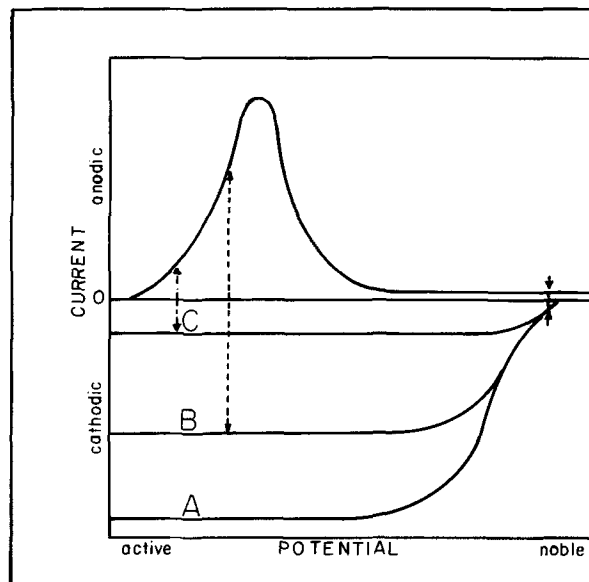


Fig. 1. Corrosion of a passivating metal in the presence of oxygen

\* Electrochemical Society Active Member.

\*\* Electrochemical Society Student Member.

Key words: corrosion, differential aeration, current distribution.

studies have also been conducted on corrosion-like configurations of fixed anode/cathode geometry. Waber *et al.* (6) calculated the primary and secondary current distributions in "local cells" having two-dimensional adjacent coplanar cathodic and anodic strips of fixed size. This method of calculation has been recently extended to other geometries including coplanar concentric rectangles (7) and circular strips (8). Wagner (9) included the role of mass transport limitations on local cell action for cases where the cathodic reaction was diffusion limited. Along somewhat different lines, Levich (10) employed a convective diffusion model to predict the rate of dissolution of inclusions of known size in both horizontal and vertical surfaces. A discussion of several of the foregoing aspects may be found in the book by Vetter (11). All of the foregoing studies assumed, however, that the anodic and/or cathodic regions were of known shape and size. One cannot make such assumptions and, at the same time, ask for the conditions under which the anodic corrosion region is extremely localized. Only a limited number of current distribution studies have been conducted on systems where localized anodic and cathodic regions coexist on adjacent regions of a single bipolar conductive surface. These studies consider bipolar resistive wires (12), bipolar porous diaphragms (13), and corroding iron disks (14). The last-mentioned study is particularly noteworthy, since it examines the consequence of differential aeration caused by nonuniform rates of oxygen transport to a corrodable surface.

By expanding upon these studies of bipolar current distribution phenomena, the following investigation arrives at a simple model for elucidating corrosion behavior of a passivating surface undergoing differential aeration corrosion. To be sure, the theoretical model does not take sufficient account of many complexities which may arise during an actual corrosion situation. For example, the effect of pH and of accelerator ions (such as  $\text{Cl}^-$ ) upon the passivation kinetics has not been included. However, the model does contain many of the most important salient features of differential aeration corrosion and can thereby serve as a basis both for developing more sophisticated studies, as well as for refining one's intuitive grasp of a complex situation.

### Derivation of the Mathematical Model

A metal surface may experience differential aeration from a wide variety of causes. A stationary meniscus, or stagnant pools and droplets of liquids in idle equipment, for example, can lead to attack. Uneven electrolyte agitation or local temperature differences may be the cause. Uneven aeration may also arise owing to the presence of a scale deposit, a block of wood lying on a tank bottom, a crevice formed by improper gasket fitting, or within a porous metal such as used for bone implants. The following theoretical model confines itself to a rather simple moist film configuration which may be thought of as akin to the region in the vicinity of a meniscus. Figure 2 illustrates the geometry of the system under investigation. The metal is covered by an electrolyte-moistened film of locally variable thickness. Oxygen diffuses from the atmosphere through the moist film to the metal surface where it is reduced. Simultaneously, the metal corrodes anodically. Electrical current flows in the moist film between the anodic and cathodic regions along the metal surface. The driving force behind the localized corrosion process under study is the difference in oxygen concentration at various positions along the metal surface. The moist film, which leads to the onset of corrosion, may eventually accumulate corrosion products and thereby change its form and nature. The following model does not account for such transient structural variations, either within the moist film or in the corroding metal surface. The applicability of the model lies in clarifying conditions under which the onset of localized corrosion is likely to occur.

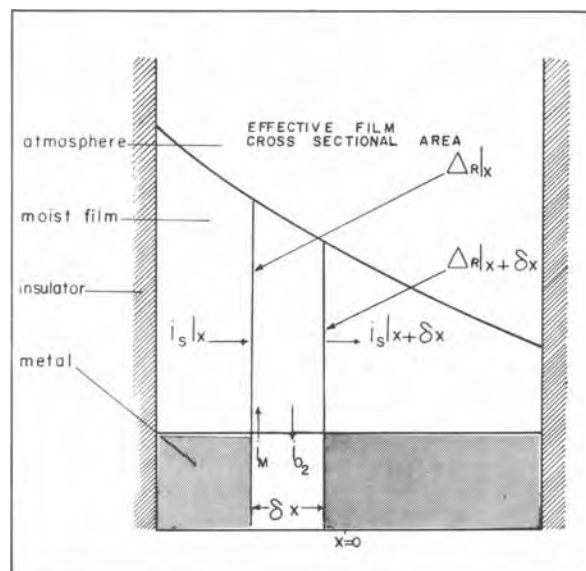


Fig. 2. System configuration for differential aeration corrosion study.

Because rigorous calculations are not necessary for a useful preliminary analysis, several simplifying assumptions have been introduced: (i) The corroding system is confined by two insulating planes as shown in Fig. 2. (ii) The potential within the corroding metal is uniform owing to the high conductivity of the metal phase. (iii) Current flows in the moist film parallel to the corroding surface. (iv) Oxygen diffuses through the moist film along paths which are perpendicular to the surface. (v) The film thickness varies with position in an exponential manner. (vi) The concentration of ionic species is uniform. Although these assumptions restrict somewhat the range of validity of the model, they do not obviate many essential features of behavior which are of interest.

The partial reactions which occur during corrosion proceed at rates which depend upon the local potential difference across the metal-film interface. Over the range of potential of interest, the current-potential behavior typical of many active-passive metals can be modeled by the function

$$i_M(x) = a \left\{ \frac{1 - \beta}{\left[ (V - \phi_s(x)) - V_R \right]^2} + \beta \right\} \quad [1]$$

The quantity,  $a$ , gives the maximum current density in the active region;  $\beta$  is the fraction of the maximum active current density which is exhibited in the passive plateau;  $s$  is related to the width of the hump which appears in the active region. Other nomenclature are compiled at the end of the text. Oxygen reduction has been modeled by a Tafel equation which includes consideration of mass transport limitations

$$i_{O_2}(x) = k \cdot \frac{c(x)}{c^0} \cdot \exp \left\{ \frac{-\alpha F}{RT} [V - \phi_s(x)] \right\} \quad [2]$$

The steady-state concentration of oxygen along the metal surface,  $c(x)$ , can be eliminated from Eq. [2] with use of Fick's first law of diffusion written locally along the film

$$i_{O_2}(x) = - \frac{4FD[c^0 - c(x)]}{\Delta_m(x)} \quad [3]$$

The local thickness of the film through which oxygen must diffuse,  $\Delta_m(x)$ , has been chosen to have the form

$$\Delta_m(x) = \delta_m \exp \left( - \frac{x}{l} \right) \quad [4]$$

Owing to local imbalances in anodic and cathodic rates, a net current may flow along the film. The current passing along the film obeys Ohm's law

$$i_s(x) = -\kappa \frac{d\phi_s(x)}{dx} \quad [5]$$

The current density flowing in the film,  $i_s(x)$ , may vary with position along the metal surface for several reasons. Figure 2 illustrates a differential slice of film having width  $\Delta x$ . Within this region, the current density flowing in the film changes owing to the change in cross-sectional area, as well as to a local imbalance of anodic and cathodic reactions. In differential form, the situation corresponds to a conservation of charge equation

$$\frac{d[i_s(x) \cdot \Delta_R(x)]}{dx} = i_{O_2}(x) + i_M(x) \quad [6]$$

The function  $\Delta_R(x)$  represents the effective cross-sectional area through which current flows. The one-dimensional flow of current, however, would not be a good approximation if the film is very thick in some regions. It should be recognized that the two-dimensional current lines, which might actually prevail, would be most dense near the corroding surface where the distance between anodic and cathodic regions is small. In view of these considerations, the function  $\Delta_R$  has been chosen to have the form

$$\Delta_R(x) = \delta_R \left[ 1 - \tanh\left(\frac{x}{l}\right) \right] \quad [7]$$

That is, the choice of the hyperbolic tangent function represents a way of confining the lines of current flow to the region near the electrode surface, even when the film may be quite thick. An exponential function for  $\Delta_R$  would perhaps be more consistent with Eq. [4], but would be less realistic in view of the two-dimensional nature of current flow which may occur under thicker portions of the film.

In order to reduce the number of independent parameters, it is convenient to introduce dimensionless variables

$$\begin{aligned} X &= \frac{x}{l} \\ \Phi &= (V - \phi_s) \frac{F}{RT} \\ C &= \frac{c}{c^0} \\ \sigma &= \left( \frac{F}{RT} \right)^2 s \\ \Phi_R &= \frac{V_R F}{RT} \end{aligned} \quad [8]$$

The model may then be rendered highly compact by combining Eq. [1]-[8] to obtain the dimensionless relation

$$\frac{d^2\Phi}{dX^2} - (1 + \tanh X) \frac{d\Phi}{dX} = \frac{\xi}{(1 - \tanh X)} \left\{ \left[ \frac{1 - \beta}{\frac{(\Phi - \Phi_R)^2}{\sigma} + \beta} \right] - \left[ \frac{\xi e^{-\alpha\Phi}}{\xi \Gamma e^{-X} e^{-\alpha\Phi} + 1} \right] \right\} \quad [9]$$

The dimensionless parameters which thereby appear in Eq. [9] are

$$\begin{aligned} \Gamma &= \frac{a\delta_m}{4FDc^0} \\ \xi &= \frac{Fl^2a}{RT\kappa\delta_R} \\ \zeta &= \frac{k}{a} \end{aligned} \quad [10]$$

The term on the right side of Eq. [9] is the net reaction rate which, for conditions of uniform corrosion, would have the value of zero everywhere along the surface. On physical grounds, Eq. [9] indicates that current flows into the film in the net anodic regions, flows along the moist film while suffering ohmic resistance and cross-sectional strictions, and flows out of the film into the net cathodic regions of the surface. A detailed treatment of the physical significance of the important parameters, Eq. [10], will be provided in the Results and Discussion Section which follows.

The only unknown quantity in Eq. [9] is  $\Phi(X)$ , the potential distribution along the metal surface. Since the differential equation is of second order, two boundary conditions must be specified; in accord with the arrangement depicted in Fig. 2, these are

$$\begin{aligned} \frac{d\Phi}{dX} &= 0 \quad \text{at } X = -\lambda \\ \frac{d\Phi}{dX} &= 0 \quad \text{at } X = +\lambda \end{aligned} \quad [11]$$

Equation [11] also defines the parameter  $\lambda$ . To be consistent with Eq. [8], the characteristic length  $l$  must be defined as

$$l = \frac{L}{\lambda} \quad [12]$$

where  $L$  is the dimensional length of the corroding surface. Effectively, the value of  $\lambda$  determines how sharply the functions  $\Delta_m$  and  $\Delta_R$  vary from one end of the interval to the other.

Once the potential distribution is found from Eq. [9] and [11], one may return to calculate the local reaction rates from Eq. [1] and [2], and the oxygen concentration distribution from Eq. [3]. In dimensionless form, the quantities are given by

$$\frac{i_M}{a} = \frac{1 - \beta}{\frac{(\Phi - \Phi_R)^2}{\sigma} + \beta} + \beta \quad [13]$$

$$\frac{i_{O_2}}{a} = \frac{\xi e^{-\alpha\Phi}}{\xi \Gamma e^{-X} e^{-\alpha\Phi} + 1} \quad [14]$$

$$\frac{c}{c^0} = \frac{1}{\xi \Gamma e^{-X} e^{-\alpha\Phi} + 1} \quad [15]$$

The theoretical model outlined above has extended previous current distribution studies to include multiple reactions occurring at bipolar electrode surfaces. The model does not require *a priori* specification of where the anodic and cathodic regions exist. In clear contrast to previous current distribution studies on corroding systems, the foregoing model allows the basic parameters of the corroding system to define the location of anodic and cathodic regions along the metal surface. As a consequence, the model is capable of predicting the conditions under which the anodic corrosion rate may be very localized.

#### Method of Solution

Equation [9], along with its boundary conditions, was solved numerically with use of an IBM 1800 digital computer. The equation was linearized about a trial solution and then set into finite difference form. The



trial distribution matrix was inverted (15), and the solution of the nonlinear equation was gained by iteration with successive correction of the trial distribution. The criterion for testing convergence was that values of the solution at the beginning, middle, and end of the spatial interval should not change by more than 0.001% of their absolute values upon successive iterations. It was found that the final solutions obtained were not noticeably affected by the mesh size when between 80 and 160 points were used, depending upon parameter values. Convergence was usually achieved smoothly within about five iterations.

In certain regions of parameter space, it was found that the choice of the first trial distribution was crucial in determining whether successful convergence would be achieved. Also, as will be discussed below, multiple solutions were obtained in certain regions of parameter space. The first trial distribution usually determined to which solution the program would converge for a given set of parameters. Convergence within such delicate regions was achieved by first obtaining a converged solution with "nearby" values of the system parameters. The values of the system parameters were then changed slightly; the "nearby" converged solution was then used as a first trial in attaining convergence at the newest set of parameters. By making only slight changes in the parameter values, and by obtaining a converged solution with every change, it was possible to explore large regions of parameter space.

The method used in this study for attaining convergence enjoys both advantages and disadvantages. During iterative steps, the trial potential distribution homes into a correct solution in a manner which, in some respects, is reminiscent of the physical response the system might have following an upset in operating conditions. As a consequence, the procedure used here usually converges onto stable solutions (16). On the other hand, the method has the disadvantage that one cannot know how many such solutions exist, except by finding them.

### Results and Discussion

Calculations based on the preceding theoretical model have been conducted in order to evaluate the computational method and in order to gain an understanding of characteristic features of differential aeration corrosion systems. Since the model contains a large number of system properties, and because the investigation is preliminary in nature, it would be cumbersome to report detailed parameter studies for every possible case. Only a few aspects which appear to be of special interest have been chosen for discussion. Table I gives the values used for those dimensionless parameters which were not varied in this investigation.

Under conditions of uniform corrosion, the local anodic and cathodic currents are in balance and the right-hand side of Eq. [9] equals zero everywhere along the surface. Up to three roots of the algebraic equation are possible, as illustrated qualitatively in Fig. 1 by curves B or C. If three roots exist, then the middle root, on the descending side of the polarization curve (i.e., having negative charge-transfer resistance), is unstable and will usually not be observed in actual systems. It is important to make a clear distinction between the number of algebraic roots of the right side of Eq. [9], and the number of solutions to the differential equation. Although up to three algebraic roots may be found from the right side, such information bears no direct relation to the number of solutions which the differential equation may exhibit.

Table I. Values of dimensionless parameters kept constant in this study

$\sigma$	=	0.15
$\kappa$	=	0.5
$\alpha$	=	0.5
$\beta$	=	0.01
$\Phi_B$	=	-7.75

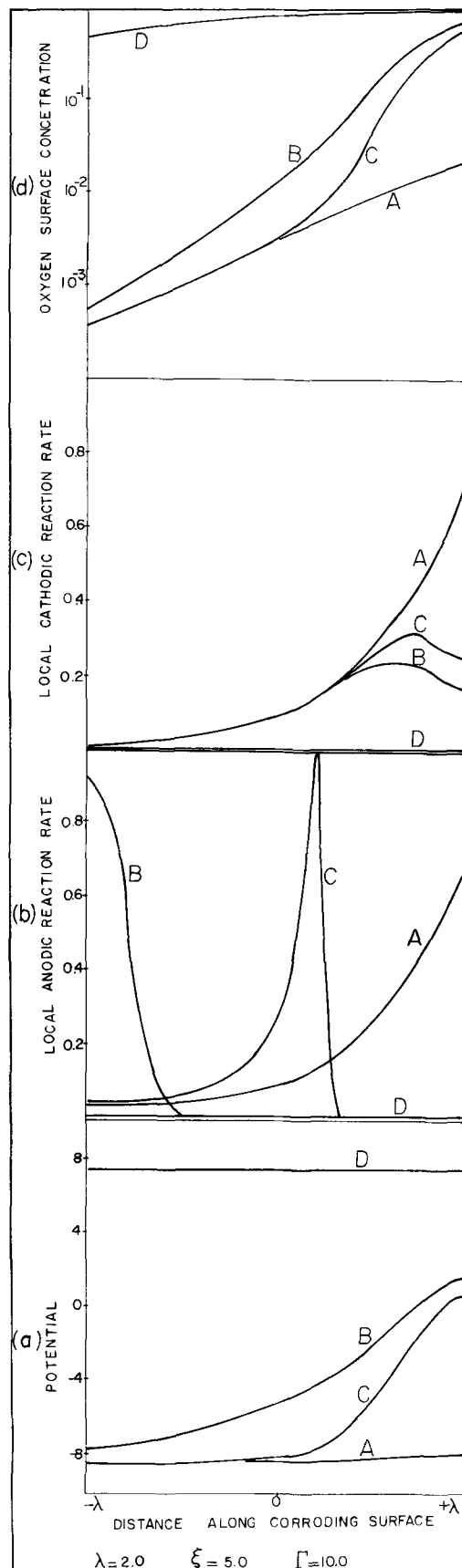


Fig. 3. Distributions satisfying Eq. [9] found for a single set of parameters. (a) Potential of the metal relative to the solution, (b) anodic dissolution rate, (c) cathodic reduction rate, (d) oxygen concentration at the surface.

*The occurrence of multiple solutions.*—In certain regions of parameter space, as many as four independent solutions of Eq. [9] have been found for a single



set of system parameters. For example, in Fig. 3, four sets of potential, current, and concentration distributions are shown for the parameter values  $\lambda = 2.0$ ,  $\xi = 5.0$ , and  $\Gamma = 10.0$ . The quantities which are plotted are given by Eq. [13], [14], and [15]. The right side of Fig. 2 ( $X = +\lambda$ ) corresponds to the thinner edge of the moist film, consistent with Fig. 1. The four potential distributions shown in Fig. 3a illustrate, in accord with introductory remarks, that the most cathodic region of the metal surface is at the more oxygenated end on the right side. The range of the potential distribution over the metal surface is seen to vary markedly from one solution to another. As a consequence, it is to be expected that the current distributions associated with each solution may be very different from each other. Figure 3b shows the four different anodic dissolution rate distributions which correspond to the four solutions. For solution A, the metal is in the active potential range everywhere and, accordingly, the local anodic dissolution rate increases with decreasing film thickness. Solution D corresponds to a fully passive situation at a very positive potential. Solutions B and C correspond to intermediate cases where one portion of the surface is passive while another portion is reactive. Solution B lies entirely on the decreasing branch of the anodic polarization curve and so is monotonic with distance. For some metals, the decreasing branch may be ill-defined so that a B-type solution may not exist. Solution C, on the other hand, varies all the way from the mildly active region to the passive region and thereby exhibits a strong maximum. Naturally, solution C is especially interesting since it indicates an obvious possibility for highly localized corrosion at intermediate positions under the moist film. It should be mentioned that, for certain parameter values, solutions A and B can also exhibit highly nonuniform dissolution rates, but the location of the maximum rate is always at or very near the extremities of the film. The average corrosion rate is related to the area under the anodic current distribution. Continuing to Fig. 3c, the cathodic reaction rate also varies with position owing in part to the potential variation and, in part, to the oxygen concentration along the surface. The cathodic current distributions given by solutions B and C are particularly noteworthy since they exhibit maxima owing to the competing effects of oxygen accessibility and distance from the net anodic region. The oxygen concentration distributions, shown in Fig. 3d, are consistent with the aforementioned behavior. Oxygen depletion does not occur to any large extent for the passive solution (D), whereas marked depletion occurs for the active solution (A). Solutions B and C are characterized by intermediate behavior.

The current flowing along the moist film is sustained by a net imbalance of local anodic and cathodic rates. As may be seen by subtracting the respective distributions in Fig. 3b and 3c, the net anodic region is always under the thick side of the film, where the oxygen concentration is the lowest. The current flowing through the film will be small for both solutions A and D, whereas it will be large for intermediate solutions B and C.

*The role of oxygen diffusion.*—Now let us turn to the influence of variations of system parameters upon the distributed variables, beginning with the parameter

$$\Gamma = \frac{a\delta_M}{4FDc^0}$$

From its definition, it may be expected that very small values of  $\Gamma$  correspond to rapid diffusion of oxygen so that the surface concentration would be essentially uniform, near the saturated value. One may see the situation by referring to the rightmost bracketed term of Eq. [9] in which  $\Gamma$  appears in the denominator. As the value of  $\Gamma$  approaches zero, the oxygen reaction

rate depends solely upon the potential, not concentration. In this limiting case, only "uniform" corrosion would be found, since the *raison d'être* for differential aeration no longer exists. For the value  $\xi = 0.5$  used in this study, only the passive root exists when  $\Gamma = 0$ , as shown schematically by curve A of Fig. 1.

On the other hand, for very large values of  $\Gamma$ , the sluggish diffusion of oxygen renders the surface concentration very low so that the surface may be active everywhere, but the corrosion rate would nevertheless be low because of the limited rate of supply of oxygen. Referring once again to the rightmost bracketed term of Eq. [9] illustrates the point. As  $\Gamma$  increases, the average cathodic rate decreases since  $\Gamma$  appears in the denominator. In the limit, the rightmost term behaves as  $1/\Gamma e^{-X}$  so that differential aeration exists, but the average corrosion rate would be exceedingly small owing to the paucity of oxygen.

Only over intermediate values of  $\Gamma$  will situations be found which correspond to appreciable rates of localized corrosion. Figure 4 illustrates the effect of  $\Gamma$  upon the anodic current distributions of solutions A, B, and C. By examining the areas under the curves, it is observed that the act of increasing  $\Gamma$  has the effect of lowering the average corrosion rate since the surface concentration of oxygen is also lowered. Solution A, which lies entirely in the active region of the metal polarization curve, responds by approaching the "rest potential" of the metal and becoming very inactive. Solution B lies primarily on the descending branch and passive region of the metal polarization curve. Solution B has the characteristic that the maximum anodic rate is always at or near the left (thick) side of the film, while the maximum cathodic rate is at or near the right (thin) side. Because the distance between anodic and cathodic regions thus remains essentially constant, and because increasing the parameter  $\Gamma$  has the effect of reducing the average anodic current, then the potential gradients along the surface become smaller. As a consequence of increasing  $\Gamma$ , the anodic current distribution becomes more uniform and the area under the distribution becomes less. One unusual characteristic of the B solution is that when  $\Gamma$  is increased, the potential in the solution shifts to more positive values under the thick part of the film and to more negative values under the thin part. This behavior is different from the other three solutions. Solution C has the characteristic of a very wide range of potential which passes through the potential of maximum anodic dissolution rate. Therefore solution C always exhibits a maximum in its anodic current distribution. Thus, since an increase in  $\Gamma$  reduces the average corrosion current, the effect on the anodic distribution is to render it more and more highly localized.

*The role of film resistivity.*—The parameter  $\xi$  characterizes the resistivity of the moist film

$$\xi = \frac{F l^2 a}{RT \kappa \delta_R}$$

and thus is an indication of the ease with which current flows between net anodic and net cathodic regions. A very small value of  $\xi$  corresponds to a film of very high conductivity. As a consequence, the potential drop along the film tends to be very small, and the metal thus corrodes "uniformly" at a local rate determined only by oxygen accessibility. That is, the high conductivity counteracts the potential driving force made available by differential aeration. On the other hand, a very large value of  $\xi$  corresponds to a film of very low conductivity. In this case, in spite of the possibility of a large range of potential along the film (owing to differential aeration) the film is not capable of carrying appreciable current between local anodic and cathodic sites. For intermediate values of  $\xi$ , the existence of highly nonuniform anodic attack is possible, and the potential distribution takes on values which

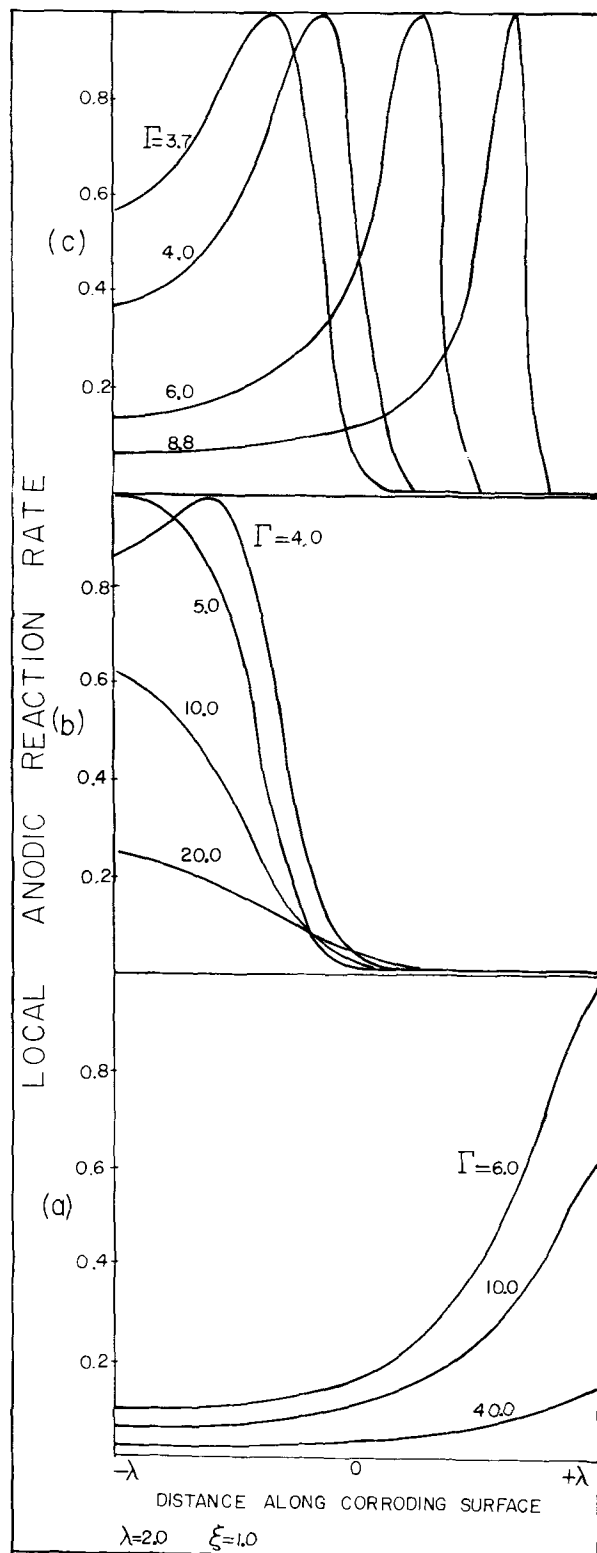


Fig. 4. The effect of  $\Gamma$  on the anodic dissolution rate distributions associated with solutions (a) A, (b) B, (c) C.

are intermediate between the potential distributions for  $\xi \rightarrow 0$  and  $\xi \rightarrow \infty$  (11).

Figure 5 illustrates the effect of parameter  $\xi$  on the anodic current distribution given by solutions A, B, and C. As  $\xi$  increases, current flow in the film becomes more difficult so that the potential gradients increase. Thus, smaller portions of the metal surface remain in the highly active anodic state. That is, for all three solutions the current distributions tend to be more localized for large values of  $\xi$  than for small values. In addition large values of  $\xi$  correspond to a wide range

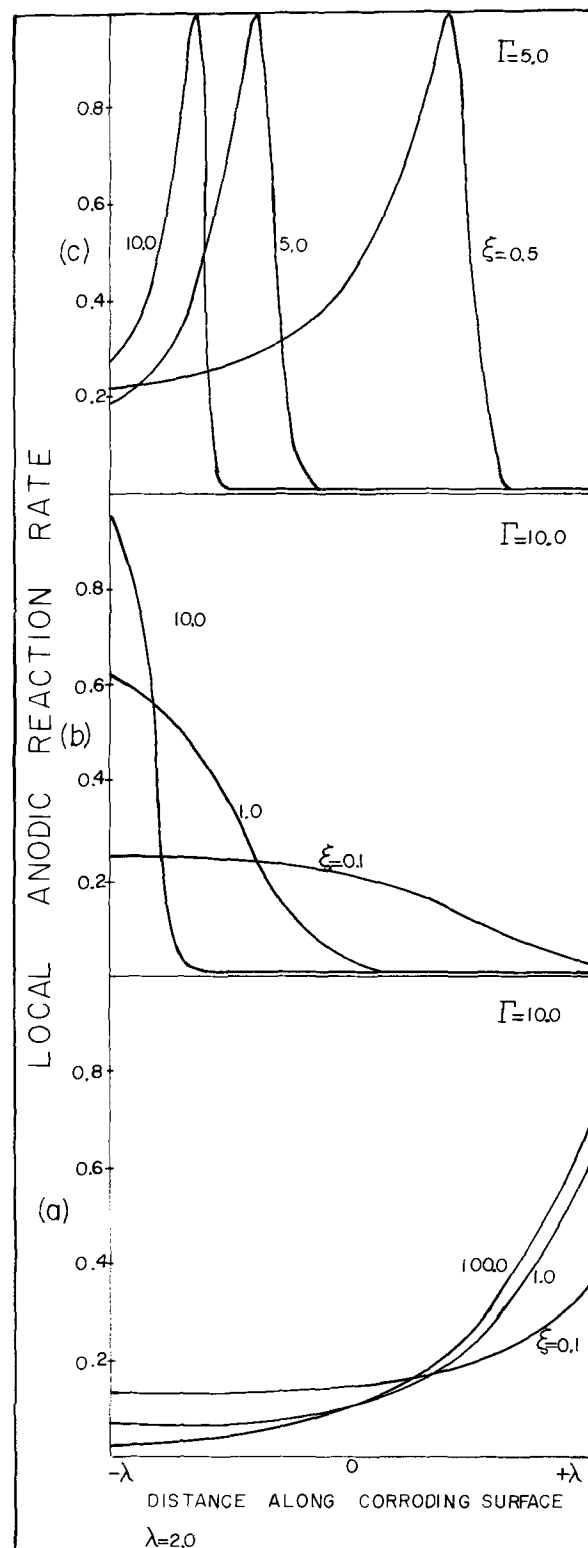


Fig. 5. The effect of  $\xi$  on the anodic dissolution rate distributions associated with solutions (a) A, (b) B, (c) C.

of potential from one end of the film to the other. In other words, an increase in  $\xi$  acts to impede the system's ability to corrode at high rates, as evidenced by examining the areas under the anodic distributions of Fig. 5. Because, for large  $\xi$ , the system cannot pass current along the film, the potential energy made available by differential aeration is stored within the system. For example, at large  $\xi$ , solutions A and B both exhibit more localized dissolution (large potential gradients) as well as large maximum dissolution rates (large potential range). Solution C, on the other hand,

cannot increase its maximum dissolution rate any further, and so responds by increasing the distance between anode and cathode.

Because the corrosion model is highly nonlinear, changes in values of one parameter affect the influence of the other parameters. Figure 6a provides an example when  $\xi$  is small; "C" solutions are found only over a small range of  $\Gamma$ . However, for larger values of  $\xi$ , as in Fig. 6b, solutions were found over a larger range of  $\Gamma$  values.

*The role of differential aeration.*—A measure of the difference in oxygen availability between one end of the electrode surface and the other end is embodied in the parameter

$$\lambda = \frac{L}{l}$$

which appears in the boundary conditions, Eq. [11]. A large value of  $\lambda$  corresponds to a large differential aeration and thereby enhances tendencies toward localized corrosion. For the value  $\lambda = 3$  and  $\xi = 1.0$ , Fig. 7 provides the anodic current distributions for solutions A and C for several values of  $\Gamma$ . These results may be compared to the distributions given in Fig. 4, for  $\lambda = 2$ ,  $\xi = 1.0$ . The comparison illustrates that when  $\lambda$  is increased, localized corrosion situations may be expected to occur over wider ranges of the other system parameters.

**Conclusions**

The investigation has shown that a relatively simple model of differential aeration corrosion may be use-

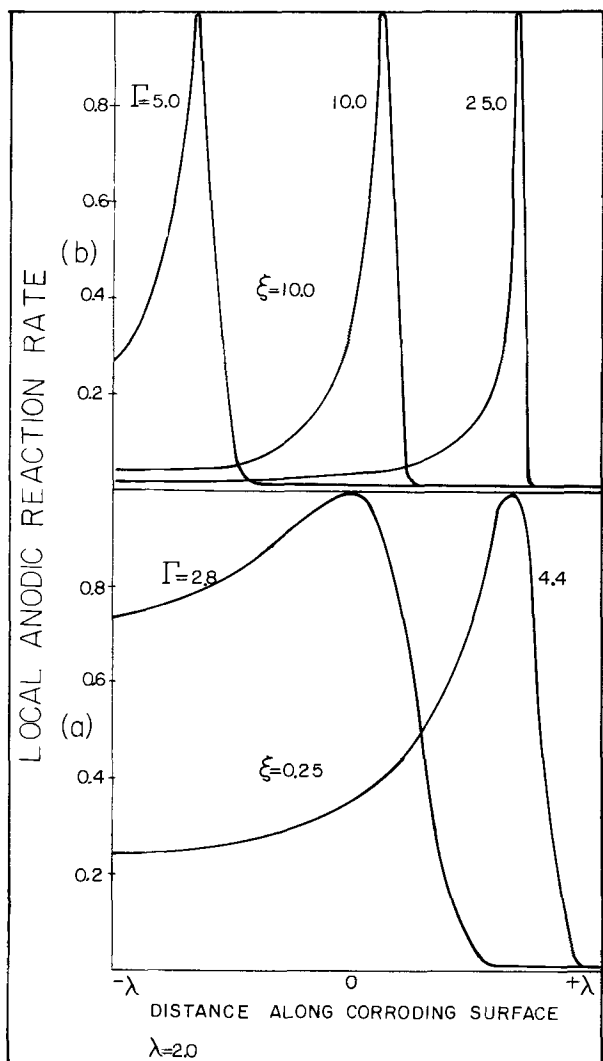


Fig. 6. The effect of  $\Gamma$  on the anodic dissolution rate distributions associated with solution C at (a) low  $\xi$  (b) high  $\xi$ .

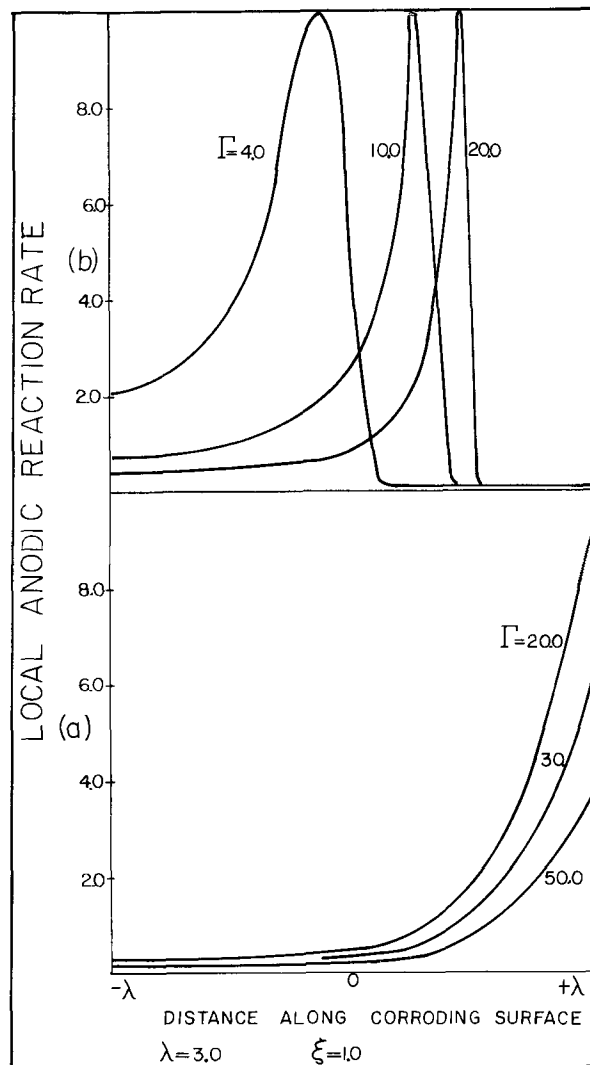


Fig. 7. Anodic dissolution rate distributions for  $\lambda = 3$  associated with solutions (a) A, (b) C.

ful for elucidating conditions under which localized attack may be expected; the model indicates both the location and the local rate of corrosive attack. The response of the model to changes in system parameters is in agreement with intuitive expectations. The reasonable behavior of the model supports the expectation that the solutions reported above are stable solutions. Unstable solutions generally behave opposite to one's intuition owing, in essence, to the negative-resistance aspect which is the source of their instability. However, as noted above, solution B is perhaps suspect because of its potential response upon variation of  $\Gamma$ , and because its potential range lies primarily on the descending branch of the anodic polarization curve, a region of negative charge-transfer resistance.

The central purpose of the foregoing study was to organize several important aspects of differential aeration corrosion systems in order to improve intuitive understanding of this complex phenomenon. Therefore, it is important to emphasize the assumptions upon which the model rests. A considerable flexibility is available for adjusting the specific details involved in the anodic rate equation, the cathodic rate equation, the shape, and cross-sectional area of the moist film. However, a major omission of the model is that it does not include consideration of concentration variations of several important constituents, particularly pH and  $Cl^-$  effects. It would be possible, in principle, to modify existing theoretical models of porous electrodes in order to investigate pH and  $Cl^-$  effects during corrosion of porous metals, flanges, and slotted regions. On

the other hand, such studies would involve eighth order systems of coupled nonlinear differential equations having, perhaps, multiple solutions. Another significant omission is that the model does not take account of the effect the substrate may have on passivation kinetics. For example, grain boundary regions may exhibit a different passivation current than other regions of the surface.

The foregoing analysis has arranged the corrosion system parameters into a small number of dimensionless groups and has illustrated how over-all system behavior is affected upon variation of these groups. Under certain regions of parameter space, at least four multiple solutions are possible. The characteristic behavior of the solutions differ from each other because each solution exhibits a different range of potential along the surface. Solution A always has potentials which are on the active branch of the metal polarization curve. The qualitative behavior of solution A is therefore expected to resemble that of nonpassivating metals undergoing differential aeration corrosion.

One of the four solutions (C) is particularly striking since it exhibits a strong maximum in the anodic current distribution. In attempting to avoid localized corrosion, one is not so much concerned with the over-all corrosion rate as with the current distribution over the surface. Therefore, it seems important to develop computational methods for ascertaining the regions of parameter space over which highly nonuniform current distributions are possible. The iterative method used in the present study is not particularly convenient since convergence upon the desired solution often depends upon one's skill in providing an initial guess of the desired solution; that is, one is not assured that a certain type of solution does not exist simply because one cannot converge upon it. Alternative solution-seeking methods are available, however, which generally find all possible solutions. Additional methods are also available for investigating the stability of the solutions.

One finds repeated comments throughout the experimental literature which emphasize the importance of establishing a definite order of operations for conducting corrosion experiments in order to obtain reproducible and consistent results. On the basis of the present investigation of one type of corroding system, it should be recognized that, if multiple steady-state situations exist, then the particular steady solution which is arrived at depends upon the start-up conditions which precede attainment of steady state. Therefore, with respect to differential aeration corrosion, ominous implications may exist for experimental procedures aimed at corrosion testing and at scale-up of corrosion tests to field situations. Not only would the corrosive test environment need to be similar to the field situation, but the events leading to establishment of the corrosion conditions would also need to be simulated. Once again, the conclusion seems clear that a method should be developed for elucidating parameter regions where highly localized attack is possible. With such information at hand, a corrosion engineer would have a better criterion for evaluating prospective designs so as to avoid altogether those potentially hazardous corrosion conditions.

#### Acknowledgments

The authors benefited greatly from discussions with Professor John Newman, University of California at Berkeley. The investigation received partial support from the National Science Foundation (Grant GK-36623).

Manuscript submitted July 5, 1973; revised manuscript received Sept. 19, 1973. This was Paper 101 presented at the Boston, Massachusetts, Meeting of the Society, Oct. 7-11, 1973.

Any discussion of this paper will appear in a Discussion Section to be published in the December 1974 JOURNAL.

#### NOMENCLATURE

$a$	maximum anodic current density, A/cm <sup>2</sup>
$c$	oxygen concentration at corroding surface, g-mole/cm <sup>3</sup>
$c^0$	oxygen concentration at film-atmosphere interface, g-mole/cm <sup>3</sup>
$D$	oxygen diffusion coefficient, cm <sup>2</sup> /sec
$F$	Faraday constant, 96,500 coulombs/g-equiv
$i_{O_2}$	local cathodic current density, A/cm <sup>2</sup>
$i_M$	local anodic current density, A/cm <sup>2</sup>
$i_s$	current density in film, A/cm <sup>2</sup>
$k$	oxygen reaction rate constant, A/cm <sup>2</sup>
$l$	characteristic length, cm
$L$	length of corroding surface, cm
$R$	gas constant, 8.31 joules/g-mole °K
$s$	parameter characteristic of anodic polarization curve width, V <sup>2</sup>
$T$	temperature, °K
$V_R$	potential of metal where anodic dissolution rate is maximum, V
$V - \phi_s$	potential of metal relative to solution close to the metal surface, V
$x$	distance along corroding surface, cm

#### Greek Characters

$\alpha$	transfer coefficient
$\beta$	anodic current density on passive plateau
$\delta_m$	mass transport layer thickness at $x = 0$ , cm
$\Delta_m$	local mass transport layer thickness, cm
$\Delta_R$	effective cross-sectional area at $x = 0$ , cm
$\delta_R$	local effective cross-sectional area, cm
$\kappa$	film electrolytic conductivity, (ohm-cm) <sup>-1</sup>

#### REFERENCES

1. C. Wagner and W. Traud, *Z. Elektrochem.*, **44**, 391 (1938).
2. M. G. Fontana and N. D. Greene, "Corrosion Engineering," Chap 10, McGraw-Hill Book Co., New York (1967).
3. U. R. Evans, "The Corrosion and Oxidation of Metals: First Supplementary Volume," p. 50, St. Martin's Press, New York (1968).
4. H. Kaesche, *Werkstoffe Korrosion*, **15**, 379 (1964).
5. J. S. Newman, "Electrochemical Systems," Part D, Prentice-Hall, Inc., Englewood Cliffs, New Jersey (1973).
6. J. T. Waber, *This Journal*, **101** 271 (1954); J. T. Waber and M. Rosenb'uth, *ibid.*, **102**, 344 (1955); J. T. Waber and B. Fagan, *ibid.*, **103**, 64 (1956); J. T. Waber, J. Morrissey, and J. Ruth, *ibid.*, **103**, 138 (1956); J. T. Waber, *ibid.*, **103**, 567 (1956); E. Kennard and J. T. Waber, *ibid.*, **117**, 880 (1970).
7. J. A. Simmons, S. R. Coriell, and F. Ogburn, *ibid.*, **114**, 782 (1967).
8. L. Gal-Or, Y. Raz, and J. Yahalom, *ibid.*, **120**, 598 (1973).
9. C. Wagner, *ibid.*, **107**, 445 (1960).
10. B. Levich, "Physicochemical Hydrodynamics," p. 343 ff, Prentice-Hall, Inc., Englewood Cliffs, New Jersey (1962).
11. K. J. Vetter, "Electrochemical Kinetics," p. 741 ff., Academic Press, New York (1967).
12. K. Nagata, T. Akimoto, and N. Fujise, *Denki Kagaku*, **38**, 763 (1970).
13. R. Alkire, *This Journal*, **120**, 900 (1973).
14. N. Vahdat and J. Newman, LBL-896, Lawrence Berkeley Laboratory, University of California, Berkeley, California, July, 1972.
15. J. S. Newman, *Ind. Eng. Chem. Fundamentals*, **7**, 514 (1968).
16. L. L. Kirkby and R. A. Schmitz, *Combustion and Flame*, **10**, 205 (1966).

# Anodic Behavior of Mild Steel in NaClO<sub>3</sub> at High Current Densities

Kao-Wen Mao\* and Der-Tau Chin\*

Electrochemistry Department, Research Laboratories, General Motors Corporation, Warren, Michigan 48090

## ABSTRACT

The IR-free anode potential and the current efficiency were studied for the electrochemical machining of mild steel in NaClO<sub>3</sub>. The results show that an electronically conductive oxide film is present in the low current density region where the current is consumed in oxygen generation. With increasing current density, the film begins to break up with the formation of pits in the film. The film finally disappears in the high current density region where the metal dissolution takes place with a current efficiency greater than 100% and the metal surface is polished due to the presence of a precipitated salt layer with high ionic conductivity.

In order to compete with conventional methods of metal removal, it is important for an electrochemical machining (ECM) process to provide the workpiece with good dimensional control and surface finish. For ECM of steels, NaClO<sub>3</sub> has been found to be superior to the commonly used NaCl solution (1). It has been suggested that the excellent dimensional control and surface finish obtained with steel in NaClO<sub>3</sub> are associated with anodic passivation (2, 3). Recently, it also has been pointed out that dimensional control in a passivating ECM electrolyte is related to the metal dissolution efficiency (4, 5).

In the present work, the anodic polarization and the current efficiency for ECM of mild steel in NaClO<sub>3</sub> were studied by carrying out the experiments in flow-channel cells. The results of this work should provide further information for future improvement of the ECM process.

## Experimental

**Anodic polarization measurements.**—The experiments for studying the anodic polarization of mild steel<sup>1</sup> in NaClO<sub>3</sub> were carried out in flow cell I previously described (6). A current interruption technique was employed to measure the IR-free anode potential. The current was interrupted after machining 0.6–3 sec (at constant current) depending upon the current density.<sup>2</sup> The experimental techniques and procedures are identical to those previously described (6, 7).

The NaClO<sub>3</sub> used had a NaCl content less than 0.04%. Distilled water was used to prepare the electrolyte. Experiments were conducted at 26° ± 2°C under the following conditions: Re = 16,000<sup>3</sup> (flow velocity, U = 2000 cm/sec) and 4000 (U = 500 cm/sec) in 4M NaClO<sub>3</sub>; Re = 19,500 (U = 2000 cm/sec) and 4000 (U = 410 cm/sec) in 2M NaClO<sub>3</sub>.

**Anodic current efficiency measurements.**—The current efficiency measurements were conducted in flow cell II, previously described (5). The details of the experimental procedures and techniques have been given elsewhere (5, 7).

Two kinds of mild steel were used for the study.<sup>4</sup> Mild Steel II was richer in carbon and phosphorus than Mild Steel I. The anodes were machined at a constant current and the dissolution time was varied from 5 sec at 100 A/cm<sup>2</sup> to 120 sec at 2 A/cm<sup>2</sup>. The electrolytes

used were 1–4M NaClO<sub>3</sub>; the flow rate was kept at Re = 7000 (or U = 1000 cm/sec). All the runs were made at 21° ± 1°C. The anode was weighed before and after the dissolution test to determine the amount of metal removal, and the current efficiency was calculated on the basis of ferrous ion as the dissolution product.

## Results

**Anodic polarization.**—The oscillogram of the anodic potential decay was enlarged 10 times for the determination of the initial slope of the decay trace. The initial slope was used for a linear extrapolation of the trace to zero time to determine the IR potential drop.

The IR-free anode potentials as a function of current density are given in Fig. 1. The data in the figure represent the average values of two or more runs. The difference between the results of replicate runs is less than 5%. The results represented by open symbols were obtained in 4M NaClO<sub>3</sub> at Re = 16,000 and in 2M NaClO<sub>3</sub> at Re = 19,500. It was found that the rate of

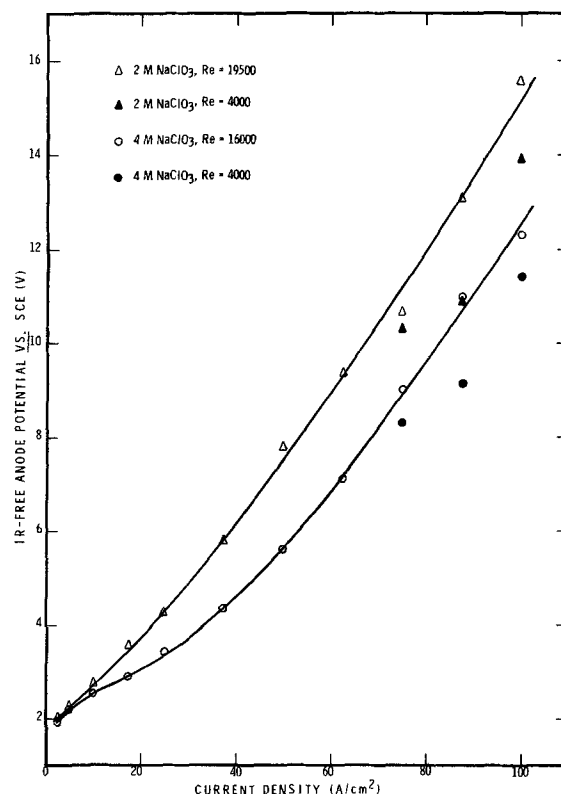


Fig. 1. IR-free anode potential vs. current density

\* Electrochemical Society Active Member.

Key words: current interruption, potential decay, current efficiency, electrochemical polishing.

<sup>1</sup> Composition (other than Fe) of the mild steel anode: C, 0.07%; Mn, 0.4%; P, 0.008%; S, 0.018%; Ni, 0.005%; Si, 0.005%; Co, 0.003%.

<sup>2</sup> In the present system, a steady state was reached in less than 0.5 sec.

<sup>3</sup> Re represents the Reynolds number which is defined as hydraulic diameter × flow velocity/kinematic viscosity.

<sup>4</sup> Compositions other than Fe: Mild Steel I = C, 0.08%; Mn, 1.05%; P, 0.057%; S, 0.25%; Ni, 0.1%; Si, 0.004%; Co, 0.05%. Mild Steel II = C, 0.12%; Mn, 1.10%; P, 0.082%; S, 0.27%; Ni, 0.1%; Si, 0.005%; Co, 0.05%.

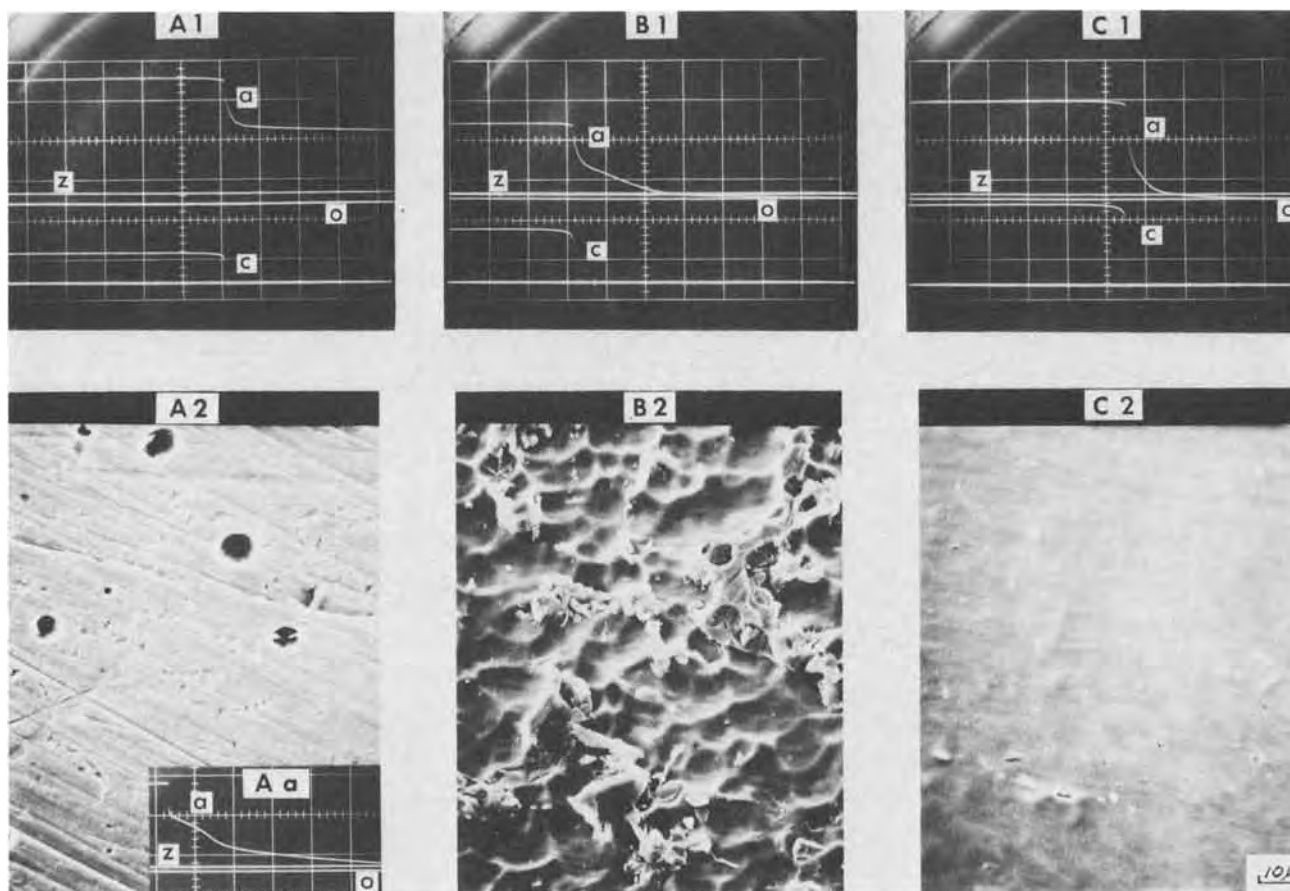


Fig. 2. Anodic potential decays and machined surfaces obtained with 4M NaClO<sub>3</sub> at Re = 16,000. Current density: Aa—2.5 A/cm<sup>2</sup>; A1, A2—10 A/cm<sup>2</sup>; B1, B2—17.5 A/cm<sup>2</sup>; C1, C2—25 A/cm<sup>2</sup>. Time scale: Aa—0.2 sec/div.; A1, B1, C1—20 μsec/div. Trace a, anodic potential decay: Aa, A1—1 V/div.; B1, C1—2 V/div. Trace z—zero point. Trace O—open-circuit potential. Trace C—cell current.

electrolyte flow had no significant effect on polarization when the current density was lower than 60 A/cm<sup>2</sup>. However, for current densities greater than 60 A/cm<sup>2</sup>, the anodic potentials at Reynolds numbers less than 4000 became significantly lower as shown by the filled symbols in Fig. 1.

Figure 2 shows the anodic potential decay traces and the machined surfaces obtained in 4M NaClO<sub>3</sub> at Re = 16,000. In Fig. 2Aa and 2B1, the anodic potential decay shows two arrests: the first arrest starts at 1.6V vs. SCE, and the second arrest starts at about 0.5V vs. SCE, corresponding to the reduction potential of Fe<sub>2</sub>O<sub>3</sub> to Fe<sup>++</sup> (8). Such a wave plateau was always observed at current densities between 2.5–17.5 A/cm<sup>2</sup> (the second arrest is not shown in Fig. 2A1 because of the large time scale used). At the present time, there is no reasonable explanation why the first arrest starts at 1.6V vs. SCE. Since this arrest potential was also observed in NaNO<sub>3</sub> (7) over a range of current densities where oxygen was generated on the electrode surface, it is probably caused by absorbed oxygen on the anode surface.

Figure 2A2 shows that the machined surface obtained at 10 A/cm<sup>2</sup> was covered with a layer of oxide film with localized pits occurring randomly in the film. It should be noted that pitting in the film was not observed until the current density reached about 5 A/cm<sup>2</sup>. As the current density was increased, more pits appeared, and the film started to break up as shown in Fig. 2B2. At this time the wave plateau in the potential decay curve became significantly shorter (Fig. 2B1). When the current density was further increased to 25 A/cm<sup>2</sup>, the oxide film was completely broken up (Fig. 2C2) and no arrest was observed (Fig. 2C1). The surface at this stage was polished and brightened.

**Current efficiency.**—The current efficiencies for ECM of Mild Steel I in 1, 2, and 4M NaClO<sub>3</sub> solutions at dif-

ferent current densities are given in Fig. 3. The results clearly show that the current efficiency increased with the concentration and with the current density. For each curve, iron was not dissolved until the current density reached a value indicated by point a in the figure. This value varied from 1.5 A/cm<sup>2</sup> for 4M NaClO<sub>3</sub> to 3 A/cm<sup>2</sup> for 1M NaClO<sub>3</sub>. Then, there was a rapid increase in current efficiency as the current density was increased. As the current density reached point b on the curves (approximately 15 A/cm<sup>2</sup> for 4M and 30 A/cm<sup>2</sup> for 1M solutions), the efficiency became greater than 100%. These results were obtained at Re = 7000, with a linear flow velocity of 1000 cm/sec. Experiments carried out at a lower flow rate indicate

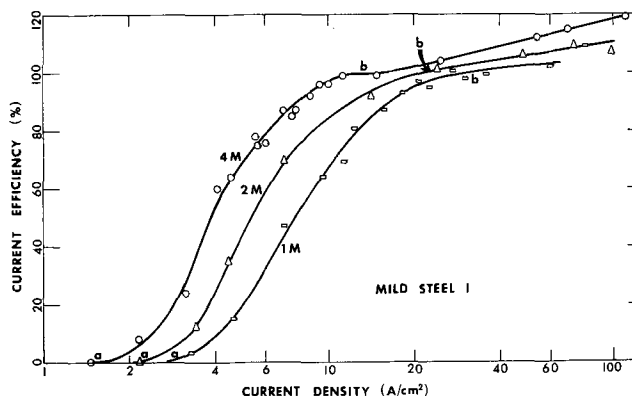


Fig. 3. Current efficiency vs. current density for Mild Steel I. Three reaction stages can be seen on each curve. The region to the left of point a is the oxygen generation stage; the region between points a and b is the transition region; and the region to the right of point b is the metal dissolution stage.

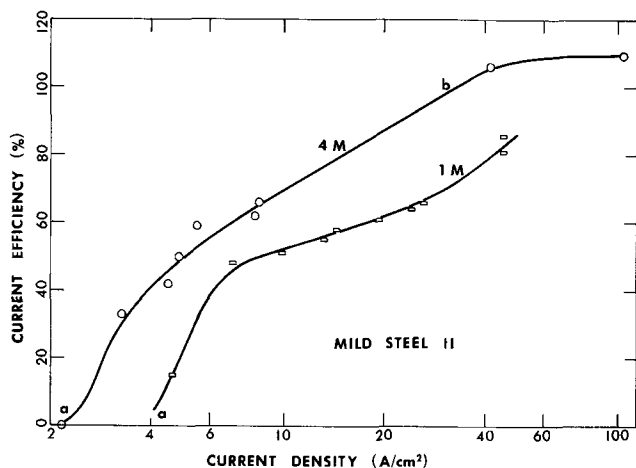


Fig. 4. Current efficiency vs. current density for Mild Steel II. Three reaction stages can be seen on each curve. The region to the left of point a is the oxygen generation stage; the region between points a and b is the transition region; and the region to the right of point b is the metal dissolution stage.

that the flow rate has little effect on the current efficiency (5).

Figure 4 presents the current efficiency results obtained with Mild Steel II in 1M and 4M NaClO<sub>3</sub>. These current efficiencies tend to be lower than those found for Mild Steel I (Fig. 3). The main difference between the two steels employed is that Mild Steel II has higher contents of carbon and phosphorus (see footnote 4). This is in agreement with the results of Freer and his co-workers (9). They found that in NaCl solution, the

current efficiency became lower as the carbon content increased.

Photomicrographs of the machined surfaces obtained in the current efficiency study are presented in Fig. 5; this shows that the surfaces obtained at equal current efficiencies are very much alike despite the differences in the concentration and the current density. The surfaces obtained at 70% current efficiency are pitted (Fig. 5A, D). As the efficiency increases the surfaces start to become polished (Fig. 5B, E). Finally, the surfaces are highly polished when the current efficiency is greater than 100% (Fig. 5C, F).

It is interesting to note that in Fig. 5C and F, flow streaks are observed on the anode surface. The appearance of the flow streaks is due to recession of the anode surface from the electrically inert flow-channel wall during metal dissolution (10). In the case of low current efficiencies, flow streaks are not observed because of oxygen generation which provides the solution with "micro" agitation.

### Discussion

Based on the results of this current efficiency study, the transpassive region for mild steel dissolution in NaClO<sub>3</sub> can be divided into three stages: (i) oxygen generation; (ii) transition; and (iii) metal dissolution stages.

*Oxygen generation stage.*—The oxygen generation stage for current densities below point a on the current efficiency curves: According to Fig. 3, this stage occurred at current densities lower than 2-3 A/cm<sup>2</sup>, depending on the concentration. In this stage the metal is not dissolved and current is expended for oxygen generation (11) on the surface of a protective oxide film. This oxide film is probably a layer of  $\gamma$ -Fe<sub>2</sub>O<sub>3</sub> (12). Since the current is consumed by the discharge of H<sub>2</sub>O

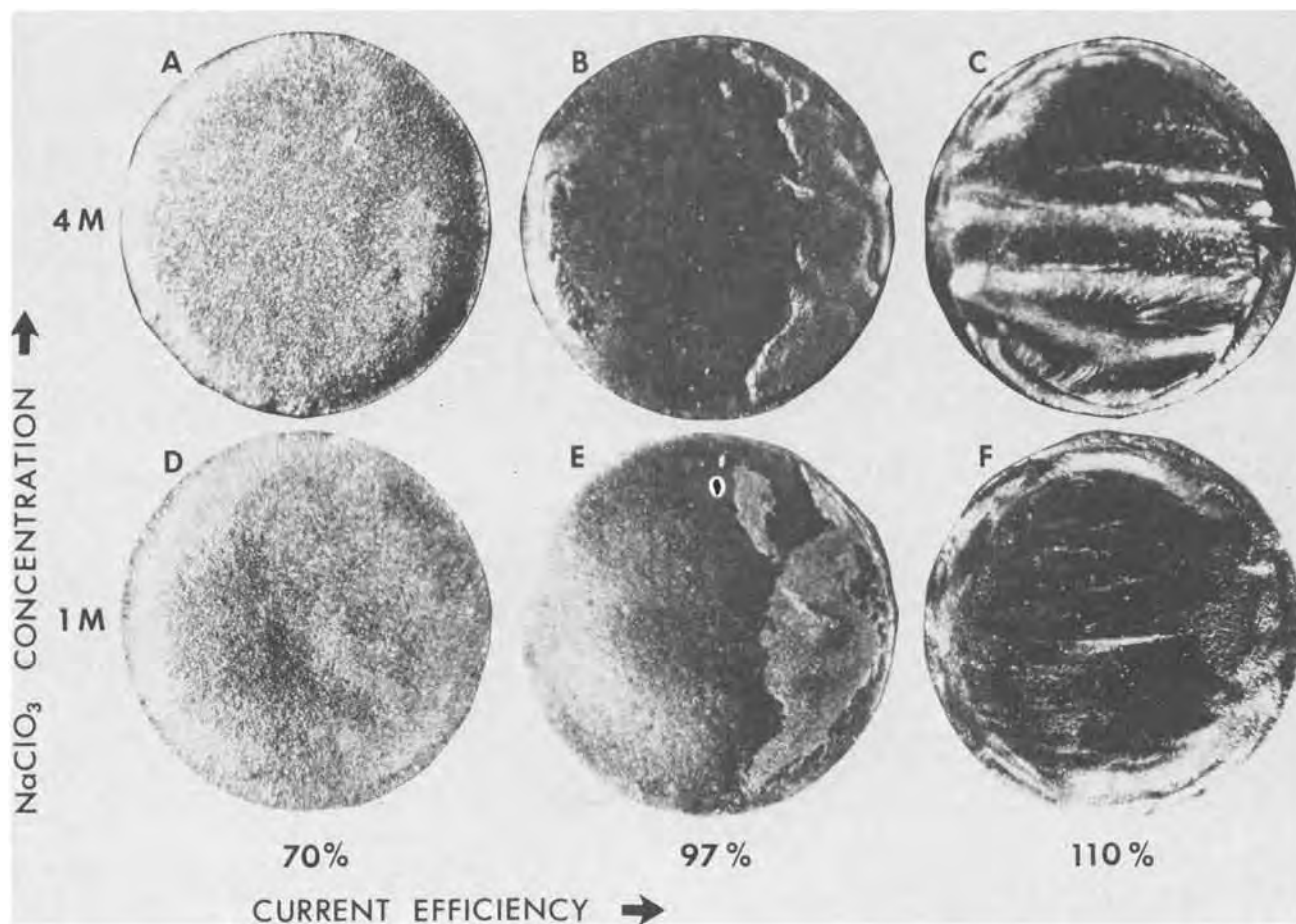


Fig. 5. ECM machined surfaces of Mild Steel I: the effect of current efficiency and NaClO<sub>3</sub> concentration. The current densities for the surfaces shown are: A, 4.6 A/cm<sup>2</sup>; B, 9.4 A/cm<sup>2</sup>; C, 54 A/cm<sup>2</sup>; D, 11 A/cm<sup>2</sup>; E, 21 A/cm<sup>2</sup>; and F, 80 A/cm<sup>2</sup>.



to  $O_2$ , the film has to be electronically conductive. In  $NaNO_3$  an electronically conductive film was also found, which was thought to be  $Fe_3O_4$  (7, 13).

**Transition stage.**—The transition stage for current densities between points a and b on the current efficiency curves: This stage corresponds to the region in Fig. 3 and 4 where the current efficiency increases from nearly 0 to 100% as the current density increases.

It was found in a previous mass balance study (11) that the total current efficiency for metal dissolution plus oxygen generation is 100%. The increase in the metal removal efficiency results from the breakup of the oxide film which starts with the formation of localized pits in the porous film (14).

At present, there are three models given in the literature to explain how the anodic oxide film is broken up in the transpassive region. They are the penetration (15), the mechanical mechanism (16), and the ion exchange (13) models. In this report no attempt is made to discuss these models. However, it is interesting to note that all three models suggest that the breakup of the anodic oxide film has to be initiated by the process of anion adsorption. Thus, the degree of the breakdown is proportional to the anion concentration and the anode potential (or current density), in agreement with the results of this current efficiency study. Here, due to breakdown of the film, the current efficiency increases with not only the anode potential (or current density) but also with the  $NaClO_3$  concentration. Similar phenomena were also observed during ECM of mild steel in  $NaNO_3$  (7).

**Metal dissolution stage.**—The metal dissolution stage for current densities above point b on the current efficiency curves: In this stage, the anode surface is highly polished, the current efficiency is greater than 100%, and no oxygen is formed. The absence of oxygen formation in this stage is also supported by the absence of a potential plateau at 1.6V (vs. SCE) (Fig. 2C1). At the present time there is no evidence on which to base an explanation of why the current efficiency is greater than 100%. There are two possible reasons: one is due to severe grain boundary attacks and the other is metal dissolution by chemical oxidation. However, grain boundary attack may be unlikely since a bright, polished surface is obtained.

For electropolishing, Hoar and his co-workers (15) have suggested that brightness results from the presence of a thin "contaminated" anodic layer which is ionically conductive and, thus, provides an even attack on differently oriented grains. Based on this electropolishing theory, the bright surface obtained in the metal dissolution stage of the transpassive region can be attributed to the presence of an anodic layer with high ionic conductivity. This layer, which is different from the previously mentioned electronically conductive oxide film, is probably formed by salt precipitation from a saturated solution (5, 14).

The nearly parallel relationship between the polarization curves for 2 and 4M  $NaClO_3$  in the metal dissolution stage indicates that the rate of iron dissolution is proportional to the chlorate concentration. The decrease in anode potential when Re was reduced to 4000

(Fig. 1) can be associated with an increase in the acidity of the solution near the anode (17). The  $H^+$  concentration can influence the solubility of the salt and, thus, the layer structure. However, such a change does not affect the ECM performance significantly because there are no apparent changes in the surface finish or in the current efficiency on reducing the flow rate.

### Conclusions

From the results of this study, it may be concluded that the transpassive dissolution of mild steel in  $NaClO_3$  takes place in three reaction stages depending on current density (applied potential). In the first stage, at low current densities, the mild steel surface is covered with an electronically conductive oxide film, and the current is consumed in oxygen evolution. In the second stage, at higher current densities, the oxide film is broken apart and the metal starts to dissolve into the electrolyte. The breakdown of the oxide film is started by the formation of localized pits in the film. In the third stage at still higher current densities, the oxide film has completely disappeared, and the high-rate metal dissolution takes place with a current efficiency greater than 100%. The metal surface after dissolution in this final stage is found to be highly polished probably due to the presence of a precipitated salt layer on the anode.

Manuscript submitted May 24, 1973; revised manuscript received Sept. 4, 1973.

Any discussion of this paper will appear in a Discussion Section to be published in the December 1974 JOURNAL.

### REFERENCES

1. M. A. LaBoda and M. L. McMillan, *Electrochem. Technol.*, **5**, 340 (1967).
2. J. P. Hoare, *Nature*, **219**, 1034 (1968); *This Journal*, **117**, 142 (1970).
3. J. P. Hoare, K.-W. Mao, and A. J. Wallace, Jr., *Corrosion*, **27**, 211 (1971).
4. D. Landolt, *This Journal*, **119**, 708 (1972).
5. D. T. Chin and A. J. Wallace, Jr., *ibid.*, **120**, 1487 (1973).
6. K.-W. Mao, *ibid.*, **120**, 1056 (1973).
7. D. T. Chin and K.-W. Mao, *J. Appl. Electrochem.*, In press.
8. A. M. Sukhotin and K. M. Kartashova, *Corrosion Sci.*, **5**, 393 (1965).
9. H. E. Freer, J. B. Hanley, and G. D. S. MacLellan, in "Fundamentals of Electrochemical Machining," C. L. Faust, Editor, p. 103, The Electrochemical Society Softbound Symposium Series, Princeton, N. J. (1971).
10. D. Landolt, R. H. Muller, and C. W. Tobias, *This Journal*, **118**, 36 (1971).
11. K.-W. Mao, *ibid.*, **118**, 1870 (1971).
12. J. P. Hoare, M. A. LaBoda, M. L. McMillan, and A. J. Wallace, Jr., *ibid.*, **116**, 199 (1969).
13. K.-W. Mao, M. A. LaBoda, and J. P. Hoare, *ibid.*, **119**, 419 (1972).
14. D. T. Chin, *ibid.*, **118**, 174 (1971).
15. T. P. Hoar, D. C. Mears, and G. P. Rothwell, *Corrosion Sci.*, **5**, 279 (1965).
16. T. P. Hoar, *ibid.*, **7**, 341 (1967).
17. R. W. Powers and J. F. Wilfore, in "Fundamentals of Electrochemical Machining," C. L. Faust, Editor, p. 135, The Electrochemical Society Softbound Symposium Series, Princeton, N. J. (1971).



# The Effect of Ion Implantation upon the Dissolution of Anodic Tantalum Oxide in Buffered Hydrogen Fluoride

J. P. S. Pringle\*

Chalk River Nuclear Laboratories, Atomic Energy of Canada Limited, Chalk River, Ontario, Canada

## ABSTRACT

A very precise sectioning technique for measuring concentration profiles in anodic tantalum oxide is based on the slow dissolution of the oxide in HF almost saturated with  $\text{NH}_4\text{F}$ . Since many of the profiles to be measured were for radioactive isotopes incorporated by ion implantation, it was necessary to establish whether ion implantation had any effect on the technique. To this end, several stable isotopes were implanted at fluences up to  $10^{17}$  ions/cm<sup>2</sup>. It was found that heavy ions gave rise to sputtering and accelerated the stripping of the oxide; by contrast, hydrogen ions gave no sputtering and decelerated the stripping. The accelerated stripping was attributed to the physical presence of the implanted ions, while the decelerated stripping may be due to the formation of hydrogen bonds between neighboring oxygen atoms in the oxide. When  $10^{17}$  ions/cm<sup>2</sup> of hydrogen were implanted, a carbonaceous deposit formed on the oxide surface due to the radiative polymerization of adsorbed pump oil molecules; this deposit prevented the oxide from dissolving at all. Implantations involving radioactive species were usually much less than  $10^{15}$  ions/cm<sup>2</sup>, and the accelerated stripping was often negligible; when present, it had no effect on the profile measurements.

A fundamental problem in metal oxidation is the nature of the atomic movements leading to the formation of an oxide film. To study these movements, tracer species must be incorporated, and their concentration profiles determined before and after the oxidation event. In the present series of experiments, the tracer species are usually incorporated in anodic tantalum oxide by ion implantation, and the profiles measured by means of the highly precise sectioning technique described previously (1). Range profiles for implanted ions have been surveyed elsewhere (2), and these constitute the initial profiles for the tracers. By studying the changes that occur on further anodization, information on the tantalum and oxygen movements has been obtained (3, 4).

The sectioning technique is based on slow dissolution of the oxide in HF almost saturated with  $\text{NH}_4\text{F}$  and depends for its success on the uniformity of the dissolution (1). Etching processes are, however, notoriously sensitive to the experimental conditions, as Vermilyea (5) has demonstrated for the anodic oxide itself. He annealed samples at different temperatures for varying times and found that the etching rate decreased with both increasing temperature and increased time at a particular temperature. These studies were performed with concentrated HF as etchant, but similar results have been obtained here using the HF- $\text{NH}_4\text{F}$  reagent. Hill (6) has implanted 15 keV electrons and observed that the dissolution rate in HF- $\text{NH}_4\text{F}$  decreased. Ion implantation was therefore very likely to have an effect, and because the extreme precision of the technique was important for subsequent work, it became necessary to find out what it was.

Effects due to implantation were readily apparent in the course of the range profile measurements reported elsewhere (2). These measurements were made with radioactive isotopes, and so the implantation fluences were relatively small ( $< 10^{15}$  ions/cm<sup>2</sup>). Nevertheless, an image of the implanted area would frequently develop on sectioning, due to the formation of different interference colors on the implanted and nonimplanted areas. Since the interference color is determined by

film thickness, the oxide on the implanted area was dissolving at a different rate; from the character of the interference colors, this dissolution could be either faster or slower.

To study the process under more favorable conditions, the anodic oxide was implanted with stable isotopes to much higher fluences ( $10^{16}$ - $10^{17}$  ions/cm<sup>2</sup>). This greatly enhanced the effects and allowed their nature to be elucidated. At the same time, another phenomenon became apparent, for an image of the implanted area would now appear solely as the result of implantation. Comparison of the interference colors showed that the apparent thickness of the implanted oxide could again be either greater or less than that of the surrounding nonimplanted oxide. Several different effects therefore occurred as a result of implantation.

The present paper examines these effects with particular reference to their influence on the sectioning procedure.

## Experimental Methods

*Preparation, anodization, and sectioning of experimental samples.*—Tantalum coupons,  $3.5 \times 1.0$  cm<sup>2</sup>, were cut from 0.015 in. (0.037 cm) sheet supplied by the Fansteel Metallurgical Corporation, and chemically polished as described previously (1). Anodizations were normally performed at a constant current density of 1 mA/cm<sup>2</sup> in 0.1M  $\text{H}_2\text{SO}_4$  maintained within 0.2°C of 25°C by means of a water bath. When oxides thicker than 3500Å were required, the electrolyte was changed to 0.01M butyric acid. The anodic films were sectioned by dissolving successive layers in concentrated HF almost saturated with  $\text{NH}_4\text{F}$ . Full details have been presented elsewhere (1).

*Film thickness measurement.*—Oxide thicknesses were measured by means of the spectrophotometric method due to Young (7). The wavelength,  $\lambda$ , for the  $n$ th order interference minimum was measured and related to the oxide thickness,  $h$ , by

$$\lambda = 2\eta \cdot \cos \phi \cdot (h - X) / (n - \frac{1}{2}) \quad [1]$$

where  $\eta$  is the refractive index of the oxide,  $\phi$  the angle of refraction in the oxide, while  $X$  accounts

\* Electrochemical Society Active Member.

Key words: tantalum, anodic oxidation, oxide dissolution, ion implantation, concentration profiles.

for the phase changes on reflection at the metal/oxide and oxide/air interfaces. Both  $\eta$  and  $X$  are functions of  $\lambda$ , and so the variation of  $h$  with  $\lambda$  had to be calibrated (7, 1). This meant, in effect, that the variation of  $\eta$  and  $X$  with  $\lambda$  had to be calibrated, and the success of the calibration showed that these variations were effectively independent of the oxide thickness. The calibration could be strictly applied, of course, only to oxide films formed under the same conditions; in this case, 1 mA/cm<sup>2</sup> in 0.1M H<sub>2</sub>SO<sub>4</sub> at 25°C (1). It was assumed, however, that the films formed in 0.01M butyric acid would be similar, and indeed there was no reason to think otherwise.

Masing, Orme, and Young (8) have shown that the refractive index varies slightly with temperature and current density when the anodization is performed in 0.1M H<sub>2</sub>SO<sub>4</sub>, and Dell'Oca and Young (9) have shown that it decreases when phosphorus is incorporated from 0.23N H<sub>3</sub>PO<sub>4</sub> electrolyte. It seemed very probable, therefore, that insertion of the foreign atoms by ion implantation would also change the optical properties of the oxide, and ellipsometric measurements with J. Ord at the University of Waterloo showed that this was indeed so.

Anodized tantalum coupons were implanted with  $3.8 \times 10^{16}$  to  $2.5 \times 10^{17}$  <sup>40</sup>Ar<sup>+</sup>/cm<sup>2</sup> at 39 keV so that thicknesses measured spectrophotometrically could be compared with those measured ellipsometrically. The agreement was within experimental error for the non-implanted areas, but the ellipsometric measurements on the implanted area were abnormal; this clearly showed that the optical properties of the oxide had been changed by the implantation. The abnormality decreased with decreasing implantation fluence, and extrapolation of the results suggested that it would disappear at a fluence of about  $10^{16}$  Ar<sup>+</sup>/cm<sup>2</sup>. Since most of the implantations reported here were made with fluences at or below this figure, the use of the spectrophotometric method to measure oxide thicknesses on the implanted areas should generally be satisfactory. When a specimen implanted to  $5.6 \times 10^{16}$  <sup>40</sup>Ar<sup>+</sup>/cm<sup>2</sup> was reanodized, however, the abnormality was much increased; considerations of time and distance precluded a more detailed investigation.

Thickness errors quoted in the present paper are standard errors, calculated according to the second procedure described in the previous paper (1).

*Testing for the uniformity of the effects due to ion implantation.*—The interference color developed by an anodic film on tantalum is very intense, and its hue is proportional to the film thickness. Near 420, 1760, and 3180Å, the hue changes very rapidly as the first, second, and third order interference minima traverse the middle region of the visible spectrum. These rapid changes, from brown (420Å) or red at thicknesses below the specified thicknesses to blue just above, proved very useful for monitoring the uniformity of the thickness on the implanted area, and hence for monitoring the uniformity of the effects associated with ion implantation. Thickness differences as small as 10Å could readily be detected in these favored regions; gross differences could of course be detected at any thickness.

*Implantation method.*—Ion implantation by means of the mass separator at Chalk River has been discussed in previous papers from this laboratory (10, 11). Positive ions are accelerated electrostatically to 40 keV and then passed through a magnetic field which separates them into their isotopic components. The latter were focused into lines 4 cm high  $\times$  0.1 cm wide on a fluorescent screen (12) in front of the target; a hole in this screen allowed the desired isotope to strike the target.

Since it was very important that the stable isotopes be implanted at uniform intensity over the specified area, the following procedure was adopted. Rutherford scattering experiments by Bellavance (13), using <sup>209</sup>Bi implanted in Si, had shown that the intensity of the isotopic beams varied along their 4 cm height, reach-

ing a plateau-like crest between 2 and 2.5 cm from the top. The hole in the fluorescent screen was therefore stopped down to this 0.5 cm in height, and to 0.8 cm in width. By modulating the magnet current, it was possible to sweep the beam horizontally across this width every 30 sec, thus obtaining a uniform dose over an area of  $0.5 \times 0.8$  cm<sup>2</sup>. This was just enough for the spectrophotometric method of measuring oxide thickness, which requires an area of  $0.2 \times 0.8$  cm<sup>2</sup> (1). Except as noted in the individual experiments, the interference colors on the implanted areas were just as uniform as those on the nonimplanted areas.

The total charge deposited in the target was used as a measure of the implantation fluence. For this purpose, the targets were mounted at the bottom of Faraday cups, 2 cm deep, behind a grid made of 0.0005 in. tungsten wire; the grid was maintained at -90V to suppress the emission of secondary electrons. Difficulties connected with the measurement of heavy ion beam currents are notorious; in estimating the fluence, it was necessary to assume that the beam consisted entirely of singly charged positive ions, and that the Faraday cups were 100% efficient. The first assumption is approximately correct, at least for radioactive species, since the range profile measurements in the next paper (2) show that less than 10% of the nuclei implant as neutral atoms. The efficiency of the Faraday cups was, however, in considerable doubt.

The insulation of the cups was not sufficient to permit retarding potentials on the target holder, and so really low implantation energies were unattainable (10). By varying the accelerating voltage, however, implantations were performed at 25, 40, and 55 keV. The maximum fluence that could be implanted in an hour, using the most abundant isotope, 99.6% <sup>40</sup>Ar, was about  $10^{17}$  ions/cm<sup>2</sup>; the minimum fluence obtained with a stable isotope was  $10^{11}$  ions/cm<sup>2</sup>, using the 0.090% abundant <sup>120</sup>Xe.

The reproducibility of the results was found to depend markedly on the way in which the implantations were performed. Normally, several specimens at a time were mounted in the mass separator and implanted in succession. Such specimens gave excellent reproducibility amongst themselves, but the results could differ by as much as 50% from similar implantations on other occasions. This suggested a lack of consistency in measuring the beam currents, but its origin was uncertain. When making comparisons, therefore, it is necessary to specify whether the results were obtained in the same series of implantations or in different series.

*Presentation of the results.*—A special format has been used to present the results. The independent variable is the change in oxide thickness on the nonimplanted area as a consequence of further treatment; thinning by dissolution in the HF-NH<sub>4</sub>F reagent or thickening by anodizing. The dependent variable is the implantation differential, which is defined as the oxide thickness on the implanted area less that on the non-implanted area. A positive implantation differential, therefore, shows that the implanted area exists as a mesa in the surrounding nonimplanted area, while a negative differential indicates that it is present as a depression.

In sectioning experiments, this format provides an integral record of the difference between the stripping rates on the implanted and nonimplanted areas, so that the difference itself is proportional to the slope of the record. Since the stripping rate of the nonimplanted oxide is constant (1), any changes in the slope are due to changes in the stripping rate on the implanted area. A downward slope shows that the implanted oxide is dissolving faster; in what follows, this situation is described as accelerated stripping. By analogy, an upward slope is described as decelerated stripping. Three other terms are used. The initial implantation differential is the differential observed as the result of implantation alone, while the final implantation differential refers

to the constant value obtained at the end of an experiment. The magnitude of the accelerated or decelerated stripping is then defined as the difference between these two differentials.

Ellipses drawn around each experimental point define the 95% confidence limits; the major and minor radii are equal to twice the appropriate standard errors. The latter are somewhat larger than those recorded elsewhere in these experiments (2-4), since they correspond to errors in the differences between two thickness measurements, not to errors in the thickness measurements themselves.

### Experimental Results

**Implantations with xenon.**—The general features of the results obtained with heavy ions are illustrated in Fig. 1. When  $^{136}\text{Xe}^+$  ions were implanted at 40 keV to a total fluence of  $10^{16}/\text{cm}^2$ , the initial implantation differential was found to be  $-68\text{\AA}$ . This thickness of oxide had therefore been removed, obviously by sputtering. On sectioning the oxide, the implanted area began by dissolving faster, so that accelerated stripping (downward slope) was observed. After a small amount of decelerated stripping (upward slope), which may not be a real effect since it was only observed on two occasions, the implantation differential reached its constant final value of  $-138\text{\AA}$ .

The sputtering and accelerated stripping are obviously a function of the implantation fluence, since no such effects were observed in the sample implanted with  $10^{12}$   $^{126}\text{Xe}^+/\text{cm}^2$  at 40 keV. Additional experiments showed that accelerated stripping would only become noticeable (final implantation differential  $\sim -10\text{\AA}$ ) at  $10^{14}$  ions/ $\text{cm}^2$ , and sputtering (initial implantation differential  $\sim -10\text{\AA}$ ) only at  $10^{15}$  ions/ $\text{cm}^2$ .

**Implantations with krypton.**—A more detailed examination of these effects was performed with krypton, since this could be labeled conveniently with the long-lived radioisotope,  $^{85}\text{Kr}$ . Samples of this fission product were obtained from Oak Ridge, and because the volume of gas was insufficient for the operation of the separator, they had to be diluted with stable gas. By diluting with xenon, the  $^{85}\text{Kr}^+$  could be implanted in almost carrier-free form, with an implantation fluence

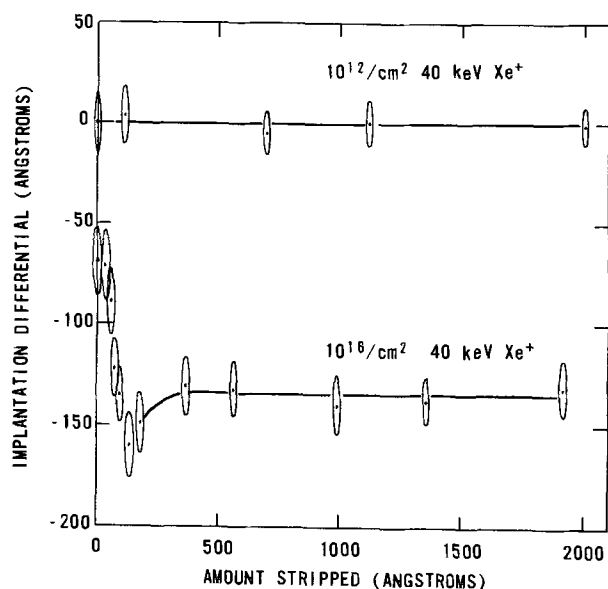


Fig. 1. Implantation differentials observed with xenon to illustrate the form of the results obtained. The amount stripped is the thickness of oxide dissolved from the nonimplanted portion of the specimen; the implantation differential is the thickness of oxide remaining on the implanted area less that remaining on the nonimplanted area. Error ellipses have been drawn at twice the standard errors round each point to indicate the 95% confidence limits. Same series of implantations.

of  $10^{13}$  ions/ $\text{cm}^2$  or less. To obtain higher fluences, the  $^{85}\text{Kr}$  sample was diluted with stable krypton; by sweeping the mass 84 and mass 85 beams over the surface of the target,  $^{84}\text{Kr}^+$  (natural abundance 56.90%) and  $^{85}\text{Kr}^+$  could be implanted together. Under these conditions, of course, the vast majority of the implanted ions were  $^{84}\text{Kr}$ , the  $^{85}\text{Kr}$  merely acting as a tracer.

Figure 2 shows the results obtained when  $10^{16}$  ions/ $\text{cm}^2$  of  $^{84}\text{Kr}^+$  and  $^{85}\text{Kr}^+$  were implanted together at 40 keV. The initial implantation differential was  $-78\text{\AA}$ , very similar to that observed with xenon at the same fluence. Like the latter, therefore, it was attributed to sputtering. To show that material really had been removed from the specimen, an oxide film was implanted with 40 keV  $^{85}\text{Kr}^+$  only, and the activity counted;  $10^{16}$   $^{84}\text{Kr}^+/\text{cm}^2$  were then implanted into exactly the same area, and the  $^{85}\text{Kr}$  activity recounted. Two such specimens gave identical results; only 68% of the original  $^{85}\text{Kr}$  activity remained after the  $^{84}\text{Kr}$  implantation.

The experiment in Fig. 2 also showed that accelerated stripping would cease when all the krypton had been removed, since the fraction of the  $^{85}\text{Kr}$  activity remaining at the last two points in the figure was 1.2 and 0.2%. A fraction of 1.2% is equivalent to approximately  $10^{14}$  ions/ $\text{cm}^2$ , which is just about the detection limit for accelerated stripping as determined from the xenon experiments. Once the krypton had been removed, the oxide remaining on the implanted area was oxide that had not been implanted at all, and so its stripping rate should be the same as that on the nonimplanted area. The constancy of the final implantation differential, as illustrated in Fig. 1, showed that this was indeed the case.

Accelerated stripping is thus related to the presence of the implanted ions and can be interpreted in two ways. It could be a radiation damage effect, in which the breaking of the tantalum-oxygen bonds leads to more rapid dissolution of the individual atoms; effects of this type have been reported in semiconductors (14). Alternatively, it could be due to the physical presence of the implanted atoms themselves. Three experiments were performed to distinguish between these possibilities.

The first experiment was to reanodize a specimen implanted with krypton. Both tantalum and oxygen migrate during the reanodization (3), and all the oxygen atoms take part in this process (4); it may reasonably be inferred that all the tantalum atoms would behave likewise (3). On reanodization, then, all

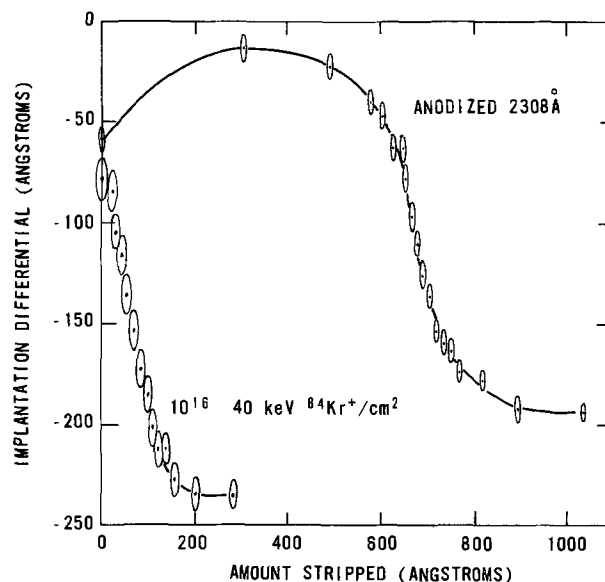


Fig. 2. Implantation differentials with krypton to illustrate the effect of reanodization on an implanted noble gas. Different series of implantations.

the atoms in the oxide rearrange to new positions, and so any structural damage should anneal out. If, therefore, the accelerated stripping is due to radiation damage, it should quickly disappear on further anodization. If, on the other hand, it is related to the physical presence of the implanted krypton atoms, it will still be associated with them after reanodization.

Another specimen was implanted with 40 keV  $^{84}\text{Kr}^+$  and  $^{85}\text{Kr}^+$  to  $10^{16}$  ions/cm<sup>2</sup> and then reanodized so that the oxide was thickened by 2308Å. On sectioning, most of the  $^{85}\text{Kr}$  label was lost as between 600 and 700Å of oxide was being removed from the nonimplanted area. Reference to Fig. 2 will show that this is just the region in which accelerated stripping was found. The latter is therefore still present after reanodization, to much the same extent as before, and still associated with the krypton atoms.

This argument is not quite conclusive, however, because it could be argued that the radiation damage gives rise to "dead" oxide; that is, oxide which does not take part in the rearrangement process. Such dead oxide would presumably approximate rather well to an inert immobile marker on further anodization, and since krypton behaves similarly (3), they would both fortuitously finish up at the same place in the final oxide. To resolve this ambiguity, the experiment was repeated with an implant known to migrate out of the oxide entirely on reanodization.

**Implantations with copper.**—The element chosen was copper, and two samples were implanted with 40 keV  $^{63}\text{Cu}^+$  and  $^{64}\text{Cu}^+$  by sweeping over both mass numbers as before. The stable  $^{63}\text{Cu}^+$ , natural abundance 69.09%, provided the implantation fluence of  $10^{16}$  ions/cm<sup>2</sup>, while the radioactive  $^{64}\text{Cu}^+$ , prepared by ( $n,\gamma$ ) reaction in the NRX reactor, acted as the tracer. One sample had an initial implantation differential of -62Å, and was sectioned to establish that accelerated stripping would indeed occur with copper implants. Figure 3 shows that it did, the final implantation differential being -129Å. The other sample, with an initial implantation differential of -63Å, was then reanodized to thicken the oxide by 1360Å. No copper remained after this treatment, as demonstrated by the complete absence of  $^{64}\text{Cu}$  activity. On sectioning, no definite evidence for accelerated stripping was obtained either (Fig. 3). The accelerated stripping must therefore be due to the physical presence of the implanted ions.

**Implantations with argon.**—The third experiment was to implant to the same fluence at different energies, and to different fluences at the same energy. If accelerated stripping is due to radiation damage, its magnitude should depend not only on the number of atoms implanted, but also on their energy; if, however, it is merely due to their physical presence, it should depend on number only. Since comparisons are involved, it is first necessary to establish the reproducibility of the results obtained in the same series of implantations under the same conditions. Three samples were implanted with  $10^{16}$   $^{40}\text{Ar}^+$ /cm<sup>2</sup> at 39 keV, whereupon the initial implantation differentials were found to vary from -14 to -18Å, and the final differentials from -213 to -220Å; these results are therefore identical within the experimental standard error of 3Å. Figure 4 then indicates that the magnitude of the accelerated stripping is independent of energy, while Fig. 5 shows that there most certainly is a dependence on number. The hypothesis that the accelerated stripping is due to the physical presence of the implanted atoms is therefore confirmed.

One further test for the nature of the accelerated stripping was to heat the oxide. Radiation damage frequently anneals on heating, and Kelly and Brown (15) have shown that no significant amounts of implanted noble gas are lost from the anodic oxide below 600°C. An oxide film implanted with  $10^{16}$   $^{40}\text{Ar}^+$ /cm<sup>2</sup> at 39 keV was therefore heated to 250° for one day,

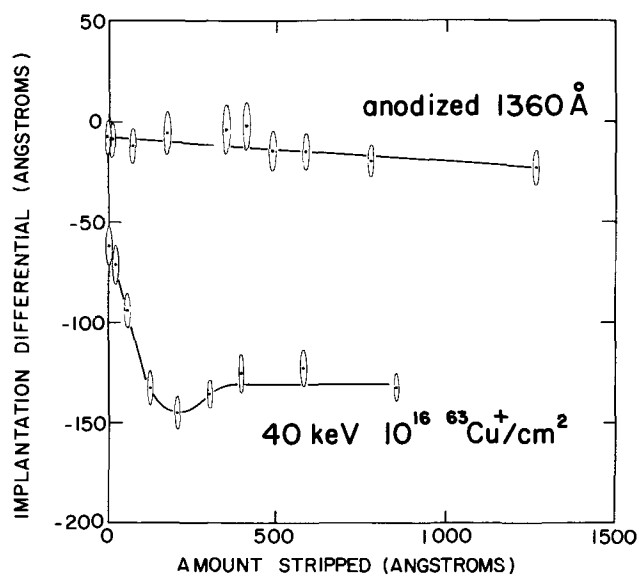


Fig. 3. Implantation differentials with copper to illustrate the effect of reanodization when the implanted species migrates out of the oxide. Same series of implantations.

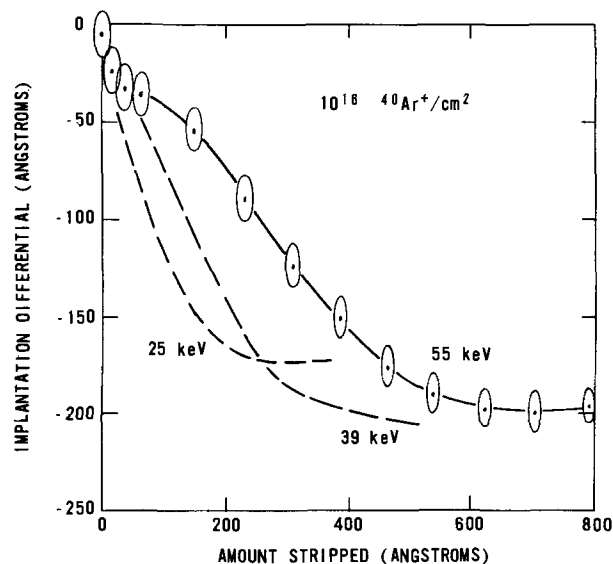


Fig. 4. Implantation differentials with argon to demonstrate the effect of varying the implantation energy. To avoid confusion, a trend line only has been drawn for the results at 25 and 39 keV. Same series of implantations.

with the results illustrated in Fig. 6. Accelerated stripping is present and is even more pronounced than for an unheated specimen; the final implantation differential is in fact about twice as great and is reached after the removal of only about half the usual amount of oxide. As Vermilyea (5) has shown, heating to 250°C for one day causes the nonimplanted oxide to dissolve at half its normal rate. The observed results can then be interpreted by assuming that the oxide on the implanted area continues to dissolve at the same rate as before, so that heating has no effect on the acceleration in the stripping. This is certainly consistent with the continued presence of the implanted atoms, but not conclusive evidence against radiation damage because the rate at which the latter would anneal out is impossible to predict.

If the accelerated stripping is due to the physical presence of the implanted atoms, it should be possible to demonstrate a relationship with their concentration profile. This is possible and will be discussed in a later paper (16).

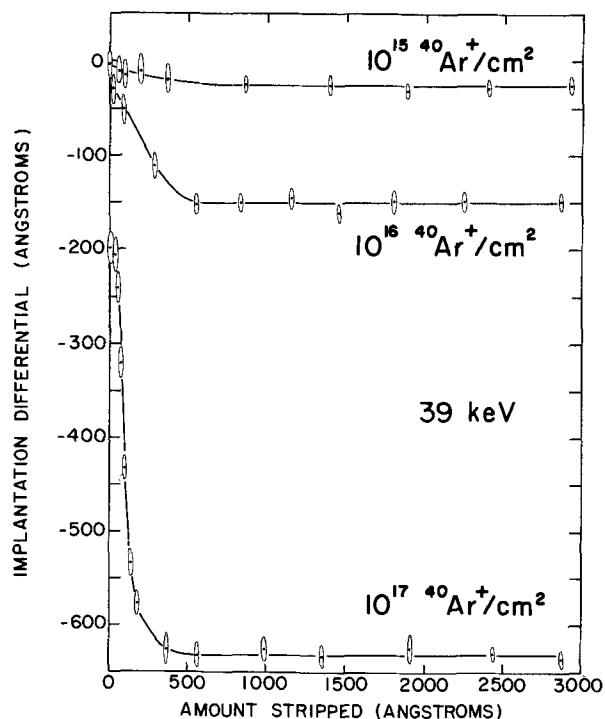


Fig. 5. Implantation differentials with argon to demonstrate the effect of implantation fluence. Same series of implantations.

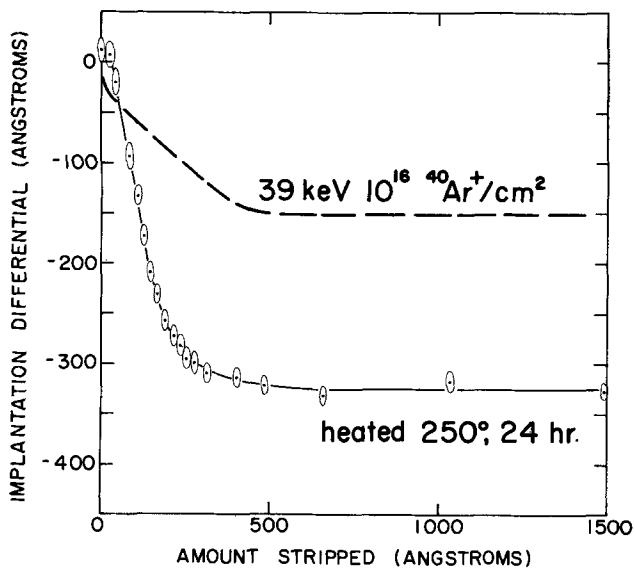


Fig. 6. Implantation differentials with argon to illustrate the effect of heating an implanted sample. Different series of implanted samples.

The initial implantation differentials in Fig. 5 were effectively 0, -10, and -195Å for the  $10^{15}$ ,  $10^{16}$ , and  $10^{17}$   $^{40}\text{Ar}^+/\text{cm}^2$  implantations, respectively. Sputtering was therefore negligible at  $10^{15}$   $^{40}\text{Ar}^+/\text{cm}^2$  and barely detectable at  $10^{16}$   $^{40}\text{Ar}^+/\text{cm}^2$ , in marked contrast to the results with  $^{63}\text{Cu}^+$ ,  $^{84}\text{Kr}^+$ , and  $^{136}\text{Xe}^+$  at the same fluence. This observation is much as expected, since the sputtering efficiency is known to decrease with decreasing mass (17). At  $10^{17}$   $^{40}\text{Ar}^+/\text{cm}^2$ , the effect of the sputtering was clear and unmistakable; some preliminary experiments indicated that it was probably not proportional to fluence, at least between  $10^{16}$  and  $10^{17}$  ions/ $\text{cm}^2$ .

Argon-40 ions were implanted at 39 keV rather than 40 keV for a trivial reason connected with the operation of the mass separator.

*Implantation with carbon.*—Accelerated stripping has been observed thus far with a metallic implant, copper, and with several noble gases. The chemical nature of the implant therefore appeared of small importance, and additional confirmation was obtained by implanting the nonmetal carbon. Accelerated stripping of the usual magnitude was observed with this species also.

*Implantation with hydrogen.*—Hydrogen implantations were performed with  $^1\text{H}_2^+$  instead of  $^1\text{H}^+$ , owing to its greater beam current in the mass separator. Unlike all the other species investigated, hydrogen implants decelerated the stripping.

When  $10^{17}$   $^1\text{H}_2^+/\text{cm}^2$  were implanted at 40 keV, the initial implantation differential was found to be +99Å, as shown in Fig. 7. On sectioning, the implanted area failed to dissolve at all, and so the implantation differential increased by the rate at which oxide was being removed from the nonimplanted area. The positive differential at the start, coupled with this failure to dissolve, suggested that the oxide surface was covered with a layer of contaminant, and that this inhibited the dissolution in the  $\text{HF-NH}_4\text{F}$  reagent. As sectioning proceeded, however, the oxide on the implanted area did eventually start to dissolve, but the dissolution was slow and very nonuniform, as demonstrated by the interference colors of the remaining oxide. So nonuniform did these become, in fact, that further thickness measurements were impossible.

Very similar effects were observed in the reanodization experiment depicted in Fig. 8. Though implanted to the same nominal  $10^{17}$  ions/ $\text{cm}^2$  dose as before, the initial implantation differential was only +53Å; this illustrates the reproducibility between different series of implantations. When the oxide thickness on the nonimplanted area was reanodized to 10Å, the implantation differential jumped to +143Å; such a large increase must be attributed to a change in the optical properties of the contaminant layer.

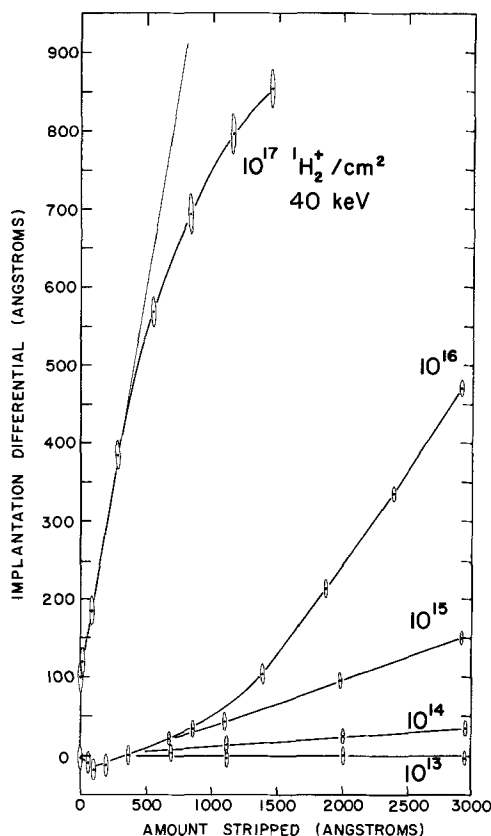


Fig. 7. Implantation differentials observed with hydrogen to demonstrate the effect of implantation fluence. The straight line tangent to the curve at  $10^{17}$   $^1\text{H}_2^+/\text{cm}^2$  indicates zero stripping on the implanted area. Same series of implantations.

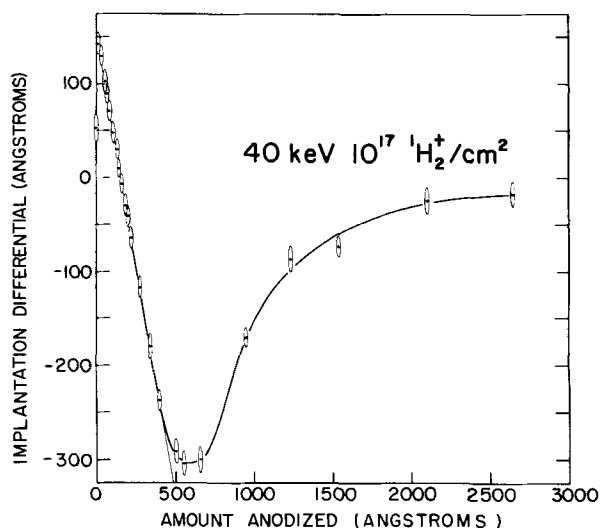


Fig. 8. Implantation differentials with hydrogen to illustrate the effect of reanodization. The abscissa is the thickness increase on the nonimplanted area.

Thereafter, the implantation differential decreased as fast as the oxide thickness on the nonimplanted area increased, until it became strongly negative. As in the initial stages of stripping, the oxide on the implanted area had been protected against further anodization by the contaminant layer; its thickness therefore remained constant, and its interference color unchanged. On continued anodizing, however, the protection again broke down at certain places, so that the resulting thickness variations gave rise to a non-uniform interference color on the implanted area. As the breakdown became more general, these thickness variations disappeared owing to the self-healing properties of the anodization process (1); the interference color was then again uniform, and the same as that on the nonimplanted area.

Sewell kindly verified the presence of carbon in the contaminant by detecting the characteristic K x-ray emitted during bombardment with 1800 eV electrons (18). An anodized tantalum specimen was implanted with  $5 \times 10^{16}$ ,  $10^{17}$ , and  $2 \times 10^{17}$   $^1\text{H}_2^+/\text{cm}^2$  on different areas of the surface, and Sewell found the carbon deposited in each area to be 0.40, 0.56, and 0.96 mg/cm<sup>2</sup>, respectively; the standard error in these figures is relatively large, at about 25%, owing to the difficulty of obtaining accurate standards for calibration. If the fractional density of the carbon in the contaminant layer is assumed unity, the thickness of the layers will be 40, 56, and 96 Å, respectively. The figure of 56 Å for  $10^{17}$   $^1\text{H}_2^+/\text{cm}^2$  agrees rather well with the 99 and 53 Å recorded by the spectrophotometric technique, but the agreement is fortuitous.

Almost certainly, therefore, the contaminant was a polymer produced by the radiation decomposition of adsorbed hydrocarbons (2); the latter would be present in the atmosphere of the mass separator as vapor from the pump oils used to maintain the vacuum. The polymer would not itself be attacked by the hydrofluoric acid, but would probably contain weak spots through which the acid could penetrate to dissolve the oxide, and through which the current could start flowing on reanodization. Polymer formation would also occur during the implantation of heavy ions, but in this case, typified by the  $10^{17}$  39 keV  $^{40}\text{Ar}^+/\text{cm}^2$  sample of Fig. 5, the contaminant layer would be removed by sputtering as fast as it was formed.

At implantation fluences of  $10^{16}$   $^1\text{H}_2^+/\text{cm}^2$  or less, the situation was entirely different. The initial implantation differential was essentially zero, and no decelerated stripping occurred immediately; the effect developed only as sectioning was prolonged. Furthermore, the interference color on the implanted area was al-

ways uniform. This decelerated stripping cannot, therefore be due to the presence of a contaminant layer, but must be related in some way to the presence of the hydrogen itself. The mean range for 20 keV  $^1\text{H}^+$  ( $\equiv$  40 keV  $^1\text{H}_2^+$ ) can be estimated from data in the literature (19) as being about 3000 Å. Up to this point, therefore, the hydrogen concentration will increase, and any effect associated with its presence should likewise increase, as observed in Fig. 7.

When the implantation energy was reduced to 25 keV, the range of the hydrogen ions decreased, and a more complete record of the decelerated stripping effect could be obtained. The result (Fig. 9) appears to be an S-shaped curve similar to those observed with accelerated stripping. Furthermore, comparison of Fig. 4 and 9 will show that the effect of varying the implantation energy seems much the same for both types of stripping, always provided that due allowance is made for the much greater range of the hydrogen ions. Despite the incompleteness of the evidence, therefore, it seems reasonable to conclude that the magnitude of the decelerated stripping effect is independent of the implantation energy, while Fig. 7 shows that there is once again a most definite dependence on the implantation fluence.

This form of decelerated stripping can therefore be interpreted in the same two ways as accelerated stripping, and the same arguments apply. The independence of implantation energy suggests that it is the physical presence of the hydrogen ions rather than radiation damage that is responsible; confirmatory evidence from reanodization or heating experiments unfortunately cannot be obtained, because the behavior of the implanted hydrogen ions under these conditions is not known. Since decelerated stripping is not observed with any of the other species, it must be related to some special property of the hydrogen itself. Presumably this is the ability to form hydrogen bonds between nearest neighbor oxygen atoms.

*Implantations with hydrogen and argon.*—To find out whether there was any interaction between accelerated and decelerated stripping,  $10^{16}$   $^1\text{H}_2^+/\text{cm}^2$  were implanted at 40 keV, followed by  $10^{16}$   $^{40}\text{Ar}^+/\text{cm}^2$  at

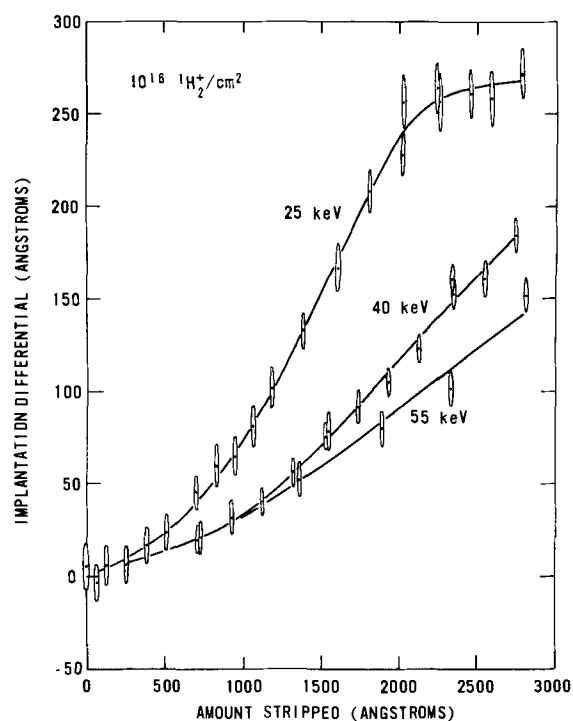


Fig. 9. Implantation differentials with hydrogen to demonstrate the effect of varying the implantation energy. Same series of implantations.

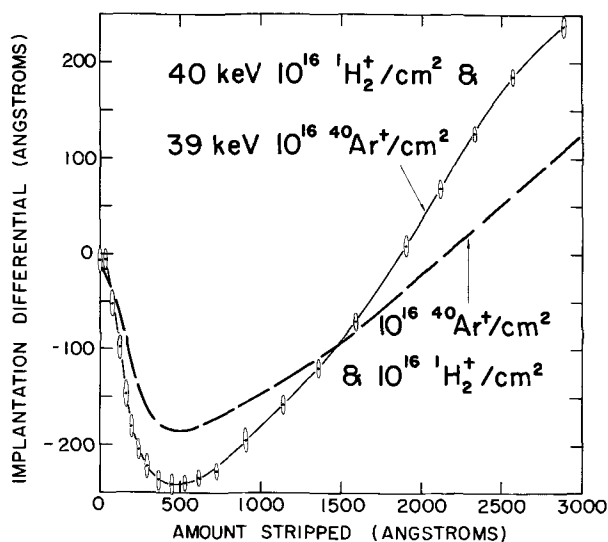


Fig. 10. Implantation differentials observed with both argon and hydrogen to demonstrate the absence of an interaction between the accelerated and decelerated stripping. Different series of implantations.

39 keV into exactly the same area; in a second experiment the implantation order was reversed. The reproducibility of the results in Fig. 10 is rather poor, but characteristic of implantations made during different series; compare, for instance the  $10^{16}$  39 keV  $^{40}\text{Ar}^+/\text{cm}^2$  samples in Fig. 4 and 5, and the  $10^{16}$  40 keV  $^1\text{H}_2^+/\text{cm}^2$  samples in Fig. 7 and 9. Within the experimental uncertainty, therefore, the effects are independent of one another, a conclusion consistent with their proposed natures.

**Implantation with radioactive isotopes.**—The range profile measurements reported elsewhere (2) were performed with radioactive isotopes, and these were normally prepared by  $(n,\gamma)$  reactions on the stable precursors. The radioactive atoms had, therefore, to be separated from a very much larger number of stable atoms. Previous experience with the mass separator had shown that the separation was by no means complete (11) and that the vast majority of the ions implanting at the radioisotope focus were in fact defocused stable isotopes (20). The fluences of these stable isotopes could be gauged from the measured beam currents, their isotopic abundances, and the known beam profiles (11), and were on occasion as much as  $10^{15}$  ion/ $\text{cm}^2$ . Accelerated stripping effects could therefore be expected, and were indeed observed; their incidence and magnitude were in excellent accord with the previous observations of this paper. Two exceptional results were however obtained, both with krypton.

The first attempt to measure 0.5-2.0 keV range profiles with radioactive  $^{85}\text{Kr}$  was performed with a total (stable  $^{84}\text{Kr}$ ) fluence of about  $10^{15}$  ions/ $\text{cm}^2$ . Implantation differentials of about  $+7\text{\AA}$  were observed on receipt from the separator, and though accelerated stripping was observed, it was so nonuniform that no meaningful profiles could be obtained; indeed, it appeared from the interference colors as though some portions of the implanted area had not stripped at all. These results can be interpreted as accelerated stripping due to the presence of the krypton, combined with the presence of a carbonaceous polymer protecting the oxide against dissolution; the latter might well be present at very low energies only where the sputtering efficiency of the krypton markedly decreases. When the total implantation fluence was reduced to about  $10^{13}$  ions/ $\text{cm}^2$ , these effects disappeared, and satisfactory range profiles were obtained.

The other exceptional result was observed in the specimen implanted with 160 keV  $^{85}\text{Kr}^+$ . To obtain this

energy, a  $-40$  kV accelerating voltage was applied to the target holder, so that the total accelerating voltage was 80 kV; by using the  $^{85}\text{Kr}^{++}$  beam, the implantation energy was doubled. The intensity of the  $^{85}\text{Kr}^{++}$  beams was, from the implanted activity, about an order of magnitude less than that for  $^{85}\text{Kr}^+$  and no accelerated stripping was observed. When some 1800 $\text{\AA}$  of oxide had been removed, however, an implantation differential of  $+20\text{\AA}$  was obtained. Since the interference color on the implanted area was uniform, this decelerated stripping would appear to be similar to that observed with hydrogen implants. It is in fact quite possible that some hydrogen was present, for krypton hydride beams have been observed in the mass separator; the most common species,  $^{84}\text{KrH}^{++}$ , would of course implant at the mass 85 position.

The most important question for the present investigations (2-4) was whether these variations in stripping rate would affect the measurement of range profiles. The experimental data for the latter consisted of a series of counts remaining vs. oxide thickness left on the implanted area, and so any variations in the overall magnitude of the stripping rate were of no consequence; what did matter was that the variation should be the same all over the  $2.0 \times 0.4$  cm area implanted. From the behavior of the interference colors, this was certainly not true for the  $^{85}\text{Kr}^+$  implanted at very low energy and high fluence, but it did appear to be true for the accelerated stripping. This was confirmed by comparing range profiles for  $^{134}\text{Cs}^+$ , obtained in the presence of about 15 $\text{\AA}$  of accelerated stripping, with those for  $^{125}\text{Xe}^+$  obtained in its absence. Since xenon and cesium have almost the same atomic mass, the range profiles are expected to be almost identical; the results reported elsewhere (2) will show that they were.

#### Comparison with Related Studies

The sputtering of anodic tantalum oxide leads to a decrease in the film thickness, and hence to a change in the interference color. This property can be used to establish the geometry of a sputtering beam, as Nielsen and Shepherd (21) have suggested; the sensitivity of the technique could be much enhanced by making use of the accelerated or decelerated stripping effect as well. Nghi and Kelly (22) have investigated the sputtering process by comparing changes in interference color with a standard color gauge; the magnitude of the effect they observed is consistent with that reported here.

Hill (6) bombarded anodic tantalum oxide with 15 keV electrons, and observed decelerated stripping in the  $\text{HF-NH}_4\text{F}$  reagent. His irradiations were conducted in an oil-pumped vacuum system at  $5 \times 10^{-6}$  Torr, with the sample surrounded by a cold finger at liquid nitrogen temperature; the latter was intended to prevent the adsorption of pump oil molecules on the specimen surface. A similar cold finger was present in the target chamber of the oil-pumped mass separator used in the present experiments and the pressure approached  $1 \times 10^{-6}$  Torr; nevertheless, decelerated stripping due to a carbonaceous polymer was still observed in the absence of sputtering. Since Hill noted that his etching was somewhat uneven, his decelerated stripping can definitely be attributed to the presence of a carbonaceous contaminant.

#### Conclusions

The effect of ion implantation on anodic tantalum oxide has been examined with the following results.

1. Implantation with heavy ions led to sputtering. The effect decreased with decreasing ion mass and implantation fluence, and was not observed with hydrogen.

2. On sectioning a specimen implanted with heavy ions, the implanted area was found to dissolve more rapidly in the  $\text{HF-NH}_4\text{F}$  reagent. This accelerated stripping has been attributed to the physical presence of the implanted ions.



3. When  $^1\text{H}_2^+$  was implanted to a fluence of  $10^{17}$  ions/cm<sup>2</sup>, a carbonaceous contaminant, some 50-100Å thick, was formed on the oxide surface, due to the radiative decomposition of adsorbed pump oil molecules. The resulting polymer protected the oxide against further anodization and against dissolution in HF-NH<sub>4</sub>F.

4. When  $^1\text{H}_2^+$  was implanted to fluences between about  $10^{13}$  and  $10^{16}$  ions/cm<sup>2</sup>, the implanted area dissolved more slowly. This decelerated stripping was attributed to the presence of the hydrogen itself, possibly by forming hydrogen bonds between neighboring oxygen atoms.

5. No accelerated or decelerated stripping was observed with fluences of  $10^{13}$  ions/cm<sup>2</sup> or less.

6. Implantations with radioisotopes showed that accelerated stripping had no effect on the sectioning procedure, at least for implantation fluences below  $10^{15}$  ions/cm<sup>2</sup>.

#### Acknowledgments

The author expresses his thanks to O. Westcott for the ion implantations and to D. Phillips for sectioning the oxides. He is grateful to J. Ord at the University of Waterloo, Waterloo, Canada, for the ellipsometric measurements, and to P. B. Sewell of the National Research Council, Ottawa, Canada, for using his x-ray technique to detect the carbon in the contaminant. J. A. Davies and D. Santry read the manuscript, and made valuable suggestions for improvement.

Manuscript submitted March 19, 1973; revised manuscript received Aug. 10, 1973.

Any discussion of this paper will appear in a Discussion Section to be published in the December 1974 JOURNAL.

#### REFERENCES

1. J. P. S. Pringle, *This Journal*, **119**, 482 (1972).
2. J. P. S. Pringle, *ibid.*, **121**, 45 (1974).
3. J. P. S. Pringle, *ibid.*, **120**, 398 (1973).
4. J. P. S. Pringle, *ibid.*, **120**, 1391 (1973).
5. D. A. Vermilyea, *ibid.*, **104**, 485 (1957).
6. B. H. Hill, *ibid.*, **116**, 668 (1969).
7. L. Young, *Proc. Roy. Soc. A*, **244**, 41 (1958).
8. L. Masing, J. E. Orme, and L. Young, *This Journal*, **108**, 428 (1961).
9. C. J. Dell'Oca and L. Young, *ibid.*, **117**, 1545 (1970).
10. J. A. Davies, F. Brown, and M. McCargo, *Can. J. Phys.*, **41**, 829 (1963).
11. I. Bergström, F. Brown, J. A. Davies, J. S. Geiger, R. L. Graham, and R. Kelly, *Nuclear Instr. Methods*, **21**, 249 (1963).
12. D. A. Hall, *Rev. Sci. Instr.*, **36**, 1512 (1965).
13. G. R. Bellavance, Private communication.
14. J. F. Gibbons, E. O. Hechtl, and T. Tsurushima, *Appl. Phys. Letters*, **15**, 117 (1969).
15. R. Kelly and F. Brown, *Acta Met.*, **13**, 169 (1965).
16. J. P. S. Pringle, Submitted to *This Journal*.
17. O. Almén and G. Bruce, *Nuclear Instr. Methods*, **11**, 279 (1961).
18. P. B. Sewell and D. F. Mitchell, *J. Appl. Phys.*, **42**, 5879 (1971).
19. J. F. Janni, U.S. Dept. of Commerce Report AD 643 837 (1966).
20. F. Brown and J. A. Davies, *Can. J. Phys.*, **41**, 844 (1963).
21. R. E. Nielsen and W. B. Shepherd, *Rev. Sci. Instr.*, **35**, 123 (1964).
22. L. O. Nghi and R. Kelly, *Can. J. Phys.*, **48**, 137 (1970).

## Nucleation of Copper Electrodeposits on Thin (111) Films of Evaporated Copper

Yasusada Ueno, Nobuyuki Kidokoro, and Masayasu Tsuiki\*

Department of Industrial Chemistry, Cifu University, Kagamihara, Gifu, Japan

#### ABSTRACT

Electrodeposited nuclei and defect structures on thin (111) films of evaporated copper were studied by means of electron and optical microscopes and electron diffraction, as a part of an investigation of copper nucleation from sulfate baths. The roles of noncoherent twin boundaries on the films were of limited significance in the nucleation. Macroscopic defects such as notches and macrosteps on the surface with mirror luster were preferential nucleation sites. The rate of nucleation in the initial stage was evaluated under various overpotentials.

In studies of nucleation of copper electrodeposits, it is necessary to determine whether defect structures on the cathode surface are responsible for nucleation or not. The single-crystal film of evaporated copper would be suitable as cathode substrates for this purpose because the deposited nuclei and defect structures on the film can be observed simultaneously by transmission electron microscope. Fundamental studies on the preparation of the epitaxial film of evaporated copper under high vacuum and on the electrodeposition of copper on the film have been carried out (1-3). Electrocrystallization of copper from sulfate solution on the thin (111) film of evaporated copper, which contains noncoherent twin boundaries and macrosteps as well as mechanical notches, is described in this paper. Distribution of nuclei in the vicinity of these defects were observed by electron and optical micro-

scopes. The number of deposited nuclei on the cathode, which did not contain macroscopic defects, was counted with time during potentiostatic cathodic polarization. Distribution of nuclei near twin boundaries and the effects of surface defects on nucleation and its rate are also discussed.

#### Experimental

The vacuum apparatus for the preparation of copper (111) film was the same as the one in the previous report (1). Thin film of 500-1000Å was prepared for transmission electron microscopy so as to facilitate penetration of an electron beam. On the other hand, thick film was made use of in other experiments. The surface of the epitaxial (111) films was optically mirror-smooth except for cleaved steps, when the films were prepared on a freshly cleaved mica substrate held at about 200°C under  $1 \times 10^{-5}$  Torr of residual gas pressure and with an evaporation rate of the order of about 10 Å/sec. The (100) films were also pre-

\* Electrochemical Society Active Member.  
Key words: electrocrystallization, copper single-crystal film, nucleation.



pared on a cleaved surface of potassium bromide by the same procedure, if necessary. Presence of noncoherent twin boundaries in the films was ascertained by transmission electron micrographs and diffraction patterns of the sample removed from the substrate.

Epitaxial copper films of about  $1.5 \times 1.5 \text{ cm}^2$  area were cut with a mica base and were used as the cathode. Specimens were cleaned with trichloroethylene under ultrasonic vibration for 2 min, rinsed in a stream of alcohol, and finally with triply distilled water prior to experiment. The surface still kept a mirror luster. The cathode assembly and the plating cell used are shown in Fig. 1. The specimen was placed at least 3 mm from the cell bottom so as to keep uniform current distribution. Observation of nucleation was also carried out simultaneously. A potentiostat (Hokuto Model P.S. 1000) was used as the power source. The cathode was polarized in the range of 20-90 mV vs. the static potential of a pure copper electrode immersed in a solution of the same composition as that of the plating solution. The current with time was recorded during electrolysis (with a Rikendenshi Model 42 X-Y recorder).

In order to avoid dissolution of electrodeposited nuclei and cathode films, a neutral solution containing only 200 g/liter copper sulfate was prepared. Then, the solution was treated with active carbon, and its pH was adjusted to about 2 by pre-electrolysis with a platinum anode. The solution was stored in contact with a piece of metallic copper. Nevertheless,  $\text{Cu}_2\text{O}$  deposition from this electrolyte was hardly possible at the initial stage of electrolysis. Color change of cathodic surface based on  $\text{Cu}_2\text{O}$  deposition is easily detectable by *in situ* optical observation. The unexpected results obtained from such oxidized specimens were entirely excluded. But a trace amount of non-detectable codeposition of  $\text{Cu}_2\text{O}$  may be ignored.

The electrodeposited layer for transmission electron microscopy was washed immediately with water, dried in air, and then coated with an acetone solution of cellulose acetate. Since the copper layer adhered strongly to the coated layer, it could be stripped off the mica substrate by pulling one end of the coated layer. After the dissolution of the coated layer in acetone, the residual copper film was held on a sheet

mesh and examined by electron microscope (Nihondenshi Model JEM T-7).

### Results and Discussion

*Electrodeposited nuclei on very thin films.*—Noncoherent twin boundaries parallel to the  $\langle 110 \rangle$  direction on the (111) plane of the fcc lattice is observed only when the electron beam is perpendicularly incident on the film surface. Observation is not always possible due to nonuniformity of the fine structure. A typical example of the thin (111) film of evaporated copper, about 500 Å thick, is shown in Fig. 2. A selected area diffraction pattern in this region is shown in Fig. 3. In this figure, extra diffraction spots of  $n/3\{4\bar{2}2\}$  type were recognized in the positions not expected from the perfect fcc lattice. Such extra spots had already been explained as an evidence of noncoherent twin boundaries in silver films by Allpress and Sanders (4). Similar explanations in copper films are also possible, and extra spots found in Fig. 3 are attributable to the diffraction from the three sets of the boundaries, which are parallel to the  $\{211\}$  plane; these planes are normal to the film surface and mutually inclined by  $120^\circ$ . It is, therefore concluded that noncoherent twin boundaries in Fig. 2 arise from the mutual contact of copper nuclei which occupied a double position (5) on a mica substrate during evaporation. Since the atomic arrangement on such a disturbed region is different from that of the perfect fcc structure, vacancies or interstitials must appear from mismatching between boundaries and bulk parts. This atomic configuration of boundaries is described by constructing a marble ball model as shown in Fig. 4. The dislocation density in the vicinity of such boundaries is much larger than that in other parts, and hence, the boundary region would become an active site of nucleation for electrocrystallization. An example supporting this concept had been demonstrated as a result of preferential

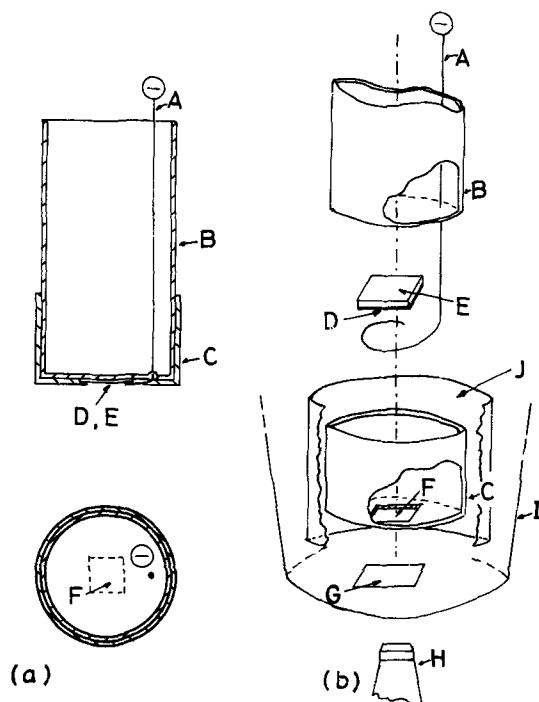


Fig. 1. Cathode assembly and plating cell. (a) Projected view, (b) exploded view. A, Pt-lead; B, plastic cylinder; C, plastic cover; D, evaporated Cu(111) film; E, substrate; F, window; G, cover glass; H, objective lens; I, cell; J, anode.

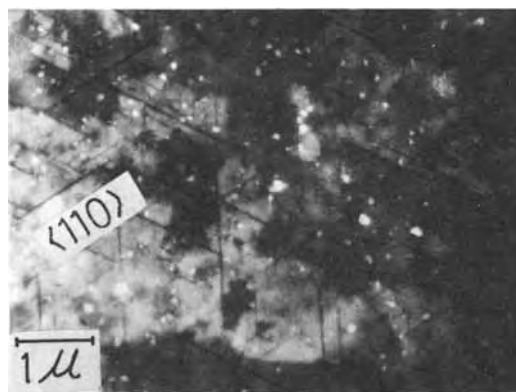


Fig. 2. Transmission electron micrograph of noncoherent twin boundaries in a thin (111) film of copper.



Fig. 3. Selected area diffraction pattern obtained from the specimen of Fig. 2.



Fig. 4. Marble ball model of a noncoherent twin boundary. N, normal position; T, boundary position.

nucleation of silver deposits on twin or high angle grain boundaries of annealed silver surfaces by Kilner and Plumtree (6). On the electrodeposition of copper on a (100) film of evaporated copper, Sard and Weil (7) suggested correlation between the twin density of the substrate and the extended pyramidal growth. Therefore, electrocrystallization of copper was performed in our experiment to explore the role of a noncoherent twin boundary in the nucleation of the deposits.

Figure 5 shows an electron micrograph of nuclei electrodeposited at 25°C with polarization of 70 mV on a surface region containing noncoherent twin boundaries. Some other experiments were carried out under 20–70 mV, and similar results were obtained. The electrodeposited nuclei on the film surface were widely distributed in nature, and aggregation of deposits along the noncoherent twin boundaries was not necessarily observed in this case.

When the cathodic overpotential decreases, noncoherent twin boundaries are expected to become more sensitive nucleation sites. A typical photomicrograph at 25 mV of polarization is shown in Fig. 6. The percentage of the number of nuclei in contact with noncoherent twin boundaries in the total number of nuclei can be determined from Fig. 6 and other photomicrographs obtained at the same overpotential. In this instance, the nuclei smaller than  $0.05 \mu\text{m}$  in diameter are liable to be confused with faults, so such small nuclei are not counted. The percentage is shown by open circles in Fig. 7 as a function of twin boundary density. It is noticed that these values do not exceed 16%.

On the other hand if we assume that nucleation sites are independent of the presence of noncoherent twin boundaries, then the percentage of the number of nuclei in contact with noncoherent twin boundaries on

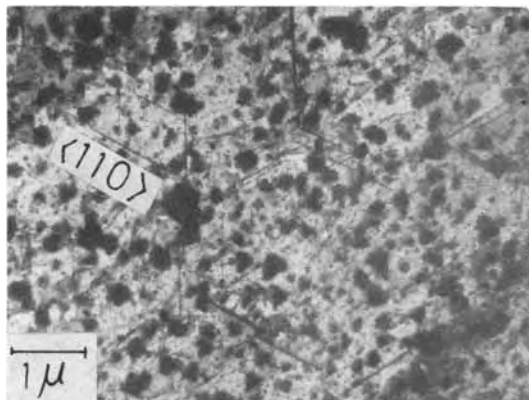


Fig. 5. Electrodeposited nuclei on the region containing noncoherent twin boundaries. Overpotential: 70 mV, (111) surface. Charge passed, 0.06 coulomb/cm<sup>2</sup>.

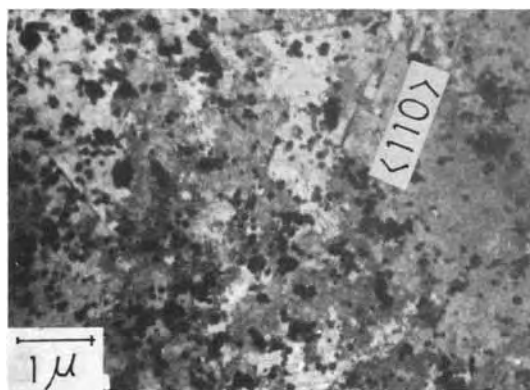


Fig. 6. Electrodeposited nuclei on the region containing noncoherent twin boundaries. Overpotential: 25 mV, (111) surface. Charge passed, 0.033 coulomb/cm<sup>2</sup>.

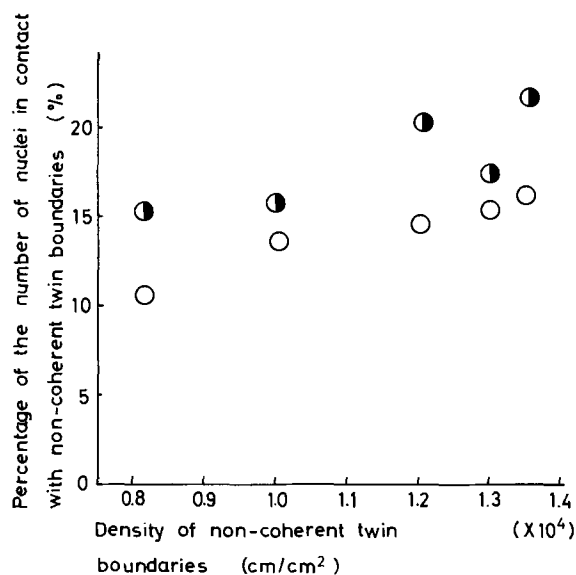


Fig. 7. Ratio of nuclei in contact with noncoherent twin boundaries to the total number of nuclei per unit area. Overpotential, 25 mV. Charge passed, 0.033 coulomb/cm<sup>2</sup>. ○, Observed value; ◐, calculated value.

the electrodeposited surface can be evaluated by Eq. [1]

$$N_c/N_t = (L\bar{D} + n\pi\bar{D}^2/4)/\text{cm}^2 \quad [1]$$

where the size of the nuclei is constant and the distribution of the nuclei is homogeneous.  $N_c$  and  $N_t$  are the number of nuclei in contact with twin boundaries and the total number of nuclei per unit area, respectively.  $L$  and  $n$  are the total length and the number of intersection lines between a twinning plane and the film surface, respectively, in the observed area.  $\bar{D}$  is the average diameter of deposited nuclei. Percentages estimated from Eq. [1] are represented by the semifilled circles in Fig. 7. Although these estimated values are somewhat higher than the values determined from the photomicrographs, the difference between the two sets of data is within 35%. In addition, the observed number of nuclei in contact with twin boundaries was always less than that expected from Eq. [1]. Consequently, it seems that the noncoherent twin boundary is less sensitive as a nucleation site than other active sites such as a step with screw dislocation.

On the contrary, Sard and Weil have shown that coherent twin boundaries on thin (100) films of evaporated copper played important roles for pyramidal or rooftop growth under galvanostatic conditions. A further experiment was made on copper electrodeposition on the (100) films with coherent twin boundaries

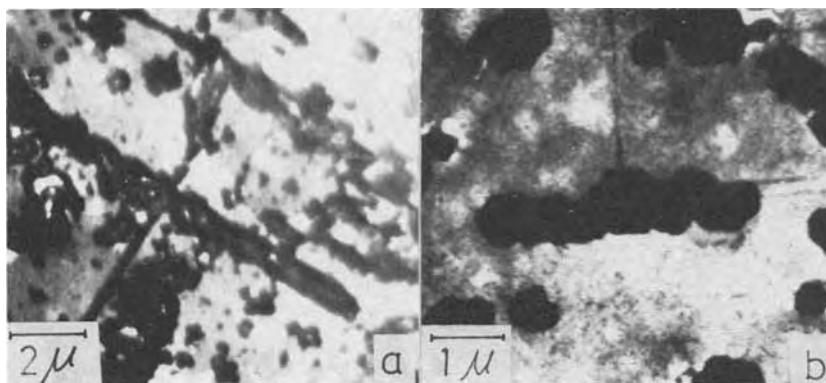


Fig. 8. Electrodeposited nuclei on (100) films of evaporated copper. Overpotential: a, 70 mV; b, 20 mV.

under potentiostatic conditions. The results obtained at 70 and 20 mV are shown in Fig. 8a and b. It can be seen that nucleation occurs on the coherent twin boundaries in the  $\langle 110 \rangle$  direction and in the vicinity of canals, which arise during the evaporation of the film. Thus the contribution of twin boundaries is much more evident on a (100) plane than on a (111) plane. Although the comparison of roles as nucleation sites of twin boundaries on the (111) plane with that on the (100) plane is interesting, it is difficult to interpret the role of twin boundaries themselves in the above results because the film contains other defect structures such as narrow canals between island structures, at the film thickness, which permitted the observation of twin boundaries. It is, however estimated that the nucleation rate on the (111) planes in a fcc lattice is larger than that on the (100) planes (8) and the nucleation energy of a two dimensional nucleus with (111) preferred orientation at lower overpotential is lower than that of the (100) preferred orientation (9). Thus it is presumed that the contribution of microscopic defects to preferential nucleation is of limited significance on the (111) planes, where nucleation occurs easily.

**Effects of macroscopic defects on preferential nucleation.**—Macroscopic defects on (111) films of evaporated copper, such as mechanical notches and macrosteps which depend on cleavage steps of the mica substrate, will also be regarded as preferential nucleation sites for electrodeposition. For this observation, highly perfect films, more than 5000Å thick, were used as substrates to avoid fracture of the film due to notched lines or macrosteps. Electrodeposits on such a surface consist of relatively few nuclei with larger size than those on very thin films, whereby optical microscopy is available for observation of deposits.

Figure 9 shows an optical micrograph of deposits along mechanical notches scratched by a knife edge. It was found that preferential nucleation occurred in the distorted region on the notches. Similar results

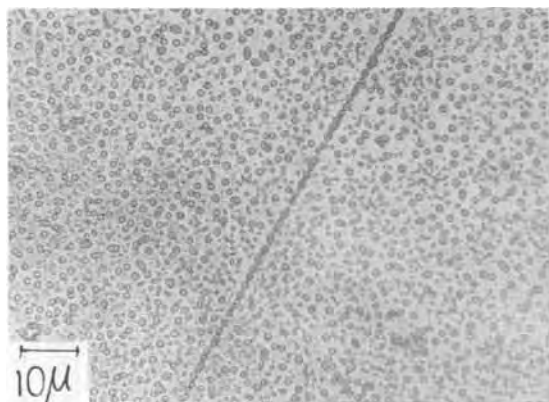


Fig. 9. Nuclei electrodeposited along a mechanical notch scratched by a knife edge. Overpotential, 70 mV.

were obtained by the observation of electrodeposits on the specimen containing macrosteps, which conformed to the cleaved step of a substrate as shown in Fig. 10. From these photographs, it was revealed for preferential nucleation of electrodeposits that the effect of macroscopic defects is larger than that of microscopic defects such as twin boundaries on (111) films of copper.

Now, for the investigation of nucleation rate, it is necessary to perform the electrodeposition on the surface, which is free from mechanical notches or macrosteps. Noncoherent twin boundaries presumably do not affect the preferential nucleation in this case. But the forms of nuclei were affected strongly by the topography of film surfaces. Isolated nuclei with geometrical forms emerged from the film with a mirror-smooth surface as shown in Fig. 11, but the number of nuclei on an uneven film was no longer countable in the photomicrograph. On such a surface, layer growth developed after a long time deposition, as shown in Fig. 12. Therefore, former types of evaporated films

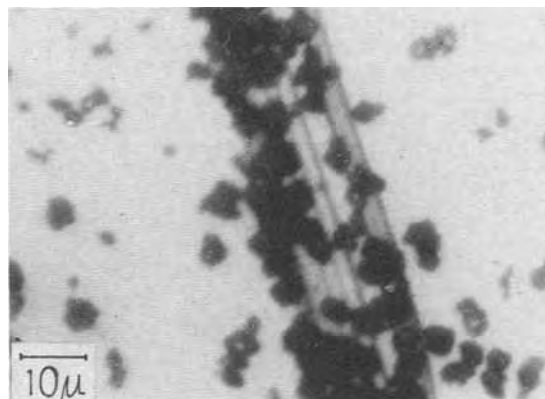


Fig. 10. Nuclei electrodeposited along the macrosteps which conformed to a cleaved step of mica. Overpotential, 50 mV.



Fig. 11. Isolated nuclei on a mirror-smooth surface. Overpotential, 30 mV. a, Surface topography; b, trigonal pyramids.

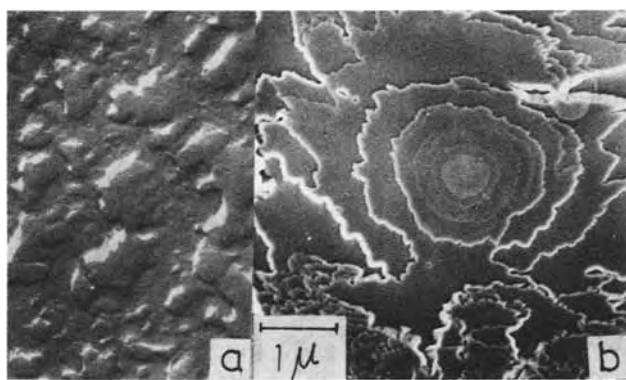


Fig. 12. Layer growth on a coarse surface. Overpotential, 30 mV. a, Surface topography; b, layer growth.

were selected as cathode specimens in the observation of the nucleation process. In this case, electrodeposited nuclei were distributed uniformly on the film surface.

**Nucleation process at the initial stage of electrodeposition.**—Figure 13 shows the density of electrodeposited nuclei as a function of deposition time in a 200 g/liter (0.8M) copper sulfate solution. The data in a dilute solution (0.27M) is shown in Fig. 14. The number of nuclei rapidly increased in the initial stage of deposition and then gradually decreased via a maximum value due to coalescence of growing nuclei. After the nucleation was completed at the initial overpotential, increasing the overpotential abruptly caused nucleation of the second stage. Then the nucleation continued until nucleation sites were saturated at the higher potential. It is noticed that the number of effective nucleation sites is held constant at an applied potential. However, the maximum values of effective nucleation sites differ from one substrate to another due to non-uniformity of the fine structure, even at the same condition. Therefore, the data presented above were those obtained by the measurement on a set of specimens which were cut off from the substrate with an epitaxial copper piece of mirror-smooth surface topography. If we assume that the nucleation process obeys the first order kinetics, the reaction rate is as follows

$$\frac{dN}{dt} = A(N_0 - N) \quad [2]$$

$$N = N_0(1 - e^{-At}) \quad [3]$$

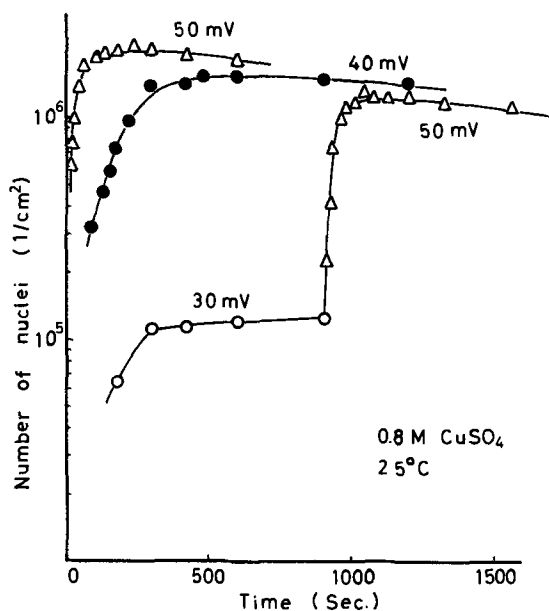


Fig. 13. Number of nuclei as a function of depositing time

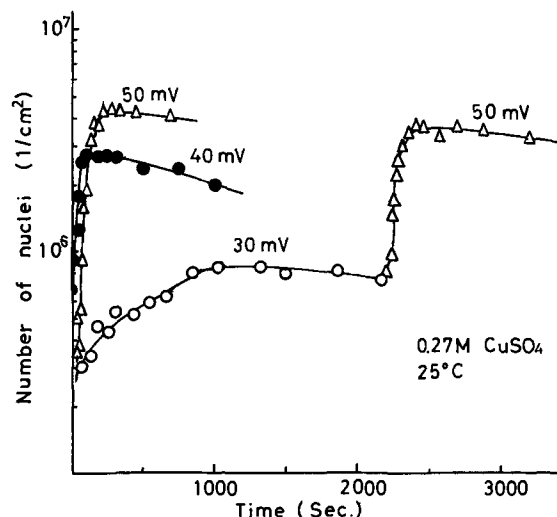


Fig. 14. Number of nuclei as a function of depositing time

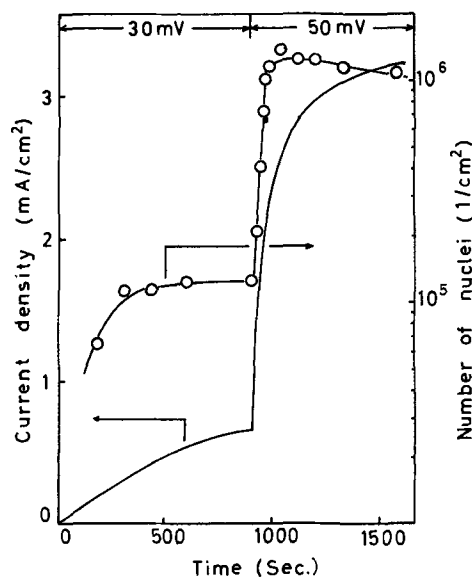


Fig. 15. Current density and number of nuclei vs. depositing time (overpotential was changed abruptly in the course of deposition).

or

$$A = \frac{1}{t} \ln \frac{N_0}{N_0 - N} \quad [4]$$

where  $N$  is the number of deposited nuclei at time  $t$ , and  $N_0$  the maximum number of nuclei evaluated from the figure. The rate constant,  $A$ , from Eq. [4] is summarized in Table I. These values are useful for calculation of the number of nuclei over the rapid nucleation processes. Therefore, it is roughly assumed that multiplication of depositing nuclei on the cathode film with mirror-smooth surface obeys the first order process. From Table I, it is noted that the nucleation process is enhanced by the increase of the overpotential and the decrease in the metal ion concentration in the electrolyte. Finally, Fig. 15 shows an example of vari-

Table I. Rate constants of nucleation  $A$  (1/sec)

Overpotential, mV	0.8M CuSO <sub>4</sub>	0.27M CuSO <sub>4</sub>
30	—	0.036
40	0.0039	0.053
50	0.020	0.065
50*	0.021	0.10

\* Values obtained after the applied overpotential changed from 30 to 50 mV.

ation of current density and number of nuclei with depositing time. Since the deposition current is sensitive to the change in the number of nuclei, it is likely that the step propagation process or layer growth scarcely occurred and the formation or the growth of nuclei was dominant.

### Summary

1. Deposited nuclei and noncoherent twin boundaries on thin (111) films of evaporated copper were simultaneously observed by transmission electron microscopy under limited conditions.

2. Number of nuclei in contact with noncoherent twin boundaries was less than 16% of that of the total deposited nuclei at 25 mV of overpotential.

3. Mechanical notches and macrosteps on the film provide the nucleation sites for preferential deposition.

4. Nucleation rate obeys the first order kinetics in the initial stage.

### Acknowledgments

The authors wish to thank Dr. F. Hine, Dr. K. Yamakawa, and Dr. T. Fukutomi for their encouragement and support in this investigation.

Manuscript submitted March 23, 1973; revised manuscript received ca. Sept. 1, 1973.

Any discussion of this paper will appear in a Discussion Section to be published in the December 1974 JOURNAL.

### REFERENCES

1. M. Tsuiki and Y. Ueno, *Denki Kagaku*, **36**, 676 (1968).
2. Y. Ueno and M. Tsuiki, *ibid.*, **39**, 840 (1971).
3. Y. Ueno and M. Tsuiki, *ibid.*, **40**, 825 (1972).
4. J. G. Allpress and J. V. Sanders, *Phil. Mag.*, **14**, 937 (1966).
5. R. Hashiguchi and S. Chikazumi, "Hakumaku Hyomen Gensho" ("Phenomena of the Surface on Thin Films"), p. 49, Asakura, Tokyo (1969).
6. T. Kilner and A. Plumtree, *This Journal*, **115**, 929 (1968).
7. R. Sard and R. Weil, *Electrochim. Acta*, **15**, 1977 (1970).
8. U. Bertocci, *This Journal*, **119**, 822 (1972).
9. N. A. Pangarov, *Electrochim. Acta*, **9**, 721 (1964).

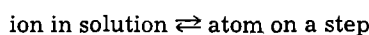
## Mechanism of Electrocrystallization

T. Vitanov, A. Popov, and E. Budevski

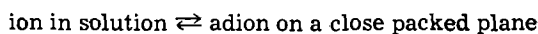
Division of Electrochemical Power Sources, Bulgarian Academy of Sciences, Sofia, Bulgaria

### ABSTRACT

The mechanism of silver deposition on electrodes representing a cubic plane of silver single crystal with known surface topography was investigated. The exchange current densities on dislocation-free intact planes and on stepped planes with exactly known step density were obtained by impedance measurements at high frequencies. It has been found that the exchange current density  $i_{o,st}$  of the charge transfer reaction



is about three orders of magnitude higher than the exchange current density  $i_{o,ad}$  of the reaction



The comparison between experimental and calculated values of both the rate of propagation of monolayers and the slope of current-square overvoltage relation has shown that the direct transfer mechanism plays a predominant role in metal deposition. The contribution of surface diffusion is negligible.

Two possible ways of ion incorporation into the crystal lattice can be considered in the process of metal deposition: (i) ions are discharged at any site of the crystal surface and are transported afterwards by surface diffusion to the sites of growth where they are incorporated, this is what we call the surface diffusion mechanism; (ii) ions are directly discharged on a growth step or on a growth site with simultaneous incorporation, this we call the direct transfer mechanism.

Although the question which of these two possible paths prevails in metal deposition is of crucial interest for the understanding of the process, no answer to the problem can be considered adequate as yet. In earlier theoretical treatments the second path has been shown to be connected with prohibitively high activation energy (1) and was completely disregarded. Inspired by some experimental results of the authors of this paper a new approach to the problem was recently made by Despic (2) who showed that the second path is by no

means negligible. Anyway, the theoretical treatment appears to be rather complicated and uncertain.

The experimental investigation of the process also failed to give a clear answer to the problem. This is mainly due to the fact that the crystallographic character of the electrode surface under normal experimental conditions is completely unknown not to mention the detailed surface topography.

### Theoretical Background

The idea that surface diffusion can be considered as rate controlling in electrochemical metal deposition was suggested by Brandes (3) as early as 1929. The first quantitative treatment was given by Lorenz (4) who adapted the theory of Burton, Cabrera, and Frank (5) to the case of metal deposition. Later, the problem was treated by Vermilyea (6), Fleischmann and Thirsk (7), Damjanovic and Bockris (8), and Schnittler (9), who brought the theory of surface diffusion mechanism to its present state.

The equation which describes the overvoltage dependence of the current at steady-state conditions has

generally the form

$$i = i_{o,ad} \left[ e^{\frac{\alpha z F}{RT} \eta} - e^{-(1-\alpha) \frac{z F}{RT} \eta} \right] \frac{\lambda_o}{x_o} \tanh \frac{x_o}{\lambda_o} \quad [1]$$

where

$$\lambda_o = (z F D_s C_{o,ad} / i_{o,ad})^{1/2} e^{-\frac{\alpha z F}{2RT} \eta}$$

is the surface diffusion penetration,  $D_s$  is the surface diffusion coefficient,  $C_{o,ad}$  the equilibrium concentration of adions,  $i_{o,ad}$  the exchange current density of ions in solution with adions and  $2x_o$  the average step distance. The latter can be expressed also by the step density (number of steps per unit length in  $\text{cm}^{-1}$ ) or the equivalent quantity  $L$ , the total length of growth steps per unit area in  $\text{cm}/\text{cm}^2$ ;  $2x_o = 1/L$ .

Two limiting cases can be distinguished:

(i) The surface diffusion penetration is greater than the average step distance ( $\lambda_o \gg x_o$ ). For that case Eq. [1] gives the Butler-Volmer relation, i.e., the charge transfer dominates the process.

(ii) The surface diffusion penetration is smaller than the average step distance ( $\lambda_o \ll x_o$ ). For that case we obtain from [1]

$$i = i_{o,ad} \left[ e^{\frac{\alpha z F}{RT} \eta} - e^{-(1-\alpha) \frac{z F}{RT} \eta} \right] \frac{\lambda_o}{x_o} \quad [2]$$

The surface diffusion has a predominant role. The current is strongly influenced by the step density.

The direct transfer mechanism was suggested for the first time by Volmer (10) and was discussed later in the works of Lorenz (4), Fleischmann and Thirsk (7), Gerischer (11), Mott and Watts-Tobin (12), and others. A quantitative expression for this case can be derived in a very simple way and can be found, e.g., in (13). Denoting with  $i_{o,st}$  the exchange current density of ions in solution with atoms on a step (or kink) the current density is given by

$$i = i_{o,st} 2r_o L \left[ e^{\frac{\alpha z F}{RT} \eta} - e^{-(1-\alpha) \frac{z F}{RT} \eta} \right] \quad [3]$$

where  $r_o$  is the atomic radius in the crystal lattice.

It can be easily seen that no clear distinction between the two mechanisms can be obtained using steady-state measurements only. In both cases the over-all exchange current density obtained from the slope of the current-overvoltage relation for small overvoltage

$$i_o = \frac{RT}{zF} \left( \frac{di}{d\eta} \right) \quad [4]$$

contains the step length  $L$ . In the case of surface diffusion

$$i_o = i_{o,ad} 2L \lambda_o \tanh \frac{1}{2L \lambda_o} \quad [5]$$

and in the case of direct transfer

$$i_o = i_{o,st} 2r_o L \quad [6]$$

In the second case  $i_o$  is proportional to  $L$  regardless of step density. In the first case a proportionality exists only for small densities ( $2L \lambda_o < 1$ ). For higher step densities  $i_o$  becomes independent of  $L$  and the process is purely charge transfer controlled. It is clear that in the case where the surface diffusion is manifested, no distinction between the two mechanisms can be made.

Transient and high frequency impedance measurements can give additional information in that respect. The frequency dependence of impedance in the case of electrocrystallization was treated first by Lorenz (4) and later by other authors (7, 14, 15). At high frequencies the equivalent circuit of the charge transfer reaction can be represented by a resistance parallel to the double layer capacitance. It can readily be shown

[c.f. Vetter (13)] that in the case of surface diffusion this resistance is given by

$$R_{F,SD} (\omega \rightarrow \infty) = \frac{RT}{zF} \cdot \frac{1}{i_{o,ad}} \quad [7]$$

At high frequencies the surface diffusion penetration becomes negligible in comparison to the step distance and the contribution of the surface diffusion to the impedance can be neglected; the exchange current density does not depend on step density.

Contrary to this the parallel resistance  $R_F$  in the case of direct transfer will be given by

$$R_{F,DT} (\omega \rightarrow \infty) = \frac{RT}{zF} \cdot \frac{1}{i_{o,st} 2r_o L} \quad [8]$$

and should depend on the step density. This gives a possibility to distinguish between the two mechanisms, and with a known value of  $L$  to obtain the exchange current density  $i_{o,st}$  of ions on a step or kink site.

### Experimental Technique

The experimental technique for the preparation of electrodes representing a single-crystal plane only (16-19) offers the possibility for a very detailed investigation of the mechanism of electrocrystallization. The most remarkable advantage of these electrodes is that they can be prepared with an exactly known surface topography and number of screw dislocations, or even without screw dislocations. Three very important surface configurations can be obtained: (i) Dislocation-free plane with atomically smooth surface (18, 19). (ii) Dislocation-free plane with a monoatomic step of known length; on a dislocation-free plane a new monoatomic step can be produced by nucleation and growth of a new lattice net (18-20). The propagation of the monolayer can be stopped at any desired position by switching off the current. (iii) Stepped plane with a known uniform step density: a plane with few screw dislocations (low dislocation density) can be grown at a constant overvoltage until a regular pyramidal growth pattern is obtained.

According to Frank's theory the distance between successive turns of the spiral is inversely proportional to the overvoltage. For a polygonal spiral growth from simple geometrical reasoning one obtains the relation (5b, 21)

$$2x_o = \frac{1}{L} = \frac{\gamma \epsilon V_m}{zF h \eta} \quad [9]$$

where  $V_m$  is the molar volume,  $\epsilon$  the specific edge energy,  $\gamma$  a coefficient depending on the spiral geometry, and  $h$  the step height. From the experiments described in (18, 19), it follows that the current is proportional to the length  $L$  of the growing step and the overpotential

$$i = K L \eta \quad [10]$$

In the case of a spiral growth the total step length per unit area  $L$ , i.e., the step density, can be given by  $\frac{1}{2x_o}$ , so that for the current density from [9] and [10] we obtain

$$i = K \frac{zF h}{\gamma \epsilon V_m} \eta^2 \quad [11]$$

This equation was experimentally verified in the case of silver deposition from aqueous solutions and melts of silver nitrate on cubic and octahedral planes of silver single crystals (22, 23).

### Mechanism of Metal Deposition

Information obtained from dislocation-free planes.— A dislocation-free intact plane behaves as an ideally polarizable electrode in the region between 0 and 10 mV cathodic overvoltage. Double layer capacity is

easily determined by impedance or galvanostatic transient measurements. A typical value of

$$C_{DL} = 30 \mu\text{F}\cdot\text{cm}^{-2}$$

was found for the cubic plane of silver in 6N silver nitrate solution.

Impedance measurements at high frequencies allow one to estimate the resistance of the charge transfer reaction

ion in solution  $\rightleftharpoons$  adion on a close packed plane

For this resistance which is parallel to the double layer capacity a value of 0.45 ohm-cm<sup>2</sup> was found. From this value the corresponding exchange current density

$$i_{o,ad} = 0.060 \pm 0.001 \text{ A cm}^{-2}$$

of the charge transfer reaction of adions on a perfect cubic plane of silver in 6M silver nitrate solution was obtained (25, 26).

The frequency dependence of the impedance and galvanostatic transients could be used to estimate the adsorption capacity and the adion concentration, respectively. The frequency dependence of impedance and the transients are however far too complex to permit an easy interpretation (26).

A very rough estimation of the adion concentration from galvanostatic transients can be made as follows: the time constant for double layer charging calculated from double layer capacity and the resistance of the charge transfer reaction is approximately 13  $\mu\text{sec}$ . The slope of the galvanostatic transient (Fig. 1) at twice that time gives a capacity of ca. 40-50  $\mu\text{F cm}^{-2}$ , leaving for the adsorption capacity a maximum value of 10-20  $\mu\text{F cm}^{-2}$ . This corresponds to an adion concentration  $C_{ad} = (2-5) \times 10^{-12} \text{ mol cm}^{-2}$ .

*Information obtained from stepped planes.*—Impedance measurements on stepped planes have shown that the charge transfer resistance depends strongly on step density. It can be therefore assumed that two parallel charge transfer reactions are taking place

(i) ion in solution  $\rightleftharpoons$  adion on a close packed plane

(ii) ion in solution  $\rightleftharpoons$  atom on a step

with exchange C.D.  $i_{o,ad}$  and  $i_{o,st}$ , respectively. The over-all exchange current density is then the sum of both.

The results of two sets of measurements performed on a cubic plane of a silver single crystal in 6M AgNO<sub>3</sub> at 45°C are shown in Table I. The first two columns in Table I present the preparation conditions of the plane.

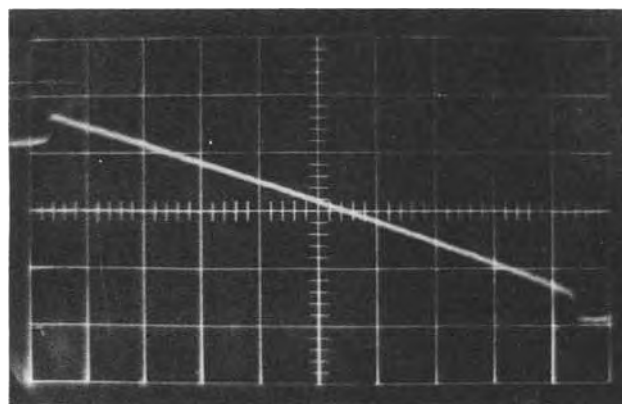


Fig. 1. Overvoltage transient on a dislocation-free cubic plane.  $i = 2.7 \times 10^{-2} \text{ A cm}^{-2}$ ; vertical sensitivity: 5 mV/cm; time base: 2  $\mu\text{sec/cm}$ .

The third column gives the overvoltage corrected for the ohmic drop and concentration polarization. The correction is made on the assumption (22) that for low  $\eta$  values both terms depend linearly on current density, while according to Eq. [11] the discharge overpotential term is proportional to  $\sqrt{i}$ . Plotting  $\frac{\Delta E}{i}$

as function of  $\frac{1}{\sqrt{i}}$  one obtains a straight line, where the

slope is equal to  $\left( K \frac{zFh}{\gamma \epsilon V_m} \right)^{-1/2}$  and the intercept

contains the coefficients of the linear terms. The additional terms connected with the semicylindrical configuration of the mass transport to the steps is negligible as can be calculated from equations given by Gerischer (11) having in mind the small step distance ( $2x_0 < 10^{-4} \text{ cm}$ ) in this case. The fourth column gives the over-all exchange current densities  $i_o$  measured immediately after switching off the growth current.<sup>1</sup>

<sup>1</sup> It is assumed that the step density does not change after switching off the growth current and during the measurements. This assumption for (100) plane is backed by the constancy of the surface topography and the impedance values during 30 min after switching off the cathodic current. Similar observations on the (111) plane show a visible flattening of the pyramids' tops accompanied by a strong change of the impedance with time. Therefore it was not possible to measure the dependence of  $i_o$  on  $L$  on the (111) plane.

Table I. Dependence of the exchange current density on the preparation conditions

Electrode 1						
Current density, $i$ (mA cm <sup>-2</sup> )	Preparation conditions		Over-all exchange current density, $i_o$ (A cm <sup>-2</sup> )	Exchange current density due to the steps $\Delta i_o = i_o - i_{o,ad}$ (A cm <sup>-2</sup> )	$\frac{\Delta i_o}{\eta}$ (AV <sup>-1</sup> cm <sup>-2</sup> )	$i_{o,st}$ (A cm <sup>-1</sup> )
	Overvoltage as measured, $\Delta E$ (mV)	Corrected overvoltage, $\eta$ (mV)				
1	2	3	4	5	6	7
1.1	0.44	0.4	0.14	0.08	$0.20 \times 10^3$	$5.1 \times 10^{-6}$
4.4	1.06	0.8	0.19	0.13	0.16	4.2
8.8	1.50	1.0	0.28	0.22	0.22	4.4
17.6	2.60	1.6	0.37	0.31	0.19	5.0
35.2	4.25	2.3	0.53	0.47	0.20	5.4
52.9	5.74	2.8	0.64	0.58	0.21	5.4
Electrode 2						
1	2	3	4	5	6	7
1.1	0.44	0.4	0.15	0.09	$0.22 \times 10^3$	$5.8 \times 10^{-6}$
4.4	1.00	0.7	0.25	0.19	0.27	5.3
8.8	1.50	1.0	0.28	0.22	0.22	4.4
17.6	2.43	1.4	0.36	0.30	0.21	4.2
35.2	4.13	2.2	0.60	0.54	0.25	5.9
52.9	5.53	2.6	0.68	0.62	0.24	5.4
Dislocation-free plane			$i_{o,ad} = 0.06$	0	—	—

Mean value:  $0.21 \times 10^3 \pm 0.01$   $5.1 \times 10^{-6} \pm 0.7$



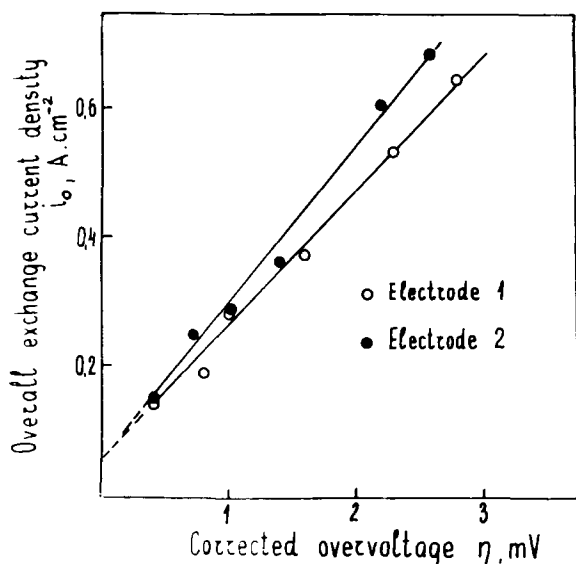


Fig. 2. Dependence of the exchange current density on a stepped cubic plane on the preparation conditions.

It is clearly seen (Fig. 2) that there is a linear dependence between the over-all exchange current density and the overvoltage at which the plane was prepared. The limiting value of  $i_o$ , determined by the intercept of the  $i_o/\eta$  relation is numerically equal to the value of  $i_{o,ad}$ , measured on a dislocation-free atomically smooth plane. The fifth column gives the difference  $\Delta i_o$  between the over-all exchange current density and  $i_{o,ad}$  and the next one, the ratio  $\frac{\Delta i_o}{\eta}$ , which is constant over the entire range of overvoltages studied.

Since according to Frank's theory the step density  $L$  is proportional to  $\eta$  (Eq. [9]), the constancy of  $\frac{\Delta i_o}{\eta}$  shows that a magnitude characteristic for the steps has been obtained. This magnitude can be expressed as exchange current per unit step length

$$i_{o,st}^* \equiv \frac{\Delta i_o}{L} \text{ [A} \cdot \text{cm}^{-1}\text{]}$$

From [9]

$$i_{o,st}^* = \frac{\Delta i_o}{L} = \frac{\Delta i_o}{\eta} \frac{\gamma \epsilon V_m}{z F h} \quad [12]$$

The term  $\frac{\gamma \epsilon V_m}{z F h}$  can be eliminated using Eq. [11] so that  $i_{o,st}^*$  can be determined from

$$i_{o,st}^* = K \Delta i_o \frac{\eta}{i} \quad [13]$$

The constant  $K$  in Eq. [13] was obtained by measuring the dependence of the propagation rate  $\theta$  of steps from overvoltage according to (23) (Fig. 3), while

$$\theta = K \frac{V_m \eta}{z F h} \text{ [cm} \cdot \text{sec}^{-1}\text{]} \quad [14]$$

A value of  $1.77 \times 10^{-4} \text{ ohm}^{-1} \text{ cm}^{-1}$  was found for  $K$ .

The values of  $i_{o,st}^*$  at different preparation conditions are represented in column 6. It is clearly seen that  $i_{o,st}^*$  is a constant which does not depend on the preparation conditions. This quantity is related to the exchange current density  $i_{o,st}$  of the direct transfer reaction. Assuming that the ion exchange takes place at a distance from the step edge not exceeding the thickness of one atomic row added to the step, the current density of the direct charge transfer reaction can be obtained by dividing  $i_{o,st}^*$  with this thickness, which

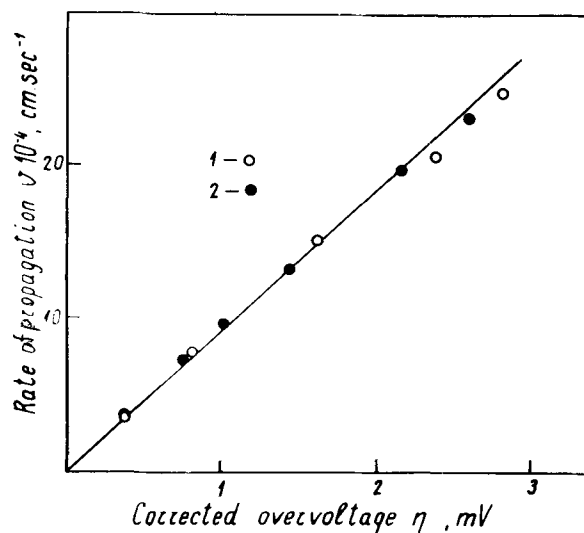


Fig. 3. Overvoltage dependence of the propagation rate of spiral steps on a cubic plane.

for the cubic plane is equal to the diameter of the silver atom in the crystal lattice  $2r_o = 2.88 \cdot 10^{-8} \text{ cm}$ , i.e.

$$i_{o,st} = 180 \pm 24 \text{ A cm}^{-2}$$

This value is about three orders of magnitude higher than the  $i_{o,ad}$  value for adions. This fact might be considered as contradicting the theoretical calculations of Conway and Bockris (1). However considering the case of ion discharge on the edge of a growth step, Despic (2) showed recently that the discharge on a step can proceed almost barrierless.

*Steady-state deposition mechanism.*—We can now return to the case of a steady state, to discuss which of the two mechanisms is prevailing in metal deposition: (i) the surface diffusion mechanism or (ii) the direct transfer mechanism.

The experimental current-square overvoltage dependence on a plane with screw dislocations has shown that the current is proportional to the step length. This fact is consistent with mechanism (ii), but agrees also with mechanism (i) under the condition that the surface diffusion penetration  $\lambda_o$  is smaller than the minimum value of the half distance of the steps over the entire range of experimental conditions, where the validity of the current-square overvoltage law was confirmed, i.e.

$$\lambda_o < x_{o,min} = \frac{\gamma \epsilon V_m}{2z F h \eta_{max}} \quad [15]$$

In order to distinguish between the two mechanisms, it is necessary to know not only the value of  $i_{o,ad}$  and  $i_{o,st}$ , but also that of  $\lambda_o$ . The estimation of the latter is however impossible since the value of  $D_s$  is unaccessible. An evaluation of the maximal value of  $\lambda_o$  nevertheless is feasible with the aid of the relation

$$x_{o,min} = \frac{K}{2} \frac{1}{\left(\frac{di}{d\eta^2}\right) \eta_{max}} \quad [16]$$

which is obtained from Eq. [9] and [11]. With  $\frac{di}{d\eta^2} = 7.2 \times 10^3 \text{ AV}^{-2} \text{ cm}^{-2}$  (Fig. 4),  $K = 1.77 \times 10^{-4} \text{ ohm}^{-1} \text{ cm}^{-1}$ , and  $\eta_{max} = 3 \text{ mV}$ , one obtains  $\lambda_o < 4 \times 10^{-6} \text{ cm}$ .

We can now compare the contributions of the surface diffusion and that of direct transfer to the deposition process using experimental and calculated values of the propagation rate of monosteps. From the measurements of the kinetics of advance of monolayers (24) and the rate of propagation of spiral steps (Fig. 3)



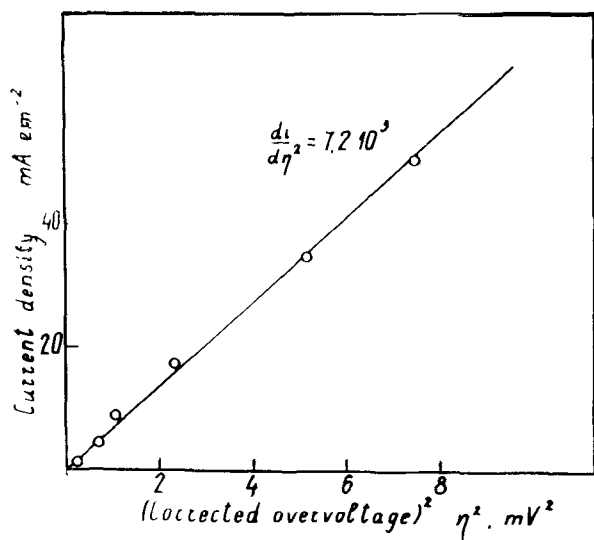


Fig. 4. Current-square overvoltage plot obtained on a cubic plane

a value  $\theta_{\text{exp}} = (0.92 \text{ to } 1.04) \times \eta \text{ cm} \cdot \text{sec}^{-1}$  ( $\eta$  in volts) was found.<sup>2</sup>

The rate of propagation can be calculated from the current density  $i$  and step density  $L$  according to

$$\theta = \frac{iV_m}{zFhL}$$

in the case of direct transfer and surface diffusion using the theoretical  $i/\eta$  relations [2] and [3].

For small  $\eta$  values in the case of surface diffusion we have

$$\theta_{\text{SD}} = \frac{i_{0,\text{ad}} V_m 2\lambda_0}{RT h} \eta \quad [17a]$$

and in the case of direct transfer

$$\theta_{\text{DT}} = \frac{i_{0,\text{st}} V_m 2r_0}{RT h} \eta \quad [17b]$$

A comparison between calculated and experimental results can also be made in terms of the current-square overvoltage law

$$i = B\eta^2$$

The experimental value of  $B$  is  $7.2 \times 10^3 \text{ AV}^{-2} \text{ cm}^{-2}$  (Fig. 4). The constant  $B$  can be calculated for both mechanisms using the values of  $i_{0,\text{ad}}$  and  $\Delta i_0/\eta$ , determined by impedance measurements.

In the case of surface diffusion after linearization for low  $\eta$  values and having in mind relation [15], Eq. [2] yields

$$i < \frac{i_{0,\text{ad}}}{\eta_{\text{max}}} \frac{zF}{RT} \eta^2 \quad [18a]$$

For direct transfer the constant  $B$  can be estimated from the relation

$$i = \frac{\Delta i_0}{\eta} \frac{zF}{RT} \eta^2 \quad [18b]$$

which is derived from Eq. [3] after linearization at low  $\eta$  values and taking into account that  $i_{0,\text{st}} = \Delta i_0/2r_0L$ .

Calculated and experimental values of the propagation rate constant  $d\theta/d\eta$  and the current-square overvoltage relation constant  $B = di/d\eta^2$  are given in Table II.

It can readily be seen that the direct transfer in our case plays a predominant role and is sufficiently rapid

<sup>2</sup> The similarity in the propagation rates for both monolayers and spiral steps gives reason to suggest that the latter are also monoatomic.

Table II. Calculated and experimental values of the propagation rate constant  $\frac{d\theta}{d\eta}$  and the current-square overvoltage relation constant  $B$  for the cubic plane of silver in 6M  $\text{AgNO}_3$  (45°C)

	Propagation rate constant, $\frac{d\theta}{d\eta}$ (cm sec <sup>-1</sup> V <sup>-1</sup> )	Current-square overvoltage constant, $B$ (AV <sup>-2</sup> cm <sup>-2</sup> )
		Calculated values*
Surface diffusion mechanism	Acc. Eq. [17] <0.094	Acc. Eq. [18] <0.74 × 10 <sup>3</sup>
Direct transfer mechanism	1.01 ± 0.14	(7.8 ± 0.5) × 10 <sup>3</sup>
	Experimental values	
Rate of propagation of monolayers (24)	1.04	—
Spiral growth	0.92 ± 0.61	(7.2 ± 0.9) × 10 <sup>3</sup>

\*  $i_{0,\text{ad}} = 0.060 \pm 0.001 \text{ A cm}^{-2}$ ;  $i_{0,\text{st}} = 180 \pm 24 \text{ A cm}^{-2}$ ;  $\lambda_0 < 4 \times 10^{-6} \text{ cm}$ ;  $\frac{\Delta i_0}{\eta} = (0.21 \pm 0.01) \times 10^3 \text{ AV}^{-1} \text{ cm}^{-2}$ ;  $\eta_{\text{max}} = 3 \text{ mV}$ .

to supply ions for the rate of advance as found experimentally.

It appears that, at least in the case of silver deposition from concentrated silver nitrate solutions, the contribution of the surface diffusion mechanism is negligibly small.

Manuscript submitted Dec. 19, 1972; revised manuscript received June 14, 1973. This was Paper 119 presented at the Cleveland, Ohio, Meeting of the Society, Oct. 3-7, 1971.

Any discussion of this paper will appear in a Discussion Section to be published in the December 1974 JOURNAL.

#### REFERENCES

- B. Conway and J. O'M. Bockris, *Proc. Roy. Soc., Ser. A.*, **248**, 394 (1958).
- A. Despic, *Croat. Chem. Acta*, **42**, 265 (1970).
- H. Brandes, *Z. Phys. Chem.*, **142 A**, 97 (1927).
- W. Lorenz, *Z. Naturforsch.*, **9a**, 716 (1954).
- 5a. N. Cabrera and W. Burton, *Discussions Faraday Soc.*, **5**, 40 (1949).
- 5b. W. Burton, N. Cabrera, and F. Frank, *Phil. Trans. Roy. Soc.*, **243 A**, 299 (1951).
- D. Vermilyea, *J. Chem. Phys.*, **25**, 1254 (1956).
- M. Fleischmann and H. Thirsk, *Electrochim. Acta*, **2**, 22 (1960).
- A. Damjanovic and J. O'M. Bockris, *This Journal*, **110**, 1035 (1963).
- Ch. Schnittler, *Z. Phys. Chem.*, **234**, 77, 379 (1967).
- M. Volmer, "Das electrolytische Kristallwachstum," Herman, Paris (1934).
- H. Gerischer, "Protection Against Corrosion by Metal Finishing," p. 11, Forster Verlag AG Zürich (1967).
- N. Mott and R. Watts-Tobin, *Electrochim. Acta*, **4**, 79 (1961).
- K. Vetter, "Elektrochemische Kinetik," Springer-Verlag, Berlin (1961).
- M. Fleischmann, S. K. Rangarajan, and H. Thirsk, *Trans. Faraday Soc.*, **63**, 1251 (1967).
- Ch. Schnittler, Habilitation, T. H. Ilmenau, September 1969.
- E. Budevski and W. Bostanov, *Electrochim. Acta*, **9**, 477 (1964); W. Bostanov, A. Kotzeva, and E. Budevski, *Bull. Inst. Chim. Phys., Acad. Bulgare Sci.*, **6**, 33 (1967).
- E. Budevski, T. Vitanov, and W. Bostanov, *Phys. Status Solidi*, **8**, 369 (1965).
- E. Budevski, W. Bostanov, T. Vitanov, Zdr. Stoinov, A. Kotzeva, and R. Kaishev, *Phys. Status Solidi*, **13**, 577 (1966); *Electrochim. Acta*, **11**, 1697 (1966).
- R. Kaischew and E. Budevski, *Contemp. Phys.*, **8**, 489 (1967).
- E. Budevski, *Electrochim. Metal.*, **1**, 1 (1966).
- R. Kaischew, E. Budevski, and J. Malinovski, *Z. Phys. Chem.*, **204**, 348 (1955).
- W. Bostanov, R. Roussinova, and E. Budevski, *Comm. Dept. Chem., Bulg. Acad. Sci.*, **2**, 885 (1969).

23. W. Bostanov, G. Staikov, E. Budevski, and R. Kaischew, *ibid.*, **4**, 311 (1971).  
 24. W. Bostanov, R. Roussinova, and E. Budevski, In press.  
 25. T. Vitanov, E. Sevastianov, W. Bostanov, and E. Budevski, *Elektrokhimiya*, **5**, 451 (1969).  
 26. T. Vitanov, E. Sevastianov, Zdr. Stoinov, and E. Budevski, *ibid.*, **5**, 238 (1969).

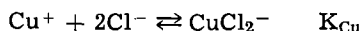
## Electrochemical Studies on Ag, Fe, and Cu Species in AlCl<sub>3</sub>-NaCl Melts

L. G. Boxall,\* H. L. Jones, and R. A. Osteryoung\*

Department of Chemistry, Colorado State University, Fort Collins, Colorado 80521

### ABSTRACT

The electrochemical behavior of the Ag/Ag<sup>+</sup>, Fe/Fe<sup>2+</sup>, Fe<sup>2+</sup>/Fe<sup>3+</sup>, and Cu/Cu<sup>+</sup>, Cu<sup>+</sup>/Cu<sup>2+</sup> systems in the equimolar region of AlCl<sub>3</sub>-NaCl melts has been investigated using potentiometry, pulse polarography, cyclic voltammetry, chronoamperometry, and chronopotentiometry. In contrast to the Al electrode, the emf of the Ag<sup>+</sup>/Ag electrode was found to be virtually independent of the melt composition. The Ag<sup>+</sup> was found to undergo reversible deposition at a tungsten electrode. However, in cyclic voltammetric experiments, the stripping process showed a marked dependence on Ag<sup>+</sup> concentration, temperature, and sweep rate. Possible explanations for this dependence are presented. The diffusion coefficient for Ag<sup>+</sup> at 175°C was found to be  $3.01 \times 10^{-6}$  cm<sup>2</sup> sec<sup>-1</sup>. The Fe<sup>3+</sup>/Fe<sup>2+</sup> couple was found to be reversible while the Fe<sup>2+</sup>/Fe couple showed typical deposition-stripping behavior. Above an initial FeCl<sub>3</sub> concentration of 5 mM the deposition process became concentration independent while the stripping process was found to involve two different electrode reactions. This behavior was consistent with the low solubility of FeCl<sub>2</sub> in the equimolar region. Nernst plots for the anodization of Cu gave low n-values in Cl-rich melts, while n-values of 1 were obtained in AlCl<sub>3</sub>-rich melts. These results are best explained by introducing the following equilibrium reaction



for which a value of  $6.5 \times 10^4$  was calculated for  $K_{\text{Cu}}$ . The two Cu couples were well behaved electrochemically.

Electrochemical studies of metal/metal ion systems in molten AlCl<sub>3</sub>-alkali halides have received considerable attention in recent years (1-10). These studies have been carried out almost exclusively in AlCl<sub>3</sub>-rich melts where, in several cases (11-14), unusually low oxidation states are stabilized because of the high acidity of the solvent. To our knowledge studies of metal/metal ion systems in NaCl-rich or equimolar chloroaluminate melts, where the greatest change in acidity occurs, have gone unreported.

In the present investigation we have studied the electrochemical behavior of the Ag/Ag<sup>+</sup>, Fe/Fe<sup>2+</sup>, Fe<sup>2+</sup>/Fe<sup>3+</sup>, and Cu/Cu<sup>+</sup>, Cu<sup>+</sup>/Cu<sup>2+</sup> systems in the equimolar region of AlCl<sub>3</sub>-NaCl melts. The recently devised aluminum titration technique has allowed us to adjust the acidity of the melt to any desired value (16). The marked dependency of the Al reference electrode on the composition of the melt led us to look at the Ag/Ag<sup>+</sup> and Cu/Cu<sup>+</sup>, Cu<sup>+</sup>/Cu<sup>2+</sup> systems while the possibility of iron impurities in these melts led us to study the Fe/Fe<sup>2+</sup>, Fe<sup>2+</sup>/Fe<sup>3+</sup> system. The electrochemistry of these melts is characterized by the use of cyclic voltammetry, pulse polarography, chronoamperometry, and chronopotentiometry.

### Experimental

All of the experimental work was carried out in a nitrogen-filled dry box (Vacuum Atmosphere, Inc.) to protect the melts from moisture and oxygen. All of the glassware was heated to 500°C for several hours and then allowed to cool in the evacuated antechamber of the dry box.

\* Electrochemical Society Active Member.

Key words: fused salts, AlCl<sub>3</sub>-NaCl melt, metal/metal ion systems, pulse polarography, cyclic voltammetry.

To facilitate the ease and rate at which an individual experiment could be carried out, a special electrochemical cell (Fig. 1) incorporating a glass bottom and a tight fitting Teflon top was constructed. Several holes were drilled in the Teflon top and various sizes of ground joints were press-fitted in these holes. The typical cell top contained a 6 mm hole for a thermocouple well, a 10/18 joint for a counterelectrode, a 14/20 joint for the reference electrode compartment, and a 25 mm hole with an O-ring groove around the top for the working electrode compartment. Together with a standard tube furnace, small ring furnaces were built to fit around the Teflon tops. By maintaining the temperature of the tops between 175° and 200°C, the build-up of AlCl<sub>3</sub> in the cooler portions of the cell was eliminated. This feature is of utmost importance when measurements are made in the AlCl<sub>3</sub>-rich melts.

Temperature controllers (Thermo Electric Model 32422) were used to control the temperatures of the melts to within  $\pm 0.5^\circ\text{C}$ . The temperature was measured using a Chromel-Alumel Pyrex-sheathed thermocouple and a Leeds & Northrup Student Potentiometer. The precision of the potentiometer was better than  $\pm 0.1$  mV compared to a precision voltage source.

All electrochemical measurements were made with a multipurpose instrument (15) interfaced to a Digital Equipment Corporation PDP-12 computer. Read-out of the data was by either a Hewlett-Packard Model 7004-B X-Y recorder, a Hewlett-Packard Model 7030-AM X-Y recorder with point plotting capabilities, or a Tektronics Model 564 oscilloscope with a Type 3A3 and Type 2A63 plug-ins. A Sargent Model IV coulometric current source was used for all of the anodization of the metals in the melt. The purity of all the metals was better than 99.99%.

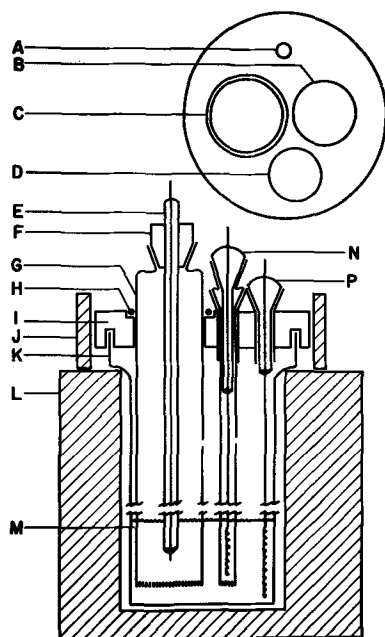


Fig. 1. Experimental electrochemical cell. A, Thermocouple well; B, 19/22 ground joint for reference electrode; C, 25 mm hole for working electrode compartment; D, 14/20 ground joint for counter-electrode; E, working electrode; F, Teflon adaptor; G, fritted working electrode compartment; H, O-ring; I, Teflon cell top; J, ring furnace; K, Pyrex glass cell; L, furnace; M, melt; N, reference electrode compartment and Al electrode; P, tungsten counterelectrode.

**Melt purification.**—Chemical analysis of the Fluka (A.G., anhydrous iron free) aluminum chloride and the Fluka (A.G.) sodium chloride found their purity to be better than 99.5%. The fusion of Fluka (A.G., anhydrous, iron free) aluminum chloride and Fluka (A.G.) sodium chloride usually produced a faintly yellow-colored melt which would slowly turn gray in color on standing for a period of several days. Rather than use a pair of Pt electrodes for purification electrolysis (where  $\text{Cl}_2$  is produced at the anode during electrolysis), a pair of aluminum electrodes was used. The net result during the electrolysis, thus, is either the replacement of impurities in the melt with the aluminum ion or the transfer of Al from one electrode to the other. The simple displacement of the impurities using Al metal failed due to the coating of the metal surface by a film formed by the displaced metal impurities which effectively stopped further displacement. The transfer of Al metal in the electrolysis procedure continually replenishes the Al surface and prevents the passivation of the aluminum. The normal procedure is to electrolyze the melt in the temperature range  $225^\circ\text{-}250^\circ\text{C}$  for at least 24 hr at a current density of  $1.5 \text{ mA cm}^{-2}$ .

In carrying out the work described below, the normal procedure was to prepare a 150 mliter melt in a cell placed in a furnace containing a window so that the bottom of the cell could be seen. After purification, the 7 mm fine-porosity sintered-glass fritted reference electrode compartment was placed into the melt. The aluminum reference electrode consisted of a spiral of aluminum wire connected to a short piece of tungsten wire sealed in the glass plug in the top of the reference compartment. The counterelectrode consisted of a large tungsten wire spiral sealed into a  $\text{T} 10/18$  glass plug. The working electrode compartment consisted of a 20 mm medium-porosity sintered glass frit at one end, a 25 mm piece of glass tubing in the middle, and a  $\text{T} 14/20$  ground joint at the top. A tightly fitting O-ring around the 25 mm glass barrel of the compartment both supported and sealed it in the Teflon top. Teflon adapters were used to seal the electrodes into the compartment as well as adjust the level of the

electrode in the compartment. The working electrode compartment was filled to approximately 10 mliters either by flow through the frit from the bulk of the melt, or by transferring melt from a second furnace by means of a preheated pipette. All of the compartments were adjusted so that all of the melt levels in the cell were equal. It was necessary to blow a small hole 5-7 cm above the melt level in each of the cell compartments to equalize any differences in the vapor pressures above the various melts.

**Pretreatment of the micro tungsten indicator electrodes.**—If the tungsten wire was found to be very splintery due to longitudinal holes in the wire, or to contain excessive amounts of gas, it was not used in the manufacture of the electrodes. The wire was sealed into 6 mm Pyrex glass tubing using a bead of uranium glass. The button electrodes were ground flat on an emery wheel and then polished with 600 grit silicon carbide powder. All the tungsten electrodes were then electrolyzed for 15 sec at 4-5V a.c. in a 25% sodium hydroxide solution. After rinsing with water, the electrodes were dried under vacuum at  $110^\circ\text{C}$  for several hours. It was necessary to cycle the electrode from +0.5 to +1.5V in the melt for several minutes to remove the final traces of the oxide film on the metal electrode surface. This electrolysis procedure produced a reasonably reproducible indicator electrode.

**Reference electrode.**—The potential of the aluminum electrode in the fritted reference compartment vs. Al in an equimolar  $\text{AlCl}_3\text{-NaCl}$  melt was determined by the aluminum titration technique (16). The potential of this arbitrary, but stable, reference electrode system was normally about 170 mV negative of the Al electrode in the 1:1 melt.<sup>1</sup> A variation of less than  $\pm 2 \text{ mV}$  was observed for a given reference electrode over a period of 2 months.

Aluminum anodization was used to adjust the acidity of the melt in the working electrode compartment to any desired value. This enabled us to determine the acid dependency of each electrode system being studied.

## Results and Discussion

All of the potentials are reported with respect to an aluminum reference electrode in an equimolar  $\text{AlCl}_3\text{-NaCl}$  melt.

Cyclic voltammetry was used to determine the current-voltage characteristics of the melt before (Fig. 2a) and after (Fig. 2b) purification. The final melt was completely colorless and exhibited no irregularities in the current-voltage curves using either a tungsten button or a hanging mercury drop indicator electrode.

<sup>1</sup> Throughout this paper the expression "1:1 melt" refers to a melt consisting of 50:50 m/o (mole per cent)  $\text{AlCl}_3\text{:NaCl}$  while a 2:1 melt refers to 66.34 m/o  $\text{AlCl}_3\text{:NaCl}$ .

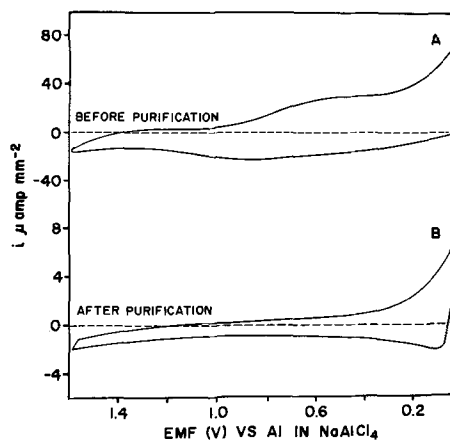


Fig. 2. Cyclic voltammetry of  $\text{NaAlCl}_4$  background on tungsten,  $175^\circ\text{C}$ ,  $\nu = 0.5 \text{ V/sec}$ .

After a week's storage of the melt, open to the atmosphere in the dry box, no detectable changes were observed. Under similar experimental conditions the background current reported by Torsi and Mamantov (13) is about ten times larger than what we have observed. Unfortunately, most of the other workers have not published their background currents; hence, many of the discrepancies in the literature may be due to impure melts.

Most of the experimental measurements were made using either tungsten button or wire indicator electrodes. The useful potential range of these electrodes was from 0.3 to 1.5V. On carrying out voltammetric experiments beyond this range, it appeared as if the electrode increased in area resulting in a background current of about four to five times the magnitude of the original values. No significant changes were observed in the shape of these enhanced voltammograms except for the increase in magnitude by a constant factor.

An apparent differential capacity,  $C_d$ , for the indicator electrode in a pure melt was determined from the slope of a plot of current *vs.* sweep rate at a given potential. The plots for the tungsten electrodes at sweep rates greater than 1.0 V-sec<sup>-1</sup> gave consistent  $C_d$  values with respect to sweep rate; however, the  $C_d$  values increased as the applied potential decreased. The  $C_d$  values increased from 50-80  $\mu\text{F cm}^{-2}$  at 0.8V to 160-200  $\mu\text{F cm}^{-2}$  at 0.1V. Slow sweep rates (0.05-0.5 V-sec<sup>-1</sup>) produced capacitances which were abnormally high and very dependent on the preparation of the electrode. At slow sweep rates any faradaic reaction, such as filming or alloying, could make an appreciable contribution to the observed current. The degree of roughness of the solid electrode will change the effective capacitance area of the tungsten electrodes and, hence, the calculated  $C_d$  value.

The background cyclic voltammogram using a platinum button electrode exhibited two anodic and two cathodic waves between +0.3 and +1.1V; however, at potentials more anodic than +1.1V, the electrode appeared to be well behaved. Continued cyclic sweeps caused the anodic and cathodic peaks for one couple to grow and the peaks for the other couple to decrease in height. As the sweep rate was increased, the growth phenomenon shifted from the couple at 0.9V to the one at 0.6V. The fact that stirring had no effect on the voltammogram and that none of the other electrode materials exhibited peaks in this region suggested one of two things: (i) the peaks may arise from some surface reaction involving a platinum chloride film, or (ii) some impurity is strongly adsorbed and the reaction is catalyzed on the platinum surface. For these reasons the platinum electrode received only limited use as an indicator electrode in the chloroaluminate melts.

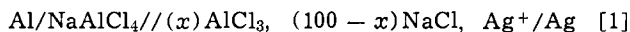
Cyclic voltammograms in which the sweep rate varied from 0.05 to 100 V-sec<sup>-1</sup> exhibited a useful working range from +0.1 to +1.0V for a hanging mercury drop electrode. Shifting the cathodic limit from +0.10 to +0.05V produced an anodic peak at +0.55V which disappeared as soon as the cathodic limit was returned to +0.10V. The shift in the useful working range for the mercury electrode with increasing melt acidity is identical to that observed for the aluminum reference electrode. Plots of current, measured at various potentials, *vs.* the sweep rate (0.05-100 V-sec<sup>-1</sup>) gave consistent capacitance values of  $\sim 14 \mu\text{F cm}^{-2}$  for the mercury electrode in the NaAlCl<sub>4</sub> melt at 175°C. The main disadvantages of this electrode are the mechanical problems and the fact that most of the metals of interest are electroactive at potentials in excess of 1.0V. The advantages are the use of a nonsolid electrode and the fact that observed capacitance is about one-tenth that of the tungsten electrodes.

**Silver.**—Silver(I) was generated coulometrically in the chloroaluminate melts with 100% current effi-

ciency at current densities from 1 to 30 mA cm<sup>-2</sup>. All of the Ag<sup>+</sup> solutions were clear and colorless under all experimental conditions. The polarization of the silver wire never exceeded 200 mV during any of the electrolysis. An average value for  $n$  of  $0.99 \pm 0.02$  was obtained either from Nernst plots (Fig. 3) or chemical analysis for silver in the melt. The  $E_M^0$  (molarity scale obtained by extrapolation of Nernst plots) values for silver in the 1:1 and 2:1 melts at 175°C *vs.* Al in the 1:1 melt are  $1.086 \pm 0.010$  and  $1.106 \pm 0.010\text{V}$ , respectively. The major portion of the 10 mV uncertainty in these values is due to the errors in determining the actual potential of the experimental Al reference electrode with respect to an Al electrode in an exact 1:1 melt. A plot of  $E_M^0$  *vs.* temperature (175°-250°C) for silver in a 1:1 melt showed no hysteresis and gave a value for  $dE_M^0/dt$  of  $-0.63 \pm 0.05 \text{ mV deg}^{-1}$ . This value is to be compared with the value of  $-0.44 \text{ mV deg}^{-1}$  reported for silver in the ternary [66:20:14 m/o (mole per cent) AlCl<sub>3</sub>:NaCl:KCl] melt (6).

Good agreement was found between our  $E_M^0$  (1.106V) value for silver in a 2:1 melt at 175°C and the value of 1.132V derived from Plambeck and co-workers (6) who reported  $E_M^0$  values of 0.695 and 0.714V in the ternary melt at 135° and 150°C, respectively. This conversion was accomplished using the authors'  $dE_M^0/dt$  value, and the assumption that the potential of the Al electrode in ternary melt is equivalent to the Al electrode in the 2:1 (AlCl<sub>3</sub>:NaCl) melt (*i.e.*, 455 mV *vs.* Al in the 1:1 melt). The 26 mV difference may be easily attributed to the effect of changing the cations in the melt from just sodium to a mixture of sodium and potassium ions. This effect has been observed in other melts as well (17).

The response of the potential of the silver electrode to a change in the composition of the melt at 175°C was determined using the cell



and is shown in Fig. 4. The response of an Al electrode is included for comparison. The mole per cent AlCl<sub>3</sub> was varied from 66 to 49.7% by the addition of known aliquots of NaCl to the 2:1 melt. The  $E_M^0$  values determined from Nernst plots in which the AlCl<sub>3</sub> content had been adjusted by the anodization of an aluminum wire are in accord with the values in Fig. 4.

The difference of 20 mV in the  $E_M^0$  values for silver in the two melts is almost negligible compared to the 455 mV observed for the aluminum electrode. The indifference of the silver electrode potential to the 4.5 orders of magnitude of change in the chloride ion concentration indicates that the silver ion is a much weaker acid than the AlCl<sub>3</sub> in these chloroaluminate melts. It is evident that the silver electrode would be a much better reference electrode for these melts than is the aluminum electrode.

Typical pulse polarograms and cyclic voltammograms for the deposition of Ag<sup>+</sup> at a tungsten electrode

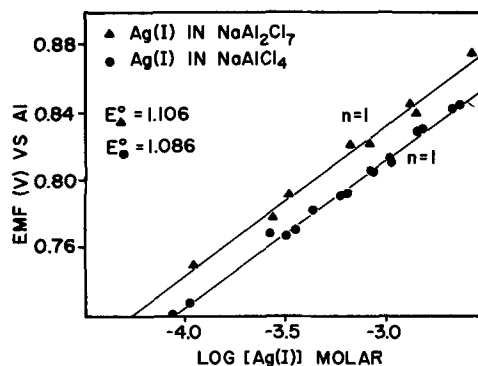


Fig. 3. Nernst plot for silver in the 1:1 and 2:1 AlCl<sub>3</sub>-NaCl melts at 175°C. An Al reference in NaAlCl<sub>4</sub> melt for both plots.

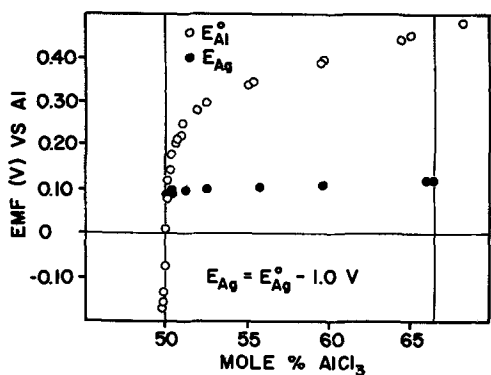


Fig. 4. Standard electrode potentials for aluminum and silver as a function of  $\text{AlCl}_3$ - $\text{NaCl}$  ratio at  $175^\circ\text{C}$ .

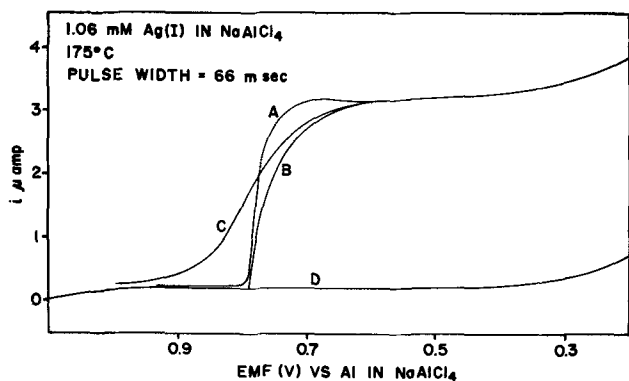


Fig. 5. Normal pulse polarogram of  $\text{Ag}^+$  in  $\text{NaAlCl}_4$ . Area of tungsten indicator electrode =  $0.785 \text{ mm}^2$ . A, Experimental curve; B, theoretical for deposition of a solid  $\sim E = E_{1/2} + \frac{RT}{F} \ln(i_d - i)$ ; C, theoretical for formation of diffusing species  $\sim E = E_{1/2} + \frac{RT}{F} \ln \frac{(i_d - i)}{i}$ ; D, background.

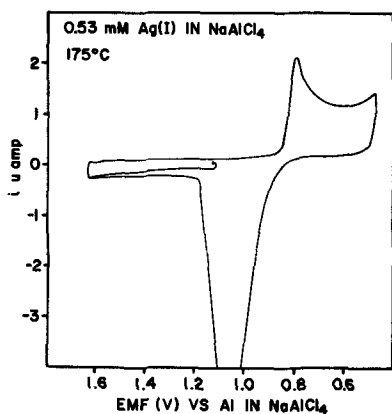


Fig. 6. Cyclic voltammogram of  $\text{Ag}^+$  in  $\text{NaAlCl}_4$ . Area of tungsten indicator electrode =  $0.785 \text{ mm}^2$ .  $\nu = 0.5 \text{ V/sec}$ .

are shown in Fig. 5 and 6, respectively. Plots of the observed currents vs. pulse width (Fig. 7), and  $\text{Ag}^+$  concentration (Fig. 8) were linear (18). Values for  $i_p/\nu^{1/2}$  and  $E_p$  remained constant when the cyclic voltammetric sweep rate was varied from 0.01 to  $100 \text{ V-sec}^{-1}$ . The experimental pulse polarogram is most closely approximated by the theoretical plot (Fig. 5) for the deposition of an insoluble product. A value for the diffusion coefficient of  $3.01 \times 10^{-6} \text{ cm}^2 \text{ sec}^{-1}$  was calculated from the pulse polarographic data using the Cottrell equation.

Although the shape of the cathodic peak for  $\text{Ag}^+$  reduction in the observed cyclic voltammograms was unaffected by changes in temperature and/or concen-

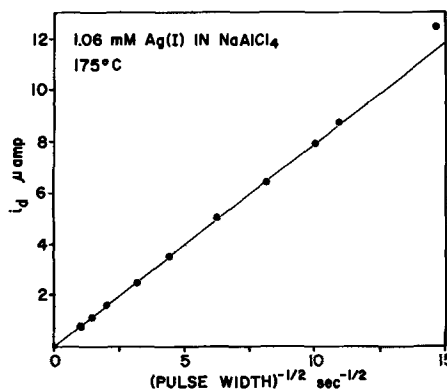


Fig. 7. Normal pulse diffusion current for  $\text{Ag}^+$  vs. pulse width. Area of tungsten electrode =  $0.785 \text{ mm}^2$ .

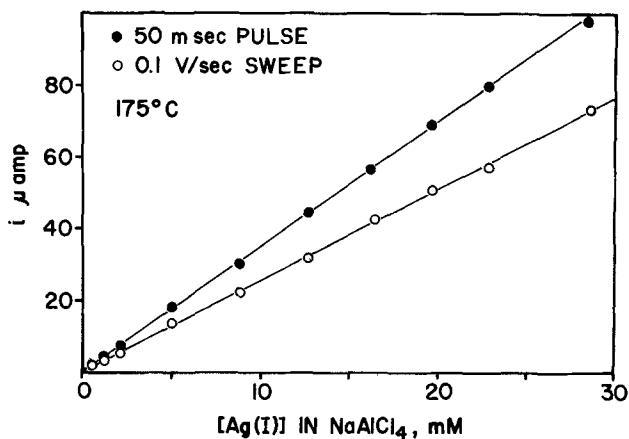


Fig. 8. Normal pulse diffusion current and cyclic voltammetry peak current vs.  $\text{Ag}^+$  concentration in  $\text{NaAlCl}_4$ . Area of tungsten indicator electrode =  $0.785 \text{ mm}^2$ .

tration, marked differences occurred in the anodic portion. A second sharp anodic stripping peak positive to the main stripping peak was observed as a result of increased  $\text{Ag}^+$  concentrations or lowered temperatures (Fig. 9). At  $175^\circ\text{C}$  this peak does not appear during a single continuous cycle until the  $\text{Ag}^+$  concentration exceeds  $\approx 1 \text{ mM}$ . If the sweep is held momentarily at  $0.5 \text{ V}$ , the second anodic peak can be observed at lower  $\text{Ag}^+$  concentrations. Regardless of the  $\text{Ag}^+$  concentration, the second anodic peak could not be observed without first sweeping through the region of silver deposition and dissolution. The position of this peak shifts anodically with a decrease in temperature and to a lesser degree with an increase in the  $\text{Ag}^+$  concentration. At temperatures of  $200^\circ\text{C}$  and above, this peak collapses completely to form a single broad stripping

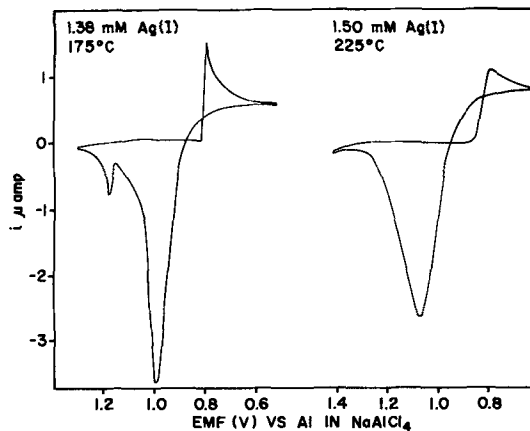


Fig. 9. Cyclic voltammograms of  $\text{Ag}^+$  in  $\text{NaAlCl}_4$ .  $\nu = 0.05 \text{ V/sec}$ . Area of tungsten indicator electrode =  $0.785 \text{ mm}^2$ .

peak. Cyclic voltacoulograms show that the area under the small anodic peak corresponds to the quantity of silver on the electrode surface ranging from less than half a monolayer to that stripped off in the first peak. The size of the peak is directly proportional to the amount of silver being stripped off the electrode. Cyclic voltammograms in the 2:1 melt exhibit only the single large anodic stripping peak regardless of the  $\text{Ag}^+$  concentrations or switching potential. The charge under the small anodic peak is directly proportional to the amount of silver being stripped off the electrode. Also, the ratio of the areas of the second peak to that of the first stripping peak increases with both  $\text{Ag}^+$  concentration and sweep rate.

This anodic behavior suggests that there may be two different electrode reactions by which the silver metal is stripped from the indicator electrode. The first reaction is not diffusion limited when only small amounts of silver are anodized; however, at a higher rate of silver anodization, the local concentration of the anionic species is depleted and the electrode reaction shifts to the more anodic reaction. The product from the second reaction then reacts in the solution to form a single dominant silver species in solution, hence a single deposition peak. The Nernst data indicates that the  $\text{Ag}^+$  ion is not complexed with the  $\text{Cl}^-$  ion leaving only the  $\text{AlCl}_4^-$  and/or the  $\text{Al}_2\text{Cl}_7^-$  anions to take part in the electrode reaction. It does not appear likely that the  $\text{AlCl}_4^-$  anion would be diffusion limited due to its high concentration in the melt. The  $\text{Al}_2\text{Cl}_7^-$  concentration is low enough in the 1:1 melt to exhibit this diffusion-limiting effect. The increase in the  $\text{Al}_2\text{Cl}_7^-$  concentration in the  $\text{AlCl}_3$ -rich melts and the increase in its diffusion coefficient would produce changes in the stripping peak consistent with the experimental data. A temperature increase from 175° to 250°C will also triple the  $\text{Al}_2\text{Cl}_7^-$  concentration in the melt (16).

The second stripping peak may be the formation of the uncomplexed  $\text{Ag}^+$  ion or an  $\text{Ag}(\text{AlCl}_4)_{n-1}^-$  complex. The ratio of the area under the second peak to that under the first stripping peak increases with both sweep rate and the silver concentration. This is consistent with the premise that the first peak may become diffusion limited. The small cathodic wave at about 1.15V in Fig. 9 (175°C) becomes more prevalent at higher sweep rates, higher  $\text{Ag}^+$  concentrations, and when the anodic switching potential is moved closer to that of the second stripping peak. If the anodic switching potential is moved cathodic of the second peak, this small cathodic wave disappears completely.

No explanation is available at the present which will satisfy all of the experimental data.

**Iron.**—A number of methods were tried to introduce an iron species into a 1:1 melt. Ferrous chloride was found to be virtually insoluble and anodization of an iron wire at current densities as low as  $2 \text{ mA cm}^{-1}$  polarized the electrode to such an extent ( $\approx 2\text{V}$ ) that chlorine evolution occurred. However, ferric chloride was found to be readily soluble. Also, a steady current of  $500 \mu\text{A}$  could be realized by potentiostating the iron wire at +1.6V vs. the aluminum reference electrode. None of the above problems were encountered when adding iron to a 2:1 melt. The inability to anodize an iron wire appeared to be caused by filming of the electrode (insoluble  $\text{FeCl}_2$ ). The insolubility of the lower oxidation states of other metals has been noted before when the chloroaluminate melts were of low acidity (7).

In a 2:1 melt a Nernst plot for the  $\text{Fe}^{2+}/\text{Fe}$  system gave a value of 0.98V for  $E^0_M$ . The slope was 0.042V compared to the theoretical value of 0.044V for a two-electron process. A temperature coefficient of  $-0.77 \text{ mV deg}^{-1}$  over a range of 175°-225°C was found. Our  $E^0_M$  value of 0.95V at 218°C is in good agreement with the published value (2) of 0.97V.

A normal pulse polarogram for the reduction of  $\text{FeCl}_3$  in a 1:1 melt is shown in Fig. 10. The height of

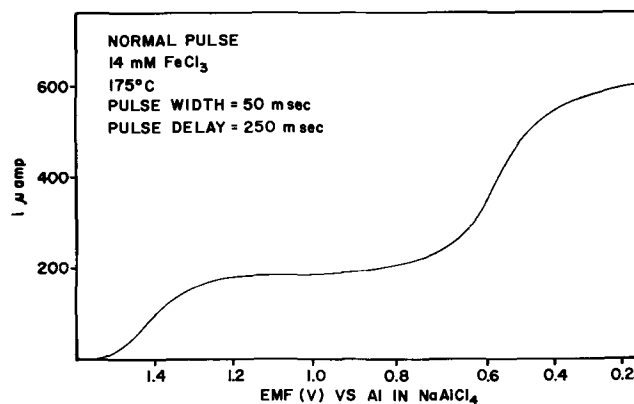


Fig. 10. Normal pulse polarogram of  $\text{Fe}^{3+}$  in  $\text{NaAlCl}_4$ . Area of tungsten indicator electrode =  $1.79 \text{ mm}^2$ .

the wave attributed to the  $\text{Fe}^{2+}/\text{Fe}$  couple ( $E_{1/2} = 0.509 \pm 0.005\text{V}$ ) is twice that for the  $\text{Fe}^{3+}/\text{Fe}^{2+}$  couple ( $E_{1/2} = 1.406 \pm 0.005\text{V}$ ). Linear plots of diffusion current vs. concentration gave a slope for the  $\text{Fe}^{2+}/\text{Fe}$  couple which was twice that for the  $\text{Fe}^{3+}/\text{Fe}^{2+}$  couple.

The cathodic and reverse anodic scans from double potential step pulse polarography (19) for the  $\text{Fe}^{3+}/\text{Fe}^{2+}$  couple are presented in Fig. 11. In this technique a generating pulse is applied causing the *in situ* reduction of  $\text{Fe}^{3+}$  to  $\text{Fe}^{2+}$ . Each generating pulse is followed by a normal pulse polarographic analysis pulse with a pulse width of one-tenth or less that of the generating pulse, thus insuring that the concentration profile of the generated material may be considered flat within the diffusion layer region established by the analysis pulse. The cathodic and anodic  $E_{1/2}$ 's differ by only 9 mV and the average  $i_d^c/i_d^a$  ratio over a range of concentrations is 0.91 where the theoretical values for completely reversible systems are 0 and 0.962 mV, respectively. The good fit of the experimental polarogram to the theoretical polarogram in Fig. 11 further indicates a high degree of reversibility in the  $\text{Fe}^{3+}/\text{Fe}^{2+}$  couple.

A typical cyclic voltammogram (sweep rate  $0.05 \text{ V sec}^{-1}$ ) of  $\text{FeCl}_3$  in a 1:1 melt is shown in Fig. 12. The  $\text{Fe}^{3+}/\text{Fe}^{2+}$  couple at  $E_{1/2} = 1.40\text{V}$  appears to be reversible while  $\text{Fe}^{2+}/\text{Fe}$  couple with  $E^0_M = 0.62\text{V}$  shows typical deposition-stripping behavior. The peak currents for the  $\text{Fe}^{3+}/\text{Fe}^{2+}$  couple were concentration dependent over the range of 0.5-2.0 mM while they were not for the  $\text{Fe}^{2+}/\text{Fe}$  couple above an initial  $\text{FeCl}_3$  concentration of 5 mM. The peak separation of 100 mV for the  $\text{Fe}^{3+}/\text{Fe}^{2+}$  couple is slightly greater than the

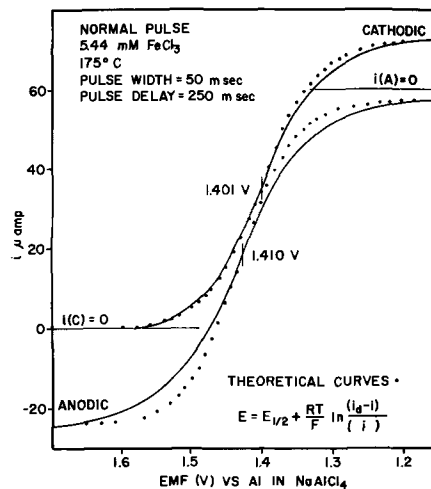


Fig. 11. Normal pulse polarograms of  $\text{Fe}^{3+}$  in  $\text{NaAlCl}_4$ . Anodic polarogram using double pulse polarography. Area of tungsten indicator electrode =  $1.79 \text{ mm}^2$ .

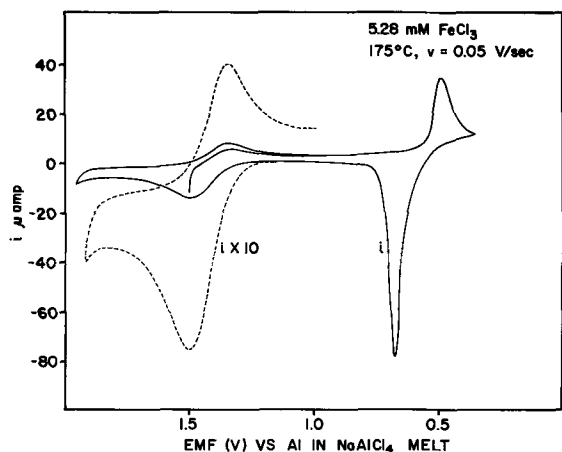


Fig. 12. Cyclic voltammogram of  $\text{Fe}^{3+}$  in  $\text{NaAlCl}_4$ , dashed curve-scale expanded by 10. Area of tungsten indicator electrode =  $1.79 \text{ mm}^2$ .

theoretical value of 84 mV for a one-electron reversible system at  $175^\circ\text{C}$ . As the sweep rate was increased, the anodic stripping peak split into two peaks (see Fig. 13) at 0.690 and 0.730V with their relative heights becoming reversed. The second peak at 0.730V became more predominant with increasing  $\text{FeCl}_3$  concentration or more cathodic switching potentials. At  $\text{FeCl}_3$  concentrations below 5 mM only a single anodic stripping peak was observed. This behavior is similar to that exhibited by silver.

The above observations indicate that the stripping process involves two different electrode reactions. The reaction occurring at 0.690V is well behaved as long as the concentration of iron on the electrode surface is not too high. We attribute this reaction to the oxidation of Fe to  $\text{FeCl}_2$ . When the rate of production of  $\text{Fe}^{2+}$  reaches a certain value, the reaction producing  $\text{FeCl}_2$  becomes limited possibly due to the depletion of  $\text{Cl}^-$  in the vicinity of the electrode. Consequently, the second reaction at 0.730V takes place. We believe that this process involves the oxidation of Fe to  $\text{Fe}^{2+}$  which diffuses out into solution. Furthermore, as only one deposition peak is observed, the two anodic processes must give rise to a single species in solution. It is very likely that the predominant Fe(II) species in these melts are chloroaluminate complexes ( $\text{Fe}(\text{AlCl}_4)_{m-2}$  or  $\text{Fe}(\text{Al}_2\text{Cl}_7)_{m-2}$ ) and when  $\text{FeCl}_2$  is added it must give a similar complex. A likely reaction for the process is

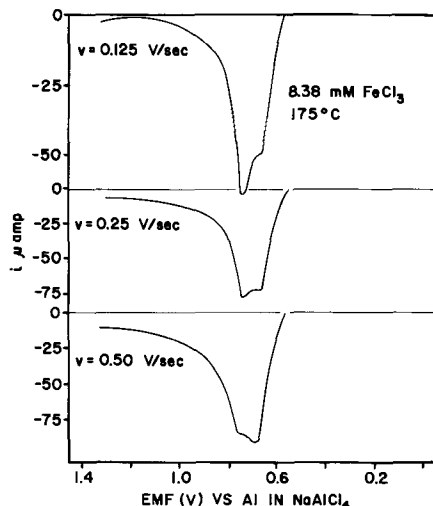
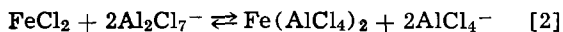


Fig. 13. Partial cyclic voltammograms for the dissolution of Fe from a tungsten electrode. Area of tungsten electrode =  $1.79 \text{ mm}^2$ . Potential program  $1.7 \rightarrow 0.3 \rightarrow 1.7\text{V}$  vs. Al.

which is also consistent with the solubility behavior of  $\text{FeCl}_2$  (in 1:1 melt low concentration of  $\text{Al}_2\text{Cl}_7^-$ , low solubility of  $\text{FeCl}_2$ ; in 2:1 melt high concentration of  $\text{Al}_2\text{Cl}_7^-$ , high solubility of  $\text{FeCl}_2$ ).

The  $\text{Fe}^{2+}$  species was found to be soluble in the 2:1 melt at  $175^\circ\text{C}$  and an overpotential of only 150 mV resulted when the iron wire was anodized at a current density of  $5 \text{ mA cm}^{-2}$ . The separation between the two anodic stripping peaks (0.76 and 0.93V) is considerably greater in the 2:1 melt than in the 1:1 melt (Fig. 14). No peaks corresponding to the  $\text{Fe}^{3+}/\text{Fe}^{2+}$  couple were observed for potentials cathodic of +2.2V. The small anodic peak at +1.14V and the cathodic prewave at  $\approx +1\text{V}$  are present in the background sweeps and are not due to the iron in the melt. The distortion of the reduction peak is due in part to other small pre-aluminum deposition waves which can be observed in the background.

The Nernst plot for the  $\text{Fe}^{2+}/\text{Fe}$  couple had a slope of 0.0371V compared to the theoretical value of 0.0444V for a two-electron process. The  $E_M^0$  for  $\text{Fe}^{2+}/\text{Fe}$  at  $175^\circ\text{C}$  in the 2:1 melt is 1.04V with a temperature coefficient of  $-0.77 \text{ mV deg}^{-1}$  over a temperature range of  $175^\circ\text{C}$ - $225^\circ\text{C}$ .

Several reverse current chronopotentiograms were recorded in an attempt to confirm our results. The irreproducibility of the data obtained did not warrant interpretation except that there is an apparent couple between 0.4 and 0.3V. This may be due to a codeposition of iron and aluminum on the electrode which is in keeping with the results of Yntema *et al.* (2).

An average diffusion coefficient of  $9.1 \pm 0.9 \times 10^{-6} \text{ cm}^2 \text{ sec}^{-1}$  for  $\text{Fe}^{3+}$  in a 1:1 melt at  $175^\circ\text{C}$  was calculated from chronoamperometric and pulse polarographic data. This is in good agreement with a value of  $2.2 \times 10^{-5} \text{ cm}^2 \text{ sec}^{-1}$  at  $250^\circ\text{C}$  (10) (2% change in  $D$  per degree change in  $T$ ).

**Copper.**—Copper(I) was most conveniently introduced into the 1:1 chloroaluminate melts by anodization of a copper wire. A current density of  $10 \text{ mA cm}^{-2}$  polarized the wire about 200 mV anodic of its equilibrium potential. Although  $\text{CuCl}$  dissolved very slowly, electrochemical results identical to those for the coulometric generation of  $\text{Cu}^+$  were obtained. While  $\text{CuBr}_2$  was completely insoluble,  $\text{CuCl}_2$  was soluble to an extent of 5 mM in a 1:1 melt at  $175^\circ\text{C}$ . In  $\text{AlCl}_3$ -rich melts no solubility problems were encountered.

The Nernst plots for duplicate sets of  $\text{Cu}^+/\text{Cu}$  emf measurements made in both a  $\text{Cl}^-$ -rich melt (49.87 m/o  $\text{AlCl}_3$ ) and an  $\text{AlCl}_3$ -rich melt (50.25 m/o  $\text{AlCl}_3$ ) are shown in Fig. 15. While an  $n$ -value of  $0.98 \pm 0.02$  was obtained for the couple in the  $\text{AlCl}_3$ -rich melt, an approximate  $n$ -value of only 0.8 was obtained in the  $\text{Cl}^-$ -rich melt. The low  $n$ -value in effect means

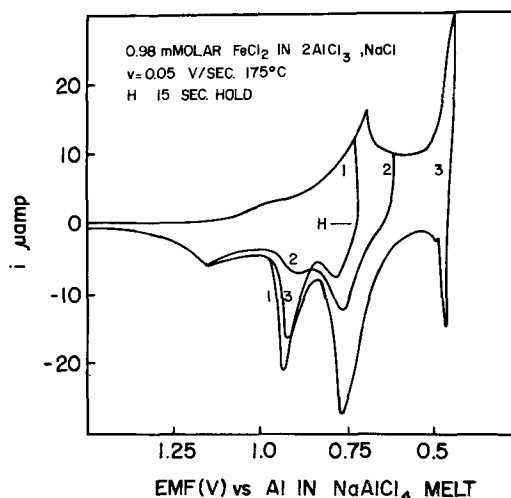


Fig. 14. Cyclic voltammogram of 0.98 mM  $\text{FeCl}_2$  in a 2:1  $\text{AlCl}_3$ - $\text{NaCl}$  melt. Area of tungsten indicator electrode =  $1.79 \text{ mm}^2$ .

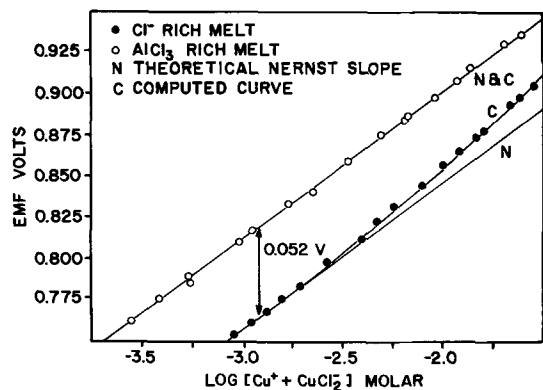


Fig. 15. Nernst plots for  $\text{Cu}^+$  in  $\text{NaAlCl}_4$  melts at  $175^\circ\text{C}$ . Reference electrode is Al in a 1:1  $\text{AlCl}_3$ - $\text{NaCl}$  melt.

that the observed electrode potential changed too rapidly, i.e., the apparent concentration of  $\text{Cu}^+$  in the vicinity of the electrode is too high. An explanation for this is presented below.

As  $\text{Cu}^+$  is added to the melt, a certain amount of chloride ion will be tied up according to the following equation



As the  $\text{Cl}^-$  concentration decreases, reaction [3] shifts to the left producing more  $\text{Cu}^+$  with respect to the amount expected from anodization of the copper electrode and, therefore, a higher potential. Using an iterative technique (where  $K_{\text{Cu}}$  and  $m$  are varied) similar to that previously developed for determining the acid base properties of these melts (16), we have calculated the shift in the over-all melt composition and the concentration of the individual species in the melt after each addition of  $\text{Cu}^+$ . At fixed values of  $m$  the value for  $K_{\text{Cu}}$  was varied until a minimum deviation between the calculated and experimental emf values was obtained. The best fit was obtained for  $K_{\text{Cu}} = 6.5 \times 10^4$  with a value for  $m$  equal to 2. A partial list of the calculated species concentrations and electrode potentials are given in Table I and plotted in Fig. 16.

The copper concentration at which the deviation occurs is dependent on the initial composition of the melt. Above 49.99 m/o  $\text{AlCl}_3$  no deviation will be observed as illustrated by the  $\text{AlCl}_3$ -rich Nernst plot in Fig. 15. As the melt becomes richer in  $\text{NaCl}$ , the greater is the quantity of copper required to change the composition of the melt into the range where the Nernst deviation occurs (49.89 to 49.99 m/o  $\text{AlCl}_3$ ). The deviation from the Nernst slope in this region is equivalent to an increase of 42 mV in the calculated  $E_M^0$  for the  $\text{Cl}^-$ -rich region to that for the  $\text{AlCl}_3$ -rich melts. The computed  $E_M^0$  from the  $\text{Cl}^-$ -rich region ( $n = 1$ ) is  $1.027 + 0.042 = 1.069\text{V}$  compared to the  $1.077\text{V}$  calculated from the  $\text{AlCl}_3$ -rich Nernst slope data.

A cyclic voltammogram for  $\text{CuCl}$  in a chloride-rich  $\text{NaAlCl}_4$  melt at  $175^\circ\text{C}$  is shown in Fig. 17. At low  $\text{CuCl}$  concentrations ( $< 2 \text{ mM}$ ) the  $\text{Cu}^{2+}/\text{Cu}^+$  couple is obscured by the evolution of chlorine. An increase in the  $\text{CuCl}$  concentration shifts the chlorine evolution to

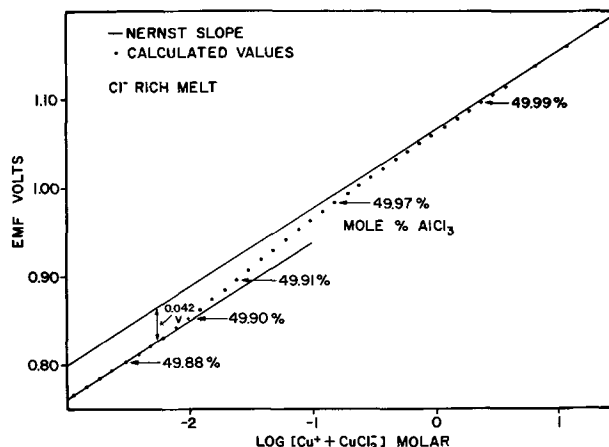


Fig. 16. Calculated  $\text{Cu}^+/\text{Cu}$  electrode potentials vs. total  $\text{Cu}^+$  concentration in a  $\text{Cl}^-$ -rich melt at  $175^\circ\text{C}$ .

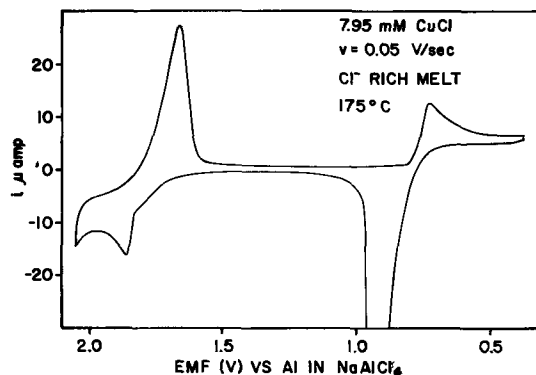


Fig. 17. Cyclic voltammogram of  $\text{Cu}^+$  in a  $\text{NaAlCl}_4$  melt. Mole per cent  $\text{AlCl}_3 = 49.87\%$ . Area of tungsten indicator electrode =  $0.656 \text{ mm}^2$ .

more anodic potentials as a result of the decrease in chloride ion concentration. The  $\text{Cu}^{2+}/\text{Cu}^+$  redox couple appears to be a reversible electrode process with no insoluble species. At  $\text{CuCl}$  concentrations in excess of  $5 \text{ mM}$ , the peak for the reduction of the cupric species becomes enhanced and resembles the shape of a stripping peak. Integration of the cyclic voltammogram shows that the amount of reduction products and oxidation products at the  $\text{Cu}^+/\text{Cu}$  couple are equal while there is about 6% excess of oxidation products at the  $\text{Cu}^{2+}/\text{Cu}^+$  couple on each cycle. This is probably the result of the somewhat irreversible oxidation of  $\text{Cl}^-$ .

The cathodic peak current for the  $\text{Cu}^+/\text{Cu}$  couple is linear with  $\text{Cu}^+$  concentration and the  $i_p/\nu^{1/2}$  at a given concentration was found to be constant over the sweep rate range  $0.05$ - $1.0 \text{ V}\cdot\text{sec}^{-1}$ . The shift in the  $E_p$  peak of copper deposition is  $0.087\text{V}$  per decade change in concentration compared to the theoretical value of  $0.089\text{V}$  for a one-electron process at  $175^\circ\text{C}$ .

Evolution of  $\text{Cl}_2$  distorts the anodic peak for the oxidation of  $\text{Cu}^+$  and makes measurement of the anodic peak potential somewhat arbitrary; however, the peak separation of  $100 \text{ mV}$  is still in reasonable agreement with the theoretical value (20) of  $84 \text{ mV}$  for a reversible one-electron process. The cathodic peak potential shifts from  $1.75$  to  $1.67\text{V}$  when the solubility of the  $\text{CuCl}_2$  is exceeded. At  $\text{Cu}^+$  concentrations less than  $5 \text{ mM}$ , the cathodic  $E_p$  for the  $\text{Cu}^{2+}/\text{Cu}^+$  couple is independent of sweep rate over the range  $0.05$ - $1.0 \text{ V}\cdot\text{sec}^{-1}$ . The peak currents for the deposition of  $\text{Cu}^+$  and for the oxidation of  $\text{Cu}^+$  were of equal magnitude.

The observed pulse polarograms for the reduction of  $\text{Cu}^+$  in 1:1 melts gave linear plots for  $i_p$  vs.  $[\text{Cu}^+]$  and  $i_p$  vs.  $(\text{pulse width})^{-1/2}$ . The shift in  $E_{1/2}$  for the  $\text{Cu}^+$  reduction wave with increasing copper concentration obeyed the expected Nernstian behavior for a one-

Table I. Structure of  $\text{CuCl}$ - $\text{NaAlCl}_4$  melt at  $175^\circ\text{C}$

Mole fraction			Over-all m/o $\text{AlCl}_3$	Expt.	EMF, V	
$[\text{Cu}^+]$ $\times 10^4$	$[\text{CuCl}_2^-]$ $\times 10^4$	$[\text{Cl}^-]$ $\times 10^3$			$K_{\text{Cu}} =$ $6.5 \times 10^4$	$K_{\text{Cu}} = 0^*$
0	0	5.2	49.87	—	—	—
1.2	1.8	4.8	49.88	0.798	0.797	0.795
1.9	2.6	4.7	49.89	0.814	0.813	0.810
4.2	4.9	4.2	49.90	0.844	0.845	0.837
9.8	8.2	3.6	49.91	0.877	0.878	0.864
16.5	10.5	3.1	49.92	0.899	0.898	0.879
131	18.9	1.5	49.97	—	0.978	0.946
2976	25.5	0.4	49.99	—	1.088	1.061

\*  $K_{\text{Cu}} = 0$  equivalent to normal Nernst calculation.



Table II. Properties of metals in NaAlCl<sub>2</sub> melt

Parameter	Melt	System	Value
$n$ , Nernst plot	1:1	Ag <sup>+</sup> /Ag	0.98 ± 0.03
	2:1	Ag <sup>+</sup> /Ag	0.99 ± 0.05
$E^0_M$ , V	1:1	Ag <sup>+</sup> /Ag	1.086 ± 0.010
	2:1	Ag <sup>+</sup> /Ag	1.106 ± 0.010
	2:1 <sup>(a)</sup>	Ag <sup>+</sup> /Ag	1.132 ± 0.010
$dE^0_M/dt$ , mV/°C	1:1	Ag <sup>+</sup> /Ag	-0.63 ± 0.05
	2:1 <sup>(a)</sup>	Ag <sup>+</sup> /Ag	-0.44 ± 0.03
$D \times 10^6$ cm <sup>2</sup> /sec	1:1	Ag <sup>+</sup>	3.01
$E_a$ , kcal/mole <sup>(b)</sup>	1:1	Ag <sup>+</sup>	3.5
$n$ , Nernst plot	2:1	Fe <sup>2+</sup> /Fe	2.1 ± 0.1
$E^0_M$ , V	1:1	Fe <sup>2+</sup> /Fe	0.63 ± 0.03
	1:1	Fe <sup>3+</sup> /Fe <sup>2+</sup>	1.44 ± 0.03
	2:1	Fe <sup>2+</sup> /Fe	0.95 ± 0.02
	2:1	Fe <sup>3+</sup> /Fe <sup>2+</sup>	1.89 ± 0.03
$dE^0_M/dt$ , mV/°C	2:1	Fe <sup>2+</sup> /Fe	-0.77
$D \times 10^6$ cm <sup>2</sup> /sec	1:1	Fe <sup>3+</sup>	8.8
$E_a$ , kcal/mole <sup>(b)</sup>	1:1	Fe <sup>3+</sup>	5.1
$n$ , Nernst plot	2:1	Cu <sup>+</sup> /Cu	1.01 ± 0.03
$E^0_M$ , V	1:1	Cu <sup>+</sup> /Cu	1.073 ± 0.005
	2:1 <sup>(a)</sup>	Cu <sup>+</sup> /Cu	1.134
	1:1	Cu <sup>2+</sup> /Cu <sup>+</sup>	1.817 ± 0.005
	2:1 <sup>(a)</sup>	Cu <sup>2+</sup> /Cu <sup>+</sup>	2.311
$dE^0_M/dt$ , mV/°C	1:1	Cu <sup>+</sup> /Cu	-0.73 ± 0.01
$D \times 10^6$ cm <sup>2</sup> /sec	1:1 <sup>(c)</sup>	CuCl <sub>2</sub> <sup>-</sup>	6.93
	1:1 <sup>(d)</sup>	Cu <sup>+</sup>	7.34
	2:1 <sup>(a)</sup>	Cu <sup>+</sup>	6.01
$E_a$ , kcal/mole <sup>(b)</sup>	1:1 <sup>(c)</sup>	CuCl <sub>2</sub> <sup>-</sup>	4.35
	1:1 <sup>(d)</sup>	Cu <sup>+</sup>	2.46
$K_{Cu}$ (mole fractions)	1:1	Cu <sup>+</sup> + 2Cl <sup>-</sup> = CuCl <sub>2</sub> <sup>-</sup>	(6.5 ± 0.1) × 10 <sup>4</sup>

All potentials in volts vs. Al in NaAlCl<sub>2</sub>.

<sup>(a)</sup> Ternary melt ref. (6) (135°C).

<sup>(b)</sup>  $D = A \exp(-E_a/RT)$ .

<sup>(c)</sup> 49.9 m/o AlCl<sub>3</sub>.

<sup>(d)</sup> 50.2 m/o AlCl<sub>3</sub>.

electron deposition process. Normal pulse polarograms for the oxidation of Cu<sup>+</sup> were ill defined; however, a double potential step pulse polarogram for a Cu<sup>+</sup> solution clearly showed the reduction of both Cu<sup>2+</sup> and Cu<sup>+</sup>.

Well-behaved chronopotentiograms containing a small nucleation peak were observed for the reduction of Cu<sup>+</sup> in 1:1 melts. The nucleation peak was considerably smaller than the one observed for the deposition of silver on the tungsten electrode.

A summary of the electrochemical data is given in Table II.

#### Acknowledgments

This work was supported by the Air Force Office of Scientific Research under Grant No. AFOSR 71-1995 and by N.A.S.A. Grant No. NGR-06-002-088. The com-

puter employed for the pulse polarographic studies was purchased in part by funds from an N.S.F. Equipment Grant No. GP-18219. The National Research Council of Canada provided a Postdoctoral Fellowship for L. G. Boxall.

Manuscript submitted May 2, 1973; revised manuscript received Aug. 24, 1973. This was Paper 258 presented at the Chicago, Illinois, Meeting of the Society, May 13-18, 1973.

Any discussion of this paper will appear in a Discussion Section to be published in the December 1974 JOURNAL.

#### REFERENCES

- W. H. Wade, G. O. Twellmeyer, and L. F. Yntema, *Trans. Electrochem. Soc.*, **78**, 77 (1940).
- E. Marshall and L. F. Yntema, *J. Phys. Chem.*, **46**, 353 (1942).
- R. G. Verdick and L. F. Yntema, *ibid.*, **46**, 344 (1942).
- R. Martin de Fremont, R. Rosset, and M. Leroy, *Bull. Soc. Chem., France.*, 706 (1964).
- M. Francini, S. Martini, and C. Manfrini, *Electrochem. Met.*, **2**, 3 (1967).
- U. Anders and J. A. Plambeck, *Can. J. Chem.*, **47**, 3055 (1969).
- K. W. Fung and G. Mamantov, *J. Electroanal. Chem.*, **35**, 27 (1972).
- H. A. Oye, *Acta Chem. Scand.*, **26**, 1646 (1972).
- T. Koaal and H. A. Oye, *ibid.*, **26**, 1647 (1972).
- W. G. Chovnyk and M. V. Myshalov, *Sov. Electrochem.*, **6**, 1583 (1970).
- T. C. F. Munday and J. D. Corbett, *Inorg. Chem.*, **5**, 1263 (1966).
- D. A. Hames and J. A. Plambeck, *Can. J. Chem.*, **46**, 1727 (1968).
- G. Torsi and G. Mamantov, *J. Electroanal. Chem.*, **30**, 193 (1971).
- G. Torsi, K. W. Fung, G. M. Begun, and G. Mamantov, *Inorg. Chem.*, **10**, 2285 (1971).
- G. Lauer, H. Schlein, and R. A. Osteryoung, *Anal. Chem.*, **35**, 1789 (1963).
- L. G. Boxall, H. L. Jones, and R. A. Osteryoung, *This Journal*, **120**, 223 (1973).
- L. G. Boxall and K. E. Johnson, *Trans. Faraday Soc.*, **67**, 1433 (1971).
- E. P. Parry and R. A. Osteryoung, *Anal. Chem.*, **37**, 1634 (1965).
- R. A. Osteryoung (Colorado State University, Fort Collins, Colorado), "Electrochemical Studies in Aluminum Chloride Melts," Report to NASA, February 1971, Contract No. NGR 06-002-088.
- R. S. Nicholson and I. Shain, *Anal. Chem.*, **36**, 706 (1964).

# Effects of the Active Chlorine and the pH on Consumption of Graphite Anode in Chlor-Alkali Cells

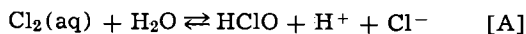
F. Hine,\* M. Yasuda, I. Sugiura,<sup>1</sup> and T. Noda

Nagoya Institute of Technology, Nagoya 466, Japan

## ABSTRACT

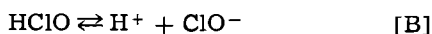
Corrosion tests of graphite anodes in saturated NaCl solution at 40°C have been carried out at 100 A/dm<sup>2</sup>. The corrosion rate was a small function of the pH between 2 and 9, but affected by the active chlorine. Electrochemical formation of chlorate is a side reaction and is limited by slow diffusion of HClO and/or ClO<sup>-</sup>. While chlorate does not affect degradation of graphite anode either electrochemically or chemically, the carbon surface oxide, which forms during electrochemical formation of chlorate from hypochlorite, is the largest factor in consumption of graphite anode in chlor-alkali cells.

It has been pointed out that the graphite anode is largely consumed by chemical oxidation with physical degradation when it is electrolyzed in alkali chloride solution containing hypochlorite ions (1, 2). A part of the chlorine dissolved in the anolyte may convert into HClO and ClO<sup>-</sup>, depending on the pH, due to the chemical equilibrium shown by reactions [A] and [B]



$$K_1 = 4.66 \times 10^{-4} \text{ at } 25^\circ\text{C} \quad (3)$$

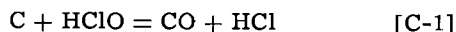
and



$$K_2 = 3.2 \times 10^{-8} \text{ at } 25^\circ\text{C} \quad (3)$$

where  $K_1$  and  $K_2$  are the dissociation constants for reactions [A] and [B], respectively.

Since graphite has many micropores, the charge-transfer reaction of Cl<sup>-</sup> in the pore might be controlled by diffusion because of low concentration of Cl<sup>-</sup> in comparison with the bulk solution. It causes formation of HClO due to hydrolysis of Cl<sub>2</sub>, and oxidation of carbon or graphite occurs



and

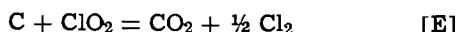


Kokhanov *et al.* studied the electrochemical consumption of graphite anodes of chlorine and chlorate cells (pH 3.3-7), and they considered that the effect of the active chlorine (sum of Cl<sub>2</sub> dissolved, HClO, and ClO<sup>-</sup>) was negligible (4, 5). They also found that corrosion of graphite in the brine without electrolysis was affected by the active chlorine, but was almost independent of the pH. Therefore, they concluded that the electrochemical consumption of graphite was caused by discharge of H<sub>2</sub>O.

Since the H<sup>+</sup> concentration of solution in the graphite pore reached 0.1-0.12N in the chlorate cell (6), it was considered that the graphite anode was oxidized by ClO<sub>2</sub> instead of HClO



and



Influence of the pH on degradation of graphite anodes has been studied by many authors (7-11), but they have not been attentive to the active chlorine.

The active chlorine is being maintained naturally in a chlorate cell as an important factor for cell reaction (12, 13). From these experimental works and practical experience, it is known that the corrosion rate of

graphite anodes attains a maximum in neutral solutions, although the mechanism of consumption is still unclear.

Laboratory testing of corrosion of the graphite anodes in concentrated NaCl solutions has been carried out for many years. The influence of pH and active chlorine are described.

## Experimental Procedure

The flowsheet of the system used is shown in Fig. 1. The pH (controlled within ±0.2), the temperature (usually 40°C), and the concentration of active chlorine are controlled in the brine reservoir (50 liters) located at about 1m below the cell level, then the brine is pumped up to the level tank at about 1.5m above the cell. A part of the brine is supplied to the anode compartment of the test cell by gravity, then sent back to the reservoir with the chlorine, where chlorine gas is separated from the brine. The gas is carried away by vacuum. Since the flow rate is more than 1 liter/min, change of the NaCl concentration by electrolysis is negligible (less than 1% decomposition). A part of the anolyte permeates to the cathode compartment through a porcelain diaphragm. The difference of the level of the anolyte-to-catholyte was about 2 cm. The catholyte and hydrogen are swept out by vacuum. Back migration of alkali causes difficulty of control of the concentration of active chlorine in the anode compartment.

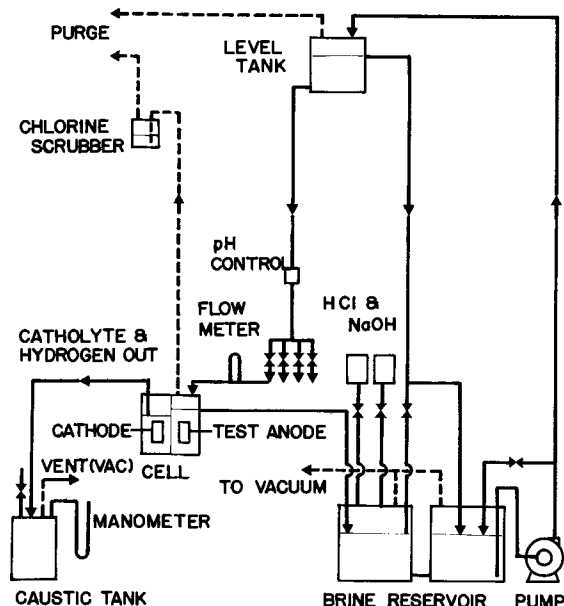


Fig. 1. Flowsheet for measurement of anode consumption

\* Electrochemical Society Active Member.

<sup>1</sup> Present address: Yamanashi Plant, Nippon Carbon Company, Yamanashi 405, Japan.

Key words: graphite anode, consumption of graphite anode, graphite corrosion testing, carbon surface oxide.

The pH was varied between 2 and 9, and the concentration of active chlorine was from  $10^{-3}$  to  $10^{-2}$ M. The chlorine content was titrated and controlled every 30 min, whereas the pH was recorded continuously. Addition of NaClO solution and dechlorination were carried out if necessary.

There are some papers on the effects of oxyacid ions such as  $\text{ClO}_3^-$  on corrosion behavior of graphite anodes (14). However, results of our preliminary experiments showed no effect of  $\text{ClO}_3^-$  on the corrosion rate.

The test cell made of titanium is illustrated in Fig. 2. A titanium cathode is located at the center within a porcelain diaphragm. Three anode assemblies are arranged around the cathode. The anode lead rod, also of titanium, as shown in Fig. 3A, is able to contact three to four graphite specimens (Fig. 3C). A commercial graphite (specific gravity, 1.71; resistivity,  $55 \times 10^{-5}$  ohm-cm; vanadium content, 3 ppm; ash less than 0.1%) was machined: 12 mm outer diameter and 10 mm long, and it had a center hole of 5 mm diam for fitting (Fig. 3B).

The corrosion rate is evaluated from the slope of the weight loss vs. time curve such as Fig. 5. Generally, electrolysis was carried out for 50 hr, and the corrosion rate was evaluated by the method of least squares. Desalting of a graphite specimen is the most important and time-consuming work prior to weighing. Immer-

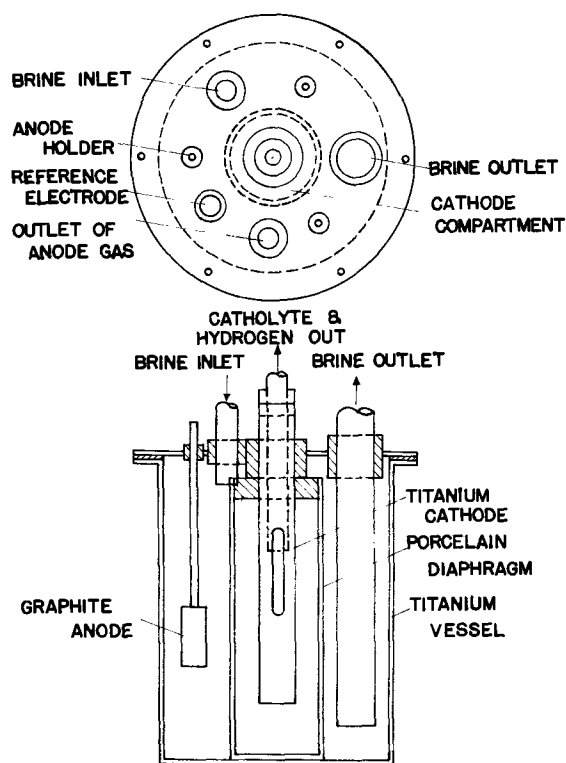


Fig. 2. Electrolytic cell for measurement of anode consumption

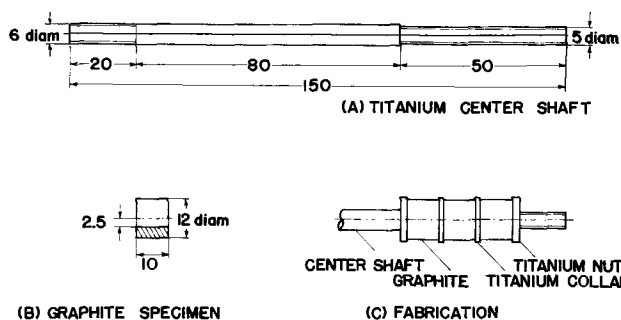


Fig. 3. Graphite specimen and center shaft for measurement of anode consumption.

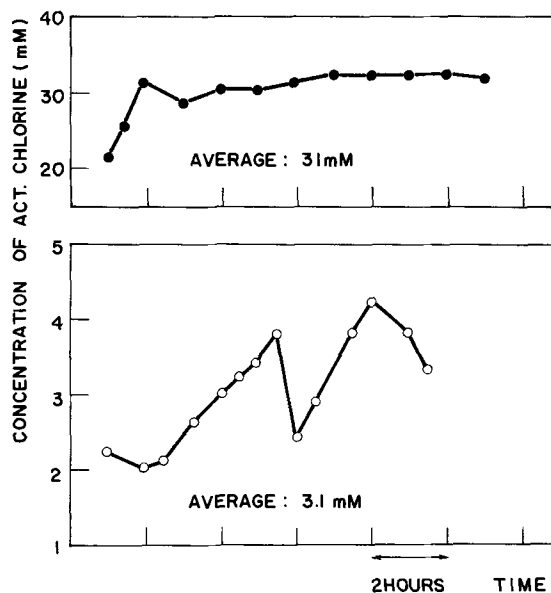


Fig. 4. Examples of the chlorine concentration vs. time curve during electrolysis (pH ca. 6).

sion and washing with hot water at about  $80^\circ\text{C}$  for 3-4 days was needed for complete removal of  $\text{Cl}^-$ . The sample was dried at  $110^\circ\text{C}$  for 2 hr and cooled in a desiccator. Since some deviations of weight loss were determined, experiments under the same conditions were repeated at least three times.

Most experiments were carried out in saturated NaCl solutions at  $40^\circ\text{C}$ , and the current density was constant at  $100 \text{ A/dm}^2$ . Operating temperature, current density, and brine composition are all important factors affecting the graphite anode.

The steady-state polarization curves of a graphite anode have been obtained under various conditions of the brine composition. The IR drop between the working electrode and the Luggin probe was calibrated by the current interruption technique. To minimize the bubble effect, a small rotating cylinder was used as the working anode ( $1 \text{ cm}^2$  area). A saturated calomel electrode was used as reference.

Results

Table I summarizes the corrosion rate with respect to operating conditions such as the concentration of active chlorine and the pH. The standard deviation of the concentration of active chlorine is also given.

Figure 4 shows an example of the variation of the concentration of active chlorine during electrolysis. Control at the  $10^{-2}$ M level is relatively easy in comparison with lower levels such as  $10^{-3}$ M. Generally, deviation of the concentration of active chlorine is large in a solution at high pH ranges containing dilute active chlorine. An example of the weight loss vs. time

Table I. Corrosion rate of a graphite anode in saturated NaCl at  $40^\circ\text{C}$  and  $100 \text{ A/dm}^2$

Exp. No.	pH	Average corrosion rate (mg/A-hr)	Average concentration of active chlorine (mM)	Standard deviation (mM)
1	2	0.12	0.62	—
2	4	0.14	2.8	0.6
3	4	0.14	2.6	0.55
4	5	0.15	3.4	0.62
5	5	0.31	30	2.3
6	6	0.17	16	—
7	6	0.34	43	5.9
8	6	0.23	29	5.3
9	6	0.14	3.1	0.29
10	6	0.26	31	—
11	8	0.34	30	2.8
12	9	0.15	5.6	—
13	9	0.38	32	3.3
14	9	0.35	31	3.9

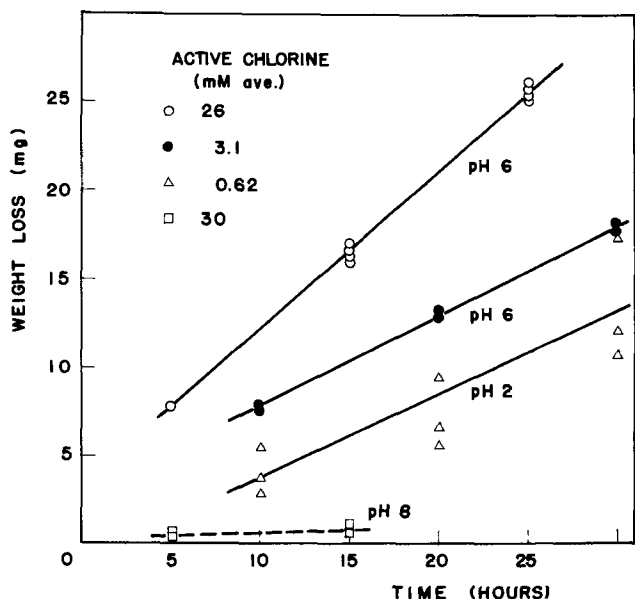


Fig. 5. Weight loss vs. time curves in saturated NaCl at 40°C. Current density, 100 A/dm<sup>2</sup>; surface area of specimen, 3.8 cm<sup>2</sup>. Broken line shows the data without electrolysis.

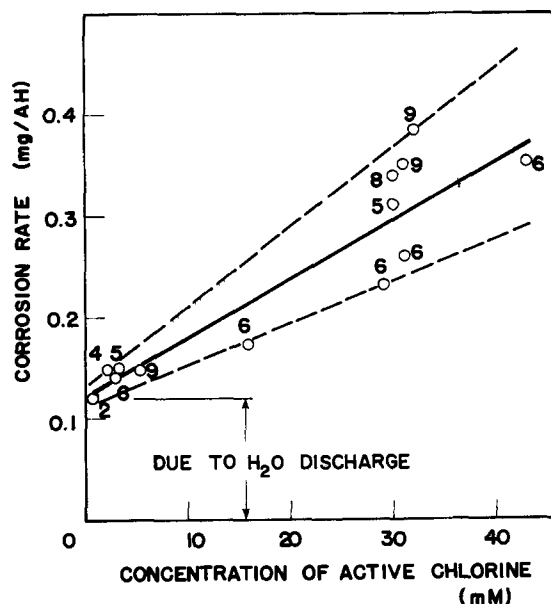


Fig. 7. Corrosion rate vs. concentration of active chlorine at 100 A/dm<sup>2</sup>. Label shows the brine pH.

curve is shown in Fig. 5. The weight loss is almost linear with time except the first stage, probably due to physical loss of fine powders from the anode surface.

The corrosion rate depends on the concentration of active chlorine and is a weak function of the pH. A broken line in the figure shows the data of consumption due to chemical oxidation in the brine containing 30 mM of active chlorine at pH 8.

Another experiment for chemical oxidation of graphite was carried out in which fine graphite powder (less than 60 mesh) was immersed in 0.1M NaClO (pH 4.2 and 9.7) at 50°C for 5 hr. The weight loss was recorded to be only 0.4-0.6% or less. It was, therefore, concluded that the chemical oxidation is negligible compared to the electrochemical consumption.

Figure 6 shows the corrosion rate vs. the ClO<sub>3</sub><sup>-</sup> concentration. The corrosion rate is almost independent of ClO<sub>3</sub><sup>-</sup> but is affected by active chlorine.

The corrosion rate as a function of the concentration of active chlorine is shown in Fig. 7. Most data have been obtained in the solution of pH 6. The corrosion rate is about linear with the concentration of chlorine. The data obtained in the solution containing a relatively high level of chlorine deviates because of the fluctuation of the chlorine concentration.

Figure 8 shows the corrosion rate vs. pH curves. The labels in the figure show the concentration of active chlorine on the order of 10<sup>-2</sup>M (closed points) or 10<sup>-3</sup>M (open points). It is clear that the corrosion rate is almost independent of the pH over a relatively wide range.

The steady-state polarization curves of the rotating graphite cylinder anode after corrosion tests are shown in Fig. 9 and 10. There is no effect of ClO<sub>3</sub><sup>-</sup> (Fig. 9), and hence ClO<sub>3</sub><sup>-</sup> would not discharge on the graphite anode. On the other hand, the potential

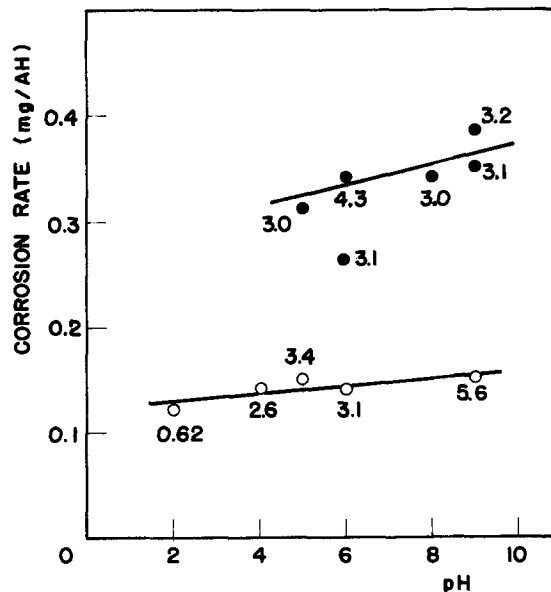


Fig. 8. Corrosion rate vs. brine pH under given concentration of active chlorine. Current density, 100 A/dm<sup>2</sup> at 40°C. Label shows the concentration of active chlorine. The values in the labels are to be multiplied by 10<sup>-2</sup>M (closed points) and 10<sup>-3</sup>M (open points).

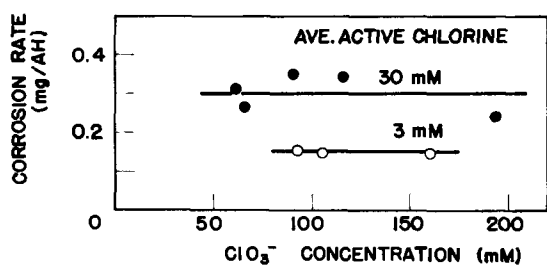


Fig. 6. Corrosion rate vs. ClO<sub>3</sub><sup>-</sup> concentration

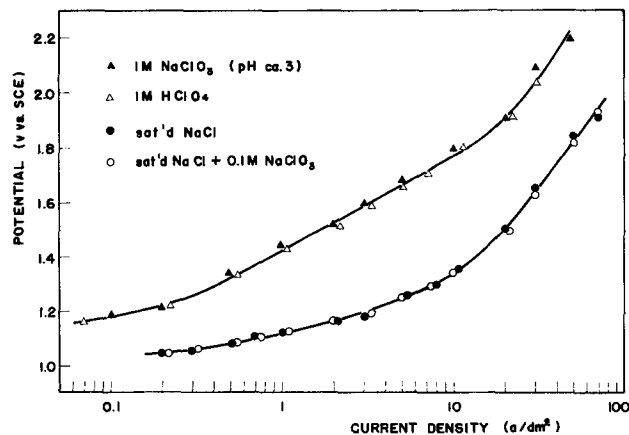


Fig. 9. Steady-state polarization curves of a rotating graphite anode.

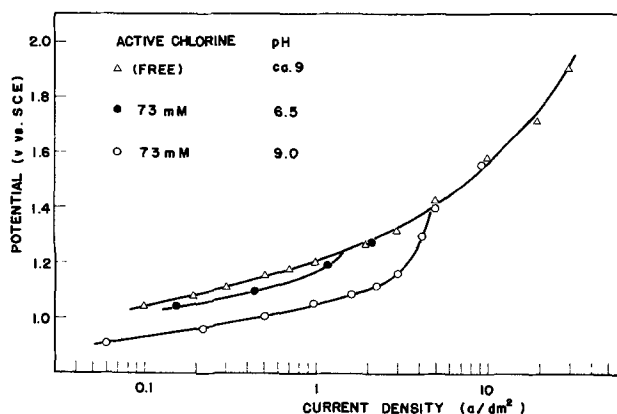


Fig. 10. Steady-state polarization curves of a rotating graphite anode.

is quite sensitive to addition of chlorine (Fig. 10) and also depends on the pH and the rotating speed.

### Discussion

A part of the chlorine generated from the graphite anode by electrolysis dissolves into the solution and forms HClO and ClO<sup>-</sup> by hydrolysis as shown by reactions [A] and [B]. The distributions of Cl<sub>2</sub> dissolved, HClO, and ClO<sup>-</sup> in the saturated NaCl at 25°C as functions of the pH are shown in Fig. 11. Since the ordinate is the mole fractions of these species, it is only a function of the brine pH, but is independent of the total concentration of active chlorine. The experiment has been carried out under given concentrations of active chlorine over a wide range of pH, or with much less than 1 atm of Cl<sub>2</sub> pressure. It is recognized the necessity of this at higher pH's but at pH 1-3, as occurs in chlorine cells, it could have been possible to saturate the anolyte with chlorine. The distribution between Cl<sub>2</sub> dissolved and HClO under 1 atm of Cl<sub>2</sub> partial pressure in the low pH range has been calculated by Barr (31). The HClO concentration increases with the pH but the Cl<sub>2</sub> concentration remains almost constant up to pH 3. A careful study in this pH range of 1-4 would have been most applicable to chlorine cells. The range 6-8 would be applicable to chlorate cells but the active chlorine is unstable in this range, going either to chlorate or oxygen, or both. The condition at the electrode must be different from the bulk of electrolyte under these unstable conditions. From Fig. 11, at about 2.5 of the pH, half of the active chlorine converts into HClO. In a range of pH 5-6, almost all chlorine dissolves as HClO, whereas ClO<sup>-</sup> is stable

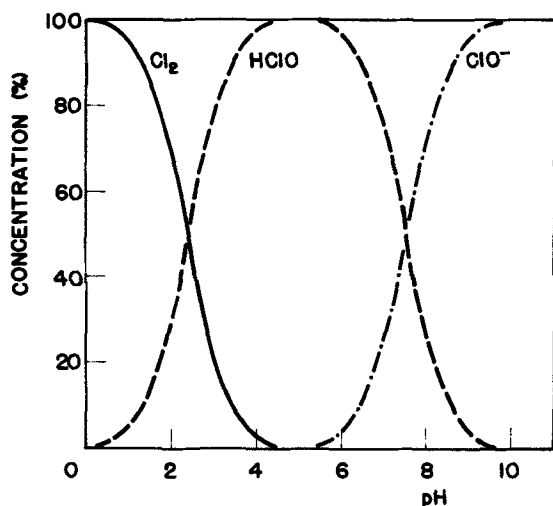


Fig. 11. Concentration ratio of three components of active chlorine in the brine as a function of the pH at 25°C.

at high pH ranges. It agrees well with the results by Cowley *et al.* (32), who have obtained the polarization curves of a graphite cathode in a solution 5M NaCl + 10<sup>-2</sup>M HCl saturated with chlorine. The diffusion limiting current density of Cl<sub>2</sub> dissolved is about the same as that of HClO.

As shown in Fig. 8, the corrosion rate is almost constant across a wide range of pH if the concentration of active chlorine is kept constant. Therefore, during electrolysis, the graphite anodes seem to be corroded by active chlorine in the bulk solution, but the species in the vicinity of the anode are unknown. However, it is well known that the graphite anode is durable in concentrated HCl solution, also the current efficiency for the Cl<sub>2</sub> formation at the graphite anode in concentrated and acidified (pH ca. 2) NaCl solution is more than 99% over wide ranges of the current density (16). The graphite anode must be corroded by HClO and/or ClO<sup>-</sup>, and not by Cl<sub>2</sub>.

It is well known that the graphite anode is oxidized into carbon surface oxide (as an intermediate) with CO and CO<sub>2</sub> in the electrolytic solution free from Cl<sup>-</sup>. The process is believed to be due to charge-transfer of H<sub>2</sub>O and OH<sup>-</sup> in acidic and alkaline solutions, respectively (17-22). Formation of CO and CO<sub>2</sub> depends on the operating conditions of electrolysis (23-25). The oxygen electrode reaction is in competition with the chlorine formation depending on the Cl<sup>-</sup> concentration and is important for corrosion of the graphite anodes. The oxygen electrode process on the graphite anodes and the carbon surface oxides will be discussed in detail in the separate papers by the same authors (23-25).

Vaaler has studied the effect of the pH on the consumption of graphite anodes in the range of pH 3-4.2 (10). He pointed out that the amount of the CO<sub>2</sub> formation increased with the pH. Wallen studied the mixed solution of 50 g/liter NaCl and 300 g/liter NaClO<sub>3</sub> in the pH range of 2-10, but he did not pay attention to the concentration of active chlorine (11, 26).

Kokhanov *et al.* proposed the discharge of H<sub>2</sub>O (to form CO and CO<sub>2</sub> with the O<sub>2</sub> formation) as a cause of graphite corrosion from the experimental results, *i.e.*, that the electrochemical weight loss minus the chemical loss was independent of the pH in the range of 3.3-7 (5). Others showed the "critical potential," at which the graphite consumption was minimized (27-29). The critical potential depends on the temperature: 1.63V *vs.* SHE at 25°C, 1.57V at 40°C, and 1.52V at 60°C. It is important that it agrees well with the potential at which the higher oxide, designated as (C-O<sub>H</sub>) by the author of this paper, would form on the graphite anode (23).

Since Cl<sub>2</sub> formation is the main reaction in concentrated NaCl at high current densities, the rate of discharge of H<sub>2</sub>O is relatively small. By projection of the line in Fig. 7 to zero concentration of active chlorine, the corrosion rate owing to discharge of H<sub>2</sub>O is estimated to be about 0.12 mg/A-hr under the conditions of 100 A/dm<sup>2</sup> at 40°C.

Formation of chlorate from hypochlorite takes place both chemically and electrochemically depending on operating conditions such as temperature, pH, and the electrode potential (12, 13).

The operating conditions of the corrosion test under discussion here (also in practical chlorine cells) are feasible for chlorate formation as a side reaction. Deviation of the polarization curve at relatively low current densities with addition of chlorine in the electrolyte is, therefore, reasonable as shown in Fig. 10. The diffusion limiting current density depends on the pH and the chlorine concentration which agrees with the results of Filippov and Ibl who have studied the anodic oxidation of hypochlorite with Pt and graphite (12, 13, 30).

Because the electrode potential was high enough during our corrosion tests, the formation of the car-

bon surface oxide as an intermediate is quite possible with formation of chlorate and evolution of oxygen.

Weight loss of graphite immersed in NaCl solution saturated with chlorine is negligible. The weight loss of the graphite during electrolysis at high current density (100 A/dm<sup>2</sup>) depends on the chlorine concentration and is a relatively small function of the pH. The effect of chlorate on graphite corrosion is also negligible. It is, therefore, concluded that the carbon oxide as an intermediate for electrochemical formation of chlorate from HClO and/or ClO<sup>-</sup> is the largest factor in consumption of a graphite anode, while some electrochemical oxidation of the graphite anode with discharge of H<sub>2</sub>O or OH<sup>-</sup> may also take place.

The corrosion rate described in this paper (e.g., Table I) is relatively low (0.1-0.3 kg/ton-Cl<sub>2</sub>) in comparison with in the practical cells (2-3 kg/ton), because the corrosion test was carried out in the saturated brine free from SO<sub>4</sub><sup>2-</sup> at low temperature (40°C).

While chlorate does not affect degradation of graphite anode, the carbon surface oxide forms simultaneously with electrochemical formation of chlorate from hypochlorite and is the largest factor of consumption of graphite anode in chlor-alkali cells.

Vaaler has reviewed the data in this paper and has worked out a regression analysis by computer. With the data of Table I, he has obtained the results shown in Table II and in Fig. 12 and 13. Although the regression coefficient  $b_2$  associated with pH is not defined very accurately, the  $F$  ratio shows that pH has a definite effect on corrosion rate. The plots in Fig. 12 show that scatter around the regression line is moderate and that the effect of pH, considered from a practical standpoint, is not large (33).

The authors have no doubts about his conclusion. However, the polarization measurements show that diffusion of HClO, ClO<sup>-</sup>, and OH<sup>-</sup> are limited under operating conditions of the practical chlorine cells, and the main reaction is formation of Cl<sub>2</sub>. The brine pH also has an effect on the corrosion rate of graphite anodes, while the slope of the corrosion rate vs. pH curves (Fig. 8) is small.

In conclusion, the effect of the active chlorine on corrosion of graphite anodes has been emphasized in this paper because the effect is large in comparison with the pH effect both during experimental work as well as in practical cells.

### Acknowledgment

This work has been directed with the support of Olin Research Center, New Haven, Connecticut. Graphite samples were supplied by Nippon Carbon Company, Tokyo. Titanium equipment was given by Kobe Steel Works, Kobe. The authors also wish to express many thanks to Dr. W. C. Gardiner and Dr. L. E. Vaaler for their kind suggestions and advice for preparation of this report. The Ph.D. thesis of M. Y. at Kyoto University (1972) involves a part of this work.

Manuscript submitted March 26, 1973; revised manuscript received Aug. 29, 1973. This was Paper 233 presented at the Chicago, Illinois, Meeting of the Society, May 13-18, 1973.

Table II. Regression analysis by L. E. Vaaler (33)

Corrosion rate =  $b_1 + b_2 \times \text{pH} + b_3 \times \text{concentration}$   
of active chlorine  
 $b_1 = 0.0753$ , standard deviation = 0.0308  
 $b_2 = 0.00926$ , standard deviation = 0.00551  
 $b_3 = 5.300$ , standard deviation = 0.7685

	Sum of squares	Degress of freedom	Mean square	F ratio
Due to pH regression	0.04441	1	0.04441	33.6
Due to active Cl <sub>2</sub> regression	0.06235	1	0.06235	47.5
About regression	0.01443	11	0.00131	—
Total	0.1212	13	—	—

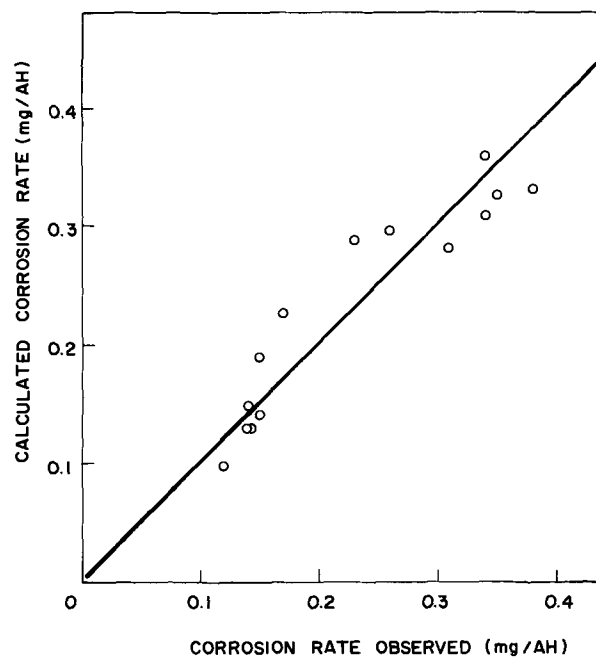


Fig. 12. Regression analysis with the data of Table I by L. E. Vaaler.

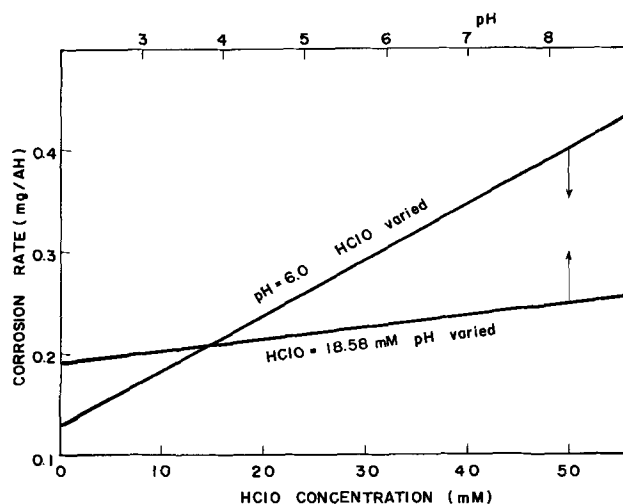


Fig. 13. Calculated corrosion rate vs. pH and HClO concentration by L. E. Vaaler.

Any discussion of this paper will appear in a Discussion Section to be published in the December 1974 JOURNAL.

### REFERENCES

- N. J. Johnson, *Trans. Electrochem. Soc.*, **86**, 127 (1944).
- M. Janes, *ibid.*, **92**, 23 (1947).
- W. M. Latimer, "Oxidation Potentials," 2nd ed., p. 51, Prentice-Hall Book Co., Englewood Cliff, N. J. (1952).
- G. N. Kokhanov and L. A. Khanova, *Élektrokhimiya*, **6**, 866 (1970).
- G. N. Kokhanov and L. A. Khanova, *ibid.*, **6**, 1492 (1970).
- V. I. Éberil', D. V. Kokoulina, L. I. Krishtalik, and L. M. Elina, *ibid.*, **5**, 336 (1969).
- L. I. Krishtalik, G. L. Melikova, and E. G. Kalinina, *Zh. Prikl. Khim.*, **34**, 1537 (1961).
- L. I. Krishtalik, G. L. Melikova, and E. G. Kalinina, *ibid.*, **34**, 1543 (1961).
- L. I. Krishtalik, *ibid.*, **34**, 1807 (1961).
- L. E. Vaaler, *This Journal*, **107**, 691 (1960).
- B. Wallén and G. Wranglén, *Electrochim. Acta*, **10**, 43 (1965).
- N. Ibl and D. Landolt, *This Journal*, **115**, 713 (1968).
- D. Landolt and N. Ibl, *Electrochim. Acta*, **15**, 1165 (1970).

14. H. Thile and E. Weise, *Z. Elektrochem.*, **55**, 193 (1951).
15. F. Hine and M. Yasuda, *Denki Kagaku (J. Electrochem. Soc. Japan)*, **39**, 530 (1971).
16. L. E. Vaaler, *Electrochem. Technol.*, **5**, 170 (1967).
17. H. Binder, A. Köhling, K. Richter, and G. Sandstede, *Electrochim. Acta.*, **9**, 255 (1964).
18. P. Drossbach and P. Schmittinger, *ibid.*, **9**, 1391 (1964).
19. L. I. Krishtalik and Z. A. Rotenberg, *Zh. Fiz. Khim.*, **39**, 168 (1965).
20. L. J. J. Janssen and J. G. Hoogland, *Electrochim. Acta*, **14**, 1097 (1969).
21. G. N. Kokhanov and N. G. Milova, *Élektrokhimiya*, **5**, 93 (1969).
22. G. N. Kokhanov and N. G. Milova, *ibid.*, **6**, 73 (1970).
23. F. Hine, M. Yasuda, and M. Iwata, In course of publication.
24. F. Hine and M. Yasuda, In course of publication.
25. F. Hine and M. Yasuda, In course of publication.
26. G. Wranglén, B. Sjödin, and B. Wallén, *Electrochim. Acta*, **7**, 577 (1962).
27. V. I. Éberil' and F. V. Kupovich, *Élektrokhimiya*, **6**, 332 (1970).
28. V. I. Éberil' and L. M. Elina, *ibid.*, **6**, 782 (1970).
29. V. I. Éberil' and L. M. Elina, *ibid.*, **6**, 1010 (1970).
30. T. S. Filippov and Yu. V. Dobrov, *ibid.*, **5**, 1046 (1969).
31. L. Barr, *This Journal*, **101**, 497 (1954).
32. W. E. Crowley, B. Lott, and J. H. Entwisle, *Trans. Inst. Chem. Engrs.*, **41**, 372 (1963).
33. L. E. Vaaler, Private communication.

## Hydrogen Evolution Reaction on Vanadium, Chromium, Manganese, Cobalt

A. Bélanger\*

*Energy Centre of the National Institute for Scientific Research,  
University of Quebec at Varennes, Province of Quebec, Canada*

and Ashok K. Vijh\*\*

*Hydro-Quebec Institute of Research, Varennes, Province of Quebec, Canada*

### ABSTRACT

The electrolytic hydrogen evolution reaction (HER) has been studied on V, Cr, Mn, and Co in sulfuric acid-sulfate solutions. The data consist of Tafel slopes, exchange current densities, apparent heats of activation, corrosion rates, corrosion potentials, and, in some cases, reaction order derivatives. Attempts were also made to obtain information on the electrode coverage by transient techniques. The presence of corrosion, however, makes the possible electrode coverage by adsorbed hydrogen inaccessible. By combining these electrode kinetic data with the gas-phase hydrogen adsorption behavior of these metals, it is suggested that the HER proceeds by means of the initial discharge mechanism on V and Mn whereas on Cr and Co, the radical-ion mechanism has been concluded.

In a previous theoretical study (1) of the electrocatalysis of the hydrogen evolution reaction (HER) by the metals of the periodic table of elements, it was found that reliable electrode kinetic data for the hydrogen evolution reaction on V, Cr, Mn, and Co were rather scarce in the literature. It was decided to obtain these values and the results of these investigations are presented here.

### Experimental

The HER was investigated on V, Cr, Mn, and Co in a three-compartment all-Pyrex cell containing suitable gas inlets and outlets. The hydrogen bubbled in the working and reference compartments and the helium in the counter compartment were purified by the purification trains described previously (2) and were led into the cell by means of glass-to-glass connections. The gas outlets from the cell had water-filled bubblers in order to eliminate the diffusion of atmospheric oxygen into the cell. The stopcocks separating the three compartments of the cell had long necks and were solution-sealed. The cell was thoroughly cleaned in chromic acid with subsequent several washings and soakings in conductivity water. The conductivity water was obtained by eliminating first the ionic and organic impurities of the tap water by passage over suitable

commercial cartridges and then by distilling twice over alkaline  $\text{KMnO}_4$  in two consecutive all-Pyrex stills. The electrolyte solutions were prepared, from  $\text{H}_2\text{SO}_4$  (Ultrex, J. T. Baker Chemical Corporation) and  $\text{Na}_2\text{SO}_4$  (Fischer A.C.S.), by adding various quantities of  $\text{H}_2\text{SO}_4$  (to fix the pH) to  $\text{Na}_2\text{SO}_4$ , the sodium sulfate acting as the supporting electrolyte to maintain a high conductivity. Buffers, which necessitate the use of weak acids such as acetic, formic, phosphoric, etc. for the preparation of acidic solutions, were avoided in order not to introduce traces of contaminants (either in the acid to start with, or produced in the counter compartment during electrolysis with the consequent migration to the working compartment even if the compartments are isolated by means of closed solution-sealed stopcock) or ions which might undergo contact adsorption. Throughout the experiments, solutions were agitated by bubbling hydrogen gas in the working compartment. When limiting currents were to be studied (e.g., proton discharge at low acidic concentrations), the agitation was however stopped in the corresponding region. Solutions were subjected to a cathodic pre-electrolysis on a sacrificial electrode (area  $\approx 1 \text{ cm}^2$ ) of the same material as the working electrode. This pre-electrolysis was conducted first at a low current density (ca.  $0.1 \text{ mA cm}^{-2}$ ) for 10-12 hr to remove any organics followed by a second one at around  $100 \text{ mA cm}^{-2}$  for 2 hr. The electrode was then pulled out of the solution when still under po-

\* Electrochemical Society Student Associate.

\*\* Electrochemical Society Active Member.

Key words: hydrogen evolution reaction, transition metals, corrosion, active dissolution.

larization. The second pre-electrolysis at 100 mA cm<sup>-2</sup> was first tried for 12-hr periods. It was noticed that it yielded Tafel lines identical with those obtained by pre-electrolysis for 2 hr. This longer pre-electrolysis was thus avoided because it resulted in change of pH in solutions of higher (from 1.9 → 4) pH values. The working electrodes were fabricated from spectroscopically pure metals obtained from A. D. Mackay, Inc., New York, and were mounted into heat-shrinkable Teflon as described previously (3). The working electrodes were polished either mechanically (Mn, Cr) or chemically (Co, V) and were thoroughly and repeatedly cleaned, the final cleaning being in boiling trichloroethylene. Hydrogen reference electrodes and iridium counterelectrodes were employed. Routine potentiostatic and potentiodynamic procedures (4) were used, and in some runs, an automatic steady-state polarization method was employed (5). The circuits used in the measurement of charging curves and open-circuit decays were as described previously (2).

The various potentiostatic plots have been corrected for the IR drop. This ohmic drop has been determined by the oscillographic method (6, 7). Checks were made to establish that this IR drop was a linear function of the current density.

### Results

The electrode kinetic parameters for the HER obtained on the four metals, together with some other related information, have been presented in Tables I-IV. Since the relevant data are contained in these tables, it is unnecessary to present these results in details in various figures. It would appear sufficient, therefore, to show here some representative figures only, as follows:

In Fig. 1, steady-state potentiostatic Tafel lines on vanadium at different temperatures are shown. An examination of these data shows that the Tafel slope is generally around  $2.3 \times 2RT/F$  at each temperature, although showing some scatter around this value. The curvature at higher current densities, exhibited by

Table I. HER on vanadium: kinetic parameters and some other characteristics

Parameter	Value	Comments
1. Tafel slope (25°C)	145 mV/decade	In the descending direction of potentials (more cathodic → less cathodic) pH = 0.7
2. Exchange current density (25°C)	$5.3 \times 10^{-7}$ A · cm <sup>-2</sup>	Extrapolation of the Tafel plot at 25°C to $\eta = 0$
3. Apparent heat of activation	11.6 kcal · mole <sup>-1</sup>	Calculated from the plot of $(-\log i)$ vs. $1/T$ at pH = 0.7 $\eta = -0.4V$
4. Reaction order derivative	$\left(\frac{\partial \log i}{\partial \text{pH}}\right)_{\phi = -0.7V} = -0.84$	Where $\phi$ refers to the electrode potential against the standard hydrogen electrode (SHE)
5. Corrosion potential (25°C)	-130 mV	For pH = 0.7, in 1N H <sub>2</sub> SO <sub>4</sub> + 2N Na <sub>2</sub> SO <sub>4</sub>
6. Corrosion current (25°C)	$2.8 \times 10^{-8}$ A · cm <sup>-2</sup>	Determined by Stern-Geary analysis (26)
7. Electrode coverage by hydrogen	No positive evidence	Masking by the associated dissolution reaction
8. Hydrogen adsorption in gas phase	$\Delta H_{\text{ads. H}} < 52$ kcal · mole <sup>-1</sup>	Does not spontaneously adsorb hydrogen (25)

Table II. HER on chromium: kinetic parameters and some other characteristics

Parameter	Value	Comments
1. Tafel slope (25°C)	120 mV/decade	For both ascending and descending directions of potentials in solution of pH = 0.7
2. Exchange current density (25°C)	$5.0 \times 10^{-8}$ A · cm <sup>-2</sup>	Extrapolation of the Tafel plot to $\eta = 0$
3. Apparent heat of activation	(a) 9.8 kcal · mole <sup>-1</sup> (b) 10.2 kcal · mole <sup>-1</sup>	(a) Obtained between 21° and 70°C from the plot of $(-\log i)$ vs. $1/T$ $\eta = -0.62V$ (b) Obtained from the relation $\left(\frac{\partial E_{\text{corr}}}{\partial 1/T}\right) = \left(\frac{\partial (E_{\text{HER}})}{\partial 1/T}\right)$
4. Reaction order derivative	—	No reaction order for the proton discharge is available because of chromium corrosion
5. Corrosion potential (25°C)	-500 mV	At pH = 0.7, in 1N H <sub>2</sub> SO <sub>4</sub> + 2N Na <sub>2</sub> SO <sub>4</sub> solution
6. Corrosion current (25°C)	1 mA · cm <sup>-2</sup>	As determined by the Stern-Geary analysis (26)
7. Electrode coverage by hydrogen	No clear evidence	General masking of any information concerning the hydrogen adsorption
8. Hydrogen adsorption in gas phase	$\Delta H_{\text{ads. H}} = 74$ kcal · mole <sup>-1</sup>	As given in ref. (25).

Table III. HER on manganese: kinetic parameters and some other characteristics

Parameter	Value	Comments
1. Tafel slope (25°C)	140 mV/decade	This value is obtained for H <sub>2</sub> O discharge in 0.1N H <sub>2</sub> SO <sub>4</sub> + 2N Na <sub>2</sub> SO <sub>4</sub> solution (pH = 1.9)
2. Exchange current density (25°C)	$3.98 \times 10^{-12}$ A · cm <sup>-2</sup>	Also for water discharge
3. Apparent heat of activation	8.1 kcal · mole <sup>-1</sup>	Calculated from the plot of $(-\log i)$ vs. $1/T$ $\eta = -1.4V$
4. Reaction order derivative	—	No reaction order for the proton discharge because of corrosion
5. Corrosion potential (25°C)	-1.04V	In a solution of 0.1N H <sub>2</sub> SO <sub>4</sub> + 2N Na <sub>2</sub> SO <sub>4</sub> (pH = 1.9)
6. Corrosion current (25°C)	17 mA · cm <sup>-2</sup>	Determined by the chemical analysis of dissolved Mn <sup>2+</sup> in the working compartment
7. Electrode coverage by hydrogen	—	The corrosion of Mn leads to a general masking of any information on the coverage by H
8. Hydrogen adsorption in gas phase	$\Delta H_{\text{ads. H}} < 52$ kcal · mole <sup>-1</sup>	Not detectable by calorimetric methods (25)

Table IV. HER on cobalt: kinetic parameters and some other characteristics

Parameter	Value	Comments
1. Tafel slope (25°C)	115 mV/decade	In the descending direction of potentials (high → low current densities) in 1N H <sub>2</sub> SO <sub>4</sub> + 2N Na <sub>2</sub> SO <sub>4</sub> (pH = 0.7)
2. Exchange current density (25°C)	$6.25 \times 10^{-7}$ A · cm <sup>-2</sup>	For proton discharge from the extrapolation of the Tafel plot at $\eta = 0$
3. Apparent heat of activation	14.8 kcal · mole <sup>-1</sup>	Obtained from the plot of $(-\log i_0)$ vs. $1/T$
4. Reaction order derivative	—	No Tafel behavior in acidic solutions. For water discharge the reaction order is near 0 (see text)
5. Corrosion potential (25°C)	-114 mV	Open-circuit potential in 1N H <sub>2</sub> SO <sub>4</sub> + 2N Na <sub>2</sub> SO <sub>4</sub> (pH = 0.7)
6. Corrosion current (25°C)	$5.4 \times 10^{-6}$ A · cm <sup>-2</sup>	By the use of Stern-Geary equation (26)
7. Electrode coverage by hydrogen	No positive evidence	Masking by the concomitant corrosion reaction
8. Hydrogen adsorption in gas phase	$\Delta H_{\text{ads. H}} = 64$ kcal · mole <sup>-1</sup>	Ref. (25)



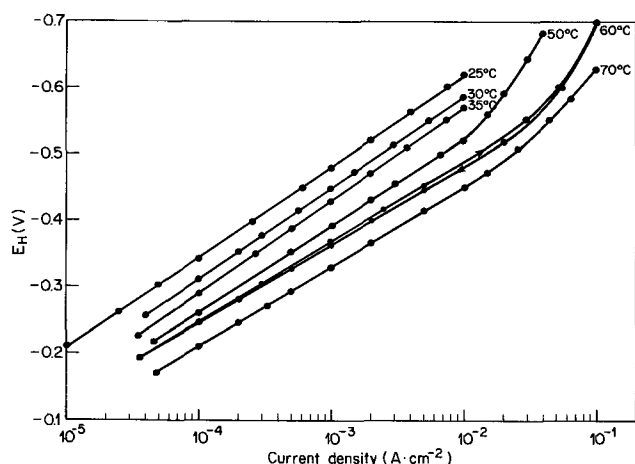


Fig. 1. Tafel relations for the HER on vanadium in 1N H<sub>2</sub>SO<sub>4</sub> + 2N Na<sub>2</sub>SO<sub>4</sub> (pH = 0.70) at different temperatures. All Tafel plots taken in the descending direction of the potential. Ascending and descending lines shown for one typical temperature, however.

some lines in Fig. 1, does not arise from the  $IR$  effects nor does it appear to be a limiting current. It is probably associated with the formation of some surface hydride phase. This curvature was also noticed by Kudryashov (8) (at  $i > 10^{-2}$  A·cm<sup>-2</sup>) in a study intended to show the influence of crystal structure of vanadium on Tafel plots for the HER in 1N H<sub>2</sub>SO<sub>4</sub>. Our results, on the polycrystalline samples are comparable to those observed on the (1,1,0) face by Kudryashov, i.e.,  $b = 140$  mV and  $i_0 = 5.8 \times 10^{-6}$  A·cm<sup>-2</sup>.

For obtaining apparent heat of activation for the HER on V, an attempt has been made to plot the logarithm of the exchange current density ( $-\log i_0$ ) values against  $1/T$ , where  $T$  is the absolute temperature. These data showed an enormous scatter and the  $\Delta H^*$  value corresponding to the line drawn is incredibly low, viz., 2 kcal·mole<sup>-1</sup>. The origin of this spurious value for an activation-controlled reaction lies in the fact that the Tafel lines in Fig. 1 are not parallel, and the long extrapolations involved in obtaining the  $i_0$  values yield a convergence at the reversible potential owing to different  $b$  values associated with the lines in Fig. 1. To circumvent this problem it was decided to extract a representative  $\Delta H^*$  value from Fig. 1 by plotting the logarithm of the current density at a typical potential (actually at  $-0.4$ V, which corresponds, roughly, to the center of the Tafel lines) against the  $1/T$  values (Fig. 2). The  $\Delta H^*$  thus obtained is 11.6 kcal·mole<sup>-1</sup>, which is quite consistent with the values usually associated with the activation-controlled electrode reactions (9).

Figure 3 contains steady-state potential-log current density relationships on chromium at various temperatures. Linear Tafel regions are obtained only at more cathodic potentials whereas at less cathodic potentials, vanishingly small polarization values are observed, owing to appreciable participation of the corrosion (dissolution) reaction. The experimental Tafel slope decreases with the increasing temperature contrary to theoretical expectations for the variation of  $2.3 \times RT/\beta F$  with the value of  $\beta = 0.5$ . One possible way to explain this would be to suppose that at low temperatures, high  $b$  values are observed because of the presence of a surface oxide on Cr; at higher temperatures, this oxide probably becomes hydrated and thus "short-circuited" as far as its kinetic participation in the charge transfer events is concerned, leading thereby to small slopes. This explanation, however, is highly speculative. The HER on chromium has also been studied previously (10-13). Our results shown in Table II may be compared at room temperature to the ones obtained by the following authors: Slope of 107

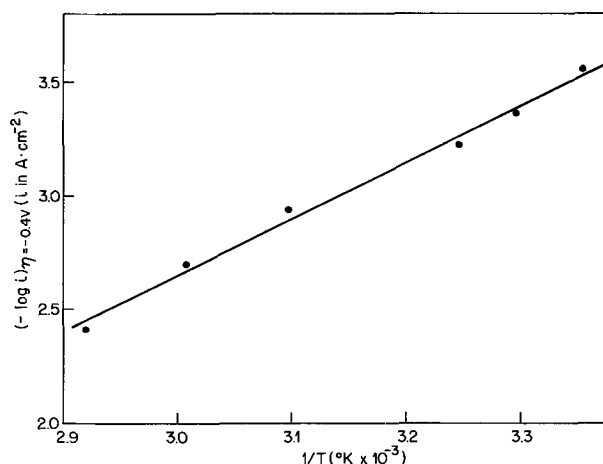


Fig. 2. Plot of  $(-\log i)_{\eta=-0.4V}$  vs.  $1/T$  for obtaining the derivative  $\left(\frac{\partial(-\log i)_{\eta=-0.4V}}{\partial(1/T)}\right)$  for the HER on vanadium in 1N H<sub>2</sub>SO<sub>4</sub> + 2N Na<sub>2</sub>SO<sub>4</sub>. Data used are taken from Fig. 1. The value of  $\Delta H^*$  thus obtained is 11.6 kcal·mole<sup>-1</sup>.

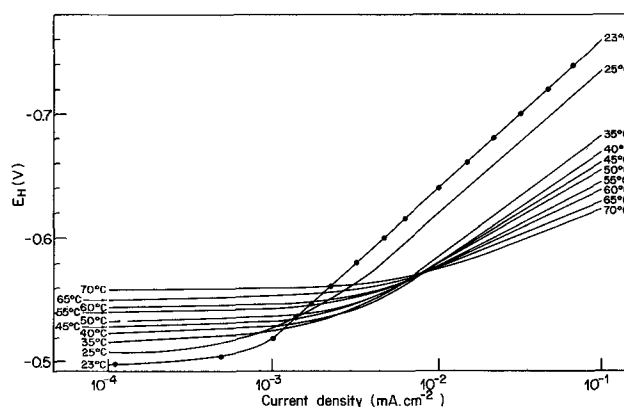


Fig. 3. Tafel relationships for the HER on chromium in 1N H<sub>2</sub>SO<sub>4</sub> + 2N Na<sub>2</sub>SO<sub>4</sub> (pH = 0.7) solution at different temperatures. The curves shown represent the ascending and descending directions of both the potential and temperature. Data were recorded at 20 mV intervals in most cases. These curves are used to evaluate the apparent heat of activation of the reaction. Typical experimental points have been shown at one curve.

mV was observed in 1N H<sub>2</sub>SO<sub>4</sub> with  $i_0 = 3.5 \times 10^{-8}$  A·cm<sup>-2</sup> by Ho Nhok Ba *et al.* (11). De Becdelièvre *et al.* (12) obtained a slope of 123 mV and  $i_0 = 5.9 \times 10^{-7}$  A·cm<sup>-2</sup> for the face (1,0,0) of chromium in 1N H<sub>2</sub>SO<sub>4</sub>, and finally a slope of 126 mV and  $i_0 = 4 \times 10^{-7}$  A·cm<sup>-2</sup> for active chromium in 1N H<sub>2</sub>SO<sub>4</sub> by Wilde and Hodge (13). From the plot of  $\log i$  (at  $\eta = -0.62$ V) vs.  $1/T$  we obtained a value of 9.8 kcal·mole<sup>-1</sup> for the apparent heat of activation (Table II).

It is of interest in the present context to examine the plot of the open-circuit mixed corrosion potentials vs.  $1/T$  values as taken from Fig. 3. One may estimate the  $\Delta H^*$  value from this plot by assuming, as in a previous publication (14), that the mixed corrosion potential is determined almost entirely by the cathodic conjugate partial reaction (i.e., the HER).

With this assumption,  $\left(\frac{\partial E_{\text{corr}}}{\partial(1/T)}\right)$  value is 129 mV

(and roughly equal to 120 mV at room temperature, i.e., equal to ca.  $2.3 \times 2RT/F$ ) and that this change in  $E_{\text{corr}}$  corresponds roughly to 1 decade change in the current density, one may estimate a  $\Delta H^*$  value from these data as equal to 10.2 kcal·mole<sup>-1</sup>. This value agrees well with the one calculated from  $\log i$  vs.  $1/T$ , the plot as obtained above. On "active" chromium, Wilde and Hodge (13) got a much higher value

from their Arrhenius plot, *i.e.*,  $38.4 \text{ kcal}\cdot\text{mole}^{-1}$  in  $1N \text{ H}_2\text{SO}_4$  while they obtained  $11 \text{ kcal}\cdot\text{mole}^{-1}$  for their passive chromium in the same solution. From the magnitudes of our corrosion potential and the corrosion current density and of those observed by Wilde and Hodge (13), it is clear that our data for the HER refer to a nonpassivated chromium surface. The values of  $\Delta H^*$  observed by Wilde and Hodge (13) for the active chromium are, however, enormously higher than those obtained by us; the magnitude of their  $\Delta H^*$  values for this case ( $38.4 \text{ kcal}\cdot\text{mole}^{-1}$ ) appears much too high in comparison with the  $\Delta H^*$  values generally observed for the HER on various metals.

In Fig. 4, steady-state potentiostatic Tafel plots for the HER on Mn in  $0.1N \text{ H}_2\text{SO}_4 + 1N \text{ Na}_2\text{SO}_4$  ( $\text{pH} = 1.9$ ), at the shown temperatures, are presented. At the lower cathodic potentials, no Tafel plot is obtained because of the vigorous open-circuit corrosion reaction. Around  $10^{-2} \text{ A}\cdot\text{cm}^{-2}$ , a limiting current density for the discharge of  $\text{H}_3\text{O}^+$  is reached, as also noted in some previous work (15), followed by a long Tafel region, at all temperatures, associated with the evolution of hydrogen by the discharge of  $\text{H}_2\text{O}$ . The Tafel slopes for these lines are *ca.*  $140 \text{ mV}/\text{decade}$  and may hence be roughly assumed to be  $2.3 \times 2RT/F$ . An attempt was made to obtain the apparent heat of activation  $\Delta H^*$ , from these Tafel lines by plotting the current density values at  $-1.4V$  vs.  $1/T$ . It was observed the

$\left(\frac{\partial \log i}{\partial 1/T}\right)_{\eta=-1.4V}$  is  $8.1 \text{ kcal}\cdot\text{mole}^{-1}$ . Melendez and Brenet (16) have reported a Tafel slope of  $152 \text{ mV}$  in buffered phosphate solutions ( $\text{pH} = 7.6$ ) which also corresponds to water discharge. Hurlen and Valand (17) obtained a slope of  $117 \text{ mV}$  in sulfuric acid-potassium sulfate solutions but these experiments (17) were conducted in a single compartment cell which would make them of questionable validity due to the possible contamination by oxygen formed at the anode. In  $0.1N \text{ H}_2\text{SO}_4$ , Gamali and Stender (18) obtained a slope of  $120 \text{ mV}$  with an exchange current density of  $1.8 \times 10^{-12} \text{ A}\cdot\text{cm}^{-2}$ .

In Fig. 5 steady-state potentiostatic Tafel plots for the HER on Co are presented. They cover a range of temperatures and were taken in  $1N \text{ H}_2\text{SO}_4 + 1N \text{ Na}_2\text{SO}_4$  ( $\text{pH} = 0.7$ ) solutions. Reproducible Tafel lines over several decades of current densities are obtained only if one prepolarizes the electrode for about 30 min at the highest current density and traces the Tafel slopes in the descending (more cathodic  $\rightarrow$  less cathodic) direction of potentials. Even under these conditions, the marginal "second" Tafel region at higher cathodic potentials is not very reproducible and will not be discussed further here. It should be emphasized that this lack of reproducibility in the upper Tafel

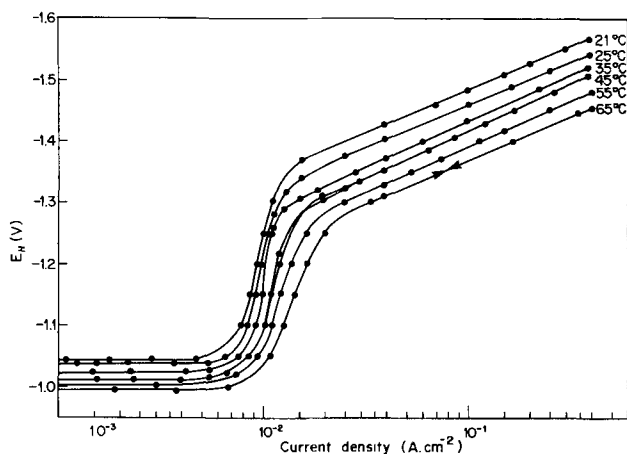


Fig. 4. Tafel relationships for the HER on manganese in  $0.1N \text{ H}_2\text{SO}_4 + 2N \text{ Na}_2\text{SO}_4$  ( $\text{pH} = 1.9$ ) at different temperatures. These curves were used to calculate the apparent heat of activation.

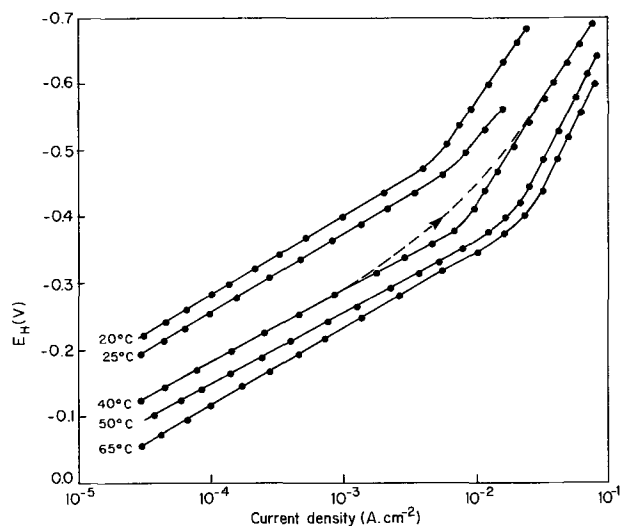


Fig. 5. Tafel relationships for the HER on cobalt in  $1N \text{ H}_2\text{SO}_4 + 2N \text{ Na}_2\text{SO}_4$  ( $\text{pH} = 0.70$ ) at different temperatures. All Tafel plots are in the descending direction of the potential but a typical ascending curve is shown (in dashes) for one temperature ( $40^\circ\text{C}$ ). Data are:  $b_{20} = 117 \text{ mV}$ ;  $b_{25} = 115 \text{ mV}$ ;  $b_{40} = 106 \text{ mV}$ ;  $b_{50} = 105 \text{ mV}$ ;  $b_{65} = 115 \text{ mV}$ .

region is not due to the impurities in the solution since good Tafel lines are obtained in the potential range,  $-0.05$  to  $-0.5V$  at all temperatures. It appears that cathodic polarization leads to some profound change in the cobalt surface which results in their stability, and hence reproducibility after the prepolarization. The hysteresis between the ascending and descending Tafel plots (on the conditioned electrodes, of course) is shown only for  $40^\circ\text{C}$  in Fig. 5; it is least pronounced for  $65^\circ\text{C}$  and assumes higher magnitudes for lower temperatures.

An attempt has been made to deduce the apparent heat of activation,  $\Delta H^*$ , by plotting  $-\log i_0$  values against the corresponding  $1/T$  value. The parent data for this plot are extracted from Fig. 5. The  $\Delta H^*$  obtained is  $14.8 \text{ kcal}\cdot\text{mole}^{-1}$ . All the results presented here and summarized in Table IV may be compared with the following ones. Iofa *et al.* (19) obtained a slope of  $147 \text{ mV}$  and an  $i_0$  of  $1.9 \times 10^{-5} \text{ A}\cdot\text{cm}^{-2}$  in  $0.1N \text{ H}_2\text{SO}_4$ ; Mottern and Myers (21) give a value of  $125 \text{ mV}$  for the cathodic Tafel slope and  $1.3 \times 10^{-5} \text{ A}\cdot\text{cm}^{-2}$  for the exchange current density with  $E_{\text{corr}}$  being  $-0.31V$  (SCE) in  $1N \text{ H}_2\text{SO}_4$ .

A typical determination of the chemically significant reaction order derivative,  $\left(\frac{\partial \log i}{\partial \text{pH}}\right)_{\phi=-0.7V, \psi, T}$  is depicted in Fig. 6, for the case of V; here  $\phi$  refers to the electrode potential against standard hydrogen electrode (also see Table IV), and  $\psi$  is the potential drop across the diffuse double layer.

**Potentiodynamic and transient studies.**—A complete study of the behavior of the four metals under dynamic variation of potential was carried out. The techniques used were the following: (i) potentiodynamic profiles for various sweep rates, temperatures, and  $\text{pH}$  values; (ii) open-circuit decay of the electrode potential; (iii) galvanostatic cathodic charging curves from the open-circuit potential; and (iv) galvanostatic forced decay (22) curves at high anodic or cathodic current densities. These experiments were conducted with a view to obtain some information on the coverage of the electrodes by chemisorbed hydrogen. In general, very high pseudo-capacitance values characteristic of a significant corrosion reaction were observed in all cases. The studies could not bring out, therefore, any evidence of the chemisorption (or lack of it) of atomic hydrogen on these electrodes during the HER.

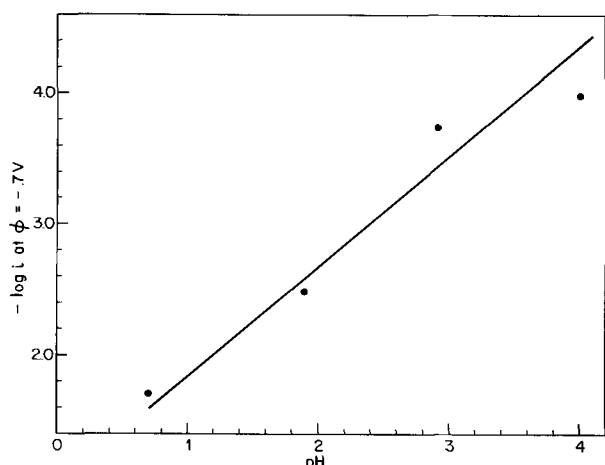
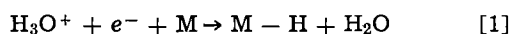


Fig. 6. Plot of  $-\log i$  at  $\phi = -0.7V$  vs.  $pH$  for the vanadium electrode in  $xH_2SO_4 + 2N Na_2SO_4$  solutions ( $1N > x > 10^{-4}N$ );  $\phi$  is the value of the electrode potential against standard hydrogen electrode (SHE).

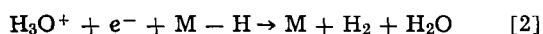
### Discussion

For V, Cr, and Co the corrosion rates in the highly acidic ( $pH = 0.7$ ) solutions are not high enough to prohibit the measurement of Tafel regions for the HER proceeding by the discharge of  $H_3O^+$  (Fig. 1, 3, and 5). For the case of Mn, however, the corrosion rate is of very high magnitude so that a Tafel line for the HER by proton discharge is not obtained even in solutions with  $pH = 1.9$  (Fig. 4). In this case, a limiting current for the  $H_3O^+$  discharge is obtained around  $10^{-2} A \cdot cm^{-2}$ , which is followed by a Tafel region for the HER by water discharge at higher cathodic potentials (Fig. 4).

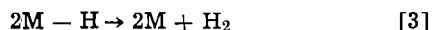
The evolution of hydrogen on V, Cr, and Co, from the acidic solutions can involve the following elementary steps (14, 23, 24)



followed by

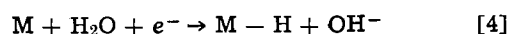


or

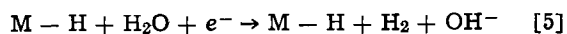


The values of the Tafel slope for these three metals (Table I, II, and IV) exclude the possibility of step [3] as the rate-determining step (rds). The experimental values observed (ca.  $2.3 \times 2RT/F$ ) would indicate either step [1] (with electrode coverage  $\theta \rightarrow 0$ ) or step [2] (with electrode coverage  $\theta \rightarrow 1$ ) as the rds. Since direct evidence on the electrode coverage by electrochemical transient studies cannot be obtained for these metals because of the interference by metal dissolution and oxide formation (or reduction) etc., it is difficult to distinguish between the choice of step [1] or step [2] as the rds. Some light may be thrown on this point, however, by the behavior of these metals toward the adsorption of  $H_2$  in the gas phase (Tables I, II, and IV), as discussed previously in the theoretical considerations of the HER (1, 23, 24). Since Cr (Table II) and Co (Table IV) are good catalysts for adsorbing hydrogen (25), it is likely that the HER proceeds on an electrode covered by adsorbed hydrogen. This fact would indicate step [2] as the rds for Co and Cr. It is found, however, that vanadium does not adsorb hydrogen from the gas phase (Table I). It is likely that because of its rather noncatalytic nature in the gas phase (25), the vanadium electrode is not covered by chemisorbed hydrogen during the HER; this would suggest step [1] as the rds for V.

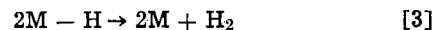
For the case of Mn, the Tafel line is observed only for the discharge of  $H_2O$  for the solutions examined (Fig. 4). The steps involved in the HER on Mn would then be



followed by



or



The value of Tafel slope (Table III) would exclude, again, step [3] as the rds. The direct knowledge on the electrode coverage by adsorbed H, during the HER, is again not accessible. However poor adsorbent properties of Mn for the  $H_2$  in the gas phase (Table III) would lead one to suggest that the electrode coverage during the HER is probably not significant. One would thus tend to conclude step [4] as the rds on Mn in the Tafel region in Fig. 4.

The relevance of other experimental data (Tables I to IV) to the proposed mechanisms may now be examined. The value of  $i_0$  for V is rather high (9, 23) for the suggested initial discharge mechanism whereas the magnitudes of reaction order and the heat of activation are not incompatible with it (Table I). For the case of chromium, the  $i_0$  and  $\Delta H^*$  values are not inconsistent with the proposed mechanism (14, 23). The attempts to measure reaction order on Cr by examining the current-potential relations at  $pH$  values of 0.7, 1.9, 3, and 4 were not successful; this arises because at higher  $pH$  values (1.9, 3, and 4), the Tafel line (obtained between the open-circuit corrosion potential and the potential for the change-over to  $H_2O$  discharge) for the  $H_3O^+$  discharge is too small to be significant.

For the case of Mn (Table III) the exchange current density value observed clearly confirms the suggested mechanism (14, 23, 24), although the  $\Delta H^*$  is rather low though not inconsistent (4) with the proposed mechanism. Here the reaction order could not be determined since the Tafel lines are obtained for the discharge of water only (Fig. 4).

The exchange current density for Co (Table IV) is of the same magnitude as is generally observed for metals proceeding with step [2] as the rds (1, 14, 23, 24). The heat of activation is not so high as would militate against the proposed mechanism. The reaction order could not be determined owing to the reasons very similar to those mentioned for chromium above.

In conclusion, it is suggested that HER on V and Mn proceeds with steps [1] and [4] as the rds, respectively. For the case of Co and Cr, step [2] appears to be the likely rds.

### Acknowledgments

Thanks are due to the Hydro-Quebec Institute of Research, the National Research Council of Canada, and the National Institute for Scientific Research, University of Quebec for the financial support of this work. Dr. P. Lenfant is thanked for his interest and encouragement.

Manuscript submitted Aug. 10, 1972; revised manuscript received Aug. 20, 1973.

Any discussion of this paper will appear in a Discussion Section to be published in the December 1974 JOURNAL.

### REFERENCES

1. A. K. Vijh and A. Bélanger, *Z. Phys. Chem.. N. F.*, **83**, 173 (1973).
2. B. E. Conway and M. Dzieciuch, *Can. J. Chem.*, **41**, 21, 38, 55 (1963).
3. R. S. Alwitt and A. K. Vijh, *This Journal*, **117**, 413 (1970).
4. A. K. Vijh and B. E. Conway, *Chem. Rev.*, **67**, 623 (1967).
5. G. Bélanger, *This Journal*, **118**, 583 (1971).
6. J. D. E. McIntyre and W. F. Peck Jr., *ibid.*, **117**, 747 (1970).
7. D. R. Flinn, M. Rosen, S. Schuldiner, and J. D. Fahey, *ibid.*, **117**, 79 (1970).

8. I. V. Kudryashov and E. G. Chekunov, *Soviet Electrochem.*, **6**, 1729 (1971); *Zh. Vses. Khim. Obshchestva*, **14**, 234 (1969).
9. B. E. Conway and M. Salomon, *Electrochim. Acta*, **9**, 1599 (1964).
10. S. G. Christov and N. A. Pavgarov, *Z. Electrochem.*, **61**, 113 (1957).
11. Ho Ngok Ba and Nguyen Dyk Vi, *Soviet Electrochem.*, **4**, 894 (1968).
12. J. de Becdelièvre, A. M. de Becdelièvre, and G. Bouyssoun, *C. R. Acad. Sci. Paris*, **268**, Sér. 1988 (1969).
13. B. E. Wilde and F. G. Hodge, *Electrochim. Acta*, **14**, 619 (1969).
14. A. K. Vijh, *J. Phys. Chem.*, **72**, 1148 (1968); **73**, 506 (1969).
15. M. Breiter, in "Symposium on Electrode Processes," E. Yeager, Editor, John Wiley & Sons, Inc., New York (1959).
16. M. Melendez and J. Brenet, *Electrochim. Acta*, **16**, 61 (1971).
17. T. Hurlen and T. Valand, *ibid.*, **9**, 1077 (1964).
18. I. V. Gamali and V. V. Stender, *Zh. Priklad. Khim.*, **35**, 271 (1962).
19. Z. A. Iofa, V. V. Batrakov, and Cho-Ngok-Ba, *Electrochim. Acta*, **9**, 1645 (1964).
20. I. V. Kudryashov and E. S. Burmistrov, *Soviet Electrochem.*, **6**, 722 (1970).
21. M. M. Mottern and J. R. Myers, *Corrosion*, **24**, 197 (1968).
22. W. Mehl, M. A. Devanathan, and J. O'M. Bockris, *Rev. Sci. Instr.*, **29**, 180 (1958).
23. B. E. Conway, "Theory and Principles of Electrode Processes," Ronald Press, New York (1965).
24. J. O'M. Bockris and A. K. N. Reddy, "Modern Electrochemistry," Vol. 2, Plenum Press, New York (1970).
25. G. Ehrlich, in "Third Congress on Catalysis," Vol. 1, W. M. H. Sachtler, G. C. A. Schuit, and P. Zwietering, Editors, North Holland Pub. Co., Amsterdam (1965).
26. M. Stern and A. L. Geary, *This Journal*, **104**, 56 (1957).

## Hydrogen and Nitrogen Evolution Reactions in Acid Liquid Ammonia

M. H. Miles\* and C. A. Yates

*Department of Chemistry, Middle Tennessee State University, Murfreesboro, Tennessee 37130*

### ABSTRACT

The hydrogen and nitrogen evolution reactions were investigated on various electrode surfaces in acid ( $\text{NH}_4\text{NO}_3$ ) liquid ammonia solutions at temperatures ranging from  $20^\circ$  to  $-60^\circ\text{C}$ . Tafel slopes, transfer coefficients, and exchange currents were determined from the potential-current measurements. The relative rates of the hydrogen evolution reaction on various surfaces in liquid ammonia is in the order  $\text{Pt, Ir} \gg \text{Ni}_2\text{B, Au} > \text{Mo, Cr, W} \gg \text{Ta}$ , similar to the relative reactivities found in aqueous solutions. The Tafel slopes for the cathodic reaction are also similar to Tafel slopes determined in aqueous solutions at comparable temperatures. However, the apparent cathodic transfer coefficients tend to decrease significantly at low temperatures. On platinum surfaces, the slow step appears to change from the chemical recombination of adsorbed hydrogen atoms to an electrochemical process as the temperature decreases. Studies of the nitrogen evolution reaction are complicated by possible interfering anodic reactions. However, the results indicate that there is an extremely high overvoltage associated with the nitrogen evolution reaction, and that electrochemical process rather than chemical recombination steps control the reaction rate.

Investigations of the hydrogen evolution reaction (h.e.r.) in liquid ammonia solutions (1-3) have been surprisingly few, especially when compared with the numerous studies of the h.e.r. in aqueous solutions (4, 5). The literature indicates that the Tafel parameters for the h.e.r. in liquid ammonia solutions have been determined only for nickel and platinum electrodes (1, 3). The only detailed study reported of the nitrogen evolution reaction (n.e.r.) in liquid ammonia was made using a platinum electrode in several acid salt solutions at  $-50^\circ\text{C}$  (6). In our study, Tafel parameters were determined for the h.e.r. on various electrodes in  $\text{NH}_4\text{NO}_3$  solutions in liquid ammonia at temperatures of  $20^\circ$ ,  $0^\circ$ , and  $-60^\circ\text{C}$ . The nitrogen evolution reaction on several electrodes was also investigated at  $0^\circ\text{C}$ .

### Experimental

The liquid ammonia solutions were prepared from anhydrous ammonia (99.99%) and vacuum-dried, reagent grade  $\text{NH}_4\text{NO}_3$  using methods similar to those described previously (2, 7). At  $0^\circ$  and  $20^\circ\text{C}$ , the mole ratio of  $\text{NH}_3$  to  $\text{NH}_4\text{NO}_3$  is about 1.5 in the ammoniate of this salt (8). At  $-60^\circ\text{C}$ , approximately 5M solu-

tions of  $\text{NH}_4\text{NO}_3$  were used. A dry ice-chloroform bath was used for measurements at  $-60^\circ\text{C}$  to provide temperature control of  $\pm 1^\circ\text{C}$ . Recent work has verified that the lead-saturated lead nitrate (SLN) reference electrode used works well in liquid ammonia solutions (9).

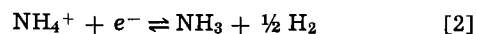
All potential-current measurements were made using a Beckman Electroscan 30 instrument. Prior to each run, the electrode received a pretreatment by sweeping the potential in the positive direction until nitrogen evolution occurred, then in the negative direction until hydrogen evolution appeared. This procedure was repeated several times, always allowing hydrogen to be evolved before the actual run started. In each run, the potential was swept in the direction of interest at a rate of 0.5 mV/sec.

### Results

The linear regions of the log  $i$  vs. potential plots suggested by Tafel's equation

$$|\eta| = |E - E_0| = a + b \log |i| \quad [1]$$

for all electrodes studied is shown in Fig. 1 for the hydrogen evolution reaction



\* Electrochemical Society Active Member.

Key words: exchange current, Tafel slopes, transfer coefficients, overvoltage.

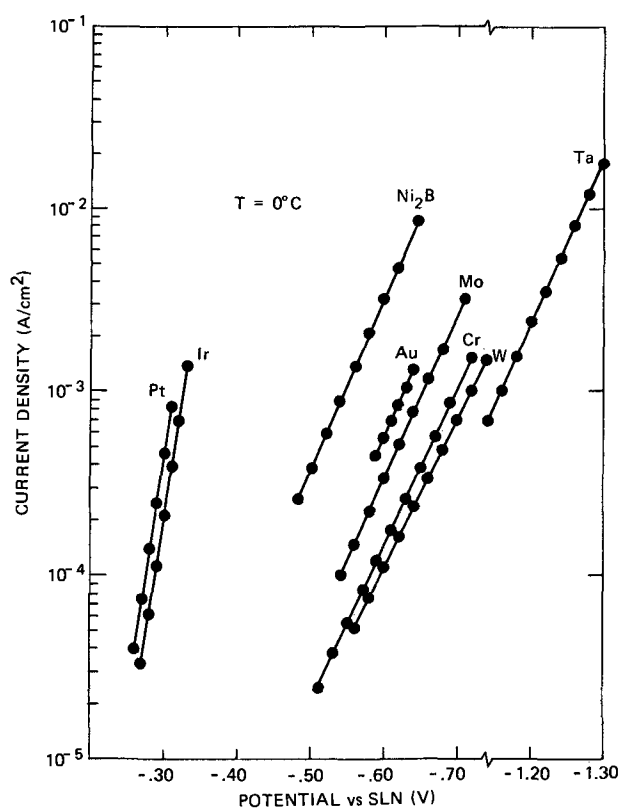


Fig. 1. Linear Tafel regions for the hydrogen evolution reaction on various electrode surfaces in acid ( $\text{NH}_4\text{NO}_3$ ) liquid ammonia solutions at  $0^\circ\text{C}$ .

in  $\text{NH}_4\text{NO}_3$  solutions in liquid ammonia at  $0^\circ\text{C}$ . The current density,  $i$ , was determined using the geometrical area of the electrode. Except for platinum and iridium, the slopes of these plots are about the same for each electrode material. However, the overvoltage,  $\eta$ , required for a given current density varies greatly with the metal used. This indicates that the ranking of these electrodes as electrocatalysts for the above reaction is in the order  $\text{Pt} > \text{Ir} \gg \text{Ni}_2\text{B} > \text{Au} > \text{Mo} > \text{Cr} > \text{W} \gg \text{Ta}$ , with Pt being the best electrocatalyst. The Tafel parameter,  $b$ , and the apparent cathodic transfer coefficient,  $\beta$ , can be determined from Fig. 1 using the relationships

$$b = \frac{d|\eta|}{d \log |i|} = \frac{2.303RT}{\beta F} \quad [3]$$

Knowledge of the equilibrium potential,  $E_0$ , for reaction [2] is required before the determination of the Tafel parameter,  $a$ , can be made. Due to indicated difficulties with the hydrogen reference electrode in liquid ammonia (9) involving rather long initial settling down periods (10), no attempt was made to measure the equilibrium potential directly for our solutions. However, the equilibrium potential can be estimated to be about  $-0.25\text{V vs. SLN}$  for the solutions at  $0^\circ\text{C}$ , based upon the current-potential measurements using the platinum electrode. Using this estimated value for  $E_0$ , both the Tafel parameter,  $a$ , and the apparent exchange current,  $i_0$ , can be determined for the h.e.r. in liquid ammonia. These results are given in Table I for the various electrodes used. Using the apparent exchange currents gives almost the same ranking as above for the electrodes as electrocatalysts for reaction [2].

Figure 2 shows Tafel plots at  $20^\circ$ ,  $0^\circ$ , and  $-60^\circ\text{C}$  for the hydrogen evolution reaction on molybdenum in acid liquid ammonia solutions. Similar studies at these three temperatures were made using platinum, gold, and tungsten electrodes. Values for the apparent cathodic transfer coefficients,  $\beta$ , for the h.e.r. were cal-

Table I. Tafel parameters for the hydrogen evolution reaction at various electrodes in  $\text{NH}_3\text{-NH}_4\text{NO}_3$  solutions at  $0^\circ\text{C}$

Electrode material	$a$ (Volts)	$b$ (Volts)	$i_0$ ( $\text{A}/\text{cm}^2$ )
Pt	0.15	0.031	$2 \times 10^{-5}$
Ir	0.16	0.032	$10^{-5}$
$\text{Ni}_2\text{B}$	0.59	0.10	$10^{-6}$
Au	0.71	0.12	$10^{-6}$
Mo	0.71	0.11	$4 \times 10^{-7}$
W	0.81	0.12	$2 \times 10^{-7}$
Cr	0.79	0.11	$10^{-7}$
Ta	1.21	0.10	$10^{-12}$

Table II. Apparent cathodic transfer coefficients for the hydrogen evolution reaction in  $\text{NH}_3\text{-NH}_4\text{NO}_3$  solutions at  $20^\circ$ ,  $0^\circ$ , and  $-60^\circ\text{C}$

Electrode material	$\beta$ ( $20^\circ\text{C}$ )	$\beta$ ( $0^\circ\text{C}$ )	$\beta$ ( $-60^\circ\text{C}$ )
Pt	2.15	1.75	0.47
Au	0.58	0.48	0.26
Mo	0.45	0.52	0.32
W	0.45	0.46	0.28

culated from the Tafel slopes using Eq. [3]. The results given in Table II show that the values for  $\beta$  vary with the temperature. For Au, Mo, and W electrodes, the values for  $\beta$  range from about 0.5 at  $20^\circ\text{C}$  to about 0.3 at  $-60^\circ\text{C}$ . For Pt,  $\beta$  ranges from about 2 at  $20^\circ\text{C}$  to about 0.5 at  $-60^\circ\text{C}$ .

Figure 3 shows Tafel plots at  $0^\circ\text{C}$  for the anodic or nitrogen evolution reaction on various electrodes in acid liquid ammonia solutions. Although formation of gas bubbles is directly visible on all the electrodes at the higher current densities, it is also possible that the anodic current includes components due to direct oxidation of the electrode itself or due to formation of interstitial nitrides of the metal. Gessler and Pleskov (6) have demonstrated that in acid salt solutions in liquid ammonia at  $-50^\circ\text{C}$ , about 6% of a constant current density of  $10^{-5} \text{ A}/\text{cm}^2$  is consumed by dissolution of the platinum anode, assuming platinum is trans-

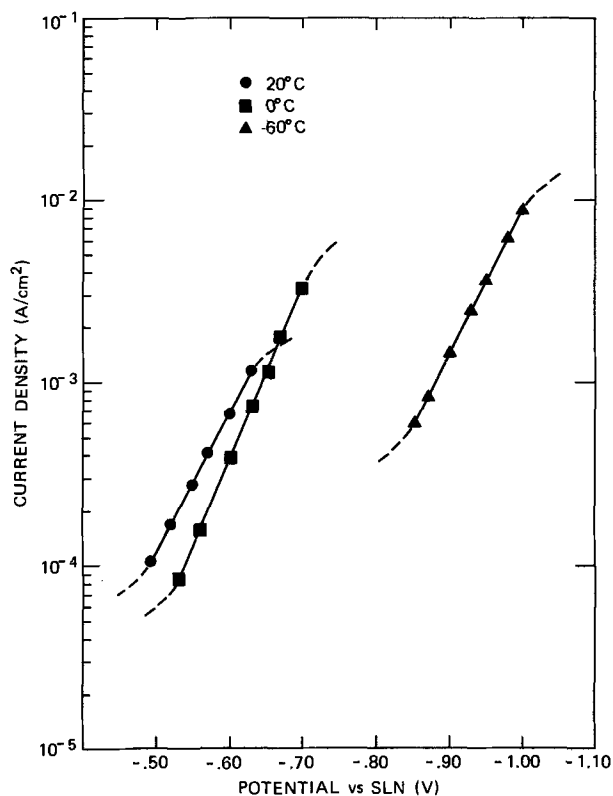


Fig. 2. Linear Tafel regions for the hydrogen evolution reaction on molybdenum in acid ( $\text{NH}_4\text{NO}_3$ ) liquid ammonia solutions at  $20^\circ$ ,  $0^\circ$ , and  $-60^\circ\text{C}$ .

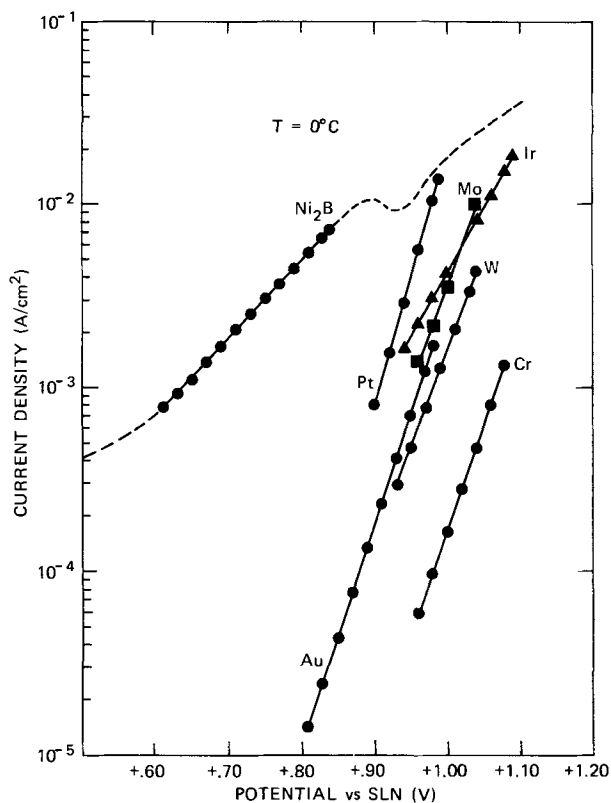
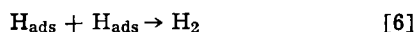
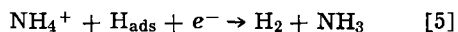
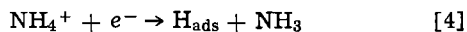


Fig. 3. Linear Tafel regions for the anodic or nitrogen evolution reaction on various electrode surfaces in acid ( $\text{NH}_4\text{NO}_3$ ) liquid ammonia solutions at  $0^\circ\text{C}$ .

ferred to the solution in the form of tetravalent ions. Such dissolution would likely be larger for the less-noble metals. The apparent anodic transfer coefficient calculated from the Tafel slopes in Fig. 3 are 0.2 for  $\text{Ni}_2\text{B}$ , 0.4 for Ir, 0.6 for Mo, W, and Cr, and 0.7 for Au and Pt. The Tafel slopes reported by Gessler and Pleskov (6) indicate an apparent anodic transfer coefficient of 0.5 for the n.e.r. on platinum at  $-50^\circ\text{C}$ .

### Discussion

At normal temperatures, the hydrogen evolution reaction in acid liquid ammonia appears to be kinetically similar to the h.e.r. in acid aqueous solutions. The reaction steps to be considered in the mechanism of reaction [2] are likely



For most transition metals, the h.e.r. proceeds with significant steady-state adsorption of hydrogen (11, 12), hence either reaction [5] or [6] would probably be rate-determining. Judging from the Tafel slopes (Tables I and II), reaction [6] appears to be rate-determining on Pt and Ir surfaces at temperatures  $0^\circ\text{C}$  or above ( $\beta \approx 2$ ), while reaction [5] is likely rate-determining on the other surfaces. The unusually large decrease in  $\beta$  with decreasing temperature to a value of about 0.5 at  $-60^\circ\text{C}$  suggests that reaction [5] becomes rate-determining on Pt at extremely low temperatures.

The reactivity scale for the h.e.r. on various metals appears to be about the same in acid ammonia solutions as observed in acid aqueous solutions. Trasatti (12) has indicated that the solvent would not interfere substantially with the h.e.r., except for shifting the absolute scale of reactivity. Studies of the results for the h.e.r. in aqueous solutions suggest that there is a linear correlation between  $\log i_0$  and the heat of adsorption of hydrogen on the electrode,  $\Delta H_{\text{ads}}$  (12, 13).

Omitting Ta, the measured exchange currents in acid liquid ammonia show a linear relationship between  $\log i_0$  and  $\Delta H_{\text{ads}}$  with  $d \log i_0 / d \Delta H_{\text{ads}} \approx 0.3$ , while a slope of 0.6 was found for aqueous solutions (13). Although the measured exchange currents in acid ammonia solutions generally tend to increase with increasing work function of the metal, the relationship between  $\log i_0$  and the work function is not clearly linear as suggested by Trasatti (12). The possibility of producing persistent interstitial nitrides during the electrode pretreatment might account for the lack of linearity. It should also be noted, however, that Kuhn *et al.* (13) question proposed correlations between the rate of the h.e.r. and the work function.

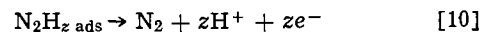
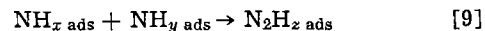
A temperature dependence of  $\beta$  similar to that shown in Table II has been observed in other studies of the h.e.r. at low temperatures (14-16). It has been proposed that either  $\beta$  is a function of temperature, or

$$b = C - \frac{2.303RT}{\beta F} \quad [7]$$

where  $C$  and  $\beta$  are constants, to account for observed increases in  $b$  with decreasing temperature (16). This anomalous temperature dependence of  $b$  can be rationalized in terms of specific adsorption of anions, presence of surface films, solvent structure effects in the double layer, or by proton tunneling at low temperatures (16, 17). It is interesting to note that a proton tunneling mechanism predicts a Tafel slope corresponding to  $\beta \approx 0.25$  (17), which is close to the experimental values at  $-60^\circ\text{C}$  (Table II) for the h.e.r. on W, Mo, and Au. Lamarre and Vijn (3) observed a similar Tafel slope for the h.e.r. on Pt at  $-73^\circ\text{C}$  in liquid ammonia and suggested the possibility of a proton tunneling mechanism. However, detailed studies of the h.e.r. in methanolic and ethanolic acid solutions at low temperatures give very little evidence for a proton tunneling mechanism (14-16).

The calculated thermodynamic dissociation voltage of liquid ammonia corresponding to evolution of hydrogen at the cathode and nitrogen at the anode is only 0.04V at  $25^\circ\text{C}$  (2, 6). Using this to estimate an equilibrium potential of  $-0.2\text{V}$  vs. SLN for the n.e.r., the data in Fig. 3 indicate that the kinetics are very slow for the nitrogen evolution reaction in liquid ammonia. The exchange current density for the n.e.r. on platinum is calculated to be only about  $10^{-19}$  A/cm $^2$  at  $0^\circ\text{C}$  in acid liquid ammonia solutions. Gessler and Pleskov (6) have also shown that a high nitrogen overvoltage exists for the n.e.r. on platinum in liquid ammonia.

Possible steps in the reaction mechanism for the n.e.r. in liquid ammonia include



where  $x$  and  $y$  are integers ranging from 0 to 3 with  $x \geq y$  and  $0 \leq z \leq 4$ . Simple kinetic considerations predict an anodic transfer coefficient value of  $\alpha = 2$  when processes involving chemical recombination of adsorbed species are rate determining. If interfering anodic reactions can be neglected, then the experimental values for  $\alpha$ , which range from 0.2 to 0.7, suggest that neither reaction [9] nor the recombination of adsorbed nitrogen atoms is rate determining. Since the electrochemical oxidation of hydrazine occurs readily in liquid ammonia (7), it seems unlikely that reaction [10] would be rate determining. Therefore, the rate-determining step for the n.e.r. in liquid ammonia must be some electrochemical process represented by Eq. [8]. Similar conclusions were reached by Gessler and Pleskov (6) in their studies in liquid ammonia, and by Gerischer and Mauerer (18) in their investigations in aqueous KOH solutions. In basic aqueous solutions, the participation of adsorbed OH-radicals promotes the electrochemical oxidation of ammonia. In both aqueous

ous and liquid ammonia acid solutions, where  $\text{OH}^-$  species are rare or absent, the electrochemical oxidation of ammonia is extremely slow.

### Conclusions

The Tafel slopes, reaction mechanisms, and relative reactivities for the h.e.r. on various electrodes in acid liquid ammonia show expected similarities to the h.e.r. in acid aqueous solutions at comparable temperatures. However, the apparent cathodic transfer coefficients tend to decrease at low temperatures, and on platinum there is evidence that a change in the rate-determining step occurs at low temperatures.

There is an extremely high overvoltage associated with the nitrogen evolution reaction in acid liquid ammonia solutions. The Tafel slopes suggest that an electrochemical step rather than a chemical recombination step is rate determining for the anodic reaction.

### Acknowledgment

The financial support of this work by the Faculty Research Committee at Middle Tennessee State University is gratefully acknowledged.

Manuscript submitted April 11, 1973; revised manuscript received Sept. 27, 1973.

Any discussion of this paper will appear in a Discussion Section to be published in the December 1974 JOURNAL.

### REFERENCES

1. V. A. Pleskov, *Acta Physicochim. U.R.S.S.*, **11**, 305 (1939).
2. M. H. Miles and P. M. Kellett, *This Journal*, **115**, 1225 (1968).
3. C. Lamarre and A. K. Vijh, *ibid.*, **120**, 85 (1973).
4. K. J. Vetter, "Electrochemical Kinetics," pp. 516-614, Academic Press, New York (1967).
5. J. O'M. Bockris and A. K. N. Reddy, "Modern Electrochemistry," Vol. 2, pp. 1231-1250, Plenum Press, New York (1970).
6. N. M. Gessler and V. A. Pleskov, *Zh. Fiz. Khim.*, **24**, 445 (1950).
7. M. H. Miles and P. M. Kellett, *This Journal*, **117**, 60 (1970).
8. D. E. Sellers and G. W. Leonard, *Anal. Chem.*, **34**, 1457 (1962).
9. D. Larkin, N. Hackerman, A. E. Buck, and L. K. Thompson, *This Journal*, **119**, 189 (1972).
10. J. Baldwin, J. B. Gill, and Ann Prescott, *J. Inorg. Chem.*, **33**, 2103 (1971).
11. A. K. Vijh, *This Journal*, **118**, 263 (1971).
12. S. Trasatti, *J. Electroanal. Chem.*, **39**, 163 (1972).
13. A. T. Kuhn, C. J. Mortimer, G. C. Bond, and J. Lindley, *ibid.*, **34**, 1 (1972).
14. B. E. Conway and M. Salomon, *J. Chem. Phys.*, **41**, 3169 (1964).
15. B. E. Conway and D. J. MacKinnon, *This Journal*, **116**, 1665 (1969).
16. B. E. Conway, D. J. MacKinnon, and B. V. Tilak, *Trans. Faraday Soc.*, **66**, 1203 (1970).
17. B. E. Conway, *Can. J. Chem.*, **37**, 178 (1959).
18. H. Gerischer and A. Mauerer, *J. Electroanal. Chem.*, **25**, 421 (1970).

## A Radiometric Study of Carbon Dioxide Adsorption on Platinum

H. B. Urbach,\* L. G. Adams, and R. E. Smith

Naval Ship Research and Development Center, Annapolis, Maryland 21402

### ABSTRACT

The adsorption of  $\text{CO}_2$  on platinum covered with adsorbed hydrogen atoms gives rise to an adsorbate called "reduced  $\text{CO}_2$ ," written  $(\text{CO}_2)_r$ . The steady-state adsorption of  $(\text{CO}_2)_r$  (the isoconcs) and its initial adsorption kinetics (Tafel plots) were studied by radiometric methods employing  $\text{C}^{14}$ -labeled  $\text{CO}_2$ . Radiometric results and selected reported electrochemical results appear to be compatible provided the adsorbate  $(\text{CO}_2)_r$  is assumed to be a carbonyl species that is bridged on two adjacent platinum sites. Isoconcs (coverage vs. potential relation) reveal a gaussian curve with a steady-state adsorption peak between 0.00 and 0.10V (RHE). Both the steady-state adsorption and kinetic rates increase with pH. No current is observed during the formation of  $(\text{CO}_2)_r$ . The character of the isoconcs and the initial kinetic rates are predicted by a reaction scheme based on cathodic reduction of carbon dioxide and anodic oxidation of adsorbed hydrogen atoms in equal amounts.

The reaction of  $\text{CO}_2$  with chemisorbed hydrogen on platinum electrodes was first studied by Giner (1). He concluded that he was observing a redox reaction and called the final adsorbed product "reduced  $\text{CO}_2$ " [henceforth referred to as  $(\text{CO}_2)_r$ ]. His studies, conducted at room temperature in an acidic electrolyte, indicated that  $\text{CO}_2$  adsorbs below 0.25V with the resultant adsorbate oxidizing above 0.5V during linear potential sweeps. In subsequent studies of the adsorption of organic materials and saturated hydrocarbons (3) he reported  $(\text{CO}_2)_r$  as part of the partially oxidized residue of these reactants.

Further studies by Niedrach *et al.* (4) indicated the presence of  $(\text{CO}_2)_r$  on platinum fuel-cell electrodes exposed to low molecular weight hydrocarbons, im-

plicating  $(\text{CO}_2)_r$  as a detrimental factor (4) affecting fuel-cell operation. Additional experiments were subsequently undertaken by other researchers (5-27) to further the characterization of reactions producing  $\text{CO}_2$  and its adsorbate. Each of these experiments has provided further insight into the basic properties of  $(\text{CO}_2)_r$  using purely electrochemical means.

Concern for the detrimental effects of  $(\text{CO}_2)_r$  on the behavior of fuel-cell anodes using carbonaceous fuels (4, 7) has prompted this radiometric investigation of the adsorption phenomenon to gain thereby further understanding of the conditions causing fuel-cell impairment. This report describes and reinterprets previously reported data in the light of these independent nonelectrochemical methods. The experiments described herein are a continuation of radiometric studies involving  $\text{C}^{14}$ -tagged formic acid (report in preparation) undertaken at this laboratory. The radiometric

\* Electrochemical Society Active Member.

Key words: reduced carbon dioxide, carbonyl electroadsorption, bridged carbon adsorbates.

techniques are modifications of methods described by Bockris and co-workers (28, 29).

### Experimental

The definition of the surface coverage parameter,  $\theta$ , employed herein is an experimental quantity equal to the ratio of the charge obtained by oxidation of the organic adsorbate divided by the charge associated with the oxidation of a clean layer (supposedly a saturated layer) of adsorbed hydrogen on the surface in question. The oxidation charge of the organic adsorbate is derived from measurement of the radioactivity of radioactive molecules of the adsorbate. The definition is simplistic and, as discussed below, subject to much error. However, the critical feature of the computation of  $\theta$  in this paper is the radiometric method which as will be seen, makes rigorous, clear-cut demands on the adsorbate model.

**Radiometric methods.**—Details of the experimental cell and the working (window) electrode were described previously (12). The experimental cell was a typical three-electrode cell of all glass and Teflon components. Both the counterelectrode and the reference electrode [a dynamic hydrogen electrode (30)] consisted of isolated platinized platinum grids. The working electrode was a thin, platinized, gold-polyester electrode, prepared by evaporative vacuum-deposition of a thin layer of gold on a polyester film, and subsequent electrodeposition of platinum. (The reverse side also received a very thin gold layer to eliminate static charge build-up). The resultant thin electrodes have a high transmission efficiency ( $\approx 5\%$ ) for the  $\beta$ -radiation emanating from the radiolabeled adsorbate, providing the basis for the radiometric procedure described below. The detection efficiency was established at the end of each experiment by using a standard radiation source (31). Standard electrolytes of 1.0N HClO<sub>4</sub> and 0.1N HClO<sub>4</sub> with 0.9N NaClO<sub>4</sub> were used with approximate pH values of 0 and 1, respectively. Sodium perchlorate was introduced in the latter electrolyte to maintain constant ionic strength. When the platinized side of the electrode was placed in contact with the electrolyte, it performed the simultaneous functions of an electrode and radiation counter "window" to monitor radioisotope-tagged species adsorbed at the electrode-electrolyte interface. Predetermined quantities of C<sup>14</sup>-tagged Na<sub>2</sub>CO<sub>3</sub> were injected through an isolated septum into the electrolyte cell. The desired CO<sub>2</sub> concentration was varied from test to test from approximately 10<sup>-7</sup> to 10<sup>-3</sup> molar in the standard electrolytes. However, a decrease in CO<sub>2</sub> concentration occurred during each test due to a slow exchange between radiolabeled CO<sub>2</sub> in the cell and inert CO<sub>2</sub> diffusing into the cell. Therefore the concentration was evaluated and recorded at 15-60 min intervals during the course of the experiment by assaying 100- $\mu$ liter aliquots of the electrolyte with a liquid scintillation spectrometer. Implicit in some previous studies and in this work is the assumption of virtually complete (although sometimes slow) conversion of the H<sub>2</sub>CO<sub>3</sub> to CO<sub>2</sub> (32, 33).

The potential of the working electrode was applied and maintained at a constant value by a fast-rise Wenking potentiostat, which was in turn controlled by a programmable potential stepping device (PPSD). The working electrode potential was measured with respect to the reversible hydrogen electrode (RHE).

Injection of the Na<sub>2</sub>CO<sub>3</sub> solution was executed at 0.9V, a potential determined from preliminary work to be sufficiently high that no adsorption occurs. The background count,  $\beta$ -radiation from the bulk solution, was thus established. Adsorption of the tagged CO<sub>2</sub> was then monitored at potentials and for periods of time programmed into the PPSD.

Two different adsorption procedures were used for these experiments. The first procedure involved stepping sequentially from 0.8 to -0.1V in 0.1V decrements.

Adsorption at each potential was independent of that at any previous potential because a "precleaning" potential sequence was applied prior to establishing the adsorption potential.

In the second procedure no "precleaning" sequence was applied prior to adsorption at each potential so that measurements represented an accumulative adsorption.

The roughness factor of the electrode was determined before and after a particular experiment from analysis of galvanostatic charging curves (34) at 100 mA. A linear relation between roughness factor and time was assumed between these measurements when variation was observed. From a measurement of the roughness factor and known geometric area the effective surface area of the electrode was calculated (12).

**Electrochemical methods.**—Experiments were conducted to detect net charge transfer resulting from the introduction of CO<sub>2</sub> into the electrolyte at the adsorption potential. The apparatus used for this measurement was a typical three-electrode cell of glass and Teflon components. The working electrode was a perforated platinized platinum electrode of large geometric surface area ( $\sim 20$  cm<sup>2</sup>). A gas inlet was connected to a CO<sub>2</sub> and He manifold. A bubble-off and valve served to regulate gas release from the cell.

With the potential of the cell maintained at 0.8V where reactants are inactive, helium was bubbled through the electrolyte to remove CO<sub>2</sub> and O<sub>2</sub>. When the cell current reached a low, steady-state value, the potential was stepped to 0.1V where the cell current was permitted, again, to approach a steady value. Then, after appropriate flushing of lines to remove impurities, CO<sub>2</sub> was admitted into the cell while the cell current was continually recorded on a Speedomax strip-chart recorder.

### Results

As stated above, the adsorption of CO<sub>2</sub> on precleaned platinum in acid media yields an adsorbate referred to as "reduced CO<sub>2</sub>." Coverage of this adsorbate,  $\theta$ , is plotted in Fig. 1a and b as a function of electrode potential for different bulk concentrations of CO<sub>2</sub>. The adsorption time at each potential was 10 min. The electrolytes were the standard solutions 1.0N HClO<sub>4</sub> and 0.1N HClO<sub>4</sub>, 0.9N NaClO<sub>4</sub> mentioned previously (henceforth referred to as 1.0N HClO<sub>4</sub> and 0.1N HClO<sub>4</sub>). Gaussian-shaped curves are similar at each pH with an apparent peak of adsorption between 0.05 and 0.10V. Coverage increases as the concentration is increased, for the same adsorption time and potential. At corresponding values of potential and concentration, a higher degree of coverage is observed at the higher pH.

An attempt was made to duplicate concentrations at several points. This was not possible because the concentration of CO<sub>2</sub> was under constant flux due to gas evolution on the electrodes and loss of CO<sub>2</sub> by diffusion through the liquid seal. However, in one case (see Fig. 1b) the concentrations 8.5 and 8.0  $\times 10^{-4}$ M CO<sub>2</sub> were sufficiently approximate to permit an estimate of the standard deviation from four sets of duplicate points. The relative standard deviation is 25% for the experiments in Fig. 1b and this value is assumed for other measurements.

Cumulative adsorption behavior (adsorbates were not removed by precleaning the electrode) is shown in Fig. 2a and b for 1.0 and 0.1N HClO<sub>4</sub> electrolytes, respectively. Adsorption time was again 10 min. The direction of the voltage stepping sequence is indicated by the arrows. No adsorption was observed at 0.3V or higher in the cathodic portion of the voltage sequence for either pH. Coverage was first observed at 0.2V, but because of the restricted time allowed for adsorption at each potential, full coverage was not achieved at 0.2V. The coverage continues to increase during the remainder of the cathodic portion and during the



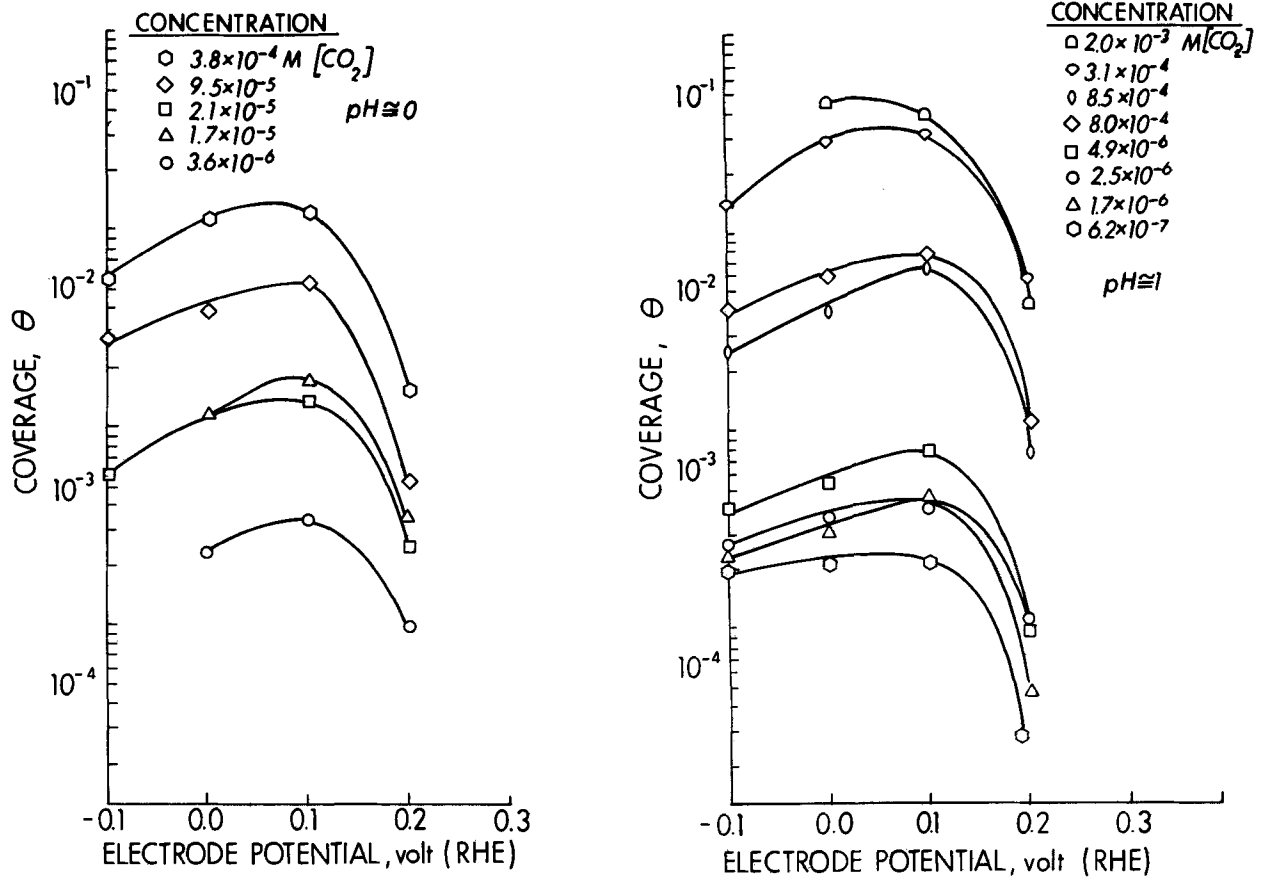


Fig. 1. Electrode coverage as a function of potential at constant  $\text{CO}_2$  concentration; adsorption time at each potential is 10 min. Electrolytes are: (a, left) 1.0N  $\text{HClO}_4$ ; (b, right) 0.1N  $\text{HClO}_4$  with 0.9N  $\text{NaClO}_4$ .

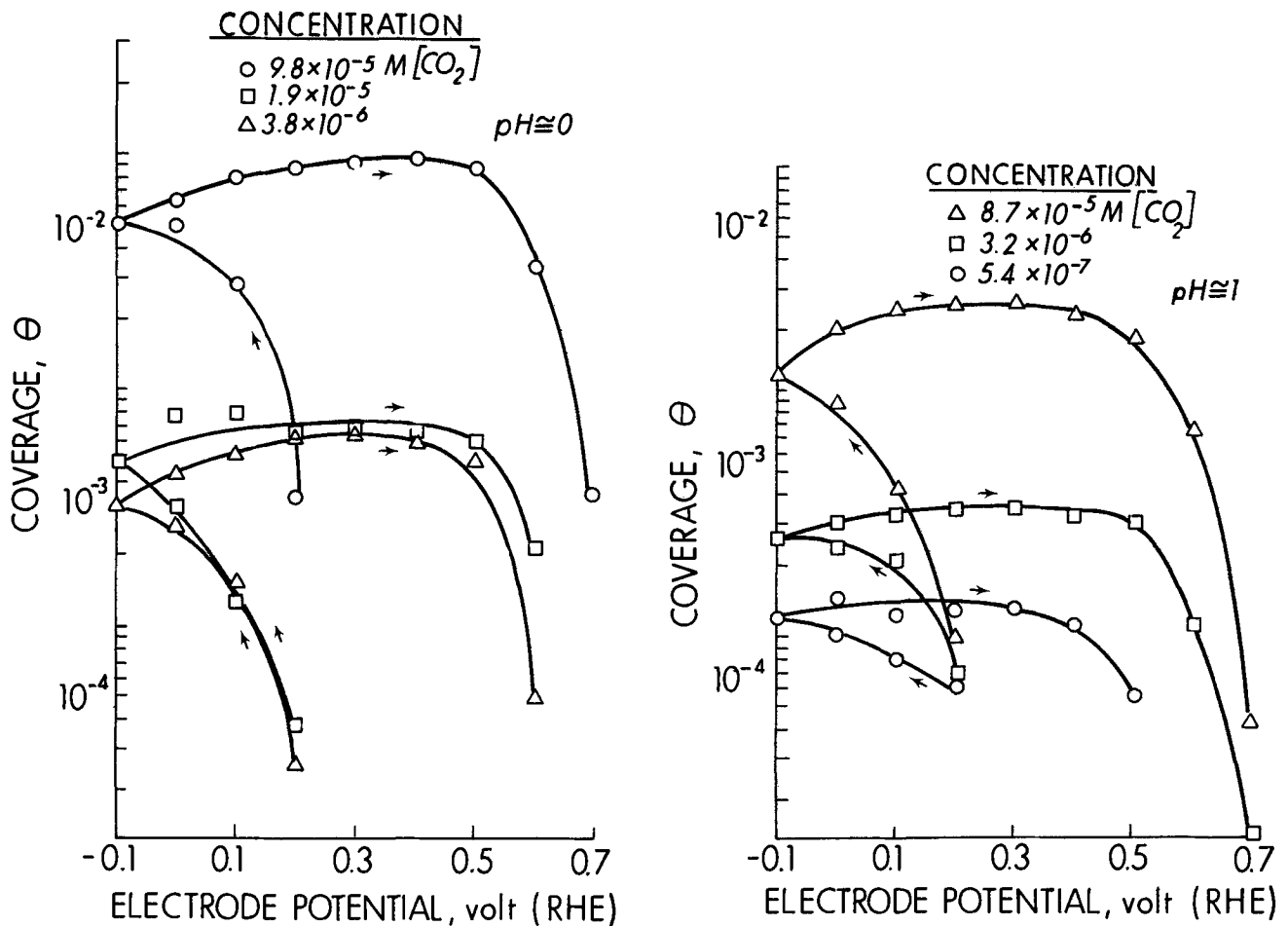


Fig. 2. Cumulative coverage as a function of potential at constant  $\text{CO}_2$  concentration. Adsorption time at each potential is 10 min without precleaning. Electrolytes are: (a, left) 1.0N  $\text{HClO}_4$ ; (b, right) 0.1N  $\text{HClO}_4$  with 0.9N  $\text{NaClO}_4$ .

anodic portion to 0.2V. The coverage remains relatively flat from 0.2 to 0.5V and then it decreases.

The decrease in coverage increases exponentially with potential so that desorption is essentially complete after 10 min at 0.8V in all observed cases. Thus, the curves exhibit a "hysteresis" in the anodic and cathodic isoconcs. The cumulative anodic curves are similar to cumulative anodic isoconcs obtained with methanol (11). Also, coverage increases with concentration as was observed above in Fig. 1a and b. In this respect there is evidence of scatter in the 1.0N HClO<sub>4</sub> data.

The effect of adsorption time is shown in Fig. 3a and b for comparably high ( $\sim 10^{-3}$  molar) CO<sub>2</sub> concentrations. For 1.0 and 0.1N HClO<sub>4</sub>, respectively, the coverage increases with time approaching a steady-state coverage at each potential. The peak of adsorption may shift from the apparent peak near 0.1V to a value which is closer to 0.0V.

Figures 4a and b indicate more clearly how coverage varies with concentration for the 1.0 and 0.1N HClO<sub>4</sub> electrolytes, respectively. The semilogarithmic relations (Langmuir plots) are given for fixed potentials from -0.1 to 0.2V. The coverage increases slowly at first, but increases rapidly above a coverage of 0.02. Finally, at the highest experimental concentration (in the 0.1N HClO<sub>4</sub>) a negative curvature indicates possible approach to saturation coverage. The Langmuir plots of Fig. 4b and 5 show the effect of different adsorption times of 10 and 40 min, respectively. Again, a slight negative curvature indicates a trend toward saturation for the 40-min case. However, in the 40-min case, a more pronounced negative curvature is expected but not observed.

Values of the calculated Tempkin factor,  $f$ , were obtained from the linear portions of the Langmuir plots of Fig. 4b and 5. Values for the 10-min (Fig. 4b) and

40-min (Fig. 5) adsorption times, 1.9 and 2.2, respectively, show reasonable agreement (considering experimental scatter).

Figure 6 shows the build-up of the adsorbate with time at 0.0 and 0.1V for  $2.0 \times 10^{-3}$ M CO<sub>2</sub>. The coverage appears to approach a steady-state value. (Lack of reversibility with respect to activity and potential indicates a nonequilibrium condition.) The existence of the steady-state coverage was verified by measuring the increments in coverage,  $\Delta\theta$ , for each two-fold increase in time. For each doubling of adsorption time  $\Delta\theta$  decreased geometrically. Thus, series summation for coverage at 0.0V yielded the asymptotic  $\theta$  value 0.62 represented in Fig. 6 by the dashed line.

Figure 7 shows the initial adsorption rate (in monolayers per second) as a function of the potential, concentration, and pH. These curves indicate an increasing rate from -0.1V to a maximum below 0.1V and then a decrease above 0.1V. The rate appears to be higher in the 0.1N HClO<sub>4</sub> electrolyte, the less acid case, when other parameters are comparable. The ascending and descending portions of the kinetic curves form linear Tafel plots according to the electrochemical results (7). If these slopes are assumed to be Tafel slopes, the radiometric data yield ascending slopes of  $400 \pm 80$  mV and descending slopes of  $85 \pm 10$  mV.

An electrochemical experiment was performed to determine whether the formation of (CO<sub>2</sub>)<sub>r</sub> obtained from the reaction of CO<sub>2</sub> with hydrogen adsorbed on platinum was associated with a cathodic current. A very small steady-state diffusion current, probably caused by O<sub>2</sub> reduction, did not change significantly (either cathodically or anodically) upon admission of CO<sub>2</sub> to the platinum electrode. (It is also possible that a small hydrogen ion reduction current may occur to replace adsorbed H.) Thus, it is evident that formation of (CO<sub>2</sub>)<sub>r</sub> involves no net faradaic charge transfer.

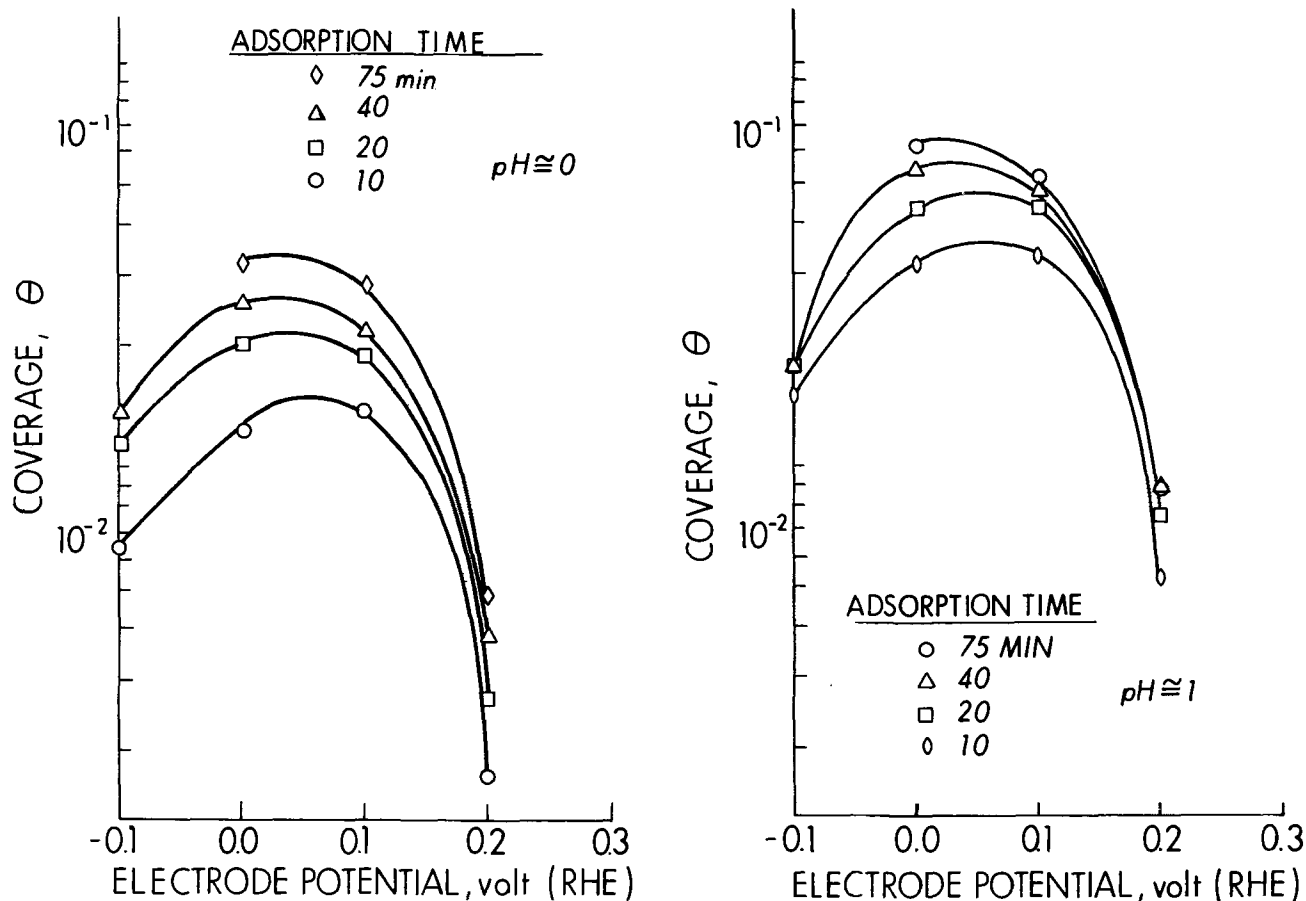


Fig. 3. Coverage-time dependence; electrode coverage as a function of potential at varying adsorption times. Bulk CO<sub>2</sub> concentrations are: (a, left)  $3.8 \times 10^{-4}$ M; (b, right)  $3.1 \times 10^{-4}$ M. Electrolytes are: a, 1.0N HClO<sub>4</sub>; b, 0.1N HClO<sub>4</sub> with 0.9N NaClO<sub>4</sub>.

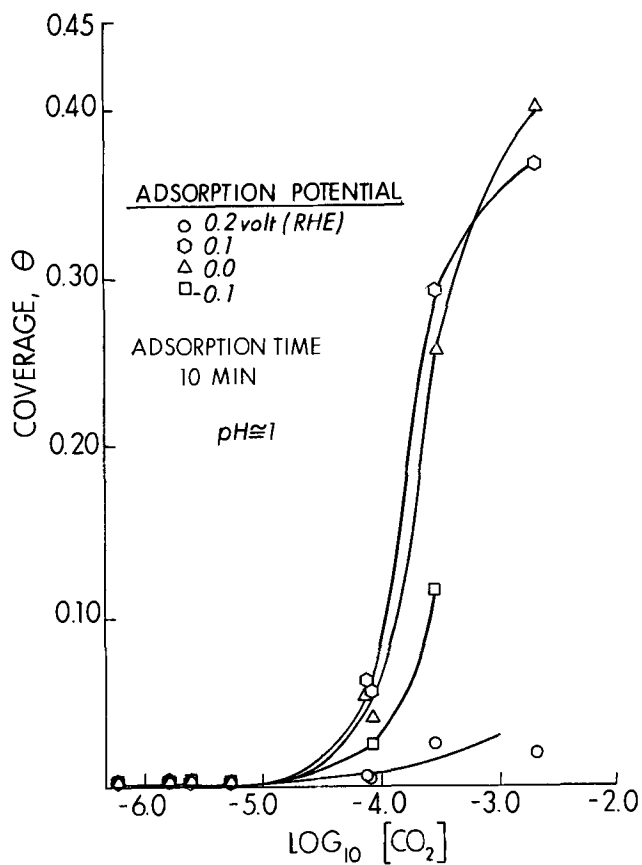
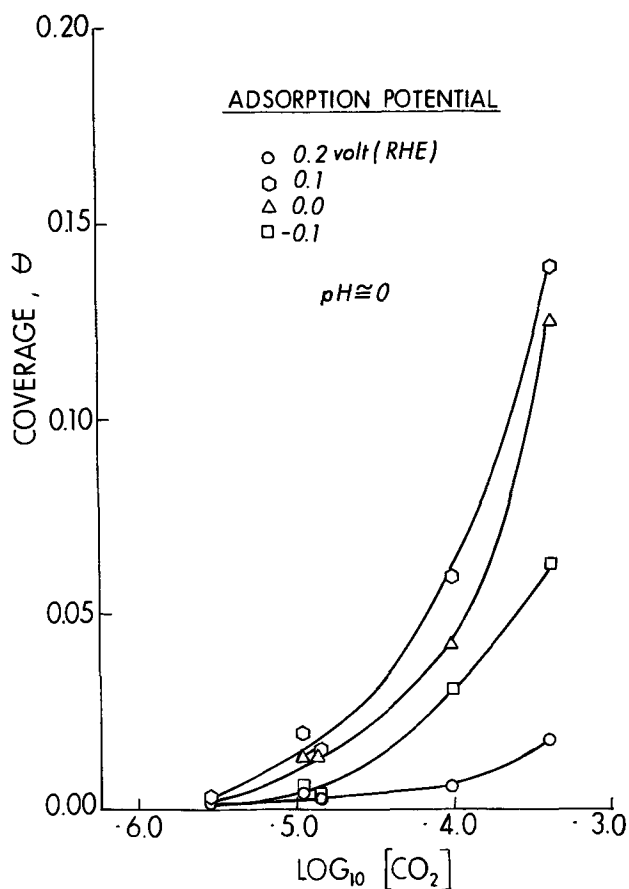
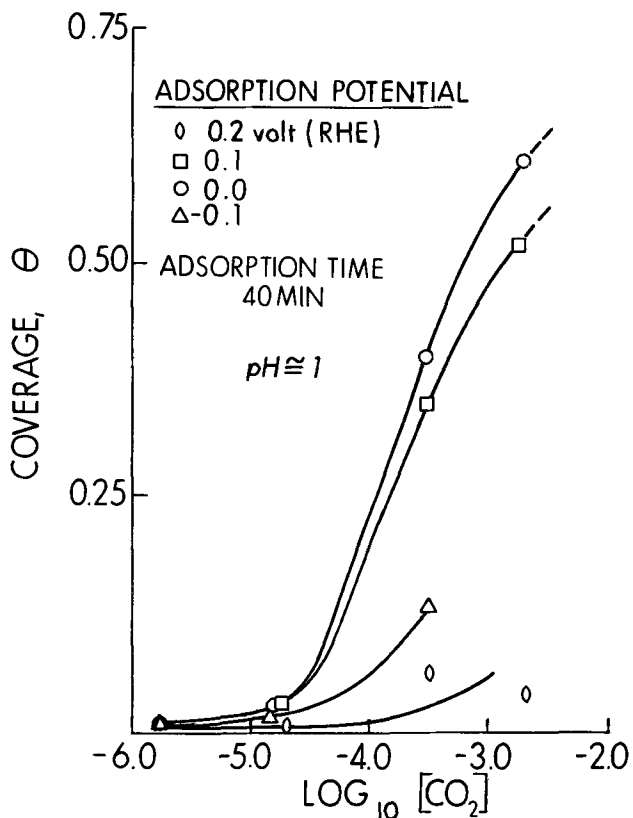


Fig. 4. Effect of CO<sub>2</sub> concentration at constant adsorption potential. Adsorption time is 10 min. Electrolytes are: (a, left) 1.0N HClO<sub>4</sub>; (b, right) 0.1N HClO<sub>4</sub> with 0.9N NaClO<sub>4</sub>.



To verify adsorption of the CO<sub>2</sub>, a galvanostatic charging curve was obtained at a current of 100 mA. The resultant curve, when compared with that of a "clean" electrode, displayed an arrest characteristic of the oxidation of the adsorbate, (CO<sub>2</sub>)<sub>r</sub>.

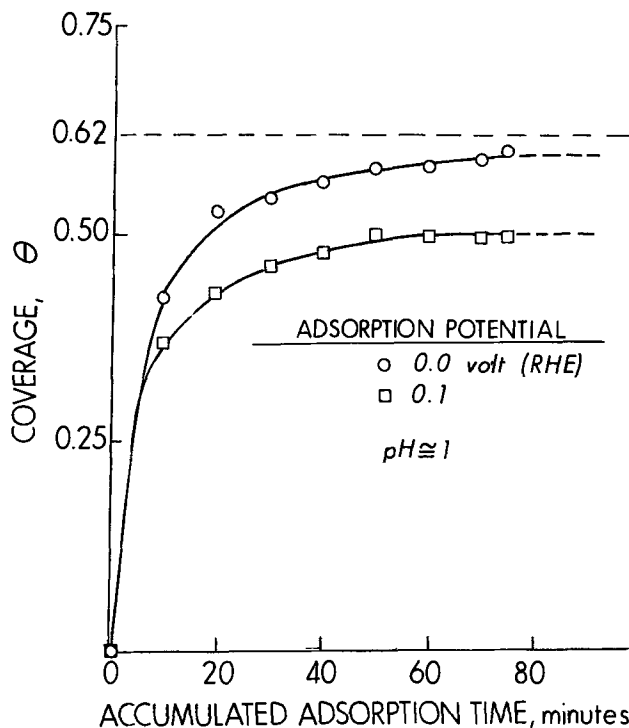


Fig. 5. Langmuir plot for 40-min adsorption time at constant adsorption potential. Electrolyte is 0.1N HClO<sub>4</sub> with 0.9N NaClO<sub>4</sub>.

Fig. 6. Coverage as a function of time at maximum experimental concentration, (CO<sub>2</sub>) = 2.0 × 10<sup>-3</sup>M.

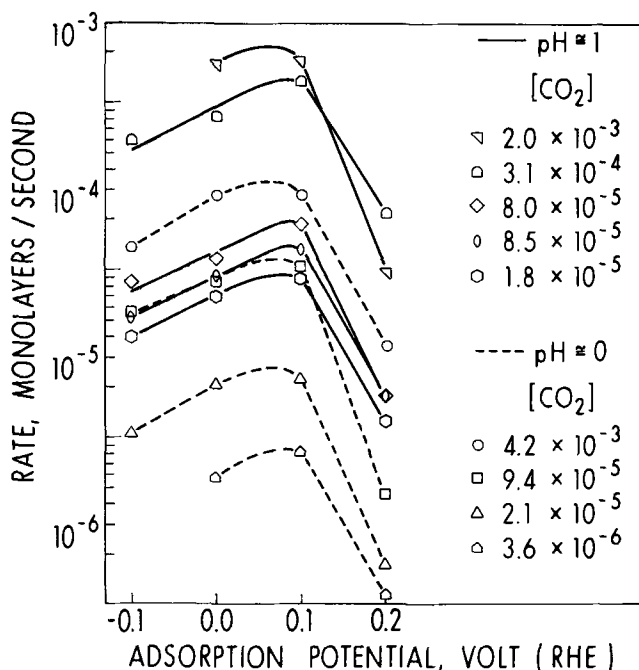


Fig. 7. Initial adsorption rate as a function of potential at constant  $\text{CO}_2$  concentration. Adsorption time is 10 min.

### Discussion

A particularly desirable objective of this study would be the achievement of a theoretical and experimental consistency between the radiometric and electrochemical adsorption data and kinetic interpretations. A total harmony between the methodologies has not existed in the past (35, 36). Fortunately, several correlations and anomalies of the experimental data of the two methods appear amenable to analysis. The following discussion is concerned with significant generalizations involving controversial aspects of adsorbed  $\text{CO}_2$ . These include the nature of the adsorbate, a comparison of radiometric and electrochemical data, and kinetic behavior. A plausible hypothesis on the structure of the adsorbate makes possible an evaluation of the coverage of the adsorbate species. Since this number is essential to the radiometric determination of the coverages, the nature of the adsorbate is discussed first.

**Nature of the adsorbate.**—Published experimental results on the characteristics and behavior of reduced  $\text{CO}_2$  are voluminous. They impose a highly restrictive set of conditions with which any hypothetical adsorbate structure must conform. For example, Breiter (6) has determined by means of a chromatographic technique employed in conjunction with anodic stripping that the average number of electrons per carbon atom is  $2.1 \pm 0.2$ . Piersma, Warner, and Schuldiner (5) reported the anodic charge associated with the stripping of adsorbate to be  $260 \pm 35 \mu\text{C}/\text{cm}^2$  while Brummer and Cahill (7) reported that this charge is  $220 \pm 10 \mu\text{C}/\text{cm}^2$ . Brummer *et al.* (7) reported 1.05 electrons per site which is sensibly equal to unity for the adsorbate and a saturation coverage of 0.68 (cathodic hydrogen coverage was 0.32, since  $\theta_{\text{CO}_2} = 1 - \theta_{\text{H}}$  in Brummer's calculations). Such numbers give rise to conclusions that there are 2.0 sites per carbon.

One may propose surface structures which incorporate many of the above constraints. These include several configurations employing the carbonyl group which has been popular with several authors (6, 7, 17, 22). The simple bridged carbonyl form  $\text{Pt}_2 = \text{CO}$  would normally yield a platinum-site, carbon ratio of two. However, one logical difficulty arises. The saturation limit of 0.68 is difficult to explain since there is no factor other than repulsive neighbor-neighbor interactions restricting total saturation of the surface with carbonyl

groups. Such neighbor-neighbor interactions are possible though not evident from the calculated  $f$  factors. (The  $f$  factor may be a measure of this interaction only if the adsorption data represents equilibrium.) It is assumed here that as far as  $(\text{CO}_2)_r$  is concerned there are no restricted sites and two sites per carbon are available. The resultant average valence state of each platinum site would, therefore, normally be equivalent to 1.0 electron per site even when summed over  $(\text{CO}_2)_r$  and hydrogen. A reduction in site occupancy produced by steric factors could result in a third of bare sites coverable by hydrogen atoms and would yield 1.0 electron per site and a carbon-hydrogen ratio of 1.5. Moreover, the hydrogen coverage would be  $70 \mu\text{C}/\text{cm}^2$  in good agreement with the reported hydrogen coverage of 0.32 and in agreement with the conclusions of Brummer [see footnote on p. 467 of ref. (7)]. Experimental results yielding a high total carbon and hydrogen charge of  $280 \mu\text{C}/\text{cm}^2$  may be explained on the basis of low values of area determination (7, 27).

The model suggested above is based on the empirical result that the adsorption energy of  $(\text{CO}_2)_r$  is large in comparison with the adsorption energy of hydrogen. [This assumption appears well supported by the irreversibility of the adsorption (12) and the high anodic potential ( $>0.5\text{V}$ ) required to oxidize  $(\text{CO}_2)_r$ .] A second assumption is that the adsorption energy for hydrogen atoms be relatively small in the neighborhood of the  $(\text{CO}_2)_r$  adsorbate. Also the adsorption energy is overcome when steric factors make their appearance at large ( $\theta > 0.52$ ) values of  $(\text{CO}_2)_r$  coverage (37-42).

The nature of the potential arrest observed during anodic galvanostatic stripping of reduced  $\text{CO}_2$  would suggest that only one species is predominately present [Brummer and Cahill consider only the predominant type I adsorbate (7)] or that several species of similar oxidation energy are present. The proposal that hydrated as well as unhydrated forms of the carbonyl species, *i.e.*,  $\text{Pt}_2 = \text{CO}$  and  $\text{Pt}_2 = \text{C}(\text{OH})_2$ , occupy the surface simultaneously might be in conflict with the above conclusion. This is particularly true if the oxidation energy of the carbon-platinum bonds were modified in the hydrated form. The relative stability of monomeric formaldehyde in dilute aqueous solution indicates that the hydrated formaldehyde species is formed without appreciable energy change. A similar behavior might be expected in  $(\text{CO}_2)_r$ .

A brief remark about the order of the adsorbed molecular configurations is appropriate. Several models of a random nature could be exhibited. They differ only in the choice of pairs of platinum atoms employed as substrate for the organic adsorbate. Since the more disordered array of pairs would have the greater entropic energy contribution, the disordered array should be preferred unless ordering forces are present. The appearance of Temkin effects in the adsorption energy of the carbon bond would suggest that ordering forces are in fact absent. The disordered state of adsorption would account for the large surface fraction which apparently remains uncovered by  $(\text{CO}_2)_r$ .

The utility of the radiometric method is strongly dependent on a valid estimate of the number of carbon-containing species formed from the reduction of  $\text{CO}_2$ . Any estimate must yield values of saturation and coverages consistent with those produced by electrochemical methods. The number of carbon species used in the radiometric calculations,  $6.55 \times 10^{14}$  atoms/ $\text{cm}^2$ , is consistent with the assumption of two sites per carbon-containing adsorbate, one carbon per adsorbate, and  $1.31 \times 10^{15}$  effective sites/ $\text{cm}^2 \pm 20\%$  (from  $210 \mu\text{C}/\text{cm}^2$  for hydrogen coverage). Having once assumed two sites per carbon, the requirement for a bridged molecular adsorbate follows.

**Comparison with previous work.**—Saturation effects.—The behavior of the coverage-time curves in Fig. 6 suggests that asymptotic steady-state values of coverage may be attained. [In the nonelectrochemical

sense that ultimately mass and energy gradients vanish, a quasi-equilibrium between  $(\text{CO}_2)_r$  and  $\text{CO}_2$  is possible. Reversibility with respect to electrode potential does not exist of course.] Stationary steady-state values imply a steady-state oxidation of  $(\text{CO}_2)_r$ . That the asymptotic values (in Fig. 6) are indeed physical is deduced from the convergence of the sum of terms representing the coverage increment with each doubling of adsorption time (the incremental terms form a convergent geometric series). An examination of the electrochemically observed time-dependent coverages indicates that the reaction rates of Brummer and Cahill (7) were favored with a small boundary layer (good stirring) as well as a ten-fold higher concentration of  $\text{CO}_2$ . Thus, the electrochemically derived data (7) exhibited evidence of saturation in the form of well-defined adsorption plateaus after less than 10 min.

The radiochemically determined values of coverage based on  $6.55 \times 10^{14}$  carbon atoms/cm<sup>2</sup> (two sites per carbon) show little evidence of saturation at values in the neighborhood of 0.62. The coverage-time plots of Fig. 6 show at 0.0 and 0.1V a consistent difference of 0.13 [compared with a total range of 0.063 in the scatter of coverage values in Fig. 2 of ref. (7)]. If, indeed, saturation coverage were established in the data of Fig. 6, the long-time values of coverage would approximate each other.

Evidence of saturation is positively provided by the appearance of a negative curvature in Langmuir plots such as Fig. 4b and 5. The Langmuir plot at 0.1V (see Fig. 4b) for adsorption times of 10 min suggests, because of the crossover of the plots, that a degree of negative curvature exists. However, Fig. 5, where adsorption time was 40 min, shows no crossover in the plots with only a slight negative curvature indicative of the fact that saturation is far from complete even at a  $\theta$  value in the neighborhood of 0.60. It is evident that the arbitrary use of a number based on three sites per carbon atom would force the  $\theta$  values dangerously close to unity but the negative curvatures of Fig. 4b and 5 would not be enhanced. Such behavior in the radiometric model represents confirmation of the proposed two sites per carbon model of the adsorbate.

*Shape of the isoconcs.*—Evidence of saturation may be inferred from the appearance of plateau-like isoconcs (7). In Fig. 3b no evidence of a plateau is observed, although the  $\theta$ -value at 75 min surpasses 0.5. The curves exhibit peaks with the maximum lying between 0.0 and 0.1V. Electrochemical data (7) for adsorption periods less than 25 sec show peaks between 0.10 and 0.15V in agreement with the radiometric results of Fig. 4b and 5. No such agreement can be claimed for similar measurements in ref. (5). The data in these figures indicate in the crossover of the curves, that the potential of maximum adsorption shifts toward lower values as reaction time increases. However, the data are too scattered for certainty.

Since no plateau is evident,  $\theta$  values of 0.62 do not appear to be representative of saturation in the radiometric results in contrast with the electrochemical results.

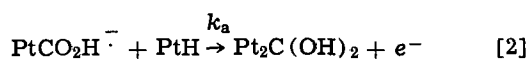
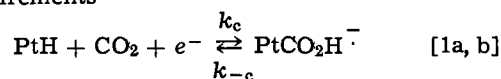
*Kinetic data.*—The electrochemical measurements of Brummer and Cahill (7) yield initial adsorption rates which are a maximum at about 0.1V. The radiometric data of Fig. 7 indicate kinetic maxima between 0.04 and 0.1V in fair agreement with the electrochemical data considering the smaller number of radiometric measurements.

Some electrochemical data (7) exhibit well-defined Tafel slopes of 80 mV/decade above 0.1V. The radiometric Tafel slopes between 0.1 and 0.2V are based on only two points one of which is located near the peak so that the slopes must be somewhat on the low side. Moreover, some of the points show considerable scatter. Ignoring two  $\text{CO}_2$  concentrations,  $9.4 \times 10^{-5}$  and  $2 \times 10^{-3}$ M, where scatter is obvious, the slopes appear to lie between 75 and 95 mV (closer to the low end) in

fair agreement with the electrochemical slopes of 80 mV (7). Corrected for variation in  $\theta_H$  the Tafel slopes are 120 mV by both methods.

There is considerable deviation, however, in the slopes of the left-hand side of the peaks in Fig. 7 which are of the order of 400 mV. The electrochemical slopes are of the order of 180 mV. Disagreement may be due to failure to correct ohmic errors in potential.

*Kinetic mechanism.*—Hypothetical mechanisms invoked to explain the observed kinetics must be consistent with the experimental observation of this study that net charge transfer does not occur during the formation of  $(\text{CO}_2)_r$ . Based on the ad hoc-requirement of 2.1 oxidation electrons per carbon (6), it is essential that two adsorbed hydrogen atoms per  $\text{CO}_2$  be consumed in the over-all reaction. According to Fig. 8, the reaction expression should be first order in  $\text{CO}_2$ . Finally, it should be first order in adsorbed hydrogen (7). The following proposed reaction scheme fulfills these requirements



The adsorbed atomic hydrogen, PtH, is represented by

$\theta_H$ , the activated ion-radical complex,  $\text{PtCO}_2\text{H}^-$ , is represented by  $\theta_c$ , and the  $k$ 's are the specific electrochemical reaction rate constants associated with each reaction. Reaction [1a] will be recognized as the cathodic reaction proposed previously by Brummer and Cahill (7). Reaction [1b] indicates a degree of reversibility not indicated for reaction [2] which is highly irreversible. Under some conditions the concentration of the ion radical may thus be described by a quasi-equilibrium. According to the arguments above  $\text{Pt}_2\text{C}(\text{OH})_2$  is closely related to  $(\text{CO}_2)_r$  or is one of the hydrated forms of  $(\text{CO}_2)_r$ .

The imposition of the condition of zero-charge transfer is obeyed by reactions [1] and [2] provided the over-all sum of the anodic and cathodic rate proc-

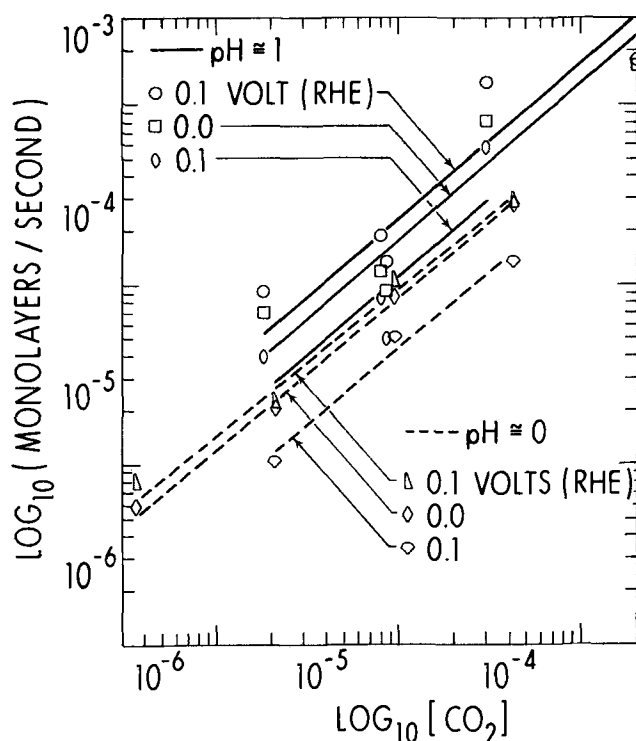


Fig. 8. Determination of the stoichiometric factor for  $\text{CO}_2$ ; initial adsorption rate as a function of concentration.

esses vanishes. Imposing this condition there is obtained

$$0 = \frac{d\theta_c}{dt} = k_c\theta_H(\text{CO}_2) \exp(-\alpha_c FE/RT) - k_{-c}\theta_c \exp(f_c\theta_c) \exp[(1-\alpha_c)FE/RT] - k_a\theta_H\theta_c \exp(\alpha_a FE/RT) \quad [3]$$

where  $t$  is the time,  $\alpha_c$  and  $\alpha_a$  are the transfer coefficients associated with the reactions indicated in the subscript,  $F$  is Faraday's constant,  $E$  is the potential at which adsorption occurs,  $R$  is the gas constant,  $T$  is the temperature, and  $f_c$  is the Temkin  $f$ -factor for the activated ion-radical complex. Equation [3] also represents the condition that the concentration of the activated complex be invariant. Temkin  $f$ -factor terms are included only in the second term of the right-hand member because [1b] is nonactivated (43); i.e., the Temkin symmetry factor,  $\alpha$ , is unity [see Conway (43) for discussion of activation]. The implication of the unit  $\alpha$ -factor is that the activation energy on the adsorption side of the reaction barrier is potential independent. Only the desorption involves a large potential and coverage dependent energy.

Equation [3] may be rearranged to facilitate deduction of the behavior of the activated complex,  $\theta_c$ , with respect to potential

$$\theta_c \exp(f_c\theta_c) = \frac{k_c\theta_H(\text{CO}_2) \exp(-\alpha_c FE/RT)}{k_{-c} \exp((1-\alpha_c)FE/RT) + k_a\theta_H \exp(\alpha_a FE/RT) \exp(-f_c\theta_c)} \quad [4]$$

The dominant term in the denominator will depend on the exponential  $\theta_c$ -factor. Whichever term predominates,  $\theta_c$  is seen to increase as  $E$  decreases. For qualitative reasoning we can approximate the  $\theta_c - E$  relation by the expression  $\theta_c \cong b - ME$ , where  $b$  and  $M$  are constants and  $M$  is positive. Thus, at high potential the factor  $\exp(-f_c\theta_c) \cong \exp(-f_cb + Mf_cE)$  causes the second term in the denominator to predominate if  $Mf_c$  is large. Thus

$$\theta_c \cong (k_c/k_a) (\text{CO}_2) \exp(-(\alpha_c + \alpha_a)FE/RT) \quad [5]$$

and  $\log \theta_c$  is seen to decrease exponentially with  $E$  with slope of  $-59$  mV [assuming that  $\alpha_a$  as well as  $\alpha_c$  (7) is 0.5]. The pattern of behavior of  $\theta_c$  is thus qualitatively similar to the behavior of  $\theta_H$ .

The rate of product formation is given by

$$\frac{d\theta}{dt} = k_a\theta_H\theta_c \exp(\alpha_a FE/RT) \quad [6]$$

Equation [6] does not contain the Temkin  $f$ -factor in accordance with the above logic. Equation [5] may be used to eliminate the surface concentration  $\theta_c$ , whence

$$\frac{d\theta}{dt} = k_c\theta_H(\text{CO}_2) \exp(-\alpha_c FE/RT) \quad [7]$$

Equation [7] is seen to be identical with the kinetic expression of Brummer and Cahill (7) which may be regarded as a special extremum of the more general reactions [1] and [2]. The kinetic equation is first order in  $\text{CO}_2$  and in adsorbed hydrogen as required. That Eq. [7] is in excellent agreement with the experimental data has been adequately demonstrated (7) (provided correction is made for varying  $\theta_H$ ).

At low potentials the first term in the denominator of [4] predominates and the expression for  $\theta_c$  becomes

$$\theta_c \cong K\theta_H(\text{CO}_2) \exp(-f_c\theta_c) \exp(-FE/RT) \quad [8]$$

where  $K$  is the equilibrium constant for Eq. [1] so that  $\theta_c$  is approximated by a quasi-equilibrium expression. Thus, as the potential decreases, the exponential rise in  $\theta_c$  becomes linear in  $E$  with some slope  $-M'$  ( $M'$  is not necessarily equal to  $M$ ). At low potentials, the kinetic rate expression is given by

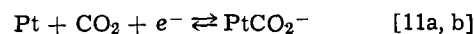
$$\frac{d\theta}{dt} = k_aK(\text{CO}_2)\theta_H^2 \exp(-f_c\theta_c) \exp[(\alpha_a - 1)FE/RT] \quad [9]$$

after substitution of Eq. [8] for  $\theta_c$  in [6]. Now for potentials less than 0.07V,  $0.97 > \theta_H > 0.91$ ,  $\theta_H^2$  may be assumed constant (43) with respect to exponential potential terms below 0.07V. The exponential  $f$ -factor becomes  $\exp(-bf_c + M'f_cE)$  whence taking the logarithm of Eq. [9] there is obtained

$$\log \frac{d\theta}{dt} = K_0 + \frac{1}{2.303} ((\alpha_a - 1)F/RT + M'f_c)E \quad [10]$$

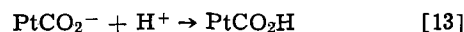
where  $K_0$  is  $\log k_aK(\text{CO}_2)\theta_H^2 - bf_c$ . With  $M'f_c$  equal to 25, the Tafel slope of [9] and [10] is  $+400$  mV in agreement with the experimental range of slopes.

According to Fig. 7 and 8 the rates of reaction are a half-order of magnitude faster at high pH. The higher rate of reaction is reflected in the higher coverages in the isoconcs at high pH values. These facts explain in part why better performance of carbonaceous fuel electrodes is achieved in strongly acid media. It is possible to explain the effect of pH in both the steady-state coverage and the kinetics by noting that Eq. [1a] represents a complex reaction which could be written more fundamentally as

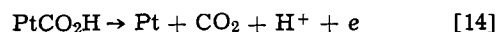


Equations [11] and [12] give rise to the over-all reaction indicated by [1a].

Formation of the ion-radical  $\text{PtCO}_2\text{H}^\cdot$  could be prevented by competing reactions, i.e.



Since the singly bonded species  $\text{PtCO}_2\text{H}$  is apparently less stable, we expect decomposition to the reactants



In essence it is proposed that formation of the ion radical via reaction with adsorbed hydrogen in [12] is contraverted by reaction with hydrogen ions according to [13]. Thus, hydrogen ions would be expected to exhibit a kinetic stoichiometry which is dependent on the relative rates of reactions in [12] and [13]. The dependence of the rate would therefore not be first order in the hydrogen ion concentration as is confirmed in Fig. 8.

The close similarity between the shape of the isoconcs and the Tafel plots warrants consideration. The obvious correlation between the steady-state adsorption behavior in Fig. 1a and b and the kinetic rates in Fig. 7 suggests that the rate of oxidation or removal of  $(\text{CO}_2)_r$  is roughly independent of potential below 0.3V. Certainly above 0.4V the data of Piersma, Warner, and Schuldiner (5) demonstrate a clear exponential dependence of the adsorbate oxidation on potential. However, below 0.3V no information on the oxidation (or removal) rate of the adsorbate is known except what can be inferred from the argument here.

### Summary

The adsorption of  $\text{CO}_2$  on platinum covered with adsorbed hydrogen atoms gives rise to an adsorbate called "reduced  $\text{CO}_2$ " or  $(\text{CO}_2)_r$ . The steady-state adsorption of  $(\text{CO}_2)_r$  (the isoconcs) and its initial adsorption kinetics (Tafel plots) were studied by radiometric methods employing  $\text{C}^{14}$ -labeled  $\text{CO}_2$ . The isoconcs of  $(\text{CO}_2)_r$  are roughly gaussian in form with a

peak between 0.05 and 0.10V. The initial adsorption kinetics are similar in form to the isoconcs. For example, the initial adsorption rate is maximum between 0.05 and 0.10V. Both the adsorption and rates increase with pH.

The radiometric isoconcs exhibit no evidence of saturation even at coverage values of 0.62. The radiometric results and selected electrochemical reports appear to be compatible provided the adsorbate,  $(\text{CO}_2)_r$ , is assumed to be a carbonyl species that is bridged to two adjacent sites each of which is capable of forming an additional half bond with adsorbed hydrogen.

No current is observed during the conversion of  $\text{CO}_2$  to  $(\text{CO}_2)_r$ . The character is the isoconcs and the kinetics are predicted by a reaction scheme based on cathodic reduction of  $\text{CO}_2$  and anodic oxidation of adsorbed hydrogen atoms in equal amounts.

Manuscript submitted Feb. 6, 1973; revised manuscript received July 16, 1973.

Any discussion of this paper will appear in a Discussion Section to be published in the December 1974 JOURNAL.

#### REFERENCES

- J. Giner, *Electrochim. Acta*, **8**, 857 (1963).
- J. Giner, *ibid.*, **9**, 63 (1964).
- J. Giner, Paper presented at 15th CITCE Meeting, London, 1964.
- L. W. Niedrach, S. Gilman, and I. Weinstock, *This Journal*, **112**, 1161 (1965).
- B. J. Piersma, T. B. Warner, and S. Schuldiner, *ibid.*, **113**, 841 (1966).
- M. W. Breiter, *Electrochim. Acta*, **12**, 1213 (1967).
- S. B. Brummer and K. Cahill, *J. Electroanal. Chem.*, **21**, 463 (1969).
- S. B. Brummer, *Soviet Electrochem.*, **4**, 215 (1968).
- M. W. Breiter, *J. Electroanal. Chem.*, **19**, 131 (1968).
- C. W. Fleischmann, G. K. Johnson, and A. T. Kuhn, *This Journal*, **111**, 602 (1964).
- R. E. Smith, H. B. Urbach, and N. L. Hatfield, *J. Phys. Chem.*, **71**, 4121 (1967).
- R. E. Smith, H. B. Urbach, J. H. Harrison, and N. L. Hatfield, *ibid.*, **71**, 1250 (1967).
- P. R. Johnson and A. T. Kuhn, *This Journal*, **112**, 599 (1965).
- W. T. Grubb and M. E. Lazarus, *ibid.*, **114**, 360 (1967).
- V. S. Bagotzky and Yu. B. Vassilyeu, *Electrochim. Acta*, **12**, 1323 (1967).
- C. Liang and T. C. Franklin, *ibid.*, **9**, 517 (1964).
- S. Gilman, *J. Phys. Chem.*, **68**, 70 (1964).
- T. Biegler and D. F. A. Koch, *This Journal*, **114**, 904 (1967).
- V. S. Bagotzky and Yu. B. Vassilyeu, *Electrochim. Acta*, **12**, 1323 (1967).
- Yu. A. Chizmadzhev and V. S. Markin, *Soviet Electrochem.*, **4**, 105 (1968).
- O. A. Khazova, Yu. B. Vasilyev, and V. S. Bagotzskii, *ibid.*, **2**, 249 (1966).
- O. A. Petry, B. I. Podlovchenko, A. N. Frumkin, and K. Lal, *J. Electroanal. Chem.*, **10**, 253 (1965).
- M. H. Gottlieb, *This Journal*, **111**, 465 (1964).
- N. Minakshisandaram, Yu. B. Vasilyev, and V. S. Bagotzskii, *Soviet Electrochem.*, **3**, 193, 283 (1967).
- S. B. Brummer and K. Cahill, *J. Electroanal. Chem.*, **16**, 207 (1968).
- S. B. Brummer and M. J. Turner, *J. Phys. Chem.*, **71**, 2825, 3902 (1967).
- S. Gilman, *ibid.*, **67**, 78 (1963).
- E. Blomgren and J. O'M. Bockris, *Nature*, **186**, 305 (1960).
- H. Dahms and M. Green, *This Journal*, **110**, 1075 (1963).
- J. Giner, *ibid.*, **111**, 376 (1964).
- W. F. Libby, *Anal. Chem.*, **19**, 2 (1947).
- F. N. Pannamperuma, *Soil Sci.*, **103**, 90 (1967).
- D. M. Kern, *J. Chem. Educ.*, **37**, 14 (1960).
- S. Gilman, "Electroanalytical Chemistry," p. 126-146, A. J. Bard, Editor, Marcel Dekker, Inc., New York (1967).
- M. W. Breiter, "Electrochemical Processes in Fuel Cells," pp. 126-129, Springer-Verlag, New York (1969).
- E. Gileadi, L. Duic, and J. O'M. Bockris, *Electrochim. Acta*, **13**, 1915 (1968).
- M. W. Breiter, Ref. 35, pp. 64-65.
- S. Gilman, *J. Phys. Chem.*, **67**, 78 (1963): see also Ref. 35, pp. 64-66.
- M. W. Breiter, *Electrochim. Acta*, **8**, 447 (1963): see also Ref. 35, pp. 64-66.
- D. A. Khasova, Yu. B. Vasilev, and V. S. Bagotzskii, *Soviet Electrochem.*, **1**, 70 (1965).
- B. I. Podlovchenko and V. F. Stenin, *ibid.*, **3**, 576 (1967).
- M. W. Breiter, Private communication, March 27, 1970.
- B. E. Conway "Theory and Principles of Electrode Processes," p. 122, Ronald Press Co., New York (1965).

## Current Distribution on a Rotating Sphere below the Limiting Current

Kemal Nisancioğlu\* and John Newman\*\*

Inorganic Materials Research Division, Lawrence Berkeley Laboratory, and Department of Chemical Engineering, University of California, Berkeley, California 94720

#### ABSTRACT

The current distribution on a rotating spherical electrode is calculated at appreciable fractions of the limiting current. Numerical results are given for Tafel kinetics and for high rotation speeds. The current distribution depends only on the specified current level and becomes uniform when this level is set below 68% of the limiting current at high rotation speeds. In general, the results disclose a number of complementary aspects of the spherical electrode alongside the disk electrode in electroanalytical applications.

The sphere has been employed in the past as an important electrode geometry in electrochemical research such as the investigation of the double-layer structure on mercury drops (1) and the study of the overpotential and reaction kinetics on copper electrodes by tran-

sient methods (2). The effects of diffusion were either eliminated or ignored in that work. The rotating sphere has been proposed anew as a potential tool in studies of mass transfer and reaction kinetics in electrochemical systems (3, 4). The convective diffusion equation for a thin diffusion layer at limiting current conditions has been solved recently (3, 5, 6) and compared successfully with experimental data (7).

\* Electrochemical Society Student Member.

\*\* Electrochemical Society Active Member.

Key words: current distribution, mass transfer, electrode kinetics.

The present interest in the rotating sphere arises from the fact that the mass transfer and current distribution characteristics of the disk and the sphere turn out to be rather complementary in some respects. For instance, the rotating disk exhibits a uniform limiting current distribution (8), which makes it attractive for mass transfer work. The disk electrode, however, has a highly nonuniform primary distribution (9), and consequently serious errors may result in the assessment of exchange current densities in investigations of reaction kinetics (10). The spherical electrode does not have the same drawback, owing to its uniform primary distribution. The disk electrode can be polished very easily, but the surface preparation for the spherical electrode does not seem to be just as straightforward without deforming its shape. On the other hand, in high-rate metal deposition or dissolution studies the spherical electrode maintains its geometry, whereas the disk rapidly forms a step between the insulating surface and the metal, thereby altering seriously the hydrodynamic conditions prevailing at its surface (3). Below the limiting current, the current distribution on a rotating disk is nonuniform (11, 12). It is possible, in principle, to attain a uniform distribution of current on a rotating sphere below the limiting current even in the presence of concentration variations at the surface as will be shown in this paper.

The mathematical treatment of thin diffusion layers with the complicating effect of nonuniform current distribution has become possible in the last decade. The underlying theory has been discussed in detail (13-16) and applied to a number of electrode geometries (11, 12, 17-20). The same theory and numerical techniques are employed here to investigate mass transfer and current distribution on a rotating spherical electrode at appreciable fractions of the limiting current. The following assumptions are made:

(i) The rotating sphere is suspended and allowed to rotate with respect to a fixed axis in an otherwise stagnant electrolyte. The analysis also applies to a hemispherical cap on an insulating plane (3).

(ii) Dilute solution theory is applicable with constant transport and thermodynamic properties.

(iii) For simplicity, the analysis is restricted to metal deposition from a single salt solution and electrode reactions with an excess of supporting electrolyte. Migration is not accounted for explicitly. Results can be obtained for more complex systems, and corrections can be made for migration effects, if necessary, with added numerical effort (15).

(iv) The fluid flow around the sphere is laminar, and the hydrodynamic boundary layer is thin (high Reynolds numbers), so that the boundary layer solution of the Navier-Stokes equations (21) is an adequate description of the hydrodynamic conditions near the surface. The dimensionless shear-stress distribution is given by (5)

$$B(\theta) = \beta_0 v^{1/2} / r_0 \Omega^{3/2} = 0.51023 \theta - 0.1808819 \theta^3 - 0.040408 \sin^3 \theta \quad [1]$$

where  $\beta_0$  is the velocity derivative  $\partial v_x / \partial y$  at the surface. The boundary layer approximation is known to break down at a region near the equator (22) with the magnitude  $0(1/\text{Re})$ , but the size of this region can be rendered small by increasing the Reynolds number.

(v) Diffusion in the direction parallel to the electrode surface can be neglected whenever the diffusion layer is thin compared to the size of the sphere. It is further assumed that the diffusion layer is thin compared to the hydrodynamic boundary layer (high Schmidt numbers), so that the fluid velocity inside the diffusion layer can be approximated by

$$v_x = \beta_0 y, v_y = -\frac{1}{2} y^2 \frac{1}{R} \frac{dR\beta_0}{dx} \quad [2]$$

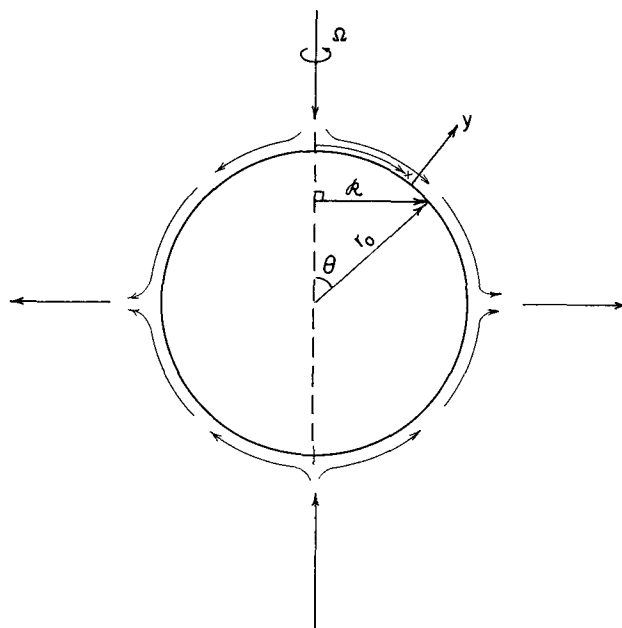


Fig. 1. The rotating sphere

where  $x$  is the distance along the electrode from its upstream end,  $y$  is the perpendicular distance from the electrode surface, and  $R$  is the distance of the axisymmetric surface from the axis of symmetry (see Fig. 1).

### Mathematical Formulation

In light of the above assumptions, the convective diffusion equation can be written in the form

$$y\beta_0 \frac{\partial c}{\partial x} - \frac{1}{2} y^2 \frac{1}{R} \frac{dR\beta_0}{dx} \frac{\partial c}{\partial y} = D \frac{\partial^2 c}{\partial y^2} \quad [3]$$

where  $c$  is the concentration of the reactant. The boundary conditions are

$$\left. \begin{aligned} c &= c_\infty \text{ as } y \rightarrow \infty \\ \partial c / \partial x &= 0 \text{ at } x = 0 \end{aligned} \right\} \quad [4]$$

$$i = \frac{nFD}{1-t} \frac{\partial c}{\partial y} \text{ at } y = 0 \quad [5]$$

where  $i$  is the normal current density at the electrode surface,  $n$  is the number of electrons produced when a reactant ion or molecule reacts, and  $t$  is the transference number. The solution satisfying the first set of boundary conditions (Eq. [4]) can be expressed as an integral equation for the concentration at the surface (15, 16, 19)

$$\left. \frac{\partial c}{\partial y} \right|_{y=0} = -\frac{\sqrt{R\beta_0}}{\Gamma\left(\frac{4}{3}\right)} \int_0^x \frac{dc_0}{dx} \Big|_{x=x'} \frac{dx'}{\left[9D \int_{x'}^x R\sqrt{R\beta_0} dx\right]^{1/3}} \quad [6]$$

or equivalently

$$c_0(x) - c_\infty = -\frac{(D/3)^{1/3}}{\Gamma\left(\frac{2}{3}\right)} \int_0^x \left. \frac{\partial c}{\partial y} \right|_{y=0, x=x'} \frac{R dx'}{\left[\int_{x'}^x R\sqrt{R\beta_0} dx\right]^{2/3}} \quad [7]$$

The current density is assumed to be related to the surface overpotential by the Butler-Volmer expression



$$i = i_o \left( \frac{c_o}{c_s} \right)^\gamma \left[ \exp \left\{ \frac{\alpha z F}{RT} \eta_s \right\} - \exp \left\{ - \frac{\beta Z F}{RT} \eta_s \right\} \right] \quad [8]$$

where  $i_o$  is the exchange current density at the bulk concentration, and  $\alpha$ ,  $\beta$ , and  $\gamma$  are kinetic parameters. The surface overpotential is in turn related to the electrode potential by

$$\eta_s = V - \Phi_o - \eta_c \quad [9]$$

where  $\Phi_o$  is the potential in the solution just outside the diffusion layer, and  $\eta_c$  is the concentration overpotential given by

$$\eta_c = \frac{RT}{ZF} \left[ \ln \left( \frac{c_o}{c_s} \right) + t \left( 1 - \frac{c_o}{c_s} \right) \right] \quad [10]$$

The parameter  $Z$  is equal to  $-z_+z_-/(z_+ - z_-)$  for a single salt and  $-n$  with supporting electrolyte. The transference number  $t$  is zero if excess supporting electrolyte is present.

The potential in the solution satisfies Laplace's equation

$$\nabla^2 \Phi = 0 \quad [11]$$

and the boundary conditions are

$$\left. \begin{aligned} \Phi &= 0 \text{ as } y \rightarrow \infty \\ \partial \Phi / \partial \theta &= 0 \text{ at } \theta = 0, \pi/2 \\ -\kappa \partial \Phi / \partial y &= i \text{ at } y = 0 \end{aligned} \right\} \quad [12]$$

where  $\kappa$  is the conductivity of the bulk solution. At  $y = 0$ , the solution can be expressed as

$$\Phi_o = \frac{RT}{ZF} \sum_{m=0}^{\infty} B_m P_{2m}(\cos \theta) \quad [13]$$

where  $P_{2m}(\cos \theta)$  is the Legendre polynomial of order  $2m$ . The coefficients  $B_m$  are given by

$$B_m = \frac{ZF r_o}{\kappa RT} \frac{4m + 1}{2m + 1} \int_0^1 i P_{2m}(\cos \theta) d(\cos \theta) \quad [14]$$

Equations [5], [6], [8], [9], [10], [13], and [14] are solved numerically for the unknowns  $c_o$ ,  $(\partial c / \partial y)_{y=0}$ ,  $i$ ,  $\eta_s$ ,  $\eta_c$ ,  $\Phi_o$ , and  $B_m$ . One has the freedom to specify the electrode potential  $V$  or the current level  $i / (i_{lim})_{avg}$ . Equivalently, one can instead fix the concentration or the current density at a given point on the sphere, such as the pole. This last choice avoids an additional iteration loop in the numerical procedure.

**Results for Tafel Kinetics**

A scaling of all parameters which appear in the problem suggests that the results can be best presented in terms of the dimensionless quantities

$$J = \frac{i_o r_o Z F}{RT \kappa} \quad [15]$$

$$N = - \frac{n Z F^2 D c_o}{RT \kappa (1 - t)} \sqrt{\frac{r_o^2 \Omega}{\nu}} \left( \frac{\nu}{9D} \right)^{1/3} \quad [16]$$

in addition to the kinetic parameters  $\alpha$ ,  $\beta$ , and  $\gamma$ , and the transference number  $t$ . Since the primary distribution is uniform, the secondary current distribution, which is obtained by ignoring the concentration polarization, is also uniform regardless of the reaction kinetics. Unless there are concentration gradients, there is no reason for the current density to be different at different parts of the sphere. As a consequence, the results do not depend strongly upon the dimensionless exchange current density  $J$  even when concentration polarization is present. Our numerical calculations for different  $J$  values, although not shown here, confirm this conclusion. Current and concentration distribu-

tions thus largely depend on  $N$ , which can be regarded as a dimensionless limiting current, and on the specified current level with respect to the average limiting current. In view of these observations, and because mass transfer effects are important at high current densities, we have chosen to report results for Tafel kinetics, thus, for the parameter  $J$  tending toward zero.

Figures 2 and 3 show the current and concentration distributions, respectively, for various current levels at  $N = 10$ . All other parameters are arbitrarily set at 0.5. The current becomes more nonuniform as the limiting current is approached whereas the concentration shows marked deviations from its average value at intermediate current levels. Figures 4 and 5 show the effect of increasing  $N$  (or increasing rotation speed) on the current and concentration distributions for a fixed concentration ( $c_o = 0.5 c_s$ ) at the pole. The

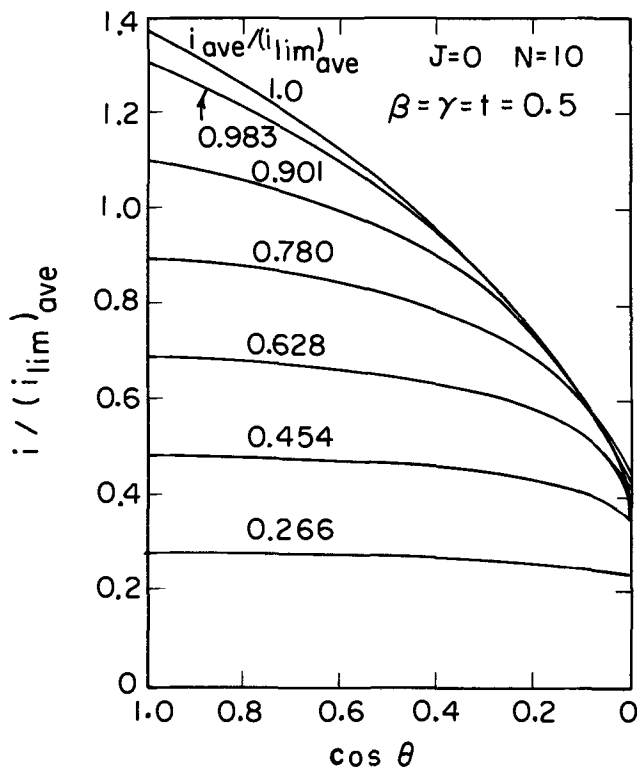


Fig. 2. Current distribution for Tafel kinetics

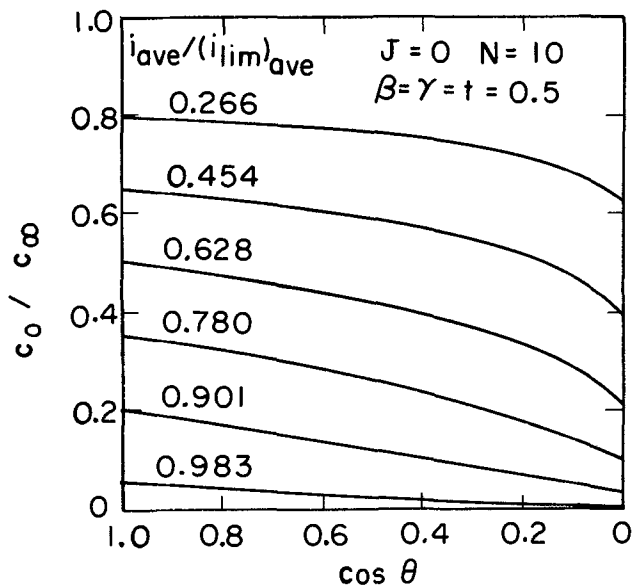


Fig. 3. Concentration distribution for Tafel kinetics

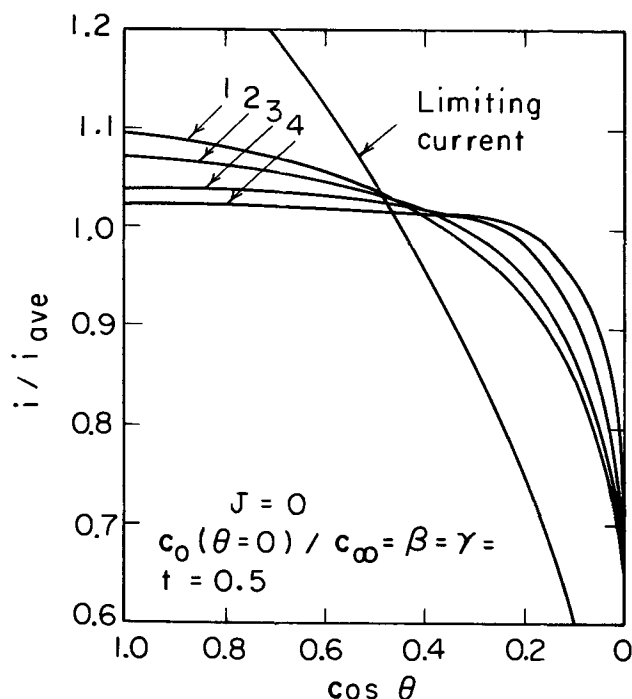


Fig. 4. The effect of rotation speed on the current distribution for Tafel kinetics: curve 1,  $N = 10$ ,  $i_{\text{avg}}/(i_{\text{lim}})_{\text{avg}} = 0.6277$ ; curve 2,  $N = 20$ ,  $i_{\text{avg}}/(i_{\text{lim}})_{\text{avg}} = 0.6432$ ; curve 3,  $N = 50$ ,  $i_{\text{avg}}/(i_{\text{lim}})_{\text{avg}} = 0.6623$ ; curve 4,  $N = 100$ ,  $i_{\text{avg}}/(i_{\text{lim}})_{\text{avg}} = 0.6722$ .

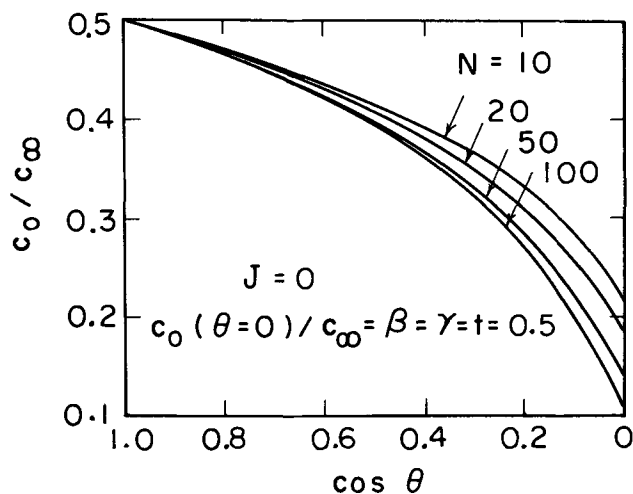


Fig. 5. The effect of rotation speed on the concentration distribution for Tafel kinetics.

current density exceeds the limiting current locally close to the equator. This can also be observed in Fig. 2 for large enough current levels. The same phenomenon has been reported for other geometries under similar conditions (11, 17, 18). With increasing  $N$ , the concentration distribution becomes slightly more nonuniform and appears to be approaching an asymptotic profile. Meanwhile, the current distribution becomes more uniform, and the current level tends toward a limiting value different from the limiting current distribution. This represents a contrast to what has been observed for the disk (11) and plane electrodes (17, 18), where the diffusion layer is completely depleted of the reactant near the trailing edges for large enough flow rates, thereby limiting the local current density. The present results suggest the possibility of attaining a uniform current distribution for large  $N$  on a rotating sphere in the presence of appreciable concentration polarization. Further investigation is in order below.

### Conditions at High Rotation Speeds

If a constant-flux situation prevails on the surface of the sphere, the concentration derivative inside the integral in Eq. [7] is constant and related to the uniform current density by Eq. [5]. After scaling the current with respect to the average limiting current density (5), Eq. [7] reduces to

$$1 - c_0/c_\infty = 0.230825 F(\theta) i / (i_{\text{lim}})_{\text{avg}} \quad [17]$$

where

$$F(\theta) = \int_0^\theta \frac{\sin \theta' d\theta'}{[\int_{\theta'}^\theta \sin \theta \sqrt{B \sin \theta} d\theta]^{2/3}} \quad [18]$$

This function  $F(\theta)$  increases from the value 3.14768 at  $\theta = 0$  (the pole) to the value 6.36850 at  $\theta = \pi/2$  (the equator). Since the surface concentration is always positive or zero, Eq. [17] can be satisfied over the entire surface if and only if

$$i / (i_{\text{lim}})_{\text{avg}} \leq 0.680267 \quad [19]$$

It also follows from Eq. [17] that for currents restricted by condition [19] the concentration at the pole will be given by

$$c_0(0)/c_\infty \geq 0.505742 \quad [20]$$

Equation [19] or [20] is the condition, therefore, for which a uniform distribution of current is possible on the sphere. The corresponding concentration distribution is given by Eq. [17].

If condition [19] or [20] is not met, the concentration becomes zero at a certain angle  $\theta^*$ , which can be determined from Eq. [17] by setting  $c_0 = 0$ . The current becomes limited for  $\theta > \theta^*$  due to this zero concentration distribution and is expected to be non-uniform. Hence Eq. [17] is no more applicable in this region. Under these circumstances, the current density can be calculated from Eq. [6]. After combining with Eq. [5] and [17] and some rearrangement, this becomes

$$\frac{i(\theta)}{(i_{\text{lim}})_{\text{avg}}} = 0.379408 [1 - c_0(0)/c_\infty] \sqrt{B \sin \theta} \times \int_0^{\theta^*} \frac{dF}{d\theta} \Big|_{\theta=\theta'} \frac{d\theta'}{[\int_{\theta'}^\theta \sin \theta \sqrt{B \sin \theta} d\theta]^{1/3}} \quad (\theta > \theta^*) \quad [21]$$

Numerical calculations for various current levels yield the interesting results depicted in Fig. 6 and 7.

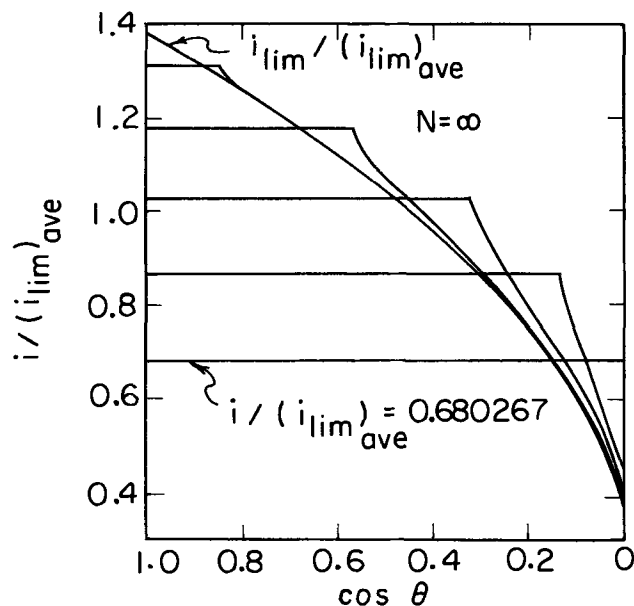


Fig. 6. Current distribution at high rotation speeds

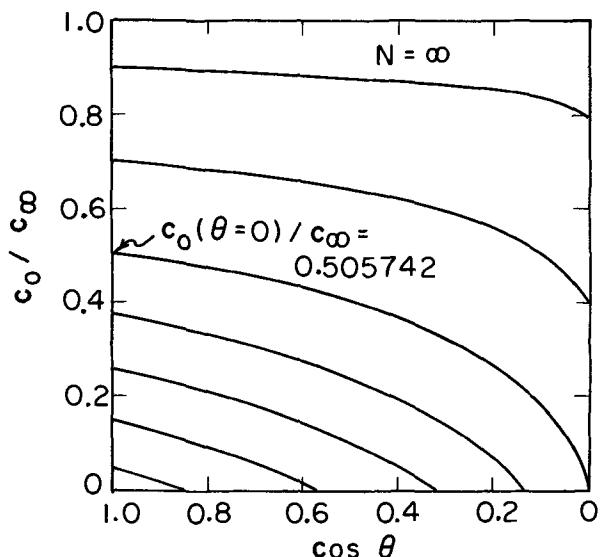


Fig. 7. Concentration distribution at high rotation speeds

Note that Eq. [17] and [21] do not depend on any of the kinetic parameters or the exchange current density; the current and concentration distributions are determined only by the specified current level for a galvanostatic process. The reaction parameters are necessary, however, to calculate the overpotential, or conversely, to calculate the current level if the electrode potential is fixed (potentiostatic process). These remarks are also true for the secondary distribution. In fact, the results of this section map out the transition from the secondary current distribution, which is uniform, to the limiting current distribution, which is nonuniform.

At low current levels ( $|i| \ll i_{lim}$ ), the secondary distribution prevails, and the surface concentration is equal to the bulk concentration. As a result, the concentration overpotential is negligible, and the electrode potential is due to the surface overpotential and the ohmic drop in the solution, the latter being given by

$$\Phi = \frac{I}{4\pi\kappa r} \quad [22]$$

where  $I$  is the total applied current. As the current level increases, the ohmic drop rises linearly with  $I$  according to Eq. [22], and the surface overpotential increases as  $\ln I$  according to the Tafel expression. If there are no mass transfer limitations, the concentration overpotential does not vary significantly. Therefore, the current distribution is controlled by the large ohmic drop, which remains uniform at the surface in the absence of mass transfer limitations, and the current distribution is also uniform. The concentration becomes zero at the equator once a critical current level is reached as specified by Eq. [19]. With increasing current, the depleted portion of the diffusion layer grows from near the equator toward the poles, and correspondingly the region of uniform current density shrinks in the same direction. Finally, the limiting current distribution is attained.

The present results are significant, first of all, in high rate dissolution or deposition studies because the spherical electrode maintains its geometry, especially when the current level is kept below  $0.68 (i_{lim})_{ave}$ , and high rotation speeds are applied. Secondly, the placement of the reference electrode is not as crucial as for the disk (9, 10) because the potential distribution is uniform if constant flux prevails at the surface. If the reference electrode is close to the surface, a correction for radial position is required. This consists of a simple extrapolation to infinity since the primary distribution (Eq. [22]) is a function of radial displacement

only. Under these conditions, the assessment of the ohmic drop by the interrupter technique, which measures the value corresponding to the primary distribution (23), is also much more straightforward (2) in comparison to the disk electrode (10, 24).

Ohmic effects due to a nonuniform potential distribution near the surface of an electrode may become important in electroanalytical work. A nonuniform ohmic drop can result in a loss of control of the electrode potential in potentiostatic applications (25, 26), cause waste of current due to hydrogen evolution during the cathodic protection of metals against corrosion, or render difficult the anodic protection of metals with active-passive kinetics (27, 28). The potential variations near the surface of a sphere are at a maximum level at the limiting current (Fig. 8). The maximum potential difference between the pole and the equator is

$$\Delta\Phi_0 = 0.546 \tau_0 i_{avg} / \kappa \quad [23]$$

This formula should be helpful in design calculations to determine the permissible values of  $\tau_0$ ,  $i_{avg}$ , and  $\kappa$  for a maximum allowable potential variation near a spherical electrode. Problems due to a nonuniform potential distribution can of course be eliminated by operating close to the conditions which guarantee a uniform current and at the same time a uniform potential distribution on the sphere as discussed in this section.

Conclusions

The current and concentration distributions below the limiting current have been calculated for a rotating spherical electrode employing a general theoretical and numerical approach applied earlier to the disk and plane electrodes. Mass transfer is assumed to be restricted to a thin diffusion layer near the electrode surface so that the potential distribution can be obtained by solution of Laplace's equation in the bulk and convective diffusion equation in the diffusion layer.

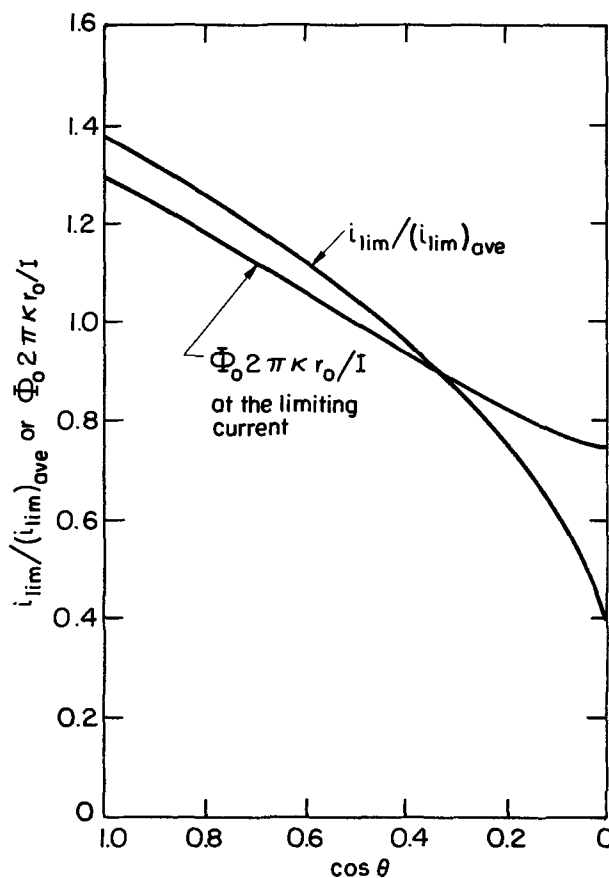


Fig. 8. Current and potential distributions at the limiting current on a spherical electrode.

The two solutions are matched according to the conditions at the electrode surface including complex electrode kinetics.

Numerical results indicate that the current distribution becomes more nonuniform with increasing mass transfer limitations, and that the exchange current density is not an important parameter, in contrast to the previous results obtained for the disk and planar geometries. Furthermore, the current density is shown to reach a uniform distribution below a certain current level, suggesting the possibility of operating at uniform flux below the limiting current even if the concentration distribution may be nonuniform.

### Acknowledgment

This work was supported by the U.S. Atomic Energy Commission.

Manuscript submitted June 15, 1973; revised manuscript received Sept. 27, 1973.

Any discussion of this paper will appear in a Discussion Section to be published in the December 1974 JOURNAL.

### LIST OF SYMBOLS

$B$	dimensionless velocity derivative at the surface
$B_m$	coefficients in series for the potential
$c$	concentration of reactant, mole/cm <sup>3</sup>
$c_0$	concentration of reactant at the electrode surface, mole/cm <sup>3</sup>
$c_\infty$	concentration of reactant in the bulk, mole/cm <sup>3</sup>
$D$	diffusion coefficient of the reactant, cm <sup>2</sup> /sec
$F$	Faraday's constant, 96,487 coulomb/equiv.
$F(\theta)$	see Eq. [18]
$i$	current density, A/cm <sup>2</sup>
$i_0$	exchange current density, A/cm <sup>2</sup>
$I$	total applied current, A
$J$	dimensionless exchange current density
$n$	number of electrons transferred in the electrode reaction
$N$	dimensionless limiting current density
$P_{2m}$	Legendre polynomial of order $2m$
$r$	radial coordinate, cm
$r_0$	radius of sphere, cm
$R$	universal gas constant, 8.3143 joule/mole-deg.
$\mathcal{R}$	normal distance of surface from axis of symmetry, cm
$Re$	$r_0^2\Omega/\nu$ , rotational Reynolds number
$t$	transference number of reactant
$T$	absolute temperature, °K
$v_x, v_y$	velocity components, cm/sec
$V$	electrode potential, V

$x$	distance along electrode from its upstream end, cm
$y$	normal distance from the electrode surface, cm
$Z$	see Eq. [10]
$\alpha, \beta, \gamma$	parameters in kinetic expression (see Eq. [8])
$\beta_0$	velocity derivative at the surface, sec <sup>-1</sup>
$\Gamma(4/3)$	0.89298, the gamma function of 4/3
$\eta_c$	concentration overpotential, V
$\eta_s$	surface overpotential, V
$\kappa$	conductivity of the bulk solution, ohm <sup>-1</sup> -cm <sup>-1</sup>
$\nu$	kinematic viscosity, cm <sup>2</sup> /sec
$\Phi$	potential in the bulk solution, V
$\Phi_0$	potential in the bulk extrapolated to the electrode surface, V
$\Omega$	angular rotation speed, radians/sec
$\theta$	angle from the pole of the sphere

### REFERENCES

1. D. C. Grahame, *J. Am. Chem. Soc.*, **63**, 1207 (1941).
2. E. Mattsson and J. O'M. Bockris, *Trans. Faraday Soc.*, **55**, 1586 (1959).
3. Der-Tau Chin, *This Journal*, **118**, 1434 (1971).
4. Der-Tau Chin, *ibid.*, **120**, 631 (1973).
5. John Newman, *ibid.*, **119**, 69 (1972).
6. Der-Tau Chin, *ibid.*, **119**, 1049 (1972).
7. Der-Tau Chin, *ibid.*, **118**, 1764 (1971).
8. V. Levich, *Acta Physicochim. U.R.S.S.*, **17**, 257 (1942).
9. John Newman, *This Journal*, **113**, 501 (1966).
10. W. H. Tiedemann, J. Newman, and D. N. Bennion, *ibid.*, **120**, 256 (1973).
11. J. Newman, *ibid.*, **113**, 1235 (1966).
12. J. Newman, *ibid.*, **114**, 239 (1967).
13. J. Newman, *Intern. J. Heat Mass Transfer*, **10**, 983 (1967).
14. J. Newman, *Ind. Eng. Chem.*, **60**, 12 (April 1968).
15. J. Newman, "Electrochemical Systems," Prentice-Hall, Inc., Englewood Cliffs, N. J. (1973).
16. J. Newman, in "Electroanalytical Chemistry," Volume 6, A. J. Bard, Editor, pp. 187-352, Marcel Dekker, Inc., New York (1973).
17. W. R. Parrish and J. Newman, *This Journal*, **116**, 169 (1969).
18. W. R. Parrish and J. Newman, *ibid.*, **117**, 43 (1970).
19. W. H. Smyrl and J. Newman, *ibid.*, **119**, 212 (1972).
20. R. Alkire and A. A. Mirarefi, *ibid.*, **120**, 1507 (1973).
21. L. Howarth, *Phil. Mag. (7th Ser.)*, **42**, 1308 (1951).
22. K. Stewartson, in "Boundary Layer Research," IUTAM Symposium, pp. 59-71 (1957).
23. J. Newman, *This Journal*, **117**, 507 (1970).
24. K. Nisancioglu and J. Newman, *ibid.*, **120**, 1339 (1973).
25. J. E. Harrar and I. Shain, *Anal. Chem.*, **38**, 1148 (1966).
26. J. Newman and J. E. Harrar, *This Journal*, **120**, 1041 (1973).
27. W. H. Smyrl and J. Newman, *ibid.*, **119**, 208 (1972).
28. N. Vahdat and J. Newman, *ibid.*, **120**, 1682 (1973).



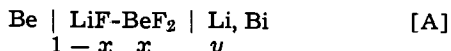
## Lithium-Bismuth Alloy Electrodes for Thermodynamic Investigation of Molten LiF-BeF<sub>2</sub> Mixtures

D. D. Sood<sup>1</sup> and J. Braunstein

Reactor Chemistry Division, Oak Ridge National Laboratory, Oak Ridge, Tennessee 37830

We wish to report here Nernst response of dilute Li-Bi alloy electrodes and their applicability for studies of thermodynamic and transport properties of molten LiF-BeF<sub>2</sub> mixtures employing emf cells with and without transference (1-3). Such electrodes have the advantage that: by controlling the alloy composition, the electrode may be made more noble than, say, a Be electrode; they are simpler to employ than gas electrodes such as H<sub>2</sub>, HF; they may avoid possible solubility difficulties with recently developed LaF<sub>3</sub> membrane electrodes (4).

We wish also to report a new calculation of the limiting excess chemical potential of Li in Bi. Previous evaluations of this thermodynamic quantity have been based on measurements in chlorides or chloride-fluoride mixtures where Li metal is soluble, and furthermore Nernst behavior has not been previously experimentally demonstrated for the dilute alloy electrodes. An independent re-evaluation was therefore desirable. We employed the cell



in which the second electrode was metallic Be.

It is almost an axiom of electrochemistry that a cell with metal electrodes reversible to two different ions cannot be stable, since the more active metal will reduce the ion of the more noble one. For example, pure molten Li would reduce Be<sup>2+</sup> to Be and there could be no stable emf. However the activity coefficient of Li in dilute solutions in molten Bi is of the order of 10<sup>-5</sup> (5), and the activity may thus be reduced sufficiently by dissolution that Li in Bi is more noble than pure Be. Furthermore Be is insoluble in Bi and remains at unit activity. With the Li in Bi more noble than Be, it is thermodynamically possible for Be to reduce Li<sup>+</sup> to Li in Bi. (It cannot reduce Li<sup>+</sup> to liquid Li, the latter being more active.) If a pathway for this process existed, e.g., via dissolution of Li<sup>o</sup>, Be<sup>o</sup>, or Be<sup>+</sup> in the salt, followed by diffusion to the Bi anode, it would act as a chemical short circuit of the cell, with the Li content in Bi increasing until the cell emf approached zero. We find, however, that the emf of cell [A] is stable (for periods of observation up to 24 hr), which suggests that the solubility of reduced species in the melt in contact with metallic Be must be extremely low.

### Experimental

The experimental arrangement of the cell is indicated in Fig. 1. A stainless steel envelope which can be evacuated or provided with an inert gas blanket contains a Mo cup in which the molten salt floats on a layer of molten Bi. Be electrodes are inserted through Teflon packed Swagelok<sup>2</sup> fittings in the risers. The pur-

pose of the Mo tubular (reference) compartment is to trap salt of fixed composition; on subsequently changing the salt composition in the bulk compartment, constancy of the alloy composition can be ascertained by constancy of the emf measured between the Be electrode in the reference compartment and the Mo tube in contact with the Li-Bi alloy.

Bi of 69 grade from Cominco American is employed (about 500g in a cell) without further purification. BeF<sub>2</sub> is purified by sublimation. Single-crystal LiF is fused and treated with HF in a nickel vessel, sparged with H<sub>2</sub> and then He. Purity of the materials is essential to avoid corrosion of the Be electrodes. A typical impurity analysis is, in ppm: O<sub>2</sub>, 120; K, 7; Na, 70; Al, 70; Mg, 30; Cr, 10; Ti, 5; Fe < 1.

After several attempts to prepare Li-Bi alloys of known composition, or to analyze samples of the alloy after Li had been added, it was found that only by forming the alloy electrolytically *in situ* and determining the concentration by coulometry could sufficient precision be obtained to test adherence to the Nernst equation for cell [A] at a fixed salt composition. The electrolysis was carried out by connecting leads from the Be and Bi electrodes to the terminals of a twenty ohm resistor, across which the potential drop was recorded as a function of time and integrated to determine the quantity of electricity passed and of Li de-

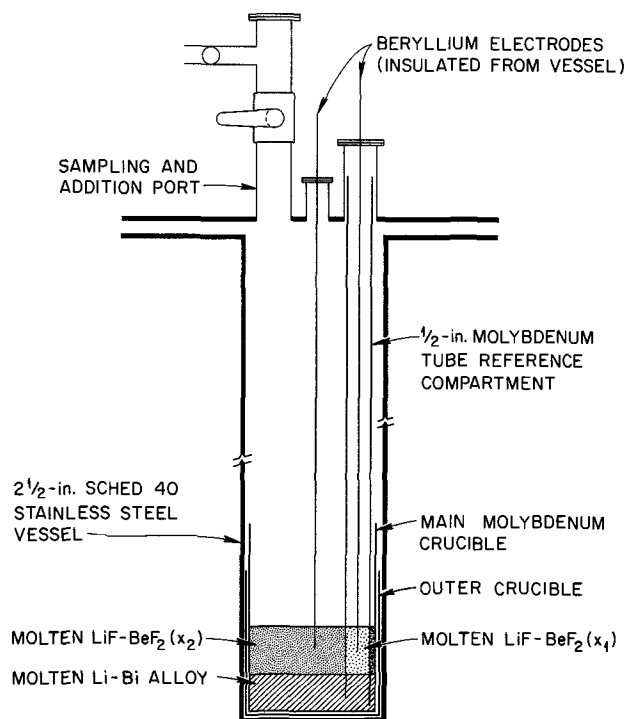


Fig. 1. Concentration cell without transference

<sup>1</sup> Guest scientist from the Bhabha Atomic Research Centre, Bombay, India.

Key words: alloys, bismuth, electrodes, lithium, molten salt.

<sup>2</sup> Crawford Fitting Company, Solon, Ohio.

posited in the Bi. Even without stirring the alloy, a steady emf was obtained within about a minute and remained constant (within several tenths of a millivolt) for periods of observation up to a day. Since Li has a very low activity in dilute solution in Bi, the alloy pool apparently provides an effective sink for the Li.

### Results and Discussion

The emf of the alloy concentration cell with fixed salt composition varies, with changing alloy composition, as

$$\Delta E = \frac{RT}{F} \ln \frac{a_{\text{Li}}(y)}{a_{\text{Li}}(y + \Delta y)}$$

Figure 2 shows the emf of the cell in a typical experiment as a function of mole fraction of Li in Bi, together with the calculated Nernst slope. (From measurements of the emf at different salt compositions, a small correction was applied for the virtually negligible change of salt composition resulting from the electrolysis.)

The fit of the Nernst equation in the Li mole fraction demonstrates that the activity coefficient of Li is constant in this concentration range, and that therefore the solution of Li in Bi follows Henry's law. Previously reported values of the excess chemical potential of Li at infinite dilution in Bi were based on extrapolation of measurements of two separate cells with higher concentrations of Li (5) ( $\geq 5\%$ ), and Nernst behavior of the electrode at low Li composition was not demonstrated experimentally. The present measurements, together with activity coefficients in LiF-BeF<sub>2</sub> mixtures (2), provide an independent estimate of the limiting excess chemical potential of Li in Bi with the aid of the cycle shown in Table I. In Table I  $\mu_{\text{Li}}^{\text{E}}$  is the excess chemical potential of Li in Bi,  $\gamma_{\text{Li}}$  is the activity coefficient,  $\mu_{\text{Li}}^{\text{E}} = RT \ln \gamma_{\text{Li}}$ , the  $\gamma$  being referred to pure liquid lithium.  $x$  is the mole fraction of BeF<sub>2</sub> in the melt used for the investigation.  $T$  is

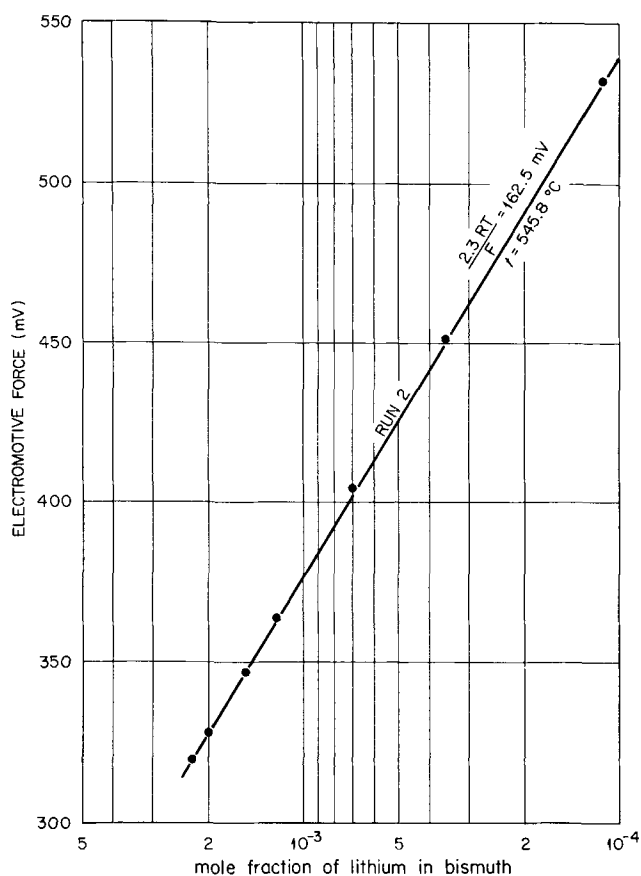


Fig. 2. Electromotive force and Nernst slopes of the cell  $\text{Be} | \text{LiF, BeF}_2 | \text{Li, Bi}$  at fixed salt composition,  $x_{\text{BeF}_2} = 0.3275$ .

Table I. Evaluation of the limiting excess chemical potential of Li in Bi at 819°K

	$\Delta G/\text{kcal mole}^{-1}$
$\frac{1}{2}\text{Be}(c) + \text{LiF}(c) \rightarrow \frac{1}{2}\text{BeF}_2(c) + \text{Li}(l);$	$\frac{1}{2}\Delta G_f^{\circ}(\text{BeF}_2, c) - \Delta G_f^{\circ}(\text{LiF}, c); +21.0^a$
$\text{Li}(l) \rightarrow \text{Li}(y, \text{Bi});$	$RT \ln y + RT \ln \gamma_{\text{Li}} = -11.241 + \mu_{\text{Li}}^{\text{E}} (y = 10^{-3}, \text{Bi})$
$\text{LiF}(x) \rightarrow \text{LiF}(x'); RT \ln [(1-x')\gamma'_{\text{LiF}}/(1-x)\gamma_{\text{LiF}}] = +0.612^{b,c}$	
$\text{LiF}(x') \rightarrow \text{LiF}(c); \Delta G = 0$	
$\frac{1}{2}\text{BeF}_2(c) \rightarrow \frac{1}{2}\text{BeF}_2(x'); \Delta G = 0$	
$\frac{1}{2}\text{BeF}_2(x') \rightarrow \frac{1}{2}\text{BeF}_2(x); \frac{1}{2}RT \ln x\gamma_{\text{BeF}_2}/x'\gamma'_{\text{BeF}_2} = -2.290^{b,c}$	
$\text{Li}(y, \text{Bi}) + \frac{1}{2}\text{BeF}_2(x) \rightarrow \text{LiF}(1-x) + \frac{1}{2}\text{Be}(c); \text{FE} = +8.716$	
$\Sigma \Delta G = 0$	
$x = 0.3275$ (experimental composition)	
$x' = 0.2935$	
$x'' = 0.975$ $E(y = 10^{-3}) = 0.378\text{V}$	

<sup>a</sup> Free energies of formation from Ref. (6).

<sup>b</sup> Phase data from Ref. (3).

<sup>c</sup> Activity coefficients from Ref. (2).

the temperature at which the emf is measured (819°K).  $x'$  is the mole fraction of BeF<sub>2</sub> at the LiF liquidus composition, and  $x''$  is the mole fraction of BeF<sub>2</sub> at the BeF<sub>2</sub> liquidus composition at the same temperature. At these compositions, the chemical potential of LiF in the melt is equal to that of pure crystalline LiF and the chemical potential of BeF<sub>2</sub> in the melt is equal to that of crystalline BeF<sub>2</sub>. These relations are indicated in Fig. 3 for the particular value  $x = 1/3$ .

The resulting value  $\mu_{\text{Li}}^{\text{E}}(\text{Bi}) = -16.82$  kcal/mole is in agreement with the value  $-16.96$  kcal/mole calculated from the results of Foster, Wood, and Crouthamel (5). The difference of 0.14 kcal corresponds to an emf discrepancy of only 3 mV, which is remarkably good since the uncertainty of 1 kcal/mole in  $\Delta G_f^{\circ}(\text{BeF}_2)$  (6) would correspond to an emf error of 20 mV.

Figure 4 shows an emf isotherm taken from measurements at a series of LiF-BeF<sub>2</sub> compositions and a fixed alloy composition, compared with previously reported results of emf measurements with transference cells.

The emf equation for the isotherm of cell [A] is

$$2F \frac{dE}{dx} = \frac{1+x}{1-x} \frac{d\mu_{\text{BeF}_2}}{dx}$$

while that for the transference cell is

$$2F \frac{dE}{dx} = t_{\text{Li}} \frac{1+x}{1-x} \frac{d\mu_{\text{BeF}_2}}{dx}$$

The equivalence of the emf results from the two cells confirms that the transference number of Be<sup>2+</sup> is zero, and that the Be electrode transference concentration cell may be used in this region to determine solution thermodynamic properties.

### Conclusions

The response of the Li-Bi electrode suggests its potential usefulness for a sensitive test of the unicationic (electrical) conduction mechanism in alkali fluoride-beryllium fluoride mixtures. A knowledge of the extent of the concentration range in which this mechanism is valid is important for the interpretation of anodic chronopotentiometry at a Be microelectrode in alkali fluoride-beryllium fluoride melts (7). The emf of

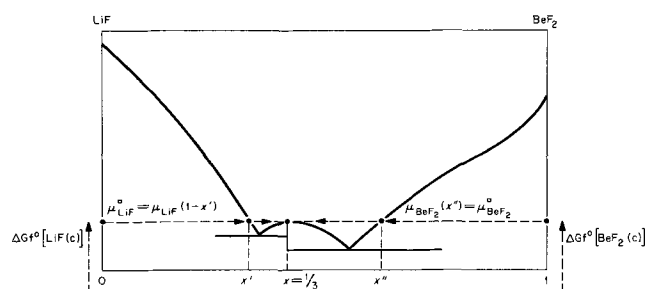


Fig. 3. Relations among free energies of formation and phase data

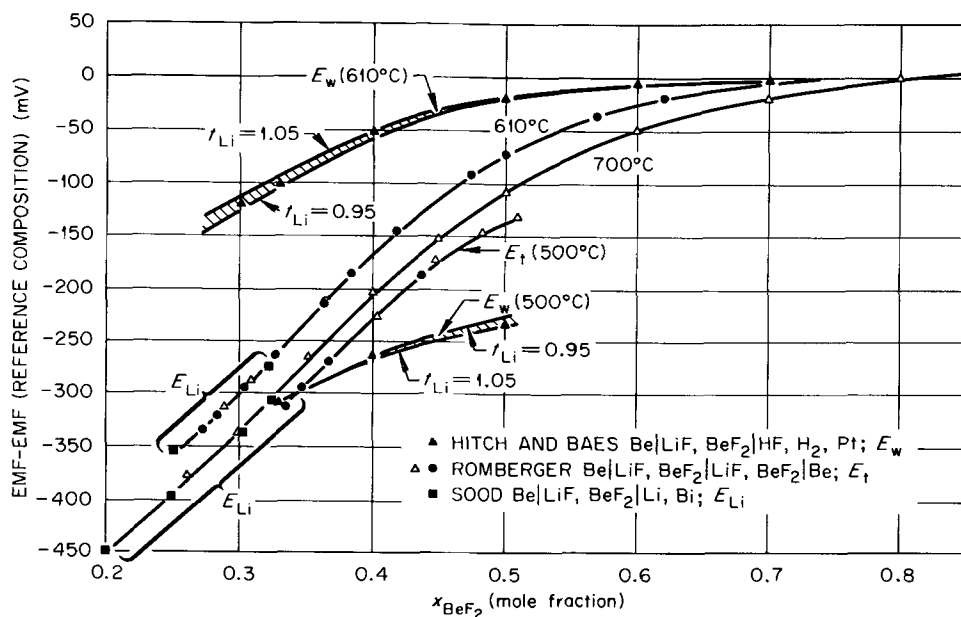
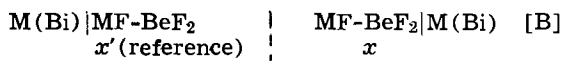


Fig. 4. Electromotive force of LiF-BeF<sub>2</sub> concentration cells.

a transference cell with an M-Bi alloy electrode in melts of varying concentrations of BeF<sub>2</sub>



would be given by

$$\frac{dE}{dx} = t_{\text{Be}} \frac{1+x}{1-x} \frac{d\mu_{\text{BeF}_2}}{dx}$$

Thus the emf of such a cell should be zero, and hence the cell would provide a sensitive indication of deviations from unicationic conduction; a negative slope would indicate anionic transport of beryllium ion relative to fluoride.

The Nernst response of the dilute Li-Bi alloy electrode, agreement with an independent value of the excess chemical potential of Li in Bi at infinite dilution, and agreement with transference cell measurements with Be electrodes, taken together, demonstrate that this electrode may be used with confidence for thermodynamic measurements.

#### Acknowledgment

We are pleased to acknowledge the cooperation of Dr. Helen Braunstein and Harry Bronstein during the course of this work.

This research was sponsored by the U.S. Atomic Energy Commission under contract with the Union Carbide Corporation.

This work was presented at the 3rd Romanian National Physical Chemistry Conference, Bucharest, Romania, September 3-7, 1972.

Manuscript submitted June 3, 1973; revised manuscript received Sept. 24, 1973.

Any discussion of this paper will appear in a Discussion Section to be published in the December 1974 JOURNAL.

#### LIST OF SYMBOLS

$a_i(y)$	activity of component $i$ at composition $y$
$E$	electromotive force
$F$	96,487 coulombs
$G$	Gibbs free energy
$\Delta G_f^\circ$	free energy of formation
$t_j$	transference number of constituent $j$
$x$	mole fraction of BeF <sub>2</sub>
$y$	mole fraction of Li in Bi
$\gamma_i$	activity coefficient of component $i$
$\mu_i$	chemical potential of component $i$
$\mu_i^E$	excess chemical potential of component $i$

#### REFERENCES

- W. K. Behl and J. J. Egan, *J. Phys. Chem.*, **71**, 1765 (1967).
- B. F. Hitch and C. F. Baes, *Inorg. Chem.*, **8**, 201 (1969).
- K. A. Romberger and J. Braunstein, *ibid.*, **9**, 1273 (1970); K. A. Romberger, J. Braunstein, and R. E. Thoma, *J. Phys. Chem.*, **76**, 1143 (1972).
- H. R. Bronstein and D. L. Manning, *This Journal*, **119**, 125 (1972).
- M. S. Foster, S. E. Wood, and C. E. Crouthamel, *Inorg. Chem.*, **3**, 1428 (1964). [See also J. J. Egan and R. H. Wiswall, *Nucleonics*, **15**, 104 (1957); L. M. Ferris, J. C. Mailen, and F. J. Smith, *J. Inorg. Nucl. Chem.*, **33**, 1325 (1971).]
- "JANAF Thermochemical Tables," D. R. Stull, Editor, PB 168 370, Clearing House for Federal Scientific and Technical Information, Springfield, Virginia, August 1965.
- J. Braunstein, H. R. Bronstein, and J. Truitt, *J. Electroanal. Chem.*, **44**, 463 (1973).

## Potentiostatic Anodic Synthesis of Ferrate(VI)

A. S. Venkatadri,<sup>1</sup> H. H. Bauer,\* and W. F. Wagner

Department of Chemistry, University of Kentucky, Lexington, Kentucky 40506

Ferrate(VI) production by electrolysis at iron anodes was observed as early as 1841 by Poggendorf

\* Electrochemical Society Active Member.

<sup>1</sup> Present address: Department of Metallurgical Engineering, Banaras Hindu University, Varanasi-5 (V.P.), India.

Key words: ferrate synthesis, iron(VI) synthesis, anodic dissolution, electrochemical synthesis.

(1). Since that time, ferrate has been used as a strong oxidizing agent in certain situations (2, 3), and electrochemical preparation has been a standard procedure. However, the preparation has been empirically developed and the electrode potential was not controlled (2, 4). It seemed worthwhile, therefore, to study the

yield of ferrate obtainable under potentiostatic conditions.

Comparatively recently, the influence of a number of experimental variables was studied by Tousek (5) with controlled currents: ferrate production was found to be greatest in 40% sodium hydroxide solution, at 20°-25°C, and at a current density of about 5 mA/cm<sup>2</sup>. At lower current densities, iron(III) was the main product, while at higher current densities oxygen was increasingly produced. In that work, the electrode potential varied appreciably over the course of the electrolysis. In the present communication, results are reported concerning the current efficiency for ferrate formation in relation to the electrode potential.

### Experimental

Controlled-potential electrolysis was carried out with a Princeton Applied Research Corporation (P.A.R.) Model 170 Electrochemistry System. The same instrument was used to determine ferrate concentration by voltammetry at a rotating iron disk electrode (6).

For ferrate synthesis, the anode consisted of four iron rods (99.7%, A. D. Mackay Inc.), 1/2 in. diameter immersed to a depth of 2 in. For determination of ferrate, an iron disk electrode (1/4 in. diameter) fitted to a Beckman Rotating Electrode Assembly was used. The counterelectrode in both cases was a platinum gauze, and the reference electrode was Hg/HgO/10.5M KOH.

The electrolyte was 10.5M KOH; "Baker Analyzed" potassium hydroxide was treated to remove oxidizable impurities as previously described (6). Controlled potential electrolysis was carried out in a water-jacketed cell for temperature control, and the solution was stirred with a magnetic stirrer. The amount of ferrate formed was calculated from the volume of the solution and from the ferrate concentration determined voltammetrically as previously described (6). The total charge passed during electrolysis was obtained directly with the P.A.R. instrument in the integrated readout mode.

### Results

Ferrate decomposes spontaneously. Electrolyses carried out over periods of 10-15 hr showed a decrease with time in the apparent current efficiency for ferrate production. This decrease is due at least in part to decomposition of the synthesized ferrate; however, the results of Tousek (5) indicate that passivation of the anode may also contribute to this effect under certain conditions.

Some studies were made of the kinetics of decomposition of ferrate, but the process is a complicated one; the decomposition is influenced by the presence of iron(III), and it did not appear that corrections for decomposition of ferrate during electrolysis could be made reliably over lengthy electrolysis times. Therefore the data reported here refer only to ferrate synthesis at electrolysis times up to 1 hr; during that period, spontaneous decomposition of ferrate was not sufficiently great as to influence the results appreciably (in more dilute KOH, however, the rate of decomposition of ferrate is greater, and corrections would have to be made).

Results are shown in Fig. 1. It is evident that maximum production of ferrate is observed in a quite narrow range of potentials (<50 mV). Moreover, the maximum coulombic efficiency (62 ± 4%) is significantly less than 100%, indicating that competing electrode reactions are occurring throughout the potential range where ferrate is formed. Tousek (5) had observed concurrent formation of iron(III) and of oxy-

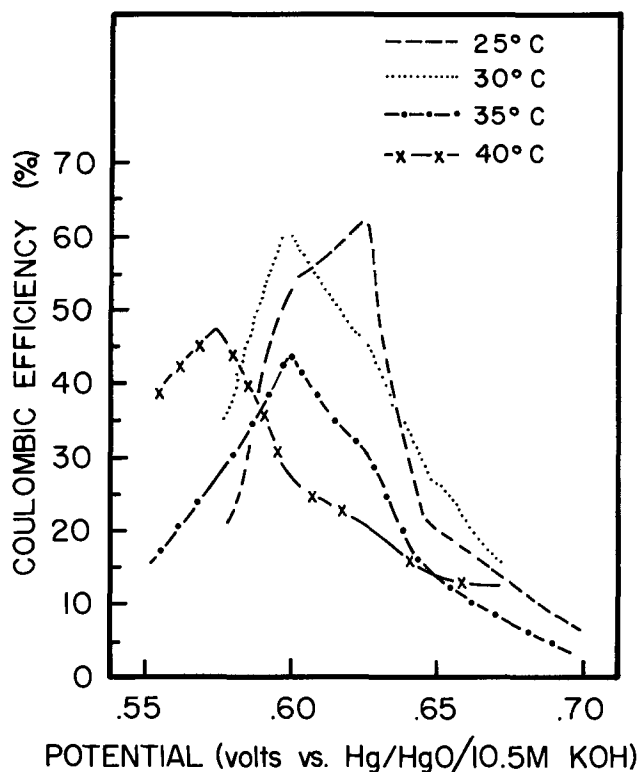


Fig. 1. Effect of potential on efficiency of ferrate (VI) production

gen in his constant-current investigations; the present studies show that these processes cannot be effectively prevented by control of the electrode potential to produce exclusively ferrate. The formation of bubbles of oxygen at the anode was seen in the present work at potentials about 70 mV less anodic than the potentials at which ferrate production was maximal.

Figure 1 indicates that the potential for maximal ferrate formation becomes less anodic as the temperature increases from 25° to 40°C, but the maximum coulombic efficiency decreases above 30°C. [These results are in good agreement with those of Tousek (5) who obtained a maximum coulombic efficiency of 60-70%, at 20°-25°C.]

### Acknowledgment

This work forms part of an investigation of electrochemical processes under Project Themis Contract DAABO7-69-C-0366 with the Department of Defense.

Manuscript submitted April 23, 1973; revised manuscript received Sept. 25, 1973.

Any discussion of this paper will appear in a Discussion Section to be published in the December 1974 JOURNAL.

### REFERENCES

1. J. C. Poggendorf, *Ann. Chem.*, **54**, 372 (1841).
2. J. W. Mellor, "Comprehensive Treatise on Inorganic and Theoretical Chemistry," Vol XIII, p. 929, Longmans, Green and Company, London, New York, Toronto (1934).
3. R. Scholder and H. V. Bunsen, German Pat. 1,013,272; *Chem. Abstr.*, **54**, 16762c (1960).
4. G. Grube and H. Gmelin, *Z. Electrochem.*, **26**, 153 (1920).
5. J. Tousek, *Coll. Czech. Chem. Commun.*, **27**, 914 (1962).
6. A. S. Venkatadri, W. F. Wagner, and H. H. Bauer, *Anal. Chem.*, **43**, 1115 (1971).



# Automatic, Sparkless Gas Pump for Gas Electrodes

Leonard F. Silvester and Peter A. Rock

Department of Chemistry, University of California, Davis, California 95616

A variety of pumps suitable for use with gas electrodes, in which recirculation of the gas is necessary, have been described (1-5). Gas recirculation may be required for several reasons, among which are: (i) the gas is expensive (*e.g.*,  $D_2$ ) and cannot be continuously discarded; (ii) the cell must be operated under strictly anhydrous, controlled atmosphere conditions; or (iii) the cell is being studied on a vacuum line.

A very brief description of each of the gas pumps designed for use with gas electrodes follows.

The Bollen pump (1) is a clever stirring device based on the Bernoulli principle that sucks gas into the solution from the vapor space above the solution as the stirrer operates. The pump can be used with a small volume of gas, but it is not suited for use where vacuum operation is necessary or where organic vapors are present, or where high speed stirring is undesirable.

The Harned-Scholes pump (2) consists of two mercury-filled cylinders activated by a plunger that is driven by an electric motor through a series of pulleys, gears, and cams in such a way that when one cylinder fills with mercury the other cylinder is emptying. In principle, the pump should circulate gas at a constant pressure; in practice, condensation of solvent vapor usually occurs because of the large volume change within each cylinder. The pump is not designed for vacuum-line applications.

The Curry-Hugus gas pump (3) is a simple, inexpensive device specifically designed for use with the hydrogen electrode in aqueous solutions. The pump can be made quite small and placed in a thermostat, except for the upper gas loop which must be maintained at a higher temperature than the pumping mechanism in order to prevent solvent condensation. The heart (and weakness) of the pump is a Bunsen valve made from a rubber medicine dropper. Adjustments to this valve are made on a trial and error basis. Because of the numerous rubber connections, the pump is not suited for vacuum applications, or for use with most organic solvents.

The Schuldiner-Hoare gas pump (4) is a stainless steel, aquarium-type circulating pump. The pump is protected from acid spray on the outlet and inlet by fritted glass disks. The design on this pump prevents its use on a vacuum line or with organic vapors that will damage the diaphragms on the pump.

The Johnson-Glover pump (5) consists of two Toepler pumps connected in parallel and operating one-half cycle apart to provide for continuous gas delivery at constant pressure. The pump employs electrical contacts in the stream of circulating gas. The pump employs eight check valves and six electrical contacts which must all function with the proper phasing to maintain correct pump operation. The pump may be used for vacuum operation, but it is difficult to adjust and maintain in operation with the proper phasing.

The gas pump described in this work is a Toepler-type pump in basic design that incorporates several novel and useful features. These features are: automatic operation, small displacement, continuous delivery of gas, wide-range working pressures, compactness, ease of adaptability, and the absence of an upper electrical contact (this feature reduces the chance of a spark-initiated explosion in a gas mixture). The pump is constructed from Pyrex glass and Teflon-core valves (stopcocks); it can be used in conjunction with a vacuum line and its operation is unaffected by organic vapors and most inorganic vapors.

Key words: pump, hydrogen, gas electrode.

Figure 1 shows the pump layout. The parts and their functions are described below.

A is the pump vessel; it consists of a 300 ml spherical flask that serves as the mercury reservoir. The vessel has four openings. The bottom one for mercury delivery to the check valves (F); an opening (C) for the working gas used to pump the mercury; and two openings (B and D) for electrical contacts.

B is the lower contact, whose height is adjustable to compensate for various mercury levels that result from varying pressures of the pumped gas.

B is shown in an enlarged view as follows: a is an 8-32 NPT brass screw; b is a 1/2 in. diameter hexagonal brass bar tapped for an 8-32 thread and drilled to receive a 7 mm glass tube at the other end; c is an "O" ring seal to prevent escape of working gas during a pump-up cycle; d is a 7 mm gas support tube attached to the mercury storage vessel and cemented with Torr-

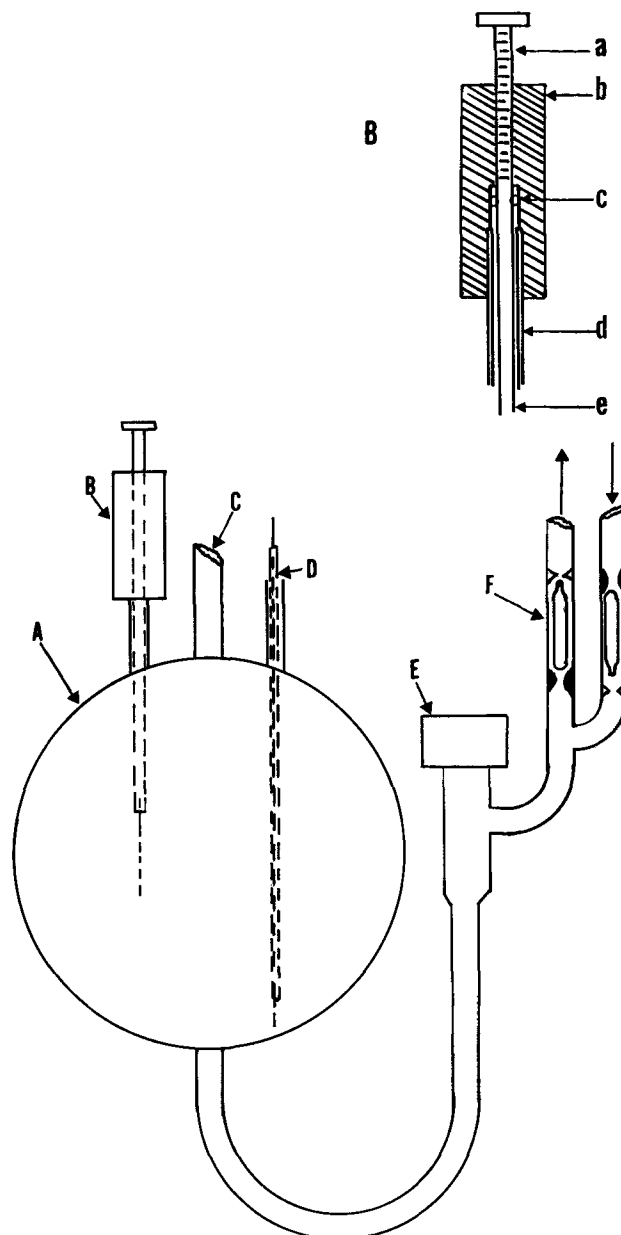


Fig. 1. Pump layout

Seal to B; and e is a  $\frac{1}{8}$  in. diameter nickel-plate-brass tube soldered to the adjusting screw with a tungsten metal contact to mercury soldered in the lower end.

C is the inlet-outlet tube for the working gas. C is connected either to vacuum for low gas pressure or to pressurized gas (e.g., tank nitrogen) for high gas pressure.

D is the common contact; it is a nonadjustable contact made by sealing tungsten wire in a 3 mm Pyrex tube and cementing the upper end with Torr-Seal to the associated support tube. (This connection could be placed near the bottom of the vessel exciting with a glass-to-metal seal.)

E is a Kontes 0-4 mm Teflon valve. This valve may be used to control the rate of rise and fall of mercury in the valving part of the pump. It has been used, however, in the present work as an isolating valve so that the entire gas recirculating system may be evacuated.

F is the check valve assembly. These valves control the direction of gas flow, as indicated by the arrows in Fig. 1. On the present pump the jackets are approximately 9 mm in diameter, with an orifice of approximately 4 mm. The exhaust valve plungers are one-half filled with mercury which acts as a weight to seal the valve during the intake cycle. (The mercury may be replaced with an iron bar so that the valve may be held open with a magnet.) The intake plungers float free; they are not mercury filled. The plunger head and valve seat are ground one upon the other to form a matched unit that provides an effective seal.

For automatic operation an electrical switching circuit is needed. This is outlined along with the working gas control system in Fig. 2. The parts and their functions are listed below.

A is the control box. This is a separate unit with banana-plug-type outlets for connection to the pump, and a Cinch-Jones connector from the control box to the Timer, B. Power is 115V,  $\sim$  60 cps, a.c. The electrical power connection, P, for the control box plugs into an electrical junction box which plugs directly into the timer unit, B. (Connection of the junction box is into the red outlet on the timer. The control box and timer could be conveniently placed in one unit.) a is a 1A fuse, connected to a double-pole, single-throw switch and a neon on-off indicator lamp; b is a single-pole single-throw relay.

B is the timer unit: a Time-Lite, Model M-59 automatic reset darkroom timer modified to start by remote signal. c is a solenoid whose plunger activates the timer start switch via a lever; d is the timer motor and automatic switching and reset mechanism of the timer (not modified), where there is a connection to the solenoid via a Cinch-Jones two-prong connector from the control box.

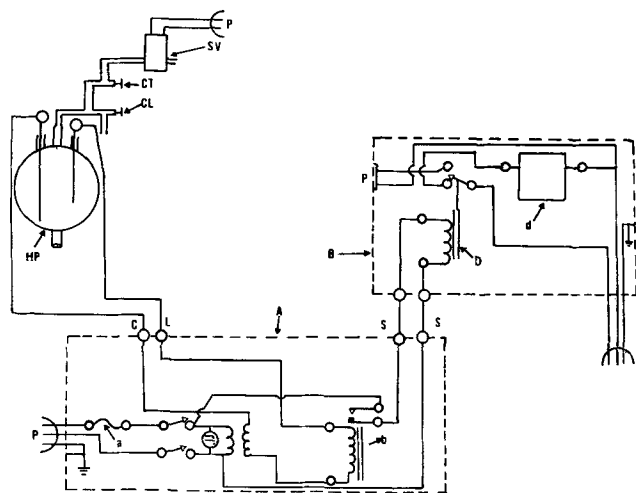


Fig. 2. Electrical switching circuit

CT, CL are the working gas control valves, Fisher-Porter 0-4 mm Teflon needle valves, for control of the incoming and outgoing flow rates. CL connects to a source of working gas.

SV is the electrical valve for the exhaust of the working gas to the atmosphere, and connection to plug P on timer unit B via a junction box.

For operating a pressure greater than atmospheric no modifications are necessary. Only the valve CT controlling the exhaust flow of the working gas through the electric valve SV need be adjusted such that the mercury falls slowly. This will prevent the gas from bubbling out of the pump through the mercury delivery tube before the working gas can come to the operating pressure.

For operations less than atmospheric pressure, i.e., 700 mm and less, solenoid SV is replaced with a three way valve; one to the pump, one to vacuum, the other to air or tank gas. The valve CL, as shown in Fig. 2, which connects to the working gas, is eliminated, while the other valve, CT, is placed on the air inlet of the electric valve to control the rate of rise of mercury (another valve may be placed on the vacuum outlet if the rate of fall of mercury is to be controlled).

The operation of the pump for automatic cycling is as follows. Suppose the pump-exhaust cycle has been completed and that the mercury is falling. Mercury continues to fall; this causes the level to rise in the vessel, A, until contact is made with the lower contact, B. Upon making contact, relay b is closed and this activates solenoid c, closing the timer-start switch. This deactivates the electric valve, SV, and the control unit, A, redirecting the working gas flow to vessel A, causing mercury to rise in the valve section, F. Mercury continues to rise at a rate set by the intake control valve and for a period of time that is preset on the timer. After the preset time, the timer action resets and in so doing activates the electric valve SV, and control unit A, exhausting the working gas to the atmosphere. Mercury falls until contact with B is again made to restart the cycle. Though the pump is presently used for recirculating gas, it may be used in the conventional manner for pumping gas into a collection flask by merely attaching the assembly to the pump exhaust port.

As noted earlier, the pump has no upper contact, and as such eliminates any possibility of electrical sparks resulting from mercury making and breaking contact during a pumping cycle, as happens with standard Toepler pumps on automatic mode employing the upper contact.

Because of this feature, explosive gaseous mixtures, or those subject to chemical reactions initiated by electrical spark discharge, or possibly contaminated by some such reaction initiated by electrical spark discharge, may be safely handled. Also the pumping system, because of the relatively simple design, is amenable to custom fabrication for the volume and rate of gas flow in question.

On automatic control, because the rate of rise of mercury in the pump (and its fall) and the period of duration of this rise are easily controlled, the volume of gas per pump cycle and the pumping cycle with periods of 2 sec to 1 min are easily selected (longer periods are possible by choice of a suitable timer).

Continuous flow is obtained by short pump-cycle times and because the volume of mercury displaced is small, surging effects and pressure fluctuations are very low. This permits gas-phase chemical reactions to be studied using the pump to supply a continuous flow of one of the reactants.

Two working models of the pump exist and have been in trouble-free operation for nearly 2 years. The pumps have run on automatic mode continuously for periods of up to 1 week without any failures or missing of pumping cycles.

Manuscript submitted Aug. 13, 1973; revised manuscript received Sept. 24, 1973.

Any discussion of this paper will appear in a Discussion Section to be published in the December 1974 JOURNAL.

## REFERENCES

1. W. B. Bollen, *Ind. Eng. Chem., Anal. Ed.*, **3**, 203 (1931).
2. H. S. Harned and S. R. Scholes, Jr., *J. Am. Chem. Soc.*, **63**, 1706 (1941).
3. J. Curry and Z. Z. Hugus, Jr., *Ind. Eng. Chem., Anal. Ed.*, **16**, 585 (1944).
4. S. Schuldiner and J. P. Hoare, *This Journal*, **105**, 278 (1958).
5. M. F. L. Johnson and J. A. Glover, *Anal. Chem.*, **22**, 204 (1950).

# Brief Communication



## Variable Composition of Basic Lead Sulfates

R. F. Dapo<sup>\*1</sup>

*Gould Incorporated, Gould Laboratories, Energy Technology, Mendota Heights, Minnesota 55118*

During the study of the compounds in the cured pastes of the lead-acid battery, procedures were developed for the preparation of pure basic lead sulfates. These methods were based on using the calculated stoichiometric ratio of sulfuric acid to lead monoxide for a given basic lead sulfate and obtaining a product having only the x-ray diffraction lines reported for that basic sulfate.

The method of preparing tetrabasic lead sulfate ( $\text{PbSO}_4 \cdot 4\text{PbO}$ ) is as follows: 250g of Baker Analyzed yellow lead monoxide was suspended in 1.0 liter of deionized water by means of rapid stirring. To this was added 31.0 ml of 1.400 sulfuric acid from a burette. The suspension was stirred and heated at 80°C for 4 hr. The solid was separated by filtration, washed and dried at 110°C. This intermediate solid, A, was ground and transferred to a nickel crucible. The solid was heated at 550°C for 4 hr to obtain the product.

The x-ray diffraction pattern of the resulting product showed only the lines of tetrabasic lead sulfate (1). Chemical analyses were also performed: total lead as  $\text{PbO}$ , 92.94 weight per cent (w/o);  $\text{SO}_3$ , 6.58 w/o; and  $\text{H}_2\text{O}$ , 0.32 w/o. Thus the total weight accounted for was 99.84 w/o. A number of preparations using this method were made, the product was always found to be only tetrabasic lead sulfate. The true density of the tetrabasic lead sulfate was measured by means of an air pycnometer. A density of  $8.04 \pm 0.06 \text{ g/cm}^3$  was found. This compares to a literature value (2) of  $8.15 \text{ g/cm}^3$ . No peaks were found on the differential thermal analysis curve except the melting point near 895°C. This melting point of 895°C agrees with the literature value of 897°C. However, this is claimed in Figure 1139 of Phase Diagrams for Ceramist to be the tribasic lead sulfate rather than the tetrabasic lead sulfate. Thus Figure 1139 is in error.

In the above method of preparation, the question was raised as to the purpose of the heating period at 550°C as no comparable heating has been required in reported preparations (3, 4). The intermediate solid, A, obtained after the digestion and before the heat-treatment at 550°C should be pure tetrabasic lead sulfate. X-ray examinations showed that the intermediate solid was always a mixture of tri- and tetrabasic lead sulfates. The amount of tribasic lead sulfate was estimated to be as much as 60 w/o of the total sample. As tribasic

lead sulfate was present in large amounts, lead monoxide or monobasic lead sulfate should be present to satisfy the stoichiometry. As neither lead monoxide nor monobasic lead sulfate could be identified in the intermediate solid, the possibility of biased x-ray results was considered. The x-ray results could be biased due to large particle size of the sample along with a poor x-ray penetration, or the results could be biased due to an amorphous form of either lead monoxide or monobasic lead sulfate.

In order to see if large particles having tri- or tetrabasic lead sulfates covering lead monoxide or monobasic lead sulfate might be responsible for the x-ray results, microscopic examination was used. Average size of the particles was estimated as  $3\mu$ . The x-ray penetration of the copper  $K_\alpha$  radiation was calculated to be  $20\mu$  (90% critical depth). Thus the x-ray diffraction results were not biased due to large particle size.

The possibility of an amorphous component of either lead monoxide or monobasic lead sulfate was considered unlikely because of the low specific surface area of the intermediate solid,  $0.48 \text{ m}^2/\text{g}$ . For lead compounds, a specific surface area of greater than  $20 \text{ m}^2/\text{g}$  appears necessary for the loss of intensity of x-ray diffraction lines. Thus the x-ray data was considered valid and a different explanation of the data was sought.

It was found that when a weighed sample of the intermediate solid was heated at 550°C, cooled, and reweighed, a weight loss occurred. Such a weight loss could be due to the loss of the water of hydration of the tribasic lead sulfate. However, chemical analysis showed that a large fraction of the weight loss on heating at 550°C consisted of carbon dioxide. Thus a reasonable explanation of the data was considered; the possibility existed that carbonate ion in the intermediate was obtained from atmospheric carbon dioxide. This carbonate ion replaced, in part, the sulfate ions in the basic lead sulfate lattice structure. As x-ray diffraction indicates the crystal lattice structure, carbonate ion might replace some sulfate ion in the lattice, hence causing the apparent violation of the stoichiometric calculations based only on the amount of sulfate. Such a substitution of one ion by another without a change in the lattice structure of a crystal is not unknown, a classical case is that of alums.

This possible explanation was investigated by the addition of ammonium carbonate to the usual preparation of tetrabasic lead sulfate, in an amount such that if carbonate replaced sulfate in the basic lead

\* Electrochemical Society Active Member.

<sup>1</sup> Present address: General Electric Company, Columbia, South Carolina 29202.

Key words: lead sulfates, lead carbonates, lead oxide reactions.

sulfate lattice, only the tribasic lattice would be evident by x-ray diffraction. Thus upon decomposition of this material at 550°C, water and carbon dioxide would be lost leaving chemically pure tetrabasic lead sulfate. In contrast to such behavior, chemically pure tribasic lead sulfate forms a 1:2 mixture of mono- and tetrabasic lead sulfates when heated at 550°C.

The procedure used follows: 250g lead monoxide, Baker Analyzed reagent, yellow powder was suspended in 2 liters of deionized water. To this was added 31.0 ml of 1.400 sulfuric acid with rapid stirring to effect suspension. The mixture was heated to 80°C. Sixteen grams of ammonium carbonate were added and the mixture allowed to digest at 80°C for 4 hr. The solid was separated by filtering, washed, and dried at 110°C. The following chemical analysis was found for this material:

	Weight per cent	Mole Ratio
PbO	88.4	4.00
SO <sub>3</sub>	6.27	0.791
CO <sub>2</sub>	2.76	0.632
H <sub>2</sub> O	2.53	1.42

The data indicate that a sufficient amount of CO<sub>2</sub> is present for the formation of the tribasic lead sulfate crystal lattice. The x-ray diffraction pattern of this material showed only the lines of tribasic lead sulfate (5).

When this material was heated at 550°C there was a weight loss of 5.29 w/o. This loss of weight corresponds to the loss of water and CO<sub>2</sub>. The heated solid was analyzed. The amount of CO<sub>2</sub> remaining was determined as 0.11 w/o. Neglecting this amount of CO<sub>2</sub>, the mole ratio of PbO:SO<sub>3</sub> was calculated to be 5:1. The resulting material showed only the x-ray diffraction pattern of tetrabasic lead sulfate. This proves that carbonate ion substitutes for sulfate ion in the tribasic lead sulfate crystal lattice.

The possible role of carbonate ion in the tetrabasic lead sulfate crystal structure was next considered. The same procedure as described above was used, but different amounts; 20.0 ml 1.400 acid, 9.29g ammonium carbonate. These amounts were calculated such that only a tetrabasic crystal structure in which about 40% substitution of carbonate ion for sulfate ion could occur.

The x-ray diffraction pattern of the product showed only the pattern of tetrabasic lead sulfate. For a synthetic mixture of pure tetrabasic lead sulfate and 15 w/o of basic lead carbonate, basic lead carbonate lines were present in the x-ray pattern. The true density of the product was measured as 8.04 g/cm<sup>3</sup> by an air pycnometer. This corresponds to the true density of pure tetrabasic lead sulfate, 8.04 ± 0.06 g/cm<sup>3</sup>. This value of the true density rules out the possibility of small amounts of basic lead carbonate ( $d = 7.55$  g/cm<sup>3</sup>) as an impurity. The chemical composition was determined and the results are listed below with the calculated mole ratios:

	Weight per cent	Mole Ratio
PbO	92.2	5.00
SO <sub>3</sub>	4.21	0.637
CO <sub>2</sub>	1.44	0.395
H <sub>2</sub> O	0.595	0.400

The composition indicated by these analytical results and having the tetrabasic lead sulfate lattice structure might be written as



where  $x$  is the degree of substitution, 0.4 in this case.

When this material was heated at 550°C, 2.04 w/o was lost. The x-ray diffraction pattern of this heated material showed only tetrabasic lead sulfate and lead monoxide in the amounts expected. The heated material, when analyzed, contained only 0.20 w/o carbon dioxide. In contrast to this behavior, pure tetrabasic lead sulfate would be stable at 550°C. Thus the carbonate substitution for sulfate ion in the tetrabasic lead sulfate crystal lattice was proven.

Additional preparations were performed to establish the possible range of carbonate substitution for sulfate ( $x$ , above) in the tetrabasic lead sulfate crystal lattice. Above  $x = 0.4$ , basic lead carbonate appears in the x-ray diffraction patterns of the resulting products. Although the ion sizes may be close, enough stress is apparently induced in the lattice with increasing amounts of carbonate, such that the more stable basic lead carbonate is formed. Preliminary experiments have shown that other anions, such as sulfite and oxalate, behave in the same fashion as carbonate in the basic lead sulfate lattice structures.

Note that the amounts of carbon dioxide in the analysis of these compounds is small when in terms of weight per cent. However, when the amounts of either carbon dioxide or water is expressed in terms of mole per cent, the magnitude assumes its appropriate importance. As pointed out above, a 1.44 w/o of carbon dioxide in a sample represented about 40 m/o of the anionic material other than oxide in the sample. Small amounts of carbon dioxide have been found in cured pastes. This is reasonable because a wet paste is basic, and may be flashed dried by an open flame. Vinal (6) asserts that carbon dioxide may be important to the hardness and strength of the cured pastes. What role these compounds might play in terms of physical or electrochemical properties is yet to be assessed.

### Acknowledgment

The author wishes to extend his appreciation to W. Cook, C. Fillmore, and J. Wiczorek for the analytical data.

Manuscript submitted May 22, 1973; revised manuscript received Sept 24, 1973.

Any discussion of this paper will appear in a Discussion Section to be published in the December 1974 JOURNAL.

### REFERENCES

1. ASTM Card No. 6-0308.
2. J. Burbank, *This Journal*, **113**, 10 (1966).
3. R. V. Biagetti and M. C. Weeks, *Bell System Tech. J.*, **49**, 1305 (1970).
4. J. J. Lander, *This Journal*, **95**, 174 (1949).
5. ASTM Card No. 6-0282.
6. G. W. Vinal, "Storage Batteries," 4th ed., p. 10, John Wiley and Sons, Inc., New York (1967).



## Ionic and Electronic Conductivity in $Y_2O_3$ -Doped Monoclinic $ZrO_2$

M. M. Nasrallah\*<sup>1</sup> and D. L. Douglass

*School of Engineering, University of California, Los Angeles, California 90024*

### ABSTRACT

The electronic and ionic conductivities of  $ZrO_2$  were determined as a function of temperature, oxygen partial pressure, and trivalent dopant content. The experimental observations were in reasonable agreement with the proposed defect structure model. Ionic conductivity for undoped zirconia was attributed to doubly ionized oxygen interstitials at high oxygen pressures and to doubly ionized oxygen vacancies at the lower extreme of the oxygen partial pressure. Doped zirconia, contrary to the undoped sample, showed maximum ionic transport at intermediate oxygen pressures. The ionic conductivity, due to extrinsic dopant effects, increased by increasing the amount of dopant and its range extended over a wider oxygen partial pressure. The observed decrease in activation energy for ionic conductivity upon doping was attributed to the formation of anion vacancies whose concentration is directly proportional to the dopant content. The 1 mole per cent (m/o)  $Y_2O_3$  sample showed predominant ionic transport.

According to the Wagner-Schottky-Hauffe semiconductor valence approach (1), appropriate additions of foreign ions<sup>2</sup> will alter the defect concentration in an oxide. The addition of higher valent cations to an n-type oxide causes a decrease in the ionic defect concentration whereas, the electron concentration is increased. Similar additions to a p-type oxide cause an increase in the ionic defect concentration and a decrease in the electron hole concentration. The opposite effect occurs in each oxide type for lower valent dopants. This approach may in principle be applied to the oxidation of metals which form n- or p-type oxide scales. The theory involving this behavior was first given by Wagner (2) and has been verified experimentally for numerous pure metals.

Previous work on  $ZrO_2$  showed that its defect structure varies across the scale depending on the oxygen pressure. Mallett and Albrecht (3) detected a negative thermoelectric power on oxide films formed on Zr-Sn alloys and suggested that zirconia is an n-type semiconductor. However, from electrical conductivity data as a function of oxygen partial pressure, Rudolph (4) found a positive pressure dependence on the conductivity over the range  $10^{-3}$  to  $10^3$  mm Hg. This p-type conductivity was also confirmed by his thermoelectric power measurements. Vest, Tallan, and Tripp (5) measured the electrical conductivity as a function of oxygen pressure from 1 to  $10^{-23}$  atm and concluded that zirconia is an amphoteric oxide with the transition from n-type to p-type conductivity occurring at about  $10^{-16}$  atm. They observed a 1/5 slope at high oxygen partial pressure and attributed it to completely ionized zirconium vacancies. Kofstad (6) stated that the presence of zirconium vacancies is inconsistent with the

phase diagram considerations and suggested an alternative interpretation in which the oxide predominantly contains oxygen vacancies which under the experimental conditions are determined by substitutionally dissolved cations of lower valence. Kofstad and Ruzika (7) also observed p- and n-type conductivity at different oxygen partial pressures and suggested an ionic conduction mechanism in which both anion vacancies and interstitials exist.

From partial electrical conductivity data, Poulton and Smeltzer (8) reported that at  $990^\circ C$  hot-pressed monoclinic zirconia is an n-type electronic conductor at oxygen partial pressures below  $10^{-18}$  atm and a p-type electronic conductor at pressures above  $10^{-10}$  atm oxygen. Oxygen ion transport predominates at intermediate pressures. Kumar *et al.* (9) measured the transference numbers and electrical conductivity as a function of oxygen pressure and temperature and suggested that the defect structure of monoclinic zirconia in the temperature range of  $700^\circ$ - $1000^\circ C$  involves doubly ionized oxygen vacancies at pressures below  $10^{-19}$  atm, and singly ionized oxygen interstitials at pressures above  $10^{-9}$  atm.

Kröger (10) further discussed the results of Vest *et al.* (5) and suggested a Schottky-type model involving both isolated oxygen vacancies and zirconium vacancies singly associated with oxygen vacancies. A detailed analysis was given by Douglass and Wagner (11) who proposed an anti-Frenkel model based on the assumption that the ionic defect structure of zirconia is similar to that of  $CaF_2$ . These models (10, 11) have been found (12) to be mathematically equivalent if the doubly ionized oxygen interstitial of the anti-Frenkel model is replaced by a doubly ionized pair of zirconium and oxygen vacancies.

The fact that  $ZrO_2$  is n-type at low oxygen pressures and is p-type at high oxygen pressures, means that a p-n junction exists within the scale, which junc-

\* Electrochemical Society Student Member.

<sup>1</sup> Present address: Pahlavi University, Shiraz, Iran.

Key words: defect structures, anion vacancies, interstitial oxygen, anti-Frenkel disorder.

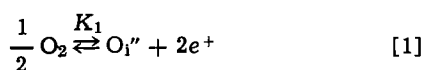
<sup>2</sup> Foreign ions are assumed to dissolve substitutionally in the parent oxide.

1974

tion would obviously affect the transport of electrons and ions across the scale. Therefore, Wagner's theory involving the change in defect concentration with dopant cannot be applied to an amphoteric oxide as zirconia. The inconsistencies in all these results can be accounted for if one considers the different materials, oxidant purity, methods of specimen preparation, and the techniques involved by various investigators. The presence of foreign cations, either in the form of impurities or intentionally added, may significantly alter the concentration of native defects. It was the objective of this work to determine the ionic and electronic conductivities of dense monoclinic zirconia containing small additions of yttria.

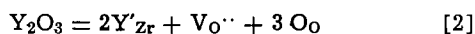
### Proposed Defect Structure

Assuming that anti-Frenkel type disorder prevails in monoclinic zirconia, the predominant type of defects at high oxygen partial pressure will be oxygen interstitials and electron holes. Furthermore, for simplicity, only doubly ionized defects will be considered, hence



by applying the law of mass action and the electro-neutrality condition that  $[e^+] = 2[\text{O}_i'']$ . The concentration of doubly ionized oxygen interstitials or electron holes will have a 1/6 power dependence on oxygen partial pressure.

If one assumes that, upon doping, the  $\text{Y}^{+3}$  enters the  $\text{ZrO}_2$  lattice substitutionally for  $\text{Zr}^{+4}$  according to the equation



The dopant cation will have one effective negative charge. Thus,  $\text{Y}_2\text{O}_3$  additions will cause an increase in the anion vacancy concentration which, even in the high oxygen partial pressure region, will be greater than the concentration of oxygen interstitials. Following Lasker's and Rapp's (13) analysis on  $\text{Y}_2\text{O}_3$ -doped  $\text{ThO}_2$ , expressions for the partial conductivities can be obtained, where

$$\kappa_{e^+} = \text{const } P_{\text{O}_2}^{1/4} [\text{Y}_2\text{O}_3]^{1/2} \quad [3]$$

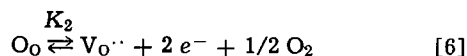
and

$$\kappa_i = 2|e|\mu_v [\text{Y}_2\text{O}_3] \quad [4]$$

From Eq. [3] and [4] the dependence of  $\text{Y}_2\text{O}_3$  content and  $P_{\text{O}_2}$  on the ionic transference number is given by

$$\tau_i = \frac{1}{1 + \text{const } P_{\text{O}_2}^{1/4} [\text{Y}_2\text{O}_3]^{-1/2}} \quad [5]$$

Similarly, in the low oxygen partial pressure region, the predominant defects in undoped  $\text{ZrO}_2$  will be doubly ionized oxygen vacancies and free electrons according to



the concentration of defects will then have a  $-1/6$  power dependence on oxygen partial pressure. Upon  $\text{Y}_2\text{O}_3$  additions the free electron conductivity and ionic transference number will be expressed by

$$\kappa_{e^-} = \text{const } P_{\text{O}_2}^{-1/4} [\text{Y}_2\text{O}_3]^{-1/2} \quad [7]$$

and

$$\tau_i = \frac{1}{1 + \text{const } P_{\text{O}_2}^{-1/4} [\text{Y}_2\text{O}_3]^{-3/2}}$$

This shows that the addition of  $\text{Y}_2\text{O}_3$  might affect the native defect equilibrium (extrinsic region), hence the ionic conductivity will be proportional to the dopant content and is independent of the oxygen partial pressure, Eq. [4]. Whereas the electron hole and free electron conductivities will have a  $+1/4$  and  $-1/4$  dependence on oxygen partial pressure according to Eq. [3] and [4], respectively. However, if the foreign ca-

tions do not affect the native defect equilibrium, (intrinsic region), the dependence of the concentration of electronic and ionic defects on oxygen partial pressure will be represented by Eq. [1] and [6].

### Experimental Procedures

*Sample preparation.*—The starting materials were Wah Chang Zirconia Powder [compositional analysis given in Ref. (9)] and  $\text{Y}_2\text{O}_3$  99.99% pure. Batches of 100g of undoped zirconia and zirconia containing 0.5 mole per cent (m/o)  $\text{Y}_2\text{O}_3$  and 1 m/o  $\text{Y}_2\text{O}_3$  were prepared. To insure homogeneity, the doped powders were thoroughly mixed in a blender for 24 hr. Isostatic compaction of the powders was performed at 60,000 psi for 5 min in glycerine. Slices, about 1.3 cm in diameter and 0.5 cm thick, were cut off the pressed samples. The disks were vacuum-sintered, in an NRC vacuum resistance furnace, at  $10^{-5}$  Torr and  $2300^\circ\text{C}$  for 3 hr. Zirconia powder sintered at  $2250^\circ\text{C}$ , was used as a spacer between the disks and the furnace base plate to prevent contamination and sticking of the disks to the tungsten base plate. The furnace temperature was measured by a disappearing filament optical pyrometer. The sintered, black, oxygen-deficient disks were embedded in zirconia powder and oxidized in air at  $850^\circ\text{C}$  for 3 days. The disks were polished on fine SiC paper. The density of the undoped zirconia sample was determined by measuring dimensions and by the water displacement methods, values ranging from 5.53 to  $5.67 \text{ g/cm}^3$  were obtained. These values correspond to 96-98% of the theoretical x-ray computed density ( $5.77 \text{ g/cm}^3$ ).

X-ray diffraction (with filtered  $\text{Cu-K}_\alpha$  radiation) and metallographic analyses were performed on all samples before and after conductivity measurements to check the structure and morphology of the samples. X-ray analysis revealed the monoclinic structure whereas metallographic examination showed a single phase with no evidence of microcracks.

Electron vapor-deposition techniques were used to apply thin platinum film electrodes to the disk faces. The samples were heated during deposition at  $850^\circ\text{C}$  in vacuum ( $2 \times 10^{-5}$  Torr). High-temperature vapor deposition was essential to obtain optimum contact between the platinum film and the zirconia samples. Films deposited were 0.5 cm in diameter and about  $15\mu$  thick.

*Electrical conductivity and transference number assembly.*—The a-c electrical conductivity vs. temperature measurements were performed at a test frequency of 1000 Hz using a General Radio Model 1608A impedance bridge. The samples were maintained in compression by means of spring-loaded platinum electrode assemblies which gave optimum contact through the deposited platinum thin films on the samples.

Two-probe conductivity measurements were employed. As a check on the two-probe technique Strickler and Carlson (14) measured the conductivity of several  $\text{M}_2\text{O}_3$ - $\text{ZrO}_2$  systems using both the two- and four-probe techniques, their results for both techniques agreeing within experimental error. Similarly, Mittoff (15) did not observe any substantial difference between both techniques from his conductivity measurements on MgO single crystal.

The sample holder was designed to completely isolate the two chambers on each face of the sample. By this setup it was possible to conduct both total electrical conductivity and galvanic cell transport measurements at different oxygen pressures and temperature on the same sample *in situ* prior to its replacement. Interruption of measurements might give inconsistent results and rupture the platinum thin film. The resistance of the platinum leads was found to be negligible. The sample was isolated from the furnace heating elements by means of a quartz tube, the furnace was kept at low impedance to ground. A

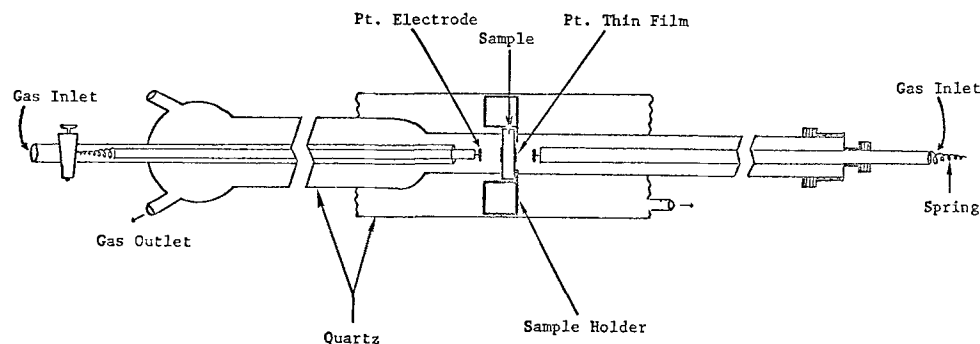


Fig. 1. Conductivity and emf assembly

schematic representation of the apparatus is shown in Fig. 1.

Transference number measurements were performed by maintaining a difference in oxygen pressure on both sides of the sample. This has been achieved by the use of gas trains which have been described elsewhere (9). Gas mixtures and their corresponding oxygen partial pressure within the temperature range of this investigation have been previously reported (16). The emf generated was measured by an L&N K-3 potentiometer. The potentiometer was also used to eliminate thermoelectric effects by reversing the polarity. The furnace had a 1.5 in. constant temperature zone at the center where the sample was located, the average temperature gradient within 2 in. from each face of the sample was 2°C; the temperature was measured by a Pt-Pt-10Rh thermocouple. A 0-100 mV chart recorder was connected from the output of the potentiometer and used to facilitate the prompt detection of steady-state conditions.

All samples were heated at 900°C for 48 hr after insertion into the apparatus and prior to the measurements.

The electrochemical cell is  $P_{O_2}^I, Pt|ZrO_2|Pt, P_{O_2}^{II}$  or  $P_{O_2}^I, Pt|ZrO_2-Y_2O_3|Pt, P_{O_2}^{II}$ . Such cells may be employed to discriminate between ionic and electronic conductivity in solids as described by Wagner (1).

The principle is to establish different oxygen activities at opposite sides of the oxide. The potential developed is measured with a potentiometer when no current is supplied to or drawn from the cell. Provided the electrodes are completely reversible and the two sides of the sample are in equilibrium with the corresponding partial pressure of oxygen, then the measured potential across the oxide,  $E_e$ , is given by

$$E_e = \tau_i \frac{kT}{4e} \ln \frac{P_{O_2}^I}{P_{O_2}^{II}} \quad [9]$$

where  $\tau_i$  represents the average ionic transport number for the ionic conductivity between the limits II and I and is evaluated from the values of  $E_e$ ,  $P_{O_2}^{II}$ , and  $P_{O_2}^I$ . When the oxide is an electronic conductor the cell is short-circuited and  $E_e = 0$ . By using Pt electrodes, only the potential difference due to separation of ionic charges is measured. The maximum value of  $\tau_i = 1$ , in which case Eq. [9] becomes

$$E = \frac{kT}{4e} \ln \frac{P_{O_2}^I}{P_{O_2}^{II}} \quad [10]$$

The difference in oxygen partial pressure ( $P_{O_2}^I$  and  $P_{O_2}^{II}$ ) on both sides of the sample was maintained at about one order of magnitude.

By combining Eq. [9] and [10]

$$\tau_i = \frac{E_e}{E} \quad [11]$$

accordingly, the average ionic transference number could be obtained from knowledge of the experimentally determined potential and that theoretically calculated for purely ionic conductor.

From total electrical conductivity and transference number data, the partial ionic and electronic conductivities can be determined according to

$$\kappa_i = \tau_i \sigma_T \quad [12]$$

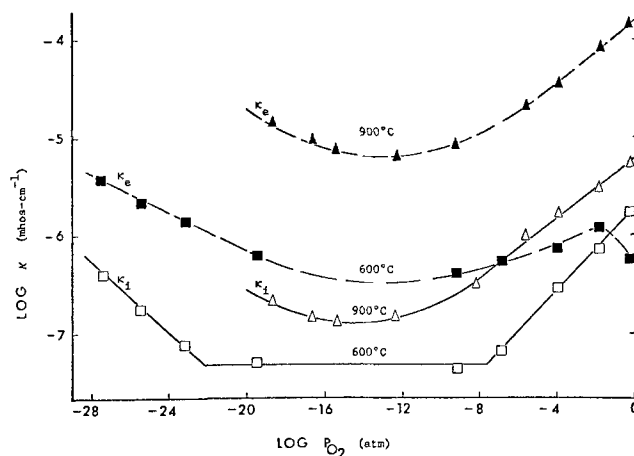
and

$$\kappa_e = \sigma_T - \tau_i \quad [13]$$

Conductivity and open circuit emf measurements were conducted at various oxygen partial pressures ranging from  $10^{-25}$  to 1 atm and at temperatures between 600°-900°C.

### Results and Discussion

The electronic and ionic conductivities for all three samples at both temperature extremes of this investigation are shown in Fig. 2, 3, and 4. With the exception of the high  $P_{O_2}$  region (0.21-1 atm) and at lower temperatures, the conductivity of the undoped sample was mainly due to electrons. This has been reported previously by Vest and Tallan (5) and by Kumar *et al.* (9). The ionic, pressure-independent region for the undoped sample at 600°C is attributed to equal concentrations of doubly ionized oxygen vacancies and interstitials as predicted from Eq. [1] and [6]. The decrease in electronic conductivity with increasing oxygen pressure from 0.21-1 atm at 600°C, has been previously observed (9). This observation is difficult to rationalize. A possible explanation is that zirconium dioxide has a tendency to lose oxygen, as verified experimentally from the volumetric measurements (16). Thus, an appreciable amount of oxygen deficiency may occur initially which results in the formation of anion vacancies or free electrons, but long exposure times will be required at low temperatures before equilibrium is attained. Furthermore, since the undoped sample was predominantly electronically conducting, it is expected that this inherent behavior was attributed to the initial free-electron conductivity giving rise to the observed n-type behavior. This is further supported by the fact that the initial n-type conductivity does not appear in the electronic plot at 900°C, a temperature that is high

Fig. 2. Ionic and electronic conductivities of undoped  $ZrO_2$

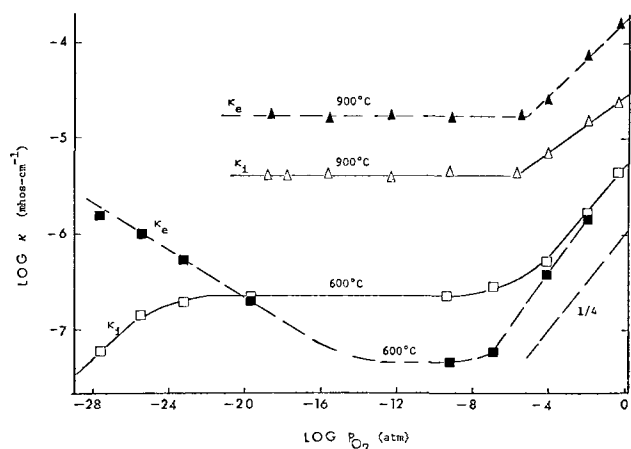


Fig. 3. Ionic and electronic conductivities of  $ZrO_2 + 0.5 \text{ m/o } Y_2O_3$

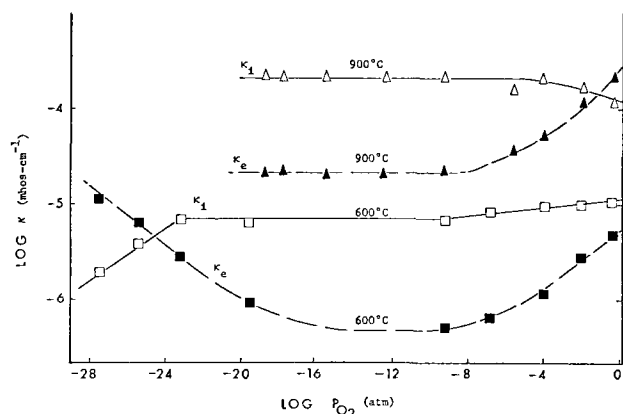


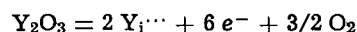
Fig. 4. Ionic and electronic conductivities of  $ZrO_2 + 1 \text{ m/o } Y_2O_3$

enough to attain equilibrium after short exposure times yielding the p-type effect directly. At 900°C the electronic conductivity decreases with decreasing  $P_{O_2}$  with a 1/6 slope, the conductivity in this region is attributed to electron holes as indicated in Eq. [1], the plot achieves a minimum at about  $10^{-14}$  atm followed by an increase in electronic conductivity with further decrease in  $P_{O_2}$  which is attributed to free electron conductivity according to Eq. [6]. The 0.5 m/o  $Y_2O_3$  sample showed predominant ionic conductivity at 600°C and at oxygen partial pressures above  $10^{-20}$  atm. At lower oxygen pressures, however, the reverse was observed; this predominant electronic conductivity had been observed also at 900°C (Fig. 3). Apparently the amount of trivalent additive was insufficient at higher temperatures to produce predominantly ionic conductivity. Thus, inherent electronic conductivity was observed. The 1 m/o  $Y_2O_3$  sample showed mainly ionic conductivity at oxygen pressures down to  $10^{-24}$  atm at 600°C, and at oxygen pressures between  $10^{-20}$ – $10^{-4}$  atm at 900°C as shown in Fig. 4. The predominant ionic conductivity which prevailed upon doping was attributed to the extrinsic effect of trivalent additives as predicted from the defect-structure model. The pressure-independent range for the electronic conductivity of doped zirconia at high temperature was attributed to equal concentrations of free electrons and electron holes. The 1/4 oxygen pressure dependence on electron-hole conductivity for doped samples, as predicted from Eq. [3], is clearly shown for the 0.5 m/o  $Y_2O_3$  sample (Fig. 3), whereas, this effect is not clearly identified for the 1 m/o  $Y_2O_3$  sample. The increase in electronic conductivity with decreasing oxygen partial pressure below  $10^{-16}$  atm for the doped samples was attributed to free electron conductivity and seems to be consistent with the theoretical prediction at 600°C, yet the exact determination

of the slope was difficult to verify. At higher temperature, the negative pressure dependency on the electronic conductivity was not observed probably due to the extension of the  $P_{O_2}$ -independent region beyond our experimental limits.

The observed decrease in ionic conductivity with decreasing oxygen partial pressure upon doping in the low-pressure region and at lower temperatures is inconsistent with the theoretical predictions from which an increase in anion vacancy concentration is expected upon the addition of  $Y_2O_3$ . This behavior has been previously observed by Keneshea and Douglass for undoped  $ZrO_2$  (12). A possible explanation is that the high concentration of anion vacancies causes clustering (14) or vacancy-impurity interaction (17) which could cause an appreciable decrease in the anion-vacancy mobility. Although the concentration of interstitial anions is expected to be low in this region, their mobility may be higher than that for anion vacancies, resulting in the observed interstitial-controlled oxygen ion conductivity at the lower extreme of oxygen pressure.

This positive pressure dependence of ionic conductivity on oxygen partial pressure can also be interpreted in terms of interstitial  $Y^{3+}$  cations in the  $ZrO_2$  lattice at low oxygen partial pressures, the defect equation is given by



This equation predicts an increase in the free-electron concentration and a decrease in the anion vacancy concentration. Accordingly, the concentration of oxygen interstitials will be expected to increase giving rise to the observed behavior at very low oxygen pressure.

The oxygen pressure dependence of the ionic conductivity of undoped monoclinic zirconia is shown for several temperatures in Fig. 5. Two pressure-dependent regions can be observed at high and low oxygen pressures, representing interstitial and vacancy-controlled oxygen ion conductivity, respectively. The ionic conductivity in the high-pressure range ( $10^{-8}$ – $1$  atm) follows a 1/6 dependence to a good approximation, particularly at higher temperatures, and may be attributed to doubly ionized oxygen interstitials. Similarly, in the very low pressure range ( $P_{O_2} \cong 10^{-23}$  atm) the conductivity seems to follow a -1/6 dependence on oxygen pressure at 600°C which might be due to doubly ionized oxygen vacancies; however, the lack of sufficient experimental points in the low-pressure range makes it difficult to determine exactly the type of pressure dependence. A pressure-independent plateau is clearly identified at lower temperatures and gradually disappears as the temperature is increased. This plateau may be attributed to either equal concentrations of cationic and anionic defects or to aliovalent impurity effects. The disappearance of the pressure-independent region at 900°C, as op-

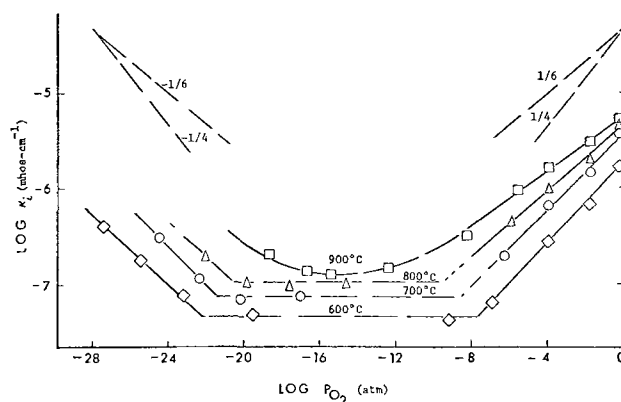


Fig. 5. Ionic conductivity for undoped zirconia



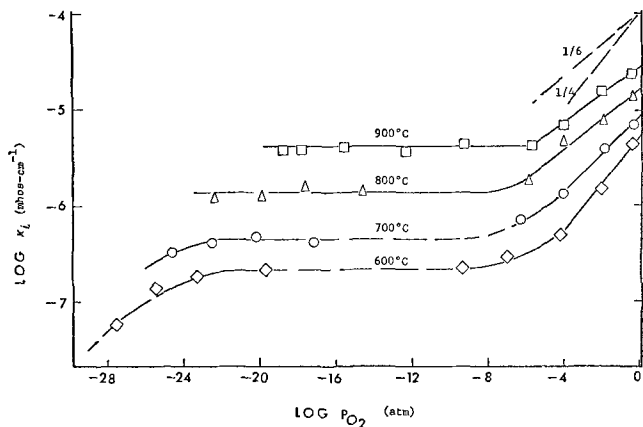


Fig. 6. Dependence of ionic conductivity on  $P_{O_2}$  and temperature for  $ZrO_2 + 0.5$  m/o  $Y_2O_3$ .

posed to earlier work (9), might be due to the lower impurity level achieved in this work during the sintering operation.

The 0.5 m/o  $Y_2O_3$  sample showed an initial decrease in ionic conductivity with decreasing oxygen pressure over the range of 1 to about  $10^{-6}$  atm, indicating anion interstitial-controlled conductivity as shown in Fig. 6. The slope in this region seems to fit a  $1/4$  dependence on oxygen pressure at lower temperatures however, as the temperature is increased, the slope deviates from the  $1/4$  dependency and seems to follow  $1/6$  dependency at  $900^\circ C$ . The p-type region is followed by a pressure-independent region which seems to spread over a wider  $P_{O_2}$  range as the temperature is increased from  $600^\circ$ – $900^\circ C$ . A decrease in ionic conductivity was observed below  $10^{-24}$  atm, indicative of p-type conductivity. This behavior was not observed at temperatures above  $700^\circ C$ , probably due to the extension of the pressure-independent region beyond the lower  $P_{O_2}$  limit of this work. Although the experimental points are insufficient to determine the slope exactly, it seems, however, that the slope is approximated best by a  $1/4$  dependence.

Doping with 1 m/o  $Y_2O_3$  caused a barely detectable, if any, change in ionic conductivity at temperatures between  $700^\circ$ – $900^\circ C$  and throughout the entire range of oxygen pressure, except in the region between  $10^{-2}$  and 1 atm, where a slight decrease in conductivity with increasing oxygen pressure was detected as shown in Fig. 7. At  $600^\circ C$  there was a slight increase in ionic conductivity with increasing oxygen pressure from  $10^{-7}$  to 1 atm, and at  $P_{O_2}$  below  $10^{-23}$  atm the ionic conductivity decreased with  $P_{O_2}$ .

An Arrhenius plot of  $\log(\kappa_i T)$  vs. reciprocal temperature for the zirconia sample doped with 1 m/o  $Y_2O_3$  is shown in Fig. 8. The isobar chosen is at an

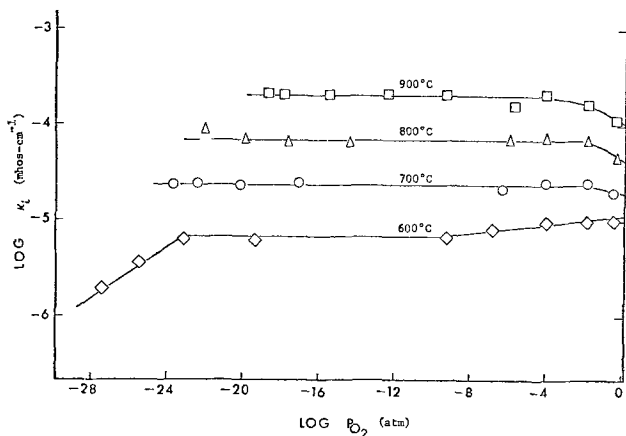


Fig. 7. Dependence of ionic conductivity on  $P_{O_2}$  and temperature for  $ZrO_2 + 1$  m/o  $Y_2O_3$ .

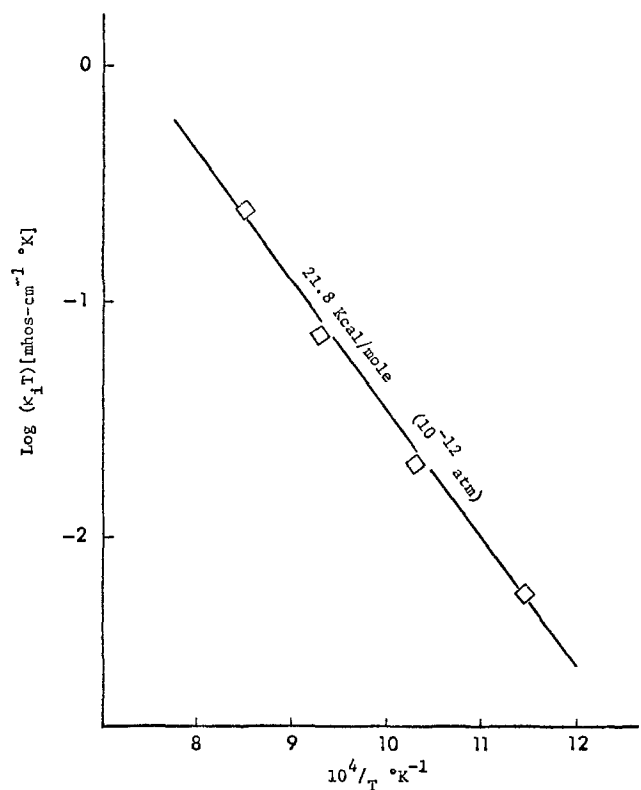


Fig. 8. Arrhenius plot for  $ZrO_2 + 1$  m/o  $Y_2O_3$  at  $10^{-12}$  atm

intermediate oxygen pressure, because ionic conductivity values at both extremes of oxygen pressure cannot be derived with high accuracy from Fig. 7, and consequently, their corresponding Arrhenius plots might be misleading. From Fig. 8, a continuous increase in ionic conductivity with increasing temperature can be observed. The data fit a straight-line relationship with an activation energy of 21.8 kcal/mole, which is lower than most of the reported values for undoped  $ZrO_2$ . Hussey and Smeltzer (21) reported an activation energy value of 31.9 kcal/mole from their Arrhenius plot of  $\log$  parabolic rate constant  $K_p$  vs.  $1/T$  at temperatures between  $400^\circ$  and  $850^\circ C$ , Gulbransen and Andrew (22) obtained a value of 28.6 kcal/mole. This is attributed to the increase in ionic defects as predicted from Eq. [2].

By comparing Fig. 5, 6, and 7, one can observe the effect of dopant on the ionic conductivity of monoclinic zirconia. The ionic conductivity increased with increasing dopant concentration which behavior is consistent with Eq. [4]. Doping with 0.5 m/o  $Y_2O_3$  resulted in a change of slope from  $1/6$  to  $1/4$  in the p-type region at high oxygen partial pressure and at lower temperatures. The undoped sample showed an increase in ionic conductivity with decreasing oxygen pressure below  $10^{-23}$  atm, whereas, the  $Y_2O_3$ -containing samples exhibited a decrease in ionic conductivity with decreasing oxygen pressure; this behavior has been discussed previously.

Increasing temperature resulted in a decrease in the pressure-independent range for the undoped sample, whereas, the opposite was observed for the doped specimens. Furthermore, the pressure-independent region extended over a wider range as the amount of dopant increased. This interesting observation identifies the role of trivalent additives. The low-temperature behavior at intermediate oxygen partial pressures for undoped zirconia can be attributed to either extrinsic factors or to equal concentrations of doubly ionized oxygen vacancies and interstitials. The disappearance of this plateau at high temperatures suggests that the intrinsic, thermally generated defects dominate as the temperature is increased.

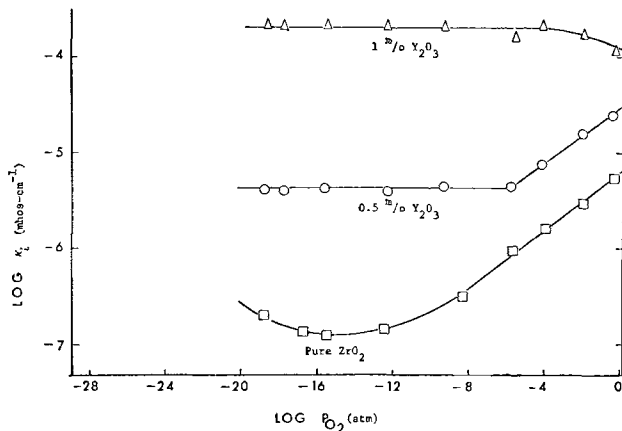


Fig. 9. Ionic conductivity as a function of dopant content and  $P_{O_2}$  at 900°C.

A cross plot for all three samples at 900°C is shown in Fig. 9. The ionic conductivity for undoped  $ZrO_2$  is due primarily to intrinsic ionic equilibria for which oxygen interstitials predominate at high  $P_{O_2}$  and to oxygen vacancies at low  $P_{O_2}$ , as shown by Eq. [1] and [6], respectively. The theoretical derivation predicts that the pressure-independent plateau is due primarily to dopant effects. The stoichiometric composition for undoped  $ZrO_2$  will yield a pressure-independent region; however, this plateau was not observed in the case of undoped  $ZrO_2$  at high temperatures where a minimum in the conductivity curve at about  $10^{-14}$  atm, was observed indicating a transition from predominant oxygen interstitials to oxygen vacancy conductivity as the  $P_{O_2}$  is lowered. Alternatively,  $Y_2O_3$ -containing samples had a pressure-independent plateau for ionic conductivity as predicted from Eq. [4]. The shift of the pressure-independent plateau towards higher oxygen pressures, and consequently the extension of the pressure-independent region over a wider  $P_{O_2}$ -range, is in agreement with Lasker's and Rapp's (13) results on  $Y_2O_3$ -doped  $ThO_2$ . The addition of 1 m/o  $Y_2O_3$  to  $ZrO_2$  is sufficient to produce essen-

tially ionic conductivity over the pressure range studied. Burke and co-workers (22) predicted that the ionic conductivity for thoria doped with 10 m/o  $Y_2O_3$ , in the temperature range of 900°-1100°C, should be independent of oxygen pressure from  $10^{-25}$ -1 atm. Similar behavior was reported (23) for  $ZrO_2$  doped with 16.5 m/o CaO at 1000°C. Patterson *et al.* (24) found that the ionic conduction for  $Zr_{0.85}Ca_{0.15}O_{1.85}$  was pressure-independent over the range of  $10^{-27}$ -1 atm oxygen at 800°-1000°C.

The change in ionic transference number with temperature as a function of dopant content is represented in Fig. 10. Figure 10A shows the ionic transference number data obtained at oxygen pressures between  $10^{-3}$  and 0.21 atm. An increase in ionic transference number with increasing dopant content was observed in agreement with Eq. [5]. As the temperature was increased, the ionic transference number decreased, however, this became less pronounced as the amount of  $Y_2O_3$  increased. Undoped  $ZrO_2$  exhibited exclusive electronic conductivity at 900°C as reported earlier by Kumar *et al.* (9); however, zirconia doped with 1 m/o  $Y_2O_3$  was primarily an ionic conductor at the same temperature and at intermediate oxygen partial pressures. The change in transference number with temperature in the pressure-independent region ( $10^{-12}$  atm) is shown in Fig. 10B. Generally, the ionic transference number values are lower than those obtained in the higher pressure region for the undoped sample, whereas, the opposite effect was observed for the  $Y_2O_3$ -containing samples. The ionic transference number for the undoped zirconia was about 0.1 at 600°C with a slight decrease as the temperature increased from 600°-900°C. Accordingly, electronic transport prevails at intermediate oxygen partial pressures, and the conductivity is primarily due to equal concentrations of free electrons and electron holes. A wide variation in transference number was observed for the sample doped with 0.5 m/o  $Y_2O_3$ . The latter had a value of 0.5 at 600°C and decreased to about 0.2 at 900°C. The observed mixed conductivity suggests that the amount of dopant was insufficient to produce the expected ionic transport and that temperature was the rate-controlling factor. Doping with 1 m/o  $Y_2O_3$  increased the ionic transference number to about 0.92 at 600°C.

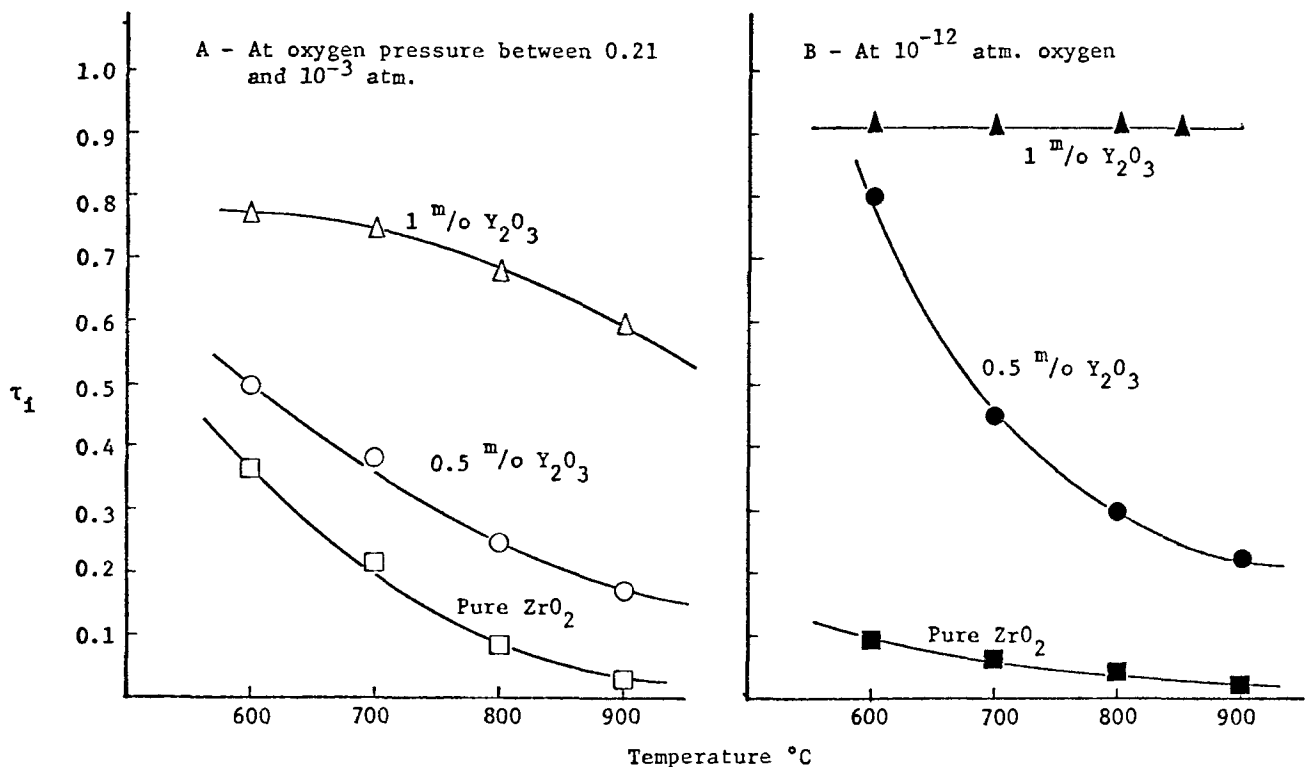


Fig. 10. Ionic transfer number as a function of temperature and  $Y_2O_3$  content

This value remained virtually unchanged over the entire temperature range of this investigation.

The dependence of ionic transference number on oxygen pressure at 600°C is shown in Fig. 11. The ionic transference number for pure zirconia increased from 0.1 to 0.8 as the oxygen pressure increased from  $10^{-8}$ -1 atm. The transference number remained almost unchanged at pressures between  $10^{-23}$  and  $10^{-18}$  atm. Below  $10^{-23}$  atm a slight increase in transference number was observed with decreasing oxygen pressure. The sample doped with 0.5 m/o  $Y_2O_3$  showed an increase in ionic transference number from about 0.2 to 0.85 with decreasing oxygen pressure from  $1 \cdot 10^{-7}$  atm. A further decrease in oxygen pressure resulted in a slight plateau of constant transference number between  $10^{-7}$ - $10^{-10}$  atm, followed by a rapid decrease in ionic transference number. For the 1 m/o  $Y_2O_3$  sample, the ionic transference number initially increased from 0.6 to 0.9 between 1 and  $10^{-5}$  atm. This was followed by a pressure-independent region between  $10^{-5}$ - $10^{-19}$  atm. A further decrease in oxygen pressure resulted in a decrease in the ionic transference number. Figure 11 shows that the range of constant ionic transference number in the higher oxygen pressure region shifted towards higher oxygen pressure as the amount of dopant increased. The relationship between ionic transport and dopant concentration is predicted from Eq. [5] and [8] at the higher and lower limits of the oxygen partial pressure, respectively. In the intermediate pressure range, the ionic conductivity is due primarily to anion vacancies whose concentration is directly proportional to the amount of trivalent dopant. This extrinsic effect should be pressure-independent for a fixed dopant content.

The agreement between the model and experimental observations is visualized from Fig. 12 which shows the change in ionic transference number as a function

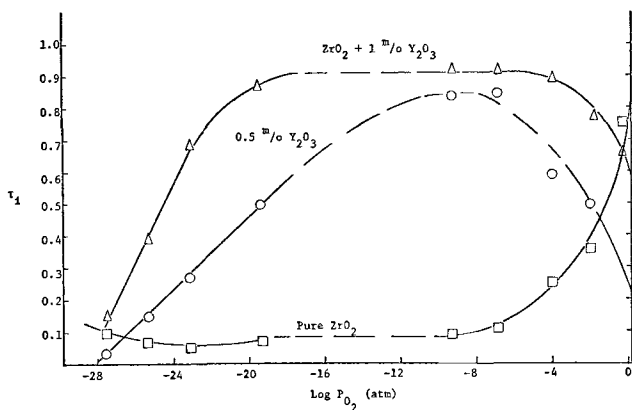


Fig. 11. Dependence of ionic transfer number on  $P_{O_2}$  and  $Y_2O_3$  content at 600°C.

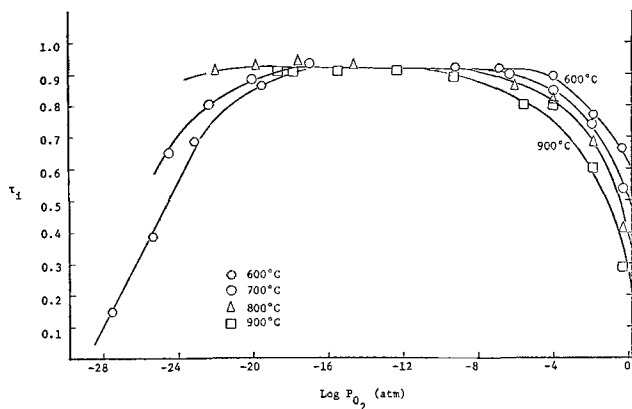


Fig. 12. Transfer number dependence of  $P_{O_2}$  and temperature for  $ZrO_2 + 1$  m/o  $Y_2O_3$ .

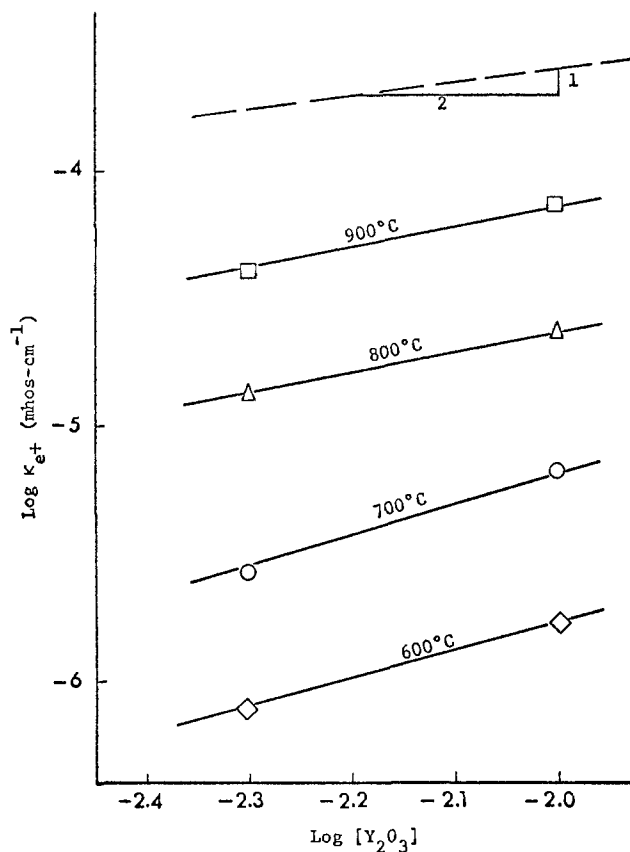


Fig. 13. Electron hole conduction as a function of  $Y_2O_3$  content and temperature at  $10^{-3}$  atm.

of oxygen pressure and temperature for zirconia doped with 1 m/o  $Y_2O_3$ . The figure clearly shows that doping with 1 m/o  $Y_2O_3$  results in predominant ionic transport in the intermediate oxygen pressure range, which is independent of both oxygen pressure and temperature. A theoretical prediction, of an increase in ionic transport with decreasing oxygen pressure at high  $P_{O_2}$  and a decrease in ionic transport with further decrease in  $P_{O_2}$  at low oxygen pressure, was experimentally verified in Fig. 12. The figure also shows that the ionic transport at both oxygen pressure extremes decreased with increasing temperature.

From Eq. [3] it is predicted that the electron hole conductivity should obey a  $1/2$  dependence on  $Y_2O_3$  content. A plot of  $\log \kappa_{e^+}$  vs.  $\log [Y_2O_3]$  for several isotherms of 0.5 and 1 m/o  $Y_2O_3$  containing samples is shown in Fig. 13. Although this work was limited to only two dopant compositions, a verification of the above dependence was observed, and the electron hole conduction mechanism is in reasonable agreement with the theoretical model.

### Conclusions

A model of the defect structure of zirconia was proposed. The model predicts the dependence of ionic and electronic conductivities on oxygen pressure and dopant content.

Undoped zirconia showed predominant electronic transport over the entire temperature range except at 600°C in the high  $P_{O_2}$  region. The ionic transport number decreased with decreasing oxygen pressure, achieves a minimum and then remains essentially constant upon further decrease in  $P_{O_2}$ , at the same temperature. Conductivity at high oxygen pressure was attributed to doubly ionized oxygen interstitials and electron holes, whereas, at low oxygen pressure, conductivity was due to doubly ionized oxygen vacancies and free electrons. The stoichiometric composition, detected by a pressure-independent plateau for undoped zirconia, occurred at intermediate oxygen pressures.

The absence of a plateau at high temperatures was attributed to the decrease in impurity content of the  $ZrO_2$  powder by the sintering operation.

The  $Y_2O_3$ -doped zirconia samples showed an increase in ionic transference number with decreasing oxygen pressure in the high oxygen pressure region and a decrease in ionic transference with further decrease in oxygen pressure at the lower extreme of the oxygen pressure range. Increasing the dopant content caused an increase in ionic transference number and extended its range over a wider oxygen pressure. The 1 m/o  $Y_2O_3$  sample showed mostly ionic transport, i.e., 90%, which was independent of temperature at intermediate oxygen pressures. These observations were in good agreement with the proposed model.

Ionic conductivity, due to the extrinsic dopant effect, was found to be independent of oxygen pressure, increased with increasing the amount of dopant and extended over a wider oxygen pressure range as the amount of dopant increased. This was attributed to anion vacancy formation and was in good agreement with the proposed model.

The interstitial-controlled oxygen ion conductivity for the  $Y_2O_3$ -doped specimens at low temperatures and oxygen partial pressures was attributed to either vacancy clustering and vacancy-dopant interaction or to the presence of dopant cations in interstitial sites. This behavior was not observed at higher temperatures probably due to the extension of  $P_{O_2}$ -independent region beyond the lower limits of this work.

The observed activation energy for oxygen diffusion in the doped sample was lower than the published values for undoped  $ZrO_2$ ; this is in agreement with the theoretical predictions. The theoretical model was qualitatively verified for the ionic transport at various oxygen partial pressures and dopant content, moreover, the model was in good agreement with the observed relation between electron-hole conductivity and dopant content.

#### Acknowledgment

This work is based on a portion of the dissertation of one of the authors (M.M.N.) in partial fulfillment of the requirements for the degree of Doctor of Philosophy in Engineering, University of California, Los Angeles, 1972.

Manuscript submitted Feb. 6, 1973; revised manuscript received Sept. 11, 1973.

Any discussion of this paper will appear in a Discussion Section to be published in the December 1974 JOURNAL.

#### LIST OF SYMBOLS

$O_o$  neutral oxygen on a normal lattice site  
 $O_i^{..}$  doubly ionized oxygen interstitial  
 $V_o^{..}$  doubly ionized oxygen vacancy

$e^-$  free electron  
 $e^+$  electron hole  
 $K$  equilibrium constant  
 $[ ]$  concentration  
 $\kappa_i$  partial ionic conductivity  
 $\kappa_{e^-}$  free electron conductivity  
 $\kappa_{e^+}$  electron hole conductivity  
 $\sigma_T$  total electrical conductivity  
 $\tau_i$  average ionic transference number  
 $Y_{Zr}$  replacement of  $Zr^{4+}$  by  $Y^{3+}$  on a normal lattice site  
 $Y_i^{..}$  interstitial trivalent cation in  $ZrO_2$  lattice  
 $U_v$  mobility of vacancies  
 $k$  Boltzmann constant

#### REFERENCES

1. P. Kofstad, "High Temperature Oxidation of Metals," pp. 265-266, John Wiley & Sons, New York (1966).
2. C. Wagner, *Z. Physik. Chem.*, **B21**, 25 (1933).
3. M. W. Mallett and W. M. Albrecht, *This Journal*, **102**, 407 (1955).
4. J. Rudolph, *Z. Naturforsch.*, **14a**, 727 (1959).
5. R. W. Vest, N. M. Tallan, and W. C. Tripp, *J. Am. Ceram. Soc.*, **47**, 635 (1964).
6. P. Kofstad, "Non-Stoichiometry, Diffusion and Electrical Conductivity in Binary Metal Oxides," pp. 153-158, John Wiley & Sons, New York (1972).
7. P. Kofstad and D. J. Ruzika, *This Journal*, **110**, 181 (1963).
8. D. J. Poulton and W. W. Smeltzer, *ibid.*, **117**, 378 (1970).
9. A. Kumar, D. Rajdev, and D. L. Douglass, *J. Am. Ceram. Soc.*, **55**, 439 (1972).
10. F. A. Kröger, *ibid.*, **49**, 215 (1966).
11. D. L. Douglass and C. Wagner, *This Journal*, **113**, 671 (1966).
12. F. J. Keneshea and D. L. Douglass, *Oxidation of Metals*, **3**, 1 (1971).
13. M. F. Lasker, and R. A. Rapp, *Z. Physik, Chimie, N.F.*, **49**, 198 (1966).
14. D. W. Stickler and W. G. Carlson, *J. Am. Ceram. Soc.*, **48**, 286 (1965).
15. S. P. Mittoff, *J. Chem. Phys.*, **31**, 1261 (1959).
16. M. M. Nasrallah, Ph.D. Dissertation, UCLA, School of Engineering, December 1972.
17. F. A. Kröger, "The Chemistry of Imperfect Solids," p. 275, North Holland Publishing Company, Amsterdam (1964).
18. J. Debuigne, and P. Lehr, *Mém. Sci. Rev. Met.*, **60**, 911 (1963).
19. T. Smith, *This Journal*, **112**, 560 (1965).
20. C. J. Rosa, and W. C. Hagel, *J. Nucl. Mater.*, **27**, 12 (1968).
21. J. Hussey and W. W. Smeltzer, *This Journal*, **111**, 564 (1964).
22. E. A. Gulbransen and K. F. Andrew, *J. Metals*, **9**, 394 (1957).
23. L. D. Burke, H. Rickert, and R. Steirner, *Z. Physik. Chimie, N.F.*, **74**, 146 (1971).
24. J. Patterson, E. C. Bogren, and R. A. Rapp, *This Journal*, **114**, 752 (1967).

# Ellipsometric Study of the Plasma Oxidation of Tantalum

J. D. Leslie<sup>1</sup>

Centre de Recherches sur les Très Basses Températures, Grenoble, France

and K. Knorr

Institut Von Laue-Langevin, Grenoble, France

## ABSTRACT

We have shown that it is possible to grow a uniform Ta oxide film up to a thickness of 1500Å by plasma oxidation. The average speed of growth was 0.1 Å/sec, which is comparable to earlier studies. Our experiments show that there is no significant contamination of the oxide due to sputtering from the cathode and that there is no evidence of sputter etching of the sample oxide due to the sample facing the cathode. These results are in opposition to the reports of earlier investigators. We find that our ellipsometric measurements on the oxide growth indicate that the Ta oxide being formed is a single, uniform layer with an index of refraction of 2.21. This result is in contrast to the earlier work of Lee *et al.*, who fitted their ellipsometric measurements on plasma-grown Ta oxide with a two-layer model with layer indices of 1.89 and 2.22.

In this paper we would like to report on an ellipsometric study of the plasma oxidation of tantalum. Since the pioneering work of Miles and Smith (1) on the formation of oxides in an oxygen glow discharge there have been several studies of the plasma oxidation of tantalum (2-4). One of the main problems with these earlier studies has been the technique used to measure the oxide thickness. Capacitance measurements (2,3) require a value of the dielectric constant to be assumed, and just as for optical-step measurements (2), the growth of the oxide has to be stopped at particular points and the thickness of the oxide determined in a separate measurement. Ellipsometry (5) allows *in situ* optical measurements to be made during the growth of the oxide, which can later be analyzed to yield a thickness calibration and a value of the index of refraction of the oxide. However, the previous *in situ* ellipsometric study of the plasma oxidation of Ta by Lee *et al.* (4) may have suffered from the fact that a manual ellipsometer was used. Since it requires an appreciable time, perhaps 2-3 min, to take a reading on a manual instrument, it is necessary to stop the oxidation at particular points in the growth so that oxide thickness data can be taken. If ellipsometric measurements are made while the film is growing, the long nulling time of a manual instrument will cause significant errors in the optical data, particularly in those regions where the optical data are changing rapidly with time.

The instrument used in the present study is an automated ellipsometer (6) that is capable of taking a reading every second. This allowed optical data to be taken continually during the growth of the oxide. Consequently this has led us to some observations on better ways to grow these oxides which are at variance with the recommendations of previous experimenters, and has allowed us to collect enough optical data during the growth of the oxide to be able to get a value of the index of refraction of the oxide that fits the experimental data very well.

## Experimental Procedures

Figure 1 shows schematically the experimental arrangement. The light source, L, is a He-Ne laser ( $\lambda = 6328\text{Å}$ ) with Brewster windows. The first quarter-wave plate,  $Q_1$ , is just to convert the linearly polarized laser light to circularly polarized. The polarizer, P, and the analyzer, A, are Glan-Thompson prisms

mounted so that they can be rotated around the optic axis by stepping motors. The output signal from the photomultiplier, PM, controls a special purpose digital computer which drives the P and A stepping motors in a sequence which finds and displays digitally the angular position of P and A for a null condition at PM. The optical alignment is done via pinholes. The sample, S, is mounted on a sample holder, SM, which can rotate from the vertical position shown to a horizontal position. The latter is used when it is desired to prepare a thin-film sample by using a source that evaporates vertically upward through a hole in the baseplate of the vacuum chamber, C. The orientation of the sample with respect to the optic axis is defined by pressing the sample holder, SM, in the vertical position against three alignment screws. The angle of incidence,  $\theta_i$ , was measured to be  $59.5^\circ$ . The laser light enters and leaves the vacuum chamber, C, via two glass windows mounted on bellows so that they can be aligned appropriately with respect to the optic axis.

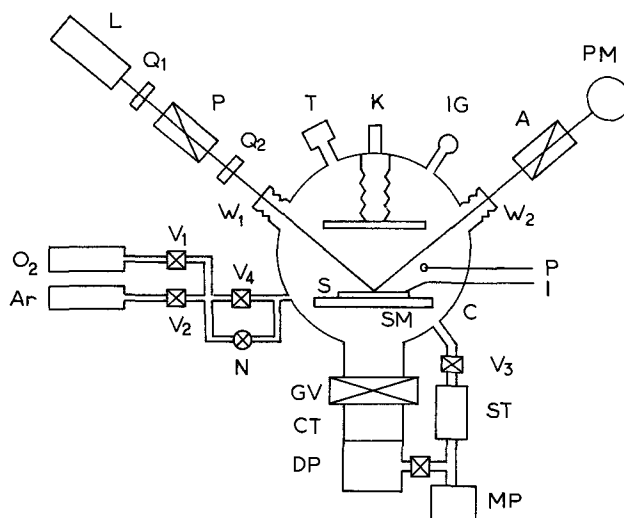


Fig. 1. Schematic diagram of the experimental arrangement. The components are: laser (L), two quarter-wave plates ( $Q_1$ ,  $Q_2$ ), polarizer (P), analyzer (A), photomultiplier (PM), sample (S), sample mount (SM), windows (W), drive current wire (I), voltage probe (V), vacuum chamber (C), valves (V), needle valve (N), gate valve (GV), sorption trap (ST), liquid nitrogen cold trap (CT), mechanical pump (MP), diffusion pump (DP), thermocouple gauge (T), ionization gauge (IG), and the glow discharge cathode (K).

<sup>1</sup> Present address: Department of Physics, University of Waterloo, Waterloo, Ontario, Canada.

Key words: ellipsometry, tantalum, oxidation, plasma.

The vacuum chamber, C, can be evacuated to  $10^{-3}$  Torr by a mechanical pump, MP, connected through a sorption trap, ST, to eliminate the possibility of hydrocarbon contamination, and the valve, V3. To attain pressures of  $10^{-7}$  Torr, *e.g.*, for evaporation of a thin-film sample, the chamber, C, can be pumped by a diffusion pump, DP, through a liquid nitrogen cooled cold trap, CT, and a gate valve, GV. Pressures higher than  $10^{-3}$  Torr are measured with a thermocouple gauge, T, and pressures lower than  $10^{-3}$  Torr are measured with an ionization gauge, IG. Oxygen or argon gas can be leaked into the vacuum chamber while being pumped out through valve V3 via the mechanical pump so that a constant pressure in the  $10^{-3}$ - $10^{-1}$  Torr range can be maintained dynamically under flow conditions.

The cathode, K, for the glow discharge is mounted on a high voltage feed-through and consists of an aluminum plate, 10 by 4 by 0.5 cm covered with a 0.1 mm tantalum foil, with the 40 cm<sup>2</sup> face of the plate facing the sample which is 8 cm away. The cathode is normally operated at between -600 and -1000V during plasma oxidation. A wire, I, which is insulated throughout its length as it passes through the vacuum space from a feed-through to the sample where it makes contact, is used to supply current to the sample and to measure its voltage during plasma oxidation. A Au probe, P, located close to the sample was used to measure the voltage of the plasma adjacent to the sample. The intent was to use the voltage measured with the wire I and the voltage measured with the probe P to arrive at the voltage across the oxide, but this is not too reliable a procedure, since one cannot be sure that the voltage measured with the probe P is really the voltage at the oxide-plasma interface.

One of the main differences in experimental technique between the present measurements and those of previous investigators besides the use of an automated ellipsometer, concerns the location of the glow discharge electrode, K, relative to the sample, S. In the pioneering work of Miles and Smith (1), the glow discharge electrode was an aluminum wire circular loop located so that the front face of the sample was facing away from the source of the plasma. Initially we tried an electrode arrangement similar to that of Miles and Smith. However, we found that the resulting glow discharge was very weak and nonuniform, so that the growth of the oxide, which could be observed directly with the ellipsometer, was very slow. If the cathode voltage was increased sufficiently, the plasma density increased and the plasma oxidation process speeded up, but the whole vacuum system, and in particular the cathode, became hot and the glow discharge changed color suggesting that impurities were being released. The P,A readings of the oxide being grown, by comparison with later results, confirmed that the oxide was being contaminated with impurities. We decided to try a cathode with a flat plate geometry located directly in front of the sample, and this certainly produced a strong uniform plasma between the cathode and the sample as was expected. Initially we tried a cathode consisting of an aluminum plate 10 by 4 by 0.5 cm thick.

The objections in the literature to the sample seeing the source of the plasma are, first, that material sputtered directly or reactively from the cathode will contaminate the oxide being grown (7), and second, that ion bombardment from the cathode will sputter etch the anodic oxide being formed and limit the maximum oxide thickness attainable (8). With *in situ* measurements with an automated ellipsometer it was possible to test for both these effects.

To investigate the cathode sputtering proposal we evaporated a Au film onto a glass slide mounted on the sample mount and then tipped it up into the vertical position to make the optical measurements. We took P,A readings of the freshly prepared Au surface, and then we proceeded to observe the P,A readings

of the Au surface in an oxygen plasma produced by applying -1000V to the Al cathode. If Al was being sputtered off the cathode and reaching the gold film, then we would expect to see a gradual change in the P,A readings corresponding to a Au surface moving towards the P,A readings characteristic of an Al surface. If Al from the cathode were reaching the sample as an aluminum oxide layer due to reactive sputtering, then we should see the P,A readings trace out a loop as an aluminum oxide layer is deposited on the Au substrate. The result of this test was that, even when the Au sample was left in an oxygen glow discharge for several hours, we could detect no change in the initial P,A readings within the experimental error of a few steps of  $0.01^\circ$  in P and A. This corresponds to less than 1Å of aluminum oxide on the Au surface in the 15,000 sec needed to grow 1500Å of tantalum oxide in our actual experiment. We thus concluded that under our experimental operating conditions, sputtering from the cathode was not a problem as regards contamination of the growing oxide film.

In contrast, O'Hanlon (7) states that, with a sample a few centimeters from and facing the cathode he observed sputtering deposition rates of 2.5 Å/min and higher in the case of an Al cathode. He does not give details of how these deposition rates were measured or about the voltage of the cathode.

Although the Al cathode worked quite well, occasionally we saw a little flickering of the plasma at the surface of the cathode. We found that covering the aluminum cathode with a sheet of 0.1 mm Ta foil, so that no Al could be seen by the plasma, eliminated this flickering. Since Ta has an even lower sputtering rate than Al (8), we were reducing even further the possibility of any problem from sputtering. The ellipsometry test for cathode sputtering onto a Au surface was repeated with the Al cathode covered with the Ta foil, and the same results were obtained as for the bare Al cathode. The use of a thin Ta foil as the active cathode over the Al plate allowed us to make another check on the possibility of cathode sputtering.

After operating the cathode for a total running time of more than 2000 hr over a period of 9 months, during which the plasma oxidation of Ta and a number of other materials were studied, we measured the thickness of a part of the Ta foil exposed to the plasma. We compared it with the thickness of a part of the same Ta foil that was folded under so that it did not see the plasma, and with the thickness of a piece of Ta foil from the same roll. Within experimental accuracy of 1%, the thicknesses were all the same. In contrast, if the Ta were being removed from the foil at the rate of 2.5 Å/min as found by O'Hanlon for an Al cathode, we would have expected to find a 30% change in the foil thickness in 2000 hr. Naturally, weighing the foil before and after would have been an even more sensitive test, but unfortunately we did not weigh the foil before mounting it. However, we feel that this result together with the result of our ellipsometer test strongly support our conclusion that cathode sputtering and resultant oxide contamination is negligible with our experimental conditions.

Subsequent to the previously described tests, a neutron activation analysis has been carried out by R. Henkelmann, Institut Max Von Laue-Paul Langevin, in order to detect whether any Ta is sputtered from the cathode and incorporated into the growing oxide in our plasma oxidation experiments. We produced a 2000Å aluminum oxide film on a piece of bulk Al (Johnson-Matthey, 99.999% pure) in our experimental apparatus using the Al cathode covered with the sheet of 0.1 mm Ta foil. The neutron activation analysis was carried out on this Al + 2000Å aluminum oxide sample and a pure Al sample for comparison. The results indicate that the Ta concentration in the plasma grown aluminum oxide layer is below the level of detection, which is 0.1 atomic per cent (a/o) of the alu-

minum oxide, under the special circumstances of this measurement.

As mentioned earlier, the other problem supposedly connected with the sample seeing the cathode is the sputter etching of the anodic oxide due to energetic neutrals and/or negative ions emanating from the cathode striking the sample surface (9). To test the importance of this effect in our experimental arrangement, we applied a driving current to a sample, *e.g.*, a Ta foil, and grew an oxide up to some particular thickness, as measured by the P,A readings of our ellipsometer. Then the driving current was reduced to zero, but the sample was left exposed to the oxygen plasma, while the ellipsometer took readings. If the oxide were being sputter etched, we would have expected to see the P,A readings head towards the bare surface values as oxide was being removed. Although the sample was left for 1 hr in this condition there was no change in the P,A readings. Even when the sample was biased positively, but at a voltage less than that to which it had been grown, there was still no change in the P,A readings with time. A change of  $0.01^\circ$  in the P reading would have indicated a change of  $0.2\text{\AA}$  in the oxide thickness. The same type of experiments were performed on an aluminum oxide layer grown on an evaporated Al sample, with the same negative results. Of course, while our sample sees the cathode, the particular geometry may have helped to minimize this effect, since O'Hanlon (9) states that the sputtering yield is greatest for obliquely incident particles, and most of the ions coming from the cathode would be striking the sample approximately vertically. While this effect may be important for materials which are sputtered easily, with our geometry we have not observed the effect even for aluminum oxide in contrast to what has been reported in the literature (10).

The sample for the plasma oxidation study of Ta was a piece of 0.1 mm thick capacitor grade Ta sheet obtained from Metallwerke Plansee, Austria. The sample, with the drive current wire, I, spotwelded to it, was insulated from the sample holder by one sheet of mica and held in place with a covering sheet of mica. This top mica sheet has a rectangular hole, 9 by 18 mm, which defined the active area of the sample on which the oxide was grown. The mica sheets also shielded the edges of the sample from the plasma.

With the ellipsometer it was possible to test various treatments of the surface of the sample to find the one that gave the cleanest surface possible prior to growth of the plasma oxide. The criterion used was that the best surface treatment should produce the highest P reading possible and a stable A reading, because if the initial surface is pictured as a perfectly clean surface covered by a thin layer of oxide or dirt, the presence of this thin layer would act primarily to lower the P reading from its true "clean" value and shift the A value by a much smaller amount, either up or down depending on whether the layer was nonabsorbing or absorbing, respectively. A number of different surface treatments were tried, including mechanical polishing followed by electropolishing, but the best treatment was found to be heating the sample, without any prior surface treatment, to a white heat in a  $10^{-7}$  Torr vacuum. This was done by mounting a piece of the Ta foil in the evaporator section of the apparatus and passing a large current through the sample after the chamber had been pumped down to the low pressure. The sample was then cut out of this piece of cleaned Ta foil and mounted. P,A readings were taken before and after the system was pumped down. Then argon gas was admitted to a pressure of 0.05 Torr and a short glow cleaning was employed by putting  $-600\text{V}$  on the glow discharge cathode K. This glow cleaning did not change the P,A readings much but was just to ensure that no water or dust particles were on the sample. Typically, the

initial heat-treatment gave P,A readings of  $24.0^\circ$  and  $31.0^\circ$ , respectively, and the final Ar glow cleaning changed these values by a further  $0.1^\circ$ . After this cleaning technique, we certainly still had a thin oxide on the sample, because we saw no spontaneous oxidation when the oxygen was admitted to the cleaned sample (something that we saw in measurements on freshly evaporated Al films), but this cleaning process was very reproducible and we were able to allow for the still present thin oxide layer (probably not more than  $20\text{\AA}$ ) in our ellipsometer fit.

Once the surface had been cleaned, the argon was pumped out of the chamber. The chamber was then flushed several times with oxygen to ensure that all the argon was removed. Finally, a dynamic equilibrium was established with oxygen flowing into the chamber through the needle valve, N, and being pumped out with the mechanical pump, MP. The oxygen gas used was Air Liquide Grade N 48. During all this process, the automatic ellipsometer was taking readings that indicated that the state of the surface was not changing. Once the state of dynamic equilibrium of pressure was reached, the voltage was applied to the cathode and the constant drive current was injected into the sample to initiate the plasma oxidation.

Several runs were made with pressures in the range 0.05-0.07 Torr, cathode voltages between  $-800$  and  $-1000\text{V}$ , and drive currents between 5 and 15 mA. The data that we are presenting here were obtained with a pressure of 0.055 Torr, a cathode voltage of  $-900\text{V}$ , and a drive current of 10 mA. The automatic ellipsometer displayed the P,A readings digitally and these digital readings were recorded. In addition, digital to analog converters were used to convert the digital P,A readings to voltages proportional to the digital readings so that the curve in the P,A plane could be plotted directly on an X-Y recorder during the experimental run. The voltage of the sample and the voltage of the nearby probe in the plasma were measured and recorded during a run. The output of a digital clock, together with the constant value of the drive current being supplied to the sample, allowed the total charge,  $q$ , passed through the sample to be measured. Normally P,A readings were taken for a period of 15,000 sec to grow  $1500\text{\AA}$  of oxide, and with a time of approximately 5 sec to take a P and A reading we ended up with 3000 P,A points to characterize a run. At the end of a run, after the glow discharge and drive current had been stopped, final P,A readings were taken. Then the oxygen pressure was brought up to the atmospheric, and P,A readings were taken again and were found to be identical within experimental error.

## Results and Discussion

Figure 2 shows typical P,A data on the plasma oxidation of Ta as it appears on our X-Y recorder. The folding back of the P,A curve at  $P = 0$  is just the result of the fact that our digital to analog converters plot the absolute value of P or A, and so when P goes negative, the positive value  $-P$  is plotted. The steps

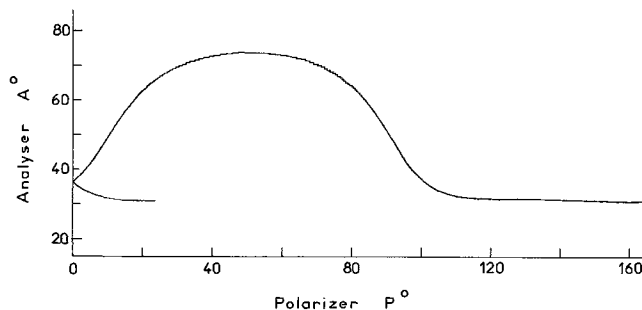


Fig. 2. Typical P,A data on the plasma oxidation of Ta as it appears on the X-Y recorder.

in the plot, which are most apparent at high A values, are just the result of the sequential way in which the P null value is updated and then the A null value is updated, with the X-Y recorder pen always in contact with the paper. The reproducibility of the data is so good that data from different runs can be superimposed on each other within the envelope given by the step structure. Indeed, if the step structure is removed by drawing a smooth curve through the midpoints of the steps, the smooth curves obtained from different runs fall almost exactly on top of each other.

To get the best fit to our experimental P,A data on the plasma oxidation of Ta shown in Fig. 2, we had to shift our bare surface P value from the experimentally measured value of  $24.0^\circ$  to  $25.6^\circ$  while leaving our bare surface A value at the experimentally measured value of  $31.3^\circ$ . This shift in the bare surface P value by  $1.6^\circ$  corresponds to the assumption that our surface treatment of the Ta sample left a  $20\text{\AA}$  layer of Ta oxide on the surface. This is certainly consistent with our observation that there was no spontaneous oxidation of the Ta surface when the oxygen was first admitted to the chamber after the final cleaning stage with the Ar glow discharge. Using initial P,A values of  $25.6^\circ$  and  $31.3^\circ$ , respectively, the index of refraction of Ta at  $6328\text{\AA}$  is found to be  $2.3 - i 2.6$ . The angle of incidence was  $59.5^\circ$ .

The P,A data of Fig. 2 could be fitted with an oxide of a constant, real, index of refraction of 2.21 growing on the bare Ta surface with initial P,A values of  $25.6^\circ$  and  $31.3^\circ$ , respectively. This fit was obtained initially by varying the index of refraction of the oxide in a standard ellipsometer program (5) while keeping all other parameters fixed, and determining the fit visually by superimposing the theoretical P,A curve plotted on one sheet of paper on the experimental P,A curve plotted on another sheet of paper. Doing this, we discovered the need to shift the initial value of P, representing the "true bare surface," by  $1.6^\circ$  otherwise the theoretical and experimental P,A curves were always displaced slightly from each other by a small amount in P. The fit obtained visually was checked later by an automatic nonlinear least squares fitting ellipsometer program which obtained the best fit between the experimental and theoretical curves by adjusting the real and imaginary parts of the index of refraction of the oxide film to minimize the least squares deviation between the experimental and theoretical values of P and A for a selected set of points on the experimental curve. Using this program, we found almost the same index of refraction for the Ta oxide film, i.e.,  $n = n_r - ik$ , with  $n_r = 2.215 \pm 0.015$  and  $k = 0.003 \pm 0.003$ . Since the error in k is as large as its value, we suggest that it is as valid to take k to be zero within experimental error.

Because a number of people presenting ellipsometer curves do so only in the form of  $\Delta$  and  $\psi$ , we have replotted our experimental data and the theoretical fit in this form and presented them in Fig. 3. In this form we can compare our results more directly with those of Lee *et al.* (4), who have made the only other ellipsometric study of the plasma oxidation of Ta. Our Fig. 3 should be compared with Fig. 3 of Lee *et al.* Their experimental data consist of 10 points that were taken with a manual ellipsometer, operating at  $5461\text{\AA}$  and at an angle of incidence of  $65^\circ$ , and the experimental points were probably taken by stopping the oxidation process at particular points to make ellipsometric measurements, although this is not stated. Our experimental data were obtained with an automated ellipsometer, operating at  $6328\text{\AA}$  and at an angle of incidence of  $59.5^\circ$ , that took data points at least every 5 sec while the oxidation process was proceeding at a constant sample driving current. Our experimental data are presented as a solid line through the approximately 3000 data points defining our curve.

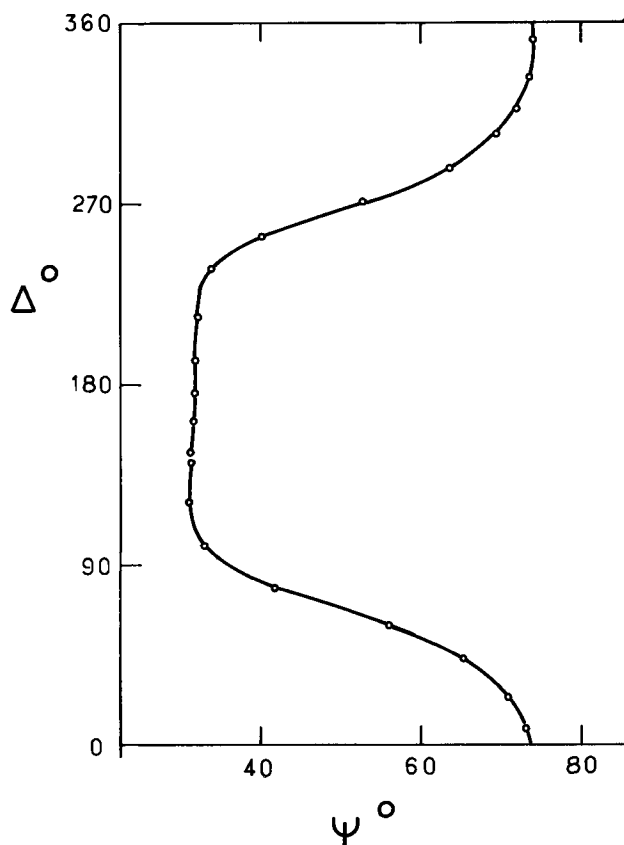


Fig. 3. Ellipsometric results for the plasma oxidation of Ta. The solid curve represents the experimental results and the open circles denote the theoretical fit obtained using a refractive index of 2.21 for the Ta oxide. Experimental conditions: sample area  $162\text{ mm}^2$ , constant drive current 10 mA, oxygen pressure 0.055 Torr, cathode voltage  $-900\text{V}$ , wavelength  $6328\text{\AA}$ , and angle of incidence  $59.5^\circ$ .

Lee *et al.* fitted their data with a model consisting of two layers: an outer layer with an index of 1.89 and an inner layer with an index of 2.22, with the outer layer comprising 43% of the total thickness of the two layers at any stage of the growth. Their fit is presented as a solid curve with the experimental data as superimposed points. As discussed earlier, we have been able to fit our ellipsometer data by a single uniform Ta oxide layer of index 2.21. For clarity, our theoretical fit is presented in Fig. 3 as a series of theoretical points superimposed on our solid experimental curve. In comparing the fit between our experimental curve and theoretical points with the fit between the theoretical curve and experimental points of Lee *et al.*, it is perhaps most revealing to note that in the regions where  $\psi$  is varying most rapidly, i.e.,  $60^\circ \cong \Delta \cong 0^\circ$  and  $360^\circ \cong \Delta \cong 280^\circ$ , Lee *et al.* in their Fig. 3 have only three experimental points and their theoretical fit passes through only two of them. From their theoretical fit it would appear that Lee *et al.* had a residual oxide layer of  $80\text{\AA}$  on their Ta sample after electropolishing, which is in agreement with our observations that electropolishing did not give as clean an initial surface as heating out the sample in a vacuum which left a residual oxide layer of only  $20\text{\AA}$ .

In Fig. 4 we present our electrical measurements during the growth of the plasma oxide on Ta in the form of plots of time, total charge passed,  $q$ , and sample voltage,  $V$ , vs. oxide thickness. As can be seen in Fig. 4 the time or  $q$  vs. oxide thickness plot is well represented by a straight line passing almost through the starting point ( $20\text{\AA}$  of residual oxide at  $t = 0$ ). The current efficiency,  $\eta$ , was calculated from Eq. [1] of Dell'Oca *et al.* (11), assuming that the oxide being formed is  $\text{Ta}_2\text{O}_5$  with a molecular weight of 442 and a density of  $8.7\text{ g/cm}^3$ . A value of  $\eta = 0.4\%$  was found



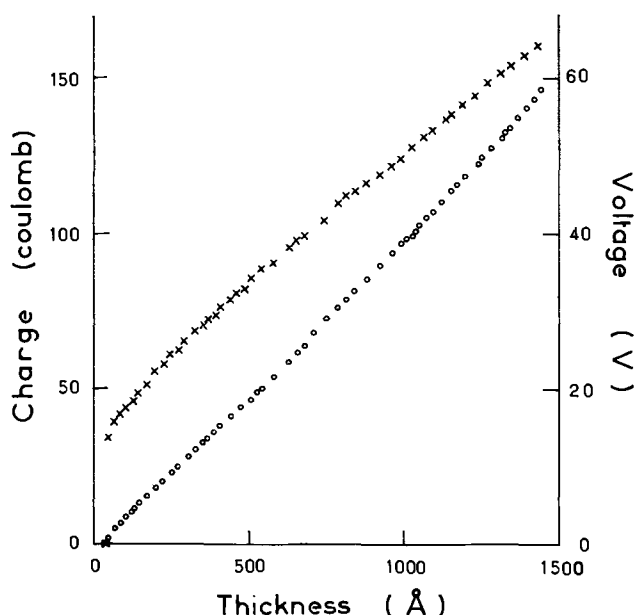


Fig. 4. Electrical measurements for the plasma oxidation of Ta. The open circles denote the total charge passed through the sample vs. the oxide thickness. The crosses denote the voltage of the sample with respect to a Au probe nearby in the plasma vs. the oxide thickness.

and this is consistent with the value of 0.5% found by Lee *et al.* The voltage  $V$  of the sample with respect to a Au probe nearby in the plasma can be seen in Fig. 4 to increase fairly quickly to a certain value at low thicknesses and then increase linearly with thickness thereafter. The interpretation of these voltage readings is complicated by the fact that it is not certain exactly what voltage is being measured by the probe in the plasma. Therefore it is difficult in Fig. 4 to separate the voltage across the oxide from the voltage drop in the plasma between the probe and the oxide-plasma interface. Since the voltage measured is so sensitive to the pressure, and this is apparently the cause of the scatter of the voltage readings in Fig. 4, we feel that the voltage drop in the plasma is a significant effect, and consequently it is dangerous to attempt to use such voltage measurements to obtain the voltage across the oxide layer.

We have not attempted to fit a model of oxide growth to our ellipsometric and electrical measurements. Since the current efficiency is so low, the ionic current, which is connected with oxide growth, is much smaller than the electron current, whose effect on oxide growth is unknown. The voltage measurements are affected by voltage drop in the plasma and also the electron current passing through the oxide, so it is difficult to determine what is the effective electric field in the oxide producing growth. We feel that at the present time with so many important quantities unknown, it would be meaningless to attempt to fit a model of oxide growth to our data. Perhaps in the

future it will be possible to improve the present techniques and supplement them with some other types of experiments to yield information on the unknown quantities, and thus make it fruitful to analyze plasma oxidation results in terms of a growth model.

In conclusion, we have shown that it is possible to grow a uniform Ta oxide layer, up to 1500Å in thickness, on a Ta foil by plasma oxidation with the sample facing the cathode. Our experimental results show that there is no significant contamination of the oxide due to sputtering from the cathode, as has been suggested by earlier investigators. Also, we find that there is no evidence for sputter etching of the oxide due to the cathode facing the sample. We have been able to fit our Ta oxide film with a single index of refraction of 2.21, in contrast to the work of Lee *et al.* who fitted their ellipsometric data with a double layer model, consisting of an outer layer of index 1.89 and an inner layer of index 2.22, with the outer layer comprising 43% of the total thickness of the two layers at any stage of the growth. Our electrical measurements, in conjunction with our ellipsometric results, show that the oxide grows at a constant rate and with a constant current efficiency of 0.4%. The sample voltage  $V$  also shows a linear dependence on thickness or time, after an initial jump.

#### Acknowledgments

The authors would like to thank Dr. R. Henkelmann of I.L.L. for carrying out the neutron activation analysis of the Al samples. One of the authors (J. D. L.) would like to thank M. Lacaze, Directeur C.R.T.B.T., for the financial assistance in bringing the author's equipment with him on his sabbatical leave, and all the members of the laboratory for their hospitality.

Manuscript submitted May 2, 1973; revised manuscript received July 16, 1973.

Any discussion of this paper will appear in a Discussion Section to be published in the December 1974 JOURNAL.

#### REFERENCES

1. J. L. Miles and P. H. Smith, *This Journal*, **110**, 1240 (1963).
2. T. A. Jennings and W. McNeill, *ibid.*, **114**, 1134 (1967).
3. D. Husted, L. Gruss, and T. Mackus, *ibid.*, **118**, 1989 (1971).
4. W. L. Lee, G. Olive, D. L. Pulfrey, and L. Young, *ibid.*, **117**, 1172 (1970).
5. F. L. McCrackin, E. Passaglia, R. R. Stromberg, and H. L. Steinberg, *J. Res. Natl. Bur. Std.*, **67A**, 363 (1963).
6. Similar to the ellipsometer described by J. L. Ord, *Surface Sci.*, **16**, 155 (1969).
7. J. F. O'Hanlon, *This Journal*, **118**, 270 (1971).
8. G. Carter and J. S. Colligon, "Ion Bombardment of Solids," p. 315, American Elsevier Publishing Company, New York (1968).
9. J. F. O'Hanlon, *Appl. Phys. Letters*, **14**, 127 (1969).
10. L. D. Locker and L. P. Skolnick, *ibid.*, **12**, 396 (1968).
11. C. J. Dell'Oca, D. L. Pulfrey, and L. Young, in "Physics of Thin Films," Vol. 6, M. H. Francombe and R. W. Hoffman, Editors, pp. 1-79, Academic Press, New York (1971).

# Effect of Chloride on Growth of an Anodic Film

J. Zahavi\* and M. Metzger\*

Department of Metallurgy and Mining Engineering and Materials Research Laboratory,  
University of Illinois at Urbana-Champaign, Urbana, Illinois 61801

## ABSTRACT

Al was anodized in 2.4M H<sub>2</sub>SO<sub>4</sub> at 5 mA/cm<sup>2</sup> and electronmicroscopic studies made of breakdown and formation of pits beneath the film after various surface treatments or after additions of up to 0.05M Cl<sup>-</sup> to the acid and selection of those specimens which had remained in the film-growth stage before stable pits grew. An electron-opacity technique was developed for studying film growth. Even in the absence of Cl<sup>-</sup>, there was a continued incidence of breakdown and a substantial time-dependent direct-dissolution current. With Cl<sup>-</sup>, cell voltage tended to be lower. Film formation efficiency and geometrical structure were correlated directly with average cell voltage and not directly with Cl<sup>-</sup> concentration. Cl<sup>-</sup> was interpreted as having only an indirect effect on film growth by stabilizing concurrent pit growth, which reduced the film-forming current. Possible modes of pitting beneath the film are discussed.

In a recent paper (1), the authors presented electronmicroscopic evidence that during galvanostatic anodizing of aluminum in sulfuric acid many small breakdown-repair (B-R) or breakdown-pitting-repair (B-P-R) events occurred at the base of the film concurrently with porous film growth and that these events were not generally associated with substrate lattice defects or impurity clusters. As part of a program concerned with the mechanism of pit initiation, this was followed in the present work by studies of: (i) the possible influence of the surface preparation on the incidence of breakdown and (ii) the effects of Cl<sup>-</sup> additions to the anodizing bath. The previous results and those of Part (i) directed attention not to the production by Cl<sup>-</sup> of breakdown, which occurred in its absence, but to its reduction of the effectiveness of repair. This might be due to an effect of Cl<sup>-</sup> on film growth rate or structure. Conditions favorable for examining this question were obtained by adjusting the Cl<sup>-</sup> concentration in the bath to the highest level at which film growth would not be immediately short-circuited by growth of optically visible stable pits. Observations had been made identifying the transition in behavior with increasing Cl<sup>-</sup> concentration (2).

The surface treatment before anodizing was of concern specifically because with the perchloric acid-ethanol electropolishing bath employed a residual film was known to be present after rinsing and this film presumably contained Cl, which has been detected by Auger analysis on surfaces polished in this bath (3). Such surfaces have been reported to yield films of low ionic resistance after forming (4).

The processes occurring in this system were such that the microtopographic features most accessible to observation were not those of growing pits but those of repair zones in the film and of the pore structure at various stages of growth. Comparisons were effectively made by examining the film after anodizing times at which it contained evidence of the previous occurrence of a high density of small (~0.1 μm) B-P-R or B-R "events," and the nature of the geometry deduced is illustrated schematically in Fig. 1 for one type of B-P-R (no implication is intended concerning the mechanism of pit initiation). The events occurred at the base of the film and were not evident in external-surface replicas. The projecting regions of repair film seen in film-underside replicas were prominent for recent events, but the ones which had occurred substantially before the time of observation had become shallower in the course of continuing general film

growth although tending to remain visible in transmission because of the alteration of the local pore structure. In addition to these events, the film showed a much lower density of larger open repaired pits usually 1/2-1 μm across.

In the present work, the apparent effect of Cl<sup>-</sup> was not to alter the basic character of the processes occurring but to increase the portion of the charge passed going to metal dissolution rather than film growth. The magnitude of the direct dissolution current associated with pitting in B-P-R events and growing pits could not be readily determined through microscopy, but over-all formation efficiency was investigated by measuring the electron opacities of the films, which give a measure of their relative mass-thicknesses. Opacity techniques have been employed effectively for studying amorphous-film growth (4) as well as for other purposes such as measurement of gas pressure in an environmental chamber (5).

## Experimental

As in a previous paper (1), coarse-grained sheet specimens of 99.999% Al (Lot III-A) were anodized for 10-900 sec at 5 mA/cm<sup>2</sup> in 2.4M H<sub>2</sub>SO<sub>4</sub> at 25.0° ± 0.2°C in a stirred bath with a Pt cathode. NaCl was added up to 0.1M.

*Surface preparation.*—The reference procedure as used previously (1) included etching off the oxide film from annealing in 10% HF, electropolishing at 0.1 A/cm<sup>2</sup> in 20 volume per cent (v/o) 70% HClO<sub>4</sub> in ethanol at -10° to -15°C and rinsing with a jet of ethanol (treatment A). This provided a featureless or almost featureless surface which facilitated observation of B-R, B-P-R, or stable pitting events and of any possible associations with structural features of the substrate such as grain boundaries (1, 2); it had been used earlier in examining the structure-related free-corrosion behavior of this material (6). HClO<sub>4</sub> electropolishing baths have also been used in several major studies of the classical pore structure (7, 8). To investigate whether ClO<sub>4</sub><sup>-</sup> or other ions containing Cl present in the residual film influence subsequent film formation, two approaches were made. The first was to remove the electropolishing film by either (B) a 2 min etch in 10% HF at 24°C or (C) use of the film stripping solution containing 35 ml 85% H<sub>3</sub>PO<sub>4</sub> and 20g CrO<sub>3</sub> per liter at 80°C for 4.5 min. The second was to avoid exposure to ClO<sub>4</sub><sup>-</sup> or F<sup>-</sup> by giving no treatment other than (D) a chemical polish at 85°C for 3 min in a solution containing 150 ml of 96% H<sub>2</sub>SO<sub>4</sub>, 800 ml of 85% H<sub>3</sub>PO<sub>4</sub>, and 50 ml of 70% HNO<sub>3</sub> or (E) an etch in 1M NaOH for 35 min at 25°C and a 1 sec dip in 50%

\* Electrochemical Society Active Member.

Key words: film growth, pitting, aluminum, chloride, electron opacity.

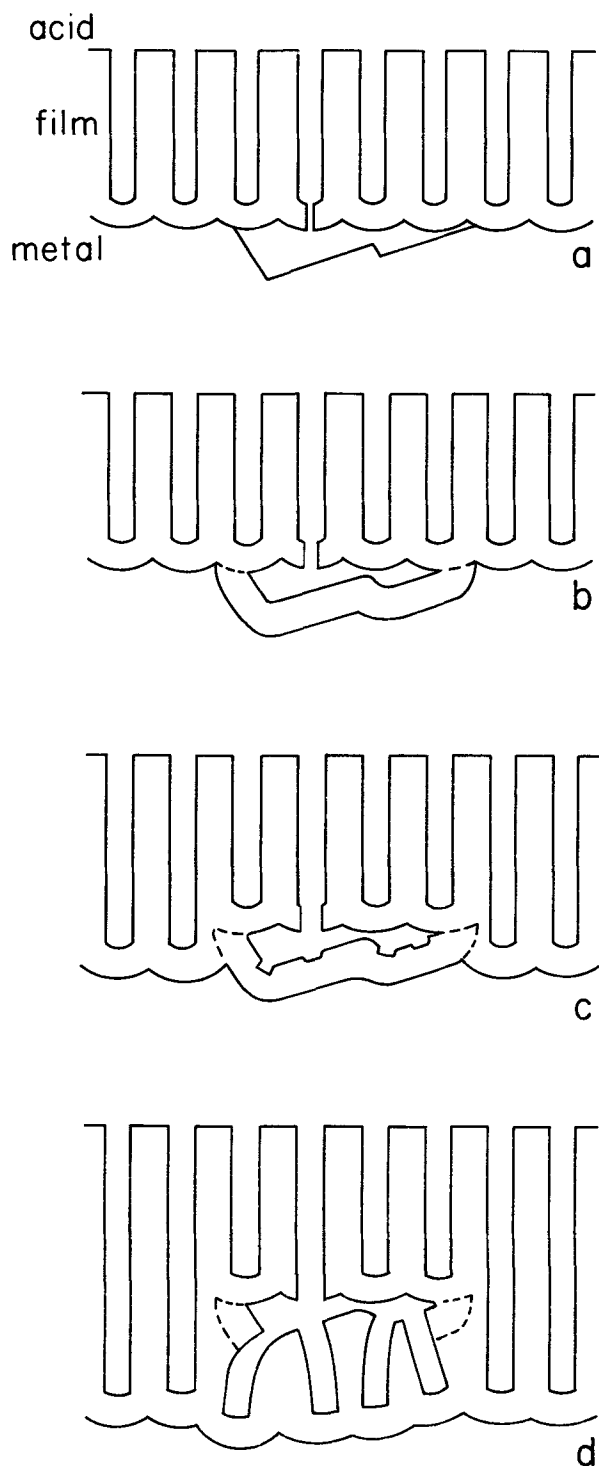


Fig. 1. Schematic of type 2 pitting repair. (a) Small geometric pit grows rapidly, (b) film just after reanodization of pit surface, (c) initiation of pores in the repair film and continuation of film growth at the other pores, (d) film growth now proceeding over the whole front.

$\text{HNO}_3$  at  $70^\circ\text{C}$  [(E) is based on a recommended alternative to electropolishing (4) but was modified to ensure removal of the annealing film]. The final step in each case was a distilled water rinse. A change in surface treatment necessarily introduces the possibility of surface contamination by ions other than  $\text{ClO}_4^-$ , even with reagent grade chemicals. (B) and (D) (and the distilled water supply) had been evaluated and found acceptable earlier in corrosion studies sensitive to metallic ion contamination (6, 9). A recent note on some Auger studies did not report contamination from  $\text{NaOH}$  or  $\text{HNO}_3$  treatments [as in (E)] but indicated

that (C), while removing most or all of the  $\text{Cl}$ , leaves detectable amounts of  $\text{P}$  and  $\text{Cr}$  (3).

**Electron microscopy.**—Several samples were taken from each specimen to permit observations in different grains. Certain B-P-R events occurring in films formed for  $t > 25$  sec were displayed strongly in transmission of the detached film, which normally remained thin enough up to approximately 150 sec, and this mode of observation was especially suited to making comparisons. Carbon replicas, preshadowed lightly with  $\text{Pt}$  at  $35^\circ$ – $45^\circ$ , were taken of film external surface, of film underside, and of the metal surface exposed by removing the anodic film with the  $\text{H}_3\text{PO}_4$ – $\text{CrO}_3$  solution used in treatment (C). Because even a slight attack on the metal by this solution could have produced significant extraneous features, the metal–film interface was examined mainly on the film underside. High magnification transmission studies of pore structure were made with special attention to defining focus (to avoid phase-contrast effects) in a series of through-focus photographs. At the time of examination, the films appeared “amorphous” by electron diffraction. Thus any crystals of precipitate, such as  $\text{Al}_2(\text{SO}_4)_3$ , which were still trapped in a repaired pit at the termination of anodizing had been dissolved during the thorough washing.

**Electron opacity.**—This can be measured in the electron microscope in several ways, the empirical coefficient which relates it to the mass-thickness of amorphous film depending on the method and instrumental factors. The opacity  $\alpha$  is  $\ln(I_o/I_c)$ , where  $I_o$  is the incident current and  $I_c$  is that part of the emergent current collected by the technique employed. One method makes use of a Faraday cage below the specimen (4) and this collects the undeviated beam plus the beam scattered within the aperture of the cage. What was measured in the present work was the current absorbed by the specimen,  $I_{ab}$ . In this case  $I_c$  is obtained by difference as  $I_o - I_{ab}$  and is the total emergent current. Measurements were made with a HU-11A microscope at 100 kV by substituting in the specimen chamber a current measuring specimen holder (CMSH) built by R. J. Anderson. This was insulated from the column and grounded through an electrometer, which read  $I_{ab}$ . The geometry of the CMSH was such that it effectively functioned as a Faraday cage when the beam was intercepted by an opaque object, such as an anodized  $500 \mu\text{m}$  aluminum disk or a crossbar of the grid on which the specimen film was mounted. Either of these gave the same beam current  $I_o$  as was read when a conventional Faraday cage was substituted for the CMSH. It was essential to combine the measurements with microscopy of the film to provide assurance that the opacity was being determined in a region of the film free from folds, cracks, or other defects. This was done as follows. A suitable area of film ( $\approx 7 \mu\text{m}$  diam) having been selected after scanning the neighborhood, the objective aperture was retracted (to avoid electron backscatter to the CMSH) and the second condenser current adjusted to the setting giving the beam C.D. ( $\approx 50 \text{ mA}/\text{cm}^2$ ) used for opacity measurements.  $I_{ab}$  was then read, the CMSH immediately displaced so that the beam intercepted a grid bar, and  $I_o$  read at several positions. This allowed the  $I_o$  corresponding to each reading of  $I_{ab}$  to be determined without being influenced by drift in the instrument and with greater precision than could be achieved merely from a predetermined calibration of  $I_o$  vs. second condenser current. The procedure was then repeated in different regions of the film. The opacity technique reveals variations in local mass-thickness not indicated by other methods of measuring thickness, e.g., weighing. The instrument’s anticontamination devices were found adequate to prevent buildup of significant contamination layers in the irradiated area.

With the opacity calculated from

$$\alpha = \ln[I_o/(I_o - I_{ab})] \quad [1]$$

the fractional error is

$$\Delta\alpha/\alpha = [-(\Delta I_o/I_o) + (\Delta I_{ab}/I_{ab})] I_{ab}/(I_o - I_{ab})\alpha \quad [2]$$

and is lowest at low opacity. In the low opacity approximation,  $\alpha \approx I_{ab}/I_o \ll 1$ , Eq. [2] simplifies to

$$\Delta\alpha/\alpha \approx -(\Delta I_o/I_o) + (\Delta I_{ab}/I_{ab}) \quad [3]$$

and this expression can be used up to the highest opacity measured, 0.28, at which it differs from the exact expression by only 15%. The short-time stability of  $I_o$  and  $I_{ab}$  was good and the Keithley 610B electrometer (accuracy 2%) could be read to better than 1%, so that from Eq. [3] the measurement of  $\alpha$  had precision 2% and accuracy 4% independent of  $\alpha$  over the range covered.

In the Appendix, the significance of the technique is discussed further and an analysis presented for the opacity of a porous film.

### Results and Discussion

**Surface preparation.**—Cell voltage-time curves for specimens subjected to the different surface treatments are given in Fig. 2a and b. Except for treatment (C), most differences in the curves fell within the range of variation of replicate runs with the same treatment and systematic differences worthy of comment were not apparent. The steady-state voltages at  $t > 50$  sec exhibited in  $>50$  runs with (A) ranged from 6.5 to 7.6V, and the values for (B), (D), and (E) fell within this range. In the case of (C), there was more variation from run to run. The plateau voltage tended to be lower and ranged from 7.6 to 4.9V. The initial voltage rise was usually distinctly faster, as in Fig. 2b, although sometimes the same.

The thickness and the structure of the film varied with surface treatment to a minor degree at most, and these aspects are discussed later together with the observations on films formed in acid containing  $\text{Cl}^-$ . In this section, consideration is given to the specific question whether B-P-R events occur with the same frequency, intensity, and apparent character after treatments (B)-(E) as after (A). The evidence pertinent to this question is illustrated concisely in low magnification transmission micrographs, where recent "events" appear as dark patches. Some examples for films formed in 2.4M  $\text{H}_2\text{SO}_4$  after different surface treatments are given in Fig. 3a, c, d (25 sec anodizing), Fig. 4a, b, c (84 sec), and Fig. 5a, b (150 sec) (the average plateau voltage,  $\bar{V}$ , has been given in these figures for later reference). These figures illustrate the result that for all treatments the events began only after about 25 sec and varied with time in a rather similar manner. The widely scattered holes in the film, as shown for (A) in Fig. 3a, represented the positions of some

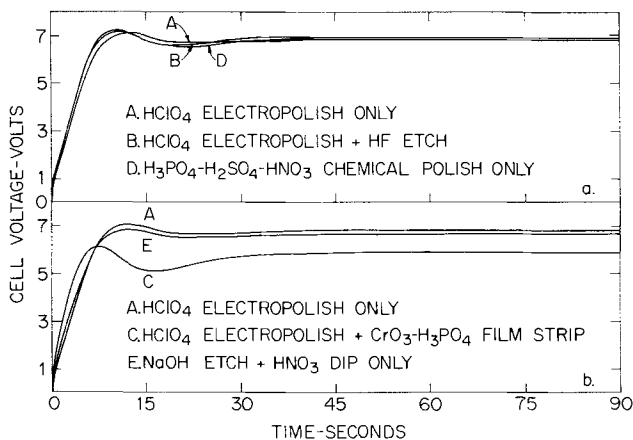


Fig. 2. Cell voltage time in 2.4M  $\text{H}_2\text{SO}_4$  for various surface treatments.

transient  $\sim 1/2 \mu\text{m}$  pits formed during anodizing and were found with all treatments.

The typical appearance of the events for the several surfaces may have been slightly different, to about the degree illustrated in Fig. 3a, c, d; Fig. 4a, b, c; and Fig. 5a, b. Any such differences were never much greater than those in any one specimen from one grain to an-

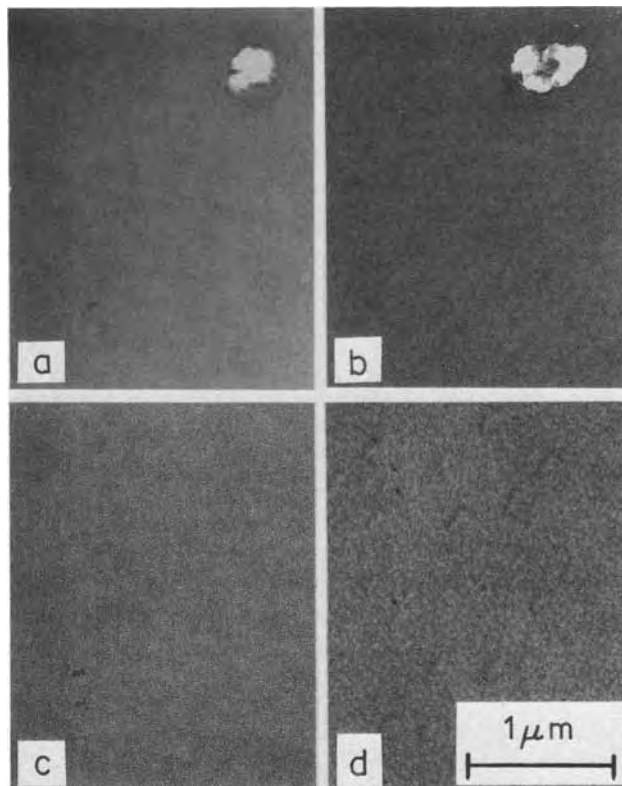


Fig. 3. Low density of events in transmission micrographs of 25 sec films. (a) Treatment A:  $\bar{V} = 7.0\text{V}$ . (b) Treatment A: 0.01M  $\text{Cl}^-$  added;  $\bar{V} = 6.4\text{V}$ . (c) Treatment B:  $\bar{V} = 6.9\text{V}$ . (d) Treatment C:  $\bar{V} = 5.8\text{V}$ .

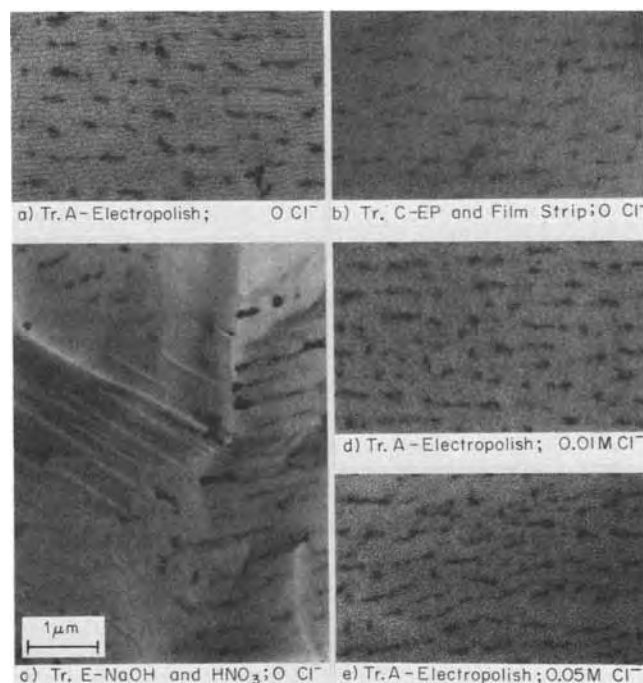


Fig. 4. Similarity of events in transmission micrographs of 84 sec films formed at relatively high plateau voltages under various conditions.  $\bar{V}$  was (a) 7.1V, (b) 6.7V, (c) 6.6V, (d) 5.9V, (e) 6.8V.

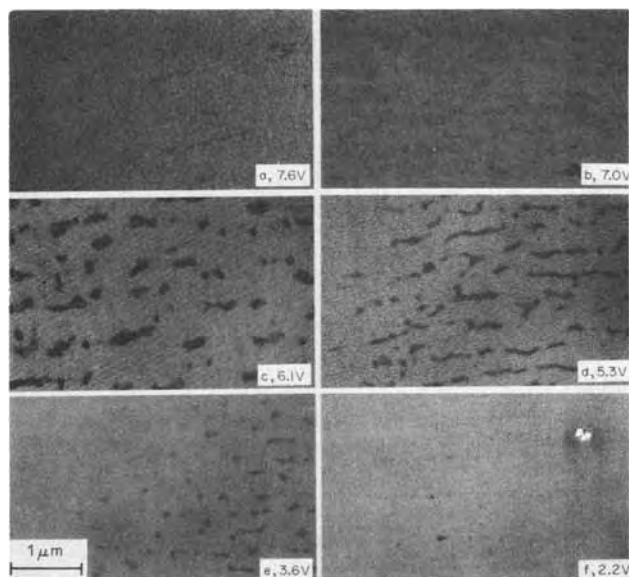


Fig. 5. Appearance of events in 150 sec films as a function of average plateau voltage,  $\bar{V}$ . (a) and (b), 0  $\text{Cl}^-$ ; (c)-(f), 0.01M  $\text{Cl}^-$ . Treatment A was used except for (b) which was given treatment (B).

other. In replica studies, no substantial differences were noted. It was concluded that events of the same general character occurred with roughly the same frequency for all surface treatments examined and thus that the high incidence of breakdown originally noted with treatment (A) (1) was not the result of special conditioning of the surface by this treatment but was an intrinsic characteristic of film growth under the present conditions.

Apart from the events, the anodic film replicated the original surface. The granular or furrow structure (dimensions  $\sim 0.1 \mu\text{m}$ ) characteristically produced by  $\text{HClO}_4$  electropolishing baths (10) was visible to a varying degree, e.g., Fig. 4a, and this was not altered by stripping the electropolishing film with treatment (C), Fig. 3d and 4b. This treatment tended to produce some shallow pits  $\leq 0.3 \mu\text{m}$  across, as replicated in Fig. 3d. The granular structure was no longer visible after the HF etch employed in (B), Figs. 3c and 5b, because this etch removes  $\leq 1 \mu\text{m}$  of metal (it also produces scattered shallow pits which do not appear in these fields) (11).

Treatment (E) was the only one yielding a surface with asperities sufficient to examine their possible influence on breakdown (12, 13). In this surface, the NaOH etch had produced craters with large smooth areas on which some geometric etching was superimposed, as replicated by the anodic film in Fig. 4c. It can be seen in this figure that most of the events were associated with smooth areas of the surface, and that most of the asperities, such as edges or corners of intersecting facets, had not given rise to events. Thus any influence of asperities on breakdown here appeared small in comparison with the breakdown tendencies intrinsic to flat surfaces.

**Effects of  $\text{Cl}^-$  additions.**—Simple electropolishing, treatment (A), was employed for further studies because it yielded a surface with a minimum of geometrical features and facilitated the observation of pits formed during anodizing.

The effect of adding  $\text{Cl}^-$  to the 2.4M  $\text{H}_2\text{SO}_4$  first became pronounced at 0.01M. At this level, pits did not grow to macroscopic size immediately but there was an initial period of film growth varying in duration from a few minutes to almost an hour. In this film-growth stage, the cell voltage varied considerably from one test to another and usually showed severe short-

and long-period fluctuations in the course of the test. Several examples are given in Fig. 6a. In comparison with the behavior without  $\text{Cl}^-$  additions (curve 1), the cell voltage often ran for a time in a similar manner at a slightly lower level (curve 2a) but more frequently ran from the start at a substantially lower level in a fluctuating fashion (curves 2b and 2c). Sometimes, a curve such as 2b would, after fluctuating severely in the 3-5V range during the first few minutes, drift upward and run with only mild fluctuations in the 5-6V range for a considerable period. A considerable voltage drop below 2V, as at the end of curve 2c, marked the growth of stable pits. With 0.05M  $\text{Cl}^-$ , an occasional specimen ran for a minute or two with a curve like 2b or 2a, but typically at 0.05M and 0.1M there was little or no film-growth stage, curve 3.

For studying the effect of  $\text{Cl}^-$  on film growth and structure, to obtain the highest concentration at which film growth was not immediately short-circuited by stable pitting, the  $\text{Cl}^-$  was set at 0.01M (to a limited extent 0.03M), many specimens were run various times, and from the  $V-t$  curves a selection was made of those which had remained in the film-growth stage throughout the anodizing. This normally included only curves which had not fallen, such as 2a and 2b in Fig. 6a, but two specimens with curves such as 2c, where the voltage had fallen at the very end of the run, were included to provide films formed at lower average voltages than were otherwise obtained.

An appropriate parameter for over-all characterization of the  $V-t$  curve was the average plateau voltage,  $\bar{V}$ . This was determined starting from the time of the voltage maximum (which provided the only suitable reference point near the plateau level) as indicated in Fig. 6b. Averaging cell voltage from  $t = 0$  would have given a misleading time-dependent index having lower values for short times just beyond the maximum even when the plateau was relatively flat. It is to be noted that although cell voltage eventually became constant for  $\bar{V} \geq 6\text{V}$ , this was achieved only after 40-50 sec anodizing, well beyond the voltage maximum at 7-13 sec (curves 1 and 2a of Fig. 6a, also Fig. 2).

**Rate of film growth by electron opacity.**—Large differences in opacity were found for films from different specimens formed for the same time with 0.01M  $\text{Cl}^-$  additions. Additional sampling and checking showed differences in opacity to be related consistently to differences in average plateau voltage,  $\bar{V}$ , during forming, and additional specimens anodized with various  $\text{Cl}^-$  concentrations or surface treatments were chosen to

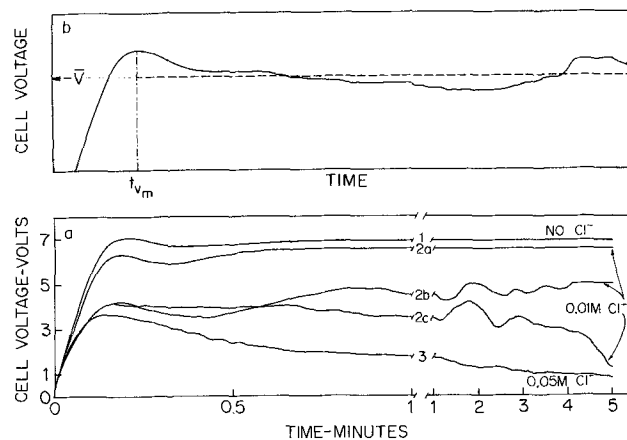


Fig. 6. (a) Cell voltage time in 2.4M  $\text{H}_2\text{SO}_4$  at 5  $\text{mA}/\text{cm}^2$  showing typical behavior without  $\text{Cl}^-$  (curve 1) and at 0.05M  $\text{Cl}^-$  (curve 3) and range of behavior exhibited at 0.01M  $\text{Cl}^-$  (curves 2a, 2b, 2c). (b) Schematic showing method of defining average plateau voltage,  $\bar{V}$ .

permit determination of opacity-time curves at various  $\bar{V}$ .

In any opacity measurement, the region of film sampled never included holes (as in Fig. 3a or b) or large ( $> 1/2 \mu\text{m}$ ) repaired pits, but the small B-P-R events (Fig. 4 and 5) were closely spaced so that the  $7 \mu\text{m}$  diameter beam necessarily included many of them, and the opacity was a measure of mass-thickness averaged over the main body of the film and the events in that region. The average opacity was typically determined from readings in ten regions in two grids with film patches taken from different parts of the specimen. The range of values in one grid overlapped that in others. The range in the sample of ten was as high as 16% of the average, and it was considered likely that the mean opacity determined here from a necessarily limited sample could deviate from the ideal mean opacity averaged over the whole area of the film by 10% or more.

Opacity vs.  $\bar{V}$  was studied primarily at 150, 300, and 900 sec and the data are given in Fig. 7. This plot was populated by first taking at each time electropolished specimens [treatment (A)] anodized either in acid without  $\text{Cl}^-$  additions at  $\bar{V}$  near 7V (open circles) or in acid with 0.01M  $\text{Cl}^-$  (half-filled circles) at various lower  $\bar{V}$ , the range of which was covered by anodizing many specimens and selecting appropriate ones for opacity measurement. For anodizing at other than 0.01M  $\text{Cl}^-$ , it was not possible to check the whole range of  $\bar{V}$  effectively, but individual examples could be run to find whether or not the films showed the same dependence of opacity on  $\bar{V}$ . These examples included one for 0.003M  $\text{Cl}^-$  (one-quarter filled circle), at which  $\bar{V}$  was always  $> 6\text{V}$ , two for 0.03M  $\text{Cl}^-$  (filled circles), at which  $\bar{V}$  varied but specimens rarely remained in the film-growth stage for times of interest, and several films formed in acid without  $\text{Cl}^-$  additions for 300 sec after treatments (B-E) (triangles, square, and diamond) and for 150 and 900 sec after treatment (B) (erect triangle). It can be seen in Fig. 7 that at each anodizing time the data for all conditions scatter around a single relation between opacity and  $\bar{V}$ . Thus, for example, in the 300 sec data opacities obtained with treatment (A) and 0.01M  $\text{Cl}^-$  at 3, 4-1/2, and 6-1/2V are close to opacities obtained near these  $\bar{V}$  with dif-

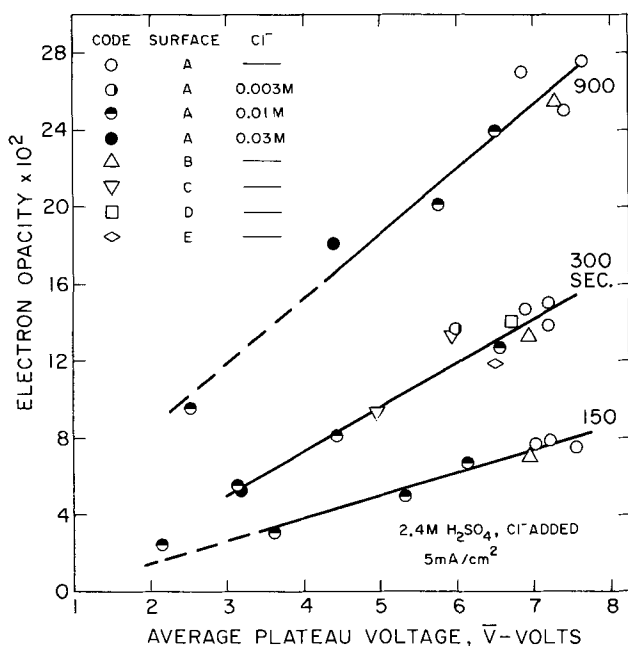


Fig. 7. Electron opacity vs. average plateau voltage for films formed 150, 300, and 900 sec under various conditions.

ferent surface treatments and/or different  $\text{Cl}^-$  levels. When all data were averaged, the relation between opacity and  $\bar{V}$  appeared to be linear and is so represented in Fig. 7. For  $V > 3\text{V}$ , the deviations of the points from the lines in Fig. 7 correspond to differences in opacity of less than 10% except for one difference of 13% and one of 15%. Most of this scatter was attributed to the sampling problem discussed above. This scatter completely overshadowed any differences which might have existed between specimens given different surface treatments and thus initially bearing films of different thickness. In the case of the electropolishing film (which was too fragile for a direct measurement), the opacity could be estimated from an extrapolation in Fig. A-1 of the Appendix as only  $\approx 0.002$ , so that any extra opacity in anodized treatment (A) specimens due to the persistence of the electropolishing film would not have been detectable in Fig. 7.

Opacity-time curves for various  $\bar{V}$  were constructed from values taken from the lines fitted to the data of Fig. 7 at 150, 300, and 900 sec and from some additional values at  $\bar{V}$  near 6 or 7V measured in specimens anodized 25 and 84 sec, Fig. 8. The behavior in unmodified  $\text{H}_2\text{SO}_4$ , which can be compared with other studies, is shown in the 7V data, and the formation efficiency vs. time was analyzed for these as discussed below.

*Film-formation efficiency.*—Cherki and Siejka (14) have most recently considered how the current (or charge) per unit area passed through the cell,  $I_{\text{tot}}$  (or  $Q_{\text{tot}}$ ), is partitioned, and their notation is used here. If the quantity of porous film present corresponds to charge  $Q_{\text{ox}}$ , then all losses are grouped as  $Q_{\text{diss}} = Q_{\text{tot}} - Q_{\text{ox}}$ . The electronic current can be assumed negligible in cases of interest here [so that  $Q_{\text{diss}}$  is determinable from the  $\text{Al}^{3+}$  in the acid and is the quantity measured by certain workers (15, 16)].  $Q_{\text{diss}}$  includes  $Q_{\text{dec}}$  which formed the oxide previously in pores and which was electrochemically decomposed [“field-assisted dissolution” at pore bases (17)] in the course of pore growth,  $Q_{\text{ch}}$  from the oxide subsequently lost by purely chemical dissolution from pore walls and film external surface, and  $Q_{\text{Al}}$  the charge associated with direct transport of cations into solution (this never went to form oxide). Cherki and Siejka used nuclear microanalysis techniques to study films formed on Al at 10V in 1.5M  $\text{H}_2\text{SO}_4$  at 15°C. For the constant current stage of their anodizing, they found that  $I_{\text{diss}}$  was 0.47  $I_{\text{tot}}$  and was not time-dependent.  $I_{\text{ch}}$  having been found to be negligible for  $t \leq 600$  sec, and  $I_{\text{dec}}$  having been calculated from previous measurements of pore dimensions,  $I_{\text{Al}}$  was found by difference to be  $\approx 0.38 I_{\text{tot}}$ . The presence of a substantial direct-dissolution current had been pointed out earlier by Nagayama, Tamura, and Takahashi (16) under the name, “extra-dissolution (electrochemical) at the pore base.”

An exact treatment of these questions is not obtained from the opacity data, but certain conclusions of interest can be drawn from the 7V data in Fig. 8 with the aid of the formalism described in the Appendix relating opacity to the geometrical parameters of a classical porous film. The calculations are described in the Appendix and their applications noted here. It was convenient to use as a reference the calculated  $\alpha$ -t curve of a film which continued to thicken, at its initial rate, by simple pore lengthening (allowance for  $Q_{\text{dec}}$  thus being built into the model). The initial thickening rate was derived from the early part of the experimental 7V curve and a hypothetical  $\alpha$ -t curve calculated for continued pore lengthening at this rate. This curve was insensitive to reasonable variations in the values of the parameters employed in the fit, and it is shown in Fig. 8. That the experimental curve fell increasingly below this calculated curve after about 84 sec indicated that losses from  $Q_{\text{ch}}$  and/or  $Q_{\text{Al}}$  became relatively important at longer times. The uncertainties

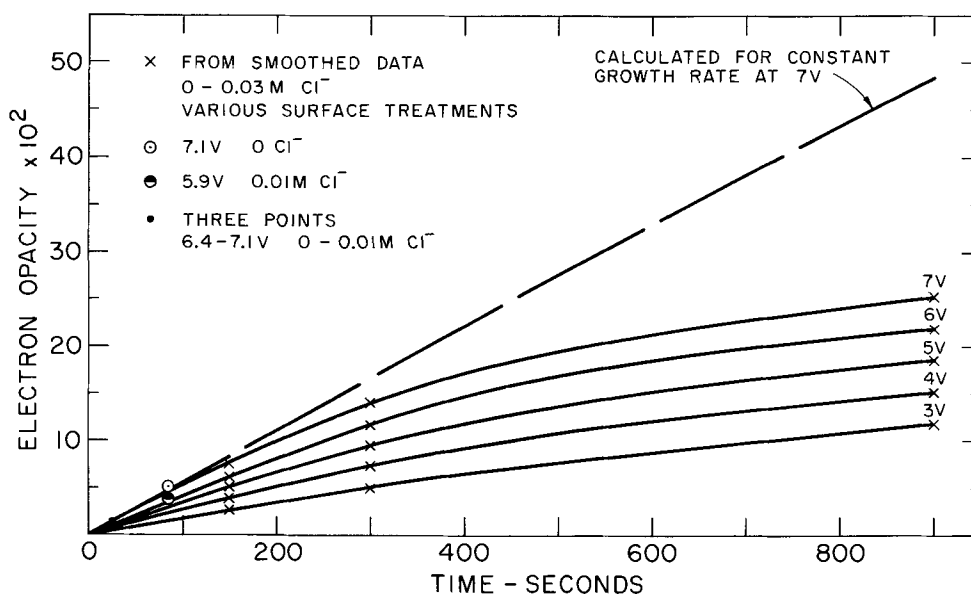


Fig. 8. Opacity time at several mean plateau voltages. The opacity of any film present at  $t = 0$  would not be visible on this scale. The dashed curve is a calculated curve for a 7V film which continued to grow at its initial rate.

of the present treatment are regarded as insufficient to place this conclusion in doubt. In particular, a non-classical distribution of pores should not have a major influence on the calculated opacity because in the low opacity range this depends only on mass-thickness, *i.e.*, on thickness and void volume fraction but not on void distribution (see Appendix).

At 900 sec, the measured 7V opacity in Fig. 8 was 48% of the calculated constant-thickening-rate value. The increasing difference between these curves may have been due to chemical dissolution, which always has negligible influence initially and becomes more important with time, and/or direct dissolution, which conceivably became more important at longer times in these experiments. For chemical dissolution, recent measurements have given linear dissolution rates from 0.75 Å/min (1M  $H_2SO_4$ , 27°C) (15) to 0.2 Å/min (1.5M, 15°C) (14) and 1 Å/min was taken as an upper limit for both pore-wall and external-surface dissolution. From the changes in film thickness and average pore area produced by this dissolution rate, the hypothetical 7V constant growth-rate opacity curve was recalculated to include the effect of chemical dissolution. Its effect was found to be small at times of interest, the hypothetical opacity being reduced at most by 2.2% at 300 sec and 8.4% at 900 sec. The major part of the 48% difference at 900 sec then had to be attributed to direct-dissolution processes,  $Q_{Al}(t)$ , which became relatively more important with time.

For films formed in solutions containing  $Cl^-$  at  $\bar{V} < 6V$ , the lower opacities cannot be attributed to an increased chemical-dissolution rate in view of results of Diggle *et al.* showing this rate to be comparable in  $SO_4^{2-}$  and  $Cl^-$  solutions at low pH (18). That the lower opacities of such films did not include a substantial loss from oxygen evolution in pits was indicated qualitatively by optical microscope observations of bubble evolution during anodizing (these also ruled out any substantial contribution to  $Q_{tot}$  from the hydrogen evolution possible in a pit beneath the film where the potential was momentarily low enough). Thus the lower opacities could be attributed only to a larger direct-dissolution loss,  $Q_{Al}/Q_{tot}$ .

The analysis cannot at present be extended with confidence from a relative to an absolute basis to yield values of the ratio  $Q_{Al}/Q_{tot}$  at various times. The early rate of porous film growth at 7V could be estimated from the data as 25 Å/sec by making use of the linear scattering coefficient determined for a compact film formed in borate solution, but the film formed in sulfuric acid differs in incorporating substantial quantities of  $SO_4^{2-}$  (14, 19) and may also differ in degree of hydration. Calculated formation rates for porous films

are subject to uncertainties related to their  $SO_4^{2-}$  content as discussed by Cherki and Siejka (14). It is sufficient here to point out that if the film were  $Al_2O_3$  of density 3.17 g/cm<sup>3</sup> forming at 5 mA/cm<sup>2</sup> at the highest possible efficiency ( $I_{Al} = I_{ch} = 0$ ) it would thicken at 27.2 Å/sec, so that the estimated 25 Å/sec is of acceptable magnitude.

The 7V opacity results indicated that  $Q_{Al}/Q_{tot}$  underwent a transition from some constant value to larger values after roughly 84 sec anodizing and that this ratio had a substantial value at 900 sec; there were too few points for analysis of its time dependence after the transition. Other evidence of a transition near this time was shown by the  $V-t$  curves, in which the cell voltage became constant after 40-50 sec, and by the electron microscopy, which revealed events occurring with high frequency in the period  $25 < t < 65$  sec and with much lower frequency thereafter. This transition did not represent pore initiation, which started as early as 5 sec and produced a well-developed pore structure no later than 15 sec.

The reason Cherki and Siejka (14) did not observe a transition in formation efficiency may have been that their analysis started only after 30 sec when the current became constant. Extensive studies of formation efficiency were made some years ago over ranges of C.D. (usually  $>5$  mA/cm<sup>2</sup>) temperature and  $H_2SO_4$  concentration (usually 1.5M) from the changes in specimen weight on forming and on stripping the film, the efficiency usually being given as the "coating ratio" (20-22). Because this ratio averages efficiency from the start of anodizing and because the first ratios obtained in these studies represented  $t \cong 1$  min, an early transition could not have been displayed distinctly in their plots. However, the plots did show coating ratios decreasing with time at relatively short times under conditions for which chemical-dissolution effects would be minimal and thus were broadly consistent with a time-dependent  $Q_{Al}/Q_{tot}$  as found here.

The previous workers (14, 16) were concerned to establish the existence of a substantial  $I_{Al}$  but did not examine its nature. Now  $I_{Al}$  conceivably originates in (i) a uniform direct-dissolution current,  $I_{Al-u}$ , across the intact barrier layer at the base of every pore (this current coexists with the currents in this layer producing growth) and/or (ii) a pitting current,  $I_{Al-p}$ . The latter is the average over the surface of the instantaneous rate of charge input to scattered transient or stable pits growing beneath the film through individual channels or cracks in the barrier layer providing paths of electrolyte extending to the metal (*e.g.*, as in Fig. 1). In principle, pit size and density hence total pit volume can be examined by microscopy. However,



pit dimensions and geometry in the present specimens did not permit determination of the extent to which pitting was responsible for low film formation efficiencies, as discussed below.

**Microscopic evidence of pitting.**—In the film-growth stage of anodizing, evidence was found for three categories of pits beneath the main film, as follows [the stable pits accompanying a fall in cell voltage in solutions containing  $\text{Cl}^-$  (2) are not dealt with here]:

1. Repaired open partly geometric pits mainly  $1/2$ - $1 \mu\text{m}$  across, some of which were visible relatively early in the anodizing (25 sec).

2. "Events" mainly  $\sim 0.1 \mu\text{m}$  across visible in the transmission micrographs (Fig. 4 and 5) thought to represent repaired shallow geometric and nongeometric pits beneath the film, many of which formed between 25 and 65 sec for  $\bar{V} \geq 6\text{V}$ .

3. Smooth broad and shallow pits beneath the film, apparently triggered by type 1 or 2 pits, which did not soon repair and which were generally not visible in the film structure or even prominent in the metal-surface topography.

The pitting here was time-dependent and complex and the processes in initiation, growth, and repair have not been established. Only the type 3 pits appeared able to persist long enough to account for a substantial direct-dissolution current,  $I_{\text{AI-p}}$ . The evidence discussed below pertains mainly to films formed at  $\bar{V} \geq 6\text{V}$ , for which many samples were available. Evidence pertaining to the film-substrate interface was preferably obtained from film-underside replicas because the  $\text{CrO}_3\text{-H}_3\text{PO}_4$  solution used to expose the metal surface for replication could introduce some shallow pits, as noted above and as has been mentioned by previous workers (23).

**Type 1.**—Figure 9a shows an external-surface replica of a 900 sec film in which the geometrically etched pit surface was visible. Here a patch of the pre-existing overlying film had been lost thus permitting direct replication of part of the pit surface, and the remainder of the pre-existing film had collapsed into the pit and conformed to the contours of the terraced pit surface thus permitting indirect replication of these contours. That the pit surface bore a repair film could be deduced from evidence of the pore mouths on the uncovered part of this surface similar to those on the main area of the external surface. Underside replicas, even for short anodizing times, showed the convex undersides of the repair film over pits, as in the region of a 25 sec film containing several repaired  $1/2 \mu\text{m}$  pits shown in Fig. 9b, indicating that pit growth was of short duration. The film overlying type 1 pits is thought generally to have cracked during anodizing (as in Fig. 9a) leaving the pit at least partly open. This is consistent with observations in transmission on detached films. In transmission, there was the possibility that additional damage to the film had occurred during detaching and washing. Thus, in 25 sec films usually only holes in the film were left, as in Fig. 3a and b. Apparently at this time the repair film was still too thin and fragile to survive the treatments used.

Note that Fig. 9a and b and 3a and b represent fields illustrating type 1 pits and are not typical fields. The density of these pits was perhaps  $\sim 10^2$  per  $\text{cm}^2$  for sulfuric acid anodizing and was not much greater when  $\text{Cl}^-$  had been added, and it is estimated that their formation had consumed a negligible fraction of  $Q_{\text{tot}}$ . This type of repaired pit was at least in part strongly geometric (Fig. 9a and b), which suggested an active dissolution mode. The low metal-surface potential required for this dissolution mode would not have been possible without large  $IR$  drops in the electrolyte. Even with a high local transient pitting current,  $IR$  drops of the magnitude required would be possible only if the pit had been fed initially through an extremely fine

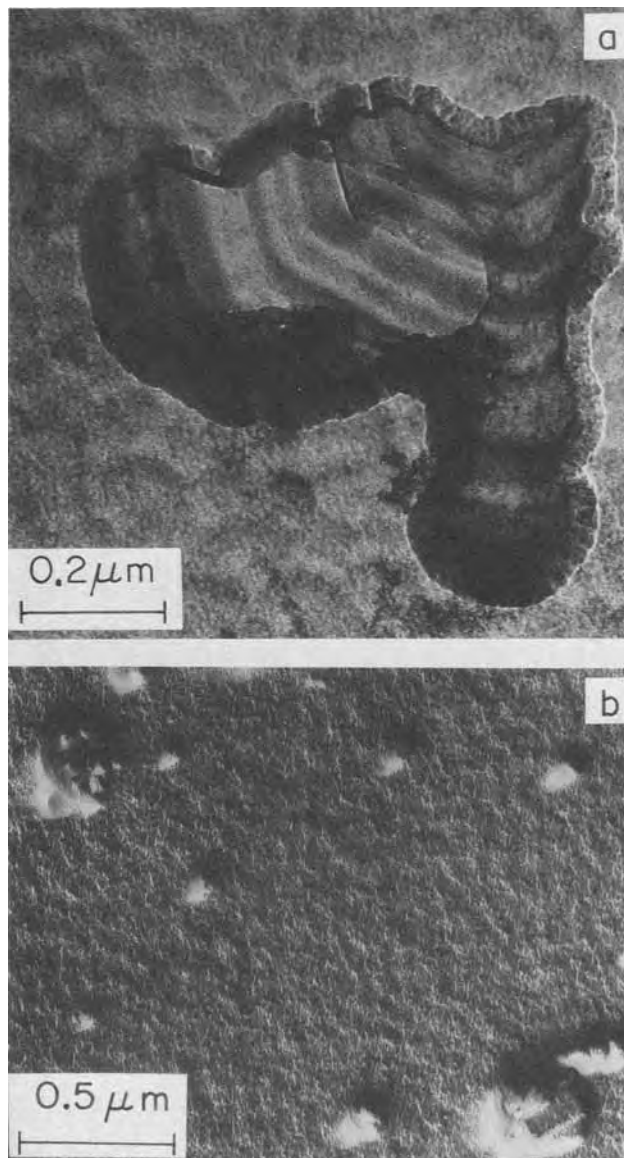


Fig. 9. Examples of type 1 pits ( $\sim 1/2 \mu\text{m}$  across) in specimens formed with  $0.01\text{M Cl}^-$  additions. (a) External-surface replica showing partly open repaired pit in 900 sec film.  $\bar{V} = 6.2\text{V}$ . (b) Film-underside replica of a region in a 25 sec film (shadowed with Au-Pd).  $\bar{V} = 5.7\text{V}$ .

channel or crack in the barrier layer. This situation would be unlikely to persist, the channel becoming enlarged or the overlying film becoming grossly cracked by one of several processes possible as the pit grew. The size of the  $IR$  drop would then have fallen sharply, thus returning the metal surface to a high potential and leading to repair (dispersion of the electrolyte in the pit may also have been important). This scheme would account for the transient nature of this mode of pitting.

**Type 2.**—The numerous "events" prominent in Fig. 4 and 5 were part of a sequence of phenomena which began after  $\geq 25$  sec anodizing (for  $\bar{V} \geq 6\text{V}$ ), these events themselves occurring with lower frequency for  $t > 65$  sec. There were also much smaller events, as discussed in the previous paper (1) in relation to individual pore appearance at high magnification in 25 sec films and diagnosed as B-R, but these are not discernible in the present micrographs and are not considered further here. Distinction between forms of B-R and of B-P-R, uncertain in earlier observations (1), now appears possible and an interpretation of the breakdown processes occurring and of the characteris-



tic arrangement of the events of Fig. 4 and 5 in stringers or streamers will be attempted in a later paper. An interpretation of the repaired geometric pitting aspect of these events is given in Fig. 1. This differs from type 1 pitting in that the pit was smaller and shallower and the overlying film was apparently intact except for a narrow path in the barrier layer assumed to be present although it was not identifiable in the electron micrographs. For example the external surface replica of a 900 sec film in Fig. 10 shows the undulant topography from the original electropolished surface and evidence of pore mouths but no indication of the processes which had occurred at the base of the film except for occasional patches of slightly different appearance (as at the upper center of Fig. 10), which may have represented part of the film overhanging a pit. Attention is directed below to the two kinds of evidence that the events in Fig. 4 and 5 were associated at least in part with pitting-repair:

1. The events as seen on the film underside tended to exhibit some angular or geometric character and no process appears capable of yielding this except repair of small geometric pits somewhat as represented in Fig. 1. Some examples from 300 sec film underside replicas are given in Fig. 11. For all conditions of anodizing (including various surface treatments, Fig. 11a and b, or anodizing in acid containing  $\text{Cl}^-$ , Fig. 11c) certain events had considerable angular or geometric character, and their outlines tended to lie in parallel directions as though they formed in the same substrate grain and had geometries related to the same crystal orientation. It is to be noted that although geometric character in an event is taken as evidence of pitting preceding repair, its absence does not establish that no pitting was involved.

2. The events were arranged in streaks running preferentially in certain directions, as in Fig. 4, and these were related to substrate orientation and changed direction at a grain boundary. Studies in progress in single crystals indicate that more than one factor is involved in the streaking, but one is a tendency for the streak to extend parallel to the surface trace of a  $\{100\}$  plane. Trenches growing along the surface in these directions have been observed during pitting of alumi-

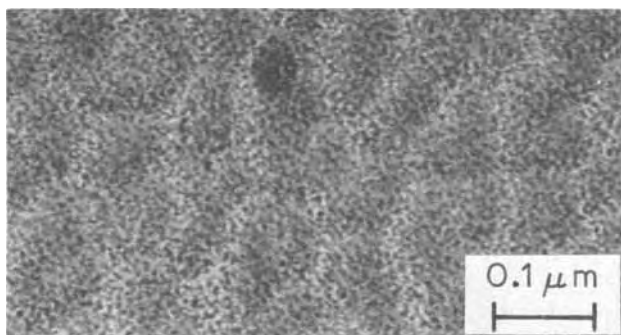


Fig. 10. External surface replica of a 900 sec film formed with  $0.01\text{M Cl}^-$  addition.  $\bar{V} = 6.2\text{V}$  Cf. Fig. 5b of Ref. (1).

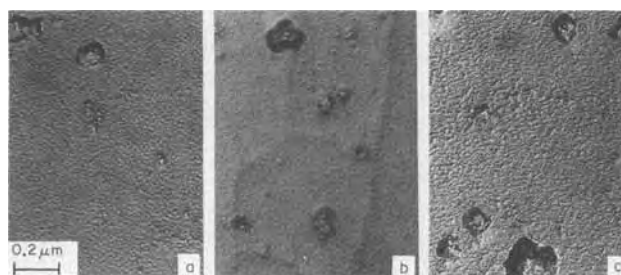


Fig. 11. Appearance of events in underside replicas of 300 sec films. (a)  $\text{NaOH-HNO}_3$  treatment (E),  $0 \text{ Cl}^-$ ,  $6.5\text{V}$ . (b) Chemical polish (D),  $0 \text{ Cl}^-$ ,  $6.7\text{V}$ . (c) Electropolish (A),  $0.01\text{M Cl}^-$ ,  $6.4\text{V}$ .

num in  $\text{HCl}$  solutions (24, 25). One also recalls the tunnel pits, in chloride solutions or tap water, growing in  $\langle 100 \rangle$  directions (26, 27).

The period of pit growth in the active dissolution mode implied by the geometric aspects of the events would have tended to be short because the severe constriction in the electrolyte path required for the large  $IR$  drop would be unlikely to persist, as discussed above for type 1 pits. It is also possible pit growth was interrupted by the inability of the acid to flow through the constriction at a sufficient rate. The pitting may have ceased through repair, or it may have continued in some other mode. There is evidence (for  $\bar{V} < 6\text{V}$ ) that some of the events were followed by a type 3 pitting not apparent in these micrographs, as discussed below. A feature of type 2 pits which may have been important was that the overlying film did not crack and the strongly occluded pit geometry (which permits an electrolyte of different character to develop within the pit) was retained. The basic character of type 2 and type 1 pits shown by microscopy did not appear altered by the presence of  $\text{Cl}^-$ .

Estimation of the charge consumed by type 2 pitting from the apparent volume of the shallow events was subject to considerable uncertainty, as seen from the interpretation of pitting-repair geometry in Fig. 1. After rapid growth to a certain size (Fig. 1a) there is reanodization of the pit surface, this occurring by constant-voltage anodizing while the system is on the plateau of the  $V-t$  curve. If this anodizing is tentatively idealized following Hoar and Yahalom (28), there is initially a rapid formation of a compact film of limiting thickness (Fig. 1b) followed by a stage of slow growth and pore formation associated with the minimum in the current-time curve (28). In this stage, continuing film growth at the bases of the other pores tends to level the film underside profile (Fig. 1c). A little later, film growth is again occurring over the whole front (Fig. 1d). At this point the event may not be prominent as a perturbation in the film underside or metal surface profile but may still be visible in transmission as a darker patch because of the nonalignment of old and new pores, the local pores having smaller apparent sizes or showing lower contrast. Thus, while occurrence of the event was readily detected and its lateral dimensions could be estimated, there was no way of establishing how much its depth had been reduced by film growth around it (Fig. 1b vs. 1d).

The most generous estimate possible of the total pit volume in visible events (using maximum depths observed in shadows on underside replicas) gave  $Q_{\text{Al}} \leq 0.1 Q_{\text{tot}}$  at 84 sec (just after the frequency of events declined) and a smaller fraction of  $Q_{\text{tot}}$  at longer times, so that the visible events themselves could not have been responsible for the substantial  $Q_{\text{Al}}/Q_{\text{tot}}$  at 900 sec indicated by the analysis of the opacity data.

**Type 3.**—A simplified geometry for a type of possibly more persistent pitting under the anodic film labeled type 3 is shown schematically in Fig. 12. It is assumed that this unrepaired pit is stabilized by what may be classified as an electropolishing film and that this is lost during film detaching or washing operations and is

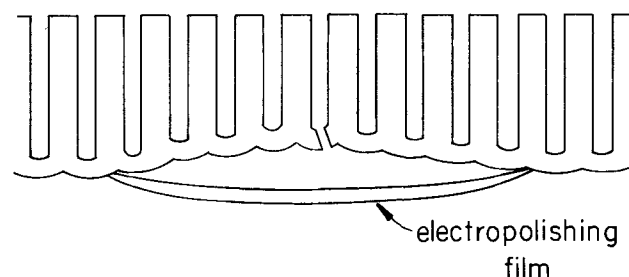


Fig. 12. Schematic geometry for a smooth pit spreading under the anodic film (type 3).

thus not detected in the electron micrographs. The distinctive features envisioned here are the smooth growth front and the spreading relatively slow growth. A shallow tapered depression is left in the anodic film underside through the progressive cessation of film growth as the pit spreads (this differs from Fig. 1a where pit growth in the active geometric mode is idealized as occurring so rapidly that there is negligible film growth in the interval). An unrepaired pit of the shape shown in Fig. 12 would be difficult to identify and characterize through replicas of metal surface and film underside because the topographic features are gently sloped, and the only feature favorable for observation is the tapering of the overlying film, which if sufficient could give rise to substantial contrast when the detached film was examined in transmission. Unambiguous evidence of this feature was not found in films formed at 7V for 300 or 900 sec, but Fig. 13 shows, in a film formed at 2.5V, a  $\sim 5 \mu\text{m}$  diameter area with the contrast expected. A number of such areas were visible in the films formed at lower  $\bar{V}$ , usually with a weaker photographic density gradient than the one in Fig. 13 indicative of a more gradual film thickness variation. In metal surface replicas some smooth craters consistent with Fig. 12 were noted but a positive characterization of all shallow surface features was not achieved. Evidence for the presence of unrepaired pits of significant extent was provided by testing for film adherence with replica tape, and it was found that patches of film could be removed, in accordance with Fig. 12. Repaired shallow type 3 pits could have been present incorporated into the film structure (analogous to Fig. 1) and not have been identifiable because with the pit shape visualized the patch of repair film would not at any stage appear as a prominent projection on the film underside. The question to what extent the charge  $Q_{\text{Al-p}}$  consumed in such pitting processes could have been responsible for the lower film formation efficiency for longer anodizing times at 7V or all anodizing times at lower  $\bar{V}$  cannot be answered directly from these observations.

The proposed type 3 is visualized as a possibly persistent mode of pitting which can be triggered by incompletely repaired type 1 or 2 pitting (not shown in Fig. 12) and which does not require a severely constricted electrolyte path and large  $IR$  drop. This is consistent with evidence such as that in Fig. 13 where the light area includes  $1/2 \mu\text{m}$  type 1 "repaired" pit which has a  $0.2 \mu\text{m}$  gap in the repair film at the bottom of the pit (not visible in this print). A type 3 pit conceivably grows in a transpassive "bright pitting" or

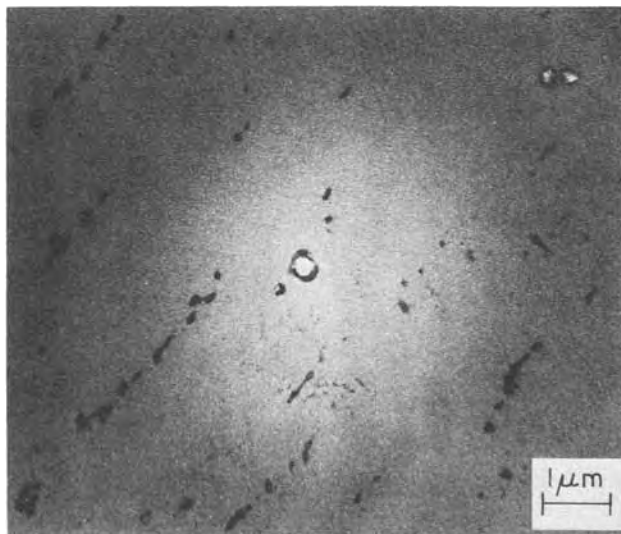


Fig. 13. Region of tapering film thickness in a film formed 900 sec in acid containing  $0.01\text{M Cl}^-$ .  $\bar{V} = 2.5\text{V}$ .

electrobrightening mode (29) [as occurs, for example, in electrochemical machining of Fe (30, 31)], the electropolishing film being stable in the special environment within the occluded pit. The change from crystallographic to brightened pits with increasing potential has been noted for Al in KCl solution (32).

*Effect of  $\text{Cl}^-$  on film growth and structure.*—The results of adding  $0.01\text{M Cl}^-$  to the anodizing bath were variable in that cell voltage tended to fluctuate with time and that  $\bar{V}$  and opacity varied from one run to another, and this behavior cannot be plausibly attributed to changes in a uniform direct-dissolution current. Therefore, the behavior with  $\text{Cl}^-$  is attributed to a greater persistence of the pitting processes concurrent with film growth, which are inherently variable, even though it was not possible to demonstrate this directly. It could not be concluded that  $\text{Cl}^-$  caused more persistent pitting by affecting film growth so as to inhibit repair, i.e., reanodization, of pits in view of the observation that films could grow at  $\bar{V} > 6\text{V}$  yielding opacities similar to those of films grown at  $0 \text{ Cl}^-$  and geometrical structures which were indistinguishable, as noted in the following paragraph. The action of  $\text{Cl}^-$  was therefore interpreted as a tendency to stabilize pit growth (type 3). Its effect on film growth was then an indirect one resulting from an increased fraction of the total current consumed by pitting leaving less available for film growth. Thus in specimens anodized with  $0.01\text{M Cl}^-$  at a nominal  $5 \text{ mA/cm}^2$  with  $\bar{V} = 2.5\text{V}$  the effective film-forming current was much lower,  $< 2 \text{ mA/cm}^2$  to judge from the relation observed between C.D. and plateau voltage for films formed without  $\text{Cl}^-$ .

It was possible to examine the question whether  $\text{Cl}^-$  had a direct effect visible in the geometrical structure of the film by selecting, for comparison with previously described films formed without  $\text{Cl}^-$  additions at 6.5 to 7.6V (1), those which had grown in the presence of  $0.01\text{M Cl}^-$  at  $\bar{V} > 6\text{V}$  and thus had reached comparable thickness at a given anodizing time. At higher magnification in transmission, the pore structures of 84 and 150 sec films (Fig. 14) were nonclassical and similar to those previously described, i.e., the pores did not appear round, of uniform size and arranged in a hexagonal pattern but they had irregular shapes, a range of sizes and they sometimes ran in strings. Their appearance is attributed to the numerous B-P-R (and B-R) events which had occurred a little earlier and had become incorporated into the film (e.g., as suggested in Fig. 1) with the result that pores were jogged and had sloping segments, the net appearance in transmission at this time then varying from one pore to another according to the details of its geometry. Structures visible at high magnification after 15 or 25 sec

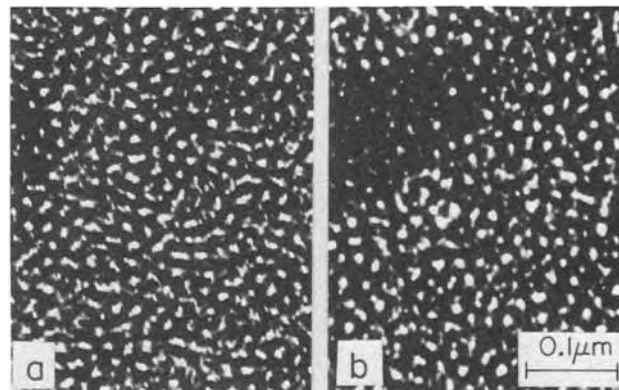


Fig. 14. Nonclassical appearance of pores in transmission micrographs of films formed with  $0.01\text{M Cl}^-$  addition for (a) 84 sec ( $\bar{V} = 6.3\text{V}$ ) and (b) 150 sec ( $\bar{V} = 6.1\text{V}$ ). Cf. Fig. 4c and d of Ref. (1).

anodizing (not shown) before the onset of the prominent events were also much the same as those previously described (1) as were the external surface structures (Fig. 10). In addition to these 0.01M Cl<sup>-</sup> films, a few samples grown at higher Cl<sup>-</sup> levels were available such as the 0.05M Cl<sup>-</sup>, 6.8V film of Fig. 4e, which showed events and pores of appearance similar to those of the 0 Cl<sup>-</sup>, 7.1V film of Fig. 4a.

These comparisons could be extended to films grown with 0.01M Cl<sup>-</sup> at low  $\bar{V}$  by making them not at the same anodizing time but at the same electron opacity. On this basis, the scale of the pore structure decreased with decreasing  $\bar{V}$  as expected from the relationships established at higher cell voltages (7), but the appearance and distribution of the events in film formed with and without Cl<sup>-</sup> was similar. Figure 5 shows events in 150 sec films at various  $\bar{V}$ . For  $\bar{V} < 7V$ , the 150 sec films were similar to those in 7V films formed for shorter times. Thus for the 5.3V-150 sec film in Fig. 5d the opacity and events were close to those of the  $\approx 7V$ -84 sec films in Fig. 4, the 3.6V-150 sec film in Fig. 5e was comparable with a 7V-45 sec film (not shown) where prominent events had occurred over only part of the surface, and the 2.2V-150 sec film in Fig. 5f had an opacity only slightly higher than that of a 7V-25 sec film and was similar in relative freedom from events to the 25 sec films of Fig. 3. The comparisons of this type suggested that the sequence of events contributing to the evolution of film structure was much the same whether films were formed with or without Cl<sup>-</sup> additions. Thus none of the microscopic observations revealed evidence that the Cl<sup>-</sup> had a direct effect on film structure.

#### Further Discussion

These results represent initial steps in examining and interpreting questions of film stability and pit initiation through observations of geometrical fine structure, and the resolution of many of the questions raised awaits further study. There are nonetheless certain implications of general interest. One is that film growth and forms of pitting on a fine scale may be concurrent and mutually interacting processes which must be considered simultaneously even if this involves a wide and unwieldy range of phenomena, as in this paper. The need for microscopy to accompany film-growth studies is satisfied within one experimental technique whenever the latter can be followed by electron opacity. A few comments on the relation of the present results to other studies are given below.

**Pore structure.**—The classical model of a porous film proposed by Keller *et al.* (33) was generally confirmed and further refined by Wood and O'Sullivan (7, 8) who showed among other observations, sections of thick films with arrays of long straight pores of roughly circular section, as for 45  $\mu$ m films in Fig. 4 of Ref. (7). It is not inconsistent with this that the present work, in transmission micrographs of much thinner films, emphasized the events and consequent nonclassical aspects of apparent pore shape, size, and distribution in 7V 84 and 150 sec films (Fig. 14). After longer anodizing times, the layers of the film perturbed by the high density of events which had occurred at  $25 < t < 65$  sec occupied a smaller fraction of its total thickness and further events occurred at much lower frequency, so that in 300 sec films, which could still be examined in transmission despite fogging of the background, the general pore appearance was much closer to that expected from the classical model. Films formed at 25 mA/cm<sup>2</sup> were also examined in transmission and the pore appearance was found to pass through similar stages although on a coarser scale corresponding to the higher cell voltage. A comparison could be made at the same  $Q_{tot}$  i.e., the progression from nonclassical to near classical appearance occurring at 17, 30, and 60 sec at 25 mA/cm<sup>2</sup> corresponded to that at 84, 150, and 300 sec at 5 mA/cm<sup>2</sup>.

Thus previous workers (7, 34) investigating the pore structure (of films formed at 20°C in H<sub>2</sub>SO<sub>4</sub> of the same or slightly lower concentration) at C.D.  $\approx 10$  mA/cm<sup>2</sup> would not have seen a distinctly nonclassical pore appearance except at short anodizing times. Their 30 or 45 sec transmission micrographs (prepared for making pore-density counts) actually did show some nonclassical pore appearance consistent with the present results, Fig. 7 of Ref. (7) and Fig. 6 of Ref. (34).

**Pitting.**—The present work was designed to examine film-growth questions relating to pitting phenomena. Although the experimental conditions differ from those in the main body of Al pitting studies, which involve electrochemical measurements and low-magnification (by present standards) microscopy in near-neutral Cl<sup>-</sup> solutions usually at  $\sim -1/2V$  vs. S.H.E. [see the recent review by Kaesche (35)], some of the present conclusions are thought likely to have rather general pertinence to pitting of Al. That "micropitting phenomena" occurred concurrent with film growth for various initial surfaces and in the absence of Cl<sup>-</sup> indicates attention should be directed not to breakdown but to pit growth vs. repair. That Cl<sup>-</sup> did not exert a detectable direct effect on film growth or structure directs attention to its role in stabilizing pit growth. These conclusions are consistent with those of Richardson and Wood (32) noted below, but they are not reconcilable with notions involving degradation of the electrical or mechanical properties of the film above the "breakthrough potential" from some form of Cl<sup>-</sup> penetration (29).

The details of micropitting phenomena will depend on the experimental conditions. The view given for the film-growth stage in this paper is that at the cell voltages prevailing any low-potential pitting in an active mode was of very short duration and any persistent pitting had to be of a high-potential transpassive type. An attempt to interpret the pitting and repair processes in more detail is not made here, but it may be pointed out that the very small size and severely occluded geometry of the pits visualized in Fig. 1 and 12 give rise to certain constraints not present with larger pits.

Richardson and Wood (32) studied by scanning microscopy pit growth beneath a pre-existing film for Al in 1M KCl at pH 6. They concluded that the film was not destroyed by Cl<sup>-</sup> but was relatively inert. Pits would grow without delay from pre-existing "mechanical-" or "residual-flaws" in the film (conceived as resulting from film growth at scratches, impurity-rich regions, bubbles, etc.) whenever electrochemical conditions were favorable, so that the basic question was not one of pit initiation but of pit growth. The conclusions of the present work are consistent with theirs but would argue further that knowledge of film growth is also required for understanding why pit growth occurs instead of repair and the origin and nature of the flaws.

#### Acknowledgments

This work was sponsored by the U. S. Army Research Office—Durham. In the use of the electron-microscope facilities of the Materials Research Laboratory, which were supervised by R. J. Anderson, it also received substantial support from the U.S. Atomic Energy Commission.

Manuscript received July 23, 1973.

Any discussion of this paper will appear in a Discussion Section to be published in the December 1974 JOURNAL.

#### APPENDIX

##### Significance of the Electron Opacity

For a homogeneous compact amorphous film, the electron opacity is proportional to mass-thickness  $w$  if the single scattering treatment may be used and the collected current follows the exponential law

$$I_c = I_0 \exp(-S_c w) \quad [A-1]$$

Here  $I_c$  is the part of the emergent current collected and  $S_c$  is the total empirical cross section ( $\text{cm}^2/\text{g}$ ) for scattering out of the aperture of the collector. The electron opacity,  $\alpha = \ln(I_0/I_c)$ , is then  $S_c w$  or, in terms of film thickness  $h$  and linear scattering coefficient  $\mu_c$ , is  $\mu_c h$  ( $\mu_c$  being  $S_c$  times film mass-density). A discussion of the exponential law and certain scattering parameters was given by Hall in connection with image formation (36).

The significance of the opacity is not different with the method of measurement used here even though  $I_c$  is obtained by difference from the current  $I_{ab}$  absorbed in the specimen and the opacity is calculated as  $\ln[I_0/(I_0 - I_{ab})]$ . The method is distinctive in that the effective collector aperture is large and  $I_0 - I_{ab}$  is the total emergent current so that only a small fraction of the scattering events in the film are sensed,  $S_c$  representing the cross section for scattering above a minimum angle near  $90^\circ$ . This should make the technique less sensitive to short-range crystallinity in "amorphous" films. As a check on the validity of the exponential law, Eq. [A-1], for these conditions, compact films were formed on electropolished specimens by anodizing in a  $\text{Na}_2\text{B}_4\text{O}_7$  solution at  $2 \text{ mA}/\text{cm}^2$  to several voltages without current decay. These films appeared compact in transmission microscopy and a special examination of 60V films at high magnification did not reveal incipient pores or cell structure. The opacity was found to be linear in cell voltage (Fig. A-1) with a small intercept at the value corresponding to equilibrium attributed to the persistence of a residual (non-compact) layer from the electropolishing. Figure A-1 is qualitatively similar to the results of Beck *et al.* (4) for opacities of compact alumina films measured at 75 kV with a Faraday cage below the specimen, but their line yields a linear scattering coefficient two orders of magnitude larger, the difference reflecting the smaller collector aperture of their technique.

Although the linearity in Fig. A-1 represents a check of the exponential law to the extent compact film thickness may be taken as proportional to formation voltage, the scattering parameters are not determinable precisely because of uncertainties in the values of one or more of the quantities required, *e.g.*,  $h/V$  at a given C.D. or film density. The values of the parameters in the growth law for compact films were considered recently by Siejka, Nadai, and Amsel (37) and from their figures for polished Al samples, the  $h/V$  for the present film was taken to be approximately  $12 \text{ \AA}/\text{V}$ . From Fig. A-1, one then obtains  $\mu_c = 2.5 \times 10^3 \text{ cm}^{-1}$  ( $4 \mu\text{m}$  per unit opacity).

#### Opacity of a Porous Amorphous Film

The general case of a void, assumed disk shaped, is reviewed first. If the void occupies a fraction  $f_i$  of the area sampled by the beam and its height is a fraction  $g_i$  of the film thickness,  $h$ , the opacity will depend on the shape or orientation of the void (although not on its location in the film) in the general case. However, in the low opacity range, the opacity can be written

$$\alpha \approx \mu_c h (1 - f_i g_i), \quad \mu_c h \ll 1 \quad [\text{A-2}]$$

and for a given film thickness it depends only on the

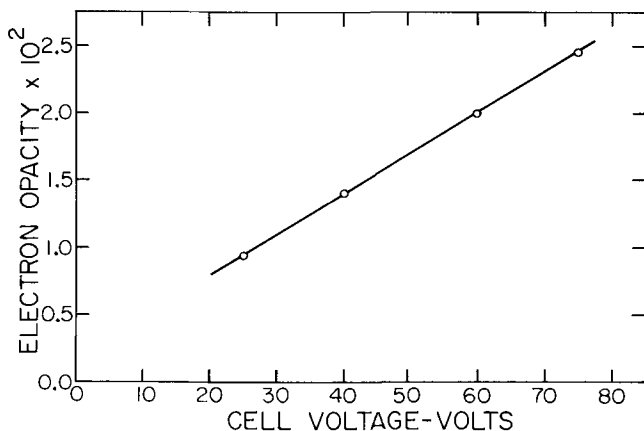


Fig. A-1. Test of the exponential law for compact anodic films formed in 1%  $\text{Na}_2\text{B}_4\text{O}_7$  at  $2 \text{ mA}/\text{cm}^2$ .

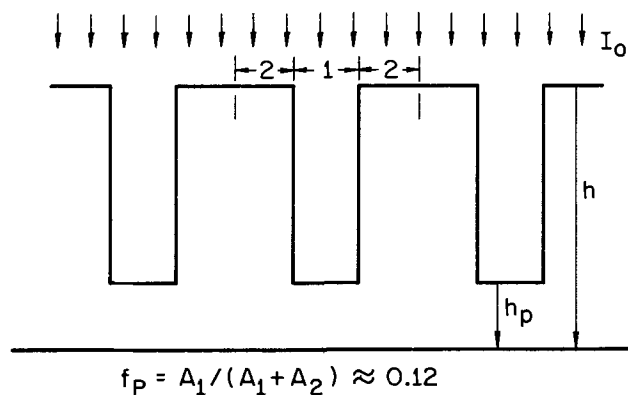


Fig. A-2. Idealization of the classical pore structure for calculation of electron opacity vs. film thickness.

void volume fraction, *i.e.*, it is proportional to mass-thickness.

In films growing through pores, the fractional porosity changes with time and it is convenient to set the problem in the specific geometry of the classical pore structure as idealized in Fig. A-2. The linear scattering coefficient of the film material is assumed the same for cell walls and barrier layer. If  $f_p$  is the fraction of area presented to the beam as pores (region 1) and the barrier layer at the bases of pores has thickness  $h_p$ , the contribution to the "collected" beam from electrons passing down the pores is  $I_0 f_p \exp(-\mu_c h_p)$  and from the electrons traversing the main body of the film (region 2) is  $I_0 (1 - f_p) \exp(-\mu_c h)$ , and the opacity is then, for  $h \geq h_p$

$$\alpha = \ln [f_p \exp(-\mu_c h_p) + (1 - f_p) \exp(-\mu_c h)] \quad [\text{A-3}]$$

In the low opacity range, this becomes

$$\alpha \approx \mu_c [f_p h_p + (1 - f_p) h], \quad \mu_c h \ll 1 \quad [\text{A-3a}]$$

These expressions are useful for analysis of film thickening at constant voltage (as on the plateau of the cell voltage-time curve) where according to the classical model  $h_p$ , which is scaled to the voltage (7, 8), remains constant.  $f_p$  is constant if pore tapering by chemical dissolution of its walls is assumed, for the moment, negligible, so that only  $h$  increases with time.  $f_p$  is taken as 0.12 from the recent measurements of Wood and O'Sullivan (7) and  $h_p/V$  as  $10 \text{ \AA}/\text{V}$  from their data for films formed in  $\text{H}_3\text{PO}_4$  (8), no microscopic measurement being available for  $\text{H}_2\text{SO}_4$ . The form of the  $\alpha$ - $h$  relation given by Eq. [A-3] is shown in Fig. A-3 by plotting  $\alpha$  vs.  $h/h_p$  for  $\mu_c h_p = 1 \times 10^{-3}$ , a level appropriate to the present experiments, and for  $1 \times 10^{-2}$ . The opacity-thickness relation is initially linear, as seen from Eq. [A-3a], and then curves slightly. The  $\alpha$ - $t$  curve would have the same shape for constant  $dh/dt$ .

#### Application to 7V Opacity Data

Although the microscopy emphasized that the pore structure had distinctly nonclassical features during the early stages of anodizing, this did not prohibit application of the opacity analysis based on the classical model because the measured opacities were low and thus, as noted above, were substantially uninfluenced by the distribution of porosity, the opacity being determined by film mass-thickness whether pores were straight, sloped, or jogged. Because  $\mu_c$  has not been measured directly for the porous film, there was minimum uncertainty in applying Eq. [A-3] when a curve-fitting procedure was employed to show how film growth-rate changed with time.

In the 7V  $\alpha$ - $t$  data in Fig. 8, the early linear region extending up to about 84 sec can be fitted with a theoretical curve for thickening at a constant rate by pore growth. A period of nonporous growth for a few seconds at the start of anodizing would not have introduced nonlinearity detectable here. From the microscopy, it was known that the pore structure required  $\leq 15$  sec to become fully developed and was present for the bulk of the linear period. It was also known that many "events" involving in part type 2 pitting-repair processes occurred at  $25 < t < 65$  sec. However, despite their prominence in transmission micrographs these were shallow and could have consumed at most

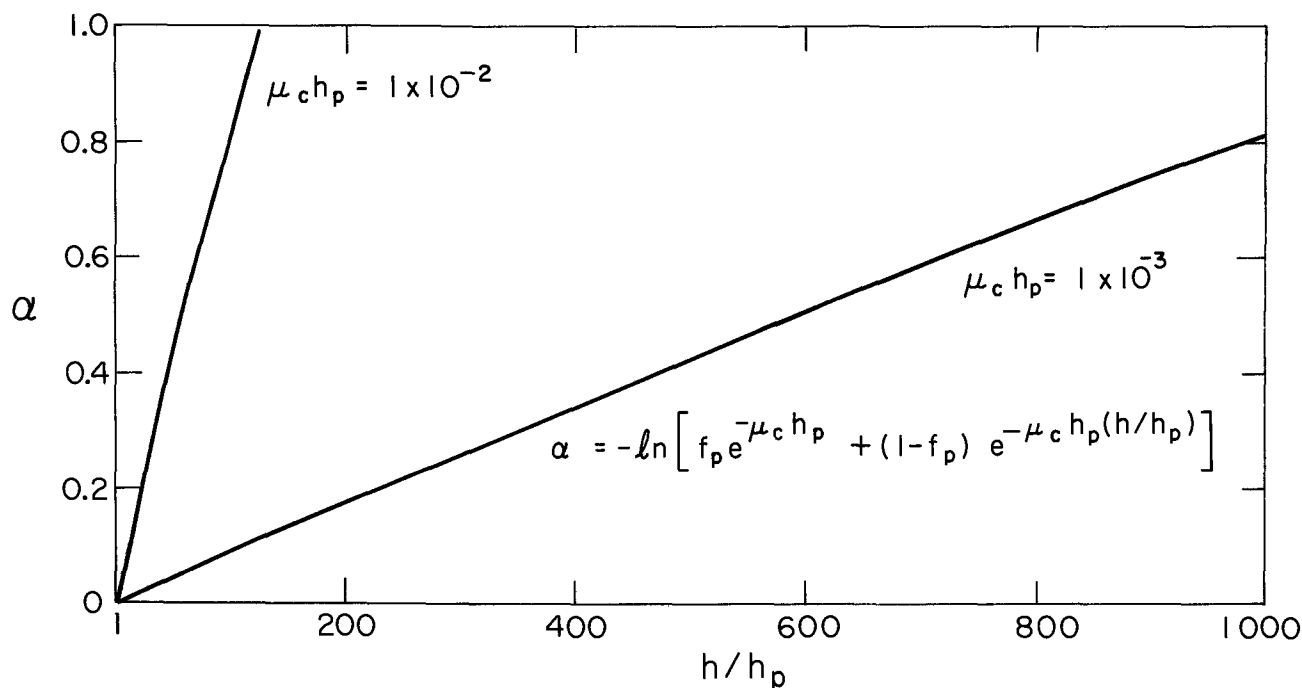


Fig. A-3. Electron opacity vs. thickness of a porous film calculated for two values of parameter  $\mu_c h_p$ .

a small fraction of the charge passed (see text), so that their presence did not contradict the supposition of an approximately constant rate of thickening by pore growth up to about 84 sec.

The initial slope of the  $\alpha$ - $t$  curve given by Eq. [A-3] is

$$(d\alpha/dt)_i = \mu_c(1 - f_p)(dh/dt)_i \quad [A-4]$$

The initial slope of the experimental 7V curve in Fig. 8, was used to calculate the product  $\mu_c(dh/dt)_i$ . For continued thickening at the initial rate, this was integrated to yield  $\mu_c h(t)$  (plus a constant of integration which could be neglected according to a fit of the data). For the other product,  $\mu_c h_p$ , required in Eq. [A-3], the  $\mu_c$  determined above for a compact alumina film was employed and  $h_p$  was taken from the cell voltage as 70Å. The  $\alpha$ - $t$  curve for constant thickening rate at 7V so calculated from Eq. [A-3] is shown dashed in Fig. 8. This curve is insensitive to the choice of values of  $\mu_c$  or  $f_p$ , e.g., doubling  $\mu_c$  would change the calculated opacity at 900 sec by 0.1%. The  $(dh/dt)_i$  derived included in principle the chemical dissolution effect on the external surface, but this was negligible here.

In the low opacity range, the effect of chemical dissolution of film external surface (at rate  $v_2$ ) and pore walls (at rate  $v_1$ ) during anodizing can be treated within the formalism of Eq. [A-3] by modifying the parameters  $h$  and  $f_p$ . The  $h(t)$  calculated from the growth rate assumed is reduced by  $v_2 t$ . The effective  $f_p$  is increased by an enlargement of pore diameter varying linearly from  $2v_1 t$  at the external surface to zero at the pore base, and the sectional area of the pore is averaged to yield  $\bar{f}_p(t)$  as a product of the original value, 0.12, and a function of  $v_1 t$ .

#### REFERENCES

- J. Zahavi and M. Metzger, *This Journal*, **119**, 1479 (1972).
- J. Zahavi and M. Metzger, "Proceedings of the U. R. Evans International Conference on Localized Corrosion," To be published.
- C. G. Dunn and L. A. Harris, *This Journal*, **11**, 81 (1970).
- A. F. Beck, M. A. Heine, E. J. Caule, and M. J. Pryor, *Corrosion Sci.*, **7**, 1 (1967).
- P. R. Swann, in "Electron Microscopy and Structure of Materials," G. Thomas, Editor, p. 878, University of California Press, Berkeley, Calif. (1972).
- J. A. Isasi and M. Metzger, *Corrosion Sci.*, **11**, 631 (1971).
- G. C. Wood and J. P. O'Sullivan, *Electrochim. Acta*, **15**, 1865 (1970).
- J. P. O'Sullivan and G. C. Wood, *Proc. Roy. Soc. (London)*, **A317**, 511 (1970).
- O. P. Arora and M. Metzger, *Trans. Met. Soc. AIME*, **236**, 1205 (1966).
- N. C. Welsh, *J. Inst. Metals*, **85**, 129 (1956).
- L. E. Hendrickson and M. Metzger, *Trans. Met. Soc. AIME*, **242**, 2329 (1968).
- L. Young, *Acta Met.*, **5**, 711 (1957).
- T. A. Renshaw, *This Journal*, **108**, 185 (1961).
- C. Cherki and J. Siejka, *ibid.*, **120**, 784 (1973).
- M. Nagayama and K. Tamura, *Electrochim. Acta*, **12**, 1097 (1967).
- M. Nagayama, K. Tamura, and H. Takahashi, *Corrosion Sci.*, **12**, 133 (1972).
- T. P. Hoar and N. F. Mott, *J. Phys. Chem. Solids*, **9**, 97 (1959).
- J. W. Diggle, T. C. Downie, and C. W. Goulding, *Electrochim. Acta*, **15**, 1079 (1970).
- R. B. Mason, *This Journal*, **102**, 671 (1955).
- R. B. Mason and C. J. Slunder, *Ind. Eng. Chem.*, **39**, 1602 (1947).
- R. B. Mason and P. E. Fowle, *This Journal*, **101**, 53 (1954).
- R. C. Spooner, *ibid.*, **102**, 156 (1955).
- D. J. Stirland and R. W. Bicknell, *ibid.*, **106**, 481 (1959).
- M. Metzger, G. R. Ramagopal, and O. P. Arora, *Trans. Met. Soc. AIME*, **221**, 250 (1961).
- M. Metzger and O. P. Arora, *ibid.*, **227**, 1305 (1963).
- E. C. Pearson, H. J. Huff, and R. H. Hay, *Can. J. Tech.*, **30**, 311 (1952).
- C. Edeleanu, *J. Inst. Met.*, **89**, 90 (1960).
- T. P. Hoar and J. Yahalom, *This Journal*, **110**, 614 (1963).
- T. P. Hoar, *Corrosion Sci.*, **7**, 341 (1967).
- J. P. Hoare, *This Journal*, **117**, 142 (1970).
- K-W Mao, M. LaBoda, and J. P. Hoare, *ibid.*, **119**, 419 (1972).
- J. A. Richardson and G. C. Wood, *Corrosion Sci.*, **10**, 313 (1970).
- F. Keller, M. S. Hunter, and D. L. Robinson, *This Journal*, **100**, 411 (1953).
- G. Paolini, M. Masoero, F. Sacchi, and M. Paganelli, *ibid.*, **112**, 32 (1965).
- H. Kaesche, "Proceedings of the U. R. Evans International Conference on Localized Corrosion," To be published.
- C. E. Hall, *J. Appl. Phys.*, **22**, 655 (1951).
- J. Siejka, J. P. Nadai, and G. Amsel, *This Journal*, **118**, 727 (1971).

# Structure of Anodically Decorated npn Bipolar Transistors

M. V. Kulkarni,\* P. J. Smith, G. A. A. James, and H. A. Troutman

IBM System Products Division, East Fishkill Facility, Hopewell Junction, New York 12533

## ABSTRACT

Examining transistors which were anodically decorated in HF solution to reveal pipes, we found that large differences in emitter-collector leakage currents are mainly due to the different number of leakage paths in each transistor. Resistance associated with each leakage path was in the 12,000-20,000 ohm range; different resistances were detected both electrically and by electrochemical etching behavior in the  $n^+$  region. From their behavior during electrochemical etching, it was determined that the leakage paths seemed to consist of narrow regions of  $n^+$  material extending from the emitter through the base into the collector. The leakage paths occurred both in and at the edge of the emitter (at the vertical emitter-base junction). No direct relation between pipes and crystallographic defects could be made, but it is shown that not all crystallographic defects cause serious junction leakages.

Several techniques have recently been developed which use electrochemical reactions to delineate devices with electrical defects (1). A silicon wafer is placed in an electrochemical cell and anodically biased. Cell conditions are adjusted so that a reaction product develops only on devices with particular electrical characteristics. Thus, a wafer can be electrically mapped for an electrical defect by examining the decorated wafer optically. This technique allows the testing of very small devices which could not be probed electrically. Considerable data can also be obtained in a relatively short time on the distribution of electrical defects, both within a wafer and on a wafer-to-wafer basis.

Our purpose was to investigate the structure of npn transistors which were shown to contain collector-to-emitter electrical leakage by anodic decoration in HF electrolyte (1). After removing the reaction product, the surface features of the decorated transistors were observed in the SEM; the defect structure within the transistors was studied using a high-voltage (1 MV) TEM.

## Experimental Procedure

Transistors of two different geometries were produced in phosphorus-doped  $n^-$  epitaxial silicon on  $p^-$  substrates with arsenic-doped subcollector diffusions. The base region was obtained through a boron diffusion; the phosphorus-diffused emitters were embedded in the base regions. For electrical measurements and SEM observation, emitter diffusions approximately  $9 \text{ mil}^2$  were made in slightly larger base areas. The TEM observations were made mainly on devices which had rows of  $1 \text{ mil}^2$  emitters embedded in a common base. Contact windows were etched in the surface oxide to expose silicon in the emitter, base, and collector contact areas. Electrical contact was established by affixing a copper plate to the back surface of the silicon wafer. After coating the wafer with wax (Fig. 1), it was made an anode in an electrolytic cell, using a 5% HF solution as the electrolyte. In the case of an n-p-n transistor under these conditions, the collector-base junction is reverse biased, so that if the cell voltage is lower than the collector-base breakdown voltage, the current density at the base and emitter regions is essentially zero, and no reaction deposits (brown amorphous Si) will develop. However, if there is an emitter-collector leakage (pipe), or if the collector-base junction has a premature breakdown, current will flow across the junction and an electrochemical reaction takes place at the device surface. Thus, a reaction product at the device surface will identify those devices with an electrical defect.

The voltage across the cell was adjusted well below collector-base breakdown so that no reaction occurred within the emitter and base contacts. Within the  $n^+$  diffusion windows in the collector region, however, the current density was sufficient to produce a reaction product within a few minutes. Under these conditions, it has been shown that emitters with emitter-collector leakages will be decorated (1).

After anodic decoration, the devices were examined by optical microscopy to determine the location of the decorated transistors. The dark brown product deposited on  $n^+$  emitter regions was removed by dipping the sample momentarily in a 3:2:1 mixture of acetic, nitric, and hydrofluoric acids, and the transistor surfaces beneath the deposits were examined in the SEM for details.

TEM samples were prepared from these wafers using an electrochemical technique (2) to provide large thinned areas. The  $p^-$  substrate and the  $p^+$  isolation areas were selectively removed by anodic dissolution, leaving the  $n^-$  epitaxial layer containing the device junctions (Fig. 2). Final sample thinning was performed by chemically etching the sample in a 3:3:5 mixture of acetic, hydrofluoric, and nitric acids. The transistor array was thinned from the substrate side

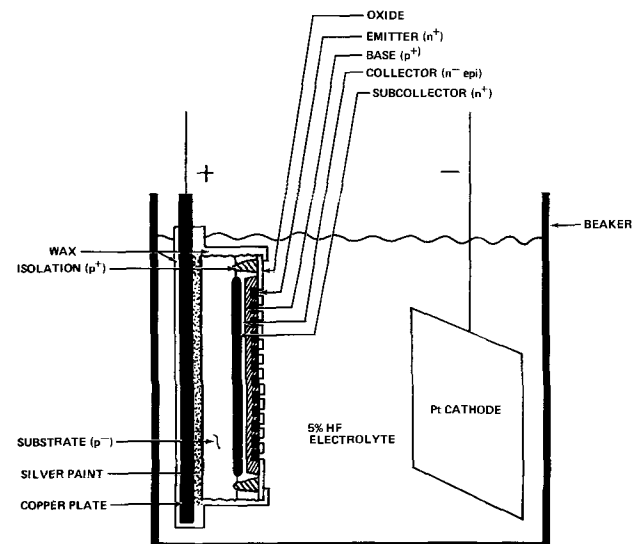


Fig. 1. Anodic decoration of transistor array. Electrical contact is made to the substrate of the wafer using a copper plate. When the sample is anodically biased, the collector-base junction is reverse-biased and no reaction product develops on the emitter. If a pipe (emitter-collector leakage) is present, current flows to the emitter and a reaction product forms on the surface.

\* Electrochemical Society Active Member.

Key words: anodic decoration, electrical leakage, bipolar transistor, crystal defects, emitter-collector leakage, junction leakage.



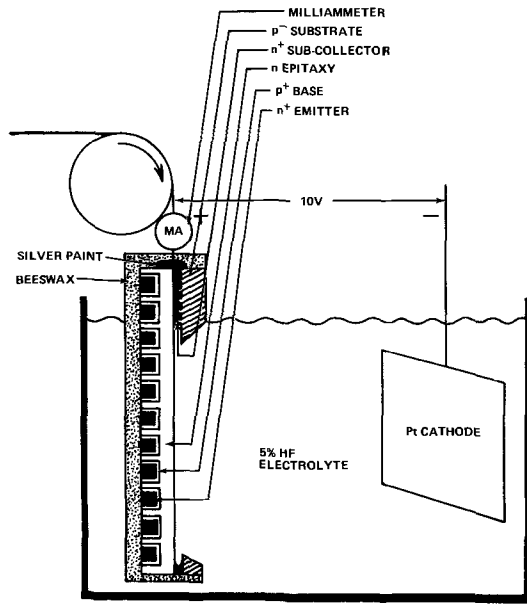


Fig. 2. Electrochemical thinning of the transistors. The sample was lowered into the electrolyte at a controlled rate to produce uniform thinning.

to approximately 2-3  $\mu\text{m}$  and examined at 1 MV; thus the TEM sample contained the entire emitter and base regions, and part of the collector. During thinning the top side was protected to insure no further etching of the emitter areas.

**SEM Examination of Decorated Emitter Surfaces**

After 5 min of anodic decoration, the emitter areas containing a collector-emitter electrical leakage (pipe) developed a brownish surface deposit (Fig. 3); the correspondence between decorated transistors and transistors with collector-emitter electrical leakage has been previously demonstrated (1). In the case of transistors with collector to emitter leakage, the brown deposit is formed as a result of the electrochemical

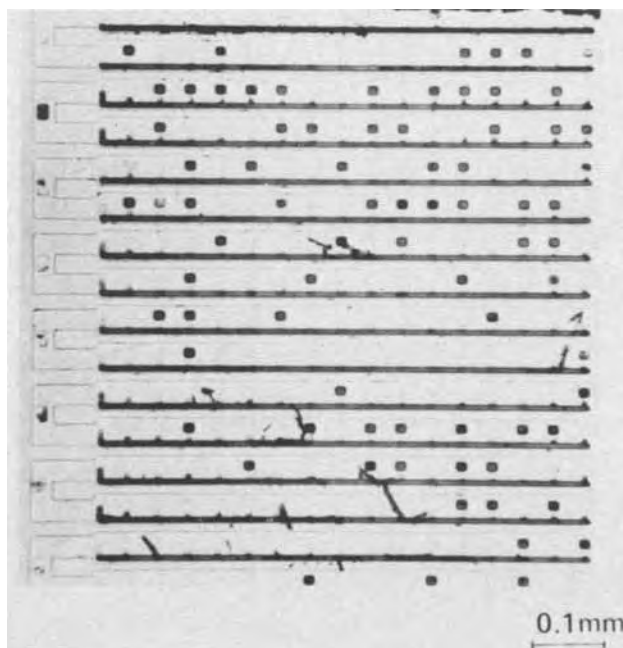


Fig. 3. Decorated transistor array. In each row the emitters are embedded in a common base. The dark emitters have been anodically decorated showing that they each contain a pipe.

conversion of  $\text{n}^+$  emitter silicon to amorphous silicon. This deposit of amorphous silicon is then removed by etching for a few seconds with 3:2:1 acid mixture described previously. The transistors with no emitter to collector leakage did not have any amorphous silicon deposit on  $\text{n}^+$  emitters. The etching did not cause any significant removal of  $\text{n}^+$  silicon on these undecorated emitters. Within the decorated emitter areas, a noticeable amount of material was removed as a result of electrochemical reaction. Of 61 emitters with pipes, 58 emitters contained small square etched areas (Fig. 4). The  $\approx 4 \mu\text{m}^2$  etched areas occurred both within the emitters and at the emitter-base junction. In some transistors, two etched areas were present (Fig. 4b). No detail in the etched areas could be resolved in the SEM. In the three other emitters with pipes which did not contain distinct etched areas there was evidence of substantial etching around the emitter-base junction. None of the emitters without pipes contained etched areas, nor was there any visible etching at the emitter-base junction (Fig. 5).

By anodically decorating large (9 mil<sup>2</sup>) emitter transistors in which the leakage currents were measured electrically, it was shown that each of the etched areas in the emitter region was associated with a leakage current through the transistor (cf. Table I and Fig. 6). For transistors with emitter-collector leakages in the 0-10  $\mu\text{A}$  range, at 3V reverse bias, no decoration was observed in the emitter areas. From 10-43  $\mu\text{A}$  the emitters were decorated, but no localized etched areas were present. Above 150  $\mu\text{A}$ , approximately 4  $\mu\text{m}^2$  etched areas were observed on the transistors; the number of etched areas increased with leakage current. From Table I it can be seen that many of the etched areas corresponded to a leakage current of approximately 150-250  $\mu\text{A}$ . In the transistor with 1650  $\mu\text{A}$  leakage currents (Fig. 6), some of the etched areas were substantially smaller than the typical 4  $\mu\text{m}^2$  area (cf. Fig. 5), indicating less leakage was associated with those particular leakage paths. In general, however, the number of parallel leakage paths within a transistor is a major influence on the total leakage current, especially in the high leakage range.

**TEM Examination of Decorated Transistors**

After thinning to approximately 3  $\mu\text{m}$ , the transistor array was examined at 1 MV. At the surface the etched areas form squares, with the sides along  $\langle 110 \rangle$  directions (Fig. 7). Stereomicrographs show that the etched areas are square only near the top surface, becoming roughly conical with increasing depth. The shape of the etched area can also be obtained from the thickness contours visible in the larger etched area in Fig. 7. The alternating light and dark fringes are a result of thickness variations in the sample; each fringe represents an area of constant thickness. If a 1 sec Sirtl etch is used to remove anodization product rather than the 3:2:1 etchant solution, the etched area is roughly circular. Thus no conclusions can be drawn about the

Table I. Relation between leakage current and number of etched areas in large-emitter transistors anodically decorated at 1V for 2 min in HF

Leakage current ( $\mu\text{A}$ ) at 3V reverse bias	Number of etched spots within decorated emitter area	Comments
10	None	Not decorated*
13	None*	Redecoration possible; therefore, emitter partially removed.
21	None*	
40	None*	
150	1**	Redecoration not possible; therefore, entire emitter removed.
370	2**	
1650	6**	
3400	12**	

\* Examined optically and in SEM.  
 \*\* Visible at 500x.

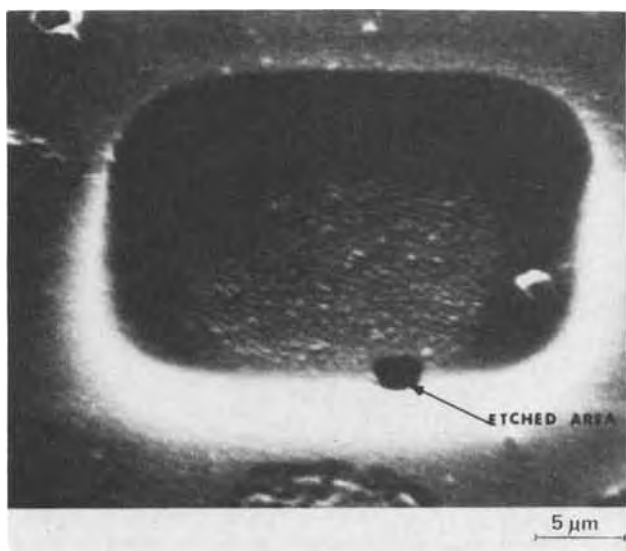


Fig. 4a. Scanning electron micrograph of an emitter with a pipe. The reaction product has been removed revealing an etched area under the emitter.

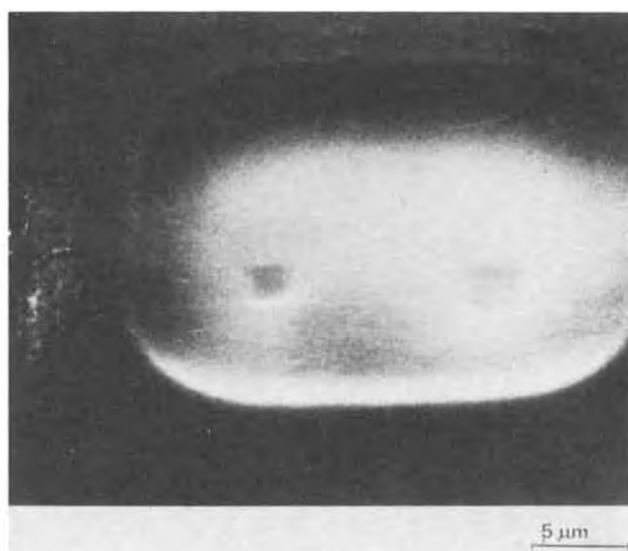
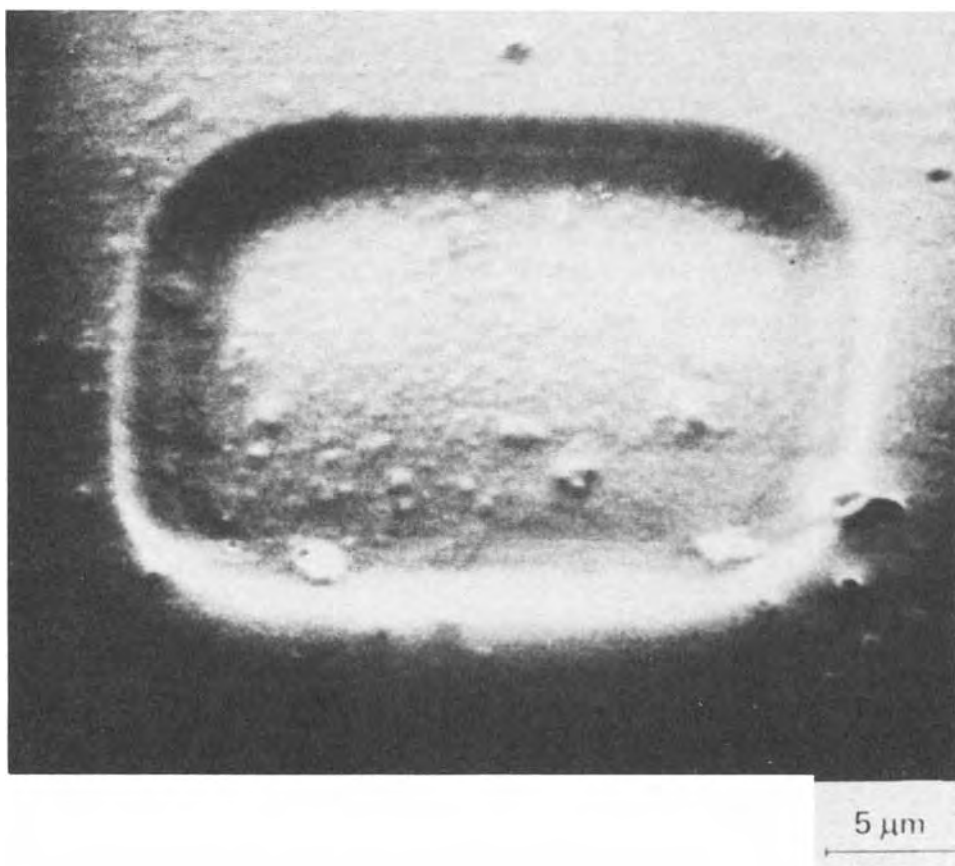


Fig. 4b. Scanning electron micrograph of an emitter with two etched areas.

Fig. 5. Scanning electron micrograph of a device that did not contain a pipe.



geometry of the etch pits in the anodically decorated emitters.

Two-dimensional defects were observed within several emitter areas (Fig. 8); similar defects were also observed outside the emitter areas. These defects were identified by Booker and Tunstall (3) as extrinsic stacking faults which grew from the top surface into the silicon wafer during oxidation. A curved Frank partial dislocation forms the boundary between the stacking fault and the nonfaulted matrix. If the TEM sample is sufficiently thin, the stacking fault will intersect the bottom surface as in this case. Recognizing the flat shape of the stacking fault at the bottom surface (lower right edge), the sample thickness can be calculated from the projected width of the stacking fault.

The amount of material removed from an emitter with a pipe can be estimated from the stacking fault shown in Fig. 7, which terminates at the upper right edge of the emitter. Assuming the stacking fault originally extended laterally into the emitter region, the thickness of material removed from the emitter is at least as great as the depth of penetration of the stacking fault into the wafer. The distance from the top surface to the bottom of the stacking fault is

$$d = w \tan \theta$$

where  $w$  is the projected width and  $\theta$  is the angle between the surface plane and the fault plane, which is always a (111) plane. For a (100) surface and the (111) fault plane,  $\theta = 54.7^\circ$ . For the stacking fault in



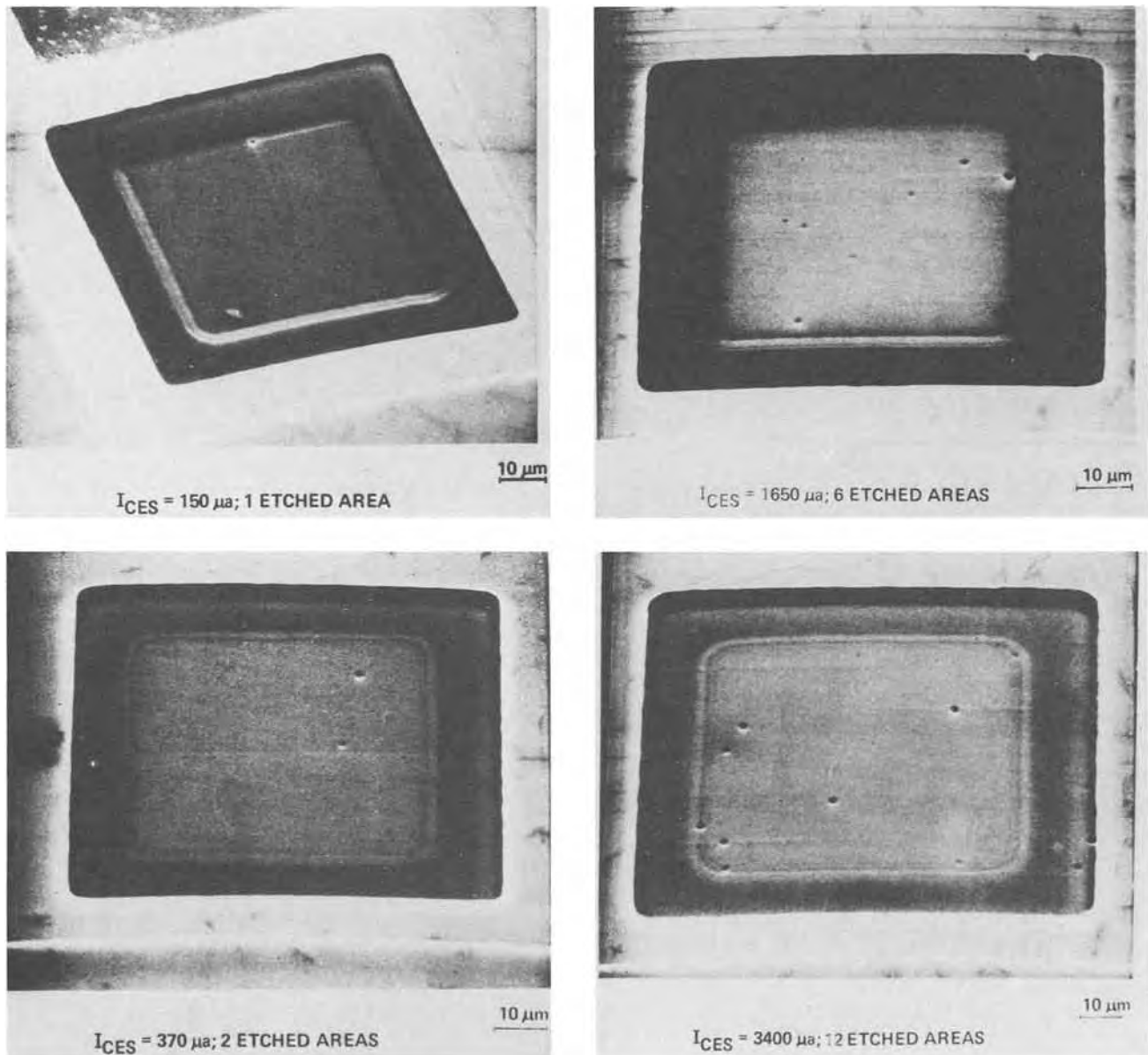


Fig. 6. Scanning electron micrographs of large-kerf transistors which had been electrically probed prior to anodic decoration. The number of etched areas within the emitter increases with increasing emitter-collector leakage.

Fig. 7,  $w = 1.25 \mu\text{m}$ , so  $d = 1.75 \mu\text{m}$ . Since the emitter-base junction depth is  $1.7 \mu\text{m}$ , it is reasonable to conclude that the  $n^+$  silicon from the entire emitter region of the transistor was converted to amorphous silicon during anodic decoration. This explains why transistors with a leakage current larger than  $150 \mu\text{A}$  cannot be redecorated after removing the initial decoration with an acid mixture (Table I).

The thickness contours at the edge of the etched area could be used to approximate the depth to which the etched area extended into the device. Assuming a two-beam condition, the extinction distance for the (220) reflection at 1 MV is approximately  $0.13 \mu\text{m}$  (4). The ten thickness fringes within the etched area show the etched area extends  $1.3 \mu\text{m}$  below the surface. We have previously shown that during anodic decoration the amount of  $n^+$  material converted was at least as great as the entire depth of the emitter region for transistors with etch pits in the emitter. We expect that conversion of  $n^+$  material to amorphous silicon should stop when the active donor concentration decreases below a certain level (see next paragraph), so that none of the material below the junction is expected to be removed during anodic decoration. Therefore, the top of the etched area is at the emitter-base junction,

and the etched area extends through the base and well into the collector region. (The base width is  $0.4 \mu\text{m}$ .)

The fact that the anodic decoration caused etching in the collector shows that localized, high  $n^+$  donor concentrations extend into the  $n^-$  collector. M. J. J. Theunissen *et al.* (5) have shown that in the range between  $3 \times 10^{18}$  and  $2 \times 10^{16}$  donors/ $\text{cm}^3$  (0.01-0.3 ohm-cm), only partial dissolution of the  $n^-$  silicon occurred at a cell voltage of 10V and the rate of anodic dissolution decreased at the lower concentrations. The  $n^-$  epitaxial silicon in the collector region of our devices had a donor concentration of  $1 \times 10^{17}$  donors/ $\text{cm}^3$  (0.09 ohm-cm). As stated above, the electron microscope samples from these device wafers were prepared by selective anodic etching of p material at 10V; the  $n^-$  epitaxy regions did not substantially dissolve even at cell voltages of 10V. In our present work, we have also noticed that the  $n^-$  collector regions did not etch when exposed to the electrolyte during the anodic decoration. However, the depth measurements of the etched areas have shown that in the region of the pipe the collectors are electrochemically etched. The presence of the etched areas in the  $n^-$  collector indicates dopant concentrations higher than the epitaxial dopant concentration. Thus, the enhanced donor

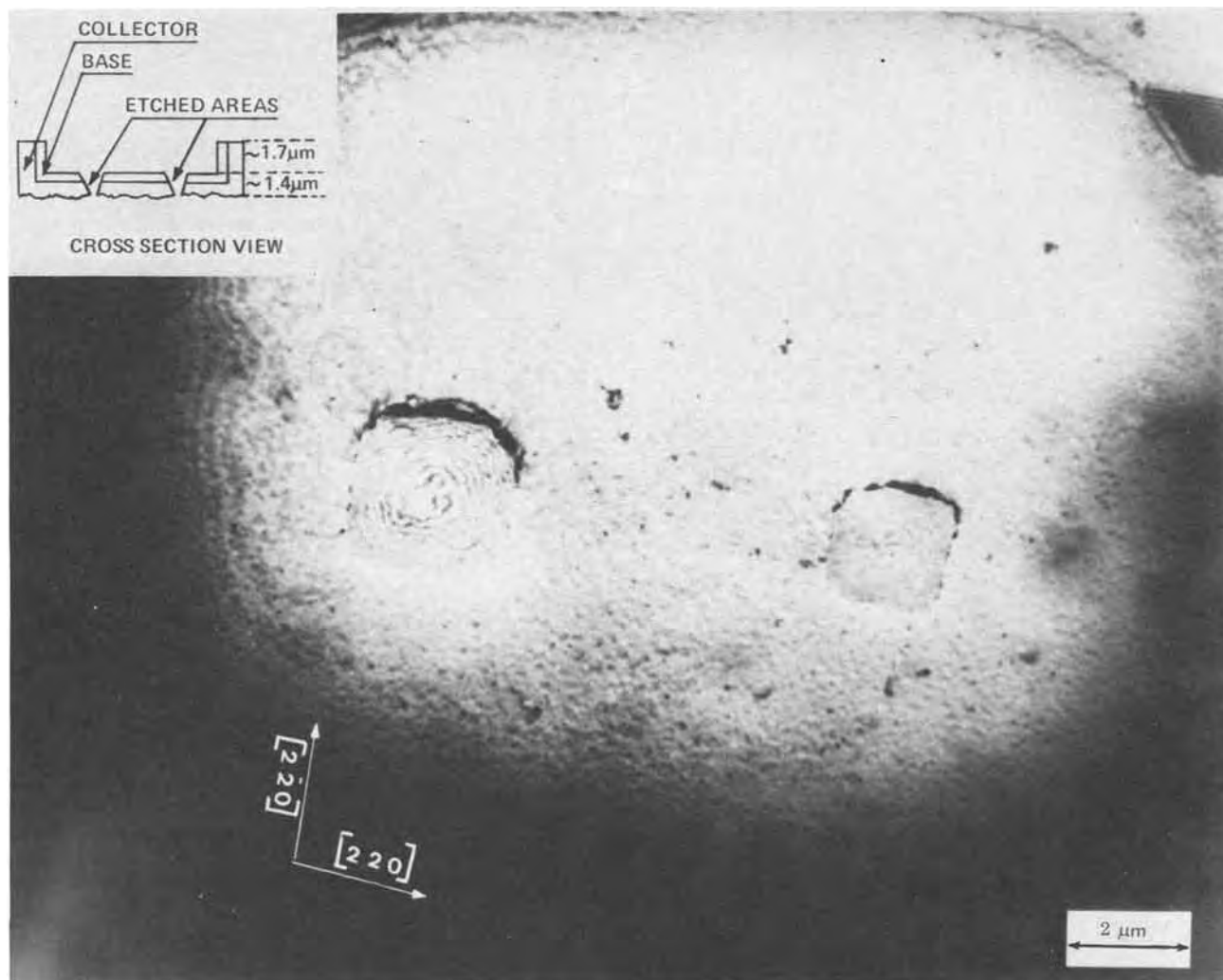


Fig. 7. Transmission electron micrograph of the device in Fig. 4b. Thickness fringes are visible both within the etched areas and at the edge of the device. The emitter has been removed during anodic decoration. An oxidation-induced stacking fault terminates at the edge of the device.

concentration, shown by Barson *et al.* (6) to be associated with the pipe in the base region, is also present in the  $n^-$  collector.

The calculation of thickness using thickness fringes could contain substantial errors due to uncertainty in deviation from the true Bragg condition (4). However, if one used the thickness contours at the edge of the emitter area to calculate the relative thickness of the base and emitter regions, a difference in thickness of  $1.2 \mu\text{m}$  is obtained, which is reasonably close to the value of  $1.7 \mu\text{m}$  obtained using the projected width of the stacking fault. Thus, it is clear that the above calculation on the depth of the etched area is sufficiently accurate to conclude that the etched area does extend from the emitter to collector, and corresponds to the actual location of the pipe.

The fact that not all crystallographic defects which cross junctions cause significant electrical problems is well illustrated by the transistor containing two oxidation-induced stacking faults (Fig. 8). From the lack of anodic decoration it is known that the emitter-collector leakage current is less than  $10 \mu\text{A}$  which is equivalent to a pipe resistance  $\cong 330 \text{ kohm}$ . The offset of the top fringe of the stacking fault as it crosses the emitter-base junction shows the emitter surface is  $0.54 \mu\text{m}$  below the surface of the adjacent base. Of this value, approximately  $0.05 \mu\text{m}$  of silicon was consumed during the formation of phosphosilicate glass during the emitter diffusion cycle. Therefore, the remaining  $0.5 \mu\text{m}$  of  $n^+$  silicon was removed during the anodic decoration, showing that an electrochemical reaction

occurred at the emitter surface, but was not strong enough to produce visible decoration.

From the projected width of the stacking fault within the emitter region, we calculated that the larger stacking fault extends at least  $3 \mu\text{m}$  into the device. Since the emitter-base and collector-base junctions are  $1.7$  and  $2.1 \mu\text{m}$  deep, respectively, the stacking fault and the bounding Frank partial dislocation extend from the emitter region through the base and into the collector region without causing a significant leakage current. Further, from the shape of the etched areas in decorated transistors, it is reasonable to conclude that they were not produced at the ends of oxidation-induced stacking faults. If the etched areas had been produced at stacking faults, one would expect the etched areas to follow the direction of the bounding Frank partial dislocation, which, in the base and collector region, tends to become parallel to the wafer surface. However, the etched area is roughly conical with the long axis approximately normal to the wafer surface and thus, does not seem to have been generated by an oxidation-induced stacking fault.

Thus, the oxidation-induced stacking faults in these devices caused no substantial leakage currents across the junctions. Obviously, no conclusions about the presence or absence of other crystallographic defects within the devices can be drawn since the leakage path was removed during decoration.

The presence of the stacking faults in devices with no appreciable leakage currents is in agreement with the hypothesis that crystalline defects degrade device

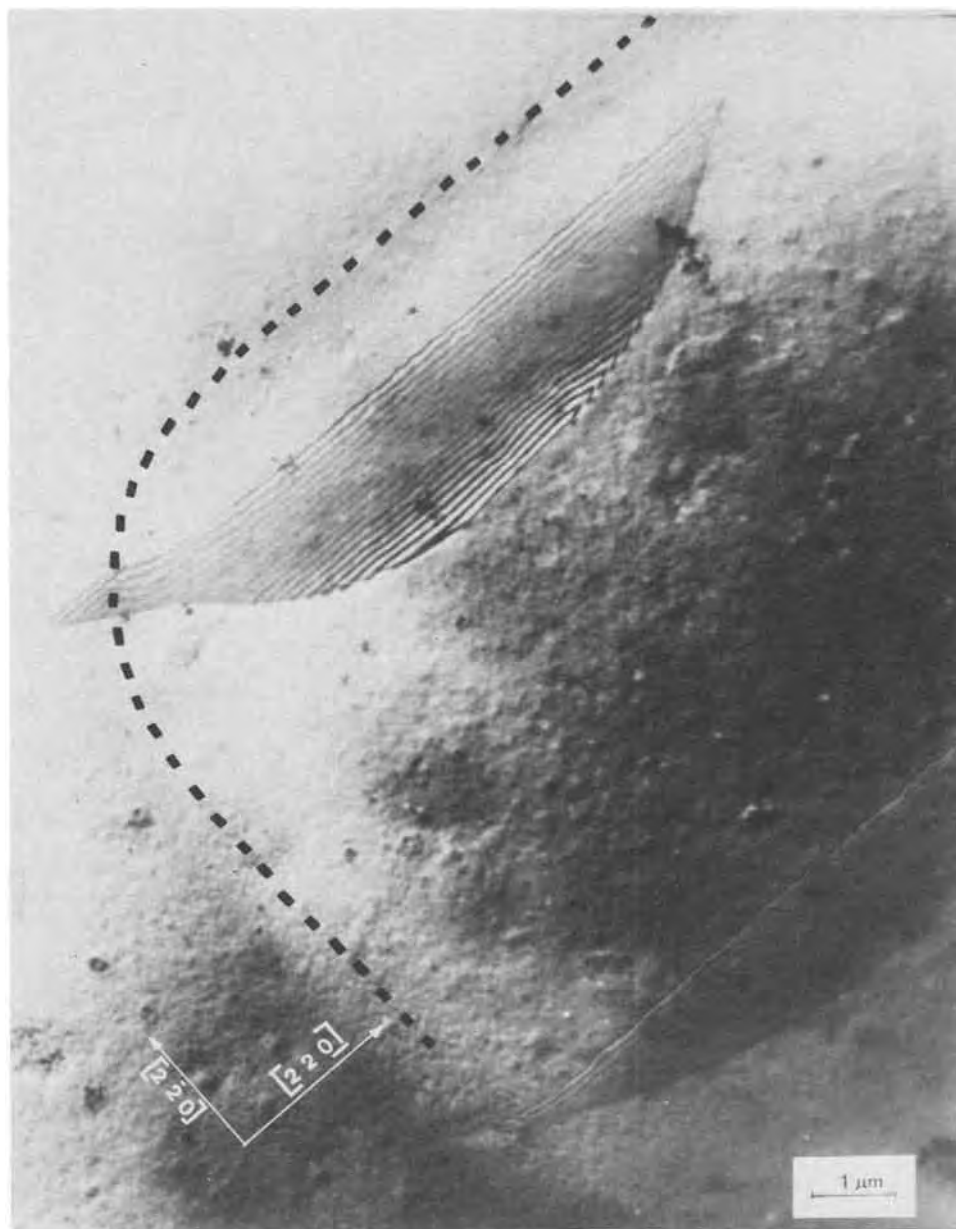


Fig. 8. Transmission electron micrograph of a transistor with a leakage current less than  $10 \mu\text{A}$ . The dotted line delineates the emitter area. The upper oxidation-induced stacking fault extends through the emitter and base regions and into the collector; the smaller stacking fault is in the lower right corner of the emitter.

properties only when there is an impurity present at the defect. Studies by Barson (6) showed that individual pipes, identified by microsectioning and staining, were often associated with stacking faults nucleated in the epi-substrate interface. Since not all stacking faults caused pipes and since the number of pipes increased if a gold diffusion was included, they concluded that a defect-impurity interaction was responsible for pipe formation. Parekh (7) also observed that increased densities of dislocations and stacking faults only caused increased pipe densities when a gold diffusion step was included.

### Summary and Conclusions

By examining transistors which had been anodically decorated in HF solution to reveal the presence of pipes, we found that large differences in the magnitude of the emitter-collector leakage current are mainly due to the different number of leakage paths existing in each transistor. The resistance associated with each leakage path was in the 12,000-20,000 ohm range; differences in resistance were detected both by electrical testing and by electrochemical etching behavior of the  $n^+$  region. From their behavior during electrochemical etching, the leakage paths have been shown to consist of narrow regions of  $n^+$  material extending from the emitter through the base into the collector. The leak-

age paths occurred both at the edge of the emitter region (at the vertical emitter-base junction) and within the emitter region.

Since electrochemical decoration removed the material in the immediate area of a pipe, no direct relation between a pipe and crystallographic defects could be made. Oxidation-induced stacking faults were observed crossing the emitter-base and collector-base junctions of a transistor. The emitter-collector leakage current of the transistor was very low, equivalent to a pipe resistance  $\cong 330,000$  ohms, illustrating that not all crystallographic defects cause serious junction leakages.

### Acknowledgments

We would like to thank J. Kent Howard and F. Reisert for the scanning electron micrographs, the staff at the United States Steel Research Center for assistance with the transmission electron microscopy, and Doris Braddock for the sample preparation.

Manuscript submitted March 16, 1973; revised manuscript received Sept. 14, 1973. This was Paper 64 presented at the Chicago, Illinois, Meeting of the Society, May 13-18, 1973.

Any discussion of this paper will appear in a Discussion Section to be published in the December 1974 JOURNAL.

## REFERENCES

1. M. V. Kulkarni, J. C. Hasson, and G. A. A. James, *IEEE Trans. Electron Devices*, **ED-19**, 1098 (1972).
2. P. J. Smith, M. V. Kulkarni, and H. A. Troutman, *29th Ann. Proc. Electron Microscopy Soc. Amer.*, p. 148 (1971).
3. G. R. Booker and W. J. Tunstall, *Phil. Mag.*, **13**, 71 (1966).
4. P. B. Hirsch, A. Howie, R. B. Nicholson, D. W. Pashley, and M. J. Whelan, "Electron Microscopy of Thin Crystals," Butterworths Inc., Washington, D.C. (1965).
5. M. J. J. Theunissen, J. A. Appels, and W. H. C. G. Verkuylen, *This Journal*, **117**, 959 (1970).
6. F. Barson, M. Hess, and M. Roy, *ibid.*, **116**, 304 (1969).
7. P. C. Parekh, *Solid State Electron.*, **14**, 273 (1971).

## Diffusion in Thin Silicon Films Formed by Electrochemical Etching

T. I. Kamins

Research and Development Laboratory, Fairchild Camera and Instrument Corporation, Palo Alto, California 94304

### ABSTRACT

The diffusion of dopant atoms into thin silicon films formed by an electrochemical-etching technique has been investigated. Dopant atoms have been diffused from boron- and phosphorus-doped, vapor-deposited oxides into both thin-film samples of the opposite conductivity type and into bulk control wafers. The diffusion characteristics of the impurity atoms are generally similar in the thin films and in bulk wafers. Second-order effects include slightly higher sheet conductances in the thin films than in the bulk control wafers and slightly shallower diffusion of phosphorus into p-type films than into bulk wafers. The oxidation rate of the thin films is the same as that of bulk silicon.

Thin silicon films on insulating substrates have received considerable attention recently because of the reduced d-c and a-c interactions between adjacent devices fabricated in the films. Most interest has been focused on silicon layers heteroepitaxially deposited on sapphire or spinel (1, 2), although the low minority-carrier lifetimes found in these films have limited their application to majority-carrier MOS transistors. One alternative to this approach is to form the thin silicon film from a thick, epitaxial, single-crystal silicon wafer by an electrochemical-etching process which terminates at a well-defined, epi-substrate interface (3). A thick, insulated layer of polycrystalline silicon, added by chemical vapor deposition before the electrochemical-thinning process, serves as a mechanical support for the single-crystal silicon film (Fig. 1). Since this system is not limited by the inherent mismatches of a heteroepitaxial deposition, the minority-carrier lifetime is significantly greater than in the silicon-on-sapphire system. Films of a quality suitable for bipolar, as well as MOS, integrated circuits can readily be fabricated (4).

A series of experiments was conducted in order to determine if the diffusion of dopant impurities into the thin, single-crystal silicon films formed by the electrochemical-etching process differs from that in bulk wafers. Diffusion of both boron and phosphorus was considered. The oxidation rate of the thin films was also examined. Unlike the cases of polycrystalline-silicon films (5) or silicon on sapphire, no gross differences were expected between the thin-film wafers and bulk samples because of the high crystal quality of these thin films.

### Experimental Method

After the appropriate conducting and insulating layers were added to the starting wafers, the films were formed by electrochemical etching (3) so that the final structure appeared as shown in Fig. 1. Then approximately 2  $\mu\text{m}$  of silicon was removed from each sample by vapor etching in order to avoid possible

Key words: silicon films, thin films, diffusion.

effects of a surface region with a different dopant concentration than the remainder of the film. The final thickness of each silicon film was approximately 6-7  $\mu\text{m}$ .

Impurities were diffused into the (111)-oriented silicon films and into similarly doped (111)-oriented, bulk control wafers from doped, vapor-deposited, silicon-dioxide films. The use of these doped oxides allowed direct comparison of diffusion into the thin films and into the bulk control wafers since the amount of dopant which entered the silicon from the doped oxide was primarily controlled by diffusion in the oxide while the diffusion depth was controlled by the diffusivity of the dopant in the silicon (6). The doped oxide films were deposited by the oxidation of silane and either diborane or phosphine at a substrate temperature of approximately 400°C and were about 1  $\mu\text{m}$  thick. The diffusions were performed in a dry nitrogen ambient, with each thin-film sample being placed in the diffusion furnace between two similarly doped, bulk control samples of approximately the same size. A diffusion temperature of 1100°C was used since diffusion at this temperature is generally more reproducible than diffusion at lower temperatures.

Surface concentrations of the dopant atoms were calculated by reference to previous work on diffusion from boron-doped oxides (6) and phosphorus-doped oxides (7). The boron-doped oxide contained about 5%  $\text{B}_2\text{O}_3$  or  $2 \times 10^{21} \text{ cm}^{-3}$  boron atoms, which should produce a surface concentration of about  $5 \times 10^{19}$

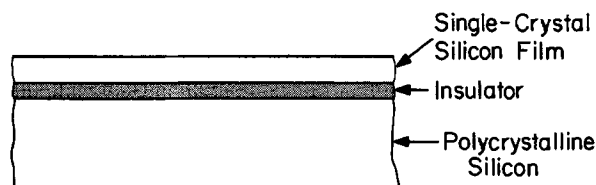


Fig. 1. Cross section of composite substrate after electrochemical etching.

cm<sup>-3</sup> boron atoms in the silicon. The phosphorus-doped oxide contained about 10% P<sub>2</sub>O<sub>5</sub> or 2 × 10<sup>21</sup> cm<sup>-3</sup> phosphorus atoms so that the surface concentration in the silicon was about 8 × 10<sup>19</sup> cm<sup>-3</sup>.

The diffusion times were chosen so that the sheet conductance and the junction depth of the diffused layer could be plotted as functions of the square root of the diffusion time for both the single-crystal films and the control samples. As discussed by Barry and Olofsen (6), this method of presentation allows ready calculation of the diffusivity of the dopant impurity.

After diffusion the sheet resistivity was measured with a four-point probe in several spots on each sample. Junction depths were measured by optical interferometric techniques after delineation by grooving and staining with a nitric-hydrofluoric acid solution (70% HNO<sub>3</sub>:49% HF:H<sub>2</sub>O = 1:500:500 by volume).

**Experimental Results**

The sheet conductances measured after the diffusions were approximately linearly proportional to the square root of the diffusion times, although the agreement was better for phosphorus diffusion into p-type samples than for boron into n-type samples. The deviation from a linear relationship seen in the latter case may be similar to that observed by Barry and Olofsen at high boron surface concentrations (C<sub>s</sub> > 10<sup>20</sup> cm<sup>-3</sup>). Figures 2(a) and 2(b) are plots of the sheet conductances in the thin films as functions of the sheet conductances in the simultaneously diffused bulk samples. In both cases the data points lie above a line with unity slope, indicating a consistent tendency for somewhat higher sheet con-

ductances in the thin films than in the bulk samples. In some cases the value in the thin film was the same as that in the bulk samples, but in no case was the value in the thin film less than that in the corresponding bulk samples. The dashed lines in Fig. 2 indicate that the sheet conductances were approximately 10% higher in the thin films for boron diffusion and about 6% higher for phosphorus diffusion.

The measured values of junction depth were also plotted as functions of the square root of the diffusion time with reasonable fit to a linear relationship. Clear, well-defined junctions were obtained in the case of phosphorus diffusion into p-type films while difficulty was occasionally encountered obtaining clear stain lines on some of the n-type films after boron diffusion.

Figures 3(a) and 3(b) show the junction depths in the thin films as functions of those in the bulk samples. In both cases the junction depths were the same in the thin films and in the bulk samples for shallower diffusions (x<sub>j</sub> < 4 μm). For the longer phosphorus diffusions, however, the junction depths in the thin films became appreciably less than those in the bulk samples. This trend was seen in three separate series of diffusions and is probably not a statistical error. The dashed line in Fig. 3(b) indicates that the junction depths were approximately 8% less in the thin films than in the bulk control samples after prolonged phosphorus diffusion.

In order to find any difference in the oxidation rate of the thin films from that of bulk silicon wafers, films were oxidized together with bulk control samples. The oxides were formed under conditions controlled by the surface reaction rate rather than by the diffusion of oxygen through the already formed oxide, since any differences caused by the thin-film structure would be most easily observed in the former case. Wafers were oxidized at 920°C in both dry oxygen

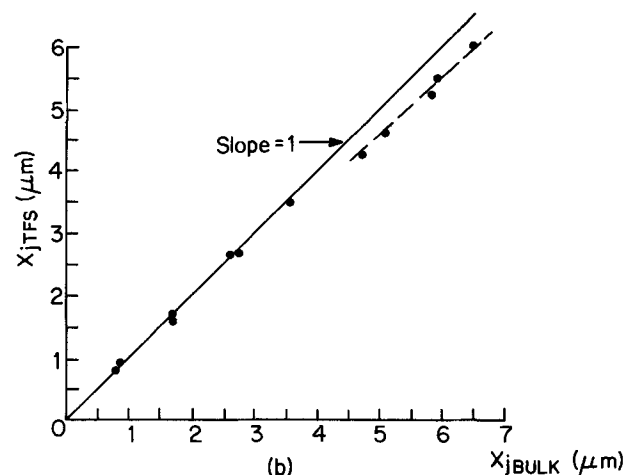
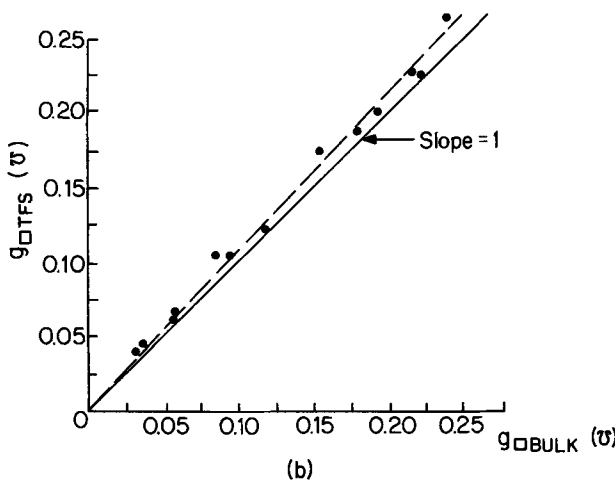
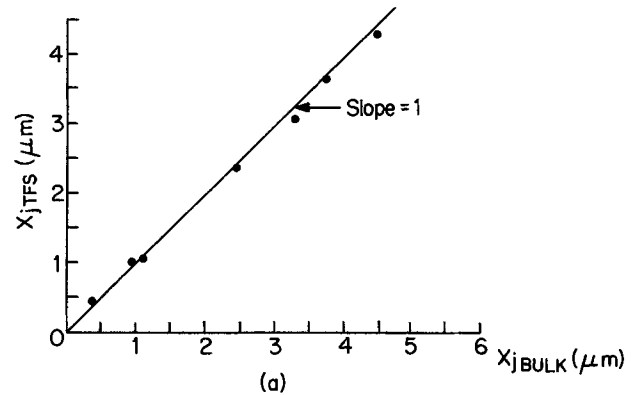
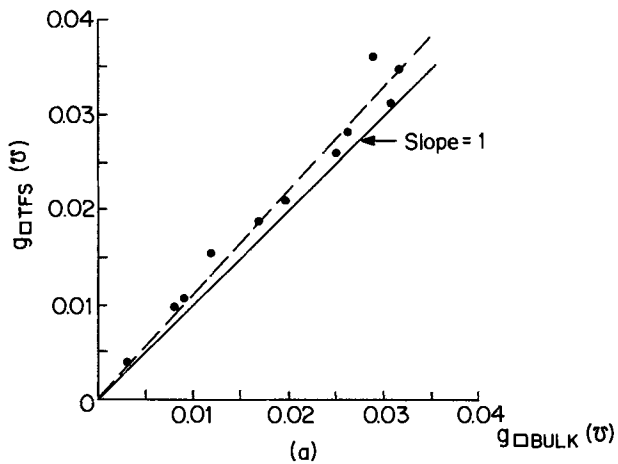


Fig. 2. Sheet conductance in thin films after diffusion as a function of sheet conductance in corresponding bulk wafers: (a) boron diffusion into n-type samples; (b) phosphorus diffusion into p-type samples.

Fig. 3. Junction depth in thin films after diffusion as a function of junction depth in corresponding bulk wafers: (a) boron diffusion into n-type samples; (b) phosphorus diffusion into p-type samples.

and "stream"<sup>1</sup> ambients. The oxide thicknesses were measured with an ellipsometer at the center of each sample. Unoxidized thin-film samples were also measured with the ellipsometer to confirm that the light ( $\lambda = 6328\text{\AA}$ ) did not penetrate through the silicon film to the underlying oxide layer and invalidate the results of the ellipsometer measurements. In most cases the oxide thickness on the thin-film sample was within 1% of that on the bulk samples, indicating that the oxidation rate of the thin films does not differ to any significant degree from the oxidation rate of bulk silicon wafers.

### Discussion

The data obtained from these experiments may be interpreted on the basis of the theory developed by Barry and Olofsen (6), which relates the diffusivity  $D$  and the segregation coefficient  $m$  of the dopant in the silicon to the measured sheet conductances and junction depths. Figures 3(a) and 3(b) indicate that the diffusivities of both phosphorus and boron are the same in the thin films and in bulk wafers, at least for the shallower diffusions. From the  $x_j$  vs.  $\sqrt{t}$  data,  $\sqrt{D}$  in the silicon film was calculated to be  $0.22 \mu\text{m}/\text{hr}^{1/2}$  for boron diffusion and  $0.30 \mu\text{m}/\text{hr}^{1/2}$  for the shallower phosphorus diffusions, in good agreement with the values previously obtained under similar conditions in bulk silicon (6, 7).

Possible causes of the shallower junction depths measured in the thin-film samples than in bulk wafers after the longer phosphorus diffusions should be briefly considered. Since the phosphorus atoms only have a finite thickness of silicon into which to diffuse, the boundary condition of the diffusion equation will be different from that usually encountered. As the junction depth approaches the film thickness, the impurity atoms will start to pile up near the bottom surface. The solution to the diffusion equation for the case of a finite film thickness and a constant surface dopant concentration is given by (8)

$$\frac{C}{C_s} = \sum_{n=0}^{\infty} (-1)^n \left[ \operatorname{erfc} \frac{2n x_f + x}{2\sqrt{Dt}} + \operatorname{erfc} \frac{2(n+1)x_f - x}{2\sqrt{Dt}} \right] \quad [1]$$

where  $x$  is the distance from the top surface of the silicon film and  $x_f$  is the film thickness. As a worst case we find that the concentration  $1 \mu\text{m}$  from the back of a  $7 \mu\text{m}$ -thick film is approximately 0.1% higher than the value found for the semi-infinite case. Consequently, the finite thickness of the silicon film cannot lead to the shallower junction depths observed in the thin films. In fact, the pile-up of impurity atoms near the back of the film should eventually lead to deeper junction depths in the thin films since the concentration at a given depth into the film will be increased above its value for the semi-infinite case. The shallower phosphorus junction depths may be related to the properties of the silicon film near the bottom surface, including the possibility of a stressed layer near the Si-SiO<sub>2</sub> interface or the precipitation of impurities. Subtle differences in the staining behavior may also influence the measured junction depth.

The differences in sheet conductance between the thin films and the bulk samples (Fig. 2) must arise from either a greater mobility or a larger number of charge carriers in the thin films. Consideration of

mobility changes expected from stress effects (9-11) indicates that the change should be in the opposite direction and markedly less in n-type diffused layers than in p-type diffused layers while the experimental behavior shows that the difference in sheet conductance is about the same for n-type and p-type diffused layers. In addition, stress measurements (12) indicate an upper bound of about  $5 \times 10^8$  dynes/cm<sup>2</sup> on the stress in the films. The corresponding maximum change in conductance should be less than about 1.5% in the boron diffused layers and less than about 0.2% in the phosphorus diffused layers—much less than the experimentally observed differences. Consequently, the differences in sheet conductance between the thin films and the bulk wafers cannot result solely from straightforward stress effects. Since Eq. [1] indicates that the finite film thickness should not significantly affect the dopant distribution for any case considered, a larger number of charge carriers in the thin film most likely results from a higher surface concentration and, hence, a greater segregation coefficient. (Further measurements on bulk samples which were either vapor etched or mechanically polished before phosphorus diffusion from doped oxides did not indicate any significant differences; therefore, any difference in segregation coefficient between the thin films and the bulk samples cannot be related solely to the vapor etch treatment given the electrochemically etched films.)

### Conclusions

From these measurements we may conclude that, to first order, the diffusion characteristics of dopant impurities are similar in the electrochemically etched thin films and in bulk wafers. Possible second-order effects include slightly higher sheet conductances in the thin films than in bulk control wafers and slightly shallower diffusion of phosphorus into p-type thin films than into bulk control wafers. The oxidation rate of the thin films is the same as that of bulk silicon.

### Acknowledgment

This research was supported by the Advanced Research Projects Agency under Contract DAHC 15-72-C-0171.

Manuscript submitted May 31, 1973; revised manuscript received Sept. 27, 1973.

Any discussion of this paper will appear in a Discussion Section to be published in the December 1974 JOURNAL.

### REFERENCES

1. D. J. Dumin *et al.*, *RCA Rev.*, **31**, 620 (1970).
2. K. H. Zaininger and C. C. Wang, *Solid-State Electron.*, **13**, 943 (1970).
3. H. J. A. van Dijk and J. de Jonge, *This Journal*, **117**, 553 (1970); R. L. Meek, *ibid.*, **118**, 1240 (1971).
4. T. I. Kamins, *Proc. IEEE (Lett.)*, **60**, 915 (1972).
5. T. I. Kamins, J. Manoliu, and R. N. Tucker, *J. Appl. Phys.*, **43**, 83 (1972).
6. M. L. Barry and P. Olofsen, *This Journal*, **116**, 854 (1969).
7. M. L. Barry, *ibid.*, **117**, 1405 (1970).
8. H. S. Carslaw and J. C. Jaeger, "Conduction of Heat in Solids," p. 309, Oxford University Press, London (1959).
9. H. Schlotterer, *Solid-State Electron.*, **11**, 947 (1968).
10. O. N. Tufté and E. L. Stelzer, *J. Appl. Phys.*, **34**, 313 (1963).
11. "Integrated Silicon Device Technology", Vol. 5: "Physical/Electrical Properties of Silicon," p. 61, Research Triangle Institute, Durham, N. C. (1964).
12. T. I. Kamins and E. S. Meieran, *J. Appl. Phys.*, **44**, 5064 (1973).

<sup>1</sup> Oxygen bubbled through 97°C water.



# Investigation of Imperfections in Silicon Substrates Using Copper Displacement Technique

M. J. Grieco\*<sup>1</sup>

IBM Components Division, East Fishkill Facility, Hopewell Junction, New York 12533

## ABSTRACT

A copper displacement etching system (1) has been used as an effective and sensitive technique for the delineation and evaluation of crystal imperfections in polished silicon substrates. X-ray topographs of the substrate prior to and after epitaxial deposition show a relationship between subsurface damage and/or contamination and defects in the epitaxial film.

Clean surfaces are essential in the fabrication of semiconductor devices. Any contaminants in the surface or subsurface could affect subsequent processing steps and thus influence the performance, yield, reliability, and quality of the semiconductor devices. Epitaxial spikes and/or mounds, for instance, on the surface would impact the subsequent photolithographic and masking operations resulting in device yield loss.

A technique is described to reveal damaged semiconductor material and to remove embedded material and surface contaminants to produce a clean surface.

## Experimental

For all experiments, vendor material and IBM Chem-Mech polished p-type,  $\langle 111 \rangle$  10-20 ohm-cm were used (2). Prior to delineation of subsurface damage with the copper displacement reaction,<sup>2</sup> the wafers were degreased in trichloroethylene, rinsed in acetone, deionized water, and heated in nitric acid ( $\text{HNO}_3$ ). The wafers were then rinsed in distilled water, rinsed in methanol, and blown dry with filtered  $\text{N}_2$ . The copper displacement process is performed at room temperature in a Teflon or polyethylene beaker. All photomicrographs were taken using Nomarski interference contrast.

In order to minimize artifacts produced during the copper displacement process and to remove controlled amounts of silicon, a 10 or 20 times dilution of the stock solution with distilled water is used. A 10:1 and

\* Electrochemical Society Active Member.

<sup>1</sup> Present address: Bell Laboratories, Murray Hill, New Jersey 07974.

Key words: imperfections, silicon substrates, copper displacement, x-ray topography.

<sup>2</sup> The copper displacement stock solution has a composition of: 55g  $\text{CuSO}_4 \cdot 5 \text{H}_2\text{O}$ ; 50 ml HF (49%); 950 ml  $\text{H}_2\text{O}$ . Approximately 1500 A/min of silicon is removed with this composition.

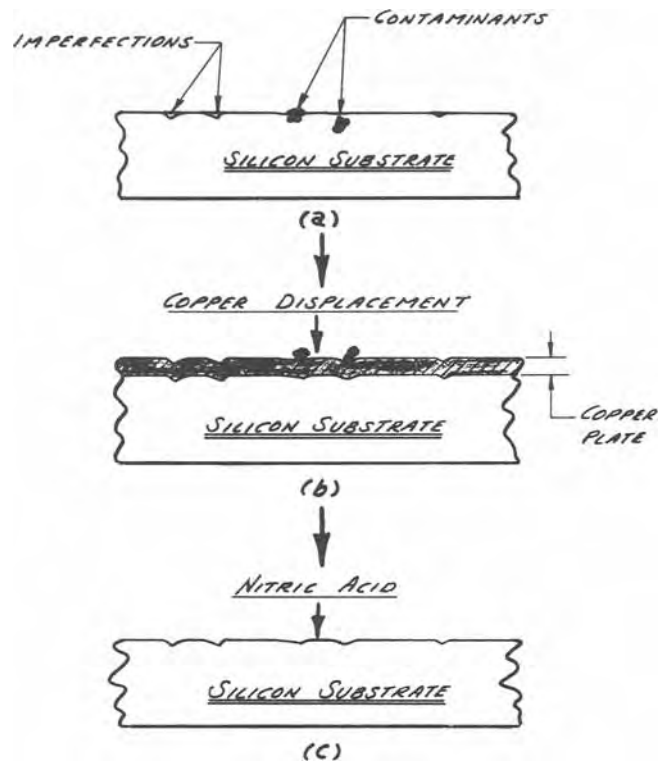


Fig. 1. Schematic representation of the mechanism involved in the copper displacement of silicon surfaces for determining crystal quality.

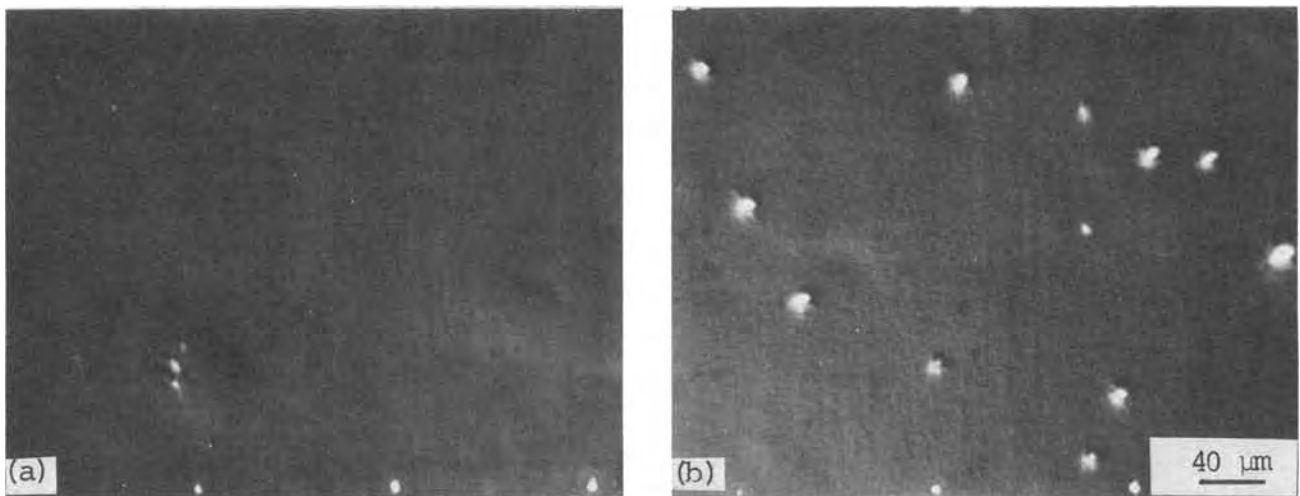
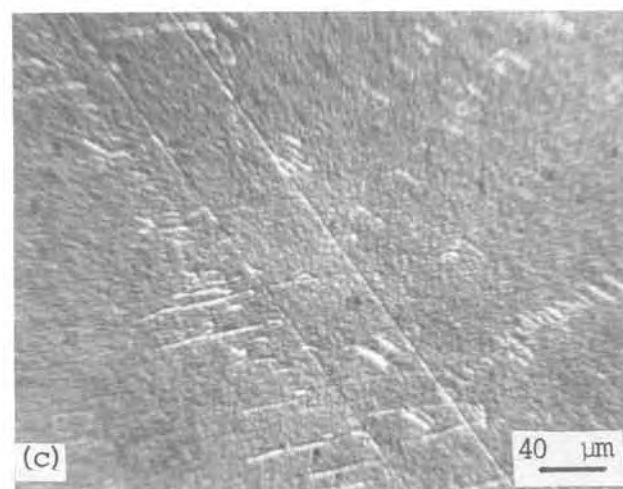
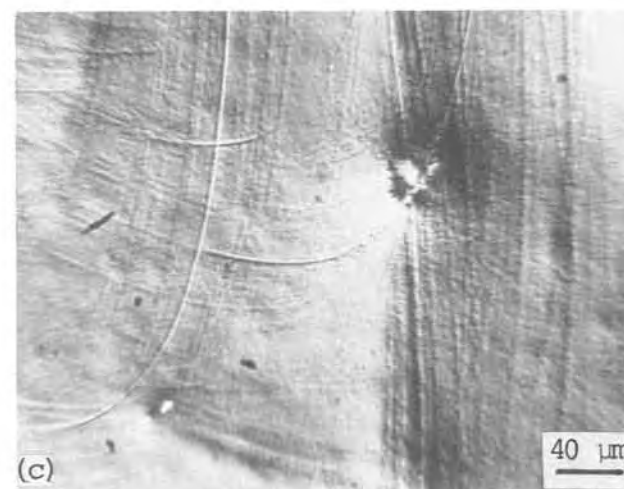
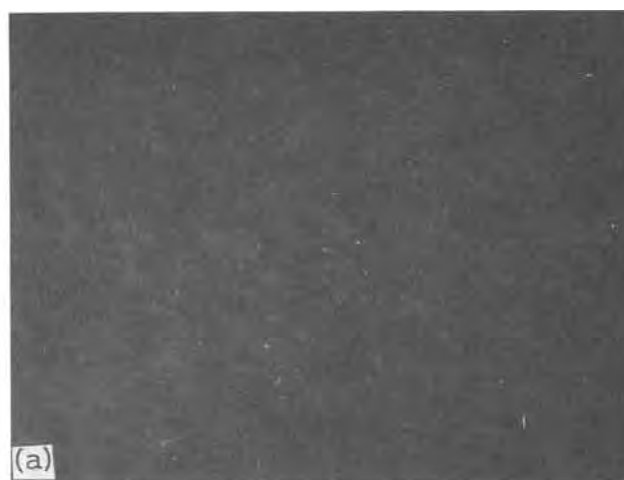


Fig. 2. Photomicrograph of silicon substrate containing embedded material. a, Original surface; b, embedded material revealed after 1 min copper displacement.



**Fig. 3.** Photomicrograph of silicon substrate containing crystallographic imperfections. a, Original surface; b, imperfections delineated after 1 min copper displacement; c, twinning delineated after 1 min copper displacement.

20:1 dilution removes approximately 800 and 400 Å/min of silicon, respectively. Unless otherwise noted, all wafers were copper displaced for 1 min using the 10:1 dilution system. The copper plating is stopped by quenching the wafers with water. The copper film is then removed by dissolving in concentrated nitric acid ( $\text{HNO}_3$ ) and rinsing in distilled water. Adequate care

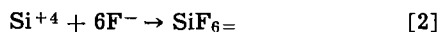
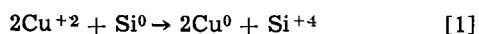


**Fig. 4.** Photomicrograph of silicon substrate containing work damage. a, Original surface; b, work damage delineated after 1 min copper displacement; c, work damage delineated after 5 min copper displacement.

must be taken to insure that all copper plating solution is removed prior to removal of the copper film with  $\text{HNO}_3$ . If this is not done, continued etching of the surface will occur due to the  $\text{HNO}_3$ -HF mixture. This will cause anomalous results and interpretation of data will be difficult due to a leveling of imperfection sites revealed by the copper displacement reaction.



The dissolution of silicon and the simultaneous plating of copper takes place according to the following reactions



The displacement process involves an oxidation-reduction reaction, in which the copper ions are reduced to copper and the silicon is oxidized (Eq. [1]). The oxidized silicon is brought into solution by a suitable complexing agent such as fluoride ions (Eq. [2]).

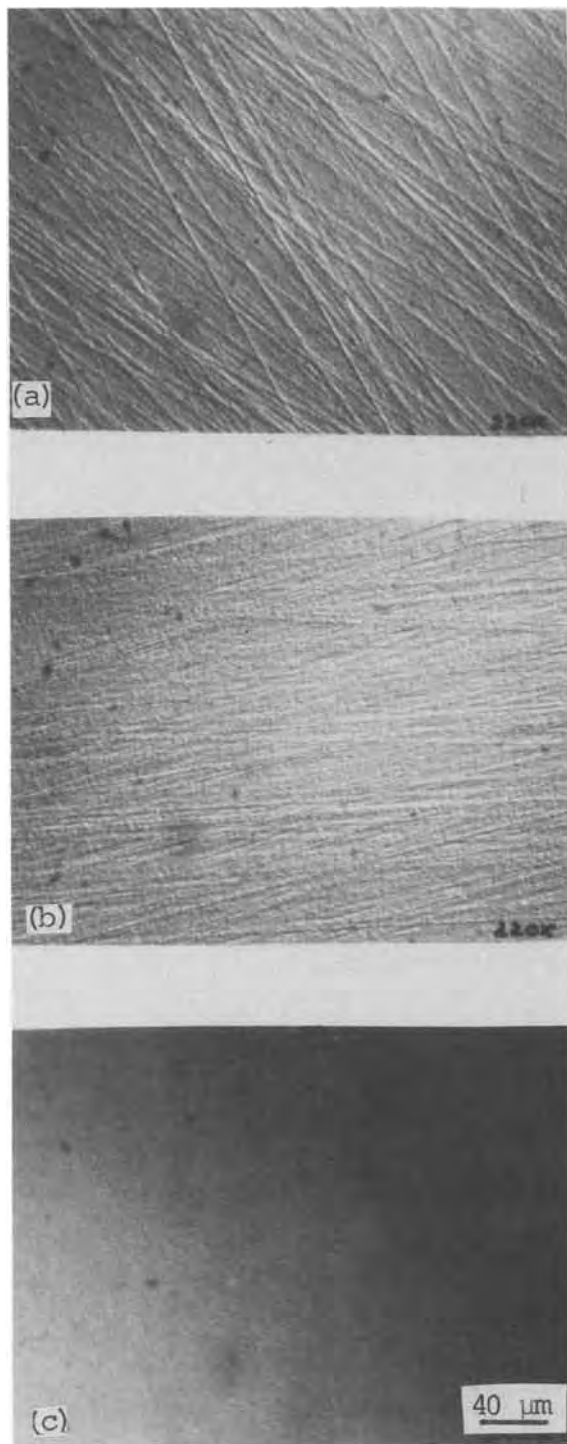


Fig. 5. Evaluation of different surface cleaning techniques and their effect on surface quality. a, Solvent clean after 1 min copper displacement; b, solvent and acid clean after 1 min copper displacement; c, solvent, acid, and HF clean after 1 min copper displacement.

## Results and Discussion

Figure 1 shows a schematic representation of the mechanism involved in the copper displacement of silicon surfaces for the delineation of subsurface damage, crystallographic imperfections, and removal of surface contaminants. Figure 1(a) represents a wafer containing subsurface damage, embedded material, and surface contamination. During the copper displacement process [Fig. 1(b)], copper plates the entire platable silicon surface. However, there is an enhanced displacement of silicon under and around the nonplatable material and a copper layer is formed between the silicon surface and the subsurface or surface contaminants. There is also an enhanced displacement of silicon at crystallographic imperfections and regions where there is surface damage. This enhanced displacement is caused by small changes in surface energy and subsequent higher etch rates in these regions. When the copper layer is removed by a suitable reagent, the surface contaminants are removed and surface imperfections are delineated [Fig. 1(c)]. In the regions where particulate matter was present, small craters were revealed.

After delineation with the copper displacement technique, the types of surfaces obtained can be grouped into three types: (i) embedded or occluded material, (ii) crystallographic defects such as imperfections and twinning, and (iii) work damage caused by the sawing or lapping operation prior to polishing the silicon substrate. Figure 2 shows a photomicrograph of a silicon surface prior to and after copper displacement in which the embedded material in the subsurface has been delineated. These particles are 10-12  $\mu\text{m}$  in diameter. An attempt was made to identify these embedded particles with an electron microprobe. Aluminum well above the background level was found in these areas. The embedded particles were also observed in the scanning electron microscope (SEM), to "pop out" of the surface due to electrostatic charge up of the dielectric. This evidence indicates that the particles in question are most probably  $\text{Al}_2\text{O}_3$  (5), a material used in the wafer shaping operation having a typical size of 10-12  $\mu\text{m}$  in diameter.

Figure 3 shows a photomicrograph of a silicon surface which contains crystallographic defects. Imperfections and twinning can be seen in Fig. 3(b) and 3(c), respectively, after copper displacement of the original silicon surface.

During the wafer shaping operation, if sufficient material is not removed during the lapping or polishing operation, work damage will still be present in the silicon crystal [Fig. 4(b, c)]. Figure 4(b) shows a photomicrograph of a silicon surface containing work damage after copper displacement. After removing a total of 1  $\mu\text{m}$  from this surface [Fig. 4(c)], additional work damage is delineated that was present in the silicon crystal and not removed during the polishing operation.

As a final step in the silicon wafer shaping operation, some silicon wafer vendors "buff" their wafers on a polishing cloth. Although this removes any sur-

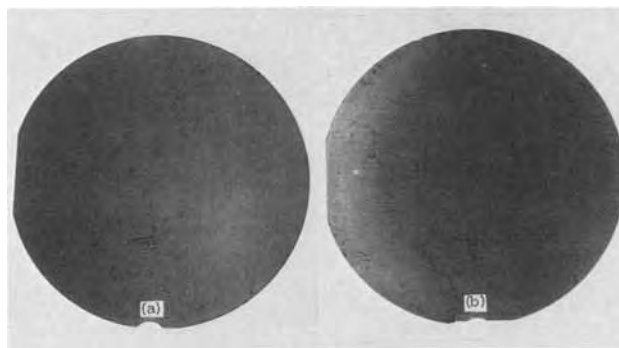


Fig. 6. X-ray topographs of: a, as-received silicon substrate; and b, after deposition of 7  $\mu\text{m}$  epitaxial film.

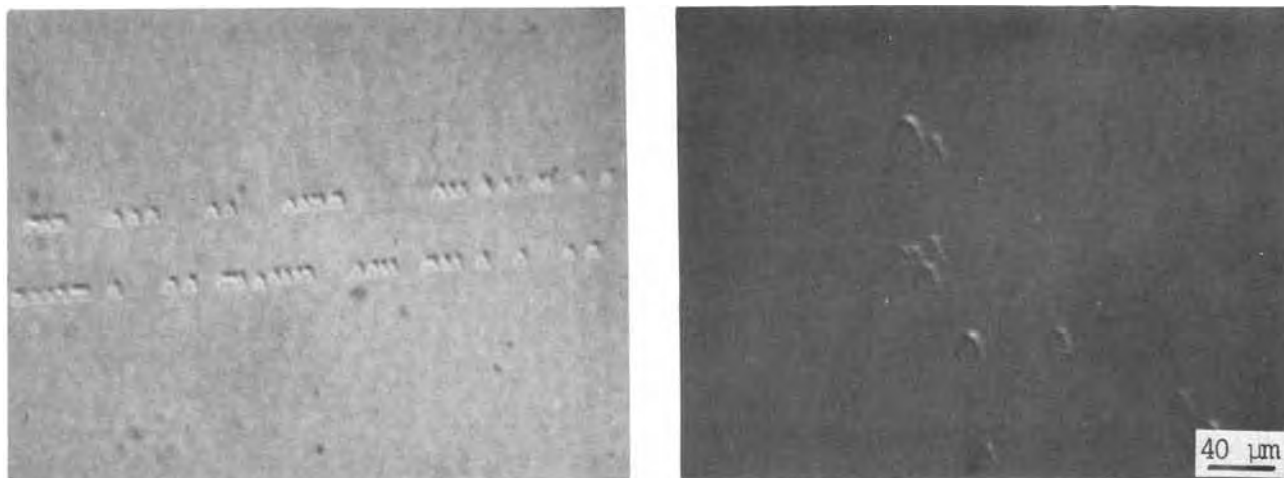


Fig. 7. Photomicrograph of film quality obtained after deposition of 7  $\mu\text{m}$  epitaxial film shown in Fig. 6

face particulate contamination, this process produces "wipe marks." It is felt that the "wipe marks" are caused by a smearing of a chemically removable residue that is present in the polishing cloth. This is evidenced by the fact that wafers from the same vendor not receiving the "buffing" step did not exhibit "wipe marks." The copper displacement technique was used to evaluate different surface cleaning techniques and their effect on surface quality and the removal of "wipe marks." Wafers known to contain "wipe marks" each received a different cleaning technique. After a copper displacement, the surface quality was evaluated.

Wafers received a solvent clean of trichloroethylene for 10 min at 60°C. Also used was the trichloroethylene/acetone/alcohol sequence (this sequence for water miscibility), and in all cases "wipe marks" were present after copper displacement [Fig. 5(a)]. When trichloroethylene (60°C, 10 min) plus sulfuric/nitric acid (sulfuric/nitric was used for the removal of organic contaminants) (100°C, 10 min) was used, the surface produced after copper displacement had a substantial reduction in the amount of "wipe marks" [Fig. 5(b)]. A combination cleaning of trichloroethylene (60°C, 10 min), sulfuric acid (100°C, 10 min), plus concentrated hydrofluoric acid (RT, 10 min) produced a featureless surface as seen in Fig. 5(c).

X-ray topographs [scanning oscillating technique, (SOT)] (3, 4) were performed on silicon wafers to determine by another technique if there was any crystal imperfections, subsurface damage, and embedded material in the silicon substrates. This x-ray technique scans across the wafer and reveals local variations in crystal perfection and orientation. The beam size used in this study was  $\approx 0.5$  mm in diameter.

Figure 6(a) shows an x-ray topograph of an as received wafer in which subsurface damage and con-

taminants present in the wafer are revealed. A 7  $\mu\text{m}$  epitaxial film was deposited and Fig. 6(b) shows a SOT in which the damage and contamination from Fig. 6(a) have propagated and are revealed in greater detail.

Figure 7 is a photomicrograph of the wafer shown in Fig. 6 after deposition of a 7  $\mu\text{m}$  epitaxial film. Stacking faults and imperfections were revealed in the epitaxial film and most defects in the epitaxial film could be correlated to defects/contaminants seen in the x-ray topograph prior to epitaxial deposition.

Contaminants on wafer surfaces were plotted prior to epitaxial growth. After epitaxial growth, the same regions were replotted and, in 65% of the cases, spikes/mounds were found.

X-ray topographs were also used to determine the extent of removal of embedded particles and surface contaminants when using the copper displacement technique. X-ray topographs were taken of the substrate prior to copper displacement. The contaminants revealed by the x-ray topograph can be seen in Fig. 8(a). Approximately 2  $\mu\text{m}$  of material was then removed from this surface by the copper displacement technique and x-ray topographs were taken of the resulting surface. As can be seen in Fig. 8(b), there is freedom from contaminants as seen in the silicon substrate prior to copper displacement.

### Conclusions

The copper displacement technique is a sensitive and suitable method for the delineation of subsurface damage and crystallographic imperfections in polished silicon substrates. This technique can also be used as a rapid method for evaluating and determining the crystalline quality of silicon substrates. X-ray topographs of the substrates prior to and after the copper displacement technique have shown that this technique does remove unwanted contaminants and that these contaminants do affect the quality of epitaxial films.

### Acknowledgments

I would like to thank D. L. Klein for helpful discussions and W. A. Westdorp for the performance and interpretation of the x-ray topographs.

Manuscript submitted March 1, 1972; revised manuscript received Aug. 20, 1973. This was Paper 187 presented at the Cleveland, Ohio, Meeting of the Society, Oct. 3-7, 1971.

Any discussion of this paper will appear in a Discussion Section to be published in the December 1974 JOURNAL.

### REFERENCES

1. R. Lieberman, W. Bracht, and D. L. Klein, *This*

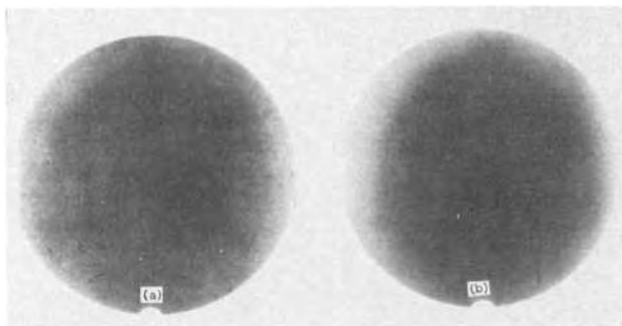


Fig. 8. X-ray topograph of a wafer prior to and after copper displacement technique. a, As-received silicon substrate; b, after 2  $\mu\text{m}$  material removed.

- Journal*, **111**, 62C (1964).  
 2. L. H. Blake and E. Mendel, *Solid State Technol.*, **13**, 42 (1970).  
 3. G. H. Schwuttke, *J. Appl. Phys.*, **36**, 2712 (1965).  
 4. G. H. Schwuttke, "X-ray Diffraction Microscopy of Imperfections in Semiconductor Crystals," AFCRL 64-545, Contract No. 19(604), 7313 (1964).  
 5. W. A. Westdorp, Private communication.

## Gas-Phase Etching of Sapphire

### III. Chlorotrifluoromethane

H. M. Manasevit\*

Rockwell International Electronics Group, Electronics Research Division, Anaheim, California 92803

#### ABSTRACT

The ever increasing interest in the use of sapphire ( $\alpha$ - $\text{Al}_2\text{O}_3$ ) as a substrate for the heteroepitaxial growth of various materials has prompted a re-examination of gas-phase etching as an effective means for improving the surface of  $\text{Al}_2\text{O}_3$ . Based on a previous investigation (1) in which several fluorinated hydrocarbons were found effective as etchants for  $\text{Al}_2\text{O}_3$ , chlorotrifluoromethane was selected for further study for several  $\text{Al}_2\text{O}_3$  orientations. It was found to be a good etch-polish agent for  $(01\bar{1}2)$ ,  $(0001)$ , and  $\sim(11\bar{2}0)$   $\text{Al}_2\text{O}_3$ .

The ever increasing interest in the use of sapphire ( $\alpha$ - $\text{Al}_2\text{O}_3$ ) for the heteroepitaxial growth of various materials has prompted a re-examination of gas-phase etching as a means for removal of work damage from the surfaces of several  $\text{Al}_2\text{O}_3$  orientations that show promise for the epitaxial growth of Si. Several years ago we described the use of sulfur fluorides (2) and fluorinated hydrocarbons (3) for the etch-polishing of  $\alpha$ - $\text{Al}_2\text{O}_3$ . Since then several other reports have appeared which have described chemical polishing methods involving molten salt (4-6) and liquid phase etchants (7-8). Reisman and co-workers (8) recently described their success in using air annealing combined with chemical polishing with  $\text{H}_2\text{SO}_4$ - $\text{H}_3\text{PO}_4$

mixtures to effect scratch-free  $\text{Al}_2\text{O}_3$  and MgAl spinel surfaces. Their results are encouraging; yet, the simplicity afforded by a gas-phase method which is compatible with the epitaxial growth system should not be overlooked.

We chose to investigate more in depth the effect of etching mechanically polished Verneuil and Czochralski-grown  $\alpha$ - $\text{Al}_2\text{O}_3$  with chlorotrifluoromethane,  $\text{CClF}_3$  (Freon-13), which from our previous studies (3) seemed to be less orientation dependent in its etch-polishing ability than most of the other fluorinated hydrocarbons superficially examined. In the studies to be described, particular attention was given to the etching characteristics of  $(01\bar{1}2)$   $\text{Al}_2\text{O}_3$ , which controls  $(100)$ Si growth, and  $(10\bar{1}4)$ ,  $(0001)$ , and

\* Electrochemical Society Active Member.  
 Key words: substrates, sapphire, etching, etch rate.

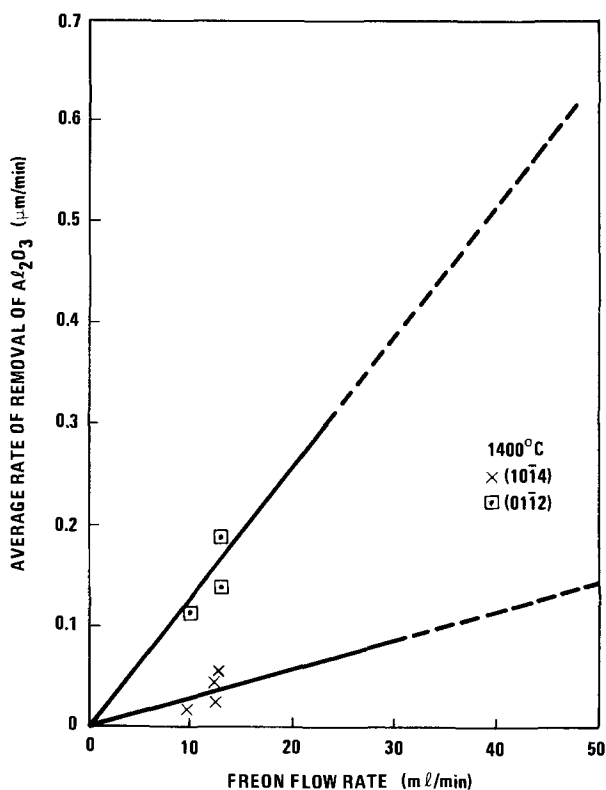


Fig. 1. Rate of etching of  $\text{Al}_2\text{O}_3$  by Freon at 1400°C

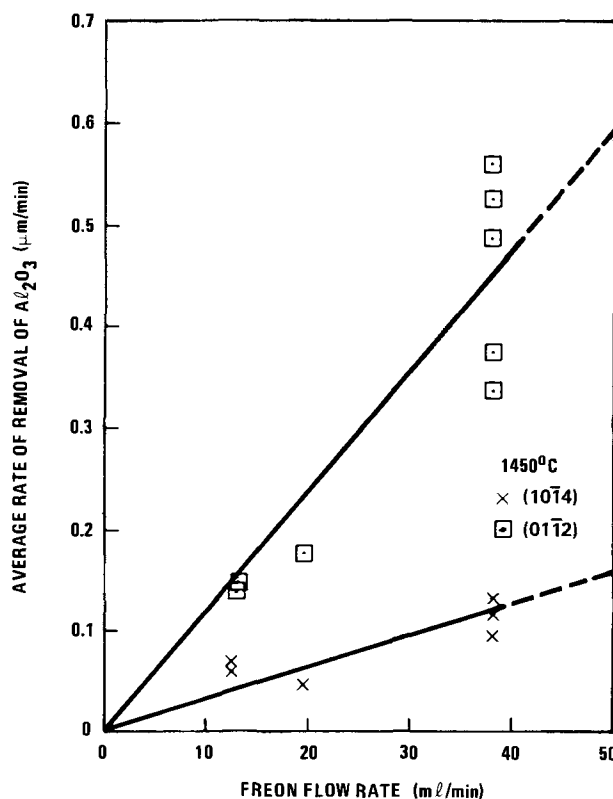


Fig. 2. Rate of etching of  $\text{Al}_2\text{O}_3$  by Freon at 1450°C

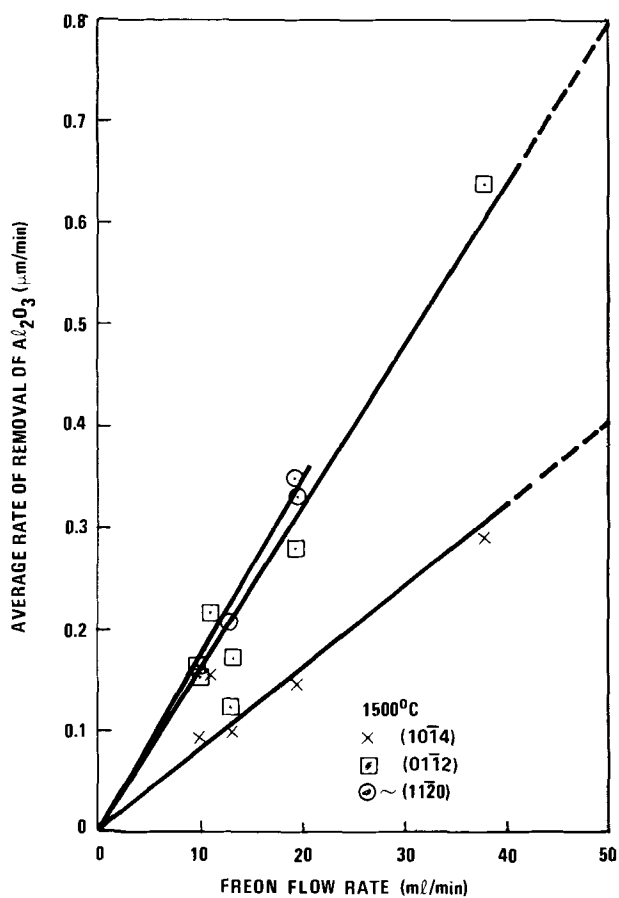


Fig. 3. Rate of etching of  $\text{Al}_2\text{O}_3$  by Freon at 1500°C



Fig. 4. Defects in Verneuil (01 $\bar{1}$ 2)  $\text{Al}_2\text{O}_3$  revealed by etch-polishing with Freon-13 (about 8  $\mu\text{m}$  removed).

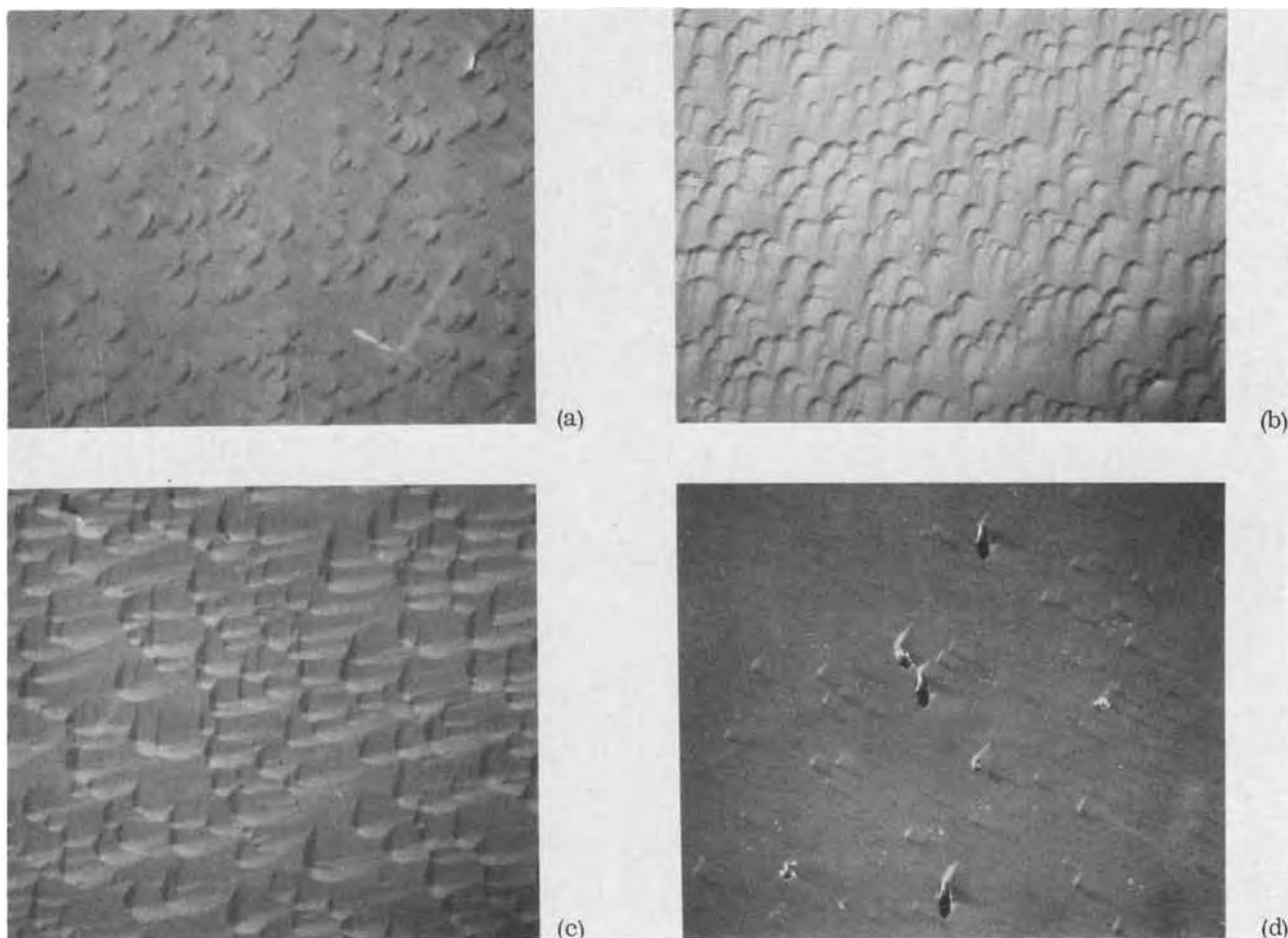


Fig. 5. The surface of Czochralski-grown (01 $\bar{1}$ 2)  $\text{Al}_2\text{O}_3$  after etching at 1500°C with Freon at a flow rate of 13 ccpm for (a) 25 min, (b) 50 min, (c) 75 min, and (d) 100 min. (All 110X).

$\sim(11\bar{2}0)$   $\text{Al}_2\text{O}_3$ , which control (111)Si growth. Cuts were made several degrees off of the  $(11\bar{2}0)$  plane in order to provide a surface orientation which would assure the growth of approximately (111)Si rather than (110)Si (9). The other  $\text{Al}_2\text{O}_3$  orientations were within 2 degrees of their designated planes.

### Experimental

Studies were performed in a vertical reactor system similar to that previously used (3). It includes a tank of inert carrier gas, such as helium, upstream from a tank of the "etchant" to be studied. These are connected via Matheson No. 607 and No. 600 flowmeters, respectively, to a stainless steel manifold joined to the quartz reactor by a Teflon connector. Carrier gas flow rates were set at 6 liters/min. The gases were passed over substrates resting on an  $\text{Al}_2\text{O}_3$  spacer covering a carbon pedestal inductively heated to the etching temperature. The spacer seemed to help provide a more even temperature distribution and to reduce reaction between the Freon-13 and the carbon pedestal. Pedestal temperatures were measured with an optical pyrometer, and uncorrected values are reported. The actual substrate temperature is estimated to be 50-100° lower than the observed 1400°-1550°C etching temperature used to establish the etch-polishing ability of Freon-13. The photomicrographs shown in the figures were made using a Nomarski interference objective on the microscope.

Etch-rate data for  $\alpha\text{-Al}_2\text{O}_3$  as a function of the flow rate of Freon-13 gas are recorded in Fig. 1-3 for uncorrected pedestal temperatures of 1400°, 1450°, and 1500°C. These preliminary data indicate that

$(01\bar{1}2)$   $\text{Al}_2\text{O}_3$ , etches at a greater rate than  $(10\bar{1}4)$   $\text{Al}_2\text{O}_3$ , the rate ratio being  $\sim 4:1$  at 1400°C and 1450°C but  $\sim 2:1$  at 1500°C. The spread in the data points is mostly due to the fact that the etch rate was calculated from the weight loss of a 15 mil thick slice, and 0.1 mg error can represent a considerable error in the etch rate, particularly when the measured weight loss was normally less than 2 mg for a sample weighing about 225 mg. (No correction was made for the weight loss from the edges and sides of the substrate or from the outer edge of the underside of the wafer, which normally is reached by the gas stream).

Etch temperature, substrate orientation, and etch rate were found to have an effect on surface quality, particularly on  $(01\bar{1}2)$   $\text{Al}_2\text{O}_3$ . The condition of the etched surface indicated that 1500°C is preferred to either 1400° or 1450°C for etch-polishing  $(01\bar{1}2)$   $\text{Al}_2\text{O}_3$  at Freon flows of  $\sim 13$  ml/min, even though the etch rate is approximately the same for the three temperatures. Structural defects appeared on the samples etched at 1400° and 1450°C, but only faint scratches were evident on the substrate etched at  $\sim 1500^\circ\text{C}$ . If these scratches were not propagated by the etching, then work damage was present even after 9  $\mu\text{m}$  of the thickness had been removed. Greater Freon flows, such as 20 ml/min and 40 ml/min, caused selective etching rather than polishing of the  $(01\bar{1}2)$ -oriented surface.

Etching was also sensitive to the quality of the crystals. Different etch patterns were often obtained on opposite sides of grain boundaries, as revealed

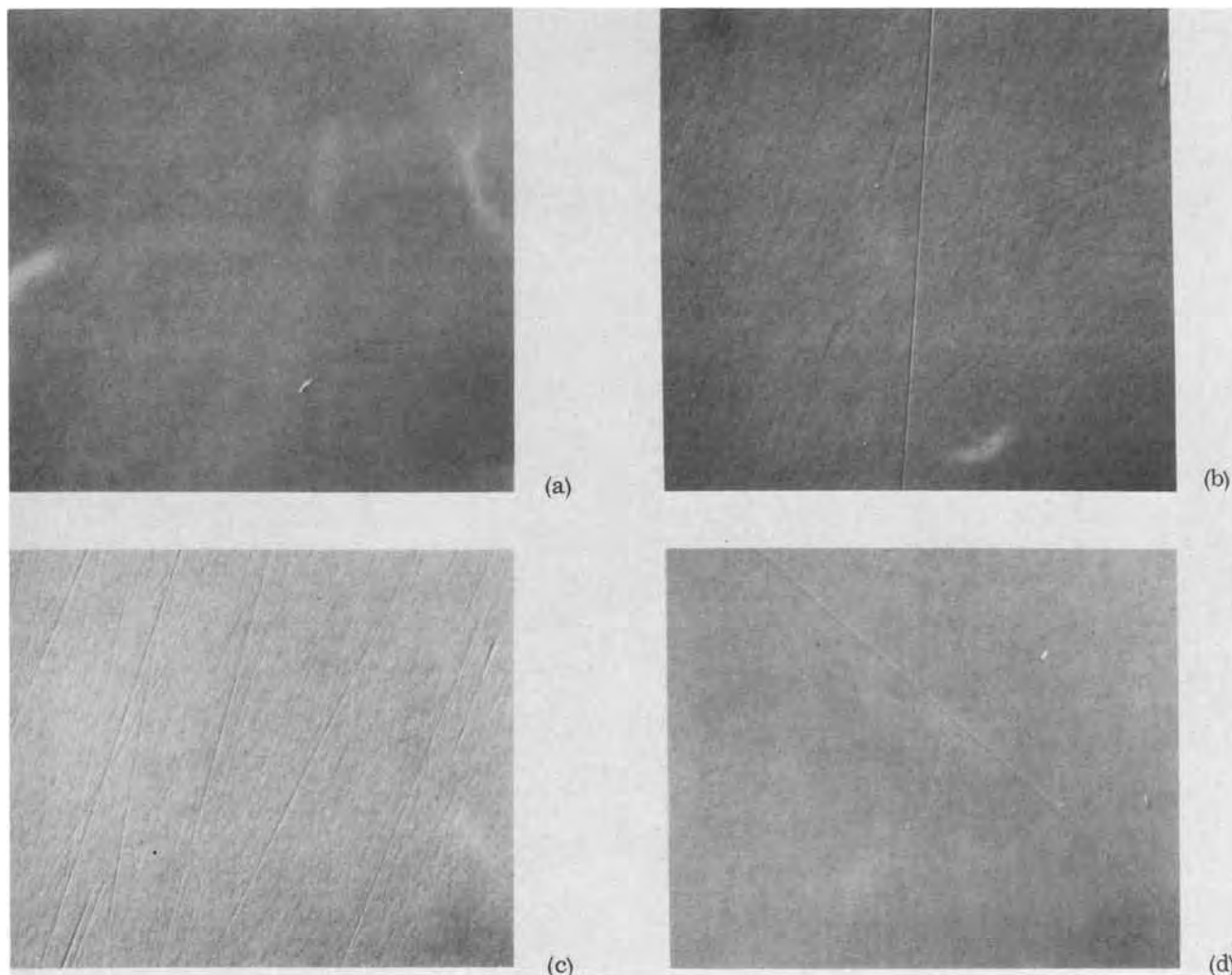


Fig. 6. The surface of different substrates of Verneuil-grown  $\sim(11\bar{2}0)$   $\text{Al}_2\text{O}_3$  after etching at 1500°C with Freon at a flow rate of 13 ccpm for (a) 25 min, (b) 50 min, (c) 75 min, and (d) 100 min.

in Fig. 4 for a  $(01\bar{1}2)$ -oriented slice of Verneuil  $\text{Al}_2\text{O}_3$  from which  $\sim 8 \mu\text{m}$  of thickness has been removed. The etch rate of Czochralski-grown  $\text{Al}_2\text{O}_3$  also appeared to be somewhat slower than that of Verneuil-grown  $\text{Al}_2\text{O}_3$ , for the same substrate orientation.

Figure 5 shows that gas-phase etching of Czochralski-grown  $(01\bar{1}2)\text{Al}_2\text{O}_3$  can also produce considerable etching of the crystal planes, but the etch pattern is relatively uniformly distributed. Etching to a  $\sim 20 \mu\text{m}$  depth led to a smoother surface, which may have resulted either from the removal of surface work damage or the exposure of a plane of  $\text{Al}_2\text{O}_3$ , oriented slightly different from the original plane, that is more susceptible to gas-phase polishing than to etching.

Etching of good quality Verneuil  $\text{Al}_2\text{O}_3$  oriented to  $\sim(1\bar{1}20)$  (Fig. 6) seems to reveal primarily the work damage produced by mechanical polishing; however, some areas of the Verneuil-grown substrate did possess a relatively high density of diamond-shaped etch pits (not shown in the figure). Czochralski-grown  $\text{Al}_2\text{O}_3$  oriented near  $(1\bar{1}20)$  seemed to polish well with Freon-13 except when the work damage in the vendor-polished slices was very deep. In some cases the removal of  $\sim 5 \mu\text{m}$  of surface seemed sufficient; for other substrates, the removal of at least  $12 \mu\text{m}$  was still insufficient to remove obvious work damage. These results suggest that close control of the sawing and mechanical polishing processes used in earlier stages of substrate preparation is necessary.

Si films,  $2 \mu\text{m}$ -thick, were grown simultaneously on the various substrate surfaces shown in Fig. 5 and 6 and on unetched  $(01\bar{1}2)\text{Al}_2\text{O}_3$ . Essentially identical

carrier mobilities were found, suggesting that the Si overgrowth is able to "overcome" much of the substrate imperfection during its growth, with the actual mobility-limiting factor being the stress-producing thermal contraction and/or lattice mismatch between the two substrates.

The same set of etch-polish conditions proved to be helpful in preparing smooth surfaces on  $(0001)\text{Al}_2\text{O}_3$ , shown in Fig. 7. After 25 min of etching, scratches were still visible. After 50 min the scratches were essentially gone, and the surface remained smooth after 75 and 100 min of etching. However, a number of hexagonal etch pits are evident. These may be characteristic of defects in the substrate or caused by reaction with the substrate of impurities in the etchant and/or those that may have been introduced into the etching atmosphere by reaction of the Freon with the carbon pedestal. Figure 7c is included to show the selectivity of the gas-phase process to certain types of defect structure present in these substrates cut from Verneuil-grown  $\text{Al}_2\text{O}_3$ .

As was the experience of Reisman *et al.* (8),  $(10\bar{1}4)\text{Al}_2\text{O}_3$  did not lend itself readily to gas-phase polishing, for a pit-free surface was not obtained under any of the experimental conditions used. Figure 8 indicates the effect of temperature on  $(10\bar{1}4)$ -oriented surfaces after removal of  $\sim 3 \mu\text{m}$  of material. The substrate as received from the vendor appeared to be essentially featureless but, after removal of 2-3  $\mu\text{m}$  or less of material, the scratch density was revealed. A majority of these scratches can be removed; light scratches seem to be removable, but major ones are either propagated by the etching or are so deep

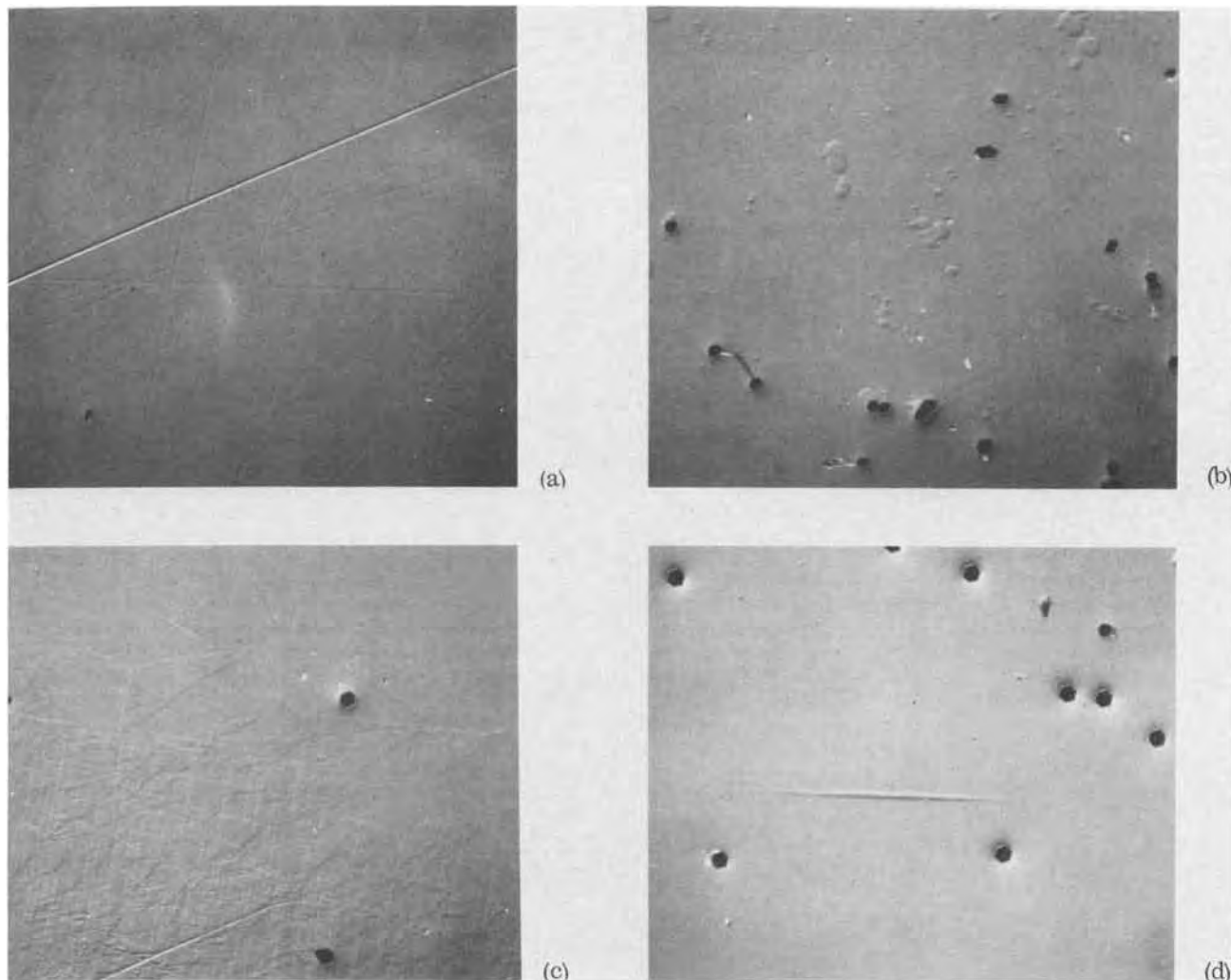


Fig. 7. The surface of  $(0001)\text{Al}_2\text{O}_3$  after etching at  $1500^\circ\text{C}$  with Freon at a flow rate of 13 ccpm for (a) 25 min, (b) 50 min, (c) 75 min, and (d) 100 min.



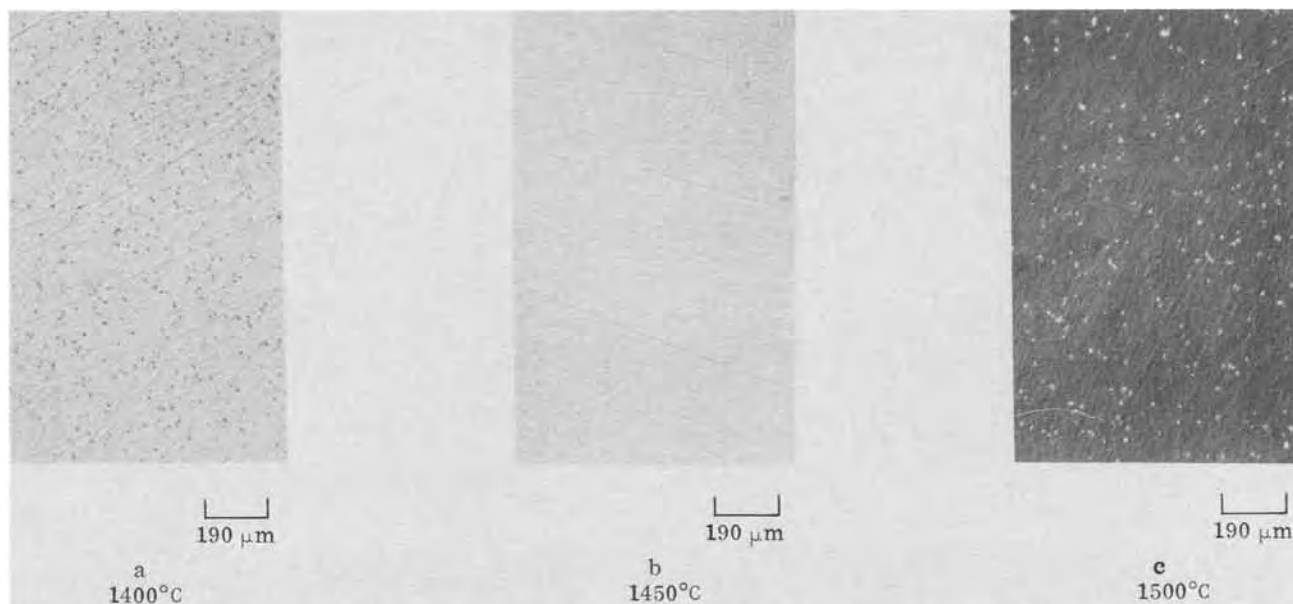


Fig. 8.  $(10\bar{1}4)Al_2O_3$  surface after etch-polishing with Freon at flow rate of 13 ml/min at various temperatures. Approximately  $3 \mu m$  of surface removed from each substrate.

as to require removal of major quantities of the substrate surface. This, in turn, usually causes deep pitting of the surfaces. However, even though Freon-13 has not been effective in providing an etch pit-free surface on  $(10\bar{1}4)Al_2O_3$ , it has been useful as a means for helping evaluate mechanical polishing techniques for this orientation and others. The low etch rates possible with Freon-13 permit very good control of surface removal in order to correlate studies of polishing with the formation and presence of work damage.

#### Conclusion

Freon-13 appears to be a good etch-polish agent for  $(01\bar{1}2)$ ,  $\sim(11\bar{2}0)$ , and  $(0001)Al_2O_3$  and useful for removing work damage from  $(10\bar{1}4)Al_2O_3$ . A combination of slow etch rate and high etch temperature seems to provide the best surfaces for the above  $Al_2O_3$  orientations. A work-damage free surface, however, does not necessarily lead to Si films with improved mobilities.

#### Acknowledgment

The author wishes to express his thanks to F. M. Erdmann, who helped in the etching experiments, to G. W. Johnson for taking some of the photomicrographs, and to R. P. Ruth for his most helpful discussions and review of this paper.

This research was supported in part by ARPA under Order 1585, monitored by USAMICOM, Redstone Arsenal, AL, under Contract No. DAAH01-70-C-1311.

Manuscript submitted May 2, 1973; revised manuscript received July 16, 1973. This was Paper 221RNP presented at the Houston, Texas, Meeting of the Society, May 7-12, 1972.

Any discussion of this paper will appear in a Discussion Section to be published in the December 1974 JOURNAL.

#### REFERENCES

1. H. Manasevit, *This Journal*, **115**, 434 (1968).
2. H. Manasevit and F. L. Morritz, *ibid.*, **114**, 204 (1967).
3. H. Manasevit, *ibid.*, **115**, 434 (1968).
4. P. H. Robinson and C. W. Mueller, *Trans. Met. Soc. AIME*, **236**, 268 (1968).
5. T. A. Zeveke, L. M. Kornev, and V. A. Tolomasov, *Soviet Phys-Cryst. (English Transl.)*, **13**, 493 (1968).
6. C. C. Wang, *J. Appl. Phys.*, **40**, 3433 (1969).
7. R. Aeschlimann, F. Gassmann, and T. P. Woodman, *Mater. Res. Bull.*, **5**, 167 (1970).
8. A. Reisman, M. Berkenblit, J. Cuomo, and S. A. Chan, *This Journal*, **118**, 1653 (1971).
9. H. M. Manasevit, R. L. Nolder, and L. A. Moudy, *Trans. Met. Soc. AIME*, **242**, 465 (1968).

# Chemically Vapor Deposited Tungsten for Semiconductor Metallizations

C. M. Melliar-Smith, A. C. Adams,\* R. H. Kaiser, and R. A. Kushner

Bell Laboratories, Murray Hill, New Jersey 07974

## ABSTRACT

The properties of CVD tungsten films, produced by the hydrogen reduction of  $WF_6$  or  $WCl_6$ , have been investigated to determine the suitability of the films for use as silicon integrated circuit metallizations. Both low pressure and atmospheric pressure flow systems have been investigated.

The tungsten films show excellent adhesion to silicon substrates, have resistivities between 6 and 15  $\mu\text{ohm-cm}$  depending on thickness, and are easily etched into submicron patterns. In addition, data on the contact resistance to silicon and MOS properties of tungsten films from both deposition reactions have been measured.

The use of chemical vapor deposition (CVD) to deposit thin tungsten films for integrated circuit metallizations has been investigated for several years (1, 2). Usually the tungsten is deposited using the hydrogen reduction of tungsten hexafluoride at temperatures between 600° and 800°C. The process is easily controlled and produces excellent tungsten films which are suitable for some integrated circuit applications (2).

However, the corrosive nature of the reactants and products tends to degrade the thermally oxidized silicon wafers used for the integrated circuits. This fact has generated additional interest in the use of tungsten hexachloride, which is less corrosive toward  $SiO_2$ , and has been used to deposit tungsten films in a similar manner to the hexafluoride (3, 4) although less information is available on their subsequent use for integrated circuit metallizations.

Consequently we have compared the two reactions for application to silicon integrated circuits, extending previous studies to include the use of CVD tungsten as a gate metallization for unipolar devices.

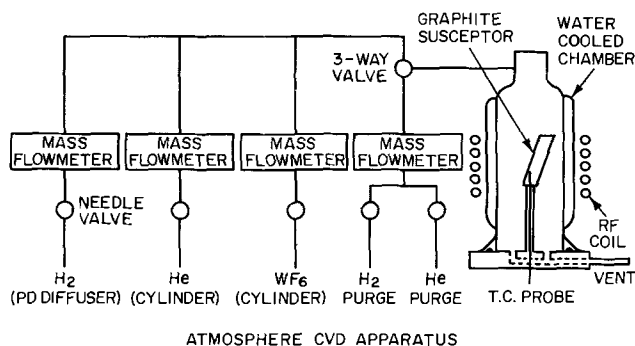
## Experimental

Tungsten films were deposited in both atmospheric and low pressure (1-10 Torr) flow systems from the hexafluoride and at atmospheric pressure from the hexachloride. Schematic diagrams of the deposition systems are shown in Fig. 1 and 2. The systems were rf heated using graphite or molybdenum susceptors. The temperature was controlled by a thermocouple embedded in the susceptor. The low pressure system proved somewhat unsatisfactory for two reasons. Firstly, at low pressure good thermal contact between the susceptor and the substrate is difficult to achieve and an inevitable uncertainty exists as to the substrate surface temperature in a fast flow system. Secondly, the use of rf heating at low pressure resulted in a plasma in the deposition chamber, the effect of which could result in ion bombardment damage to sensitive substrates.

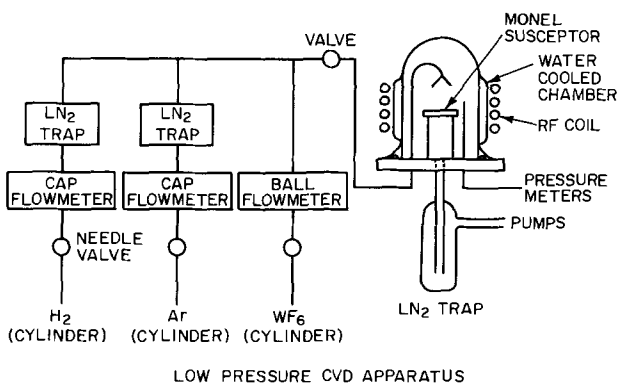
The tungsten hexachloride saturator and the gas lines leading from the saturator to the reaction chamber were heated to  $150^\circ \pm 5^\circ\text{C}$ . Chemicals used were: hydrogen, purified using a palladium diffuser; argon, purified using a titanium chip furnace; helium (99.9999%); hydrogen chloride (99.99%); tungsten hexafluoride (99.5%); and tungsten hexachloride (59%). The major impurity in the tungsten hexachloride was tungsten oxychloride ( $WOCl_4$ ) which was removed by sublimation at 100°C. The thickness of the deposited tungsten was measured by the  $\beta$ -backscatter technique.

## Results and Discussion

**Deposition.**—Typical deposition conditions are shown in Table I. The deposition temperature was varied from



ATMOSPHERE CVD APPARATUS



LOW PRESSURE CVD APPARATUS

Fig. 1. Apparatus used for the chemical vapor deposition of tungsten from tungsten hexafluoride.

420° to 800°C for the hexafluoride reaction, and from 550° to 950°C for the hexachloride process. The effect of substrate temperature on the deposition rate is shown in Fig. 3 for the hexachloride reaction. At deposition temperatures below 600°C the rate falls off rapidly, rises to a maximum between 700° and 900°C and subsequently falls off again above 900°C. The results are similar to those published by Mehalchick and MacInnis (4) who found a maximum deposition rate at 600°C. The temperature dependence of the deposition

Table I. Conditions for depositing tungsten

Pressure	1 Torr	1 atm.	1 atm.
Temperature	700°C	700°C	700°C
Ar	0.2 liter/min	—	30 liter/min
He	—	3 liter/min	—
H <sub>2</sub>	0.1 liter/min	1 liter/min	5 liter/min
WF <sub>6</sub>	0.009 liter/min	0.004 liter/min	—
WCl <sub>6</sub>	—	—	0.5 liter/min*
Dep. rate	3000 Å/min	1000 Å/min	1000 Å/min

\* Electrochemical Society Active Member.

Key words: metallization, tungsten, semiconductors, CVD.

\* An Ar flow of 0.5 liter/min through the  $WCl_6$  saturator at 150°C.



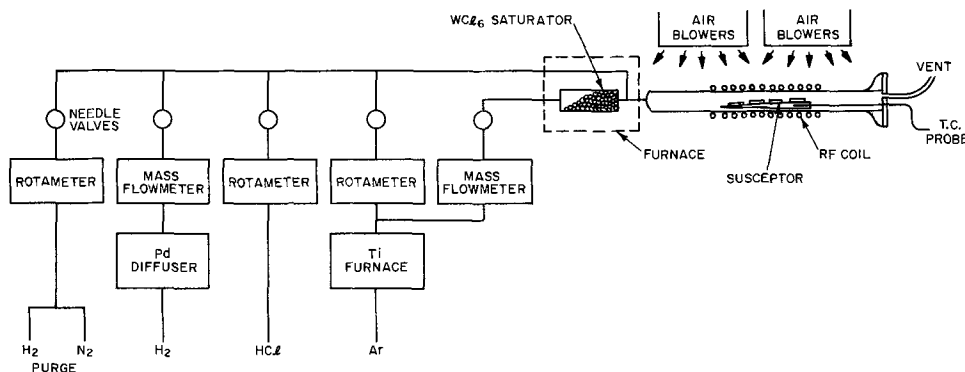


Fig. 2. Apparatus used for the chemical vapor deposition of tungsten from tungsten hexachloride.

rate can be rationalized as follows: at low temperatures the reaction behaves as a normal, thermally dependent, surface reaction. As the substrate temperature is raised, the deposition rate becomes more and more limited by gas-phase diffusion of the reactants to the surface, and consequently approaches a region of temperature independence. A further increase in temperature results in a drop in the deposition rate as measured by the thickness of the substrate. This is a result of the combined effects of the onset of a homogeneous gas-phase reaction and deposition on the walls of the reaction chamber.

For both chemical reactions, the deposition rate could be varied between 200 and 3000 Å/min by changing the concentration of the tungsten hexafluoride or tungsten hexachloride. The thickness of the tungsten films ranged up to 3  $\mu\text{m}$ .

Tungsten films can be deposited selectively at a silicon surface by reducing tungsten hexafluoride with silicon in an inert atmosphere (1, 2). The reaction proceeds until a limiting tungsten thickness of 300 to 400 Å is reached. The selective deposition of tungsten onto silicon from hexachloride proved very slow, and useful films cannot be produced unless hydrogen is used as the reducing agent.

**Film structure and analysis.**—CVD tungsten from the hydrogen reduction of tungsten hexachloride deposits on  $\text{SiO}_2$  with a bcc structure and a slight  $\langle 110 \rangle$  orientation as shown by pole figure x-ray measurements. The preferred orientation is enhanced if the

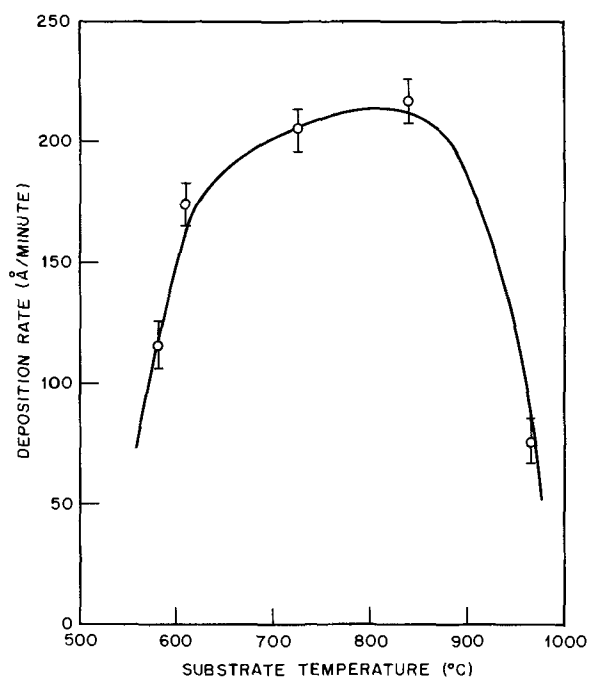


Fig. 3. Deposition rate as a function of substrate temperature using tungsten hexachloride.

samples are annealed in vacuum at 900°C for 60 min. The  $\langle 100 \rangle$  texture is observed in films deposited by the tungsten hexafluoride reaction. X-ray diffraction and transmission electron diffraction show no evidence for the presence of the  $\beta$ -phase in tungsten produced by either reaction.

The grain size of the films has been measured by transmission and replica electron microscopy. The surface grain size increases with increasing thickness as shown in Fig. 4. In addition, thicker films appear to have much larger individual crystals growing on the surface, some as large as 1  $\mu$  in a 3200 Å film.

Stress measurements in films of CVD tungsten deposited on  $\text{SiO}_2$  have been made by both x-ray and substrate bending techniques. All films have low residual stress levels, less than  $1 \times 10^{10}$  dynes/cm<sup>2</sup>. Films deposited from tungsten hexafluoride tended to be in compression, while films from tungsten hexachloride had tensile stress. Grain size and stress data are summarized in Table II.

No impurities were detected in the tungsten films by electron microprobe analysis, but spark mass spectrometry showed the presence of a number of trace elements, the major impurity being fluorine or chlorine (0.05-0.1%) from the fluoride and chloride reduction reactions, respectively.

**Film adhesion.**—Adherent tungsten films, 160-30,000 Å thick, have been deposited on silicon, silicon dioxide, and sapphire. More than 300 films were deposited from tungsten hexachloride and none showed evidence of poor adherence. Eleven samples were subjected to a 5 min boiling water treatment and to rapid thermal cycling from boiling water to liquid nitrogen. None of the samples failed these tests. Samples annealed in vacuum at 1000°C for 60 min showed no loss in adherence to silicon dioxide or sapphire; however, adhesion to silicon was lost due to tungsten silicide formation.

Tungsten films deposited on silicon from tungsten hexafluoride at atmospheric pressure were initially found to be nonadherent due to the formation of a thin ( $\sim 20$  Å) black film. The film was analyzed by electron diffraction and found to be polycrystalline silicon which is produced when the hydrogen fluoride by-product reacts with the native oxide film on the silicon surface

Table II. Grain size and stress in CVD tungsten

Dep. temp. (°C)	Thickness (Å)	Grain size (Å)	Stress (dynes/cm <sup>2</sup> )
<b>WF<sub>6</sub></b>			
600	2300	500-1000	$8 \times 10^9$ compressive
700	2300	500-1000	$2 \times 10^9$ compressive
800	2500	500-1000	$< 1 \times 10^9$
<b>WCl<sub>6</sub></b>			
550	2300	500-1000	$3 \times 10^9$ tensile
600	2600	200-2000	$4 \times 10^9$ tensile
650	2400	500-1000	$6 \times 10^9$ tensile
700	2000	500-1000	$10 \times 10^9$ compressive

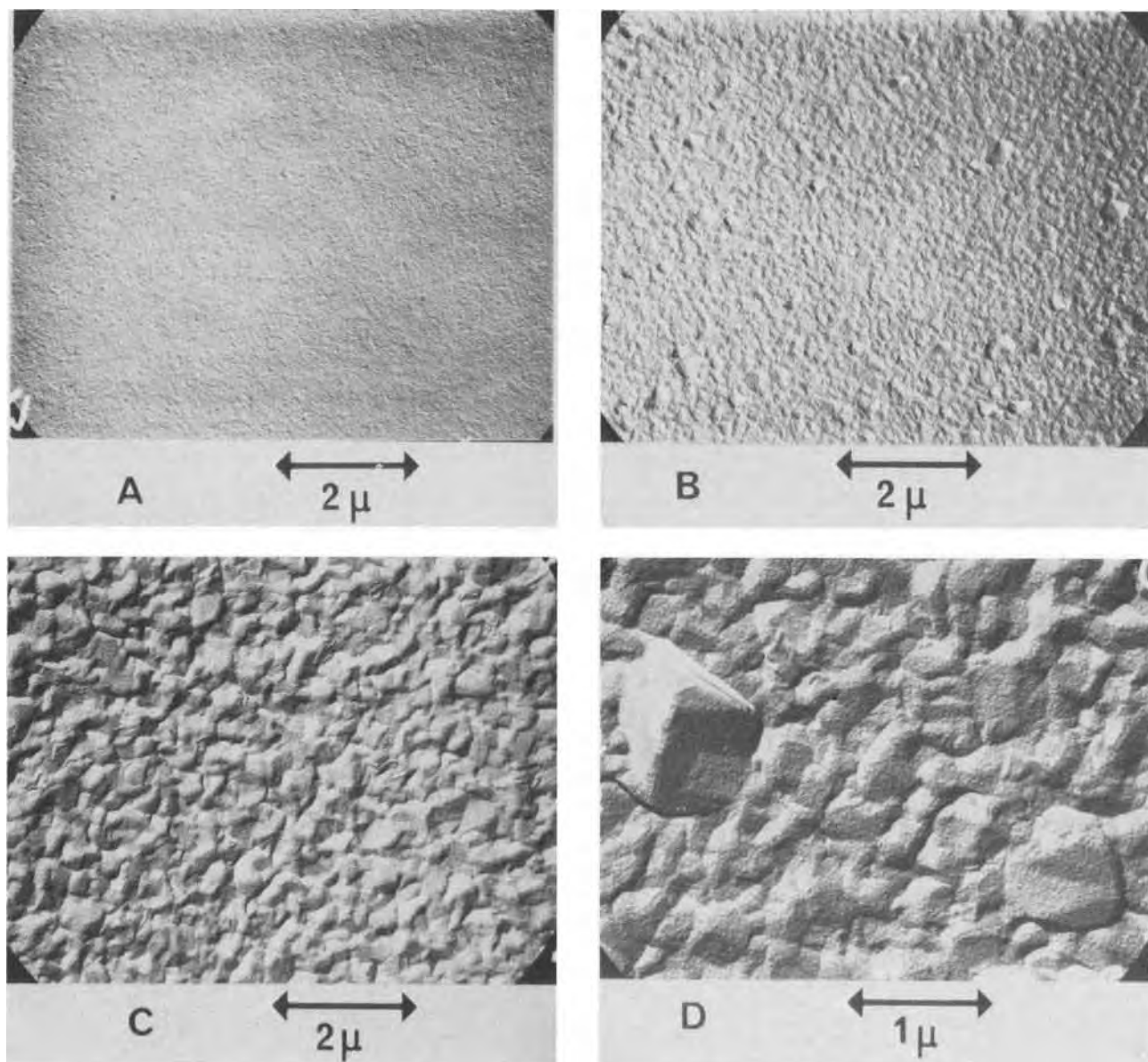
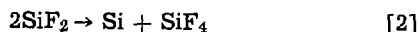


Fig. 4. Carbon replica electron micrographs of tungsten films on oxidized silicon substrates, produced by the hydrogen reduction of tungsten hexachloride. A, B, and C show rapid increase in surface grain size with increasing thickness (tungsten thickness: A, 400Å; B, 1700Å; C, 3200Å). D showing surface crystallite growth and fine particle nucleation on surface defects (tungsten thickness, 3200Å).



This reaction scheme is supported by several observations. The polycrystalline silicon forms only at the Si-W interface and not at the SiO<sub>2</sub>-W interface. This indicates that the silicon is required in the reactions. The polycrystalline silicon does not form when WF<sub>6</sub> in helium reacts with silicon; however, it does form when the WF<sub>6</sub> is reduced by hydrogen. The polycrystalline silicon has also been produced by passing dilute (0.01%) hydrogen fluoride in helium over a tungsten-coated silicon sample at 700°C. These observations indicate that the hydrogen fluoride diffuses through the tungsten to react at the Si-W interface. Finally, where silicon samples are coated with sputtered tungsten after removal of the native oxide by backspattering and the samples exposed to WF<sub>6</sub> in hydrogen at 750°C, the polycrystalline silicon is not formed. However, the polycrystalline silicon is formed when the experiment is repeated using silicon samples coated by atmospheric pressure CVD or E-gun evaporation techniques, where the native oxide film is not removed. These observations are consistent with reactions [1] and [2] in which silicon reacts with an ox-

dizing agent in the presence of hydrogen fluoride to form SiF<sub>2</sub> which disproportionates to form SiF<sub>4</sub> and polycrystalline silicon.

The formation of the polycrystalline silicon can be prevented by using high flow rates where the hydrogen fluoride is removed before it can react at the interface, or by using an *in situ* HCl etch which removes the native oxide.

The polycrystalline silicon does not form when tungsten hexachloride is used as the source of tungsten.

*Etching and step coverage.*—CVD tungsten may be delineated into high resolution patterns by standard lithography and etching techniques. Submicron lines have been produced using electron beam lithography and a buffered KOH/K<sub>3</sub>Fe(CN)<sub>6</sub> etch. The finest lines obtained were 2500Å wide. Figure 5a shows a grid pattern of 5000Å wide tungsten lines.

Step coverage was measured by depositing 2000Å of tungsten over 10 μm wide stripes etched into a 6000Å thick thermal oxide. The tungsten was delineated into 5 μm wide stripes perpendicular to the oxide bars. Step coverage was checked by measuring electrical continuity or by viewing with a scanning electron micro-

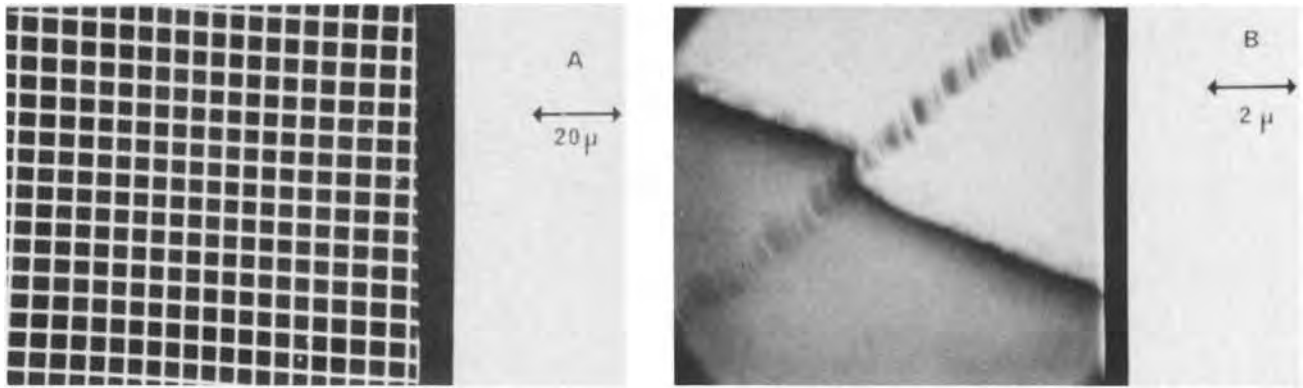


Fig. 5. A, Scanning electron micrographs of 5000Å wide grid pattern in 1400Å of CVD tungsten; B, scanning electron micrograph of 5 μm wide tungsten line passing over a 6000Å high oxide step.

scope (Fig. 5b). No failures in step coverage were observed.

**Resistivity.**—The resistivity of the tungsten films was found to be dependent on the thickness of the film, as shown in Fig. 6. The resistivity ranged from about three times the bulk value for films less than 1000Å thick to the bulk value (5.4 ohm-cm) for film thicknesses greater than 1 μm. No difference in resistivity was observed between films deposited from tungsten hexafluoride and from tungsten hexachloride. Annealing tungsten films on SiO<sub>2</sub> at 1000°C in vacuum for 60 min produced no detectable change in the resistivity.

A very similar dependence of resistivity on film thickness for polycrystalline CVD tungsten has been observed by Mayadas *et al.* (5) which they attribute to grain size effects. The work of Sheng *et al.* (6) on sputtered tungsten films (2500Å thick), however, suggests that the presence of vacancies and interstitial impurities is an additional cause of the residual resistivity above the bulk value.

**Contact resistance.**—The contact resistance of W-Si structures has been investigated by depositing tungsten on highly doped silicon through 11 × 14 μm holes in a 2000Å thick oxide film. The tungsten is then delineated into pads around each contact window and the I-V characteristics obtained from pad to pad measurements. The values for the contact resistance are dependent on the silicon doping concentration as shown

in Table III. In this table, the contribution from the spreading resistance has not been subtracted from the experimental values, so the true contact resistance is smaller than the values reported.

The contact resistance is independent of deposition temperature for films deposited from tungsten hexafluoride; however, the contact resistance is strongly dependent on deposition temperature when tungsten hexachloride is used as the source material. Samples deposited from tungsten hexachloride between 600° and 800°C are characterized by a high, nonohmic contact resistance; as the deposition temperature increases in this range, the I-V characteristics of the contacts become more nearly ohmic and the contact resistance decreases. Samples deposited at 850°C are ohmic with a low contact resistance (Table III). The temperature dependence suggests the presence of a detrimental interfacial layer between the tungsten and the silicon. This layer may be a native oxide film present on the silicon surface before deposition, or an oxide layer may be formed in the deposition chamber by the reaction of silicon with impurities in the tungsten hexachloride or in the carrier gas. Where tungsten is deposited at 850°C, the oxide layer may not prevent contact formation due to rapid diffusion of tungsten and/or silicon through the thin oxide. However, at 850°C the formation of tungsten silicide is rapid which may result in nonadherent films.

The contact resistance is markedly affected by subsequent heat-treatment. Tungsten as deposited on silicon shows evidence for only a very small amount of tungsten silicide and little change is observed in the contact resistance on annealing up to 800°C. Annealing above 800°C, however, causes silicide formation to proceed rapidly (7, 8) and 30 min at 900°C is sufficient to cause considerable deterioration in the contact resistance. The failure mechanism appears to be due to excessive tungsten silicide formation in the contact region. This compound formation results in a volume change in the contact metallization leading to severe mechanical stresses which can cause cracks to develop at the base of the contact window.

Forward bias measurements on n-type, 1-10 ohm-cm Schottky diode structures using tungsten deposited from tungsten hexafluoride give values of 0.66 eV for

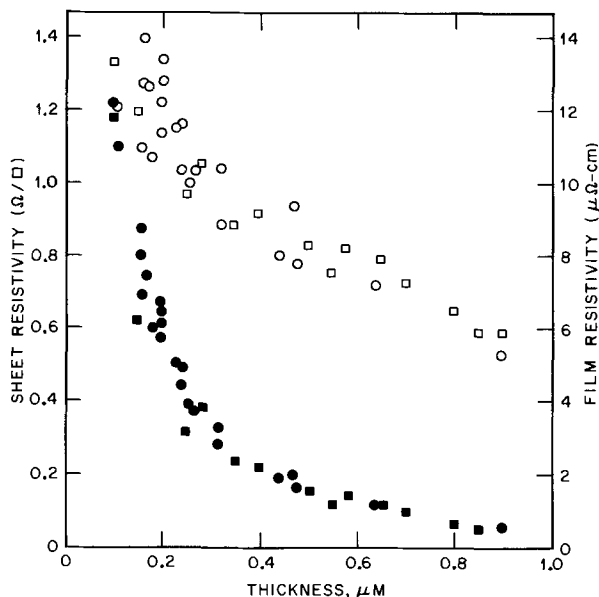


Fig. 6. Sheet and film resistivity curves as a function of film thickness for CVD tungsten. (Film resistivity points: ○, WCl<sub>6</sub>; □, WF<sub>6</sub>. Sheet resistivity points: ●, WCl<sub>6</sub>; ■, WF<sub>6</sub>.)

Table III. Contact resistance for CVD tungsten

Substrate	R <sub>c</sub> experimental (ohm-cm <sup>2</sup> )	R <sub>c</sub> theoretical (θ) (ohm-cm <sup>2</sup> )
WF <sub>6</sub> at 700°C		
2 × 10 <sup>19</sup> p-type	3 × 10 <sup>-5</sup>	1 × 10 <sup>-6</sup>
6 × 10 <sup>19</sup> p-type	2 × 10 <sup>-6</sup>	1 × 10 <sup>-7</sup>
1 × 10 <sup>20</sup> n-type	3 × 10 <sup>-6</sup>	6 × 10 <sup>-7</sup>
WCl <sub>6</sub> at 860°C		
5 × 10 <sup>19</sup> p-type	1 × 10 <sup>-5</sup>	2 × 10 <sup>-7</sup>
6 × 10 <sup>19</sup> p-type	7 × 10 <sup>-5</sup>	1 × 10 <sup>-7</sup>
9 × 10 <sup>19</sup> p-type	7 × 10 <sup>-6</sup>	8 × 10 <sup>-8</sup>

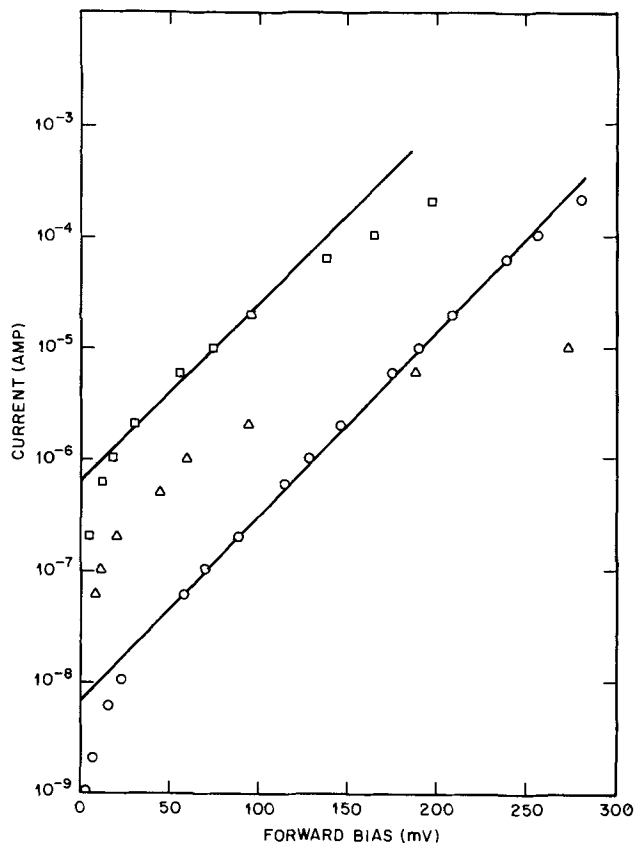


Fig. 7. Forward current as a function of applied voltage for CVD tungsten-silicon diode.  $\circ$ :  $\text{WF}_6$  at  $575^\circ\text{C}$ , 3 mil diode,  $n = 1.02$ ,  $\phi = 0.66$  eV.  $\square$ :  $\text{WCl}_6$  at  $700^\circ\text{C}$ , 10 mil diode,  $n = 1.07$ ,  $\phi = 0.59$  eV.  $\triangle$ :  $\text{WCl}_6$  at  $600^\circ\text{C}$ , 3 mil diode.

the barrier height and 1.02 for  $n$  (Fig. 7). Both values are in good agreement with data in the literature (1). If the tungsten is deposited from tungsten hexachloride, the forward bias measurement depends on the deposition temperature. Structures deposited at  $850^\circ\text{C}$  have I-V characteristics identical to those for the hexafluoride films ( $n = 1.03$ ,  $\phi = 0.65$  eV); for deposition at  $700^\circ\text{C}$ ,  $n = 1.07$  and  $\phi = 0.59$  eV. For depositions at  $600^\circ\text{C}$ , the I-V characteristics become too nonlinear for  $n$  and  $\phi$  to be determined (Fig. 7).

**MOS properties.**—The MOS characteristics of W/ $\text{SiO}_2$ /Si structures have been established by (i) 1 MHz C-V measurements; (ii) quasistatic C-V measurements with a 50 mV/sec sweep rate and  $\pm 10$  V sweep range; (iii) triangular voltage ramp ionic drift measurements with a 45 mV/sec sweep rate and  $\pm 6$  V sweep range at a temperature of  $300^\circ\text{C}$ ; and (iv) bias-temperature stressing at  $300^\circ\text{C}$  for 5-15 min, with  $\pm 10$  V on the field plate and cooling the sample under bias. The samples had 1200 Å of dry oxide grown in oxygen containing 1% hydrogen chloride on  $\langle 100 \rangle$ , 0.5 ohm-cm, n-type substrates. Prior to tungsten deposition, 200 Å of oxide was removed by etching in dilute hydrofluoric acid. The MOS capacitors were 20 or 25 mils in diameter and were formed by standard photolithography and etching techniques. Evaporated aluminum was used as the back contact. None of the samples were annealed.

The MOS characteristics are summarized in Table IV. MOS dots formed from tungsten hexafluoride were usually shorted or very leaky. This resulted from attack of the oxide by the tungsten hexafluoride during the metal deposition. Decoration of the MOS oxide after removing the tungsten showed pinhole densities as great as  $10^7/\text{cm}^2$ . Because of the large number of pinholes, the tungsten hexafluoride reaction is not suitable for gate metallizations over  $\text{SiO}_2$ .

Shorted and leaky dots do not form when tungsten is deposited from tungsten hexachloride, and the MOS

Table IV. MOS properties of CVD tungsten

Property	Source material	
	$\text{WF}_6$	$\text{WCl}_6$
% shorts	50-75%	0
Flatband voltage, $V_{\text{FB}}$	-0.5 to +0.1V	+0.2 to +0.5V
$\Delta V_{\text{FB}}$ after B-T stress	—	-0.1V
Fixed charge, $Q_{\text{ss}}$	$2-3 \times 10^{10} \text{ cm}^{-2}$	$1-3 \times 10^{10} \text{ cm}^{-2}$
Mobile charge, $N_{\text{a}}$	$2-3 \times 10^{11} \text{ cm}^{-2}$	$1-5 \times 10^{10} \text{ cm}^{-2}$
Fast-state density, $N_{\text{ss}}$ (Midgap)	$8-10 \times 10^9 \text{ cm}^{-2} \text{ eV}^{-1}$	$2-4 \times 10^{10} \text{ cm}^{-2} \text{ eV}^{-1}$

properties of the W/ $\text{SiO}_2$ /Si structures are nearly ideal. The flatband voltage is 0.2-0.5V; this implies that the fixed charge,  $Q_{\text{ss}}$ , is very low ( $1-3 \times 10^{10} \text{ cm}^{-2}$ ). The fast-state density distribution, shown in Fig. 8, is independent of the deposition temperature. There are no unusual or irregular peaks across the bandgap, and at midgap the fast-state density is  $2-4 \times 10^{10} \text{ cm}^{-2} \text{ eV}^{-1}$  for all the samples. The mobile charge, which ranged from  $1 \times 10^{10}$  to  $5 \times 10^{12} \text{ cm}^{-2}$ , is very dependent on deposition conditions. However, consistent values of  $1-5 \times 10^{10} \text{ cm}^{-2}$  were obtained by adding 0.1% hydrogen chloride to the carrier gas during deposition. The addition of hydrogen chloride had no effect on the other properties of the tungsten films.

### Summary

Tungsten films have been deposited by hydrogen reduction of tungsten hexafluoride or tungsten hexachloride, and the two systems have been compared for applications for silicon integrated circuits. Films with thicknesses as great as 30,000 Å have been deposited from both chemical sources at rates up to 3000 Å/min. The films from both sources have low residual stress,

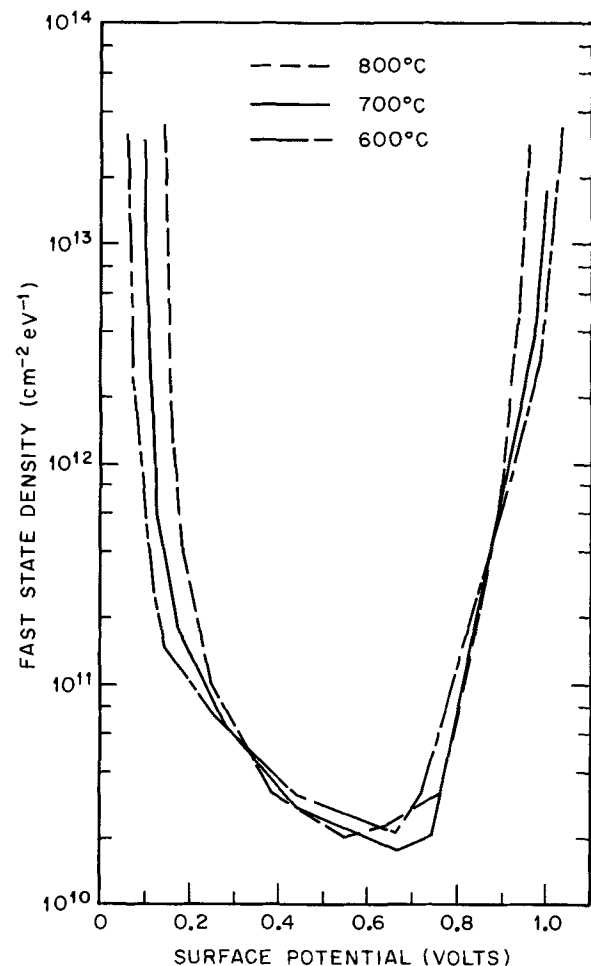


Fig. 8. Fast-state density distribution as a function of substrate temperature during deposition ( $600^\circ\text{C}$ - $800^\circ\text{C}$ ) for the  $\text{WCl}_6$  reaction.

good step coverage, are easily etched into fine resolution patterns, and have resistivities between one and three times the bulk value. Films deposited from tungsten hexafluoride have excellent W-Si contacts; however, tungsten hexafluoride attacks SiO<sub>2</sub> which results in shorted or leaky MOS structures. Consequently, tungsten hexafluoride cannot be used for a gate metallization on SiO<sub>2</sub>. In contrast, films deposited from tungsten hexachloride have nearly ideal MOS properties; however, the W-Si contacts are poor unless the metal is deposited at high temperatures (850°C). At high temperatures, the formation of tungsten silicide is rapid and the films frequently develop cracks due to the volume change associated with the silicide formation. Consequently, tungsten hexachloride has not been used in metallizations that require the formation of a W-Si contact.

#### Acknowledgments

The authors wish to acknowledge the assistance of P. Petroff, T. T. Sheng, and Miss S. E. Koonce for electron microscopy data, of D. L. Malm for analytical assistance, of L. F. Thompson for SEM pictures, of B. C. Wonsiewicz and N. N. Axelrod for pole figure and stress measurements, of M. H. Hanes for Schottky diode measurements, and of Mrs. K. E. Weis and V. Kuman for contact resistance measurements.

Manuscript received May 21, 1973. This was Paper 224 presented at the Boston, Massachusetts, Meeting of the Society, Oct. 7-11, 1973.

Any discussion of this paper will appear in a Discussion Section to be published in the December 1974 JOURNAL.

#### REFERENCES

1. C. R. Crowell, J. C. Sarace, and S. M. Sze, *Trans. Met. Soc. AIME*, **233**, 478 (1965).
2. J. M. Shaw and J. A. Amick, *RCA Rev.*, **31**, 306 (1970).
3. C. F. Powell, J. H. Oxley, and J. M. Blocher, Jr., Editors, "Vapor Deposition," pp. 322-326, John Wiley and Sons, Inc., New York, New York (1966).
4. E. J. Mehalchick and M. B. MacInnis, *Electrochem. Tech.*, **6**, 66 (1968).
5. A. F. Mayadas, J. J. Cuomo, and R. Rosenberg, *This Journal*, **116**, 1742 (1969).
6. T. T. Sheng, R. B. Marcus, and W. A. Reed, *Thin Solid Films*, **14**, 289 (1973).
7. L. D. Locker and C. D. Capio, To be published.
8. A. K. Sinha and T. E. Smith, To be published.
9. M. P. Lepselter and J. M. Andrews, in "Ohmic Contacts to Semiconductors," B. Schwartz, Editor, pp. 159-186, The Electrochemical Society Softbound Symposium Series, New York, New York (1969).

## Technical Notes



### Luminescence of Mn<sup>2+</sup> in Alpha-LiAlSiO<sub>4</sub>

K. R. Laud, T. Y. Tien,<sup>1</sup> E. F. Gibbons, and H. L. Stadler

Scientific Research Staff, Ford Motor Company, Dearborn, Michigan 48121

Synthetic lithium aluminum orthosilicate, LiAlSiO<sub>4</sub>, exists in two crystallographic forms (1, 2). The high temperature β-form has a β-quartz type structure and transforms to the low temperature α-form under hydrothermal conditions. The α-form is found in nature as α-eucryptite and has a phenacite (Be<sub>2</sub>SiO<sub>4</sub>) structure (2, 3). The α ⇌ β inversion temperature at atmospheric pressure is reported as 848°C (2).

The objective of the work reported here is to synthesize α-LiAlSiO<sub>4</sub>:Mn<sup>2+</sup> phosphor. Since this phosphor can be prepared only under hydrothermal conditions, a wide variation of pressure and temperature is possible in the phosphor preparation.

#### Experimental

Chemically pure lithium carbonate, aluminum hydroxide, silicic acid, and manganous carbonate were used as starting materials. The batch was formulated as LiAlSiO<sub>4</sub>:Mn<sup>2+</sup> where the Mn<sup>2+</sup> concentration was maintained at as low as 0.005 atom per cent (a/o) (i.e., 2 Mn replacing 'Li + Al').

The weighted batch was wet mixed in acetone, dried, and slowly calcined to 800°C for 18 hr. The calcined mixture was melted in a platinum crucible at 1400°C for 20 min and was eventually quenched to obtain glass for use in hydrothermal experiments. The glass was crushed and passed through a 325 mesh

screen. Approximately 1.5g of glass powder was packed in a gold tube (3/8 in. I.D., 1 in. long) which was placed in a hydrothermal pressure vessel. The hydrothermal apparatus is described elsewhere (4). The phosphor specimens were prepared in the entire α-eucryptite region of the P-T diagram shown in Fig. 1. Holding times at 14,000, 7,500, and 2,000 psi pressure were 48, 84, and 120 hr, respectively.

The cathodoluminescence (C.L.) data were obtained in a demountable electron beam gun system operated at 3 kV. Samples were mounted at the focal point of an optical system which then refocused the emitted light on the entrance slit of a 3/4m Czerny-Turner spectrometer. The output from a photomultiplier (P.M.) tube, located at the exit slit of the spectrometer, was amplified by means of a synchronous detector and displayed on an x-y recorder. The required periodic signal for the P.M. tube was obtained by applying a 13 Hz square wave to the horizontal deflection plates of the electron beam gun, thus providing a 50% excitation duty cycle on the sample. The same square-wave generator provided the reference signal for the synchronous detector.

The excitation and emission spectra were taken in a system using a xenon light source focused through a monochromator with a mechanical light chopper after the exit slit. The phosphor emission was focused on the entrance slit of a 3/4m Czerny-Turner spectrometer and again the output of a P.M. tube located at the exit slit was amplified by means of a syn-

<sup>1</sup> Present address: University of Michigan, Materials and Metallurgical Engineering Department, Ann Arbor, Michigan 48104.

Key words: orthosilicate phosphor, phenacite structure, luminescence, Mn<sup>2+</sup> activator, hydrothermal.

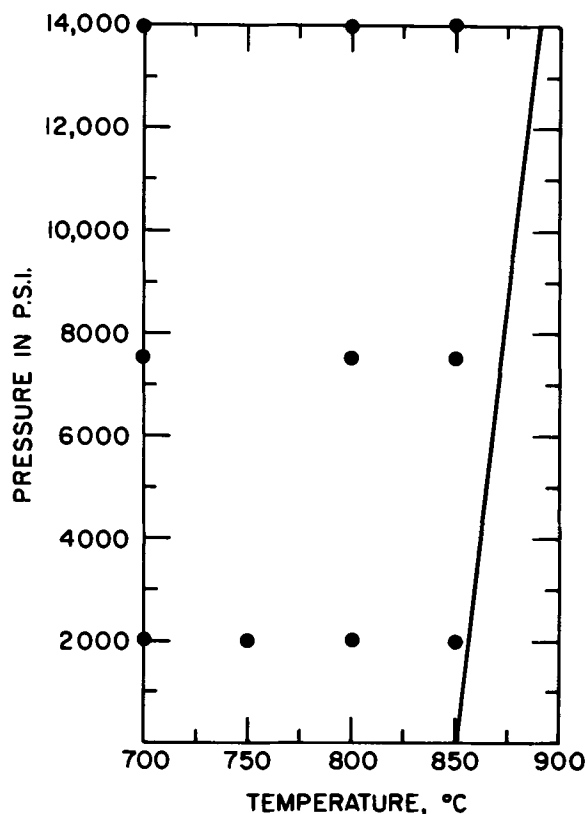


Fig. 1. Pressure-temperature diagram for the reaction  $\alpha\text{-LiAlSiO}_4 \rightleftharpoons \beta\text{-LiAlSiO}_4$  [after Isaacs and Roy (2)]. Solid circles represent the hydrothermal pressure and temperature of the phosphors prepared in this work.

chronous detector and displayed on an x-y recorder. For excitation spectra, the spectrometer was set at the desired emission peak and the monochromator was scanned over the appropriate range, while for emission spectra, the desired excitation wavelength was chosen by the monochromator and the spectrometer was scanned over the emission band. Appropriate filters were used in front of and behind the phosphor sample.

### Results

In all, ten phosphors were prepared in the  $\alpha\text{-LiAlSiO}_4$  area of the P-T diagram (Fig. 1). The x-ray diffraction patterns indicated all the phosphors to be composed entirely of  $\alpha\text{-LiAlSiO}_4\text{:Mn}$ .

Figure 2 shows the C.L. emission spectra for three phosphors prepared under different hydrothermal conditions. In nine phosphors, two C.L. emission bands

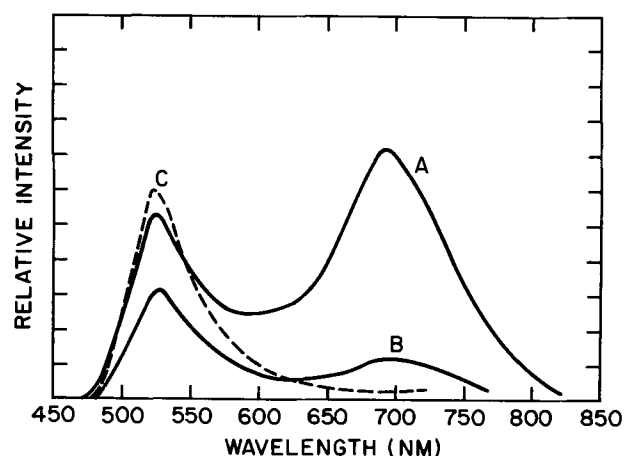


Fig. 2. C.L. emission spectra for  $\alpha\text{-LiAlSiO}_4\text{:Mn}^{2+}$  phosphors prepared under hydrothermal conditions. A, 14,000 psi, 700°C, 48 hr; B, 7,500 psi, 800°C, 84 hr; and C, 2,000 psi, 850°C, 120 hr.

appear with peak positions at 5230Å in the green region and 6900Å in the red region of the spectrum. In only one phosphor, prepared at 2000 psi and 850°C, a 5230Å band predominates. The ratio of the peak intensities of green to red bands decreases with increasing pressure but increases with increase in temperature. This indicates that low pressure and high temperature conditions favor the green band but high pressure and low temperature are suitable for the red band to appear.

For a phosphor, prepared at low pressure and high temperature, the excitation and photoluminescence spectra are shown in Fig. 3 and 4, respectively. The excitation peak positions are at 2750Å and 3750Å for the 6900Å and 5230Å emission settings of the spectrometer, respectively. In the photoluminescence spectrum two bands appear. For the 3750Å excitation wavelength, an emission peak appears at 5230Å and for the 2750Å excitation wavelength, an emission peak is located at 6900Å. The excitation and photoluminescence spectra for a phosphor prepared at high pressure and low temperature were identical to those shown in Fig. 3 and 4 except in peak intensities.

The excitation and photoluminescence spectra (Fig. 3 and 4) suggest that the emission occurs from two separate systems. In one system, the excitation is at the 3750Å level and emission occurs in a band whose peak is at 5230Å. In the other system, the excitation is at the 2750Å level and emission is from the 6900Å

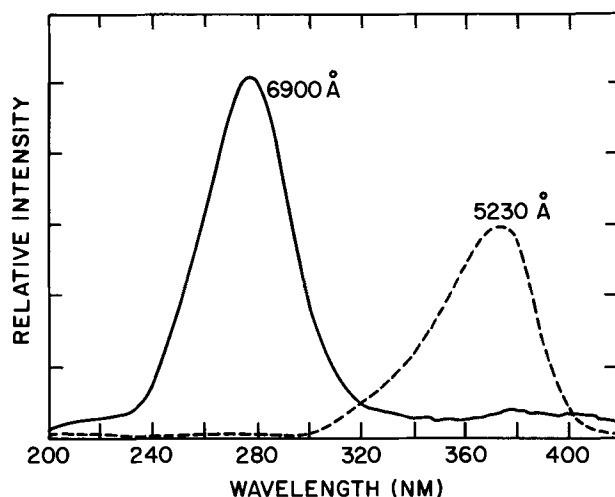


Fig. 3. Excitation spectra for 5230 and 6900Å emission of  $\alpha\text{-LiAlSiO}_4\text{:Mn}^{2+}$  phosphor (prepared at 2000 psi, 850°C, 120 hr).

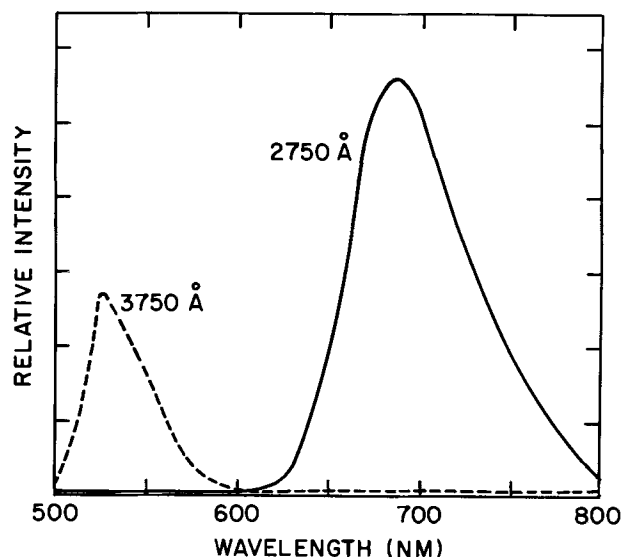


Fig. 4. Photoluminescence spectra for  $\alpha\text{-LiAlSiO}_4\text{:Mn}^{2+}$  phosphor (prepared at 2000 psi, 850°C, 120 hr) exciting at 3750 and 2750Å.

level. However, there is no evidence of energy transfer occurring between these two systems.

Manuscript submitted July 2, 1973; revised manuscript received Sept. 28, 1973. This was Paper 80 presented at the Houston, Texas, Meeting of the Society, May 7-11, 1972.

Any discussion of this paper will appear in a Discussion Section to be published in the December 1974 JOURNAL.

## YVO<sub>4</sub>:Eu,Tb—An Efficient High Pressure Mercury Vapor Lamp Phosphor

S. Faria\* and E. J. Mehalchick

GTE Sylvania Incorporated, Chemical and Metallurgical Division, Towanda, Pennsylvania 18848

Enhancement of  $Eu^{3+}$  emission by relatively high concentrations of  $Tb^{3+}$  was reported by Van Uitert *et al.* (1) in the alkali rare earth tungstates and by Ropp (2) in yttrium oxide. The increase in  $Eu^{3+}$  emission was described as a resonance transfer of energy absorbed by the  $Tb^{3+}$  center. Using relatively low concentrations of  $Tb^{3+}$  Mehalchick *et al.* (3) showed a significant increase in the cathode ray brightness of YVO<sub>4</sub>:Eu. This work shows that moderate amounts of  $Tb^{3+}$  are also effective in enhancing the  $Eu^{3+}$  emission of YVO<sub>4</sub>:Eu, when the phosphor is used as a color corrector in high pressure mercury vapor (HPMV) lamps (4). The improvement is most readily observed at the high operating temperature of the HPMV lamps, thus indicating that the energy transfer from  $Tb^{3+}$  to  $Eu^{3+}$  is thermally activated (5).

### Experiments and Results

Series of YVO<sub>4</sub>:Eu and YVO<sub>4</sub>:Eu,Tb phosphors were prepared by the usual solid-state reaction described in a previous paper (6). All the phosphors were evaluated in HPMV lamps operating at 400W. The red emission was measured using a Corning red filter number 2418 (CS-2-62) and is expressed in per cent relative to the control sample. Unless otherwise stated, the Eu concentration was maintained at 5 mole per cent (m/o), although other concentrations were also evaluated (4).

### Tb<sup>3+</sup> Concentration

In Table I we report the lumens per watt (LPW) and the per cent red for 0 and 100 hr of lamp operation as a function of  $Tb^{3+}$  concentration. Note that increasing the  $Tb^{3+}$  appreciably affects the per cent red as well as the LPW. The optimum  $Tb^{3+}$  concentration varied between 50 and 750 ppm by weight and depended on the purity of the yttrium oxide lots. The spectral energy distribution at 0 hours of samples 1 and 2 are shown in Fig. 1.

Further investigation on the effect of  $Tb^{3+}$  on  $Eu^{3+}$  was evaluated by using a high purity lot of yttrium oxide. The results shown in Table II were obtained by adding 250 ppm and 300 ppm  $Tb^{3+}$  to a 99.999% pure yttrium oxide lot.

The increase in the red output was again observed in a yttrium oxide lot containing 25 ppm Tb as an impurity. When we added 250 ppm Tb, an increase from 112% to 150% was obtained. The large differences in per cent red output shown in Tables I, II, and III are mainly due to the variation in Y<sub>2</sub>O<sub>3</sub> lots and their impurity contents.

\* Electrochemical Society Active Member.

Key words: energy transfer, rare earth phosphors.

### REFERENCES

1. R. Roy, D. M. Roy, and E. F. Osborn, *J. Am. Ceram. Soc.*, **33**, 152 (1950).
2. T. Isaacs and R. Roy, *Geochim Cosmochim. Acta*, **15**, 213 (1958).
3. H. G. F. Winkler, *Beitr. Mineral. Petrog.*, **4**, 233 (1954).
4. R. Roy and O. F. Tuttle, "Physics and Chemistry of the Earth," Vol. I, p. 138-80, Pergamon Press Inc., New York (1956).

Table I. Terbium variation

Sample No.	Tb, ppm	LPW	0 hr % Red	LPW	100 hr % Red
1	0	100	100	100	100
2	50	104	115	103	107
3	250	105	119	102	103
4	500	105	119.5	99	108
5	750	105	119.5	102	109
6	1000	105	115.0	100	103

Table II. Terbium addition to high purity Y<sub>2</sub>O<sub>3</sub>

Control	No Tb	100% Red at 0 hr
Test A	250 ppm Tb	140% Red at 0 hr
Test B	300 ppm Tb	153% Red at 0 hr

### Effect of Dysprosium

Many of the tested yttrium oxide lots contain Dy as well as other rare earth impurities. In many instances, the Dy content was determined to be as high as 400 ppm. To establish the effect of Dy on the overall performance of the HPMV lamps, various Dy concentrations were evaluated with or without Tb.

Table III shows the results obtained without Tb, with Tb, with Dy, and with Tb + Dy. The results indicate that levels of Dy equal to or lower than Tb do not appreciably affect the total lumen output or the per cent red.

YVO<sub>4</sub>:Eu,Tb phosphor prepared from lots containing relatively high Dy as an impurity were almost as efficient as those prepared from low Dy.

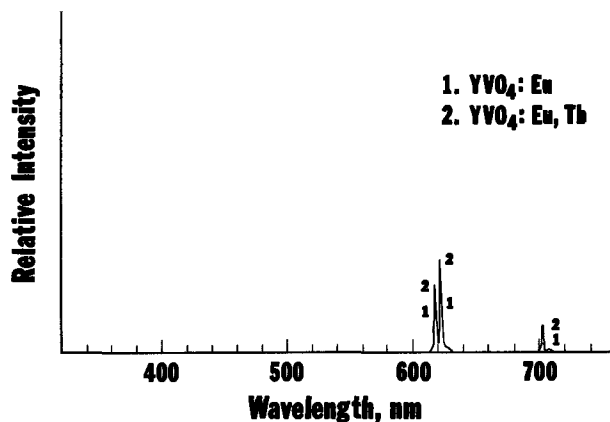


Fig. 1. Spectral energy distribution of YVO<sub>4</sub>:Eu,(1) and YVO<sub>4</sub>:Eu,Tb(2) in 400W HPMV lamps.

Table III. Effect of Dy and Dy + Tb on % red and LPW

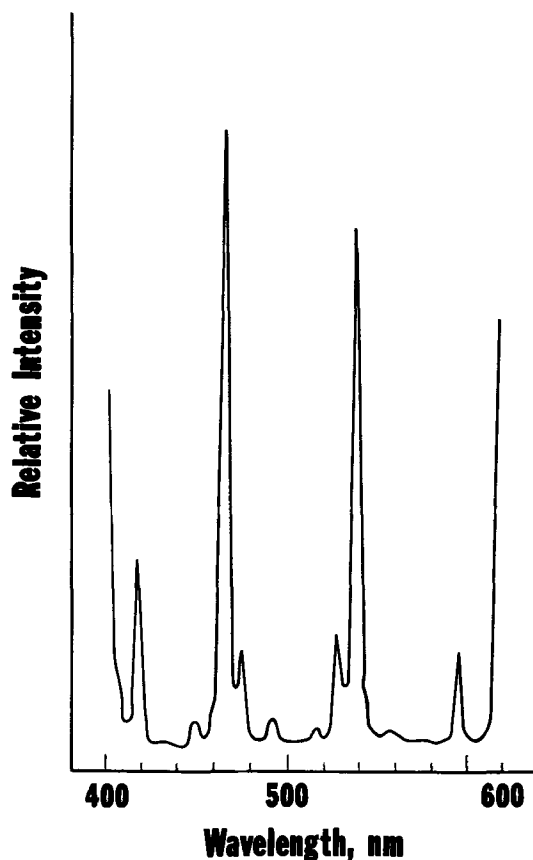
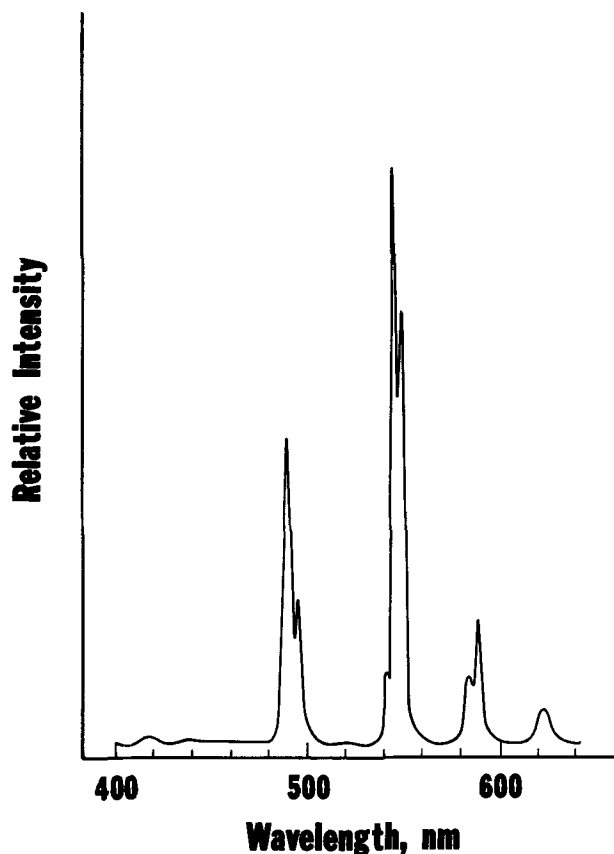
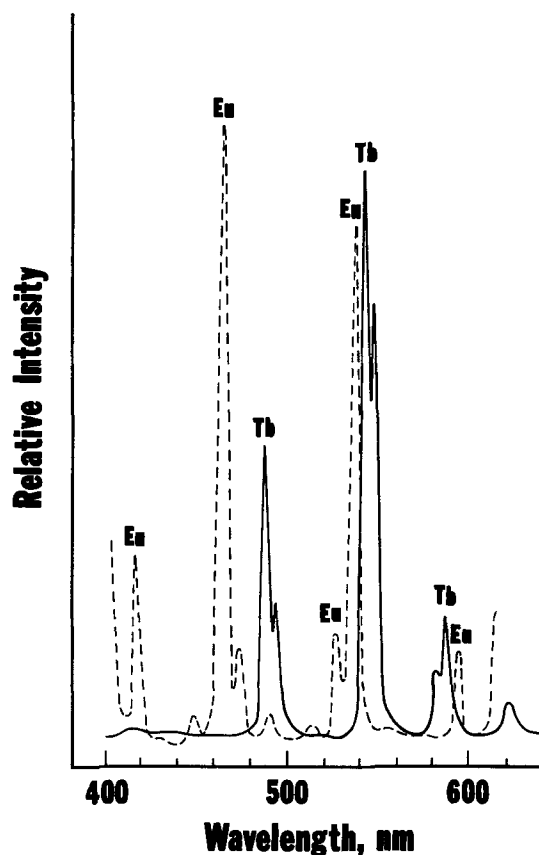
Description	LPW	% Red
Control test	100	100
Test + 150 ppm Tb	108	138
Test + 300 ppm Tb	104	149
Test + 150 ppm Dy	100	100
Test + 150 ppm Dy + 150 ppm Tb	105	128
Test + 150 ppm Dy + 300 ppm Tb	106	143
Test + 300 ppm Dy	100	97.0

The particle size was also taken into consideration when optimizing the system for HPMV lamp application. Best output in lumens and per cent red were obtained when the particle size ranged between 6 and  $10\mu$  as measured by the Fisher Sub-Sieve-Sizer (FSSS). In general, the small particle size phosphor always showed a slight gain in red output, but at a slight loss in LPW.

### Discussion

Blasse (7) and Palilla (8) have described the very strong optical absorption of  $YVO_4$  for both short and long ultraviolet radiation. Incorporation of  $Eu^{3+}$  in this matrix results in luminescence through a rather efficient host transfer mechanism. The efficient Eu emission arises from the large overlap between the visible matrix emission band and Eu visible absorption levels. These Eu absorption lines are clearly shown in Fig. 2.

Although we do not know the actual mechanism for the Eu enhancement, it would appear that when Tb is also incorporated in the matrix, a similar energy interaction between Tb emission and Eu absorption levels could exist. In Fig. 3, we show the visible emission lines of Tb in  $YPO_4$  since Tb emission does not occur in  $YVO_4$  (9), even though both  $YVO_4$  and  $YPO_4$  have similar structures (both matrices being tetragonal-xenotime). Figure 4 shows the possible energy overlap that would exist for Eu absorption in  $YVO_4$  and Tb emission as it appears in  $YPO_4$ .

Fig. 2. Excitation spectrum of Eu in  $YVO_4$ Fig. 3. Spectral energy distribution of  $YPO_4:Tb$  showing characteristic Tb emission.Fig. 4. Combined excitation spectrum of Eu in  $YVO_4$  and the emission spectrum of Tb in  $YPO_4$ .

The enhancement of  $Eu^{3+}$  emission in  $YVO_4$  by  $Tb^{3+}$  has been described. We believe that the same energy



transfer mechanism may apply here as suggested by Ropp for Tb<sup>3+</sup> and Eu<sup>3+</sup> in Y<sub>2</sub>O<sub>3</sub>.

Manuscript submitted July 2, 1973; revised manuscript received Oct. 5, 1973. This was Paper 59 presented at the Los Angeles, California, Meeting of the Society, May 10-15, 1970.

Any discussion of this paper will appear in a Discussion Section to be published in the December 1974 JOURNAL.

#### REFERENCES

1. L. G. Van Uitert and R. R. Soden, *J. Chem. Phys.*, **36**, 1289 (1962).

2. R. C. Ropp, *J. Opt. Soc. Am.*, **57**, 213 (1967).
3. E. J. Mehalchick, F. F. Mikus, and J. E. Mathers, *This Journal*, **116**, 1017 (1969).
4. S. Faria and E. J. Mehalchick, U.S. Pat. 3,480,819 (1969).
5. L. G. Van Uitert, E. F. Dearborn, and H. M. Marcos, *J. Appl. Phys. Letters*, **9**, 255 (1966).
6. S. Faria and D. T. Palumbo, *This Journal*, **116**, 157 (1969).
7. G. Blasse, *J. Chem. Phys.*, **45**, 2356 (1966).
8. F. C. Palilla, *Electrochem. Technol.*, **6**, 39 (1968).
9. R. G. Losh, T. Y. Tien, E. F. Gibbons, P. J. Zecmanidis, and H. L. Stadler, *J. Chem. Phys.*, **53**, 681 (1970).

## A Scanning Electron Microscope Investigation of Glass Flow in MOS Integrated Circuit Fabrication

W. E. Armstrong and D. L. Tolliver\*

Motorola Semiconductor Products Division, Phoenix, Arizona 85008

A formidable problem in the fabrication of multilayer metal bipolar integrated circuits and MOS circuits has been the discontinuity in metal interconnections over steep or even retrograde steps (1-3). These steps result from three primary sources: (i) metal or poly silicon interconnects which lie under an insulating oxide; (ii) thick oxide steps; and (iii) oxide windows or contact holes which have been etched open to allow connection between metal and an underlying surface. In a study of multilayer metalization problems, Santoro and Tolliver (4) outlined techniques for reducing step problems associated with deposited oxides over aluminum metal layers. One of the points presented in that work was "step profiling can result in ideal (metal) coverage even with non-ideal (oxide) deposition control." When profiles involve deposited oxides over steps other than etched aluminum metalization, new degrees of profiling steps are attainable. A method for controlling the profile steps resulting from deposition of oxide on MOS poly silicon interconnections was discussed in a recent work by C. T. Nabor (5). The profile control of oxide over poly silicon steps or etched oxide steps is achieved by doping the oxide to lower its softening point and annealing at a temperature above that point. This work reports on a study of related conditions that can be used to control oxide profiles in MOS integrated circuits. The effects of impurity concentration in the glass, time and temperature of the anneal, and annealing ambient on the step profile are investigated. The application of the technique to "contact window" steps as well as poly silicon steps is discussed.

### Effects of Impurity Concentration

It has long been known that phosphorous oxide doping of vapor deposited glass films changes important chemical and physical properties. Among these properties are etch rate, thermal coefficient of expansion, and viscosity-temperature characteristics. The measurement of phosphorous concentration in this work is referenced to a diffusion technique, and utilizes a typical 10<sup>16</sup> background p-type wafer. A minimum 6000Å phosphorous doped glass film is deposited on the surface. The wafer is then diffused for a sufficient time at 1100°-1200°C to achieve an easily measured junction depth in the order of 3-4μ. Using Irvin's curves (6), the surface concentration of the wafer is then calculated. Figure 1 is a set of scanning electron micrographs of the step formed when an

8000Å phosphosilicate glass film (6 × 10<sup>20</sup> atom/cm<sup>3</sup>) which corresponds to approximately 7 weight per cent (w/o) phosphorus is deposited over a 5000Å poly silicon step and subsequently annealed in nitrogen at 1050°C for times from 0 to 120 min. The flow becomes apparent first as a smoothing and restructuring of the oxide surface and eventually creates a new profile of the oxide step. In Fig. 2-5, the 8000Å phosphosilicate glass was deposited on a steep, recessed, 1μ oxide step. Note that very high phosphorous concentration (2.2 × 10<sup>21</sup>) has such a low viscosity that it loses physical stability. In the last micrograph of each anneal time, the heavily phosphorous enriched layers have vigorously boiled off, so as to completely alter the pattern and partly vaporize it along with the highly volatile phosphorous oxide. There are, of course, many other problems with the use of such a film. These include: (i) The formation of strong acid due to the hygroscopic nature of heavily doped phosphosilicate glass. This phosphoric acid formed from low level moisture in room ambient with high glass phosphorous concentrations can attack aluminum metalization or cause photoresist layers to lift and make subsequent processing impossible. (ii) Solubility or corrosion in "cleaning acids" (e.g., chromic or nitric acid) or even in water. The phosphorous concentration must be properly controlled to avoid attack by frequent immersions in integrated circuit cleaning and rinsing agents. (iii) Polarization under temperature-bias stress. Polarization of high concentration films under temperature bias stress can result in circuit failures caused by changing characteristics of parasitic devices. Fortunately, with proper stoichiometric control good step profiles can still be obtained by annealing lower concentration glass films.

### Effects of Ambient and Temperature

The effects of different ambients are demonstrated in Fig. 6 and 7. Glass was deposited on a steep, 1μ oxide step and annealed at 1050°C. A comparison of these figures with Fig. 1 shows that for the given temperature, the viscosity is lowest for a steam ambient ("highest flow") and greatest for a nitrogen ambient ("lowest flow") with oxygen falling somewhere between the two. In Fig. 8, the same glass/step system was used to demonstrate the effect of annealing at lower temperature (1000°C). A comparison of Fig. 8 (1000°C) with Fig. 6 (1050°C) shows that the same profile can be achieved at lower temperature, but at the expense of a longer anneal time.

\* Electrochemical Society Active Member.

Key words: glass, flow, MOS integrated circuit.

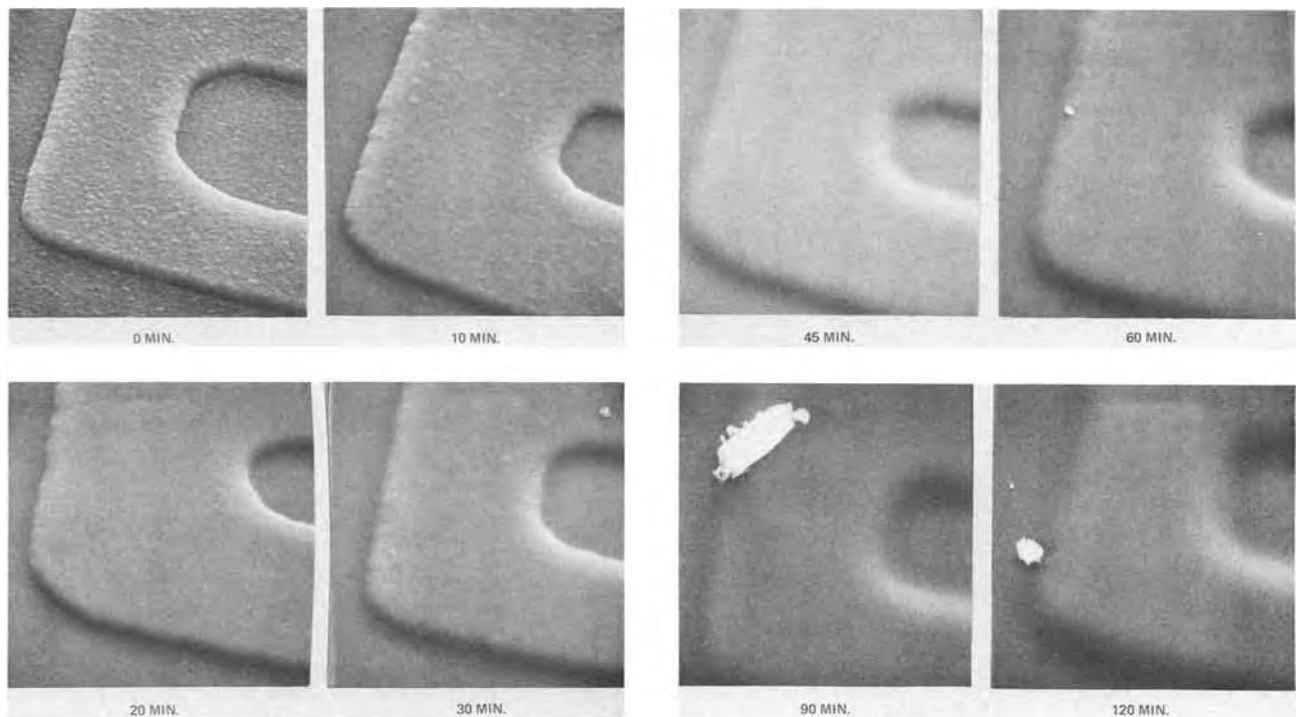


Fig. 1. 1050°C N<sub>2</sub> anneal of an 8000Å phosphosilicate glass film deposited over a 5000Å poly silicon step

### Discussion

Figure 9 is a photomicrograph of a "contact window" etched in a 8000Å, phosphosilicate glass. With conventional metal evaporation, this step is typically steep enough to cause the microcracks shown in Fig. 9b. If the oxide window is annealed after the window is opened as in Fig. 9c, the step will be reprofiled and the microcracks will not appear. There are, of course, photoresist or deposition techniques which will cause the profile of the oxide to be improved as it is etched; but the profile is generally not as reproducible. However, these less reproducible techniques may still be more effective in cases where

the anneal may cause other problems. For example, if the contact window opens into a P<sup>+</sup> diffused area, the area may be converted by phosphorous autodoping during the anneal.

Figure 9d shows the metal coverage achievable when the glass film which isolates poly silicon from metal is profiled with a steam anneal. If this anneal were done after the contact windows were opened as just discussed, the steam anneal would grow an oxide in the windows. This oxide would then have to be etched out before metal could be evaporated. Even if the anneal is performed before the contact windows are opened, there are still several other

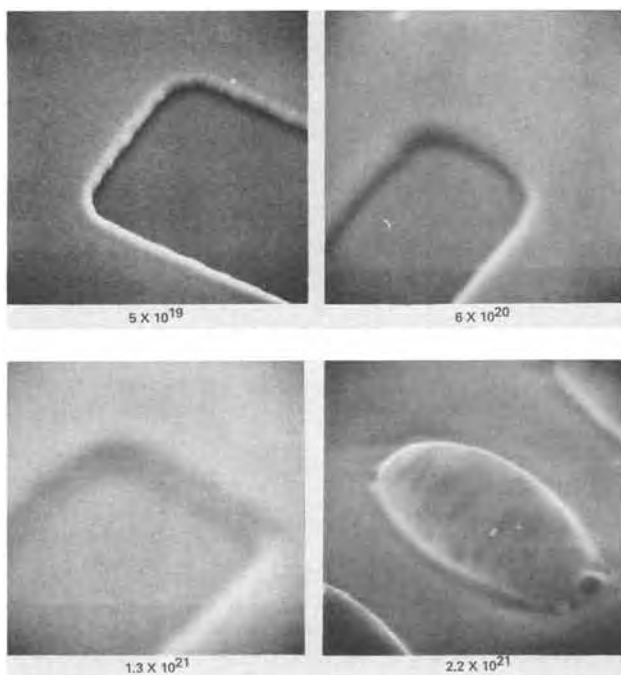


Fig. 2. 8000Å phosphosilicate glass deposited for 10 min at 1050°C (N<sub>2</sub>) on a steep, recessed, 1μ oxide step.

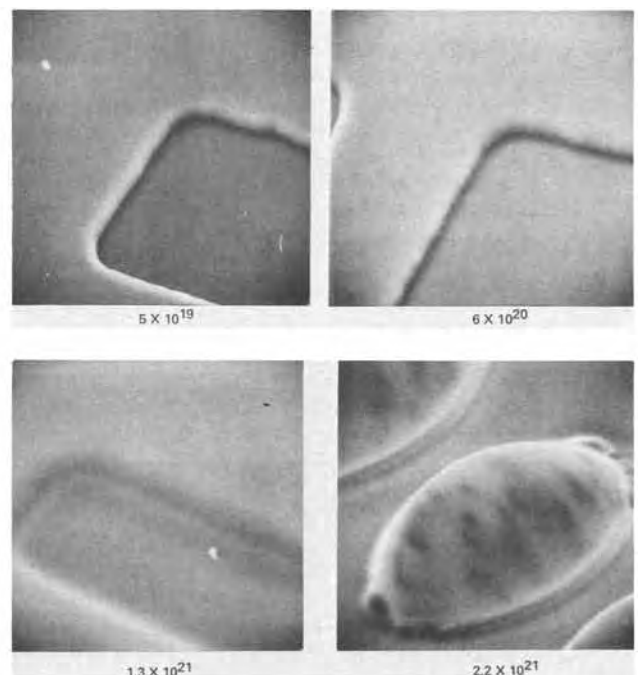


Fig. 3. 8000Å phosphosilicate glass deposited for 20 min at 1050°C (N<sub>2</sub>) on a steep, recessed, 1μ oxide step.

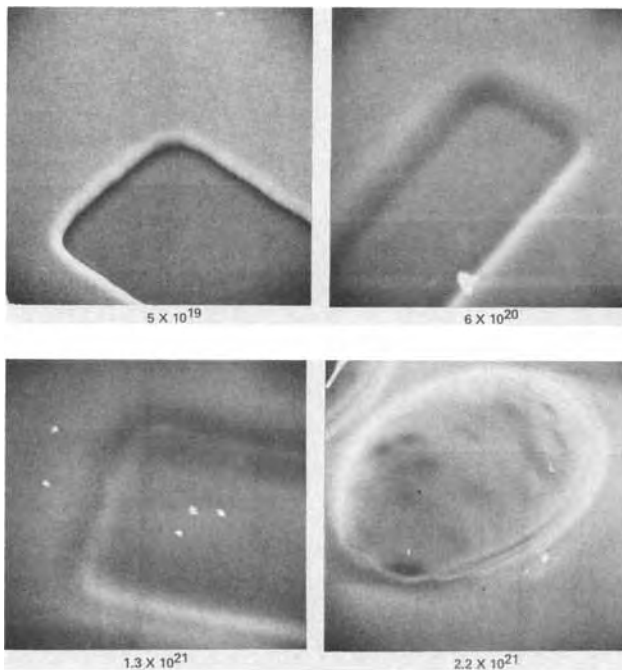


Fig. 4. 8000Å phosphosilicate glass deposited for 40 min at 1050°C ( $N_2$ ) on a steep, recessed,  $1\mu$  oxide step.

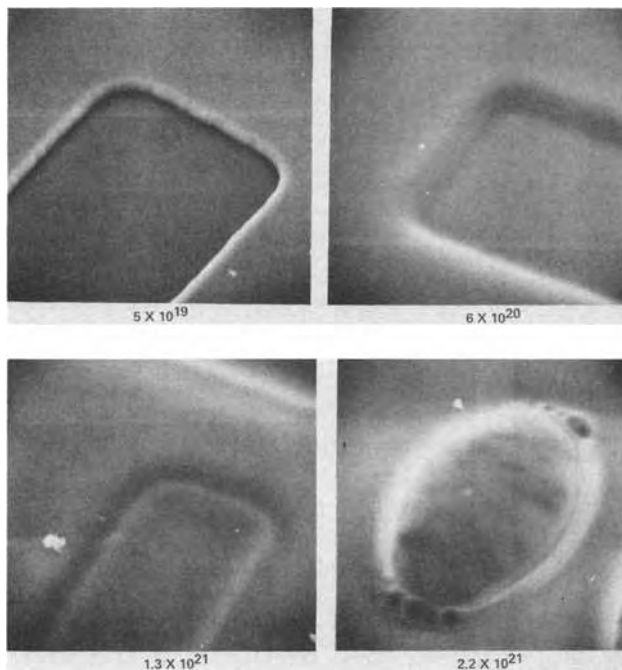


Fig. 5. 8000Å phosphosilicate glass deposited for 60 min at 1050°C ( $N_2$ ) on a steep, recessed,  $1\mu$  oxide step.

problems which must be considered: (i) the additional diffusion time (regardless of the ambient) will change the effective source-drain space as well as the space between unrelated diffusions; (ii) ambients such as steam or oxygen will change surface conditions and affect device or even parasitic thresholds; (iii) if the time required to achieve a given profile is shortened by increasing the phosphorous content of the glass, photoresist adhesion or film stability may suffer; and (iv) steam annealing of p-channel devices will result in hydrogen-aided boron diffusion through the gate oxide (thus reducing the threshold below desirable limits). In spite of these disadvantages, the technique is probably more widely used than might be expected from the amount of relevant information available in the literature. In many cases the authors believe advantageous profiles will be obtained during

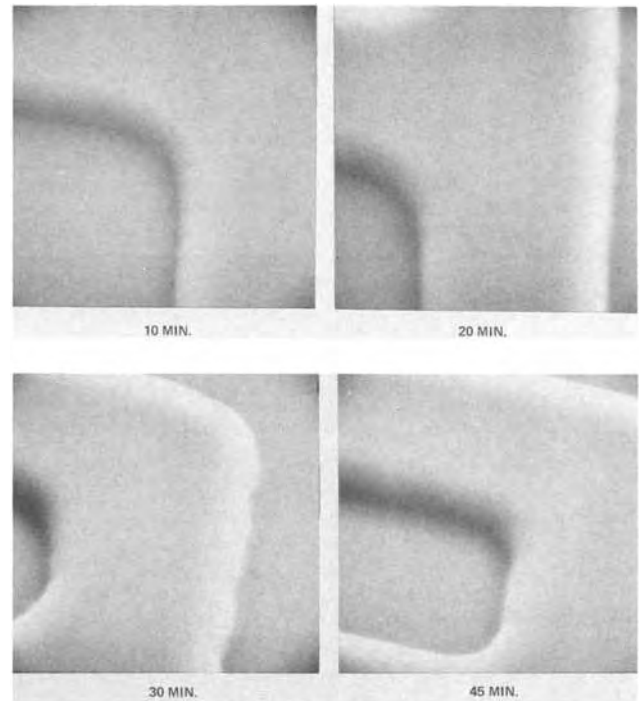


Fig. 6. 1050°C anneal of an 8000Å phosphosilicate glass film deposited over a steep,  $1\mu$  oxide step.

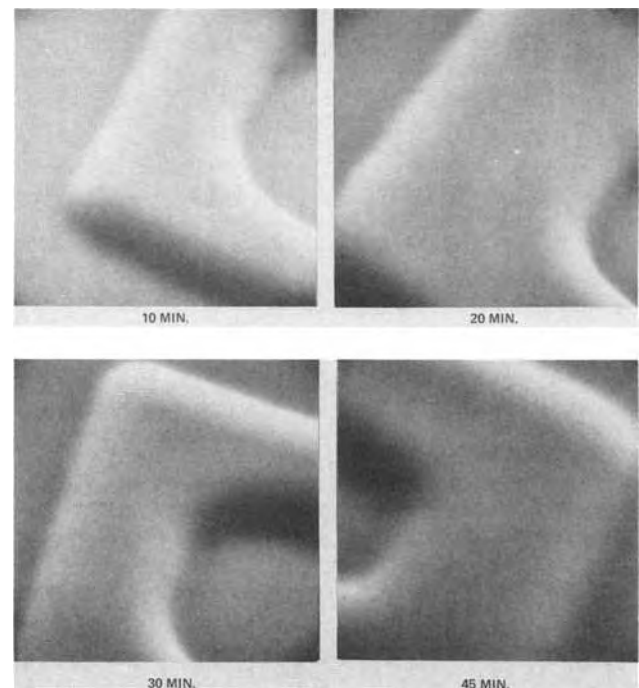


Fig. 7. 1050°C steam anneal of an 8000Å phosphosilicate glass film deposited over a steep,  $1\mu$  oxide step.

processing without direct intent to create them, by using deposited oxide films in conventional processing sequences.

### Conclusions

It has been shown that an increase in the concentration of phosphorous in a vapor-deposited oxide can change the viscosity-temperature characteristics of the film to cause "flow" at temperatures as low as 1000°C. In addition, this oxide flow can be further enhanced by annealing the glass in oxygen or steam ambients rather than in inert gases. Finally, the technique was shown to improve step profiles as it was applied to (i) steps from poly silicon lying under the

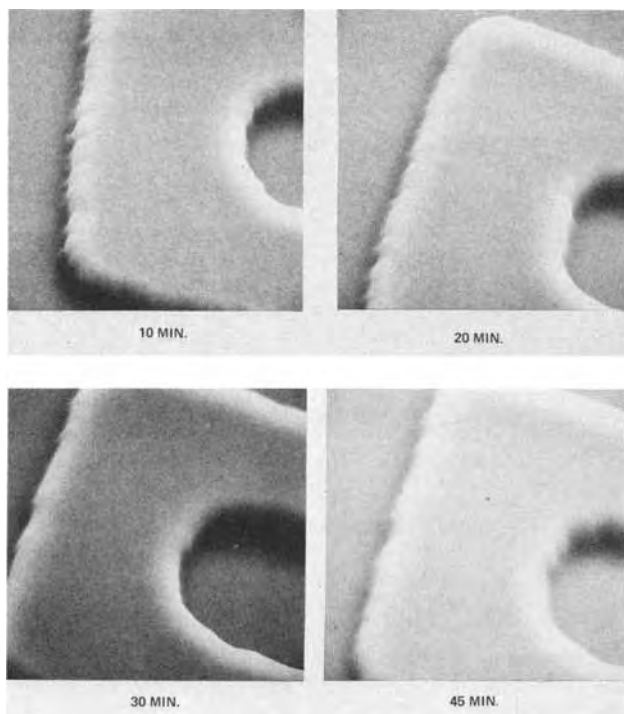


Fig. 8. 1000°C O<sub>2</sub> anneal of 8000Å phosphosilicate glass film deposited over a steep, 1μ oxide step.

phosphosilicate glass film, (ii) thick oxide steps, and (iii) "contact window" openings.

Manuscript submitted May 23 1973; revised manuscript received Sept. 27, 1973.

Any discussion of this paper will appear in a Discussion Section to be published in the December 1974 JOURNAL.

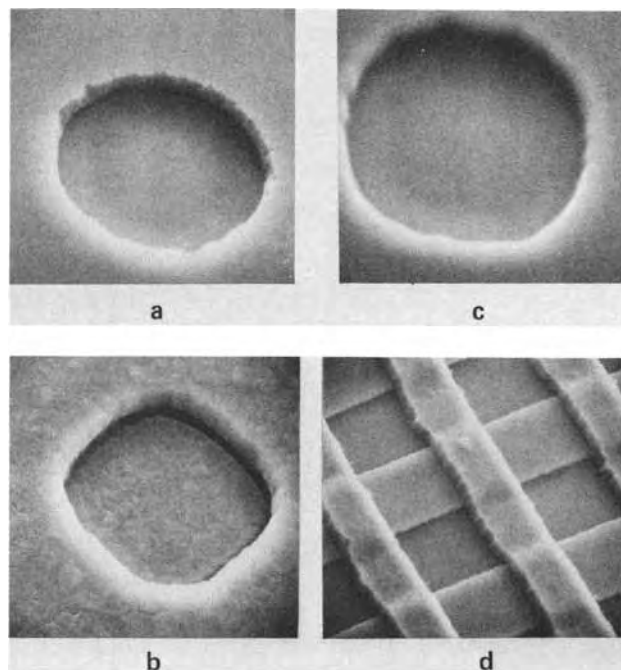


Fig. 9. Applications to MOS integrated circuit fabrication

#### REFERENCES

1. J. F. Campbell and W. H. Shepherd, Paper 198 presented at Electrochemical Society Meeting, Detroit, Michigan, Oct. 5-9, 1969.
2. W. H. Shepherd, J. F. Campbell, and I. A. Blech, Paper presented at Reliability Physics Symposium, April 1970.
3. I. A. Blech and E. S. Meieran, *J. Appl. Phys.*, **40**, 485 (1969).
4. C. J. Santoro and D. L. Tolliver, *Proc. IEEE*, **59**, 1403 (1971).
5. C. T. Naber, Paper 351RNP presented at Electrochemical Society Meeting, Miami Beach, Florida, Oct. 8-13, 1972.
6. T. C. Irvin, *Bell Systems Tech. J.*, **41**, 387 (1962).

## Germanium Surface Cleaning—An Auger Analysis

D. A. Kiewit,<sup>\*1</sup> I. J. D'Haenens, and J. A. Roth

Hughes Research Laboratories, Malibu, California 90265

A variety of methods have been used to clean germanium surfaces in order to insure the removal of lifetime killing impurities (e.g., Cu) prior to high temperature processing. Much of the older literature recommends the use of cyanide solutions or chelating agents in the cleaning process, while more recent studies have suggested the use of basic and acidic peroxide solutions (1). We have used Auger electron spectroscopy to study several methods embodying both approaches, and have also measured the etch rates associated with some of these cleaning agents in order to assess their suitability for use with partially processed wafers containing thin doped regions. For all the experiments reported here we used chemically polished, (111) oriented, 10 ohm-cm n-type germanium wafers.

Etch rates were measured on germanium wafers that were partially masked with Apiezon W wax, exposed to the cleaning solution for 10 min, stripped of the mask, and examined interferometrically to measure the etch step, if any. The results of these measurements

appear in Table I and indicate a substantial etch rate for many of these cleaners. The data for the acidic peroxide solutions in particular, are in good agreement with etch rate studies made by Primak *et al.* (2) on germanium surfaces exposed to peroxide solutions of varying pH.

Most of the samples that were used in the subsequent cleaning studies were given an initial standard preclean consisting of boiling in xylene; washing in trichloroethylene, acetone, methanol, and deionized water; and cleaning first in NH<sub>4</sub>OH:H<sub>2</sub>O<sub>2</sub>:H<sub>2</sub>O (1:1:5) and then in HCl:H<sub>2</sub>O<sub>2</sub>:H<sub>2</sub>O (1:1:5), for 1 min at 24°C. These samples were then rinsed in deionized water and blown dry with nitrogen. Following the preclean, each of these samples was subjected, for 1 min, to a variable cleaning step which is listed in Table I. With the exception of the sample cleaned with acetone (MA) which was blown dry immediately, all of these samples were subsequently rinsed in ten changes of deionized water and then blown dry with nitrogen. One other sample (FL) was not subjected to the standard preclean sequence, but was cleaned with trichloroethylene, acetone, methanol, and deionized water, soaked in HF,

\* Electrochemical Society Active Member.

<sup>1</sup> Present address: Gould Electrical and Electronics Laboratory, Rolling Meadows, Illinois 60008.

Key words: germanium, surface preparation, cleaning, Auger electron spectroscopy.

Table I.

Sample ident.	Variable cleaning step	Etch rate	Species observed by AES*
STD	HCl:H <sub>2</sub> O <sub>2</sub> :H <sub>2</sub> O (1:1:5)	200 A/min	Ca [C] [O]
SC	HCl:H <sub>2</sub> O <sub>2</sub> :H <sub>2</sub> O (1:1:60) + 1% Na <sub>2</sub> EDTA	50	Ca, low [C] [O]
ED	1% Na <sub>2</sub> EDTA	0	low [C] [O]
CN	10% NaCN	75	— [C] [O]
AS	Aurostrip®†	5-10	low [C] [O]
MA FL	Methanol, acetone HF	0 0	P F

\* In addition to Ge, O, N, and C.  
† Sel-Rex Chemical Company.

rinsed in deionized water, and then blown dry. No intentionally contaminated samples were employed.

The organic solvents, HF, and disodium ethylenediamine-tetracetic acid (Na<sub>2</sub>EDTA) were either reagent or electronic grade. The deionized water used for rinsing had a resistivity of at least 18 Mohm and was passed through both activated carbon and 0.22 μm particle filters prior to use. Pyrex labware, which has been previously noted as a source of boron contamination on silicon wafers (3), was used in all wet steps not employing HF. HF rinses were done in polypropylene beakers.

Within 2 hr after cleaning, the samples were loaded into a Physical Electronics Industries LEED/Auger system and pumped down to 10<sup>-8</sup> Torr without bake-out. Auger derivative spectra were taken from each sample and plotted out automatically. These data are summarized in Table I, and representative Auger derivative spectra for samples STD, SC, and MA are shown in the figure.

The total list of elements present at detectable levels (i.e., in excess of 10<sup>11</sup>-10<sup>12</sup> cm<sup>-2</sup>)<sup>2</sup> were: Ge, O, N, C, Ca, F, and P, although the last three named were seen only on some of the samples, as indicated in Table I. It should be noted that none of the common lifetime killers, such as copper, were found.

A fluorine contamination on the order of 10<sup>11</sup>-10<sup>12</sup> cm<sup>-2</sup> was seen only on the samples that were washed in HF prior to water rinses. Kern (4), who used radiochemical tracer methods to study semiconductor cleaning methods, reported a fluorine contaminant level on germanium of about 10<sup>17</sup> cm<sup>-2</sup> immediately after HF immersion and about 10<sup>15</sup> after a water rinse. The discrepancy of three orders of magnitude between our results and his may be due to differences in the final washing procedures, faster desorption of the residual fluorine *in vacuo*, or to electron desorption of the fluorine by the Auger primary beam. [Chou *et al.* (5), for example, have recently reported electron desorption of halides during Auger studies.] Sample MA, which was washed with methanol and acetone after an immersion in HF, did not show a detectable level of fluorine contamination. This agrees with Kern's observation that acetone is very effective in desorbing fluorine.

Calcium was noted only on samples STD and SC for which the variable cleaning step employed an acidic peroxide solution, and phosphorus was found only on sample MA which had a final acetone rinse. The Auger spectra from these three samples are given in Fig. 1. Both the phosphorous and calcium impurities are believed to be due to reagent contamination.

The use of chelating agents and cyanide leads to changes in the amounts of carbon and oxygen that

<sup>2</sup> Estimated on the basis of an Auger sensitivity of ~1% of a monolayer.

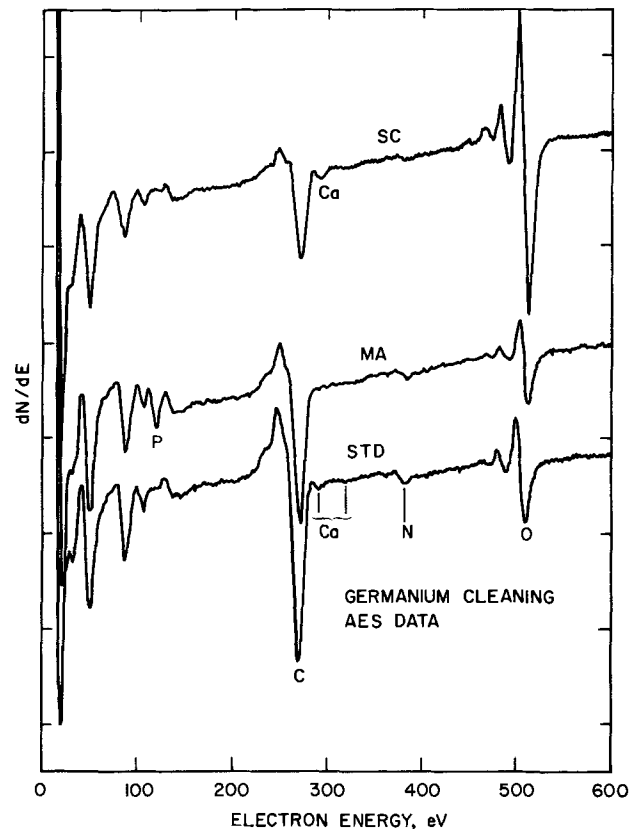


Fig. 1. Auger derivative spectra for Ge samples STD, SC, and MA

were observed on the surfaces. These treatments decreased the carbon level by about 1/2 and/or increased the oxygen concentration to about 3 or 4 times the value otherwise observed, as may be seen from Fig. 1 by comparing the spectrum from sample SC with those from samples STD and MA. These effects could be due to the formation of an oxide film, to increased water adsorption, or to decreased hydrocarbon contamination.

We conclude that for many applications, such as the in-process cleaning of germanium devices containing thin doped regions, germanium cleaning methods that employ either concentrated cyanide solutions or acidic peroxides are of limited utility due to concomitant etching. The recommended procedure, when etching is to be avoided, is to employ organic solvents to remove gross contaminations such as wax residues, and to then use a chelating agent such as EDTA.

#### Acknowledgment

This work was partially supported by the U.S. Army, Night Vision Laboratories, under contract DAAK02-72-C-0442.

Manuscript submitted Aug. 6, 1973; revised manuscript received Oct. 12, 1973. This was Paper 60 presented at the Chicago, Illinois, Meeting of the Society, May 13-18, 1973.

Any discussion of this paper will appear in a Discussion Section to be published in the December 1974 JOURNAL.

#### REFERENCES

1. W. Kern and D. Puotinen, *RCA Rev.*, **31**, 187 (1970).
2. W. Primak, R. Kampwirth, and Y. Dayal, *This Journal*, **114**, 88 (1967).
3. R. C. Henderson, *ibid.*, **119**, 772 (1972).
4. W. Kern, *Solid State Technol.*, **15**, 34 (1972).
5. N. J. Chou, C. M. Osburn, Y. J. van der Meulen, and R. Hammer, *Appl. Phys. Letters*, **22**, 380 (1973).



## Comments on the Article

### "On the Theory of Thermal Quenching of Luminescence"

by H. Payen de la Garanderie and D. Curie

R. Pappalardo

GTE Laboratories Incorporated, Waltham, Massachusetts 02154

Fluorescence, as the radiative deactivation of an excited species (atom or molecule) is one of several deactivation paths. Other decay processes involve instead of atom-photon interactions the coupling of the excited species with the phonon field (nonradiative deactivation). The increase in system temperature, by enhancing the phonon field favors in general the nonradiative relaxation to the expense of the radiative process. This adverse effect of temperature on the fluorescence properties of an emitting species can be quite important to the design of new gas lasers (1) and high-temperature phosphors.

In the case of vapors of "complex" aromatic molecules, the operating temperature (150°-250°C) of the envelope of the discharge tube is expected to favor intersystem crossing (2), by comparison with the situation existing at room temperature in dye-solution lasers. For longer lived emitting species in solid matrices, the temperature increase raises the probability of multiphonon relaxation and of potential-curve crossing.

In view of the commonly adverse effect of temperature on fluorescence, it was of considerable interest to find in the literature statements to the effect that the fluorescence intensity can be enhanced by temperature increases.

Payen de la Garanderie and Curie (3) consider a common, simplified model of an activator center as characterized by potential curves for the ground and excited electronic state and conclude, within the framework of the model used, that the radiative intensity  $I_r$  is not a constant quantity, but that on the contrary "it increases with increasing temperature." The physical reason for this effect is identified as follows: "the effective number of states leading to a light transition increases with temperature."

The conclusion that  $I_r$  increases with temperature would be quite pertinent to the area of high-temperature phosphors. Our contention is that the conclusions reached by the two authors are erroneous, as it will be shown in what follows.

The model for the activator center used by Payen de la Garanderie and Curie is now briefly summarized. The ground and excited electronic states are described by potential curves with vibrational levels characterized in the excited electronic state by a regular energy spacing  $h\nu_e$ . Excitation from the ground state is assumed to lead to the  $j_0$  vibrational level of the excited state, located at  $E_{j_0} = j_0 h\nu_e$  above the corresponding potential minimum. The over-all pumping intensity to  $j_0$  is characterized by a constant term  $q$ .

Single-phonon processes in the excited electronic state are responsible for a fast redistribution of the population among the vibrational levels, in times that

are much shorter than the radiative deactivation. A quasi-Boltzmann distribution of population over the vibrational levels ensues. The radiative transition probability  $p$  is assumed constant for all vibrational levels  $j$ . A very fast radiationless deactivation occurs at energy  $j_1 h\nu_e \gg j_0 h\nu_e$ .

The authors then proceed to calculate the over-all intensity of radiative emission  $I_r$ , assuming a Boltzmann distribution for the vibrational levels of the excited state, and they find

$$I_r = pn_0 \frac{1 - e^{-j_1 h\nu_e/kT}}{1 - e^{-h\nu_e/kT}} \sim pn_0 \frac{1}{1 - e^{-h\nu_e/kT}} \quad [1]$$

$n_0$  being the population of the lowest vibrational level of the excited electronic state. The factor multiplied by  $pn_0$  reflects a population summation carried over the levels not affected by radiationless deactivation, using the condition that  $j_1 h\nu_e \gg kT$ . The authors point out that on increasing  $T$  the value of  $I_r$  increases, in particular at the Debye temperature  $kT = h\nu_e$  one has  $I_r = 1.58 pn_0$ .

Our criticism is as follows. Given a constant pump intensity  $q$  and a radiative transition probability  $p$  which is constant over the vibrational levels considered,  $I_r$  should not be affected by the vibrational distribution of the population. The only conceivable effect resulting from a temperature increase is an enhanced contribution of the radiationless deactivation, resulting in a decrease of  $I_r$ .

The authors assume implicitly in the expression for  $I_r$  shown above, that  $n_0$  will remain constant with variations of the temperature. This is of course physically meaningless. Equation [1] cannot be used because its derivation is based on a wrong normalization constant. The vibrational-level populations  $n_j$  have in effect been expressed in terms of  $n_0$ , the population of the lowest vibrational level in the excited manifold. An expression of this type is only appropriate when ratios of population are considered. As soon as absolute values of population come into play, the normalization constant should contain the total population, which in this case is expressed by the constant pump term  $q$ . If the vibrational level populations are expressed as

$$n_j = \frac{q}{\sum_{j=0}^{j_1} e^{-jh\nu_e/kT}} e^{-jh\nu_e/kT} \quad [2]$$

instead of Eq. [1], one finds

$$I_r = pq \quad [3]$$

as intuitively anticipated. The conclusion that  $I_r$  increases with temperature is unacceptable.

Key words: luminescence, temperature dependence, theory.

## REFERENCES

1. S. Ahmed and R. Pappalardo, *IEEE J. Quantum Electron.*, **8**, 525 (1972).
2. N. A. Borisevich, *Vozbyzhdenie Sostoyaniya Slozhnikh Molekul v Gazovoi Faze*, Nauka i Tekhnika, Minsk (1967).
3. Payen de la Garanderie and D. Curie, "Luminescence of Organic and Inorganic Materials," Kallmann and Marmor-Spruch, Editors, p. 334, John Wiley and Sons, New York (1962).

## A Flux Step Boundary Condition Solution to the Diffusion Equation Corresponding to the Error Function Complement Profile

M. A. Fullenwider\*<sup>1</sup>

B-B Laboratory, Carlisle, Pennsylvania 17013

One of the solutions of the diffusion equation

$$\frac{\partial C}{\partial t} = D \frac{\partial^2 C}{\partial x^2} \quad [1]$$

which is basic to semiconductor diffusion is the error function complement profile (1)

$$\frac{C(x, t)}{C_0} = \operatorname{erfc} \frac{x}{2(Dt)^{1/2}} \quad [2]$$

where  $x$  is the distance into a semi-infinite specimen,  $t$  is the time of diffusion,  $C(x, t)$  is the concentration at  $x$  and  $t$ ,  $C_0$  is the maximum concentration within the specimen, constant in Eq. [2], and  $D$  is the diffusion coefficient. This solution is based on the simple boundary conditions for the diffusion equation

$$C(x, t) = 0, \quad x \rightarrow \infty \quad [3]$$

$$C(x, t) = 0, \quad t = 0 \quad [4]$$

$$C(0, t) = C_0, \quad t > 0 \quad [5]$$

Now Eq. [5] which corresponds to a step function in concentration at  $x = 0$  and for times greater than zero is a carry-over from the theory of heat conduction where no other condition would be reasonable under these circumstances.

In the flux of matter (diffusion), however, there is the possibility of another condition which will replace Eq. [5]. It is that of a flux step at  $x = 0$

$$-D \left( \frac{\partial C}{\partial x} \right)_{x=0} = j, \quad t > 0 \quad [6]$$

where  $j$  is the time constant flux at the surface due to kinetic control of a chemical nature, and where it has been assumed that the quantity of diffusing substance available to the surface is constant.

It is the purpose of this paper to show that this boundary condition and solutions resulting from it, different from Eq. [2], will produce concentration profiles which, with the exception of the value of the diffusion coefficient and behavior as a function of time, are very similar to Eq. [2].

Recent work (2) with the hydrogen-palladium system has shown that Eq. [6] obtains for diffusion through thin membranes as according to the analysis of Schmidt and Siegenthaler (3). This was a new and previously unsuspected result for the system. Rate limited diffusion of impurities into semiconductors has been reported previously (4-6) for the case of rate limitation due to a physical barrier at the surface. Of the two cases, physical and chemical rate limita-

tion, the first is probably the more general since it may be applied to such nonchemical situations as, for example, diffusion through an impeding film into a substrate. However, expressions derived from considerations on the second case (where it applies) are simpler and involve fewer parameters, and where both might apply, it can be difficult to distinguish between them experimentally.

From Eq. [1], [3], [4], and [6] with the method of the Laplace transformation we obtain

$$C(x, t) = 2j \left( \frac{t}{\pi D} \right)^{1/2} e^{-x^2/4Dt} - j \frac{x}{D} \operatorname{erfc} \frac{x}{2(Dt)^{1/2}} \quad [7]$$

or

$$C(x, t) = 2j \left( \frac{t}{D} \right)^{1/2} i \operatorname{erfc} \frac{x}{2(Dt)^{1/2}} \quad [8]$$

and since

$$C(0, t) = C_0 = 2j \left( \frac{t}{\pi D} \right)^{1/2} \quad [9]$$

we have

$$\frac{C(x, t)}{C_0} = e^{-x^2/4Dt} - \frac{x}{2} \left( \frac{\pi}{Dt} \right)^{1/2} \operatorname{erfc} \frac{x}{2(Dt)^{1/2}} \quad [10]$$

Figures 1 and 2 show plots of Eq. [2] and [10], respectively, for identical times and diffusion coefficients. The curves of Fig. 2 can be seen to lie well below those of Fig. 1. However, simply dividing the diffusion coefficient of Eq. [2] by a factor of 1.7 results in curves which are very similar (see Fig. 3). Thus the mistaken use of Eq. [2] where Eq. [10] applies will result in an error in the estimation of the diffusion coefficient of a factor of 1.7.

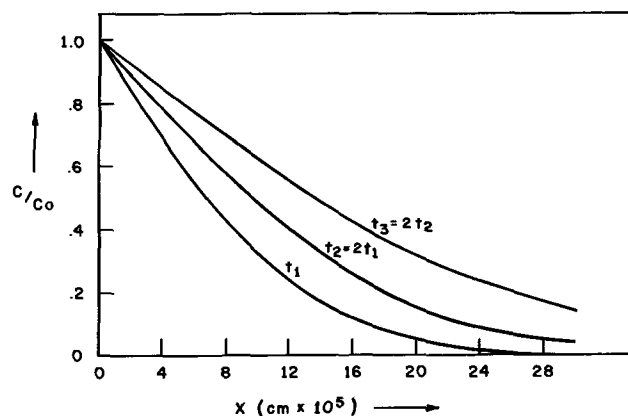


Fig. 1.  $C(x, t) = C_0 \operatorname{erfc} \frac{x}{2(Dt)^{1/2}}$

\* Electrochemical Society Active Member.

<sup>1</sup> Present address: 2970 MacArthur Road, Whitehall, Pennsylvania 18052.

Key words: error function complement profile, flux step boundary condition, concentration dependent diffusion, semiconductor diffusion.



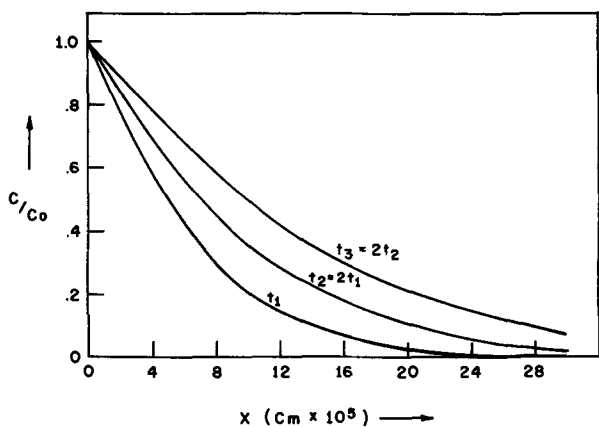


Fig. 2.  $C(x, t) = C_0 \left[ e^{-x^2/4Dt} - \frac{x}{2} \left( \frac{\pi}{Dt} \right)^{1/2} \operatorname{erfc} \frac{x}{2(Dt)^{1/2}} \right]$

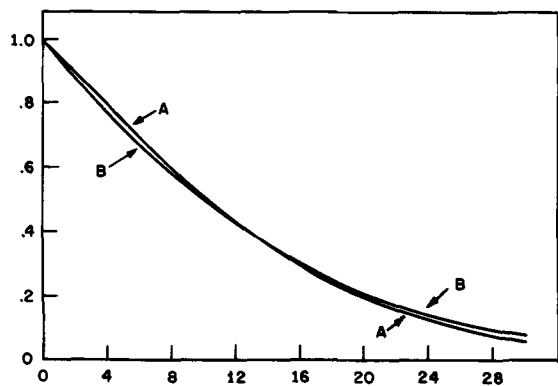


Fig. 3. A,  $C(x, t) = C_0 \operatorname{erfc} \frac{x}{2 \left( \frac{D}{1.7} t \right)^{1/2}}$ . B,  $C(x, t) =$

$$C_0 \left[ e^{-x^2/4Dt} - \frac{x}{2} \left( \frac{\pi}{Dt} \right)^{1/2} \operatorname{erfc} \frac{x}{2(Dt)^{1/2}} \right].$$

Experimentally the two cases can be distinguished simply by comparing profiles for the same system at different values of  $t$ , since the  $C_0$  of Eq. [10] should have the time functionality of Eq. [9], if it applies.

A diffusion coefficient should never be assigned to a system from analysis of a single profile.

Another point is that eventually equilibrium must be established at the interface, since  $C_0$  of Eq. [9] cannot, of course, go to infinity. At equilibrium, Eq. [5] will apply. At small times for a system Eq. [6] will always apply, and the rate at which equilibrium is established will depend upon the magnitude of  $j$ . If the time to equilibrium is finite, however, the system will have obeyed Eq. [10] during this time interval, and the final result will not be Eq. [2], but a combination of Eq. [10] and [2]. This behavior could easily be mistaken for concentration dependent diffusion, i.e., if Eq. [2] were to be used for all times  $D$  would appear to increase with time after equilibrium had been established.

It is of interest to compare these expressions with those for physical rate limitation. The expression similar to Eq. [9] is (5)

$$\frac{C_0}{C_e} = 1 - e^{Kx/D} \operatorname{erfc} K \left( \frac{t}{D} \right)^{1/2} \quad [11]$$

where  $C_e$  is the equilibrium concentration within the substrate, a constant, and  $K$  is a rate constant defined in terms of transport across a physical barrier. Also for the concentration profile (5)

$$\frac{C(x, t)}{C_e} = \operatorname{erfc} \frac{x}{2(Dt)^{1/2}} - e^{(Kx+K^2t)/D} \operatorname{erfc} \left[ \frac{x}{2(Dt)^{1/2}} + K \left( \frac{t}{D} \right)^{1/2} \right] \quad [12]$$

Manuscript submitted June 5, 1973; revised manuscript received Oct. 5, 1973.

Any discussion of this paper will appear in a Discussion Section to be published in the December 1974 JOURNAL.

#### REFERENCES

1. J. Crank, "The Mathematics of Diffusion," p. 12, Oxford (1956).
2. To be published.
3. E. Schmidt and H. Siegenthaler, *Helv. Chim. Acta*, **53**, 321 (1970).
4. F. M. Smits, *Proc. IRE*, **46**, 1049 (1958).
5. F. M. Smits and R. C. Miller, *Phys. Rev.*, **104**, 1242 (1956).
6. R. N. Ghoshtagore, *Solid-State Electron.*, **15**, 1113 (1972).





## Nonaqueous Lithium-Bromine Secondary Galvanic Cell

J. L. Weininger\* and F. W. Secor

General Electric Corporate Research and Development, Schenectady, New York 12301

### ABSTRACT

A nonaqueous secondary cell consists of a negative lithium electrode and a positive bromine electrode. This combination is made possible by the use of an ultrafine, porous polyethylene separator. It reduces the diffusion of bromine to the lithium electrode to tolerable levels. The cell was tested with 90 min charge-discharge cycles. Based on the utilization of lithium deposited on the anode, the current efficiency was 90% for the first 100 cycles, 70% up to cycle 300, and above 30% for the duration of the cell life of 1785 cycles. Self-discharge was sufficiently slow so that an open-circuit stand up to 2 hr did not show appreciable loss of charge. The over-all cell mechanism is complex. It consists of the interaction of the electrode reactions, the propylene carbonate solution properties, and the effect of the porous separator. Within this framework a bromine shuttle mechanism has been identified which explains the long life of the cell in spite of a small but measurable self-discharge.

In recent years many attempts have been made to extend battery technology to nonaqueous solvents in order to take advantage of the high-energy density inherent in the use of alkali and alkaline earth metals (1). Lithium is generally recognized as the most satisfactory material for the negative electrode (anode on discharge) in a nonaqueous cell. Although there remain some problems in its use, the phenomenology, if not the state-of-the-art, of a lithium electrode is equivalent to that of other metal electrodes in aqueous systems; for example, zinc in alkaline solution. Until now, however, there has not been a satisfactory material for the positive electrode (cathode on discharge) which is to be paired with the lithium electrode in a rechargeable cell.

The difficulties encountered with cathode materials are lack of complete and repeated utilization of conventional electrodes as well as lack of chemical compatibility and their increased electrical resistivity in the organic environment.

Halogens have been frequently proposed as cathode materials in fuel cells and galvanic cells. Their application failed because of their chemical reactivity with materials of construction (for example, the separator) and with the counterelectrode, resulting in self-discharge. Homogeneous ion-exchange membranes can be used, but failed in nonaqueous solvents because of their greatly increased resistivity.

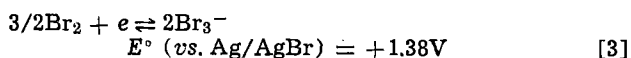
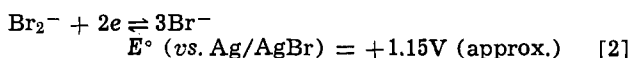
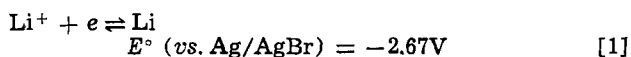
We have set as our goal the application of a halogen electrode to the lithium nonaqueous system, and we now describe below the mechanism, design, and performance of a lithium-bromine cell.

### Mechanism of the Cell

Figure 1 is a schematic diagram of the cell. The negative electrode is an inert nickel substrate on which lithium is alternately deposited and discharged while bromine undergoes the electrode reactions at a positive

porous carbon electrode. The tribromide ion is much more stable in the organic solvent, propylene carbonate (PC), than in water. Lithium bromide and lithium perchlorate are added as solutes, as shown in the diagram.

During operation of the cell, the lithium couple  $\text{Li}/\text{Li}^+$  undergoes reversible electrode reactions with fairly high exchange currents. The four reactions in which the bromide species participate involve only relatively small overvoltages so that very large cell voltages can be obtained from the electrode reactions



Combination of reactions [1] and [2] gives a cell voltage of 3.82V and a theoretical energy density of 320

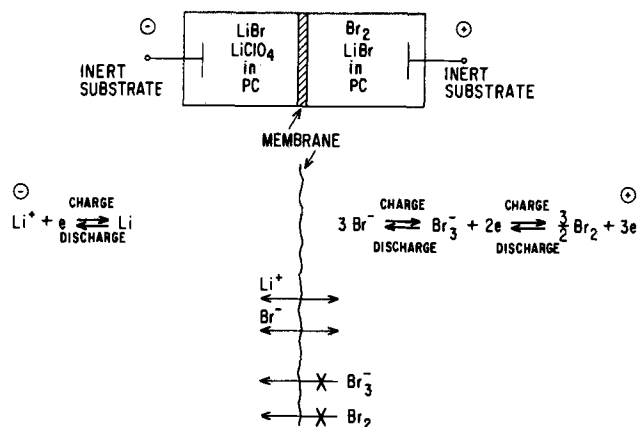


Fig. 1. Schematic of lithium-bromine cell

\* Electrochemical Society Active Member.  
 Key words: electrochemistry, nonaqueous batteries, lithium anodes, halogen electrodes, propylene carbonate solvent.

Whr/lb; combination of reactions [1] and [3] increases the initial open-circuit voltage to 4.05V and the theoretical energy density to 504 Whr/lb. In practical use, voltages close to the theoretical values are obtained on open circuit and during discharge. As for the energy density, only a small fraction of the theoretical value is realized in the present cell which is designed for developmental purposes and not for maximizing energy density.

The use of bromine at the positive electrode takes advantage of favorable electrode potentials and kinetics. The control of the rate of the electrode reaction is changed from ionic diffusion in a solid, as in AgCl/Ag or CuF<sub>2</sub>/Cu electrodes, to diffusion control in the solution. The greater solubility of bromine in the organic solvent is important in two respects: it increases the available electroactive material in dissolved form, and it also reduces the chemical attack of bromine on the materials of cell construction. The single, most important disadvantage in the use of bromine is its reaction with lithium. As indicated in Fig. 1, the self-discharge of the cell by the tarnishing reaction must be avoided; the oxidized bromine species, Br<sub>2</sub> and Br<sub>3</sub><sup>-</sup>, may not enter the negative electrode chamber.

The early part of this study was therefore concerned with a search for a barrier for dissolved and solvated bromine molecules. When a porous Vycor glass disk with pore diameters of 60Å was used as a separator in a lithium-bromine cell (2) diffusion of Br<sub>2</sub> or Br<sub>3</sub><sup>-</sup> was prevented. This was attributed to the relatively large size of the solvated complexes of Br<sub>2</sub> and Br<sub>3</sub><sup>-</sup> with propylene carbonate. The literature contains information on a variety of stable molecular complexes of the alkali metal salts of polyhalide anions, e.g., in benzonitrile KI<sub>3</sub>·2C<sub>6</sub>H<sub>5</sub>CN and LiI<sub>3</sub>·4C<sub>6</sub>H<sub>5</sub>CN (3). The bromine species were therefore expected to complex in propylene carbonate, but the extent to which this would retard bromine diffusion remained to be seen.

The present cell has an ultrafine, porous polyethylene membrane (4) which prevents most of the bromine diffusion. It has about 50% porosity and an average pore size of 40-120Å. The limited migration of Br<sub>2</sub> and Br<sub>3</sub><sup>-</sup> can be tolerated, provided the cell is not required to stand on open charge for more than a few hours. This is predicated on a shuttle mechanism similar to those occurring in aqueous battery systems. The tarnishing of the lithium electrode is controlled by the diffusion of the bromine species to the lithium. This results in self-discharge with LiBr as the product, identical to the product of the galvanic cell reaction. Therefore, as the LiBr concentration increases in the solution contained in the negative electrode compartment, it saturates that solution. The chemical concentration gradient with respect to the positive compartment (bromine electrode) produces the back diffusion of bromide ions. This completes the shuttle. In the present cell, the process is slow enough so as not to decrease unduly the current efficiency of the cell.

### Cell Composition

Different cell designs and variations in the concentration of the cell components have been tested. Preliminary experiments were performed with small cells having 2.54 cm diameter electrodes. Life tests were performed on larger cells, for which only one of twelve tests is reported here. The following cell was used  $\ominus$  Li(Ni foam)/0.2M LiBr + 0.8M LiClO<sub>4</sub> in PC/UF polyethylene membrane/1.5M Br<sub>2</sub> + 1.6M LiBr in PC/porous C  $\oplus$

**Electrodes.**—Figure 2 is a sketch of the external view and cross section of the cell. Nickel and carbon were used as inert electrodes. The anode was Foamet<sup>®</sup> nickel, a 95% porous metal structure, prepared by the Metallurgical Products Department, General Electric Company. The porous carbon cathode was made of material supplied by the Pure Carbon Company. It was a fuel cell grade (FC-22) carbon with 60% porosity, a

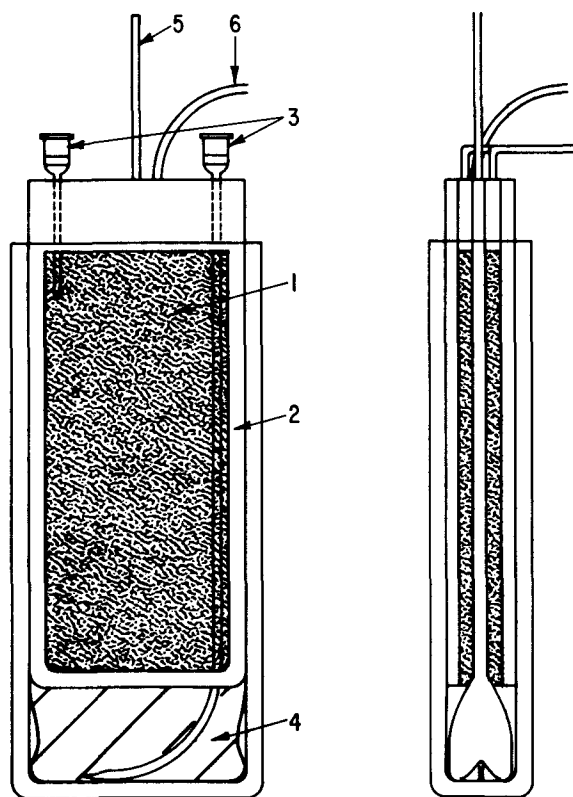


Fig. 2. External and cross-sectional view of lithium-bromine cell. 1, Porous carbon cathode; 2, PTFE cathode frame; 3, PTFE syringes for filling and venting; 4, UF polymer separator bag; 5, anode; 6, Ag/AgBr reference electrode.

surface area of 600 m<sup>2</sup>/g, and a median pore diameter of 11 μm.

A brominated silver wire was immersed in the anode chamber as a reference electrode. This gives a potential sufficiently stable to determine the polarization of the respective electrodes. However, the Ag/AgBr couple is not stable in the solution containing bromine (cathode chamber) because AgBr is slightly soluble due to the formation of the AgBr<sub>2</sub><sup>-</sup> complex.

**Solvent.**—The distillation of propylene carbonate is run continuously for about 80 hr in a glass column packed with 1 in. diameter stainless steel helices at a pressure of 26.5 mm and boiling point of 120°C. During the first stage the column is on total reflux for 1 hr. Then the first 10% cut, approximately 300 cm<sup>3</sup>, is discarded. This is followed by the sample collection. After each cut the material is poured directly from the still into a molecular sieve (Linde 5A) column. It is then allowed to stay for more than 16 hr over the molecular sieve until it is placed in the oven-dried receiver at 50 drops. Before use, the molecular sieve is heated to 220°C for 36 hr under nitrogen flow and cooled with nitrogen. It is used for two consecutive distillations before it is discarded. This procedure yielded solvent free of water at the limit of detection of vapor phase chromatography (less than 10 ppm).

**Solute.**—Lithium bromide and lithium perchlorate were recrystallized and vacuum dried. The active cathode material, bromine, was used as-received. The concentrations were chosen for convenience and not for maximum conductivity. In the anode chamber, LiClO<sub>4</sub> was added to the solution to bring the Li<sup>+</sup> ion concentration up to 1M. In the cathode chamber the bromine concentration was less than that of LiBr so as to have almost all of Br<sub>2</sub> complexed as the tribromide. This increased the chemical stability of the system.

The conductivity could be increased, first of all, by addition of other solutes such as LiBF<sub>4</sub>. For the given system LiBr + Br<sub>2</sub> in PC the conductivity and solu-

bility of the electrolyte are illustrated in Fig. 3. One curve represents the conductivity of the solution, saturated with LiBr, as a function of Br<sub>2</sub> concentration. The numbers of the data points of the curve represent the molarity of saturated LiBr corresponding to the given Br<sub>2</sub> concentration. Thus at the maximum conductivity of 0.0083 mho/cm the concentrations are 2.23N (1.115M) Br<sub>2</sub> and 1.17M LiBr. For the solution used in the cathode compartment the conductivity is 0.0067 mho/cm. In the absence of bromine the solubility of LiBr in PC is limited to 0.203M. Other and larger values reported in the literature can be attributed to the probable presence of water in those systems. If bromine is added to the 0.2M LiBr solution without further addition of LiBr the lower conductivity curve of Fig. 3 is obtained.

During the lifetime of the cell, the initial concentrations will undergo substantial changes in the two compartments. Except for the presence of bromine in the cathode chamber and the existence of the bromine-bromide shuttle, described above, the supporting electrolyte will tend to equalize in the two compartments. Because of the shuttle, the anode chamber will be saturated with LiBr and provisions must be made to accommodate some precipitated LiBr in that compartment.

**Separator.**—The porous 0.01 cm thick polyethylene was heat-sealed to form a bag containing the lithium electrode. This membrane material was characterized by a porosity of 43%, a flow rate of nitrogen per cm<sup>2</sup> at 5.6 and 65.6 psi of 1.2 and 4.0 ml/min/cm<sup>2</sup>, and a conductivity of  $0.76 \times 10^{-3}$  mho/cm when filled with 1M KCl in water.

### Cell Performance

The cell was tested in 90 min cycles with charge-discharge times divided into 60:30, 42:48, and 48:42 min half cycles. Constant current levels of 30-100 mA were used, which corresponded to charge transfer of 252-360 coulombs on charge and 108-324 coulombs on discharge (the electrode dimensions were  $10.4 \times 4.2$  cm, resulting in a current density of 1.15 mA/cm<sup>2</sup> equivalent to 100 mA). Occasionally steady-state current voltage measurements were made. These were carried out at different points in the cycle and reflected the relative state of charge of the cell. Simultaneous measurements of the individual electrode potentials with respect to a Ag/AgBr reference electrode indicated the sources of overpotential.

Figure 4 shows several current-voltage curves. Symbols C and D indicate whether these steady-state measurements, which include both charging and discharging conditions, were actually made at a time when the cell was nearly fully charged or discharged. Curves C53 and D67 are typical polarization curves for about the first hundred cycles when there was little polarization due to activation and diffusion control. The slope of about 5 ohms was indicative of the electrolyte and membrane impedance. This is also reflected

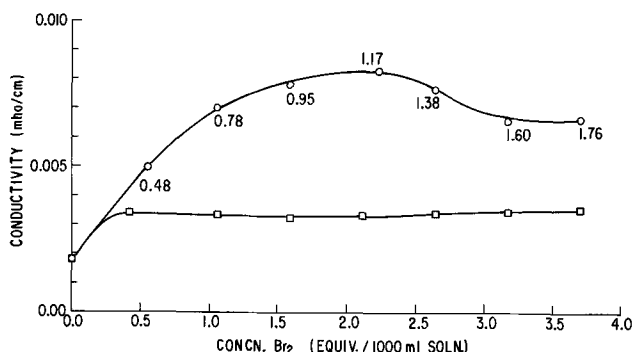


Fig. 3. Conductivity of bromine-containing solution of propylene carbonate as a function of bromine and lithium bromide concentration. □, 0.2M LiBr solution; ○, solution saturated with LiBr.

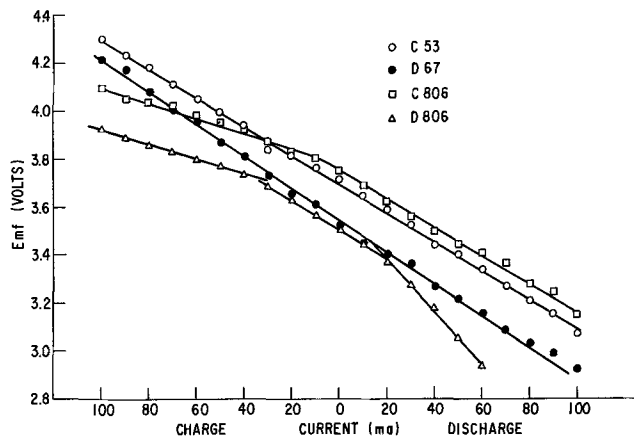


Fig. 4. Current-voltage curves for lithium-bromine cell. C53 at end of charge, cycle 53; D67 at end of discharge, cycle 67; C806 and D806 at end of charge and discharge of cycle 806.

in the constant-current cycling discussed below. At cycle 806, curve C806 indicates an equally good cell capability at end of charge (start of discharge). The reason for the change in slope (to 3 ohms) for the charging part of the  $i$ - $E$  curve is not known. It may be due to the presence of nickel ions in solution, lowering the potential of the lithium electrode, or to a change in the electrolyte concentration in either the anode compartment or in the membrane due to the operation of the bromine shuttle. On the other hand, D806 shows considerable polarization during discharge of a nearly discharged cell. Here both electrodes are under diffusion and activation control, resulting in a slope for the  $i$ - $E$  curve of about 12 ohms. This is brought out more clearly in Fig. 5 where the individual cell potentials are shown for comparable conditions during cycle 1017.

Constant-current cycling of the cell was followed by observing the cell voltage as a function of time at various stages in the life of the cell, during charge and discharge cycles, and with different current levels and ratios of time at charge and discharge. Consequently, the depths of discharge were also varied.

Originally there was no bulk lithium present and all of the lithium deposited in one cycle on the inert nickel foam substrate could be discharged in the same cycle, subject only to aging and deterioration of the cell. With incomplete discharge, the active electrode mate-

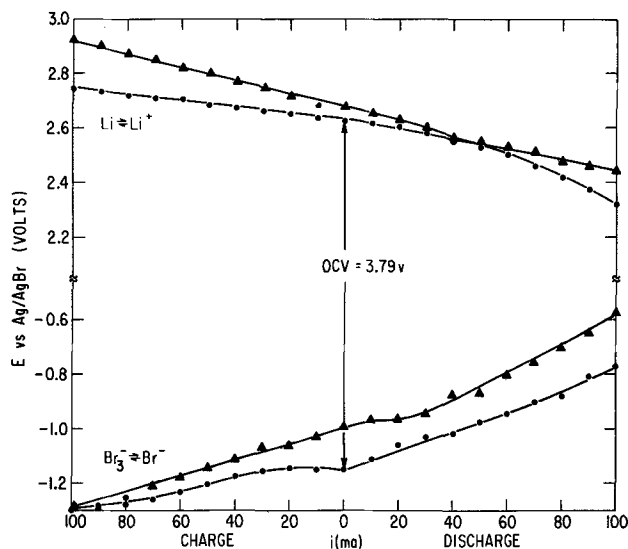


Fig. 5. Current-voltage curves for individual electrodes vs. Ag/AgBr reference electrode. Cycle 1017: ○, end of charge; △, after partial discharge.

Table I. Utilization (current efficiency) of lithium-bromine cell on continuous cycling

Cycle No. Approx. % utilization	0-100	100-300	300-1785
	90	70	30

rials, lithium and bromine, are not completely used up and create activation and diffusion barriers in subsequent charge. The actual utilization of lithium, which was in limited supply, given as the percentage of charge recovered on discharge, was a function of cycle life. Approximate values which depend on the lithium electrode, are shown in Table I.

Deep discharge cycles, or even current reversal, had no deleterious effects on the cell. Cycle 917 showed complete discharge of the lithium electrode. Cycle 918 even reversed polarity. Significantly, this improved the charge acceptance and discharge of the following cycle.

The effect of open-circuit stand on the cell was also tested. The cycling regime was changed for cycles 222-230 to a 60 min, 90 mA charge half-cycle and a 30 min 90 mA discharge half-cycle. The discharge was interrupted after 15 min and the cell was left on open circuit for various times: 10, 30, 60 min, 2 hr, and overnight (8 hr and 40 min). Only in the last case was there a noticeable effect due to open-circuit stand. On other occasions the cell was left on open circuit for several days, in which case the cell self-discharged but readily accepted a fresh charge and showed good subsequent performance.

After a final open-circuit stand of 6 days after cycle 1785 the cell failed to accept reasonable charge. Its life, therefore, was 1785 cycles, in almost continuous operation over a period of 4 months.

### Conclusions

A lithium-bromine cell can be repeatedly charged when an ultrafine, porous separator is used. The sepa-

separator retards the diffusion of bromine to the lithium electrode, thereby allowing a short open-circuit stand in the charge condition.

The mechanism of the cell is understood in general terms. The long cell life could only be achieved because of the bromine shuttle. However, the individual electrode reactions have not yet been elucidated nor is the cell mechanism completely understood in terms of the presently found cell polarization.

The cell design is convenient for testing lithium anodes with nickel metal foam substrates, UF membranes as separators, and porous carbon cathodes. It made no pretention at achieving high-energy density. The latter will require a careful balance of active materials and inert electrode substrates. In the present case bromine was kept in excess so that the utilization or current efficiency reported above refers to the lithium electrode. This is justified by the smaller chemical stability of the lithium electrode in spite of its higher rates of electrode reactions, as compared with the lower rates and less reversible kinetics of the bromine electrode. In fact, after 4 months of operation, the bromine electrode was still completely serviceable, whereas the lithium electrode in the form of a deposit on the nickel metal foam had partly disintegrated.

Manuscript submitted Aug. 24, 1973; revised manuscript received Nov. 5, 1973.

Any discussion of this paper will appear in a Discussion Section to be published in the December 1974 JOURNAL. All discussions for the December 1974 Discussion Section should be submitted by Aug. 1, 1974.

### REFERENCES

1. R. J. Jasinski, *Electrochem. Technol.*, **6**, 28 (1968).
2. J. L. Weininger and R. J. Charles, Unpublished.
3. J. H. Martin, *J. Chem. Soc.*, **1932**, 2640 (1932).
4. J. L. Weininger and F. F. Holub, *This Journal*, **117**, 340 (1970).

## Redox Couple Behavior on Lithiated Nickel Oxide Electrodes

Dennis M. Tench\*<sup>1</sup> and Ernest Yeager\*

Chemistry Department, Case Western Reserve University, Cleveland, Ohio 44106

### ABSTRACT

The rotating electrode technique has been used to study the kinetics of various redox couples [ $\text{Fe}(\text{CN})_6^{4-}/\text{Fe}(\text{CN})_6^{3-}$ ,  $\text{Fe}^{2+}/\text{Fe}^{3+}$ ,  $\text{Cr}^{2+}/\text{Cr}^{3+}$ , and quinone/hydroquinone] on mosaic lithiated nickel oxide electrodes in sulfate solutions. At potentials cathodic to the flatband potential, the redox reactions are very inhibited. At potentials anodic to the flatband potential, the oxidation of the ferrocyanide ion exhibits a transfer coefficient of  $\alpha = 1/2$  with an apparent standard rate constant approximately two orders of magnitude smaller than on Pt. The other couples exhibit abnormal transfer coefficients under these conditions, probably because of specific adsorption on the oxide electrode surface.

The kinetics of various redox reactions have been examined on lithiated mosaic nickel oxide electrodes with the objective of comparing the behavior of these couples on this compound semiconductor with that on metals. With  $\text{NiO}(\text{Li})$  electrodes, the heterogeneous electron transfer is expected to involve rather localized valency states within the electrode phase [i.e.,  $\text{Ni}^{2+}(3d^8)$  and  $\text{Ni}^{3+}(3d^7)$ ] rather than the wide bands

involved with metal and some other semiconductor electrodes.

The electronic properties of  $\text{NiO}(\text{Li})$  have been discussed by various authors [see, e.g., Ref. (1) and (2)]. Although the conduction process appears to involve a narrow valence band carrier mechanism, the band width may still be sufficiently narrow that the electron transfer across the interface can be reasonably well approximated as involving localized valency states within the electrode phase.

Information concerning the potential distribution at the semiconductor-electrolytic solution interface is a

\* Electrochemical Society Active Member.

<sup>1</sup> Present address: Fritz-Haber Institut der Max-Planck-Gesellschaft, D-1 West Berlin-33, Germany.

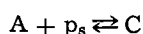
Key words: nickel oxide electrodes, semiconductor electrochemistry, redox couples, electrode kinetics.

prerequisite to redox kinetic studies at such interfaces. In earlier work (3) the charge and potential distributions at the NiO(Li)-sulfate electrolyte interface were examined using a-c impedance measurements. At potentials more than  $\sim 0.5V$  cathodic to the voltammetry peak at 1.00-0.059 pH volts re SHE [designated as peak I in Ref. (3)], linear Mott-Schottky plots (see Appendix) were obtained, indicating that virtually all of any change in electrode potential occurs across the space charge region within the semiconductor. Peak I is attributed to the  $Ni^{2+}-Ni^{3+}$  surface reaction and hence is attended by a large change in surface charge. As the potential becomes more anodic, an increasing fraction of any electrode potential change occurs across the Helmholtz region. At potentials anodic to peak I virtually all of the potential change occurs across this region. Under these circumstances the redox kinetics would be expected to approach those on metal electrodes except for possible differences in the free energies of activation arising from the involvement of localized valency states in the electrode phase.

Earlier workers (4,5) have examined the kinetic behavior of redox couples on NiO(Li). Rouse and Weininger (4), using chronopotentiometry, reported apparent Tafel slopes for the ferro-ferricyanide couple on mosaic NiO(Li) which varied between 69 and 153 mV/decade for Li concentrations of 0.21-2.74 cation % Li in sulfate solutions of pH  $\sim 3$  even at potentials where electrode potential changes should be almost entirely across the Helmholtz region. Yohe *et al.* (5), using the rotating disk technique, found values of the Tafel slope for this couple which increased with rotation rate (e.g., for  $5 \cdot 10^{-3}M$   $Fe(CN)_6^{3-}$  -  $5 \cdot 10^{-3}M$   $Fe(CN)_6^{4-}$  in 0.5M  $K_2SO_4$ , the anodic Tafel slope increased from 90 mV/decade at 64 rpm to 220 mV/decade at 6400 rpm). This effect was attributed by Yohe *et al.* to the series contribution of the potential drop associated with the back electrical contact to the NiO(Li). As the rotation rate increased and the current becomes higher, more of the potential drop occurred at the back junction of the crystal, rather than just at the semiconductor-solution interface, and the Tafel slope increased. The electrical contacts used in the earlier work of Yohe *et al.* and also that of Rouse and Weininger (cured Ag epoxy resin) appear to be unsatisfactory for measurements of this kind with NiO(Li) electrodes.

The fused Ag electrical contact used in the present work has eliminated this problem. With this contact the Tafel slopes did not vary with rotation rate, when ohmic losses within the NiO(Li) electrodes were negligible and the kinetics were principally under charge transfer control at potentials anodic to voltammetry peak I.

For a redox reaction involving surface p carriers ( $p_s$ )



the kinetics may be represented as follows (6)

$$i = i_o \cdot \left[ \frac{i_a - i}{i_a} \exp f(\alpha \Delta \phi_H + \Delta \phi_S) - \frac{i_c + i}{i_c} \exp - f\beta \Delta \phi_H \right] \quad [1]$$

where  $\alpha$  and  $\beta$  are the anodic and cathodic transfer coefficients,  $\Delta \phi_H$  and  $\Delta \phi_S$  are the contributions to the overpotential from the potential drops across the Helmholtz layer and semiconductor space charge region, respectively;  $i_a$  and  $i_c$  are the anodic and cathodic diffusion limiting current densities;  $i_o$  is the exchange current density (uncorrected for ionic double layer effects); and  $f = F/RT$ . Equation [1] involves the assumption that only p-carriers are involved in the redox reactions and that the p-carrier surface concentrations can be described by a simple Boltzmann distribution. Equation [1] can also be expressed in the form

$$\eta = \frac{RT/F}{1 - (1 - \alpha)\gamma} \cdot \ln \left\{ \frac{i}{i_o} / \left[ \left( 1 - \frac{i}{i_a} \right) - \left( 1 + \frac{i}{i_c} \right) \exp - f\eta \right] \right\} \quad [2]$$

where  $\eta$  is the overpotential, ( $\eta = \Delta \phi_H + \Delta \phi_S$ ),  $\gamma = \Delta \phi_H/\eta$ , and  $\alpha + \beta = 1$ . At potentials cathodic to voltammetry peak I,  $\gamma \rightarrow 0$  and the Tafel slope approaches  $RT/F$ ; at potentials in the vicinity of this peak and anodic to it,  $\gamma \cong 1$  and the Tafel slope is  $RT/(\alpha F)$ .

Very high carrier concentration are involved with the NiO(Li) electrodes used in the present study ( $\sim 10^{20}$  carriers/cm<sup>3</sup>). This, together with the high concentration of surface states expected as voltammetry peak I is approached, makes it unlikely that Eq. [1] will be followed except when  $\gamma \rightarrow 1$ .

### Experimental Procedures

Procedures used in preparing the mosaic NiO(Li) electrodes and the electrolytes (except alkaline solution) have been described previously (3). The redox couple solutions were prepared using recrystallized reagent grade chemicals. The alkaline electrolyte (0.497M  $K_2SO_4$  + 0.01M NaOH) was purified by *in situ* pre-electrolysis of 100 ml of solution for 16 hr using passivated Ni electrodes having areas of  $\sim 4$  cm<sup>2</sup> each at potentials of about  $-0.40$  and  $0.83V$  re SHE. Platinum pre-electrolysis electrodes are not acceptable because of possible Pt contamination of the NiO(Li) electrode surface. All electrolytes were saturated with helium which was passed through hot copper turnings to remove  $O_2$  and traps containing Linde molecular sieves (3A and 13X) at liquid  $N_2$  temperatures to remove other contaminants.

The NiO(Li) electrodes were prepared as described previously (3) and compression molded into Kel-F cylindrical holders for use with the rotating disk method. The exposed NiO(Li) surface was near square shaped ( $\sim 0.1$  cm<sup>2</sup>) rather than circular because of fabrication problems. Earlier studies (5) with metal electrodes have shown that the use of square rather than circular electrodes does not lead to appreciable errors in kinetic studies with the rotating disk method. The lithium concentrations in the NiO(Li) electrodes listed in this paper were obtained from the slopes of the Mott-Schottky plots. These values have been shown to be essentially the same as those from flame photometric analyses (3).

The Pyrex cell (Fig. 1) consisted of a main compartment containing the NiO(Li) working electrode and separate compartments for the reference and platinum counterelectrode. Temperature control was achieved through the circulation of thermostated water through a jacket surrounding the bottom of the main compartment. A Teflon gasket was used between the ground surfaces of the lid and body of the cell with a screw clamp to apply pressure.

The potential of the NiO(Li) electrode was controlled with a Wenking potentiostat in conjunction with a slow linear potential sweep scanner and a Hewlett Packard/Moseley 7030A x-y plotter to record the current-potential data.

The reference electrode was  $Hg|HgSO_4$  in acid and neutral solutions and  $Hg|HgO$  in basic solutions with the same electrolyte as used for the supporting electrolyte in the main compartment, with the exception of the measurements in neutral solution. For the 0.50M  $K_2SO_4$  redox solutions the reference compartment contained 0.495M  $K_2SO_4$  + 0.005M  $H_2SO_4$ . All potentials reported have been converted to the standard hydrogen electrode (SHE) scale.

### Results and Discussion

The results presented in this paper are representative of those found for electrodes containing 0.2-0.5 cation % Li. Electrodes which were less highly doped

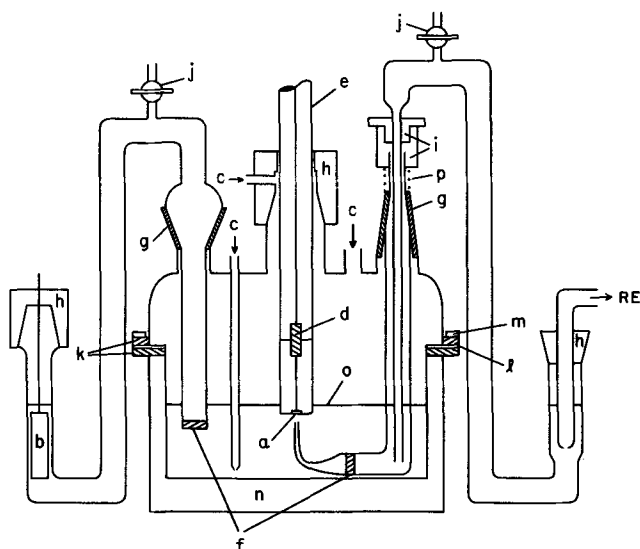


Fig. 1. Electrochemical cell for use with rotating electrode assembly. a, NiO(Li) electrode (WE); b, Pt foil (external CE); c, helium gas inlets; d, spring-cap electrical contact; e, rotating shaft (Teflon sleeve); f, sintered glass plugs; g, standard taper glass joints; h, Teflon plug fittings to standard taper joints; i, Teflon plugs (press-fit); j, Teflon-glass stopcocks; k, ground glass lips or rims; l, Teflon gasket; m, brass ring; n, water jacket; o, electrolyte level; p, spring.

(<0.1 cation % Li) generally exhibited Tafel slopes which were considerably higher and dependent on rotation rate and at high current densities also on potential. These effects are attributed to errors in the measured electrode potential due to ohmic losses within the bulk of the electrode. This conclusion is in accord with the a-c impedance results which yielded values for the bulk electrode resistance as high as 1000 ohms at 1 kHz corresponding to a resistivity of  $\sim 10^4$  ohm-cm for 0.05 cation % Li. While results are presented only for rather highly doped electrodes, the Tafel slopes obtained for the less highly doped samples generally agree with those for the more heavily doped electrodes within 10-20% if a correction is applied for bulk resistivity as an adjustable parameter.

The dissolution rates of mosaic NiO(Li) are very slow even in concentrated acid solutions. For a potential of 1.0V re SHE in 1N H<sub>2</sub>SO<sub>4</sub> at 95°C, Lee and Yeager (7) report the dissolution rate of NiO (0.88 cation % Li) to be  $\sim 10^{-5}$  g/cm<sup>2</sup>-hr. On the basis of the temperature dependence found in this work, the dissolution rates would be expected to be several orders of magnitude slower at room temperature (i.e.,  $\sim 10^{-8}$  g/cm<sup>2</sup>-hr). Taking into account the potential dependence of the dissolution rate observed by Lee and Yeager, the amount of NiO lost through dissolution even in the most acid solution involved in the present work (1N H<sub>2</sub>SO<sub>4</sub>) would not be expected to exceed  $10^{-7}$  g/cm<sup>2</sup> (the equivalent of approximately 1 monolayer) over the times (5-10 min) required to record the current-potential curves, scanning in any one direction.

**Ferro-ferricyanide couple.**—This couple was chosen for the majority of the study because the reactants are moderately stable over a wide pH range, the salts are easily recrystallized for purification purposes, and the couple has a reversible potential near the flatband potential for NiO(Li), thus affording an opportunity to examine the effects of changes in the space charge within the semiconductor on the kinetics. This couple has been found to be relatively fast on various metals in sulfate solutions at various pH (8), with the rate increasing as the hydrogen ion is replaced by alkali metal cations such as Na<sup>+</sup> or K<sup>+</sup>.

The current-potential behavior of the ferro-ferricyanide reaction on NiO(Li) electrodes at various rotation rates is illustrated in Fig. 2-5 for sulfate solutions at pH from 0.5 to 12.0. Appreciable hysteresis was observed in the voltammetry curves for the ferro-ferricyanide reaction only in neutral solution (see Fig. 4) and this may be due to pH changes at the interface and/or the specific adsorption of some solution species. Unless otherwise indicated, only the current-potential curves obtained with sweeps in the cathodic direction are shown in the graphs.

For the strongly acidic medium, the cathodic branch is very inhibited but becomes progressively less inhibited at higher pH. The anodic branch also is somewhat inhibited at low overpotentials in acidic solutions but this effect becomes less pronounced at higher pH. The inhibition of the cathodic reaction arises because the depletion of charge carriers in the vicinity of the electrode surface leads to a small value of  $\gamma$  in Eq. [2], i.e., a large potential drop across the space charge region. Studies on a-c impedance have shown that protons on the electrode surface strongly affect the potential distribution [see Ref. (3)] and that the depletion of charge carriers becomes less severe as the pH is increased. At more anodic potentials, protons are desorbed from the surface and hence the depletion of charge carriers is less with the result that the anodic reaction proceeds faster.

In acid solutions the cathodic currents are independent of the rotation rate (Fig. 2 and 3) but this is not the case at higher pH values (Fig. 4 and 5). Even at pH 12.0, however, the cathodic limiting currents at 0.264V re SHE are not completely diffusion controlled as is evident from the plot of  $1/i_L$  vs.  $1/(\omega)^{1/2}$  in Fig. 6. For a diffusion controlled reaction this curve should pass through the origin.

The limiting currents for the anodic branches are not very clearly defined, especially at the higher rotation rates and lower pH values. A possible cause for this effect may be that, with the near square rather than circular exposed electrode surfaces used in this work, the current distribution on the rotating electrode may not be uniform even at the diffusion limiting current. Yohe *et al.* (5), however, have shown experimentally that rotating near-square electrodes yield electrochemical results for redox reactions which do not differ significantly from those obtained on rotating

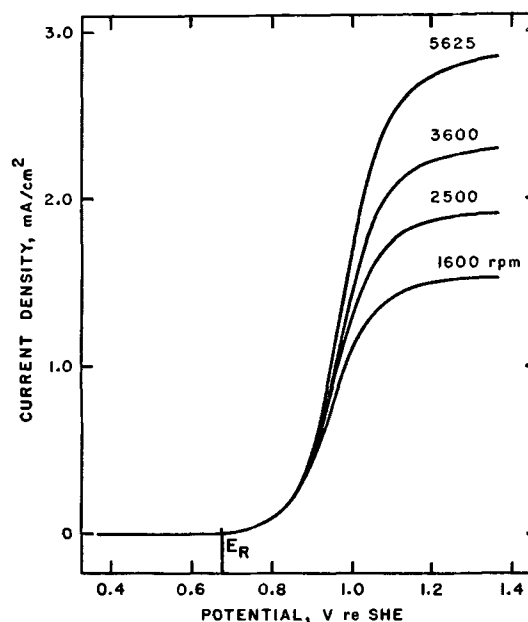


Fig. 2. Current-potential curves at various rotation rates for mosaic NiO(0.36 cation % Li) in He-saturated 1.0N H<sub>2</sub>SO<sub>4</sub> [2.5 mM K<sub>4</sub>Fe(CN)<sub>6</sub> and 2.5 mM K<sub>3</sub>Fe(CN)<sub>6</sub>] at 25°C. Electrode area, 0.128 cm<sup>2</sup>; sweep rate, 2 V/min; E<sub>R</sub> = 0.672V re SHE.

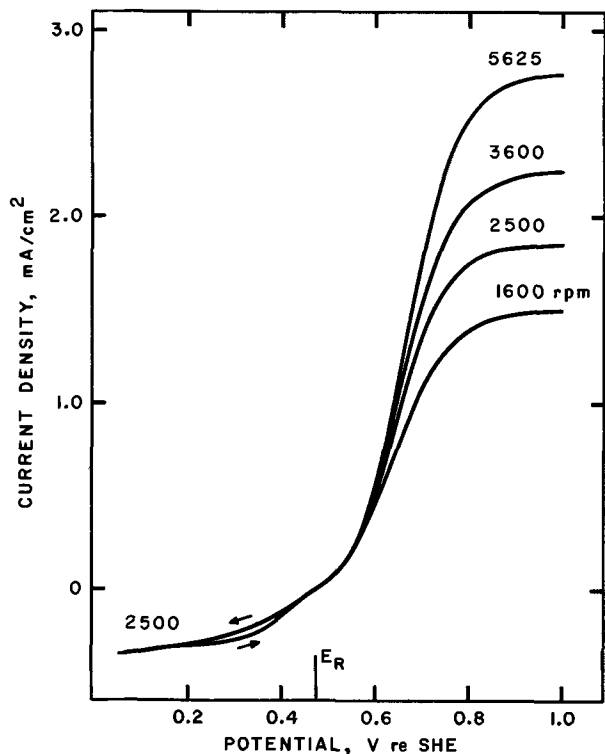


Fig. 3. Current-potential curves at various rotation rates for mosaic NiO(0.36 cation % Li) in He-saturated 0.495M  $K_2SO_4$  + 0.005M  $H_2SO_4$  [2.5 mM  $K_4Fe(CN)_6$  and 2.5 mM  $K_3Fe(CN)_6$ ] at 25°C. Electrode area, 0.128  $cm^2$ ; sweep rate, 1 V/min;  $E_R = 0.470V$  re SHE.

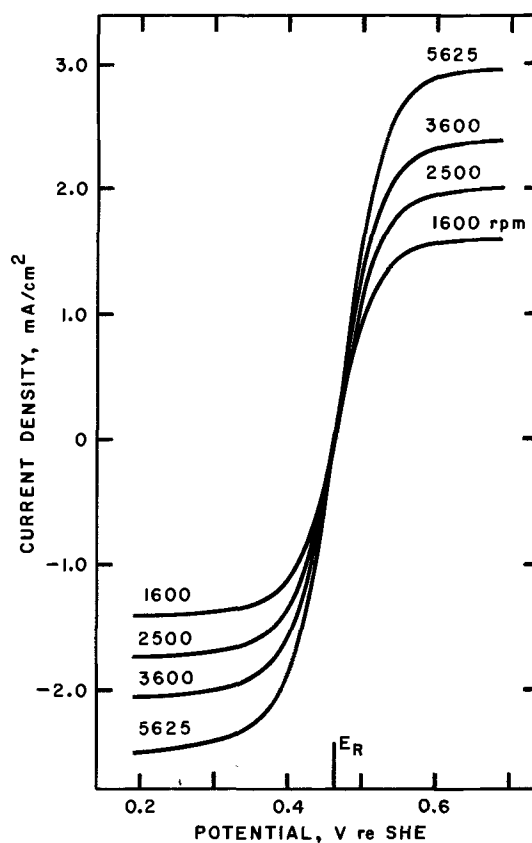


Fig. 5. Current-potential curves at various rotation rates for mosaic NiO(0.48 cation % Li) in He-saturated, pre-electrolyzed 0.497M  $K_2SO_4$  + 0.01M NaOH [2.5 mM  $K_4Fe(CN)_6$  and 2.5 mM  $K_3Fe(CN)_6$ ] at 25°C. Electrode area, 0.0416  $cm^2$ ; sweep rate, 1 V/min;  $E_R = 0.461V$  re SHE.

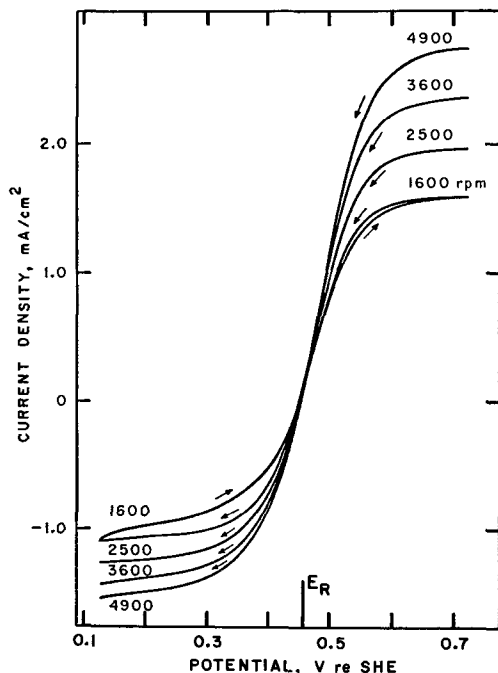


Fig. 4. Current-potential curves at various rotation rates for mosaic NiO(0.36 cation % Li) in He-saturated 0.50M  $K_2SO_4$  [2.5 mM  $K_4Fe(CN)_6$  and 2.5 mM  $K_3Fe(CN)_6$ ] at 25°C. Electrode area, 0.128  $cm^2$ ; sweep rate, 4 V/min;  $E_R = 0.460V$  re SHE.

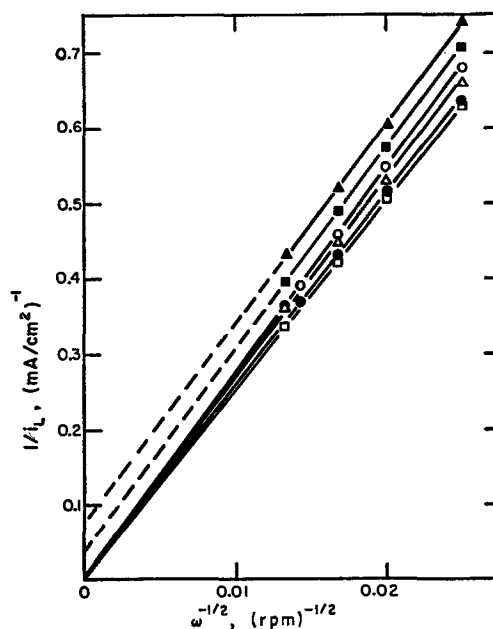


Fig. 6. Plots of  $1/i_L$  vs.  $\omega^{-1/2}$  for the ferro-ferricyanide couple on mosaic NiO(0.36 cation % Li) in He-saturated sulfate solutions [2.5 mM  $K_3Fe(CN)_6$  and 2.5 mM  $K_4Fe(CN)_6$ ] for various pH at 25°C.  $\Delta$ ,  $\blacktriangle$  = 1.0N  $H_2SO_4$ ; oxidation at 1.22 and 1.07V re SHE, respectively; pH:0.5.  $\circ$  = 0.495M  $K_2SO_4$  + 0.005M  $H_2SO_4$ ; oxidation at 0.92V; pH:2.9.  $\bullet$  = 0.50M  $K_2SO_4$ ; oxidation at 0.70V.  $\square$ ,  $\blacksquare$  = 0.497M  $K_2SO_4$  + 0.01M NaOH; oxidation at 0.664V and reduction at 0.264V, respectively; pH:12.0.

disk electrodes. Furthermore, there is no reason to believe that current distribution effects at the diffusion limiting current density should be markedly dependent on the pH of the solution. A more likely explanation for the ill-defined anodic limiting currents is interference from the surface reaction associated with voltammetry peak I [see Fig. 1 in Ref. (1)]. The potential of peak I lies near that for the anodic limiting

currents (see Table I) in acid but not neutral and alkaline solutions.

In spite of difficulties encountered in determining the anodic limiting current densities exactly, Fig. 6 verifies that the experimental values chosen for each rotation rate at a given potential for each solution are essentially the diffusion limiting current densities.<sup>2</sup> The potentials at which the diffusion limiting currents were determined are given in the legend to this figure. For comparison, a plot for the solution of pH = 0.5 is also given in Fig. 6 at a fixed potential of 1.07V re SHE, corresponding to a region well below the limiting current.

Anodic plots of  $\ln[i/(i_a - i)]$  vs. potential are shown in Fig. 7 for various rotation rates for the 1.0N H<sub>2</sub>SO<sub>4</sub> solution. Linearity is to be expected when the back reaction is negligible and  $\gamma$  is constant or negligible (see Eq. [2]). Above 0.8V the plots of  $\ln[i/(i_a - i)]$  vs.  $E$  are linear with a constant slope of 120 mV/decade at all rotation rates. The slope of these plots indicates that in this potential region all of the change in electrode potential is across the Helmholtz region with no appreciable space charge effects within the semiconductor and also no appreciable ionic double layer effects despite the relatively high charge of the species undergoing oxidation. This is the kind of behavior usually observed for a redox couple on a metal electrode with the reaction under combined kinetic and diffusion control with  $\alpha = 1/2$ .

At potentials cathodic to 0.8V, the anodic Tafel plots deviate from linearity. These deviations are almost certainly related to a change in the potential distribution at the interface with an appreciable fraction of the change in electrode potential occurring across the space charge region within the semiconductor. The intercept of the Mott-Schottky plot for this electrode at 1 kHz in 1.0N H<sub>2</sub>SO<sub>4</sub> is at  $\sim 1.1$ V with  $1/C_{sc}^2$  becom-

<sup>2</sup> The points on this and subsequent graphs in this paper correspond to the particular values calculated using arbitrarily chosen specific points from the continuously recorded current-potential curves.

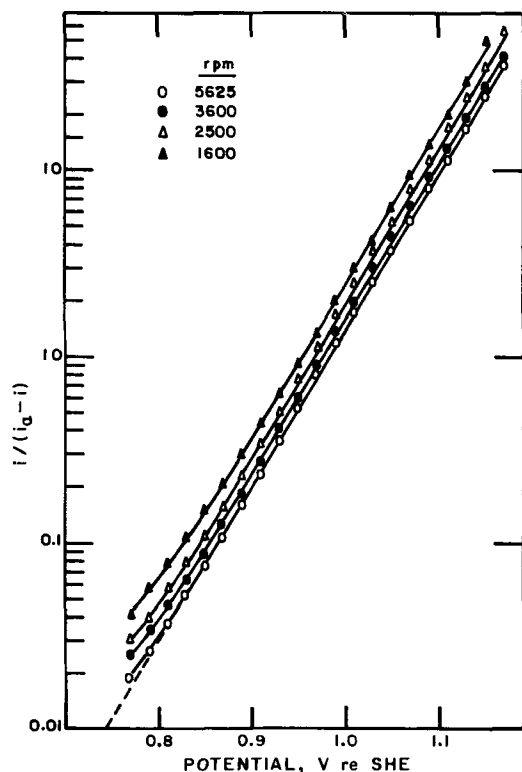


Fig. 7. Tafel plots for oxidation of ferrocyanide on mosaic NiO(0.36 cation % Li) in He-saturated 1.0N H<sub>2</sub>SO<sub>4</sub> [2.5 mM K<sub>4</sub>Fe(CN)<sub>6</sub> and 2.5 mM K<sub>3</sub>Fe(CN)<sub>6</sub>] at 25°C.  $E_R = 0.672$ V re SHE;  $b = 120$  mV/decade (all rotation rates).

ing appreciable at  $\sim 0.8$ V ( $C_{sc} =$  space charge capacitance; see Appendix, Fig. A-1).

Extrapolation of the linear portions of the Tafel plots to the reversible potential ( $E_R = 0.672$ V re SHE) yields a value for the apparent exchange current density of  $6.6 \pm 0.1 \mu\text{A}/\text{cm}^2$ . If all of the potential drop occurs in the space charge region of a p-type semiconductor, the cathodic current should reach a limiting value which corresponds to  $i_0$ , the exchange current density. Although the cathodic current actually increases slowly at more cathodic potentials, there is a sharp "leveling off" which should yield an approximate value for the exchange current density. For comparison, the value of  $i_0$  determined in this way is about  $8.6 \mu\text{A}/\text{cm}^2$ .

In solutions of higher pH, the back reaction term in Eq. [2] cannot be neglected. In Fig. 8, a typical plot according to Eq. [2] is shown for the oxidation of ferrocyanide on NiO(Li) in 0.495M K<sub>2</sub>SO<sub>4</sub> + 0.005M H<sub>2</sub>SO<sub>4</sub>. The cathodic diffusion limiting current density  $i_c$  has been assumed to be equal to the anodic value  $i_a$  in making this plot. At potentials cathodic to 0.75V, the points on the graph for different rotation rates superimpose. The slight divergence at more anodic potentials is probably due to the inaccuracy inherent in this type of plot at current densities approaching  $i_a$ , coupled with the uncertainty involved in determining the  $i_a$  value. The linear portion of this plot has a slope of 120 mV/decade which indicates that  $\alpha = 0.5$  and that all of the potential change occurs across the Helmholtz layer. At potentials cathodic to about 0.6V, the points deviate from linearity. This is probably because an appreciable potential change occurs across the space charge region.

Extrapolation of the linear portion of the Tafel plot to the reversible potential [ $E_R = 0.470$ V re SHE] for the 0.495M K<sub>2</sub>SO<sub>4</sub> + 0.005M H<sub>2</sub>SO<sub>4</sub> solution yields a value for the exchange current density of  $64 \mu\text{A}/\text{cm}^2$ . This is considerably larger than the value observed in 1.0N H<sub>2</sub>SO<sub>4</sub> ( $6.6 \mu\text{A}/\text{cm}^2$ ). The rate of reaction would be expected to be faster at higher pH because the electrode surface is less protonated and the depletion of p-carriers near the surface does not become pronounced until more cathodic potentials. The kinetics of the ferro-ferricyanide couple also are highly de-

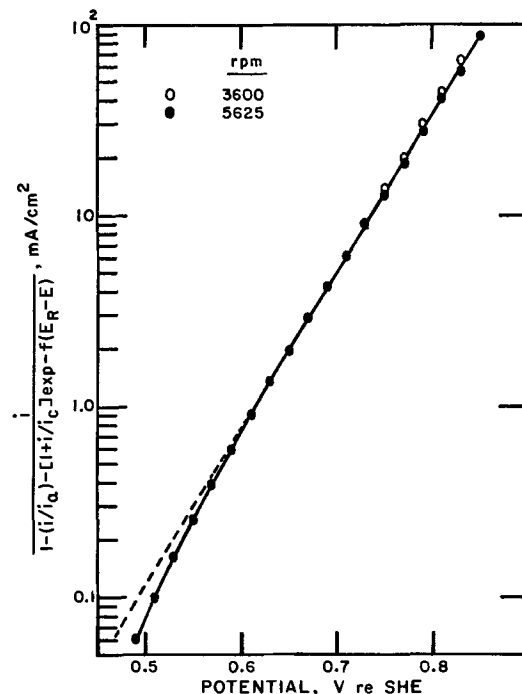


Fig. 8. Tafel plots for oxidation of ferrocyanide on mosaic NiO(0.36 cation % Li) in He-saturated 0.495M K<sub>2</sub>SO<sub>4</sub> + 0.005M H<sub>2</sub>SO<sub>4</sub> [2.5 mM K<sub>4</sub>Fe(CN)<sub>6</sub> and 2.5 mM K<sub>3</sub>Fe(CN)<sub>6</sub>] at 25°C.  $E_R = 0.470$ V re SHE;  $b = 120$  mV/decade.



pendent on the pH and the cations. The rates are very fast with polarizable cations such as  $\text{Cs}^+$  and relatively slow with less polarizable cations such as  $\text{Li}^+$  or  $\text{H}^+$  as the principal cations on metal electrodes such as gold (9). A similar cation effect has also been observed on the homogeneous rate constants for this couple (10). Both effects are probably a consequence of the association of the cations with the anions of the couple, particularly the ferrocyanide ion with its charge otherwise of  $-4$  (11, 12). Polarizable cations may facilitate the electron transfer through some type of outer sphere, bridged activation complex between couples or to the surface. The replacement of the  $\text{H}^+$  or  $\text{Li}^+$  ions associated with the  $\text{Fe}(\text{CN})_6^{4-}$  by more polarizable cations may also reduce the outer sphere contribution to the free energy of activation within the framework of the Marcus-Hush (13) and Levich-Dogonadze (14) theories of electron transfer. In the present work, ion association alone, however, cannot explain the pH dependence of the exchange current density since the dependence of the apparent rate constant continues to be great outside the range where proton association with the ferrocyanide is predominant (see Table I).

In Fig. 9 are plots based on Eq. [2] for near neutral solutions ( $\text{pH} = 6.5$ ) with  $0.5\text{M}$   $\text{K}_2\text{SO}_4$  as the supporting electrolyte. The cathodic diffusion limiting current densities have been taken as equal to the anodic values since the space charge effects interfere with the direct determination of the cathodic values from Fig. 4. From Fig. 9, it is evident that the plots are no longer linear and the slopes are dependent on the concentration of the redox couple as well as the rotation rate at higher anodic current densities. Thus at the higher ferro- and ferricyanide concentrations ( $5 \times 10^{-3}\text{M}$ ) and the highest rotation rate (5625 rpm) in Fig. 9, the slope is  $105\text{ mV/decade}$  whereas at  $2.5 \times 10^{-3}\text{M}$  and 1600 rpm, the slope is  $\sim 70\text{ mV/decade}$  at higher anodic potentials.

Theoretically, Eq. [2] is applicable regardless of whether the electrochemical reaction rate is controlled by electron transfer, diffusion, or both. When the reaction rate approaches pure diffusion control ( $i_o > i_a$  or  $i_c$ ) however, practical application of Eq. [2] becomes tenuous. Because of the magnitude of  $i_o$ , small errors in the value of  $i_a$  or  $i_c$  become very significant

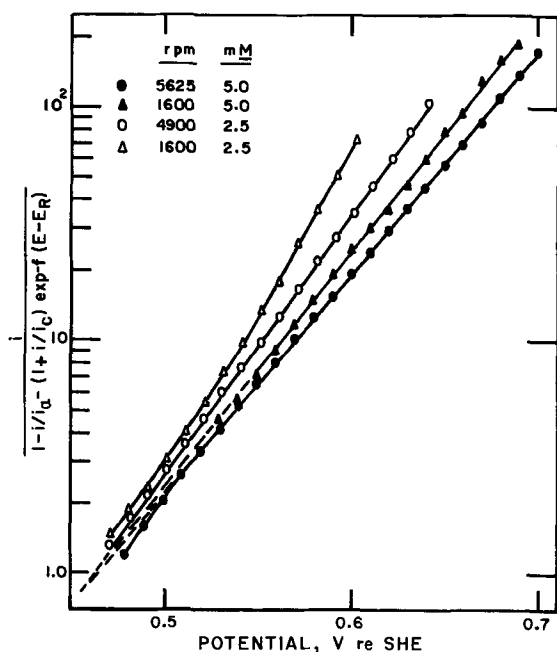


Fig. 9. Tafel plots for oxidation of ferrocyanide on mosaic NiO(0.36 cation % Li) in He-saturated  $0.5\text{M}$   $\text{K}_2\text{SO}_4$  [ $2.5$  and  $5.0\text{ mM}$   $\text{K}_4\text{Fe}(\text{CN})_6$  and  $\text{K}_3\text{Fe}(\text{CN})_6$ ] at  $25^\circ\text{C}$ .  $\text{pH} = 6.5$ ;  $E_R = 0.460\text{V}$  re SHE.

and deviations can occur in plots of the type given in Fig. 9. This is the probable explanation for the deviations at more anodic potentials in this figure. In the near neutral solutions, even the minute amount of NiO which dissolves under these conditions may result in an appreciable pH change adjacent to the electrode surface. Such changes in pH could change the state of protonation of the electrode surface and hence also change the exchange current density for the redox couple, thus disturbing the apparent Tafel slope in Fig. 9.

Only at the higher redox couple concentrations ( $5 \times 10^{-3}\text{M}$ ) and highest rotation rate (5625 rpm) is the plot in Fig. 9 sufficiently linear to permit extrapolation to the reversible potential ( $E_R = 0.461\text{V}$ ) to obtain an estimated exchange density of  $i_o \cong 0.9\text{ mA/cm}^2$ .

In more alkaline solutions (*i.e.*,  $\text{pH} = 12$ ) the kinetics have become sufficiently fast that the oxidation and reduction are under almost pure diffusion control and quantitative values for the exchange current densities and Tafel slopes could not be obtained with the rotating disk technique.

The apparent exchange current densities, Tafel slopes, and diffusion coefficients evaluated from the present study are listed in Table I. The diffusion coefficient determined from the anodic limiting current density for the ferrocyanide is in reasonably good agreement with the value of  $7.2 \times 10^{-6}\text{ cm}^2/\text{sec}$  reported by Jahn and Vielstich (16) on Pt in  $0.5\text{M}$   $\text{K}_2\text{SO}_4$  at  $25^\circ\text{C}$ . The rest potentials were always the same ( $\pm 2\text{ mV}$ ) as the values observed on platinum and agree quite well with the literature (15).

The apparent standard rate constants for the ferro-ferricyanide couple on NiO(Li) are considerably slower than on metals such as platinum and gold even at low pH values where protonation of the ferrocyanide leads to less reversibility [see *e.g.*, (17-23)]. Using a-c methods, Randles and Sommerton (20) obtained an apparent standard rate constant of  $1.3 \times 10^{-1}\text{ cm}^2/\text{sec}$  in  $0.5\text{M}$   $\text{K}_2\text{SO}_4$  at  $20^\circ\text{C}$ . The apparent  $k_o$  value for this reaction on NiO(Li) at  $25^\circ\text{C}$  is  $1.9 \times 10^{-3}\text{ cm}^2/\text{sec}$  or approximately two orders of magnitude less.

**$\text{Fe}^{2+}$ - $\text{Fe}^{3+}$  couple.**—Typical voltammetry curves at various rotation rates are shown in Fig. 10 for the  $\text{Fe}^{2+}$ - $\text{Fe}^{3+}$  couple on NiO(Li) in  $0.495\text{M}$   $\text{K}_2\text{SO}_4 + 0.005\text{M}$   $\text{H}_2\text{SO}_4$  ( $\text{pH} = 2.9$ ). Pronounced inhibition is evident for the cathodic branch and also for the anodic branch at low overvoltages. At more anodic potentials the current increases to a limiting value, which is rotation dependent. At about  $1.6\text{V}$  re SHE, the current again increases, due to the onset of oxygen evolution. Values of  $i_L$  determined at  $1.50\text{V}$  are diffusion limited, as shown in Fig. 11. For comparison, current densities at  $1.27\text{V}$  are also plotted in this figure. Tafel plots with corrections for diffusion of reactants using  $i_L$  evaluated at  $1.50\text{V}$  are shown in Fig. 12. These plots are linear over at least two decades of current with a slope of

Table I. Summary of data for the ferro-ferricyanide couple at  $25^\circ\text{C}$  on NiO(Li) electrodes in aqueous solution

pH	C <sup>(a)</sup> (mM)	E <sub>R</sub> <sup>(b)</sup> (V)	E <sub>P</sub> <sup>(c)</sup> (V)	b <sup>(d)</sup> (cmV/ decade)	k <sub>o</sub> <sup>(e)</sup> (cm <sup>2</sup> /sec)	D × 10 <sup>6(f)</sup> (cm <sup>2</sup> /sec)
0.5	2.5	0.672	0.95	120	$2.8 \times 10^{-5}$	6.7
2.9	2.5	0.470	0.83	120	$2.7 \times 10^{-4}$	6.4
6.5	2.5	0.460	0.62	—	—	7.1
6.5	5.0	0.461	0.62	105	$1.9 \times 10^{-3}$	—
12.0	2.5	0.461	0.29	—	—	7.3

(a) C = concentration of  $\text{K}_4\text{Fe}(\text{CN})_6$  and  $\text{K}_3\text{Fe}(\text{CN})_6$  (both equal).

(b)  $E_R$  = measured rest potential (corresponding to reversible value) re SHE.

(c)  $E_P$  = potential of the voltammetry peak I re SHE.

(d) b = Tafel slope or slope for plots according to Eq. (2).

(e)  $k_o$  = apparent standard rate constant (no double layer correction).

(f) D = diffusion coefficient of ferrocyanide calculated from slope of  $1/i_a$  vs.  $\omega^{-1/2}$  plots, using  $0.0095$  for the kinematic viscosity (15).

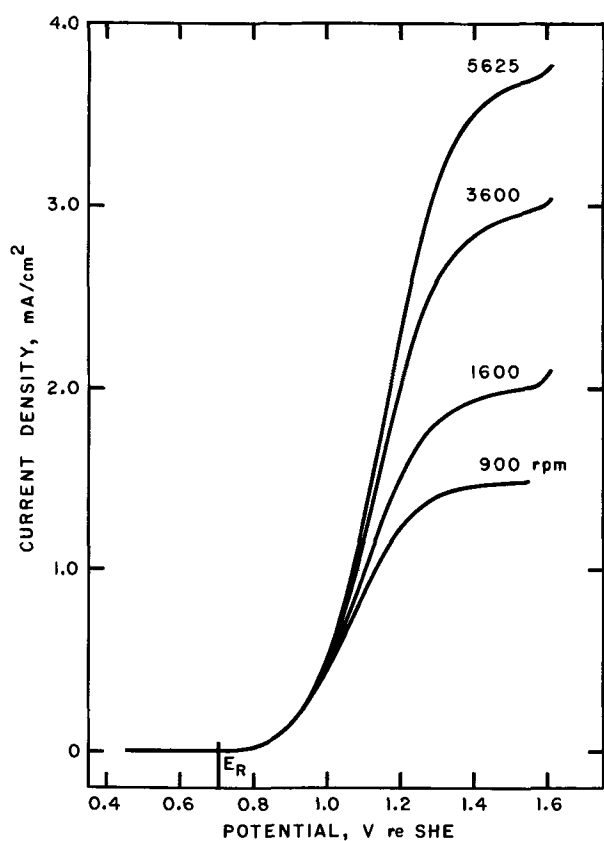


Fig. 10. Current-potential curves at various rotation rates for mosaic NiO(0.36 cation % Li) in He-saturated 0.495M  $K_2SO_4$  + 0.005M  $H_2SO_4$  [2.5 mM  $FeSO_4$  and 2.5 mM  $Fe_2(SO_4)_3$ ] at 25°C. Electrode area, 0.128  $cm^2$ ; sweep rate, 1 V/min;  $E_R = 0.706V$  re SHE.

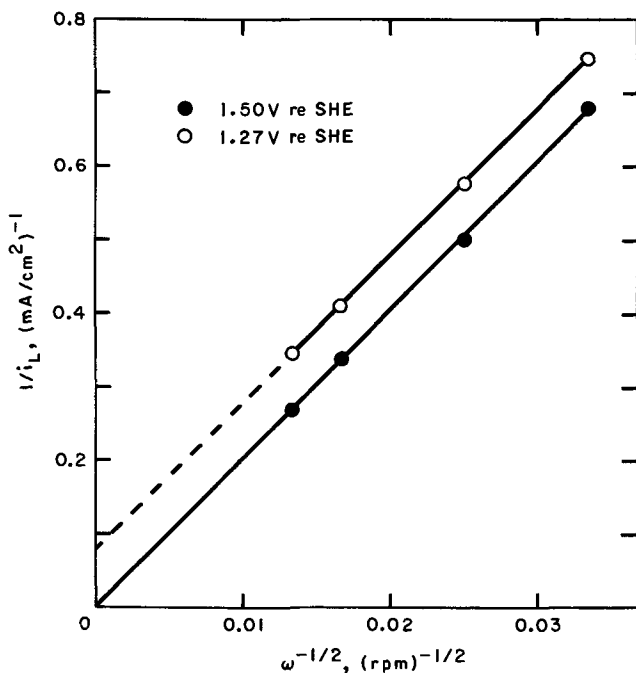


Fig. 11. Plots of  $1/i_L$  vs.  $\omega^{-1/2}$  for oxidation of ferrous ion on mosaic NiO(0.36 cation % Li) in He-saturated 0.495M  $K_2SO_4$  + 0.005M  $H_2SO_4$  [2.5 mM  $FeSO_4$  and 2.5 mM  $Fe_2(SO_4)_3$ ] at 25°C. Electrode area, 0.128  $cm^2$ .

200 mV/decade, independent of rotation rate. The dependence of the intercept on rotation rate is that anticipated for this type of plot according to Eq. [2].

The Tafel slope of 200 mV/decade is considerably higher than found for this couple on metals such as

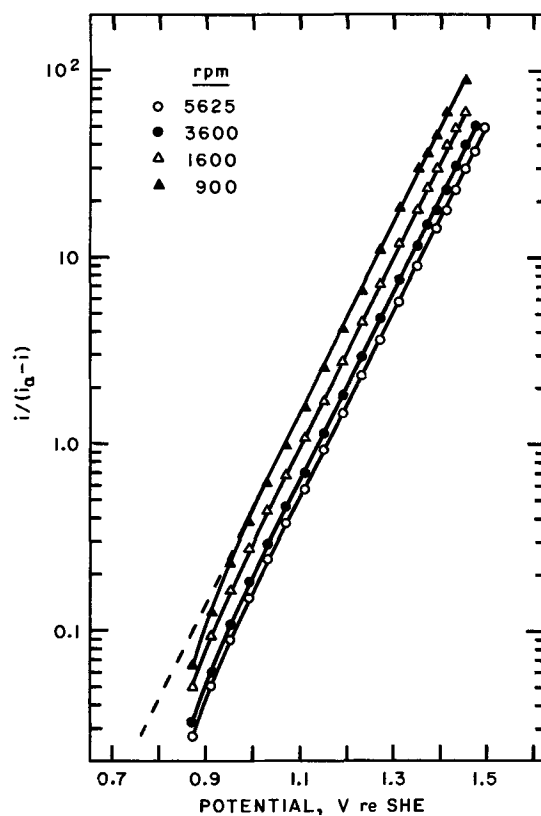


Fig. 12. Tafel plots for oxidation of ferrous ion on mosaic NiO(0.36 cation % Li) in He-saturated 0.495M  $K_2SO_4$  + 0.005M  $H_2SO_4$  [2.5 mM  $FeSO_4$  and 2.5 mM  $Fe_2(SO_4)_3$ ] at 25°C.  $E_R = 0.706V$  re SHE;  $b = 200$  mV/decade (all rotation rates).

platinum. Gerischer (24) has reported an apparent anodic transfer coefficient of 0.42 corresponding to a Tafel slope of 143 mV/decade and an apparent standard rate constant of  $3 \times 10^{-3}$  cm/sec for this couple in 1M  $H_2SO_4$  on platinum. Other workers have confirmed these results (8). The apparent standard rate constant evaluated from the plots in Fig. 12 is  $8.3 \times 10^{-5}$  cm/sec or approximately two orders of magnitude smaller than the value on platinum. Note, however, that the supporting electrolytes and pH are not the same.

The lack of any appreciable current for the reduction of ferric ion on NiO(Li) and evidence of inhibition at low anodic overpotentials are somewhat surprising since the reversible potential for the ferrous-ferric couple is 0.706V re SHE and more anodic than that for the ferro-ferricyanide couple. On the basis of the a-c impedance studies in the same supporting electrolyte (3), the onset of the exhaustive depletion region would not have been expected at potentials less cathodic than 0.5V re SHE.

Both the slope of 200 mV/decade and the pronounced cathodic inhibition for this system may be explained by considering specific adsorption of Fe ions. The interaction of Fe ions with the electrode surface may involve sharing of an  $H_2O$  from the inner coordination sphere of Fe with a Ni ion on the surface or replacement of an  $H_2O$  in the inner coordination sphere of iron by surface O<sup>=</sup> or OH<sup>-</sup> ions. The adsorption of either  $Fe^{+2}$  or  $Fe^{+3}$  ions will modify the potential distribution and  $Ni^{3+}$  concentration at the surface. The depletion of p-carriers produced by the adsorption of  $Fe^{2+}$  or  $Fe^{3+}$  ions will lead to a relatively large potential drop across the space charge region at electrode potential considerably less cathodic than otherwise would be necessary for such a depletion effect.

Much of the anodic branch occurs at potentials more positive than the voltammetry peak I where a substantial fraction of the surface nickel ions appear to be

converted to the +3 valency state. In the anodic branch, therefore, most of the potential drop should be across the Helmholtz region and hence available to drive the electrochemical oxidation. Consequently the p-carrier surface concentration would not be expected to depend strongly on the electrode potential in this region. Under these circumstances the behavior of the  $\text{Fe}^{+2}\text{-Fe}^{+3}$  couple should approach that on a metal. The higher than usual anodic slope of 200 mV/decade may reflect the specific adsorption of  $\text{Fe}^{+2}$  and/or  $\text{Fe}^{+3}$  ions (even at potentials anodic to voltammetry peak I).

**Hydroquinone-quinone couple.**—The current-potential curves for  $1.0 \times 10^{-3}\text{M}$  quinhydrone were examined in He-saturated  $1.0\text{N H}_2\text{SO}_4$  on an NiO(0.48 cation % Li) electrode at various rotation rates (1600-5625 rpm). The rest potential was unsteady, although the expected value of 0.67V re SHE was obtained on Pt electrodes in these solutions. The cathodic branch on the NiO(Li) electrode was very inhibited. No current was evident from -0.7 to 0.9V re SHE but at more anodic potentials the current increased reproducibly to a well-defined diffusion limited value at 1.6V. Plots of  $\log i/(i_a - i)$  vs.  $E$  were linear over two decades of current with a slope of 170 mV/decade, independent of rotation rate.

Assuming that all of the potential drop occurs in the Helmholtz region at anodic potentials, the corresponding anodic transfer coefficient is 0.35 for a rate-determining step involving only one electron change. The values agree quite well with the limiting value for  $\alpha$  of 0.37 obtained by Vetter (8) above pH 5 for this electrode reaction on platinum.

**$\text{Cr}^{2+}\text{-Cr}^{3+}$  couple.**—The behavior of the  $\text{Cr}^{2+}\text{-Cr}^{3+}$  couple was examined on the NiO(Li) electrodes in perchlorate solutions using slow linear sweep voltammetry. The reversible potential ( $E^\circ = -0.41\text{V}$  re SHE) of this couple is very cathodic compared to the flatband potential or potentials where the capacitance contribution from the space charge region in the semiconductor first becomes appreciable. In a  $0.5\text{M NaClO}_4$  solution containing  $0.02\text{M Cr}^{2+}$  and  $0.02\text{M Cr}^{3+}$  plus sufficient  $\text{HClO}_4$  to adjust the pH to 1.2, the slow sweep voltammetry curves (4 V/min) were the same as in the absence of the  $\text{Cr}^{2+}\text{-Cr}^{3+}$  couple over the voltage range -0.8 to +1.5V re SHE. Oxidation or reduction current densities of even a few  $\mu\text{A}/\text{cm}^2$  would have been detectable.

In the absence of halide ions the  $\text{Cr}^{2+}\text{-Cr}^{3+}$  couple is quite irreversible even on metals such as Hg and Pt. None the less at overpotentials of several tenths of a volt, currents in the  $\text{mA}/\text{cm}^2$  range are observed [see e.g. Ref. (25)]. The much more pronounced irreversibility of the  $\text{Cr}^{2+}\text{-Cr}^{3+}$  couple in NiO(Li), therefore, must be attributed to the electrode.

The introduction of halide anions into the perchlorate solution greatly increases the reversibility of the oxidation of  $\text{Cr}^{2+}$  and also the reduction of  $\text{Cr}^{3+}$  on metal electrodes if the halide anion is present in the inner coordination sphere of the  $\text{Cr}^{3+}$  (25). The halide is believed to facilitate the charge transfer through anion bridging. With the NiO(Li) electrode, the introduction of  $10^{-3}\text{M NaCl}$  into the  $\text{NaClO}_4\text{-HClO}_4$  solution resulted in a substantial oxidation current, for the  $\text{Cr}^{2+}\text{-Cr}^{3+}$  couple at potentials anodic to 0.75V re SHE where the depletion layer is not involved. Quantitative steady-state data for the kinetics of the oxidation are not available in the presence of the  $\text{Cl}^-$  but the behavior appears similar to that on metal electrodes at anodic potentials.

#### Comparison of Redox Behavior on NiO(Li) and Metal Electrodes

The rates of the various redox couples examined in this work are substantially slower on the NiO(Li) electrode than on metals such as Pt and Au. Factors which may be responsible for the difference in rates include: (a) semiconductor effects, (b) ionic double

layer effects, (c) differences in surface roughness, and (d) contribution of the electrode phase directly to the free energy of activation for the charge transfer.

At potentials appreciably cathodic to the flatband potential, most of the potential drop is across a depletion layer within the NiO(Li). Under such circumstances, pronounced inhibition of cathodic and anodic processes is to be expected. This has been observed not only for the couples already cited, but also a number of other processes including the oxidation of CO and organic acids (26). At potentials anodic to the flatband potential, all the couples studied in the present work were still slower even in the anodic branch than on metals such as Pt. For the ferro-ferricyanide couple, the ratio of the standard rate constants on NiO(Li) and Pt electrodes in  $0.5\text{M K}_2\text{SO}_4$  is  $1.5 \times 10^{-2}$ . For the  $\text{Fe}^{2+}\text{-Fe}^{3+}$  couple this ratio is  $2.7 \times 10^{-2}$  although the comparison is not fully valid since the electrolyte used with the NiO(Li) electrode was  $0.5\text{M K}_2\text{SO}_4 + 0.005\text{M H}_2\text{SO}_4$ , whereas that for the Pt was  $1\text{M H}_2\text{SO}_4$  (24).

Differences in the ionic double layers on the two electrodes would be expected to cause some difference in the apparent rate constants but it is doubtful whether ionic double layer effects would cause differences of  $\sim 2$  orders of magnitude. Further the double layer effects would act in opposite directions for the ferro-ferricyanide and ferrous-ferric couples because of the differences in the charge of the reacting ions. The constancy of the Tafel slopes and in the instance of the ferro-ferricyanide couple the finding of a transfer coefficient of 0.5 are further arguments against large ionic double layer effects.

For surface roughness to be the major factor responsible for the two orders of magnitude difference in rate constants on NiO(Li) and Pt would require a roughness factor of  $\sim 10^2$  for the Pt used by such workers as Randles and Sommerton (20) and Gerischer (24). This seems unlikely with bright platinum electrodes of the type used by these authors.

The most probable explanation for the two orders of magnitude difference in rate constants at potentials anodic to the flatband potential is that the electrode phase contributes significantly to the free energy of activation for the charge transfer process. According to the Marcus-Hush theory (13) of heterogeneous electron transfer the true standard first order rate constant  $(k_0)_t$  (corrected for double layer effects) is given by

$$(k_0)_t = A \exp - \frac{\Delta F^*}{RT} = \kappa Z \exp - \frac{\Delta F^*}{RT} \quad [3]$$

where  $\kappa$  is the transmission coefficient (taken as unity by Marcus),  $\Delta F^*$  is the free energy of activation, and  $Z$  is the collision frequency factor. Assuming all sites on the electrode surface equally accessible,  $Z$  is given<sup>3</sup> by Marcus as

$$Z = [kT/(2\pi m^*)]^{1/2} \quad [4]$$

where  $m^*$  is the effective mass of the reactant. For a species such as  $\text{Fe}(\text{CN})_6^{4-}$ ,  $Z \cong 4 \times 10^4$  cm/sec.

The activation free energy for a redox couple on a metal is as follows

$$\Delta F^* = \Delta F^*_i + \Delta F^*_o + \Delta F^*_e \quad [5]$$

where  $\Delta F^*_i$  is the contribution from rearrangement (prestraining) of the inner sphere ligands,  $\Delta F^*_o$  is the contribution from the outer sphere and more remote ion-solvent environment, and  $\Delta F^*_e$  is any electronic quantum mechanical contribution. For a metal,  $\Delta F^*_e$  is usually taken to be zero but with a semiconductor, particularly involving rather localized electronic states  $\Delta F^*_e$  may not be zero because of possible spin inversion attending the electron transfer.

<sup>3</sup>The validity of this expression given by Marcus for  $Z$  has been challenged by Bockris (27). At the best, the term is probably not more accurate than to an order of magnitude. In the present discussion, only the ratio of the values between the NiO(Li) electrode and metal electrodes such as Pt is important.

With semiconductor electrodes, the pre-exponential term  $A$  in Eq. [3] (or alternatively the exponential term  $\Delta F^*$ ) must be modified to take into account the carrier concentration in the electrode surface. At potentials anodic to peak I in the voltammetry curve (3, 5), however, the surface concentration of  $\text{Ni}^{3+}$  is estimated to be  $\sim 1/4$  of that of the atoms on the surface of a metal such as Pt. This estimate is based on the number of coulombs/square centimeter associated with voltammetry peak I. Since the rate constants on the  $\text{NiO}(\text{Li})$  electrodes are principally based on kinetic data at potentials anodic to this peak, the pre-exponential term  $A$  in Eq. [3] would not be expected to differ from that on Pt by more than four-fold, assuming that  $\kappa$  is still  $\sim 1$  for the  $\text{NiO}(\text{Li})$  electrode. Redox species such as the ferrocyanide anions are expected to undergo electron transfer with distances of 7-10 Å between their centers and those of the  $\text{Ni}^{3+}$  on the electrode surface. Consequently the electron transfer probably should not require the aligning of the redox species with sites on the electrode surface and hence the difference in  $A$  may be much smaller than a factor of 4.

If the pre-exponential terms  $A$  for  $\text{NiO}(\text{Li})$  and Pt are assumed to be the same,  $\Delta F^*$  must be  $\sim 3$  kcal/mole larger for the  $\text{NiO}(\text{Li})$  electrodes than for the platinum electrodes. Possible sources for such an additional activation free energy are (i) contributions to  $\Delta F^*$ ; and  $\Delta F^*_e$  for the electrode phase and (ii) spin problems resulting in an appreciable value for  $\Delta F^*_e$ . The latter seems unlikely since spin inversion would probably produce a much larger contribution to  $\Delta F^*_e$  than just a few kcal/mole. Significant contributions to  $\Delta F^*$ ; and  $\Delta F^*_e$  from the prestressing of the environment of the  $\text{Ni}^{3+}$  states at the electrode surface appear more likely.

On the other hand, dielectric loss measurements in  $\text{NiO}(\text{Li})$  as well as resistivity, Hall, and Seebeck coefficient measurements have indicated that any activation energy for  $\text{Ni}^{3+}$  hole mobility in  $\text{NiO}(\text{Li})$  is less than 200 cal/mole [see Ref. (2) for a summary of the evidence]. The conductivity has an activation energy which is much larger but this activation energy corresponds to the dissociation of  $\text{Li}^+-\text{Ni}^{3+}$  or  $\text{Ni}^{3+}$ -cation vacancy pairs to yield highly mobile p-carriers. The lack of any appreciable activation energy for the free p-carriers in  $\text{NiO}$  is probably the result of  $\text{Ni}^{3+}-\text{O}^{2-}-\text{Ni}^{2+}$  interactions which facilitate electron transfer from a  $\text{Ni}^{2+} e_g$  orbital to an  $\text{Ni}^{3+} e_g$  orbital of parallel spin (2); i.e., the equivalent of the anion bridge mechanism for redox species in solution. For charge transfer across the interface between  $\text{Ni}^{3+}$  in the electrode phase and a redox species, the situation would be substantially different and such strong interactions between orbitals of  $\text{Ni}^{3+}$  and those of the redox species would not be expected, particularly with redox species such as ferro-ferricyanide which have stable inner coordination spheres and which are probably not specifically adsorbed. Thus a contribution of several kcal/mole to  $\Delta F^*$  from prestressing of the environment of the surface  $\text{Ni}^{3+}$  ions is quite possible.

If such is the situation, then the charge transfer between the  $\text{Ni}^{3+}$  states in  $\text{NiO}(\text{Li})$  and a redox species in the electrolyte is rather analogous to charge transfer between two different redox couples in solution. Such a model has been considered for this system by the authors (28) using the Marcus theory (13) for homogeneous rates of redox reaction. Calculations with this model, however, are limited by the lack of adequate data for use in calculating  $\Delta F^*_1$  and  $\Delta F^*_e$  for the surface  $\text{Ni}^{3+}$  ions as well as difficulties in evaluating the coulombic interactions.

#### Acknowledgment

The authors are pleased to acknowledge the support of this research by the United States Office of Naval Research.

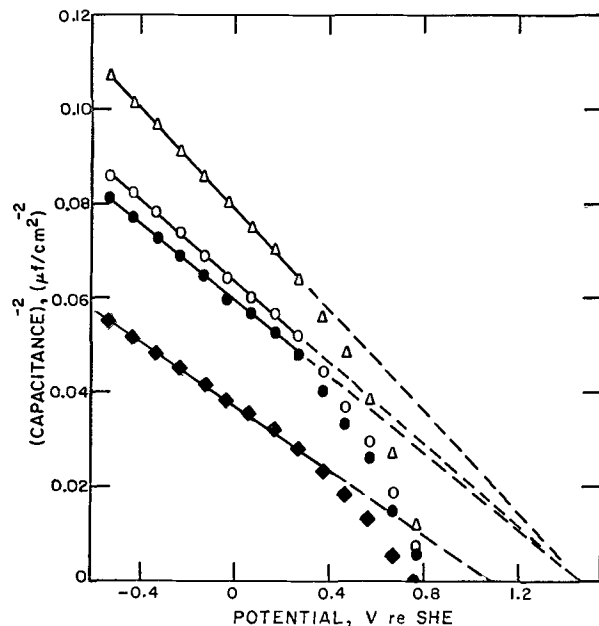


Fig. A-1. Plots of  $1/C^2$  vs.  $E$  at various frequencies for mosaic  $\text{NiO}(0.48 \text{ cation } \% \text{ Li})$  in He-saturated  $1.0N \text{ H}_2\text{SO}_4$  at  $25^\circ\text{C}$ . Electrode area,  $0.0416 \text{ cm}^2$ . Curves without Helmholtz capacitance correction:  $\bullet = 1 \text{ kHz}$ ;  $\circ = 2 \text{ kHz}$ ;  $\triangle = 20 \text{ kHz}$ . With Helmholtz capacitance correction:  $\blacklozenge = 1 \text{ kHz}$ .

Manuscript submitted July 17, 1973; revised manuscript received Oct. 4, 1973.

Any discussion of this paper will appear in a Discussion Section to be published in the December 1974 JOURNAL. All discussions for the December 1974 Discussion Section should be submitted by Aug. 1, 1974.

#### APPENDIX

##### Helmholtz Capacitance Correction in A-C Impedance Studies of $\text{NiO}(\text{Li})$

In the a-c impedance measurements reported earlier (1), no correction was made for the Helmholtz layer capacitance in the calculation of the space charge capacitance for the  $\text{NiO}(\text{Li})$  electrodes. Unfortunately information is lacking as to the value of the Helmholtz capacitance. Since the observed capacitance was much smaller than the normal Helmholtz capacitance, the assumption was made that the series Helmholtz capacitance could be neglected for purposes of preparing Mott-Schottky plots with only a minor error.

The omission of the correction for the Helmholtz layer capacitance, however, may lead to a substantial error in the intercepts in the Mott-Schottky plot for highly doped  $\text{NiO}(\text{Li})$  electrodes. If the value of this capacitance is taken to be  $\sim 20 \mu\text{f}/\text{cm}^2$  at potentials cathodic to the apparent flatband potential, the intercept is shifted to more cathodic potentials by  $\sim 0.35\text{V}$  for the 0.36 and 0.48 cation % Li electrodes in both the acid and near neutral sulfate electrolytes used in the earlier work (3), see Fig. A-1. The slopes also are slightly decreased numerically by  $\sim 15\%$  and the linear region slightly extended.

With this correction, the intercepts coincide approximately with the potentials of the first peak in the voltammetry curves corresponding to the  $\text{Ni}^{2+}-\text{Ni}^{3+}$  potential.

#### REFERENCES

1. D. Adler, "Solid State Physics," Vol. 21, pp. 1-115, F. Seitz, D. Turnbull, and H. Ehrenreich, Editors, Academic Press, New York (1968).
2. J. B. Goodenough, in "Progress in Solid State Chemistry," Vol. 5, pp. 271-276, H. Reiss, Editor, Pergamon Press, New York (1971).
3. D. Tench and E. Yeager, *This Journal*, **120**, 164 (1973).
4. T. O. Rouse and J. L. Weininger, Report No. 68-C-222, General Electric Co., Schenectady, N. Y., July 1968.
5. D. Yohe, A. Riga, R. Greef, and E. Yeager, *Electrochem. Acta*, **13**, 1351 (1968); see also D. Yohe, E. Yeager, R. Greef, and A. Riga, Tech. Report

- No. 3, Western Reserve University, Cleveland, Ohio, U.S. Office of Naval Research, Contract Nonr 1439 (09), Project NR 056-451, July 1, 1967.
- V. A. Myamlin and Y. V. Pleskov, "Electrochemistry of Semiconductors," Plenum Press, New York (1967).
  - C. H. Lee and E. Yeager, Tech. Report No. 5, Case Western Reserve University, Cleveland, Ohio, U.S. Office of Naval Research, Contract Nonr 1439(09), Project NR 359-451, Oct. 1, 1969.
  - K. J. Vetter, "Electrochemical Kinetics," Academic Press, New York (1967).
  - J. Kuta and E. Yeager, To be submitted for publication.
  - See e.g., A. C. Wahl and C. F. Deck, *J. Am. Chem. Soc.*, **76**, 4054 (1954); A. C. Wahl, *Z. Electrochem.*, **64**, 90 (1960).
  - J. Jordan and G. Ewing, *Inorg. Chem.*, **1**, 587 (1967).
  - "Stability Constants of Metal-Ion Couples," The Chemical Society (London), Special Publ. No. 17, London (1964).
  - See e.g., R. A. Marcus, *J. Chem. Phys.*, **24**, 966 (1956); **26**, 867 (1957); **67**, 853 (1963); **43**, 679 (1965).
  - See e.g., V. C. Levich, in "Physical Chemistry," Vol. IXB, "Electrochemistry," H. Eyring, Editor, chap. 12, Academic Press, New York (1970).
  - International Critical Tables of Numerical Data, Vol. III and V, McGraw Hill Book Co., New York (1928-1929).
  - D. Jahn and W. Vielstich, *This Journal*, **109**, 849 (1962).
  - J. J. Lingane and I. M. Kolthoff, *J. Am. Chem. Soc.*, **61**, 825 (1939).
  - H. A. Laitinen and I. M. Kolthoff, *J. Phys. Chem.*, **45**, 1061 (1941).
  - J. V. Petrocelli and A. A. Paolucci, *This Journal*, **98**, 291 (1951).
  - J. E. B. Randles and K. W. Sommerton, *Trans. Faraday Soc.*, **48**, 937 (1952).
  - P. Delahay and C. C. Mattax, *J. Am. Chem. Soc.*, **76**, 874 (1954).
  - J. Jordan and R. A. Javick, *Electrochim. Acta*, **6**, 22 (1962).
  - Z. Kublik, *J. Electroanal. Chem.*, **5**, 450 (1963).
  - H. Gerischer, *Z. Elektrochem.*, **54**, 366 (1960).
  - S. Donovan and E. Yeager, Tech. Report No. 24, Case Western Reserve University, Cleveland, Ohio, U.S. Office of Naval Research Contract N00014-67-C-0389, Project NR 359-277, Oct. 1, 1969; see also R. Parsons and E. Passeron, *J. Electroanal. Chem.*, **12**, 524 (1966).
  - P. Longhi and E. Yeager, Unpublished research.
  - J. O'M Bockris, Private communications.
  - D. Tench and E. Yeager, Tech. Report 28, Case Western Reserve University, Cleveland, Ohio, U.S. Office of Naval Research Contract N00014-67A-0404-0006, Project No. NR 359-451. Sept. 15, 1970.

## Cell Dimensions and Electrical Properties of the Solid Solutions: $1-x\text{ZnS}/x\text{CuAlS}_2$ and $1-x\text{ZnSe}/x\text{CuAlSe}_2$ where $x = 0$ to $0.33$

P. C. Donohue and P. E. Bierstedt

Central Research Department, E. I. du Pont de Nemours and Company, Wilmington, Delaware 19898

### ABSTRACT

Sphalerite-type solid solutions were prepared in the systems  $1 - x\text{ZnS}/x\text{CuAlS}_2$  and  $1 - x\text{ZnSe}/x\text{CuAlSe}_2$  for  $x = 0$  to  $0.33$ . The cell dimensions initially increase with  $x$  between  $x = 0$  and  $\sim x = 0.01$  followed by a decrease with further increase in  $x$ . The resistivities are high at low values of  $x$  and decrease with increasing  $x$ . Seebeck coefficients indicate that p-type conduction occurs with  $x$  as low as  $0.05$  for the sulfides and  $0.1$  for the selenides.

Attempts to prepare light-emitting diodes from the sphalerite-type II-VI compounds have been frustrated by the inability to achieve good p-type conductivity. It has recently been reported that chalcopyrite-type  $\text{CuAlS}_2$  and  $\text{CuAlSe}_2$  are p-type conductors (1, 2). Since the chalcopyrite and sphalerite structures are similar, we decided to investigate the properties of solid solutions in these systems. Of special interest was the amount of chalcopyrite needed to impart p-type conduction to the usually n-type sphalerite compounds. Solid solutions in the  $1 - x\text{ZnS}/x\text{CuAlS}_2$  system have been recently reported (3); however, their electrical properties were not reported, and the region between  $x = 0$  and  $0.2$  was not investigated.

### Experimental

Compositions were prepared starting with high-purity ZnS or ZnSe, Cu, Al, and S or Se which were weighed in stoichiometric proportions and sealed in evacuated silica tubes with about  $5 \text{ mg I}_2/\text{cm}^3$ .

The tubes were heated in a natural gradient tube furnace, and the temperature was increased gradually over a period of several days until all the chalcogen reacted. The tubes were then cooled and opened; the products were reground and then sealed in evacuated silica tubes. These products were reheated for several

days in a gradient of about  $1000^\circ\text{-}800^\circ\text{C}$ , and in most cases, millimeter size crystals were transported to the cooler region. To obtain single compositions, the products were reground, sealed in silica, and heated at  $1000^\circ\text{C}$  with no gradient.

The products were characterized by Debye-Scherrer x-ray powder diffraction, and the cell dimensions were refined by a computerized least squares analysis of the data. The standard deviations are  $0.001\text{\AA}$  or less.

Electrical resistivities ( $\rho$ ) and Seebeck coefficients ( $\alpha$ ) were measured on individual crystals using a two-probe method. Small copper probes attached to two micromanipulators were positioned at opposite ends of the crystal being investigated. A heating element was wound around one of these probes and both probes were attached by a differential copper-constantan thermocouple (electrically isolated but thermally linked to the probes). Passing a current through the heating element resulted in thermal voltages being developed by both the sample and the thermocouple, and these voltages were displayed on the axes of an X-Y recorder. The Seebeck coefficients were calculated from the slope of the resulting Seebeck voltage vs. temperature difference plot. This technique is similar to that described by Berglund and Beirsto (4).

The electrical resistivities were measured using a Keithley 610A electrometer, operating in the resistance mode, with the copper probes used in the Seebeck co-

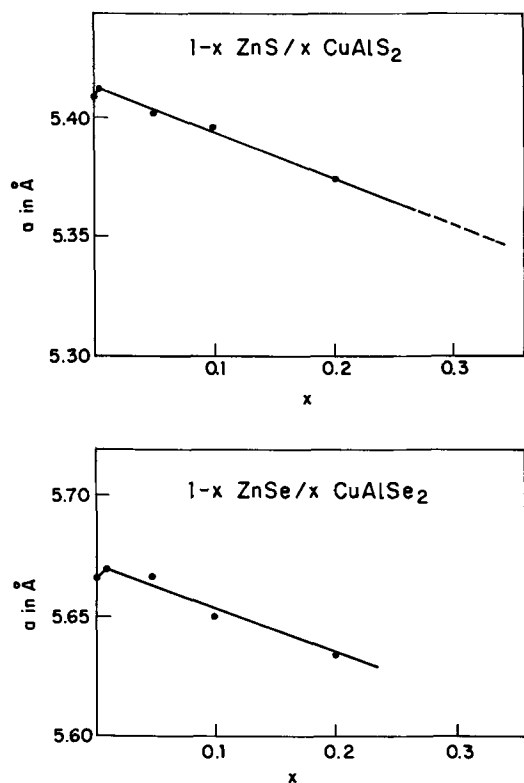


Fig. 1. Lattice parameter  $a$  vs.  $x$  for  $1 - x\text{ZnS}/x\text{CuAlS}_2$  and  $1 - x\text{ZnSe}/x\text{CuAlSe}_2$

efficient serving as the current probes. Air dry silver paint was used to improve and strengthen the contact with the copper probes. All manipulations were performed with the aid of a microscope, and with irregular shaped crystals the use of silver paint was necessary to insure stability.

### Results and Discussion

The cell dimensions and some pertinent electrical parameters for compositions in the systems  $1 - x\text{ZnS}/x\text{CuAlS}_2$  and  $1 - x\text{ZnSe}/x\text{CuAlSe}_2$  are given in Table I. Graphs of  $a$  vs.  $x$  for both systems are shown in Fig. 1. The compositions marked with an asterisk in Table I were used to construct the graph for the sulfides and were those heated at constant temperature to obtain single-phase material. In spite of the lack of a gradient in these cases, the products tended to transport and form a range of compositions. Thus the points on the graph are not precisely defined in  $x$ . Crystals used for

electrical characterization were picked from transported crystalline aggregates. The compositions of the sulfide crystals were derived from the graph and not from the ratio of starting materials. In the case of the selenides, the compositions were assumed to be the same as the starting ratio. The general trends and conclusions, however, are not influenced by this assumption.

The cell dimensions in both systems show a small rise with increasing  $x$  for values of  $x \approx 0.01$ . This is followed by the expected decrease in  $a$  with further increase in  $x$ . At  $x = 0.33$ , a symmetry change to tetragonal was observed in the sulfide system.

The sample impedances at low values of  $x$  were too high to obtain Seebeck coefficients with our present apparatus. Above  $x \approx 0.05$  in the sulfides and  $\approx 0.1$  in the selenides, the resistivities were low enough to measure Seebeck coefficients and positive  $\alpha$  values were obtained. With further increase in  $x$ , the resistivities became progressively lower and the  $\alpha$  values became more positive. In our experience, two-probe resistivity measurements indicate values about an order of magnitude higher than four-probe measurements made on crystals with soldered indium contacts.

The sulfides were black, probably because of iron impurities since the black color of  $\text{CuAlS}_2$  has been found to be due to iron (5). As we found with  $\text{CuAlS}_2$  (5), the color of these compositions can be removed by annealing in the presence of excess Al or preparing the phases with excess Al (see Table I).

Thus we have found that small quantities of  $\text{CuAlS}_2$  in  $\text{ZnS}$  and  $\text{CuAlSe}_2$  in  $\text{ZnSe}$  can yield relatively low resistivity p-type compositions. Because of the similarity in lattice constants, these p-type solid solutions may be used in combination with the n-type end members for the preparation of pn junctions.

### Acknowledgments

Mr. D. W. Reutter assisted in sample preparation and Mr. B. F. Gordon assisted in electrical measurements. Dr. J. F. Whitney and his staff in their x-ray diffraction department are thanked for their help in obtaining powder patterns and carrying out refinements of lattice constants. This was Contribution 2066 from the Central Research Department, E. I. du Pont de Nemours and Company, Wilmington, Delaware.

Manuscript submitted Sept. 4, 1973; revised manuscript received Sept. 28, 1973.

Any discussion of this paper will appear in a Discussion Section to be published in the December 1974 JOURNAL. All discussions for the December 1974 Discussion Section should be submitted by Aug. 1, 1974.

Table I. Electrical properties and cell dimensions in the systems  $1 - x\text{ZnS}/x\text{CuAlS}_2$  and  $1 - x\text{ZnSe}/x\text{CuAlSe}_2$

$x$	$a$ in Å	Color	$\rho(25^\circ\text{C})$ (2 probe) (ohm-cm)	$\alpha$ ( $\mu\text{V}/^\circ\text{C}$ )
<b><math>1 - x\text{ZnS}/x\text{CuAlS}_2</math></b>				
0.0	5.4093	White	—	n type
0.005	5.411	Black	$>10^8$	—
0.01	5.412	Black	$>10^8$	—
0.05*	5.402	Black	—	—
0.045	5.406	Black	$6.0 \times 10^8$	+12
0.10*	5.396	Black	—	—
0.12	5.386	Black	$1.4 \times 10^4$	+24
0.20*	5.374	Black	—	—
		Yellow, made with excess Al	—	—
$\sim 0.32$	5.347	—	$1.5 \times 10^9$	+34
0.33	Tetragonal $a =$ 5.332Å, $c =$ 10.429Å	—	—	—
<b><math>1 - x\text{ZnSe}/x\text{CuAlSe}_2</math></b>				
0.0	5.6676	Yellow	—	n type
0.01	5.670	Dark red	$>10^8$	—
0.05	5.668	Red	$>10^8$	—
0.1	5.650	Red	$2.1 \times 10^9$	+5
0.2	5.636	Red	$6.7 \times 10^9$	+93

\* No crystals obtained.

## REFERENCES

1. W. N. Honeyman, *J. Phys. Chem. Solids*, **30**, 1935 (1969).
2. B. Tell, J. L. Shay, and H. M. Kasper, *J. Appl. Phys.*, **43**, 2469 (1972).
3. M. Robbins and M. A. Miksovsky, *J. Solid State Chem.*, **5**, 462 (1972).
4. C. N. Berglund and R. C. Beairsto, *Rev. Sci. Instr.*, **38**, 66 (1967).
5. P. C. Donohue, J. D. Bierlein, J. E. Hanlon, and H. S. Jarrett, Submitted to *This Journal*.

## Critical Overpotential and Induction Time of Dendritic Growth

A. R. Despić and M. M. Purenović

*Faculty of Technology and Metallurgy, University of Beograd  
and Institute for Chemistry, Technology and Metallurgy, Beograd, Yugoslavia*

### ABSTRACT

Relationships developed earlier (1) for the dependence of the rate of appearance and propagation of dendrites on the properties of the system and overpotential, have been used to develop a quantitative theory of induction period and critical overpotential of dendritic growth. It has been shown that the thermodynamic concept of critical overpotential is applicable to metals of high exchange current density only. The limitations in the appearance of dendrites in metals of low exchange current density are of kinetic character and can be represented by a kinetically defined critical overpotential. The theory has been verified experimentally by following the yield of dendritic deposit of zinc from alkaline zincate solutions as a function of concentration of depositing ions, of overpotential, and of time of deposition.

For some time now it has been known that metallic dendrites appear in electrochemical deposition of metals only if a certain current density and overpotential of deposition are surpassed. Even then, some time is known to pass from the beginning of deposition till the first dendrites can be observed. Wranglen (2) introduced the concept of critical current density. On the other side, Barton and Bockris (3) in a comprehensive theory of dendritic growth introduced the concept of critical overpotential maintaining this to be the basic factor governing the appearance of dendrites, because of being associated with the energy needed to start the dendritic growth (nucleate the crystal or start turning a screw-dislocation). They found this to be of the order of 3 mV for the deposition of silver from nitrate melts. They also noted the increase in dendrite length to be linear with time over the period in which it could be observed and defined the induction period as the time at which the dendrite length extrapolates to zero.

More recently, Despić, Diggle, and Bockris (1, 4) as well as Diggle and Damjanović (5) investigated dendritic growth of zinc from alkaline zincate solution and found the critical overpotential in that system to be about 60-80 mV, while Tajima and Ogata (6) investigating the appearance of dendrites in deposition of nickel, cobalt, and iron found the necessary cell voltage to be of the order of several volts.

The thermodynamic concept of critical overpotential could be criticized on two grounds. First, energy is needed to start any crystal growth other than that occurring by continuation of already established crystal layers (layer growth). Hence, growth of compact deposits should as well require a certain minimum overpotential under the same conditions.

One could maintain here that nuclei required for the development of dendritic crystal are different than those for compact growth and requiring increased overpotential to raise the probability of their appearance. Indeed, Justinijanović and Despić (7) have found zinc dendrites to grow always along the  $\langle 11\bar{2}0 \rangle$  axis while compact zinc exhibited close to the substrate always  $\langle 0001 \rangle$  oriented texture. The work of Panjarov *et al.* (8) has shown that two-dimensional nu-

cleation of the  $(11\bar{2}0)$  nuclei requires a higher degree of supersaturation by adatoms than the  $(0001)$  nuclei, i.e., higher crystallization overpotential. Hence, in such cases the thermodynamic concept of critical overpotential seems to be fully justified.

The second criticism, however, seemed more difficult to counteract: no difference in crystal properties (lattice energies etc.) between, e.g., silver, zinc, and nickel, could account for the large differences in critical overpotential as observed in experiments. Moreover, the fact that those are in the same sequence as the exchange current densities for the deposition of those metals, indicated that some kinetic factors may also be responsible for the phenomenon of critical overpotential. Indeed, one of us (A.D.) has presented (9) a quantitative kinetic concept of that property based on the theory of dendritic growth of metals with relatively slow electron exchange reaction of Despić, Diggle, and Bockris outlined in their work on dendritic growth of zinc (1, 4) [cf. also Despić and Popov (10)].

It is the purpose of this communication to give the details of the derivation of the kinetic definition of the critical overpotential, to show how it superimposes on the thermodynamic one, and to report about its verification by the results of a study of the yield of dendritic zinc in the electrochemical deposition from alkaline zincate solutions.

### Experimental

Zinc has been deposited onto a stainless steel circular electrode which was a base of a cylinder imbedded in Teflon, 0.2 cm<sup>2</sup> in surface area. The cell used is shown in Fig. 1. Vertical position of the cathode allowed a free escape of codeposited hydrogen, provided a fairly reproducible diffusion layer thickness and also made it possible to shave off any disperse deposit into a mercury pool at the bottom of the cell by a Teflon blade. The yield of dendritic deposit has been determined much in the same way as in the experiments of Romanov (11). The amount of zinc in the pool as well as that of compact zinc remaining on the steel cathode have been determined coulometrically by anodic stripping, and the yield obtained as the ratio of the former to the sum of both.

Key words: kinetic definition of critical overpotential, theory of (equations for) induction time, yield of dendritic deposit of zinc, function of zincate concentration, function of overpotential, overpotential of zero dendrite yield.

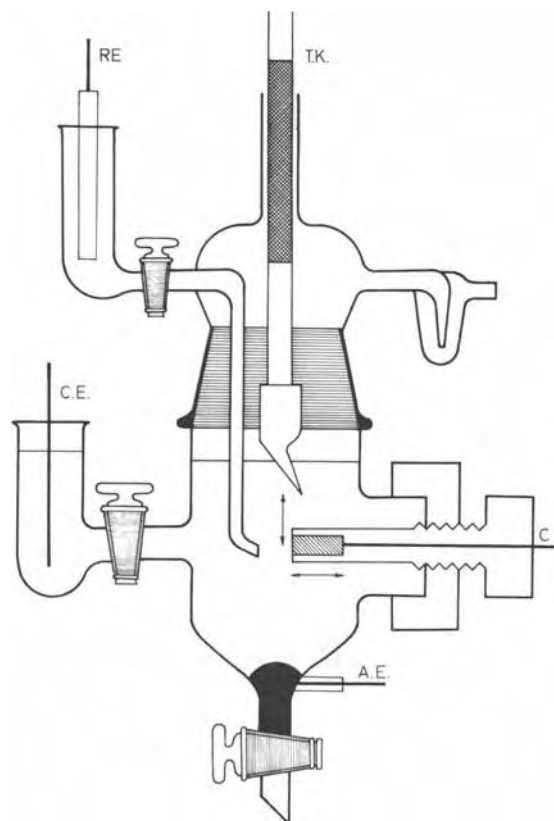


Fig. 1. Cell for determining the yield of disperse deposit. C, cathode; A.E., auxiliary electrode; CE, counterelectrode; RE, reference electrode; T.K., Teflon knife.

Solution of KOH (5*N*) has been used as the electrolyte, and varying amounts of zinc oxide have been dissolved in it to make solutions range from 0.025 to 0.5*M* in zincate. Analytical grade reagents have been used and no additional purification has been carried out after Diggle and Damjanović (5) have shown this to have no effect on the deposition in the investigated system. It was then confirmed in our experiments, as well, that the morphology of the deposit remains the same, whether it is obtained from a fresh electrolyte or from one which has been subjected to prolonged electrolysis.

The experiments consisted of setting the electrode at a constant potential negative to the reversible potential of zinc, by means of a Wenking potentiostat, for a chosen period of time. The development of a disperse deposit could be observed visually. The electrode has then been disconnected for a brief period of time to shave the deposit off, and then submitted to an anodic potential rendering suitable anodic dissolution current which has been followed as a function of time till falling to zero. The same has been done then with the mercury pool at the bottom of the cell.

### Results

**Current-time relationships.**—As already noted and discussed by some authors (1, 5, 12) current-time relationships are known to reflect the establishment of a fixed diffusion layer and the development of a disperse deposit. A typical relationship is shown in Fig. 2. The initial fall in current indicated that the selected potential provided for the appearance of appreciable difficulties in transport of depositing ions, while the ascending part is due to the contribution of the growing crystals penetrating through the diffusion layer. The rather irregular nature of the increase in current past the minimum reflects the properties of the dendrite growth function: for each individual dendrite the latter consists of an initial exponential part and a subsequent linear one (10). Since, the current is determined by the sum of growth rates of all

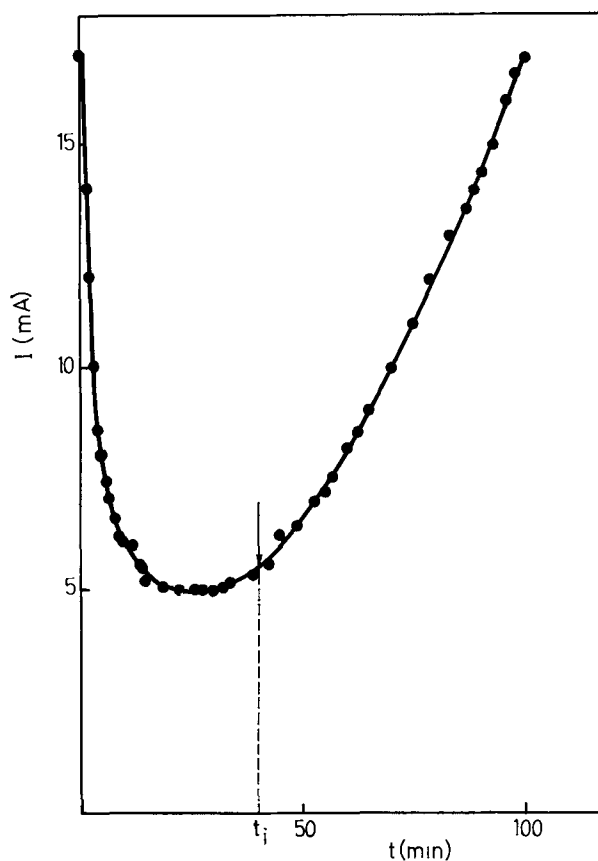


Fig. 2. Typical current-time relationship during the deposition of dendritic deposit at a constant overpotential (100 mV).  $t_i$ —induction time recorded at the 10% increase in current.

the dendrites at different stages of growth and the appearance of each one is an accidental event, the fluctuations in the increase in the value of the current are not unexpected. Also, it is quite possible that hydrogen evolution (bubble formation and departure) makes its own contribution to such irregularity. For all these reasons the curves are not amenable to quantitative theoretical interpretation for obtaining the time constants of dendritic growth. Instead, they were used to note the time at which the amount of dendrites at the surface becomes so large as to make a noticeable contribution to the current over that used for compact deposition. A 10% increase in current is used as a criterion for recording this type of initiation time. The result is shown in Fig. 7 as a function of overpotential.

**Current-potential relationships.**—These have been extracted from the current-time curves by plotting the current minima as functions of potential for different concentrations of zincate ions. A plot is shown in Fig. 3. The dispersion of points is indicative of a fair degree of reproducibility of the diffusion layer thickness.

The absence of limiting currents indicates that all the investigated potentials remained in the region of mixed activation and diffusion control.

**Dendrite yield as a function of time.**—This is shown in Fig. 4 for different constant overpotentials at a constant zincate concentration of 0.5*M*, and in Fig. 5 for different zincate concentrations at a constant cathodic overpotential of 100 mV. Linear extrapolation of these functions to zero yield rendered the initiation time of dendritic growth. This extrapolation rests on the assumption that even at the shortest time of observations the majority of dendrites is already in the phase of constant rate of growth.

**Dendrite yield as a function of overpotential.**—For a given time of observation the yield of dendrites was



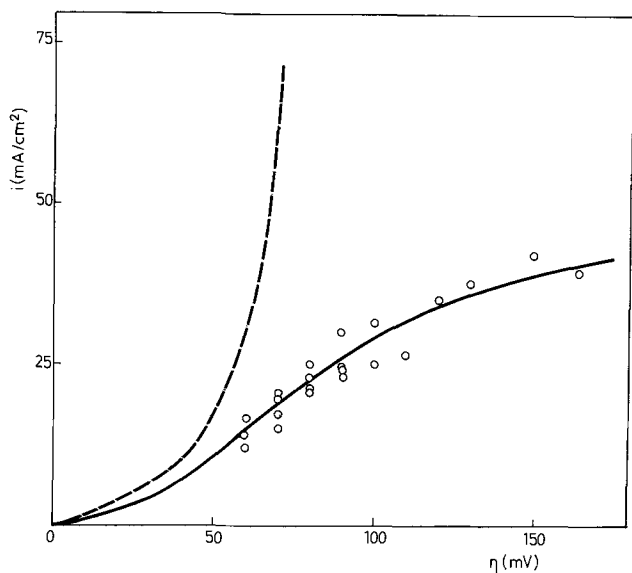


Fig. 3. Current density overpotential relationship for the deposition of zinc from 0.5M alkaline zincate solution. Dashed line—expected relationship in the absence of concentration polarization.

traced as a function of overpotential. The resulting dependence is shown in Fig. 6 for the zincate concentration of 0.5M. The decrease of the functions to zero yield defines the overpotentials of zero yield below which compact deposition should be taking place.

*Induction times and overpotentials of zero yield.*—

The induction times extracted from the results of Fig. 4 and 5 are shown in Fig. 7 and 8 as functions of

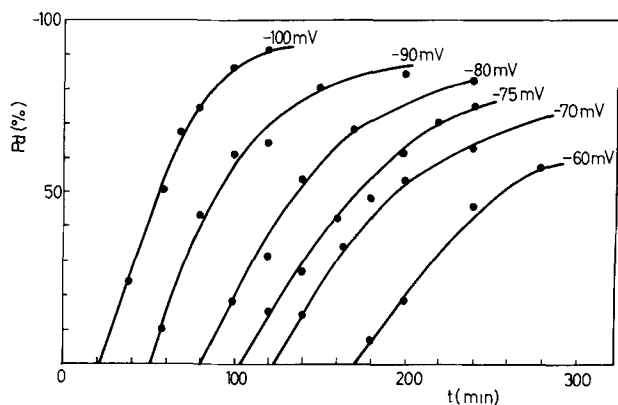
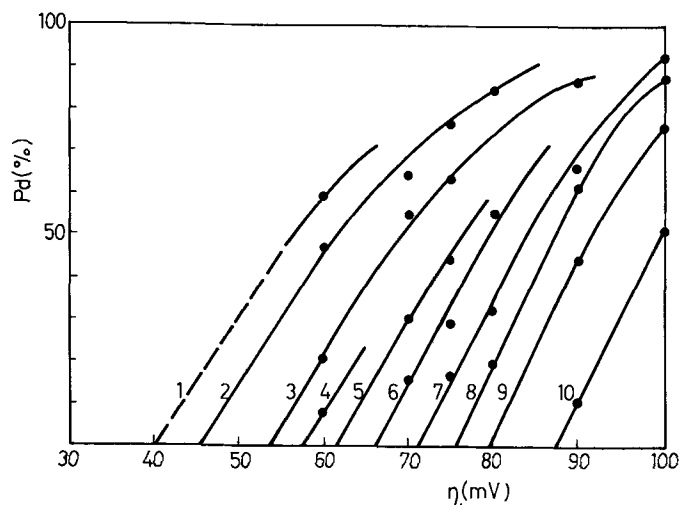


Fig. 4. Yield of dendrites as a function of time at different constant overpotentials at a zincate concentration of 0.5M.



- 1 = 280 min    6 = 140 min
- 2 = 240 min    7 = 120 min
- 3 = 200 min    8 = 100 min
- 4 = 180 min    9 = 80 min
- 5 = 160 min    10 = 60 min

Fig. 6. Yield of dendrites as a function of overpotential for different times of observation (zincate concentration 0.5M).

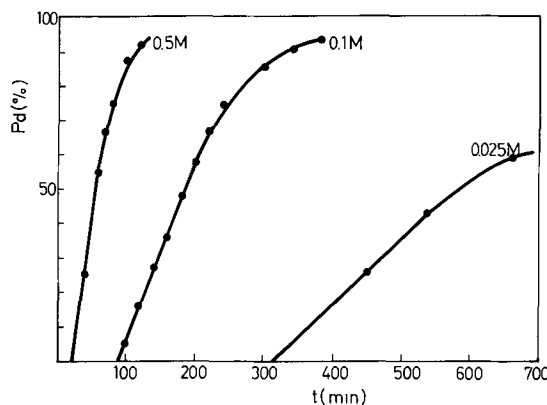


Fig. 5. Yield of dendrites as a function of time at different alkaline zincate concentrations at a constant overpotential of 100 mV.

overpotential (at zincate ion concentration of 0.6M) and of zincate ion concentration (at  $\eta = 100$  mV), respectively.

Figure 7 shows also the overpotential of zero yield as obtained from Fig. 6 as a function of the time of observation, as well as the induction times obtained from current minima (cf. Fig. 2).

**Discussion**

The plot of Fig. 7 justifies once more the contention that the current increase is indicative of the appearance of dendritic deposit, for the times of 10% current increase practically coincide with the induction times obtained from the zero yield.

More significant, however, is the finding indicated by the same plot, that the induction period function of overpotential coincides with the zero yield overpotential as a function of the time of observation. It seems justified to identify the zero yield overpotential with the known critical overpotential of dendritic growth for it is the overpotential below which dendrites do not appear within the time of experiment. However, the fact that the critical overpotential should depend on the time of observation, does not seem to be in accordance with the concept of the critical overpotential used so far and obviously calls for a more detailed analysis of the problem.

This can be made in terms of the theory of dendritic growth as set by Barton and Bockris (3) and developed by Despić, Diggle, and Bockris (14).

That theory has rendered equations for the rate of growth of dendrites (tip current density) under mixed activation and diffusion control as a function of concentration of depositing ions,  $C_o$ , diffusion layer thickness,  $\delta$ , and overpotential,  $\eta$ , [cf. Despić and Popov

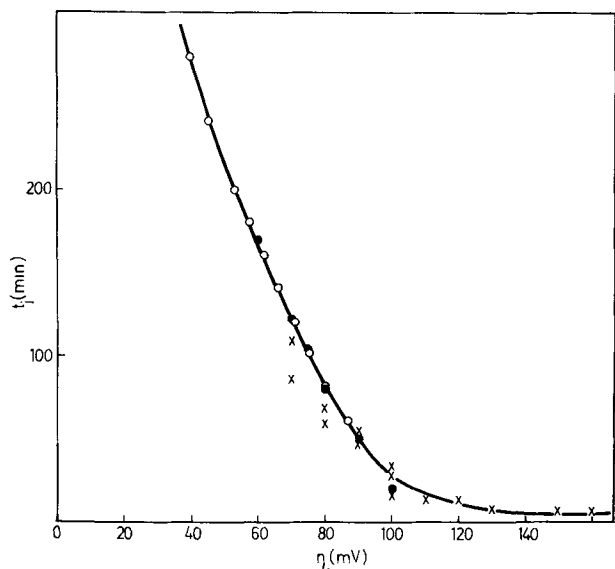


Fig. 7. The induction time as a function of overpotential at a zincate concentration of 0.5M. x, from current minima; ●, from plots of yield vs. time; ○, from zero yield overpotentials.

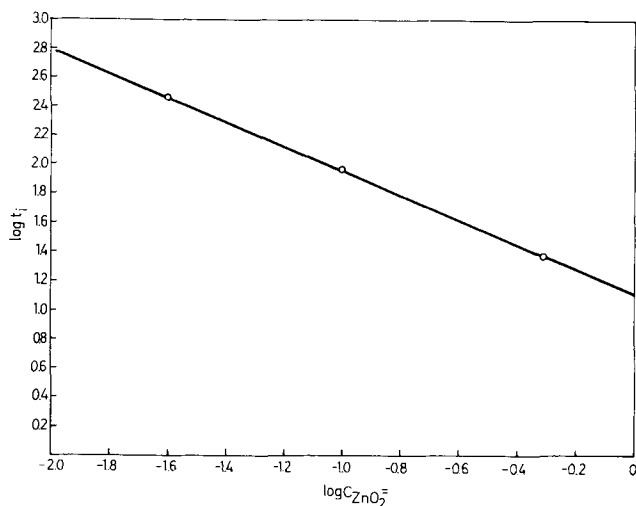


Fig. 8. Induction time as a function of zincate concentration at a constant overpotential of 100 mV.

(10)]. From those, taking the case of divalent metal ion discharge one could derive a complete equation (without some simplifying assumptions made in the original work) for the relationship between dendrite height,  $h$ , and time,  $t$ .

$$\frac{nF}{V} \frac{r}{i_L} (1 + \beta) \frac{[(1 - f_{ac}) + (1 - f_{ac}K(r))\beta + f_{ac}(1 - K(r))]}{[(1 - f_{ac}K(r))\beta + f_{ac}(1 - K(r))]^2} \left\{ \ln \frac{h - h_c}{h_0 - h_c} + \frac{h - h_0}{h_c - r\beta} \right\} = t \quad [1]$$

where

$$\beta = \frac{i_0 f_c(\eta)}{i_L} \quad [2]$$

$$f_{ac} = \frac{f_a(\eta)}{f_c(\eta)} \quad [3]$$

$$h_c = \frac{r\beta(1 - f_{ac})}{(1 - f_{ac}K(r))\beta + f_{ac}(1 - K(r))} \quad [4]$$

and

$$f_c(\eta) = \exp \left[ -\frac{\alpha_c F}{RT} \eta \right] \quad [5]$$

$$f_a(\eta) = \exp \left[ \frac{\alpha_a F}{RT} \eta \right] \quad [6]$$

$$K(r) = \exp \left[ \frac{2\sigma V}{RT\rho/2} \right] \quad [7]$$

Here  $h_0$  is the height of the dendrite precursor, while  $r$  is a quantity reflecting the tip radius. If one approximated the situation by a paraboloidal diffusion law, this would be

$$r = \frac{\rho/2}{\nabla f'} \quad [8]$$

where  $\rho$  is the radius of curvature of the paraboloid at the tip of  $\nabla f'$  is a function [cf. Ref. (10), Fig. 19] of depositing ion concentration. In fact,  $\nabla f'$  is not too sensitive to the latter and in the concentration range which may be encountered in practice, taking a constant value of 0.1 would be a fairly good approximation.  $i_0$  is the exchange current density and  $\alpha_c$  and  $\alpha_a$  the transfer coefficients of the electrochemical reaction;  $i_L$  is the diffusion limiting current density for linear diffusion through limited diffusion layer thickness,  $\delta$ ;  $K(r)$  is the Kelvin-effect term where  $\sigma$  is the surface tension of the metal.

A typical dependence arising from this relationship is shown in Fig. 9. This demonstrates the physical meaning of the following quantities, which may be determined by experiment:

(i) The time constant of growth,  $\tau_s$ , is the constant of the exponential part of the growth and could be ob-

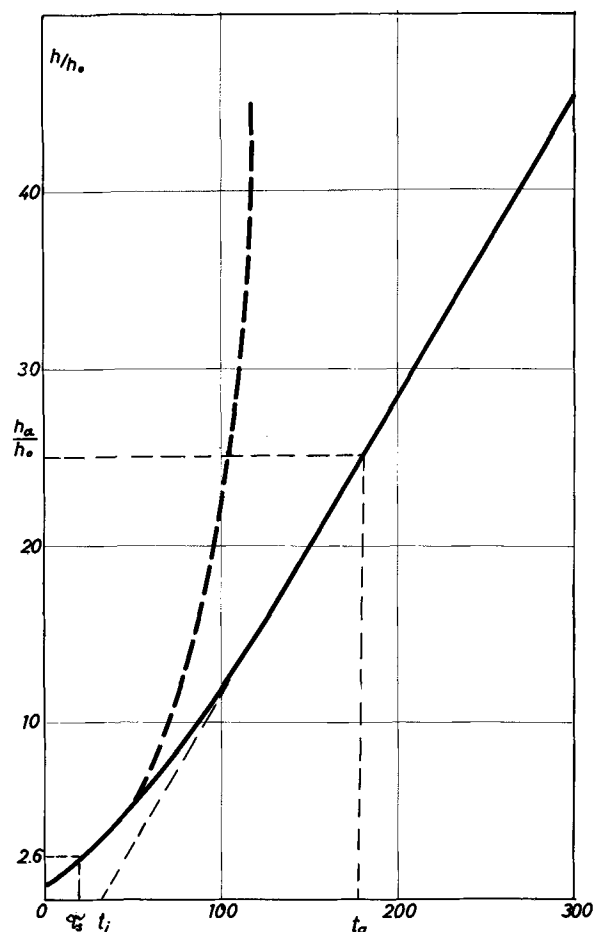


Fig. 9. Time dependence of a dendrite height.  $h_0$ , initial height;  $\tau_s$ , time constant of the exponential growth;  $t_i$ , induction time;  $t_a$ , time of appearance.

tained in principle from the slope of the plot of log height vs. time if that phase of growth could be found experimentally.

(ii) The induction period,  $t_i$ , is obtained by extrapolation of the linear phase of growth to zero height.

(iii) The time of appearance,  $t_a$ , is the time in which a dendrite reaches a height,  $h_a$ , detectable by the method used.

Simple relationships exist between the three quantities.

Equation [1] reveals directly the factors determining  $\tau_s$ , i.e.

$$\tau_s = \frac{nF}{V} \frac{r}{i_L} (1 + \beta) \frac{[(1 - f_{ac}) + (1 - f_{ac}K(r))\beta + f_{ac}(1 - K(r))]}{[(1 - f_{ac}K(r))\beta + f_{ac}(1 - K(r))]^2} \quad [9]$$

The initiation time,  $t_i$ , can be obtained from the following reasoning. It was shown earlier (2) that, as an experimental quantity, it is found by extrapolation of the linear growth function to zero dendrite height. This function could be derived theoretically for the growth of dendrite outside the diffusion layer boundary on the basis of the tip current density [cf. Ref. (10)] as

$$h = \frac{V}{nF} i(\text{tip}) (t - t_i) = \frac{V}{nF} \frac{i_L i_o [f_c(\eta) - K(r) f_a(\eta)]}{i_L + \frac{r}{\delta} i_o f_c(\eta)} (t - t_i) \quad [10]$$

At the very exit from the linear diffusion layer ( $h = \delta$ ) this function must coincide with the function presented above (Eq. [1]) for the growth of the dendrite from the start up to the diffusion layer boundary. Equating the two, one can eliminate  $t$  and solve the equation for  $t_i$ . The result is

$$t_i = \tau_s \left\{ \ln \frac{\delta - h_c}{h_o - h_c} - \frac{h_o}{h_c + r\beta} + \frac{\delta}{h_c + r\beta} \left[ 1 + \frac{r\beta}{h_c} \cdot \frac{\left(1 + \frac{r}{\delta} \beta\right)}{(1 + \beta)} \right] \right\} \quad [11]$$

The time of appearance,  $t_a$ , is directly given by Eq. [1] when  $h$  is replaced by  $h_a$ .

It is of interest now to analyze any one of these quantities for its dependence on the operational parameter  $\eta$ , for different values of the basic properties of the system as are the  $i_o$  and the concentration of depositing ions. One could assume certain values of the diffusion coefficient of depositing ions ( $D = 10^{-5} \text{ cm}^2 \text{ sec}^{-1}$ ) and the diffusion layer thickness ( $\delta = 10^{-3} \text{ cm}$ ) determining the diffusion limiting current density  $i_L$  as well as of the height of the dendrite precursor ( $h_o = 10^{-4} \text{ cm}$ ) and the radius of the dendrite tip ( $r = 10^{-5} \text{ cm}$ ). The cathodic transfer coefficient  $\alpha_c$  is known to be about 0.5 and the anodic one  $\alpha_a$  about 1.5 for most divalent metal deposition reactions. With the  $r$  value taken, the Kelvin effect, as given by Eq. [7] is negligible, i.e., the factor  $K(r)$  sufficiently close to unity. This simplifies considerably Eq. [11] for computational purposes. Hence, the dependence of the induction time on overpotential was obtained using the simplified Eq. [11] with the above set of parameters. This is shown in Fig. 10 on a log-log scale, for a number of different  $i_o$  values ranging from 1 to  $10^{-8} \text{ A/cm}^2$  and in Fig. 11 for concentrations ranging from 1 to  $10^{-4} \text{ M}$ . In Fig. 12 two values of the tip radius have been taken differing by a power of ten.

Several characteristics features should be noted:

(i) In the high overpotential region all the curves for different  $i_o$  values and the same concentration of depositing ions converge to a single one, with an asymptotic tendency to a level inversely dependent on concentration. This is obviously the region of prevailing diffusion control.

The limiting value of the induction time is obtained from [11] as

$$t_{i,1} = \frac{nF}{V} \cdot \frac{r}{i_L} \ln \left( \frac{\delta - r}{h_o - r} \right) = \left[ \frac{\delta}{VD} \ln \left( \frac{\delta - r}{h_o - r} \right) \right] \frac{r}{C_o} \quad [12]$$

(ii) In the low overpotential region linear functions with the slope of  $-1$  are obtained, indicating the first order relationship between inverse induction time and overpotential. This is the region of prevailing activation control.

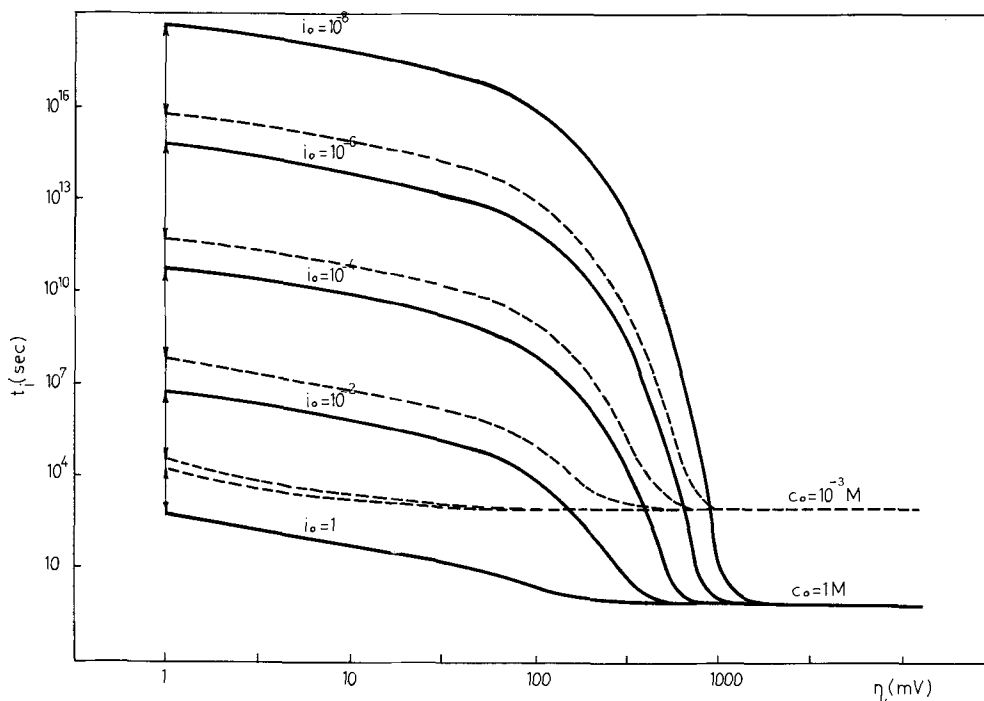


Fig. 10. The induction time as a function of overpotential (theoretical relationship, Eq. [11]) for different constant  $i_o$  and zincate concentrations.

Fig. 11. The induction time as a function of overpotential (theoretical relationship, Eq. [11]), for different constant zincate ion concentrations and  $i_0$  values of  $10^{-2}$  A/cm<sup>2</sup> (full line) and  $10^{-6}$  A/cm<sup>2</sup> (dashed line).

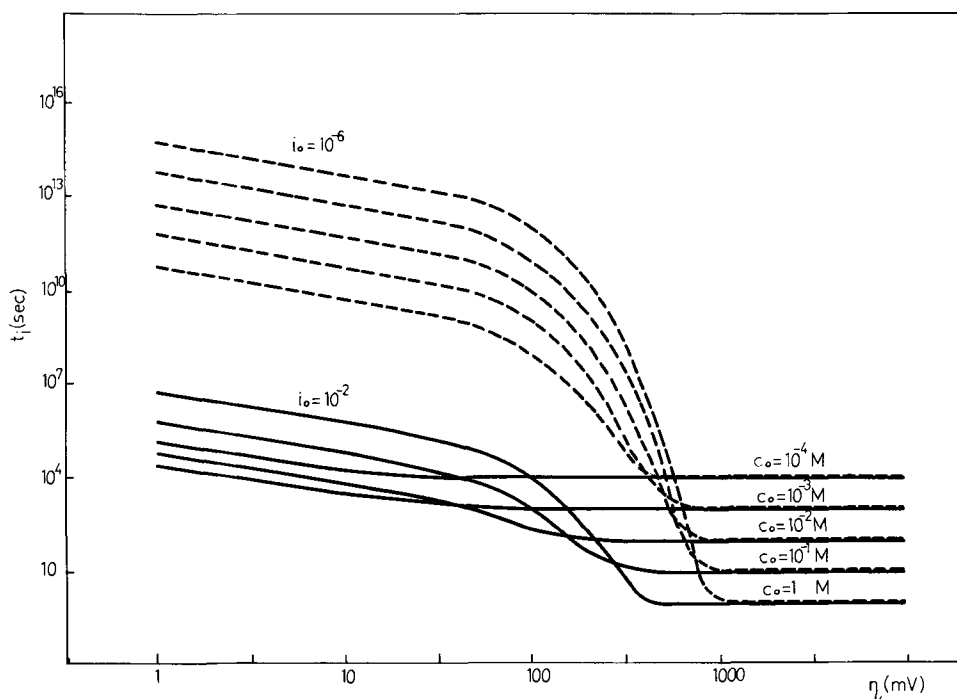
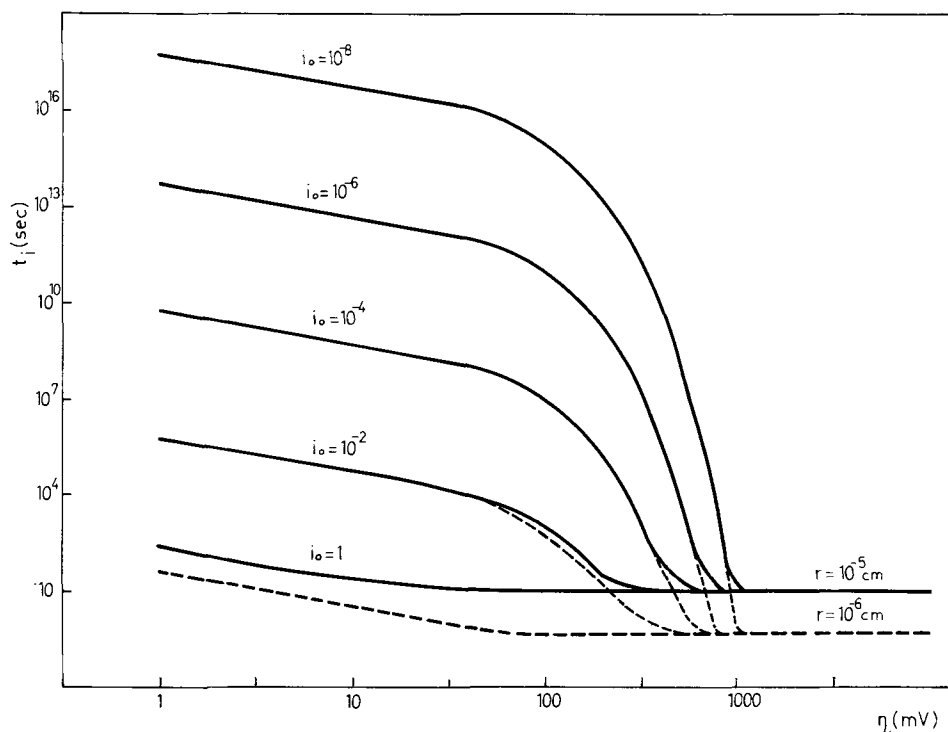


Fig. 12. The induction time as a function of overpotential for two different values of the dendrite tip radius ( $C_o = 10^{-1}$  M).



(iii) The tip radius has no effect in the activation controlled region, while the limiting induction time level at high potentials is directly proportional to it.

(iv) There is a transition region in which the change in the induction time with overpotential can be very sharp. It is sharper the lower the  $i_0$  value and the higher the concentration.

(v) In the transition region, in systems of low  $i_0$  value and at high concentration of depositing ions, decreasing the overpotential in a relatively narrow range can result in a change of the induction time by so many powers of ten as to bring it to values unattainable under normal experimental conditions ( $10^8$  to  $10^{10}$  sec).

In view of these findings one should consider the problem of the critical overpotential. In systems of high  $i_0$  values and at high concentrations of depositing ions the induction time does not increase much with

decreasing overpotential and it should always be possible to extend the experimental observation to times far outside the possible induction time limits. Hence, if no dendrites appear in such time intervals one could maintain to have carried out the deposition at the overpotential below the true, i.e., thermodynamic critical overpotential value. The proper way to ascertain the latter would be to establish the dependence of the inverse of induction time on overpotential. In the absence of critical overpotential with decreasing overpotential this should extrapolate to zero. Any critical overpotential should show as a non-zero intersection with the abscissa.

In the case of systems with high  $i_0$  values, however, when operating at ever decreasing overpotentials one is likely to enter the region of sharp change in induction time. At still lower overpotentials one would record no dendrites within reasonable time and the over-

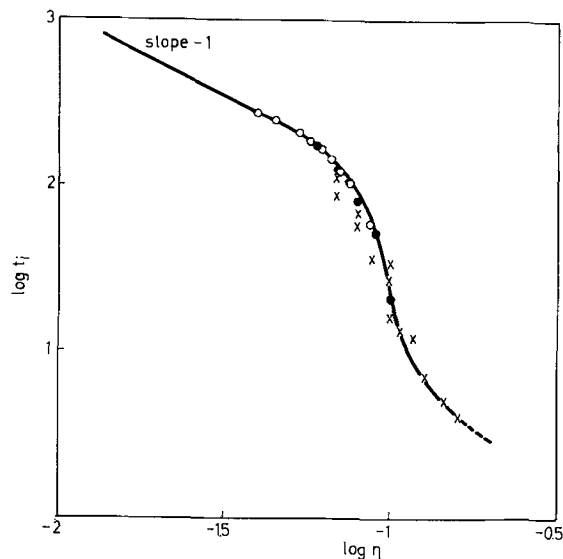


Fig. 13. The induction time as a function of overpotential—experimental relationship based on data of Fig. 7.

potential at which that transition takes place would have the character of a critical overpotential. Obviously, extending the existing definition of the critical overpotential is indicated. Beside the true thermodynamic critical overpotential, one should define also an apparent or kinetic critical overpotential as the overpotential at which the induction time sharply rises to high values unattainable under normal conditions of experiment.

If one takes as the kinetic critical overpotential that overpotential at which the induction time becomes  $x$ -fold (e.g., 100 times) larger than the limiting induction time value,  $t_{i,L}$ , one can derive by contrasting Eq. [11] and [12], that for reasonably high  $r$  values

$$-\eta_{c,k} = \frac{2.3 RT}{\alpha_c F} \log \frac{nFD}{\delta(x^{1/2} - 1)} + \frac{2.3 RT}{\alpha_c F} \log \frac{C_o}{i_o} \quad [13]$$

In view of these conclusions one should consider the results of the present experimental investigations. The data of Fig. 7 are replotted in Fig. 13, to match the presentation of the theoretically derived functions. The similarity is evident. This plot indicates that the critical overpotential of dendritic growth of zinc from zincate solution reported in the literature to be between 60 and 80 mV, is a kinetic critical overpotential. It is interesting to note that this system is on the limit at which the thermodynamic critical overpotential could also be determined from the same plot but from the low overpotential region. It is seen that the last few points indicate a linear dependence with the theoretically predicted slope of  $-1$ . Hence, a graph of  $1/t_i$  vs.  $\eta$  is constructed, as shown in Fig. 14, and the extrapolation to  $1/t_i = 0$  is made. The precision of such an extrapolation is necessarily rather poor. Nevertheless, one could maintain with a fair degree of certainty that the thermodynamic critical overpotential, if any, is not larger than 10 mV.

At the end one should note that the above theory should also be applicable to other transport controlled phenomena in metal deposition and in particular to the phenomenon of the amplification of surface roughness (13).

In that context it was possible to show that the above analysis could be carried out with respect to current density of deposition rather than to overpotential, which for many a practical purpose is a more easily controllable operational parameter. It was shown that the concept of critical current density can also be

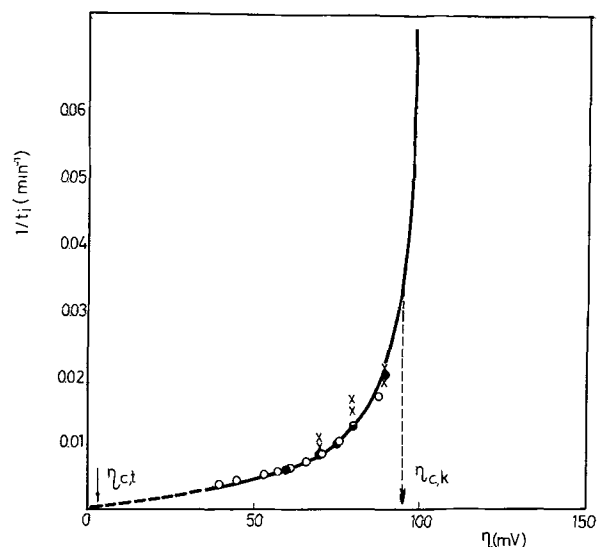


Fig. 14. Inverse induction time as a function of overpotential:  $\eta_{c,t}$ , thermodynamic critical overpotential;  $\eta_{c,k}$ , kinetic critical overpotential.

given a kinetic background similar to that derived above for the critical overpotential.

#### Acknowledgments

The authors gratefully acknowledge the financial support of the National Science Foundation (U.S.A.) (contract No. GF-31057 under the PL 480 Programme), as well as that of the Fund for Scientific Research of the SR Serbia, which have made this work possible. The authors are also indebted to Dr. S. Bingulac for the aid in the mathematics and computing relevant to this paper.

Manuscript received March 13, 1973. This was Paper 120 presented at the Cleveland, Ohio, Meeting of the Society, Oct. 3-7, 1971.

Any discussion of this paper will appear in a Discussion Section to be published in the December 1974 JOURNAL. All discussions for the December 1974 Discussion Section should be submitted by Aug. 1, 1974.

#### REFERENCES

1. A. R. Despić, J. Diggle, and J. O'M. Bockris, *This Journal*, **115**, 507 (1968).
2. G. Wrangien, *Electrochim. Acta*, **2**, 130 (1960).
3. J. L. Barton and J. O'M. Bockris, *Proc. Royal Soc.*, **A 268**, 485 (1962).
4. J. W. Diggle, A. R. Despić, and J. O'M. Bockris, *This Journal*, **116**, 1503 (1969).
5. J. W. Diggle and A. Damjanović, *ibid.*, **117**, 65 (1970).
6. S. Tajima and M. Ogata, *Electrochim. Acta*, **13**, 1845 (1968); *ibid.*, **15**, 61 (1970).
7. I. Justinijanović and A. R. Despić, *Electrochim. Acta*, **18**, 709 (1973).
8. cf. N. A. Pangarov and V. Velinov, *Electrochim. Acta*, **13**, 1909 (1968).
9. A. R. Despić, Paper 120 presented at Electrochemical Society Meeting, Cleveland, Ohio, Oct. 3-7, 1971.
10. A. R. Despić and K. I. Popov, in "Modern Aspects of Electrochemistry," Vol. 7, Chap. 4, B. E. Conway and J. O'M. Bockris, Editors, Plenum Press, New York (1972).
11. V. V. Romanov, *Zh. Prikl. Khim.*, **34**, 2693 (1961).
12. N. Ibl, and K. Schadegg, *This Journal*, **114**, 54 (1967).
13. A. R. Despić, "Proceedings of the 8th Congress Internat. Union Electrodep. and Surface Finishing, Basel, 1972," p. 89, Forster Verlag, Zürich (1973).

# Amalgam Decomposition

## I. Theoretical Relations for Decomposition Kinetics of Sodium Amalgam in Tower Decomposer

I. Roušar,\* S. Rajasekaran,<sup>1</sup> and V. Cezner

Department of Inorganic Technology, Institute of Chemical Technology, Prague, Czechoslovakia

### ABSTRACT

Relationships between the amalgam decomposition rate in a tower decomposer, concentration of sodium in the amalgam, and mass flow of the amalgam through the tower were derived. The dependence of the reaction rate on the rate of flow exhibits a maximum.

Problems of the kinetics of amalgam decomposition in tower decomposers were studied by Hine and co-workers (1-7) who derived equations for calculation of the local and average decomposition rate in a tower with the use of several simplifying assumptions. Their equations are in good agreement with experimental data only at low or medium rates of flow of the amalgam (8). Hine's experimental data (7) indicate that the amalgam decomposition rate decreases when a certain "optimum" flow rate is exceeded. However, Hine's theory (7) ceases to be satisfactory at amalgam flow rates beyond optimum, because it still would predict an increase of amalgam decomposition rates. We therefore attempted to describe the amalgam decomposition in a tower completely and to derive theoretically the dependence of the decomposition rate on the rate of flow, which would satisfy the experimental data in a broader range of flow rates than Hine's theory. Nevertheless, the presented theory is restricted to systems where amalgam drops are formed and therefore is not valid for flooded systems (with water in the dispersed phase).

### Basic Assumptions

During decomposition, the amalgam is brought into contact with graphite and a sodium hydroxide solution. Thus, a local hydrogen-amalgam cell is formed, where the amalgam functions as anode and graphite as cathode. A positive electric current flows from the amalgam to the electrolyte, passes through the latter, enters into the graphite and through the graphite-amalgam interface returns into the amalgam. Along every closed line of current, the reversible voltage of the amalgam-hydrogen cell ( $\tau U$ ) is compensated by anodic and cathodic overvoltages and by ohmic losses in the electrolyte, amalgam, graphite, and contact resistance between the amalgam and graphite.

The anodic overvoltage ( $\eta_A$ ) during dissolution of the sodium amalgam is due to an insufficiently rapid transport of sodium from the bulk to the amalgam-electrolyte interface (9-11)

$$\eta_A = (RT/F) \ln (a_{Na^0}/a_{Na^s}) \quad [1]$$

Here  $a_{Na^0}$  and  $a_{Na^s}$  denote activities of sodium in the bulk of the amalgam and at the interface, respectively. The flux of sodium to the interface is given by unidirectional diffusion

$$\bar{i}/F = -N_{Na} D_{Na} d \ln a_{Na}/dz \quad [2]$$

where  $\bar{i}$  denotes average current density on the drop surface ( $A/cm^2$ ),  $N_{Na}$  bulk concentration of sodium ( $mol/cm^3$ ),  $D_{Na}$  its diffusion coefficient ( $cm^2/sec$ ), and  $z$  distance perpendicular to the amalgam surface ( $cm$ ). In further calculations, we shall express  $N_{Na}$  and  $a_{Na}$  by molar fraction of sodium in the amalgam,  $X_{Na}$ ; because  $\eta_A$  reaches significant values if  $X_{Na^0} \rightarrow 0$  we

shall use the assumption  $X_{Na} \rightarrow 0$ . Then

$$N_{Na} = X_{Na}/V_{AM} M_{Hg} \quad [3]$$

where  $M_{Hg}$  is the molecular weight of mercury and  $V_{AM}$  denotes specific volume of the amalgam ( $cm^3/mol$ ), which can be expressed (12) as a function of  $X_{Na}$ ; for  $X_{Na} \rightarrow 0$

$$V_{AM} = V_{Hg} \quad [4]$$

Here  $V_{Hg}$  denotes specific volume of mercury ( $cm^3/mol$ ) at the given temperature. On introducing Eq. [4] into [3], we obtain

$$N_{Na} = X_{Na}/V_{Hg} M_{Hg} \quad [5]$$

The activity of sodium in the amalgam is given by (13)

$$a_{Na} = X_{Na} \exp (A + BX_{Na} + CX_{Na}^2) \quad [6]$$

and for  $X_{Na} \rightarrow 0$  we obtain from Eq. [6]

$$a_{Na} = X_{Na} \exp (A) \quad [7]$$

where  $A = 9505.4 \ln 10/T^{1.16}$ ,  $B = 214.3 \ln 10/T^{0.46}$ , and  $C = (14.7 - 0.027T) \ln 10$ . On introducing Eq. [5] and [7] into [2] and rearranging we obtain

$$(\bar{i}/F) dz = - (D_{Na}/V_{Hg} M_{Hg}) dX_{Na} \quad [8]$$

Integration of this equation from  $X_{Na^s}$  ( $z = 0$ ) to  $X_{Na^0}$  ( $z = \delta$ ) yields

$$(\bar{i}/F) (\delta V_{Hg} M_{Hg}/D_{Na}) = - (X_{Na^s} - X_{Na^0}) \quad [9]$$

( $X_{Na^s}$  denotes mean molar fraction of sodium in amalgam on the drop surface and  $\delta$  thickness of Nernst layer for sodium diffusion to the interface). Rearranging Eq. [9] and using Eq. [7] we obtain

$$a_{Na^s}/a_{Na^0} = 1 - (\bar{i} \delta V_{Hg} M_{Hg}/D_{Na} F X_{Na^0}) \quad [10]$$

The value of  $(a_{Na^s}/a_{Na^0})$  thus found enables one to calculate  $\eta_A$  (Eq. [1]). The overvoltage during hydrogen evolution,  $\eta_K$ , on a graphite cathode is given by the Tafel equation

$$\eta_K = a_K - b_K \ln i, \quad \eta_K < 0 \quad [11]$$

where  $i$  denotes current density,  $a_K$  and  $b_K$  Tafel constants (V) to be determined experimentally (14) for the given sort of graphite, concentration, and temperature of electrolyte.

The ohmic voltage drop in the electrolyte between the anode and cathode is given by the specific resistance of the mixture of hydrogen bubbles and electrolyte in the space between the electrodes and by the geometry of this space. If the specific resistance is constant the Laplace equation applies

$$\nabla^2 \phi = 0 \quad [12]$$

with suitable boundary conditions on the interfaces. However, the solution of this equation is rendered impossible by insufficient knowledge of the distribution

\* Electrochemical Society Active Member.

<sup>1</sup> Present address: Chemical Engineering Department, Indian Institute of Technology, Kanpur-16, India.

Key words: amalgam decomposition, tower decomposer.

of amalgam flow in the bed. We therefore used for a quantitative description of the processes during amalgam decomposition the drop model described below.

### Drop Model for Amalgam Decomposition

We assume that the amalgam flows down through the graphite bed in the form of half-sphere-shaped droplets of radius  $r_o$  independent of the rate of flow. The droplets are distributed evenly in the bed at a density of  $N_1$  droplets per unit height of the bed; a circular area of graphite of radius  $r_f$  corresponds to every drop. The situation during decomposition of an amalgam drop in contact with graphite is illustrated in Fig. 1 showing a closed line of current which passes the ohmic resistances and interfaces. The voltage balance for this line of current is

$$(f_1 L_{EPE} + f_2 L_{ELPE} + L_{CG} + L_{AMPAM})i + 2\rho_{SL} L_{SL} \bar{i} + \epsilon_A - \epsilon_K = 0 \quad [13]$$

Here  $L_E$ ,  $L_{EL}$ ,  $L_G$ ,  $L_{AM}$ , and  $L_{SL}$  (cm) denote lengths of the current line in the bulk of electrolyte, in the layer of electrolyte-bubble mixture at the graphite surface, in the graphite, in the amalgam, and in the amalgam-graphite interface, respectively;  $\rho_E$ ,  $\rho_G$ ,  $\rho_{AM}$ , and  $\rho_{SL}$  (ohm · cm) specific resistances of the pure electrolyte (without bubbles), graphite, amalgam, and amalgam-graphite interface, respectively;  $i$  (A/cm<sup>2</sup>), anodic current density on the given point of the amalgam surface;  $\epsilon_A$ ,  $\epsilon_K$  (V), local anodic and cathodic potentials;  $f_1$ , ratio of the specific resistance of the electrolyte-bubble mixture in the bulk of electrolyte to that of the pure electrolyte; and  $f_2$  the same ratio for the electrolyte-bubble mixture at the graphite surface. The term  $2L_{SL}\rho_{SL}\bar{i}$  represents the voltage loss on the contact resistance between amalgam and graphite. The factor of 2 follows from the assumption that the amalgam drops have a hemispherical shape during contact with graphite; the contact area is then  $\pi r_o^2$  whereas the surface area to which the anodic current is referred is  $2\pi r_o^2$ . As illustrated in Fig. 1, and Eq. [13], we assume that the only surface on which the evolution of hydrogen can occur is the free surface area of graphite. In fact a small fraction of hydrogen also evolves under the amalgam drop because the graphite surface is covered with a thin layer of caustic. Hydrogen evolution in this contact area leads to an increase of resistance under the amalgam drop. Therefore it is necessary that the voltage balance be extended by a term taking account of this effect, i.e., the term  $2L_{SL}\rho_{SL}\bar{i}$ .

The voltage balance can be rewritten with the use of the equations

$${}_rU = r\epsilon_A - r\epsilon_K \quad [14]$$

$$\eta_A = \epsilon_A - r\epsilon_A \quad [15]$$

$$\eta_K = \epsilon_K - r\epsilon_K \quad [16]$$

where the index  $r$  refers to the equilibrium state;  $\eta_A$ ,  $\eta_K$  (V) local anodic and cathodic overpotentials; and  ${}_rU$  reversible voltage of the amalgam-hydrogen cell. Thus, Eq. [13] gives

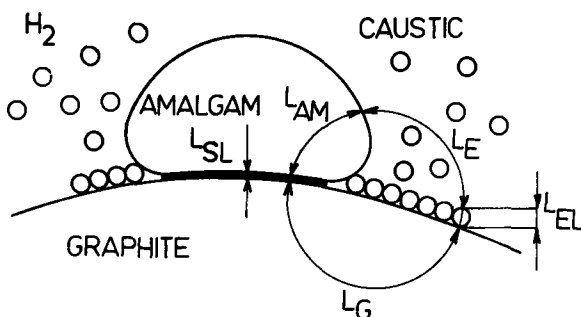


Fig. 1. Drop model (course of a current line)

$$-{}_rU = f_1 L_{EPE}i + f_2 L_{ELPE}i + L_{CG}i + 2L_{SL}\rho_{SL}\bar{i} + L_{AMPAM}i + \eta_A - \eta_K \quad [17]$$

Here we can neglect the terms corresponding to the voltage drop in the graphite and amalgam since  $\rho_G$  and  $\rho_{AM}$  are by about three orders of magnitude smaller than  $\rho_E$ . We assume that the length of the lines of current in the electrolyte is given as

$$L_E = r - r_o \quad [18]$$

where  $r$  denotes distance from the center of the drop measured along the graphite surface. This simplifying assumption is important since the true value of  $L_E$  can be computed only after solving Eq. [12] for a given geometry and boundary conditions. Thus, the assumption that  $L_E$  is known implies that the solution of the Laplace equation for the given system is also known. Equation [17] can be rearranged as follows

$$-{}_rU + a_K - (RT/F) \ln (a_{Na^o}/a_{Na^s}) - 2\rho_{SL}L_{SL}\bar{i} = f_1\rho_E(r - r_o)i + f_2\rho_{EL}L_{EL}i + b_K \ln i \quad [19]$$

The terms that are independent of coordinates are on the left side, those which depend on position (on the drop surface and its proximity) are on the right side.

The current density on the graphite surface attains its maximum value,  $i = i_{max}$ , for  $r = r_o$ , which can be found from Eq. [19]

$$-{}_rU + a_K - (RT/F) \ln (a_{Na^o}/a_{Na^s}) - 2\rho_{SL}L_{SL}\bar{i} = f_2\rho_{EL}L_{EL}i_{max} + b_K \ln i_{max} \quad [20]$$

By subtracting Eq. [20] from [19] we obtain

$$f_1\rho_E(r - r_o)i + f_2\rho_{EL}L_{EL}(i - i_{max}) + b_K \ln (i/i_{max}) = 0 \quad [21]$$

We now define the following dimensionless criteria and simplexes

$$K_D = f_1\rho_E r_o i_{max}/b_K \quad [22]$$

$$K_{SL} = f_2\rho_{EL}L_{EL}i_{max}/b_K \quad [23]$$

$$i_R = i/i_{max} \quad [24]$$

$$r_R = r/r_o \quad [25]$$

The term  $\ln (i/i_{max})$  in Eq. [21] can be expanded in series for  $i \approx i_{max}$  and the terms of higher order can be neglected

$$\ln (i/i_{max}) = \ln (1 + (i - i_{max})/i_{max}) \approx ((i - i_{max})/i_{max}) - \frac{1}{2} ((i - i_{max})/i_{max})^2 \quad [26]$$

On introducing Eq. [22]-[26] into [21] we obtain

$$K_D(r_R - 1)i_R + K_{SL}(i_R - 1) + (i_R - 1) - (\frac{1}{2})(i_R^2 - 2i_R + 1) = 0 \quad [27]$$

and after rearranging the dependence of  $i_R$  on  $r_R$  is found as

$$i_R = 2 + K_D(r_R - 1) + K_{SL} - [(2 + K_D(r_R - 1) + K_{SL})^2 - 3 - 2K_{SL}]^{1/2} \quad [28]$$

This equation gives the local current density on the graphite surface. The average current density on the amalgam surface,  $\bar{i}$ , and that on the graphite surface,  $i_p$ , is found by integrating over the free graphite surface as

$$\bar{i} 2\pi r_o^2 = i_p \pi (r_f^2 - r_o^2) = 2\pi r_o^2 i_{max} \int_1^{r_f/r_o} i_R r_R dr_R \quad [29]$$

whence follows the relation

$$\bar{i} = 0.5 i_p [(r_f/r_o)^2 - 1] = i_{max} \int_1^{r_f/r_o} i_R r_R dr_R = i_{max} P_1 \quad [30]$$

where

$$P_1 = \int_1^{r_f/r_o} i_R r_R dr_R \quad [31]$$

After introducing  $i_R$  from Eq. [28] into [31] we obtain

$$P_1 = \int_1^{r_f/r_o} (2 + K_D r_R - K_D + K_{SL}) r_R dr_R - \int_1^{r_f/r_o} (a r_R^2 + b r_R + c)^{1/2} r_R dr_R \quad [32]$$

where

$$a = K_D^2 \quad [33a]$$

$$b = 4K_D - 2K_D^2 + 2K_D K_{SL} \quad [33b]$$

$$c = K_D^2 - 2K_D K_{SL} + K_{SL}^2 - 4K_D + 2K_{SL} + 1 \quad [33c]$$

$$a + b + c = (K_{SL} + 1)^2 \quad [33d]$$

The integrals in Eq. [32] can be evaluated as

$$\int_1^{r_f/r_o} (2 + K_D r_R - K_D + K_{SL}) r_R dr_R = 0.5(K_{SL} - K_D + 2) [(r_f/r_o)^2 - 1] + (K_D/3) [(r_f/r_o)^3 - 1] \quad [34]$$

$$\int_1^{r_f/r_o} (a r_R^2 + b r_R + c)^{1/2} r_R dr_R = (1/3a) (a (r_f/r_o)^2 + b (r_f/r_o) + c)^{3/2} - K_{SL} + 1)^3 - (b/8a^2) \{ [(2a(r_f/r_o) + b) a (r_f/r_o)^2 + b (r_f/r_o) + c]^{1/2} - (2a + b) (K_{SL} + 1) \} - (b(4ac - b^2))/(16a^{5/2}) \cdot \ln \left\{ \frac{2a^{1/2}(a(r_f/r_o)^2 + b(r_f/r_o) + c)^{1/2} + 2a(r_f/r_o) + b}{2a^{1/2}(K_{SL} + 1) + 2a + b} \right\} \quad [35]$$

The final equation for  $P_1$  is

$$P_1 = a_1 - b_1 + c_1 - d_1 \quad [36]$$

where  $a_1$  denotes right side of Eq. [34],  $b_1$ ,  $c_1$ , and  $d_1$  the three terms in Eq. [35]; the average current density on the free graphite surface (not covered with amalgam drops) is

$$i_p = 2P_1 i_{\max} / [(r_f/r_o)^2 - 1] \quad [37]$$

The current referred to unit height of tower,  $I$  (A/cm) depends on  $i_p$  as follows

$$I = i_p \pi (r_f^2 - r_o^2) N_1 \quad [38]$$

where  $N_1$  denotes number of amalgam drops in unit tower height ( $\text{cm}^{-1}$ ). The latter value can be calculated from the balance of the surface on which the amalgam decomposition proceeds

$$N_1 \pi r_f^2 = S_T (S_G/V_T) f_S \quad [39]$$

where  $S_T$  denotes inner cross section of tower ( $\text{cm}^2$ ),  $S_G/V_T$  total surface area of the graphite bed in unit volume of tower ( $\text{cm}^2/\text{cm}^3$ ),  $f_S$  a factor proportional to utilization of the graphite surface in the amalgam decomposition (supposing, that the lower part of the graphite spheres is ineffective  $f_S \approx 0.6$ ).

The rate of amalgam decomposition,  $r_{\text{Na}}$  [mol Na/( $\text{cm}^3 \cdot \text{sec}$ )] at a given height of tower is given by

$$r_{\text{Na}} = I / (\mathbf{F} \cdot S_T) \quad [40]$$

where  $\mathbf{F}$  is 96,496 coulombs.

After introducing  $I$  from Eq. [38] and  $N_1$  from [39] we obtain

$$r_{\text{Na}} = (i_{\max}/\mathbf{F}) (r_o/r_f)^2 (S_G/V_T) f_S 2P_1 \quad [41]$$

This equation can be directly used in calculating the tower height,  $H$  (cm) (assuming homogeneous, piston flow of amalgam through the tower)

$$H \cdot S_T/M = - \int_{Y_1}^{Y_2} dY/r_{\text{Na}} \quad [42]$$

Here  $M$  denotes rate of flow of mercury (mol Hg/sec),  $Y$  concentration of sodium in the amalgam (mol Na/mol Hg),  $Y_1$  and  $Y_2$  values of  $Y$  at the inlet and outlet, respectively.

To calculate the ratio  $r_f/r_o$  in Eq. [41], the volume balance for the amalgam is expressed as

$$N_1 (2/3) r_o^3 w_{\text{Hg}} = M (\bar{V}_{\text{Hg}} + Y \bar{V}_{\text{Na}}) \quad [43]$$

where  $w_{\text{Hg}}$  (cm/sec) denotes apparent velocity of fall of amalgam drops through the tower referred to the motion along  $z$  axis;  $\bar{V}_{\text{Hg}}$  and  $\bar{V}_{\text{Na}}$  partial molar volumes of mercury and sodium in the amalgam ( $\text{cm}^3/\text{mol}$ ). The velocity  $w_{\text{Hg}}$  involves also the exchange effect of amalgam between drops flowing down through the bed and those forming a stationary portion held up in the bed;  $w_{\text{Hg}}$  is, therefore, smaller than the measured velocity of amalgam drops in the tower. By eliminating  $N_1$  from Eq. [39] and [43] we obtain

$$r_f/r_o = [(2/3) r_o w_{\text{Hg}} (S_G/V_T) f_S] / [(M/S_T) (\bar{V}_{\text{Hg}} + Y \bar{V}_{\text{Na}})]^{1/2} \quad [44]$$

With increasing rate of flow of the amalgam, the free surface area of graphite on which the amalgam decomposition can proceed decreases gradually until a certain rate of flow (which can be denoted as maxi-

mum from the point of view of amalgam decomposition) the total available surface of the graphite is flooded with the amalgam.<sup>2</sup> We denote this rate of flow as  $(M/S_T)_{\max}$ ; for this case is  $r_o = r_f$  and Eq. [44] gives

$$(M/S_T)_{\max} = [(2/3) r_o w_{\text{Hg}} (S_G/V_T) f_S]^2 / (\bar{V}_{\text{Hg}} + Y \bar{V}_{\text{Na}}) \quad [45]$$

We introduce relative rate of flow,  $(M/S_T)_{\text{rel}}$ , defined as

$$(M/S_T)_{\text{rel}} = (M/S_T) / (M/S_T)_{\max} \quad [46]$$

and from Eq. [44]-[46] follows the expression

$$r_f/r_o = 1 / (M/S_T)_{\text{rel}}^{1/2} = [(M/S_T)_{\max} / (M/S_T)]^{1/2} \quad [47]$$

which can be introduced into Eq. [41] to give the expression for the reaction rate in the form suitable for calculation

$$r_{\text{Na}} = (i_{\max}/\mathbf{F}) (M/S_T)_{\text{rel}} (S_G/V_T) f_S 2P_1 \quad [48]$$

Equation [48] was verified by measurement of the dependence of the decomposition rate on amalgam concentration at constant rate of flow of the amalgam through the tower as well as by measurement of the decomposition rate on the rate of flow at constant amalgam concentration (15).

### Discussion of Results

We shall use the following values of the constants in calculating the rate of amalgam decomposition:  $f_S = 0.6$ ;  $(M/S_T)_{\max} = 0.025$  mol Hg/( $\text{cm}^2 \cdot \text{sec}$ );  $f_1 r_o = 0.4$  cm;  $\delta = 4.23 \times 10^{-4}$  cm. For a reactor containing 40% NaOH at 80°C we calculated the dependences shown in Fig. 2 and 3 with  $a_K = -0.604V$ ,  $\alpha = 0.411$ ,  $f_2 L_{\text{EL}} = 0.35$  cm,  $\rho_{\text{SL}} L_{\text{SL}} = 0.35$  ohm  $\cdot \text{cm}^2$  ( $b_K = RT/(1 - \alpha)\mathbf{F}$  and  $\beta = 1 - \alpha$ ).

<sup>2</sup> The reaction rate calculation ought to include a term representing amalgam decomposition at the amalgam-graphite contact area. This term is small for systems where the free surface area of graphite is comparable with the contact area. For systems with small free surface area of graphite (the so-called flooded systems) this new term predominates and represents practically the whole reaction rate of amalgam decomposition. Since our analysis is restricted to the former systems, we neglected this additional term in calculating the reaction rate. Nevertheless, we still use the expression "reaction rate for flooded system," meaning only that fraction of the reaction rate due to hydrogen evolution on the free surface area of graphite, rather than the whole reaction rate.



The dependence of the rate of amalgam decomposition on the concentration of sodium for  $M/S_T = 0.01$  mol Hg/(cm<sup>2</sup> · sec) is shown in Fig. 2. Its slope in bilogarithmic coordinates at higher sodium concentrations is close to 0.2; at concentrations <0.05 weight per cent (w/o) Na the slope increases and approaches 1.0 at 0.001%. The value of 0.2 can be attributed to the influence of the resistances of the bubble layer and interelectrode space—without these effects the slope should be about 0.5 (for  $\alpha = 0.5$ ). At low sodium concentrations in the amalgam the rate determining step is diffusion of sodium toward the drop surface, hence the reaction rate becomes linearly dependent on the sodium concentration.

The dependence of the rate of amalgam decomposition on the mass flow of the amalgam ( $M/S_T$ ) at a sodium concentration of 0.1915 w/o is shown in Fig. 3. It exerts a flat maximum at about 0.012 mol Hg/(cm<sup>2</sup> · sec), which can be attributed to the fact that with increasing number of drops per volume unit of tower (with increasing wetting) the surface area of the bed available for hydrogen evolution diminishes. For high values of  $M/S_T$  the drop model fails; the reaction rate in this region is therefore represented by the dashed portion of the curve in Fig. 3.

The influence of a change of hydrogen overvoltage,  $a_T$ , from  $-0.604V$  to  $-0.469V$  and a simultaneous change of  $\alpha$  from 0.411 to 0.517 is illustrated in Fig. 4. As a result, the reaction rate increases by about 40% (in the maximum). Thus, materials with a lower hydrogen overvoltage enable one to obtain higher reaction rates.

Figure 5 shows the influence of a change of the quantity  $\rho_{SL}L_{SL}$  from 0.35 to 0.01 ohm-cm<sup>2</sup> (curves 1 and 2) and  $f_2L_{EL}$  from 0.35 to 0.01 cm (curves 1 and 3). It is seen that the decrease of the resistance at the interface (i.e., the contact resistance on the graphite surface and the surface coverage with evolved gas)

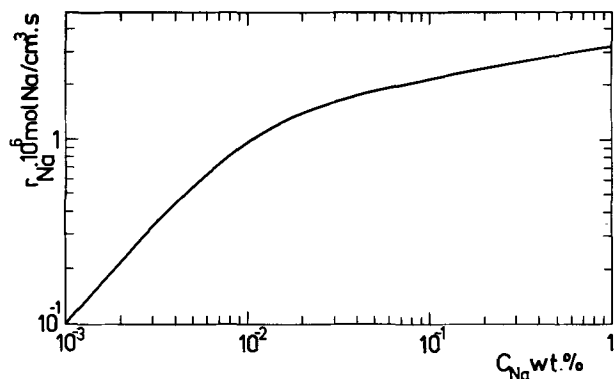


Fig. 2. Dependence of the rate of amalgam decomposition on concentration of sodium for  $M/S_T = 0.01$  mol cm<sup>-2</sup> sec<sup>-1</sup>.

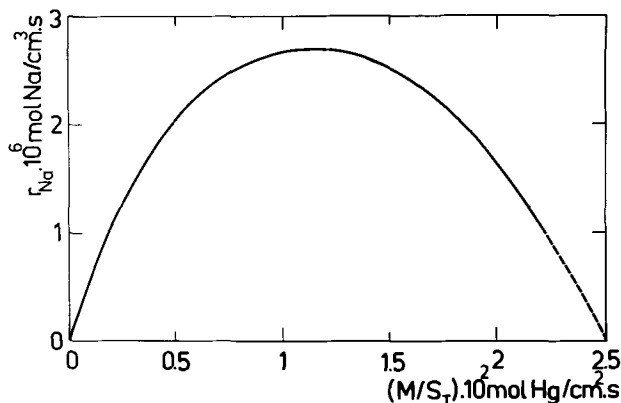


Fig. 3. Dependence of the rate of amalgam decomposition on specific wetting of the bed with amalgam at 0.1915 weight per cent Na.

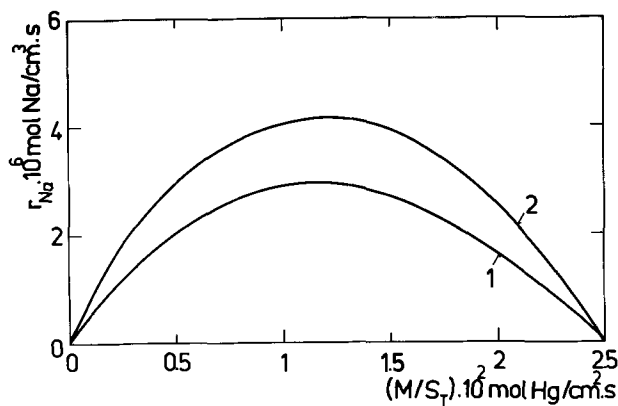


Fig. 4. Influence of hydrogen overvoltage on graphite changing from  $a_T = -0.604V$  (curve 1) to  $a_T = -0.469V$  (curve 2).

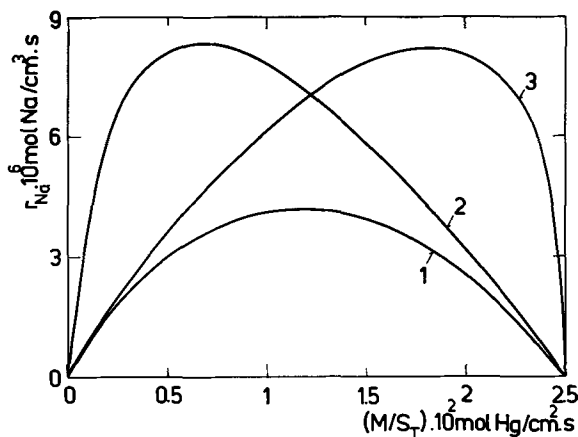


Fig. 5. Influence of  $\rho_{SL}L_{SL}$  changing from 0.35 to 0.01 ohm-cm<sup>2</sup> (curves 1 and 2) and  $f_2L_{EL}$  changing from 0.35 to 0.01 cm (curves 1 and 3) for  $a_T = -0.469V$ ,  $\alpha = 0.517$ .

causes a marked increase of the reaction rate. A good material of the bed should have a low resistance in contact with the amalgam and the gas bubbles should be easily removable from it.

**Use of the Theory in Calculating the Tower Height**

It is advantageous that the dependence of  $\log r_{Na}$  on  $\log c_{Na}$  can be in the technically interesting region replaced by two straight lines. The resulting dependence has therefore the form

$$r_{Na} = kc_{Na}^n \text{ or } r_{Na} = k_1Y^n \quad [49a, b]$$

Both  $k$  and  $n$  depend on the rate of flow of the amalgam and other factors used in the calculation. Their values were found from the dependence in Fig. 2 to be

$$k = 3.452 \times 10^{-6}, n = 0.21308 \text{ for } 0.02 \leq c_{Na} \leq 0.2 \quad [50a]$$

$$k = 1.479 \times 10^{-5}, n = 0.58496 \text{ for } 0.01 \leq c_{Na} \leq 0.02 \quad [50b]$$

The relation between  $c_{Na}$  and  $Y$  is

$$Y \approx (c_{Na}/100) (M_{Hg}/M_{Na}) = c_{Na} \cdot 0.087251 \quad [51]$$

hence

$$dY = 0.087251 \cdot dc_{Na} \quad [52]$$

where  $c_{Na}$  denotes weight concentration of sodium in the amalgam. If Eq. [52] is introduced in [42] the following expression for the tower height results

$$H = -\frac{M}{S_T} 0.087251 \int_{c_1}^{c_2} \frac{dc_{Na}}{k \cdot c_{Na}^n} = \frac{M}{S_T} \frac{0.087251}{k} \frac{1}{1-n} [c_1^{1-n} - c_2^{1-n}] \quad [53]$$

Hence, the tower height for the given parameters ( $c_{Na,1} = 0.2$ ;  $c_{Na,2} = 0.01$ ) is equal to 82.2 cm in good accord with the experiment (15). It follows that the parameters used in the calculation will be close to those obtained from experimental data.

Manuscript submitted June 1, 1973; revised manuscript received Sept. 17, 1973. This was Paper 232 presented at the Chicago, Illinois, Meeting of the Society, May 13-18, 1973.

Any discussion of this paper will appear in a Discussion Section to be published in the December 1974 JOURNAL. All discussions for the December 1974 Discussion Section should be submitted by Aug. 1, 1974.

#### REFERENCES

1. F. Hine and S. Yoshizawa, *J. Electrochem. Soc. Japan, Overseas Ed.*, **27**, E-176 (1959).
2. F. Hine and S. Yoshizawa, *ibid.*, **27**, E-205 (1959).
3. F. Hine, S. Yoshizawa, J. Kushiro, and Y. Noriyuki, *ibid.*, **28**, E-6 (1960).

4. F. Hine and S. Yoshizawa, *ibid.*, **28**, E-22 (1960).
5. F. Hine and S. Yoshizawa, *ibid.*, **28**, 115 (1960).
6. F. Hine and S. Yoshizawa, *ibid.*, **28**, E-129 (1960).
7. F. Hine, *Electrochem. Technol.*, **2**, 79 (1964).
8. M. Matušek, Private communication.
9. E. Yeager, in "Fuel Cells," W. Mitchell, Jr., Editor, p. 299, Academic Press, New York (1963).
10. J. O'M. Bockris, "Modern Aspects of Electrochemistry," Vol. 1, Chap. 4, Butterworths, London (1954).
11. G. I. Volkov, "Proizvodstvo chlora i kaustičeskoj sody metodom elektroliza s rtutnym katodom," p. 53, Chimija, Moskva (1968).
12. J. Balej, I. Paseka, and J. Vondrák, *Collection Czech. Chem. Commun.*, **28**, 528 (1963).
13. M. L. Iverson and H. L. Recht, *J. Chem. Eng. Data*, **12**, 262 (1967).
14. J. Hostomský, S. Rajasekaran, I. Roušar, and V. Cezner, *Collection Czech. Chem. Commun.* In press.
15. S. Rajasekaran, I. Roušar, and V. Cezner, *This Journal*, **121**, 340 (1974).

## Amalgam Decomposition

### II. Measurement of Amalgam Decomposition Rate in Tower Decomposer

S. Rajasekaran,<sup>1</sup> I. Roušar,\* and V. Cezner

Department of Inorganic Technology, Institute of Chemical Technology, Prague, Czechoslovakia

#### ABSTRACT

The rate of amalgam decomposition in a laboratory tower decomposer with 40% NaOH was measured at 80°C in dependence on concentration and rate of flow of the amalgam. The dependence of the reaction rate on the rate of flow shows a maximum, which was explained theoretically and the constants in the equation for the rate of decomposition were evaluated. The bed material consists of graphite balls.

The object of present work was to verify the theoretical relations for the rate of decomposition derived previously (4). The independent variables are temperature, concentrations of amalgam and of the alkali hydroxide, and rate of flow of the amalgam. We preferred the measurement of the dependence of the decomposition rate on concentration and rate of flow of the amalgam. The tower was filled with graphite balls (Tohoku Kyowa Carbon Corporation, Japan) of a diameter of 1.1 cm and composition: carbon 97-98%, ash 1.2-2.5%, volatile compounds 0.5%, vanadium 20-50 ppm, manganese 20-50 ppm. The graphite was activated with FeCl<sub>3</sub> by the manufacturer.

#### Experimental

*Apparatus.*—The apparatus used in measuring the decomposition rate is shown schematically in Fig. 1. It consists of two circuits, one for the amalgam, the other for alkali hydroxide. The amalgam was pumped from reservoir, 1, by centrifugal pump, 2, into overflow vessel, 3. A part of the amalgam from this vessel was returned into the reservoir through conduit, 4, filled with Raschig rings, which retarded the flowing amalgam and thus functioned as a shock absorber. The main portion of the amalgam was led from vessel, 3, through heat exchanger, 5, (a steel tube heated electrically) and thermometer, 8, to the inlet of decomposition tower, 10. The flow of the amalgam was controlled by stopcock, 6, and measured so that the amalgam was for a given time led through three-way stopcock, 7, into a calibrated vessel. Samples of the amalgam were taken at the inlet and outlet of the tower in places 9 and 14.

The temperature of the amalgam at the outlet was measured by thermometer, 13.

The cylindrical part of the decomposition tower (10.2 cm ID) was made of organic glass and its ends were closed with steel fittings. A Teflon disk provided with holes was placed at the bottom to support the bed. The height of the active graphite bed was only 4.1 cm so that the decomposer functioned as a differential one. The remaining volume of the tower was filled up with glass balls. The amalgam was distributed over the bed by means of a steel dish provided with 104 openings 1.5 mm in diameter and 9 mm in distance from one another. The amalgam flowed from the tower to electrolyzer, 12, in the form of a horizontal Plexiglas channel of dimensions 60 × 6 × 3 cm. The amalgam functioned as a cathode, the anode was a platinum sheet. Thus, the amalgam which had been partly decomposed in the tower was enriched again. The current lead to the amalgam was a sheet of steel fastened in the bottom of the electrolyzer so as to be wholly covered by the flowing amalgam. The passage of the steel through the electrolyzer wall was cemented with a solution of Plexiglas in chloroform. The current source was a rectifier of the type CKD 30 V/600 A. The maximum possible current that could be safely used was 300A.

The alkali hydroxide solution was circulated by means of air lift, 16, (Fig. 1) where the supporting gas was electrolytic hydrogen which passed through water cooler, 18, into the atmosphere. The electrolyte was pumped from reservoir, 15, into overflow vessel, 17, and flowed through regulation stopcock, 19, rotameter, 20, and heat exchanger, 21 (of same type as 5), into the decomposer. The temperature of the electrolyte at the inlet was measured by thermometer, 22, and

\* Electrochemical Society Active Member.

<sup>1</sup> Present address: Chemical Engineering Department, Indian Institute of Technology, Kanpur-16, India.

Key words: amalgam decomposition rate, tower decomposer.

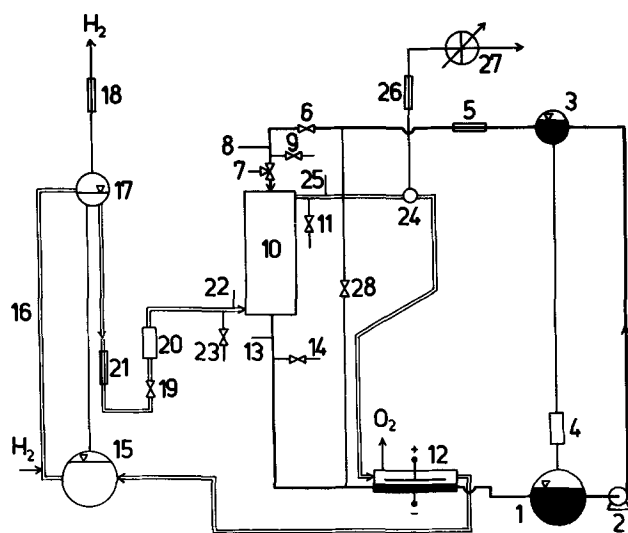


Fig. 1. Scheme of the apparatus for measuring decomposition rates. 1, Amalgam reservoir; 2, centrifugal pump; 3, overflow of amalgam; 4, bed of Raschig rings (shock absorber); 5 and 21, electric heating; 6, stopcock to regulate amalgam flow; 7, three-way stopcock to enable measurement of amalgam flow; 8, 13, 22, and 25, thermometers; 9, 11, 14, and 23, outlets for taking samples of amalgam and electrolyte; 10, decomposition tower; 12, electrolyzer; 15, electrolyte reservoir; 16, air lift; 17, overflow of electrolyte; 18, 26, cooling of hydrogen; 19, electrolyte flow controller; 20, rotameter; 24, hydrogen separator; 27, gasmeter.

electrolyte samples were taken at 23. The alkali hydroxide solution passed through the tower counter-currently with respect to the amalgam; its outlet temperature was measured by thermometer, 25, and outlet solution samples were taken at 11. The hydrogen formed during decomposition of the amalgam was collected in separator, 24, and the electrolyte was led into the electrolyzer. The level heights of the amalgam and electrolyte in the electrolyzer and decomposer were controlled by means of the overflow vessels, 3 and 17. The rate of amalgam decomposition was determined from the rate of hydrogen evolution in the tower. The hydrogen was led from the separator, 24, through water cooler, 26, into gasmeter, 27.

**Method of measurement.**—The apparatus was filled with distilled mercury and 38–42% NaOH from an electrolysis plant (Spolana, Neratovice, Czechoslovakia: the solution was taken from a conduit leading from the decomposer to the reservoir); the same solution was used also in measuring the hydrogen overvoltage. After the circulation of the mercury and electrolyte started, the amalgam was electrolytically prepared and the temperature in the apparatus was raised gradually to 80°C. When a chosen concentration of the amalgam was attained, the current in the electrolyzer was controlled so as to maintain the amalgam concentration constant, i.e., to compensate for the decomposition of the amalgam in the tower as well as for its spontaneous decomposition elsewhere. The flow rate and temperature of the caustic were also maintained constant (3.26 ml/sec and 80°C). The measurement proper concerned the rate of hydrogen evolution in the decomposer (gasmeter, 27, Fig. 1). When this rate attained a constant value, samples of the amalgam and electrolyte at the inlet and outlet were taken. The concentration of the amalgam was determined by measuring the voltage of the cell  $\text{NaHg} | \text{NaOH } 40\% | \text{HgO}, \text{Hg}$  on the one hand and by dissolving in 0.1N HCl and retitrating with 0.1N NaOH with use of methyl orange on the other hand. The concentration of NaOH was determined (after the carbonate had been precipitated with 0.5N  $\text{BaCl}_2$ ) by titration of a diluted sample with 0.1N HCl with the use of phenolphthalein as indicator. The molar rate of flow of mercury ( $\text{mol}/\text{cm}^2 \text{ sec}$ ) was

Table I. Comparison of theoretical reaction rates (Eq. [48], Part I) with experimental data

Temperature $79.5 \pm 1^\circ\text{C}$ , caustic concentration $37.4 \pm 1 \text{ w/o}$				
Flow rate $\times 10^3$ ( $\text{mol}/\text{cm}^2 \text{ sec}$ )	Amalgam conc (%)	$r_{\text{Na}} \times 10^6$ Theory	Experiment ( $\text{mol}/\text{cm}^2 \text{ sec}$ )	Relative deviation (%)
6.26	0.323	2.518	2.649	-4.9
	0.169	2.237	2.178	2.7
	0.092	1.999	1.954	2.3
	0.078	1.938	1.838	5.4
	0.064	1.855	1.735	7.5
7.63	0.266	2.633	2.627	0.3
	0.230	2.593	2.591	0.1
	0.057	2.007	1.970	1.9
	0.036	1.817	1.836	-1.0
	0.015	1.197	1.576	-24.0
10.84	0.151	2.563	2.252	13.8
	0.172	2.555	2.386	7.1
	0.091	2.274	2.224	2.2
	0.031	1.819	1.735	4.8
	0.024	1.743	1.506	15.7
	0.015	1.445	1.162	24.3
14.05	0.176	2.497	2.465	1.3
	0.106	2.249	2.146	4.8
	0.048	1.941	1.922	1.0
	0.021	1.609	1.566	2.8
	0.016	1.435	1.481	-3.1
16.45	0.299	2.496	2.686	-7.1
	0.190	2.250	2.494	-9.8
	0.120	2.103	2.336	-10.0
	0.067	1.855	2.111	-12.2
	0.042	1.686	1.970	-14.4

calculated as

$$M/S_T = 13.15 Q_{\text{am}}/200.47 S_T \quad [1]$$

where  $Q_{\text{am}}$  means measured rate of flow of the amalgam ( $\text{cm}^3/\text{sec}$ ). We assumed that the density of the amalgam is constant ( $13.15 \text{ g}/\text{cm}^3$ ) since it was dilute. The rate of decomposition,  $r_{\text{Na}}$  ( $\text{mol}/\text{cm}^3 \text{ sec}$ ), was calculated from the rate of hydrogen evolution in the tower,  $Q_{\text{H}_2}$  ( $\text{cm}^3/\text{sec}$ )

$$r_{\text{Na}} = Q_{\text{H}_2} 273.16 (p_{\text{tot}} - p_{\text{H}_2\text{O}})/(11,214 THS_T) \quad [2]$$

Here  $H$  denotes height of active layer of the bed (cm),  $p_{\text{tot}}$  total pressure in the gasmeter, and  $p_{\text{H}_2\text{O}}$  tension of water vapor over the NaOH solution (atm) calculated from the equations used previously (4).

**Results and discussion.**—Experimental data and some calculated values (using Eq. [48], Part I, p. 338) are shown in Table I and in diagrams, Fig. 2 and 3. The dependence of the rate of decomposition on amalgam concentration  $c_{\text{Na}}$  (weight per cent) for  $c_{\text{Na}} > 0.05\%$  and  $M/S_T = \text{const.}$  can be also expressed by the em-

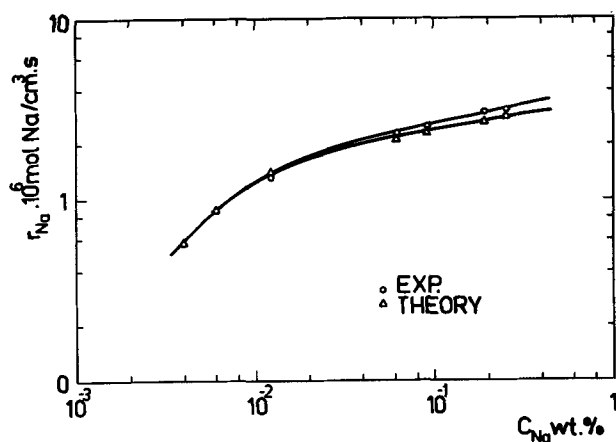


Fig. 2. Dependence of decomposition rate on amalgam concentration. Temperature  $79.5 \pm 1^\circ\text{C}$ , caustic conc.  $37.4 \pm 1 \text{ w/o}$ , rate of amalgam flow  $12.68 \times 10^{-3} \text{ mol}/\text{cm}^2 \text{ sec}$ ;  $\Delta$ , theory;  $\circ$ , experiments.

pirical equation

$$r_{\text{Na}} = kC_{\text{Na}}^n \quad [3]$$

The value of  $n$  is in the range 0.18-0.23. The values of  $r_{\text{Na}}$  for less than 0.05% were measured only in several cases. It is seen from Fig. 2 that in this concentration region the value of  $n$  increases with decreasing amalgam concentration until it reaches the value of 1.0, i.e., the transport of sodium from the bulk of the amalgam to the interface becomes rate-controlling.

Figure 3 shows the dependence of the decomposition rate on the rate of flow of the amalgam at an average concentration of 0.22% Na. The rate of decomposition shows a maximum at a certain rate of flow, which is optimum with respect to the amalgam decomposition.

The experimental data were used in evaluating the following unknown parameters occurring in the theoretical equations for the rate of decomposition derived previously (4): rate of flow of the amalgam at which the tower becomes flooded,  $(M/S_T)_{\text{max}}$ ; the factor of utilization of the graphite surface,  $f_s$ ; correction for the influence of bubbles in the electrolyte,  $f_1 r_o$ , and at the graphite surface,  $f_2 L_{\text{EL}}$ ; contact resistance between the amalgam and graphite,  $\rho_{\text{SL}} L_{\text{SL}}$ ; thickness of the diffusion layer for transport of sodium in the amalgam,  $\delta$ .

The best agreement between experimental and theoretical decomposition rates (with an average deviation of 8.7%) was obtained for the following values of the parameters:  $(M/S_T)_{\text{max}} = 0.025$  mol/cm<sup>2</sup> sec,  $f_s = 0.6$ ,  $f_1 r_o = 0.4$  cm,  $f_2 L_{\text{EL}} = 0.35$  cm,  $\rho_{\text{SL}} L_{\text{SL}} = 0.35$  ohm cm<sup>2</sup>,  $\delta = 4.23 \times 10^{-4}$  cm. The values of the rates of decomposition calculated on the basis of these constants are in Table I together with other quantities (see also Fig. 2 and 3). The calculations involved the experimentally (5) found dependence of hydrogen overvoltage on current density, concentration of NaOH, and temperature; the average value of  $\beta$  was set equal to 0.589.

The conductivity of NaOH solution as a function of temperature and concentration was calculated from data in Ref. (1).

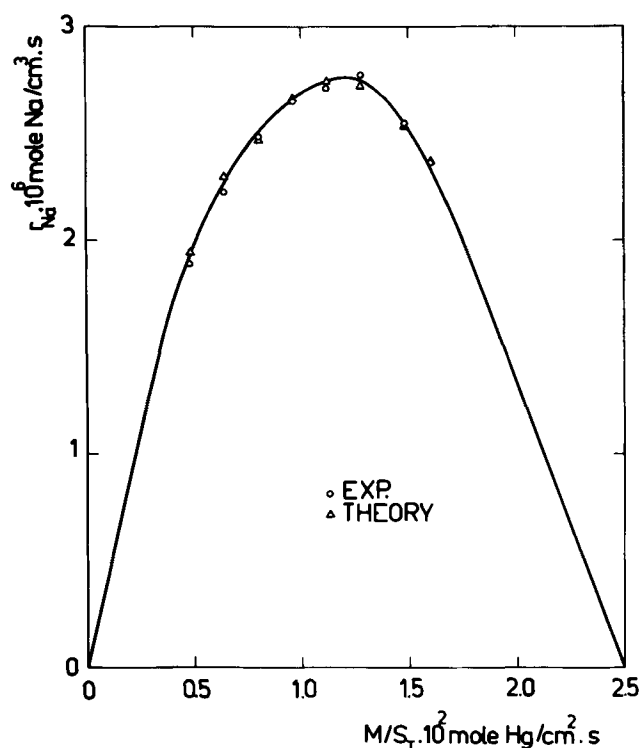


Fig. 3. Dependence of decomposition rate on amalgam flow. Temperature  $79.5^\circ \pm 1^\circ\text{C}$ , caustic conc.  $37.4 \pm 1$  w/o, amalgam concentration 0.22% Na;  $\Delta$ , theory;  $\circ$ , experiments.

The agreement between experimental and theoretical values was especially good for the dependence of the decomposition rate on the rate of amalgam flow (average deviation 1.69%) (Fig. 3).

The indicated parameter values are plausible from the physical point of view or comparable with literature data. The value of  $(M/S_T)_{\text{max}} = 0.025$  mol/cm<sup>2</sup> sec was taken from Hine (2) and at the same time was found by extrapolation of the decomposition rate function of  $M/S_T$  to zero. Also the value of  $f_s = 0.6$  is acceptable since the lower parts of the graphite balls are probably not utilized in the reaction. The value of  $f_1 r_o = 0.4$  cm can be accepted since the radius of the amalgam drops was in the range 0.1-0.3 cm, and the ratio of the gas emulsion resistance to the electrolyte resistance could be about 2 (e.g., if the relative volume of gas in the mixture  $g = 0.4$ , then according to the Meredith-Tobias equation

$$\rho_M/\rho_E = (4 + g)(4 - g)/8(2 - g)(1 - g) \quad [4]$$

the specific resistance of the mixture  $\rho_M = 1.93 \rho_E$ ). Further, if we assume that the length of the line current in the bubble layer at the graphite surface  $L_{\text{EL}} \approx 0.02$ -0.05 cm (approximately equal to the bubble diameter), then from the found value of  $f_2 L_{\text{EL}} = 0.35$  cm it follows that  $f_2 \approx 7$ -15.5, i.e., after Eq. [6] the relative volume of the gas in the layer  $g = 0.75$ -0.90. The value of  $\rho_{\text{SL}} L_{\text{SL}}$  gives the contact resistance between the amalgam and graphite referred to unit contact surface area and is not known as yet. Finally, the thickness of the diffusion layer  $\delta = 4.23 \times 10^{-4}$  cm corresponds to common values of  $\delta$  under the conditions of a turbulent flow (3).

The values of reaction rates in Table I were obtained after one and a half-year operation of the decomposer and were on the average by 15-20% lower than those obtained after a one-month operation.

*Fitting of measured data by an empirical equation.*—For practical purposes, the dependence of the reaction rate of amalgam concentration is conveniently expressed by Eq. [3] where  $k$  and  $n$  are empirical parameters. The measured data for different rates of flow were evaluated by the least squares method except for the points for concentrations below 0.05 w/o Na, which were dropped. The results are shown in Table II. It is seen that the value  $n$  for concentrations above 0.05 w/o Na does not depend significantly on the rate of flow, the deviations from the average being random in character.

From the data also used in Fig. 3, values of the rate constant  $k$  were calculated assuming  $n = 0.2$  (see Table III). The value of  $k$  depends obviously on the

Table II. The dependence of  $n$  (Eq. [3]) on amalgam flow rate

$M/S_T \times 10^2$ (mol cm <sup>-2</sup> sec <sup>-1</sup> )	$n$
0.4817	0.2434
0.6262	0.2589
0.6422	0.2047
0.7622	0.1852
0.8429	0.2127
1.084	0.1656
1.266	0.2242
1.405	0.1876
1.485	0.1985
1.646	0.1590

average:  $n = 0.2006$

Table III. The dependence of  $K$  (Eq. [3]) on amalgam flow rate

$M/S_T \times 10^2$ (mol cm <sup>-2</sup> sec <sup>-1</sup> )	$k \times 10^6$ (mol cm <sup>-2</sup> sec <sup>-1</sup> )	$M/S_T \times 10^2$ (mol cm <sup>-2</sup> sec <sup>-1</sup> )	$k \times 10^6$ (mol cm <sup>-2</sup> sec <sup>-1</sup> )
0.482	2.550	1.124	3.675
0.642	3.011	1.284	3.761
0.803	3.365	1.485	3.447
0.963	3.592	1.605	3.139

rate of flow of the amalgam and attains its maximum at 0.01284 mol/cm<sup>2</sup> sec. The empirical Eq. [3] is more suitable in calculating the height of the tower than the exact equations given in the preceding paper (4).

Manuscript submitted June 1, 1973; revised manuscript received Sept. 17, 1973.

Any discussion of this paper will appear in a Discussion Section to be published in the December 1974 JOURNAL. All discussions for the December 1974 Discussion Section should be submitted by Aug. 1, 1974.

## REFERENCES

1. R. Burian, Research Report, Spolek pro chemickou a hutní výrobu, Ústí n. Labem (1962).
2. F. Hine, S. Yoshizawa, J. Kushiro, and N. Yokota, *J. Electrochem. Soc. Japan*, **28**, E-6 (1960).
3. A. Regner, "Technická Electrochemie I," p. 208, Academia, Prague (1967).
4. I. Rousar, S. Rajasekaran, and V. Cezner, *This Journal*, **121**, 336 (1974).
5. J. Hostomský, S. Rajasekaran, I. Roušar, and V. Cezner, *Collection Czech. Chem. Commun.*, In press.

## Amalgam Decomposition

### III. Comparison of Different Sorts of Graphite Bed for Decomposition of Amalgam in Tower Decomposer

I. Roušar,\* V. Cezner, M. Krajča,<sup>1</sup> and K. Kolařík

Department of Inorganic Technology, Institute of Chemical Technology, Prague, Czechoslovakia

## ABSTRACT

Four sorts of graphite bed in a laboratory tower reactor for amalgam decomposition were compared. Measurements were performed at 80°C, concentration of NaOH 40%, rate of flow of amalgam 0.0125 mol/cm<sup>2</sup> sec, and concentration of sodium in amalgam 0.03-0.7 weight per cent; decomposition of the amalgam was maximum with crushed graphite of the firm Sigri (West Germany).

In preceding communications (1, 2), the problem of calculating the decomposition rate of sodium amalgam in a tower reactor filled with graphite balls was treated. It followed that the reaction rate is directly proportional to the specific surface area of the bed (in cm<sup>2</sup>/cm<sup>3</sup> of bed). The object of the present work was to substantiate this dependence experimentally by measurements on beds with different specific surface areas.

#### Theoretical

The dependence of the rate of amalgam decomposition on the concentration of sodium in the amalgam was evaluated from the following empirical equation

$$r_{\text{Na}} = k c_{\text{Na}}^n \quad [1]$$

where  $k$  and  $n$  are empirical parameters;  $c_{\text{Na}}$ , concentration of sodium in weight per cent w/o; and  $r_{\text{Na}}$ , rate of decomposition. The values of  $k$  and  $n$  were calculated by the least squares method for every sort of graphite and Eq. [1] was used in calculating the tower height according to

$$H = -(M/S_T) \int_{Y_1}^{Y_2} r_{\text{Na}}^{-1} dY \quad [2]$$

where  $M/S_T$  denotes flow of amalgam in mol Hg/cm<sup>2</sup> sec and  $Y$  its concentration in mol Na/mol Hg, which can be expressed as

$$Y = 0.08725 c_{\text{Na}} \quad [3]$$

By introducing Eq. [1] and [3] into [2] and integrating we obtain the final relation

$$H = \frac{0.08725 M}{k(1-n)S_T} (c_{\text{Na},1}^{1-n} - c_{\text{Na},2}^{1-n}) \quad [4]$$

where  $c_{\text{Na},1}$  and  $c_{\text{Na},2}$  denote inlet and outlet concentra-

tion of the amalgam flowing into or out from the tower.

#### Experimental

The apparatus and measurement of parameters were described in the preceding work (2). All measurements were made after 14 days of operation of apparatus. Three sorts of graphite were used: Sigri (West Germany), ZEW Raciborz (Poland), and Tohoku Kyowa (Japan), the specifications of which are as follows:

1. Crushed Sigri graphite, marked EHK, particle size 9-16 mm, vanadium content less than 2.5 ppm, porosity 14%, apparent density 1.73 g/cm<sup>3</sup> (given by the manufacturer), specific surface area about 5-6 cm<sup>2</sup>/cm<sup>3</sup> of bed.
2. ZEW Raciborz graphite cylinders (a) hollow, 10.2 mm in height, 9.6 mm outer diameter, diameter of hole of irregular shape 3.6-4.6 mm, bulk density 0.814 g/cm<sup>3</sup>, specific surface area 4.41 cm<sup>2</sup>/cm<sup>3</sup> of bed; (b) solid, 10 mm in height, 9.8 mm in diameter, bulk density 1.042 g/cm<sup>3</sup>, specific surface area 3.695 cm<sup>2</sup>/cm<sup>3</sup> of bed.
3. Tohoku Kyowa Carbon balls containing C 98-99%, ash 0.5-1%, V 10-20 ppm, Mn 20-30 ppm; diameter 10.7 mm, bulk density 0.916 g/cm<sup>3</sup>, specific surface area 2.876 cm<sup>2</sup>/cm<sup>3</sup> of bed.

The diameter of the bed in the decomposition tower was 102 mm and its height 40 mm; its lid was provided with 104 openings of a diameter of 1.5 mm. The amalgam was circulated by a centrifugal pump. The electrolyte was electrolytic 40% sodium hydroxide solution (Spolana Neratovice, CSSR). Mercury was purified by distillation before use. The temperature of the tower was 80°C unless otherwise indicated.

#### Results of Measurements

Experimentally found values are presented in Fig. 1 and 2 for the different graphite sorts along with theoretical values corresponding to Eq. [1]. The values of

\* Electrochemical Society Active Member.

<sup>1</sup> Present address: Spolek pro chemickou a hutní výrobu n.p., Ústí nad Labem, Czechoslovakia.

Key words: amalgam decomposition, graphite bed, tower decomposer.

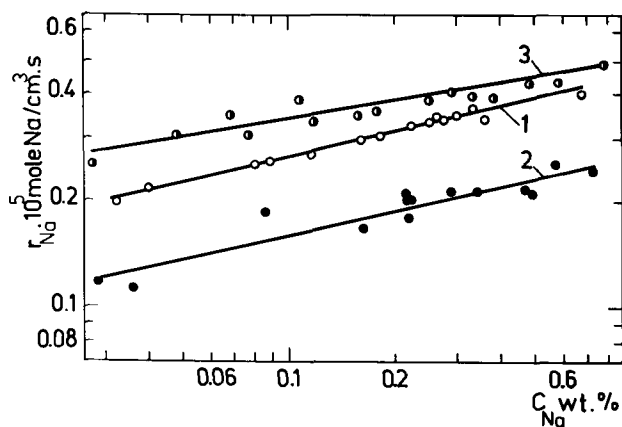


Fig. 1. The dependence of reaction rate on amalgam concentration for ZEW Raciborz graphite for 80°C and 40 w/o NaOH. Curve 1, hollow cylinders, amalgam flow rate  $1.25 \times 10^{-2}$  mol Hg/cm<sup>2</sup> sec; curve 2, solid cylinders, amalgam flow rate  $1.25 \times 10^{-2}$  mol Hg/cm<sup>2</sup> sec; curve 3, hollow cylinders, amalgam flow rate  $1.5 \times 10^{-2}$  mol Hg/cm<sup>2</sup> sec.

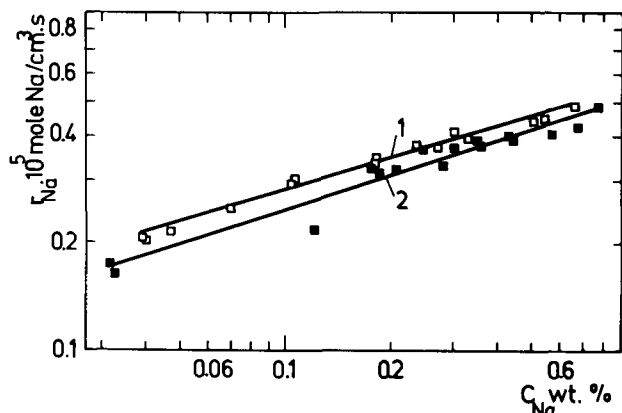


Fig. 2. The dependence of reaction rate on amalgam concentration for 80°C and 40 w/o NaOH. Amalgam flow rate  $1.25 \times 10^{-2}$  mol Hg/cm<sup>2</sup> sec. Curve 1, crushed Sigri graphite; curve 2, graphite balls of Tohoku Kyowa Carbon.

$k$  and  $n$  are given in Table I and were used in calculating the tower height on the assumption that the inlet and outlet concentrations of sodium in the amalgam were 0.2 or 0.4 and 0.01%, respectively. The results given in Table II indicate that the specific surface area (for different sorts of graphite) is not inversely proportional to the tower height, as it should be according

Table I. Values of  $k$  and  $n$  for different beds

Graphite sort	$10^2 M/S_T$ (mol/cm <sup>2</sup> sec)	$10^6 k$ (mol/cm <sup>3</sup> sec)	$n$
Raciborz, solid cylinders	1.25	2.683	0.2219
Sigri, crushed	1.25	5.613	0.3017
Tohoku Kyowa, balls	1.25	5.213	0.3211
Raciborz, hollow cylinders	1.25	4.380	0.2321
Raciborz, hollow cylinders	1.50	4.866	0.1632

Table II. Height of tower decomposer for different graphite sorts and outlet concentration of amalgam 0.01% Na, temperature 80°C, caustic concentration 40 w/o

Graphite sort	$10^2 M/S_T$ (mol/cm <sup>2</sup> sec)	Tower height (cm) for inlet amalgam conc (0.2 w/o) (0.4 w/o)	
Raciborz, solid cylinders	1.25	134	240
Sigri, crushed	1.25	79	135
Tohoku Kyowa, balls	1.25	90	151
Raciborz, hollow cylinders	1.25	85	150
Raciborz, hollow cylinders	1.50	77	142

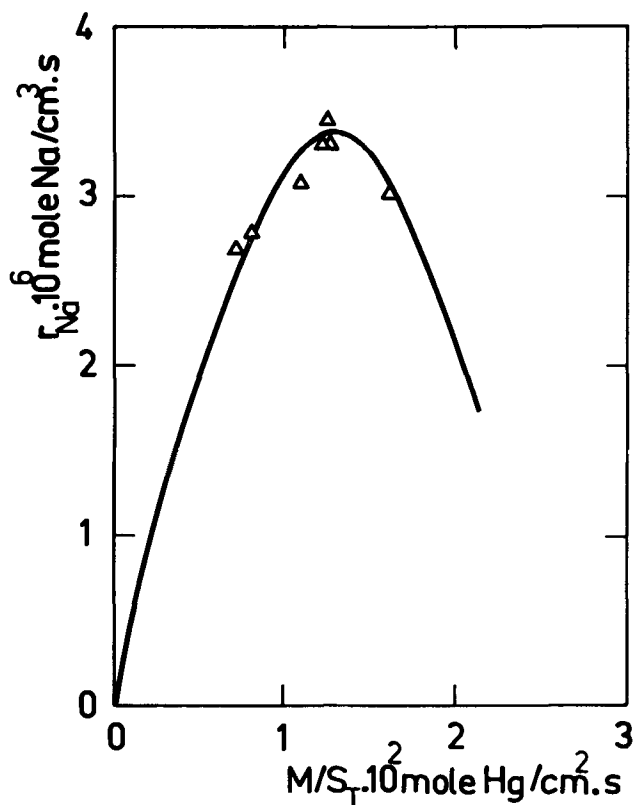


Fig. 3. The dependence of reaction rate on amalgam flow for Tohoku Kyowa graphite for 0.2 w/o Na, 80°C and 40 w/o NaOH.

to the theory (1). It means that also the content of heavy metals, such as Mo, V, Co, Fe, etc., in graphite exerts an important effect on the rate of decomposition. Nevertheless, for one sort of graphite (see Fig. 2, curves 1 and 2) the measured dependence is not far from theoretical predictions. Indeed, Table II shows that for ZEW Raciborz graphite, the ratio of tower heights for solid and hollow cylinders is  $1.35/0.85 = 1.58$  and the ratio of specific surfaces is  $4.41/3.7 = 1.19$ . The difference between these values can be explained by the fact that the amalgam hold-up is higher for hollow than for solid cylinders.

The dependence of the reaction rate on amalgam flow through the tower was measured on the Tohoku Kyowa graphite ball bed. The dependence  $r_{Na} = f(M/S_T)$  is shown in Fig. 3.

### Conclusions

It follows from the comparison of the tower heights at a rate of flow of  $1.25 \times 10^{-2}$  mol Hg/cm<sup>2</sup> sec that the most suitable material for the bed is crushed graphite of the Sigri firm, then comes the ZEW Raciborz graphite (hollow cylinders), and finally Tohoku Kyowa graphite (balls). The least suitable were the solid graphite cylinders of ZEW Raciborz. A comparison of graphites of the same sort but with different geometry (ZEW Raciborz) suggests that the reaction rate increases with increasing specific surface area of the bed ( $S_G/V_T$ ).

Manuscript submitted June 1, 1973; revised manuscript received Sept. 17, 1973.

Any discussion of this paper will appear in a Discussion Section to be published in the December 1974 JOURNAL. All discussions for the December 1974 Discussion Section should be submitted by Aug. 1, 1974.

### REFERENCES

1. I. Roušar, S. Rajasekaran, and V. Cezner, *This Journal*, **121**, 336 (1974).
2. S. Rajasekaran, I. Roušar, and V. Cezner, *ibid.*, **121**, 340 (1974).

# Nicotinamide and N'-Methylnicotinamide: Electrochemical Redox Pattern

## Behavior of Free Radical, Dimeric, and Dihydropyridine Species

Conrad O. Schmakel,<sup>1</sup> K. S. V. Santhanam,<sup>2</sup> and Philip J. Elving\*

The University of Michigan, Ann Arbor, Michigan 48104

### ABSTRACT

The mechanisms for the electrochemical reduction of nicotinamide (3-carbamoylpyridine) and N'-methylnicotinamide [3-(N-methylcarbamoyl)-pyridine] in aqueous media, as well as those for reduction and oxidation of intermediate and final products, have been investigated. Both compounds involve the same redox pattern of two successive one-electron additions. The initial step involves simultaneous addition of an electron and a proton to form a free radical (only an electron in the pH range where the compound is protonated), which rapidly dimerizes to an apparent 6,6' species; oxidation of the free radical can be seen at pH 9. At more negative potential, the nicotinamide is reduced to an apparent 1,6-dihydropyridine species (the dimer is stable to reduction in the available potential range); the two polarographic waves begin to merge above pH 8 and are completely merged by pH 12.  $E_{1/2}$  for both electron-transfer processes becomes more negative with increasing pH between pH 4 and 9. The rate constants for dimerization of the initially produced free radicals are  $1.8 \times 10^6$  and  $4.9 \times 10^6$  liter mol<sup>-1</sup> sec<sup>-1</sup> for nicotinamide and N'-methylnicotinamide, respectively, at 30° and pH 9. Adsorption of both compounds and their reduction products at the mercury-solution interface is negligible. Both dimer and dihydropyridine species are oxidized to the original nicotinamide but at considerably more positive potentials than those necessary for their formation.

Nicotinamide (3-carbamoylpyridine) (Fig. 1) is widely distributed in plant and animal tissues and is an essential dietary factor for nearly all mammalian systems. Its absence, along with that of nicotinic acid and other members of the B complex, results in pellagra. The essential role of nicotinamide undoubtedly stems from its importance in the production of certain types of pyridine nucleotides,<sup>3</sup> e.g., NAD<sup>+</sup> and NMN<sup>+</sup>, under physiological conditions. The function of such nucleotides in biological systems, e.g., the role of NAD<sup>+</sup> as a coenzyme, generally involves oxidation-reduction of the pyridine ring. For this reason, redox processes involving nicotinamide and its derivatives are of obvious interest.

Nicotinamide itself differs from the pyridine nucleotides in having a ring nitrogen, which is basic due to the presence of the lone electron pair. Consequently, its redox behavior would be expected to show a pH-dependence differing from those of the pyridine nucleotides except in the pH region where the ring nitrogen is protonated.

The polarography of nicotinamide has been previously studied (1-4). Essentially, nicotinamide is reported to yield in acidic media two rather ill-defined polarographic waves having half-wave potentials,  $E_{1/2}$ , close to one another, which have been ascribed (5, 6) to the protonated and neutral species, presumably in an acid-base equilibrium of a type frequently seen in polarography. Others (7) observed nearly the same behavior except that the double wave was not noted. Above pH 8, a single well-defined wave was reported (5-7), whose  $E_{1/2}$  became 40 mV more negative per pH unit. These and related results were considered to indicate that the wave was an irreversible two-electron (2e) process (number of electrons apparently estimated from diffusion current constant,  $I$ ) with at

least one proton taking part in the electrode reaction (two in the total reduction). The product has been postulated to be either a 2,3- or 3,4-dihydropyridine species (5-8). The polarographic assay of nicotinamide (niacinamide) in pharmaceutical preparations has been described (9).

In general, the polarography of nicotinamide was primarily investigated (5, 6, 10-13) from the viewpoint of the catalytic hydrogen current<sup>4</sup> which it produces; its fundamental behavior has been only meagerly interpreted and the reduction mechanism has not been fully understood. Consequently, the electrochemical reduction of nicotinamide and N'-methylnicotinamide [3-(N-methylcarbamoyl)pyridine] in aqueous medium, as well as the nature, reduction, and oxidation of intermediate and final products, e.g., free radical,

<sup>4</sup> A catalytic hydrogen evolution reaction occurs when a compound is present whose protonated adduct under the experimental conditions is more easily reducible, i.e., has a lower activation energy in respect to net addition of an electron to the proton, than the uncomplexed proton itself.

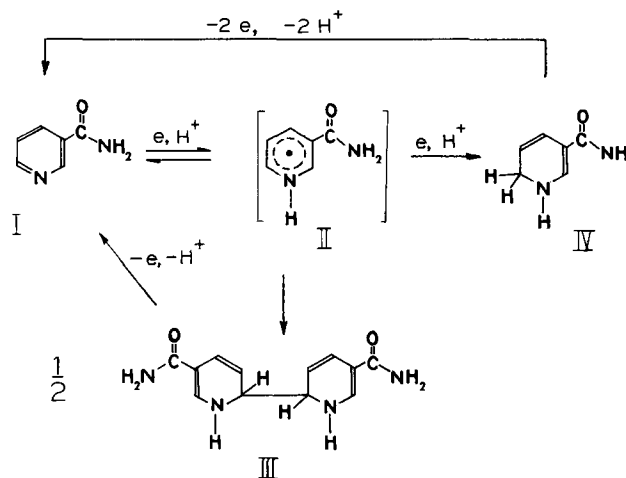


Fig. 1. Reaction paths for the electrochemical behavior of nicotinamide and its reduction products.

\* Electrochemical Society Active Member.

<sup>1</sup> Present address: Abbott Laboratories, Scientific Divisions, North Chicago, Illinois 60064.

<sup>2</sup> On leave of absence from the Tata Institute of Fundamental Research, Bombay 5, India.

<sup>3</sup> NAD<sup>+</sup> represents nicotinamide-adenine-dinucleotide, which is also referred to as diphosphopyridine nucleotide (DPN<sup>+</sup>) or coenzyme I; NMN<sup>+</sup> represents nicotinamide mononucleotide.

Key words: dihydropyridines, dimerization, free radicals, N'-methylnicotinamide, nicotinamide.

dimer, and dihydropyridine species, has been investigated by a variety of electrochemical techniques. These included controlled-potential electrolysis to provide solutions of products suitable for chemical, electrochemical, and spectrophotometric examination, and rapid perturbation techniques such as cyclic voltammetry and phase-selective a-c polarography to investigate chemical steps intervening in the redox process, e.g., free radical formation and dimerization.

The choice of *N*'-methylnicotinamide is based partially on the expectation that its basic  $pK_a$  would be similar to that of nicotinamide and partially on the behavior of  $NAD^+$  and  $NADP^+$  (1, 4). If a nicotinamide free radical produced in the initial one-electron (1e) process dimerizes similarly to  $NAD^+$ , the site for dimerization would be expected to be at the 4 or 6 position. Molecular models of the free radicals indicate dimerization at the 4 position in *N*'-methylnicotinamide to be sterically hindered due to free rotation of the methyl group.

### Experimental Procedure

**Chemicals.**—The reported analytical data and spectrophotometric assay indicated sufficient purity of the nicotinamide and *N*'-methylnicotinamide (Sigma) for polarographic study. Neither spectrophotometry nor polarography revealed any impurities.

Buffer solutions (Table I) were prepared from analytical reagent grade chemicals. Nitrogen used for deoxygenating was purified and equilibrated by bubbling it successively through acidic (HCl) V(II) kept over heavily amalgamated zinc, saturated CaO, and distilled water.

**Apparatus.**—Current-voltage and current-time curves were recorded with three-electrode potentiostats and Moseley Model 7001A(S) and 7005B X-Y recorders.

The potentiostats were multipurpose instruments (14-16), based on solid-state operational amplifiers, with only certain functions being used in any given mode; details of construction, operation, and performance are given elsewhere (17). A conventional arrangement was employed for d-c polarography; for phase-selective a-c polarography, a Princeton Applied Research Model 122 lock-in amplifier was incorporated. Automatic compensation for series resistance was achieved by positive feedback (18, 19). Rapidly occurring events were recorded with a Tektronix Type 502 oscilloscope and C-12 camera system; the oscilloscope was also utilized as a general purpose monitoring device. Potentials were accurately monitored with a Hewlett-Packard Model 3430A digital voltmeter.

Voltammetric measurements were made in a water-jacketed three-compartment cell (20), kept at  $25.0^\circ \pm 0.1^\circ C$  unless otherwise stated. Agar salt bridges were inserted on the counter and reference sides of the medium porosity glass frits separating the compartments. The reference compartment contained a saturated calomel reference electrode (SCE); the counter compartment contained a platinum mesh electrode immersed in saturated KCl solution. The DME capillaries (marine barometer tubing) had drop-times, measured

at potentials of interest, between 3 and 6 sec, and  $m$  values of 1.2 to 2.4 mg/sec (open circuit). Sargent S-2931-30 and home-made hanging mercury drop electrodes (HMDE) were employed in the stationary electrode studies.

Coulometry and macroscale electrolysis used a mercury pool electrode (3 or 5 cm<sup>2</sup>) at  $25.0^\circ \pm 0.1^\circ C$  in a water-jacketed cell (25 mliter capacity), fitted with a Teflon cap, which allowed introduction of sample, salt bridges, and deaeration tubing. Reference and counter-electrodes were thermostated and identical to those used for voltammetry except that they were connected to the cell via saturated KCl salt bridges prepared from polyethylene tubes (2.5 mm ID) fitted at the cell end with 5-mm lengths of Vycor glass rod (Corning Code 7930 porous glass). The number of coulombs passed during electrolysis was found by measuring the area of the current-time curve with a Gelman Model 39231 compensating polar planimeter.

Ultraviolet spectra were obtained with Beckman Model DB and DU spectrophotometers. All pH measurements were made with a Beckman Model G pH meter.

**Voltammetric procedures.**—Test solutions were prepared by diluting known volumes of stock solutions in volumetric flasks with the desired buffer. About 10 mliters of test solution were transferred to the cell, purged with  $N_2$  for 15 min, and then examined electrochemically with  $N_2$  passing over the solution. The test solution pH was measured after voltammetry. Except where indicated, the background current, obtained on an identically treated buffer solution, was subtracted algebraically from the total current.

A natural drop-time was employed for d-c polarography;  $E_{1/2}$  and  $i_d$  were determined graphically, utilizing the average recorder trace. For a-c polarography, the instantaneous a-c current amplitude at the end of a controlled 3-sec drop-life was recorded; in the frequency variation studies, a natural drop-time and a 10 mV peak amplitude were used. For single sweep and cyclic runs at the HMDE, one or two drops of Hg were collected from the DME and hung on the hanging drop assembly; the HMDE (0.030 cm<sup>2</sup>) was allowed to equilibrate for 15 sec before the voltammetric scan was begun. Scan rates ranged from 0.1 to 32 V/sec.

**Macroscale electrolysis procedures.**—Twenty milliliters of buffer solution were added to the cell and deoxygenated for 20 min; Hg was then introduced and the stirred solution electrolyzed at a potential identical to that at which the electrolysis was to be run, until the current fell to a minimum value (0.01-0.03 mA). The potential was then shifted to  $-0.6V$  and a 5-ml aliquot of stock solutions containing only the electroactive species added;  $N_2$  was again vigorously bubbled through the solution until the current level dropped to zero (5 min); the electrolysis was then switched to the desired potential. Nitrogen was continuously passed through the cell during electrolysis. Current was automatically recorded as a function of time; suitable correction was made for background current.

Immediately before and after each electrolysis, an aliquot of the electrolysis solution was examined spectrophotometrically after dilution with the buffer used for electrolysis;  $Et_4NCl$ /carbonate solutions were diluted with carbonate buffer. An identical concentration of buffer was used in the reference cell.

### Results

Since the observed electrochemical behavior patterns of nicotinamide and *N*'-methylnicotinamide are generally similar, the discussion is focused on nicotinamide with reference being made to *N*'-methylnicotinamide only where significant factors are involved.

**D-C polarography.**—In acidic media, nicotinamide yields two closely adjacent waves (Table II; Fig. 2); wave II, which is less well-defined than wave I, occurs just prior to a catalytic wave.<sup>4</sup> In pH 5.0 acetate buffer,

Table I. Buffer and background electrolyte solutions<sup>(a)</sup>

Buffer No.	pH range	Composition
1	0.0-1.0	HCl + KCl
2	2.0-8.0	$Na_2HPO_4 \cdot 7H_2O$ + citric acid monohydrate + KCl
3	3.3-6.0	$KHC_2H_3O_4$ + HCl or NaOH
4	3.9-5.9	HOAc + NaOAc
5	7.8-10.0	$H_2BO_3$ + NaOH + KCl
6	9.0-10.0	$K_2CO_3$ + $KHCO_3$
7	9.0-10.0	$K_2CO_3$ + $KHCO_3$ + KCl <sup>(b)</sup>
8	9.0-10.0	$K_2CO_3$ + $KHCO_3$ + $Et_4NCl$ <sup>(c)</sup>
9	9.0-10.0	$NH_3$ + $NH_4Cl$
10	11.0-12.0	KOH + KCl

<sup>(a)</sup> The final ionic strength of test solutions was 0.5M unless otherwise stated.

<sup>(b)</sup> KCl concentration: 0.4M.

<sup>(c)</sup>  $Et_4NCl$  concentration: 0.4M.



Table II. Variation in polarographic behavior of nicotinamide and N'-methylnicotinamide with pH

Buffer No.	pH	$-E_{1/2}$ , V	Wave slope, <sup>(a)</sup> mV	$I$ <sup>(b)</sup>
Nicotinamide <sup>(c)</sup>				
2	3.2 <sup>(b)</sup>	I 1.10	—	4.2
		II 1.20	—	4.0
2	3.6 <sup>(b)</sup>	I 1.11	—	3.0
		II 1.22	—	4.3
2	3.7 <sup>(b)</sup>	I 1.13	—	3.3
		II 1.25	—	5.1
2	4.4 <sup>(b)</sup>	I 1.15	—	2.3
		II 1.27	—	5.6
4	5.0 <sup>(b)</sup>	I 1.20	—	2.2
		II 1.31	—	4.8
2	7.0 <sup>(b)</sup>	I 1.39	—	2.0
		II 1.51	—	2.5
2	8.0 <sup>(d)</sup>	1.57	120	3.7
6	9.2	1.59	55	3.9
6	9.4	1.60	55	3.8
8	9.6 <sup>(d)</sup>	1.61	76	3.4
6	9.7	1.60	43	3.7
10	12.0	1.70	34	3.8
N'-Methylnicotinamide <sup>(e)</sup>				
1	1.8	I 1.08	—	—
1	2.2	I 1.08	—	—
3	3.3	I 1.08	40	1.1
	4.3	I 1.08	47	1.4
4	5.0	I 1.21	44, 44	1.7, 1.9
		II 1.38	—	—
3	6.0	I 1.23	44	2.0
		II 1.40	—	—
5	7.5	I 1.43	43	1.5
		II 1.51	—	—
7	9.0	I 1.60	—	2.1
10	10.5	I 1.62	—	—

<sup>(a)</sup> Wave slope calculated as  $(E_{1/4} - E_{3/4})$ .

<sup>(b)</sup> Both nicotinamide waves are ill-defined and are not necessarily diffusion controlled due to the presence of a catalytic hydrogen wave at slightly more negative potential; diffusion current constant ( $I = i_1/Cm^{2/3}t^{1/6}$ ) values have been calculated for comparison with the wave in alkaline solution. It is especially difficult to measure wave II.

<sup>(c)</sup> Nicotinamide concentration: 0.35 mM. Roman numerals refer to the two waves.

<sup>(d)</sup> Wave is treated as a single wave; actually two closely adjacent electron-transfer steps are involved.

<sup>(e)</sup> N'-methylnicotinamide concentration: 0.49 to 2.58; concentrations used at pH 5.0: 1.63 and 0.58 mM. Wave I is generally well-defined; wave II is always poorly defined.

background discharge (at the 2- $\mu$ A level) occurs 0.26V more positive than for background electrolyte alone, i.e., the rising portion of the catalytic wave serves as discharge. All three waves have been noted previously

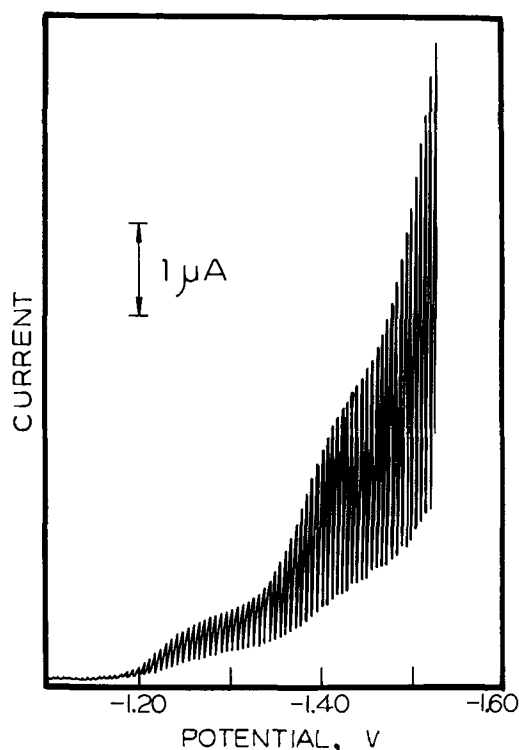


Fig. 2. D-C polarogram of nicotinamide (5.3 mM) in pH 5.0 acetate buffer.

(5, 6), but only the catalytic wave has been adequately studied; consequently, it will not be further considered in the present study.

$E_{1/2}$  for wave I (Table II; Fig. 3) is nearly pH-independent below pH 4 and above pH 9, and varies linearly with pH between pH 4 and 9 (following is based on Table II, pH 3.7 and 7.0)

$$E_{1/2} = -0.73 - 0.079 \text{ pH} \quad [1]$$

N'-methylnicotinamide shows an identical pattern (Fig. 3).

Between pH 3 and 7, the height of wave II varies between 1 and 2.5 times the height of wave I (this variation may result from uncertain knowledge of the base current due to the close proximity of the catalytic wave to wave II);  $E_{1/2}$  for both waves becomes more negative with a constant separation of about 0.1-0.2V. The catalytic wave disappears between pH 7 and 8. The apparently single 2e wave observed at pH 8.0 at low nicotinamide concentration shows an inflection about half way up the wave, i.e., it appears to consist of two merging 1e waves; the wave height is slightly less than the sum of the two waves at pH 7. With increasing pH (pH 8-12 in the absence of tetraethylammonium salts), the inflection disappears,  $E_{1/2}$  becomes slightly more negative, the wave slope ( $E_{1/4} - E_{3/4}$ ) approaches a more reversible value, and the diffusion current constant ( $I$ ) remains constant.

The nearly merged wave (Fig. 4) is markedly altered on addition of a tetraalkylammonium cation (Fig. 5); addition of  $\text{Et}_4\text{NCl}$  to pH 9.4 carbonate buffer shifts  $E_{1/4}$  ( $E_{1/2}$  of wave I) more positive (-1.57 to -1.55V) and  $E_{3/4}$  ( $E_{1/2}$  of wave II) more negative (-1.64 to 1.68V) so that two waves of equal height are formed. The wave split is much more pronounced at 1.27 than at 0.13 mM. The total current in  $\text{Et}_4\text{NCl}$  solution is diffusion controlled ( $i_1$  proportional to  $h^{1/2}$ ) and proportional to concentration (0.13-1.25 mM); the slightly lower  $I$  of 3.44 is due to a viscosity effect. Despite some uncertainty due to the small potential separation, the slopes of both waves at 1.27 mM nicotinamide are the same as that expected for reversible electron-transfer steps.

**Cyclic voltammetry.**—The behavior of nicotinamide is consistent with the DME pattern. In acidic media, the initial sweep to more negative potential produces peaks Ic and IIc (Table III; Fig. 6); these are ill-defined, appearing as shoulders or inflections on the side of background discharge which occurs at more positive potential than for background electrolyte alone. Small differences in  $E_p$  between Table III and Fig. 6 are due to differences in nicotinamide concentration; the wave separation seems to increase with concentration (cf. previous paragraph).

The magnitude of the peak IIc current compared to that of peak Ic suggests that the over-all wave Ic product is not further reduced, i.e., most of the nicotinamide in the vicinity of the electrode has been converted to the 1e product by the time the potential for formation of the 2e product is reached, and that peak

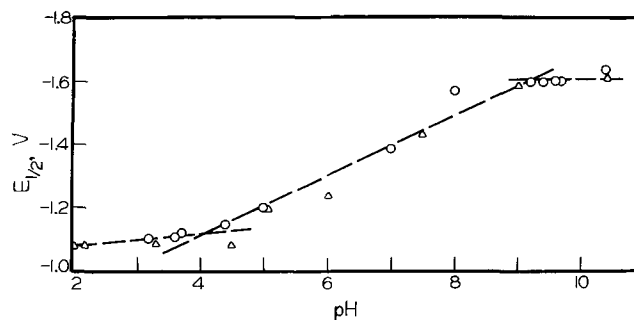


Fig. 3. Variation with pH of the half-wave potential,  $E_{1/2}$ , for the first cathodic polarographic wave of nicotinamide (circles) and N'-methylnicotinamide (triangles).

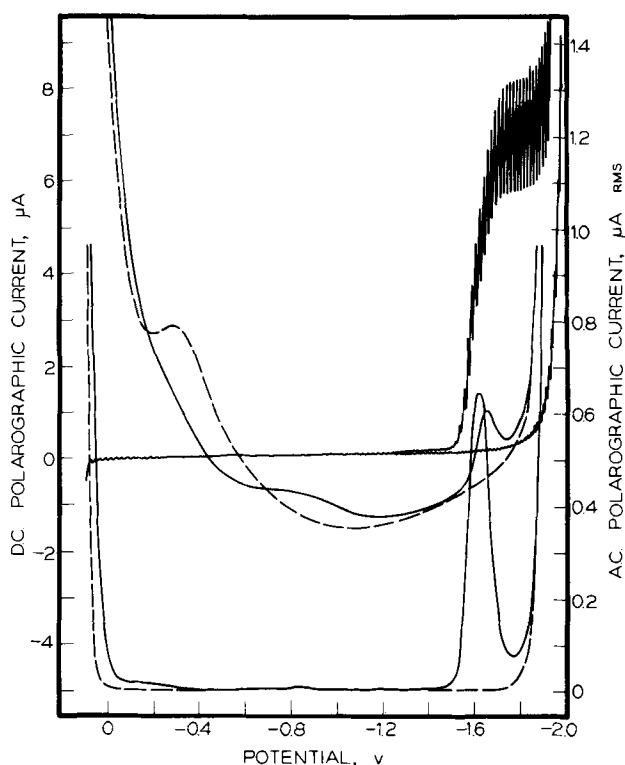


Fig. 4. D-C and a-c polarograms of nicotinamide (1.27 mM) in carbonate buffer (pH 9.4). The upper pair of curves result from d-c polarography (test and background solutions). The intermediate pair of curves represent the quadrature a-c component; the lowest pair of curves the in-phase a-c component; dashed lines are for background solution alone.

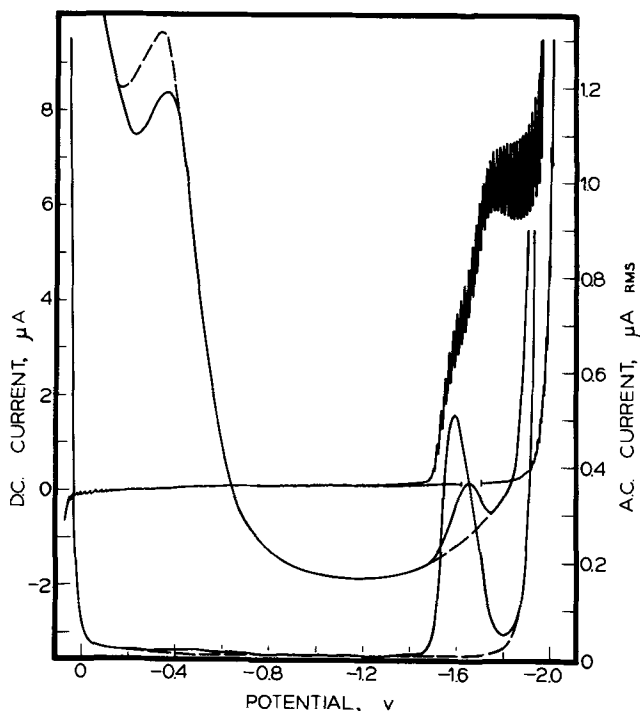


Fig. 5. D-C and a-c polarograms of nicotinamide (1.27 mM) in  $\text{Et}_4\text{NCl}$ /carbonate buffer (pH 9.4) (see Fig. 4 caption for curve identification).

IIC then results from two successive  $1e$  reductions of nicotinamide in the partially depleted layer at the interface.

Both peak potentials become more negative with increasing pH. Since the pH-dependence of peak Ic is greater than that of IIC (Eq. [2]), the two peaks

Table III. Cyclic voltammetry of nicotinamide and N'-methylnicotinamide: cathodic peaks<sup>(a)</sup>

Sweep rate, $v$ , V/sec	Peak I			Peak II	
	$-E_p$ , V	$i_p$ , $\mu\text{A}$	$i_p/v^{1/2}$	$-E_p$	$i_p$
Nicotinamide <sup>(b)</sup>					
0.10	1.30	5.5	17.4	1.43	7.0
0.15	1.32	7.0	18.1	1.43	8.8
0.21	1.32	8.0	17.5	1.43	12.0
0.48	1.32	12.0	17.4	1.43	14.0
1.00	1.32	14.7	14.7	1.40	16.8
2.50	1.32	26.0	10.4	1.40	34.0
N'-methylnicotinamide <sup>(c)</sup>					
0.10	1.29	7.8	24.4		
0.15	1.29	9.5	24.5		
0.20	1.29	10.8	24.4		

<sup>(a)</sup> Data are for pH 5.0 acetate buffer solutions, where nicotinamide wave II contains a contribution from catalytic hydrogen evolution and N'-methylnicotinamide wave II is very poorly defined.

<sup>(b)</sup> Concentration: 1.18 mM.

<sup>(c)</sup> Concentration: 1.63 mM.

begin to merge at *ca.* pH 7, although the merging into a single peak is not complete until pH 12. Above pH 8, the cathodic peak current increases to a maximum at pH 12, where it is about twice that of peak Ic in acid solution.

$$\text{Peak IIC: } E_p = -1.02 - 0.065 \text{ pH} \quad [2]$$

The pattern obtained on the reverse sweep to more positive potential depends on the pH. If the sweep at pH 12 is reversed after the single cathodic peak ( $E_p = -1.72\text{V}$ ), a single anodic peak IIa occurs at  $-0.21\text{V}$ , which is due to oxidation of the  $2e$  reduction product. At pH 9.4, sweep reversal immediately following the apparently single cathodic peak produces two anodic peaks (Fig. 7). Peak IIa represents the  $2e$  oxidation just discussed; peak Ia represents oxidation of the  $1e$  reduction product; both oxidation steps produce nicotinamide. Repetitive scanning (12 V/sec) around the single cathodic peak and either peak Ia at pH 9.4 or peak IIa at pH 12 establishes a relatively high steady-state nicotinamide concentration at the

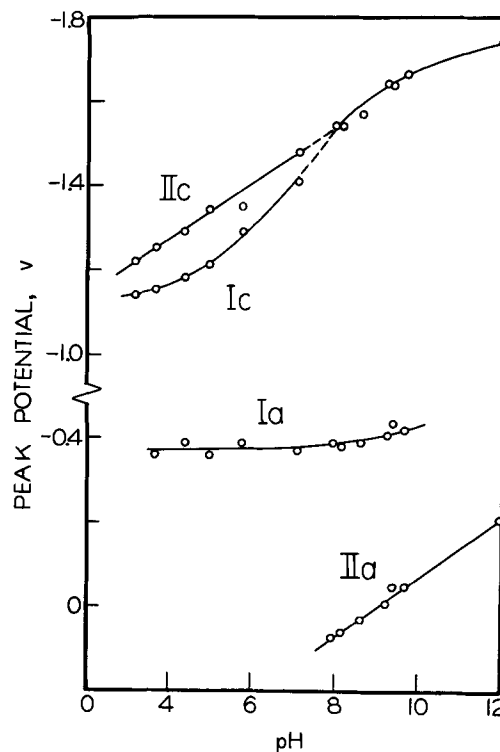


Fig. 6. Variation of peak potentials with pH for nicotinamide (0.35 mM) on cyclic voltammetry at the HMDE. Roman numerals refer to waves, a to anodic, and c to cathodic. Scan rate is 100 mV/sec.

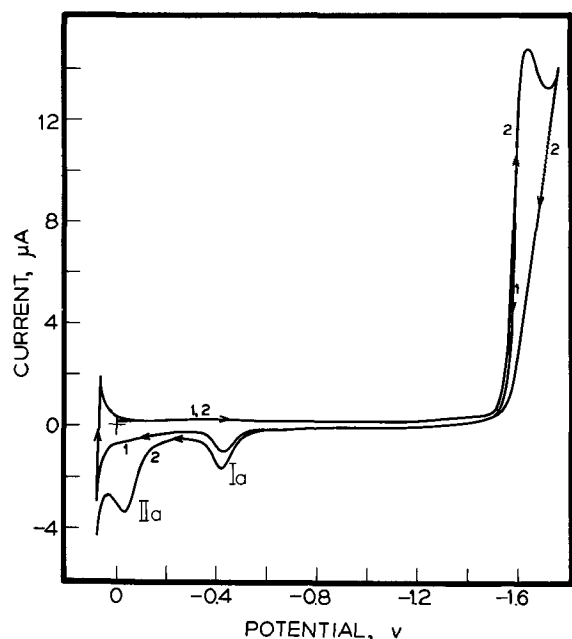


Fig. 7. Cyclic voltammogram of nicotinamide (1.27 mM) in pH 9.4 carbonate buffer at the HMDE. Roman numerals refer to waves; Arabic numerals to sweep. Scan rate is 100 mV/sec.

interface; however, the cathodic peak decreases if the anodic peak is excluded from the repetitive cycle.

The formation of two anodic peaks from an apparently single cathodic peak process is obviously due to the latter actually being the fusion of two processes. The fact that the first wave (1e) reduction product is mainly formed at potentials on the rising portion of the cathodic peak and the second wave (2e) reduction products at more negative potential, is illustrated in Fig. 7. If the first sweep to more negative potential is reversed before the peak potential is reached, only peak Ia appears; if the second sweep is reversed past the cathodic peak, both Ia and IIa are seen. Consistent with the DME results, the two processes separate in the presence of  $\text{Et}_4\text{NCl}$  to yield two closely spaced cathodic peaks (Fig. 8).

The oxidation processes producing peaks Ia and IIa yield a proton or protons during electron transfer, since the peak potentials become more positive with

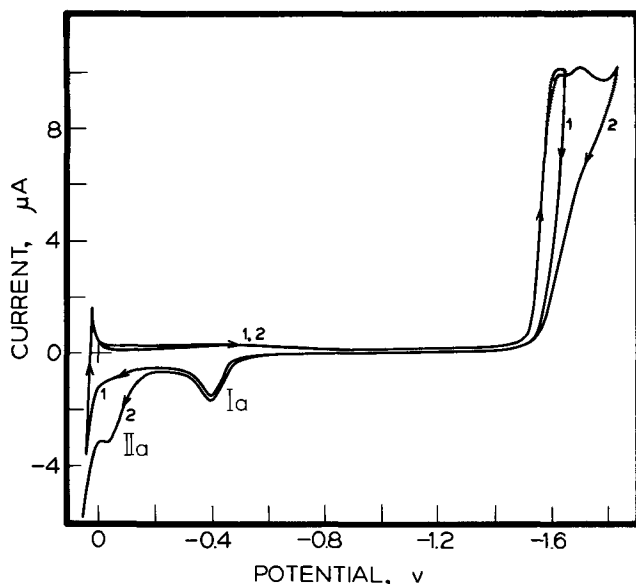


Fig. 8. Cyclic voltammogram of nicotinamide (1.27 mM) in pH 9.4  $\text{Et}_4\text{NCl}$ /carbonate buffer at the HMDE. Roman numerals refer to waves; Arabic numerals to sweep. Scan rate is 100 mV/sec.

decreasing pH (Fig. 6). The pH-dependence of peak potential Ia is nonlinear and much less pronounced than that for IIa

$$\text{Peak IIa: } E_p = 0.62 - 0.07 \text{ pH} \quad [3]$$

In neutral or acidic solution, reversing the potential sweep after either peak Ic or IIc yields only peak Ia; peak IIa is masked by mercury discharge, e.g., Eq. [3] predicts  $E_p$  for the IIa process to be 0.13V at pH 7.1, but mercury discharge occurs at 0.10V at pH 7.1.

Magnitudes of the two anodic peak currents depend to some extent on the potential of sweep reversal and are poorly reproducible. However, definite trends are established with change in pH. The peak IIa current increases with increasing pH, since the 2e reduction process is then favored. The peak Ia current reaches a maximum at pH 7-8; the decrease at higher pH is due to the decreased 1e reduction process and at lower pH to instability of the 1e reduction product.

A similar pattern involving two cathodic peaks is observed for N'-methylnicotinamide; peak II is obscured by background discharge below pH 5 (Table III).

*Detection of radical intermediate.*—In order to confirm formation of the radical intermediate during the first 1e step, repetitive fast-scan cyclic voltammetry was employed.

In pH 9.0 carbonate buffer, an anodic peak ( $E_{pa} = -1.65\text{V}$ ) (Fig. 9) was seen for nicotinamide at  $v$  between 14 and 32 V/sec, which was complementary to the cathodic peak ( $E_{pc} = -1.71\text{V}$ ) in involving formation of a free radical on reduction and oxidation of the latter back to the original species; the 60-mV difference in the cathodic-anodic peak potentials is characteristic of a 1e reversible redox couple. A similar redox couple was observed for N'-methylnicotinamide between 8 and 25 V/sec ( $E_{pc} = -1.66\text{V}$ ;  $E_{pa} = -1.60\text{V}$ ) (Fig. 9).

The dimerization rate of the free radical was determined from Nicholson's (21) curves relating the  $i_{pc}/i_{pa}$  ratio to the kinetic term  $k_d C^0 \tau$ , where  $k_d$  is the rate constant for a dimerization reaction following an electron-transfer process,  $C^0$  is the bulk concentration of the original electroactive species, and  $\tau$  is the switching time, i.e., the time necessary to scan from  $E^0$  for the

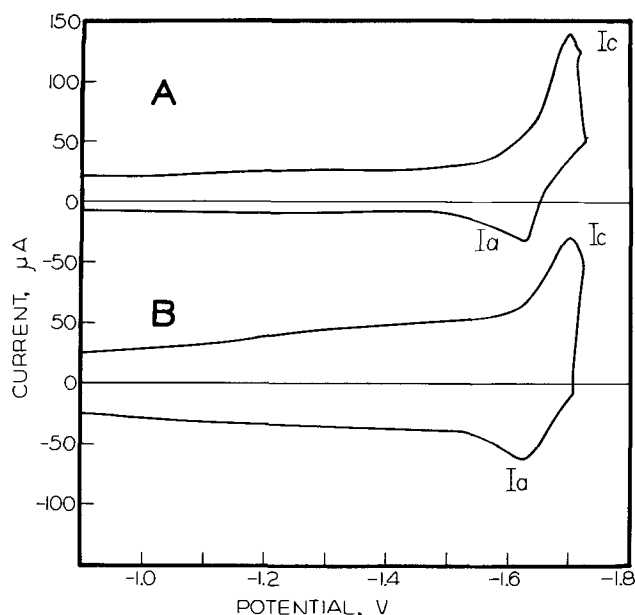


Fig. 9. Cyclic voltammograms of (A) nicotinamide (scan rate = 23 V/sec) and (B) N'-methylnicotinamide (scan rate = 18 V/sec) in pH 9.0 carbonate buffer, showing the reversible cathodic-anodic peak couple for the first electron-transfer process present at high sweep rates.

initial electrode process to the switching potential ( $E^\circ$  is assumed to be close to  $E_{1/2}$ ).

At 30°,  $k_d$  is  $(1.8 \pm 1.1) \times 10^6$  liter mol<sup>-1</sup> sec<sup>-1</sup> (mean and standard deviation for five measurements) for nicotinamide, and  $(4.9 \pm 1.2) \times 10^6$  liter mol<sup>-1</sup> sec<sup>-1</sup> (six measurements) for N'-methylnicotinamide. Measurement of  $k_d$  between 15° and 50° gave Arrhenius plots of  $\log k_d$  vs.  $T^{-1}$ , whose slopes corresponded to activation energies of 24 kcal mol<sup>-1</sup> for nicotinamide and 14 kcal mol<sup>-1</sup> for N'-methylnicotinamide.

**Controlled potential electrolysis and coulometry.**—Electrolyses were primarily carried out on pH 10 solutions (1.25 mM nicotinamide; 0.4M Et<sub>4</sub>NCl; 0.1M carbonate buffer).

**Wave I process.**—In accord with the indication that the over-all wave I process would be irreversible, electrolysis at a potential (−1.60V) slightly more negative than  $E_{1/2}$  of wave I in order to minimize formation of wave II product, went to completion for a faradaic  $n$  of 1.09. A greenish-yellow color appeared and reached maximum intensity when the electrolysis was about two-thirds complete; the completely electrolyzed solution was clear and only faintly yellow. The transient color is not due to the free radical (based on indication of a rather short half-life); it may be due to formation of an unstable by-product. When electrolysis was complete, shift of the potential to −1.8V produced no additional current flow other than background, confirming that the final wave I product is not an intermediate in the formation of wave II.

A polarogram of the electrolyzed solution revealed the absence of the two nicotinamide cathodic waves and the presence of two anodic waves, one of which ( $E_{1/2} = -0.45V$ ) had a limiting current about three times that of the other ( $E_{1/2} = -0.11V$ ); these correspond to the cyclic voltammetric anodic peaks. Thus, due to the small potential separation of the two reduction processes, some 2e reduction product is obtained; this is consistent with the  $n$  value.

The initial solution had a single absorption maximum at 261 nm ( $\epsilon = 2980$ ). The completely electrolyzed solution had maxima at 266 and 346 nm (Fig. 10); on dilution with McIlvaine buffer (final pH = 7.4), the two maxima slowly disappeared and a new band appeared at 280 nm.

On exposure of the electrolyzed solution to air, the 346-nm band decreased by 11% after 1 hr. After 24 hr, the 261-nm nicotinamide band reappeared; a small shoulder at about 280 nm suggested presence of some decomposition product similar to that formed in Mc-

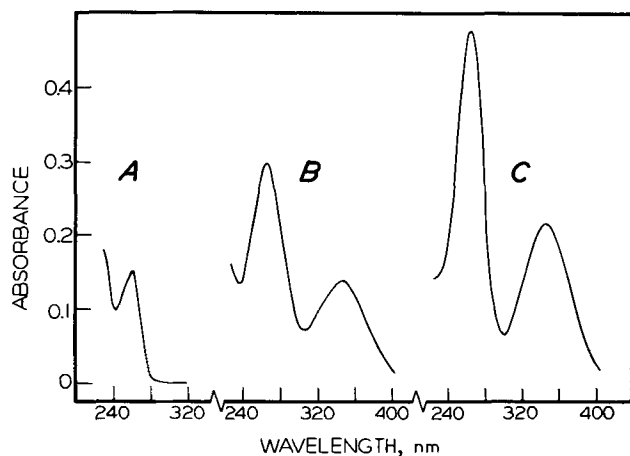


Fig. 10. Absorption spectra obtained on electrolysis of nicotinamide (1.25 mM) in pH 10 Et<sub>4</sub>NCl/carbonate buffer. Spectra obtained by a 1/25 dilution of electrolysis solutions with pH 10 carbonate buffer: A, before electrolysis; B, after electrolysis at −1.60V; C, after electrolysis at −1.80V.

Ilvaine buffer. Polarographic examination of the 24-hr solution revealed disappearance of the two anodic waves, regeneration of nicotinamide at about 91% of its original height, and presence of a broad wave characteristic of hydrogen peroxide.

**Wave II process.**—Electrolysis at −1.80V (limiting portion of wave II) gave an  $n$  of 1.82; no transient color was observed. The colorless electrolyzed solution had absorption maxima at 265 and 346 nm (Fig. 10) and exhibited the two anodic waves seen after electrolysis at the wave I  $E_{1/2}$ ; however, since the first wave height was only about 6% that of the second, mostly the 2e reduction product was obtained.

Exposure of the electrolyzed solution to air (room temperature; 24 hr) caused a 95% decrease in 346-nm absorption and appearance of a 272-nm band; this can best be explained by assuming disappearance of the 2e reduction product via two paths, similar to the 1e reduction product, i.e., the 272-nm band is a combination of bands due to nicotinamide ( $\lambda_{max} = 261$  nm) and a decomposition product ( $\lambda_{max} = 280$  nm). Polarography revealed absence of the anodic waves, 51% regeneration of nicotinamide, and a broad H<sub>2</sub>O<sub>2</sub> wave.

Reoxidation of the freshly electrolyzed solution at 0.0V, which corresponds to the 2e anodic wave limiting portion, gave a faradaic  $n$  of 1.69 based on the original nicotinamide content; the nicotinamide wave reappeared at 91% of its original height.

**Electrolysis at pH 9.**—Electrolysis of 1.80 mM nicotinamide in pH 9.0 carbonate buffer gave results comparable to those obtained at pH 10.0.

Electrolysis at −1.60 gave a faradaic  $n$  of one. Electrolysis at −1.72V gave an  $n$  of 1.80 and a solution with absorption maxima at 260 and 340 nm, and an anodic wave at −0.06V, whose height was 91% of the combined cathodic wave I and II heights before electrolysis. Oxidation of the latter solution gave an  $n$  of 1.90 and a solution with the characteristic nicotinamide polarographic and spectrophotometric patterns.

**Electrolysis of N'-methylnicotinamide.**—Electrolysis of 0.58 mM N'-methylnicotinamide in pH 5.0 acetate buffer at −1.35V gave an  $n$  of one and a solution with absorption maxima at 270 and 350 nm, and a polarographic pattern which lacked the features of the original compound but had an anodic wave at −0.01V. Oxidation of the latter solution regenerated the original compound; coulometry indicated that about half of the reduction product had decomposed chemically.

Electrolysis of 0.91 mM N'-methylnicotinamide in pH 9.0 carbonate buffer at a wave I potential (−1.63V) gave an  $n$  of 1.10; a yellow color appeared and reached maximum intensity when electrolysis was about three-fourths complete. Shifting of the potential to −1.8V on completion of electrolysis gave only background current flow. A polarogram of the electrolyzed solution revealed the absence of both cathodic waves and the presence of two anodic waves, one of which ( $E_{1/2} = -0.57V$ ) was about three times as large as the other ( $E_{1/2} = -0.15V$ ). The original solution had an absorption maximum at 260 nm; the electrolyzed solutions had maxima at 265 and 346 nm.

Oxidation of the reduced solution at −0.40V gave an  $n$  of 0.92 per original N'-methylnicotinamide molecule and a solution with the polarographic and spectrophotometric patterns characteristic of N'-methylnicotinamide.

**A-C polarography.**—The in-phase and quadrature components of the alternating current in the presence and absence of nicotinamide and of Et<sub>4</sub>NCl at pH 9.4 are shown in Fig. 4 and 5; the presence of Et<sub>4</sub>NCl has only minor effect. A single faradaic peak (in-phase component) occurs at −1.62V (at −1.59V in presence of Et<sub>4</sub>NCl); the corresponding quadrature components occur at −1.66V.

Table IV. A-C polarography of nicotinamide and N'-methylnicotinamide: faradaic peaks<sup>(a)</sup>

Compound	Frequency, Hz	Peak I		Peak II	
		-E <sub>s</sub> , V	Δi <sub>s</sub> , μA	-E <sub>s</sub> , V	Δi <sub>s</sub> , μA
Nicotinamide (5.32 mM)	50	1.25	1.05	1.40	1.05
	100	1.25	1.22	1.40	1.05
	200	1.25	1.20	1.40	1.05
N'-methylnicotinamide (1.63 mM)	500	1.25	0.85	1.42	0.70
	50	1.25	0.43	—	—
	100	1.25	0.31	—	—

<sup>(a)</sup> In-phase current component response for pH 5.0 acetate buffer solutions.

Nicotinamide is only slightly surface-active even at relatively high concentration (1.27 mM), *i.e.*, the differential double layer (DL) capacity in the potential region immediately prior to the first reduction wave is identical in both systems to that for the corresponding background electrolyte alone, showing an absence of adsorption phenomena involving nicotinamide.<sup>5</sup> The absence or presence of adsorption phenomena involving its reduction products cannot be ascertained with certainty due, for example, to the close proximity of the waves to background discharge in carbonate buffer. The quadrature current component in this potential region shows no capacitance depressions or anomalous peaks which might be attributed to adsorption-desorption (tensammetric) phenomena.

In Et<sub>4</sub>NCl/carbonate buffer (Fig. 5), both components of the a-c faradaic response are likely to be primarily due to the first 1e step, although a small inflection or shoulder on the more negative potential side of the in-phase component is probably due to the second 1e faradaic process. This interpretation is consistent with the fact that Et<sub>4</sub>NCl addition shifts both E<sub>1/2</sub> and E<sub>s</sub> (peak potential of the total alternating faradaic current) of wave I to more positive potential and E<sub>1/2</sub> of wave II to more negative potential, and that the total a-c faradaic response occurs in a potential region more clearly associated with wave I than wave II, *e.g.*, the absolute difference E<sub>s</sub> - E<sub>1/2</sub> is only 34 mV for wave I, but 95 mV for wave II. [Interestingly, E<sub>p</sub> for wave I is not markedly shifted on Et<sub>4</sub>NCl addition (Fig. 7 and 8).]

The a-c polarographic results for nicotinamide are in contrast to the reported positive shift of the electrocapillary maximum (ecm) in pH 6 solutions of nicotinamide (5, 6).

The a-c polarographic behavior of N'-methylnicotinamide is essentially similar to that of nicotinamide, *e.g.*, in showing only slight surface activity. Thus, at pH 5.0, both compounds show faradaic peak I at -1.25V (Table IV). The faradaic current for nicotinamide at first increases with increasing a-c frequency and then decreases, reflecting behavior common to systems where the initial electrochemical product is involved in a rapid chemical reaction. That of N'-methylnicotinamide starts to decrease at a lower frequency, reflecting the difference in rates of the follow-up chemical reaction at pH 5.

Nicotinamide shows a second faradaic peak at -1.40V at pH 5.0; that for N'-methylnicotinamide is obscured by background discharge.

### Discussion

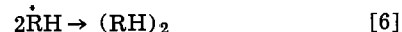
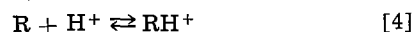
**Redox pattern.**—The potential separation of the two electron-transfer reactions for the electrochemical reduction of 3-carbamoylpyridine (nicotinamide) in aqueous media never exceeds *ca.* 0.12V; that for 3-(N-methylcarbamoyl)pyridine (N'-methylnicotinamide) is difficult to evaluate due to obscuring of its wave II by background discharge but it may be as large as 0.2V in alkaline solution. The two nicotinamide polaro-

graphic waves evident in acidic solution shift to more negative potential with increasing pH and start to merge above pH 8; however, the merging process is not entirely complete until pH 12 or 13. Thus, while an apparently single 2e wave is observed at pH 9.4 (Fig. 4), the process occurring on the initial rising portion of the wave leads to the dimeric 1e reduction product; Et<sub>4</sub>NCl addition separates the two processes and two waves of equal height are seen (Fig. 5). The reason for the separation, which results from a shift in potential of both waves, is unclear. The surface-activity of Et<sub>4</sub>N<sup>+</sup> is probably a factor, but its role does not appear to be related to adsorption phenomena involving any of the electrode reaction participants. The waves may be shifted by Et<sub>4</sub>N<sup>+</sup> through its effect on the rate of the dimerization reaction.

**Redox mechanism.**—The reaction scheme outlined in Fig. 1 seems to fit best the electrochemical, chemical, and spectral data for nicotinamide (I) and N'-methylnicotinamide.

At pH above the pK<sub>a</sub> of nicotinamide [3.3 at 20° (22)], the initial reduction can be regarded as uptake of an electron and a proton to form a neutral free radical (II) (source of polarographic wave I). This is followed by irreversible dimerization to an apparent 6,6' dimer (III). At the potential of wave II, nicotinamide is reduced to an apparent 1,6-dihydropyridine species (IV), which is equivalent to a further 1e reduction of the free radical; the dimer is not further reduced at this potential. At a potential considerably more positive than that of reduction wave I, the dimer is oxidized to nicotinamide. At still more positive potential, the dihydropyridine species is also oxidized to nicotinamide.

The pH-dependencies of the two electrochemical reductions and the two electrochemical oxidations are compatible with the proposed mechanistic scheme. Below pH 4 (Fig. 3), the wave I reduction process should show only slight pH-dependence because most of the nicotinamide will be protonated at N(1) and the unprotonated compound will rapidly protonate as the protonated form is reduced. Under the conditions of cyclic voltammetry (Fig. 6), peak potential I<sub>c</sub> does not become less pH-dependent as the pH is lowered. The essential reactions in the wave I process are, consequently, as follows, where R represents nicotinamide

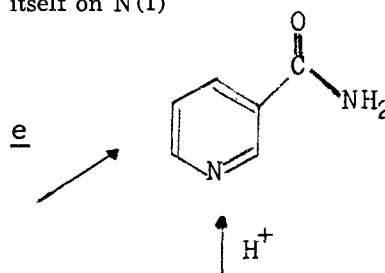


The assumption that protonation is essentially complete before electron transfer is supported by the relatively slight pH-dependence of E<sub>1/2</sub> and by the closeness of E<sub>1/2</sub> for nicotinamide (-1.11V) and N'-methylnicotinamide (-1.08V) to that for 1-methyl-3-carbamoylpyridinium ion (-1.03V) (23), where the nitrogen lone pair is not available and the electroactive species exists as a cation.

The wave II process involves the previous reactions plus reduction of the free radical (the following may proceed stepwise)



Above pH 4, the energy-controlling step in the reduction involves simultaneous addition of an electron entering the ring electronic system and of a proton localizing itself on N(1)



[8]

<sup>5</sup> In potential regions where there is no a-c faradaic process, the quadrature a-c current component is proportional to the differential double layer capacity at the solution-electrode interface, which would reflect adsorption of nicotinamide at the interface.

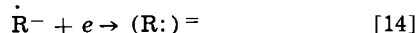
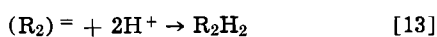
The distribution of electron density in the nicotinamide ring based on resonance structures supports this model (24). In the slightly acidic to slightly alkaline region (Fig. 3), the protonation is sufficiently rapid that it is not a limiting factor. The essential steps in the wave I process are, accordingly



The pH-dependence of 79 mV/pH unit for  $E_{1/2}$  of wave I between pH 4 and 9 (60 mV expected for an uncoupled reversible  $1e$  reaction) probably results from the rapid follow-up reaction as well as possible protonation subsequent to electron transfer (cf. reversibility).

Dimerization of the neutral free radical produced in acidic to slightly alkaline media must be exceedingly rapid since an anodic peak corresponding to its oxidation is not seen even at high scan rates on cyclic voltammetry.

Since oxidation of the free radical is seen at pH 9 and above (Fig. 9), the latter process probably involves the negatively charged radical anion, whose dimerization would be slowed down due to electrostatic repulsion. Protonation would be expected to be a slow process. However, the radical, once formed, is essentially more easily reduced than the original electroactive species as indicated by the behavior at pH 12 where the two electrons add almost simultaneously, producing a polarographic wave which has a slope only slightly less than that expected for a reversible  $2e$  wave. The following reactions are, accordingly, involved



The rate constants for the dimerization of the radical anions in aqueous alkaline solution ( $1.8 \times 10^6$  and  $4.9 \times 10^6$  liter mol<sup>-1</sup> sec<sup>-1</sup> for nicotinamide and N'-methylnicotinamide, respectively, at 30°) are comparable to that observed for the pyrimidine radical anion in acetonitrile [ $8 \times 10^5$  liter mol<sup>-1</sup> sec<sup>-1</sup> at 25° (25)].

**Reversibility.**—Evaluation of the reversibility of the electron-transfer processes involved in the nicotinamide redox patterns is complicated by rapid follow-up chemical reactions, which result in the over-all irreversibility of the electrode process. A claim of reversibility can be made for the first  $1e$  addition to nicotinamide, based on wave slope and reversible oxidation of the radical intermediate. Observation for the first faradaic process of less than 3% of the alternating current theoretically expected for a reversible  $1e$  process, is accounted for by the period of the alternating voltage used (20 msec) being much greater than the half-life of the nicotinamide radical, which is considerably less than 1 msec; thus, most of the radicals dimerize before they can be reoxidized.

Similar claims can be made for the first N'-methyl-nicotinamide wave. For example, cyclic voltammetric peak I shows a difference of 42–44 mV in peak to half-peak potentials, compared to the 39 mV theoretically expected for a dimerization reaction following reversible  $1e$  transfer (21). Similarly, polarographic wave I has a slope ( $E_{1/4} - E_{3/4}$ ) of ca. 44 mV compared to the theoretically expected 46 mV for reversible  $1e$  transfer followed by dimerization (26).

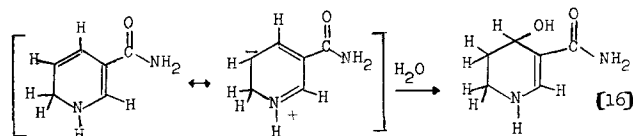
The fact that, at any pH, nicotinamide wave I becomes increasingly more evident with increasing concentration is in agreement with theory for an irreversible chemical reaction following a reversible charge

transfer, i.e., as the nicotinamide concentration is increased, the rate of the dimerization reaction increases, altering the ratio of concentrations of oxidized and reduced species at the electrode surface and thus causing the wave to shift to more positive potential.

**Characterization of the reduction products.**—Identification of the stable products of the  $1e$  and  $2e$  processes is based on ultraviolet absorption spectra, chemical behavior, and electrochemical oxidation, as previously described, e.g., postulation of the 6,6' dimer and the 1,6-dihydropyridine species is based on the absorption bands observed in the 240–400 nm region. Before reduction, 1-substituted 3-carbamoylpyridinium species generally show a single absorption band at about 265 nm; the dihydropyridine reduction products show single bands at about 410 nm for the 1,2 species and 350 for the 1,4 species, and two bands at about 265 and 360 nm for the 1,6 product; similarly, the 4,4' dimers absorb at about 350 nm and the 6,6' dimers at about 265 and 360 nm (27–33). These patterns have also been theoretically predicted (30).

Although the 1,6 isomers appear to be the major products, it is not inconceivable that other isomers might also be present, since the final electrolyzed solutions were not examined for product homogeneity. In the case of the  $2e$  product, for example, the 1,4 isomer cannot be readily excluded because it would be expected to exhibit a single absorption band at about the same wavelength as the long wavelength band of the 1,6 isomer. The 1,2 isomer can probably be excluded, because the electrolyzed solution was colorless. In the case of the  $1e$  product, at least six different dimeric structures are possible but, because of the two asymmetric carbons at the point of dimerization, as many as 21 stereoisomers may exist (3 *meso* forms and 9 *dl*-pairs). Furthermore, the validity of using the same spectral arguments for assigning the position of dimerization in partially reduced pyridines has not been thoroughly tested. Using the above criteria, structures have been readily assigned (32) to dimers of nicotinamide model compounds prepared by zinc reduction, but others have suggested caution (34). Nevertheless, in view of the available evidence, it is felt that the 1,6 isomers are the major products of the electrochemical reduction of nicotinamide.

The two reduction products of each compound undergo acid-catalyzed decomposition even in solutions as alkaline as pH 10. With decreasing pH, the rate of decomposition increases; at any given pH, the dimer is less stable than the dihydropyridine species. The decomposition involves hydrolysis of the 4,5 double bond and can be regarded as an instance of enamine nucleophilicity (35, 36)



Thus, the two nicotinamide products decompose in the presence of a proton donor such as  $H_2PO_4^-$  at pH 7.4 to give a single absorption band at 280 nm; the same reaction occurs more slowly in pH 10  $Et_4NCl^-$ /carbonate buffers. The hydrolytic reaction of Eq. [16] accounts for loss of the 266- and 346-nm bands and for the concomitant increase in 280-nm absorption due

to the  $HN-C=C-C=O$  chromophore (37).

Hydrolysis of the 5,6 double bond of a 1,4 reduced pyridine species would also be expected to lead to the same chromophore (28, 35), but hydrolysis of a 1,2 reduced pyridine species produces no new increase in absorption (28).

During decomposition, the anodic voltammetric waves characteristic of each reduction product are lost.

Since in alkaline solution the two reduction products of each compound are directly oxidized by molecular oxygen to the original species, two decomposition pathways are possible on exposure to air. For the species derived from nicotinamide, both pathways appear to be equally important for the dihydropyridine species since only half of the original nicotinamide is recovered; the dimer, on the other hand, is more easily oxidized by oxygen than the dihydropyridine species, which is consistent with their electrochemical oxidation potentials, and most of the original nicotinamide is recovered.

#### Acknowledgment

The authors thank the National Science Foundation, which helped support the work described.

Manuscript submitted June 11, 1973; revised manuscript received Sept. 27, 1973.

Any discussion of this paper will appear in a Discussion Section to be published in the December 1974 JOURNAL. All discussions for the December 1974 Discussion Section should be submitted by Aug. 1, 1974.

#### REFERENCES

1. B. Janik and P. J. Elving, *Chem. Rev.*, **68**, 295 (1968).
2. J. Kuthan, V. Simonek, and V. Volveo, *Z. Chem.*, **11**, 111 (1971).
3. K. K. Lovecchio, *Dissertation Abstr.*, **30B**, 5397 (1970).
4. P. J. Elving, J. E. O'Reilly, and C. O. Schmakel, in "Methods of Biochemical Analysis," D. Glick, Editor, Vol. 21, pp. 287-465, Interscience Publishers, New York (1973).
5. E. Knobloch, *Chem. Listy*, **39**, 54 (1945).
6. E. Knobloch, *Collection Czech. Chem. Commun.*, **12**, 407 (1947).
7. P. C. Tompkins and C. L. A. Schmidt, *Univ. Calif. (Berkeley) Publ. Physiol.*, **8**, 247 (1943).
8. I. M. Kolthoff and J. J. Lingane, "Polarography," Vol. II, p. 814, Interscience Publishers, New York (1952).
9. J. M. Moore, *J. Pharm. Sci.*, **58**, 1117 (1969).
10. V. Moret, *Arch. Sci. Biol. (Bologna)*, **39**, 456 (1955).
11. E. Peingor and G. Farsang, *Acta Chim. Acad. Sci. Hung.*, **27**, 175 (1961).
12. J. Sancho, P. Salmeron, and J. G. Hurtado, *Anales Real Soc. Espan. Fis. Quim. (Madrid) Ser. B*, **55**, 23 (1959).
13. S. Yamada and Y. Kikugawa, *Chem. Ind.*, **52**, 2169 (1966).
14. D. D. DeFord, Division of Analytical Chemistry, 133rd National Meeting, Am. Chem. Soc., San Francisco, Calif. (1958).
15. W. M. Schwarz and I. Shain, *Anal. Chem.*, **35**, 1770 (1963).
16. D. E. Smith, in "Electroanalytical Chemistry," A. J. Bard, Editor, Vol. I, pp. 1-155, Marcel Dekker, New York (1966).
17. C. O. Schmakel, Ph.D. Thesis, University of Michigan (1971).
18. P. Delahay and I. Trachtenberg, *J. Am. Chem. Soc.*, **80**, 2094 (1958).
19. R. DeLevie and A. A. Husovsky, *J. Electroanal. Chem.*, **20**, 181 (1969).
20. J. E. Hickey, M. S. Spritzer, and P. J. Elving, *Anal. Chim. Acta.*, **35**, 277 (1966).
21. M. L. Olmstead, R. G. Hamilton, and R. S. Nicholson, *Anal. Chem.*, **41**, 260 (1969).
22. D. D. Perrin, "Dissociation Constants of Organic Bases in Aqueous Solution," Butterworths, London (1965).
23. C. O. Schmakel, K. S. V. Santhanam, and P. J. Elving, Work in progress.
24. B. Pullman and A. Pullman, "Quantum Biochemistry," Interscience Publishers, New York (1963).
25. J. E. O'Reilly and P. J. Elving, *J. Am. Chem. Soc.*, **93**, 1871 (1971).
26. R. Bonnaterre and G. Cauquis, *J. Electroanal. Chem.*, **32**, 199 (1971).
27. S. Chaykin, *Ann. Rev. Biochem.*, **36**, 161 (1967).
28. S. Chaykin, L. King, and J. G. Watson, *Biochim. Biophys. Acta.*, **124**, 13 (1966).
29. S. Chaykin and L. Meissner, *Biochem. Biophys. Res. Commun.*, **14**, 233 (1964).
30. G. Maggiora, H. Johansen, and L. L. Ingraham, *Arch. Biochem. Biophys.*, **131**, 352 (1969).
31. H. Sund, in "Biological Oxidations," T. P. Singer, Editor, p. 603, Interscience Publishers, New York (1967).
32. K. Wallenfels, *Ciba Found. Study Group*, **2**, 10 (1959).
33. K. Wallenfels and H. Shüly, *Ann.*, **621**, 106 (1959).
34. R. W. Burnett and A. L. Underwood, *Biochemistry*, **7**, 3328 (1968).
35. E. M. Kosower, "Molecular Biochemistry," p. 166, McGraw-Hill Book Co., New York (1962).
36. D. J. McClemens, A. K. Garrison, and A. L. Underwood, *J. Org. Chem.*, **34**, 1867 (1969).
37. R. M. Burton and N. O. Kaplan, *Arch. Biochem. Biophys.*, **101**, 150 (1963).

# The Control of Oxygen Activities in Argon-Oxygen Mixtures by Coulometric Titration

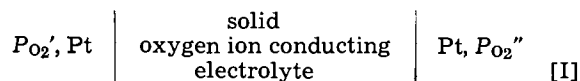
Yogesh K. Agrawal, David W. Short, Roger Gruenke, and Robert A. Rapp\*

Department of Metallurgical Engineering, The Ohio State University, Columbus, Ohio 43210

## ABSTRACT

High-temperature electrochemical cells based on stabilized zirconia as a solid electrolyte with porous platinum electrodes may be used either to monitor oxygen activities by open-circuit measurements or else to pump oxygen into or out of stationary or streaming gas mixtures. In this work, a feed-back control unit (potentiostat) in combination with a zirconia-base solid electrolyte tube was used to simultaneously control and measure the oxygen partial pressure in a flowing inert carrier gas (argon). The oxygen activity of "tank" argon was controlled to desired levels between  $2 \times 10^{-2}$  and  $10^{-16}$  atm oxygen. A four-electrode double cell arrangement is shown to be superior to a three-electrode arrangement.

The  $ZrO_2$ -base electrolytes exhibit a  $P_{O_2}$ -independent predominant oxygen ion conduction over a range of oxygen pressures from above 1 atm to about  $10^{-25}$  atm (depending on temperature). The oxygen ion conducting electrolytes may be used in combination with two separated metallic (generally platinum) electrodes, which are at equilibrium with different oxygen partial pressures to form a high-temperature galvanic cell as follows



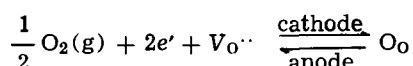
where  $P_{O_2}'$  and  $P_{O_2}''$  represent the oxygen partial pressures at the cathode and anode, respectively, with  $P_{O_2}' < P_{O_2}''$ .

At open circuit, the voltage of this cell indicates the ratio in oxygen chemical potentials at the electrodes according to the equation

$$E_{o.c.} = \frac{RT}{4F} \ln \frac{P_{O_2}''}{P_{O_2}'} \quad [1]$$

if the electrolyte exhibits exclusive ionic conduction ( $t_{ion} > 0.99$ ) over the oxygen pressure range between the two electrodes. If  $P_{O_2}''$  is considered to be a time-independent and known reference electrode (e.g., air with  $P_{O_2} = 0.21$  atm), then the galvanic cell can indicate the unknown or variable  $P_{O_2}'$  with high accuracy.

Within the  $P_{O_2}$ -range of predominant ionic conduction, essentially all of the current passed through cell [1] should correspond to the transport of oxygen ions through the solid electrolyte from the cathode (at negative polarity) to the anode. At the anode and cathode, respectively, the loss or gain of electrons from the external circuit accomplishes the formation or dissociation of oxygen molecules according to the reaction<sup>1</sup>



If a voltage ( $V$ ) is externally superimposed onto the open-circuit, "chemical" voltage of Eq. [1], then oxygen may be passed from the reversible reference electrode at  $P_{O_2}''$  into the phase of variable  $P_{O_2}'$ , or, alternatively in the opposite direction, depending on the sign and magnitude of the net voltage across the elec-

trolyte. The rate at which oxygen is locally transferred would depend on the ionic conductivity and geometry or cell constant (length/area) of the electrolyte, the local open-circuit cell voltage, the voltage applied across the electrolyte, and any voltage losses through polarization ( $\eta$ )

$$V - E_{o.c.} - \eta = I_{ion}\Omega_{ion} \quad [2]$$

in which equation the polarity of the applied voltage is denoted as positive when it opposes  $E_{o.c.}$ ;  $\Omega_{ion}$  is the ionic resistance of the electrolyte and  $I_{ion}$  the ionic current.

At temperatures between 530° and 800°C, Yuan and Kröger (2) have used a stabilized zirconia tube to pump residual oxygen from a streaming mixture of nitrogen plus oxygen. Downstream open-circuit gauges on the same tube indicated the extent of the pumping. In some cases, pumping voltages ( $V$ ) far in excess of the decomposition voltage of zirconia were used; the buffering effects of  $H_2O$  and  $CO_2$  molecules were studied. In the current study, a different electrode arrangement is used and subsequently compared to that of Yuan and Kröger.

Kleitz *et al.* (3, 4) have previously reported on the use of a series combination of an oxygen pump and an oxygen meter whereby each of these elements consisted of separate closed-end stabilized zirconia tubes. The application of a voltage to the upstream pump effected a change in the oxygen content of an inert carrier gas which was measured by the downstream oxygen gauge. However, the pump and meter were not otherwise connected by a device to effect automatic control.

Beekmans and Heyne (5, 6) have introduced a feed-back control circuit between an oxygen pump and meter on a single zirconia electrolyte tube to effect the automatic control of oxygen in flowing gas streams. Except for work at very low  $P_{O_2}$ , the authors used a three-electrode arrangement whereby the electrodes for the pump and the meter within the tube were common. The control of the temperature of the system was accomplished by an auxiliary monitoring of the electrical resistance of a section of the electrolyte tube. The direct current-voltage characteristics of the device were not described.

Spacil *et al.* (7, 8) have also introduced a feed-back control unit between an oxygen pump and gauge on a single zirconia tube. Their specific application for this device was the determination of the composition of the gaseous products of combustion reactions.

\* Electrochemical Society Active Member.  
Key words: oxygen control, zirconia, potentiostat, coulometric titration, solid-state electrochemistry.

<sup>1</sup> The defect notation of Kröger and Vink (1) has been used.



Hickam and Witkowski (9) have recently described an apparatus for the control of oxygen in flowing fluids. Some pumping characteristics of their system were presented.

Many authors (10-14) have previously reported on the direct current-voltage characteristics and the associated polarization behavior of stabilized zirconia cells with porous platinum electrodes. These previous mechanistic studies have employed electrode arrangements and experimental procedures which were better suited to fundamental interpretation than the relatively long pumping cells used here. While the electrode polarization behavior observed in this work is qualitatively similar to that previously reported, we have not attempted to interpret these results in terms of the fundamental mechanisms involved.

Based on the previously described characteristics of zirconia electrolyte cells to function as an oxygen pump and gauge, we have in this work built and tested an electrochemical system and an associated feed-back control device for the simultaneous measurement and control of oxygen activities (partial pressures) in stagnant and flowing gaseous environments at high temperatures (600°-1200°C) (15). This electrochemical system is based on the calcia-doped zirconia electrolyte with two sets of porous Pt electrodes, together with electronic circuitry in closed loop, which was used to regulate the oxygen partial pressures in flowing Ar-O<sub>2</sub> gas mixtures. A special component was introduced to allow the control of oxygen activity independent of temperature fluctuations in the electrochemical system.

### Experimental Apparatus and Procedure

**Oxide electrolyte cells.**—Fully stabilized [7½ w/o (weight per cent) calcia] and partially stabilized (3-4 w/o calcia) zirconia electrolyte tubes purchased from Zircoa (Solon, Ohio) were used. The composite cell system is shown schematically in Fig. 1. A pair of short (1 cm) porous Pt electrodes (III and IV) formed a downstream, open-circuit cell to monitor continuously the oxygen activity of the exiting gas mixture. A pair of longer (22 cm) porous Pt electrodes (I and II) served as an upstream pumping cell. This electrode configuration is different from that of Yuan and Kröger (2) who used three electrodes (a common inner electrode) instead of four while working with N<sub>2</sub>-O<sub>2</sub> mixtures at lower temperatures.

The open-circuit measuring cell of electrodes III and IV was used as a sensor for the control system. Platinum wires were wrapped around electrodes I and III, and platinum wires were laid loosely inside the tube to form the electrical leads for electrodes II and IV. The zirconia tube was sealed to soft glass at both ends and further to Pyrex through graded glass seals. A Pt/Pt-10% Rh thermocouple was placed inside the tube to measure the gas temperature at the measuring cell. The thermocouple and the Pt leads to the inner electrodes were sealed through the soft glass tubes at the two ends.

To insure that the oxygen activity measured by the inner electrode of the downstream sensor cell was indeed the average  $P_{O_2}$ ' of the gas mixture, and not some steady-state  $P_{O_2}$ ' resulting from laminar flow in the tube and the presence of a stagnant gas film at the

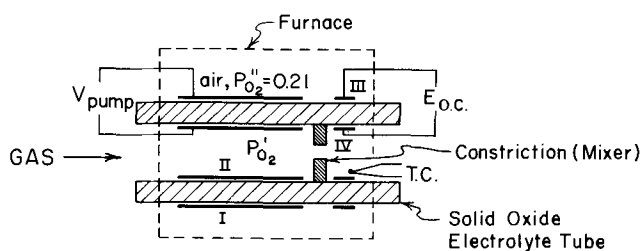


Fig. 1. Four-electrode zirconia electrolyte system for control of oxygen activity in flowing gases.

wall, a constriction was placed inside the tube between the pumping and the measuring or reference cell. This ceramic constriction (mixer) was a hollow cylinder approximately 10 mm long and 3 mm ID, which fitted snugly into the 12 mm ID CaO-stabilized zirconia electrolyte tube and was positioned between electrodes II and IV as indicated in Fig. 1. This constriction was assumed to create sufficient turbulence in the gas stream so that the downstream cell indicated the average  $P_{O_2}$ ' of the gas phase after coulometric pumping by the upstream cell. In fact, during the course of the work, the use of this constriction was found to be unnecessary because of the rapid interdiffusion in the flowing gas. This result agrees with the calculation provided by Yuan and Kröger (2).

**Closed-loop control system.**—The detailed circuit diagrams of different blocks of the system as represented in Fig. 2 are shown in Fig. 3-5. Figure 3 indicates the cell amplifier and the thermocouple amplifier. Figure 4 consists of the divider circuit, set points, summing junction, and amplifier/integrator circuit. Figure 5 shows the power amplifier and limiter circuitry.

As is clear from Eq. [1], the open-circuit emf  $E_{O.C.}$  is proportional to the absolute temperature,  $T$  (°K), as

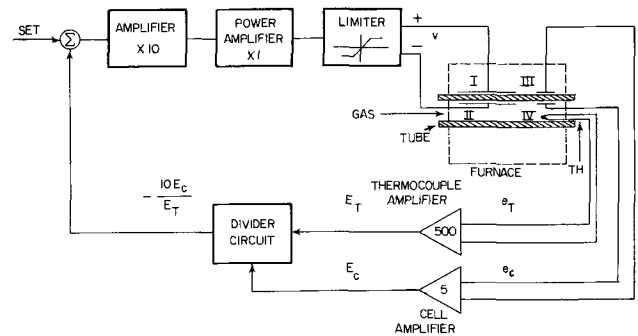


Fig. 2. Block diagram of closed-loop, feed-back control unit for oxygen activity in gases.

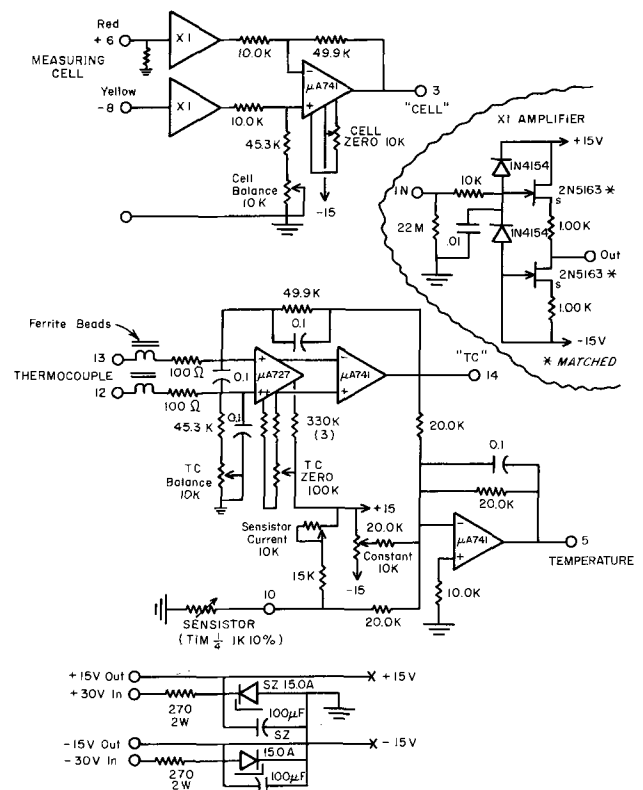


Fig. 3. Cell amplifier and thermocouple amplifier of control unit

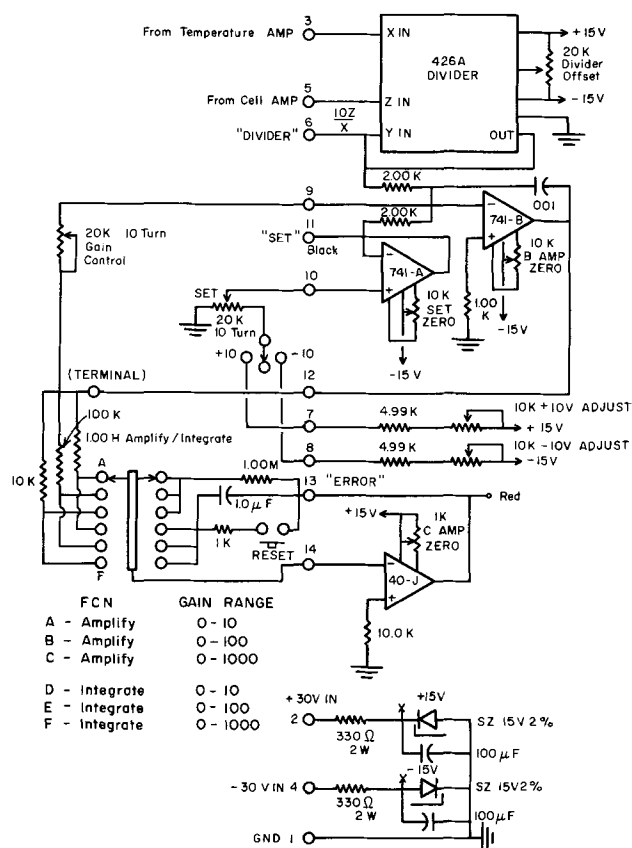


Fig. 4. Circuitry of components in control unit

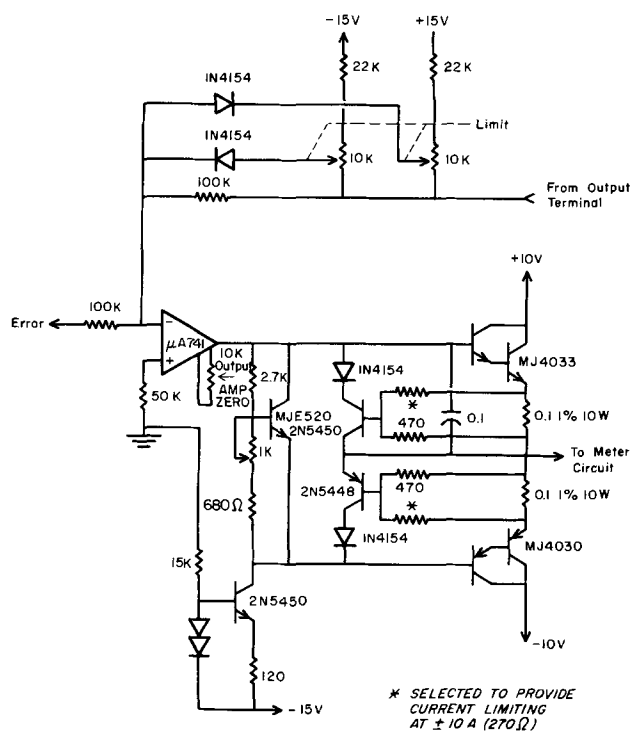


Fig. 5. Power amplifier and limiter circuitry of control unit

well as  $\log P_{O_2}'$ . To remove the undesirable effect of variation in furnace temperature, the parameter  $E/T$ , which is only dependent on  $P_{O_2}'$ , was chosen as the control variable. The thermocouple output was used to compensate for incremental variations in furnace temperature during operation. The signal to the thermocouple amplifier includes a room temperature cold-junction correction by means of a "sensistor" as shown in Fig. 3. Also, since  $T$  of Eq. [1] is the absolute tem-

perature in degrees Kelvin, an additional emf correction corresponding to an additive  $273^\circ$  was built into the thermocouple amplifier such that the output was proportional to  $T(^{\circ}K)$ . The two compensations to the thermocouple signal were accomplished by assuming linear  $E$  vs.  $T$  behavior for the thermocouple about the temperature of expected use ( $850^\circ C$ ), and the extrapolation of this behavior to zero  $^{\circ}K$ . The high gain of the thermocouple amplifier (500X) makes the system quite sensitive to variation in the furnace temperature.

As is seen in Fig. 2, the open-circuit emf between electrodes III and IV is amplified and subsequently divided by the compensated and amplified thermocouple emf. The divider circuit has a built-in gain of 10. The output of the divider circuit is compared with the set value of  $E/T$  to produce an error signal, which in turn, is amplified and applied to the pumping cell (electrodes I and II). The amplification of a steady-state error classifies this device as a "type zero" control system. The polarity of the voltage applied to the pumping cell is automatically selected and the gain in the amplification of the error signal is manually chosen so that the error signal is minimized, i.e., so that the desired  $P_{O_2}'$  is essentially achieved downstream. By controlling the quantity  $E/T = R/4F \ln P_{O_2}''/P_{O_2}'$  of Eq. [1], the desired oxygen activity  $P_{O_2}'$  is achieved and the dependence on cell temperature is removed over a wide temperature range (as long as the thermocouple output is essentially linear with  $T$ ).

As used in our work, the limiter circuit (Fig. 5) allowed a maximum of only  $\pm 2.0V$  to be applied to the electrolyte tube, which, however, could be changed to  $\pm 5V$  by adjusting potentiometers shown by "Limit" in Fig. 5. This limiter was introduced to restrict the voltage applied to the pumping cell to a value beyond which the tube would be expected to pass excessive electronic current and perhaps otherwise degrade by partial reduction or electrolysis.

Argon- $O_2$  mixtures were dried of water vapor with magnesium perchlorate and passed through the electrolyte tube. Because of the temperature gradient in the furnace, the middle of the pump was at a temperature of  $910^\circ C$  and the measuring cell at  $800^\circ C$ . This temperature difference represented a steady-state condition with gas flowing at a rate of  $2 \text{ cm}^3/\text{sec}$ . Only a few centimeters past the measuring cell, the electrolyte tube was cooled through a steep gradient to ambient temperature. The results for our four-electrode system were compared with that of a three-electrode cell by shorting the inner electrodes II and IV externally.

## Results

The Ar- $O_2$  mixture was passed through the electrolyte tube at a flow rate of  $2 \text{ cm}^3/\text{sec}$  and a steady-state open-circuit emf at the measuring cell was measured. From this emf and Eq. [1] the oxygen content in the gas mixture was calculated. Prior to the testing of the control unit, the characteristics (interrelation of  $V_{\text{pump}}$ ,  $E_{O.C.}$ , and  $I$ ) of the four-electrode arrangement were established for a given flow rate of Ar- $O_2$  mixture and a given temperature. From a constant voltage supply, different voltages were applied at the pump electrodes, and the current passing through the pump, as well as the open-circuit emf resulting at the measuring cell, were measured. Thus, by initially using the pumping voltage,  $V_{\text{pump}}$ , as the independent variable, values for  $I_{\text{pump}}$  and  $E_{O.C.}$  (or  $-\log P_{O_2}'$ ) vs.  $V_{\text{pump}}$  are presented as Fig. 6-8.

Experiments were conducted to demonstrate that the pumping and measuring cells were electrically independent, i.e., that the application of a voltage to the pumping cell did not result in an electrical (voltage) input to the measuring cell. Upon the application of one volt to the downstream (measuring) cell, no change in the open-circuit voltage of the upstream cell was observed. The flow of gas was also reversed and the same observation was made. Thus, the two cells

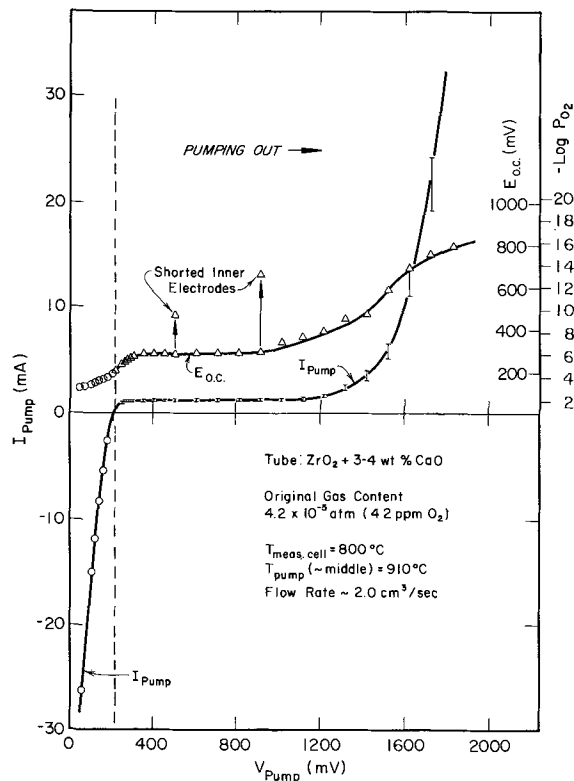


Fig. 6. Electrical characteristics of four-electrode cell arrangement using  $V_{pump}$  as independent variable.

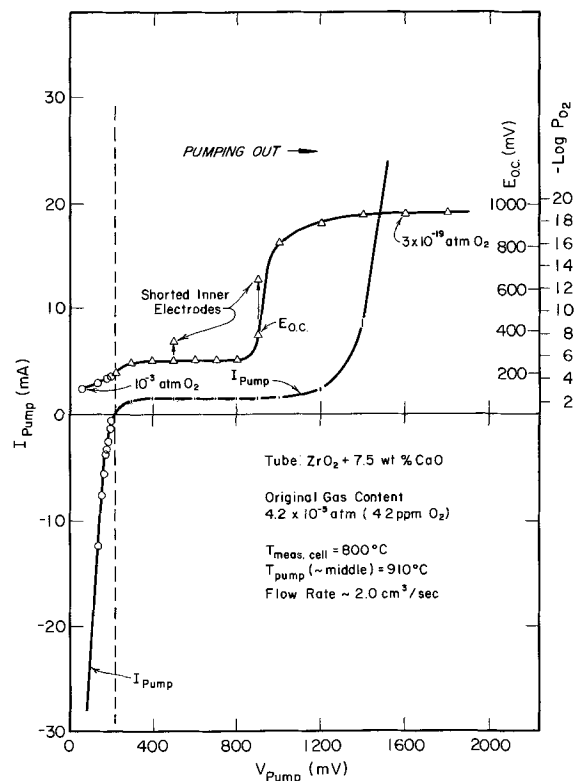


Fig. 8. Electrical characteristics of four-electrode cell arrangement using  $V_{pump}$  as independent variable.

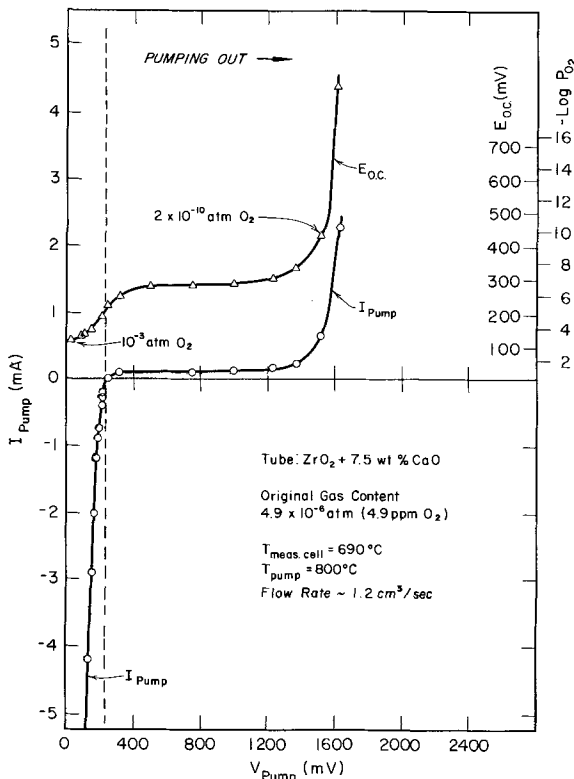


Fig. 7. Electrical characteristics of four-electrode cell arrangement using  $V_{pump}$  as independent variable.

were electrically independent. Furthermore, upon shorting the inner electrodes to form a three-electrode cell, the electrical characterization tests resulted in significant voltage changes in the open-circuit cell. Upon shorting the inner electrodes II and IV, the emf of the measuring cell rose almost instantaneously. Examples of this effect are shown in Fig. 6 and 8.

After the electrical characteristics of the system had been established using  $V_{pump}$  as the independent variable, the previously described feed-back control device was inserted between the measuring and pumping cells. This "potentiostat for gases" automatically applied a variable voltage to the upstream pumping cell in proportion to an error signal corresponding to the difference between the actual signal ( $E/T$ ) of the downstream open-circuit measuring cell and a desired value which is selected and read into the device. This type-zero control unit was used to reproduce the cell characteristics previously obtained and already presented as Fig. 6-8. In contrast to the characterization experiments, the use of the control unit involves the use of  $E_{oc}$  as the independent variable with  $V_{pump}$  and  $I_{pump}$  as the dependent variables. An example of the excellent agreement found is shown in Fig. 9 where the data points resulting from the use of the control unit are compared with the results from Fig. 8 which are given as dotted lines. In Fig. 9, values for  $I_{pump}$  are shown by brackets because some fluctuation in these values was observed. The agreement of the two sets of data of Fig. 8 and 9, and similar agreement for the test conditions of Fig. 6 and 7, demonstrates that the potentiostat operated effectively. Thus, in the closed-loop, type-zero, mode of operation, the system effected the automatic control of oxygen activity in flowing argon.

To check further the accuracy of the  $P_{O_2}$  achieved by the potentiostat as indicated by the measuring cell, the  $P_{O_2}$  was independently measured by another  $ZrO_2$ - $CaO$  probe far downstream in another furnace. For  $10^{-9} < P_{O_2} < 10^{-3}$  the values observed at this probe were essentially the same as those indicated at the measuring cell. Hence, the gas composition as indicated by the emf of the measuring cell is real and there is no electrical coupling between the electrodes of the pumping cell and those of the measuring cell.

In a few experiments involving the "potentiostat," the inner electrodes II and IV were again shorted to simulate a three-electrode cell. As shown in Fig. 9, anomalous results, equivalent to those previously ob-

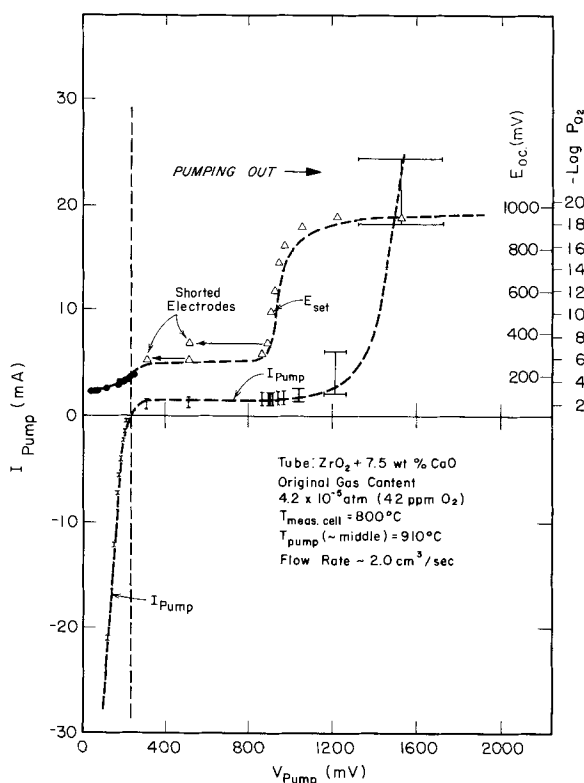


Fig. 9. Response of four-electrode cell arrangement to closed-circuit control unit (results from previous characterization experiments are indicated by dashed lines).

served in the characterization experiments, were again observed.

### Discussion

The polarization behavior indicated in Fig. 6-8 is similar to that reported previously (3, 10-14). However, the values of  $I_{pump}$  reported here (as a function of  $V_{pump}$ ) are "integrated" values over a long electrode, along which there exists a gradient in  $P_{O_2}$ . Such data (2) are not ideally suited for an interpretation of the electrochemical mechanisms. Moreover, in this work, fluxed platinum electrodes were used (because of their superior tenacity to the electrolyte), and such electrodes are known to exhibit higher polarization than nonfluxed porous platinum or sputtered Pt films (13). As previously observed, in attempting to pump residual oxygen out of the inert gas, plateaus in both pumping current and  $E_{O.C.}$  are experienced until substantial external voltage ( $V_{pump} \approx 1$  volt at our temperatures of study) has been applied to the pumping cell. As shown in Fig. 6-8, the realization of  $\log P_{O_2} < -6$  is achieved only upon the introduction of significant electronic conduction (rapid rise in  $I_{pump}$  with  $V_{pump}$ ) into the electrolyte. The accepted "high-voltage model," that oxygen is reduced and inserted directly into highly reduced zirconia at points adjacent to the otherwise effective triple-points of Pt-zirconia-gas, seems to be a consistent explanation (11, 12).

The ultimate realization of very low  $P_{O_2}$  on the order of  $10^{-20}$  atm is only possible through the presence of a small content of a buffering gaseous constituent like  $H_2$  or CO. In fact, to improve the buffer capacity of the gas at very low  $P_{O_2}$ , a few parts per million or more of residual hydrogen or water vapor could be admitted to the pump in the inert carrier gas (2). Obviously, the high proportion of electronic conduction in the "high-voltage" range provides a low Faradaic pumping efficiency.

In high-temperature service, many electrolyte tubes, especially those "partially stabilized" by 3-4 w/o CaO, have been found to leak molecular oxygen at reproducible rates which are quite temperature dependent.

In our system, the electrolyte tube was cooled immediately downstream from the measuring cell, thereby eliminating any oxygen leak after the meter.

Upon the addition of oxygen to the argon gas, some polarization is exhibited for small net voltages,  $O > (V_{pump} - E_{O.C.}) > -50$  mV. However, for greater net voltages, the oxygen pump exhibited ohmic behavior. By the use of large negative values of  $V$ , higher than those shown in Fig. 6-8, the oxygen content in the argon was driven up to as high as  $P_{O_2} = 0.02$  atm.

For the tube geometry and temperatures of our study, the necessity to use separate internal electrodes for the pump and gauge was proven. The electrical "crosstalk" between the pump and gauge should become less important for cells at lower temperature and for gases with oxygen  $O_2$  contents exceeding  $\sim 10^{-5}$  atm. Nevertheless, the use of four electrodes is generally advisable. We believe that the interference in the performance of the gauge when it shares an electrode common to the pump is a result of polarization. When these electrodes are common, the pumping voltage draws a small current (oxygen flux) from or to the gauge electrode, despite a very disadvantageous cell geometry. For measurements in the range of  $P_{O_2} \sim 10^{-6}$ , polarization can result in a large error in the value of oxygen activity reported by the gauge cell. For this reason, the extremely low values of  $P_{O_2}$  reported by Yuan and Kröger (2) for a three-electrode arrangement must be considered suspect.

The closed-loop system of Fig. 2 could be schematically represented as in Fig. 10(A). The transfer function for the solid electrolyte tube was determined to first-order approximation to be

$$G(s) = \frac{e_c}{e_p} = \frac{0.167(40s + 1)}{(160s + 1)(2.5s + 1)} = 0.167 G_1(s)$$

where  $s$  is the Laplace Transform operator  $d/dt$ ,  $e_p$  the input signal (input to pump),  $e_c$  is the output signal (reference cell output), and in Fig. 10A.,  $\xi_{ss}$  is the steady-state error signal.

The system of Fig. 10(A) can be more simply represented as a unity feed-back system as in Fig. 10(B), where  $G'(s) = KG_1(s)$  and  $K$  is the gain including that of amplifier, power amplifier, tube, and divider circuit. Thus

$$\frac{C}{R_{set}} = \frac{G'(s)}{1 + G'(s)}; C = Ae_c$$

where the gain of the amplifier is ten, the equivalent gain of the divider circuit is  $A$ , the gain of the limiter is unity, and the gain of the tube is 0.167. In general  $G'(s)$  has the form as below

$$G'(s) = \frac{K(z_1s + 1)(z_2s + 1)}{s^j(p_1s + 1)(p_2s + 1)(p_3s + 1)}$$

where  $z$ 's and  $p$ 's are constants, and  $j = 0, 1, 2$ , and so on, and the system is referred to as type zero, type one, type two, and so on, respectively. The steady-state

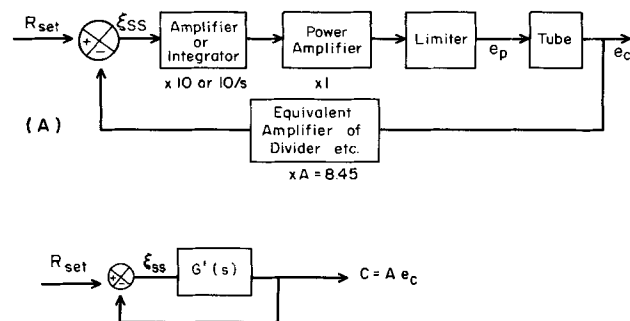


Fig. 10. (A) Schematic representation of closed-loop, type-zero control system. (B) Simplified schematic diagram of control system.

error,  $\xi_{ss}$ , for an input of  $R_{set}$ , defined as a step function of magnitude  $R$ , is given by the following for a unity feedback system as shown in Fig. 10 (B)

$$\begin{array}{lll} j = 0 & \text{type zero} & \xi_{ss} = \frac{R}{1 + K} \\ j = 1 & \text{type one} & \xi_{ss} = 0 \\ j = 2 & \text{type two} & \xi_{ss} = 0 \end{array}$$

$\xi_{ss} = 0$  for higher order systems.

Potentiostat circuitry can provide a factor  $1/s$  which is simply an integrator in the forward path so that

$$G'(s) = K \frac{G_1(s)}{s}$$

which is a type-one system and, therefore  $\xi_{ss} = 0$  for step inputs.

In general, it is desirable to use a control system having a type-one mode of operation, but the possibility of instabilities (overshoot, undamped oscillations, unbound output for a bounded input) in the network increases markedly with an increase in the value of  $j$ , the mode designation number. In our research, we have investigated both type-zero and type-one control systems. The following example calculation computes the steady-state error in the measuring cell for type-zero operation.

At 800°C, the thermocouple emf is 7.328 mV and 4.513 mV is added for the correction to Kelvin degrees. Hence, the thermocouple amplifier output is  $5.9205V$  ( $7.328 + 4.513$ )  $\times 500$ . For incremental variations around the quiescent point in the inputs to the divider, the equivalent amplifier of the cell, as shown in Fig. 3 and 4, has a gain of  $10 \times 5/5.92 = 8.45$ . With a gain of 10 in the amplifier of the forward path, the loop gain  $K$  is  $8.45 \times 10 \times 0.167 = 14.1$ . For  $R_{set} = (10E_c/E_t)$  of 2.392V the emf of the open-circuit cell should be 0.2832V for  $P_{O_2}' = 10^{-6}$  atm. However  $\xi_{ss} = R_{set}/(1 + K) = 2.392/15.10 = 0.1584V$  and therefore, the cell voltage =  $0.1584 \times 10 \times 0.167 = 0.2645V$ . The corresponding steady-state error of the measuring cell is therefore 18.6 mV. However, with a previous knowledge of the expected steady-state error, it is a simple matter to adjust the set point to compensate for the small error in  $E_{O,c}$ .

In an attempt to eliminate the  $\xi_{ss}$ , a type-one system was also investigated. This system featured an integrator instead of an amplifier in the forward path. However, the closed-loop, type-one system was found to be unstable; it could perhaps be made stable by circuit compensation but this further work was not thought to be worthwhile. For a given electrolyte tube the type-zero potentiostat could be calibrated with little difficulty and then be used for controlling the oxygen activities.

While the electrical characteristics and polarization behavior of zirconia-Pt-O<sub>2</sub> cells are of fundamental interest, in fact, the effective use of the feed-back control unit described here to establish oxygen activities in flowing argon does not depend on the details of the electrical characteristics of the pump, nor on the current efficiency of the pumping. If the flowing gas arriving at the downstream meter should deviate in oxygen activity from the desired level, a voltage as high as that allowed by the limiter is automatically applied to the pump until the error signal is minimized. Obviously, it is possible by the use of high flow rates, low cell temperatures, and highly buffered gas mixtures (CO/CO<sub>2</sub> and H<sub>2</sub>/H<sub>2</sub>O) to exceed the operational range of the system, i.e., the combination of electrolyte resistance and polarization can be too great to accomplish a desired oxygen activity from a given starting activity. Therefore, the utility of the instrument and the system will be realized only within a certain range of operating conditions. However, because the system is specific to oxygen activity, in principle, the unit could be used alternately for establishing the oxygen

activity in any sort of inert gas, or in buffered gas mixtures like CO/CO<sub>2</sub> or H<sub>2</sub>/H<sub>2</sub>O, etc., so long as excessively large pumping currents are not required to accomplish the desired activities.

In our laboratory, we have used the described system in several geometries to support several sorts of high-temperature investigations. In a study of tracer diffusion in oxides, the specimens were enclosed in a closed-end zirconia tube which was initially filled with a partial atmosphere of argon. The oxygen activity within the closed tube was controlled over many days at either  $10^{-2}$  or  $10^{-5}$  atm by use of the four-electrode system. A similar "enclosure" arrangement was used to control the oxygen activity and prevent oxidation in a high-temperature study of the creep of nickel wires. In an "open" flowing system, the evaporation of ZnO crystals was studied as a function of  $P_{O_2}$  in an inert carrier gas whose oxygen activity was established in the manner described here.

Potentially, the kinetics of oxygen addition or removal from an enclosed system at known and fixed oxygen activity could be measured by the recording of the current passed through the pumping cell. However, for this application, extreme care must be exercised that the pumping ability of the system is adequate, and that the Faradaic current efficiency is unity. Furthermore, the unavoidable molecular leakage of oxygen through the tube and the seals may contribute in only a minor way compared to the current passed in the pumping cell. The electrochemical semipermeability of oxygen ions resulting from electronic conduction in the electrolyte should not lead to inaccurate gauge readings. Finally, rapid desorption of oxygen from the pump and adequate mixing of gas in the enclosure are required to eliminate gradients within the chamber. The development of "perfect" high-temperature seals has proven difficult, and the use of a low-temperature seal for the enclosure requires the complication of a nonisothermal system. In short, the use of the control unit to measure kinetics will require a reaction of the proper rate, the careful design of a tight high-temperature enclosure, and an experimental demonstration that only oxygen ions are passed through the electrolyte.

### Acknowledgments

This research was supported under Contract F 33615-70-C-1103 which is an ARPA contract administered through the Materials Laboratory of Wright-Patterson Air Force Base. The authors appreciate the help and discussions with E. Mogollon.

Manuscript submitted April 2, 1973; revised manuscript received Oct. 25, 1973.

Any discussion of this paper will appear in a Discussion Section to be published in the December 1974 JOURNAL. All discussions for the December 1974 Discussion Section should be submitted by Aug. 1, 1974.

### REFERENCES

1. F. A. Kröger and H. J. Vink, "Solid State Physics," Vol. 3, Academic Press, New York (1956).
2. D. Yuan and F. A. Kröger, *This Journal*, **116**, 594 (1969).
3. M. Kleitz, C. Deportes, and P. Fabry, *Rev. Générals de Thermique*, **97**, 19 (1970).
4. J. Besson, C. Deportes, and M. Kleitz, Brevet (Patent) Français 1,580,819 (1969).
5. N. M. Beekmans and L. Heyne, *Philips Tech. Rev.*, **31**, 112 (1970).
6. N. M. Beekmans, L. Heyne, and A. T. Vink, U.S. Pat. 3,654,112 (1972).
7. H. S. Spacil, *Metal Progr.*, **96**, 5, 106 (1969).
8. H. S. Spacil, J. F. Elliott, D. L. Schroeder, and D. W. White at General Electric, U.S. Pat. 3,514,377 (1970).
9. W. M. Hickam and R. E. Witkowski, U.S. Pat. 3,650,934 (1972).
10. M. Kleitz, "Electrode Reactions in Solid Oxide Electrolytes," Thesis, Grenoble, 1968.
11. M. Kleitz, J. Besson, and C. Deportes, *Rev. Energ.*

- Primaire*, 3, 35 (1966); Proc. Journées Int. Études Piles Combust., 2nd, Bruxelles, S.E.R.A.I., 354 (1967).
12. H. Yanagida, R. J. Brook, and F. A. Kröger, *This Journal*, 117, 594 (1970).
13. R. J. Brook, W. L. Pelzmann, and F. A. Kröger, *ibid.*, 118, 185 (1971).
14. T. H. Etsell and S. N. Flengas, *ibid.*, 118, 1890 (1971).
15. R. A. Rapp, U.S. Pat. 3,699,032 (1972).

## A Dissolution-Redeposition Mechanism for the Roughening of Platinum Electrodes by Cyclic Potential Programs

D. F. Untereker\*<sup>1</sup> and S. Bruckenstein\*

Chemistry Department, State University of New York at Buffalo, Buffalo, New York 14214

### ABSTRACT

Rotating platinum disk-gold ring and platinum disk-platinum ring electrodes were used to study the roughening of platinum produced by a triangular wave potential program. The rate of roughening was found to decrease with increasing rotation speed and/or decreasing potential scan rate. The amount of soluble platinum collected on the gold ring electrode during the roughening process increased with angular velocity. The data obtained are consistent with a mechanism in which soluble platinum produced during both the anodic and cathodic disk potential scans is redeposited on the electrode surface at cathodic potentials.

Much has recently been published about the roughening of platinum electrodes caused by potential cycling (1-7). Although this phenomenon has been known for a number of years [see (1)], its mechanism has never been conclusively established. Gilman (4) assumed that the roughening mechanism involves the making and breaking of Pt-O bonds because both the oxidation and reduction of platinum had been reported in nearly all experiments that increase the electrode roughness. The roughening process was thought to be related to the migration of platinum species on the electrode surface. The activation energy for this migration process was said to arise as a result of the simultaneous reduction of a large amount of platinum oxide. Hoare (3), however, reported that roughening of platinum electrodes occurs only when the electrode potential went into the hydrogen evolution region and attributed this result to a mechanism involving hydrogen embrittlement.

Biegler (7) gave a very complete discussion of platinum electrode roughening and characterized the process in considerable detail. He concluded that (a) the roughening rate increased with the anodic limit of the potential scan; (b) hydrogen adsorption had little, or a negative, effect on the electrode roughening rate; (c) only potential programs which involved rapid reduction of platinum oxide caused roughening, and, in fact, those which did not caused smoothing; (d) the roughening rate decreased when the solution was stirred; and (e) dissolved platinum was observed in the solution after prolonged roughening of a platinum electrode. The last two observations are not explained by the previously proposed roughening mechanisms.

Since soluble platinum species have been detected along with electrode roughening (7), it seemed probable to us that a link between the two existed. Biegler rejected dissolution and redeposition of platinum as a possible mechanism because he found that platinum particles were not removed from the electrode when he made electron micrograph replicas of the surface. He reasoned that a mechanism involving deposition of

soluble platinum would form an epitaxial layer, which would be readily removed from the electrode surface. Evidence, presented below, however, shows conclusively that the roughening mechanism does involve the soluble platinum species *via* a solution/redeposition mechanism.

Rotating disk and ring-disk electrodes seemed to be excellent experimental tools to study the details of the roughening of platinum and were used in the experiments described below.

### Experimental

**Equipment.**—A conventional four electrode potentiostat, cell, and rotator were used. The electrode rotator was supplied by the Pine Instrument Company, of Grove City, Pennsylvania. An EAI XYY' Variplotter was used to record the experimental data.

A platinum disk-gold ring electrode (PDGRE) and platinum disk-platinum ring electrode (PDPRE), both made in our laboratory, were used in the experiments reported below.

All potentials are reported *vs.* the saturated calomel electrode (SCE).

**Solutions.**—The supporting electrolyte was 1M H<sub>2</sub>SO<sub>4</sub>.

Solutions were deoxygenated by bubbling N<sub>2</sub> gas through them for 20 min preceding the start of experiments. The supporting electrolyte was also bubbled with N<sub>2</sub> during cyclic potential scanning and anodic potential halt experiments in order to remove oxygen generated at anodic potentials. Data were recorded with N<sub>2</sub> passing over, not through, the solution.

Solutions were prepared from triply distilled water and Baker reagent grade sulfuric acid.

**Electrode pretreatment.**—The electrode pretreatment consisted of polishing the electrode with a slurry of 0.05 $\mu$  alumina and water before introducing it into the cell, then potential cycling it several times between -0.2 and 1.6V at 2500 rpm. This procedure yielded reproducible *i*-*E* curves, and was used between each experimental determination of disk electrode roughness.

**Measurement of surface area.**—The roughness factor of the platinum disk of the PDGRE, pretreated as

\* Electrochemical Society Active Member.

<sup>1</sup> Present address: Chemistry Department, University of North Carolina, Chapel Hill, North Carolina 27514.

Key words: platinum roughening, platinum dissolution, platinum redeposition, ring disk.

described above, was always about 1.8 as measured by the hydrogen desorption charge.

The data reported in Fig. 1 were calculated as follows. After the cyclic potential program had been applied for the required time, the total disk electrode anodic charge, obtained on a linear potential sweep between  $-0.27$  and  $0.4V$ , was determined. This value was then divided by the analogous charge obtained at the start of the experiment. This calculated ratio, the "roughness ratio," is an accurate measure of any change in the surface area of the disk electrode produced by potential cycling it.

### Results and Discussion

#### *Effect of angular velocity on electrode roughening.*—

A platinum disk electrode was roughened in  $1M H_2SO_4$  by applying a repetitive triangular sweep voltage program for various times at four selected rotation speeds. The electrode was cycled between  $0.0$  and  $1.8V$  vs. SCE at  $25$  Hz, i.e., at  $90$  V/sec.

Figure 1 shows the plot of the roughness ratio,  $R/R_0$ , as a function of cycling time for angular velocities of  $400$ ,  $900$ ,  $1600$ , and  $2500$  rpm. (The roughness ratio of the electrode is defined in Experimental.) The maximum absolute roughness shown in Fig. 1 is about  $3.2$

The rate of roughening increases with decreasing angular velocity. Although not shown in Fig. 1, the rate of roughening also increases with cycling rate and anodic disk potential limit.

Our polished electrode, with its initial roughness factor of  $1.8$  was mirror-like. However, after the electrode roughened about  $50\%$ , its surface became slightly dull. This dulling increased until, at values of  $R/R_0$  greater than  $2$ , the surface had a hazy appearance. The haze was easily removed from the electrode surface by hand polishing with  $0.05\mu$  alumina, provided the electrode was still wet, but it required considerable effort to remove the haze after the electrode surface had dried. This observation may explain why Biegler (7) found no platinum particles on his electron micrograph replicas.

Biegler also mentions that his data were not very reproducible (7), not only for different electrodes, but also for repetitive experiments using the same electrode. Similar behavior was also found by us. When data were obtained during an experiment, such as reported in Fig. 1, the roughness ratio sometimes changed randomly. This phenomenon was usually observed for  $R/R_0$  values larger than those shown in Fig. 1. In such situations, if a mirror was placed under the cell in order to observe the rotating electrode surface while the roughening process was occurring, the surface would become hazy and dark, and then golden in appearance. The golden color slowly intensified, provided electrode potential cycling was continued, but quickly

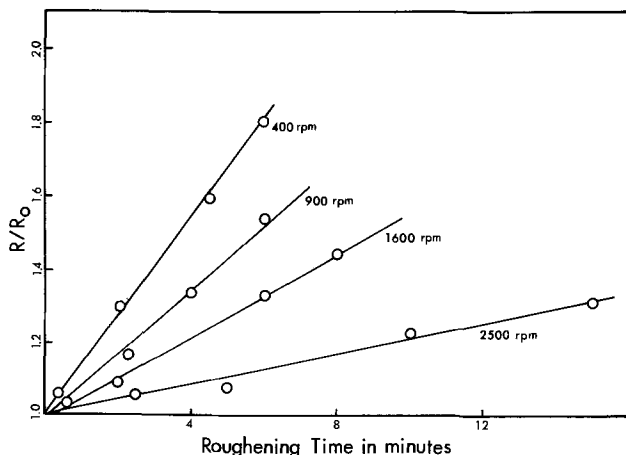


Fig. 1. Relative rates of roughening of platinum disk electrode as a function of time at selected angular velocities.  $1M H_2SO_4$ . Potential cycled between  $0.0$  and  $1.8V$  at  $25$  Hz.  $R_0 \approx 1.8$  at  $t = 0$  for each angular velocity.

(in about 1 sec) changed to a gray deposit when the cycling was stopped at  $0.0V$ . If the electrode potential was cycled for a long period of time, the golden deposit became orange and had the electrochemical properties attributed to phase platinum oxide (8). Data resulting from experiments where phase platinum oxide was formed were not used, since the roughening phenomena of concern to us did not involve phase oxide formation.

*Proposed mechanism of roughening.*—The rate of roughening, as determined from Fig. 1, depends on angular velocity. Therefore, a soluble species must be involved in the rate-determining step for the roughening process. If only surface rearrangements of platinum atoms occurred, as had been previously postulated, no such angular velocity dependence would be observed.

Since the only soluble species produced during cyclic potential scans in  $1M H_2SO_4$  at platinum electrodes are hydrogen, oxygen, Pt(II) (9), and Pt(IV) (10), the angular velocity dependence would have to be associated with the production of one or more of these species.

From Gilman's (4) and Biegler's (7) results, and confirmed by our data, hydrogen evolution need not occur to roughen a platinum electrode, contrary to Hoare's views (3).

It also seems unlikely that oxygen is involved in the actual roughening process since evolving oxygen at a platinum electrode for long periods of time caused no appreciable roughening. Also, there would seem to be little connection between oxygen evolution and the observation that the rate of roughening depends on the cathodic potential scan program (4, 7).

Finally, although hydrogen need not be evolved to roughen a platinum electrode, the cathodic potential limit must reach about  $0.3V$ , or no roughening occurs.

These observations can only be rationalized if at least one soluble platinum species is taking part in the roughening process.

Two different processes, involving soluble platinum, could lead to roughening. Either platinum dissolves from the electrode surface (forming pits), or it dissolves and redeposits on the electrode surface (forming hills and pits). Figure 1 is not consistent with the first possibility since more soluble platinum would be carried away from the disk electrode surface at higher angular velocities than at low ones, and thus, Fig. 1 would show higher roughening rates at higher, not lower angular velocities. Also, the previously reported dependence of roughening on the potential scan program (4, 7) is not consistent with a mechanism solely involving dissolution. Experimental results (4, 7), in fact, show that under conditions where only dissolution of platinum would occur (slow cathodic scans), smoothing of the platinum surface results. Finally, the roughened surface could not be wiped off an electrode if only pits were formed.

A mechanism involving both platinum dissolution and redeposition at cathodic potentials is consistent with Fig. 1 and the other data. This mechanism also predicts that the increased rate of roughening found by Biegler (7), as the anodic potential scan limit is made more anodic, must result from a larger quantity of soluble platinum species being produced.

Probably both Pt(II) and Pt(IV) species are involved in the roughening process. The relative contribution from each species is dependent on convection-diffusion and the potential cycling program, i.e., the amount of platinum that can be redeposited at the electrode depends on the amount of soluble platinum species in the diffusion layer when the electrode potential becomes sufficiently negative to reduce the platinum to Pt(0). The contribution of the Pt(II) species to roughening should be somewhat larger than that from the Pt(IV) species since the Pt(II) is produced on the cathodic potential scan (9), much nearer to the redeposition potential.

For this reason, the quantity of soluble Pt(II) produced during reduction of the platinum oxide (9) that was formed at increasing anodic potentials was determined.

**Effect of anodic scan potential limit on Pt(II) formation.**—The disk of a platinum disk-platinum ring electrode was oxidized for 60 sec at several anodic potentials,  $E_a$ , in 1M  $H_2SO_4$ . After the oxidation, the disk potential was linearly scanned at 100 mV/sec from  $E_a$  to 0.0V at 2500 rpm, while the ring electrode was held at 1.2V. At this ring potential any Pt(II) produced by the disk electrode will be oxidized to Pt(IV) (9). The ring electrode current-disk potential curves recorded during the linear cathodic voltage sweep of the disk electrode were integrated and the resulting charge plotted vs.  $E_a$ . Figure 2 shows the experimental results obtained on the two consecutive days. The data in this figure support a dissolution-redeposition mechanism since, as predicted, the amount of soluble Pt(II) produced increases with increasing anodic potential scan limit.

**Rate of electrode area increase.**—Further evidence supporting the dissolution-redeposition mechanism was obtained by quantitatively correlating the amount of soluble platinum produced during the roughening with the increase in electrode surface area. In this experiment the amount of platinum dissolved was determined using the gold ring of a gold ring-platinum disk electrode (PDGRE). The gold ring electrode was held at 0.0V while the disk electrode was potential cycled under the conditions in Fig. 1. The amount of platinum dissolved from the disk electrode at each rotation speed was calculated from the collection efficiency of the ring-disk electrode and the amount of platinum oxide formed by oxidizing the gold ring electrode at 1.3V (12). It was assumed that all platinum deposited on the gold was available for oxidation.

At 3600 rpm,  $8 \times 10^{-7}$  mg/cycle of platinum dissolved. A negligible change in the area of disk electrode was observed.

At 400 rpm much less soluble platinum was collected on the gold ring, i.e., only about  $1.2 \times 10^{-7}$  mg/cycle dissolved from the disk. However, the rate of surface area increase of the disk was significant, i.e.,  $9.2 \times 10^{-5}$  cm<sup>2</sup>/cycle.

The difference between the amount of soluble platinum leaving the disk electrode at 3600 and at 400 rpm corresponds to the extra amount of soluble platinum redeposited at 400 rpm as compared to 3600 rpm. This difference,  $6.8 \times 10^{-7}$  mg Pt/cycle, divided into the difference in rates of area change between 400 and 3600 rpm,  $9.2 \times 10^{-5}$  cm<sup>2</sup>/cycle, gives the surface area increase per milligram of platinum involved in roughening,  $\sim 1.4 \times 10^2$  cm<sup>2</sup>/mg.

Feltham and Spiro (12) recently investigated the deposition of platinum under a variety of electrochemical conditions. Their Table I indicates that a surface area increase of about  $100 \pm 25$  cm<sup>2</sup>/mg of platinum deposited would be typical. Our result of  $\sim 1.4 \times 10^2$  cm<sup>2</sup>/mg, based on the dissolution-redeposition hypo-

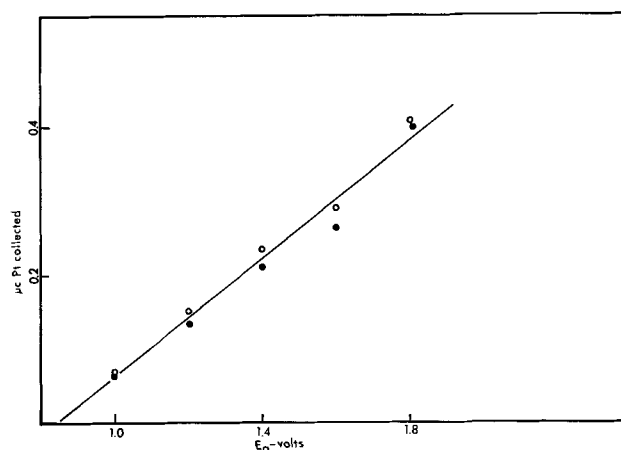


Fig. 2. Amount of soluble Pt(II) collected at ring electrode during reduction of platinum oxide formed at various anodic potentials ( $E_a$ ). Filled and unfilled circles represent data obtained on two consecutive days. Oxidation time is 60 sec at each  $E_a$ . Supporting electrolyte is 1M  $H_2SO_4$ .

thesis for roughening of platinum, agrees well with their values.

Thus, not only does the dissolution-redeposition mechanism for roughening qualitatively describe all aspects of roughening of platinum electrodes by potential cycling, but it also gives quantitative agreement with other literature concerned with platinum deposition.

#### Acknowledgment

This research was supported by the United States Air Force Office of Scientific Research under Grant No. AFOSR 70-1832.

Manuscript submitted July 27, 1973; revised manuscript received Oct. 15, 1973.

Any discussion of this paper will appear in a Discussion Section to be published in the December 1974 JOURNAL. All discussions for the December 1974 Discussion Section should be submitted by Aug. 1, 1974.

#### REFERENCES

1. S. Shibata, *J. Chem. Soc. Japan*, **79**, 239 (1958).
2. F. C. Anson and D. M. King, *Anal. Chem.*, **34**, 362 (1961).
3. J. P. Hoare, *Electrochim. Acta.*, **9**, 599 (1964).
4. S. Gilman, *J. Electroanal. Chem.*, **9**, 276 (1965).
5. S. B. Brummer, J. I. Ford, and M. J. Turner, *J. Phys. Chem.*, **69**, 3424 (1965).
6. T. Biegler, *This Journal*, **114**, 1261 (1967).
7. T. Biegler, *ibid.*, **116**, 1131 (1969).
8. S. D. James, *ibid.*, **116**, 1681 (1969).
9. D. C. Johnson, D. T. Napp, and S. Bruckenstein, *Electrochim. Acta.*, **15**, 1493 (1970).
10. D. A. Rand and R. Woods, *J. Electroanal. Chem.*, **35**, 209 (1972).
11. D. F. Untereker, Ph.D. Thesis, State University of New York at Buffalo, Buffalo, New York, chap. VI.
12. A. M. Faltham and M. Spiro, *J. Electroanal. Chem.*, **35**, 181 (1972).



# A Chalcogenide Glass Electrode Sensitive to Cupric Ions

Raymond Jasinski,\* Isaac Trachtenberg,\* and Gary Rice

Texas Instruments Incorporated, Dallas, Texas 75222

## ABSTRACT

Electrodes formed from the chalcogenide glass,  $\text{Cu-As}_2\text{S}_3$ , are selective to cupric copper in concentrated solutions of chloride, bromide, nitrate, and acetate over the concentration range of  $10^{-1}$  to at least  $10^{-6}\text{M}$  copper. Nernstian slopes of approximately 30 mV/decade concentration changes were observed in nitrate and acetate solutions; slopes of 50 mV/decade were observed in 1M chloride and bromide electrolytes. A slope of 40 mV/decade was observed in 0.1M chloride solution. The active phase in the electrode material appears to be "sinnerite" ( $\text{Cu}_6\text{As}_4\text{S}_9$ ); data on the sensing mechanism are presented.

The development of ion-selective electrodes is an active area of analytical electrochemistry (1-3). One of the more technologically important measurements amenable to this technique is that for copper in process streams and waste waters. A variety of sensor electrodes have been suggested (4-9); a few are available commercially (10). All are based on cuprous or cupric sulfide and differ primarily according to the specific technique used to achieve a reasonable electronic conductivity within the sensor element and the technique used to form the active element.

The present paper discusses the preparation, performance, and properties of a copper sensitive chalcogenide glass electrode prepared from copper and arsenic trisulfide. Information will also be presented relative to the cupric ion sensing mechanism for this electrode.

## Experimental

Arsenic trisulfide was prepared by heating the elements (99.9999 pure) in a sealed quartz ampul at  $525^\circ\text{C}$  for about 90 hr. The resulting glass was deep red and, in 50 mil slices, was transparent. The infrared spectrum of the material prepared as described agreed with that published for arsenic trisulfide. Glasses prepared from commercial arsenic trisulfide were often opaque to the infrared and led to erratic copper sensors. Both effects were ascribed to residual impurities in the starting chemicals.

To prepare the sensor material, the crushed glass was mixed with the appropriate amount of copper metal, cupric oxide, or cupric sulfide, placed in a quartz ampul which was evacuated, sealed, and placed in a furnace for 70 hr at  $700^\circ\text{C}$ . The temperature was then reduced to  $400^\circ\text{C}$  for 1 hr and the ampul was air quenched to room temperature.

Electrodes were formed in the manner described previously (11). The majority of the  $\text{Cu}^{+2}$  concentration measurements were taken with an ohmic contact made directly to the sensor glass slice. Entirely equivalent data were obtained when the membrane configuration was used, i.e., when the glass slice was used to separate the solution being studied from an internal solution of constant composition; electrical contact was then made via a commercial reference electrode placed in the internal solution.

Potentials were also measured as previously described (11). An Orion Ag/AgCl reference electrode was used in the double junction mode to minimize contamination of some test solutions; 10%  $\text{KNO}_3$ , was used as the outer filling solution. Standard copper solutions were prepared by dissolving the appropriate copper salt in the following supporting electrolytes:

- (i) 1M KCl, pH 2
- (ii) 3M KCl, pH 2

- (iii) 1M KCl + 1M HCl
- (iv) 1M NaBr, pH 2
- (v) 0.1M  $\text{KNO}_3$ , pH 2
- (vi) 1M sodium acetate, pH 4
- (vii) 0.1M sodium acetate + 0.9M  $\text{NaNO}_3$ , pH 4

No attempt was made to remove residual copper contamination from the supporting electrolytes; it was not necessary to deaerate the solutions.

Three test electrodes were monitored simultaneously in order to sort out spurious electrode effects and spurious solution effects; for simplicity of presentation, the data from only one electrode in each set will be presented here.

Unless otherwise indicated, all measurements were taken in stirred solutions, which was accomplished with a paddle stirrer (275 rpm). The consequences of stirring will be discussed.

In order to obtain a reproducible surface before each series of measurements, the electrodes were etched with 10% KOH, rinsed with the appropriate electrolyte, re-etched, and rerinsed. The electrode was then equilibrated before use in  $10^{-1}\text{M}$  cupric ion solution for 1 hr. The chemistry involved in this important activation step will be discussed.

Measurements were also taken with two commercially available copper sensitive electrodes, the Coleman "Copper Ion-Sensitive Electrode," No. 3-804, and the Orion Model 94-29A. The purpose here was not to criticize or evaluate commercial electrodes *per se*, but to determine if significant differences in performance existed relative to the copper-arsenic trisulfide electrodes.

## Results and Discussion

*Electrode composition.*—Visual observation of the glasses indicated a heterogeneous multiphase system with crystalline material distributed randomly throughout an amorphous matrix.

The strongest lines in all x-ray diffraction patterns were those ascribable to "sinnerite," a recently reported mineral (12, 14). In no case was it possible to confirm the presence of copper metal, cupric sulfide, cuprous sulfide, or the oxides, even when the initial source of copper was cupric sulfide or cupric oxide.

Sinnerite is reported to exist in two crystalline modifications, cubic  $\text{Cu}_6\text{As}_4\text{S}_9$  ( $3\text{Cu}_2\text{S}\cdot\text{As}_2\text{S}_3$ ) and triclinic  $\text{Cu}_{6.3}\text{As}_1\text{S}_9$ . Both modifications were found in the melt containing 0.25 mole fraction added copper. At lower concentrations of copper, the phase found depended on the age of the sample. This was correlatable with the preparative conditions, according to the following argument. The initial precipitate which formed on quenching the melt was the cubic phase, and was metastable at room temperature. On standing, copper slowly diffused through the glass forming the more stable triclinic distorted material near the

\* Electrochemical Society Active Member.  
Key words: arsenic trisulfide, sinnerite, copper sulfide, potentiostatic activation, electrodes, ion selective.

$\text{Cu}_{6.3}\text{As}_4\text{S}_9$  composition. Indeed the triclinic lines were visible primarily in the diffraction patterns of the oldest samples and in the slow-cooled samples. The optical micrographs were consistent with such a crystal growth mechanism, in that a long (> 18 hr) reaction time at 550°C gave needle-like dendritic growth while the slow-cooled sample gave large crystals.

Resistivity measurements (d-c) were taken as described previously (11), i.e., with 1 to 2 mm thick slices onto which gold had been evaporated. As shown in Table I, resistivity decreased with increasing additions of copper; the same effect was obtained regardless of the form of the initially added copper. This is consistent with the x-ray data in that the conductive crystalline material formed in the melt was independent of the starting copper compound.

The primary conclusion to be drawn from the data of Table I is that the conductivity of the high copper-content glasses is sufficient in itself for stable electrochemical operation and that the addition of conductive binders such as  $\text{Ag}_2\text{S}$  or graphite is not necessary.

The spread in the data represent the spread in resistivities measured for different slices taken from the same melt. Obviously the slices are also heterogeneous along the length of the melt as well as along the surface of a slice. However this variation in resistivity decreased as the copper content of the melt was increased above mole fraction 0.2, as would be expected if the conductivity were due primarily to the crystalline phase.

A rigorous correlation of electrode performance with electrode composition, crystalline phase, or physical properties was not attempted. It was generally observed however that electrodes containing a mole fraction of copper at or less than 0.2 were less sensitive to changes in  $\text{Cu}^{++}$  concentration below  $10^{-4}\text{M}$  than electrodes containing larger amounts of copper. Unless otherwise noted, all data presented in this paper were taken with electrodes containing 0.25 mole per cent (m/o) copper.

Since electrode performance depended significantly upon the type of supporting electrolyte the experimental results will be grouped according to this parameter.

**Performance in nitrate and acetate solutions.**—The first series of electrochemical measurements to be described are those taken with 0.1M  $\text{KNO}_3$  as the supporting electrolyte; complex ion formation is minimal (13), and soluble cuprous species are unstable.

Shown in Fig. 1 are the potential-concentration relationships for an electrode operated in the following manner. The electrode was first etched and then placed directly into  $10^{-6}\text{M}$  cupric nitrate, followed by solutions of increasing copper ion concentration. Data were recorded when potential drift was less than 2 mV/min. After exposure to  $10^{-2}\text{M}$   $\text{Cu}^{++}$ , the electrode was exposed to decreasing concentrations of copper (in order of magnitude changes) to  $10^{-6}\text{M}$ , and then to concentrations increasing to  $10^{-1}\text{M}$ . After 30 min at this concentration, the copper content was decreased incrementally to  $10^{-6}\text{M}$  and increased incrementally to  $10^{-1}\text{M}$ .

The slope of the first of these potential-concentration curves is "super-Nernstian," i.e., with a slope greater than 30 mV/decade; the return to lower concentrations gave a slope of less than 30 mV/decade. On subsequently increasing concentration, Nernstian

Table I. Resistivities of copper-arsenic trisulfide glasses

Mole fraction copper	Resistivity (ohm-cm)	
	CuO added	Cu added
0.05	$3 \times 10^8$ to $6 \times 10^{10}$	$2 \times 10^7$ to $4.3 \times 10^7$
0.10	$3 \times 10^8$ to $3 \times 10^8$	$4.1 \times 10$ to $4 \times 10^4$
0.15	$4 \times 10^8$ to $1 \times 10^9$	$4 \times 10^2$ to $3 \times 10^3$
0.20	$1 \times 10^2$ to $8 \times 10^3$	$4 \times 10^2$ to $3 \times 10^3$
0.25	46 to 50	64 to 69
0.30	—	36 to 37

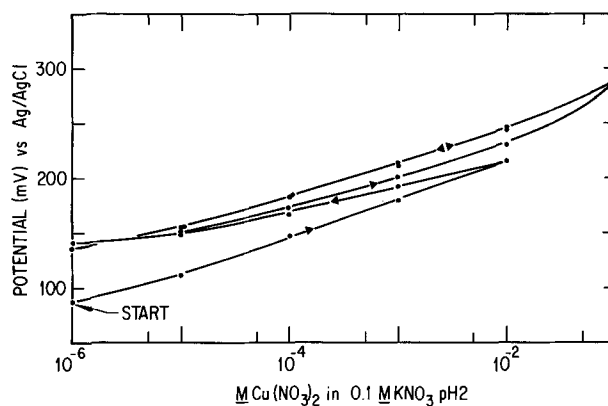


Fig. 1. Performance of a freshly etched, not activated copper-arsenic trisulfide electrode.

behavior was observed from  $10^{-4}$  to  $10^{-2}\text{M}$ ; the potential at  $10^{-2}\text{M}$  showed a slow but real drift to more positive values; the potential change between  $10^{-2}$  and  $10^{-1}$  was 60 mV. The next cycle between  $10^{-1}$  and  $10^{-6}\text{M}$   $\text{Cu}^{++}$  showed no hysteresis of the type described and showed Nernstian behavior from  $10^{-2}$  and  $10^{-5}\text{M}$  copper. Such measurements formed the basis for the activation procedure described, i.e., to obtain a stable, reproducible, and reversible sensor, the freshly etched electrode first had to be exposed to high concentrations of cupric ion.

The time for activation in  $10^{-1}\text{M}$  cupric nitrate (in 0.1M  $\text{KNO}_3$ ) was evaluated by measuring the potential-concentration dependencies after the electrodes were etched and exposed to the solution for periods of 45 min, 1 hr, 2.5 hr, and overnight. There was little difference in the slopes of the response curves and the sensitivity to low  $\text{Cu}^{++}$  concentrations, although, as exposure time was increased, the curves were always displaced to higher potentials. There was also considerable hysteresis, after the electrode had been equilibrated in  $10^{-1}$  cupric nitrate for more than 2.5 hr, between the first exposures of the electrode from  $10^{-1}$  to  $10^{-6}\text{M}$  cupric nitrate relative to subsequent cycles in concentration between these limits.

Shown in Fig. 2 are the concentration-potential relationships determined in nitrate solutions for a properly activated electrode; included for comparison are the performances of the commercial electrodes. Below  $10^{-2}\text{M}$  copper, the Orion electrode and the copper-arsenic sulfide electrodes were essentially identical in performance, with Nernstian slopes of 31 and 27 mV/decade, respectively. Above  $10^{-2}\text{M}$  copper, the copper-arsenic trisulfide electrode showed a slight super-Nernstian response. Below  $10^{-4}\text{M}$  copper, this particular Coleman electrode showed little sensitivity

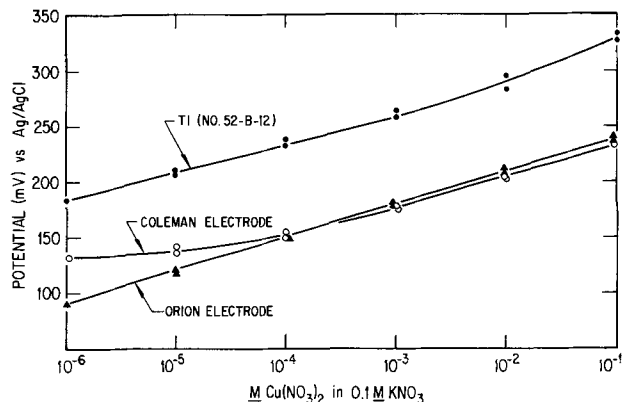


Fig. 2. Steady-state responses of a copper arsenic trisulfide electrode, and two commercial electrodes, to varying copper ion concentrations in a supporting electrolyte of 0.1M  $\text{KNO}_3$ .

to changing copper ion concentration; above  $10^{-4}\text{M}$  copper the two commercial electrodes were essentially identical in response.

Response times for all electrodes were good, e.g., at  $10^{-4}\text{M}$  copper, steady state was achieved within 1-3 min; here steady state is defined as a potential stable to less than 1 mV drift in 3 min.

The three electrodes showed little dependence on stirring. For example, 2 min after stirring of the  $10^{-2}\text{M}$  copper solution was terminated, the potentials of the Cu-As<sub>2</sub>S<sub>3</sub>, Orion, and the Coleman electrodes decreased by 1.9, 1.8, and 0.2 mV, respectively.

The effect of pH on sensor response in nitrate solution is shown in Fig. 3. In the absence of Cu<sup>++</sup>, the electrode is pH sensitive, probably due to some absorption or reaction of the surface with hydroxyl ion. However in the presence of cupric ion, the electrode response is independent of pH until cupric hydroxide begins to precipitate. Even as this takes place, the electrode potential followed the remaining copper in solution until the detection limit of the electrode was reached. The data shown were for an electrode prepared from CuO; identical results were obtained for an electrode prepared from copper metal, as would be expected in view of the x-ray studies described above.

Responses of the Cu-As<sub>2</sub>S<sub>3</sub> electrodes in the acetate solutions are summarized in Fig. 4; included for comparison is a response curve for the electrode in 0.1 nitrate solution. Prior to each run the electrode was etched and activated to remove possible complications from prior history.

At and below  $10^{-3}\text{M}$  added copper, the slopes of the curves were basically identical, with slopes of approximately 30 mV/decade. The curves did shift to lower potentials with increasing acetate concentration at a fixed added concentration of copper. Qualitatively this is consistent with the argument that the electrode responds to uncomplexed cupric ion which decreases in concentration as acetate increases (13). A rigorous calculation of the shifts in potential with changing acetate concentration was not done due to shifts in  $E_0$  of the electrodes by virtue of the re-etching procedure

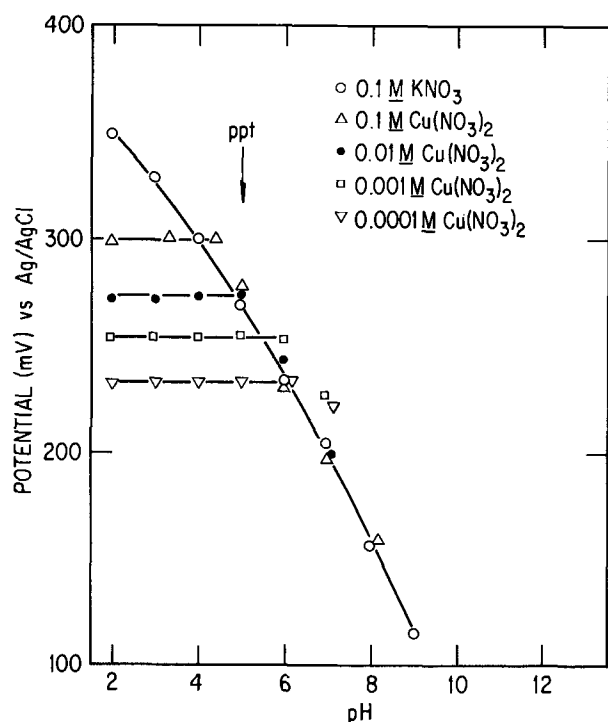


Fig. 3. Response of a  $(\text{CuO})_{0.15}(\text{As}_2\text{S}_3)_{0.85}$  electrode, in the membrane configuration, to varying cupric ion concentration as a function of pH. All solutions were 0.1M KNO<sub>3</sub>.

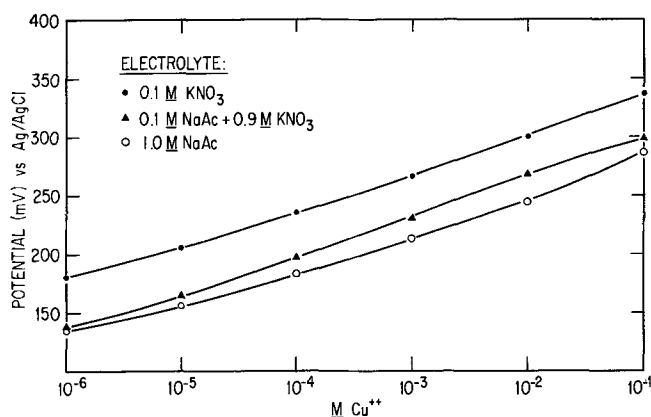


Fig. 4. Responses of a copper arsenic trisulfide electrode in nitrate solution, in 0.1M sodium acetate solution and in 1.0M sodium acetate solution.

followed between each series of concentration measurements.

*Performance in chloride and bromide solutions.*—Copper-arsenic trisulfide electrodes operated in these solutions also required the activation step before stable Nernstian response could be obtained. There was little difference between electrodes equilibrated in  $10^{-4}\text{M}$  cupric chloride solutions (1M KCl, pH 2) for 1 hr and those equilibrated for 5 hr. Electrodes equilibrated overnight were less sensitive to changes in cupric ion concentration at and below  $10^{-5}\text{M}$ . After a 40 hr exposure to  $10^{-1}\text{M}$  CuCl<sub>2</sub>, all electrodes showed a significant loss in activity below  $10^{-4}\text{M}$  copper, i.e., a lowering in sensitivity to changes in cupric ion concentration.

Shown in Fig. 5 are the steady-state responses to varying cupric ion concentrations in 1M KCl for a copper-arsenic trisulfide electrode and, for comparison, an Orion and a Coleman electrode. The copper-arsenic trisulfide electrode showed Nernstian behavior over the range of  $10^{-5}$  to  $10^{-2}\text{M}$  copper, but with a slope of  $49 \pm 2$  mV/decade, rather than  $\sim 30$  mV/decade. The Nernstian slope for the Coleman electrode was 55 mV/decade from  $10^{-4}$  to  $10^{-1}\text{M}$  cupric ion; the potentials oscillated  $\pm 2$  mV at steady state. The Orion electrode demonstrated a saturation effect at high copper concentrations in this high chloride containing solution. This was predicted by the operations manual supplied with the electrode and is apparently due to the reaction (17)



The film of AgCl would cover the active surface of the electrode, giving sensitivity to Cl<sup>-</sup> rather than Cu<sup>++</sup>. Between  $10^{-6}$  and  $10^{-4}\text{M}$  copper, the potential change of the Orion electrode gave slopes in the 35-50 mV range. Thus the performance of these electrodes at high chloride ion and low Cu<sup>++</sup> concentrations are more complicated than predicted from the standard solubility product mechanism.

All copper-arsenic sulfide electrodes showed a stirring dependence when operated in 1M KCl and 1M NaBr solutions. The most sensitive copper arsenic trisulfide electrodes generally showed a drop in potential of 30 mV 2 min after stirring was stopped in the  $10^{-1}\text{M}$  copper chloride solution; smaller changes were observed at the lower copper containing solutions, e.g., 15 mV at  $10^{-4}$  cupric ion. This stirring dependence also varied from electrode to electrode, in the best case being only 10 mV/2 min at  $10^{-1}\text{M}$  cupric and 3.3 mV/2 min at  $10^{-3}\text{M}$ . However these electrodes were less sensitive to changes in cupric ion concentration at low levels of copper (e.g.,  $10^{-5}\text{M}$ ). A tentative explanation for this stirring dependence will be given below. A correlation of potential with stirring rate was not made.

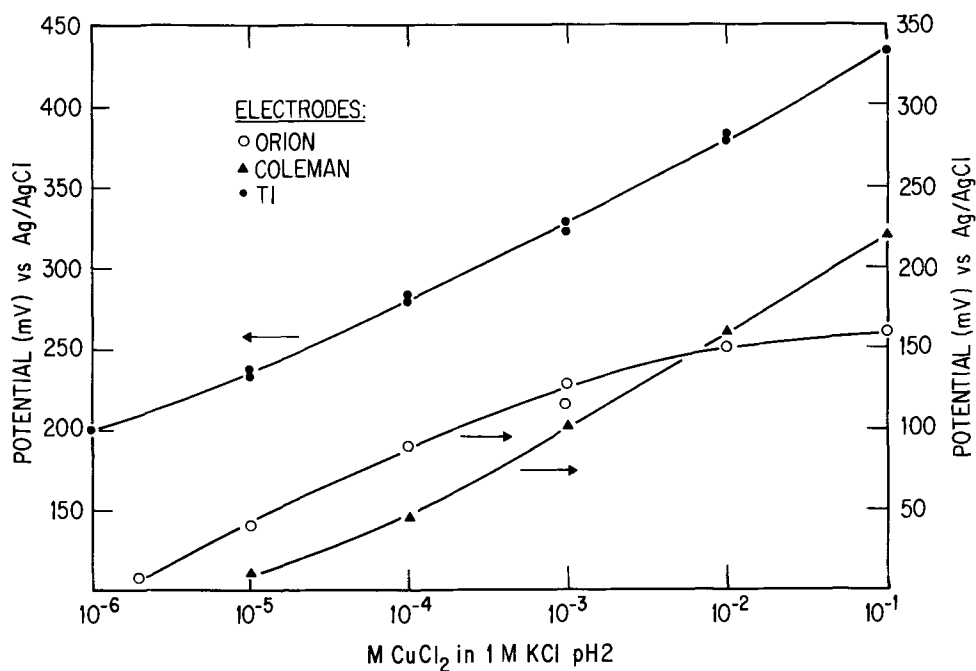


Fig. 5. Steady-state potential-concentration responses of a copper arsenic trisulfide electrode, and two commercial electrodes, in 1M KCl, pH 2. The arrows indicate the appropriate potential scales.

The Coleman electrode showed a stirring effect of the same magnitude but in the opposite direction, *i.e.*, the potential increased after the stirring was shut-off. For one Orion electrode a potential increase of 2 mV was observed 2 min after stirring was terminated in  $10^{-5}$ M cupric chloride. However, two other electrodes showed stirring dependencies similar to those found with the Coleman electrode.

Since the slopes observed in 1M chloride were higher than those observed in nitrate and in acetate, a study was made on the effect of chloride ion concentration on electrode response. Accordingly, electrodes were exposed to varying copper concentrations in supporting electrolytes of 3M KCl, 1M KCl, 0.1M KCl + 0.9M  $\text{KNO}_3$ , and 0.1M NaCl; pH was maintained at 2 in all cases.

Within the accuracy of the experiments the Nernstian slopes in the 3M and the 1M KCl were identical. In all cases the slopes for the 0.1M KCl solution was lower, approximately 40 mV/decade. The actual potentials measured in the 3M KCl were about 50 mV higher than those measured in 1M KCl. Some of these data, together with the performance in zero chloride ion concentration (0.1N  $\text{KNO}_3$ ) are shown in Fig. 6.

An evaluation was made of the electrode properties in bromide solution, which has a different distribution of complex ions with cupric ion (13) and in which cuprous ions are still stable (15). The electrodes were etched, stored overnight in  $10^{-1}$ M cupric nitrate solution, and exposed to varying cupric ion concentrations in 1M NaBr and in 1M KCl. In all cases the slope of the potential-concentration dependence appeared to be higher in bromide than in chloride by about 2 mV, however this is well within the accuracy of the data. Stirring dependencies were also observed in bromide electrolytes, and these were slightly greater than in chloride solutions of the same added copper concentration. In all cases the actual potentials of the bromide solutions were higher than those in the chloride solutions. According to Ref. (13) the copper-bromide complexes are weaker than the copper-chloride complexes so that at any given total added copper the available cupric ion concentration will be greater in bromide and could, at least in part, account for the differences observed in the actual potentials (assuming that the electrode responds only to uncomplexed cupric ion).

**Electrode selectivity.**—The response of the copper-arsenic trisulfide electrode to other soluble ionic spe-

cies was evaluated. Univalent ions such as  $\text{Na}^+$ ,  $\text{K}^+$ , and  $\text{H}^+$  do not give a response in the presence of cupric ion other than via ionic strength effects. Some interference does result when excessive amounts of ferric ion are present. This is illustrated in Fig. 7. Each plot represents the response of a  $\text{Cu-As}_2\text{S}_3$  electrode immersed in solutions of constant ferric ion concentration but with varying cupric ion concentrations. These curves indicate that the ferric ion must be at least ten times greater than the cupric ion concentration before significant interference is observed.

The response of the sensor to other ions is shown in Fig. 8. Varying amounts of calcium, nickel, and

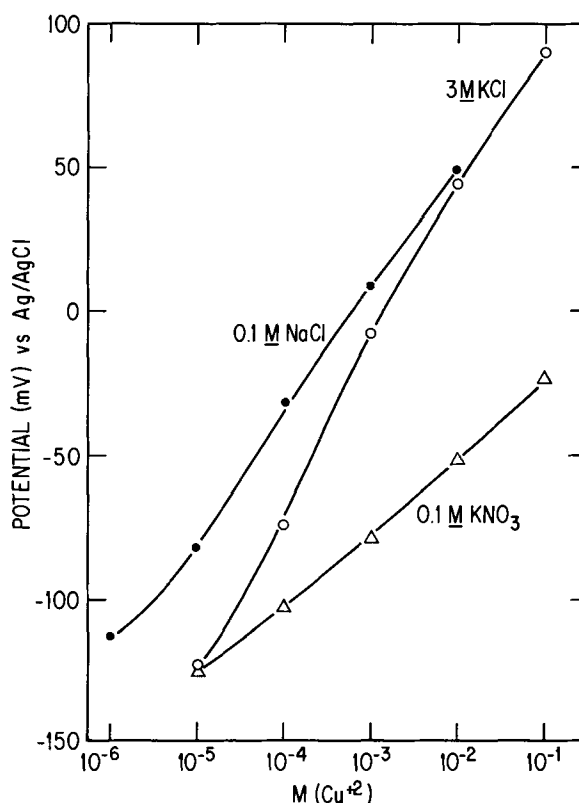


Fig. 6. Potential-log copper concentration relationships shown by a  $\text{CuO-As}_2\text{S}_3$  electrode in 3M KCl, 0.1M NaCl, and zero molar chloride (0.1M  $\text{KNO}_3$ ).

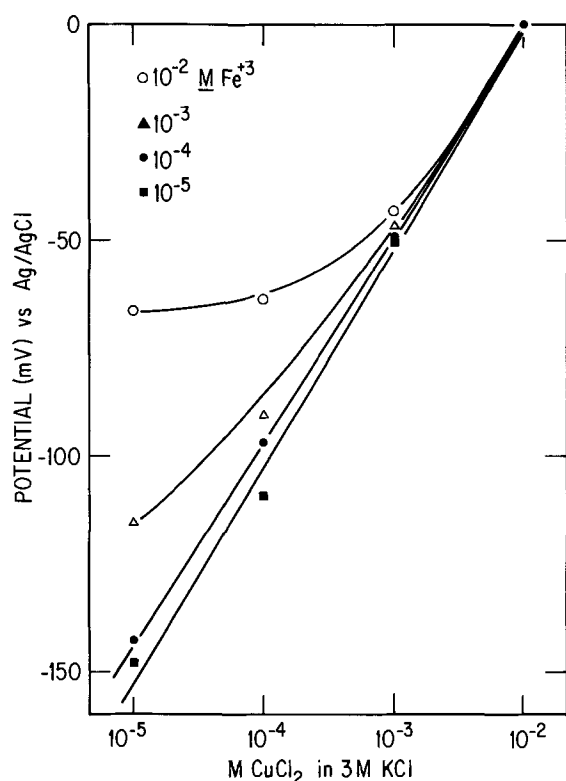


Fig. 7. Response of  $(\text{CuO})_{0.15}(\text{As}_2\text{S}_3)_{0.85}$  electrode, in the membrane configuration, to cupric ion in the presence of varying ferric ion concentrations.

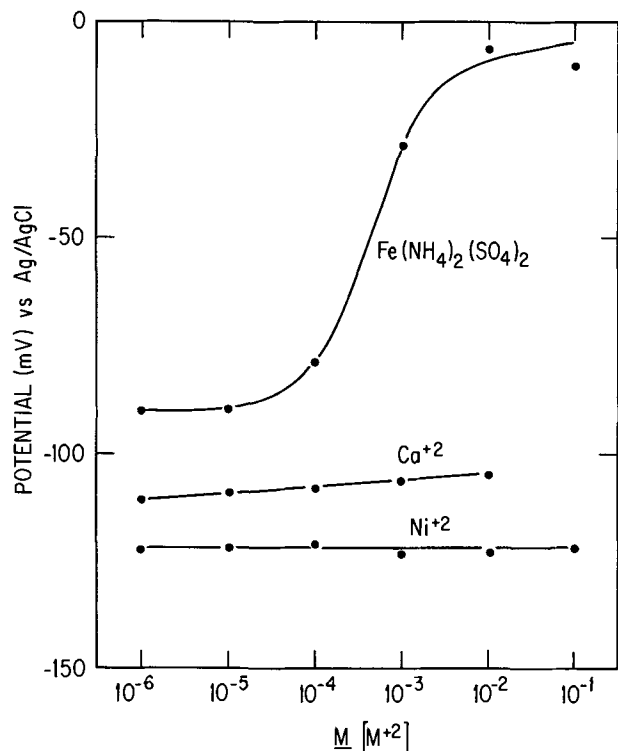


Fig. 8. Response on a copper-arsenic trisulfide electrode to varying concentrations on the indicated ions, in millimolar cupric nitrate.

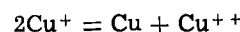
ferrous ion were added to a  $10^{-3}\text{M}$  cupric nitrate solution. The results indicate no interference due to either calcium or nickel. The effect of ferrous ion suggests a titration curve, whereby cupric ion is reduced and ferric ion is generated. There are also no interferences from  $\text{Pb}^{+2}$ ,  $\text{Mn}^{+2}$ , or  $\text{Zn}^{+2}$ . Interference was found with silver ion.

**Sensing mechanism.**—It is apparent that the behavior characteristics of these electrodes are not consistent with the usual solubility product type of ion sensing formalism. A series of experiments were carried out in the hope of clarifying the mechanism operating for the copper-arsenic trisulfide electrodes.

The first feature considered then was the electrode activating mechanism, *i.e.*, whereby a freshly etched electrode surface must first be exposed to high concentrations of cupric ion before stable Nernstian responses can be obtained. Exposures of the electrode to  $10^{-1}\text{M}$   $\text{Cu}^{++}$  solutions obviously present the electrode with a high concentration of cupric ion, but this also presents the electrode with a high positive potential, which can possibly oxidize the electrode surface.

In order to sort out the relative importance of these two factors, the following experiment was carried out. Electrodes were freshly etched and then potentiostated at the potential of  $10^{-1}$   $\text{CuCl}_2$ , but in the absence of cupric ion; all other components of the solution were identical to those used in the chemical activation procedure, *i.e.*, 1M KCl, pH 2. An anodic current, independent of stirring, was observed, so that chemical oxidation of the electrode surface must take place during the activation procedure. After the anodic current had decreased to less than  $1\ \mu\text{A}$ , the electrode was exposed to  $10^{-6}\text{M}$  cupric chloride and to incrementally increasing copper concentrations in the usual manner used to test the electrodes. The nature of the response was similar to that shown in Fig. 1, *i.e.*, super-Nernstian responses until high cupric ion concentrations were reached. Thus a high potential alone is not sufficient to activate the electrode surface.

It is not difficult to understand a chemical oxidation-activation mechanism occurring in chloride solution where cuprous ion, the necessary soluble product of the surface oxidation reaction, is chemically stable. However the same chemical activation process takes place in nitrate solution where cuprous ion is unstable according to the reaction



However, according to the equilibrium constant for the above disproportionation reaction the concentration of cuprous ion is  $2.5 \times 10^{-4}\text{M}$  in the solutions used. Approximately 2.5 Asec of charge would pass before this concentration was exceeded and copper metal was formed. Since this is in excess of the total charge passed during the potentiostatic oxidation of the electrode, it is possible, even in nitrate solution, for the cupric ion to oxidize the electrode and produce a small amount of cuprous ion in solution.

The potentiostatically oxidized surface still demonstrated super-Nernstian behavior which is indicative of more than a one or two electron process, *i.e.*, indicative of further interaction of the copper sensing surface. This interaction between cupric ion and the electrode surface could take a variety of forms, such as compound formation to generate the active sites, or irreversible reaction with strongly adsorbing sites, or both. In any event, this final surface then comes into reversible equilibrium with the cupric ion content of the electrolytes, providing stable Nernstian slopes to changing  $\text{Cu}^{+2}$  concentration.

A fundamental difference in this sensing mechanism must exist between halide solutions, and nitrate solutions, since the Nernstian slopes in halide are a nominal 50 mV/decade and are a nominal 30 mV/decade in nitrate. Furthermore there is some dependence of slope on the halide concentration. A major difference in the chemistry of these solutions is the increased stability of cuprous ion in halide electrolytes.

The response of the electrode to cuprous ion was therefore considered. Electrodes were etched and activated as described. Activity was confirmed by exposure to solutions of varying cupric ion concentration

in 1M KCl. The electrodes were then washed with supporting electrolyte and exposed to solutions of cuprous chloride in the same electrolyte. Electrode potential readings were somewhat erratic but always less than that expected from  $10^{-6}$ M cupric chloride. It must therefore be concluded, particularly when considering the difficulties in preventing cuprous chloride from air oxidizing to cupric chloride, that the response of the electrode to  $\text{Cu}^{+1}$  species is minor.

This then precludes any "solubility product" sensing mechanism involving the participation of sulfide ion in solution. Cuprous sulfide, like silver sulfide is highly insoluble and should have given rise to a potential shift equivalent to a high cupric ion concentration (low sulfide ion).

The electrode was then washed with supporting electrolyte and exposed to  $10^{-4}$ M  $\text{CuCl}_2$  in 1M KCl. Increments of cuprous chloride were added to determine whether the electrode does respond to the cupric/cuprous couple. As potentials were recorded there was some drift upwards as, apparently, the cuprous ion was slowly oxidized by air. The data obtained are shown in Table II; similar results were obtained when the starting cupric ion concentration was  $10^{-3}$ M.

Obviously cuprous ion suppressed the potential normally generated by a fixed amount of cupric ion; the depression increased as cuprous ion concentration increased, but not in a well-defined manner and not to the extent expected from the cuprous/cupric couple (60 mV/decade).

This depression may afford a pragmatic explanation for the stirring dependencies observed with the copper-arsenic trisulfide electrodes in halide solution. It can be argued that a reduced material, presumably cuprous ion, dissolves slowly off the electrode surface and reacts with cupric ion, thus depressing the amount of cupric ion in the vicinity of the electrode and hence depressing the electrode potential. (If cupric ion dissolved off the electrode potential would have increased.) On stirring, the cuprous copper is swept away from the electrode vicinity and the potential takes on a value more characteristic of the cupric ion in solution. The amounts of cuprous ion are sufficiently small however to prevent any easily detectable increase in total copper ion concentration in the test solution. Consistent with this dissolution mechanism then is the observation that those electrodes demonstrating the most pronounced stirring dependence were also the most pitted after prolonged use.

It is necessary, in using this explanation, to account for the chemistry of a reaction between cuprous and cupric copper in solution. It has been shown by optical absorption spectroscopy (16) that a weak but well-defined complex exists in solution between cuprous and cupric chlorides in the range of chloride concentration used in the electrode studies. Thus cuprous ion may well dissolve off the electrode, complex the cupric copper in the vicinity of the electrode, and thus lower the available concentration of cupric copper at the electrode surface. As a result, potential falls.

More direct evidence for dissolution of a reduced species from electrodes in halide solution was obtained as follows. A copper arsenic trisulfide electrode was etched, activated in  $10^{-1}$ M cupric nitrate and transferred to a deaerated solution of  $10^{-3}$ M cupric chloride; a platinum screen electrode was placed about the copper electrode. In the absence of the copper

Table II. Potential response vs. cuprous chloride concentration  
(Original solution: 100 ml  $\text{CuCl}_2$  + 1M KCl)

Molar ratio ( $\text{Cu}^{++}/\text{Cu}^{+}$ )	Electrode potential (mV)
$\infty$	287.8
100/1	278.9
10/1	248.1
0.9/1	230.8

Table III. Arsenic contents of equilibration solutions

Solution	Arsenic concentration (ppb)
$10^{-3}$ M $\text{KNO}_3$	<10
$10^{-3}$ M $\text{KNO}_3$ + $10^{-2}$ M $\text{Cu}^{++}$	<10
1M KCl	35
1M KCl + $10^{-4}$ M $\text{Cu}^{++}$	35
1M KCl + $10^{-2}$ M $\text{Cu}^{++}$	65

electrode the potential of the platinum electrode was relatively stable at about +430 mV. After insertion of the copper electrode the potentials of the platinum electrode were well poised, i.e., showing no oscillations, and continuously drifted to more negative values. The drift rate at steady state (after 60 min) was 4.3 mV/hr. Thus, a reduced species, presumably cuprous ion, is indeed dissolving off the electrode surface. The solution was then changed to  $10^{-5}$ M cupric chloride; the final drift rate of the platinum electrode was 1.8 mV/hr. Thus, the cuprous ion dissolution rate is inversely proportional to the cupric ion concentration. (Identifying the "reduced species" as cuprous ion is based on the difference in electrode performance between halide and nitrate solutions, and the stability of  $\text{Cu}^{+1}$  in halide solutions.)

This proportionality was checked by direct chemical analysis of the solution. Since the copper concentrations involved are small and hence difficult to detect in the presence of the higher ambient concentrations, analysis was made for arsenic. The results are shown in Table III.

Thus there can be little doubt that the electrodes are more soluble in chloride than in nitrate, and that the solubility is higher in the presence of high cupric ion concentrations. All of this is consistent with the stirring dependences discussed above.

The next question is whether this soluble reduced material (presumably cuprous ion) is involved in the cupric ion sensing mechanism, or whether this dissolution reaction is merely incidental. Accordingly, freshly etched electrodes were potentiostated at increasingly positive potentials (in 1M NaBr, pH 2) to more completely oxidize the electrodes surface, then equilibrated in  $10^{-1}$ M cupric nitrate (0.1M  $\text{NaNO}_3$ ), and exposed to solutions of 1M NaBr, pH 2 varying in cupric ion content. The results are shown in Fig. 9; included for comparison are the responses of a chemically activated electrode.

The behavior of the chemically activated electrode and the electrode potentiostated at +600 mV are essentially identical. The effect of higher potentials is obvious, i.e., as potential is made more positive, the subsequent sensitivity of the electrode to change in copper concentration below  $10^{-4}$ M decreases. It was

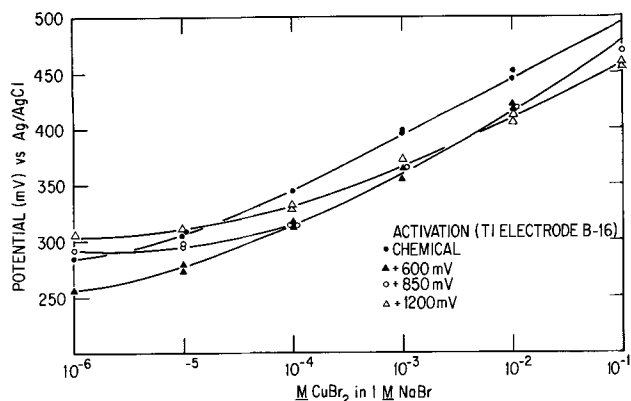


Fig. 9. Steady-state responses of a copper arsenic trisulfide electrode to varying concentrations of cupric bromide after chemical activation and after potentiostatic treatment at the potentials shown.

also observed that electrodes exposed to +1200 mV would oscillate  $\pm 4$  mV when subsequently equilibrated with copper halide solutions. The stirring dependences decreased with increasing potential applied to the electrode. Note however that sensitivity to low levels of copper concentration decreases at the same time. This is similar to observations made earlier that electrodes which had the lower stirring dependencies also had the lower sensitivities. Application of high potential to such electrodes completely deactivated the electrode. It is thus apparent that the "reduced material" is indeed involved in the potential sensing mechanism.

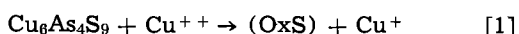
As indicated previously, the electrode is at least a two-phase system, *i.e.*, crystalline sinnerite imbedded in an amorphous phase. The participation of the amorphous phase in the sensing process was evaluated by comparing the performances of pure sinnerite electrodes with those of  $\text{Cu}_{0.25}(\text{As}_2\text{S}_3)$  electrodes.

Accordingly samples of sinnerite material were compounded by mixing  $\text{Cu}_2\text{S}$  and  $\text{As}_2\text{S}_3$  in a mole ratio of 3:2. The mixture was placed in ampul, evacuated, sealed, and heated to 700°C for 1 hr. The temperature was then lowered to 500° for 1 hr and finally raised to 550°C and maintained at this latter temperature for 90 hr. The resulting sample was then air quenched to room temperature. Resistivity as measured on two slices was 3.04 and 3.22 ohm-cm indicating that the sinnerite is indeed a conducting material. Three sinnerite electrodes were prepared from this material. The electrodes were etched, stored overnight in  $10^{-3}\text{M}$  cupric nitrate, and exposed first to cupric nitrate solutions over the range of  $10^{-3}$  to  $10^{-6}\text{M}$ . A Nernstian slope of 30 mV/decade was obtained. The experiment was repeated in 1M KCl over the range  $10^{-1}$  to  $10^{-6}\text{M}$   $\text{CuCl}_2$ . A Nernstian slope of approximately 55 mV/decade was obtained between  $10^{-1}$  and  $10^{-3}\text{M}$  cupric chloride. However between  $10^{-4}\text{M}$  and  $10^{-6}\text{M}$   $\text{CuCl}_2$ , the response was super-Nernstian of the order of 100 mV/decade. The electrodes also showed a greater stirring dependence at and below  $10^{-4}\text{M}$ .

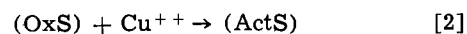
These responses in nitrate (between  $10^{-3}$  and  $10^{-6}\text{M}$ ) and in chloride solutions (at and above  $10^{-3}\text{M}$   $\text{CuCl}_2$ ) are equivalent to those for the two phase system so that it can be concluded that either the amorphous phase is not involved in the potential sensing *per se* or that its role is entirely equivalent to that of the sinnerite. This is consistent with the observations that all the copper-arsenic trisulfide electrodes behaved in an equivalent manner, regardless of the initial chemical form of the copper put into the melt. Since the crystalline phase was always sinnerite, the amorphous phase must have differed in composition. If it were involved then it would have been expected that the electrode behavior would also have varied with the form of the initial copper.

The abnormal behavior of the sinnerite electrodes at low concentrations of cupric chloride was similar in form to that obtained for  $\text{Cu}_{0.25}(\text{As}_2\text{S}_3)_{0.75}$  electrodes exposed to varying  $\text{Cu}^{++}/\text{Cu}^+$  ratios. This performance then can be rationalized in terms of the sinnerite electrode depositing abnormally high concentrations of cuprous ion in the vicinity of the electrode and reaching concentration ratios where the cuprous ion exerts a significant effect on observed electrode potential. Furthermore, the pronounced higher stirring dependence for the sinnerite electrodes is what would be expected from the dissolution of greater quantities of cuprous ion.

The conclusions of these semiquantitative mechanistic studies can be summarized by the following formalism. The active electrode material ( $\text{Cu}_6\text{As}_4\text{S}_9$ ) is first oxidized by cupric ions (potentiostated sinnerite developed a high initial anodic current), *i.e.*



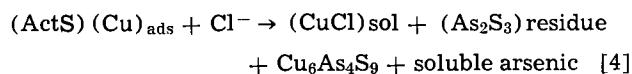
This oxidized surface, (OxS), then reacts with cupric ion to form the active sites (ActS) which come into equilibrium with the cupric ion concentration of the test solutions, *i.e.*



and



A second and irreversible process such as reaction [2] is required to account for the super-Nernstian slope observed only initially with oxidized electrodes. It is envisioned that as the sites are formed they then interact with cupric ion according to reaction [3]. It is postulated that this active copper site with adsorbed copper dissolves in halide solution to inject cuprous ion (or some other reduced specie which can remove  $\text{Cu}^{+2}$  ions) into the electrolyte. Participation of this site is indicated by virtue of the proportionality between cupric ion concentration and electrode solubility. Also formed during this dissolution process is a soluble arsenic species, a sulfur-arsenic residue and some fresh sinnerite surface



The involvement of chloride ion in this reaction, due to its stabilizing influence on cuprous ion, accounts for the dependence of the Nernstian slope on the chloride ion concentration. The sinnerite so exposed can then proceed through the reactions illustrated by Eq. [1] and [2]. Since at least one of these involves electron transfer, a slope greater than 30 mV/decade is obtained. The extent of this reaction is dependent upon cupric ion concentration via the participation of the adsorbed copper sites in reaction [4], so that the over-all response of the electrode is dependent upon cupric ion concentration of the solution. Reaction [4] should lead to an eventual deactivation of the electrode in chloride solutions via the accumulation of the residue, and a deactivation is observed. Furthermore this deactivation should be less important in nitrate solution due to the lower solubility; this is also observed. By the law of mass action it would be expected, from Eq. [3], that deactivation should take the form of lowering sensitivity to low concentrations of cupric ion, and this is also observed.

### Summary

Fusing arsenic trisulfide with copper, cupric oxide, or cupric sulfide generates an electronically conductive glass which is sensitive to changes in cupric ion concentration over the ranges of at least  $10^{-1}$  to  $10^{-6}\text{M}$  copper in molar solutions of chloride, bromide, nitrate, and acetate. The electrochemically active component of the glass is apparently "sinnerite" ( $\text{Cu}_6\text{As}_4\text{S}_9$ ). Stable, Nernstian responses were obtained only after the electrode surface was etched in caustic and equilibrated with high ( $>10^{-3}\text{M}$ ) concentrations of cupric ion; excessive oxidation of the surface ( $> +600$  mV *vs.* Ag/AgCl) decreased electrode sensitivity to low levels of copper ion concentration.

In the presence of cupric ions, the electrode response was independent of hydrogen ion concentration from pH 2 to a value at which copper hydroxide precipitation takes place. Even as copper precipitated the electrode potential followed the remaining copper in solution until the limit of detection of the electrode was reached.

In nitrate and acetate solutions the slopes of the potential-log concentration plots were 27 mV/decade; for the 1, 2, and 3M chloride and bromide solutions the slopes were 50 mV/decade; the slope in 0.1M KCl was 40 mV/decade. The commercial electrodes studied also showed differences in slope between the nitrate and chloride solutions.

The response of the copper-arsenic trisulfide electrodes were independent of stirring in the nitrate and

acetate electrolytes. However in chloride and in bromide solutions, stirring led to an increase in electrode potential. Stirring dependencies were also found for the commercial electrodes studied but in the opposite direction.

The copper-arsenic trisulfide electrodes did not respond to cuprous ion *per se*, or to the  $\text{Cu}^{++}/\text{Cu}^+$  couple. No interference was found from  $\text{Ca}^{++}$ ,  $\text{Pb}^{++}$ ,  $\text{Zn}^{++}$ ,  $\text{Ni}^{++}$ , or  $\text{Mn}^{++}$ . Ferric ion, when present in a ten fold excess, interferes;  $\text{Ag}^+$  also interferes.

Qualitative studies of the electrode activation process indicated that direct oxidation of the surface by cupric ion takes place followed by two or more chemical reactions between cupric ion in solution and this oxidized surface. It is this final surface configuration which is involved in cupric ion sensing.

#### Acknowledgments

Financial support of this work by the Office of Saline Water, U.S. Department of the Interior, is gratefully acknowledged. The authors also wish to thank Dr. L. Swink for performing and interpreting the x-ray diffraction analysis, as well as Mr. Roy DeViney for assisting in the electrochemical studies.

Manuscript submitted May 2, 1973; revised manuscript received Aug. 14, 1973.

Any discussion of this paper will appear in a Discussion Section to be published in the December 1974 JOURNAL. All discussions for the December 1974 Discussion Section should be submitted by Aug. 1, 1974.

#### REFERENCES

1. R. Durst, Editor, "Ion Selective Electrodes," Nat. Bur. Std. Special Publ. 314 (Nov. 1969).
2. E. Pungor and K. Toth, *Analyst*, **95**, 625 (1970).
3. G. Eisenman, Editor, "Glass Electrodes for Hydrogen and other Cations: Principles and Practice," Marcel Dekker, New York (1967).
4. P. Ruetschi and R. Amlie, *This Journal*, **112**, 665 (1965).
5. H. Hirata, K. Higashiyama, and K. Date, *Anal. Chim. Acta*, **51**, 209 (1970).
6. H. Hirata and M. Arai, U.S. Pat. 3,669,862 (1972).
7. H. Hirata and K. Date, *Talanta*, **17**, 883 (1970).
8. M. Mascini and A. Liberti, *Anal. Chim. Acta*, **53**, 202 (1971).
9. J. Ruzicka and C. Lamm, *ibid.*, **53**, 206 (1971).
10. R. Durst, Editor, "Ion Selective Electrodes," Nat. Bur. Std. Special Publ. 314, p. 80 (Nov. 1969).
11. C. Baker and I. Trachtenberg, *This Journal*, **118**, 571 (1971).
12. F. Marumo and W. Nowacki, *Schweiz Mineral. Petrog. Mitt.*, **44**, 439 (1964).
13. L. Sillén and A. Martell, "Stability Constants of Metal-Ion Complexes," Special Publ. No. 17, The Chemical Society London (1964).
14. L. Cambi and M. Elli, *Chim. Ind. (Milan)*, **49**, 606 (1967).
15. W. Latimer, "Oxidation States of the Elements and their Potentials in Aqueous Solutions," 2nd ed., Prentice-Hall Book Co., New York (1952).
16. H. McConnell and N. Davidson, *J. Am. Chem. Soc.*, **72**, 3168 (1950).
17. J. Koryta, *Anal. Chim. Acta*, **61**, 329 (1972).

## Interferometric Study of the $\text{Zn}/\text{ZnSO}_4/\text{Zn}$ System

### II. Concentration Gradients under Convectionless Transport

R. N. O'Brien\*

Department of Chemistry, University of Victoria, Victoria, British Columbia, Canada

J. Leja

Department of Mineral Engineering, University of British Columbia, Vancouver, British Columbia, Canada

and E. A. Beer\*

Institute of Gas Technology, I. I. T. Center, Chicago, Illinois

#### ABSTRACT

The Laplace transform solution of the unsteady state diffusion equation which describes the concentration gradients in a convectionless system has been compared to experimentally obtained values. The experimental values were obtained as multiple beam Fizeau-type fringes from an electrolysis cell which was also a Fabry-Perot interferometer using a laser as the light source. The electrochemical system was  $\text{Zn}/\text{ZnSO}_4/\text{Zn}$ , at 0.5-0.05M concentration at room temperature at constant currents ranging from 1.0 to 0.1  $\text{mA cm}^{-2}$ . At the middle ranges of times and current densities quite good agreement is found. In general the calculated and experimental values differed more than the expected experimental error. A "passivated" set of electrodes was used and gave much lower concentration changes for similar current densities than the normal electrodes.

In Part I the effect of natural convection on concentration gradients and the potential required for a constant current density was evaluated (1). It was shown that for vertical electrodes natural convection limited the diffusion layer to values of about 0.01-0.03 cm. In the anode over cathode horizontal electrode configuration convection was evident within 15 sec for the lowest current densities (0.37  $\text{mA}/\text{cm}^2$ ). Again with hori-

zontal electrodes the diffusion layer constantly increased in depth with time since no limiting process was present. Interferometry was demonstrated to be efficacious in detecting concentration gradients and the effect of convection. In this part the convectionless system is considered.

Measurements of concentration gradients at working electrodes have become reasonably common (2-4). In general, quite good agreement has been found between the concentration calculated from the solution of the

\* Electrochemical Society Active Member.  
Key words: Zn anode, Zn cathode, convectionless transport, interferometry.



differential equation of Fick's second law due to Rosebrugh and Miller (5) or variations of it (2) and the experimentally determined values. Some anomalous results have been reported (6): in particular there seemed to be an abrupt discontinuity at 0.07 cm electrode separation of a plot of voltage to maintain a constant current density at a given electrode separation for all electrode arrangements with and without convection. The first complete calculation of a concentration gradient under convectionless conditions (3) was for the system Cu/CuSO<sub>4</sub>/Cu and the agreement between calculated and observed values was good at short times (i.e., ~15 sec). At longer times (~150 sec) the order of magnitude was correct but use of the accepted transport number for the sulfate ion required that a diffusion constant lower than the accepted one be used. The diffusion constant derived from old electrochemical methods (Sand's data) without allowance made for ion-pair formation gave the best agreement.

In the present work on the Zn/ZnSO<sub>4</sub>/Zn system some anomalies were anticipated because of the expected pH changes [as calculated by Wagner (7) and observed by Polukarpov (8)] at the electrodes and the amphoteric behavior of zinc ion on either side of pH 7.

In Part III anomalous results obtained for low Zn<sup>++</sup> (metal ion) concentration will be presented. In this part experimental results for both anode and cathode are presented, but only calculations for the cathode are discussed. The experimental concentration changes are found not to be symmetrical at the two electrodes, whereas calculated results based on constant transport parameters are. The differences between the two electrodes are more marked at lower concentration and hence will be discussed more fully in Part III. In Part III anomalous results obtained for low ZnSO<sub>4</sub> concentration will be presented.

### Experimental Arrangements

The ZnSO<sub>4</sub> stock solution was made from Analar grade material and water (four times distilled), then titrated with EDTA and diluted to the required concentration, and used at its natural pH. Concentrations were checked once per week for several weeks until it became obvious that no change occurs in stoppered volumetric flasks kept in the dark. Zinc 99.99% pure was donated by Cominco, Trail, British Columbia. The temperature was 25° ± 0.3°C.

The cell used was a modification (4, 9) of that used in Part I, the distance between electrodes, 2*l*, being 0.3 cm which was the same as the thickness of electrode. The cell represented a modified Fabry-Perot interferometer which contained the solid Zn electrodes and the electrolyte. The cathode was in horizontal position above the horizontal anode. The light source was a He-Ne 1 mW laser, of 632.8 nm wavelength. Refractive indices of the solutions at other wavelengths and pH's have been published (10). Those at 632.8 nm were obtained using the laser and a precision Abbé refractometer (Table I) by a technique recently published (11).

A constant current was provided by a 6V lead acid battery at 5/8th charge with an external variable resistance in series with the cell whose resistance was always less than 200 ohms. The current was monitored

by a voltmeter with 10<sup>7</sup> ohms/V input resistance across a calibrated standard resistance of 100 ohms also in series in the circuit. Current densities from 0.1 to 1 mA/cm<sup>2</sup> in steps of 0.1 mA were investigated at both 0.5 and 0.05M. Interferograms were recorded with a 35 mm camera. These were then projected onto a plotting table and hand drawn on large-size millimeter graph paper at 50 and 100 times magnification. Fringe perturbations were converted to concentration contours by the method previously outlined (4).

### Theory

The theory of electrolyte concentration near working electrodes was worked out by Rosebrugh and Miller in 1910 (5) using Fourier analysis methods. O'Brien published data on the Cu/CuSO<sub>4</sub>/Cu system obtained interferometrically (3) and compared these with the values obtained using an expression based on a Laplace transform solution.

A modified form of the solution which is easier to analyze by inspection and is more complete will now be presented.

Following the review of Tobias, Eisenberg, and Wilke (12), the rate of transfer of ions in the *x* direction taken perpendicular to the working surface of a planar, horizontal electrode is

$$N_t = CU \frac{\partial \Psi}{\partial x} - D \frac{\partial C}{\partial x} + VC \quad [1]$$

where *N<sub>t</sub>* is the total rate of transfer, gram ions cm<sup>-2</sup> sec<sup>-1</sup>; *C* is gram ions cm<sup>-3</sup>; *U* is mobility, cm<sup>2</sup> sec<sup>-1</sup> V<sup>-1</sup>;  $\Psi$  = potential, V; *x* is distance in direction of transfer, cm; *D* is the diffusion constant for the salt derived from conductivity measurement, cm<sup>2</sup> sec<sup>-1</sup>; and *V* = velocity for the steady-state conditions, cm sec<sup>-1</sup>. We eliminate the third term by ensuring experimentally that *V* = 0 (exactly horizontal electrodes, cathode above) and the first term by multiplying the second term by the transport number of the anion following Newman (13), resulting in a single term expression corresponding to Fick's first law, or the steady-state concentration gradient. For semi-infinite diffusion (as contrasted to limited diffusion) the achievement of the steady state requires very long times. Accordingly, all experiments can be regarded as being transient (or unsteady state and Fick's second law applies) thus the solution of the equation

$$\frac{\partial C}{\partial t} = D \frac{\partial^2 C}{\partial x^2} \quad [2]$$

is sought with the initial condition that at *t* = 0, *C* = *C*<sub>0</sub> at all *x* from 0 to *l* where 2*l* is the distance between the two electrodes and the boundary conditions that  $\Delta C = 0$ , *x* = *l*, *t* > 0, and  $\partial \Delta C / \partial t = \text{constant}$  at *x* = 0, *t* > 0.

The electrochemical form of the solution by Laplace transform method is for cathode concentration changes

$$\Delta C_{(x,t)} = \frac{2It_-}{nF\sqrt{D}} \sqrt{t} \left[ \text{ierfc} \left( \frac{(2l-x)}{2\sqrt{Dt}} \right) - \text{ierfc} \left( \frac{x}{2\sqrt{Dt}} \right) \right] \quad [3a]$$

which for short times (> 180 sec) reduces to

$$\Delta C_{(x,t)} = \frac{-2It_-}{nF} \sqrt{t/D} \text{ierfc} \frac{x}{2\sqrt{Dt}} \quad [3b]$$

in which *I* is the current density, A/cm<sup>-2</sup>; *n* the charge on the ion; *F* the Faraday, coulombs; *t* the time in seconds; *t*<sub>-</sub> the transport number of the anion;  $\Delta l$  the change in concentration (M cm<sup>-3</sup>); and *ierfc* the complement of the integrated error function tabulated by Carslaw and Jaeger as 2 *ierfc*. The previously published equation had typographical errors and should

Table I. Aqueous ZnSO<sub>4</sub> refractive indices at 25°C and 632.8 nm

Concentration, M	Refractive index, <i>n</i>	Slope $\frac{\partial n}{\partial c}$ , M <sup>-1</sup>
0.000	1.33128	
0.0125	1.33172	0.0352
0.03	1.33224	0.0297
0.2	1.33688	0.0273
0.25	1.33824	0.0271
0.50	1.34465	0.0258

have been identical to [3b] after algebraic simplification.

For a given starting or bulk concentration  $C_0$ , providing the current density is not too high or the time of electrolysis not too long, both  $D$  and  $t_-$  will be effectively constant. These are really the initial assumptions made in the solution of Eq. [2]. At constant times, the expression then becomes the difference of the two ierfc terms. Under the experimental conditions used, the first ierfc term is negligible at all times [the four place table in Carslaw and Jaeger (14) gives zero] while for the second term it varies from 0.5643 to zero. The value of  $l$  is 0.15 cm and obviously must be at least an order of magnitude smaller to affect terms containing it and hence change the results significantly ( $D$  is of the order of  $10^{-6}$  and  $t \sim 180$  and  $x$  is always small relative to  $l$  under these conditions).

In the previous calculation of concentration gradients in the Cu/CuSO<sub>4</sub>/Cu system it was shown that if the accepted transport numbers were used, a value of the diffusion constant derived from electrochemical measurements without the usual allowances for activity gave the best fit. Accordingly the values derived from conductivities measured by Harned and Hudson (15) using the well-known expression

$$D = \frac{RTA}{F^2} \quad [5]$$

rather than the values calculated by them allowing for ion-pair (15) formation were used. A test of the fit with the larger values obtained when ion-pairs are allowed for confirmed the suitability of the choice as would be expected.

Since the variation in temperature between runs was only  $\pm 0.3^\circ\text{C}$  (except for the passivated run and the one in Fig. 4) no allowance was made in the diffusion constant, transport number, or refractive index.

### Results and Discussion

A very large number of runs were done. A selection of results only is presented. Obviously with a motion picture camera running at 16 fps vastly more data than are presented were obtained, in fact about 10 frames/100 ft or one in 4000 was analyzed. Most of the results presented are those in which the electrodes were assembled quickly into the cell and the electrolysis begun immediately. If this was not done a type of passivation occurred which will be dealt with later.

Data were originally taken from interferograms of the type shown in Fig. 1-3 and compared in tables against calculated values. Both sets of values were then plotted as  $\log \Delta C$  vs.  $x$  in Fig. 4. Figure 1 is for 0.5M ZnSO<sub>4</sub> pH 5.6 electrolyzed at 25.3°C at a current density of 0.5 mA/cm<sup>2</sup>,  $2l = 0.3$  cm. The optical anomalies reported by Ibl (16) and treated in detail by Beach (17) resulting from unequal refraction of the light in a concentration gradient would cause only about 1% error for the most severe experimental conditions used or for most cases they are smaller than other experimental errors. Figure 2 is taken from Fig. 1 and shows the 120-sec concentration contour. The calculated points are also plotted to show that the agreement is quite good. Figure 3 is the 90-sec concentration contour at 0.5M and 1 mA/cm<sup>2</sup> current density and calculated points showing poor agreement, the point at  $x = 0.01$  cm being only about one-half the experimental value, and the  $x = 0.04$  cm value is also about one-half the experimentally observed one.

In Fig. 4-8, the calculated values appear as a curve since the error function is only partly exponential in nature. Figure 4 in which the experimental results at 27°C, 0.1 mA/cm<sup>2</sup>,  $5 \times 10^{-2}$ M at 30, 90, and 120 sec are compared with the calculated values, the best fit of experimental points is two straight lines, which also appears to be the case in Fig. 5, but not in Fig. 6-8 where the concentration is higher. At 0.1 mA/cm<sup>2</sup> the long time value is always above the calculated, at 90

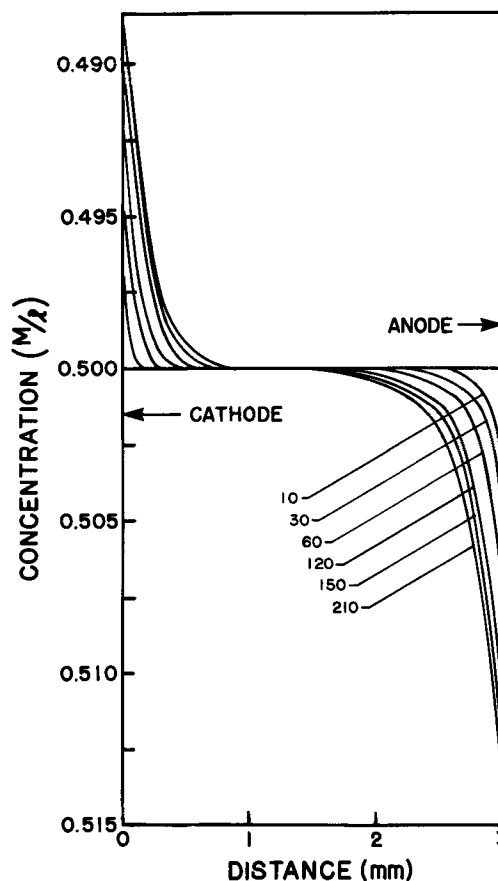


Fig. 1. Concentration contours at various times redrawn from interferograms of 0.5M ZnSO<sub>4</sub> solution at pH 5.6 electrolyzed at 25.3°C at 0.5 mA/cm<sup>2</sup>.

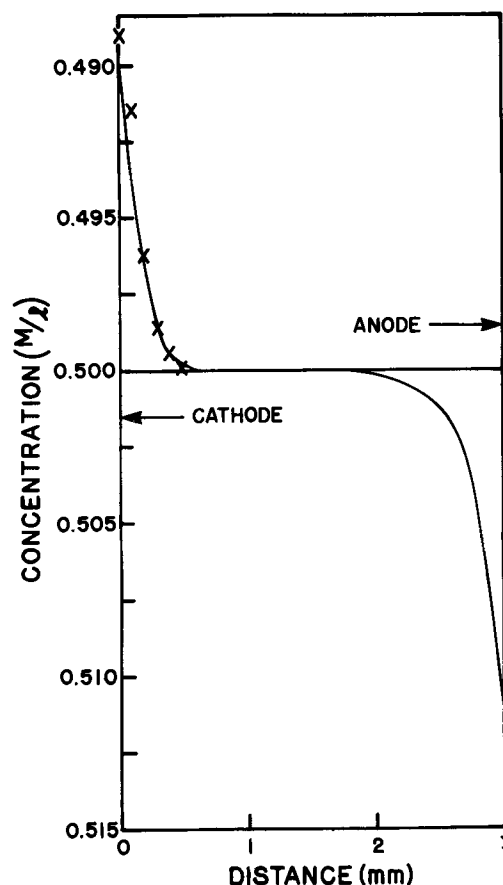


Fig. 2. The 120-sec concentration contour from Fig. 1. The points are calculated from Eq. [3].

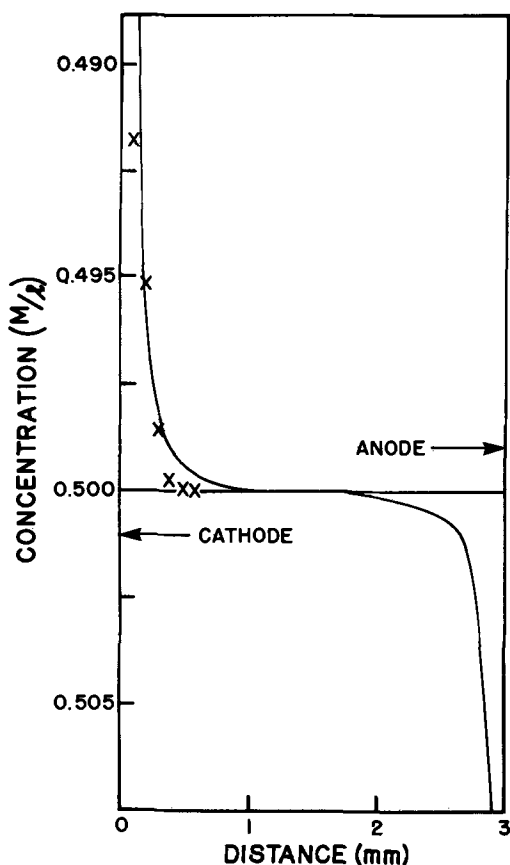


Fig. 3. The 90-sec concentration contour in 0.5M ZnSO<sub>4</sub> at 24.7°C electrolyzed at 1 mA/cm<sup>-2</sup>.

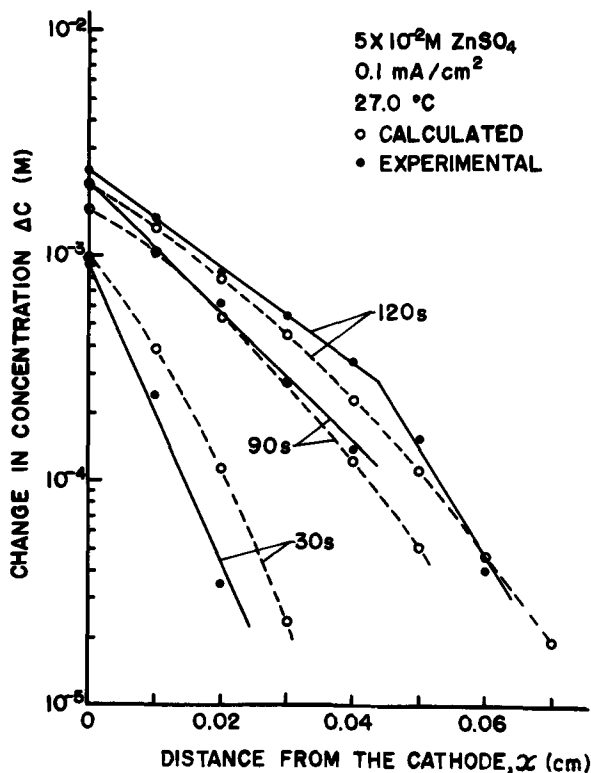


Fig. 4. The logarithm of the concentration change at the cathode in 0.05M ZnSO<sub>4</sub> at 27°C and 0.1 mA/cm<sup>-2</sup> at various times.

sec they are almost equal and at 30 sec the experimental values are considerably less. At the larger current density (0.5 mA/cm<sup>2</sup>, Fig. 5) the 30-sec values are nearly equal, the 90-sec values cross at about one-half

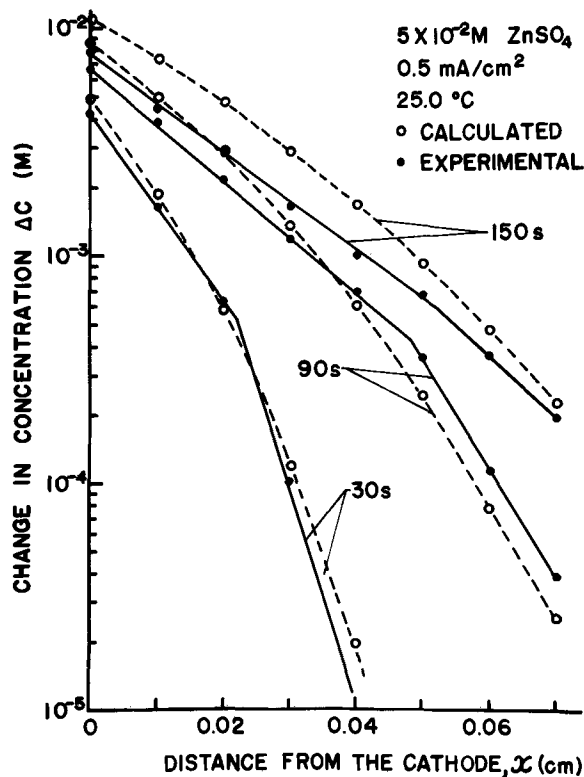


Fig. 5. The logarithm of the concentration change at the cathode in 0.05M ZnSO<sub>4</sub> at 24.7°C and 0.5 mA/cm<sup>-2</sup> at various times.

way through the diffusion layer (calculated being higher at the electrode), and at 150 sec the calculated values are everywhere higher.

In Fig. 6-8, the higher concentration solution (0.5M), the results have a more general pattern. At all short times (10 and 15 sec) the agreement between calculated and experimental values is quite good. At the longer times (30 and 90 sec) and higher current densi-

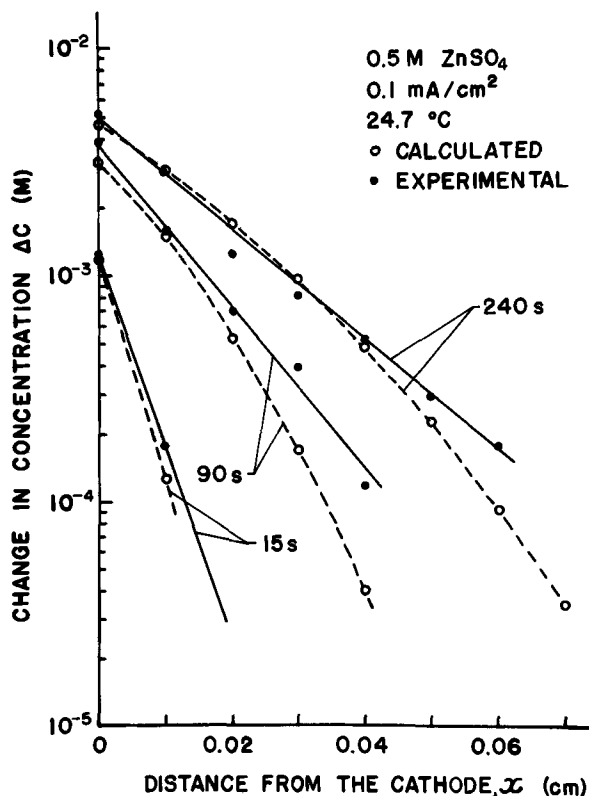


Fig. 6. The logarithm of the concentration change at the cathode in 0.5M ZnSO<sub>4</sub> at 24.7°C and 0.1 mA/cm<sup>-2</sup> at various times.

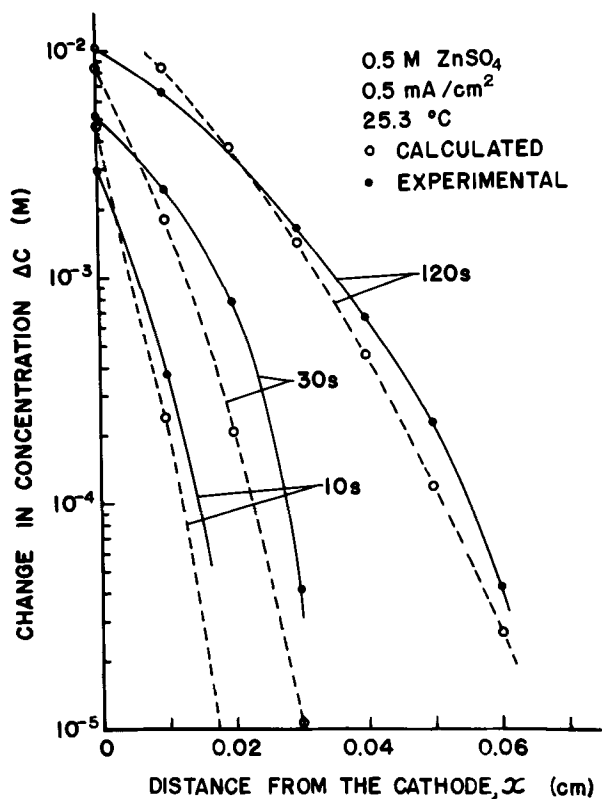


Fig. 7. The logarithm of the concentration change at the cathode in 0.5 mA/cm<sup>2</sup> at 25.3°C at various times.

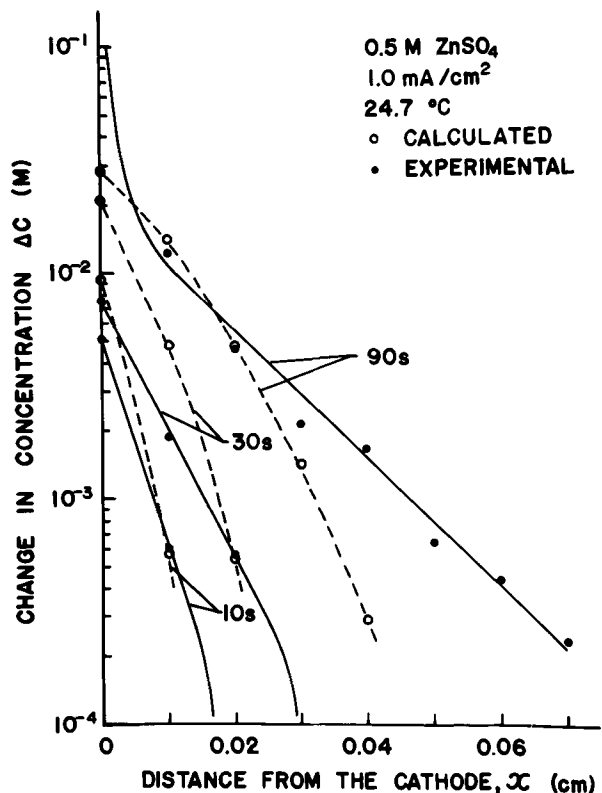


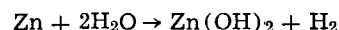
Fig. 8. The logarithm of the concentration change at the cathode in 0.5M ZnSO<sub>4</sub> at 24.7°C and 1.0 mA/cm<sup>2</sup> at various times.

ties the agreement deteriorates, but usually there is agreement at some distance, the plots either crossing (0.5 and 1.0 mA/cm<sup>2</sup>) or approaching closely (0.1 mA/cm<sup>2</sup>). At the longest times shown (120 and 240 sec) this condition still holds for the lower C.D.'s even up to 240 sec for 0.1 mA/cm<sup>2</sup> but the 120-sec experimental value at  $x = 0$  was unmeasurable and  $> 10^{-2}$ M and

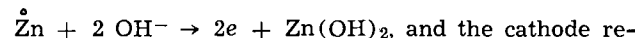
shows that the depletion of the innermost layer is now proceeding at a higher rate (and well above the calculated rate) than in the outer parts of the diffusion layer.

In general at lower concentrations, at low current densities, and at short times of electrolysis near the electrode, the agreement is good, i.e., in the range of 5-10%. This is greater than the experimental error expected which is estimated to be less than 3% at the electrode in all but the lowest current densities at the shortest times where it may reach 10% at 0.1 mA/cm<sup>2</sup> at less than 30 sec. Large per cent deviations at greater distances arise because the limit of detection experimentally is often reached before ierfc goes to zero in the four place table. The limits of detection are typically in the range of 10<sup>-5</sup>M, varying with the fringe spacing which is controlled by the wedge angle between the interferometer's flats.

Figure 9 shows the concentrations observed when an electrode and the electrolyte were in contact for about 2 hr before the run began. The solution was 0.05M, pH 5.6 electrolyzed at 0.8 mA/cm<sup>2</sup> at 26°C. The concentration gradients are much less steep and much less intensive. If the assumption is made that Zn(OH)<sub>2</sub> was deposited on both electrodes by the reaction



and that the anode reaction during electrolysis was



and the cathode reaction was  $\text{Zn}(\text{OH})_2 + 2e \rightarrow \text{Zn} + 2\text{OH}^-$ , and if one further assumes only OH<sup>-</sup> diffuses, that its transport number is about 0.80, and that its diffusion constant is about  $2.6 \times 10^{-5}$  cm<sup>2</sup> sec<sup>-1</sup> (OH<sup>-</sup> single ion refractive index is about 5.15 compared to 1/2 Zn<sup>2+</sup> at 0.305 which would decrease the refractive index slightly at the pH's expected), then at  $x = 0$ ,  $t = 90$  sec,  $\Delta C_{\text{calc}} = 1.72 \times 10^{-3}$ , and  $\Delta C_{\text{exp}} = 1.66 \times 10^{-3}$ M in reasonable agreement. The anode arm of the concentration gradient begins to increase markedly between 600 and 1200 sec of electrolysis. The pH would be expected to increase at the anode and the Zn(OH)<sub>2</sub> go into solution as the hydroxide complex as previously observed (18). The cathode meanwhile still shows a low concentration change. If the suggested reaction is correct then for there to be still some Zn(OH)<sub>2</sub> on the surface the

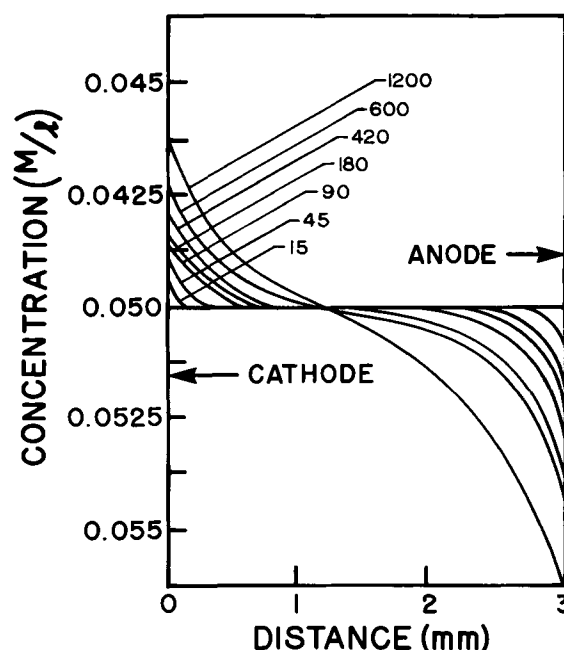


Fig. 9. The "passivation" of electrodes left in contact with the solution for 2 hr before electrolysis began, 0.05M at 26°C and 0.8 mA/cm<sup>2</sup>.

thickness at the beginning of electrolysis must have been at least 1000 molecular diameters thick.

### Conclusions

Even in a system exhibiting amphotericism the Laplace transform (and Fourier transform) solution obviously fits the experimentally observed concentration gradients. An unexplained but previously observed (19, 20) sudden change in agreement with predicted values occurs often at about 0.03 cm distant from the electrode at longer times. An electrode, assumed passivated by long times of immersion (by for example a slow, film producing, corrosion reaction) in the electrolyte before electrolysis began has much lower concentration gradients and gives reasonable agreement with calculated values if Zn(OH)<sub>2</sub> is assumed to be one of the reacting substances at each electrode.

### Acknowledgments

The authors wish to thank S. Levine and W. Michalik for valuable discussions. This work was supported by the Defense Research Board of Canada.

Manuscript submitted Sept. 11, 1972; revised manuscript received Aug. 20, 1973.

Any discussion of this paper will appear in a Discussion Section to be published in the December 1974 JOURNAL. All discussions for the December 1974 Discussion Section should be submitted by Aug. 1, 1974.

### REFERENCES

1. R. N. O'Brien, W. F. Yakymyshyn, and J. Leja, *This Journal*, **110**, 820 (1963).
2. Limin Hsueh, Ph.D. Thesis, University of California,

- nia, Lawrence Radiation Laboratory, Berkeley, Calif., UCRL-18597.
3. R. N. O'Brien, *This Journal*, **113**, 389 (1966).
4. R. N. O'Brien, *Rev. Sci. Instr.*, **35**, 803 (1964).
5. T. R. Rosebrugh and W. L. Miller, *J. Phys. Chem.*, **14**, 816 (1910).
6. R. N. O'Brien and K. Kinoshita, *This Journal*, **112**, 951 (1965).
7. Carl Wagner, J. (and Trans.) *Electrochem. Soc.*, **95**, 161 (1949).
8. N. N. Polukarpov, *Zh. Obshch. Khim.*, **18**, 1249 (1958).
9. R. N. O'Brien, E. A. Beer, K. Beach, J. Leja, S. Weiner, and K. S. Spiegler, UCRL-17002 Preprint, Lawrence Radiation Laboratory, Berkeley, Calif., A.E.C. Contract W-7405, Eng. 48.
10. R. N. O'Brien, *J. Chem. Eng. Data*, **13**, 2 (1968).
11. R. N. O'Brien, F. P. Dieken, and A. Glasel, *ibid.*, **18**, 142 (1973).
12. C. W. Tobias, M. Eisenberg, and C. R. Wilke, *This Journal*, **99**, 359C (1952).
13. John Newman, in "Advances in Electrochemistry and Electrochemical Engineering," Delahay and Tobias, Editors, Vol. 5, Chapt. 2, Interscience, New York (1967).
14. H. S. Carslaw and J. C. Jaeger, "Conduction of Heat in Solids," 2nd ed., p. 485, Oxford University Press (1959).
15. H. S. Harned and R. M. Hudson, *J. Am. Chem. Soc.*, **73**, 3781 (1951).
16. N. Ibl, Proceedings of the 7th Meeting C.I.T.C.E., Lindau, Butterworths, London (1955).
17. K. Beach, Ph.D. Thesis, University of California, Lawrence Radiation Laboratory, Berkeley, Calif., UCRL-20324, A.E.C. Contract W-7405, Eng. 48.
18. W. F. Yakymyshyn, M.Sc. Thesis, University of Alberta, Edmonton, Canada, 1962.
19. R. N. O'Brien, C. A. Rosenfield, K. Kinoshita, W. F. Yakymyshyn, and J. Leja, *Can. J. Chem.*, **43**, 3304 (1965).

## Technical Notes



# The Use of D-C Resistance and A-C Impedance Measurements on Discharged and Undischarged Cathodes as a Measure of the Relative Electronic and Ionic Conductance

M. L. Kronenberg\*

Union Carbide Corporation, Battery Products Division, Cleveland, Ohio 44101

Dry cell cathodes are normally compacted mixes containing electronically conducting powders (i.e., acetylene black and graphite plus MnO<sub>2</sub>) and ionically conducting solutions (i.e., solutions of NH<sub>4</sub>Cl-ZnCl<sub>2</sub> or KOH). In attempting to understand the mode of discharge of cathodes, it is helpful to know how the conductivity of this mixture is shared by the electronically and ionically conducting phases in fresh and in discharged cells. In this investigation a method was devised to distinguish between ionic and electronic conductivity. The system was regarded as an electronically conducting matrix (MnO<sub>2</sub> + acetylene black and/or graphite) permeated by an ionically conduct-

ing phase (solutions of ZnCl<sub>2</sub> + NH<sub>4</sub>Cl or KOH). The two types of conductivity were considered to be in parallel. A simple, electrical model of a cathode, therefore, could be approximated by a platinum wire immersed in a conducting solution. The d-c resistance of the wire would be independent of whether or not the wire was immersed in electrolyte as long as no Faradaic reaction takes place. Total resistance (ionic + electronic), as measured by an a-c bridge, depends on whether an ionic path is in parallel with the electronic one, i.e., whether the wire is immersed or not. In the work reported here, measurements were made on fresh and discharged cathodes, not on complete cells. These were obtained from commercial "D" size Leclanché, alkaline MnO<sub>2</sub>, and mercuric oxide cells.

\* Electrochemical Society Active Member.

Key words: electronic conductivity, ionic conductance, Leclanché cells, alkaline manganese dioxide cells, mercuric oxide cells.

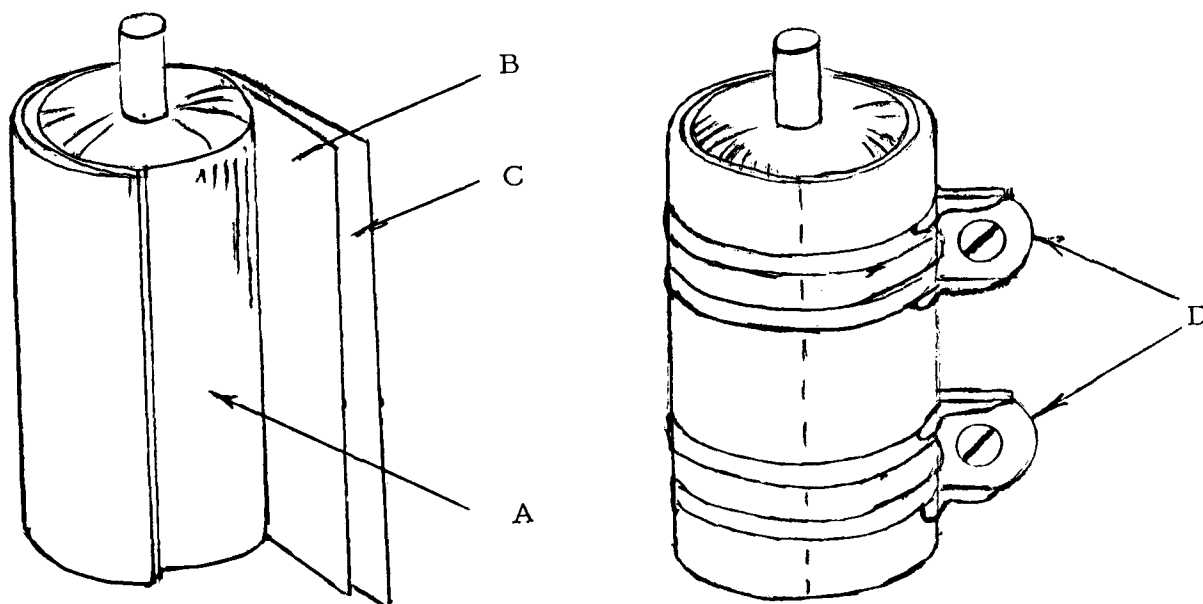


Fig. 1. Experimental arrangement for resistance measurements for Leclanché cell cathodes. A, Bobbin; B, graphite cloth; C, platinum foil; D, adjustable clamps.

### Experimental

Cathode resistance was always measured across the thickness of the cathode. For a Leclanché cell bobbin (see Fig. 1, point A), this was between the center carbon rod and graphite cloth (point B) held under pressure by platinum foil (point C). The platinum foil was clamped with adjustable ring clamp (point D). This procedure was evolved after trying many others that were not satisfactory because too much contact resistance was included in the measurement.

The components used for electrical measurements on alkaline  $MnO_2$  and mercuric oxide cells are illustrated in Fig. 2. For these cells, graphite cloth (Fig. 2, point C) was pressed into the inside cathode surface (point D) by a uniformly expanding sleeve (point B) and tapered mandrel (point A). The sleeve had to be gold plated because steel wool and platinum, which were tried first, showed a large frequency dependence when resistance was measured with an a-c bridge. Virtually no frequency dependence is noted with this present procedure.

Cells referred to as discharged Leclanché and alkaline  $MnO_2$  were discharged at a high rate in excess of their rated capacities to below 0.7V. Leclanché cathodes were discharged continuously through a 20

ohm resistor for 73 hr (231 A-min). Alkaline  $MnO_2$  cells were discharged through a 10 ohm resistor for 115 hr (680 A-min). Mercuric oxide cells were discharged through a 2 ohm resistor to about 1.08V for 5¼ hr which corresponds to about 25-30% of their rated capacity (120 A-min). Mercuric oxide cells were not completely discharged because excessive mercury product would be lost from the discharge site, and anode removal becomes difficult with complete discharge.

The total resistance ( $R_T$ ) was measured using a Wheatstone resistance bridge. A schematic of this bridge is shown in Fig. 3. The a-c signal input to the bridge was normally 100 mV or lower and resistance

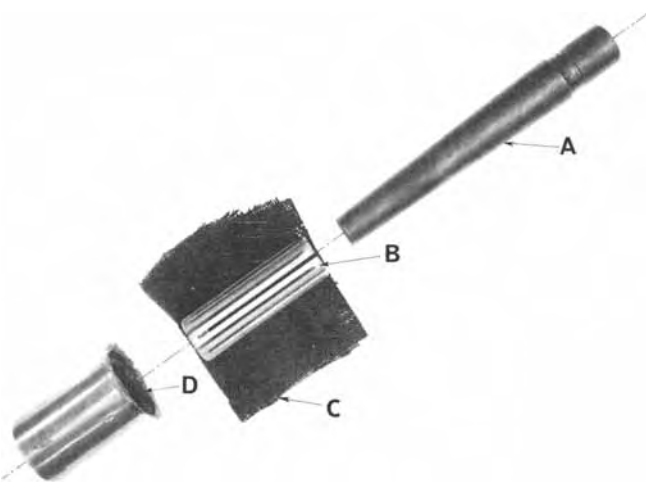


Fig. 2. Experimental arrangement for resistance measurements on alkaline  $MnO_2$  and mercuric oxide cell cathodes. A, Tapered mandrel; B, expanding sleeve; C, graphite cloth; D, inside cathode surface.

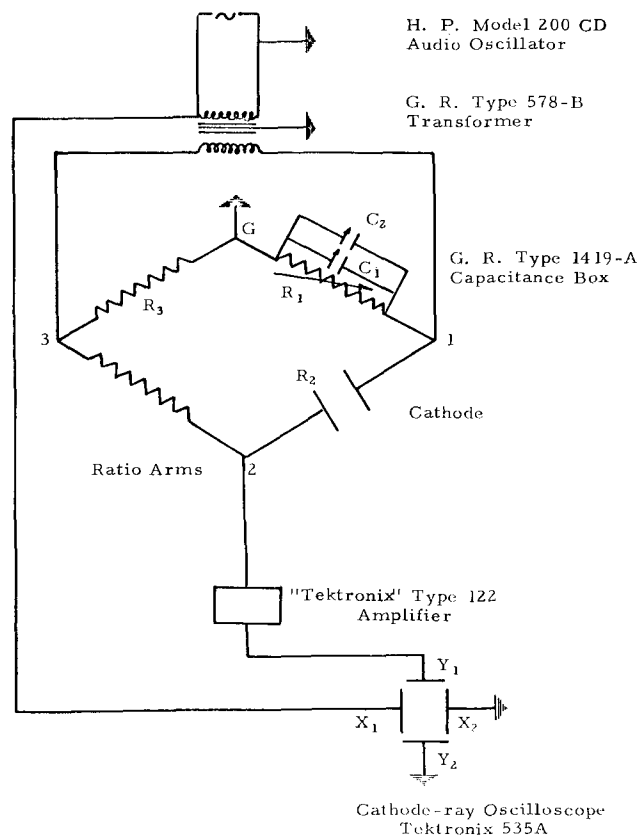


Fig. 3. Bridge circuit used for measurement of total resistance ( $R_T$ ).

measurements were obtained at frequencies ranging from 1 to 10 kHz. Frequency independence was used to reassure the experimenter that no unexpected changes had taken place along the collector-cathode interface, such as openings developing in the gold-plated platinum which would have led to frequency dependence as was previously noted.

Electronic resistance ( $R_e$ ) was obtained from the voltage-current slope ( $E/i$ ) in a potential sweep below the Faradaic range (no appreciable reaction, 0-100 mV). The slope was constant, retraceable up and down, and independent of sweep rate over the range 1-50 mV/sec. A Physical Dynamics Corporation potentiostat and auxiliary voltage scanning unit were used for the potential sweep. The results were recorded on a Honeywell 520 XY recorder. A typical sweep used to obtain  $R_e$  on a Leclanché cathode is shown in Fig. 4.

Ionic resistance,  $R_i$ , was calculated from  $R_T$  and  $R_e$  using a parallel circuit analysis as follows

$$\frac{1}{R_i} = \frac{1}{R_T} - \frac{1}{R_e} \quad [1]$$

or

$$R_i = R_e R_T / (R_e - R_T)$$

The ratio of electronic conductance to ionic conductance ( $\kappa_e/\kappa_i$ ) is equal to  $R_i/R_e$ .

### Experimental Results

Preliminary experiments were conducted with a platinum wire immersed in 9N KOH and in  $ZnCl_2-NH_4Cl$  solutions to test the model. The electrical equivalent of an  $MnO_2$  bobbin was approximated by this technique before beginning work on cathodes from the three different types of cells.

To provide an example of the way in which the data were tabulated, results of resistance measurements on fresh and discharged alkaline  $MnO_2$  cathodes are summarized in Tables I and II, respectively. In Table III, the average values for  $R_e$ ,  $R_i$ , and  $\kappa_e/\kappa_i$  expressed to the 95% confidence limit are summarized for six different categories of fresh and discharged cathodes.

Fresh Leclanché cathodes have an electronic-to-ionic conductance ratio of 3.37; whereas, discharged Leclanché cathodes have a value close to unity for this same ratio. Electronic resistance increased by a factor of 3-4 upon heavy discharge, while ionic resistance did not change significantly.

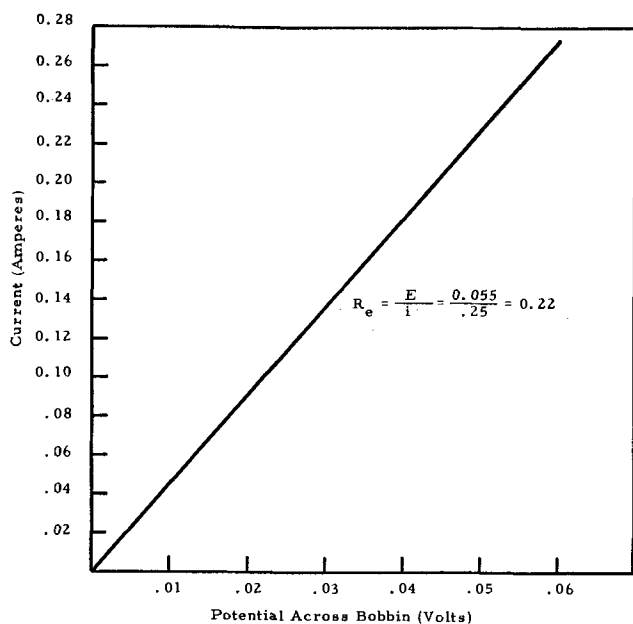


Fig. 4. Example of electronic resistance determination ( $R_e$ ) on a Leclanché cathode from potential sweep data.

Table I. Resistance measurements on ten undischarged alkaline  $MnO_2$  cathodes

Cell No.	$R_T$	$R_e$	$R_i = \frac{R_e R_T}{R_e - R_T}$
123	0.05	0.100	0.100
126	0.07	0.123	0.162
129	0.05	0.085	0.121
131	0.04	0.062	0.112
133	0.05	0.076	0.146
134	0.06	0.104	0.142
135	0.05	0.081	0.131
136	0.04	0.063	0.110
137	0.05	0.076	0.150
138	0.04	0.076	0.084

Table II. Resistance measurements on ten discharged alkaline  $MnO_2$  cathodes

Cell No.	$R_T$	$R_e$	$R_i$
159	0.22	0.828	0.300
160	0.25	1.123	0.322
161	0.28	1.639	0.338
162	0.22	1.175	0.271
163	0.28	1.127	0.372
164	0.24	1.189	0.301
165	0.24	2.140	0.270
166	0.29	1.757	0.347
167	0.25	2.095	0.284
168	0.24	1.640	0.281

Table III. Electronic and ionic conductance measurements on Leclanché, alkaline  $MnO_2$ , and mercuric oxide cathodes

Description	$R_e$ , ohms	$R_i$ , ohms	$R_i/R_e = \kappa_e/\kappa_i$
Leclanché, fresh	0.233 ± 0.014	0.786 ± 0.141	3.37 ± 0.85
Leclanché, completely discharged	0.890 ± 0.151	0.830 ± 0.165	0.932 ± 0.317
Alkaline $MnO_2$ , fresh	0.0845 ± 0.014	0.126 ± 0.019	1.49 ± 0.14
Alkaline $MnO_2$ , completely discharged	1.471 ± 0.319	0.309 ± 0.025	0.210 ± 0.056
Mercuric oxide, fresh	0.138 ± 0.019	0.069 ± 0.010	0.527 ± 0.119
Mercuric oxide, partially discharged	0.087 ± 0.023	0.119 ± 0.026	1.367 ± 0.052

Alkaline  $MnO_2$  cathodes have an electronic-to-ionic conductance ratio of 1.49 before discharge and a ratio of 0.2 after heavy discharge. While there was some change in ionic conductance, it is seen that the electronic resistance increases by more than one order of magnitude upon heavy discharge.

Fresh mercuric oxide cells had an electronic-to-ionic conductance ratio of 0.527. With partially discharged cells this ratio increased to 1.367.

### Discussion of Results

The sharp increase in electronic resistance upon discharge for both alkaline  $MnO_2$  and Leclanché cells is in agreement with the well-known fact that the resistivity of manganese oxides increases as reduction proceeds. Results in this current work suggest that electronically conducting powder (*i.e.*, acetylene black and graphite) in the cathode mix do not form continuous paths across the width of the cathode in parallel with  $MnO_2$  but that most of their conductance occurs in series with  $MnO_2$  particles. Otherwise the increase in manganese oxide resistance upon discharge would not change the over-all electronic resistance.

The decrease in electronic resistance for mercuric oxide cathodes upon discharge is due to formation of a higher conductivity reduction product (Hg). Similar results would probably be characteristic of silver oxide cathodes but these have not yet been tried.

### Acknowledgment

The author wishes to acknowledge the able assistance of Mr. Frank Dagata who carried out many of the experimental measurements.

Manuscript submitted June 27, 1973; revised manuscript received Oct. 29, 1973.

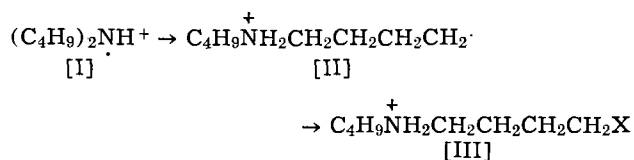
Any discussion of this paper will appear in a Discussion Section to be published in the December 1974 JOURNAL. All discussions for the December 1974 Discussion Section should be submitted by Aug. 1, 1974.

# Electrochemical Oxidation of Secondary Amines

S. Wawzonek\* and S. M. Heilmann

Department of Chemistry, The University of Iowa, Iowa City, Iowa 52242

The similarity in intermediates [I] postulated in the electrolytic oxidation of aliphatic amines (1) and in the Hofmann-Loeffler reaction of N-haloamines (2, 3) suggested the present investigation of the electrolytic oxidation of dibutylamine and methylisohexylamine as a possible method of preparing intermediates which could be converted into pyrrolidines



Differences between the electrolytic method and the Hofmann-Loeffler reaction would occur in the third step of the reactions; the radical formed by rearrangement of [I] would require an external reagent in the electrolysis to produce a species [III] which could be converted to a pyrrolidine by base. Electrolyses were therefore studied in methanol at a carbon anode and in the presence of bromotrichloromethane. The former conditions were investigated to determine whether the radical [II], if formed, would be converted to a carbonium ion that would react with methanol and form a methyl ether. Cleavage of this product with hydrogen bromide would give [III] (X = Br). Electrolysis in the presence of bromotrichloromethane would lead to this product ([III], X = Br) directly by an abstraction of a bromine atom from this compound by [II].

Secondary amines (1) studied electrolytically thus far contained alkyl groups which were unsuitable sterically (4) for the hydrogen abstraction step necessary for this series of reactions.

## Experimental

Voltammetric studies were carried out with a Beckman Electroscan 30 using a rotating microplatinum electrode or a stationary 10H pencil. The cathode was a platinum wire mesh cylinder and the reference electrode was a silver wire in a 0.1M solution of silver nitrate in 90% methanol. Irreversible oxidation waves were found for dibutylamine at 0.70V (Ag|Ag<sup>+</sup>) at platinum and 0.72V (Ag|Ag<sup>+</sup>) at graphite, and for methylisohexylamine at 0.62V (Ag|Ag<sup>+</sup>) at graphite.

Large scale electrolyses were carried out in two types of cells. A 600 ml Berzelius beaker was fitted with a stirrer, platinum cathode (foil cylinder, 1.5 in. high and 1 in. in diameter), platinum wire screen (2 in. high, 0.5 in. in diameter) anode, or graphite rod (5.5 in. high and 1 in. in diameter) anode, and a Ag|Ag<sup>+</sup> (0.1M) reference cell in the appropriate solvent. The reference cell was separated from the cell by a sintered glass disk. No diaphragm was employed between the anode and cathode.

The second cell was similar to the flow-through cell used by Rüetschi and Trümpler (5) with the following modification. A graphite fiber cylindrical anode (0.8 in. high, 1.2 in. in diameter) was placed on the sintered glass disk and the platinum cathode (disk, 0.8 in. in diameter) was positioned above the anode.

### Electrolytic Oxidation of Dibutylamine

(i) A solution of dibutylamine (10 ml, 0.059 mole) in methanol-water (90:10) (400 ml) containing benzyl-

trimethylammonium tetrafluoroborate (19.0g, 0.08 mole) was electrolyzed in the first cell at a platinum anode and at a constant potential of +0.9V using a PAR Model 173 automatic potentiostat. The initial current of 0.9A decreased to 0.75A after 5 hr of electrolysis. A plot of current *vs.* time corresponded to the utilization of 2.5 electrons per molecule of dibutylamine. The resulting solution was acidified with dilute hydrobromic acid and the methanol was removed. The residue was refluxed with concentrated hydrobromic acid for 6 hr and then made basic with concentrated sodium hydroxide. The resulting solution was steam distilled until the distillate was neutral. The distillate was acidified with 12N hydrochloric acid, evaporated to dryness, and the amines were liberated with 10% sodium hydroxide and treated with p-toluenesulfonyl chloride, and then dilute acid. Extraction of the sulfonamides with ether was followed by removal of the ether and chromatography on silica gel using benzene and benzene-ethyl acetate mixtures as eluants. The following p-toluenesulfonamides were isolated and characterized by thin layer chromatography (tlc) migration times and comparison of infrared spectra with authentic samples: N-butyl (bis) p-toluenesulfonamide (0.25g, 1.7%), N,N-dibutyl-p-toluenesulfonamide (8.8g, 52.5%), N-butyl-p-toluenesulfonamide (2.88g, 22.6%), N-methyl-p-toluenesulfonamide (0.29g, 3.4%), p-toluenesulfonamide (0.44g, 5.1%).

The hydrochloric acid solution upon basification and extraction with pentane gave a mixture of tertiary amines (0.27g). Examination by vapor phase chromatography (vpc) using a 6 ft × 1/8 in. column packed with 15% Carbowax 4000 on 100-120 mesh Chromosorb P indicated the presence of only trace amounts of benzyldimethylamine and dibutylmethylamine. Identification was made by comparison of migration times with those of known samples. No 1-butylpyrrolidine was present.

The residue from the steam distillation was extracted with ether and gave a brown oil (0.04g) which by vpc and tlc analyses was shown to be a mixture and was not investigated further because of the small amount present.

Electrolysis of a similar solution at a carbon anode gave identical products. The tertiary amine mixture (0.38g) contained dibutylmethylamine and benzyldimethylamine in a ratio of 60:40.

(ii) A solution of dibutylamine (10 ml, 0.059 mole) and bromotrichloromethane (10 ml) in 90% methanol (100 ml) containing tetrabutylammonium tetrafluoroborate (6.58g, 0.02 mole) was passed through a flow-through cell at uncontrolled potential. The current observed was 0.6A at an externally applied potential of 30V. The products obtained were similar to those given in (i) above. The tertiary amines (0.2g) contained traces of dibutylmethylamine and tributylamine.

The use of methylene chloride as a solvent in this electrolysis gave similar products. This electrolysis had to be interrupted twice to remove a black substance which coated the cathode.

### Electrolytic Oxidation of N-Isohexyl-N-methylamine

Isohexylmethylamine (6) (7.4g) was oxidized at a carbon anode in 90% methanol-water (400 ml) containing 0.2M benzyltrimethylammonium tetrafluoroborate at a constant potential of +0.80V in a cell similar to that used in part (i) above for dibutylamine. The initial current of 0.66A decreased to 0.05A after 21 hr. A plot of current *vs.* time corresponded to the use of

\* Electrochemical Society Active Member.  
Key words: cation radicals, Hofmann-Loeffler reaction, disproportionation.



slightly more than one electron for each molecule of amine. The resulting solution was treated in a similar fashion to that given in part (i) above for dibutylamine. The mixture of amines obtained was extracted with pentane. Removal of the pentane gave a yellow liquid (5.10g), which, when examined by gas chromatography, did not contain any of the desired pyrrolidine. Distillation of the oil gave 2.5g of a clear liquid which was subjected to a Hinsberg separation; no tertiary amines were present. Two toluenesulfonamides were isolated and identified as isohexyl(bis)toluenesulfonamide (0.95g) and N-methyl-N-isohexyltoluenesulfonamide (3.22 g).

Isohexyl(bis)toluenesulfonamide was a white solid which melted at 91.5°-92.5°C after crystallization from hexane; infrared(Nujol) 8.60 $\mu$  (SO<sub>2</sub>); nmr(CDCl<sub>3</sub>)  $\delta$  0.80(d, 6H, C(CH<sub>3</sub>)<sub>2</sub>, J = 6 cps), 0.90-1.90(m, 5H, CHCH<sub>2</sub>CH<sub>2</sub>), 2.42(s, 6H, ArCH<sub>3</sub>), 3.68(t, 2H, NCH<sub>2</sub>, J = 8 cps), 7.33(d, 4H, C<sub>6</sub>H<sub>2</sub>, J = 8 cps), 7.94(d, 4H, C<sub>6</sub>H<sub>2</sub>, J = 8 cps); mass spectrum *m/e* 338 (M-C<sub>5</sub>H<sub>11</sub>); 254 (M-CH<sub>3</sub>C<sub>6</sub>H<sub>4</sub>SO<sub>2</sub>).

*Analysis*.—Calculated for C<sub>20</sub>H<sub>27</sub>NS<sub>2</sub>O<sub>4</sub>: C, 58.65; H, 6.65; N, 3.42. Found: C, 58.68; H, 6.66; N, 3.44.

N-Methyl-N-isohexyltoluenesulfonamide was a colorless viscous oil; infrared(neat) 8.72 $\mu$ (SO<sub>2</sub>); nmr(CDCl<sub>3</sub>)  $\delta$  0.86(d, 6H, C(CH<sub>3</sub>)<sub>2</sub>, J = 6 cps), 1.00-1.70(m, 5H, CHCH<sub>2</sub>CH<sub>2</sub>), 2.40(s, 3H, ArCH<sub>3</sub>), 2.70(s, 3H, NCH<sub>3</sub>), 2.97(t, 2H, NCH<sub>2</sub>, J = 6 cps), 7.34(d, 2H, C<sub>6</sub>H<sub>2</sub>, J = 8 cps), 7.70(d, 2H, C<sub>6</sub>H<sub>2</sub>, J = 8 cps); mass spectrum *m/e* 269(M).

*Analysis*.—Calculated for C<sub>14</sub>H<sub>23</sub>NSO<sub>2</sub>: C, 62.41; H, 8.60; N, 5.20. Found: C, 62.66; H, 8.52; N, 5.25.

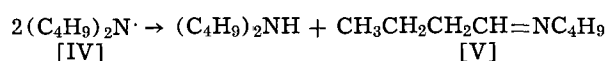
*Benzyltrimethylammonium tetrafluoroborate*.—A solution of 40% benzyltrimethylammonium hydroxide in methanol (208g) was treated with 48% fluoroboric acid (92g) and the resulting solution was evaporated to dryness using reduced pressure. The addition of 400 ml of benzene followed by distillation to remove water gave a solution which upon cooling gave yellowish crystals (120g). Recrystallization from 1:1 ethanol-ethyl acetate gave white needles melting at 132°-133°C.

*Analysis*.—Calculated for C<sub>10</sub>H<sub>16</sub>NBF<sub>4</sub>: C, 50.66; H, 6.80; N, 5.91. Found: 50.53; H, 6.70; N, 5.95.

### Results and Discussion

Electrolysis of dibutylamine in 90% methanol at platinum and graphite at controlled and uncontrolled potentials in an undivided conventional cell using benzyltrimethylammonium tetrafluoroborate as the supporting electrolyte gave butylamine, methylamine, and ammonia with traces of methylidibutylamine and benzyldimethylamine as products. The oxidation of methylisohexylamine, which would form a cation radical more susceptible to rearrangement because of the tertiary hydrogen present, gave mainly isohexylamine at a graphite anode.

These results indicated that the cation radical [I] was reacting with the parent amine, or with the methanol before it could rearrange, and forming the dibutylamino free radical [IV]



This radical [IV] undergoes a bimolecular disproportionation to dibutylamine and the Schiff's base [V] (7). Hydrolysis of the Schiff's base [V] would form butylamine which by a similar sequence of reactions would form ammonia. This type of disproportionation occurs only to a slight extent in the Hofmann-Loeffler reaction because of the strong acids used as solvents.

The use of an undivided cell did not complicate the products obtained at the anode. Reduction of the supporting electrolyte at the cathode would produce trimethylamine and toluene as the main products with benzyldimethylamine and methane as side products. The oxidation of these tertiary amines occurs at approximately the same point as that of dibutylamine and at more positive potentials than that of isohexylmethylamine. The coulometric analysis for the oxidation of dibutylamine was therefore high and that for isohexylmethylamine corresponded to the use of one electron per molecule of amine.

The source of the trace amounts of methylamine and methylidibutylamine isolated is not actually known; participation of methanol or its conjugated acid as a methylating agent is implied.

In order to minimize the effect of the amine on the oxidation product [I], the electrolysis was carried out in a modified flow-through cell (5) using a graphite fiber anode and a platinum cathode placed above the anode. The products from dibutylamine in this cell were again butylamine, ammonia, and traces of dibutylmethylamine indicating that the methanol was basic enough to convert [I] to [IV]. Substitution of methylene chloride for the methanol did not aid in the stabilization of the cation radical [I] and butylamine was again the main product.

### Acknowledgment

This work was part of the Ph.D Thesis of one of the authors (S. M. H.), University of Iowa, 1973.

Manuscript submitted April 9, 1973; revised manuscript received Sept. 4, 1973.

Any discussion of this paper will appear in a Discussion Section to be published in the December 1974 JOURNAL. All discussions for the December 1974 Discussion Section should be submitted by Aug. 1, 1974.

### REFERENCES

1. P. J. Smith and C. K. Mann, *J. Org. Chem.*, **34**, 1821 (1969).
2. S. Wawzonek and P. J. Thelen, *J. Am. Chem. Soc.*, **72**, 2118 (1950).
3. S. Wawzonek and T. P. Culbertson, *ibid.*, **81**, 3367 (1959).
4. E. J. Corey and W. R. Hertler, *ibid.*, **82**, 1657 (1960).
5. P. Rüetschi and G. Trümpler, *Helv. Chim. Acta*, **36**, 1649 (1953).
6. S. Wawzonek and S. M. Heilmann, *Org. Prepn. Proced. Int.*, **5**, 195 (1973).
7. S. Wawzonek and J. D. Nordstrom, *J. Org. Chem.*, **27**, 3726 (1962).



## Oscillatory Interface Instability During Czochralski Growth of Heavily Doped Germanium

R. Singh,<sup>\*1</sup> A. F. Witt,<sup>\*\*</sup> and H. C. Gatos<sup>\*\*</sup>

Department of Metallurgy and Materials Science,  
 Massachusetts Institute of Technology, Cambridge, Massachusetts 02139

### ABSTRACT

Oscillatory interface instability associated with constitutional supercooling was established during growth of germanium single crystals from gallium-doped melts by the Czochralski technique. The wavelength and phase velocity of the instability were determined and found to be consistent with theory. The effects of pulling and rotation rates on oscillatory instability were quantitatively correlated with the interface stability theory. It was shown that during rotational pulling under conditions leading to constitutional supercooling, the destabilizing effects of rotation dominate its stabilizing effects for moderate rates of rotation in the presence of thermal asymmetry.

During crystal pulling from a doped melt, the region ahead of the growth interface may become constitutionally supercooled if the distribution coefficient of the solute differs from one. The original criterion for constitutional supercooling of Rutter and Chalmers (1) and Tiller *et al.* (2) was derived from static considerations. Constitutional supercooling during crystal growth from stirred melts was first investigated by Hurle (3). Dynamic theories for small perturbations were subsequently developed in the linear approximation by Mullins and Sekerka (4) and by Voronkov (5). Calculations of the conditions leading to instability of solid-liquid interfaces have recently received considerable attention (6-13). In these investigations the melt was considered to be stationary with diffusion being the only means of mass transport; convection effects were excluded. Hurle (13) considered the effects of convective mixing of solute in the melt (expressed in terms of boundary layer thickness) and concluded that the spatial frequency of the first appearing instability is a function of convective mixing. Delves (14, 15), in a recent analysis of interface stability during growth from stirred melts, has predicted oscillatory behavior of the growth interface for convection controlled solute transport encountered in Czochralski growth. Some experimental results consistent with this theoretical treatment have been reported (16).

In the present paper a detailed analysis of an experimental investigation on interface instability during Czochralski growth is reported and discussed in the light of the prevailing theoretical models.

### Experimental Procedure

Single crystals of germanium were grown in the  $\langle 111 \rangle$  direction by the Czochralski technique from gallium-doped melts. The pulling rate, the rotation

rate, and the dopant concentration in the melt were adjusted so that the growth interface came to the verge of instability at some point during growth. The diameter of the crystals was maintained between 1.5 and 2 cm over a length of 4-6 cm. The effects of pulling rate and rotation rate were studied in the range of 2.9-6 cm/hr and 13-70 rpm, respectively. The crystals were cut along the growth axis; the sections were polished (0.06  $\mu\text{m}$  particle size alumina) and chemically etched (1.5 min in 1 part HF, 1 part  $\text{H}_2\text{O}_2$ , and 2.5 parts water, by volume) to reveal impurity heterogeneities which were studied with interference contrast microscopy.

### Theory

The theory of interface instability for a two-component system solidifying with planar front under conditions of constitutional supercooling has been developed by a number of investigators. If  $\Phi(x, t)$  describes the shape of the perturbed interface, it can be expressed by a Fourier integral (12)

$$\phi(x, t) = \frac{1}{2\pi} \int_{-\infty}^{\infty} e^{i\omega x} \Phi_0(\omega) e^{t f(\omega)} d\omega \quad [1]$$

and

$$\frac{\dot{\Phi}}{\Phi} \equiv \left( \frac{d\Phi}{dt} \middle/ \Phi \right) = f(\omega) \quad [2]$$

where  $\Phi_0(\omega)$  is the Fourier transform of the initially perturbed shape of the interface,  $\Phi$  is the Fourier transform of  $\phi$ , and  $\omega$  is the spatial frequency associated with the perturbation;  $f(\omega)$  is not strongly time dependent, provided the system is just on the verge of instability (12).

A stability criterion can be established based on the values of  $f(\omega)$ ; it can be positive, negative, or complex corresponding to enhancement, decay, or oscillation of a perturbation, respectively. On the basis of this analysis the stability criterion derived for systems with rotational stirring takes the form (15)

\* Electrochemical Society Student Member.

\*\* Electrochemical Society Active Member.

<sup>1</sup> Present address: Allied Chemical Company, P.O. Box 1021R, Morristown, New Jersey 07960.

Key words: interface instability, germanium, constitutional supercooling, crystal growth.

$$\frac{K_1 G_1 + K_s G_s}{(K_1 + K_s) G_1} > S \left(-\frac{D}{\nu}\right)^{1/30.75} \quad [3]$$

where  $K_1$  and  $K_s$  are the thermal conductivities of the liquid and the solid, respectively;  $G_1$  and  $G_s$  are the thermal gradients near the interface in the liquid and the solid;  $\nu$  is the kinematic viscosity of the melt;  $D$  is the diffusion coefficient of the solute in the melt; and  $S$  is the constitutional supercooling parameter defined as

$$S = \frac{C_1 - C_s}{\frac{D}{V} G_1} \left| \frac{dT}{dC} \right| \equiv \frac{m G_c}{G_1} \\ = \frac{-m(1-k)VC_0}{G_1 D [k + (1-k) \exp -\delta V/D]} \quad [4]$$

where  $C_1$  and  $C_s$  are the impurity concentrations in the liquid and the solid, respectively, near the interface;  $V$  is the instantaneous microscopic growth rate;  $m$  is the slope of the liquidus in the phase diagram;  $k$  is the equilibrium distribution coefficient;  $C_0$  is the impurity concentration in the bulk of the melt; and  $\delta$  is the thickness of the boundary layer.  $G_c$  is the concentration gradient in the liquid just ahead of the advancing interface given by

$$G_c = \frac{-(1-k)VC_0}{D[k + (1-k) \exp -\delta V/D]} \quad [5]$$

Thus, the stability criterion becomes

$$\frac{-m(1-k)VC_0}{D[k + (1-k) \exp -\delta V/D]} \left| \frac{D}{\nu} \right|^{1/3} 0.75 < \frac{K_1 G_1 + K_s G_s}{(K_1 + K_s)} \quad [6]$$

If the pulling rate  $V_0$ , and the impurity concentration,  $C_0$ , in the melt are adjusted so that the system is at the verge of instability (i.e., left-hand side of inequality (Eq. [6]) just exceeds the right-hand side), then during rotational pulling the instantaneous microscopic growth velocity (17),  $V$ , is given by

$$V = V_0(1 - \alpha \cos 2\pi R t) + \frac{d\phi}{dt} \quad [7]$$

where  $\alpha = 2\pi R \Delta T / G_1 V_0$ ;  $\Delta T$  is the temperature variation for a given point at the growth interface over the rotational cycle; and  $R$  is the rotational rate. The first term (Eq. [7]) represents the growth rate fluctuations associated with the rotational pulling in a thermally asymmetric system;<sup>2</sup> the second term is the derivative of the perturbation (Eq. [1]) which arises from the instability due to constitutional supercooling. This second term is relatively small and associated with a spatial frequency.

**Growth interface shape in time and space.**—For a perturbation of constant spatial frequency, by integrating Eq. [1] and employing a delta function, one obtains

$$\phi(x, t) = \frac{1}{2\pi} \Phi_0(\omega) e^{i\omega x} e^{f(\omega)t} \quad [8]$$

If  $f(\omega)$  is complex, say,  $f(\omega) = p_j(\omega) = \text{Re}[p_j(\omega)] + i\text{Im}[p_j(\omega)]$ , then the shape of the growth interface is given by either the real or imaginary parts of Eq. [9]

$$\phi(x, t) = \Phi_0(\omega) e^{\text{Re}[p_j(\omega)]t} \sin\{\omega x + \text{Im}[p_j(\omega)]t\} \quad [9]$$

where  $\phi_0(\omega) = \Phi_0(\omega)/2\pi$ . [The notation adopted here is used by Delves (15).] If the growth rate is constant and the system is on the verge of instability (i.e., inequality, Eq. [6], is just reversed and  $\text{Re}[p_j(\omega)]$  is small or zero) the general equation representing the one-dimensional growth interface moving in the  $z$

direction can be found by integrating Eq. [7] with respect to  $t$

$$z = V_0 t + \Phi_0(\omega) \sin\{\omega x + \text{Im}[p_j(\omega)]t\} \quad [10]$$

This equation describes the dynamics of the growth interface with oscillatory instabilities of a wavelength  $2\pi/\omega$  and phase velocity  $\text{Im}[p_j(\omega)]/\omega$ . On the basis of Delves's theory (15), the onset of oscillatory instability in Ge for the present experimental conditions should be associated with  $\lambda = 80\text{--}90 \mu\text{m}$  and  $\text{Im}[p_j(\omega)] = 0.5\text{--}1.0 \text{ sec}^{-1}$ . If the growth interface, during rotational pulling, advances with periodically varying velocity,  $V$ , the general equation representing a one-dimensional growth interface moving in the  $z$  direction assumes the form

$$z = V_0 t - \frac{\alpha V_0}{2\pi R} \sin 2\pi R t + \Phi_0(\omega) e^{\text{Re}[p_j(\omega)]t} \sin\{\omega x + \text{Im}[p_j(\omega)]t\} \quad [11]$$

## Results

During crystal pulling by the Czochralski technique the onset of constitutional supercooling in melts with moderately high doping levels can be delayed by seed rotation since boundary layer thickness is decreased. In the absence of constitutional supercooling, the growth interface remains stable and the microscopic growth rate in the  $z$  direction varies in a quasisinusoidal mode within each rotational cycle because of unavoidable thermal asymmetry (first term of Eq. [7]). In the presence of pronounced thermal asymmetry, partial remelting takes place during passage of the interface through the hottest region in the system and "remelt" rotational striations are formed which appear as "smooth" parallel lines delineating the shape of the growth interface at the moment of their formation. During crystal pulling from melts doped to very high levels, constitutional supercooling cannot be suppressed by rotation, for any appreciable growth period, and the interface becomes unstable.

Based on the preceding theoretical considerations, constitutional supercooling depends strongly on the microscopic growth rate (Eq. [4]); thus, sinusoidal growth rate variations associated with rotation may bring the system, within each rotation, periodically to the verge of constitutional supercooling; as a result, oscillatory instability can be brought about and be sustained for prolonged periods of growth.

**Oscillatory instability.**—The behavior discussed above was experimentally observed as seen in Fig. 1, which depicts an outer region of the grown crystals. The rotational striations, normally "smooth" parallel lines, appear here as "wavy" lines, indicating oscillatory instability without interface breakdown. Since the rotational striations are of the remelt type, the observed amplitude of the elevations and depressions is, of course, less than the maximum amplitude encountered during growth. As is seen in Fig. 1, protrusions of the interface into the melt (maxima) on one striation develop (during growth associated with a  $360^\circ$  rotation) into depressions (minima) on the next striation, while the minima develop into maxima.

This behavior might be interpreted as a "stationary" oscillatory instability with the sinusoidal growth rate variations (resulting from seed rotation) being modulated by an oscillatory instability component. However, examination of the instability as observed in Fig. 2-4 indicates that the behavior observed in Fig. 1 is not typical. The growth direction being normal to the striations, these figures show that the maxima on one striation are displaced laterally on the subsequent striation; the extent of such displacement varies depending on the growth conditions. Such lateral displacement of the oscillatory instability is also consistent with the nonperpendicular alignment of the segregation inhomogeneities within successive striations (see, for example, Fig. 2). These periodic segrega-

<sup>2</sup> The effect of sinusoidal temperature fluctuations on the microscopic growth rate has been independently derived by Hurle et al. (18).

1988

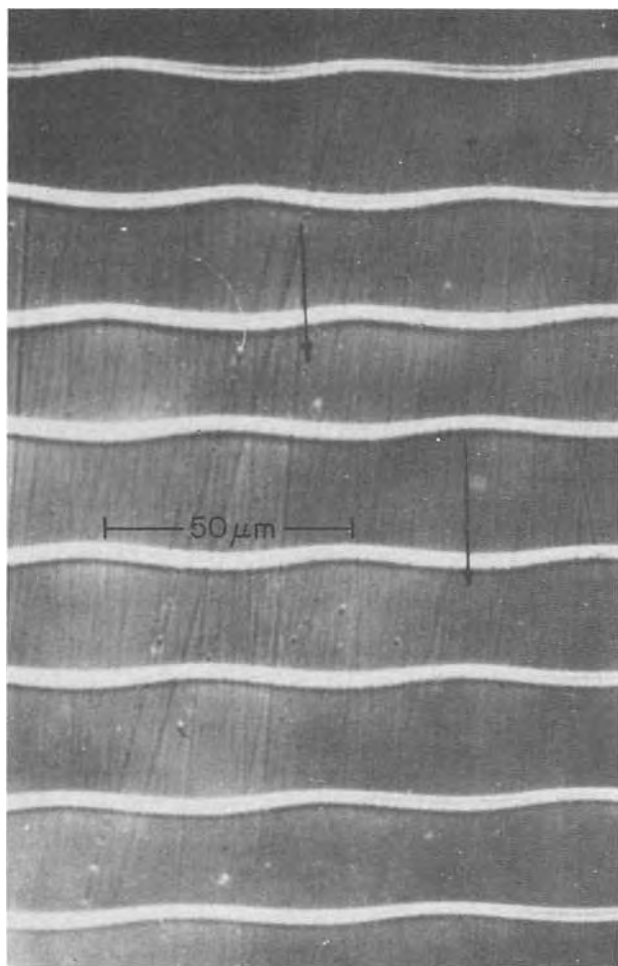


Fig. 1. Rotational remelt striations in a Ga-doped germanium single crystal pulled in the  $\langle 111 \rangle$  direction (3.15 cm/hr; 26 rpm). The depicted segment is from an outer region of the crystal and shows oscillatory instability of the growth interface. The arrows indicate the direction of growth.

tion inhomogeneities reflect the periodic development and decay of the instability resulting from the sinusoidal growth rate variations within each rotational cycle. Accordingly, it is concluded that the observed oscillatory instability is of a "traveling wave" nature with a characteristic phase velocity (15) and not stationary as could be assumed from Fig. 1.

Using the cylindrical coordinates system, the oscillatory perturbation can be resolved into two oscillatory components, in the radial and tangential directions, with wavelengths  $\lambda_r$  and  $\lambda_\theta$ , respectively. The wavelengths of the oscillations in the radial direction ( $\lambda_r$ ) were determined on planes exposed by cutting the crystal along the rotational axis. The wavelengths in the tangential direction ( $\lambda_\theta$ ) were obtained from cuts perpendicular to the above; since there is an inherent uncertainty in obtaining cuts precisely through the axis of rotation, the measured  $\lambda_r$  and  $\lambda_\theta$  values do not necessarily represent the pure radial and tangential components. The phase velocity of the oscillations was determined from the horizontal displacements of the segregation inhomogeneities between successive striations (see Fig. 2) and the rotational rates. It can alternatively be obtained from the displacement of the maxima or minima between successive striations. The values of the experimental data are summarized in Table I.

A direct application of the theory to the present experiments could not be made because not all experimental variables controlling the constitutional supercooling parameter,  $S$ , Eq. [4] could be determined. However, since the numerical values assumed in Ref.

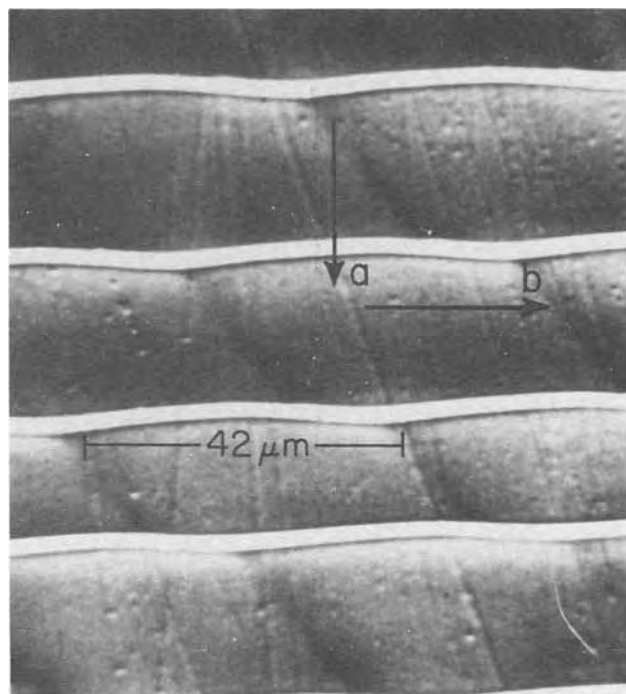


Fig. 2. Oscillatory instability and associated segregation inhomogeneities (inclined dark bands between successive rotational striations). Note lateral displacement of inhomogeneities indicating the traveling wave nature of instability (3.5 cm/hr; 25 rpm). Arrow (a) indicates growth direction and arrow (b) indicates the direction of lateral phase displacement of the oscillation.

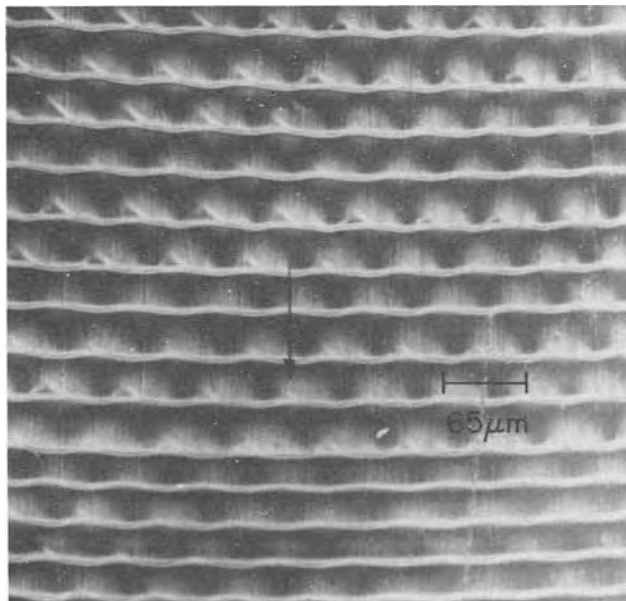


Fig. 3. Effect of rotational rate on interface instability. Depicted segment was pulled at 3.38 cm/hr; the upper and lower regions were rotated at 15 and 20 rpm, respectively (see text).

(15) are sufficiently close to those encountered in the present experiments a comparison between theory and the experimental results is considered reasonable. Thus, the theoretically predicted values of  $\lambda_\theta$  given in Table I were obtained from Fig. 3 in Ref. (15), assuming that the fluid velocity in the tangential direction is approximately equal to the macroscopic fluid velocity  $2\pi rR$  (19) (a reasonable approximation for the distances from the rotational axis at which  $\lambda$  was measured). It is seen that the experimentally determined values of  $\lambda_\theta$  are in reasonable agreement with those predicted from theory for the onset of oscillatory in-

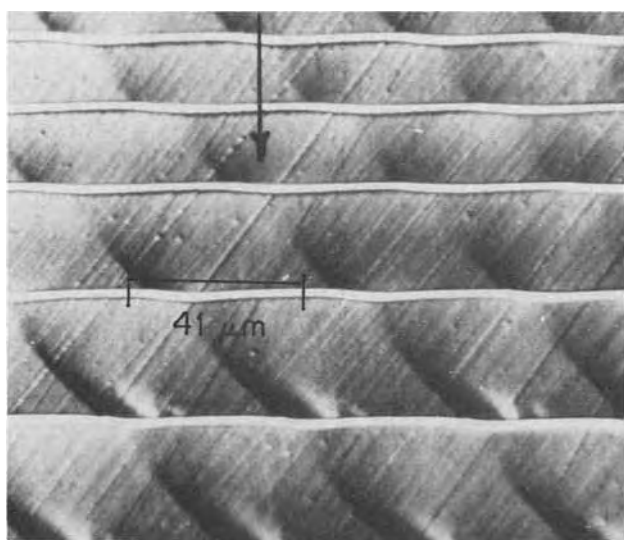


Fig. 4. Effect of pulling rate on interface instability. Depicted segment was rotated at 25 rpm. The upper region was pulled at 2.9 cm/hr (see text).

stability. A similar comparison of  $\lambda_r$  could not be made since a parabolic velocity distribution (assumed in theory) is not applicable for the radial fluid flow.

**Effects of pulling rate and seed rotation on oscillatory instability.**—The effects of the pulling rate were investigated in crystals grown at fixed seed rotation (25 rpm) with pulling rates ranging from 2.9 to 6.0 cm/hr. The effects of seed rotation were studied in crystals pulled at rates of 2.9 and 3.38 cm/hr with seed rotation ranging from 20–41 and 13–70 rpm, respectively. Since the experimental conditions necessary for the onset of oscillatory instability cannot be arrived at directly from theoretical considerations, the gallium dopant levels were adjusted by trial and error so that the system reached the verge of instability at some time during growth. Amounts of melt several times larger than those corresponding to the size of the crystals pulled were used to insure the occurrence of sustained instability.

The effect of increasing the rate of rotation on the growth process is clearly seen in Fig. 3. Here the depicted upper and lower segments were rotated at 15 and 20 rpm, respectively. While oscillatory instability prevails throughout both segments, the complexity of the segregation inhomogeneities (reflecting the degree of instability) is noticeably reduced in the region grown at the higher rate of rotation. This stabilizing

effect reflects a decrease of the average value of the constitutional supercooling parameter,  $S$ , due to enhanced stirring. The characteristics of the instability during rotational and nonrotational pulling are compared below.

The effect of the pulling rate on interface instability is shown in Fig. 4. From the spacing of the rotational striations it can be seen that the pulling rate was increased by a factor of about two in the segment of the crystal depicted in the lower part of the figure. This increase in pulling rate clearly resulted in further developed dopant inhomogeneities. It should be noted that the rate of development of the inhomogeneities following each rotational striation is the same in the upper and lower segments of the crystal. The relationship between the observed inhomogeneities and the amplitude of the perturbation is not known in the present case. In view of the pronounced dependence of interface stability on the microscopic growth rate, the behavior observed in Fig. 4 implies that the increase in the pulling rate by a factor of two did not result in a corresponding increase in the microscopic rate of growth during the initial stages of growth following remelting.

### Discussion

**Theoretical considerations.**—The applicability of the interface stability theory to the presently observed oscillatory instability is tested on the basis of typical experimental data employing Eq. [11]. The effects of thermal asymmetry are examined taking  $\alpha = 0$  (no thermal asymmetry);  $\alpha = 0.9$  (thermal asymmetry, no backmelting); and  $\alpha = 1.1$  (backmelting). The growth interface behavior is graphically presented and discussed on the basis of experimental observations. The experimental values employed are: pulling rate,  $V_0 = 12.5 \mu\text{m/sec}$ ; rate of rotation,  $R = 25 \text{ rpm}$ ; distance of instability from rotational axis = 0.6 cm.

When growth takes place in a thermally symmetric environment,  $\alpha = 0$ , then Eq. [11] reduces to

$$z = 12.5t + 5 \sin \left[ \left( \frac{2\pi x}{70} \right) + 1.2t \right] \quad [12]$$

A graphic representation of Eq. [12] depicting the dynamics of the growth interface, at time intervals of 0.28 sec, is shown in Fig. 5. It is seen that the traveling wave nature of the oscillation (lateral displacement component) modulates the microscopic growth rates thus resulting in periodic regions of decreased and increased growth rates which appear as narrow and wide bands inclined to the advancing growth interface ( $z$  direction). The angle of inclination is controlled by the phase velocity of the perturbation. The growth behavior, as shown in Fig. 5, corresponding to

Table I. Wavelengths and phase velocities associated with interface oscillations during Czochralski-type growth of gallium-doped germanium

Crystal number	Rotation rate (rpm)	Pulling rate, $V_0$ (cm/hr)	Initial amount of melt (g)	Radius of the crystal, $r_0$ (cm)	Radial distance of oscillatory instability (cm)	Macroscopic fluid velocity, $V = 2\pi rR$ (cm/sec)	Experimental $\lambda$ ( $\mu\text{m}$ )		Theoretical $\lambda_\theta$ (15) ( $\mu\text{m}$ )	Experimental phase velocity ( $\mu\text{m/sec}$ )
							$\lambda_r$	$\lambda_\theta$		
1	25	2.92	312	0.80	$0.5 \pm 0.1$	$1.31 \pm 0.15$	$48 \pm 3$		80	$9.6 \pm 0.3$
2	25	2.93	290	0.75	$0.6 \pm 0.1$	$1.51 \pm 0.20$	$49 \pm 3$		68	$10.6 \pm 0.3$
3	25	3.38	350	0.80	$0.7 \pm 0.1$	$1.90 \pm 0.20$	$50 \pm 3$	$65 \pm 3$	63	$14.0 \pm 0.4$
4	25	3.50	516	0.95	$0.5 \pm 0.2$	$1.37 \pm 0.15$	$59 \pm 3$	$70 \pm 3$	79	$11.0 \pm 0.5$
5*	25	3.50	400	0.95	$0.85 \pm 0.1$	$2.36 \pm 0.10$	$41 \pm 3$	$58 \pm 3$	56	$8.9 \pm 0.4$
6	25	4.50	346	0.75	$0.6 \pm 0.1$	$1.51 \pm 0.25$	$62 \pm 3$	$70 \pm 3$	69	$13.9 \pm 0.4$
7	25	5.50	336	0.75	$0.7 \pm 0.1$	$1.76 \pm 0.25$	$64 \pm 3$		64	$13.6 \pm 0.4$
8	25	5.80	325	0.75	$0.6 \pm 0.1$	$1.51 \pm 0.25$	$61 \pm 4$		69	$13.8 \pm 0.4$
9	20	2.93	310	0.75	$0.6 \pm 0.1$	$1.26 \pm 0.20$	$52 \pm 3$	$75 \pm 3$	85	$8.7 \pm 0.3$
2	25	2.93	290	0.75	$0.6 \pm 0.1$	$1.64 \pm 0.20$	$49 \pm 3$		68	$10.6 \pm 0.3$
10	33	2.93	270	0.75	$0.6 \pm 0.1$	$2.10 \pm 0.30$	$40 \pm 3$		58	$11.0 \pm 0.3$
11	41	2.93	250	0.75	$0.6 \pm 0.1$	$2.67 \pm 0.30$	$41 \pm 3$		55	$14.0 \pm 0.4$
12**	13	3.38	504	0.85	$0.6 \pm 0.1$	$0.84 \pm 0.15$	$75 \pm 3$	$82 \pm 3$	112	$13.4 \pm 0.6$
3	25	3.38	350	0.80	$0.7 \pm 0.1$	$1.90 \pm 0.20$	$50 \pm 3$	$65 \pm 3$	63	$14.0 \pm 0.4$
13	55	3.38	429	0.85	$0.6 \pm 0.1$	$3.47 \pm 0.35$	$34 \pm 3$	$45 \pm 3$	39	$15.6 \pm 0.4$
14	70	3.38	432	0.85	$0.6 \pm 0.1$	$4.40 \pm 0.50$	$27 \pm 3$	$40 \pm 3$	30	$22.4 \pm 0.5$

\* Ga concentration in the melt in atoms per cent:  $C_{1_1}$  (start),  $2.56 \pm 0.1$ ;  $C_{1_2}$  (end),  $3.30 \pm 0.12$ .

\*\* Ga concentration in the melt in atoms per cent:  $C_{1_1}$  (start), 1.53;  $C_{1_2}$  (end),  $1.77 \pm 0.01$ .

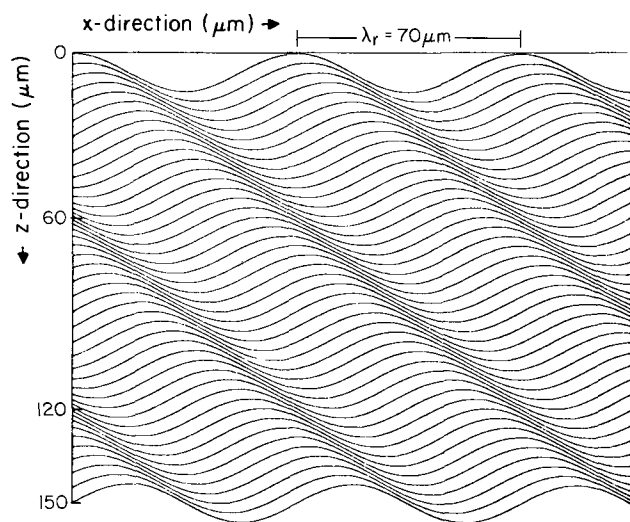


Fig. 5. Graphic presentation of oscillatory growth interface instability (Eq. [12]) in the absence of thermal asymmetry;  $\alpha = 0$ . The time interval between successive lines is 0.28 sec. (For numerical values used in Eq. [12] see text).

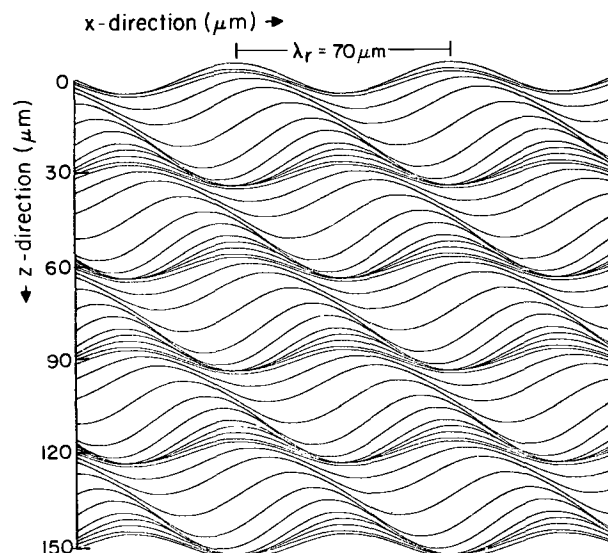


Fig. 6. Graphic presentation of oscillatory growth interface instability in the presence of thermal asymmetry ( $\alpha = 0.9$ ). The interval between successive lines is 0.24 sec (see text).

rotational pulling in the absence of thermal asymmetry, is never encountered in real systems.

In the presence of thermal asymmetry ( $\alpha > 0$ ) the exact solution of Eq. [11] requires the knowledge of the constitutional supercooling parameter (which changes continuously during rotation) since  $Re[p_j(\omega)]$  is a function of  $S$ .

This behavior is a result of the growth rate dependence of the constitutional supercooling parameter,  $S$ ; changes in  $S$  lead to corresponding changes in  $Re[p_j(\omega)]$  between positive and negative values averaging about zero. Depending on whether  $Re[p_j(\omega)]$  assumes positive or negative values for extended periods of time, the system will "break down" or revert to stability, respectively. In the presently considered situation characterized by oscillatory instability, the values of  $Re[p_j(\omega)]$  remain close to zero. The amplitude of the interface instability, in contrast to that in Fig. 5, is not constant but increases and decreases periodically with the variation of the microscopic growth rate within each rotational cycle. Concurrent with the variation  $Re[p_j(\omega)]$ , the phase velocity  $Im[p_j(\omega)]$  varies periodically; these variations, however, are small. Since  $S$  and its variations, during rotation, could not be determined, a graphic representation of a realistic situation ( $V_o = 4.5$  cm/hr,  $R = 25$  rpm, and  $\lambda_r = 70$   $\mu\text{m}$ ) was obtained by selecting reasonable values of the phase velocity (ranging from 0 to 30  $\mu\text{m}/\text{sec}$ ) and amplitude of perturbation (ranging from 4 to 8  $\mu\text{m}$ ) for  $\alpha = 0.9$  (Fig. 6). The individual lines represent the dynamics of the growth interface morphology at time intervals of 0.24 sec. In this case the microscopic growth rate,  $dz/dt$  (which is constant in the absence of thermal asymmetry and oscillatory instability) is modulated simultaneously by: (i) the sinusoidal growth rate variation along the  $z$  direction (independent of  $x$ ) resulting from thermal asymmetry and (ii) the periodic growth rate variation along both the  $x$  and  $z$  directions resulting from the traveling wave nature of the oscillatory instability.

When the average value of  $Re[p_j(\omega)]$  becomes positive, oscillatory instability can no longer be sustained and the amplitude of the perturbation increases continuously as shown in Fig. 7 and ultimately leads to interface breakdown.

The dynamic behavior of the growth interface under conditions leading to remelting ( $\alpha = 1.1$ ) is presented in Fig. 8. Since in this case the variation of the microscopic growth rate within each rotational cycle is larger than in the case  $\alpha = 0.9$ , the corresponding variations in phase velocity and amplitude of the per-

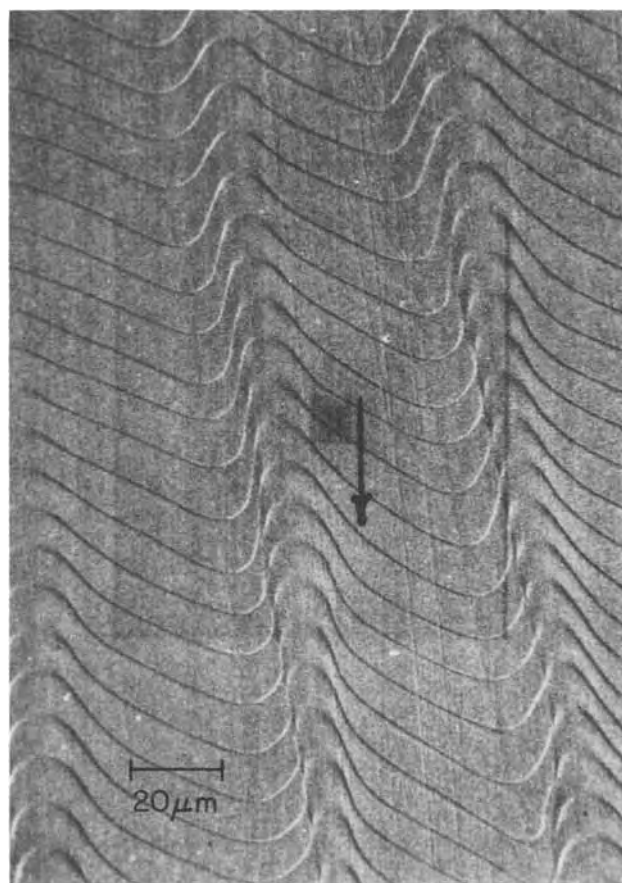


Fig. 7. Interface instability in Ga-doped Ge for growth conditions where the average value of  $Re[p_j(\omega)]$  is positive. Oscillatory instability is not sustained; note progressive increase (from top to bottom) of the amplitude of the perturbation.

turbation are expected to be larger. Accordingly, the values for the phase velocity were selected to range from 0 to 35  $\mu\text{m}/\text{sec}$  and those of the amplitude ranged from 4 to 10  $\mu\text{m}$ . The dotted lines within each rotational cycle represent the grown regions which were remelted during rotation through the hot region of the melt (17). The onset of growth following remelting is indicated in Fig. 8 by heavy lines which correspond to remelt striations (see for example Fig. 2). These



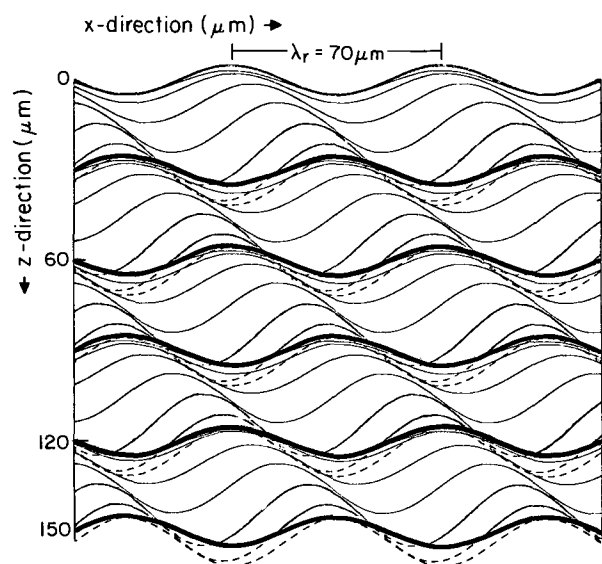


Fig. 8. Graphic presentation of oscillatory growth interface instability under partial remelt conditions ( $\alpha > 1$ ). The dotted lines, within each rotational cycle, represent the grown regions which were remelted. The heavy lines represent the remelt rotational striations. (For comparison with the experimental findings of Fig. 2, see text.)

remelt striations have the wavelength of the oscillatory instability but not its amplitude (the resulting amplitude is significantly reduced).

*Comparison with experimental results.*—All results in this investigation were obtained on crystals grown in the presence of thermal asymmetry leading to remelting; thus, comparison with theory will be focused on conditions as depicted in Fig. 8. This comparison is based on the premise that the experimentally observed segregation behavior is controlled by the microscopic growth rate.

Consistent with the theoretical considerations outlined above, sustained oscillatory interface instability ("wavy" remelt striations) is observed in all crystals investigated (Fig. 1-4). The traveling wave nature of the oscillation, as predicted from theory, is confirmed by the lateral displacement of the maxima (and the minima) in successive rotational striations, as seen in Fig. 2; the direction of the phase displacement is in agreement with that predicted from theory. The "inclined" segregation inhomogeneities within rotational cycles (between successive rotational striations) seen in Fig. 2 are readily explained on the basis of the preceding analysis; as seen in Fig. 8, the microscopic growth rate,  $dz/dt$ , varies along the  $x$  direction during each rotational cycle; thus, the traveling wave nature of the oscillations results in the formation of "cells" (between successive remelt striations) bounded laterally by regions of decreased growth rate (inclined bands). The complex segregation inhomogeneities between rotational striations in Fig. 3 cannot be explained exclusively on the basis of growth rate controlled segregation, as discussed below.

*Theoretical assumptions and experimental conditions.*—The preceding comparison must be viewed in the light of the following basic assumptions underlying the theoretical model (14): (i) the growth system is at steady state; (ii) the perturbations at the growth interface are small, so that the linearized theory is applicable; (iii) fluid flow at the momentum boundary layer is laminar with a parabolic velocity distribution within the boundary layer (diffusion of heat and convective solute transport are dominant); (iv) kinetic supercooling is absent; (v) there are no radial temperature and concentration gradients.

During rotational crystal growth by the Czochralski technique "steady state" [assumption (i)] prevails on a macroscopic level for conditions of constant pulling rate and constant crystal diameter (constant macroscopic growth rate). However, since thermal asymmetry is inherent in Czochralski growth, the microscopic growth rate is not constant but varies periodically within each rotational cycle.

When  $\alpha < 1$  the effects of varying microscopic growth rates on interface instability can in principle be quantitatively accounted for through corresponding variations of the constitutional supercooling parameter,  $S$ . The growth and segregation behavior under such conditions has been discussed in the previous section. When  $\alpha > 1$ , as in the presently discussed experiments, partial remelting takes place within each rotational cycle. Since the solute redistribution within the boundary layer associated with the remelt process cannot be assessed, the magnitude of the constitutional supercooling parameter cannot be determined and the applicability of the instability theory cannot be quantitatively tested. The good agreement between theory and experiment in the case of Fig. 2 is attributed to marginal remelt conditions ( $\alpha$  very close to 1).

The exact amplitude of the perturbations at the growth interface [assumption (ii)] could not be experimentally determined. However, the fact that the oscillatory perturbations were sustained over a considerable period of growth, without leading to interface breakdown, is direct evidence that, even during maximum microscopic growth rate (within each rotation), the amplitude of the perturbation was small enough to keep the system on the verge of instability.

The condition of laminar flow and parabolic velocity distribution in the momentum boundary layer [assumption (iii)] was met, in the present system, at the pulling rates (2.0-5.8 cm/hr) and the rotational rates (13-40 rpm) employed. Apparently, under these conditions diffusion of heat and convection controlled solute transport were dominant (15).

The presence of oscillatory instability in all crystals investigated was limited to their outer regions where kinetic supercooling [assumption (iv)] approaches zero; oscillatory instability was never encountered in "facet" regions.

Radial temperature and concentration gradients do exist in Czochralski growth; however, their magnitude is small over the regions investigated and can be neglected [assumption (v)].

The theoretical treatments of interface instability indicate that crystal rotation during Czochralski pulling has a stabilizing effect through changes in the characteristics of the boundary layer. This conclusion is based on the assumption that rotation takes place in a thermally symmetric environment in which rotation does not affect the microscopic growth rate. Since, however, thermal asymmetry is inherent in Czochralski growth, this assumption is valid only at high rates of rotation since increased stirring tends to minimize thermal asymmetry. At moderate rates of rotation (say, up to 50 rpm) the microscopic growth rate does not remain constant, particularly under remelt conditions where the actual growth rate ranges from negative values (remelting) to positive values which may exceed the pulling rate by more than a factor of ten. It is, thus, clear that in this range of rotational rates, the modulation of the microscopic growth rate can have pronounced destabilizing effects on the growth system. These effects can dominate the concurrent stabilizing effects of stirring. In fact, at moderate rates, seed rotation will induce interface instability rather than have the expected stabilizing effects.

### Acknowledgment

The authors are indebted to the National Science Foundation for financial support and to Mr. Clifford J. Herman for his skillful assistance in the growth of the single crystals.

Manuscript submitted June 4, 1973, revised manuscript received Sept. 30, 1973.

Any discussion of this paper will appear in a Discussion Section to be published in the December 1974 JOURNAL. All discussions for the December 1974 Discussion Section should be submitted by Aug. 1, 1974.

### REFERENCES

1. J. W. Rutter and B. Chalmers, *Can. J. Phys.*, **31**, 15 (1953).
2. W. A. Tiller, K. A. Jackson, J. W. Rutter, and B. Chalmers, *Acta Met.*, **1**, 428 (1953).
3. D. T. J. Hurle, *Solid-State Electron.*, **3**, 37 (1961); W. Bardsley, J. M. Callan, H. A. Chedzey, and D. T. J. Hurle, *ibid.*, **3**, 142 (1961).
4. W. W. Mullins and R. F. Sekerka, *J. Appl. Phys.*, **35**, 44 (1964).
5. V. V. Voronkov, *Soviet Phys.-Solid State*, **6**, 2378 (1965).
6. R. F. Sekerka, *J. Appl. Phys.*, **36**, 264 (1965).
7. R. T. Delves, *Phys. Status Solidi*, **16**, 621 (1966); *ibid.*, **17**, 119 (1966).
8. R. F. Sekerka, in "Crystal Growth," H. S. Peiser, Editor, p. 691, Pergamon Press, Oxford, England (1967).
9. S. R. Coriell and R. L. Parker, *ibid.*, p. 703.
10. L. A. Tarshis and W. A. Tiller, *ibid.*, p. 709.
11. G. R. Kotler and W. A. Tiller, *ibid.*, p. 721.
12. R. F. Sekerka, *J. Crystal Growth*, **3**, 4, 71 (1968).
13. D. T. J. Hurle, *ibid.*, **5**, 162 (1969).
14. R. T. Delves, *ibid.*, **3**, 4, 562 (1968).
15. R. T. Delves, *ibid.*, **8**, 13 (1971).
16. R. Singh, A. F. Witt, and H. C. Gatos, *J. Appl. Phys.*, **41**, 2730 (1970).
17. K. Morizane, A. F. Witt, and H. C. Gatos, *This Journal*, **113**, 51 (1966); *ibid.*, **114**, 738 (1967); *ibid.*, **115**, 747 (1968).
18. D. T. J. Hurle, E. Jakeman, and E. R. Pike, *J. Crystal Growth*, **3**, 4, 633 (1968).
19. Y. G. Levich, "Physicochemical Hydrodynamics," Prentice-Hall, Inc., Englewood Cliffs, N. J. (1962).

## A Diffusion Model for Oxidation of Nickel-Iron Alloys at 1000°C

A. D. Dalvi\*<sup>1</sup> and W. W. Smeltzer\*

Department of Metallurgy and Materials Science, McMaster University, Hamilton, Ontario, Canada

### ABSTRACT

A generalized diffusion model involving ternary oxides is used to formulate the oxidation mechanism of Ni-Fe alloys containing 2 and 4 weight per cent Fe. A defect structure, adopted for the inner nickel oxide layer containing iron, yields the variation of its cation diffusion coefficients which, when substituted in the diffusion equations, yield the cation concentration and the oxygen activity profiles in the oxide and the oxidation constants for the respective alloy. Thermodynamic considerations are used in deriving the oxygen activity profile in the outer two-phase nickel oxide-spinel layer of an external scale. A solution to the diffusion problem in the alloy is considered. The experimentally derived composition path in an alloy and the scale is superimposed on the Fe-Ni-O phase diagram. This path is shown to be consistent with the structural observations and composition determinations, and it is also consistent with thermodynamic and kinetic considerations.

In an earlier work (1) the present authors discussed the kinetics and morphological development of the oxide scales formed at 1000°C on Ni-Fe alloys containing 0-25 weight per cent (w/o) Fe. It was demonstrated that continuous and reproducible long-time kinetic curves could be obtained in dry oxygen. Since the over-all reaction kinetics and growth of individual layers followed a parabolic time dependence, it is reasonable to assume that conditions of ambipolar diffusion and local equilibrium at interfaces would occur at this high temperature. Accordingly one may postulate a mechanism based on diffusion through the different phases. The purpose of this paper is to present experimental results for the iron and nickel distributions in the various phases present during the oxidation of these alloys and to rationalize the oxidation kinetics for these alloys on the basis of a ternary diffusion model.

### Experimental Procedures and Results

The alloys oxidized contained 0-25 w/o Fe. The samples, which were in the form of  $1 \times 2 \times 0.1$  cm

plates, were sectioned after oxidation and mounted and polished for metallographic examination and electron-probe microanalyses. Oxidation was carried out at 1000°C in pure oxygen contained in a volumetric apparatus at 400 Torr pressure. Details of the experimental procedures are given in Ref. (1). The nominal and actual compositions of the alloys of interest here are reproduced in Table I.

Concentration profiles of nickel and iron across the samples were determined from samples oxidized for various periods up to 55 hr. The instrument used was a CAMECA MS-24 Model electron microprobe. Counts on Ni and Fe  $K_{\alpha}$  x-rays were taken at regular intervals across the samples and the concentrations were obtained using the pure metals as standards and a procedure described in Ref. (2).

Table I. Compositions of the investigated alloys based upon wet chemical analyses for nickel and iron

Nominal composition	Actual composition	
	w/o Fe	w/o Ni
Ni-2% Fe	1.85	98.15
Ni-4% Fe	4.5	95.5
Ni-6% Fe	6.6	95.4
Ni-8% Fe	8.3	91.7

\* Electrochemical Society Active Member.

<sup>1</sup> Present address: J. Roy Gordon Research Laboratory, The International Nickel Company of Canada Limited, Mississauga, Ontario, Canada.

Key words: Ni-Fe alloys, NiO, (Ni,Fe)<sub>3</sub>O<sub>4</sub>, alloy oxidation, diffusion model.



In a diffusion controlled process, the solutions to the equations are parametric such that all concentrations can be described by an expression of the type

$$C_i = C_i(\lambda); \lambda = \lambda(x, t) \quad [1]$$

where  $x$  is the distance coordinate and  $t$  is the time coordinate. For parabolic kinetics, the parametric function  $\lambda$  is given by

$$\lambda = x/\sqrt{t} \quad [2]$$

Hence all concentration profiles are invariant with respect to  $\lambda$ . Accordingly, the experimental results for the metal concentrations across an oxidized sample are plotted against this parameter.

For the scale, a dimensionless parameter,  $y$ , is used instead of  $\lambda$  where

$$y = x/x_s \quad [3]$$

Here  $x$  is the distance from the metal/oxide interface and  $x_s$  is the total thickness of the external scale. Since the scaling of the alloys follows parabolic kinetics

$$x_s = k\sqrt{t}; y = x/k\sqrt{t} \quad [4]$$

Thus  $y$  has the same parametric form as  $\lambda$  except for the constant  $k$  which is the parabolic rate constant for thickening of the scale.

Concentration profiles for iron across the sample are illustrated in Fig. 1-4 for alloys containing 2, 4, 6, and 8 w/o iron, respectively. The nickel profile is essentially complementary to that of iron. This is shown for the Ni-6 w/o Fe alloy (Fig. 3). It is seen from these plots that the metal concentration profiles are indeed invariant in  $\lambda$ -space. Profiles at times significantly lower than 50 hr could not be obtained for the Ni-8

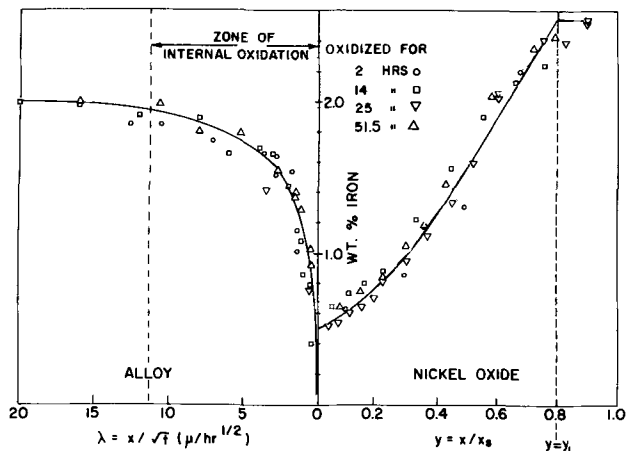


Fig. 1. Concentration profile for iron in alloy and external scale plotted in the  $\lambda$ -space for the Ni-2 w/o Fe alloy.

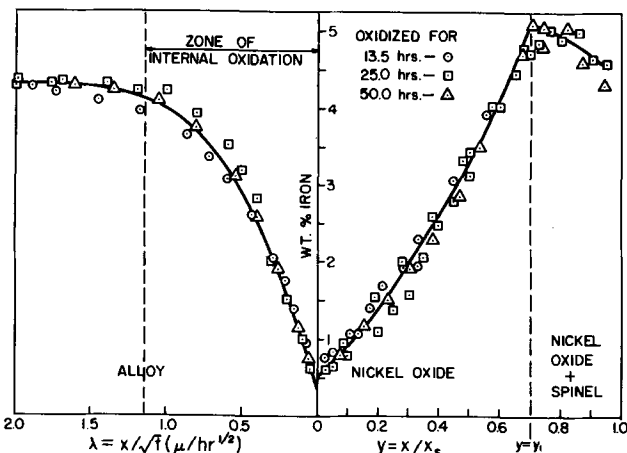


Fig. 2. Concentration profile for iron in alloy and external scale plotted in the  $\lambda$ -space for the Ni-4 w/o Fe alloy.

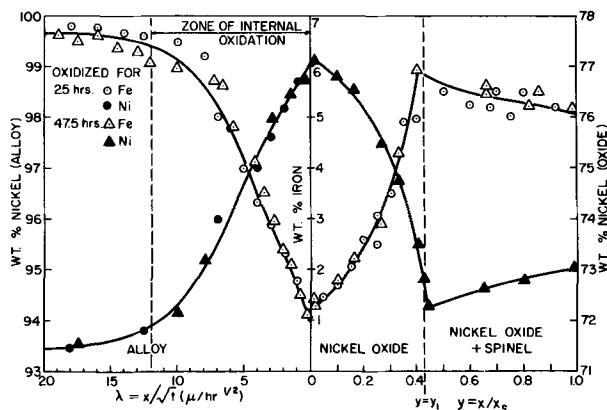


Fig. 3. Concentration profile for iron in alloy and external scale plotted in the  $\lambda$ -space for the Ni-6 w/o Fe alloy.

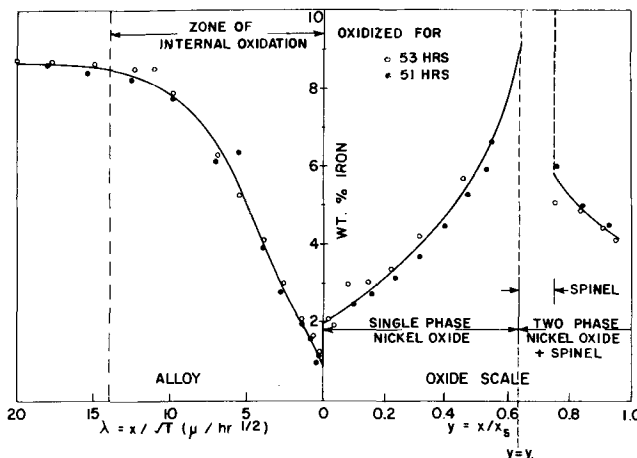


Fig. 4. Concentration profile for iron in alloy and external scale plotted in the  $\lambda$ -space for the Ni-8 w/o Fe alloy.

w/o Fe alloy due to spalling of the scale upon quenching.

Four distinct zones could be observed in all samples: the unoxidized alloy matrix, a zone of internal oxidation near the metal/scale interface, an inner single-phase nickel oxide layer, and an outer two-phase spinel-nickel oxide layer. This typical structure is illustrated by the micrograph in Fig. 5 of an oxidized Ni-8 w/o Fe alloy. As can be seen from Fig. 1-4, iron is severely depleted from the alloy in the zone of internal oxidation. Its concentration at the alloy surface was below 1 w/o; this concentration is low enough to stabilize nickel oxide in the external scale (2). The concentration of iron increases toward the outer surface in the nickel oxide layer and it then decreases within the nickel oxide matrix of the outer spinel-nickel oxide layer. Thus iron diffuses against its concentration gradient in the innermost nickel oxide layer and down the concentration gradient within nickel oxide matrix in the outer two-phase layer. This peculiar behavior of iron is discussed in the following sections.

### Theory and Analysis

Wagner (3) has published a theory for binary alloy oxidation which applies to situations in which an alloy of metals A and B forms a scale consisting of a solid solution of the corresponding oxides, A(O) and B(O). Coates and Dalvi (4) have reviewed and, to some extent, generalized, Wagner's analysis. The model discussed by these authors can be applied to the present results as it has been done previously for Ni-Co and Fe-Mn alloys (5, 6) with some modification of the boundary conditions for diffusion.

*Oxide defect structure model.*—Before considering the diffusion model, it is necessary to establish the

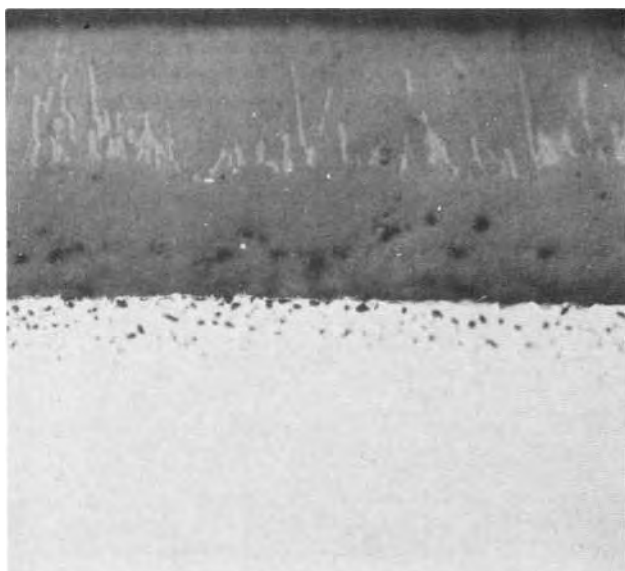
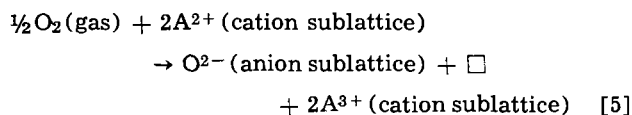


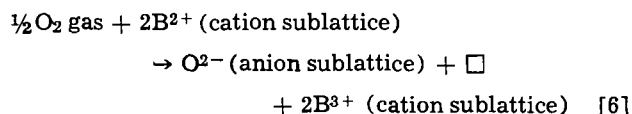
Fig. 5. A cross section of a Ni-8% Fe alloy oxidized for 48.5 hr at 1000°C illustrating the zone of internal oxidation, the inner single phase nickel oxide layer, and the outer spinel-nickel oxide scale layer.

effect of solute cations on the defect structure and consequently on the diffusivities of cations in mixed oxides when the solute cations exhibit variable valence. Zintl (7) has considered the general case for an oxide solid solution containing two transition metals.

If association of positive holes and vacancies may be neglected, the defect equation for a pure p-type oxide AO may be written as



where  $\square$  represents a cation vacancy. Substitution of a divalent cation  $B^{2+}$  for  $A^{2+}$  would sustain electrical neutrality. If the energy required for the formation of trivalent  $B^{3+}$  from its divalent cation is much less compared to the corresponding energy for an A cation, then reaction [5] will shift to the right and lead to a higher vacancy concentration. The corresponding reaction for B ion is



For electrical neutrality in the mixed AO-BO oxide

$$2X_{\square} = X_{\bullet} = X_{A^{3+}} + X_{B^{3+}} \quad [7]$$

where  $X$ 's are atom fractions. If ideal solution behavior is assumed, the variation of vacancy concentration with the composition and oxygen pressure is given by

$$X_{\square} = (K_6/4)^{1/3} (P_{O_2})^{1/6} \xi^{2/3} \quad [8]$$

In Eq. [8]  $\xi$  is the mole fraction of the solute oxide BO and  $K_6$  is the equilibrium constant for reaction [6]. It is assumed here that the tendency of the cation  $A^{2+}$  to go into the trivalent state is much smaller than the corresponding tendency for the solute cation  $B^{2+}$ .

The diffusion coefficient  $D_M$  for a cation  $M^{2+}$  is given by

$$D_M = D_{\square} (M^{2+}) X_{\square} \quad [9]$$

where  $D_{\square} (M^{2+})$  is the vacancy mobility in the sublattice of  $M^{2+}$  ions. From Eq. [8] and [9] we obtain

expressions for the self-diffusion coefficients of A and B in the oxide solid solution. Thus

$$D_A = D^{\circ}_A (P_{O_2})^{1/6} \xi^{2/3} \quad [10]$$

$$D_B = D^{\circ}_B (P_{O_2})^{1/6} \xi^{2/3} \quad [11]$$

where

$$D^{\circ}_M = D_{\square} (M^{2+}) (K_6/4)^{1/3} \quad M = A, B \quad [12]$$

The proportionality constants  $D^{\circ}_A$  and  $D^{\circ}_B$  thus contain the mobility terms for the respective cations. Equations [10]-[12] are used for the iron and nickel self-diffusion coefficients in (Ni, Fe)O. In this case  $\xi$  is the FeO mole fraction.

**Diffusion model.**—We may give a theoretical basis to our results utilizing the diffusion theory and the thermodynamics of the Fe-Ni-O system. Although the qualitative aspects of the diffusion model are valid for all the alloys, quantitative analysis is attempted only for the dilute alloys. For the underlying assumptions and the mathematical formalism the reader is referred to Ref. (3-5).

As noted earlier, a scale consists of two layers. The outer layer consists of spinel precipitates in a nickel oxide matrix and the inner layer is composed only of nickel oxide. For the purpose of simplifying the mass balance to obtain a tractable mathematical solution, we assume that the amount of spinel in the outer layers of the scales formed on the 2 and 4 w/o Fe alloys is negligible. We also assume that the matrix composition in the outer layer is nearly constant. These assumptions are justified for the dilute alloys from the experimental observations, notwithstanding the observed compositional variations as explained in the following discussion; this is because the observed variations do not affect the mass balance seriously. The proposed diffusion model and the metal concentration profiles are illustrated in Fig. 6.

Although the metal concentrations in the outer layer are assumed constant for the solution of the equations describing diffusion in the inner layer, they can be qualitatively predicted from thermodynamic considerations. There is only one degree of freedom in this two-phase layer from the Gibb's phase rule. Hence specification of the local oxygen activity automatically specifies the corresponding metal concentration from the following reaction

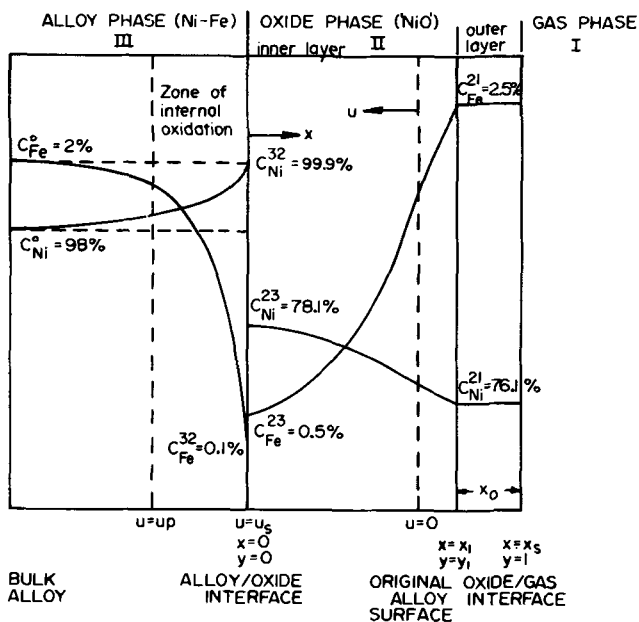
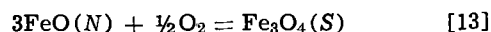


Fig. 6. Diffusion model for the oxidation of a Ni-2 w/o Fe alloy in oxygen at 1000°C.  $u = 0$  is the original alloy surface.

where  $N$  and  $S$  denote the (Fe, Ni)O solid solution and spinel, respectively. The equilibrium constant for reaction [13],  $K_{13}$ , is

$$K_{13} = \frac{a_{\text{Fe}_3\text{O}_4}}{a_{\text{FeO}}^3} \quad [14]$$

where  $a$ 's denote activities;  $a_{\text{O}} \equiv P_{\text{O}_2}^{1/2}$ . Equation [14] could be rewritten as

$$\frac{(N_{\text{FeO}})^3}{N_{\text{Fe}_3\text{O}_4}} = \frac{K}{a_{\text{O}}} \quad [15]$$

where

$$K = \frac{\gamma_{\text{Fe}_3\text{O}_4}}{(\gamma_{\text{FeO}})^3 K_{13}} \quad [16]$$

$\gamma_{\text{Fe}_3\text{O}_4}$  and  $\gamma_{\text{FeO}}$  are activity coefficients of  $\text{Fe}_3\text{O}_4$  and  $\text{FeO}$  in the coexisting (Ni, Fe) $_3\text{O}_4$  and (Ni, Fe)O solid solution phases, respectively.

Thermodynamically, with decreasing value of  $N_{\text{FeO}}$ , the value of  $N_{\text{Fe}_3\text{O}_4}$  also decreases (2, 8). It can be shown that the decrease in the values of  $N_{\text{FeO}}$  in NiO and  $N_{\text{Fe}_3\text{O}_4}$  in the spinel phase are similar, i.e.  $N_{\text{FeO}} \simeq \text{const. } N_{\text{Fe}_3\text{O}_4}$ . Hence, Eq. [15] may be written as

$$(N_{\text{FeO}})^2 \simeq K''/a_{\text{O}} \quad [17]$$

$N_{\text{FeO}}$  is thus inversely proportional to  $(P_{\text{O}_2})^{1/4}$  in the outer two-phase layer. Since the values of  $N_{\text{FeO}}$  and  $a_{\text{O}}$  are known in the three-phase spinel-nickel oxide-alloy region (2, 8), the value of  $K''$  could be estimated. For  $a_{\text{O}} = 5 \times 10^{-6}$  and  $N_{\text{FeO}} = 0.15$ ,  $K'' \simeq 10^{-7}$ . Hence

$$N_{\text{FeO}} = \frac{3.2 \times 10^{-4}}{(P_{\text{O}_2})^{1/4}} = \frac{3.2 \times 10^{-4}}{a_{\text{O}}^{1/2}} \quad [18]$$

The observed boundary compositional values for the alloys containing 2-8 w/o Fe are given in Table II. The oxygen activities at  $y = 0$  and  $y = y_1$  may then be calculated from Eq. [14] and [18], respectively.

*Diffusion equations for the nickel oxide layer.*—One arrives at Eq. [19] and [20] by an analysis similar to that in Ref. (3-6) using the functional values of  $D_{\text{Ni}}$  and  $D_{\text{Fe}}$  as given in Eq. [10]-[12] where Ni  $\equiv$  A and Fe  $\equiv$  B in the flux equations for these species in the oxide, and applying the mass balance condition at the interface given by  $y = y_1$  (see Fig. 6). These expressions are differential equations describing the variation of the mole fraction of FeO,  $\xi$ , and oxygen activity,  $a_{\text{O}}$ , in the inner nickel oxide layer of the scale

$$\frac{d \ln a_{\text{O}}}{dy} = \left[ \frac{k'}{\xi^{2/3} a_{\text{O}}^{1/3}} + (p-1) \frac{d\xi}{dy} \right] \Bigg|_{[1 + (p-1)\xi]} \quad [19]$$

and

$$[1 + (p-1)\xi] \xi \frac{d^2 \xi}{dy^2} + \frac{2}{3} \left( \frac{d\xi}{dy} \right)^2 + \left( \frac{\xi''}{\xi} \right)^{-1/3} \left( \frac{a_{\text{O}}''}{a_{\text{O}}} \right)^{1/3} \left\{ \frac{y[1 + (p-1)\xi]^2 - 2p/3}{(p-1)(1-\xi'')} \right\} \left( \frac{d\xi}{dy} \right)_{y=y_1} \left( \frac{d\xi}{dy} \right) = 0 \quad [20]$$

where  $y_1$  is the value of  $y$ , a dimensionless parameter defined in Eq. [3] at the boundary between the inner and outer layers in the scales (see Fig. 6),  $\xi'' = \xi(y = y_1)$  and  $a_{\text{O}}'' = a_{\text{O}}(y = y_1)$ .  $p$  is the ratio of jump frequencies of iron and nickel cations, respectively, to an adjacent vacancy. That is

$$p = \frac{D_{\text{Fe}}^{\circ}}{D_{\text{Ni}}^{\circ}} \quad [21]$$

where  $D_{\text{Fe}}^{\circ}$  and  $D_{\text{Ni}}^{\circ}$  are defined by Eq. [12].  $p$  is assumed to be constant at all concentrations.  $k' = k/D_{\text{Ni}}^{\circ}$  where  $k$  is the parabolic scaling constant for the external scale defined in Eq. [4].

Equations [19] and [20], which are simultaneous, nonlinear, differential equations in the dependent variables  $\xi$  and  $a_{\text{O}}$ , can be solved in the same manner as in Ref. (4). The values of the concentrations in nickel oxide obtained as a function of  $x$  by the electron microprobe can be converted to mole fractions of FeO and NiO. This yields the boundary values  $\xi(y = 0)$  and  $\xi(y = y_1)$ . The oxygen activity  $a_{\text{O}}'' = a_{\text{O}}(y = y_1)$  is obtained from Eq. [18] after substituting the experimental value of  $\xi$ , i.e.,  $N_{\text{FeO}}$  at that point. The value of  $k$  defined in Eq. [4] is obtained from the experimental weight gain curves (1). The constant  $k$  is related to  $k_p$  in  $\text{g}^2/\text{cm}^4\text{-sec}$  as follows

$$k = (k_p/2)(V/16)^2 \text{ cm}^2/\text{sec} \quad [22]$$

where  $V$  is the molar volume of the oxide. Thus for the Ni-2 w/o Fe alloy,  $k = 4.44 \times 10^{-10} \text{ cm}^2/\text{sec}$  and for the Ni-4 w/o Fe alloy,  $k = 6.8 \times 10^{-10} \text{ cm}^2/\text{sec}$ . Equations [19] and [20] need only three boundary conditions for the solution; viz., the values of  $\xi'$ ,  $\xi''$ , and  $a_{\text{O}}''$ , where  $\xi' = \xi(y = 0)$  and  $\xi''$  and  $a_{\text{O}}''$  have been defined earlier. However, if an additional boundary condition  $a'_{\text{O}} = a_{\text{O}}(y = 0)$  is utilized, these equations yield the value of  $k'$  and consequently of  $D_{\text{Ni}}^{\circ}$  since

$$k' = k/D_{\text{Ni}}^{\circ} \quad [23]$$

The value of  $a'_{\text{O}}$  may be estimated from the oxidation reaction for pure Ni, Eq. [14], as discussed earlier and from the displacement reactions between FeO and NiO. This procedure yields the following expression for  $a'_{\text{O}}$  as function of  $\xi'$

$$a'_{\text{O}} = (1 - 0.966\xi') 6.7 \times 10^{-6} \quad [24]$$

One of the parameters of the diffusion equations is the ratio,  $p$ , of the mobilities of iron and nickel in the nickel oxide layer. We estimate the value of  $p$  as follows (7). The self-diffusion coefficients  $D_{\text{M}}$  are related to the vacancy diffusivity  $D_{\square}$  and the vacancy concentration by Eq. [9]. For pure nickel oxide, the value of  $D_{\text{Ni}}$  at  $1000^{\circ}\text{C}$  and  $P_{\text{O}_2} = 1 \text{ atm}$  is  $10^{-11} \text{ cm}^2/\text{sec}$  (9-12). The corresponding value of  $X_{\square}$  at 1 atm is  $\sim 10^{-4}$  (13-14). Thus from Eq. [9]

$$D_{\square}(\text{NiO}) = 10^{-7} \text{ cm}^2/\text{sec} \quad [25]$$

The value of  $D_{\text{Fe}}$  in FeO in equilibrium with Fe corresponding to  $P_{\text{O}_2} = 1.32 \times 10^{-14} \text{ atm}$  at  $1000^{\circ}\text{C}$  is  $3.5 \times 10^{-8} \text{ cm}^2/\text{sec}$  (15, 16). The value of  $X_{\square}$  is 0.05 (11). Thus

$$D_{\square}(\text{FeO}) = 7.0 \times 10^{-7} \text{ cm}^2/\text{sec} \quad [26]$$

Table II. Interfacial compositions for Ni-Fe alloys containing 2-8 w/o Fe, oxidized at  $1000^{\circ}\text{C}$

Bulk alloy composition (microprobe analyses)	Interfacial compositions			
	Alloy phase		Oxide phase	
	$C(\lambda = \lambda_1)$	$C(y = 0)$	$\xi(y = 0)$	$\xi(y = y_1)$
Ni-2 w/o Fe	1.9 w/o Fe	0.2 w/o Fe ~150 ppm O	0.0068	0.034
Ni-4.3 w/o Fe	4.2 w/o Fe	0.35 w/o Fe ~150 ppm O	0.0069	0.066
Ni-6.6 w/o Fe	6.4 w/o Fe	0.65 w/o Fe ~150 ppm O	0.017	0.075
Ni-8.5 w/o Fe	8.4 w/o Fe	0.9 w/o Fe ~150 ppm O	0.026	0.090

$\lambda = \lambda_1$ , position of the boundary between unoxidized alloy and the zone of internal oxidation.  
 $y = 0$ , alloy-oxide interface.  
 $y = y_1$ , position of the boundary between inner single-phase zone and outer two-phase zone.  
 $C$ , alloy composition.  
 $\xi$ , mole fraction of FeO in FeO-NiO solid solution.

Table III. Data for the solution of diffusion equations in NiO-FeO mixed oxide and the resultant solution

Ni-2 w/o Fe alloy	
$p = D_{Fe}^{\circ}/D_{Ni}^{\circ} = 3$	
$y_1 = 0.8$	
$\xi^* = \xi(y = y_1) = 0.0340$ ;	$a''_O = a_O(y = y_1) = 1.1 \times 10^{-4}$
$\xi^* = \xi(y = 0) = 0.0068$ ;	$a'_O = a_O(y = 0) = 6.65 \times 10^{-4}$
$k = 4.7 \times 10^{-10}$ cm <sup>2</sup> /sec	
$D_{Ni}^{\circ} = 6.7 \times 10^{-8}$ cm <sup>2</sup> /sec;	$k' = k/D_{Ni}^{\circ} = 0.0070$
$\left(\frac{d\xi}{dy}\right)_{y=y_1} = 0.0385$ ;	$\left(\frac{d\xi}{dy}\right)_{y=0} = 0.0148$

These values of  $D_{Ni}$  (NiO) and  $D_{Fe}$  (FeO) involve one order of magnitude uncertainties. From Eq. [25] and [26] we obtain

$$p = \frac{D_{Fe}(\text{FeO})}{D_{Ni}(\text{NiO})} \approx 7 \quad [27]$$

For iron to accumulate at the outer interface, it is necessary that the ratio  $p$  be greater than unity (3). In solving the differential Eq. [19] and [20] the value which resulted in best fit to the data was chosen. This yielded  $p = 3.0$ .

Using the above values of the various parameters, Eq. [19] and [20] were solved numerically with the aid of a computer to obtain  $\xi$  and  $a_O$  as functions of  $y$  in the scale formed on the Ni-2 w/o Fe alloy. The boundary values and values of required parameters and the resultant solution are given in Table III. The calculated and observed values of  $\xi$  as a function of  $y$  are illustrated in Fig. 7. The corresponding values of the oxygen activity in the nickel oxide layer are given in Fig. 8. By comparing the value of  $a'_O$  obtained from the solution of Eq. [19] and [20] to the value obtained from Eq. [24], the value of  $k'$  can be obtained by an iterative process. For this alloy, the value of  $k'$  was 0.0070. Since  $k$  is known,  $D_{Ni}^{\circ}$  could be calculated. This yields  $D_{Ni}^{\circ} = 6.4 \times 10^{-8}$  cm<sup>2</sup>/sec.

The above analysis lacks a true experimental closure. This is because  $p$  and  $D_{Ni}^{\circ}$  were obtained from the analysis using experimental data as boundary conditions. Equations [19] and [20], however, can be solved for the scale on the Ni-4 w/o Fe alloy with similar assumptions using the same values of the above parameters. The solution obtained should show agreement with the experimental data since the form of these equations remain the same for (Ni,Fe)O formed on the alloys because the ratio of cation jump frequencies remains constant if interaction correlations do not prevail. The various boundary values could be obtained in the manner discussed above. The boundary values, the

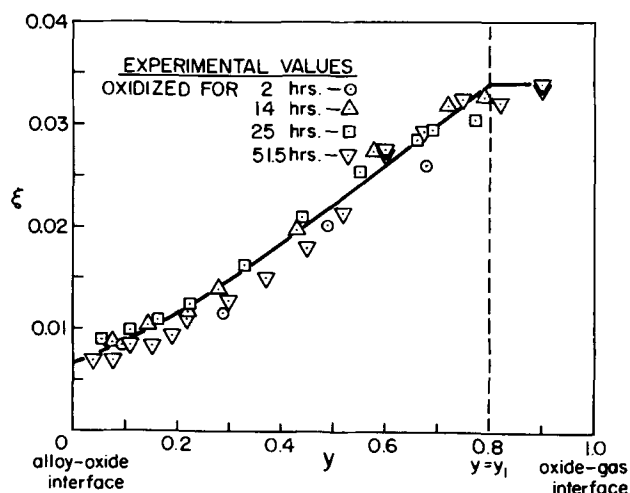


Fig. 7. Mole fraction of FeO,  $\xi$ , vs. the normalized distance coordinate  $y$  in the (Ni, Fe)O scale layer formed on the Ni-2 w/o Fe alloy. The solid curve represents calculated values from Eq. [19] and [20].

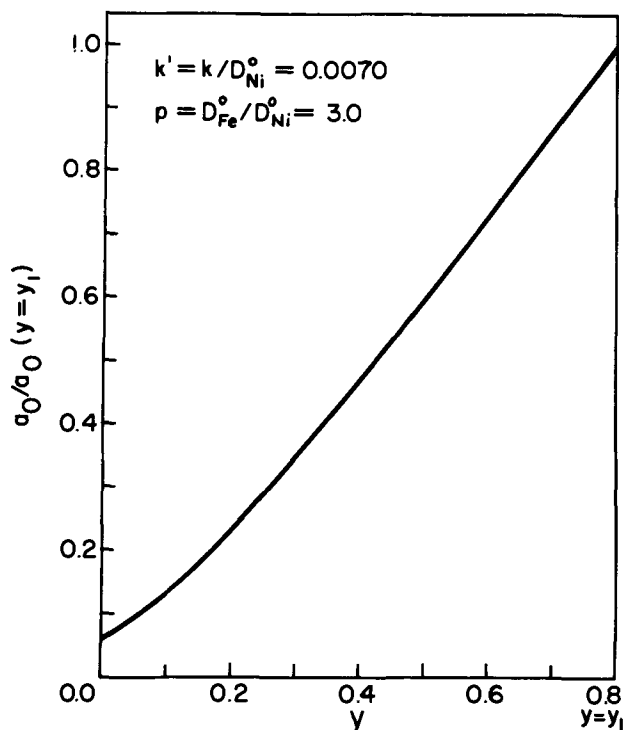


Fig. 8. Oxygen activity vs. normalized distance coordinate  $y$  in the (Ni,Fe)O oxide layer formed on the Ni-2 w/o Fe alloy calculated from Eq. [19] and [20].

values of required parameters, and solution to the equation for the 4 w/o Fe alloy are summarized in Table IV. The calculated and observed values of  $\xi$  as a function of the normalized distance parameter  $y$  are given in Fig. 9. Excellent agreement is obtained between these values. The corresponding oxygen activity profile is given in Fig. 10. The value of  $D_{Ni}^{\circ}$  was also calculated and for the value  $k' = 0.0089$ ,  $D_{Ni}^{\circ} = 7.8 \times 10^{-8}$  cm<sup>2</sup>/sec. This value agrees within 25% of the values obtained from the analysis for the Ni-2 w/o Fe alloy.

*Diffusion in the alloy.*—Estimates may be made for the concentration profiles in the alloy when an internal oxidation zone is present. Kirkaldy (17) has shown that if the variation of oxygen solubility in an alloy with respect to the concentration of the alloying element is negligible, *i.e.*,  $dC_O/dC_B \ll 1$ , then the effective diffusion coefficient in the internal oxidation zone is the interdiffusion coefficient of the metallic constituents where diffusion is regarded as being uninfluenced by the oxide precipitate particles. An estimate of this interdiffusion coefficient,  $D_{alloy}$ , can be made from the solution of the diffusion equation for the alloying element (iron).

Let the parameter  $\alpha$  be defined as

$$u_s = \alpha\sqrt{t} \quad [28]$$

where  $u_s$  is the coordinate of the alloy-oxide interface with respect to the original alloy surface. Therefore  $\alpha$  defines the recession rate of the alloy/oxide interface with respect to the original alloy surface. The solu-

Table IV. Data for the solution of diffusion equations in NiO-FeO mixed oxide and the resultant solution

Ni-4 w/o Fe alloy	
$p = D_{Fe}^{\circ}/D_{Ni}^{\circ} = 3$	
$y_1 = 0.7$	
$\xi^* = \xi(y = y_1) = 0.0660$ ;	$a''_O = a_O(y = y_1) = 2.9 \times 10^{-4}$
$\xi^* = \xi(y = 0) = 0.0069$ ;	$a'_O = a_O(y = 0) = 6.56 \times 10^{-4}$
$k = 6.3 \times 10^{-10}$ cm <sup>2</sup> /sec	
$D_{Ni}^{\circ} = 6.7 \times 10^{-8}$ cm <sup>2</sup> /sec;	$k' = k/D_{Ni}^{\circ} = 0.0089$
$\left(\frac{d\xi}{dy}\right)_{y=y_1} = 0.099$ ;	$\left(\frac{d\xi}{dy}\right)_{y=0} = 0.0069$

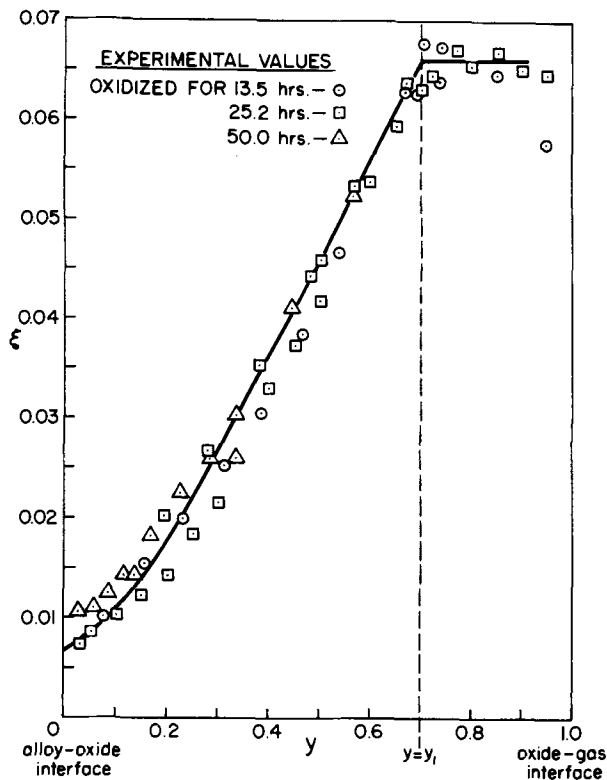


Fig. 9. Mole fraction of FeO,  $\xi$ , vs. the normalized distance coordinate  $y$  in the (Ni, Fe)O scale layer formed on the Ni-4 w/o Fe alloy. The solid curve represents calculated values from Eq. [19] and [20].

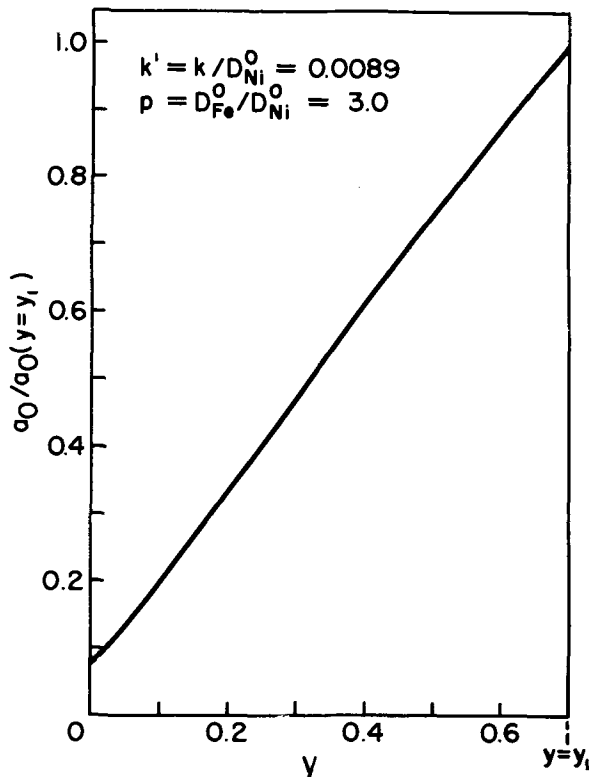


Fig. 10. Oxygen activity vs. normalized distance coordinate  $y$  in the (Ni, Fe)O oxide layer formed on the Ni-4 w/o Fe alloy calculated from Eq. [19] and [20].

tion to the diffusion equation assuming  $D_{\text{alloy}}$  to be constant is

$$C_{\text{Fe}} = C'_{\text{Fe}} + (C^{\circ}_{\text{Fe}} - C'_{\text{Fe}}) \frac{\text{erfc}(x/2\sqrt{D_{\text{alloy}}t})}{\text{erfc}(\alpha/2\sqrt{D_{\text{alloy}}})} \quad [29]$$

where  $x$  is the distance from the alloy/oxide interface and  $C'_{\text{Fe}}$  and  $C^{\circ}_{\text{Fe}}$  are the concentrations at the alloy/oxide interface and in the bulk alloy (4). Since  $\text{erfc}$  denotes the complimentary error function, we obtain from Eq. [29]

$$\frac{dC_{\text{Fe}}}{d\lambda} = \frac{(C^{\circ}_{\text{Fe}} - C'_{\text{Fe}})}{\text{erfc}(\alpha/2\sqrt{D_{\text{alloy}}})} \cdot \frac{1}{2\sqrt{D_{\text{alloy}}}} \exp\left(-\frac{\lambda^2}{4D_{\text{alloy}}}\right) \quad [30]$$

where  $\lambda = x/\sqrt{t}$

At the alloy/oxide interface,  $x = 0$  and hence

$$\left(\frac{dC_{\text{Fe}}}{d\lambda}\right)_{\lambda=0} = \frac{(C^{\circ}_{\text{Fe}} - C'_{\text{Fe}})}{\text{erfc}(\alpha/2\sqrt{D_{\text{alloy}}})} \cdot \frac{1}{2\sqrt{D_{\text{alloy}}}} \quad [31]$$

If the values of  $C^{\circ}_{\text{Fe}}$ ,  $C'_{\text{Fe}}$ ,  $(dC_{\text{Fe}}/dx)_{x=0}$ , and  $\alpha$  are known, Eq. [31] can be solved for  $D_{\text{alloy}}$ . An estimate for  $D_{\text{alloy}}$  may now be made from the experimental results for the alloys containing 2 and 8 w/o Fe (1). The values of  $\alpha$  for these alloys are  $2.4 \times 10^{-5}$  and  $1.8 \times 10^{-5}$  cm/sec<sup>1/2</sup>, respectively. From the values of  $C^{\circ}_{\text{Fe}}$ ,  $C'_{\text{Fe}}$ , and  $(dC_{\text{Fe}}/d\lambda)_{\lambda=0}$  in Fig. 1 and 4,  $D_{\text{alloy}}$  is estimated to be  $\sim 10^{-10}$  cm<sup>2</sup>/sec. This value is an order of magnitude higher compared to the literature data (16, 17) but the agreement may be regarded as a first approximation considering the difficulty involved in estimating the value of error functions for large arguments and the approximation made that boundaries between the oxide precipitates and the alloy play no role in the diffusion mechanism.

*Oxygen solubility in Ni-Fe alloys and internal oxidation.*—No results are available on the maximum oxygen solubility in the solid alloys as a function of composition. This solubility for pure iron and nickel at 1000°C is 3 ppm (18) and 150 ppm (19), respectively. From these terminal values, the oxygen solubility curve for the alloys can be estimated by a method given by Smith (20). Using the Gibbs-Duhem equations for the oxide and alloy phases in equilibrium and the Wagner formalism (21) for the activity coefficients, the variation of oxygen solubility with alloy composition can be determined in terms of the compositions of the alloy and oxide phases and the interaction parameters  $\epsilon_{ij}$  in the alloy defined by

$$\epsilon_{ij} = \frac{\partial \ln \gamma_i}{\partial X_j} \quad [32]$$

Here,  $\gamma_i$  is the activity coefficient of species  $i$  and  $X_j$  is the mole fraction of species  $j$ . In the limiting case where the oxygen solubility is very small, i.e.,  $X_{\text{O}}^{\text{A}} \ll 1$ , the slope of the solubility curve is given by

$$\left. \frac{dX_{\text{O}}}{dX_2} \right|_{X_2 \rightarrow 0} = [1 - (1 + \epsilon_{12})X_{\text{O}}^{\text{ox}}] \frac{X_{\text{O}}^{\circ}}{X_{\text{O}}^{\text{ox}}} \quad [33]$$

where  $X_{\text{O}}^{\circ}$  is the oxygen solubility in pure metal 1, and 2 is the solute metal.  $X_{\text{O}}^{\text{ox}} = 0.5$  for an MO type compound and  $X_{\text{O}}^{\text{ox}} = 4/7$  for an M<sub>3</sub>O<sub>4</sub> compound. This equation may be applied in the nickel oxide-alloy region since the maximum iron content of the alloy is less than 1%. Since  $X_{\text{O}}^{\circ} \ll 1$ ,  $dX_{\text{O}}/dX_{\text{Fe}} \sim 0$  from Eq. [33], and the oxygen solubility line in this region may be drawn parallel to the Fe-Ni binary axis. Since the Fe-Ni system is nearly ideal (2, 8), the interaction parameters  $\epsilon_{ij}$  are expected to be small. Grundmann (22) has found the interaction parameter  $\epsilon_{\text{O}}^{\text{Ni}} = 1.64$  for  $N_{\text{Ni}} < 0.5$  and  $\epsilon_{\text{O}}^{(\text{Ni})} = 3.34$  for  $N_{\text{Ni}} > 0.5$ , in liquid Fe-Ni alloys at 1600°C. These values are expected to increase with decreasing temperature. This interaction parameter, however, would not be expected to be much greater than unity, and the change in oxygen solubility with nickel content over the wustite-alloy region as given by Eq. [33] would be negligible.

The oxygen solubility curve for the alloys based upon the above considerations may be plotted semi-quantitatively as illustrated in Fig. 11. This behavior

Table V. Equilibrium oxygen pressures over phases in the Fe-Ni-O system at 1000°C (2, 8)

Equilibrium phases	Oxygen partial pressure, atm
Fe/FeO	$1.32 \times 10^{-15}$
Alloy/wustite/spinel	$3.26 \times 10^{-14}$
Alloy/nickel oxide/spinel	$4.03 \times 10^{-11}$
Ni/NiO	$4.48 \times 10^{-11}$

Table VI. Self-diffusion coefficients of iron, nickel, and oxygen in the metallic and oxide phases at 1000°C

Diffusion species	Diffusion phase	Self-diffusion coefficient, cm <sup>2</sup> /sec	Reference
Fe	$\gamma$ -Fe	$1.0 \times 10^{-12}$	23
Fe	Fe-32 w/o Ni	$6.2 \times 10^{-12}$	24
Ni	Ni	$2.5 \times 10^{-12}$	25
Ni	Ni-20 w/o Fe	$9.4 \times 10^{-12}$	26
Ni	Ni-30 w/o Fe	$1.1 \times 10^{-11}$	26
Ni	Fe-19.3 w/o Ni	$2.4 \times 10^{-12}$	27
O	$\gamma$ -Fe	$6.8 \times 10^{-7}$	18
Fe	Spinel Ni <sub>0.8</sub> Fe <sub>2.2</sub> O <sub>4</sub>	$1 \times 10^{-11}$	28
Ni	NiO	$1 \times 10^{-11}$ ( $P_{O_2} = 1$ atm)	9-12, 29
Ni	(Fe,Ni)O; $N_{FeO} \sim 0.01$	$7 \times 10^{-10}$ ( $P_{O_2} = 1$ atm)	Present work
Fe	(Fe,Ni)O; $N_{FeO} \sim 0.01$	$2 \times 10^{-9}$ ( $P_{O_2} = 1$ atm)	Present work
O	NiO	$5.3 \times 10^{-15}$	30

may also be inferred from the corresponding equilibrium oxygen pressures given in Table V. The variation in the oxygen pressure over the nickel oxide-alloy region is small. Its variation over the wustite-alloy region is about one order of magnitude, whereas the variation over the spinel-alloy region is about three orders of magnitude.

The diffusion coefficients of iron, nickel, and oxygen in the various phases are given in Table VI. The diffusion coefficient of oxygen in the metal is more than four orders of magnitude higher than that for iron or nickel. This will result in a steep concentration gradient for the alloying elements (Fig. 1-4) and a shallow gradient for oxygen. For the shape of the solubility curve illustrated in Fig. 11, this will easily result in constitutional supersaturation and hence internal oxidation. Figure 11 also shows schematic virtual diffusion paths for the alloys containing 5 and 20 w/o Fe, consistent with the above consideration. It can be seen from the shape of the oxygen solubility curve in the spinel-alloy region that constitutional supersaturation is readily attained even for this steepest range of the oxygen concentration gradient. As a consequence supersaturation could be easily produced in the alloys

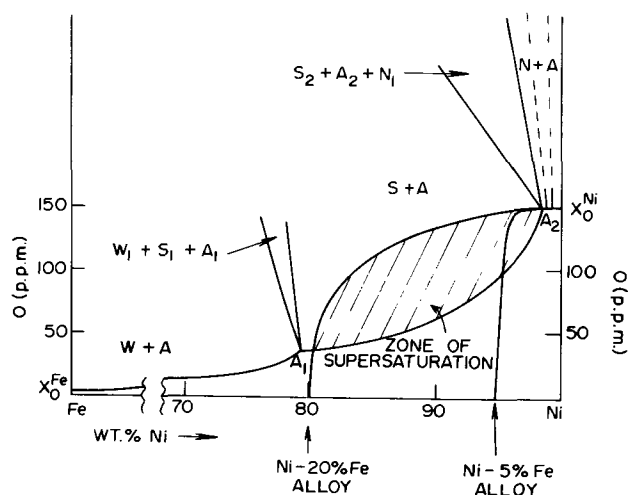


Fig. 11. Oxygen solubility curve for Fe-Ni alloys at 1000°C and the virtual diffusion paths in the alloy phase for the alloys containing 5 and 20 w/o Fe. Phase notations are: W-wustite, (Ni,Fe)O; S, spinel, Ni<sub>2</sub>Fe<sub>3-2</sub>O<sub>4</sub>; A, iron-nickel alloy; N, nickel oxide solid solution, (Fe,Ni)O. Phase compositions are: S<sub>2</sub>-Ni<sub>0.8</sub>Fe<sub>2.2</sub>O<sub>4</sub>; N<sub>1</sub>-Fe<sub>0.15</sub>Ni<sub>0.85</sub>O; A<sub>2</sub>-Fe<sub>0.01</sub>Ni<sub>0.99</sub>.

investigated (0-25 w/o Fe) with the extent of internal oxidation increasing with increasing alloy iron content.

**Composition paths.**—The results in Fig. 1-4 show that the concentration profiles in the phases of the oxidized samples are invariant in  $\lambda$ -space. Since a solution of the diffusion equation is parametric in  $\lambda$ , the concentration profile can be transposed onto the phase diagram by eliminating  $\lambda$ . This transposition reflects the condition of mass conservation and monotonic activity gradients for the diffusing species.

A composition path for an investigated alloy is stationary-state oxidation consistent with metallographic and electron-probe observations is shown in Fig. 12. The oxide layer adjacent to the gas contains spinel and nickel oxide since a single phase of nickel oxide containing a high iron concentration cannot be sustained at high oxygen potentials. Below this two-phase layer, nickel oxide exists as the innermost layer in which iron is enriched toward the outer interface due to its higher mobility (corresponding to  $p = 3$ ). The metal-external scale interface corresponds to nickel oxide-alloy equilibrium. The composition path then crosses over to the spinel-alloy region via the three-phase spinel-nickel oxide-alloy region. This corresponds to the internal oxidation zone where the alloy and spinel compositions are given by the corresponding ends of the tielines which are cut. Since the iron content of spinel increases with increasing iron content of the bulk alloy, the spinel particles in the internal oxidation zone are enriched in iron with increasing penetration distance into the alloy. The final segment of the composition path is traversed in the region corresponding to the unoxidized alloy.

This composition path shows monotonically decreasing values of oxygen activity from the outer oxide surface to the bulk alloy, as required from thermodynamic considerations. The flux equations for the cations in the oxide phase from which Eq. [19] and [20] were derived are written in terms of decreasing cation activities toward the oxide/gas interface. Equations [19] and [20] are therefore consistent with monotonically decreasing cation activities outward. Recall that the concentration profiles in the nickel oxide-spinel layer satisfy the thermodynamic relation given by Eq. [18] consistent with a decreasing oxygen activity inward. Interfacial compositions corresponding to the depicted composition path in Fig. 12 for alloys contain-

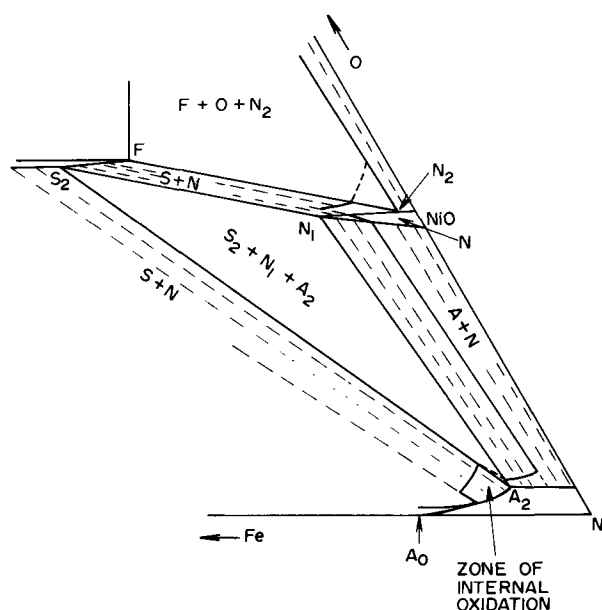


Fig. 12. A typical composition path for an oxidized alloy (distorted scale). Phase notations and compositions are as in Fig. 11. Additional compositions are: F-nickel ferrite, NiFe<sub>2</sub>O<sub>4</sub>; N<sub>2</sub>-Fe<sub>0.01</sub>Ni<sub>0.99</sub>O. A<sub>0</sub> is the bulk alloy composition.

ing 2-8% Fe are given in Table II from which the actual paths can be estimated.

Application of Eq. [18] to the oxide/gas interface indicates that the wustite content of nickel oxide should be  $\sim 0.03$  mole per cent (m/o). However, the experimental results (Fig. 1-4) show that the concentration of wustite is much higher, up to within a few microns of the interface. Consequently the iron concentration gradient is extremely steep near the scale/gas interface but its exact shape could not be determined in this region due to experimental limitations. An oxygen activity profile through a section of the oxidation zones of the alloy is illustrated in Fig. 13. It is drawn such that the spinel-nickel oxide-alloy equilibrium occurs at the interface of alloy and the external scale. However, this three-phase equilibrium need not actually correspond to the alloy-external scale interface since a slight amount of nickel oxide containing iron could occur as internal precipitates (as corresponding to the diffusion path illustrated in Fig. 12). This would not significantly affect the oxygen activity at the above interface since the variation in oxygen activity in the alloy-nickel oxide region is very small.

### Discussion

In this investigation, Eq. [19] and [20] giving the cation distributions and oxygen activity in the scale were derived from the ternary diffusion analysis. The effect of ternary interactions in causing uphill diffusion of cations is well demonstrated in this system through these equations. The driving force for cation diffusion through the scale is associated with the vacancy gradient caused by the variation in oxygen activity. Although iron diffuses against its concentration gradient in the nickel oxide layer it is actually diffusing down its activity gradient. This situation merely suggests the importance of writing diffusion fluxes in terms of activity gradients in mixed oxide systems. Wagner (3) has postulated a formalism which showed that the cation with the higher mobility (iron in the present case) is the one that preferentially concentrates toward the oxide/gas interface. In a ternary system at constant temperature and pressure, a single phase region has two degrees of freedom one of which is fixed at any coordinate point by the oxygen pressure. The extra degree of freedom thus cannot be fixed by a pure thermodynamic parameter and hence a kinetic parameter (relative jump frequency for cations) comes into play and determines the distribution of cations in the oxide.

The effect of an oxygen activity gradient and the relative jump frequencies of iron and nickel are such

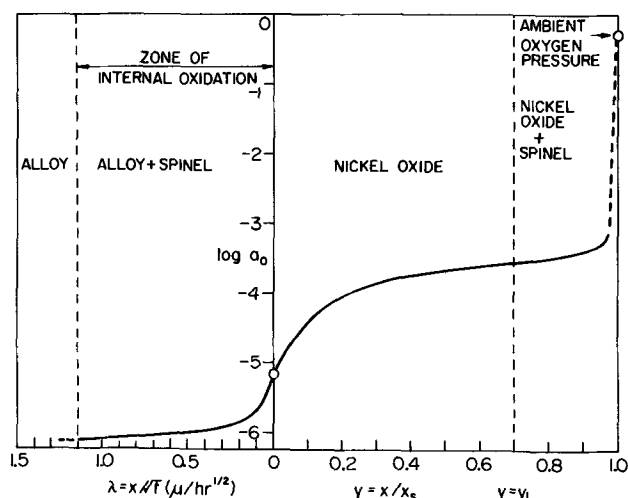


Fig. 13. An oxygen activity profile through a section of the oxidation zones of an oxidized Ni-4 w/o Fe alloy. The dashed section of the oxygen activity profile near the surface of the oxide scale has been extrapolated to ambient oxygen pressure.

as to preferentially concentrate iron toward the outer interface of nickel oxide. However, when this concentration becomes high, spinel precipitates from nickel oxide. The explanation for this is as follows. At very low oxygen potentials iron in nickel oxide is present in the form of ferrous ions. Since this does not require creation of additional vacancies, solubility of iron in this oxide is high at low oxygen potentials (2, 8). Iron tends to pass from the ferrous to the ferric state with increasing oxygen potential. Since nickel oxide cannot incorporate ferric iron in large concentrations without sustaining a high concentration of vacancies, the iron solubility rapidly decreases with increasing oxygen pressure. Iron solubility in nickel oxide is negligible at  $P_{O_2} \sim 1$  atm, and correspondingly iron is preferentially concentrated in the spinel phase which can accommodate ferric ion easily in its crystal lattice. Most of the spinel in the external scale appears to be precipitated at a value of the spatial coordinate where nickel oxide first supersaturates with respect to iron (the location nearest the source), and hence the peculiar scale structure seen in Fig. 5.

The experimental closure of the theoretical analysis is not entirely satisfactory. This situation arises mainly due to lack of independent measurements on the relative jump frequencies of iron and nickel in nickel oxide. In the absence of these values, constancy of these parameters has to be assumed for a closure which neglects any correlation effects in the system. Thus it is assumed that the jump frequency of a cation into a vacancy is independent of the composition gradient and that the vacancies do not show preferential affinity for one or the other cation. The extent to which these assumptions are valid for nickel oxide containing dissolved iron is not presently known.

### Summary

Ni-Fe alloys containing up to 25 w/o Fe upon exposure to oxygen at  $1000^\circ\text{C}$  form by parabolic kinetics a zone of internal oxidation containing spinel particles and an external scale consisting of an inner nickel oxide layer and an outer two-phase nickel oxide-spinel layer. The concentration gradients of iron and nickel in the alloys and reaction product layers could be determined by electron-probe microanalyses. The oxidation phenomena were interpreted by a diffusion model which is consistent with diffusional parameters for the various phases and thermodynamics of the Fe-Ni-O system. The composition paths in an alloy and the scale were superimposed on the ternary isotherm. Sufficient results were available to demonstrate that the ternary diffusion equations in conjunction with a defect model for nickel oxide containing iron quantitatively predicted the cation concentration and the oxygen activity profiles in the nickel oxide layer and the parabolic oxidation constants for the alloys containing 2 and 4 w/o Fe.

### Acknowledgments

This work forms part of the thesis submitted by A. D. Dalvi to McMaster University in partial fulfillment of the requirements for the award of the Ph.D. degree. He gratefully acknowledges the award of the International Nickel Company of Canada Fellowship for graduate research. The authors are indebted to D. E. Coates and J. S. Kirkaldy for helpful discussions. This research was carried out under auspices of the National Research Council of Canada.

Manuscript submitted Dec. 22, 1972; revised manuscript received Sept. 17, 1973.

Any discussion of this paper will appear in a Discussion Section to be published in the December 1974 JOURNAL. All discussions for the December 1974 Discussion Section should be submitted by Aug. 1, 1974.

### REFERENCES

1. A. D. Dalvi and W. W. Smeltzer, *This Journal*, **118**, 1978 (1971).

2. A. D. Dalvi and W. W. Smeltzer, *ibid.*, **117**, 1431 (1970).
3. C. Wagner, *Corrosion Sci.*, **9**, 91 (1969).
4. D. E. Coates and A. D. Dalvi, *J. Oxidation Metals*, **2**, 331 (1970).
5. A. D. Dalvi and D. E. Coates, *ibid.*, **3**, 203 (1971).
6. P. Mayer and W. W. Smeltzer, *This Journal*, **119**, 626 (1972).
7. G. Zintl, *Z. Physik. Chem. N.F.*, **48**, 340 (1966); *ibid.*, **54**, 110 (1967).
8. Haydn Davies and W. W. Smeltzer, *This Journal*, **119**, 1362 (1972).
9. R. L. Lindner and A. Akerstrom, *Discussions Faraday Soc.*, **23**, 133 (1957).
10. M. T. Shim and W. J. Moore, *J. Chem. Phys.*, **26**, 802 (1957).
11. J. B. Price and J. B. Wagner, Jr., *Z. Physik Chem. N.F.*, **49**, 257 (1966).
12. M. L. Volpe and J. Reddy, *J. Chem. Phys.*, **53**, 1117 (1970).
13. S. P. Mitoff, *ibid.*, **35**, 882 (1961).
14. Y. D. Tretyakov and R. A. Rapp, *Trans. AIME.*, **245**, 1235 (1969).
15. L. Himmel, R. F. Mehl, and C. E. Birchenall, *ibid.*, **197**, 827 (1953).
16. R. E. Carter and F. D. Richardson, *ibid.*, **200**, 1244 (1954).
17. J. S. Kirkaldy, *Can. Met. Quart.*, **8**, 35 (1969).
18. J. Swisher and E. T. Turkdogan, *Trans. AIME*, **239**, 626 (1967).
19. M. Hansen, "Constitution of Binary Alloys," p. 1024, McGraw-Hill Book Co., New York (1958).
20. P. N. Smith, Ph.D. Thesis, p. 82, McMaster University (1970).
21. C. Wagner, "Thermodynamics of Alloys," Addison-Wesley Publishing Co., Inc., Reading, Mass. (1952).
22. R. Grundmann, Ph.D. Thesis, p. 41, Technische Hochschule, Aachen (1967).
23. P. L. Gruzin, J. W. Kornew, and G. W. Kurdjumor, *Dokl. Akad. Nauk. SSSR*, **80**, 49 (1951).
24. M. Badia and A. Vignes, *Compt. Rend.*, **264**, 1528 (1967).
25. I. V. Ivantsov, *Fig. Metal. Metalloved.*, **22**, 725 (1966).
26. E. W. de Reza and C. Pampillo, *Acta Met.*, **15**, 1263 (1967).
27. G. F. Hancock and G. H. Leak, *Met. Sc. J.*, **1**, 33 (1967).
28. R. H. Condit, M. J. Brabers, and C. E. Birchenall, *Trans. AIME*, **218**, 768 (1960).
29. K. Fueki and J. B. Wagner, Jr., *This Journal*, **112**, 384 (1965).
30. M. O'Keefe and W. J. Moore, *J. Phys. Chem.*, **65**, 1438 (1961).

## A Study of SnO<sub>2</sub> Thin Films Formed by Sputtering and by Anodizing

Enrico Giani and Roger Kelly\*

*Institute for Materials Research, McMaster University, Hamilton, Ontario, Canada*

### ABSTRACT

SnO<sub>2</sub> films have been prepared by reactive sputtering in an oxygen-containing glow discharge, by ion-beam sputtering in an accelerator, and by anodizing with an ethylene-glycol-based electrolyte. The sputtered films were amorphous if deposited on KCl or Ta at temperatures from -100° to +200°C, though were crystalline if deposited on SnO<sub>2</sub> at 200°C. The anodic films were variously crystalline or microcrystalline, though clearly nonamorphous. The crystallization temperatures ranged from <200°C for crystalline SnO<sub>2</sub> substrates, to 250°-300°C for KCl substrates, to 400°-450°C for Ta substrates, to 475°-550°C for unsupported films. The crystallization product was consistently cassiterite (*i.e.*, rutile type). The thickness (*d*) of the reactively sputtered films was estimated by noting the interference colors when using a Ta substrate and assuming the validity of the relation  $n_{\text{SnO}_2}d_{\text{SnO}_2} = n_{\text{Ta}_2\text{O}_5}d_{\text{Ta}_2\text{O}_5}$ , where *n* is the index of refraction. The thickness of the anodic films was estimated by sputtering the films with 20-keV Kr ions until metal was exposed and noting the weight change. The anodization of Sn has a rather low efficiency (4-21%), and this could be shown to be due to electronic conduction rather than to dissolution.

SnO<sub>2</sub> is nearly unique among electronic materials in being a fairly good conductor when oxygen deficient yet in having a high degree of transparency to visible light (1). By contrast, oxides such as MoO<sub>3</sub>, Nb<sub>2</sub>O<sub>5</sub>, or V<sub>2</sub>O<sub>5</sub> are strongly absorbing when oxygen deficient and therefore conductive (2, 3). This has led to a considerable amount of work on the electrical and optical properties of SnO<sub>2</sub>, and has resulted in SnO<sub>2</sub> being proposed, among other things, for transparent heating elements (4), for transparent antistatic coatings (5), and for making transistors or other devices where transparency was required (6, 7).

Typically, three different approaches have been used to form SnO<sub>2</sub> films. (i) Most commonly the films have been formed chemically, for example by passing SnCl<sub>4</sub> or SnCl<sub>4</sub> plus water vapor over a substrate held at 500°-750°C (8, 9) or by a similar procedure involving

other volatile tin compounds (9, 10). (ii) In other work vacuum evaporation of SnO<sub>2</sub> (11) has been used so as to take advantage of the unusually high vapor pressure (12). Closely related is the reactive evaporation of Sn (9). (iii) Finally, SnO<sub>2</sub> films have been successfully prepared by reactive sputtering either of Sn cathodes (6, 13-17) or of SnO<sub>2</sub> itself (18).

There has been an enormous amount of electronic and optical characterization in this work, though notably lacking has been structural characterization. Thus present knowledge is largely confined to two results: chemically deposited layers are invariably crystalline (8-10), while evaporated or reactively sputtered layers are normally (6, 9, 11, 13, 14, 16, 17) though not always (15, 17, 18) amorphous. Evidently the range of crystallization temperatures for supported SnO<sub>2</sub> films lies in the interval between the substrate temperatures used in chemical deposition and those used in evaporation or sputtering. We regard structural characterization to

\* Electrochemical Society Active Member.

Key words: tin, thin films, sputtering, anodization, amorphousness.



be nearly as important as other characterization in view of the fact that both the magnitude of conductivity, as well as its temperature stability, are affected by crystallinity. Striking examples of this interdependence occur with V<sub>2</sub>O<sub>3</sub> and VO<sub>2</sub> (19).

Also lacking has been virtually any degree of success in producing SnO<sub>2</sub> films by anodizing Sn at high voltages. Work with both acidic (20-22) and basic (23-25) electrolytes has generally involved low voltages ( $\leq 5V$ ) and never values ( $\gg 5V$ ) characteristic of the growth of thick, uniform, protective films analogous to those formed on Si (26) and Ge (27). More specifically, Hampson and Larkin (21) showed that the capacitances of anodically polarized Sn had values appropriate to perhaps a monolayer of oxide when acidic electrolytes were used. Kerr (23), by contrast, obtained thick films (up to 10<sup>5</sup>Å) with basic electrolytes but the films neither showed interference colors nor supported a significant voltage. Only Bianchi (28) appears to have succeeded in polarizing Sn at a high voltage. Using an electrolyte of water with NaOH and potassium silicate he reached 100V, though the film was described as a thick, black crust.

We would propose in the present work to explore the properties of 500-5000Å SnO<sub>2</sub> films as formed by reactive sputtering, ion-beam sputtering, and high-voltage anodizing. These properties will include the crystal form, crystallization behavior, thickness, and anodizing efficiency. Other properties, especially those relating to radiation damage, will be treated separately (29).

### Experimental

**Reactive sputtering.**—The preparation of SnO<sub>2</sub> films by reactive sputtering is an already well-understood process. In the present work the equipment was of the diode type (e.g., 15, 17), with a 50 mm diameter Sn cathode. The substrates, consisting of pieces of chemically polished Al, Ta, or V, or of cleaved KCl, or of air-annealed SnO<sub>2</sub>, were laid on a 42 mm diameter anode table placed 30 mm beneath the cathode. The dark-space region of the discharge usually extended about 20 mm away from the cathode when the gas pressure was about  $1 \times 10^{-2}$  Torr. The gas was a 1:1 mixture of oxygen and argon which was purified by being passed through a liquid-nitrogen trap. Applied d-c voltages ranged from 1000 to 3000 and the discharge current was typically 10 mA. Those films which were deposited on KCl could be stripped using water.

**Ion-beam sputtering.**—SnO<sub>2</sub> films were also prepared by sputtering Sn anodized to 50V with 10-30 keV Kr ions at doses ranging from 25 to 200  $\mu\text{Amin}/\text{cm}^2$ . The sputtering was performed using a high-current ion accelerator and collecting the deposit on unheated KCl (30). This method of film preparation involves a vacuum of  $10^{-6}$  Torr and the sputtered particles therefore reach the substrate with their full energy [1-60 eV (31)] and without contamination.

**High-voltage anodizing.**—Finally, anodizing was considered. The anode was a chemically degreased 20  $\times$  30 mm Sn sheet, while the cathode was either a 20  $\times$  30 mm Al sheet or a 23 mm ID Pt cylinder. Previous work (20-25, 28) has shown that water-based electrolytes, whether acidic or basic, do not permit Sn to be anodized to high voltages, and an organic-based one was therefore chosen. It consisted of 330 g/liter of ammonium pentaborate in ethylene glycol which was varied by adding water (subsequently indicated in units of ml/liter). Most films were formed using a preset voltage of 50 and a preset current of 10 mA/cm<sup>2</sup> as obtained with a Hewlett-Packard Model 6186B constant-current power supply.

The difference between electrolytes with different additions of water is brought out in Fig. 1. Electrolyte (a) (0 ml/liter) yields opaque, white films, though the time variation of current and voltage is sometimes unpredictable. Electrolyte (b) (150 ml/liter) gives opaque, gray films. Electrolyte (c) (300 ml/liter) leads

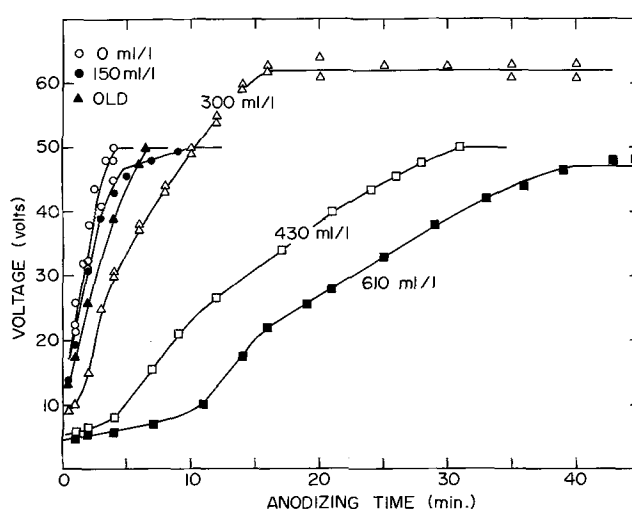


Fig. 1. Voltage-time curves for anodizing Sn at 10 mA/cm<sup>2</sup> in electrolytes consisting of ethylene glycol, 330 g/liter of ammonium pentaborate, and varying amounts (indicated in ml/liter) of water. "Old" refers to an electrolyte containing 300 ml/liter water which had aged owing to use. The upper voltage limit is due to presetting in all cases except "Δ" and "■", where it is a true upper limit.

to a voltage rise of 50-65 and the films show interference colors over approximately six orders, in agreement with the behavior of most other substances which permit anodizing to high voltages.

Electrolyte (c) is subject to aging, through use or storage. This gives rise to electrolyte (c'), yielding opaque, white films. Electrolyte (d) (430 ml/liter) gives films which show slight interference effects though are better described as opaque, yellowish brown. Finally, electrolyte (e) (610 ml/liter) gives opaque, grayish brown films.

Contrary to previous work, Sn can evidently be anodized in a "normal" manner provided a correct electrolyte is chosen. The normalcy is further shown by the existence of a well-defined fall in current when the preset voltage is reached (Fig. 2).

We have centered our attention on films obtained using electrolytes (c) and (c'), subsequently referred to as "colored" and "white." When necessary, the films were stripped by placing the specimens in 1% HCl for several hours.

### Results

**Film continuity and crystal form.**—The state of the films that were obtained was determined using transmission electron microscopy as well as electron diffraction.

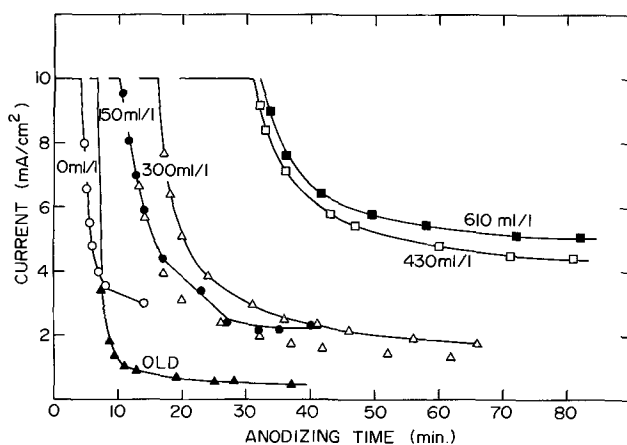


Fig. 2. Current-time curves for anodizing Sn when both current and voltage are preset. The anodizings are the same as in Fig. 1 in all cases except "Δ" and "■", where the preset voltages are 50 and 40V. Note that, to avoid crowding, only one set of points "Δ" has been joined.

tion. Some 400 specimens were examined, the main trends being as follows:

(i) Reactive sputtering onto KCl substrates at  $-100^{\circ}\text{C}$  gave amorphous films, sometimes with an island structure and sometimes continuous (Fig. 3). Though the island structure is not understood, the amorphousness is a reasonable result given that most oxides deposit amorphously at low temperatures (16, 30).

(ii) Reactive sputtering onto KCl or Ta at  $25^{\circ}$  or  $200^{\circ}\text{C}$ , as well as ion-beam sputtering onto KCl at  $25^{\circ}\text{C}$ , gave amorphous films which were continuous (Fig. 4). Apparently  $25^{\circ}$  and  $200^{\circ}\text{C}$  also constitute "low" temperatures as far as  $\text{SnO}_2$  is concerned.

(iii) Reactive sputtering onto  $\text{SnO}_2$  single crystals or sintered pellets at  $200^{\circ}\text{C}$  gave finely polycrystalline films with the structure of cassiterite. This result is consistent with the ready availability of crystallization nuclei in spite of the temperature being "low."

(iv) Colored anodic films, as formed with electrolyte (c), were continuous and showed a characteristic cellular structure with mean dimensions of  $200\text{--}700\text{\AA}$  (Fig. 5). The diffraction pattern was borderline between showing halos and rings, though was judged to be more nearly of a ring type with d spacings corresponding to cassiterite. Note that the grains are much smaller than the cells.

(v) White anodic films, as formed with electrolyte (c'), were polycrystalline with the structure of cassiterite (Fig. 6). Though continuous they were characterized by a variation in thickness as if random crystal growth had occurred.

In effect,  $\text{SnO}_2$  films can be formed in either an amorphous or crystalline state, the result depending on whether sputtering or anodizing is used, and in addition depending on the substrate and/or temperature.

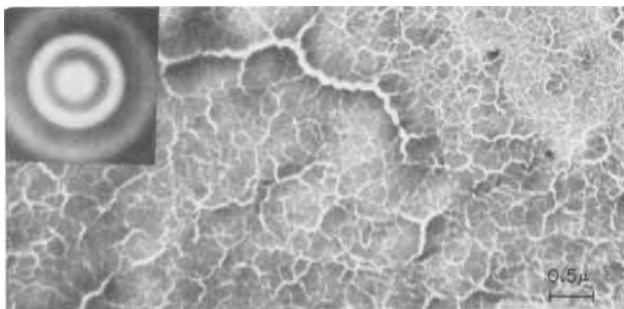


Fig. 3. Micrograph with mag. 22,000 of  $\text{SnO}_2$  film formed by reactive sputtering onto KCl at  $-100^{\circ}\text{C}$ . The example is amorphous (obvious from the diffraction pattern) and shows an island structure, though in other instances the films were amorphous and continuous.

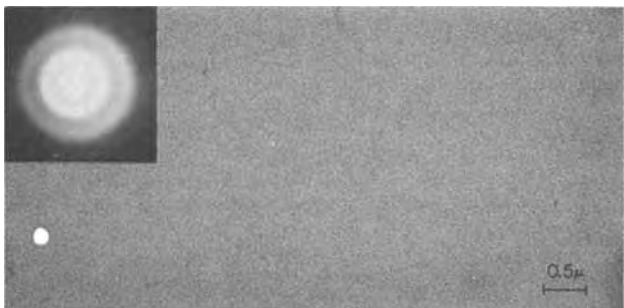


Fig. 4. Micrograph with mag. 22,000 of  $\text{SnO}_2$  film formed by reactive sputtering onto KCl at  $200^{\circ}\text{C}$ . Films formed at  $200^{\circ}\text{C}$  were always amorphous (again obvious from the diffraction pattern) and continuous.

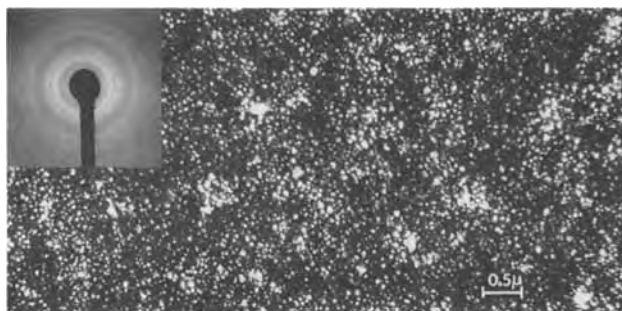


Fig. 5. Micrograph with mag. 22,000 of  $\text{SnO}_2$  film formed by anodizing Sn using electrolyte (c). The film has a cellular structure on a scale of  $\sim 500\text{\AA}$  but consists of crystallites on a much smaller scale. The diffraction pattern was judged to be more nearly indicative of crystallinity than amorphousness.

*Crystallization behavior.*—Amorphous  $\text{SnO}_2$  shows four well-defined halos at low angles together with others at greater angles. It was found that these halos persisted when specimens were heated to gradually increasing temperatures (6 min hold times) until they split abruptly to yield the ring pattern of cassiterite. This splitting has been taken as signalling the onset of crystallization, with the main trends as follows:

(i) Unsupported amorphous films, whether formed by reactive or ion-beam sputtering, crystallized at  $475^{\circ}\text{--}550^{\circ}\text{C}$  (Fig. 7) to yield grains having sizes of  $100\text{--}250\text{\AA}$  (shown in dark-field photographs). A similar crystallization temperature was obtained for heating both in air and vacuum ( $10^{-5}$  Torr).

(ii) Supported films showed reduced crystallization temperatures, with a value of about  $400^{\circ}\text{--}450^{\circ}\text{C}$  when

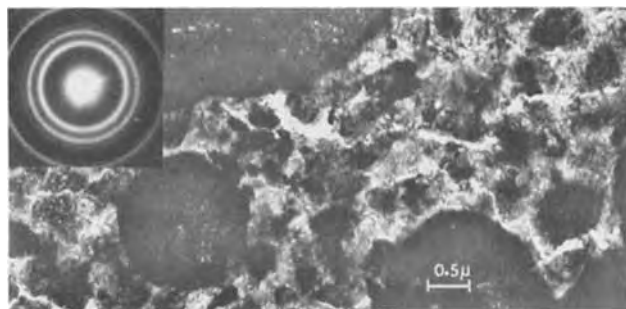


Fig. 6. Micrograph with mag. 22,000 of  $\text{SnO}_2$  film formed by anodizing Sn using electrolyte (c'). The film consists in part of thin regions and in part of thick regions, the latter appearing as large black areas. Such films had better defined crystallinity than those of Fig. 5 and the diffraction pattern could be readily shown to be that of cassiterite.

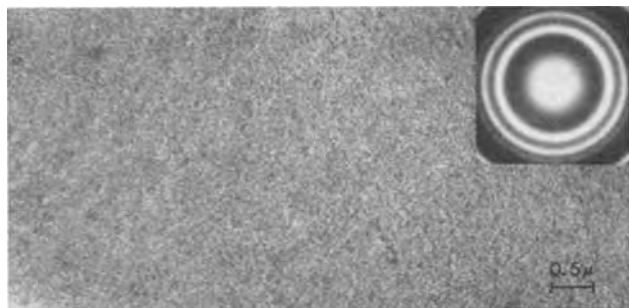


Fig. 7. Bright-field micrograph with mag. 22,000 of  $\text{SnO}_2$  film formed by reactive sputtering onto KCl at  $200^{\circ}\text{C}$ . The film was stripped and then heated for 10 min in air at  $600^{\circ}\text{C}$  in an unsupported state. The corresponding diffraction pattern (given) was that of cassiterite, while dark-field views (not given) revealed grains with a size range of  $100\text{--}350\text{\AA}$ .

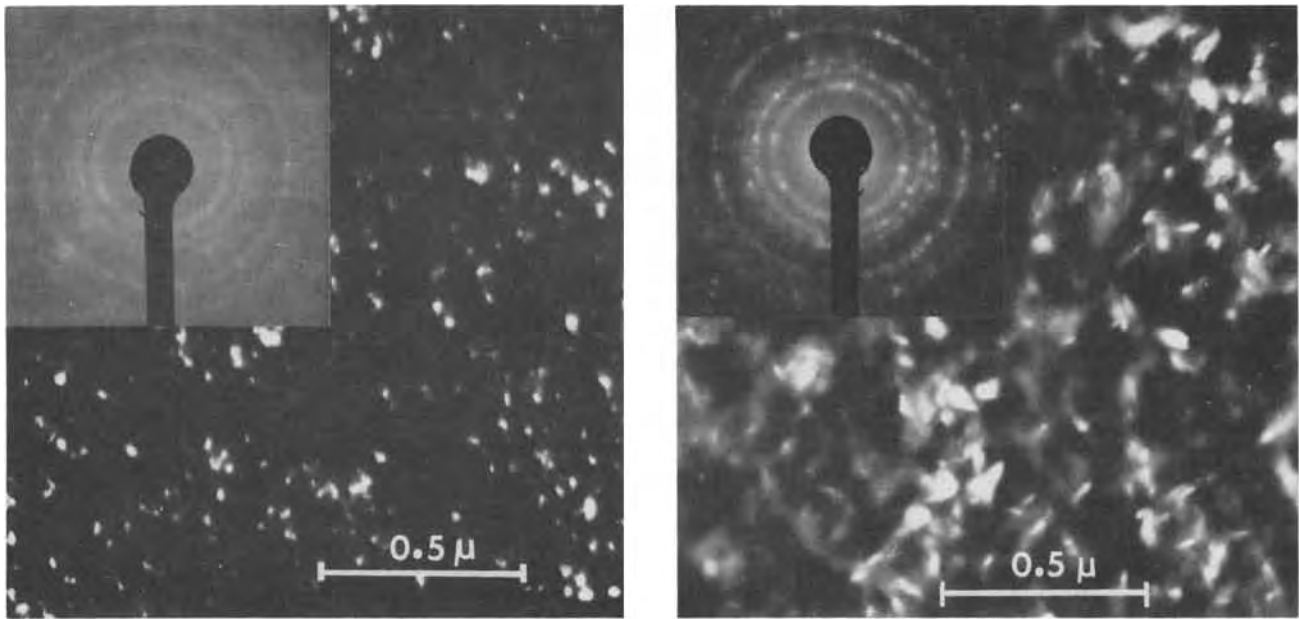


Fig. 8. (a, left) Bright-field micrograph with mag. 54,000 of SnO<sub>2</sub> film formed by anodizing Sn using electrolyte (c). The film was stripped and then heated for 6 min in air at 1000°C in an unsupported state. The diffraction pattern is still best described as consisting of rings. (b, right) As in (a) but dark-field and heated at 1100°C. The diffraction pattern now shows a tendency to be spotty.

in contact with Ta, 250°–300°C when in contact with KCl, and <200°C (thence crystalline as deposited) when in contact with crystalline SnO<sub>2</sub>. The grains formed had a broad range of sizes from 200 to 1500 Å and were therefore larger than those formed in unsupported films. The differences in crystallization temperature and in grain size suggest that nucleation rather than growth is the rate-controlling step in the crystallization of SnO<sub>2</sub>.

(iii) Colored anodic films which had been stripped were found to undergo a continuous increase in the sharpness of the rings with increasing temperature. This can be taken as confirming their polycrystalline nature in the sense that an amorphous film would have shown an abrupt increase in ring sharpness.

Higher temperatures led to relatively little change until 1000°C was exceeded. For example, the films retained their island-type or continuous form, the diffraction patterns persisted as rings corresponding to cassiterite, and the grains remained small (e.g., 100–400 Å in Fig. 8A). Only once a temperature of 1100°C was reached was there evidence for major grain growth. The diffraction patterns became spotty and dark-field photographs revealed larger grains (e.g., 500–1000 Å in Fig. 8B).

*Thicknesses of reactively sputtered films.*—In order to determine the thicknesses of the reactively sputtered films, substrates of Al, Sn, Ta, and V were included among the KCl cleavings on the anode table. It was hoped that well-defined interference colors would develop, and indeed satisfactory results were obtained with Ta. The colors for SnO<sub>2</sub> on Ta were then described in terms of a voltage such that when a was anodized to this voltage the same color was obtained. It was then assumed that the films had a similar "optical thickness," i.e.

$$n_{\text{SnO}_2} d_{\text{SnO}_2} = n_{\text{Ta}_2\text{O}_5} d_{\text{Ta}_2\text{O}_5}$$

where  $n$ , the index of refraction, was taken as 1.95 for SnO<sub>2</sub> (1) and 2.20 for Ta<sub>2</sub>O<sub>5</sub> (32). Since the thickness of anodic Ta<sub>2</sub>O<sub>5</sub> is given by 16.7 Å/V (33), we finally have

$$d_{\text{SnO}_2} \approx 19 \text{ Å/V} \quad [1]$$

where the voltage refers to that to which Ta is anodized. The results are summarized in Table I.

*Thicknesses of anodic films.*—The film thicknesses on anodized Sn were estimated in several ways. (i) They were judged in the first place to be nearly independent of voltage between 6 and 50V on the grounds that the interference colors changed only slightly with voltage for specimens anodized as in Fig. 2. (ii) Explicit thicknesses were obtained by measuring the weight increases due to anodizing and interpreting them in the light of the result (see below) that dissolution during anodizing is normally unimportant (column 2 of Table II). (iii) Explicit thicknesses were also deduced by a sputtering technique in which anodized specimens are bombarded with 20-keV Kr until the metal is exposed. The thicknesses follow gravimetrically (column 3 of Table II), while one obtains as an extra benefit values for the sputtering coefficient (29).

The inferred independence of thickness and voltage is seen to be fairly well, though not completely, borne

Table I. Thicknesses of reactively sputtered SnO<sub>2</sub> films

Interference color of SnO <sub>2</sub> on Ta	Voltage to which Ta must be anodized to show same color <sup>(a)</sup>	Thickness of SnO <sub>2</sub> film from Eq. [1] (Å)
Dark blue	24	470
Intermediate blue	40	760
Light blue	48	910
Blue with bit of yellow	54	1030
Yellow with bit of red	80	1520
Purple	85	1620
Yellowish green	120	2280

<sup>(a)</sup> The Ta was anodized for 3 min in 0.2% KF.

Table II. Thicknesses of anodic SnO<sub>2</sub> films<sup>(a)</sup>

Anodizing voltage (V)	Thickness as inferred from weight increase due to anodizing (Å)	Thickness as inferred from weight loss due to sputtering (Å)
6	3700 ± 300	3100 ± 300
8	6900 ± 100	6200 ± 600
15	4300 ± 700	4400 ± 400
25	2800 ± 500	3000 ± 300
35	2500 ± 500	4200 ± 400
50	2600 ± 300	4700 ± 500

<sup>(a)</sup> The current density was initially 6.5 or 10 and finally 2 mA/cm<sup>2</sup>. The conversion from μg/cm<sup>2</sup> to angstroms was made using the assumed value 6.95 μg/cm<sup>2</sup> for the density of SnO<sub>2</sub>; the real density would be somewhat lower.

Table III. Anodizing efficiency

Anodizing voltage (V)	Charged passed (coulombs/cm <sup>2</sup> )	Anodizing efficiency (%)	Hypothetical weight loss if low efficiency is due to dissolution (μg/cm <sup>2</sup> )
6	2.7	20 ± 2	600
8	5.25	21 ± 2	1200
15	7.92	10 ± 1	2100
25	8.64	6 ± 1	2500
35	11.8	6 ± 1	3400
50	21.2	4 ± 0.5	6200

(a) The current density was initially 6.5 and finally 2 mA/cm<sup>2</sup>.

out. In fact the films are thickest for a voltage in the vicinity of 8-15, an effect which will be studied in future work.

**Anodizing efficiency.**—The anodic-film thicknesses are of additional interest in that they enable the anodizing efficiency to be deduced. To this end it is sufficient to compare the film weights as obtained by integrating current-time curves as in Fig. 2 with observed weights. The results are summarized in Table III (columns 2 and 3). The efficiency is 20% for a 6V film but decreases with increasing voltage.

A low efficiency can arise either from electronic conduction or from film dissolution. These can be distinguished firstly from the fact that anodized specimens tended to gain weight approximately as required from the explicit film weights (columns 2 and 3 of Table II). Evidently electronic conduction is occurring, for had dissolution been important there would have been pronounced weight losses as in column 4 of Table III.

The origin of the low efficiency can be shown secondly from an experiment in which a specimen is first labeled with 30-keV Kr<sup>85</sup> and is then anodized to 50V as in Fig. 2. During the anodizing about 30 ± 10% of the activity is lost from colored films and about 90 ± 6% is lost from white films. Such losses can be expressed in terms of Sn dissolution provided the integral depth distribution of the 30-keV Kr is known. The relevant relation is

$$C^{\text{int.}} \approx \frac{1}{2} \operatorname{erfc} \left[ \frac{x - \langle x \rangle}{2^{1/2} \Delta x} \right] \quad [2]$$

where  $\langle x \rangle$  is the mean projected ion range [10.1 μg/cm<sup>2</sup> as for CdTe (34)] and  $\Delta x$  is the mean projected ion straggling [5.8 μg/cm<sup>2</sup> (34)]. This relation is shown graphically in Fig. 9, from which we conclude that the amount of Sn dissolving is 7-21 μg/cm<sup>2</sup>. Such an amount is small compared with the 350 μg/cm<sup>2</sup> of Sn contained in a 5000Å film and one again concludes that the low efficiencies are due mainly to electronic conduction.<sup>1</sup>

### Discussion

**Reactive sputtering.**—The preparation of SnO<sub>2</sub> by reactive sputtering has a long precedent in the literature and we have little to add, at least from the point of view of preparation as an end in itself. The structural characteristics of SnO<sub>2</sub> films have, on the other hand, been largely neglected. Even such a basic concept as the crystallization temperature has not been previously determined in a satisfactory way. The work has in all cases applied to supported films (where nucleation problems enter) and the temperature was normally given as a limit [e.g., >280°C (9), <400°C (13), <500°C (8)]. The present work suggests that the crystallization temperature depends on the nucleation conditions as governed by the substrate, varying from <200°C for crystalline SnO<sub>2</sub> substrates, to 250°-300°C

<sup>1</sup> Equation [2] is strictly valid only if channeling is minimal. Nothing is known about channeling in Sn, and the estimated dissolution loss of 7-21 μg/cm<sup>2</sup> should therefore be regarded as a lower limit.

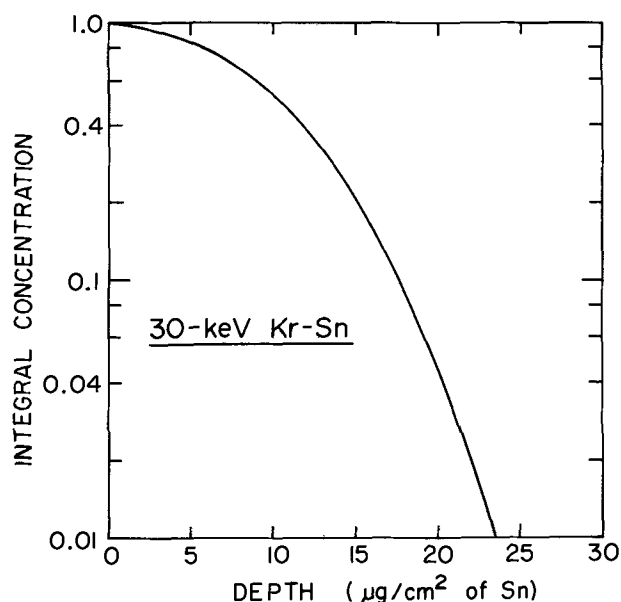


Fig. 9. Integral depth distribution of 30-keV Kr in Sn according to Eq. [2]. The range parameters  $\langle x \rangle$  and  $\Delta x$  in Eq. [2] were assigned values as for CdTe (34), which has a mean mass similar to that of Sn.

for KCl substrates, to 400°-450°C for Ta substrates, to 475°-550°C for unsupported films.

As far as agreement with other work on SnO<sub>2</sub> is concerned, the range 250°-450°C for crystallization on KCl or Ta substrates is compatible with virtually all previous work (8-10, 13, 15, 16) except that of Hecq and Portier (17) and of Yamanaka and Oohashi (18). The former authors obtained crystalline SnO<sub>2</sub> films at 90°C for sufficiently large anode-cathode separations. The argument was made that the density of nucleation sites should be low (leading to a crystalline film) for low sputtered-particle energies such as would result with large anode-cathode separations. A similar effect may have occurred also with Ref. (18), as the product (pressure) × (separation) was here as large as with Ref. (17).

By way of comparison with substances other than SnO<sub>2</sub>, we would first of all point out that certain other amorphous oxides also show a substrate effect. They include the following examples:

oxide	Al <sub>2</sub> O <sub>3</sub> (35)	SiO <sub>2</sub> (36, 37)	Nb <sub>2</sub> O <sub>5</sub> (38)	Ta <sub>2</sub> O <sub>5</sub> (38)
cryst. temp. in contact with metal (°C)	500	700	475	550
cryst. temp. when unsupported (°C)	680	>1300	590	715

SiO<sub>2</sub>, GeO<sub>2</sub>, and SnO<sub>2</sub> constitute a homologous series and here the main feature to emphasize is that the crystallization temperatures decrease along the series. For example, we have >1300°C for SiO<sub>2</sub> (37) ~630°C for GeO<sub>2</sub> (39), and 475°-550°C for SnO<sub>2</sub> (present work), in all cases for unsupported material.

**Anodizing.**—While SnO<sub>2</sub> is frequently prepared by reactive sputtering, there is as far as we know no precedent for films being formed by high-voltage anodizing except for the instance in which a "thick black crust" was obtained (28). This lack of success is not really surprising when it is remembered that Mo and V, for example, were long regarded as being incapable of supporting high anodizing voltages yet have been recently found to yield uniform, protective films with thicknesses of ~1200Å at 100V. The key lay in choosing an appropriate nonaqueous electrolyte (40-42). The present work makes it clear that, though the process is far from perfect, high-voltage film growth is readily achieved with Sn. The main problem still to overcome is probably that of exploring alternative electrolytes or anodizing cycles until one is found which yields

Table IV. The crystallization products of amorphous oxides

Oxide	Crystallization product	Stability	Ref.
Al <sub>2</sub> O <sub>3</sub>	Gamma	Always metastable	(46)
Nb <sub>2</sub> O <sub>5</sub>	Low temp. form	Always metastable	(47)
Ta <sub>2</sub> O <sub>5</sub>	Low temp. form	Always metastable	(38)
TiO <sub>2</sub>	Anatase	Always metastable	(48)
Bi <sub>2</sub> O <sub>3</sub>	Cubic	Stable above 717°C	(16)
GeO <sub>2</sub>	Hexagonal	Stable above 1033°C	(39)
HfO <sub>2</sub>	Cubic	Stable above ~2700°C	(49)
WO <sub>3</sub>	Orthorhombic	Stable above 330°C	(16)
ZrO <sub>2</sub>	Cubic	Stable above 2285°C	(30)

films which, due either to their structure or to doping, show the expected linearity between thickness and voltage.

Unexpected was the result that anodic SnO<sub>2</sub> is crystalline as formed, for anodic films are nearly invariably amorphous. ZrO<sub>2</sub> appears to be an exception, as it forms in the cubic modification (38), while anodic BeO (43) and TiO<sub>2</sub> (44) are sometimes crystalline. Perhaps there is precedent in the work of Lakhiani and Shreir (45), where normally amorphous anodic Nb<sub>2</sub>O<sub>5</sub> was shown to crystallize at high voltages due to voltage breakdown. Alternatively, it is a simple temperature effect governed by the current (43, 44).

The low anodizing efficiency found here for Sn (4-21%) finds a parallel in the behavior of Si and Ge. Thus the value 2% has been quoted for Si (26) and 11-17% for Ge (27). The low efficiency with Sn was attributed to electronic conduction, a result which is not surprising in view of the numerous examples where the carrier densities in SnO<sub>2</sub> films have been found to be nearly as high as in metals. Groth *et al.* (1), for example, found carrier densities of  $1-6 \times 10^{20}$  electrons/cm<sup>3</sup>.

*Polymorphism in SnO<sub>2</sub>.*—A consistent result in this work has been that amorphous SnO<sub>2</sub>, formed by either reactive or ion-beam sputtering, crystallized to cassiterite. Likewise SnO<sub>2</sub> films formed anodically were cassiterite as formed. In view of the fact that other amorphous oxides often yield metastable or high-temperature phases when crystallized (Table IV), a possible conclusion is that SnO<sub>2</sub> lacks metastable or high-temperature phases. Whether or not this conclusion is warranted will be shown in part when the phase relations of SnO<sub>2</sub> in the still unstudied region above about 1600°C are determined.

#### Acknowledgments

The authors are grateful to Dr. J. P. Marton (McMaster University) for discussions on the properties of SnO<sub>2</sub> and in particular for having supplied SnO<sub>2</sub> single crystals.

This research was supported by a grant from the Defence Research Board, Ottawa.

Manuscript submitted June 4, 1973; revised manuscript received Aug. 13, 1973.

Any discussion of this paper will appear in a Discussion Section to be published in the December 1974 JOURNAL. All discussions for the December 1974 Discussion Section should be submitted by Aug. 1, 1974.

#### REFERENCES

1. R. Groth, E. Kauer, and P. C. v.d. Linden, *Z. Naturforschung*, **17a**, 789 (1962).
2. H. M. Naguib and R. Kelly, *J. Phys. Chem. Solids*, **33**, 1751 (1972).
3. D. K. Murti and R. Kelly, To be published.
4. J. W. Ward, *Appl. and Ind.*, **16**, 408 (1955).
5. L. Holland and G. Siddal, *Vacuum*, **3**, 375 (1953).
6. Anonymous, *Nature*, **169**, 829 (1952).
7. H. A. Klasens and H. Koelmans, *Solid-State Electron.*, **7**, 701 (1964).
8. K. Ishiguro, T. Sasaki, T. Arai, and I. Imai, *J. Phys. Soc. Japan*, **13**, 296 (1958).
9. F. v.d. Maesen and C. H. M. Witmer, Proc. 7th Intern. Conf. on the Phys. of Semiconductors, p. 1211, Paris (1964).
10. V. Caslavská and R. Roy, *J. Appl. Phys.*, **40**, 3414 (1969).
11. M. Shiojiri, H. Morikawa, and E. Suito, Sixth Intern. Cong. for Electron Microscopy, p. 467, Kyoto (1966).
12. R. Colin, J. Drowart, and G. Verhaegen, *Trans. Faraday Soc.*, **61**, 1364 (1965).
13. W. R. Sinclair and F. G. Peters, *J. Am. Ceram. Soc.*, **46**, 20 (1963).
14. W. R. Sinclair, F. G. Peters, D. W. Stillinger, and S. E. Koonce, *This Journal*, **112**, 1096 (1965).
15. V. M. Vainshtein, *Simp. Protessy Sin. Rosta Krist. Plenok Poluprov. Mater., Tezisy Dokl.*, p. 296, Novosibirsk (1965).
16. M. L. Lieberman and R. C. Medrud, *This Journal*, **116**, 242 (1969).
17. M. Heq and E. Portier, *Thin Sol. Films*, **9**, 341 (1972).
18. S. Yamanaka and T. Oohashi, *Jap. J. Appl. Phys.*, **8**, 1058 (1969).
19. T. N. Kennedy and J. D. Mackenzie, *J. Non-Cryst. Sol.*, **1**, 326 (1969).
20. R. Kerr and D. J. MacNaughtan, *J. Electrodep. Tech. Soc.*, **12**, 19 (1937).
21. N. A. Hampson and D. Larkin, *This Journal*, **115**, 612 (1968).
22. A. Jeanne and D. Laforgue-Kantzer, *Compt. Rend. Acad. Sci. Paris*, **271C**, 1502 (1970).
23. R. Kerr, *J. Soc. Chem. Ind.*, **57**, 405 (1938).
24. A. M. Shams el Din and F. M. Abd el Wahab, *Electrochim. Acta.*, **9**, 883 (1964).
25. M. Pugh, L. M. Warner, and D. R. Gabe, *Corrosion Sci.*, **7**, 807 (1967).
26. M. A. Wilkins, Harwell (U.K.) Report AERE-R5875 (1968).
27. S. Zwerdling and S. Sheff, *This Journal*, **107**, 338 (1960).
28. G. Bianchi, *Chim. Ind.*, **29**, 295 (1947).
29. E. Giani and R. Kelly, To be published; see also E. Giani, M.Sc. Thesis, McMaster University (1971).
30. H. M. Naguib and R. Kelly, *J. Nucl. Mater.*, **35**, 293 (1970).
31. B. W. Farmery and M. W. Thompson, *Phil. Mag.*, **18**, 415 (1968).
32. L. Young, *Proc. Roy. Soc.*, **A244**, 41 (1958).
33. R. E. Pawel, *Rev. Sci. Instr.*, **35**, 1066 (1964).
34. W. S. Johnson and J. F. Gibbons, "Projected Range Statistics in Semiconductors," Stanford University Bookstore, Stanford, Calif. (1969).
35. G. Hasz, *Optik*, **1**, 134 (1946).
36. H. Matzke, *Phys. Status Solidi.*, **18**, 285 (1966).
37. F. W. Ainger, *J. Mater. Sci.*, **1**, 1 (1966).
38. P. H. G. Draper and J. Harvey, *Acta Met.*, **11**, 873 (1963).
39. J. Drowart, F. Degrève, G. Verhaegen, and R. Colin, *Trans. Faraday Soc.*, **61**, 1072 (1965).
40. M. R. Arora and R. Kelly, *This Journal*, **119**, 270 (1972).
41. R. G. Keil and R. E. Salomon, *ibid.*, **115**, 628 (1968).
42. M. R. Arora and R. Kelly, *ibid.*, **120**, 128 (1973).
43. M. L. Levin, *Trans. Faraday Soc.*, **54**, 935 (1958).
44. D. G. Brandon, J. Zahavi, A. Aladjem, and J. Yahalom, *J. Vacuum Sci. Technol.*, **6**, 783 (1969).
45. D. M. Lakhiani and L. L. Shreir, *Nature*, **188**, 49 (1960).
46. R. G. Frieser, *This Journal*, **113**, 357 (1966).
47. F. Holtzberg, A. Reisman, M. Berry, and M. Berkenblit, *J. Am. Chem. Soc.*, **79**, 2039 (1957).
48. M. Shiojiri, *J. Phys. Soc. Japan*, **21**, 335 (1966).
49. I. A. El Shanshoury, V. A. Rudenko, and J. A. Ibrahim, *J. Am. Ceram. Soc.*, **53**, 264 (1970).

# The Relation Between Environmental pH, Porosity, and the Impedance of Anodic Aluminum Oxide Films

T. A. Libsch and O. F. Devereux\*

Department of Metallurgy, Institute of Materials Science, University of Connecticut, Storrs, Connecticut 06268

## ABSTRACT

The capacitance and resistance of an electrochemical cell have been measured to determine the effect of the pH (3.6-8.2) of aqueous potassium nitrate and perchlorate electrolytes upon 360Å thick anodic oxide films formed on polycrystalline 99.99% aluminum. While the film has been found to be quite stable upon exposure to electrolytes having pH values in the range 5.1-8.2, frequency dependent capacitance increases and resistance decreases have been observed during a 3000 min test period for cells having electrolytes of pH 3.6. The data for electrochemical cells having 1.0M KNO<sub>3</sub> electrolytes of pH 3.6 have been corrected for the presence of the electrolyte by two electrical analogs. This corrected aluminum cell data represent average anodic oxide film properties. The authors have interpreted the large capacitance increases and resistance decreases of electrochemical cells having an electrolyte of pH 3.6 in terms of the growth of pores in the anodic oxide film. The data for cells having 1.0M KNO<sub>3</sub> electrolytes of pH 3.6 have been quantitatively analyzed as a function of exposure time and frequency by modeling the electrochemical cell as a parallel combination of two parallel RC circuits in series with a third parallel RC circuit. Transmission electron microscopy of films before and after testing supports the interpretation of the data in terms of a porous film structure. Some comments are forwarded on the defect structure of the film before and after environmental exposure.

Oxide surface films, formed in air at elevated temperatures, or formed anodically, provide substrate metals with corrosion protection, but concurrently affect substrate mechanical properties (1, 2). Several investigators (3-7) have proposed the existence of these surface films and their interaction with the environment to play a significant role in the engineering problems of stress corrosion cracking, corrosion fatigue, and creep rupture. Forty and Humble (8) have proposed a repeated film formation-film rupture mechanism to be operative in the stress corrosion cracking of  $\alpha$ -brass in ammoniacal solutions. A similar mechanism has been proposed by McEvily (9) for the elevated temperature creep rupture behavior of Cu, Cu-7Al, and Al-Zn-Mg alloys. A more thorough knowledge of environment-surface film interactions is a necessary prerequisite to an understanding of the elusive mechanisms which control these engineering problems.

Previous investigations have revealed that liquid environments are capable of modifying the defect structure of and/or deteriorating anodic oxide films formed on the valve metals. Vermilyea (10-12) has determined that in acidic electrolytes the capacitance of thin niobium, tantalum, tungsten, titanium, and antimony anodic oxide films is a marked function of the electrical potential difference applied across the film during measurement. Vermilyea proposed that these capacitance changes were the result of changes in a space charge which was created by the evaporation of protons at the oxide/electrolyte interface into the oxide film. Anodic aluminum, beryllium, and zirconium oxide films did not exhibit these capacitance changes, presumably due to lower proton mobility. Pryor and co-workers (13-17) have reported the effects of aqueous environments of sodium chloride, sodium fluoride, and sodium chromate on the dielectric properties of anodic aluminum oxide films. These studies suggest that fluoride, chloride, and hydroxyl ions from aqueous electrolytes can penetrate anodic aluminum oxide films by exchange with oxide ions in the film lattice. Pryor and co-workers determined that chromate solutions in the pH range 7-9 uniformly thin the anodic oxide to a passive layer thickness of 20-25Å without modifying the film during the

dissolution process. This result enabled these investigators to examine the ionic and electronic resistivity as a function of film thickness, and also the changes in the resistivity-thickness profiles resulting from pre-exposure of films to other aqueous electrolytes. Richardson *et al.* (18-20) have examined the effect of near neutral chromate, dichromate, chloride, bromide, iodide, fluoride, and sulfate aqueous electrolytes on the dielectric characteristics of anodic and air-formed aluminum oxide films. These investigators found that chromate and dichromate electrolytes heal flaws originally present in air-formed films and thin anodic oxide films to a passive thickness of 25Å. Bromide, chloride, and iodide electrolytes were purported to pit the substrate metal at the base of film flaws. Little attack occurred in sulfate solution, whereas in fluoride the film was rapidly removed and replaced by a complex oxyfluoride.

The aforementioned investigations have been primarily oriented toward the effects which electrolytes of near neutral pH have upon uniform anodic aluminum oxide films. The purpose of the current investigation was to determine the effect of the pH of aqueous electrolytes upon these films (21). Potassium nitrate and potassium perchlorate electrolytes were chosen as environments because potassium, nitrate, and perchlorate ions had previously been reported to be indifferent to the surface of alumina (22). Impedance measurements were made on electrochemical cells having anodized aluminum electrodes as a function of exposure time over the frequency range  $5 \times 10^2$  to  $5 \times 10^4$  Hz. A frequency range was utilized since resulting frequency dispersions are useful in analyzing both modifications in the film defect structure and nonuniform film deterioration (14, 15). Platinum specimens were utilized as dummy specimens in order to determine the impedance attributable to the electrolytic double layer, solution, and counterelectrode. The platinum data were subsequently used to correct measurements made on cells having anodized aluminum specimens.

## Experimental Procedure

Small cylindrical specimens of 99.99% aluminum and 99.5% platinum were machined and mechanically polished. The surface of each aluminum specimen was stress-relieved by heat-treatment for a short period

\* Electrochemical Society Active Member.  
Key words: aluminum, anodic oxidation, impedance, porosity.



at 345°C in argon (23) and subsequently chemically polished using the sodium hydroxide-nitric acid method (24). Electropolishing was avoided as a means of surface preparation due to reports by previous investigators that films formed on electropolished surfaces yield erratic impedance data (18, 20). Electrode assembly is illustrated in Fig. 1.

Anodizing and test electrolytes were prepared with double distilled water and reagent grade chemicals. Several electrolytes, e.g., boric acid (13) and tartaric acid (25), have been used by previous investigators to form barrier layer anodic oxide films on aluminum. The anodizing electrolyte employed in this investigation was that used by McMullen and Pryor (13) and Richardson and Wood (20), i.e., an aqueous 3.0 weight per cent (w/o) solution of ammonium tartrate adjusted to pH 7.0 by the addition of several drops of dilute ammonium hydroxide. Three test electrolytes were prepared. The pH of 0.1M and 1.0M potassium nitrate solutions was adjusted to values of 3.6, 5.1, 6.6, or 8.2 by the addition of several drops of dilute nitric acid or potassium hydroxide. The pH of the 0.1M potassium perchlorate solution was adjusted to the same pH values by the addition of several drops of dilute perchloric acid or potassium hydroxide. Test electrolytes were stored under a nitrogen atmosphere to prevent carbon dioxide absorption and resulting pH uncertainty (22).

Anodizing was performed in the cell of Fig. 1, which was maintained at  $30.0^\circ \pm 0.3^\circ\text{C}$  by a constant temperature water bath. The potential between the aluminum specimen and platinum grid counterelectrode was raised to 30V in such a manner that the current surge did not exceed  $1\text{ mA/cm}^2$ . The importance of maintaining a current limit in the initial stages of a constant voltage anodizing procedure has not been well established. Many investigators do not report a current limit, and the current limits that have been reported vary widely, e.g., McMullen and Pryor (13) used  $5\text{ mA/cm}^2$ , while Smith (26) used  $20\text{ mA/cm}^2$ .

The 30V potential was maintained for 45 min during which time the current normally decayed to less than  $30\text{ }\mu\text{A/cm}^2$ . Specimens having leakage currents in excess of this value were discarded. McMullen and Pryor (13) have used  $20\text{ }\mu\text{A/cm}^2$  as an upper limit of leakage current for acceptable anodized specimens. This value, however, applies to 99.995% aluminum substrates rather than 99.99% as used in this investigation. Anodization constants for barrier layer anodic aluminum oxide films vary by several A/V depending primarily on the anodizing electrolyte utilized. Utilizing the anodization constant of 12.0 A/V determined by McMullen and Pryor (13) for a 3.0 w/o ammonium tartrate electrolyte of pH 7.0, the anodization procedure formed a 360Å thick barrier layer anodic aluminum oxide film on the cylindrical aluminum surface. While a film formed in this manner is normally regarded as uniform, several investigators (27, 28) have suggested that a slight tendency exists toward a cellular structure and porosity.

Testing was also performed in the cell of Fig. 1 maintained at a constant temperature of  $30.0^\circ\text{C}$ . The dielectric properties of test cells having anodized aluminum or platinum electrodes were measured with a General Radio capacitance measuring assembly consisting of a Type 1310-B oscillator, a Type 1615-A capacitance bridge, a Type 1232-A null detector, a Type 1419-B decade capacitor, and a Type 1434-QC decade resistor. A 2 mV peak to peak signal was applied to the test cell in all cases. Utilizing the test electrolytes of different pH values, the dielectric properties of test cells having anodized aluminum or platinum electrodes were measured as a function of applied frequency ( $\frac{1}{2}$ , 1, 5, 10, 20, 50 kHz) and test time (0-4000 min). The terms aluminum cell and platinum cell will be used for convenience in subsequent sections to designate a test cell having an anodized aluminum specimen or a platinum specimen, respectively.

## Results

**Aluminum cell data.**—Negligibly small capacitance increases and resistance decreases were recorded during the 3000 min test period for aluminum cells having electrolytes of pH 5.1, 6.6, or 8.2. This result suggests that little film-environment interaction occurs under these conditions. Large capacitance increases and resistance decreases were recorded during the same test period for aluminum cells having electrolytes of pH 3.6. Time related capacitance increases and resistance decreases indicate some type of film-environment interaction, i.e., uniform film thinning, non-uniform film deterioration, and/or a modification of the film defect structure.

The capacitance and resistance values for all the aluminum cells are presented in Fig. 2 and 3, respectively. In Fig. 3, the resistance has been plotted as resistance times frequency for graphical convenience. Several general comments apply to both figures. Each figure has been constructed from thirty-six average curves—each average curve being characterized by an electrolyte concentration and composition (1.0M  $\text{KNO}_3$ , 0.1M  $\text{KNO}_3$ , or 0.1M  $\text{KClO}_4$ ), a pH value (3.6, 5.1, 6.6, or 8.2), and a frequency value ( $\frac{1}{2}$ , 10, or 50 kHz). Each average curve was determined from three specimens, except for the average curves determined from cells having 1.0M  $\text{KNO}_3$  electrolytes of pH 8.2, in which case the average was ascertained from two specimens. In both figures a number of the average curves lie in close proximity; in such cases the curves were condensed into bands. The scatter brackets included represent data extremes except for the scatter brackets on the two curves labeled 0.1, 1.0M  $\text{KNO}_3$ , 0.1M  $\text{KClO}_4$ ; pH (5.1, 6.6, 8.2) and 1.0M  $\text{KNO}_3$ ; pH (5.1, 6.6, 8.2) in Fig. 3. In these two cases the scatter brackets illustrate the extremes of average curves.

**Platinum cell data.**—Capacitance and resistance values were measured for platinum cells having 1.0M

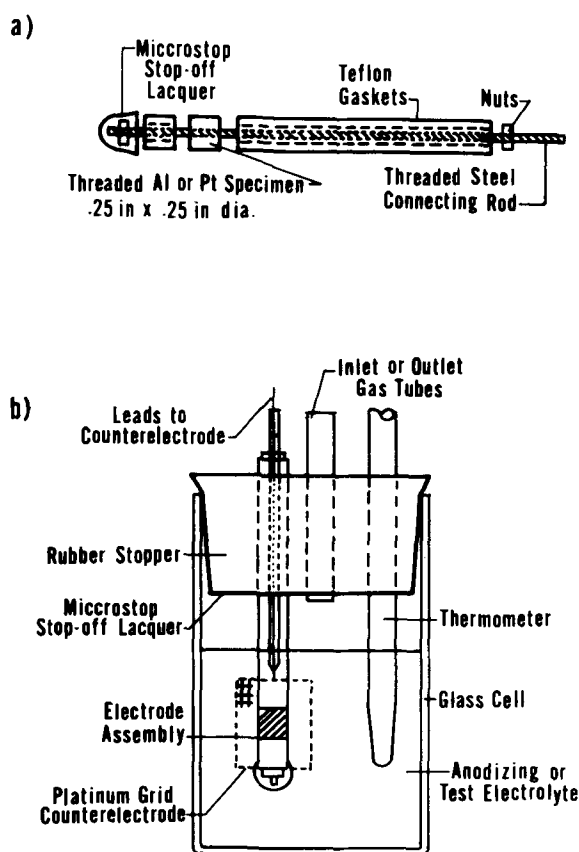


Fig. 1. (a) Electrode assembly diagram (expanded view). (b) Electrochemical cell used for anodizing and testing.

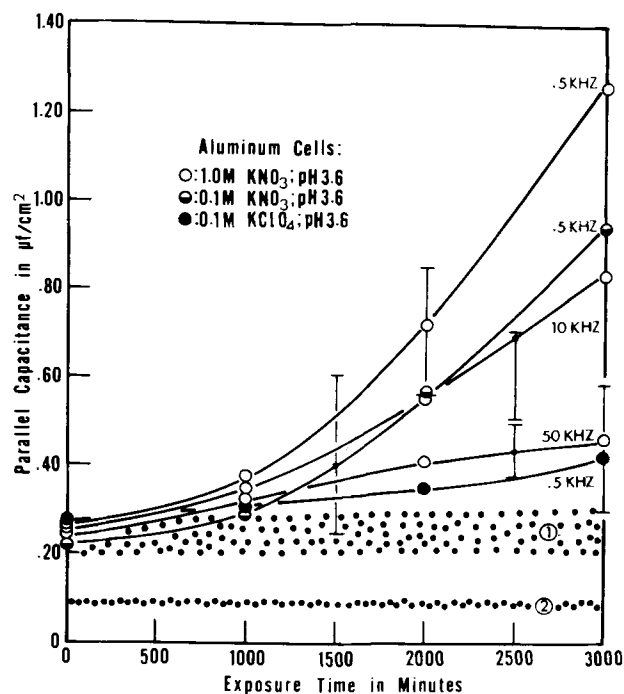


Fig. 2. Average capacitance-time relationships at  $\frac{1}{2}$ , 10, and 50 kHz for aluminum cells having 1.0M  $\text{KNO}_3$ , 0.1M  $\text{KNO}_3$ , and 0.1M  $\text{KClO}_4$  electrolytes of pH 3.6, 5.1, 6.6, and 8.2. Band 1 contains the averages: 1.0M  $\text{KNO}_3$ , pH (5.1, 6.6, 8.2), ( $\frac{1}{2}$ , 10, 50 kHz); 0.1M  $\text{KNO}_3$ , 0.1M  $\text{KClO}_4$ , pH 3.6, 10 kHz; 0.1M  $\text{KNO}_3$ , 0.1M  $\text{KClO}_4$ , pH (5.1, 6.6, 8.2), ( $\frac{1}{2}$ , 10 kHz). Band 2 contains the averages: 0.1M  $\text{KNO}_3$ , 0.1M  $\text{KClO}_4$ , pH (3.6, 5.1, 6.6, 8.2), 50 kHz. Error bars typical.

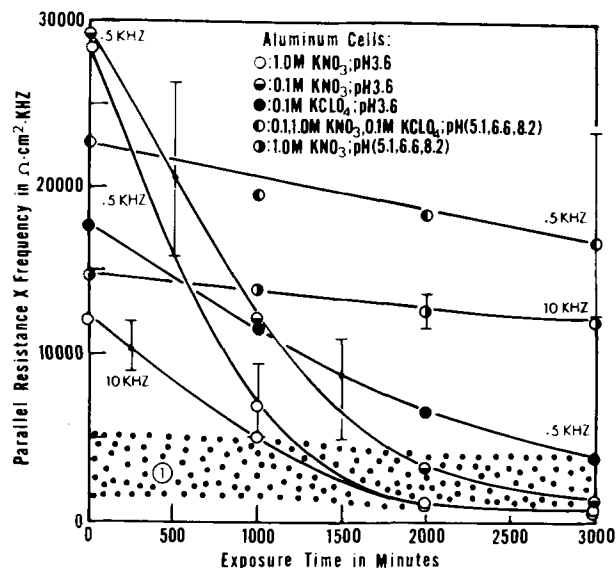


Fig. 3. Average resistance-time relationships at  $\frac{1}{2}$ , 10, and 50 kHz for aluminum cells having 1.0M  $\text{KNO}_3$ , 0.1M  $\text{KNO}_3$ , and 0.1M  $\text{KClO}_4$  electrolytes of pH 3.6, 5.1, 6.6, and 8.2. Band 1 contains the averages: 1.0M  $\text{KNO}_3$ , pH (3.6, 5.1, 6.6, 8.2), 50 kHz; 0.1M  $\text{KNO}_3$ , 0.1M  $\text{KClO}_4$ , pH (3.6, 5.1, 6.6, 8.2), (10, 50 kHz). Error bars typical.

$\text{KNO}_3$  electrolytes as a function of electrolyte pH, exposure time, and applied frequency. No definitive effect of electrolyte pH was observed. At constant frequency, the dielectric properties of platinum cells were observed to stabilize after a short induction period. Frequency effects were pronounced. Table I lists the average steady-state values (4000 min) of parallel capacitance ( $C_{p2}$ ), parallel resistance ( $R_{p2}$ ), and series resistance ( $R_{s2}$ ) on a unit area basis for three platinum cells having 1.0M  $\text{KNO}_3$  electrolytes of pH 3.6 as a function of the applied frequency.  $R_{s2}$  values were calculated from  $C_{p2}$  and  $R_{p2}$  values from the equation

Table I. Values of parameters used in Analog 1, Analog 2, and Analog 3

$\omega$ (rad/sec)	$C_{p2}^*$ ( $\mu\text{f}/\text{cm}^2$ )	$R_{p2}^*$ (ohm $\cdot$ $\text{cm}^2$ )	$R_{s2}^*$ (ohm $\cdot$ $\text{cm}^2$ )	$\rho_{s2}^*$ (ohm $\cdot$ $\text{cm}$ )
$3.14 \times 10^3$	11.1	114	6.78	$5.17 \times 10^6$
$6.28 \times 10^3$	9.88	49.9	4.70	$2.34 \times 10^6$
$3.14 \times 10^4$	5.22	7.00	3.03	$2.81 \times 10^5$
$6.28 \times 10^4$	2.75	3.99	2.71	$1.07 \times 10^5$
$1.26 \times 10^5$	0.978	2.88	2.57	$8.02 \times 10^4$
$3.14 \times 10^5$	0.042	2.44	2.44	$3.75 \times 10^4$

$d_s$  (original film thickness):  $3.60 \times 10^{-8}$  m (360Å)  
 $d_i$  (film thickness at pore base):  $3.94 \times 10^{-9}$  m (40Å)  
 $\kappa$  (film dielectric constant): 10  
 $\epsilon_0$  (permittivity constant):  $8.85 \times 10^{-12}$  f/m  
 $A_s$  (total film area):  $8.09 \times 10^{-5}$  m<sup>2</sup>  
 $A_o$  (rate constant for the growth of the porous area of the film):  
 $1.40 \times 10^{-15}$  m<sup>2</sup>/sec<sup>2</sup>

\* Definitions can be found in the list of symbols.

$$R_{s2} = R_{p2} / (1 + \omega^2 C_{p2}^2 R_{p2}^2)$$

These values will be subsequently used to correct and interpret the data of aluminum cells having 1.0M  $\text{KNO}_3$  electrolytes of pH 3.6.

An unsuccessful attempt was made to determine the capacitance and resistance of platinum cells having 0.1M  $\text{KNO}_3$  and 0.1M  $\text{KClO}_4$  electrolytes. Proper bridge balances could not be made for these cells at frequencies greater than 10 kHz, presumably due to the fact that the bridge was designed to measure capacitance with resistance as a minor component.

*Correction procedures for aluminum cell data.*—The authors have corrected the aluminum cell capacitance and resistance because it was necessary to determine the series film resistivity as a function of frequency to explain the capacitance increases and resistance decreases of aluminum cells having 1.0M  $\text{KNO}_3$  electrolytes of pH 3.6. Also, regardless of the type of film-environment interaction occurring, the corrected aluminum cell capacitance and resistance values would represent average data for the film alone.

Two analogs were investigated for correcting the aluminum cell data. These analogs, their equivalent circuits, and the notation utilized are illustrated in Fig. 4 under the headings Analog 1 and Analog 2. A complete list of parameters and definitions is provided at the end of the paper. Analog 1 models the aluminum cell as a resistor in series with a parallel RC circuit—the resistor representing the electrolyte and the RC circuit representing the anodic oxide film. Analog 2 is similar but somewhat more sophisticated in that the electrolyte has been modeled as a parallel RC circuit instead of a simple resistance. Both Heine and Pryor (15) and Richardson *et al.* (18), have suggested Analog 2 to represent an aluminum cell of the type utilized in this investigation.

The experimental data recorded for the aluminum cells represent coupled film-electrolyte properties. In order to employ Analogs 1 and 2 the electrolyte properties must be determined in some manner. Richardson *et al.* (18) suggest the three following methods for determining electrolyte properties: (i) measurement with a dummy electrode of low impedance, (ii) calculation from the cell geometry and specific conductivity of the electrolyte, and (iii) extrapolation of a plot of series resistance *vs.* reciprocal frequency to infinite frequency. Both Heine and Pryor (15) and Richardson *et al.* (18) chose to determine electrolyte properties by using a dummy platinum electrode. This technique has also been utilized in this investigation.

The corrected aluminum cell data derived from Analog 1 can be determined from the equations

$$C_{p1} = C_{s5} / [1 + \omega^2 (R_{s5} - R_{s2})^2 C_{s5}^2]$$

$$R_{p1} = 1 / [\omega^2 (R_{s5} - R_{s2}) C_{s5} C_{p1}]$$

where  $C_p$ ,  $C_s$ ,  $R_p$ , and  $R_s$  represent the parallel ca-



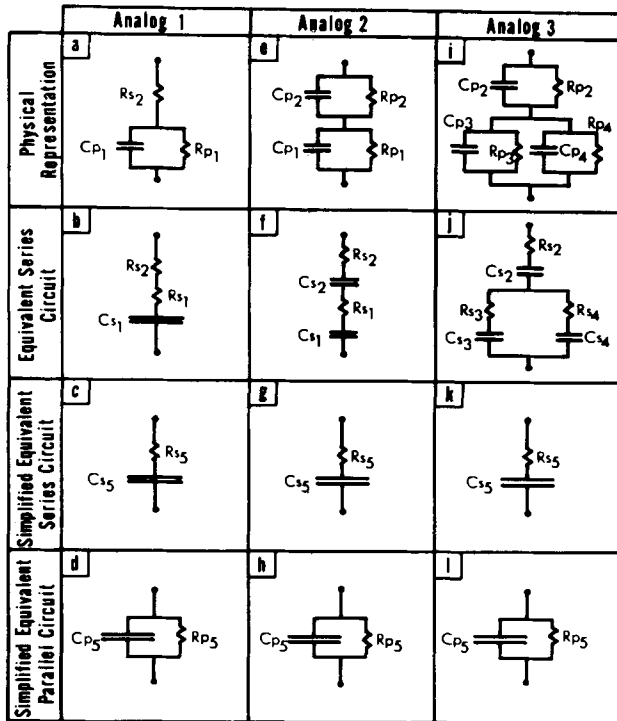


Fig. 4. Electrical analogs, equivalent circuits, and notation. Analogs 1 and 2 have been used to correct the measured aluminum cell data for the presence of electrolyte; Analog 3 has been used to interpret the large capacitance and resistance variations of aluminum cells having electrolytes of pH 3.6.

capacitance, series capacitance, parallel resistance, and series resistance, respectively, and the subscripts 1, 5, and 2 refer these quantities to a corrected aluminum cell, a measured aluminum cell, and a platinum cell, respectively. The corrected aluminum cell data derived from Analog 2 can be determined from the equations

$$Cp_1 = Cs_2Cs_5 / \{ (Cs_2 - Cs_5) \{ 1 + [ (Cs_2D_5 - Cs_5D_2) / (Cs_2 - Cs_5) ]^2 \} \}$$

$$Rp_1 = (Cs_2 - Cs_5) / [\omega Cp_1 (Cs_2D_5 - Cs_5D_2)]$$

where *D* represents the dissipation factor and the remainder of the notation is identical to that described above. Calculations for both Analog 1 and Analog 2 were performed on a unit area basis in the MKS system of units.

As mentioned previously, data could not be obtained for platinum cells having 0.1M KNO<sub>3</sub> or 0.1M KClO<sub>4</sub> electrolytes. The correction procedure has consequently been confined to aluminum cells having 1.0M KNO<sub>3</sub> electrolytes using the platinum cell data listed in Table I. Figures 5 and 6 show the corrected aluminum cell data derived from both Analogs 1 and 2 for aluminum cells having 1.0M KNO<sub>3</sub> electrolytes of pH 3.6. Both analogs provide the same general corrections listed below. The difference between the corrected and measured aluminum cell capacitance is observed to increase at constant frequency with increasing exposure time, and to increase at constant exposure time with increasing frequency. The difference between the corrected and measured aluminum cell resistance is observed to increase at constant frequency with decreasing exposure time, and to increase at constant exposure time with increasing frequency. The resistance curves for Analogs 1 and 2 are virtually identical and have not been differentiated in Fig. 6.

**Discussion**

*Analog 3.*—The interpretation given to the large capacitance increases and resistance decreases observed for aluminum cells having electrolytes of pH 3.6 (Fig.

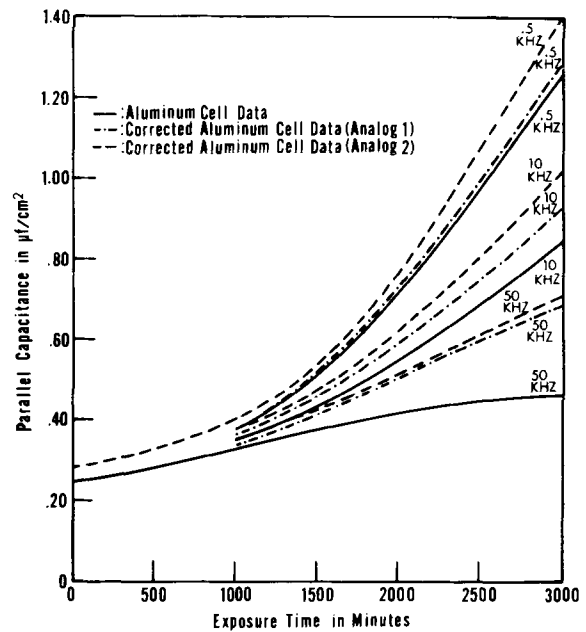


Fig. 5. The average measured and corrected capacitance of aluminum cells having 1.0M KNO<sub>3</sub> electrolytes of pH 3.6 as a function of exposure time and frequency.

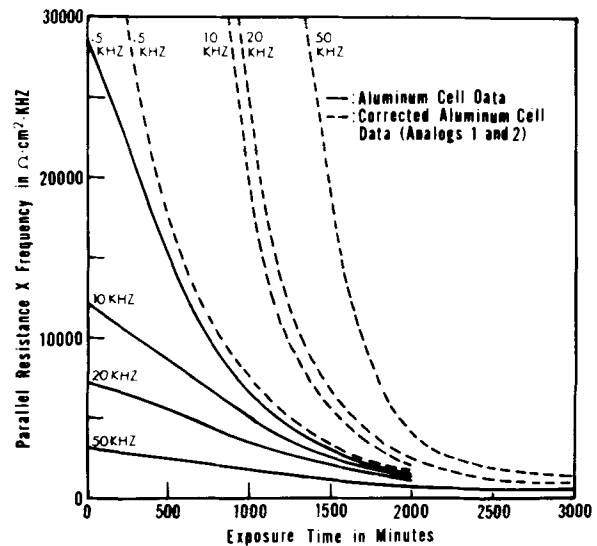


Fig. 6. The average measured and corrected resistance of aluminum cells having 1.0M KNO<sub>3</sub> electrolytes of pH 3.6 as a function of exposure time and frequency.

2 and 3) is based upon the growth of pores in the oxide film. A model has been developed in such a manner as to furnish the average capacitance and resistance of the aluminum cell as a function of exposure time and frequency. Only aluminum cells having 1.0M KNO<sub>3</sub> electrolytes of pH 3.6 have been quantitatively analyzed with Analog 3 because (i) data was unavailable for platinum cells having 0.1M KNO<sub>3</sub> or 0.1M KClO<sub>4</sub> electrolytes, and (ii) little film-environment interaction occurs during the 3000 min test period for aluminum cells having 1.0M KNO<sub>3</sub> electrolytes of pH 5.1, 6.6, or 8.2.

The electrical analog selected to represent the aluminum cell, circuits equivalent to it, and the symbols employed in the analysis are illustrated in Fig. 4 under the heading Analog 3. The physical representation of the aluminum cell is presented in Fig. 4i. The parallel combination of two parallel RC circuits represents the oxide film—one RC circuit represents the region of nonporous film, the other, the pores. The parallel RC circuit in series with the film represents the electro-

lyte. Figure 4j shows the equivalent circuit in terms of series capacitances and resistances. The following notation has been used in Fig. 4j:  $Cs_2, Rs_2$ : series capacitance, series resistance of platinum cell;  $Cs_3, Rs_3$ : series capacitance, series resistance of the nonporous area of the film;  $Cs_4, Rs_4$ : series capacitance, series resistance of the porous area of the film. Figures 4k and 4l show simplified series and parallel RC circuits equivalent to Fig. 4j. The following notation has been used in Fig. 4k:  $Cs_5, Rs_5$ : series capacitance, series resistance of the aluminum cell. Calculations for Analog 3 were performed on the total electrode area ( $A_5$ ) in the MKS system of units, and subsequently transformed to a unit area basis.

$Cs_2$  was determined from the measured parallel capacitance ( $Cp_2$ ) and parallel resistance ( $Rp_2$ ) of the platinum cell (Table I) from the expression

$$Cs_2 = Cp_2 + 1/(\omega^2 Rp_2^2 Cp_2)$$

The calculation of  $Rs_2$  from  $Cp_2$  and  $Rp_2$  has been described previously. Expressions for  $Cs_3, Rs_3, Cs_4,$  and  $Rs_4$  as functions of exposure time ( $t$ ) were formed in the following manner. Immediately subsequent to immersion in the testing electrolyte the film was considered to possess  $n$  cylindrical pores, uniformly distributed, of constant depth, and of zero radii. It was further considered that the radius of each pore ( $r$ ) grew linearly with increasing exposure time, i.e.,  $r = R_0 t$ , where  $R_0$  is a radial growth constant for pores. The porous area of the film ( $A_4$ ) as a function of exposure time is then given by the expression  $A_4 = n\pi R_0^2 t^2 = A_0 t^2$ , where  $A_0$  is the rate constant for the growth of the porous area of the film. The nonporous area of the film ( $A_3$ ) as a function of exposure time is given by the expression  $A_3 = A_5 - A_0 t^2$ , where  $A_5$  represents the total film area. The capacitance and resistance of the nonporous film area ( $Cs_3, Rs_3$ ) and porous film area ( $Cs_4, Rs_4$ ) can be given as functions of exposure time by

$$Cs_3 = \kappa \epsilon_0 (A_5 - A_0 t^2) / d_3$$

$$Rs_3 = \rho_s d_3 / (A_5 - A_0 t^2)$$

$$Cs_4 = \kappa \epsilon_0 A_0 t^2 / d_4$$

$$Rs_4 = \rho_s d_4 / (A_0 t^2)$$

where  $\kappa$  is the dielectric constant,  $\epsilon_0$  the permittivity constant,  $d_3$  the original film thickness,  $\rho_s$  the series resistivity, and  $d_4$  the thickness of the film at the pore base.

An a-c circuit analysis (29, 30) of the analogs in Fig. 4j and 4k yields  $Rs_5$  and  $Cs_5$  to be

$$Rs_5 = s_2 \cos \theta_2 + s_3 s_4 \cos \theta_3 / (s_3 + s_4)$$

$$Cs_5 = 1 / \{ \omega [s_2 \sin \theta_2 + s_3 s_4 \sin \theta_3 / (s_3 + s_4)] \}$$

where

$$s_2 = [Rs_2^2 + 1/(\omega^2 Cs_2^2)]^{1/2}$$

$$s_3 = d_3 (1 + \omega^2 \kappa^2 \epsilon_0^2 \rho_s^2)^{1/2} / [\omega \kappa \epsilon_0 (A_5 - A_0 t^2)]$$

$$s_4 = d_4 (1 + \omega^2 \kappa^2 \epsilon_0^2 \rho_s^2)^{1/2} / (\omega \kappa \epsilon_0 A_0 t^2)$$

$$\theta_2 = \tan^{-1} [1/(\omega Rs_2 Cs_2)]$$

$$\theta_3 = \tan^{-1} [1/(\omega \rho_s \kappa \epsilon_0)]$$

$Cs_5$  and  $Rs_5$  of Fig. 4k have been transformed to the parallel capacitance ( $Cp_5$ ) and parallel resistance ( $Rp_5$ ) of Fig. 4l and put on a unit area basis by the following expressions

$$Cp_5/A_5 = Cs_5 / [A_5 (1 + \omega^2 Rs_5^2 Cs_5^2)]$$

$$Rp_5 A_5 = A_5 (1 + \omega^2 Rs_5^2 Cs_5^2) / (\omega^2 Cs_5^2 Rs_5)$$

Table I lists the values of the parameters used to analyze the average data for aluminum cells having 1.0M  $KNO_3$  electrolytes of pH 3.6 (Fig. 2 and 3). The parameters listed in Table I, where applicable, represent

the average data of three aluminum or platinum cells having 1.0M  $KNO_3$  electrolytes of pH 3.6. The only exception is the series resistivity values which were determined from the corrected aluminum cell data (Analog 2). The series resistivity values were calculated at time zero before the film was subject to nonuniform deterioration.

A computer analysis of Analog 3 was performed in the following manner. First, values for the rate constant for the growth of the porous area of the film ( $A_0$ ) and the pore depth ( $d_3 - d_4$ ) were selected such that the  $\frac{1}{2}$  kHz capacitance-time curve of Analog 3 fit the  $\frac{1}{2}$  kHz measured aluminum cell curve in Fig. 5. An  $A_0$  value of  $1.40 \times 10^{-15} \text{ m}^2/\text{sec}^2$  and a pore depth of 320Å yielded good results. Using these values, the frequency dependence of the capacitance and resistance were generated. Figure 7 illustrates the results of the model compared to the average aluminum cell data. The  $A_0, d_3 - d_4$  pair utilized in Fig. 7 does not appear to be unique, i.e., for any value of  $A_0$  a value of  $d_3 - d_4$  can be located such that the  $\frac{1}{2}$  kHz capacitance-time curve of Analog 3 fits the corresponding aluminum cell curve. However, the value of the rate constant for the growth of the porous area of the film ( $A_0$ ) is bounded in that physically it cannot be much greater than  $1.40 \times 10^{-15} \text{ m}^2/\text{sec}^2$  (corresponding to complete consumption of the area by the pores in 4000 min) and as it decreases the pore depth ( $d_3 - d_4$ ) increases to unrealistic values, i.e., the pores extend nearly to the substrate metal. The frequency dependence remains virtually unchanged for acceptable  $A_0, d_3 - d_4$  pairs.

While it is difficult to distinguish in Fig. 7, at time zero the capacitance and resistance of Analog 3 are slightly less than and greater than, respectively, the corresponding aluminum cell data. A more sophisticated model considering the time dependence of radial pore growth to be  $r = r_0 + R_0 t$ , where  $r_0$  is the initial pore radius, would create somewhat better agreement at time zero while creating a negligible change at greater exposure times.

*Consideration of defects at test initiation.*—Figure 8 portrays the zero time capacitance-pH relationships for 1.0M  $KNO_3$ , 0.1M  $KNO_3$ , and 0.1M  $KClO_4$  aluminum cells at  $\frac{1}{2}$  kHz. Each symbol used in this figure represents the average of the data of three aluminum cells. The symbols have been slightly displaced from pH values of 3.6, 5.1, 6.6, or 8.2 for graphical clarity.

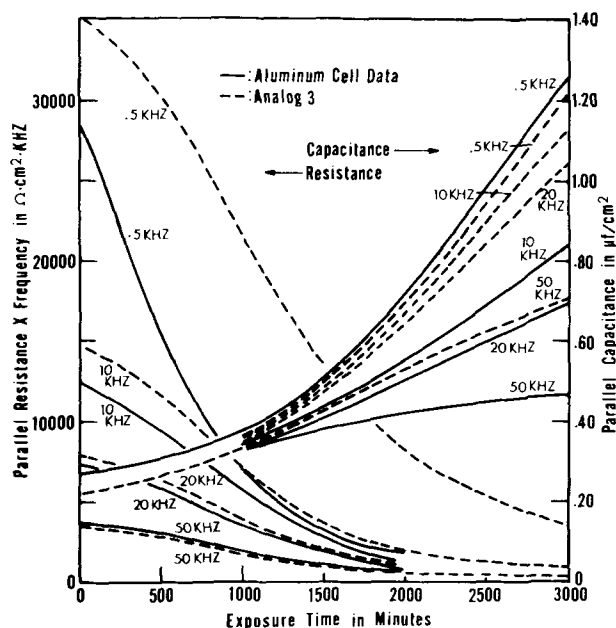


Fig. 7. Capacitance and resistance data calculated from Analog 3 for aluminum cells having 1.0M  $KNO_3$  electrolytes of pH 3.6 as a function of exposure time and frequency. The measured aluminum cell data for these conditions have been added for comparison.

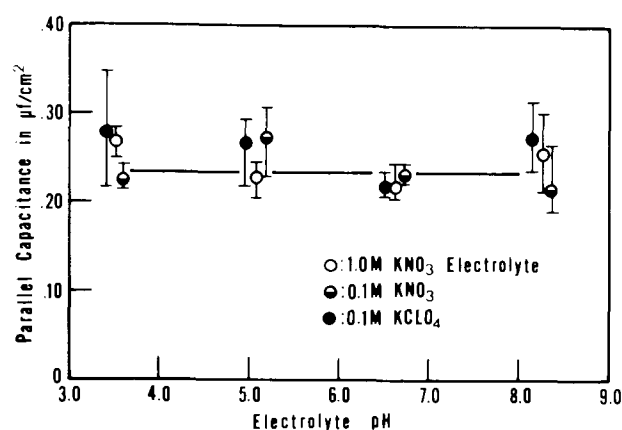


Fig. 8. Capacitance-pH relationship at  $\frac{1}{2}$  kHz and time zero for aluminum cells having 1.0M  $\text{KNO}_3$ , 0.1M  $\text{KNO}_3$ , and 0.1M  $\text{KClO}_4$  electrolytes.

The data illustrated in this figure, while that of the aluminum cell, can be regarded with negligible error as that of the film. The corrected aluminum cell relationships in Fig. 5 substantiate this. The capacitance is observed to be independent of electrolyte pH. The data scatter present in this figure is attributed to slight variations between specimens rather than to an effect of electrolyte pH. This conclusion was drawn by successively immersing one anodized aluminum electrode in electrolytes of the same concentration and composition, but increasing pH. No capacitance variations were observed in these tests.

The charge density at the film/electrolyte interface is known to be a function of the electrolyte pH (31). One would expect the motion of film defects to become limited as the magnitude of the surface charge is increased, thereby altering the measured film capacitance. Apparently even the maximum surface charge at pH 3.6 is insufficient to cause enough defect immobility to be recorded as a capacitance change. The maximum surface charge in an experiment of this type is limited by two phenomena. First, the surface charge is zero at the zero point of charge of the oxide ( $\sim$ pH 8.0) (32) and its magnitude increases when the pH is either increased or decreased. Second, the pH range is practically limited to that studied since electrolytes of very low or very high pH cause rapid film deterioration resulting in capacitance variations not associated with defect mobility. The result of the present investigation, i.e., the capacitance is independent of electrolyte pH, is in accord with the work of Vermilyea (11) cited previously.

**Consideration of defects with increasing exposure time.**—Two aspects of the present investigation strongly suggest that the defect structure of the anodic aluminum oxide film is modified upon continued exposure to electrolytes of pH 3.6. First, it is apparent by comparison of the derived and measured aluminum cell capacitance curves in Fig. 7 that the growth of film pores cannot fully account for the frequency dispersion of capacitance in the experimental data, i.e., at constant exposure time for any frequency change, the change in the proposed model capacitance (Analog 3) is less than the corresponding change in the measured aluminum cell capacitance. The frequency effect of the model would more closely resemble the experimental data if the model were amended to include the continuous absorption of defects, characterized by relatively long relaxation times, from the electrolyte. Film defects can be generally classified as either ionic or electronic in nature (14). Each ionic or electronic defect has a distribution of relaxation times. There is, however, a mean relaxation time for each defect, and this value is many orders of magnitude greater for an ionic defect than for an electronic defect. Pryor and co-

workers (14, 15) have cited slightly less than  $10^{-5}$  sec as an approximate relaxation time for several ionic defects in anodic aluminum oxide films. In order for defects to create any capacitance dispersion in the frequency range under consideration, the defects must necessarily be ionic in nature. As the frequency is increased at a constant exposure time an increasing fraction of the ionic defects will no longer be able to alternate their position in accordance with the applied alternating potential, and their capacitance will thus be lost to the recorded measurement. It is in this manner that absorbed ionic defects can create a capacitance dispersion.

The second aspect of this investigation suggesting a modification of the defect structure is the result of limited reversibility testing of the phenomenon occurring at pH 3.6. Reversibility testing has been conducted by transferring anodized aluminum electrodes which have been tested in electrolytes of pH 3.6 to electrolytes in the pH range 5.1-8.2. This testing indicates that a small fraction of the capacitance increases and resistance decreases are in fact reversible. Continued efforts are being made into the area of reversibility in order to clarify the modifications in defect structure which have occurred. Vermilyea (11, 12), Onoda and deBruyn (33), McMullen and Pryor (13), and Richardson and Wood (20) have previously suggested that ions from an electrolyte may penetrate anodic oxide films resulting in a modification of the film defect structure.

**Microscopic examination of films.**—It was deemed advisable to test the interpretation given to the large capacitance increases and resistance decreases of aluminum cells having electrolytes of pH 3.6 by examining the films microscopically. Freshly anodized and tested films were prepared for transmission electron microscopy by stripping in saturated mercuric chloride solution, rinsing in double distilled water, and mounting on 100 mesh copper screens (34). Mercuric chloride solution is purported to remove the film without deterioration. Transmission electron micrographs (100 kV) of the film before and after a 3000 min test period in Fig. 9a and 9b, respectively. It should be noted in regard to these figures that light areas in transmission electron microscopy of amorphous films generally represent areas of lesser mass thickness (34, 35). In this regard, the freshly anodized film appears to possess a minor degree of surface roughness as suggested by Franklin (28) and others. The tested film (Fig. 9b) appears porous. Three points should be noted in regard to Fig. 9b: (i) the pores are generally cylindrical in shape and many have coalesced after 3000 min exposure time, (ii) the darker halos around the pores are presumed to be the result of electron diffraction from the pore walls, and (iii) the surface roughness of the freshly anodized films is absent. Considering the pore structure of Fig. 9b in relation to Analog 3, one finds the rate constant for radial pore growth ( $R_o$ ) to be  $1.75 \times 10^{-13}$  m/sec and the number of pores per unit area ( $n/A_s$ ) to be  $1.80 \times 10^{10}/\text{cm}^2$ , i.e.,  $A_o = \pi n R_o^2 = 1.40 \times 10^{-15}$  m<sup>2</sup>/sec<sup>2</sup>.

### Summary and Conclusions

The authors have measured the capacitance and resistance of an electrochemical cell to determine the effect of the pH of aqueous potassium nitrate and perchlorate electrolytes upon 360Å thick anodic oxide films formed on polycrystalline 99.99% aluminum. Negligible capacitance and resistance variations were observed over the 3000 min test period for films exposed to aqueous potassium nitrate and perchlorate electrolytes in the pH range 5.1-8.2. The authors conclude that little film-environment interaction occurs under these conditions. Large capacitance increases and resistance decreases were recorded during the same test period for electrochemical cells having elec-

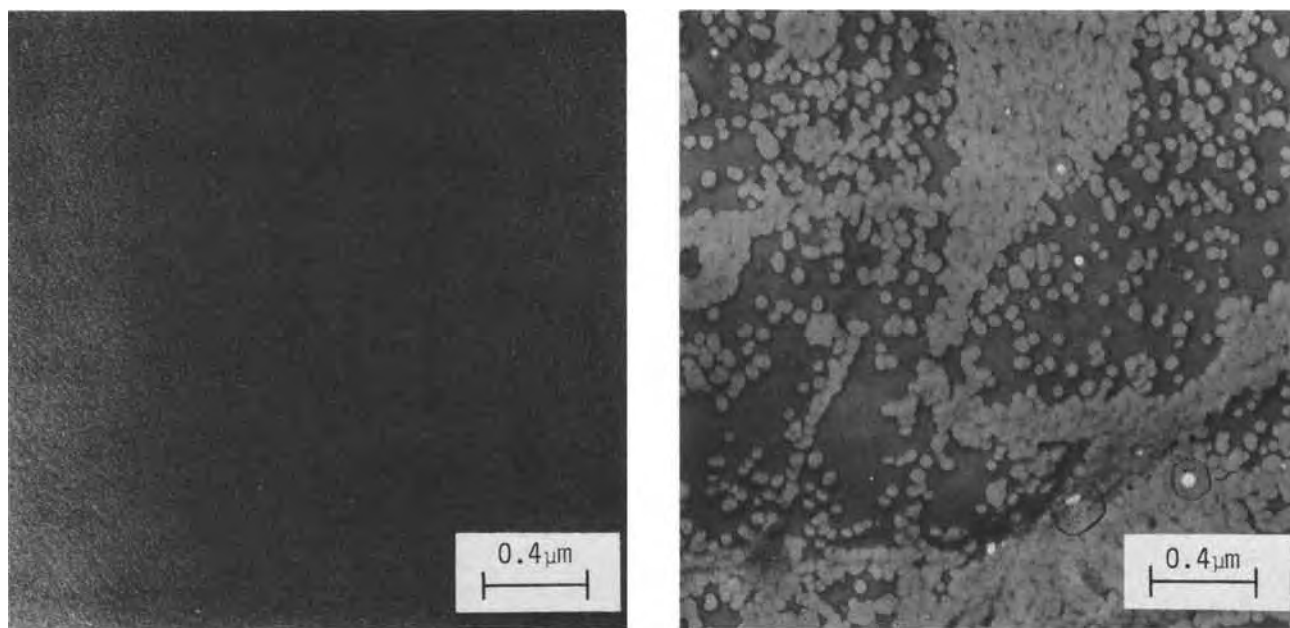


Fig. 9. Transmission electron micrographs of the anodic oxide film: (a, left) subsequent to anodizing, (b, right) subsequent to 3000 min exposure to 1.0M  $\text{KNO}_3$  electrolyte of pH 3.6.

trolytes of pH 3.6. At this pH, the dielectric property changes for cells having potassium nitrate electrolytes were greater than those having potassium perchlorate electrolytes. The data for electrochemical cells having 1.0M  $\text{KNO}_3$  electrolyte of pH 3.6 have been corrected for the presence of the electrolyte by two electrical analogs. The corrected cell data represent average properties for the film alone. Both analogs show the film capacitance and resistance to be greater than the same properties of the electrochemical cell, the amount of difference varying with the exposure time and frequency.

The authors have interpreted the large capacitance increases and resistance decreases of electrochemical cells having electrolytes of pH 3.6 to be due to the growth of pores within the anodic oxide film. The data for cells having 1.0M  $\text{KNO}_3$  electrolytes of pH 3.6 have been quantitatively analyzed as a function of exposure time and frequency by modeling the electrochemical cell as a parallel combination of two parallel RC circuits in series with a third parallel RC circuit. The results of this analog show that the experimental data can be explained by the growth of deep cylindrical pores whose radii are a linear function of exposure time. The interpretation of the data in this manner has been supported by transmission electron microscopy of freshly anodized and tested films. The model and limited reversibility testing indicate that in addition to pore growth, films exposed to electrolytes of pH 3.6 continually absorb defects of ionic nature from the electrolyte.

#### Acknowledgments

The authors thank the anonymous reviewers of this paper for suggesting that a porous film structure could be responsible for the observed capacitance and resistance dispersions. The authors thank the National Science Foundation and the University of Connecticut Research Foundation for financial support. This work was performed under NSF grants GK 20017 and GH 35580.

Manuscript submitted March 13, 1973; revised manuscript received Oct. 5, 1973.

Any discussion of this paper will appear in a Discussion Section to be published in the December 1974 JOURNAL. All discussions for the December 1974 Discussion Section should be submitted by Aug. 1, 1974.

#### LIST OF SYMBOLS (MKS Units)

$A_0$	rate constant for the growth of the porous area of the film, $\text{m}^2/\text{sec}^2$
$A_3$	nonporous area of the film, $\text{m}^2$
$A_4$	porous area of film, $\text{m}^2$
$A_5$	total area of film, $\text{m}^2$
$Cp_1$	corrected parallel capacitance of aluminum cell, f
$Cp_2$	steady-state parallel capacitance of platinum cell (at 4000 min), f
$Cp_3$	parallel capacitance of the nonporous area of the film, f
$Cp_4$	parallel capacitance of the porous area of the film, f
$Cp_5$	measured parallel capacitance of the aluminum cell, f
$Cs_1$	corrected series capacitance of the aluminum cell, f
$Cs_2$	steady-state series capacitance of the platinum cell (at 4000 min), f
$Cs_3$	series capacitance of the nonporous area of the film, f
$Cs_4$	series capacitance of the porous area of the film, f
$Cs_5$	measured series capacitance of aluminum cell, f
$d_3$	original film thickness, m
$d_4$	film thickness at pore base, m
$D_2$	steady-state dissipation factor of platinum cell (at 4000 min), unitless
$D_5$	measured dissipation factor of aluminum cell, unitless
$\epsilon_0$	permittivity constant, f/m
$\kappa$	dielectric constant of anodic aluminum oxide, unitless
$n$	number of film pores, unitless
$\omega$	angular frequency, rad/sec
$\rho_s$	series resistivity determined from corrected aluminum cell data at time zero, $\text{ohm}\cdot\text{m}$
$r_0$	initial pore radius, m
$r$	pore radius, m
$R_0$	rate constant for the growth of the pore radius, m/sec
$Rp_1$	corrected parallel resistance of aluminum cell, ohms
$Rp_2$	steady-state parallel resistance of platinum cell (at 4000 min), ohms
$Rp_3$	parallel resistance of the nonporous area of the film, ohms
$Rp_4$	parallel resistance of the porous area of the film, ohms
$Rp_5$	measured parallel resistance of aluminum cell, ohms

$R_{s1}$	corrected series resistance of aluminum cell, ohms
$R_{s2}$	steady-state series resistance of platinum cell (at 4000 min), ohms
$R_{s3}$	series resistance of nonporous area of the film, ohms
$R_{s4}$	series resistance of porous area of the film, ohms
$R_{s5}$	measured series resistance of the aluminum cell, ohms
$t$	exposure time, sec

## REFERENCES

- J. C. Grosskreutz, *Surface Sci.*, **8**, 173 (1967).
- J. C. Grosskreutz, *This Journal*, **116**, 1232 (1969).
- R. W. Staehle, *Fund. Aspects Stress Corros. Cracking*, NACE, **3** (1969).
- H. H. Uhlig, *Fund. Aspects Stress Corros. Cracking*, NACE, **86** (1969).
- A. J. Forty, *Fund. Aspects Stress Corros. Cracking*, NACE, **64** (1969).
- J. C. Grosskreutz, *Proc. Intern. Conf. Corros. Fatigue*, NACE, **201** (1972).
- B. F. Brown, C. T. Fujii, and E. P. Dahlberg, *This Journal*, **116**, 218 (1969).
- A. J. Forty and P. Humble, *Phil. Mag.*, **8**, 247 (1963).
- A. J. McEvily, Jr., *Fund. Aspects Stress Corros. Cracking*, NACE, **72** (1969).
- D. A. Vermilyea, *Surface Sci.*, **2**, 444 (1964).
- D. A. Vermilyea, *J. Phys. Chem. Solids*, **26**, 133 (1965).
- D. A. Vermilyea, *This Journal*, **115**, 177 (1968).
- J. J. McMullen and M. J. Pryor, "Proc. 1st Intern. Congress on Metallic Corrosion," p. 52, Butterworths, London (1961).
- A. F. Beck, M. A. Heine, D. S. Keir, D. van Rooyen, and M. J. Pryor, *Corros. Sci.*, **2**, 133 (1962).
- M. A. Heine and M. J. Pryor, *This Journal*, **110**, 1205 (1963).
- M. A. Heine, D. S. Keir, and M. J. Pryor, *ibid.*, **112**, 24 (1965).
- M. J. Pryor, *Oxid. Metals*, **3**, 523 (1971).
- J. A. Richardson, G. C. Wood, and A. J. Breen, *Thin Solid Films*, **16**, 81 (1973).
- J. A. Richardson, G. C. Wood, and W. H. Sutton, *ibid.*, **16**, 99 (1973).
- J. A. Richardson and G. C. Wood, *This Journal*, **120**, 193 (1973).
- T. A. Libsch, M.S. Thesis, University of Connecticut (1972).
- J. A. Yopps and D. W. Fuerstenau, *J. Colloid Sci.*, **19**, 61 (1964).
- Metals Handbook, 1, "Properties and Selection of Materials," ASM (1971).
- P. M. Deeley, "Electrolytic Capacitors," Recorder Press, Plainfield, N. J. (1938).
- G. Haas, *J. Opt. Soc. Am.*, **39**, 532 (1949).
- A. W. Smith, *Can. J. Phys.*, **37**, 591 (1959).
- J. E. Lewis and R. C. Plumb, *This Journal*, **105**, 496 (1958).
- R. W. Franklin, *Nature*, **180**, 1470 (1957).
- V. Del Toro, "Principles of Electrical Engineering," Prentice-Hall, Inc., Englewood Cliffs, N. J. (1965).
- General Radio Company, "Instruction Manual for Type 1615-A Capacitance Bridge," G. R. Co. (1963).
- G. A. Parks and P. L. deBruyn, *J. Phys. Chem.*, **66**, 967 (1962).
- R. Fricke and H. Keefer, *Z. Naturforsch.*, **4A**, 76 (1949).
- G. Y. Onoda and P. L. deBruyn, *Surface Sci.*, **4**, 48 (1966).
- F. Keller, M. S. Hunter, and D. L. Robinson, *This Journal*, **100**, 411 (1953).
- J. Zahavi and M. Metzger, *ibid.*, **119**, 1479 (1972).

## Optimized Spectral Power Distributions for Mercury Vapor Lamps

Thomas F. Soules and Mary A. Maier

General Electric Company, Lighting Research and Technical Services Operation, Nela Park, Cleveland, Ohio 44112

### ABSTRACT

Ways of optimizing the spectral power distribution (SPD) of mercury vapor lamps by adding spectral lines and bands to the discharge spectrum are investigated. The performance of simulated SPD's is judged on the basis of luminous efficiency and color rendition. Maximum performance and the highest value for the color rendition index (CRI) is achieved by adding narrow gaussian bands at 490 and 620 nm to the discharge spectrum. This is true for lamps with colors at 6500°, 4000°, and 3000°K on the Planckian locus. However, for the lower color temperatures, 4000° and 3000°K, it is necessary to filter some of the radiation from the mercury lines in the blue. For maximum efficiency without regard to color rendition, a band should be added around 590 nm. The spectral power distributions of phosphors are also investigated. In addition to the CRI, we evaluated the color rendering ability of spectral power distributions by computing changes in hue, chroma, and value of Munsell color samples under different test sources.

During the past few years a number of papers have been written on optimum spectral power distributions (SPD's) for lamps. White light can be composed of two or more spectral wavelengths of continuous distributions. An optimum spectral power distribution is one having maximum lumen efficiency and good or "preferred" color rendition. Ivey (1) showed that two asymmetric gaussian emission bands give the highest luminous efficiency when the two bands have their peaks near 445 and 580-590 nm. For maximum efficiency, these bands have small widths at half-maxi-

mum (WHM). However, this two-component spectral power distribution has poor color rendition. Einhorn and Einhorn (2) showed that for a continuous SPD, restricting the wavelength range from about 440 to 660 nm improves the luminous efficiency without significantly reducing the color rendition. Walter (3) found that good performance, i.e., high luminous efficiency and good color rendition, could be obtained with two-component SPD's consisting of a broad band in the blue-green region and a narrow red band to form white light. Thornton (4) showed that higher luminous efficiency and quite good color rendition

Key words: mercury vapor lamps, color rendition, phosphors.

could be achieved with a SPD consisting of three narrow bands: one in the red at 610 nm, one in the green around 540 nm, and one in the blue near 450 nm. Koedem and Opstelten (5) and Koedem, Opstelten, and Radielovic (6) investigated similar three-line SPD's for high pressure discharge lamps. In these studies the color rendering capability of the light was measured by the color rendition index (CRI) (7).

The purpose of this study is to find the optimum SPD for high pressure mercury vapor (HPMV) lamps. HPMV lamps are used for street lighting and other commercial applications. The SPD's of these lamps are dominated by the atomic mercury lines in the visible region of the spectrum. However, phosphors are used in HPMV lamps to improve color and color rendition. Cadmium and zinc metals and some metal iodides have also been added to the discharge to improve color rendition and luminous efficiency. Hence, it is important to ask, What is the optimum SPD for these lamp types? Ivey (8) found the addition of two phosphor components with emission bands near 445 and 590 nm to yield the highest output for a white HPMV lamp. These same wavelengths were found to give the maximum output for white light in the absence of the visible mercury line spectrum. Wanmaker *et al.* (9) suggested two phosphor components with peaks in the blue-green between 480 and 510 nm and in the red between 610 and 635 nm would increase the CRI of the HPMV lamp to between 60 and 70. In our study, both the luminous efficiency and CRI of SPD's are evaluated.

### Method of Calculation

The spectrum of the HPMV lamp was obtained from a prototype 400W lamp manufactured by the General Electric Company. The SPD of the clear mercury lamp is shown in Fig. 1. It consists of the intense atomic mercury lines in the visible region and much weaker continuous emission. When operated at 120V, the lumen output of this lamp was measured at 21,500 lumens. The color rendition of the HPMV lamp is poor, CRI  $\approx$  23.

Using a computer program, one and two spectral lines and bands were added to the SPD of the HPMV lamp. The relative intensity of the added emissions was determined by prescribing suitable chromaticity coordinates for the lamp (1-5).

For each simulated SPD, the four response variables shown in Table I are computed.  $Q$  is the quantum conversion fraction. It is the fraction of ultraviolet photons available which are converted to visible radiation. The uv from a 400W mercury vapor lamp was mea-

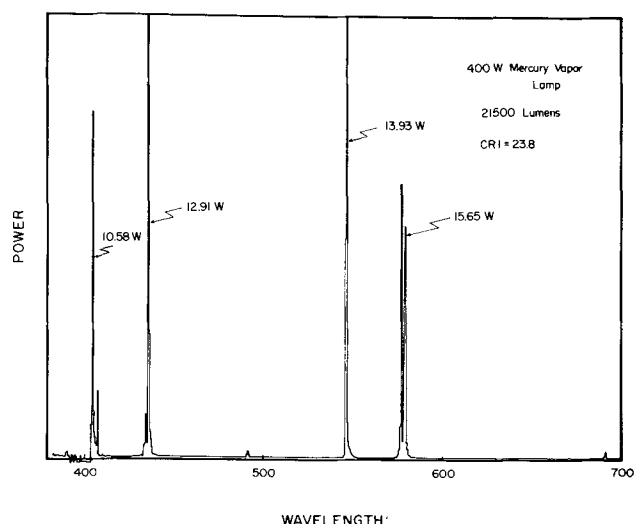


Fig. 1. The visible spectral power distribution of a mercury vapor lamp (400W). Power is measured in units of W/0.5Å. The numbers indicate the total power radiated in the dominant mercury lines.

Table I. Response variables utilized in this study. Integrals were evaluated numerically between 400 and 700 nm unless otherwise indicated. The effect of the mercury line emission was added separately after the integration.

L.E. (Luminous Efficiency)	$\frac{\int P(\lambda) \bar{y}(\lambda) d\lambda}{\int P(\lambda) d\lambda}$
Lumens	$\int P(\lambda) \bar{y}(\lambda) d\lambda$
Q (Quantum Efficiency)	$\frac{\int P(\lambda) \lambda d\lambda}{\int_{250}^{420} P(\lambda) \lambda d\lambda}$
CRI (Color Rendering Index)	

sured between 250 and 420 nm<sup>1</sup> and the results were used to compute the denominator in the expression for  $Q$ . (If there is a significant amount of radiation below 250 nm which is transmitted through the arc tube, more photons may be available. However, a reasonable value for  $Q$  is probably 0.85. This is the value found for a mercury vapor lamp with a heavy coating of the standard deluxe phosphor.) The color rendition index, CRI, is evaluated according to CIE interim method (10).

### Results on Adding Gaussian Bands

Data was obtained for all combinations of the mercury vapor lamp SPD plus one and two gaussian distributions.<sup>2</sup> Color temperatures of 3000°, 4000°, 5000°, and 6500°K were investigated. However, the lower color temperatures of 3000° and 4000°K are of greater commercial interest. The added gaussian bands were chosen to have representative WHM of 5, 30, and 100 nm and the peaks were spaced at about 10 nm. Zero, 30, 50, and 70% filters were simulated to remove the indicated amounts of radiation from the mercury discharge between 400 and 450 nm. For the lower color temperatures, 3000° and 4000°K, it is necessary to remove some of the blue radiation from the discharge to attain the color points on the Planckian locus, and as we will show, to obtain high CRI values. The response variables were plotted on graphs, *e.g.*, Fig. 2, which is a plot of CRI *vs.* luminous efficiency. Lamps with maximum performance have the highest values of the CRI and luminous efficiency. Hence, only the outer envelope of points is shown for 3000° and 4000°K SPD's. For SPD's of maximum performance, it is seen that a high luminous efficiency results at the expense of high CRI. As shown in the figure, 3000°K SPD's with the highest values of the CRI have 70% of

<sup>1</sup> The authors gratefully acknowledge the General Electric Company Product Testing Section at Nela Park for making these measurements.

<sup>2</sup> When one gaussian band was added, the intensity was computed for different correlated color temperatures.

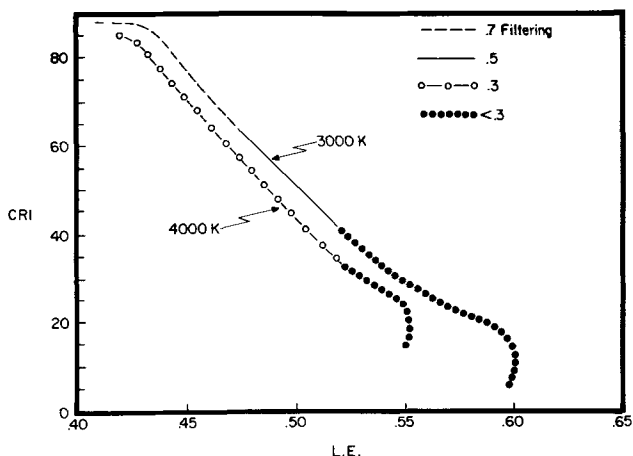


Fig. 2. The effect of adding one or two gaussian bands to the HPMV lamp spectrum. CRI is plotted against luminous efficiency. The envelopes indicate the maximum performance SPD's at 3000° and 4000°K.

the blue radiation from the discharge removed while a high CRI at 4000°K is achieved with about 30% of this radiation removed. Similar results are obtained for higher color temperatures with no filter. For narrow emission bands, Fig. 3 and 4 show the CRI to be a sensitive function of the peak positions of the added bands. The CRI peaks sharply when emission bands are added near 490 and 620 nm. This is true for 3000°-6500°K color temperatures. However, maximum luminous efficiency occurs with the addition of a peak

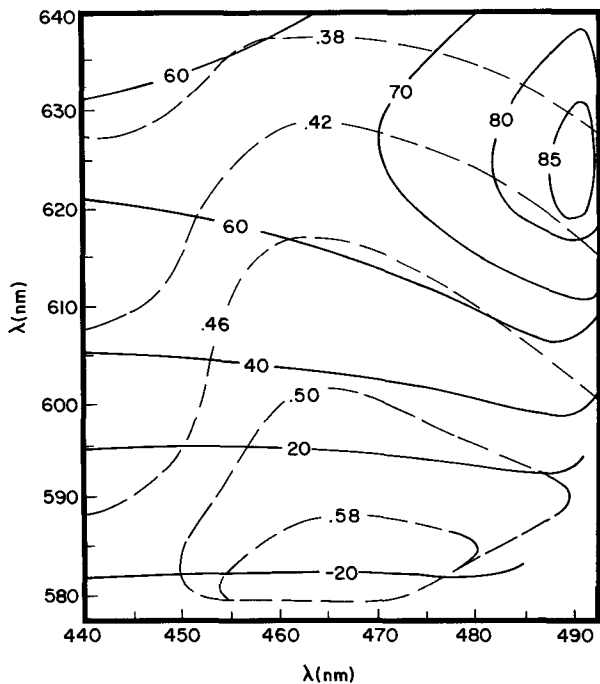


Fig. 3. The effect of adding two narrow Gaussian bands to the mercury vapor lamp spectrum to form white light at 3000°K. Contours indicate the value of the CRI (solid line) and luminous efficiency (dashed lines). The x and y axes label the wavelengths of the added emission bands. The bands have a width-at-half-maximum (WHM) of 5 nm. 70% of the mercury radiation in the blue between 400-450 nm is removed.

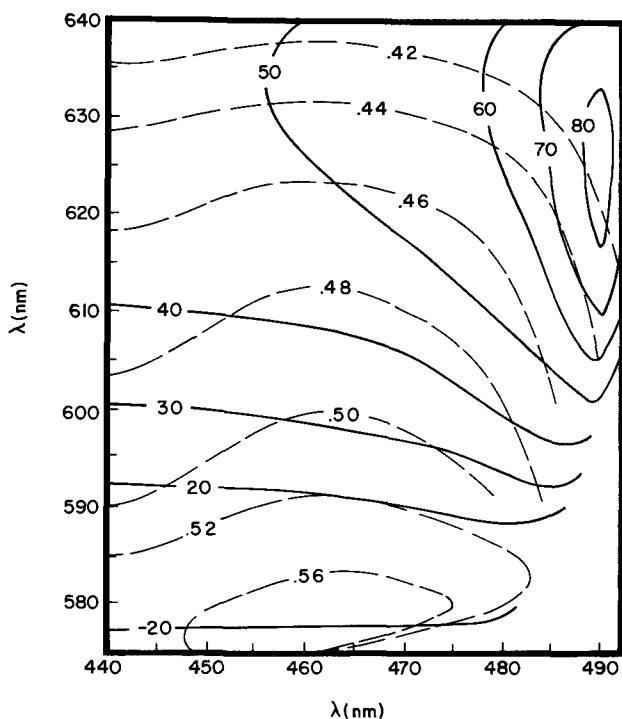


Fig. 4. The same as Fig. 3 for 4000°K. 30% of the mercury radiation in the blue is removed.

at 580-590 nm and a peak between 450 and 470 nm depending on the color temperature.

Figure 5 shows the spectra of lamps having the highest CRI and maximum luminous efficiency at a source color corresponding to 4000°K. The spectrum with the highest CRI has two narrow bands added at 490 and 620 nm. Broad Gaussian bands were not selected for maximum performance. The spectra are, in fact, very similar to optimized five-line spectra found by Mahr (10) to give excellent color rendition and higher luminous efficiency than continuous spectra of comparable color rendition.

The spectrum corresponding to the highest luminous efficiency and maximum performance has a broader band centered at 590 nm (WHM = 30 nm). The single broad band in this case extends the emission into regions of higher luminous efficiency and provides a higher CRI than a narrow band at comparable luminous efficiency.

In Fig. 6 and 7, CRI is plotted vs. lumen output, and contours of maximum performance are indicated at different computed values of  $Q$ . The figures show that the highest values of the CRI are not attainable for 4000° and 3000°K chromaticities with quantum efficiencies restricted to 1 or less. The maximum CRI is around 65 for both 3000° and 4000°K. For quantum efficiencies between 0.6 and 0.8, the CRI does not significantly improve until a quantum efficiency of near 1 is reached. On the other hand, the lumen output of

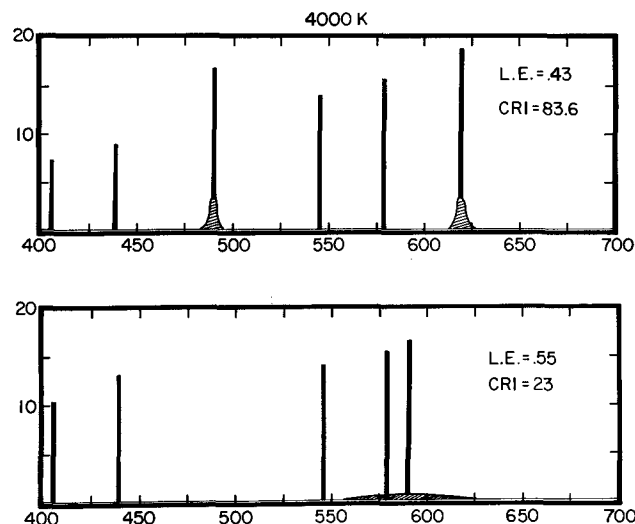


Fig. 5. The spectra giving the highest CRI (top) and highest luminous efficiency (bottom) for a color temperature of 4000°K. The intensities of the added Gaussian bands are indicated by the lines above them. The total power radiated in mercury lines and added bands is given on the y-axis (in watts).

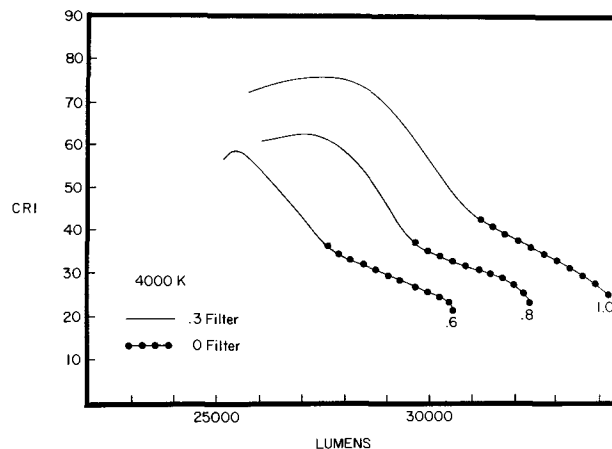


Fig. 6. Envelopes of maximum performance SPD's with contours indicating the quantum conversion fraction for 4000°K.

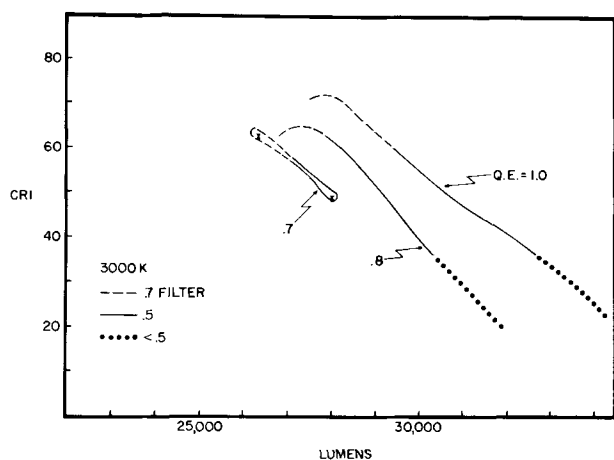


Fig. 7. Envelopes of maximum performance SPD's with contours indicating the quantum efficiency for 3000°K.

the maximum performance SPD's increases significantly for both color temperatures with increasing quantum efficiencies. Efficiencies up to around 80 lumens/W are theoretically possible if the quantum efficiency of 0.8 is reached.

In Fig. 8 we show the spectrum with maximum color rendition and lumen output for a lamp at 4000°K with the quantum efficiency restricted to 0.6 or less. In general, restricting the quantum efficiencies reduces the intensity of the red emission and the blue-green emission in SPD's with the highest CRI. The blue-green emission also moves to shorter wavelengths.

If the quantum efficiency is restricted to  $\sim 0.7$  for a 3000°K lamp, the choice of emission bands is very limited. All the radiation must be added in the red region to color-correct the mercury lamp. Maximum lumen output is achieved with a narrow band peaking near 610 nm. Higher CRI is attained by shifting the band just slightly toward 620 nm and filtering more of the blue radiation from the discharge. Broad red bands cannot be used nor can emission bands at wavelengths longer than 620 nm. These will not sufficiently shift the color of the mercury lamp. Except for the filtering in the blue, these spectra are very similar to the standard deluxe white lamps.

### Discussion

Phosphors employed in HPMV lamps must: (i) be efficient at the operating outer bulb wall temperature which for a 400W lamp is between 300° and 400°C

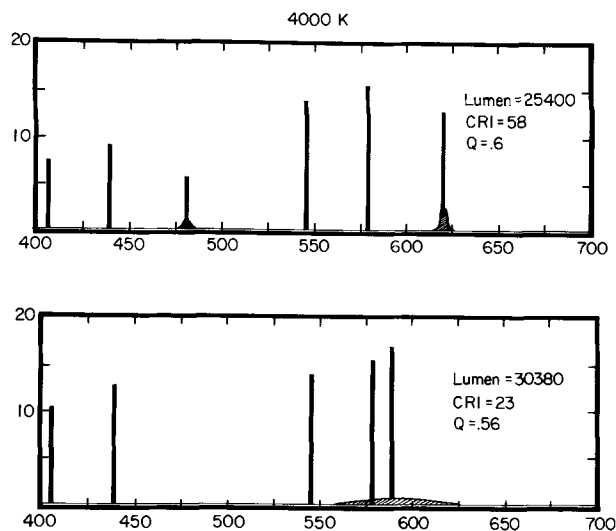


Fig. 8. The spectra corresponding to maximum CRI (top) and maximum lumen output (bottom) for 4000°K lamps with the quantum conversion fraction of added emission bands limited to  $Q < 0.6$ .

and (ii) be excited by the long wavelength ultraviolet radiation of the high pressure mercury discharge. Because of these limitations, only a few practical phosphors for such applications are known today. Table II shows a list of phosphors considered in this study. Not all of these phosphors are equally suitable for use in HPMV lamps but they do give a range of peak positions and half-widths in the red and blue regions of the spectrum.

Calculations were performed in which all possible combinations of one and two of these phosphors are taken together with the mercury discharge spectrum for lamp colors at 3000° and 4000°K. No account was taken of absorption of visible radiation by the phosphor except in the case of the  $Mn^{4+}$  activated magnesium germanate. Magnesium germanate and a similar magnesium arsenate phosphor have significant absorption in the blue region of the spectrum. To study phosphor combinations including the magnesium germanate phosphor, two lamps were made with different weights of the germanate phosphor. The spectral power distributions of these lamps were then used in combinations with the other phosphors.

The optimum spectral power distributions cannot be achieved with the existing commercial phosphors in Table II. In fact, our computed results show that the maximum lumen output with a relatively high CRI is attained with the standard deluxe phosphor for color temperatures of 3500°-4000°K. A higher lumen output at some expense to color rendition should be achieved by adding a yellow emitting phosphor in combination with the yttrium vanadate-phosphate phosphor. The calculated results show that the  $Dy^{3+}:YVO_4$  phosphor may be used for this purpose. However, in practice, the  $Dy^{3+}$  activated phosphor is much too inefficient.

The merits of adding a blue or blue-green emitting phosphor are questionable. Combinations employing the europium-activated strontium chlorapatite phosphor and the standard deluxe phosphor give only a small improvement in the CRI, 43 vs. 38, at a color temperature of 4000°K. Values of the CRI of 50-52 are achieved with blends containing the tin-activated, pyrophosphate or the strontium chlorosilicate phosphor together with the standard deluxe phosphor. However, color temperatures are generally greater than 4000°K. Also, a rather high quantum conversion fraction,  $Q \geq 0.9$ , is computed for combinations with either phosphor. A mixture of the chlorosilicate phosphor, the standard deluxe phosphor, and either a filter to remove 30% of the mercury radiation in the blue or the  $Mn^{4+}$ -activated phosphor, whose SPD strongly resembles Fig. 8, requires a quantum conversion fraction of 1.3 when real phosphor emission bands are used.

On the other hand, values for the CRI of approximately 50 can be achieved at lower color temperatures, 3500°-3100°K, with combinations consisting of the standard deluxe phosphor and either the  $Mn^{4+}$ :magnesium germanate or magnesium arsenate or a filter for some of the blue radiation from the discharge. The  $Mn^{4+}$  phosphors have the additional advantage of using the radiation in the blue mercury lines and re-emitting it in the red, making the lower color temperatures possible. Blue or blue-green phosphors cannot be used if the lower color temperatures are desired.

Table II. Phosphors whose spectra were used in the calculations

Phosphors		
Description	Main peak (nm)	Range (nm)
$Eu^{3+}:YVO_4:YPO_4$	618	617-620
$Mn^{4+}$ :magnesium germanate	660	625-676
$Sn^{2+}$ :strontium orthophosphate	630	570-700
$Dy^{3+}:YVO_4$	575	565-585
$Eu^{2+}$ :strontium chloroapatite	450	435-465
$Eu^{2+}$ :strontium chlorosilicate	485	450-530
$Sn^{2+}$ :strontium pyrophosphate	465	410-525



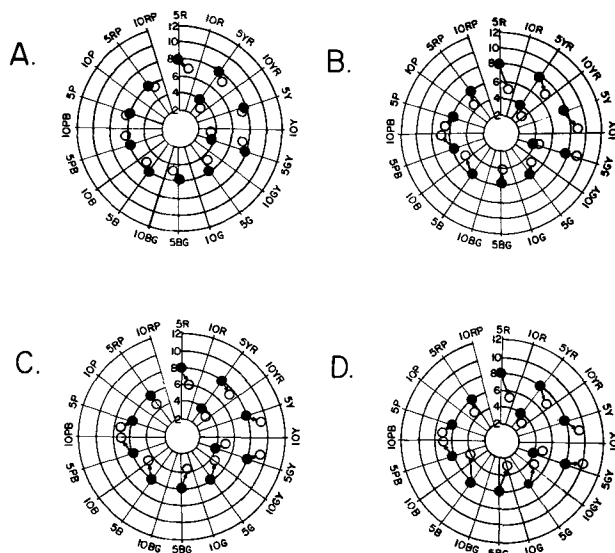


Fig. 9. Calculated color shifts of twelve Munsell samples under four different SPD's whose color coordinates are at or near 4000°K. A, The SPD in Fig. 5 (top) consisting of HPMV lamp and two narrow gaussian bands at 490 nm and 620 nm; B, the SPD in Fig. 8 (top); C, a simulated deluxe lamp with the standard deluxe phosphor plus  $Mn^{4+}$ : magnesium germanate; D, a commercial deluxe white lamp with a heavy coating of the deluxe phosphor. The open circles show the color shifts relative to a 4000°K Plankian illuminant. Color shifts are calculated as described in the text.

In Fig. 9, we show color shifts for some of the spectral power distributions investigated on hue *vs.* chroma Munsell diagrams. The CIE color coordinates, X, Y, and Z, were calculated in the usual way for Munsell color chips under both the reference and test illuminants. The color coordinates are then transformed to Munsell color space using the modification of Adam's "chromatic value space" given by Saunderson and Milner (11). The set of Munsell color chips is the same as that chosen by Eastman, Allen, and Brecher (12). These colors were chosen to span the entire hue circle plus the CIE colors representing foliage (5GY4/14) and skin complexion (5YR8/4).

Color shifts on the Munsell diagram were computed to give a more complete description of the color rendering properties of SPD's studied. The CRI is a single number representing the average displacement of eight CIE colors on the uv diagram relative to a Plankian reference source.

The Munsell color space has the advantage of being more uniform than the CIE-UCS and being familiar to most workers in the field of color. It also has the advantage that the source color is always at the center of the cylindrical color system. A von Kries type of transformation to correct for chromatic adaptation to different source colors is built into the transformation to chromatic value space. The consequences of chromatic adaptation to different source colors have been investigated by many workers using different experimental methods (13-16) although corrections for chromatic adaptation do not agree (6, 16). In a future report, we will show that some of the results of recent experiments by Eastman and Brecher (17) and Eastman, Allen, and Brecher (12) to measure the effects of chromatic adaptation are accounted for by the transformation to chromatic value space. On the other hand, chromatic adaptation is not accounted for on the CIE-UCS except by simply subtracting the difference in source colors.

In Fig. 9, the test lamp colors are at or near 4000°K. The reference illuminant is a 4000°K Plankian radiator.<sup>3</sup> Figure 9A shows that the SPD with the high CRI,

<sup>3</sup> The colors under the reference are not at the nominal notations indicated which were assigned by Munsell when the colors were viewed under the Standard Illuminant C. This does not effect the measured or calculated color shifts.

shown in Fig. 5, shifts the Munsell colors only very slightly relative to their appearance under the Plankian radiator. This is true even though the source in Fig. 5 is very much different from a Plankian radiator and, in fact, has no broad emission bands. The color chips shown in the figure are a greater sampling of the entire hue circle and are more saturated than those used in computing the CRI. They would be expected to emphasize differences between the test and reference illuminants.

Figure 9B shows the calculated color shifts under the spectral power distribution given in Fig. 8. Unlike the results for the high CRI SPD, colors viewed under this test source are significantly different from when viewed under a Plankian radiator illuminant. Reds become much less saturated and shift in hue toward the yellow as a result of the decreased emission in the added red band. The shift of the chip representing flesh tones toward the yellow-red region is probably undesirable (18). Blues and blue-greens are shifted toward the deeper blue colors of the mercury lines. Also, most of the colors appear less saturated or shifted toward lower chroma values than under the Plankian radiator. Only the yellow and yellow-green colors appear more saturated or more vivid. The shift of the foliage chip toward a deeper and more saturated green is probably not undesirable (18).

Figures 9C and 9D show calculated color shifts from two phosphor coated HPMV lamps. The two SPD's include: (C) a simulated combination of the standard europium-activated yttrium vanadate-phosphate phosphor and the  $Mn^{4+}$ :magnesium germanate phosphor and (D) an SPD from a commercial lamp with a heavy coating of the deluxe phosphor. Neither SPD has any added emission in the blue or blue-green region. Most of the color shifts are the same as those discussed above for Fig. 9C. The only color chip which appears to be better rendered by the blue-green emission is 5BG6/6. When comparing the two phosphor coatings, the phosphor blend consisting of the standard deluxe phosphor and the  $Mn^{4+}$ -activated phosphor which also filters some of the blue radiation from the discharge, appears to be somewhat better in its color rendering ability.

## Conclusions

Various ways of optimizing the SPD of HPMV lamps were investigated by computer calculations. By adding gaussian emission bands of varying position and half-width, we found that emission bands located near 490 nm in the blue-green and 620 nm in the red region of the spectrum result in the greatest improvement in color rendition. In fact, excellent color rendition and good luminous efficiency are achieved if sufficient radiation can be added in narrow bands in these regions. For lamps with the color temperatures of 4000° and 3000°K, it is necessary to remove some of the discharge radiation in the blue region. The highest luminous efficiency is not obtained with the red and blue-green emission bands but rather by the addition of radiation near 590 nm.

Present commercial phosphors do not provide the optimum SPD for a HPMV lamp. While the  $Eu^{3+}$ : $YVO_4$ : $YPO_4$  phosphor is a natural choice for providing some of the red emission in order to improve the color rendition of the lamp, it is not clear whether a blue-green emitting phosphor should be used, especially if low color temperatures are desired. Little effort appears to have been made in finding a yellow emission source to provide a lamp with considerably higher luminous efficiency.

By calculating changes in hue, chroma, and value for Munsell colors, we provide a more complete description of the color rendering properties of the SPD's studied. In general, the effects of colorimetric shifts can be calculated for lamps which vary in spectral quality but have the same source color. Halstead, Palmer, and Stainsby (19) carefully studied CIE color rendering tolerances. They observed that just

noticeable differences in color rendition did correlate with calculated color shifts of individual color samples on a uniform chromaticity scale. Furthermore, the just noticeable color differences under their experimental conditions, which involved viewing the samples in optically isolated sections of a room, correspond to approximately 5.5 times the minimum perceptible color differences of the MacAdam's observer. This is about  $1\frac{1}{2}$  units of length in the Munsell system. With current phosphor coatings, calculated color shifts are of this magnitude for the red, blue-green, and blue hues.

### Acknowledgments

The authors would like to thank Michael Haynesworth for doing the drawings and Carmy Beggs and Clarence Sanders for their help in preparing the manuscript.

Manuscript submitted July 30, 1973; revised manuscript received Oct. 31, 1973. This was Paper 31 presented at the Chicago, Illinois, Meeting of the Society, May 13-18, 1973.

Any discussion of this paper will appear in a Discussion Section to be published in the December 1974 JOURNAL. All discussions for the December 1974 Discussion Section should be submitted by Aug. 1, 1974.

### REFERENCES

1. H. Ivey, *J. Opt. Soc. Am.*, **53**, 1185 (1963).
2. H. D. Einhorn and F. D. Einhorn, *IES*, **62**, 154 (1967).
3. W. Walter, *Appl. Opt.*, **10**, 1108 (1971).
4. W. A. Thornton, *J. Opt. Soc. Am.*, **61**, 1155 (1967).
5. M. Koedam and J. J. Opstelten, *Lighting Res. Technol.*, **3**, 205 (1971).
6. M. Koedam, J. J. Opstelten, and D. Radielovic, *Illum. Eng. Soc. Conf.*, Chicago, August, 1971.
7. IES Subcommittee on Color Rendering, *Illum. Eng.*, **57**, 471 (1962); Committee Internale de l'Eclairage (CIE), CIE Publication No. 13 (E-1.3.2), Bureau Central de la CIE, Paris, France (1965).
8. H. Ivey, *J. Opt. Soc. Am.*, **62**, 814 (1972).
9. W. L. Wanmaker, J. J. Opstelten, and D. Radielovic, *Extended Abstract 75*, p. 200, Electrochemical Society Extended Abstracts, Spring Meeting, Houston, Texas, May 7-11, 1972.
10. K. Mahr, *ibid.*, Abstract 76, p. 202.
11. J. L. Saunderson and B. I. Milner, *J. Opt. Soc. Am.*, **36**, 36 (1946).
12. A. A. Eastman, C. J. Allen, and G. A. Brecher, *J. Illum. Eng. Soc.*, **1**, 23 (1972).
13. H. Helson, D. B. Judd, and M. H. Warren, *Illum. Eng.*, **47**, 221 (1952); *ibid.*, **51**, 329 (1956).
14. R. W. Burnham, R. M. Evans, and S. M. Newhall, *J. Opt. Soc. Am.*, **42**, 597 (1952); *ibid.*, **47**, 35 (1957).
15. R. W. Burnham, *ibid.*, **49**, 254 (1959).
16. D. Nickerson, *ibid.*, **50**, 57 (1960).
17. A. A. Eastman and G. A. Brecher, *J. Illum. Eng. Soc.*, **1**, 239 (1972).
18. Not all color shifts are necessarily undesirable. In particular, color shifts toward a more saturated color may be preferred. Also, familiar objects may have preferred colors which are different from the colors actually observed under daylight or a Plankian reference illuminant. See, for example, D. B. Judd, *Illum. Eng.*, **593** (1967); G. B. Back and H. C. Froelich, *ibid.*, **53**, 27 (1948).
19. M. B. Halstead, D. A. Palmer, and A. G. Stainsby, *Lighting Res. Technol.*, **2**, 99 (1971).

## Preparation and Properties of Boron Arsenide Films

T. L. Chu\* and A. E. Hyslop

Electronic Sciences Center, Southern Methodist University, Dallas, Texas 75222

### ABSTRACT

Boron arsenide films have been deposited on the basal plane of hexagonal silicon carbide and {111} oriented sodium fluoride and silicon substrates at 800°-850°C by the thermal decomposition of a diborane-arsine mixture in a hydrogen atmosphere. Adherent films were deposited on silicon carbide substrates and were identified by electron diffraction as boron arsenide with random orientations. Boron arsenide deposits on sodium fluoride substrates were not adherent due to the large differences in their thermal expansion coefficients. Boron arsenide films deposited on silicon substrates were found to be amorphous by electron diffraction. Optical absorption measurements implied that boron arsenide is a direct gap material with a room temperature energy gap of about 1.45 eV. The current-voltage characteristics of metal-boron arsenide-silicon structures have indicated that the current-controlling mechanism is similar to that of an insulator containing traps of uniform energy. The density of traps was calculated to be approximately  $10^{17}/\text{cm}^3$  eV.

Boron forms two arsenides. The direct combination of the elements at 800°-850°C yields the cubic monoarsenide, BAs, with a lattice parameter of 4.777Å and an optical energy gap of 1.46 eV (1, 2). The monoarsenide is stable up to 920°C and undergoes irreversible decomposition to an orthorhombic subarsenide, B<sub>13</sub>As<sub>2</sub>, at higher temperatures (3). Thus, boron monoarsenide can only be formed at temperatures below 920°C, and chemical vapor growth techniques are most suited for the preparation and crystal growth of boron monoarsenide. For example, the reversible reaction between boron monoarsenide and boron triiodide has been used for the growth of boron monoarsenide crystals at 850°C by the chemical transport technique (4). Chemical reactions between gaseous boron and

arsenic compounds may also be used for the preparation of boron monoarsenide. Since the hydrides of boron and arsenic are thermochemically unstable at room temperature and above, the thermal decomposition of a diborane-arsine mixture is feasible for the preparation of boron monoarsenide.

In this work, the thermal decomposition of a diborane-arsine mixture in a hydrogen atmosphere was used for the deposition of boron monoarsenide, referred to as boron arsenide hereafter, on the basal plane of hexagonal silicon carbide platelets and sodium fluoride and silicon substrates of {111} orientation. Sodium fluoride and hexagonal silicon carbide were selected on the basis of crystal symmetry and lattice parameter considerations. Sodium fluoride crystallizes in the sodium chloride structure with a lattice parameter of 4.62Å as compared with 4.777Å for boron arsenide. The

\* Electrochemical Society Active Member.

Key words: conduction, deposition, semiconductor, substrate.

basal plane of silicon carbide has a sixfold symmetry with an interatomic distance of 3.095Å which is approximately 8.2% lower than that of boron arsenide in a {111} plane. The structural and electrical properties of the deposited films were studied. The experimental procedures and results are summarized in this paper.

### Preparation of Boron Arsenide Films

The deposition of boron arsenide was carried out in a gas flow system by the thermal decomposition of a diborane-arsine mixture in a hydrogen atmosphere using the apparatus shown schematically in Fig. 1. The flow of various gases was directed by using appropriate valves and measured with flowmeters. Hydrogen was purified by diffusion through a palladium-silver alloy. Diborane and arsine were in the form of hydrogen-hydride mixtures, each containing about 5% of the hydride. These hydrides decompose rapidly at 500°C and above, thereby promoting the gas-phase nucleation and yielding nonadherent deposits. Thus, the gas-phase nucleation must be suppressed by optimizing the experimental conditions such as the use of a water-cooled reaction tube, a low partial pressure of hydrides in the reactant, and a high gas velocity over the substrate surface.

The substrates, sodium fluoride, hexagonal silicon carbide, and silicon, were supported on a boron arsenide coated graphite susceptor in a water-cooled reaction tube of 55 mm ID, and the susceptor was heated externally with an rf generator. The sodium fluoride substrates were in the form of platelets with cleaved faces of a {111} orientation, and water was used as an etchant. The silicon carbide substrates were also in the form of platelets with main faces parallel to the basal plane, and molten potassium hydroxide was used as an etchant. The silicon substrates were of a {111} orientation, p-type, and 0.01 ohm-cm resistivity; a 5:3:3 nitric acid-hydrofluoric acid-acetic acid mixture was used as an etchant. The mechanically polished and chemically etched substrates were thoroughly cleaned and were heated *in situ* in a hydrogen atmosphere before the deposition of boron arsenide. Boron arsenide was usually deposited at 800°-850°C. Typical flow rates of hydrogen, diborane, and arsine were  $2 \times 10^4$ , 2, and 8 ml/min, respectively (a large As/B ratio was always used to prevent arsenic deficiencies in the deposit). The deposition rate was 3-4  $\mu\text{m/hr}$  as measured directly on angle-polished boron arsenide-silicon carbide and boron arsenide-silicon structures.

The deposition of adherent boron arsenide films on sodium fluoride substrates was not successful. The deposits always cracked off during the cooling process, due mainly to the difference in the thermal expansion coefficients of the two materials.

Adherent and uniform boron arsenide films have been deposited reproducibly on the basal plane of hexagonal silicon carbide substrates under a wide range of experimental conditions. No structural fea-

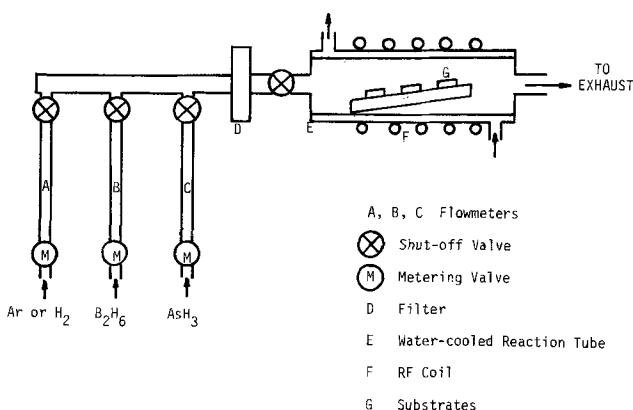


Fig. 1. Schematic diagram of apparatus for the deposition of boron arsenide film.

tures were observed when the as-deposited films were examined with an optical microscope. Reflection electron diffraction examinations with a Hitachi Hu-11B2 electron microscope indicated that films deposited at 800°-850°C were all boron arsenide with random orientations. Figure 2 shows the reflection electron diffraction pattern of a boron arsenide film deposited on the silicon face of a hexagonal silicon carbide substrate at 850°C. The lack of single crystallinity is presumably related to the large difference in lattice parameters of boron arsenide and silicon carbide and to the relatively low temperature used in the deposition process.

The boron arsenide films deposited on silicon substrates at 800°-850°C at rates of a few micrometers per hour were highly adherent and were found to be amorphous by the electron diffraction technique. If a boron arsenide film of 10  $\mu\text{m}$  or greater in thickness is deposited on a silicon substrate of 400  $\mu\text{m}$  thickness, the resulting structure became convex upon cooling, indicating that the thermal expansion coefficient of amorphous boron arsenide is smaller than that of silicon. Amorphous boron arsenide is chemically inert, insoluble in aqueous acids and alkalis at room temperature and above. It can be etched in a 1:9 sodium peroxide-sodium hydroxide molten mixture at about 400°C at a rate of approximately 1  $\mu\text{m/min}$ .

### Properties of Amorphous Boron Arsenide Films

Due to the chemical inertness of boron arsenide, the silicon substrate can be readily etched off from the boron arsenide-silicon structures by using a mixture of nitric acid and hydrofluoric acid. The resulting film transmitted dark red light. A boron arsenide film of about 2  $\mu\text{m}$  thickness was placed between two quartz plates, and its optical absorption was measured using a Perkin-Elmer Model E-1 monochromator. The results are shown in Fig. 3 where the square and the square root of the absorption coefficient,  $\alpha$ , are plotted vs. photon energy, E. The dependence of the absorption coefficient on photon energy can be used to distinguish between direct and indirect electron transitions (5). In practice, the plot of  $\alpha^2$  vs. photon energy



Fig. 2. Reflection electron diffraction pattern of a boron arsenide film deposited on the silicon face of a hexagonal silicon carbide substrate at 850°C.

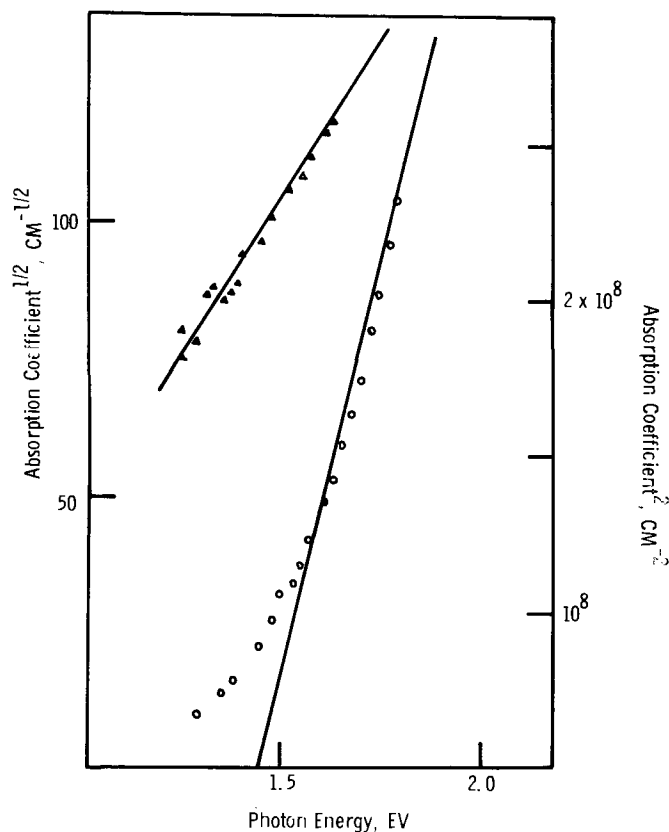


Fig. 3. Optical absorption data of a boron arsenide film. The circles and triangles represent, respectively, the square and the square root of the absorption coefficient.

gives a straight line for direct transitions, and the intercept on the energy axis gives the bandgap for direct transitions. For indirect transitions, the plot of  $\alpha^{1/2}$  against photon energy gives a straight line, and the intercept on the energy axis gives the bandgap for indirect transitions. The energy gap of boron arsenide deduced from the  $\alpha^2$  vs.  $E$  plot in Fig. 3 is approximately 1.45 eV, while the plot of  $\alpha^{1/2}$  vs.  $E$  yields an energy gap of only 0.67 eV. Since the former is in agreement with the reported optical bandgap of microcrystalline boron arsenide, 1.46 eV (2), boron arsenide presumably is a direct gap material.

The electrical conduction mechanism in amorphous boron arsenide films was studied by measuring the current-voltage characteristics of metal-boron arsenide-silicon structures over a wide temperature range. Boron arsenide films of various thicknesses deposited on 0.01 ohm-cm, p-type silicon substrates were used. Aluminum contacts were deposited on silicon, and aluminum or gold contacts of 1 mm diameter were deposited on boron arsenide by evaporation. The specimens were scribed and mounted on TO-5 headers. Aluminum wire was bonded onto the metal electrodes by an ultrasonic bonder, and the header was sealed. The current-voltage characteristics of these units were then taken in the temperature range 100°–400°K.

Typical current-voltage characteristics of aluminum-boron arsenide-silicon structures are shown in Fig. 4 where the current-voltage relations over a wide temperature range for a boron arsenide film of 1  $\mu\text{m}$  thickness are plotted on logarithmic scales. At low bias levels, the slope is unity designating the ohmic region, and the room temperature resistivity of boron arsenide is approximately  $10^7$  ohm-cm. The slope of the plot of the logarithm of the conductance vs. the reciprocal temperature yielded an activation energy of about 0.24 eV, indicating that the electronic conduction is responsible for the ohmic behavior. As the bias is increased, the slope of the  $\log I$  vs.  $\log V$  plot increases to two, indicating a space-charge-limited cur-

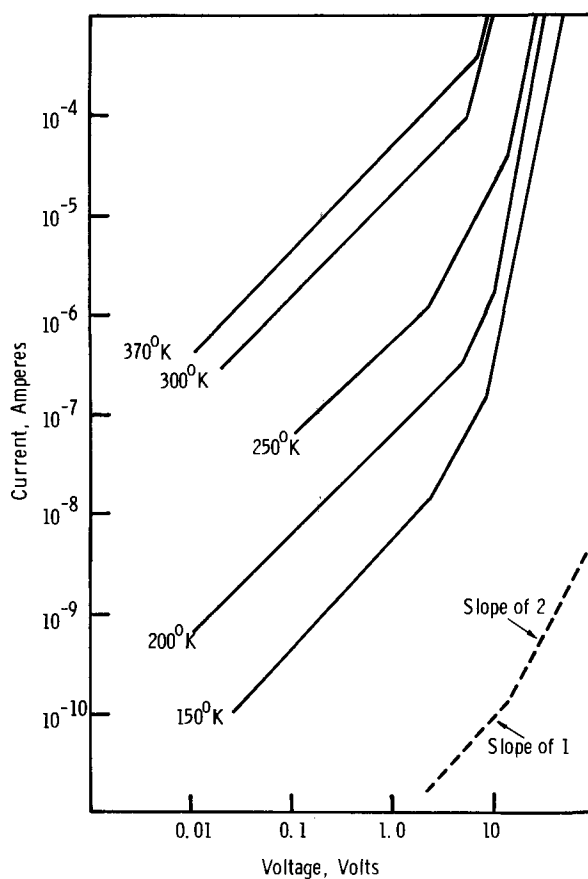


Fig. 4. Typical current-voltage characteristics of an aluminum-boron arsenide-silicon structure with a boron arsenide film of 1  $\mu\text{m}$  thickness.

rent situation. This is expected because of the relatively large energy gap of boron arsenide. At lower temperatures, further increase in bias results in a large increase in slope which subsequently decreases to two (this decrease in slope is not shown in Fig. 4).

The high slope region could be related to Schottky emission, Poole-Frenkel emission, tunneling, internal field emission, and space-charge-limited currents in the presence of traps. However, the Schottky and Poole-Frenkel emissions are both associated with a lowering of the metal-insulator barrier height under the influence of an electric field, and the logarithm of the current varies linearly with the square root of the voltage. Also, if any of these mechanisms except the space-charge-limited current were to occur, their effect on the current-voltage characteristics would continue to prevail at still larger bias. However, the  $\log I$  vs.  $V^{1/2}$  plot of the data in the high slope region did not yield a straight line, and the high slope region subsequently reverts back to a square law at higher bias. The space-charge-limited current mechanism therefore prevails, and the current-voltage characteristics are influenced by the presence of traps of a concentration much greater than the equilibrium carrier concentration. This region has been designated as the trap filled limit (TFL) region. Extensive theories for insulators containing traps have been developed, and current-voltage characteristics attributable to this type of trapping mechanism have been reported (6).

The reasoning for the appearance of the high slope region is briefly as follows. As the bias is increased, the quasi-Fermi level for the charge carrier moves away from its thermal equilibrium value toward its respective band. If, for example, there is one discrete trap level, single-carrier space-charge-limited current should behave as  $I \propto V^2$  until the quasi-Fermi level moves within a few  $kT$  of the trap level. When the quasi-Fermi level is at the trap level, the injected

charge will be condensed into this trap level, thus giving a sharp rise in current, the TFL region. Since a discrete trap level is assumed, the slope of the  $\log I$  vs.  $\log V$  plot in the TFL region should be very large because the excess injected charge will only go into this trap level over an exceedingly small voltage range while the current increases by orders of magnitude. As the bias is increased further, the quasi-Fermi level moves away from the trap level, and the current again becomes proportional to the square of the applied voltage.

The slope of the  $\log I$  vs.  $\log V$  plot in the TFL region and its temperature dependence are determined by the energy distribution of traps. Detailed analysis has been carried out for the situation where an exponential energy distribution of traps exists in the forbidden band, and the current-voltage relationship has been deduced (7). Attempts to correlate this relationship with the current-voltage data on amorphous boron arsenide produced no meaningful results, suggesting that a different energy distribution of traps should be used. Assuming that all traps have the same energy according to the relation

$$N_T(E_T) = N_n/\text{cm}^3 \text{ eV}$$

The current-voltage relation for such a distribution is (8)

$$J = 2qn_0\mu(v/L) \exp(2eV/N_nkTqL^2)$$

where  $n_0$  is the equilibrium carrier density,  $\mu$  is the carrier mobility,  $L$  is the insulator thickness, and  $\epsilon$  is the dielectric constant. The slope of the  $\log I$  or  $\log J$  vs.  $\log V$  plot in the TFL region is

$$m = \frac{d \log J}{d \log V} = 1 + \frac{2eV}{2.3 N_n k T q L^2}$$

for which a temperature variation in slope should be

$$\frac{1}{m-1} = \left[ \frac{2.3 N_n k T q L^2}{2eV} \right] T$$

Using current-voltage characteristics shown in Fig. 4, the quantity  $1/(m-1)$ , is plotted vs. the absolute temperature in the range 200°-300°K in Fig. 5. This linear relationship indicates that the traps presumably have a uniform energy distribution in the temperature range under consideration. The density of traps calculated from the slope of this line is approximately  $10^{17}/\text{cm}^3 \text{ eV}$ .

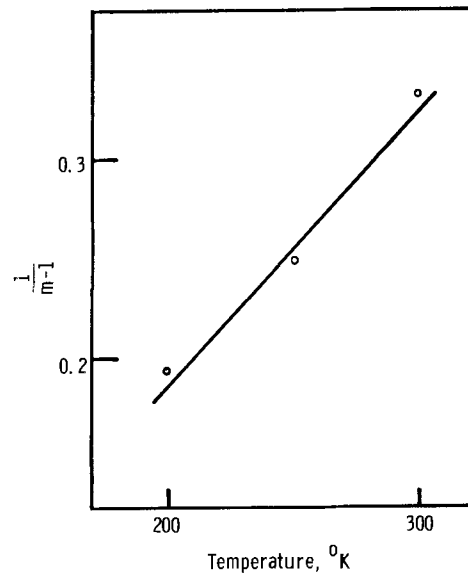


Fig. 5. A plot of  $1/(m-1)$  vs. absolute temperature of data shown in Fig. 4.

### Acknowledgment

This research was supported by the Robert A. Welch Foundation, Houston, Texas, under Grant N-298.

Manuscript submitted Jan. 4, 1973; revised manuscript received March 30, 1973.

Any discussion of this paper will appear in a Discussion Section to be published in the December 1974 JOURNAL. All discussions for the December 1974 Discussion Section should be submitted by Aug. 1, 1974.

### REFERENCES

1. A. J. Perri, S. LaPlaca, and B. Post, *Acta Cryst.*, **11**, 310 (1958).
2. S. K. Ku, *This Journal*, **113**, 813 (1966).
3. F. V. Williams and R. A. Ruehrwein, *J. Am. Chem. Soc.*, **82**, 1330 (1960).
4. T. L. Chu and A. E. Hyslop, *J. Appl. Phys.*, **43**, 276 (1972).
5. See, for instance, R. H. Bube, "Photoconductivity of Solids," p. 214, John Wiley & Sons, New York (1960).
6. M. A. Lampert and P. Mark, "Current Injection in Solids," Academic Press, New York (1970).
7. M. A. Lampert and P. Mark, *ibid.*, p. 72.
8. M. A. Lampert and P. Mark, *ibid.*, p. 77.

# Growth and Characterization of GaAsSb-GaAlAsSb Lattice-Matched Heterojunctions

G. A. Antypas\* and R. L. Moon\*

Corporate Research Laboratories, Varian Associates, Palo Alto, California 94303

## ABSTRACT

Liquid phase epitaxial layers of  $\text{Ga}_{1-y}\text{Al}_y\text{As}_{1-x}\text{Sb}_x$  on GaAs (100) substrates were grown from beginning growth temperatures of 760° and 720°C, and have been characterized by electron microprobe, x-ray, and photoluminescence measurements. The solubility of As as a function of Al was experimentally determined at  $x_{\text{Sb}}^1/x_{\text{Ga}}^1 = 0.178$  for 760° and 720°C. In the concentration range and temperatures investigated, the distribution coefficient of As was found to vary drastically as a function of Al concentration. For layers grown at 720°C the distribution coefficient of As varied between 78 and 220 for  $x_{\text{Al}}^1$  of 0 and  $0.3 \times 10^{-2}$ , respectively. However, the distribution coefficient of Sb appeared to be practically independent of the Al concentration in the liquid. Thermodynamic and physical properties of the quaternary liquid and solid solutions were compared whenever possible with ternary AlGaAs (the case of zero Sb) properties.

The solid solution properties of III-V compounds have promoted the development of solid-state light emitting diodes, near-infrared photoemitters and detectors, and solid-state heterojunction lasers. In most instances, however, the epitaxial growth of ternary solid solutions on binary III-V substrates results in junctions with high dislocation and stacking fault densities. In cases where the heterojunction is an active part of the device, such as heterostructure lasers, super-lattice formation, transmission photocathodes, etc., a high defect density at the interface results in high recombination losses.

With the exception of the Al-Ga-V ternary compounds, which exhibit lattice matching over the whole concentration range, other ternary compounds cannot be grown on III-V binary substrates without the introduction of appreciable mismatch dislocations at the interface. This limitation of the ternary solid solutions can be relaxed by the addition of a fourth component that introduces an extra degree of freedom and permits the independent variation of lattice constant and bandgap. Thus lattice matching in III-V quaternary systems can be achieved over a wide range in bandgap energy.

From a practical point of view, however, the fabrication of lattice-matched heterojunction on commercially available substrates is limited to the growth of  $\text{Al}_x\text{Ga}_{1-x}\text{V}$  alloys on Ga-V substrates, the quaternaries  $\text{In}_{1-y}\text{Ga}_y\text{As}_{1-x}\text{P}_x$  on InP or GaAs and  $\text{In}_{1-y}\text{Ga}_y\text{As}_{1-x}\text{Sb}_x$  on GaSb or InAs. The ternary-quaternary lattice-matched structures, although theoretically extending over the whole concentration range, are limited by the nonavailability of appropriate substrates. So for systems such as GaAlAsP-GaAsP, and GaAlAsSb-GaAsSb, a buffer layer is usually grown on the substrate in order to minimize the effects of lattice mismatch between the substrate and the active epitaxial layer.

Liquid phase epitaxy has been used for the growth of  $\text{GaAs}_x\text{Sb}_{1-x}$  alloys for photoemission (1) and light emission applications (2). In both cases layers of good crystallinity could only be grown having GaSb concentration of less than 20%. This is primarily due to the large lattice mismatch between GaAs and GaSb (7.8%). Sugiyama and Saito (3) using growth procedures and a boat design similar to that used by Panish *et al.* (4) for the growth of GaAs-GaAlAs heterojunctions, prepared a GaAsSb-GaAlAsSb heterostructure laser. The growth of GaAlAsSb-GaAsSb heterojunctions is very similar to the GaAlAsP/GaAsP sys-

tem reported by Burnham and co-workers (5). In these systems the variations in heterojunction barriers are controlled by the  $x_{\text{Ga}}^{\text{Sb}}$  to  $x_{\text{Al}}^{\text{Sb}}$  ratio while constancy of the lattice parameter across the junction is controlled by the  $x_{\text{As}}^{\text{Sb}}$  to  $x_{\text{P}}^{\text{Sb}}$  or  $x_{\text{As}}^{\text{Sb}}$  to  $x_{\text{Sb}}^{\text{Sb}}$  ratios.

## Growth and Materials Characterization

Consistent with our earlier work on GaAsSb, the epitaxial layers were grown on (100) oriented GaAs substrates. A horizontal growth system using a palladium purified hydrogen environment and a graphite boat similar in design reported by Rosztochy *et al.* (6) was used. Epitaxial layers were grown in the temperature range of 720° and 760°C with a cooling rate of 1°C/min over a temperature interval of 20°C. Layer thicknesses were between 10 to 15 $\mu$ .

In addition to the epitaxial growth experiments, As solubility experiments were performed at 720° and 760°C by initially preparing a Ga-Al-Sb solution and saturating with As from a GaAs substrate. The weight loss of the GaAs substrate establishes the solubility limit of As. Interpretation of this type of solubility experiment implicitly assumes that the prevention of complete dissolution of the saturating source is due to a quaternary layer which is in equilibrium with the melt at the saturating temperature.

Figure 1 shows the resulting liquidus isotherms at 720° and 760°C for a liquid of  $x_{\text{Ga}}^1$  and  $x_{\text{Sb}}^1$  of 0.84 and 0.15, respectively. The solubility behavior of As in Ga-Sb solutions as a function of Al concentration in the liquid is very similar to the case of the ternary Al-Ga-As system. For comparison, the data of Alferov *et al.* (7) for the GaAlAs system at 712° and 757°C are shown. In both cases the As solubility limit decreases rapidly with the addition of small amounts of Al.

In order to achieve lattice match across the heterojunction between GaAlAsSb and GaAsSb a constant  $x_{\text{Sb}}^{\text{Sb}}/x_{\text{As}}^{\text{Sb}}$  ratio must be maintained. Due to the lack of any phase diagram calculation and the drop in As solubility upon adding Al to the solution, the growth of lattice-matched heterojunctions requires some experimentation. To investigate this, a series of epitaxial layers were grown from solutions with constant Ga and Sb concentrations while varying the As concentration by saturating at 720° and 760°C. The epitaxial layers were characterized by microprobe, x-ray, and photoluminescence measurements to determine the composition of the solid solution, the lattice constant, and bandgap.

Detailed characterization of the epitaxial layers is shown in Table I. For the layers grown at 720°C the

\* Electrochemical Society Active Member.  
Key words: III-V quaternary alloys, lattice matching, heterojunctions, LPE (liquid phase epitaxy).

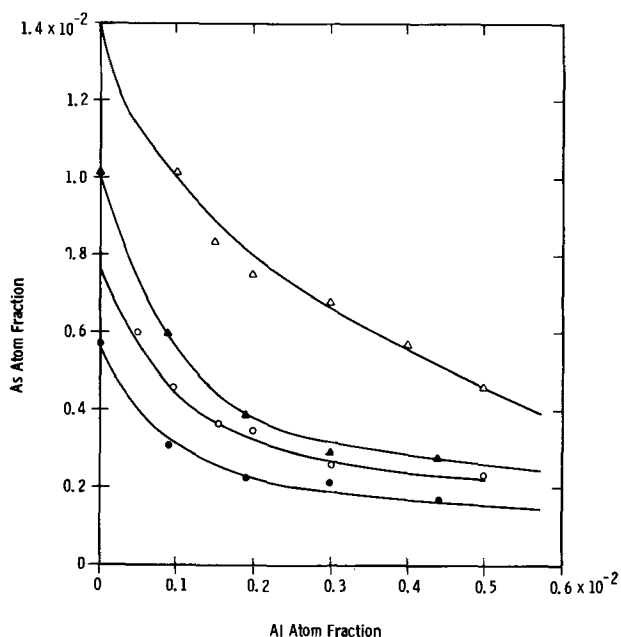


Fig. 1. Liquidus isotherms for the GaAlAs and GaAlAsSb ( $x_{Sb}^l/x_{Ga}^l = 0.178$  in the liquid) systems:  $\Delta$ , 757°C (7);  $\circ$ , 712°C GaAlAs (7); and  $\blacktriangle$ ,  $\bullet$ , this work at 760° and 720°C, respectively, for GaAlAsSb.

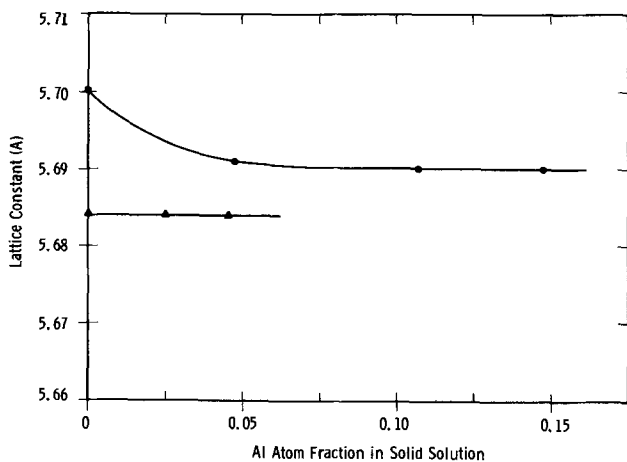


Fig. 2. Dependence of lattice parameter on the Al concentration in the solid solution, for layers grown at  $\blacktriangle$ , 760°C; and  $\bullet$ , 720°C.

distribution coefficient of Sb decreased slightly as a function of Al concentration, while at 760°C it appeared to remain practically constant. This change in the distribution coefficient of Sb is also reflected on the lattice parameter of the epitaxial layers. The series of layers grown at 720°C indicated a decrease in the lattice constant as a function of Al, while for those grown at 760°C the lattice parameter remained constant. The dependence of the lattice parameter on the Al concentration is shown in Fig. 2 for both series of runs.

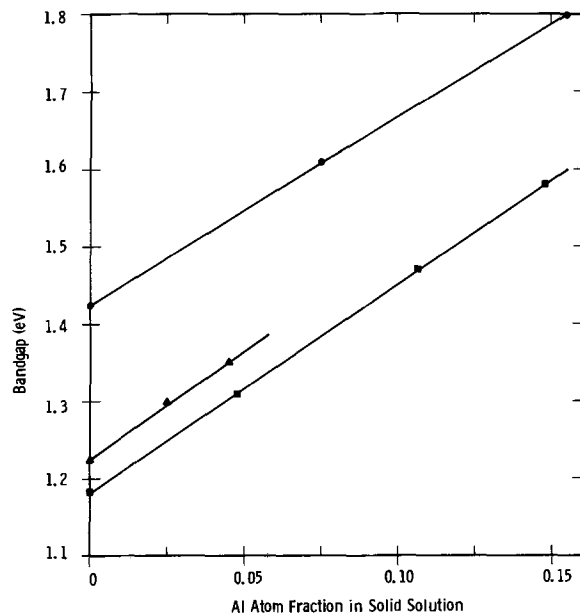


Fig. 3. Dependence of the room temperature bandgap on the Al concentration in the solid solution for  $\bullet$ , AlGaAs (8) and GaAlAsSb layers grown from solutions with  $x_{Sb}^l/x_{Ga}^l = 0.178$  at  $\blacktriangle$ , 760°C and  $\blacksquare$ , 720°C.

The bandgap energy was determined by photoluminescence measurements at 77° and 300°K. The excitation source was a chopped 0.5W argon ion laser. A Perkin-Elmer 301 spectrophotometer was used with a dry-ice-cooled S-1 photomultiplier. The PL spectra of all the layers consisted of intense near-bandgap radiation, along with a defect line of lower energy. Figure 3 shows the variation of bandgap on the Al concentration in the solid. The linear dependence of bandgap on Al for the two series of runs is almost identical to the GaAlAs case as indicated by the slopes  $2.65$  and  $2.55 \times 10^{-2}$  eV per Al atom per cent, for the GaAlAsSb and GaAlAs lines, respectively.

The reproducible growth of heterojunctions requires detailed knowledge of the distribution coefficient of the various components. For the growth of GaAlAsSb, epitaxial Al and As have appreciably higher distribution coefficients than either Ga or Sb. Furthermore, since these epitaxial layers normally are grown from As saturated solutions the distribution coefficient of As is strongly dependent on the Al concentration in the liquid solution. This behavior is shown in Fig. 4 and 5. Figure 4 simply shows the distribution of Al for quaternary epitaxial layers grown at 760° and 720°C. For comparison, the data of Alferov *et al.* (7) are shown for the distribution coefficient of Al in GaAlAs. From microprobe measurements the distribution coefficient of Sb remains practically independent from the Al concentration in the liquid, and since the As solubility decreases drastically by the presence of Al in the solution, the effective distribution coefficient of As increases as a function of Al. This behavior is

Table I. Growth and characterization parameters for GaAlAsSb liquid phase epitaxial layers

Run No.	Growth temp. (°C)	Melt composition* (g)			Solid composition (atom per cent)		Lattice parameter (Å)	Bandgap eV (RT)
		Ga	Sb	Al	$x_{Sb}^s$	$x_{Al}^s$		
1	720-700	4.00	1.25	0	6.5	0	5.701	1.18
2	720-700	4.00	1.25	0.0015	5.8	4.7	5.691	1.31
3	720-700	4.00	1.25	0.0035	5.4	10.7	5.690	1.47
4	720-700	4.00	1.25	0.0055	4.8	14.7	5.690	1.58
5	760-740	4.00	1.25	0	4.3	0	5.684	1.23
6	760-740	4.00	1.25	0.0015	4.1	2.4	5.684	1.30
7	760-740	4.00	1.25	0.0035	4.0	4.4	5.686	1.35

\* Solutions saturated in As.

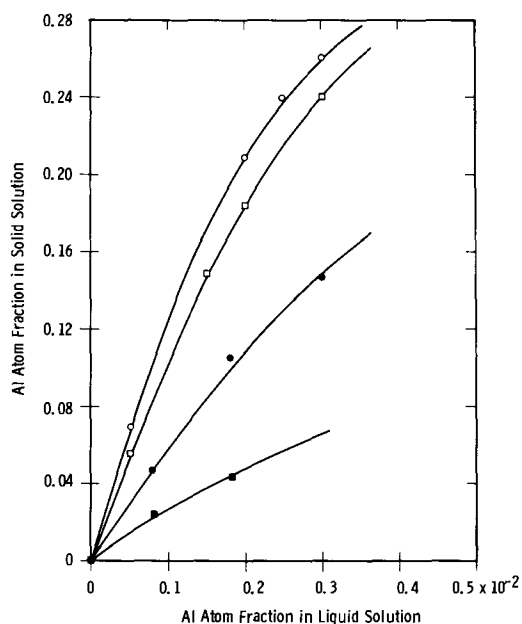


Fig. 4. Distribution of Al for GaAlAs at ○, 707°C (7) and □, 756°C (7), and GaAlAsSb grown from solutions with  $x_{\text{Sb}}/x_{\text{Ga}} = 0.178$  at ●, 720°C and ■, 760°C.

shown in Fig. 5 for the epitaxial layer grown at 760° and 720°C.

### Conclusions

During this investigation we have shown that GaAlAsSb layers can be prepared by liquid phase epitaxy similarly to the procedures developed for the growth of GaAsSb. Furthermore, it was observed that although the addition of Al in the liquid solution results in a decrease in the As solubility limit, the concentration ratio of Sb to As in the solid solution remains practically constant in the concentration range and temperatures investigated. This implies that lattice-matched heterojunctions in this system can be routinely grown from solutions having constant Ga and Sb concentrations and varying Al concentrations necessary for the desired heterojunction barrier. In order for this type of behavior to occur the activity of As in the solution must increase in the presence of Al to counteract the decrease in the solubility limit.

### Acknowledgments

The authors would like to express their appreciation to L. Garbini, J. von Szeremy, and S. Hikido for their technical assistance.

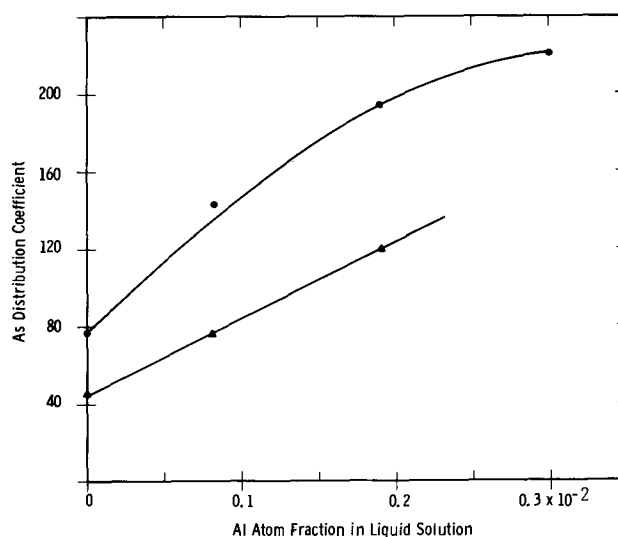


Fig. 5. The distribution coefficient of As for GaAlAsSb layers grown from solutions with  $x_{\text{Sb}}/x_{\text{Ga}} = 0.178$  at ●, 720°C and ▲, 760°C.

This work was supported by the U.S. Army Night Vision Laboratory, Fort Belvoir, Virginia 22060.

Manuscript submitted April 9, 1973; revised manuscript received Aug. 31, 1973.

Any discussion of this paper will appear in a Discussion Section to be published in the December 1974 JOURNAL. All discussions for the December 1974 Discussion Section should be submitted by Aug. 1, 1974.

### REFERENCES

1. G. A. Antypas and L. W. James, *J. Appl. Phys.*, **41**, 2165 (1970).
2. T. Mitsuhashi, in "Proceedings of the 3rd Conference on Solid State Devices, Tokyo," p. 110, Japan. Soc. of Appl. Phys. (1971).
3. K. Sugiyama and H. Saito, *Japan. J. Appl. Phys.*, **11**, 1056 (1972).
4. M. B. Panish, S. Sumski, and I. Hayashi, *Met. Trans.*, **A12**, 795 (1971).
5. R. D. Burnham, N. Holonyak, Jr., and D. R. Scifres, *Appl. Phys. Letters*, **17**, 455 (1970).
6. F. E. Rosztochy, J. F. Caldwell, J. Kinoshita, and M. Omori, *ibid.*, **22**, 525 (1973).
7. Zh. I. Alferov, V. M. Andreyev, S. G. Konnikov, V. G. Nikitin, and D. N. Tret'yakov, in "Proceedings of the International Conference on Heterojunctions I," p. 93, Academy of Sciences, Budapest (1971).
8. O. Berolo and J. C. Woolley, *Can. J. Phys.*, **49**, 1335 (1971).



# Microprobe Technique for Determination of Thickness and Phosphorous Concentration of Gate Oxide Phosphosilicate Glass in FET Devices

Giulio DiGiacomo

IBM System Products Division, East Fishkill Facility, Hopewell Junction, New York 12533

## ABSTRACT

This microprobe technique is capable of determining the thickness and phosphorous concentration of the phosphosilicate glass in FET gate oxide. The technique is equally applicable to wafers and devices. The latter application is unique since there is no other way, at present, to obtain this information on actual FET gates. In addition to the extended capability to real devices, this technique yields the phosphorous concentration with a precision of  $\pm 0.1$  mole per cent about one order of magnitude better than that obtainable by the etch rate method. The oxide and phosphosilicate thickness are determined with a precision of  $\pm 5\text{\AA}$ , comparable to that achieved by ellipsometry, with the advantage of applicability to actual devices.

It is necessary to measure accurately the phosphorous concentration and thickness of the PSG and the thickness of the total gate oxide in FET devices. The PSG serves as a stabilizer since it traps impurity ions such as  $\text{Na}^+$  which otherwise would drift to the oxide/silicon interface and affect the electrical properties of the device; e.g., threshold voltage shift. If the phosphorous concentration of the PSG is increased, say, from 4%  $\text{P}_2\text{O}_5$  m/o (mole per cent), its ability to retain trapped ions improves since the activation energy required for  $\text{Na}^+$  ion release increases greatly with phosphorous concentration (1-3). However, a higher phosphorous concentration will produce significant polarization effects, affecting the voltage threshold, causing it to shift in the same direction observed with  $\text{Na}^+$  drift. The manufacture of stable devices requires a compromise at an intermediate PSG composition sufficient to minimize threshold voltage shifts resulting from either polarization or ion drift effects.

Since threshold shifts depend strongly on phosphorous concentration an accurate knowledge of the phosphorous concentration is imperative for studying the ion-drift and polarization effects and establishing a criterion for quality control. On the basis of recent works (1-3), predictions on the threshold shifts can be made if the phosphorous and  $\text{Na}^+$  ion concentrations are known accurately. The present microprobe technique applies directly to the problem of phosphorous polarization (P concentration measurement) and indirectly to  $\text{Na}^+$  ion drift, since phosphorous controls  $\text{Na}^+$  ion trapping and the activation energy for ion release. At temperatures of  $200^\circ\text{C}$  or higher, the polarization is strongly dependent on temperature and the polarization rate appears to be proportional to the concentration squared. No polarizability saturation is noted at these temperatures at  $\text{P}_2\text{O}_5$  mole concentrations of less than 12% for a few hundred hours (2). At temperatures lower than  $120^\circ\text{C}$ , the polarizability saturates quickly and therefore one is concerned with the saturated value which is proportional to the threshold shift and which depends on the square of the P concentration. At low, as well as high temperatures, the ratio of PSG thickness to total  $\text{SiO}_2$  and PSG thickness is of importance since the threshold shift depends also on this ratio. One can assume a linear dependence at small ratios such as those prevailing in the FET's. At the higher temperature, an analysis of the data reported in this recent work (2) shows an activation energy of 0.37 eV/atom. From the same data the voltage thresh-

old shift relationship was evaluated to be

$$\Delta V = \Delta V(1 \text{ hr}, T) + 750 e^{-0.37/kT} \log t \quad [1]$$

For a  $\text{P}_2\text{O}_5$  concentration of 4%, temperature of  $140^\circ\text{C}$ , and a ratio,  $t_{\text{PSG}}/t_{\text{SiO}_2}$  of 0.14, the threshold shift due to polarization is  $\sim 0.1\text{V}$  for 1000 hr. Concentration and thickness ratio factors can be included in the above relationship to take into consideration their effects.

## Experimental

**Method.**—Full characterization of the PSG in terms of phosphorous concentration and thickness requires the measurements of both phosphorous and oxygen characteristic radiation before and after a layer of the PSG is removed by etching. The removal produces x-ray intensity decrements of both elements proportional to the thickness of the layer removed and makes possible, with the original intensity values, the calculation of thickness and phosphorous concentration of the PSG and the total thickness of the gate oxide. An illustration of the principle of the microprobe approach appears in Fig. 1a which also defines the x-ray values measured and shows the thickness and concentration quantities. The proportionality constants between these quantities and the x-ray intensities have been determined experimentally utilizing samples of known phosphorous content and oxide thickness. X-ray intensities yielded straight lines as expected when plotted against phosphorous content and oxide thickness. For thin films these relationships are linear at sufficiently high voltage. Figure 1a also shows that the electron beam penetration is greater than the thickness of the silicon oxide. Figure 1b shows the x-ray intensi-

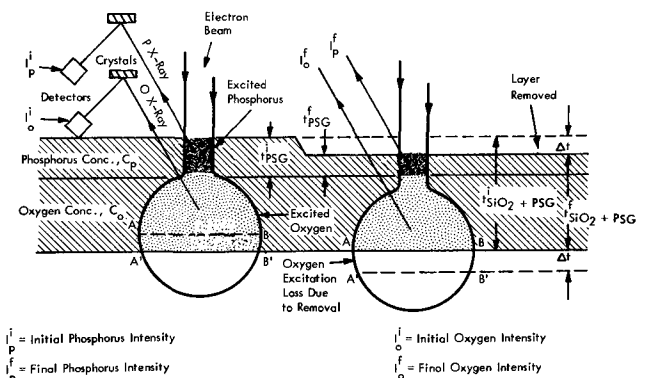


Fig. 1a. Principle of microprobe technique

Key words: polarization, ion drift, voltage threshold, ion trapping,  $\text{SiO}_2$ -silicon interface.

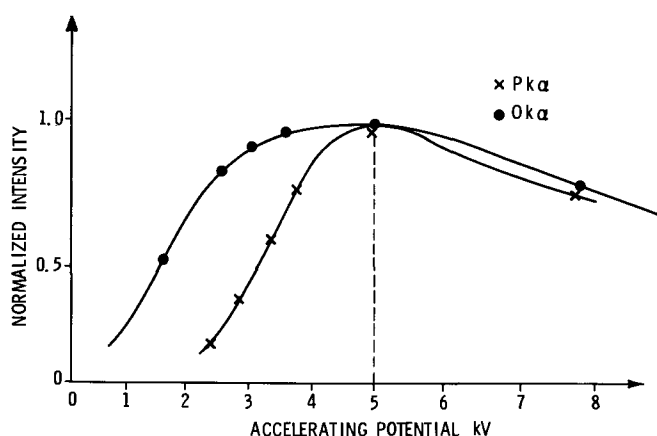


Fig. 1b. Intensity optimization

ties of both elements vs. the accelerating potential. From the plot it is evident that approximately 5 kV gives maximum intensities. At this potential we also obtain optimum detectability. At higher keV, the detectability degenerates quite fast because of a rising background and decreasing ionization cross section; at lower voltages the ionization efficiency is low.

Figure 1a exhibits the initial x-ray measurements of both elements  $I_0$  and  $I_p$ . These two intensity values when used in Fig. 2 and 3, respectively, yield the initial oxide plus PSG thickness,  $t_{\text{SiO}_2 + \text{PSG}}$ , and the initial phosphorous content in terms of thickness  $\times$  concentration units,  $t_{\text{PSG}} \cdot C_p$ . After the x-ray measurement is completed, the wafers are etched for 1½ min with DP etchant to remove approximately 40Å of PSG which contains ~4%  $\text{P}_2\text{O}_5$ . (The etchant is a dilute solution of HF and  $\text{HNO}_3$  acids, 3 parts of HF and 2 parts of  $\text{HNO}_3$  in 645 parts of water.) Having etched a part of the PSG, a second microprobe measurement is made for both elements. The intensities  $I_0'$  and  $I_p'$ , thus obtained are again used in Fig. 2 and 3 to determine the new oxide thickness,  $t_{\text{SiO}_2 + \text{PSG}}'$ , and the new phosphorous content  $t_{\text{PSG}}' \cdot C_p$  (refer to Fig. 1a also). It is to be noted that the technique requires PSG removals equal or less than the total PSG thickness. From the above measured values, the thickness and phosphorous concentration of the PSG are determined in the following manner

$$t_{\text{SiO}_2 + \text{PSG}} - t_{\text{SiO}_2 + \text{PSG}}' = \Delta t_{\text{SiO}_2 + \text{PSG}} = \Delta t_{\text{PSG}} \quad [2]$$

$$t_{\text{PSG}} \cdot C_p - t_{\text{PSG}}' \cdot C_p = \Delta t_{\text{PSG}} \cdot C_p \quad [3]$$

$$I_p - I_p' = \Delta I_p \propto \Delta t_{\text{PSG}} \cdot C_p \quad [4]$$

$$I_0 - I_0' = \Delta I_0 \propto \Delta t_{\text{PSG}} \quad [5]$$

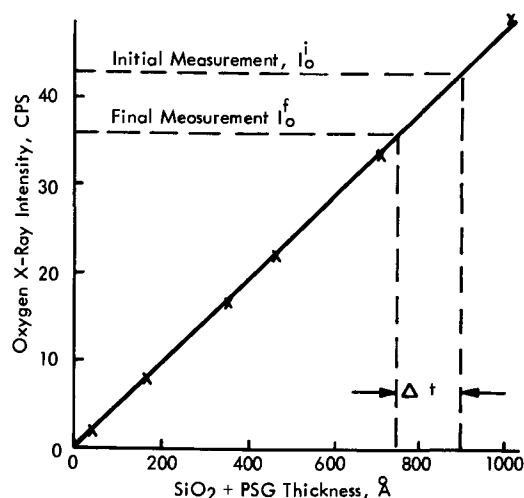


Fig. 2. Determination of PSG layer removed

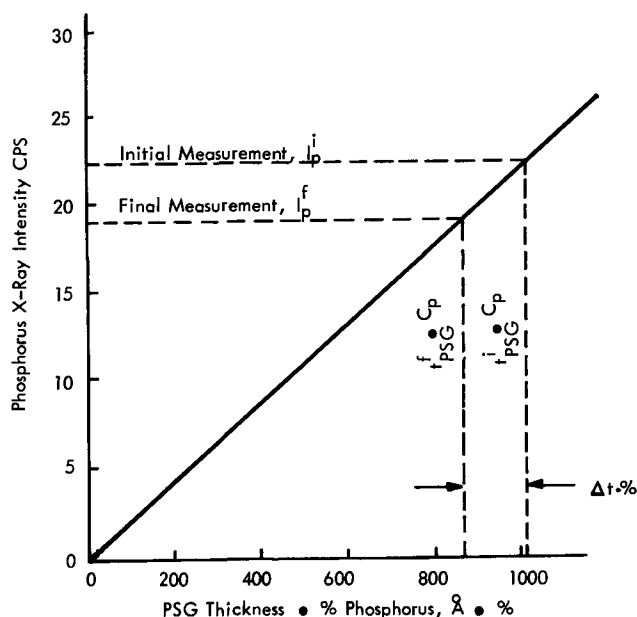


Fig. 3. Determination of phosphorous content in Å · % units

The two values of thickness and phosphorous content,  $\Delta t_{\text{PSG}}$  and  $\Delta t_{\text{PSG}} \cdot C_p$ , are read directly from the calibration curves. Having obtained  $C_p \cdot \Delta t_{\text{PSG}}$  from phosphorus and  $\Delta t_{\text{PSG}}$  from oxygen intensities, division of the former by the latter yields the phosphorous concentration. Having obtained the phosphorous concentration, one can obtain the thickness  $t_{\text{PSG}}$  from the graph of phosphorous intensity vs. mass thickness, by dividing the initial mass thickness of phosphorus by the concentration as obtained above

$$C_p = \frac{\Delta t_{\text{PSG}} \cdot C_p}{\Delta t_{\text{PSG}}} \quad [6]$$

and

$$t_{\text{PSG}} = \frac{t_{\text{PSG}} \cdot C_p}{C_p} \quad [7]$$

and

$$\text{Thickness ratio} = \frac{t_{\text{PSG}}}{t_{(\text{SiO}_2 + \text{PSG})}} \quad [8]$$

$C_p$  and the thickness ratio are the two parameters needed for determining the polarization. Measurement of both PSG thickness and composition are thus obtained with two microprobe measurements and only one etching operation. To perform the above measurements in one operation, black wax is used to cover a portion of the region to be analyzed before the PSG is removed such that the covered PSG is not etched. Upon removal of the black wax, the probe analysis is performed on both etched and unetched portions. Thus, all microprobe information is obtained with a minimum of error. This refers to errors due to time-dependent instabilities.

**Procedure and results.**—To obtain calibration curves for both phosphorous and oxygen, eleven wafers with known oxide thicknesses were analyzed by the probe. The  $\text{SiO}_2$  thicknesses which ranged from 30 to 2000Å has been determined by the ellipsometry method. The x-ray intensities obtained from these samples by microprobe were plotted vs. the known thicknesses. The plot was a straight line passing through the origin and having a slope of about 0.05 cps (counts per second)/Å, which is the x-ray sensitivity for  $\text{SiO}_2$  thickness. In other words one needs a 20Å thick layer of  $\text{SiO}_2$  to get 1 cps intensity at electron beam conditions of 5 kV and  $10^{-7}\text{A}$ . The minimum detectable limit was found to be 5Å for a 1 min x-ray count. The analysis was performed with an ARL probe which has a take-off angle of 52°. Lead stearate and ADP

crystal monochromators were used for determining oxygen and phosphorous, respectively.

A similar linear plot was obtained with phosphorous content *vs.* x-ray intensity using a set of samples which had been analyzed by neutron activation or compared to neutron activation standards. Since thickness multiplied by concentration is a convenient and practical measure of phosphorous content the concentration-thickness unit,  $\text{\AA}\cdot\%$ , was adopted. Following the method of analysis outlined, the phosphorous sensitivity was determined to be  $0.023 \text{ cps}/\text{\AA}\cdot\%$  which yields a minimum detectable limit of  $15 \text{ \AA}\cdot\%$  for 100 sec of x-ray count. (There are  $4.4 \times 10^{12} \text{ at}/\text{cm}^2/\text{\AA}\cdot\%$ .) This means that the thickness of a PSG having 3% P concentration can be determined within  $5\text{\AA}$ . The accuracies for phosphorous and oxygen are comparable although it requires a slightly longer x-ray count for phosphorous determination. The counting time requirement for a desired accuracy is dictated by the x-ray statistics which are based on the photon distribution in time. The minimum detectable limit (MDL) for both elements was calculated according to the following relationship

$$\text{MDL} = \frac{\left(\frac{1}{t_p} + \frac{1}{t_b}\right)^{1/2} B^{1/2}}{S} \quad [10]$$

where  $T_p$  = time to count the peak signal for a fixed total count (sec),  
 $t_b$  = time to count background for the same total count (sec),  
 $B$  = background in counts per second (cps), and  
 $S$  = concentration sensitivity in  $\text{cps}/\text{\AA}\cdot\%$ .

The background was measured in both sides of the peak and averaged. This agreed with the calibration line intercept on the intensity axis. By increasing the total count and therefore  $t_p$  and  $t_b$ , the MDL is made sufficiently small to meet the desired accuracy. There is a limit, however, to how far one can increase the total count or counting time since there are other factors such as equipment power instability and carbon build-up on the specimen which finally limit the MDL. Carbon build-up is minimized by a decontaminator. Contamination is minimized by circulating liquid nitrogen in the water cooling coils of the objective lens (ARL probe), which promotes vapors condensation. This reduces contamination by more than a factor of ten. The effect of carbon build-up is within experimental error which is reflected in the accuracy stated.

Since we are dealing with x-ray signals just above background, the minimum detectable limit as calculated above is also the precision with which a measurement is made and, when a sample of known composition and thickness is used as a control it represents the accuracy. Dozens of samples, wafers and devices alike, have been analyzed to show in practice that the accuracy calculated on the basis of the x-ray statistics was indeed attainable. The reproducibility of the x-ray readings, and therefore the accuracy of the oxide thickness and phosphorous content, were found to be within the MDL calculated. Figures 4 and 5 show how oxygen and phosphorous x-ray intensities from the above samples plot linearly against  $\text{SiO}_2$  thickness and phosphorous content. Considering the composition and thickness ranges, the calibration lines in both cases are satisfactorily straight. The samples have been analyzed many times and the straight lines reproduced each time. Figure 6 is another graph obtained from a number of  $\text{SiO}_2$  samples analyzed later. The graph includes also three samples originally used in the intensity-thickness calibration curve shown in Fig. 4. The original samples were included to show the reproducibility at a different time. In Fig. 5,

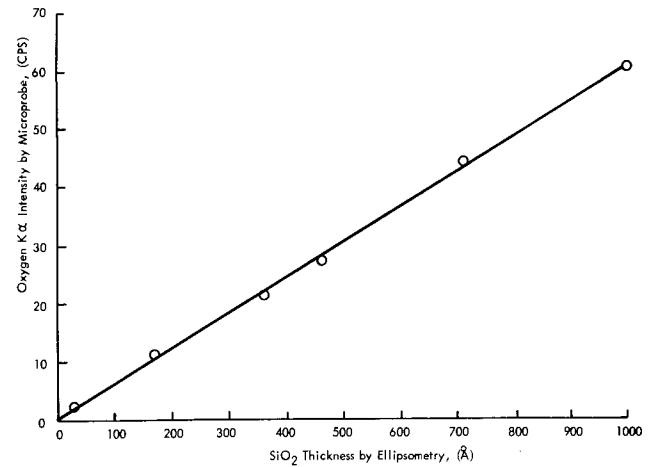


Fig. 4.  $\text{SiO}_2$  thickness calibration curve

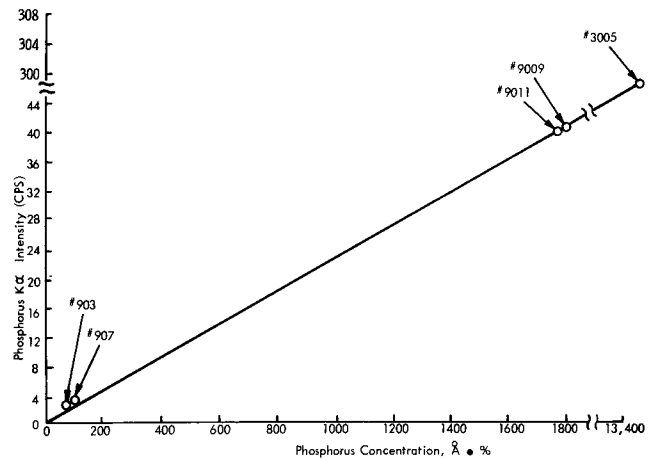


Fig. 5. Calibration curve for PSG phosphorous content

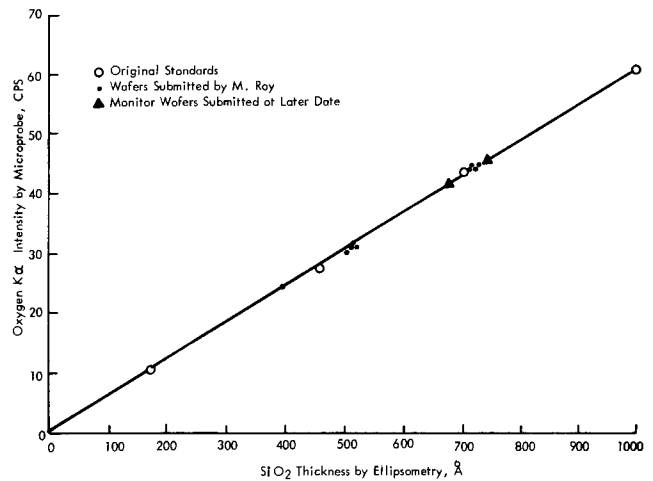


Fig. 6. FET gate oxide and PSG measurement of samples

only one sample (No. 3005) was analyzed directly by the neutron activation method; the others were simultaneously analyzed by the x-ray fluorescence technique with standards of comparable composition whose phosphorous content had been determined by neutron activation analysis. These wafer samples were analyzed within an accuracy of  $\pm 5\%$  of the amount of phosphorous. Hundreds of wafers and devices have been fully analyzed by this technique recently. Each of them has gone through the etching and microprobe measurement steps. Typical oxide removals of  $\sim 60\text{\AA}$  have been obtained with etching times of about 2 min. The technique has become, therefore, part of the characterization process of wafers and devices.

### Discussion and Conclusions

Measurements of the SiO<sub>2</sub> thickness are based, as already indicated, on the intensity of the oxygen K $\alpha$  x-ray generated in the oxide layer as a result of electron bombardment. At 5 kV, the x-ray intensity is directly proportional to the oxide thickness for oxide layers <2000Å. Since oxygen is present in both SiO<sub>2</sub> and PSG, the x-ray technique gives the total thickness of SiO<sub>2</sub> and PSG. There is a slight difference, however, in the oxygen content between SiO<sub>2</sub> and the PSG because of the presence of a few per cent of phosphorous. This difference is either small (3% or less) and therefore neglected, or it is easily accounted for when a high phosphorous concentration warrants it. For thin gate oxide PSG's, this correction is not necessary. After going through the zeroing procedure, the electron beam current is adjusted to give 100 nA specimen current. The adjustment is made on the specimen itself. The P<sub>2</sub>O<sub>5</sub> and SiO<sub>2</sub> standards (measured originally by the independent method as specified) are analyzed simultaneously with the specimen under the same conditions to standardize the intensity values and generate calibration curves for both phosphorus and oxygen as illustrated in Fig. 2 and 3. It is important that the specimen current remains constant during the test.

The phosphorous analysis, as already indicated, is carried out simultaneously with oxygen using a different spectrometer. This is advantageous in terms of time and accuracy because the x-ray intensities of both elements come from sample volumes irradiated and analyzed at the same time, thus, allowing a faster analysis and preventing any error that might arise from possible inhomogeneities and an instrumental power instability.

Because of the linearity with which x-ray intensities are related to the thickness and the phosphorous concentration of the PSG, and because of the accuracy with which the x-ray intensity can be measured, this

technique can be used with little effort to evaluate other techniques such as the etch-rate technique which is known to have an accuracy on the order of  $\pm 1\%$  P<sub>2</sub>O<sub>5</sub>. The microprobe technique has revealed upon extensive application that this error is at times greater than  $\pm 1\%$ . Consequently it is concluded that (i) the etch rate technique may not be adequate when applied to study the effects of phosphorous polarization and Na<sup>+</sup> ion drift, and (ii) the present microprobe technique is unique for determining silicon oxide thickness in FET gate oxide, PSG thickness, and PSG phosphorous concentration within the accuracy required in the study of P-polarization and Na<sup>+</sup> ion drift for finished devices.

### Acknowledgment

The author wishes to acknowledge J. J. Gniewek for his guidance, helpful suggestions, and assistance in procuring the materials and Watson Research Center, Yorktown, for the wafer sample analyses. Mr. Maurice Roy and Mrs. Donna Bouer are acknowledged for providing the oxide and PSG wafers used in this work. The assistance of D. Stabell in providing the help for etching the wafers and devices is appreciated.

Manuscript submitted April 2, 1973; revised manuscript received Aug. 15, 1973.

Any discussion of this paper will appear in a Discussion Section to be published in the December 1974 JOURNAL. All discussions for the December 1974 Discussion Section should be submitted by Aug. 1, 1974.

### REFERENCES

1. J. M. Eldridge and D. R. Kerr, "Sodium Ion Drift Through Phosphosilicate Glass-SiO<sub>2</sub> Films," Aug. 10, 1970 (IBM Technical Report).
2. J. M. Eldridge, R. B. Laibowitz, and P. Balk, *J. Appl. Phys.*, **40**, 4 (Nov. 1968).
3. E. H. Snow and B. E. Deal, *This Journal*, **113**, 263 (1966).

## Some Device Applications of Spreading Resistance Measurements on Epitaxial Silicon

Bernard L. Morris

*Bell Telephone Laboratories, Incorporated, Allentown, Pennsylvania 18103*

### ABSTRACT

Thin epitaxial silicon should not be characterized by simply specifying a thickness and resistivity. The success of a device can depend on knowledge of the entire epitaxial impurity profile. In most cases the complete profile can only be obtained by the spreading resistance technique. The information obtained by this method should then be correlated with the results of the more commonly used characterization techniques; infrared thickness measurement and diode capacitance-voltage profiling. Examples of such correlations are presented for a number of thin epitaxial device structures such as GIMIC, OXIM, a 50 GHz IMPATT diode, a PIN phase modulator, and a large area power Schottky diode.

If a flat circular voltage probe of radius  $a$  is brought into contact with a semi-infinite conducting material, practically all of the potential drop occurs within  $1.5 \times a$  of the point of contact (1). For a metal-semiconductor contact in which the surface barrier resistance (Schottky resistance) may be neglected, the resistance of the contact, which is called the spreading resistance, is

$$R_s = \rho/4a \quad [1]$$

Key words: spreading resistance, epitaxial silicon, resistivity profiles, integrated circuits.

where  $\rho$  is the semiconductor resistivity. Since real metal-semiconductor contacts can have appreciable barrier resistance, an empirical calibration of  $R_s$  vs.  $\rho$  is necessary. For silicon with a given value of resistivity, the spreading resistance depends on the conductivity type, orientation, and surface finish. Calibration curves have been constructed by measuring both  $\rho$  and  $R_s$  on a large number of samples, both N and P, <111> and <100>, with resistivities from approximately 0.001 to 100 ohm-cm. All of the calibration samples are Syton polished.

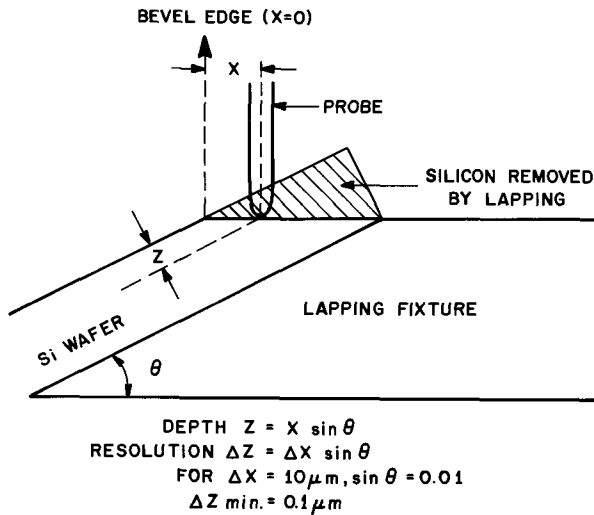


Fig. 1. Side view of spreading resistance profiling technique

The spreading resistance (SR) set used in this work is the model ASR-100 built by Solid State Measurements, Inc.<sup>1</sup> The probes are made of an osmium-tungsten alloy, and pressure is applied by 45g weights. The sample is placed on an X-Y stage, and the X drive is automatically stepped after each measurement; the step sizes used vary from 10 to 250  $\mu\text{m}$ . If a measurement of the uniformity of surface resistivity is required, the sample is either waxed onto a block or held on a vacuum chuck, and the SR is automatically scanned and recorded with the selected step size. If a resistivity profile in depth is desired, the sample must be angle lapped on a special fixture supplied with the ASR-100. This is shown in Fig. 1. Since the  $\rho$ - $R_s$  calibration is strongly dependent on the surface finish (2), the initial lapping with Linde-A is followed by a final polish with Syton.

The assumption of semi-infinite material from which Eq. [1] was derived does not hold for thin epitaxial layers. A thin film correction factor (CF) must be used, so that Eq. [1] now reads

$$\rho_{\text{corr}} = 4aR_s/CF \quad [2]$$

The value of the CF depends on the relative resistivities and types of the epitaxial layer and substrate, and on the ratio  $t/a$  where  $t$  is the epitaxial layer thickness, and  $a$  is the effective contact radius as defined by Eq. [1]. Values of the CF for different types of profiles are available in the literature (3, 4). The two limiting cases for the CF are shorting and insulating boundaries. The former is a good representation of steep N/N<sup>+</sup> (or P/P<sup>+</sup>), while the latter holds for a P/N (or N/P) epi-substrate boundary. These CF's are shown schematically in Fig. 2.

The contact radius of the ASR-100 probes is approximately 3  $\mu\text{m}$ . For insulating boundaries, Fig. 2 shows that the CF begins to change rapidly for  $t/a \lesssim 5$ , that is for  $t \lesssim 15 \mu\text{m}$ . Due to the uncertainty in the (calculated) CF in this range, the errors in the calculated values of  $\rho$  will tend to become large as the junction is approached. For N/N<sup>+</sup> (or P/P<sup>+</sup>) the actual resistivity profile can be more accurately determined, since the CF tends toward unity as the resistivity of the epitaxial layer approaches the substrate resistivity. Therefore as the N-N<sup>+</sup> boundary (which in practice is always graded) is approached,  $\rho_1$  smoothly approaches  $\rho_2$ , and even though  $t/a$  becomes very small the CF goes to unity.

The over-all accuracy of the SR profile depends on: the measurement of the depth,  $z$ ; the reproducibility of the measured spreading resistance,  $R_s$ ; the accuracy of the  $\rho$ - $R_s$  calibration; and the accuracy of the CF calculation. The error in depth measurement is  $dz =$

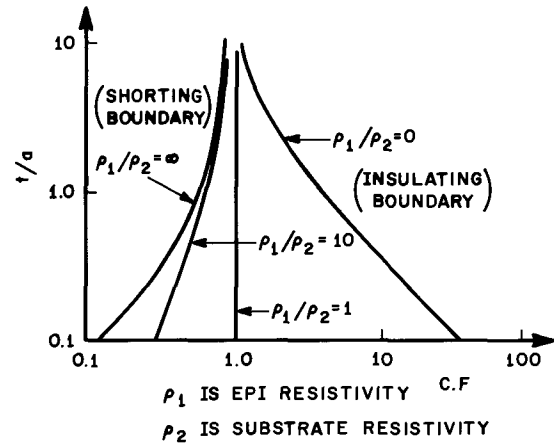


Fig. 2. Spreading resistance correction factors

$\pm (0.05 \times z + 0.1) \mu\text{m}$ , where  $z$  is the depth in micrometers. The first term,  $\pm 5\%$  of  $z$ , is the error in  $\theta$  (see Fig. 1) and the second term, 0.1  $\mu\text{m}$ , is due to possible alignment error and error in the definition of the bevel edge.

The reproducibility of  $R_s$  is better than  $\pm 5\%$  for  $\rho \lesssim 5 \text{ ohm-cm}$ . At higher resistivities  $R_s$  is increasingly influenced by adsorbed water and by minor variations in surface quality.

There is no simple way of judging the accuracy of the  $\rho$ - $R_s$  calibration or the CF calculations. The best measure of the accuracy of the SR technique is to compare its results with those of diode C-V profiles. Such comparisons suggest an over-all accuracy of  $\pm 10\%$  for N/N<sup>+</sup> or P/P<sup>+</sup> profiles, and  $\pm 20\%$  for P/N or N/P profiles.

#### Measurement of Effective Epitaxial Thickness

In the days when Si epitaxial thickness was typically  $\gtrsim 8 \mu\text{m}$ , with an (assumed) flat resistivity profile, the exact definition of the thickness was not a problem. Angle lap and stain and/or infrared (IR) thickness measurements were used to define  $t$ , and the resistivity was usually defined at a single point on the profile.

Device technology has now advanced to the point where many epitaxial thicknesses are in the region 1-4  $\mu\text{m}$ , with the newest IMPATT diodes requiring submicron epitaxial layer,  $t = 0.6-0.8 \mu\text{m}$ .

For this thin epitaxial material, it is not enough to specify a thickness and a resistivity; the complete profile must be known.

Every device design assumes some number which is supposed to characterize the epitaxial thickness. This is the electrical or effective epitaxial thickness,  $t_{\text{eff}}$ . For epitaxial layers with a conductivity type different than that of the substrate (or buried layer), this thickness usually corresponds to the point at which the net carrier concentration is zero. For N/N<sup>+</sup> (or P/P<sup>+</sup>) structures  $t_{\text{eff}}$  will correspond to some value of  $N_D$  (or  $N_A$ ) on the (graded) boundary profile.

Once the desired thickness ( $t_{\text{eff}}$ ) is known, the next step is to correlate it with a practical production technique.

The two methods commonly used for epitaxial layer thickness measurement are IR and angle lap and stain. The former technique is nondestructive, fast (5 sec/measurement with the FTG-12<sup>2</sup>), operator independent, accurate, and reproducible to within  $\pm 0.1 \mu\text{m}$ . Angle lap and stain is destructive, slow, operator and stain dependent, with a multi-laboratory precision of  $\pm (0.15t + 0.5) \mu\text{m}$  (5). For these reasons the use of the IR thickness is preferred.

It must be emphasized that the correlation between  $t_{\text{eff}}$  and  $t_{\text{IR}}$  for a particular device depends on the

<sup>1</sup> Solid State Measurements Inc., Murrysville, Pennsylvania.

<sup>2</sup> Digilab Inc., Cambridge, Massachusetts.

epitaxial resistivity profile. This depends on the reactor time-temperature cycle and the surface impurity concentration of the substrate or buried layer. If any of these parameters are changed, the correlation must be re-established. Two specific examples of the application of SR to the  $t_{\text{eff}}-t_{\text{IR}}$  correlation will now be discussed.

The Oxim (Oxide Isolated Monolithic) structure has epitaxial specifications similar to those of thin CDI (6). The epitaxial layer is low resistivity P-type,  $t_{\text{IR}} = 2.0 \mu\text{m}$ , grown over a standard Sb diffused buried layer. The effective thickness of this device is the point at which the material changes from P- to N-type, that is the point of maximum resistivity. This is shown in Fig. 3. This figure also shows the IR and stain thicknesses. Note that  $t_{\text{IR}}$  thickness falls at the point of maximum impurity concentration (minimum value of SR). This has been found always to be the case when the substrate, or buried layer, concentration is in the region of  $10^{19} \text{ cm}^{-3}$ , which is the range of the standard Sb diffused buried layer. It is also obvious that the stain depth,  $t_{\text{st}}$ , does not coincide with  $t_{\text{eff}}$  as is often assumed. Since  $t_{\text{eff}}$  corresponds to an easily identifiable point on the SR profile, it is not necessary to calculate the resistivity (or carrier concentration) profile.

Another device, GIMIC (Guard Ring Implanted Monolithic Integrated Circuit) (7) is shown in Fig. 4. In both GIMIC and Oxim as in CDI, the epitaxial layer forms the base region. In CDI and Oxim the base doping is determined by the epitaxial resistivity. In GIMIC the epitaxial layer is grown with the highest possible resistivity, and the effective base doping (the Gummel number) is implanted into this "intrinsic" layer. The actual transition between the intrinsic epitaxial layer and the heavily doped buried layer is quite graded. It was decided that  $t_{\text{eff}}$  for this device corresponds to the point on the outdiffusion profile

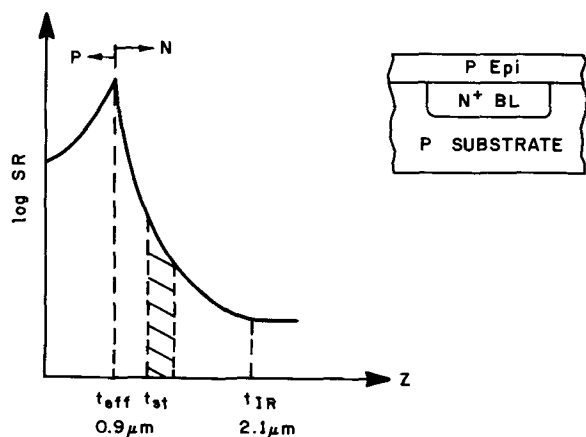


Fig. 3. Spreading resistance profile of Oxim-II epitaxial layer

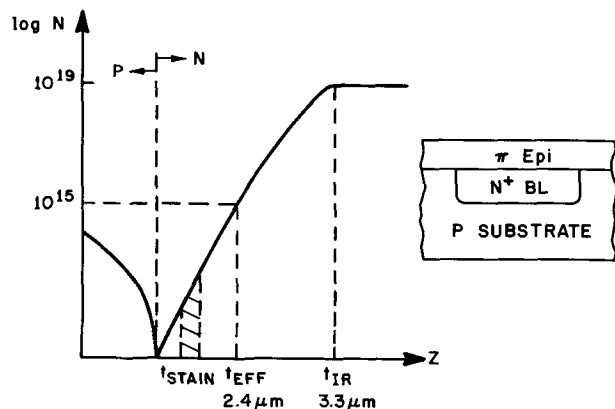


Fig. 4. Spreading resistance profile of GIMIC epitaxial layer

where the concentration is  $10^{15} \text{ cm}^{-3}$ , all material from this point to the surface is considered intrinsic. For six different epitaxial runs, the correlation of  $t_{\text{eff}}$  and  $t_{\text{IR}}$  had a maximum spread of  $\pm 0.1 \mu\text{m}$ , that is,  $(t_{\text{IR}} - t_{\text{eff}}) = 0.9 \pm 0.1 \mu\text{m}$  in all cases. The same correlation between  $t_{\text{eff}}$  and  $t_{\text{st}}$  had a maximum spread of  $\pm 0.4 \mu\text{m}$ . Since  $t_{\text{eff}}$  corresponds to a specific concentration, the raw SR data had to be converted to a concentration profile. As the critical area can be considered to be an  $N/N^+$  structure, the  $CF$  is sufficiently well known to do this conversion with the necessary accuracy.

### Measurement of the Complete Epitaxial Profile

For  $N/N^+$  or  $P/P^+$  epitaxial structures, the diode capacitance-voltage ( $C-V$ ) method is often used to determine the carrier concentration profile (8). Analog methods such as the Copeland (9) or Miller Feedback Profilers (10) use the same basic phenomenon as the  $C-V$  method to record the profile.

All of these methods are quite useful as they provide a direct measure of the carrier concentration profile  $N(x)$  without the necessity of calibration curves for different materials. However, they all suffer the same basic limitation; the minimum and maximum depths over which  $C-V$  profiles may be obtained are limited respectively by the zero bias depletion width and the depletion width at breakdown. The minimum value of the depletion width is obtained using simple evaporated Schottky diodes; however, these have an inherently soft breakdown, so the maximum depth reached falls short of the theoretical one.

For many types of profiling these limitations are not serious, but if the resistivity at the true surface, or the exact shape of the epitaxial-substrate interface are needed,  $C-V$  techniques cannot be relied upon.

A 50 GHz IMPATT diode requires an epitaxial structure with the following specifications: substrate—As doped,  $\rho \lesssim 0.0015 \text{ ohm-cm}$ ; epitaxial layer—As doped,  $N_D = 5.3 \times 10^{16} \text{ cm}^{-3}$  ( $\pm 10\%$ ); and  $t_{\text{eff}} = 1.5 \mu\text{m}$ .

It is required that the carrier concentration,  $N_D$ , in the epitaxial layer be constant from the true surface to  $t_{\text{eff}}$ . After that point  $N_D$  should rise as sharply as possible. At  $N_D = 5.3 \times 10^{16} \text{ cm}^{-3}$ , the total distance that a  $C-V$  profile can cover is approximately  $0.35 \mu\text{m}$ . To measure a complete profile of this epitaxial layer using  $C-V$  techniques, five different diodes with diffusion depths ranging from  $0.0 \mu\text{m}$  (i.e., a Schottky diode) to  $1.3 \mu\text{m}$  would be needed. Even then the first  $0.2 \mu\text{m}$  could not be measured. Figure 5 shows  $N(x)$  profiles of two attempts to fabricate this structure. The  $C-V$  data were obtained by combining the results of two different diode diffusion depths. The first structure would make good devices while the second would not. This last fact, however, is not readily apparent from the  $C-V$  data.

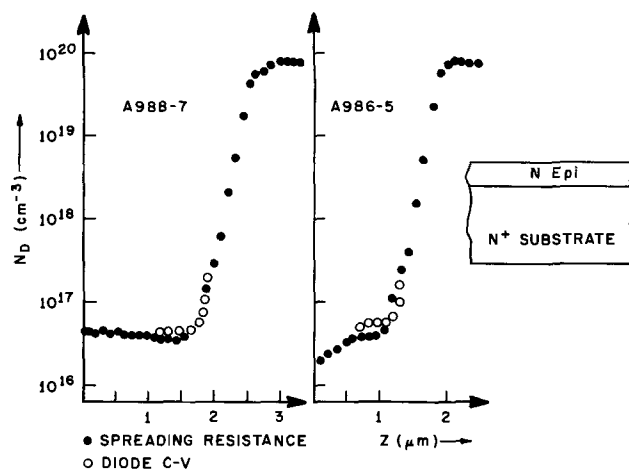


Fig. 5. Spreading resistance and diode  $C-V$  profiles of IMPATT diode epitaxial layers.

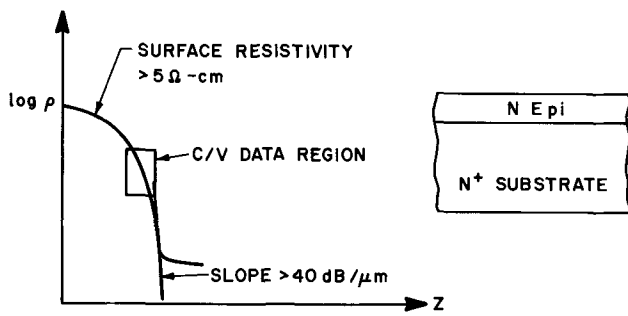


Fig. 6. Spreading resistance profile of PIN phase modulator

The epitaxial profile required for a new PIN phase modulator is shown in Fig. 6. This device requires that the epitaxial resistivity be  $\geq 5$  ohm-cm near the surface, and that the resistivity rise sharply at the epitaxial-substrate interface,  $\Delta\rho/\Delta X \cong$  two orders of magnitude (40 db) per micron. Only a small region of this profile is accessible to C-V profiling, as the zero bias depletion width is typically  $1\mu$ , and the breakdown voltage is quickly reached as the epitaxial resistivity starts to decrease. Figure 6 shows schematically the complete profile as determined by SR, and the small portion of the profile accessible to C-V methods.

**Outdiffusion and Autodoping**

The ability of SR to measure the entire epitaxial substrate interface makes it a powerful tool to study outdiffusion and autodoping. For the purposes of this paper, outdiffusion is defined as the change in the resistivity profile resulting from solid-state diffusion mechanisms. This process occurs during both epitaxial growth and subsequent heat-treatments. Autodoping is defined as the change in resistivity profiles due to impurities which are evaporated from the substrate and reintroduced into the solid during epitaxial growth. The effective diffusion constant of the substrate during epitaxial growth can be two orders of magnitude greater than the usual solid-state diffusion constant. In Fig. 3 the total outdiffusion is  $t_{IR} - t_{eff} = 1.2 \mu\text{m}$ . The epitaxial layer was grown over an Sb buried layer heated for 13 min at  $1050^\circ\text{C}$ . The corresponding solid-state diffusion length,  $2\sqrt{DT}$ , in the literature (11) is  $0.066 \mu\text{m}$ . The "effective" diffusion is approximately 180 times greater than this. This enhancement is in good agreement with recent calculations (12) of autodoping-outdiffusion effects over Sb substrates. Detailed knowledge of this phenomenon can be vitally important in the design of new devices utilizing thin epitaxial material.

The initial epitaxial profile will be altered by heat-treatments associated with oxidation and diffusion during processing. Two examples of this on actual device structures are shown in Fig. 7 and 8. Figure 7 shows that in Oxim the average change in  $t_{eff}$  after heating is  $0.15 \mu\text{m}$ . Figure 8 shows that after the GIMIC

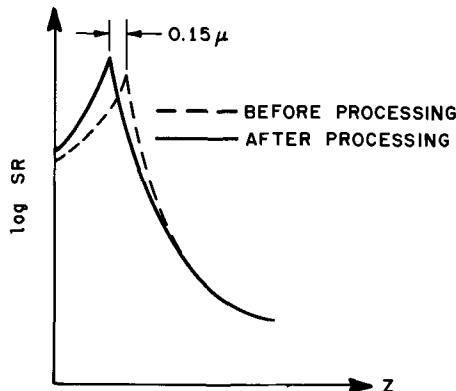


Fig. 7. Oxim-II profile after heat-treatments

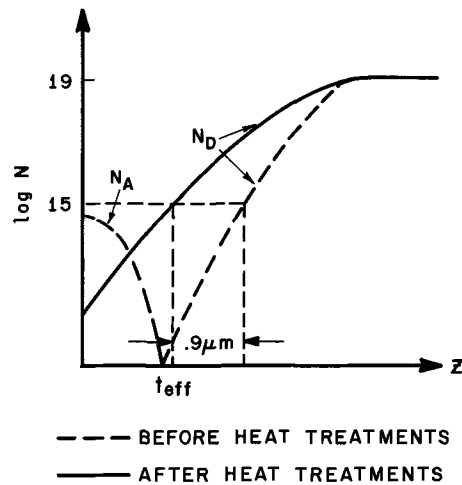


Fig. 8. GIMIC profile after processing heat-treatments

heat-treatments the effective thickness has changed by  $0.9 \mu\text{m}$ , and the "surface" layer has changed from p-type to n-type.

**Measurements of Completed Devices**

In order to make SR profile measurements in a material  $t$  microns thick, a minimum area of approximately  $1.5 \text{ mm} \times 150t \mu\text{m}$  is needed. The first limit is due to the 1 mm spacing between the two probes, the second comes from the 100X magnification of the angle lap. For epitaxial layers grown over a low resistivity substrate (no buried layer) this is not a problem, but for most buried layer patterns this limit cannot be easily satisfied, and a blanket diffused control wafer must be used.

This area limit makes it difficult to do SR profile measurements on most completed device structures; however, measurements can be made on these wafers if there is a large control bar, or if the device itself is one with a large area. An example of the second case is shown in Fig. 9. A power Schottky diode with a large area ( $160 \text{ mil}$  diameter) had been designed for low series resistance and medium breakdown voltages. It was found that the BV map of some completed wafers was very nonuniform, and it was suspected that inhomogeneities in the epitaxial resistivity profile could be the cause of the soft breakdowns. One wafer which showed both good and bad breakdowns was profiled. The measurement results, as shown in Fig. 9, showed that the epitaxial profiles were identical in both diodes, and thus the "soft" breakdowns are not due to nonuniformity of the resistivity profile.

**Uses in a Manufacturing Area**

The discussion of SR up to this point has emphasized its use as an aid in the development of new epitaxial devices. In addition to these uses, SR measurements can be of use in production environments.

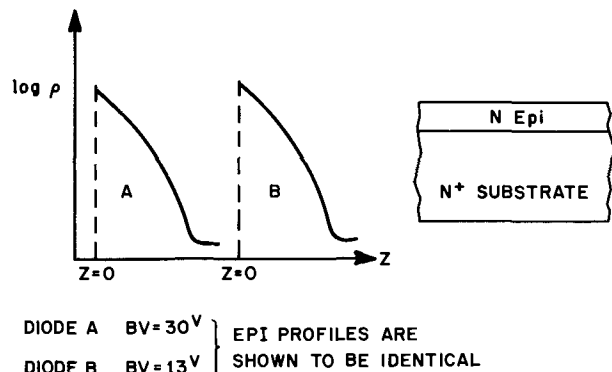


Fig. 9. Spreading resistance used as diagnostic tool

There are two distinct uses of SR in manufacturing; measurement of epitaxial surface resistivity and measurement of the complete epitaxial profile. The first use merely requires placing a wafer in a vacuum chuck in the ASR-100 and measuring  $R_s$  at a few points on the epitaxial surface, which has a finish equivalent to a Syton polished surface (2). No angle lapping is required. This measurement is basically nondestructive, the total surface damage being limited to the probe marks which are roughly 8  $\mu\text{m}$  in diameter. In order to calculate the actual resistivity, the layer thickness must be known from IR measurements. Total measurement time for this technique is less than 1 min per wafer, and it may be used on either control or product wafers.

The second use of SR in production requires that a chip be scribed from a wafer for angle lapping. The complete profile of the epitaxial material could then be measured. This technique would take approximately 10-20 min per profile and would thus be limited to a small sample size.

Since this method would significantly contribute to the total wafer cost, its use would be justified only where control of the complete epitaxial profile is vital to the success of the device.

### Conclusions

Thin epitaxial material should not be characterized by simply specifying a thickness and resistivity. An awareness of the entire resistivity profile can be essential to the success of the device. In most cases the complete profile can only be obtained by the SR technique.

Once the profile has been established, a correlation of the "effective" epitaxial thickness and the IR thickness may be made. The results of diode C-V profiling, which necessarily covers a limited thickness range, may also be compared to the SR results. Once established, these correlations should remain constant as long as the epitaxial growth conditions and the substrate impurity concentration are unchanged. Changes in the heat-treatment schedule during device processing can also affect these correlations.

### Acknowledgment

Thanks are expressed to P. H. Langer for his aid with the thin film correction factor computer program, and to K. E. Benson for his continuing guidance.

Manuscript submitted May 14, 1973; revised manuscript received Aug. 15, 1973. This was Paper 76 presented at the Chicago, Illinois, Meeting of the Society, May 13-18, 1973.

Any discussion of this paper will appear in a Discussion Section to be published in the December 1974 JOURNAL. All discussions for the December 1974 Discussion Section should be submitted by Aug. 1, 1974.

### REFERENCES

1. R. Holm, "Electric Contacts Handbook," Springer, Berlin (1967).
2. D. C. Gupta, J. Y. Chan, and P. Wang *Rev. Sci. Instr.*, **41**, 1681 (1970).
3. P. A. Schumann, Jr. and E. E. Gardner, *Solid State Electron.*, **12**, 371 (1969).
4. E. E. Gardner, P. A. Schumann, Jr., and E. F. Gorey, "Measurement Techniques for Thin Films," p. 258, B. Schwartz and N. Schwartz, Editors, The Electrochemical Society Softbound Symposium Series, New York (1967).
5. Method F 110, "Thickness of Epitaxial or Diffused Layers in Silicon by the Angle Lapping and Staining Technique," 1969 Book of ASTM Standards, part 8.
6. B. T. Murphy, V. H. Glinski, P. A. Gary, and R. A. Pedersen, *Proc. IEEE*, **57**, 1523 (1969).
7. J. Agraz-Guerena, Int. Electron Device Meeting, December 1972, Washington, D.C.
8. C. O. Thomas, D. Khang, and R. C. Manz, *This Journal*, **109**, 1055 (1962).
9. J. Copeland, *IEEE Trans. Electron Devices*, **ED-16**, 445 (1969).
10. G. L. Miller, *ibid.*, **ED-19**, 1103 (1972).
11. A. S. Grove, "Physics and Technology of Semiconductor Devices," John Wiley & Sons, Inc., New York (1967).
12. P. H. Langer and J. I. Goldstein, Paper 259 presented at Miami Beach, Florida, Meeting of the Society, Oct. 8-13, 1972.

## Fabrication of GaAs IMPATT Devices Using Electroplated Heat Sinks

### II. Control of Wafer Curvature

G. A. Rozgonyi,\* J. V. DiLorenzo,\* and E. Heinlein

Bell Laboratories, Murray Hill, New Jersey 07974

### ABSTRACT

It has been found that wafer curvature due to the use of electroplated heat sinks in the processing of Pt/GaAs IMPATT device material can be kept to levels low enough to make an essential difference in the yield of processed devices. This has been achieved in a two-step procedure. First, the stresses in the metal layers are determined using an x-ray lattice curvature technique, then a thin metal film with a stress of the opposite sign, compressive tungsten in this case, is used to compensate the bending due to the initial layers. As a result of the multilevel, stress-compensating approach, large area electroplated wafers have been successfully thinned to less than 15  $\mu\text{m}$  without cleaving. Also, preliminary device data show efficiencies and degradation properties comparable to the best data reported thus far for equivalent GaAs material.

Discrete silicon solid-state devices which require low thermal impedance for the dissipation of high

input power have traditionally been fabricated by thermal compression (TC) bonding the device to a heat sink of high thermal conductivity. The silicon IMPATT device, where a mesa is TC bonded to a

\* Electrochemical Society Active Member.

Key words: GaAs devices, plated heat sinks, wafer curvature.



diamond heat sink (1), is a good example of the application of TC bonding technology. It was, therefore, logical that TC bonding be used in the initial fabrication of compound semiconductor devices such as GaAs Gunn effect (2), IMPATT (3), and heterojunction laser (4) devices. Recently, however, there have been reports (5-8) that the TC bonding processing step leads to material degradation such as dislocation generation and the formation of acceptor states which adversely effect the electrical performance of III-V devices. This is not unexpected since the yield stress in GaAs is considerably lower than that in silicon (9, 10) and dislocation generation is much more likely to occur in the compound. In addition, Brantley and Harrison (11) have found that the degradation rate of electroluminescent GaAs diodes increases by an order of magnitude when the diodes are mechanically stressed beyond a reproducible threshold level. This stress correlated with that necessary for dislocation generation.

Because of the above-mentioned problems of TC bonding applied to compound semiconductors, an alternate approach using electroplated heat sinks (PHS) has been pursued in order to reduce the thermal resistance of GaAs IMPATT devices. The PHS approach has recently been used by DiLorenzo (12) in the fabrication of Gunn diodes of exceptionally high power, efficiency, and uniformity. Carey (13), in a comparison of Gunn devices fabricated by TC bonding and PHS, concluded that the efficiency and yield of PHS devices were consistently better than TC bonded devices.

Although the PHS technology has also improved the reproducibility of the thermal resistance of GaAs IMPATT's (14) new problems have arisen because the stresses inherent in the thin-film platinum Schottky barrier contact and electroplated gold or silver layers cause the GaAs substrate to warp severely. Using x-ray diffraction lattice curvature measuring procedures (15) radii of curvature of less than 1m are typically observed for 0.004 in. thick PHS's on 0.010 in. thick GaAs substrates.<sup>1</sup>

After electroplating, the original GaAs substrate must be removed by lapping and polishing the back side of the wafer. During the thinning step two problems are encountered. First, it has been observed that the GaAs substrate breaks apart by cleaving into as many as a dozen separate pieces after thinning. Although the PHS does serve to hold the pieces of GaAs together, the yield per wafer is necessarily reduced. A second problem arises because a 2 cm wide substrate bent to a radius of curvature,  $R$ , equal to 1m has a center to edge deflection of  $\sim 25\mu$ . Therefore, the wafer will not lie flat on the polishing block during the GaAs substrate thinning procedure. These variations are quite serious since the thickness of the final GaAs thin

<sup>1</sup> It should be noted that this is an elastic phenomenon and no permanent damage or plastic flow are observed at this stage, contrary to the case with TC bonding procedures.

film/substrate combination is eventually reduced to 10-20 $\mu$ .

In the present report we first identify the origins of certain mechanical problems such as wafer warpage and fracture. A particular solution using a multilayer, stress-compensation, thin-film approach is then described. Electrical data are also presented to show that by properly monitoring each stage of device metalization, measurable improvements in the over-all yield and uniformity of actual devices can be achieved. At the same time the efficiency and degradation properties have been as good as the best results reported thus far.

### Wafer Curvature in Multilayer Systems

In this section, the substrate lattice curvature due to sputtered platinum films and electroplated gold layers is discussed along with procedures for achieving flat wafers using a multilayer deposition scheme. Initially, the stresses in Pt layers were tensile and varied from 8 to 14  $\times 10^9$  dynes  $\text{cm}^{-2}$  (see Table I, samples K404 and K398). This was enough for a 0.2  $\mu\text{m}$  film to bend a 0.010 in. GaAs substrate to a radius of curvature  $R_{\text{Pt}} = +6\text{m}$ , where the plus sign signifies a tensile film stress. Although the average tensile stress in an electroplated Au layer was only from 2 to 4  $\times 10^8$  dynes  $\text{cm}^{-2}$ , the 75-100  $\mu\text{m}$  thick Au layer required resulted in an  $R_{\text{Au}}$  of less than 1m. Since the Au stress was also tensile the  $R_{\text{Pt}+\text{Au}}$  was reduced further. Subsequent work by Murarka (16) showed that compressive Pt films could be deposited by proper control of the sputtering plasma. Although this did serve to counteract the tensile Au plate, the magnitude of the compressive stress required, which would be greater than  $10^{10}$  dynes  $\text{cm}^{-2}$  for films less than 1 $\mu$  thick has not yet been achieved.

Concurrent with the attempts to control the sign and magnitude of the Pt film a multilayer scheme was proposed which took advantage of the fact that sputtered tungsten films can be grown with an intrinsic compressive stress of greater than  $10^{10}$  dynes  $\text{cm}^{-2}$  (15). Initially, a wafer was processed as outlined in Table I, sample K404. As shown, the compressive W film does serve to compensate the effects of the tensile Pt and Au layers. The calculated Au plate required to obtain an  $R_{\text{Au}} = +3\text{m}$  was 22  $\mu\text{m}$ . However, due to an unusually severe taper in the Au plate a thickness variation of 17.5-30  $\mu\text{m}$  was obtained. The taper resulted in the GaAs wafer having regions of positive or negative curvature depending on whether  $R_{\text{Au}}$  was locally greater or less than +3m. The measured values of  $R_{\text{Pt}+\text{W}+\text{Au}}$  varied from +120m to -13m. This represents an improvement of more than an order of magnitude over a nontungsten coated sample. Since the Au surface is made parallel to the back surface of the GaAs substrate in a later processing step, the taper, if present, can be used to pinpoint the optimum thickness for an  $R > 100\text{m}$ . Unfortunately, because of adherence problems between the Au PHS and the stress-compen-

Table I. Stress and curvature data on PHS materials

Sample ( $t_{\text{substrate}}$ in.)	Film	Thick- ness ( $\mu\text{m}$ )	R (m)	Thin-film stress (dynes $\text{cm}^{-2} \times 10^8$ )	Comments
K404 $t_s = 0.010$	Pt	0.2	+6.4	86 (T)	Model Shop Pt Heinlein W Tapered layer Model Shop Pt
	W	0.3	-3.0	180 (C)	
	Au	17.5-30	-13 + 120	2 (T)	
K398 $t_s = 0.014$	Pt	0.2	+8.2	140 (T)	Single pumpdown in Heinlein system Very thick Ag Single pumpdown for 3 layers
	W	0.3	-8.3		
	Pt	0.05	+1.5		
	Ag	250	-8.46		
S220 $t_s = 0.016$	Pt	0.2	+2.8	1.8 (T)	After thinning as shown in Fig. 1(a) Single pumpdown for 3 layers
	W	0.4	0.15-0.60		
	Pt	0.2	-1.2		
$t_s < 0.001$	Au	87	+2.0	1.8 (T)	PHS too thick After thinning PHS
	Pt	0.2	+13-500		
	W	0.4			
	Ag	100			
S272B $t_s = 0.0083$	Pt	0.2			
	W	0.4			
	Pt	0.2			

sating W film the PHS separated from the W during subsequent processing of K404. This problem was easily solved by backsputter cleaning the W and then depositing a 2000Å encapsulating layer of Pt over the W. Seventy-five microns of Au were then plated over the Pt cap and no further adherence problems were encountered. Device data on K404 are discussed below.

Because of the incompatibility of Au PHS's and W, and also the high tensile stress in the Pt, two more samples were prepared in a system capable of sequentially sputtering low tensile Pt and highly compressive W. Tungsten-stress compensated, Pt capped structures were then obtained as shown in Table I, samples K398 and S220. In these samples the stress compensation was not as close as in K404 due to the much thicker PHS. Therefore, improvements of only  $\sim 3$  times that of a non-W coated sample were obtained. However, good PHS adherence was obtained to the top Pt film. Sample S220 was successfully processed through the substrate thinning operation without undergoing any cleavage or fractures. The mechanical stability of the sample is illustrated in Fig. 1(a) which shows that even after thinning to the point where complete removal of GaAs has occurred over a portion of the wafer, thereby exposing part of the Pt layer, the remaining GaAs has not failed. The final GaAs thickness was  $15 \mu\text{m}$  at the top of the wafer shown in Fig. 1(a) tapering off to zero when the Pt metalization was reached.

For comparison, a 0.010 in. thick GaAs sample with a 0.005 in. thick PHS and no stress-compensating W film is shown in Fig. 1(b). Note that this sample, which has not yet been thinned, has already cleaved in at least eight places (see arrows C and white lines orthogonal to C and  $45^\circ$  to C). The radius of curvature of this sample was 0.8m. The calculated maximum stress in the substrate for the sample shown in Fig. 1(b) is only  $\sim 1 \times 10^8$  dynes  $\text{cm}^{-2}$ , which is well below the yield point of GaAs. However, close examination of plated wafers which have spontaneously cleaved indicates that the failure is usually initiated at a flaw near the edge of the wafers. Therefore, it is believed that local stresses can be significantly higher than the

average stress calculated from the radius of curvature. The stress in the chemically thinned sample shown in Fig. 1(a) is estimated to be  $\sim 2 \times 10^9$  dynes  $\text{cm}^{-2}$ . The absence of cleavage and the elastic character of the sample is partly attributed to stress relief by chemical etching of damage at potential cleavage sites during the chemical thinning operation. The actual stress profile in a multilayer, stress-compensated structure depends on the relative thicknesses of the layers and the exact position of the neutral axis, as well as possible gradients in the stress as a function of individual layer thickness. More detailed analyses of the quantitative aspects of this problem will be presented in a separate report. The main point to be emphasized here is that the only two GaAs IMPATT wafers to be successfully thinned without mechanical failure have been stress-compensated, multilayered structures (see Table I S220 and S272B).

Although sample S220 did not cleave, the substrate thinning did not proceed uniformly, as shown in Fig. 1(a). This is due, in part, to the fact that the wafer curvature, at just under 3m, is still significant enough to cause center-to-edge deflections comparable to the final thickness of the GaAs device, e.g.,  $5\text{--}15 \mu\text{m}$ . However, this is not considered to be a serious problem since recent results show that much larger radii of curvature can be obtained by careful attention to each step of the process. For example, the final sample listed in Table I, S272B, was processed using the dual target sputtering station to obtain a Pt-W-Pt metalization which yielded a  $-1.2\text{m}$  radius of curvature. This was followed by a  $100 \mu\text{m}$  thick Ag PHS layer which brought the radius over to  $+2.0\text{m}$ . Calculation of the average stress in the Ag layer necessary to effect this bending yielded a value of  $1.8 \times 10^8$  dynes  $\text{cm}^{-2}$ . Further calculations showed that thinning the Ag PHS to  $\sim 55 \mu\text{m}$  would more effectively balance the compressive stress of the W film. This was done and a sample was obtained with a final radius of 500m over several millimeters of the wafer.

### Electrical Characteristics

*Device structures and Schottky barrier data.*—In this section device data on three wafers, K404, S272B, and S220, processed using the multilayer, stress-compensated PHS technique are discussed. Sample K404 was fabricated into single mesa IMPATT devices  $125 \mu\text{m}$  in diameter on a PHS with dimensions  $0.625 \text{ in.} \times 0.625 \text{ in.} \times 75 \mu\text{m}$  thick. Slices S220 and S272B were processed into distributed four mesa structures ( $14$ ) with each  $150 \mu\text{m}$  diameter mesa connected by  $8 \mu\text{m}$  Au leads on a  $1.25 \text{ mm}$  diameter PHS (Au PHS for S220 and Ag PHS for S272B).

The reverse I-V characteristics of a representative device from slice K404 are presented in Fig. 2. A negligible amount of leakage current is observed prior to breakdown at approximately  $-62\text{V}$  for both  $10 \mu\text{A}$  and  $10 \text{ mA}$  per division sensitivities. The abruptness of this reverse characteristic at both current values indicates that the Schottky barrier resulting from the Pt-W-Pt PHS IMPATT is free of microplasmas. The absence of microplasmas at the edge of the mesas on sample K404 at reverse biases up to  $55\text{V}$  was recently confirmed by S. E. Haszko of these laboratories during a series of electron beam induced current studies of GaAs IMPATT's with the scanning electron microscope.

Ten devices from slice K404 were bonded into diamond V-3 packages using an Au-Sn eutectic bond. These devices were RF tested at X band ( $10\text{--}11 \text{ GHz}$ ). The efficiencies (and performance) of these devices at  $10.8 \text{ GHz}$  were very uniform giving values from 11% yielding  $1.5\text{W}$  out for  $13.7\text{W}$  in, to as high as 15% for  $6.8\text{W}$  input. The efficiency of these units is equal to the best obtained to date for single mesa devices with Pt Schottky barriers. The power output of these devices was limited primarily because of size and package limitations and not for any fundamental reason. Eight devices from slice S272B were bonded into V-8

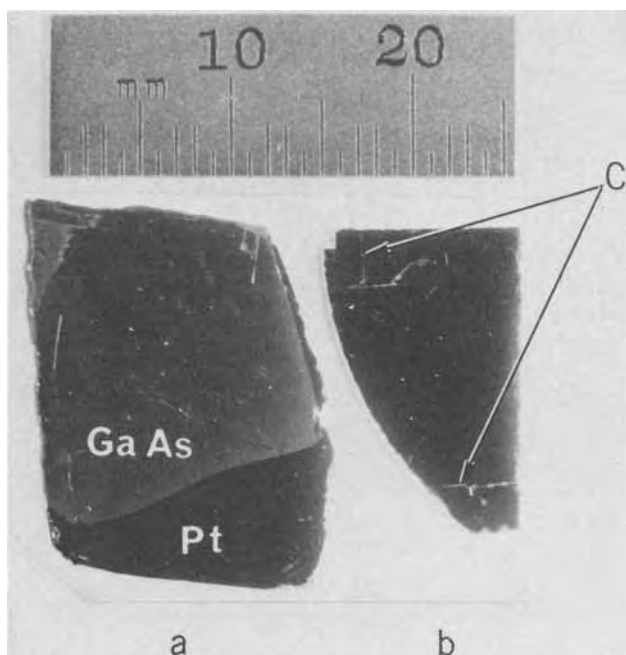


Fig. 1. a, Plated heat sink Pt/W/Pt on GaAs IMPATT wafer after chemical thinning GaAs to remove substrate. The GaAs remaining is tapered from 0 to  $\sim 15 \mu\text{m}$  at the top of the wafer. b, Plated heat sink Pt/GaAs IMPATT wafer which spontaneously cleaved, see arrows C, due to handling highly stressed wafer. Substrate has not yet been thinned.

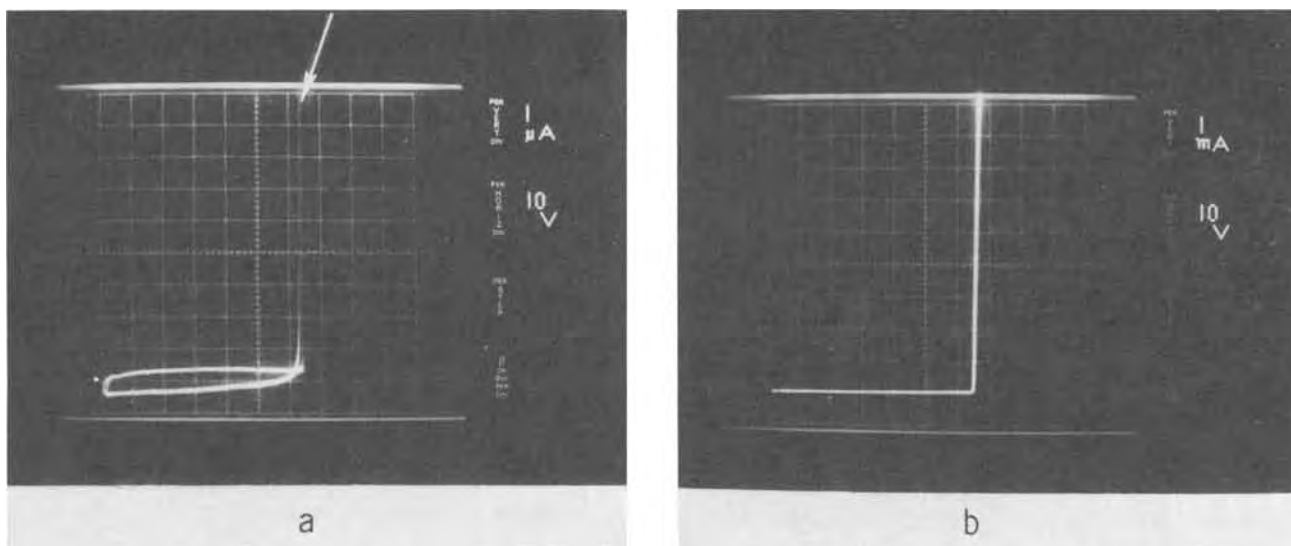


Fig. 2. Reverse I-V characteristics of representative device from slice K404. a, 1.0  $\mu\text{A}/\text{cm}$  sensitivity; b, 1.0  $\text{mA}/\text{cm}$  sensitivity.

Cu packages (14) and RF tested at C band ( $\approx 4\text{-}6$  GHz). The average peak efficiency of these devices was 11.6% at 5.4 GHz with 18W input, and  $\approx 10\%$  at 32W. The performance of the multimesa devices from S272B is comparable to single mesa TC bonded diodes on diamond heat sinks.

Units from slice S220 also had extremely sharp reverse I-V characteristics and were bonded into packages for reliability tests which are discussed below.

*Preliminary aging data.*—Recently great emphasis has been placed on obtaining an estimate of the expected life of a GaAs IMPATT diode at a junction temperature of  $200^\circ\text{C}$ . One approach which has been used is to monitor the softening of the d-c characteristics of a packaged diode at an elevated temperature as a function of time. Based on previous data of this type from Irvin (17) for Pt/GaAs single mesa IMPATT devices, aged at temperatures of  $350^\circ$  and  $323^\circ\text{C}$ , the expected life, or time to failure,<sup>2</sup> of an IMPATT should be approximately 500 hr<sup>3</sup> at  $300^\circ\text{C}$  and greater than  $10^6$  hr at  $200^\circ\text{C}$ . The six diodes packaged from sample S220 were aged for 532 hr at  $300^\circ\text{C}$  and resulted in only one diode failure. Therefore, following Irvin's analysis, the extrapolated life of the remaining diodes would be greater than  $10^6$  hr.

### Discussion and Conclusions

Although the primary objective of this work was to maintain the mechanical integrity of a wafer by keeping it from warping or cleaving during processing, it is important to note that the final product, assuming a balanced stress compensation has been achieved, will have an epitaxial GaAs layer with very low stress. This is due to the fact that the initial deposit is a stress-free, homoepitaxial layer. Stresses in the layer are encountered only after metalization, and the maximum GaAs stress generated, even for a Pt film stress of  $1 \times 10^{10}$  dynes  $\text{cm}^{-2}$ , would be less than  $5 \times 10^7$  dynes  $\text{cm}^{-2}$  for a final GaAs thickness of 20  $\mu\text{m}$ , provided the wafer is kept flat. Although the initial device performance is not expected to be critically dependent on stress, many of the degradation mechanisms proposed for device failure invoke phenomena which are enhanced by stress and strain.

Summarizing the results described above, it has

<sup>2</sup> Failure is defined here to mean a 2% reduction in the reverse voltage needed to draw 10  $\mu\text{A}$  current.

<sup>3</sup> Five hundred hours based on an activation energy of 1.9 eV and 1000 hr for an activation energy of 1.0 eV.

been shown that the wafer curvature introduced during the processing of GaAs IMPATT device material using plated heat sink technology can be kept to levels low enough to make an essential difference in the processing yield. This has been achieved by proper characterization of the stresses in the Pt and Au or Ag layers, and by the introduction of a stress compensating W thin film. As a result of the multilayer, stress-compensating approach, wafers have been successfully thinned to less than  $15\mu$  without undergoing any cleavage or fracture. Initial electrical data show extremely hard I-V characteristics with uniformly high breakdown voltages. Also, the degradation properties and efficiencies are comparable to the best data reported thus far for similar GaAs IMPATT devices. Finally, it is noted that the analytical procedures used for film stress studies and wafer curvature control would generally be applicable to a wide variety of semiconductor devices which are subjected to processing conditions which bend the device wafer, e.g., heterojunction lasers and silicon integrated circuits.

### Acknowledgments

The authors would like to thank T. J. Ciesielka for performing curvature measurements and J. R. Velebir for the electroplated Au and Ag layers. Comments on the final manuscript by R. B. Marcus are also appreciated.

Manuscript received July 6, 1973.

Any discussion of this paper will appear in a Discussion Section to be published in the December 1974 JOURNAL. All discussions for the December 1974 Discussion Section should be submitted by Aug. 1, 1974.

### REFERENCES

1. S. M. Sze, "Physics of Semiconductor Devices," John Wiley & Sons, Inc., pp. 254-259, New York (1969).
2. T. J. Riley, "GaAs, Proceedings of the 2nd International Symposium," pp. 173-178, Institute of Physics and the Physical Society, London (1969).
3. J. C. Irvin, D. J. Coleman, W. A. Johnson, I. Tatsuguchi, D. R. Decker, and C. N. Dunn, *Proc. IEEE*, **59**, 1212 (1971).
4. J. E. Ripper, J. C. Dymont, L. A. D'Asaro, and T. L. Paoli, *Appl. Phys. Letters*, **18**, 155 (1971).

5. S. Mitsui and O. Ishihara, *Japan J. Appl. Phys.*, **11**, 603 (1972).
6. F. Hasegawa and H. Ito, *Appl. Phys. Letters*, **21**, 107 (1972).
7. W. A. Brantley and D. A. Harrison, *This Journal*, **120**, 1281 (1973).
8. R. L. Hartman and A. R. Hartman, *Appl. Phys. Letters*, **23**, 147 (1973).
9. N. P. Sazhin, M. G. Mil'Vidskii, V. B. Osvenskii, and O. G. Stolyarov, *Soviet Phys.-Solid State*, **8**, 1223 (1966).
10. H. Alexander and P. Haasen, *Solid State Phys.*, **22**, 27 (1968).
11. W. A. Brantley and D. A. Harrison, *Proc. IEEE Rel. Phys. Symp.*, April, 1973, IEEE Cat. No. 73, CHO, pp. 755-759 (1973).
12. J. V. DiLorenzo, *IEEE Trans.*, **ED-19**, 123 (1972).
13. R. C. Carey, Unpublished data.
14. J. V. DiLorenzo, W. C. Niehaus, J. R. Velebir, and D. E. Iglesias, Paper 24.8, IEDM, Washington, D.C. (1973).
15. G. A. Rozgonyi and T. J. Ciesielka, *Rev. Sci. Instr.*, **44**, 1053 (1973).
16. S. P. Murarka, Unpublished data.
17. J. C. Irvin, Cornell Conference on Microwave Devices, Circuits and Applications (Aug. 1973).

## The Reaction Between Silica and Aluminum

K. Prabruptaloong and M. R. Piggott

Department of Chemical Engineering and Applied Chemistry,  
Materials Research Centre, University of Toronto, Toronto 5, Ontario, Canada

### ABSTRACT

Earlier studies on this reaction, using thin aluminum films on silica substrates, have been extended to temperatures below the melting point of aluminum, and the effect of crystallinity in the silica has also been investigated. Electron and x-ray diffraction were used for detection and identification of reaction products. Between 400° and 850°C the reaction obeys the Arrhenius equation, but suffers an abrupt change of activation energy at the melting point of aluminum. With quartz, the activation energy is greater and the reaction rate is less than with vitreous silica. The main products of reaction are  $\theta$ - $\text{Al}_2\text{O}_3$  and Si below the melting point of aluminum, but above the melting point a volatile oxide of aluminum is formed (probably  $\text{Al}_2\text{O}$ ) when thin films are used. The reaction seems to be influenced very little, if at all, by the physical form of the film, or by the presence of water or air.

Solid-state reactions are important in at least two areas. In the field of electronics, solid-state circuitry is in widespread use, and often involves potentially reactive materials in close contact, e.g., the aluminum contacts on oxidized silicon (1). In the field of structural materials, fibrous composite materials are being considered for use in turbines and in other high temperature applications (2). Nearly all combinations being considered are potentially reactive. (The only exceptions are the directionally solidified off-eutectic alloys which contain long fibers or platelets of the eutectic alloy in a matrix of the excess metal.)

Some studies on the solid-state reaction between aluminum and silica have already been carried out. Cratchley and Baker (3) observed some reaction product when they examined etched sections of silica fiber reinforced aluminum in the microscope after 500 hr at 500°C. This was thought to account for the drastic reduction in strength of the material at this temperature. Silverman (4) examined the electrical resistance of 0.2 $\mu$  thick condensed aluminum films on various types of silica substrates after heating to temperatures between 400° and 625°C in various atmospheres, for periods of from 1 to 21 hr. X-rays were used to analyze the products on some of the specimens. He found that moisture either on the silica, or in the atmosphere had a considerable effect on the reaction rate, as determined by resistivity changes, but did not report detecting any reaction below 550°C. X-rays only re-

vealed Si as reaction product. Chou and Eldridge (1) did detect some reaction product ( $\gamma$ - $\text{Al}_2\text{O}_3$ ) after 2 hr at 500°C using electron diffraction and microprobe analysis.

Moisture in the silica was also felt to be important by Standage and Gani (5), who did experiments above the melting point of Al and used light microscopy to determine reaction rates, and x-rays to determine products of reaction. Their x-ray results indicate that more than one crystallographic form of  $\text{Al}_2\text{O}_3$  was produced by the reaction, as well as Si. They observed an induction time before reaction started, which they ascribed to the effect of moisture, but which was later shown (6) to be due to adventitious oxide on the molten Al surface.

Silica fiber reinforced aluminum is weaker at 400°C than at room temperature (7), and the effect is probably due to a solid-state chemical reaction, since storing the material at this temperature for a period of 3 months halves the room temperature strength (8). The reaction is therefore worth investigating in more detail at temperatures lower than 550°C, and with more sensitive techniques than hitherto. Prabruptaloong and Piggott (9) have demonstrated the sensitivity of electron diffraction for this purpose at temperatures above 700°C, and the work described here is an extension of those studies down to a temperature of 400°C.

### Experimental Method

The apparatus used has already been described in detail (8). The experimental method consisted of

evaporating a sufficient amount of high purity (99.999%) aluminum wire to condense a film of about  $0.1\mu$  thick on a piece of silica (also 99.999% pure). Two forms of silica were used: vitreous silica ("Suprasil II" obtained from Amersil Incorporated) having a density of  $2.2\text{ g/cm}^{-3}$ , and quartz single crystals. The surfaces used for the reaction were polished to optical smoothness. The quartz crystal surface was a (0001) plane, and the crystal was initially the low temperature ( $\alpha$ ) form. Heating prior to reaction caused its transformation to the high temperature ( $\beta$ ) form. The silica was solvent cleaned, and was placed inside a box made of thin tantalum strip that could be heated and cooled very rapidly. Prior to the condensation, water absorbed at or near the surface was removed by heating the silica to  $800^\circ\text{C}$  for at least 10 min in vacuum, except in cases where the effect of absorbed water on the reaction was being investigated.

Condensation was carried out at the reaction temperature and at room temperature. The reaction was allowed to take place in air, as well as in vacuum ( $\sim 10^{-6}$  Torr). For the experiments in air, the specimen was cooled rapidly immediately after condensation, when this had been carried out at reaction temperature, so that a significant amount of reaction product was not formed during the condensation process. The specimen was then transferred to a small commercial laboratory furnace for the reaction. For reactions in vacuum the same chamber was used as for the condensation.

After the reaction experiment was completed, the specimen was transferred to an electron diffraction camera for examination. The topography of some films was also examined in the light microscope, and using palladium shadowed carbon replicas, in the electron microscope. In addition, x-ray patterns were obtained from the reaction products by grinding several similar specimens together and removing glassy particles under a light microscope.

Air-formed oxides on aluminum were also examined. They were made by first condensing aluminum on rock salt, then oxidizing the aluminum while on the salt.

### Experimental Results

Figure 1 shows the results for the reaction in different environments, *i.e.*, for films condensed on hot substrates, on cold ( $\sim 20^\circ\text{C}$ ) substrates, and on water-soaked cold substrates. (Water soaking was carried out by immersion in water at room temperature for 1 week.) The substrates in all these cases were vitreous silica, and the reaction rate was evaluated by determining the time required to produce enough silicon to be detected by electron diffraction.

It can be seen that in air the reaction seems to take place slightly more slowly than in vacuum. Condensation onto cold substrates also resulted in a slight decrease in reaction rate, but these differences were barely any greater than the spread of results. The reduction in reaction rate due to water soaking appears to be more significant, however.

The films formed by condensation at the reaction temperature were in the form of droplets, while those condensed at room temperature were continuous, whether or not the silica contained substantial amounts of water (Fig. 2-4). The appearance of the films after reaction for 15 hr at  $500^\circ\text{C}$  is also shown in Fig. 2-4. It will be seen that, while the appearance of the film condensed on the hot substrate showed very little change as a result of the reaction, both continuous films changed considerably. The film on the initially dry substrate was still substantially continuous, but became very uneven, while the film on the water-

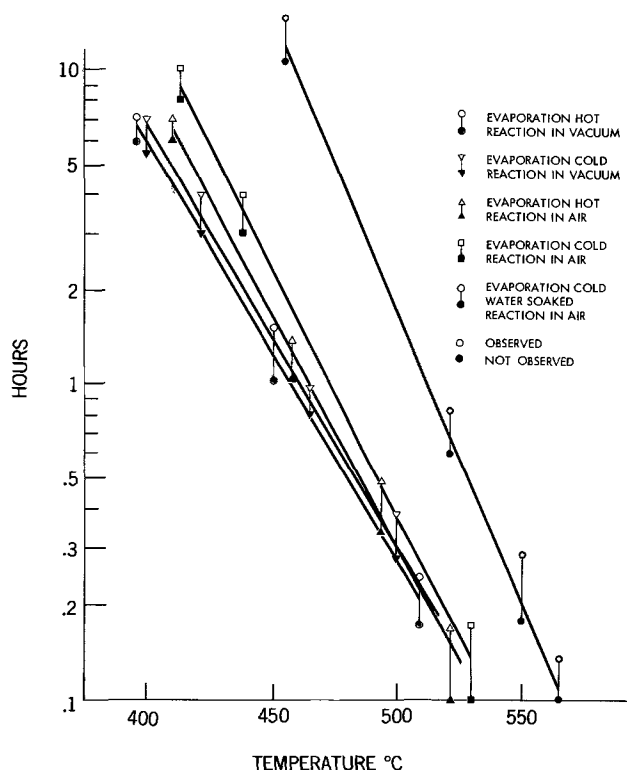


Fig. 1. Curves showing time of first appearance of reaction products in thin-film reaction under different experimental conditions.

soaked substrates broke up into disconnected, irregular patches, a few microns in extent.

Quartz crystals were also used as substrates, and were found to react more slowly than vitreous silica under the same conditions. All the results in the temperature range  $400^\circ\text{C}$ - $850^\circ\text{C}$ , for vitreous as well as crystalline silica, are summarized in the Arrhenius plot shown in Fig. 5.

No crystalline alumina was observed as a result of the air oxidation of the thin aluminum films. The electron diffraction pattern, all rings which were due to elementary aluminum, became less distinct as a result of the oxidation, but no extra rings were observed (Fig. 6).

However, the oxide formed as a result of the  $\text{Al-SiO}_2$  reaction below the melting point was crystalline, and consisted mainly of  $\theta\text{-Al}_2\text{O}_3$ , with traces of  $\alpha\text{-Al}_2\text{O}_3$ . Si was also detected in the reaction products. A typical electron diffraction pattern, obtained after the reaction had been allowed to proceed almost to completion, is shown in Fig. 7. The detection of  $\theta$ - and  $\alpha\text{-Al}_2\text{O}_3$  was confirmed by x-ray examination of the crushed reaction products. The only product observed from the reaction above the melting point of the aluminum was Si.

### Discussion

The results reported here appear to be in good agreement with the earlier electron diffraction work (9), except for the anomalous result that had been obtained at  $700^\circ\text{C}$ . This result appears to have been slightly in error, and it now seems likely that the change in slope of the Arrhenius plot occurs at the melting point of aluminum (Fig. 5). The activation energies indicated by the slopes of the lines in this figure are:

vitreous silica

31 kcal/mole ( $T < T_m$ )

17 kcal/mole ( $T > T_m$ )

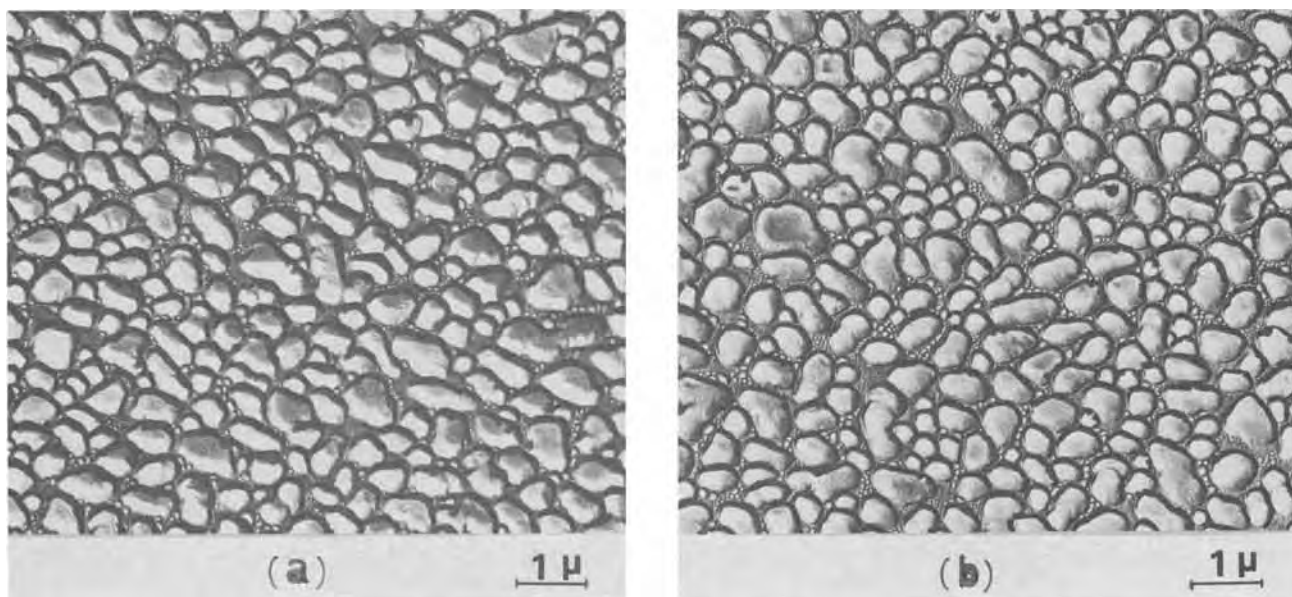


Fig. 2. Micrographs of Al films evaporated onto hot silica substrate (a) before and (b) after reaction at 500°C for 15 hr.

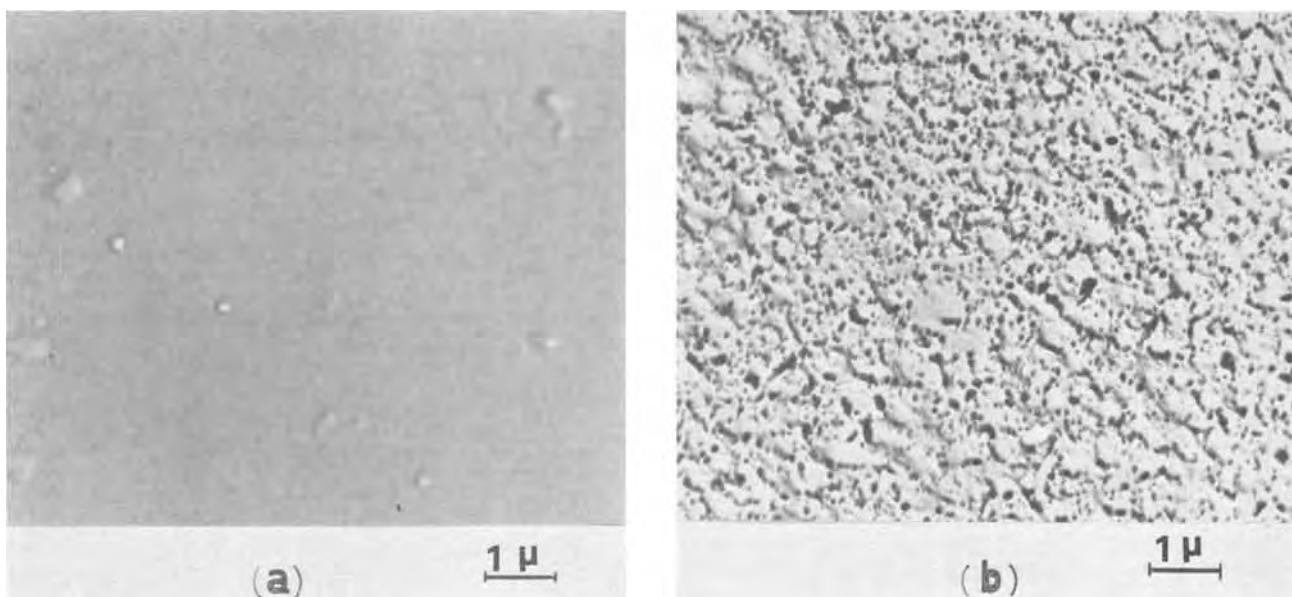


Fig. 3. Micrographs of Al film evaporated onto silica substrate at room temperature (a) before and (b) after reaction at 500°C for 15 hr.

64 kcal/mole ( $T < T_m$ ) quartz  
27 kcal/mole ( $T > T_m$ )

(all results accurate to about  $\pm 10\%$ ).

The higher activation energies and lower reaction rates observed when the silica is crystalline are in keeping with the observation that quartz is the least reactive form of silica (10), but the differences between the activation energies (above) seem not to be related in any simple way to the heat of fusion of quartz, or to differences in the heats of formation of the different forms of silica.

The products of reaction also change abruptly at the melting point of aluminum when thin films are used. Below the melting point, the products are  $\theta$ -Al<sub>2</sub>O<sub>3</sub>, traces of  $\alpha$ -Al<sub>2</sub>O<sub>3</sub>, together with elemental Si. Above the melting point, the only product observed has been silicon, whether the silica was vitreous or crystalline. The oxide of aluminum produced above the melting point was probably the volatile Al<sub>2</sub>O (9), but attempts to detect it with a mass spectrometer have not, so far, been successful. [This lack of success is not surprising since the Al<sub>2</sub>O would condense on any cool surface it

met (e.g., the walls of the vacuum vessel) and the quantity produced would anyway be very small.] The reaction with quartz gave the same products as the reaction with silica under the same conditions.

In the case of the reaction below the melting point, the bulk reaction, and the thin-film reaction above the melting point, direct formation of Al<sub>2</sub>O vapor at the SiO<sub>2</sub>-Al interface and its escape should be impossible (its vapor pressure, even at 800°C, is sufficient only to support a column of aluminum 5Å high). The reaction is therefore considered to take place as follows (9). First the Si-O bond is ruptured, and Si and O go into solution in the aluminum. When the aluminum is liquid and in the form of a thin layer, the O can quickly diffuse to the surface and escape as Al<sub>2</sub>O. In the case of the bulk reaction, the diffusion of oxygen is not sufficiently fast since the distance it has to go is much greater than in the thin-film case, and the rate of formation of  $\theta$ -Al<sub>2</sub>O<sub>3</sub> becomes significant. The results obtained for the reaction below 660°C suggest that, in this case also, the rate of diffusion of oxygen atoms to the surface of the film is slower than the rate of formation of Al<sub>2</sub>O<sub>3</sub>.



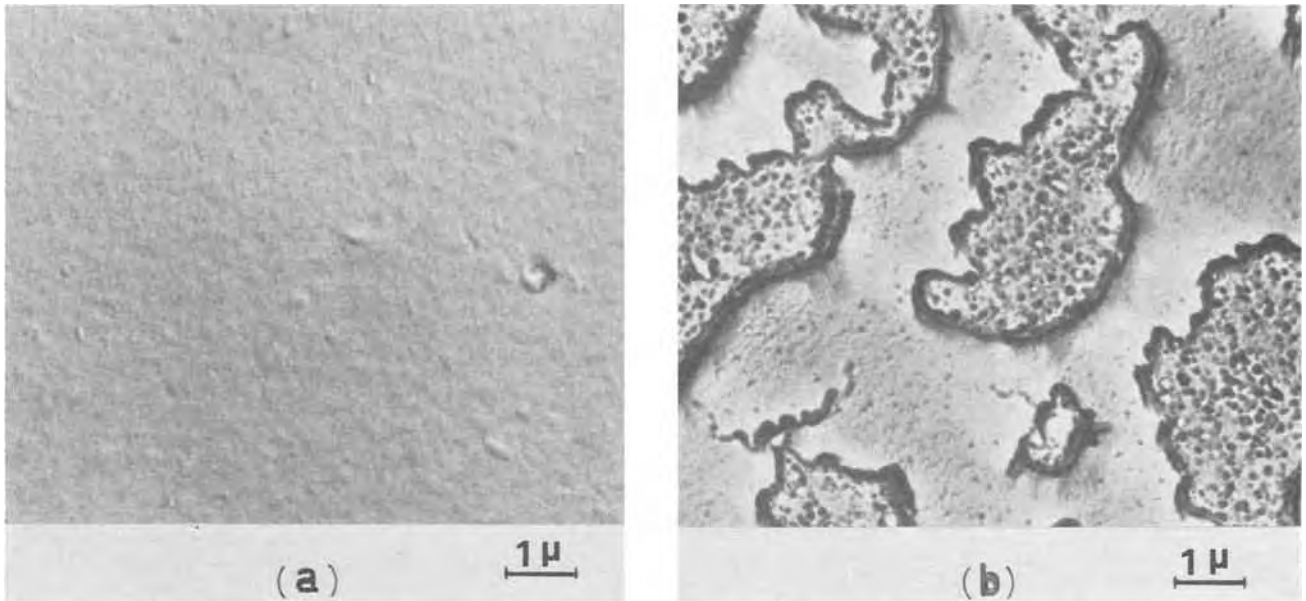


Fig. 4. Micrographs of Al film evaporated onto water-soaked silica substrate at room temperature (a) before and (b) after reaction at 500°C for 15 hr.

The lowering of the melting point of aluminum by solution of silicon<sup>1</sup> does not appear to influence the reaction significantly. The discontinuity in activation energy does not occur at the Al-Si eutectic point; drawing lines through the experimental points of Fig. 5 on the assumption that the change in slope occurs at

<sup>1</sup>We are grateful to the referee for drawing this point to our attention.

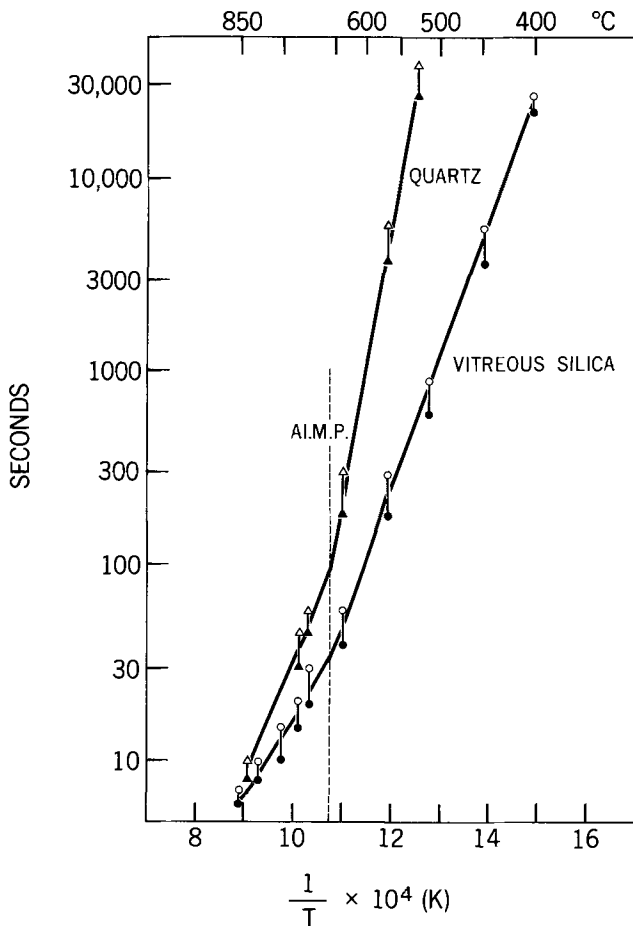


Fig. 5. Arrhenius plots of reactions between Al and quartz and silica at temperatures both above and below the melting point of Al.

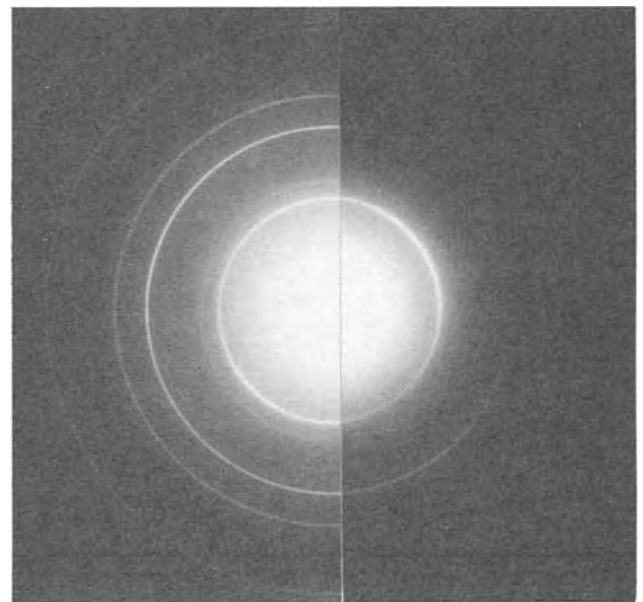


Fig. 6. Electron diffraction patterns of Al film (left) before and (right) after being oxidized by air.

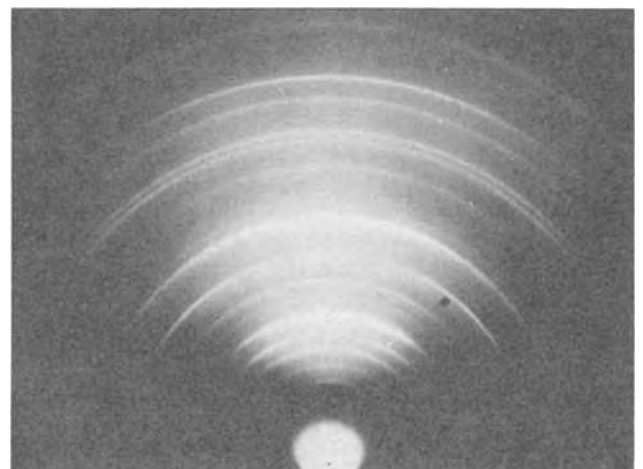


Fig. 7. Typical electron diffraction pattern of reacted Al film showing Si, α-Al<sub>2</sub>O<sub>3</sub>, and traces of θ-Al<sub>2</sub>O<sub>3</sub>.

577°C gives a very poor fit, especially in the case of the quartz crystals. This suggests that the role of the oxygen produced when the first few atomic layers of silica decomposes must be decisive. If it can diffuse away (the thin-film, molten aluminum case), Al<sub>2</sub>O<sub>3</sub> is formed. If it cannot diffuse sufficiently quickly (the solid aluminum case) the Al<sub>2</sub>O<sub>3</sub> barrier is formed before sufficient silicon has been produced to significantly lower the melting point of aluminum.

The effect of condensation conditions on the reaction was very small, despite the difference in physical form of the film. The presence of water in the silica, however, did have a significant effect, but this may well have been due simply to the water lifting the aluminum film off the silica surface; it certainly appears to have caused disruption of the film (Fig. 4).

The presence of air during the reaction had very little effect. This conflicts with the results of Silverman. However, Silverman failed to detect any reaction at all at temperatures below 550°C, so his method seems not to have been very sensitive. It could be that the method he used is not reliable either; disruption of the film, observed when the silica contained some water, would certainly lead to misleading electrical resistance values. So would sintering of the film, which is very likely to occur at 550° and 600°C. Such disruption could also account for some of the visual changes he described. Finally, x-ray diffraction is not sensitive enough to detect the very small quantities of reaction products very reliably; this is confirmed by Silverman's failure to detect  $\theta$ -Al<sub>2</sub>O<sub>3</sub>, which electron diffraction shows is produced in similar quantities to the Si.

The apparent lack of much effect due to the presence of air is not surprising. Air can be expected to affect the thickness of the amorphous oxide film on the side of the aluminum exposed to the atmosphere (such an increase in thickness of this oxide was indirectly observed, Fig. 6). However, such films are good barriers to further oxygen penetration, so the aluminum should contain little oxygen from this source compared with the amount available from reduction of the silica. Similarly, it seems unlikely that water vapor in the environment or in the silica has much effect. The results of Standage and Gani (5) and Silverman (4) appear to be in conflict on this point, while the results herein reported suggest that water in the silica only has a slight effect even when there is enough water for physical disruption of the aluminum film.

## Conclusion

Reaction between aluminum and silica occurs below the melting point of aluminum with the formation mainly of  $\theta$ -Al<sub>2</sub>O<sub>3</sub> and Si. The rate is governed by the Arrhenius equation

$$R = R_0 e^{-E/kT}$$

where  $E$  has the value  $31 \pm 3$  kcal/mole for vitreous silica, and  $64 \pm 6$  kcal/mole for quartz. This equation is obeyed at least down to 400°C. The activation energy for the reaction decreases abruptly at the melting point of the aluminum, and a volatile oxide (probably Al<sub>2</sub>O) is formed.

The water content of the silica has only a slight effect on the reaction, and this effect may be entirely due to disruption of the film by escaping water vapor when the specimen is heated. Under clean conditions, the physical form of the film has little effect on the reaction, and whether the reaction is carried out in air or in vacuum ( $10^{-6}$  Torr) has very little effect on the results.

Manuscript submitted April 2, 1973; revised manuscript received Sept. 11, 1973.

Any discussion of this paper will appear in a Discussion Section to be published in the December 1974 JOURNAL. All discussions for the December 1974 Discussion Section should be submitted by Aug. 1, 1974.

## REFERENCES

1. N. J. Chou and J. M. Eldridge, *This Journal*, **117**, 1287 (1970).
2. R. J. Glenny, *Proc. Roy. Soc.*, **A319**, 33 (1970).
3. D. Cratchley and A. A. Baker, *Am. Ceram. Soc. Bull.*, **46**, 191 (1967).
4. R. Silverman, *This Journal*, **115**, 674 (1968).
5. A. E. Standage and M. S. Gani, *J. Am. Ceram. Soc.*, **50**, 101 (1967).
6. K. Prabripataloong and M. R. Piggott, *ibid.*, **56**, 184 (1973).
7. D. Cratchley and A. A. Baker, *Metallurgia*, **69**, 154 (1964).
8. M. R. Piggott and A. Hunton, *J. Nucl. Mater.*, **29**, 334 (1969).
9. K. Prabripataloong and M. R. Piggott, *J. Am. Ceram. Soc.*, **56**, 177 (1973).
10. A. S. Berezhnoi, "Silicon and Its Binary Systems," pp. 136-137, Translated from Russian, Consultants Bureau, New York (1960).

# Interaction Between Phosphosilicate Glass Films and Water

Naoyuki Nagasima, Hisako Suzuki, Keizo Tanaka, and Sumio Nishida

Semiconductor and Integrated Circuits Division, Hitachi, Limited, Kodaira, Tokyo, Japan

## ABSTRACT

Phosphosilicate glass (PSG) films were deposited onto silicon substrates by the oxidation of SiH<sub>4</sub> and PH<sub>3</sub> at 350°C. Densities, phosphorus oxide concentrations, and infrared absorption spectra were measured for the evaluation of the film structure. It was found that nearly all the phosphorus oxide in a PSG film containing more than about 8 mole per cent P<sub>2</sub>O<sub>5</sub> was dissolved into water by exposing to saturated water vapor at 120°C. By heating at elevated temperatures, the phosphorus oxide concentration value at which phosphorus oxide began to dissolve shifted toward the higher concentration region. Water absorption in the PSG film also can be lessened considerably by heat-treatment.

Since Kerr *et al.* (1) reported in 1965 that a phosphosilicate glass film (PSG film) is effective for stabilizing

Key words: PSG film, activation analysis, phosphorus concentration, infrared absorption, moisture resistance.

the surface of silicon planar transistors, it has been confirmed by many investigators to decrease surface instabilities due to ionic drift (2). However, application of a PSG film to silicon devices has been accom-



panied by some problems. One of them is the influence of water on the PSG film, which is the subject dealt with in this paper.

Corl *et al.* (3) and Esch *et al.* (4) examined the water stability of their PSG films by infrared absorption spectroscopy. Yamada *et al.* (5) reported that the dissolution of phosphorus oxide in their passivated film on a transistor into water resulted in degradation of the p-n junction. Daghir (6) used a PSG layer as a moisture detector to evaluate overcoatings of rf-sputtered and CVD SiO<sub>2</sub> films.

Phosphorus oxide concentration is an important parameter of the PSG film. It is known empirically that, as the phosphorus oxide concentration increases, the film will absorb water more easily. However, to our knowledge, no report concerning the effect of phosphorus oxide concentration on interaction between PSG film and water vapor has been made available.

In the present paper, the influence of water on CVD PSG films having various phosphorus oxide concentrations are treated. Some considerations on the structure of the PSG film are also given.

### Experimental Procedure

PSG films used in the present study were prepared on Si surfaces by oxidizing SiH<sub>4</sub> (diluted to 4% by N<sub>2</sub>) and PH<sub>3</sub> (diluted to 1% by N<sub>2</sub>), using an apparatus shown schematically in Fig. 1. The Si substrate was p-type (B-doped), 10 ohm-cm, cut parallel to the (111) plane or (100) plane, and mirror polished. The flow rates of SiH<sub>4</sub>, O<sub>2</sub>, and N<sub>2</sub> were 0.04, 0.35, and 25 liters/min, respectively; phosphorus oxide concentration in the PSG film was controlled by changing the flow rate of PH<sub>3</sub>. The substrate temperature was kept at 350°C during the film formation.

The phosphorus content in the PSG film was measured by means of neutron activation analysis. The sample together with the standard sample (NH<sub>4</sub>H<sub>2</sub>PO<sub>4</sub>) were irradiated for 5 hr in the atomic reactor with a thermal neutron flux of about  $2 \times 10^{12}$  n cm<sup>-2</sup> sec<sup>-1</sup>, and then cooled for about two weeks for reducing the <sup>31</sup>Si activity (the half-value periods of <sup>31</sup>Si and <sup>32</sup>P are 2.62 hr and 14.3 days, respectively). After cooling, the β-activity of the <sup>32</sup>P was measured by a gas flow GM counter. The phosphorus content was also measured by means of an electron probe microanalyzer. In this measurement, the sample whose phosphorus content was determined by neutron activation analysis was used as a standard sample, and correction of the phosphorus content was made in consideration of the penetration depth of electrons into the PSG film.

Immediately after deposition, the sample was weighed on a Mettler microbalance with an accuracy of 1 μg, and the infrared absorption spectrum was taken by a Hitachi 225 double-beam spectrophotometer. The moisture test was conducted by exposing a sample to the saturated water vapor at 120°C (vapor pressure, 1.96 atm.) for 4 hr. After exposure, the sample was kept in the room at a temperature of 20°C and a relative humidity of 50% for 24 hr, and then the

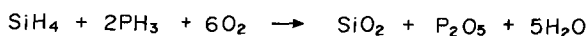
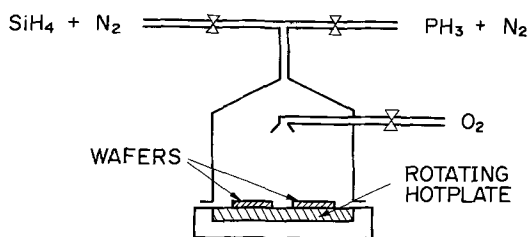


Fig. 1. Schematic drawing of apparatus for vapor deposition of PSG films.

weight and infrared absorption spectrum were measured again. The thickness of the PSG film was determined by means of a Taylor-Hobson stylus instrument "Talystep 1" of which the resultant accuracy was  $\pm 30\text{\AA}$  in the range of 0.5-1 μ. Electron microscopic observation was also made.

### Results

Figure 2 shows an example of the relationship between the PH<sub>3</sub>/SiH<sub>4</sub> ratio and the phosphorus oxide concentration in the PSG film. Figure 3 shows electron microphotographs of PSG film surfaces, CVD SiO<sub>2</sub> and thermally grown SiO<sub>2</sub> films are also shown for comparison. Surfaces of the thermally grown SiO<sub>2</sub> and CVD SiO<sub>2</sub> films appear rather smooth, but the PSG film surface is coarse. It seems that surface roughness of the PSG film is not very dependent on the phosphorus content.

The change of film density after the moisture test is shown in Fig. 4, together with the result of the moisture test of the PSG film heat-treated in dry N<sub>2</sub> at 900°C for 15 min. In the range of the low phosphorus concentration, the as-deposited PSG film after the moisture test did not show a change in density. However, in the range where the phosphorus oxide concentration exceeded about 8 mole per cent (m/o), the film density showed a remarkable decrease by the moisture test.

It is well known that SiO<sub>2</sub> film deposited at low temperatures decreases in thickness when heated at a higher temperature. In the present case, when the sample was heated for 15 min in dry N<sub>2</sub> at 900°C, the film thickness was reduced by about 7% irrespective of phosphorus oxide concentration. The phosphorus oxide concentration value at which phosphorus oxide began to dissolve shift towards the higher concentration region by heating.

To find the cause of density change by the moisture test, the phosphorus oxide concentration of PSG films before and after the moisture test were measured. The results are shown in Fig. 5. In the figure, the abscissa shows the phosphorus oxide concentration before the moisture test, while the ordinate shows that after the moisture test. This figure indicates that the data point will be plotted on the 45° angle straight line in the case where there is no change in phosphorus oxide concentration by the moisture test. It was revealed that phosphorus oxide in the PSG film with

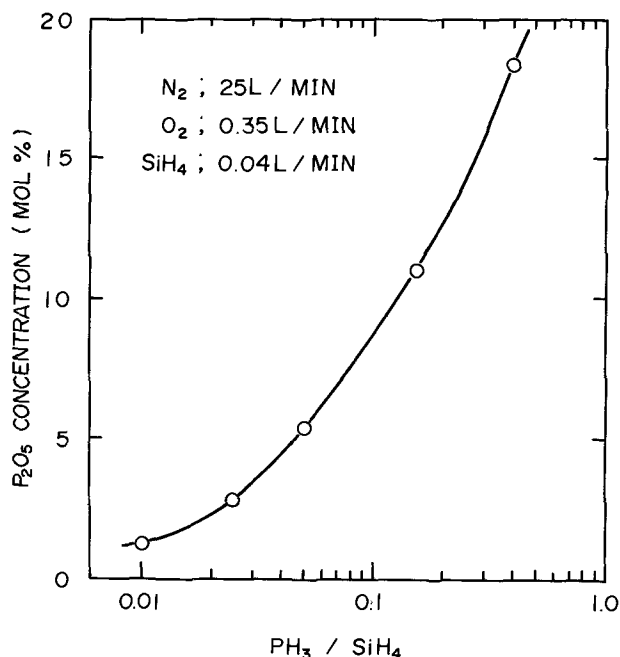
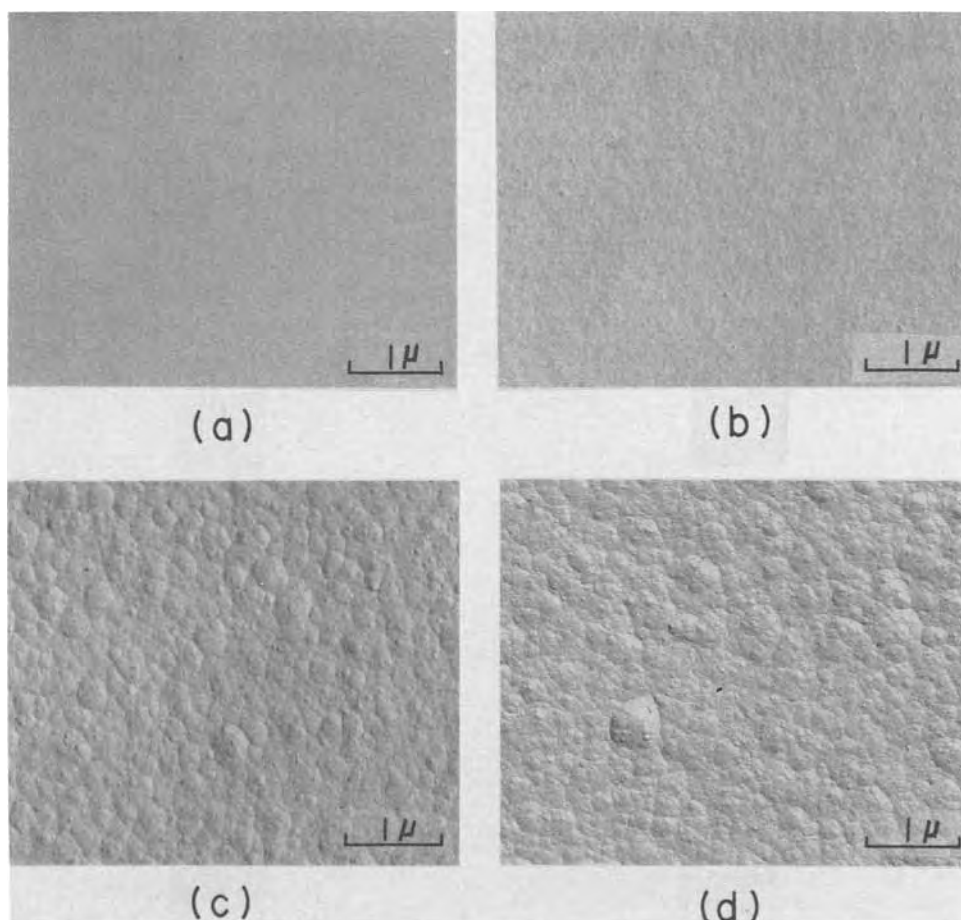


Fig. 2. Phosphorus oxide concentration in PSG film vs. PH<sub>3</sub>/SiH<sub>4</sub> volume ratio.

Fig. 3. Electron micrographs of surfaces of (a) thermally grown  $\text{SiO}_2$ , (b) CVD  $\text{SiO}_2$ , (c) PSG film containing 2.8 m/o  $\text{P}_2\text{O}_5$ , and (d) PSG film containing 10.5 m/o  $\text{P}_2\text{O}_5$ .



the concentration above a certain value is mostly dissolved into water by exposing to the saturated water vapor at  $120^\circ\text{C}$  for 4 hr. This concentration value is conveniently termed the "critical concentration" in the present paper. The critical concentration corresponds with the point in Fig. 4 at which the film density begins to decrease by the moisture test. Figure 6 shows the relationship between heating temperatures and the critical concentrations of PSG films heat-treated in dry  $\text{N}_2$ . As an ambient for heat-treatment, dry  $\text{O}_2$  was proved to have the same effect as dry  $\text{N}_2$  in improving resistance to moisture. Here, we named the  $\alpha$ -phase the region (0-8 m/o) where phosphorus oxide in the as-deposited film does not dissolve by the moisture test, the  $\beta$ -phase the region (more than 8 m/o) where phosphorus oxide dissolves, and the  $\alpha\beta$ -

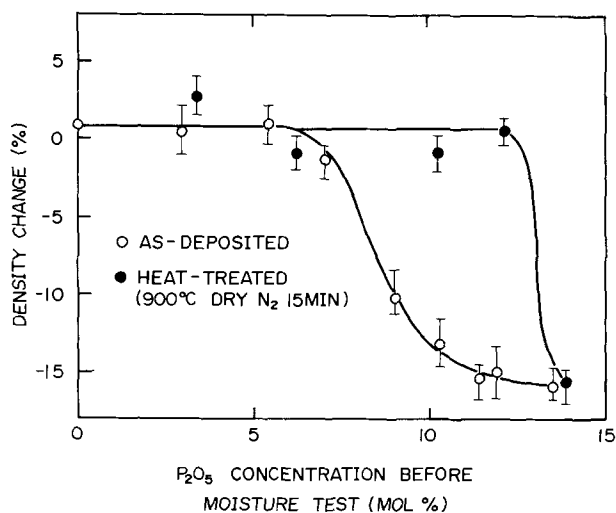


Fig. 4. Change of film density after moisture test

phase the region where dissolving ceases to occur by heat-treatment.

Figures 7(a) and 7(b) show the infrared absorption spectra of the PSG films before and after heating at  $900^\circ\text{C}$ . The intensity of the P-O absorption peak at  $1300\text{ cm}^{-1}$  increases with an increase in the phosphorus oxide concentration, and the Si-O absorption band near  $1100\text{ cm}^{-1}$  is influenced by the existence of phosphorus oxide. In the film which allowed the phosphorus oxide to dissolve by the moisture test, the P-O peak disappeared. At the same time, absorption peaks emerged in the neighborhood of  $3700\text{ cm}^{-1}$  and  $910\text{ cm}^{-1}$ , because of the existence of the water and silanol. Except for the absorption peaks due to water

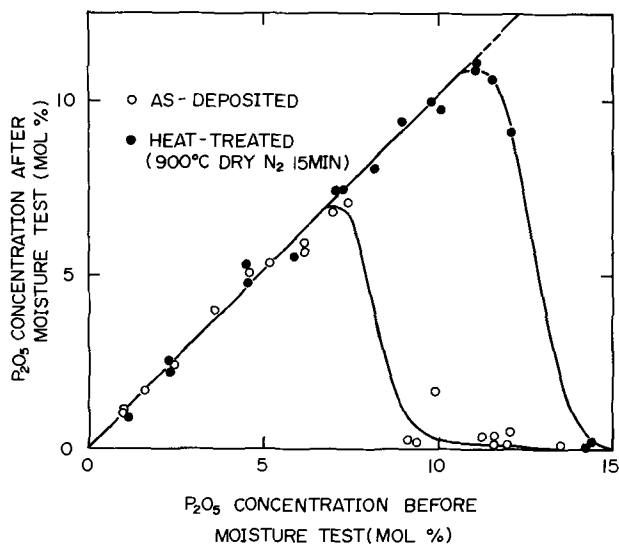


Fig. 5. Change of phosphorus oxide concentration after moisture test.

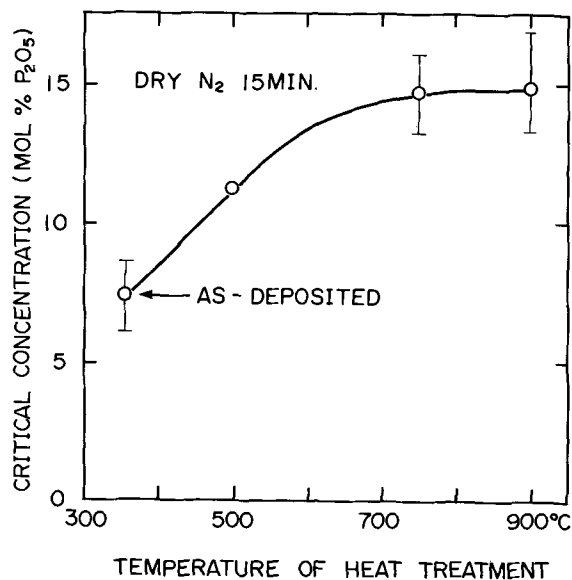


Fig. 6. Relationship between critical concentration of phosphorus oxide in PSG film and heating temperatures.

and silanol, the infrared absorption spectra of a film in which phosphorus oxide dissolved out resemble those of CVD SiO<sub>2</sub> films.

While the heat-treatment causes the infrared absorption peaks to shift slightly towards the higher frequency side, it is difficult to observe any variation in the shape of spectrum. As can be seen in Fig. 7(b), the infrared absorption spectrum of a film belonging to the  $\alpha$ -phase did not cause any noticeable change by the moisture test. Also, no absorption due to water occurred. On the other hand, in the case of film with a higher phosphorus oxide concentration ( $\beta$ -phase), heat-treatment could not prevent the P-O peak from disappearing by the moisture test, and the absorption peaks due to water and silanol occurred.

It has been confirmed that beyond the critical concentration, the phosphorus in the PSG film is reduced below the detecting limit by the moisture test. Thus, the quantity of water absorbed in the film was calculated by considering changes of the phosphorus oxide concentration and film weight by the moisture test. In this calculation, phosphorus oxide was assumed to be lost in the form of P<sub>2</sub>O<sub>5</sub>. Figure 8 shows the results of calculation. As can be seen from the figure the quantity of water contained in the heat-treated film

is negligibly small as compared with that of the as-deposited film.

### Discussion

As a result of the present study, it became evident that the phosphorus oxide in the PSG film is not allowed to dissolve out into water in the range where the phosphorus oxide concentration is low; however, in the range where the phosphorus oxide concentration exceeds the critical concentration, the phosphorus oxide tends to begin dissolving by the moisture test, and that such critical concentration can be raised by heat-treatment.

Since electron diffraction of the PSG film gives halo pattern in every case, as shown in Fig. 9, sufficient knowledge of the film structure has not yet been obtained. A phase diagram of SiO<sub>2</sub>-P<sub>2</sub>O<sub>5</sub> system has been reported by Tien *et al.* (7), by saturated equilibration and quenching technique on bulk materials. Eldridge *et al.* (8) dealt with PSG films which were formed by the reaction of SiO<sub>2</sub> film with gaseous P<sub>2</sub>O<sub>5</sub> over a temperature range from 800° to 1200°C. According to their results, small, water-soluble crystallites were formed on the surface of a film formed at 870°C or less, and from the SiO<sub>2</sub>-P<sub>2</sub>O<sub>5</sub> phase diagram of Tien *et al.*, these small crystallites were assumed to be 2SiO<sub>2</sub>·P<sub>2</sub>O<sub>5</sub> or SiO<sub>2</sub>·P<sub>2</sub>O<sub>5</sub>.

The PSG films used in the present experiment were formed at a relatively low temperature of 350°C. Therefore, phosphorus in the film can be considered to be in such a state that small particles of phosphorus oxide P<sub>2</sub>O<sub>5</sub>, rather than a compound such as 2SiO<sub>2</sub>·P<sub>2</sub>O<sub>5</sub> or SiO<sub>2</sub>·P<sub>2</sub>O<sub>5</sub>, are dispersed in the SiO<sub>2</sub> matrix. At low phosphorus oxide concentration in the PSG film, the SiO<sub>2</sub> matrix which is water-insoluble protects the phosphorus oxide from being attacked by water vapor. However, as the phosphorus oxide concentration increases to the critical concentration, the volume fraction of phosphorus oxide to the SiO<sub>2</sub> matrix increases, and the SiO<sub>2</sub> matrix is no longer effective in protecting the phosphorus oxide from a moisture attack. The SiO<sub>2</sub> matrix has a larger angular distribution width of Si-O-Si bond because it is formed at low temperature (9). Also, it is highly porous (10). This probably allows water to penetrate into the film with ease causing phosphorus oxide to dissolve. These considerations are based on the fact that apparent film thickness does not change by the moisture test, and that the infrared absorption spectrum of a sample whose phosphorus oxide is dissolved by the moisture test closely resembles that of CVD SiO<sub>2</sub> film which never contained phosphorus. Thus, the film deprived of phosphorus oxide by the moisture test becomes to

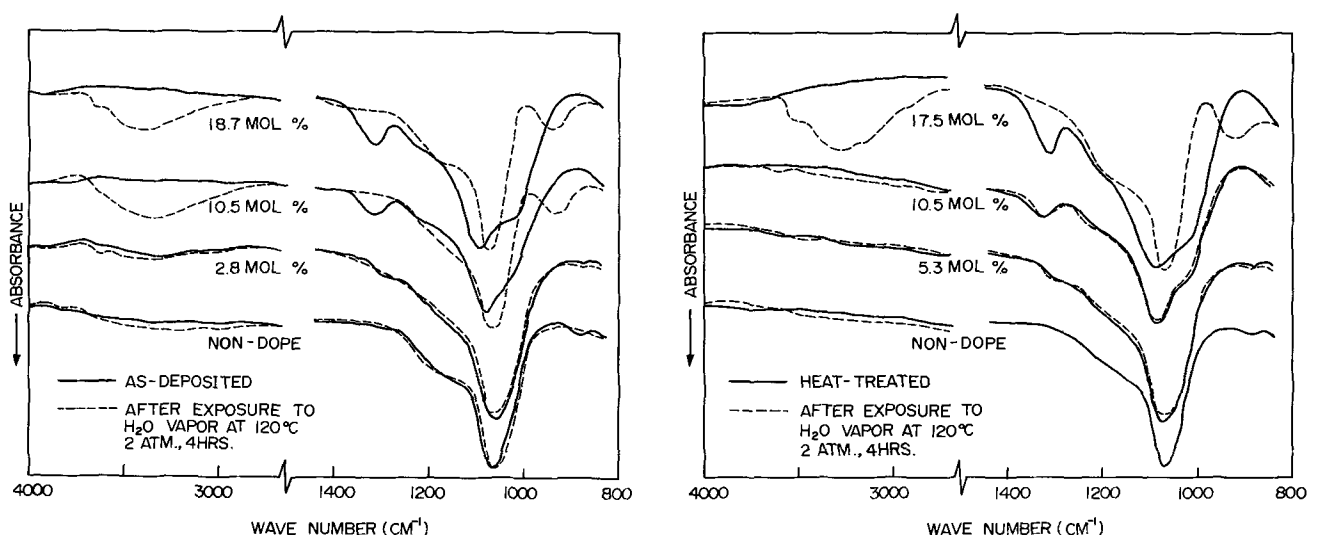


Fig. 7. Infrared absorption spectra of (a) as-deposited films and (b) heat-treated films

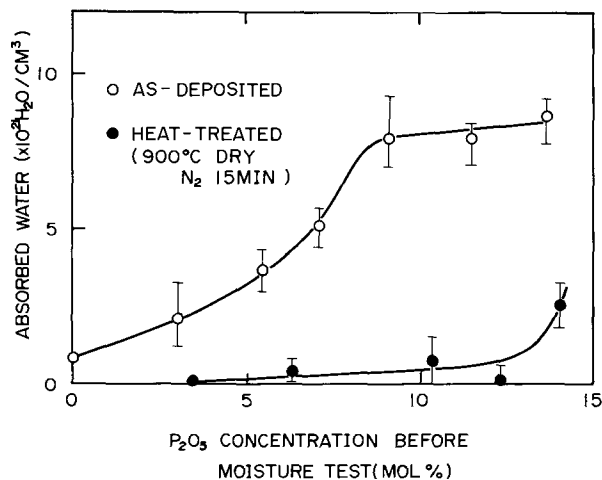


Fig. 8. Water absorbed in PSG film as a result of moisture test



Fig. 9. Reflecting electron diffraction pattern of PSG film

have a sponge-like structure and is capable of absorbing much water. That is, water replaces phosphorus oxide, and so the infrared absorption peak appears in the neighborhood of  $3700\text{ cm}^{-1}$  which is characteristic of the OH stretch.

Heat-treatment densifies the  $\text{SiO}_2$  matrix, which in turn makes it hard for water vapor to diffuse and attack the phosphorus oxide. It is likely that heat-treatment leads to reaction of the phosphorus oxide

with the  $\text{SiO}_2$  matrix, and results in formation of a water-insoluble compound such as  $(\text{SiO}_2)_x(\text{P}_2\text{O}_5)_y$ . Further detailed discussions on this problem will be made when the analysis of film structure is completed.

The as-deposited film is not soluble in water as long as its phosphorus oxide concentration is less than about 8 m/o, but it absorbs a fairly large quantity of water depending on the phosphorus oxide concentration, as shown in Fig. 8. This water absorption can be considerably lessened by heat-treatment. This may be attributed to the narrowing of the angular distribution width of the Si-O-Si bond, the resulting decrease in porosity, and the phase transformation.

#### Acknowledgments

The authors wish to express their thanks to Dr. K. Sugawara for his support in preparing samples, and to Messrs. H. Enari and Y. Shimizu for their aid in electron microscopic study.

Manuscript submitted July 11, 1973; revised manuscript received Oct. 15, 1973. This was Paper 34 presented at the Houston, Texas, Meeting of the Society, May 7-11, 1972.

Any discussion of this paper will appear in a Discussion Section to be published in the December 1974 JOURNAL. All discussions for the December Discussion Section should be submitted by Aug. 1, 1974.

#### REFERENCES

1. D. R. Kerr, J. S. Logan, P. J. Burkhardt, and W. A. Pliskin, *IBM J.*, **8**, 376 (1965).
2. For example, M. M. Schlacter, E. S. Schlegel, R. S. Keen, R. A. Lathlaen, and G. L. Schnabel, *IEEE*, **ED17**, 1077 (1970).
3. E. A. Corl and W. E. Reese, *Met. Trans.*, **1**, 747 (1970).
4. R. P. Esch and W. A. Pliskin, original work unpublished but some results were referenced by W. A. Pliskin in "Semiconductor Silicon 1973," H. R. Huff and R. R. Burgess, Editors, p. 521, The Electrochemical Society Softbound Symposium Series, Princeton, N. J., (1973).
5. E. Yamada, S. Ito, K. Yamada, and K. Sugawara, Paper 33 presented at Electrochemical Soc. Meeting, Houston, Texas, May 7-11, 1972.
6. K. S. Dagher, Paper 268 presented at the Electrochemical Soc. Meeting, Miami Beach, Florida, Oct. 8-13, 1972.
7. T. Y. Tien and F. A. Hummel, *J. Am. Ceram. Soc.*, **45**, 422 (1962).
8. J. M. Eldridge and P. Balk, *Trans. Met. Soc. AIME*, **242**, 539 (1968).
9. N. Nagasima, *J. Appl. Phys.*, **43**, 3378 (1972).
10. W. A. Pliskin and H. S. Lehman, *This Journal*, **112**, 1013 (1965).

# Growth and Evaluation of Epitaxial GaAs for Microwave Devices

Ferenc E. Rosztochy\* and Joshyo Kinoshita\*

Varian Associates, Palo Alto, California 94303

## ABSTRACT

Using liquid phase epitaxy (LPE), single, double, and triple epitaxial layers are grown. The layers have well-controlled, uniform thicknesses and good surface characteristics on wafers 1½ in. long. Individual layers in multi-layer structures are grown with thicknesses from 0.3 to 30 μm. Hall mobilities at 77°K vary from 73,800 cm<sup>2</sup> V<sup>-1</sup> sec<sup>-1</sup> ( $N = 1.4 \times 10^{15}$  cm<sup>-3</sup>) to 24,000 ( $N = 1.3 \times 10^{16}$  cm<sup>-3</sup>). A segregation coefficient for the net carrier concentration vs. Sn concentration in the melt is calculated as  $7.9 \times 10^{-5}$  for <100> GaAs and  $2.6 \times 10^{-4}$  for <111B> GaAs substrates. Gunn devices fabricated from this material using conventional flip chip design give up to 4% cw efficiency at 54 GHz, gradually increasing to 12.5% cw efficiency at 9-10 GHz. This technique has also been successfully used to grow epitaxial layers for varactors, avalanche diodes, FET devices, and photocathodes.

The great potential of GaAs Gunn diodes or transferred electron devices is well documented (1). Although the experimentally measured cw data for these devices are rapidly improving, there is still a significant gap between the predicted limits, i.e., 30% efficiency for Gunn devices (1) compared to the best published experimental results of 12.5% for Gunn diodes (2). The relatively low experimental values are due in a great extent to shortcomings in circuit design and heat sinking, but the quality of the epitaxial layer and the contacting technology are also important limiting factors. Quality includes such properties as: crystalline perfection, minimum amount of unwanted impurities and deep level traps, good uniformity, well-controlled, smooth doping profile, and exact carrier concentration and thickness. For example, in the case of avalanche devices <0.5 μm thick layers are required with the above properties, including a thickness control of ±0.05 μm and carrier concentration ±5% or better.

The purpose of this paper is to describe in detail the growth of GaAs by liquid phase epitaxy in our laboratory for microwave application; to describe studies related to the distribution coefficient of Sn in GaAs when grown from Ga solutions, as well as the orientation dependence of this distribution coefficient; and to correlate GaAs epitaxial crystal quality with rf device performance for both Gunn and avalanche devices.

Epitaxial GaAs has been grown from liquid or vapor phase. For large scale mass production, like the GaAsP LED requirements, the cheaper, more efficient vapor phase technology is preferred. For microwave applications where high quality is important and cost is secondary, liquid phase epitaxy has significant advantages.

Since its introduction in 1963 (3) and later its application to grow GaAs with high Hall mobility (4) liquid phase epitaxy went through numerous changes. The simple tipping technique was replaced by wiping (5-7), dipping (8), or rotating (9).

A version of the wiping technique was developed at Varian four years ago (10). The results indicate that it is suitable for growing high quality epitaxial GaAs for microwave specifications (2, 11).

## Epitaxial Crystal Growth

*Growth apparatus.*—To obtain low doped material with well-controlled, flat doping profile, special care is taken to operate a vacuum-tight, leak-tested gas

train from the palladium diffused hydrogen purifier to the low vapor pressure oil bubbler. The gas train is made of stainless steel and quartz. There is no intentional temperature gradient applied to the boat in any direction. A temperature, constant within ±0.1°C along the boat, is sought. To assure such a flat temperature profile during the dynamic temperature program of the epitaxial growth, a three-zone furnace with three controlling thermocouples is used. To assure flat doping profiles, the hydrogen is saturated with the partial pressure of arsenic from high purity GaAs dendrites inside the hot furnace just prior to reaching the graphite boat.

For different applications there are some variations in the design of the graphite boat. A schematic drawing of the basic boat design has been published (11). Figure 1 presents a photograph of a slightly different design. The boats are approximately 6-8 in. long, precision machined from the highest purity graphite available and carefully cleaned prior to melt preparation, including degreasing, acid cleaning and high temperature vacuum and hydrogen firing. As the figure indicates, the substrate wafers are recessed in the bottom of the boat. A movable slider with three or five compartments containing two melts is kept in exact position by special railing. The typical growth area varies between 0.75-1.8 in. (2). The slider is positioned with a quartz push rod within ±0.3 mm.

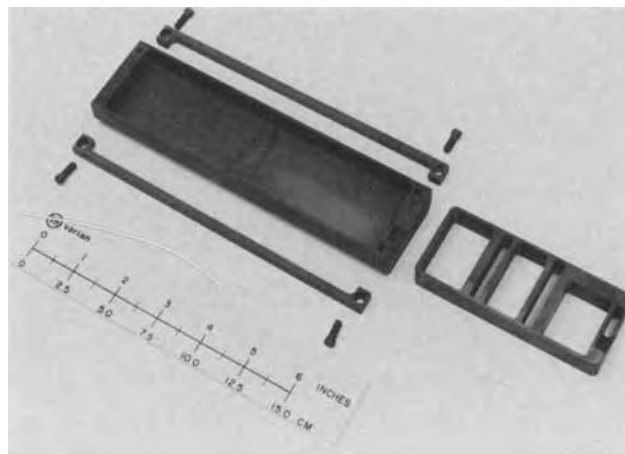


Fig. 1. Graphite boat with five-compartment slider to grow epitaxial GaAs double or triple layers.

\* Electrochemical Society Active Member.

Key words: gallium arsenide, crystal growth, liquid phase epitaxy, distribution coefficients in GaAs, microwave devices.

**Growth technique.**—The transient method is employed with starting temperatures usually around 725°C and the cooling rates, usually 0.2–2°C/min, are calculated in such a way that the growth of a single layer should take 3–30 min. The procedure for growing the epitaxial layer structures consists of the following steps:

1. Dendrite preparation. To obtain better quality epitaxial layers, the GaAs source material is prepared "in-house" by crystallizing GaAs from Ga solution.

2. Melt preparation. The melts contain gallium, Sn as the donor or Ge as the acceptor dopant and slight excess of GaAs to saturate the melt at growth temperature. Precautions are taken to drive out all oxygen and/or other volatile contaminants from the melts prior to growth and to keep the unwanted Si contamination to a minimum. One hundred hours at 900°C for a 50g melt is used prior to the first growth. Twelve to sixteen hours at 900°C is used prior to subsequent growths.

3. Substrate preparation. The substrates are Czochralski grown Sn-doped GaAs with carrier concentrations in the  $5\text{--}10 \times 10^{17} \text{ cm}^{-3}$  range, or Cr-doped semi-insulating crystals. Efforts are made to use substrates with the lowest possible unwanted impurity concentrations, especially avoiding Si. The wafers are  $\langle 100 \rangle$  oriented, rectangular-shaped according to  $\langle 110 \rangle$  cleavage faces and Br<sub>2</sub>-methanol polished.

4. Substrate cleaning. The method described by Di-Lorenzo is used and gives satisfactory results (12).

5. Melt saturation. The freshly cleaned substrates are placed in the slots on the bottom of the boat. For Hall measurements, a small, Cr-doped semi-insulating wafer is also included. The system is flushed with hydrogen for at least 30 min, then heated to  $\sim 10^\circ\text{C}$  above the desired growth temperature, and kept there for 30 min. The system is then cooled with the pre-selected cooling rate.

6. Layer growth. To grow an  $n^+ \text{--} n^- \text{--} n^+$  triple layer, the appropriate melts are positioned over the substrate as the system is being cooled. After the last growth, the wafers are wiped clean and the system is quenched to room temperature.

7. Removal and cleaning. When the system is under 35°C, it is opened, the wafers are taken out and evaluated for breakdown voltage, then boiled in concentrated HCl to dissolve any excess Ga.

**P-N junction growth.**—According to the literature, most GaAs p-n junctions are prepared through Zn diffusion. This technique gives satisfactory results for LED application, but has definite limitations regarding carrier concentration profiles, compensation in the p layer, and precipitate formation (13). For microwave applications, the quality of the epitaxial GaAs is very important. The epitaxial layers have to be uncompensated with well-controlled uniform carrier concentrations and a high degree of crystalline perfection. The liquid phase epitaxial technology described above can be used to grow n and p layers of GaAs consecutively in one heat cycle, with the required quality, if suitable dopants are selected (11). To insure minimum or zero cross-contamination and compensation, the dopants must have low vapor pressure and low distribution coefficient under the epitaxial growth conditions.

Table I compares the vapor pressure (14) and the distribution coefficient of the best known uncompensated dopants of GaAs (7, 9, 15, 16). Sn and Ge have the lowest distribution coefficients and also have vapor pressure many orders of magnitude lower than the other dopants. To insure uncompensated layers and an abrupt junction, Sn and Ge are selected as dopants.

When Ge-doped epitaxial GaAs layers are grown from Ga solution under 900°C, the Ge atoms act as uncompensated acceptors like Zn in the crystal (6, 16). The distribution coefficient for Ge is  $8 \times 10^{-3}$  and its

Table I. Vapor pressure and distribution coefficients for dopants in GaAs when grown from Ga solution

Donors	Vapor pressure (14) (in Torr, at 1000°K)	Distribution coefficient
Te	$8 \times 10$	3 (15)
Se	$1 \times 10^9$	10 (15)
Sn	$5 \times 10^{-8}$	$8 \times 10^{-15}$ (9)
Acceptors		
Zn	$1 \times 10^2$	$1 \times 10^{-2}$ (7)
Ge	$6 \times 10^{-10}$	$8 \times 10^{-3}$ (16)

vapor pressure at 1000°K is  $7 \times 10^{-10}$  Torr compared with 90 Torr for Zn. The distribution coefficient for Sn is  $8 \times 10^{-5}$  and the vapor pressure at 1000°C is  $7 \times 10^{-8}$  Torr.

### Wafer Evaluation

**Breakdown voltage measurement.**—The simplest, fastest qualitative evaluation of GaAs is done by measuring the point breakdown voltage between two tungsten probes. Figure 2 presents some of our empirical data. The semi-insulating substrates have breakdown voltage over 200V. The  $n^+$ , approximately  $1 \times 10^{18}$ , substrates have breakdown voltages around 4–5V. The typical  $n^-$  layer for Gunn devices with carrier concentrations between  $1 \times 10^{15}$  and  $5 \times 10^{15} \text{ cm}^{-3}$  has breakdown voltage between 30 and 70V.

**Thickness measurements.**—Each wafer is cleaved and stained to measure the thickness of the epitaxial layer under a microscope. Figure 3 shows the photograph of a cleaved and stained epitaxial triple layer. The buffer layer is about 2  $\mu\text{m}$ , the  $n^-$  active layer is 10  $\mu\text{m}$  and the contact layer is 5  $\mu\text{m}$ . Notice the relatively stronger line between the substrate and the buffer layer compared to the lines defining the interfaces between the three epitaxial layers. This gives a qualitative indication of the relative defect and impurity concentrations at the different interfaces,

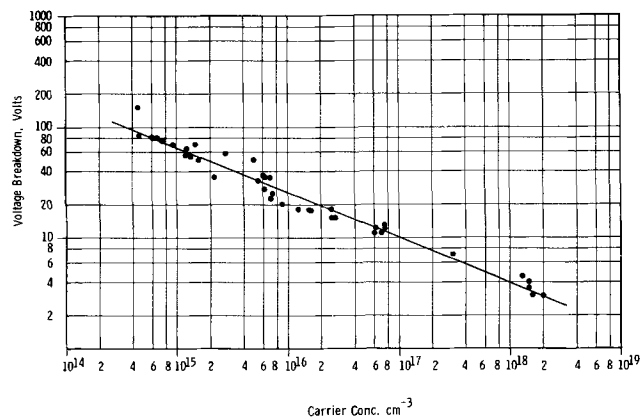


Fig. 2. Variation of breakdown voltage with carrier concentration in n-type GaAs as determined on an I-V scope between two tungsten point contacts.

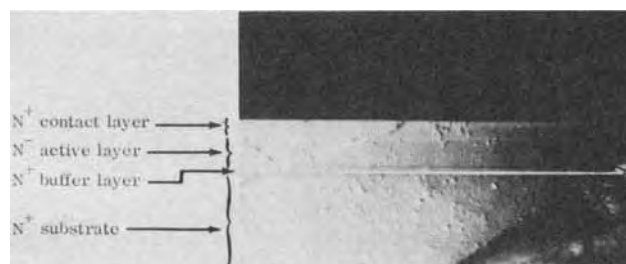


Fig. 3. Cleaved and stained GaAs  $N^+ / N^- / N^+$  triple layer on  $N^+$  GaAs substrate.

showing the beneficial effect of introducing the buffer layer to separate the relatively high concentration "surface" defects and impurities from the active layer.

If the layer structure is  $n^-$  on  $n^+$ , then IR spectrum measurements are also used to determine thickness uniformity across the wafer. For  $n^-$  layers, 7-30  $\mu\text{m}$  thick, the thickness is determined by measuring the distance between interference fringes in the 16-40  $\mu\text{m}$  wavelength range (17).

Figure 4 is a photograph showing the surface quality of GaAs layers with epitaxial thickness of approximately 20  $\mu\text{m}$ . The thickness uniformity for a high percentage of the wafers is better than  $\pm 2.5\%$  in.<sup>-1</sup> or  $\pm 0.10 \mu\text{m}$  in.<sup>-1</sup>, whichever is higher, for 90-95% of the surface area. For example, X-band wafers are prepared with 8  $\mu\text{m}$  active layer length uniform within  $\pm 0.2 \mu\text{m}$ .

**Doping profiles.**—Gold or gold-tin Schottky barriers of 20 mils diameter are evaporated on the GaAs and the doping profiles are determined using the capacitance depletion technique. This is done by measuring capacitance vs. voltage manually and then using a computer program to calculate carrier concentration vs. depth.

Figure 5 shows the doping profile of an epitaxial triple layer and the substrate. The individual layer thicknesses are determined by the cleave and stain technology. The carrier concentrations in the contact layer and in the substrate are established by Hall mea-

surements. The doping profile of the n-layer is determined by depletion capacitance measurements.

**Hall measurements.**—Van der Pauw crosses, 100  $\times$  100 mils, are used for Hall measurements (18) with a 1200 gauss magnetic field. The Hall mobility, carrier concentration and resistivity are measured at room temperature and at 77°K using Cr-doped substrate pieces added to each growth.

The combination of the room temperature and 77°K Hall mobility vs. carrier concentration data is a good way to judge the quality of GaAs layers. The higher and closer to the theoretical value these data are, the better is the epitaxial GaAs.

Figure 6 presents data for various n-layers grown in our laboratory for microwave applications along with various published experimental and theoretical data. The data of DiLorenzo (19) and Wolfe *et al.* (20) are based on vapor phase epitaxy, while those of Vilms and Garrett (9) and our laboratory are based on liquid phase epitaxy.

### Distribution Coefficient of Sn for <100> and <111B> Substrates

Figure 7 presents some representative data showing how the free carrier concentration determined by room temperature Hall measurements varies with increasing Sn concentration in the growth solution. The growth temperature is around 725°C for these layers and the substrates are <100> oriented. For comparison, recently published data by other authors are also presented (9, 24, 25). Based on our data, the distribution coefficient for GaAs grown from Ga solutions at 725°C is  $7.9 \times 10^{-5}$  for <100> substrates, where the distribution coefficient is defined  $k = n/(Sn_1)$ . This is in good agreement with prior work, which indicates a decreasing distribution coefficient with decreasing temperature. Migitaka *et al.* (26) recently reported  $k = 8.2 \times 10^{-5}$  at 730°C.

To determine the orientation dependence of the distribution coefficient, epitaxial layers are grown on <100> and <111B> Cr-doped substrates side-by-side from the same melts at the same temperature. Figure 8 presents the data showing 3.3 times higher carrier con-

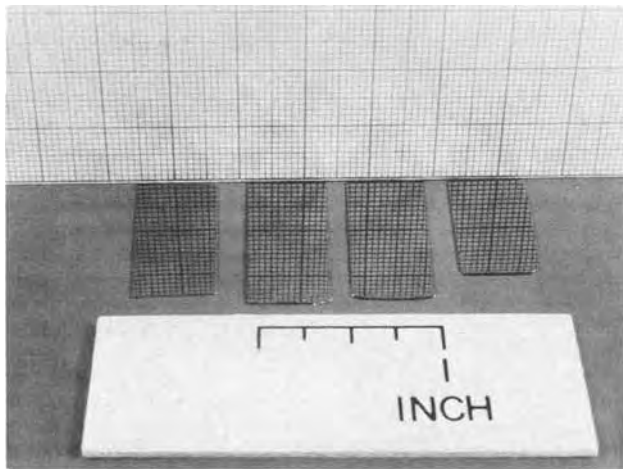


Fig. 4. Surface quality of LPE GaAs

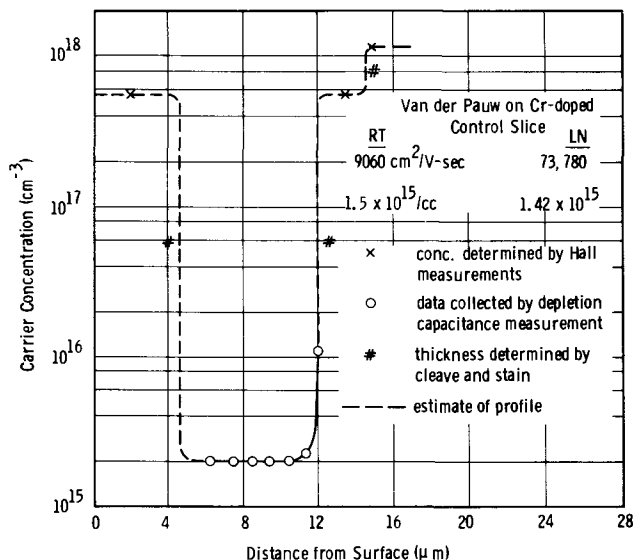


Fig. 5. Doping profile of epitaxial GaAs with triple layers

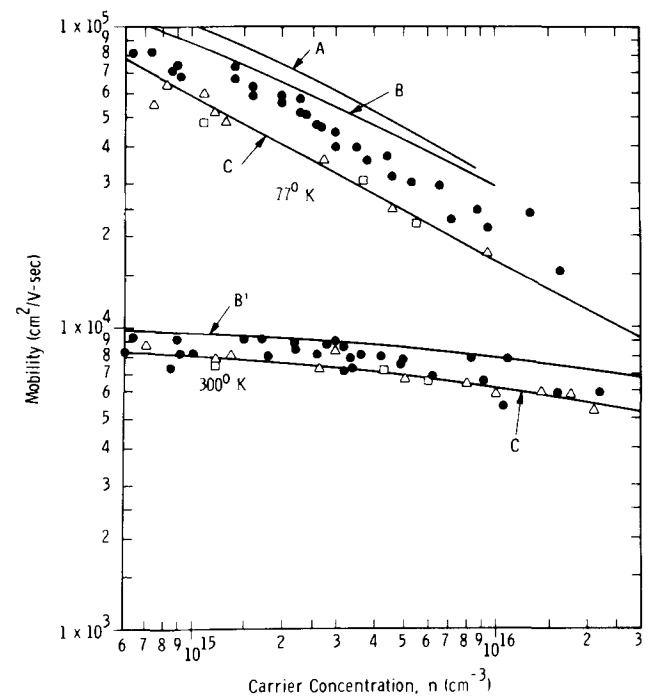


Fig. 6. This figure compares theoretical maximum mobility curves from Wolfe *et al.* (21) (A), drift mobility (B), and Hall mobility (B') from Rode and Knight (22, 23), with experimental data by Wolfe *et al.* (20) (C), DiLorenzo (19) ( $\square$ ), Vilms and Garrett (9) ( $\triangle$ ), and this work ( $\bullet$ ).

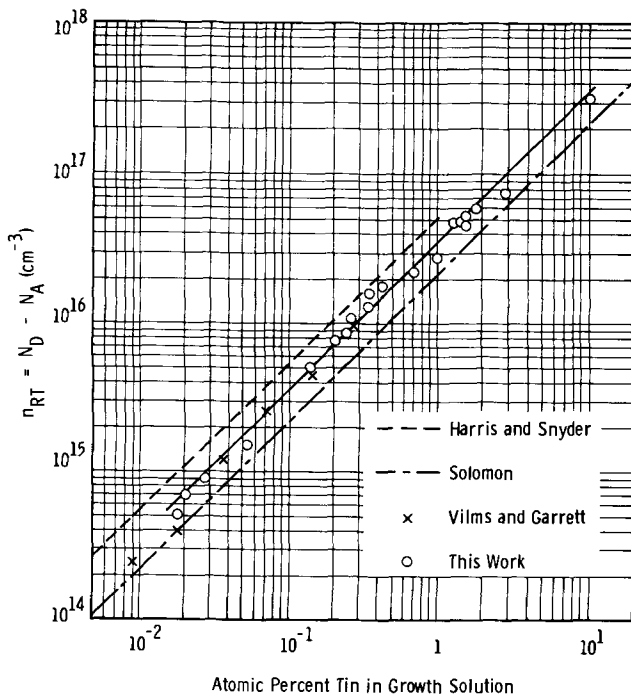


Fig. 7. Carrier concentration in <100> GaAs vs. Sn-concentration in GaAs-Ga melt.

centration on the <111B> substrates. This indicates a distribution coefficient of  $2.6 \times 10^{-4}$  at 725°C for  $n$  vs. Sn in the melt for <111B> oriented substrate crystals. This is in good agreement with the work of Kang and Greene (27), which is reported in terms of resistivity vs. carrier concentration for various orientation of GaAs substrates, and implies a value of approximately 3 for <111B> vs. <100>. Vogel (28) estimated a ratio of distribution coefficients of  $k_{111B}/k_{100} = 2$  at 770°C for the incorporation of Sn.

**Gunn Diodes**

Figure 9 shows the cross section of a typical Gunn diode. The results reported in this paper are based on devices made with the simple flip-chip technology, where the GaAs chip is thermo-compression or ultrasonically bonded epi down to the heat sink (2). The alloyed contacts are AuGeNi. As Fig. 9 indicates, the buffer layers on both sides of the N active layer are considered optional. The carrier concentration of the buffer layers is  $1-10 \times 10^{17} \text{ cm}^{-3}$ . The buffer layers not only reduce the defect density at the two sides of the active layer but (i) they also protect the active layer from out-diffusion of unwanted impurities from the substrate, (ii) diminish bonding damages to the active layer, and (iii) make it easier to form good ohmic contact between the metals and the GaAs. The regrown contact, i.e., the buffer layer on the surface of the active layer, adds unwanted thermal resistance to the device, reducing cw efficiency, and it is also suspected to have detrimental effects on the boundary

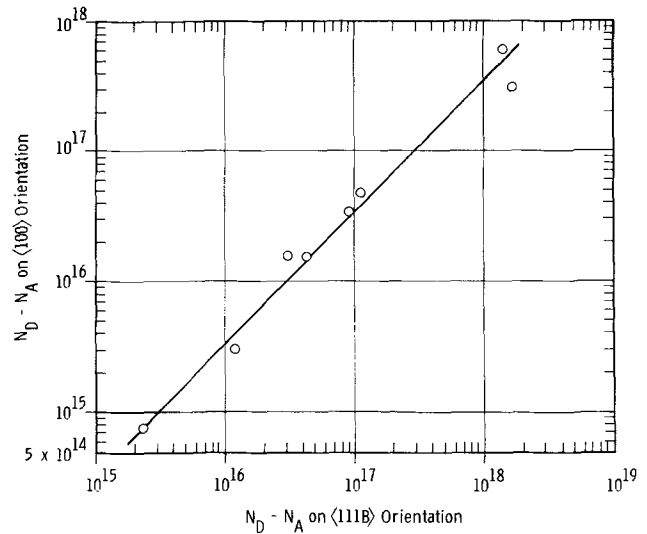


Fig. 8. <100> vs. <111B> orientation dependence of the carrier concentration in Sn-doped GaAs grown around 725°C by LPE.

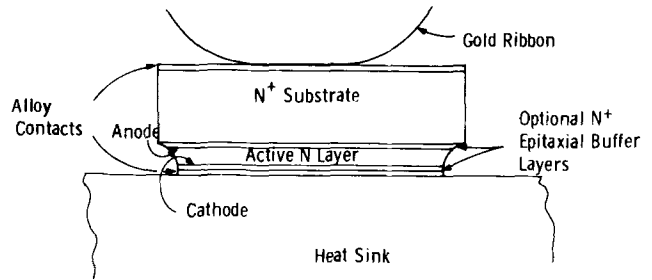


Fig. 9. Typical epitaxial Gunn diode structure

definition on the cathode side, which becomes significant in the case of mm-wave devices, with active layer thickness around 2.0-2.5 μm only.

In Fig. 10 experimental data are presented to show the threshold voltage ( $V_{th}$ ) vs. active layer length ( $l$ ) relationship for Gunn devices. The  $V_{th}$  values are measured pulsed with < 1% duty cycle. For comparison, the data measured on wafers with regrown contact are presented with a different symbol ( $\Delta$ ) as data measured on wafers with metallic contact ( $\circ$ ). The majority of the thickness data is based on cleave and stain measurements on production-run wafers prior to contacting, but in a few cases completed diodes are cross sectioned after the determination of  $V_{th}$ , to measure  $l$  more accurately. The symbols  $\blacktriangle$  and  $\bullet$  denote these corresponding points in Fig. 10. The points measured on regrown wafers ( $\Delta$  and  $\blacktriangle$ ) tend to be higher than the ones measured on wafers with metallic contact ( $\circ$  and  $\bullet$ ) indicating shorter  $l$  values for the same  $V_{th}$  on regrown wafers.

Table II summarizes certain key parameters to fabricate high efficiency or wide-tuning Gunn devices. It lists for the different frequency bands the optimum carrier concentration ( $n$ ), active layer length ( $l$ ) and

Table II. Nominal device parameters for Gunn diodes

Frequency band (GHz)	Active layer length (μm)	Carrier conc. (n <sub>cm<sup>-3</sup>)</sub>	Type of contact	Application	n × l product (× 10 <sup>12</sup> cm <sup>-2</sup> )	V <sub>th</sub> (Volts)
C-band, 4-8	10-20	1.6 × 10 <sup>15</sup>	Regrown	High efficiency	2.4	4-7
		8.5 × 10 <sup>14</sup>	Regrown	Wide tuning	1.3	
X-band, 8-12.4	8.0	2.9 × 10 <sup>15</sup>	Metal	High efficiency	2.3	3-3.6
		1.7 × 10 <sup>15</sup>	Regrown	Wide tuning	1.3	
Ku-band, 12.4-18	5.8	4 × 10 <sup>15</sup>	Metal	High efficiency	2.3	2.5-3.0
		2.5 × 10 <sup>15</sup>	Regrown	Wide tuning	1.3	
K-band, 18-26	4.2	5.5 × 10 <sup>15</sup>	Metal	High efficiency	2.3	2.1-2.5
		3.7 × 10 <sup>15</sup>	Regrown	Wide tuning	1.3	
Ka-band, 26-40	2.8	8.2 × 10 <sup>15</sup>	Metal	High efficiency	2.3	1.7-2.1
		4.6 × 10 <sup>15</sup>	Metal	Wide tuning	1.3	
V-band, 40-80	2.1	~1.1 × 10 <sup>16</sup>	Metal	High efficiency	2.3	1.5-1.8
		6 × 10 <sup>15</sup>	Metal	Wide tuning	1.3	



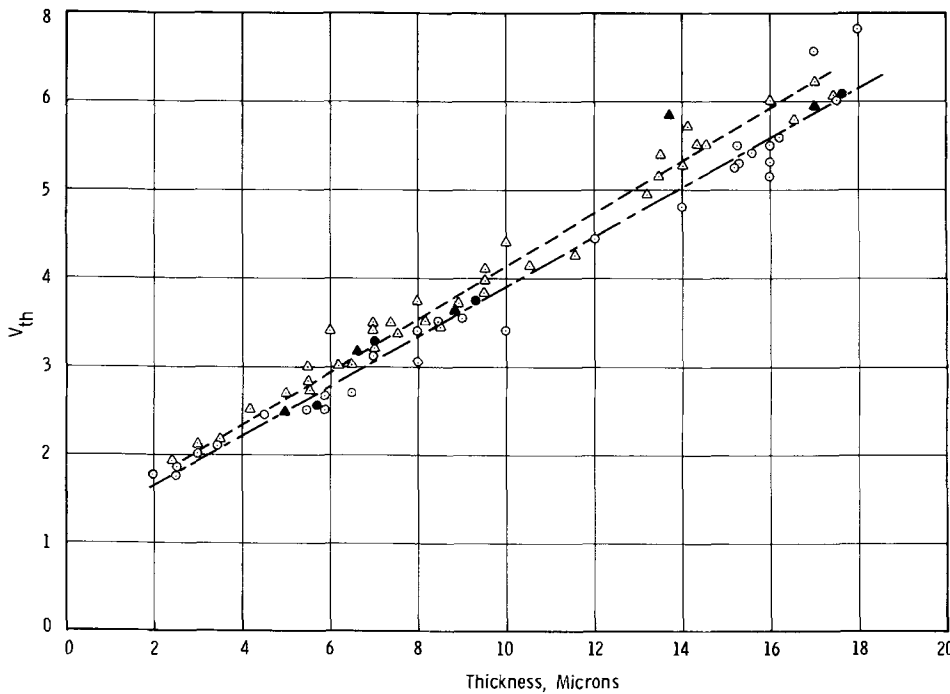


Fig. 10. Pulse threshold voltage vs. active layer thickness for GaAs Gunn diodes.  $\Delta$ ,  $\blacktriangle$ , and --- represent results with regrown contact, while  $\circ$ ,  $\bullet$ , and — are based on data with direct metal contact.  $\triangle$  and  $\circ$  represent average values on epitaxial wafers.  $\blacktriangle$  and  $\bullet$  are based on cross sectioning individual diodes.

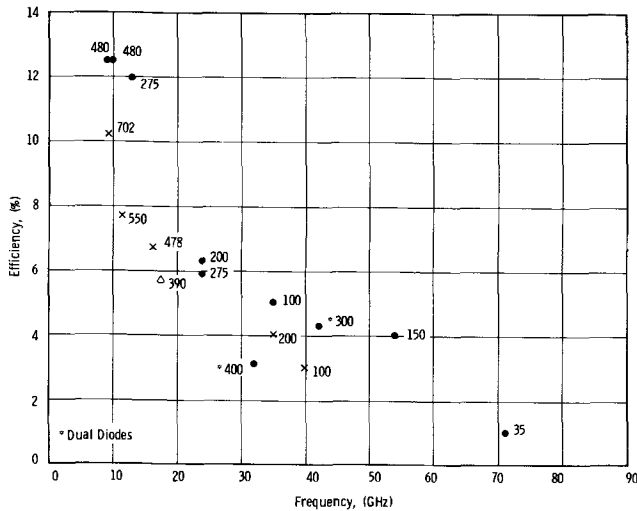


Fig. 11. Cw efficiency vs. frequency is plotted for Gunn diodes and the power output in mW is listed alongside each data point. The results of this work ( $\bullet$ ) are compared with those of Hasty *et al.* (30) (X) and DiLorenzo (19) ( $\Delta$ ). \* is for two diodes measured in a dual diode circuit.

corresponding  $V_{th}$ . For high efficiency devices the optimum  $n \times l$  product is about  $2.3 \times 10^{12} \text{ cm}^{-2}$  and with the exception of C-band devices, metallic contacts are recommended. For wide-tuning applications on the other hand, the optimum  $n \times l$  product is around  $1.3 \times 10^{12} \text{ cm}^{-2}$  and regrown contacts are preferred up to 26 GHz.

Table III. RF performance data for GaAs microwave devices

Type of diodes	Frequency (GHz)	Efficiency (%)	$P_o$ (mW)
Gunn devices	9-10	12.5	480
	13	11.9	275
	24	6.3	200
	35	5.0	100
	54	4.0	150
	71	1.0	35
	Double drift avalanche devices	8.9	16.3
8.9		15.8	3000
10.3		19.6	2200

Device Performance

The ultimate judgment on epitaxial wafer quality for microwave applications must be based on the rf performance of the resulting devices. It is the main objective of this paper to describe the crystal growth technology and the properties of the epitaxial wafers together with the rf performance data of the corresponding devices. Figure 11 charts the rf performance of the Gunn diodes. Cw efficiency vs. frequency is plotted and the cw output power is listed alongside each data point. The best efficiency, 12.5%, is measured at 9 and 10 GHz, with output power of 480 mW (2). At 54 GHz, 4% efficiency is observed with 150 mW power output. At 71 GHz, 1% efficiency and 30 mW is the best recorded data (29). For comparison, the best published results by DiLorenzo (19) and Hasty *et al.* (30) are also presented.

Table III summarizes the most notable rf data on our microwave devices. Besides the Gunn device data, results with double drift and high-low structure avalanche devices are also listed. Double-drift avalanche devices are fabricated with 20.7% pulsed and 16.3% cw efficiency and power outputs of 4.1W and 2.35W, respectively, in X-band (11, 31). High-low avalanche devices give 19.6% efficiency and 2.2W cw at around 10 GHz (32). These results are only preliminary data and significant improvements are imminent.

Using some of the above described Gunn diodes, transferred electron amplifiers are built with 110 mW saturated power output and 3 GHz bandwidth at 35 GHz; 13 db small-signal gain and 16.2 db noise figure are observed (33).

Acknowledgments

The authors wish to thank F. B. Fank and R. E. Goldwasser for their initial review of the manuscript and C. Casau and S. Lombardi for their help with the experiments.

Manuscript submitted Aug. 7, 1973; revised manuscript received Oct. 17, 1973. This was Paper 229 presented at the Miami Beach, Florida, Meeting of the Society, Oct. 8-13, 1972.

Any discussion of this paper will appear in a Discussion Section to be published in the December 1974 JOURNAL. All discussions for the December 1974 Discussion Section should be submitted by Aug. 1, 1974.

REFERENCES

1. J. A. Copeland, *Proc. IEEE*, 57, 1666 (1969).

2. J. F. Caldwell and F. E. Rosztochy, "Proc. Fourth Int. Symp. on GaAs and Related Compounds," Boulder, Colorado (1972) p. 240, The Institute of Physics, London (1973).
3. H. Nelson, *RCA Rev.*, **24**, 603 (1963).
4. C. S. Kang and P. E. Greene, *Appl. Phys. Letters*, **11**, 171 (1967).
5. J. Konoshita, W. W. Stein, G. F. Day, and J. B. Mooney, "Proc. Second Int. Symp. on GaAs," Dallas, Texas (1968) p. 22, The Institute of Physics, London (1969).
6. F. E. Rosztochy, F. Ermanis, I. Hayashi, and B. Schwartz, *J. Appl. Phys.*, **41**, 264 (1970).
7. K. Keller and W. Muench, *Solid-State Electron.*, **14**, 526 (1971).
8. H. Rupprecht, "Proc. (First) Int. Symp. on GaAs," Reading, England (1966), p. 57, The Institute of Physics, London (1967).
9. J. Vilms and J. P. Garrett, *Solid-State Electron.*, **15**, 443 (1972).
10. F. E. Rosztochy, J. Kinoshita, M. Omori, and B. Fank, 1971 Workshop on Compd. Semicond. for Microwave Devices, Jan. 28-29, 1971, New York.
11. F. E. Rosztochy, J. F. Caldwell, J. Konoshita, and M. Omori, *Appl. Phys. Letters*, **19**, 525 (1973).
12. J. V. DiLorenzo, *This Journal*, **118**, 1645 (1971).
13. W. C. Rhines, "Stanford Materials Science and Engineering Report No. SU-DMS-72-T-137," Stanford University, Palo Alto (1972).
14. R. E. Honig and D. A. Kramer, *RCA Rev.*, **30**, 285 (1969).
15. P. D. Greene, To be published.
16. F. E. Rosztochy and K. B. Wolfstirn, *J. Appl. Phys.*, **42**, 426 (1971).
17. M. P. Alberts and J. F. Combs, *This Journal*, **109**, 709 (1962).
18. L. J. Van der Pauw, *Philips Res. Rept.*, **13**, 1 (1958).
19. J. V. DiLorenzo, *IEEE Trans. Electron Devices*, **ED-19**, 123 (1972).
20. C. M. Wolfe, A. G. Foyt, and W. T. Lindley, *Electrochem. Technol.*, **6**, 208 (1968).
21. C. M. Wolfe, G. E. Stillman, and W. T. Lindley, *J. Appl. Phys.*, **41**, 3088 (1970).
22. D. L. Rode and S. Knight, *Phys. Rev. B.*, **3**, 3 (1971).
23. D. L. Rode, Private communication.
24. J. S. Harris and W. L. Snyder, *Solid-State Electron.*, **12**, 337 (1969).
25. R. Solomon, "Proc. Second Int. Symp. on GaAs," Dallas, Texas (1968) p. 11, The Institute of Physics, London (1969).
26. M. Migitaka, A. Doi, and M. Miyazaki, "Proc. Fourth Int. Symp. on GaAs and Related Compounds," Boulder, Colorado (1972) p. 249, The Institute of Physics, London (1973).
27. C. S. Kang and P. E. Greene, "Proc. Second Int. Symp. on GaAs," Dallas, Texas (1968) p. 18, The Institute of Physics, London (1969).
28. K. H. Zschauer and A. Vogel, "Proc. Third Int. Symp. on GaAs and Related Compounds," Aachen, Germany (1970) p. 100, The Institute of Physics, London (1971).
29. F. E. Rosztochy, R. E. Goldwasser, and T. G. Ruttan, *Microwave J.*, **16**, 51 (1973).
30. T. E. Hasty, T. G. Blocker, D. W. Shaw, and D. N. McQuiddy, "Proc. 3rd Cornell Elec. Eng. Conf.," Ithaca, N. Y., p. 325 (1971).
31. M. Omori, F. E. Rosztochy, and R. Hayashi, *Proc. IEEE*, **61**, 255 (1973).
32. R. E. Goldwasser, Private communication.
33. R. E. Goldwasser and F. E. Rosztochy, *Proc. IEEE*, **61** (1973).

## Preliminary Results of an Ion Scattering Study of Phosphosilicate Glass Gettering

R. L. Meek\* and C. F. Gibbon

*Bell Laboratories, Murray Hill, New Jersey 07974*

### ABSTRACT

Phosphosilicate glass gettering of silicon wafers in which diodes had been formed has been studied. The amount and identity of the gettered impurities were determined by means of Rutherford backscattering of 2 MeV He<sup>+</sup> ions. The principal gettered impurities are Cu and Fe ( $\sim 10^{15}$  cm<sup>-2</sup>) and a heavy mass species in the range Pt-Pb, presumably Au ( $\sim 10^{13}$  cm<sup>-2</sup>). Gettering behavior is correlated with diode properties; the diode quality increases with increased amounts of gettered impurities.

In view of the renewed interest in the role of transition metals and other impurities, either initially present in the material (1) or introduced by the process, in the degradation of p-n junction properties, we have initiated a study of phosphosilicate glass gettering, using ion backscattering as the diagnostic technique. Phosphosilicate glass gettering has long been used to remove unwanted electrically active impurities from silicon wafers (2-7). The purpose of the present work is to identify, qualitatively and quantitatively, the impurities present in typically processed device wafers and to examine their effect on diode properties as an aid to subsequent studies where controlled amounts of appropriate impurities are intentionally introduced.

### Experimental

*Diode preparation.*—Two groups of wafers were studied; both were p-type (111) slices with  $3\mu$  of 0.5

ohm-cm n-type epi grown on them. One group (from epi run H2114) gave nearly 100% very soft base-collector junctions when boron was diffused from either a BN or ion-implanted source. (A soft junction is one whose I-V characteristic on a curve tracer clearly shows curvature below the avalanche breakdown voltage on the 10  $\mu$ A/cm<sup>2</sup> scale.) The other group of wafers, having substrate material different from the group just described (from epi run H2067), gave much better properties with 80% of the junctions being hard as diffused.

After reoxidation to protect the base from phosphorous diffusion, wafers were gettered for various times in a 1000°C, PBr<sub>3</sub> phosphorous furnace in which the bare back side of the wafer was exposed to the phosphosilicate glass. The glass was stripped off, the diode properties remeasured, and the ion scattering spectrum was taken.

*Ion scattering.*—The Rutherford backscattering technique for chemical analysis was pioneered by Davies

\* Electrochemical Society Active Member.  
Key words: gettering, soft junctions, phosphosilicate glass, ion backscattering.

et al. (8), and Bogh (9) and has been recently reviewed by Buck and Wheatley (10) and by Nicolet et al. (11).

For energetic ions undergoing Rutherford scattering from a target atom the scattering yield per unit solid angle is given by

$$\frac{dn}{d\Omega} = \frac{n_0 N b^2}{16} \sin^{-4} \left( \frac{\theta_c}{2} \right) \quad [1]$$

where

$$b = \frac{Z_1 Z_2 e^2}{\frac{1}{2} \left( \frac{M_1 M_2}{M_1 + M_2} \right) V^2} \quad [2]$$

$Z_1$  and  $Z_2$  are the atomic numbers of incident particle and target atom,  $M_1$  and  $M_2$  are the respective masses, and  $\theta_c$  is the center of mass scattering angle;  $e$  is the electronic charge,  $V$  is the velocity of the incident ion,  $n_0$  is the number of incident ions, and  $N$  is the number of target atoms  $\text{cm}^{-2}$ . The center of mass and laboratory scattering angles are related by

$$\sin(\theta_c - \theta_L) = \frac{M_1}{M_2} \sin \theta_L \quad [3]$$

Since the scattering is elastic, ions scattered from a target atom of given mass at a given  $\theta_L$  have a characteristic energy,  $E$ , given by

$$\frac{E}{E_0} = \frac{M_1^2}{(M_1 + M_2)^2} \left\{ \cos \theta_L + \left( \frac{M_2^2}{M_1^2} - \sin^2 \theta_L \right)^{1/2} \right\}^2 \quad [4]$$

where  $E_0$  is the ion energy before the scattering event.

For scattering from target atoms of given mass distributed in a substrate, the energy scale may be converted to a depth scale by use of the kinematic energy loss and the specific energy loss rate in the material; namely

$$\Delta t = \Delta E \left\{ \left( \frac{dE}{dx} \right)_{E_{in}} \left( \frac{E_{out}}{E_{in}} \right) + \left( \frac{dE}{dx} \right)_{E_{out}} \frac{1}{|\cos \theta_L|} \right\}^{-1} \quad [5]$$

which relates the energy shift  $\Delta E$  to thickness increment  $\Delta t$ .

In these experiments a beam of 2 MeV  $\text{He}^+$  ions collimated to  $\sim 0.05^\circ$  through two Ta collimators 1 mm in diameter about 2m apart was used. The backscattered He ions were detected at  $\theta_L = 177^\circ$  in a 50  $\text{cm}^2$  surface barrier detector having an energy resolution of 16 keV. This energy resolution corresponds to a depth resolution of about 200Å. Secondary electron suppression and pile-up rejection electronics were used. Samples were surrounded by a baffle cooled to liquid nitrogen temperature and were mounted in a two axis goniometer. The scattering chamber was maintained at  $10^{-6}$  Torr and the He ion fluence was typically  $10^{16}$   $\text{cm}^{-2}$ .

### Results

Ion scattering spectra from the back side of typical wafers before phosphosilicate glass gettering are seen in Fig. 1 for the poorer material and in Fig. 2 for the better. After reoxidation to protect the base from phosphorus diffusion and a 60 min getter in a 1000°C,  $\text{PBr}_3$  phosphorus furnace in which the bare back side of a Si wafer from the poor group was exposed to phosphosilicate glass, about 25% of the junctions had become hard. This glass was stripped off and the spectrum taken. It is presented in Fig. 3.

In Fig. 2 and 3 particularly, impurities are seen at energies corresponding to transition and heavy metals. From the shape and magnitude of the spectra [especially the channeled spectra which separate lattice-

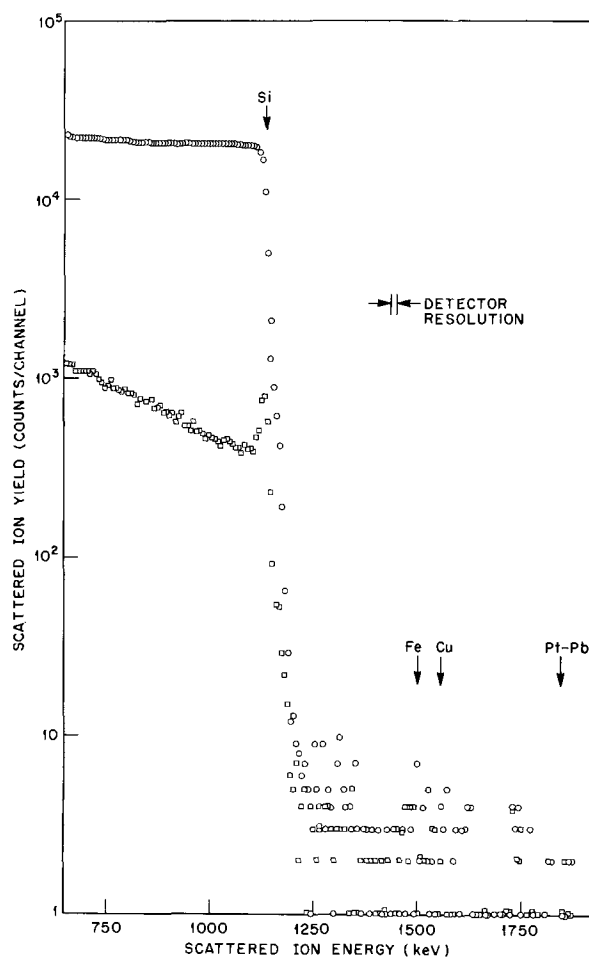


Fig. 1. Scattered ion spectrum from the back side of material which formed poor diodes (before gettering).

site and off-lattice-site scatterers and shows in some cases two separate peaks (see Fig. 3), the upper edges of which correspond to Fe and Cu] we conclude that the transition metals present include Cu and Fe. (Secondary ion mass analysis confirms this.) The impurities are contained in a layer about 2000Å wide at the back surface (determined from Eq. [5]). The heavy metal present lies in the Pt-Pb range and we presume it is Au. Figure 1 (the poor material before gettering) shows a maximum of  $2(10)^{14}$   $\text{cm}^{-2}$  of Cu and Fe and  $10^{13}$   $\text{cm}^{-2}$  Pt-Pb near the back surface. After gettering (Fig. 3) there are  $2(10)^{15}$   $\text{cm}^{-2}$  of Cu and Fe and  $4(10)^{13}$   $\text{cm}^{-2}$  of the Pt-Pb group. Since the glass was removed before the spectra were taken, no information is available on the impurities contained in the glass itself. This will be discussed in a future publication (12), where it will be shown that they are in fact almost entirely in the silicon.

Figure 2 is for ungettered material which originally produced good diodes. Note that impurities are apparently already "self-gettered" to the back surface by some mechanism [ $(10)^{15}$   $\text{cm}^{-2}$  of Cu and Fe and  $2(10)^{13}$   $\text{cm}^{-2}$  of Pt-Pb]. The implications of and the possible reasons for this are under study. It is tentatively suggested that it may be due to residual damage or defects left at the back surface. The silicon  $\langle 110 \rangle$  minimum yield was 2% for the poor material and 3% for the good material before any phosphosilicate glass gettering. After gettering it is 3%. After diffusion gettering of the good material 80-100% of the diodes are hard and the amounts of impurities on the back surfaces are essentially unchanged.

In Fig. 4 is plotted the gettered impurity concentration vs. gettering time for the material which initially formed soft diodes. The number in parentheses beside each data point is the ratio of counts in the (110) chan-

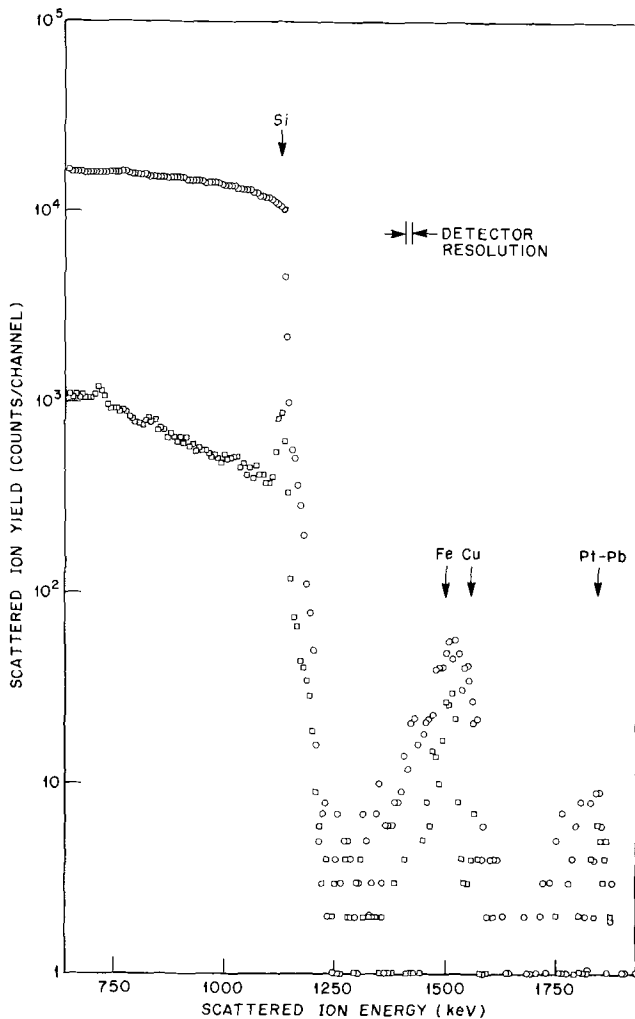


Fig. 2. Scattered ion spectrum from the back side of material which formed good diodes (before gettering).

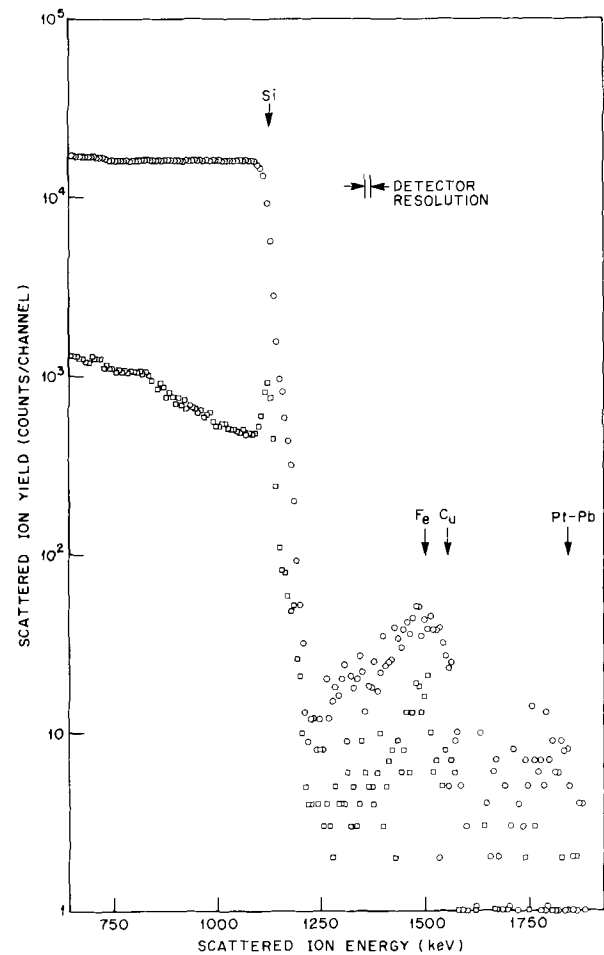


Fig. 3. Scattered ion spectrum from the back side of material which formed poor diodes before gettering, after phosphosilicate glass gettering (1000°C, 1 hr) and removal of glass from back side.

neled spectrum to those in the random spectrum and gives essentially the fraction of the impurity atoms which lie off silicon lattice sites. Since the effective diffusion coefficient for Cu in silicon (13) is  $\sim 10^{-4}$   $\text{cm}^2 \text{sec}^{-1}$  and that for Fe and Au (14, 15) is  $\sim 10^{-8}$   $\text{cm}^2 \text{sec}^{-1}$ , it is fair to assume that all of the Cu should have been gettered even in the shortest gettering time. (The characteristic time for Cu to diffuse across the wafer thickness is  $\sim 1$  sec and for Fe and Au is  $\sim 1$  hr.) Since a steady increase in the amount of gettered impurity Cu and Fe is observed for times up to 1 hr, it appears that most of the Cu + Fe is in fact Fe. The shape of the spectra also appears to support this interpretation, the peak occurring at Fe, not Cu. In the case of Au, the high value on the ungettered material is felt likely to be due to surface contamination. In fact examination of the spectrum (Fig. 1) indicates that a significant fraction of the counts attributed to Au might in fact be due to a lighter surface impurity.

Figure 5 shows the median voltage at 10  $\mu\text{A}$  leakage current (the "10  $\mu\text{A}$  breakdown voltage") for 96 diodes after each gettering treatment. An avalanche breakdown voltage of 25-30V would be expected on this material for a hard diode. There is a clear trend to lower leakage currents at a given voltage indicated on this curve which corresponds to increased accumulation of impurities on the backs of the slices shown on Fig. 4.

The question of course arises as to where the impurities originate. Previous work on polishing and pre-oxidation cleaning has shown that they should not originate with these steps (18). Furthermore, gettering of unprocessed wafers indicates that such large amounts of impurities are not likely to be present in

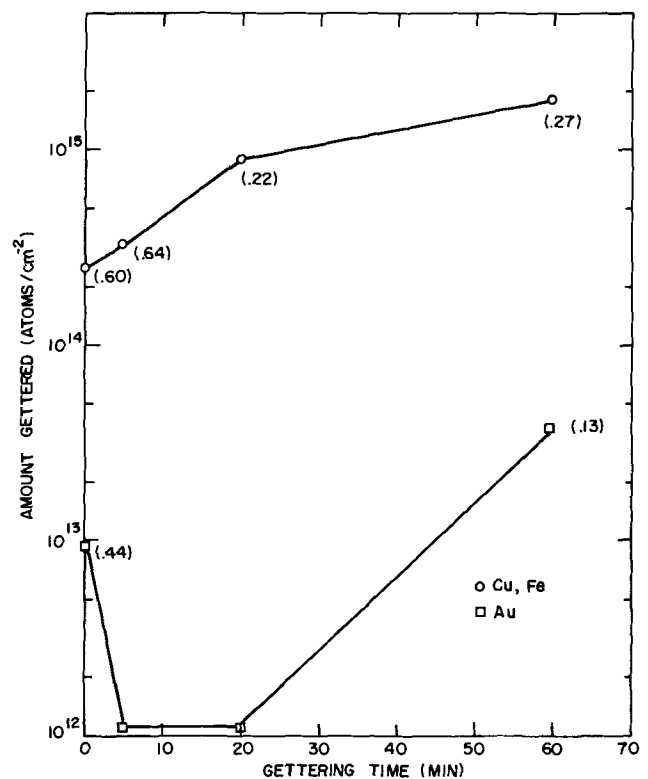


Fig. 4. Gettered impurity concentration vs. gettering time at 1000°C for material which initially formed poor diodes.

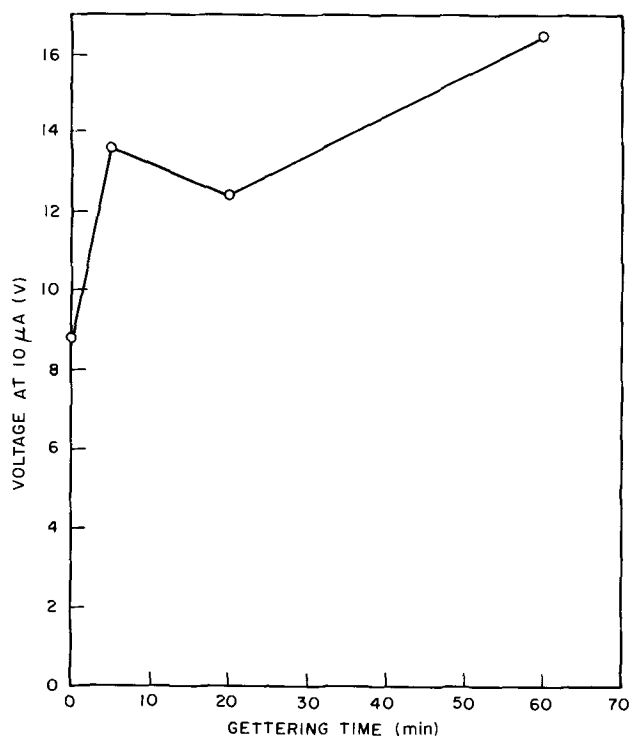


Fig. 5. Breakdown voltage vs. gettering time for the same material as Fig. 4.

the starting material (12). Further work is in progress in an attempt to identify the point in the processing sequence at which the impurities are introduced. However, we have noted that often cleaning procedures are ineffectually applied and that furnaces sometimes become contaminated with Cu or Au (12). Ion scattering from control sample surfaces furnishes a fast, reliable quality control technique for determining when

such processing steps are resulting in contaminated wafers (18, 19).

Manuscript submitted Nov. 13, 1972; revised manuscript received Sept. 4, 1973.

Any discussion of this paper will appear in a Discussion Section to be published in the December 1974 JOURNAL. All discussions for the December 1974 Discussion Section should be submitted by Aug. 1, 1974.

#### REFERENCES

1. A. Mayer, *Solid State Technol.*, **15**, 38 (1972).
2. A. Goetzberger and W. Shockley, *J. Appl. Phys.*, **31**, 1821 (1960).
3. S. W. Ing, R. E. Morrison, R. E. Alt, and R. W. Aldrich, *This Journal*, **110**, 533 (1963).
4. L. A. Murray and H. Kressel, *Electrochem. Technol.*, **5**, 406 (1967).
5. T. M. Buck, H. C. Casey, J. V. Dalton, and M. Yamin, *Bell System Tech. J.*, **47**, 1827 (1968).
6. M. Nakamura, T. Kato, and N. Oi, *Japan. J. Appl. Phys.*, **7**, 512 (1968).
7. J. L. Lambert and M. Reese, *Solid State Electron.*, **11**, 1055 (1968).
8. J. A. Davies, J. Denhartog, L. Erikson, and J. W. Mayer, *Can. J. Phys.*, **45**, 4053 (1967).
9. E. Bogh, *ibid.*, **46**, 653 (1968).
10. T. M. Buck and G. H. Wheatley, *Surface Sci.*, **33**, 35 (1972).
11. M. A. Nicolet, J. W. Mayer, and I. V. Mitchell, *Science*, **177**, 841 (1972).
12. T. E. Seidel and R. L. Meek, "3rd. Int. Conf. on Ion Implantation," B. L. Crowder, Editor, p. 305, Plenum Press, New York (1973).
13. R. N. Hall and J. H. Racette, *J. Appl. Phys.*, **35**, 379 (1964).
14. W. R. Wilcox and T. J. LaChapelle, *ibid.*, **35**, 240 (1964).
15. J. D. Struthers, *ibid.*, **27**, 1560 (1956).
16. C. B. Collins, R. O. Carlson, and C. J. Gallaghen, *Phys. Rev.*, **105**, 1168 (1957).
17. C. B. Collins and R. O. Carlson, *Phys. Rev.*, **108**, 1409 (1957).
18. R. L. Meek, T. M. Buck, and C. F. Gibbon, *This Journal*, **120**, 1241 (1973).
19. R. L. Meek, *ibid.*, **121**, 172 (1974).

# Segregation Behavior in a Stationary Vertical Zone with Converging Interfaces: Pressure-Induced Segregation Effects

K. M. Kim, A. F. Witt,\* and H. C. Gatos\*

Department of Metallurgy and Materials Science,  
Massachusetts Institute of Technology, Cambridge, Massachusetts 02139

## ABSTRACT

Crystal growth and segregation behavior in a confined, vertical melt zone in an InSb system were studied by allowing the upper and lower crystal-melt interfaces to converge through controlled power reduction. Segregation inhomogeneities during the initial stages of solidification appeared exclusively in the upper crystal segment which grew under destabilizing thermal gradients. At decreased zone height, irregular dopant inhomogeneities, identical in appearance, were simultaneously formed in both the upper and lower crystal segments. With continuing solidification the irregular and random inhomogeneities became periodic (oscillatory) in nature. Periodic dopant striations of decreasing frequency were observed to the coalescence point of the two interfaces. The random and periodic segregation inhomogeneities, which formed simultaneously at the converging growth interfaces, were attributed to isostatic pressure effects which originate in the volume expansion of the confined solidifying melt.

It has been found that during stationary vertical crystal growth under destabilizing thermal gradients (1), with decreasing height, the melt exhibits successively, turbulent convection, oscillatory instability, and thermal stability. Both turbulent convection and oscillatory thermal instability in the melt lead to corresponding characteristic dopant inhomogeneities in a growing crystal. On the other hand, under stabilizing thermal gradients, uniform dopant distribution has been observed (2).

In the present study, crystal growth and segregation were investigated in a confined vertical melt zone in which the upper solid-melt interface advanced under destabilizing and the lower under stabilizing thermal gradients.

## Experimental Procedure

The technique reported earlier (1) for crystal growth by controlled power reduction was employed in the present study, modified as shown in Fig. 1. A wire-wound resistance heater (1.5 cm ID and 1.5 cm long) was placed coaxially inside the longer external heater. Both heat sources were operated (in series) by proportional power control with the control thermocouple in the external heater. The solid-melt interfaces were made to converge by decreasing the furnace temperature at a constant rate of 0.54°C/min.

Two tin-doped ( $10^{17}$  atoms/cm<sup>3</sup>) InSb single crystals with  $\langle 111 \rangle$  orientation were machined and etched to fit into the quartz tube (0.8 cm ID). The lower crystal was placed on a graphite holder and the upper was mounted on a water-cooled holder. Polycrystalline charge, heavily doped with tin (about  $10^{20}$  atoms/cm<sup>3</sup>), was placed between the two crystals and was melted together with a portion of both crystals. After melting, the upper crystal segment was lowered to establish a cylindrical melt zone. The molten zone (about 1.3 cm long) was held at temperature to achieve homogenization before proceeding with solidification.

"Time markers" were introduced simultaneously in both growing crystals by applying current pulses (18A) of 50 msec duration at a repetition rate of 20 sec through leads attached to the upper and lower crystal. Each current pulse caused Peltier cooling on one crystal-melt interface (electron flow: melt to solid) and

simultaneously Peltier heating on the other crystal-melt interface (electron flow: solid to melt).

The growth and segregation characteristics of the system were studied on etched (211) planes exposed by cutting the solidified zone along the  $\langle 111 \rangle$  growth axis.

## Experimental Results

*Interface morphology and growth rate.*—The photomicrograph of an etched (211) plane from a typical solidification experiment is shown in Fig. 2. In the figure, the solid-liquid interface with the destabilizing thermal gradient advanced from the top down (crystal segment A) while the solid-liquid interface with stabilizing thermal gradient advanced from the bottom up (crystal segment B). The A and B time markers bearing the same numbers grew simultaneously. The pronounced time markers appearing alternately in the two crystal segments were introduced by pulsed Peltier

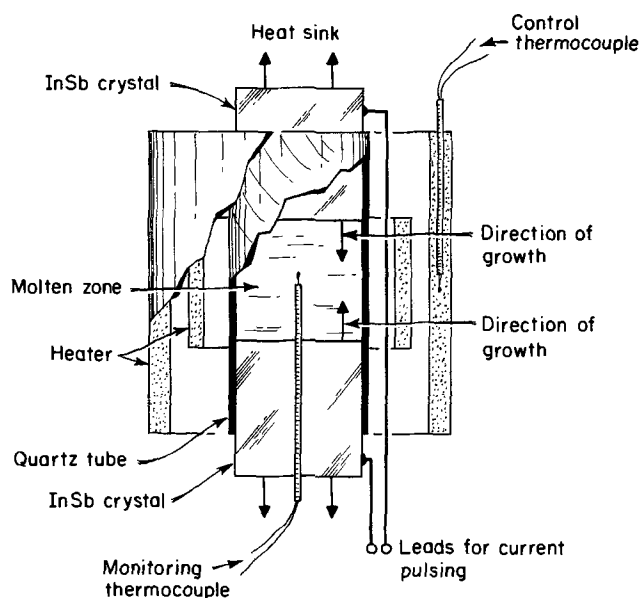


Fig. 1. Schematic diagram of the apparatus used for concurrent crystal growth under stabilizing and destabilizing thermal gradients.

\* Electrochemical Society Active Member.  
Key words: indium antimonide, segregation, pressure effects, solidification.

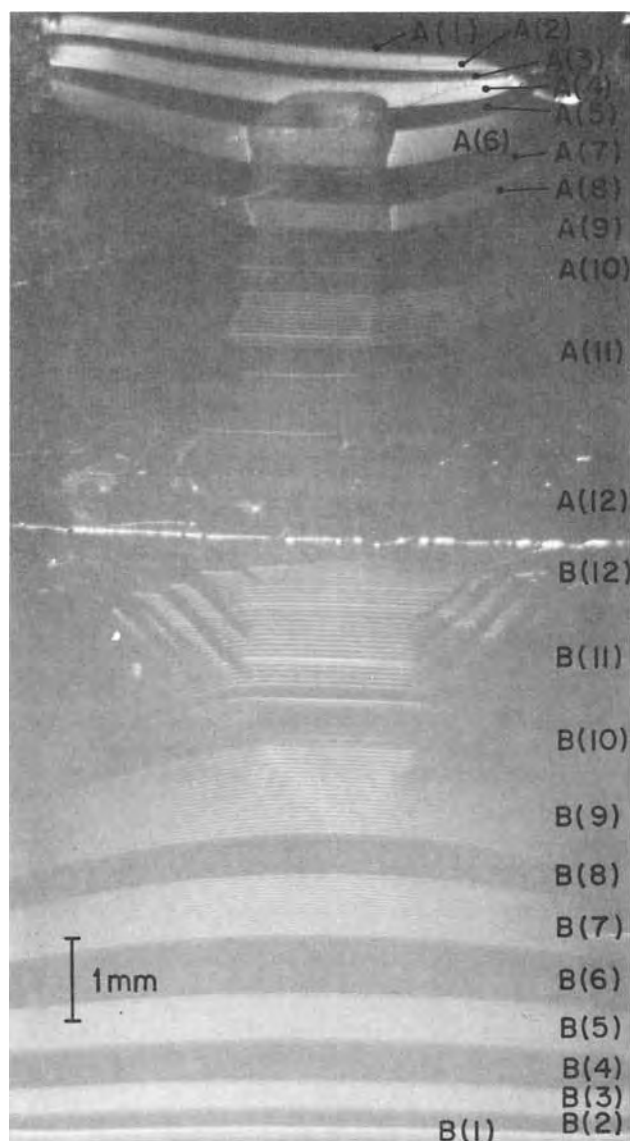


Fig. 2. Photograph of an etched cut along the growth axis. The upper crystal segment grew (downwards) under destabilizing and the lower grew (upwards) under stabilizing thermal gradients. The coalescence plane of the two growth interfaces is clearly visible between regions A(12) and B(12). The A and B regions bearing the same number grew simultaneously in time. The striations across the crystal are "time markers" introduced by current pulses (see text).

cooling. Time markers due to Peltier heating are not pronounced; thus, to insure the formation of clearly visible time markers in both solidifying segments the polarity of the current pulses was reversed at predetermined intervals. Since the time markers reflect the interface morphology at the instant of their incorporation, Fig. 2 shows that initially both growth interfaces were virtually flat, but became increasingly convex, toward the melt, with continuing growth. This behavior reflects the presence of radial temperature gradients which increase with decreasing zone height. The occurrence of facet growth (core formation) at both advancing interfaces is clearly visible. It is of interest to note that in all experiments facet growth occurred earlier at the upper, water-cooled, crystal segment with the larger thermal gradient in the melt. The coalescence of the two interfaces took place in a virtually horizontal front and was preceded by off-core interface breakdown due to high dopant concentration in the melt.

The microscopic growth rates of both solidifying segments were determined from the spacing of the time markers in the inner region of the crystal. Their values

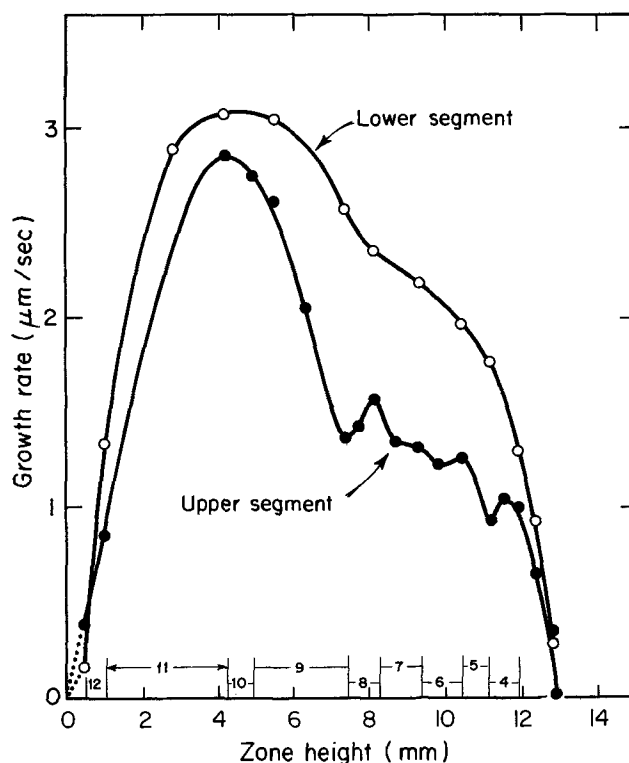


Fig. 3. Microscopic growth rates of the upper and lower crystal segments as a function of zone height. The regions (4 to 12) indicated on the horizontal axis correspond to the regions shown in Fig. 2 and in subsequent photomicrographs.

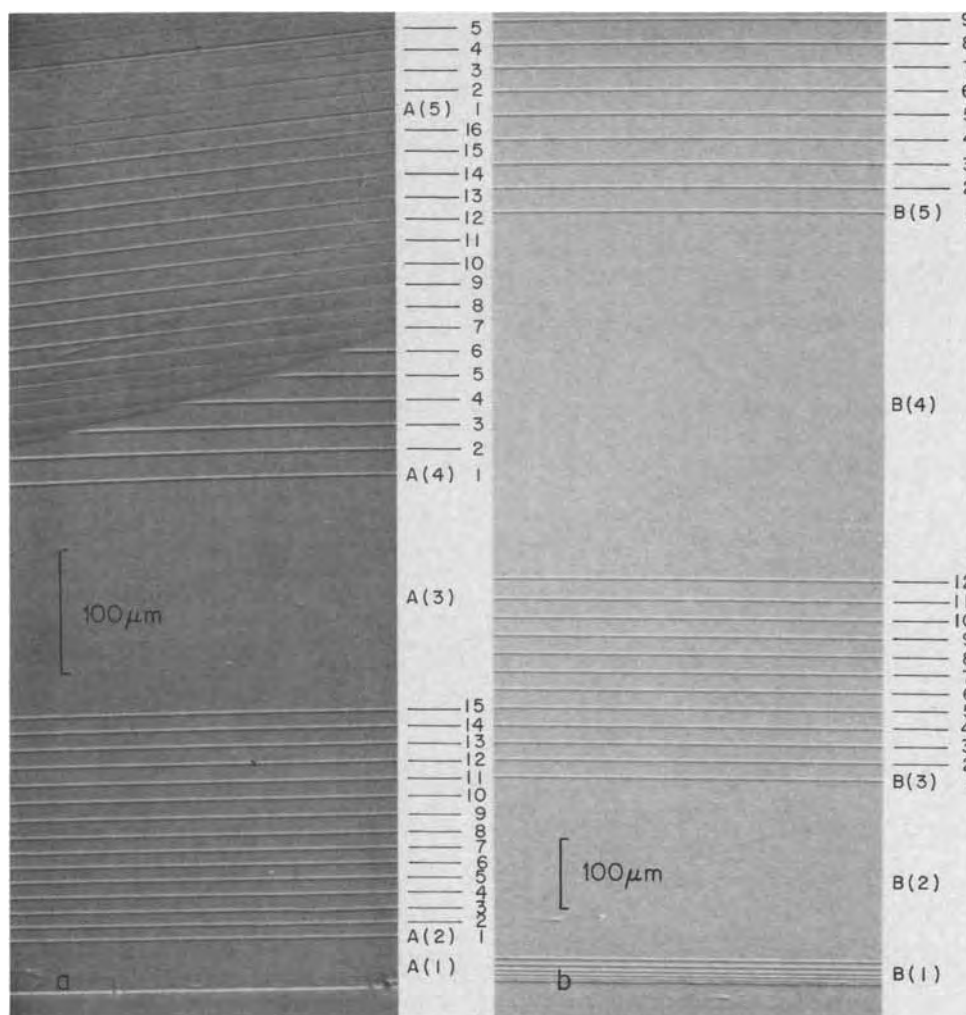
are plotted in Fig. 3 as a function of zone height. It can be seen that the over-all growth behavior of the two interfaces is the same: the growth rate is initially small, increases with decreasing zone height, and decreases again prior to coalescence. The consistently lower microscopic growth rate of the upper crystal segment is due to the prevailing steeper thermal gradient in the upper melt zone.

It can also be seen that the growth rate of the upper segment, with destabilizing thermal gradient in the melt, exhibits significant fluctuations in contrast to that of the lower crystal segment which grows under stabilizing thermal gradients.

*Dopant segregation.*—The segregation behavior during the initial stages of growth is the same at both advancing interfaces as seen in Fig. 4. The dopant distribution, as revealed by etching, is uniform (the regularly spaced striations are the time markers introduced by Peltier cooling). Dopant inhomogeneities appear first in the upper segment as seen in Fig. 4a, region A(4), and coincide with core formation. Since this upper segment grows under destabilizing vertical and radial thermal gradients in the melt, the observed dopant inhomogeneities are attributed to thermal convection (3). The uniform dopant segregation observed at the simultaneously grown region of the lower segment, Fig. 4b, indicates that convection under the present experimental conditions does not affect the thermally stable melt region and is, thus, confined to the melt region subjected to destabilizing thermal gradients.

With continuing growth a striking change in the segregation behavior takes place; dopant inhomogeneities appear in both the upper and the lower segments as shown in Fig. 5. These inhomogeneities (striations) form simultaneously in both growth segments and are identical in detail [see for example regions A(9)-14/15 and B(9)-14/15]. They are at the onset irregular in intensity and periodicity and become periodic with continuing growth (Fig. 5 and 6). These periodic inhomogeneities persist to the point of coalescence of the interfaces and resemble in all respects segregation be-

Fig. 4. Photomicrographs of etched cuts along the growth axis of the crystal segments grown concurrently under destabilizing (a) and stabilizing (b) thermal gradients. For convenience, the growth direction of both segments is here shown from bottom to top. In segment b, dopant inhomogeneities are absent. In segment a, random inhomogeneities are visible (between successive time markers) beginning with region A(4). The onset of core formation appears in the same region.



havior associated with oscillatory thermal instability (1). Their frequency, initially 0.8/sec, decreases to 0.5/sec near the point of coalescence.

### Discussion

The appearance of segregation inhomogeneities in the upper crystal segment during the early stages of growth can be explained as the result of convective melt flow due to the presence of destabilizing thermal gradients (1). Since the simultaneously grown lower crystal segment exhibits uniform dopant distribution, it is apparent that convective instability is confined to the melt region with a destabilizing thermal gradient and does not propagate into the thermally stable lower part of the molten zone.

The ensuing simultaneous incorporation of irregular dopant inhomogeneities, which are identical in detail in both the upper and the lower crystal segments, cannot be attributed to convective instability; temperature and melt composition are time-dependent variables in convective systems, thus the simultaneous formation of identical, random segregation effects at interfaces which are several millimeters apart cannot be reconciled with convective behavior. Moreover, the presence of such periodic segregation inhomogeneities at both crystal segments cannot be explained on the basis of thermal oscillatory instability since they are formed up to the point of interface coalescence where the Rayleigh number of the melt approaches zero (1). Temperature measurements in the center of the melt zone (by means of a thermocouple inserted through the lower crystal segment) showed that the melt was thermally stable (within  $\pm 0.01^\circ\text{C}$ ) during the growth period in question; accordingly, the present segregation inhomogeneities are not due to thermal convective instability.

In the present confined system, with fixed geometric boundaries, solidification of InSb must lead to pronounced pressure build-up since it is associated with a  $\sim 14\%$  volume increase (4). It is, thus, believed that the growth and segregation inhomogeneities formed simultaneously on both crystal segments are due to isostatic pressure effects. Indeed excessive pressure build-up caused, in seven out of fifteen growth experiments, during the late stages of solidification, breakage of the quartz tube (1 mm wall thickness) containing the melt zone.

During the early stages of growth the volume expansion was apparently accommodated by corresponding retraction of the upper and/or lower crystal segments since the normally expected segregation behavior was observed: absence of dopant inhomogeneities in the lower segment grown with stabilizing gradients in the melt and dopant inhomogeneities in the upper segment in which growth took place under destabilizing gradients.

As solidification proceeds, further retraction of the crystal segments in the present experimental arrangement is expected to be increasingly impeded, and, thus pressure must build up in the molten zone. The pressure build-up, with continuing growth, is rapid since the compressibility of solid InSb is small ( $2.4 \times 10^{-6}/\text{kg cm}^{-2}$ ) (5). Due to the pressure dependence of the melting point of InSb ( $-0.008^\circ\text{C}/\text{atm}$ ) (6), any pressure increase will in turn affect the established growth rate. Under the present experimental conditions, involving a continuous temperature decrease (constant growth rate), the pressure increase associated with the convergence of the growth interfaces must lead to a slow-down or even a temporary arrest of the growth process. Under continuing temperature decrease the growth interfaces must continue to converge. The as-



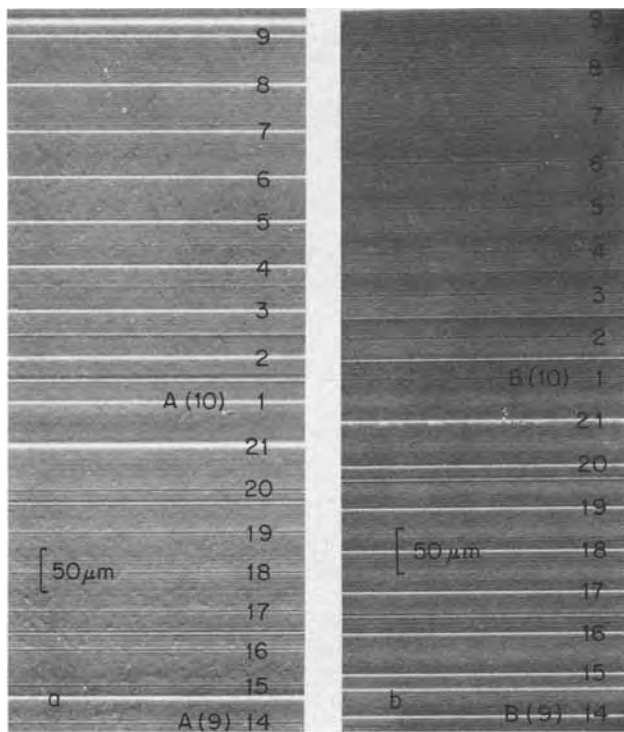


Fig. 5. Photomicrographs of etched cuts along the growth axis of the crystal segment grown under destabilizing (a) and stabilizing (b) thermal gradients (growth direction of both segments is here shown from bottom to top). Dopant inhomogeneities identical in detail are simultaneously incorporated in both segments (grown at slightly different rates, see Fig. 3) beginning with region A(9)14 and B(9)14. Note for example the pronounced striation between time markers 14 and 15 (see text).

sociated pressure increase will either lead to forced retraction of the crystal segments or to breakage of the quartz tube.

The dopant inhomogeneities formed simultaneously in both advancing interfaces can be explained on the basis of pressure induced segregation effects. In the early stages of pressure build-up abrupt, "jerky," retraction of the crystal segments results in irregular isotatic pressure fluctuations which thus affect simultaneously the growth rate at both interfaces. Since temperature fluctuations as low as 0.01°C have been shown to result in segregation inhomogeneities (1), pressure fluctuations in excess of 1 atm (corresponding to a melting point decrease greater than 0.01°C) are expected to cause detectable segregation inhomogeneities. The periodic inhomogeneities, which persist to the point of the interface coalescence, may be in-

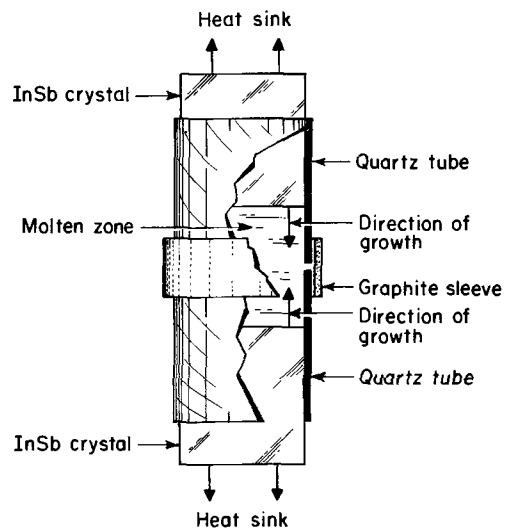


Fig. 7. Schematic diagram of the apparatus used to provide continuous pressure release during growth. The upper and lower quartz tubes were tight-fitted into a graphite sleeve exposing the melt to a "graphite window" 1 mm in height.

terpreted as the result of periodic, discontinuous crystal retraction (periodic increase and decrease in pressure). Alternatively, the retraction may be continuous and the inhomogeneities reflect "oscillatory pressure instability." As seen in Fig. 3, in the region of the periodic segregation inhomogeneities, the microscopic growth rate decreases steadily. Although it is unlikely, the decreasing growth rate could be attributed to changing characteristics of the thermal gradients in the melt; it is more likely that this growth rate behavior is the result of a steadily increasing pressure which is only partially released through retraction of the crystal segments.

To confirm the origin of the periodic segregation inhomogeneities, growth experiments were performed in a system with identical geometry as in Fig. 1, in which continuous pressure release (constant pressure) during growth was provided for by a 1 mm thick annular "graphite window" located in the region of coalescence of the converging growth interfaces (Fig. 7). In this configuration, constant (moderate) pressure prevailed during growth, since the volume expansion was accommodated by continuous leakage of liquid InSb through the graphite window. The growth and segregation behavior under these conditions is shown in Fig. 8. It can be seen that dopant segregation remains uniform to the point of coalescence with no evidence of dopant inhomogeneities (Fig. 8a). It is seen further that the

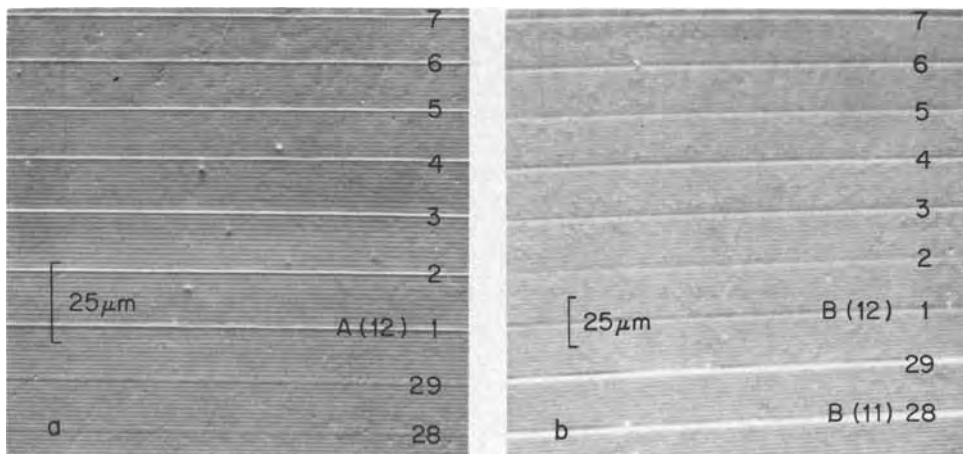


Fig. 6. Photomicrographs of etched cuts along the growth axis of the crystal segment grown under destabilizing (a) and stabilizing (b) thermal gradients (growth direction of both segments is here shown from bottom to top). Note periodic (oscillatory) inhomogeneities, in both segments, persisting to the coalescence of the two interfaces (see Fig. 2 and text).

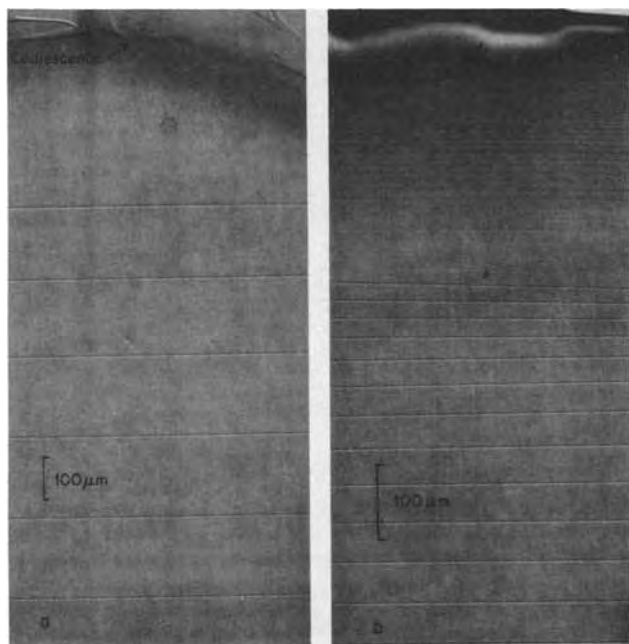


Fig. 8. Photomicrographs of etched cuts along the growth axis of a crystal segment grown in the apparatus providing for continuous pressure release (a) and a segment grown in the confined arrangement of Fig. 1. Note that in (a), the distance between the time marker remains constant to the point of interface coalescence in contrast to the segment (b), where the microscopic rate decreases gradually. The periodic inhomogeneities (between successive time markers) in segment (b) are visible at the lower region of the segment but with decreasing growth rate their spacing in the upper region is beyond resolution.

microscopic growth rate remained virtually constant (virtually constant spacing of time markers) to the point of the interface coalescence. This behavior is in pronounced contrast to that seen in Fig. 3 where the growth rates approach zero at the interface coalescence. Thus, it is concluded that the dopant inhomogeneities incorporated simultaneously in the two crystal segments are due to pressure effects and that the continuous growth rate decrease is the result of a steadily increasing hydrostatic pressure.

#### Acknowledgment

The authors are indebted to Dr. J. R. Carruthers who suggested that the presently observed segregation behavior could be attributed to pressure effects. The authors are also indebted to the National Aeronautics and Space Administration and the National Science Foundation for financial support.

Manuscript submitted May 18, 1973; revised manuscript received Aug. 7, 1973.

Any discussion of this paper will appear in a Discussion Section to be published in the December 1974 JOURNAL. All discussions for the December 1974 Discussion Section should be submitted by Aug. 1, 1974.

#### REFERENCES

1. K. M. Kim, A. F. Witt, and H. C. Gatos, *This Journal*, **119**, 1218 (1972).
2. K. M. Kim, A. F. Witt, and H. C. Gatos, *J. Mater. Sci.*, **6**, 1036 (1971).
3. J. R. Carruthers, *Can. Met. Quart.*, **5**, 55 (1966).
4. N. H. Nachtrieb and N. Clement, *J. Phys. Chem.*, **62**, 747 (1958).
5. M. D. Banus and M. C. Lavine, *J. Appl. Phys.*, **40**, 409 (1969).
6. R. E. Hanneman, M. D. Banus, and H. C. Gatos, *J. Phys. Chem. Solids*, **25**, 293 (1964).

## Technical Notes



### Field Effect Modulated Photoluminescence in ZnO

T. O. Sedgwick\*

IBM Thomas J. Watson Research Center, Yorktown Heights, New York 10598

The photoluminescent intensity of ZnO has been modulated by the surface adsorption of the gases H<sub>2</sub> and O<sub>2</sub> (1, 2). It is known that adsorbed O<sub>2</sub> raises the surface potential and therefore depletes the normally n-type ZnO surface. U.V. excitation of the ZnO produces hole-electron pairs and it has been postulated that the photoluminescence (or luminescence) results from the recombination of the minority carrier holes with a luminescent center. The decrease in photoluminescent intensity upon O<sub>2</sub> adsorption is thought to occur because the field induces transport of the holes away from the luminescent centers and to the surface where they undergo recombination with radiationless recombination centers (1). Hydrogen adsorption, on the other hand, results in electron accumulation at the ZnO surface and causes the photoluminescence to increase since the holes are repelled from the radiationless recombination centers at the surface.

\* Electrochemical Society Active Member.

Key words: corona charged ZnO, interface traps, SiO<sub>2</sub>-ZnO oxide semiconductor structure.

However, it is difficult to know whether the changes in emitted light-intensity are due to surface potential changes alone or whether they depend on the presence of the adsorbed gases directly. Conceivably, the adsorbed gases could act as recombination centers or alternatively, they could react chemically with surface recombination centers already present and hence render them inactive. In this note we report on the observed modulation of photoluminescence in ZnO coated with a SiO<sub>2</sub> film whose surface is charged with a corona to produce the modulating field at the ZnO surface and thus completely avoid the effects of gas ambients.

Photoluminescent measurements were made on samples of single crystal ZnO and layers of ZnO powder about 1 cm<sup>2</sup> in area. Some samples were coated with 3000-3500Å pyrolytic SiO<sub>2</sub> deposited at 420°C in oxygen (3). The single crystal ZnO was supplied by Airtron and was lightly doped with Li (the Li concentration was estimated to be ca. 100 ppm by electron spin

resonance which did not agree for some unknown reason with a determination of  $< 3$  ppm Li by emission spectroscopy). The measured surface was the oxygen face,  $000\bar{1}$ , which had been polished down  $\sim 5$  mils to remove cutting damage using  $\frac{1}{4}\%$  conc HCl in  $H_2O$  on a Pellon cloth. The back surface of the  $SiO_2$  coated single crystal sample exhibited high resistivity after  $SiO_2$  deposition so it was annealed at  $510^\circ C$  for 1 hr in  $10\% H_2$  in  $N_2$  to increase the conductivity. The four point probe resistivity of the back surface after annealing was 11 ohm-cm which agrees with that found by Thomas and Lander (4) for a similar exposure of ZnO crystals to hydrogen. A contact was made with gallium to the back of the sample for subsequent electrical measurements.

The ZnO powder was a commercial P-15 phosphor supplied by Sylvania which was settled without binder onto Ta plates before coating with  $SiO_2$ . The powder samples were used without further treatment.

The photoexcitation was made (Fig. 1) using radiation from a medium pressure mercury lamp filtered through Corning filters 7-51 and 7-737 to give a band centered at  $3600\text{\AA}$ . The photoluminescence was measured with a 1P21 phototube after passage through a Corning 3-72 filter to remove radiation of wavelength shorter than  $4400\text{\AA}$ .

Before making photoluminescent measurements on the  $SiO_2$ -coated single crystal sample, 2 mm diameter Pd dots were evaporated on the  $SiO_2$  surface and capacitance-voltage (C-V) measurements (5) were made at 150 kHz and room temperature. Although most devices were leaky due to the large area dots, several C-V curves were obtained and one is shown in Fig. 2. The capacitance was constant from 0 out to  $+60V$  but showed the expected decrease for an n-type sample at sufficiently negative voltage. The existence of the capacitance drop shows that the applied voltage of  $-40$  to  $-80V$  does in fact deplete the n-type ZnO surface. The gradual drop of capacitance with voltage over the whole negative voltage range indicates the presence of a large density of surface states ( $\sim 4 \times 10^{12}/cm^2$ ) which become positively charged as a result of the applied field. The Pd dots were then removed with a KI-I<sub>2</sub> solution.

The sample surfaces were charged in air either positive or negative using a  $\pm 4$  kV corona charging wire held for 1-10 sec about 1-2 cm from the surface. Although the surface potential of these particular oxide films was not measured, we have found that thermally grown  $SiO_2$  films retain surface charge densities corresponding to fields across them of  $\pm 5-10 \times 10^6$  V/cm for days after charging (6). Even  $SiO_2$  films which have been etched and otherwise handled showed a minimum retention field of  $1 \times 10^6$  V/cm. If we assume that the present films could support a field of  $1-10 \times$

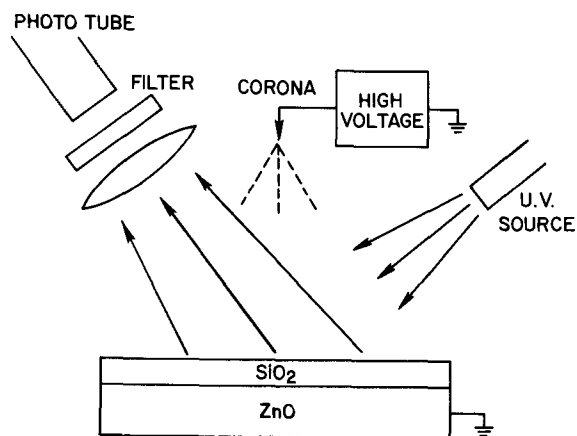


Fig. 1. Schematic of sample charging and photoluminescent measuring apparatus.

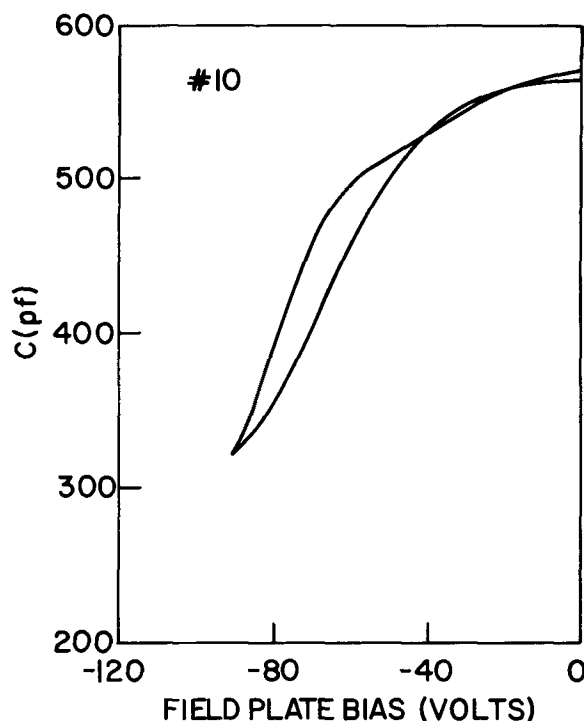


Fig. 2. Capacitance-voltage curve of Pd field plate/3000-3500Å  $SiO_2/ZnO$  single crystal measured at 150 kHz in room light at  $300^\circ C$ .

$10^6$  V/cm, then the potential on the surface which could be retained for a long time was 30-350V.

The basic experimental result that we would like to present is shown in Fig. 3a for the  $SiO_2$  coated single crystal ZnO sample. The initial luminescence of the uncharged sample is constant in time. Upon negative charging the intensity decreases immediately and drastically. When the charging is terminated the luminescent intensity rises slowly, henceforth called the "luminescent relaxation" and reaches a new constant value which is lower than for the uncharged sample. Upon positive charging the luminescence immediately rises to a level higher than that of the uncharged sample and remains essentially constant although a slight decrease is often observed in time. All the subsequent figures show data using the same experimental sequence. Figure 3b shows a very similar result at ten times the luminous intensity and Fig. 3c shows that a structure without any  $SiO_2$  does not exhibit any appreciable modulation of intensity as a result of charging. In Fig. 3a time was indicated schematically since the time elapse was not exactly recorded.

Similar measurements were made on powder ZnO samples in Fig. 4 and with similar results. The last data point of Fig. 4a taken at  $\sim 110$  min shows that the luminescent intensity is stable after the initial and relatively short duration ( $\sim 10$  min) "luminescent re-

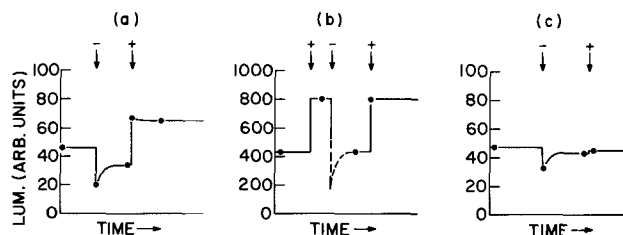


Fig. 3. Photoluminescent intensity as a function of time (schematic) for single crystal ZnO samples. (a)  $SiO_2$  coated, (b)  $SiO_2$  coated at 10X intensity, (c) no  $SiO_2$  on ZnO;  $\downarrow$ ,  $\uparrow$  indicates first measurement of intensity after negative or positive charging, respectively.

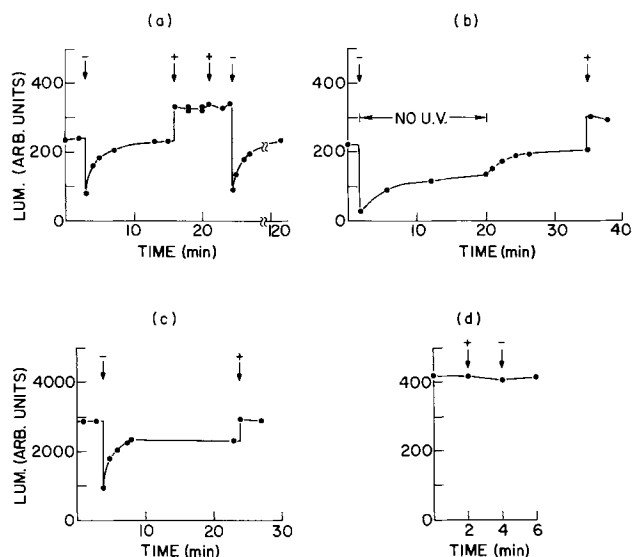


Fig. 4. Photoluminescent intensity as a function of time for powder ZnO samples (a) SiO<sub>2</sub> coated, (b) SiO<sub>2</sub> coated, u.v. was blocked from sample from 1½-20 min except during measurement of data points, (c) SiO<sub>2</sub> coated at 10X intensity, (d) no SiO<sub>2</sub> on ZnO.

laxation." The time required for this relaxation to occur is significantly increased when the u.v. radiation is blocked (Fig. 4b) or significantly decreased when the u.v. intensity is increased (Fig. 4c). No modulation in luminescent intensity was observed in a sample without SiO<sub>2</sub> coating (Fig. 4d). Although not shown in Fig. 4, it was also determined that repeated sequential negative charging always was followed by the "luminescent relaxation" process. It was not possible to lower either the initial or stable intensity level by repeated negative charging.

The ratio of the intensity after the "luminescent relaxation" to the intensity after positive charging for all SiO<sub>2</sub> coated samples varied from about 1.3 to 1.9. If instead the initial intensity after negative charging is used, the ratio is typically 3 or 4 and can be as high as 10 (Fig. 4b).

These results show that the luminescent intensity of both single crystal and powder ZnO samples can be significantly modulated by the application of either a negative or a positive bias to the surface via an oxide layer where gas adsorption on the ZnO surface plays no role. The change in intensity is consistent (depletion lowers intensity) with what was observed previously for H<sub>2</sub> and O<sub>2</sub> modulation of surface potential (1). Thus photoluminescent intensity changes are primarily a function of surface potential changes and not gas-solid interactions.

There is a stable difference between the photoluminescent intensity of the negatively and positively charged surfaces which is, at least to first order, independent of u.v. intensity and for which we have a satisfactory explanation given immediately below. On the other hand, the rate of change of the initial "luminescent relaxation" is clearly dependent on u.v. intensity and is not so readily explained.

The stable change in photoluminescence with applied field may be explained conveniently using Fig. 5. Figure 5a shows the photoluminescent process in a field free structure, where the holes produced by u.v. excitation are neither preferentially drawn to nor repelled from the ZnO-SiO<sub>2</sub> interface. Hence moderate luminescence results. (We are not specifying the actual photoluminescent mechanism other than to assume that hole density is related to the light production process.) Figure 5b shows that when the SiO<sub>2</sub> is positively charged the holes are repelled from the surface and hence are relatively more available for the luminescent process than for radiationless recombination at the re-

combination centers and hence the luminescence is more intense. Initially after negative charging (Fig. 5c or 5e), holes move preferentially to the interface. They are consumed at the radiationless recombination centers (circles) and by other nonradiative processes and the luminescent intensity is at a minimum.

There are, however, two basic models which account for the "luminescent relaxation" and although we feel the "oxide discharge" model (Fig. 5e and f) is more consistent with our data we cannot rule out a "trapping model" (Fig. 5c and d). In the "trapping model" we envision that some of the holes moving toward the

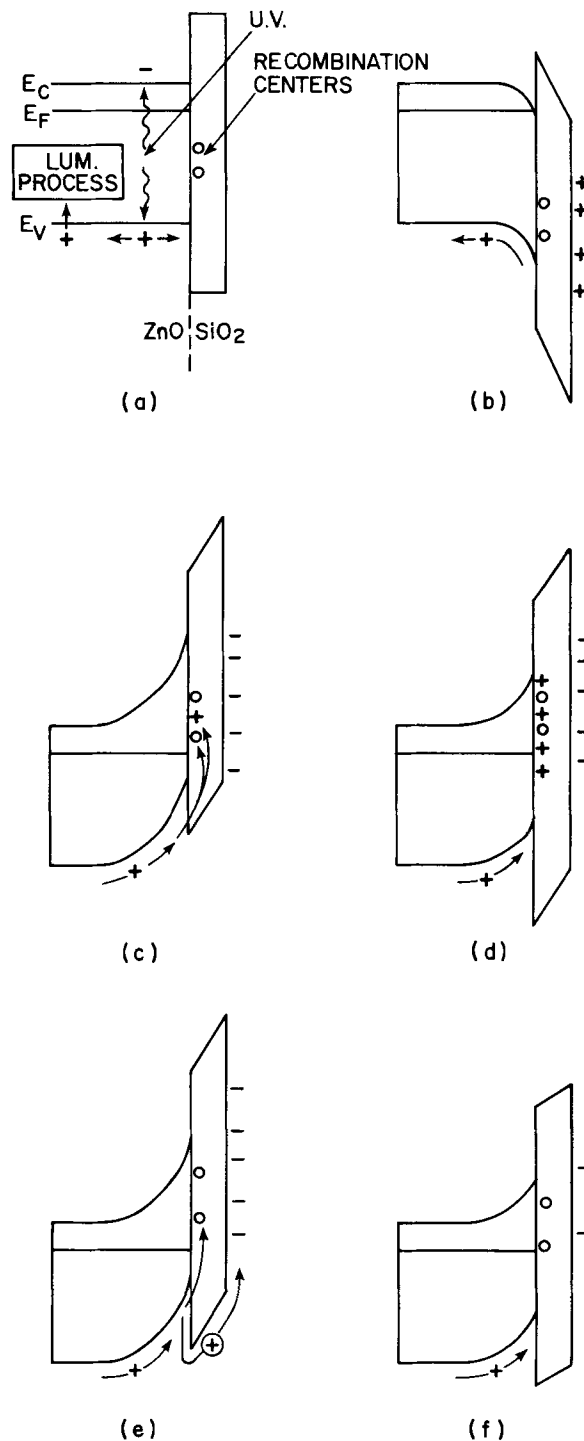


Fig. 5. Schematic of band model of SiO<sub>2</sub>-ZnO structure to explain field effect modulation of photoluminescence after the surface was charged as follows: (a) none; (b) positive, "trapping model;" (c) negative initial configuration; (d) negative after "luminescent relaxation;" "SiO<sub>2</sub> discharge model;" (e) negative initial; (f) negative after "luminescent relaxation."

surface, due to the electric field, become trapped in interface states and result in a slow build up of positive charge at the interface. As the positive charge increases, the electric field in the semiconductor decreases. In turn the preferential flow of holes toward the surface is lowered, and hence the photoluminescence decreases. The extent of the "luminescent relaxation" would be dependent on the hole supply and hence on u.v. intensity, and would probably stop when the traps are saturated or the trapping rate becomes insignificant because of the lowered surface potential. The existence of hole traps at the ZnO interface is consistent with the capacitance voltage data obtained on the single crystal sample. If this model is correct, subsequent repeated negative charging of this structure (Fig. 5d) should no longer produce an initial "luminescent relaxation" because the SiO<sub>2</sub> already supports the maximum field across it. Our experimental results indicate clearly that the "luminescent relaxation" recurs after every new negative charging. Thus, we feel that the charge on the SiO<sub>2</sub> is probably discharged by excitation of holes (Fig. 5e) from the ZnO into the valence band of the SiO<sub>2</sub> and which finally neutralize the negative charge on the surface of the SiO<sub>2</sub>. The structure (Fig. 5f) could then be recharged with the corona and returned to the state indicated in Fig. 5e and could exhibit the "luminescent relaxation" repeatedly which is observed experimentally. The valid-

ity of the "oxide discharge" model could be resolved unambiguously by making surface potential measurements of the SiO<sub>2</sub> surface as a function of time and luminescent intensity to determine whether the charge on the SiO<sub>2</sub> is in fact discharged by the u.v.

#### Acknowledgment

The author would like to thank B. Kazan for many helpful discussions and suggestions. He is indebted to E. Bassous for depositing the SiO<sub>2</sub> films, C. Kircher for depositing the Pd field plate dots, and to B. Agule who made many of the measurements.

Manuscript submitted July 26, 1973; revised manuscript received Sept. 21, 1973.

Any discussion of this paper will appear in a Discussion Section to be published in the December 1974 JOURNAL. All discussion for the December 1974 Discussion Section should be submitted by Aug. 1, 1974.

#### REFERENCES

1. R. Nink, *Z. Naturforsch.*, **24a**, 1329 (1969).
2. J. O'Hanlon and W. Pennebaker, Submitted to *J. Appl. Physics*.
3. S. Krongelb, *Electrochem. Technol.*, **6**, 251 (1968).
4. O. G. Thomas and J. J. Lander, *J. Chem. Phys.*, **25**, 1136 (1956).
5. T. O. Sedgwick, *J. Appl. Phys.*, **39**, 5066 (1968).
6. T. O. Sedgwick, M. E. Cowher, I. F. Chang, and J. F. O'Hanlon, *J. Electronic Materials*, **2**, 309 (1973).

## Controlled Chemical Etching of GaP

Lillian Rankel Plauger

Bell Laboratories, Murray Hill, New Jersey 07974

Gallium phosphide electroluminescent diodes suitable for inclusion in alphanumeric matrix displays have been described recently (1, 2). One of the important requirements in the fabrication of beam lead gallium phosphide electroluminescent diodes (1) is the development of a technology for the controlled chemical etching of GaP. Chemical etching procedures are required for the formation of light emitting mesas on the GaP, for air isolation of diodes, for final separation of individual display devices from the wafer, and also for shaping of the matrix array (see Fig. 1 and 2). Although there are many techniques available for mesa etching such as SiO<sub>2</sub> masking following etching with aqua regia (1), Br<sub>2</sub> in MeOH (3), or Cl<sub>2</sub> in MeOH (3), these etches are unsatisfactory for separation etching of beam lead diodes since they attack gold beam leads. An etching solution is needed that: (i) rapidly etches GaP and results in a polished unpitted surface; (ii) does not attack dielectrics such as SiO<sub>2</sub> or Ti-Pd-Au beam lead metalizations.

Both (111) and (100) oriented GaP are used for diodes. There is a significant difference between the {111} surface (Ga plane A-face) and the  $\{\bar{1}\bar{1}\bar{1}\}$  (P plane B-face). The outermost surface layer of atoms consists of either Ga or P atoms which are triply bonded to the lattice. This leads to pronounced chemical differences between the (111) or A-face and the  $\{\bar{1}\bar{1}\bar{1}\}$  or B-face (4, 5). For the (100) oriented GaP, the {100} planes are made up of Ga and P atoms and therefore are chemically the same.

During this study, it was found that alkaline ferricyanide solutions in certain concentration ranges (KOH: 0.25-3.0M and K<sub>3</sub>Fe(CN)<sub>6</sub>: 0.50-1.00M) polished all faces of GaP except the Ga-face (which developed a smooth "orange-peel" texture), and did

Key words: polishing GaP, masking GaP, alkaline ferricyanide etching, LED, separation etching.

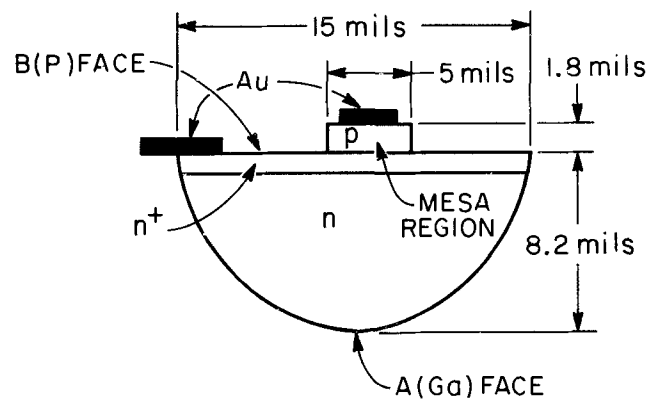


Fig. 1. GaP beam lead diode

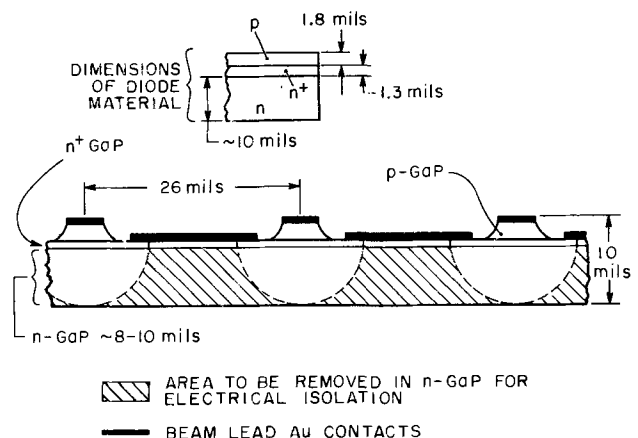


Fig. 2. Planar beam lead devices

not attack gold. Solution systems of this type have been previously used to mechanically polish (6) or reveal dislocations and stacking faults (7) in (111) GaP. Masking materials such as SiO<sub>2</sub> (silane deposited and sputtered), Ti (evaporated and sputtered), and Biwax were evaluated to determine compatibility with alkaline ferricyanide solutions.

### Experimental

Both n-type (selenium-doped) and p-type (zinc-doped) (111) and (100) oriented GaP slices were used for this study. Before use, all mechanically polished material was further polished using a solution of 0.5M KOH + 1.0M K<sub>3</sub>Fe(CN)<sub>6</sub> at 95°C for 10 min [the Ga-face of (111) material was not so etched]. This chemical polishing step removes surface damage and abrasive particles from the mechanical polishing step. This results in less undercutting of all the masking materials evaluated for selective GaP etching (see Table I for a listing of masking materials). Forty-eight per cent fluoroboric acid (J. T. Baker Chemicals) was used to remove Ti metal masking material. Ten to fifteen seconds in fluoroboric acid at room temperature dissolved 1000-3000Å Ti layer with no attack of the GaP, dielectrics, or gold metallization.

Reagent grade Fisher Chemicals were used to prepare the etching solutions listed in Table II. All solutions were maintained at a constant temperature using a Corla Model I NB Temperature Bath circulation through jacketed beakers. During this investigation, the concentrations of K<sub>3</sub>Fe(CN)<sub>6</sub> and KOH were varied to optimize the etch rate of GaP. Some of the concentration ranges listed in Table II could only be achieved at temperatures greater than 40°C.

Measurements of the depth of etching were made with a calibrated microscope using a SiO<sub>2</sub> mask as a reference point. The separation of individual diodes from a large piece of material is accomplished by a partial saw cut into the Ga face of n-GaP (Fig. 3a),

Table I. Masking material lifetime\*

Masking material	(111) n-GaP	(100) n-GaP
Silane SiO <sub>2</sub> -5000A <sup>a</sup>	0.5 hr	1.5 hr
Sputtered SiO <sub>2</sub> -6000A <sup>b</sup>	0.8 hr	0.8 hr
Sputtered SiO <sub>2</sub> with Biwax solution	1.5 hr	>2.0 hr
Ti 1000A evaporated	1.0 hr	2.0 hr
Ti 3000A sputtered	>2.0 hr	>2.0 hr
Ti 1000A evaporated photoresist <sup>c</sup>	2.0 hr	>2.0 hr
Biwax solution <sup>d</sup>	1-2 hr	>2.0 hr

\* 0.5M KOH + 1.0M K<sub>3</sub>Fe(CN)<sub>6</sub> etching solution at 80°C with stirring where end of lifetime value represents breakdown of ~25% of the masking material.

<sup>a</sup> SiO<sub>2</sub> deposited in a hot plate vertical reactor at 185°C with the following flow rates: 2400 cc/min of 0.5% silane in N<sub>2</sub>, 800 cc/min of N<sub>2</sub>, and 30 cc/min of O<sub>2</sub> where deposition rate was 500 Å/min.

<sup>b</sup> Low frequency RF sputtered with a fused quartz target (carried out below 200°C).

<sup>c</sup> KMER (1:1) photoresist 0.5μ thick.

<sup>d</sup> 50% by volume Biwax No. B-6507 in a solution of 1:1 toluene: ethanol that is baked ½ hr in 80°C vacuum oven.

Table II. Etching of n-GaP

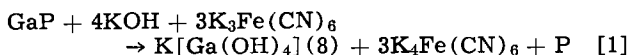
Etching solutions	(111) n-GaP (Ga face)		(100) n-GaP	
	No stirring (μ/hr)	Stirring (μ/hr)	No stirring (μ/hr)	Stirring (μ/hr)
0.25M KOH + 1.0M K <sub>3</sub> Fe(CN) <sub>6</sub> 80°C		55		115
0.50M KOH + 1.0M K <sub>3</sub> Fe(CN) <sub>6</sub> 60°C		50		102
80°C		115	115	210
95°C		(260μ)*		235
1.0M KOH + 1.0M K <sub>3</sub> Fe(CN) <sub>6</sub> 80°C	100	118	126	187
95°C	225	210	175	262
3M KOH + 0.5M K <sub>3</sub> Fe(CN) <sub>6</sub> 80°C	100		80	125

\* P face of (111) n-GaP.

and chemically etching the remaining GaP. Air isolation of individual diodes results (Fig. 3b).

### Results and Discussion

K<sub>3</sub>Fe(CN)<sub>6</sub> + KOH is an excellent etch for n-GaP where etch rates of 100-250 μ/hr can be obtained by adjustment of solution concentration and temperature (see Table II). Since p-GaP was found to etch at the same rate as n-GaP, n-GaP was used more extensively because of availability. The P-face of (111) GaP etched about two times faster than the Ga-face of the (111) material [see Table II for etch rate of (111) P-face at 95°C]. In this etching solution, GaP probably dissolves in the following manner



where P dissolves chemically to PH<sub>3</sub> and H<sub>3</sub>PO<sub>4</sub> (9), being easily oxidized by K<sub>3</sub>Fe(CN)<sub>6</sub>. All etching solutions studied were of pH > 13. At these high pH values the gallium ion exists as GaO<sub>3</sub><sup>-3</sup> where compounds of gallium such as K[Ga(OH)<sub>4</sub>], KGaO<sub>2</sub> · 1½H<sub>2</sub>O, and KGaO<sub>2</sub> · H<sub>2</sub>O have been isolated from KOH solutions, and four or six coordinate species such as [Ga(OH)<sub>4</sub>]<sup>-</sup> or [Ga(OH)<sub>4</sub>(H<sub>2</sub>O)<sub>2</sub>]<sup>-</sup> can form in solution (10, 11). These complexes are sparingly soluble (8) but since large volumes of etching solution are used (100 ml) to dissolve small pieces of GaP (wt < 0.1g), no precipitation of gallium complexes could be detected.

The activation energy E<sub>a</sub> calculated from the data in Table II for basic ferricyanide stirred solutions was found to be ~10 kcal/mole for the Ga-face of (111) n-GaP and ~6 kcal/mole for (100) oriented n-GaP. It was also found that stirring the etching solution does not appreciably affect the etch rate of the Ga-face of (111) material while the etch rate is increased by a factor of ~1.5 for (100) n-GaP in stirred solution. From this one can conclude that dissolution of the Ga-face of (111)-GaP is limited by the rate of heterogeneous chemical reaction, and is independent of diffusion processes. (100) n-GaP dissolution is diffusion limited which is to be expected for covalently bonded substances (12). The bonding of gallium atoms to underlying phosphorus atoms on the Ga-face of the (111)-surface has a slightly ionic or metallic nature (4, 5, 13) which accounts for the higher E<sub>a</sub> value.

Etching solution No. 2 [0.5M KOH + 1.0M K<sub>3</sub>Fe(CN)<sub>6</sub>] was chosen as the best solution for selectively etching GaP. With this solution it is possible to dissolve the most GaP [4-9 mils/hr on the Ga-face and up to 15 mils/hr on P-face of (111)-material, and up to 10 mils/hr on (100)-material] with the least attack on the masking materials listed in Table I. The optimum temperature is 80°C when using unprotected SiO<sub>2</sub> or 1000Å Ti masking (see Table I). With thicker Ti metal layers or Biwax protected SiO<sub>2</sub>, higher temperatures can be used without corrosion of the masking layer so that a slightly faster etch rate of GaP can be obtained. In all cases, masking material adheres better to (100) n-GaP than to the Ga-face of (111) n-GaP.

After partial saw cutting, chemical etching is used to complete the air isolation of individual diodes in the matrix array (see Fig. 3b). The gold metallization, that can be seen under the GaP diodes in Fig. 3b, is not attacked during this separation etching step. When thinner GaP (2-5 mils) is used for diode fabrication, partial saw cutting could be eliminated and selective shadow mask defined Ti used for a separation etching mask. Shadow mask defined Ti metal is a one step procedure which eliminates photoresist processing. The Ti metal can easily be removed in 10-15 sec with 48% fluoroboric acid (with no attack to the device structure).

### Summary

Alkaline ferricyanide solutions such as 0.5M KOH + 1.0M K<sub>3</sub>Fe(CN)<sub>6</sub> are excellent etches for (100) and

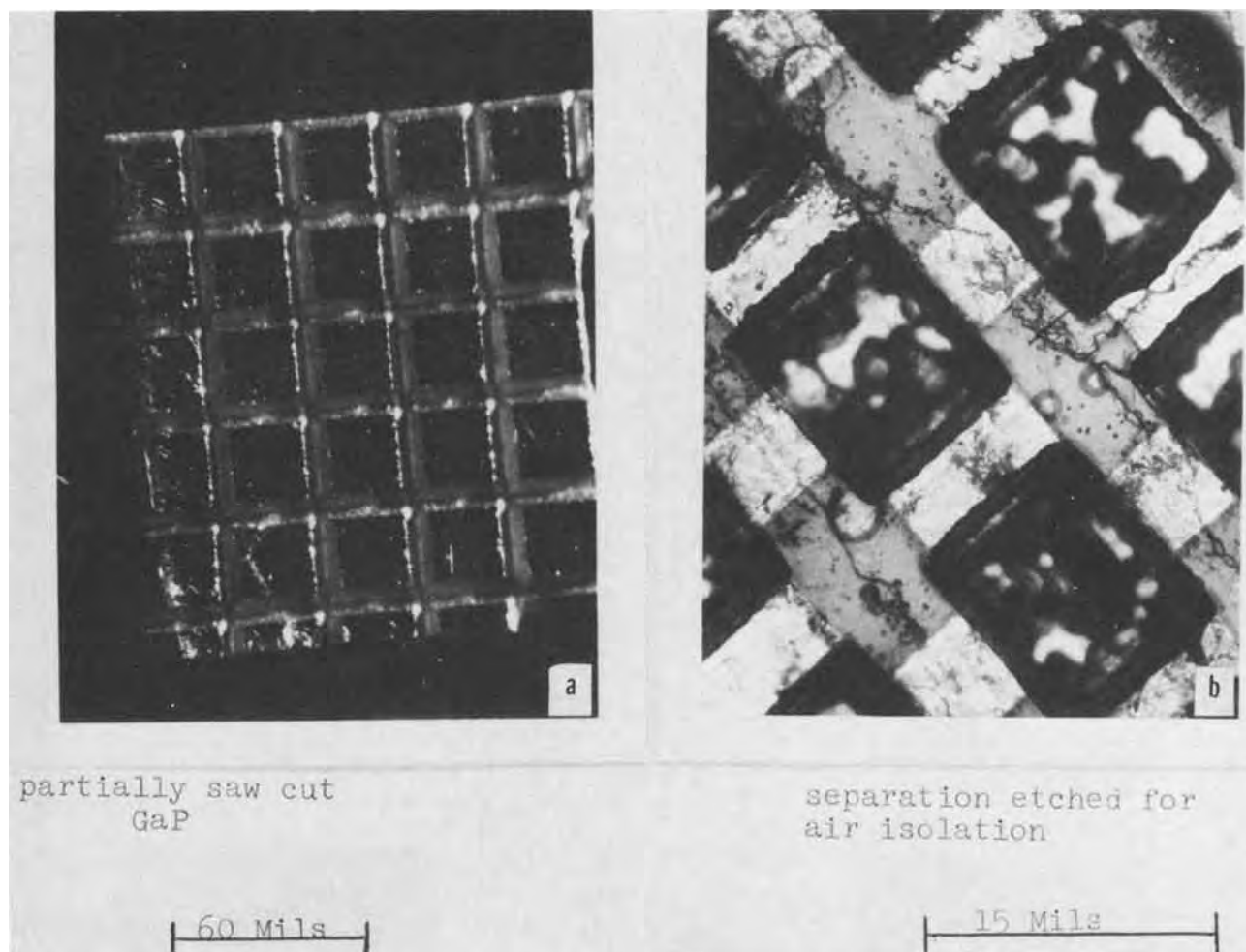


Fig. 3. Separation etching with alkaline ferricyanide solution

(111) oriented GaP diode processing because a fast rate can be obtained 4-9 mils/hr ( $\sim 100-200 \mu\text{m/hr}$ ), a polished surface results on all faces (except the Ga-face), compatible masking materials such as sputtered  $\text{SiO}_2$  and Ti are available (Ti can be shadow-mask defined), and no attack of the dielectrics or Ti-Pd-Au metallization of the device structure occurs.

#### Acknowledgments

The author wishes to acknowledge N. E. Schumaker for his useful comments on the manuscript, as well as help throughout this study. Discussion of this work with D. E. Koontz, L. A. Koszi, and D. R. Turner is appreciated.

Manuscript submitted June 14, 1973; revised manuscript received Oct. 12, 1973. This was Paper 49 presented at the Chicago, Illinois, Meeting of the Society, May 13-18, 1973.

Any discussion of this paper will appear in a Discussion Section to be published in the December 1974 JOURNAL. All discussion for the December 1974 Discussion Section should be submitted by Aug. 1, 1974.

#### REFERENCES

1. N. E. Schumaker, M. Kuhn, and R. A. Furnanage, *IEEE Trans. Electron Devices*, **ED-18**, 627 (1972).
2. W. Rosenzweig, B. H. Johnson, and N. E. Schumaker, *ibid.*, **ED-18**, 633 (1972).
3. C. S. Fuller and H. W. Allison, *This Journal*, **109**, 880 (1962).
4. J. P. Suchet, "Chemical Physics of Semiconductors," Chap. 6 and 7, D. van Nostrand Co., New York (1965).
5. N. N. Sirota, "Chemical Bonds in Semiconductors and Solids," pp. 7-50, Consultants Bureau, New York (1967).
6. A. Siemens and G. Halske, German Pat. 1,227,307 (1966).
7. M. D. Val'Kovskaya and Y. Boyarskaya, *Soviet Phys. Sol. State*, **8**, 1976 (1967).
8. F. A. Cotton and G. Wilkinson, "Advanced Inorganic Chemistry," Chapter 18, John Wiley and Sons, New York (1966).
9. R. Memming and G. Schwardt, *Electrochim. Acta*, **13**, 1299 (1968).
10. M. Poubaix, "Atlas of Electrochemical Equilibria in Aqueous Solutions," pp. 428-435, Pergamon Press, New York (1966).
11. B. N. Ivanov-Ernin and Y. Rabovik, *J. Gen. Chem. USSR*, **17**, 1061 (1947).
12. G. M. Orlova and L. D. Tikhomirova, *Zh. Obsheh. Khim.*, **35**, 1336 (1965).
13. T. Tokuda and M. B. Ives, *This Journal*, **118**, 1404 (1971).





## Decomposition Reaction of Concentrated Lithium-Ammonia Solutions

M. H. Miles<sup>\*,1</sup> and W. S. Harris<sup>\*,2</sup>

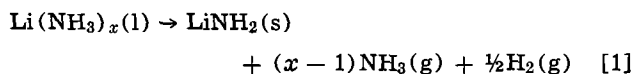
*Naval Weapons Center, Corona Laboratories, Corona, California 91720*

### ABSTRACT

The self-decomposition reaction of concentrated solutions of lithium in ammonia at atmospheric pressure was studied at various temperatures in polyethylene and in glass containers by observing the change in weight of the solution. The reaction follows a first-order rate law and is apparently heterogeneous. An unusually large, negative value for the activation entropy and a relatively low activation energy is found for this reaction. Possible explanations for these results include the concepts that the solvated electron is involved in the decomposition reaction and that electron transfer occurs by a tunneling mechanism.

Lithium, like other alkali metals, forms solutions with ammonia which have very unusual properties. For example, a solution saturated with lithium in ammonia has a metallic, bronze-like luster, an electrical conductivity approaching that of metals, and the lowest density of any known liquid (1-5). These concentrated metal-ammonia solutions are generally believed to contain solvated metal ions and free or solvated electrons (2-9). The electronic properties of the concentrated solutions are similar to those of liquid metals (5).

With the high energy theoretically available from lithium, concentrated lithium solutions in ammonia, represented by  $\text{Li}(\text{NH}_3)_x$ , could be an electrochemical fuel of exceptional interest for fuel cells or batteries. The usefulness of such a fuel would be limited by the parasitic decomposition reaction



which takes place in the liquid. Of prime interest in this work is the study of the self-decomposition reaction in concentrated lithium solutions where the equilibrium vapor pressure of  $\text{NH}_3$  is maintained at about 1 atm.

### Experimental

Lithium is capable of forming solutions with ammonia through exposure of the metal to dry ammonia gas at ambient conditions of temperature and pressure (1). Both the formation of the concentrated lithium-ammonia solutions and the self-decomposition reaction involve large weight changes which can be correlated with the reactions taking place. Metallic lithium was exposed to a stream of ammonia gas at atmospheric pressure, and weight *vs.* time was recorded by using a specially modified du Pont 950 thermogravimetric analyzer. By means of an electronic

adapter (consisting of a power supply and op-amp follower), the output of the electrobalance was recorded on a Honeywell 10 in. strip chart recorder. Weights of greater precision were obtained from a digital voltmeter and were manually recorded on the chart at various times. Figure 1 shows detailed views of parts of the apparatus and a flow diagram for the complete system. The lithium was contained in a special sample boat constructed entirely of polyethylene with baffles to prevent loss of material by effervescence during the reactions. The ammonia gas, after passing over the boat, was vented through an oil bubbler to the atmosphere. The flow rate used was approximately 80 ml/min. The thermostat jacket was supplied with circulating fluid by an external constant temperature bath to maintain accurate temperature control within the Pyrex furnace tube containing the sample boat.

Additional studies of the decomposition reaction of lithium-ammonia solutions were made in 5 ml soft glass vials modified with baffles consisting of several indentions on the sides. The vials were soaked overnight in warm, concentrated nitric acid, rinsed well with distilled water and acetone, and then taken inside an inert atmosphere dry box where a known weight of lithium was added to each. The vials were then placed in a wide mouth stainless steel bomb which was sealed, removed from the dry box to a constant temperature bath, and connected to a vacuum line. After evacuating the bomb, ammonia gas was admitted through the vacuum line to form the metal-ammonia solution. The pressure inside the bomb was maintained at about 1-3 atm by frequent venting of excess gas. Later the decomposition reaction was interrupted by again using the vacuum line to remove the ammonia and hydrogen present. The bomb containing the vials was taken back into the dry box, opened, and the weight of the contents,  $\text{Li} + \text{LiNH}_2$ , in each vial was determined. Using the known weight of  $\text{Li}$  added initially, the extent of the reaction in each vial could then be calculated.

In a third experiment, three larger glass vials (30 ml) with known weights of lithium were placed inside

<sup>\*</sup> Electrochemical Society Active Member.  
<sup>1</sup> Present address: Department of Chemistry, Middle Tennessee State University, Murfreesboro, Tennessee 37130.  
<sup>2</sup> Present address: Chemistry Laboratory, Mare Island Naval Shipyard, Vallejo, California 94592.  
 Key words: activation entropy, fuel, solvated electron.



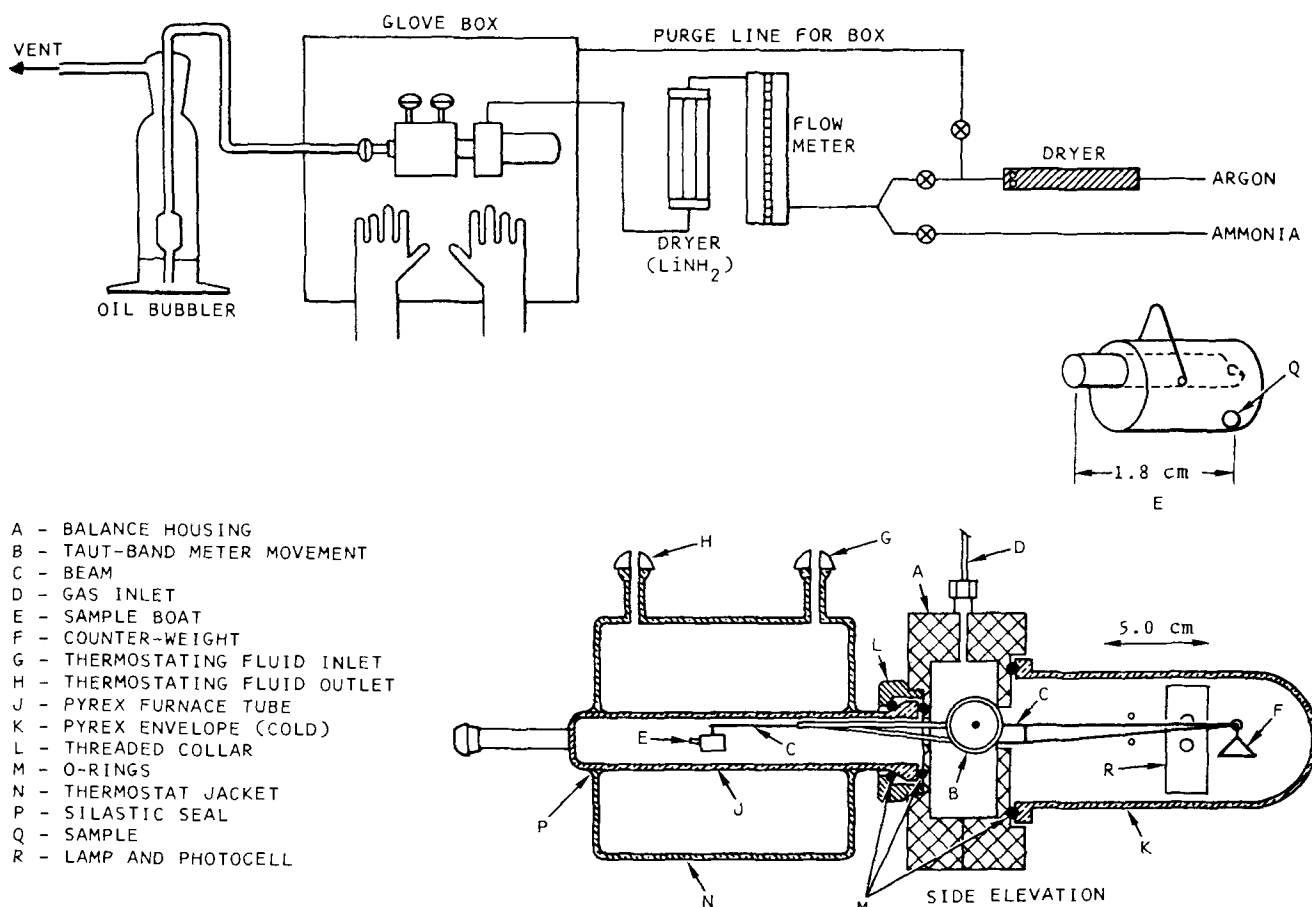


Fig. 1. Modified du Pont 950 thermogravimetric analyzer and flow diagram

a glass vacuum system and exposed to flowing ammonia gas vented through an oil bubbler. This arrangement permitted visual observation of the changes occurring. Upon admitting ammonia gas at atmospheric pressure, the bronze lithium-ammonia solution forms readily at 25°C, usually being completely formed within 1 or 2 hr.

### Results and Discussion

A relatively large and rapid weight increase is observed as the bronze-colored, lithium-ammonia solution forms according to the reaction



where  $x$  is about 4 for saturated lithium solutions in ammonia at atmospheric pressure (3, 10). A much more gradual loss of weight is observed as the self-decomposition reaction occurs (reaction [1]), and the gaseous products of  $\text{NH}_3$  and  $\text{H}_2$  are swept out of the system leaving only unsolvated  $\text{LiNH}_2$ . Although the decomposition reaction of alkali metals in liquid ammonia is reversible (11, 12), the continuous removal of hydrogen by the flowing ammonia gas in this open system ensures that the reaction goes to completion.

At an instant the weight,  $W$ , is given by

$$W = n_1M_1 + n_2M_2 + n_3M_3 \quad [3]$$

where  $n_1$ ,  $n_2$ ,  $n_3$ , and  $M_1$ ,  $M_2$ ,  $M_3$  represent the number of moles and molecular weights of  $\text{Li}$ ,  $\text{Li}(\text{NH}_3)_x$ , and  $\text{LiNH}_2$ , respectively. Here  $\text{Li}(\text{NH}_3)_x$  represents the bronze-colored, concentrated lithium-ammonia solution. After the first few hours required for complete formation of  $\text{Li}(\text{NH}_3)_x$ ,  $n_1 = 0$  and

$$W = n_2M_2 + (n - n_2)M_3 \quad [4]$$

where  $n$  represents the number of moles of lithium initially present. The rate of change of  $W$  is then given

by

$$\frac{dW}{dt} = (M_2 - M_3) \frac{dn_2}{dt} \quad [5]$$

Assuming that reaction [1] obeys a first-order rate law with respect to the amount of  $\text{Li}(\text{NH}_3)_x$  present, then

$$\frac{dn_2}{dt} = -kn_2 = -k \left( \frac{W - nM_3}{M_2 - M_3} \right) \quad [6]$$

where Eq. [4] was used to obtain the last expression. Substituting Eq. [6] into Eq. [5] and integrating gives

$$\log(W - W_\infty) = \frac{-kt}{2.303} + \text{constant} \quad [7]$$

where  $W_\infty = nM_3$  and represents the weight when all the lithium has been converted into  $\text{LiNH}_2$ . This first-order rate law can also be expressed in terms of the volume of the  $\text{Li}(\text{NH}_3)_x$  solution since this volume is directly proportional to the amount present.

The test of assumption of first-order kinetics which leads to Eq. [7] is shown in Fig. 2 for experiments in the polyethylene sample boat at 0° and 50°C. Two linear segments are observed in each experiment suggesting that the self-decomposition reaction is indeed first-order and that a change to a slower rate later occurs. Similar results were observed by Jackman and Keenan in dilute lithium-ammonia solutions using a spectrophotometer to follow the reaction (13, 14). They report two linear, first-order segments and that the change to the slower rate occurs at about the time  $\text{LiNH}_2$  begins to precipitate on the walls of the reaction vessel. In fact, the decomposition reactions of all alkali metal-ammonia solutions seem to take place at the cell walls since the homogeneous reaction is apparently immeasurably slow (13, 14). The observed linearity in Fig. 2 may simply reflect that the rate is propor-

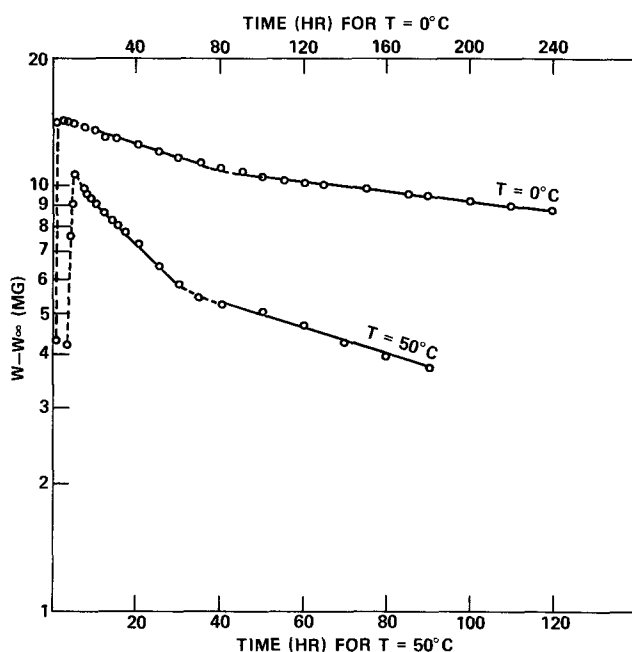


Fig. 2. First-order plot for the decomposition of lithium-ammonia solutions at 0° and 50°C. Initial weights of lithium were 1.72 and 1.48 mg, respectively.

tional to the surface area of the cell walls in contact with the solution since this surface area would likely be proportional to the amount of  $\text{Li}(\text{NH}_3)_x$  present.

Eventually, as the self-decomposition reaction nears completion, the experimental sample weight should approach the weight calculated for complete conversion of the sample to unsolvated  $\text{LiNH}_2$ . Although several long duration experiments gave approximate agreement with the calculated weight of  $\text{LiNH}_2$ , complex processes which tend to occur in late stages of the reaction made it difficult to verify this result accurately. Growth of solid  $\text{LiNH}_2$  in a branching, tree-like fashion was often observed late in the decomposition reaction. Frequently the  $\text{LiNH}_2$  "tree" would grow right out of the tube of the sample boat forcing discontinuation of the experiment due to loss of material. Occasionally, a shift of the bronze solution to new surfaces free of  $\text{LiNH}_2$  was observed which produced a perceptible increase in the rate of self-decomposition. When any such complex processes occurred, the data was not used to calculate any kinetic parameters. Fortunately, the reactions were usually well-behaved for at least the first half-life.

Further experiments were conducted at 50°C where small amounts of  $\text{LiI}$ , a typical electrolyte readily soluble in liquid ammonia, were intentionally added to the reaction mixture. No large change was observed in the rate of the self-decomposition reaction during the early stages of the reaction. In fact, a slight decrease in rate was detected in the presence of the  $\text{LiI}$ . This result is significant for any use of lithium in ammonia in fuel cells or batteries where there is contact of this fuel with the electrolyte.

For the experiments in the glass vials, the extent of the self-decomposition reaction can be determined by the relationship

$$\alpha = \frac{W - W_0}{W_\infty - W_0} = \frac{\% \text{ weight increase}}{231\%} \quad [8]$$

where  $\alpha$  represents the fraction reacted,  $W$  is the weight of  $\text{Li}$  and  $\text{LiNH}_2$  present after pulling off the ammonia,  $W_0$  is the initial weight of lithium added to the vial, and  $W_\infty$  is the weight when all lithium is converted into  $\text{LiNH}_2$ .

Table I presents the kinetic data for the self-decomposition reaction in the three different reaction vessels.

Table I. Kinetic data for the reaction  $\text{Li}(\text{NH}_3)_x(\text{l}) \rightarrow \text{LiNH}_2(\text{s}) + (x - 1) \text{NH}_3(\text{g}) + \frac{1}{2} \text{H}_2(\text{g})$  during the first half-life.

Temp, °C	Rate constant, sec <sup>-1</sup>	Standard deviation	Reaction vessel
25.0	$1.1 \times 10^{-6}$	$\pm 0.06 \times 10^{-6}$	5 ml glass vials
25 ± 1	$0.9 \times 10^{-6}$	$\pm 0.02 \times 10^{-6}$	30 ml glass vials
0.0	$0.97 \times 10^{-6}$	About ± 5%	Polyethylene boat
50.0	$6.2 \times 10^{-6}$	About ± 5%	Polyethylene boat

Thirteen experiments in the small glass vials with initial weights of lithium ranging from 18 to 159 mg established that the fraction reacted after 117 hr is independent of the initial amount present. This result supports a first-order rate law. Running the experiments for longer times in the glass vials indicated also that a change to a slower rate later occurs. The "Student t" statistical test indicates that the average rate constants for the large and small glass vials differ significantly at the 90% confidence level. The slightly larger rate constant for the small vials may reflect a somewhat larger ratio of surface area per unit volume for the smaller vials. However, experimental conditions also differed somewhat for these two measurements. The rate constants for the reaction in the polyethylene container were calculated from the data in Fig. 2 by using the method of least squares to determine the slopes of the linear regions. Other measurements in the polyethylene container established that these results are reproducible with a standard error of about ±5%. Surface effects are again indicated by the fact that the reaction is faster in the polyethylene containers than in the glass containers.

From the Arrhenius equation and the Eyring equation

$$k_r = A e^{-E_a/RT} = \frac{kT}{h} e^{\Delta S^\ddagger/R} \cdot e^{-\Delta H^\ddagger/RT} \quad [9]$$

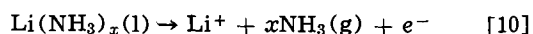
values for  $E_a$ ,  $\Delta S^\ddagger$ ,  $\Delta H^\ddagger$ , and  $\Delta G^\ddagger$  can be determined from the experimental rate constant,  $k_r$ , determined at two different temperatures assuming a transmission coefficient of unity (15, 16). Using the experimental rate constants at 0° and 50°C given in Table I for the polyethylene container, an unusually large, negative value is calculated for the activation entropy,  $\Delta S^\ddagger$  ( $-65 \text{ cal deg}^{-1} \text{ mole}^{-1}$ ), for this reaction while the activation energy,  $E_a$ , is relatively low (6 kcal/mole). The probable error is ±0.5 kcal/mole for  $E_a$  and ±2 cal deg<sup>-1</sup> mole<sup>-1</sup> for  $\Delta S^\ddagger$ . In terms of the Arrhenius equation,  $k_r = 15.3 \times 10^{-2} \text{ sec}^{-1} e^{-6500/1.987T}$  during the earlier stages of the reaction and changes to  $k_r = 1.9 \times 10^{-2} \text{ sec}^{-1} e^{-5900/1.987T}$  during the later stages. The rare reactions with such strikingly small frequency factors show some tendency to be heterogeneous reactions with sensitivity to the reaction-vessel surface (17). As in electrochemical kinetics, the kinetic parameters can still be determined for heterogeneous reactions whenever surface conditions are constant. The eventual precipitation of  $\text{LiNH}_2$  on the walls of the reaction vessel, which changes the surface, produces slight changes in the kinetic parameters.

Experiments in water-ammonia mixtures indicate that the rate of the solvated electron reaction is controlled mainly by the entropy of activation which likely decreases to large negative values as the ammonia content increases (18). Lepoutre *et al.* (19-21) have shown that the absolute entropy of the ammoniated electron is abnormally high. Their interpretation is that the electron breaks the hydrogen-bonded structure of ammonia in order to become "ammoniated." During the self-decomposition reaction, the electron loses its high entropy as the loose solvent structure collapses and hydrogen bonds reappear in the activated complex.

The fact that reaction [1] involves the transfer of an electron to a surrounding ammonia molecule sug-

gests that quantum-mechanical tunneling through the potential-energy barrier is possibly an important factor in this reaction. A tunneling mechanism would account for the first-order rate law observed. Anbar (22) suggests that the low, nearly constant values of activation energies found for reactions involving solvated electrons is due to an electron-tunneling mechanism, and that the different rates observed are due to different probabilities for this tunneling. Eyring (23) and Laidler (24) indicate that electron-transfer reactions occurring by a tunneling mechanism will be characterized by apparent negative entropies of activation if the energy of activation is low. As the tunneling distance increases, the apparent entropy of activation becomes more negative. It is reasonable that for the unusually low density lithium-ammonia solution, the tunneling distance would be relatively large. The abnormally small frequency factor found for this decomposition reaction is predicted for reactions where there is tunneling (25). Perhaps the observed surface effects on the reaction rate result from a favored tendency by adsorbed  $\text{NH}_3$  to accommodate the tunneling electron. Jackman and Keenan propose that an ammonia molecule bound to a surface acid group is more open to attack by a solvated electron (14). The eventual precipitation of the Lewis base,  $\text{LiNH}_2$ , would tend to neutralize surface acid groups, thus causing a decrease in the rate.

The electrochemical oxidation reaction of concentrated lithium solutions in liquid ammonia can be represented as



where the electrons produced enter the electrode. The potential-energy barriers for both reactions [1] and [10] are probably similar since both involve destruction of the unusual electronic structure of  $\text{Li}(\text{NH}_3)_x$  and incorporation of the electron into another substance. Therefore, a large Gibbs free-energy of activation,  $\Delta G^\ddagger$ , resulting from a large, negative entropy of activation,  $\Delta S^\ddagger$ , can also be expected for reaction [10]. Studies of the electrode reaction of solvated electrons in hexamethylphosphoric triamide support this conclusion (26). The heat of activation is much too small (4.2 kcal/mole) for the observed rate constant, and a large and negative entropy of activation is postulated.

#### Acknowledgment

Financial support of this work was by the Naval Air Systems Command, Code AIR 310C. The experimental measurements were performed by the authors at the former Corona Laboratories of the Naval Weapons Center.

Manuscript submitted Feb. 2, 1973; revised manuscript received Nov. 12, 1973.

Any discussion of this paper will appear in a Discussion Section to be published in the December 1974 JOURNAL. All discussions for the December 1974 Discussion Section should be submitted by Aug. 1, 1974.

#### APPENDIX

The Franck-Condon principle implies that tunneling cannot occur until the structure of the  $\text{Li}(\text{NH}_3)_x$  system is modified in such a way that transfer of the electron leaves the total energy unchanged. The rate will be determined by a compromise between the tunneling probability,  $W$ , and the free energy of rearrangement (23),  $\Delta G^\ddagger_r$ , hence

$$k = \frac{kT}{h} \cdot W \cdot e^{-\Delta G^\ddagger_r/RT} \\ = \frac{kT}{h} \cdot W \cdot e^{-\Delta S^\ddagger_r/R} \cdot e^{-\Delta H^\ddagger_r/RT} \quad [A-1]$$

The subscripts r and t will be used to indicate contributions due to rearrangement and tunneling, respec-

tively. Comparing this equation with Eq. [9] above gives

$$\Delta H^\ddagger_{\text{exp}} = \Delta H^\ddagger_r + \Delta H^\ddagger_t = \Delta H^\ddagger_r \quad [A-2]$$

since  $\Delta H^\ddagger_t = 0$ , hence an experimental heat of activation reflecting only the rearrangement energy would account for the low activation energies observed in reactions involving tunneling. Furthermore

$$\Delta S^\ddagger_{\text{exp}} = \Delta S^\ddagger_r + \Delta S^\ddagger_t = \Delta S^\ddagger_r + R \ln W \quad [A-3]$$

For a rectangular energy barrier of height  $E - E_0$

$$\Delta S^\ddagger_t = R \ln W = -R \frac{4\pi a}{h} [2m(E - E_0)]^{1/2} \quad [A-4]$$

The actual height of the energy barrier involved must be greater than  $\Delta G^\ddagger_{\text{exp}}$ ; otherwise the rate due to crossing over the barrier would exceed the rate due to tunneling. Taking a lower limit of

$$E - E_0 \approx \Delta G^\ddagger_{\text{exp}} = 24 \text{ kcal/mole}$$

and using the separation between electron cavities (5) to estimate  $a \approx 8 \text{ \AA}$  gives a value of

$$\Delta S^\ddagger_t \approx -17 \text{ cal/deg mole} \quad [A-5]$$

More negative values for  $\Delta S^\ddagger_t$  would result if larger estimates of  $E - E_0$  were used. Despite the approximations used, this result indicates that a tunneling mechanism could contribute significantly to the experimental  $\Delta S^\ddagger$ . Assuming that the reacting electron loses its high entropy in the structure rearrangement (20, 21)

$$\Delta S^\ddagger_r = -S^\circ_{e, \text{am}} \approx -30 \text{ cal/deg mole}$$

Hence  $\Delta S^\ddagger_r$  might also contribute significantly to the large, negative entropy of activation observed experimentally.

#### REFERENCES

1. M. M. Markowitz, *J. Inorg. Nucl. Chem.*, **24**, 1475 (1962).
2. J. L. Dye, *Sci. Am.*, **216**, (2), 76 (1967).
3. R. E. Lo, *Z. Anorg. Allgem. Chem.*, **344**, 230 (1966).
4. J. F. Suttle, "Comprehensive Inorganic Chemistry," Vol. VI, pp. 22-32, M. C. Sneed and R. C. Brasted, Editors, D. Van Nostrand Co., New York (1957).
5. M. H. Cohen and J. C. Thompson, *Adv. Phys.*, **17**, 857 (1968).
6. U. Schindewolf, *Angew. Chem.*, **80**, 165 (1968).
7. J. C. Thompson and C. R. Ore-Ore, *J. Chem. Phys.*, **54**, 2279 (1971).
8. K. G. Breitschwerdt and H. Radscheit, *Z. Angew. Phys.*, **32**, 276 (1971).
9. W. S. Glaninger, S. Zolotov, and M. J. Sienko, *J. Chem. Phys.*, **56**, 4756 (1972).
10. R. Bridges, A. J. Ingle, and D. E. Bowen, *ibid.*, **52**, 5106 (1970).
11. E. J. Kirschke and W. L. Jolly, *Inorg. Chem.*, **6**, 855 (1967).
12. U. Schindewolf, R. Vogelsgesang, and K. E. Bödiker, *Angew. Chem.*, **79**, 1064 (1967).
13. D. Y. P. Chou, M. J. Pribble, D. C. Jackman, and C. W. Keenan, *J. Am. Chem. Soc.*, **85**, 3530 (1963).
14. D. C. Jackman and C. W. Keenan, *J. Inorg. Nucl. Chem.*, **30**, 2047 (1968).
15. S. Glasstone, K. Laidler, and H. Eyring, "The Theory of Rate Processes," pp. 184-201, McGraw-Hill Book Co., New York (1941).
16. J. F. Bunnett, "Technique of Organic Chemistry," Vol. VIII, Part I, 2nd Ed., pp. 199-210, S. L. Friess, E. S. Lewis, and A. Weissberger, Editors, Interscience Publishers, New York (1961).
17. S. W. Benson, "The Foundations of Chemical Kinetics," pp. 250-257, McGraw-Hill Book Co., New York (1960).
18. R. Olinger and U. Schindewolf, *Ber. Bunsenges. Phys. Chem.*, **75**, 693 (1971).
19. A. Demortier, P. Chieux, G. Lepoutre, G. Billaud, B. David-Gnanhui, and P. Van Nguyen, *Bull. Soc. Chim. Fr.*, 3421 (1971).
20. G. Lepoutre and A. Demortier, *Ber. Bunsenges. Phys. Chem.*, **75**, 647 (1971).
21. G. Lepoutre and J. Jortner, *J. Phys. Chem.*, **76**, 683 (1972).
22. M. Anbar, *Quart. Rev.*, **22**, 578 (1968).

23. R. J. Marcus, B. J. Zwolinski, and H. Eyring, *J. Phys. Chem.*, **58**, 432 (1954).  
 24. K. J. Laidler, *Can. J. Chem.*, **37**, 138 (1959).  
 25. K. J. Laidler, "Theories of Chemical Reaction Rates," pp. 59-63, McGraw-Hill Book Co., New York (1969).  
 26. Y. Kanzaki and S. Aoyagui, *J. Electroanal. Chem.*, **36**, 297 (1972).

## The Effect of Additives on the Reaction Mechanism of the Pb/PbSO<sub>4</sub> Electrode

A. C. Simon\*

Naval Research Laboratory, Washington, D. C. 20375

S. M. Caulder\*

International Lead Zinc Research Organization Research Associate at the Naval Research Laboratory

and P. J. Gurlusky and J. R. Pierson

Globe-Union, Incorporated, Milwaukee, Wisconsin 53201

### ABSTRACT

An investigation has been made of the effect of lignin and BaSO<sub>4</sub> on the capacity and life of the negative plate. BaSO<sub>4</sub> alone, lignin alone, and combinations of the two improved cycle life. Of the combinations tested, 0.5% BaSO<sub>4</sub> and 1.0% lignin gave the greatest improvement on SAE cycle life tests. Lignin alone was as effective as the lignin-BaSO<sub>4</sub> combination in high-rate, low-temperature discharges. Lignin decreased the diameter of the lead particles and passivated portions of the lead surface, so that lead sulfate crystal growth was away from the surface, leaving considerable open space in the mass of crystals at the end of discharge. Without lignin the lead particles were larger, more closely spaced, and lead sulfate grew solidly along the lead surfaces, so that there was little void space at the end of charge. Microscopic examination showed nothing to explain the beneficial effect of BaSO<sub>4</sub>.

The effect of lignin and its derivatives on the performance of the negative plate, specifically under the conditions of low-temperature and high-discharge rate, has been reported by a number of investigators (1-6). This work has been recently reviewed (7). Despite these investigations, however, there is still considerable uncertainty about the exact function of an organic expander, such as lignin, and a question as to why it should function better in the company of an inorganic material such as BaSO<sub>4</sub>.

Several years ago, a cooperative investigation was undertaken by Globe Union, Incorporated and the Naval Research Laboratory in an attempt to elucidate the function of the negative plate additives. More recently, the International Lead Zinc Research Organization has supported this project, among others, by maintaining a Research Associate at the Naval Research Laboratory.

As a result of this cooperative effort, it has been found that when lignin is present in the paste, it modifies the structure of the lead crystals that grow during the formation process. The modifying action produces crystals of smaller diameter with larger surface area and a more porous structure. BaSO<sub>4</sub>, on the other hand, had no appreciable effect on the growth of the lead crystals during the formation process (1).

The present paper reports on further investigations made to determine the function of lignin and BaSO<sub>4</sub> during low-temperature, high-rate discharge of the cell, and their effect on the SAE cycle life and negative electrode morphology.

### Experimental Method

It was decided that nine different active material compositions would be adequate to study the effect of

lignin alone, BaSO<sub>4</sub> alone, and practical combinations of the two. The amount of lignin or BaSO<sub>4</sub> used in the nine pastes are shown in Table I. The BaSO<sub>4</sub> had a mean particle size of 5.2 μm. The lignin used in the experiments was sodium lignosulfonate, marketed under the trade name of Maracell E by the Marathon Paper Company.

With the exception of the different amounts of lignin and BaSO<sub>4</sub>, the paste mixes were as identical to one another in preparation and composition as could be managed. All pastes were very nearly of the same weight and paste density, and every step in the preparation, from mixing to formation, was carefully controlled to eliminate as many extraneous variables as possible. The negatives so prepared were matched with production type positive plates and then assembled. When assembled, each cell contained 5 negatives and 4 positives. The nominal capacity of the batteries used was 50 A-hr. In the various phases of the investigation the samples used for analysis, microscopic examination, and other tests were taken from the center of the negative group. The two end plates were always discarded.

A series of plates was placed on cycling life test, using the procedure outlined in SAE specification

Table I. Amounts of additives used in the experimental plates

Mix No.	BaSO <sub>4</sub> (%)	Lignin (%)
1	none	none
2	none	0.5
3	none	1.0
4	0.5	none
5	0.5	0.5
6	0.5	1.0
7	1.0	none
8	1.0	0.5
9	1.0	1.0

\* Electrochemical Society Active Member.

Key words: expander, additives, lead electrode, lead morphology, lignin, BaSO<sub>4</sub>, PbSO<sub>4</sub>.

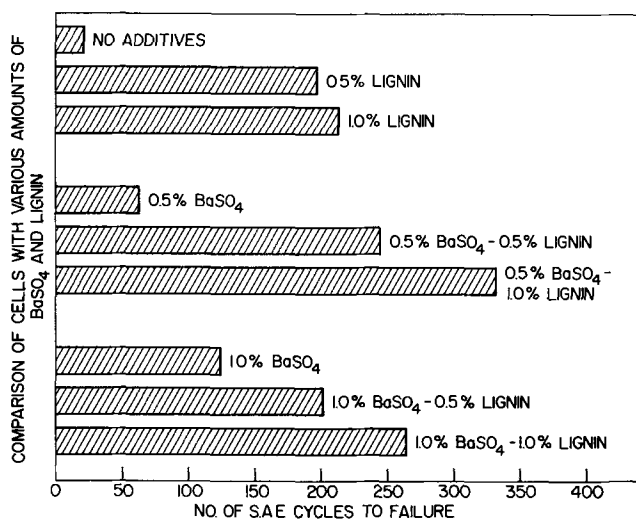


Fig. 1. Comparison of cycle life obtained by the use of various additive combinations. Termination of the bars represent the end of cycle life.

J537d. Using this procedure, there were 27 cycles per week, and low temperature ( $-17.8^{\circ}\text{C}$ ), 150A discharges were made initially and at the 54th and 135th cycles. Sufficient cells were included in the series so that representative samples of the plates were available at the end of life, at the end of low-temperature discharge, and at the end of the recharge that followed the low-temperature discharge.

Since cycling itself had an effect on the microstructure of the lead crystals, a series was also run where a low-temperature, high-rate discharge followed only 5 SAE discharge-charge cycles.

Each of these series involved the use of cells containing the nine different paste compositions shown in Table I, and enough cells were constructed to insure samples for removal at the various designated points during the cell tests. In addition, individual cells of the series were run through duplicate testing when the first results seemed ambiguous.

Samples of each of the series were removed at the points indicated above and were impregnated with plastic,<sup>1</sup> polished, and examined by microscopy.

### Results of Experiment and Examination

*Effects noted in the SAE life cycle test.*—As shown in Fig. 1, BaSO<sub>4</sub> alone produced a considerable increase in cycle life with each 0.5% addition. Lignin alone produced a more marked effect with the first 0.5% addition than did the BaSO<sub>4</sub>, but the contrast between the 0.5 and the 1.0% addition was much less than for BaSO<sub>4</sub>. Also evident was the fact that BaSO<sub>4</sub> and lignin were more effective in increasing life when used together, although this effectiveness decreased when too much BaSO<sub>4</sub> was used. The addition of 1.0% lignin was in all cases more effective than 0.5%. Since the battery industry uses between 0.1 and 0.5% lignin in its negative plates, the use of 1.0% lignin seemed high when planning this investigation. It now appears that even higher amounts might have proven to be beneficial.

Although lignin was found to increase cycle life in SAE tests, when discharge was at the 20 hr rate (Table II), neither lignin nor BaSO<sub>4</sub> caused any appreciable increase in initial capacity, either before or after a 150A discharge.

Microscopic examination of the cycled plates, in the charged state, revealed that the lead crystals were influenced by the lignin in the same manner as they had been in the formation process. The lead dendrites in plates containing lignin were much smaller with

Table II. Comparison of discharges at the 20 hr rate

Mix No.	Initial discharge (A-hr)	After cold test (A-hr)
1	60.9	57.5
2	59.3	58.3
3	59.8	58.7
4	60.2	58.6
5	58.9	58.3
6	58.7	58.3
7	56.9	55.9
8	59.5	58.9
9	59.5	58.9

individual branches of smaller diameter than were those seen in the plates without lignin. Repeated cycling tended to destroy this effect, as the size of the lead particles increased with the amount of cycling. However, even in this case, the particles remained smaller in the plates containing lignin than in those with no additives. There was a general tendency for the lead particles to increase in size and to become roughly spherical as the cycling continued. One effect of the lignin was to retard this lead particle size increase.

The lignin-free plates showed many needle-like dendritic arms growing in parallel arrangement and extending for considerable distance. These growing needles extended in such a manner as to form long and quite narrow channels between the individual branches. Since this type of structure seemed to be nearly absent from the lignin-containing plates, and since in this case the small particles showed little relation to one another, another apparent function of the lignin is to restrict the extent of growth of dendritic arms in the individual crystals, during the conversion of PbSO<sub>4</sub> to Pb.

The above description refers to the structural effect that lignin produced on the lead dendrites which appeared in the charged plates. The effect of lignin on the structure of the PbSO<sub>4</sub> crystals formed during discharge was somewhat more difficult to observe clearly with the optical microscope. The PbSO<sub>4</sub> crystals grew close together, so that individual outlines were difficult to separate from the group. In addition, the cross sections of the crystals, as seen in the polished sections, bore little relation to their actual three-dimensional shapes, so that comparisons, based on these cross sections, left a considerable amount to the imagination. Certain facts were evident, however.

Cycled plates, of similar capacity, discharged at the 20 hr rate, showed PbSO<sub>4</sub> crystals grouped around the lead particles, evidently of about the same amount, size, and shape, whether or not the plates contained lignin. There was a marked difference, however, in the manner in which the PbSO<sub>4</sub> crystals were arranged. Those PbSO<sub>4</sub> crystals in the lignin-free plates were tightly grouped close to the surface of the lead dendrites in a continuous layer (Fig. 2). Those PbSO<sub>4</sub> crystals in the lignin-containing plates were much more loosely attached and extended further from the surface (Fig. 3).

Since the charged, lignin-free plates had dendritic lead crystals of large diameter, and since these tended to form parallel and closely spaced dendritic branches, the growth of the PbSO<sub>4</sub> during discharge acted to block the resulting channels as well as to leave a large amount of unreacted lead at the core of the particles. In the lignin-containing plates, on the other hand, the lead particles were smaller and the PbSO<sub>4</sub> crystals were more openly spaced and less unreacted lead was left at the core of the particles. Under the condition of discharge at the 20 hr rate it seemed that passivation was more dependent upon a sufficient diameter being present in the lead particle so that a PbSO<sub>4</sub> layer of sufficient thickness could be built up to cause passivation to occur before all the lead was utilized, rather than upon the formation of PbSO<sub>4</sub> crystals of a particular small size.

The so-called expansion of the plates was another noteworthy effect of SAE cycling that could be at-

<sup>1</sup> Vacuum impregnation of dried plate with catalyzed polyester resin, Gr-28V, obtainable from W. R. Grace Company, Marco Chemical Division, Linden, New Jersey 07036.

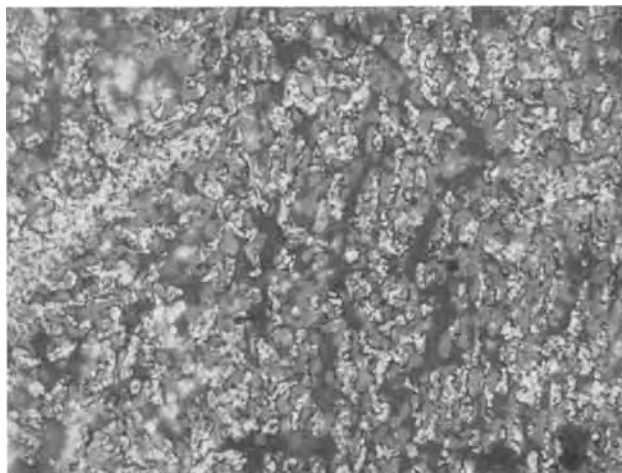


Fig. 2. Appearance of a negative that failed at 19 cycles, had no additives, and is shown in the discharged condition. Note the large amount of lead (bright particles). The PbSO<sub>4</sub> (light gray) is close packed around the lead surfaces and there is relatively little void space (dark gray) shown. Original magnification 1000 $\times$ .

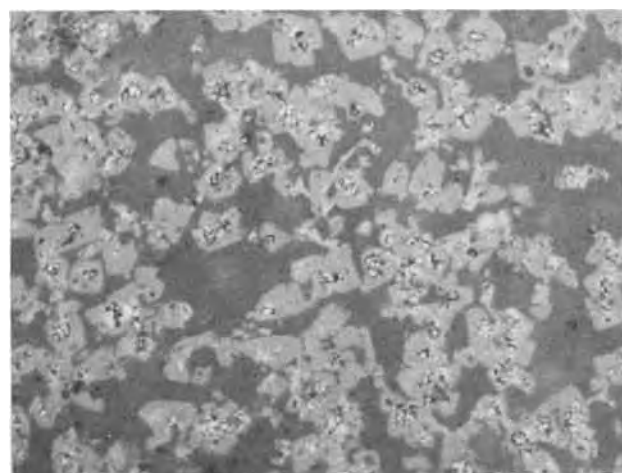


Fig. 3. Appearance of a negative plate containing 0.5% BaSO<sub>4</sub> and 1.0% lignin, that has not yet failed but is shown discharged at 27 cycles. Note the large void spaces (dark gray), the small amount of lead (bright particles), and the relatively ungrouped spacing of the PbSO<sub>4</sub> crystals (light gray). Original magnification 1000 $\times$ .

tributed to lignin and which was evident on a macro-scale. Those plates which were lignin-free maintained practically the same thickness and density throughout their cycle life (Fig. 4). No large voids were formed, and the size and spacing of the dendrites seemed to remain constant, or nearly so. The plates containing BaSO<sub>4</sub> expanded only slightly during cycle life. They showed a few small voids and there was a very slight increase in the separation between particles at the end of life.

The lignin-containing plates behave quite differently. During their life there was a remarkable increase in the thickness of the plate, the interiors became filled with large and interconnected voids, and the particles themselves became more separated (Fig. 5). The increase in thickness and the decrease in density were gradual. At 5 cycles hardly any change could be detected from the appearance that was shown by the freshly formed plates, but the difference became more marked with increasing cycling. Low-magnification examination of the surface of the lignin-containing plates revealed many volcano-like, cone-shaped openings, with raised rims and an accumulation of particles around them. This was not found in the lignin-free plates. Cross sections showed such openings at the surface were connected with the internal large



Fig. 4. The appearance of a cross section of a negative plate containing no lignin but 0.5% BaSO<sub>4</sub> after 27 cycles. Compare thickness of plate with that of Fig. 5. Magnification 17 $\times$ . Plate is charged.

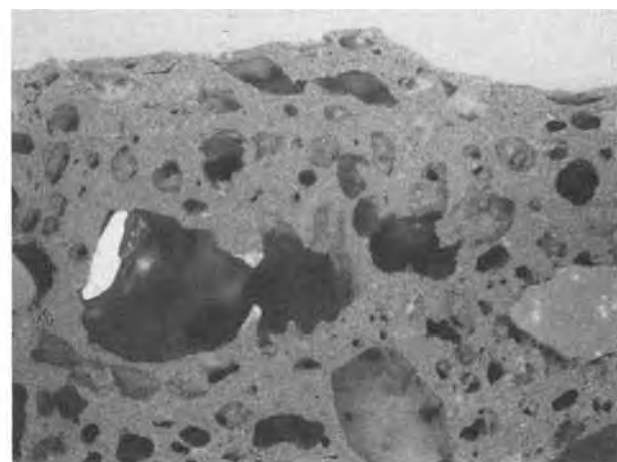


Fig. 5. The appearance of a cross section from a negative plate containing 0.5% BaSO<sub>4</sub> and 1.0% lignin, after 27 cycles. Note the wide cross section and the numerous large voids. Magnification is 17 $\times$ . Plate is charged.

voids. The appearance left no doubt that these large voids were the result of gas action, and that the same process had caused the voids that were present throughout the plates.

Since the observation has been made repeatedly that additives increase both the cell potential and the overvoltage at the negative electrode, it was hard to explain why the gassing should be greater on the plates containing lignin. Careful examination of the plates led to the conclusion that the small size and open-spaced structure of the dendrites in the plates with lignin made them structurally weaker than the large diameter branches of the plates without lignin. For this reason the surface tension effects produced by the formation of large bubbles literally blasted the lignin-containing plates apart, while an equivalent amount of gassing was without effect on the lignin-free plates.

In SAE cycle tests, such as were run here, the negative is not usually expected to limit the reaction. It is obvious from Fig. 1, however, that the cycle life test results were, in fact, influenced by whether or not the negative contained lignin. The termination of life for a given cell is determined by the loss of a definite proportion of its initial capacity. It is evident from Table II that the presence or absence of lignin or BaSO<sub>4</sub> did not initially affect the capacity of these

cells, so that it is logical to think that the effect on capacity must have been from something that occurred during the continued cycling. The most evident effect of the lignin was to limit the growth of the lead dendrites that were formed during charge. In order for the lead sulfate film, formed during the discharge, to become passivating, it must build up to a definite thickness, produced at the expense of the underlying lead. If the diameter of the lead particle is small enough, complete reaction can take place before a film of sufficient thickness can build up. Conversely, too large a particle will form a passivating film before the original lead is all converted to lead sulfate and this condition reduces the available capacity. It is precisely this condition that the lignin prevents by limiting the diameter of the lead particles.

A secondary effect of the lignin is to limit the normally extensive growth of individual crystals. This extensive growth frequently produces parallel-growing dendritic filaments that in turn produce long, narrow, or complex channels in the active material. Such channels are undoubtedly easily clogged with growing  $\text{PbSO}_4$  crystals, thus rendering portions of the active material relatively inactive.

A third effect may involve a change in the mode of crystal growth, since the observation was made repeatedly that the lead sulfate crystals were less densely packed and extended from the surface of the lead particle when lignin was present in the plate.

It is evident that the so-called expander action is of little value, since the least expansion of the plate occurs at the beginning, when the capacity is the greatest. When the expansion is the greatest, the capacity has dropped to a very low value.

In SAE cycling, the most important function of the lignin appears to be the regulation of the size of the lead dendritic crystals.

*Effects noted in the low-temperature, high-rate discharges.*—The results of the  $-17.8^\circ\text{C}$  temperature, 150A discharges are shown in Fig. 6 as obtained initially, and after 5, 54, and 135 cycles. The graph represents the averages of several results. It can be seen that additions of  $\text{BaSO}_4$  resulted in only slight improvement in capacity, whereas lignin produced a considerable increase in capacity over that obtained in its absence. However, a combination of lignin and  $\text{BaSO}_4$  produced little if any, improvement over the use of lignin alone.

Microscopic examination revealed no  $\text{PbSO}_4$  crystals around the lead dendrites in the plates which contained no additives, except for an occasional large crystal that was probably an unconverted remainder from a previous discharge at the normal rate. Examination with polarized light is usually extremely effective

in detecting films of any sort, because of the light scattering caused by the latter, but it was ineffective in this case. In the plates containing lignin, lead sulfate crystals were found present in sufficient abundance to account for the capacity obtained (at the best, about one fifth of that obtained at the 20 hr rate). In those plates containing no additives or only  $\text{BaSO}_4$  as an additive, the amount of  $\text{PbSO}_4$  would be about 3-5g per 100g of lead. Considering the large surface area of lead in the negative plate, it is not surprising that this amount could not be detected with the optical microscope.

The self-passivation of the lead electrode is a well-known phenomena that has been studied by a number of investigators (8-11), and it is very likely that all charged lead electrodes become covered with a layer of lead sulfate crystals as soon as the charging current is removed. After any prolonged stand the number of such crystals would increase rapidly. None of these, of course, have been seen with the optical microscope. Kabonov and co-workers (4) showed that lead sulfate crystals of about 400-500Å in size formed on pure lead sheet in the absence of additives. Pavlov and Popova (11) report that on lead without additives, the effective thickness of the layer which causes passivation was between 800 and 5000Å. Both of these investigations revealed the presence of individual crystals, with open spaces in between.

According to Pavlov and Popova (11) the growth of  $\text{PbSO}_4$  crystals leads to a decrease of the free lead surface, bringing an increase in current density at those points. When the  $\text{Pb}^{+2}$  ions formed exceed the flux of the  $\text{SO}_4^{-2}$  ions flowing toward the lead surface, the solution at the active metal surface becomes alkaline in order to remain electroneutral. With the increase in pH, basic lead sulfates and lead oxide are formed. These compounds then proceed to fill the spaces between the  $\text{PbSO}_4$  crystals, and thus a continuous layer is formed which passivates the electrode. When the current is interrupted, these basic sulfates rapidly disappear. These authors postulate that the rate of passivation depends in part upon the number and area of intercrystalline spaces. Such a mechanism would explain how a thin and discontinuous layer of small  $\text{PbSO}_4$  crystals could become passivating and would also explain our inability to detect a lead sulfate layer in the sections examined.

Otherwise, it is extremely difficult to accept that such a thin layer of lead sulfate could become passivating. Considering the excessive supersaturation that would exist at the negative plate under the onset of a 150A discharge, it is inconceivable that relief of this supersaturation would not lead to dendritic growth in the  $\text{PbSO}_4$  crystals. Such dendritic growth has already been observed at both the negative (12) and positive electrode (13) under much less severe current densities. It would be logical to expect nucleation to proceed to a two-dimensional dendritic growth along the lead surface because of the very steep concentration gradient developing immediately following the relief of supersaturation. Such dendritic structures would not be ideal candidates for the formation of an impervious layer unless a mechanism such as that of Pavlov and Popova was in operation.

While it was evident that lignin had a decided effect on the lead crystal structure during SAE cycling, and that this would also be effective during the high rate discharge, it was not evident what mechanism caused the  $\text{BaSO}_4$  to become effective. Nothing in the microscopic examination indicated that any physical change took place as a result of the presence of  $\text{BaSO}_4$ . However, since it was difficult to determine the true shapes of the  $\text{PbSO}_4$  crystals, it is possible that  $\text{BaSO}_4$  had some effect that was not detected.

Certainly, if  $\text{BaSO}_4$  provides nucleating points for the growth of  $\text{PbSO}_4$  crystals, as has been suggested by previous investigators, the prevention of supersaturation should act to promote the growth of finer and larger crystals. It has been evident throughout

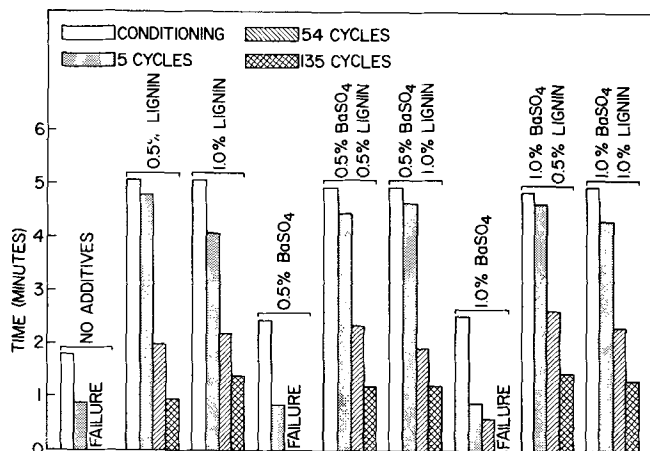


Fig. 6. Relative times of discharge at  $-18.8^\circ\text{C}$  and the 150A rate, with and without the use of additives. Shows the effect of additives on high-rate discharge at the beginning of cycle life and after 5, 54, and 135 cycles.



this examination, however, that whatever effect BaSO<sub>4</sub> has on the discharge process, this effect cannot be detected with the optical microscope.

### Conclusions

The data on cycling and low-temperature discharge agreed in general with previously reported work, although BaSO<sub>4</sub> and lignin, when used together, did not provide as great an increase in effectiveness as some previous reports would lead one to expect.

A new effect of lignin, modification of the structure of the lead particles in the charged electrode, has been found as a result of this investigation. It appears that lignin provides lead particles of sufficiently small diameter to permit their complete conversion to PbSO<sub>4</sub> before a sufficiently thick film can be formed to cause passivation. Lignin also appears to retard the growth of the larger lead particles that are the result of continuous cycling. These effects were noted during formation and SAE cycling.

During SAE cycling, lignin also produced a difference in the manner of deposition of lead sulfate crystals, those electrodes containing lignin having a more open and porous crystalline deposit than those containing no lignin. Although details of this deposit were somewhat obscure using optical microscopy, there was no evidence of a marked difference in lead sulfate crystal size in those plates with lignin as compared with those without.

In low-temperature, high-rate discharges, the optical microscope failed to show any evidence of lead sulfate crystal formation in those plates containing no lignin, although a definite crystalline film could be easily observed in those electrodes in which lignin was present. Failure to detect any lead sulfate might be used as evidence that crystals of extremely small size, forming an extremely thin passivating film, were formed, as postulated by Willihnganz (6), but would not be conclusive as the small amount of reaction product formed would be difficult to detect with the microscope in any case.

No effect of BaSO<sub>4</sub> on either the structure of lead or of lead sulfate was detected, although the data indicated that BaSO<sub>4</sub> in some manner increased reactivity slightly, both alone and in the presence of lignin.

### Acknowledgments

The authors wish to thank the Naval Research Laboratory, Globe-Union, Incorporated, and the International Lead Zinc Research Organization for permission to publish this report and for their cooperation and support that have made this investigation possible.

Manuscript submitted March 19, 1973; revised manuscript received Nov. 26, 1973. This was Paper 29 presented at the Miami Beach, Florida, Meeting of the Society, Oct. 8-13, 1972.

Any discussion of this paper will appear in a Discussion Section to be published in the December 1974 JOURNAL. All discussions for the December 1974 Discussion Section should be submitted by Aug. 1, 1974.

### REFERENCES

1. J. R. Pierson, P. Gurlusky, A. C. Simon, and S. M. Caulder, *This Journal*, **117**, 1463 (1970).
2. G. W. Vinal, "Storage Batteries," 3rd ed., p. 26, John Wiley & Sons, Inc., New York (1945).
3. A. C. Zachlin, *This Journal*, **98**, 325 (1951).
4. E. G. Yampol'skaya, M. I. Ershova, I. I. Astakhov, and B. N. Kabanov, *Elektrokhimiya*, **2**, 1327 (1966); Ya. B. Kasparov, E. G. Yampol'skaya, and B. N. Kabanov, *Zh. Prikl. Khim.*, **37**, 1936 (1964); Ya. B. Kasparov, E. G. Yampol'skaya, and B. N. Kabanov, *Tr. 4-go (Chetvertogo) Soveshch. po Elektrokhim.*, Moscow, 1956, pp. 747-747 (1959).
5. W. Simon, *Bosch Technische Berichte*, **1**, 234 (1966).
6. E. Willihnganz, *This Journal*, **79**, 243 (1941); National Lead Company Research Report 46 (1941); National Lead Company Research Report 63 (1942).
7. J. Burbank, A. C. Simon, and E. Willihnganz, in "Advances in Electrochemistry and Electrochemical Engineering," P. Delahay and C. W. Tobias, Editors, Vol. 8, Chap. 3, pp. 157-251, Wiley-Interscience, New York (1971).
8. E. J. Casey and K. N. Campney, *This Journal*, **102**, 219 (1955).
9. K. Ekler, *Can. J. Chem.*, **42**, 1355 (1964).
10. H. F. Haring and U. B. Thomas, *This Journal*, **68**, 293 (1935).
11. D. Pavlov and R. Popova, *Electrochim. Acta*, **15**, 1483 (1970).
12. A. C. Simon, *Electrochem. Technol.*, **3**, 307 (1965).
13. T. Chiku and K. Nakajima, *This Journal*, **118**, 1395 (1971).

## Initiation of Pitting at Sulfide Inclusions in Stainless Steel

Göran S. Eklund

*Swedish Institute for Metal Research, Stockholm, Sweden*

### ABSTRACT

Equilibrium calculations on some sulfide systems actual in commercial stainless steel have shown that the sulfides cannot thermodynamically exist at the potential of the passive steel. The ions released by the dissolution of the sulfides give rise to an acid solution in microareas. A pitting corrosion mechanism based on the sulfides themselves is suggested. The sulfides are polarized to the potential of the passive steel surface and tend to dissolve. During the dissolution a virgin metal surface is exposed to the environment. When the solution in the microarea thus developed has reached a certain composition, the contacting metal can no longer passivate and the metal starts to dissolve.

It is well accepted that pitting of stainless steels is effected in two steps: one initiating step and one propagating step (1). The initiation is still the subject of contention, and no mechanism for the pitting of stainless steels has been developed to the point that

**Key words:** initiation of pitting corrosion, sulfide equilibria in aqueous solutions, diagram of manganese sulfide potential-pH.

one can make quantitative predictions pertaining to the pitting resistance.

Most of the proposed mechanisms involve either an activating ion, such as chloride, penetrating and destroying the passive film locally, or the activating ion being adsorbed at the metal/solution interface displacing the adsorbed passive layer and thus destroying



the passivity locally. The potential setup between the locally disrupted film and the rest of the surface leads to anode formation and attack of the metal at some point (2-4). In both mechanisms the adsorption of the anion is important.

The composition of the oxide film on the metal surface, which depends sensitively on the production history of the steel (5-8), must also have a great influence on the adsorption. It is therefore difficult to attempt a quantitative treatment, especially since information on the energies involved is not readily available.

Based on another approach, Vermilyea (9) has developed a theory that allows a semiquantitative prediction of pitting potentials. He assumes that the pitting potential is the potential at which the protective metal oxide, the salt of the metal, and the aggressive anion are in equilibrium. The theory successfully predicts the critical potential for Al, Mg, Fe, and Ni. However, it does not say which ions should be aggressive. It also appears difficult to apply this treatment to alloys.

The experimental determination of the pitting potential also seems to be very difficult and values reported by different authors for the same system differ greatly. The critical potential is evidently a function of time, film history, and metal surface preparation. In addition, the early history of the steel, such as deoxidation practice, speed of solidification, and heat-treatment, also exerts a certain influence.

The sites at which pitting starts on a stainless steel surface have been the subject of much discussion. It has been suggested that local disturbances in the oxide layer at grain boundaries and other inhomogeneities should make these areas more accessible to adsorption of the chloride ions. Streicher (3) and Uhlig (10) indicated that nonmetallic inclusions could be possible sites for pit nucleation. Lately it has been shown that pitting starts almost exclusively at nonmetallic inclusions and that the sulfides are especially detrimental (11-13). One can then assume that the oxide layer close to inhomogeneities such as inclusions has a composition slightly different from the rest of the surface. This means that a potential difference can exist which then is amplified by preferential adsorption of the anions. Further, in the presence of microcrevices pitting can also be induced by a crevice corrosion mechanism. The evidence for such mechanisms is, however, inadequate.

Another explanation of the initiation of a pit and its subsequent propagation is based on the sulfides themselves (13). It is known that the sulfides in a commercial stainless steel containing manganese comprise manganese sulfides with variable amounts of dissolved iron and chromium. The sulfides are electronic conductors and can be polarized to the potential of a passive stainless steel surface. At this potential the sulfides, as shown below, are not thermodynamically stable and tend to dissolve.

When such a dissolution takes place, virgin metal is exposed to the environment. The solution developed in that microarea must, as a result of the dissolution, have a different composition to that of the bulk. The metal ions from the sulfide, manganese, iron, and chromium, can undergo complex reactions and give rise to a low pH as well as a certain concentration of hydrogen sulfide and its protolyzed products. At a certain composition of the solution, the exposed metal can no longer passivate and metal ions enter the solution and the potential drops drastically, thus becoming more active. The metal ions thus released develop their own environment and maintain the attack provided the geometrical conditions are such that a dilution of the solution is prevented.

In order to establish if a pit initiation mechanism based on the sulfides themselves is thermodynamically justified, equilibrium calculations on manganese sulfides and manganese sulfides with iron substitutionally

dissolved have been carried out. Thermodynamic data on CrS are not available and so calculations on (MnCr)S systems have not been possible; however, since chromium can be of importance for the formation of an acid solution from the dissolution of chromium-containing sulfides, the system Cr-H<sub>2</sub>O-Cl has been considered.

To test the validity of the calculations some experiments with synthetic sulfides were carried out as well as studies of corroded steel samples.

### Equilibrium Calculations

The calculations were made using a program developed by Sillén and co-workers (14). The program calculates the equilibrium concentration of any number of species in mixtures of any number of components, which in turn can form any number of complexes and solid phases. In the calculations, concentrations are used postulating that the activity coefficient *f* (on moles per liter concentration scale) is equal to unity. The equilibrium data must be known and enough data be given about the gross composition. From the input information the program itself devises an efficient plan for solving the simultaneous equations. The program also provides an efficient means for finding out which of many possible solid phases can actually appear in a certain equilibrium mixture.

All calculations are based on a given input concentration of Cr<sup>2+</sup>, Mn<sup>2+</sup>, Fe<sup>2+</sup>, SO<sub>4</sub><sup>2-</sup>, Cl<sup>-</sup>, H<sup>+</sup>, and e<sup>-</sup> where the latter here is considered as an ion. The concentration of any species can be changed stepwise and the concentration of the complexes and solid phases can be calculated for any point of the system. For the construction of potential-pH diagrams, the pH has been kept constant and *pe* has been changed stepwise; *pe* is here the negative logarithm of the electron activity defined as

$$pe \equiv \frac{EF}{RT \ln 10} \quad [1]$$

In short, the program handles the electrons in such a way that no redox process takes place at equilibrium, which means that no electron transfer is effected. It is the equilibrium composition at that particular *pe* which is calculated.

The symbols and reactions used in the calculations are found in the List of Symbols below.

Equilibrium constants for the reactions used in this paper are given in Table I.

*MnS-H<sub>2</sub>O-Cl*.—In the calculations, the total concentrations of Mn, S, and Cl<sup>-</sup> are each 0.1 mole/liter. This means that at any point of the diagram, the sum of, for example, manganese is 0.1 mole irrespective of whether the manganese is present as a solid phase, ion, or complex. The same is valid for sulfur and chloride. In the calculations  $\Delta G_f^\circ = -48,750$  calories/mole has been used for the free energy of formation of MnS (15). The numbers and symbols in Fig. 1 and 4 refer to the reactions listed in Table II.

From Fig. 1 it is seen that MnS can exist between pH 4.8 and 13.8 (lines 6 and 8). At pH values less than 4.8, MnS dissolves forming H<sub>2</sub>S, Mn<sup>2+</sup>, and MnCl<sup>+</sup>. The concentration of the latter complex is about 10<sup>-2</sup> mole/liter. One-tenth of the total amount of the manganese is thus present as MnCl<sup>+</sup>. At pH values higher than 13.8, MnS dissolves forming S<sup>2-</sup>, Mn(OH)<sub>2</sub>, and HMnO<sub>2</sub><sup>-</sup>. Line 7, at pH 10.2, corresponds to the formation of Mn(OH)<sub>2</sub> due to the increase in solubility of MnS when the pH is raised.

The domain of MnS at higher potentials is limited by the formation of Mn(OH)<sub>2</sub> and SO<sub>4</sub><sup>2-</sup> (line 5). At still higher potentials, MnS dissolves without forming any solid substance (line 4). The highest potential at which MnS can exist is about -100 mV (line 3). The dissolution at this potential takes place with the formation of sulfur.

Table I. Equilibrium constants for reactions used in the calculations

	log K
<b>Ligand e-</b>	
<b>Dissolved substances</b>	
$\text{Cr}^{2+} = \text{Cr}^{3+} + e^-$	6.90 <sup>a</sup>
$\text{Cr}^{2+} + \text{H}_2\text{O} = \text{CrOH}^{2+} + \text{H}^+ + e^-$	3.40 <sup>a</sup>
$2\text{Cr}^{2+} + 2\text{H}_2\text{O} = \text{Cr}_2(\text{OH})_2^{4+} + 2\text{H}^+ + 2e^-$	9.80 <sup>a</sup>
$\text{Cr}^{2+} + 4\text{H}_2\text{O} = \text{Cr}(\text{OH})_4^- + 4\text{H}^+ + e^-$	-19.50 <sup>a</sup>
$\text{Cr}^{2+} + 4\text{H}_2\text{O} = \text{CrO}_4^{2-} + 8\text{H}^+ + 4e^-$	-66.43 <sup>a</sup>
$2\text{Cr}^{2+} + 7\text{H}_2\text{O} = \text{Cr}_2\text{O}_7^{2-} + 14\text{H}^+ + 8e^-$	-121.40 <sup>a</sup>
$\text{Cr}^{2+} + 4\text{H}_2\text{O} = \text{HCrO}_4^- + 7\text{H}^+ + 4e^-$	-59.92 <sup>a</sup>
$\text{Cr}^{2+} + 4\text{H}_2\text{O} = \text{H}_2\text{CrO}_4 + 6\text{H}^+ + 4e^-$	-59.92 <sup>a</sup>
$6\text{Cr}^{2+} + 12\text{H}_2\text{O} = \text{Cr}_6(\text{OH})_{12}^{6+} + 12\text{H}^+ + 6e^-$	27.0 <sup>a</sup>
$\text{Cr}^{2+} + \text{SO}_4^{2-} = \text{Cr}^{3+}\text{SO}_4^{2+} + e^-$	11.70 <sup>a</sup>
$\text{Cr}^{2+} + \text{Cl}^- = \text{Cr}^{3+}\text{Cl}^- + e^-$	7.80 <sup>a</sup>
$\text{Cr}^{2+} + \text{Cl}^- = \text{CrCl}^{2+} + e^-$	7.20 <sup>a</sup>
$\text{Cr}^{2+} + 2\text{Cl}^- = \text{CrCl}_2^{2+} + e^-$	6.40 <sup>a</sup>
$\text{Cr}^{2+} + 3\text{H}_2\text{O} + \text{Cl}^- = \text{CrO}_2\text{Cl}^- + 6\text{H}^+ + 4e^-$	-63.70 <sup>a</sup>
$\text{Cr}^{2+} + 2\text{Cl}^- + \text{H}_2\text{O} = \text{CrCl}_2\text{OH} + \text{H}^+ + e^-$	0.40 <sup>a</sup>
$\text{Mn}^{2+} = \text{Mn}^{3+} + e^-$	-25.53 <sup>b</sup>
$\text{Mn}^{2+} + 4\text{H}_2\text{O} = \text{MnO}_4^{2-} + 8\text{H}^+ + 4e^-$	-117.90 <sup>a</sup>
$\text{Mn}^{2+} + 4\text{H}_2\text{O} = \text{MnO}_4^- + 8\text{H}^+ + 5e^-$	-127.49 <sup>a</sup>
$\text{Fe}^{2+} = \text{Fe}^{3+} + e^-$	-13.02 <sup>a</sup>
$\text{Fe}^{2+} + \text{H}_2\text{O} = \text{FeOH}^{2+} + \text{H}^+ + e^-$	-15.22 <sup>a</sup>
$\text{Fe}^{2+} + 2\text{SO}_4^{2-} = \text{Fe}(\text{SO}_4)_2^{2-} + e^-$	-7.62 <sup>a</sup>
$\text{Fe}^{2+} + \text{SO}_4^{2-} = \text{FeSO}_4^{2+} + e^-$	-8.92 <sup>a</sup>
$\text{Fe}^{2+} + \text{H}^+ + \text{SO}_4^{2-} = \text{FeHSO}_4^{2+} + e^-$	-9.26 <sup>a</sup>
$\text{Fe}^{2+} + \text{Cl}^- = \text{FeCl}^{2+} + e^-$	-11.52 <sup>a</sup>
$\text{H}_2\text{S aq} + 4\text{H}_2\text{O} = \text{SO}_4^{2-} + 10\text{H}^+ + 8e^-$	-41.00 <sup>a</sup>
$\text{HS}^- + 4\text{H}_2\text{O} = \text{SO}_4^{2-} + 9\text{H}^+ + 8e^-$	-34.00 <sup>a</sup>
$\text{S}^{2-} + 4\text{H}_2\text{O} = \text{SO}_4^{2-} + 8\text{H}^+ + 8e^-$	-20.00 <sup>a</sup>
<b>Solid substances</b>	
$\text{Cr}^{2+} + 3\text{H}_2\text{O} = \text{Cr}(\text{OH})_3 + 3\text{H}^+ + e^-$	-5.10 <sup>a</sup>
$3\text{Mn}^{2+} + 4\text{H}_2\text{O} = \text{Mn}_3\text{O}_4 + 8\text{H}^+ + 2e^-$	-61.72 <sup>a</sup>
$2\text{Mn}^{2+} + 3\text{H}_2\text{O} = \text{Mn}_2\text{O}_3 + 6\text{H}^+ + 2e^-$	-48.80 <sup>a</sup>
$\text{Mn}^{2+} + 2\text{H}_2\text{O} = \text{MnOOH} + 3\text{H}^+ + e^-$	-31.90 <sup>a</sup>
$\text{Mn}^{2+} + 2\text{H}_2\text{O} = \text{MnO}_2 + 4\text{H}^+ + 2e^-$	-41.56 <sup>a</sup>
$\text{MnS} + 4\text{H}_2\text{O} = \text{Mn}^{2+} + \text{SO}_4^{2-} + 8\text{H}^+ + 8e^-$	-31.58 <sup>b,c</sup>
$\text{Fe}^{2+} + 3\text{H}_2\text{O} = \text{Fe}(\text{OH})_3 + 3\text{H}^+ + e^-$	-17.87 <sup>a</sup>
$\text{Fe}^{2+} + 2.7\text{H}_2\text{O} + 0.3\text{Cl}^- = \text{Fe}(\text{OH})_2 \cdot \text{Cl}_{0.3} + 2.7\text{H}^+ + e^-$	-15.97 <sup>a</sup>
$(\text{Mn}_{0.8}\text{Fe}_{0.1})\text{S} + 4\text{H}_2\text{O} = 0.9\text{Mn}^{2+} + 0.1\text{Fe}^{2+} + 8\text{H}^+ + 8e^- + \text{SO}_4^{2-}$	-32.74 <sup>b,c</sup>
$\text{S} + 4\text{H}_2\text{O} = \text{SO}_4^{2-} + 8\text{H}^+ + 6e^-$	-36.24 <sup>a</sup>
<b>Ligand OH-</b>	
<b>Dissolved substances</b>	
$\text{H}_2\text{O} = \text{H}^+ + \text{OH}^-$	-14.00 <sup>a</sup>
$\text{Mn}^{2+} + 3\text{H}_2\text{O} = \text{Mn}(\text{OH})_3^- + 3\text{H}^+$	-34.20 <sup>a</sup>
$\text{Mn}^{2+} + 2\text{H}_2\text{O} = \text{HMnO}_2^- + 3\text{H}^+$	-34.39 <sup>a,b</sup>
$\text{Fe}^{2+} + \text{H}_2\text{O} = \text{FeOH}^+ + \text{H}^+$	-9.20 <sup>a</sup>
$\text{Fe}^{2+} + \text{H}_2\text{O} = \text{Fe}(\text{OH})_2^- + 3\text{H}^+$	-32.00 <sup>a</sup>
<b>Solid substances</b>	
$\text{Cr}^{2+} + 2\text{H}_2\text{O} = \text{Cr}(\text{OH})_2 + 2\text{H}^+$	-11.00 <sup>a</sup>
$\text{Mn}^{2+} + 2\text{H}_2\text{O} = \text{Mn}(\text{OH})_2 + 2\text{H}^+$	-15.20 <sup>a</sup>
$\text{Fe}^{2+} + 2\text{H}_2\text{O} = \text{Fe}(\text{OH})_2 + 2\text{H}^+$	-12.90 <sup>a</sup>
<b>Ligand SO<sub>4</sub><sup>2-</sup></b>	
<b>Dissolved substances</b>	
$\text{SO}_4^{2-} + \text{H}^+ = \text{HSO}_4^-$	1.96 <sup>a</sup>
$\text{Mn}^{2+} + \text{SO}_4^{2-} = \text{MnSO}_4$	2.30 <sup>a</sup>
<b>Ligand Cl-</b>	
<b>Dissolved substances</b>	
$\text{Mn}^{2+} + \text{Cl}^- = \text{MnCl}^+$	0 <sup>a</sup>
$\text{Fe}^{2+} + \text{Cl}^- = \text{FeCl}^+$	1.0 <sup>a</sup>
$\text{Fe}^{2+} + 2\text{Cl}^- = \text{FeCl}_2$	1.40 <sup>a</sup>

<sup>a</sup> Denotes data taken from Sillen and Martell (24, 25).

<sup>b</sup> Denotes data taken from Pourbaix (26).

<sup>c</sup> Denotes values calculated from  $\Delta G^\circ_f$  for the sulfides.

Figures 2 and 3 show the correlation between concentration and potential at equilibrium in a mixture containing 0.1 mole each of  $\text{Mn}^{2+}$ ,  $\text{SO}_4^{2-}$ , and  $\text{Cl}^-$ . The domain for the solid phases is shown above the diagrams. For simplicity two figures are drawn, one containing the manganese complexes and the other the sulfur complexes. Going from left to right in these it is clear that the concentration of the different species is constant up to  $-400$  mV. The concentrations then begin to increase and the coexistence of  $\text{Mn}(\text{OH})_2$  and  $\text{MnS}$  ceases. pH 10.2 and  $\log \text{H}^+ = -10.2$  correspond to line 7 in Fig. 1. The concentrations of  $\text{Mn}^{2+}$  and  $\text{MnCl}^+$  increase with the potential up to  $-100$  mV and are then constant up to  $+300$  mV, where the formation of  $\text{MnSO}_4$  makes these decrease slightly.

The formation of sulfur takes place at  $-100$  mV. At the same potential the  $\text{H}_2\text{S}$  concentration reaches a

Table II. Reaction and equilibrium formula

a	$\text{H}_2 = 2\text{H}^+ + 2e^-$ $E = 0.0 - 0.0591 \text{ pH}$
b	$2\text{H}_2\text{O} = \text{O}_2 + 4\text{H}^+ + 4e^-$ $E = 1.228 - 0.0591 \text{ pH}$
1	$\text{S} + 4\text{H}_2\text{O} = \text{SO}_4^{2-} + 8\text{H}^+ + 6e^-$ $E = 0.357 - 0.0788 \text{ pH} + 0.0098 \log \text{SO}_4^{2-}$
2	$\text{H}_2\text{S} = \text{S} + 2\text{H}^+ + 2e^-$ $E = 0.142 - 0.0591 \text{ pH} - 0.0295 \log \text{H}_2\text{S}$
3	$\text{MnS} = \text{Mn}^{2+} + \text{S} + 2e^-$ $E = -0.122 + \log \text{Mn}^{2+}$
4	$\text{MnS} + 4\text{H}_2\text{O} = \text{Mn}^{2+} + \text{SO}_4^{2-} + 8\text{H}^+ + 8e^-$ $E = 0.223 + 0.0074 \log \text{Mn}^{2+} + 0.0074 \log \text{SO}_4^{2-} - 0.0591 \text{ pH}$
5	$\text{MnS} + 6\text{H}_2\text{O} = \text{Mn}(\text{OH})_2 + \text{SO}_4^{2-} + 10\text{H}^+ + 8e^-$ $E = 0.349 + 0.0073 \log \text{SO}_4^{2-} - 0.0738 \text{ pH}$
6	$\text{MnS} + 2\text{H}^+ = \text{Mn}^{2+} + \text{H}_2\text{S}$ $\log \text{Mn}^{2+} = 8.9 - \log \text{H}_2\text{S} - 2 \text{ pH}$
7	$\text{Mn}^{2+} + 2\text{H}_2\text{O} = \text{Mn}(\text{OH})_2 + 2\text{H}^+$ $\log \text{Mn}^{2+} = 17.82 - 2 \text{ pH}$
8	$\text{MnS} = \text{Mn}^{2+} + \text{S}^{2-}$ $\log \text{Mn}^{2+} = -13.60 - \log \text{S}^{2-}$
9	$\text{Mn}_2\text{O}_3 + \text{H}_2\text{O} = 2\text{MnO}_2 + 2\text{H}^+ + 2e^-$ $E = 0.573 - 0.0591 \text{ pH}$
10	$2\text{Mn}_3\text{O}_4 + \text{H}_2\text{O} = 3\text{Mn}_2\text{O}_3 + 2\text{H}^+ + 2e^-$ $E = 0.689 - 0.059 \text{ pH}$
11	$3\text{Mn}(\text{OH})_2 = \text{Mn}_3\text{O}_4 + 2\text{H}_2\text{O} + 2\text{H}^+ + 2e^-$ $E = 0.240 - 0.059 \text{ pH}$
12	$\text{Mn}^{2+} + 2\text{H}_2\text{O} = \text{MnO}_2 + 4\text{H}^+ + 2e^-$ $E = 1.228 - 0.1182 \text{ pH} - 0.0591 \log \text{Mn}^{2+}$
13	$2\text{Mn}^{2+} + 3\text{H}_2\text{O} = \text{Mn}_2\text{O}_3 + 6\text{H}^+ + 2e^-$ $E = 1.900 - 0.1773 \text{ pH} - 0.0591 \log \text{Mn}^{2+}$
14	$3\text{Mn}^{2+} + 4\text{H}_2\text{O} = \text{Mn}_3\text{O}_4 + 8\text{H}^+ + 2e^-$ $E = 1.824 - 0.2364 \text{ pH} - 0.0886 \log \text{Mn}^{2+}$
15	$\text{HSO}_4^- = \text{SO}_4^{2-} + \text{H}^+$ $\log \text{SO}_4^{2-} = -1.91 + \text{pH} + \log \text{HSO}_4^-$
16	$\text{HS}^- + 4\text{H}_2\text{O} = \text{SO}_4^{2-} + 9\text{H}^+ + 8e^-$ $E = 0.252 - 0.0665 \text{ pH} + 0.0074 \log \text{SO}_4^{2-} - 0.0074 \log \text{HS}^-$
17	$\text{H}_2\text{S} = \text{HS}^- + \text{H}^+$ $\log \text{HS}^- = -7 + \text{pH} + \log \text{H}_2\text{S}$
18	$\text{Fe}^{2+} + 2\text{H}_2\text{O} = \text{Fe}(\text{OH})_2 + 2\text{H}^+$ $\log \text{Fe}^{2+} = 13.29 - 2 \text{ pH}$
19	$\text{Fe}^{2+} + 3\text{H}_2\text{O} = \text{Fe}(\text{OH})_3 + 3\text{H}^+ + e^-$ $E = 1.057 - 0.1773 \text{ pH} - 0.0591 \log \text{Fe}^{2+}$
20	$\text{Fe}^{2+} + 2.7\text{H}_2\text{O} + 0.3\text{Cl}^- = \text{Fe}(\text{OH})_2 \cdot \text{Cl}_{0.3} + 2.7\text{H}^+ + e^-$ $E = 0.944 + 0.0591 \log \text{Fe}^{2+} + 0.0177 \log \text{Cl}^- - 0.1595 \text{ pH}$

maximum of  $10^{-2}$  mole/liter. This potential also corresponds to the boundary between the domains for  $\text{MnS}$  and  $\text{S}$  as shown above Fig. 2 and 3. The equilibrium pH at this particular point is 5.8 as can be seen

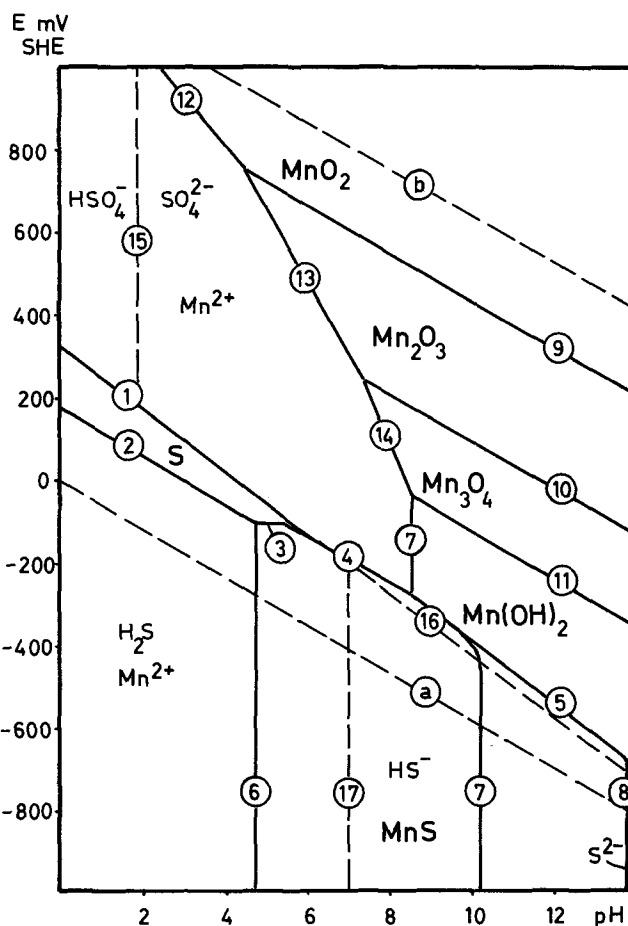


Fig. 1. Potential-pH diagram for the system  $\text{MnS-H}_2\text{O-Cl}^-$  calculated on basis of 0.1 mole/liter for  $\text{SO}_4^{2-}$ ,  $\text{Cl}^-$ , and  $\text{Mn}^{2+}$ , respectively.

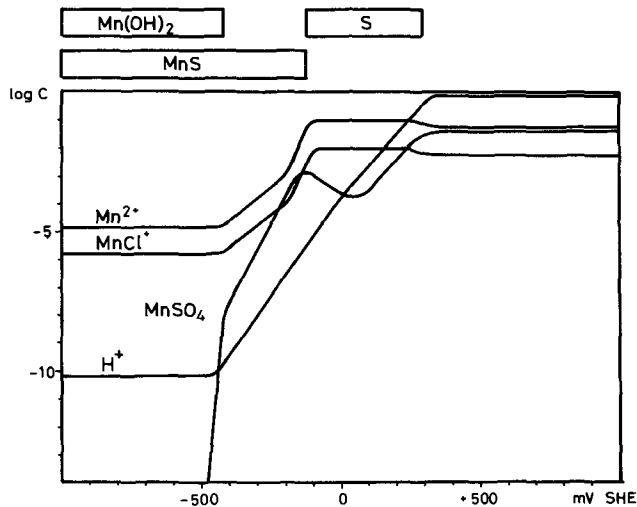


Fig. 2. Equilibrium potential-concentration diagram for the  $\text{MnS-H}_2\text{O-Cl}^-$  system at a total concentration of 0.1 mole/liter for  $\text{SO}_4^{2-}$ ,  $\text{Cl}^-$ , and  $\text{Mn}^{2+}$ . For clarity only manganese compounds are drawn. The stability ranges for the solid phases are shown over the diagram.

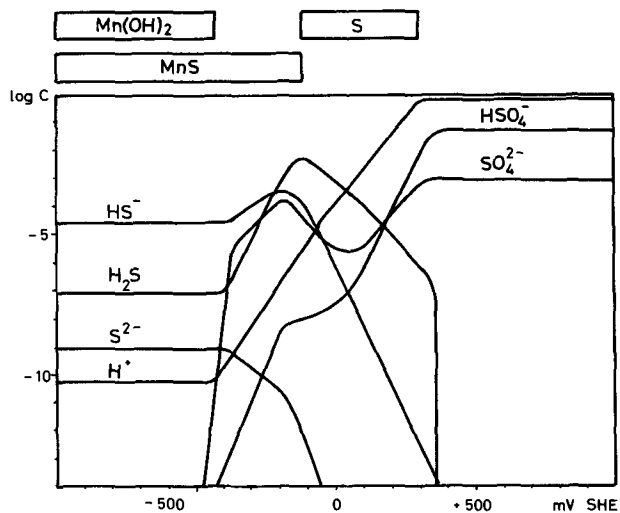


Fig. 3. Equilibrium potential-concentration diagram for the same system as in Fig. 2, only sulfur-containing complexes are shown.

from the  $\text{H}^+$  lines in the figures. At +100 mV all the sulfur containing complexes reach a minimum, which means that most of the sulfur is present in elemental form.

$(\text{Mn}_{0.9}\text{Fe}_{0.1})\text{S-H}_2\text{O-Cl}^-$ .—The thermodynamic data for the free energy of formation and the entropy of mixing of  $\text{MnS}$  and  $\text{FeS}$  available in the literature are very inconsistent. For this reason it was considered justified to add the free energies for each sulfide in their proportions. The value for  $(\text{Mn}_{0.9}\text{Fe}_{0.1})\text{S}$  thus obtained is  $-46\,200$  calories/mole. By using this value and the data listed in Table I, Fig. 4 has been calculated. The total amount of the metal ions is 0.1 mole/liter in addition to the other components.

Comparing Fig. 1 and 4, it is evident that the domain of the sulfide is smaller and that the domain of the complete solubility has been considerably reduced due to the formation of  $\text{Fe}(\text{OH})_2$ ,  $\text{Fe}(\text{OH})_3$ , and  $\text{Fe}(\text{OH})_{2.7}\text{Cl}_{0.3}$ . This latter compound has earlier been described as  $\beta\text{-FeOOH}$ , but investigations by Biedermann and Chow (16) have shown that  $\beta\text{-FeOOH}$  is in fact the hydroxy-chloride complex  $\text{Fe}(\text{OH})_{2.7}\text{Cl}_{0.3}$ .

The equilibrium pH follows, as in the aforementioned case, the lines of coexistence between sulfide and hydroxide (line 18) and at higher potentials lines 4 and 1.

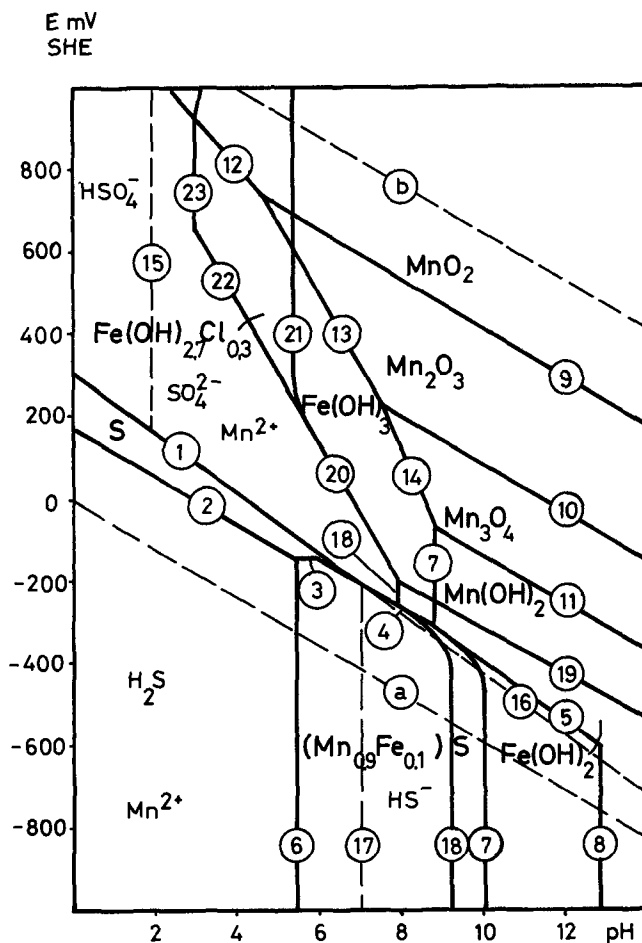


Fig. 4. Potential-pH diagram of the system  $(\text{Mn}_{0.9}\text{Fe}_{0.1})\text{S}$  calculated on the basis of 0.09 mole/liter  $\text{Mn}^{2+}$ , 0.01 mole/liter  $\text{Fe}^{2+}$ , 0.1 mole/liter  $\text{SO}_4^{2-}$ , and 0.1 mole/liter  $\text{Cl}^-$ .

$\text{Cr-H}_2\text{O-Cl}^-$ .—The manganese sulfides in stainless steel usually contain chromium to some extent. Chromium ions must therefore enter the solution when the sulfide is dissolved, and when these enter a solution containing chloride several different complex reactions can take place.

In order to find how the pH and the concentration of the complexes can vary with the potential, equilibrium calculations on the  $\text{Cr-H}_2\text{O-Cl}^-$  system at different concentrations of  $\text{Cr}^{2+}$  and  $\text{Cl}^-$  have been carried out.

Figures 5 and 6 show how the pH, the chloride, and the hydroxy complexes vary with the potential at equilibrium. The diagrams are based on a total concentration of 0.1 mole/liter of  $\text{Cr}^{2+}$  and  $\text{Cl}^-$ .

When the potential is raised, the formation of hydroxy complexes will give an increase in hydrogen ion concentration. At potentials higher than  $-400$  mV, coinciding with the equilibrium between  $\text{Cr}^{2+}$  and  $\text{Cr}^{3+}$ , the concentration of the complexes does not change with the potential.

A solution containing chromium in contact with an electrode will thus tend to a low pH at potentials higher than  $-400$  mV. The acidity of the solution is dependent on the chromium concentration as shown in Fig. 7 where the equilibrium pH has been calculated at different  $\text{Cr}^{2+}$  concentrations. The curve is only valid for potentials higher than  $-400$  mV. The concentration of the chloride ions does not influence the pH since the amount of the chloride-containing hydroxy complexes is small.

#### Discussion

Figure 1 shows the range of stability for  $\text{MnS}$ . From this it is clear that  $\text{MnS}$  cannot exist at potentials higher than  $-100$  mV, and since the potential of a

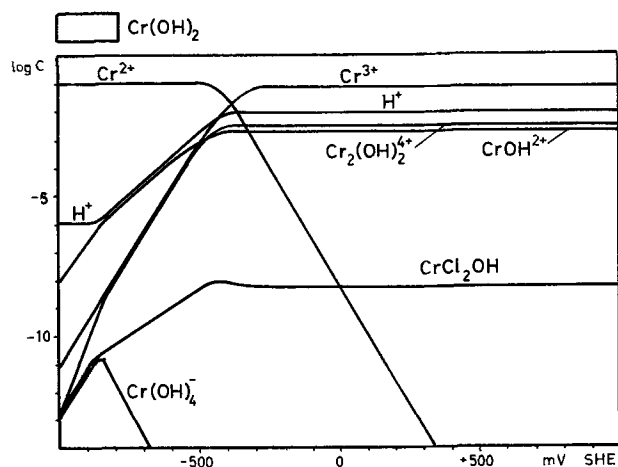


Fig. 5. Equilibrium potential-concentration diagram of the  $\text{Cr-H}_2\text{O-Cl}^-$  system at a total concentration of 0.1 mole/liter for  $\text{Cr}^{2+}$  and  $\text{Cl}^-$ . The stability range for the solid phase is shown over the diagram. Only hydroxy complexes are drawn in this diagram.

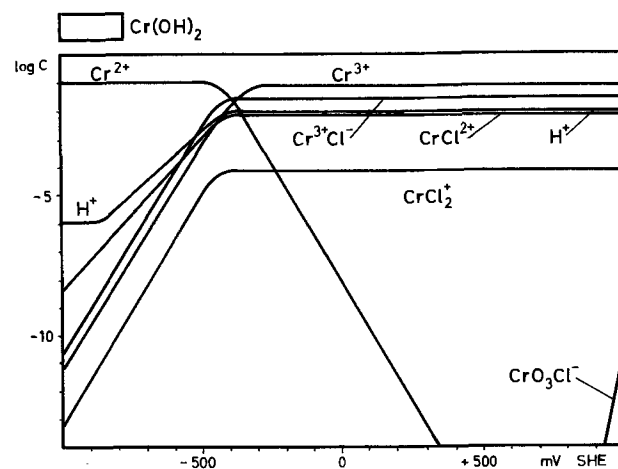


Fig. 6. Equilibrium potential-concentration diagram for the same system as in Fig. 5. Only chloride complexes are drawn.

passive stainless steel surface is considerably higher, the embedded  $\text{MnS}$  particles should tend to dissolve.

When a manganese sulfide was polarized to +200 mV in an air-free, unbuffered 0.1M NaCl solution, the sulfide dissolved and elemental sulfur in the form of small spherical particles was formed on the surface (Fig. 8). The preparation of the sulfides and the apparatus used are described elsewhere (17). The pH of the solution decreased to 5.8 after 6 days, a value corresponding to the equilibrium  $\log C_{\text{H}^+}$  at the  $\text{MnS/S}$  boundary as shown in Fig. 2 and 3. The current, of the order of 0.1 mA/cm<sup>2</sup>, was constant with time indicating that the sulfur did not form any compact layer. When the same experiment was carried out at pH 6.5, x-ray investigations of the layer showed no evidence as to the presence of any manganese compound. Addition of  $\text{BaCl}_2$  to the solution gave a precipitate of  $\text{BaSO}_4$ , which showed that some of the sulfur was oxidized to  $\text{SO}_4^{2-}$ . When the  $\text{MnS}$  electrode was polarized to +200 mV at pH 10, no elemental sulfur could be observed.

Experiments with manganese sulfide electrodes containing ca. 6% Cr and ca. 8% Fe substitutionally dissolved showed the same behavior as pure  $\text{MnS}$ . Elemental sulfur was formed on the surface when the electrodes were polarized to +200 mV in the same solution as above. The pH in the unbuffered solution changed with time and reached a value of ca. 4 for the sulfide containing Cr. It is therefore assumed that the sulfides containing Fe and Cr dissolve in a similar

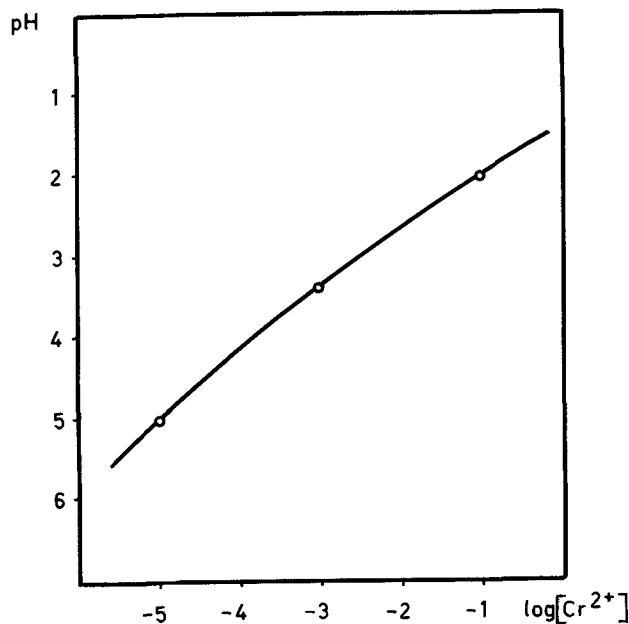


Fig. 7. pH as a function of total  $\text{Cr}^{2+}$  concentration. The  $\text{Cl}^-$  concentration at all points, 0.1 mole/liter. The diagram is only valid for potentials higher than -400 mV SHE.

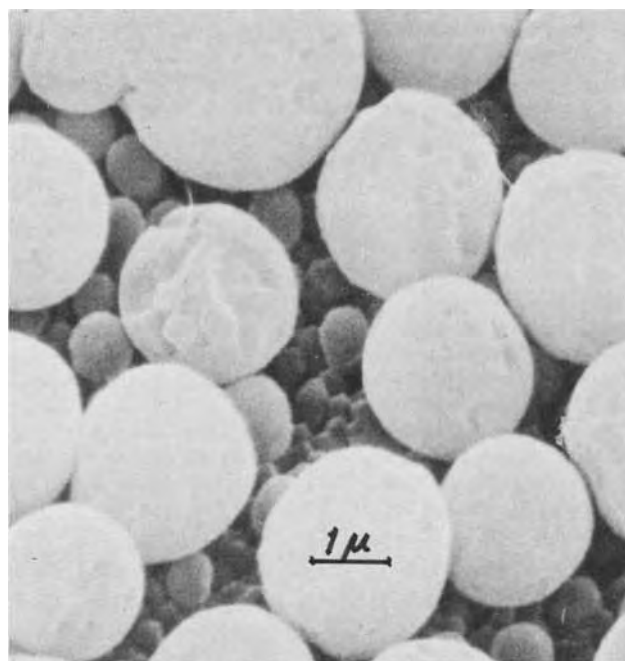
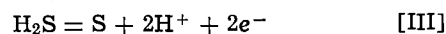
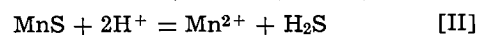
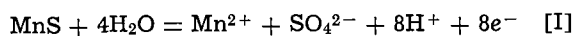


Fig. 8. Surface of  $\text{MnS}$  after polarization at +200 mV SHE in 0.1M NaCl-solution. The discreet sulfur particles suggest their formation via the solution. The size of the particles decrease somewhat with depth.

way to pure  $\text{MnS}$ . In addition, the complex reactions and hydrolysis of the metal ions released decrease the pH of the solution.

It seems unlikely that the elemental sulfur particles shown in Fig. 8 should be the result of a surface diffusion mechanism associated with the dissolution of  $\text{MnS}$  to elemental sulfur and  $\text{Mn}^{2+}$ . The form of the sulfur suggests that it is precipitated from the solution. For this reason the following mechanism is suggested for the dissolution of  $\text{MnS}$  when polarized in a positive direction in an unbuffered solution.



At the moment when the sulfide is polarized, reaction [I] takes place. Due to the oxidation of MnS to  $\text{SO}_4^{2-}$  the pH at the interface will decrease making reaction [II] possible. The hydrogen sulfide thus released will form S and sufficient hydrogen ions to continue the dissolution according to reactions [II] and [III]. The reaction takes place at the MnS interface making the electron transfer for reaction [III] possible and the sulfur layer will be built up from underneath.

Analysis of inclusions from commercial steels, mainly based on isolates, show that the sulfides are MnS with various amounts of Fe and Cr substitutionally dissolved (18, 19). The Fe and Cr substituted sulfides have a higher S content than that corresponding to the formula  $(\text{Mn,Fe,Cr})\text{S}$  (20). The sulfide lattice of these solid solutions apparently has metal vacancies, which are formed to compensate for the change in valency when Mn(II) is substituted by metals of valency III; this makes the sulfides p-type semiconductors. Investigations of the solubility of the transition metals in MnS have shown that it is possible to substitute as much as 60-70 weight per cent (w/o) Cr and Fe in the  $\alpha$ -MnS lattice (18). In a commercial 18-8 steel the composition of the sulfides can vary from one inclusion to another but the manganese sulfides usually contain from 10 to 40 w/o substitutionally dissolved Cr and Fe, the exact amounts depending on the way the steel is produced, heat-treated etc.

In this connection, it can be mentioned that the metal at the interface between the sulfides and the matrix cannot have any oxide layer since the sulfides are formed directly from the melt. A dissolution of a sulfide will therefore reveal a virgin metal surface.

As mentioned in the introduction, pitting on a stainless steel surface starts preferentially at sulfide inclusions. When such a steel is subject to a potentiostatic pitting corrosion test only a few pits will develop per unit area despite the fact that the number of sulfide inclusions on the same area is several orders of magnitude greater. The number of pits will increase with the applied potential as the latter is increased from the critical potential. This is probably due to the different chemical behavior of the sulfides because of compositional differences. The higher the potential, the more sulfide inclusions will become active.

The corrosion process within a pit is a unique type of anodic reaction and produces conditions which are both stimulating to, and indeed necessary for, continuing activity of the pit. In the pit itself there is a high concentration of metal and chloride ions and as a result of hydrolysis, a high concentration of hydrogen ions. The question is how a low pH is created.

The exposed surface of the inclusions is small compared with the surface of the passive steel. When a piece of steel is submerged in a solution the potential against the solution changes to a rather noble value, usually above 250 mV in a neutral aerated sodium chloride solution. As the inclusions are electronic conductors to some extent they will be polarized towards the potential of the steel surface. Thus the sulfides are polarized to a potential at which they cannot exist thermodynamically.

Since the electronic conductivity of the sulfides is lower than for the metal matrix, the dissolution takes place preferentially at the boundary between the sulfide and the matrix and for this reason a small crevice will develop (Fig. 9). This crevice has two walls, one consisting of the sulfide and the other of the metal matrix. In the beginning, the metal matrix will immediately passivate, but as the reaction proceeds, the dissolution of the sulfide in the crevice will increase the metal ion content and ion complexing and hydrolysis reactions can take place in the microarea. On the metal wall the dissolved ions, e.g., iron, can form  $\text{Fe}(\text{OH})_2 \cdot 7\text{Cl}_{0.3}$ , as shown earlier, thus lowering the pH locally. Furthermore, the chromium ions can undergo

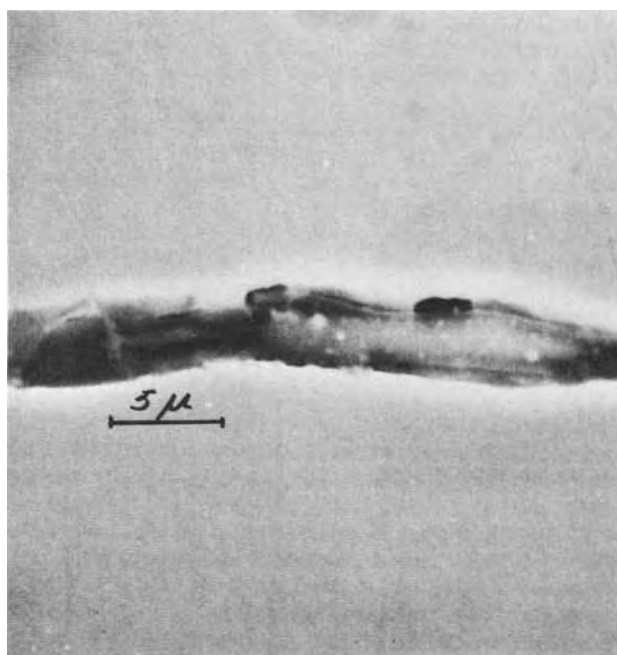


Fig. 9. 18-8 steel with 2.5 Mo containing 0.28 S galvanostatically corroded at  $0.1 \text{ mA/cm}^2$ .  $800 \text{ mAs/cm}^2$  has passed the sample. The dissolution of the sulfide has preferably taken place close to the metal matrix.

hydrolysis and contribute to the formation of hydrogen ions; the higher the chromium content the lower the pH as shown in Fig. 7. When the pH decreases in this local region the passivation of the exposed metal will be difficult. At a certain moment metal atoms from the metal lattice will enter the solution and the potential will drop drastically and the pit turn active (21, 22). The electrochemical dissolution of the sulfide will then stop since the potential is now within the domain of thermodynamic stability. If the rate of formation of hydrogen ions from the increased metal ion hydrolysis exceeds that of the chemical dissolution reaction of the sulfide itself, a sustaining pit will develop, otherwise the hydrogen ions will be neutralized by the formation of  $\text{H}_2\text{S}$  and the bared metal will passivate. This reaction probably takes place at a number of sites on the metal surface. These pitting attempts can be observed as potential drops when a steel is left to corrode freely and the potential is followed with time (Fig. 10).

This means that initiation of pitting is a kinetic problem in which the formation and neutralization of hydrogen ions are of importance. If attack occurs at the wall between the metal and the sulfide, the pit can continue to propagate as long as the solution is

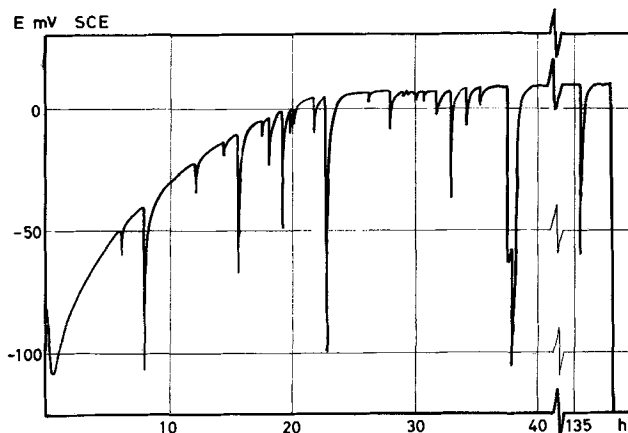


Fig. 10. Potential-time relation for an 18-8, 0.25 S stainless steel corroding freely in  $0.1\text{M NaCl}$  solution.

not diluted or neutralized, which means that certain geometrical conditions must be fulfilled; here the presence of oxide particles in the sulfides can be significant.

Figure 11 shows a pit developed at the boundary between a sulfide particle and the matrix; the sulfide is partly dissolved and some sulfur particles can be observed on the surface. The pits spread from these points and propagate under the metal surface. In certain places, the attack will reach the surface giving

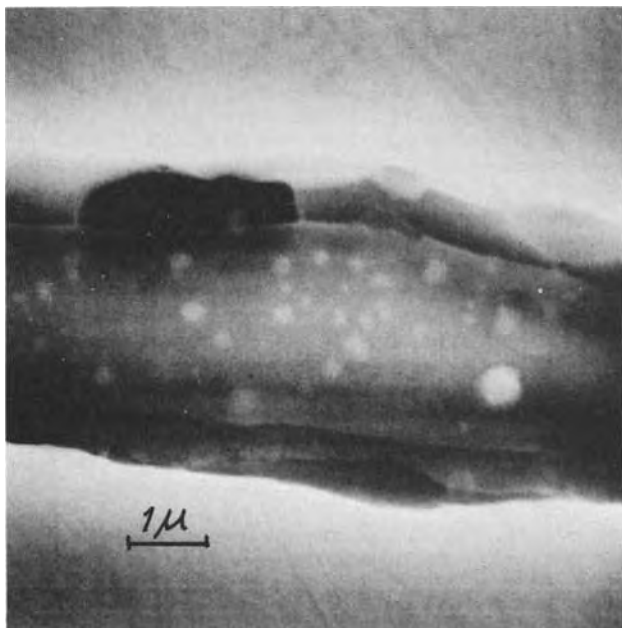


Fig. 11. Same steel and inclusion as in Fig. 9. Notice the beginning of a pit (dark area) at the metal wall in the ditch between the sulfide and the metal matrix. Elemental sulfur particles are visible on the sulfide surface.

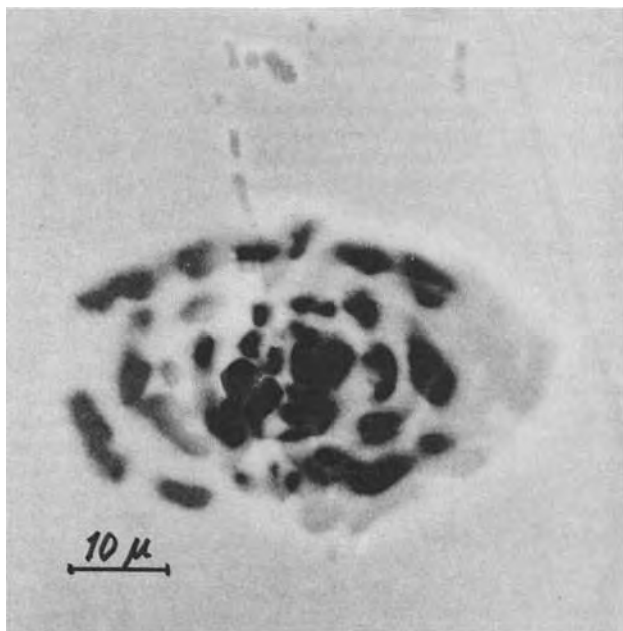


Fig. 12. Same steel as in Fig. 9 corroded at 1 mA/cm<sup>2</sup>. 800 mAs/cm<sup>2</sup> has passed the sample. The corrosion pit has started at the sulfide inclusion. The metal is dissolved from underneath and the passive layer still remains at some places as light gray parts of the lacelike pattern.

rise to an irregular network (Fig. 12). The passive layer usually remains intact but probably breaks down mechanically when the size of the subsurface pit becomes too great. The solid parts of the lacelike lattice are metal covered by the passive layer (23, 13).

The pitting or critical potential should then refer to the potential at which the metal oxide and the solution within the microarea are in equilibrium. Since the composition of the solution in the microarea will depend on the original composition of the sulfide inclusion, the critical potential will be dependent on factors influencing the composition of the sulfides.

It must, however, be remembered that the proposed mechanism is not limited to sulfides only, but can also be applied to other inclusions provided they are capable of being polarized and releasing metal ions.

#### LIST OF SYMBOLS

$p_e$	negative logarithm of the electron activity
$E$	potential vs. SHE
$F$	Faraday's constant
$R$	gas constant
$T$	temperature, °K
$\Delta G^\circ_f$	standard free energy of formation
$\log K$	equilibrium constant
$f$	activity factor

Manuscript submitted May 17, 1973; revised manuscript received Nov. 1, 1973.

Any discussion of this paper will appear in a Discussion Section to be published in the December 1974 JOURNAL. All discussions for the December 1974 Discussion Section should be submitted by Aug. 1, 1974.

#### REFERENCES

- N. D. Greene and M. G. Fontana, *Corrosion*, **15**, 25t (1959).
- T. P. Hoar, *Corrosion Sci.*, **7**, 341 (1967).
- M. A. Streicher, *This Journal*, **103**, 375 (1956).
- T. P. Hoar, D. C. Mears, and G. P. Rothwell, *Corrosion Sci.*, **5**, 279 (1965).
- T. P. Hoar and W. R. Jacob, *Nature*, **216**, 1299 (1967).
- T. N. Rodin, *Corrosion*, **12**, 123t (1956).
- C. Leygraf, S. Ekelund, and G. Schön, *Scand. J. Metallurgy*, **2**, 313 (1973).
- C. T. H. Stoddart and E. D. Hondros, *Nature Phys. Sci.*, **237**, 90 (1972).
- D. A. Vermilyea, *This Journal*, **118**, 529 (1971).
- H. H. Uhlig, *Trans. Am. Inst. Min. Met. Engrs.*, **140**, 411 (1940).
- B. E. Wilde and J. S. Armijo, *Corrosion*, **208**, 208 (1967).
- Z. Szklarska-Smialowska, A. Szummer, and M. Janik-Czachor, *Brit. Corrosion Sci.*, **5**, 159 (1970).
- G. Eklund, *Jernkontorets Ann.*, **155**, 637 (1971).
- N. Ingri, W. Kakolowicz, L. G. Sillén, and B. Warnqvist, *Talanta*, **14**, 1261 (1967).
- O. Kubaschewsky and J. A. Catterall, "Thermochemical Data of Alloys," Pergamon Press, New York (1956).
- G. Biedermann and J. T. Chow, *Acta Chem. Scand.*, **20**, 1376 (1966).
- G. Eklund, *Scand. J. Metallurgy*, **1**, 301 (1972).
- K. Sano and M. Inoye, *J. Iron Steel Inst. (Japan)*, **45**, 9 (1959).
- I. S. Brammar and R. W. K. Honeycombe, *J. Iron Steel Inst.*, **202**, 335 (1964).
- R. Kiessling and N. Lange, *ibid.*, **202**, 761 (1963).
- L. Rosenfeld and S. Danilow, *Corrosion Sci.*, **7**, 129 (1967).
- H. Pickering and D. Frankenthal, *This Journal*, **119**, 1297 (1972).
- H. Pickering and D. Frankenthal, *ibid.*, **119**, 1305 (1972).
- L. G. Sillén and A. E. Martell, Special Publication 17, The Chemical Society, London (1964).
- L. G. Sillén and A. E. Martell, Special Publication 25, The Chemical Society, London (1971).
- M. Pourbaix, "Atlas of Electrochemical Equilibria in Aqueous Solutions," Pergamon Press, London (1966).

# Optical and Electrochemical Studies of Underpotential Deposition of Lead on Gold Evaporated and Single-Crystal Electrodes

Radoslav Adzic,<sup>1</sup> Ernest Yeager,\* and B. D. Cahan\*

Chemistry Department, Case Western Reserve University, Cleveland, Ohio 44106

## ABSTRACT

Linear sweep voltammetry and reflectance spectroscopy have been used to examine the underpotential deposition of lead on gold in  $Pb^{2+}$  containing  $HClO_4$  solutions. The voltammetry curves and reflectance-change data provide evidence that the lead is first deposited as ions although their effective ionic charge is probably reduced substantially from +2 through their strong interaction with the band structure of the gold substrate. At more cathodic potentials, still well below the reversible potential of bulk lead, a sharp transition is observed over a 5-10 mV range. On the basis of the reflectance and voltammetry data, this transition appears to involve a two-dimensional phase transition leading to a metalliclike lead layer. Adsorption isotherms have been evaluated from the reflectance changes. Alternating potential electro-modulation techniques and complex plane analysis have been used to examine the kinetics of the lead adsorption-desorption and to evaluate the apparent exchange current density for the process.

The underpotential deposition (UPD) of various metals on foreign metal substrates involves monolayer or submonolayer formation at potentials anodic to that for the reversible electrodeposition of the bulk metal. UPD is particularly important to the understanding of the early stages of metal electrodeposition and also electrocatalysis. This phenomenon has received the attention of a number of electrochemists (1-11). Early work has been reviewed by Rogers (3).

UPD is clearly the result of a strong interaction between the monolayer and the substrate. Breiter (5) and also Tindal and Bruckenstein (6) have found large differences between the first and subsequent layers of copper on platinum. Schultze (10) has concluded that the copper in monolayer or submonolayer amounts on platinum is only partially discharged. Schmidt and Gyax (4), however, believe that UPD involves the formation of a metallic monolayer of electrically neutral atoms. The Mossbauer spectroscopic data of Bowles and Cranshaw (8), obtained *in situ*, indicates that tin is in the metallic state on platinum, although this finding is not necessarily applicable to the UPD of other metals on other substrates. Astley *et al.* (9) have expressed the view that the UPD is not just an adsorption process but may involve the formation of a crystalline phase.

Despite the rather extensive electrochemical studies already reported in the literature on UPD, many questions still remain to be answered, *i.e.*, What are the state of charge and the nature of the interactions among the species within the layer and between the species of the layer and the substrate metal and electrolyte phase? How are these interactions influenced by electrode potential? Is there ordering within the layer? What is the origin of the multiple peaks observed in linear sweep voltammetry in the potential regime corresponding to UPD?

Substantial information is available concerning these questions in the instance of foreign layers at metal-vacuum interfaces. For example, field emission studies (12, 13) have helped to identify the nature of the electronic interactions involved with alkali and

alkali earth metals adsorbed on tungsten. A quantum mechanical picture of the valency orbitals of the adsorbate with the conduction and valence bands of the substrate metal has been developed [see, for example, Ref. (14)]. LEED studies of such monolayers have often shown ordering in such systems [see, for example, Ref. (15)]. Unfortunately these findings are not transferable to the corresponding electrochemical interfaces since solvent interactions with the monolayer are usually strong and are expected to modify substantially the interactions of the monolayer with the foreign metal substrate.

Ordinary electrochemical techniques are able only to provide very limited atomic level information concerning UPD and consequently use has been made of *in situ* specular reflectance spectroscopy in the present work. During a linear potential sweep, specular reflectance measurements allow changes of the electronic properties of the adsorbed layer to be followed continuously with increasing coverage, from submonolayer to monolayer and multilayer amounts of foreign metal. Prior studies (16, 17) have already shown that UPD of various metals on gold causes a pronounced change of reflectance with an interesting wavelength dependence.

In the present investigation specular reflectance spectroscopy together with linear sweep voltammetry have been used to study the UPD of lead on evaporated gold electrodes. Some voltammetry experiments have also been performed with single-crystal gold electrodes. A-C electromodulation reflectance measurements and complex plane analysis (18) have been used to check on the extent to which kinetic *vs.* diffusion control are involved and to evaluate the coverage with lead. Some complementary *non-in situ* information concerning the lead layers on gold also has been obtained from x-ray photoelectron spectroscopy (ESCA).

## Experimental

The specular reflectance measurements have been carried out with the optical system<sup>2</sup> shown in Fig. 1. The electrochemical cell was constructed from an optically ground Pyrex cylinder<sup>3</sup> of 5 cm ID. The light source was a tungsten-halogen 150W lamp, operated with a Power Mate Corporation regulated power sup-

\* Electrochemical Society Active Member.

<sup>1</sup> Present address: Institute for Chemistry, Technology and Metallurgy, Belgrade, Yugoslavia.

Key words: underpotential deposition, reflectance spectroscopy, lead deposition, adsorption isotherms.

<sup>2</sup> This optical system was designed by J. Horkans and B. Cahan.

<sup>3</sup> The internal and external grinding of this cylinder was carried out by Potts Optics, Tulsa, Oklahoma.



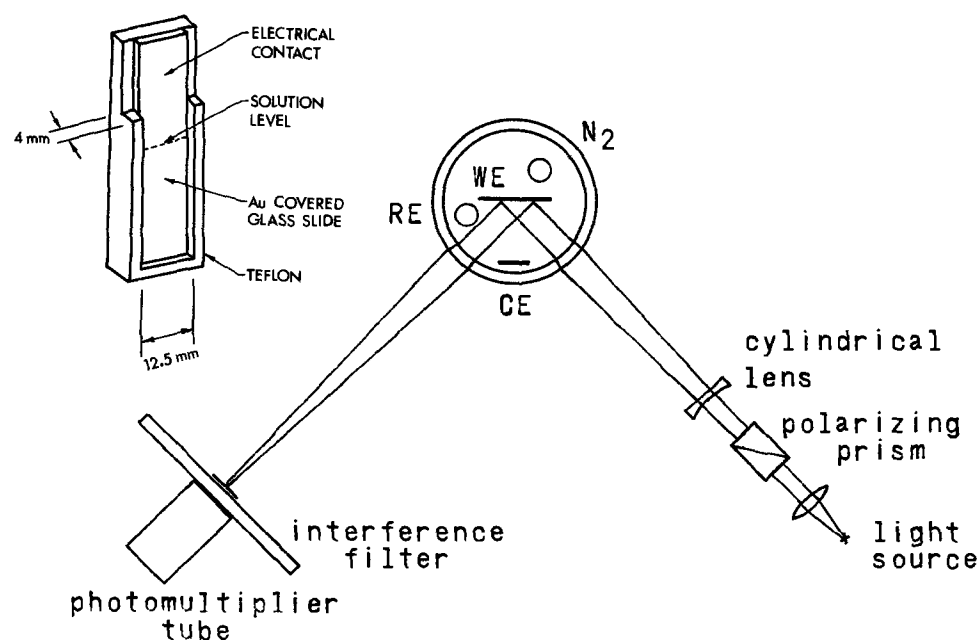


Fig. 1. Optical electrochemical cell with associated optics. Inset: evaporated gold electrode mount for a-c electromodulation reflectance measurements.

ply. All measurements herein reported were carried out at an angle of incidence of  $45^\circ$  with the light polarized parallel to the plane of incidence with a Nicol prism. A cylindrical concave lens together with the cylindrical wall of the optical-electrochemical cell collimated the light incident on the electrode. Wavelengths in the visible were selected through the use of a linear second-order interference wedge with a half-band width of 12 nm. The whole system was mounted on a  $\theta$ - $2\theta$  goniometer.

For some experiments the d-c signal from a Hamamatsu R-374 photomultiplier was amplified and then directly recorded on an X-Y recorder during the linear sweep of the electrode potential with a Wenking potentiostat. In the a-c electromodulation reflectance measurements, the electrode potential was modulated with a sinusoidal potential of 20-30 mV p-p, in some instances superimposed on a linear sweep (typically 20 mV/sec), using an IR drop compensated potentiostat.<sup>4</sup> Both the in- and out-of-phase components of the signal from the photomultiplier were measured with a PAR-129A lock-in amplifier together with an X-Y recorder.

These studies have been carried out in 1M HClO<sub>4</sub> containing  $10^{-6}$  to  $10^{-2}$ M Pb<sup>2+</sup>. The solutions were prepared from Baker reagent grade HClO<sub>4</sub> and triply distilled water with the first distillation from alkaline permanganate. The lead salt was Johnson-Matthey spectrographic standard Pb(NO<sub>3</sub>)<sub>2</sub>. In some experiments the HClO<sub>4</sub> was pre-electrolyzed by circulating it for 24 hr over  $8 \times 8$  cm, 52 mesh gold gauze electrodes, wrapped on a glass rod and fitted within a glass tube. The applied voltage across the gold electrodes was 1.1-1.3V. At 1.3V some dissolution of gold at the anode and deposition of gold black at the cathode were observed but no detrimental effects on the subsequent measurements of lead UPD were detected.

The evaporated gold electrodes were prepared by vapor-depositing gold to a thickness of  $0.5$ - $1\mu$  in a vacuum evaporator on a glass slide with an undercoating of Nb, which provides good adhesion and has no detrimental electrochemical or optical effects (19). This glass slide electrode (WE) was mounted at the center of the cell with an area of  $6.3$  cm<sup>2</sup> in contact with the electrolyte (without any mask) for the linear sweep voltammetry measurements and simultaneous reflectance measurements. For the a-c electromodulation reflectance measurements, four successive gold evaporations were used to obtain gold films of  $2$ - $4\mu$ , so

as to reduce IR drop in the films. The gold-coated glass slides were fitted into the Teflon mask, shown in Fig. 1, to obtain more uniform current distribution. The area in contact with electrolyte was  $\sim 3$  cm<sup>2</sup>.

Single-crystal gold electrodes with (111), (110), and (100) orientations, and polycrystalline bulk gold electrodes, were pressure-fitted into Teflon rods and polished mechanically to obtain a mirror finish. The final polishing was performed electrolytically in a cyanide solution to remove the cold-worked surface layer. After polishing, the electrodes were washed with KOH and HNO<sub>3</sub> solutions and stored in triply distilled water. The gold electrodes used in the ESCA experiments were bulk gold plates, which were mechanically polished and then treated in the same way as the single-crystal electrodes but not electrochemically polished.

The counterelectrode (CE) in the electrochemical measurements was a hydrogen-saturated palladium plate, mounted parallel to the working electrode at a distance of 2 cm, just outside the optical path. The reference electrode (RE) was an  $\alpha$ -PdH bead of 1 mm diameter mounted on the end of a fine glass tube with the center of the bead located typically at a distance of 1.0 mm from the working electrode.

Nitrogen gas, purified by passing it over treated copper turnings and then through molecular sieves (Linde 4A and 13X), was bubbled through the solution before measurements to remove dissolved O<sub>2</sub>, and a N<sub>2</sub> atmosphere was maintained above the solution during the measurements. All measurements were carried out at room temperatures ( $22^\circ$ - $23^\circ$ C).

Before measurements, the potential of the gold electrode was cycled several times up to 1.6V re RHE.<sup>5</sup> This procedure substantially improved the reproducibility of the measurements, probably through the redistribution of gold on the surface to form a reproducible surface microtopography and also perhaps the removal of adsorbed organic impurities.

## Results

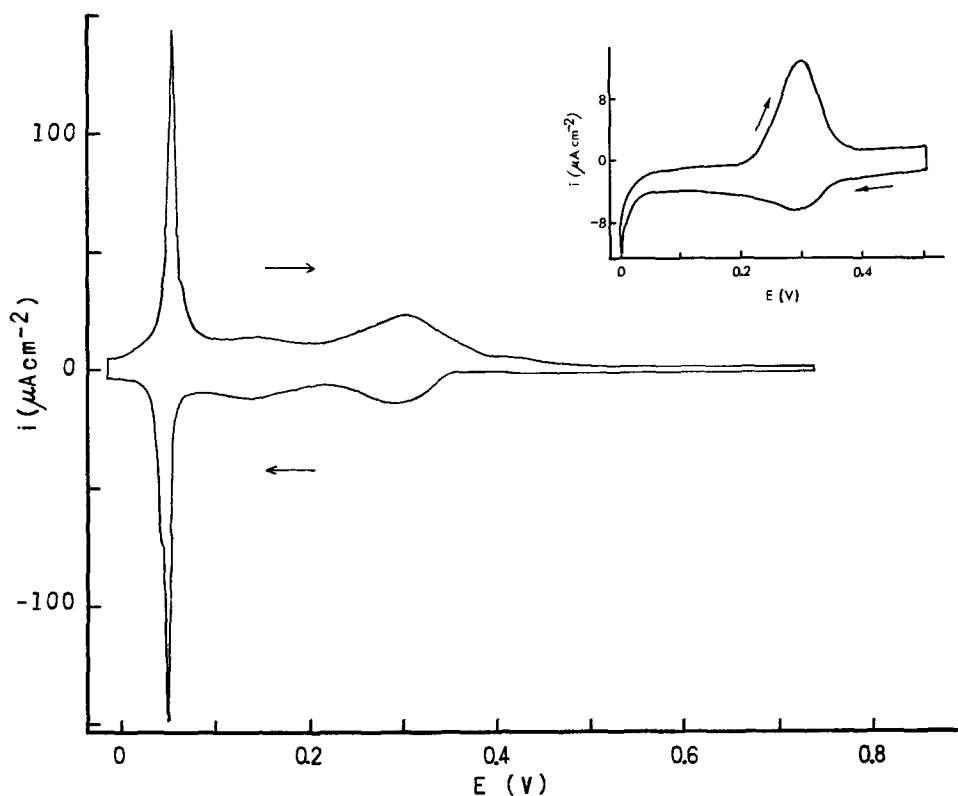
**Linear sweep voltammetry.**—The linear sweep voltammetry curve (Fig. 2) for evaporated gold with  $1 \cdot 10^{-3}$ M Pb<sup>2+</sup> indicates two principal peaks, the first at  $\sim 0.30$ V and the second at  $\sim 0.05$ V. The first peak is predominantly under diffusion control for Pb<sup>2+</sup> concentrations of up to  $10^{-3}$ M at a sweep rate of 20 mV/sec. This peak is more drawn out and more rounded than expected for adsorption under Langmuir behavior. At lower concentrations of Pb<sup>2+</sup>, the anodic and cath-

<sup>5</sup> Unless otherwise indicated, all potentials are stated relative to a reversible hydrogen electrode in the same solution.

<sup>4</sup> Specially designed by B. D. Cahan.



Fig. 2. Voltammetry curve for the UPD of lead on evaporated gold in 1 mM  $\text{Pb}(\text{NO}_3)_2$  + 1M  $\text{HClO}_4$ . Sweep rate, 20 mV/sec. Insert: behavior in  $1 \times 10^{-5}\text{M}$   $\text{Pb}^{2+}$ .



odic peaks differ in height and shape, as is to be expected as diffusion control becomes more predominant (see insert in Fig. 2).

The second peak observed with  $10^{-3}\text{M}$   $\text{Pb}^{2+}$  is extraordinarily narrow for the gold electrode shown in Fig. 2, with a half-width of  $\sim 10$  mV and a peak separation between anodic and cathodic sweeps of  $\sim 5$  mV. The narrowness of this peak indicates that it is not an adsorption-desorption peak despite the substantial charge ( $70\text{--}90 \mu\text{Coulombs/cm}^2$ ) associated with it. A surface transformation appears to be involved, which is not dependent on the transport of further  $\text{Pb}^{2+}$  ions to the electrode surface. The finite peak width and separation are probably caused almost entirely by surface heterogeneity and nonuniform current distribution.

Close examination of the anodic sweep in Fig. 2 indicates that the second peak may actually consist of two peaks and further work is required to establish this fine structure with certainty.

The width and general shape of the second voltammetry peak are very sensitive to electrode pretreatment as well as potential sweep range, as is evident from a comparison of Fig. 2 and 3. The greater peak width in Fig. 3 probably results from more surface heterogeneity. The potential and shape of the second peak are rather insensitive to sweep rate for 5-100 mV/sec at a  $\text{Pb}^{2+}$  concentration of 1 mM. As the  $\text{Pb}^{2+}$  concentration is decreased, the peak height decreases but the effective width and anodic-cathodic sweep peak separation are relatively insensitive to  $\text{Pb}^{2+}$  concentration for  $C_{\text{Pb}^{2+}} \geq 10^{-4}\text{M}$ . At concentrations below  $10^{-4}\text{M}$   $\text{Pb}^{2+}$ , the second peak completely disappears for a sweep rate of 20 mV/sec (see insert in Fig. 2).

The voltammetry curves in Fig. 3 also indicate further minor peaks at 0.13 and  $-0.08\text{V}$ . The voltammetry curves for polycrystalline gold are similar to those shown in Fig. 3. A large change in reflectivity is observed at  $\sim -0.22\text{V}$  where the deposition of mossy or dendritic lead occurs. The total surface charge is only  $\sim 300 \mu\text{Coulombs/cm}^2$  (apparent area) corresponding to less than a monolayer of lead atoms when this three-dimensional crystal growth commences.

The voltammetry curves on the (100), (110), and (111) faces of single-crystal gold (Fig. 4) are quite

distinctive. The first voltammetry peak is evident at  $\sim 0.3\text{V}$  for each orientation but its relative height and shape are highly dependent on the orientation. An additional very pronounced peak is evident for the (111) orientation although its potential is approximately 25 mV more cathodic than that of the second peak for the evaporated gold electrodes (Fig. 2 and 3) or for ordinary polycrystalline gold. A peak is observed for the (110) orientation at the same potential as for the (111) but is far less pronounced. The base current also is larger and not as well defined for these voltammetry curves as for the evaporated gold. Clavilier *et al.* (20) have noted a similar effect in their studies of single-crystal gold and have attributed it to a layer of electrolyte between the Teflon holder and the gold crystal.

While the over-all surface orientation of the single-crystal electrodes is known, information is lacking as to the microstructure of the surface. The cycling of the electrode potential several times up to 1.6V prior to

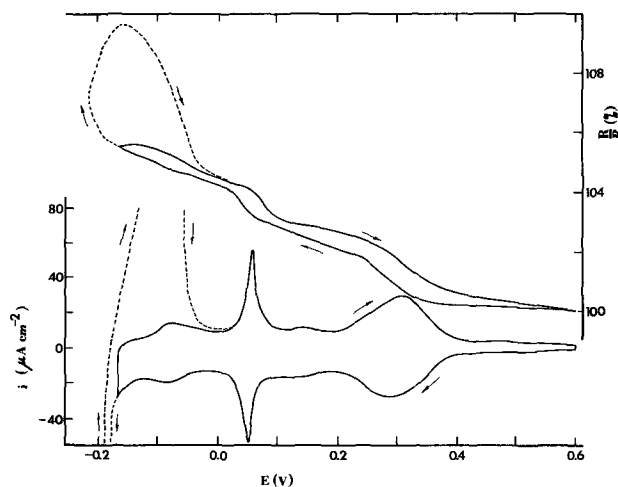


Fig. 3. Voltammetry and specular reflectance curves for UPD of lead on evaporated gold in 1 mM  $\text{Pb}(\text{NO}_3)_{1/2}$  + 1M  $\text{HClO}_4$ . Sweep rate, 20 mV/sec; wavelength, 431 nm. Differences between Fig. 2 and this figure are due to differences in potential sweep range and minor variations in pretreatment.

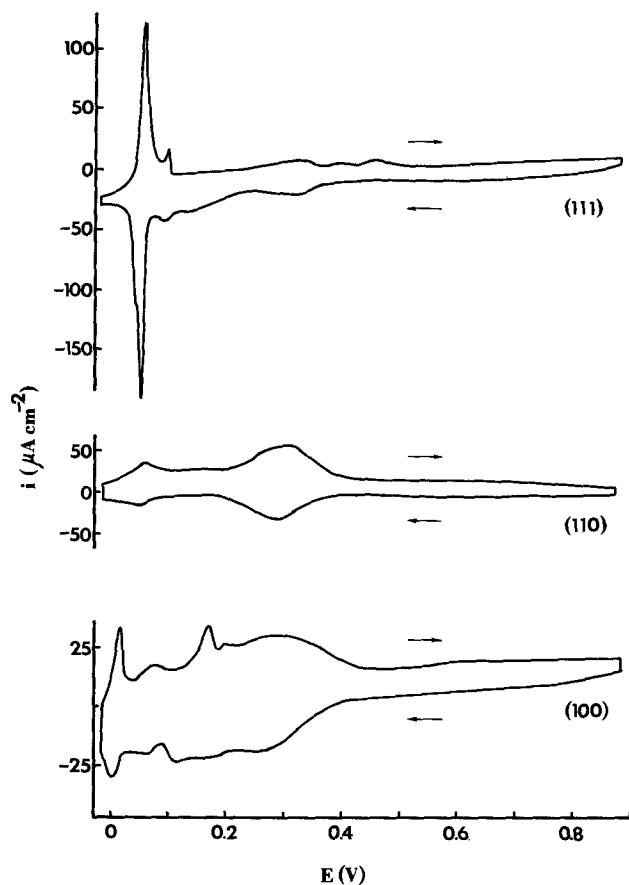


Fig. 4. Voltammetry curves for single-crystal gold electrodes with (100), (110), and (111) orientations in 1 mM  $\text{Pb}(\text{NO}_3)_2$  + 1M  $\text{HClO}_4$ . Sweep rate, 20 mV/sec.

recording the voltammetry curves probably modified the micro-orientation of the single-crystal surfaces. The microsurface structures of the single-crystal gold electrodes probably involved several orientations and hence the relative complex peak structure is not surprising, particularly for the (100) orientation. On the basis of the voltammetry curves, however, it appears that the surface of the evaporated gold electrode used for Fig. 2 was at least as homogeneous as that of either the (111) or (110) orientations of the gold single crystals and much more homogeneous than that of the (100) orientation.

The charge density *vs.* potential curves for the UPD of lead on evaporated and single-crystal gold (Fig. 5) have been calculated by integrating the voltammetry

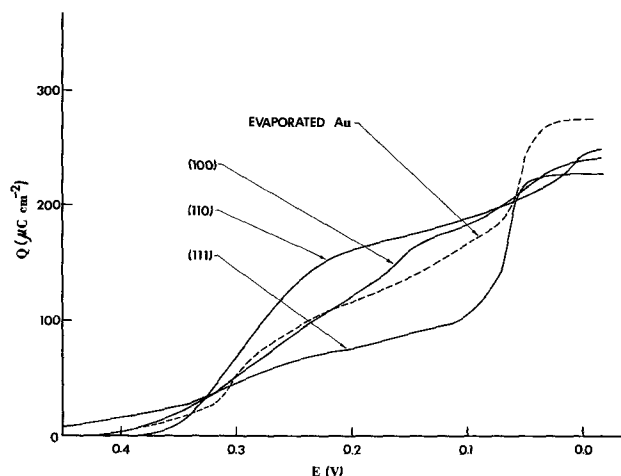


Fig. 5. Charge density *vs.* potential curves for the UPD of lead, obtained from the voltammetry curves in Fig. 2 and 4.

curves as a function of potential, and then subtracting the charge obtained from the voltammetry curves for gold in the absence of lead. This procedure involves the dubious assumptions that the charge associated with the formation of the lead layer and ordinary double-layer charging can be separated, and that the double-layer charging of the gold and lead-covered gold surfaces are the same. It is difficult, however, to avoid this or some equally dubious assumption in calculating the charge density associated with the formation of the lead layer. In any event the implications of the charge density-potential curves are not affected by this assumption since the charge associated with the formation of the lead layer is large compared to the ordinary double-layer charge. All three of the single-crystal surfaces approach 225-250  $\mu\text{C}/\text{cm}^2$  (apparent area) at 0.00V. A slightly higher value of  $\sim 275 \mu\text{C}/\text{cm}^2$  is approached at this potential for the evaporated gold surface but this may reflect differences in the ratio of true-to-apparent area. Each of the charge-potential curves are otherwise quite distinctive indicating differences in these surfaces and the UPD on them. For the (110) orientation, the majority of the charge is associated with the first peak, whereas for the (111) orientation much of the charging occurs at more cathodic potentials.

*Specular reflectance.*—The specular reflectance measurements on evaporated gold electrodes indicate that the voltammetry peaks are attended by large changes in the reflectance (Fig. 6). For the measurements reported in this figure, the reflectance has been normalized to unity at 0.5V for each wavelength. The hysteresis is, for the most part, the result of the response time ( $\sim 1$  sec) of the filter used to suppress noise in the recording system. The changes in reflectance are particularly pronounced at  $\sim 0.05\text{V}$  where the second peak in the voltammetry curve occurs, indicating that a very large change in the optical properties of the layer occurs, most likely as a result of a change in the elec-

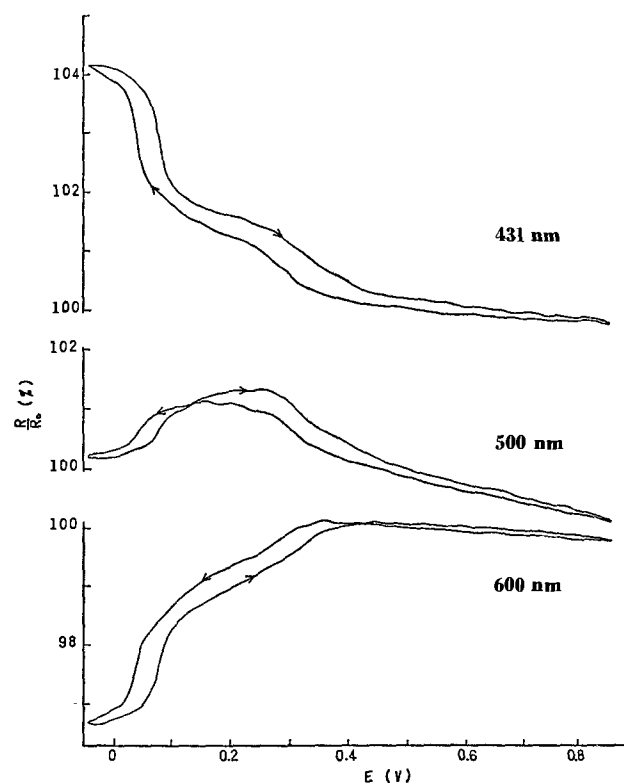


Fig. 6. Reflectance *vs.* potential curves for UPD of lead in evaporated gold at three wavelengths. Conditions the same as for Fig. 3.

tronic properties of the surface lead layer and its interaction with the gold substrate and solvent molecules.

Figure 6 indicates that the reflectance changes attending the UPD are highly wavelength dependent. The wavelength dependence of the relative reflectance changes are given in Fig. 7 for various  $Pb^{2+}$  ion concentrations in 0.2M  $HClO_4$  at a potential of 0.33V, which corresponds to the first voltammetry peak in this electrolyte. The values on the ordinate correspond to the difference in the reflectance of the polished bulk gold electrode at 0.33V in the  $Pb^{2+}$  containing solutions normalized at 0.5V, and the corresponding value for this electrode in a lead-free solution, also normalized to 0.5V. The various  $Pb^{2+}$  ion concentrations correspond to different surface coverages with lead, as will be evident from a consideration of the adsorption isotherms discussed below. Similar results have been obtained with evaporated gold. The reflectance spectrum of the lead layer on the gold is strongly influenced by the absorption edge of gold at  $\sim 500$  nm. The reflectance increases with the formation of the lead partial monolayer at wavelengths below the absorption edge of gold and decreases at longer wavelengths. This effect, however, is quite potential dependent (see the 500 nm curve in Fig. 6).

All the curves in Fig. 7 have a nearly common intersection at  $\sim 510$  nm. This behavior is rather analogous to the isobestic point encountered in absorption spectroscopy when the sum of the concentrations of two forms of an absorbing species is constant. The analogous situation for the reflectance spectra are the occupied and unoccupied surface sites, the sum of which is a constant. Apparently at 0.15V the contribution to the reflectance from occupied and unoccupied sites is the same at  $\lambda \cong 510$  nm.

The dependence of the normalized reflectance change on charge density is shown for three wavelengths for

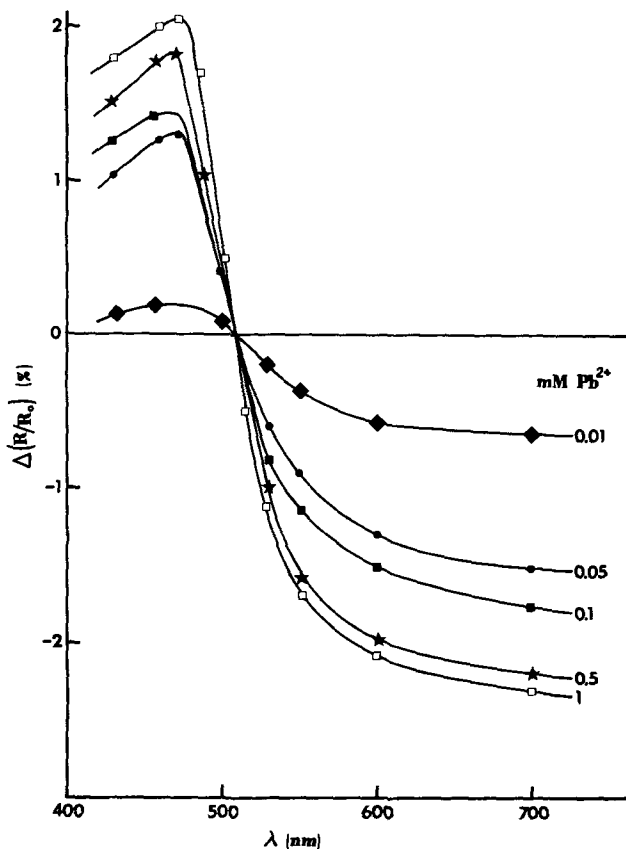


Fig. 7. Wavelength dependence of normalized reflectance change for the UPD of lead on polished bulk gold for various  $Pb(NO_3)_2$  concentrations in 0.2M  $HClO_4$  at 0.33V. Data evaluated from reflectance vs. potential curves obtained with sweep rate of 20 mV/sec.

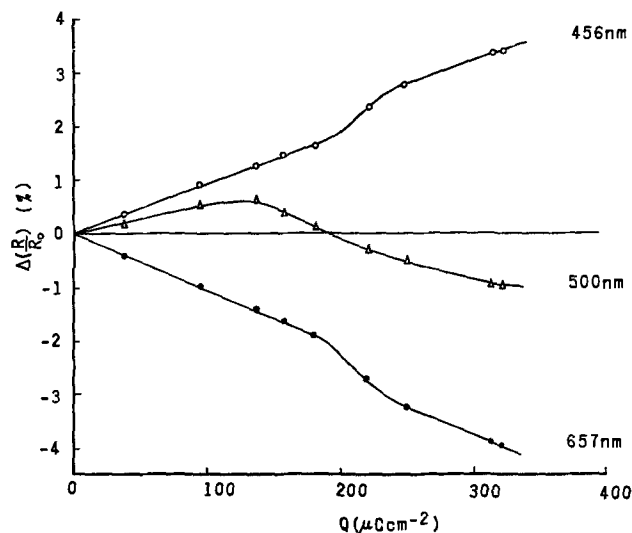


Fig. 8. Normalized change in reflectance vs. charge density for the UPD of lead on evaporated gold in 1 mM  $Pb(NO_3)_2$  + 1M  $HClO_4$ . Charge density evaluated as in Fig. 5.

evaporated gold in a 1 mM  $Pb(NO_3)_2$  + 1M  $HClO_4$  solution in Fig. 8. The charge density, obtained from the integration of the voltammetry curves with the lead-free gold surface as a reference, should be at least approximately proportional to the amount of lead on the gold surface if all of the adsorbed lead species on the surface have the same charge. The outer Helmholtz plane and diffuse layer contributions to the total charge density should be small compared to the charge associated directly with the formation of the lead layer, regardless of whether the latter is faradaic, non-faradaic, or partially both. Consequently, the linearity in Fig. 8 up to a charge density of  $\sim 175$   $\mu\text{Coulombs/cm}^2$  (apparent area) for wavelengths of 456 and 657 nm implies that the reflectance changes under these conditions are proportional to the amount of lead adsorbed. This proportionality facilitates the determination of adsorption isotherms from reflectance measurements, but care must be exercised to avoid wavelengths near the absorption band edge of gold where linear behavior is not observed over any appreciable range of charge densities.

At  $\sim 200$   $\mu\text{Coulombs/cm}^2$  an abrupt change in slope occurs in Fig. 8 at 456 and 657 nm. This charge density corresponds to the occurrence of the second voltammetry peak and is indicative of a large change in the electronic structure of the lead layer.

The dependence of the differential reflectance coefficient [ $\chi = (1/R)(dR/dE)$ ] on potential and wavelength also has been examined using the a-c electro-modulation technique (18). The in-phase component of the reflectance is given as a function of potential for three wavelengths in Fig. 9 for a 70 Hz, 30 mV p-p sinusoidal modulation of the electrode potential superimposed on a 20 mV/sec linear voltage sweep. At this modulation frequency, the out-of-phase component is not small compared to the in-phase component in the potential regime corresponding to the UPD of lead. Consequently, the potential dependence of  $\chi$  is influenced by the dependence of the adsorption-desorption kinetics on potential as well as the change of the optical properties of the surface with coverage and potential. The hysteresis in Fig. 9 is the result of the relatively long time constant (1 sec) of the filter used to minimize noise. The changes in sign and magnitude of  $\chi$  at these wavelengths and at the various potentials are as would be expected from the d-c reflectance data in Fig. 6.

The wavelength dependence of the in-phase component of  $\chi$  is shown in Fig. 10 for the same conditions as for Fig. 9. While these derivative curves have some similarity to those for the integral reflective

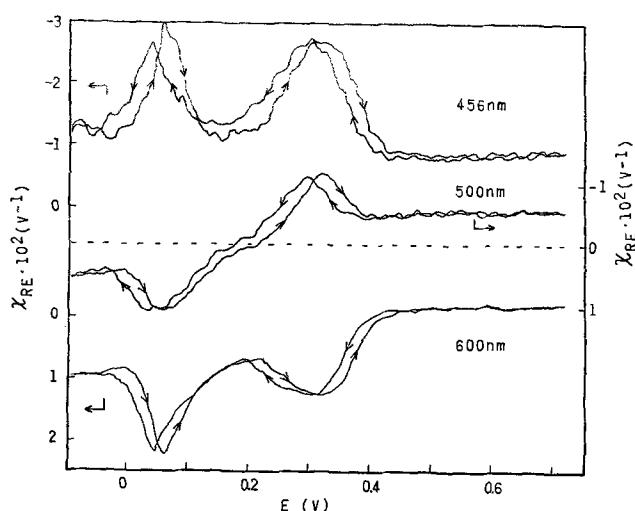


Fig. 9. Differential reflectance-potential curves for the UPD of lead on evaporated gold. Only the in-phase component is shown. A-C modulation potential, 30 mV p-p; 70 Hz, sweep potential rate, 20 mV/sec; electrolyte, 5 mM  $\text{Pb}(\text{NO}_3)_2$  + 1M  $\text{HClO}_4$ .

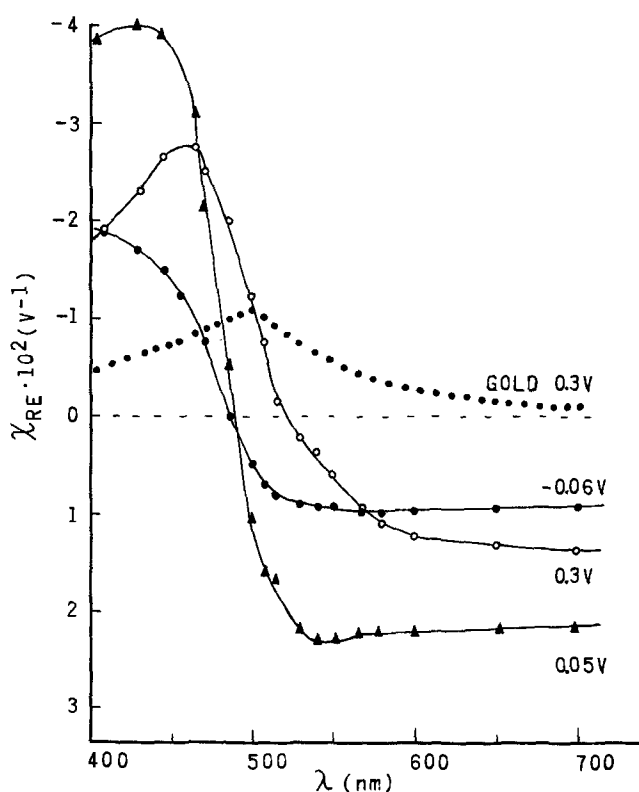


Fig. 10. Differential reflectance spectra for the UPD of lead on evaporated gold at three potentials. Conditions the same as for Fig. 9. Dotted line, differential reflectance spectrum of gold in 1M  $\text{HClO}_4$  in the absence of  $\text{Pb}^{2+}$ .

changes in Fig. 7, the common crossover or isobestic point is no longer found. This is a consequence of the fact that the curves have been evaluated at potentials above and below the second voltammetry peak where marked changes occur in the electronic properties of the lead layer. For comparison purposes, the differential reflectance spectra of evaporated gold in the absence of  $\text{Pb}^{2+}$  is also shown. The UPD of lead on the surface produces layers whose optical properties are quite dependent on potential and coverage, and quite different from that of gold. The comparison of the lead-free gold and lead-covered surfaces, however, must be made with caution. The differential electro-modulation reflectance  $\chi$  is given by

$$\chi = \frac{1}{R} \left( \frac{dR}{dE} \right) = \frac{1}{R} \left[ \left( \frac{\partial R}{\partial E} \right)_{N_i} + \sum_i \left( \frac{\partial R}{\partial N_i} \right)_E \frac{dN_i}{dE} \right] \quad [1]$$

where  $N_i$  represents the surface concentration of the various types of lead species on the surface. For the lead-free systems, the second summation term within the bracket is zero, whereas for the lead-covered surfaces involved in Fig. 10, the second term is predominant at low modulation frequencies. Evidence as to the relative magnitudes of these terms from complex plane analysis is presented below. Much of the variation of  $\chi$  with potential at  $\lambda = 456$  and 600 nm in Fig. 9 results from the potential dependence of  $(dN_i/dE)$ .

**Adsorption isotherms.**—The adsorption isotherms have been determined from the reflectance data at 600 nm for potentials well anodic to the second voltammetry peak and are given in Fig. 11. After sweeping the potential several times up to 1.6V, the potential was maintained constant at the potential specified on the curve in Fig. 11 so as to allow sufficient time for adsorption equilibrium to be reached. The normalized reflectance change was then determined by comparing the reflectance of the partially lead-covered gold electrode with that of the lead-free gold surface.

Linear behavior of the reflectance change, and hence lead surface concentration on  $\log C_{\text{Pb}^{2+}}$  is evident in Fig. 11 over the concentration range  $C_{\text{Pb}^{2+}} = 3 \times 10^{-6}$  to  $5 \times 10^{-4}M$ , as is to be expected if the lead adsorption obeys a Temkin isotherm. The slopes of these portions of the plots are indicative of the Temkin parameter. The potential dependence of these slopes is not surprising since the interaction between the adsorbed species and therefore the Temkin parameter would be expected to depend on electrode potential, particularly for charged adsorbed species.

Rather surprising, however, is the abrupt leveling off of the isotherms at concentrations of  $\sim 5 \times 10^{-4}M$   $\text{Pb}^{2+}$  for all three potentials. The surface coverage even at 0.12V only corresponds to  $\sim 100 \mu\text{Coulombs/cm}^2$  and is much less for the other two more anodic potentials. Rather similar leveling off of the adsorption isotherms at well below monolayer coverage has been observed by Bagotzky *et al.* (21) for  $\text{Cl}^-$  on Pt although not so abruptly. The precision of the points in Fig. 9 makes it unlikely that this abrupt feature of the curves is the result of a statistical variation.

**Specular reflection study of adsorption-desorption kinetics.**—The kinetics of UPD of lead have been investigated with both the potential step method and complex plane analysis of a-c electromodulation measurements, using reflectivity as a readout. The potential step measurements were performed by stepping

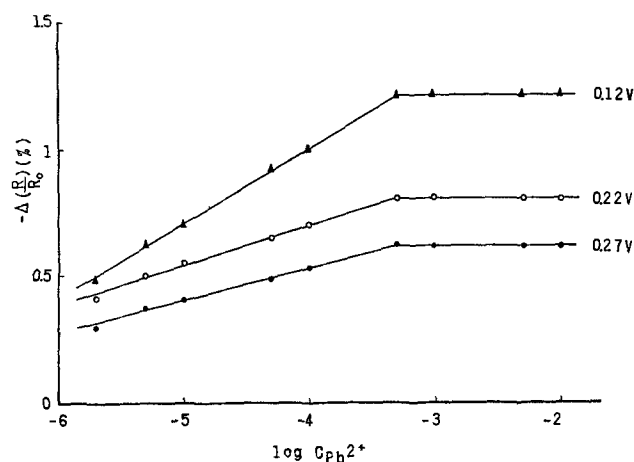


Fig. 11. Adsorption isotherm for lead UPD on gold in 1M  $\text{HClO}_4$  evaluated from reflectance measurements on evaporated gold at 600 nm. Potentials indicated on curves.

the potential from 0.5 to 0.1V where UPD of lead occurs. The change of reflectivity with time was followed with an X-Y recorder. Such curves show initially a virtually instantaneous change of reflectivity which corresponds to the intrinsic dependence of reflectivity of gold on potential. This is followed by a gradual change of reflectivity attending the deposition of lead. The plots of  $\Delta(R/R_0)$  vs. square root of time for various concentrations of  $Pb^{2+}$  are linear (Fig. 12). This indicates diffusion control and also confirms the linearity of the change of reflectivity with the surface concentrations of lead. The ratios of the slopes correspond experimentally to the ratios of the solution concentrations of  $Pb^{2+}$ , as is to be expected for pure diffusion control of the adsorption process.

The kinetics of the UPD of lead have been examined using complex plane analysis of the in-phase and out-of-phase components of the change of reflectivity as a function of frequency obtained in a-c electromodulation experiments. This technique was more attractive than attempting to extend the potential step method to shorter times because of a better signal-to-noise ratio and the possibility of following faster processes. The complex plane analysis of electromodulation reflectance data has been described elsewhere (18). The plot of the out-of-phase vs. in-phase components at various frequencies yields a semicircle for pure kinetic control for an adsorption process and a quarter circle for pure diffusion control. With mixed control, an intermediate curve is obtained, which approaches perpendicular to the in-phase axis of the plot at the high frequency end of the complex plane curve and at  $45^\circ$  at the low frequency end. The intercept with the in-phase axis at the high frequency end should correspond to the term  $(\partial R/\partial E)_{N_i}$  in Eq. [1], while the low frequency intercept with the in-phase axis corresponds to the total derivative  $(dR/dE)$ .

Complex plane plots are presented in Fig. 13 for the UPD of lead on evaporated gold in 1 mM  $Pb(NO_3)_2$  + 1M  $HClO_4$  for two potentials. The high frequency intercepts with the real axis indicate that  $(1/R) (\partial R/\partial E)_{N_i}$  is  $-8 \times 10^{-3}/V$  at a potential of 0.268V, and  $-2 \times 10^{-3}/V$  at 0.00V at 600 nm. These values are three- and twofold larger, respectively, than the corresponding values for lead-free gold surfaces (evaporated) at the corresponding potentials, indicating that the presence of lead on the surface substantially modifies the intrinsic electromodulation coefficient. Further measurements are needed to establish the wavelength dependence of this coefficient. The low frequency limiting values of the in-phase component of  $\chi$  verify that at both potentials the change of reflectance with potential is mostly due to the  $\Sigma_i (\partial R/\partial N_i) dN_i/dE$  term in Eq. [1].

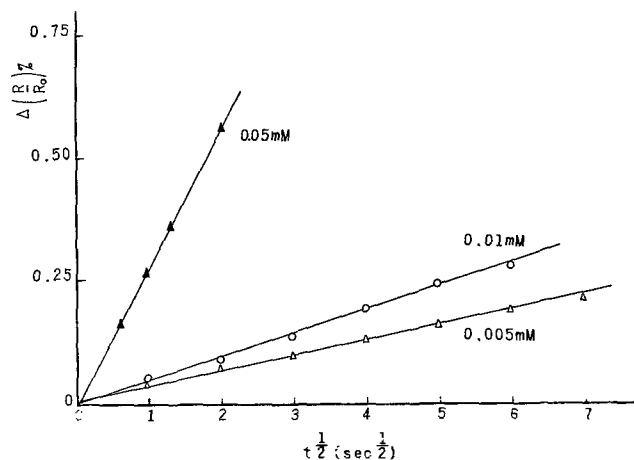


Fig. 12. Time dependence of the reflectance change at 431 nm attending the UPD of lead on evaporated gold following a potential step from 0.5 to 0.1V at various  $Pb^{2+}$  concentrations in 1M  $HClO_4$ . ( $Pb^{2+}$  concentrations indicated on curves.)

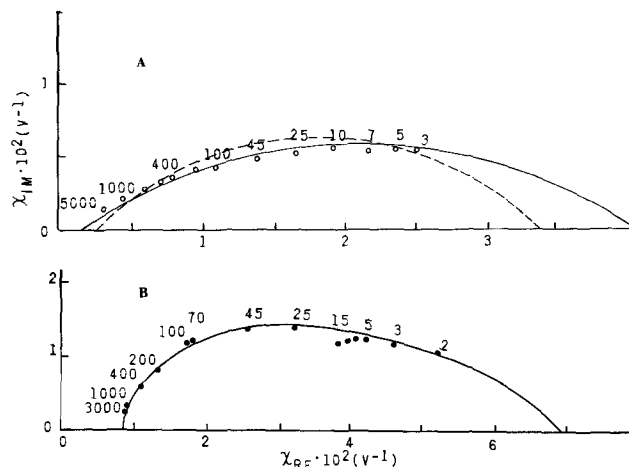


Fig. 13. Complex plane analysis of electromodulation reflectance data for the UPD of lead on evaporated gold in 1 mM  $Pb(NO_3)_2$  + 1M  $HClO_4$  at  $\lambda = 600$  nm. A, potential = 0.00V; solid curve, best portion of circle through points; dashed curve, quarter circle; B, potential = 0.268V. Numbers in figure correspond to frequencies in Hertz.

The curve for 0.268V in Fig. 13 corresponds to mixed kinetic and diffusion control.<sup>6</sup> The equation describing the electromodulation coefficient  $\chi$  under such circumstances is (18)

$$\chi = \frac{1}{R} \left[ \left( \frac{\partial R}{\partial E} \right)_N + \left( \frac{\partial R}{\partial q} \right)_E \cdot \frac{1}{j\omega Z_{ad}} \right] \frac{Z_{int}}{Z} \quad [2]$$

assuming only a single type of adsorbed species, where  $\chi = (1/R) (dR/dV)$ ,  $R$  is the reflectance,  $E$  is the potential across the interface,  $q$  is the charge associated with the UPD of the lead,  $\omega$  is the angular frequency of the modulation signal,  $Z_{ad}$  is the adsorption impedance,  $Z_{int}$  is the over-all impedance of the interface, and  $Z$  is the total impedance (including ohmic drop within the solution) across which the modulation potential ( $V$ ) is applied. With the  $IR$  drop compensated potentiostat used in the present study,  $Z = Z_i$ . The impedance  $Z_{ad}$  involves the following series components: the capacitance  $C_{ad}$ , the kinetic resistance  $r$ , and the Warburg impedance  $W$ , where

$$W = L(1 - j)/\sqrt{\omega} \quad [3]$$

with

$$L = \frac{RT}{z^2 F^2 \sqrt{2}} \cdot \frac{1}{C_{Pb^{2+}} + \sqrt{D_{Pb^{2+}}}} \quad [4]$$

where  $C_{Pb^{2+}}$  and  $D_{Pb^{2+}}$  are the concentration and diffusion coefficient of the  $Pb^{2+}$  ion,  $z = 2$ , and the other symbols have their usual meaning. Thus

$$Z_{ad} = \frac{1}{j\omega C_{ad}} + r + \frac{L(1 - j)}{\sqrt{\omega}} \quad [5]$$

Equation [2] can be rearranged, using Eq. [3]-[5], to the form

$$\chi = \frac{1}{R} \left[ \left( \frac{\partial R}{\partial E} \right)_{N_i} + \left( \frac{\partial R}{\partial q} \right) \cdot \frac{(1 + x) - j(1 + r\sqrt{\omega}/L)x}{(1 + x)^2 + (r\sqrt{\omega}/L + 1)^2 x^2} \right] \quad [6]$$

where  $x = LC_{ad}\sqrt{\omega}$ . Using  $D_{Pb^{2+}} = 0.98 \times 10^{-5} \text{ cm}^2 \text{ sec}^{-1}$  (22) yields  $W = 15(1 - j)/\sqrt{\omega} \text{ ohm-cm}^2$ . The data for 0.268V in Fig. 13 yield a value of  $C_{ad} \approx 3 \times 10^{-3} \text{ farad/cm}^2$  and  $r = 1.0 \text{ ohms-cm}^2$ . The apparent

<sup>6</sup> The curve for 0.268V in Fig. 13 differs from the experimental curve for lead adsorption on gold at 0.30V in Ref. (18) because in the earlier experimental work the a-c electromodulation data were recorded without complete compensation for  $IR$  drop and with the sinusoidal potential modulation superimposed on a linear potential sweep rather than at a fixed potential.

exchange current density corresponding to this value of  $r$  is

$$i_0 = \frac{\nu RT}{nF} \cdot \frac{1}{r} = 1.3 \cdot 10^{-2} \text{A/cm}^2 \quad [7]$$

where  $\nu$  is the stoichiometric number for the over-all adsorption (assumed to be 1) and  $n$  is the charge transferred (taken as 2).

The potential of 0.00V used for the other plot (A) in Fig. 13 is cathodic to the second voltammetry peak where a transition in the electronic properties of the layer appears to occur. These data cannot be fitted closely to a quarter circle (dashed line). Although part of a circle (solid curve) can be drawn through the points, the center is well below that for the quarter circle predicted by theory for pure diffusion control. Such deviation may be the result of having two forms of lead on the surface or an instrumental artifact such as slight overcompensation of the solution phase  $IR$  drop. Further work is required to clarify this point.

**ESCA.**—Some preliminary measurements were made with ESCA in an attempt to establish whether any differences could be found between the lead monolayer in gold and that of the surface of bulk lead. The lead layer was formed on bulk gold at 0.02V. The electrode was then withdrawn from solution at this potential and washed with  $H_2$  saturated methanol in an attempt to prevent the reoxidation and loss of lead in the rinse upon removal of the potential control. The electrode was subsequently allowed to dry in a  $N_2$  atmosphere. The sample was then transferred into the vacuum of the ESCA spectrometer (Varian VIEE-15, with MgK ( $\alpha$ ) x-ray source) without exposure to air.

The sample exhibits peaks at 138.5 eV ( $4f_{7/2}$ ) and 143.6 eV ( $4f_{5/2}$ ), as shown in Fig. 14. These values are much higher than those for pure metal lead [137 eV ( $4f_{7/2}$ ) obtained with this instrument] and comparable to the values reported recently for lead film evaporated on gold after exposure to oxygen for an extended time (23). Thus the lead monolayer film formed electrochemically is not lost during the washing in hydrogen saturated methanol but it is apparently oxidized in subsequent operations. The peak width in Fig. 14 is broader than can be attributed to instrument broadening, probably as a result of surface heterogeneity and adsorbed water molecules in the modest vacuum ( $10^{-7}$  Torr) obtained with the ESCA equipment in this study.

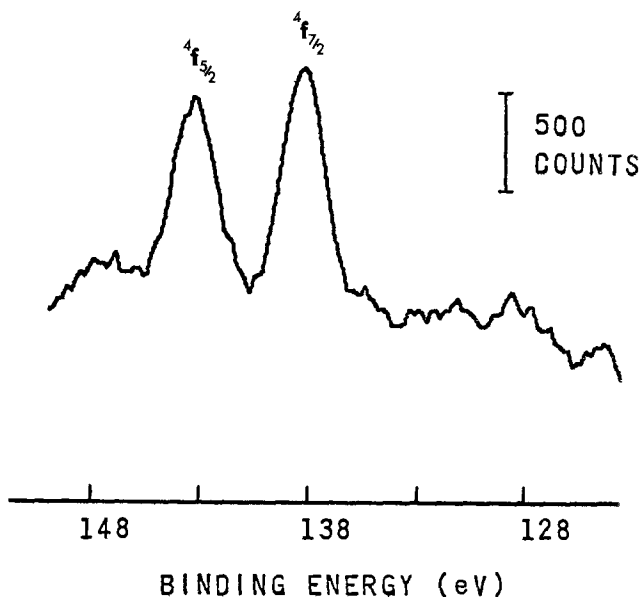
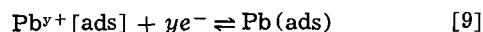
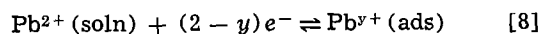


Fig. 14. ESCA spectrum (4 farads) for partial monolayer of lead on gold.

## Discussion

On the basis of the linear sweep voltammetry and reflectance studies, it is proposed that the UPD of lead involves two processes



The first is the adsorption of lead, probably in ionic form. This process appears to occur over a wide range of potentials, commencing with the first cathodic voltammetry peak at  $\sim 0.3$ V. In solutions of less than  $10^{-3}M$   $Pb^{2+}$  at a sweep rate of 0.02 V/sec, reaction [8] is under diffusion control. The second process (reaction [9]) appears to be a phase transition attended by a change in the state of charge within the adsorbed layer since it is characterized by a quite sharp peak in the voltammetry curves and is not under diffusion control. Theoretically a potential sensitive reversible phase transition within a two-dimensional layer should occur at a single potential, but surface heterogeneity and lack of complete reversibility can easily smear this peak out over a range of potentials. The disappearance of the second voltammetry peak at concentrations below  $10^{-4}M$   $Pb^{2+}$  for a sweep rate of 20 mV/sec can be explained by the fact that the diffusion control of the process in reaction [8] prevents the surface coverage from reaching the critical value necessary for this transition.

The pronounced difference in the second voltammetry peak on the various gold single-crystal surfaces is not surprising since this phase transition leading to a metallic layer should be dependent on crystallographic orientation. Apparently the recycling of the evaporated gold surface produced a relatively homogeneous surface at least with respect to this phase transition.

The charge of the adsorbed species resulting from the first process is expected to be substantially less than the +2 charge of the lead ions in solution. While it is not possible to distinguish between the charge of a faradaic process and that of nonfaradaic ionic adsorption in the voltammetry experiments, nonetheless, the 100–200  $\mu\text{coulombs/cm}^2$  or more of charge passed before reaching the second voltammetry peak is too high for simple ion adsorption, even with strong interaction between the adsorbed ions and the substrate.

The additional charge (70–90  $\mu\text{coulombs/cm}^2$ ) involved in the second peak is too high to be associated with a change in the charge of the outer Helmholtz and diffuse ionic layers attending the phase transition within the lead layer. Consequently, the phase transition is accompanied by a change in the charge of the adsorbed lead species, most likely to zero charge. This behavior and the pronounced change in the reflectivity and its wavelength dependence accompanying the second voltammetry peak can be readily explained by having the phase transition involve the formation of a metallic lead layer in which the valence bands of the lead merge with the band structures of the gold substrate.

A monolayer or near monolayer of a metalliclike lead layer on gold should have optical properties which differ substantially from those of bulk lead because of the two-dimensional nature of the layer and the strong interaction with the band structure of the gold substrate. Nonetheless, it is interesting to compare the reflectance changes calculated for a metallic lead layer using the refractive index of bulk lead with the experimental values at potentials cathodic to the second voltammetry peak (Fig. 15). The calculation has been carried out with the following equation (24)

$$\left(\frac{\Delta R}{R}\right)_p = \frac{8\pi d n_1 \cos \phi_1}{\lambda} \text{Im} \left\{ \frac{\epsilon_2 - \epsilon_3}{\epsilon_1 - \epsilon_3} A \right\} \quad [10]$$

$$\text{where } A = \frac{1 - [\epsilon_1 / (\epsilon_2 \epsilon_3)] (\epsilon_2 - \epsilon_3) \sin^2 \phi_1}{1 - (1/\epsilon_3) (\epsilon_1 + \epsilon_3) \sin^2 \phi_1} \quad [10a]$$

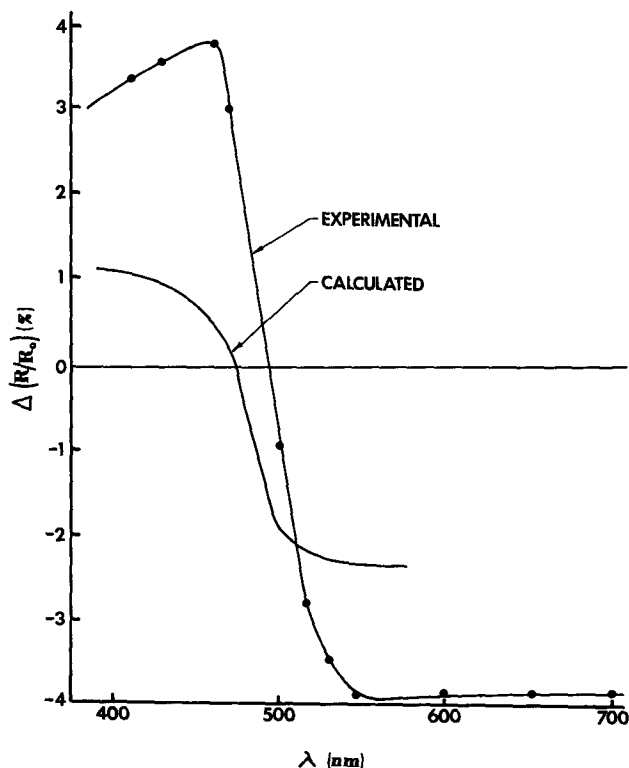


Fig. 15. Comparison of experimental values for the reflectance change with calculated values for a 3Å thick layer of lead on gold with the optical properties of the layer taken as those of bulk lead. Experimental data for a potential of 0.00V in 1 mM  $\text{Pb}(\text{NO}_3)_2 + 1\text{M HClO}_4$  at angle of incidence of  $45^\circ$ .

$\hat{\epsilon}_1$ ,  $\hat{\epsilon}_2$ , and  $\hat{\epsilon}_3$  are the complex dielectric constants of the solution, lead layer, and gold substrate, respectively, at the wavelength  $\lambda$  (in vacuo);  $n_1$  is the refractive index of the solution;  $d$  is the thickness of the lead layer; and  $\phi_1$  the angle of incidence. For the  $45^\circ$  angle of incidence used in the present work, the term  $A$  contributes relatively little to the wavelength dependence compared to the other term within the bracket in Eq. [10] and will be approximated as 1 for the purposes of this discussion of wavelength dependence. Equation [10] can be rearranged to the form

$$\left(\frac{\Delta R}{R}\right)_p = U[X(\epsilon_2' - \epsilon_3') + Y(\epsilon_2'' - \epsilon_3'')] \quad [11]$$

$$X = \left[ (\epsilon_1' - \epsilon_3') \left( \frac{\epsilon_1' - \epsilon_3'}{\epsilon_1'' - \epsilon_3''} + \frac{\epsilon_1'' - \epsilon_3''}{\epsilon_1' - \epsilon_3'} \right) \right]^{-1} \quad [11a]$$

$$Y = - \left[ (\epsilon_1'' - \epsilon_3'') \left( \frac{\epsilon_1' - \epsilon_3'}{\epsilon_1'' - \epsilon_3''} + \frac{\epsilon_1'' - \epsilon_3''}{\epsilon_1' - \epsilon_3'} \right) \right]^{-1} \quad [11b]$$

$$U = (8\pi d n_1 \cos \phi_1) / \lambda \quad [11c]$$

The values of  $U$ ,  $X$ , and  $Y$  have been calculated from the values of  $\epsilon_3'$  and  $\epsilon_3''$  for pure gold (see Table I), evaluated from the ellipsometric measurements of

Horkans (25) for evaporated gold and with the layer thickness taken as  $\sim 3\text{\AA}$ . The values of  $\epsilon_2'$  and  $\epsilon_2''$  (Table I) have also been calculated from the complex refractive index data determined ellipsometrically for a bulk lead sample by Horkans (25). This lead sample was not of high optical quality, but the calculation is relatively insensitive to small errors in the refractive index data for lead.

The calculated changes in reflectance for a metallic lead layer are compared with the experimental values corresponding to the difference in the reflectance with and without the lead layer at 0.00V for an evaporated gold electrode on 1 mM  $\text{Pb}^{2+}$  solution in Fig. 15. As indicated earlier, this subtraction assumes that the intrinsic dependence of the reflectance on potential for the lead-covered gold electrode is the same as for pure gold. This certainly is not true, but the error should be small except in the vicinity of crossover (475-500 nm) in Fig. 15 where the change of the reflectance with lead coverage passes through zero. At wavelengths remote to this region, the change of reflectance associated with the lead layer is due principally to the term  $(\partial R / \partial N_i)_E (dN_i / dE)$  in Eq. [1] and not to the intrinsic electromodulation term  $(\partial R / \partial E)_{N_i}$ . While the calculated reflectance change passes through zero, the values at  $\lambda$  remote from 500 nm are in large discrepancy. This is not surprising since the optical properties of the monolayer should be quite different from those of lead. Further, the electronic properties and optical constants of the surface layer of gold should be strongly perturbed by the lead.

Even at the less cathodic potentials where the lead is believed to have much ionic character, the interaction of the lead with the substrate gold must be very strong. The first voltammetry peak occurs at potentials of +0.3-0.4V anodic to the potential of zero charge, which is estimated to be -0.1V in 1M  $\text{HClO}_4$  on the basis of the work of Bockris and co-workers (26). This and the relatively high charge density ( $\sim 200 \mu\text{coulombs/cm}^2$  prior to the second voltammetry peak) indicate strong specific adsorption with no water interposed between the lead and the gold substrate. Such specific adsorption requires not only the displacement of water molecules on the gold surface but also the removal or at least gross distortion of water in the inner coordination sphere of the lead ions. On the basis of the behavior of similar divalent ions (27), the heat of hydration of  $\text{Pb}^{2+}$  should be at least 400 kcal/mole of which approximately one-half is associated with the inner coordination sphere. All things considered, the minimum energy required to reorganize the inner coordination sphere of the lead ions to accommodate the direct interaction with the gold substrate is certainly at least 20 kcal/mole if the lead retains its +2 charge, and probably much more, particularly if the charge of the adsorbed lead ions is effectively reduced through interaction with the band structure of the gold. Consequently, the strength of the interaction of the lead and gold is at least 20 kcal/mole.

Prior to the sharp transition associated with the second peak, the lead should be distributed randomly on various adsorption sites with water molecules surrounding each lead ion on the surface. Direct inter-

Table I. Optical data involved in the calculation of the reflectance change attending the formation of a lead monolayer on gold with the monolayer having the refractive index of pure bulk lead

$\lambda$ , nm	$n_2$	$k_2$	Lead <sup>a</sup>		$n_3$	$k_3$	Gold <sup>a</sup>		Calc. $\Delta(R/R_0)$ , %
			$\epsilon_2'$	$\epsilon_2''$			$\epsilon_3'$	$\epsilon_3''$	
400	1.50 <sup>b</sup>	3.52	-10.1	10.6	1.56	2.13	-2.10	6.65	+1.14
450	1.92	3.66	-9.71	14.1	1.45	1.87	-1.39	5.42	+0.72
475	2.04	3.73	-9.75	15.2	1.25	1.78	-1.61	4.45	0.00
500	2.15	3.80	-9.82	16.3	0.78	1.90	-3.00	2.96	-1.94
550	2.28	3.95	-10.4	18.0	0.30	2.61	-6.72	1.57	-2.31

<sup>a</sup>  $n_2$ ,  $k_2$ ,  $n_3$ ,  $k_3$  are from Ref. (25).  $\epsilon' = n^2 - k^2$ ,  $\epsilon'' = 2nk$ .

<sup>b</sup> Value extrapolated to 400 nm.

actions (horizontal) between the adsorbed lead ions would be expected to be coulombic and relatively weak under these circumstances. Indirect interactions (vertical) between adsorbed lead ions resulting from modifications in the surface electronic structure of the gold are probably more important. Even so, the linearity of the reflectance changes *vs.* charge density (Fig. 8) up to  $\sim 175 \mu\text{coulombs/cm}^2$  (apparent area) at wavelengths remote from 500 nm indicates that the interactions among the adsorbed lead species are small, whether direct or indirect, for coverages up to 0.4-0.5. [The charge density of  $175 \mu\text{coulombs/cm}^2$  corresponds to 0.4 on the (111) plane and 0.46 on the (100) plane, assuming two charges per lead adsorbed, one adsorption site per gold surface atom, and a true-to-apparent area ratio of unity.] At and near the wavelength (500 nm) corresponding to the threshold for the 5d-6s interband transition of gold, the reflectance is extremely sensitive to small changes in the surface electronic properties of the gold and hence the much more limited range of linearity at 500 nm in Fig. 8 is not surprising.

The reflectivity change *vs.* wavelength data in Fig. 7 indicate an increment in reflectance with formation of the adsorbed layer at wavelengths less than 500 nm and a decrease at longer wavelengths for a potential of 0.15V where the layer should have substantial ionic character. A simple adsorbed ionic layer without any appreciable imaginary refractive index component ( $k$ ), however, cannot explain this wavelength behavior. Consideration of Eq. [11] indicates that for  $k_2 = 0$  and  $n_2 > n_1$ , only a negative change in reflectance with layer formation is possible, contrary to observation. Taking into account the electronic polarizability of the core  $\text{Pb}^{2+}$  ion [ $4.34 \times 10^{-24} \text{cm}^3$  at 589 nm, based on measurements for  $\text{Pb}^{2+}$  in ionic salts of cubic symmetry (28)],  $n_2$  for an ionic layer should certainly be greater than that of the bulk solution. The explanation for the wavelength dependence in Fig. 7 must lie in either a substantial value of  $k_2$  for the lead layer as a consequence of the lead-gold interaction and/or a failure of the three-layer model upon which Eq. [11] is based because of pronounced changes in the surface electronic properties of the gold.

The authors have refrained from speculating as to the origin of the shallow maxima in the reflectance changes *vs.* wavelength curves in Fig. 7 and 15. The three-layer model used in obtaining Eq. [11] is too oversimplified to be used to interpret relatively minor features of the reflectance *vs.* wavelength curves.

A probable model for the interactions of the adsorbed lead with the gold substrate and other adsorbed lead ions or atoms is presented in Fig. 16A and B for low and moderate coverage where the lead is ionic and in Fig. 16C and D for high coverage where the lead is metallic. The representation is that usually employed for adsorption at metal-gas interfaces (29) and makes no attempt to show solvent states. Further, these figures are applicable at or near the pzc where the potential gradients associated with differences in the potentials of the metal and solution phases are small compared with those intrinsic to the electronic structure of the interface. Figures 16A and C represent the potential energy profiles perpendicular to the gold surface through the center of a lead ion or atom while Fig. 16B and D represent the corresponding profiles parallel to the surface through the center of nearest neighbor lead ions or atoms. The dashed lines represent the potential energy of an electron when there is no interaction, electrostatic or otherwise, between the gold and lead. The solid curves are the combined potential energy curves. In Fig. 16A and C the potential energy curve between the metal surface and the lead is lowered near the intersection of the two separate curves by resonance splitting. At high coverages, this resonance splitting is much larger than at low coverages because of the three-dimensional aspect as

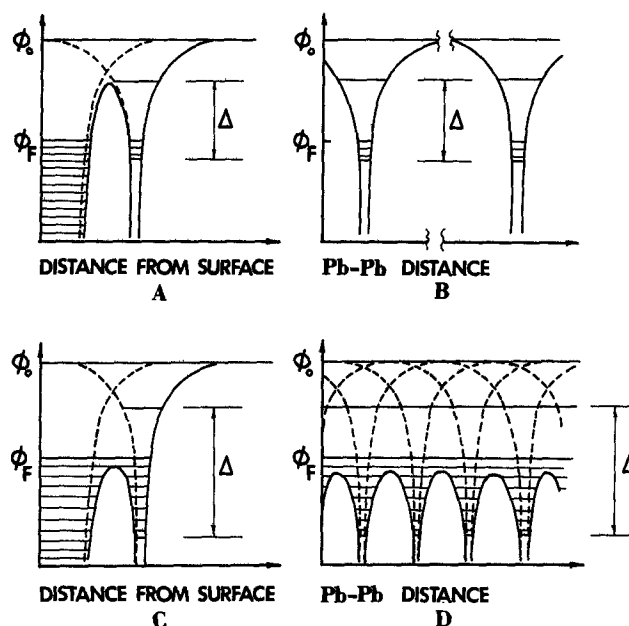


Fig. 16. Energy level diagram for lead on gold. A and B, Behavior at low and moderate coverage. C and D, Behavior at high coverage. A and C, Perpendicular to surface. B and D, Parallel to surface.  $\phi_0$ , Potential energy of electron in unbound state;  $\phi_F$ , Fermi energy;  $\Delta$ , band width in Pb. Solid curves, combined metal-substrate-lead potential curves; dashed lines, parallel curves with no interactions of lead with gold substrate or other adsorbed lead.

lead-lead as well as lead-gold interactions become important.

In Fig. 16A the valence orbitals (6p) of the adsorbed lead are broadened through interaction with the orbitals of the gold with part of the lead valence orbital band below the Fermi level. This results in a charge on the adsorbed lead of less than +2. The depression of the potential energy barrier between the lead and gold, however, is not sufficient to reduce the top of the barrier below the Fermi level and thus in this case, the lead-gold interaction is not yet metalliclike. The energy of the gold valence and conduction bands is modified even remote from the intersection of the two potential energy curves because of interaction of the lead with these orbitals with the result that substantial changes in the real and imaginary components of the optical dielectric constant of the gold are to be expected, as seems to be the situation from the relatively large changes in reflectivity and its wavelength dependence even at low coverage. (No attempt has been made to represent the valence and conduction bands of the gold substrate in Fig. 16.) The possibility that the barrier has been pulled down below the Fermi level, even at low coverages, cannot be ruled out at this time without separate values for  $n$  and  $k$  for the surface layer, but this is unlikely without the three-dimensional interactions within the layer as well as between the layer and the substrate.

Such three-dimensional interactions are to be expected at high coverages. In Fig. 16C and D, the barriers are shown depressed below the Fermi level, i.e., the lead layer is metallic. The phase transition to which the second voltammetry peak is ascribed serves to bring the lead spheres into the close proximity required to achieve metallic properties for the layer.

The potential energy plots in Fig. 16 will change with electrode potential, at least qualitatively, in a manner similar to that used to represent the situation in field emission at metal-vacuum interfaces (29). In Fig. 16A, the barrier will be lowered as the electrode potential is driven cathodic. Once the barrier falls below the Fermi level, however, the fraction of the electrode potential difference felt by this barrier will become very small because of the metallic properties



of the lead and the smallness of the Thomas-Fermi screening distance.

Figure 16 is qualitative. To convert this figure to quantitative diagrams for lead on gold and other similar systems requires far more information than is presently available. A next step is the *in situ* measurement of the real and imaginary components of the refractive index as a function of wavelength using ellipsometry.<sup>7</sup>

#### Acknowledgment

This research has been supported by the Office of Naval Research. One of the authors (R.A.) expresses appreciation to the Republicka zajednica za naucni rad S. R. Serbia, Yugoslavia, for a research fellowship in 1971. The authors also express appreciation to Miss J. Horkans for help in matters relating to the optical equipment and optical measurements, and to Dr. G. Mateescu in the ESCA measurements.

Manuscript received Sept. 25, 1973. This was Paper 108 presented at the Houston, Texas, Meeting of the Society, May 7-11, 1972.

Any discussion of this paper will appear in a Discussion Section to be published in the December 1974 JOURNAL. All discussions for the December 1974 Discussion Section should be submitted by Aug. 1, 1974.

<sup>7</sup> Ellipsometric measurements have been carried out by J. Horkans (25) on underpotential deposited lead on gold and will be the subject of a separate paper.

#### REFERENCES

1. See, for example, *Symp. Faraday Soc.*, No. 4 (1970).
2. M. Haissinsky, *Experientia*, **8**, 125 (1952).
3. L. B. Rogers, *Record Chem. Progr.*, **16**, 197 (1955).
4. E. Schmidt and H. R. Gygas, *J. Electroanal. Chem.*, **12**, 300 (1966).
5. M. W. Breiter, *This Journal*, **114**, 1125 (1967).
6. G. W. Tindall and S. Bruckenstein, *Anal. Chem.*, **40**, 1051 (1968).
7. J. T. Byrne and L. B. Rogers, *This Journal*, **98**, 457 (1951).
8. B. J. Bowles and T. E. Granshaw, *Phys. Letters*, **17**, 258 (1965).
9. D. J. Astely, J. A. Harrison, and H. R. Thirsk, *J. Electroanal. Chem.*, **19**, 325 (1968).
10. J. W. Schultze, *Ber. Bunsenges. Physik. Chem.*, **74**, 705 (1970).
11. B. Vassos and H. B. Mark, *J. Electroanal. Chem.*, **13**, 1 (1967).
12. L. D. Schmidt and R. Gomer, *J. Chem. Phys.*, **42**, 705 (1970).
13. J. W. Gadzuk, *Phys. Rev.*, **B**, **1**, 2110 (1970).
14. J. W. Gadzuk, *Surface Sci.*, **6**, 133 (1967).
15. J. Henrion and G. E. Rhead, *ibid.*, **29**, 20 (1972).
16. T. Takamura, K. Takamura, W. Nippe, and E. Yeager, *This Journal*, **117**, 626 (1970).
17. T. Takamura, Y. Sato, and K. Takamura, *J. Electroanal. Chem.*, **11**, 31 (1973).
18. R. Adzic, B. D. Cahan, and E. Yeager, *J. Chem. Phys.*, **58**, 1780 (1973).
19. R. Adzic, J. Horkans, B. D. Cahan, and E. Yeager, *This Journal*, **120**, 1219 (1973).
20. J. Clavilier, A. Hamelin, and G. Valette, *C. R. Acad. Sci. Paris*, **C265**, 221 (1967).
21. V. S. Bagotzky, Y. B. Vassilyev, J. Weber, and J. N. Pirtskhalava, *J. Electroanal. Chem.*, **27**, 31 (1970).
22. R. Parsons, "Handbook of Electrochemical Constants," p. 79, Butterworths Scientific Publications, London (1959).
23. K. S. Kim and N. Winograd, *Chem. Phys. Letters*, **19**, 209 (1973).
24. J. McIntyre and D. Aspnes, *Surface Sci.*, **24**, 417 (1971).
25. J. Horkans, Ph.D. Thesis, Case Western Reserve University, Cleveland, Ohio, June 1973.
26. J. Bockris, S. D. Argade, and E. Gileadi, *Electrochim. Acta*, **14**, 1259 (1969); see also, J. P. Carr and N. A. Hampson, *This Journal*, **119**, 325 (1972).
27. B. E. Conway, "Electrochemical Data," p. 132, American Elsevier Publishing Co., Inc., New York (1952).
28. F. C. Frank, *Trans. Faraday Soc.*, **33**, 513 (1937).
29. See, for example, J. W. Gadzuk, *Phys. Rev.*, **B**, **1**, 2110 (1970).

## Electrical Resistivity of Silver Deposited by Aerosol Spray

W. R. Momyer\* and D. J. Levy\*

Lockheed Palo Alto Research Laboratory, Lockheed Missiles & Space Company, Incorporated,  
Palo Alto, California 94304

#### ABSTRACT

The silver ligands and reducing agents found most effective for producing low resistivity silver films by spray chemical reduction are in the order:  $\text{NH}_3$ , en, EDTA for ligands and  $\text{HCHO}$ ,  $\text{N}_2\text{H}_4$  for reductants. No silver was deposited from  $\text{Ag}^+$  complexed with  $\text{CN}^-$  or  $\text{I}^-$ , and deposition rates were low with  $\text{SCN}^-$  and  $\text{Br}^-$ . Reduction of  $(\text{EDTA})_x\text{Ag}^+$  with  $\text{N}_2\text{H}_4$  results in deposits with a high (20-35  $\mu\text{ohm-cm}$ ) initial resistivity due to inclusion of  $\text{Ag}_2\text{O}$  and an unstable bluish coating which appears to be a silver carboxylate.  $(\text{NH}_3)_2\text{Ag}^+$  reduced with  $\text{HCHO}$  produces deposits with the lowest initial resistivity (1.7  $\mu\text{ohm-cm}$ ). The resistivity of all films can be reduced to 1.6  $\mu\text{ohm-cm}$  (pure silver) by thermal treatment within the 120°-300°C range. en is the preferred ligand because of the possibility of forming explosive compounds when using  $\text{NH}_3$ . Silver deposition rate is linear with  $(\text{en})_2\text{Ag}^+$  up to at least 1.6  $\mu\text{m/min}$ . The optimum molar composition of the silver solution is  $\text{en}/\text{Ag}^+ = 2.5$  at pH 10.6. The reductant composition should be prepared with the molar ratios  $\text{HCHO}/(\text{en})_2\text{Ag}^+ = 9$  and  $\text{NaOH}/\text{HCHO} \sim 0.08$ .

Aerosol plating was known even before the turn of the century (1) but it was not perfected for commercial use (silvering mirrors) until some 40 years later. Silvering processes that have been widely used include the dual-spray chemical reduction of ammoniacal silver nitrate,  $(\text{NH}_3)_2\text{Ag}^+$ , with hydrazine (2), for-

maldehyde (3), glyoxal (4), and dextrose (5), and the reported use of hydroxylamine (6).

Upton *et al.* (7) studied the  $(\text{NH}_3)_2\text{Ag}^+$ -HCHO system and determined the deposition rate and efficiency as a function of solution concentration and spray conditions. The effect of atomization parameters on deposition rate and efficiency of an aerosol plating process has also been reported (8).

\* Electrochemical Society Active Member.  
Key words: silver, resistivity, aerosol plating, spray plating, formaldehyde, hydrazine.

Copper (9) and gold (10) films with the electrical resistivity of the pure dense metal can be aerosol plated under proper conditions. This fact, plus the observation that plating will not initiate on unsensitized nonconductors, suggests that deposition may sometimes proceed via an autocatalytic plating mechanism.

The present study was undertaken in an effort to evaluate the quality of aerosol-plated silver films as determined by electrical resistivity measurements. Ethylenediamine (en) and ethylenediamine-NNN'N'-tetra-acetic acid (EDTA) were the principal ligands evaluated with either formaldehyde or hydrazine as the reducing agent. However, some plating was performed with the ammoniacal silver complex for comparison, and bromide, iodide, cyanide, and thiocyanate ligands were evaluated in the initial experiments. Consideration was also given to the hazard of forming explosive silver compounds in the metal solution.

### Experimental

**Apparatus.**—The plating solutions were sprayed with a stainless steel, dual-nozzle, pneumatic atomizing spray gun fitted with glass siphon cups. A Binks Manufacturing Company Model 181 SS Spray Gun with 0.5 mm (0.022 in.) liquid orifices and 66SH air nozzles was used. All surfaces in contact with the metal solution were plastic or plastic coated. Metal and reductant solution flow rates were each 50 ml/min and plating was conducted at 22°C using exhaust ventilation. Filtered compressed air was used at ca. 0.04 kg/mm<sup>2</sup> (60 psig) for atomization. These conditions were previously determined (8) to yield efficient aerosol plating.

The pH of the silver solutions was adjusted using a Beckman Model H2 meter in conjunction with a multipurpose glass electrode (0-14 pH, 0-100°C) and a silver/silver chloride reference electrode. Unstable pH readings were sometimes encountered when adjusting pH of the (en)<sub>2</sub>Ag<sup>+</sup> complex. This instability was due to the deposition of silver and/or silver chloride in the capillary of the reference electrode. The problem was circumvented by coupling the reference electrode to the circuit through a sodium nitrate-agar gel bridge.

More accurate pH adjustment was required when studying stability of the (en)<sub>2</sub>Ag<sup>+</sup> complex. An Orion Research Model 601 digital pH meter with a Beckman "Perma-Probe" silver/silver chloride solid-state reference electrode and a multipurpose glass electrode was used for this study. The gel bridge was again used in the reference circuit and a dual-buffer standardization technique was employed. Readings were accurate to ±0.02 pH unit with this system.

A Hewlett Packard Model 5750 gas chromatograph with a Poropak Q column and thermal conductivity detector was used to analyze the gases evolved during thermal treatment of some aerosol-plated silver films. Helium was used as the carrier gas. The silver was deposited on fiber glass knit mesh substrates in order to provide a high silver surface area per unit volume. The fiber glass substrates were heat-cleaned at 650°C before silver plating in order to remove any organic contaminants (sizing, lubricants, etc.). The silver-plated panels were then placed in a vacuum-tight container of known volume, evacuated, given a thermal treatment at 125°C for 2 hr to decompose the unstable compound, and the gases evolved analyzed both qualitatively and quantitatively.

**Materials.**—The reductant solutions were prepared with purified grade 64% hydrazine and U.S.P. 37% formaldehyde. The formaldehyde solutions were prepared fresh daily to minimize the effects of the Cannizzaro reaction (12). The silver complexes were prepared with 98-100% en, 99% EDTA (tetrasodium salt), and reagent grade ammonium hydroxide. Additional en purification is required if the (en)<sub>2</sub>Ag<sup>+</sup> complex is to be stored for several weeks before use. Ninety-nine and eight tenths per cent silver nitrate was used in prepa-

ration of the metal solutions and all other chemicals were of reagent grade quality. The substrates were 5 × 5 cm frosted borosilicate glass panels.

**Procedure.**—The substrate panels were cleaned in chromic acid, heated to 200°C for 1 hr, cooled, and weighed to the nearest 0.1 mg. The glass squares were then sensitized with stannous chloride (0.25 g/liter), rinsed with deionized water, and aerosol silver plated for 30 sec unless specified otherwise. The panels were again rinsed, dried, and reweighed to the nearest 0.1 mg after plating. In some instances the silver films were heated before reweighing when it was found that film resistivity was sensitive to postbake temperature. An average film thickness was calculated using the density of pure silver, 10.5 g/cm<sup>3</sup> at 20°C (13), and the geometrical area. Electrical resistance of the silver film was measured with a 4.4 cm square, parallel bar probe (gold plated to minimize contact resistance) and a Hewlett-Packard Model 412A d-c vacuum tube voltmeter. Electrical resistivity was calculated using the measured resistance and the calculated film thickness. A comparison with the accepted resistivity for pure silver, 1.60 μohm-cm at 22°C (13), gives a good indication of film quality (density and purity).

Frosted glass substrates were used in these tests in order to obtain adequate adhesion of the aerosol silver film to the glass. It might be expected, therefore, that the calculated resistivity values would be higher than the true values because the actual surface area of frosted glass is somewhat greater than the geometrical area. However, this difference was not observed in practice and, evidently, the geometrical area is quite close to the true area for the silver thickness deposited. A reported resistivity value is the average of several measurements which normally varied less than ±0.1 μohm-cm for any given set of spray conditions.

### Selection of Silver Complexes for Aerosol Plating

The silver complex is one of the principal factors determining both the plating rate and the quality of the silver deposit in this process. The silver ion activity must be maintained at a low value in order to prevent silver oxide from forming in the metal solution either prior to or during spraying. Natarajan and Krishnan (14) recently surveyed the literature and found a broad spectrum of silver complexes effective for electrodeposition. Table I lists the instability constants for the more important silver complexes found in this survey. However, only the cyano and, to a lesser extent, the iodo silver complexes have been used commercially for electroplating.

Aerosol plating places greater restrictions on the choice of the silver complex than electroplating. The cyano and iodo silver complexes are too stable and no metal deposition is observed in aerosol plating.

Thiocyanato and bromo silver complexes produce bright, metallic deposits but the plating rates are rather low. High quality silver deposits are obtained at rapid plating rates with NH<sub>3</sub>, en, and EDTA silver complexes. The EDTA complex is anionic and is slightly less stable than the ammonia complex (15). Silver complexes with instability constants from 10<sup>-7</sup> to 10<sup>-8</sup>, therefore, appear to be optimum for aerosol plating. It is not possible to use silver complexes with instability constants greater than 10<sup>-7</sup> because silver

Table I. Instability constants of silver complexes

Complex	K
Ag(CN) <sub>2</sub> <sup>-</sup>	8.0 × 10 <sup>-22</sup>
AgI <sub>4</sub> <sup>-3</sup>	1.8 × 10 <sup>-14</sup>
Ag(S <sub>2</sub> O <sub>3</sub> ) <sub>2</sub> <sup>-3</sup>	3.5 × 10 <sup>-14</sup>
Ag(CSN <sub>2</sub> H <sub>4</sub> ) <sub>3</sub> <sup>+</sup>	7.0 × 10 <sup>-14</sup>
Ag(CSN) <sub>4</sub> <sup>-3</sup>	9.3 × 10 <sup>-11</sup>
AgBr <sub>4</sub> <sup>-3</sup>	6.3 × 10 <sup>-10</sup>
Ag(en) <sub>2</sub> <sup>+</sup>	1.5 × 10 <sup>-8</sup>
Ag(SO <sub>3</sub> ) <sub>2</sub> <sup>-2</sup>	4.5 × 10 <sup>-8</sup>
Ag(NH <sub>3</sub> ) <sub>2</sub> <sup>+</sup>	9.3 × 10 <sup>-8</sup>
AgCl <sub>4</sub> <sup>-3</sup>	1.2 × 10 <sup>-8</sup>

oxide precipitates in the alkaline media used for aerosol plating.

The EDTA complex is probably in the form of the ethylenediamine tetraacetato silver ion  $(\text{EDTA})\text{Ag}^{-3}$ . However, the designation  $(\text{EDTA})_x\text{Ag}^+$  is used since it was beyond the scope of this work to establish the number of coordinated ligands. The ammoniacal silver complex was invariably chosen in the past although it is not a particularly desirable complex because of possible side reactions which can form explosive compounds. In preparing  $(\text{NH}_3)_2\text{Ag}^+$  only a slight excess of ammonia is used over that required to redissolve the silver oxide precipitate which forms during mixing. Under this condition, and particularly in the presence of additional alkali, explosive compounds may form in solution.  $\text{Ag}(\text{NH}_3)_2\text{OH}$  is a soluble strong base which forms a highly explosive nitride, probably  $\text{Ag}_3\text{N}$  (silver azide) or  $\text{Ag}_2\text{NH}$  (silver imide), upon standing (16).

### Aerosol Silver Plating with Hydrazine

The silver-EDTA complex produced the most specular deposits on smooth glass surfaces in preliminary screening experiments with hydrazine. The spray formulations were therefore optimized using this complex. Initial tests indicated that the resistivity of the deposited silver film was not constant with time. The resistivity immediately after plating was quite high but decreased substantially over a period of 1 week to a value only 4-5 times that of pure silver (Fig. 1). A similar observation without data was reported by Ollard (17) in the discussion comments of another paper. Silver had been deposited from a Rochelle salt bath onto glass and it was found that the electrical resistance "fell after a few hours to half its value."

Figure 2 shows that heating the films decreases the time required to reach a steady-state resistivity and produces a lower final value (resistivity of pure silver at 300°C). It is not difficult to explain the resistivity decrease observed at 200° and 300°C. Silver oxide is unstable at elevated temperatures with the partial

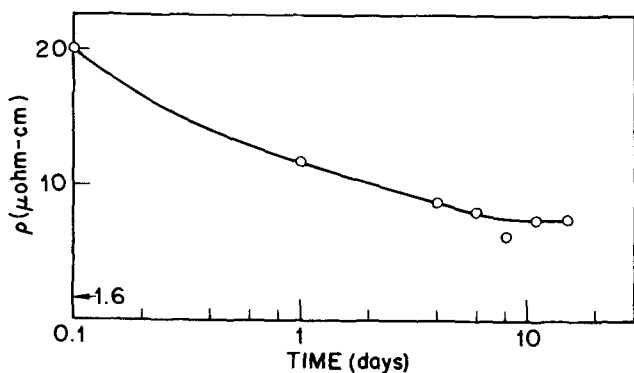


Fig. 1. Change in electrical resistivity of silver deposit at 22°C. 0.3  $\mu\text{m}$  Ag (on smooth glass). Plating solutions: 0.02M  $\text{Ag}^+$ , 0.08M EDTA, pH 10.5; 0.5M  $\text{N}_2\text{H}_4$ , 0.03M NaOH.

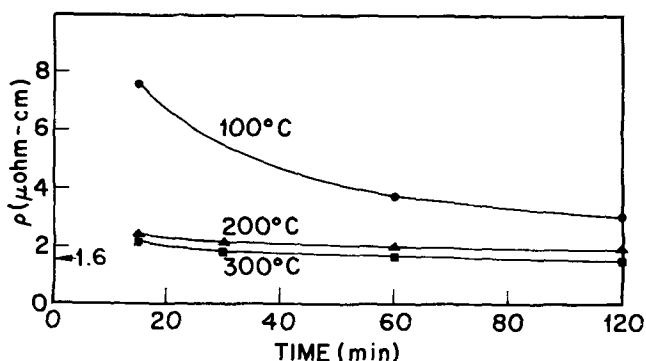
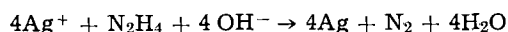


Fig. 2. Thermal treatment of silver. Plating solutions: 0.04M  $\text{Ag}^+$ , 0.12M EDTA, pH 10.5; 0.5M  $\text{N}_2\text{H}_4$ , 0.03M NaOH.

pressure of oxygen over silver oxide reaching 1 atm at 184°C (16). Decomposition of the oxide is also catalyzed by metallic silver. However, the decrease in resistivity at room temperature is not due to oxide decomposition.

These silver films were observed with a scanning electron microscope in the as-plated condition and after heating at 100°C. There was no apparent change in film morphology either with time or the 100°C bake. A weight loss of 0.5-1.0 mg is typically observed upon heating to 100°C and the silver films have a whiter luster. The weight loss observed is also independent of film thickness. Therefore it appears that a compound is deposited on the surface of the silver that is either volatile or decomposes to silver and a volatile compound.

It is generally undesirable and in many cases impossible to heat-treat a silver deposit at 300°C to achieve the resistivity of pure silver. However, it is often possible to lower the resistivity of the metal film by proper adjustment of the reactant concentrations. The net reaction for the reduction of silver ion by hydrazine can be presented by the following equation



Although this equation does not show all the steps involved in the actual reduction of silver ion by hydrazine, it does indicate that such factors as silver ion activity, hydrazine concentration, and reaction pH will be important in determining plating rate and film quality (oxide content, porosity, etc.)

Figure 3 shows the effect of hydrazine concentration on silver plating rate at several concentrations of the silver-EDTA complex. Hydrazine has little effect on plating rate above a molar ratio of 10. This is in marked contrast to the dependence observed when aerosol plating copper with hydrazine (9). The slight increase in plating rate at the higher hydrazine concentrations is due to an increase in the total alkalinity of the reductant by the additional hydrazine. The silver film resistivity did not vary appreciably over  $\text{N}_2\text{H}_4/\text{Ag}^+$  molar ratios from 10 to 100.

Figure 4 illustrates the dependence of plating rate on concentration of the  $(\text{EDTA})_x\text{Ag}^+$ . There is no substantial difference in film resistivity over the range of plating rates investigated (0.3 to 0.9  $\mu\text{m}/\text{min}$ ).

The silver ion activity in the metal solution can be decreased by increasing the ligand/metal ion ratio. Figure 5 indicates that the film resistivity decreases with decreasing silver ion activity. However, this is an inefficient method by which to decrease film resistivity because the plating rate also decreases substantially. Figure 6 indicates that the plating rate at the high ligand/metal ion ratio can be increased slightly without adversely affecting silver resistivity by increasing the pH of the silver-EDTA solution. The plating rates are somewhat lower in this test because the metal

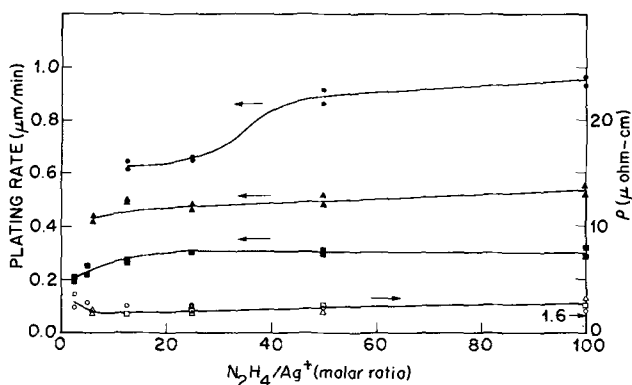


Fig. 3. Effect of  $\text{N}_2\text{H}_4/\text{Ag}^+$  on plating rate and resistivity. 0.4-0.6  $\mu\text{m}$  Ag, 200°C bake. Plating solutions: 4 EDTA/ $\text{Ag}^+$ ; pH 10.5; 0.04M NaOH.  $\text{Ag}^+$ : 0.02M,  $\square$ ; 0.04M,  $\triangle$ ; 0.08M,  $\circ$ .

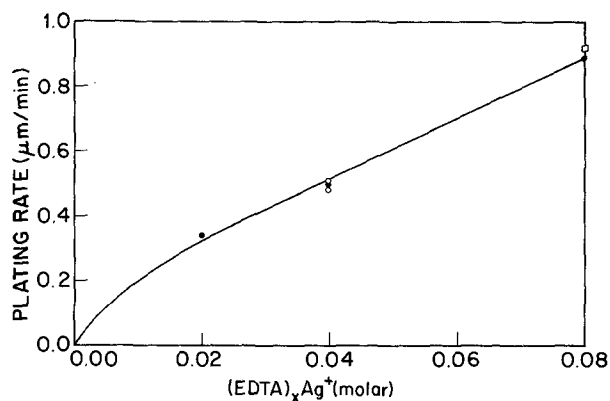


Fig. 4. Effect of  $(\text{EDTA})_x\text{Ag}^+$  concentration on plating rate using  $\text{N}_2\text{H}_4$ . Metal solution: 4  $\text{EDTA}/\text{Ag}^+$ , pH 10.5.  $\text{N}_2\text{H}_4/\text{Ag}^+$ : 50, ●; 25, □○. NaOH: 0.04M, ●; 0.06M, □; 0.10M, ○.

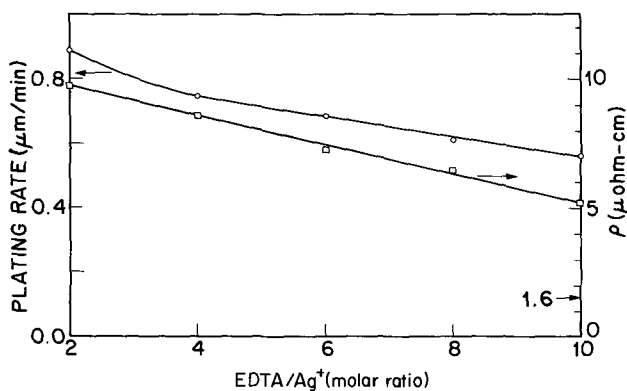


Fig. 5. Influence of  $\text{EDTA}/\text{Ag}^+$ . Plating solutions: 0.08M  $\text{Ag}^+$ , pH 10.3; 1.0M  $\text{N}_2\text{H}_4$ , 0.1M NaOH. 45 ml/min, 120°C bake.

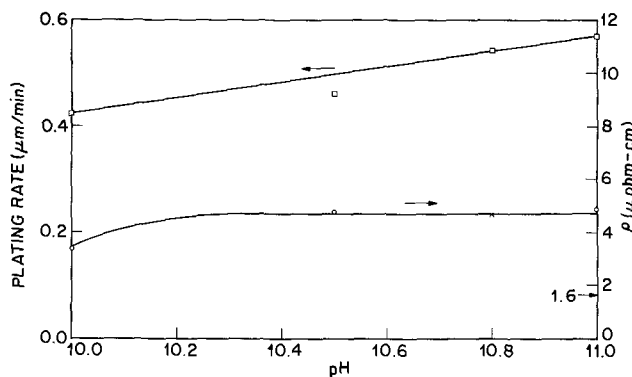


Fig. 6. Effect of pH of metal solution. Plating solutions: 0.08M  $\text{Ag}^+$ , 0.8M EDTA; 1.0M  $\text{N}_2\text{H}_4$ , 0.1M NaOH. 43 ml/min, 120°C bake.

solution flow was about 10% lower than desired. The optimum molar ratio of  $\text{EDTA}/\text{Ag}^+$  would appear to be from 2 to 4 on the basis of both plating rate and film resistivity.

The most critical parameter in aerosol silver plating is the pH of the spray mixture. Changes in atomization and mixing conditions, liquid flow rates, pH of the metal solution, and sodium hydroxide in the reductant all affect this reaction parameter. The pH of the silver-EDTA complex was controlled to  $\pm 0.1$  pH unit in this work. Plating rate was adjusted to the desired value with sodium hydroxide additions to the reductant. Figure 7 shows plating rate and film resistivity as a function of sodium hydroxide additions to the hydrazine solution. A substantial increase in plating rate is obtained upon increasing the sodium hydroxide concentration from 0.03 to 0.05M. However, more silver oxide is codeposited with the silver at the higher sodium hydroxide concentrations.

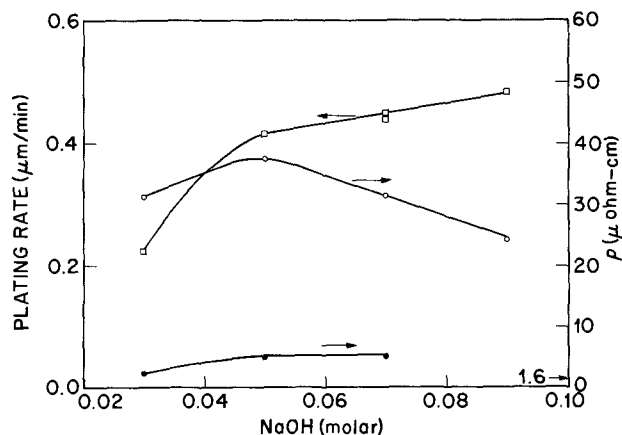


Fig. 7. Effect of  $\text{OH}^-$  concentration in  $\text{N}_2\text{H}_4$  solution. Plating solutions: 0.04M  $\text{Ag}^+$ , 0.16M EDTA, pH 10.5; 0.5M  $\text{N}_2\text{H}_4$ . Resistivity: initial, ○; 200°C bake, ●.

Pure silver films were not obtained with the silver-EDTA complex by adjustment of either the hydrazine concentration, silver and EDTA concentration, or reaction pH. The steady-state resistivity of the deposited silver films typically ranged from 4 to 10  $\mu\text{ohm-cm}$ . The deposits have a metallic appearance but evidently some silver oxide and an unstable silver compound are codeposited with the silver. The film resistivity of pure silver can only be achieved by a thermal treatment at 300°C.

Aerosol silver plating with the en and ammonia complexes was also evaluated with hydrazine using the optimum reducing conditions found for the EDTA complex. Table II compares typical plating results of the three silver complexes with hydrazine. The silver-en complex was tested at an en/ $\text{Ag}^+$  molar ratio of 2 and pH 10.5 while the silver-ammonia complex was tested at a  $\text{NH}_3/\text{Ag}^+$  molar ratio of 4 without pH adjustment (pH slightly greater than 11). It is evident that the ammonia and en complexes are far superior to the EDTA complex for aerosol plating silver with hydrazine. The plating rates are much more rapid and the resistivities substantially lower. However, even the silver films deposited from the en and ammonia complexes exhibit a significant decrease in resistivity during a thermal treatment at 120°C. There also appears to be some silver oxide codeposited with the silver as evidenced by the final resistivity readings after the 120°C bake.

#### Aerosol Silver Plating with Formaldehyde

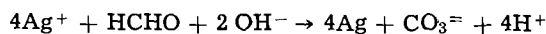
Aerosol silver films deposited with formaldehyde are considerably brighter than those deposited with hydrazine. A milky brown cast generally develops on thick silver films deposited with hydrazine, indicating the presence of silver oxide. Initial aerosol plating experiments with formaldehyde indicated that en was a suitable ligand for the silver but that EDTA was not. Blue deposits were obtained with the EDTA complex which have quite high resistivities (greater than 1000  $\mu\text{ohm-cm}$ ). A thermal treatment at 120°C reduces the resistivity to about 20  $\mu\text{ohm-cm}$  but the deposit is still of poor quality. The aerosol silver process was therefore optimized with the silver-en complex.

Table II. Aerosol silver plating\* with hydrazine

Ligand	Plating rate ( $\mu\text{m}/\text{min}$ )	$\rho$ ( $\mu\text{ohm-cm}$ )	
		22°C	120°C
EDTA	0.9	7	3-5
en	1.3	3-4	1.8
$\text{NH}_3$	1.9	2.8	1.9

\* 0.08M silver complexes. Resistivity at ambient temperature and after heating.

The net reaction for the reduction of silver ion by formaldehyde can be represented by the following equation if complete oxidation of formaldehyde is assumed



The reduction of silver ion by formaldehyde is analogous to the hydrazine reduction and therefore the same general reaction parameters can be expected to affect plating rate and film quality. Lower plating rates are obtained with formaldehyde because it is a slightly weaker reducing agent than hydrazine (18). The most important parameter is again the pH of the reaction mixture.

Figure 8 shows that the silver plating rate varies directly with the concentration of alkali in the reductant. Unlike the hydrazine process, the resistivity of pure silver can be achieved by a thermal treatment at 120°C. This indicates that the silver oxide content of the deposit is quite low under the proper plating conditions. In this test, the silver oxide content of the film is significant only at sodium hydroxide concentrations above 0.06M. However, the films still exhibit a resistivity 2-3 times greater than pure silver in the as-plated condition. A 0.5-1.0 mg weight loss is also noted after a 120°C bake.

Figure 9 shows that the formaldehyde concentration is not very critical in this process. A molar rate of HCHO/Ag<sup>+</sup> near 9 appears to be the optimum. The decrease in plating rate at the higher formaldehyde concentration is a pH effect. Commercial formaldehyde is marketed as a mildly acidic solution to minimize chemical decomposition. Total alkalinity of the reductant is therefore lower at higher formaldehyde concentrations when a fixed amount of sodium hydroxide is added.

An attempt was made to identify the unstable compound deposited with the silver during aerosol plating.

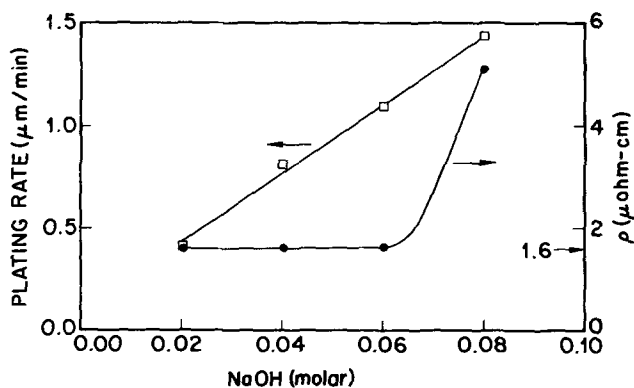


Fig. 8. Effect of OH<sup>-</sup> concentration in HCHO solution. Plating solutions: 0.08M Ag<sup>+</sup>, 0.16M en, pH 10.5; 0.75M HCHO. 120°C bake.

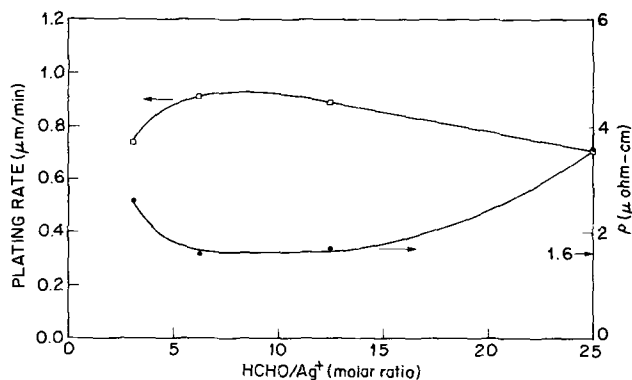


Fig. 9. Effect of HCHO/Ag<sup>+</sup>. Plating solutions: 0.08M Ag<sup>+</sup>, 0.16M en, pH 10.5; 0.05M NaOH. 120°C bake.

The silver films in the as-plated condition generally have a blue-gray tint, the degree dependent upon which spray solutions are used. The films become noticeably whiter after a thermal treatment at 120°C and exhibit a corresponding weight loss and decrease in resistivity. The weight loss is independent of sample size in the range from 0.4 to 1.8g silver and the weight loss is greater in films deposited from the EDTA complex (3-6 mg) than from the en complex (1-2 mg).

Gas chromatographic analysis of the gases evolved during thermal treatment of the silver films indicates that carbon dioxide is the principal species. The carbon dioxide detected was a hundredfold higher than the background level in silver films deposited from the en complex and a hundredfold higher from the EDTA complex. Water, oxygen, and nitrogen were also generally detected but those constituents were not substantially higher than the background levels. Immersing the films in a dilute sulfuric acid solution after plating produced a significant decrease in resistivity and a weight loss. The films were also noticeably whiter. The carbon dioxide detected after thermal treatment was 50-75% less for silver films immersed in sulfuric acid. These data suggest that the unstable material is either silver carbonate or a silver carboxylate compound.

It is unlikely that the unstable compound is silver carbonate. Silver carbonate is a brilliant yellow-green color and decomposes at a temperature of 218°C (13). The material in the silver films is a blue-gray color and decomposes rapidly at 120°C. The silver films after thermal treatment have the metallic white luster of silver and exhibit the electrical resistivity of pure silver. If silver carbonate were decomposing at this low temperature it would yield silver oxide (brown) and the films would not exhibit the resistivity of pure silver. The resistivity data and color observations would, therefore, tend to eliminate silver carbonate as the contaminant.

The unstable material in the aerosol silver films would appear to be a silver carboxylate, probably silver formate in the case of the en-HCHO system. Formate is present in the HCHO reductant as a result of both the Cannizzaro reaction (12) and incomplete HCHO oxidation during reduction of the silver complex. The color of pure silver formate would probably be white; however, some metallic silver in the material might tend to impart color (analogous to AgCl). Formic acid is a weaker reducing agent than HCHO (18) but is capable of reducing silver in alkaline media. The addition of sodium formate to the (en)<sub>2</sub>Ag<sup>+</sup> complex produced no visible reaction at a pH of 10.6. Increasing the pH to 11.5 produced a gray powder and the solution had a light bluish cast. Thermal decomposition of silver formate would yield only metallic silver, carbon dioxide, and hydrogen. Hydrogen was not detected in the gas chromatographic analysis due to the helium carrier gas.

The silver-en complex is not as stable to decomposition as either the silver-ammonia or silver-EDTA complexes. Part of the difficulty appears to arise from impurities in the commercial 98-100% en and further purification (19) is desirable for best solution stability. The stability of the silver-en complex is also affected by molar ratio of en/Ag<sup>+</sup>, pH, and mixing conditions. The complex is not very stable at a ligand/metal ion molar ratio below 2.5 but good stability is achieved at a molar ratio of 5. Figure 10 shows a substantial reduction in plating rate at the higher molar ratio although film resistivity does not change appreciably over the range of molar ratios from 2 to 8. Stability of the silver solution is diminished at pH values below 10 or above 11. In preparing the (en)<sub>2</sub>Ag<sup>+</sup>, the pH of the en solution should be adjusted to 10.60 with nitric acid and cooled to 23°C before addition of the silver nitrate. During addition of the silver nitrate, maintain pH near 10.6 by adjustment with sodium hydroxide.

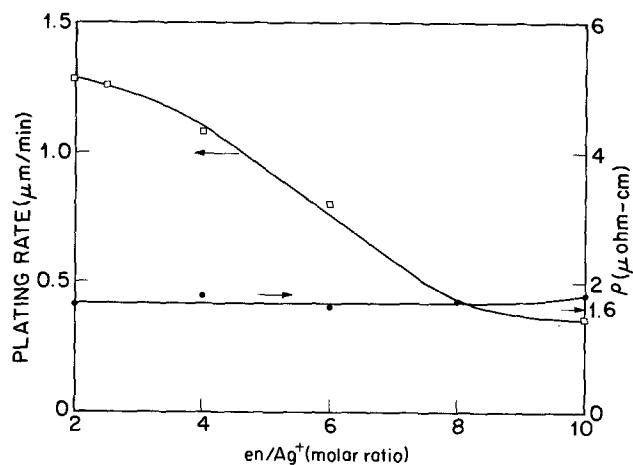


Fig. 10. Influence of  $en/Ag^+$ . Plating solutions: 0.08M  $Ag^+$ , pH 10.5; 0.75M HCHO; 0.06M NaOH. 120°C bake.

Filter the solution through a glass frit if any silver decomposition (black precipitate) is noted within 24 hr after preparation. A moderately stable metal solution is obtained at an  $en/Ag^+$  molar ratio of 2.5 by this procedure. The pH of the solution remains constant at  $10.60 \pm 0.02$  over a period of 1 week without silver decomposition, although the plating rate tends to decrease somewhat with solution age.

Figure 11 shows the relationship between plating rate and silver-en concentration when an attempt is made to neutralize the acid added with the formaldehyde. A linear dependence is apparent and good quality films are obtained over the entire concentration range. The data obtained in this test indicate that the molar ratio of NaOH/HCHO should be near 0.08. The data points at 0.02 and 0.04M silver-en concentrations were at NaOH/HCHO molar ratios of 0.17 and 0.11, respectively. Higher plating rates than 1.6  $\mu m/min$  can be achieved by using silver-en concentrations greater than 0.12M. However, aerosol plating efficiency (7, 8) generally decreases with increasing metal ion concentration and economics of the process will be affected accordingly.

The deposition efficiency of the  $en$ -HCHO spray formulation was determined at 0.15M  $Ag^+$ . At this concentration, 55% of the  $Ag^+$  sprayed was obtained in the deposit. It should be possible to increase efficiency slightly by reducing the  $Ag^+$  concentration and optimizing spray parameters. However, 60-70% efficiency would appear to be the practical upper limit for aerosol plating processes (7, 8).

Table III summarizes the plating results with formaldehyde. The EDTA complex is unsuitable with this reducing agent. The ammonia complex produces the purest deposits in the as-plated condition and the rates are somewhat higher than with the  $en$  complex. How-

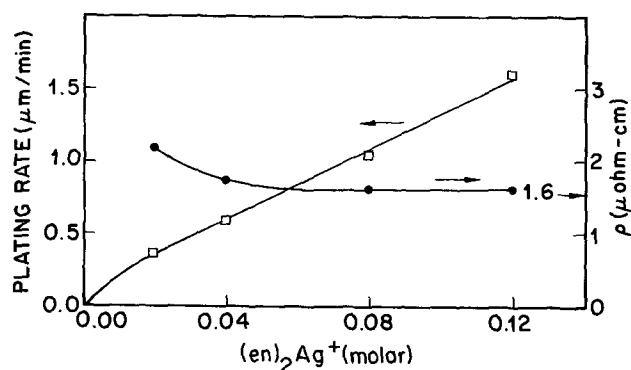


Fig. 11. Effect of  $(en)_2Ag^+$  concentration on plating rate using HCHO. Plating solutions: 2.5  $en/Ag^+$ , pH 10.5; 9 HCHO/ $Ag^+$ , variable NaOH. 120°C bake.

Table III. Aerosol silver plating\* with formaldehyde

Ligand	Plating rate ( $\mu m/min$ )	$\rho$ ( $\mu ohm-cm$ )	
		22°C	120°C
EDTA	0.3	>1000	22
en	1.1	3-4	1.6
NH <sub>3</sub>	1.4	1.7	1.6

\* 0.08 molar silver complexes. Resistivity at ambient temperature and after heating.

ever, care must be exercised in storage of this complex to prevent the formation of the explosive silver imide or azide. The  $en$  complex produces plating results comparable to the ammoniacal complex and may be less hazardous. Silver- $en$  solutions have been stored for periods in excess of 1 year without any difficulty.

### Summary

Aerosol silver films deposited with formaldehyde have a lower electrical resistivity than those deposited with hydrazine (compare Tables II and III). The electrical resistivity of pure silver can be achieved with deposits from formaldehyde by a brief thermal treatment at 120°C. The films as deposited appear to contain a small amount of some compound, probably silver carboxylate, on the surface which decomposes to silver and carbon dioxide at temperatures above 22°C. Films deposited with hydrazine also exhibit a weight loss and decrease in resistivity in this temperature range. Some silver oxide is also codeposited with the silver in the hydrazine process and a thermal treatment at 200°-300°C is required to achieve the resistivity of pure silver.

The ligand used in the aerosol process has an effect on the electrical resistivity of the deposited film. EDTA produces the highest resistivity films while  $en$  and ammonia produce deposits with or near the resistivity of pure silver. Ammonia is not preferred because it has the potential to form explosive compounds in the silver solution upon standing.

The recommended aerosol silver process for producing low resistivity films utilizes  $en$  as the silver ligand and formaldehyde as the reducing agent. This system produces deposits comparable in quality to those obtained from the ammonia complex and the metal solution may not be as hazardous. The optimum composition of the silver solution is  $en/Ag^+$  molar ratio  $\geq 2.5$ . The pH should be maintained at 10.5-10.6 for best stability. The reductant consists of a mixture of formaldehyde and sodium hydroxide with the molar ratio of NaOH/HCHO near 0.08. The optimum molar ratio of HCHO/ $Ag^+$  is near 9. Plating rates from 0.3 to 1.6  $\mu m/min$  have been obtained by varying the concentration of the silver- $en$  complex from 0.02 to 0.12M. As-plated films have an electrical resistivity twice that of pure silver. A brief thermal treatment at 120°C reduces resistivity to the value for pure silver.

Manuscript submitted Oct. 1, 1973; revised manuscript received Dec. 7, 1973. This was Paper 214 presented at the Miami Beach, Florida, Meeting of the Society, Oct. 8-13, 1972.

Any discussion of this paper will appear in a Discussion Section to be published in the December 1974 JOURNAL. All discussions for the December 1974 Discussion Section should be submitted by Aug. 1, 1974.

### REFERENCES

1. A. Barnes, U.S. Pat. 625,733 (1899).
2. W. Peacock, U.S. Pat. 2,214,476 (1940).
3. H. Schneider, U.S. Pat. 2,136,024 (1938).
4. W. Peacock, U.S. Pat. 2,363,354 (1944).
5. Private communication.
6. W. Peacock, British Pat. 537,987 (1941).
7. P. B. G. Upton, G. W. Soundy, and G. E. Busby, J. Electrodepos. Tech. Soc., 28, 103 (1952); Metal Finishing, 51, 65 (1953).

8. D. J. Levy and E. F. Delgado, *Plating*, **52**, 1127 (1965).
9. W. R. Momyer and D. J. Levy, *Electrochem. Technol.*, **5**, 293 (1967).
10. D. J. Levy and W. R. Momyer, Unpublished data.
11. D. J. Levy, *Tech. Proc. Am. Electroplaters' Soc.*, **51**, 139 (1964).
12. C. R. Noller, "Chemistry of Organic Compounds," p. 218, W. B. Saunders Co., Philadelphia (1952).
13. "Handbook of Chemistry and Physics," 52nd ed., pp. B-134 and E-72, The Chemical Rubber Co., Cleveland (1971).
14. S. R. Natarajan and R. Krishnan, *Metal Finishing*, **69**, 51 (1971).
15. L. G. Sillen and A. E. Martell, "Stability Constants of Metal-Ion Complexes," p. 634, The Chemical Society, Metcalfe and Cooper Ltd., London (1964).
16. W. M. Latimer and H. H. Hildebrand, "Reference Book of Inorganic Chemistry," Revised Edition, p. 114, The Macmillan Co., New York (1949).
17. Ollard, *J. Electrodepos. Tech. Soc.*, **17**, 11 (1941).
18. W. M. Latimer, "Oxidation Potentials," 2nd ed., pp. 99 and 130, Prentice-Hall, Inc., Englewood Cliffs, N. J. (1952).
19. W. C. Fernelius, "Inorganic Syntheses," Vol. II, p. 196, McGraw-Hill Book Co., New York (1946).

## Carbon in Gold Electrodeposits

H. A. Reinheimer\*

*Bell Laboratories, Incorporated, Reading, Pennsylvania 19604*

### ABSTRACT

Gold electrodeposits plated from pure phosphate and citrate buffered  $\text{KAu}(\text{CN})_2$  solutions can become contaminated with carbonaceous material which originates from the metal complex. The level of impurity in gold foils can be made to vary in a range from essentially 0 to 1300 ppm of carbon as a function of plating temperature, and, at room temperature, as a function of solution pH, current density, and buffer ion composition. The morphological characteristics of the deposited gold surface, however, were found to be influenced by the extent of bath usage, and such plating parameters as current density and bath temperature, rather than by carbon content. Hardness and brittleness increase with carbon content.

It has been recognized in recent years that carbonaceous materials can be incorporated into electrodeposited gold (1-10). Primary attention was paid to baths containing hardening agents, such as cobalt and nickel, as it became apparent that in deposits plated from such formulations rather large quantities of carbon were imbedded, namely as much as tenths of a per cent by weight.

In this investigation so-called pure, soft-gold bath formulations were utilized exclusively, which contain only potassium cyanaurate(I) and a buffer system in aqueous solution.

Objectives of this work were (i) to establish relationships between the appearance of electrodeposited gold and its content of carbonaceous contaminants; (ii) to determine the conditions under which incorporation of such carbon-containing materials are enhanced; and (iii) to trace the origin of these contaminants.

In order to analyze for carbon in gold a commercially available apparatus<sup>1</sup> was used, which combines a classical type of combustion with a gas chromatographic means of detection, and an automatic readout by which it is capable of detecting as little as 1 ppm. With metallic samples (such as standard steel materials supplied by the National Bureau of Standards) at a 20 ppm level a precision of  $\pm 1.5$  ppm was generally achieved.

Observations of surface features were performed with a scanning electron microscope (MAC 700).

### Results and Discussion

*Aging of baths operated at 65°C.*—It is commonly known that the appearance of gold electrodeposits undergoes undesirable changes from bright yellow to dark brown as the age of a bath increases with use, although all operating parameters are kept constant or within a narrow range during the deposition process.

Two different buffer systems similarly operated [a potassium phosphate buffer at pH 10, and an ammonium citrate buffer at pH 4.7 (Table I)] were used to study these changes in morphology of the deposits and the carbon incorporation in the gold. Hardness and brittleness characteristics were also determined.

From 1.5 liters of the phosphate buffered plating solution, sets of two gold-struck Rodar<sup>2</sup> disks (10 cm<sup>2</sup> each) and one molybdenum rectangle (2.5 × 5 cm) were plated at 7.5 mA/cm<sup>2</sup> to yield sufficient gold (approx. 1g) on the molybdenum substrate for carbon analyses and a thickness of more than 30 μm on the disks to determine hardness. A total of 23 sets were plated from the phosphate-buffered solution. The bath was replenished whenever it had been depleted by ~30% of its original gold metal content. By replenishing the bath four times, a total of 65g of gold was plated out, corresponding to 95g of gold potassium dicyanoaurate(I). The objective of working the bath to this extent was to enhance any side reactions that might occur, such as the formation of polymeric material, which could lead to subsequent incorporation of carbon into the gold deposit. The anode was a platinum wire (0.08 mm diameter). Vigorous agitation was provided by attaching the cathode specimens horizontally onto a vertical moving impeller (3 cm vertical stroke at ~250 rpm). A small anode area was found to provide much more uniformly plated deposits when used with this type of agitation than those obtained with a larger geometry. This effect may be due to the rapidly changing position of the cathode.

The cathodic current efficiencies were found to be 95-99+, except for the plating of the last 4 sets when the bath was electrolyzed to full depletion of its gold content. Since pH changes were minute (slight increases), corrections were made only when the bath was replenished.

Carbon analyses of the foils indicated practically no organic contamination. As the age of the solution in-

\* Electrochemical Society Active Member.

Key words: carbon in gold, morphology of electrodeposited gold, electrodeposition of gold.

<sup>1</sup> Low Carbon Analyzer, Laboratory Equipment Corporation.

<sup>2</sup> Rodar, a commercially available alloy, is composed of approximately 54% iron, 29% nickel, and 17% cobalt.



Table I. Aging of 65°C baths

Composition	Bath 1	Bath 2
	20 g/liter KAu(CN) <sub>2</sub> 40 g/liter KH <sub>2</sub> PO <sub>4</sub> 10 g/liter K <sub>2</sub> HPO <sub>4</sub> KOH to adj. pH	20 g/liter KAu(CN) <sub>2</sub> 50 g/liter NH <sub>4</sub> -citr.* 50 g/liter (NH <sub>4</sub> ) <sub>2</sub> SO <sub>4</sub> citric acid to adj. pH
Operating conditions		
Temperature		65° ± 2°C
Current density		7.5 mA/cm <sup>2</sup> d.c.
Plating time		75 min
pH	10	4.75
Current efficiency:		
average	97%	95%
range	95-99 + %	91-99 + %
Thickness range of gold on		
Rodar disks	35-50 μm	35-45 μm
Total No. of sets plated	23	23
Total amount of gold plated	64g	59.6g

\* NH<sub>4</sub>-citr. = dibasic ammonium citrate.

creased with use, no increase of carbon was found in the deposits (see Fig. 1). The general level was 0-20 ppm with maxima approaching slightly over 30 ppm.<sup>3</sup>

The morphology of the deposits, however, exhibited marked alterations as the age of the bath increased, when the gold concentration was replenished, or when solution purification by charcoal treatments were applied.

As the plating process was continued at a constant current density of 7.5 mA/cm<sup>2</sup>, the structure gradually changed from a lateral smooth weblike type growth with high reflectivity or bright appearance to an acicular outward type growth with low reflectivity and brown color (see SEM micrographs, Fig. 2, parts 1-8, representing deposits plated in sequence). The latter structure is very similar to what can be observed when a current density higher than ~10 mA/cm<sup>2</sup> is applied with a freshly made-up bath. As the gold concentration is restored to its original level, some brightening of the color, and consequently decreased acicular features, may be observed in the SEM micrograph (Fig. 2, part 4). However, very soon after less than 10% of further gold has been removed, (Fig. 2, part 5), the rough surface characteristic returns, and additional replenishments made later in the aging process do not reproduce the brightening effect (Fig. 2, part 6).

Thus, a decrease in gold concentration which occurs during continuous plating at constant current density is not the only reason for morphological changes. Since the deposited gold does not contain any increased amounts of imbedded organic materials, there is an implication that constituents are generated in solution which cause alterations in the deposition process, or alternatively, an inherently present species is being depleted.

Upon further continued plating and without implementation of a purification treatment, the deposit will only appear darker (Fig. 2, part 7). Once the gold

<sup>3</sup> Handling of the parts (rinsing, boiling in deionized water, drying, bottling, weighing, transferring, etc.) should be regarded as a potential source of contamination at this very low level. Great care was taken to avoid any contact with organic contaminants from outside origins.

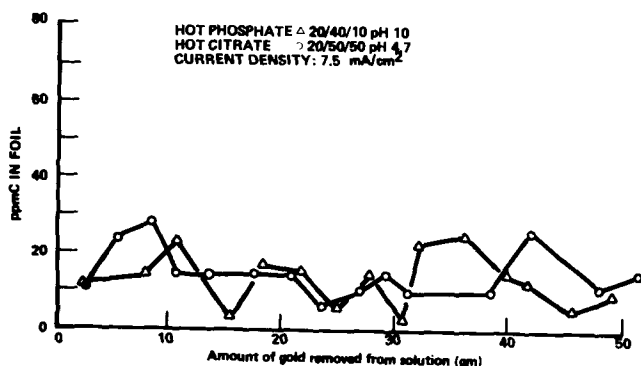


Fig. 1. Carbon content of gold deposits as a function of bath age

concentration reaches very low levels near the depletion of the bath, the gold becomes almost dendritic, discontinuous, and very dark in appearance (Fig. 2, part 8).

The change in morphology is also accompanied by a change in the cathodic deposition potential. When operating a bath at constant current density and a narrow range of gold concentration (e.g., 12.5 g/liter ±10%) the deposition potential after an initial stabilization period decreases slowly toward more negative values, e.g., at pH 10, 65°C, and 7.5 mA/cm<sup>2</sup>, a cathodic potential<sup>4</sup> range from approximately -800 to -980 mV can be observed during an aging process that involves several turnovers of the original gold content of the bath. At potential readings between approximately -800 and -900 mV a bright surface develops, whereas an off color or brownish deposit is obtained once the deposition potential drops below -900 to -930 mV.

Chemical analysis of the depleted bath supplied information about polymeric matter, free cyanide ions, and residual gold concentration. Extraction of the major portion of the depleted solution with ethyl acetate yielded a small quantity (<100 mg/liter) of oily yellowish polymeric material, which was characterized by IR (see Experimental Appendix) and found to be similar to samples, which were isolated from potassium cyanide solution polymerization reactions. At high pH and 65°C most of the liberated cyanide would undergo hydrolysis to formate and carbonate, as was reported by Silver (8); consequently, the concentration of free cyanide ion in solution would vary with its rate of hydrolysis. In this bath, immediately after completion of the plating experiments, a total of 6.7 g/liter of free cyanide ions was found by titration with silver nitrate (potassium iodide as indicator) to account for almost 40% of all cyanide liberated. After storing the solution for several days, much less free cyanide was found. The residual gold concentration in solution was determined to be 0.015 g/liter.

Hardness data were found to vary between 85 and 100 Knoop<sup>5</sup> for a 25g load. No up or downward trends were observed, although large morphological variations were found. The deposits are very ductile and pass wire wrap tests (see Experimental Appendix).

The second series of hot bath aging experiments was done with a citrate formulation as shown in Table I, bath composition 2. Plating conditions were the same as for the phosphate bath, namely 7.5 mA/cm<sup>2</sup> current density, at 65°C. Sets of 2 rodar disks and 1 molybdenum rectangle were plated from 1.5 liters solution volume. A total of 60g of gold was plated from the bath, corresponding to 88g of KAu(CN)<sub>2</sub>. Cathodic efficiency was 91-99%.

Basically the same information was obtained, namely, very low carbon content (Fig. 1), and gradu-

<sup>4</sup> Cathodic potentials referred to calomel electrode.

<sup>5</sup> These values are high, due to the manner of agitation, as explained in Table II.



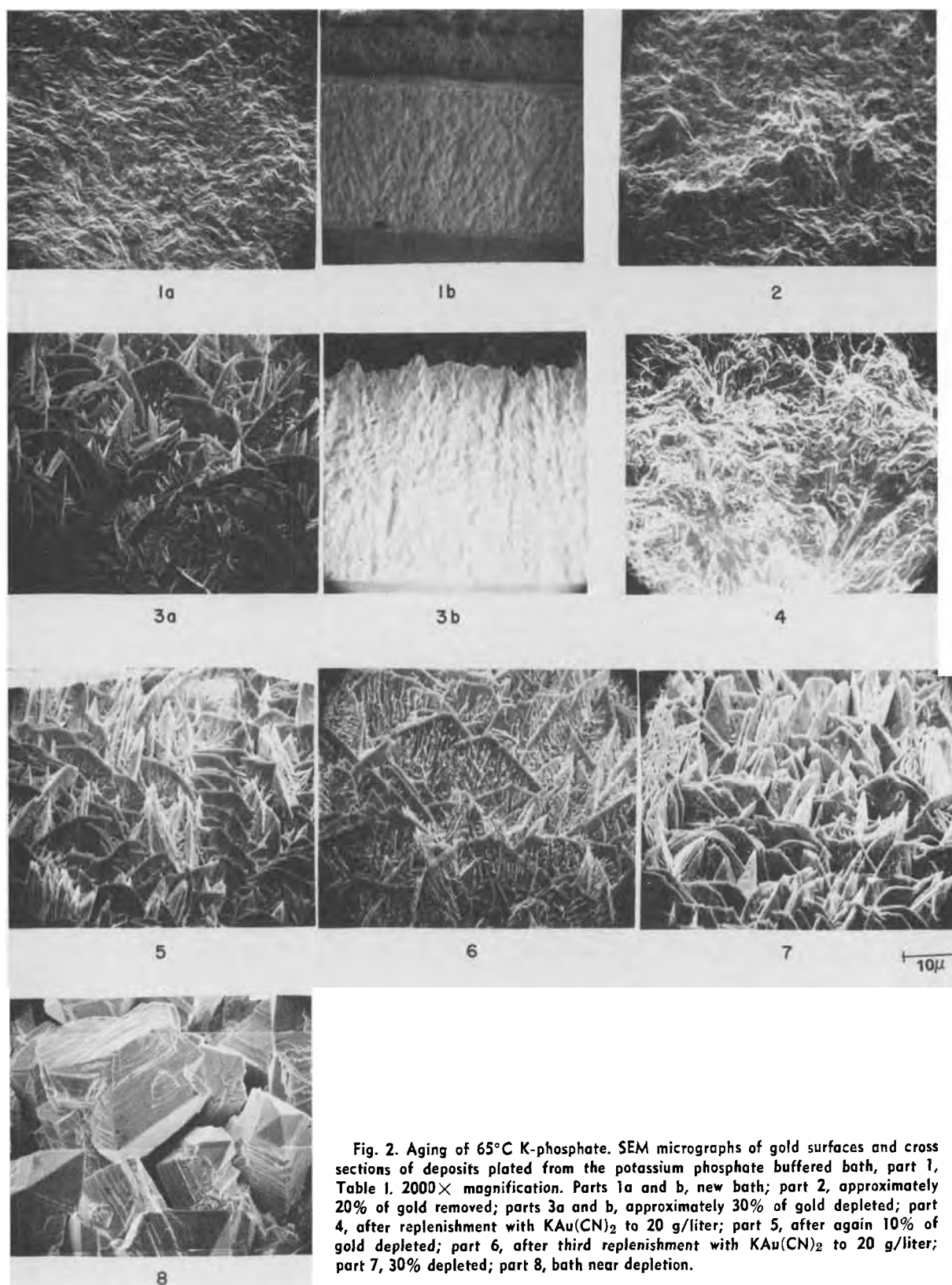


Fig. 2. Aging of 65°C K-phosphate. SEM micrographs of gold surfaces and cross sections of deposits plated from the potassium phosphate buffered bath, part 1, Table I. 2000 $\times$  magnification. Parts 1a and b, new bath; part 2, approximately 20% of gold removed; parts 3a and b, approximately 30% of gold depleted; part 4, after replenishment with  $\text{KAu}(\text{CN})_2$  to 20 g/liter; part 5, after again 10% of gold depleted; part 6, after third replenishment with  $\text{KAu}(\text{CN})_2$  to 20 g/liter; part 7, 30% depleted; part 8, bath near depletion.

ally changing surface features from a lateral crystalline to an outward type growing pattern (Fig. 3, parts 1-4).

Hardness values obtained were between 99 and 109 Knoop for a 25g load. The average thickness of the deposits was 40  $\mu\text{m}$ .

The results of chemical analysis of the depleted solution diverged somewhat from what was found in the phosphate bath. It was observed that after removal of about 20% of gold by electrolysis, the solution had turned visibly to clear yellow. Extraction of the de-

pleted citrate gold bath with ethyl acetate now showed a small quantity of a product, which was identified and shown to consist of a mixture of a product due to a citrate degradation and a cyanide derivative. Separation of both constituents was not undertaken since the quantity was too small. A similar discoloration was obtained when a solution of dibasic ammonium citrate alone was electrolyzed. Anodically, the citrate is oxidatively attacked to form an orange brownish oil, which could be isolated from electrolyzed pure dibasic ammonium citrate solutions. Ex-

Table II. Properties of deposits from hot baths

Bath	pH	Current (mA/cm <sup>2</sup> )	Appearance*	Hardness** (Knoop)	Brittleness	ppm C*** (avg)
K-phos. 40/100	4.5	3	5	99	D	50
		15	8	108	D	30
	7.0	3	4	67	D	~10
		15	8	102	D	~10
	10.0	3	4	65	D	<10
		15	7-8	96	D	~10
12.0	3	5	66	D	<10	
	15	5-6	79	D	<10	
NH <sub>4</sub> -phos. 40/100	4.5	3	8	90	D	25
		15	10	105	D	20
		3	4-5	77	D	~10
NH <sub>4</sub> -citr. 40/100	4.5	3	7	112	D	<10
		15	7			

D = ductile, no cracks upon wrapping a plated wire.

\* See Table III for explanation.

\*\* The hardness data appear generally high which is due to the vigorous vertical mode of agitation. It was established that these values are generally about 20% higher than those which are observed by stirring with magnetic spinbars. However, since all experiments employed the former mode of agitation, the numbers are valid for comparison.

\*\*\* Carbon content in gold deposit.

K-phos. = potassium phosphate buffer.

NH<sub>4</sub>-phos. = ammonium phosphate buffer.

NH<sub>4</sub>-citr. = ammonium citrate buffer.

40/100 = 40 g/liter KAu(CN)<sub>2</sub>, 100 g/liter buffer salt.

cept for IR spectroscopic characterization further identification was not pursued.

Free cyanide was present to only 0.05 g/liter (after the pH was adjusted to 11 in the analysis sample), indicating that free hydrogen cyanide (HCN) does not accumulate to high concentrations in the bath at pH 4.7. A strong smell was recognized during the operation of the bath, indicating the probable escape of HCN.

Although the basic bath composition changed in a different way with respect to the free cyanide and citrate constituents, electrolysis of the bath produced similar changes in the morphology of the deposits. Also, the yellow oily citrate derivative, isolated from electrolyzed dibasic ammonium citrate solutions, proved to be cathodically inactive and did not change morphological characteristics when added to a fresh plating bath.

In view of these results, effort was directed toward obtaining information about the material which causes the change in the deposition process to promote the undesirable outward-type growth of deposit. Since it was not codeposited in sufficient quantities for routine characterization, an indirect approach was adopted.

*Contamination of a bath with organic materials.*—A variety of materials, which can be derived from cyanide ions in an aqueous environment, was purposely added to a phosphate bath to study the influence upon

the appearance of the deposit. The Hull cell represents a sensitive tool for such tests, because a current density range from 0 to 22 mA/cm<sup>2</sup> can be obtained on one panel (10 × 6.8 cm). Thus, the current density at which the deposit changes from a bright to a dark appearance can readily be observed on the rectangularly shaped panel. Quantities of approximately 500 mg of each of the following materials per 550 ml solution (size of Hull cell) were added to samples of a fresh phosphate buffered bath and allowed to dissolve:

CN <sup>-</sup>	free cyanide ions as potassium cyanide
HCN	hydrogen cyanide
HCONH <sub>2</sub>	formamide
HCO <sub>2</sub> K	potassium formate
H <sub>2</sub> CO	formaldehyde
(HCN) <sub>4</sub>	tetramer of HCN, diaminomaleonitrile
CN-polymer	isolated from KCN polymerization by extraction
(CONH <sub>2</sub> ) <sub>2</sub>	oxamide
(CONHOH) <sub>2</sub>	oxalhydroxamic acid
H <sub>2</sub> NCH <sub>2</sub> COOH	glycine
C <sub>5</sub> N <sub>5</sub> H <sub>5</sub>	adenine

Subsequently, a panel was plated at 0.5A total current for 5 min plating time.

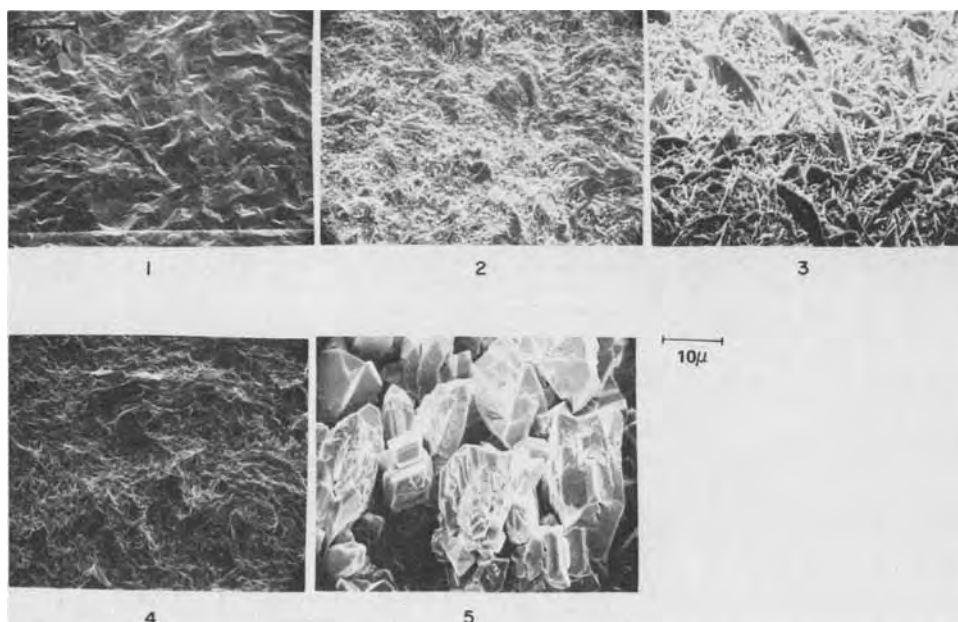


Fig. 3. Aging of 65°C ammonium citrate. SEM micrographs of gold surfaces of deposits plated from the ammonium citrate buffered bath 2, Table I. 2000× magnification. Part 1, new bath; part 2, after approximately 20% of gold was depleted; part 3, after approximately 30% of gold was depleted; part 4, after first replenishment with KAu(CN)<sub>2</sub> to 20 g/liter; part 5, bath near depletion.

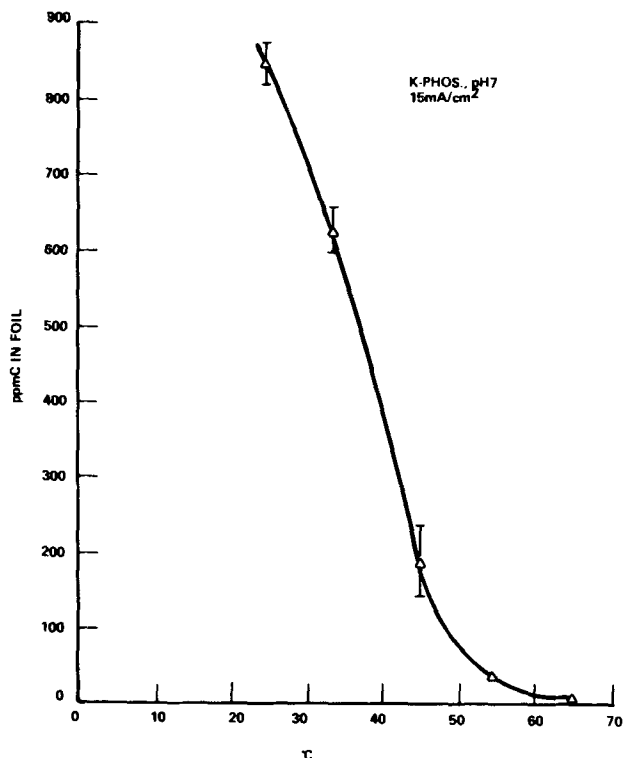


Fig. 4. Carbon content in gold deposits vs. bath temperature

None of the components listed influenced the appearance of the deposit visibly. This rather negative result suggests that either the electrochemically active species would be a chemically unstable intermediate, or that a new bath would contain a hitherto unde-

Table III. Appearance classification

No.	Visual		SEM	
	Appearance	Color	Characteristics	Growth
1	bright, glossy	yellow	sectional, sphericals	lateral
2	bright, hazy	yellow	sphericals, irregular	lateral
3	matte, hazy	ochre	needle-type	outward
4	bright	yellow	crystalline	lateral
5	matte, smooth	yellow	"webblike"	lateral
6	matte	dark yellow	transitional*	lateral/ outward
7	matte	ochre	mostly acicular	outward
8	dull	brownish	acicular or spherical or crystalline	outward
9	dull	brown	same as 8**	outward
10	dark	brown	same as 8**	outward

\* Beginning structural change from lateral to outward type.  
\*\* Increase in vertical growth and discontinuity.

tected desirable species, which quite independent of any buildup of organic materials, is continuously depleted during the electrodeposition, and thereby would cause the change in morphology.

**Fresh baths.**—When using freshly made up solutions under a variety of conditions at  $65^\circ \pm 2^\circ\text{C}$  as outlined in Table II (hot baths), it was determined that none or very small amounts of carbon were contained in the deposits. Dark deposits plated at high current density were found to be equally pure as compared to bright deposits plated at low current density.

However, when the plating temperature was lowered in steps of  $10^\circ\text{C}$ , a subtle increase of carbon in the gold deposits was discovered. Figure 4 shows this as an example for a potassium phosphate buffered bath at pH 7, operated at a current density of  $15\text{ mA/cm}^2$ .

A repetition of all plating experiments at  $25^\circ\text{C}$  instead of  $65^\circ\text{C}$ , gave insight into the conditions under which the incorporation of carbonaceous matter appeared to be enhanced, such as increasing current density, decreasing solution pH, and changing buffer ions. Table IV summarizes the experimental findings. Specifically, the relationships of the carbon incorporation into the deposit vs. current density and solution pH are depicted in Fig. 5 and 6 for the potassium phosphate and ammonium citrate buffered formulations, respectively.

An increase of current density increases the carbon, though the gradient of the increase is not constant. There is a pH dependency, notably in acidic and neutral media, where the current density affects the level of contamination significantly. At increasing alkalinity of the solution, the carbon contamination diminishes. In deposits from a potassium phosphate system at pH 12 and  $3\text{ mA/cm}^2$ , a minimum of approximately 300 ppm, and at pH 4.5 and  $15\text{ mA/cm}^2$ , a maximum of around 1300 ppm, were detected (Fig. 5). When ammonium ion acts as the cation of the buffering salt, then a much lower level of carbonaceous contamination is obtained. The same general trends, however, are observed: an increase of carbon content with increasing current density, and a slight increase of contamination with decrease of pH. However, the maximum now is only about 600 ppm of carbon, whereas the minimum contents are below 100 ppm at low current densities (Fig. 6).

Bright, glossy, yellow deposits can be obtained, e.g., from a phosphate or citrate buffered formulation at  $10\text{ mA/cm}^2$  to approximately  $50\text{ mA/cm}^2$ , although at the high current densities (higher than  $20\text{ mA/cm}^2$ ), it becomes more and more dependent on the mode of agitation. Vigorous agitation is required to obtain best results. "Bright" in this context means glossy yellow, as compared to the matte crystalline yellow appear-

Table IV. Properties of deposits from baths at  $25^\circ\text{C}$

Bath	pH	Current (mA/cm <sup>2</sup> )	Appearance*	Hardness** (Knoop)	Brittleness	ppm C*** (avg)
K-phos. 40/100	4.5	3	8	168	B	780
		15	1-2	168	B	1200
	7.0	3	10	147	D	440
		15	1-2	172	B	890
	10.0	3	10	138	D	330
		15	1-2	159	B	415
NH <sub>4</sub> -phos. 40/100	4.5	3	8	127	D	320
		15	1-2	134	B	360
	7.0	3	10	168	D	190
		15	1-2	175	B	600
	10.0	3	10	144	D	190
		15	1-2	166	D	405
NH <sub>4</sub> -citr. 40/100	4.5	3	8	161	D	120
		15	1-2	176	D	370
	7.0	3	10	138	D	70
		15	1-2	160	B	380
	10.0	3	10	139	D	520
		15	6	162	B	525

D = ductile (does not show cracks upon wrapping a plated wire).

B = brittle (shows cracks upon wrapping a plated wire).

\* See Table III for explanation.

\*\* See footnote in Table II.

\*\*\* Carbon content in gold deposits.

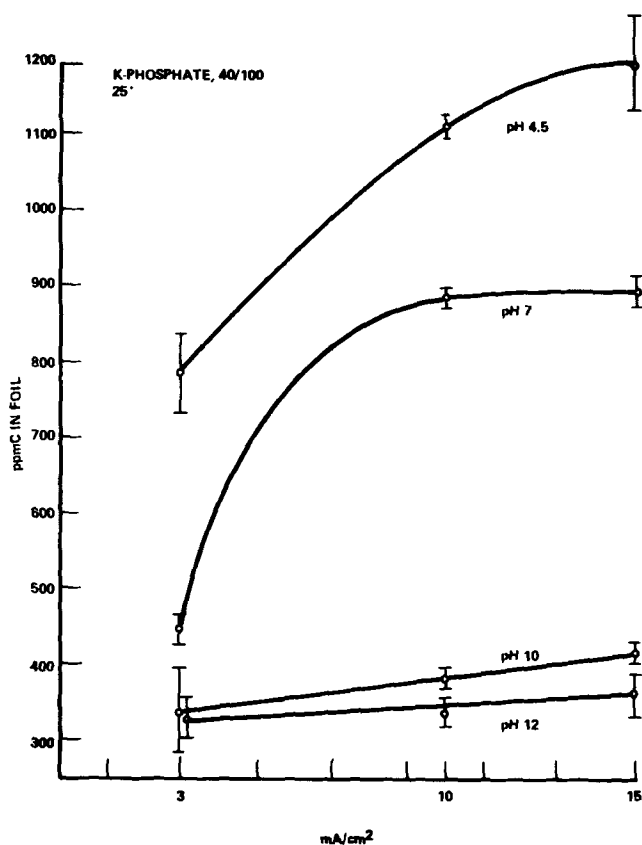


Fig. 5. Carbon content in gold deposits vs. current density

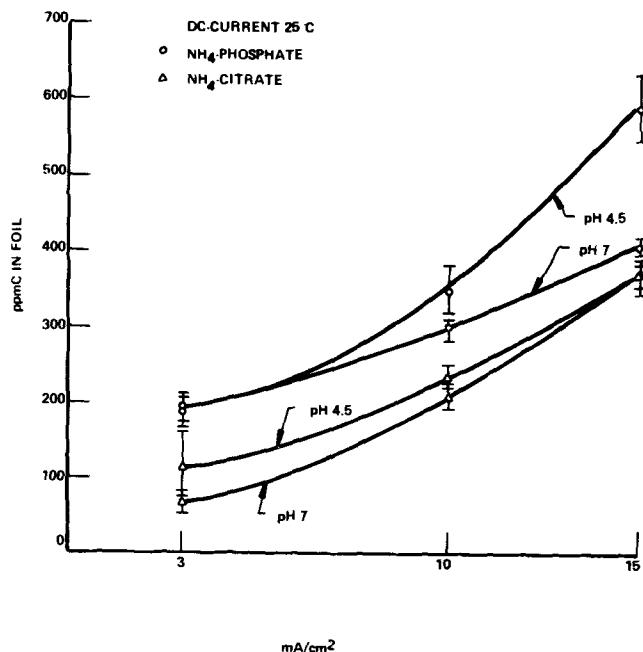


Fig. 6. Carbon content in gold deposits vs. current density

ance of deposits from hot baths (Table III, parts 1 and 4).

Morphological differences as viewed by the scanning electron microscope are pronounced as well. Whereas surfaces of hot bath plates are crystalline with lateral growths, a rather featureless topography characterized with spherical segments is observed on deposits from room temperature baths (Fig. 7, part 2; Fig. 8, part 1; Fig. 9, part 1).

The bulk of the deposit, as shown in Fig. 8 and 9, is very homogeneous, displays columnar type growth, and does not contain any layers of foreign material.

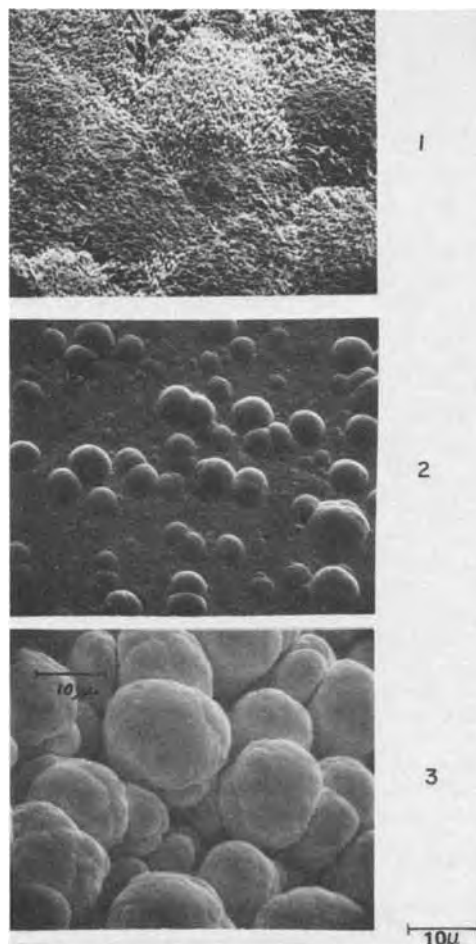


Fig. 7. SEM micrographs of gold surfaces of deposits generated in a potassium phosphate buffered bath at room temperature (100 g/liter  $\text{KH}_2\text{PO}_4$ , 40 g/liter  $\text{KAu}(\text{CN})_2$ , pH 4.5). Part 1 at 3 mA/cm<sup>2</sup>; part 2 at 25 mA/cm<sup>2</sup>; part 3 at 60 mA/cm<sup>2</sup>.

Dark deposits are obtained both at low current densities (<5 mA/cm<sup>2</sup>) and at very high current densities (>50 mA/cm<sup>2</sup>). It should be noted that this differs significantly from the behavior of the hot plating baths, which exhibit yellow crystalline deposits preferably at very low current densities, and extend only to a general maximum of about 10 mA/cm<sup>2</sup>. The matte brownish surface observed at low current densities is shown in Fig. 7, part 1. This is a typical outward-type growth of very fine needlelike features, less than 1 μm in width. Quite different from this is the growth at the very high current densities, which consists of discrete sphericals packed randomly on top of one another, and resulting in a very weakly adherent, porous deposit. The particle size varies between 1 and 15 μm and the color of the surface appears brown as well (Fig. 7, part 3).

Further information about the physical properties of gold deposits was gained by determination of hardness and brittleness (See Tables II and IV).

The following relationships could be established for deposits plated from baths at 25° and 65°C:

(i) Much harder deposits result from high as well as low current density plating at room temperature vs. plating at 65°C.

(ii) Hardness increases with current density for both 25° and 65°C baths.

(iii) Hardness decreases with an increase in pH. A similar trend exists for the carbon content in foils plated from cold baths, although no direct relationship with hardness could be established.

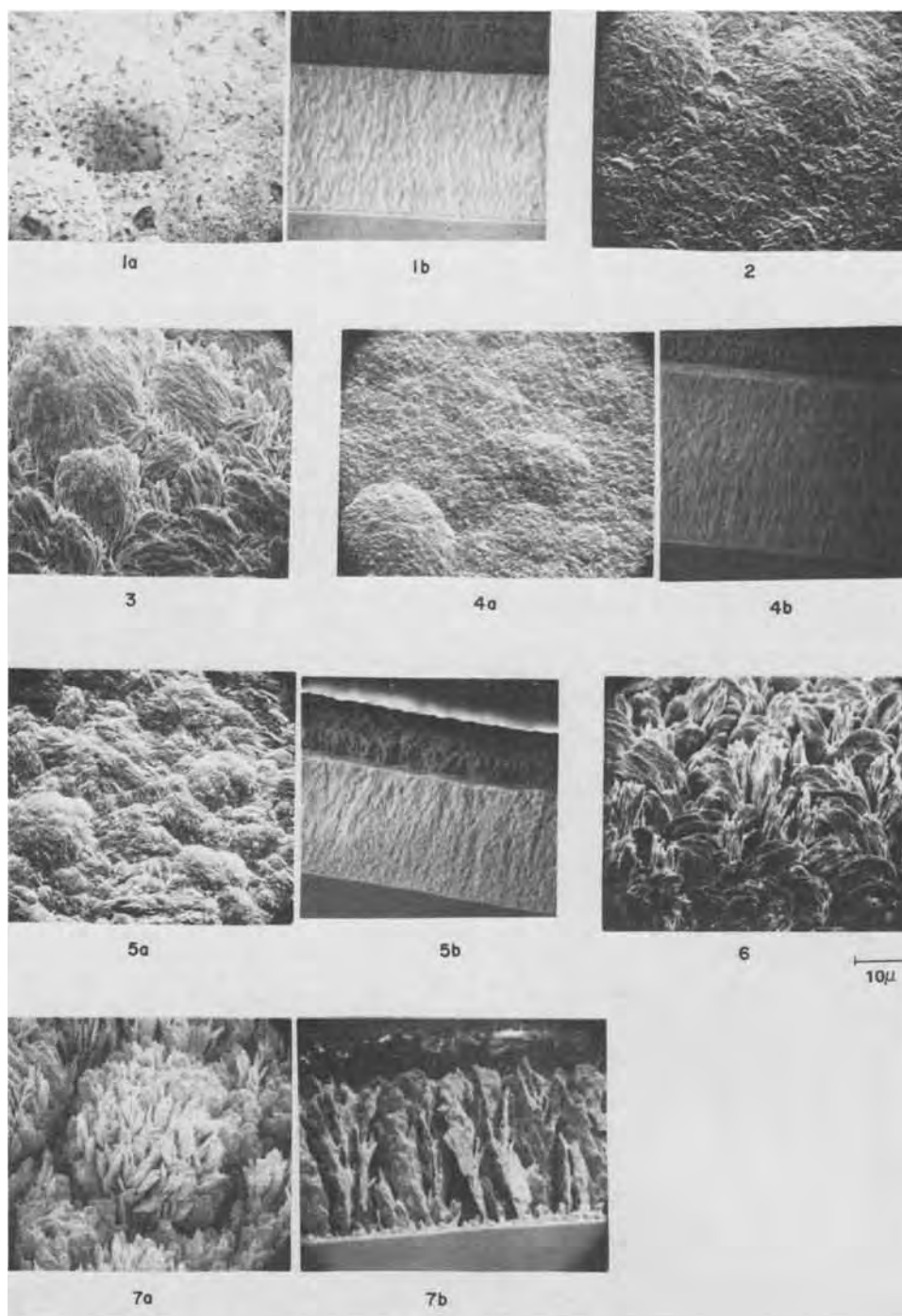


Fig. 8. Aging of 25°C K-phosphate. SEM micrographs of gold surfaces (a) and cross sections (b) of deposits plated from the potassium phosphate buffered bath 1, Table VI. Part 1, fresh bath; part 2, after approximately 20% of gold depleted; part 3, approximately 30% gold depleted; part 4, bath replenished with  $\text{KAu}(\text{CN})_2$  to 40 g/liter; parts 5 and 6, further increased age of the bath; part 7, bath near depletion.

(iv) The hardness of a deposit does not depend on the kind of buffering salt. Ammonium salts delivered a hardness similar to that of potassium salts, when plated under identical conditions. The carbon content, however, does depend strongly upon the kind of cation used. Thus, it can be concluded that the similarity in trend between carbon content and hardness is coincidental.

Brittleness of deposits from cold baths, however, appears to show a relationship to the level of carbonaceous contamination (Table V). All foils from hot baths, containing very low quantities of organic materials, as well as all deposits from cold formulations, which contained less than 350 ppm of carbon, passed wire wrap tests. All coatings with more than 520 ppm of carbon very clearly appeared to be brittle, and resulted in cracking upon wrapping. In the range between 350 and 500 ppm inconsistent results were obtained with some of the deposits exhibiting definite

cracks, and others showing only slight evidence of cracking.

Undoubtedly it is surprising to discover that relatively large quantities of carbon-containing materials can be codeposited electrolytically, especially when working with freshly prepared cold baths. Therefore, it was essential to determine if any change in the content of this unknown material in gold deposits would occur as the bath was exposed to continuous use.

*Aging of baths operating at room temperature.*—Experiments were carried out with both baths at room temperature (see Table VI for formulations and plating conditions). From the phosphate bath, 26 sets of 2 rodar disks and 1 molybdenum sheet were plated, corresponding to a total of 75.8g of gold removed from a 1.5 liter solution volume. From the citrate formulation a total of 33 sets of parts were plated with a total of 70g of gold from the same solution volume.

A carbon analysis was obtained from every set, so that it was possible to follow the change or possible

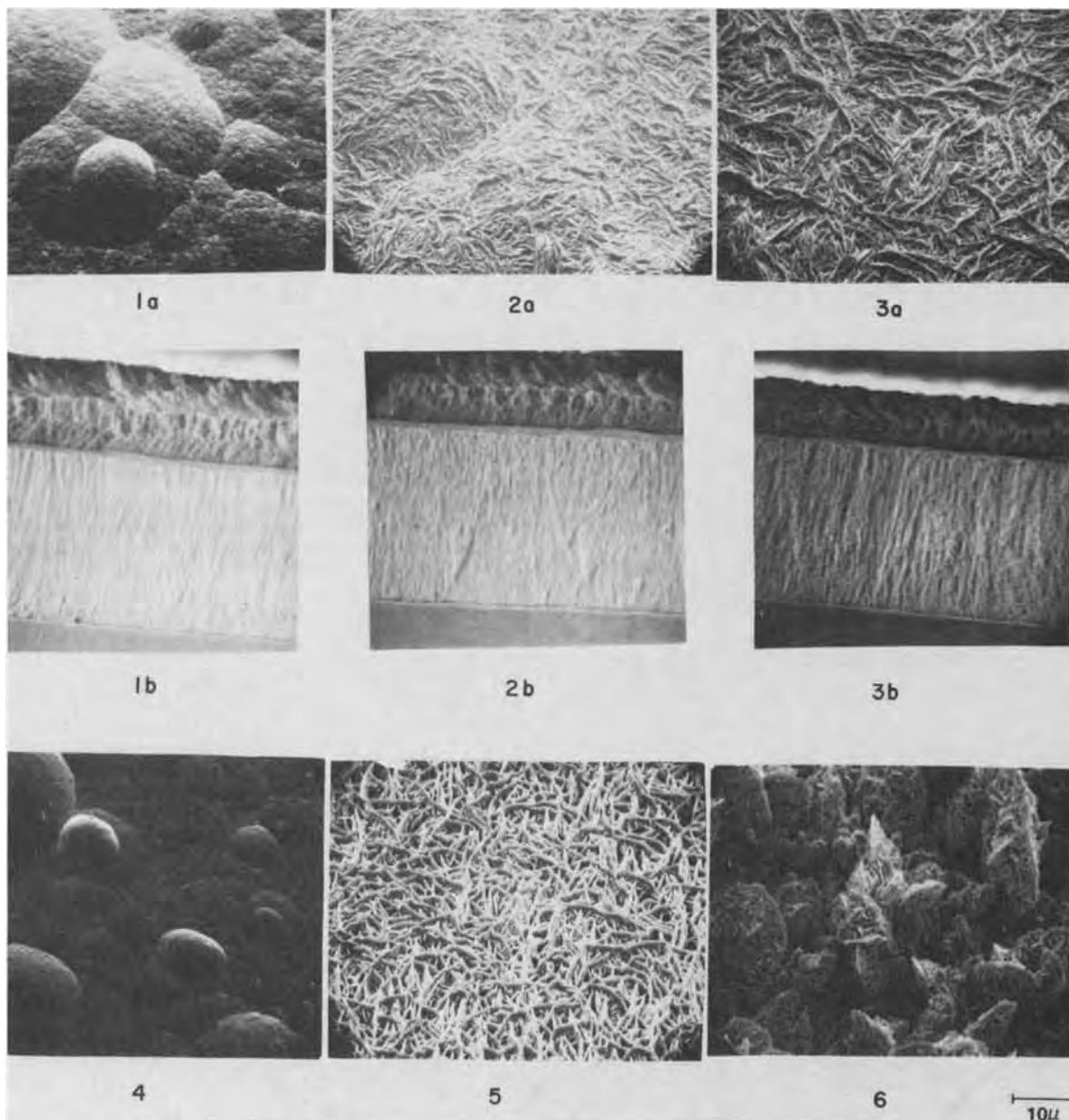


Fig. 9. Aging of 25°C citrate. SEM micrographs of gold surfaces (a) and cross sections (b) of deposits plated from the dibasic ammonium citrate buffered bath 2, Table VI. Part 1, fresh bath; parts 2 and 3, increased age of solution (approximately 20 and 30% gold depleted); part 4, bath replenished with  $\text{KAu}(\text{CN})_2$  to 40 g/liter; part 5, after further 20% of depleting; part 6, bath near depletion.

increase of carbon in the gold as a function of accumulation of organic materials in solution with increasing age of the bath.

Foils plated from the phosphate bath contained on the average 1000 ppm of carbon, including those plated at the initial stages (Fig. 10). Towards the end of the experimental series, when the gold concentration dropped to very low levels, the carbon content in the foil decreased markedly. At the same time the cathodic efficiency decreased drastically, since more and more hydrogen was evolved.

The citrate bath produced somewhat different results for the codeposition of this carbonaceous material. As found earlier with fresh baths in the presence of ammonium ions, a lower concentration of carbon was found initially. After about 15g (25%) of gold were plated from the bath, a significant increase in carbon content occurred which averaged about 800 ppm. Though somewhat lower in carbon content than the foils plated from the phosphate bath, the carbon level remained high with fluctuations until toward the end of the experiment when the depletion of gold was ap-

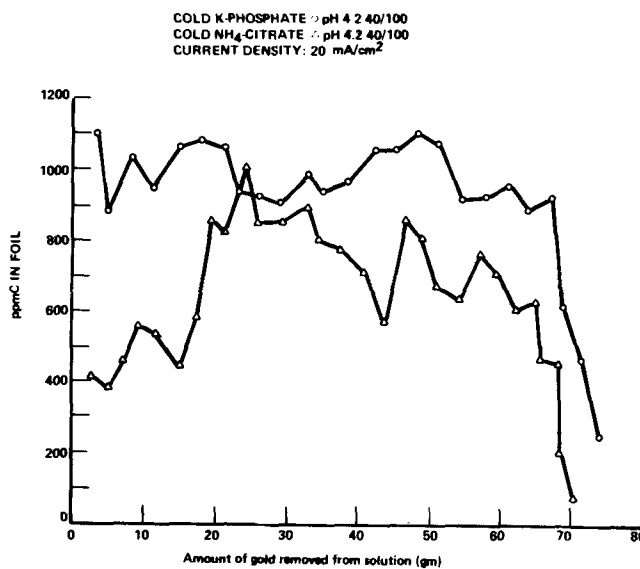


Fig. 10. Carbon content of gold deposits as a function of bath age



Table V. Brittleness vs. carbon content in gold deposits

Bath	pH	mA/cm <sup>2</sup>	Brittleness	ppm C
Hot baths	4.5-12	3 and 15	all D	<50
Cold baths				
NH <sub>4</sub> -citr.	7	3	D	70
NH <sub>4</sub> -citr.	4.5	3	D	120
NH <sub>4</sub> -phos.	7	3	D	190
NH <sub>4</sub> -phos.	4.5	3	D	190
K-phos.	12	3	D	320
K-phos.	10	3	D	330
K-phos.	12	15	B	360
NH <sub>4</sub> -citr.	4.5	15	D	370
NH <sub>4</sub> -citr.	7	15	B	380
NH <sub>4</sub> -phos.	7	15	D	405
K-phos.	10	15	B	415
K-phos.	7	3	D	440
K-citr.	7	3	D	520
K-citr.	7	15	B	525
NH <sub>4</sub> -phos.	4.5	15	B	600
K-phos.	4.5	3	B	780
K-phos.	7	15	B	890
K-phos.	4.5	15	B	1200

D = ductile.  
B = brittle.

proached. The carbon content together with the current efficiency then decreased rapidly.

It is of interest to note that the carbon content was not markedly changed when either of the baths were replenished after depleting about 30-40% of the original gold concentration. The variation of carbon level is due to inconsistencies probably in the deposition process, which have not yet been ascertained. Plating conditions were maintained constant within experimental capability from one set to the next. Contamination from handling can be considered negligible at a level higher than several 100 ppm.

Successive plating from room temperature baths results in very similar morphological changes to those which are observed in hot baths. (For deposits from the potassium phosphate formulation, see Fig. 8, parts 1-8, and for the dibasic ammonium citrate buffered bath see Fig. 9, parts 1-6.)

Initially, the surface of deposits from the phosphate bath are very glossy yellow, exhibiting flat spherical segments without crystalline features (Fig. 3, part 1). The cross-sectional micrograph shows a very homogeneous bulk of columnar appearance (Fig. 8, part 1b). As the age of the bath increases, a loss in smoothness can be noticed and a randomly oriented outward-type growth occurs (Fig. 8, part 1-3). When the bath is replenished, a definite brightening effect becomes apparent (Fig. 8, part 4a). Characteristics of the bulk of the metal remain practically unchanged. Depleting of about 30-40% of the original gold concentration and replenishing is related to a marked brightening of the deposit the first time only. The second time replenishment is made, the deposit does not regain its initial bright appearance, and with further successive additions, hardly any brightening, or none at all, is observed. Again the carbon content in the foil is not apparently related to the structural changes on the surface. As the gold concentration approaches depletion, the deposit becomes discontinuous and dendritic

(Fig. 8, part 7a) which is also demonstrated in a cross-sectional micrograph (Fig. 8, part 7b). Hydrogen is the major cathodic product under these conditions, and does not allow the gold to form an adherent deposit.

Hardly any different information was obtained when the citrate formulation was substituted. The initial deposit appears highly lustrous, but as the plating process is carried on, the coatings get dull and the morphological features again change towards an outward-type growth pattern. Similarly, the homogeneity in the bulk of the gold becomes less, as can be seen from cross-sectional micrographs (Fig. 9, part 1b-3b). The first replenishment then brings back the very smooth and glossy surface, which changes into a brown-appearing, acicularly crystallized deposit (Fig. 9, part 5). Again as the gold in solution approaches very low concentrations, a discontinuous almost dendritic growth is observed. This deposit is dark brown and easily mechanically destructible (Fig. 9, part 6).

*Plating in a cell with separated anode and cathode compartments.*—In order to decide whether the carbon constituent in gold deposits is of anodic or cathodic origin, a cell with separated anodic and cathodic compartments was employed. Plating solution was used as the bridge electrolyte, and the cell separation was implemented by use of semipermeable membranes at each end of the bridge. A potassium phosphate and an ammonium phosphate buffered solution, respectively [40 g/liter KAu(CN)<sub>2</sub> and 100 g/liter buffer salt], were used for the experiments at 25°C. In the potassium phosphate buffered solution, a maximum cathodic current density of only 4.5 mA/cm<sup>2</sup> was obtained because of bridge resistance, while 6 mA/cm<sup>2</sup> was achieved in the ammonium phosphate buffered bath. The initial pH was adjusted to 4.5 in both solutions. Two gold foils of 3g each were plated from the potassium phosphate bath, and one foil of 4g from the ammonium phosphate bath.

The following results were obtained by carbon analyses: (i) potassium phosphate bath, first foil—945 ppm carbon, second foil—746 ppm carbon; (ii) ammonium phosphate bath, 349 ppm carbon.

These data unequivocally demonstrate that the co-deposition of this carbon-containing material observed in gold foils plated from room temperature baths is a cathodically formed product. In fact, both the pH sensitivity and the cation dependency are also reflected in these figures. In a bridged cell the pH stability upon exposure to electrolysis is very low, resulting in a marked increase of pH in the cathodic compartment and an equivalent decrease of pH in the anodic compartment. It was found that the pH in the potassium phosphate bath rose from 4.5 to 5.6 after plating of both foils. Consequently, the carbon content of the second foil is somewhat lower, as would be predicted in accordance with the relationship of carbon vs. pH given in Fig. 5. Also, the result from the ammonium phosphate bath at pH 4.2 and 6 mA/cm<sup>2</sup> falls fairly well in the expected range, being well below the values obtained from the potassium phosphate system.

Table VI. Aging of 25°C baths

Composition	Bath 1	Bath 2
	40 g/liter KAu(CN) <sub>2</sub> 100 g/liter KH <sub>2</sub> PO <sub>4</sub> KOH to adj. pH	40 g/liter KAu(CN) <sub>2</sub> 100 g/liter NH <sub>4</sub> -citr. citric acid to adj. pH
Operating conditions		
Temperature		25° ± 2°C
Current density		20 mA/cm <sup>2</sup> d.c.
Plating time	30 min	27 min
pH		4.3-4.5
Cathode efficiency:		
average	90%	85%
range	85-98%	80-96%
(last 4 measurements excluded)		
Thickness range of gold on Rodar disks	40-50 μm	35-50 μm
Total No. of sets plated	26	33
Total amount of gold plated	75.8g	70g

### Conclusions

Our study of gold electrodeposits plated from pure buffered potassium gold cyanaurate(I) solutions lead to the following facts:

1. At solution temperatures of 65°C and above the incorporation of carbonaceous contaminants into cathodic deposits is minimized and practically negligible. Varying any operating parameters, as well as changing the concentration of solution components, does not increase the carbon content in the gold, as long as the bath temperature remains high.

Even, as the used age of a bath increases and the appearance of the deposit changes from bright yellow to dull brown, the carbon content of these deposits stays unchanged and very low. Undoubtedly this marked change of morphological characteristics is related to a simultaneous alteration of the solution composition. However, there are indications that the cathodic liberation of cyanide ions, and the subsequent buildup of known hydrolysis and polymerization products are not the only cause of the change in morphology of the deposits.

It was further found that characteristic surface morphologies are generated at certain cathodic deposition potentials, whereby bright yellow deposits are formed at less negative potentials than dull brown ones, e.g., in a pure phosphate buffered bath at pH 10 and 65°C, bright yellow gold is plated to as low as -900 mV and at values of -950 mV and more negative, typically dark gold is cathodically deposited. As a bath is operated at constant current density and its used age increases, the gradual darkening of the deposit is also accompanied by a potential shift towards more negative values. If organic buildup in the bath were the sole cause for this phenomenon, intentional addition of hydrolysis or polymer products derived from cyanide ions should then effect similar changes. However, hardly any morphological changes or potential deviations were observed upon addition of such derivatives to freshly prepared solutions. Similarly, a change of appearance and deposition potential could also be expected, if a hitherto unknown inherent species would be depleted from the bath as electrolysis proceeds.<sup>6</sup>

2. By lowering the bath temperature below 60°C a subtle increase of carbon in the deposit was discovered, which reaches a maximum of approximately 1300 ppm at 25°C, pH 4.5, and high current density (15 mA/cm<sup>2</sup>). Solution pH, current density, and solution composition affect the degree of carbonaceous incorporation at room temperature (see Fig. 5 and 6). At the same time a change in morphology is also observed. The surface, however, is bright, glossy yellow characterized by spherical segments. Bright deposits can be obtained even at very high current densities (up to approximately 50 mA/cm<sup>2</sup>) when vigorous agitation is provided.

Other properties such as hardness and brittleness are also changed. Deposits plated from 65°C baths are soft and ductile (see Table II) in contrast to those plated from 25°C baths which are much harder and brittle where the carbon content is high (see Table IV and V).

By plotting the carbon content *vs.* bath age (or amount of gold plated) it was learned that, at least in the case of the phosphate buffered solution at 25°C, there was no increase of carbon in the deposit. Once the bath was no longer replenished with potassium cyanaurate(I) there was indeed a marked decrease of carbon in the deposited gold with decreasing gold concentration in solution (see Fig. 10). This result clearly reveals that the amount of incorporated carbonaceous material is not related to the accumulation of free cyanide or subsequently formed reaction products. Although the carbon content throughout the main part of the experiment was found to remain at around

1000 ± 100 ppm, a gradual change in appearance was observed also here extending from lustrous yellow to dark brown.

The carbon data obtained from the ammonium citrate formulation at 25°C were more inconsistent (see Fig. 10), suggesting interaction of the ammonium ions in some unknown way. Principally, however, similar results were obtained, namely, deposits of lustrous yellow appearance gradually darkening as the age of the bath increased, and high hardness and brittleness at high current density, together with relatively high carbon content.

3. Further, the fact that carbon was also found in deposits where anode and cathode were placed in separate compartments excludes that anodically oxidized or polymerized cyanide derivatives would contribute to the carbon content in electroplated gold.

Most likely, therefore, cyanide, as potassium cyanide, gold(I) cyanide, potassium cyanaurate, and hydrogen cyanide are incorporated into the metal during the deposition process.

### Acknowledgments

The author wishes to thank Dr. M. J. Elkind for many helpful and stimulating discussions during the course of this work and Mr. K. Yoshida for the elaborate scanning electron microscope work.

Manuscript submitted June 15, 1973; revised manuscript received Nov. 20, 1973. This was Paper 199 presented at the Miami Beach, Florida, Meeting of the Society, Oct. 8-13, 1972.

Any discussion of this paper will appear in a Discussion Section to be published in the December 1974 JOURNAL. All discussions for the December 1974 Discussion Section should be submitted by Aug. 1, 1974.

### EXPERIMENTAL APPENDIX

#### Sample Preparation for Carbon Analysis

Onto a molybdenum substrate (2.5 × 5 cm) gold was plated to accumulate generally approximately 1 or 2g of metal. The deposits were rinsed thoroughly with deionized (DI) water and peeled from the substrate, again rinsed, then immersed in approximately 100 ml DI water, boiled for 5 min, and subsequently rinsed with cold DI water to assure complete removal of bath residues. For drying, the foil was placed into a clean oven for approximately 2 hr at 125°C. If not analyzed immediately the gold was stored in clean glass containers. Approximately 1g was used per analysis.

#### Wire Wrap Test

Annealed Dumet<sup>7</sup> wire (0.45 mm) was plated to approximately 6.5 μm with gold, rinsed, air-dried, and subsequently, with the help of a mechanical tool wrapped around a gold-plated brass mandrel of a square cross section (0.1 cm side length). A ductile deposit as defined here must not show any cracks in the gold surface at 20X optical magnification.

#### Solution Extraction

Five hundred milliliters of solution (electrolyzed potassium cyanide solution, dibasic ammonium citrate solution, or depleted plating bath) was placed into a separatory funnel. Approximately 150 ml of distilled ethyl acetate were then added and shaken energetically. The organic phase was separated and new ethyl acetate added to the aqueous phase. Three extractions were sufficient to remove organic materials quantitatively. After combining all solvent portions, ethyl acetate was stripped off on a rotatory evaporator, and the residual oily or greasy materials transferred into a crystallization dish in which they were dried in a desiccator over CaCl<sub>2</sub> or silica gel.

Due to small quantities obtained from most of the operations, no further purifications were undertaken. IR spectra of the products were recorded.

IR absorptions were determined of products isolated by ethyl acetate extraction from the following: (i)

<sup>7</sup> Dumet: a 57% iron, 42% nickel, and 1% manganese alloy wire core with copper cladding.

<sup>6</sup> A publication of this study is in preparation.



KCN solution polymerization (orange brownish partially crystalline oil), 3320s, 2955s, 1672w, 1446m, 1375s, 1320m, 1186m, 1122s, 1089s, 1043s, 944m, 926m, 878w, 842m, 792w; (ii) electrolyzed dibasic ammonium citrate solution (yellow brownish oil), 3150s br, 2630sh, 1728s, 1380s br, 1250v br, 1178sh br, 1048m; (iii) depleted potassium phosphate plating bath (65°C, pH 10), (brownish, partially crystalline oil), 3260s, 2195w, 1668w, 1445m, 1375w, 1229m, 1046s, 1010m, 793s; (iv) depleted dibasic ammonium citrate plating bath (65°C, pH 4.7), (brownish oil), 3150s br, 2640sh, 2210s, 2170w, 1728s br, 1428s, 1380s, 1263m, 1165sh br, 1098m, 1049m, 1022sh, 873w br, 802s br.

## REFERENCES

1. G. B. Munier, *Plating*, **56**, 1151 (1969).
2. C. K. Kim and M. J. Vasile, *Anal. Chim. Acta*, **56**,

- 339 (1971).
3. S. Dzetaveckiene, J. Butkevicius, and R. Visomirskis *Lietuvos TSR Mokslu Akad. Darbai, Ser. B*, **3(66)**, 15 (1971).
4. D. R. Mason and A. Blair, *Trans. Inst. Metal Finishing*, **50**, 138 (1972).
5. L. Holt and J. Stanyer, *ibid.*, **50**, 24 (1972).
6. D. J. Huettnner and R. C. Sanwald, *Plating*, **59**, 750 (1972).
7. H. G. Silver, *This Journal*, **116**, 591 (1969).
8. H. G. Silver, *ibid.*, **116**, 26C (1969).
9. L. Holt, *J. Inst. Nucl. Eng.*, **13**, 42 (1972).
10. E. Raub, Ch. J. Raub, A. Knödler, and H. P. Wiel, *Werkstoffe Korrosion*, **23**, 643 (1972).

## The Surface Tension of the Molten Binary System LiCl-KCl

D. A. Nissen and R. W. Carlsten

Exploratory Power Supplies Division 2523, Sandia Laboratories, Albuquerque, New Mexico 87115

## ABSTRACT

Surface tension measurements are reported for the binary molten salt system LiCl-KCl over the composition range 10-90 mole per cent KCl and at temperatures ranging from the melting point to 850°C. All measurements were made using the maximum bubble pressure method. The surface tension is linearly dependent on temperature, and the experimental results for the mixture at constant temperature are best explained on the basis of regular solution behavior. However, there is an indication that some local structure exists in the melt.

The physical-chemical properties of molten salts are of interest because they can reveal the type and extent of ionic interactions in these systems. The entire spectrum of ionic interactions can be obtained in molten salt mixtures: from the NaNO<sub>3</sub>-KNO<sub>3</sub> system which approximates ideal behavior (1) to those which deviate considerably from ideal behavior and have been explained on the basis of complex ion formation (2) or polarization effects due to large differences in cation size (1, 3, 4). The correlation of solution behavior with surface properties has been a common and fruitful approach.

Even though molten LiCl-KCl has been used extensively as a solvent in both electrochemical and chemical studies, little is known about its physical properties. Except for the rather sparse data of Mizuno (5) and Jaeger (6), studies that have been made of the surface tension of the binary alkali metal halides (1, 2) have not included the LiCl-KCl system in spite of the fact that deviations from ideal solution behavior may exist as indicated by the conductivity data of Van Artsdalen (7). The purpose of the present study is to extend the available surface tension data to include mixtures of LiCl and KCl and to examine these data in the light of current models of molten salt mixtures.

## Experimental

Of the numerous techniques available for determining the surface tension of molten salts, the maximum bubble pressure method was chosen for this investigation. This method is capable of giving precise results at high temperatures in a moderately corrosive medium, and has been used in many investigations of the surface tension of molten salts. It involves the slow formation of a bubble at the inner diameter of a very

carefully fabricated capillary orifice immersed in the liquid of interest. Simultaneously, the pressure of the gas used to form the bubble is measured in order to determine the maximum pressure developed inside the bubble, i.e., at the minimum radius of curvature.

Schrödinger (8) showed that the relationship between the pressure and surface tension is given by the equation

$$\gamma = \frac{\bar{p}r}{2} \left[ 1 - \frac{2}{3} \frac{r}{h} - \frac{1}{6} \left( \frac{r}{h} \right)^2 \dots \right]$$

where  $\gamma$  is the surface tension in dynes/centimeter,  $\bar{p}$  is the maximum pressure difference between the inside and outside of the bubble,  $r$  is the radius of the capillary, and  $h = \bar{p}/g (D - d)$ , where  $g$  is the acceleration due to gravity,  $D$  is the density of the liquid, and  $d$  is the density of the vapor. If the density of the vapor phase is disregarded, it is possible to express the above equation in the more tractable form (9)

$$\gamma = \frac{\tau g}{2} (hd_1 - id_2) - \frac{1}{3} d_2 r^2 g - \frac{1}{12} \frac{r^3 g d_2^2}{hd_1 - id_2}$$

where  $h$  is the height of the manometer column,  $d_1$  is the density of the manometer fluid,  $i$  is the depth of immersion of the capillary, and  $d_2$  is the density of the liquid under study. The third term was not used in our calculations since it is negligible,  $<10^{-4}$  dyne/cm.

Sugden (10, 11) has objected to the use of Schrödinger's equation because it assumes an elliptical bubble profile and thus should only be applied to small bubbles. However, Tripp (12) has pointed out that if the bubbles are formed slowly, about five bubbles per minute, the mathematical theory is in accordance with experiment and has criticized Sugden's conclusions on the grounds that the bubble rate used in his experi-

\* Key words: regular solution, molten salts, coulombic interaction, solution theory.

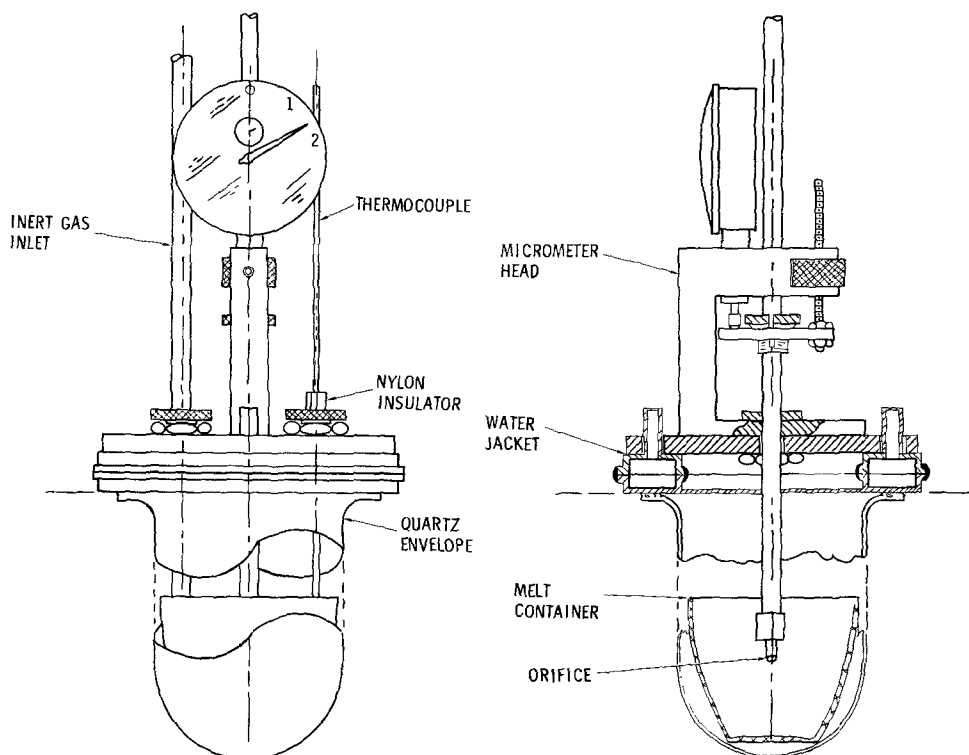


Fig. 1. Experimental apparatus

ments was too high. Since our surface tension data for both  $\text{NaNO}_3$  and  $\text{KNO}_3$  (13) agree with that obtained by other investigators using both the maximum bubble pressure method (9) and the Wilhelmy slide plate technique (14), any errors involved in the use of Schrödinger's equation for surface tension appear to be negligible for slow bubble rates.

The literature provides a more extensive review of the historical background, theory, and practice of this technique for measuring surface tension (9, 12).

**Apparatus.**—The apparatus used in this investigation was similar to that of Dahl and Duke (2, 9) and is shown in Fig. 1. In this investigation the capillary tip was fabricated from pure gold and was 2.25 cm long with an orifice approximately 0.8 mm in diameter. It was joined to the graphite gas delivery tube by means of a graphite collar.

In order to obtain precise results, it is necessary that careful attention be paid to the capillary tip. We have found that the bore must be as accurately round as possible, the end flat and perpendicular to the axis of the capillary, and the edge of the orifice very sharp. Furthermore, this condition must be maintained throughout the measurements. For accurate, reproducible results, these requirements cannot be too strongly emphasized.

A Lietz Ortholux microscope was used to check the condition and the diameter of the orifice. The capillary tip was magnified  $60\times$  and photographed with a superimposed filar, ruled to 0.01 mm. This photograph was then used to measure the diameter of the capillary and determine its condition. All measurements were corrected for thermal expansion of the capillary orifice (15).

The graphite tube which supported the gold capillary was rigidly clamped to the micrometer head which allowed the depth of immersion of the tip to be measured within  $\pm 0.01$  mm. The level of the vapor-liquid interface was determined by measuring the resistance between the capillary and a gold-sheathed thermocouple placed in the melt as the tip was being slowly lowered by means of the adjustment screw attached to the micrometer head.

A dibutyl phthalate manometer was used to measure the gas pressure in the system. Its temperature was maintained at  $25^\circ \pm 0.1^\circ\text{C}$  by a constant temperature

bath. The height of the meniscus was read by a cathetometer accurate to  $\pm 0.001$  mm.

The temperature of the melt was measured with a gold-sheathed Chromel-Alumel thermocouple and was maintained constant within  $\pm 0.5^\circ\text{C}$  of the set temperature. The vertical temperature gradient through the sample was less than  $1.0^\circ\text{C}$ .

**Materials.**—Both the LiCl and KCl used in these experiments were of analytical purity and were carefully vacuum dried before use. The appropriate composition was made up by accurately weighing the dried salts directly into the container. After the salts were melted, they were further purified by the use of chlorine and hydrogen chloride gas (16). All weighing and other manipulations of the dried salts were done in an atmosphere whose water content was less than 100 ppm. After a set of measurements on a sample was finished, the sample was analyzed for both lithium and potassium by atomic absorption to determine its exact composition to within  $\pm 0.1$  weight per cent (w/o). In every case the weighed composition agreed with the analyzed composition to within  $\pm 0.2$  mole per cent (m/o).

Purified argon was used to form the bubbles and to maintain an inert atmosphere over the sample. The argon was purified by passing over hot copper turnings and  $\text{Mg}(\text{ClO}_4)_2$ .

### Results

Prior to determining the surface tension of LiCl-KCl mixtures, we measured the surface tension of both  $\text{NaNO}_3$  and  $\text{KNO}_3$ . The agreement between our results and the accepted literature values (17) is within 1% (13). To check the accuracy of our measurements on the LiCl-KCl system, we periodically remeasured the surface tension of  $\text{KNO}_3$ . In each case the agreement was well within a reasonable experimental error ( $\pm 0.2$  dyne/cm,  $\sim \pm 0.2\%$ ).

For each composition the surface tension shows the usual linear temperature dependence,  $\gamma = A - Bt$ , where  $t$  is the temperature in degrees centigrade. Table I summarizes these results analytically. The equations which relate the surface tension and temperature are the result of a least squares computer analysis of the data points. The standard deviation of the points about the line is shown in the last column in Table I and is about 0.3 dyne/cm.

Table I. LiCl-KCl<sup>(a)</sup>

KCl, m/o	$\gamma$ , dyne/cm	$s$ , dyne/cm
10	164.9-0.0676t	0.275
21	164.4-0.0714t	0.496
31	165.4-0.0755t	0.308
42	165.3-0.0780t	0.215
50	165.3-0.0808t	0.275
60	166.4-0.0846t	0.376
70	167.2-0.0869t	0.262
78	166.9-0.0857t	0.193
85	165.6-0.0840t	0.287
90	166.2-0.0850t	0.357

<sup>(a)</sup> Density data used in calculating these surface tensions were taken from Van Artsdalen and Yaffee (7).

With the exception of the rather sparse data of Mizuno (5) and Jaeger (6), there are no other surface tension data on the LiCl-KCl system in the literature that can be used for comparison. Mizuno (5) reports surface tension data for the compositions 20, 40, and 60 m/o KCl. For these compositions, his values are about 4-5% higher at 800°C than ours. Jaeger (6) reports only one data point for 447°C and a composition of 42 m/o KCl; it is 5% lower than our value for the same composition. Based on the agreement between our values for the surface tension of KNO<sub>3</sub> and NaNO<sub>3</sub> (13) and those reported by Janz (17), and the precision of all our data for the surface tension of LiCl-KCl for which we estimate an accuracy of better than  $\pm 1\%$ , we are unable to explain the differences between our values and those of Mizuno and Jaeger.

### Discussion

Figure 2 shows a plot of surface tension as a function of composition at a constant temperature of 800°C. It can readily be seen that there is a large deviation from additive behavior, reaching a maximum of 7.7 dyne/cm at 50 m/o KCl. There is a pronounced minimum in the curve in the region of 65-70 m/o KCl.

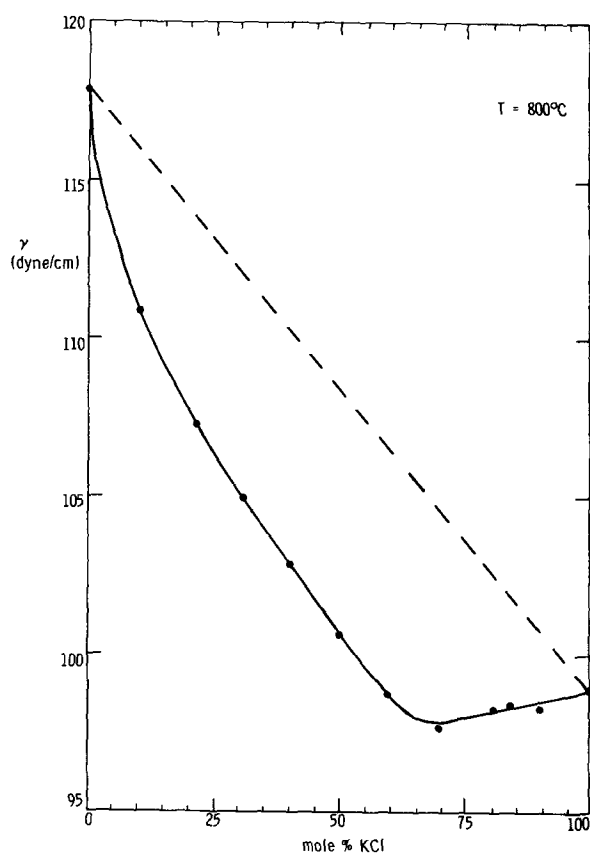


Fig. 2. Isothermal surface tension curve for the LiCl-KCl system at 800°C.

There have been a number of theoretical treatments of the surface tension of mixtures (18, 19) whose object it has been to evolve a model which would allow the prediction of the surface tension of a mixture at constant temperature, for any composition, provided the surface tensions of the pure components are known. These models and their correlation with our experimental data are discussed below.

The surface tension of nearly all binary mixtures deviates negatively from additivity; behavior which is, in fact, predicted by Guggenheim's equation for the surface tension of an ideal solution (18). The surface tension of the LiCl-KCl system similarly exhibits negative deviations from additivity. However, neither Guggenheim's equation for ideal solutions nor modifications of it (20, 21) are able to describe the LiCl-KCl experimental surface tension isotherm. This is not particularly surprising since the heat of mixing studies of Aukrust, *et al.* (22) show that mixtures of LiCl and KCl exhibit considerable negative deviations.

In a series of studies of the surface tension of binary molten salt systems, Bertozzi (14, 23, 24) advocated the use of the semiempirical expression

$$\gamma = x_1\gamma_1 + x_2\gamma_2 - \beta x_1x_2 \quad [1]$$

to represent the data. In this equation  $x_i$  is the mole fraction of component  $i$ ,  $\gamma_i$  is the surface tension of pure component  $i$ , and  $\beta$  is a constant which may be empirically determined. For those mixtures which behave as ideal solutions,  $\beta$  is, of course, equal to zero.

If deviations from ideal behavior are considered to be purely coulombic in origin, the constant  $\beta$  can be expressed as a size parameter

$$\beta = \frac{-e^2}{2a} \left( \frac{1}{d_1} + \frac{1}{d_2} \right) \left( \frac{d_1 - d_2}{d_1 + d_2} \right)^2 \quad [2]$$

where  $d_i$  is the sum of the radii of the cation and anion of the pure salt indicated,  $e$  is the electronic charge, and  $a$  is the mean area of the molecules and is given by the formula

$$a = \frac{1}{2} \left[ \left( \frac{V_1}{N} \right)^{2/3} + \left( \frac{V_2}{N} \right)^{2/3} \right]$$

where  $N$  is Avogadro's number and  $V_i$  is the molar volume of the  $i$ th component. This form of  $\beta$  is the result of calculations made by Forland (25) on the energy change which results from mixing a linear array of ions, considering only nearest and next neighbor interactions. Equations [1] and [2] were used by Kleppa to represent heat of mixing data for alkali nitrate systems (26, 27).

Using the cation-anion distances obtained by Levy and Danford from their diffraction studies of molten salts (28) and Van Artsdalen's values of the molar volumes of LiCl and KCl (7), we calculate a value of  $\beta = 17.7$  dynes/cm. A computer fit of Eq. [1] to the experimental data using  $\beta$  as an adjustable parameter was made and is shown in Fig. 3. It was found that the best fit was obtained for a value of  $\beta = 32.5$ , considerably larger than that calculated from Eq. [2].

Equation [1] predicts that, if deviations from ideal behavior are coulombic in nature, then for a given composition, the deviation from ideal behavior,  $\Delta\gamma = \gamma - (x_1\gamma_1 + x_2\gamma_2)$ , should be approximately a linear function of the size parameter  $[(d_1 - d_2)/(d_1 + d_2)]^2$ ;

since the factor  $\frac{1}{a} \left( \frac{1}{d_1} + \frac{1}{d_2} \right)$  is nearly constant for the various binary alkali chlorides shown in Fig. 4. Figure 4 shows the deviation from ideal behavior,  $\Delta\gamma$ , at a composition of 0.5 mole fraction plotted against the size parameter,  $[(d_1 - d_2)/(d_1 + d_2)]^2$ , for several different binary alkali chloride systems (2, 5, 23). This plot shows that a model based on a one-dimensional array of the ions and purely coulombic considerations cannot completely describe the deviations of the surface

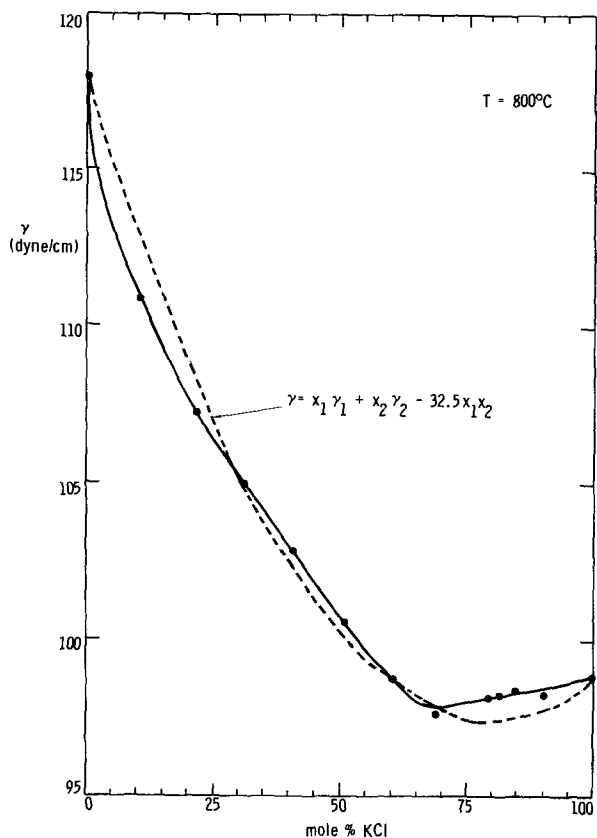


Fig. 3. Comparison of the experimental surface tension with that calculated from Eq. [1] for  $\beta = 32.5$  dynes/cm at  $800^\circ\text{C}$ .

tension from ideal behavior in all binary molten salt systems with a common anion. If polarization effects were taken into account as well as an extension of the one-dimensional model for coulombic interaction into three dimensions, it is possible that this model would more closely parallel the experimental results. This conclusion is similar to that suggested by Grojtheim (20) in his study of the surface tension of binary mixtures of alkali and alkaline earth chlorides, and discussed by Blander (29).

Based on calculations of the activity of molten salt mixtures with a common ion, Bloom (30) has shown that these mixtures may be treated as regular solutions.

Guggenheim (18) and Prigogine (19) have derived an equation for the surface tension of regular solutions based on a quasi-crystalline model in which each molecule in the liquid is treated as though it were arranged on a lattice and on the zeroth approximation in which it is assumed that there is complete randomness in both the bulk and in the surface layer. In this case the surface tension is given by

$$\begin{aligned} \gamma &= \gamma_1 + \frac{kT}{a} \ln \frac{x_1'}{x_1} + \frac{wl}{a} [(x_2')^2 - (x_2)^2] \\ &\quad - \frac{wm}{a} (x_2)^2 \\ &= \gamma_2 + \frac{kT}{a} \ln \frac{x_2'}{x_2} \\ &\quad + \frac{wl}{a} [(x_1')^2 - (x_1)^2] - \frac{wm}{a} (x_1)^2 \quad [3] \end{aligned}$$

where  $l$  and  $m$  refer to the fraction of nearest neighbors which occupy the same lattice plane and an adjacent lattice plane, respectively, and satisfy the relationship  $l + 2m = 1$ ,  $w$  is the interaction parameter in the theory of regular solutions, and the primed quantities refer to the surface layer.

According to Prigogine (19), if one neglects the adsorption of atmospheric gases, or excludes them from the experimental system, an extreme value of the surface tension can occur from which it follows that the equilibrium surface phase at this point has the same composition as the bulk solution, i.e.,  $x_1' = x_1$  and  $x_2' = x_2$ . In these circumstances, Eq. [3] reduces to

$$\gamma_{\text{extr.}} = \gamma_1 x_1 + \gamma_2 x_2 - \frac{wm}{a} x_1 x_2 \quad [4]$$

Inserting the appropriate experimental values of  $\gamma_{\text{extr.}}$ ,  $x_1$  and  $x_2$  into Eq. [4], we obtain  $wm/a = 32$  dynes/cm and  $wm/kT = 0.352$  for  $T = 1073^\circ\text{K}$ .

With the value of  $wm/a$  calculated from Eq. [4], we used Eq. [3] to calculate values of the surface tension for various LiCl-KCl compositions. A computer was used to do the actual calculations and the program was written so that the ratio  $l/m$  could be varied. The best fit to the experimental surface tension data was obtained for the ratio  $l/m = 2$ . Table II and Fig. 5 show a comparison of the experimental and calculated values of the surface tension. The minimum in the calculated curve comes at about 80 m/o KCl as against 65-70 m/o KCl in the experimental curve; otherwise the agreement is excellent, lending support to the idea that the LiCl-KCl system behaves as a regular solution.

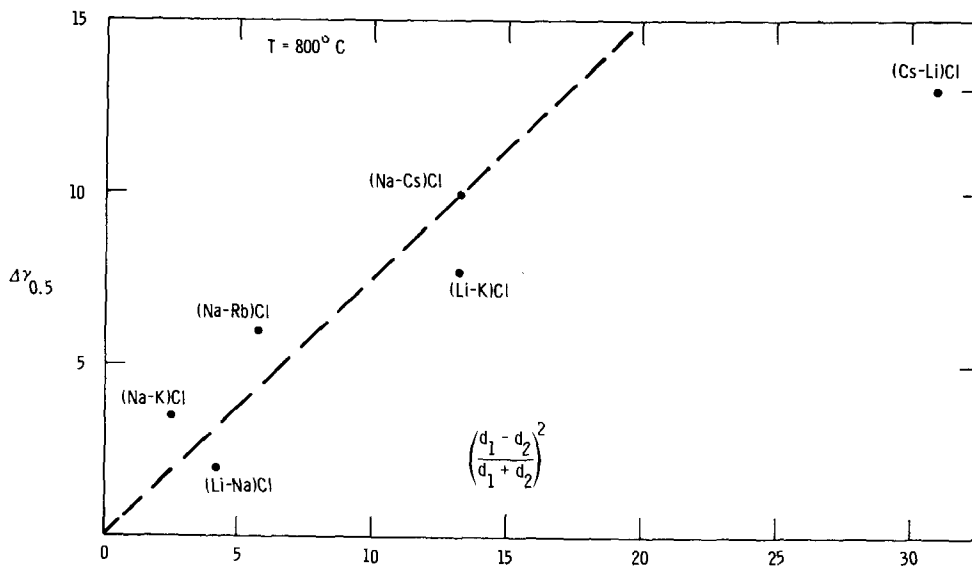


Fig. 4. Deviation from ideal behavior at 0.5 mole fraction as a function of the size parameter  $(d_1 - d_2/d_1 + d_2)^2$  for several binary alkali metal chloride systems.

Table II. Comparison of calculated and experimental values of the LiCl-KCl surface tension at 800°C

KCl, m/o	$\gamma$ (calc., Eq. [3]), dyne/cm	$\gamma$ (expt'l.), dyne/cm
10	111.76	110.91
20	107.04	107.29
30	103.63	104.98
40	101.24	102.90
50	99.58	100.62
60	98.44	98.72
70	97.75	97.68
80	97.50	98.30
90	97.81	98.20

We believe, however, that there are indications of some type of specific interaction in the LiCl-KCl mixture. Van Artsdalen's measurements of the conductivity of the LiCl-KCl system (7) show a pronounced minimum in the equivalent conductance isotherm in the region of 70-80 m/o KCl. In a similar fashion, the surface tension isotherm shows a minimum between 65-70 m/o KCl, cf. Fig. 2. Furthermore, our calculations of the surface entropy  $S^\gamma$  and surface energy  $E^\gamma$  show maxima at about 67 m/o KCl, Fig. 6. These facts suggested evaluation of a model which considers possible specific interaction between the components of the mixture.

Kaufman (31) has shown that molecular-type aggregates or clusters of ions which possess unique stoichiometric relationships to one another are theoretically capable of producing minimum or maximum values of the surface tension. A molecular type which is surface active will cause a minimum and one which concentrates in the bulk phase will cause a maximum value of the surface tension. Based on the Gibbs adsorption isotherm and using a restrictive equation for the chemical potential of the surface active-species, Kaufman (31) derived an equation of the form

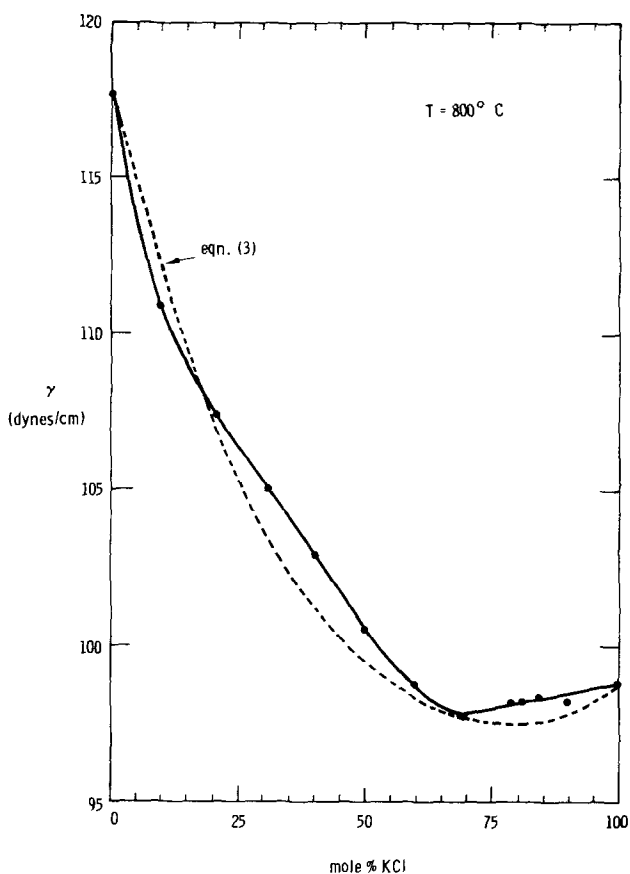


Fig. 5. Comparison of experimental surface tension with that calculated from Eq. [3] at 800°C.

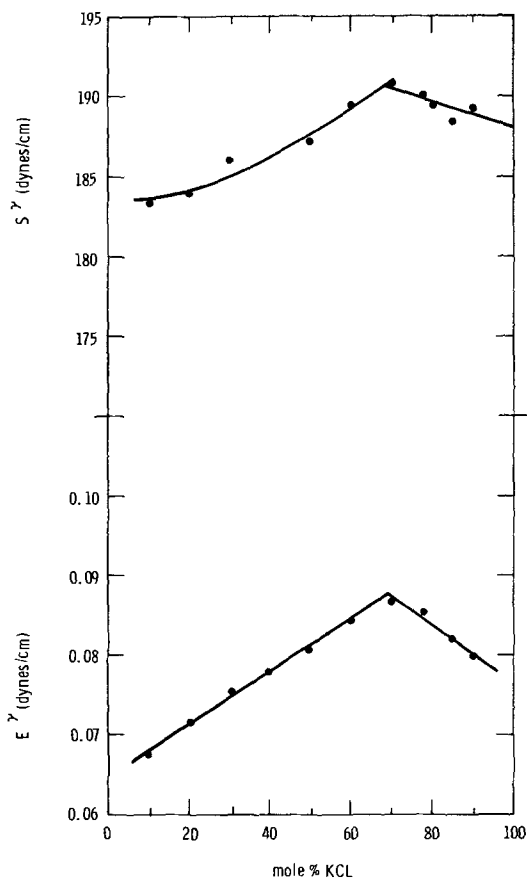


Fig. 6. Surface entropy,  $S^\gamma$  and surface energy  $E^\gamma$  as a function of composition for the LiCl-KCl system at 800°C.

$$\gamma = x_1\gamma_1 + x_2\gamma_2 + \left(\frac{x_1}{r_1}\right)^{r_1} \left(\frac{x_2}{r_2}\right)^{r_2} (r_1 + r_2)^{(r_1 + r_2)} + \left(\frac{f_1}{f_1 \max}\right)^{r_1} \left(\frac{f_2}{f_2 \max}\right)^{r_2} [(\gamma_c - \gamma_1) + (\gamma_1 - \gamma_2)]x_2 \quad [5]$$

In this equation  $r_1$  and  $r_2$  are constants and represent the stoichiometric ratios in which the various components occur in a particular aggregate,  $f_1$  and  $f_2$  are the activity coefficients of the two components, and  $\gamma_c$  is the surface tension of the bulk at a composition corresponding to some particular stoichiometric ratio. In the limit of weak interactions between the constituents of the mixture, the surface-active species can be assumed to behave like pure solute in the unassociated state and Eq. [5] can be shown to reduce to a form similar to Eq. [4] (31); i.e., in the limit of weak interaction the mixture will behave as a regular solution.

Equation [5] was used to calculate the surface tension of the LiCl-KCl mixture. For this calculation it was assumed that the minimum in the isothermal surface tension curve, cf. Fig. 2, could be ascribed to the presence of a surface-active species in the melt, and the values of  $\gamma_1$ ,  $\gamma_2$ , and  $\gamma_c$  were chosen accordingly. Thus,  $\gamma_1 = 1$ ,  $\gamma_2 = 2$ , and  $\gamma_c = 97.5$  dyne/cm. It was also assumed that  $f_1/f_1 \max = f_2/f_2 \max = 1$ .

The results of this calculation are shown in Fig. 7 superimposed on the experimentally measured isothermal surface tension curve. The agreement between the calculated and experimental values of the surface tension, particularly in the region of the minimum, is quite reasonable considering the approximations involved.

We do not believe that any sort of complex-ion in the generally accepted sense, e.g.,  $\text{AlCl}_4^-$ ,  $\text{BeF}_4^{2-}$ ,  $\text{CdCl}_4^{2-}$ , etc., is formed in the LiCl-KCl melt. How-

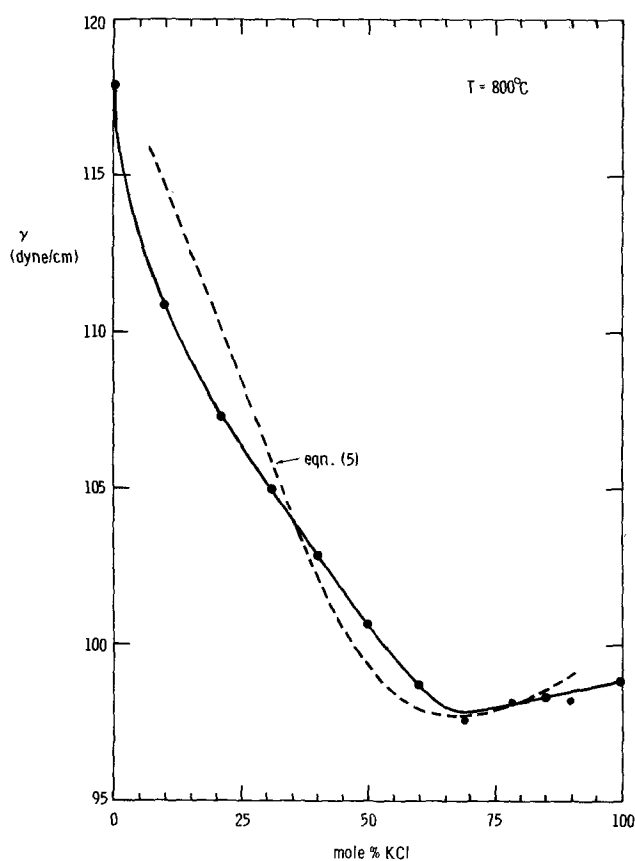


Fig. 7. Comparison of the experimental surface tension with that calculated from Eq. [5] at 800°C.

ever, the correspondence between the calculated and experimental data shown in Fig. 7 do suggest that some sort of loose aggregation or "complex-like" arrangement of the ions is formed in the melt, and that this entity is surface active. The strong polarizing power of the lithium ion is probably responsible for changes in local structure about itself.

In the NaCl-KCl system, where the sodium ion is much less strongly polarizing than the lithium ion, there appears to be no evidence of local structure or preferential ion groupings in the melt (5, 9). The essential features of this association model have also been proposed to explain the observed heats of mixing in binary alkali metal halide systems (32).

The preferential ion groupings discussed above have not been observed experimentally, and therefore, the conclusions based on their existence are speculative. Furthermore, as Kaufman (33) points out, because these compound like groups of ions can have effects on surface properties orders of magnitude greater than might be expected from their relative influence on bulk properties, they might represent only an insignificant fraction of the total mass of liquid. However, a model in which these ion groupings are assumed does seem to account for the LiCl-KCl surface tension data, cf. Fig. 7, and may also explain the conductivity data for this same system.

### Conclusion

We have attempted to fit our surface tension data for the LiCl-KCl system to four different theoretical models of the surface tension of mixtures. The first of these is Guggenheim's model for ideal behavior. The second, an outgrowth of heat of mixing studies on binary molten systems, considers that deviations from ideal solution behavior are due to purely coulombic interactions. The third is Guggenheim's zeroth approximation treatment of regular solutions which

assumes complete randomness in the surface layer as well as the bulk. In the fourth model, the regular solution model is, in essence, modified by assuming compositional variations at the interface which could be completely specified by the preferential adsorption of a stoichiometric multi-atomic species from the bulk phase.

Our experimental data cannot be adequately described by either the ideal solution model or by the coulombic interaction model, most probably because these models do not take into account the polarization effects which undoubtedly exist in the LiCl-KCl system.

The experimental surface tension data are well fitted by Guggenheim's regular solution model of liquid mixtures except that the positions of the minima in the calculated and experimental isothermal surface tension curves are displaced from each other.

Because values of the surface tension calculated from the fourth of these models which assumes discrete atom groupings fit the experimental data reasonably well, particularly in the region of the minimum, we believe that, while regular solution theory can adequately explain our results, there may be some local structure in the LiCl-KCl melt. That is, the constituents of the melt, at least at the interface, do not seem to be randomly distributed. This view is also supported by the plots of surface entropy and total surface energy against composition which show maxima at 67 m/o KCl.

### Acknowledgment

The authors are indebted to Mr. T. R. Rhinehart for the design and fabrication of the surface tension apparatus, to Dr. J. G. Eberhart and Dr. B. H. Van Domelen for helpful discussions, and to Mr. L. B. Brace for help with the computer programming.

Manuscript submitted Aug. 27, 1973; revised manuscript received Nov. 7, 1973. This was Paper 275 presented at the Chicago, Illinois, Meeting of the Society, May 13-18, 1973.

Any discussion of this paper will appear in a Discussion Section to be published in the December 1974 JOURNAL. All discussions for the December 1974 Discussion Section should be submitted by Aug. 1, 1974.

### REFERENCES

1. N. K. Boardman, A. R. Palmer, and E. Heymann, *Trans. Faraday Soc.*, **51**, 277 (1955).
2. J. L. Dahl and F. R. Duke, *J. Phys. Chem.*, **62**, 1468 (1958).
3. H. Bloom, F. G. Davis, and D. W. James, *Trans. Faraday Soc.*, **56**, 1179 (1960).
4. V. K. Semenchenko and L. P. Skikhobalova, *Zh. Fiz. Khim.*, **21**, 1387 (1947).
5. M. Mizuno, Y. Matsumura, S. Sugino, and Y. Tanaka, *Sukyokai-Shi*, **16**, 488 (1968).
6. F. M. Jaeger, *Z. Anorg. Chem.*, **101**, 1 (1917).
7. E. R. Van Artsdalen and I. S. Yaffee, *J. Phys. Chem.*, **59**, 118 (1955).
8. E. Schrödinger, *Ann. Physik*, **46**, 413 (1917).
9. J. L. Dahl, "Surface Tension of Some Binary Fused Salt Systems," Ph.D. Thesis, Iowa State College, 1957.
10. S. Sugden, *J. Chem. Soc.*, **121**, 858 (1922); **123**, 27 (1924).
11. S. Sugden, "The Parachor and Valency," Alfred Knopf, New York (1930).
12. H. P. Tripp, "The Maximum Bubble Pressure Method for the Measurement of Surface Tension," Ph.D. Thesis, University of Chicago, 1934.
13. D. A. Nissen and R. W. Carlsen, *J. Chem. Eng. Data*, **18**, 75 (1973).
14. G. Bertozzi and G. Sternheim, *J. Phys. Chem.*, **68**, 2908 (1964).
15. S. P. Clark, "Handbook of Physical Constants," p. 78, Geological Society of America, New York (1966).
16. D. A. Nissen, *J. Inorg. Nucl. Chem.*, **28**, 1740 (1966).
17. G. S. Janz and C. G. Dijkhuis, "Molten Salts," Vol. 2, pp. 93-94, U.S. Dept. of Commerce, National Bureau of Standards (1969).

18. E. A. Guggenheim, "Mixtures," Oxford at the Clarendon Press, London (1952).
19. R. Defay, I. Prigogine, A. Bellemans, and D. H. Everett, "Surface Tension and Adsorption," p. 179, John Wiley & Sons, Inc., New York (1966).
20. K. Grjotheim, J. L. Holm, B. Lilleburn, and H. A. Øye, *Acta Chem. Scand.*, **26**, 2050 (1972).
21. J. G. Eberhart, *J. Phys. Chem.*, **70**, 1183 (1966).
22. E. Aukrust, B. Björge, H. Flood, and T. Forland, *Ann. N. Y. Acad. Sci.*, **79**, 830 (1960).
23. G. Bertozzi, *J. Phys. Chem.*, **69**, 2606 (1965).
24. G. Bertozzi and G. Soldani, *ibid.*, **70**, 1838 (1966).
25. T. Forland, *ibid.*, **59**, 152 (1955).
26. O. J. Kleppa and L. S. Hersh, *J. Chem. Phys.*, **34**, 351 (1961).
27. O. J. Kleppa and L. S. Hersh, *Discussions Faraday Soc.*, **32**, 99 (1961).
28. H. A. Levy and M. D. Danford, in "Molten Salt Chemistry," M. Blander, Editor, John Wiley & Sons, Inc., New York (1964).
29. M. Blander, in "Molten Salt Chemistry," M. Blander, Editor, John Wiley & Sons, Inc., New York (1964).
30. H. Bloom and B. J. Welch, *Discussions Faraday Soc.*, **32**, 116 (1961).
31. S. M. Kaufman, *Acta Met.*, **15**, 1089 (1967).
32. L. Lumsden, *Discussions Faraday Soc.*, **32**, 138 (1961).
33. S. M. Kaufman and T. J. Whalen, *Acta Met.*, **13**, 797 (1965).

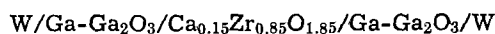
## Oxygen Transfer Kinetics Between Ga-Ga<sub>2</sub>O<sub>3</sub> Electrodes and the Solid Electrolyte Calcia-Stabilized Zirconia

L. F. Donaghey\* and Raymond Pong\*\*

*Inorganic Materials Research Division of the Lawrence Berkeley Laboratory and the Department of Chemical Engineering of the University of California, Berkeley, Berkeley, California 94720*

### ABSTRACT

The kinetics of oxygen transfer between Ga-Ga<sub>2</sub>O<sub>3</sub> composite electrodes and the solid electrolyte calcia-stabilized zirconia, ZrO<sub>2</sub>(CaO), were studied with the symmetric, galvanic cell



over the temperature range from 800° to 900°C. Chronopotentiometric studies were conducted using current densities from 0.3 to 130 μA/cm<sup>2</sup> to obtain overpotentials for faradaic oxidation and reduction reactions at the Ga-Ga<sub>2</sub>O<sub>3</sub>/ZrO<sub>2</sub>(CaO) interface. A linear dependence of the overpotential on current density was obtained, corresponding to a local electrode resistance of 3.8 ohm/cm<sup>2</sup> of electrode-electrolyte interface at 800°C. The data are in agreement with a solution-diffusion mechanism of oxygen transport through liquid Ga in the electrode between the ZrO<sub>2</sub>(CaO) electrolyte and Ga<sub>2</sub>O<sub>3</sub> particles.

Solid electrolytes have become important in recent years for use in thermodynamic and kinetic studies with solid-state electrochemical cells (1-4) and more recently, in fuel cells and other power sources (5-11). Major areas of concern in kinetics and power source applications of solid electrolytes are the structure of the solid electrolyte-electrode interface and the electrochemical, rate-controlling process for ionic transport across this interface (12). Considerable theoretical and experimental work has been reported concerning space charge polarization in liquid and solid systems where it is well established that static concentration gradients of ionic species and diffuse, charged double layers play an important roll (13-17). Most previous investigations of electrode processes in solid systems have been limited to single-phase electrodes (18) in asymmetric cells containing both nonpolarizable and polarizable electrodes (19). The oxygen transfer between the two-phase, liquid metal-metal oxide electrode Ga<sub>(l)</sub>-Ga<sub>2</sub>O<sub>3</sub>, and the solid electrolyte ZrO<sub>2</sub>(CaO) is studied in the present paper.

Oxygen transfer kinetics at interfaces between two-phase electrodes and solid electrolytes is important in many electrochemical applications. Metal-metal oxide mixtures are the most commonly used reference electrodes in thermodynamic studies with solid-state galvanic cells (3), where electrode polarization is undesirable. Kinetic studies with such cells require oxygen transfer for coulombic titration experiments (20), for

measurements of oxygen diffusion in liquid and solid metals (1,3), and for phase boundary reaction rate determinations (21).

Oxygen transfer kinetics from metal-metal oxide electrodes to solid electrolytes has only recently received attention. The reversibility of electrode polarization in symmetric cells has been studied by Steele (22) for several such electrodes. Recently Worrell and Iskoe (23) measured overpotentials for Cu-Cu<sub>2</sub>O, Fe-FeO, and Ni-NiO electrodes in symmetric cells and found that the steady-state overpotentials were independent of the direction of current flow. These authors have shown that the magnitude of the overpotential for a given current is consistent with an oxygen transfer mechanism which is kinetically limited by bulk diffusion of oxygen through the metal component of the electrode.

The oxygen transfer kinetics from liquid metal-metal oxide electrodes to solid electrolytes has not been studied previously. If the same or similar mechanism limits oxygen transfer for such electrodes as for solid metal-metal oxide electrodes, then the measured overpotentials should be significantly lower for the liquid metal-metal oxide electrodes, owing to the high oxygen permeability of liquid metals. On this assumption, kinetics for the Ga<sub>(l)</sub>-Ga<sub>2</sub>O<sub>3</sub> electrode should be exceptionally fast because of the exceptionally high oxygen diffusivity in liquid gallium.

In this study the oxygen transfer kinetics of Ga<sub>(l)</sub>-Ga<sub>2</sub>O<sub>3</sub> electrodes to ZrO<sub>2</sub>(CaO) is studied in a nearly symmetric cell. Because no reference electrode is included, the cell arrangement does not allow the inde-

\* Electrochemical Society Active Member.

\*\* Electrochemical Society Student Member.

Key words: emf measurements, solid electrolyte, oxygen transfer kinetics.

pendent measurement of overpotentials at individual electrode-electrolyte interfaces. It will be shown, however, that measurement of the total overpotential is sufficient to test alternative kinetic mechanisms provided that oxygen diffusion is rate controlling and that the solid electrolyte is an oxygen anionic conductor. Study of the oxygen transfer kinetics of the  $\text{Ga}_{(l)}\text{-Ga}_2\text{O}_3$  electrode has become important because of the increasing application of this electrode in solid-state electrochemical cells for thermodynamic and kinetic studies (24, 25). The understanding of transfer kinetics for this electrode system should provide a basis for employing liquid metal-metal oxide electrodes in electrochemical systems.

### Experimental

**Materials.**—Gallium metal<sup>1</sup> of 99.9999% purity and  $\text{Ga}_2\text{O}_3$  powder<sup>2</sup> (-325 mesh) of 99.99% purity for co-existence electrodes and the  $\text{ZrO}_2(\text{CaO})$  electrolyte<sup>3</sup> were obtained from commercial sources. High purity, recrystallized  $\text{Al}_2\text{O}_3$  was used in the remaining components of the cell assembly. An inert purge gas manifold was constructed of stainless steel throughout with KEL-F sealed, bellows valves. Viton and rubber O-rings were employed in seals between steel and ceramic components.

**Apparatus.**—The experimental cell configuration is shown schematically in Fig. 1. A closed-end, 0.64 cm diameter  $\text{ZrO}_2(15 \text{ mol per cent [m/o] CaO})$  solid electrolyte tube separated one electrode contained within it from a second  $\text{Ga-Ga}_2\text{O}_3$  electrode supported on  $\text{Ga}_2\text{O}_3$  powder within a 1.5 cm ID alumina crucible. This assembly was contained in a closed-end alumina reaction tube which was sealed at the top by an O-ring seal contained in a water-cooled stainless steel cap. The cap contained two additional O-ring seals through which the electrolyte tube, a thermocouple protection tube, and a purge gas inlet tube passed. Two of these tubes were also sealed at their tops by O-ring closures to a purge gas manifold. The tube assembly was positioned in a Kanthal A-1 alloy resistance furnace whose temperature was regulated by a triac-controlled, integrating proportional controller. The cell temperature was held constant ( $\pm 0.5^\circ\text{C}$ ) at the electrode assembly by a control thermocouple placed outside the alumina reaction tube. Convection in the liquid gallium was prevented by maintaining a vertical thermal gradient of  $0.3^\circ\text{C}/\text{cm}$  over the electrode assembly. Electrical interference from current transients in the furnace winding was prevented by encasing the reaction tube in an electrically grounded stainless steel tube to shield the electrode circuit from induced potentials.

<sup>1</sup> Cominco Company, Seattle, Washington.

<sup>2</sup> Alfa Inorganic.

<sup>3</sup> Zirconium Corporation of America, Solon, Ohio.

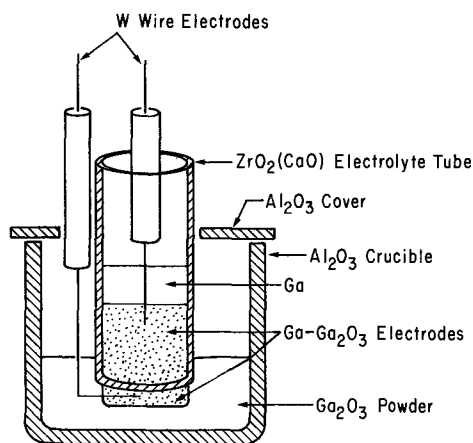


Fig. 1. Galvanic cell configuration

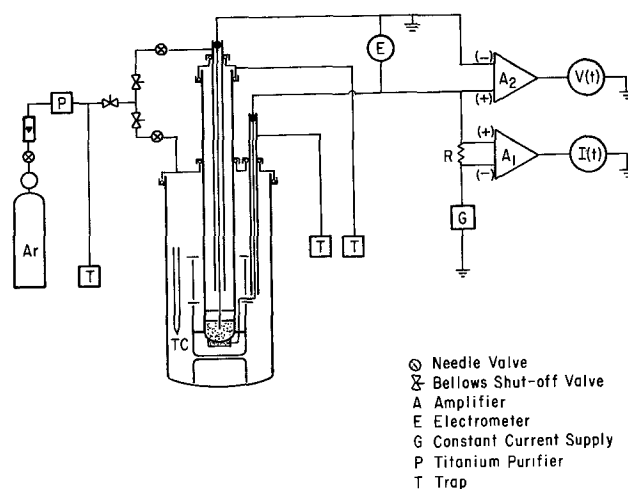


Fig. 2. Schematic of the gas manifold and electrical circuit employed in chronopotentiometric experiments.

The electrical circuit and purge gas manifold are shown schematically in Fig. 2. The emf of a Chromel-Alumel thermocouple used to measure the cell temperature was determined with a Leeds and Northrup K-3 potentiometric facility. The tungsten wire contacts to the  $\text{Ga-Ga}_2\text{O}_3$  electrodes were passed through De Khotinsky cement and glass seals to isothermal copper connectors, then to coaxial cables. Cell currents were produced with an Electronics Measurements, Model C636 constant current power supply (G, Fig. 2). The ohmic component of the voltage response to current changes was measured with a dual beam Tektronic Type RM35A oscilloscope with a high speed Type G differential input preamplifier plug-in ( $A_2$ , Fig. 2). The cell emf was measured with a Keithley 610C electrometer (E, Fig. 2) having a sensitivity of  $\pm 0.02 \text{ mV}$  and an offset current of  $5 \times 10^{-15} \text{ A}$ .

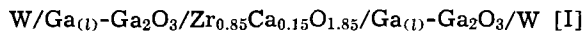
**Procedure.**—Following assembly, the cell was well purged with flowing argon. Both electrode compartments were leak tight, as checked with a He leak detector. The initially 99.998% pure Ar was purified by passing it through a Centorr gas-purification furnace containing Ti chips heated to  $800^\circ\text{C}$ . After thorough purging, the cell temperature was raised to the operating temperature at  $75^\circ\text{C}/\text{hr}$  to minimize thermal stress on the  $\text{ZrO}_2(\text{CaO})$  electrolyte. The cell was equilibrated overnight at the working temperature to anneal the electrodes and to allow a check on cell emf stability. During measurements both electrode compartments were sealed off from the gas manifold to prevent emf errors from gas flow sources.

Experiments were conducted with constant current density pulses between 0.3 and  $130 \mu\text{A}/\text{cm}^2$ . The open cell voltage was measured after equilibration and before current was applied. The ohmic voltage was measured from the abrupt change in oscilloscope trace occurring when the current to the cell was applied or terminated. Following the onset of each pulse the cell voltage was monitored intermittently for a period of 10-20 min during which the current was applied, followed by intermittent voltage measurements with no current for an additional 10-30 min period during which equilibrium was established. After all experiments were completed the cell temperature was lowered at  $70^\circ\text{C}/\text{hr}$  under flowing Ar. The cell was then dismantled for inspection of the electrodes and electrode-electrolyte interface to insure that the electrode remained two-phase during the experiments, and that wetting of the electrolyte by liquid gallium had occurred.

### Results

Chronopotentiometric studies were carried out with the cell





Wagner (1) has shown that the cell emf is a function of the oxygen partial pressure at the two electrode-electrolyte interfaces

$$\text{emf} = \frac{RT}{4F} \int_{\ln P_{\text{O}_2}''}^{\ln P_{\text{O}_2}' } t_{\text{ion}} d \ln P_{\text{O}_2} \quad P_{\text{O}_2}' > P_{\text{O}_2}'' \text{ [1]}$$

where  $t_{\text{ion}}$  is the ionic transference number. Thus, for the symmetric cell [I] at equilibrium, the cell emf should be zero. In practice, however, a small emf,  $V_0$ , can arise from small differences in temperature, composition, or ambience between the two electrodes. When a current density,  $i$ , is passed through the cell, an oxygen ion flux of magnitude  $i/2$  flows in the opposite direction for which an ohmic voltage component  $L\rho i$  appears across the electrolyte of thickness  $L$  and resistivity  $\rho$ . In addition a local overpotential,  $\eta$ , appears at each of the two electrode-electrolyte interfaces which, for small oxygen partial pressure gradients, are

$$\eta' = \frac{RT}{4F} \ln (P_{\text{O}_2}'/P_{\text{O}_2}'^e) \text{ [2a]}$$

$$\eta'' = \frac{RT}{4F} \ln (P_{\text{O}_2}''/P_{\text{O}_2}''^e)^{-1} \text{ [2b]}$$

where  $P_{\text{O}_2}'^e$  and  $P_{\text{O}_2}''^e$  are the oxygen partial pressures far from the electrolyte in electrodes 1 and 2, respectively. Thus, the cell voltage measured during current flow is

$$V = V_0 + \eta' + \eta'' + L\rho i \text{ [3]}$$

The total, steady-state overpotential  $\eta_t = \eta' + \eta''$  is a function of current density whose magnitude depends on the oxygen transfer kinetic mechanism. The magnitude of  $\eta_t(i)$ , and thus information on this mechanism, is readily deduced from  $V(i)$  measurements and independent determinations of  $V_0$ ,  $L$ , and  $\rho$ .

The cell voltage response to a long galvanostatic pulse is shown schematically in Fig. 3a. The experimentally measured voltages during, and following a

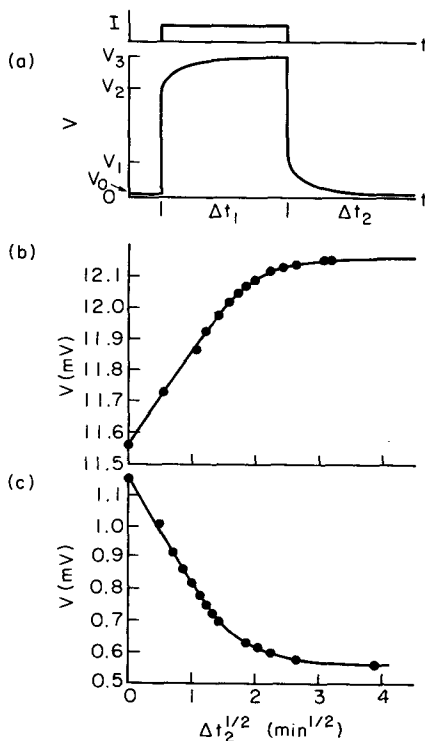


Fig. 3. Cell voltage response to a galvanostatic pulse of  $56 \mu\text{A}/\text{cm}^2$  and long duration. (a) Schematic time dependence; (b) galvanostatic voltage rise following current initiation; (c) voltage decline following current termination.

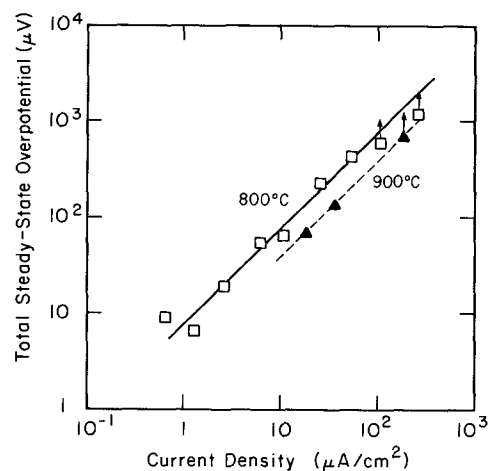


Fig. 4. Total steady-state overpotential as a function of current density for the cell  $\text{Ga-Ga}_2\text{O}_3/\text{ZrO}_2(\text{CaO})/\text{Ga-Ga}_2\text{O}_3$ .

pulse of  $56 \mu\text{A}/\text{cm}^2$  are shown in Fig. 3b and c, respectively. The data are plotted as a function of the square root of the incremental time following the current change to show the parabolic time dependence of the voltage transients.

The total steady-state overpotential  $\eta_t$  was calculated for each chronopotentiometric experiment from the magnitude of the galvanostatic voltage transient ( $V_3 - V_2$ , in Fig. 3a). The dependence of  $\eta_t$  on current density passed through the cell at  $800^\circ\text{C}$  is shown in Fig. 4. Measurements at current densities well above  $100 \mu\text{A}/\text{cm}^2$  were hindered by the failure of the overpotential to reach steady state in a convenient period of time. On the other hand, measured overpotentials below  $\sim 25 \mu\text{V}$  were in error because of the finite noise level in the measurement circuit. A linear dependence of  $\eta_t$  on  $i$  was observed which, at  $800^\circ\text{C}$ , had a slope of  $7.6 \pm 2 \text{ ohms}/\text{cm}^2$  of electrode-electrolyte interface. Measurements of steady-state overpotentials at  $900^\circ\text{C}$  also showed a linear dependence of  $\eta_t$  on  $i$  with a slope of  $4 \pm 2 \text{ ohms}/\text{cm}^2$  of interface.

## Discussion

**Oxygen transfer mechanisms.**—During passage of current between electrodes, charge-carrying oxygen ions are transferred across the solid electrolyte. Gallium oxidation occurs at the positive cell electrode and oxide reduction, at the negative electrode.

Several mechanisms for oxygen transfer between the electrodes operate in parallel, and these are summarized in Fig. 5. Oxygen flowing from the solid electrolyte into liquid gallium saturates the metal after charge transfer. In the solution-diffusion mechanism I the dissolved oxygen diffuses across a narrow liquid layer to an oxide surface where oxidation is assumed to take place. The oxide can form on the solid electrolyte if a nucleation and growth mechanism II is operative. Alternately, the dissolved oxygen can adsorb onto and diffuse along the solid electrolyte-liquid metal interface, III, to an oxide grain contacting the electrolyte. At points of three phase contact a metal-oxide-electrolyte reaction mechanism IV can operate without diffusion.

Oxygen transfer across the electrolyte-oxide interface can also occur by point defect migration through the oxide. For the anion diffusion mechanism V, interstitial oxygen ions diffuse to metallic regions, or alternately, oxygen vacancies diffuse from the metal following local oxidation toward the electrolyte. In the cation diffusion mechanism VI, interstitial cations diffuse from the metal to the electrolyte where oxidation displaces the oxide phase in the direction away from the solid electrolyte.

Each oxygen transfer mechanism involves the series of kinetic steps. The charge transfer and oxidation

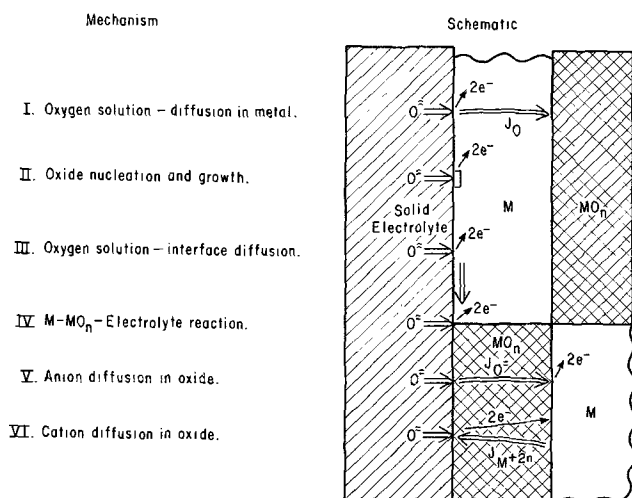


Fig. 5. Mechanisms for charge transfer from a solid electrolyte to a metal-metal oxide electrode.

processes are common to all oxygen transfer mechanisms, while dissolution and liquid-phase or solid-state diffusion are required by several. Usually one step will be rate limiting.

Several of the oxygen transfer mechanisms do not contribute significantly to the total oxygen flux. Oxide nucleation by mechanism II cannot operate at sufficiently low oxygen supersaturation of the liquid phase ( $10^{-2}$  in this study). The oxygen solution-interface diffusion mechanism III is probably rate limited by the interfacial diffusion process for which the interfacial oxygen permeability is less than that for the bulk liquid phase. The extent to which the metal-oxide-electrolyte reaction mechanism IV can operate is limited by the amount of oxide contacting the electrolyte.

For the oxygen transfer mechanisms V and VI, diffusive transport of point defects should be rate limiting. Cation interstitial diffusion is known to predominate over anion diffusion mechanisms in  $\text{Ga}_2\text{O}_3$ . In a study of the oxidation kinetics of GaAs (27), an oxide film of  $\text{Ga}_2\text{O}_3$  was found to form after evaporation of arsenic. Further oxidation proceeds by interstitial diffusion of Ga through the oxide layer. This mechanism is corroborated by Rosenberg (28) for InSb oxidation. The Sb remains metallic because the diffusivity of Sb as well as oxygen is much lower than that of the trivalent metal in the oxide. Thus, the anion diffusion mechanism V is virtually inoperative compared to the cation diffusion mechanism VI. The cation diffusivity of the oxide, however, is significantly lower than the oxygen diffusivity of liquid gallium (29).

A study of the mechanisms shown schematically in Fig. 5 indicates that the solution-diffusion mechanism I should predominate in the temperature range studied, owing to the large permeability of liquid gallium. This mechanism is explored in the following section.

**Solution-diffusion model.**—The solution-diffusion model for aqueous reactions between sparingly soluble reagents and conducting electrodes has been investigated extensively by Dunning *et al.* (30) and studied experimentally by Katan *et al.* (17). The numerous local complex reaction paths operating at the electrode-electrolyte interface can easily be combined by expressing the over-all rate constant  $k$  as a function of the rate constants for the  $i^{\text{th}}$  step,  $k_i$

$$k = [\sum_i A_i k_i^{-1}]^{-1} \quad [4]$$

The numerical value of the coefficients, however, must be determined experimentally, unless the rate-controlling step can be deduced by relative magnitude esti-

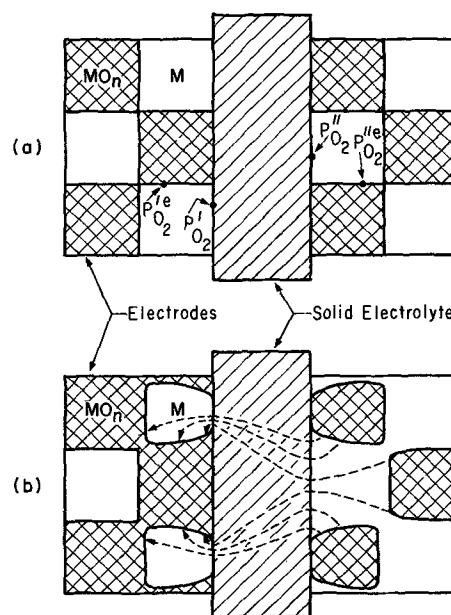


Fig. 6. Schematic of a symmetric liquid metal-metal oxide electrode, solid-state galvanic cell. (a) Before current flow; (b) after current flow assuming a solution-diffusion mechanism for oxygen transfer.

mates. Such estimates suggest that liquid-phase diffusion of dissolved oxygen is rate controlling in the Ga-Ga<sub>2</sub>O<sub>3</sub> electrode, and thus the over-all rate constant  $k$  is approximately  $D_0$ , the diffusivity of oxygen in liquid gallium. This estimate of the rate-controlling step is supported by a recent study of oxygen transfer between solid metal-metal oxide electrodes and solid electrolytes, where oxygen diffusion in the metal was found to be rate controlling (23).

Oxygen transport through the experimental cell by mechanism I under a galvanostatic driving force is shown schematically in Fig. 6. The overpotential at each electrode can be calculated from Eq. [2] and [3] with the oxygen partial pressures at the electrolyte surfaces,  $P_{\text{O}_2}'$  and  $P_{\text{O}_2}''$ , and from the equilibrium partial pressures at the metal-metal oxide interfaces within the electrode,  $P_{\text{O}_2}'^e$  and  $P_{\text{O}_2}''^e$ . The average partial pressure drops within the electrodes can be defined by  $\overline{\Delta P}' = P_{\text{O}_2}' - P_{\text{O}_2}'^e$  and  $\overline{\Delta P}'' = P_{\text{O}_2}''^e - P_{\text{O}_2}''$ . The electrode overpotentials in the electrodes are then

$$\eta' = \frac{RT}{4F} \ln \left( 1 + \frac{\overline{\Delta P}'}{P_{\text{O}_2}'} \right) \simeq \frac{RT}{4F} \frac{\overline{\Delta P}'}{P_{\text{O}_2}'} \quad [5a]$$

$$\eta'' = \frac{RT}{4F} \ln \left( 1 - \frac{\overline{\Delta P}''}{P_{\text{O}_2}''} \right)^{-1} \simeq \frac{RT}{4F} \frac{\overline{\Delta P}''}{P_{\text{O}_2}''} \quad [5b]$$

The oxygen partial pressures can be converted to oxygen molar solubilities by Sievert's law from which it follows, for the reaction  $\text{O}_2 \rightarrow 2 \text{O}_{\text{diss}}$ , that the solubility is proportional to  $P_{\text{O}_2}$  and, therefore,  $\Delta c/c = \frac{1}{2} \Delta P/P_{\text{O}_2}$ .

The oxygen solubilities at the electrolyte surfaces will differ from the equilibrium solubility  $c_0$  at the cell temperature. However, in the limit of small supersaturations, the overpotential for electrode 1 becomes

$$\eta' = \frac{RT}{2F} \frac{\overline{\Delta c}'}{c_0} \quad [6]$$

The oxygen ion molar flux  $J$  is related to the cell current density by Faraday's law, which for divalent ions is  $i_{\text{ion}} = 2FJ$ . The oxygen flux within the electrode metal phase is related to the oxygen diffusivity by Fick's first law

$$J = -D \frac{\partial \bar{c}}{\partial z} \Big|_{z=0} = D \frac{\Delta c}{l} \quad [7]$$

where  $\bar{c}$  is the average concentration gradient at the electrolyte and  $l$  is a characteristic length. The dependence of the solubility drop on cell current is then

$$\Delta c = \frac{it_{\text{ion}} l}{2FD} \quad [8]$$

Finally, the dependence of the electrode overpotentials on cell current is obtained by combining Eq. [6] and [8]

$$\eta' = \frac{RT}{4F^2 D c_0} t_{\text{ion}} i \quad [9]$$

An identical expression applies to the second electrode. The ratio  $\eta'/i$  is the specific electrode resistance  $R_{\eta}$ .

All coefficients in Eq. [9] are experimentally known except for the oxygen permeability of liquid gallium,  $D_{\text{O}}$ , and the characteristic diffusion lengths,  $l$ .

The oxygen permeability of liquid gallium can be deduced from the measured oxygen solubility  $c_0$  and the liquid-phase diffusivity  $D$ . The solubility of  $\text{Ga}_2\text{O}_3$  in liquid gallium was determined by Foster and Scardefield (30) by a gravimetric method over the temperature range from 900° to 1200°C. Their experimental data on oxide mole fraction is represented here by the relation

$$x_{\text{Ga}_2\text{O}_3} = 1.175 \times 10^2 \exp [(-35,850 \pm 1,140)/RT] \quad [10]$$

The solubility of atomic oxygen is then found by assuming that the dissolved oxide dissociates into atomic components, from which it follows that the molar solubility  $c_0$  ( $\approx 3x_{\text{Ga}_2\text{O}_3} d_{\text{Ga}}/M_{\text{Ga}}$ ) is

$$c_0 = 30.63 \exp [(-35,850 \pm 1,140)/RT] \quad [11a]$$

The activation energy for dissolution is 35,850 ± 1,140 cal for the available data, and thus the extrapolation of the oxygen solubility to low temperatures produces an error which increases with the extent of extrapolation. The diffusivity of oxygen in liquid gallium was measured by Klinedinst (29) by galvanostatic titration experiments. The diffusion coefficient was expressed by the equation

$$D_{\text{O,Ga(l)}} = (3.68 \pm 0.42) \times 10^{-3} \exp [(-8,370 \pm 0.25)/RT] \quad [11b]$$

The permeability of atomic oxygen in liquid gallium is, finally

$$D_{\text{cO}} = 0.11273 \exp [(-44,220 \pm 1,140)/RT] \quad [12]$$

Thus, the permeabilities at 800° and 900°C are  $1.11 \times 10^{-10}$  and  $6.49 \times 10^{-10}$ , respectively.

A general dependence of the local overpotential on temperature and current density for the solution diffusion model can now be found by combining the permeability Eq. [12] with Eq. [9], for  $t_{\text{ion}} \approx 1$

$$\eta' = (1.98 \times 10^{-9}) l' i T \exp(44,220/RT) \quad [13]$$

Again, the diffusion length  $l'$  depends on the electrode structure. The Ga- $\text{Ga}_2\text{O}_3$  electrode resistivity associated with the local overpotential can be defined by

$$\rho_{\eta'} \equiv \frac{\eta'}{l' i} = (1.98 \times 10^{-9}) T \exp(44,220/RT) \quad [14]$$

Unlike the overpotential resistance per unit area ( $R_{\eta} = \eta'/i$ ), the local electrode resistivity is independent of the electrode structure and is a property of the oxygen transfer through the liquid phase.

**Ga- $\text{Ga}_2\text{O}_3$  electrode properties.**—If the solution-diffusion mechanism controls oxygen transfer between the Ga- $\text{Ga}_2\text{O}_3$  electrode and the solid electrolyte with

dissolved oxygen diffusion in liquid gallium as the rate-controlling step, then the interfacial transfer resistivity  $\rho_{\eta'}$  should be given by Eq. [14]. This rate control can be tested by comparing experimental data for  $\eta'/i$  with  $\rho_{\eta'}$ , calculated from Eq. [14]. The effective diffusion length required is then given by

$$l' = 5.05 \times 10^8 T^{-1} \exp(-44,220/RT) \cdot (\eta'/i)_{\text{meas.}} \quad [15]$$

At 800°C,  $\rho_{\eta'}$  equals 2162 ohm-cm, whereas the measured  $\eta'/i$  is 3.8 ohm-cm<sup>2</sup>. The diffusion length deduced from these data is then

$$l' = 1.76 \times 10^{-3} \text{ cm}$$

This diffusion length is consistent with the actual electrode structure in which loosely packed  $\text{Ga}_2\text{O}_3$  particles with an average diameter of  $2.5 \times 10^{-3}$  cm are infused with liquid gallium. The experimental data at 900°C indicates an effective diffusion length of  $5.0 \times 10^{-3}$  which is somewhat larger than expected for diffusion-limited kinetics, but within the limits of error and reproducibility of the electrode structure.

Another test of the mechanism and rate control lies in the time dependence of the overpotential following initiation of a constant cell current. Transport of oxygen ions through the electrolyte causes a local supersaturation of dissolved oxygen which, in the quasi-steady state, can be shown to be related to the diffusion flux  $J$  and time  $t$  by

$$\Delta c \approx J \sqrt{2t/D} \quad [16]$$

The time dependence of the local electrode overpotential is then

$$\eta'(t) \approx \eta'(\infty) \sqrt{2Dt}/l' \quad [17]$$

A linear dependence of  $\eta'$  on  $t^{1/2}$  for short times was observed in all experiments, again supporting the diffusion-limited kinetics.

The measured overpotentials were independent of the direction of current flow to within 5%. The asymmetry of the experimental cell was minimized by limiting the interfacial area of the outer electrode in contact with the electrolyte tube. The dependence of overpotential on the direction of current flow is assumed to indicate differences in oxide packing within the two Ga- $\text{Ga}_2\text{O}_3$  electrodes.

The total oxygen flux transferred during the experiments is not expected to significantly alter the electrode structure at the solid electrolyte interface according to mechanism I. A calculation, based on the fact that 1 coulomb passing through the cell transfers  $5.18 \times 10^{-6}$  moles of oxygen, shows that an oxide thickness of only 200 Å/cm<sup>2</sup> of electrode-electrolyte interface was transferred during all experiments. For the idealized interface structure shown in Fig. 6, the ratio of oxide-metal area to metal-electrolyte area is 2.5, and thus the average oxide-metal interface displacement is only 80Å. Most of the oxide-metal interface displacement takes place near the electrolyte where the diffusion distance is short, however, and this effect leads to the current-modified electrode structure shown in Fig. 6b. For the actual electrode containing irregular oxide particles in a liquid matrix, the oxide transfer processes has less effect on the electrode structure because of limited three-phase contact.

A comparison of the present results with earlier studies shows that the Ga- $\text{Ga}_2\text{O}_3$  electrode exhibits an exceptionally low overpotential-associated resistance. Worrell and Iskoe (23) have measured the dependence of steady-state overpotentials on cell current for symmetric cells of the type  $M\text{-MO}_n/\text{ZrO}_2(\text{CaO})/M\text{-MO}_n$ , in which the  $M\text{-MO}_n$  electrodes were Ni-NiO, Fe-FeO, and Cu-Cu<sub>2</sub>O. The steady-state overpotentials per unit area of electrode-electrolyte interface calculated from their data are shown in Fig. 7 along with the measurements from this study. From this comparison it can be seen that the Ga- $\text{Ga}_2\text{O}_3$  electrode exhibits a lower

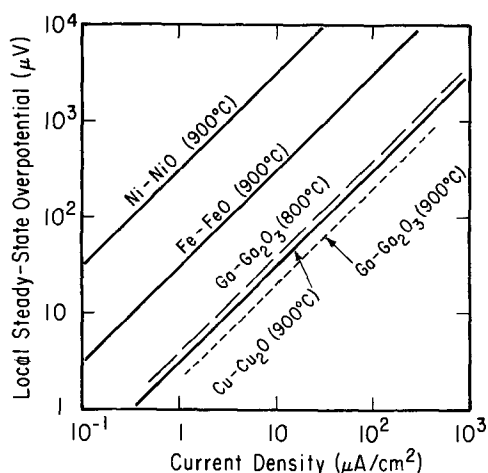


Fig. 7. Local steady-state overpotentials as a function of current density for Ni-NiO, Fe-FeO, Cu-Cu<sub>2</sub>O, and Ga-Ga<sub>2</sub>O<sub>3</sub> electrodes.

electrode overpotential than do the three most commonly employed reference electrode and, therefore, promises to be a superior reference electrode for kinetics and phase equilibria applications in the low partial pressure range.

#### Acknowledgments

The financial support of the United States Atomic Energy Commission is gratefully acknowledged. The authors wish to thank Dr. W. L. Worrell for copies of his manuscript prior to publication.

Manuscript submitted Sept. 12, 1973; revised manuscript received Nov. 9, 1973.

Any discussion of this paper will appear in a Discussion Section to be published in the December 1974 JOURNAL. All discussions for the December 1974 Discussion Section should be submitted by Aug. 1, 1974.

#### SYMBOLS

$c_0$	molar solubility, moles/cm <sup>3</sup>
$D$	diffusion coefficient, cm <sup>2</sup> /sec
$F$	Faraday constant, 96,489 coulomb/equiv., or 23,061 cal/V-equiv.
$J$	oxygen ion flux, moles/cm <sup>2</sup> -sec
$L$	electrolyte thickness, cm
$l'$	characteristic diffusion length, cm
$P_{O_2}$	oxygen partial pressure, atm
$R$	gas constant, 1.987 cal/mole °K
$R_n$	local electrode resistance, ohm
$T$	absolute temperature, °K
$t_{ion}$	ionic transference number
$V$	cell voltage, V
$V_0$	open cell voltage, V
$x_i$	mole fraction of component $i$
$\eta'$	local electrode overpotential, V
$\eta_t$	total cell overpotential, V
$\rho$	electrolyte resistivity, ohm-cm
$\rho_n$	local electrode resistivity, ohm-cm
$\tau$	relaxation time constant, sec

#### REFERENCES

- D. O. Raleigh, in "Progress in Solid State Chemistry," Vol. III, Chap. 3, H. Reiss, Editor, Pergamon Press, New York (1967).
- C. B. Alcock, Editor, "Electromotive Force Measurements in High-Temperature Systems," American Elsevier Publishing Co., New York (1968).
- R. A. Rapp and D. A. Shores, in "Physicochemical Measurements in Metals Research, Part 2," R. A. Rapp, Editor, p. 123, Wiley-Interscience, New York (1970).
- H. Schmalzreid and A. D. Pelton, "Annual Review of Material Science," Vol. 2, p. 143, R. Huggins, Editor, Annual Review Inc., Palo Alto, Calif. (1972).
- B. Reuter and K. Hardel, *Naturwiss.*, **48**, 161 (1961).
- T. Takahashi and O. Yamamoto, *Electrochim. Acta*, **11**, 779 (1966).
- J. N. Bradley and P. D. Greene, *Trans. Faraday Soc.*, **62**, 2069 (1966); **63**, 424 (1967).
- B. B. Owens and G. R. Argue, *Science*, **157**, 308 (1967).
- R. T. Foley, *This Journal*, **116**, 13C (1969).
- H. Wiedersich and S. Geller, "Chemistry of Extended Defects in Non-Metallic Solids," Proc. Symp. Scottsdale, Ariz., April 21, 1969.
- W. van Gool, Editor, "Fast Ion Transport in Solids; Solid State Batteries and Devices," North-Holland Publishing Co., Amsterdam (1973).
- N. H. Michael and A. A. Pilla, *This Journal*, **118**, 72 (1971).
- F. C. Anson, *J. Phys. Chem.*, **71**, 3605 (1967).
- C. G. J. Baker and E. R. Buckle, *Trans. Faraday Soc.*, **64**, 469 (1968).
- R. P. Buck, *J. Electroanal. Chem.*, **23**, 219 (1969).
- J. R. Macdonald, *Trans. Faraday Soc.*, **66**, 943 (1970).
- T. Katan, S. Szpak, and D. N. Bennion, *This Journal*, **120**, 883 (1973).
- D. O. Raleigh, in "Electroanalytical Chemistry—A Series of Advances," Vol. VI, pp. 87-186, A. J. Bard, Editor, Marcel-Dekker Press, New York (1967).
- S. V. Karpachev and A. T. Filyaev, *Elektrokhimiya*, **2**, 617 (1966); **4**, 498 (1968).
- B. C. H. Steele, in "Mass Transfer in Oxides," J. B. Wachtman and A. D. Franklin, Editor, Nat. Bur. Std., Spec. Publ. 296, p. 165 (1968).
- F. A. Kröger, *This Journal*, **120**, 75 (1973).
- B. C. H. Steele, in "Electromotive Force Measurements in High-Temperature Systems," C. B. Alcock, Editor, pp. 17-18, Inst. of Mining and Met. Pub., London (1968).
- W. L. Worrell and J. L. Iskoe, in "Fast Ion Transport in Solids, Solid State Batteries and Devices," W. van Gool, Editor, p. 513, North-Holland Publishing Co., Amsterdam (1973).
- A. U. Seybolt, *This Journal*, **111**, 697 (1964).
- K. A. Klinedinst, M. V. Rao, and D. A. Stevenson, *ibid.*, **119**, 1261 (1972).
- C. Wagner, *Z. Physik. Chem.*, **B21**, 25 (1933).
- H. T. Minden, *This Journal*, **109**, 733 (1962).
- A. J. Rosenberg, *J. Phys. Chem. Solids*, **14**, 175 (1960).
- K. A. Klinedinst and D. A. Stevenson, *This Journal*, **120**, 304 (1973).
- L. M. Foster and J. Scardefield, *ibid.*, **116**, 494 (1969).

# The Triangular Voltage Sweep Method for Determining Double-Layer Capacity of Porous Electrodes

## III. Porous Nickel in Potassium Hydroxide

E. G. Gagnon\*

Electrochemistry Department, Research Laboratories, General Motors Corporation, Warren, Michigan 48090

### ABSTRACT

The effects of faradaic current and distributed capacity on the measurement of double-layer capacity of porous nickel were analyzed as a function of electrode thickness and temperature. Faradaic current observed with electrodes at  $-46^{\circ}\text{C}$  was negligible compared to results obtained at  $22^{\circ}\text{C}$ . Distributed capacity effects increased with electrode thickness and with decreasing temperature; the results agreed well with values predicted from a previously developed model. In the potential range of 0 to  $-0.40\text{V}$  vs.  $\text{Hg}/\text{HgO}$ , the capacity based on the BET area of the electrode was about  $30 \mu\text{F}/\text{cm}^2$ .

The electrochemically active surface area of a porous electrode can be determined directly and simply from double-layer capacity (DLC) measurements. Faradaic currents and distributed reactions, however, may interfere with the analysis. Unless these effects can be eliminated or minimized, spurious results will be obtained. This paper shows how faradaic current and/or distributed capacity effects can be handled using a triangular voltage sweep (TVS) technique. The system investigated was porous nickel in 31 weight per cent (w/o) KOH.

### Theory

The physical model of the porous electrode-electrolyte system considered was discussed before (1). Triangular voltage sweep results, where DLC is constant, will be analyzed for cases where faradaic current,  $i_F$ , and/or distributed capacity effects are present.

Faradaic currents are often caused by processes which are complex and difficult to describe mathematically (e.g., removal of impurities on an electrode or the adsorption of species present in the electrolyte). The results are difficult to analyze because the electrode reactions are often unsteady-state processes.

Distributed capacity effects arise when the outer surface of a porous electrode charges or discharges faster than the interior. Increasing the resistance of the electrolyte in the pores of the electrode enhances this effect. Four cases for the TVS method will now be discussed.

**Case A:** Faradaic current and distributed capacity effects negligible.

In the absence of faradaic current,  $i_F$ , and distributed capacity effects, an electrode which behaves as a plane capacitor will produce a current-time curve of the type illustrated in Fig. 1A; DLC is calculated simply from

$$C = i_c/k \quad [1]$$

where  $i_c$  is the capacitive current (milliamperes);  $C$  is capacity (farads); and,  $k$  is the sweep rate (millivolts/second).

**Case B:** Faradaic current significant, but distributed capacity effects negligible.

If the electrode is passing faradaic current,  $i_F$ , the total measured current is  $i = i_c + i_F$ . Thus, the resulting  $i-t$  curve is illustrated in Fig. 1B. If  $i_F$  is not too large compared to  $i_c$ ,  $i_F$  will have about the same value just before and after the reversal point of the sweep. Then,  $i_1 = i_F + kC$  and  $i_2 = kC - i_F$ . It can be easily seen that

$$C = (i_1 + i_2)/2k \quad [2]$$

and a capacity corrected for  $i_F$  is obtained.

**Case C:** Distributed capacity effects significant, but faradaic current negligible.

In the absence of  $i_F$  effects, distributed capacity gives rise to behavior illustrated in Fig. 1C. It has already been shown (1) that the current density (milliamperes/square centimeter) at the face of the electrode,  $i(L)$ , may be predicted in region abcd (Fig. 1C) from

$$i(L) = \beta_1 k C' \quad [3]$$

where

$$\beta_1 = 1 - \sum_{n=1}^{\infty} \exp\left[-M_n^2 \frac{t}{\rho_e C' L}\right] \left[\frac{2\psi^2}{M_n^2(\psi^2 + M_n^2 + \psi)}\right]$$

$$\psi = \frac{L\lambda}{d} = \frac{\rho_e}{R_e A} = M_n \tan M_n \quad [4]$$

$$\rho_e = \rho\lambda \quad [5]$$

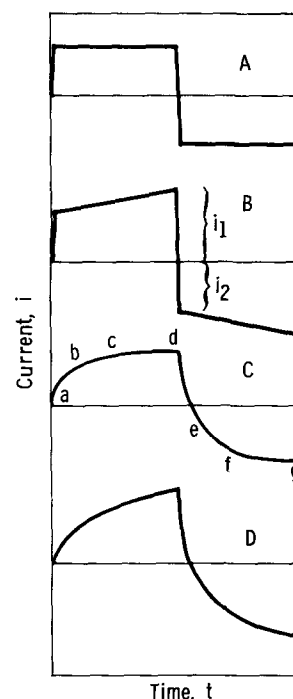


Fig. 1. TVS results illustrating faradaic and/or distributed capacity effects. A,  $i_F$  and distributed capacity effects negligible; B,  $i_F$  effects significant; C, distributed capacity effects significant; D,  $i_F$  and distributed capacity effects significant.

\* Electrochemical Society Active Member.

Key words: porous electrodes, double-layer capacity, nickel electrode.

and  $k$  is sweep rate (millivolts/second);  $C'$  is capacity (farads/square centimeter) based on the geometric area,  $A$  (square centimeters), of the electrode;  $L$  is electrode thickness (centimeters);  $t$  is time (seconds);  $\rho$  is the specific resistance (ohm-centimeter) of the bulk electrolyte;  $\rho_e$  is the specific resistance (ohm-centimeter) of the electrolyte in the pores of the electrode;  $R_e$  is the resistance (ohms) of the bulk electrolyte;  $\lambda$  is the labyrinth factor;  $d$  is the distance (centimeters) between the surface of the electrode and the tip of the Luggin capillary;  $M_n$  are the various roots of the transcendental equation  $\psi = M_n \tan M_n$ . Clearly, as time decreases, as electrode thickness increases, or as the specific resistance of the electrolyte increases, distributed capacity effects become more significant.

At the reversal point of the TVS, the current density at the face of the porous electrode was also predicted (1) from

$$i(L) = \gamma k C' \quad [6]$$

where

$$\gamma = \beta_1 - \beta_2$$

and

$$\beta_2 = \sum_{n=1}^{\infty} \exp \left[ -M_n^2 \frac{t}{\rho_e C' L} \right] \cdot \left[ \frac{2(\psi^2 + M_n^2)}{M_n^2(\psi^2 + M_n^2 + \psi)} \right] \sin^2 M_n$$

Case D: Faradaic current and distributed capacity effects significant.

When both faradaic current and distributed capacity effects are significant, the  $i$ - $t$  curve obtained is illustrated in Fig. 1D. This case is difficult to handle mathematically. If possible, it is best to handle the situation experimentally by selecting the experimental conditions to minimize one or both of the effects.

### Experimental

The electrochemical cell and instrumentation used in this study were discussed previously (1). The test electrodes were punched from a sheet of sintered, porous nickel battery plaque. They were disk-shaped, had a thickness of about 0.046 cm, a diameter of 3.5 cm, and a BET area of 0.049 m<sup>2</sup>/g. Electrodes of different thicknesses were obtained by stacking a number of the 0.046 cm thick disks into a special electrode holder (2); only one face of the electrode was exposed to the electrolyte.

All measurements were performed using an Hg/HgO (31 w/o KOH) reference electrode with a Luggin capillary positioned about 10 mm from the face of the test electrode. The cell and the reference electrode were placed in a constant temperature cabinet; measurements were made at 22° and -46° ± 0.5°C.

### Results and Discussion

Figures 2-5 show results obtained using electrodes of different thickness at 22° and -46°C. In all cases, a starting potential of -0.10V vs. Hg/HgO was used; a sweep excursion of about 200 mV was selected to keep  $i_F$  not too large compared to  $i_c$ . In all of the work reported here, a sweep rate of 86.5 mV/sec was used. The  $i$ - $t$  results obtained may be categorized according to the four cases, illustrated in Fig. 1; the results are summarized in Table I.

Table I. Characterization of  $i$ - $t$  data as a function of electrode thickness and temperature

Electrode thickness (cm)	Case types	
	22°C	-46°C
0.046	A	C
0.092	B	C
0.137	B	C
0.183	D	C

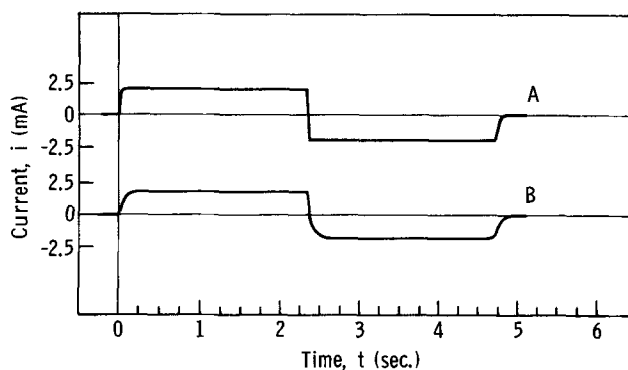


Fig. 2. Sweep data obtained for a 0.046 cm thick porous nickel electrode using a sweep rate of 86.5 mV/sec. A, At 22°C; B, at -46°C.

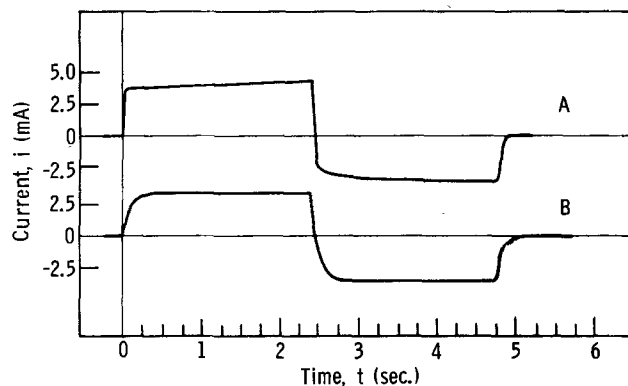


Fig. 3. Sweep data obtained for a 0.092 cm thick porous nickel electrode using a sweep rate of 86.5 mV/sec. A, At 22°C; B, at -46°C.

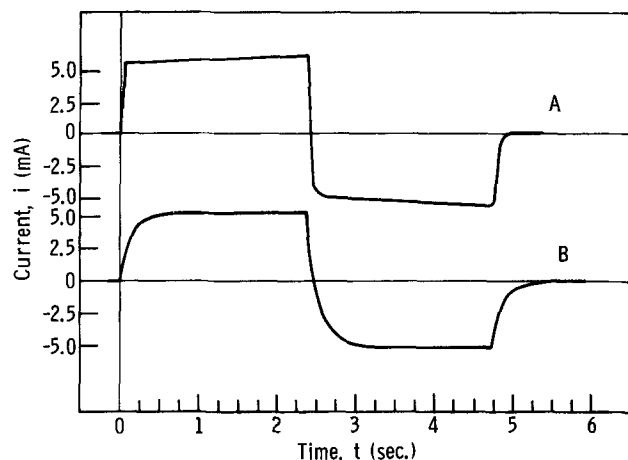


Fig. 4. Sweep data obtained for a 0.137 cm thick porous nickel electrode using a sweep rate of 86.5 mV/sec. A, At 22°C; B, at -46°C.

At 22°C, the  $i$ - $t$  curve for the thinnest electrode (Fig. 2A) was essentially symmetrical about zero current and approximated the square wave illustrated in Fig. 1A. This is characteristic of an electrode behaving as a plane capacitor. The capacity of the electrode,  $C$ , was calculated (using Eq. [1]) to be 0.021 farads which, based on the BET area of the electrode, gives a value of 30  $\mu$ F/cm<sup>2</sup>. A similar shape was observed at -46°C (Fig. 2B) except that some rounding effects were noted at the start and at reversal point of the sweep, showing the presence of some distributed reactions. The calculated capacity was the same as at room temperature.

As the electrode thickness increased, faradaic current effects also increased; the thickest electrode (Fig. 5A) showed signs of distributed reactions in addition to faradaic current effects (Case D, Fig. 1D).

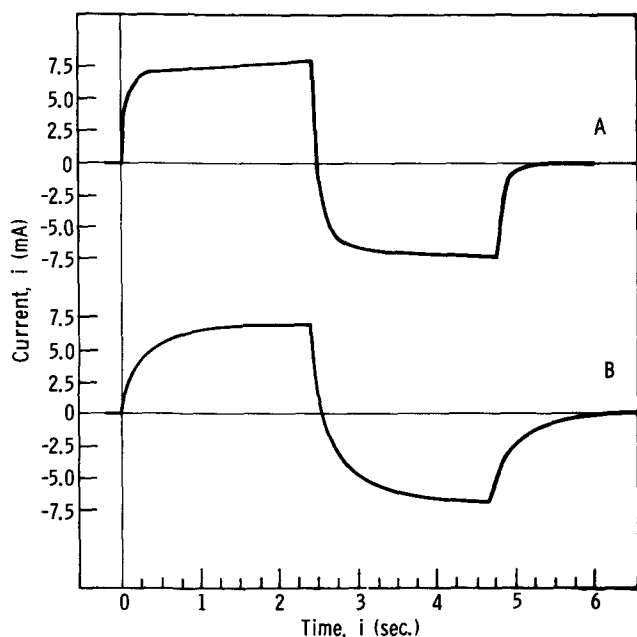


Fig. 5. Sweep data obtained for a 0.183 cm thick porous nickel electrode using a sweep rate of 86.5 mV/sec. A, At 22°C; B, at -46°C.

At -46°C, all four electrode thicknesses (Fig. 2B, 3B, 4B, and 5B) displayed the same general shape illustrated in Fig. 1C; the time, however, for the current to reach a steady value both at the start and after the reversal point of the sweep increased with electrode thickness. A plot of the steady current as a function of electrode thickness at -46°C, given in Fig. 6, is linear. This is expected since the double-layer capacity of an electrode is proportional to electrode area in the absence of distributed capacity and  $i_F$  effects.

**Distributed capacity effects.**—To test if the times observed initially and at the reversal point of the sweep at -46°C could be predicted from Eq. [3] and [6], respectively, estimates of the parameters  $\psi$ ,  $\lambda$ ,  $d$ , and  $\rho_e$  were made to calculate  $\beta$  and  $\gamma$ , for each electrode thickness.

The distance,  $d$ , was obtained, as in earlier work (3), using galvanostatic transient measurements performed at temperatures ranging from 22° to -46°C. Ohmic polarization, taken as the discontinuity on the oscilloscopic potential-time trace, was found to be due primarily to the resistance of the electrolyte between the electrode and the tip of the Luggin capillary. The

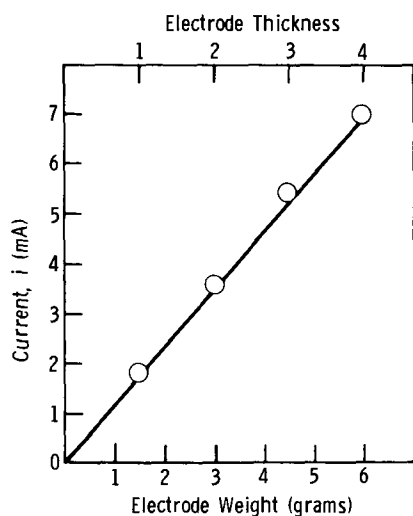
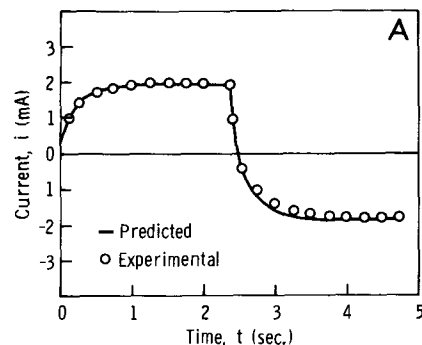


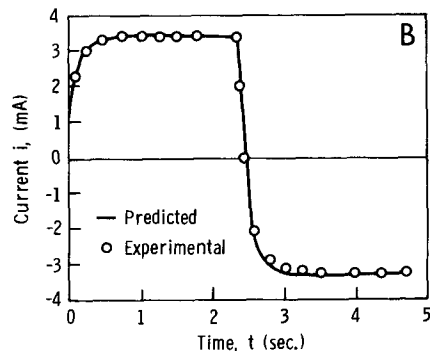
Fig. 6. Capacitive current vs. electrode thickness

distance  $d$ , was then estimated from  $d = R_e A / \rho$ ; a value of  $d = 0.94$  cm was determined.

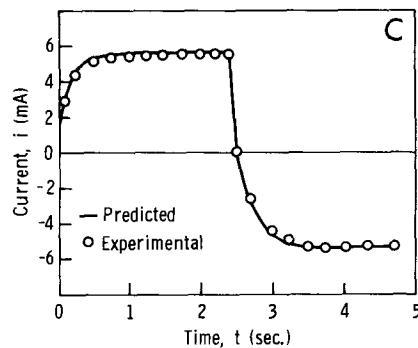
A labyrinth factor,  $\lambda$ , of 1.3 was estimated similarly to earlier work with porous silver (1). It was accomplished by matching one set of experimental results (Fig. 2B) with data predicted from Eq. [3] and [6], thus fixing a value of  $\psi$ . These parameters were then used to predict  $i-t$  results for other electrode thickness. Predicted and experimental  $i-t$  results obtained as a function of electrode thickness are shown in Fig. 7



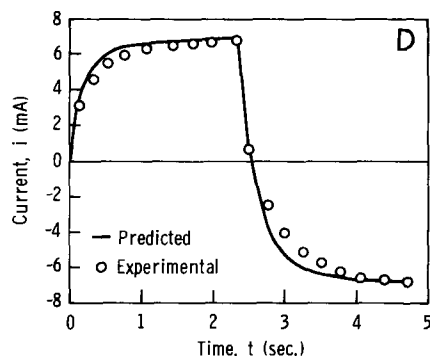
A. 0.046 cm thick



B. 0.092 cm thick



C. 0.137 cm thick



D. 0.183 cm thick

Fig. 7. Predicted and experimental data for electrodes of different thickness at -46°C.

Table II. Parameters used in the distributed capacity predictions

Thickness (cm)	Predicted		Experimental Capacity, C (farads)
	$\psi$	Capacity, C (farads)	
0.046	0.063	—	0.021
0.092	0.126*	0.042*	—
0.137	0.190*	0.063*	—
0.183	0.253*	0.084*	—

\* Values predicted using the 0.046 cm thick electrode data at  $-46^{\circ}\text{C}$  and a value of  $\lambda = 1.3$ .

Table III. A comparison of capacitive currents corrected for  $i_F$  effects at  $22^{\circ}\text{C}$  vs. values measured at  $-46^{\circ}\text{C}$ 

Electrode thickness (cm)	Capacitive currents	
	$22^{\circ}\text{C}^*$	$-46^{\circ}\text{C}^{**}$
0.046	1.8	1.8
0.092	3.4	3.6
0.137	5.0	5.4
0.183	4.3	7.1

\* Corrected.  
\*\* Experimental.

A-D. Table II gives some of the important parameters used.

**Faradaic current effects.**—Calculations using Eq. [2], which correct for faradaic current, were made for all electrode thicknesses at  $22^{\circ}\text{C}$ . The capacitive currents corrected for  $i_F$  are compared to the low temperature data in Table III.

The  $i_F$  corrected capacitive currents calculated for the first three electrode thicknesses agreed reasonably well with the low temperature values; for the thickest electrode, however, a significant deviation was noted. The discrepancy noted with the thickest electrode was due to distributed capacity effects which interfered with analysis of the data (i.e., excessive rounding of the  $i$ - $t$  curve after sweep reversal). The faradaic current observed was a transient effect, since the current just prior to the start of the sweep was zero.

**Effect of potential.**—Apparent capacities were calculated from a series of  $i$ - $t$  curves where the start of each sweep was at a different potential, but each was run in the cathodic direction at the same sweep rate,  $k$ , of  $86.5\text{ mV/sec}$ ; conditions were such as to minimize

distributed capacity and faradaic current effects. The capacity, based on the BET area of the electrode, appears to be nearly constant at about  $30\ \mu\text{F/cm}^2$  in the potential range of 0 to  $-0.40\text{V vs. Hg/HgO}$ .

### Summary and Conclusions

This work showed that by properly selecting the test conditions, effects due to distributed capacity and for faradaic current could be minimized, thus enabling one to measure the double-layer capacity of porous nickel in 31 w/o KOH. With very thin electrodes, at  $22^{\circ}\text{C}$ , faradaic current and distributed capacity effects were negligible, and the electrode behaved simply as a plane capacitor. As the thickness of the electrode increased, transient faradaic currents also increased at  $22^{\circ}\text{C}$ , which made it somewhat difficult to estimate the capacity using the conventional approach. At  $-46^{\circ}\text{C}$ , however, faradaic current effects were found to be negligible, but distributed capacity effects became more predominant with increasing electrode thickness. It was shown that the distributed capacity effects could be predicted using a mathematical model which had been previously developed.

When faradaic current effects were significant and distributed capacity effects were negligible, the capacity corrected for faradaic current at the reversal point of the sweep was about the same as the capacity determined at  $-46^{\circ}\text{C}$ .

The capacity based on the BET area of the electrode was nearly constant at about  $30\ \mu\text{F/cm}^2$  in the potential range of 0 to  $-0.40\text{V vs. Hg/HgO}$ . This compares well with a value of  $29\ \mu\text{F/cm}^2$  in  $1\text{M Na}_2\text{SO}_4$  at  $-0.4\text{V vs. SCE}$  (4).

Manuscript submitted May 31, 1973; revised manuscript received Nov. 12, 1973. This was Paper 44 presented at the Boston, Massachusetts, Meeting of the Society, Oct. 7-11, 1973.

Any discussion of this paper will appear in a Discussion Section to be published in the December 1974 JOURNAL. All discussions for the December 1974 Discussion Section should be submitted by Aug. 1, 1974.

### REFERENCES

1. E. G. Gagnon, *This Journal*, **120**, 1052 (1973).
2. E. G. Gagnon and L. G. Austin, HDL-065-4, U.S. Army Materiel Command, Harry Diamond Laboratories, Washington, D. C., September 1971.
3. E. G. Gagnon and L. G. Austin, *This Journal* **118**, 497 (1971).
4. R. J. Brodd and N. Hackerman, *ibid.*, **104**, 704 (1957).



# Polarographic Behavior of *p*-Dihalosubstituted Benzenes and Related Compounds

S. Wawzonek\* and S. M. Heilmann

Department of Chemistry, University of Iowa, Iowa City, Iowa 52240

## ABSTRACT

*p*-Diodobenzene and *p*-iodophenyltrimethylammonium iodide show a normal polarographic behavior in dimethylformamide in contrast to that reported for *p*-dibromobenzene. 9,10-Dibromoanthracene and 9-bromoanthracene gave an abnormal polarographic behavior which suggested the intermediacy of dibenzo Dewar benzene in the electrode reaction. Macro electrolyses of 9-bromoanthracene were unsuccessful in preparing this compound.

*p*-Dibromobenzene has been reported (1) to show an unusual polarographic behavior in dimethylformamide and acetonitrile. The second reduction wave occurred at a slightly more positive potential than that for bromobenzene and the diffusion current was larger than that observed for the corresponding wave for *m*-dibromobenzene. This behavior was considered to be caused by the synergistic effect of the intermediate anion on the reduction of the second halogen with the possible formation of *p*-dehydrobenzene.

The work has now been extended to a study of the reduction of *p*-diiodobenzene, *p*-iodophenyltrimethylammonium iodide, and 9,10-dibromoanthracene to determine whether the tendency for *p*-dehydrobenzene would be increased. The first two compounds have better leaving groups than *p*-dibromobenzene and the last compound would possibly form a *p*-dehydrobenzene which would be stabilized by resonance.

## Experimental

The solutions were studied in a cylindrically shaped cell with a mercury pool anode and fitted with side arms for the admission of nitrogen and for the anode connection. All measurements were made in a water thermostat at  $25^\circ \pm 0.1^\circ\text{C}$ .

The current-voltage curves were obtained with a Sargent Model XXI Polarograph.

The dropping mercury electrodes were operated at 70 cm pressure and had drop times of (i) 6.10 and (ii) 5.0 sec in dimethylformamide (open circuit). The  $m^{2/3}t^{1/6}$  values were (i) 1.36 and (ii) 1.71  $\text{mg}^{2/3} \text{sec}^{-1/2}$ , respectively.

Cyclic voltammetric studies were made using a Beckman Electroscan 30 and a Chemtrix Model SSP-2 Polarograph with a Tektronix Oscilloscope.

The compounds used were obtained from a stock with the exception of *p*-iodophenyltrimethylammonium iodide (2), phenyltrimethylammonium iodide (3), 9,10-dibromoanthracene (4), and hexamethylbicyclo[2,2,0]hexa-2,5-diene. The first three were prepared by methods given in the literature and the fourth compound was purchased from Columbia Chemical Company.

**Electrolytic reduction of 9-bromoanthracene.**—A solution of 9-bromoanthracene (3.0g) in dimethylformamide (100 ml) containing 0.2M tetrabutylammonium tetrafluoroborate was reduced at a controlled potential of  $-1.65$  (SCE) at a mercury cathode ( $19.6 \text{ cm}^2$ ). The cathode compartment was connected to a saturated calomel electrode by a 70% dimethylformamide-agar bridge. The anode compartment was separated from the cathode compartment with a medium porosity glass frit and contained a platinum foil cylinder anode. The initial current of 60 mA decreased to 1 mA in 4.5 hr

and was terminated. A plot of current vs. time indicated the use of one electron per molecule of 9-bromoanthracene. The mercury was separated and the catholyte was filtered. The yellow solid (0.33g) obtained melted at  $356^\circ\text{--}358^\circ$  [dec. lit. (5)  $> 300^\circ$ ] and was identified as bis-9-anthryl-mercury by its ir and mass spectra:  $m/e$  556, (M), 197-202 (Hg).

The red filtrate when poured into a mixture of water (400 ml) and hexane (400 ml) gave a solid which was filtered; yield, 0.69g. This solid upon preparative chromatography on silica gel plates using hexane and methylene chloride as eluting solvents gave anthracene (0.55g), trace amounts of 9,9'-bianthryl and anthraquinone (0.02g). Identification of the last two solids was made by comparison with authentic samples.

The hexane extract was separated from the water layer and upon removal of the solvent gave 1.5g of a yellow solid. This solid which showed many components by thin layer chromatography (tlc) on silica using hexane was dissolved in a minimal amount of benzene and adsorbed on silica gel. The silica gel was dried and upon extraction with hexane for 36 hr in a Soxhlet extractor gave 0.96g of anthracene. Further extraction of the silica gel with chloroform gave 0.11g of a yellow solid. Preparative chromatography on two silica plates gave anthracene-9-mercuribromide (0.02g) and anthraquinone (0.03g). Identification was made by comparison with authentic samples. Other components were present in amounts too small to characterize.

The use of uncontrolled potential in this reduction gave bis-9-anthrylmercury (4%), anthracene (63%), anthraquinone (trace), and 9,10-dihydroanthracene (trace). An applied potential of 37V gave an initial current of 55 mA which decreased to 18 mA after 12 hr when the electrolysis was terminated.

Reduction at a platinum cathode using uncontrolled potential gave a dark brown semisolid residue. Tlc analysis of the crude mixture showed seven components. The only solid isolated was anthracene (76%). The applied potential of 20V gave a current of 80 mA which decreased to 26 mA at the termination of the electrolysis (12 hr).

**Anthracene-9-mercuribromide.**—A solution of anthracene (8.9g) and trichloroacetic acid (16.3g) in carbon tetrachloride was treated with yellow mercuric oxide (10.9g) and the resulting mixture was stirred at room temperature for 12 hr. The yellow solid obtained was filtered, washed with methanol, suspended in methanol (200 ml), and treated with a solution of sodium bromide (20.6g) in water (100 ml). Filtration of the resulting yellow green mixture gave a solid (13.33g) which upon crystallization from benzene gave yellow needles melting at  $272^\circ\text{--}275^\circ$ . ir (KBr) 3.28, 3.30, 3.38, 6.10, 6.95, 7.65, 7.90, 8.75, 9.90, 10.85, 11.20, 11.90, 12.10, 13.05, 13.70, 13.90, 16.40, 19.70, 27.00 $\mu$ ; mass spectrum,  $m/e$  459.

\* Electrochemical Society Active Member.

Key words: *p*-diiodobenzene, *p*-iodophenyltrimethylammonium iodide, 9,10-dibromoanthracene, dibenzo Dewar benzene.

Table I. Polarographic behavior of halogenated aromatic compounds in dimethylformamide containing 0.2M tetrabutylammonium bromide

Compound	$E_{1/2}$ (Hg pool)	$I_d$
<i>p</i> -Dibromobenzene	-1.73	3.64
	-2.02	3.35
Bromobenzene	-2.03	3.46
<i>p</i> -Diiodobenzene	-1.12	4.40
	-1.30	2.78
Iodobenzene	-1.31	5.10
<i>p</i> -Iodophenyltrimethylammonium	-1.00	2.31
	-1.79	2.81
Iodide	-2.08	1.74
Phenyltrimethylammonium Iodide	-1.79	3.78
	-2.08	2.28
9,10-Dibromoanthracene <sup>a</sup>	-0.80	2.98
	-1.02	3.10
	<sub>b</sub>	
9-Bromoanthracene <sup>a</sup>	-1.93	0.93
	-1.01	3.51
	<sub>b</sub>	0.82
	-1.90	0.99
9-Bromoanthracene <sup>c</sup>	-1.02	3.62
	<sub>b</sub>	1.41
	-2.02	1.10
Anthracene <sup>a</sup>	-1.39	1.45
	-1.96	1.06

<sup>a</sup> Results were obtained using capillary 2; all other data were obtained with capillary 1.

<sup>b</sup> Poorly defined wave.

<sup>c</sup> In the presence of excess phenol.

Anal. Calc for C<sub>14</sub>H<sub>9</sub>HgBr: C, 36.73; H, 1.98. Found: C, 36.90; H, 1.91.

### Results

The polarographic behavior of various halogenated aromatic compounds in dimethylformamide containing 0.2M tetrabutylammonium bromide is given in Table I.

To aid in formulating a mechanism of reduction for 9-bromoanthracene macro scale reductions were performed and the results are given in the Experimental Section.

### Discussion of Results

Examination of the data in Table I indicates that the reduction of *p*-diiodobenzene and *p*-iodophenyltrimethylammonium iodide is normal and proceeds stepwise with no synergistic effect of the intermediate anion formed by the reduction of the iodine on the reduction of the second group.

The polarographic behaviors of 9,10-dibromoanthracene and 9-bromoanthracene were unusual and are shown in Fig. 1 and 2. The diffusion current for the first wave of anthracene resulting from the reduction of the halogen decreased to a point which was less or slightly higher than that of the reduction wave for 9-bromoanthracene.

Cyclic voltammetry of 9-bromoanthracene at a platinum cathode showed three cathodic peaks and one anodic peak for the oxidation of the anion radical of anthracene. A similar study at a stationary mercury

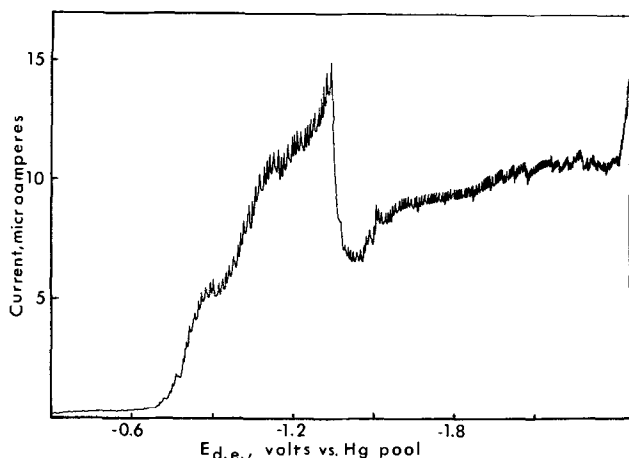


Fig. 1. Polarogram of 1.0 mmole 9,10-dibromoanthracene in dimethylformamide-0.2M tetrabutylammonium bromide.

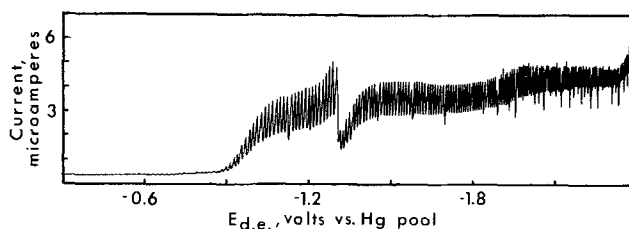
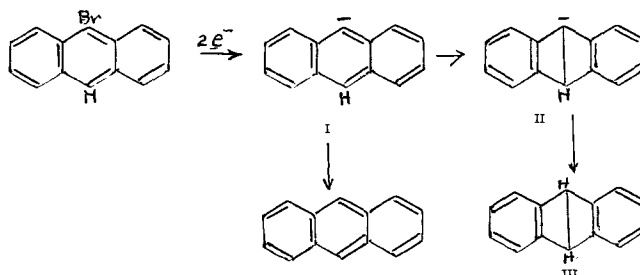


Fig. 2. Polarogram of 0.5 mmole 9-bromoanthracene in dimethylformamide-0.2M tetrabutylammonium bromide.

electrode was normal at a fast scan rate (10 V/sec) but showed an inverted peak for the 9-bromoanthracene portion at a slow scan rate (0.5 V/sec). Such inverted peaks have been observed in the one-electron reduction of oxymethyls (6), and cyanopropyltriphenylphosphonium bromide (7) and have been ascribed to the formation of rapidly absorbed radical intermediates (6). This type of explanation is unlikely for a two-electron reduction wave and was not substantiated by adsorption studies. The electrocapillary curve for the reduction of 9-bromoanthracene was similar to that obtained for the supporting electrolyte using either tetrabutylammonium bromide or perchlorate.

Another possible explanation for the unusual behavior of 9-bromoanthracene is formation of a Dewar benzene III



The intermediate carbanion I formed by the reduction of 9-bromoanthracene protonates directly to anthracene or rearranges to the carbanion II which on protonation would give the Dewar benzene III. This compound (III) would probably be stable to further reduction since hexamethylbicyclo[2,2,0]-hexa-2,5-diene was not polarographically active under similar conditions.

Studies of the polarographic behavior of 9-bromoanthracene in the presence of excess phenol favored such reactions. In the presence of excess phenol, which would increase the rate of protonation of carbanion I the dip in the diffusion current was reduced and the diffusion current for the first anthracene wave became normal.

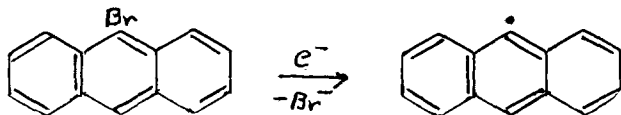
Attempts to isolate the Dewar benzene III by macro-scale electrolytic reductions of 9-bromoanthracene were not successful. Electrolysis at controlled potential at a mercury cathode using a potential before the drop in current gave a complex mixture of products. Plotting the current used *vs.* electrolysis time indicated that only one electron was transferred per molecule of 9-bromoanthracene. Products isolated and identified were anthracene (73%), di-9-anthrylmercury (10%), anthraquinone (1%), bis-9-anthryl (trace), and 9-anthrylmercuric bromide (trace). The use of uncontrolled potential at the same electrode gave anthracene (63%), 9,10-dihydroanthracene (trace), di-9-anthrylmercury (4%), and anthraquinone (trace).

In order to avoid the formation of mercury compounds electrolysis was carried out at a platinum cathode at uncontrolled potentials and gave anthracene (76%) as the only isolable product.

Separations of products were made in all cases by chromatography on silica gel. The assumption was made that such treatment would not isomerize the

Dewar benzene III since other Dewar benzenes have been isolated by chromatography on both silica gel (8) and alumina (9). The Dewar benzene III is a bent molecule and in contrast to its planar isomer anthracene should interact less strongly with silica than the latter, and migrate more readily than anthracene. A similar relationship has been found in other Dewar benzene-aromatic systems (10).

If the assumptions made about the stability of the Dewar benzene III are valid, then this compound is not produced by the macroscale reduction of 9-bromoanthracene. The conditions for the latter are no longer diffusion controlled and products are obtained mainly from the carbanion I and from a one electron reduction of 9-bromoanthracene which results in the 9-anthryl radical.



This radical is the precursor of the mercury compounds and di-9-anthryl isolated. This radical may also react with traces of oxygen and form anthraquinone.

#### Acknowledgments

This paper is based on the Ph.D. Thesis of S. M. Heilmann (December 1973). The research was sup-

ported by the National Science Foundation, Grant GP17317.

Manuscript submitted Sept. 25, 1973; revised manuscript received Nov. 16, 1973.

Any discussion of this paper will appear in a Discussion Section to be published in the December 1974 JOURNAL. All discussions for the December 1974 Discussion Section should be submitted by Aug. 1, 1974.

#### REFERENCES

1. S. Wawzonek and J. H. Wagenknecht, *This Journal*, **110**, 420 (1963).
2. T. H. Reade and S. A. Sim, *J. Chem. Soc.*, 157 (1924).
3. F. J. Welcher, "Organic Analytical Reagents," Vol. I, p. 505, D. Van Nostrand Co., New York (1947).
4. *Org. Syntheses. Coll. Vol. I*, 207 (1941).
5. J. Loevenich, W. Becker, and T. Schroeder, *J. Prakt. Chem.*, **127**, 248 (1930).
6. B. Fleet and R. D. Jee, *J. Electroanal. Chem.*, **25**, 397 (1970).
7. D. A. Tysee, *ibid.*, **30**, App. 14 (1971).
8. E. E. Van Tamelen and S. Pappas, *J. Am. Chem. Soc.*, **84**, 3789 (1962).
9. R. Weiss and C. Schlierf, *Angew. Chem.*, **83**, 887 (1971).
10. E. E. Van Tamelen and S. Pappas, *J. Am. Chem. Soc.*, **85**, 3297 (1963).

## Electrochemistry in N,N-dimethylformamide

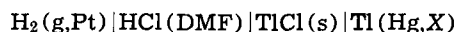
### I. The $H_2(g, Pt) | HCl(DMF) | TlCl(s) | Tl(Hg)$ Cell

Leonard F. Silvester and Peter A. Rock

Department of Chemistry, University of California, Davis, California 95616

#### ABSTRACT

This paper reports the results of our electrochemical measurements on the cell



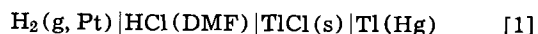
where DMF is the solvent N,N-dimethylformamide. The cell was found to behave reversibly over the HCl concentration range of 0.017-0.24M, and over the  $H_2(g)$  pressure range of 550-750 Torr. Data obtained from this cell were combined with literature data for the activity of Tl in Tl(Hg) and for the dissociation of HCl in DMF to obtain the standard cell voltage,  $\mathcal{E}^\circ$ , of the cell



The value obtained is  $\mathcal{E}^\circ_{ion} = -886.8 \pm 2.0$  mV at 296.7K [molality composition scale, and strong electrolyte standard states for HCl(DMF)]. The behavior of the hydrogen electrode in DMF is discussed.

N,N-dimethylformamide (DMF) shows considerable promise as an aprotic solvent for use in electrochemical cells (1-4). DMF has a high dielectric constant (36.7 at 25°C), a low vapor pressure (3.7 Torr at 25°C), and it is not difficult to prepare in a high purity, anhydrous state (3, 5).

We have investigated the cell



as part of an electrochemical study of the thermodynamics of hydrogen-isotope-exchange reactions (6). This paper reports the results of our electrochemical measurements for reversible cells of type [1]. The hydrogen electrode has been found to behave reversibly in anhydrous HCl (DMF) solutions.

Key words: N,N-dimethylformamide, hydrogen electrode, aprotic solvents, thallium electrode, reversible cell.

#### Experimental

Because of the need to exclude oxygen and water from the cell, the entire cell was set up and studied as a closed system on the vacuum line (6, 7).

Samples of  $H_2(g)$  [99.999 atomic per cent (a/o)] were obtained from the Matheson Chemical Company. The purity of the  $H_2(g)$  was checked by mass spectrometry. Before use in the emf cells, the  $H_2$  was run through a "DEOXO" hydrogen purifier (Englehard Industries) and then through  $CaSO_4$  drying towers. Thallium amalgams were prepared from weighed quantities of reagent grade Tl (precleaned with 0.01M  $H_2SO_4$ ) and reagent grade Hg. The amalgam was washed with dilute (0.001M)  $HNO_3$ , thoroughly dried under high vacuum, and stored in a reservoir on the vacuum line. The DMF used was Mallinckrodt analytical reagent grade, and it was purified as follows

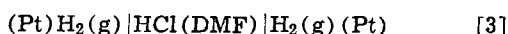
(8): The DMF was stored over 4A molecular sieves for at least 1 week; the DMF was then transferred to the distillation apparatus on the vacuum line and 30g of P<sub>2</sub>O<sub>5</sub> was added per 400 ml of DMF; the DMF was then vacuum distilled with a pot temperature of about 80°C and a head temperature of 33°-49°C. The distillation column was a ¾ in. Pyrex tube 4 ft in length that was packed with 3 × 5 mm Raschig rings. Only the middle 60% of the distillate was used to make the cell solutions. The purified DMF was stored on the vacuum line in a reservoir which was painted black to inhibit the photochemical decomposition of DMF (9). Samples of HCl(g) were prepared on the vacuum line via the reaction of H<sub>2</sub>O(l) with PCl<sub>5</sub>(s). [This is a violent reaction and the water must be added dropwise to the PCl<sub>5</sub> with cooling. This method is a convenient and economical way to prepare just the desired amount of anhydrous HCl(g) or DCl(g).]

The evolved gas was run first through a dry ice ethanol trap and then through three CaSO<sub>4</sub> drying towers (each 30 cm × 25 mm). The resulting anhydrous gas was then run into purified DMF in a mixing flask on the vacuum line (10). The HCl (DMF) solution was stored in the mixing flask on the vacuum line until its introduction to the cell. Samples of TlCl were obtained by bubbling anhydrous HCl(g) into a solution of TlNO<sub>3</sub> in purified DMF under a nitrogen atmosphere. The resulting TlCl(s) was thoroughly washed with purified DMF, vacuum dried at room temperature, and stored over CaSO<sub>4</sub>. Cells of the type



had emf values < |0.005| mV when set up with TlCl(s) prepared as described above. Cells of this type set up with commercial, reagent grade TlCl gave emf values in the range 0.1-0.6 mV. Consequently, the commercial TlCl was not used.

The hydrogen electrodes were prepared as follows (11). Four feet of 0.020 in. diameter gold wire was wound in a closed-loop coil 40 mm in length and 11 mm in diameter. The coil leads were fused about 25 mm above the top of the coil to a platinum lead that exited via a Pt-to-soft-glass seal through the top of the hydrogen electrode cell compartment. The coils were cathodically cleaned in 3M H<sub>2</sub>SO<sub>4</sub>(aq), washed with distilled water, and given a coating of Pt black in a 2% PtCl<sub>4</sub> in 2M HCl(aq) plating solution; 15 min at 20 mA, followed by 5 min at 40 mA. The platinized electrodes were washed several times with distilled water and vacuum dried at room temperature. Cells of type



with identical hydrogen pressures rapidly gave emf values < |0.004| mV; the cells maintained these low emf values for periods ranging from 12 hr to several days. However, all such cells eventually gave rise to much larger, unstable emf values. The development of instability was always a rapid process which took place over a 1-2 hr period. The onset of such instabilities was readily recognized in cells of type [1], and the data reported here were obtained from the cells in their stable period.

The cell construction was of the simple H-type with a central large-bore stopcock. The cell was set up to operate as an automatically controlled, closed system on the high vacuum line. Samples of Tl(Hg), TlCl(s), and HCl(DMF) were run into the cell from their respective storage compartments after the cell was mounted on the vacuum line. The H<sub>2</sub>(g) was continuously recycled through the cell by means of a Toepler-type, short-stroke, small displacement (10 cm<sup>3</sup>/min<sup>-1</sup>) pump (12). The gas bubbling rate in the hydrogen electrode compartment was set at about 2-3 bubbles per second. Pressure fluctuations from the operation of the pumps were observed to be less than 0.05 Torr at the pressures used in our cells. Pressures

were measured on a differential manometer with a cathetometer; atmospheric pressure was read with a barometer.

The emf measurements were made with a Keithley 630 potentiometric electrometer, and an L and N certified K-3 potentiometer and L and N 9834 electronic null detector. All cells were run at room temperature (23.5° ± 1°C), which was periodically recorded while the measurements were in progress. The cells must be run at room temperature or below in order to prevent condensation of the vapor phase in the pump systems or the manometers.

The molalities of the HCl(DMF) cell solutions were determined as follows. Samples of the cell solution were obtained from the cells and weighed; the weighed samples were then added to water and rapidly titrated with standardized, carbonate-free sodium hydroxide (0 ~ 0.01M) solution to a methyl red plus bromocresol green end point (pH ~ 5.4); the NaOH solution was standardized against an HCl(aq) solution of known concentration, which was obtained by dilution of constant-boiling HCl(aq). The possible interference of DMF with the analysis was ruled out by titration of known quantities of standardized HCl(aq) in the presence and absence of added DMF. The mole fraction of thallium, X<sub>Tl</sub>, in the thallium amalgams was determined by a slightly modified version of the acidimetric method of Richards and Daniels (13, 10). The calculations described in the Results section were carried out in double precision on a DEC PDP-8 computer.

## Results

The results of our measurements on cells of type [1] are presented in Table I. The emf, pressure, and temperature measurements were taken at 1 hr intervals during the life of the cell and the results were averaged. The period of stability of the cells ranged from 12 to 170 hr with a mean lifetime of 110 hr. The pressures reported have been corrected for the vapor pressure of the cell solutions (~ 3.5 Torr). Barometer location and temperature corrections have also been applied.

Reversibility checks (emf vs. meter scale position) gave no evidence of a hysteresis loop; this is strong evidence that the cells were operating under reversible conditions.

Measurements are reported only for the period during which the emf measurements with the gas bubblers on agreed within experimental error with those with the gas bubblers off. When this condition was not met the cells deteriorated rapidly, and the measured emf drifted when the gas bubblers were turned off.

The values of ln γ<sub>Tl</sub> given in Table I (where γ<sub>Tl</sub> is the activity coefficient of thallium in mercury relative to the hypothetical ideal unit mole fraction solute

Table I. Results of measurements on the cell  
(Pt)H<sub>2</sub>(g) | HCl(M,DMF) | TlCl(s) | Tl(Hg,X<sub>Tl</sub>)  
where T = 296.7 ± 1K

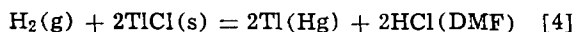
P <sub>H<sub>2</sub></sub> , Torr	m <sub>HCl</sub> , mol · kg <sup>-1</sup>	X <sub>Tl</sub>	ln γ <sub>Tl</sub>	E, mV (exp.)*	E, mV (calc.)†
561.0	0.1189	0.1128	1.119	-554.4 ± 0.3	-553.4
562.2	0.03890	0.1128	1.119	-527.1 ± 0.1	-526.9
553.8	0.02499	0.1152	1.134	-515.5 ± 0.03	-517.2
720.4	0.06454	0.09975	1.029	-531.3 ± 0.1	-530.4
744.2	0.09525	0.1022	1.049	-540.5 ± 0.1	-540.3
543.4	0.2398	0.1242	1.194	-573.6 ± 0.2	-574.1
564.6	0.1131	0.1128	1.119	-553.7 ± 0.3	-552.1
560.6	0.03170	0.1128	1.119	-521.2 ± 0.1	-521.9
554.0	0.02921	0.1152	1.134	-521.5 ± 0.05	-521.0
712.0	0.05836	0.09975	1.029	-527.0 ± 0.1	-528.2
743.3	0.09206	0.1022	1.049	-538.6 ± 0.3	-539.5
540.3	0.2201	0.1241	1.194	-570.1 ± 0.2	-572.2

\* The last six cells in this table were run with 99.5% D<sub>2</sub> and 99.9% DCl, rather than H<sub>2</sub> and HCl. The reported emf values for the deuterium cells were converted to hydrogen cells by subtracting 7.64 mV from the measured emf value (see Ref. (6) and (15)).

† The values of E given in this column were calculated from Eq. [9] using E<sub>°<sub>10n</sub></sub> = 854.0 mV and 2ωA = 187.3 mV.

standard state) were obtained from a large-scale graph of  $\ln \gamma_{\text{Tl}}$  vs.  $X_{\text{Tl}}$  at 23.5°C. The graph was constructed using the emf data on thallium amalgams of Richards and Daniels (13); the details of the method are described in the literature (14, 10).

The postulated cell reaction for cell [1] is



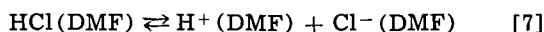
Application of the Nernst equation to this reaction yields ( $\omega = RT/F$ )

$$\mathcal{E} = \mathcal{E}^{\circ}_{\text{neut}} - \frac{\omega}{2} \ln \left\{ \frac{a_{\text{Tl}(\text{Hg})}^2 a_{\text{HCl}(\text{DMF})}^2}{a_{\text{H}_2(\text{g})} a_{\text{TlCl}(\text{s})}^2} \right\} \quad [5]$$

where the subscript neut refers to undissociated HCl in DMF. If we take  $a_{\text{H}_2(\text{g})} \approx (P_{\text{H}_2}/760)$ ,  $a_{\text{Tl}(\text{Hg})} = X_{\text{Tl}}\gamma_{\text{Tl}}$ , and  $a_{\text{TlCl}(\text{s})} = 1$ , then

$$\mathcal{E} = \mathcal{E}^{\circ}_{\text{neut}} + \frac{\omega}{2} \ln \left( \frac{P_{\text{H}_2}}{760} \right) - \omega \ln X_{\text{Tl}}\gamma_{\text{Tl}} - \omega \ln a_{\text{HCl}(\text{DMF})} \quad [6]$$

Hydrochloric acid in DMF is a weak electrolyte; the dissociation constant on the molality composition scale for the reaction



is  $K_{\text{d}} = 2.68 \times 10^{-4}/0.9458 = 2.83 \times 10^{-4}$  (15) at 25°C, and

$$K_{\text{d}} = \frac{a_{\text{H}^+} a_{\text{Cl}^-}}{a_{\text{HCl}}} = \frac{m_{\text{ion}}^2 \gamma_{\pm}^2}{a_{\text{HCl}}} \quad [8]$$

Substitution of Eq. [8] into Eq. [6] yields

$$\mathcal{E} - \frac{\omega}{2} \ln \left( \frac{P_{\text{H}_2}}{760} \right) + \omega \ln \gamma_{\text{Tl}} X_{\text{Tl}} + 2\omega \ln m_{\text{ion}} = \mathcal{E}_{\text{H}} \quad [9]$$

where  $\mathcal{E}_{\text{H}}$  is the Hitchcock extrapolation function. The value of  $m_{\text{ion}}$  was estimated at each value of  $m$  from the expression

$$2.83 \times 10^{-4} \approx \frac{m_{\text{ion}}^2}{m - m_{\text{ion}}} \quad [10]$$

The value of  $\ln \gamma_{\pm}$  should be given at low concentrations by the Debye-Hückel equation

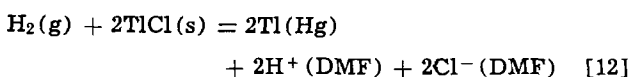
$$\ln \gamma_{\pm} \approx -3.593 m^{1/2}_{\text{ion}} / (1 + m^{1/2}_{\text{ion}}) \quad [11]$$

Thus a plot of  $\mathcal{E}_{\text{H}}$  vs.  $m^{1/2}_{\text{ion}} / (1 + m^{1/2}_{\text{ion}})$  should have a slope of (Eq. [9])  $2\omega A = 2 \times 25.562 \times 3.593 = +183.7$  mV at 23.5°C and an intercept of  $\mathcal{E}^{\circ}_{\text{ion}} = \mathcal{E}^{\circ}_{\text{neut}} + \omega \ln K_{\text{d}}$ . A least-squares analysis of the data in Table I in terms of Eq. [9], [10], and [11] yields a slope of  $187.3 \pm 31.2$  mV and an intercept of  $\mathcal{E}^{\circ}_{\text{ion}} = -854.0 \pm 2.0$  mV at 23.5°C.

The agreement between the experimental and theoretical slopes provides strong evidence that we have reliably established the value of  $\mathcal{E}^{\circ}_{\text{ion}}$ .

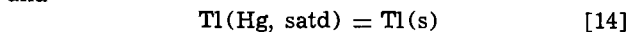
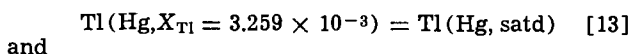
### Discussion

The value of  $\mathcal{E}^{\circ}_{\text{ion}} = -854.0$  mV for the reaction

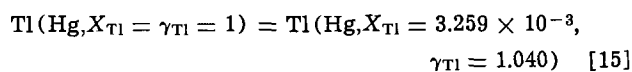


can be combined with the value of  $K_{\text{d}} = 2.83 \times 10^{-4}$  to compute a value of  $\mathcal{E}^{\circ}_{\text{neut}} = \mathcal{E}^{\circ}_{\text{ion}} - \omega \ln K_{\text{d}} = -645.2$  mV at 23.5°C. The value of  $\mathcal{E}^{\circ}_{\text{neut}}$  refers to reaction [4] with undissociated HCl(DMF).

The emf values for the reactions



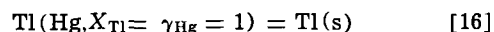
are (13)  $\mathcal{E}_{13} = -175.6$  mV at 23.5°C and  $\mathcal{E}_{14} = -2.6$  mV. The emf value for the reaction



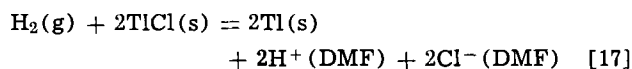
is (23.5°C)

$$\mathcal{E}_{15} = 25.562 \ln (3.259 \times 10^{-3} \times 1.040) = +145.4 \text{ mV}$$

Consequently, the emf of the reaction



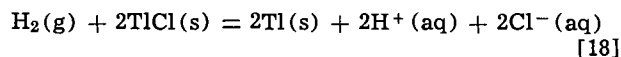
is  $\mathcal{E}_{16} = \mathcal{E}_{13} + \mathcal{E}_{14} + \mathcal{E}_{15} = -32.8$  mV, and the standard potential for the reaction



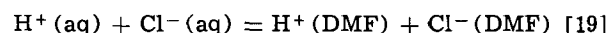
is  $\mathcal{E}^{\circ}_{\text{ion}} = -854.0 - 32.8$  mV =  $-886.8$  mV at 23.5°C.

The hydrogen electrode is the most important reference electrode in aqueous solution, and there has been considerable interest in the development of the hydrogen electrode as a reference electrode in non-aqueous media as well (3). In addition to its use as a reference electrode, the hydrogen electrode can be used in nonaqueous media to obtain Gibbs energies of transfer for Brønsted acids between aqueous and non-aqueous solvents. Gibbs energies of transfer can be used to test various models for the nature of the solvated proton in such media. Of special interest in this connection are aprotic organic solvents, because of the inherent freedom of the solvent molecules from intermolecular hydrogen bonding.

The standard potential for the reaction



is  $\mathcal{E}^{\circ} = -556.8$  mV at 25°C (16). Combination of this result with our value of  $\mathcal{E}^{\circ}$  for reaction [17] yields, for the reaction



a value of  $\Delta G^{\circ} \approx 31.8$  kJ · mol<sup>-1</sup> for the standard Gibbs energy of transfer of HCl from water to DMF. The positive value of  $\Delta G^{\circ}$  reflects the much stronger solvation of the proton in water than in DMF.

### Acknowledgment

This work was supported by NSF Grant GP33264.

Manuscript submitted Aug. 13, 1973; revised manuscript received Dec. 1, 1973.

Any discussion of this paper will appear in a Discussion Section to be published in the December 1974 JOURNAL. All discussions for the December 1974 Discussion Section should be submitted by Aug. 1, 1974.

### REFERENCES

1. L. W. Marple, *Anal. Chem.*, **39**, 846 (1967).
2. J. C. Synnott and J. N. Butler, *ibid.*, **41**, 1890 (1969).
3. J. N. Butler, in "Advances in Electrochemistry and Electrochemical Engineering," Vol. 7, P. Delahay and C. W. Tobias, Editors, pp. 77-175, Interscience Publishers, New York (1970).
4. V. J. Puglisi and A. J. Bard, *This Journal*, **120**, 755 (1973).
5. R. S. Kittila, "Dimethylformamide Chemical Uses," E. I. du Pont de Nemours and Co., Wilmington, Delaware (1967).
6. L. F. Silvester, J. J. Kim, and P. A. Rock, *J. Chem. Phys.*, **56**, 1863 (1972).
7. G. Singh, J. C. Hall, and P. A. Rock, *ibid.*, **56**, 1855 (1972).
8. C. D. Ritchie and G. H. Megerle, *J. Am. Chem. Soc.*, **89**, 1447 (1967).
9. F. Oehme, *Chemiker Ztg.*, **82**, 33 (1958); *Chem. Abstr.*, **52**, 8419f.
10. L. F. Silvester, Ph.D. Dissertation, University of California, Davis, California (1972).
11. G. J. Hills and D. J. G. Ives, in "Reference Electrodes," D. J. G. Ives and G. J. Janz, Editors, Chap. 2, Academic Press, New York (1961).
12. L. F. Silvester and P. A. Rock, *This Journal*, **121**, 251 (1974).

13. T. W. Richards and F. Daniels, *J. Am. Chem. Soc.*, **41**, 1732 (1919).
14. G. N. Lewis and M. Randall, "Thermodynamics," 2nd ed., revised by K. S. Pitzer and L. Brewer, pp. 257-260, McGraw-Hill Book Co., New York (1961).
15. L. F. Silvester and P. A. Rock, *J. Chem. Eng. Data*, **19**, 98 (1974).
16. A. J. de Bethune and N. A. Swendeman Loud, "Standard Aqueous Electrode Potentials and Temperature Coefficients at 25°C," C. A. Hempel, Skokie, Illinois (1964).

## An Asymptotic Solution for the Warburg Impedance of a Rotating Disk Electrode

Robert V. Homsy and John Newman\*

*Inorganic Materials Research Division, Lawrence Berkeley Laboratory, and Department of Chemical Engineering, University of California, Berkeley, California 94720*

### ABSTRACT

The Warburg impedance of a rotating-disk electrode is treated by a regular perturbation expansion valid for large alternating-current frequencies. This solution agrees well with the exact numerical solution, the error in the Warburg impedance being less than 2% for a dimensionless frequency of 10.

When an electrode is subjected to an alternating current, the concentration on the surface and thus the concentration overpotential vary in a time-dependent manner. This variation gives rise to what is known as the Warburg impedance. Early studies of the frequency dependence of this impedance were made around the start of the century by Warburg (1). More recently (2), the impedance of a rotating-disk electrode was studied and numerical results presented for large Schmidt numbers. We investigate here the asymptotic behavior of the Warburg impedance for large frequencies.

It is assumed in the treatment of the problem that the Schmidt number is large and that radial convection and diffusion are negligible. The radially dependent problem is currently being studied at this laboratory (3). It is further assumed that dilute-solution theory, with constant transport and thermodynamic properties, is applicable, and that there is an excess of supporting electrolyte so that migration effects are negligible.

### Mathematical Formulation

The dimensionless, time-varying equation of convective diffusion is given by

$$\frac{\partial^2 c}{\partial \zeta^2} + 3\zeta^2 \frac{\partial c}{\partial \zeta} - \frac{\partial c}{\partial t^*} = 0 \quad [1]$$

where  $c$  is the concentration of reactant,  $\zeta = y\sqrt{\Omega/\nu}(a\nu/3D)^{1/3}$  is a dimensionless distance from the disk,  $a = 0.51023$  is a constant (4), and  $t^* = t\Omega D(a\nu/3D)^{2/3}/\nu$  is a dimensionless time. We may express the concentration as a sum of its steady and time-varying contributions

$$c = \bar{c} + \tilde{c} \quad [2]$$

The steady problem was first treated by Levich (5). For an alternating current of frequency  $\omega$ , the time-varying concentration may be expressed as<sup>1</sup>

$$\tilde{c} = A e^{jKt^*} \theta \quad [3]$$

where  $K = \omega\nu(3D/a\nu)^{2/3}/\Omega D$  is a dimensionless frequency. Substitution into the convective diffusion equation yields the complex equation

\* Electrochemical Society Active Member.

Key words: Warburg impedance, rotating disk.

<sup>1</sup> Strictly speaking, one takes the real part of such complex expressions:  $\tilde{c} = \text{Re}(A e^{jKt^*} \theta)$ .

$$\theta'' + 3\zeta^2 \theta' - jK\theta = 0 \quad [4]$$

subject to the boundary conditions

$$\theta = 1 \text{ at } \zeta = 0, \theta \rightarrow 0 \text{ as } \zeta \rightarrow \infty \quad [5]$$

The Warburg impedance is related to the concentration overpotential by the expression

$$Z_w = \frac{\tilde{\eta}_c}{i} = \frac{RT\sqrt{\nu/\Omega}}{n^2 F^2 \bar{c}_0 D \theta'(0)} \left( \frac{3D}{a\nu} \right)^{1/3} \quad [6]$$

where  $\tilde{\eta}_c = RT\tilde{c}_0/nF\bar{c}_0$  is the time-varying concentration overpotential (valid for  $\tilde{c}_0 \ll \bar{c}_0$ ).

*Asymptotic solution.*—We are concerned here with the behavior of Eq. [4] and [5] for large  $K$ . This system appears to comprise a singular perturbation problem (6); however, a closer examination shows that the solution is regular for large  $K$  if we modify the variables. If we let

$$\theta = \exp\{-(jK)^{3/4} Y(x)\} \quad [7]$$

and

$$x = \zeta/(jK)^{1/4} \quad [8]$$

Eq. [4] and [5] become

$$(Y')^2 - 3x^2 Y' - 1 = Y''/(jK)^{3/4} \quad [9]$$

$$Y = 0 \text{ at } x = 0, \text{Re}\{(jK)^{3/4} Y\} \rightarrow \infty \text{ as } (jK)^{1/4} x \rightarrow \infty \quad [10]$$

$Y$  can evidently be expanded in a regular expansion in  $K^{-3/4}$

$$Y = Y_0(x) + (jK)^{-3/4} Y_1(x) + (jK)^{-3/2} Y_2(x) + 0(K^{-9/4}) \quad [11]$$

Substituting this expansion into Eq. [9] and equating terms of equal order in  $K$ , we obtain relatively simple differential equations for  $Y_0, Y_1, Y_2$ , etc. Solving these, we have that  $Y'_0(0) = 1$  and  $Y'_2(0) = 3/4$ , while odd terms give no contribution to  $Y'(0)$ . The concentration derivative on the surface of the disk is thus given by

$$\theta'(0) = -\sqrt{jK} Y'(0) = -\sqrt{jK} + 3j/4K + 0(K^{-5/2}) \quad [12]$$

so that we may write

$$\text{Re} \left\{ \frac{1}{\theta'(0)} \right\} = \frac{4K(2\sqrt{2} K^{3/2})}{16K^3 - 6\sqrt{2} K^{3/2} + 9} \quad [13]$$

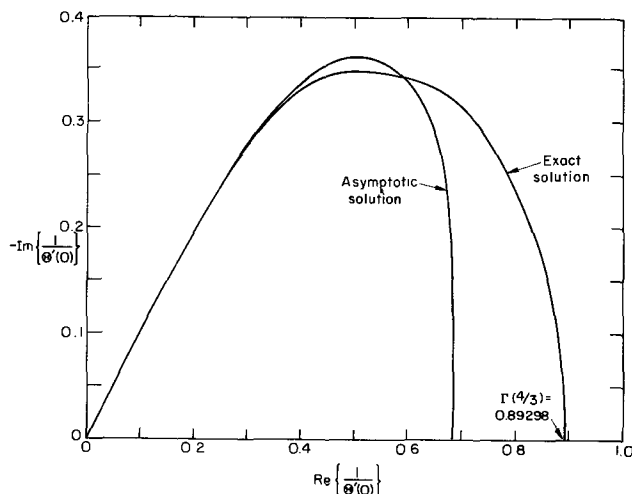


Fig. 1. The complex  $1/\theta'(0)$  plane showing the asymptotic and exact numerical solutions.

$$-Im \left\{ \frac{1}{\theta'(0)} \right\} = \frac{4K(2\sqrt{2}K^{3/2} - 3)}{16K^3 - 6\sqrt{2}K^{3/2} + 9} \quad [14]$$

These latter expressions may be used to evaluate the real and imaginary parts of the Warburg impedance (see Eq. [6]).

### Results and Discussion

Figure 1 shows  $1/\theta'(0)$  plotted on the complex plane with the dimensionless frequency  $K$  as a parameter. The exact numerical solution is shown along with the asymptotic solution represented by Eq. [13] and [14]. These results are summarized in Table I. Also shown in the table is the impedance of a stagnant Nernst diffusion layer (7)

$$\frac{1}{\theta'_N(0)} = \Gamma\left(\frac{4}{3}\right) \frac{\tanh \sqrt{j\omega\delta^2/D}}{\sqrt{j\omega\delta^2/D}} = \frac{\tanh\left(\Gamma\left(\frac{4}{3}\right)\sqrt{jK}\right)}{\sqrt{jK}} \quad [15]$$

where the Nernst diffusion layer thickness,  $\delta$ , is taken to be

$$\delta = \Gamma\left(\frac{4}{3}\right) \sqrt{\frac{\nu}{\Omega}} \left(\frac{3D}{a\nu}\right)^{1/3} \quad [16]$$

At large  $K$  the asymptotic expansion agrees well with the exact solution, the error in the Warburg impedance for  $K = 10$  being less than 2% for both real and imaginary parts. As  $K$  decreases, the asymptotic solution departs radically from the exact solution. It should be pointed out that it is in the region of intermediate to large values of  $K$  that the Nernst diffusion-layer approximation is most in error in predicting the Warburg impedance. It appears, therefore, that the asymptotic expansion developed here offers an improved approximate solution in this region of  $K$ .

### Summary

A regular perturbation expansion valid for large alternating-current frequencies has been developed to predict the Warburg impedance of a rotating-disk electrode. This asymptotic solution compares favorably with the exact solution and offers an improvement over the Nernst diffusion-layer approximation in the region of intermediate to large  $K$ .

### Acknowledgment

Charles M. Mohr assisted in the numerical calculations for the Nernst diffusion layer and exact solutions. This work was supported by the United States Atomic Energy Commission.

Manuscript received Sept. 17, 1973.

Any discussion of this paper will appear in a Discussion Section to be published in the December 1974 JOURNAL. All discussions for the December 1974 Discussion Section should be submitted by Aug. 1, 1974.

### LIST OF SYMBOLS

$a$	0.51023
$A$	amplitude of the time-varying concentration, mole/cm <sup>3</sup>
$c$	concentration of reactant, mole/cm <sup>3</sup>
$\tilde{c}$	steady concentration of reactant, mole/cm <sup>3</sup>
$c$	time-varying concentration of reactant, mole/cm <sup>3</sup>
$c_\infty$	bulk concentration of reactant, mole/cm <sup>3</sup>
$D$	diffusion coefficient, cm <sup>2</sup> /sec
$F$	Faraday's constant, 96,487 coulomb/equiv
$\tilde{i}$	normal alternating current density at electrode surface, A/cm <sup>2</sup>
$j$	$\sqrt{-1}$
$K$	$\omega\nu(3D/a\nu)^{2/3}/\Omega D$ , dimensionless frequency
$n$	number of electrons produced when one reactant ion or molecule reacts
$R$	universal gas constant, 8,3143 joule/mole-deg
$t$	time, sec
$t^*$	$t\Omega D(a\nu/3D)^{2/3}/\nu$ , dimensionless time
$T$	absolute temperature, °K
$Sc$	$\nu/D$ , Schmidt number
$x$	see Eq. [8]
$y$	normal distance from the disk, cm
$Y$	see Eq. [7]
$Y_m$	expansion functions (see Eq. [11])
$Z_w$	Warburg impedance, ohm
$\Gamma(4/3)$	0.89298, the gamma function of 4/3
$\delta$	$\Gamma(4/3)\sqrt{\nu/\Omega}(3D/a\nu)^{1/3}$ , Nernst diffusion layer thickness
$\zeta$	$y\sqrt{\Omega/\nu}(a\nu/3D)^{1/3}$ , dimensionless distance normal to the disk
$\tilde{c}$	time-varying concentration overpotential, V
$\theta$	complex, dimensionless, time-varying concentration
$\nu$	kinematic viscosity, cm <sup>2</sup> /sec
$\omega$	frequency of alternating current, rad/sec
$\Omega$	rotation speed of disk, rad/sec

### Subscripts

( )<sub>0</sub> ( ) evaluated at the electrode surface

Table I. Solutions for the real and imaginary parts of  $1/\theta'(0)$

K	Asymptotic solution		Exact solution		Nernst layer solution	
	$Re \left\{ \frac{1}{\theta'(0)} \right\}$	$-Im \left\{ \frac{1}{\theta'(0)} \right\}$	$Re \left\{ \frac{1}{\theta'(0)} \right\}$	$-Im \left\{ \frac{1}{\theta'(0)} \right\}$	$Re \left\{ \frac{1}{\theta'(0)} \right\}$	$-Im \left\{ \frac{1}{\theta'(0)} \right\}$
1.5	0.65758	0.27793	0.72406	0.30195	0.75500	0.28926
2.0	0.56637	0.35398	0.64160	0.33934	0.67925	0.33682
3.5	0.40549	0.33980	0.45610	0.34736	0.48538	0.37104
5.0	0.33041	0.29907	0.35557	0.31151	0.36695	0.34060
7.5	0.26468	0.25101	0.27346	0.25876	0.26868	0.27945
10	0.22729	0.21967	0.23143	0.22396	0.22266	0.23537
20	0.15905	0.15716	0.15999	0.15812	0.15656	0.15788
50	0.10015	0.09985	0.10030	0.10000	0.10004	0.10001
100	0.07075	0.07087	0.07079	0.07072	0.07071	0.07071

## REFERENCES

1. E. Warburg, *Ann. Physik*, **67**, 493 (1899); **6**, 125 (1901).
2. E. Levart and D. Schuhmann, *Collection Czech. Chem. Commun.*, **36**, 866 (1971).
3. Peter Appel and John Newman, Unpublished results.
4. John Newman, *This Journal*, **113**, 1235 (1966).
5. B. Levich, *Acta. Physicochim. U.R.S.S.*, **17**, 257 (1942).
6. John Newman, in "Electroanalytical Chemistry," A. J. Bard, Editor, Vol. 6, pp. 187-352, Marcel Dekker, Inc., New York (1973).
7. Daniel Schuhmann, *Compt. Rend.*, **262C**, 624 (1966).

## The Short-Time Response of a Disk Electrode

Kemal Nisancioğlu\* and John Newman\*

*Inorganic Materials Research Division, Lawrence Berkeley Laboratory, and  
Department of Chemical Engineering, University of California, Berkeley, California 94720*

### ABSTRACT

An asymptotic treatment of the transient response of a disk electrode is given for short times. Results are obtained by expressing the potential in terms of an integral equation at the surface. A similar formulation is used also to calculate the steady-state current distribution for large exchange-current densities.

The authors have recently reported (1, 2) a theoretical study of the transient behavior of a disk electrode in the presence of faradaic and capacitive effects. Series expressions were obtained for the potential and the current under galvanostatic and potentiostatic control, respectively. Those results are readily applicable to describe the long-time response of the disk and determine the relaxation time of the overpotential after a step change in the applied current or the current decay after a step change in the potential. However, a large number of terms need to be included in the series to express the short-time behavior accurately. This can be accomplished more efficiently by deriving an asymptotic solution to the problem valid at small times.

Shortly after the cell current is switched on, the current distribution on the surface is given by the primary distribution (3, 4) everywhere except at a small region near the edge of the disk. Since the primary current density is infinite at the edge, the double-layer capacity is charged more rapidly in this region than at other parts of the disk, so that the current density is reduced to a finite value.

From a mathematical standpoint, we have a singular perturbation problem at hand. A similar problem at high frequencies for the alternating-current distribution on a disk electrode has been treated earlier (5). We follow here the same guidelines in the mathematical formulation as developed in that paper. Another problem of the same type is encountered for large values of the exchange-current density (6). The singular nature of this problem has been recognized (5); however, its consequences were not of immediate interest. It nevertheless conforms with the context of the present paper, and an analysis is outlined in Appendix II, thereby rendering more complete the over-all treatment of the secondary current distribution at a disk electrode.

### Mathematical Model

The potential in the solution satisfies Laplace's equation

$$\nabla^2\Phi = 0 \quad [1]$$

The current density vanishes on the insulating plane of the disk, which implies

$$\frac{\partial\Phi}{\partial z} = 0 \text{ at } z = 0, r > r_0 \quad [2]$$

Away from the edge region, the potential in the solution is given by the primary distribution,  $\Phi^p$ . Furthermore, at the surface, the passage of current is primarily due to the charging of the electric double layer

$$i = -\kappa \frac{\partial\Phi}{\partial z} = C \frac{\partial(V - \Phi)}{\partial t} \text{ at } z = 0, r \leq r_0 \quad [3]$$

where  $V$  is the potential of the electrode,  $\kappa$  is the conductivity of the solution, and  $C$  is the double-layer capacity. Charge transfer may also occur by means of a faradaic reaction. This effect is small at short times as long as the exchange-current density is not too large, and it is neglected here. The other extreme, where the faradaic reaction dominates over the double-layer charging, is discussed in Appendix II. Diffusion is also neglected. The transient response of a rotating-disk electrode under mass transfer controlled situations has been treated elsewhere (7, 8).

### Analysis and Results

In terms of the rotational elliptic coordinates, the potential distribution outside the edge region with the counterelectrode placed at infinity is given by (3)

$$\Phi^p/\Phi^p_0 = 1 - \frac{2}{\pi} \tan^{-1}\xi \quad [4]$$

where  $\Phi^p_0$  is the potential in the solution adjacent to the electrode surface corresponding to the primary distribution (1). If the electrode potential is kept at a constant value  $V$ , then  $\Phi^p_0 = V$ . If, however, the electrode is under galvanostatic control,  $\Phi^p_0 = I/4r_0\kappa$ . With this difference in mind, the present analysis applies to both galvanostatic and potentiostatic cases unless stated otherwise. For small  $\xi$ , Eq. [4] can be approximated by

$$\Phi/\Phi^p_0 = 1 - 2\xi/\pi \quad [5]$$

which may be regarded as the outer solution for the potential, with which the potential in the edge region must match. For instance, in the inner region, the potential approaches Eq. [5] asymptotically as  $\xi \rightarrow \infty$  and also as  $t \rightarrow 0$ . The rotational elliptic coordinate system reduces to parabolic coordinates in the edge region (5), and Laplace's equation can be expressed as

\* Electrochemical Society Active Member.  
Key words: singular perturbation, galvanostatic control, potentiostatic control, exchange-current density, current distribution.



$$\frac{\partial^2 \Phi}{\partial \eta^2} + \frac{\partial^2 \Phi}{\partial \xi^2} = 0 \quad [6]$$

Let us now introduce the stretched variables appropriate to the edge region

$$\bar{\phi} = \frac{\pi}{2\sqrt{\theta}} \left( \frac{V - \Phi}{\Phi^{\nu_0}} \right) \quad [7]$$

$$\bar{\eta} = \eta/\sqrt{\theta}, \quad \bar{\xi} = \xi/\sqrt{\theta} \quad [8]$$

where  $\theta = \kappa t/\tau_0 C$  is the dimensionless time. Equation [7] represents a separation of variables, such that  $\bar{\phi}$  is a function of  $\bar{\eta}$  and  $\bar{\xi}$  only. When the basic equations are transformed into the stretched coordinates, the problem reads

$$\frac{\partial^2 \bar{\phi}}{\partial \bar{\eta}^2} + \frac{\partial^2 \bar{\phi}}{\partial \bar{\xi}^2} = 0 \quad [9]$$

$$\frac{\partial \bar{\phi}}{\partial \bar{\xi}} = \frac{1}{2} \bar{\eta} \bar{\phi} - \frac{\bar{\eta}^2}{2} \frac{\partial \bar{\phi}}{\partial \bar{\eta}} \quad \text{at } \bar{\xi} = 0 \quad [10]$$

$$\frac{\partial \bar{\phi}}{\partial \bar{\eta}} = 0 \quad \text{at } \bar{\eta} = 0 \quad [11]$$

$$\bar{\phi} \rightarrow \bar{\xi} \quad \text{as } \bar{\eta}^2 + \bar{\xi}^2 \rightarrow \infty \quad [12]$$

These results indicate that the inner region is of order  $r_0 \theta$  in the original, cylindrical coordinate system. Moreover, the dimensionless potential is of order  $\sqrt{\theta}$ , and the dimensionless current density, given by

$$\frac{i r_0}{\kappa \Phi^{\nu_0}} = - \frac{V - \Phi_0}{2 \Phi^{\nu_0} \theta} \quad [13]$$

is of order  $1/\sqrt{\theta}$ .

One possible way of solving the system of Eq. [9] to [12] is by finite-difference methods (9). This scheme did not prove to be straightforward in converging to a stable solution due to the complex nature of the surface boundary condition, Eq. [10]. The problem for the potential at the surface can also be expressed (see Appendix I) in terms of the integral equation

$$\bar{\phi}_0(\bar{\eta}) = \frac{1}{\pi} \int_0^\infty \ln |\bar{\eta}_*^2 - \bar{\eta}^2| \left[ \frac{\bar{\eta}_*}{2} \bar{\phi}_0(\bar{\eta}_*) - \frac{\bar{\eta}_*^2}{2} \frac{\partial \bar{\phi}_0}{\partial \bar{\eta}} \Big|_{\substack{\bar{\xi}=0 \\ \bar{\eta}=\bar{\eta}_*}} - 1 \right] d\bar{\eta}_* \quad [14]$$

In order to bring the problem into a finite domain, the integral can be written in the form

$$\bar{\phi}_0 = \frac{1}{\pi} \int_0^{\eta_s} \ln |\bar{\eta}_*^2 - \bar{\eta}^2| \left( \frac{\bar{\eta}_*}{2} \bar{\phi}_0 - \frac{\bar{\eta}_*^2}{2} \frac{\partial \bar{\phi}_0}{\partial \bar{\eta}_*} - 1 \right) d\bar{\eta}_* + \frac{1}{2\pi} \int_0^{1/\eta_s^4} \ln \left| \frac{1}{\sqrt{x_*}} - \frac{1}{\sqrt{x}} \right| \frac{1}{x_*^{3/4}} \frac{\partial \bar{\phi}'_0}{\partial x_*} dx_* \quad [15]$$

where

$$\bar{\phi}'_0 = (\bar{\phi}_0 - 1/\bar{\eta})/\bar{\eta}, \quad x = 1/\bar{\eta}^4 \quad [16]$$

and  $\eta_s$  is a convenient breaking point. Equation [15] can now be integrated for the entire range of  $\bar{\eta}$ , whereas Eq. [14] has to be truncated at some point with the possibility of neglecting an important contribution to the integral. Numerical solution of this integral equation (10) turned out to be more efficient than the finite-difference technique in obtaining results for the present problem.

The results are shown in Fig. 1. The shape of the curves is also characteristic of the current distribution near the edge since the dimensionless potential  $\bar{\phi}_0$  is proportional to the current density as indicated by Eq.

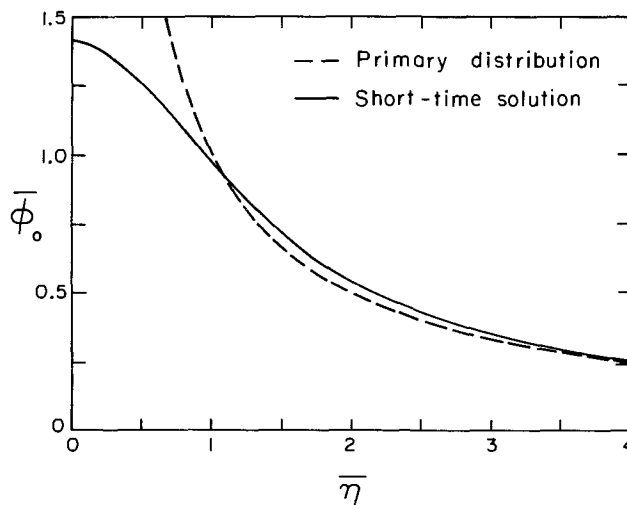


Fig. 1. The surface potential distribution at short times near the edge of a disk electrode.

[13]. The current distribution approaches the primary distribution toward the center of the disk. However, it remains finite and much more uniform than the primary distribution in the edge region; the finite capacity of the electric double layer does not allow it to become infinite.

The electrode potential for the galvanostatic case or the applied current for the potentiostatic case is given by

$$\left. \begin{aligned} & \text{(galvanostatic) } V/\Phi^{\nu_0} - 1 \\ & \text{(potentiostatic) } 1 - I/4r_0\kappa\Phi^{\nu_0} \end{aligned} \right\} = \int_0^1 \left( \frac{V - \Phi_0}{\Phi^{\nu_0}} \right) d\bar{\eta} \quad [17]$$

Substitution of the stretched variables and integration yields

$$\int_0^1 \left( \frac{V - \Phi_0}{\Phi^{\nu_0}} \right) d\bar{\eta} = -\frac{1}{\pi} \theta \ln \theta + A \theta \quad [18]$$

where (5)

$$A = \frac{2}{\pi} \left\{ \int_0^b \bar{\phi}_0 d\bar{\eta} + \int_b^\infty \left( \bar{\phi}_0 - \frac{1}{\bar{\eta}} \right) d\bar{\eta} - \ln b \right\} \quad [19]$$

The integral is broken up this way as a convenience in numerical calculation since the first integral does not converge as  $b \rightarrow \infty$  and the second integral as  $b \rightarrow 0$ . Equation [19] was integrated (10) for the whole range of  $\bar{\eta}$  using the numerical solution obtained from Eq. [15], and the value of  $A$  was thus found to be 0.841. Equation [18] is plotted in Fig. 2 using this value and compared to previous calculations (1,2). The long-time series approaches the present short-time solution as an asymptote for small values of  $\theta$ .

### Conclusions

The present work demonstrates once more the efficiency and convenience of the singular perturbation method in obtaining asymptotic solutions to problems which would otherwise be laborious to solve numerically. In electroanalytical applications, one usually focuses attention on the conditions at the electrode surface, and the conditions in the bulk can be accounted for adequately by using the expression for the primary distribution, Eq. [4]. Therefore, expressing the surface potential in terms of an integral equation provides additional economy in the numerical work since the bulk of the solution does not enter the calculations explicitly.

The results reported above are universally applicable since no parameters appear in the problem, and

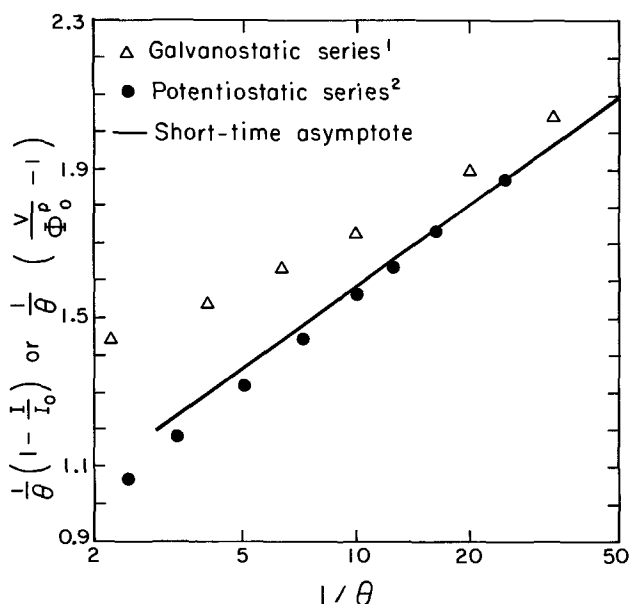


Fig. 2. Comparison of the short-time solution and the long-time series (1, 2) for the transient response of a disk.

numerical calculations need not be repeated. Furthermore, the results are independent of the disk geometry because the formulation is confined to a small region near the edge. Hence, they can also be made to apply under similar conditions to any electrode geometry embedded in an insulating plane.

**Acknowledgment**

This work was supported by the United States Atomic Energy Commission.

Manuscript received Oct. 1, 1973.

Any discussion of this paper will appear in a Discussion Section to be published in the December 1974 JOURNAL. All discussions for the December 1974 Discussion Section should be submitted by Aug. 1, 1974.

**APPENDIX I**

*Integral Representation for the Potential at Short Times*

It is possible to solve Laplace's equation by superposing solutions due to current sources on an electrode. For a disk, this is given by (11)

$$\Phi(r, z) = \frac{2}{\pi\kappa} \int_0^{r_0} \frac{i(r_*)K(m)r_*dr_*}{\sqrt{z^2 + (r + r_*)^2}} \quad [A-1]$$

where  $K(m)$  is the complete elliptic integral of the first kind (12)

$$K(m) = \int_0^{\pi/2} \frac{d\alpha}{\sqrt{1 - m \sin^2 \alpha}} \quad [A-2]$$

and

$$m = \frac{4rr_*}{z^2 + (r + r_*)^2} \quad [A-3]$$

After converting into the rotational elliptic coordinates (3) and substituting Eq. [3], one obtains

$$\frac{\Phi_0}{\Phi^{p_0}} = \frac{2}{\pi} \int_0^1 \frac{K(m)}{1 + \sqrt{1 - \eta_*^2}} \frac{\partial}{\partial \theta} \left( \frac{V - \Phi_0}{\Phi^{p_0}} \right) \eta_* d\eta_* \quad [A-4]$$

where the assumption  $\eta \ll 1$  has been introduced for the edge region. The assumption cannot be applied to the dummy variable  $\eta_*$  because the integration has to be carried over the entire surface of the disk.

Define

$$F(\eta, \eta') = \frac{2}{\pi} \int_0^{\eta'} \frac{K(m)}{1 + \sqrt{1 - \eta_*^2}} \frac{\partial}{\partial \theta} \left( \frac{V - \Phi_0}{\Phi^{p_0}} \right) \eta_* d\eta_* \quad [A-5]$$

The potential distribution in the outer region is approximated by Eq. [5]. Substitution into Eq. [3] and integration gives

$$\frac{V - \Phi_0}{\Phi^{p_0}} = \frac{2}{\pi} \frac{\theta}{\eta} \quad [A-6]$$

Hence, for the outer region, Eq. [A-5] can be written as

$$\tilde{F}(\eta, \eta') = F(\eta, 1) - \frac{4}{\pi^2} \left[ \int_0^1 \frac{K(m)}{1 + \sqrt{1 - \eta_*^2}} d\eta_* - \int_0^{\eta'} \frac{K(m)}{1 + \sqrt{1 - \eta_*^2}} d\eta_* \right] \quad [A-7]$$

The first integral in the brackets corresponds to the primary distribution. Proof:

Let us write Eq. [A-1] for the primary distribution by replacing  $\Phi$  with  $\Phi^p$  and  $i$  with the primary current density (3)

$$\Phi^{p_0} = I/4\kappa r_0 = \frac{2}{\pi\kappa} \int_0^{r_0} \frac{I}{\pi r_0^2} \frac{0.5}{\sqrt{1 - (r_*/r_0)^2}} \frac{K(m)r_*dr_*}{r + r_*} = \frac{4\Phi^{p_0}}{\pi^2} \int_0^1 \frac{K(m)}{\sqrt{1 - \eta^2 + \sqrt{1 - \eta_*^2}}} d\eta_* \quad [A-8]$$

Thus, independent of the value of  $\eta$ , we have

$$\frac{4}{\pi^2} \int_0^1 \frac{K(m)}{\sqrt{1 - \eta^2 + \sqrt{1 - \eta_*^2}}} d\eta_* = 1 \quad [A-9]$$

For small values of  $\eta'$ , the second integral in Eq. [A-7] can be approximated by

$$\int_0^{\eta'} \frac{K(m)}{1 + \sqrt{1 - \eta_*^2}} d\eta_* \approx \int_0^{\eta'} \ln \frac{4}{\eta} d\eta = \eta' \left( \ln \frac{4}{\eta'} + 1 \right) \quad [A-10]$$

Equation [A-7] for the outer region therefore reduces to

$$\tilde{F}(\eta, \eta') = F(\eta, 1) - 1 + \frac{4\eta'}{\pi^2} \left( \ln \frac{4}{\eta'} + 1 \right) \quad [A-11]$$

In the inner region, Eq. [A-5] can be expressed in the form

$$\bar{F}(\eta, \bar{\eta}') = \frac{\sqrt{\theta}}{\pi^2} \int_0^{\bar{\eta}'} K(m) \left[ \bar{\phi}_0(\bar{\eta}_*) - \bar{\eta}_* \frac{\partial \bar{\phi}_0}{\partial \bar{\eta}} \Big|_{\bar{\eta}=\bar{\eta}_*} \right] \bar{\eta}_* d\bar{\eta}_* \quad [A-12]$$

Both  $\eta$  and  $\eta_*$  are small in the inner region. Therefore

$$\lim_{\eta, \eta_* \rightarrow 0} K(m) = \lim_{\eta, \eta_* \rightarrow 0} \frac{1}{2} \ln \frac{16}{1 - m} = \ln \frac{16/\theta}{|\bar{\eta}^2 - \bar{\eta}_*^2|} \quad [A-13]$$

Equation [A-12] can now be broken up into several parts

$$\bar{F}(\bar{\eta}, \bar{\eta}') = \frac{2\sqrt{\theta}}{\pi^2} \left\{ \int_0^\infty \ln(16/\theta) G(\bar{\eta}_*) d\bar{\eta}_* - \int_0^\infty \ln|\bar{\eta}_*^2 - \bar{\eta}^2| G(\bar{\eta}_*) d\bar{\eta}_* - \int_{\eta'}^\infty \ln \frac{16/\theta}{|\bar{\eta}_*^2 - \bar{\eta}^2|} G(\bar{\eta}_*) d\bar{\eta}_* + \int_0^{\bar{\eta}'} \ln \frac{16/\theta}{|\eta_*^2 - \eta^2|} d\eta_* \right\} \quad A-14$$

where

$$G(\eta_*) = \frac{\bar{\eta}_*}{2} \phi_0(\eta_*) - \frac{\bar{\eta}_*^2}{2} \frac{\partial \bar{\phi}_0}{\partial \eta} \Big|_{\eta=\eta_*} - 1 \quad [A-15]$$

In the original unstretched coordinate system, the first

integral can be expressed as

$$\begin{aligned} \ln(16/\theta) \int_0^\infty G(\bar{\eta}_*) d\bar{\eta}_* &= -\frac{\ln(16/\theta)}{\sqrt{\theta}} \\ &\int_0^1 \left( \frac{\pi}{2\Phi_{P_0}} \frac{\partial \Phi}{\partial \xi} \Big|_{\xi=0} + 1 \right) d\eta \\ &= \frac{\ln(16/\theta)}{\sqrt{\theta}} \left( \frac{1}{4\kappa r_0 \Phi_{P_0}} \int_0^{r_0} 2\pi r dr - 1 \right) \\ &= \frac{\ln(16/\theta)}{\sqrt{\theta}} \left( \frac{I}{4\kappa r_0 \Phi_{P_0}} - 1 \right) \quad [\text{A-16}] \end{aligned}$$

Under galvanostatic control,  $I = 4\kappa r_0 \Phi_{P_0}$ , and the integral is identically zero. For potentiostatic control, the current is given by Eq. [18], and the integral is therefore of order  $\sqrt{\theta}$  and still small compared to the second integral, which is of order unity. For large  $\bar{\eta}'$ , the last integral in Eq. [A-14] can be approximated by

$$\int_0^{\bar{\eta}'} \ln \frac{16/\theta}{|\bar{\eta}_*^2 - \bar{\eta}^2|} d\bar{\eta}_* \approx \bar{\eta}' \ln \frac{16}{\theta} - \bar{\eta}' \ln \bar{\eta}^2 + 2\bar{\eta}' \quad [\text{A-17}]$$

Equation [A-14] for the inner region thus becomes at large  $\bar{\eta}'$

$$\begin{aligned} \bar{F}(\bar{\eta}, \bar{\eta}') &= -\frac{2\sqrt{\theta}}{\pi^2} \left\{ \int_0^\infty \ln |\bar{\eta}_*^2 - \bar{\eta}^2| G(\bar{\eta}_*) d\bar{\eta}_* \right. \\ &+ \int_{\bar{\eta}'}^\infty \ln \frac{16/\theta}{|\bar{\eta}_*^2 - \bar{\eta}^2|} G(\bar{\eta}_*) d\bar{\eta}_* \\ &\left. - \bar{\eta}' \ln \frac{16}{\theta} + \bar{\eta}' \ln \bar{\eta}^2 - 2\bar{\eta}' \right\} \quad [\text{A-18}] \end{aligned}$$

Finally, the matching condition

$$\lim_{\bar{\eta}' \rightarrow 0} \bar{F}(\bar{\eta}, \bar{\eta}') = \lim_{\bar{\eta} \rightarrow 0} \bar{F}(\bar{\eta}, \bar{\eta}') \quad [\text{A-19}]$$

has to be satisfied. Substitution of Eq. [A-11] and [A-18] gives, after canceling the matching terms

$$\bar{\phi}_0(\bar{\eta}) = \frac{1}{\pi} \int_0^\infty \ln |\bar{\eta}_*^2 - \bar{\eta}^2| G(\bar{\eta}_*) d\bar{\eta}_* \quad [\text{A-20}]$$

which is identical to Eq. [14].

## APPENDIX II

### Current Distribution on a Disk Electrode at Large Exchange-Current Densities

Previous numerical calculations for the rotating disk (6) have shown that the secondary current distribution approaches the primary distribution as the exchange-current density goes to infinity. For large but finite exchange-current densities, the current distribution approximates closely the primary distribution on the disk except near the edge, where the faradaic impedance is large enough to force the current density to remain finite.

When the current density is small compared to the exchange-current density ( $i \ll |i_0|$ ), one may assume linear kinetics (6). The dimensionless, exchange-current density can then be defined as

$$J = (\alpha_a + \alpha_c) \frac{i_0 r_0 \Gamma}{RT\kappa} \quad [\text{A-21}]$$

where  $\alpha_a$  and  $\alpha_c$  are the kinetic parameters of the general kinetic expression for an electrode reaction (11). The condition at the electrode surface can be expressed by

$$i = -\kappa \frac{\partial \Phi}{\partial z} \Big|_{z=0} = J(V - \Phi_0) \quad (r \leq r_0) \quad [\text{A-22}]$$

The stretched variables appropriate for this problem are

$$\bar{\phi} = \frac{\pi}{2} \left( 1 - \frac{\Phi}{V} \right) \sqrt{J} \quad [\text{A-23}]$$

$$\bar{\eta} = \eta \sqrt{J}, \quad \bar{\xi} = \xi \sqrt{J} \quad [\text{A-24}]$$

Substitution into Laplace's equation and the boundary conditions gives a system identical to Eq. [9], [11], and [12], and the condition at the surface becomes

$$\frac{\partial \bar{\phi}}{\partial \bar{\xi}} \Big|_{\bar{\xi}=0} = \bar{\eta} \bar{\phi} \quad [\text{A-25}]$$

The finite-difference method by successive over-relaxations was successful in this case in obtaining a stable solution. The results are plotted in Fig. 3.

The steady-state current or potential can be calculated from

$$\begin{aligned} 1 - \frac{\Phi_{P_0}}{V} &= 1 - \frac{I}{4r_0 \kappa V} = \int_0^1 \left( 1 - \frac{\Phi_0}{V} \right) d\eta \\ &= \frac{1}{\pi J} \ln J + \frac{A}{J} \quad [\text{A-26}] \end{aligned}$$

where  $A$  has the same form as Eq. [19] and the numerical value of 0.708. The quantity  $V/\Phi_{P_0}$  can be characterized as a dimensionless, effective, direct-current resistance (5),  $4r_0 \kappa R_{\text{eff}}$ , and is fixed once  $J$  is specified. A few values were reported earlier (1, 5), and these are reproduced in Table I along with some additional results. These results are compared with the present asymptotic solution in Fig. 4.

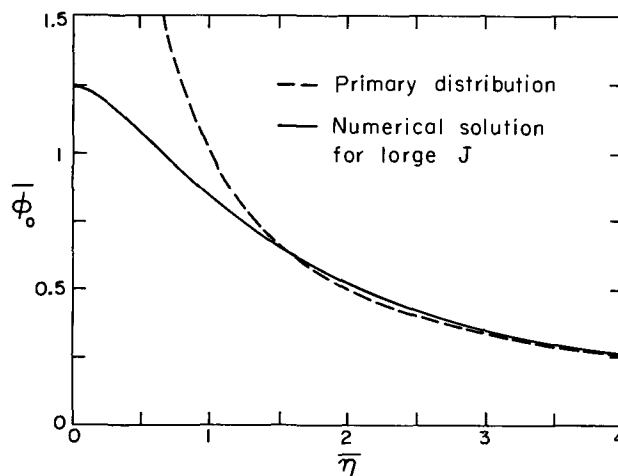


Fig. 3. The surface potential distribution for large values of the kinetic parameter  $J$  near the edge of a disk electrode.

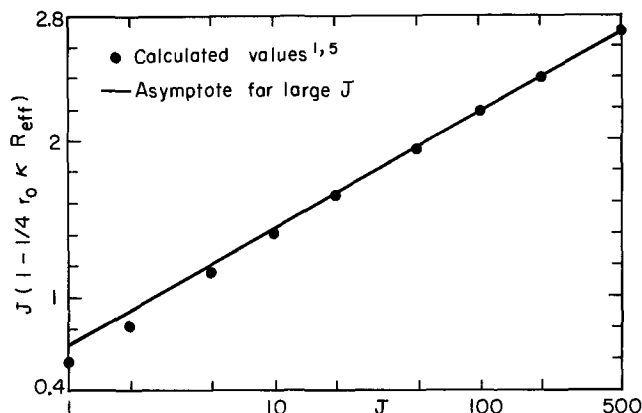


Fig. 4. The dependence of the effective direct-current resistance on the kinetic parameter  $J$ .

Table I. The effective cell resistance at different values of the parameter,  $J$ 

$J$	$4r_0kR_{eff}$
0.1	13.81194
0.2	7.44458
0.5	3.62161
1	2.34368
2	1.69962
5	1.30375
10	1.16459
20	1.09002
50	1.04072
100	1.02231
200	1.01217
500	1.00543

## LIST OF SYMBOLS

$A$	constant defined in Eq. [18]
$C$	double-layer capacity, farads/cm <sup>2</sup>
$F$	Faraday's constant, coulomb/equiv
$F(\eta, \eta')$	function defined by Eq. [A-4]
$G(\eta_*)$	function defined by Eq. [A-14]
$i$	current density, A/cm <sup>2</sup>
$I$	total current, A
$J$	dimensionless parameter for linear electrode kinetics
$K(m)$	complete elliptic integral of the first kind
$r$	radial position from axis of disk, cm
$r_0$	radius of disk, cm
$R_{eff}$	effective direct-current resistance, ohm
$t$	time, sec
$V$	electrode potential, V
$z$	distance from plane of disk, cm

$\kappa$	conductivity of the solution, ohm <sup>-1</sup> ·cm <sup>-1</sup>
$\eta$	rotational elliptic coordinate
$\phi$	dimensionless potential in the solution
$\Phi$	potential in the solution, V
$\Phi_0$	potential in the solution adjacent to the electrode, V
$\Phi^D$	potential in the solution corresponding to the primary distribution, V
$\xi$	rotational elliptic coordinate
$\theta$	dimensionless time

## REFERENCES

1. Kemal Nişancıoğlu and John Newman, *This Journal*, **120**, 1339 (1973).
2. Kemal Nişancıoğlu and John Newman, *ibid.*, **120**, 1356 (1973).
3. John Newman, *ibid.*, **113**, 501 (1966).
4. John Newman, *ibid.*, **117**, 507 (1970).
5. John Newman, *ibid.*, **117**, 198 (1970).
6. John Newman, *ibid.*, **113**, 1235 (1966).
7. V. S. Krylov and V. N. Babak, *Soviet Electrochem.*, **7**, 626 (1971). [*Elektrokhimiya*, **7**, 649 (1971)].
8. Kemal Nişancıoğlu and John Newman, Submitted to *J. Electroanal. Chem.*
9. J. A. Klingert, S. Lynn, and C. W. Tobias, *Electrochim. Acta*, **9**, 297 (1964).
10. Kemal Nişancıoğlu, Dissertation, University of California, Berkeley, California (1973).
11. John Newman, in "Electroanalytical Chemistry," Allen J. Bard, Editor, Vol. 6, pp. 187-352, Marcel Dekker, Inc., New York (1973).
12. Milton Abramowitz and Irene A. Stegun, Editors, "Handbook of Mathematical Functions," p. 608, National Bureau of Standards, Washington, D.C. (1964).

## Characterization of the Deposition of Iron Oxides on a Platinum Ring Electrode

Der-Tau Chin\*

Electrochemistry Department, Research Laboratories, General Motors Corporation, Warren, Michigan 48090

## ABSTRACT

A potentiostatic transient study has been made of the deposition of iron oxides on a rotating platinum ring electrode from pH 4-5 ferrous sulfate solutions. The current-time relation is described by a two-dimensional nucleation and growth model for the formation of a monomolecular layer of an oxide film. The rate of film deposition is found to increase with ferrous concentration, pH, and rotational speed. The results indicate that the oxide deposition is a diffusion-controlled process, possibly due to the transport of FeOH<sup>+</sup> ions to the ring surface and of H<sup>+</sup> ions to the bulk of the electrolyte. The use of the potentiostatic transient as a simple diagnostic method for identifying passivity mechanisms on iron and carbon steels is discussed.

Deposition of iron oxides on a platinum substrate from neutral ferrous sulfate solution was recently studied by Leibenguth and Cohen (1) and by Ehrenfreund and Leibenguth (2). Using x-ray and electron diffraction methods, these authors have found that the oxide is a thin layer of  $\gamma$ -FeOOH, and is formed by the anodic oxidation of FeOH<sup>+</sup> ions in the solution. This evidence suggests the use of a ring-disk or a ring hemisphere (3) for the study of iron dissolution reactions in which FeOH<sup>+</sup> complex ion has been assumed to be a reaction intermediate (4). By properly setting the potential of a platinum ring electrode within the region for the iron oxide deposition reaction, it is possible to detect the soluble FeOH<sup>+</sup> species produced by iron dissolution at the central disk or hemispherical electrode.

For this reason, a series of runs has been made in this laboratory to determine the characteristics of the iron oxide deposition reaction under the convective conditions. This paper reports the results of these studies in ferrous sulfate solutions.

## Experimental

The experimental setup was the same as described in a previous ring hemisphere study (3). The rotating ring hemispherical electrode used consisted of a platinum ring and a gold hemisphere of smaller diameter, mounted concentrically on a Teflon support. The platinum ring was 0.798 cm ID  $\times$  1.003 cm OD, and had a surface area of 0.291 cm<sup>2</sup> exposed to the electrolyte. In the present study, the gold hemispherical electrode was kept at open circuit; its purpose was to provide a hydrodynamic condition similar to that in the subsequent dissolution experiments.

\* Electrochemical Society Active Member.  
Key words: iron oxides from ferrous sulfate solutions, limiting current for the oxidation of ferrous to ferric ions, potentiostatic transient, passivation of iron and carbon steels.

A potentiostatic transient method was used to study the anodic deposition of ferric oxide from 0.01-0.1M  $\text{FeSO}_4$  solutions. Nitrogen-saturated 1-2M  $(\text{NH}_4)_2\text{SO}_4$  was used as the supporting electrolyte. The pH of these solutions was maintained at a constant value (between 4 and 5) by adding proper amounts of  $\text{NH}_4\text{OH}$  and  $\text{H}_2\text{SO}_4$  during the experiments. For each run, the surface of the platinum ring electrode was polished with a 600 grit wet grinding paper, cleaned with ethanol and 6N HCl, and cathodically treated in 2M NaOH for 2 min followed by a rinse in running water. The clean electrode was then installed on a high speed rotator, and transferred immediately to a 2 liter acrylic cell equipped with a saturated calomel reference electrode and a platinum counterelectrode. At this point, a constant speed was selected for the rotator, and the ring potential was examined with a strip-chart recorder. After the potential reached a steady-state value at open circuit, a constant anodic potential pulse of 0.9V vs. SCE (controlled by a Magna 4700M potentiostat) was applied to the ring, and the current transient was recorded on a Sanborn 296 recorder. All the experiments were performed at a constant temperature of  $24^\circ \pm 1^\circ\text{C}$ .

### Results and Discussion

**Polarization measurements.**—Before the transient measurements, a voltametric sweep was made for the platinum ring electrode to determine the potential range within which meaningful results could be obtained with the potential pulse method. The sweep procedures were described in a previous report (3). Figure 1 is a set of anodic sweep curves obtained in a pH 4 solution containing 0.01M  $\text{Fe}^{++}$  and 1M  $(\text{NH}_4)_2\text{SO}_4$  at a scan rate of 1.2 V/min. It is seen that the limiting current potentials for the oxidation of  $\text{Fe}^{++}$  to  $\text{Fe}^{+++}$  are within 0.7-1.2V vs. SCE. The curve at 2500 rpm is interesting because the current began to decrease after reaching a maximum value at 0.8V vs. SCE. Apparently at the limiting current potentials, in addition to the  $\text{Fe}^{++}/\text{Fe}^{+++}$  oxidation reaction, there is a parallel reaction for the deposition of a thin layer of an iron oxide on the ring surface. The current consumption for the iron oxide deposition reaction is very small as compared to that of the  $\text{Fe}^{++}/\text{Fe}^{+++}$  reaction; however, the oxide film reduces the active area available to the  $\text{Fe}^{++}/\text{Fe}^{+++}$  oxidation reaction, thus resulting in a decrease of the current. For these reasons, a limiting current potential of 0.9V vs. SCE was chosen for the transient experiments reported in this paper.

**Typical transient results.**—The two-reaction scheme discussed can be more clearly seen in Fig. 2, where a series of current transient curves in response to the potential pulse of 0.9V vs. SCE is given for the same electrolyte at various rotational speeds. Notice that

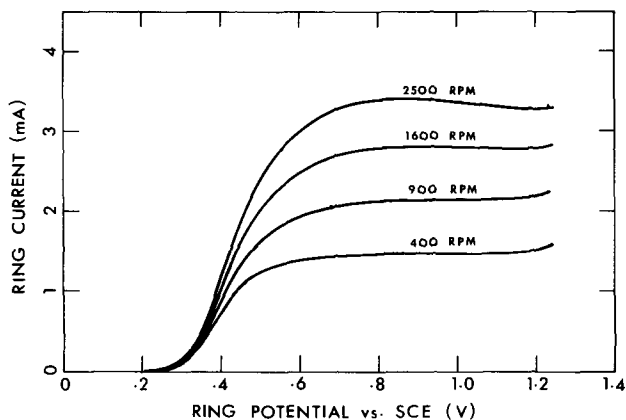


Fig. 1. Anodic sweep curves for a platinum ring electrode in a pH 4 solution containing 0.01M  $\text{Fe}^{++}$  and 1M  $(\text{NH}_4)_2\text{SO}_4$ . The scan rate was 1.2 V/min.

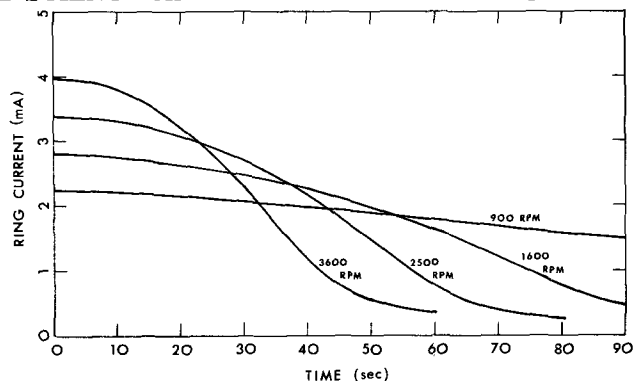


Fig. 2. Recorder traces of transient ring current in response to a constant potential pulse of 0.9V vs. SCE in a pH 4 solution containing 0.01M  $\text{Fe}^{++}$  and 1M  $(\text{NH}_4)_2\text{SO}_4$ .

the time scale in Fig. 2 is 10 sec/div; thus the curves should represent a steady-state current under the mass transfer conditions.<sup>1</sup> For each rotational speed, the current jumps to a limiting current level for the oxidation of  $\text{Fe}^{++}$  to  $\text{Fe}^{+++}$  ions at the onset of the transient, and then decreases with time due to the deposition of the iron oxide on the ring surface. The rate of current drop increases with increasing rotational speeds, implying that the oxide deposition reaction is also a diffusion limited process.

Some insight into the composition of the iron oxide can be gained by observing the typical potential decay curves shown in Fig. 3. These curves were obtained in a pH 4 ferrous sulfate solution after switching off the cell current. The curves exhibit a potential arrest at 0.25V vs. SCE (indicated by the crosses) before it reaches a steady-state value at open circuit. This arrest potential corresponds to the reduction of  $\text{Fe}_2\text{O}_3$  to  $\text{FeO}$  (6), which is subsequently dissolved in the slightly acidic electrolyte. Since the arrest time increases with decreasing rotational speeds, the dissolution of  $\text{FeO}$  is probably the rate-controlling step for the reduction of the oxide film after switching off the current. That the oxide film is a layer of  $\text{Fe}_2\text{O}_3$  is supported by the works of Leibenguth and Cohen (1) and Ehrenfreund and Leibenguth (2), who investigated the deposition of the iron oxides on a platinum substrate from ferrous sulfate solutions at pH 6.5-9.5. Using the electron diffraction method these authors have found that the oxide film is a hydrated  $\text{Fe}_2\text{O}_3$ , identified as  $\gamma\text{-FeOOH}$ .

**Interpretation of transient results with a two-dimensional film model.**—It was found that during the current drop period, the logarithm of the transient current varied linearly with the cube of time. Figure 4 is a semilogarithmic plot of ring current vs. cube of time for each of the curves shown in Fig. 2. The exact linear relationship suggests that the oxide deposition reaction follows a two-dimensional nucleation and growth model developed by Thirsk and his associates (7-9). The model was used to describe the formation of a monomolecular layer of passive films during anodic

<sup>1</sup> According to a ring theory (5), the transient time under conditions of mass transfer control can be calculated from the following equation

$$\tau \approx \frac{3}{0.510^{2/3}} \frac{(\nu/D)^{1/3}}{\omega}$$

Using  $\nu/D = 1000$  and  $\omega = 100$  rad/sec, corresponding to typical conditions in the present experiments,  $\tau$  is equal to 0.47 sec.

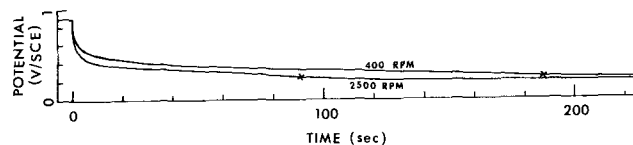


Fig. 3. Typical ring potential decay curves after switching off the current. These curves were obtained in a pH 4 ferrous sulfate solution.

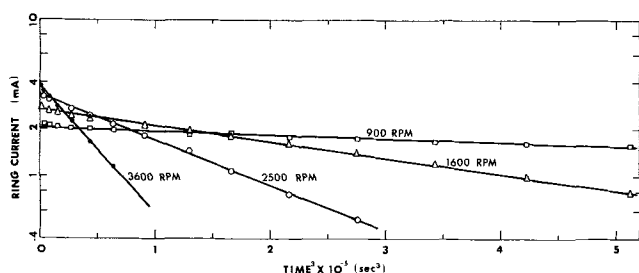


Fig. 4. Interpretation of transient currents with a two-dimensional nucleation and film growth model. The data shown here were obtained from a pH 4 solution containing 0.01M  $\text{Fe}^{++}$  and 1M  $(\text{NH}_4)_2\text{SO}_4$ .

dissolution of metals. Since the model treated the metal dissolution and the passive film formation as two parallel reactions, we may analogously formulate the following equations to describe the current/time transients obtained in the present study:

(i) current due to the deposition of a monolayer of ferric oxide on the ring electrode

$$I_1 = Q_{\text{mon}} \pi v^2 N t^2 \exp\left(-\frac{\pi}{3} v^2 N t^3\right) \quad [1]$$

(ii) current for the oxidation of ferrous to ferric ions on the oxide-free portion of the ring electrode

$$I_2 = I_{\text{lim}} \exp\left(-\frac{\pi}{3} v^2 N t^3\right) \quad [2]$$

(iii) current for the oxidation of ferrous to ferric ions on the oxide-covered ring surface

$$I_3 = I_{\infty} \left[1 - \exp\left(-\frac{\pi}{3} v^2 N t^3\right)\right] \quad [3]$$

The total current for each potential pulse is the sum of Eq. [1]-[3]. In the present study,  $I_1$  and  $I_3$  were too small to be observed under the experimental conditions, and the current during the drop period directly obeyed Eq. [2] as shown in Fig. 4.

Equation [2] implies that the limiting current for the oxidation of ferrous to ferric ions on the clean ring electrode can be obtained from the current transient curves by extrapolating the  $\ln(I)$  vs.  $t^3$  plot to  $t = 0$ . Figure 5 is a plot of limiting current vs. square root of rotational speed for various ferrous concentrations in a 1M  $(\text{NH}_4)_2\text{SO}_4$  supporting electrolyte. The curve for 0.01M  $\text{Fe}^{++}$  is given for two pH values. As expected, changes in the pH of the supporting electrolyte had no effect on the limiting current values. It is seen that the data points for each ferrous concentration fall on a straight line passing through the origin as predicted by the ring theory (5). For a narrow ring, the following relation gives a good approximation of the limiting current (10)

$$I_{\text{lim}} = 0.645 n F A [\text{Fe}^{++}] (\tau_i/\Delta\tau)^{1/3} D^{2/3} v^{-1/6} \omega^{1/2} \quad [4]$$

This equation indicates that the diffusion coefficient of ferrous ion in 1M  $(\text{NH}_4)_2\text{SO}_4$  can be calculated from the slopes of the straight lines in Fig. 5. The average diffusion coefficient thus obtained is  $5.0 \times 10^{-6} \text{ cm}^2/\text{sec}$ , in good agreement with a value of  $5.7 \times 10^{-6} \text{ cm}^2/\text{sec}$  for ferrous ion in 1M  $\text{KClO}_4$  (11).

**Kinetic considerations of the iron oxide deposition reaction.**—The mathematical model discussed above reveals that the deposition of iron oxides from ferrous sulfate solutions is initially characterized by formation of a monolayer of  $\gamma\text{-FeOOH}$  on the electrode surface. According to Eq. [2], the product,  $\pi v^2 N/3$ , is the slope of the straight lines in Fig. 4; the cube root of  $v^2 N$  can be regarded as a composite rate constant for the overall monolayer deposition process.

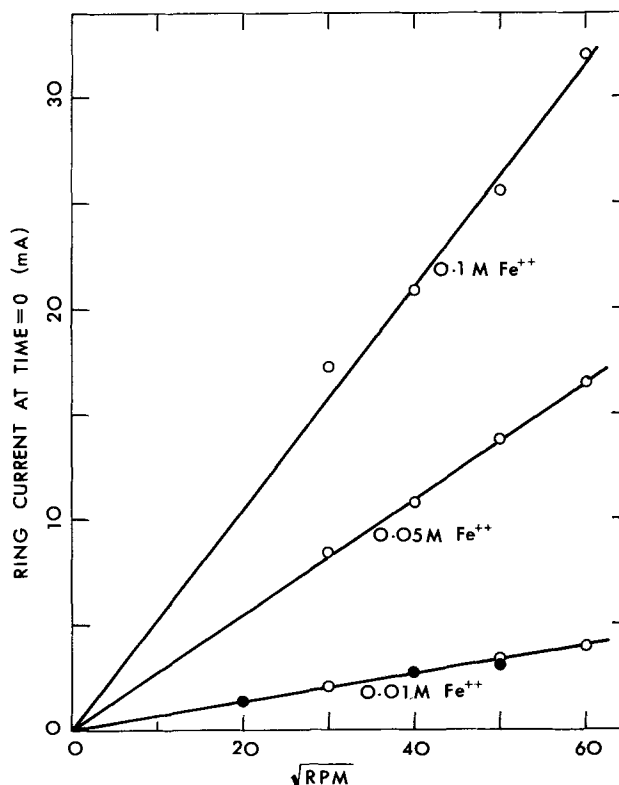


Fig. 5. Limiting current for the oxidation of ferrous to ferric ions vs. the square root of rotational speeds for three different ferrous concentrations. The supporting electrolyte was 1M  $(\text{NH}_4)_2\text{SO}_4$ . The pH of the solution was 4 for the open circles and 5 for the filled circles.

Figure 6 is a linear plot of  $\sqrt[3]{v^2 N}$  vs. ferrous ion concentrations for three different rotational speeds. The supporting electrolyte was pH 4, 1M  $(\text{NH}_4)_2\text{SO}_4$ . It is seen that the composite rate constant increases linearly with concentration of ferrous ion; it also increases with increasing rotational speed. No direct correlation was found between the composite rate constant and the limiting current for the oxidation of ferrous to ferric ions. The effect of pH and of concentration of  $(\text{NH}_4)_2\text{SO}_4$  on the composite rate constant are shown in Fig. 7 and 8, respectively. In these two figures,  $\sqrt[3]{v^2 N}$  is plotted against rotational speed on a log-log scale, and the data points are seen to fall on a straight line. The slopes of the straight lines are approximately equal to 1; it increases slightly with increasing pH and  $\text{Fe}^{++}$  concentrations. Figure 7 shows that an increase of pH from 4 to 5 results in a fivefold increase in  $\sqrt[3]{v^2 N}$ . Changes in the concentration of the supporting electrolyte apparently have no effect on the composite rate constant (Fig. 8). This implies that  $\text{SO}_4^{--}$  ions are not participating in the film deposition reaction.

Previous works have shown that the  $\gamma\text{-FeOOH}$  film is formed from  $\text{FeOH}^+$  ions (1, 2). In a slightly acidic or a neutral electrolyte, the following ionic equilibria are the possible cause for the formation of  $\text{FeOH}^+$  ions and the film deposition reaction



The equilibrium constant for reaction (5) is given (12) as

$$K = \frac{[\text{FeOH}^+][\text{H}^+]}{[\text{Fe}^{++}]} \simeq 10^{-8} \text{ mole/liter} \quad [7]$$

Using  $[\text{Fe}^{++}] = 10^{-2}\text{-}10^{-1} \text{ mole/liter}$ , and  $[\text{H}^+] = 10^{-5}\text{-}10^{-4} \text{ mole/liter}$ , corresponding to the experimental conditions shown in Fig. 6-8,  $[\text{FeOH}^+]$  can be cal-

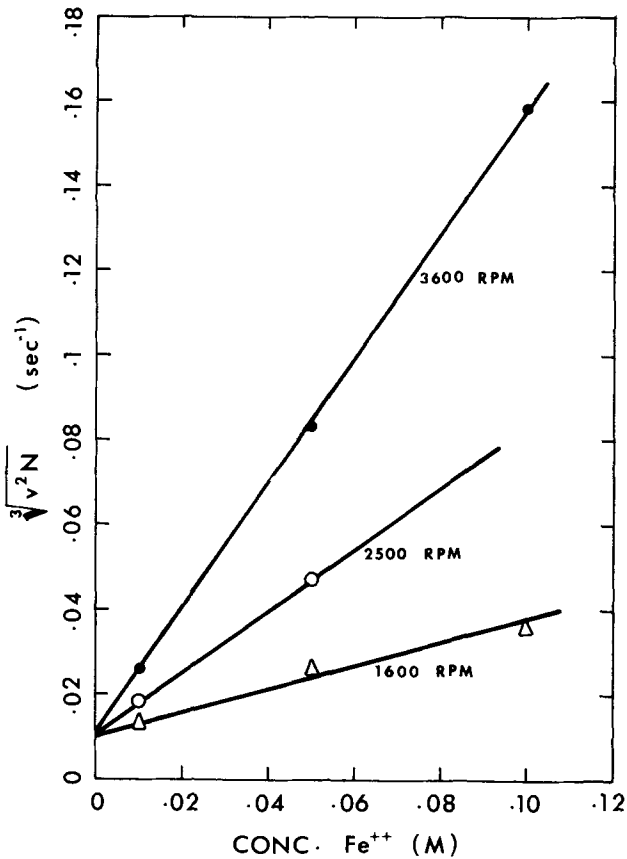


Fig. 6. Rate of oxide deposition as a function of ferrous concentration in pH 4 1M  $(\text{NH}_4)_2\text{SO}_4$ .

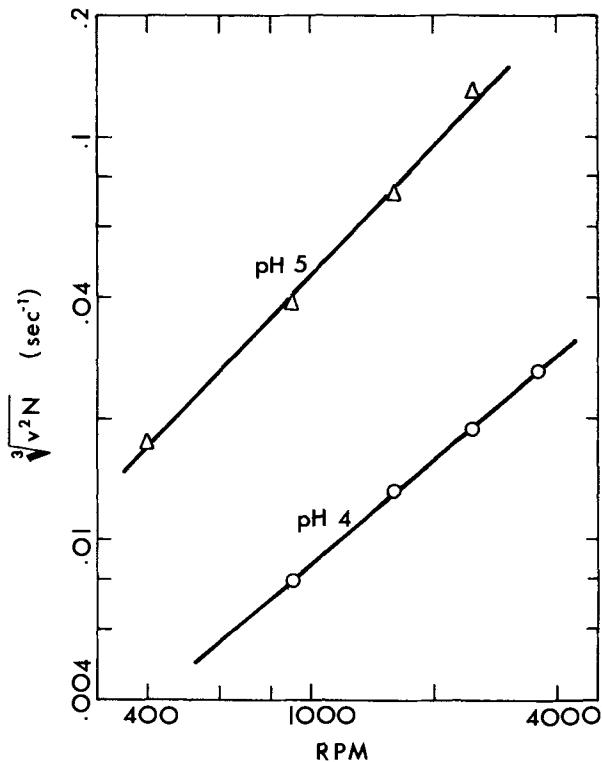


Fig. 7. Rate of oxide deposition vs. rotational speeds for two different pH values. The electrolyte used was 0.01M  $\text{Fe}^{++}$  and 1M  $(\text{NH}_4)_2\text{SO}_4$ .

culated to be approximately  $10^{-6}$ - $10^{-5}$  mole/liter. This concentration is of the same order of magnitude as that of hydrogen ion in these solutions. Thus, it is possible that transport of  $\text{FeOH}^+$  ions to the ring surface and of  $\text{H}^+$  ions to the bulk of the electrolyte are

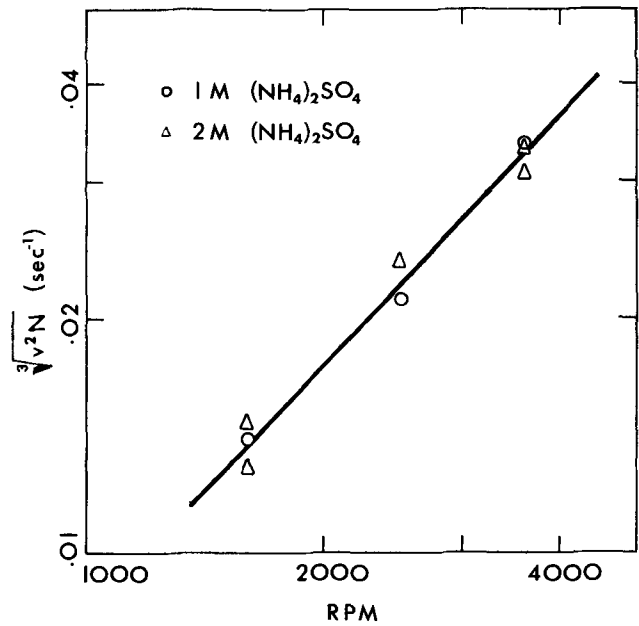


Fig. 8. Rate of oxide deposition vs. rotational speeds for two different sulfate concentrations at pH 4. The concentration of ferrous ion was 0.015M.

the rate-determining steps for the film deposition process under the present experimental conditions.

**Application to passivation studies.**—The cause of passivity on iron and its alloys has been generally attributed to one of the following processes: (i) solid-phase anodic oxidation in which the metal reacts with adsorbed anions to form an oxide without the metal ion entering the solution; (ii) dissolution precipitation in which the passivity is initiated by precipitation of a dissolution product from its supersaturated solution in the immediate neighborhood of the anode; and (iii) anodic deposition of oxides (1) in which a soluble dissolution product, such as  $\text{FeOH}^+$  ion, is further oxidized at the anode to form a monolayer of passive film. How to distinguish these mechanisms has been a controversial subject discussed extensively in the literature (13-17). The distinction between mechanisms (ii) and (iii) is especially difficult, for both are preceded by a metal dissolution reaction. However, the potentiostatic transient seems to be a simple diagnostic criterion for identifying these two mechanisms. A typical example of mechanism (ii) is the passivation of mild steels in neutral sulfate and perchlorate solutions, in which the current/time relation is described by Muller's dissolution precipitation model and the active/passive transition potential is convection dependent (18). The present results suggest that for mechanism (iii), the transient current in response to a potential step in the passive region should follow Eq. [1]-[3]. The onset of passivation for mild steels in neutral nitrate solutions is a good example of this third mechanism; in this system, the logarithm of the transient current has been found to vary linearly with the cube of time (19).

### Summary

A study has been made of the deposition of  $\gamma\text{-FeOOH}$  on a rotating platinum ring electrode from ferrous sulfate solutions at pH 4-5. It is found that the transient current in response to a potential step in the limiting current region for the oxidation of ferrous to ferric ions, follows a two-dimensional nucleation and growth model for the formation of a monolayer of oxide on the electrode surface. The rate of film formation increases with increasing concentrations of ferrous ion, pH of electrolytes, and rotational speeds of the ring electrode. The results imply that the oxide deposition reaction is a diffusion-controlled process under the

present experimental conditions, possibly due to the transport of  $\text{FeOH}^+$  ions to the ring and of  $\text{H}^+$  ions to the bulk of the electrolyte. The diffusion coefficient of ferrous ion as calculated from the limiting current measurement, is  $5.0 \times 10^{-6}$  cm<sup>2</sup>/sec. The use of the potentiostatic transient as a simple diagnostic method for identifying the mechanisms of passivity on iron and carbon steels was discussed.

Manuscript submitted July 11, 1973; revised manuscript received Oct. 19, 1973.

Any discussion of this paper will appear in a Discussion Section to be published in the December 1974 JOURNAL. All discussions for the December 1974 Discussion Section should be submitted by Aug. 1, 1974.

#### LIST OF SYMBOLS

A	surface area of ring electrode, cm <sup>2</sup>
D	diffusion coefficient, cm <sup>2</sup> /sec
F	Faraday constant, 96,500 coulombs/g-equiv
$I_1$	current for deposition of a monomolecular layer of iron oxides on ring electrode, A
$I_2$	current for oxidation of ferrous to ferric ions on the oxide-free portion of ring electrode, A
$I_3$	current for oxidation of ferrous to ferric ions on the oxide-covered portion of ring electrode, A
$I_{lim}$	limiting current for oxidation of ferrous to ferric ions on ring electrode whose entire surface is free from oxide contamination, A
$I_{ss}$	steady-state current of $I_3$ , A
$n$	number of electrons transferred in electrode reactions, g-equiv/g-mole
N	rate of nucleation of two-dimensional centers, nuclei/cm <sup>2</sup> /sec
$Q_{mon}$	charge required to form a monomolecular layer of oxide on ring surface, coulombs
$r_i$	inner radius of ring electrode, cm
$\Delta r$	width of ring electrode, cm
t	time, sec

$v$	rate of film spreading from nucleus centers, cm/sec
$\tau$	transient time required to reach a steady state, sec
$\nu$	kinematic viscosity of electrolyte, cm <sup>2</sup> /sec
$\omega$	angular velocity of ring electrode, rad/sec
[X]	bulk concentration of species X, g-mole/cm <sup>3</sup> or g-mole/liter

#### REFERENCES

- J.-L. Leibenguth and M. Cohen, *This Journal*, **119**, 987 (1972).
- M. Ehrenfreund and J.-L. Leibenguth, *Bull. Soc. Chim. Fr.*, **7**, 2590 (1972).
- D-T Chin, *This Journal*, **120**, 631 (1973).
- J. O'M. Bockris, D. Drazic, and A. R. Despic, *Electrochim. Acta*, **4**, 325 (1961).
- W. J. Albery and M. L. Hitchman, "Ring-Disc Electrode," Oxford University Press, London (1971).
- A. M. Sukhotin and K. M. Kartushova, *Corrosion Sci.*, **5**, 393 (1965).
- A. Bewick, M. Fleischman, and H. R. Thirsk, *Trans. Faraday Soc.*, **58**, 2200 (1962).
- M. Fleischman and H. R. Thirsk, *Electrochim. Acta*, **9**, 757 (1964).
- R. D. Armstrong, D. F. Porter, and H. R. Thirsk, *J. Phys. Chem.*, **72**, 2300 (1968).
- D-T Chin and M. Litt, *This Journal*, **119**, 1338 (1972).
- D. Jahn and W. Vielstich, *ibid.*, **109**, 849 (1962).
- J. Bjerrum, G. Schwarzenbach, and L. G. Sillen, "Stability Constants of Metal-Ion Complexes. Part II: Inorganic Ligands," The Chemical Society, London (1958).
- R. D. Armstrong, *Corrosion Sci.*, **11**, 693 (1971).
- R. D. Armstrong, *J. Electroanal. Chem.*, **28**, 221 (1970).
- A. K. N. Reddy, *ibid.*, **28**, 217 (1970).
- U. Ebersbach, K. Schwabe, and K. Ritta, *Electrochim. Acta*, **12**, 927 (1967).
- O. L. Riggs, Jr., *Corrosion*, **25**, 130 (1969).
- D-T Chin, *This Journal*, **119**, 1043 (1972).
- D-T Chin, *ibid.*, **119**, 1182 (1972).

## Technical Note



### Influence of Active Material Thickness on Positive Grid Corrosion in the Pb-Acid Battery

A. C. Simon\*

Electrochemistry Branch, Naval Research Laboratory, Washington, D. C. 20375

and S. M. Caulder\*

International Lead Zinc Research Organization Research Associate at the Naval Research Laboratory

The problem of Pb/Sb grid corrosion due to repeated anodizations and acid attack has been the subject of numerous investigations (1-5). However, all of these investigations were made on alloys which were unprotected by a covering of the active material. No report has been found in which the possible beneficial effect of an active material covering over the grid was investigated or discussed. In a pasted plate the active material surrounds the grid member and, since these plates are often overpasted, the grid may lie buried at some depth

below the surface. This depth is not the same at all grid bars because of unequal pasting, bent grids, or other problems of manufacture. With this unequal covering it is likely that there could be a direct correlation between corrosion and the thickness of the active material covering at each point of the grid.

The positive plate offers the means for determining the effect of such a covering. When a battery plate is cross sectioned (Fig. 1), the horizontal grid bars will usually appear in the section as small isosceles triangles. The apex of each triangle is at or near the surface of the plate and the base of the triangle is at or parallel to the center line of the plate. Since these

\* Electrochemical Society Active Member.

Key words: lead-acid battery, lead-antimony corrosion, active material protection.



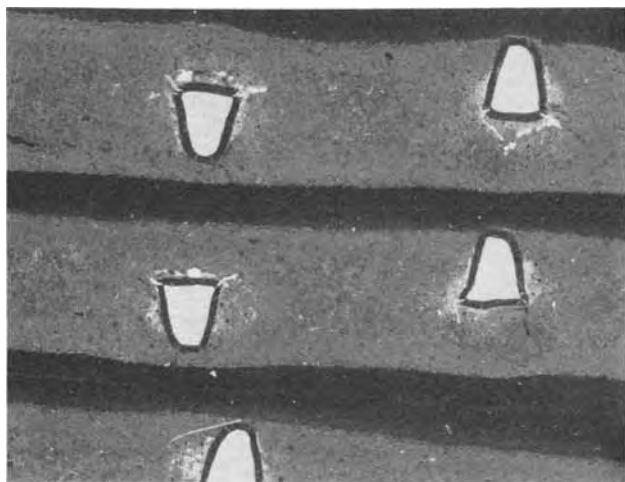


Fig. 1. Cross-sectioned battery plate showing relative positions of grid bars.

horizontal grid bars are alternately placed to one or the other side of the center line of the plate, the plate is approximately twice the thickness of the individual grid bars (measured from apex to base). In many cases the plate is also overpasted so that an additional layer of active material then covers the apex of the grid triangle or adds to the thickness between the base and the surface on the other side of the plate. Most important is the fact that the depth of active material covering the grid triangle at the apex and at the base will be quite different, as measured from the surface of the plate. Advantage can be taken of this difference in thickness to determine if the thickness of the corrosion product is different at these two points, as would be the case if the active material offers a protection that varies with its thickness.

In cross sections of grid bars, the width of the corrosion product is an accurate measure of the extent of the grid corrosion that has taken place. In lead-antimony grid alloys, the corrosion product is very clearly defined and is distinct from both the metal from which it forms and from the active material which surrounds it. If the plate has not received too many cycles, the corrosion product is still firmly attached to the metal and has not separated into layers.

The lead dioxide plates used in the measurements reported here were of two paste formulations. One plate group contained an 80-20% litharge-red lead mechanical blend and the other group contained a persulfate "watermix" mechanical blend with 18% red lead. Both of these paste formulations were prepared in two paste densities and all were pasted on 6% Pb-Sb grid alloys.




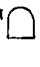
The metallurgical specimens used for measurements consisted of three or four pieces from the same plate, each piece containing five or six horizontal grid bar cross sections, and all the pieces were contained in the same plastic mount. Most of the bars in the metallurgical section met the requirements for measurement and each of these was measured for thickness of corrosion product.

The plates selected for measurement had an average corrosion layer thickness that varied from approximately 60 to 150  $\mu\text{m}$ , depending upon active material composition and porosity. Three corrosion thickness measurements were made on each side of the triangle and base at the  $\frac{1}{4}$ ,  $\frac{1}{2}$ , and  $\frac{3}{4}$  position along its length. Measurements were also made at the apex of the triangle, where it was nearest to the surface.

### Results and Comments

The corrosion thickness data obtained from the two electrodes of different active material composition but with the same number of charge-discharge cycles, are given in Table I. From these data, which were typical

Table I. Grid corrosion product measurements

Grid bar	Average ( $\mu$ )			
				
80-20 litharge-red lead mechanical blend	80.0	72.9	87.3	71.5
	81.3	72.9	89.7	70.6
	81.3	79.1	90.2	76.0
Persulfate "water mix" mechanical blend containing 18% red lead	119.1	112.6	108.8	115.5
	116.9	112.8	106.2	112.9
	110.2	108.8	107.9	113.7

of all other samples examined, no significant difference in corrosion thickness was observed at different depths in the active material. Measurements made on a series of plates containing different oxide blends, of which two are reported here, indicated that the amount of corrosion might be influenced to some extent by the plate composition (Fig. 2 and 3).

The corrosion product around the grid section builds up during continued cycling to a point where internal stress generated within the film is relieved by cracking which extends outwards from the grid at the points of critical stress. This stress is then transferred to the active material and may result in dislodgment of the pellet. While not dependent on a definite thickness, the presence of overpasting may help to prevent this radial cracking until a later stage in the corrosion process.

The active material composition, and to a certain extent, the original paste density, are in some manner related to the corrosion process. It was found that, in some cases, the protective lead dioxide layer did not form immediately when the plate was cycled. This inability to form the adherent and dense  $\text{PbO}_2$  layer on the surface of the grid resulted in the intermediate formation of a film that consisted of large  $\text{PbSO}_4$  crys-

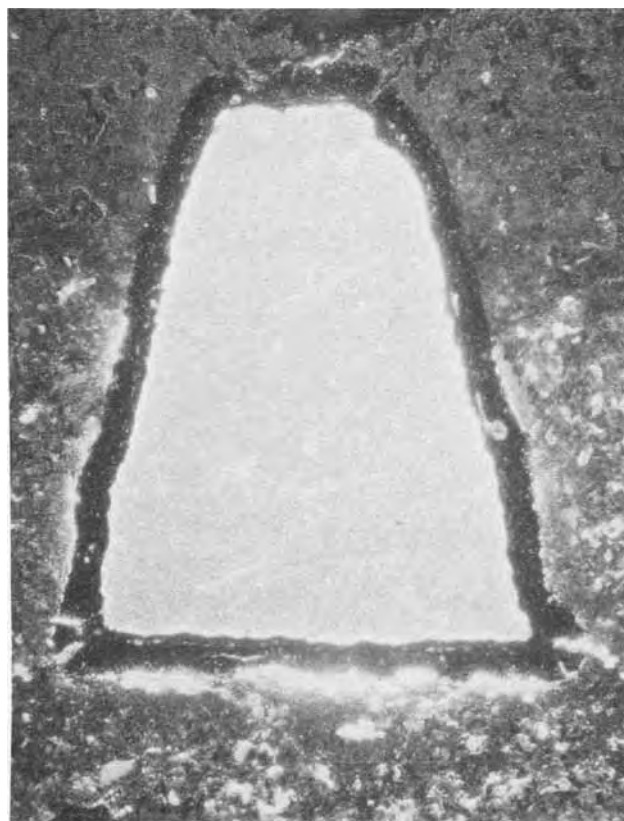


Fig. 2. Corrosion product of grid bars pasted with a 80-20 litharge-red lead mechanical blend.

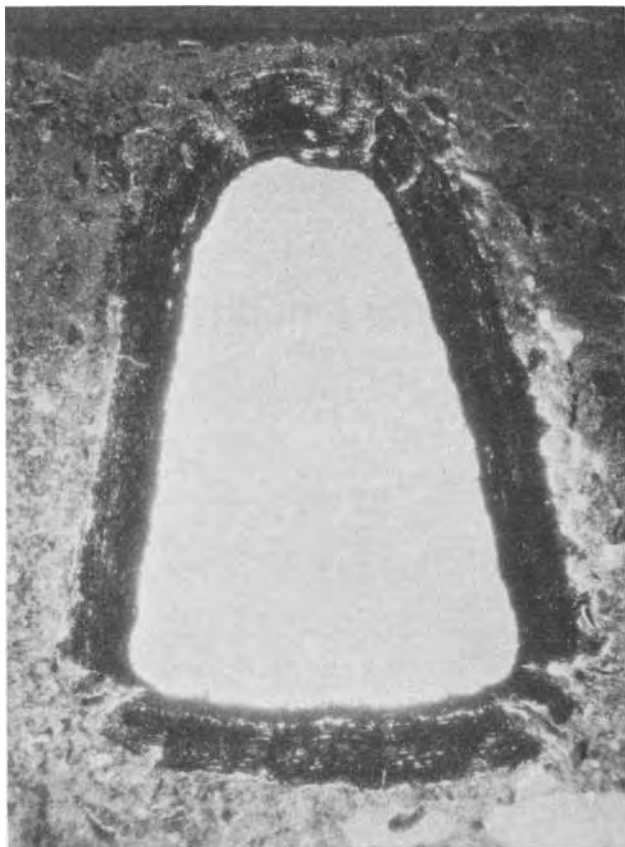


Fig. 3. Corrosion product of grid bars pasted with a persulfate "water mix" mechanical blend containing 18% red lead.

tals which were subsequently converted to  $PbO_2$  upon continued cycling.

In a case where a high and low density paste were both used by the same manufacturer, the grids of the

plate with the high density paste showed this inability to form a protective layer on the first cycle, while the grids of the low density paste developed a  $PbO_2$  corrosion layer in a normal manner. However, after eleven capacity cycles, no appreciable difference in the amount of corrosion product was observed between high and low density plates.

### Conclusions

Attempting to gain protection against corrosion by overpasting the grid or by increasing the thickness of the active material above the grid is ineffective. The composition of the paste from which the active material is made, or the paste density, has an effect on the thickness of the corrosion product during the first few cycles, but the thickness of the active material does not. Any possible effect of overpasting is due to mechanical support of the corrosion product at the critical stress areas which thus may delay cracking and delay dislodgment of active material.

### Acknowledgment

The authors wish to thank the International Lead-Zinc Research Organization, Incorporated, and the Naval Research Laboratory for their support of this research.

Manuscript submitted March 12, 1973; revised manuscript received Nov. 26, 1973. This was Paper 32 presented at the Miami Beach, Florida, Meeting of the Society, Oct. 8-13, 1972.

Any discussion of this paper will appear in a Discussion Section to be published in the December 1974 JOURNAL. All discussions for the December 1974 Discussion Section should be submitted by Aug. 1, 1974.

### REFERENCES

1. J. J. Lander, *This Journal*, **98**, 220 (1951).
2. J. B. Burbank and A. C. Simon, *ibid.*, **100**, 11 (1953).
3. J. Burbank, *ibid.*, **104**, 693 (1957).
4. P. Ruetschi and B. Cahan, *ibid.*, **105**, 369 (1958).
5. D. Pavlov, M. Boton, and M. Stoyanova, *Izv. Inst. Fizikokhim, Bulgar. Akad. Nauk*, **5**, 55 (1965).

## Errata

In the paper "Stability and Stirring in Crystal Growth from High-Temperature Solutions" by Hans J. Scheel and D. Elwell which appeared on pp. 818-824 in the June 1973 JOURNAL, Vol. 120, No. 6, the line drawings given as Fig. 7 and Fig. 8 on page 823 are interchanged.

In the paper "The Nucleation with  $SnCl_2$ - $PdCl_2$  Solutions of Glass Before Electroless Plating" by C. H. de Minjer and P. F. J. v.d. Boom which appeared on pp. 1644-1650 in the December 1973 JOURNAL, Vol. 120, No. 12, the micrographs given as Fig. 1 and Fig. 2 on page 1645 are interchanged.



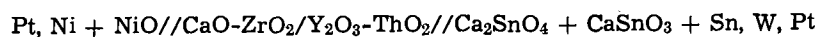
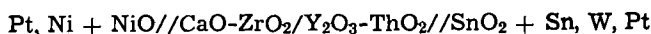
## Electrochemical Determination of the Stability of Mono- and Dicalcium Stannates

K. T. Jacob and J. C. Chan<sup>1</sup>

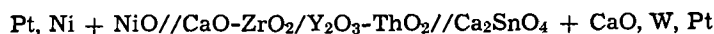
*Department of Metallurgy and Materials Science, University of Toronto, Ontario, Canada M5S 1A4*

### ABSTRACT

The thermodynamic properties of mono- and dicalcium stannates have been determined in the temperature range 973°-1423°K from the electromotive force measurements on solid oxide galvanic cells



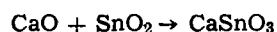
and



The Gibbs free energy changes accompanying the formation of the stannates from component oxides may be represented by the equations



$$\Delta G^\circ = -17,040 + 0.85T (\pm 300) \text{ cal}$$



$$\Delta G^\circ = -17,390 + 2.0T (\pm 300) \text{ cal}$$

The partial pressures of the tin bearing oxide species resulting from the decomposition of the stannates have been calculated as a function of the oxygen partial pressure by combining the results of this study with published information on the partial pressures and composition of oxide species over stannic oxide.

Quantitative information on the stability of calcium stannates is of importance in the pyrometallurgy of tin and its alloys. Tin smelting slags frequently contain considerable amounts of calcium oxide. Recently Shelley and Shelley (1) have illustrated the importance of calcium oxide in increasing the solubility of stannic oxide in glassy matrix. The traditional use of stannic oxide as an opacifier in glass is related to its precipitation as  $\text{CaSnO}_3$ ,  $\text{CaSnTiO}_5$ , etc. Application of alkaline-earth stannates as dielectric materials (2) has raised considerable interest in the stability of these compounds under different environmental conditions. The tendency of these compounds to change composition at high temperatures and reducing conditions, due to the volatilization of  $\text{SnO}$  and its polymeric forms, can be quantitatively assessed from an accurate knowledge of the stabilities and published information (3) on the vapor composition and pressures over  $\text{Sn} + \text{SnO}_2$  mixtures.

The phase diagram (2,4) indicates the occurrence of two compounds in the  $\text{CaO-SnO}_2$  system; mono- and dicalcium stannates. The oxygen chemical potential

in equilibrium with tin and stannic oxide was measured by Belford and Alcock (5) using a galvanic cell incorporating a yttria-doped thoria electrolyte and  $\text{Ni} + \text{NiO}$  reference electrode, in the temperature range 773°-1023°K. In this study the Gibbs free energies of formation for calcium stannates were measured using a similar technique. Equilibration of tin with two adjoining phases of the  $\text{CaO-SnO}_2$  system fixes the oxygen potential, measurement of which permits the calculation of the partial and integral thermodynamic properties of the system.

### Experimental

*Materials.*—The stannic oxide was supplied by the British Drug House Limited and was 99.95% pure. Calcium oxide was prepared by calcination of calcium carbonate, 99.99% pure, supplied by the Electronic Space Products Incorporated. The stannates were prepared by mixing fine powders of the component oxides in the required stoichiometric ratio, compacting the mixture into pellets, and sintering at 1273°K in oxygen atmosphere for 8 hr in a closed platinum dish. X-ray diffraction analysis of the products confirmed the formation of the stannates.

<sup>1</sup> Present address: Canada Wire and Cable Limited, 147 Laird Drive, Toronto, Ontario, Canada.

Key words: thermodynamics, solid electrolyte, galvanic cell, calcium stannates, vaporization.

Tin of 99.99+ purity was supplied by the Fisher Scientific Company. Calcia-stabilized zirconia tubes were supplied by the Zirconia Corporation of America. Thoria pellets stabilized by 15 mole per cent (m/o) yttria, were prepared from mixed nitrate solution by evaporation and subsequent decomposition. The resulting powder was pressed into pellets at a pressure of 30 tons/sq in.<sup>-1</sup>, and sintered under an atmosphere of 90% N<sub>2</sub> + 10% H<sub>2</sub> at 2073°K. The argon gas used as the atmosphere for the emf runs was 99.98% pure, and was dried by passing through magnesium perchlorate and deoxidized by passage through a column of titanium granules maintained at 1170°K.

**Apparatus.**—It has been observed in earlier studies (6,7) that at temperatures above 1273°K the calcia-stabilized zirconia electrolyte is corroded by pure stannic oxide in equilibrium with tin. Preliminary studies indicated that yttria-doped thoria electrolyte, used by Belford and Alcock (5) up to a temperature of 1023°K, is suitable in contact with pure stannic oxide till 1173°K and in contact with the stannates till 1423°K. At higher temperatures, discoloration of the electrolyte was noticed.

A schematic diagram of the apparatus is shown in Fig. 1. The Ni + NiO reference electrode was placed inside a closed end, flat bottomed, lime-zirconia tube, with a platinum wire spring loaded against the reference electrode. The platinum lead is enclosed in an alumina sheath, through which prepurified argon gas is passed at a rate of 100 ml/min<sup>-1</sup>. The lime-zirconia tube is placed inside an alumina tube, one end of which is attached to a yttria-doped thoria pellet by means of alumina cement and glass seals. The outer end of the lime-zirconia tube and the surfaces of the yttria-thoria pellets were polished with diamond paste to facilitate good contacts when pressed together. The entire assembly was mounted inside a reaction tube in a vertical molybdenum wound resistance furnace in such a way that the assembly could be moved up and down through a sliding rubber seal.

Pellets of Sn + SnO<sub>2</sub> were made by compacting a mixture of their powders in the molar ratio 1:2. The pellet was placed inside an alumina crucible which was supported on an alumina tube. The pellet was pressed down against the bottom of the alumina crucible with a spring loaded ring sleeve of alumina. When the Sn + SnO<sub>2</sub> pellets of 1:2 mixture were heated under inert gas, fine droplets of molten tin were found to be held against the yttria-thoria pellet by surface tension. They do not settle to the bottom of the alumina crucible unless the ratio of tin in the pellets is increased.

Electrical contact between the Sn + SnO<sub>2</sub> pellet and the platinum wire passing over the outside of the alumina tube, *e*, was affected by lowering the overhanging electrolyte-tube onto the pellet. Attack of the platinum contact by the molten tin was observed, but was minimized by recessing the platinum lead in a small groove cut into the yttria-thoria pellet and then adding a 1 cm long tungsten wire extension to the platinum-lead to make contact with the Sn + SnO<sub>2</sub> pellet. Times varying from 30 min to 3 hr were found necessary to attain equilibrium emf's. The emf's were measured with "Solartron" digital voltmeter, which has an input impedance of 10<sup>12</sup> ohms. The design of the emf cell permitted the electrolyte material to be detached from the Sn + SnO<sub>2</sub> pellet during heating and cooling periods. Pellets containing tin and a mixture of stannates were prepared in a manner similar to the Sn + SnO<sub>2</sub> pellets; the respective stannates being mixed in 1:1 molar ratio. Reversible emf's of the following cells were measured as a function of temperature

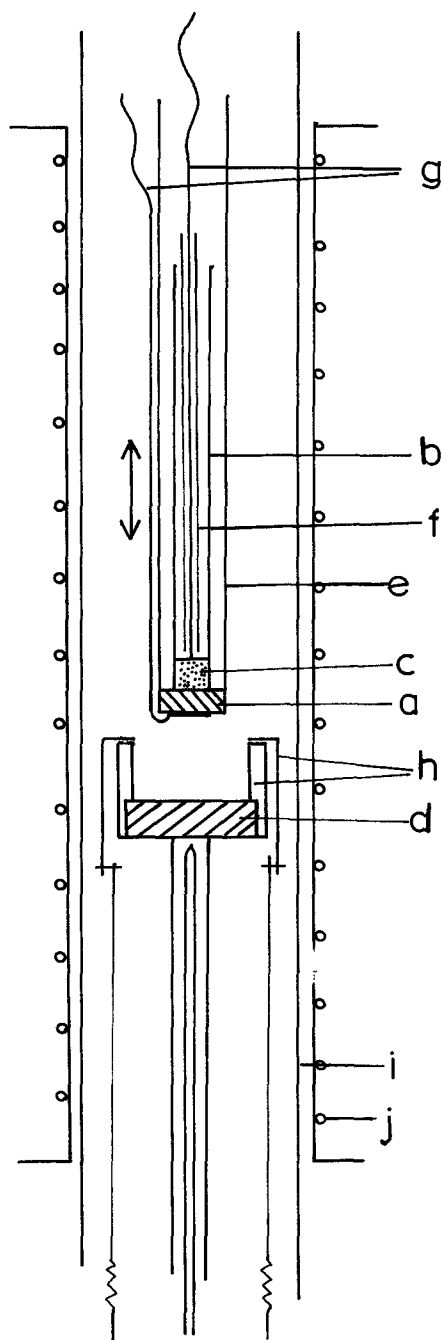
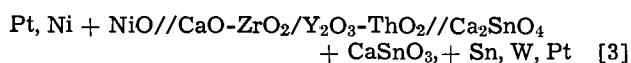
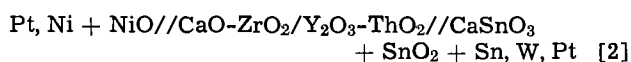
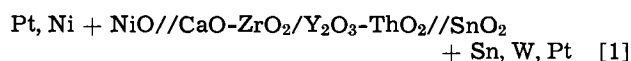
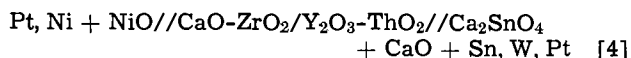


Fig. 1. Schematic diagram of the electrochemical cell assembly; (a) Y<sub>2</sub>O<sub>3</sub>-ThO<sub>2</sub> pellet, (b) CaO-ZrO<sub>2</sub> tube, (c) Ni + NiO reference electrode, (d) Sn + SnO<sub>2</sub> electrode, (e) alumina tube, (f) alumina sheath (argon inlet), (g) platinum leads, (h) alumina crucibles and rings for spring loading the Sn + SnO<sub>2</sub> electrode against the alumina container, (i) alumina reaction tube, (j) molybdenum resistance furnace.



and



The reversibility of the cells was checked by passing a small current ( $\approx 50 \mu\text{A}$ ) through the cell for 2-5 min in either direction, and it was found that the emf

returned to its initial value in a few minutes, after which it remained constant for up to 8 hr. Emf's were also found to be independent of the flow rate of inert gas through the cell.

### Results and Discussion

The emf's were reproducible within  $\pm 2$  mV on repeated temperature cycling. The emf's of cells [3] and [4] were found to be a linear function of temperature, as shown in Fig. 2, in the temperature range 975°-1423°K. At lower temperatures higher emf's were observed which tend to increase with time, suggesting that equilibrium may not have been attained. The emf's of cells [1] and [2] varied linearly with temperature in the range 875°-1175°K, above which the emf's were found to decrease with time. Reproducible emf's could not be obtained once the cells were heated above 1175°K. Examination of the cell components indicated that SnO vapor penetrated the  $Y_2O_3$ - $ThO_2$  pellets and the supporting alumina tube above 1175°K.

The emf of cell [2] was on the average 2.5 mV above the emf of cell [1]. If the solid solubility of calcium oxide in stannic oxide is negligible, the emf's of cells [1] and [2] should be identical. While the slightly higher emf obtained with cell [2] indicates some solid solubility, it is not possible to calculate the solubility limit accurately from the present results because of a scatter of  $\pm 2$  mV in the measured emf. The variation of the emf's of cells [1], [3], and [4] with temperature may be represented by the equations

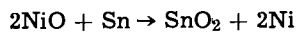
$$E_1 = 300.5 - 0.1088T (\pm 2) \text{ mV}$$

$$E_3 = 492.7 - 0.143T (\pm 2) \text{ mV}$$

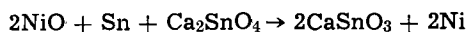
$$E_4 = 485.2 - 0.1032T (\pm 2) \text{ mV}$$

The emf of cell [1] obtained in this study is almost identical to that reported by Belford and Alcock (5). Recent work by Carbo-Nover and Richardson (7) have confirmed that both solid and liquid SnO are

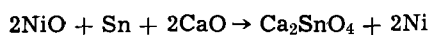
unstable below 1373°K and decompose to a mixture of Sn and  $SnO_2$ . Above 1373°K, liquid SnO is the stable phase in equilibrium with tin. Information on electrolytic conduction domains for both calcia-zirconia and yttria-thoria has been reviewed by Patterson (8). An analysis of the emf of bioelectrolyte cells has been proposed by Shores and Rapp (9), which indicates that at the oxygen potentials prevailing at the electrodes employed in this study, significant electronic contributions to the total conductivity of the electrolyte would be absent. Therefore, the standard free energy changes accompanying the following cell reactions can be calculated from the measured emf



$$\Delta G^\circ = -27,720 + 10.04T (\pm 200) \text{ cal}$$



$$\Delta G^\circ = -45,455 + 13.19T (\pm 200) \text{ cal}$$

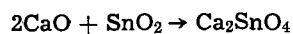


$$\Delta G^\circ = -44,765 + 10.89T (\pm 200) \text{ cal}$$

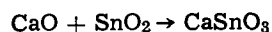
Using a value of

$$\Delta G^\circ = -55,965 + 20.29T \text{ cal}$$

for the standard free energy of formation of NiO (10), the free energy of formation of calcium stannates from the component oxides can be obtained from the above equations



$$\Delta G^\circ = -17,040 + 0.85T (\pm 300) \text{ cal}$$



$$\Delta G^\circ = -17,390 + 2.0T (\pm 300) \text{ cal}$$

Figure 3 shows the integral free energy and enthalpy of mixing in the CaO-SnO<sub>2</sub> system. The uncertainty limits on second law enthalpies are also indicated on the diagram. Within experimental error limits the integral heat of formation of dicalcium stannate is a linear additive function of the heats of formation of monocalcium stannate and pure calcium oxide. A slightly higher entropy of formation appears to be responsible for the high temperature stability of the dicalcium stannate with respect to monocalcium stannate and calcium oxide.

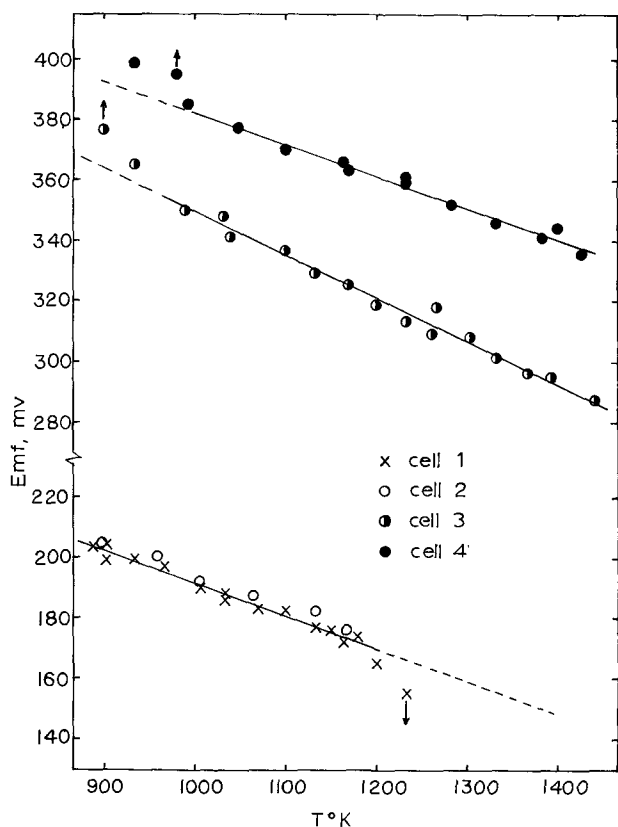


Fig. 2. The temperature dependence of the emf's of cells [1], [2], [3], and [4].

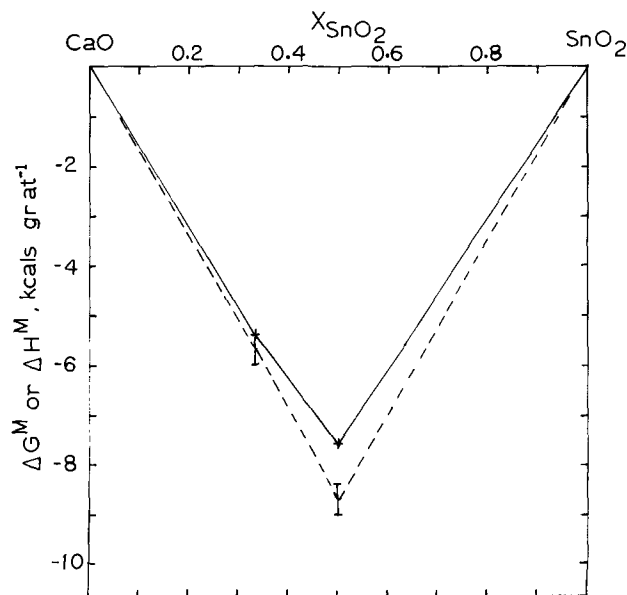


Fig. 3. The integral free energy and enthalpy of mixing in the CaO + SnO<sub>2</sub> system; —  $\Delta G^M$ , 1000°K; - - -  $\Delta H^M$ .

Table I. Standard free energy change accompanying the volatilization of SnO<sub>2</sub> (3)

Reaction	$\Delta G^\circ$ , cal
$\text{SnO}_2(\text{s}) \rightarrow \text{SnO}(\text{g}) + \text{O}_2(\text{g})$	$138,420 - 60.947T$
$2\text{SnO}(\text{g}) \rightarrow \text{Sn}_2\text{O}_2(\text{g})$	$-64,570 + 30.76T$
$3\text{SnO}(\text{g}) \rightarrow \text{Sn}_3\text{O}_3(\text{g})$	$-131,740 + 67.84T$
$4\text{SnO}(\text{g}) \rightarrow \text{Sn}_4\text{O}_4(\text{g})$	$-200,220 + 102.68T$

The mass-spectrometric studies of Colin, Drowart, and Verhaegen (3) have shown that the vapor above stannic oxide consists of Sn, SnO, Sn<sub>2</sub>O<sub>2</sub>, Sn<sub>3</sub>O<sub>3</sub>, and Sn<sub>4</sub>O<sub>4</sub> species. On the basis of their mass-spectrometric measurements and earlier studies of the vapor pressures over Sn + SnO<sub>2</sub> mixtures, the standard free energy changes for the reactions involved in the vaporization of stannic oxide have been derived (3), and are summarized in Table I. Due to the change in the stoichiometry of the oxide during vaporization, the volatility of stannic oxide and the stannates would be dependent on the oxygen partial pressure as discussed by Kellogg (11). The partial pressures of the oxide species over mono- and dicalcium stannates can readily be calculated by combining the information in Table I with the results of the present study. Figure 4 shows the variation of the partial pressure of the various gaseous species over mono- and dicalcium stannates with the oxygen partial pressure at 1400°K. The pressures of SnO and its polymeric forms increase as the oxygen partial pressure decreases, until pure liquid tin is obtained as a separate phase by the reduction of the stannates. A further decrease in the oxygen partial pressure results in a decrease in the partial pressure of the oxide species. The main contribution to the total pressure arises from SnO species. The relative contribution of the polymeric species to the total pressure increases as the oxygen pressure is reduced, and attains a maximum value at the oxygen partial pressure corresponding to the reduction of the stannates to form liquid tin. The total

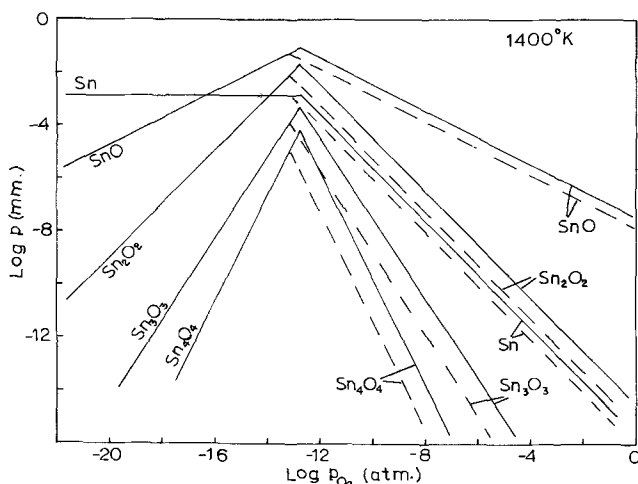


Fig. 4. The partial pressures of the tin bearing oxide species in equilibrium with the stannates at 1400°K as a function of the oxygen partial pressure; — monocalcium stannate, - - - - dicalcium stannate.

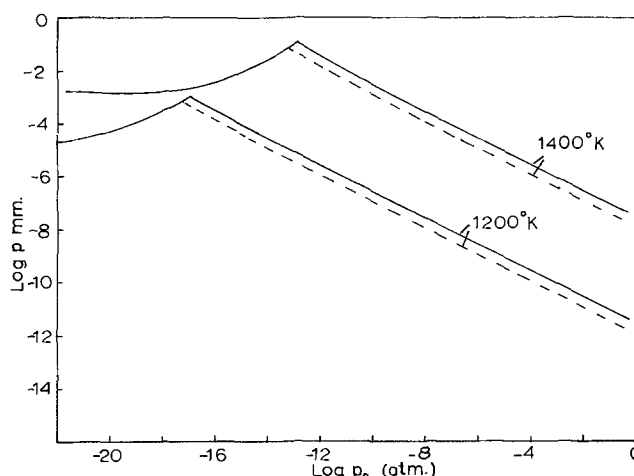


Fig. 5. The total vapor pressure over the stannates as a function of the oxygen partial pressure; — monocalcium stannate, - - - - dicalcium stannate.

pressure, obtained as a summation of the individual partial pressures over mono- and dicalcium stannates, is shown in Fig. 5, as a function of the oxygen partial pressure. If the stannates are kept under an inert gas or in vacuum, the volatility would be restricted by the requirement that  $P_{\text{SnO}} = 2P_{\text{O}_2}$ . The values for the partial and total pressures of the tin bearing oxide species, shown in Fig. 4 and 5, enable the estimation of the composition changes upon prolonged use of the stannates at high temperatures.

#### Acknowledgment

The authors wish to express their appreciation to Professor C. B. Alcock, at whose laboratories this work was undertaken.

Manuscript submitted Aug. 10, 1973; revised manuscript received Nov. 9, 1973.

Any discussion of this paper will appear in a Discussion Section to be published in the December 1974 JOURNAL. All discussion for the December 1974 Discussion Section should be submitted by Aug. 1, 1974.

#### REFERENCES

1. T. R. Shelley and R. Shelley, *Trans. Inst. Min. Met.*, **82**, C54 (1973).
2. L. W. Coughanour, R. S. Roth, S. Marzullo, and F. E. Sennett, *J. Res. Nat. Bur. Std.*, **54**, 149 (1955).
3. R. Colin, J. Drowart, and G. Verhaegen, *Trans. Faraday Soc.*, **61**, 1364 (1965).
4. Y. Tanaka, *J. Chem. Soc. Japan*, **62**, 199 (1941).
5. T. N. Belford, and C. B. Alcock, *Trans. Faraday Soc.*, **61**, 443 (1965).
6. K. T. Jacob, S. K. Seshadri, and F. D. Richardson, *Trans. Inst. Min. Met.*, **79**, C274 (1970).
7. J. Carbo-Nover and F. D. Richardson, *ibid.*, **81**, C63 (1972).
8. J. W. Patterson, *This Journal*, **118**, 1033 (1971).
9. D. A. Shores and R. A. Rapp, *ibid.*, **118**, 1107 (1971).
10. B. C. H. Steele, "Electromotive Force Measurements in High Temperature Systems," C. B. Alcock, Editor, *Inst. Min. Met.*, London (1968).
11. H. H. Kellogg, *Trans. Met. Soc. AIME*, **236**, 602 (1966).

# Diffusional Growth of Cobaltous-Ferrous Oxide Scales on Cobalt-Iron Alloys

P. Mayer\*<sup>1</sup> and W. W. Smeltzer\*\*

Department of Metallurgy and Materials Science, McMaster University, Hamilton, Ontario, Canada L8S 4M1

## ABSTRACT

Co-Fe alloys containing up to 10 weight per cent Fe oxidize parabolically by formation of a cobaltous-ferrous oxide scale when exposed at 1200°C to oxygen at  $10^{-4}$  and  $10^{-3}$  atm. The values of the parabolic oxidation constants were directly dependent on the iron contents of the alloys. Scale iron contents corresponded to those in the bulk alloys. The iron gradients within the scales increased with increasing outward distance due to iron migrating more rapidly than cobalt. A diffusion model based on equations derived by Wagner for metal transport through a scale under chemical activity gradients leads to a correlation between the parabolic oxidation constants and the iron gradients.

There is only limited knowledge available on the distributions of cations in metal conducting scales on binary alloys which is sufficiently extensive for interpretation by a diffusion model describing metal transport under chemical activity gradients. Wagner (1) has advanced methods for calculating these distributions in scales grown by parabolic kinetics. Dalvi and Coates (2) and Dalvi and Smeltzer (3) have demonstrated that the cobalt and iron profiles in nickel oxide scales formed on Co-Ni and Fe-Ni alloys, respectively, are consistent with ternary diffusional properties. Cobalt and iron were enriched toward the outer surfaces in these scales due to mobilities higher than that for nickel. Mayer and Smeltzer (4) have also employed this model to describe growth of the manganese-wustite scale on Fe-Mn alloys and to evaluate the metal self-diffusion coefficients and the nonstoichiometry of manganese-wustite as a function of manganese content. In this case, the metal gradients were small and linear due to very small differences in the cation mobilities.

Formation of the cobaltous-ferrous oxide [(FeCo)O] scales on Co-Fe alloys has not been investigated. Carter and Richardson (5, 6) have shown that cobalt diffusion in cobalt oxide and growth of this oxide on cobalt at high temperatures can be interpreted by the Wagner theory for parabolic scaling (7). Crow (8) has determined the tracer diffusion coefficients of cobalt and iron in (CoFe)O. At 1200°C, the ratio  $D_{Fe}/D_{Co}$  equals 1.6 at an oxygen pressure of  $10^{-3}$  atm, and it equals 0.7 at pressures greater than  $10^{-1}$  atm. Thermodynamic properties and compositions of (CoFe)O have been determined by Aukrust and Muan (9, 10).

Metal diffusion in (CoFe)O is much more rapid than in Co-Fe alloys (8, 11). One would therefore expect that a superficial scale would form as the major reaction product with only a relatively small degree of internal oxidation when these alloys are oxidized at high temperatures. In the present work, the reaction kinetics, morphological development, and compositions of the scales have been determined upon exposing cobalt alloys containing up to 10 weight per cent (w/o) Fe to oxygen atmospheres at 1200°C. These alloys were found to oxidize parabolically at  $10^{-4}$  and  $10^{-3}$  atm. Consequently, an attempt could be made to interpret these results by equations deduced from the ternary diffusion model for oxidation of a binary alloy using metal diffusional determinations for (CoFe)O and thermodynamic properties of the Co-Fe-O system.

## Experimental

Oxidation kinetics of the alloys were determined gravimetrically by exposing metal disks, 10 mm diameter and 2 mm thick, to a flowing atmosphere of research grade oxygen, <25 ppm impurities. The reaction assembly is schematically represented in Fig. 1. Zero time for initiation of a test was taken as the instant when the specimen was lowered into the reaction chamber. The atmospheric pressure was monitored by Pirani

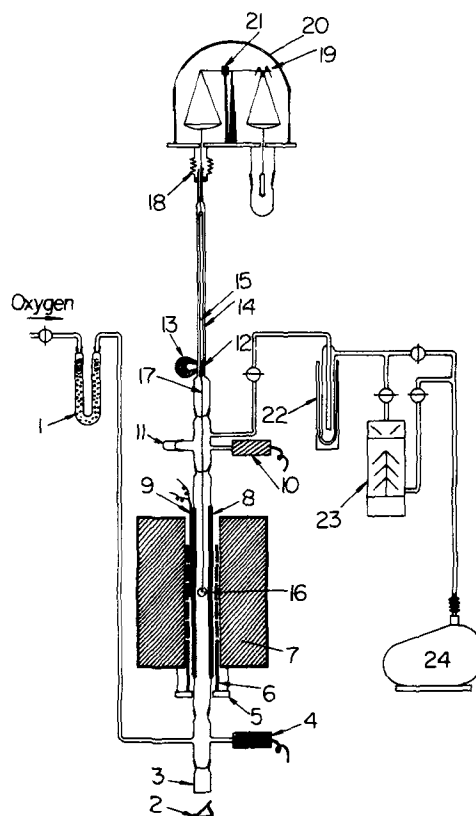


Fig. 1. Schematic of reaction assembly containing RV Ainsworth continuously recording semiautomatic microbalance. 1, Oxygen purifier containing silica gel; 2, reflection mirror; 3, observation window; 4, Pirani gauge; 5, supporting ring for heating element; 6, silicon carbide heating element; 7, furnace; 8, mullite tube; 9, thermocouples; 10, Pirani gauge; 11, loading inlet; 12, soft iron core; 13, magnet; 14, outer tube; 15, suspension tube; 16, specimen; 17, suspension wire; 18, expansion bellow; 19, automatically switched weights; 20, glass bell; 21, transducer; 22, cold trap; 23, diffusion pump; 24, mechanical pump.

\* Electrochemical Society Student Member.

\*\* Electrochemical Society Active Member.

<sup>1</sup> Present address: Ontario Research Foundation, Sheridan Park, Mississauga, Ontario, Canada.

Key words: Co-Fe alloy oxidation, cobaltous-ferrous oxide, diffusional scale growth.

gauges located at the entrance and exit of the reaction tube. A pressure drop was not detected through the reaction tube at the experimental pressures of  $10^{-4}$  and  $10^{-3}$  atm. Temperature of the reaction zone was controlled to  $1200 \pm 2^\circ\text{C}$ . At completion of a run, the specimen was quenched by rapidly raising it into the section of the reaction tube maintained at room temperature by means of a magnetic device.

Alloys were prepared as rods, 8 cm in length and 14 mm in diameter, by vacuum melting in required proportions of cobalt (>99.997 w/o pure) and iron (>99.875 w/o pure). Actual iron contents of the nominal 1, 2, 4, 6, 8, and 10 w/o Fe alloys were 0.93, 2.1, 4.1, 5.5, 7.7, and 9.6 w/o Fe, respectively. The rods were sealed in quartz tubes containing argon and annealed for periods up to 10 days at  $1200^\circ\text{C}$  to homogenize the compositions. They were then machined to uniform diameter and cut into disks with a multiple wire saw. The disks were finally metallographically polished to  $1\mu$  diamond abrasive using kerosene as lubricant, washed with petroleum ether, and stored in acetone.

Oxidized specimens for metallographic observations and microprobe analyses were mounted in room-setting epoxy resin and the cross sections polished to  $1\mu$  diamond abrasive using kerosene as lubricant. Specimens subjected to analyses were covered by an evaporated thin carbon film. The analyses were carried out using a Cameca electron probe microanalyzer operating at 15 keV and a specimen current of 100-150 nA. Standards for constructing alloy calibration curves for (CoFe)O were constructed according to the method given by Friskney and Howarth (12) and consisted of successively applying atomic number (13), absorption (14), and fluorescence (15, 16) corrections to a composition set.

**Results**

Figures 2 and 3 show the oxidation curves plotted in parabolic form for cobalt and the six alloys containing up to 10 w/o Fe exposed to oxygen at  $10^{-4}$  and  $10^{-3}$  atm. It is seen that parabolic kinetics describe scale growth. The parabolic oxidation constants calculated from the slopes of these plots are shown in Fig. 4; they were accurate to within  $\pm 10\%$  based on the deviations from the average value for four runs completed on each alloy. These constants show a direct dependence on the iron contents of the alloys and larger values at the higher oxygen pressure. The parabolic constants of cobalt are in good agreement with previously reported values (17).

Internal oxidation was insignificant. This behavior is illustrated by the photomicrographs shown in Fig.

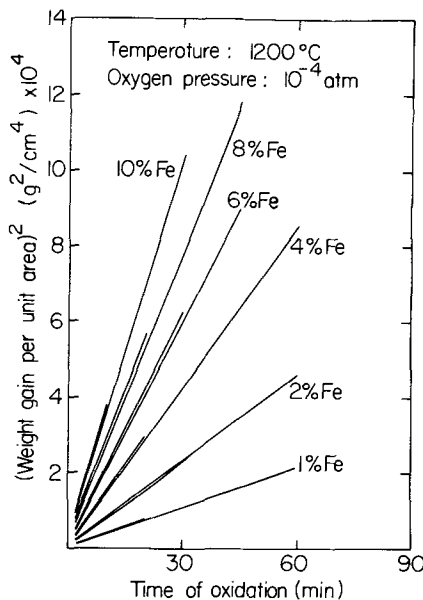


Fig. 2. Oxidation kinetics plotted in parabolic form of the Co-Fe alloys exposed at  $1200^\circ\text{C}$  in oxygen at  $10^{-4}$  atm.

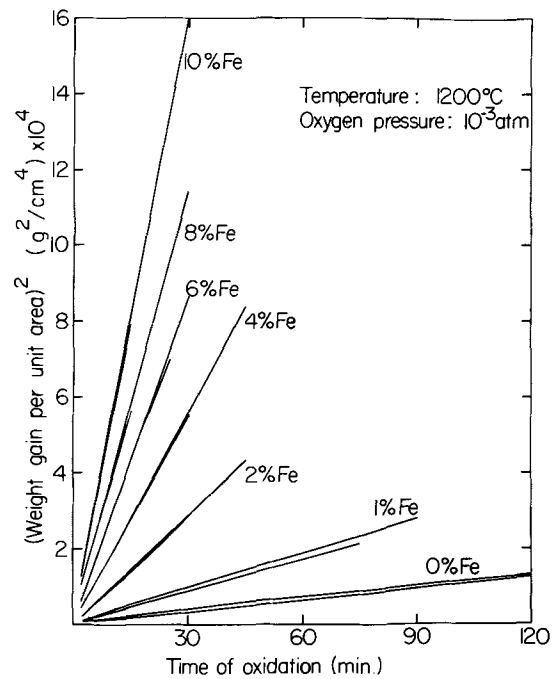


Fig. 3. Oxidation kinetics plotted in parabolic form of the Co-Fe alloys exposed at  $1200^\circ\text{C}$  in oxygen at  $10^{-3}$  atm.

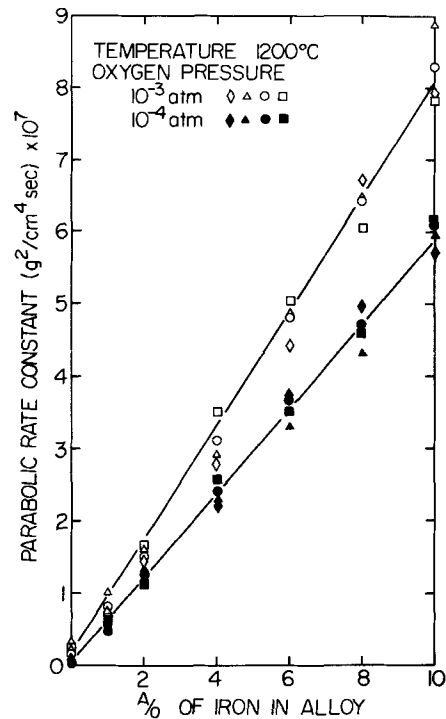


Fig. 4. Variation of the parabolic oxidation constants with alloy iron contents. The designated symbols refer to the evaluations of the parabolic oxidation constants obtained at  $10^{-3}$  and  $10^{-4}$  atm for various time periods of oxidation.

5 and 6 of the oxidized alloy specimens containing the maximum iron concentration of 10 w/o. The scales were compact and uniformly thick except for small irregularities of the outer surfaces associated with development of the individual oxide grains. Based on microscopic measurements at different regions, positions within scales could be reproduced within  $\pm 10\%$ . X-ray diffraction lattice parameter measurements on the powdered scales confirmed that they were composed of (CoFe)O.

Iron compositions within the scales formed on each alloy at the two investigated pressures are shown in



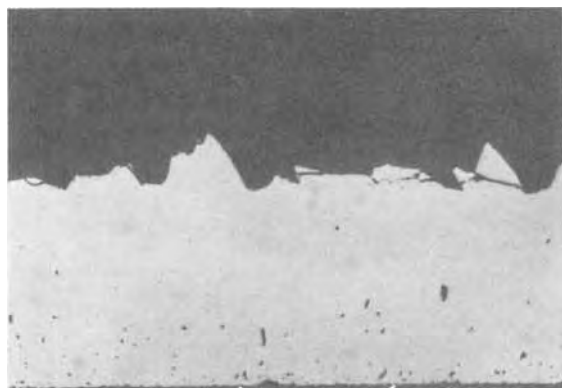


Fig. 5. Cross section of a Co-10 w/o Fe alloy specimen oxidized at  $10^{-4}$  atm oxygen pressure for 10 min ( $\times 200$ ).

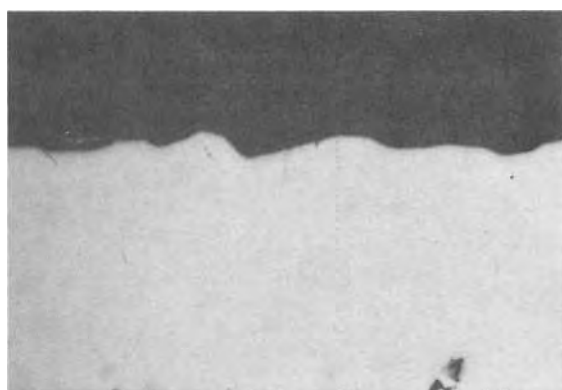


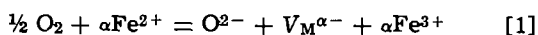
Fig. 6. Cross section of a Co-8 w/o Fe alloy specimen oxidized at  $10^{-3}$  atm oxygen pressure for 15 min ( $\times 200$ ).

Fig. 7a, 7b, 8a, and 8b. These determinations are based on analyses taken from scales formed on four specimens of each alloy using the electron microprobe point count method at normalized distances  $y = x/x_s$ , where  $x_s$  is a total scale thickness. The iron content increased with increasing outward distance and the average content of a scale corresponded to the alloy content.

### Discussion

A correlation between the reaction kinetics and the normalized iron profiles within scales are quantitatively assessed by means of the ternary diffusion model advanced by Wagner. To complete this analysis it is necessary to obtain an empirical relationship for the nonstoichiometry of  $(\text{CoFe})\text{O}$  as a function of iron content and oxygen activity. This nonstoichiometry, in turn, is related to the metal diffusivities in order to obtain differential equations describing the metal gradients. The equations are subsequently numerically integrated using the experimentally determined parabolic rate constants to generate the iron profiles within the scales.

Cobalt oxide behaves as a p-type semiconductor containing metal vacancies in the singly and doubly ionized states, the former state being predominant over a major portion of its oxygen stability range (18-20). Iron substituted into this oxide is considered to give rise to the following defect equilibrium



where the designated iron and oxygen ions occupy normal lattice sites and  $V_{\text{M}}^{\alpha-}$  and  $\alpha \text{Fe}^{3+}$  represent metal vacancies and ferric ions with effective charges  $\alpha-$  and  $+1$ , respectively. There are insufficient results, however, for analyzing this defect equilibrium in detail. It is reasonable, nevertheless, to suggest that the vacancies occur predominantly from the influence of

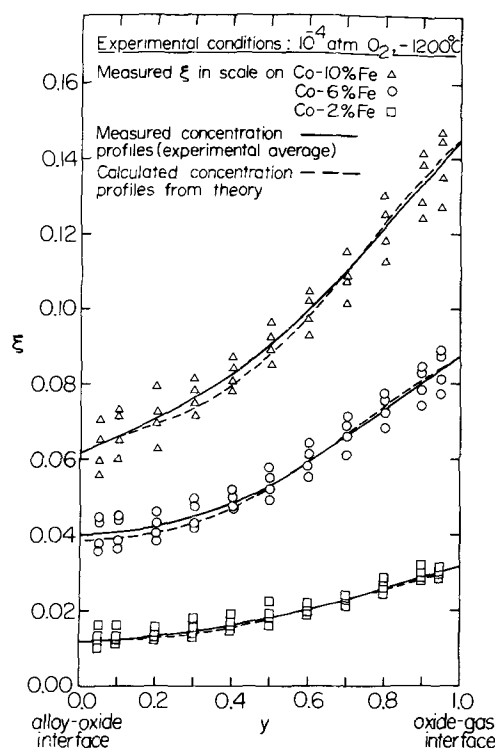


Fig. 7a. Iron composition within the  $(\text{CoFe})\text{O}$  scales formed on the Co-10 w/o, 6 w/o, and 2 w/o Fe alloys at  $10^{-4}$  atm oxygen pressure.

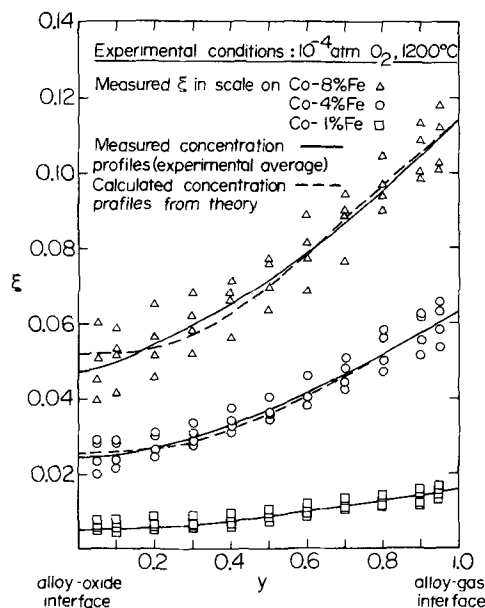


Fig. 7b. Iron composition within the  $(\text{CoFe})\text{O}$  scales formed on the Co-8 w/o, 4 w/o, and 1 w/o Fe alloys at  $10^{-4}$  atm oxygen pressure.

iron by the displacement of the above reaction far to the right. Assuming to a first approximation that the fraction of the total iron content ionized to the ferric state remains constant, at fixed oxygen activity, the atom fraction of vacancies is of the form

$$N_{\text{V}} = \gamma a_{\text{O}}^n \xi \quad [2]$$

Here,  $a_{\text{O}}$  is the oxygen activity,  $\xi$  is the iron fraction in the cation sublattice of  $(\text{CoFe})\text{O}$ ,  $\gamma$  and  $n$  are empirical constants.

Vacancy concentrations were calculated from the compositions of  $(\text{CoFe})\text{O}$  reported by Aukrust and Muan (9) using the formula  $N_{\text{V}} = (X - 1)/X$  where  $X$  is the oxygen atom fraction per metal atom fraction

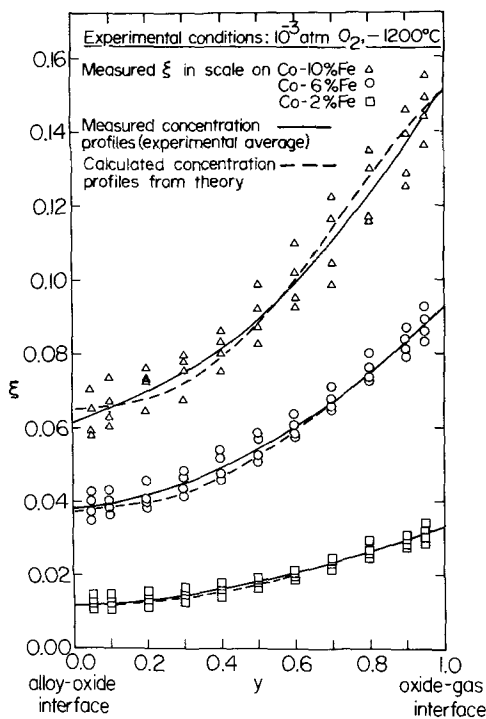


Fig. 8a. Iron composition within the (CoFe)O scales formed on the Co-10 w/o, 6 w/o, and 2 w/o Fe alloys at  $10^{-3}$  atm oxygen pressure.

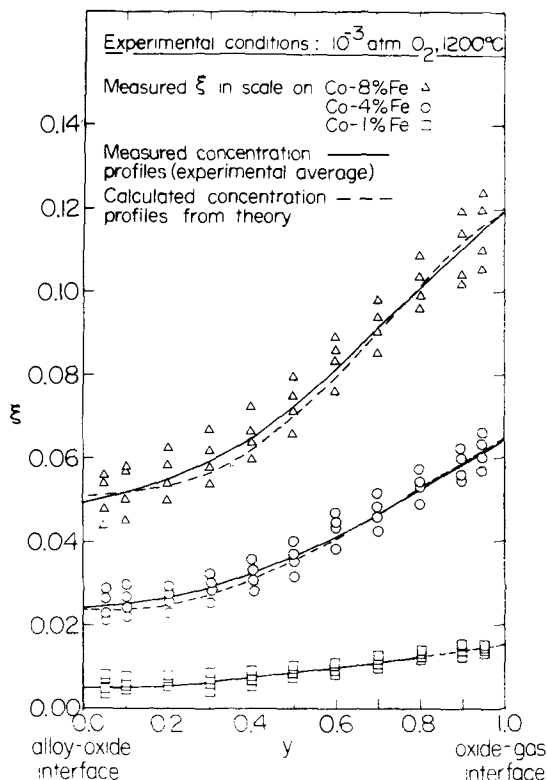


Fig. 8b. Iron composition within the (CoFe)O scales formed on the Co-8 w/o, 4 w/o, and 1 w/o Fe alloys at  $10^{-3}$  atm oxygen pressure.

$X = (O/(Fe + Co))$ .  $N_V$  is plotted vs.  $\xi$  for several values of oxygen pressure in Fig. 9. Linear plots relate these variables for the oxide compositions encountered in the present investigation (Fig. 7a, 7b, 8a, and 8b). Figure 10 shows the vacancy concentration expressed as  $N_V/\xi$  at each pressure on logarithmic scales. It is seen that a constant power relationship for the oxygen activity dependence is an adequate approximation al-

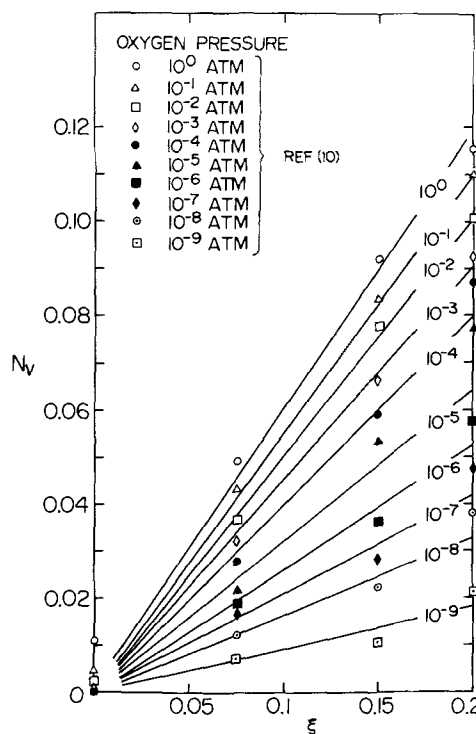


Fig. 9. Metal vacancy concentration plotted vs. iron atom fraction in (CoFe)O for several oxygen pressures ranging from  $10^{-9}$  to 1 atm. The experimental results were obtained from Ref. (9) and (10).

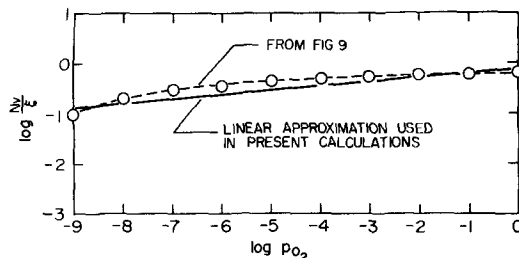


Fig. 10. Atom fraction of vacancies per atom fraction of iron in (CoFe)O plotted vs. oxygen pressure. The experimental results were obtained from Ref. (9) and (10).

though the additionally depicted plot exhibiting a small curvature may account in a more factual manner for the vacancy behavior. Accordingly, the constants in Eq. [2] are expressed as  $\gamma = 0.60 \pm 0.11$  and  $n = 0.15 \pm 0.03$ .

It is essential to represent the metal self-diffusion coefficients by appropriate analytical expressions involving their dependence on the iron concentrations and oxygen activities in order to numerically integrate the differential equations to be subsequently introduced. These diffusion coefficients are therefore expressed as the product of the individual vacancy diffusivities and the vacancy concentration

$$D_{Co} = D^V_{Co} N_V = D^o_{Co} \gamma a_o^n \xi \quad [3]$$

$$D_{Fe} = D^V_{Fe} N_V = D^o_{Fe} \gamma a_o^n \xi \quad [4]$$

and

$$p = D_{Co}/D_{Fe} = D^o_{Co}/D^o_{Fe} \quad [5]$$

Carter and Richardson (6) expressed the tracer diffusion coefficient of cobalt in cobalt oxide as a function of oxygen activity by a constant power relationship. Using this result and those reported by Fisher and Tannhauser (18) for the dependence of the cobalt vacancy concentration on oxygen activity, the cobalt vacancy diffusivity at  $1200^\circ\text{C}$  was calculated to be  $D^o_{Co} = 1.46 \pm 0.04 \times 10^{-6}$  cm<sup>2</sup>/sec. The constant  $p$ , the rates of the cobalt and iron vacancy diffusivities, was determined from the results obtained by Crow (8) for the

tracer diffusivities as a function of oxygen activity. The ratio of these diffusivities was  $p = 1.63 \pm 0.03$  at pressures of  $10^{-4}$  and  $10^{-3}$  atm.

Equations to describe growth of a metal conducting scale on a binary alloy are now invoked. The formalism of Wagner is used and the reader is referred to the original paper for mathematical derivations. The (CoFe)O scale growth is determined by the outward diffusion of cobalt and iron via vacancies and Eq. [11] from Ref. (1) for the parabolic oxidation constant becomes

$$D_{Co}(1-\xi) \left( \frac{-d \ln a_{CoO}}{d\xi} \frac{d\xi}{dy} + \frac{Z_{Co}}{Z_o} \frac{d \ln a_o}{dy} \right) + D_{Fe}\xi \left( \frac{-d \ln a_{FeO}}{d\xi} \frac{d\xi}{dy} + \frac{Z_{Fe}}{Z_o} \frac{d \ln a_o}{dy} \right) = k \quad [6]$$

In this expression,  $D$  is a metal self-diffusion coefficient,  $a$  is a local activity,  $Z$  is a valency,  $\xi$  is the atom fraction of iron or mole fraction of wustite in (CoFe)O, and  $y = x/x_s$  is the normalized scale thickness.

The solubility of wustite in cobalt oxide exhibits Henrian solution behavior (10). Hence, the Gibbs-Duhem equation for this solid solution leads to

$$\frac{d \ln a_{FeO}}{d\xi} = \frac{1}{\xi}; \quad \frac{d \ln a_{CoO}}{d\xi} = \frac{-1}{1-\xi} \quad [7]$$

Substituting Eq. [2], [5], and [7],  $Z_{Co} = Z_{Fe} = |Z_o| = 2$  and  $k' = k/D_{Co}\gamma$  in Eq. [6] yields

$$\frac{d \ln a_o}{dy} = \left[ \frac{k'}{a_o^n \xi} + (p-1) \frac{d\xi}{dy} \right] / [1 + (p-1)\xi] \quad [8]$$

Equation [19] from Ref. (1), which describes the metal gradient in a scale using the divergence equation for the metal flux, becomes

$$yk \frac{d\xi}{dy} = \frac{-d}{dy} \left[ D_{Fe}\xi \left( \frac{d \ln a_{FeO}}{d\xi} \frac{d\xi}{dy} - \frac{d \ln a_o}{dy} \right) \right] \quad [9]$$

Upon substituting into Eq. [9] parameters from Eq. [2], [5], and [7]

$$yk' \frac{d\xi}{dy} = -p \frac{d}{dy} \left[ a_o^n \xi \left( \frac{1}{\xi} \frac{d\xi}{dy} - \frac{d \ln a_o}{dy} \right) \right] \quad [10]$$

An expression including the parabolic oxidation constant and the limiting iron concentrations and gradients in (CoFe)O at either the inner or outer scale interface serves as an auxiliary equation for solving Eq. [8] and [10]. Since an insignificant degree of internal oxidation occurred, the ratio for the flux of cobalt to iron in the scale at its inner interface is equivalent to the metal ratio in the bulk alloy. Equation [35] in Ref. (1) for material balance at this interface gives upon substituting Eq. [2], [5], and [7]

$$\left( \frac{d\xi}{dy} \right)_{y=0} = \frac{k'}{a_o^n \xi'} \left\{ \frac{p\xi' - [1 + (p-1)\xi'] \xi_{alloy}}{p} \right\} \quad [11]$$

where the prime refers to the inner scale surface and  $\xi_{alloy}$  is the atom fraction of iron in the alloy.

Iron concentration and oxygen activity profiles in the scales were generated within the range from  $y = 0$  to  $y = 1$  by simultaneously numerically integrating Eq. [8] and [10] with boundary values at  $y = 0$  established by Eq. [11] using a computer knowing the values of the constants  $D_{Co}$ ,  $p$ ,  $\gamma$ ,  $n$ , the experimental values of  $a_o'$ ,  $\xi'$ , and the parabolic constant  $k$ . The calculated iron profiles in the scales formed on each alloy at  $10^{-4}$  and  $10^{-3}$  atm are shown in Fig. 7a, 7b, 8a, and 8b. They correspond to those experimentally determined in both magnitude and form. The typical shape of the oxygen activity gradient is illustrated by the plot in Fig. 11

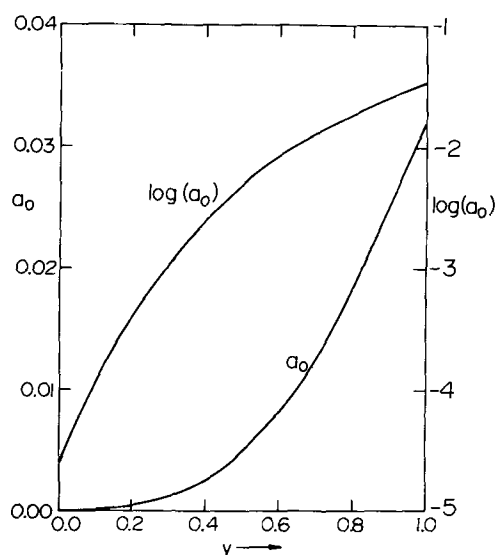


Fig. 11. Oxygen activity profile in (CoFe)O scale formed on the Co-10 w/o Fe alloy at  $10^{-3}$  atm oxygen pressure.

for the scale formed on the Co-10 w/o Fe alloy at  $10^{-3}$  atm. Iron was most significantly enriched in the outer region of a scale where the influence of the oxygen activity gradient was most pronounced on the more rapidly diffusing iron cations.

An excellent correlation has been obtained by the diffusion analysis for the parabolic reaction kinetics and the normalized metal profiles in the scales formed on the alloys containing up to 10 w/o Fe at oxygen pressures of  $10^{-4}$  and  $10^{-3}$  atm. The analysis based on ternary diffusion equations, nevertheless, is to be regarded as a simplified empirical description of the oxidation phenomena. A more fundamental analysis cannot be attempted until additional definitive knowledge becomes available on the structures, thermodynamics, and mobilities of the lattice defects in (CoFe)O. Because of the paucity of information, the nonstoichiometry of this oxide was directly related to estimates for the vacancy concentration in the cation sublattice. These vacancies, moreover, were assumed to exhibit Henrian solution behavior and constant mobilities. This type of solution behavior is only a suitable approximation for analysis purposes as illustrated by the empirical expression (Eq. [2]) used to relate vacancy concentration to iron and oxygen activities. Also, the metal mobilities can be regarded as constant within the framework of presently available results only to the upper investigated pressure of  $10^{-3}$  atm since the tracer diffusivities of cobalt and iron in (CoFe)O undergo variations between oxygen pressures of  $10^{-3}$  to  $10^{-1}$  atm (8).

#### Acknowledgments

This work was carried out by P. Mayer in partial fulfillment of the requirements for award of the Ph.D. degree by McMaster University under auspices of the National Research Council of Canada. He wishes to acknowledge the award of a National Research Council of Canada Bursary for graduate studies.

Manuscript submitted July 17, 1973; revised manuscript received Nov. 2, 1973.

Any discussion of this paper will appear in a Discussion Section to be published in the December 1974 JOURNAL. All discussions for the December 1974 Discussion Section should be submitted by Aug. 1, 1974.

#### REFERENCES

1. C. Wagner, *Corrosion Sci.*, **2**, 91 (1969).
2. A. D. Dalvi and D. E. Coates, *J. Oxidation Metals*, **3**, 203 (1971).
3. A. D. Dalvi and W. W. Smeltzer, *This Journal*, **121**, 386 (1974).

4. P. Mayer and W. W. Smeltzer, *ibid.*, **119**, 626 (1972).
5. R. E. Carter and F. D. Richardson, *Trans. AIME*, **200**, 1244 (1954).
6. R. E. Carter and F. D. Richardson, *ibid.*, **203**, 336 (1955).
7. C. Wagner, "Atom Movements," p. 153, American Society for Metals, Cleveland (1951).
8. W. B. Crow, Report ARL-70-0090, Project No. 7021, Office of Aerospace Research, United States Airforce, Wright-Patterson Air Force Base, Ohio (1970).
9. E. Aukrust and A. Muan, *Trans. AIME*, **230**, 1395 (1964).
10. E. Aukrust and A. Muan, *ibid.*, **227**, 1378 (1963).
11. M. Badia, Thesis, p. 47, Univ. Nancy, France (1969).
12. C. A. Friskney and N. Haworth, *Brit. J. Appl. Phys.*, Sec. 2, **1**, 873 (1968); *J. Sci. Instr.*, Sec. 2, **1**, 753 (1968).
13. P. Duncumb and S. J. B. Reed, *Nat. Bur. Std. (U.S.)*, *Spec. Publ.* 298 (1968).
14. J. Philibert, Proc. Third Int. Symp., "X-Ray Optics and X-Ray Microanalysis," Academic Press, New York (1963).
15. P. Duncumb and P. K. Shields, "The Electron Microprobe," I. D. McKinley, K. R. J. Heimlich, and D. B. Whitby, Editors, John Wiley & Sons, Inc., New York (1966).
16. M. Green and V. E. Cosslet, *Proc. Phys. Soc. (London)*, **78**, 1206 (1961).
17. F. Morin and M. Rigaud, *Can. Met. Quart.*, **9**, 521 (1971).
18. B. Fisher and D. S. Tannhauser, *J. Chem. Phys.*, **44**, 1663 (1966).
19. W. G. Eror and J. B. Wagner, Jr., *J. Phys. Chem. Solids*, **29**, 1597 (1968).
20. I. Bransky and J. M. Wimmer, *ibid.*, **33**, 801 (1972).

## Oxygen and Metal Activities of the Chromium-Nickel-Oxygen System Between 900° and 1100°C

Haydn Davies\*<sup>1</sup> and W. W. Smeltzer\*\*

*Department of Metallurgy and Materials Science, McMaster University, Hamilton, Ontario, Canada L8S 4M1*

### ABSTRACT

The equilibrium oxygen pressures for Cr-Ni alloys existing as the alpha ( $\alpha$ ) and gamma ( $\gamma$ ) phases and coexisting with chromium oxide ( $\text{Cr}_2\text{O}_3$ ), nickel oxide (NiO), and nickel chromite ( $\text{NiCr}_2\text{O}_4$ ) were determined at 900°, 1000°, and 1100°C using an electrochemical cell with a calcia-zirconia electrolyte. These pressures were related to compositional determinations of the solid phases and the Cr-Ni-O isotherms. The free energies of formation of chromium oxide and nickel chromite were determined. With increasing nickel content of the alloy, the oxygen pressure increases from the dissociation pressure of pure chromium oxide to that of the univariant phase field,  $\alpha$ - $\gamma$ - $\text{Cr}_2\text{O}_3$ , with chromium oxide containing <0.2 weight per cent (w/o) nickel. At higher oxygen pressures, the  $\gamma$ - $\text{Cr}_2\text{O}_3$  phase field extends up to the univariant  $\gamma$ - $\text{NiCr}_2\text{O}_4$ - $\text{Cr}_2\text{O}_3$  phase field. Nickel chromite was essentially stoichiometric the nickel content of chromium oxide was  $\sim 0.5$  w/o, and the  $\gamma$ -alloy contained only a very small chromium content,  $\sim 10^{-4}$  w/o. No variation was detected in the spinel composition across the  $\gamma$ - $\text{NiCr}_2\text{O}_4$  region but the chromium content of the alloy decreased to  $\sim 10^{-8}$  w/o at the univariant  $\gamma$ - $\text{NiCr}_2\text{O}_4$ -NiO phase field, with nickel oxide containing 4.5 w/o Cr.

The thermodynamic behavior of the Cr-Ni-O system has not been extensively investigated, probably due to the very low oxygen activities encountered and to the consequent experimental difficulties. The free energy of formation and dissociation pressures of nickel oxide have been well defined (1-3), but these parameters for chromium oxide are less accurately known (1, 4-9). The Cr-Ni phase diagram has often been investigated but its shape above 1200°C is still controversial. The diagram determined by Bechtoldt and Vacher (10) is judged to be the most accurate; the maximum solubilities of chromium in the  $\alpha$ (bcc) and  $\gamma$ (fcc) alloy phases at the eutectic temperature of 1345°C are 40 and 58 atom per cent (a/o), respectively. An isothermal section of the Cr-Ni-O system has been proposed by Croll and Wallwork (11) based upon chemical analyses of five binary Cr-Ni alloys that were oxidized and equilibrated at 1000°C for periods up to 5 days. They found very small solubility of chromium in nickel oxide and of nickel in chromium oxide, and a nickel chromite of stoichiometric composition. Gas equilibration (12), electrochemical cells (9, 13), and Knudsen cell (14, 15) techniques have been used to

determine the alloy chromium and nickel activities, but the results show wide divergences. There is a need, therefore, for systematic determinations of the thermodynamic parameters governing phase equilibria in this system. Accordingly, we have determined the equilibrium oxygen pressure diagram for the Cr-Ni-O system and the compositions of the phases coexisting at temperatures in the range 900°-1100°C.

### Experimental

A solid-state electrochemical technique was used to determine the dissociation pressures of the oxides. The cell assembly, which we have described (16), contained a 12 in. long tube of calcia stabilized zirconia (B grade) which acted as the electrolytic membrane between the separated anode and cathode compartments.

Electromotive force measurements were made on the following cells

Fe, FeO	electrolyte	Cr <sub>2</sub> O <sub>3</sub> , Cr	[I]
Cr, Cr <sub>2</sub> O <sub>3</sub>	electrolyte	Cr <sub>2</sub> O <sub>3</sub> , (Cr-Ni) $\gamma$	[II]
Cr, Cr <sub>2</sub> O <sub>3</sub>	electrolyte	Cr <sub>2</sub> O <sub>3</sub> , (Cr-Ni) $\gamma$ , (Cr-Ni) $\alpha$	[III]
Fe, FeO	electrolyte	Cr <sub>2</sub> O <sub>3</sub> , NiCr <sub>2</sub> O <sub>4</sub> , (Cr-Ni) $\gamma$	[IV]
Fe, FeO	electrolyte	NiCr <sub>2</sub> O <sub>4</sub> , NiO, (Cr-Ni) alloy	[V]

Since a cell reaction involves oxygen transfer across

\* Electrochemical Society Student Member.

\*\* Electrochemical Society Active Member.

<sup>1</sup> Present address: J. Roy Gordon Research Laboratory, The International Nickel Company of Canada Limited, Mississauga, Ontario, Canada.

Key words: Cr-Ni-O thermodynamics; Cr, Ni, and O activities; Cr<sub>2</sub>O<sub>3</sub> and NiCr<sub>2</sub>O<sub>4</sub> free energies of formation.

the electrolyte, a cell emf is (17)

$$E = \frac{RT}{4F} \ln (P_{O_2}''/P_{O_2}') \quad [1]$$

where  $R$  is the gas constant,  $F$  is Faraday's constant,  $P_{O_2}''$  and  $P_{O_2}'$  are the dissociation pressures of the oxides in the cathode and anode compartments.

The electrodes were fabricated as tablets 0.25 in. diameter by 0.10 in. thick by compressing, at 15,000 psi, powders of iron, nickel [99.99 weight per cent (w/o) pure], and chromium (>99.95 w/o pure) in predetermined proportions with one, or more, of the oxides (99.6 w/o pure) magnetite, nickel oxide, and nickel chromite. Two tablets of the same composition were sealed into a quartz capsule under  $10^{-4}$  Torr purified argon and annealed for at least 30 days at 1000°C. Samples representing three-phase equilibria were also annealed at 1100°C. Capsules containing tablets for these latter systems contained chromium powder to act as an oxygen getter. After annealing, the samples were quenched, reaching room temperature within 1 min. One tablet was used in the cell while the other tablet was analyzed. Tablets were mounted in epoxy cold-setting resin; best polishing was obtained using a Rotopol mechanical polisher, the lubricant being a slurry of  $0.3\mu$  alumina in water. The oxides were readily etched in a solution of 10 volume per cent (v/o) concentrated hydrochloric acid in ethanol with the exception of nickel chromite which required etching in a solution containing 50 v/o concentrated hydrochloric acid. The  $\alpha$  and  $\gamma$  alloy phases were easily distinguished without etching. The calibration of the electron probe microanalyzer consisted of sequentially applying atomic number, absorption, and fluorescence corrections (18,19). The calibration curves were checked using materials of known compositions, i.e., Ni-Cr alloys and pure oxides analyzed by wet chemical methods.

The compositions of the solid phases in the electrode compartments must remain unchanged for measurement of reversible potentials by the galvanic cell technique (16). The coulometric technique introduced by Diaz and Richardson (20) was used to determine these reversible potentials in this investigation. A cell was disturbed from any supposed equilibrium state by passing a small current equivalent to 0.04 coulombs and the emf value subsequently determined from the plateau in the cell emf vs. time curves. Work was initially carried out using cell [I] to verify the reliability of the electrolyte for use at oxygen pressures below  $10^{-20}$  atm since this cell generated the maximum voltages ranging up to 500 mV. The emf was measured at five temperatures, allowing 2 days for equilibration at each temperature. Since the emf always slowly decreased at a constant temperature, the cell was coulometrically disturbed and the reversible potential determined from the plateau value which lasted for approximately 1 hr. Cell temperatures were then cycled over the range 900°-1100°C and the emf was recorded immediately upon attaining temperature stabilization. These values agreed within  $\pm 2\%$  of the plateau values obtained from coulometry.

Equilibrium oxygen pressures of chromium oxide coexisting with Cr-Ni alloys were measured with cell [II]. The emf values at five temperatures were measured using coulometric disturbance; the emf did not decrease by more than 1 mV from the plateau values even after 2 hr. The temperature was cycled and emf values also noted on immediately attaining temperature stability, and alternate values were checked by coulometric disturbance. Cell [III] was used to determine the oxygen pressure for the phase field  $\alpha$ - $\gamma$ -Cr<sub>2</sub>O<sub>3</sub> with each of three electrode tablets which had been annealed at 900°, 1000°, and 1100°C for 60 days. For each tablet, the cell emf was measured at the corresponding annealing temperature. Cells [IV] and [V] were used

Table I. Compositions of Cr-Ni alloys used in electrochemical cell [II], based upon wet chemical and electron probe analyses

Alloy	Alloy composition		
	w/o Cr	w/o Ni	a/o Cr
NC1	2.5 ± 0.3	97.5 ± 0.4	2.8 ± 0.3
NC2	5.0 ± 0.3	95.0 ± 0.5	5.6 ± 0.3
NC3	9.7 ± 0.2	90.3 ± 0.4	10.8 ± 0.2
NC4	12.0 ± 0.2	88.0 ± 0.3	13.3 ± 0.2
NC5	18.1 ± 0.2	81.9 ± 0.3	20.0 ± 0.2
NC6	19.8 ± 0.3	80.2 ± 0.3	21.8 ± 0.3
NC7	25.4 ± 0.4	74.6 ± 0.5	27.8 ± 0.4
NC8	28.8 ± 0.3	71.2 ± 0.3	31.3 ± 0.3
NC9	33.5 ± 0.3	66.5 ± 0.4	36.3 ± 0.3
NC10	37.2 ± 0.4	62.8 ± 0.5	40.1 ± 0.4

to measure the oxygen pressures of the phase fields alloy NiCr<sub>2</sub>O<sub>4</sub>-Cr<sub>2</sub>O<sub>3</sub> and alloy NiCr<sub>2</sub>O<sub>4</sub>-NiO, respectively. The oxygen pressures of the tablets which had been annealed at 1100°C for 50 days were determined only at this temperature over periods of 8 days. The samples annealed at 1000°C for 60 days were held at this temperature for 10 days to measure the cell potentials, and then at 900°C for 16 days during which the emf was again measured.

### Results

Cell [I].—The variation with temperature of the emf is shown in Fig. 1, and the deviation of the reported values is within  $\pm 2\%$  of the least-squares line

$$E(\text{mV}) = 534.5(\pm 6.7) - 0.0874(\pm 0.0223)T (\pm 3.4 \text{ mV}) \quad [2]$$

Cell [II].—Emf vs. temperature plots for results governing alloy-Cr<sub>2</sub>O<sub>3</sub> equilibria are given in Fig. 2-4 and the compositions of the designated alloys are recorded in Table I. The least-squares analyses of emf measurements between 900° and 1100°C are given in Table II and in all cases, the correlation coefficients exceeded 0.99.

Cells [III]-[V].—The emf's representing the univariant equilibria  $\alpha$ - $\gamma$ -Cr<sub>2</sub>O<sub>3</sub>,  $\gamma$ -NiCr<sub>2</sub>O<sub>4</sub>-Cr<sub>2</sub>O<sub>3</sub>, and  $\gamma$ -NiCr<sub>2</sub>O<sub>4</sub>-NiO are listed in Table III. The compositions of the solids are recorded in Tables IV-VI. The

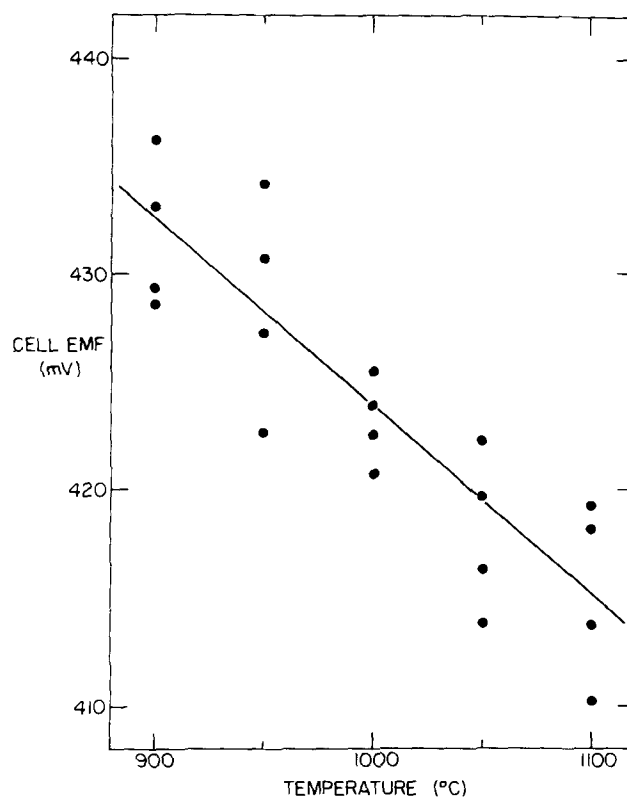


Fig. 1. Variation of the emf of cell [I] with temperature

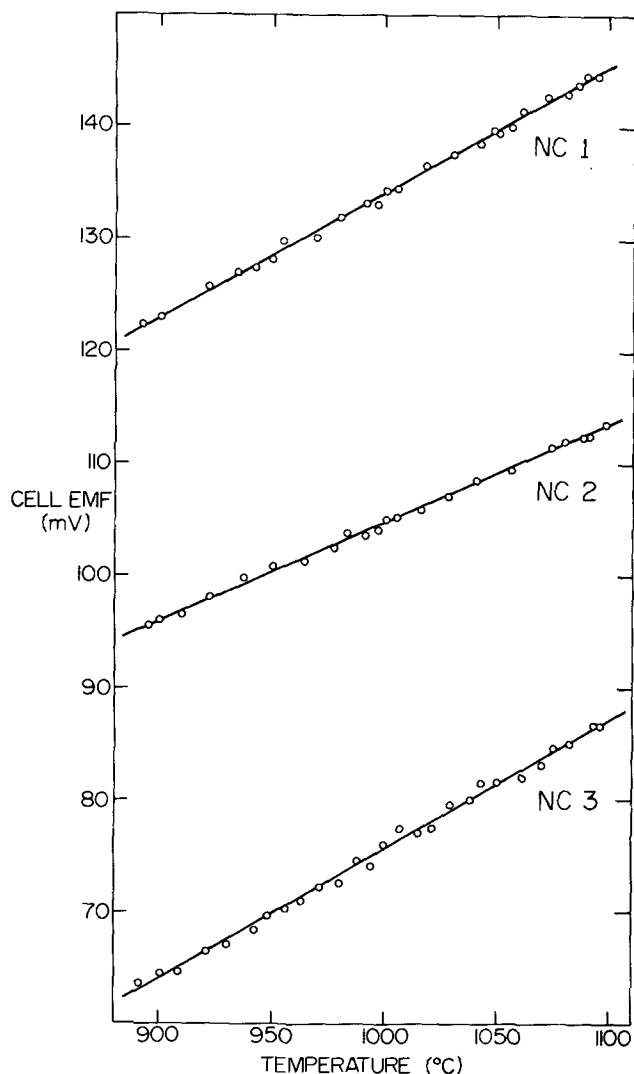


Fig. 2. Variation of the emf of cell [II] with temperature for Ni-Cr alloys, NC1-NC3, equilibrated with Cr<sub>2</sub>O<sub>3</sub>.

values in Table IV for the compositions of the equilibrated  $\alpha$ - $\gamma$  alloy phases are in agreement with those selected by Shunk (21).

**Discussion**

The Fe,FeO electrode was used as a reference to determine the potential of the Cr,Cr<sub>2</sub>O<sub>3</sub> electrode, and these two electrodes were subsequently used to determine the dissociation pressures of oxides co-existing with Cr-Ni alloys. As a consequence, the variation of the oxygen activity over the Cr-Ni-O isotherms at the several investigated temperatures can be obtained. Each phase field within this ternary system is discussed and, in addition, thermodynamic in-

Table II. Least-squares analyses of electromotive force measurements in the alloy-Cr<sub>2</sub>O<sub>3</sub> phase field

$$\text{Cell emf (mV)} = A + B T (^{\circ}\text{K})$$

Sample	A (mV)	B (mV/°K)	Standard deviation (mV)
NC1	-8.5 ± 0.5	0.1120 ± 0.0021	0.4
NC2	-7.7 ± 0.5	0.0883 ± 0.0020	0.3
NC3	-71.3 ± 1.0	0.1154 ± 0.0035	0.6
NC4	-73.5 ± 1.0	0.1135 ± 0.0035	0.5
NC5	-61.6 ± 0.6	0.0840 ± 0.0018	0.6
NC6	-73.1 ± 0.9	0.0886 ± 0.0039	0.6
NC7	-62.3 ± 0.6	0.0684 ± 0.0020	0.4
NC8	-88.7 ± 0.8	0.0829 ± 0.0028	0.6
NC9	-62.6 ± 0.6	0.0566 ± 0.0018	0.6
NC10	-48.3 ± 0.6	0.0424 ± 0.0021	0.5

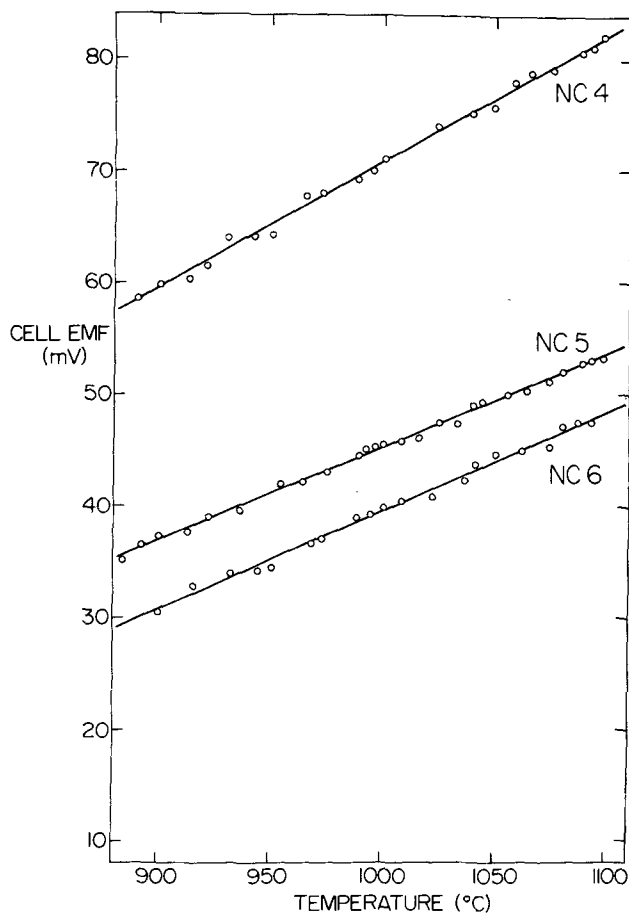


Fig. 3. Variation of the emf of cell [II] with temperature for Ni-Cr alloys, NC4-NC6, equilibrated with Cr<sub>2</sub>O<sub>3</sub>.

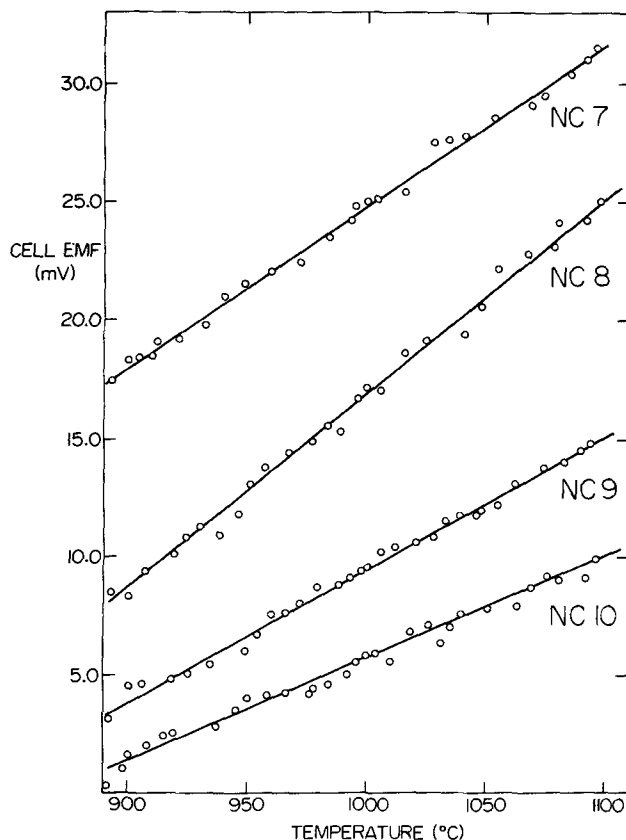


Fig. 4. Variation of the emf of cell [II] with temperature for Cr-Ni alloys, NC7-NC10, equilibrated with Cr<sub>2</sub>O<sub>3</sub>.

Table III. Emf determinations for the three-phase fields in the Cr-Ni-O system

Sample	Cell	Cell emf (mV)		
		900°C	1000°C	1100°C
$\alpha$ -alloy + $\gamma$ -alloy + Cr <sub>2</sub> O <sub>3</sub>	[III]	1.0	1.5	4.2
		0.6	2.0	3.3
		mean = 0.8 (±0.2)	mean = 1.7 (±0.3)	mean = 3.7 (±0.5)
$\gamma$ -alloy + spinel + Cr <sub>2</sub> O <sub>3</sub>	[IV]	93.5	121.0	141.5
		96.5	123.5	142.0
		98.5	122.0	141.0
		97.5	121.5	140.5
		mean = 96.5 (±3.0)	mean = 122.0 (±1.5)	mean = 139.0 (±1.5)
$\gamma$ -alloy + spinel + NiO	[V]	274.0 (±1.0)	283.5 (±1.5)	294 (±1.0)

formation is given which can be calculated by appropriate assumptions and approximations.

*Cr-Cr<sub>2</sub>O<sub>3</sub> equilibrium.*—The variation of the emf of cell [I] with temperature, Eq. [2], may be combined with the corresponding relationship for the Fe, FeO electrode (2,16) to obtain the emf of the Cr, Cr<sub>2</sub>O<sub>3</sub> electrode

$$E \text{ (mV)} = 1371.3 - 0.340T \text{ (}\pm 2.7 \text{ mV)} \quad [3]$$

The free energy of formation of chromium oxide is therefore

$$\Delta G_f^\circ \text{ (cal/mole Cr}_2\text{O}_3) = -263,350 + 59.15T \text{ (}\pm 610 \text{ cal)} \quad [4]$$

Table IV. Compositions of Cr-Ni alloys in cell [III]

Temperature (°C)	Alloy phase	Composition		
		w/o Cr	w/o Ni	a/o Cr
900	$\alpha$	97.2 ± 0.5	3.0 ± 0.5	97.5 ± 0.5
900	$\gamma$	39.8 ± 0.3	60.6 ± 0.4	42.5 ± 0.4
1000	$\alpha$	93.4 ± 0.6	6.9 ± 0.3	94.2 ± 0.6
1000	$\gamma$	41.8 ± 0.4	58.3 ± 0.5	45.0 ± 0.5
1100	$\alpha$	86.5 ± 0.5	13.7 ± 0.2	88.2 ± 0.5
1100	$\gamma$	44.7 ± 0.4	55.4 ± 0.4	47.5 ± 0.4

Table V. Electron probe microanalyses of three-phase sample, spinel-alloy-chromium oxide

Phase		Nickel (w/o)	Chromium (w/o)
Chromium oxide	(i)	0.5 ± 0.3	67.9 ± 0.2
	(ii)	0.5 ± 0.2	67.9 ± 0.3
Spinel	(i)	26.0 ± 0.3	45.8 ± 0.4
	(ii)	25.9 ± 0.3	45.6 ± 0.5
Alloy	(i)	>99.99	<0.01
	(ii)	>99.99	<0.01
Cr <sub>2</sub> O <sub>3</sub>	*	—	68.4 ± 0.2
NiCr <sub>2</sub> O <sub>4</sub>	*	25.9 ± 0.2	45.9 ± 0.2

(i) Sample annealed at 1000°C.

(ii) Sample annealed at 1100°C.

\* The specimens Cr<sub>2</sub>O<sub>3</sub> and NiCr<sub>2</sub>O<sub>4</sub> were prepared from the pure materials (>99.8% purity) and had been annealed at 1100°C in 10<sup>-4</sup> Torr purified argon.

Table VI. Electron probe microanalyses of three-phase sample, spinel-alloy-nickel oxide

Phase		Nickel (w/o)	Chromium (w/o)
Nickel oxide	(i)	72.7 ± 0.6	4.7 ± 0.4
	(ii)	73.0 ± 0.8	4.3 ± 0.4
Spinel	(i)	26.1 ± 0.4	45.7 ± 0.6
	(ii)	25.8 ± 0.5	45.7 ± 0.4
Alloy	(i)	>99.99	<0.01
	(ii)	>99.99	<0.01
NiO	*	78.4 ± 0.2	—
NiCr <sub>2</sub> O <sub>4</sub>	*	25.8 ± 0.2	45.8 ± 0.3

(i) Sample annealed at 1000°C.

(ii) Sample annealed at 1100°C.

\* The specimens NiO and NiCr<sub>2</sub>O<sub>4</sub> were prepared from the pure materials (>99.8% purity) and had been annealed at 1100°C in 10<sup>-4</sup> Torr purified argon.

These results were combined with previous work, as shown in Fig. 5, and a least-squares analysis of all data gave

$$\Delta G_f^\circ \text{ (cal/mole Cr}_2\text{O}_3) = -265,020 (\pm 1960) + 60.15 (\pm 5.40) T \quad [5]$$

over 1173°-1373°K, with a standard deviation of ±980 cal. The results of this investigation are within this estimate which supports the validity of the use of the calcia-zirconia electrolyte. The dissociation pressure of chromium oxide can thus be expressed as

$$\log (P_{O_2} \text{ atm}) = \frac{-38,619 (\pm 286)}{T} + 8.765 (\pm 0.787) \quad [6]$$

*Variation of equilibrium oxygen pressure with alloy composition.*—The results given in Table VII are shown in Fig. 6 for 900°, 1000°, and 1100°C. The maximum nickel solubility in chromium oxide equilibrated with the Ni-Cr alloys was found to be 0.5 w/o and the oxygen pressure of the oxide varied over approximately two orders of magnitude at constant temperature. The analyses of the very small nickel contents of chromium

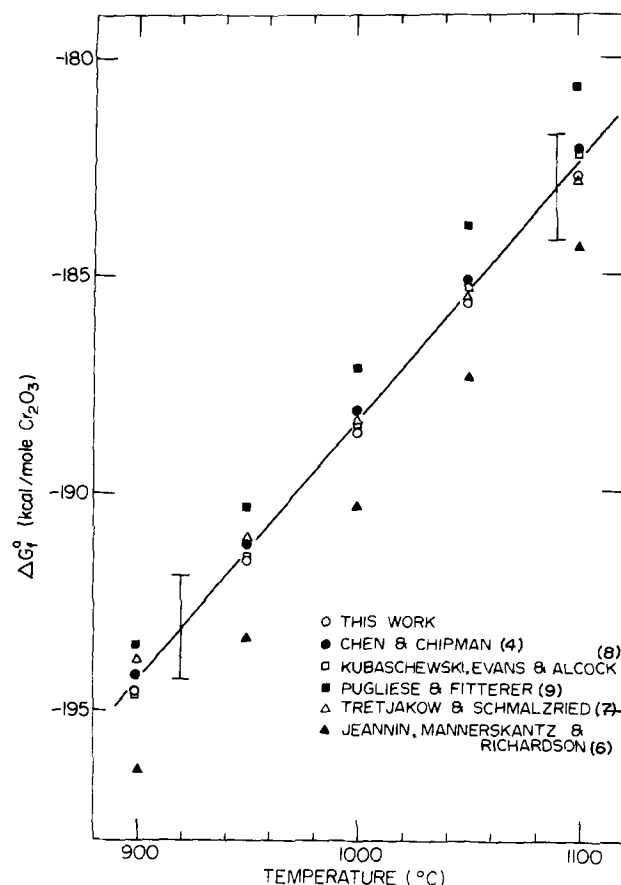


Fig. 5. Experimental determination of the free energy of formation of pure Cr<sub>2</sub>O<sub>3</sub> as a function of temperature.

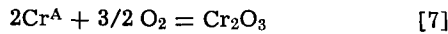
Table VII. Dissociation pressure of chromium oxide as a function of alloy composition and temperature

Atom fraction chromium	-log (P <sub>O<sub>2</sub></sub> atm)		
	900°C	1000°C	1100°C
0.028	22.045	19.448	17.229
0.056	22.509	19.913	17.694
0.108	23.057	20.374	18.083
0.133	23.133	20.447	18.154
0.200	23.523	20.854	18.574
0.218	23.628	20.943	18.650
0.278	23.850	21.180	18.900
0.313	24.011	21.305	18.994
0.363	24.093	21.422	19.141
0.401	24.133	21.482	19.217
0.425	24.146		
0.975*			
0.450		21.543	
0.942*			
0.475			19.310
0.882*			
1.00	24.158	21.572	19.363

\* Three-phase field, α + γ + Cr<sub>2</sub>O<sub>3</sub>.

oxide showed large relative errors and no attempt was made to describe its dependence upon oxygen pressure.

**Thermodynamics of Cr-Ni alloys.**—Equilibrium between chromium oxide and the Cr-Ni alloy can be represented as



Then, for a particular temperature, and assuming  $a_{Cr_2O_3} \approx 1$  (maximum nickel content was 0.5 w/o)

$$a_{Cr^A} = (P^*_{O_2}/P_{O_2})^{0.75} \quad [8]$$

where  $a_{Cr^A}$  is the chromium alloy activity, and  $P^*_{O_2}$  and  $P_{O_2}$  are the dissociation pressures for chromium oxide equilibrated with pure chromium and an alloy,

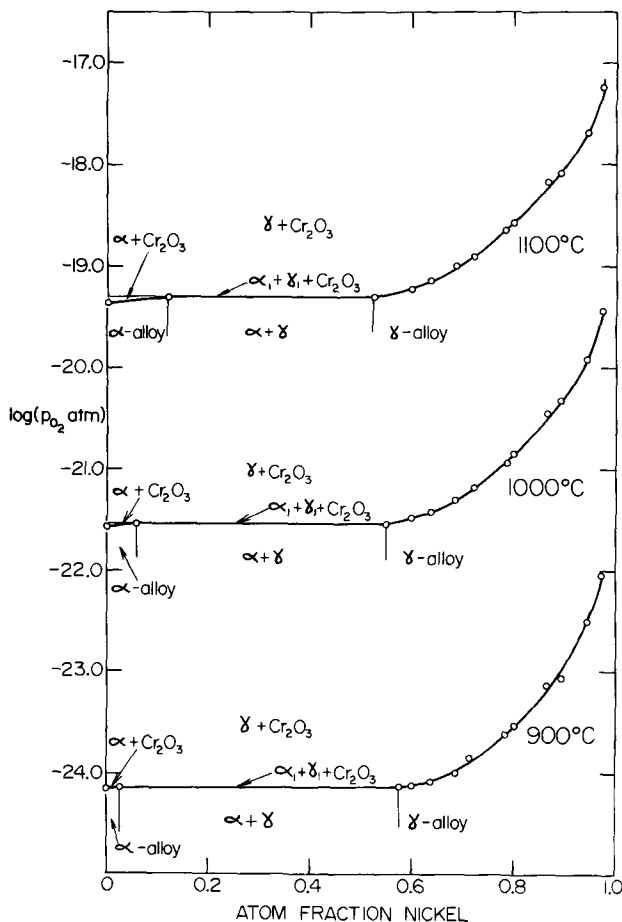


Fig. 6. Dissociation pressures of Cr<sub>2</sub>O<sub>3</sub> coexisting with Cr-Ni alloys at 900°, 1000°, and 1100°C.

respectively. The emf's of cells [II] and [III] using Eq. [1] and [8] can therefore be expressed as

$$E = - \frac{RT}{3F} \ln a_{Cr^A} \quad [9]$$

Values of chromium activities calculated using this equation and data of Tables I, II, and IV are given in Table VIII; uncertainties in the values were estimated for an error of ±1 mV, which is larger than the standard deviations from the least-squares lines, and a ±5°C temperature error. The nickel activities recorded in Table VIII were determined from the chromium activities and compositions by numerically integrating the Gibbs-Duhem equation, following a method described previously (16).

Typical behavior of the metal activities over the investigated temperature range is illustrated by the plots in Fig. 7.<sup>2</sup> When the chromium activity is taken as one for the pure metal in the bcc structure, chromium shows positive deviations from ideality at compositions  $N_{Cr^A} > 0.08$  and small negative deviations at lower concentrations. The activity curves from pure chromium to the terminal α-phase composition are only tentatively proposed since the experimental method is not sufficiently sensitive in this region.

Mean values for the partial heats of metal mixing in the γ-alloy and the integral heats of solution are recorded in Table IX. For chromium,

$$\Delta\bar{G}_{Cr} = RT \ln a_{Cr} = \Delta\bar{H}_{Cr} - T\Delta\bar{S}_{Cr} = 3F(A + BT) \quad [10]$$

when the emf results in Table II are represented by  $E = A + BT$ .  $\Delta\bar{G}_{Cr}$ ,  $\Delta\bar{H}_{Cr}$ , and  $\Delta\bar{S}_{Cr}$  are the partial free energy, heat, and entropy of mixing of chromium, respectively. The corresponding partial heats of mixing of nickel could be evaluated from its activity data and the relationship

$$\Delta\bar{H}_{Ni} = \frac{RT_1T_2}{T_2 - T_1} \ln a_{Ni(T_1)}/a_{Ni(T_2)} \quad [11]$$

<sup>2</sup>Determinations of chromium and nickel activities in Ni-Cr alloys have been reported during course of this paper's publication by F. N. Mazandarany and R. D. Pehlke (22).

Table VIII. Chromium and nickel activities in Cr-Ni alloys at 900°, 1000°, and 1100°C

Atom fraction Chromium	Atom fraction Nickel	Activity		Temperature (°C)
		Chromium	Nickel	
0.028	0.972	0.026 ± 0.001	0.972 ± 0.002	900
0.028	0.972	0.026 ± 0.001	0.972 ± 0.002	1000
0.028	0.972	0.026 ± 0.001	0.972 ± 0.002	1100
0.056	0.944	0.058 ± 0.002	0.940 ± 0.003	900
0.056	0.944	0.057 ± 0.002	0.940 ± 0.003	1000
0.056	0.944	0.056 ± 0.001	0.940 ± 0.002	1100
0.108	0.892	0.149 ± 0.004	0.870 ± 0.005	900
0.108	0.892	0.127 ± 0.003	0.882 ± 0.005	1000
0.108	0.892	0.110 ± 0.002	0.886 ± 0.004	1100
0.133	0.867	0.171 ± 0.005	0.85 ± 0.01	900
0.133	0.867	0.144 ± 0.004	0.86 ± 0.01	1000
0.133	0.867	0.124 ± 0.003	0.87 ± 0.01	1100
0.200	0.800	0.335 ± 0.010	0.74 ± 0.02	900
0.200	0.800	0.290 ± 0.008	0.75 ± 0.02	1000
0.200	0.800	0.256 ± 0.006	0.76 ± 0.02	1100
0.218	0.782	0.401 ± 0.012	0.71 ± 0.02	900
0.218	0.782	0.338 ± 0.009	0.72 ± 0.02	1000
0.218	0.782	0.293 ± 0.006	0.73 ± 0.02	1100
0.278	0.722	0.587 ± 0.017	0.63 ± 0.02	900
0.278	0.722	0.507 ± 0.013	0.63 ± 0.02	1000
0.278	0.722	0.448 ± 0.011	0.63 ± 0.02	1100
0.313	0.687	0.775 ± 0.023	0.56 ± 0.03	900
0.313	0.687	0.630 ± 0.017	0.58 ± 0.03	1000
0.313	0.687	0.528 ± 0.013	0.59 ± 0.03	1100
0.363	0.637	0.893 ± 0.026	0.52 ± 0.03	900
0.363	0.637	0.772 ± 0.021	0.52 ± 0.03	1000
0.363	0.637	0.682 ± 0.018	0.52 ± 0.03	1100
0.401	0.599	0.960 ± 0.028	0.50 ± 0.03	900
0.401	0.599	0.858 ± 0.023	0.49 ± 0.03	1000
0.401	0.599	0.780 ± 0.018	0.48 ± 0.03	1100
0.425	0.575*	0.98 ± 0.02	0.49 ± 0.03	900
0.975	0.025**	0.98 ± 0.02	0.49 ± 0.03	900
0.450	0.550*	0.955 ± 0.025	0.46 ± 0.03	1000
0.942	0.058**	0.955 ± 0.025	0.46 ± 0.03	1000
0.475	0.525*	0.912 ± 0.022	0.43 ± 0.03	1100
0.882	0.118**	0.912 ± 0.022	0.43 ± 0.03	1100

\* Three-phase field α + γ + oxide, nickel-rich alloy.

\*\* Three-phase field α + γ + oxide, chromium-rich alloy.



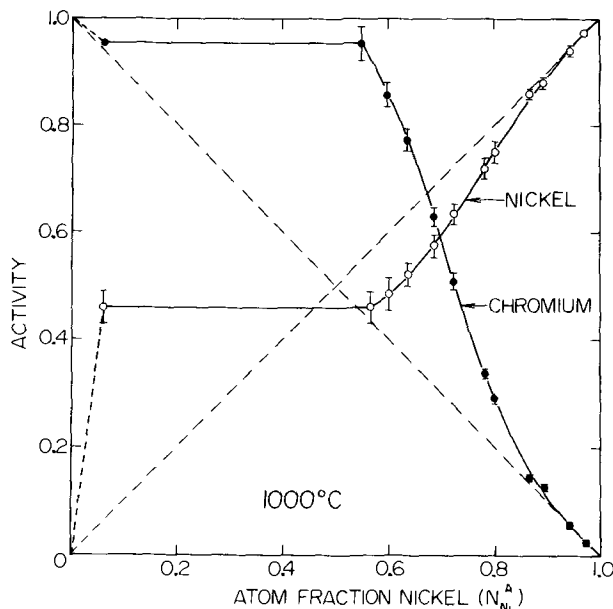


Fig. 7. Chromium and nickel activities in Cr-Ni alloys at 1000°C

Integral heats of mixing were calculated from the relationship

$$\Delta\bar{H} = N_{Cr}\Delta\bar{H}_{Cr} + N_{Ni}\Delta\bar{H}_{Ni} \quad [12]$$

where the  $N$ 's are mole fractions in the alloy.

There is an uncertainty of  $\pm 70$  cal/gram atom in  $\Delta\bar{H}_{Cr}$  for an error of  $\pm 1$  mV in the determination of the coefficient  $A$ . Although the standard deviation for each determination of this coefficient, Table II, is within this error limit, the values show that this deviation is larger and that it does not vary systematically with compositions of the alloy samples ranging from 10.8 to 40.1 a/o Cr. Average values of  $A$  and  $\Delta\bar{H}_{Cr}$  can, therefore, only be given for this alloy composition range equal to  $67.7 \pm 12.0$  mV and  $4690 \pm 830$  cal/gram atom, respectively. The corresponding average value for  $\Delta\bar{H}_{Ni}$  is  $-380 \pm 290$  cal/gram atom.

**Alloy-NiCr<sub>2</sub>O<sub>4</sub>-Cr<sub>2</sub>O<sub>3</sub> phase field.**—The oxygen pressures were calculated from the emf's of cell [IV]. This field is the upper bound, with respect to oxygen pressure, of the  $\gamma$ -Cr<sub>2</sub>O<sub>3</sub> equilibria and so the value of  $a_{Cr}$  at this terminal composition can be calculated using Eq. [9]. These activities are  $1.6(\pm 0.4) \times 10^{-7}$ ,  $3.4(\pm 0.4) \times 10^{-7}$ , and  $8.0(\pm 0.5) \times 10^{-7}$  at 900°, 1000°, and 1100°C, respectively. Compositional results (Table V) show the chromium contents of the alloy to be  $< 0.01$  w/o which taken together with the values of the activities demonstrate that the terminal alloy chromium compositions of the  $\gamma$ -Cr<sub>2</sub>O<sub>3</sub> phase field are  $\approx 1$  ppm.

The free energy of formation of nickel chromite can be obtained from the reaction

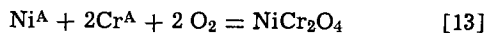


Table IX. Partial and integral heats of mixing in Cr-Ni alloys

Atom fraction		Partial heat of mixing (cal/gram atom)		Integral heat of mixing (cal/gram atom)
Cr	Ni	Cr	Ni	
0.028	0.972	560	0	20
0.056	0.944	530	0	30
0.108	0.892	4930	-290	270
0.133	0.867	5090	-370	350
0.200	0.800	4270	-430	510
0.218	0.782	5060	-450	760
0.278	0.722	4310	0	1200
0.313	0.687	6130	-840	1350
0.363	0.637	4330	0	1570
0.401	0.599	3340	-650	1730

The analytical data (Table V) permit one to assume  $a_{Ni^A} > 0.999$  and  $a_{NiCr_2O_4} > 0.99$ , and so

$$\Delta G_f^0(NiCr_2O_4) = 9.150T [\log a_{Cr} + \log P_{O_2}] \quad [14]$$

giving  $\Delta G_f^0(NiCr_2O_4)$  equal to  $-234.9$ ,  $-226.1$ , and  $-217.7$  kcal/mole at 900°, 1000°, and 1100°C. The estimated error in these values is  $\pm 1.2$  kcal. This analysis can be extended to determine the free energy change,  $\Delta G_f^0$ , for the formation of nickel chromite from nickel oxide and chromium oxide, where

$$\Delta G_f^0 = \Delta G_f^0(NiCr_2O_4) - \Delta G_f^0(NiO) - \Delta G_f^0(Cr_2O_3) \quad [15]$$

The values of  $\Delta G_f^0$  are  $-8300$ ,  $-7500$ , and  $-7200$  cal/mole NiCr<sub>2</sub>O<sub>4</sub> at 900°, 1000°, and 1100°C, respectively, with an estimated uncertainty of  $\pm 1300$  cal.

**Alloy-NiCr<sub>2</sub>O<sub>4</sub>-NiO phase field.**—Oxygen pressures calculated from the emf's of cell [V] were  $9.5(\pm 0.6) \times 10^{-13}$ ,  $4.2(\pm 0.3) \times 10^{-11}$ , and  $1.0(\pm 0.05) \times 10^{-9}$  atm at 900°, 1000°, and 1100°C. The dissociation pressures of pure nickel oxide at these temperatures are  $1.02 \times 10^{-12}$ ,  $4.43 \times 10^{-11}$ , and  $1.11 \times 10^{-9}$  atm. Since the chromium content of the alloy is less than the critical value of  $10^{-4}$  w/o determined for the alloy Cr<sub>2</sub>O<sub>3</sub> equilibrium, the relationship

$$P_{O_2} = P^*_{O_2}(a_{NiO})^2 \quad [16]$$

describes this system, giving a value of  $\sim 0.97$  for  $a_{NiO}$  at the three investigated temperatures. The chromium contents of nickel oxide given by the electron probe determinations of samples annealed at 1000° and 1100°C (Table VI) correspond to 0.955 atom fraction nickel oxide.

The chromium activity in the  $\gamma$ -alloy can be estimated from Eq. [14] as  $1 \times 10^{-10}$ ,  $8 \times 10^{-10}$ , and  $5 \times 10^{-9}$  at 900°, 1000°, and 1100°C. Thus, the alloy existing with nickel chromite and nickel oxide is almost pure nickel.

**Equilibrium oxygen pressure diagram for the Cr-Ni-O system.**—This diagram, which has the same shape between 900° and 1100°C, is shown only as a schematic in Fig. 8 because several of the experimentally determined parameters are too small to be represented graphically. With increasing nickel content of the alloy,  $N_{Ni^A}$ , the oxygen pressure increased from the dissociation pressure of pure chromium oxide to that associated with the univariant phase field,  $\alpha$ - $\gamma$ -Cr<sub>2</sub>O<sub>3</sub>, with chromium oxide containing  $< 0.2$  w/o Ni. The compositions of the  $\alpha$  and  $\gamma$  alloy phases at 900°, 1000°, and 1100°C were 97.5 and 42.5, 94.2 and 45.0, and 88.2 and 47.5 a/o Cr, respectively. The  $\alpha$ -alloy is unstable at larger oxygen pressures and  $\gamma$ -Cr<sub>2</sub>O<sub>3</sub> phase field extended up to the univariant phase field,  $\gamma$ -spinel-Cr<sub>2</sub>O<sub>3</sub>. At both 1000° and 1100°C the nickel chromite spinel was found to be essentially stoichiometric, the nickel content of chromium oxide was 0.2 w/o while the chromium content of the  $\gamma$ -alloy phase,  $A_1$ , was estimated to be in the order of  $10^{-4}$  w/o. The measurements did not detect any variation in the spinel composition across the two-phase field, alloy-spinel, but the chromium content of the alloy decreased to  $\sim 10^{-8}$  w/o, i.e., alloy  $A_2$  is effectively pure nickel and spinel  $S_2$  is NiCr<sub>2</sub>O<sub>4</sub>, at the three-phase  $\gamma$ -NiCr<sub>2</sub>O<sub>4</sub>-NiO univariant oxygen pressure. The maxi-

Table X. Equilibrium oxygen pressures for the univariant phase equilibria of the Cr-Ni-O system

	-log (P <sub>O<sub>2</sub></sub> atm)		
	900°C	1000°C	1100°C
Cr-Cr <sub>2</sub> O <sub>3</sub>	24.158	21.572	19.363
$\alpha$ - $\gamma$ -Cr <sub>2</sub> O <sub>3</sub>	24.15	21.54	19.31
$\gamma$ -Cr <sub>2</sub> O <sub>3</sub> -NiCr <sub>2</sub> O <sub>4</sub>	15.085	12.950	11.242
$\gamma$ -NiCr <sub>2</sub> O <sub>4</sub> -NiO	12.02	10.38	9.00
Ni-NiO	12.000	10.354	8.954

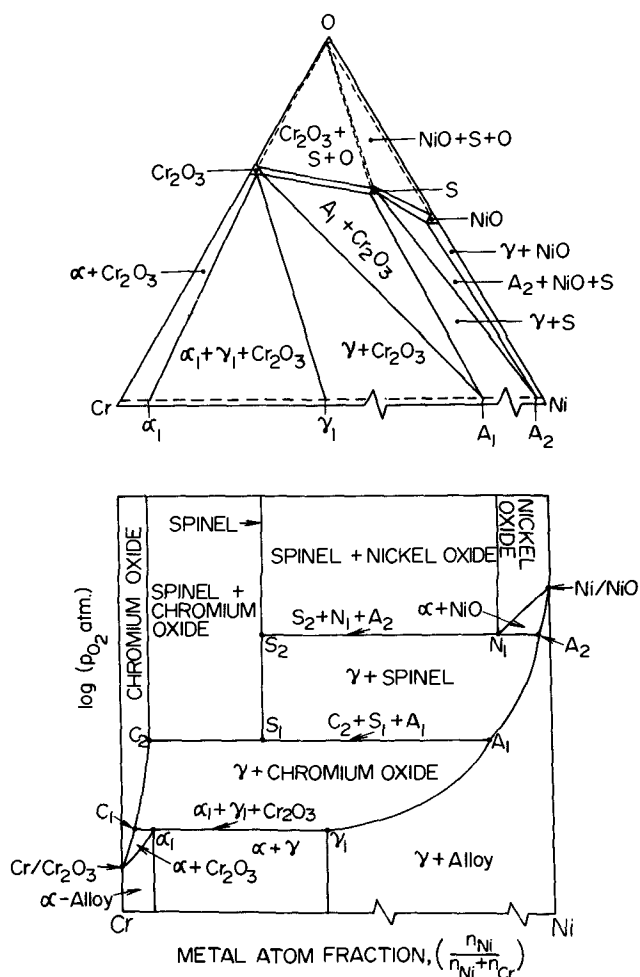


Fig. 8. Schematic representation of the equilibrium oxygen pressure diagram of the Cr-Ni-O system between 900° and 1100°C.

mum chromium content of nickel oxide was 4.5 w/o at 1000° and 1100°C. The oxygen pressures for the univariant phase equilibria of the Cr-Ni-O system at the three investigated temperatures are summarized in Table X.

**Acknowledgments**

This work was carried out by one of the authors (H. D.) in partial fulfillment of the requirements for award of the Ph.D. degree at McMaster University under auspices of the National Research Council of

Canada. He wishes to acknowledge the award of a Pier Fellowship, National Research Council of Canada.

Manuscript submitted June 2, 1973; revised manuscript received Nov. 15, 1973.

Any discussion of this paper will appear in a Discussion Section to be published in the December 1974 JOURNAL. All discussions for the December 1974 Discussion Section should be submitted by Aug. 1, 1974.

**REFERENCES**

1. J. Elliott and M. Gleiser, "Thermochemistry for Steelmaking," Vol. 1, Addison-Wesley Publishing Co., Inc., Reading, Mass. (1960).
2. B. C. H. Steele, in "Electromotive Force Measurements in High Temperature Systems," C. B. Alcock, Editor, American Elsevier Publishing Co., Inc., New York (1968).
3. C. G. Charette and S. J. Flengas, *This Journal*, **115**, 796 (1968).
4. H. M. Chen and J. Chipman, *Trans. ASM*, **38**, 70 (1947).
5. J. P. Coughlin, *U.S. Bur. Mines, Bull.*, **542** (1954).
6. Y. Jeannin, C. Mannerskantz, and F. D. Richardson, *Trans. AIME*, **227**, 300 (1963).
7. J. D. Tretjakow and H. Schmalzried, *Ber. Bunsengesellschaft Phys. Chem.*, **69**, 396 (1965).
8. O. Kubaschewski, E. L. Evans, and C. B. Alcock, "Metallurgical Thermochemistry," Pergamon Press, Inc., Elmsford, N. Y. (1967).
9. L. A. Pugliese and G. R. Fitterer, *Met. Trans.*, **1**, 1997 (1970).
10. C. J. Bechtold and H. C. Vacher, *Trans. AIME*, **221**, 14 (1961).
11. J. E. Croll and G. R. Wallwork, *J. Oxidation Metals*, **1**, 55 (1969).
12. G. Grube and M. Flad, *Z. Elektrochem.*, **48**, 377 (1942).
13. M. B. Panish, F. R. Newton, W. R. Grimes, and F. R. Blankenship, *J. Phys. Chem.*, **62**, 980 (1958).
14. E. Z. Vintaikin, *Dokl. Akad. Nauk. SSR* (English translation), **129**, 951 (1959).
15. O. Kubaschewski, W. A. Dench, and G. Heymer, *Z. Elektrochem.*, **64**, 801 (1960).
16. H. Davies and W. W. Smeltzer, *This Journal*, **119**, 1362 (1972).
17. K. Kiukkola and C. Wagner, *ibid.*, **104**, 379 (1957).
18. C. A. Friskney and C. W. Haworth, *Brit. J. Appl. Phys.*, Ser. 2, **1**, 873 (1968).
19. P. Duncumb and S. J. B. Reid, *Nat. Bur. Std., Special Publ.*, **298** (1968).
20. C. M. Diaz and F. D. Richardson, in "Electromotive Force Measurements in High Temperature Systems," C. B. Alcock, Editor, p. 29, American Elsevier Publishing Co., Inc., New York (1968).
21. F. A. Shenk, "Constitution of Binary Alloys," Second Supplement, p. 274, McGraw-Hill Book Co., New York (1969).
22. F. N. Mazandarany and R. D. Pehlke, *Met. Trans.*, **4**, 2067 (1973).

# A Rutherford Scattering Analysis of Anodic Tantalum-Silicon Oxides

P. J. Silverman<sup>1</sup>

*Bell Laboratories, Indianapolis, Indiana 46206*

and N. Schwartz\*

*Bell Laboratories, Murray Hill, New Jersey 07974*

## ABSTRACT

Reactively sputtered films consisting of ~65 atom per cent (a/o) Ta and ~35 a/o Si are of considerable interest for forming thin film capacitors and resistors. Oxides have been anodically grown on Ta-Si films and examined by the Rutherford backscattering technique. This analysis revealed that the outer layer of the oxide is greatly enriched in Ta and almost devoid of Si, while the inner layer has a lower Ta:Si ratio than the as-sputtered film. This indicates that Ta cations are very mobile within the oxide and are migrating to the surface under the influence of the applied field during anodization. No appreciable dissolution of either Ta or Si takes place. The Ta:Si:O stoichiometry of the oxide is consistent with a film composed of Ta<sub>2</sub>O<sub>5</sub> and SiO<sub>2</sub>.

At the present time in tantalum thin-film circuit technology (1), anodized  $\beta$ -tantalum (2, 3) is used for capacitors, while reactively sputtered tantalum nitride (4) is used for resistors. The fabrication of these circuits would be greatly simplified if a single thin film starting material were utilized for both of these components, especially if higher stability devices were obtained. Studies have been performed to use tantalum alloy compositions to improve the properties of capacitors. Alloys of tantalum with carbon, nitrogen, and oxygen (5) as well as tantalum-aluminum mixtures (6) have been investigated in the past. The use of tantalum-silicon alloys should have some considerable advantages:

1. Both elements are high melting point materials which should result in a film having high thermal and electromigration stability in resistors.

2. Some of the bulk tantalum silicides are reported to have resistivities (7) of the same order as tantalum nitride and tantalum-aluminum.

3. Both elements may be anodized (8) to form protective stable oxide films, and mixtures of them would presumably behave similarly.

4. As the tantalum-silicon alloy films can be deposited by reactive sputtering, all of the basic processes for thin film component fabrication can be retained and only the initial film material changed.

In another report (9) the initial characteristics of the tantalum-silicon alloy films were described, as well as the properties of the passive devices formed from them. In summary, however, quite stable resistors and very stable capacitors are formed from a composition in the neighborhood of 35 atom per cent (a/o) silicon.

The purpose of the present study was to determine the composition of the anodic oxide films formed on tantalum-silicon alloys. Relatively little work has been devoted to the analysis of anodic oxides grown on compounds or alloys (10); however, a recent Rutherford scattering study of anodic oxides on GaP (11) proved to be quite relevant to the present work. Rutherford ion scattering is an excellent technique for the determination of thin film composition as a function of depth. It is the only surface analytical method which will provide this information nondestructively. The technique has been used to examine a wide variety of thin film systems in addition to GaP, including the oxides of aluminum (12), silicon (13), and ni-

bium (14). In the present study, Rutherford backscattering provided depth profiles of the elements comprising the Ta-Si films and their oxides, allowing us to speculate on the oxide growth mechanism. In addition, since a small loss (~20%) in capacitance had been found for thin film Ta-Si capacitors (9) compared to  $\beta$ -tantalum capacitors, it was of interest to determine whether this capacitance change was attributable either to incorporation of a low dielectric constant material (SiO<sub>2</sub>) in tantalum oxide or to a change in film thickness.

## Experimental Procedure

*Sputtering and anodization.*—The films were prepared by d-c diode reactive sputtering of tantalum in silane-argon mixtures in a 6-in. oil diffusion pump system with a liquid nitrogen trap and a glass bell jar. Sputtering from a 36 in.<sup>2</sup> cathode was conducted at a potential of 5 kV, a current density of 0.5-1.2 mA/in.<sup>2</sup>, a gas pressure of  $1 \times 10^{-2}$  Torr, and an interelectrode spacing of 2.75 in. The deposition rate varied from 80-120 Å/min, depending on the partial pressure of silane, which ranged from  $7 \times 10^{-6}$  to  $8 \times 10^{-4}$  Torr. This technique resulted in film compositions varying from 0-92 a/o silicon. Substrates were fused silica cleaned by a trichloroethylene boil, hydrogen peroxide boil, ultrasonic detergent wash, deionized water rinse, hot nitrogen dry with a final bake at 400°C in air for 30 min. In the vacuum station, the substrates were heated to 550°C for 2 hr and then cooled for 2 hr to a temperature of 100°C. Silane was admitted into the chamber to the desired partial pressure through a needle valve, and then argon was added to a total pressure of  $1 \times 10^{-2}$  Torr. After a presputtering period of 45 min with a shutter covering the substrates, the films were deposited for 45 min. Beta-tantalum films were prepared in pure argon, and the structure was identified by x-ray diffraction.

For the anodization, the  $1 \times 3$  in. coated fused quartz slides were scribed and broken into six  $\frac{1}{2} \times 1$  in. slices. On each small slice, a thin strip of electroplaters tape was used to mask off the section where the electrolyte-air interface would form, and contact was made to the film with a small alligator clip. Anodization was performed in 0.01% citric acid using a tantalum cathode with an Electronic Measurements Inc. constant current/constant voltage power supply. Tantalum-silicon alloy films were anodized at 3-4 mA/cm<sup>2</sup>; one set of slices was then soaked for about 20 min at constant voltage until the current dropped an order

\* Electrochemical Society Active Member.

<sup>1</sup> Present address: Bell Laboratories, Murray Hill, New Jersey 07974.

Key words: ion backscattering, thin films, anodic oxides.

of magnitude. Beta-tantalum films were anodized at 1 mA/cm<sup>2</sup> and then similarly soaked at the given anodizing voltage.

**Backscattering.**—Rutherford backscattering of <sup>4</sup>He<sup>+</sup> ions was employed to analyze the composition and to obtain depth profiles of the Ta-Si films and their anodic oxides. In this technique a well-collimated, mono-energetic beam of ions is directed onto the sample. The ions lose energy in a solid by two processes: (i) elastic scattering by the repulsive Coulomb force between the nuclei of the incident ion and a target atom; and (ii) inelastic collisions with the electrons of the material. The nuclear scattering allows identification of the constituent elements of a thin film by the amount of energy the incident ion loses to the recoil of the target atom; light atoms, such as oxygen, can take up a large portion of the energy of the ion, while heavy atoms, like tantalum, absorb relatively little energy in recoiling. The stopping power of the electrons provides information about the depth distribution of elements in the sample, since ions scattered from atoms deep in the sample will have lost more energy than those scattered from atoms of the same element at the sample surface. Interpretation of the backscattered energy spectrum thus permits a nondestructive determination of the identity and position of the elements composing a thin film.

All measurements in this experiment were performed on the Bell Laboratories Van de Graaff accelerator with 1.9 MeV <sup>4</sup>He<sup>+</sup> ions. The experimental apparatus and the basic equations pertinent to Rutherford backscattering analysis have been described elsewhere (15). Two backscattered energy spectra were taken for each sample: one on the anodic oxide and one on an adjacent unanodized area. Typically, the beam current was ~2.5 nA, and the total integrated beam charge for each spectrum was 6 μC. Because of the Z<sup>2</sup> dependence of scattering cross section, there is relatively little backscattering from the O and Si atoms present compared to that from the Ta atoms, and consequently a period of about 50 min was required to obtain a spectrum with adequate statistics (statistical uncertainties in total counts of ~1%) for the O and Si yields from a sample. The energy resolution of the system, determined mainly by the resolution of the surface barrier silicon detector, was 15 keV.

### Results

A backscattered energy spectrum for an as-sputtered Ta-Si film is shown in Fig. 1; the relatively small yields of the low energy side have been magnified by a factor of 20. The energies with which 1.9 MeV He ions are backscattered from Ta, Ar, and Si atoms at the surface are shown on the abscissa. These energies correspond to the half-heights of the leading edges of the respective scattering peaks, indicating that all of these elements are present at the sample surface.

The shaded areas give the yields corresponding to elements in the Ta-Si film. The background under the Ar yield, probably due to multiple scattering from Ta within the film, is taken simply by drawing a horizontal straight line; such long tails are always present in scattering from thin films. Because the trailing edge of the Ar yield is overlapped by the leading edge of the Si yield, it is necessary to determine (using a knowledge of the kinematics of the scattering process and the electronic stopping powers) the expected Ar peak width from the observed Ta peak width, assuming that the Ar is uniformly distributed throughout the film. For the Si, some criterion must be established to determine the position of the interface between the film and the underlying quartz (SiO<sub>2</sub>) substrate. Here we use the energy of the midpoint between the substrate and film plateaus as the energy of the half-height of the trailing film edge; Mitchell *et al.* (16) have shown this to be an accurate method. A straight line is then drawn from the leftmost point of the film

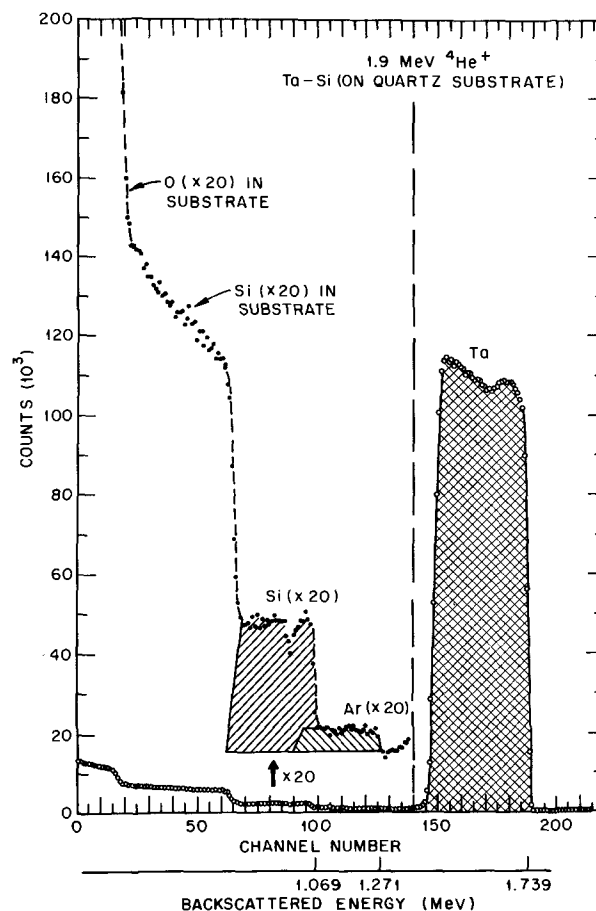


Fig. 1. Backscattered energy spectrum of 1.9 MeV <sup>4</sup>He ions from a sputtered Ta-Si film about 4200Å thick. The low energy side of the spectrum is also shown magnified by a factor of 20. The shaded areas are the scattering yields of the elements in the film. The energies with which the ions are backscattered from Ta, Ar, and Si are shown on the abscissa (energy scale = 7.5 keV/channel).

plateau through the half-height to approximate the trailing edge of the film scattering for Si.

For a thin film of uniform composition, the backscattered yield should increase with decreasing energy due to the  $E^{-2}$  dependence of the Rutherford cross section (the stopping power is essentially constant in this energy region). Thus, the slope observed in the Ta yield is expected, but the slight peak at the surface is not. This peak represents an increase in the Ta level present; the corresponding decrease in Si concentration is not as easily discerned in the scattering spectrum. Similar nonuniformities were observed in samples with different over-all compositions from sputtering runs at different silane partial pressures.

The integrated composition of a film is obtained from the elemental scattering yields after allowing for the Z<sup>2</sup> dependence of scattering cross section. The ratio of Ta:Si:Ar in the film of Fig. 1 is 2.9:1:0.10, or 72% Ta, 25% Si, and 3% Ar. The average film composition, obtained from spectra taken on six unanodized samples, was 69% Ta, 28% Si, and 3% Ar, or a ratio of 2.5:1:0.13. Argon is incorporated into the film during the sputtering process, and similar levels have been previously observed in sputtered films (17). The actual numbers of Ta, Si, and Ar atoms per square centimeter were obtained by comparing the yields to that from a bulk gold or tantalum sample. Converting these numbers to a surface density (grams per square centimeter) and dividing by the weighted average of the densities of β-Ta and bulk Si (ignoring the small amount of Ar), the film thickness was calculated to be about 4200Å.

Figure 2 is the spectrum obtained from a Ta-Si film anodized at constant current to 249V and soaked at

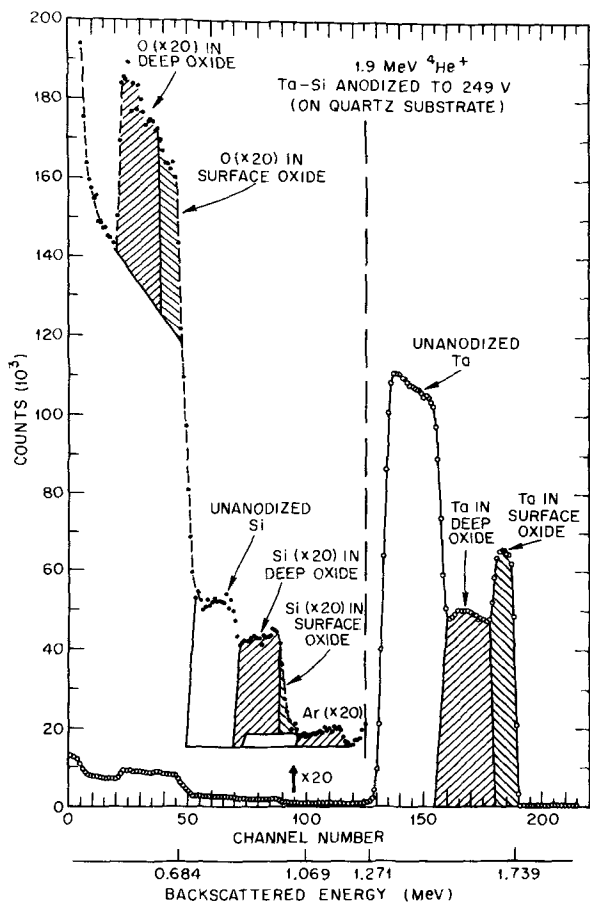


Fig. 2. Backscattered energy spectrum of 1.9 MeV  $^4\text{He}$  ions from a Ta-Si film anodized to 249V. The yields of Si and O from the surface layer are shaded the same as the surface Ta peak; similarly, the Ar, Si, O, and Ta in the deep oxide layer are shaded alike. There is essentially no Ar yield from the surface layer. Elemental yields from the unanodized Ta-Si film beneath the oxide are shown as enclosed, unshaded areas. Within experimental uncertainties, the measured amount of O corresponds to an oxide composed of  $\text{Ta}_2\text{O}_5$  and  $\text{SiO}_2$ . (Energy scale = 7.5 keV/channel.)

this voltage as previously described. Several interesting features of this spectrum are immediately apparent. The large Ta peak indicates an excess of Ta at the outer surface of the oxide. There is a corresponding deficiency of Si in this region, as shown by the difference between the observed position of the Si half-height and the position expected if Si were present at the oxide surface. Similarly, the Ar leading edge occurs at a reduced energy, indicating a lack of Ar in this surface layer. Virtually every oxide grown exhibited these nonuniformities, including oxides formed on films of other Ta-Si compositions. The small dip in the Ta yield at the back edge of the deep oxide indicates a slight Ta deficiency, although this was not observed in any other oxides.

Since the composition of the surface and deep oxide layers are obviously different, the areas corresponding to these layers have been shaded differently in Fig. 2 to facilitate interpretation. Boundaries of the Si and O yields were determined kinematically from the width of the surface Ta peak. The background under the O peak, due mainly to scattering from Si in the quartz substrate, is determined simply by extrapolating a smooth line from the points to the left of the peak. The Ta:Si:O ratio was calculated to be  $\sim 9:1:26$  for the surface layer and  $\sim 1.8:1:6.5$  for the deep layer. (Argon was not included as it was not expected to enter into stoichiometric combinations with the other elements and was present at such low levels.) Despite the large difference in Ta:Si ratios, the amount of O observed in each layer is consistent, within 6%, with the presence

Table I. Integrated stoichiometries of Ta-Si oxides produced by constant current anodization followed by a constant voltage soak period

The expected O level (relative to Si as 1), assuming an oxide composed exclusively of  $\text{Ta}_2\text{O}_5$  and  $\text{SiO}_2$ , and the agreement between the expected and observed O levels are given for each oxide.

Anodizing voltage (V)	Observed Ta:Si:O	Theoretical O:Si Expected for $\text{Ta}_2\text{O}_5$ and $\text{SiO}_2$ only	Observed O / Theoretical O $\times 100\%$
39	2.8:1:8.9	9.0	100
83	1.6:1:5.1	6.0	85
122.5	3.2:1:10.0	10.0	100
169	2.0:1:6.5	7.0	93
191	2.5:1:7.5	8.3	90
249	2.6:1:8.8	8.5	104
Average	2.5:1:7.8	8.1	96

of  $\text{Ta}_2\text{O}_5$  and  $\text{SiO}_2$ . The integrated Ta:Si:O stoichiometry for the oxide of Fig. 2 is 2.6:1:8.8. The stoichiometries of oxides produced at various voltages, and the agreement between the expected and observed levels of O, and listed in Table I. The close agreement between expected and observed O levels indicates that only  $\text{Ta}_2\text{O}_5$  and  $\text{SiO}_2$  are being formed.

Figures 3 and 4 show the elemental depth profiles extracted directly from the backscattering spectra of Fig. 1 and 2. To obtain these profiles, backgrounds were subtracted from each point of the O, Si, and Ar peaks. The number of counts represented by each of the shaded areas was normalized to allow for the Rutherford backscattering cross-section ratios for O:Si:Ar:Ta of 1:3.36:5.69:95.2. The widths of the O, Si, and Ar peaks were linearly increased by 34, 16, and 11%, respectively, relative to the Ta peak, to adjust for the kinematic decrease in width with decreasing mass; corresponding decreases of the peak heights were then made to conserve the total number of counts. Also, the  $E^{-2}$  slope of the peaks was allowed for so that a film of uniform composition would show constant concentration levels in the depth profile. The profiles reflect a depth resolution of roughly 200Å, as calculated from Bragg's additivity rule for stopping powers (18) and the 15 keV energy resolution.

The depth profile of Fig. 3 clearly shows the variation in composition of the Ta-Si film as-sputtered. The outer layer is about 75% Ta, 22% Si, and 3% Ar,

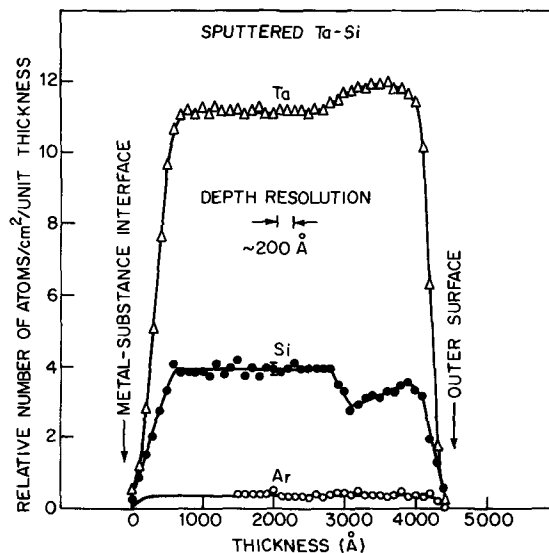


Fig. 3. Depth profile extracted from the Ta-Si spectrum of Fig. 1. The increased Ta and reduced Si concentrations at the surface of the Ta-Si film are clearly seen. A uniform distribution of Ar deep within the film is extrapolated back from the observed Ar yield not overlapped by the Si scattering. A typical error bar is shown on the Si profile; the uncertainties on the Ta and Ar are approximately the dot size.

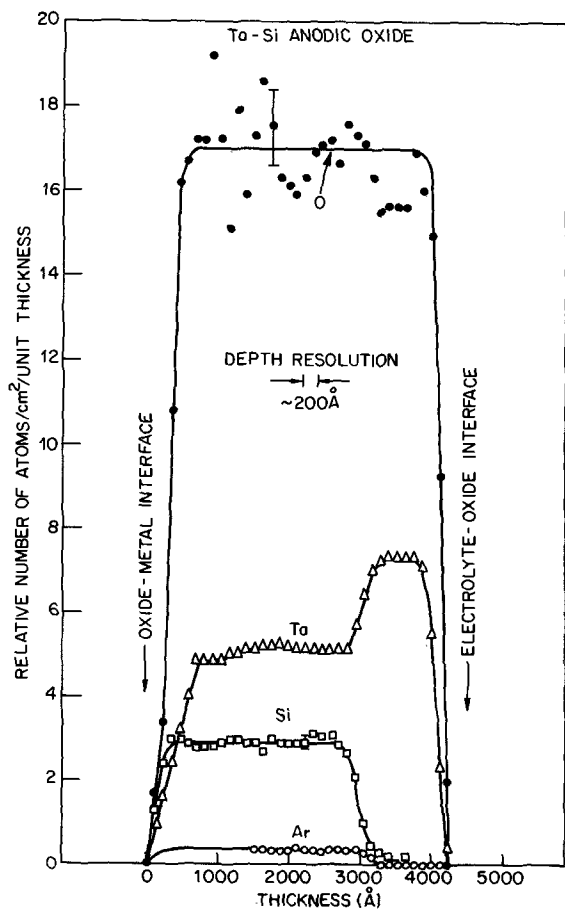


Fig. 4. Depth profile of the 249V anodic oxide layer, extracted from the spectrum of Fig. 2. The surface layer is evidently almost devoid of Si and Ar, with a correspondingly large excess of Ta. The lines are drawn simply to guide the eye, not necessarily as a best fit for the data points.

while the inner layer is composed of 70% Ta, 27% Si, and 3% Ar. This results in an over-all composition of 72% Ta, 25% Si, and 3% Ar, as noted earlier. The positive slope of the Si profile within the outer layer seems to indicate that the Si level increases near the surface. However, this slope may simply reflect a small error in the extrapolated width and shape of the Ar yield underlying the Si yield in the backscattering spectrum.

Figure 4 is the depth profile of the 249V oxide layer of Fig. 2, excluding the underlying unanodized layer. The large pile-up of Ta and the deficiency of Si at the surface are evident. Argon is apparently almost totally absent from the surface of the oxide. By comparison with Fig. 3, it can be seen that the Ta:Si ratio in the deep oxide is much smaller than in the unanodized film, while in the surface oxide the ratio is far higher than usual. Within the uncertainties of the statistics for the O yield, the level of O seems to be fairly uniform throughout the oxide.

Information about the loss of elements into solution can also be obtained from the spectrum of an anodized film. This is accomplished simply by summing the entire film scattering yield for Ta, Si, and Ar rather than just that part which corresponds to the oxide layer. The average of the values obtained in this fashion from all of the anodized film spectra was a Ta:Si:Ar ratio of 2.6:1:0.09 or about 70% Ta, 27% Si, and 3% Ar, quite close to the average composition of the unanodized films. In addition, the actual numbers of Ta atoms in the anodized films were within 2% of the numbers in the as-sputtered films, indicating that no appreciable dissolution of the constituent elements of the films occurred during anodization.

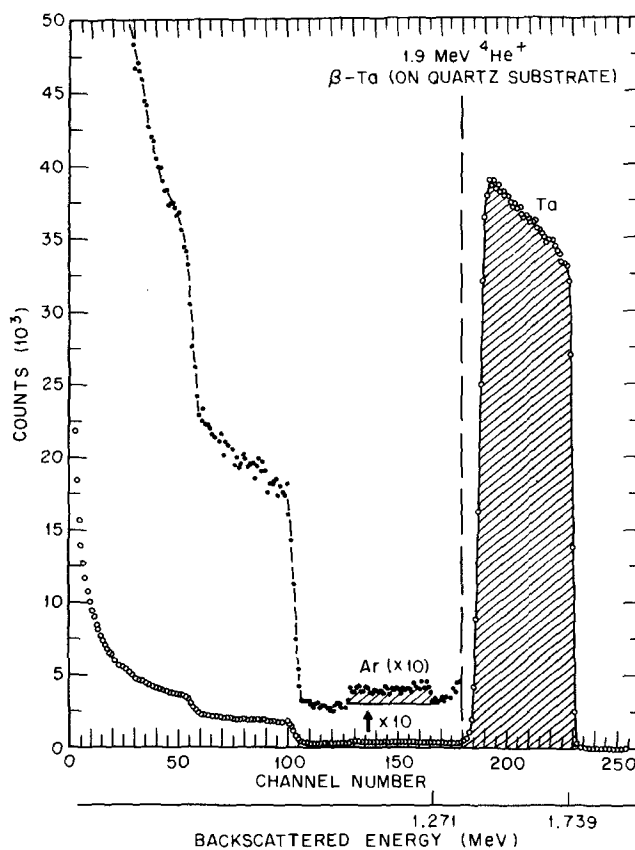


Fig. 5. Backscattered energy spectrum of 1.9 MeV  $^4\text{He}^+$  ions from a sputtered  $\beta$ -Ta film. The composition appears to be constant throughout the thickness of the film; the slope of the Ta peak is due to the  $E^{-2}$  dependence of the scattering cross section. (Energy scale = 7.5 keV/channel).

Because of the interesting nonuniformities observed in Ta-Si and its oxides, a scattering analysis of sputtered  $\beta$ -Ta film and its anodic oxide was performed. Figure 5 shows the backscattering spectrum from a sputtered  $\beta$ -Ta film. Again, the yields at low energy are shown expanded (by a factor of 10) so that the Ar present in the film may be seen more readily. It is obvious that the Ta concentration is uniform throughout the Ta film; the slope of the Ta peak is simply that expected from the  $E^{-2}$  cross-section dependence. The composition of 96% Ta and 4% Ar was essentially constant for all samples analyzed.

Figure 6 is the spectrum obtained from a Ta film anodized to 82V and soaked as before. The Ta and O levels are seen to be reasonably constant throughout the thickness of the oxide. The Ta:O ratio was found to be 1:2.4 for this oxide, corresponding closely to the  $\text{Ta}_2\text{O}_5$  stoichiometry as expected. Indeed, all measurements on  $\beta$ -Ta oxides of various thicknesses resulted in ratios within 6% of 1:2.5.

In every scattering spectrum for the  $\beta$ -Ta oxides, the leading edge of the Ar scattering fell close to or on the trailing edge of the Ta scattering and consequently was obscured, making the Ar level near the oxide surface difficult to determine. For this reason, the area corresponding to the Ar yield is not delineated in Fig. 6. Despite this uncertainty, it can be stated that in most cases more Ar is present at or near the  $\beta$ -Ta oxide surface than was found in the surface layer of the Ta-Si oxide. However, small peaks in the Ta yields, corresponding to increases of 2-3% in the amount of Ta present at the surface, were observed in the spectra of the two thickest  $\beta$ -Ta oxides, anodized to 210 and 249V. While this could be attributed to the presence of some Ta in a valence state less than +5 (and a consequent decrease in the amount of O present), we be-

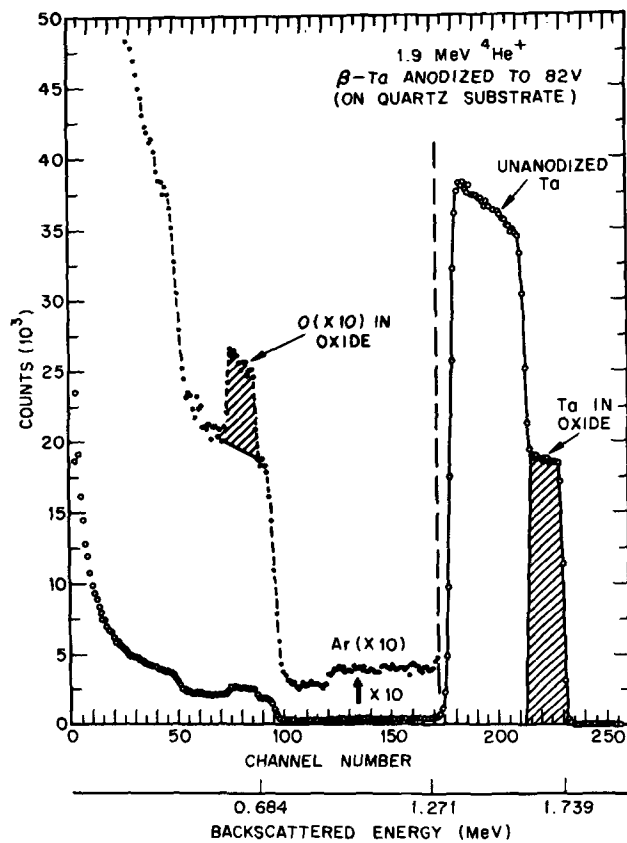


Fig. 6. Backscattered energy spectrum of 1.9 MeV He ions from a  $\beta$ -Ta film anodized to 82V. The Ta and O concentrations are uniform throughout the oxide and correspond to the  $\text{Ta}_2\text{O}_5$  stoichiometry. The Ar yield is not determined because of the overlap of its leading edge with the Ta trailing edge. (Energy scale = 7.5 keV/channel).

lieve that it is more likely to be correlated with a lack of Ar in the outer layer (about one-fourth of the total oxide thickness) similar to that seen in the Ta-Si oxides.

All of the Ta-Si oxides exhibited brilliant uniform interference colors similar to those seen in the anodic  $\text{Ta}_2\text{O}_5$  films. Thicknesses were calculated for the oxides by the method mentioned previously for the unanodized Ta-Si film: determining the number of atoms per square centimeter from the spectra, converting this to a surface density (grams per square centimeter), and dividing by the weighted average of the densities of anodic  $\text{Ta}_2\text{O}_5$  (8.0 g/cm<sup>3</sup>) (19) and anodic  $\text{SiO}_2$  (1.8 g/cm<sup>3</sup>) (20). Film thickness vs. anodized voltages is plotted in Fig. 7. The growth rate of  $\beta$ -Ta oxide was 17.5 Å/V and falls within the range of 16-18 Å/V that is usually quoted for  $\beta$ -Ta (19, 21, 22). The Ta-Si oxides formed at a somewhat higher rate, about 20 Å/V. The fact that the thickness vs. V plots intercept  $\sim 50$ -100 Å at zero volts must be due in part to experimental error, however, the statistics of the yield in Fig. 1 at the energy corresponding to oxygen atoms at the surface do not preclude the possibility of a 20 Å native oxide layer existing on the as-sputtered film.

In addition to the  $\beta$ -Ta and Ta-Si oxides produced by the usual anodizing method, Ta-Si oxides were formed simply by anodizing at constant current up to a given voltage, omitting the constant voltage soak period. The results obtained from backscattering spectra of unsoaked Ta-Si oxides showed these films to be quite similar in many respects to the soaked Ta-Si oxides; the over-all average oxide composition was the same within experimental error and similar nonuniformities in Ta levels, etc., were observed. However, as shown in Fig. 7, the growth rate of the unsoaked oxides was only 14 Å/V, much lower than for

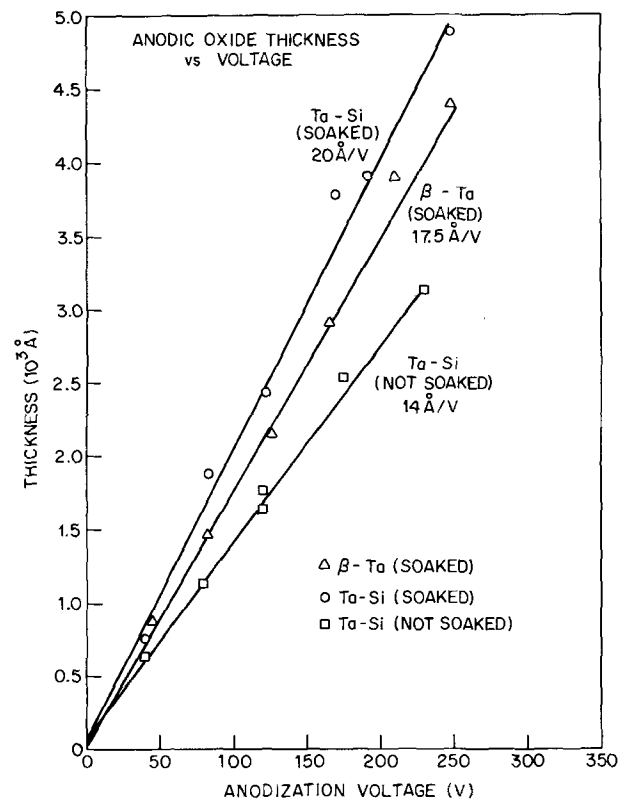


Fig. 7. Comparison of anodic oxide thickness vs. anodization voltage for  $\beta$ -Ta and Ta-Si. Ta-Si produces a thicker oxide than  $\beta$ -Ta for a given anodizing voltage when a constant voltage soak period is included in the anodization.

the films which did undergo a soak at the final anodized voltage. This is to be expected, at least qualitatively, since the soaked oxide continues to grow at a decelerating rate as the current drops when held at a constant voltage.

The rates at which the films were consumed during anodization were also calculated. About 7.5 Å of  $\beta$ -Ta or Ta-Si was consumed per volt when a constant voltage soak period was used; the value dropped to 5 Å/V for unsoaked Ta-Si. From these values it was then easy to determine the conversion factor between initial film thickness and anodic oxide thickness. It was found that 2.7 Å of oxide resulted for each angstrom of Ta-Si consumed, with or without a soak period, slightly more than the 2.3 Å of  $\text{Ta}_2\text{O}_5$  produced per angstrom of  $\beta$ -Ta.

### Discussion and Conclusions

Oxides have been anodically grown on Ta-Si films by a method typically used for forming  $\text{Ta}_2\text{O}_5$  on Ta. Our measurements indicate the following important compositional features:

1. The Ta-Si films have slightly enhanced concentrations of Ta and decreased levels of Si near the surface prior to anodization.
2. The outer layer of the Ta-Si oxide is apparently largely  $\text{Ta}_2\text{O}_5$  and is nearly devoid of Si (and Ar).
3. The inner oxide layer is probably composed of  $\text{Ta}_2\text{O}_5$  and  $\text{SiO}_2$ , with a lower Ta:Si ratio than in the unanodized film.
4. There is no appreciable dissolution of Ta or Si from the films during anodization.

The concentration nonuniformities in the as-sputtered film were seen in film samples from several sputtering runs, indicating that the effect is not just an artifact of some abnormal sputtering condition (e.g., a change in silane partial pressure) that may have occurred during a particular run. The nonuniformity indicates that less Si is being incorporated into the film toward the end of the sputtering process. This

may be caused by a rise in the substrate temperature during deposition, which might decrease the sticking coefficient of Si on Ta. In any case, the significance of the nonuniformity to our results is only that the oxides are formed mainly from a slightly Ta-rich and Si-poor layer. While none of the Ta-Si film used in this study was exactly 35% Si, a Ta-Si sintered alloy cathode may make film composition and reproducibility more easily controlled in the future.

The concentration profiles of the Ta-Si oxides are strikingly similar to those found by the backscattering technique in anodic oxides of GaP (11); unlike the GaP case, however, there is no complication of interpretation due to dissolution of the film. Apparently, the Ta cation is much more mobile than Si (or Ar) within the oxide. Under the influence of the applied anodizing electric field, a large fraction of the available Ta migrates to the surface of the oxide through a stationary matrix of Ta<sub>2</sub>O<sub>5</sub> and SiO<sub>2</sub>. In a study of the anodic oxidation of various alloys, Wood and Khoo (10) found a similar profile in Nb-Ta oxides except that Nb was the more mobile ion and was found in excess in the outer film surface. According to Pringle (23), the transport number of O is about three times that of Ta in the anodization of Ta films, so that one Ta ion migrates outward for every seven or eight O ions that move inward. Thus, the in-migration of the oxidizing species may also be a major feature of the growth mechanism of Ta-Si oxide.

It is significant that the film seems to anodize to form only Ta<sub>2</sub>O<sub>5</sub> and SiO<sub>2</sub>. While Ta will anodize in almost any solution, SiO<sub>2</sub> is considerably more difficult to form anodically in aqueous electrolytes. Although the agreement (shown in Table I) between the theoretical (assuming only Ta<sub>2</sub>O<sub>5</sub> and SiO<sub>2</sub>) and observed amounts of O is quite good, there is a large variation of the Ta:Si ratios. These variations are probably caused in part by the uncertainty (perhaps 15%) of the Si yield, a result of the procedure for determining the background counts underlying the Si portion of the spectrum; however, the near equality of the average Ta:Si ratios for the unanodized and anodized films indicates the basic validity of the measurements. Figure 7 demonstrates that the oxide film thickness for the soaked Ta-Si and  $\beta$ -Ta differ by about 2.5 Å/V for a given anodizing voltage. The lower capacitance of Ta-Si oxide capacitors, compared to those made with Ta<sub>2</sub>O<sub>5</sub>, is therefore due mainly to the greater oxide thickness, although incorporation of Si and SiO<sub>2</sub> in the oxide film may also be a contributing factor.

#### Acknowledgments

The authors are indebted to J. M. Poate, T. Buck, and P. A. Turner for their most helpful advice and discussions, to F. G. Peters for the sputtered films, and

to W. M. Augustyniak for assistance with the accelerator operation.

Manuscript submitted June 4, 1973; revised manuscript received Nov. 14, 1973.

Any discussion of this paper will appear in a Discussion Section to be published in the December 1974 JOURNAL. All discussions for the December 1974 Discussion Section should be submitted by Aug. 1, 1974.

#### REFERENCES

1. D. A. McLean, *IRE WESCON Conv. Record*, Part 6, 87 (1959).
2. R. W. Berry, and D. Sloan, *Proc. IRE*, **47**, 1070 (1959).
3. M. H. Read and C. Altman, *Appl. Phys. Letters*, **7**, 51 (1965).
4. D. Gerstenberg and E. H. Mayer, *Proc. Electron Components Conf.*, Washington, D. C., 1962, 57.
5. D. Gerstenberg, *This Journal*, **113**, 542 (1966).
6. C. A. Steidel and D. Gerstenberg, *Proc. Electron Components Conf.*, Washington, D. C., 1969, p. 372.
7. V. S. Neshpor and G. V. Samsonov, *Fiz. Tverdogo Tela.*, **2**, 2202 (1960); *C. A.*, **55**, 15030d (1961).
8. L. Young, "Anodic Oxide Films," Academic Press, New York (1961).
9. N. Schwartz and F. G. Peters, *Proc. Electron Components Conf.*, Washington, D. C., 1973, p. 255.
10. G. C. Wood and S. W. Khoo, *J. Appl. Electrochem.*, **1**, 189 (1971).
11. J. M. Poate, P. J. Silverman, and J. Yahalom, *This Journal*, **120**, 844 (1973). A complete account of the experiment is given in *J. Phys. Chem. Solids*, **34**, 1847 (1973).
12. M. Kamoshida, J. W. Mayer, and I. V. Mitchell, AFCRL-72-0319. Reference 16 is also contained within this report.
13. O. Meyer, J. Gyulai, and J. W. Mayer, *Surface Sci.*, **22**, 263 (1970).
14. J. F. Ziegler, M. Berkenblit, J. B. Light, K. C. Park, and A. Reisman, *IBM J. Res. Develop.*, **16**, 530 (1972).
15. T. M. Buck, J. M. Poate, K. A. Pickar, and C. M. Hsieh, *Surface Sci.*, **35**, 362 (1973).
16. I. V. Mitchell, M. Kamoshida, and J. W. Mayer, *J. Appl. Phys.*, **42**, 4378 (1971).
17. W. G. Guldner and R. Brown, in "Measurement Techniques for Thin Films," B. Schwartz and N. Schwartz, Editors, p. 82, The Electrochemical Society Softbound Symposium Series, New York (1967).
18. L. C. Northcliffe and R. F. Schilling, *Nuclear Data Tables*, **A7**, 233-463 (1970).
19. J. Klerer, *This Journal*, **112**, 896 (1965).
20. R. J. Archer, *J. Opt. Soc. Am.*, **52**, 970 (1962).
21. D. Gerstenberg, in "Handbook of Thin Film Technology," L. I. Maissel and R. Glang, Editors, McGraw-Hill Book Co., Inc., New York (1970).
22. D. G. Muth, *J. Vacuum Sci. Technol.*, **6**, 749 (1969).
23. J. P. S. Pringle, *This Journal*, **120**, 398 (1973).



# Diffusion of Phosphorus in Gallium Melt

Kunio Kaneko, Masaaki Ayabe, Masashi Dosen, Kenji Morizane, Setsuo Usui,  
and Naozo Watanabe

Sony Corporation Research Center, 174 Fujitsuka-cho, Hodogaya-ku Yokohama, Japan

## ABSTRACT

Crystal growth rate of GaP in the SSD (synthesis, solute diffusion) method is limited by the diffusion process of phosphorus in the gallium melt. The diffusion process was analyzed and the diffusion coefficient was derived as  $D = 1.8 \times 10^{-2} \exp(-0.65 \text{ eV}/kT) \text{ cm}^2 \text{ sec}^{-1}$ .

We have recently developed the SSD (synthesis, solute diffusion) method for growing GaP crystals (1, 2). Diffusion of the solute phosphorus in a gallium melt plays an important role in the crystal growth process of this method. Pertinent data are, however, scarce. The only published value of the diffusion coefficient is  $5 \times 10^{-5} \text{ cm}^2 \text{ sec}^{-1}$  at temperatures from 700° to 1300°C, used by Tiller (3) and by Plaskett (4). Rodot *et al.* (5) adopted a value of  $1 \times 10^{-4} \text{ cm}^2 \text{ sec}^{-1}$  from an analogy to GaAs. But a temperature dependent diffusion coefficient is not available.

In the SSD method, a thin film of GaP exists at the surface of the gallium melt, so the phosphorus concentration at the melt surface is fixed to the saturation concentration determined by the surface temperature. After a nucleus is formed at the bottom of the melt where the temperature is lower than at the surface of the melt, the concentration at the growth front is also fixed to the saturation concentration determined by the temperature at the growth front. Diffusion of phosphorus continues in the melt between these two saturation concentrations and limits the growth rate of the crystal (1).

In this paper the diffusion process of the SSD method is analyzed and the diffusion coefficient is evaluated as a function of temperature using the growth rate data obtained by this method.

## Evaluation of Diffusion Coefficient

That the growth process is limited by diffusion of the solute makes it possible to evaluate the diffusion coefficient from the experimental data of the growth rate (1), provided due assumptions and approximations are made. As the crystal grows, the growth front moves upward into a higher temperature region and at the same time the melt itself moves upward in the crucible because of volume increase which accompanies the conversion of gallium into GaP. Thus, taking a moving coordinate system which is stationary with respect to the melt, the requirements of the conservation of gallium and phosphorus at the growth front are expressed respectively as

$$(\rho^M - C^M) \frac{dR}{dt} = \rho_{\text{GaP}}^M V \quad [1]$$

and

$$D \frac{\partial C^M}{\partial x} + C^M \frac{dR}{dt} = \rho_{\text{GaP}}^M V \quad [2]$$

where  $x$  is the position variable,  $\rho^M$  is the density of the melt,  $\rho_{\text{GaP}}^M$  the density of GaP, and  $C^M$  the concentration of phosphorus in the melt (all in mole  $\text{cm}^{-3}$ ).  $D$  is the diffusion coefficient of the solute,  $R$  the position of the growth front expressed in the coordinate system as a function of time,  $t$ , and  $V$  the growth rate of the GaP crystal. Then from Eq. [1] and [2]

$$D \frac{\partial C^M}{\partial x} = \rho_{\text{GaP}}^M V \left( 1 - \frac{C^M}{\rho^M - C^M} \right) \quad [3]$$

Since the mole fraction of phosphorus,  $C$ , is defined as

**Key words:** gallium phosphide, crystal growth, diffusion coefficient, phosphorus, gallium melt.

$C = C^M/\rho^M$ , we obtain from Eq. [3]

$$V = \frac{\rho^M}{\rho_{\text{GaP}}^M} \frac{1 - C}{1 - 2C} D \frac{\partial C}{\partial x} \quad [4]$$

Equation [4] holds strictly only at the growth interface, and necessary information to evaluate  $D$  using this equation is not obtainable experimentally. However, we can simplify the treatment as follows.

The diffusion coefficient is assumed to be independent of  $C$  and  $T$  over the temperature range of each run. Although our aim is to obtain the temperature dependence of  $D$ , this assumption will be justified if the dependence is not strong. The concentration profile, which is fixed at both the growth interface and at the melt surface to the saturation concentration,  $C_P$ , becomes nearly linear, because diffusion proceeds in nearly steady fashion (the diffusion coefficient is of the order of  $10^{-4} \text{ cm}^2 \text{ sec}^{-1}$  while the growth rate is of the order of  $10^{-6} \text{ sec}^{-1}$ ). The growth front moves, as the crystal grows, from the bottom of the crucible to a height almost twice the initial depth of the melt,  $W$ , if the total gallium is exhausted. Therefore, the values of the temperature,  $T_H$ , the concentration,  $C_{PH}$ , and  $dC_P/dx$  at the initial melt surface may serve as average values for  $T$ ,  $C_P$ , and  $\partial C/\partial x$  at the growth front, respectively, taken over the whole period of growth. The left hand term of Eq. [4],  $V$ , can now be replaced by the average growth rate,  $V_{av}$ , or the length of the crystal divided by the time of growth.

Thus from Eq. [4] a new relation is obtained

$$\frac{V_{av}}{\nabla T} = KD \quad [5]$$

where  $\nabla T$  is a temperature gradient in the melt

$$\nabla T = \frac{dT}{dx} = \frac{T_H - T_L}{W}$$

and

$$K = \frac{\rho_{\text{Ga}}^M}{\rho_{\text{GaP}}^M} \frac{1 - C_{PH}}{1 - 2C_{PH}} \left( \frac{dC_P}{dT} \right)_{T=T_H}$$

$T_L$  is the temperature at the bottom of the crucible.  $\rho^M$  was approximated by the density of pure gallium,  $\rho_{\text{Ga}}^M$ , in mole  $\text{cm}^{-3}$ , because  $C_P$  was small compared to unity in the temperature regions investigated. The saturation concentration,  $C_P$ , as a function of temperature, or the liquidus of gallium-phosphorus system, has been given by M. Rubenstein (6), R. N. Hall (7), and C. D. Thurmond (8), which is approximately expressed in the form

$$C_P = C_{P0} \exp(-E_C/kT)$$

with the constants  $C_{P0} = 1.998 \times 10^{-3}$  and  $E_C = 1.28 \text{ eV}$ . Assuming that the diffusion coefficient can be expressed in the form

$$D = D_0 \exp(-E_D/kT)$$

the following relation is obtained

$$KD = \frac{\rho_{Ga^M}}{\rho_{GaP^M}} \frac{1 - C_{PH}}{1 - 2C_{PH}} C_{Po} D_o \frac{E_C}{kT_H^2} \exp \left[ - (E_C + E_D) / kT \right] \quad [6]$$

Using Eq. [5]  $KD$  was calculated from the experimental results (1), and  $\log KDT_H^2(1 - 2C_{PH}) / (1 - C_{PH})$  has been plotted as a function of  $1/T_H$  in Fig. 1. Values for  $\rho_{Ga^M}$  and  $\rho_{GaP^M}$  at room temperature,  $8.5 \times 10^{-2}$  and  $4.1 \times 10^{-2}$  mole  $cm^{-3}$ , respectively, were employed in the calculation. A straight line was drawn through the points, from which  $D_o$  and  $E_D$  were obtained using Eq. [6]. The results are

$$D_o = 1.8 \times 10^{-2} \text{ cm}^2 \text{ sec}^{-1}$$

$$E_D = 0.65 \text{ eV}$$

Figure 2 shows the same result as Fig. 1 with the ordinate changed to  $D$ . The diffusion coefficient thus obtained,  $8 \times 10^{-5} \text{ cm}^2 \text{ sec}^{-1}$  at  $1100^\circ\text{C}$  is in fair agreement with the values  $5 \times 10^{-5}$  to  $1 \times 10^{-4} \text{ cm}^2 \text{ sec}^{-1}$  adopted by Tiller (3) and other authors (4, 5). D. L. Rode recently measured the diffusion coefficient in his study of the liquid phase epitaxy process of GaP (9). He obtained  $D$  equal to  $5.7 \times 10^{-5} \text{ cm}^2 \text{ sec}^{-1}$  at  $1020^\circ\text{C}$ , which is on the extrapolated line in Fig. 2.

**Estimation of the Time of Nucleation**

The foregoing analysis is based, among others, on the approximation that the growth proceeds nearly steadily throughout a run. Actually, however, the growth does not start until the melt reaches supersaturation. Once the growth starts, its rate is at first greater than the steady-state growth rate because of the supersaturation in the melt. Thus in the calculation of the average growth rate, the error due to neglecting the time of supersaturation and that due to neglecting the transient growth should partially cancel each other, resulting in an over-all error smaller than either of the two. Therefore, it suffices to estimate the time from

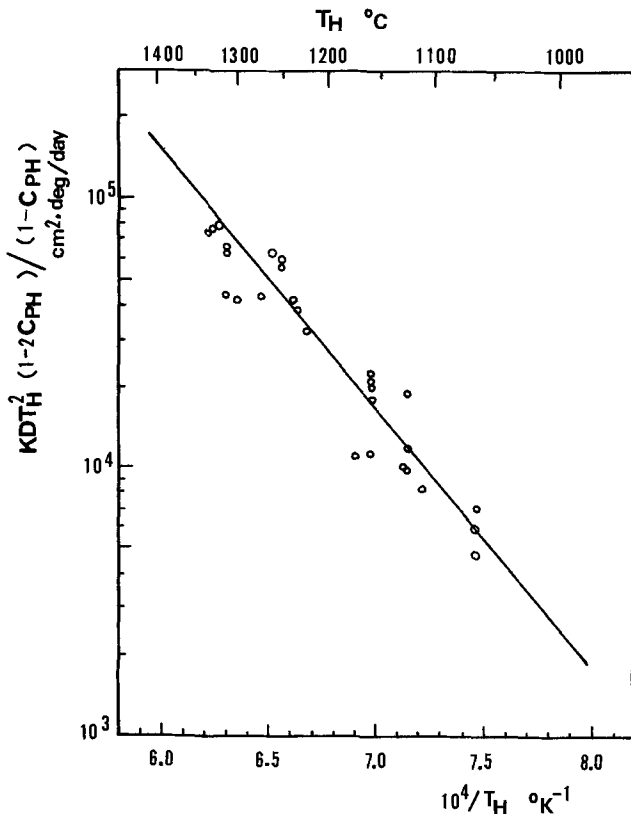


Fig. 1. Relation of  $KDT_H^2(1 - 2C_{PH}) / (1 - C_{PH})$  vs.  $1/T_H$ .  $D$  is the diffusion coefficient of phosphorus in gallium and

$$K = \frac{\rho_{Ga^M}}{\rho_{GaP^M}} \frac{1 - C_{PH}}{1 - 2C_{PH}} \left( \frac{dC_P}{dT} \right)_{T=T_H}$$

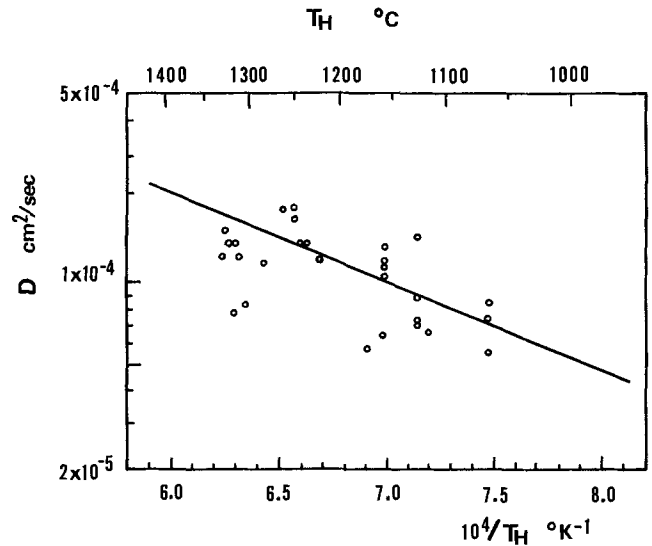


Fig. 2. Temperature dependence of the diffusion coefficient. The straight line is given by  $D = 1.8 \times 10^{-2} \exp(-0.65 \text{ eV}/kT) \text{ cm}^2 \text{ sec}^{-1}$ .

the start of the run to nucleation in order to estimate the over-all error.

Initially the concentration of phosphorus in the gallium melt is zero everywhere. At time  $t = 0$ , a thin film of GaP is formed on the surface of the melt and remains there throughout a run, thereby keeping the concentration at the surface constant. Then the concentration of phosphorus in the melt is given by Ref. (10). Here the concentration is expressed in mole fraction in place of mole  $cm^{-3}$  because the density of the melt is nearly constant in the concentration range in question.

$$C = C_{PH} \sum_{n=0}^{\infty} (-1)^n \left\{ \operatorname{erfc} \frac{(2n+1)W-x}{2\sqrt{Dt}} + \operatorname{erfc} \frac{(2n+1)W+x}{2\sqrt{Dt}} \right\}$$

where the origin of  $x$  coincides with the bottom of the crucible because no solidification occurs yet. The volume increase of gallium due to dissolution of phosphorus is ignored. Figure 3 shows the concentration profiles at various times. In Fig. 4 the concentration at the bottom of the crucible,  $C_L$ , is shown as a function of a parameter  $Dt/W^2$ . For a rough estimate take  $D = 0.9 \times 10^{-4} \text{ cm}^2 \text{ sec}^{-1}$  and  $W = 3 \text{ cm}$ , then from Fig. 4  $t \sim 10^5 \text{ sec}$  is obtained for  $C_L = 0.9C_{PH}$ , which gives a small amount of supersaturation. In our experiments the saturation concentration at the bottom,  $C_{PL}$ , ranged from  $0.5 C_{PH}$  to  $0.8 C_{PH}$ . The times necessary for  $C_{PL}$  to reach  $0.5 C_{PH}$  and  $0.8 C_{PH}$  are  $4 \times 10^4$  and  $8 \times 10^4 \text{ sec}$ , respectively. Experimentally small crystals were observed in one day's run. Since the time of a run is of

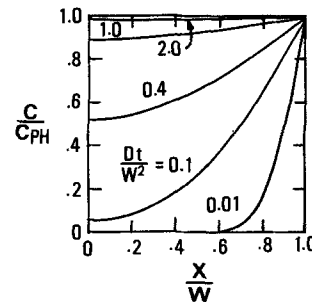


Fig. 3. Concentration of phosphorus in the melt as a function of time and position.  $W$  is the depth of the melt,  $D$  the diffusion coefficient, and  $t$  the time. The surface concentration is fixed at  $C_{PH}$ , and the initial concentration in the melt is zero.

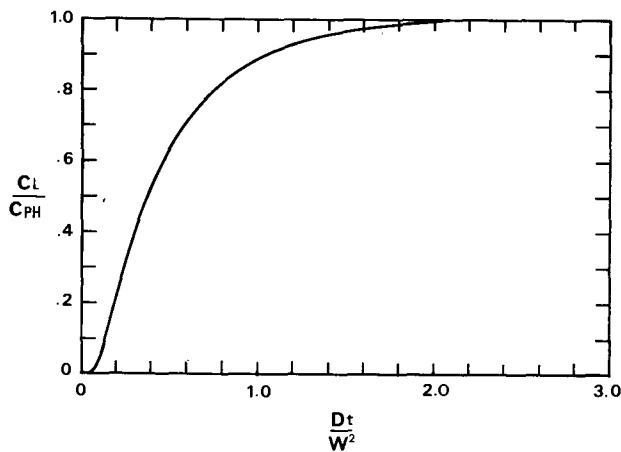


Fig. 4. Concentration of phosphorus in the melt at the bottom of a crucible as a function of time. Initial and boundary conditions are the same as those of Fig. 4.

the order of  $10^6$  sec, we may be overestimating the time of growth by less than 10% by equating it to the time of a run.

#### Conclusions

The diffusion process in SSD method was analyzed and the relation between the diffusion coefficient and the growth rate was derived. From experimental data the diffusion coefficient of phosphorus in gallium was obtained as  $D = 1.8 \times 10^{-2} \exp(-0.65 \text{ eV}/kT) \text{ cm}^2 \text{ sec}^{-1}$ . The calculated values are in fair agreement with the diffusion coefficients published by other authors.

#### Acknowledgments

We would like to express our hearty thanks to Messrs. H. Nagasawa and K. Sawada of the Research Center for their cooperation. Continual encouragement by Drs. S. Shima and Y. Kanai have been of strong support to us through this work. We also would like to express our thanks to Dr. A. Shibata for his critical comments on the manuscript.

Manuscript submitted July 31, 1973; revised manuscript received Nov. 14, 1973.

Any discussion of this paper will appear in a Discussion Section to be published in the December 1974 JOURNAL. All discussions for the December 1974 Discussion Section should be submitted by Aug. 1, 1974.

#### REFERENCES

1. K. Kaneko, M. Ayabe, M. Dosen, K. Morizane, S. Usui, and N. Watanabe, *Proc. IEEE*, **61**, 884 (1973).
2. K. Kaneko and N. Watanabe, U.S. Pat. 3,615,203; British Pat. 1,251,251; Can. Pat. 895,251.
3. W. A. Tiller, *J. Crystal Growth*, **2**, 69 (1968).
4. T. S. Plaskett, *This Journal*, **116**, 1722 (1969).
5. H. Rodot, A. Hruby, and M. Schneider, *J. Crystal Growth*, **3 & 4**, 305 (1968).
6. M. Rubenstein, Abstract 65, p. 129, Vol. 11, No. 1, Electrochemical Society Extended Abstracts, Spring Meeting, Los Angeles, Calif., May 6-10, 1962.
7. R. N. Hall, *ibid.*, **110**, 385 (1963).
8. C. D. Thurmond, *J. Phys. Chem. Solids*, **26**, 785 (1965).
9. D. L. Rode, Private communication.
10. H. S. Carslaw and J. C. Jaeger, "Conduction of Heat in Solids," 2nd ed., p. 309, Oxford University Press, England (1959).

## Implantation of Argon into $\text{SiO}_2$ Films Due to Backsputter Cleaning

F. B. Koch,\* R. L. Meek,\* and Daniel V. McCaughan<sup>1</sup>

Bell Laboratories, Murray Hill, New Jersey 07974

#### ABSTRACT

Argon in concentrations up to  $2(10)^{16} \text{ cm}^{-2}$  has been found in  $\text{SiO}_2$  after backsputter cleaning with 150V  $\text{Ar}^+$  ions in a low voltage triode sputtering apparatus. The argon has been detected directly by Rutherford backscattering analysis with 2 MeV  $\text{He}^+$  ions. The highest argon content was found in a sample subjected to 2 min of backsputtering at a rate of about 50 Å/min. Immediately after this backsputtering, 2000Å of tungsten was sputter deposited. During a subsequent vacuum anneal at 850°C for 20 min, bubbles about 10 μm in diameter appeared under the tungsten metallization. The bubbles apparently were caused by internal pressure resulting from the outdiffusion of the entrapped argon. Surface contamination of the backsputtered  $\text{SiO}_2$  by W, Cu, and Fe was also detected. This was evidently caused by redeposition of sputtered material from adjacent parts of the sputtering apparatus since these elements increased steadily in concentration with backsputtering time. The maximum contamination of  $8(10)^{14}$  copper atoms per  $\text{cm}^{-2}$  after 10 min is nearly a monolayer. Annealing experiments established that 20 min at 600°C was sufficient to reduce the argon level to near or below detection limits [ $\sim 5(10)^{13} \text{ cm}^{-2}$ ] in both backsputtered Si and  $\text{SiO}_2$ .

Low voltage triode sputtering is attractive for metallization of silicon-integrated circuits since a wide variety of metals and even insulators may be deposited. The possibility of sputter cleaning the surface by  $\text{Ar}^+$  ion bombardment immediately prior to the deposition is an important feature in certain applications such as contact metallizations where the cleanli-

ness of the Si/metal interface is crucial. The fact that all materials sputter at varying rates presents some problem in the design of a sputtering apparatus. All electrically isolated surfaces exposed to the plasma assume a negative potential (the wall potential) and are thus subject to  $\text{Ar}^+$  ion bombardment. This paper describes an application of the highly sensitive technique of Rutherford ion backscattering to evaluate the extent of surface contamination and argon implantation under typical operating conditions for a particular triode sputtering apparatus.

\* Electrochemical Society Active Member.

<sup>1</sup> Present address: Royal Radar Establishment, Great Malvern, Worcestershire, England.

Key words: backsputtering, ion trapping, metallization, sputtering.

### Experimental Procedure

**Low voltage triode sputtering.**—In a triode sputtering system, a discharge is run between an anode and a hot cathode to maintain a high density plasma. The sputtering target is an auxiliary electrode, located and biased so that it can extract ions from the plasma. In this case, the main discharge runs at 4A and is maintained by a potential of about 100V between anode and cathode. A high current discharge at low voltage is possible because the cathode is a copious source of thermionic electrons. The cathode, a 0.125 cm diameter Ta wire, is heated to incandescence by an a-c current of 65A. The pressure was fixed at 2 mTorr of high purity argon. Figure 1 illustrates the apparatus. The plasma is confined by an aluminum tunnel as shown, with openings to allow the  $\text{Ar}^+$  ions to be extracted from the plasma so that they bombard the sputtering target or the sample surface as desired. The silicon sample wafers rest on a stainless steel grid-work as shown, and can be heated to 950°C during the deposition by tantalum heater coils if so desired. Sputter deposition of tungsten at about 120 Å/min occurs when a voltage of -200V is applied to the source target (relative to the cathode) so that sputtered metal atoms pass through both tunnel openings and are deposited on the sample surface. It is also possible to sputter material (50Å of  $\text{SiO}_2$ /min) from the sample surfaces to effect a cleaning by applying an 800 kHz rf voltage to the pedestal bearing the samples (backspattering). The  $\text{Ar}^+$  ions are accelerated to the sample surface during the negative half-cycle by a voltage adjusted for a peak value of -150V relative to the cathode. Contamination of the sample surface may conceivably occur during the backspattering due to redeposition of sputtered material from structural parts of the apparatus such as the sample pedestal, the plasma confinement tube, or the tantalum cathode.

**Rutherford backscattering analysis.**—Surface analysis using Rutherford backscattering (1-3) of mega-electron volt  $\text{He}^+$  ions has been described in detail elsewhere (1, 2). Briefly, the energy of a backscattered ion identifies the mass of the atom it scattered from, and the number of backscattered ions determines the number of scattering atoms. For scattering from target atoms of a given mass, the energy scale may be converted to a depth scale through a knowledge of the kinematic energy loss and the stopping power.

In these experiments, a beam of 2 MeV  $\text{He}^+$  ions collimated to  $\sim 0.05^\circ$  through two Ta collimators 1 mm in diameter and about 2m apart was used. The backscattered He ions were detected at  $\theta_L = 177^\circ$  in a 50 mm<sup>2</sup> surface barrier detector having an energy resolution of 16 keV. This energy resolution corresponds to a depth resolution of about 200Å. Secondary electron suppression and pile-up rejection electronics were

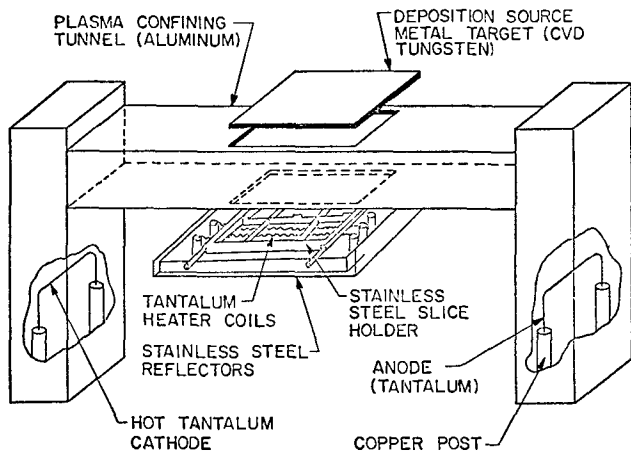


Fig. 1. Low voltage triode sputtering apparatus

used. Samples were surrounded by a baffle cooled to liquid nitrogen temperature and were mounted in a two axis goniometer. The scattering chamber was maintained at  $10^{-6}$  Torr and the He ion fluence was typically  $10^{16}$  cm<sup>-2</sup>. Typical detection limits are  $10^{13}$  cm<sup>-2</sup> for masses near Cu and  $10^{12}$  cm<sup>-2</sup> for masses near Au.

### Experimental Results

The initial impetus for the present investigation was to explain the formation of what are apparently bubbles under a 2000Å thick sputtered tungsten film. The tungsten had been deposited over a 2800Å steam oxide through which contact holes had been etched to the underlying silicon wafer. The substrate had been rf backspattered for 2 min with 150V, immediately prior to the W deposition, to remove about 100Å of the oxide. Following the deposition, the tungsten was etched to give a contact test pattern and the sample was vacuum annealed for 20 min at 850°C. During this anneal the tungsten metallization took on the microscopic appearance shown in Fig. 2. Shown are an optical micrograph (upper photograph) and a scanning electron micrograph taken at 55° sample tilt (lower photograph) showing bubbles about 10 μm in diameter and with an area concentration of about  $5(10)^5$  cm<sup>-2</sup>. Neither did a sample backspattered for 1 min only, nor did a control sample which was not backspattered show any bubbles when subjected to the same annealing treatment.

The bubbles seen in Fig. 2 are not always seen after metallization of backspattered surfaces but are not an isolated instance. They have not been observed with metal silicides (PtSi, NiSi) formed on backspattered silicon (4, 5) nor in deposition on  $\text{SiO}_2$  of metals such

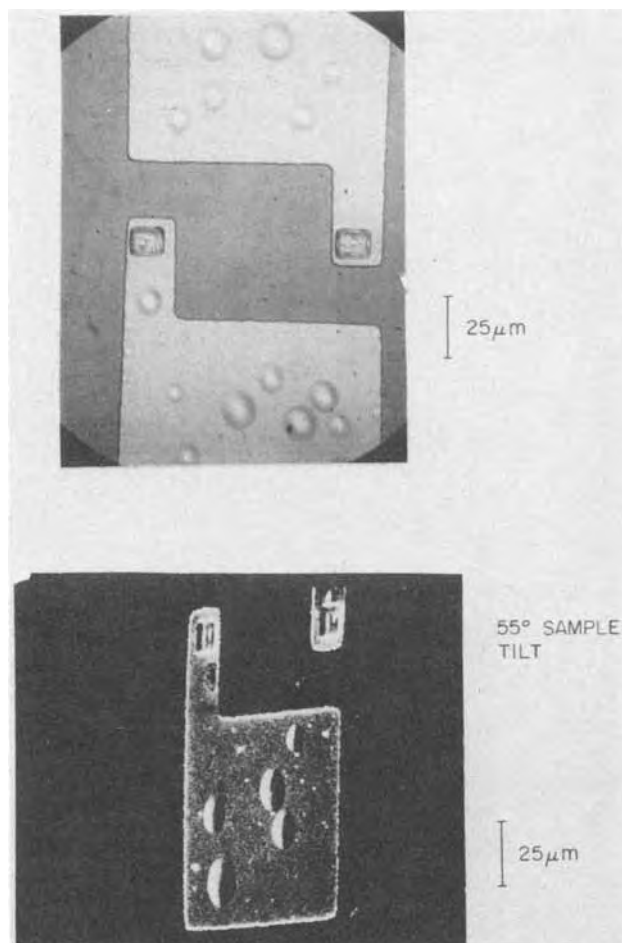


Fig. 2. Upper micrograph shows tungsten metallization at 660× where bubbles have apparently formed at the W/Si interface. Lower photograph shows SEM secondary electron images taken with sample tilt of 55°.

as Cr or Ti which react strongly with  $\text{SiO}_2$ . Bubbles have only been observed after prolonged backspattering followed by tungsten metallization.

We have attempted to investigate whether these bubbles resulted from argon entrapped in the oxide during backspattering and subsequently released during the vacuum annealing. The tungsten was etched from unannealed portions of the samples backspattered for 1 and 2 min. These samples and other backspattered samples were then analyzed by ion backscattering for argon content and surface contaminants. The analysis shows that the sample in which the bubbles were formed did indeed contain a large amount of argon, more argon, in fact, than some other samples which had been backspattered for up to five times as long.

Figure 3 shows a representative energy spectrum (scattered ion yield as counts per channel *vs.* scattered ion energy) for a sample which was backspattered for 8 min at 150V. The energy of ions scattered from oxygen, silicon, argon, iron, copper, and tungsten at the surface are indicated. The iron, copper, and tungsten undoubtedly result from redeposition of sputtered material from adjacent structures in the sputtering system since the impurity peaks grow steadily with backspattering time (as will be discussed later). The size and width of the argon peak shows that  $1.2(10)^{15}$  argon atoms have been trapped within  $200\text{\AA}$  of the surface (the resolution of the measurement).

Figure 4 is the spectrum for the sample which showed the bubbles. In this case the argon surface concentration is  $2(10)^{16}\text{ cm}^{-2}$  and the argon distribution extends considerably further into the oxide. The argon volume concentration is plotted in the insert to Fig. 4, and at the surface is  $2(10)^{21}\text{ cm}^{-3}$ . The argon distribution was confirmed by a controlled etching removal of the  $2800\text{\AA}$  oxide. Removal of  $200\text{\AA}$  of oxide gave a spectrum with only the expected small change in energy scale and peak height, whereas removal of  $1500\text{\AA}$  of oxide eliminated the peak. On the surface of

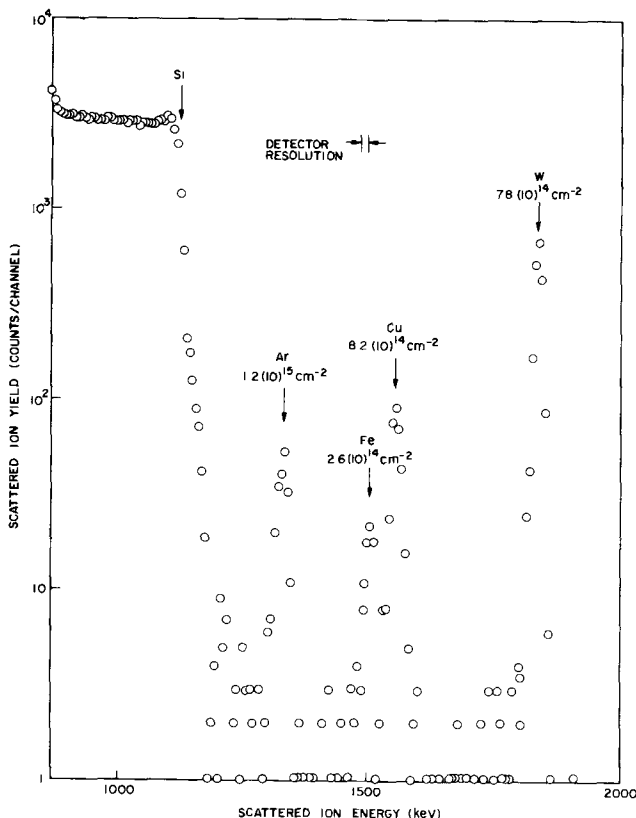


Fig. 3. Backscattered ion energy spectrum from a representative sample which had been backspattered 8 min. It shows  $1.2(10)^{15}$  argon atoms/cm<sup>2</sup>.

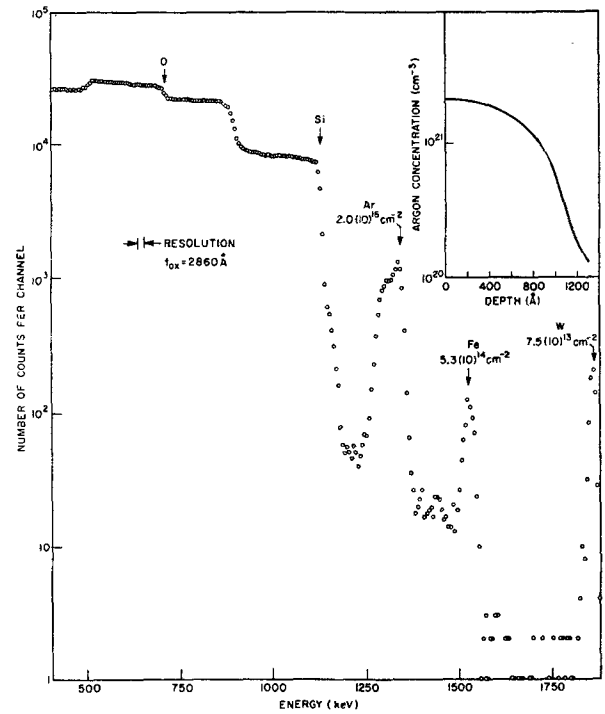


Fig. 4. Backscattered ion energy spectrum from sample which formed the bubbles shown in Fig. 2. Argon profile is indicated in the insert.

this sample iron and tungsten are present at a concentration of  $5.3(10)^{14}\text{ cm}^{-2}$  and  $7.5(10)^{13}\text{ cm}^{-2}$ , respectively.

Table I presents the measured argon content for bare and oxidized silicon samples subjected to backspattering for various times. The 2 min backspattered oxide which formed bubbles had the highest argon concentration of  $2(10)^{16}\text{ cm}^{-2}$ ; only one other sample had an argon concentration in the  $10^{16}\text{ cm}^{-2}$  range. Some samples with 3-10 min backspattering times had argon content about one order of magnitude less. This variability in argon concentration, together with the deep penetration of argon in the two samples with the high argon content, constitute some of the most interesting findings reported here. The projected range of 10 keV  $\text{Ar}^+$  in  $\text{SiO}_2$  has not been measured, but certainly would be less than  $100\text{\AA}$  since the calculated range of 10 keV  $\text{Ar}^+$  in  $\text{SiO}_2$  is only  $123\text{\AA}$  (6). In the Discussion section, the possibility will be considered that thermal diffusion of the argon during backspattering is responsible for the observed penetration depths of about  $1000\text{\AA}$  for some samples.

Figure 5 shows the buildup of surface contaminant tungsten, copper, and iron with backspattering time. This buildup with backspattering time strongly indicates that the contamination originates from redeposition of sputtered material from adjacent parts of the apparatus (7). This finding is not surprising in view of

Table I.

Substrate	Sputtering time (min)	Argon concentration ( $\text{cm}^{-2}$ )
$\text{SiO}_2$ on Si	1	$2.4(10)^{15}$
$\text{SiO}_2$ on Si	1	$2.8(10)^{15}$
$\text{SiO}_2$ on Si	2	$2.0(10)^{16}$ *
$\text{SiO}_2$ on Si	3	$1.9(10)^{15}$
$\text{SiO}_2$ on Si	5	$1.3(10)^{15}$
$\text{SiO}_2$ on Si	8	$1.2(10)^{15}$
$\text{SiO}_2$ on Si	10	$2.4(10)^{15}$
Bare Si	5	$3.0(10)^{14}$
Bare Si	10	$2.8(10)^{14}$

\* Sample which developed bubbles under the tungsten metallization.

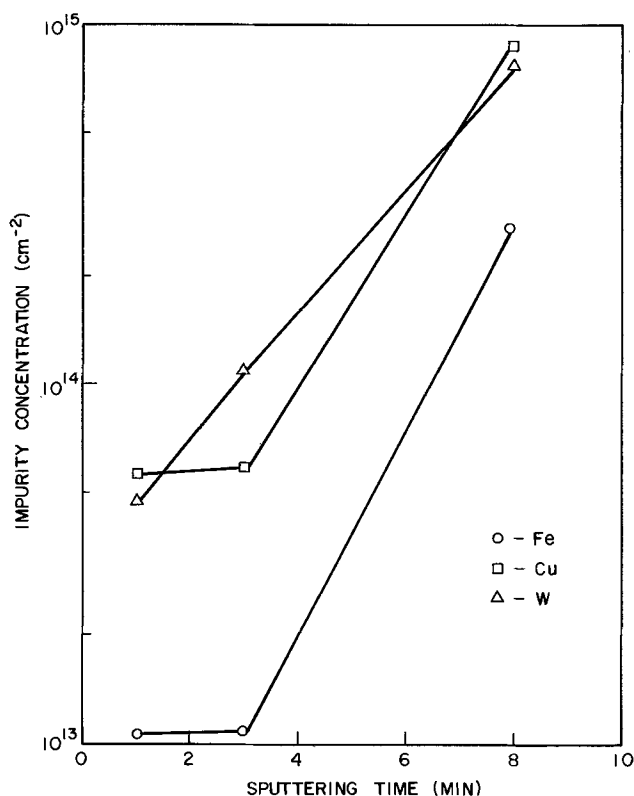


Fig. 5. Buildup of surface impurities of iron, tungsten, and copper with backsputtering time.

the results of Vossen *et al.* (8) who found sputter re-deposition of up to ten monolayers of Pt, Cu, or Mo when a silicon wafer was sputtered while resting on a plate consisting of one of these metals. The tungsten comes from that which was deposited in the apparatus on previous depositions. The copper and iron probably originate from the copper vacuum feedthroughs and the stainless steel pedestal, respectively. No Al from the tunnel was detected although the large background from silicon lowers the detection sensitivity to about  $10^{16}$  atoms per cm<sup>2</sup>. It should be noted that the observed impurity deposition rates are the net difference between an arrival rate, which might be significantly higher, and the backsputter removal rates.

Finally, we have studied argon outdiffusion during vacuum annealing as a function of temperature. Figure 6 shows the amount of argon remaining in samples of bare Si and SiO<sub>2</sub>, previously backsputtered for 10 min *vs.* the annealing temperature; portions of the sample were annealed for 20 min at each temperature. A slight decrease in argon content was observed after a 400°C anneal. The argon was no longer confined to the surface but had penetrated about 500Å. After a 600°C anneal no argon could be detected in either sample.

### Discussion

It is well known that ions used for sputtering can be incorporated into the bombarded substrate. Comas and Wolicki (9) showed that more than  $10^{16}$  argon atoms/cm<sup>2</sup> could be trapped in silicon by sputtering at less than 200 eV.

Their method, using neutron activation, gives, however, no depth information. Schwartz and Jones (10) used x-ray fluorescence to show that an argon/Si ratio of up to 0.1 could be achieved by varying sputtering parameters, but again their method gives no depth information. All this work is consistent with results on ion trapping in metals (11-13) in which it has been shown that up to many monolayers of inert gas can be incorporated in films ion bombarded at low to medium energies. We believe, however, that our work is one of the first to show accurately the location and

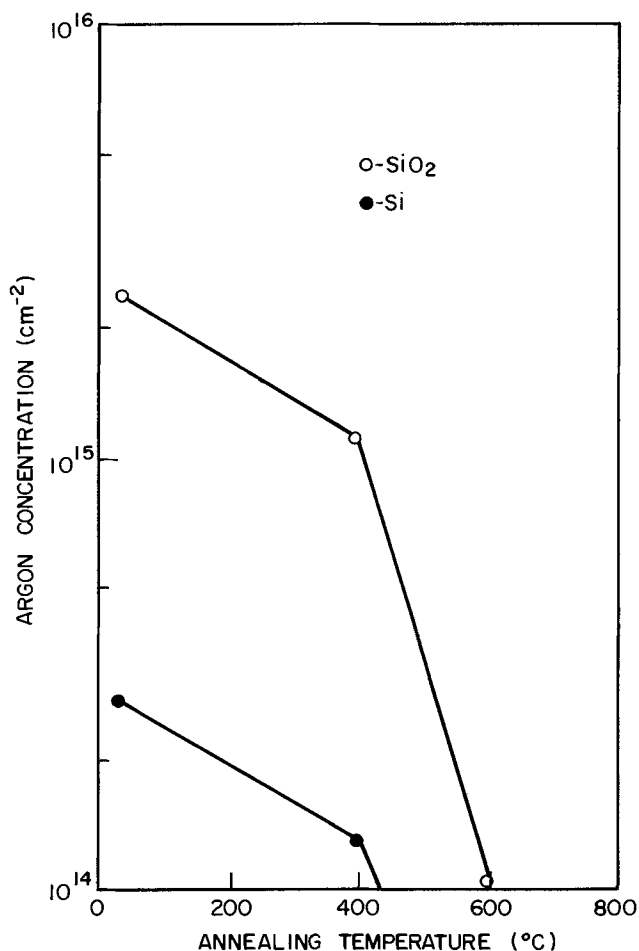


Fig. 6. Decrease in argon concentration as determined from the integrated area under the argon peak as a function of the vacuum annealing temperature. Samples of SiO<sub>2</sub> and bare Si were backsputtered for 10 min and annealed for 20 min.

concentration profile of argon buried in SiO<sub>2</sub>, and relate these parameters to bubble formation.

The best explanation for the bubbles shown in Fig. 2 seems to be that argon diffuses from the SiO<sub>2</sub> to the SiO<sub>2</sub>/tungsten interface. At a critical concentration of argon at this interface, adhesion of the metal to the insulator will be lost and a small blister will be formed under the metal. The blister will then easily grow to an observable size with further argon diffusion due to the stress concentration around the periphery. One might inquire whether a concentration of  $2(10)^{16}$  argon atoms/cm<sup>2</sup> would be sufficient for this process. If we assume that this amount of argon is confined at 850°C to the observed  $5(10)^5$  hemispherical bubbles, each with a diameter of 10 μm, the pressure inside the bubbles is calculated to be a surprisingly high 40 atm.

Thermal diffusion of argon into the film during backsputtering of the surface seems to be required to explain the large concentrations and penetration depths of argon seen in several samples. Diffusion of argon in fused silica was studied by Perkins and Begeal (14) in the temperature range 650°-900°C. They found their data could be represented by the equation  $D = D_0 \exp(-E/kT)$  where  $D_0 = 1.21 \pm 0.007$  cm<sup>2</sup> sec<sup>-1</sup> and  $E = 28,670 \pm 120$  cal/g-atom. A plot of the expected diffusion distance,  $\sqrt{2Dt}$ , *vs.* temperature for diffusion times of 2 and 20 min is shown in Fig. 7. In order to account for argon penetration of 1000Å in 2 min, a slice temperature of about 475°C would be required. The condition  $\sqrt{2Dt} < 200\text{Å}$  limits the sample temperature to a maximum of 375°C for the bulk of the samples where argon penetration was not observed.

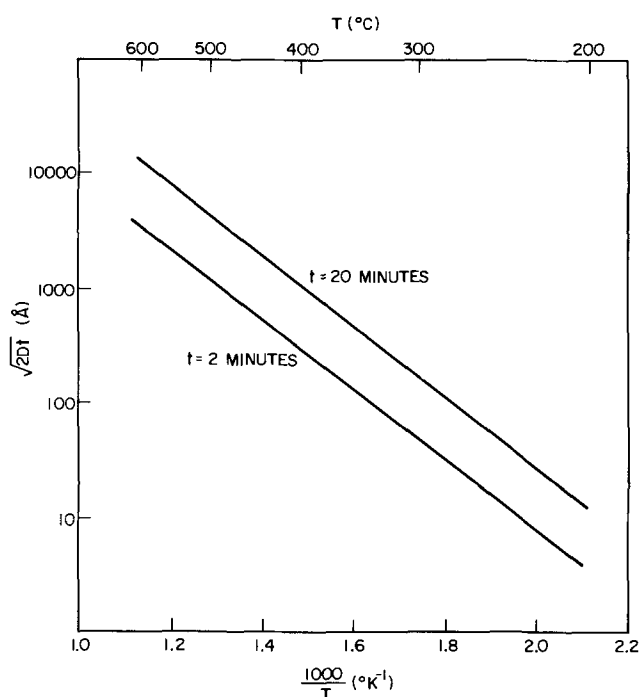


Fig. 7. The diffusion length  $\sqrt{2Dt}$  vs. the diffusion temperature for times of 2 and 20 min. The values of  $D$  as function of temperature were extrapolated from the data of Perkins and Begeal (14).

These temperatures may be compared to the substrate temperatures found in previous calibration runs using a Pt-Pt 10% Rh thin-film thermocouple to measure the heating during 150V backsputtering (15). There a temperature rise of 200°C was usually observed. On some calibration runs, however, the temperature rise was as much as 400°C. This larger temperature rise resulted in intense local melting of the thin-film thermocouple. There was some tendency for discharges to occur during the first backsputtering of an oxide after exposure to the atmosphere (16). The unusual heating of a sample during an occasional run where these discharges occurred seems to be the most likely explanation for the higher than normal argon content in some samples.

The change in argon content with vacuum annealing temperature shown in Fig. 6 is not surprising in view of the expected diffusion coefficients. Referring to Fig. 7,  $\sqrt{2Dt} = 1000\text{\AA}$  for 20 min at 400°C, so diffusion will cause considerable escape to the surface. At 600°C,  $\sqrt{2Dt} \approx 1\ \mu\text{m}$ . So it is expected that the argon which has not been lost at the surface will have diffused sufficiently into the bulk to be undetectable.

A quantitative theory for the amount of argon entrapped during backsputtering would have to take into account the total dose of  $\text{Ar}^+$  impinging on the surface, the trapping probability, the sputter removal rate of argon already entrapped, and the redistribution and surface loss caused by thermal diffusion. In this case, the flux of  $\text{Ar}^+$  is roughly  $1\ \text{mA}/\text{cm}^2$ , corresponding to a total dose of  $7.5(10)^{17}\ \text{Ar}^+\ \text{cm}^{-2}$ . Without attempting to formulate a detailed model, we note that less than 1% of the total dose of argon is usually trapped but that somewhat more than 1% was

trapped in two samples. Most samples will have an argon content limited by a steady-state concentration at the surface, but thermal diffusion away from the surface when the sample temperature is unusually high will increase the steady-state value considerably.

### Summary

We have profiled the argon concentration in rf backsputtered  $\text{SiO}_2$  films by Rutherford scattering. Some samples showed anomalously high argon concentration, up to  $2(10)^{16}\ \text{cm}^{-2}$ . In such a sample, which, after backsputtering, had 2000Å of tungsten deposited by triode sputtering, vacuum annealing for 20 min at 850°C caused lifting of the tungsten film in bubbles of  $10\ \mu\text{m}$  in diameter at an area concentration of  $5(10)^5\ \text{cm}^{-2}$ . Samples with lower argon content did not show bubble formation.

In one sample which showed an argon concentration of  $2(10)^{16}\ \text{cm}^{-2}$ , argon in the oxide was still detectable at a depth of 1200Å. In other samples with lower argon concentration, the profile did not extend below 200Å (the depth resolution limit of the measurement). Annealing in vacuum to 600°C for 20 min was in all cases sufficient to reduce the argon concentration below detection limits.

The concentration of surface contaminants has also been determined as a function of backsputtering time. Iron, copper, and tungsten have been observed on the  $\text{SiO}_2$  surface in concentrations of up to  $8.4(10)^{14}\ \text{cm}^{-2}$ . These seem to be associated with redeposition of material from surrounding surfaces onto the sample.

Manuscript submitted May 16, 1973; revised manuscript received Oct. 24, 1973. This was Paper 250 presented at the Miami Beach, Florida, Meeting of the Society, Oct. 8-13, 1972.

Any discussion of this paper will appear in a Discussion Section to be published in the December 1974 JOURNAL. All discussions for the December 1974 Discussion Section should be submitted by Aug. 1, 1974.

### REFERENCES

1. R. L. Meek, T. M. Buck, and C. F. Gibbon, *This Journal*, **120**, 1241 (1973).
2. R. L. Meek, *ibid.*, **120**, 308 (1973).
3. J. A. Davies, J. Denhartog, L. Ericksson, and J. W. Mayer, *Can. J. Phys.*, **45**, 4053 (1967).
4. J. M. Andrews and F. B. Koch, *Solid-State Electron.*, **14**, 901 (1971).
5. F. B. Koch and P. A. Byrnes, Abstract 191, p. 470, Electrochemical Society Extended Abstracts, Fall Meeting, Atlantic City, N. J., Oct. 4-8, 1970.
6. W. S. Johnson and J. F. Gibbons, "Projected Range Statistics in Semiconductors," Stanford University Press, Stanford, Calif. (1970).
7. Daniel V. McCaughan and R. A. Kushner, *Thin Solid Films*, In press.
8. J. L. Vossen, J. J. O'Neill, Jr., K. M. Finlayson, and L. J. Royer, *RCA Rev.*, **31**, 293 (1970).
9. J. Comas and E. Wolicki, *This Journal*, **117**, 1197 (1970).
10. G. E. Schwartz and R. E. Jones, *IBM J. Res. Develop.*, **14**, 52 (1970).
11. J. H. Carmichael and E. A. Trendelenberg, *J. Appl. Phys.*, **29**, 1570 (1958).
12. R. S. Nelson, *Phil. Mag.*, **9**, 343 (1964).
13. B. Jouffrey, *J. Microscopie*, **2**, 45 (1963).
14. W. G. Perkins and D. R. Begeal, *J. Chem. Phys.*, **54**, 1683 (1971).
15. F. B. Koch and P. A. Byrnes, Unpublished work.
16. D. V. McCaughan and V. T. Murphy, *J. Appl. Phys.*, **44**, 3182 (1973).

# Impurity Redistribution during Silicon Epitaxial Growth and Semiconductor Device Processing

Paul H. Langer

Bell Laboratories, Allentown, Pennsylvania 18103

and Joseph I. Goldstein

Department of Metallurgy and Materials Science, Lehigh University, Bethlehem, Pennsylvania 18015

## ABSTRACT

A model has been developed that can account for both front and back "autodoping" effects during epitaxial growth as well as impurity redistribution during further high-temperature processing. The model incorporates three dopant fluxes, *i.e.*, (i) the flux from the solid into the gas phase at the rear of the wafer, (ii) the flux from the solid to the front surface of the wafer, and (iii) the flux from the bulk gas phase into the boundary layer near the front surface of the wafer in which transport of dopant occurs by diffusion only. The redistribution of impurities both within the solid semiconductor and in the gas phase are investigated from a theoretical viewpoint. Numerical solutions are obtained using the Crank-Nicolson method. Implications of differences between this approach and previous work are discussed. Calculated results are presented to illustrate the variety of problems that may be solved using this mathematical approach.

The distribution of impurities in epitaxially grown silicon layers plays a major role in the operation of diodes, transistors, and integrated circuits. The impurity redistribution that occurs during silicon epitaxial processing and semiconductor device fabrication is dependent upon processing times and temperatures, diffusivities, evaporation rates, and segregation coefficients of the dopants in the solid and gaseous phases. A model for the redistribution process would enable one to assess the critical steps in the fabrication sequence and predict the effect of process changes on the impurity distribution in the semiconductor. A typical device processing sequence may consist of fifteen discrete high-temperature steps that affect the impurity redistribution. Since the results of the prior step form the initial conditions for the present step, analytical solutions to the diffusion or transport equations are not available. Therefore, a sequential numerical technique is the obvious choice to solve this type of processing problem. At present only fragmentary parts of this problem have been solved and no complete model exists.

## Background—Epitaxial Growth

Since the largest single unknown in calculating the impurity redistribution during device fabrication is the redistribution due to epitaxial growth, this process step will be treated in great detail. The prior efforts on modeling the substrate and layer impurity redistribution during epitaxial silicon growth can be divided into three categories based upon the source of the impurity. The first and earliest approach involved the transfer of dopant from the front surface of the substrate (1-2), mixing of this dopant with the gas phase, and subsequent reincorporation of this dopant into the growing epitaxial layer. This treatment completely ignored solid-state diffusion as the other major mechanism for dopant transport. The second approach to the redistribution involved the transport of dopant by diffusion in the solid only (3-4). The effects of the ambient gas phase were neglected. A more detailed analysis of this approach was made by Abe *et al.* (5). A numerical approach was used in order to treat the steps prior to the deposition of the epitaxial layer. The influence of the gas phase on the redistribution process was ignored and the case of slow layer growth was not successfully treated. The third approach to the redistribution prob-

lem involved the transfer of dopant from the back surface of the wafer into the ambient and its subsequent incorporation into the growing epitaxial layer (6-8). However, the effects of solid-state diffusion were ignored.

All three approaches have been used and the results of the models have been verified over a limited range of experimental conditions. The three approaches give a wide range of predictions when applied to any one common system. Since front and back surface evaporation and diffusion of dopant are all occurring simultaneously throughout the epitaxial growth and other high-temperature processing steps, a model incorporating all of the three approaches would provide a better description of the process.

The type of dopant transport phenomenon that will predominate in a given epitaxial deposition cycle is a function of the distribution of dopant in the substrate along with the dopant intentionally added to the gas phase. Three dopant fluxes must be considered to completely define the boundaries of the gas-solid composite system. The first flux is that between the solid and the gas at the back boundary. This flux is the one that has been treated by Joyce *et al.* (6), Shepherd (7), and Skelly (8) as the sole contributing factor to the "autodoping" phenomenon. A similar flux existing at the front surface of the wafer gives the rate of transfer of dopant from the solid to the front gas-solid interface. This flux is of great importance in understanding autodoping associated with the first few microns of growth.

After the first few microns of growth in normal epitaxy (*i.e.*, lightly doped layer on highly doped substrate) the back transport effect predominates. The third flux is that flux which controls the rate of transport of dopant from the bulk of the gas phase to the gas-phase boundary layer near the front interface. In the gas-phase boundary layer, diffusion is the sole transport mechanism. This flux can include intentionally added dopant as well as the dopant released at the back surface.

The following treatment will determine the three dopant fluxes and establish the boundary conditions for the problem. The doping of a layer with the same dopant as in the substrate as well as different dopant species is considered. Also nonuniform initial conditions are treated by the numerical method employed to solve Fick's Second Law in the solid.

**Key words:** silicon, epitaxy, semiconductor, device processing redistribution.



Theory

The solution of the problem will involve the treatment of three regions: (i) the bulk gas phase where all the dopant is uniformly distributed; (ii) the gas-phase boundary layer where transport of dopant is by diffusion only; and (iii) the solid where transport of dopant occurs only by diffusion. Figure 1 depicts a section of an epitaxial reactor with the wafer on a heated susceptor. The various sources of dopant are shown schematically. To reduce this situation to a one-dimensional case consider a line  $z = z_0$ , perpendicular to the wafer in the plane A-A. Figure 2 shows the concentration distribution along the line  $z = z_0$  from the wall of the reactor,  $x = w$  to the back surface of the wafer,  $x = b$ . This line also passes through the boundaries  $x = d$  and  $x = i$  which respectively separates the bulk gas phase from the gas-phase boundary layer, and the gas-phase boundary layer from the front surface of the wafer. All subsequent analysis of impurity redistribution problems will refer to the dopant movement along the line  $z = z_0$ . A mathematical model describing the redistribution sequence can be formu-

lated since the impurity redistribution within the solid and within the gas-phase boundary layer is diffusion controlled. For a diffusion-controlled process Fick's Second Law (for constant diffusivity,  $D$ ) in one dimension is

$$\frac{\partial C(x, t)}{\partial t} = D \frac{\partial^2 C(x, t)}{\partial x^2} \quad [1]$$

where  $C(x, t)$  is the concentration and  $x$  and  $t$  are the spatial and time variables, respectively. The one-dimensional assumption is applicable to the case of uniformly doped epitaxial structures normally encountered in semiconductor device fabrication since the diameter to thickness ratio of the wafer is usually greater than 150 to 1. For analysis of subdiffused substrates encountered in integrated circuit fabrication the one-dimensional analysis does not strictly apply, since transport of dopant from the diffused regions to the nondiffused areas occurs parallel to the surface of the wafer. This dopant transfer may still be analyzed in one dimension by treating the diffused and nondiffused regions as separate structures linked by an intermediate gas phase. In order to obtain the boundary condition at the front gas-solid interface ( $x = i$ ) the mass balance will be constructed about the interface. The flux  $F(i, t)$  in the solid at the interface  $x = i$  will then be expressed in terms of solid concentrations and concentrations of dopant in the bulk of the gas phase. Both of these concentrations may be measured experimentally.

As can be seen from Fig. 1 there are two sources of dopant that may enter the growing epitaxial layer by way of the gas phase. These sources are the flux of intentionally added dopant,  $F_a$  and the flux of dopant escaping from the back and sides of the wafer  $F(b, t)$ . These dopant fluxes will be used to define the time rate of change of dopant,  $Q' = dQ/dt$ , in control region 1 shown in Fig. 3. Let one consider the dopant flow into and out of region 1. This area is in the  $x-y$  plane between  $x = w$  to  $x = d$  and  $y = y_1$  to  $y = y_2$ . The dopant entering this region consists of the flux of intentionally added impurities,  $F_{ain}$ , plus some fraction ( $f_1$ ) of the flux of dopant escaping from the back of the wafer  $f_1 F(b, t)$ . Of this dopant entering region 1 across  $y_1$  some will leave in the  $y$ -direction across  $y_2$ . The rest will enter region 2 in the  $x$ -direction, toward the solid, crossing the boundary,  $x = d$ .

Therefore, the rate of change of dopant in region 1,  $Q'_1$ , may be written as

$$Q'_1 = F_{in} - F_{out} \quad [2a]$$

or

$$Q'_1 = \{F_{ain} + f_1 F(b, t)\} - \{[F_{aout} + (f_1 - f) F(b, t)] + [F(g)(d, t) + f F(b, t)]\} \quad [2b]$$

where  $f$  is the fraction of dopant from the back of the wafer that is crossing the boundary  $x = d$ , in the  $x$ -direction, and going toward the solid.  $F(g)(d, t)$  is the fraction of the intentionally added dopant also going toward the solid in the  $x$ -direction. Therefore,  $[F(g)(d, t) + f F(b, t)]$  is the flux of the dopant leaving region 1 and crossing the boundary,  $x = d$ .

SOURCES OF DOPANT FOR EPITAXIAL LAYER

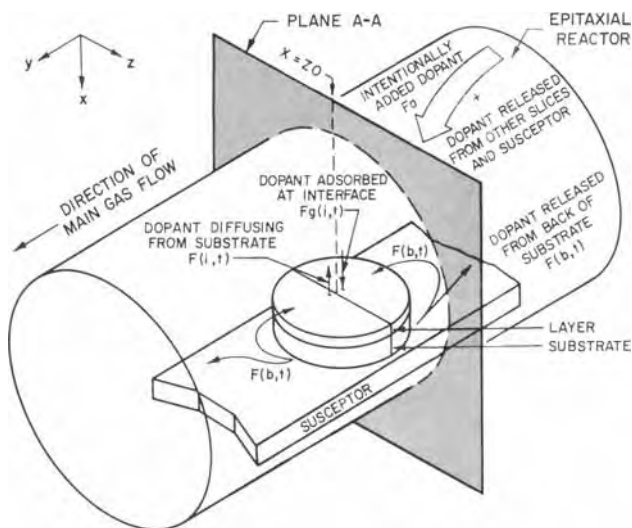


Fig. 1. Schematic representation of an epitaxial reactor showing sources of dopant.

LINE  $Z = Z_0$  IN PLANE A-A

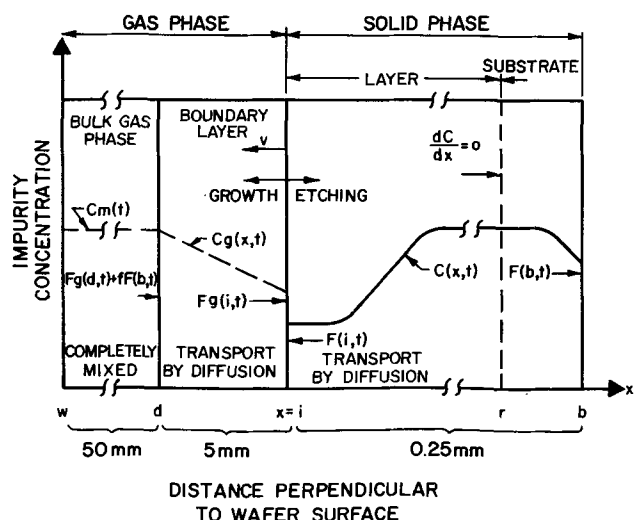


Fig. 2. The concentration distribution along the line  $z = z_0$ , in plane A-A through the epitaxial reactor from the reactor wall to the back surface of the wafer.

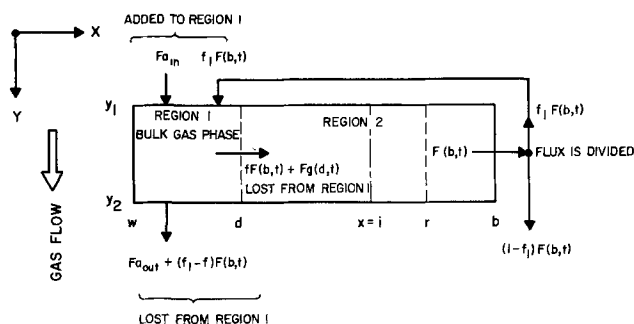


Fig. 3. Control region

Now let one consider the rate of change of dopant  $Q'_2$  (region 2, Fig. 3) in the gas-solid composite system between  $x = d$  and  $x = r$ .  $r$  is a point in the wafer where the concentration gradient is always equal to zero. For semiconductor device fabrication such a point always exists since wafers are usually  $\sim 250\mu$  thick, while diffusion lengths in the solid are almost never more than  $10\mu$ . To obtain  $Q'_2$  one first must integrate the concentration distribution in region 2 to obtain  $Q_2$ .  $Q_2$  is the total number of dopant atoms per unit area in region 2

$$Q_2 = \int_d^i C(g)(x, t) dx + \int_i^r C(x, t) dx \quad [3]$$

where the symbol (g) refers to terms in the gas, while the absence of (g) refers to terms in the solid. To obtain  $Q'_2$  one differentiates Eq. [3] with respect to time

$$Q'_2 = \int_d^i \frac{\partial C(g)(x, t)}{\partial t} dx + C(g)(i, t) \frac{di}{dt} - C(g)(d, t) \frac{dd}{dt} + \int_i^r \frac{\partial C(x, t)}{\partial t} dx + C(r, t) \frac{dr}{dt} - C(i, t) \frac{di}{dt} \quad [4]$$

The terms containing the expression  $\int_\alpha^\beta \frac{\partial C}{\partial t} dx$ , when  $\alpha$  and  $\beta$  are arbitrary limits, can be simplified using the following substitution

$$\int_\alpha^\beta \frac{\partial C}{\partial t} dx = \int_\alpha^\beta D \frac{\partial^2 C}{\partial x^2} dx = F(\alpha, t) - F(\beta, t)$$

which is the integral of Fick's Second Law for constant diffusivity. Using the above substitution in Eq. [4] and defining  $v_\alpha = d\alpha/dt$  (where  $\alpha$  is the position of a boundary in the  $x$ -direction), one obtains

$$Q'_2 = -F(g)(i, t) + F(g)(d, t) + v_1 C(g)(i, t) - v_d C(g)(d, t) - F(r, t) + F(i, t) + v_m C(r, t) - v_1 C(i, t) \quad [5a]$$

Inspecting Eq. [5a] there are a number of terms that will go to zero. Since the boundary,  $x = r$ , is not moving,  $v_m$  is zero. The velocity at  $x = d$  is set equal to zero since the movement of the front interface is small compared to thickness of the gas-phase boundary layer (9). Therefore, only the velocity  $v_1$  is not zero. Since  $x = i$  is the only moving interface, the subscript will be omitted. The flux at  $x = r$  is zero since  $r$  was defined as a point where the concentration gradient is always zero. Eliminating the zero terms from  $Q'_2$  one obtains

$$Q'_2 = -F(g)(i, t) + F(g)(d, t) - v[C(i, t) - C(g)(i, t)] + F(i, t) \quad [5b]$$

Since dopant only enters or leaves region 2 at the boundary  $x = d$ , one already knows the flux across  $d$  from the analysis of region 1, i.e.,  $[F(g)(d, t) + fF(b, t)]$ . This flux may now be set equal to  $Q'_2$  to obtain the boundary condition at the front gas-solid interface

$$F(i, t) = F(g)(i, t) + v[C(i, t) - C(g)(i, t)] + fF(b, t) \quad [6]$$

The assumptions used to simplify  $Q'$  and to derive the boundary condition at the gas-solid interface, ( $x = i$ ), are summarized as follows:

(i) The bulk gas phase is completely mixed at all times.

(ii) A linear concentration gradient exists across the stagnant gas-phase boundary layer.

(iii) Dopant transport in the solid phase can be characterized by Fick's Second Law.

(iv) The diffusivity of the dopant is independent of concentration.

(v) The dopant escaping from the back surface of the wafer is not influenced by the flux of dopant at the front interface.

(vi) During growth, etching, or oxidation steps only the front solid interface is moving.

Equation [6] implies that the flux  $F(i, t)$  is not only a function of dopant transported from the gas  $[F(g)(i, t)]$ , but is also a function of the dopant leaving the back surface or sides of the wafer  $[F(b, t)]$ , as well as the velocity of the front gas-solid interface,  $v$ .

Equation [6] contains flux terms that cannot be easily evaluated. Therefore the terms  $F(b, t)$  and  $F(g)(i, t)$  will be approximated with the following relationships

$$F(b, t) = -h[C(b, t) - kC(g)(b, t)] \quad [7]$$

and

$$F(g)(i, t) = h[C(i, t) - kC(g)(i, t)] \quad [8]$$

These equations assume that the driving force for dopant transport at the interfaces,  $x = b$  and  $x = i$ , respectively, is the concentration difference across the interface.  $k$  is the equilibrium segregation coefficient defined at zero growth rate as

$$k = \frac{C(i, \infty)}{C(g)(i, \infty)} \quad [9a]$$

and

$$k = \frac{C(b, \infty)}{C(g)(b, \infty)} \quad [9b]$$

This type of flux approximation (Eq. [7] and [8]) is used to describe a situation, at an interface, where a restriction to dopant transport exists [see Crank (9)]. The restriction coefficient  $h$  has the units of velocity, and will be referred to in this work as the "evaporation coefficient." The evaporation coefficient is a constant that depends upon the temperature, pressure, dopant species, wafer orientation, gas velocity, and reactor geometry. Small values of  $h$  effectively keep the ratio of concentrations on either side of an interface from reaching the equilibrium value as defined in Eq. [9a] and [9b]. The evaporation coefficient therefore controls the time rate of approach of the ratio of concentrations on either side of an interface to its equilibrium value.

For large values of  $h$  (i.e.,  $h \gg \sqrt{D/t}$ ) the escape of dopant will be diffusion controlled since all the dopant reaching a surface will rapidly transfer into the gas phase. Also for large  $h$  the back flux term will rapidly approach a constant value and have the same effect as an increased constant concentration level of dopant in the gas phase. For small values of  $h$  there will be a large time dependence of the flux at the front interface, resulting in a graded dopant distribution in the growing layer. Substituting Eq. [7] and [8] into Eq. [6], and regrouping terms, one obtains an equation for the flux in the solid at the front interface in terms of solid- and gas-phase concentrations and the constants  $h$ ,  $v$ , and  $f$

$$F(i, t) = h[C(i, t) - kC(g)(i, t)] - fh[C(b, t) - kC(g)(b, t)] + v[C(i, t) - C(g)(i, t)] \quad [10]$$

Equation [10] still contains terms of  $C(g)(i, t)$  and  $C(g)(b, t)$  which cannot be easily measured in practice. Since the distance between the front and back surfaces of the wafer (0.25 mm) is small compared to the total boundary layer thickness (5 mm) (10), we will assume  $C(g)(b, t) = C(g)(i, t)$ . Equations [7] and [8] still contain a term,  $C(g)(i, t)$ , which cannot be easily measured. One approach to this dilemma would be to write the flux across the gas-phase boundary layer ( $x = d$  to  $x = i$ ) as

$$F = h(g) [C_m(t) - C(g)(i, t)]$$

where  $C_m(t)$  is the mean gas-phase concentration and  $h(g)$  is the gas-phase mass transfer coefficient. Then one could simultaneously solve the above equation in conjunction with Eq. [6] to eliminate the term  $C(g)(i, t)$  in favor of the mean gas-phase concentration  $C_m(t)$ . This is a cumbersome method. Since the diffusivity in the gas is much larger (twelve orders of magnitude) than in the solid, and since the velocity of the gas-solid interface is small compared to the transport across the boundary layer, a simple relationship between the mean gas-phase concentration and the gas-phase concentration at the interface will be assumed

$$C(g)(i, t) = k_g C_m(t) \quad [11]$$

where  $k_g$  is an arbitrary constant that will depend upon the gas velocity distribution in the boundary layer. For all of the systems investigated by the authors,  $k_g$  was usually very close to unity for most conditions encountered during epitaxial growth and semiconductor processing.

Finally substituting Eq. [11] into Eq. [10] and assuming  $C(g)(b, t) = C(g)(i, t)$ , one obtains the boundary condition at the front interface in terms of readily measurable or easily calculable quantities

$$F(i, t) = h[C(i, t) - k_e C_m(t)] - fh[C(b, t) - k_e C_m(t)] + v[C(i, t) - k_g C_m(t)] \quad [12]$$

where  $k_e = k(g)$ . This flux term  $F(i, t)$  completely describes the movement of dopant both from the solid and from the gas across the front gas-solid interface. The flux of dopant will only go to zero under a set of stringent conditions. These three conditions must be met simultaneously for a zero flux to occur. (i) The velocity,  $v$ , of the gas-solid interface is zero. (ii) The concentration in the solid at the front interface must be equal to  $k_e C_m(t)$ . (iii) The concentration in the solid at the back interface must be equal to  $k_e C_m(t)$ . If one lets  $C_m(t) = 0$ , and assumes that no dopant from the back is reincorporated into the growing layer ( $f = 0$ ) then Eq. [12] reduces to

$$F(i, t) = (h + v) C(i, t)$$

which is Grove's (4) boundary condition for the solid neglecting gas-phase contributions.

An alternate approach to the solution of the composite gas-solid system involves the solution of the transport problem in both the gas-phase boundary layer and in the solid phase. This approach eliminates the assumptions about the fluxes at  $x = i$  and  $x = b$  inherent in the method outlined above. For practical reasons as outlined later, the approximation approach was chosen over the solution of the composite system.

The boundary condition at the front gas-solid interface (Eq. [12]), and the boundary condition at the back of the wafer (Eq. [7]) can be used to solve Fick's Second Law (Eq. [1]) in the solid using numerical techniques.

### Numerical Solution

A number of numerical techniques have been used in the past to obtain solutions to a parabolic partial differential equation (e.g., Eq. [1]). The simplest approach is the forward finite difference method (FFDM). This technique suffers in two major respects. The first of these is the poor approximation (only first order correct) to the time derivative of concentration. The second restriction is the limit on the stability criterion which requires that the value of the dimensionless quantity  $R = D\Delta t/(\Delta x)^2$  cannot exceed 0.5, where  $\Delta t$  and  $\Delta x$  are the time and spatial increments, respectively. This limit on  $R$  forces one to employ very small values of  $\Delta t$  (and to use extremely long computation times) if a stable solution is to be obtained. The implicit Crank-Nicholson Method (CNM) has the disadvantage of more mathematical operations than the

FFDM but offers higher accuracy for the same total expenditure of computer time. Also there is no bound on the stability parameter  $R$  for interior points (11). Some problems may occur at a boundary when large values of  $R$  are used, especially if a large concentration discontinuity exists. Since the CNM involves analogs for the various concentration derivatives centered in the time interval  $\Delta t$ , they are second order correct. Another advantage of the CNM is the ease in which  $\Delta x$  and/or  $\Delta t$  may be varied. It is this flexibility that leads to shorter run times for the same level of accuracy compared to the FFDM. For the initial stages of a problem where large changes in concentration with time are occurring one would like to use small values of  $\Delta t$ . In the final stages of the problem, where little or no concentration changes are taking place a much larger value of  $\Delta t$  would permit substantial savings in computer time. The spatial grid size  $\Delta x$  is usually only limited by the available amount of computer core storage. The finite difference equations used to solve Fick's Second Law are given in the Appendix.

A computer program called CASPER (Computer Aided Semiconductor Processing and Epitaxial Redistribution) was written to solve the diffusion equation (Eq. [1]) using the boundary conditions of Eq. [7] and [12] and nonuniform initial conditions, using the Crank-Nicholson method (17).

To test the accuracy of the CNM, a comparison was made with the known analytical solution for the moving boundary and evaporation problem (MBEP) where the gas concentration,  $C_m$ , is set equal to zero. The analytical solution to the moving boundary and evaporation problem as given by Grove *et al.* (4) is presented below

$$C(x, t) = \frac{C_s}{2} \operatorname{erfc} \left( \frac{x}{2\sqrt{Dt}} \right) - \left( \frac{h+v}{2h} \right) \cdot \exp \left[ \frac{v}{D} (vt - x) \right] \operatorname{erfc} \left[ \left( \frac{2vt - x}{2\sqrt{Dt}} \right) \right] + \left[ \frac{v+2h}{2h} \right] \cdot \exp \left\{ \left[ \frac{v+h}{D} \right] \cdot [(v+h)t - x] \right\} \operatorname{erfc} \left\{ \left[ \frac{2(v+h)t - x}{2\sqrt{Dt}} \right] \right\} \quad [13]$$

where  $C_s$  is the original concentration level in the solid.

Equation [13] was compared to the solutions obtained by the CNM for the following set of numerical conditions

dopant, boron  
temperature, 1294°C  
diffusivity, 0.0500  $\mu^2/\text{min}$   
 $0.01 \leq h/(\sqrt{D/t}) \leq 10^{10}$   
 $0.00 \leq v \leq 2.0 \mu/\text{min}$   
substrate thickness, 5.0  $\mu$   
time, 5.0 min

First let us consider the evaporation case ( $v = 0$ ) using the CNM solution. The accuracy of the CNM will depend not only upon the size of the time and spatial parameters  $\Delta t$  and  $\Delta x$ , but also upon the rate of change of concentration in the interval  $\Delta x$ . The error relative to the analytical solution is defined below

$$\text{Relative error} = \frac{C_{\text{analytical}} - C_{\text{CNM}}}{C_{\text{analytical}}} \times 100$$

A variable  $\Delta t$  Crank-Nicholson solution is used to solve Eq. [1] under the boundary conditions of Eq. [12] and the resultant numerical solution is compared to the analytical solution given in Eq. [13]. In this method, a very small value of  $\Delta t$  is initially chosen. This value corresponds to an  $R$  value of 0.0001. With each successive solution of the grid equations,  $\Delta t$  is increased by 40% until the total elapsed time is expended. This technique offers good accuracy while allowing one to minimize the amount of computer time per total cal-

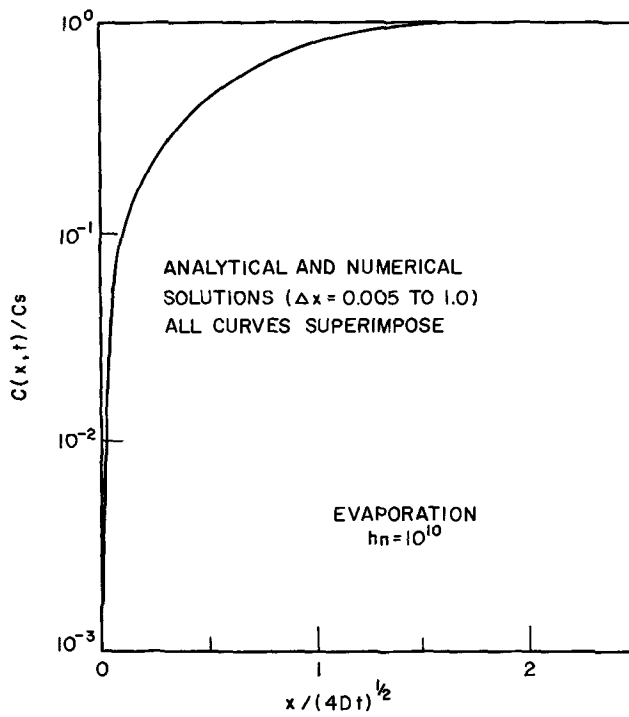


Fig. 4. Plot of relative concentration vs. normalized depth for a simple evaporation problem. The numerical and analytical solutions agree to better than 1% over the entire depth range. Time, 5 min; temperature, 1294°C; dopant species, boron.

ulation. Figure 4 graphically displays both the analytical and numerical solutions to Eq. [1] using the boundary condition of Eq. [12] with the normalized evaporation coefficient  $h_n = 10^{10}$ , where  $h_n = h/(\sqrt{D/t})$ , and  $v = 0$  (evaporation only). At the smaller values of  $h_n$  the curves tend to flatten out. For the numerical solution,  $\Delta x$  was varied from 0.005 to 1.0, i.e. the solid which was  $5\mu$  thick was divided into a number of steps which varied from 1000 to 5. Even for the largest  $\Delta x$ , the numerical solution and the analytical solution cannot be resolved on this plot. The error associated with the evaporation solution is very small over the entire range of  $\Delta x$  that was investigated. The maximum error occurs at the gas-solid interface. For a  $\Delta x$  of 0.05, which is the interval size normally used, the error at the interface is 0.4%. The variable  $\Delta t$  solution is highly accurate for the solution of the evaporation problem. This variable time interval solution is particularly useful in the treatment of long diffusion problems where little or no dopant movement occurs over a large part of the time cycle. For an 8 hr oxidation cycle at 1100°C the computer run time was reduced by a factor of 230 when using the variable  $\Delta t$  solution. If the concentration distribution was continuously varying, a fixed interval  $\Delta t$  method would be preferred over the variable  $\Delta t$  solution.

To achieve the highest level of accuracy, using the CNM, the smallest value of  $\Delta x$  consistent with the amount of computer core storage available should be chosen. For systems where the active diffusion zone is small relative to the total dimensions of the body under simulation, the smallest practical value of  $\Delta x$  that may be chosen may still be too large to give the required level of accuracy desired. Therefore, a numerical solution that allows the use of small values of  $\Delta x$  in the active diffusion region and larger values of  $\Delta x$  in regions where little or no transport of dopant is taking place, would allow one to conserve large amounts of computer core storage while significantly reducing the calculation time. When treating a problem where little change in concentration is expected to occur at the interface (e.g., an evaporation problem with  $h_n \ll 1.0$ )  $\Delta x$  may be taken large. But if one is working in a region where the concentration gradient is large, i.e., the

concentration change over  $1\Delta x$  is greater than a factor of two, then a small value of  $\Delta x$  should be used. This would result in a variable  $\Delta x$  solution where  $\Delta x$  would be small in regions of large concentration changes and would be large in regions where the concentration gradient was close to zero.

Since small values of  $\Delta x/(\sqrt{Dt})$  lead to higher accuracy, one would use this solution in regions where rapidly changing concentration gradients occur. There are savings in both computer time and core if one has a prior knowledge of where these regions of large concentration changes are occurring throughout the solid. The "split grid approach" was developed for a continuous material but it is also extremely useful in treating problems where a boundary or discontinuity exists such as the gas-solid interface or the boundary between two phases. It allows one to choose values of  $\Delta x$  in each region that will result in the minimum total error for the smallest amount of computer core and time. There may be as many breaks in the grid size as is required by the particular problem under study. An example of where this variable grid size solution would be useful is the growth (Fig. 5) of a thick epitaxial layer at very low temperatures such that the region between the layer and the substrate would have a very large concentration gradient, while in the substrate and in the layer the concentration gradient would be close to zero. If one tries to model this problem using a large value of  $\Delta x$ , the transition region appears more graded than it actually is. If one tries to employ a very fine  $\Delta x$  solution, large amounts of core are required since the regions in which the concentration gradient is zero may be  $20\mu$  thick while the transition region may only be  $2\mu$  in size. The optimum treatment of this type of problem is to use a large value of  $\Delta x$  ( $\Delta x = 0.5$ ) in the regions of small concentration change (i.e., the layer and the substrate) and to use a very fine  $\Delta x$  ( $\Delta x = 0.002\mu$ ) in the  $2\mu$  transition region. Errors in the numerical solution occurring in the region of fine  $\Delta x$  are comparable to the errors that occurred when using a uniform grid size  $\Delta x = 0.002$ . The saving in both computer run time and core storage for this particular problem is almost a factor of 10.

The errors resulting from the CNM treatment of the MBEP will now be discussed. In the growth mode, the following sequence is used to obtain a numerical solution:

(i) A growth step equal in size to  $\Delta x$  or some whole number times  $\Delta x$  is added. These steps are added on using  $C_a = ke^*C_m$  where  $C_a$  is the concentration of the added step. For most elements,  $ke$  decreases with temperature and approaches unity with increasing growth velocity (12).

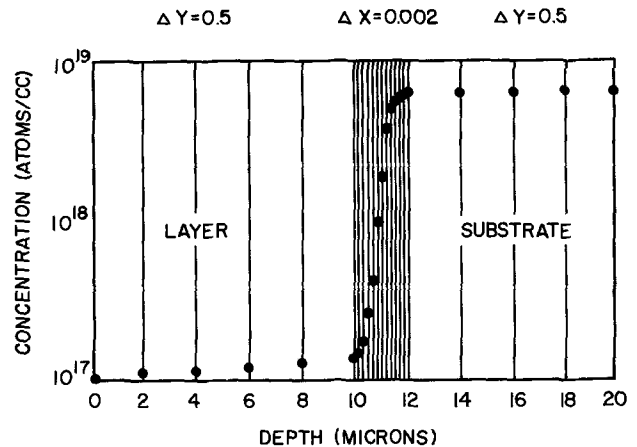


Fig. 5. Example of variable grid size solution. Concentration vs. distance plot of an epitaxial layer in which the graded region between the layer and the substrate is divided into a finer mesh size than the rest of the structure to minimize the computational errors as well as computer time.

(ii) An adjustment is made to the concentration at the prior original interface to conserve mass across the added solid step and a region of equal size already in the solid phase. This is accomplished by averaging the concentration of the added step with the prior interface concentration value.

(iii) The problem is now solved under static conditions using a fixed  $\Delta t$  method. One time iteration is usually sufficient.

(iv) Steps (i) through (iii) are repeated until the specified growth is complete.

The errors resulting from the CNM solution to the growth case are somewhat larger than one obtains from the evaporation problem. A comparison of the analytical solution and the CNM for the MBEP for a number of values of  $\Delta x$ ,  $hn = 10^{10}$ , and  $vn = v/(\sqrt{D/t})$  is shown in Fig. 6. These results, are representative of values of the normalized growth rates (0.2–2.0  $\mu/\text{min}$ ), and are typical of semiconductor epitaxial processing. Since the examples are for boron, other elements with smaller diffusivities will experience even smaller errors since  $vn \approx 50$ .

Errors in general are largest at the smallest growth rates and at larger values of  $\Delta x$ . While the errors appear larger the further one gets from the original interface ( $x = 0$ ) the concentration gradient at distances far from the interface is also large. At a depth of  $3.3\mu$  from the original boundary, the concentration may have dropped by six orders of magnitude, while the concentration change over  $0.05\mu$  is almost a factor of two. Therefore, errors less than 50% are really quite small relative to the large changes in concentration. Even when the calculated error is greater than 1000%, a lateral shift in the concentration distribution of less than  $1\Delta x$  is all that is needed for perfect agreement. For a  $\Delta x = 0.005$ , the calculated error at a concentration level ten orders of magnitude below  $C_s$  was only 4%.

In summary, a numerical model has been developed than when compared to available analytical solutions yields highly accurate results. The CNM is used to

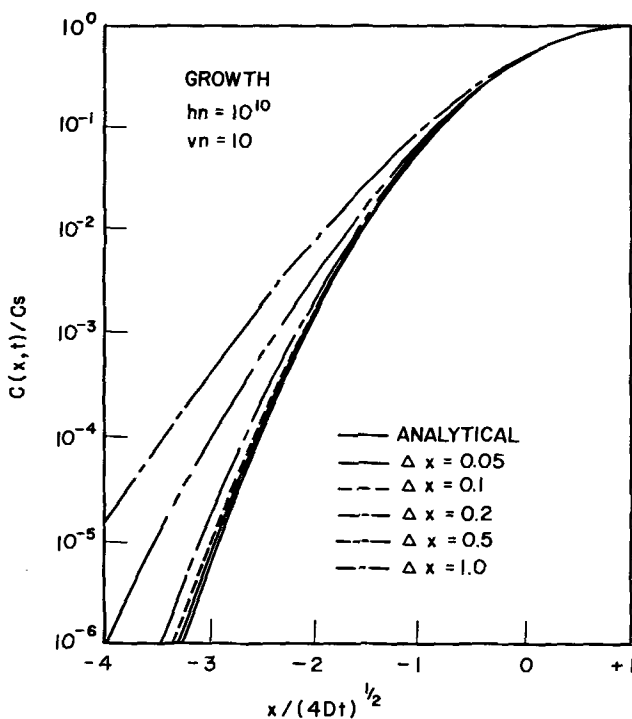


Fig. 6. Plot of relative concentration vs. normalized depth for the moving boundary and evaporation problem. The difference between the analytical and CNM solution increases for increasing values of  $\Delta x$ . Time, 5 min; temperature,  $1294^\circ\text{C}$ ; growth rate, 1.0  $\mu/\text{min}$ ; dopant species, boron.

solve the diffusion equation in the solid for arbitrary initial and boundary conditions. Savings in computer time and core storage can be realized by using a variable increment size solution.

### Analysis of Processing Problems

To design or modify a semiconductor device the single most important parameter is the concentration distribution in the wafer. This distribution affects every single electrical function of the device. Unfortunately, at present, no experimental method exists to determine this concentration distribution. The computer program CASPER offers the designer a powerful tool for performing processing experiments in a short time at a reasonable cost. With CASPER the designer can easily perturb a particular set of materials' properties or a given processing sequence to optimize the electrical characteristics of the device.

In this section CASPER is applied to actual semiconductor processing problems supplied to the author by device designers. In most cases the designers could not accurately define the boundary conditions for the diffusion and "drive-in" operations. All experimentally determined electrical parameters were obtained from the device engineers and represent averages taken over hundreds of thousands of processed devices. In treating certain steps in the device fabrication sequence, specific simplifying approximations were used. During a step involving oxidation of the silicon surface it is assumed that all n-type dopants have zero evaporation coefficients, i.e., no dopant is lost through the oxide. For p-type dopants the evaporation coefficient is modified (lowered) and 30% of the dopant consumed by the oxide is lost to the silicon. The values of the segregation coefficient,  $k$ , were taken from the work of Shepherd (12). The limiting concentration allowed in the solid in all cases is the solubility limit of the individual dopant species taken from the work of Trumbore (13). Conversions from concentration to resistivity were made using the polynomial fit developed by T. P. Lee (14) which is used in the calculation of sheet resistance. Emitter discussions were carried out under a constant surface concentration boundary condition, while base diffusions were simulated as a two-step process consisting of a predeposition at low temperature followed by a high-temperature drive-in step.

**Example 1.**—In the first example, an integrated circuit device pictured in Fig. 7 is analyzed. This example shows how CASPER is used to isolate a critical step in the processing sequence relative to a given parameter (buried layer-sheet resistance) that can be easily calculated from the resultant concentration vs. depth distribution. In this structure, the sheet resistance of the antimony buried layer must be kept below 20 ohms/square. It was found in some devices after processing that the sheet resistance had exceeded this value. Since the antimony distribution itself was formed by a deep predeposition and drive-in process, no analytical solution existed for the impurity distribution. Therefore the CNM was used to calculate this distribu-

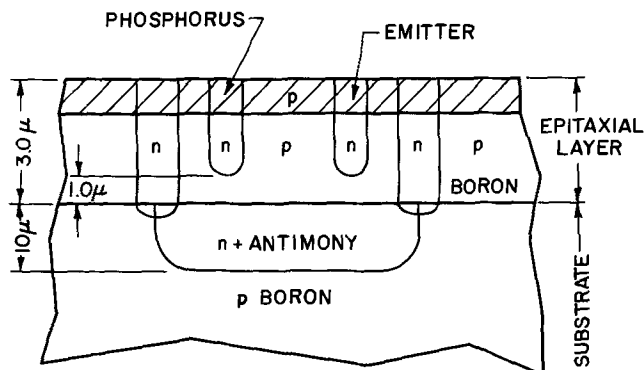


Fig. 7. Schematic of integrated circuit structure

Table I. Sheet resistance change vs. processing step

Step No.	Sb sheet resistance	Width of Sb region	Max. B.L. conc. atoms/cm <sup>3</sup>
Steam oxidation			$\times 10^{19}$
Sb predeposition	16.71	4.15	5.50
Cap. oxidation	16.48	4.30	4.52
Drive-in	13.14	9.15	1.61
HCl etch* (0.75 $\mu\text{m}$ )	17.34	8.45	1.48
Epi growth (3 $\mu\text{m}$ )	16.96	8.85	1.46
Steam oxidation	16.91	8.90	1.41
Phos. diffusion			
BN predeposition			
B drive-in			
Steam oxidation			
Emitter diffusion	16.79	9.00	1.37

\* 32% change in sheet resistance on HCl etching.

tion and subsequently integrate it to obtain the sheet resistance of the structure at all subsequent processing steps.  $R_s$  is defined below

$$R_s = \left\{ \int_{x_1}^{x_2} q \mu(x) C(x, t) dx \right\}^{-1}$$

where  $q$  is the electronic charge and  $\mu(x)$  is the majority carrier mobility. Table I shows the change in antimony sheet resistance as a function of high-temperature processing. Since this calculation established that the HCl vapor etch was the principal culprit, further analysis was undertaken to reveal the extent of this effect. Calculations were performed simulating the HCl vapor etching of the silicon surface, removing from 0 to 2  $\mu$  of silicon. Figure 8 shows both the calculated and experimental results for the percentage change in  $R_s$  vs. the amount of silicon removed. The agreement between the predicted increase in  $R_s$  and the measured values is excellent. This calculation enabled the specification of the HCl cycle as a function of the sheet resistance and therefore resulted in the more efficient utilization of the subdiffused wafers.

*Example 2.*—In the second example the movement of a minor impurity in a heavily doped substrate during epitaxial growth and subsequent high-temperature processing was explored. Again one is confronted with a problem with nonuniform initial conditions for the second and all subsequent steps. In this case the substrate was doped to  $5 \times 10^{18}$  atoms/cm<sup>3</sup> with antimony,

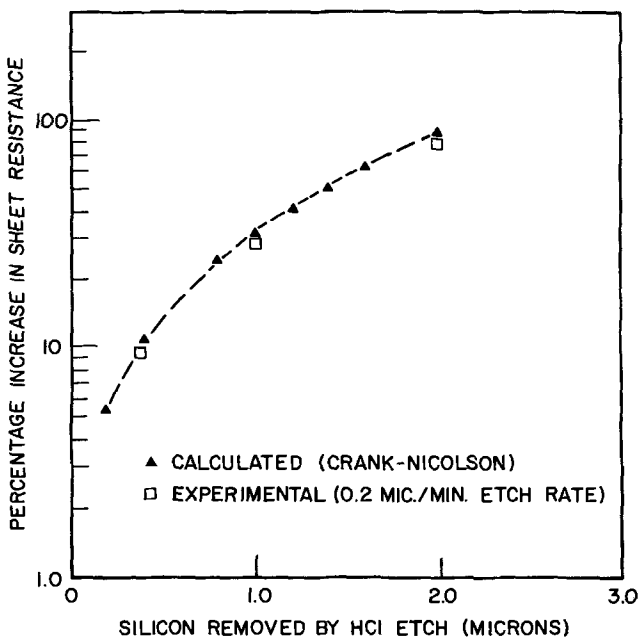


Fig. 8. Plot of change in sheet resistance vs. amount of silicon removed by HCl etching for a 0.2  $\mu$ /min etch rate. Etch temperature was 1250°C; dopant species in the diffused region was boron.

and the layer was intentionally doped with  $2 \times 10^{14}$  atoms/cm<sup>3</sup> of phosphorus. The boron in the substrate (due to contamination of the polycrystalline silicon raw material or contamination during crystal growth) was believed to diffuse out during growth and form a p-region about 1  $\mu$  from the original interface in the epitaxial layer. In some cases this region apparently escaped detection after epitaxial growth but appeared to form sometime during subsequent high-temperature processing. Figure 9 shows the calculated concentration distribution for  $1 \times 10^{16}$  atoms/cm<sup>3</sup> of boron originally in the substrate. The CNM solution showed that the p-layers did indeed grow with subsequent processing by almost a factor of 2.5. The calculation also showed that if the boron level in the substrate was less than  $5 \times 10^{15}$  atoms/cm<sup>3</sup> no layer could be detected by the MOS capacitance technique being used. This suggested that slices should be subjected to a high-temperature soak directly after epitaxial deposition to enhance the presence of the p-layers if they existed. Figure 10 shows the comparison between the calculated width of the p-region before and after the high-temperature processing steps. These calculated p-region widths are in good agreement with the boron concentrations found in the substrates using the ion microprobe (15).

*Example 3.*—The third example deals with the back autodoping phenomenon. This example shows how CASPER may be used on a problem where multiple sources of dopant are present (i.e., intentionally added to the gas phase, diffusing from the substrate into the layer, and transported through the gas phase from the sides and back of the substrate). This effect involves the transport of dopant originally in the substrate through the gas phase and back into the growing layer. Therefore epitaxial layers deposited on lightly doped substrates would have a lower layer doping level than layers deposited on heavily doped substrates in the same reactor. Dopant from one substrate may affect other wafers in the reactor with the effect decreasing as the distance from the heavily doped wafer in question. The back of the substrate which is unsealed during the deposition cycle is usually the prime source of this extra dopant after the first micron or two of growth. Subdiffused regions on the surface have been shown by Pogge (16) to also give rise to the same

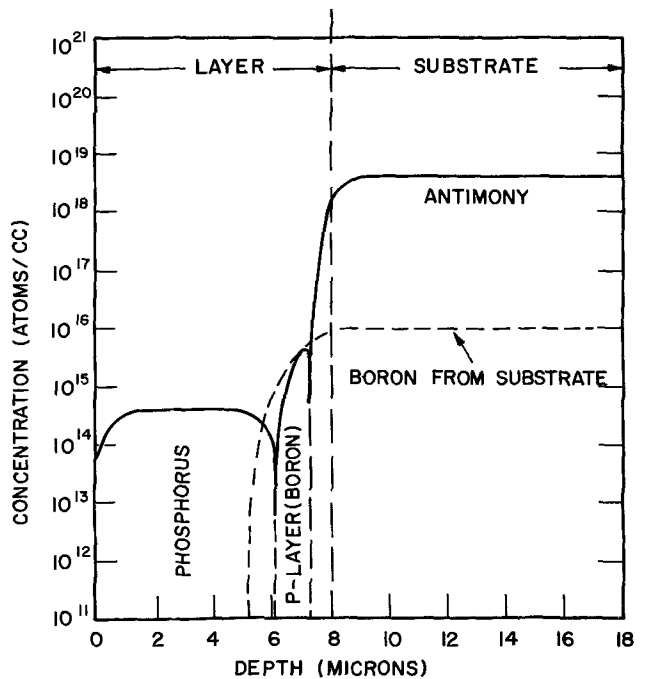


Fig. 9. Plot of impurity concentration vs. depth showing the formation of p-type region in an n-type epitaxial structure due to boron contamination in the starting substrate. Growth rate 0.8  $\mu$ /min at 1170°C for 10 min.

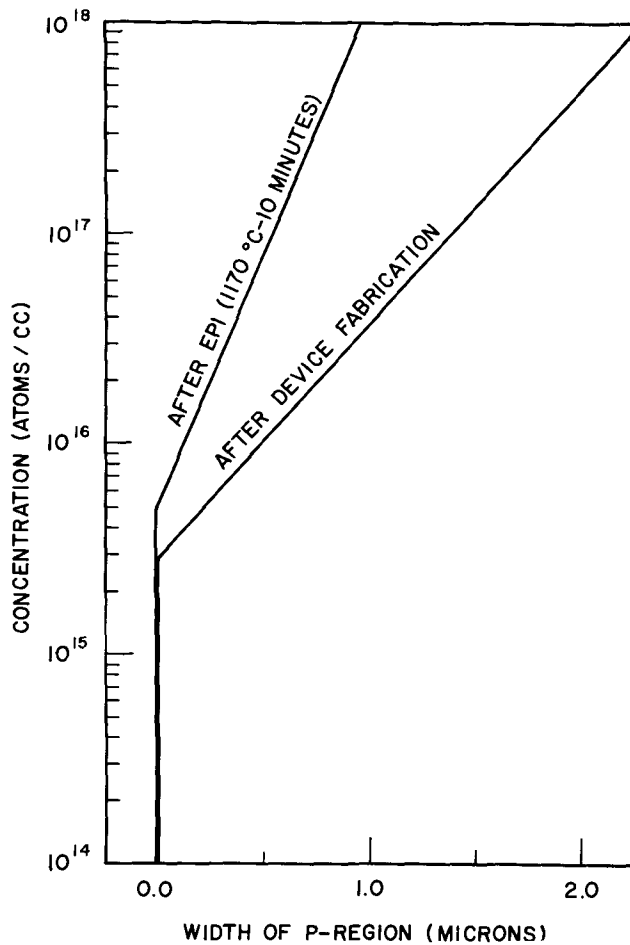


Fig. 10. Plot of boron concentration originally in the substrate vs. the width of the p-region formed after epitaxial deposition and subsequent device processing.

autodoping effect, though this source of dopant modifies the impurity profile near the original interface more than in the layer far from the interface. Shepherd (7) developed a mathematical treatment of the autodoping problem that considered the back surface of the wafer as the sole source of dopant that could enter the growing epitaxial layer over and above the transport of dopant by solid-state diffusion. Using this approach and the initial conditions that the distribution of dopant originally in the substrate was uniform, he developed a calculation that involved a knowledge of the growth rate and the transport parameters of the dopant in both the gas and solid system. His final equation ignores the effects of solid-state diffusion so that his model is applicable from about two diffusion lengths from the original interface to the surface of the epitaxial structure. Figure 11 is a comparison between the autodoping model developed by Shepherd and the CNM solution of the same problem. The agreement is quite good between the two approaches. Both calculations were performed assuming that 4% of all dopant leaving the back surface was available for re-incorporation into the growing layer. The conditions of growth were as follows: temperature 1200°C, time 6 min at a growth rate of 0.75  $\mu$ /min and 114 min at a growth rate of 0.13  $\mu$ /min. The scatter in Shepherd's data is a factor of five greater than the disagreement between his calculation and the results of the numerical model.

### Conclusions

In conclusion, a one-dimensional computer model has been developed that can predict the impurity distribution in a silicon wafer that has been subjected to a sequence of high-temperature device processing steps. Particular attention has been paid to the model-

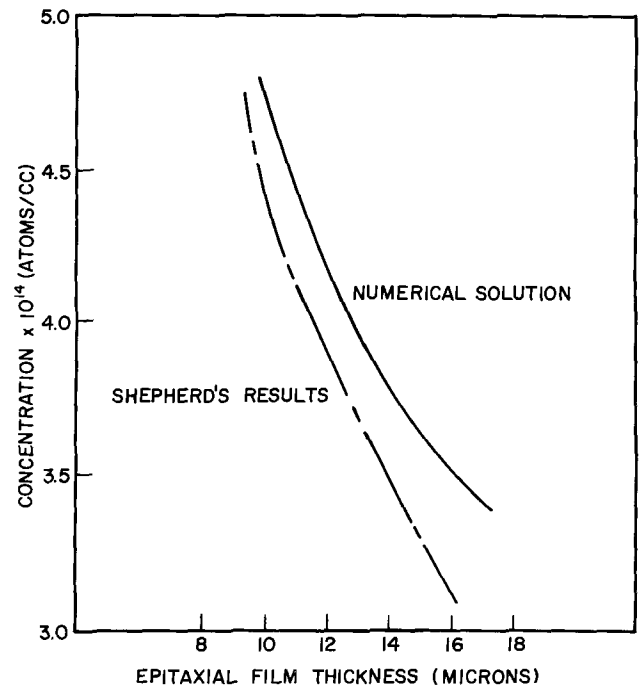


Fig. 11. Comparison between the model of Shepherd for back surface autodoping and the CNM calculation. Dopant species, arsenic.

ing of dopant transport during epitaxial growth in order to explain both front and back surface autodoping phenomena. The Crank-Nicholson method has been used to solve the resultant equations numerically to a high order of accuracy with the aid of a split grid approach to minimize computer run time. At present the accuracies of CASPER's predictions are limited only by the experimental values of the constants employed in the analysis, e.g., diffusivity, evaporation coefficient, and segregation coefficients. A better understanding of the dopant interchange at the gas-solid interface will permit extension of this model to the analysis of submicron epitaxial structures.

### Acknowledgments

The authors wish to acknowledge the help of Dr. K. E. Benson for many useful discussions.

They also wish to thank Mr. W. R. McCormack of Western Electric who allowed P. H. Langer the time and support necessary to accomplish this investigation.

This paper was submitted as a partial requirement by one of the authors (P.H.L.) for the degree of Ph.D. to the Department of Metallurgy and Materials Science, Lehigh University, Bethlehem, Pennsylvania 18015.

Manuscript submitted Oct. 5, 1972; revised manuscript received Aug. 15, 1973.

Any discussion of this paper will appear in a Discussion Section to be published in the December 1974 JOURNAL. All discussions for the December 1974 Discussion Section should be submitted by Aug. 1, 1974.

### APPENDIX

The finite difference equation used in the Crank-Nicholson method to solve Fick's Second Law (Eq. [1]) is presented below. At the front interface the equation is

$$\begin{aligned}
 C'_0 \left[ -1 - \frac{1}{R} - \frac{\Delta x(h+v)}{D} \right] + C'_{+1} \\
 = C_0 \left[ 1 - \frac{1}{R} + \frac{\Delta x(h+v)}{D} \right] - C_{+1} \\
 - \frac{2\Delta x}{D} \{hk_e C_m - fh[C_b - k_e C_m]\} + v k_g C_m \quad [A-1]
 \end{aligned}$$

Equation [A-1] is the analog to Eq. [12].

For all the interior grid lines an equation of the following type is used

$$C'_{j-1} + C' \left[ -2 - \frac{2}{R} \right] + C'_{j+1} = -C_{j-1} + C_j \left[ 2 - \frac{2}{R} \right] - C_{j+1} \quad \text{[A-2]}$$

for  $1 \leq j \leq b-1$

At the back boundary the following finite difference equation may be derived from Eq. [7]

$$C'_{b-1} + C'_b \left[ -1 - \frac{1}{R} - \frac{\Delta x h}{D} \right] = -C_{b-1} + C_b \left[ 1 + \frac{1}{R} + \frac{\Delta x h}{D} \right] - \frac{2\Delta x h k_e}{D} C_m$$

#### REFERENCES

1. C. O. Thomas, D. Kahng, and R. C. Manz, *This Journal*, **109**, 1055 (1962).
2. J. J. Grossman, *ibid.*, **110**, 1065 (1963).
3. W. Rice, *Proc. IEEE*, **52**, 284 (1964).
4. A. S. Grove, A. Roder, and C. T. Sah, *J. Appl. Phys.*, **36**, 802 (1965).
5. T. Abe, Y. Nishi, K. Sato, and N. Oi, *Denki Kagaku*, **35**, 142 (1967). Translated by Associated Technical Services (1968).
6. B. A. Joyce, J. C. Weaver, and D. J. Maule, *This Journal*, **112**, 1100 (1965).
7. W. H. Shepherd, *ibid.*, **115**, 652 (1968).
8. G. Skelly and A. C. Adams, *ibid.*, **120**, 116 (1973).
9. J. Crank, "Mathematics of Diffusion," p. 38, Oxford University Press, London (1967).
10. F. C. Evesteyn, P. J. Severin, C. H. v.d. Brekel, and H. L. Peek, *This Journal*, **117**, 925 (1970).
11. D. U. von Rosenberg, "Numerical Methods for the Solution of Partial Differential Equations," Chap. 2 and 5, and Appendix A, American Elsevier Publishing Co., Inc., New York (1969).
12. W. H. Shepherd, *This Journal*, **115**, 541 (1968).
13. F. A. Trumbore, *Bell System Tech. J.*, **39**, 205 (1960).
14. T. P. Lee, *IEEE, Trans. Electron Devices*, **13**, 881 (1966).
15. J. Edwards, Private communication (January 1972).
16. H. B. Pogge, D. W. Boss, and E. Ebert, in "Chemical Vapor Deposition, Second International Conference," John M. Blocher, Jr. and James C. Withers, Editors, p. 767, The Electrochemical Society Softbound Symposium Series, New York (1970).
17. P. H. Langer, Ph.D. Dissertation, Lehigh University (May 1973).

## Epitaxial Growth and Properties of GaAs on Magnesium Aluminate Spinel

C. C. Wang,\* F. C. Dougherty, P. J. Zanzucchi, and S. H. McFarlane III

RCA Laboratories, Princeton, New Jersey 08540

#### ABSTRACT

Heteroepitaxial GaAs films have been grown by the vapor phase organometallic process on magnesium aluminate spinel substrates prepared by various methods. The effects of variations in growth parameters on the epitaxial GaAs film characteristics have been studied. These growth parameters include substrate surface preparation, substrate composition, substrate orientation, growth temperature, gas flows, reactor geometry, and source materials. The substrate orientation and the purity of the source materials were found to play a critically important role in determining both the crystallinity and the electrical properties of the films. Unintentionally doped GaAs films with electron and hole mobilities up to 70 and 100%, respectively, of bulk GaAs values were grown in the carrier concentration range  $10^{15}$ - $10^{16}$ /cm<sup>3</sup>. The epitaxial composites have been characterized by physical and electrical methods. Information on the crystalline perfection, optical properties, and carrier transport characteristics has been obtained.

Single-crystal growth of large-area semiconductor films on oxide insulating substrates is of technical importance to many solid-state electronic devices. Extensive studies of the epitaxial growth of elemental semiconductors, silicon and germanium, on oxide insulating substrates have been reported (1-6) in the past few years. These studies have led to a basic understanding of the composite material systems and to the development of devices (7-9) constructed in silicon grown on sapphire. With the significant progress made on elemental heteroepitaxial semiconductor films, the trend of development was extended to compound semiconductors. Recently, the successful growth of several III-V and II-VI compounds has been reported (10-15), and many properties of GaAs grown on sapphire have been characterized (11, 16). In this paper research results are presented on the epitaxial

growth and properties of GaAs grown on magnesium aluminate spinel.

#### Experimental

##### Substrate Preparation

Spinel substrate wafers used for GaAs epitaxy were obtained from crystals grown at RCA Laboratories. Stoichiometric spinel (MgAl<sub>2</sub>O<sub>4</sub>) was grown by the flux (17) and the Czochralski (18) methods. Low alumina-rich spinels (MgO:1.5Al<sub>2</sub>O<sub>3</sub>-MgO:2.5Al<sub>2</sub>O<sub>3</sub>) were grown by the Verneuil method (19). Selected Czochralski spinel wafers of good quality from commercial sources were also used. Initial growth experiments indicated that single-crystal GaAs films can be grown on spinel prepared by all three methods. However, it was found that most films grown on flux spinel exhibited very high resistivities due to unintentional doping of the GaAs films by flux impurities in this

\* Electrochemical Society Active Member.

Key words: epitaxial growth, GaAs-on-spinel, heteroepitaxial semiconductor, GaAs/insulating substrates.



type of spinel, and emphasis was therefore shifted to films grown on Czochralski and Verneuil materials.

The proper preparation of substrate wafers from the spinel single crystals is of essential importance in obtaining good epitaxial growth. Orientation of the spinel crystals for cutting was determined by the x-ray Laue back-reflection method. Substrate wafers (about  $1 \text{ cm}^2 \times 0.06 \text{ cm}$  thick) of (111), (100), and (110) orientations were obtained by cutting the x-ray oriented crystals using a diamond wheel. An accuracy of better than one-quarter degree is maintained throughout the operation. The spinel substrate wafers were mechanically lapped and polished to produce the flat and smooth surface which is required for epitaxial growth. Lapping was carried out with about  $30\mu$  boron carbide abrasives to obtain a flat coplanar surface. The lapped surface was further polished using successively finer grades of alumina, ending with the  $0.05\mu$  grade. After polishing the wafers generally have a flatness of better than  $\pm 0.4 \mu/\text{cm}$ , as measured by interferometry.

#### Epitaxial Growth

Epitaxial growth of GaAs on spinel was obtained by using the reaction (15) between trimethylgallium [ $(\text{CH}_3)_3\text{Ga}$ ] and arsine ( $\text{AsH}_3$ ).

The growth system, as shown in Fig. 1, consists of a water-cooled vertical quartz reactor (6.25 cm diameter  $\times$  40 cm long) equipped with an adjustable quartz pedestal, a trimethylgallium source reservoir (kept at  $0^\circ\text{C}$ ) and dispenser, an arsine supply (10% by volume in  $\text{H}_2$ ), all stainless steel gas lines and valves, and precision gas flow controls. Hydrogen purified by a Pd-diffuser was used as the carrier gas. The growth of doped GaAs films was explored using  $(\text{C}_2\text{H}_5)_2\text{Zn}$  and  $\text{H}_2\text{Se}$  (also  $\text{H}_2\text{S}$ ) as the p- and n-dopants, respectively. A Lepel radio frequency induction heating system (with precision electronic control unit) and pyrolytic graphite or SiC-coated graphite susceptors were employed for the deposition. The substrate temperature was measured by an infrared pyrometer.

In a typical growth run, the reactor is first thoroughly flushed by  $\text{H}_2$  to purge the system of air. Predetermined and equilibrated  $\text{AsH}_3$  and  $(\text{CH}_3)_3\text{Ga}$  gas flows are then sequentially admitted to the reactor in which the substrate is heated to the growth temperature. The crystal growth is carried out for the desired length of time after which the  $(\text{CH}_3)_3\text{Ga}$  carrier gas is turned to the exhaust. The  $\text{AsH}_3$  gas valve is then turned off,

and the substrate is cooled at an average rate of about  $50^\circ\text{C}/\text{min}$  in the  $\text{H}_2$  ambient. Extensive studies were made on the growth parameters to achieve optimum properties and to develop a basic understanding of the growth process. The parameters include growth temperature, flow rates, substrate orientation, substrate surface preparation, and source material purification.

#### Physical and Electrical Characterization

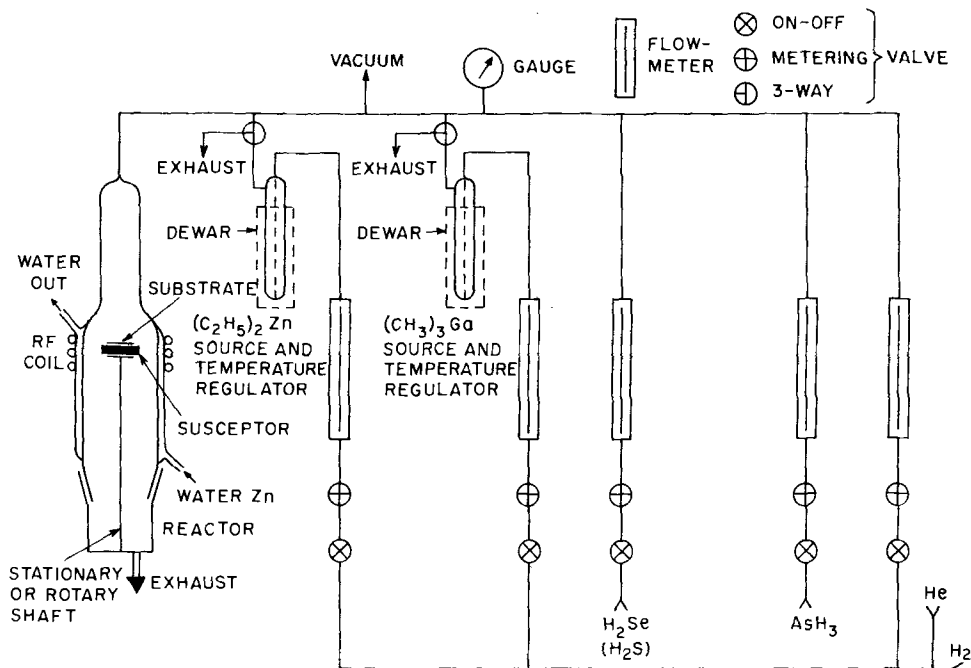
The GaAs-spinel composite structure was characterized by x-ray diffraction, electron diffraction, electron microscopy, and optical techniques. Information on the epitaxial orientation relationship, defect structures, and surface perfection has been obtained.

The conventional x-ray Laue back-reflection method has been used for the determination of orientation relationship and the assessment of crystalline perfection. In addition, x-ray diffractometric measurements were made to determine the orientation mismatch and the line broadening of the diffraction peaks as the film-substrate structure is rotated in a well-collimated beam of x-rays. A Jarrell-Ash microfocus x-ray generator and the attached diffractometric tracer has been employed for this study.

The crystalline perfection of the surface of the epitaxial GaAs films has been examined by glancing angle electron diffraction and by optical and electron microscopy. An RCA Model EMU electron microscope, a Cambridge scanning electron microscope, and a Lietz high power optical microscope were employed for this study. Optical transmission and reflection of the GaAs spinel composite were measured in the spectral range u.v. to infrared to determine a variety of properties (20-23), including film thickness, film uniformity, surface quality, doping type, and carrier concentration. These measurements were made using spectrometers (Cary 14, Perkin Elmer 457, and Perkin Elmer 301).

The carrier transport properties of epitaxial GaAs grown on spinel were determined by Hall measurements. Bridge-shaped Hall bar samples with six terminals were prepared by chemical etching and conventional photolithographic techniques. Ohmic contacts to the GaAs samples were made by an alloying process (24) at about  $500^\circ\text{C}$  in a hydrogen atmosphere. For n-type materials, In was used as the contact metal. For p-type materials, both In and Au (2% In) were used. The resistivity and Hall coefficient were experimentally measured by the conventional method (25) in a magnetic field of 3000 gauss. The Hall mobil-

Fig. 1. Epitaxial growth system.



ity was determined by the ratio of the Hall coefficient and the resistivity. The net carrier concentration was derived from the Hall mobility and resistivity using  $N = 1/(\rho e \mu)$ , where  $N$  is the carrier concentration,  $\rho$  is the resistivity,  $e$  is the electronic charge, and  $\mu$  is the Hall mobility.

## Results and Discussions

### Growth Parameters and Characteristics

**Growth temperature and gas flows.**—Single-crystal GaAs films with thicknesses up to 70  $\mu\text{m}$  were grown on spinel substrates. The flow conditions that yield the best results for the particular apparatus geometry used are:  $\text{H}_2$  carrier gas flow, 3.0 liters/min;  $\text{AsH}_3$  (10% in  $\text{H}_2$ ) flow, 200  $\text{cm}^3/\text{min}$ ; and  $\text{H}_2$  carrier gas for  $(\text{CH}_3)_3\text{Ga}$ ,<sup>1</sup> 5 cc/min. Under these conditions, the average film growth rate is about 0.5  $\mu\text{m}/\text{min}$  for 10  $\mu\text{m}$  thick films. Higher flow rates than these favor heavy deposition at the center of the substrate, while slower rates favor deposition at its periphery. The optimum growth temperatures varied with substrate orientations. A series of growth experiments was carried out in the temperature range 500°–800°C, with other variables being held constant, to determine the effect of growth temperature on the GaAs crystalline quality. The substrates were heated in  $\text{AsH}_3$  (10% by volume in  $\text{H}_2$ ) at 700°C for 3 min prior to the admission of  $(\text{CH}_3)_3\text{Ga}$  for growth.

The general trends observed were: (i) At low temperatures (<600°C), the GaAs films are polycrystalline in nature. (ii) At high temperatures (>800°C), the gases in the reactor are highly turbulent and the films tend to be inhomogeneous with high densities of growth defects. (iii) Within a limited temperature range, 680°–720°C for (111) spinel and 630°–700°C for (110) spinel, highly reflective GaAs

<sup>1</sup> Kept at 0°C.

of good crystallinity can be grown. Figures 2 and 3 show the surface structures of (111) and (100) GaAs films grown, respectively, on (111) and (110) spinel at various temperatures. The growth rate (determined from infrared film thickness measurements) was varied with growth temperature, as shown in Fig. 4, until a plateau was reached corresponding to the optimum growth temperature range. The growth rate then decreased with further increasing temperature.

The growth rate and film optical quality depend also on the ratio of  $\text{AsH}_3/(\text{CH}_3)_3\text{Ga}$  introduced into the system. This is illustrated in Fig. 5, which shows plots of growth rate and optical reflectance factor ( $Q$ ) of (111) GaAs films ( $\sim 10 \mu\text{m}$  thick) vs. the  $\text{H}_2$  carrier gas setting for  $(\text{CH}_3)_3\text{Ga}$ . The  $\text{AsH}_3$  (10% in  $\text{H}_2$ ) gas flow was held constant (200  $\text{cm}^3/\text{min}$ ). The growth rate (film thickness) was determined by infrared reflection measurement, and  $Q$  was derived from the measured and calculated reflectivities ( $R_m$  and  $R_{\text{calc}}$ ) as defined in Eq. [1]. It is seen that there is an optimum range of source gas ratios at which high-quality films are grown.

$$Q = \left( 1 - \frac{R_{\text{calc}} - R_m}{R_{\text{calc}}} \right) \times 100 \quad [1]$$

**Effect of substrate orientation.**—Extensive studies revealed that the substrate orientation plays a critical role in the ease with which the epitaxial layers grow. The ease of growth of GaAs on spinel increases with spinel orientation in the order (111) > (110) > (100) under normal growth procedures described above. The epitaxy<sup>2</sup> of (100) GaAs on (110) spinel is more sensitive to substrate surface quality than that of (111) GaAs on (111) spinel. Moreover, the films tend to grow epitaxially at relatively lower temperatures (see

<sup>2</sup> The (100)GaAs || (110)spinel relationship was previously noted (11). Details of the GaAs-spinel orientation relationship are discussed in the section on Orientation Relationship and Crystallinity.

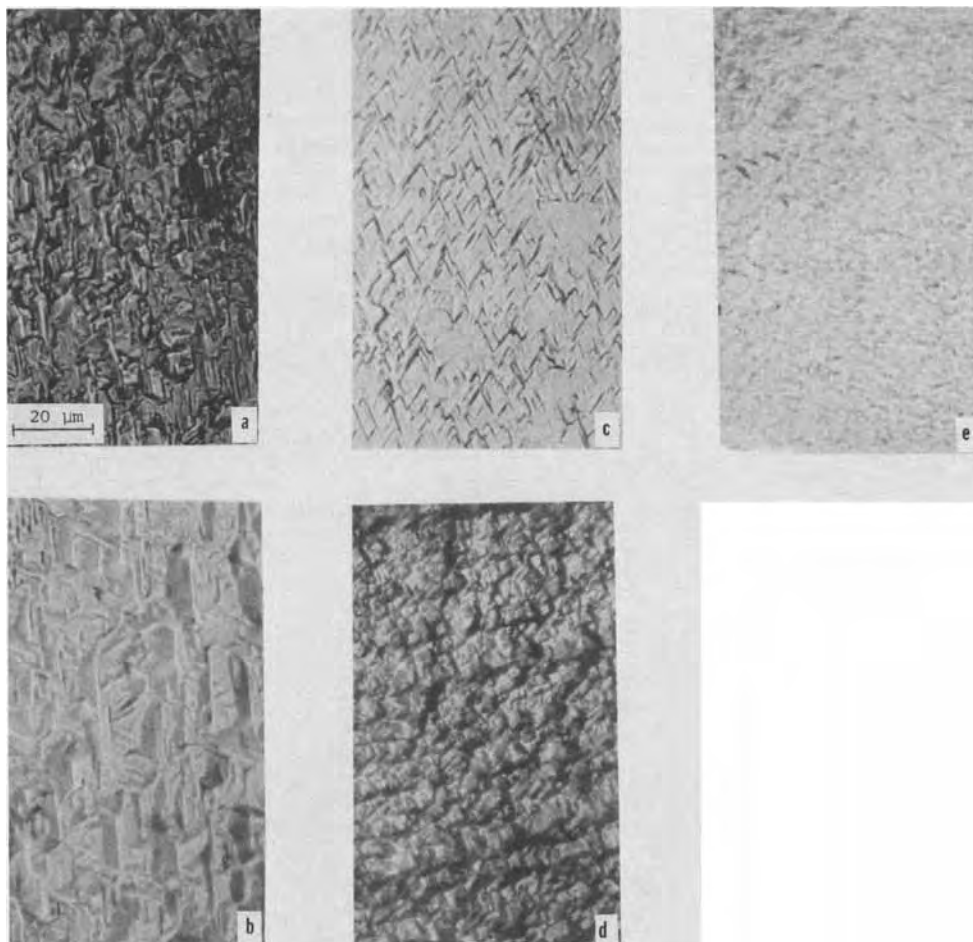
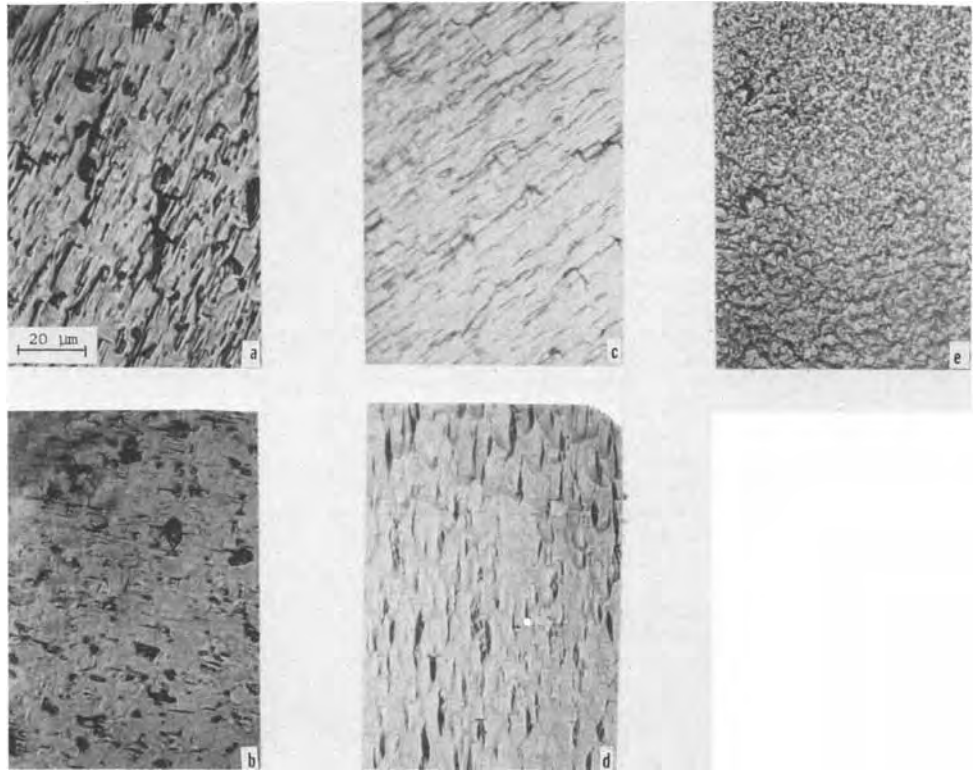


Fig. 2. Optical micrographs of (111) GaAs grown on (111) spinel at various temperatures. (a) 780°C, (b) 750°C, (c) 700°C, (d) 620°C, and (e) 550°C. Film thickness,  $\sim 10 \mu\text{m}$ .

Fig. 3. Optical micrographs of (100) GaAs grown on (110) spinel at various temperatures. (a) 780°C, (b) 750°C, (c) 700°C, (d) 620°C, and (e) 550°C. Film thickness,  $\sim 10 \mu\text{m}$ .



section on Growth temperature and gas flows). The (100) GaAs grown on substrates with generally inferior surface quality exhibits fairly well-defined band or strip structures across the crystal with a high degree of crystallite misorientation (26). Scanning electron micrographs of GaAs films grown on (111), (110), and (100) spinel in Fig. 6 show the crystalline structures. The films were grown simultaneously onto the substrates at 700°C. The oriented single-crystal growth was obtained on both (111) and (110) spinel orientations, but not on (100) orientation. Films grown on (100) spinel substrates were polycrystalline with isolated (100) GaAs single-crystal areas (see section on Orientation Relationship and Crystallinity).

The effect of substrate orientation on the GaAs growth characteristics was further studied by growth on off-oriented substrates. Substrate wafers were prepared with off-orientations [in  $\langle 211 \rangle$  for (111) and (110);  $\langle 110 \rangle$  for (100)] up to  $5^\circ$  from the (111), (100), and (110) major orientations. Epitaxial growth was carried out using the three sets of substrates under, respectively, the most favorable conditions previously determined for the individual orientations.

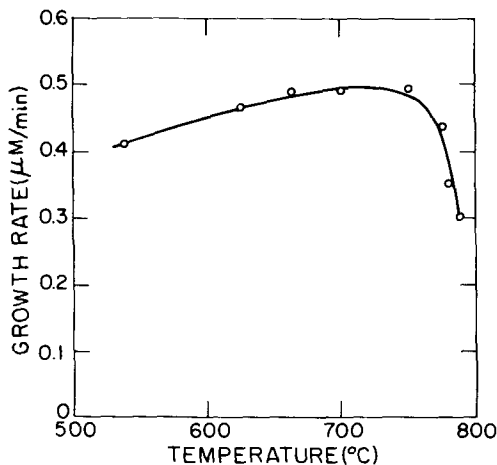


Fig. 4. Growth rate as a function of growth temperature of (111) GaAs.

The films (10-15  $\mu\text{m}$  thick) were examined by x-ray Laue back-reflection and by scanning electron microscopy to determine the crystalline nature and the surface perfection. Infrared reflection measurements were further made on the films providing an assessment of the film surface quality.

The experimental results are presented in Table I. The significant surface structures of the three sets of films are shown in the scanning electron micrographs (Fig. 7). A general trend is observed for all three orientations. Smooth epitaxial surfaces with the least surface imperfections were obtained on misoriented substrates. The optimum degree of misorientation, as shown in Table I, is slightly different for the three major surfaces studied. The improvement of epitaxial surface crystallinity by growth on substrates with off-orientation was previously reported (27) for the homoepitaxial growth of GaAs and Ge, and for the heteroepitaxial GaAs/Ge growth. Another important and interesting finding in this study is on the growth characteristics of films on (100) spinel. As reported above, the growth of (100) GaAs on (100) spinel was difficult, and the grown films were polycrystalline in

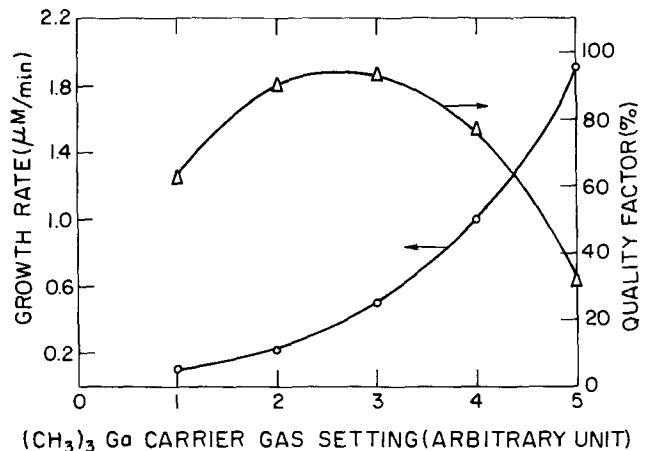


Fig. 5. Growth rate and quality factor as a function of  $(\text{CH}_3)_3\text{Ga}$  feed rate.

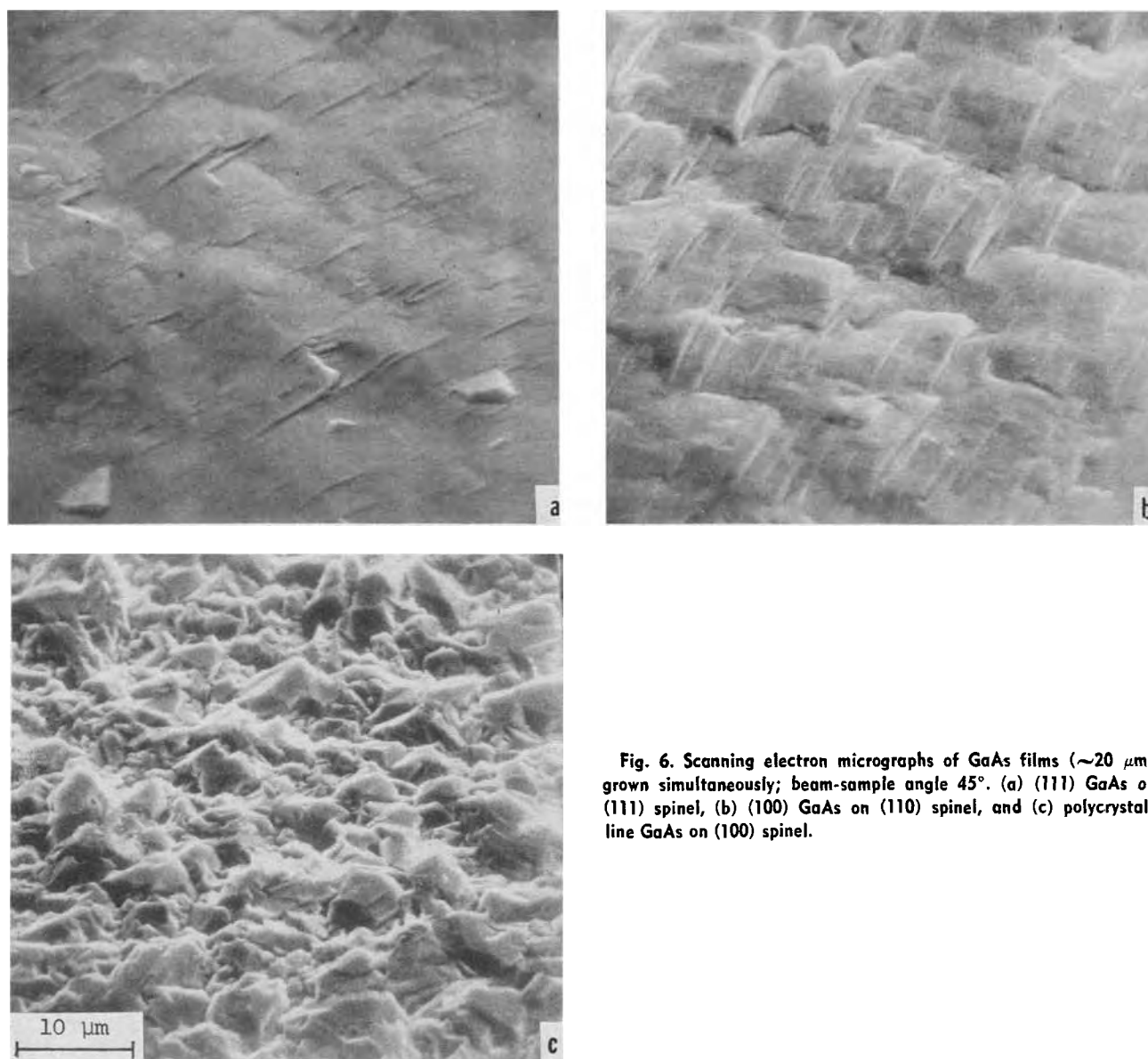


Fig. 6. Scanning electron micrographs of GaAs films ( $\sim 20 \mu\text{m}$ ) grown simultaneously; beam-sample angle  $45^\circ$ . (a) (111) GaAs on (111) spinel, (b) (100) GaAs on (110) spinel, and (c) polycrystalline GaAs on (100) spinel.

nature, with isolated single-crystal areas. However, with a substrate off-orientation as small as  $1^\circ$ , the growth was enhanced remarkably with (111) GaAs grown on (100) spinel. GaAs grown on (100) and  $1^\circ$  off-(100) spinel orientations exhibits a pronounced difference in crystallinity.

Because of the lack of a center of symmetry, there exist the (111)A and (111)B faces for GaAs (28). The physical and chemical characteristics of the two faces

are distinctly different. Simultaneous growth on (111) and off-oriented (100) spinel substrates and on the (111)A and (111)B faces of GaAs reveals that the surface of (111) GaAs grown on spinel resembles the growth on the (111)A face of GaAs. The (111)A face of GaAs grown on spinel was further confirmed by studying the etching behavior (see section on Optical Properties) of the GaAs films and bulk materials.

*Effect of substrate surface preparation.*—Substrate surface perfection has a direct effect on the GaAs heteroepitaxy. The quality of the mechanical polishing was critically important for obtaining good GaAs growth. It was found that surface scratches on the substrates provide preferential nucleation sites. Adsorbed layers and impurity aggregates on the substrate surfaces can also cause defects in the GaAs films.

The effect of preannealing of substrate on the film crystallinity was studied. (111) and (100) GaAs films (about  $10 \mu\text{m}$  thick) were grown, respectively, on (111) and (110) spinel substrates preannealed at  $1200^\circ\text{C}$  in  $\text{H}_2$  for 20 min and on substrates without this treatment. The growth conditions were those optimized for the (111) and (110) orientations. This annealing has been used (4, 6, 19) to improve the surface crystallinity of spinel for silicon epitaxy. Annealing at high temperatures (in air at  $1500^\circ\text{C}$ ) followed by chemical polishing was also reported to minimize mechanical damage of oxide substrates (29). Experimental results indicate that the films grown on preannealed

Table I. Effect of substrate off-orientation on film characteristics

Substrate orientation	Apparent film orientation	Optical reflectance factor, $Q$ (at $2.5 \mu\text{m}$ ) (%)
(111)	(111)	80
$1^\circ$ off (111)	(111)	70
$2^\circ$ off (111)	(111)	92
$3^\circ$ off (111)	(111)	100
$4^\circ$ off (111)	(111)	100
$5^\circ$ off (111)	(111)	100
(110)	(100)	86
$1^\circ$ off (110)	(100)	93
$2^\circ$ off (110)	(100)	90
$3^\circ$ off (110)	(100)	85
$4^\circ$ off (110)	(100)	72
$5^\circ$ off (110)	(100)	18
(100)	(100)	20
$1^\circ$ off (100)	(111)	100
$2^\circ$ off (100)	(111)	100
$3^\circ$ off (100)	(111)	83
$4^\circ$ off (100)	(111)	83
$5^\circ$ off (100)	(111)	52

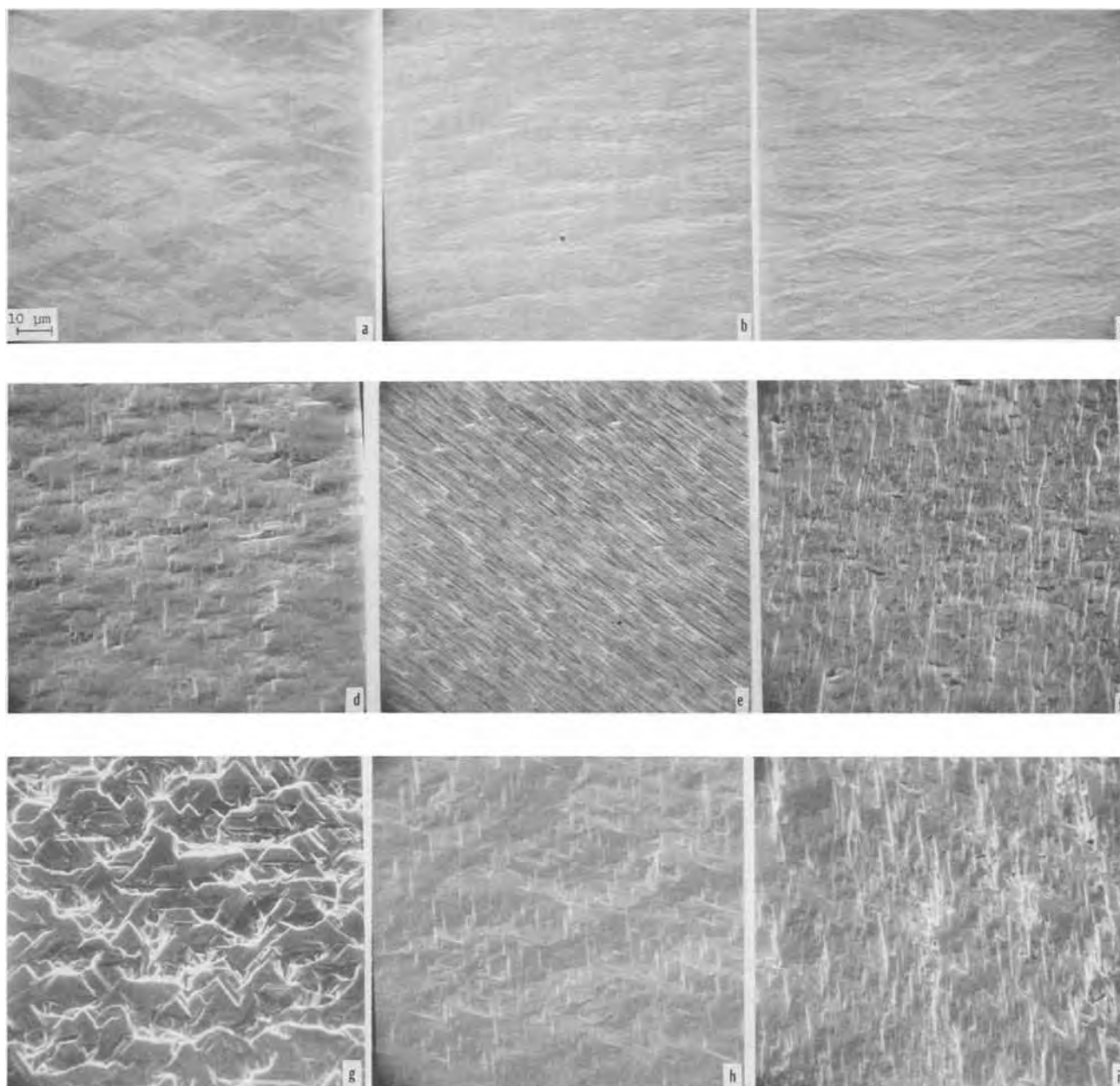


Fig. 7. Scanning electron micrographs of GaAs films ( $\sim 10 \mu\text{m}$  thick) grown on off-oriented spinel substrates. (a) (111)  $0^\circ$  off, (b) (111)  $2^\circ$  off, (c) (111)  $5^\circ$  off, (d) (110)  $0^\circ$  off, (e) (110)  $2^\circ$  off, (f) (110)  $5^\circ$  off, (g) (100)  $0^\circ$  off, (h) (100)  $2^\circ$  off, (i) (100)  $5^\circ$  off.

substrates are always inferior in quality and that the hydrogen annealing of the substrate is, therefore, not desirable for the growth of GaAs by the organometallic process. Scanning electron micrographs of films grown on the unannealed and preannealed substrates are shown in Fig. 8.

*Early growth stage studies.*—The nature of the initial film growth was qualitatively explored by terminating the growth after predetermined growth periods (in the order of seconds) and examining the films by scanning electron microscopy. Experimental results indicate that the early stage of growth involves the formation of discrete nuclei which coalesce, forming growth islands. The islands finally grow together, producing complete coverage of the substrate surface. Similar growth mechanism was observed for heteroepitaxially grown Si (2, 4) and GaAs on sapphire (30). The scanning electron micrographs in Fig. 9 show the growth islands of (111) GaAs on (111) spinel just before complete coverage of the substrate. A slight difference is seen in the percentage of coverage for substrates grown by different methods. This may be due to differences in surface perfection.

The scanning electron micrograph of a typical (111) spinel substrate, grown by flame fusion, in Fig. 10(a) shows the surface structure of a substrate that was cleaned by standard procedures for epitaxial growth. The substrate was heated in  $\text{AsH}_3$  (10% by volume in  $\text{H}_2$ ) at  $700^\circ\text{C}$  for 3 min. This treatment was made on wafers prior to the admission of  $(\text{CH}_3)_3\text{Ga}$  to initiate growth. The surface structure of the substrate is shown in the scanning electron micrograph [Fig. 10(b)]. The micrographs show that the surface is featureless before the heat-treatment in  $\text{AsH}_3$ . However, after the treatment, scratches caused by polishing damage are observed. This indicates that  $\text{AsH}_3$  etches the spinel substrates at a temperature of about  $700^\circ\text{C}$ . The etched single crystalline surfaces promote the epitaxial growth of GaAs. The etching of spinel by  $\text{AsH}_3$  was also observed on flux and Czochralski-grown materials.

*Effect of substrate composition.*—Growth experiments were made to investigate the effect of substrate composition on the film characteristics. A series of (111) spinel substrates with compositions in the range  $\text{MgO}:1.5\text{Al}_2\text{O}_3$  to  $\text{MgO}:3.0\text{Al}_2\text{O}_3$  was prepared for the epitaxial growth of (111) GaAs. The substrate crystals



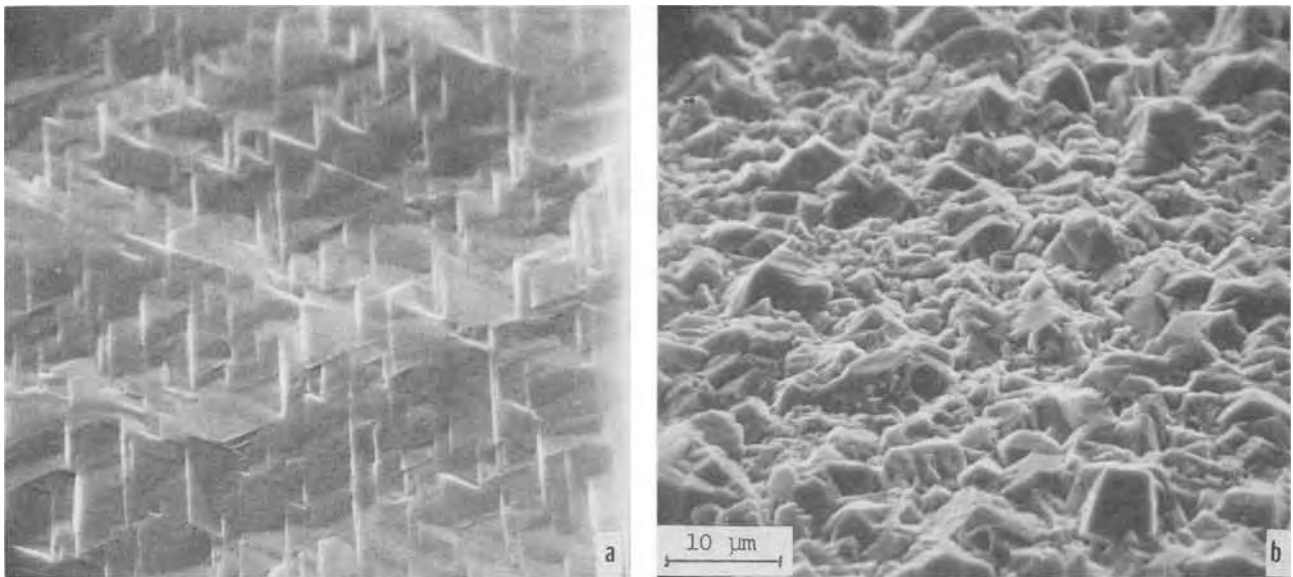


Fig. 8. Scanning electron micrographs of (111) GaAs ( $\sim 10 \mu\text{m}$  thick) grown on (111) spinel. (a) Substrate not annealed, (b) substrate annealed. Beam-sample angle  $45^\circ$ .

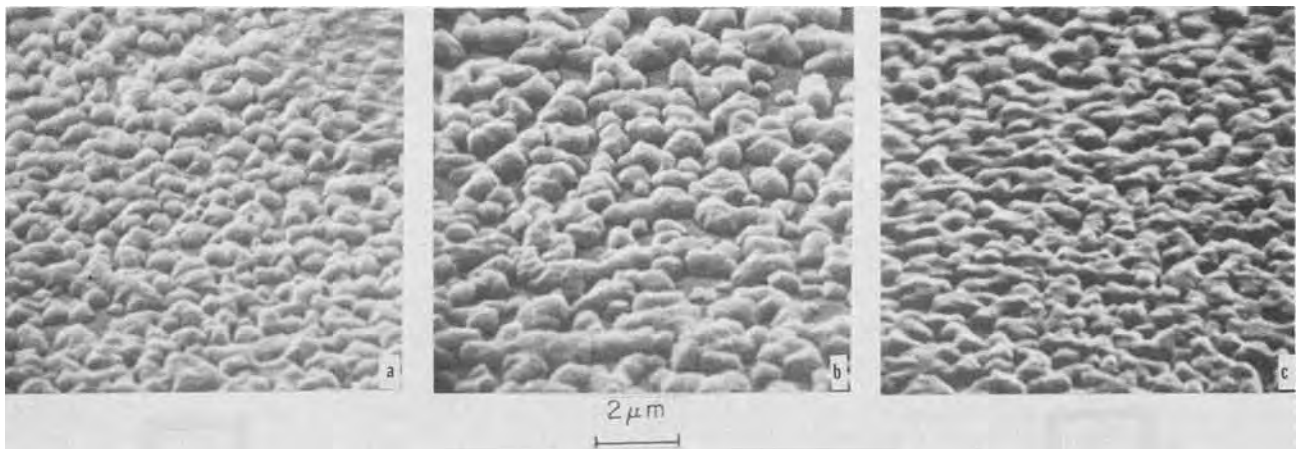


Fig. 9. Scanning electron micrograph of GaAs-on-(111) spinel showing growth islands just before complete coverage; growth rate of about  $0.8 \mu\text{m}/\text{min}$  for 8 sec; beam-sample angle  $60^\circ$ . (a) Flux-spinel substrate, (b) flame fusion spinel substrate, (c) Czochralski spinel substrate.

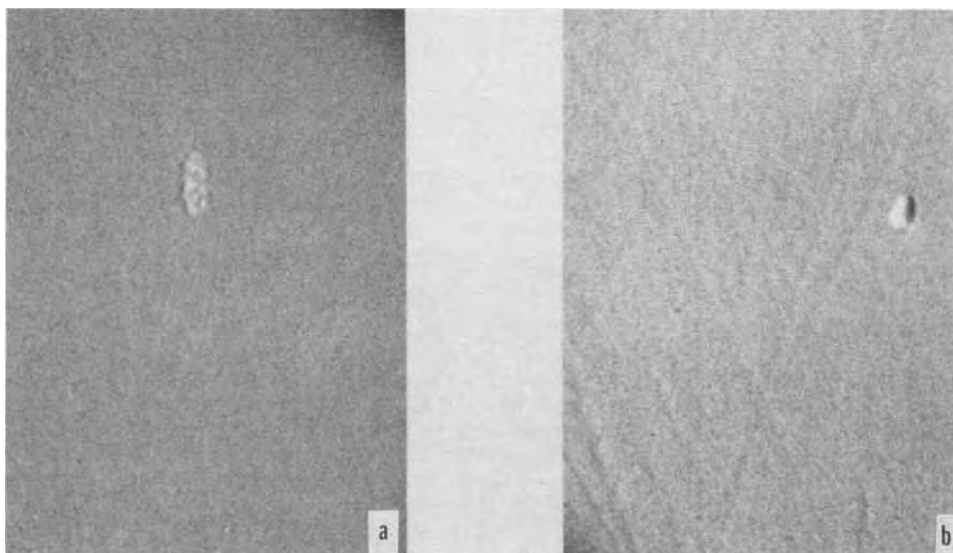


Fig. 10. Scanning electron micrographs showing surface structures of spinel substrate, beam-sample angle  $60^\circ$ . (a) Substrate before treatment, (b) substrate heated in  $\text{AsH}_3$  (10% in  $\text{H}_2$ ) at  $710^\circ\text{C}$  for 3 min.

were grown by the Verneuil method and were polished under conditions that the degree of variation in substrate polishing quality is minimized. For comparison, Czochralski  $\text{MgAl}_2\text{O}_4$  wafers were also used for this

study. The growth experiments were carried out under the optimum conditions so that the effect of substrate composition on the film quality may be elucidated. The film characteristics are shown in Table II.

Table II. Characteristics of GaAs grown on spinel of various compositions

Substrate material	Film thickness ( $\mu\text{m}$ )	Growth rate ( $\mu\text{m}/\text{min}$ )	Optical reflectance factor, $Q$ (%)	Conductivity type	Resistivity ( $\text{ohm-cm}$ )	Hall mobility ( $\text{cm}^2/\text{V-sec}$ )
MgO:Al <sub>2</sub> O <sub>3</sub>	17.2	0.29	69.9	n	0.17	3100
MgO:Al <sub>2</sub> O <sub>3</sub>	25.0	0.42	55.7	n	0.61	2200
MgO:1.5Al <sub>2</sub> O <sub>3</sub>	18.9	0.32	55.7	n	0.43	3300
MgO:1.7Al <sub>2</sub> O <sub>3</sub>	25.3	0.42	49.0	n	0.29	2100
MgO:2.0Al <sub>2</sub> O <sub>3</sub>	25.0	0.42	40.0	n	2.10	1800
MgO:2.5Al <sub>2</sub> O <sub>3</sub>	25.3	0.42	33.2	n	0.27	2600
MgO:3.3Al <sub>2</sub> O <sub>3</sub>	25.0	0.42	55.7	n	1.87	1200

It is seen that for the Verneuil substrates there is no significant trend to dependence of film electrical characteristics on substrate composition. Moreover, there is no significant difference in growth rate and quality factor between films grown on Czochralski and Verneuil substrates. The only difference between films grown on the two kinds of substrates is the physical appearance. Films grown on the Verneuil material exhibit the subgrain structures originating from the substrates, and films grown on the Czochralski substrates do not show subgrain structures. An important variable in the growth of GaAs on Verneuil spinel is the degree of misorientation (19) of subgrains. As described in the section on Orientation Relationship and Crystallinity the film surface quality depends highly on the substrate orientation. This orientation factor affects the film characteristics in addition to the composition. Substrates with minimum subgrain misorientation are desired for the epitaxial growth of GaAs.

Growth experiments were also made to study the difference between Czochralski spinel and sapphire as substrates for GaAs epitaxy. The film growth characteristics were very similar between GaAs/(111) spinel and GaAs/(0001) sapphire grown under identical conditions. However, a significant difference between sapphire and spinel for GaAs epitaxy is that (100) GaAs of good quality can be grown on (110) spinel but not on any known sapphire orientation. Besides the (0001) orientation it is relatively difficult to grow single-crystal GaAs of good quality on other sapphire orientations, and the films, in most cases, exhibit a (111) orientation. For certain device applications the (100) GaAs which can be obtained on spinel is desirable (7).

**Source materials.**—Experimental results indicate that the purity of the source material is of critical importance in determining the electrical properties of the epitaxial films. High purity AsH<sub>3</sub> is commercially available. The purity of the AsH<sub>3</sub> gas used for the GaAs growth on spinel was evaluated in a homoepitaxial GaAs growth system employing the reaction between gallium chloride and arsine (31). However, the quality of the (CH<sub>3</sub>)<sub>3</sub>Ga varies from lot to lot. The impurities generally found, by emission spectroscopy, in typical lots of (CH<sub>3</sub>)<sub>3</sub>Ga include Cu, Fe, Zn, Al, Si, and Mg on the order 10<sup>-1</sup>-10<sup>2</sup> ppm (by weight). These impurities may cause significant unintentional doping of the GaAs films. Analysis of (CH<sub>3</sub>)<sub>3</sub>Ga samples by infrared spectroscopy was also made. The results indicated that there are hydrocarbons (mainly CH<sub>4</sub> and minute higher alkanes) present in some samples with widely varying concentrations from sample to sample.

Electrical measurements of the heteroepitaxial GaAs indicate that categorically, three kinds of films (unintentionally doped), depending mainly on the quality of (CH<sub>3</sub>)<sub>3</sub>Ga, were obtained under the optimum growth conditions and using a high-purity arsine source. The first kind of films exhibited very high resistivity (>10<sup>3</sup> ohm-cm) independent of thickness. The films are highly compensated and contain localized p-n junctions. Several films in this class were angle-lapped and chemically stained to reveal the p- and n-regions. It was found for all the films examined that a p-region is next to the spinel substrate. With subsequent growth the sample either becomes n-type or forms further n-p

regions. Experiments on the homoepitaxial growth of GaAs were also carried out using the organometallic process. It has been found that the interface p-region was not present. The results indicate that the initial p-region is only formed in heteroepitaxial GaAs grown on oxide substrates such as spinel and sapphire (16). It is likely that this p-region is a result of autodoping from the substrate.

The second class of the as-grown unintentionally doped films exhibited p-type conductivity. As described above, many lots of (CH<sub>3</sub>)<sub>3</sub>Ga contain appreciable amounts of Cu and Zn which are well known to be effective acceptors in GaAs. These p-type GaAs films are most probably Cu- and/or Zn-doped. The carrier transport properties<sup>3</sup> are dependent on film thickness, crystallinity, orientation, and other parameters.

It is significant to note that the p-type films (>10  $\mu\text{m}$  thick) with mobilities ( $\sim 300 \text{ cm}^2/\text{V-sec}$ ) close to the bulk values (32) were prepared in the carrier concentration range mid-10<sup>15</sup>/cm<sup>3</sup> to low-10<sup>17</sup>/cm<sup>3</sup>. It was also found that in the p-type films the mobility gradually decreases, starting from about  $3 \times 10^{16}/\text{cm}^3$ , with increasing carrier concentration. This trend is consistent with that of the bulk GaAs.

The third class of films was n-type and was grown on spinel under the optimum growth conditions using particular lots of (CH<sub>3</sub>)<sub>3</sub>Ga and high-purity arsine sources. The electrical properties of the n-type films were less consistent than that of the p-type films. Electron mobilities (carrier 10<sup>15</sup>-10<sup>17</sup>/cm<sup>3</sup>) in the range  $1-4 \times 10^3 \text{ cm}^2/\text{V-sec}$  were measured for films with thicknesses greater than 10  $\mu\text{m}$ . The inconsistency of the electrical properties in n-type films is primarily due to the fact that the films are electrically compensated and because a p-type GaAs layer is often present during the initial film growth on a substrate. Moreover, the crystalline defects may act as charged imperfections containing an accumulation of traps, thus lowering the mobility. To date, the highest electron mobility measured has a value of 4500 cm<sup>2</sup>/V-sec which is about 70% of the bulk value. Typical results of unintentionally doped GaAs films are shown in Table III.

**Doped films.**—The growth characteristics of the Zn-doped films were found similar to those of the unintentionally doped films. The film crystallinity improves with increasing film thickness, and the substrate preparation has a pronounced effect on the film quality, in particular for thin films. The net carrier concentration of the film was found to be dependent primarily on the (C<sub>2</sub>H<sub>5</sub>)<sub>2</sub>Zn reservoir temperature and on the (C<sub>2</sub>H<sub>5</sub>)<sub>2</sub>Zn carrier gas flow. In the present study, films with a carrier concentration in the range  $8 \times 10^{18}$  to  $5 \times 10^{19}/\text{cm}^3$  were grown. Emphasis was placed on the growth of thin ( $\sim 1 \mu\text{m}$  thick) degenerate GaAs films. The thin epitaxial GaAs grown on transparent substrate is of interest for use as negative electron affinity photocathode (33).

The thin films generally exhibit hole mobilities less than the thick films. In the carrier range of  $1-3 \times 10^{19}/\text{cm}^3$  the mobility ranges from 50 to 70% of the bulk values. In an effort to eliminate the problem of the presence of a high defect region near the film/substrate

<sup>3</sup> The electrical properties of GaAs-on-spinel will be reported in detail in a separate paper.

Table III. Electrical properties of (111) epitaxial GaAs\* grown on spinel

Substrate	Film thickness ( $\mu\text{m}$ )	Conductivity type	Resistivity (ohm-cm)	Carrier concentration ( $\text{cm}^{-3}$ )	Hall mobility ( $\text{cm}^2/\text{V-sec}$ )
Flux MgAl <sub>2</sub> O <sub>3</sub> Verneuil	30	n	9	$9.4 \times 10^{14}$	740
MgO:1.7Al <sub>2</sub> O <sub>3</sub> Czocharalski	50	n	0.40	$4.1 \times 10^{15}$	3820
MgAl <sub>2</sub> O <sub>3</sub> Czocharalski	23	n	0.31	$4.7 \times 10^{15}$	4200
MgAl <sub>2</sub> O <sub>3</sub> Verneuil	26.4	p	0.58	$3.4 \times 10^{16}$	320
MgO:2.0Al <sub>2</sub> O <sub>3</sub>	39	p	4.5	$4.5 \times 10^{15}$	316

\* Unintentionally doped films.

interface, several growth experiments were carried out with encouraging results<sup>4</sup> by growing (100) thin GaAs 1  $\mu\text{m}$  thick on heteroepitaxial (100) GaP grown on either (100)Si/(1102)sapphire or (110) spinel.

Studies were also made on the growth of doped n-GaAs on (111) and (100) spinel. It was found that the control of the degree of doping was more difficult for H<sub>2</sub>Se than for H<sub>2</sub>S because the H<sub>2</sub>Se gas was not chemically stable in storage. Thick films (>10  $\mu\text{m}$ ) with carrier concentration in the range  $2 \times 10^{17}$  to  $1 \times 10^{19}/\text{cm}^3$  were grown with mobility ranges from 50 to 90% of the bulk values.

#### Orientation Relationship and Crystallinity

The film-substrate orientation relationship was determined and a preliminary assessment made of the crystalline perfection of the GaAs films, using the Laue x-ray back-reflection method. Some thin (<5  $\mu\text{m}$  thick) GaAs films were also examined by reflection electron diffraction at a glancing angle of less than 1° using a 100-kV electron beam. Laue x-ray back-reflection patterns and electron diffraction patterns are shown, respectively, in Fig. 11 and 12 for typical films grown on (111) spinel substrates prepared by different methods. It is seen that the Laue patterns show complete zone lines (superposition of film/substrate poles) of threefold symmetry and sharp Laue spots with no polycrystalline structures, indicating the good monocrystallinity of the GaAs films and the parallel orientation relationship. The electron diffraction patterns were indexed. The results obtained further confirm the (111) film/substrate parallel orientation relation-

<sup>4</sup>Electrical characteristics of the films will be reported elsewhere.

Table IV. Departure of (111) GaAs from exact parallel epitaxy

Substrate	Misorientation from exact parallel epitaxy
Flux spinel	0.15°
Czocharalski spinel	0.32°
Flame fusion spinel	0.43°

ship. As described before, the film quality improves with increasing thickness. The (111) thin films (<5  $\mu\text{m}$ ) generally exhibit a high degree of twinning about the  $\langle 111 \rangle$  directions.

The departure of the films from exactly parallel epitaxy was determined, as previously described (26), by measuring the angular separation of diffracted peaks from the layer and substrate and comparing this observed value with that expected for parallel epitaxy. Typical results are shown in Table IV. It is interesting to note that the flux spinel crystals exhibit high crystalline perfection without lattice distortion and that the GaAs grown on the flux spinel exhibits the least misorientation from exact parallel epitaxy.

Besides the (111) GaAs films, (100) GaAs films have been grown on both (100) and (110) spinel substrates. As described in the section on Growth Temperature and Gas Flows, the growth results of GaAs on (100) spinel substrate have not been consistent. Because of the lack of a film of uniform quality, the x-ray single-crystal oscillation technique (34) was employed to examine a selected single crystalline area (~30 mil diameter) of a GaAs film grown on spinel. The results indicate that the (100) GaAs exhibits the parallel epi-

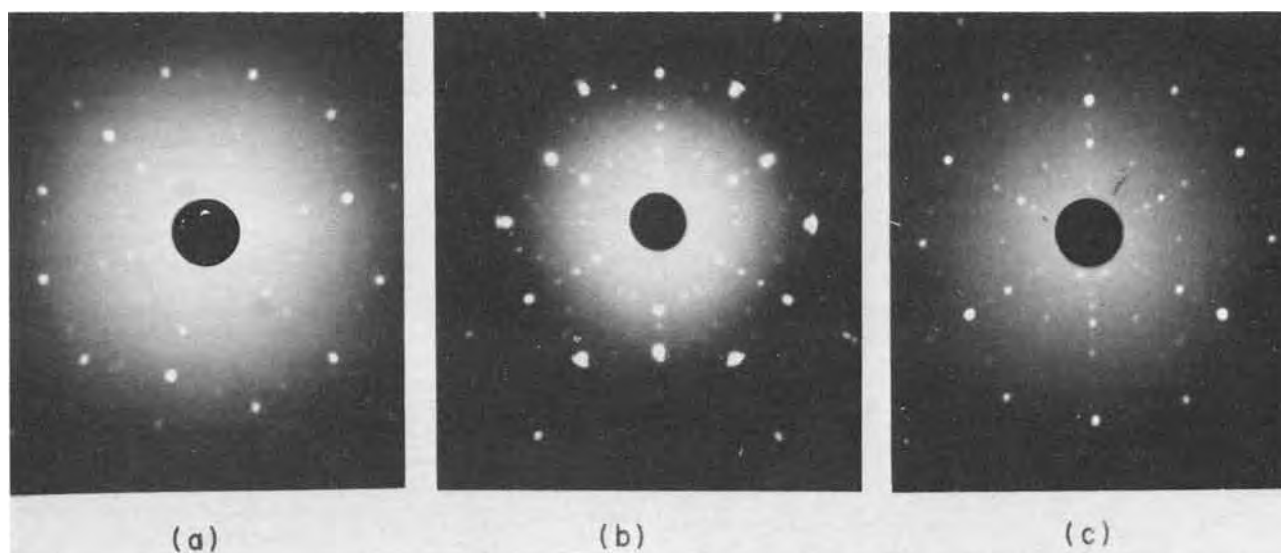


Fig. 11. Laue x-ray back-reflection patterns of epitaxial GaAs grown on (111) spinel. (a) Flame fusion spinel, (b) flux spinel, (c) Czocharalski spinel.



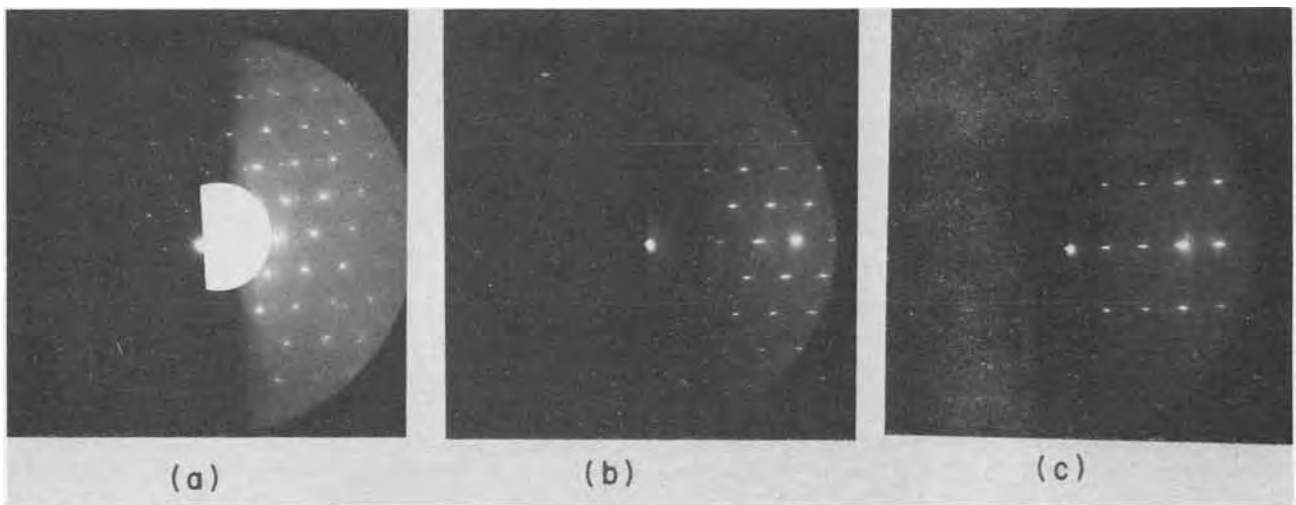
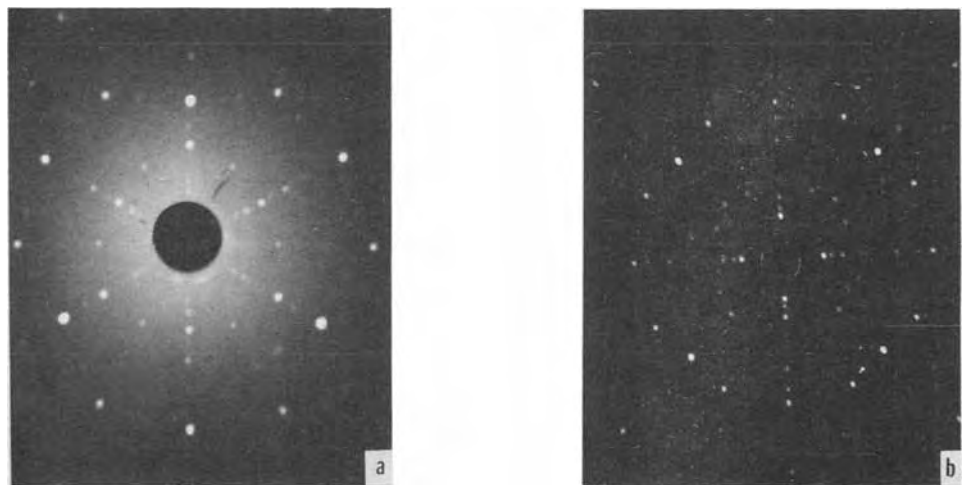


Fig. 12. Electron diffraction patterns of epitaxial GaAs grown on (111) spinel. (a) Flame fusion spinel, (b) flux spinel, (c) Czochralski spinel.

Fig. 13. Laue x-ray back-reflection patterns of (111) GaAs grown on (100) spinel substrate. (a) Film, (b) substrate.



taxial relationship with the (100) spinel substrates. The epitaxy of GaAs on (100) spinel is most interesting in that an apparent orientation relationship of (111)GaAs|| (100)spinel has also been discovered.

The experimental evidence is shown in Fig. 13(a) and (b) which are the x-ray Laue back-reflection patterns of the GaAs layer and spinel substrate sides of a sample. The substrate is (100) oriented with  $1^\circ$  off in  $\langle 110 \rangle$ . The sample was aligned optically such that it was within  $\pm \frac{1}{4}^\circ$  of being normal to the x-ray beam, and the films were taken with exposure long enough to reveal all the Laue spots. The misorientation between the film and substrate was measured, and a value of  $1^\circ$  was found from exact parallel epitaxy. Research results on the epitaxial orientation relationship between GaAs and spinel are summarized in Table V.

The crystallinity of the heteroepitaxial GaAs was characterized in detail by x-ray diffraction topography. The results (26) indicate that the single-crystal layers are composed of grains which are misoriented  $\pm 0.1^\circ$  from the nominal orientation of the layers.

Table V. Epitaxial relationship between GaAs and spinel

Parallel plane		Parallel direction	
Spinel	GaAs	Spinel	GaAs
(111)	(111)	[011]	[011]
(100)	(100)	[010]	[010]
(110)	(100)	[110]	[011]
(100) $1^\circ$ - $5^\circ$ off	(111)	[110]	[011]

### Optical Properties

Optical properties of the heteroepitaxial GaAs were studied. The transmission characteristics of (111) GaAs films grown on spinel, 0.4, 5.1, and  $14.0 \mu\text{m}$  thick, are given as a function of wavelength (in the bandgap region) in Fig. 14. It is seen that the sharpness of the absorption edge increases with increasing thickness. The absorption observed below the bandgap region is due, in part, to reflection losses from the air-GaAs interface ( $R \approx 0.28$ ), the GaAs-spinel interface ( $R \approx 0.10$ ), and the spinel-air interface ( $R \approx 0.07$ ). Reflection losses account for an apparent optical density of about 0.25, in agreement with optical density values obtained for polished, vapor-deposited GaAs films shown in Fig. 15. From Fig. 15 it is apparent that below the bandgap absorption occurs which is not due to simple reflection losses. Reflection measurements indicate that the absorption is due to light scattering from GaAs surface structures. A fundamental characteristic of as-grown, vapor-deposited GaAs films on oxide substrates is, therefore, a surface structure which scatters near infrared light. Reflection characteristics of the films in the lattice band region were also determined. The films all exhibit a sharp transition in reflectivity near  $300 \text{ cm}^{-1}$ , consistent with the characteristics for bulk material (35-36). The reflection data suggest that the  $0.4 \mu\text{m}$  thick GaAs is not significantly different from thicker vapor-deposited GaAs films. This means that the initial  $4000\text{\AA}$  of vapor-deposited GaAs is not grossly autodoped by the spinel substrate nor grossly divergent in stoichiometry and crystal structure.

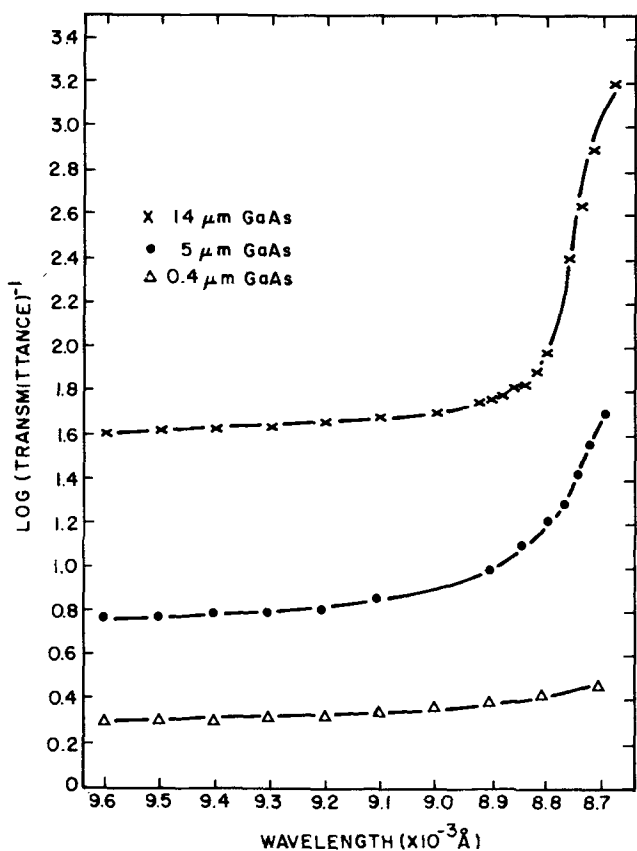


Fig. 14. Optical absorption as a function of wavelength of GaAs films.

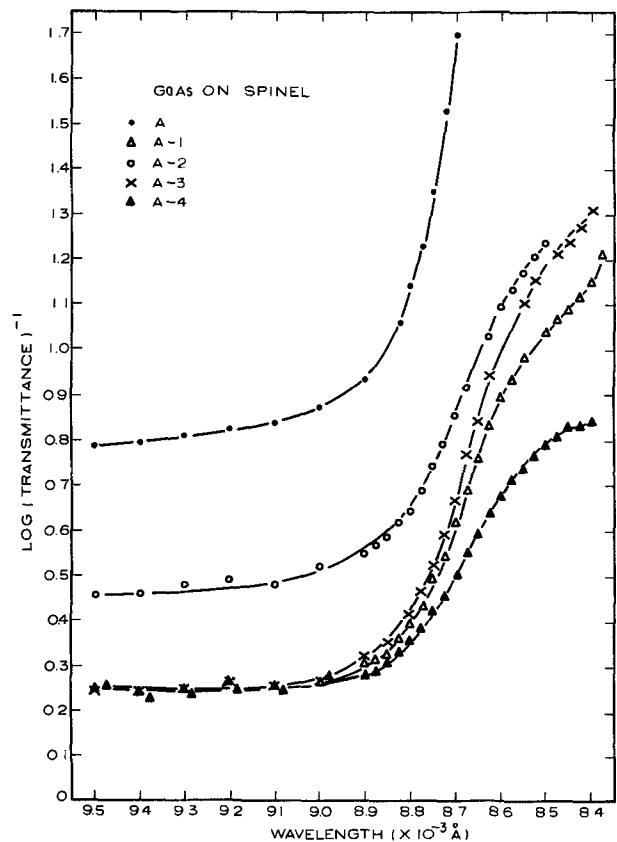


Fig. 15. Optical absorption as a function of wavelength of polished and unpolished GaAs films.

To determine the effects of various polishing methods on the optical properties of GaAs vapor-deposited films, an as-grown (111) GaAs film on (111) spinel,

Table VI. Polishing methods for GaAs

GaAs designation	Polishing method	GaAs film thickness, $\mu\text{m}$
Film A	Film as-grown, untouched	5.1
Film A-1	0.3 $\mu\text{m}$ Linde mechanical polish	2.4
Film A-2	$\text{Br}_2\text{-CH}_3\text{OH}^*$ chemical etch	1.8
Film A-3	0.3 $\mu\text{m}$ Linde mechanical polish followed by a $\text{H}_3\text{PO}_4$ chemical etch	2.5
Film A-4	$\text{H}_3\text{PO}_4^*$ chemical etch only	1.5

\*  $\text{Br}_2$  (0.5%)- $\text{CH}_3\text{OH}$ ;  $\text{H}_3\text{PO}_4$  (85%)- $\text{H}_2\text{O}$ ; etching was done at room temperature.

designated A, was split into five sections. Each section of the original GaAs film was polished by the methods conventionally used for (111) GaAs listed in Table VI.

The results showed that the film and bulk (111)A faces can be polished by  $\text{H}_3\text{PO}_4$  but not by  $\text{Br}_2\text{-CH}_3\text{OH}$ , which is a polisher for (111)B GaAs. Optical transmission and reflection characteristics of the A-film series are shown, respectively, in Fig. 15 and 16. Films A and A-2 exhibit rough surfaces, and the transmission of these samples above the absorption edge is lower than A-1, A-3, and A-4. The films designated A-1, A-3, and A-4 have a smooth surface structure and consequently have identical transmission above the absorption edge. Below the absorption edge, transmission of the A-film series is somewhat different due to differences in film thickness (see Table VI).

The reflection spectra showed that the as-grown sample, A, yields the best over-all band structure while all other spectra exhibit a degraded band structure with the reflectivity minimum shift to a higher wave number. This degradation, originated from surface damage, may cause disorder in the surface lattice structure and introduce electron traps (36).

Ellipsometric measurements were made at a wavelength of 5461Å on epitaxial GaAs grown on spinel

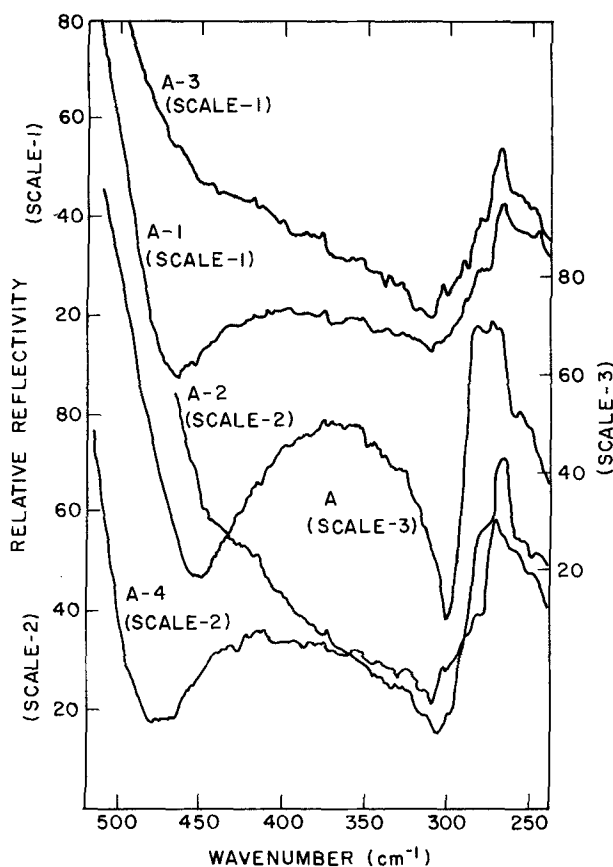


Fig. 16. Reflectivity as a function of wave number of polished and unpolished GaAs films.

Table VII. Optical and dielectric constants of epitaxial GaAs films on spinel at  $\lambda = 5461 \text{ \AA}$

Description of the sample	$\epsilon_1$	$\epsilon_2$	$n$	$k$
Epitaxial GaAs* on spinel. Film thickness = 25 $\mu\text{m}$	15.195	3.602	3.925	0.459
Epitaxial GaAs* on single crystal, bulk GaAs. Film thickness = 2 $\mu\text{m}$	15.636	3.674	3.981	0.461

\* (111) surface.

using an ellipsometer and associated equipment as described in the literature (37). Prior to the measurements, the samples were polished and etched by mechanical and chemical means so that damaged surface structure was removed if present.

The optical constants (the real and imaginary parts of the refractive index  $n-ik$ ) and the dielectric constants  $\epsilon_1$  and  $\epsilon_2$  (the real and imaginary parts of the complex dielectric constant  $\epsilon_1-i\epsilon_2$ ) were derived from the measurements. Typical values of  $n$ ,  $k$ ,  $\epsilon_1$ , and  $\epsilon_2$  of the films were compared with those obtained on epitaxial GaAs grown on bulk GaAs, as shown in Table VII. It is apparent that the optical and dielectric constants of the heteroepitaxial GaAs are quite close to that of the homoepitaxial films.

### Summary

Using the vapor-phase, organometallic deposition process, heteroepitaxial GaAs films on magnesium aluminate spinel substrates have been prepared and characterized. Data show that the GaAs epitaxial films are similar in physical and electrical properties to bulk GaAs. Ease of growth of GaAs on spinel increased with spinel orientation in the order (111) > (110) > (100). Small substrate off orientations (>1°) markedly change the ease of GaAs growth. Preanneal of the substrate in hydrogen at 1200°C prior to growth is not desirable, leading to poor film quality.

Electrical properties of the GaAs films are markedly affected by the purity of the source materials. Semi-insulating, p- and n-type GaAs films can be produced depending mainly on the impurity content of the source materials. Deliberate doping of the GaAs p-type using  $(\text{C}_2\text{H}_5)_2\text{Zn}$  or n-type using  $\text{H}_2\text{Se}$  (and  $\text{H}_2\text{S}$ ) is demonstrated. Both acceptor and donor mobilities are affected by crystalline defects in the film. The crystalline quality of the films improves with thickness. Optical properties of the films are consistent with bulk GaAs. Chemical polishing characteristics have been studied. Over-all, the characteristics of vapor-deposited GaAs films in spinel are adaptable to device fabrication.

### Acknowledgments

The authors are grateful to B. J. Seabury, R. T. Smith, and J. T. McGinn for x-ray diffraction and electron microscopy work. They also wish to thank A. N. Saxena for ellipsometric work, D. A. Kramer for optical measurements, and N. Pastal for film deposition work. Valuable discussions with G. W. Cullen are appreciated. This research was jointly sponsored by the Air Force Materials Laboratory, Wright-Patterson Air Force Base, under Contract F33615-70-C-1536 and RCA Laboratories, Princeton, New Jersey.

Manuscript submitted June 4, 1973; revised manuscript received Sept. 7, 1973.

Any discussion of this paper will appear in a Discussion Section to be published in the December 1974 JOURNAL. All discussions for the December 1974 Discussion Section should be submitted by Aug. 1, 1974.

### REFERENCES

1. A. Miller and H. Manasevit, *J. Vacuum Sci. Technol.*, **3**, 68 (1966).
2. T. S. La Chapelle, A. Miller, and F. L. Morrizz, in "Progress in Solid State Chemistry," Vol. 3, H. Reiss, Editor, Pergamon Press, Inc., London (1967).
3. J. D. Filby and S. Nielson, *Brit. J. Appl. Phys.*, **18**, 1357 (1967).
4. G. W. Cullen, *J. Crystal Growth*, **9**, 107 (1971).
5. D. J. Dumin, P. H. Robinson, G. W. Cullen, and G. E. Gottlieb, *RCA Rev.*, **31**, 620 (1970).
6. C. C. Wang, G. E. Gottlieb, G. W. Cullen, S. H. McFarlane, and K. H. Zaininger, *Trans. Met. Soc. AIME*, **245**, 441 (1969).
7. J. F. Allison, D. J. Dumin, F. P. Heiman, C. W. Mueller, and P. H. Robinson, *Proc. IEEE*, **57**, 1490 (1969).
8. C. W. Mueller, *J. Vacuum Sci.*, **7**, 147 (1970).
9. R. Ronen and P. Robinson, *Proc. IEEE*, **59**, 1506 (1971).
10. W. A. Guttierrez, H. D. Pommerrenig, and M. A. Jasper, *Solid State Electron.*, **13**, 1199 (1970).
11. H. M. Manasevit and W. I. Simpson, *This Journal*, **116**, 1725 (1969).
12. P. Rai-Choudhury, *ibid.*, **116**, 1745 (1969).
13. C. C. Wang and S. H. McFarlane III, *J. Crystal Growth*, **13-14**, 262 (1972).
14. H. M. Manasevit and W. I. Simpson, *This Journal*, **118**, 644 (1971).
15. H. M. Manasevit, *J. Crystal Growth*, **13-14**, 302 (1972).
16. A. C. Thorsen and H. M. Manasevit, *J. Appl. Phys.*, **42**, 2519 (1971).
17. C. C. Wang and S. H. McFarlane III, *J. Crystal Growth*, **3-4**, 485 (1968).
18. B. Cockayne and M. Chesswas, *J. Mater. Sci.*, **2**, 498 (1967).
19. C. C. Wang, *J. Appl. Phys.*, **40**, 3433 (1969).
20. W. G. Spitzer and M. Tannenbaum, *ibid.*, **32**, 744 (1961).
21. M. P. Albert and J. F. Combs, *This Journal*, **109**, 709 (1962).
22. C. E. Jones and A. R. Hilton, *ibid.*, **112**, 908 (1965).
23. W. G. Spitzer and J. M. Whelan, *Phys. Rev.*, **114**, 59 (1959).
24. C. W. Mueller and N. D. Ditrick, *RCA Rev.*, **17**, 46 (1956).
25. E. H. Putley, "The Hall Effect and Related Phenomena," Butterworth and Co., Ltd., London (1960).
26. S. H. McFarlane III and C. C. Wang, *J. Appl. Phys.*, **43**, 1724 (1972).
27. M. Berkenblit and A. Reisman, U.S. Pat. 3,476,592 (1969).
28. O. Madelung, "Physics of III-V Compounds," John Wiley & Sons, Inc., New York (1964).
29. A. Reisman, M. Berkenblit, J. Cuomo, and S. A. Chan, *This Journal*, **118**, 1653 (1971).
30. H. M. Manasevit and A. C. Thorsen, *Trans. Met. Soc. AIME*, **1**, 623 (1970).
31. J. J. Tietjen and J. Amick, *This Journal*, **113**, 724 (1966).
32. S. M. Sze and J. C. Irwin, *Solid State Electron.*, **11**, 599 (1968).
33. Y. Z. Liu, J. L. Moll, and W. E. Spicer, *Appl. Phys. Letters*, **17**, 60 (1970).
34. B. D. Cullity, "Element of X-Ray Diffraction," Addison-Wesley Publishing Co., Reading, Mass. (1959).
35. W. G. Spitzer and J. M. Whelan, *Phys. Rev.*, **114**, 59 (1959).
36. C. E. Jones and A. R. Hilton, *This Journal*, **112**, 908 (1965).
37. K. H. Zaininger and A. G. Revesz, *RCA Rev.*, **25**, 85 (1964).



## Microsegregation of Iron in Electrolytic Capacitor Grade Aluminum

Ronald B. Diegle

Corporate Research and Development Center, General Electric Company, Schenectady, New York 12301

Aluminum foil for use in electrolytic capacitors is customarily electrolytically and/or chemically etched to increase the surface area exposed to electrolyte. Impurity content of the Al has long been known to exert a profound influence on the response of foil to a particular etching process, *i.e.*, on its etchability.<sup>1</sup> However, although composition limits for major impurities are usually specified, there is still little understanding of how the identity, concentration, and distribution of these impurities affect the etching process.

Relatively little work is reported in the literature which elucidates the influence of trace impurities on Al etchability. Bakish *et al.* (1) noted a correlation between etchability and the concentration of major impurities in commercial grade Al, but variations in the microscopic distribution of these elements, that is, the states of microsegregation, were not investigated. (The term microsegregation as used in this paper refers to heterogeneities in impurity concentration, either in solid solution or as second-phase particles, on a microscopic scale.) Investigations into other areas of Al corrosion have also shown the importance of impurity content (2, 3), but microsegregation has not been considered. A notable exception was a two-part study by Biloni *et al.* (4) and Bond *et al.* (5), which conclusively demonstrated that distribution could be even more important than total impurity content in determining the tendency for pitting corrosion of Al in NaCl solution.

In this note preliminary results of the effect of microsegregation of Fe on the etchability of cold-rolled Al are reported. Iron was chosen as the impurity element for investigation for two reasons. First, it is the only element in the higher purity grades (Al content greater than about 99.8%) of Al for electrolytic capacitor use that precipitates extensively as a second phase during metallurgical processing. Such precipitates, nominally FeAl<sub>3</sub> from phase diagram considerations, could conceivably initiate undesirable corrosion during electroetching and thereby impair etchability (6). Second, the response of etchability to high temperature (600°-650°C) heat-treatments applied at various stages of ingot reduction was shown (7) to be both favorable, possibly indicating a detrimental role of impurity microsegregation established during casting, but quite sluggish, in accord with the very small diffusion rate of Fe in Al (8).

### Material Preparation

Extensive equilibrium and nonequilibrium microsegregation of impurities occurs during the commercial casting of Al for capacitor use (7). It was therefore desired to produce microsegregation, in this case of Fe, in a controlled manner in laboratory ingots, and to

Key words: aluminum etchability, tunnel corrosion, precipitation.

<sup>1</sup> Etchability as used here refers to the total area of foil contributing to capacitance after etching and anodic film formation. It is proportional to the specific capacitance of foils etched under identical conditions and anodically formed to a particular voltage.

preserve it to the foil stage for evaluation of its influence on etchability. Precipitation from supersaturated solid solution was chosen as the technique, both because it is more conveniently performed than controlled solidification, and because it has already been studied in detail in the Al-Fe system (9).

An Al-400 ppm (weight) Fe alloy was prepared from 99.9999% Al<sup>2</sup> and an Al-1.8 weight per cent (w/o) Fe master ingot. The melt was homogenized and vacuum chill cast, after which the ingot was sectioned into slices 0.95 by 1.41 by 0.18 cm. Some of the slices were homogenized by soaking at 645°C in air for 96 hr followed by water quenching. The quenched slices were next annealed for 1 min in a fused salt bath at 250°C to reduce the concentration of vacancies and dislocation loops formed during quenching from 645°C (9). Examination in the transmission electron microscope (TEM) of thinned sections of homogenized ingot verified that essentially all of the Fe was in solid solution. To produce different stages of nucleation and growth of FeAl<sub>3</sub>, some of the homogenized slices were aged at 350°C for times ranging from 2 to 140 hr, quenched, aged 1 min at 250°C, and again quenched. Representative aged ingot specimens were selected for examination in the TEM. The remaining slices were lightly abraded and chemically etched to provide a clean surface for rolling, and were then cold-rolled in a hand mill to 90 $\mu$  thickness, a reduction of 95%.

### Determination of Etchability

As-rolled foil specimens were sectioned into strips 1.8 cm wide and 6 cm long and electropolished in an ethanol-perchloric acid mixture to establish a standard surface condition. To evaluate the effect of this surface preparation on etchability, some foils were instead etched 1 min in 30% NaOH solution at 23°C. Electroetching was performed for 54 sec at an anodic current density of 775 mA/cm<sup>2</sup> in 20% NaCl solution at 90°C. Certain foils were electroetched only 3 sec for the purpose of studying the morphology of etch initiation. Etched specimens were washed and dried, chemically etched in nitric acid diluted 2 to 1 with water for 2 min to remove traces of chloride ion, and again washed and dried. A 50V anodic film was formed on each specimen using previously described techniques (10), and the capacitance of specimens etched for 54 sec was measured (10).

### Microstructural Evaluation

Specimens of unaged ingot and ingot aged for different times at 350°C were electrochemically thinned by conventional techniques and studied with the TEM. A nucleation time of slightly less than 48 hr was noted, since no precipitates could be resolved after 19 hr of aging, but they were beginning to develop after 48 hr. (Resolution was about 30Å.) The appearance of a few

<sup>2</sup> Purchased from United Mineral and Chemical Corporation, Metals Division, New York, New York.

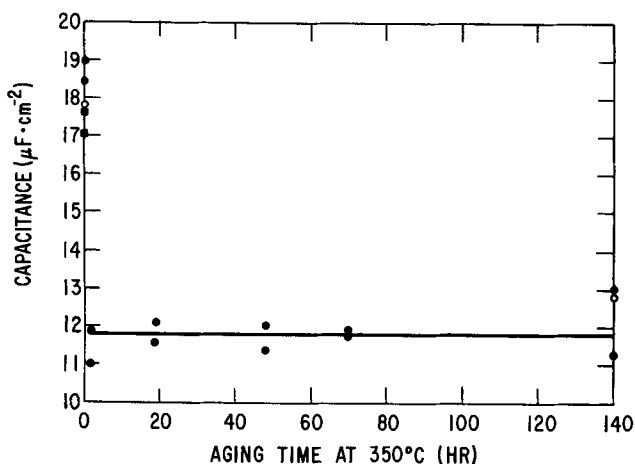


Fig. 1. Capacitance at 50V formation of cold-rolled Al-400 ppm Fe foil vs. ingot aging time at 350°C. Shaded circle, ingot homogenized and aged at 350°C for time indicated; open circle, ingot homogenized and aged for time shown, but foil etched in 30% NaOH instead of electropolished before electroetching; shaded square, ingot neither homogenized nor aged before rolling to foil.

particles after 48 hr of aging at 350°C is in good agreement with the work of Miki and Warlimont (9) who measured a nucleation time of 40-50 hr at 389°C for Al-400 ppm Fe.

Particles typically were  $0.1\mu$  long and  $0.05\mu$  wide after 48 hr of aging, and they grew to about  $0.4\mu$  by  $0.1\mu$  after 140 hr. The number of particles per unit volume, which was determined from foil thickness and areal particle densities in TEM micrographs, was within a factor of 3 of  $10^{13}\text{ cm}^{-3}$  and was independent of aging time for times of 70 hr and greater.

Since dislocation substructure influences the etchability of cold-rolled foil, it was desired to know whether different degrees of microsegregation in the ingot affected the substructure produced by cold-rolling. The very large dislocation densities produced by 95% reduction in thickness precluded any attempts to study dislocation morphology in detail, so subgrain size was chosen to characterize dislocation substructure. Subgrain sizes, which were calculated by the linear intercept method from several micrographs of each foil, were between  $0.7$  and  $0.85\mu$ . Since variations in size were within the  $\pm 10\%$  limit of experimental error, no effect of microsegregation on subgrain size was found.

#### Effects of Microsegregation on Etchability

A remarkable effect on etchability produced by microsegregation of Fe in ingot is shown in Fig. 1. Etchability decreased precipitously as a result of only 2 hr aging, which is far less than the minimum time required for homogeneous nucleation and growth of  $\text{FeAl}_3$  in this alloy. Almost as surprising is the fact that etchability was not affected by the onset of precipitation of  $\text{FeAl}_3$ , which occurred between 19 and 48 hr of aging. (The foils used in this work certainly contained a sufficient number of particles to permit evaluation of their effect on etchability. For instance, a very conservative estimate of the number of particles intersecting the surfaces of foils rolled from ingots aged 70 hr or more is  $2 \times 10^7\text{ cm}^{-2}$ , based on the assumption that the only particles which intersect lay within an imaginary layer next to the surface of depth equal to the minimum particle dimension, about  $0.02\mu$ . This is three orders of magnitude greater than the surface particle density of about  $10^4\text{ cm}^{-2}$  experimentally determined from a typical commercial foil lot of 99.88% purity. It should be noted, however, that solid-state precipitation produced particles of submicron size, whereas typical commercial casting results in precipitates several microns in diameter.)

To learn more about the effect of short time aging on etchability, oxide replicas were made of foils etched for 3 and 54 sec, lifted, and examined with the scanning electron microscope (11). Comparison of Fig. 2a and 2b shows that the formation of individual etch tunnels in the first 3 sec of electroetching was severely inhibited due to aging of the ingot for just 2 hr. The reason for the lower capacitance of fully etched foil is shown in Fig. 2c and 2d, which illustrates that a much coarser, less intricate tunnel structure developed as a result of ingot aging.

Prismatic dislocations formed by vacancy condensation during quenching from 645°C were largely removed during the first 250°C anneal, as observed by Miki and Warlimont (9) and verified in this study. Therefore, there are only two phenomena which might reasonably be expected to have occurred in ingot during the initial 2 hr of aging at 350°C. The first is clustering of Fe atoms in the Al matrix. Since particles as small as 30Å could not be detected after 19 hr, such clustering was certainly a preprecipitation or pre-nucleation phenomenon resulting only in solid solution microsegregation. (The morphology of preprecipitation in the Al-Fe system has not been studied in nearly as much detail as in, for example, the more important Al-Cu system.) The second occurrence is heterogeneous nucleation and growth of  $\text{FeAl}_3$  on such preferred sites as grain boundaries and grown-in dislocations, thus producing two-phase microsegregation. The contribution to the final particle density of  $10^{13}\text{ cm}^{-3}$  by heterogeneous nucleation within 2 hr of aging was negligible for two reasons. First, since no precipitates were detected after 19 hr, relatively few nucleated as early as 2 hr. Second, it was demonstrated by both low temperature resistivity measurements and transmission electron microscopy that only homogeneous, not heterogeneous, nucleation occurs in Al-400 ppm Fe at aging temperatures below 470°C (9). Thus the most reasonable explanation for the disruption of tunnel corrosion during electroetching is preprecipitation clustering of Fe atoms during aging times somewhat less than 48 hr. Moreover, since etchability did not increase after the transition of these clusters to discrete  $\text{FeAl}_3$  precipitates, which proceeded during aging beyond about 48 hr, it is evident that these precipitates were equally detrimental to etchability.

#### Conclusions

Evidence has been presented that microsegregation of Fe in Al occurring at the ingot stage can reduce the capacitance of cold-rolled foil by as much as 40%, or about  $7\text{ }\mu\text{farad/cm}^2$ . Such microsegregation initially was most likely caused by preprecipitation clustering of Fe atoms, but after about 48 hr of aging it was manifest as discrete submicron size  $\text{FeAl}_3$  particles. Although the postnucleation stage of microsegregation could be detected by conventional electron optical techniques, pre-nucleation stages could not. The effect of microsegregation was to impede development of the intricate tunnel network normally produced during the electroetching process. Future work should attempt to establish the precise mechanism by which microsegregation disrupts tunnel corrosion in Al, and to determine the possible effects on etchability caused by segregation of other impurities, such as Si, Mg, and Cu, normally present in capacitor grade Al.

#### Acknowledgments

The author is grateful to F. W. Daniels, Capacitor Materials Product Section, General Electric Company, Hudson Falls, N. Y., and to Dr. C. G. Dunn for providing advice and encouragement during this work. Thanks are also extended to Dr. D. A. Vermilyea for critically reviewing the manuscript.

Manuscript received Oct. 4, 1973.

Any discussion of this paper will appear in a Discussion Section to be published in the December 1974

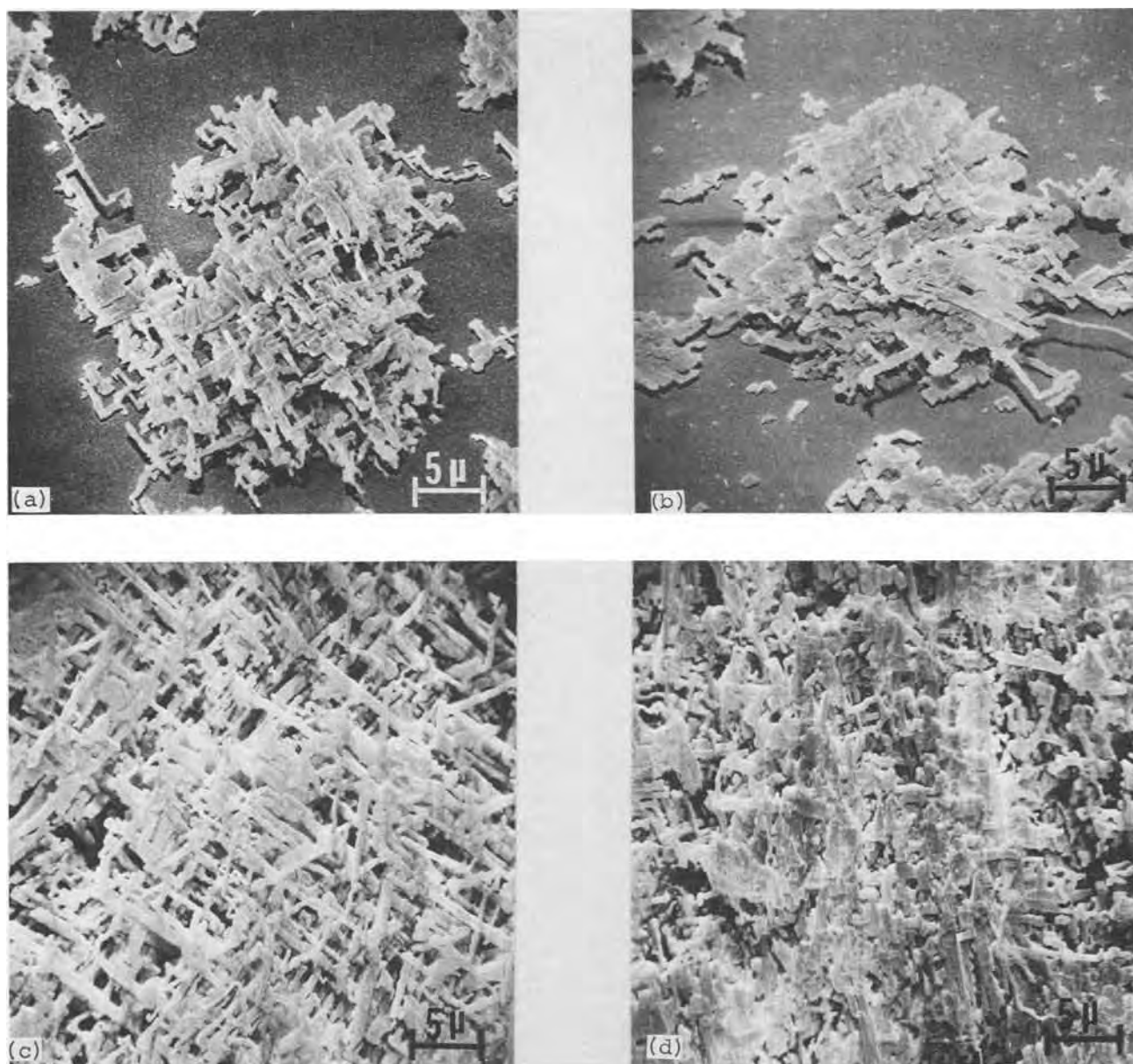


Fig. 2. SEM micrographs of gold-coated oxide replicas of electroetched foil formed to 50V. Note characteristic tunnel corrosion morphology. (a) Ingot not aged, foil electroetched 3 sec; (b) ingot aged 2 hr at 350°C, foil electroetched 3 sec; (c) ingot not aged, foil electroetched 54 sec; (d) ingot aged 2 hr at 350°C, foil electroetched 54 sec.

JOURNAL. All discussions for the December 1974 Discussion Section should be submitted by Aug. 1, 1974.

#### REFERENCES

1. R. Bakish, R. J. Kornhaas, and E. Z. Borders, *Electrochem. Technol.*, **1**, 358 (1963).
2. M. Metzger and J. Intrater, *Trans. AIME*, **197**, 820 (1953).
3. E. C. W. Perryman, *ibid.*, **203**, 1053 (1955).
4. H. Biloni, M. F. Bolling, and H. A. Domian, *TMS-AIME*, **233**, 1926 (1965).
5. A. P. Bond, M. F. Bolling, and H. A. Domian, Tech. Rep. No. SL-65-50, Ford Motor Company Scientific Laboratory (1965).
6. M. S. Hunter, *Electrochem. Technol.*, **1**, 151 (1963).
7. R. B. Diegle, Unpublished work.
8. W. B. Alexander and L. M. Slifkin, *Phys. Rev.*, **1**, 3274 (1970).
9. I. Miki and H. Warlimont, *Z. Metallk.*, **59**, 254 (1968).
10. C. G. Dunn, R. B. Bolon, A. S. Alwan, and A. W. Stirling, *This Journal*, **118**, 381 (1971).
11. C. G. Dunn and R. B. Bolon, *ibid.*, **116**, 1050 (1969).

# Optical Absorption and Electrical Conductivity of SiC Films Produced by Ion Implantation

W. Rothemund and C. R. Fritzsche\*

Institut für Angewandte Festkörperphysik der Fraunhofer-Gesellschaft, D-78 Freiburg, West Germany

Within the past few years, silicon carbide has gained increasing importance as a material for high-temperature semiconductor devices. It is as well an interesting material from a scientific point of view. The preparation of this material by conventional techniques of crystal growth is difficult, and attempts have been made to produce carbide films by reaction of solid silicon with hydrocarbons or by pyrolytic deposition (1). Temperatures of 1100°C and more are needed for these techniques. Implantation of carbon ions into silicon and subsequent annealing at 800°C and above offers an alternate method of obtaining silicon carbide (2, 3). Until now, only results of implantations with one single energy have been reported, and only isolated grains of SiC surrounded by silicon have been obtained. The present paper reports on attempts to produce continuous SiC layers by multiple implantations with various energies and provides some information on the optical absorption in the visible and infrared regions and on the electrical conductivity of these layers from which their quality can be estimated.

## Experimental

C<sup>+12</sup> ions were implanted at room temperature into 500 ohm-cm, n-type, single-crystal silicon wafers. The wafers were (111) oriented and polished on both sides. Either three or four implantations were made with energies of 50, 30, and 15 keV or 70, 50, 30, and 15 keV, respectively. Typical beam current densities were approximately 10 μA cm<sup>-2</sup> with respect to the implanted area. Fluences were chosen so that the peak concentrations for each single implantation were 10<sup>23</sup> cm<sup>-3</sup>, i.e., the single fluences were on the order of 10<sup>18</sup> cm<sup>-2</sup>. These concentrations were calculated according to the theory of Lindhard, Scharff, and Schiott (LSS) from the tables of Johnson and Gibbons (4). Since the crystal axis was tilted 7° from the beam axis, we assume that LSS theory applies in good approximation at the beginning of the implantations. When the carbon concentration becomes high, the contribution of the implanted ions to the stopping power will cause a reduction of the penetration depth. No corrections according to this effect were made.

At high fluences, as used in our work, the maximum concentration can be limited by sputtering if the surface recedes substantially. Therefore, we investigated the step appearing at the border of a limited area implanted with 15, 30, 50, or 70 keV C<sup>+12</sup> ions. While from the 15 keV implantation a sputtering coefficient of 0.2 atoms per incident ion was estimated, the other implantations did not result in a measurable surface erosion. EerNisse (5) has reported on the energy dependence of the sputtering yield of noble gas ions into silicon and his data consist well with our observations.

The effect of sputtering on the maximum ion concentration for Bi into GaAs was investigated by Tinsley *et al.* (6). They found a saturation of the retained dose at a fluence of about 5 × 10<sup>16</sup> cm<sup>-2</sup> at 60 keV. In this case, the sputtering coefficient is 4.4 atoms/ion and the projected range is 170 Å. In our 15 keV implantation, the corresponding values are 0.2 atoms/ion and 480 Å. Comparing all these data, we find that the saturation effect will be negligible at least for our 30, 50, and 70 keV implantations. This can also be concluded

from the fact that after multiple implantations the implanted surface was always above the silicon surface.

The calculated implantation profile is shown in Fig. 1. It can be seen that over a range of about 3000 Å the total ion concentration is higher than 5 × 10<sup>22</sup> cm<sup>-3</sup> and thus sufficient to convert all the silicon within this range into carbide. If the 70 keV implantation is omitted, the expected carbide range is only 2000 Å.

Annealing was made in nitrogen or vacuum so that results of the IR absorption studies could be compared to those of Borders *et al.* (2). Only vacuum annealed samples were used for the electrical measurements. IR spectra were measured with a Beckmann IR 9 spectrometer. For the electrical measurements, gold electrodes of various sizes and shapes were evaporated onto the carbide layer. Contact to the back side of the silicon was also made by evaporated gold. The spectral distribution of the photovoltaic effect of the Au-SiC-Si-Au structure was determined using the monochromator section of a Baird SF-100 spectrophotometer.

## Results

The IR absorption spectrum of the implanted silicon in the range of wave numbers 400-3600 cm<sup>-1</sup> shows only one band which can be attributed to SiC. Before annealing, this band is wide and has its peak at 750 cm<sup>-1</sup>. The effect of annealing in nitrogen is shown in Fig. 2. Isochronal 15 min anneal treatments were performed at progressively higher temperatures. The band moves towards higher wave numbers with increasing anneal temperature, and its half-width decreases considerably, both effects being most pronounced between 800° and 850°C. The band approaches the transversal optical (TO) phonon absorption at 794 cm<sup>-1</sup> (7, 8) for both α- and β-SiC and the shift is almost finished at 1000°C. The half-width, however, decreases distinctly up to at least 1300°C. When annealing was carried out in vacuum at 10<sup>-2</sup> Torr, or when the 70 keV implantation was omitted, the behavior of the TO phonon absorption was approximately the same as described by Fig. 2.

In the visible range, the optical properties cannot be investigated by transmission spectroscopy because of absorption by the silicon substrate. Reflectance was

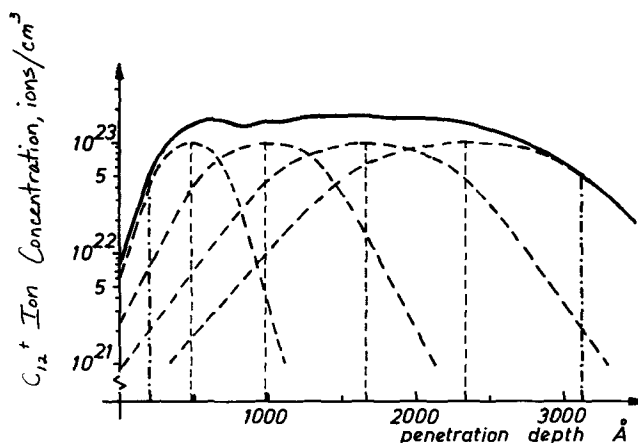


Fig. 1. Calculated implantation profile of implanted C<sup>+12</sup> ions in silicon.

\* Electrochemical Society Active Member.  
Key words: silicon carbide, ion implantation, compound formation.



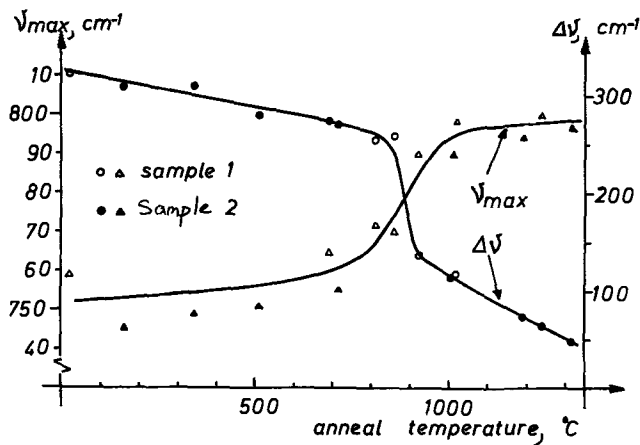


Fig. 2. Annealing of carbon implanted silicon; wave number  $\nu_{\max}$  and half-width  $\Delta\nu$  of the main IR absorption band as a function of anneal temperature.

measured and was found to be high in the range from 550 to 800 nm, but interpretation of the spectrum is difficult since reflection at the carbide as well as at the silicon surface, and consequently also absorption in the carbide, determine the reflected intensity. From the electrical measurements described below, we conclude that the range of high reflectance is determined by the transmittance of the carbide.

The electrical conductivity of layers implanted with four different energies was determined from bridge measurements between various combinations of electrodes on top of the implanted layer. After annealing for 30 min at 1300°C in vacuum of  $10^{-1}$ - $10^{-2}$  Torr, resistivities between  $10^{-2}$  and  $10^{-3}$  ohm-cm were found. No substantial current-voltage nonlinearity was observed. However, when contact is made to one electrode on top of the SiC layer and to one electrode on the back side of the silicon wafer, samples show rectifier characteristics and a photovoltaic effect on the carbide side. The devices are blocking if the carbide side is negatively biased, and the polarity of the carbide side is positive if the unbiased sample is illuminated. Because of the high conductivity of the carbide the photoelectric effect can be assumed to take place in the silicon, and we consider the device to be a Schottky diode with a transparent electrode rather than a heterojunction.

Since only a part of the silicon surface was implanted, we were able to compare photodiodes with and without a SiC cover. If the photocurrent,  $J_2$ , of the SiC-Si device is divided by that of the silicon diode,  $J_1$ , the intensity distribution of the light source as well as the spectral response of the silicon is eliminated, and the quotient is proportional to the transmittance of the carbide. The result of this evaluation is shown by the solid line in Fig. 3. The dashed line indicates the absorption edge of  $\beta$ -SiC after Lely and Kröger (9). Visually, the color of our layers is between green and yellow.

### Discussion and Conclusions

The absorption band at  $800\text{ cm}^{-1}$  in Fig. 2 corresponds to TO phonons in SiC, and the absorption edge at about 2.25 eV in Fig. 3 is close to that of cubic SiC. This indicates that implantation of carbon ions into silicon, with a profile according to Fig. 1 after annealing at 1300°C, results in silicon carbide which is similar to the cubic  $\beta$ -SiC, but probably has still a high disorder.

The infrared spectrum of our samples has some properties in common with the one reported by Borders *et al.* (2) which was obtained after single-energy implantation. In both cases, the broad, featureless absorption band at  $750\text{ cm}^{-1}$ , which is observed immediately after implantation and after annealing to temperatures less than 800°C, can be interpreted to be due

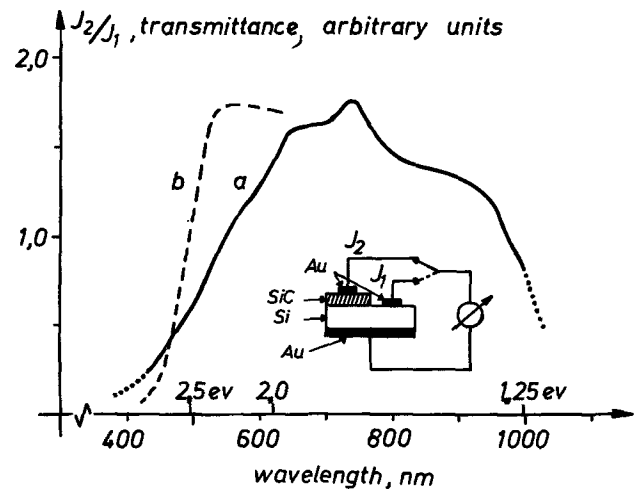


Fig. 3. (a) Transmittance spectrum of the SiC layer as estimated from photovoltage measurements. (b) Band edge of  $\beta$ -SiC, as in Lely and Kröger (9).

to Si-C stretching modes in regions of high disorder possibly overlapped by the local mode of highly concentrated carbon in silicon. In both cases, the band approaches the transversal optical frequency of SiC [see Spitzer *et al.* (7, 8)] after annealing at temperatures close to 900°C. An essential difference is found after annealing at temperatures above 900°C. While Borders *et al.* state that annealing is complete by 875°C and no change is observed in the band upon further anneals to 1000°C, we observe a pronounced decrease in the band half-width up to 1300°C. It is likely that at the carbide/silicon interface disorder and deviations from stoichiometry cannot completely be removed by annealing. A lower limit of the half-width is thus determined by the volume ratio of bulk SiC and disordered interface regions. Therefore, our results mean that the interface is relatively small in our samples and a continuous layer may have formed. That maximum order is not yet achieved, even in our samples, can be concluded from the lack of saturation in the half-bandwidth annealing curve.

As to the optical properties in the visible range, Knippenberg (10) has concluded from an investigation of several SiC polytypes that the bandgap is the smaller the lower the single-bond energy. Thus, the difference between the band edge of  $\beta$ -SiC and the edge resulting from our measurements could possibly be explained by a lower, single-bond energy in our samples. However, according to Lely and Kröger (9), the edge could also be shifted by a high nitrogen content. These authors also report that nitrogen-doped hexagonal SiC shows a narrow band at 620 nm and a broad band extending from 900 nm into the near infrared. Corresponding bands seem to appear in our material, and it may be the superposition of these bands which causes the transmittance peak at 720 nm in Fig. 3. Lely and Kröger (9) have correlated quantitatively their optical and electrical measurements with the nitrogen content. Comparison of the spectra indicates a nitrogen concentration of about  $2 \times 10^{19}\text{ cm}^{-3}$  in our samples.

Approximately the same value is obtained from the electrical measurements. For high carrier concentrations, Lely and Kröger (9) report mobilities of about 14 and  $9\text{ cm}^2/\text{V-sec}$  for electrons and holes, respectively. The resistivity of our samples is less than  $10^{-2}$  ohm-cm, hence the carrier concentration is higher than  $4.5 \times 10^{19}\text{ cm}^{-3}$  if the layer is n-type and  $7 \times 10^{19}$  if the layer is p-type. There definitely are no donors or acceptors other than nitrogen or lattice defects that could have been introduced in such high amounts during implantation or annealing. The assumption of n-type conductivity results in a better agreement of the carrier concentrations estimated from electrical and optical measurements, respectively. Nitrogen is likely



to be the donor, since its presence in our layers is indicated by the absorption spectrum as discussed above.

The high conductivity indicates that the layer cannot consist of SiC grains imbedded in low-conductive, 500 ohm-cm silicon. To get direct information on the structure, we investigated electron diffraction patterns of layers implanted only with an energy of 50 keV and of layers formed by multiple implantations. Neither of these layers showed the pattern of cubic  $\beta$ -SiC. However, in contrast to the single-energy implanted layer, the multiple-energy implanted layer showed a pattern which definitely is not caused by silicon. It resembles the pattern of a mixture of the diamond and the cubic form of graphite reported by Aust and Drickamer (11), but differs from it in the ring diameters by more than the experimental error. Whether or not this is due to a special form of SiC cannot be stated by these preliminary measurements. At least they indicate that the two types of implantations result in different layer structures.

We have shown that multiple-energy implantations of carbon into silicon result in a carbide which is amenable to more detailed physical investigations than reported until now. Because of its high conductivity and the low half-width of the TO phonon band obtained after annealing at 1300°C, the carbide is supposed to form a continuous layer. Improvement of the layer quality may be possible with respect to the nitrogen content, which is perhaps due to a pressure gradient from the pump to the hot parts of the furnace tube used for annealing. A lower nitrogen content should be obtainable with suitable experimental arrangements, as for instance annealing in argon instead of in a vacuum. Improvement of the crystal quality will be difficult, since at still higher anneal temperatures, one approaches the melting point of the silicon. Also, with respect to the lattice constant, silicon is not an ideal substrate for the growth of silicon carbide.

### Acknowledgments

Thanks are expressed to J. Baars for helpful discussions and to W. Haydl for his suggestions concerning the manuscript. We are also very indebted to P. Buck who carried out the electron diffraction investigations.

Manuscript submitted Jan. 26, 1973; revised manuscript received July 5, 1973.

Any discussion of this paper will appear in a Discussion Section to be published in the December 1974 JOURNAL. All discussions for the December 1974 Discussion Section should be submitted by Aug. 1, 1974.

### REFERENCES

1. P. Rai-Choudhury and N. P. Formigoni, *This Journal*, **116**, 1440 (1969).
2. J. A. Borders, S. T. Picraux, and W. Beezhold, *Appl. Phys. Letters*, **18**, 509 (1971).
3. G. H. Schwuttke, Final Report AFCRL-72-0176, Air Force Cambridge Research Laboratory, Cambridge, Mass. (1972).
4. W. S. Johnson and J. F. Gibbons, "Projected Range Statistics in Semiconductors," distributed by Stanford University Bookstore, Stanford, Calif. (1969).
5. E. P. EerNisse, *J. Appl. Physics*, **42**, 480 (1971).
6. A. W. Tinsley, W. A. Grant, G. Carter, and M. J. Nobes, II. Intern. Conf. Ion Implantation in Semiconductors, pp. 199-204, Garmisch-Partenkirchen, Springer-Verlag, Berlin, Heidelberg, New York (1971).
7. W. G. Spitzer, D. Kleinmann, and D. Walsh, *Phys. Rev.*, **113**, 127 (1959).
8. W. G. Spitzer, D. Kleinmann, and C. J. Frosch, *ibid.*, **113**, 133 (1959).
9. J. A. Lely and F. A. Kröger, *Proc. Intern. Colloq. Semiconductors and Phosphors*, pp. 514 and 525, Garmisch-Partenkirchen, Verlag Friedrich Vieweg u. Sohn, Braunschweig (1958).
10. W. F. Knippenberg, *Philips Res. Rept.*, **18**, 161 (1963).
11. R. B. Aust and H. G. Drickamer, *Science*, **140**, 817 (1963).

## Numerical Calculation of Impurity Redistribution during Thermal Oxidation of Semiconductors

R. H. Krambeck

Bell Laboratories, Murray Hill, New Jersey 07974

During a thermal oxidation, the impurities in a silicon wafer are redistributed; some impurity atoms are incorporated in the growing oxide and others diffuse to new locations in the silicon. By using Green's functions, Kato and Nishi (1) have obtained a solution to this problem, but a simplified numerical calculation is very much needed to obtain results quickly and cheaply. Recently this need has intensified because of the use of ion implantation followed by thermal oxidation to achieve threshold voltage control in IGFET's (2).

This note describes a calculation which solves the redistribution problem by the method of finite differences. The technique gives agreement with analytically checkable solutions to within less than 1%, an accuracy which is quite satisfactory for most applications. Moreover, the computer time used is low enough that the calculations can conveniently be carried out on a time sharing facility. The results of the calculations are in good agreement with published data (1) on the thermal oxidation of boron-doped silicon.

Key words: numerical analysis, silicon dioxide, solid-state diffusion, silicon.

### Analysis

The motion of impurities during thermal oxidation of silicon is governed by the diffusion equation, but the solution of this equation is complicated by the motion of the oxide-silicon interface. Kato and Nishi (1) have shown that if diffusion in the oxide is neglected, and the spatial coordinate is transformed so the moving interface is always at  $x = 0$ , then the impurity concentration in the silicon,  $C(x, t)$ , obeys a modified diffusion equation of this form

$$\frac{\partial C}{\partial t} = D \frac{\partial^2 C}{\partial x^2} + mf' \frac{\partial C}{\partial x} \quad [1]$$

where  $x$  is the distance into the silicon in the direction normal to the interface,  $m$  is the thickness ratio of silicon consumed to oxide grown (0.44) (3),  $f'$  is the time derivative of the oxide thickness, and  $D$  is the diffusion constant of the impurity in silicon.

At the boundary between oxide and silicon ( $x = 0$ ) the number of impurity atoms must be conserved. During a small time interval,  $\Delta t$ , the amount of silicon oxidized is  $mf' \cdot \Delta t$ . The impurities present in this layer,

$mC(0, t)f \cdot \Delta t$ , must be incorporated into the oxide or diffused into the silicon. The amount incorporated into the oxide is  $kC(0, t)f \cdot \Delta t$ , where the segregation coefficient  $k$  is the ratio at the interface of impurity concentration in the oxide to the concentration in the silicon. The amount diffused into the semiconductor is  $-D \frac{\partial C(0, t)}{\partial x} \cdot \Delta t$ . Conservation of impurity yields

$$mC(0, t)f \cdot \Delta t = kC(0, t)f \cdot \Delta t - D \frac{\partial C(0, t)}{\partial x} \cdot \Delta t$$

or

$$D \frac{\partial C(0, t)}{\partial x} = (k - m)fC(0, t) \quad [2]$$

The initial impurity distribution  $C(x, 0)$  is presumed to be a known function.

Although the diffusion equation is normally solved for the semi-infinite case in which the distance  $x$  extends to infinity, for the purposes of numerical calculation it is necessary to confine the sample mesh to a finite interval. Further, the region within a micrometer or two of the interface is of most interest, so it is desirable to concentrate the mesh points near the interface to increase both resolution and precision. These objectives have been achieved by transforming the distance  $x$ , which extends over the interval  $0 \leq x \leq \infty$ , to a new spatial variable  $u$  which is defined on the interval  $0 \leq u \leq 1$ . The particular transformation chosen was hyperbolic, since this gives the best compromise between a high density of points at the interface and a reasonable density deeper in the semiconductor

$$x = \frac{1}{A} \frac{u}{(1 - u)}$$

where  $A$  is a scaling constant. Substitution into Eq. [1] gives

$$\frac{\partial C}{\partial t} = DA^2(1 - u)^4 \frac{\partial^2 C}{\partial u^2} - 2DA^2(1 - u)^3 \frac{\partial C}{\partial u} + mf'A(1 - u)^2 \frac{\partial C}{\partial u} \quad [3]$$

for the basic equation, and from Eq. [2] the condition at the growing interface is

$$AD \frac{\partial C(0, t)}{\partial u} = (k - m)fC(0, t) \quad [4]$$

To solve Eq. [3], the interval  $0 \leq u \leq 1$  is divided into  $N$  equal segments, and the value of  $C$  at each node is designated  $C_0, C_1, \dots, C_N$ . Time is divided into appropriate increments also but these are not necessarily equal. In using the finite difference technique, the time derivative is taken to be constant over a given time increment. Since the derivative actually changes with time, it is necessary to decide what value to adopt for the calculation. The only way to obtain a stable solution is to choose the value at the end of the increment, and this is the choice that was made. When Eq. [3] is rewritten in terms of finite differences in this way, it becomes

$$\begin{aligned} & \frac{(C_{j,n+1} - C_{j,n})}{\Delta t} \\ &= DA^2(1 - u)^4 \frac{C_{j+1,n+1} + C_{j-1,n+1} - 2C_{j,n+1}}{(\Delta u)^2} \\ & - DA^2(1 - u)^3 \frac{C_{j+1,n+1} - C_{j-1,n+1}}{\Delta u} \\ & + mf'A(1 - u)^2 \frac{C_{j+1,n+1} - C_{j-1,n+1}}{2\Delta u} \quad [5] \end{aligned}$$

where the first subscript to  $C$  indicates a position on

the transformed spatial mesh and the second subscript indicates a time. Note that from Eq. [3], the right side of Eq. [5] equals the value of the time derivative at the end of the time increment, and that Eq. [5] sets the average time derivative equal to this. There are  $(N - 1)$  of these equations, corresponding to  $j = 1$  through  $j = (N - 1)$ , but there are a total of  $(N + 1)$  unknowns. One additional equation is

$$C_{N,n+1} = C_{N,n} \quad [6]$$

because  $C_N$  is the concentration at  $x = \infty$  and cannot change with time. Finally, the boundary condition, Eq. [4], provides

$$AD \frac{C_{1,n+1} - C_{0,n+1}}{\Delta u} = (k - m)fC_{0,n+1} \quad [7]$$

This set of  $(N + 1)$  equations can now be solved simultaneously for the values of  $C$  at the time  $(n + 1)$ . (The solution of the simultaneous equations is simplified by the tridiagonal nature of the matrix. The method of solution is described in the Appendix.) These values can then be used to obtain the values of  $C$  at the end of the next time increment, again using Eq. [5]-[7]. To obtain results with at least 1% accuracy, the following parameters have been used

$$N = 500$$

$$t(\text{hr}) = n^2(10^{-4})$$

$$A(\text{cm}^{-1}) = \left( \frac{0.02}{D} \right)^{1/2} (5 \times 10^4)$$

where  $D$  is in  $\mu\text{m}^2/\text{hr}$ .

The selection of a nonlinear mapping of time does not affect the solution of Eq. [5] at all, and it allows the solution to proceed expeditiously even though the diffusion process slows as time goes on.

## Results

Solutions were obtained for various conditions of oxide growth for both phosphorus- and boron-doped silicon. Two mathematical tests were made to check the accuracy of the results. For the first test,  $k$  was set equal to 0. For this value all impurities remain in the silicon, and the integral of impurity concentration must be constant. Therefore, the total change in the calculated value of this integral is a good measure of the error in the calculation. This test was used for an initial implanted doping  $0.1 \mu\text{m}$  deep with a Gaussian distribution contour and a straggle of  $0.02 \mu\text{m}$ . In Fig. 1, contours of constant error (using this test) are shown as a function of parabolic growth rate constant and diffusion constant. Also shown are representative points indicating the values of these constants for the wet and dry oxidation of phosphorus- or boron-doped silicon. The errors are generally no more than 1% in the region of interest.

For the second test, a uniform initial impurity distribution and a parabolic oxide growth rate were assumed. Under these conditions the surface concentration becomes constant at a value that can be determined analytically (4). The values obtained by using the numerical calculations did become constant. Figures 2 and 3 show the contours of constant difference between the numerical and analytical values of surface concentration for segregation coefficients of 3 and 0.03, respectively. The errors in surface concentrations calculated numerically are generally below 1%. It should be noted that the lower segregation coefficient (greater rejection of impurity by the oxide) produced larger errors than the higher coefficient. These results, together with those of the first test, indicate that the numerical solution is accurate to  $\pm 1\%$  for a wide range of conditions, including those associated with the wet or dry oxidation of silicon doped with boron or phosphorus in the temperature range  $1000^\circ - 1150^\circ\text{C}$ .

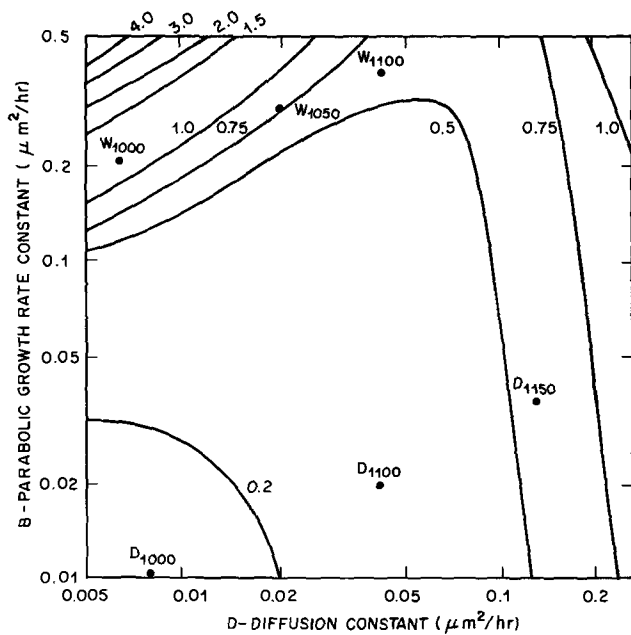


Fig. 1. Contours of constant error (as a percentage) in retained impurity dose when the oxide completely rejects the impurity ( $k = 0$ ). The error shown is the highest error found in the first hour of growth. Initially, implant depth =  $0.1 \mu\text{m}$  and spread is  $0.02 \mu\text{m}$ . Typical conditions of silicon oxidation are indicated by W for wet and D for dry with the subscript showing temperature ( $^{\circ}\text{C}$ ), using as diffusion constant the average of the diffusion constants of boron and phosphorus.

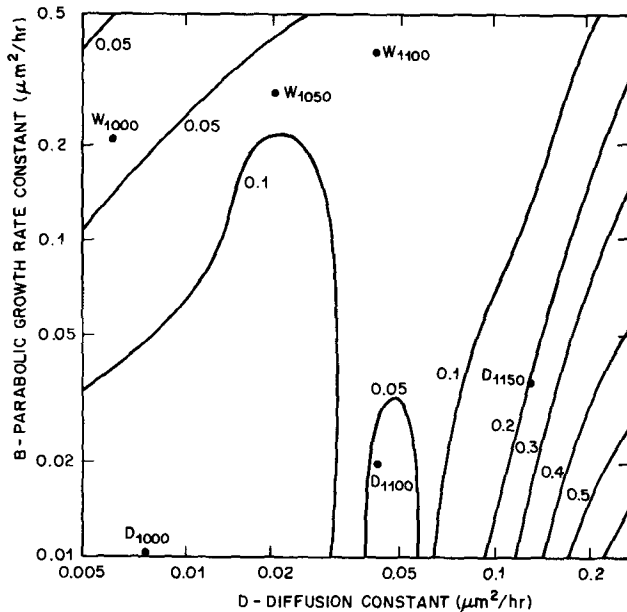


Fig. 2. Contours of constant error (as a percentage) for surface concentration, assuming parabolic oxide growth, an initially uniform impurity distribution, and a segregation coefficient of 3. The concentration was calculated for 2 hr of growth. The points labeled W and D again show typical oxidation conditions, as in Fig. 1.

Next, solutions were compared to experimental data previously published. Figures 4 and 5 show the diffusion data presented by Kato and Nishi (1). Here the predeposition of boron was made by diffusion. The diffusion constant and oxide growth rate are the same as those used by Kato and Nishi to match the data with their calculation. The segregation coefficient was found to be 8 using the method described in this paper, as compared to 10 in their work. The reason for the difference is not clear.

## Conclusions

A straightforward numerical solution has been obtained for the problem of redistribution of impurities during thermal oxidation of a semiconductor. The solution matches known analytical solutions and gives good agreement with experimental data. The fact that the program is fast enough to use on a Honeywell 600 time sharing facility with less than 1 min delay for a 2 hr oxidation should make it a valuable tool for investigation and process characterization.

## Acknowledgments

The author wishes to thank R. J. Strain and N. L. Schryer for helpful discussions on numerical analysis and R. A. Moline, C. F. Gibbon, and G. Weber for discussions about recent experimental results.

Manuscript submitted April 17, 1973; revised manuscript received Nov. 5, 1973.

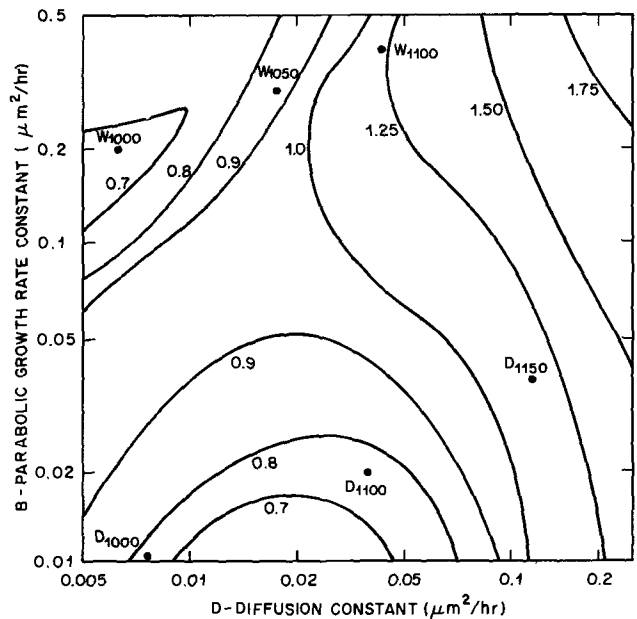


Fig. 3. The same as Fig. 2 except the segregation coefficient is changed to 0.03.

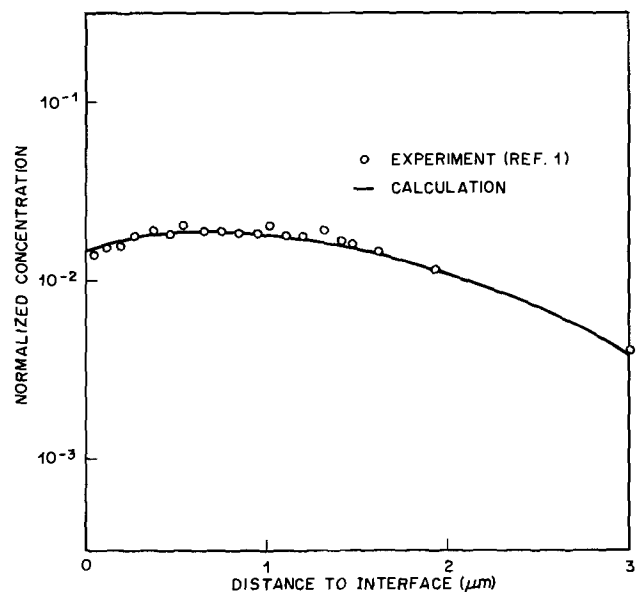


Fig. 4. Experimental data of Kato and Nishi (1) on redistribution of a boron diffusion in silicon after thermal oxidation of the silicon. Also shown is the calculated curve for  $k = 8$ ,  $D = 0.72 \mu\text{m}^2/\text{hr}$ ,  $t = 3100 \text{ sec}$ ,  $f = (0.0367 \mu\text{m}^2/\text{hr})^{1/2} \text{ cm}$ . The theoretical value for retained dose is 8.7%.

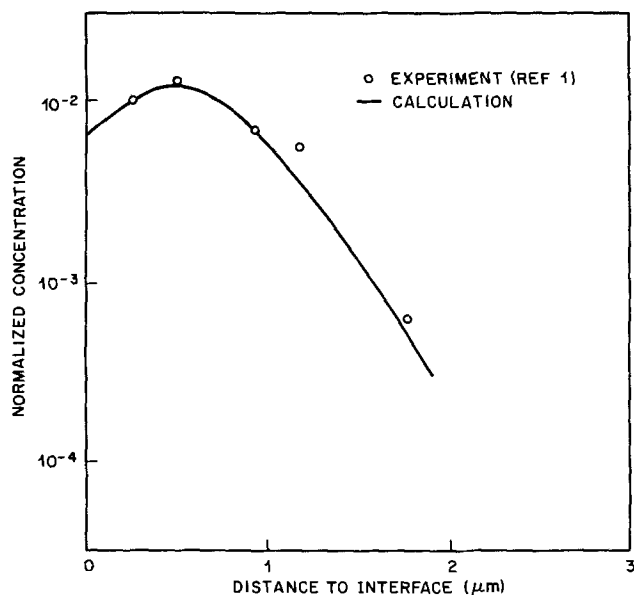


Fig. 5. As for Fig. 4 but with  $D = 0.216 \mu\text{m}^2/\text{hr}$ . The theoretical value for retained dose is 2.6%.

Any discussion of this paper will appear in a Discussion Section to be published in the December 1974 JOURNAL. All discussions for the December 1974 Discussion Section should be submitted by Aug. 1, 1974.

#### APPENDIX

The first step in solving Eq. [5]-[7] is to rewrite Eq. [5] with the unknowns on the left

$$C_{j-1,n+1}A_j + C_{j,n+1}B_j + C_{j+1,n+1}E_j = F_j \quad [\text{A-1}]$$

where

$$A_j = -DA^2(1-u)^4/(\Delta u)^2 - DA^2(1-u)^3/\Delta u + mf'A(1-u)^2/(2\Delta u) \quad [\text{A-2}]$$

$$B_j = +2DA^2(1-u)^4/(\Delta u)^2 + 1/(\Delta t) \quad [\text{A-3}]$$

$$E_j = -DA^2(1-u)^4/(\Delta u)^2 + DA^2(1-u)^3/\Delta u - mf'A(1-u)^2/(2\Delta u) \quad [\text{A-4}]$$

$$F_j = C_{j,n}/(\Delta t) \quad [\text{A-5}]$$

Thus  $F_j$  is determined by the impurity distribution at the beginning of the time increments. The other two equations are

$$C_{N,n+1} = C_{N,n} \quad [\text{A-6}]$$

and

$$\frac{C_{0,n+1}}{C_{1,n+1}} = \frac{AD/(\Delta u)}{(k-m)f' + AD/(\Delta u)} \quad [\text{A-7}]$$

The tridiagonal nature of the matrix associated with these equations makes a solution rather easy to obtain. The technique [as shown, for example, by Strain and Schryer (5)] begins with the calculation of two intermediate sets of numbers

$$G_j = -\frac{A_j}{B_j + E_j G_{j-1}} \quad [\text{A-8}]$$

and

$$H_j = \frac{F_j - E_j H_{j-1}}{B_j + E_j G_{j-1}} \quad [\text{A-9}]$$

where  $G_0$  is the ratio of  $C_{0,n+1}$  to  $C_{1,n+1}$  given by Eq. [A-7] and  $H_0 = 0$ . Values of  $G$  and  $H$  are calculated for all values of  $j$  from 1 to  $N-1$ . Next these values of  $G$  and  $H$  are used to find the new values of concentration

$$C_{j,n+1} = G_j C_{j+1,n+1} + H_j \quad [\text{A-10}]$$

where  $C_N$  is given by Eq. [A-6]. This gives values for concentration at the end of the time increment. These values can now be used to obtain new values for  $F_j$  in Eq. [A-5] and the process repeated to obtain the values of  $C$  at the end of the next time increment. This procedure can be followed very easily in a computer analysis.

#### REFERENCES

1. T. Kato and Y. Nishi, *Japan. J. Appl. Phys.*, **3**, 377 (1964).
2. R. A. Moline, G. W. Reutlinger, R. R. Buckley, A. U. MacRae, and S. E. Haszko, International Electron Device Meeting, Washington, D. C. (1972).
3. R. H. Bube, *Phys. Rev.*, **99**, 1105 (1955).
4. A. S. Grove, "Physics and Technology of Semiconductor Devices," p. 71, John Wiley and Sons, Inc., New York (1967).
5. R. J. Strain and N. L. Schryer, *Bell Syst. Tech. J.*, **50**, 1721 (1971).

## Brief Communications



### Effect of Dielectric Insert on Surface Charge Density of Electrets

K. Ikezaki, I. Fujita, and K. Wada

Department of Instrumentation, Faculty of Engineering, Keio University, Yokohama, Japan

and J. Nakamura

Research and Development Department, Aiwa Company, Limited, Tokyo, Japan

In electrets there are two kinds of surface charge, referred to as heterocharge and homocharge. The het-

Key words: FEP Teflon, spray charge, thermoelectret, homocharge.

erocharge is associated with the internal volume polarization and has the opposite polarity to that of the adjacent forming electrode. On the other hand, it is widely believed that the homocharge, which has the

same polarity as that of the electrode, is due to a sparking break down in an air gap between sample and electrode (1).

The decay of the heterocharge is so rapid as compared with that of the homocharge in most electrets, that an electret with a net homocharge has attracted much attention because of its practical application to the electret microphone (2).

In order to produce a film electret with a large homocharge without destruction of the sample by arcing during the polarization process, an appropriate dielectric is inserted between sample and electrodes (3,4). Perlman and Reedyk produced FEP Teflon film electrets with a large homocharge (about  $5 \times 10^{-8}$  coulombs/cm<sup>2</sup>) by applying a field of about 20 kV/cm at 120°C (3). They pointed out that the volume polarization of the dielectric inserts plays an important role for producing a large homocharge electret.

On the other hand, Sessler and West reported an ingenious method to get a large homocharge electret (about  $5 \times 10^{-7}$  coulombs/cm<sup>2</sup>) at higher electric fields by preventing back-discharges which occur during removal of the electrode (4).

Recently we found that a fairly large charge density (about  $2 \times 10^{-8}$  coulombs/cm<sup>2</sup>) is produced with applying relatively low fields (about 10 kV/cm) at room temperature by inserting a sheet of glass disk between a film sample and a negative (not positive) electrode. In this note we report the effect of the dielectric insert.

As we used one sheet of dielectric insert, there are two kinds of geometrical arrangement of the polarizing holder which are depicted schematically in Fig. 1: Case A, where a sheet of soda glass disk (0.75 mm thick) is inserted between the film and the negative forming electrode; and case B, where the glass disk is inserted between the film and the positive electrode.

The electret material used in this study is FEP Teflon film (12 $\mu$  thick). Electrets were produced by applying a polarizing voltage  $V_p$  across the electrodes for a period of 10 min at room temperature. The net surface charge density of the electrets was measured by the vibration electrode method developed by Reedyk and Perlman (5).

The time variations of the surface charge density on the anode side of the sample stored at room temperature are shown in Fig. 2 for two kinds of electret, both of which were produced at room temperature by applying the same polarizing voltage of 700V. The absolute value and the time variations of the surface charge density on the cathode side of the sample are almost the same as those on the anode side, so that they are not presented in the figure. As shown in Fig. 2, the value of the produced surface charge density depends strongly on the position in which the glass disk is inserted. This effect also takes place when the electret is polarized at elevated polarizing temperatures.

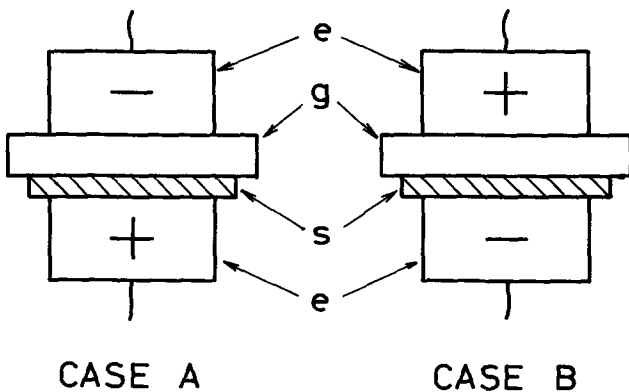


Fig. 1. Geometrical arrangements for electret forming. g, Glass disk; s, sample film; e, metal electrode.

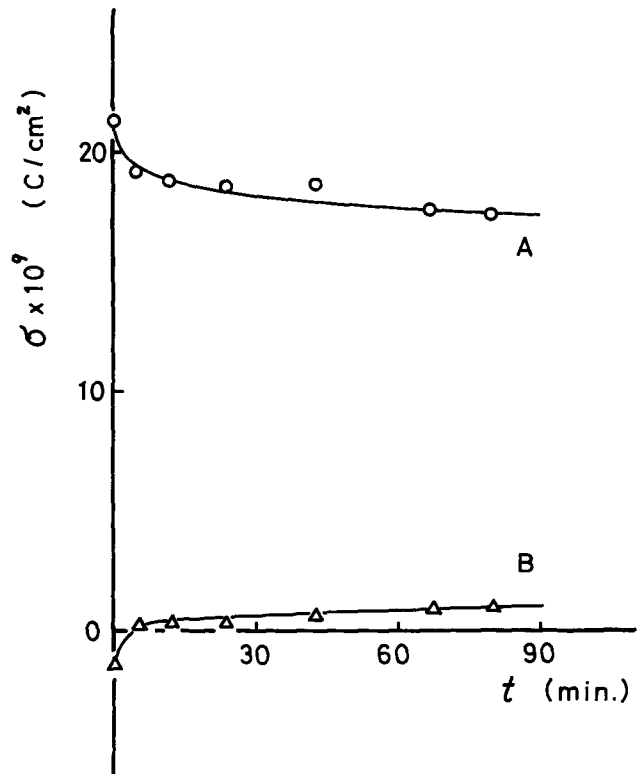


Fig. 2. Time variations of the surface charge density  $\sigma$  on the anode side of the FEP Teflon electrets. Curve A, polarized in the geometrical arrangement of case A; curve B, polarized in the geometrical arrangement of case B.

In our experimental conditions, when the polarizing voltage  $V_p$  is lower than about 300V, the produced surface charge density of the electrets was small both in case A and case B (Fig. 1). This is simply explained by the fact that the field strength in the air gap between the sample and the inserted glass disk is too low to bring about discharges in the gap. When  $V_p$  is higher than about 1000V, the surface charge density was very large in both cases. This large charge density is also explained simply by consideration of the fact that the field strength is high enough to spray charges in the gap. On the contrary, when  $V_p$  is between about 500 and 800V the value of the surface charge was different depending on the position of the inserted glass disk. Before the spray discharges occur, the field strength in the air gap between the sample and the glass disk are the same both in case A and case B. According to the theory of Perlman and Reedyk (3), applying a voltage between electrodes increases the polarization of the inserted glass disk and the field in the air gap. Eventually, this field will exceed the breakdown strength of the air in the gap and the spray discharge will occur. The homocharge deposition by this spray discharge reduces the field in the gap to a value below breakdown and the discharge is quenched. The polarization of the inserted glass then continues to increase, and the cycle repeats. Therefore, the produced surface charge should be independent of the position where the glass disk is inserted.

Polarity effects which are often observed in the electrical breakdown of solid dielectrics in the non-uniform field (6) suggest that our observed effect of the dielectric insert may be associated with the different initiation voltages for the breakdown in the gap.

The observed effect of the inserted glass disk cannot be fully explained at this stage. This problem is now under investigation.

### Acknowledgment

The authors wish to thank Mr. K. Okazaki and Mr. Y. Suzuki of the Research and Development Department, Aiwa Company, Limited for their technical help.

Manuscript submitted Sept. 18, 1973; revised manuscript received Dec. 14, 1973.

Any discussion of this paper will appear in a Discussion Section to be published in the December 1974 JOURNAL. All discussions for the December 1974 Discussion Section should be submitted by Aug. 1, 1974.

### REFERENCES

1. J. W. Wild and J. D. Stranathan, *J. Chem. Phys.*, **27**, 1055 (1957).
2. G. M. Sessler and J. E. West, *J. Acoust. Soc. Am.*, **40**, 1433 (1963).
3. M. M. Perlman and C. W. Reedyk, *This Journal*, **115**, 45 (1968).
4. G. M. Sessler and J. E. West, *J. Appl. Phys.*, **43**, 922 (1972).
5. C. W. Reedyk and M. M. Perlman, *This Journal*, **115**, 49 (1968).
6. D. L. Pulfrey, *J. Phys. D., Appl. Phys.*, **5**, 647 (1972).

## Determination of Boron and Oxygen Surface Contamination due to Common Solvents by Nuclear Microanalysis

J. C. North and E. C. Lightowers<sup>1</sup>

Bell Laboratories, Murray Hill, New Jersey 07974

During the course of our work on nuclear microanalysis (1), a source of large background signal was traced to boron contamination of sample surfaces which originated from the solvents used to "clean" the samples. Following this discovery, a systematic study has been made of several commonly used chemical solvents to determine the expected surface boron contamination from use of these solvents in cleaning wafers. Boron contamination levels can be large enough such that if a significant fraction of the boron were diffused into a Si device slice as electrically active acceptors during subsequent processing steps, the device characteristics could be adversely affected.

### Experimental

Samples were prepared from polished high purity Si wafers cleaved into pieces ~1 cm square. They were cleaned by agitating them for ~10 sec in each of the following sequence of chemicals: deionized water, HF, deionized water, HNO<sub>3</sub>, deionized water, HF, and deionized water. The cleaned slices were hydrophobic. Several of these pieces were used as controls. A new sealed bottle of each solvent to be tested was then opened, and some of the contents was poured directly over the surface of one of the Si samples while it was held from the back side by vacuum forceps. The solvent was allowed to dry on the sample. In general, as a solvent dries, it recedes to small droplets on the surface of the Si. After these droplets evaporate, several of the solvents left visible residue spots.

Nuclear microanalysis was used to determine both the surface boron and surface oxygen concentrations. Prompt  $\alpha$ -particles resulting from the reaction of 685 keV incident protons with <sup>11</sup>B and <sup>18</sup>O were detected. The nuclear reactions are

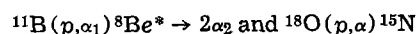
<sup>1</sup> Present address: Physics Department, King's College, London, WC2R 2LS, England.

Key words: cleaning, solvents, contamination, nuclear microanalysis.

Table I.

	<sup>11</sup> B	<sup>18</sup> O
Q value of reaction, MeV	8.7 (2)	4.0 (3)
Reaction cross section, millibarns	800 (4)	~150 (5)*
Natural abundance of this isotope, %	81 (6)	0.20 (6)

\* The value given was obtained by multiplying the differential cross section at 165° by 4 $\pi$ .



The relevant parameters of these reactions are given in Table I.

Figure 1 shows the  $\alpha$ -particle spectra obtained from calibration standards which were prepared by implantation of <sup>11</sup>B and <sup>18</sup>O at 3 keV (range ~100Å) (7) into polished Si wafers, which closely approximate surface layers. The energy of the  $\alpha$ -particles at the detector is reduced by a graded foil (1) which was used to prevent backscattered protons from reaching the detector. Figure 1 illustrates the relative sensitivity of this technique for surface <sup>11</sup>B and <sup>18</sup>O since the proton doses used were the same for both spectra and the <sup>11</sup>B and <sup>18</sup>O surface concentrations were nearly the same.

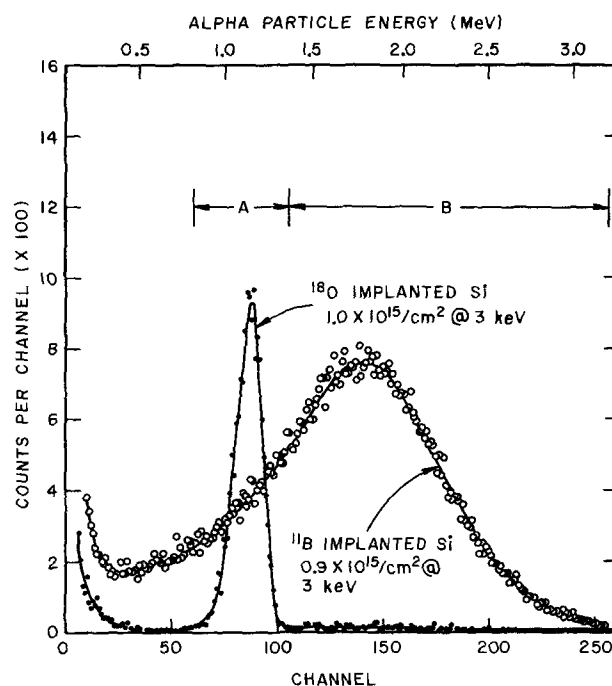


Fig. 1. Alpha-particle spectra obtained from calibration standards prepared by 3 keV implantations of <sup>11</sup>B and <sup>18</sup>O. Both spectra represent irradiations of 240  $\mu$ coulombs of 685 keV protons. The quantities of <sup>11</sup>B and <sup>18</sup>O represented by the spectra obtained from test samples were determined by comparison with these two spectra.

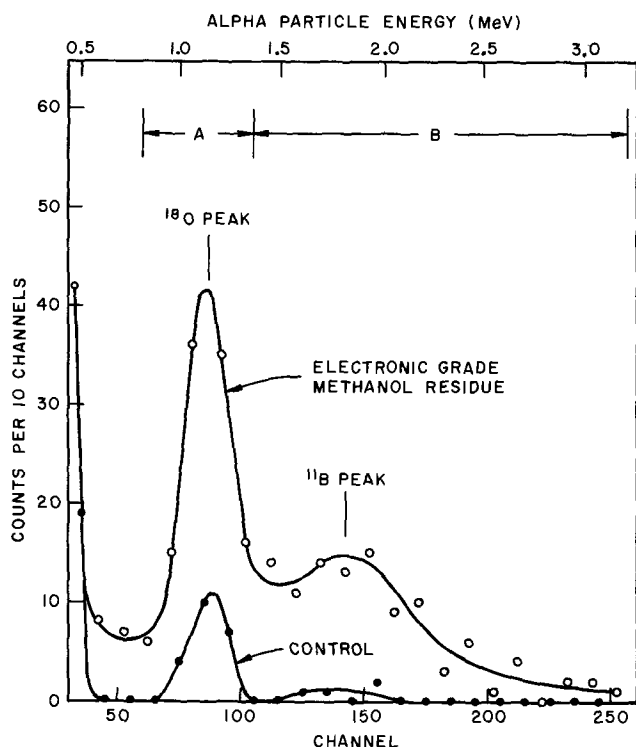


Fig. 2. Alpha-particle spectra of a control sample and a sample having residue on the surface from electronic grade methanol. The area of analysis included one of the visible residue spots left by the evaporated solvent. Both spectra represent proton irradiations of 120  $\mu$ coulombs. The average concentrations over the area of the incident proton beam for the control sample are  $0.2 \pm 0.1 \times 10^{12}$  boron/cm<sup>2</sup> and  $1.4 \pm 0.3 \times 10^{15}$  oxygen/cm<sup>2</sup>. The corresponding concentrations for the methanol contaminated sample are  $4.0 \pm 0.4 \times 10^{12}$  boron/cm<sup>2</sup> and  $5.1 \pm 0.7 \times 10^{15}$  oxygen/cm<sup>2</sup>.

Figure 2 shows spectra obtained for a control sample and a sample having residue on the surface from electronic grade methanol. The boron and oxygen concentrations are both much larger on the methanol contaminated sample.

The total surface concentration of boron or oxygen,  $N_2$ /cm<sup>2</sup>, on the test samples was calculated by comparison with the calibration spectra of Fig. 1 using the expression

$$N_2 = N_1 Q_1 n_2 / f Q_2 n_1$$

where the subscripts 1 and 2 refer to the calibration standard and test sample respectively,  $N_1$  is the concentration of <sup>11</sup>B or <sup>18</sup>O in the standard,  $f$  is the fractional natural abundance of the isotope <sup>11</sup>B or <sup>18</sup>O,  $Q$  is the proton flux, and  $n$  is the number of counts in the spectra attributable to <sup>11</sup>B or <sup>18</sup>O. With reference to Fig. 1, the count rate in spectral region B is due only to boron, while the count rate in region A is due to both oxygen and boron. Therefore, the quantities  $n$

in the above equation can be set equal to  $B$  (i.e., the number of counts in region B) for boron. For oxygen, the boron background can be subtracted by setting  $n$  equal to  $A - XB$  where  $X$  is the ratio of  $A/B$  for the boron spectrum of Fig. 1. The quantity  $X = 0.275$ .

### Results

The polished silicon wafers as received from the supplier<sup>2</sup> were found to have surface boron concentrations of  $\sim 4 \times 10^{12}$ /cm<sup>2</sup>. If a solvent such as methanol was poured onto the sample, the boron compounds were apparently dissolved by the solvent, and as the solvent evaporated the boron was collected into the residue spots. Average boron concentrations of  $> 10^{14}$ /cm<sup>2</sup> over the proton beam spot area have been observed if the beam area included one of these evaporation spots. After the samples were given the cleaning treatment described earlier, the surface boron concentrations were reduced to  $\sim 0.2 \times 10^{12}$ /cm<sup>2</sup>.

The results for the solvents tested are shown in Table II. All samples were given the same initial cleaning procedure. For the solvents tested which left visible spots, two measurements were taken, one in an area containing no visible spots and another in a region which included one or more spots. The residue spots were much smaller than the proton beam diameter of 1.5 mm. The results given are the average concentrations over the entire area analyzed by the proton beam. Therefore, the concentrations of boron and oxygen in the evaporation residue spots were greater than the numbers shown by more than an order of magnitude. The absence of visible spots does not necessarily mean that residue spots of higher concentrations do not exist.

Among the solvents tested, the lower grades of methanol were particularly bad. The evaporation spots were clearly visible, and the measured average concentrations over the incident beam area were in the mid  $10^{12}$ /cm<sup>2</sup> range, which means that the concentration in the evaporation spots was  $\sim 10^{14}$ /cm<sup>2</sup>. To appreciate the significance of these concentration levels, it should be noted that if  $10^{12}$  boron/cm<sup>2</sup> diffuses  $\sim 1 \mu$ m into the Si, the resulting volume concentration is  $\sim 10^{16}$ /cm<sup>3</sup>.

If the measured boron concentration in an area containing no visible evaporation spots is smaller than the concentration of the control samples, as in the case of isopropanol, then it cannot be concluded that the boron in the evaporation spot originated from the isopropanol. The solvent may have collected some of the residual boron that was left from the cleaning procedure from a larger area and concentrated it in the residue spot. However, if the boron concentration is higher than the controls even in those areas where there are no visible residue spots, then the additional boron must have come from the solvent tested.

The total oxygen concentration on the control samples and on the test samples in regions of no evaporation spots was  $\sim 1.5 \times 10^{15}$  oxygen atoms/cm<sup>2</sup>. This

<sup>2</sup> Western Electric Corporation, Allentown, Pennsylvania.

Table II. Average boron and oxygen surface concentrations over the incident proton beam area following evaporation of the solvents listed. When visible residue spots remained, measurements were made both in areas which included such spots and in areas free of visible spots. The errors quoted are standard errors determined from the counting statistics alone.

Solvent	Brand	Grade	Boron (10 <sup>12</sup> /cm <sup>2</sup> )		Oxygen (10 <sup>15</sup> /cm <sup>2</sup> )	
			Including spot(s)	No spots	Including spot(s)	No spots
Average of 4 controls			—	0.2 $\pm$ 0.1	—	1.6 $\pm$ 0.4
Methanol	Baker	Reagent	7.6 $\pm$ 0.5	0.5 $\pm$ 0.1	6.2 $\pm$ 0.9	1.0 $\pm$ 0.3
	Baker	Electronic	4.0 $\pm$ 0.4	0.5 $\pm$ 0.1	5.1 $\pm$ 0.7	1.3 $\pm$ 0.3
	Baker	MOS	0.3 $\pm$ 0.1	0.4 $\pm$ 0.1	0.8 $\pm$ 0.3	1.7 $\pm$ 0.4
Pure ethyl alcohol	U.S.I.	Reagent	1.3 $\pm$ 0.2	—	1.2 $\pm$ 0.4	—
Isopropanol	Baker	Reagent	2.6 $\pm$ 0.3	0.1 $\pm$ 0.1	3.1 $\pm$ 0.6	1.1 $\pm$ 0.3
Acetone	Baker	Electronic	—	0.7 $\pm$ 0.2	—	1.3 $\pm$ 0.3
Trichloroethylene	—	—	—	0.8 $\pm$ 0.2	—	1.7 $\pm$ 0.4
Cobene	Cobene	—	—	0.2 $\pm$ 0.1	—	1.1 $\pm$ 0.3
Chloroform	Baker	Reagent	—	0.1 $\pm$ 0.1	—	1.0 $\pm$ 0.3

corresponds to a  $\text{SiO}_2$  thickness of only  $\sim 3\text{\AA}$ . At least 30 min elapsed between the time that the samples were cleaned and the time that they were put in the vacuum chamber of the accelerator. The same samples were measured by ellipsometry which indicated that a film thickness of  $\sim 40\text{\AA}$  was present. In a separate series of experiments (8) it was verified that the prompt  $\alpha$ -particle technique and ellipsometry gave the same results for oxide thickness  $>50\text{\AA}$ , but diverged significantly for thinner layers.

The nature of this surface layer which appears  $\sim 40\text{\AA}$  thick by ellipsometry, but yet contains only enough oxygen to comprise  $\sim 3\text{\AA}$  of  $\text{SiO}_2$  is not yet understood.

It can be seen that in those cases where the boron concentration was large, the oxygen concentration was also much larger. The additional oxygen which appears as a result of the solvent is  $\sim 10^3$  times the additional boron concentration due to the solvent.

### Conclusions

1. Methanol, acetone, and trichloroethylene leave measurable quantities of boron on the surface of Si samples. Reagent and electronic grade methanol are particularly bad, since they leave visible evaporation residue spots having concentrations as high as  $\sim 10^{14}/\text{cm}^2$ .

2. Chemical solvents can collect an existing uniform surface boron contamination into spots of much higher concentration.

3. The  $^{18}\text{O}(p,\alpha)$  technique is a usable method of determining oxide thickness down to the  $3\text{\AA}$  range, even though  $^{18}\text{O}$  is only 0.2% abundant.

### Acknowledgments

We are grateful to A. C. Adams and R. H. Kaiser for making the ellipsometer measurements, to W. L. Brown for providing running time on the Van de Graaff, and to R. S. D'Angelo for technical assistance.

Manuscript received Oct. 1, 1973.

Any discussion of this paper will appear in a Discussion Section to be published in the December 1974 JOURNAL. All discussions for the December 1974 Discussion Section should be submitted by Aug. 1, 1974.

### REFERENCES

1. E. C. Lightowers, J. C. North, A. S. Jordan, L. Derick, and J. L. Merz, *J. Appl. Phys.*, **44**, 4758 (1973).
2. F. Aizenberg-Selove and T. Lauritsen, *Nucl. Phys.*, **11**, 45 (1959); *ibid.*, **11**, 117 (1959).
3. J. H. E. Mattauch, W. Thiele, and A. H. Wapstra, *ibid.*, **67**, 32 (1965).
4. R. E. Segal, S. S. Hanna, and R. G. Allas, *Phys. Rev.*, **139**, B818 (1965).
5. G. Amsel and D. Samuel, *Anal. Chem.*, **39**, 1689 (1967).
6. D. Strominger, J. M. Hollander, and G. T. Seaborg, *Rev. Mod. Phys.*, **30**, 585 (1958).
7. H. E. Schiott, in "Ion Implantation," F. H. Eisen and L. T. Chadderton, Editors, p. 197, Gordon & Breach Science Publishers, Inc., London, New York, Paris (1971).
8. J. C. North, A. C. Adams, and R. H. Kaiser, Unpublished work.

## Etching Solution for Revealing P-N Junctions in PbS and $\text{PbS}_{1-x}\text{Se}_x$

H. Preier and H. Pfeiffer

AEG-Telefunken Forschungsinstitut, D-6000 Frankfurt am Main, Germany

Lead salts are of great interest as materials for light detection and light emission in the infrared region. The p-n junctions of such laser and detector diodes are mainly fabricated by diffusion. However, thus far no etchants have been reported which optically display p-n junctions in lead salts. Here we will report about an etching procedure for revealing p-n junctions in  $\text{PbS}_{0.6}\text{Se}_{0.4}$  and PbS. The composition of the room temperature etch is as follows: 40 ml deionized  $\text{H}_2\text{O}$ , 1.5g  $\text{K}_2\text{Cr}_2\text{O}_7$ , 10 ml HCl (37%), 1.5 ml  $\text{H}_3\text{PO}_4$  (85%). Before use, this etching solution was diluted in water (2 parts water, 1 part etchant).

An example for an etched p-n junction in PbS is shown in Fig. 1a. Here an n-type crystal grown by sublimation from the vapor phase with the carrier concentration of  $3 \times 10^{18}/\text{cm}^3$  (77°K) was diffused in sulfur rich PbS powder ( $\text{Pb}_{0.49}\text{S}_{0.51}$ ) at 550°C for 1 hr. Diffusion and etching occurred perpendicular to as-grown (100) faces. Before etching, the crystal was embedded in an epoxy resin and mechanically polished to remove the p-layer from the exposed (100) surface. For chemical polishing an etching procedure was used which was described recently (1). The embedded crystal was then dipped into the etching solution for 3-5 sec and afterwards was quickly rinsed in deionized water and methanol. As can be seen from Fig. 1 p-type PbS is more strongly attacked by the etchant. Therefore, the junction is revealed by the step which occurs between the p- and n-region as shown in Fig. 1a. The variation of the thermoelectric power across the sur-

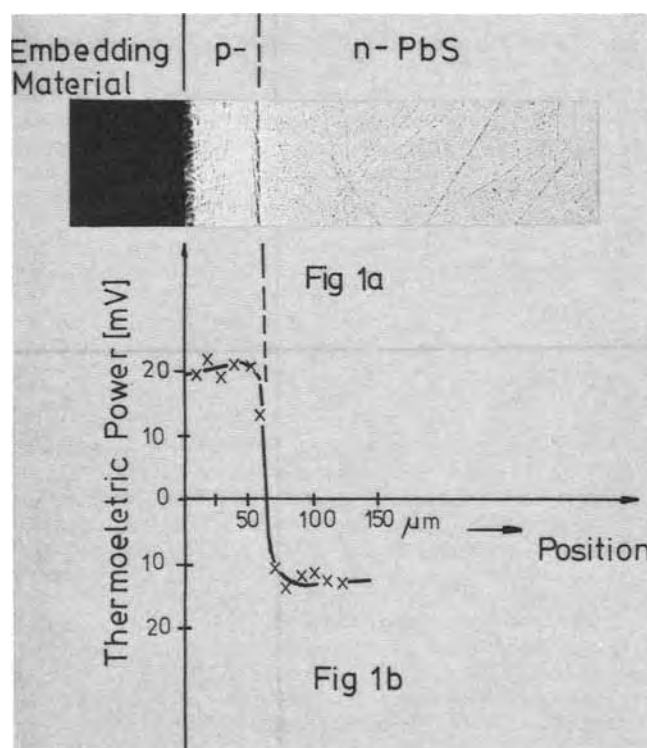


Fig. 1. a, Etched p-n junction in PbS; b, variation of the thermoelectric power across the junction.

Key words: PbS,  $\text{PbS}_{0.6}\text{Se}_{0.4}$ , etchant for revealing p-n junctions, IV-VI compounds.



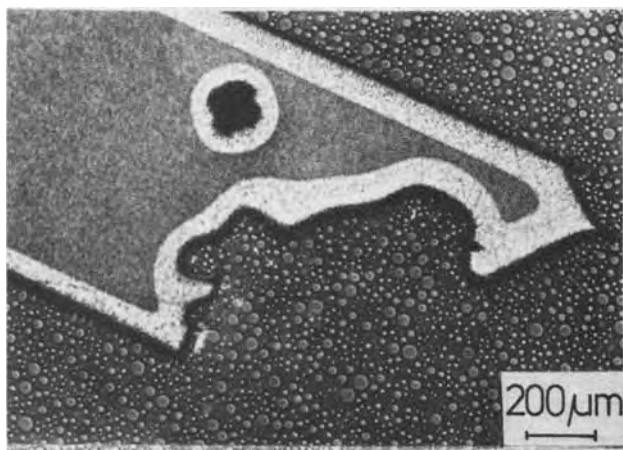


Fig. 2. Etched n-type  $\text{PbS}_{0.6}\text{Se}_{0.4}$  crystal after diffusion in chalcogenide rich powder.

face of the etched PbS crystal was used as a controlling experiment for revealing the actual position of the p-n junction. The corresponding result is shown in Fig. 1b. A change of the sign of the thermoelectric power occurs exactly at the position of the etched step. This proves the agreement of the step with the position of the p-n junction and the usefulness of this etchant.

The same etching solution was also successfully applied to ternary lead salts. Here an n-type  $\text{PbS}_{0.6}\text{Se}_{0.4}$  crystal with a carrier concentration of  $4 \times 10^{18}/\text{cm}^3$  was diffused in ( $\text{S}_{0.6}\text{Se}_{0.4}$ ) rich vapor at  $550^\circ\text{C}$  for 2 hr. An etched p-n junction in an irregularly shaped crystal is shown in Fig. 2. As can be seen, diffusion occurred also from a defect of the crystal surface. The junction depth as measured by thermal probe at  $77^\circ\text{K}$  was here about a factor of two smaller than the one revealed by etching. The latter effect is not fully understood yet and is presently being studied in detail.

#### Acknowledgment

This work was financially supported by the Ministry of Research and Technology of the Federal Republic of Germany as part of its technology program. The authors alone are responsible for the content of this paper.

Manuscript received Nov. 19, 1973.

Any discussion of this paper will appear in a Discussion Section to be published in the December 1974 JOURNAL. All discussions for the December 1974 Discussion Section should be submitted by Aug. 1, 1974.

#### REFERENCE

1. G. A. Ferrante, M. C. Lavine, T. C. Harman, and J. P. Donnelly, *This Journal*, **120**, 310 (1973).

## The High Pressure Crystal Growth of Sodium Beta-Alumina

F. H. Cocks

*Duke University, School of Engineering, Durham, North Carolina 27706*

and R. W. Stormont

*Tyco Laboratories, Incorporated, Waltham, Massachusetts 02154*

Sodium beta-alumina is of considerable interest because of the high mobility of its sodium ions (1-4). Indeed, it has been suggested that beta-alumina may be "a prelude to a revolution in solid state electrochemistry" (5). Such high ionic mobility makes possible, for example, its use as an ionic membrane separator material in high energy density batteries, such as the sodium-sulfur battery (6-9). Due to the highly anisotropic ionic conductivity of the beta-alumina crystal structure, single-crystal plates or tubes would result in membranes with improved conductivities and would also eliminate problems associated with the electrical short circuiting due to possible sodium metal diffusion along grain boundaries or through interconnected pores. For these reasons we addressed ourselves to the growth of single-crystal tubes of beta-alumina, oriented such that the high ionic conductivity planes of the resulting crystal are normal to the tube axis. There are considerable difficulties associated with the crystal growth of sodium beta-alumina, due principally to the fact that beta-alumina appears to decompose peritectically (10, 11) as well as to the high vapor pressure of sodium over beta-alumina at its decomposition temperature (11). In order to produce tubular crystals, we have made use of a recently developed crystal growth method called edge-defined, film-fed growth (EFG), which enables a variety of crystals to be grown having any constant cross-sectional shape

(12-19). To counter the problem of sodium vaporization, a high pressure (300 psi), inert gas, EFG crystal growth chamber has been constructed, and to contain the reactive melt, both the crucible and the crystal-shaping dies were fabricated from iridium.

In the basic EFG procedure for crystals having a tubular shape, the liquid melt rises by capillary action to fill the feeding orifice in the tubular die (12-15). A seed crystal is then brought into contact with the melt at the top of the capillary feed slot. After adjustment of the melt temperature and seed withdrawal rate, the melt spreads across the top surface of the die until further spreading is prevented by the  $90^\circ$  change in contact angle at both the inner and outer edges of the die. The growth of a tubular shape from a thin liquid meniscus is then established.

The design of the high pressure EFG chamber needed to suppress sodium vaporization during growth is shown schematically in Fig. 1. A water-jacketed Type 304 stainless steel chamber comprises the basic pressure vessel. This vessel is fitted with two quartz viewing ports, each 4 in. in diameter. In addition, both x-y and linear feedthroughs enable the position of the crucible and EFG die to be controlled both vertically and horizontally. The crystal withdrawal mechanism is of standard design<sup>1</sup> and has a water-cooled shaft which can apply pulling rates between 0.01 and 10

Key words: beta-alumina, crystals, membranes.

<sup>1</sup>A. D. Little, Cambridge, Massachusetts, Crystal Withdrawal Mechanism No. 3637-Q35.

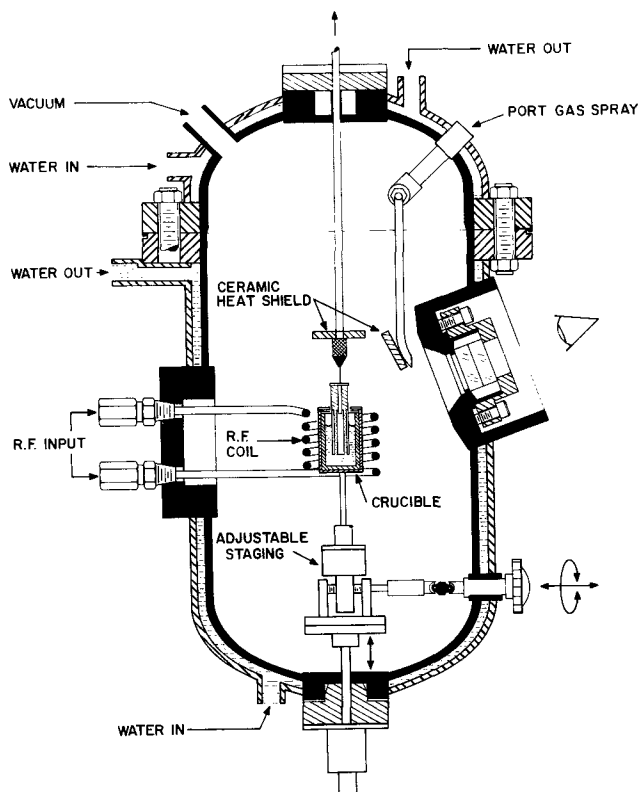


Fig. 1. Schematic drawing of the high pressure chamber and growth arrangement used to produce both alumina single-crystal tubes.

in./hr. The power feedthroughs are standard Conax fittings,<sup>2</sup> modified to accept fiberglass-reinforced Teflon pressure plugs in order to minimize localized rf heating. In order to prevent arcing from the interior coil, due to the presence of sodium vapor, the rf coil has been coated with a high dielectric constant film.<sup>3</sup> In addition, both the crucible and seed holder have been electrically insulated from the pressure chamber using boron nitride inserts. This system permits crystals to be grown under inert gas overpressures of up to 300 psig. Higher overpressures may not be useful in suppressing sodium vaporization due to gas convection effects (20).

Seeding was initiated in all cases using Monofrax H,<sup>4</sup> beta-alumina crystal pieces oriented so as to produce tubular shapes whose high sodium-ion conductivity planes are everywhere perpendicular to the tube axis. The influence of inert gas overpressure is shown in Table I, which gives the approximate relative beta-alumina and  $\text{Al}_2\text{O}_3$  composition  $\text{Na}_2\text{O} \cdot 11 \text{Al}_2\text{O}_3$ . As may be seen, there is a tendency for the relative per-

<sup>2</sup> Conax Division, Esterline Corporation, Buffalo, New York, Fitting No. EGT-250.

<sup>3</sup> American Durafilm Company, Newton Lower Falls, Massachusetts, 300 Series Enamel.

<sup>4</sup> Obtained from Harberson-Carborundum Corporation, Falconer, New York 14733.

Table I. Melt compositions and beta-alumina contents of tubes grown by EFG under inert gas overpressures. Beta-alumina compositions determined by x-ray reflection intensities and by metallographic measurement of the relative volume of  $\text{Al}_2\text{O}_3$  present.

Tube No.	Melt composition	Inert gas overpressure, psig	Per cent beta-alumina content of tubes
1	$\text{Na}_2\text{O} \cdot 11 \text{Al}_2\text{O}_3$	15 (argon)	40
2	$\text{Na}_2\text{O} \cdot 11 \text{Al}_2\text{O}_3$	100 (argon)	75
3	$\text{Na}_2\text{O} \cdot 11 \text{Al}_2\text{O}_3$	200 (argon)	85-90
4	$\text{Na}_2\text{O} \cdot 11 \text{Al}_2\text{O}_3$	300 (argon)	85-90
5	$\text{Na}_2\text{O} \cdot 4 \text{Al}_2\text{O}_3$	200 (argon)	100

centage of beta-alumina present in the crystal tube to increase as the overpressure is increased from atmospheric to a maximum of 200 psi. This limit may be due to local convection currents (20), as well as to the incongruent melting of beta-alumina. The phase diagram for the system  $\text{Na}_2\text{O} \cdot \text{Al}_2\text{O}_3/\text{Al}_2\text{O}_3$  deduced from a critical evaluation of the literature by DeVries and Roth (21) shows that beta-alumina decomposes peritectically at approximately 2000°C. The beta-alumina compositions shown in Table I were determined by comparison of the intensities of alumina ( $\text{Al}_2\text{O}_3$ ) and beta-alumina x-ray reflections observed in Debye-Scherrer photographs as well as from metallographic observations. Although a single beta-alumina crystal was used as a seed in every case, none of the tubes whose beta-alumina content was less than 100% was found to be single crystalline. In each case, these tubes showed a two-phase alumina-beta alumina structure, indicating a deficiency of  $\text{Na}_2\text{O}$ .

To prepare tubes having a 100% beta-alumina composition as well as a substantial single crystallinity, it is necessary to use melts containing an enriched concentration of  $\text{Na}_2\text{O}$ . For the case of tube No. 5 (Table I), the use of a melt composition containing 20 mole per cent  $\text{Na}_2\text{O}$  enables tubes having a 100% beta-alumina content to be grown. A photograph of two 100% beta-alumina tubes produced by this EFG growth procedure is shown in Fig. 2. X-ray analysis confirms that these tubes are single crystalline and have assumed the orientation of the seed crystal, that is, with their high conductivity (cleavage) planes normal to the tube axis. Similar single crystal, 100% beta-alumina tubes doped with 0.8 weight per cent MgO have also been produced.

The sodium and aluminum content of a 100% beta-alumina tube was determined by wet chemical analysis, and the composition of this tube was  $1.54 \text{Na}_2\text{O} \cdot 11 \text{Al}_2\text{O}_3$ . This is well within the range of  $\text{Na}_2\text{O}$  contents (1.16-1.86) determined by Harata to lie within the single-phase field of beta-alumina (22).

#### Acknowledgments

The authors gratefully acknowledge the support of this work by the National Aeronautics and Space Administration, Lewis Research Center, Contract No. NAS3-15385, the initial work on this program carried out by Dr. J. T. A. Pollock, and many helpful discussions with F. V. Wald.

Most of this work was performed while both of the authors were associated with Tyco Laboratories, Incorporated, Waltham, Massachusetts 02154.

Manuscript submitted Oct. 16, 1972; revised manuscript received Nov. 19, 1973.

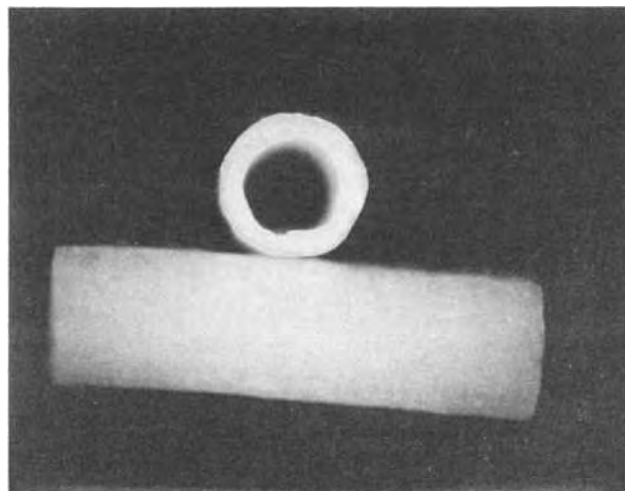


Fig. 2. Macro photograph of two single-crystal beta-alumina tubes. The outside tube diameter is 0.5 cm.

Any discussion of this paper will appear in a Discussion Section to be published in the December 1974 JOURNAL. All discussions for the December 1974 Discussion Section should be submitted by Aug. 1, 1974.

## REFERENCES

1. J. T. Kummer and Neill Webber, U.S. Pat. 3,404,035 (1968).
2. J. T. Kummer and Neill Webber, U.S. Pat. 3,404,036 (1968).
3. Yung-Fang Yu Yao and J. T. Kummer, *J. Inorg. Nucl. Chem.*, **29**, 2453 (1967).
4. M. Stanley Whittingham and Robert A. Huggins, *J. Chem. Phys.*, **54**, 414 (1971).
5. M. S. Whittingham and R. A. Huggins, National Bureau of Publications Special Publication 364, Proceedings of the 5th Materials Symposium, p. 139 (July 1972).
6. Ford Motor Co., *Mater. Design Eng.*, **64**, 19 (1966).
7. Ford Motor Co., *Science*, **154**, 828 (1966).
8. Ford Motor Co., *Mater. Design Eng.*, **65**, 14 (1967).
9. J. T. Kummer and Neill Webber, U.S. Pat. 3,413,510 (1968).
10. R. C. DeVries and V. L. Roth, *J. Am. Ceram. Soc.*, **52**, 364 (1969).
11. J. T. Kummer, *Prog. Solid State Chem.*, **7**, 141 (1972).
12. H. E. LaBelle, Jr. and A. I. Mlavsky, *Mater. Res. Bull.*, **6**, 571 (1971).
13. Bruce Chalmers, H. E. LaBelle, Jr., and A. I. Mlavsky, *ibid.*, **6**, 681 (1971).
14. H. E. LaBelle, Jr., *ibid.*, **6**, 581 (1971).
15. H. E. LaBelle, Jr., U.S. Pat. 3,471,266 (1969).
16. F. H. Cocks and R. W. Stormont, *J. Am. Ceram. Soc.*, **55**, 479 (1972).
17. F. H. Cocks and J. T. A. Pollock, *J. Appl. Phys.*, **43**, 3878 (1972).
18. H. E. Bates, F. H. Cocks, and A. I. Mlavsky, *Proc. Ninth IEEE Photovoltaic Specialists Conference*, p. 386, IEEE, New York (1972).
19. F. H. Cocks, J. T. A. Pollock, and J. S. Bailey, *Proc. Conf. on In Situ Composites*, Lakeville, Conn., Sept. 5-8, 1972, pp. 141-156, Publication NMAB-308-1, National Academy of Sciences, Washington, D. C. (1973).
20. M. Chessmas, B. Cockayne, D. T. J. Hurle, E. Jake-man, and J. B. Mullin, *J. Crystal Growth*, **11**, 225 (1971).
21. R. C. DeVries and W. L. Roth, *J. Am. Ceram. Soc.*, **52**, 364 (1969).
22. Mituo Hirata, *Mater. Res. Bull.*, **6**, 461 (1971).



## William G. Pfann—Solid State Science and Technology Award Medalist

N. Bruce Hannay<sup>1</sup>



Dr. N. Bruce Hannay delivers introductory remarks about the Solid State Science and Engineering Award Medalist

It is a great pleasure for me to be able to speak to you tonight about Bill Pfann, the first recipient of The Electrochemical Society Award in Solid State Science and Technology. In the next few minutes I hope to give you some flavor of the work he has done and an impression of the enormous impact it has had on solid-state science and technology. To those of you who are solid-state people his name is already a household word.

I shall also tell you something about Bill as a person, because he has wide-ranging talents, and he never fails to surprise his friends with his unusual approach to things. I am told that one of the people he often surprised was his mother. It seems that when Bill was of preschool age, it was not clear whether he would be left-handed or right-handed, but there were early indications that he would be left-handed, as ultimately proved to be the case. His mother, however, was encouraging him to use his right hand and in order to fix in his mind right from left, she purchased a ring for him to wear on his right hand. One day he returned home from play without the ring. When his mother asked him what had happened, he replied, "I now know my right hand from my left hand, so I threw the ring away."

This early strong display of pragmatism foretold Bill's approach to life, as well as his approach to the science that became his career. He has always been

<sup>1</sup>Introductory remarks by N. Bruce Hannay, Bell Laboratories, Murray Hill, New Jersey, on the occasion of the presentation of the first Solid State Science and Technology Medal Award to William G. Pfann on May 15, 1973, at the Chicago Meeting of the Society.

quick to find the practical solution to problems; for example, during World War II, when faced with food rationing he managed to negotiate with an associate the exchange of a used camera for 24 dozen eggs, to be delivered at weekly intervals.

Now you might think that practicality, then, is clearly the essential ingredient for extraordinary inventiveness and for success in science. But I should tell you of another side of Bill's character and that is his writing of poetry, and perhaps this reveals even more about the forces that have inspired him. Thus he has written:

The old values neither  
Pinned him down,  
Nor sustained him.

Therein lay  
His success . . .  
And his despair.

Or, as another example,

The tempo of science  
Increases with  
Each passing year.

Brilliant achievement  
Is swept away  
In the swift stream  
Of her advance,  
And sinks from sight  
Almost before  
Recognition.

Bill was born in New York City and lives in Bedminster, New Jersey. His biography next says that he graduated from Cooper Union School of Engineering with the degree of B.Ch.E. in 1940 and has been a member of the Metallurgical Research Department at Bell Labs since 1936. Now, these bare facts are worth more careful examination. Bill first came to work for Bell Labs in 1935 at the age of 17. His first job was messenger boy, and, given the prevailing economics in those years, he was glad to have the job, as well as the \$15 a week. Seven months later he received first the good news, that he was raised to \$16, but the bad news that came next was that the work week was cut, so he actually was reduced to \$14.74. Bill was undaunted, however, and he began night school at Cooper Union, graduating with a B.Ch.E. in 1940. At Bell Labs he delivered the mail so effectively that a year after he began work he was moved into the technical department, where he, of course, delivered the goods. His initial assignment was relatively modest, as a Technical Assistant, but in a few years he had reached full status as a Member of Technical Staff. I am glad to report also that he was no longer at \$14.74 a week.

Now I have told you about this for a reason. Living as we do in a day when many expect that there is something automatic about success, and that it will be handed to them merely because they are there, it is reassuring to know people like Bill, who began at the

bottom and then put together natural talents and a desire to succeed so effectively that he went on to accomplishments which have been rewarded by the Mathewson Gold Medal of the AIME in 1955 for his original papers on zone melting, a citation from Cooper Union for work in this field, the Clamer Medal of Franklin Institute in 1957, the Albert Sauveur Award of ASM in 1958, the Professional Progress Award of AICHe in 1960 for the invention and development of zone melting, the Moissan Medal from the School of Chemistry of the University of Paris in 1962, the Gano Dunn Medal for Professional Achievement of Cooper Union in 1963, the Award for Creative Invention of the American Chemical Society in 1968 (and, by the way, he was the first recipient of this award, for which the selection was made from all U.S. patents issued in the past 17 years in the chemical field) and, finally, in 1972 the Carborundum Company Award for Excellence in Non-Ferrous Materials. Many other scientific honors have also come to Bill, including Visiting Lectureships at Berkeley and at Cambridge University, where he was elected an Overseas Fellow at Churchill College.

We must then look more closely at Bill's record, to see how he went from messenger boy at Bell Labs in 1935 to these richly deserved honors, and what we find running throughout his work is a keen sense of what is important, and the simple way to do it. At least, it is simple after he has shown us what to do.

Zone melting is a particularly simple and elegant process. It revolutionized science and technology as it made possible the pure materials that not only provided the foundation for the semiconductor materials technology, that is, the cornerstone of solid-state electronics, but also launched us into an era of new understanding of the fundamental properties of solids, based on research on exceedingly pure and well-defined compositions. One measure of its impact is the approximately 1000 papers on the subject that were published in the decade immediately following Pfann's first paper. Actually, this is a completely inadequate measure, because it does not count the far larger number of papers that were possible only because of zone melting, which put pure materials in the hands of solid-state scientists and electronic device engineers for the first time.

The most important of zone melting techniques is probably zone refining, originally applied to semiconductors for the achievement of ultrahigh purities, of the order of one part in 10 billion. Purification in metals, organic materials, and other substances is also important, however, the tool is a universal one, and applicable in both research and manufacture.

There are other uses of zone melting also. One is zone leveling, a technique for distributing impurities uniformly through the solids. Another, developed by a colleague of Pfann's, is the floating zone method of crystal growth, an enormously valuable technique which eliminates the crucible in crystal growth, thus avoiding contamination.

Bill Pfann's zone melting processes have brought him his greatest fame, but his other scientific and technical achievements have also been notable. He made striking contributions to the development of silicon microwave detectors for use in radar receivers during World War II. One of the first of these followed some experiments which conclusively demonstrated that the noise output of the radar detector for use at 3000 MHz was related to surface irregularities on the point contact. These point contacts were fabricated from a 0.005 in. tungsten wire which had been sharpened in a sort of pencil sharpener grinding fixture. Pfann found that electrolytic polishing drastically reduced the noise of the detector, a factor directly related to the radar's sensitivity and range. Later he devised a process for producing the point contacts themselves by electrolytic means, and this dramatically increased the output of detectors, then in short supply to the armed services. Again we see the simplicity of Bill's approach to the solution of technical problems, in this and again in

later work on fundamental materials aspects of electrical contact erosion, in which he discovered the phenomenon of self-limiting transfer, and through this, a method of eliminating contact "bridge" erosion, a problem of long standing.

Bill conceived and developed the prototype of the first transistor to be manufactured (Type A), and he holds basic patents relating to alloying and diffusion methods of making transistors. He was co-author of the first paper describing an MOS device.

One of Bill's simplest experiments, which well illustrates the sort of spectacular result that has come naturally to him, investigated the effect of disturbing the solid-liquid interface. He did this by rubbing the interface of a solid as it was being frozen from the melt. Now you might wonder how he got the idea for this. I cannot answer that, although I can say that when he was a Churchill Fellow at Cambridge he enjoyed making rubbings of cathedral tombstones. I can also tell you how he did the experiment; he used a wire brush, and simply reached into the molten metal and scrubbed the surface of the solid as it was being frozen. That is such an unsophisticated and direct way to do an experiment that no one else would have thought of it. It worked, and he was able to make spectacular changes in the metal texture, producing an extremely fine grained eutectic alloy.

Just one more of Bill's scientific discoveries must be mentioned. If it were not for zone refining, we could well be honoring him tonight for this as it was one of the classic experiments in revealing the fundamental nature of solids. Dislocations were a concept that had to be invented to explain the mechanical properties of solids. Real solids were orders of magnitude away from what should have been found if lattices were simple, like those found in crystallography books, and so something that had never been seen was imagined to exist, to explain away these spectacular anomalies. For years dislocations were talked about as though they were real, and then Pfann and his colleagues showed that they indeed were real in the first experiments that unmistakably demonstrated the existence of dislocations using pure germanium. It had been observed that freshly etched surfaces of germanium often show rows of microscopic conical pits. This makes a beautiful photograph, which I would have shown you but our esteemed Executive Secretary told me that he would have had to employ a union operator at double-time rates for 4 hours to show the one slide, so those of you who did not see it in Bill's talk this afternoon will have to imagine it. The pits develop at the points where dislocations intersect with the surface, because the slightly disordered lattice at a dislocation is slightly more reactive chemically than is the perfect lattice. The spacing and position checked the theory beautifully, and these classic observations thus furnished a striking confirmation of dislocation theory.

Bill holds over 60 patents and he is the author of a book on "Zone Melting," as well as more than 60 papers. He has been a successful administrator of his research group, recruiting talented people and leading them so skillfully that on two occasions members of his group have won the Mathewson Gold Medal. He spent two weeks in Israel as an advisor to the National Council of Research and Development. He used to admire the Brooklyn Dodgers but gave them up in favor of the New York Mets, and he is an avid hockey fan. We could talk of many facets of Bill's character. But I return to his poetry for the final insight on the career and essential human quality of this remarkable person.

The mind goes on and on,  
Exploring a vast universe  
Of ideas  
Without end.

But the body  
Is subject to  
The rhythm of day and night,  
The need for sleep.

The mind  
Must therefore bide its time,  
And find the chance

To make that gallant leap  
Between distractions of the day  
And the magnetic pull of sleep.

## The Semiconductor Revolution<sup>2</sup>

William G. Pfann



Mr. William G. Pfann presents Solid State Science and Technology Award Address

President McKinley, ladies and gentlemen: Although I have taken part in the revolution in solid-state science and technology from its beginning, in fact, perhaps, even before most people knew it had begun, and although I have known the crescendo of scientific and technical advances of this revolution, on many fronts, I was completely overwhelmed by the news from President McKinley that I had been chosen as the first recipient of the Award for Solid State Science and Technology of this Society. The news was both heartwarming for your Society's recognition of my past achievements, and also thought-provoking because of my personal knowledge of so many other prolific contributors in this field.

In any event, I hope to share with you some of the excitement of these years of the semiconductor revolution, together with some personal anecdotes and insights which I hope may lead others to experience the joys of contributing to our society and the joy of being recognized as a person. Finally, I plan to say a few words that may be of help to future innovators in this major field.

The name of this award is very general. In the letter of notification from President McKinley I was told that the choice of subject was open, but it was recommended that the topic be chosen from my own work. This I plan to do. This is not a critical review of the field; rather, it is the field as seen through the eyes and feelings of one person.

### Prehistory

A very good review of early semiconductor research was written by G. L. Pearson and W. H. Brattain (1)

<sup>2</sup> Solid State Science and Technology Award Address delivered May 15, 1973, at the Chicago Meeting of the Society.

from which some of the following was taken. An important addition to semiconductor science was the Hall effect, discovered by E. H. Hall in 1879 (2). In 1931 A. H. Wilson (3) came up with the band theory of semiconductors, and conduction by electrons and by holes, but of course there were no materials suitable for study at that time. Tamm (4) in 1932 introduced the concept of surface states, which Bardeen took up so aptly later on. In Russia in 1938 B. Davydov (5) actually came up with the idea of diffusion of minority carriers across a p-n barrier. In 1938, but no one believed him. No one took him seriously; and even to the very month before the discovery of the transistor (W. Shockley recently gave a talk in England about that) they just did not get this idea of carrier injection. It eluded them for some subtle reason. This kind of puzzlement runs through this whole story, and all of these events. You wonder how you could have been so obtuse for so long before you saw how easy something was to do.

Just before the transistor, Mott and Gurney's "Electronic Processes in Ionic Crystals" was used as a seminar subject organized by W. Shockley. I was lucky to be in the seminar, and then the thing broke. Conyers Herring at Bell Labs is probably the best person in the country in the referencing of the literature of physics, and when the Nobel Prize for the transistor was announced he gave a talk, along with the winners, in which he used Fig. 1. I just wish to point out something that is odd about it. You notice that the number of papers culled from abstract journals was very small compared to today. You notice that in the early years the number was actually going down. In fact, the subject was sort of dying out! Then, in the postwar years, a lot of things that had been found during the war were published. There was a rise. The transistor was found in 1948. There is this later drop which Conyers could not interpret very well, and then this sudden

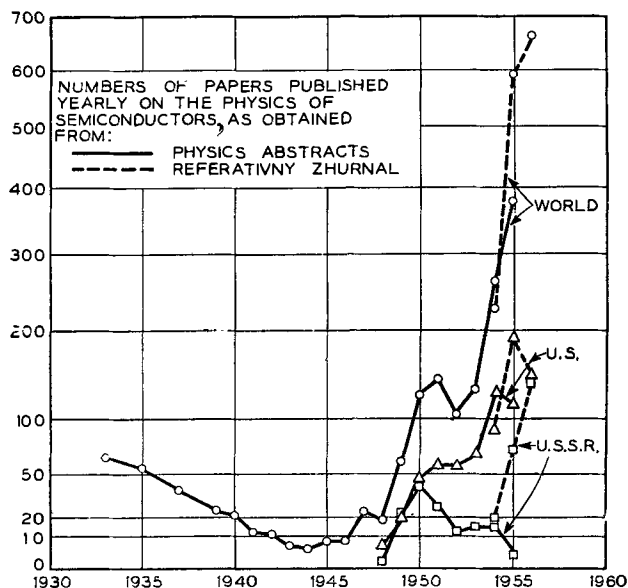


Fig. 1. Numbers of papers on the physics of semiconductors, 1933-1956 (after C. Herring).

the years many co-workers have helped shore up weak spots in my scientific training. As participation in more and more new topics has increased, so has my acquaintance with scientists the world over, and this has added to my development and led to many valued friendships. I will acknowledge the help of one man I recognized as a comer after hearing his first talk, my close friend and your incoming president, Bruce Hannay.

## REFERENCES

1. G. L. Pearson and W. H. Brattain, *Proc. I.R.E.*, **43**, 1794 (1955).
2. E. H. Hall, *Am. J. Math.*, **2**, 287 (1879).
3. A. H. Wilson, *Proc. Roy. Soc. (London)*, **A133**, 458 (1931); *ibid.*, **A134**, 277 (1931).
4. I. Tamm, *Physik. Zeit. Sowjetunion*, **1**, 733 (1932).
5. B. Davydov, *Tech. Phys. USSR*, **5**, 79 (1938).
6. J. H. Scaff, H. C. Theuerer, and E. E. Schumacher, *Trans. AIME*, **185**, 383 (1949).
7. W. G. Pfann and J. H. Scaff, *ibid.*, **185**, 389 (1949).
8. J. H. Scaff, *Metallurgical Trans.*, **1**, 561 (1970).
9. H. C. Theuerer, U.S. Patent 3,060,123 (1952); *Trans. AIME*, **206**, 1316 (1956).
10. P. H. Keck and M. J. E. Golay, *Phys. Rev.*, **89**, 1297 (1953).
11. W. G. Pfann, "Zone Melting," 2nd ed., John Wiley and Sons, Inc., New York (1966).
12. W. G. Pfann, C. E. Miller, and J. D. Hunt, *Rev. Sci. Instr.*, **37**, 649 (1966).
13. J. M. Burgers, *Proc. Phys. Soc. (London)*, **52**, 23 (1940).
14. F. L. Vogel, W. G. Pfann, H. E. Corey, and E. E. Thomas, *Phys. Rev.*, **90**, 489 (1953).
15. R. A. Logan, A. J. Goss, and M. Schwartz, *J. Appl. Phys.*, **25**, 1551 (1954).
16. A. J. Goss, K. E. Benson, and W. G. Pfann, *Acta Met.*, **4**, 332 (1956).
17. W. G. Pfann, K. E. Benson, and J. H. Wernick, *J. Electron.*, **2**, 597 (1957).
18. W. F. Pfann and R. S. Wagner, *Trans. Met. Soc. AIME*, **224**, 1139 (1962).
19. A. R. Chaudhuri, J. R. Patel, and L. G. Rubin, *J. Appl. Phys.*, **33**, 2736 (1962).
20. J. R. Patel and B. W. Batterman, *ibid.*, **34**, 2716 (1963).
21. J. H. Wernick and K. E. Benson, *J. Phys. Chem. Solids*, **3**, 157 (1957).
22. K. A. Jackson and R. S. Wagner, *J. Appl. Phys.*, **36**, 2132 (1965).
23. R. S. Wagner and W. C. Ellis, *Trans. Met. Soc. AIME*, **233**, 1053 (1965).
24. W. G. Pfann and C. G. B. Garrett, *Proc. I.R.E.*, **47**, 2011 (1959).
25. W. G. Pfann and R. N. Thurston, *J. Appl. Phys.*, **32**, 2008 (1961).
26. C. S. Smith, *Phys. Rev.*, **94**, 42 (1954).
27. C. Herring, *Bell Syst. Tech. J.*, **34**, 237 (1955).
28. W. van Roosbroeck and H. C. Casey, Jr., *Phys. Rev.*, **B5**, 2154 (1972).
29. J. A. Burton, R. C. Prim, and W. P. Slichter, *J. Chem. Phys.*, **21**, 1987 (1953).
30. W. C. Dash, *J. Appl. Phys.*, **31**, 736 (1960).
31. H. Welker, *Z. Naturforsch.*, **7a**, 744 (1952).
32. F. A. Kröger, "Chemistry of Imperfect Crystals," North Holland Publishing Company, New York (1964).
33. W. Kaiser, P. H. Keck, and C. F. Lange, *Phys. Rev.*, **101**, 1264 (1956).

## Some Problems of Electrochemical Kinetics

Benjamin G. Levich<sup>1</sup>

*Institute of Electrochemistry, USSR Academy of Sciences, Moscow, USSR*

My Dear Colleagues:

First I should like to express my gratitude to The Electrochemical Society for the high honor given me. Unfortunately, through no fault of my own, I am unable to present this paper myself and have had to be as brief as possible.

Electrochemical kinetics is a very distinctive field of research. Indeed, merely enumeration of the factors which determine the kinetics of electrode reactions—the chemistry of reagents; the structures and properties of fluid solvents; the properties of metals and semiconductors; the structural, adsorptive, and catalytic properties of their surfaces; the mechanism of charge transport in fluids; the movement of the solvent as a whole; and, finally, the mechanism of charge transfer in the elementary act of the electrode process—this listing shows that the most diverse fields of physics and chemistry converge in electrochemical kinetics. Therefore, electrochemical processes are not only very complex but also, as the present company would probably agree, very interesting.

In my paper I shall limit myself to the two aspects of the problem with which my own work has been connected, namely, studies of the macroscopic theory of the transport of species in moving solutions (diffusion kinetics) and studies of the charge transfer in the elementary act of the electrode reaction, electrode kinetics proper. Without going into details, I shall try to describe the present state of these questions, underlining the difficulties and the pressing problems that face theory and experimentation.

### Transport of Species in Solutions

The problem of the transport of species in a solution is a comparatively old one in electrochemistry. However, there has been a growing interest in it in the last twenty-five years. There are two reasons for this. First, it was the use of effective methods of modern hydrodynamics that made it possible to produce a quantitative theory of the transport of species in a moving solution. Second, the development of new experimental methods made it necessary to obtain quantitative expressions for the diffusion current under diverse conditions in the implementation of electrochemical processes. Of course, the problem of the transport of reagents in a solution is a general question in the theory of heterogeneous reactions involving liquid phases, but it was in electrochemistry that the real need first arose for formulating a quantitative theory of transport that would meet the high level of precision of electrochemical measurements. Since the molecular coefficients of diffusion in fluids are exceedingly small, the convective transport of species predominates over molecular transport at the smallest velocities of the fluid. Therefore, the theory of the transport of reagents to and from the surface of the electrode, except in some special instances (in narrow capillaries or cracks, during high-frequency processes in fluids, or with immobilizing admixtures and the like), constitutes a problem of convective diffusion. Problems of this kind are very complex and that is why the ideas of electrochemistry were for a relatively long time limited to the qualitative theory of Nernst, according to which the existence of a limiting current is related to the slowness of the diffusion process through a stationary layer of fluid adjacent to a solid electrode. Though it was perfectly clear to all that no such stationary layer can exist,

<sup>1</sup> The Palladium Medal Address was read for Professor Levich by Dr. David A. Vermilyea at the Boston Meeting of The Electrochemical Society, October 9, 1973. The medal was struck from palladium supplied by the International Nickel Company, New York, New York.



the Nernst theory was accepted as a convenient empirical description of the convective diffusion process. The quantitative solution of the convective diffusion expressions for the specific instance of a dropping mercury electrode was first disclosed in the works of Ilkovic and Rideal. Later, in our work, the general hydrodynamic theory of the boundary layer was applied to the instance of convective diffusion in fluids. As early as the beginning of this century, Prandtl demonstrated that at large Reynolds numbers the entire fluid flow can be divided into a region of basic flow, in which there is viscosity independent motion of the fluid, and a hydrodynamic boundary layer, in which there is a viscous flow at a rate that diminishes to zero at a solid surface. When an electrode reaction occurs at a solid surface, causing a change in the concentration of species at that surface, the entire moving solution may be divided into a region of constant concentration and a diffusion boundary layer. The change in concentration takes place in the latter; moreover, the transfer of species in it occurs in equal measure by convection and by molecular diffusion, as well as by migration when there are ions and there is no supporting electrolyte in the solution. Because of the smallness of the molecular diffusion coefficient, the diffusion boundary layer is several times thinner than the hydrodynamic boundary layer (for water, for example, it is 1/10 as thick). The mathematical smallness of the diffusion coefficient makes it possible to take advantage of the method developed by Poincaré for solving equations containing specific derivatives with small parameters. We used this method in dealing with a number of specific tasks. Exact solutions were obtained for problems of convective-diffusion when there was uniform accessibility of the surface (the rotating disk electrode), and later an approximate solution was found in a number of concrete instances and expressions were derived for currents in cases of mixed kinetics and limiting currents at the surfaces of electrodes of different geometries with laminar flow. A number of researchers, including present and past co-workers, have also developed the theory of convective diffusion in nonisothermal solutions, in moving thin films in phase boundaries of the fluid, in fluids with nonstationary currents and nonsteady-state conditions, in natural convection, and in a number of other cases. Along with these calculations, a theory of kinetic and catalytic currents on solid electrodes was developed. Finally, Acrivos and Chambre demonstrated that the solution of a problem in convective diffusion at an arbitrary surface may, by the law of kinetics, be reduced to the solution of an integral equation, and such an equation is convenient for obtaining a numerical solution. If one also takes into account the multitude of problems concerning diffusion and migration of species in an immobile medium that have been solved in connection with the development of a-c methods in electrochemistry, then it must be recognized that diffusion kinetics is one of the most advanced fields of electrochemistry. At present, the expression for the flow of a substance to an electrode of any geometrical shape under any and all conditions of electrode reactions is known or can be quantitatively obtained. However, this does not mean that all the problems of diffusion kinetics may be considered solved. For example, the transition to large current densities requires the transition from laminar to turbulent flow conditions and also to high solution concentrations. The question of the detailed mechanism of the convective transport of species in the turbulent flow of a fluid cannot as yet be considered as answered in full. There are two theories—the theory of Prandtl and the theory of Landau and this author, based on different concepts of the law of diminishing turbulence in proximity to a solid surface. Which of these two theories one chooses is very significant, both for obtaining the estimated formulas for the flows of species that interest electrochemists and for the general hydrodynamic theory of turbulence. It is only

very recently that, thanks to the measurements carried out by Hanratty (U.S.) and also by Kishinevsky and co-workers (USSR), it has become possible to decide in favor of our hypothesis. The transport of species in a turbulent flow is an extremely complex process, the mechanism of which is closely connected with the mechanism of the turbulent pulsations themselves. As is known, there is at present no quantitative theory of turbulence in anisotropic flows. Hence, the study of the mechanism of the transport of species to a solid surface is not only of great practical importance for electrochemistry but also of basic significance for the theory of turbulence.

### Diffusion and Migration

The diffusion and migration of ions in concentrated solutions are being studied intensively, both theoretically and experimentally, chiefly on the basis of the thermodynamics of irreversible processes. The difficulties of the theory in this field are connected primarily with the difficulties of the theory of concentrated solutions of electrolytes. However, I shall not deal with this question inasmuch as I myself have not worked on diffusion and migration in concentrated solutions. Another group of not yet elucidated but very important problems for electrochemistry are those connected with the transport of a substance in solutions containing a large number of gas bubbles, in porous media with fluid flow, and in gelatinous systems. Finding the solutions to problems of this kind, requiring a statistical approach, is now the order of the day.

### Charge Transfer

The question of the mechanism of the elementary act of the electrode process is undoubtedly a central basic problem of electrochemistry. The first theoretical approaches to this problem are associated with the names of Gurney and Horiuti and Polanyi. A new stage in the development of the problem is associated with the work of Weiss, Marcus, Zwolinsky, and others, who have emphasized the importance of the processes connected with the influence of the polar solvent. The latter direction has been developed quantitatively in the works of Marcus and of this author and his former co-workers. Since I am, naturally, unable to present our theory in detail or give a historical survey and critical analysis of other theoretical ideas, I shall restrict myself to a discussion of the general approach to the problem, the principal conclusions, and the difficulties confronting the theory.

The process of transfer of an electron between an ion and an electrode is an extremely complex one even in the simplest case of a reduction-oxidation reaction on the surface of a metal electrode, taking place without the rupture or formation of chemical bonds and not complicated by adsorption phenomena. Indeed, the ion near the electrode is surrounded by a solvation shell, which is distorted, as compared with the same kind of shell in the bulk of the solvent, by a strong double-layer electric field. The structure of the polar solvent that surrounds the ion has not been studied sufficiently. We have only very approximate knowledge of the wave functions of electrons in complex ions. The surface properties of metals and, especially, of semiconductors contiguous with the solution are far from those of the ideal surfaces that figure in the modern theory of metals. Under such conditions, it is important to understand that it would be pointless to construct a theory that claimed to give a quantitative and detailed description of the process of charge transfer. This applies even more to the more complex electrode reactions that take place with the disruption or formation of chemical bonds. In our view, it makes more sense to limit ourselves to the construction of the kind of simplified model that will correctly convey the basic qualitative characteristics of the process. What are the tasks of the model theory? First, it should provide an explanation of one fundamental fact—the extremely



low velocities of electrode processes, that is, of the origin of slow discharge. The slowness of electrode processes, to which electrochemists are accustomed, distinguishes the processes taking place in a polar solvent from all other processes where opposite charges combine. Such processes always take place at enormous velocities, as, for instance, charge recombination processes in gases. The circumstance that the rate of the reaction between an ion and electrode of the same chemical nature does not differ from the rate of the reaction between an ion and electrode of different chemical nature is closely related to the slowness of the discharge. In other words, the phenomenon of resonant charge transfer that is always present in gaseous reactions is absent from electrode processes. Second, the theory must also clarify the nature of Tafel's law, or, equivalently, the nature of Bronsted's rules for homogeneous reactions occurring with charge transfer. Finally, the most complicated of the general tasks that confront the theory according to us is that the theory must calculate the magnitude of the transfer coefficient in Tafel's law and its dependence on overvoltage. The answer to the first question on the nature of the slow discharge is to be found in very general quantum mechanical considerations. To illustrate this point, let us examine a homogeneous reaction with transfer of an electron between two identical ions with different charges. The difference in the magnitude of the charge causes a difference in the degree of solvation of the ions. This latter circumstance indicates that the energy levels of both ions, surrounded by a polarized medium, have been shifted differently with regard to their positions in vacuum (where the energy levels of identical ions coincide). The transfer of the electron from one ion to the other must be accompanied by the absorption or release of energy from the above-mentioned shift. This indicates that there is some sort of energy reservoir which ensures the appearance of a reaction situation in the system. A reaction situation occurs when the positions of the energy levels of both ions temporarily coincide. Both the slowness of the reaction and the absence of resonant phenomena are due to the inertness, the slowness of the action of the energy reservoir. Basically, either the polar solvent or the thermal energy of inner molecular oscillations (if the reagent or product of the reaction is a molecular ion) can serve as the energy reservoir.

The thermal oscillations of the polar solvent alter its polarization (the optical branch). The change in the polarization, in turn, alters the positions of the energy levels of the solvated ions. The position of the energy levels also changes as a result of inner molecular oscillations. If the energy levels of the ions become the same as the result of these fluctuations, then it is very likely that the transfer of the electron will occur at that moment. The exchange of the electron between the metal electrode and the ion takes place in exactly the same way, at least in principle, in instances of electrode reactions, too. Thus, we see that slow discharge is a purely quantum mechanical phenomenon, arising from the discrete nature of energy levels. Along with this, the task of theory becomes clear: to describe the mechanism of the action of the energy reservoir. For this it is necessary, strictly speaking, to have detailed data on the nature of the thermal movement of the solvent and on the inner molecular oscillations of the molecules in the polar solvent, both while situated in the strong double layer electric field. There are, of course, no such data at present, and it is therefore necessary, on the one hand, to devise a simplifying hypothesis, and, on the other, to develop a theory of the above-mentioned phenomena. At first, R. Marcus (U.S.) and we independently restricted ourselves to describing the bulk medium as a continuum, with exactly the same properties as a polar crystal. It was also assumed that the oscillations of the molecules of the first solvated layer were suppressed, but later we were able to reject these oversimplifications and to develop further the theory of thermal movement in a polar

fluid. In this theory the properties of the fluid are quite fully described by the dependence of its dielectric constant on frequency and wavelength. However, we do not at present know what kind of function this is near a solid surface for so complex a fluid as, say, water. In the simplest case of atomic and weakly solvated ions, only a polar solvent can serve as the energy reservoir. Its thermal fluctuations create a reaction situation. In more complex instances, as with molecular ions during the discharge of the hydronium ion and also in the case of strongly solvated ions, a significant role may be played, along with the thermal fluctuations of the solvent, by molecular excitation within the molecule as well as by oscillations along the molecule's bonds with the first hydration shell. All these processes contribute to the creation of a reaction situation. The theory of Horiuti and Polanyi took into account only inner molecular thermal excitation as the mechanism for creating a reaction situation. Actually, the relative roles of the two competing mechanisms creating the reaction situation, that is, the role of the thermal fluctuations of the solvent and the thermal fluctuations of molecular oscillations, are determined by the specific magnitudes of the frequencies and the properties of the thermal movement of the polar solvent. The latter also has certain characteristic frequencies. Hence, there is no point in counterposing the two coexisting, mutually competing mechanisms as some authors still try to do. As for the transfer of the electron, theory indicates that the corresponding probability of the process does not contribute to the temperature dependence of the current in the case of metal electrodes. However, the specific features of the energy spectra of semiconductors greatly affect the probability of the passage of the electron. At present, theory has made possible the derivation of Tafel's law, the calculation of the magnitude of the transfer coefficient, and the establishment of its dependence on overvoltage. Theory correctly conveys the nature of the isotope effect and describes the mechanism of the operation of the transfer of electrons across bridging species and several other experimental facts. Theory was applied to a number of specific electrode reactions and compared with the results of the theory of homogeneous reactions with charge transfer. Despite the favorable quantitative results of comparisons with experiment, one should not overestimate the quantitative preciseness and completeness of the theory, underestimate the crude assumptions on which it is based, or consider the theory devoid of difficulties.

Let us enumerate some of those difficulties. The theory of thermal movement of so complex a fluid as a polar solvent is only very approximate. As we have stressed, the properties of thermal movement near a solid surface differ from the properties of movement in the bulk. Yet existing theory does not take this into account. Nor does theory as yet take into account the influence of the strong, heterogeneous electric field of the double layer. The frequencies of oscillation along the bonds with solvated molecules and the dielectric constant when the waves are exceedingly short, which figure in the final formulas of the theory, together with a number of other circumstances have not yet been investigated either theoretically or experimentally. It seems to me, therefore, all the more surprising that theory has nevertheless made it possible to find a quantitative expression for the transfer coefficient and to give a qualitative description of the entire group of problems connected with electrode kinetics. The reason for this, I believe, is that the magnitude of the transfer coefficient, which is  $\frac{1}{2}$ , is related to the shape of the potential energy surface and this is influenced by the potential energy of the solvent. If there is a parabolic surface in the potential energy, corresponding to the approximation of the small oscillations, the magnitude of the transfer coefficient obtained is  $\frac{1}{2}$ , irrespective of the detailed mechanism of the process. However, in the case of hydrogen overvoltage, a trans-

fer coefficient of  $\frac{1}{2}$  is observed over such a wide range of overvoltage that it becomes very difficult to find a theoretical explanation for it. Apparently, the energy of reorganization, the basic characteristic of the fluctuation process, which was considered constant in the theory, depends, in fact, on the intensity of the electric field in the double layer. Hence, we see that de-

spite the achievements of the theory, there are still extensive unexplored fields to be investigated. At the same time, and this is extremely important, it is necessary to develop the experimental technology that would facilitate the experimental testing of a number of the detailed qualitative and quantitative predictions of the theory.



## Tribo-Ellipsometric Study of the Repassivation Kinetics of a Ti 8Al-1Mo-1V Alloy

J. R. Ambrose and J. Kruger\*

*Institute for Materials Research, National Bureau of Standards, Washington, D. C. 20234*

### ABSTRACT

The tribo-ellipsometric technique allows one to distinguish between film growth and other reactions that occur after removal of a film from a metal surface in a given environment. This technique was used to study the relationship between repassivation kinetics and stress corrosion cracking (SCC) susceptibility for Ti 8Al-1Mo-1V alloy. In these studies the effect of the rate of film growth on the amount of metal dissolution which occurs during the repassivation process was investigated by comparing the repassivation transient behavior in a 1.0N NaCl solution, where cracks have been found to propagate, to that in a 1.0N NaNO<sub>3</sub> solution where SCC susceptibility has never been detected. Film growth kinetics in both solutions were consistent with a Fleischmann-Thirsk mechanism of oxide patch nucleation and two-dimensional growth, although the film growth rate was significantly slower in the 1.0N NaCl solution. Low film growth rate led to an increase in metal dissolution in a solution where crack propagation velocities have been measured, but at an apparent rate slower than necessary to propagate such cracks by metal dissolution alone.

Theoretical treatments of the relationship between repassivation kinetics and susceptibility to stress corrosion cracking have recently been incorporated into mechanisms for cracking of a number of materials, noticeably mild steel (1) and titanium alloys (2). Studies by Beck (2) relating crack propagation velocities to anodic current densities measured following fast fracture of titanium alloy wire utilized an empirical relationship to estimate film growth rates during the repassivation transient.

The recently developed technique of tribo-ellipsometry (3, 4), with which a determination of both anodic current and film growth rates can be made following passive film removal by abrasion, makes possible a separation of the total repassivation process into film growth and metal dissolution components. The object of this technique is to simulate the production of bare metal by film rupture at the tip of a stress corrosion crack.

This work describes the results of a study comparing repassivation behavior of a commercial titanium alloy (Ti 8Al-1Mo-1V) exposed to 1.0N NaCl in solution where cracks are known to propagate and to 1.0N NaNO<sub>3</sub> where no susceptibility to cracking has been detected.

An attempt has been made to correlate measured film growth rates with the Fleischmann-Thirsk patch nucleation and growth mechanism (9) and to estimate crack propagation velocities which would result from metal dissolution during repassivation.

### Experimental

The description of the experimental apparatus and technique of tribo-ellipsometry has been presented in prior publications (3, 4).

\* Electrochemical Society Active Member.

Key words: repassivation kinetics, stress corrosion cracking, titanium alloy, tribo-ellipsometry.

A Ti 8Al-1Mo-1V commercial alloy was used in this study: 1.905 cm diameter  $\times$  0.635 cm thick cylindrical specimens were machined from rod stock and polished on silicon carbide metallographic papers followed by rotary polishing on nylon cloth with 6 $\mu$  diamond paste. Air-saturated solutions of 1.0N NaCl (pH = 6.11) and 1.0N NaNO<sub>3</sub> (pH = 6.08) were prepared from ACS reagent grade chemicals and distilled water.

Specimen potentials were controlled potentiostatically. The repassivating current pulse generated upon cessation of abrasion was used to trigger the sweep of a dual channel oscilloscope. The scope also recorded the output of the photometer system used to monitor changes in ellipsometer light intensity.

Total coulombs,  $Q_T$ , passed during the transient were determined by graphical integration of the total current,  $i_T$ ; film thickness,  $x$ , was determined from light intensity changes which were converted using predetermined calibration data.

### The Repassivation Ratio, $R_p$

Measurement of the total current,  $i_T$ , and the film thickness,  $x$ , as a function of time during the repassivation transient is relatively straightforward. However, several uncertainties exist that make it difficult to render analysis of tribo-ellipsometric data completely unambiguous and quantitative. These uncertainties are as follows:

(i) The total current involved in repassivation,  $i_T = i_a + i_c$ , is the current supplied by the potentiostat to maintain the specimen potential at some fixed value with respect to a reference electrode potential. If any cathodic reduction were also to supply current ( $i_c$ ) a determination of  $i_a$ , the anodic current used during repassivation, becomes difficult. Of course,  $i_c$  can be made negligible by operating at potentials 50 mV or so more positive than the open-circuit or corrosion potential.

However, this would defeat the point of attempting to predict susceptibility to SCC for materials immersed in specific environments.

(ii) The charge utilized in the formation of an oxide film is given by

$$Q_x = \int_0^t i_x dt = \frac{z_f F \rho_f A_f x}{10^4 M_f} \quad [1]$$

It is difficult to obtain an accurate value of area,  $A$ , for the surface where film growth (and metal dissolution) occurs since the efficiency of the abrasion process is difficult to ascertain.

To get around these difficulties a recent paper (5) expressed the experimentally measured variables of total current,  $i_T$ , and film thickness,  $x$ , in the form of a ratio, designated  $R_p$  and given by

$$R_p = \frac{\int_0^t i_T dt}{x} \quad [2]$$

Since  $\int_0^t i_T dt = Q_T$  and  $x = \frac{10^4 M_f}{z_f F \rho_f A} Q_x$ , then

$$R_p = \frac{Q_T}{k Q_x} \quad [3]$$

where  $k = \frac{10^4 M_f}{z_f F \rho_f A}$ . If we assume that  $Q_T = Q_x + Q_d$ , then

$$R_p = \frac{Q_x + Q_d}{k Q_x} = \frac{1}{k} \left[ 1 + \frac{Q_d}{Q_x} \right] \quad [4]$$

where  $Q_d =$  charge consumed by metal dissolution, and  $\frac{dQ_d}{dt} = i_d$  is the current consumed by metal dissolution.

$R_p$  is defined above using the experimentally measured total current rather than current density because an estimation of the area available for the repassivation reaction is difficult. However, it is sometimes useful to express  $R_p$  as a dimensionless variable, designated  $R_p^*$  and equal to

$$\frac{Q_t}{Q_x} = 1 + \frac{Q_d}{Q_x} \quad [5]$$

since results would be independent of the particular experimental procedures and apparatus employed. Although  $R_p$  and  $R_p^*$  differ in magnitude only by the constant,  $k$ ,  $R_p$  values are determined directly from experimental measurements; therefore, discussion and conclusions will be based on  $R_p$  values.  $R_p$  is a cumulative index of the extent of corrosion attack. Its time derivative is also useful as an indicator of any abrupt variation which might occur during the repassivation process, for example, completion of monolayer coverage. Differentiating  $R_p$  with respect to time

$$\frac{dR_p}{dt} = \frac{1}{k} \left( \frac{Q_x \frac{dQ_d}{dt} - Q_d \frac{dQ_x}{dt}}{Q_x^2} \right) \quad [6]$$

$$= \frac{1}{k} \left[ \frac{Q_x i_d - Q_d i_x}{Q_x^2} \right] \quad [7]$$

$$= \frac{1}{k} \left[ \frac{i_d}{Q_x} \right] - \frac{1}{k} \left[ \frac{Q_d i_x}{Q_x^2} \right] \quad [8]$$

In this derivation we have neglected the cathodic current,  $i_c$ . This is a reasonable assumption since it is generally quite low except in acid solutions, hence negligible compared to  $i_a$  when the anodic overvoltage is high.

The values of  $R_p$  and  $dR_p/dt$  can be used to distinguish between metal dissolution and film repair, and thus to provide parameters for predicting stress corrosion cracking susceptibility. Consider the following limiting conditions which could correspond to situations within a stress corrosion crack: (i)  $i_d \gg i_x$  and  $dR_p/dt > 0$ ; this would correspond to a situation where general corrosion without any repassivation was occurring. (ii)  $i_x \gg i_d$  and  $\frac{dR_p}{dt} \simeq \frac{1}{k} \left[ \frac{Q_d i_x}{Q_x^2} \right]$  (from

Eq. [8]); this corresponds to virtually instant repassivation with no metal dissolution and little susceptibility to SCC. (iii)  $i_x \simeq i_c$  and  $dR_p/dt \simeq 0$ . (iiia)  $dx/dt > 0$  (at large values of  $t$ ); in this case the film formed is not protective, but is similar in characteristics to (i) because general corrosion or pitting results. (iiib)  $dx/dt \simeq 0$  (at large values of  $t$ ). These conditions would be those most consistent with the initiation and propagation of stress corrosion cracks based on a metal dissolution mechanism which is dependent upon the rate of repassivation. In other words, a relatively large value of  $R_p$ , with small values of  $dR_p/dt$  and  $dx/dt$ , indicates that metal dissolution accompanies film regrowth. Repassivation eventually occurs, thus protecting the walls of the advancing crack and restricting propagation of the crack to the area directly at its tip. These conditions are summarized in Table I.

Light intensity vs. polarizer angle calibration plots were constructed prior to each experiment. From this, the ellipsometrically determined film thickness change was obtained using a proportionality constant of 0.15 nm/degree change in polarizer reading. This particular value was computed using the optical constants for film-free titanium reported by Melmed and Carroll (12) and assuming a nonabsorbing film with a refractive index of 2.75, a reasonable median value for oxides of titanium (13). Calculations show that a 20% error in this refractive index would lead to a variation of only  $\pm 0.06$  nm in the thickness of a monolayer (0.3 nm).

## Results

*Effect of anions.*—Results of the tribo-ellipsometric repassivation kinetics experiments conducted in 1N NaNO<sub>3</sub> (pH = 6.08) and 1N NaCl (pH = 6.11) solutions at -222 mV SHE<sup>1</sup> are shown in Fig. 1 and 2. At comparable film thickness, the value of the repassiva-

<sup>1</sup> This potential was the open-circuit value measured after 5 min exposure to the solution. Although corrosion potentials are extremely difficult to reproduce, depending for example, upon specimen surface treatment (6), the open-circuit potential established for the particular specimen used in these studies after several abrasion cycles was the same for Ti 8-1-1 in both solutions used and was fairly reproducible even when the specimen was repolished or solutions changed.

Table I. Prediction of type of corrosion process from measured repassivation parameters

Repassivation parameter				Significance
$R_p^*$	$dR_p/dt$	$x$	$dx/dt$	
$>1$	$\simeq 0$	$\simeq 0$	$\simeq 0$	Case (i): $i_d \gg i_x$ ; very little film growth; general corrosion attack.
$\approx 1$	$\leq 0$	$>0$	$\simeq 0$	Case (ii): $i_x \gg i_d$ ; most of current goes into formation of film; characteristic of the passive state.
$>1$	$\simeq 0$	$\simeq 0$	$\simeq 0$	Case (iiia): $i_x \approx i_d$ ; film which forms either is not protective [similar to case (i)] or grows too slowly to cover the surface, characteristic of general attack or pitting.
$>1$	$\leq 0$	$>0$	$\simeq 0$	Case (iiib): $i_x \approx i_d$ ; characteristic of a system which has eventually passivated after some metal dissolution has occurred. This would correspond to a system where the metal dissolution/film rupture model would apply.

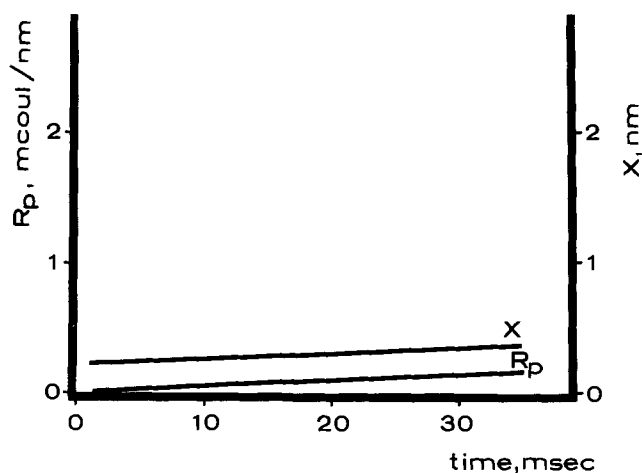


Fig. 1. Change in thickness,  $x$ , and repassivation ratio,  $R_p$ , after removal of the abrasion wheel of the tribo-ellipsometric apparatus for Ti 8-1-1 in 1N NaNO<sub>3</sub> at 25°C. The alloy is at the open-circuit (corrosion) potential  $-222$  mV (SHE).

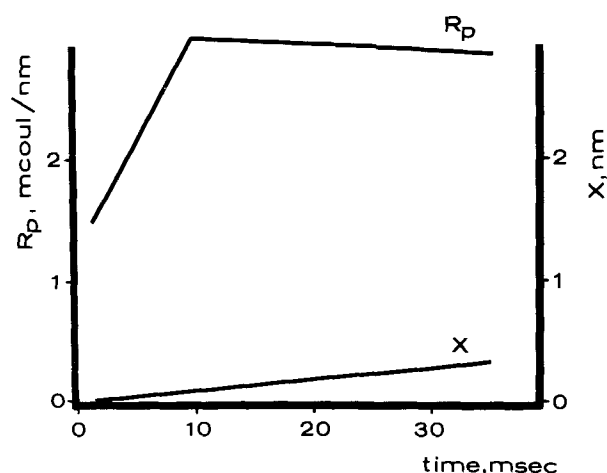


Fig. 3. Change in thickness,  $x$ , and repassivation ratio,  $R_p$ , after removal of the abrasion wheel of the tribo-ellipsometric apparatus for Ti 8-1-1 in 1N NaCl at 25°C. The alloy is at  $+706$  mV (SHE).

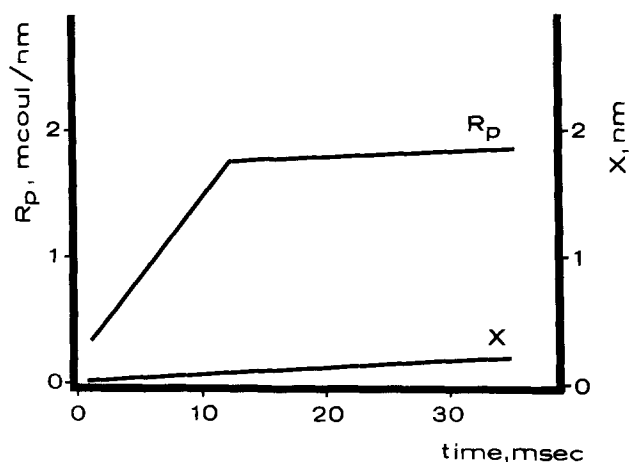


Fig. 2. Change in thickness,  $x$ , and repassivation ratio,  $R_p$ , after removal of the abrasion wheel of the tribo-ellipsometric apparatus for Ti 8-1-1 in 1N NaCl at 25°C. The alloy is at the open-circuit (corrosion) potential  $-222$  mV (SHE).

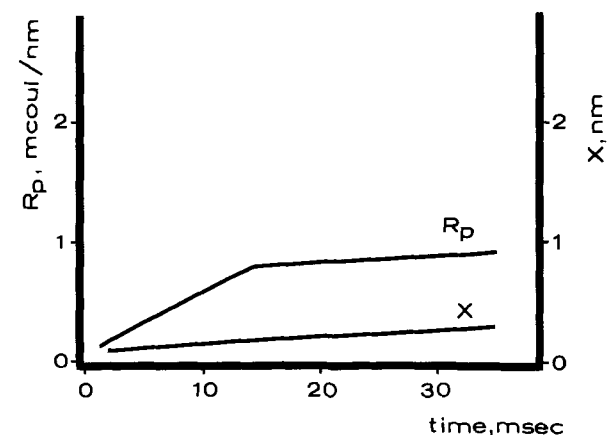


Fig. 4. Change in thickness,  $x$ , and repassivation ratio,  $R_p$ , after removal of the abrasion wheel of the tribo-ellipsometric apparatus for Ti 8-1-1 in 1N NaNO<sub>3</sub> at 25°C. The alloy is at  $+706$  mV (SHE).

tion ratio,  $R_p$ , is significantly higher in the NaCl solution than in the NaNO<sub>3</sub> solution, approaching a limiting value of about 2 mCoulombs/nm when at a monolayer coverage of 0.3 nm ( $R_{p\text{lim}} \approx 0.3$  mCoulomb/nm). The values of the ellipsometrically determined film thickness are also shown. In NaNO<sub>3</sub>, an oxide thickness of 0.30 nm is present on the metal surface by the time the abrasion wheel had retracted to allow ellipsometric measurements ( $\sim 5$  msec), indicating extremely rapid early stage film growth. In NaCl, on the other hand, film growth is so slow that a film thickness of 0.30 nm is not reached until 38 msec after cessation of abrasion.

**Effect of potential.**—The results of repassivation experiments conducted in the 1N NaNO<sub>3</sub> and 1N NaCl solutions at  $+706$  mV SHE are given in Fig. 3 and 4.  $R_{p\text{lim}}$  values are significantly higher than at open circuit in both solutions ( $\sim 3.00$  for NaCl;  $\sim 1.02$  for NaNO<sub>3</sub>). Initial film thickness growth is substantially slower at  $+706$  mV than at  $-222$  mV for the NaNO<sub>3</sub> solution. A comparison of oscilloscope tracings for Ti 8-1-1 in 1N NaCl and 1N NaNO<sub>3</sub> at 706 mV SHE appears in Fig. 5.

Peak current densities for the transients in NaCl and NaNO<sub>3</sub> were 65.0 and 18.8 mA, respectively.

A straight line and zero intercept was obtained when film thickness in chloride solution was plotted against the square root of time, but some deviation from a parabolic growth law was observed at short times for the nitrate solutions. These plots for Ti 8-1-1 in 1N

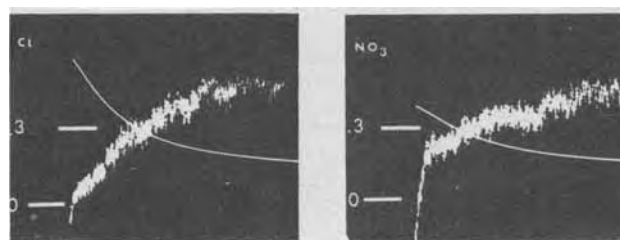


Fig. 5. A comparison of oscilloscope repassivation transients for Ti 8-1-1 in 1N NaCl (susceptible) and 1N NaNO<sub>3</sub> (nonsusceptible) solutions at  $+706$  mV (SHE) (ellipsometric film growth, jagged trace; current, solid line trace). 0 and 0.3 nm film thickness values are shown.

NaCl and 1N NaNO<sub>3</sub> at both potentials are given in Fig. 6. This particular figure is presented only to illustrate a problem of interpretation. Since data could be made to fit other growth laws ( $\ln x$  vs.  $t^2$  and  $x$  vs.  $t$ ) as well, it was necessary to exercise caution in accepting one mechanism over another. The values of  $R_p$ ,  $R_p^*$ ,  $t_m$  (the time required for obtaining 0.30 nm film thickness),  $dx/d(t^{1/2})$ , and  $i_{\text{max}}$  are given in Table II. In the calculation of  $R_p^*$ , the oxide was assumed to be TiO<sub>2</sub> ( $z = 4$ ). If lower valence oxides of titanium were to form, the net effect would be that the tabulated  $R_p^*$  could be too high by a factor of about 2. However, even if different oxides were to form in the respective solutions, the correction to  $R_p^*$  resulting from a change in  $z$ ,  $M$ , and  $\rho$  would not be large enough to account for the relative differences in  $R_p^*$  determined for the two solutions.

Table II. Repassivation parameters for Ti 8-1-1 alloy in 1N NaNO<sub>3</sub> and 1N NaCl solutions

Solution	Potential SHE (mV)	$R_p(t_m)^*$ (mCoulombs/nm)	$R_p^*(t_m)^\dagger$	$t_m$ (msec)	$\left(\frac{dR_p}{dt}\right)_{t < t_m}$ (mCoulombs/nm/msec)	$\left(\frac{dR_p}{dt}\right)_{t > t_m}$ (mCoulombs/nm/msec)	$\left(\frac{dx}{dt^{1/2}}\right)_{t < t_m}$ (nm/msec) <sup>1/2</sup>	$\left(\frac{dx}{dt^{1/2}}\right)_{t > t_m}$ (nm/msec) <sup>1/2</sup>	$i_{max}$ (mA)
1N NaNO <sub>3</sub>	-222	0.3	1.04	<5	—	+0.005	—	0.0350	4.2
1N NaCl	-222	2.0	6.94	38	+0.130	+0.004	0.0150	0.0405	24.0
1N NaNO <sub>3</sub>	+706	1.0	3.47	20	+0.052	+0.006	0.0167	0.052	18.8
1N NaCl	+706	3.0	10.4	20	+0.174	-0.005	0.0272	0.072	65.0

\* Good reproducibility was obtained for reported  $R_p$  values with a relative precision of less than  $\pm 5\%$  being obtained for all measurements. This leads, for example, to a maximum range of  $\pm 0.2$  mCoulombs/nm in the  $R_p$  determination for Ti 8-1-1 in 1N NaCl at +706 mV SHE.

† The  $R_p^*$  values reported here are based upon an approximate area of metal produced during abrasion of 0.14 cm<sup>2</sup>. This value of area was computed by assuming that  $i_T \approx i_x$  after monolayer coverage on Ti 8-1-1 in 1N NaNO<sub>3</sub> solution, when metal dissolution can be assumed low. Hence

$$\int_{t_1}^{t_2} i_T dt \approx Q_x = \frac{z_e F \rho_t A x}{10^4 M_t} \text{ or } A \approx \frac{10^4 M_t \int_{t_1}^{t_2} i_T dt}{z_e F \rho_t x}$$

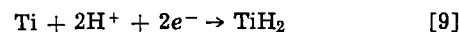
## Discussion

**Repassivation ratio and stress corrosion susceptibility.**—From Fig. 1 and Table II it can be seen that for Ti 8-1-1 in 1N NaNO<sub>3</sub> at the corrosion potential of -222 mV SHE, a low value of  $R_p$  was observed throughout the repassivation transient. Here  $dR_p/dt = 0$ . Based on the size of the oxide ion, a monolayer of TiO<sub>2</sub> would be approximately 0.30 nm in thickness; it formed in < 5 msec in this environment. These results are characteristic for a case (ii) repassivation transient in which most of the current transient is utilized in rapid film growth without significant metal dissolution. When this is compared to the results obtained in 1N NaCl at the same potential, where crack propagation velocities on the order of 10<sup>-2</sup> cm/sec have been measured (2, 7), it is seen that  $R_p$  is significantly higher as is  $dR_p/dt$ , indicating substantial metal dissolution which can be accounted for by low rates of film growth in 1N NaCl. Although monolayer coverage is not obtained until 38 msec following cessation of abrasion,  $R_p$  changes slope at about 12 msec. This indicates some inhibition of metal dissolution, perhaps by formation of a precipitated salt layer on the surface which results from saturation of the diffusion layer with TiCl<sub>3</sub> (Fig. 2). At any rate, repassivation is eventually achieved [case (iiib)]. Similarly, at an applied potential of +706 mV SHE,  $R_p$  is quite high in the chloride solution with  $R_p$  changing slope at about 10 msec which would substantiate a precipitated salt passivation mechanism since a saturated solution of TiCl<sub>3</sub> would be obtained more rapidly at these higher current densities. The time to complete monolayer coverage,  $t_m$ , is about 20 msec.  $R_p$  and  $dR/dt$  for 1N NaNO<sub>3</sub>,

although larger than at the lower potential, are far less than in the NaCl environment.

Based upon analysis of the  $R_p$ ,  $dR_p/dt$ , and  $t_m$  parameters, it appears that, at least for titanium alloys, a case (i) → case (iiib) transition in  $dR_p/dt$  with an initial high  $R_p$  predicts susceptibility to stress corrosion cracking under the experimental conditions employed.

We should, nevertheless, not rule out some mechanism involving embrittlement by hydrogen through decohesion or fracture of titanium hydride (TiH<sub>2</sub>) produced by the cathodic reduction reaction



Since the results of our study show lower repassivation rates in the environment known to be susceptible to SCC, repassivation kinetics that can control or limit access of H<sup>+</sup> to the Ti surface may still be relevant. Secondly, fractographs of titanium alloys that have undergone SCC show a great deal of cleavage (8). This could rule out metal dissolution as a factor during crack propagation. However, the significantly higher metal dissolution in Cl<sup>-</sup> solutions suggested by Beck (2) and confirmed in this study cannot be ignored. The effect of repassivation on metal dissolution must be important in the initiation stages of a crack when, because the pH of neutral chloride solutions would be near bulk solution values, the H<sup>+</sup> concentration would be too low for the reaction in Eq. [9] to play an important role. During later stages of propagation, where metal ion hydrolysis leads to pH and IR drops within the crack, hydride cleavage mechanisms must be considered in addition to the effects of environmental variations on film growth and metal dissolution kinetics.

**Film growth kinetics.**—The first stage of film growth appears to be consistent with the Fleischmann and Thirsk analysis of thin-film nucleation and growth (9). The extension of their model to interpret repassivation kinetic transient data was developed by Beck (2) who adopted the Fleischmann and Thirsk assumption of an instantaneous nucleation of  $n$  patches/cm<sup>2</sup> which spread in two dimensions until formation of an oxide monolayer is complete. His equation for the current density to the oxide patches is given by

$$i_t = 2mQ_f C t \exp[-Ct^2] \quad [10]$$

Since the patch thickness is assumed constant until complete monolayer coverage is obtained,  $Q_f$  would be constant;  $C$  would also be independent of time. This allows integration of Eq. [10] [from Ref. (2)]

$$1 - \theta = \exp[-Ct^2] \quad [11]$$

where  $\theta$  is the fraction of surface coverage.

Taking logarithms of both sides gives

$$\log[1 - \theta] = -Ct^2 \quad [12]$$

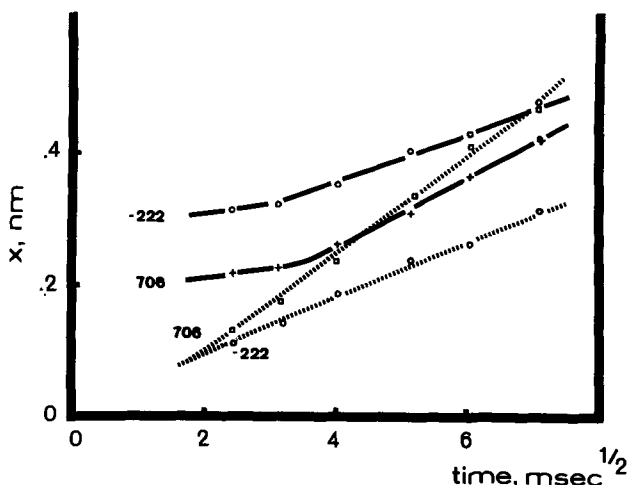


Fig. 6. Changes in film thickness,  $x$ , for Ti 8-1-1 in 1N NaNO<sub>3</sub> (dashed line) and in 1N NaCl (dotted line) at -222 and +706 mV (SHE) at 25°C.

Since  $\theta$  is proportional to the ellipsometer parameter  $\Delta$  which depends on average film thickness, hence also to  $\Delta P$  (the change in polarizer reading), a plot of  $\log \Delta P$  vs.  $t^2$  should be linear if the Fleischmann-Thirsk model is an appropriate one. Results are given in Fig. 7.

From Table II, we find that a monolayer (approximately 0.30 nm) has formed on Ti 8-1-1 in the  $\text{NaNO}_3$  solution at the open-circuit potential in less than 5 msec. A comparison with the  $\text{NaCl}$  solution at the same potential shows that monolayer coverage is not obtained until some 30 msec later, and the  $\log(1 - \theta)$  vs.  $t^2$  plot is linear, but two staged, indicating possible applicability of the Fleischmann-Thirsk model. The break in the  $-222$  mV  $\text{NaCl}$  solution plot corresponds quite well with the change in slope of  $R_p$  vs. time plot (Fig. 2) indicating some change in the film growth process, perhaps the onset of the conversion of an already present salt film to an oxide film. The break in the  $+706$  mV plot is not in good agreement with the  $R_p$  change in Fig. 3, however, indicating some delay in the onset of oxide growth. We have no explanation for this behavior. Experiments run at the higher anodic potential give approximately the same effect, that is, film growth is substantially slower in the chloride solution than in the nitrate. The fact that first stage growth rates at the higher potential are lower in the nitrate solution may be due to a localized pH lowering from solvated  $\text{Ti}^{+3}$  hydrolysis. This could measurably affect film growth kinetics. Such an effect would not be noticeable in the chloride solution where hydrolysis of the metal ions probably results in pH decreases in both potentials. The values of  $i_{\max}$  for both solutions at the two potentials would substantiate this conclusion. In  $\text{NaNO}_3$  the relative increase in peak current resulting from film removal at the higher potential is about 6:1 whereas only about a 3:1 increase is noted for chloride solution (Table II).

Simultaneous determination of both film thickness and total current allow an estimate of the amount of metal dissolution occurring during the repassivation transient. Such an estimate would allow prediction of the crack propagation velocities to be expected if propagation proceeds via an electrochemical dissolution mechanism as suggested by Beck (2).

Assuming that metal dissolution occurs by Tafel kinetics on the bare metal between patches

$$i_d = i_{d,0} \exp[\alpha(E_a - E_{o,t})/RT] \quad [13]$$

Total metal dissolution current over the entire surface is proportional to the area of bare metal exposed. It

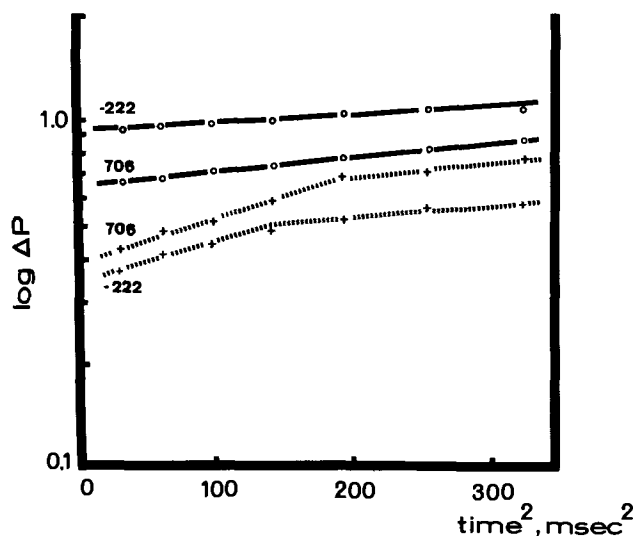


Fig. 7. Changes in  $\log_{10} \Delta P$  for Ti 8-1-1 in  $1N \text{NaNO}_3$  (dashed line) and  $1N \text{NaCl}$  (dotted line) at  $-222$  and  $+706$  mV (SHE) at  $25^\circ\text{C}$ .

can be assumed, however, that the local dissolution current density on bare metal surfaces remains constant over the span of the repassivation transient until the patches coalesce. This would allow an estimate of the maximum penetration of metal by electrochemical dissolution. Since the local dissolution current density is given by  $i_{\max}/A$ ,  $l_{p\max}$ , the maximum penetration at those areas of surface last covered by the monolayer, is given by

$$l_{p\max} = \frac{i_{\max} M_M}{10^3 z_M F \rho_M A_M} t_m \quad [14]$$

Using data from Table II for Ti 8-1-1 in  $1N \text{NaCl}$  at the open-circuit potential of  $-222$  mV SHE, we obtain a value of  $l_{p\max}$  of  $2.3 \times 10^{-7}$  cm or a maximum propagation velocity of  $6.0 \times 10^{-6}$  cm/sec assuming metal dissolution as  $\text{Ti}^{+3}$ . Even if the  $i_{\max} \approx i_d$  approximation is in error due to localized cathodic reactions, as well as overestimating bare metal surface area, propagation velocities based on electrochemical metal dissolution do not come close to the observed stress corrosion crack propagation velocities of  $8 \times 10^{-3}$  cm/sec by Beck at this potential (2).

However, propagation velocities are potential dependent,  $v_{p\max}$  being calculated as  $16.2 \times 10^{-6}$  cm/sec at a potential of  $+706$  mV SHE. From this we would predict that upon increasing the applied potential by 1V the propagation velocity would increase by a factor of three, in agreement with Beck (2). This would suggest that although metal dissolution does not account for the observed crack propagation rates, it may be a necessary condition for such propagation.

The Fleischmann-Thirsk model for patch growth, coupled with the assumption of constant metal dissolution current density at the metal surface, would, however, predict creation of localized penetration sites. The geometry of these sites would lead to increased stresses at the point of maximum penetration as well as effecting environmental composition variations due to the occluded nature of these sites (Fig. 8).

Whether crack propagation then proceeds via a dissolution-assisted, mechanical, cleavage process or by fracture of a brittle region produced by entry into the metal of hydrogen formed by cathodic reduction cannot be determined on the basis of the results presented here. The specific function of halide ions (e.g.,  $\text{Cl}^-$ ) in restricting lateral oxide growth is also highly speculative but may result from preferred ion adsorption inhibiting oxide growth kinetics. Green and Sedricks suggest that on the basis of their ellipsometric potential step experiments film growth kinetics play no part in determining SCC (7). However, they did not study film growth kinetics on bare metal surfaces, making their conclusions somewhat irrelevant to stress cracking. By varying the water content of 3.5%  $\text{LiCl}$  in dimethyl sulfoxide solutions they have been able to control crack propagation velocities in Ti 8-1-1 (10). Their results suggest the possibility of a hydrogen embrittling mechanism since no available hydrogen is present in pure DMSO; however, neglect in measuring their solution conductivities leaves open the possibility of crack propagation rates being limited by mass transfer of some rate-determining species. On the other hand, this work indicates that film growth rate and SCC susceptibility appear to be related for those environments studied.

### Conclusions

1. Ti 8-1-1 alloy repassivates rapidly in  $\text{NaNO}_3$  solution as indicated by a low  $R_p$  and  $dR_p/dt$  with a monolayer of oxide being formed in less than 5 msec.
2. Ti 8-1-1 alloy repassivates less rapidly in  $\text{NaCl}$  solution than in  $\text{NaNO}_3$  solution as indicated by a higher  $R_p$  with an initially higher  $dR_p/dt$ . Although monolayer coverage is not obtained until after 38 msec following oxide removal, a decrease in  $dR_p/dt$  is observed at 12 msec, probably to inhibition of metal dissolution by a precipitated salt layer.

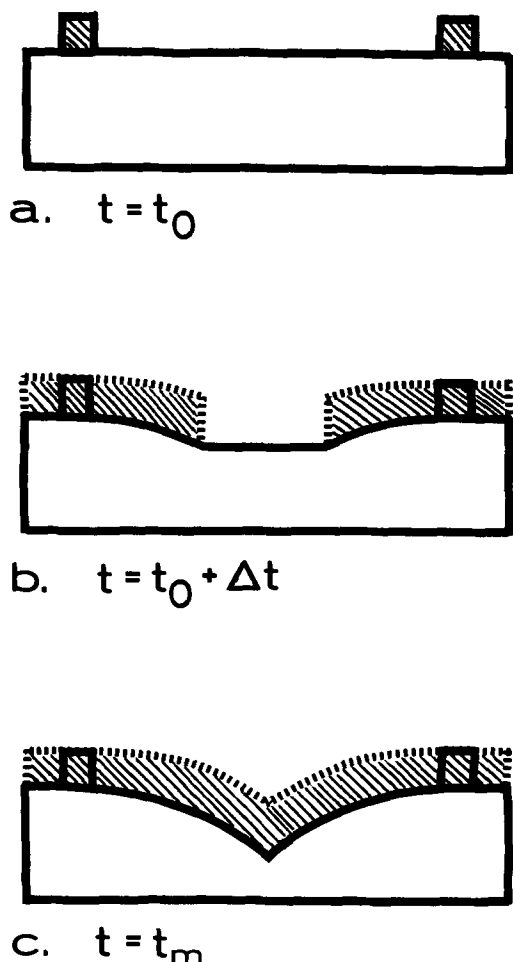


Fig. 8. Schematic of the effect of the Fleischmann-Thirsk model of oxide patch nucleation and growth on substrate penetration by metal dissolution. (a) Nucleation of oxide patches at cessation of abrasion; (b) metal dissolution during lateral patch growth resulting in formation of localized crevices where patches coalesce (c).

3. An analysis of ellipsometrically determined film growth kinetics on Ti 8-1-1 shows that the Fleischmann-Thirsk model of oxide patch nucleation and growth is applicable in both 1N NaCl and 1N NaNO<sub>3</sub> solutions.

4. A calculation of the maximum penetration resulting from Ti dissolution in Ti 8-1-1 in NaCl solution during the 38 msec time interval for oxide monolayer formation shows that crack propagation velocities observed by others cannot be accounted for by metal dissolution alone.

#### Acknowledgment

We are most grateful to the Office of Naval Research which supported this work under contract NAONR 18-89 NRO 36-082.

A portion of this work has been included in the research dissertation submitted to the University of Maryland by one of the authors (J.R.A.) in partial fulfillment of the requirements for the Ph.D. degree.

Manuscript submitted Sept. 27, 1973; revised manuscript received Dec. 31, 1973.

Any discussion of this paper will appear in a Discussion Section to be published in the December 1974

JOURNAL. All discussions for the December 1974 Discussion Section should be submitted by Aug. 1, 1974.

#### LIST OF SYMBOLS

$Q_x$	charge consumed in film formation, mcoulombs
$Q_d$	charge consumed in metal dissolution, mcoulombs
$Q_T$	total charge consumed in repassivation, mcoulombs
$i_x$	current consumed in film formation, mA
$i_d$	current consumed in metal dissolution, mA
$i_T$	total current consumed during repassivation, mA
$i_a$	anodic current component of $i_T$ , mA
$i_c$	cathodic current component of $i_T$ , mA
$z_f$	valence of metal ion in film, dimensionless
$z_M$	valence of metal ion in solution, dimensionless
$F$	Faraday constant, 96,500 coulombs/mole
$\rho_f$	density of film, g/cm <sup>3</sup>
$\rho_M$	density of metal, g/cm <sup>3</sup>
$A$	area of bare metal produced, cm <sup>2</sup>
$x$	film thickness, nm
$M_f$	molecular weight of film, g/mole
$M_M$	atomic weight of metal, g/mole
$R_p$	$Q_T/X$ repassivation ratio, mcoulombs/nm
$R_p^*$	$Q_T/Q_x$ repassivation ratio, dimensionless
$t$	elapsed time, msec
$t_m$	time for monolayer coverage, msec
$k$	$10^4 M_f/z_f F \rho_f A$ , nm/mcoulomb
$i_f$	current density, to oxide patches, A/cm <sup>2</sup>
$n$	number of monolayers, dimensionless
$Q_f$	charge density of oxide monolayer, coulombs/cm <sup>2</sup>
$C$	$\pi n (\delta_M i_z / Q_f)^2$
$n$	number of oxide patches, cm <sup>-2</sup>
$\delta_M$	thickness of monolayer, cm
$i_z$	current density at periphery of oxide patches, A/cm <sup>2</sup>
$\theta$	fractional surface coverage, dimensionless
$\Delta P$	change in polarizer angle, degrees
$i_{d,o}$	exchange current, A
$\alpha$	transfer coefficient, dimensionless
$E_a$	applied potential, V
$E_{o,t}$	equilibrium potential for metal dissolution, V
$l_{pmax}$	maximum metal penetration distance, cm

#### REFERENCES

1. T. P. Hoar and J. R. Gavele, *Corrosion Sci.*, **10**, 211 (1970).
2. T. R. Beck, in "The Theory of Stress Corrosion Cracking in Alloys," J. C. Scully, Editor, p. 64, NATO Scientific Affairs Division, Brussels, (1971).
3. J. R. Ambrose and J. Kruger, *Corrosion*, **28**, 30 (1972).
4. J. Kruger, J. R. Ambrose V. Bertocci, and G. M. Vgiansky, National Bureau of Standards Report No. 10-876, Technical Summary Report No. 3, Contract NAONR 18-69, NR 036-082 (1972).
5. J. R. Ambrose and J. Kruger, Proc. 5th Int. Congr. Met. Corr., Tokyo, 1972, To be published.
6. T. R. Beck, *This Journal*, **114**, 551 (1967).
7. J. A. S. Green and A. J. Sedricks, *Metall. Trans.*, **2**, 1807 (1971).
8. J. C. Scully, in "The Theory of Stress Corrosion Cracking in Alloys," J. C. Scully, Editor, p. 127, NATO Scientific Affairs Division, Brussels (1971).
9. M. Fleischmann and H. R. Thirsk, *Advan. Electrochem. Electrochem. Eng.*, **3**, 123 (1963).
10. J. A. S. Green and A. J. Sedricks, *Corrosion*, **28**, 220 (1972).
11. H. H. Uhlig, Proc. Int. Cong. Fundamental Aspects of Stress Corrosion Cracking, Ohio State University, 1967, p. 93, NACE, Houston (1969).
12. A. J. Melmed and J. J. Carroll, NBS Technical Note 565, p. 17, Washington, D.C. (1971).
13. "Handbook of Chemistry," N. A. Lange, Editor, p. 322, Sandusky, Ohio (1956).



# Electrodissolution Kinetics of Iron in Chloride Solutions

## IV. Alkaline Solutions Containing Benzotriazole

S. Asakura, C. C. Lu, and Ken Nobe\*

School of Engineering and Applied Science, University of California, Los Angeles, California 90024

### ABSTRACT

The anodic dissolution of iron in alkaline chloride solutions in the presence and absence of benzotriazole has been investigated by potentiostatic, galvanostatic, and potential sweep polarization. The steady-state and transient polarization experiments indicate that iron dissolution occurs in the absence (active region) and presence (prepassive region) of a porous prepassive surface film. Anodic Tafel slopes of 60 mV/decade were obtained below (active region) and above (prepassive region) the formation potential of the prepassive film on both uninhibited and inhibited iron indicating the same mechanism of iron dissolution. The results suggest that the prepassive film merely decreases the effective surface area for iron dissolution. The effect of benzotriazole is to decrease further the effective surface area.

There have been numerous investigations of benzotriazole (BTA) as a corrosion inhibitor of copper [e.g., see Ref. (1-3)] but very little work has been reported on iron. Some recent studies have shown that BTA inhibits the hydrogen evolution reaction on iron (4, 5) and steel (6). Furthermore, the results of Chin (4) indicate that the adsorbed BTA does not affect the mechanism of the h.e.r. on iron. Although Santhianandhan *et al.* (6) reported that BTA increases the anodic polarization of mild steel in acidic solutions, no attempt was made by these workers to elucidate the role of BTA in the dissolution mechanism.

A previous paper in this series (7) describes an investigation of the mechanism of iron dissolution in alkaline chloride solutions. This earlier work forms the basis for this paper which reports on the effects of benzotriazole on the kinetics and mechanism of iron dissolution in alkaline chloride solutions. Both steady-state and transient polarization techniques have been used.

### Experimental

Electrodes were prepared from Ferrovac E iron rod (1 cm diam). The cross-sectional surfaces were polished with 2/0 emery paper, and then the electrodes were degreased in detergent and washed several times with distilled water and benzene. Each electrode was sealed in Teflon tubes and inserted into electrode holders so that only one surface was exposed to the electrolyte. A three electrode, Pyrex glass, electrochemical cell was used. Specific pH values of the alkaline solutions were obtained by addition of appropriate quantities of KOH to the 1N KCl solutions. The inhibited system was prepared by the addition of 77 mM benzotriazole (BTA) to the electrolyte. The solutions were deaerated by bubbling prepurified nitrogen gas through the electrolyte for 24 hr before each experiment. The temperature was maintained at  $25^\circ \pm 1^\circ\text{C}$ .

Electrode potentials were measured with respect to the saturated calomel electrode (SCE). Linear potential sweep, potentiostatic, and galvanostatic polarization were used in the experiments.

After immersion in the electrolyte, the electrode was reduced at  $-1.5\text{V vs. SCE}$  until the cathodic current reached steady state. Subsequently, open-circuit conditions were initiated and then maintained until the rest potential was attained. After this procedure, either potential or current steps, or potential sweeps were imposed by a potentiostat coupled with function generators.

### Results

**Steady-state polarization.**—Figure 1 shows the steady-state polarization of inhibited (in the presence of BTA) and uninhibited iron in solutions of  $\text{pH} =$

12.8. For uninhibited iron (curve A) the current increased monotonically with increase in potential. Reproducibility of the data was very good. In contrast to the behavior of iron in the absence of BTA, inhibited iron showed a constant current region which was independent of the applied potential (i.e., a limiting current). This constant current value was a function of the history of the inhibited electrode since a newly immersed electrode (curve B) exhibited a larger value than an aged one (curve C).

It was observed that both an increase in immersion time and repetitive anodic polarization decreased the constant current value. After the electrode was aged sufficiently by repetitive anodic polarization and/or long immersion, it exhibited a reproducible polarization (curve C) as shown in Fig. 1.

The polarization behavior on an expanded scale is shown in Fig. 2. Both potentiostatic (closed points) and galvanostatic (open points) polarization data are given, and it is seen that good agreement is obtained. In Fig. 2, the correction for the ohmic potential drop is made in the polarization plot of uninhibited iron, and it is seen that Tafel behavior with a slope of 60 mV/decade is obtained over the entire potential region examined. That is

$$\frac{\partial \phi_a}{\partial \log i_a} = 60 \text{ mV/decade} \quad [1]$$

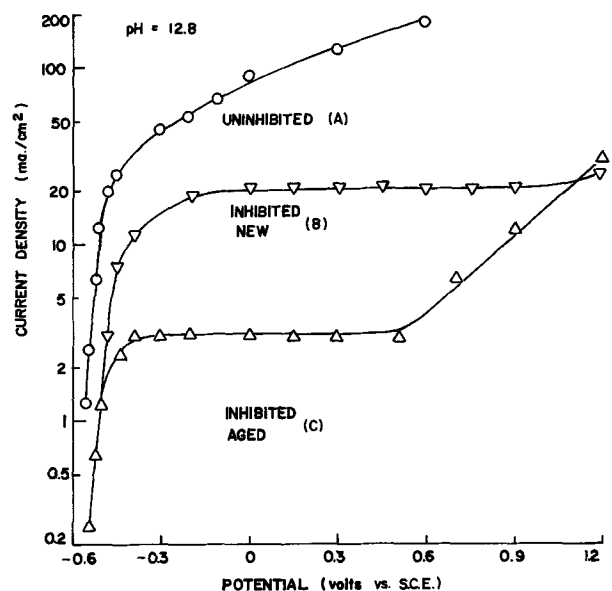


Fig. 1. Steady-state polarization of iron in chloride solutions of  $\text{pH} = 12.8$ .

\* Electrochemical Society Active Member.

Key words: inhibition, anodic dissolution, corrosion.

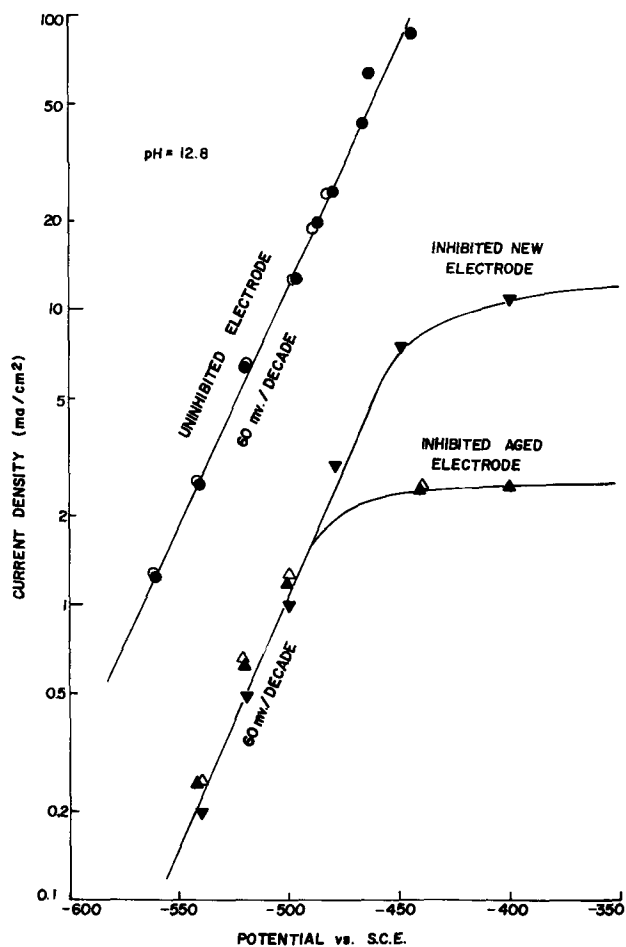


Fig. 2. Steady-state polarization of iron in chloride solutions of  $\text{pH} = 12.8$  (expanded scale). Closed and open points represent potentiostatic and galvanostatic polarization, respectively.

for uninhibited iron where  $\phi_a$  and  $i_a$  are the anodic potential (corrected for ohmic potential drop) and the steady-state anodic current, respectively. In the low current density region, inhibited iron also showed Tafel behavior with a slope of 60 mV/decade

$$\frac{\partial E_a}{\partial \log i_a} = 60 \text{ mV/decade}, \quad i_a \leq 1 \text{ mA/cm}^2 \quad [2]$$

where  $E_a$  is the apparent electrode potential. In the plots for the inhibited system, the ohmic potential drop was negligible in the low current density region. It should be noted that at  $\text{pH} = 12.8$  the electrode potential  $\phi_a$  was still within the region of active dissolution even at high current densities for the uninhibited system.

**Potential sweep.**—Figure 3 shows typical potential-current behavior of uninhibited iron in solutions of various  $\text{pH}$  obtained with a constant potential sweep rate. After the peak current, the current decreased and then increased again. Similar behavior was observed for inhibited iron. The peak current ( $i_p$ ) is plotted vs. sweep rate ( $\lambda$ ) in Fig. 4 for uninhibited iron in chloride solutions ranging from  $\text{pH} = 12.2$  to 13.8. For both uninhibited and inhibited iron,  $\log i_p$  is linearly related to  $\log \lambda$  with a slope of 1/2 for all  $\text{pH}$  values

$$\left( \frac{\partial \log i_p}{\partial \log \lambda} \right)_{\text{pH}} = \frac{1}{2} \quad [3]$$

The dependence of  $i_p$  on  $\text{pH}$  for both inhibited and uninhibited systems is shown in Fig. 5. In both cases linear relations were obtained for the  $\log i_p$  vs.  $\text{pH}$  plots with slopes of 1/2

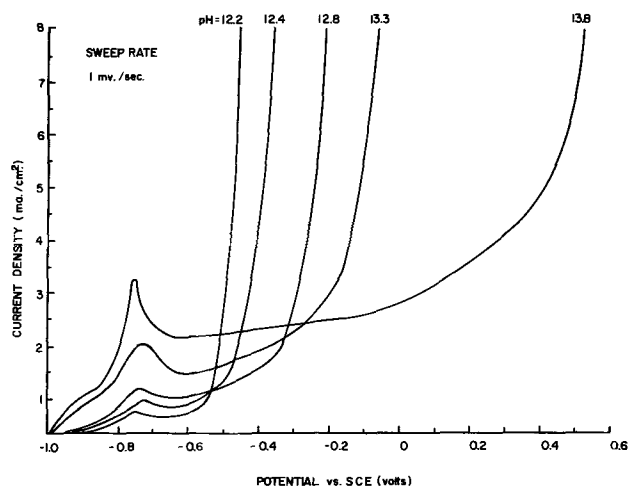


Fig. 3. Typical current-potential behavior of uninhibited iron at a constant potential sweep rate.

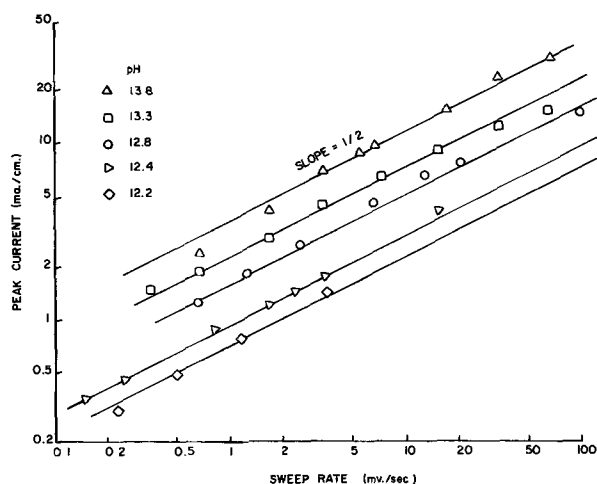


Fig. 4. Peak current vs. sweep rate of uninhibited iron

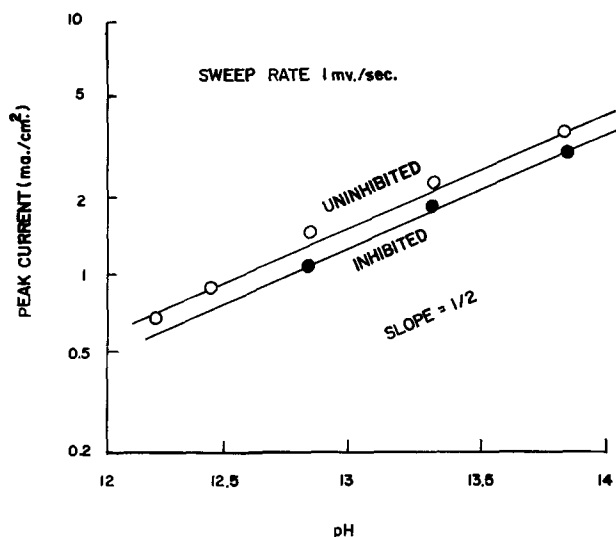


Fig. 5. Peak current vs.  $\text{pH}$  for uninhibited and inhibited iron

$$\left( \frac{\partial \log i_p}{\partial \text{pH}} \right)_{\lambda} = \frac{1}{2} \quad [4]$$

However, the  $i_p$  values were decreased by addition of inhibitor. For example, the effect of the inhibitor on the value of  $i_p$  can be expressed as

$$\frac{i_p(\text{inhibited})}{i_p(\text{uninhibited})} = 0.8 \quad \text{for } \text{pH} = 12.8 \quad [5]$$

The peak potential  $E_p$  was also dependent on the sweep rate as shown in Fig. 6 for the inhibited system. Linear relations in the  $E_p$  vs.  $\log \lambda$  plots with a slope of about 34 mV/decade were obtained for both inhibited and uninhibited iron, i.e.

$$\left( \frac{\partial E_p}{\partial \log \lambda} \right)_{pH} \approx 34 \pm 10 \text{ mV/decade} \quad [6]$$

As shown in Fig. 7,  $E_p$  did not depend on pH, i.e.

$$\left( \frac{\partial E_p}{\partial pH} \right)_{\lambda} = 0 \quad [7]$$

However,  $E_p$  values of inhibited iron were about 50 mV more positive than uninhibited iron.

**Potentiostatic transients.**—Typical current transients under potentiostatic conditions are shown in Fig. 8 and 9 in log-log plots of  $i$  and  $t$  where  $i$  and  $t$  are the transient current and time after imposition of a potential step, respectively. Electrodes used for the transient studies were aged before measurements were carried out. The  $\log i$  vs.  $\log t$  plots exhibited a linear relation with a slope of  $-1/2$  during the initial part of the transient, i.e.

$$i = A/\sqrt{t} \quad [8]$$

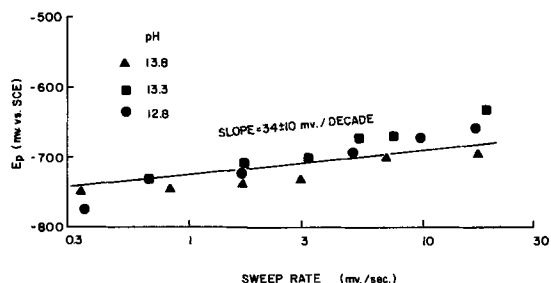


Fig. 6. Peak potential vs. sweep rate for inhibited iron

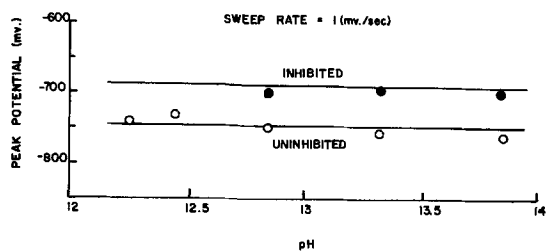


Fig. 7. Peak potential vs. pH for uninhibited and inhibited iron

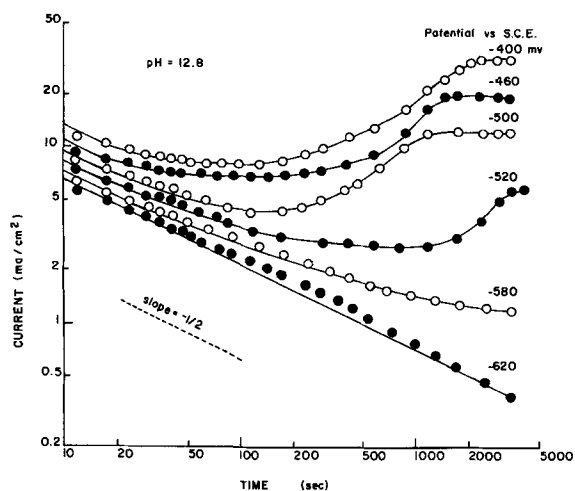


Fig. 8. Potentiostatic transients of the uninhibited system at pH = 12.8.

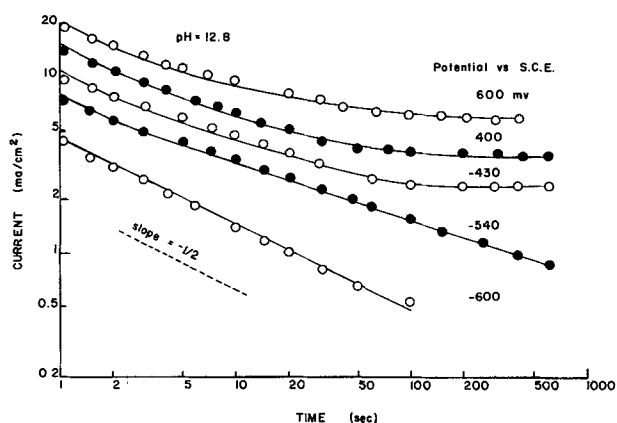


Fig. 9. Potentiostatic transients of the inhibited system at pH = 12.8.

where the constant  $A$  is a function of the potential step  $E$ .

Figure 8 shows that the current of uninhibited iron in pH = 12.8 solutions decayed initially and then increased after long polarization to steady-state values for  $E > -520$  mV. On the other hand, Fig. 9 shows that the current of inhibited iron decayed monotonically with no increase with time observed.

**Galvanostatic transients.**—The potential immediately after charging of the double layer was plotted against the applied current in Fig. 10 [see Fig. 4, Ref. (7)]. These plots exhibit Tafel behavior with a slope of 60 mV/decade for different pH solutions in the presence and absence of BTA. The pH dependence of anodic dissolution is obtained by plotting the current at  $-750$  mV vs. SCE (in Fig. 10) vs. the pH as shown in Fig. 11. For uninhibited iron the log current was linearly related to pH with a slope of  $1/2$ . Thus, the initial

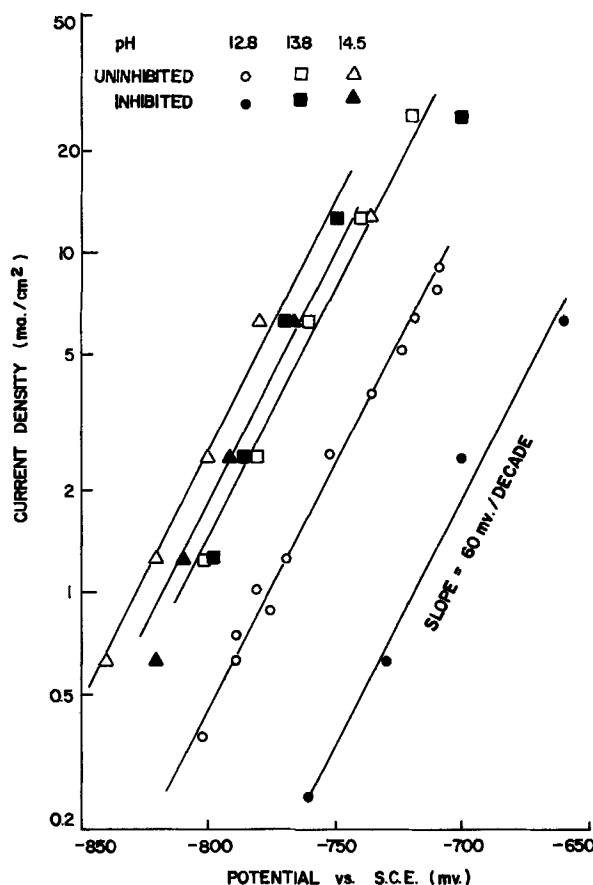


Fig. 10. Current-potential behavior immediately after galvanostatic charging of the double layer (active region).

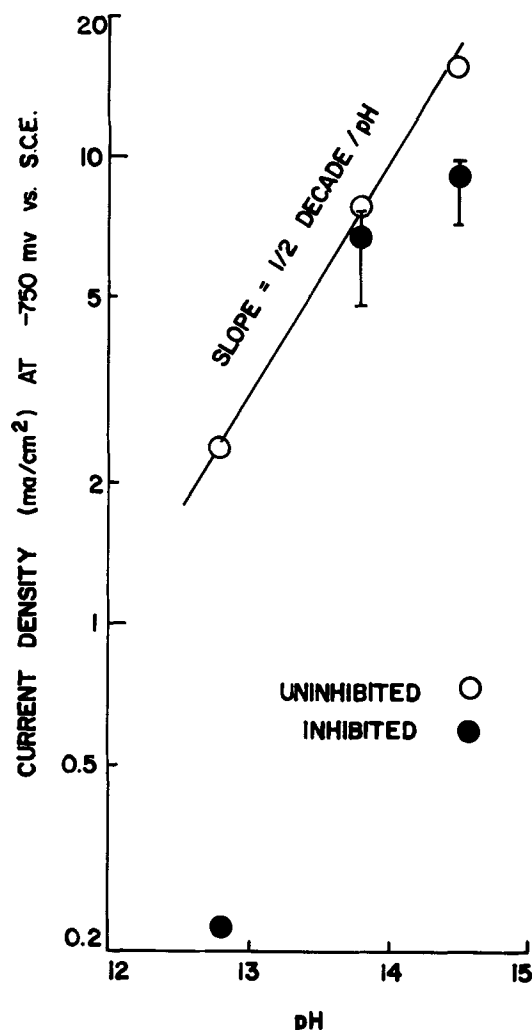


Fig. 11. The pH dependence of anodic dissolution in the active region.  $E = -750$  mV vs. SCE.

potential-current relation which represents the active dissolution of uninhibited iron can be expressed as

$$i = K_1 (\text{OH}^-)^{1/2} \exp\left(\frac{FE}{RT}\right) \quad [9]$$

For inhibited iron

$$i = K_2 \exp\left(\frac{FE}{RT}\right) \quad [10]$$

where  $K_2$  is some function of  $\text{OH}^-$  concentration.

### Discussion

**Potentiostatic and galvanostatic experiments.**—In the previous paper (7) it was concluded that active iron dissolution was followed by passivation in 1N KCl solutions of  $\text{pH} = 12.8$ , and the peak potential was identified as the primary passivation potential. The more detailed studies reported in the present paper indicated that true passivation conditions were not attained; rather, the peak potential was actually the formation potential of a prepassive film similar to the phenomenon observed for nickel in sulfuric acid by Bockris and his co-workers (8). In the present paper, the potential range below and immediately above the peak potential will be referred to as the active region and the prepassive region, respectively.

The polarization curve of uninhibited iron in Fig. 2 shows the steady-state dissolution behavior of iron covered with the porous prepassive film. On the other hand, the dissolution of iron in the active region was only attained during transient conditions as shown in previous experiments (7) and in Fig. 10. The same value of the anodic Tafel slopes, 60 mV/decade, for

iron dissolution in both the active and prepassive regions indicates that iron dissolution occurs by the same reaction mechanism. The difference in the apparent current densities of iron in the active and prepassive regions may be attributed to the difference in the effective surface area for the dissolution reaction. In other words, in the prepassive region, dissolution occurs only at that part of the surface not covered by the prepassive film.

Since Fig. 2 and Fig. 10 show iron dissolution in the prepassive and active regions, respectively, a relative measure of the surface area not covered by the prepassive film can be obtained by comparing the apparent current densities in the two regions, i.e.

$$\frac{i_{\text{prepassive}}}{i_{\text{active}}} \approx 10^{-3}, \text{ at } \text{pH} = 12.8 \quad [11]$$

In other words, during steady-state dissolution of iron, the ratio of the "true" surface area (i.e., the surface area not covered by the prepassive film) to the apparent surface area is approximately  $10^{-3}$ . The addition of BTA does not appear to change the reaction mechanism since anodic Tafel slopes remain the same. However, BTA does reduce the effective surface area for iron dissolution as seen in Fig. 2. The ratio,  $i$  (inhibited)/ $i$  (uninhibited)  $\approx 0.1$ , gives a measure of the relative effective surface areas of inhibited and uninhibited iron.

In the previous study (7), the formation of the prepassive film was attributed to the precipitation of a hydroxochloro-iron complex. In this study, it seems reasonable to suppose that the prepassive films on inhibited iron contain BTA.

The constant current (limiting current) region of inhibited iron in  $\text{pH} = 12.8$  solutions during steady-state polarization, as shown in Fig. 1 and 2, may be due to diffusion of this complex as the rate controlling step in the dissolution of iron. The mechanism of dissolution and precipitation of the prepassive film presented in Ref. (7) must be modified to include the participation of BTA for the inhibited system. The greater surface coverage of BTA on aged electrodes facilitates the precipitation of the complex on additional parts of the "bare" surface (i.e., the complex film is less porous) at the onset of the limiting diffusion current region. Thus, the aged inhibited electrodes have considerably less "bare" surface than the unaged electrodes.

The potential-current relation for the active dissolution of iron as shown in Fig. 10 has been developed theoretically by the previous analysis (7). Furthermore, the results in Fig. 11 provide the experimental verification of the pH dependence of active dissolution of iron which has been derived theoretically in the previous paper [Eq. 15, Ref. (7)]. Thus, the empirical relationship, Eq. [9], obtained for the active dissolution of uninhibited iron is consistent with the relationship deduced theoretically by applying the Temkins isotherm to the Bockris mechanism for iron dissolution.

**Potential sweep experiments.**—The functional dependence of the peak current and peak potential on both the sweep rate and pH is not affected by the presence of BTA. These relations are given by Eq. [3] and [4] for the peak current while Eq. [6] and [7] give the relations for the peak potentials of inhibited and uninhibited iron. Although the functional dependence of these two parameters on sweep rate and pH are not affected by BTA, their absolute magnitudes are affected as shown in Fig. 5 and 7. It is seen that the presence of BTA decreases the peak current and increases the peak potential.

According to the previous theoretical analysis (7), the active dissolution of iron in alkaline chloride solutions followed the relation

$$i_a = k_b'' [\text{OH}^-]^{1/2} \exp\left(\frac{FE}{RT}\right) \quad [12]$$

where  $k_b''$  is a constant and  $[\text{OH}^-]$  is the activity of hydroxyl ions. Furthermore, the peak current and peak

potential relationships were determined theoretically and confirmed experimentally as

$$i_p = 2 F k \exp(E_p/K) = 2 F C_s \sqrt{\frac{D\lambda}{K}} \quad [13]$$

and

$$E_p = \frac{K}{2} \ln \lambda + K \ln \left( \frac{C_s}{k} \sqrt{\frac{D}{K}} \right) \quad [14]^1$$

where  $K = RT/F$ ,  $k = k_b'' [\text{OH}^-]^{1/2}$ , and  $C_s$  and  $D$  are the saturated concentration and diffusion coefficient of the iron complex, respectively.

Differentiation of Eq. [13] with respect to pH gives

$$\left( \frac{\partial \log i_p}{\partial \text{pH}} \right)_\lambda = \left( \frac{\partial \log C_s}{\partial \text{pH}} \right)_\lambda \quad [15]$$

Equations [4] and [15] give

$$\left( \frac{\partial \log C_s}{\partial \text{pH}} \right)_\lambda = \frac{1}{2} \quad [16]$$

Then

$$C_s \propto [\text{OH}^-]^{1/2} \quad [17]$$

This relation can also be obtained by differentiating Eq. [14] with respect to pH

$$\left( \frac{\partial E_p}{\partial \text{pH}} \right)_\lambda = \left( \frac{\partial \ln C_s/k}{\partial \text{pH}} \right)_\lambda = 0 \quad [18]$$

Thus

$$\ln \frac{C_s}{k} = \text{constant} \quad [19]$$

Since  $k$  is proportional to  $[\text{OH}^-]^{1/2}$

$$C_s \propto k \propto [\text{OH}^-]^{1/2} \quad [20]$$

<sup>1</sup> Equation [37] in the previous paper (7) contains several typographical errors. Equation [14] in this paper is the correct form.

Equations [17] and [20] show that the pH dependence of the saturation concentration of the complex can be deduced from different experimental parameters by using the analysis described previously (7). Since the peak parameters for inhibited iron followed the relationships given in Eq. [3], [4], [6], and [7], the precipitation mechanism for prepassive film formation on both inhibited and uninhibited iron should be the same. The primary effect of BTA is to decrease the effective surface area.

#### Acknowledgment

This work was supported by a grant from the Office of Saline Water, U.S. Department of the Interior.

Manuscript submitted Oct. 2, 1972; revised manuscript received Jan. 29, 1974.

Any discussion of this paper will appear in a Discussion Section to be published in the December 1974 JOURNAL. All discussions for the December 1974 Discussion Section should be submitted by Aug. 1, 1974.

#### REFERENCES

1. J. B. Cotton, 2nd Int. Congr. Met. Corr., p. 590, NACE, Houston, Texas (1963).
2. I. Dugdale and J. B. Cotton, *Corrosion Sci.*, **3**, 69 (1963).
3. J. B. Cotton and I. R. Scholes, *Brit. Corr. J.*, **2**, 1 (1967).
4. R. J. Chin and Ken Nobe, *This Journal*, **118**, 545 (1971).
5. R. J. Chin, D. Altura, and Ken Nobe, *Corrosion*, **29**, 185 (1973).
6. B. Sathianandham, K. Balakrishnan, and N. Subramanyan, *Brit. Corr. J.*, **5**, 270 (1970).
7. S. Asakura and Ken Nobe, *This Journal*, **118**, 19 (1971).
8. J. O. M. Bockris, A. K. N. Reddy, and B. Rao, *ibid.*, **113**, 1133 (1966).

## Effect of Arsenic upon the Entry of Hydrogen into Mild Steel as Determined at Constant Electrochemical Potential

R. D. McCright\* and R. W. Staehle\*

The Ohio State University, Columbus, Ohio 43210

#### ABSTRACT

Arsenic added as arsenite ( $\text{AsO}_2^-$ ) to acid solutions promotes the entry of hydrogen into steel structures during cathodic polarization. The extent of the hydrogenation depends on electrochemical potential. At the corrosion potential of the steel, arsenite inhibits the entry of hydrogen; the reduction of arsenite to elemental arsenic suppresses the hydrogen evolution reaction. Only when the specimen is polarized to sufficiently cathodic potentials is there noticeable entry and permeation of hydrogen in steel. The greater the concentration of arsenite is in the solution, the greater is the extent of cathodic polarization needed to bring about measurable permeation. The entry of hydrogen does not depend on arsine formation; the greatest relative permeation occurs in the potential range where arsenic is the stable phase.

The purpose of this investigation was to determine the effects of additions of arsenic compounds to solutions used for hydrogen-charging steel specimens when the entry kinetics of the hydrogen are controlled potentiostatically. Compounds of arsenic and other 5-A, 6-A, and even 7-A elements are known to increase greatly the amount of hydrogen entering an iron or steel specimen polarized cathodically (1-9). However, most experiments have been carried out by applying a constant current without measuring the accompanying

electrochemical potential. Electrochemical processes such as electrodeposition, pickling, corrosion, and cathodic protection during which hydrogen can enter iron and steel occur over fairly narrow ranges of potential. Moreover, the role of potential is fundamental in explaining the mechanism whereby arsenic and the other elements enhance hydrogen entry. These elements are generically called either "promoters" because they promote hydrogenation of the specimen or "poisoners" because they poison the hydrogen evolution reaction on the metal surface.

At potentials encountered during the electrolytic production of hydrogen on an iron cathode, arsenic is

\* Electrochemical Society Active Member.

Key words: permeation of hydrogen, arsenite, hydrogenation of steel, adsorption of hydrogen, cathodic polarization.

thermodynamically stable as the metallic phase ( $As^0$ ) or as the gas, arsine ( $AsH_3$ ), at the most negative potentials. The form in which arsenic is added, arsenite ( $AsO_2^-$ ), is not stable in the regime of potentials where  $H_2$  is stable. Because arsenic is added to these solutions in an oxidized form (arsenite or arsenate), cathodic polarization reduces the compound and co-deposits the As along with the hydrogen.

Several treatments of the hydrogen evolution reaction (HER) exist (10-14). This reaction occurs in two important steps: an ionic discharge step followed by either a chemical desorption step (recombination of two adsorbed H atoms to give  $H_2$ ) or an electrochemical desorption step (adsorbed H atom +  $H^+$  to give  $H_2$ ).

The hydrogen absorption reaction (HAR) occurs as a side reaction, since the hydrogen is adsorbed as the atomic species and enters the metal:  $H_{ads} \rightarrow H_{abs}$ . Thus, the HAR competes for the same population of  $H_{ads}$  as the HER. McBreen and Genshaw (15) summarized the rate equations and the predictions of the permeation rate for control of the HER by each of the steps, considering also the effect of the adsorption energetics on the permeation rate. Although the kinetics of the HER on an iron surface are less well characterized than on platinum and palladium, one investigation (16) showed that the rate-controlling mechanism in acid solution without promoter additions is coupled discharge-chemical desorption. This means that the two steps have nearly equal activation energy barriers, and the reasonable conclusion is that arsenic and other promoters somehow increase the barrier for the chemical desorption (recombination) step and thereby favor the competing absorption step.

Explanation of the enhanced hydrogenation effect in the presence of promoters involves the formation of a stable hydride according to some previous works. For example, when carbonyl Fe wires loaded in torsion were hydrogen charged from 1N  $H_2SO_4$  containing  $As_2O_3$  (17, 18) no embrittlement occurred until the potential became more active than about  $-400$  mV<sub>H</sub>. This value corresponds to a reversible potential for As/ $AsH_3$  with As at unit activity and an  $AsH_3$  fugacity of  $10^{-7}$  atm. The conclusion reached was that arsine formation was necessary for significant hydrogenation. Using 1N  $H_2SO_4$  with various promoter additions and measuring the elongation of hydrogen-charged iron wires or coils, Smialowski and Szklarska-Smialowska (4-6) found that the relative effectiveness of the promoter element correlated well with increasing bond strength and stability of the hydride ( $H_2S > PH_3 > AsH_3$ ). Newman and Shreir (8), who reached essentially the same conclusion as in the Smialowski work, galvanostatically charged high-strength steel specimens for 24 hr and measured the hydrogen content afterwards. Having performed their experiments over a wide range of pH, they found that As and P were effective promoters at all pH's (their hydrides are stable over the entire 0-14 pH range); whereas S, Se, and Te were more effective in acid solution (their hydrides hydrolyze in more alkaline solutions). Furthermore, they obtained correlation between the pH at which hydrogenation of the specimen occurred and the  $pK_a$  for the ionization.

Radhakrishnan and Shreir (9) while hydrogenating shim steel specimens by the electropermeation technique, found that As, added as  $NaAsO_2$  to 0.1N  $H_2SO_4$  solutions, gave the highest permeation rates of all the 5-A and 6-A elements. However, the authors found that  $AsH_3$ , produced outside their permeation cell, did not enhance the hydrogen permeation rate when bubbled into the cell.

The discrepancy in the necessity of the presence of arsine in these last two papers cited (8, 9) emphasizes the need for an examination of the factors influencing the hydrogen entry in the presence of promoters. With regard to arsenic the following questions are of interest: Is arsine formation necessary for causing hydrogen to enter the metal? If so, how does the arsine ac-

complish this? Does the experimental technique used to charge or detect the hydrogen play an important role?

### Experimental Procedure

The electropermeation technique, developed by Bockris and Devanathan (19) and subsequently used in other investigations (9, 16, 20-25), was used for simultaneously hydrogenating the specimen and measuring the outflux of hydrogen. In this technique a thin specimen is simultaneously cathodically polarized at one surface and anodically polarized at the other; the hydrogen is produced at the first surface, passes through the metal, and is oxidized at the second surface. The permeation current is calculated as the difference between the current at the exit side, when the entry side is cathodically polarized, and the current in the absence of cathodic polarization.

**Instrumentation.**—The instrumentation consisted of two potentiostats (Wenking Model 66-TS-10) for maintaining potential control and measuring the currents of cathodic and anodic polarization, an electrometer (Keithley Model 610B) that served to amplify the anodic currents, and a recorder (Esterline-Angus AZAS) for registry of these currents. Special attention was paid to the grounding of all these instruments.

**Material.**—The steel used for these tests was shim stock with a composition corresponding to AISI 1010: C, 0.08-0.13%; Mn, 0.30-0.60%; P, 0.40% max; S, 0.50% max. Two-mil thick specimens ( $5 \times 10^{-3}$  cm) were used. The shim steel was cut into square coupons of 3.5 cm on the edge and vacuum annealed at 650°C for 2 hr. The structure consisted of large ferrite grains and pearlite colonies with inclusions mostly concentrated at the ferrite grain boundaries. Following annealing, the surface was cleaned in  $H_2SO_4$  solution, lightly mechanically polished, and rinsed in acetone. The surface area exposed to the solution in the permeation cell was 2 cm<sup>2</sup>.

**Solutions.**—Solutions used were 0.1N NaOH at the exit side and either 0.1N  $H_2SO_4$  or an acetate buffer (0.25N  $CH_3COOH$  and 0.20M  $CH_3COONa$ ; pH = 4.5) at the entry side. To the latter was added small amounts of sodium arsenite,  $NaAsO_2$ , as required. Reagent grade chemicals were used; no further purification of these was attempted. Solutions were deaerated by bubbling nitrogen gas for 2-3 hr in a separate cell before commencing the hydrogen charging. The solutions were transferred to the permeation cell and bubbling was continued during the permeation experiment to agitate the solutions. All experiments were performed at room temperature. Reference electrodes were saturated calomel.

In order to reduce the passivation current at the exit side, a thin plate of palladium was electrodelessly plated on this surface prior to insertion of the steel sample in the permeation cell. The palladization treatment has been discussed previously (19). Further, the Pd accelerates the kinetics of hydrogen oxidation, whereas on an Fe surface a significant part of the hydrogen undergoes the competitive recombination reaction to form molecular hydrogen. Since this last reaction is not electrochemical, it does not contribute to the measured current. Thus, the permeation current measured on a palladized steel specimen is much more nearly the true hydrogen flux.

**Ancillary experiments.**—Polarization and coulombic deposition experiments were performed to clarify important features of arsenic relative to hydrogen entry kinetics. Polarization experiments were performed on the shim steel in the sulfuric acid and acetate buffer solutions with and without additions of  $NaAsO_2$ . A special cell and holder for accommodating sheet specimens was constructed for these experiments (26). Polarization data were obtained by the potentiokinetic technique at a scan rate of 600 mV/hr, which approximates steady-state conditions. Coulombic deposition of arsenic was performed on specimens destined for study

of the effect of an As predeposit before permeation. The deposition was carried out in a more concentrated  $\text{NaAsO}_2$  solution (41,000  $\mu\text{g As/mliter}$ , pH 9) in which the deposition of hydrogen can be totally suppressed. The amount of As deposited was determined coulombically by graphically integrating the  $i-t$  plot with potentiostatic control throughout the deposition.

### Results

**Permeation experiments.**—Generally, a permeation experiment is run until the permeation current establishes a steady-state value, the permeation transient showing a plateau under steady-state conditions. However, as the charging potential is made very active or the charging current is increased, a steady-state condition does not obtain. At first, the plateau of the permeation transient ( $i_p$  as a function of time) shows only a small decrease with time. Then as the potential is made more active, the deviation from a steady-state condition becomes more and more severe and there occurs a sharp decline of the permeation current with time. This same behavior has been noted before (15, 21); the explanation offered is that blisters form under the metal surface, these blisters resulting from hydrogen recombination at internal surfaces which act as hydrogen sinks. Accordingly, the permeation rate drops since less hydrogen evolves from the exit side. Other effects tending to prevent a steady-state permeation current are the local increase in pH at the entry surface during prolonged electrolysis and formation of hydrogen gas bubbles which reduce the effective surface area. These effects become important at high charging current densities. We indicate on the appropriate graphs where the deviation from steady-state permeation occurred. Thus, to avoid the above complications, comparisons of permeation behavior are best considered at modest cathodic polarizations and/or low charging current densities.

Two ways of presenting the permeation data as a function of the applied cathodic potential are used here. The first method plots the permeation current *vs.* the potential; the second involves the calculation of the permeation efficiency  $i_p^\infty/i_c \times 100$  where  $i_p^\infty$  is the steady-state permeation current density, and  $i_c$  is the cathodic charging current density measured when the potential reached its steady-state value. The cathodic charging current is essentially equal to the hydrogen deposition current, except in the potential range where the concomitant deposition of arsenic consumes a significant part of the total current. The maximum of the permeation current density and the cathodic charging current density existing when the maximum obtains are used for calculating the permeation efficiencies when the hydrogen permeation decreased with time during cathodic charging.

The results obtained for permeation from 0.1N  $\text{H}_2\text{SO}_4$  with and without additions of arsenite are illustrated in Fig. 1, the arsenite concentration being expressed in micrograms of elemental arsenic per milliliter. Evidently, very small amounts of arsenite are quite effective in promoting hydrogenation. The slashes through the points in Fig. 1 show where the anomalous behavior of the permeation transients occurred. This behavior is particularly noticeable in the acid solution, since an increase in the over-all hydrogen reduction kinetics (more active potential) actually decreases the hydrogen permeation in the metal.

In Fig. 2 are shown the curves of the permeation efficiency as a function of the cathodic potential at the entry side. A much larger fraction of the hydrogen produced at the entry side enters the steel in the presence of arsenite. Permeation efficiency expresses a relative or normalized permeation.

According to Fig. 1 and 2 enhanced hydrogenation occurs in the region of potential where elemental arsenic is the stable phase. These figures indicate the equilibrium potential between arsenic (metallic, unit activity) and  $\text{AsH}_3$  at a fugacity of  $10^{-7}$  atm. It was at the potential corresponding to this arsine fugacity

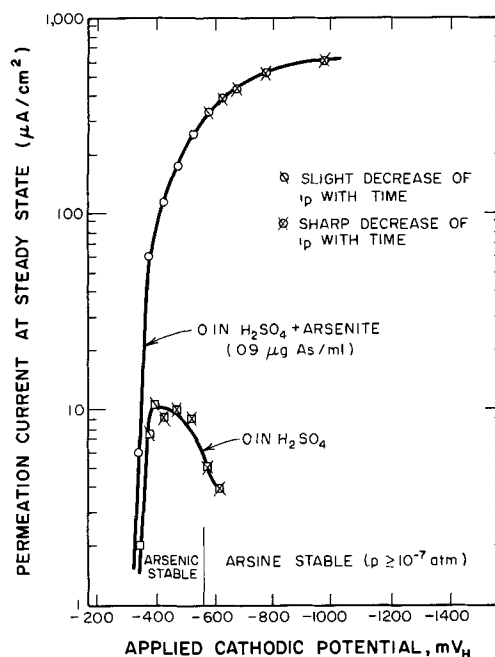


Fig. 1. Steady-state hydrogen permeation of 1010 steel as a function of applied cathodic potential in sulfuric acid solutions.

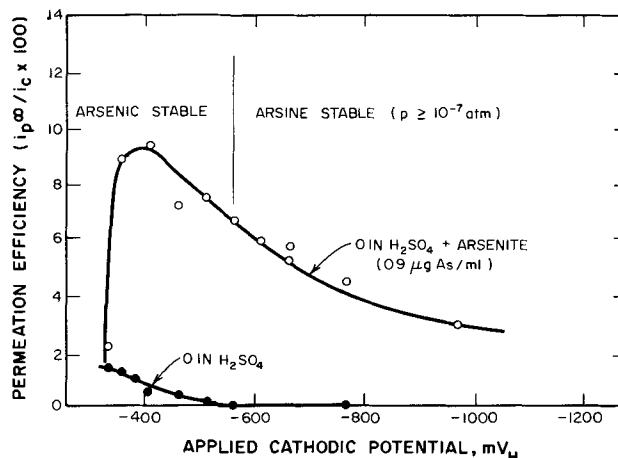


Fig. 2. Permeation efficiencies of 1010 steel as a function of applied cathodic potential in sulfuric acid solutions.

that the Polish experimenters noted hydrogenation of their specimens (embrittlement or elongation) (16, 17).

The results obtained by cathodic charging from the acetate buffer are shown in the next two figures. Figure 3 shows the permeation current density as a function of the applied cathodic potential, and Fig. 4 shows the permeation efficiency as a function of the applied cathodic potential. When these data are compared with those obtained from the  $\text{H}_2\text{SO}_4$  solution, it appears that acetate itself might act as a weak promoting anion (by comparison with sulfate), since the acetate solution without arsenite gives a higher permeation efficiency (Fig. 4) than the sulfuric acid solution (Fig. 2). Moreover, when the hydrogen was charged from an  $\text{H}_2\text{SO}_4\text{-K}_2\text{SO}_4$  solution at pH 4.5 (same pH as acetate), the permeation current was nil. A buffering system, such as acetate permits greater acidity near the cathodically polarized electrode. As the solution becomes more alkaline, the buffer produces more  $\text{H}^+$  to restore the pH. This hydrolysis cannot occur so extensively in the strongly ionized sulfate solution.

Two other effects are also shown in Fig. 3 and 4. Curves 2 and 3 in the figures show the effect of arsenite concentration on the permeation behavior. Increasing the concentration acts to shift the potential range at

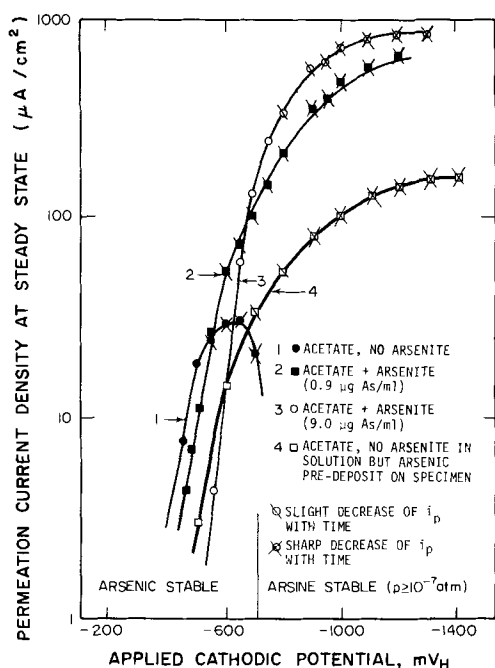


Fig. 3. Steady-state hydrogen permeation of 1010 steel as a function of applied cathodic potential in acetate solutions.

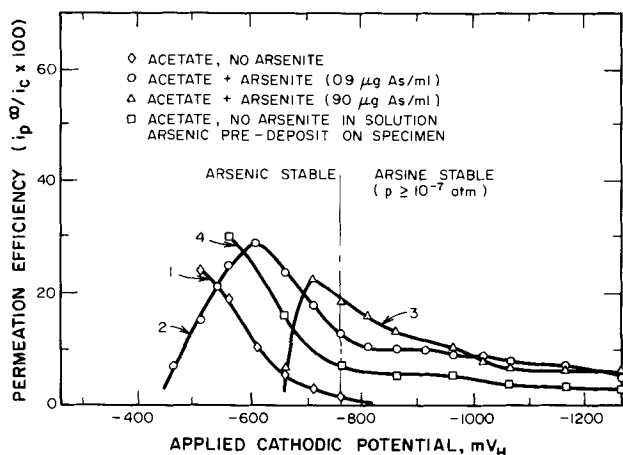


Fig. 4. Permeation efficiencies of 1010 steel as a function of applied cathodic potential in acetate solutions.

which the enhanced permeation occurs to more active values. Thus, adding arsenite in the solution suppresses hydrogen entry at the corrosion potential, although the permeation efficiency of the small amount of hydrogen produced is large. Curve 4 shows the effect of pre-deposition of arsenic where intermediate behavior is observed relative to that of pure acid (hydrogen deposition only) and the solution containing arsenite (codeposition of As and H). The amount of As pre-deposited was equivalent to 60 mcoulombs, or about 40-50 monolayers if uniformly deposited. During a typical permeation experiment this amount of As is reduced simultaneously with the production of hydrogen. However, examination of the surface verified that the surface was not uniform and tended to spall; the arsenic deposition was not crystalline. In the acetate solution, as well as in  $\text{H}_2\text{SO}_4$ , the highest permeation efficiency occurs in the potential domain where elemental arsenic is the stable phase.

When the hydrogen entry kinetics were galvanostatically controlled over a wide range of currents, the curves shown in Fig. 5 were obtained. Experimental conditions were similar to those used to obtain the data shown in Fig. 3. The highest permeation rates occurred during codeposition of As and H, the As predeposit giving significantly lower permeation currents.

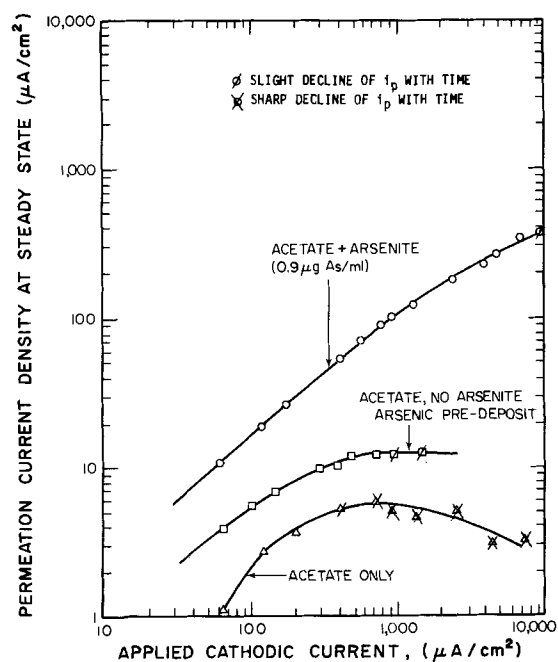


Fig. 5. Steady-state hydrogen permeation of 1010 steel as a function of applied cathodic current density in acetate solutions.

**Polarization experiments.**—Addition of arsenite shifts the corrosion potential to more noble values and particularly decreases the cathodic kinetics in the region of the corrosion potential. The influence of arsenite on the corrosion potential is seen in Fig. 6 where the experimental potential dependencies are near the 20 mV/decade value given by the Nernst equation for  $\text{AsO}_2^-/\text{As}$  equilibrium at room temperature. For the case of cathodic polarization, effects of concentration of arsenite in 0.1N  $\text{H}_2\text{SO}_4$  are shown in Fig. 7 and in acetate buffer in Fig. 8. With regard to these figures in both the sulfuric and acetate solutions the shape of the polarization curves is changed when arsenite is added. Addition of arsenite produces an S-shaped curve, which is more pronounced for the larger arsenite additions and more prominent in the acetate solution than in the sulfuric acid solution. Comparable polarization work done in the U.S.S.R. (27) in 0.1N  $\text{H}_2\text{SO}_4$  containing small  $\text{As}_2\text{O}_3$  additions yielded curves of the same general shape as in the present work.

The effect of arsenite as a corrosion inhibitor is well documented in the literature (28). In the sulfuric acid solutions addition of arsenite reduced the cathodic kinetics in the vicinity of the corrosion potential. In acetate solution the first additions of arsenite appear to accelerate the cathodic kinetics, but further addi-

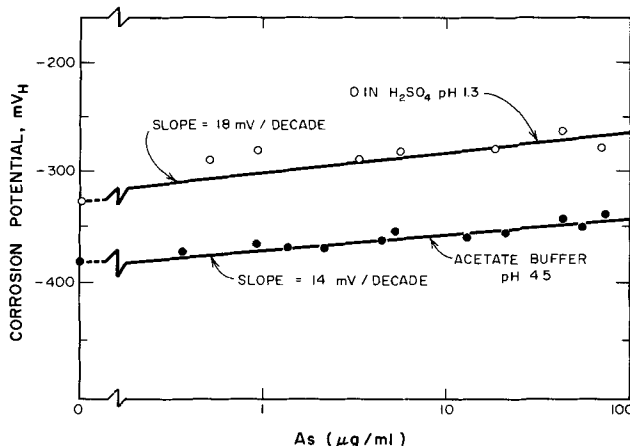


Fig. 6. Corrosion potential of 1010 steel as a function of arsenite concentration.



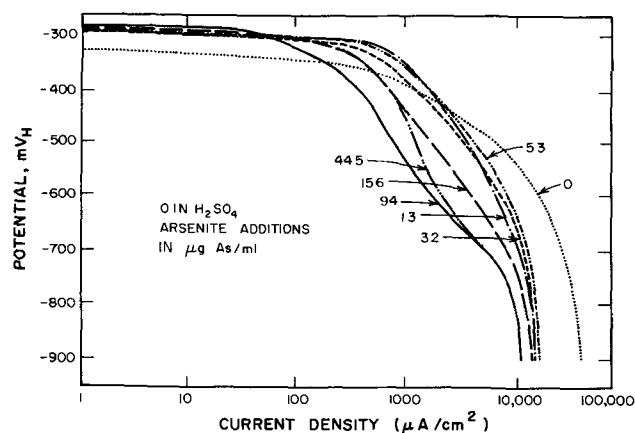


Fig. 7. Potentiokinetic polarization curves for 1010 steel in 0.1N  $H_2SO_4$  with arsenite additions.

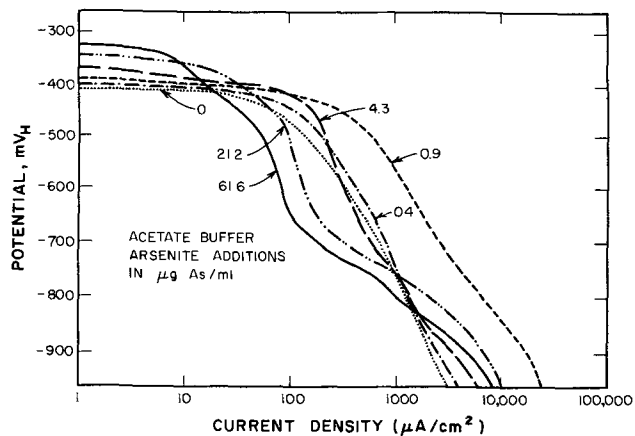


Fig. 8. Potentiokinetic polarization curves for 1010 steel in acetate solutions with arsenite additions.

tions greatly reduce the cathodic currents (Fig. 7 and 8).

In no case were we able to detect the presence of  $AsH_3$  at the potentials used in these experiments (to  $-1300$  mV<sub>H</sub>) using  $H_2O_2$  as a qualitative indicator. Arsine is appreciably soluble in water and all  $N_2$  bubbling was stopped before the determination. A review of the kinetics of arsine formation indicated that the process occurs at very low current efficiencies; Salzberg and Goldschmidt (29) found that the efficiency was only about 1-2% in acid solution. This means that significant arsine evolution occurs only after the potential is made much more active than the As/ $AsH_3$  co-existence potential. Likewise, Menzies and Owen (30) produced  $AsH_3$  only at very high currents. They attributed the low current efficiencies to concomitant hydrogen evolution and the deposition of a solid brown substance, which could have been a subhydride, on their specimens along with arsenic.

At the most negative potentials in the acetate solution containing arsenite additions (Fig. 8) the current is higher than for the acetate solution without addition. This increase could not be due to arsine formation. Rather, the effect is related to a likely acceleration of the hydrogen kinetics (evolution and absorption) after the arsenic deposition on the surface. The effect is not seen in the sulfuric acid solutions because the over-all currents are always much larger due to the lower pH.

An interesting observation which illustrates the significant suppression of the HER brought about by the addition of arsenite is shown in Fig. 9. Initially, the acetate solution contained no arsenite. At a constant potential of  $-660$  mV<sub>H</sub> the current decreased gradually with time. When  $NaAsO_2$  was added there occurred an abrupt current rise caused by the deposition of As. This

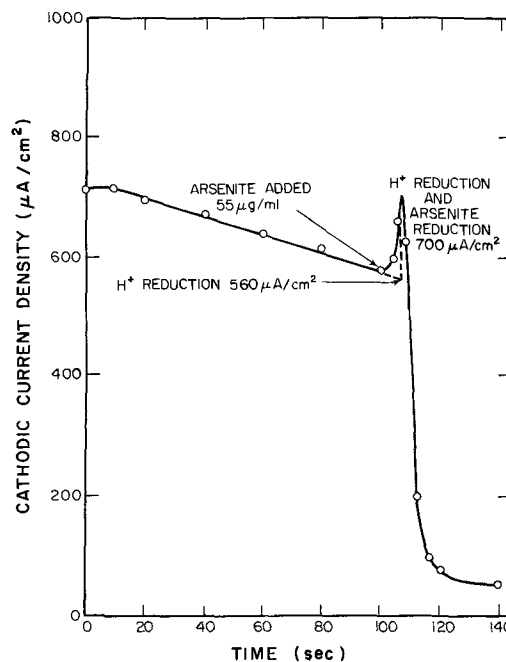


Fig. 9. Change of current upon adding arsenite to acetate solution at a potential of  $-660$  mV<sub>H</sub>.

event was followed by a sharp decrease of the current, and the subsequent depositions of As and H were hindered. The behavior in Fig. 9 is consistent with that observed in Fig. 8 where at a potential of  $-660$  mV<sub>H</sub> the cathodic current of the curve containing no arsenite is much higher than that for the curve corresponding to a concentration of  $61.6$   $\mu g$  As/mliter, which is comparable to the  $55$   $\mu g$  As/mliter concentration in Fig. 9.

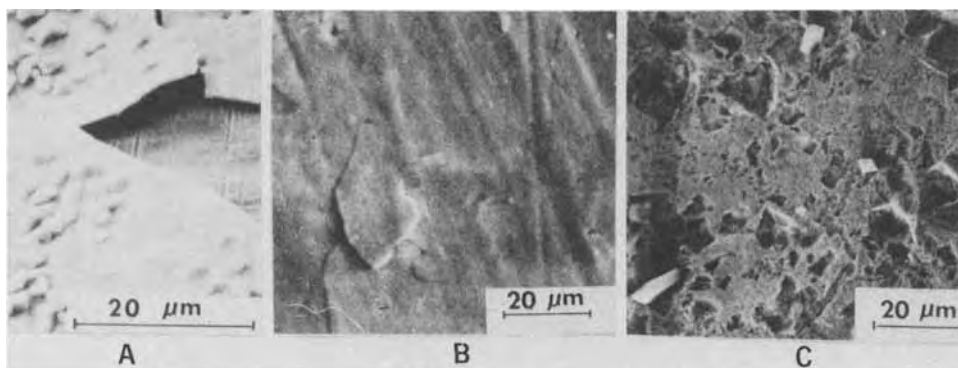
**Morphology of arsenic deposits.**—Observation of arsenized surfaces (exposed to As-containing solutions) by scanning electron microscopy illustrates some interesting features of the arsenic deposits, three examples of which are depicted in Fig. 10. In (A) the deposit is estimated at several thousand monolayers and is apparently very brittle and poorly adherent. The arsenic in this photomicrograph is crystalline; its electron diffraction pattern served as the basis for the verification of thinner As plates. The ED pattern was obtained with a replica extraction of the surface exposed to a 100 kV beam. In (B) the deposit is typical of those with thicknesses of the order 50 to a few hundred monolayers. At less than about 50 monolayers, the structure is amorphous; deposits thicker than this value are crystalline, but not all reflections are observed. The deposit shows a tendency to crack. In (C) where the specimen was exposed to a very dilute arsenite solution for a long time without applied potential, deposits of As occurred along with attack of the steel substrate.

### Discussion

The essential concern of these experiments relates to the criteria for the accelerating effect of arsenic-containing species in hydrogen absorption. The arguments in this discussion are directed toward pointing out that the stability of arsine is not critical for accelerating hydrogen entry and that there are other reasonable alternatives.

**Analysis of the polarization and permeation behavior.**—To explain the polarization behavior observed in Fig. 7 and 8, we must account for the acceleration of the cathodic kinetics in the vicinity of the corrosion potential for most of the solutions containing arsenite, the deceleration of the kinetics as the electrode is polarized cathodically, and the increase in the cathodic current as the electrode is further cathodically polarized. Aspects of the permeation behavior are related to the

Fig. 10. Morphology of arsenic deposits. (A) Thick deposit from concentrated solution; crystalline structure. (B) Thin deposit from concentrated solution; amorphous structure. (C) Specimen exposed to dilute solution; condition simulating permeation experiment.



polarization behavior. Let us consider individual reactions that influence the observed polarization and permeation currents.

1. *Hydrogen evolution on iron.*—According to Bockris, McBreen, and Nanis (21) the mechanism for the HER on an iron surface in acid solution is coupled discharge-chemical desorption (recombination). This means that the activation energy barriers for the two steps are about equal so that both steps constitute the rds. These authors postulated Langmuir adsorption kinetics for the hydrogen; therefore, the resulting Tafel slope is  $2RT/F$  or about 120 mV/decade at room temperature. This seems to be the slope which obtains for the present work, although the Tafel region does not extend over the usual 2-3 orders of magnitudes, possibly due to impurities in the solution.

2. *Hydrogen evolution on arsenic.*—The very low estimated value of the exchange current density of hydrogen on arsenic ( $10^{-12}$  A/cm<sup>2</sup>) suggests that the rds is the discharge of H<sup>+</sup>. The measured slope of the HER on an arsenic electrode is reported as 110 mV/decade, close to the theoretical  $2RT/F$  for this mechanism (31).

3. *Anionic adsorption on iron.*—The potential of zero charge occurs at about  $-400$  mV<sub>H</sub> on Fe (32). Thus, adsorption of various chemical species can take place at potentials in this vicinity. An indication of chemical adsorption on an electrode is an S-shaped polarization curve, since the adsorption process causes an overpotential effect (33, 34). On Fig. 7 and 8 such an S-shaped curve is observed in the potential region from the corrosion potential to some 200-300 mV cathodic from it. Therefore, one interpretation of the S-shape part of the polarization curves in Fig. 7 and 8 is a double layer effect of, presumably, AsO<sub>2</sub><sup>-</sup> adsorption. This effect is more noticeable in the acetate than in the sulfuric acid solutions, owing to the low ionic polarizability of sulfate ion and, thus, its lesser tendency to adsorb specifically (34). Over most of the potential region where the adsorption may occur, the hydrogen absorption reaction appears totally inhibited as the permeation current is zero or barely measurable. The hydrogen evolution reaction is also inhibited.

4. *Deposition of arsenic.*—The HAsO<sub>2</sub>/As redox potential being more positive than for H<sup>+</sup>/H<sub>2</sub>, one would expect arsenic to electrodeposit easily from aqueous solution. The exchange current density for the HAsO<sub>2</sub>/As couple ought to be around  $10^{-6}$  A/cm<sup>2</sup> according to Piontelli's classification (35, 36). Arsenic in contact with As<sub>2</sub>O<sub>3</sub> establishes equilibrium, and the couple can be used as a pH meter under certain conditions (37). However, studies of As deposition reveal that the process occurs with relatively low current efficiencies, in part due to simultaneous hydrogen evolution. As observed by Menzies and Owen (30) and by Wranglen (38), the deposition of As is governed by a film of amorphous As that stifles the further deposition of As due to its high resistivity. The resistivity of electrodeposited As was measured at  $10^8$  ohm-cm (39). Difficulties in polarographically analyzing solutions containing trivalent arsenic compounds have been ex-

plained in terms of a film that limits the reduction reaction instead of the usual diffusion limiting current (40).

On our Fig. 7 and 8 the plateau observed when the steel is polarized about 100 mV or so might seem to indicate that the electrodeposition of arsenic controls the cathodic kinetics. This reaction occurs as the arsenic deposits as the photomicrographs of Fig. 10 attest. Because of the small arsenite additions, the limiting current for the arsenite/arsenic reaction is of the order  $10^{-5}$ - $10^{-6}$  A/cm<sup>2</sup>. Thus, the current values on the order  $10^{-3}$ - $10^{-4}$  A/cm<sup>2</sup> for the plateaus in 0.1N H<sub>2</sub>SO<sub>4</sub> are larger than the limiting current for As deposition. It appears, therefore, that the double layer effects are responsible for the shape of the polarization in this region.

Piontelli and Poli (41) obtained crystalline As deposits and explained the required cell voltages as a cumulative overvoltage composed of the activation overpotential for As deposition, the activation overpotential for H reduction on As, an ohmic overpotential due to the poor conductivity of As, and perhaps an overpotential effect due to structural changes of the As. The significant factor seems to be the overpotential of H on As, which decreases with time perhaps because of a change in mechanism of the HER.

5. *Hydrogen evolution and absorption on an "arsenized" surface.*—The results described above for As electrodeposition, namely that the current efficiency with respect to As decreases and the cell voltage decreases as the current density increases, suggest that the HER proceeds on an "arsenized" surface in a manner different from that on an "unpoisoned" electrode. After polarization beyond the current plateau region where adsorption of AsO<sub>2</sub><sup>-</sup> and deposition of As take place, a sharp rise in the cathodic current occurs. Copious gas evolution is experimentally observed in this region. If the over-all HER is controlled by the recombination step, the Tafel slope is  $RT/2F$  or 30 mV/decade whether the adsorption follows Langmuir or Temkin behavior. If the discharge step controls the over-all HER kinetics, arsenite may increase  $i_0$  for the HER by its double layer effects. Either of these effects would decrease the hydrogen overpotential. The  $i_0$  for the HER has not been measured on any arsenic electrode, massive or plated. Thus, the often-stated explanation for the effect of arsenic poisoning the HER by increasing the hydrogen overpotential may be misleading. Thus, an interplay between H<sup>+</sup> and other species present in the double layer could alter the H<sup>+</sup> concentration as well as the energetics of the adsorbed monatomic H. In particular, if H<sup>+</sup> concentration increases in the double layer,  $i_0$  increases and possibly the entry rate, too. This effect tends to lower the overpotential. If the M-H bond energy is lowered with respect to H<sup>+</sup> and H<sub>2</sub>, the activation energy for discharge and for recombination is increased. This effect tends to raise the overpotential and promotes the hydrogen entry rate.

With regard to the hydrogen permeation behavior in Fig. 1-4, at the rest potential the inhibitive strength of the arsenite against hydrogenation is increased as

its concentration increases. Comparison of the polarization and permeation behaviors indicates that the higher the arsenite concentration, the more active the potential needed to hydrogenate the steel. These results are in qualitative accord with those of Hudson and Strand (42) for a mild steel in a 2N H<sub>2</sub>SO<sub>4</sub> pickling bath at 38°C. In their work an addition of 1 μg As/mliter doubled the pickling rate over the As-free acid, while the absorption of hydrogen remained constant. An addition of more than 4 μg As/mliter inhibited pickling while still hydrogenating the specimen, and an addition of more than 8 μg As/mliter inhibited the absorption of hydrogen. Both the pickling rate (and hence hydrogen evolution rate) and absorption rate decreased with time. These experiments were performed without applied potential. An explanation of these results is that the exchange current density is raised with the first arsenite additions, initially favoring the HER, but further additions of arsenite and the passage of time affect the bond energy of H<sub>ads</sub> to the metal. An applied cathodic potential is then required to stimulate both the HER and HAR. This explanation requires that trivalent arsenic compounds be specifically adsorbed, replacing H<sub>2</sub>O molecules and consequently inhibiting dissolution of the metal to corresponding aquo-ions.

We can write a mass balance for the hydrogen:  $i_d = i_r + i_p$  where the  $i$ 's represent the current equivalents for the discharge ( $d$ ), recombination ( $r$ ), and permeation ( $p$ ) reactions, respectively. The rate of permeation is given by  $k_p \theta$ , and for discharge by  $k_d(1 - \theta)$ . If recombination controls the over-all HER kinetics, then the permeation efficiency is  $i_p/(i_p + i_r)$  or  $k_p\theta/(k_p\theta + k_r\theta^2)$ . As the potential becomes more active,  $\theta$  increases. Therefore, for recombination control the permeation efficiency should be near unity for small  $\theta$  values and should decrease as  $\theta$  increases. The larger  $k_r$  is relative to  $k_p$ , the more the permeation efficiency declines with increased cathodic polarization. By contrast, discharge control yields a permeation efficiency given by  $i_p/i_d$  or  $k_p\theta/k_d(1 - \theta)$ . In this case increasing the degree of cathodic polarization increases the permeation efficiency. Evidently, recombination control prevails when  $\theta$  is large (more active potentials) since all the curves on Fig. 2 and 4 show a decrease of permeation efficiency.

However, in these experiments where arsenite adsorption, arsenic deposition, and possible hydride formation compete for the same surface sites, the above arguments for  $\theta$  are somewhat invalidated by the complicated influences of other species on hydrogen adsorption. Nevertheless, from a phenomenological point of view, the presence of arsenic in whatever form it exists on the surface serves to keep  $\theta$  less than unity over a wider range of potentials.

When a cathodic potential is applied, the effects of arsenite are more evident, as the permeation efficiency plots of Fig. 2 and 4 indicate. The curves obtained in solution containing arsenite show an ascending and descending branch. Thus, these particular curves have a permeation efficiency maximum. The ascending branch indicates the region where the effect of arsenite adsorption and its subsequent reduction to elemental arsenic dominates the cathodic kinetics. The amount of hydrogen entering and permeating the metal is not detectable until the specimen is polarized some 100-300 mV from the corrosion potential, the higher arsenite concentration requiring a greater polarization. As the potential is made more active, the hydrogen reaction becomes more dominant, hence the increase in the permeation rate. In the case of the solutions containing no arsenite and in the case of the As predeposit there is no ascending branch since hydrogen reduction is the only possible cathodic process. These show only a decline of permeation efficiency with cathodic polarization.

For the case with predeposited arsenic (curve 4, Fig. 4) the permeation efficiency at a given potential is lower than that for the codeposited case once the hy-

drogen reaction dominates over the arsenic deposition reaction, although the total amount of deposited As in both cases is approximately the same. The permeation efficiency for the codeposition goes to zero at the corrosion potential, but for the predeposited case the permeation efficiency at the corrosion potential is high. When the solution contains AsO<sub>2</sub><sup>-</sup> (curves 2 and 3) the arsenic deposited helps to protect the metal from hydrogenation, whereas in the predeposited case (no AsO<sub>2</sub><sup>-</sup> present) hydrogenation occurs at the corrosion potential. This suggests that a freely corroding steel containing an addition of As is prone to hydrogenation. Thus, arsenic is beneficial from the point of view of preventing hydrogen entry as long as the arsenic is present in the oxidized form in the solution. Upon sufficient cathodic polarization arsenic has a sinister effect as the arsenite is reduced and hydrogen evolution and absorption take place on the arsenized surface.

**6. Arsine formation.**—Arsine formation from As occurs by a series of one-electron transfer steps to form intermediate surface subhydrides or radicals (AsH and AsH<sub>2</sub>). These subhydrides disproportionate to form AsH<sub>3</sub> and As, and the current efficiency based on expected arsine formation is very low in acid solution, around 1-2% (29). During arsenic electrodeposition from HCl + As<sub>2</sub>O<sub>3</sub> solutions only traces of AsH<sub>3</sub> evolved after prolonged electrolysis at 300 mA/cm<sup>2</sup> (30). These results indicate that AsH<sub>3</sub> formation requires considerable overpotential. The value of the equilibrium potential is given by (44):  $E = -0.608 - 0.0591 \text{ pH} - 0.0197 \log p_{\text{AsH}_3}$ . This formula was used for calculating the equilibrium potential indicated on Fig. 1-4. A few remarks are needed here. Values of the free energy of formation in kilocalories of the Group V hydrides are: NH<sub>3</sub>, -3.98; PH<sub>3</sub>, +4.36; AsH<sub>3</sub>, +42.0; SbH<sub>3</sub>, +35.5; and BiH<sub>3</sub>, +55.3. In the series the value of AsH<sub>3</sub> seems too high or that of SbH<sub>3</sub>, too low. If the value for AsH<sub>3</sub> were too low, then the corresponding As/AsH<sub>3</sub> redox potential would be too active and AsH<sub>3</sub> would then be stable at potentials closer to the corrosion potential. The calculation of the redox potential is also based on unit activity of As. If As is present at an activity less than one, the redox potential is shifted to more active values. Possible dissolution of As in the steel substrate could reduce its thermodynamic activity. Notwithstanding the uncertainty of the equilibrium potential, the potential region where we first noted enhanced hydrogen permeation seems thermodynamically and kinetically unfavorable to AsH<sub>3</sub> production. Moreover, we detected no arsine formation throughout the potential region studied.

**7. Formation of arsenic subhydrides.**—Surface subhydrides are proposed as intermediates during arsine formation (29). Brown deposits, which may be lower hydrides, have been observed in connection with As electrodeposition (30). Solid arsenic hydrides of composition varying between AsH<sub>0.001</sub> to AsH<sub>0.52</sub> have been prepared by various techniques including electrochemical reduction (43). However, only small amounts of material were obtained so that the physical and chemical properties were not measured. Pourbaix reports solid arsenic lower hydrides with formulas As<sub>2</sub>H<sub>2</sub> and As<sub>4</sub>H<sub>2</sub> (44).

**8. Dissolved oxygen and other impurities.**—Residual dissolved oxygen and other impurities may influence hydrogen in the double layer in much the same way as arsenite. Their effect is probably most important near the corrosion potential.

**9. Concentration polarization of the HER.**—As the potential is made more active, hydrogen evolution eventually becomes limited by the diffusion of protons to the surface. Addition of pH buffering substances such as acetate and arsenite and alkalization of the solution near the steel electrode due to rapid hydrogen evolution complicate the appearance of a true limiting current.

**Mechanism of promotion.**—A mechanism for the hydrogenation promotion effects due to the presence of arsenic must account for the following important observations: (i) Hydrogenation of the specimen is promoted to the greatest extent (maximum permeation efficiency) in the potential region where codeposition of hydrogen and arsenic takes place. (ii) The permeation rate and efficiency are higher for the arsenic-containing solutions than for those free of arsenic. The permeation efficiency decreases as the potential becomes more active. (iii) At the corrosion potential, addition of arsenite appears to inhibit hydrogenation; however, at modest cathodic polarization potentials hydrogenation occurs regardless of the arsenite concentration. (iv) The promoter effects of arsenic operate over a range of pH.

A number of explanations regarding the phenomenon of the sharply increased entry rate have been offered (15, 21). The general conclusion is that the metal to hydrogen bond is reduced in the presence of the promoting species. Reduction of this bond energy creates a more flexible, less directional bond so that the transition from adsorbed hydrogen to absorbed hydrogen is facilitated with less activation energy. This hypothesis is based partly on the observed phenomenology that the heat of adsorption (and hence the metal-hydrogen bond energy) decreases as the metal becomes more "catalytically active." Catalytically active metals (so-called because of their ability to hydrogenate organic compounds) have a higher inherent solubility of hydrogen (Pd > Ni > Pt > Fe). The disagreements or controversies range over what causes the decrease in the metal-hydrogen bond energy. A decreased metal-hydrogen bond energy has the kinetic effect of lowering the activation energy for the absorption process relative to the barrier for the recombination process. Because these processes compete for the adsorbed hydrogen, absorption is favored. Only slight changes in the bond energy is needed for accelerating the entry rate. The question is then: How can arsenic act to change the metal to hydrogen bond entry?

Three ways in which promoter species can lower the metal-hydrogen bond have been suggested (15, 21). One possibility is a lateral interaction between adsorbed H and the promoter species so that the surface energy of atoms is modified with the result that the Fe-H bond energy is lowered due to the lateral component. Secondly, the promoter species adsorbs or deposits first at the more energetic sites, leaving hydrogen to adsorb at less energetic sites. Thirdly, an electronic effect may occur between the promoter and Fe. Promoter species are characteristically electron rich and can conceivably influence the electronic energy levels at the surface. Hydrogen is more soluble in Pd, Pt, and Ni than in Fe. According to the valence bond theory the percentage d-character of the metallic bond is slightly higher for the first elements than for Fe (45). Thus, the promoter species furnishes additional bonding electrons. The electronic effect is apparently more important than the effect of the crystallographic structure, because the solubility of H in fcc-Fe at room temperature is about 2-3 times that in bcc-Fe (extrapolation to room temperature), whereas the solubility of H in Ni, for example, is 1000 times that in bcc-Fe.

Consider now the influence of arsenic in the above three explanations. The H-As and H-Fe bond energies are of comparable magnitudes (46). Attraction of the H atom toward an As atom may then reduce the bond energy between H adsorbed on Fe. It is reasonable that As would plate out at the most active sites leaving H to deposit elsewhere. Elemental As and various As-H radicals have more electrons available for bonding than AsH<sub>3</sub>. Indeed, this fact agrees with the observation that the highest permeation efficiency effects occur where As is the stable phase. At these potentials the equilibrium partial pressure of AsH<sub>3</sub> would be infinitesimal. In view of the observation that arsine formation is relatively inefficient and that a number of subhydrides form as intermediates, the absolute per-

meation rates obtained from the arsenite solutions upon further cathodic polarization might be attributed to some As-H interaction at the surface. An As-H bond would deter recombination of the hydrogen atoms; upon further hydrogen deposition from the solution, the H atoms bonded to As could enter into the Fe lattice rather than evolve as H<sub>2</sub>. We have no evidence that the subhydrides exist; no extraneous lines were observed on the electron diffraction patterns made from surface deposits. However, the greater number of unbonded electrons or unsaturated bonds in the subhydrides could more greatly influence the electronic energy levels in the substrate than could arsine.

Another possible explanation for hindered recombination is that the surface diffusion of hydrogen atoms deposited on this surface is low. An estimate of  $D_{\text{surface}}$  for H on Fe is considerably lower than  $D_{\text{bulk}}$  for H in Fe (47). Hence, hydrogen atoms are more likely to stick where they are discharged and the likelihood of their absorption is increased because of the increased lifetime as H<sub>ads</sub>. This factor is important at low coverages because the distance an H atom must move to recombine is relatively great. Recent work by Kim and Wilde (48) established that the surface coverage of hydrogen adatoms can be low in the vicinity of the corrosion potential. The role of As in suppressing the HER extends the range over which a small  $\theta$  is possible. A small  $\theta$  value permits a high permeation efficiency, although the absolute permeation rate is not high. The excellent "throwing power" attributed to the corrosion inhibiting properties by trivalent arsenic solutions suggests a leveling of the energy of surface sites due to adsorption and discharge of As (41). Although the coverage increases with applied cathodic potential, the presence of arsenic may increase the surface coverage of hydrogen on iron by crowding hydrogen onto adjacent available iron surfaces since the discharge process on As appears to have high kinetic barriers. Another effect, according to Smialowski (7), is that strong chemisorption of the promoter species may provoke the formation of surface defects which allow an easy passage of hydrogen at the surface to the bulk of the metal.

A reaction between iron and arsenic is possible. At room temperature the solubility of As in Fe is about 5% and arsenic forms arsenides FeAs and FeAs<sub>2</sub>, at higher concentrations (49). However, Besnard (50-52) has considered that As is itself absorbed preferentially at the grain boundaries because of its lowering of the surface tension in addition to the chemical effects and believed this effect was responsible for premature cracking of the iron specimens. Absorption of arsenic could further enhance the hydrogen permeation as there would be greater opportunity for the electronic interaction between Fe and As.

An extremely useful, but lacking, piece of information is an analytical determination of the effect of arsenic on the solubility of hydrogen in iron. If arsenic raises the solubility significantly, then a higher concentration of hydrogen at the entry surface would drive a greater flux through the metal.

Considerable evidence exists in the literature that enhanced hydrogen promotion occurs in the presence of stable hydrides, such as AsH<sub>3</sub>, PH<sub>3</sub>, H<sub>2</sub>S, H<sub>2</sub>Se. In particular, the experiments of Newman and Shreir (8) correlate the hydrogen saturation very well with the stability of the hydride. Furthermore, in the case of arsenic, cathodic polarization must be applied to obtain a measurable increase of the hydrogen absorption over that occurring from the As-free solution, whereas the effects of sulfur as a hydrogen promoter are operable at the corrosion behavior. This behavior compares with the relative stabilities of the hydrides; H<sub>2</sub>S is stable at the usual corrosion potential of iron in acid, while AsH<sub>3</sub> is stable at considerably more cathodic potentials. With regard to the work cited (9), in which AsH<sub>3</sub> was externally introduced into the charging compartment of the permeation cell, the authors did not give important experimental details: Was the cell saturated with the gas? Was the specimen cathodically polarized?

These details are important in establishing the necessity of AsH<sub>3</sub> presence toward promoting hydrogenation.

Furthermore, the sensitivity of the experimental technique used to arrive at this kind of conclusion can be very important. The permeation current technique is perhaps the most sensitive of the techniques used for hydrogen charging and determination. The investigations in which it was concluded that AsH<sub>3</sub> formation was necessary for significant hydrogen entry used techniques less sensitive than the permeation technique. Therefore, higher charging currents were necessary to effect observable hydrogen entry and these occurred at potentials well into the range where AsH<sub>3</sub> should form.

The present work shows considerable hydrogen permeation at modest cathodic potentials. Also, mechanistic arguments of promotion effects are sufficiently general that other As-containing species can act in this capacity as can AsH<sub>3</sub>.

### Conclusion

1. The role of As as a promoter of hydrogenation of mild steel depends on electrochemical potential. At the corrosion potential, addition of arsenite to the solution suppresses the hydrogen reaction. Hydrogenation of the specimen occurs at potentials polarized cathodically some 100-300 mV from the corrosion potential, with the more concentrated solutions requiring greater polarization. Once sufficiently polarized, specimens exposed to solution containing arsenite are hydrogenated more than specimens exposed to solutions free of arsenite.

2. The intensity of the hydrogenation, as indicated by both the permeation efficiency and the absolute permeation rate, is highest for solutions containing arsenite so that there is codeposition of As and H. The permeation efficiency drops with application of more cathodic potentials, although the permeation current increases.

3. Hydrogen permeation occurs at potentials where metallic arsenic is stable and arsine can be present only in infinitesimal quantities. Despite the experimental conditions which appear not to favor arsine formation, considerable hydrogenation of the steel specimens occurs. Thus, arsine formation is not a necessary condition for promoted hydrogenation.

4. From discussion presented on mechanistic arguments, arsenic in trivalent form adsorbed to the surface, arsenic in elemental form deposited on the surface, and arsenic subhydrides, as well as arsine, can enhance hydrogen entry.

### Acknowledgments

This work was supported by the Air Force Materials Laboratory under contract No. F 33615-69-C-4258. The encouragement of Drs. C. T. Lynch and H. Kirkpatrick of that organization is especially appreciated.

Manuscript submitted December 1, 1972; revised manuscript received Dec. 10, 1973.

Any discussion of this paper will appear in a Discussion Section to be published in the December 1974 JOURNAL. All discussions for the December 1974 Discussion Section should be submitted by Aug. 1, 1974.

### REFERENCES

- D. I. Phalen and D. A. Vaughan, *Corrosion*, **24**, 243 (1968).
- M. E. Giles and L. L. Shreir, *Electrochim. Acta*, **11**, 193 (1966).
- K. Farrell, *Corrosion*, **26**, 105 (1970).
- M. Smialowski and Z. Szklarska-Smialowska, *Bull. Acad. Polon. Sci., Classe III*, **2**, 73 (1959).
- M. Smialowski and A. Szklarska-Smialowska, *Rockzniki Chem.*, **29**, 85 (1955).
- M. Smialowski and Z. Szklarska-Smialowska, *Bull. Acad. Polon. Sci., Classe III*, **1**, 159 (1953).
- M. Smialowski, "Hydrogené dans les Metaux," Ecole Centrale des Arts et Manufactures, 1972, Editions Science et Industrie, Paris, p. 300 (1972).
- J. F. Newman and L. L. Shreir, *Corrosion Sci.*, **9**, 631 (1969).
- T. P. Radhakrishnan and L. L. Shreir, *Electrochim. Acta*, **11**, 1007 (1966).
- P. C. Milner, *This Journal*, **111**, 228 (1964).
- R. J. Barton, 47th Tech. Proc. of the American Electroplaters' Soc., 116 (1960).
- B. E. Conway, "Theory and Principles of Electrode Processes," chap. 8, Ronald Press, New York (1965).
- B. E. Conway and J. O'M. Bockris, *J. Chem. Phys.*, **26**, 532 (1957).
- J. O'M. Bockris and A. K. N. Reddy, "Modern Electrochemistry," Vol. 2, chap. 10, Plenum Press, New York (1970).
- J. McBreen and M. A. Genshaw, "Proceedings of Conference: Fundamental Aspects of Stress Corrosion Cracking, Ohio State University, 1967," R. W. Staehle, A. J. Forty, and D. van Rooyen, Editors, p. 51, NACE, Houston (1969).
- M. A. V. Devanathan, Z. Stachurski, and W. Beck, *This Journal*, **110**, 886 (1963).
- H. Angerstein-Kozłowska, *Bull. Acad. Polon. Sci., Ser. Sci., Chim. Geol. et Geograph.*, **7**, 881 (1959).
- H. Angerstein-Kozłowska, *ibid.*, **6**, 739 (1958).
- J. O'M. Bockris and M. A. V. Devanathan, Tech. Report 4, Office of Naval Research, NR 036-078 (Feb. 1961).
- E. Gileadi, M. A. Fullenwider, and J. O'M. Bockris, *This Journal*, **113**, 926 (1966).
- J. O'M. Bockris, J. McBreen, and L. Nanis, *ibid.*, **112**, 1025 (1965).
- W. Beck, J. O'M. Bockris, J. McBreen, and L. Nanis, *Proc. Royal Soc. (London)*, **A290**, 220 (1966).
- T. P. Radhakrishnan and L. L. Shreir, *Electrochim. Acta*, **12**, 889 (1967).
- J. O'M. Bockris, M. A. Genshaw, and M. A. Fullenwider, *ibid.*, **15**, 47 (1970).
- M. A. V. Devanathan and Z. Stachurski, *Proc. Royal Soc. (London)*, **A270**, 90 (1962).
- J. R. Myers, E. G. Gruenler, and L. A. Smulczynski, *Corrosion*, **24**, 52 (1968).
- S. M. Beloglazov, *Russ. J. Phys. Chem.*, **38**, 223 (1964).
- H. C. Gatos, *Corrosion*, **12**, 332t (1956).
- H. W. Salzberg and B. Goldschmidt, *This Journal*, **107**, 348 (1960).
- I. A. Menzies and L. W. Owen, *Electrochim. Acta*, **11**, 251 (1966).
- E. A. Efimov and I. G. Erusalimchik, *Elektrokhimiya*, **1**, 1133 (1965).
- N. E. Khomotov, *Russ. J. Phys. Chem.*, **36**, 1475 (1962).
- A. N. Frumkin, "Advances in Electrochemistry and Electrochemical Engineering," Vol. 3, chap. 5, P. Delahay, Editor, Interscience Publishers, New York (1963).
- J. M. West, "Electrodeposition and Corrosion Processes," chap. 2 and 5, D. Van Nostrand Co. Ltd., London (1965).
- R. Piontelli and G. Poli, *Gazz. Chim. Ital.*, **79**, 214 (1949).
- R. Piontelli, *CITCE*, **2**, Tamburino and Milano, 1950, p. 136, Butterworth, London (1951).
- A. Riad Tourky and A. A. Mousa, *J. Chem. Soc.*, **1949**, 1297.
- G. Wranglen, *This Journal*, **109**, 551 (1962).
- G. Tammann and H. Warrentrup, *Z. Anorg. Chem.*, **228**, 92 (1936).
- D. A. Everet and G. W. Finch, *J. Chem. Soc.*, **1955**, 704.
- R. Piontelli and G. Poli, *This Journal*, **109**, 551 (1962).
- R. M. Hudson and G. L. Stragand, *Corrosion*, **18**, 259t (1962).
- W. L. Jolly, L. B. Anderson, and R. T. Beltrami, *J. Am. Chem. Soc.*, **79**, 2443 (1957).
- M. Pourbaix, "Atlas of Electrochemical Equilibria in Aqueous Solution," Pergamon Press, Oxford, and CEBELCOR, Brussels (1966).
- G. C. Bond, "Catalysis by Metals," chap. 1, Academic Press, London and New York (1962).
- H. A. Skinner, *Trans. Faraday Soc.*, **41**, 645 (1945).
- R. A. Oriani, "Proceedings of Conference: Fundamental Aspects of Stress Corrosion Cracking, The Ohio State University, 1967," R. W. Staehle, A. J. Forty, and D. van Rooyen, Editors, p. 32, NACE, Houston (1969).
- C. D. Kim and B. Wilde, *This Journal*, **118**, 202 (1971).

49. M. Hansen, "Constitution of Binary Alloys," 2nd ed., McGraw-Hill Book Co., New York (1958).  
 50. S. Besnard, *Corrosion Anti-Corrosion*, **10**, 182 (1962).  
 51. S. Besnard and J. Talbot, *Comp. Rend.*, **144**, 1193 (1957).  
 52. S. Besnard, C. Messenger, and J. Talbot, *ibid.*, **248**, 1516 (1959).

## A Comparison of the Immersion and Open-Circuit Scrape Methods for Determining the Potential of Zero Charge of Metal Electrodes

G. J. Clark, T. N. Andersen, R. S. Valentine, and H. Eyring

Department of Chemistry, University of Utah, Salt Lake City, Utah 84112

### ABSTRACT

Open-circuit potentials were measured for freshly immersed metal surfaces and for metal surfaces renewed abrasively (scraped-off) *in situ* in aqueous electrolytes. Electrode materials included Au, Ag, Cu, Pt, Ga, In, Bi, and Sn and the electrolytes included alkali halides and alkali sulfates in acid, neutral, and alkaline solutions. The fresh-surface potentials for Au, Ga, In, Bi, and Sn were approximately the same following either immersion or scraping in solution and yielded the potential of zero charge at certain pH conditions. For Ag, Cu, and Pt the immersion potentials were several hundred millivolts more positive than the scrape potentials. This is attributed to the presence of adsorbed oxygen on these metals at the instant of immersing them in solution. For Ag, Cu, and Pt the scrape potentials are interpreted as the potential of zero charge for the bare metal while the immersion potentials reflect a superimposed dipolar effect or faradaic reduction of the oxygen.

Values for the potential of zero charge (pzc) of most solid metals have suffered from irreproducibility among various methods and workers (1, 2). Much of this variance is attributed to differences of impurities or other "foreign" species (*e.g.*, H or O) on the surface, or to the crystallographic state of the metal surface resulting from different electrode pretreatments. In some cases it is difficult to verify that faradaic reactions do not interfere.

In the present work the immersion and open-circuit scrape potentials are compared for a number of metals in aqueous solutions. Although both of these methods are based on essentially the same principle, there is some disagreement on published values obtained with the two methods (*cf.* Table I). There are other methods used to measure the pzc of solid electrodes which depend on various properties of the metal such as mechanical properties or capacity of the metal-solution interphase. These methods have a different basis than the kinetic methods being compared in this work. Inasmuch as they are reviewed elsewhere (1) we need not discuss them further here.

In the dip or immersion method a fresh metal test electrode, connected to a reference electrode through

an external polarizing source, is immersed in an electrolytic solution. Upon immersion a transient potential is observed between the test and reference electrode which corresponds to charging the newly formed electrode. For the test electrode there is one state of external polarization at which the potential transient is of zero magnitude. The electrode potential at this condition is considered to be the pzc (3). In the open-circuit scrape method (5-8) the metal electrode surface is abrasively removed *in situ* with an insulating, inert scraper and the accompanying open-circuit potential is recorded. Depending on the system, reactions may or may not charge the electrode faster than the scraper removes it, and hence the recorded scrape potentials must be interpreted to determine whether or not they are the pzc. This interpretation depends on the influences of scraper speed, adsorbable ions, and pH as well as on the potential decay following scraping.

If very rapid faradaic reactions ( $i \geq 5 \times 10^{-4}$  A cm<sup>-2</sup> for present scrape methods) occur before the pzc can be established or measured, then the pzc cannot be obtained by the open-circuit scrape method. It appears that the immersion method should suffer a similar limitation, however, since it is implicitly assumed that the pzc is developed unless an external current passes through the test electrode. In Table I,

Key words: electrical double layer, zero charge, fresh metal surfaces.

Table I. Potentials of zero charge (pzc) reported from immersion measurements compared to open-circuit scrape potentials

Metal	Immersion results			Open-circuit scrape			
	pzc vs. SHE <sup>(a)</sup>	Solution	Reference	Potential V vs. SHE	Solution	pzc or not	Reference
Al	-0.523 <sup>(a)</sup>	0.01M KCl	(3)	-1.56	0.5M K <sub>2</sub> SO <sub>4</sub> , MKCl	No	(5)
Bi	-0.358	0.01M KCl	(3)	-0.34	0.01M KCl	Yes	(5)
Cu	-0.012	0.1M KCl	(3, 4)	-0.64	0.1M KCl	Yes	(8)
Ni	-0.193 <sup>(a)</sup>	0.01M KCl	(3)	-0.34	0.5M K <sub>2</sub> SO <sub>4</sub> , MKCl	No	(5)
Sn	-0.38	0.01M KCl	(3)	-0.43	0.5M K <sub>2</sub> SO <sub>4</sub>	Yes	(5)

<sup>(a)</sup> In the present study immersion potentials were obtained for Al and Ni which are substantially more negative than the above values and, in fact, are rather close to the above scrape potentials. As the presently obtained immersion values for Al and Ni are controlled by faradaic processes, they are not considered further in the present work.

<sup>(b)</sup> SHE = standard hydrogen electrode.



one notes that the open-circuit scrape potential and the dip potential agree for Bi and Sn and also purport to measure the pzc. For Cu the values differ, yet both methods are purported to measure the pzc. For Al and Ni the open-circuit scrape method yields a mixed potential while the dip method is purported to give the pzc. Even though the recorded values by the two methods are different for Ni and Al, it is not apparent why a pzc can be obtained by one method and not by the other. It is also not apparent why the pzc values for Cu are so different in the two cases. To better understand these problems we have measured immersion potentials for a variety of metals in various aqueous solutions, and have compared them with open-circuit scrape potentials. To eliminate the differences in Table I which may have been caused by impurities in the metal or by the crystal orientation of the electrode, we have used the same metal wire samples and have created the fresh metal surface in the identical manner for both methods. This method of surface renewal was by scraping the metal with a sapphire bit, while measuring the potential in the case of the open-circuit scrape and prior to immersing the electrode in the case of the dip method. It has been suggested (2) that the open-circuit scraping may produce active sites and more faradaic interference than other methods. The present work should indicate whether or not this is so.

### Experimental

The apparatus for the open-circuit scrape method has been described in previous work (5-8). Basically, this consisted of a cell containing the reference and test electrodes which were connected to a high impedance oscillographic recorder or an oscilloscope. Measurement of transient, open-circuit potentials was made while the entire metal electrode face was scraped off with a sharpened sapphire bit inserted in a high speed drill. The electrolyte was saturated with a non-reactive gas such as  $N_2$ . For the dip experiments a two-compartment cell was utilized (Fig. 1). One compartment, A, contacted the salt bridge, B, of the saturated KCl, calomel reference electrode and was separated from the main compartment, C, by a stopcock. The top of the main cell compartment was usually fitted with first a thin sheet (cover), D, of polyethylene drawn tightly over the top and then an air-tight polyethylene bag, E, in which an inert atmosphere could be maintained. The polyethylene sheet served to separate the cell atmosphere from the atmosphere of the polyethylene bag where the electrode surface was pre-

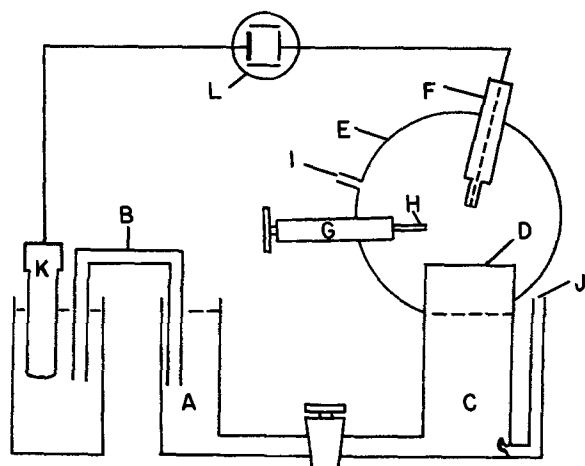


Fig. 1. Schematic diagram of experimental setup for obtaining immersion potentials: A, side compartment of cell; B, salt bridge; C, main cell compartment; D, polyethylene sheet; E, polyethylene bag; F, test electrode; G, dental handpiece; H, sharpened sapphire bit; I, gas inlet to polyethylene bag; J, gas inlet to main cell compartment; K, reference electrode; L, oscilloscope.

pared. Also fitted in the polyethylene bag was the electrode, F, and the dental handpiece, G, used to renew the metal surface prior to dipping.

The electrode for both the open-circuit scrape and immersion tests consisted of a metal wire tightly encased in a Teflon sleeve such that only its cross-sectional end was exposed to the solution (Fig. 2). Gallium electrodes required a minor modification for enclosure in Teflon as this metal liquifies at  $29.8^\circ C$ . In this case a small quantity of bulk metal was melted, placed in contact with a platinum wire fitted in the electrode for electrical connection, and then forced through a hole drilled in the Teflon sleeve (Fig. 3). Upon solidification, the gallium expanded to produce a satisfactorily sealed electrode. The entire procedure was carried out in a dry atmosphere of high-purity (99.996+%) nitrogen to prevent oxidation of the metal.

After the electrolyte and the gas compartments were purged with an inert gas, the electrode was scraped with a sharpened sapphire rod inserted in the dental handpiece in order to produce the fresh surface. Immediately (5 to 10 sec) after the scraping, the electrode was plunged through the polyethylene cover into the solution.

Open-circuit transient potentials between the open-circuit test electrode and reference electrode resulting from immersion of the test electrode were observed by internally triggering the sweep on a Tektronix Model 564 storage oscilloscope (3A3 amplifier and 2B67 time base). The "initial" potential observed on the oscilloscope screen is the pzc in the absence of very rapid faradaic reactions. The potential generally drifted or decayed positive from this initial "dip potential,"  $E_d$ . With a 10:1 input probe, the oscilloscope input impedance was approximately 11 megohms, which was considered sufficiently high to justify the open-circuit dip method employed rather than resorting to the compensation method of Jakuszewski and Kozlowski (3). For the polarizable metals (Cu, Sn, and Bi) our dip potentials agree with those of Jakuszewski and Kozlowski (3). The measured potentials were recorded relative to the standard hydrogen electrode (SHE) without correction for liquid junction potentials, which are assumed to be small compared to the precision of the results. The potential of the saturated calomel half cell was taken as  $0.242V$  vs. SHE. Also assumed insignificant are variations due to fluctuations of the ambient temperature ( $25^\circ \pm 3^\circ C$ ) under which the experiments were conducted. The purities of all the metals studied was 99.995% or better except for Sn which was 99.95% pure. Solutions were prepared from reagent grade chemicals and water twice distilled from a basic permanganate solution. The predip gas environments were 99.995+ % pure  $N_2$ ; commercial, bottled He; He which was further purified by passing through a column of molecular sieve to further remove  $O_2$ ;

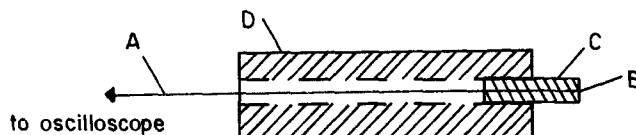


Fig. 2. Test electrode-solid metals: A, metal wire; B, wire surface to be scraped; C,  $\frac{1}{8}$  in. diameter Teflon; D,  $\frac{3}{8}$  in. diameter Teflon.

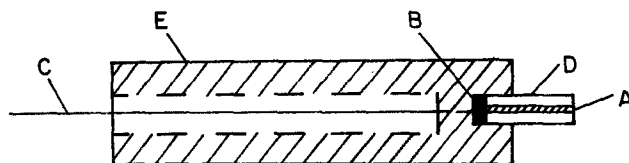


Fig. 3. Test electrode-gallium: A, gallium metal; B, Pt-Ga contact; C, Pt wire; D,  $\frac{1}{8}$  in. diameter Teflon; E,  $\frac{3}{8}$  in. diameter Teflon.

electrolytic hydrogen; and air. The electrolyte was saturated in each case with the high purity  $N_2$ .

### Results

**Values of dip and scrape potentials.**—Table II lists the dip potentials,  $E_d$ , along with the corresponding metal and solution. The third column in Table II shows the gaseous environment in which the fresh surface was produced prior to the dipping. Tests in which water vapor from the electrolyte contacted the electrode in the predip environment gave results equal to those in the corresponding dry predip environment. These tests were run by renewing the metal surface without a membrane over the mouth of the cell. The results from He were independent of whether the gas was prepurified or straight from the cylinder. The values of  $E_d$  were in general quite variable and hence the range of  $E_d$  or the individual values of  $E_d$  (if less than three experiments were performed) is shown in column 4. The number of data points determined is listed in column 5. Column 6 lists the scrape potential,  $E_{sc}$ , for the system shown on the corresponding line. The range of scrape values was generally narrower than that for dip potentials and many scrape tests were run for each system. Consequently only a single value for  $E_{sc}$  is shown in Table II.

**Transient potential decays.**—Immediately after the electrode scraping ceased, the potential decayed positive from the scrape potential ( $E_{sc}$ ) due to the reduction of impurity oxygen in the solution or to the reduc-

tion of the electrolyte. Because the concentration of dissolved oxygen was low in  $N_2$ -saturated solutions, this factor produced slow decays of the order of 10 mV/sec. Under conditions favoring the rapid reduction of  $H_3O^+$  ions (i.e., in acid solutions) or of water (e.g., Cu and Ag in neutral solutions) the decays were up to several orders of magnitude faster. After an electrode was dipped, potential decays similar to those following  $E_{sc}$  were observed. These are explicable on the basis of reduction of the solution or dissolved  $O_2$ . In addition Bi, In, Cu, and Ag frequently exhibited a very rapid (0.1-1 msec) decay of 0.1-0.2V. These rapid decays were only observed in conjunction with the more negative dip potentials. Thus dipping Bi in 1M KCl yielded an  $E_d$  value of -0.42V (Table II), and a potential decay to -0.2V occurred in 0.5 msec. However when  $E_d$  for the same system was -0.2, the very rapid decay was absent.

**Significant experimental results.**—An explanation of the results must rationalize the following observations:

1.  $E_d \approx E_{sc}$  for Au, and in most cases for In, Bi, Ga, and Sn.  $E_d$  is substantially positive of  $E_{sc}$  for Ag, Cu, and Pt.

2. The most negative values of  $E_d$  for Ag, Cu, In, and Bi are followed by a very rapid positive decay which does not appear to be explained by the reduction of solvent or of impurity  $O_2$  dissolved in the solution.

3. Both  $E_d$  and  $E_{sc}$  exhibit anion effects whether or not  $E_d$  equals  $E_{sc}$ .

Table II. Dip potentials ( $E_d$ ) under various conditions and corresponding open-circuit scrape potentials ( $E_{sc}$ ). Potentials with respect to SHE

Metal	Solution	Predip environment	$E_d$ (V) (present study)	No. of data points	$E_{sc}$ (V) and Reference
Au	0.5M $Na_2SO_4$	$N_2$	+0.21 to +0.12	3	0.12 (7)
	0.5M $Na_2SO_4$	$H_2$			0.11 (5)
	1M KF	$N_2$	0.04	3	0.13 (7)
	0.1M KCl	$N_2$	-0.05, -0.10	2	-0.08 (7)
	1M KCl, pH = 2.7 to 11	$N_2, He$	-0.07 to -0.13	20	-0.12 (7)
	1M KCl, pH = 12, 13	$N_2$	-0.15	2	-0.15 (7)
	0.1M KBr	$N_2, He$	-0.16 to -0.20	6	-0.24 (7)
	0.1M KBr	$H_2$	-0.07, -0.10	2	
	0.1M KBr	air	0.26, 0.22	2	
	1.0M KBr	$N_2$	-0.20, -0.24	3	-0.28 (7)
4.0M KBr	$N_2$	-0.24, -0.29	2		
Bi	0.1M $KClO_4$	$N_2$	-0.33	1	-0.35 (5)
	1.0M KCl, pH = 3.7 to 12	$N_2, He$	-0.21 to -0.42	12	-0.42 (5)
	1.0M KCl, pH = 2.7	$N_2$	-0.06, -0.14	2	-0.42 (5)
	1.0M KCl, pH = 1.8	$N_2$	-0.065	2	-0.40 (5)
	1.0M KCl	air	-0.085	1	
Ga	0.45M $Na_2SO_4$ + 0.05M $H_2SO_4$	$N_2$	-0.50 to -0.56	3	-0.63 (8, present)
	1M KCl + HCl, pH = 1.0	$N_2$			-0.71 <sup>(b)</sup>
	1M KCl + HCl, pH = 1.8	$N_2$			-0.70 to -0.81 <sup>(a)</sup>
	1M KCl + HCl, pH = 2.7	$N_2$			-0.79 <sup>(a)</sup> to -0.82 <sup>(a)</sup>
	1M KCl	$N_2$			-0.86 <sup>(a)</sup>
In	0.9M KBr + 0.1M HCl	$N_2$	-0.50 to -0.56	4	-0.73 (8, present)
	1M KCl, pH 3.7 to 12	$N_2$	-0.61 to -0.72	11	-0.72 (5)
	1M KCl, pH = 13	$N_2$	-0.08	2	-0.96 <sup>(a)</sup> (5)
	1M KCl, pH = 2.7 to 3.1	$N_2, He$	-0.44 to -0.50	6	-0.70 <sup>(a)</sup> (5)
	0.1M $NaClO_4$	$N_2$	-0.38, -0.43	2	-0.43 (5)
Ag	0.1M $KClO_4$	$N_2$	-0.25	1	-0.45 (7)
	0.1M $KClO_4$	air			-0.30 <sup>(a)</sup>
	0.1M KCl, pH = 2.7 to 7	$N_2$	0.12 to -0.19	4	-0.63 (7, 8)
	1.0M KCl, pH = 2.7	air	0.08, 0.04	2	
	1.0M KCl, pH = 1 to 13	$N_2$	-0.10 to -0.30	19	-0.90
	0.1M KBr	$N_2, He$	-0.36 to -0.41	5	-0.78 (7) -0.84 (8)
Cu	0.1M KBr	$H_2$	-0.22, -0.24	2	
	1.0M KBr	$N_2$	-0.47	2	-0.73 <sup>(a)</sup> (7)
	0.5M $Na_2SO_4$	$N_2$	0.09	1	-0.50, -0.31 (8)
	0.1M KCl	$N_2$	0.24 to 0.17	2	-0.51, -0.64 (8)
	1M KCl, pH = 2.7 to 11	$N_2, He$	0.04 to -0.11	22	-0.51
	1M KCl, pH = 1	$N_2$	0.08	1	
	1M KCl, pH = 13	$N_2$	-0.31	3	
	1M KCl	air	+0.04	2	
	1M KCl, pH = 13	air	-0.02, -0.10	2	
	0.1M KBr	$N_2, He, H_2$	+0.09 to 0	11	-0.65, -0.70 (8)
Pt	1M KBr	$N_2$	-0.04 to -0.12	5	-0.74
	0.01M KI	He	+0.04 to -0.06	3	
	0.5M KI	He	-0.11 to -0.16	2	
	0.5M $Na_2SO_4$	$N_2$	0.48	1	0.04 (9)
	0.5M $Na_2SO_4$	$H_2$			-0.3 <sup>(a)</sup>
	0.5M $Na_2SO_4$	air			0.15 <sup>(a)</sup>
	1M KCl	$N_2$	0.39	1	-0.08
	1M KCl, pH = 12	$N_2$	0.07	2	
	1M KCl, pH = 2.7	$N_2, He$	0.39, 0.41	2	0.02 <sup>(a)</sup> (9)
	0.1M KBr	$N_2, He$	0.26 to 0.31	4	-0.16 (9)

<sup>(a)</sup> All of the tabulated  $E_{sc}$  values are interpreted as pzc's except those with a superscript "(a)" in which cases faradaic reactions are considered to help establish the value of  $E_{sc}$ .

<sup>(b)</sup>  $E_{sc}$  values without reference in parenthesis were obtained in present study.



4. There is an intermediate pH range over which the values of  $E_d$  and  $E_{sc}$  reach a plateau and are independent of pH. In acidic solutions  $E_d$  and  $E_{sc}$  become more positive and in basic solutions they become more negative. The pH values at which  $E_{sc}$  and  $E_d$  shift from the plateau varies with the metal and also often differs between  $E_{sc}$  and  $E_d$ .

5.  $E_d$  is independent of whether the fresh surface is produced in a  $N_2$  or a He atmosphere, and whether or not this atmosphere contains water vapor.  $H_2$  also has little or no effect on  $E_d$  except for Pt, in which case there is a tendency for the reversible hydrogen electrode potential to be established.

6. When an electrode surface is produced in an air environment,  $E_d$  is almost always several hundred millivolts positive of the value obtained using  $N_2$ .

### Discussion

As the scrape potentials have been interpreted in previous studies (5-9), we first review the explanation of them and then discuss the dip results in light of the similarities and differences. After the surface of the immersed electrode is removed with its accompanying charge and double layer, the various processes of charge separation occur at the metal-liquid interphase and faradaic reactions start at a rate dependent, among other things, on the potential. The value of  $E_{sc}$  is determined by which processes occur more rapidly than the scraping process (the latter has been effected up to 500 times per second). The dipolar potentials due to electron relaxation within the metal, and solvent orientation are much faster than the scrape process. Also the specific adsorption of simple ions in most cases attains equilibrium by the time  $E_{sc}$  is detected. Therefore  $E_{sc}$  is considered to be the pzc if the faradaic reactions are slow enough. This is the case in the neutral pH range for all the metals here reported except for Ga; in that case the pzc is obtained in acid. The faradaic reactions which normally interfere with obtaining the pzc are the reduction of  $H^+$  ions in acid solutions and oxidation of metals (*i.e.*, corrosion) in basic solutions. In the present study corrosion interferes with obtaining the pzc for In, Bi, and Sn in basic solutions, and for Ga in neutral and basic solutions. For most base metals (*e.g.*, Al, Fe, Ni, Zn, Pb) corrosion occurs so rapidly at any pH that it is not possible to obtain the pzc by the scrape method (5). In acid solutions  $H^+$  ion reduction causes the rapid decay and in basic solutions there is usually no decay or only a slow decay caused by  $O_2$  reduction on a passive film.

The potential transient of gold dipped from an inert gas environment closely resembles that after scraping the electrode, and we thus interpret  $E_d$  the same as  $E_{sc}$ . All of the other metals studied behave differently from gold in that  $E_d$  is either more positive than  $E_{sc}$  or a rapid positive potential decay occurs at  $E_d$  when  $E_d = E_{sc}$ . As gold is the only metal which does not tend to chemisorb oxygen (10), we believe that adsorbed oxygen is responsible for the differences observed in the scrape and dip potential transients for the other metals. The dip and scrape potentials are so far negative of known corrosion potentials that metal oxidation does not seem probable. Also, as water vapor has no influence on the potentials, it would seem that solvent reduction is not involved in the differences. The source of oxygen is believed to be in the predip gases (which were on the order of 99.995% pure) or in grain boundaries or other imperfections in the metals, themselves. When the electrodes are dipped, weakly adsorbed molecules such as He or  $N_2$  are rapidly displaced by a layer of water molecules. Strongly adsorbed atoms such as oxygen (or hydrogen in the case of Pt) remain on the surface and may undergo faradaic reactions as contact is made with the solution.

The manner in which  $E_d$  is established for Ag, Cu, and Pt cannot be determined with certainty. However the very rapid decays observed for In, Bi, Ag, and Cu

immediately after dipping indicate that faradaic reduction of the adsorbed oxygen occurs. It is easy to rationalize the magnitude of the decay (approximately 200 mV) with very small amounts of oxygen. For example, if we assume a double layer capacity of 30  $\mu\text{Coulombs/cm}^2$  only 6  $\mu\text{Coulombs/cm}^2$  of charge is required to cause the 200 mV decay. Reduction of oxygen atoms at only 1% surface coverage could effect this charge. Many times this amount of oxygen may be present in the 50 ml or so of predip environment, which contained gases on the order of 99.995% pure or in imperfections in the metal. In the case of scrape potentials more negative values were obtained for 99.999% pure Ag than for 99.95% Ag, so that internal impurities such as oxygen can also affect  $E_{sc}$ . The average rate of oxygen reduction following  $E_d$  for Ag, Cu, Bi, and In is approximated as  $i \approx 6 \mu\text{Coulombs cm}^{-2}/10^{-4} \text{ sec} = 60 \text{ mA/cm}^2$  (where  $10^{-4} \text{ sec}$  is the average decay time). This rate does not seem excessive when one considers that the potentials involved are 0.8-1.4V more negative than the reversible oxygen potential. Tafel lines for  $O_2$  reduction on Pt (11) extrapolate to even larger values of  $i$  at such negative oxygen overvoltages.

Reduction of adsorbed oxygen can explain the rapid positive decay discussed above for Bi, In, Ag, and Cu and also the wide range of dip potentials observed for these metals. This phenomena may also be responsible for the significant differences observed for  $E_d$  and  $E_{sc}$  in the cases of Ag, Cu, and Pt. As the negative  $E_{sc}$  values are never approached by  $E_d$  values, the reduction corresponding to 400 mV (from  $E_{sc}$  to  $E_d$ ) would need to be several orders of magnitude more rapid than that following  $E_d$ . In this case an alternative explanation to oxygen reduction may be that the adsorbed oxygen contributes a dipolar potential to metals such as Ag, Cu, and Pt before the O is reduced. Then the most negative value of  $E_d$  would correspond to the potential of zero charge but for a different surface than in the case of  $E_{sc}$ . Recent measurements by Belyaeva *et al.* (12) show that the electronic work function,  $W_e$ , of silver increases as oxygen is chemisorbed onto the surface. Moreover the data of the above authors indicate that the shift in  $W_e$  is approximately 0.25V if enough oxygen is added to give a surface atom ratio of  $O/Ag = 0.06$ . These data are therefore not inconsistent with the idea that  $E_{sc}$  corresponds to the pzc on a bare surface and  $E_d$  corresponds to the pzc on a surface which is partially covered with chemisorbed oxygen. In this connection a plot of pzc vs. electronic work function was made for the metals studied in addition to Hg. The plot was drawn through Hg (at pzc = -0.2V and  $W_e = 4.5 \text{ eV}$ ) with a slope of one. When the values of  $E_{sc}$  were used with the more negative  $W_e$  values for Ag (12) and Cu (13), the experimental points fell quite close to the line. When the values of  $E_d$  were used along with the more positive  $W_e$  values for Ag and Cu, the experimental points again fell quite close to the line.

### Acknowledgment

The authors wish to thank the National Institute of Health, Grant GP 12862, National Science Foundation, Grant GP 28631, and the Army Research-Durham, Contract DA-ARO-D-31-124-72-G15, for support of this work.

Manuscript submitted Nov. 12, 1973; revised manuscript received Jan. 21, 1974.

Any discussion of this paper will appear in a Discussion Section to be published in the December 1974 JOURNAL. All discussions for the December 1974 Discussion Section should be submitted by Aug. 1, 1974.

### REFERENCES

1. R. S. Perkins and T. N. Andersen, in "Modern Aspects of Electrochemistry," Vol. 5, Chap. 3, J. O'M. Bockris and B. E. Conway, Editors, Plenum Press, New York (1969).

2. J. O'M. Bockris, S. D. Argade, and E. Gileadi, *Electrochim. Acta*, **14**, 1259 (1969).
3. B. Jakuszewski and Z. Kozlowski, *Roczniki Chem.*, **36**, 1873 (1962).
4. B. Jakuszewski and Z. Kozlowski, *Lodz. Towarz. Nauk. Wydzial III, Acta Chim.*, **9**, 25 (1964).
5. T. N. Andersen, J. L. Anderson, and H. Eyring, *J. Phys. Chem.*, **73**, 3562 (1969).
6. T. N. Andersen, R. S. Perkins, and H. Eyring, *J. Am. Chem. Soc.*, **86**, 4496 (1964).
7. D. D. Bodé, Jr., T. N. Andersen, and H. Eyring, *J. Phys. Chem.*, **71**, 792 (1967); D. D. Bodé, Jr., Ph.D. Thesis, University of Utah (1966).
8. R. S. Perkins, Ph.D. Thesis, University of Utah (1967).
9. T. N. Andersen, J. L. Anderson, D. D. Bodé, Jr., and H. Eyring, *J. Res. Inst. Catalysis, Hokkaido Univ.*, **16**, 449 (1968).
10. D. O. Hayward and B. M. W. Trapnell, "Chemisorption," second edition, Butterworths, London (1964).
11. A. Damjanovic, "Modern Aspects of Electrochemistry," Vol. 5, Chap. 5, J. O.M. Bockris and B. E. Conway, Editors, Plenum Press, New York (1969).
12. M. E. Belyaeva, T. V. Kalish, and R. Kh. Burshtein, *Elektrokimiya*, **7**, 1711 (1971).
13. *Handbook of Chemistry and Physics*, 44th Edition, p. 2656, p. 2650 The Chemical Rubber Publishing Co., Cleveland, Ohio (1963).

## Resistive Wire Electrodes

Richard Alkire\* and Richard Varjian

Department of Chemical Engineering, University of Illinois, Urbana, Illinois 61801

### ABSTRACT

Two-dimensional current and potential distributions have been calculated for cylindrical electrolysis cells having a resistive wire electrode along the cell axis. Cell behavior has been predicted for both monopolar and bipolar electrode situations. The calculations involve solving the Laplace equation for the electrolyte resistance, in conjunction with equations for charge-transfer overpotential and electrode resistance phenomena. Over a wide range of parameter space, which includes most practical applications of resistive electrodes, it was found that simple one-dimensional approximations to Laplace's equation yield reaction rate distributions which are in excellent agreement with more rigorous two-dimensional calculations. By using the one-dimensional approximations of monopolar and bipolar electrodes, it may be anticipated that future studies may be conducted with relative ease on mass transport phenomena during high-rate electrolysis at resistive wire electrodes.

During electrolysis, there may be a substantial ohmic loss in the electrode if its cross-sectional area is small. The resistive loss in the metal phase leads to a non-uniform potential in the metal which may thereby cause variations in the local reaction rate along the electrode surface. In electroplating operations it is known, for example, that deposits of high quality are usually obtained only over a certain range of current densities. As a consequence, a highly nonuniform current distribution may be detrimental to product quality owing to variations in plating thickness, adherence, hardness, composition, and appearance, to name a few. Industrial processes which involve resistive electrode effects include production of tinplate (1), plating of copper and steel wire (2), electrodeposition of magnetic alloys onto moving wires (3), manufacture of printed circuit boards (4), and copper plating on the interior of millimeter wave guides (5). In view of these practical applications, the present study has been undertaken in order to elucidate the behavior of resistive wire electrodes.

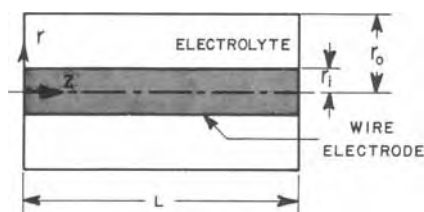
Figure 1(a) illustrates the geometry of the electrolysis cell under consideration. The wire electrode, having radius  $r_1$ , passes down the axis of a concentric tube of radius  $r_0$ . The end faces of the cylindrical region are insulated. The annular space contains electrolytic solution. Two different electrical connections, shown in Fig. 1(b) and (c), are examined in the study below. In Fig. 1(b), the resistive wire is a cathode while the concentric cylindrical tube is the counter-electrode. When a voltage is imposed on the cell, electrical current travels along the wire and passes into the electrolytic solution via electrochemical reaction at the wire surface. The applied voltage is consumed

within the electrolysis cell by several irreversible phenomena. If ohmic losses in the wire electrode are negligible, then current passes between anode and cathode such that the secondary potential distribution along the wire surface is uniform owing to the cylindrical symmetry. On the other hand, if ohmic losses in the wire electrode are appreciable, then the potential in the electrode varies with position; the remainder of the applied voltage, available for other irreversible phenomena, also varies with position. As a consequence, the charge-transfer overpotential may vary with position so that the electrode reaction may occur at different rates along the electrode surface. In most cases, the reaction rate on the wire surface will tend to be highest near the electrical contact. In Fig. 1(c), the resistive wire passes through an insulator tube containing electrolyte; current passes through the wire, from one end to the other. Owing to the wire resistance, the potential difference between the two ends of the wire may serve to drive an electrochemical reaction provided that reactive species are present. Although one portion of the wire will act as a cathode while the remainder will act as an anode, one generally has no *a priori* knowledge of the precise location of these regions. The electrode in Fig. 1(c) will be called bipolar in contradistinction to the monopolar electrode of Fig. 1(b). Within the foregoing cells, the principal phenomena which determine the current distributions at low current densities are the electrolyte resistance, electrode reaction polarization, electrode resistance, and cell geometry. At high current densities, mass transport restrictions may also arise.

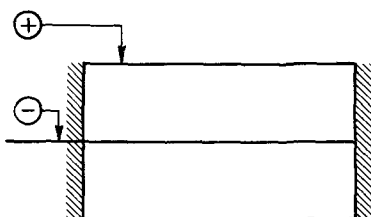
Several investigations of monopolar resistive electrodes have been conducted. With simple linear network models which included metal resistance, electrolyte resistance, and constant electrode polarization, Weisselberg (6) and Fomichev (7) predicted current

\* Electrochemical Society Active Member.  
Key words: resistive electrode, current distribution, bipolar electrode, wire electrode, potential distribution.

## (a) CELL GEOMETRY



## (b) MONOPOLAR WIRE ELECTRODE



## (c) BIPOLAR WIRE ELECTRODE

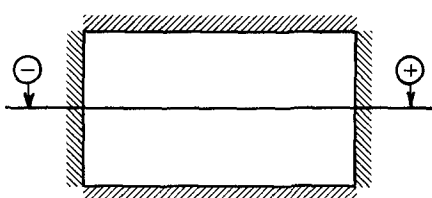


Fig. 1. Geometric configuration and electrical connections for the electrolysis cell under investigation.

distributions which were in reasonable accord with a small number of experimental data. Waber (8) recognized the need to take better account of polarization phenomena and proposed a linear model. In a series of publications, Conway *et al.* (9-11) also used more realistic polarization laws, but did not include the effect of electrolyte resistance. In an advanced treatment, Böhnlein (12) accounted for electrolyte resistance effects and applied the results to magnetic wire-plating processes. None of the foregoing studies considered mass transport limitations which arise at high current densities. The effect of convective heat- and mass-transfer to moving wires and sheets has received considerable attention in the chemical engineering literature (13-18). The effect of wall conduction on the heat transfer from a boundary layer has also received attention (19, 20). The extensive experimental studies on high-rate wire-plating by Tvarusko (21) are especially noteworthy since they demonstrate that mass transport limitations are important for the operating conditions used commercially. Alkire (22) and Alkire and Tvarusko (23) modeled mass transport of reactants to resistive electrodes under conditions of uniform stirring and of unsteady-state diffusion, respectively, but did not include electrolyte resistance effects. In sophisticated studies, Tobias and Wijsman (24) and Ishizaka *et al.* (25) accounted for electrolyte resistance by solving the Laplace equation for cells having resistive electrodes, uniform concentrations, and linear polarization laws; these two analyses were sufficiently complex that further expansion to include mass transport effects would be difficult. However, in their study of planar electrodes, Tobias and Wijsman illustrated that substantial simplifications can be made when the current flow in the electrolyte is unidirectional.

The behavior of resistive bipolar wire electrodes has been the subject of a small number of investigations. The linear network model of Harvey (26) accounted

for electrode resistance and linear polarization, while Nakata *et al.* (27) included electrolyte resistance phenomena in a one-dimensional manner. In a related work on one-dimensional bipolar porous metal diaphragms, Alkire (28) incorporated electrode and electrolyte resistance, nonlinear polarization, diffusion and convection phenomena. However, the porous diaphragm model may not be suitable for predicting behavior of bipolar resistive wire electrodes since the potential and concentration fields may not be one-dimensional.

Analyses of high-rate processes at wire electrodes need to include mass transport and electrolyte resistance phenomena as well as electrode resistance and reaction polarization effects. The foregoing survey indicates that studies to date on wire electrodes have not achieved this goal. The problem arises in coupling the solution of the Laplace equation, for the electrolyte resistance, to mass transfer processes occurring near the electrode surface. Even in the absence of electrode resistance effects, the successful studies to date (29, 30) have had to incorporate complex procedures for obtaining solutions by numerical methods. A simpler approach, initiated in the study below, is to investigate the range over which the solution of the Laplace equation may be approximated by unidirectional current flow. Over this range, it may be anticipated that the mass transport problem may be attacked with relative ease.

### Mathematical Development

The following analysis of monopolar and bipolar resistive electrodes incorporates the effects of the ohmic resistance of the wire electrode, the activation overpotential of the electrochemical reaction, the ohmic resistance of the electrolyte, and the geometry of the electrolysis cell. The voltage applied to the electrolysis cell is assumed to be held constant during electrolysis. The following assumptions outline the model: (i) the potential in the wire electrode varies along its length in a one-dimensional manner; (ii) the electrolytic solution is of uniform composition so that the potential distribution obeys Laplace's equation; (iii) a single reversible electrochemical reaction occurs in accord with Butler-Volmer kinetics; (iv) no structural or geometric changes of significance occur during electrolysis; (v) the ohmic resistance of wire electrode external to the electrolysis is negligible; and (vi) the counterelectrode is unpolarized for the monopolar electrode cell.

As indicated in Fig. 1, the  $z$ -coordinate extends down the axis of the cell, while the  $r$ -coordinate extends from the wire surface,  $r_1$ , to the outer tubular surface,  $r_0$ . The current and potential within the wire electrode are related by Ohm's law

$$i_m(z) = -\sigma \frac{d\phi_m}{dz} \quad [1]$$

The electronic current in the wire,  $i_m(z)$ , varies with position owing to the electrochemical reaction which occurs on the wire surface

$$\frac{di_m(z)}{dz} = -\frac{2}{r_1} j(z) \quad [2]$$

The local electrochemical reaction rate,  $j(z)$ , proceeds at the wire surface ( $r = r_1$ ) and is related to the potential difference between metal and solution phases by the Butler-Volmer expression

$$j(z) = i_0 \left[ \exp \left\{ \frac{\alpha n F}{RT} [\phi_m(z) - \phi_s(z)] \right\} - \exp \left\{ \frac{(\alpha - 1) n F}{RT} [\phi_m(z) - \phi_s(z)] \right\} \right] \quad [3]$$

where  $\phi_s(z)$  denotes the potential in the solution ad-

adjacent to the wire surface. For the sake of convenience, we will denote the right side of Eq. [3] as  $i_0 f[\phi_m(z) - \phi_s(z)]$ . The local reaction rate,  $j(z)$ , is also related to the potential gradient in the electrolytic solution adjacent to the wire surface

$$j(z) = -\kappa \left. \frac{\partial \phi(r, z)}{\partial r} \right|_{r=r_1} \quad [4]$$

Finally, the potential distribution in the electrolytic solution obeys the equation of Laplace

$$\frac{1}{r} \frac{\partial}{\partial r} \left[ r \frac{\partial \phi(r, z)}{\partial r} \right] + \frac{\partial^2 \phi(r, z)}{\partial z^2} = 0 \quad [5]$$

The boundary conditions which apply to the foregoing equations are

$$\left. \frac{\partial \phi}{\partial z} \right|_{z=0} = \left. \frac{\partial \phi}{\partial z} \right|_{z=L} = 0$$

$$\left. \frac{\partial \phi}{\partial r} \right|_{r=r_1} = -\frac{j(z)}{\kappa} \quad [6]$$

For the monopolar situation depicted in Fig. 1(b)

$$\left. \phi \right|_{r=r_0} = \left. \frac{d\phi_m}{dz} \right|_{z=L} = 0$$

$$\phi_m|_{z=0} = \phi_A \quad [7]$$

For the bipolar situation depicted in Fig. 1(c)

$$\left. \frac{\partial \phi}{\partial r} \right|_{r=r_0} = \left. \phi_m \right|_{z=L} = 0$$

$$\phi_m|_{z=0} = \phi_A \quad [8]$$

Equations [1], [2], [3], and [5], along with the boundary conditions, define the resistive electrode model. It is easy to recognize that the potential distribution must be determined in two separate phases: the metal and the electrolytic solution. For the general case given above, the solution to the problem is found by matching the potential distributions along the common boundary between the electrolyte and the electrode.

The procedure for obtaining a solution may be simplified a great deal if the flow of current through the electrolytic solution is approximately unidirectional. Two cases are possible, depending on whether the wire electrode is monopolar or bipolar. In order to ascertain the range of conditions under which such simplifications are appropriate, results obtained with the general model outlined above are compared with the following two approximate models.

#### Monopolar Approximation

If the current carried by the electrolytic solution travels only in the radial direction, then the  $z$ -derivative of Eq. [5] may be deleted; integration of what remains gives the result

$$\phi_s(z) = \frac{r_1}{\kappa} \ln \left( \frac{r_0}{r_1} \right) j(z) \quad [9]$$

since the potential of the counterelectrode is chosen to be zero. Combining Eq. [3] and Eq. [9] gives the algebraic expression

$$\phi_s(z) = \frac{r_1 i_0}{\kappa} \ln \left( \frac{r_0}{r_1} \right) \{f[\phi_m(z) - \phi_s(z)]\} \quad [10]$$

Furthermore, Eq. [1], [2], and [3] may be combined to obtain the result

$$\frac{d^2 \phi_m(z)}{dz^2} = \frac{2i_0}{r_1 \sigma} \{f[\phi_m(z) - \phi_s(z)]\} \quad [11]$$

Equations [10] and [11] constitute two equations hav-

ing the two unknown potential distributions  $\phi_m(z)$  and  $\phi_s(z)$ . The boundary conditions needed for Eq. [11] are given in Eq. [7] above.

#### Bipolar Approximation

If passage of current in the electrolyte is primarily in the axial direction, then Eq. [5] may be abandoned in favor of a one-dimensional form of Ohm's law written for the solution phase

$$i_s(z) = -\kappa \frac{d\phi_s(z)}{dz} \quad [12]$$

Since the ionic current carried by the electrolyte varies with axial position owing to the electrochemical reaction source at the wire, one has

$$\frac{di_s(z)}{dz} = -\frac{2r_1}{(r_0^2 - r_1^2)} j(z) \quad [13]$$

By differentiating Eq. [12] and combining the result with Eq. [3] and [13], one has for the solution phase

$$\frac{d^2 \phi_s(z)}{dz^2} = \frac{2r_1 i_0}{(r_0^2 - r_1^2) \kappa} \{f[\phi_m(z) - \phi_s(z)]\} \quad [14]$$

Equation [11] applies in the electrode phase; taken together, Eq. [11] and [14] constitute two differential equations having the two unknown potentials  $\phi_m(z)$  and  $\phi_s(z)$ . The four boundary conditions may be drawn from Eq. [6] and [8]. The one-dimensional bipolar approximation derived here is essentially identical to the treatment of bipolar porous metal diaphragms (28).

By introducing the following dimensionless variables

$$\rho = \frac{r}{r_1}, \quad \xi = \frac{z}{L}, \quad \Phi = \frac{nF}{RT} \phi, \quad J = \frac{2Lj}{r_1 i_0}, \quad \beta = \frac{nFLi_0}{\sigma RT}$$

the number of independent system parameters is reduced to the following independent dimensionless quantities

$$\psi = \frac{r_1^2 \sigma}{L^2 \kappa}, \quad \xi = \frac{2nFL^2 i_0}{\sigma r_1 RT}, \quad \rho_0 = \frac{r_0}{r_1}, \quad \gamma = \frac{r_1}{L}$$

A physical interpretation of each of these parameters will be provided in the discussion section below.

#### Methods of Solution

The equations and boundary conditions which describe the several models must be solved simultaneously. Owing to their complexity, analytical solutions are not convenient so that computations were made by numerical methods in conjunction with an IBM 360 digital computer. The method of solution varied according to the model.

#### General Monopolar and Bipolar Models

Equations [1], [2], [3], and [5], along with boundary conditions [6]-[8] define the general models. The procedure for solving the equations is complex because the equations are strongly coupled. The iterative scheme outlined below was found to converge rapidly over a wide range of parameter space.

In the electrolytic solution, Eq. [5] describes the potential distribution. Integration proceeded by separation of variables in order to obtain an expression for the potential distribution in the solution adjacent to the wire electrode surface

$$\Phi_s(\xi) = B_0 + \sum_{n=1}^{\infty} B_n \cos(\lambda_n \xi) \quad [15]$$

The details of the derivation depend on whether the wire is monopolar or bipolar, and are outlined in Appendix I. The potential distribution within the wire electrode may be found by combining Eq. [1], [2], [4], and either [A-I-3] or [A-I-4], as outlined in Appendix

II. For the monopolar wire, the result is

$$\Phi_M(\zeta) = \Phi_A - \frac{2B_0\zeta}{\psi \ln \rho_0} + \frac{B_0\zeta^2}{\psi \ln \rho_0} - \frac{2}{\psi} \sum_{n=1}^{\infty} \frac{B_n R_n'(1)}{\lambda_n^2} [1 - \cos(\lambda_n \zeta)] \quad [16]$$

while, for the bipolar wire, one finds

$$\Phi_M(\zeta) = \Phi_A + \left\{ \frac{2}{\psi} \sum_{n=1}^{\infty} \frac{B_n R_n'(1)}{\lambda_n^2} [1 - (-1)^n] - \Phi_A \right\} \zeta - \frac{2}{\psi} \sum_{n=1}^{\infty} \frac{B_n R_n'(1)}{\lambda_n^2} [1 - \cos(\lambda_n \zeta)] \quad [17]$$

The  $B$ -coefficients which appear in Eq. [15]-[17] may be calculated from a trial guess of the potential distribution within the cell; the manipulation of Eq. [3], [4], [15], [16], and [17] to accomplish this goal is outlined in Appendix III. After achieving convergence, the dimensionless form of Eq. [3] is used to calculate the current distribution

$$J(\zeta) = \frac{\xi}{\beta} [\exp\{\alpha[\Phi_M(\zeta) - \Phi_S(\zeta)]\} - \exp\{(\alpha - 1)[\Phi_M(\zeta) - \Phi_S(\zeta)]\}] \quad [18]$$

For the monopolar electrode, integration of the current distribution over the entire electrode begets the total current flowing in the system

$$\int_0^1 J(\zeta) d\zeta = 1.0 \quad [19]$$

whereas, for the bipolar electrode, the anodic and cathodic currents must balance exactly

$$\int_0^1 J(\zeta) d\zeta = 0$$

$$\beta = - \left. \frac{d\Phi_M}{d\zeta} \right|_{\zeta=0} \quad [20]$$

The iterative procedure of solution consists of the following steps:

(i) Make some reasonable initial guess of the potential distributions  $\Phi_M(\zeta)$  and  $\Phi_S(\zeta)$ . The approximate models may be employed to generate the initial guess.

(ii) From the procedure described in Appendix III, calculate trial values of the  $B$ -coefficients.

(iii) Calculate a revised trial distribution of  $\Phi_S(\zeta)$  by substituting the  $B$ -coefficients into Eq. [15].

(iv) Calculate a revised trial distribution of  $\Phi_M(\zeta)$  by substituting the  $B$ -coefficients into either Eq. [16] or [17].

(v) With the foregoing revised potential distributions in hand, return to iteration step (ii) and repeat the sequence of operations until convergence is achieved. The criterion for convergence is that two successive  $\Phi_S(\zeta)$  distributions agree everywhere to within 0.01%.

(vi) With converged potential distributions in hand, calculate  $J(\zeta)$  and  $\beta$  from Eq. [18]-[20].

It was found that the convergence scheme outlined above usually converged in less than ten iterations regardless of the crudeness of the initial guesses in step (i). If the approximate models were used to generate the first guess, convergence was generally achieved within four iterations. It was found that the results were essentially independent of mesh spacing if

fifty or more mesh points were employed. For both monopolar and bipolar electrodes, 1000  $B$ -coefficients were used.

Several other iterative schemes were tried, but none met with success over wide ranges of parameter space. For example, the  $B$ -coefficients are related to the current distribution along the wire as may be found by applying orthogonality requirements upon Eq. [A-I-3] or [A-I-4]. Thus a simple method for calculating the  $B$ -coefficients, in principle, is by appropriate integration of a trial guess of the current distribution along the wire. Knowledge of the  $B$ -coefficients can, in turn, provide a new estimate of the potential distribution along the wire surface and thereby permit calculation of a revised current distribution. During this study, several iteration schemes were developed along this line but all failed to converge, even when the approximate model was used to generate the initial guess. It seems reasonable that the difficulty in convergence is in part attributable to the nature of the reaction rate expression; even slight errors in the trial potential distributions become highly magnified since the errors appear in exponential terms. It is believed that the success of the convergence scheme used in this study is attributable to the fact that the current distribution,  $J(\zeta)$ , has been eliminated from all steps within the iterative procedure. It is not necessary to calculate the current distribution until a converged solution for the potential distributions is available.

#### Approximate Monopolar and Bipolar Models

Each approximate model consists of two equations to be solved simultaneously. The dimensionless equations which describe the two approximate models are: Monopolar

$$\Phi_S(\zeta) = \frac{\xi \psi \ln \rho_0}{2} [e^{\alpha(\Phi_M - \Phi_S)} - e^{(\alpha-1)(\Phi_M - \Phi_S)}] \quad [21]$$

$$\frac{d^2 \Phi_M(\zeta)}{d\zeta^2} = \frac{2}{\psi \ln \rho_0} \Phi_S(\zeta) \quad [22]$$

$$\Phi_M(0) = \Phi_A, \quad \frac{d\Phi_M(1)}{d\zeta} = 0$$

Bipolar

$$\frac{d^2 \Phi_M(\zeta)}{d\zeta^2} = \xi [e^{\alpha(\Phi_M - \Phi_S)} - e^{(\alpha-1)(\Phi_M - \Phi_S)}] \quad [23]$$

$$\frac{d^2 \Phi_S(\zeta)}{d\zeta^2} = - \frac{\chi}{\xi} \frac{d^2 \Phi_M}{d\zeta^2} \quad [24]$$

$$\frac{d\Phi_S(0)}{d\zeta} = \frac{d\Phi_S(1)}{d\zeta} = \Phi_M(1) = 0$$

$$\Phi_M(0) = \Phi_A$$

where

$$\chi = \frac{2 r_1 i_0 n F L^2}{(r_0^2 - r_1^2) \kappa RT}$$

The equations were solved by first linearizing them about a trial solution and then placing them into finite difference form. The resulting tridiagonal matrices were then inverted (31) in order to obtain revised potential distributions. The solution of the nonlinear problem was obtained by iteration with successive correction of the approximate potential distributions obtained by each calculation. It was found that 50 mesh points gave results which were essentially independent of mesh spacing. The criterion for convergence upon the nonlinear solution was that two successive  $\Phi_M(\zeta)$  distributions agree to within 0.001%.

#### Results and Discussion

The model described in the present investigation contains three phenomena which act to consume the applied potential: wire resistance, electrolyte resistance, and charge-transfer reaction resistance. The rel-

ative importance of these three effects is indicated by two dimensionless parameters. The first is proportional to the exchange current density divided by the metal conductivity

$$\xi = \frac{2nFL^2i_0}{\sigma r_1 RT}$$

A large value of the parameter  $\xi$  would therefore correspond to a system with a very reversible reaction occurring on an electrode of low conductivity. In such a system, the applied potential would be consumed primarily by the electrode resistance, not by charge-transfer overpotential; further, the electrochemical reaction would tend to occur primarily near the electrical contact end of the wire. That is, for large values of  $\xi$ , the ohmic resistance of the wire tends to cause a nonuniform current distribution. A second parameter contains information about the electrolytic solution

$$\psi = \frac{r_1^2 \sigma}{L^2 \kappa}$$

It is seen that if  $\psi$  has a small value (high solution conductance, low electrode conductance), then the applied potential would be consumed more by ohmic losses in the electrode phase than by ohmic losses in the electrolytic solution phase.

Two additional parameters define the geometric configuration of the cell

$$\rho_0 = \frac{r_0}{r_1}, \quad \gamma = \frac{r_1}{L}$$

#### Monopolar Electrode

Let us first discuss behavior of monopolar wire electrode models. Results given in Fig. 2, 3, and 4 were obtained with the general (two-dimensional) model. It was found that, over the entire range of parameter space investigated below, the approximate (one-dimensional) model gave current and potential distributions which agreed to within 4% of those given by the general model. As a consequence, the compilations presented in Fig. 5, 6, and 7 were performed with the approximate model. Discussion of the unusual agreement between general and approximate models will be postponed until the end of the section.

Figure 2 illustrates how the three overpotentials vary with distance along a wire electrode for one typical situation ( $\xi = 1.0$ ,  $\psi = 1.0$ ,  $\Phi_A = 3$ ,  $\rho_0 = 10$ ,  $\gamma = 10^{-3}$ ). Although the three overpotentials vary with distance along the wire, their sum is always a constant (the applied potential). The trade-off among

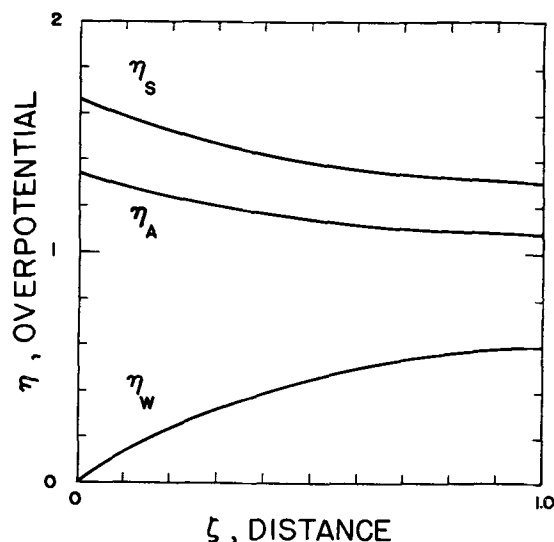


Fig. 2. Overpotential distributions along a resistive monopolar wire electrode ( $\psi = 1$ ,  $\xi = 1$ ,  $\Phi_A = 3$ ,  $\rho_0 = 10$ ,  $\gamma = 10^{-3}$ ).

the three overpotentials, and their variation with distance along the wire, depends on the relative magnitudes of the dimensionless parameters outlined previously. Consider the position  $\zeta = 0$ , the electrical contact end of the electrode; the applied potential is distributed between the charge-transfer overpotential and the ohmic loss in the electrolyte. As we depart from the contact end and move down the wire, the ohmic resistance of the metal acts to consume an ever-increasing proportion of the applied potential. The consequence is that the charge-transfer overpotential decreases with distance along the wire.

Figure 2 illustrates that the variation of charge-transfer overpotential along the wire leads to a non-uniform current distribution. The local reaction rate is always highest at the contact end of the wire, and decreases with distance along the wire. For low values of  $\psi$ , the resistance of the electrolyte is low with respect to charge-transfer and wire resistance effects; the uniformity of the current distribution then depends solely on the value of parameter  $\xi$ . If  $\xi$  is large, the ohmic loss in the metal is large and the current distribution is nonuniform; if  $\xi$  is small, then the charge-transfer overpotential predominates and the current distribution is uniform. In Fig. 3 it may be seen that as the ohmic resistance of the solution is increased (by increasing  $\psi$ ), the reaction rate distribution becomes more and more uniform. Thus, even though  $\xi$  may have a large value, the reaction distribution may nevertheless be quite uniform because of the resistance of the electrolytic solution.

Figures 2 and 3 illustrate the behavior trends of the potential and current distributions for a few typical parameter values. However, it is desirable to display a great deal of detailed data in a more convenient manner. The following figures illustrate several approaches.

The total cell current divided by the applied potential may be denoted as the over-all conductivity of the electrolysis cell. The over-all conductivity of the cell will depend on the system parameters. Figure 4 illustrates the variation of the over-all cell conductivity with the two parameters  $\xi$  and  $\psi$  ( $\gamma = 10^{-3}$ ,  $\rho_0 = 10$ ,  $\Phi_A = 3$ ). Since the applied potential has the same value for all these curves, it is recognized that the current passing through the cell depends strongly on the system parameters. By increasing  $\xi$ , the cell current tends to increase; however a tenfold increase of  $\xi$  does not increase the cell current by tenfold since the

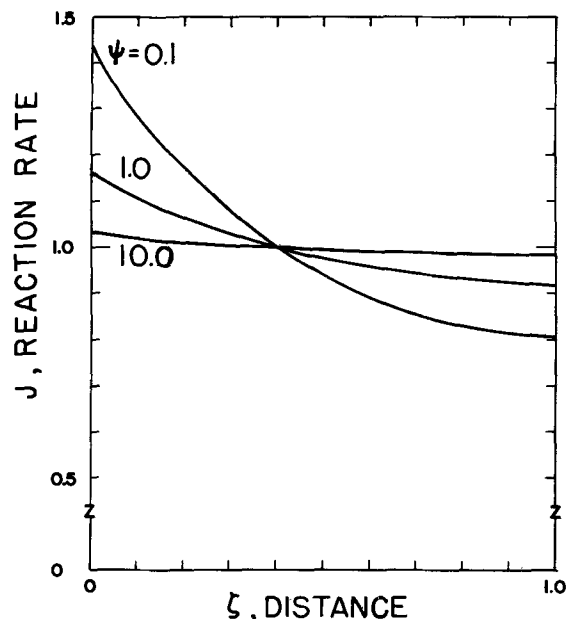


Fig. 3. Effect of electrolyte conductivity on monopolar current distribution ( $\xi = 1$ ,  $\Phi_A = 3$ ,  $\rho_0 = 10$ ,  $\gamma = 10^{-3}$ ).

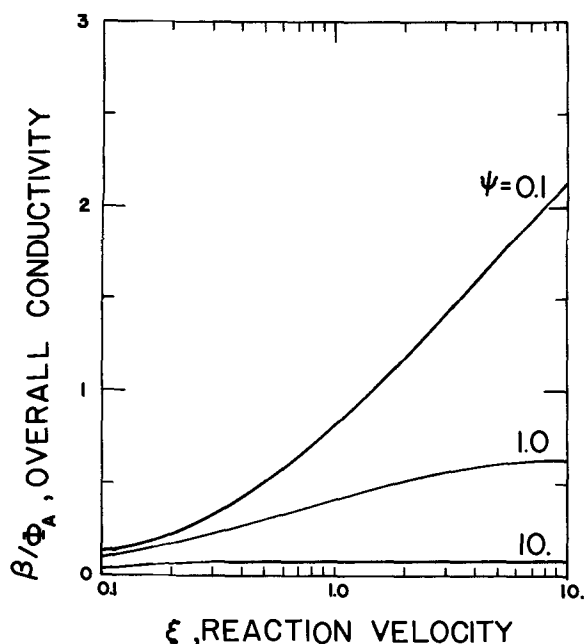


Fig. 4. Effect of exchange current density and electrolyte conductivity on monopolar cell behavior ( $\Phi_A = 3, \rho_0 = 10, \gamma = 10^{-3}$ ).

current distribution is not uniform. For small values of  $\psi$ , the electrolytic solution is highly conductive; for large values of  $\psi$ , however, the electrolyte resistance is large with respect to other resistances. Thus for systems exhibiting large  $\psi$ , increasing the exchange current density (increasing  $\xi$ ) would have little effect on cell current since the charge-transfer resistance is negligible. For intermediate values, such as  $\psi = 1.0$ , increasing  $\xi$  will act to increase the total cell current to a certain extent; however, the charge-transfer resistance may eventually become reduced to such values that further increases in  $\xi$  would have no effect on cell current. For example, one sees in Fig. 4 that the cell conductivity for  $\psi = 1.0$  increases with  $\xi$  but reaches a plateau at about  $\xi = 10$ .

The over-all conductivity also varies with geometric configuration of the electrolysis cell. The effect of parameter  $\rho_0$  on over-all conductivity is shown in Fig. 5. When  $\rho_0$  has a small value, that is, when the distance between electrodes is small, then the electrolyte resistance tends to be low so that the parameter  $\xi$  exerts a strong influence on the system behavior. On the other hand, when  $\rho_0$  is large, the ohmic resistance of the electrolyte is large, thereby decreasing the relative importance of parameter  $\xi$ . Also, it is recognized that the ohmic resistance of the electrolyte arises primarily adjacent to the wire, where the normal cross-sectional area for current flow is small. The effect may be seen in Fig. 5 wherein the downward shift of the curves becomes smaller with successively larger values of  $\rho_0$ . The effect of increasing  $\rho_0$  from 2 to 10 is thus far greater than increasing it from 100 to 1000. Because of the nonlinear reaction rate expression, Eq. [3], the curves presented in Fig. 4 and 5 will vary as the applied potential is changed. In general, an increase in applied potential will act to shift the curves upward, that is, to increase the over-all conductivity.

A somewhat different approach to compiling system behavior is also available (22). The method takes advantage of the fact that the applied potential is partitioned into three overpotentials

$$\Phi_A = \eta_s(\xi) + \eta_A(\xi) + \eta_w(\xi)$$

where  $\eta_s$  = potential consumed by electrolyte resistance,  $\eta_A$  = potential consumed by the charge-transfer process, and  $\eta_w$  = potential consumed by wire resistance.

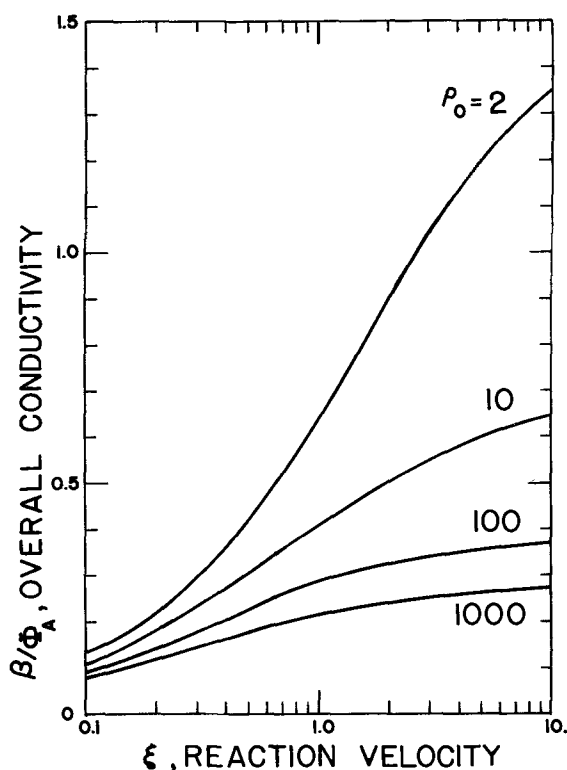


Fig. 5. Effect of exchange current density and counterelectrode radius on monopolar cell behavior ( $\psi = 1, \Phi_A = 3$ ).

Although the three overpotentials may vary in magnitude with position along the wire, they always sum to the applied potential which is a constant. As a consequence, the relative magnitude of each overpotential may be depicted on an equilateral triangular graph as illustrated in Fig. 6. Each point within the triangle, designated as a partition point, corresponds to a different partitioning of the applied potential among electrode resistance, charge-transfer, and electrolyte effects. For example, the partition point which corresponds to the insulated end of the electrode system depicted in Fig. 2 is denoted by point A in Fig. 6. The partition points at the insulated end of other systems may also be found in Fig. 6 at the intersection of the appropriate grid lines which are drawn for various values of  $\xi$  and  $\psi$ . Similarly, the partition point in Fig. 6 which corresponds to the electrical contact end of the

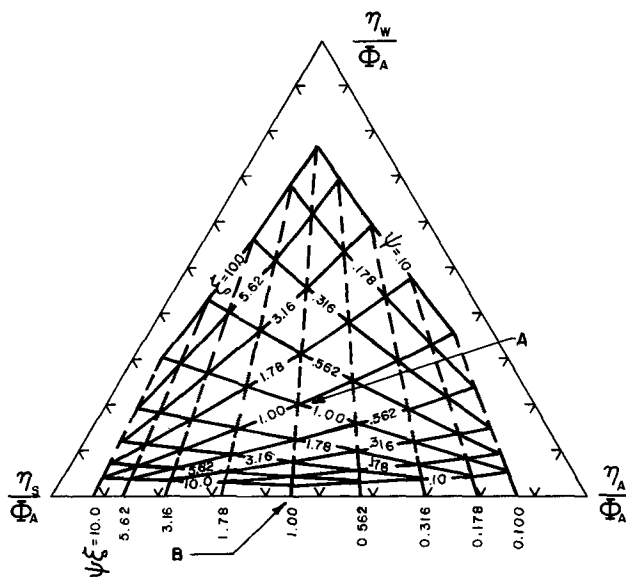


Fig. 6. Compilation of overpotential partitioning for monopolar resistive electrode ( $\Phi_A = 3, \rho_0 = 10$ ).

electrode in Fig. 2 is shown as point B. Ohmic effects are always absent at the electrical contact end, so that such partition points always fall on the  $\eta_s$ - $\eta_A$  "binary" base line at a position which is determined solely by the product  $\xi\psi$ . Therefore Fig. 6 allows us to determine the relative effects of the three overpotentials at the left and right ends of the cell.

A numerical example may illustrate the use of Fig. 6. Suppose that a particular system under consideration has the parameter values such that  $\rho_0 = 10$ ,  $\Phi_A = 3$ ,  $\psi = 1.00$ , and  $\xi = 1.00$ . The product  $\xi\psi$  is 1.00. Since, at the electrical contact end of the cell, the ohmic loss in the wire electrode is zero, we find from the  $\eta_s$ - $\eta_A$  base line that the ohmic loss in the solution equals 55% of the applied potential and the charge-transfer overpotential consumes 45% of the applied potential (point B). At the insulated end of the wire, we find the partition point where the lines intersect corresponding to  $\xi = 1.00$  and  $\psi = 1.00$  (point A). From the triangular graph, we read that the ohmic drop in the electrode has consumed 20% of the applied potential, the ohmic loss in the electrolyte has consumed 44%, and the charge-transfer overpotential has consumed 36% of the applied potential.

It is convenient to recall that the current distribution along the wire will tend to be nonuniform only if ohmic losses in the metal phase are appreciable with respect to other effects. Therefore if the insulated-end partition point lies near the  $\eta_w$  apex of Fig. 6, the current distribution will be nonuniform. If the insulated end partition point lies near the  $\eta_s$ - $\eta_A$  base line, the current distribution will be uniform. Figure 7 is a triangular graph for a cell having radii ratio  $\rho_0 = 1000$ . By comparison with Fig. 6 ( $\rho_0 = 10$ ), one may recognize that the ohmic loss in the electrolyte increases by increasing  $\rho_0$ , other conditions remaining equal. That is, an increase in  $\rho_0$  shifts the partition points toward the  $\eta_s$  apex. However, the magnitude of the shift becomes smaller as  $\rho_0$  increases, as was mentioned in conjunction with Fig. 5.

A change in applied potential affects the grids given in Fig. 6 and 7 owing to the nonlinear reaction rate equation. An increase in  $\Phi_A$  tends to reduce the relative importance of charge-transfer overpotential and thereby shift the grid away from the  $\eta_A$ -apex, that is, upward and to the left.

The approximate model of unidirectional radial current flow in the electrolyte has been found to give

current and potential distributions which are in excellent agreement with the two-dimensional model. Owing to the cylindrical geometry, it has been mentioned that the ohmic resistance of the electrolyte arises primarily near the wire surface where the cross-sectional area normal to current flow is small. Therefore it seems reasonable that differences between the two models in prediction of reaction rate distributions would depend primarily on whether unidirectional radial flow occurred near the wire surface. Far away from the wire surface, deviations from one-dimensional current flow may indeed occur, but their effect on over-all cell behavior would be minimal since the regions far from the wire surface do not contribute an appreciable ohmic resistance to the cell. In addition, it seems reasonable that differences between the two models would arise only when the resistance of the electrolyte consumed an appreciable fraction of the applied potential: that is, significant deviations from unidirectional radial flow may be anticipated when the reaction rate distribution is nonuniform and, at the same time, when the solution resistance is appreciable. On the basis of earlier discussion, the current distribution will be nonuniform when the parameter  $\xi$  has a large value. In addition, the resistance of the solution will be appreciable when  $\psi$  has a large value; however, too large a value of  $\psi$  will render the reaction rate distribution uniform as was shown in Fig. 4. Therefore deviations between one- and two-dimensional monopolar calculations are most likely to affect the predicted reaction rate distribution when  $\xi$  is large, and when  $\psi$  is in the range between 0.1 and 10.

The potential distribution in the solution is given by Eq. [A-1-3]. If the unidirectional approximation is suitable near the wire surface, then the ratio of axial to radial potential gradients must be very small everywhere along the wire surface. By appropriate differentiation of Eq. [A-1-3], one obtains the conditions

$$\frac{\partial\Phi}{\partial\xi} \Big|_{\rho=1} = \frac{-\sum_{n=1}^{\infty} B_n \lambda_n \sin(\lambda_n \xi)}{-\frac{B_0}{\ln \rho_0} + \sum_{n=1}^{\infty} B_n R_n'(1) \cos(\lambda_n \xi)}$$

$$\frac{\partial\Phi}{\partial\rho} \Big|_{\rho=1} = \frac{2 \sum_{n=1}^{\infty} B_n \lambda_n \sin(\lambda_n \xi)}{\psi \beta J(\xi)} \quad [25]$$

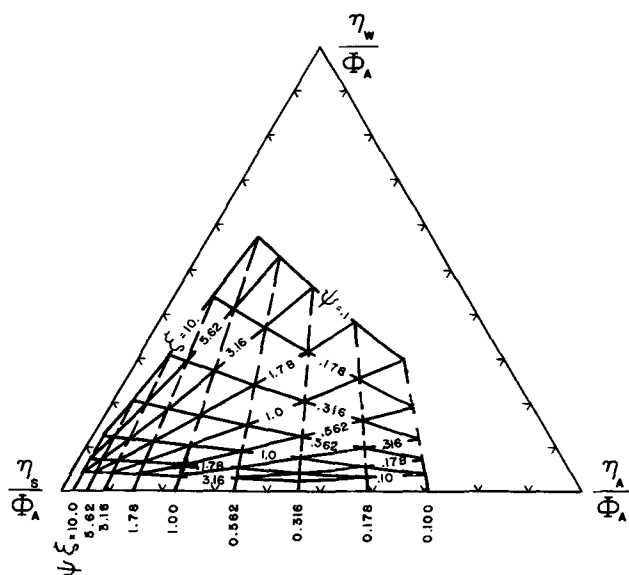


Fig. 7. Compilation of overpotential partitioning for monopolar resistive electrode ( $\Phi_A = 3$ ,  $\rho_0 = 1000$ ).

which may be evaluated if the  $B$ -coefficients are known from a converged two-dimensional solution. The ratio given by Eq. [25] is equivalent to the ratio of axial to radial current flowing near the wire surface. The ratio therefore has zero values at  $\xi = 0$  and 1, the insulating end planes, but takes on nonzero values at intermediate positions. From the right hand side of Eq. [25], it is seen that the assumption becomes worse as  $\psi$  becomes small; however, as noted above, small  $\psi$  corresponds to a situation where the electrolyte resistance is negligible so that errors would be of little consequence. For the conditions  $\xi = 100$ ,  $\psi = 1$ ,  $\rho_0 = 10$ ,  $\gamma = 10^{-3}$ , the largest axial current was found to be 0.15% of the radial current at the wire surface. Larger deviations were found for very short, fat wires, but such geometries are not commonly found among practical situations involving resistive wires. For the geometries associated with the practical applications cited in the introductory remarks, the flow of current in the electrolyte may be taken to be unidirectional in the radial direction.

When  $\rho_0$  has a small value, the current density at the counterelectrode may be large so that polarization would occur, violating assumption (vi). For unidirectional radial flow, the current density along the



counterelectrode would be

$$j_{c.e.}(z) = \frac{r_1}{r_0} j_{wire}(z)$$

If, however, the maximum current density along the counterelectrode is not to be greater than the exchange current density of the counterelectrode reaction, then

$$j_{c.e.}^{max} \leq i_{oc.e.}$$

One thereby, arrives at a criterion for judging whether the counterelectrode would be polarized

$$\rho_0 \geq \frac{\beta_{wire} j_{wire}^{max}}{\xi_{c.e.}} \quad [26]$$

#### Bipolar Electrode

The approximate bipolar electrode model has been treated in Ref. (28). Since the over-all qualitative features are discussed therein, we choose not to duplicate them here. Instead, attention will be focused on the region of validity of the one-dimensional model by comparing results with the two-dimensional bipolar model. The parameter  $\chi$ , which arises in the one-dimensional treatment is related to the parameters of the two-dimensional model by

$$\chi = \frac{\xi\psi}{\gamma^2(\rho_0^2 - 1)} \quad [27]$$

According to earlier discussion, it is anticipated that deviations between the two models will occur when two conditions are met: (I) the current distribution is nonuniform and (II) an appreciable fraction of the applied potential is consumed by electrolyte resistance effects. That is,  $\xi$  should be larger than unity, say 100. For the one-dimensional model, the range  $1 < \chi < 1000$  was found to satisfy the second condition (28).

A simple basis for comparing the models is to examine the over-all cell conductivity ( $\beta/\Phi_A$ ) predicted by the models. Figure 8 shows how the ratio of two-dimensional to one-dimensional over-all conductivity varies with the parameters  $\psi$ ,  $\gamma$ , and  $\rho_0$ . Deviations from one-dimensional behavior occur when the value of the ordinate differs from unity. Deviations always occur such that the ordinate-ratio is less than unity; that is, the two-dimensional  $\beta$  is less than the one-dimensional  $\beta$ . This observation is reasonable since the one-dimensional model does not take account of the added ohmic resistance caused by the radial component of current flow. For  $\rho_0 = 10$ , it may be seen that appreciable deviations set in when the value of  $\gamma$  exceeds 0.01, and when  $\psi$  lies in the range  $10^{-3} < \psi < 10$ . For  $\rho_0 = 1000$ , deviations occur over the range  $10^{-4} < \psi < 10$ .

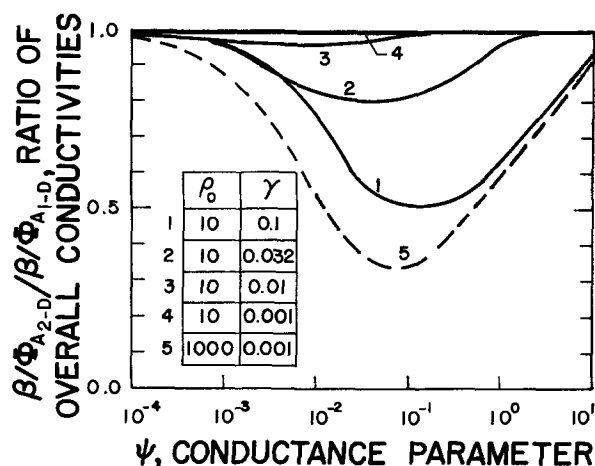


Fig. 8. Comparison of one-dimensional and two-dimensional bipolar electrode models ( $\Phi_A = 1$ ,  $\xi = 100$ ).

The basis chosen for comparing one- and two-dimensional models in Fig. 8 is arbitrary and may not be suitable for some purposes. Nevertheless, on that basis, the calculations carried out in this study indicate that the one-dimensional approximation is good provided that

$$\rho_0 \gamma < 0.1 \quad [28]$$

That is, the cell length should exceed five times the cell diameter.

#### Conclusions

The powerful method developed above for calculating current and potential distributions is reasonably flexible with respect to the underlying assumptions. In particular, alternative reaction rate expressions characteristic of special applications may easily be substituted in place of the Butler-Volmer expression. In addition, multiple electrochemical reactions, such as during alloy deposition or gassing during cyanide plating, could be incorporated with ease. The one-dimensional monopolar model may easily be expanded to include effects associated with counterelectrode polarization, counterelectrode ohmic resistance, and multiple counterelectrode contacts; excessive costs would arise in investigation of these effects by expanding the two-dimensional model.

For geometric configurations typical of practical applications, both monopolar and bipolar electrode systems may be accurately approximated by unidirectional current models. The importance of this knowledge is that a relatively straightforward path is now available for superimposing mass transport considerations onto the theoretical models. For example, by incorporating Eq. [9], the mass transport models of Alkire (22) and of Alkire and Tvarusko (23) may be expanded to account for electrolyte resistance effects. For slow moving wires where the mass transfer boundary layer exists under laminar flow conditions, the convective diffusion equation may be incorporated into the model with use of the Lighthill transformation method (30). For turbulent flow, local mass transfer coefficients may be employed following the method of Ref. (22).

By taking into account simultaneously the phenomena of mass transfer, electrolyte resistance, electrode resistance, and charge-transfer overpotential, the above-suggested expansions of the present investigation will permit the analysis of high-rate processes at wire electrodes.

#### Acknowledgment

This study constituted partial fulfillment of requirements for a Master of Science degree in the Department of Chemical Engineering, University of Illinois, Urbana-Champaign. The investigation received the support of the National Science Foundation (Grant GK-36623). Computer costs were partially supported by the University of Illinois Research Board. The authors benefited from discussions with Professor John Newman, University of California at Berkeley. Part of this study was conducted while the junior author (R.V.) received a fellowship sponsored by the Esso Research and Engineering Company.

Manuscript submitted July 30, 1973; revised manuscript received ca. Dec. 19, 1973. This was Paper 230 presented at the Chicago, Illinois, Meeting of the Society, May 13-18, 1973.

Any discussion of this paper will appear in a Discussion Section to be published in the December 1974 JOURNAL. All discussions for the December 1974 Discussion Section should be submitted by Aug. 1, 1974.

#### APPENDIX I

In dimensionless notation, Eq. [5] is

$$\frac{1}{\gamma^2 \rho} \frac{\partial}{\partial \rho} \left( \rho \frac{\partial \Phi}{\partial \rho} \right) + \frac{\partial^2 \Phi}{\partial \xi^2} = 0 \quad [A-I-1]$$

which may be solved by separation of variables

$$\Phi(\rho, \xi) = \sum_{n=0}^{\infty} R_n(\rho) Z_n(\xi) \quad [\text{A-I-2}]$$

For the monopolar electrode, the result is

$$\Phi(\rho, \xi) = B_0 \left( 1 - \frac{\ln \rho}{\ln \rho_0} \right) + \sum_{n=1}^{\infty} B_n R_n(\rho) \cos(\lambda_n \xi) \quad [\text{A-I-3}]$$

where

$$R_n(\rho) = \frac{K_0(\lambda_n \gamma \rho) - \frac{K_0(\lambda_n \gamma \rho_0)}{I_0(\lambda_n \gamma \rho_0)} I_0(\lambda_n \gamma \rho)}{K_0(\lambda_n \gamma) - \frac{K_0(\lambda_n \gamma \rho_0)}{I_0(\lambda_n \gamma \rho_0)} I_0(\lambda_n \gamma)}$$

The  $\lambda_n$  are the eigenvalues in the  $\xi$  direction. The  $B_0$ -term in Eq. [A-I-3], for  $\lambda = 0$ , provides a logarithmic radial potential distribution in the electrolyte when current distribution along the wire is uniform. For the bipolar electrode, one finds

$$\Phi(\rho, \xi) = B_0 + \sum_{n=1}^{\infty} B_n R_n(\rho) \cos(\lambda_n \xi) \quad [\text{A-I-4}]$$

where

$$R_n(\rho) = \frac{[I_1(\lambda_n \gamma \rho_0) K_0(\lambda_n \gamma \rho) + K_1(\lambda_n \gamma \rho_0) I_0(\lambda_n \gamma \rho)]}{[I_0(\lambda_n \gamma) K_1(\lambda_n \gamma \rho_0) + I_1(\lambda_n \gamma \rho_0) K_0(\lambda_n \gamma)]}$$

The  $B_0$ -term arises when  $\lambda = 0$ .

At wire surface ( $\rho = 1$ ), Eq. [A-I-3] and [A-I-4] both have the form

$$\Phi(1, \xi) = \Phi_S(\xi) = B_0 + \sum_{n=1}^{\infty} B_n \cos(\lambda_n \xi) \quad [15]$$

## APPENDIX II

By combining Eq. [1] and [2], setting them into integral form, and rendering them dimensionless, one obtains

$$\Phi_M(\xi) = \beta \int_0^{\xi} \int_0^{\xi} J(\zeta) d\zeta d\zeta \quad [\text{A-II-1}]$$

The dimensionless form of Eq. [4] is

$$-\frac{\psi \beta J}{2} = \frac{\partial \Phi}{\partial \rho} \Big|_{\rho=1} \quad [\text{A-II-2}]$$

For the monopolar wire, substitution of Eq. [A-I-3] into [A-II-2] yields

$$-\frac{\psi \beta J}{2} = -\frac{B_0}{\ln \rho_0} + \sum_{n=1}^{\infty} B_n R_n'(1) \cos(\lambda_n \xi) \quad [\text{A-II-3}]$$

Substituting Eq. [A-II-3] into Eq. [A-II-1] then gives

$$\Phi_M(\xi) = \frac{2}{\psi} \int_0^{\xi} \int_0^{\xi} \left[ \frac{B_0}{\ln \rho_0} - \sum_{n=1}^{\infty} B_n R_n'(1) \cos(\lambda_n \xi) \right] d\zeta d\zeta \quad [\text{A-II-4}]$$

where the boundary conditions are

$$\begin{aligned} \Phi_M(0) &= \Phi_A \\ \frac{d\Phi_M(1)}{d\xi} &= 0 \end{aligned}$$

After integration, the result for the monopolar wire is

$$\begin{aligned} \Phi_M(\xi) &= \Phi_A - \frac{2B_0\xi}{\psi \ln \rho_0} + \frac{B_0\xi^2}{\psi \ln \rho_0} \\ &\quad - \frac{2}{\psi} \sum_{n=1}^{\infty} \frac{B_n R_n'(1)}{\lambda_n^2} [1 - \cos(\lambda_n \xi)] \quad [\text{A-II-5}] \end{aligned}$$

An analogous result may be found for bipolar electrodes by combining Eq. [A-I-4] with [A-II-1] and [A-II-2] to obtain

$$\Phi_M(\xi) = -\frac{2}{\psi} \sum_{n=1}^{\infty} B_n R_n'(1) \int_0^{\xi} \int_0^{\xi} \cos(\lambda_n \zeta) d\zeta d\zeta \quad [\text{A-II-6}]$$

with boundary conditions

$$\begin{aligned} \Phi_M(0) &= \Phi_A \\ \Phi_M(1) &= 0 \end{aligned}$$

Integration yields

$$\begin{aligned} \Phi_M(\xi) &= \Phi_A \\ &+ \left\{ \frac{2}{\psi} \sum_{n=1}^{\infty} \frac{B_n R_n'(1)}{\lambda_n^2} [1 - (-1)^n] - \Phi_A \right\} \xi \\ &\quad - \frac{2}{\psi} \sum_{n=1}^{\infty} \frac{B_n R_n'(1)}{\lambda_n^2} [1 - \cos(\lambda_n \xi)] \quad [17] \end{aligned}$$

## APPENDIX III

The following procedure illustrates the method used to calculate the  $B$ -coefficients from trial values of the potential distribution. By eliminating the current distribution,  $J(\zeta)$ , from Eq. [18] and [A-II-2], and by incorporating the derivative of Eq. [A-I-3], one obtains, for a monopolar electrode, the result

$$\begin{aligned} -\frac{\psi \xi}{2} [e^{\alpha(\Phi_M - \Phi_S)} - e^{(\alpha-1)(\Phi_M - \Phi_S)}] \\ = -\frac{B_0}{\ln \rho_0} + \sum_{n=1}^{\infty} B_n R_n'(1) \cos(\lambda_n \xi) \quad [\text{A-III-1}] \end{aligned}$$

The exponential terms on the left side of Eq. [A-III-1] are then linearized about trial potential distributions: that is, let the unknown potential distributions be combined to form

$$\eta_A = \Phi_M - \Phi_S$$

and denote the trial distributions, known from the previous iteration step, by

$$\eta_A^* = (\Phi_M - \Phi_S)_{\text{trial values}}$$

The right hand side of Eq. [A-III-1] can then be made linear with respect to the unknown distribution,  $\eta_A$

$$\begin{aligned} -\frac{B_0}{\ln \rho_0} + \sum_{n=1}^{\infty} B_n R_n'(1) \cos(\lambda_n \xi) = \\ -\frac{\psi \xi}{2} \{ [e^{\alpha \eta_A^*} - \alpha \eta_A^* e^{\alpha \eta_A^*} - e^{(\alpha-1)\eta_A^*} \\ + (\alpha-1)\eta_A^* e^{(\alpha-1)\eta_A^*} \\ + [\alpha e^{\alpha \eta_A^*} - (\alpha-1)e^{(\alpha-1)\eta_A^*}] \eta_A \} \quad [\text{A-III-2}] \end{aligned}$$

Because subsequent equations become voluminous, only the basic outline will be described henceforth. Interested readers may find full details of the derivations in Ref. (32).

Substitute Eq. [15] and [16], for  $\Phi_M$  and  $\Phi_S$ , into the  $\eta_A$  term of Eq. [A-III-2] and denote the result as Eq. [A-III-3]. Now integrate both sides of Eq. [A-III-3] from  $\xi = 0$  to  $\xi = 1$ . The result may be solved algebraically to obtain

$$B_0 = f_1(B_n) \quad [\text{A-III-4}]$$

That is,  $B_0$  may be calculated if the  $B_n$ -coefficients are known. Now, by orthogonality, evaluate the  $B_n$ -coefficients by multiplying Eq. [A-III-3] by  $\cos(\lambda_n \xi)$  and then integrating from  $\xi = 0$  to  $\xi = 1$  in order to obtain an expression of the form

$$B_n = f_2(B_0) \quad [\text{A-III-5}]$$

That is, the  $B_n$ 's may be calculated if  $B_0$  is known. Now multiply Eq. [A-III-5] by the quantity

$$\xi[\alpha e^{\alpha\eta_A^*} - (\alpha - 1) e^{(\alpha-1)\eta_A^*}] \frac{R_n'(1)}{\lambda_n^2}$$

and sum all the  $n$ -equations; substitute the result into Eq. [A-III-4] to eliminate the  $B_n$  terms therein. The coefficients  $B_0$  may now be calculated directly from the trial distribution,  $\eta_A^*$ . In turn, the  $B_n$ 's are subsequently found from Eq. [A-III-5].

The procedure for determining the bipolar  $B$ -coefficients is identical to that given above except that Eq. [A-I-4] is used in place of Eq. [A-I-3].

#### SYMBOLS

$B_0, B_n$	coefficients of infinite series for potential distribution
$F$	Faraday's constant, 96,500 coulombs/g-equiv.
$f(z)$	quantity within large brackets in Eq. [3]
$i_m$	current density in metal electrode, A/cm <sup>2</sup>
$i_o$	exchange current density, A/cm <sup>2</sup>
$i^o$	current density in electrode at electrical contact point, A/cm <sup>2</sup>
$i_s$	current density in solution, A/cm <sup>2</sup>
$I_0, I_1$	modified Bessel functions of first kind, of order 0 and 1
$j$	local reaction rate along electrode, A/cm <sup>2</sup>
$J$	local reaction rate along electrode, dimensionless
$K_0, K_1$	modified Bessel functions of second kind, of order 0 and 1
$L$	length of wire electrode, cm
$n$	number of electrons in electrode reaction, g-equiv./g-mole
$r$	spatial variable in radial direction, cm
$r_1$	radius of wire electrode, cm
$r_o$	radius of outer cylinder as in Fig. 1, cm
$R$	gas constant, 8.31 joule/g-mole °K
$R_n$	radial component of potential field, Eq. [A-I-2]
$T$	temperature, °K
$z$	spatial variable in axial direction, cm
$Z_n$	axial component of potential field, Eq. [A-I-2]
<i>Greek characters</i>	
$\alpha$	transfer coefficient in rate equation
$\beta$	current density in wire electrode at electrical contact end, dimensionless
$\gamma$	geometric parameter, dimensionless
$\zeta$	spatial variable in axial direction, dimensionless
$\kappa$	electrolyte conductivity, (ohm-cm) <sup>-1</sup>
$\xi$	reaction velocity parameter, dimensionless
$\rho$	spatial variable in radial direction, dimensionless
$\rho_0$	geometric parameter, dimensionless
$\sigma$	electrode conductivity, (ohm-cm) <sup>-1</sup>
$\phi$	potential in electrolyte, V
$\phi_A$	applied potential, V
$\phi_m$	potential in electrode, V
$\phi_s$	potential in electrolyte adjacent to electrode, V
$\Phi$	potential in electrolyte, dimensionless
$\Phi_A$	applied potential, dimensionless
$\Phi_M$	potential in electrode, dimensionless
$\Phi_S$	potential in electrolyte adjacent to electrode, dimensionless

$\chi$  bipolar conductivity parameter, dimensionless  
 $\psi$  conductivity parameter, dimensionless

#### REFERENCES

- W. E. Hoare, E. S. Hedges, and B. T. K. Barry, "The Technology of Tinplate," St. Martin's Press, New York (1965).
- C. L. Mantell, "Electrochemical Engineering," 4th ed., p. 116 ff., McGraw-Hill Book Co., New York (1960).
- J. S. Mathias and G. A. Fedde, *IEEE Trans. Magnetics*, **MAG-5**, 728 (1969).
- R. E. Visco, Paper 227 presented at Electrochemical Society Meeting, Chicago, Illinois, May 13-18, 1973.
- R. Haynes, Paper 228 presented at Electrochemical Society Meeting, Chicago, Illinois, May 13-18, 1973.
- A. Weisselberg and Staff, *Trans. Electrochem. Soc.*, **90**, 235 (1946).
- V. Fomichev, *Soviet Electrochem.*, **4**, 708 (1968).
- J. T. Waber, *Trans. Electrochem. Soc.*, **90**, 243 (1946).
- B. Conway, E. Gileadi, and H. Oswin, *Can. J. Chem.*, **41**, 2447 (1963).
- S. Ranganajan, M. Dignam, and B. Conway, *ibid.*, **45**, 422 (1967).
- J. Wojtowicz, L. Laliberte, and B. Conway, *Electrochim. Acta*, **13**, 361 (1968).
- A. Böhnlein, *Metalloberfläche*, **6**, 210 (1970).
- B. C. Sakiadis, *A.I.Ch.E. J.*, **7**, 26, 221, 467 (1961).
- R. M. Griffith, *Ind. Eng. Chem., Fundamentals*, **3**, 245 (1964).
- L. E. Erickson, L. T. Fan, and V. G. Fox, *Ind. Eng. Chem., Fundamentals*, **5**, 19 (1966); *A.I.Ch.E. J.*, **14**, 726 (1968); **15**, 327 (1969).
- J. W. Rotte, G. L. J. Tummers, and J. L. Dekker, *Chem. Engr. Sci.*, **24**, 705, 1009 (1969).
- F. Coeuret and F. Vergnes, *C. R. Acad. Sci. Paris, Ser. C*, **273**, 580 (1971).
- J. Paukert, *Elektrotech. Časopis*, **17**, 625 (1966); *Povrchove Upravy*, **6**, 137 (1966).
- R. C. Lindberg and R. A. Schmitz, *Chem. Eng. Sci.*, **24**, 1113 (1969).
- T. Hoshino and T. Sawada, *Bull. Univ. Osaka Prefecture, Ser. A, Engr. Nat. Sci.*, **19**, 253 (1970).
- A. Tvarusko, *This Journal*, **119**, 43 (1972).
- R. Alkire, *ibid.*, **118**, 1935 (1971).
- R. Alkire and A. Tvarusko, *ibid.*, **119**, 340 (1972).
- C. Tobias and R. Wijsman, *ibid.*, **100**, 459 (1953).
- S. Ishizaka, H. Matsuda, and Y. Wada, *J. Electrochem. Soc. Japan*, **22**, 420 (1954).
- W. Harvey, *This Journal*, **109**, 638 (1962).
- K. Nakata, T. Akimoto, and N. Fujise, *Denki Kagaku*, **38**, 763 (1970).
- R. Alkire, *This Journal*, **120**, 900 (1973).
- J. Newman, *ibid.*, **113**, 1235 (1966); W. R. Parrish and J. Newman, *ibid.*, **116**, 169 (1969); W. R. Parrish and J. Newman, *ibid.*, **117**, 43 (1970).
- R. Alkire and A. Mirarefi, *ibid.*, **120**, 1507 (1973).
- J. Newman, *Ind. Eng. Chem., Fundamentals*, **7**, 514 (1968).
- R. D. Varjian, M. S. Thesis, Dept. Chem. Engr., University of Illinois, Urbana-Champaign, October 1973.

# Electrode Capacitance in Silver-Halide Solid Electrolyte Cells

## I. Room Temperature Graphite and Platinum Electrodes

Douglas O. Raleigh\*

Science Center, Rockwell International, Thousand Oaks, California 91360

### ABSTRACT

Potentiostatic chronocoulometry on polarized graphite electrodes on AgI and AgBr solid electrolytes at room temperature shows an ideally fast, almost voltage-independent, double layer charging process for both electrolytes. Results on the more highly conductive electrolyte  $2[(\text{CH}_3)_4\text{NI}] \cdot 13 \text{ AgI}$  are similar to AgI, but with moderate capacitance dispersion in the subsecond time range. For all three electrolytes, the results suggest charging by a compact, purely electrostatic, interfacial  $\text{Ag}^+$ -ion layer separated from the graphite surface by a strongly adsorbed anion layer. For platinum electrodes on AgI and AgBr, a variety of types of platinum and surface pretreatments gave the common result of a slow, broadly dispersed charging process. The Pt results are consistent with a previously proposed interface model in which charging involves both cation and anion motion, and suggests that slow charging results from the relatively immobile anions. The relationship between various types of double layer capacitance in solid electrolytes is discussed.

It has been of continuing interest in our laboratory to characterize the nature of electrode double layer capacitance in solid-electrolyte systems (1-4). Several years ago, Hull and Pilla (5) reported some intriguing findings with pressed-powder pellet cells  $\text{Ag}|\text{AgI}|\text{C}$  and  $\text{Ag}|\text{AgI}|\text{Pt}$ . It was of interest for a variety of reasons to pursue these experiments further, extending them to other  $\text{Ag}^+$ -ion electrolytes, other types of graphite and platinum electrodes, and above-ambient temperatures.

In the Hull-Pilla work, the cells were formed by successively compacting powders of their components in a cylindrical die, and included an embedded Ag wire reference electrode midway in the electrolyte, which was partially exposed after pressing. The experiments included applying small potential steps atop a polarizing d-c bias (Ag electrode negative,  $<0.5\text{V}$ ) and observing the current-time behavior oscillographically with varying degrees of electronic IR compensation. With graphite electrodes, plots of  $\log i$  vs.  $t$  were linear over several current decades for a wide range (tens of microsecond to second) of effective cell time constants, and indicated a single, bias-independent capacitance with ideally fast (undispersed) charging kinetics. With platinum electrodes,  $\log i$  vs.  $t$  plots were not linear. Large ( $\sim 10^4 \mu\text{f}/\text{cm}^2$ ), bias-dependent total capacitances were reported, with considerable dispersion on all time scales. It was suggested that the graphite capacitance,  $8.0 \mu\text{f}/\text{cm}^2$ , involved a purely electrostatic compact charge layer of  $\text{Ag}^+$  ions, while the platinum results represented large faradaic effects throughout the voltage range, involving silver and iodine deposition and stripping.

The graphite results were surprising, in view of the method of interface preparation and the capacitance dispersion generally reported for unpolished solid electrodes in aqueous systems (6). In our own laboratory, a previous study (2) showed considerable dispersion for pyrolytic graphite foil electrodes on AgBr at  $244^\circ$ - $292^\circ\text{C}$ . It was of interest to determine in the present work whether the dispersion-free behavior was specific to AgI, to graphite powder electrodes, and to ambient temperatures.

In the case of platinum, the large capacitances obtained were in contrast to our own work with polished

Pt wire electrodes in AgBr in the neighborhood of its melting point (3). In this latter work, 30-fold smaller capacitances were obtained that showed a broad time range of undispersed behavior and could be fitted to a model involving an interfacial electrolyte layer of adsorbed anions and cations. It was felt that the Hull-Pilla results might reflect faradaic impurities specific to their use of platinum black as the electrode material, and that other forms of platinum might give different results. Additionally, we noted in our own work that the platinum capacitance progressively acquired dispersion on cooling from the AgBr melting point, and suggested that this might involve an interface strain due to differing thermal contraction rates of AgBr and Pt. For both these reasons, it was of interest in the present work to determine whether a properly prepared  $\text{Pt}|\text{AgX}$  interface would show undispersed charging at room temperature.

In the present work, the electrolytes investigated were AgI, AgBr, and the recently discovered (7) composition  $2[(\text{CH}_3)_4\text{NI}] \cdot 13 \text{ AgI}$ . Silver bromide was studied in view of our previous investigations (1-3). Both AgI and AgBr have low bulk ionic conductivities at room temperature ( $\sim 10^{-8} \text{ ohm}^{-1} \text{ cm}^{-1}$ ), so their compacted powders conduct predominantly via grain boundary paths, with effective conductivities of  $10^{-4}$ - $10^{-6} \text{ ohm}^{-1} \text{ cm}^{-1}$ . Because of this, it was desirable to study an electrolyte with good room temperature bulk conductivity as well. The tetramethylammonium iodide-silver iodide (TMAI) composition has an  $\text{Ag}^+$ -ion conductivity of  $0.041 \text{ ohm}^{-1} \text{ cm}^{-1}$  at  $22^\circ\text{C}$  (7) and was selected rather than the better known  $\text{RbAg}_4\text{I}_5$ , since the moisture sensitivity of the latter (8) would seem to lead to a questionable interface composition, even with careful inert-atmosphere handling techniques.

The preferred electrochemical technique in the present work was potential-step chronocoulometry rather than chronoamperometry, since it gives a direct visual indication of the charging process over a wide range of times scales. Chronoamperometry and cyclic voltammetry were occasionally used as supplementary techniques.

### Experimental

$\text{Ag}|\text{AgX}|\text{C}$  pressed-powder pellet cells with a 10-mil Ag wire reference electrode were prepared essentially by the Hull-Pilla procedure, except that a

\* Electrochemical Society Active Member.  
Key words: solid electrolyte, silver halides, double layer, electrode capacitance.

1/4 in. rather than 1/2 in. cylindrical die was used, so weights of materials were quartered. Finely ( $-325$  mesh) powdered, 5N grades of Ag, AgI, and AgBr were used, and spectroscopic graphite powder. A sample of  $2[(\text{CH}_3)_4\text{NI}] \cdot 13 \text{ AgI}$ , which was obtained from Dr. B. B. Owens, was prepared as previously described (7). In one AgI cell, the carbon electrode was a freshly cleaved thin foil of the stress-annealed pyrolytic graphite used in the previous study (2). Additionally, two Ag|AgI compacts were pressed, leaving a smooth free AgI face which was spray-coated with a several-micron layer of Acheson "Dag 154" graphite dispersion in 1:5 methanol.

A variety of Ag|AgX|Pt cells were prepared, using AgI or AgBr. Cells employing  $-100$  mesh platinum powder, Pt filings, or Pt foil were prepared essentially as above. The filings and foil were pretreated by boiling in concentrated  $\text{HNO}_3$ , rinsing, boiling in concentrated HCl, rinsing, and air- or oven-drying. The 99.95% Pt powder was used as is. Most experiments, however, were carried out with an embedded Pt wire electrode, as shown in Fig. 1. The embedded wire was partially exposed after pressing, and the two Ag end layers were electrically connected to serve as a single large counterelectrode. In general, the wire electrode pretreatment was the same as for filings and foil, except that the HCl boil was preceded by heating the wire to orange-yellow several times in the outer part of an air-gas torch flame. Additionally, in one embedded-wire cell, no pretreatment was used and, in two others (one each AgI and AgBr), the pretreatment was followed by argon-sputtering the wire in an Auger ion-bombardment apparatus directly prior to cell preparation.

All measurements were made in the ambient laboratory atmosphere, with the cell lightly springloaded between 1/4 in. metal rods in a Micarta cell holder. An 0.25V polarizing d-c bias was placed on the cell and measurements started after the steady-state cell current settled to  $\sim 1$  nA. In some cases, current settling was hastened by applying several voltage steps. Fifty millivolt potential steps of 10- $\mu\text{sec}$  rise time in the bias voltage range 25-425 mV anodic to Ag were applied with a standard 3-electrode (2-electrode for Pt wire cells) potentiostat (2), and the current or integrated charge response followed oscillographically and by recorder. Resistance compensation was not employed. Cyclic voltammetry, when used, was carried out with a standard arrangement.

In addition, electron micrographs of the AgBr|C and AgI|C interfaces were taken, using fractured powder cells and an Etec scanning electron microscope.

### Results

**Graphite powder electrodes.**—Oscillographic charge-time curves showed the same basic charging behavior for all three electrolytes. On applying a potential step, the integrated charge rose to a flat or slightly up-sloped "plateau" in a time of several RC constants, indicating a well-defined "fast" capacitance. Figure

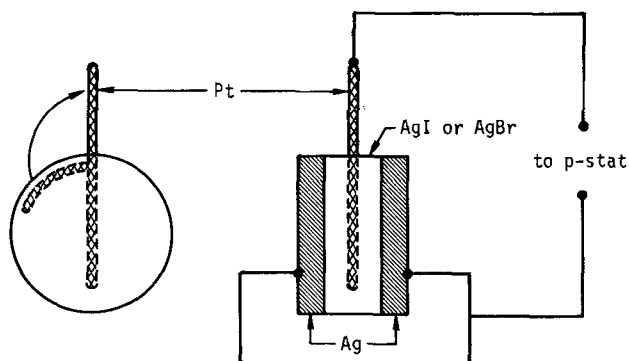


Fig. 1. Schematic of cell with embedded Pt wire electrode

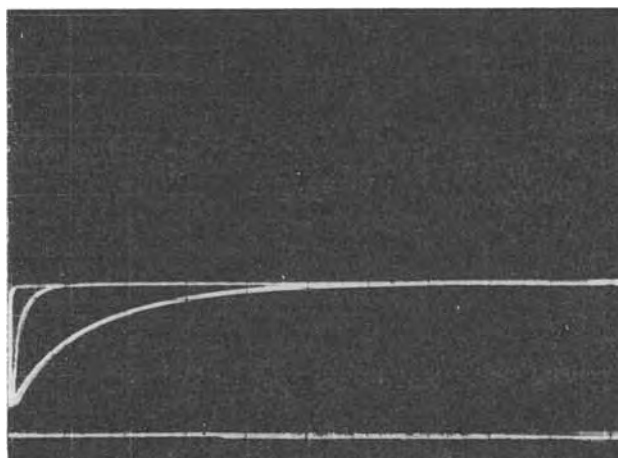


Fig. 2. Oscillographic charge-time traces for 0.25 $\rightarrow$ 0.20V step on Ag|AgI|C (pressed powder) cell. Sweep rates 5, 50, 500 msec/cm; ordinate 0.06  $\mu\text{coulomb/cm}$ . Bottom line is  $Q = 0$  reference level.

2 shows this behavior for an AgI cell over two decades of time.

For AgI and AgBr cells, supplementary measurements confirmed this picture. Potential-step oscillographic current-time data yielded exactly or closely linear  $\log i$  vs.  $t$  curves whose capacitance slopes agreed well with capacitances obtained chronocoulometrically. On longer time scales, recorder charge-time data for  $1 \leq t \leq 50$  sec and slow ( $\sim 1$  mV/sec) cyclic voltammetry showed in general 10-20% increased capacitances. However, plots of  $Q$  vs.  $t^{1/2}$  from the recorder data were linear and back-extrapolation to  $t = 0$  gave capacitances in agreement with the oscillographic data. Because of their random character from one cell to the next, these slow charge contributions are felt to reflect a diffusion-controlled faradaic impurity reaction. In view of the general slowness of impurity ion diffusion in solid electrolytes, the likely source of the impurity would be the graphite electrode. A  $Q$  vs.  $t^{1/2}$  plot from recorder data for an AgBr cell is shown in Fig. 3.

Data from some four AgI cells and seven AgBr cells show an averaged fast capacitance of  $9.3 \pm 3\%$   $\mu\text{f/cm}^2$  for the AgI|C (pressed powder) interface at the 0.225V voltage range midpoint and  $5.5 \pm 4\%$   $\mu\text{f/cm}^2$  for AgBr. The capacitances per unit area are calculated from the geometric pellet area. For AgI, data from the various cells showed a 3-8% capacitance increase over the bias range 0.05 to 0.40V, while AgBr

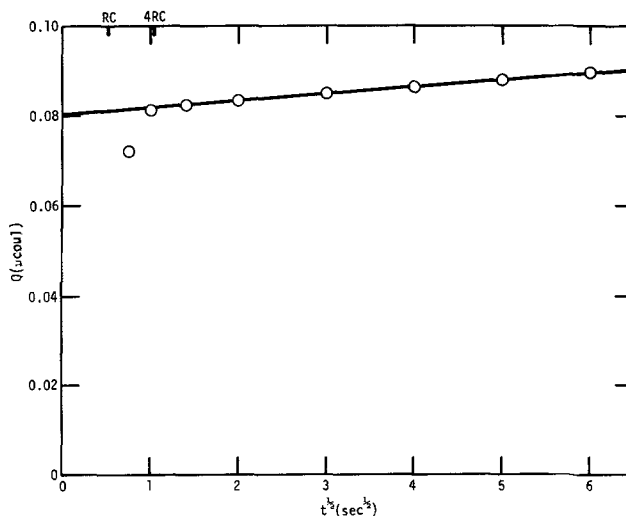


Fig. 3.  $Q$  vs.  $t^{1/2}$  plot for Ag|AgBr|C (pressed powder) cell from recorder data (0.25 $\rightarrow$ 0.20V step).

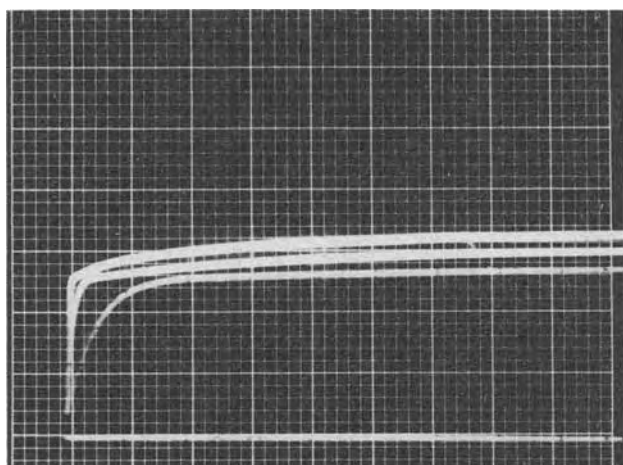


Fig. 4. Oscillographic charge-time traces for 0.25→0.20V step on Ag|TMAI|C (pressed powder) cell. Sweep rates 0.1, 0.5, and 2.0 msec/cm; ordinate 0.05  $\mu\text{coulomb/cm}$ .

cells showed no voltage dependence of capacitance within the accuracy of measurement (1-1/2%).

For the TMAI cells, the capacitance was not as cleanly describable in terms of an intrinsic "fast" component and a small, diffusion-like faradaic contribution. Figure 4 shows oscillographic charge-time traces for sweep rates of approximately 1.5, 7.5, and 30 RC rise times per centimeter for a typical cell. The fast sweep rate shows a nearly flat plateau, but slower sweeps show further charging. Chronocoulometric recorder data showed a "slow" capacitance amounting to ~50% of the total at  $t = 1$  min. The data yielded linear  $Q$  vs.  $t^{1/2}$  plots, but back-extrapolations to  $t = 0$  gave capacitance values some 6-60% higher than from various types of oscillographic data.

Table I shows capacitance data for three TMAI/C cells, using four types of capacitance determination: (A) slope of  $\log i$  vs.  $t$  plot from oscillographic current-time trace; (B) average  $Q$  value at 5-10 RC rise times from oscillographic chronocoulometry (Fig. 4); (C)  $t = 0$  back-extrapolation of  $Q$  vs.  $t^{1/2}$  plot from oscillographic data ( $0.2 \leq t^{1/2} \leq 1.0 \text{ sec}^{1/2}$ ); and (D)  $t = 0$  back-extrapolation of  $Q$  vs.  $t^{1/2}$  plot from recorder data ( $1 \leq t^{1/2} \leq 7 \text{ sec}^{1/2}$ ). As seen, individual cell values for a given type measurement agree well, but the various determinations do not suggest a well-defined "fast" capacitance. The bias dependence of the TMAI/C (pressed powder) capacitance was found to be in the range of that for AgI.

For all the graphite powder cells, some capacitance changes were seen on standing, though the direction and degree were highly variable. For AgI and AgBr cells, capacitances were stable for at least several days and, in some cases, changed only 5-10% over a two-year period. For TMAI cells, large changes often occurred, even over several days. These changes are possibly due to atmospheric contamination effects. In all cases, the data reported are initial data, which showed good agreement among duplicate cells.

**Other graphite electrodes.**—As noted before, two AgI cells were made with a spray-coated colloidal graphite electrode and one with stress-annealed pyrolytic graphite foil. Since these cells involved smooth

electrode interfaces, one purpose of studying them was to see if their data could be used to estimate a roughness factor for the pressed-powder interfaces.

The pyrolytic graphite cell gave results quite similar to the pressed-powder cells. Flat chronocoulometric plateaus from oscillographic sweeps gave a capacitance of  $8.3 \mu\text{f/cm}^2$  at 0.225V and a bias dependence of +3.5% over the full voltage range. The result suggests a factor of 1.12 greater surface for the powder cell interfaces, relative to the smooth cleavage face of the pyrolytic foil. Further justification for this comparison will be presented in the Discussion section.

The spray-coated colloidal graphite cells also showed a well-defined fast capacitance, but the value was much smaller and its bias dependence differed. Well-defined oscillographic chronocoulometric plateaus showed a capacitance of  $0.45 \pm 2\% \mu\text{f/cm}^2$  at 0.225V. Plots of  $Q$  vs.  $t^{1/2}$  from 1-25 sec recorder data were linear and the back-extrapolated  $t = 0$  capacitance agreed well with the chronocoulometric data. Oscillographic  $\log i$  vs.  $t$  plots were essentially linear, but gave capacitances some 10-15% smaller than the chronocoulometric data. Thus, some fast-time dispersion is indicated. The bias voltage dependence was negative, with capacitance at 0.40V being ~12% lower than at 0.05V. Because of the 20-fold smaller capacitance than pressed-powder cells and negative bias dependence, it was felt that more than a simple interface area reduction due to smoothness was involved. It would seem that the effect of solvent and binder residues in the spray coatings is not negligible.

**Platinum electrodes.**—A common result in all platinum electrode cells was the lack of any well-defined "fast" charging contribution. Figure 5 shows a typical set of oscillographic charge-time traces. The chronocoulometric capacitance was observed to increase continuously on all time scales from tens of microsecond to tens of second, with no plateau or "shoulder" feature. This result was common to both AgI and AgBr. to all the Pt electrode types (powder, filings, foil, wire), all surface pretreatments, and occurred throughout the voltage range. In addition,  $\log i$  vs.  $t$  plots from oscillographic current-time traces were invariably seriously curved. The picture is one of a completely dispersed charging process.

Because of this behavior, well-defined "total" capacitances could not be obtained. However, even on the longest time scale (~10-15 min), effective chronocoulometric capacitances were several orders of magnitude smaller than the  $\sim 10^4 \mu\text{f/cm}^2$  values reported by Hull and Pilla for platinum black. Effective capacitances at  $t = 0.1$  sec were of order  $300 \mu\text{f/cm}^2$  for filings, 60

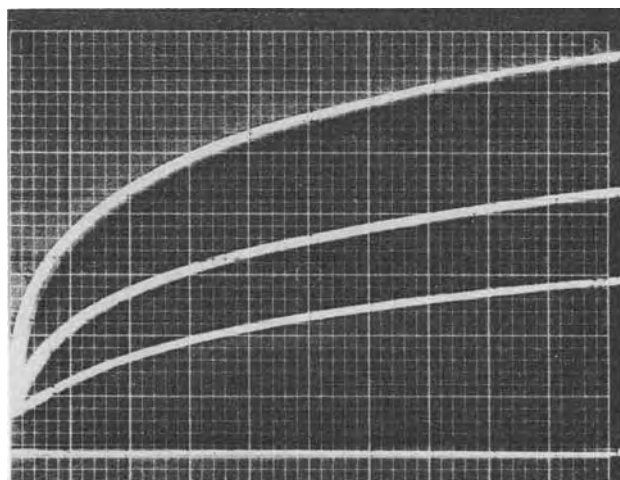


Fig. 5. Oscillographic charge-time traces for 0.25→0.20V step on Ag|AgI|Pt (embedded wire) cell. Sweep rates 0.05, 0.2, and 1.0 msec/cm; ordinate 500 pf/cm.

Table I. TMAI|C capacitances

Run	Measured capacitance ( $\mu\text{f/cm}^2$ )			
	Method A	Method B	Method C	Method D
1	6.8	8.6	9.3	10.0
2	7.2	9.0	10.6	11.0
3	6.7	8.4	11.4	12.1
Average	6.9	8.7	10.4	11.0

$\mu\text{f}/\text{cm}^2$  for powder, and  $0.3 \mu\text{f}/\text{cm}^2$  for foil and wire. Because of the uncertain effective interface areas and faradaic contributions for filings and powder, and poor adherence of the Pt foil, most experiments made use of embedded-wire cells (Fig. 1). While the electrode geometry in such cells should result in a "geometric" capacitance dispersion (16) due to nonuniform current distribution, such an effect with our geometry would involve only a small time span during the initial RC charging process. In view of the observed incompleteness of chronocoulometric charging over many decades of time, even in Pt cells with the cylindrical electrode geometry, this effect in the embedded-wire cells would be negligible. Results reported from this point are for embedded-wire cells.

It was not found possible to resolve potential-step chronocoulometric data into a partial diffusion-like contribution. Figure 6 shows a typical  $Q$  vs.  $t^{1/2}$  plot from recorder data. Most such plots from both oscilloscope and recorder data had the continuous curvature seen, with back-extrapolation to  $t = 0$  at the prevailing curvature leading toward the origin. In instances where a plot segment at the right side had a quasi-linear appearance, back-extrapolation gave a line from which the actual curve still deviated at times long compared with any estimate of RC rise time. Thus, the significance of the back-extrapolation would be in question. In several instances where a nearly linear plot was obtained, back-extrapolation brought the plot closely through the origin. The coexistence, then, of "fast" and diffusion-like charging components was not seen for the AgX|Pt interface.

Several duplicate AgI cells, in which the standard Pt wire pretreatment was used, gave similar interface charging characteristics, but gave capacitance magnitudes varying up to a factor of two among individual cells. Thus, random interface variations appear important. For a given cell, however, a consistent set of variations of capacitance behavior with voltage step direction, bias voltage, and time was observed which suggest a charging pattern in line with previous findings for the AgBr|Pt interface at elevated temperatures (3).

Figure 7 shows a set of  $Q$  vs.  $t^{1/2}$  plots from chronocoulometric recorder data for a standard-pretreatment AgI cell, using  $0.05\text{V}$  voltage steps over the full range of the bias voltage. While such plots are not generally linear, they offer a convenient means of displaying the charging behavior over an extended time span. At short times ( $t \sim 1$  sec), charge values tend to cluster together in the mid-voltage range, rise slightly at low voltage, and fall somewhat at high voltage. Though not readily seen in Fig. 7, the curvature is slightly convex upward for average voltages below

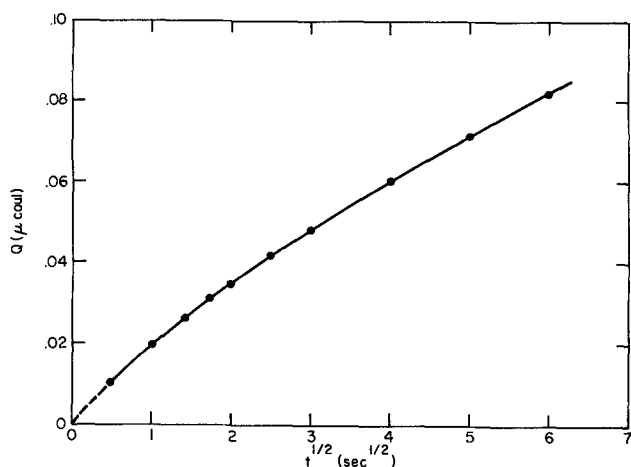


Fig. 6.  $Q$  vs.  $t^{1/2}$  plot for Ag | AgI | Pt (embedded wire) cell A from recorder data ( $0.25 \rightarrow 0.20\text{V}$  step).

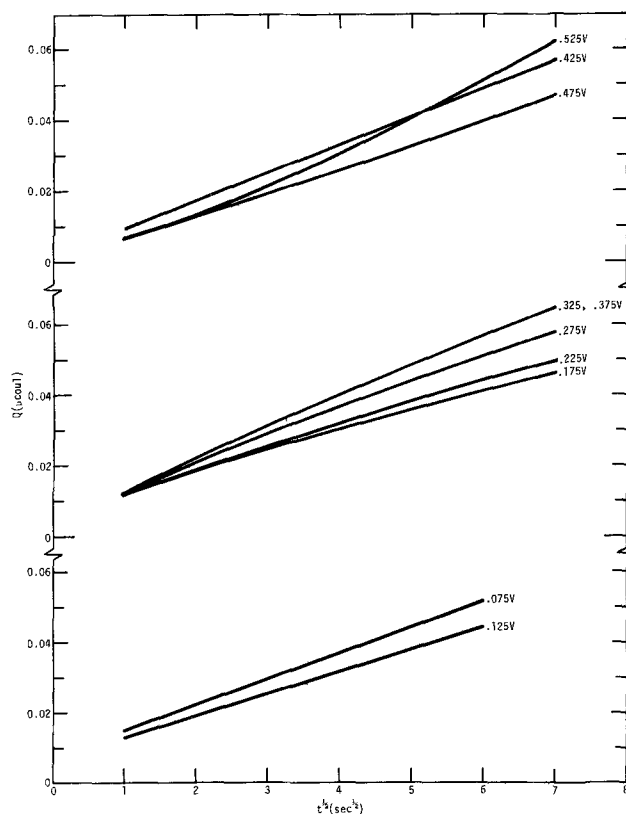


Fig. 7.  $Q$  vs.  $t^{1/2}$  plots for Ag | AgI | Pt (embedded wire) cell B for upward  $0.05\text{V}$  step at various average bias voltages (e.g.,  $0.225\text{V}$  is for  $0.20 \rightarrow 0.25\text{V}$  step). Curves displaced for clarity.

$0.425\text{V}$ , quasi-linear at  $0.425\text{V}$ , and slightly concave upward above  $0.425\text{V}$ .

Figure 8 shows the step direction dependence of charging for three voltage steps. The charging curve was always higher for the upward voltage step. The difference, however, was negligible below  $0.25\text{V}$ , in-

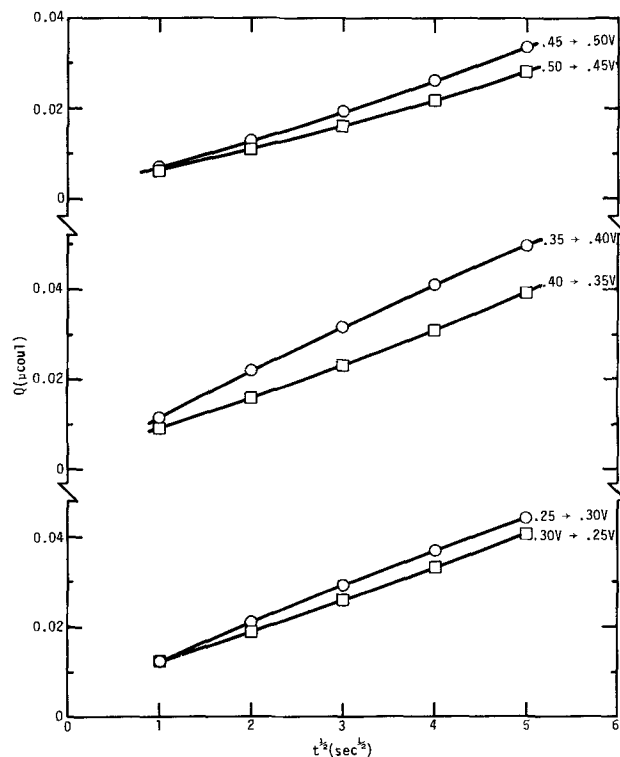


Fig. 8.  $Q$  vs.  $t^{1/2}$  plots for Ag | AgI | Pt (embedded wire) cell B for upward and downward  $0.05\text{V}$  steps at three average bias voltages. Curves displaced for clarity.



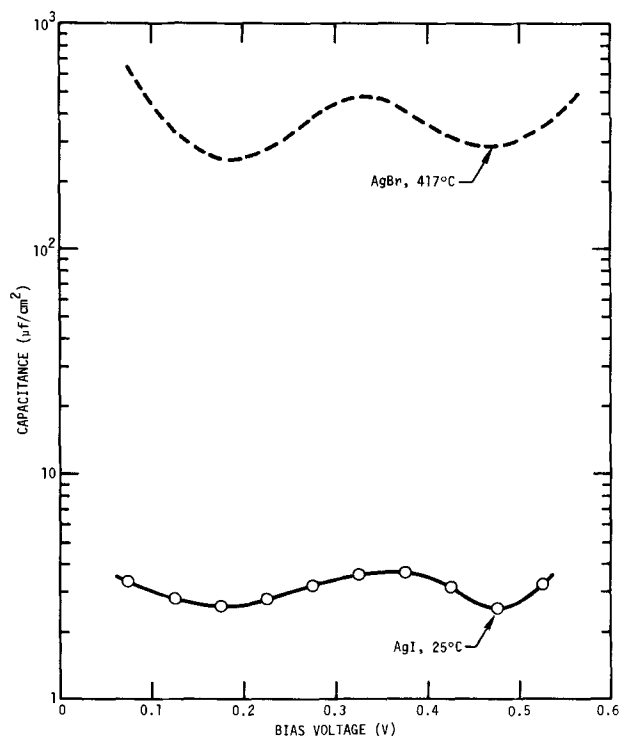


Fig. 9. A-C capacitance at 1 kHz for AgBr|Pt interface at 417° (3) compared with effective chronocoulometric capacitance for Ag|AgI|Pt cell B at  $t = 36$  sec, as function of bias voltage.

creased to a maximum at the 0.35-0.40V step, and decreased thereafter.

To get an idea of the bias voltage dependence, the capacitance corresponding to the  $Q$  value at  $t^{1/2} = 6$  (i.e., 36 sec) from Fig. 7 is plotted in Fig. 9 as a function of bias and compared with the undispersed a-c capacitance-voltage curve for AgBr|Pt at 417° from the previous study (3). We observe qualitatively the same voltage dependence, though considerably flattened, and a factor of 100 reduction in absolute magnitude. The comparison suggests that the previously observed onset of dispersion on cooling is an intrinsic property of the AgX|Pt interface rather than a result of differential thermal contraction strain. The various other features of the  $Q$  vs.  $t^{1/2}$  curves of Fig. 7 and 8 are discussed in terms of the previously proposed interface model in the Discussion section.

Results for AgBr cells were similar to those for AgI, except that serious irreproducibilities or "memory" effects were observed on bias voltage cycling unless inordinately long waiting times were employed at each voltage. Because of this, the above comparison with previous data was carried out with AgI rather than AgBr cells. However, capacitance magnitudes and the features of the  $Q$  vs.  $t^{1/2}$  plots at various biases were basically the same for AgI and AgBr cells.

Cyclic voltammetric data from an AgI cell in which there was no Pt wire pretreatment showed poor reproducibility on cycling and severalfold lowered capacitance from cells with the standard pretreatment. Hence, detailed chronocoulometric data were not taken.

For the cells in which the standard Pt wire pretreatment was followed by argon-sputtering (one each with AgI and AgBr),  $Q$  vs.  $t^{1/2}$  plots showed severalfold reduced capacitances and a slight concave-upward curvature for the 0.25 → 0.20V step data. Since these findings indicated generally reduced charging kinetics, this preparation technique was not pursued further. Results for the two cells, however, were extremely similar, again showing the basic similarity of the charging process with the two electrolytes.

As in the case of AgX|C cells, Pt electrode cells also showed capacitance changes on standing, possibly

because of atmospheric contamination. With the Pt cells, however, the change was invariably a decrease.

### Discussion

The findings for pressed-powder graphite cells with AgI and AgBr basically agree with those of Hull and Pilla in establishing that charging occurs predominantly by an intrinsically rapid process that depends but little on bias voltage. The average capacitance for AgI|C is some 16% higher than their value ( $8.0 \mu\text{f}/\text{cm}^2$ ), which may relate to the specific type of graphite used.

Hull and Pilla suggested that the capacitance arose from an ideal compact layer ("inner layer") of Ag<sup>+</sup> ions on the graphite surface, with the effective charge separation being the Ag<sup>+</sup> ionic radius and an assumed vacuum dielectric constant ( $K_D = 1$ ). This yields a theoretical parallel-plate capacitance of  $7.4 \mu\text{f}/\text{cm}^2$ . The assumption of a compact layer still seems reasonable, but the difference between AgBr and AgI capacitance (AgBr 41% lower) suggests the need for a modified picture. Further, the microscopic nature and roughness of the experimental interface needs consideration.

Figure 10 shows scan electron micrographs of an Ag|AgBr|C powder cell at two magnifications. A surprisingly flat interface is seen, with the roughness being a slight waviness at most. The AgBr crystallite particles appear to be pressed flat by a well-laminated graphite layer. The same results were seen for the AgI|C interface. An electron micrograph showed the unpressed graphite particles to be 5-10 $\mu$  diameter platelets. On pressing, it appears that the graphite flakes form an intermeshed, nearly planar front that flattens the relatively soft silver halide crystallites. On this basis, the similarity of graphite capacitances between pressed powder and pyrolytic foil seems reasonable. The 11% lower capacitance with pyrolytic foil presumably results from a slightly smoother interface.

While these results show a relatively low topographical roughness, one still expects microscopic roughness on a smaller scale, given that we have a solid-solid interface. Aqueous electrochemical studies, for instance, indicate a 1.5-2.0 microscopic roughness factor for smooth platinum electrodes (9, 10). It seems not unreasonable, then, to expect an over-all roughness factor  $\cong 2$ . Our experimental results then lead to maximal microscopic capacitances of 4.7 and 2.8  $\mu\text{f}/\text{cm}^2$  for AgI|C and AgBr|C, respectively. Using the parallel-plate capacitance expression

$$C = K_D \epsilon_0 / d \quad [1]$$

where  $C$  is the capacitance per unit area,  $K_D$  the dielectric constant,  $\epsilon_0$  the permittivity of free space, and  $d$  the plate separation, we find that even with the assumption of  $K_D = 1$ , these capacitances require  $d$  values greater than the Ag<sup>+</sup> ionic radius.

It would seem that both the electrolyte dependence of capacitance and the need for increased double layer charge separation  $d$  could be achieved by assuming a layer of strongly adsorbed anions between the Ag<sup>+</sup> cations and the graphite surface. From Eq. [1], both  $K_D$  and  $d$  help determine  $C$ . If  $d$  is the distance between the electrode surface and the centers of the mobile Ag<sup>+</sup> ions, then the larger crystal ionic radius for the iodide ion would in itself predict a larger capacitance for the AgBr cell. However, a stronger chemisorption and greater polarizability of I<sup>-</sup> than Br<sup>-</sup> may offset this by giving a substantially greater  $K_D$  for AgI. The chemisorption and polarizability of I<sup>-</sup> may also explain the observed 4-8% voltage dependence of capacitance in AgI|C cells in terms of an anion-layer electrostrictive effect. Attempts to obtain a detailed fit of our capacitance results to a simple anion-layer model involving Br<sup>-</sup> and I<sup>-</sup> ionic radii and polarizabilities were not successful, but the



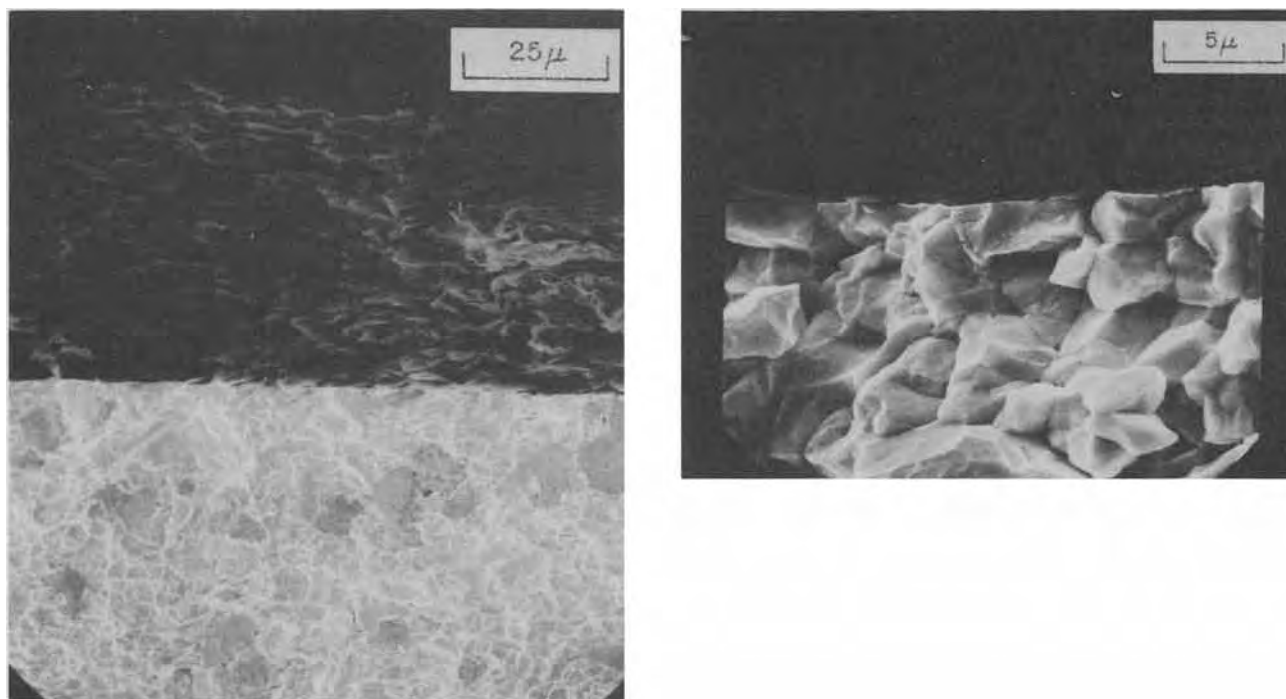


Fig. 10. Scanning electron micrographs of AgBr|C (pressed powder) interface at 800X (a, left) and 4000X (b, right). Dark areas are graphite, light areas AgBr.

general picture of an adsorbed anion layer seems useful and consistent with the experimental data.

We have noted the less clear-cut charging process in TMAI|C cells. One is struck, however, by the similar magnitudes of oscillographic capacitance in Fig. 2 and 4, the similar voltage dependence of capacitance for AgI and TMAI, and the fact the anions are  $I^-$  ions in both electrolytes. From these similarities one is disposed to suggest that the TMAI interface may be little more than a "perturbed" AgI interface, in which the altered composition and structure, or possibly an adsorbed atmospheric component, may supply the perturbation. The enlarged "slow" capacitance contribution and faster change of interface properties on standing observed with this electrolyte would favor the picture of atmospheric contamination. In all three electrolytes, we are suggesting that a fast charging process occurs which involves only  $Ag^+$  ion motion to and from a compact interfacial layer, with a fixed, intervening anion layer.

Considering now the AgX|Pt results, we have already noted that our effective capacitances for Pt wire were at least several orders of magnitude lower than observed by Hull and Pilla for Pt black. The latter workers suggested their large apparent capacitances were primarily due to Ag dissolution in Pt black at reduced activity, and that the true double layer capacitance on Pt should be the same as on graphite.

Faradaic effects due to Ag deposition should result in a sharp upturn in effective capacitance as the Ag potential is approached, because of the exponential dependence of silver activity on  $(V - V_{Ag})$ . We have observed such an upturn for solid Pt electrodes in both the present and previous (1-3) work, but only below  $\sim 0.18V$  (Fig. 9). At higher potentials, the low value of the silver activity, voltage variation of the capacitance, and, in the previous AgBr|Pt study (3) at  $417^\circ - 429^\circ C$ , the disappearance of frequency-dependent electrode capacitance, all indicate negligible Ag deposition effects for solid Pt electrodes above  $\sim 0.18V$  anodic of  $V_{Ag}$ .

Hull and Pilla reported the presence of metallic Ag in their Pt black electrodes at various potentials from microprobe measurements, but did not specify the voltage range. From the rather modest capacitance

variation they observed ( $9-16 \text{ mF/cm}^2$ ) over the voltage range  $0-0.4V$  anodic of  $V_{Ag}$ , it would seem either that Pt black displays quite different Ag dissolution characteristics from solid Pt or that a partial contribution from electroactive impurities in the Pt black may have been involved.

We feel, then, that our observed AgX|Pt capacitances over the bulk of the voltage range are true double layer capacitances, and are indeed different from the double layer capacitance on graphite. We recall the capacitance model previously (3) suggested for AgBr|Pt at high temperatures. The Pt surface is assumed to be covered by adsorbed layer of both anions and cations, whose anion:cation ratio depends only on the voltage. Capacitance (charge storage) occurs by change of the anion:cation ratio with voltage. The electrolyte behind the adsorbed first ion layer serves merely to transport charge in or out of the layer. This mechanism, however, requires both anion and cation motion in the charging process, and, in AgBr, anions are appreciably mobile only above or near the melting point. As AgBr cools in the solid state, the anions become successively more immobile. We propose that this, rather than interfacial strain, is the source of the increasing dispersion and drop in effective capacitance magnitude.

Thus, at room temperature, the graphite charging process is rapid because only the mobile  $Ag^+$  cations are involved, while platinum charging is presumably rate-limited by anion motion. The distinction in charging behavior appears to arise from the situation that halide anions are adsorbed on both types of electrodes, but  $Ag^+$  ions are adsorbed only on Pt. Thus, adsorbed anions form an immobile layer on graphite, but participate in the charging process on Pt. The adsorption of  $Ag^+$  ions on Pt and not on graphite was proposed previously (2) in connection with "preplating" or "undervoltage" behavior observed for  $Ag^+$  discharge on Pt and the dendritic nature of  $Ag^+$  discharge on graphite from AgBr electrolyte.

The previously noted features of Fig. 7 and 8 all appear explainable in terms of the above AgX|Pt interface model. From Fig. 9, we see that only a small portion of the total charging (upper curve) has occurred on the time scale of Fig. 7 and 8. Thus, these

latter figures should basically show those charging kinetics characteristic of the interface composition at the initial side of the voltage step. Since  $\text{Ag}^+$  ion motion is faster than anion motion, we assume initial kinetics will be fastest for the interface with the highest cation:anion ratio. Thus, for a given voltage step (e.g., 0.30-0.35V), the upward step should give the higher charging curve. The degree of difference, however, should increase with increasing cation:anion compositional difference at the two sides of the step. We have previously (3) suggested that the interface layer contains mostly cations at low bias, anions at high bias, and a roughly equal mixture of them at the capacitance maximum. Thus, the greatest compositional change and, as Fig. 8 shows, the greatest step direction asymmetry, should occur in this mid-bias range. Also, in Fig. 7 and 8, it seems reasonable to expect that charging should involve primarily cation motion at early times and increasing degrees of anion motion at larger  $t$  values. Thus, the clustering of the curves at  $t \leq 1$  sec may represent a fairly voltage-independent "cation surge," while greater anion involvement at longer times is required to show the voltage dependence (Fig. 9) more characteristic of the total charging process. Finally, the transition in Fig. 7 from convex-upward to concave-upward curvature with increasing voltage suggests a general reduction of initial charging kinetics with increasing interfacial anion concentration, since the convex-upward curvature suggests more early charging than the concave-upward curvature.

We have suggested, then, that AgX charging with graphite involves fast cation motion in a compact, purely electrostatic charge layer (with immobile adsorbed anions as the "dielectric") and charging on platinum involves the compositional change of a strongly adsorbed anion-cation layer. It seems useful at this point to try to explicate the relative roles of compact, diffuse, and adsorbed layer charging in solid-electrolyte systems. Figure 11 shows a suggested model, offered in a qualitative sense only. Diffuse and compact layer capacitances are in series, as is conventional.  $C_{\text{ADSORPTIVE}}$  refers to capacitive charge storage realized by the change in composition of an adsorbed charged interface layer with voltage. Since this type of charge storage represents a thermodynamic distribution of ions between sites on the electrode surface and the bulk electrolyte, dependent for a given electrolyte and temperature on the voltage only, it should be independent of other sources of charge storage and hence be considered in parallel with them. However,  $C_{\text{COMPACT}}$  and  $C_{\text{ADSORPTIVE}}$  compete for interfacial area, so  $C_{\text{COMPACT}}$  should be quite small in the case of large adsorptive capacitance.

For the graphite cells, a strongly adsorbed anion layer and nonadsorbed cations would result in  $C_{\text{ADSORBED}} = 0$ , so this capacitance could be removed. Diffuse layer capacitance in solid electrolytes was discussed in a previous publication (4). For the case of AgBr at 300°C, the entire accessible voltage range is thought to be far from the pzc and an accumulation-layer-type capacitance of several tens of microfarads/

square centimeter is predicted. One expects similar considerations to apply for AgBr and AgI at room temperature. Since our observed compact layer capacitances are at least several times smaller, and should be roughly halved by the roughness factor correction, they should dominate the series capacitance.

In the case of platinum,  $C_{\text{COMPACT}}$  should be small, as mentioned above, because of the large adsorptive capacitance. In this case, the lower branch capacitance in Fig. 11 would be dominated by  $C_{\text{COMPACT}}$  and the total capacitance by  $C_{\text{ADSORBED}}$ . Also, to be correct electrically,  $C_{\text{ADSORBED}}$  for Pt electrodes should really be replaced by a more complex resistive-capacitive circuit element to account for the slow, dispersed charging behavior. Figure 11, however, is offered merely to show the relationship between the various capacitances.

In all polycrystalline solid electrolytes, still another circuit element should be considered; one which is unique to solid electrolytes. Grain-boundary conduction, as we have said, dominates the room-temperature ionic conductivity in AgI and AgBr. Even in more highly conductive electrolytes, however, it is assuredly present (11). The effective result in any case is that planar sheets of very high local specific conductivity extend across the electrolyte bulk and intersect the electrode interface. Since such planar sheets are too conductive to support a diffuse double layer, they should effectively "short-circuit" any diffuse layer developed in the bulk. Thus we have indicated in Fig. 11 that a portion of grain-boundary resistance  $R_{\text{gb}}$  is in parallel with  $C_{\text{DIFFUSE}}$ . Here,  $L$  is the electrolyte thickness and  $\lambda$  the effective path length across the diffuse layer.

We expect, then, that diffuse layer capacitance should not be observable in polycrystalline solid electrolytes. Even in single-crystal electrolytes, however, precautions would seem necessary. Several workers (12-14) have indicated a space-charge-layer thickness of several tenths of a micron for AgBr at room temperature. If electrode attachment develops thermal or mechanical surface damage (e.g., in evaporating a metal film), such damage may breach the diffuse layer, such as by a network of cracks. On the other hand, we have seen that a sprayed graphite electrode gives anomalously small capacitance, presumably because of solvent and binder residues. It would seem that the best chance of observing diffuse layer capacitance in single-crystal solid electrolytes would be with the use of either inert liquid metal electrodes or adjacent electrolytic solutions.

Finally, in comparing our results with a recent study, we note that Armstrong and Mason (15) have measured the voltage dependence of a-c capacitance at 1-3 kHz for vitreous carbon and platinum electrodes on AgI, AgBr, and  $\text{RbAg}_4\text{I}_5$  at various temperatures. Low (1.8-3.5  $\mu\text{f}/\text{cm}^2$ ), relatively voltage-independent capacitances were reported with vitreous carbon, which were interpreted in terms of compact layer capacitance, as we have done for graphite electrodes in the present work. In the case of Pt electrodes, compact or "inner layer" capacitance was also suggested, with possible effects due to specific ion adsorption. In view of our own results on Pt, we feel their results would be better explained by our proposed anion-cation adsorption model. This would account better, for instance, for their large (45-130  $\mu\text{f}/\text{cm}^2$ ) observed capacitances for  $\alpha\text{-AgI}|\text{Pt}$  at 200°.

#### Acknowledgments

The author is grateful to Mr. W. Michael Moore for carrying out much of the experimental work, to Dr. Boone B. Owens for providing a sample of the tetramethylammonium iodide-silver iodide (TMAI) electrolyte, and to Dr. Harris Marcus and Mr. James Harris for the argon-sputtering operation on two of the platinum wire electrodes.

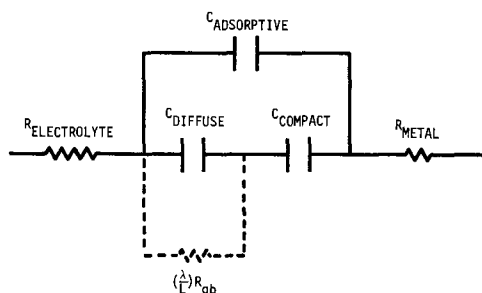


Fig. 11. Qualitative equivalent electrical circuit of solid electrolyte-inert metal interface.

Manuscript submitted July 2, 1973; revised manuscript received Oct. 25, 1973.

Any discussion of this paper will appear in a Discussion Section to be published in the December 1974 JOURNAL. All discussions for the December 1974 Discussion Section should be submitted by Aug. 1, 1974.

#### REFERENCES

1. D. O. Raleigh, *J. Phys. Chem.*, **70**, 689 (1966).
2. D. O. Raleigh, *ibid.*, **71**, 1785 (1967).
3. D. O. Raleigh and H. R. Crowe, *This Journal*, **118**, 79 (1971).
4. D. O. Raleigh, *Phys. Status Solidi*, (A), **4**, 215 (1971).
5. M. N. Hull and A. A. Pilla, *This Journal*, **118**, 72 (1971).
6. See, for instance, P. Delahay, "Double Layer and Electrode Kinetics," p. 129, Interscience Publishers, Inc., New York (1965).
7. B. B. Owens, *This Journal*, **117**, 1536 (1970).
8. W. V. Johnston, H. Wiedersich, and G. W. Lindberg, *J. Chem. Phys.*, **51**, 3739 (1969).
9. S. Gilman, in "Electroanalytical Chemistry," Vol. 2, p. 129, A. J. Bard, Editor, Marcel Dekker, New York (1967).
10. C. A. Khazova, Y. B. Vasilev, and V. S. Bagotskii, *Soviet Electrochem.*, **3**, 915 (1967).
11. D. O. Raleigh, *J. Appl. Phys.*, **41**, 1876 (1970).
12. V. I. Saunders, R. W. Tyler, and W. West, *Phot. Sci. Eng.*, **12**, 90 (1968).
13. F. Trautweiler, *ibid.*, **12**, 98 (1968).
14. J. E. Hall and L. J. Bruner, *J. Chem. Phys.*, **50**, 1596 (1969).
15. R. D. Armstrong and R. Mason, *J. Electroanal. Chem.*, **41**, 231 (1973).
16. D. C. Grahame, *J. Am. Chem. Soc.*, **68**, 301 (1946).

## Electrode Capacitance in Silver-Halide Solid Electrolyte Cells

### II. Temperature-Dependent Behavior of the AgBr-Graphite Powder Interface

Douglas O. Raleigh\*

Science Center, Rockwell International, Thousand Oaks, California 91360

#### ABSTRACT

The nature and capacitance of AgBr-graphite pressed powder interfaces prepared at room temperature and heated to various temperatures were examined at 25°-375°C, using potentiostatic capacitance measurements and electron micrography. At temperatures to 250°C, electrolyte grain growth produces irreversible capacitance increases by progressive interfacial roughening. However, the primary interface charging process remains ideally fast (undispersed) and heating to a given temperature rapidly creates a stable, reproducible degree of roughening. At ~275°C, an irreversible solid-state "wetting" process occurs, in which the electrolyte "soaks" some 170 $\mu$  into the graphite in 1-2 min. The capacitance increases 50-fold and becomes dispersed, with the charging process quantitatively following porous electrode behavior. The unique "wetting" process appears to involve a shallow network of graphite microcracks and requires a mechanism of rapid AgBr anion diffusion on graphite surfaces. Throughout the full 25°-375°C temperature range, the microscopic interface charging process appears to remain the same (Ag<sup>+</sup> compact layer capacitance).

In order to relate the capacitance results of Hull and Pilla (1), and of our own in the preceding paper (2) on AgX-graphite powder interfaces at room temperature to our previous study (3) of the AgBr-pyrolytic graphite interface at 244°-292°C, it was of interest to investigate graphite powder electrodes at above-ambient temperatures as well. The electrolyte chosen was AgBr, since it is stable and monophasic from room temperature to its melting point (425°C), and conducts by a single (Frenkel defect) ionic mechanism.

#### Experimental

Ag|AgBr|C pressed-powder cells with Ag wire reference electrodes were prepared as described in the preceding paper (2). In two cells, the graphite powder employed was first outgassed overnight at 250°C. Cells were springloaded in a Pyrex resistance furnace assembly described previously (3, 4). Various temperatures to 375°C were applied and maintained with a proportioning controller and read with a Chromel-Alumel thermocouple whose output was continuously recorded. A polarizing d-c bias, generally 0.25V, and a flowing argon atmosphere were maintained throughout a run.

The measurements carried out were potential-step chronocoulometry and chronoamperometry, using

0.05V steps in the range 0.05-0.40V anodic to Ag, as described in the preceding paper (2). Measurements were generally started at room temperature and the apparatus heated to successively higher temperatures. At each temperature, the cell current under d-c bias was allowed to settle to a steady-state value before starting measurements. These currents increased with increasing temperature, from < 1 nA at room temperature to ~ 1  $\mu$ A at most, and generally did not interfere with potential-step measurements.

In addition, electron micrographs of the AgBr|C interface, before and after cell heats, were taken as described in Ref. (2).

#### Results

*Temperatures to 250°C.*—The first result of heating the AgBr|C interface from room temperature was to raise and make less distinct the previously noted chronocoulometric plateau. Figure 1 shows oscillographic charge-time data for a given cell at 25° and 75°C, plus the indicated charging course at higher temperatures. At above-ambient temperatures, the plateau feature disappears. At temperatures to 250°C, however,  $Q$  vs.  $t^{1/2}$  plots showed fair to excellent linearity for times in excess of several RC. An example, employing both oscillographic and recorder data, is shown in Fig. 2.

In addition, potential-step oscillographic current-time curves, involving the relatively short time scale

\* Electrochemical Society Active Member.  
Key words: solid electrolytes, solid-state wetting, AgBr-graphite interface, electrode capacitance, solid-solid interface roughening.

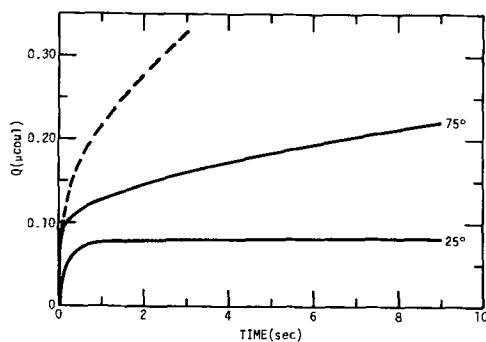


Fig. 1. Oscillographic charge-time traces for 0.25  $\rightarrow$  0.20V step on Ag | AgBr | C (pressed powder) cell at 25° and 75°C. Dotted line indicates charging course at higher temperatures.

of RC charging, gave linear  $\log i$  vs.  $t$  plots whose slope agreed well with  $t = 0$  capacitances obtained from back-extrapolating the  $Q$  vs.  $t^{1/2}$  plots. Even when the latter displayed some curvature, back-extrapolation at the prevailing curvature gave good agreement. From these results, we conclude that the AgBr|C (powder) capacitative behavior in this temperature range can still be described in terms of an ideally fast charging component plus a slower, diffusion-like contribution.

The behavior of the fast and slow charging components differed in several respects. At a given temperature, the magnitude of the slow component (as measured by the  $dQ/dt^{1/2}$  slope) often dropped considerably on standing overnight, while that of the fast component remained constant. Slow-component values scattered several-fold from cell to cell, and were lower with outgassed graphite electrodes, where fast-component values agreed to an average deviation of  $\sim 10\%$ . The slow-component value dropped several-fold over the bias voltage range 0.05-0.40V, while the fast component was roughly constant, increasing by 10-15% at most. On cycling back to a given temperature from a higher one, the slow-component contribution was considerably reduced.

Because of these findings, one again feels that the slow component represents a diffusion-controlled faradaic impurity reaction, with the impurity capable of at least partial depletion by continued electrolysis at a given temperature and bias voltage. Average values of the  $dQ/dt^{1/2}$  capacitance slope from seven different cells are plotted logarithmically vs.  $1/T$  in Fig. 3. The surprising linearity indicates that a single diffusing impurity species may predominate.

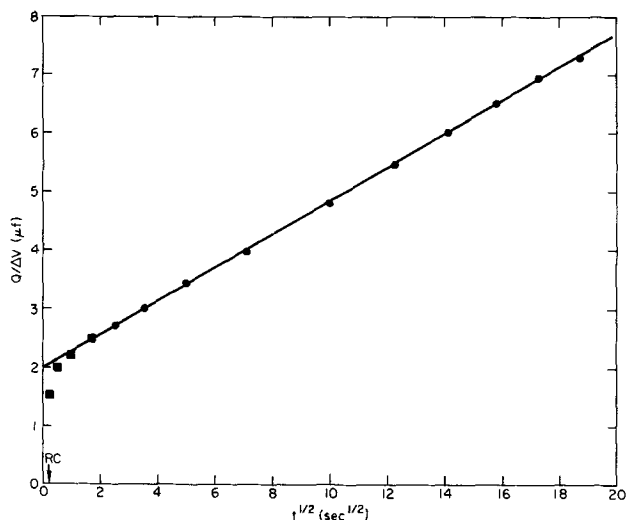


Fig. 2.  $Q$  vs  $t^{1/2}$  plot for 0.25  $\rightarrow$  0.20V step on Ag | AgBr | C (pressed powder) cell at 75°C. Squares are from oscillographic data; dots from recorder data.

Figure 4 shows a data-averaged plot of the "fast" capacitance as a function of temperature from seven different cell runs. In each run, the data employed were confined to measurements at successively increasing temperatures. As noted, the fast capacitance at a given temperature remained unchanged on overnight standing. However, on cooling to a lower temperature, the initial higher temperature capacitance was maintained. This is shown in Fig. 5 for  $Q$  vs.  $t^{1/2}$  plots for a given cell at 250°C and on cooling the cell to 150°C. One sees the already noted reduction of the slow

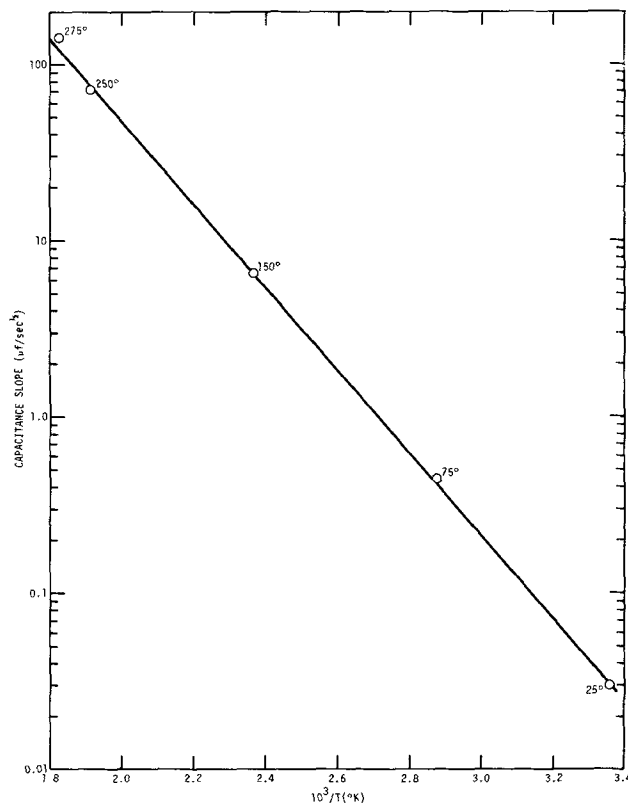


Fig. 3. Average diffusive capacitance slope  $(1/\Delta V) (dQ/dt^{1/2})$  vs. temperature.

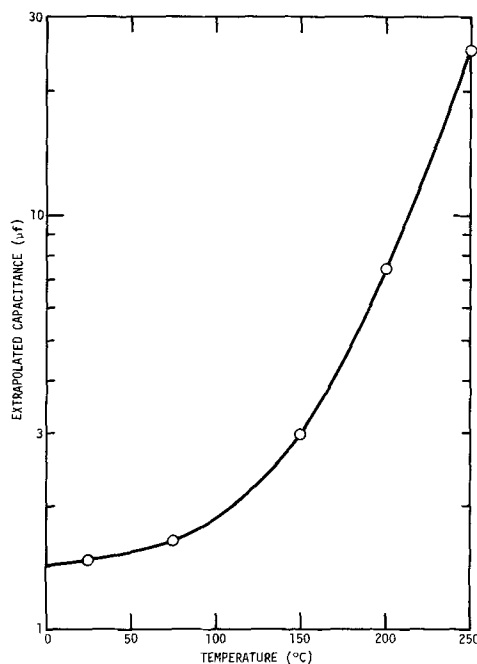


Fig. 4. Average diffusion-corrected chronocoulometric capacitance of AgBr | C (pressed powder) interface on heating to temperatures to 250°C. Capacitance irreversible on cooling.

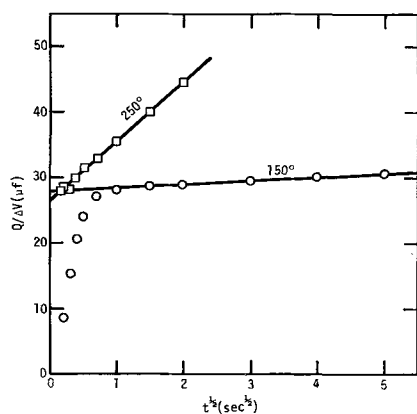


Fig. 5.  $Q$  vs.  $t^{1/2}$  plots for 0.25 → 0.20V step on Ag | AgBr | C (pressed powder) cell at 250°C and on cooling back to 150°C.

charging component, along with retention of the fast capacitance. The latter indicates that heating produces a permanent progressive change in the microphysical nature of the interface.

**Temperatures above 250°C.**—On heating to 275°C after overnight standing at 250°C, a fairly abrupt and considerable change in the qualitative nature of interface charging occurred. The effective chronocoulometric capacitance increased many-fold on all time scales. Plots of  $\log i$  vs.  $t$  from oscillographic chronoamperometry became severely curved, indicating disappearance of the well-defined fast charging component.

Figure 6 shows a  $Q$  vs.  $t^{1/2}$  plot at 275°C from oscillographic and recorder-scale chronocoulometry, using two time scales. On the longer time scale, a linear diffusion slope is still obtained, but only at times way in excess (500-fold in Fig. 6) of the RC charging time. The slope magnitude is in the line of the previous points on Fig. 3, indicating that the nature of the slow charging component is unchanged. The expanded-time plot of the initial-rise portion shows a linear slope that back-extrapolates approximately through the origin (actually, slightly below the origin because of finite RC rise time). The same type  $Q$  vs.  $t^{1/2}$  plots were obtained at higher temperatures to 375°C and on subsequent cooling to as low as 175°. Moreover, the  $t = 0$  capacitances obtained by back-extrapolating the linear diffusion slope were reproduced on temperature cycling. Thus, in contrast to results at 250°C and below, the new interface was stable to temperature cycling.

Figure 7 shows the back-extrapolated  $t = 0$  chronocoulometric capacitance (i.e., the capacitance corrected for the slow, diffusionlike component) over the full temperature range. The graph shows data from a single run at 275°C and above. A duplicate run with a new cell gave good agreement. We see that this presumed total interface capacitance increases 50-fold for 250° → 275°C and varies fairly gently with temperature thereafter. Thus, from Fig. 6 and 7 and the chronoamperometric results, the interface capacitance has both increased sharply and acquired considerable dispersion. Tests at 325°C showed the interface capacitance to be unchanged on overnight standing, or cooling to room temperature and reheating to temperature, and to be invariant (to within several per cent) to voltage step direction and bias voltage in the 0.05–0.40V range.

In view of the apparent abruptness of the capacitance increase, it was of interest to see how rapidly it occurred during the 250° → 275°C heatup and at what approximate temperature. For this purpose, a 7 Hz, 0.05V voltage square wave from the potentiostat was applied to a cell at 250°C, the  $Q$  waveform monitored visually on the oscilloscope screen, and the furnace control temperature changed to 275°C. At 270°–275°C, the expected large increase in the waveform amplitude occurred over a 1–2 min period. Thus, the increase is rapid, though not instantaneous.

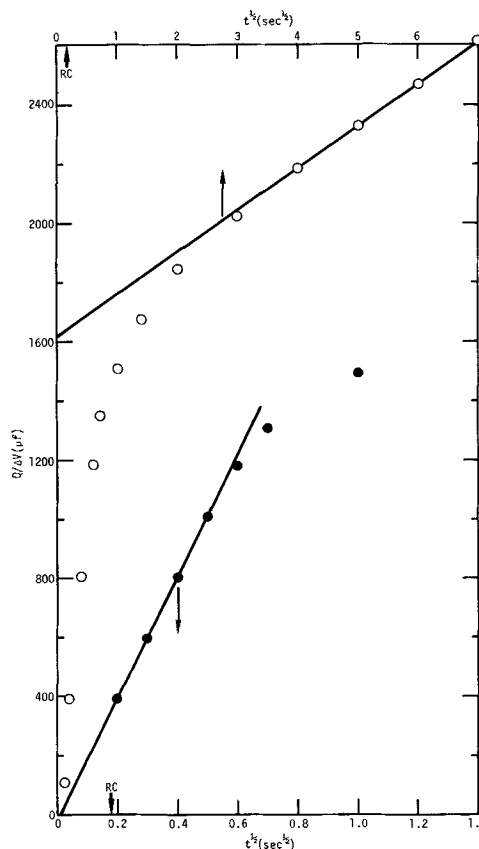


Fig. 6.  $Q$  vs.  $t^{1/2}$  plot for 0.25 → 0.20V step on Ag | AgBr | C (pressed powder) cell at 275°C (upper curve) and initial linear rise portion on 5-fold expanded abscissa (lower curve).

**Micrographic data.**—Following the capacitance studies, scanning electron micrographs of the AgBr|C in-

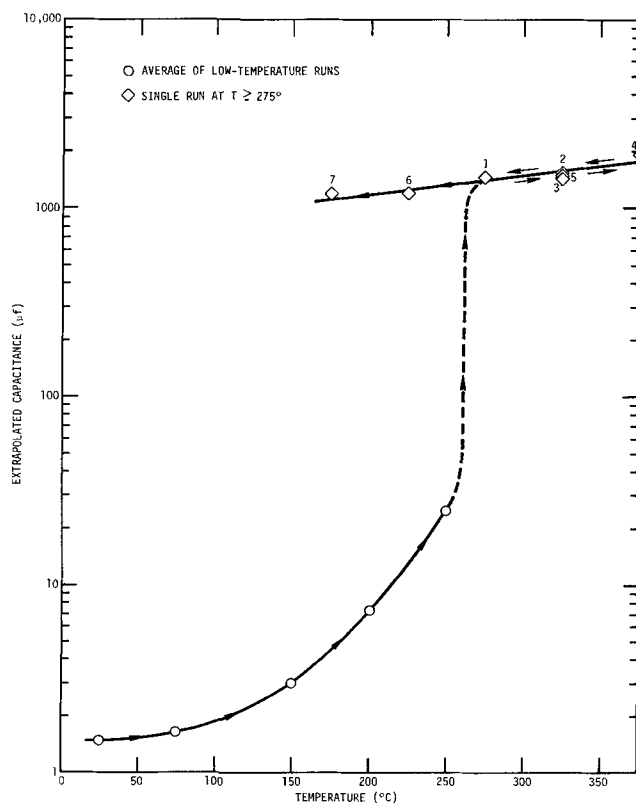


Fig. 7. Diffusion-corrected chronocoulometric capacitance of AgBr | C (pressed powder) interface as function of temperature before and after  $\sim 275^\circ\text{C}$  transition. Point numbers show temperature sequence; 2, 3 represent  $1\frac{1}{2}$  day anneal at 325°C.

interface were taken for (a) cells that had been heated to 250°C, and (b) cells heated in the 275°-375°C range.

Figure 8 shows an interface (a). We see that a well-defined phase separation is still maintained, but considerable interfacial roughening has taken place, compared with Fig. 10 of Ref. (2). Also, the AgBr appearance has changed considerably, showing a good deal of grain growth, intergranular voiding, and the appearance of plastic deformation in individual grains. In line with this altered appearance, visual examination of the cells thus heated showed considerable "bulging" (swelling) of the electrolyte layer and change of this layer from a glassy translucence to an opaque, porous appearance.

Figures 9 and 10 show the interphase appearance near the AgBr and graphite, respectively, for a cell exposed to temperatures in the 275°-375°C range. Focusing problems prevented a clear photograph of the full interphase region, but a well-defined layer, some 170 $\mu$  thick, was observed. To this degree, AgBr is seen to have penetrated or "soaked" into the graphite. Figure 11 shows a highly magnified portion of the interphase layer.

### Discussion

We noted earlier that the characteristics of the slow, diffusionlike contribution to the charging process suggest it is due to a single faradaic impurity species. The size of this component and the effect of outgassing the graphite again suggests that an impurity in the graphite, rather than the electrolyte, is involved. Further, the effect of outgassing suggests a gaseous or volatile impurity. However, since its characteristics (several-fold scatter from cell to cell, effects of bias-annealing and graphite outgassing) seem to be those of an impurity rather than an intrinsic interface component, it seems justified to drop further consideration of this contribution. We will instead consider the capacitance remaining when it is corrected for, which is presumably the intrinsic capacitance of the AgBr|C (powder) interface. Further, the approximate voltage independence of the latter capacitance throughout the entire temperature range suggests that the double layer charging process is the same as suggested in the preceding paper ( $\text{Ag}^+$  ion compact layer capacitance) and that such changes in characteristics as have been observed are due to changes in the physical nature of the interface.

Ionic conductivity studies by Shapiro and Kolthoff (5) show that pressed powder AgBr bodies exhibit



Fig. 8. Scanning electron micrograph of AgBr|C (pressed powder) interface after heating to 250°C.

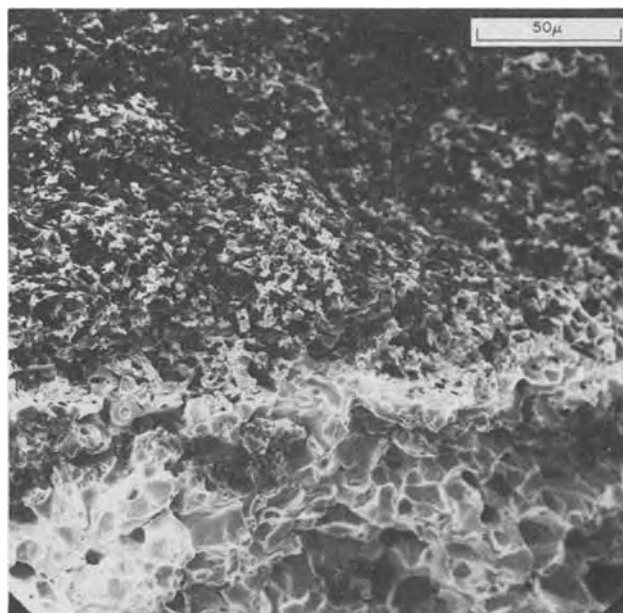


Fig. 9. Scanning electron micrograph of AgBr|C (pressed powder) interface after heating above  $\sim 275^\circ\text{C}$  transition temperature.

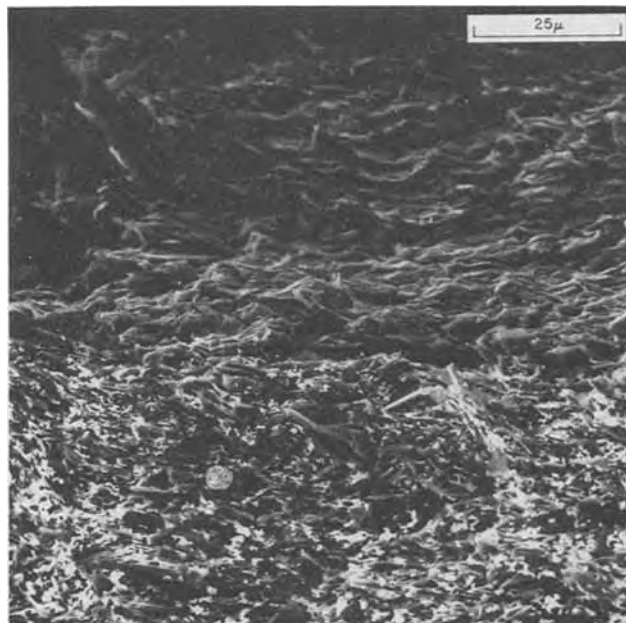


Fig. 10. Scanning electron micrograph of terminus of AgBr penetration zone in graphite after heating above 275°C transition temperature.

considerable grain growth on heating to various temperatures. Our visual and micrographic evidence shows the process to be characterized by swelling and porosity development. Thus, growth of large grains at the expense of small ones appears to enlarge grain dimensions without filling the space left by the digested grains. One expects this process to apply stress to and roughen the AgBr|C interface, both by topography change [see, for instance, Fig. 10 of Ref. (2)] and by lateral AgBr grain motion involved in the electrolyte swelling. The reduced AgBr grain size seen near the interface (Fig. 8) appears to show grain shattering associated with these stresses.

At temperatures to 250°C, the net electrical result seems merely to roughen the double layer interface without changing its fast charging characteristic. This would be expected if "necks" of electrolyte in the roughened interface are not appreciably resistive compared with the bulk electrolyte. From retention of the



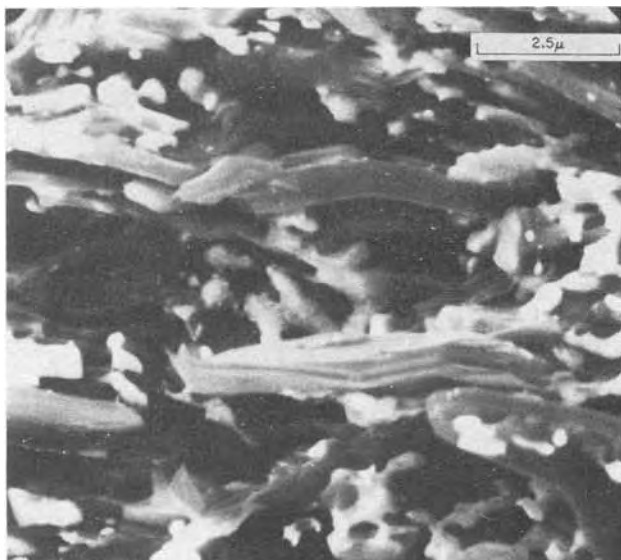


Fig. 11. Scanning electron micrograph of AgBr penetration zone in graphite in Fig. 10. Magnification 3500X.

increased capacitance on cooling (Fig. 5), the increase with temperature appears to result solely from the area increase due to roughening. From Fig. 3, heating  $25^\circ \rightarrow 250^\circ\text{C}$  is seen to produce a 16.7-fold increase in roughness factor.

It is of interest that stable increased capacitances are obtained shortly after heating to each new temperature. It would appear that each such heating rapidly produces a given degree of grain growth, interfacial stressing, and stress relaxation through roughening. While one would not *a priori* expect this result, our experimental findings are that overnight standing at, e.g.,  $150^\circ$  and  $250^\circ\text{C}$ , did not increase capacitance.

The micrographic and capacitance changes on heating to  $275^\circ\text{C}$  seem difficult to describe as other than a solid-state "wetting" process, despite the distance from the electrolyte melting point ( $425^\circ$ ). On heating, AgBr displays a continuously increasing plasticity. Comparison of Fig. 8 and 9, for instance, shows a rounding of void spaces and merging of crystallites in AgBr heated to the higher temperature. The increased capacitance and its dispersion are both strongly suggestive of a transition from compact to porous electrode behavior.

It is of interest to compare the chronocoulometric behavior after the  $\sim 275^\circ\text{C}$  transition with a model of porous electrode charging. DeLevie (6) gives, for the capacitive charging current at the mouth of a semi-infinite cylindrical electrolyte-filled electrode pore, following a potential step  $\Delta V$

$$i(0, t) = \frac{\Delta V}{R} \sqrt{\frac{RC}{\pi t}} \quad [1]$$

where  $R$  and  $C$  are the electrolytic resistance and electrode capacitance per unit pore length. For a pore radius  $r$ , we may use  $R = \rho/\pi r^2$  and  $C = 2\pi r C_0$  to obtain

$$i(0, t) = \Delta V \sqrt{\frac{2\pi r^3 C_0}{\rho t}} \quad [2]$$

where  $\rho$  is the specific electrolyte resistivity and  $C_0$  the double layer capacitance per unit microscopic area. For an arbitrary pore radius distribution,  $N = \sum n_i(r_i)$ , the current per unit electrode area, ignoring its outer surface for the moment, is

$$\begin{aligned} i(0, t) &= \Delta V \sum n_i \sqrt{\frac{2\pi r_i^3 C_0}{\rho t}} = \Delta V \sqrt{\frac{2\pi C_0}{\rho t}} \sum n_i \sqrt{r_i^3} \\ &\equiv G \Delta V \sqrt{\frac{2\pi C_0}{\rho t}} \end{aligned} \quad [3]$$

where  $G \equiv \sum n_i \sqrt{r_i^3}$  may be considered a "porosity structure factor" characterizing a given electrode. Integrating to obtain the chronocoulometric charge

$$Q(0, t) = \int_0^t i(0, t) dt = Q_0 + 2G \Delta V \sqrt{\frac{2\pi C_0}{\rho}} t^{1/2} \quad [4]$$

where the expression refers to a semi-infinite electrode, and where  $Q_0$ , the charge at the lower limit of integration, is introduced to account for any fast charging associated with the outer electrode surface. Then, for a porous electrode of finite thickness, Eq. [4] predicts a region of linear  $Q$  vs.  $t^{1/2}$  behavior as  $t \rightarrow 0$ , as we have observed. We also note that, as previously discussed, both chronocoulometric and chronoamperometric oscillographic results indicate  $Q_0$  is negligible.

Equation [4] predicts that, for a given porous electrode body and  $C_0$  temperature-independent, the linear  $Q$  vs.  $t^{1/2}$  slope for  $t \rightarrow 0$  should vary as  $\rho^{-1/2}$ , the inverse square root of the electrolyte resistivity. In Fig. 12, these slopes are plotted from chronocoulometric data for a given "post-transition" cell in the temperature range  $175^\circ$ – $375^\circ\text{C}$ . On the same graph, a "theoretical" temperature dependence line was constructed by multiplying the experimental  $dQ/dt^{1/2}$  slope at  $275^\circ\text{C}$  by  $(\rho_{275^\circ}/\rho_T)^{1/2}$  to predict the values at the other temperatures. A fair correspondence is seen, with the mid-point slopes of the two curves differing by 22%. We see, then, that the chronocoulometric results following the  $\sim 275^\circ\text{C}$  transition can be reasonably well described in terms of porous electrode behavior.

It is of interest now to consider the nature of the porosity. Both the micrographic results (e.g., Fig. 10) and the existence of stable, well-defined total capacitances, invariant to annealing and temperature-cycling, indicate the porosity is limited to a fixed interfacial zone. Thus, it seems unlikely to reflect the inherent porosity of the pressed graphite. We suggest instead that it represents a shallow network of fracture damage to the graphite surface, created by the previously described process of grain-growth-induced interfacial roughening on heating  $25^\circ \rightarrow 275^\circ\text{C}$ .

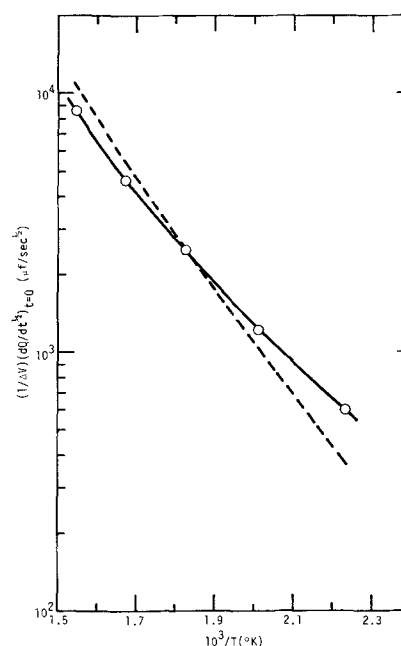


Fig. 12. Slope of initial linear rise of  $Q$  vs.  $t^{1/2}$  plots (e.g., Fig. 6) vs. temperature for cell after  $\sim 275^\circ\text{C}$  transition (smooth line), and slope curve predicted by Eq. [4] (dashed line).

At  $\sim 275^\circ\text{C}$ , an obviously rapid electrolyte "soak-in" occurs, some  $150^\circ$  below the AgBr melting point. While we may invoke high plasticity in the AgBr and capillary action in the fracture network, the abruptness of the "soak-in" requires consideration. As noted before, AgBr has no phase transition between  $25^\circ\text{C}$  and its melting point. Silver bromide and graphite are chemically inert to one another. Bulk phase properties, then, do not seem involved.

For capillary penetration of a porous solid by a liquid, it is required (7) simply that  $W_a > \gamma_L$ , where  $W_a$  is the work of adhesion and  $\gamma_L$  the liquid surface tension. Using

$$W_a = \gamma_L + \gamma_S - \gamma_{LS} \quad [5]$$

where  $\gamma_S$  refers to the surface tension of the solid and  $\gamma_{LS}$  to the interfacial tension, the criterion reduces to  $\gamma_S > \gamma_{LS}$ . Thus, if the surface tension of the solid is reduced by wetting, capillary penetration can occur. We expect, then, that  $\gamma_S$  and  $\gamma_{LS}$  for graphite and AgBr|C are different functions of temperature. Thus, it may simply be that  $\sim 275^\circ\text{C}$  marks a cross-over from  $\gamma_S < \gamma_{LS}$  to  $\gamma_S > \gamma_{LS}$ .

Since these relationships are thermodynamic ones, it makes no difference in principle whether they refer to wetting by a liquid or a mobile solid. The rapid penetration, however, seems quite unique. From the fact of penetration to  $170\mu$  in  $\sim 100$  sec, we may use  $x = 2\sqrt{Dt}$  to estimate (8) quite roughly an effective diffusion coefficient of  $(1.7 \times 10^{-2})^2/4 \times 10^2 \approx 7 \times 10^{-7}$  cm<sup>2</sup>/sec, a high value for diffusion in solids. It would seem that a mechanism of rapid anion diffusion in the graphite microcracks, followed by the smaller cations, is required. Strong anion adsorption on the graphite surface, proposed in the previous paper (2), may provide a chemical driving force for the process, with cations drawn along coulombically. At any rate, a most unusual solid-state phenomenon seems involved.

The 50-fold increase in total capacitance at  $\sim 275^\circ\text{C}$ , together with the previously noted 17-fold increase in roughness factor on heating  $25^\circ \rightarrow 250^\circ\text{C}$ , might be thought to indicate an over-all 850-fold increase in the effective interfacial area from the presumed near-planar room-temperature configuration. However, the temperature dependence of the "post-transition" capacitance (26% per  $100^\circ$ ) puts this calculation in question. It may be that the AgBr "soaks" into a wide variety of crack widths and that capacitance associated with the narrowest electrolyte paths becomes increasingly more accessible with increasing temperature, since ionic conductivity in AgBr increases rapidly with temperature (900-fold for  $175^\circ \rightarrow 375^\circ\text{C}$ ). If this is the case, the precise effective porosity factor is a function of temperature, and varies from 760 to 1220 in the  $175^\circ$ - $375^\circ\text{C}$  range.

Finally, the over-all results invite comparison with our earlier AgBr-graphite study at  $244^\circ$  and  $292^\circ\text{C}$ . In the latter work, the interface was formed by spring-loading a cylindrical AgBr single-crystal disk between silver and pyrolytic graphite foils and briefly heating the assembly above the AgBr melting point *in vacuo* to flash-melt the electrolyte to the electrodes. The cell was then cooled to the  $292^\circ$  and  $244^\circ\text{C}$  measuring temperatures. Oscillographic current-time and recorder scale charge-time data were taken, much as in the present work, except that  $Q$  vs.  $t^{1/2}$  plots were not made. Log  $i$  vs.  $t$  plots were nonlinear. The chronocoulometric data showed a slow charging process with apparent closure at long times (in excess of several minutes), so "total" capacitance values were reported. These ranged from 25 to  $45 \mu\text{f}/\text{cm}^2$  and were interpreted as a diffuse double layer capacitance.

Clearly, the large capacitances reported in the present work were not seen, despite the fact that the interface formation temperature and one of the measuring temperatures were well above the  $275^\circ\text{C}$  "transition" temperature. This is consistent with our sug-

gestion that the large capacitance results from the wetting of graphite porosity induced by surface damage from electrolyte grain growth. With single-crystal AgBr and pyrolytic graphite foil, the porosity may well be limited to that inherent in the graphite.

To examine this earlier charging process further,  $Q$  vs.  $t^{1/2}$  plots were made from the chronocoulometric recorder data for  $0.02$ - $0.30\text{V}$ ,  $244^\circ$  and  $292^\circ\text{C}$ ,  $1 \leq t^{1/2} \leq 7 \text{ sec}^{1/2}$ . The plots were linear for  $t \geq 4$  sec and back-extrapolated to an average  $t = 0$  capacitance of  $15 \mu\text{f}/\text{cm}^2$ . The oscillographic log  $i$  vs.  $t$  data could be fitted to current decay by a mixture of two RC time constants (9). The capacitance associated with the faster time constant averaged  $5.3 \mu\text{f}/\text{cm}^2$  and the total capacitance for the two components averaged  $9.9 \mu\text{f}/\text{cm}^2$ .

The fastest capacitance, then, agrees roughly with that measured for the AgBr|C interface at room temperature in the previous paper. The occurrence of an appreciably larger sum capacitance and back-extrapolated  $Q$  vs.  $t^{1/2}$  capacitance indicates a significant dispersed capacitance in the subsecond time range. This dispersed component may well reflect a small amount of natural porosity in the pyrolytic graphite foil, such as from microcracks, dislocations, and lamellar separations. In any event, the capacitance in this earlier study seems better described as some combination of fast and dispersed Ag<sup>+</sup> compact layer capacitance (with a possible diffusive impurity component), than as a diffuse layer capacitance, as previously (3) proposed.

### Conclusions

We have seen, then, that heating a pressed-powder ceramic interface (AgBr-graphite) from room temperature first produces interfacial roughening via grain growth and, later, a rapid solid-state capillary penetration of the one phase into the other. Capacitance measurements made it possible to study both of these processes in detail. In the first, the charging process remained rapid despite a 17-fold increase in roughness factor. In terms of previous discussions of roughness and capacitance dispersion in electrochemical systems (10), it is seen that the former alone does not necessarily produce the latter; rather that capillary penetration, such as into microcracks, seems required.

The solid-state capillary penetration process would appear to be unique, but not *a priori* unlikely, given the appropriate surface energy situation and a mechanism for rapid capillary diffusion. It would seem that both the roughening and penetration processes would be of interest in the area of ceramic adhesion and bonding. Given a solid-solid interface between an ionic and an electronic conductor, capacitance measurements might well make possible a detailed study of its nature.

### Acknowledgments

The author is grateful to Mr. W. Michael Moore for carrying out much of the experimental work. Special thanks are due to Mr. Leroy Hackett for the scanning electron micrographs in both these papers and for helpful discussions on their interpretation. Discussions on adhesion with Mr. D. H. Kaelble are gratefully acknowledged.

*Note Added in Proof:* The author is grateful to Dr. Kenneth Hay of Central Electricity Research Laboratories, U.K., for suggesting that at least part of the AgBr swelling, porosity development, and roughening of the interface with graphite which occurred on heating our pressed-powder cells to  $250^\circ$  may have resulted from the gradual expansion and outgassing of air entrapped in the electrolyte during the pressing process. This may explain better why heating to successively increasing temperatures in the  $25^\circ$ - $250^\circ$  range produced a stable increased degree of roughening rather quickly at each new temperature.

Manuscript submitted July 2, 1973; revised manuscript received Oct. 25, 1973.

Any discussion of this paper will appear in a Discussion Section to be published in the December 1974



JOURNAL. All discussions for the December 1974 Discussion Section should be submitted by Aug. 1, 1974.

## REFERENCES

1. M. N. Hull and A. A. Pilla, *This Journal*, **118**, 72 (1971).
2. D. O. Raleigh, *ibid.*, **121**, 632 (1974).
3. D. O. Raleigh, *J. Phys. Chem.*, **71**, 1785 (1967).
4. D. O. Raleigh, *J. Phys. Chem. Solids*, **26**, 329 (1965).
5. I. Shapiro and I. M. Kolthoff, *J. Chem. Phys.*, **15**, 41 (1947).
6. R. de Levie, *Electrochim. Acta*, **8**, 751 (1963).
7. See, for instance, D. H. Kaelble, "Physical Chemistry of Adhesion," Wiley-Interscience, New York (1971).
8. See, for instance, P. G. Shewmon, "Diffusion in Solids," pp. 8-14, McGraw-Hill Book Co., New York (1963).
9. D. O. Raleigh, *J. Phys. Chem.*, **70**, 689 (1966).
10. See, for instance, P. Delahay, "Double Layer and Electrode Kinetics," pp. 129-131, Interscience Publishers, Inc., New York (1965).

## Ring-Disk Electrode Study of Palladium Dissolution

Steven H. Cadle<sup>1</sup>

Chemistry Department, Vassar College, Poughkeepsie, New York 12601

## ABSTRACT

The corrosion rate of palladium is measured as a function of potential in 0.2M H<sub>2</sub>SO<sub>4</sub>. A typical corrosion rate is 0.35  $\mu$ A/cm<sup>2</sup> at +1.1V vs. SCE for an electrode with a roughness factor of 1.6. Passivation of the palladium dissolution occurs and is monitored by collection of Pd(II) at the ring electrode. Soluble palladium is produced simultaneously with the reduction of an oxidized electrode. This soluble palladium is separated into two categories. One category is associated with the reduction of surface palladium oxide while the other is associated with the reduction of phase oxide. Dissolution processes cause significant roughening of the electrode surface at  $E \cong +1.4V$ .

Recent investigations (1, 2) of the anodic behavior of palladium in acid solution have shown that palladium dissolution occurs. Rand and Woods (1) used atomic absorption spectroscopy to determine the quantity of palladium dissolved during a potential cycle of the electrode in 1M H<sub>2</sub>SO<sub>4</sub>. Llopis *et al.* (2) determined the corrosion rate of palladium in 1M HClO<sub>4</sub> as a function of potential using a radiochemical technique. Neither of these experimental techniques can determine the instantaneous dissolution rate since the concentration of palladium in solution must be increased over a period of time. Thus, it has not been possible to determine if palladium dissolution occurs during both the anodic and cathodic potential cycle of the electrode. Also the rate of passivation of the dissolution process could not be measured. These problems have been overcome by the use of the rotating ring-disk electrode.

### Experimental

**Equipment and solutions.**—The circuit for the ring-disk potentiostat, the cell, and the rotator are described elsewhere (3). A Beckman Electroscan 30 recorder was used.

A rotating palladium ring-palladium disk electrode (RPdRDE) was used. The collection efficiency,  $N$ , was 0.319. The projected area of the electrode was 0.452 cm<sup>2</sup>. The roughness factor of the electrode was estimated by assuming that one monolayer of oxygen is adsorbed on the electrode at +1.0V (4, 5) and corresponds to 424  $\mu$ Coulombs/cm<sup>2</sup> (6). The electrode was oxidized at +1.0V for 15 min before its potential was scanned to more negative potentials. The quantity of adsorbed oxygen was determined by integration of the palladium oxide reduction peak. On this basis the roughness factor of the electrode was 1.6.

A rotating gold ring-palladium disk electrode (RGPdRDE) was prepared by electroplating gold on the ring of the RPdRDE from a sulfuric acid solution of auric sulfate.

All solutions were prepared using triply distilled water. The 0.2M sulfuric acid supporting electrolyte was prepared from Fisher reagent grade sulfuric acid. Solutions were deoxygenated with nitrogen.

All potentials are reported vs. the saturated calomel electrode. Values of the apparent charge density

( $\mu$ Coulombs/cm<sup>2</sup>) are reported using the projected area of the electrode, uncorrected for roughness factor.

**Electrode pretreatment.**—In order to obtain reproducible current-potential curves the RPdRDE was pretreated in the following manner. The electrode was polished occasionally with Buehler 0.05 $\mu$  gamma micro-polish. The electrode was introduced into solution and both the ring and disk were oxidized for 10 min at +1.4V and then reduced at 0.0V for 5 min. The electrode potential was then cycled repeatedly between 0 and +1.4V until a reproducible current-potential curve was obtained. Approximately ten potential cycles were required.

A similar pretreatment was required for the RGPdRDE. This electrode, however, was not polished between experiments. To remove the palladium which was collected at the gold ring during an experiment, the ring electrode potential was cycled repeatedly between -0.3 and +1.6V.

**Corrosion rate determination.**—The corrosion rate was determined by collecting soluble palladium on the gold ring of a RGPdRDE. Initially, the palladium disk was reduced at 0.0V for 1 min. Then it was stepped to the potential at which the corrosion rate was to be measured and was held at this potential 15 min to allow complete oxidation of the electrode to occur. After this time the ring electrode potential was stepped from +1.2V, a potential at which no collection of palladium occurs, to 0.0V. Palladium was collected at the ring for 4 min at a rotation speed of 900 rpm. The ring potential was then stepped to +0.40V and immediately scanned in the anodic direction. The quantity of palladium collected was determined from integration of the resulting ring current-ring potential curve using a procedure developed in this laboratory (5). Since considerable roughening of the electrode occurs at  $E_D \cong +1.4V$  the roughness factor was determined after each measurement. All data were corrected to a roughness factor of 1.6. Assuming that all the palladium was collected as Pd(II) and taking into account the collection efficiency, the disk electrode current due to the Pd(II) dissolution was calculated.

### Results and Discussion

**Palladium dissolution.**—Ring-disk electrode experiments using the RPdRDE were conducted in 0.2M H<sub>2</sub>SO<sub>4</sub> in order to determine if any soluble species

<sup>1</sup> Present address: Research Laboratories, General Motors Corporation, General Motors Technical Center, Warren, Michigan 48090.  
Key words: palladium, dissolution, ring-disk electrode.

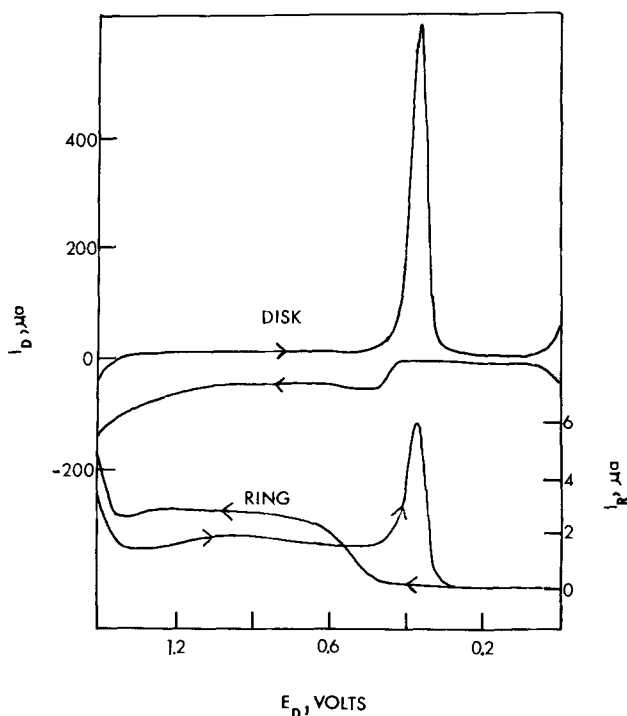


Fig. 1. Current-potential curves at a RPDRE, showing collection of Pd(II) at the ring electrode. 0.2M H<sub>2</sub>SO<sub>4</sub>, rotation speed 2500 rpm, potential scan rate 100 mV/sec,  $E_R = 0.0V$ .

could be detected during the oxidation and reduction of the palladium disk electrode. Figure 1 shows a disk current-disk potential ( $i_D-E_D$ ) curve and the corresponding ring current-disk potential ( $i_R-E_D$ ) curve obtained at a rotation speed of 2500 rpm. The potential scan rate was 100 mV/sec and the ring electrode potential was 0.0V. The  $i_D-E_D$  curve shows the oxidation of the palladium electrode at  $E_D > +0.4V$  and the corresponding reduction peak during the cathodic scan at +0.36V. The  $i_R-E_D$  curve shows that ring collection of an electroactive species commences during the anodic scan at the same potential that palladium oxide formation begins. The rapid increase in  $i_R$  at  $E_D \cong +1.13V$  is due to the collection of oxygen. During the cathodic scan a ring current peak is observed at the same potential as the palladium oxide reduction peak. It is shown below that the ring current at  $E_D \leq +1.10V$  is due to the collection of Pd(II).

$i_R-E_D$  curves were recorded at several rotation speeds under the experimental conditions of Fig. 1. No dependence on the rotation speed was observed.

**Identification of collected species.**— $i_R-E_D$  curves were obtained at a RGPDRDE under the same experimental conditions as in Fig. 1. A ring collection curve identical to the curve in Fig. 1 was obtained.

The soluble species was collected at the gold ring electrode,  $E_R = 0.0V$ , during several potential cycles of the palladium disk between zero and +1.1V. The disk electrode was then reduced at 0.0V and open circuited. An  $i_R-E_R$  curve was recorded at 100 mV/sec between 0 and +1.6V. The oxidation and reduction of thin layer palladium deposits on gold (5) were apparent, proving that palladium is collected at the ring electrode under these conditions. This procedure was repeated at a fresh electrode, with the soluble palladium being collected during only one potential cycle of the disk. Integration of the  $i_R-E_D$  curve showed that the charge required to reduce the Pd collected at the ring during one potential cycle was 34.7  $\mu\text{coulombs}$ . The quantity of palladium deposited on the ring was determined by measuring the charge required to oxidize this deposit to a known oxidation state (5). Assuming a two-electron reduction of Pd(II), it was found that 33.1  $\mu\text{coulombs}$  of palladium had been deposited. Compari-

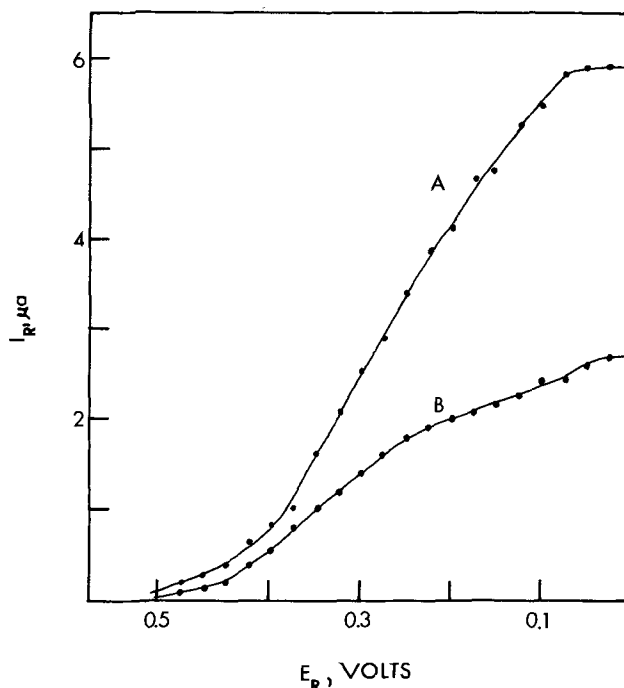


Fig. 2. Current-potential curve showing the effect of ring potential on the collection of Pd(II). 0.2M H<sub>2</sub>SO<sub>4</sub>, rotation speed 900 rpm, potential scan rate of the disk electrode 100 mV/sec. Curve A, ring current measured at  $E_D = +0.36V$  during the cathodic scan; curve B, ring current measured at  $E_D = +1.0V$  during the anodic scan.

son of these results leaves little doubt that the observed ring collection current is due to the reduction of Pd(II) under these experimental conditions.

Current-potential curves for the soluble Pd(II) were constructed from  $i_R-E_D$  curves obtained at different ring electrode potentials. Two such curves are shown in Fig. 2. The ring current for curve A was measured at the current peak observed during the cathodic scan at  $E_D = +0.36V$  (see Fig. 1). The ring current for curve B was measured at  $E_D = +1.0V$  during the anodic scan. The curves are irreversible and the shape of curve B gives some indication, although inconclusive, that more than one Pd(II) species is being collected. The limiting current is obtained by +0.05V. Thus, the collection efficiency of the soluble Pd(II) is equal to  $N$  at  $E_R \leq +0.05V$ . It must be noted that the observed ring current decreased with time if the ring electrode was not frequently oxidized at +1.2V. This rate of decrease was dependent on the rotation speed of the electrode indicating that the inhibition was due to impurity adsorption.

**Corrosion rate.**—The corrosion rate of palladium was determined as a function of potential using the procedure described above (Experimental). The data is presented in Table I. The decrease in the corrosion rate observed when the potential is increased from +0.7 to +0.9V is assumed to be due to the partial passivation of the electrode caused by the formation of palladium oxide. This data is in reasonable agreement with that of Llopis *et al.* (2), who reported a corrosion rate equivalent to 0.32  $\mu\text{A}/\text{cm}^2$  at +0.9 and +1.5V in 1N

Table I. Corrosion of palladium

Electrode potential (V)	$i_D$ ( $\mu\text{A}/\text{cm}^2$ )
+0.5	0.00
+0.7	0.360
+0.9	0.306
+1.1	0.354
+1.3	0.374
+1.5	0.442
+1.7	0.832

$\text{HClO}_4$ . A significantly higher corrosion rate than found in this study was reported at +0.75 and +1.75V (2.8 and 1.8  $\mu\text{A}/\text{cm}^2$ , respectively). The difference at +0.75V may have been caused by an enhanced corrosion rate due to the presence of a trace amount of chloride in the perchloric acid supporting electrolyte. The disagreement at +1.7V is most likely due to an increase in roughness factor of the electrode used by Llopis *et al.* The roughness factor was not measured in their work.

Comparison of the data in Table I with the ring collection curve in Fig. 1 shows that a much larger ( $\sim 30\times$ ) corrosion rate is observed at a given potential during an anodic potential scan at 100 mV/sec than is observed at the same potential after electrode oxidation is complete. Thus, it is apparent that oxidation of the electrode results in the passivation of the dissolution process, and that the corrosion rate will depend markedly on the electrode potential scan rate and the history of the electrode.

**Passivation.**—The ring electrode was used to monitor the passivation of the palladium dissolution process at disk electrode potentials where oxygen is not evolved, *i.e.*,  $E_D \leq +1.1\text{V}$ . In these experiments the disk electrode was reduced at +0.1V for 1 min before its potential was stepped to a more oxidizing potential. Palladium was collected at the ring electrode at 0.0V. The resulting ring current-time curves are shown in Fig. 3 for four different disk electrode potentials. Curve a, Fig. 3, was recorded for a potential jump to +0.4V, a potential at which no palladium dissolution occurs. The observed ring current was attributed to electroactive impurities being stripped from the disk electrode. This curve is also labeled the residual curve in Fig. 3. Curves b-d, Fig. 3, were recorded for potential steps to successively more positive potentials and show successively larger corrosion rates. The corrosion rate decreases rapidly during the first 10 sec and then more slowly for times up to 10 min. At times longer than 10 min no additional decrease in the ring col-

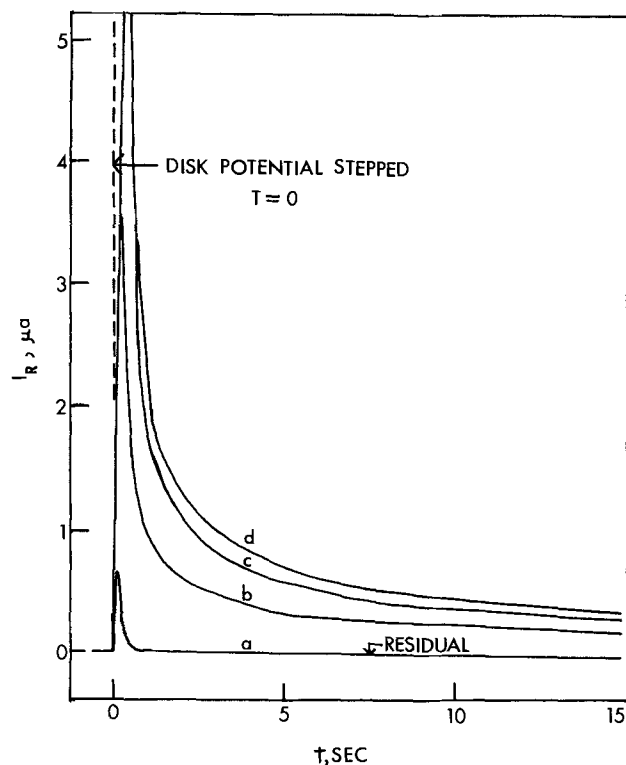


Fig. 3. Ring current vs. time curves for the collection of Pd(II). Disk potential stepped from +0.1V to  $E_D$  at time = 0. Curve a,  $E_D = +0.4\text{V}$ ; curve b,  $E_D = +0.6\text{V}$ ; curve c,  $E_D = +0.85\text{V}$ ; curve d,  $E_D = +1.1\text{V}$ . 0.2M  $\text{H}_2\text{SO}_4$ , rotation speed 900 rpm.

lection current was observed and the electrode is passivated.

**Cathodic dissolution.**—Once the electrode has been passivated via oxidation, it might be expected that no increase in palladium dissolution would occur if the electrode potential is scanned to more negative potentials. The  $i_R-E_D$  collection curves in Fig. 4 prove that this is not the case, since a much larger quantity of palladium is collected at the ring than is predicted from the corrosion rate observed at a passivated electrode. This palladium is termed cathodically soluble palladium. These curves were recorded at  $E_R = 0.0\text{V}$  after the disk electrode was oxidized for 15 min at the potential indicated in the figure. The  $i_D-E_D$  curves corresponding to Fig 4 are presented in Fig. 5.

The cathodically soluble palladium appears to be associated with two different reduction processes which occur at the disk electrode. The first is the reduction of the surface palladium oxide at  $E_D < +0.5\text{V}$ . This reduction is accompanied by the formation of soluble Pd(II) which is seen in Fig. 4 as a ring current peak, A. A similar phenomenon has been observed at both gold electrodes (7) and platinum electrodes (8). The second reduction process occurs at more positive potentials than the surface palladium oxide reduction peak (see Fig. 5). Reduction peaks at palladium electrodes have been previously reported in this potential region if the electrode is oxidized at potentials greater than +1.75V *vs.* SCE in 1M  $\text{H}_2\text{SO}_4$  (6). These peaks were shown to be due to the reduction of a phase oxide. The data in Fig. 4 and 5 indicate that small quantities of phase oxide form at  $E_D \geq +1.1\text{V}$  and that a considerable quantity of soluble palladium is generated when the phase oxide is reduced. This effect

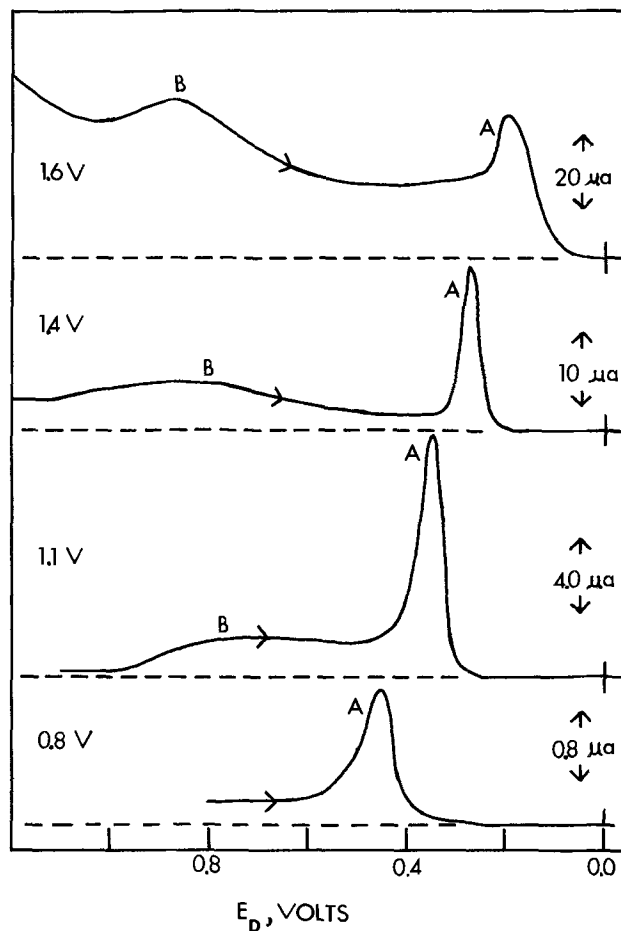


Fig. 4. Effect of disk oxidation potential on cathodic soluble palladium. Disk electrode oxidized at indicated potential for 15 min. 0.2M  $\text{H}_2\text{SO}_4$ , rotation speed 900 rpm, potential scan rate 100 mV/sec.

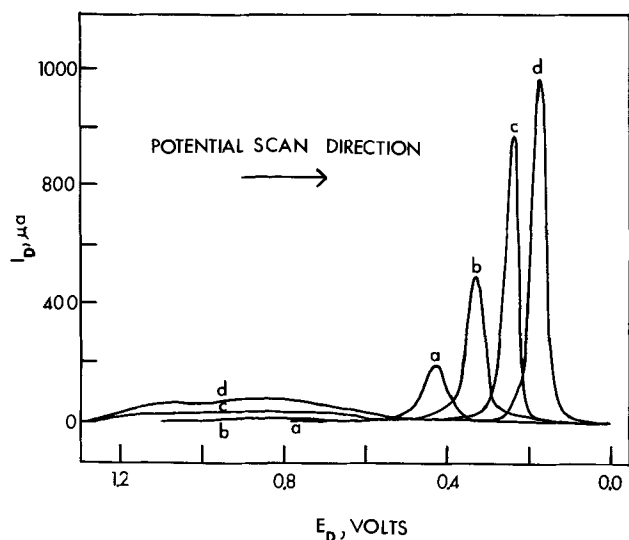


Fig. 5. Current-potential curve for a palladium disk electrode oxidized at  $E_D$  for 15 min. Curve a,  $E_D = +0.8V$ ; curve b,  $E_D = +1.1V$ ; curve c,  $E_D = +1.4V$ ; curve d,  $E_D = +1.6V$ .  $0.2M H_2SO_4$ , rotation speed 900 rpm, potential scan rate 100 mV/sec.

accounts for the tremendous increase in soluble palladium formed at  $E_D \cong +1.4V$  and helps account for the observed increases in the surface roughness when the electrode is oxidized at  $E_D \cong +1.4V$ .

The quantity of cathodically soluble palladium produced at the disk electrode was calculated from  $i_R-E_D$  curves as a function of the disk oxidation potential and is presented in Table II. The soluble palladium produced during reduction of the surface palladium oxide reduction peak is designated  $Q_A$ , while that produced during reduction of the phase oxide is  $Q_B$ . It is not possible to directly measure the soluble palladium produced at  $E_D > +1.1V$  because of the simultaneous collection of oxygen which is evolved at these potentials. Therefore,  $Q_B$  was measured between  $+1.1$  and

Table II. Cathodic soluble palladium

Electrode potential (V)	$Q_B$ ( $\mu\text{coulombs/cm}^2$ )	$Q_A$ ( $\mu\text{coulombs/cm}^2$ )	$Q_A/Q_{PdO_x}$
+0.7	3.30	3.47	0.015
+0.8	3.47	8.91	0.021
+0.9	3.67	14.5	0.029
+1.0	10.6	17.1	0.027
+1.1	36.6	24.8	0.034
+1.2	93.2	36.7	0.043
+1.3	157.0	45.7	0.050
+1.4	259.0	58.5	0.055
+1.5	812.0	84.4	0.075
+1.6	1750.0	160.5	0.126

0.0V and is not the total quantity of palladium dissolved during the cathodic scan if the disk is oxidized at  $E_D > +1.1V$ . The last column of Table II gives the ratio of  $Q_A/Q_{PdO_x}$ .  $Q_{PdO_x}$  is the number of coulombs passed for the reduction of surface palladium oxide at the disk electrode current peak,  $E_D < +0.5V$ . This quantity increases with increasing potential from 1.5% at  $+0.8V$  to 12.6% at  $+1.6V$ .

Manuscript submitted July 31, 1973; revised manuscript received Nov. 1, 1973.

Any discussion of this paper will appear in a Discussion Section to be published in the December 1974 JOURNAL. All discussions for the December 1974 Discussion Section should be submitted by Aug. 1, 1974.

#### REFERENCES

1. D. A. J. Rand and R. Woods, *J. Electroanal. Chem.*, **35**, 209 (1972).
2. J. F. Llopis, M. M. Gamboa, and L. Victori, *Electrochim. Acta*, **17**, 2225 (1972).
3. D. C. Johnson, Ph.D. Thesis, University of Minnesota (1967).
4. R. Kh. Burshtein, M. R. Tarasevich, and V. S. Vilinskaya, *Elektrokhimiya*, **3**, 349 (1967).
5. S. H. Cadle, *Anal. Chem.*, Submitted for publication.
6. D. A. J. Rand and R. Woods, *J. Electroanal. Chem.*, **31**, 29 (1971).
7. S. H. Cadle and S. Bruckenstein, *Anal. Chem.*, In press.
8. D. C. Johnson, D. T. Napp, and S. Bruckenstein, *Electrochim. Acta*, **15**, 1493 (1970).

## Experimental Determination and Calculation of Parasitic Currents in Bipolar Electrolyzers with Application to Chlorate Electrolyzer

I. Roušar\* and V. Cezner

Department of Inorganic Technology, Institute of Chemical Technology, Prague, Czechoslovakia

#### ABSTRACT

Experimental determination of parasitic currents flowing through an electrolyzer in inlet and outlet channels was performed for a bipolar electrolyzer consisting of six cells, for production of chlorates. The average deviation of experimental values from theoretical was 14%.

The problem of parasitic currents was studied theoretically in an earlier paper (1). A comparison of theoretical values of parasitic currents with experimental ones is necessary since the theory is based on a very simplified model which replaces the individual cells and connecting channels by a system of parallel and series resistances (2).

The following relations for resistances of inlet channels to every cell were derived for the so-called W

model (1)

$$R_{S1} = \rho_E (1 + 1.5 K_3 + 1.5 K_3') \left( \frac{L_1}{wd} \right) + 0.5(w + w_1)/L_2d + \rho_E (1 + 1.5 (V_{GT}/V_p)) (L_{ST}/F_{ST}) \quad [1]$$

$$R_{S2} = \rho_E (1 + 1.5 K_3') (L_1/wd) + 0.5(w + w_1)/L_2d + \rho_E (L_{SB}/F_{SB}) \quad [2]$$

and connecting channels between cells

$$R_{Q1} = \rho_E (1 + 1.5 (V_{GT}/V_p)) (S_A + S_K + D)/F_{QT} \quad [3]$$

\* Electrochemical Society Active Member.

Key words: bipolar electrolyzer, parasitic currents, chlorate electrolysis.

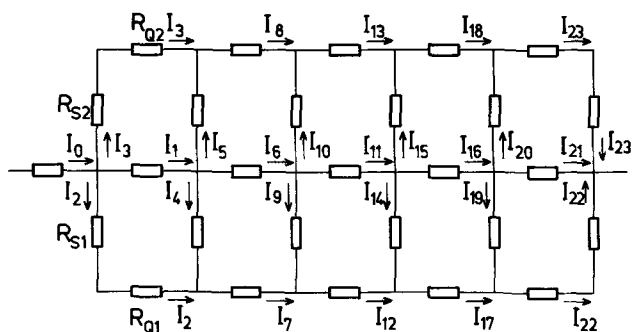


Fig. 1. Scheme of electric circuit. Resistances in the center correspond to individual cell resistances of bipolar electrolyzer.

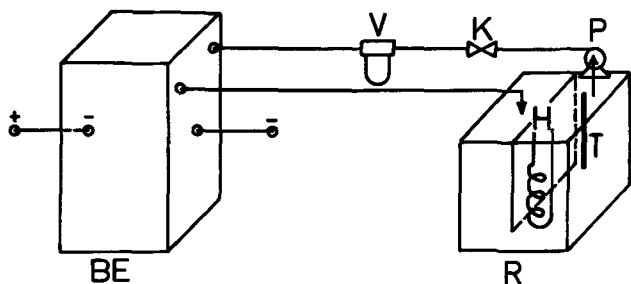


Fig. 2. Experimental setup BE, bipolar electrolyzer; V, Venturi tube; P, centrifugal pump; R, electrolyte reservoir; K, regulation stop cock; T, thermometer; H, titanium heat exchanger.

$$R_{Q2} = \rho_E(S_A + S_K + d)/F_{QB} \quad [4]$$

The single-cell voltage of the electrolyzer is given by

$$U = A + B\eta_{Sj} \quad [5]$$

The electric circuit, shown in Fig. 1, can be simplified (1) if it can be assumed that  $R_{S1} \approx R_{S2}$  and  $R_{Q1} \approx R_{Q2}$ ; however this was not the case in the present work. We introduce dimensionless parameters  $I_{Rj} = I_j/I_0$ ;  $\alpha_{R1} = A/I_0R_{S1}$ ;  $\alpha_{R2} = \alpha_{R1}R_{S1}/R_{S2}$ ;  $\beta_{R1} = R_{Q1}/R_{S1}$ ;  $\beta_{R2} = R_{Q2}/R_{S2}$ ;  $\gamma_{R1} = B/I_0R_{S1}$ ;  $\gamma_{R2} = \gamma_{R1}R_{S1}/R_{S2}$ . The currents flowing through the resistance network are determined by considering the voltage balance for every closed circuit and the current balance for every knot. The resulting system of  $5n-7$  equations for  $n$  cells can be represented by a diagonal matrix (see Table I) and solved by the Thomas method (3).

### Experimental

The bipolar electrolyzer (Fig. 2) consisted of six cells, each containing a bipolar electrode  $13 \times 58$  cm made of impregnated Acheson graphite. The flowing electrolyte was pumped by pump P from reservoir R of 120 liters holding capacity passing Venturi tube V. The reservoir was provided with a thermometer and titanium heat exchanger connected with a thermostat. The electrolyzer was fed with current from a silicon rectifier and was assembled from frames (Fig. 3) and

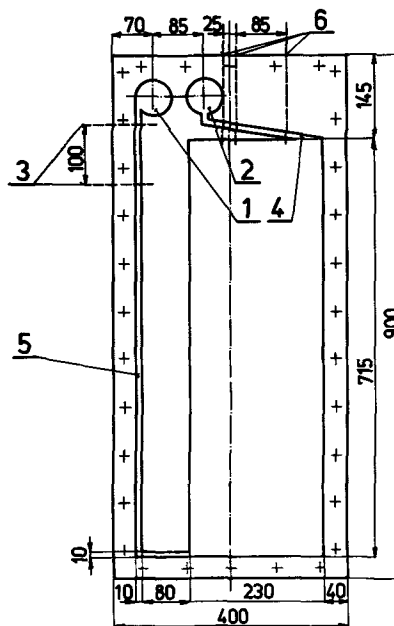


Fig. 3. Interelectrode frame. 1, main channel for electrolyte inlet; 2, main channel for outlet of electrolyte with bubbles; 3, platinum probes to measure voltage drops in inlet channel ( $U_{B12}$ ); 4, 5, connecting channels; 6, platinum probes to measure voltage drops in outlet channel ( $U_{T12}, U_{T23}$ ). Dimensions are given in millimeters.

plates (Fig. 4) made of organic glass (Plexiglas). The frames contained built-in platinized platinum wires. The voltage drop between them could be measured by a vacuum tube voltmeter and compared with the calculated voltage given by the parasitic current in the considered circuit and by the electrolyte resistance between the platinum probes. The frame assembled with the plate is shown in Fig. 5 indicating the direction of the electrolyte flow. Between the plate and the frame there was a soft rubber gasket 0.5 mm thick. The distance between the anode and the cathode in the complete assembly was 6 mm at the beginning of experiments. At the end of measurements, the electrodes were partly corroded on the anodic side and the distance between them was 7.7 mm. The electrodes were provided with platinum wires enabling measurement of the voltage,  $U$ , between individual cells.

Measurements were made at  $40^\circ\text{C}$  and pH was adjusted to 5.5-6.5 by addition of diluted hydrochloric acid. Two different electrolytes were used: (A) 600 g/liter  $\text{NaClO}_3 + 90$  g/liter  $\text{NaCl} + 3$  g/liter  $\text{Na}_2\text{Cr}_2\text{O}_7$ , (B) 500 g/liter  $\text{NaClO}_3 + 150$  g/liter  $\text{NaCl} + 10$  g/liter  $\text{Na}_2\text{Cr}_2\text{O}_7$ .

### Results

For three values of the current density, 0.03, 0.06, and 0.09  $\text{A}/\text{cm}^2$ , three rates of flow of electrolyte A or B were chosen, namely, 10, 20, and 30 kg/min. Thus, the total number of experiments amounted to 18. The resistances between probes in the outlet and inlet

Table I. Coefficients and right-hand sides of  $5n-7$  equation describing current distribution in the electric circuit in Fig. 1

$j$	1	2	3	4	5	6	7	8	9	$I_{Rj}$	10	16	17	18	19	20	21	22	23	Right-hand side	
1																					
2	$-\gamma_1$	$1 + \beta_1$	0	-1	0																$\alpha_1$
3	$-\gamma_2$	$1 + \beta_1$	$1 + \beta_2$	-1	-1	0															$\alpha_2 + \alpha_1$
4	1	0	0	-1	-1	-1	0														0
5		1	0	1	0	0	0	-1	0												0
6			1	0	1	0	0	0	0												0
7				1	0	$-\gamma_1$	$\beta_1$	0	-1	0											$\alpha_1$
8					1	$-\gamma_2$	0	$\beta_2$	0	-1											$\alpha_2$
18												1	0	0	-1	-1	-1	0	0	0	0
19													1	0	0	0	0	0	0	0	0
20														1	0	0	0	0	0	0	0
21															1	$-\gamma_1$	$1 + \beta_1$	0	0	0	0
22																1	0	0	0	0	0
23																	1	$1 + \beta_2$	1	1	1

Table II. Voltage drops in inlet and outlet channels due to parasitic currents

Cell number	$U_{B12}$ (V)			$U_{T12}$ (V)			$U_{T23}$ (V)			
	Theory	Experimental	Deviation (%)	Theory	Experimental	Deviation (%)	Theory	Experimental	Deviation (%)	
$i = 0.03 \text{ A/cm}^2$										
1	0.835	0.956	14.5	0.724	0.656	-9.4	2.461	2.490	1.2	
2	0.501	0.680	35.7	0.433	0.560	29.3	1.472	1.450	-1.5	
3	0.167	0.194	16.2	0.144	0.186	29.2	0.490	0.494	0.8	
4	-0.167	-0.138	-17.4	-0.144	-0.232	61.1	-0.490	-0.356	-27.4	
5	-0.501	-0.459	-8.4	-0.433	-0.480	10.9	-1.472	-1.402	-4.8	
6	-0.835	-0.922	10.4	-0.724	-0.656	-9.4	-2.461	-2.666	8.3	
Average deviation (%)			17.1				24.9			
$i = 0.06 \text{ A/cm}^2$										
1	0.890	0.950	6.7	0.795	0.725	-8.8	2.701	2.640	-2.3	
2	0.534	0.715	33.9	0.475	0.525	10.5	1.615	1.585	-1.9	
3	0.178	0.203	14.0	0.158	0.205	29.8	0.538	0.465	-9.9	
4	-0.178	-0.165	-7.3	-0.158	-0.185	17.1	-0.538	-0.370	-31.2	
5	-0.534	-0.480	-10.1	-0.475	-0.525	10.5	-1.615	-1.495	-7.4	
6	-0.890	-0.938	5.4	-0.795	-0.725	-8.8	-2.701	-2.845	5.3	
Average deviation (%)			12.9				14.25			
$i = 0.09 \text{ A/cm}^2$										
1	0.935	1.074	14.9	0.853	0.703	-17.6	2.900	2.847	-1.8	
2	0.561	0.519	-7.5	0.510	0.590	15.7	1.734	1.728	-0.4	
3	0.187	0.225	20.3	0.170	0.206	21.2	0.577	0.383	-33.6	
4	-0.187	-0.155	-17.1	-0.170	-0.240	41.2	-0.577	-0.535	-7.3	
5	-0.561	-0.498	-11.2	-0.510	-0.545	6.9	-1.734	-1.590	-8.3	
6	-0.935	-1.002	7.2	-0.853	-0.703	-17.6	-2.900	-2.910	0.3	
Average deviation (%)			13.03				20.03			

channel were calculated as

$$R_{T12} = \rho_E (1 + 1.5(V_G/V_p)) (L_{T12}/F_{ST})$$

$$R_{T23} = \rho_E (1 + 1.5(V_G/V_p)) (L_{T23}/F_{ST})$$

$$R_{B12} = \rho_E L_{B12}/F_{SB}$$

The distance between the platinum probes were (Fig. 3):  $L_{T12} = 2.5$  cm,  $L_{T23} = 8.5$  cm, and  $L_{B12} = 10$

cm. The voltage drops  $U_{T12}$ ,  $U_{T23}$ , and  $U_{B12}$  on the resistances  $R_{T12}$ ,  $R_{T23}$ , and  $R_{B12}$  were measured and calculated. Typical results obtained at a rate of flow of 10 kg/min and current densities of 0.03, 0.06, and 0.09  $\text{A/cm}^2$  with electrolyte B are presented in Table II. Measured values of the average cell voltage,  $U$ , at an electrode distance of 7.7 mm are given in Table III.

### Conclusions

The reproducibility of the measurement of the voltage drop using platinized platinum probes was checked for 5 couples of platinum probes built in the Plexiglas tube and using electrolyte B (without bubbles). The distance between these platinum probes was 5 cm. The reproducibility was 1% (10 mV) for a total voltage drop of about 1V. It follows that the main part of the deviation between experiments and theory is not due to the platinized platinum probes for the voltage drop measurement.

The deviations between theory and experiments are caused by the simplifications used in the mathematical description of the system and at the same time by the fact that the experimental conditions in each cell, such as local temperature and local flow rate of electrolyte, were not constant as assumed in the mathematical description. Unfortunately, it was not possible to distinguish exactly between these two sources of deviation on the basis of our data. The average deviation for the parasitic currents for the inlet channels (electrolyte without bubbles) was 14% and the same deviation was obtained for outlet channels (electrolyte with bubbles). It follows, that the presence of bubbles in the electrolyte has no influence on the average deviation.

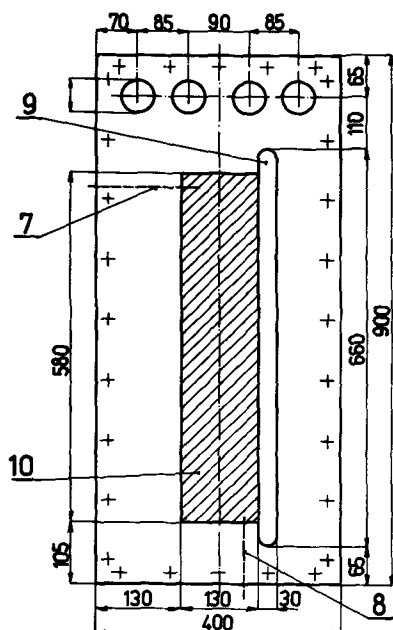


Fig. 4. Electrode frame. 7, 8, Platinum probes to measure cell voltage of electrolyzer ( $U$ ); 9, Plexiglas separator; 10, graphite electrode. Dimensions are given in millimeters.

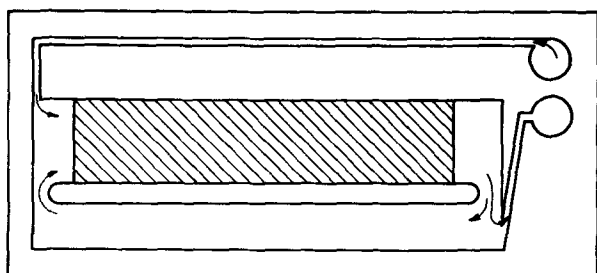


Fig. 5. Assembly of interelectrode and electrode frames. Direction of electrolyte flow is indicated by arrows.

Table III. Dependence of average cell voltage on current density and electrolyte rate of flow

Electrolyte	$\bar{i}$ ( $\text{A/cm}^2$ )	Rate of flow through 6 cells ( $\text{kg/min}$ )	Cell voltage (V)
A	0.03	10	3.027
	0.03	20	3.027
	0.03	30	2.987
	0.06	10	3.174
	0.06	20	3.164
	0.06	30	3.144
	0.09	10	3.358
	0.09	20	3.340
	0.09	30	3.330
	B	0.03	10
0.03		20	3.046
0.03		30	3.042
0.06		10	3.175
0.06		20	3.170
0.06		30	3.160
0.09		10	3.387
0.09		20	3.380
0.09		30	3.378

It is seen from the tables that the average error in all measurements was 14%. In view of the small absolute values of the parasitic currents the agreement is satisfactory. Our method therefore can be used in calculating the parasitic currents in practical bipolar electrolyzers.

Manuscript submitted April 24, 1973; revised manuscript received Nov. 1, 1973.

Any discussion of this paper will appear in a Discussion Section to be published in the December 1974 JOURNAL. All discussions for the December 1974 Discussion Section should be submitted by Aug. 1, 1974.

### SYMBOLS

(The values used are indicated in parentheses.)

$A, B$	constants in Eq. [5] <sup>1</sup>
$d$	inter-electrode distance (0.77 cm)
$d_2$	thickness of insulating wall in bubble separator compartment (1.0 cm)
$F_{SB}$	cross section of inlet electrolyte channel (0.6 cm <sup>2</sup> )
$F_{ST}$	cross section of outlet electrolyte channel (0.6 cm <sup>2</sup> )
$F_{QB}$	cross section of connecting channel for inlet of electrolyte (28.6 cm <sup>2</sup> )
$F_{QT}$	cross section of connecting channel for outlet of electrolyte (9.48 cm <sup>2</sup> )
$I_0$	current flowing through cells (A)
$\bar{i}$	average current density (0.03, 0.06, and 0.09 A/cm <sup>2</sup> )
$j$	cell number

<sup>1</sup> The values of  $A$  and  $B$  were calculated on the basis of experimental data for average cell voltage given in Table III.

<sup>2</sup> Criteria  $K_3, K_3'$ , and  $V_{GT}$  values were calculated by the method described previously (1).

$K_3, K_3'$	criteria <sup>2</sup>
$L$	height of bipolar electrode (58 cm)
$L_1$	height of insulation wall in electrode channel (4 cm)
$L_2$	height of connecting channel between inter-electrode channel and bubble separator (2.5 cm)
$L_{ST}$	length of connecting channel (above) (19 cm)
$L_{SB}$	length of connecting channel (below) (84 cm)
$L_{T12}, L_{T23}, L_{B12}$	distances between Pt probes in connecting channels (2.5, 8.5, and 10 cm)
$R_{T12}, R_{T23}, R_{B12}$	resistances between Pt probes in connecting channels (ohm)
$S_A, S_K$	thickness of anode or cathode (both 0.415 cm)
$U$	cell voltage (V)
$U_{T12}, U_{T23}, U_{B12}$	voltage drops between Pt probes in inlet channels (V)
$V_{GT}$	volume flow of gas phase on upper edge of electrode (cm <sup>3</sup> /sec) <sup>2</sup>
$V_P$	volume flow of electrolyte through cell (cm <sup>3</sup> /sec)
$w$	width of bipolar electrode (13.0 cm)
$w_1$	width of bubble separator (6.5 cm)
$\eta_{Sj}$	current efficiency in $j$ -th cell (with regard to parasitic currents)
$\rho_A, \rho_K$	specific resistances of anode and cathode (both $6.6 \times 10^{-4}$ ohm cm)
$\rho_E$	specific resistance of electrolyte (4.42 ohm cm)

### REFERENCES

1. I. Rousar, *This Journal*, **116**, 676 (1969).
2. J. R. Wilson, "Deminceralization by Electrodialysis," Butterworths, London (1960).
3. L. H. Thomas, "Elliptic Problems in Linear Difference Equations over a Network," Watson Scientific Lab., Columbia University, New York (1949).

## Cyclic Voltammetry of Copper Metal in Lithium Hydroxide Solution at Elevated Temperatures

Digby D. Macdonald<sup>1</sup>

Whiteshell Nuclear Research Establishment, Pinawa Manitoba, Canada

### ABSTRACT

A cyclic voltammetric study of copper metal in 1 mole kg<sup>-1</sup> LiOH solution at 25°, 125°, 200°, and 250°C is described. The results are consistent with the formation of both soluble (CuO<sub>2</sub><sup>2-</sup>) and insoluble (Cu<sub>2</sub>O and CuO) products at the metal surface. The formation and reduction of Cu(III) was found to occur near oxygen evolution at 25°C but not at the higher temperatures due to a sharp reduction in the oxygen evolution overpotential with temperature.

The electrochemical behavior of copper metal in alkali solution at temperatures less than 100°C has been investigated extensively (1-12). These studies have shown that two principal oxidation processes occur at the copper surface in alkaline solutions at room temperature, viz., the formation of Cu<sub>2</sub>O followed by the formation of CuO or Cu(OH)<sub>2</sub>. A third oxidation/reduction process has been observed at potentials close to oxygen evolution and was attributed to the formation of a copper(III) oxide, 'Cu<sub>2</sub>O<sub>3</sub>', (1, 7-12). However, recent cyclic voltammetry work indicates that this process may involve soluble species (8, 9).

Almost no experimental work has been reported on the electrochemical behavior of copper metal in aqueous solution at temperatures greater than 100°C. The need for studies on this system is clear, since copper

and copper-containing alloys are frequently used in industrial plants which utilize high-temperature water. In this study, the oxidation/reduction behavior of copper metal in 1 mole kg<sup>-1</sup> lithium hydroxide at 25°, 125°, 200°, and 250°C was investigated using cyclic voltammetry. This technique is capable of detecting very small amounts of charge consumed at the interface and has been used previously to investigate the electrochemical behavior of iron (13) and nickel (14) in high-temperature lithium hydroxide solutions. A thermodynamic study of the copper water system at temperatures to 300°C has been recently reported by Macdonald *et al.* (15) and provides a theoretical basis for the interpretation of the experimental electrochemical work reported here.

### Experimental

The high-temperature titanium electrochemical cell and the electronic apparatus used for the cyclic voltammetry studies have been described previously (13).

<sup>1</sup> Present address: Department of Chemistry, Victoria University of Wellington, Wellington, New Zealand.

Key words: copper, cyclic voltammetry, corrosion, elevated temperatures, lithium hydroxide.

Copper electrodes (12.7 mm long, 9.53 mm diameter, and  $3.8 \times 10^{-4} \text{ m}^2$  apparent surface area) were machined from 99.99% bar stock. Spectrographic analysis revealed the following constituents besides copper in micrograms/grams: Sb 40, As 10, B 1, Ca 20, Cr 1, Fe 10, Pb 1, Mg 5, Si 1, Ag 5, and Sn 1. The electrode surface was initially polished with No. 400 and No. 600 grit silicon carbide paper, degreased in acetone, and finally washed with distilled water.

Lithium hydroxide solutions were prepared from AR lithium hydroxide monohydrate and doubly distilled water. The solutions were stored in tightly stoppered Teflon containers to minimize contamination by atmospheric carbon dioxide. The solutions were also purged *in situ* using 99.99% nitrogen gas before heating.

All potentials reported in this work were measured with respect to a saturated calomel electrode which was maintained at 25°C. Electrolytic contact between the cell contents and the reference electrode was maintained via a compressed asbestos plug as previously described (13).

### Results

**General.**—Cyclic voltammograms for copper in 1 mole  $\text{kg}^{-1}$  lithium hydroxide solution at 25°, 125°, 200°, and 250°C are plotted in Fig. 1-4. The solid and broken lines represent the first and twentieth sweeps, respectively. In general, cyclic sweeping reduced the peak heights especially at the higher temperatures. At 25°C the peaks initially increased on cyclic sweeping although the reverse did occur if the system was swept over 50 or more cycles.

The cyclic voltammograms plotted in Fig. 1-4 show that two main anodic (I and II) and cathodic (V and VI) processes occur on copper over the potential range between hydrogen and oxygen evolution. At 25°C additional processes, corresponding to the formation and reduction of Cu(III) species, were observed close to oxygen evolution and are designated III and IV in Fig. 1. These processes were not observed at the higher temperatures due to reduction in overpotential for oxygen evolution at the metal surface (13).

At 25°C (Fig. 1) peaks II and VI frequently exhibited fine structure. This suggests that multiple redox processes occur in these regions of potential and may arise from the simultaneous existence of CuO and Cu(OH)<sub>2</sub> on the metal surface (6). At higher temperatures, the fine structure is no longer observed. This is consistent with the x-ray diffraction evidence of Bouillon *et al.* (6) which shows that only CuO is formed on copper at temperatures greater than 45°C.

A small cathodic peak (peak A, Fig. 2) with anodic "wings" (peaks B, Fig. 2) was often observed at about -0.1V vs SCE (25°C) at temperatures from 125° to 250°C. This peak occurs at too low a potential to be attributed to the process which is responsible for peak IV at 25°C and must represent an additional redox

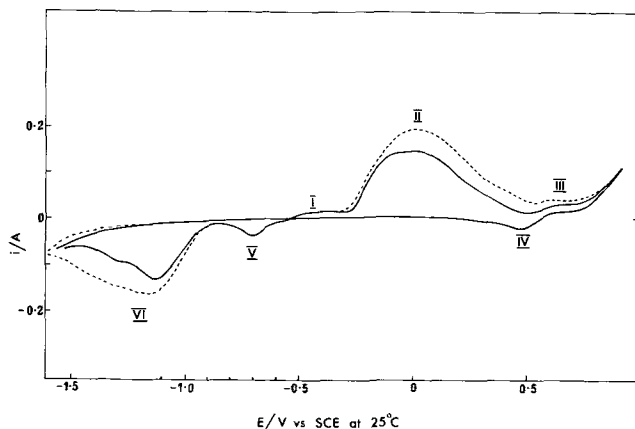


Fig. 1. Cyclic voltammogram for copper in 1 mole  $\text{kg}^{-1}$  LiOH solution at 25°C.  $dE/dt = 0.25 \text{ V/sec}^{-1}$ . Solid line, first sweep; broken line, twentieth sweep.

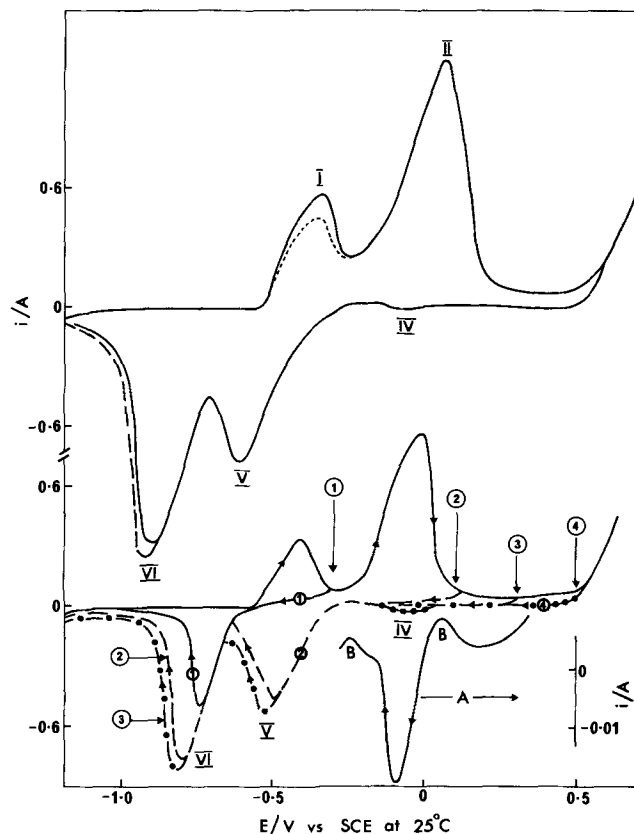


Fig. 2. Cyclic voltammograms for copper in 1 mole  $\text{kg}^{-1}$  LiOH solution at 125°C.  $dE/dt = 0.233 \text{ V/sec}^{-1}$  (upper curves),  $0.042 \text{ V/sec}^{-1}$  (lower curves). Solid line, first sweep; broken line, twentieth sweep.

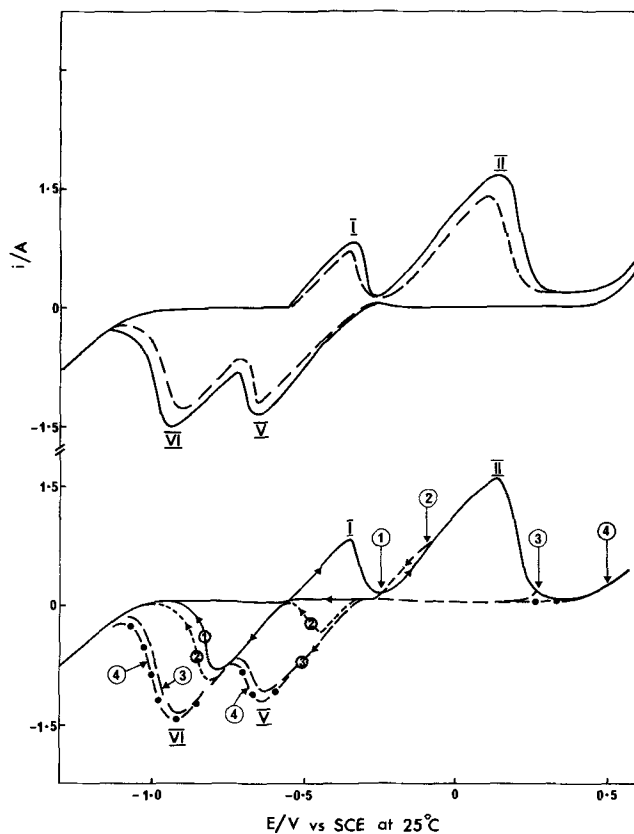


Fig. 3. Cyclic voltammograms for copper in 1 mole  $\text{kg}^{-1}$  LiOH solution at 200°C.  $dE/dt = 0.0466 \text{ V/sec}^{-1}$  (upper curves),  $0.042 \text{ V/sec}^{-1}$  (lower curves). Solid line, first sweep; broken line, twentieth sweep.



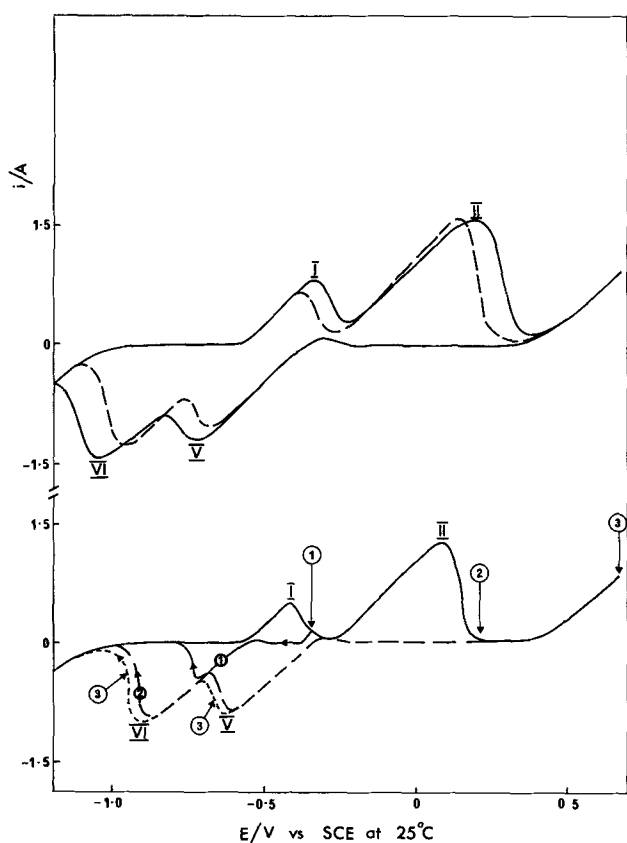


Fig. 4. Cyclic voltammograms for copper in 1 mole  $\text{kg}^{-1}$  LiOH solution at  $250^\circ\text{C}$ .  $dE/dt = 0.0466 \text{ V/sec}^{-1}$  (upper curves),  $0.042 \text{ V/sec}^{-1}$  (lower curves). Solid line, first sweep; broken line, twentieth sweep.

reaction in the system. The anodic "wings" to this peak on the anodic to cathodic scan suggest that the peak arises from a reactivation process in which the passivating film is partially reduced. However, the amount of charge consumed is small and, in view of the total charge required to completely reduce the surface (peaks V and VI), the redox process probably involves only a small fraction of the total film.

**Sweep reversal experiments.**—An important feature of this study concerned the behavior of the cathodic peaks (IV-VI) after sweep reversal on the anodic scan at selected potentials. The potentials at which the anodic scans were reversed ( $E_R$ ) are designated by vertical arrows in Fig. 2-5.

If the sweep was reversed before the start of peak I, the cathodic scan simply retraced the anodic sweep at all temperatures. The region from  $-1.0\text{V}$  to the start of peak I appears to be analogous to the "double layer" region observed on platinum (16) in which the major portion of the current is used to charge the double layer with very little being utilized in faradaic processes. At more cathodic potentials, hydrogen evolution becomes kinetically important as shown by the sweep behavior at potentials more negative than  $-1.0\text{V}$ .

Reversal of the anodic scans in Fig. 2-5 after peak I resulted in the cathodic peak designated VI. If the anodic sweeps were reversed after peak II, however, peaks V and VI resulted. Thus, we can conclude that the products formed at peaks I and II are reduced, at least to some extent, at peaks VI and V, respectively. The charges passed at peaks II and VI are considerably greater than those passed at peaks I and V. This is inconsistent with a mechanism involving simple consecutive one-electron transfer steps (e.g.,  $\text{Cu} \rightarrow \text{Cu}_2\text{O}$  and  $\text{Cu}_2\text{O} \rightarrow \text{CuO}$ ). Instead, a more complex mechanism involving parallel charge-transfer reactions in the peak regions of potentials is indicated.

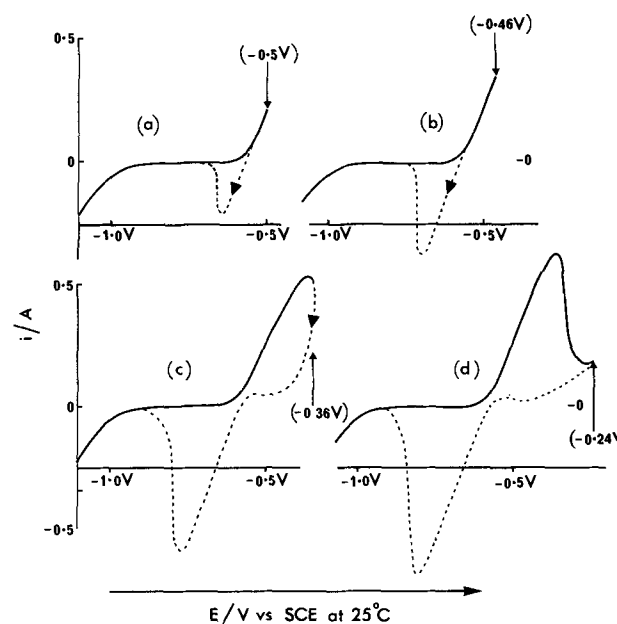


Fig. 5. Sweep reversal studies on copper in 1 mole  $\text{kg}^{-1}$  LiOH at  $250^\circ\text{C}$ .  $dE/dt = 0.042 \text{ V/sec}^{-1}$ . Solid line, cathodic to anodic sweep; broken line, anodic to cathodic sweep.

A number of experiments were carried out in which the anodic sweeps were reversed at potentials on the rising regions of peaks I and II in an attempt to ascertain the nature of the anodic processes responsible for the oxidation of copper in high-temperature hydroxide solutions. If the sweep was reversed on the rising part of peak I, then the reverse sweep retraced part of the forward sweep and then resulted in a cathodic peak as shown in Fig. 5. The cathodic charge passed on the reverse sweep, as represented by the area of the peak, was found to increase markedly as the potential of reversal on the rising part of peak I became more anodic. If the reversal potential exceeded the peak potential for peak I, then hysteresis between the ascending and descending scans in the peak I region of potential was observed. These results suggest that the electrode surface becomes completely covered with a resistive film of product at potentials greater than  $E_P$ , after which the faradaic process is essentially field-assisted film growth. The apparent reversibility of the anodic scan for  $E_R < E_P$  implies that the current-voltage curve in this region of potential is determined principally by a fast reversible process such as dissolution. The oxide film which eventually passivates the surface at  $E_R > E_P$  may then form either by direct nucleation from the metal or by precipitation of the dissolution product when the interfacial concentration exceeds the saturation value.

Sweep reversal on the ascending portion of peak II (Fig. 3) revealed that if  $E_R < E_P$ , then the current on the reverse scan was more anodic than for the forward scan. A similar phenomenon was noted by Ambrose *et al.* (8, 9) for copper in KOH solutions at  $25^\circ\text{C}$ . This observation indicates that the forward scan initially removes the passivating film formed at peak I, thus reducing the resistance to charge transfer by dissolution on the reverse sweep. Again, it was found that for  $E_R > E_P$ , hysteresis between the forward and reverse sweeps occurred, indicating the irreversible formation of a solid passivating film at the metal surface in this region of potential.

The cathodic peaks V and VI were found to shift to more negative potentials with increasingly anodic values for  $E_R$  (Fig. 2-5), or charge passed on the anodic scan. This behavior is similar to that found for the reduction of surface oxides on noble metals in 1 mole/liter $^{-1}$  perchloric acid at  $25^\circ\text{C}$  (17) in which it was concluded that the total quantity of surface

oxide is the important factor determining the peak potential in the reduction profile and the progressive hysteresis between the anodic oxide formation and the cathodic reduction profile. This same factor is presumed to contribute to the observed shifts in  $E_P$  for peaks V and VI in the present work. Resistance polarization effects associated with the ohmic resistances of the films probably also contribute to the dependence of  $E_P$  on anodic charge and hence film thickness.

**Sweep rate dependence.**—Cyclic voltammograms were obtained at a number of sweep rates over the range 0.05–0.5 V/sec<sup>-1</sup>. Both the peak currents and potentials were found to be sensitive to sweep rate at all temperatures, as has been previously observed for other metals in alkali solution at elevated temperatures (13, 14). In this work, it was found that neither the peak currents nor the peak potentials were sufficiently reproducible to determine their functional dependence on sweep rate. However, it was observed that the peak currents tended to increase with  $dE/dt$ . The potentials at which peaks occur on the forward sweep, i.e., peaks I and II (and III at 25°C) were found to become more anodic with increasing sweep rate, whereas those peaks observed on the reverse sweep shifted to more cathodic potentials. This observed sweep rate dependence of  $E_P$  is inconsistent with the operation of reversible redox processes involving adsorbed species (17). Instead, this behavior, together with the general asymmetric nature of the peaks, is consistent with the proposed irreversible formation of passivating oxide films (Cu<sub>2</sub>O and CuO) on the metal surface.

**Charge considerations.**—The total current passed at any potential during cyclic sweeping can be written as

$$i = (dq/dt)_f + CA(dE/dt) \quad [1]$$

where the first term is the current due to faradaic processes and the second represents the current associated with the nonfaradaic process of charging the double layer. Simple calculations (13) show that the charging current for sweep rates of the magnitude used here should be less than 10  $\mu$ A. Hence, the charging current can be neglected, and the total charge passed during electrolysis is attributed to faradaic processes at the interface. The change in charge,  $\Delta q$ , due to sweeping between potentials  $E_1$  and  $E_2$  is therefore given as

$$\begin{aligned} \Delta q &= \int_{E_1}^{E_2} i dE / (dE/dt) \\ &= \Delta q_D + \Delta q_F \end{aligned} \quad [2]$$

where  $\Delta q_D$  and  $\Delta q_F$  are the charges associated with dissolution and film formation processes, respectively. Although the present experimental technique does not permit resolution of the total charge into these components, we can nevertheless draw important conclusions if it is assumed that the sweep rates were sufficiently slow so that dissolution products formed on the forward (anodic) sweep have sufficient time to diffuse into the bulk of the solution before being reduced on the reverse (cathodic) sweep. Thus, any discrepancy between the total anodic and cathodic charges on cyclic sweeping can be attributed to dissolution processes.

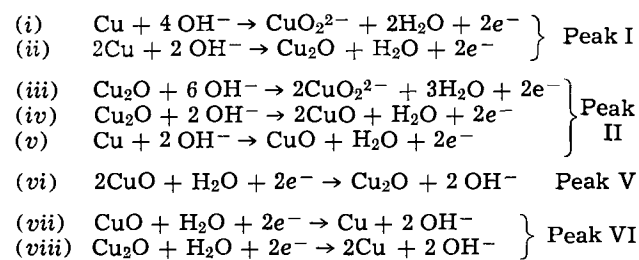
The charges passed on scanning the electrode between selected potentials were determined graphically from the recorded current/voltage curves. The total charges passed on anodic followed by cathodic sweeping were found to be not very reproducible and depended upon the previous history of the electrode. However, over a complete cycle from hydrogen evolution to oxygen evolution at 25°C, the total anodic charge passed was found to be about 10–15% greater than the total cathodic charge. This difference was found to increase slightly with temperature to about 20% at

250°C. This behavior is in sharp contrast to that observed for iron (13) and nickel (14) when it was found that the ratio of anodic to cathodic charge increased sharply with temperature between 25° and 200°C corresponding to the greater importance of dissolution processes in determining the electrochemical properties of these systems at elevated temperatures.

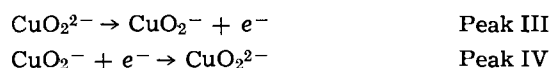
Cyclic voltammetry traces for Cu in 1 mole kg<sup>-1</sup> LiOH at 250°C as a function of reversal potential are shown in Fig. 5. The reversal potentials were chosen within the peak I region as shown. The ratio of anodic to cathodic charge over a complete cycle,  $Q_A/Q_C$ , is plotted as a function of  $E_R$  in Fig. 6. Thus, as the reversal potential increases along the ascending portion of peak I, the ratio  $Q_A/Q_C$  decreases from 1.52  $\pm$  0.05 to 1.25  $\pm$  0.05. This behavior indicates the existence of a large dissolution charge on the ascending part of the peak followed by passivation of the surface by a solid film. The same general behavior was displayed at all temperatures from 125° to 250°C.

### Discussion

**Oxidation mechanism.**—The following reactions are proposed to account for the oxidation/reduction behavior of copper metal in 1 mole kg<sup>-1</sup> LiOH at temperatures from 25° to 250°C



Ambrose *et al.* (8, 9) have proposed the following reactions to account for the oxidation/reduction peaks near oxygen evolution at 25°C



in which the copper(III) species is the ion CuO<sub>2</sub><sup>-</sup>. On the other hand, Shams El Din and El Wahab (7) considered the Cu(III) product to be an oxide "Cu<sub>2</sub>O<sub>3</sub>" rather than a soluble species. Irrespective of the identity of this product, the present work demonstrates that it is only formed before oxygen evolution at tem-

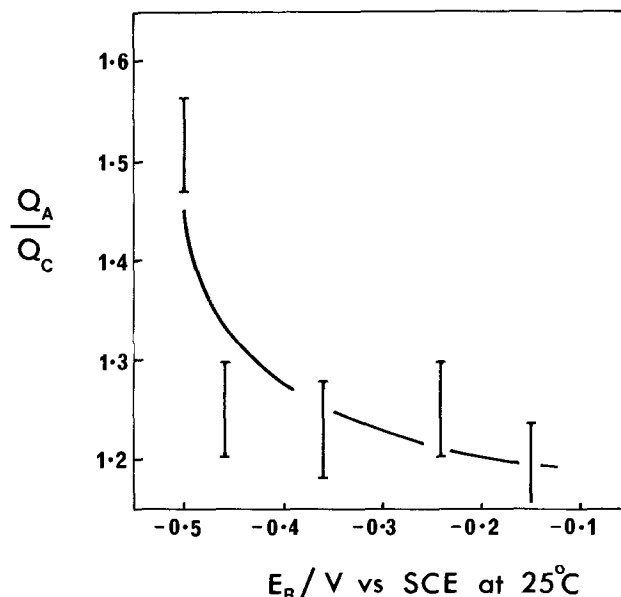


Fig. 6. Anodic to cathodic charge ratios for copper in 1 mole kg<sup>-1</sup> LiOH at 250°C.  $dE/dt = 0.042$  V/sec<sup>-1</sup>.

peratures less than 125°C. At higher temperatures, the overvoltage for oxygen evolution is reduced to such an extent that it completely masks the Cu(III) formation reaction. A similar phenomenon was found to occur at the nickel anode in 1 mole kg<sup>-1</sup> LiOH at elevated temperatures (14). Thus, at 22°C the formation and reduction of Ni(IV) oxide, possibly NiO<sub>2</sub> or non-stoichiometric NiO<sub>1.8</sub>, results in clearly defined cyclic voltammogram peaks just before oxygen evolution; even though thermodynamics show that the equilibrium potential for the Ni<sub>2</sub>O<sub>3</sub>/NiO<sub>2</sub> couple is more positive than the equilibrium potential for oxygen evolution under the conditions employed. At higher temperatures (175° and 250°C) these peaks are no longer observed due to a sharp reduction in oxygen evolution overpotential.

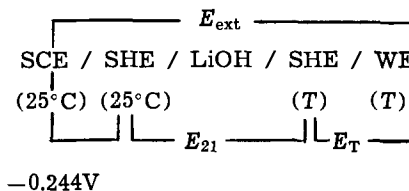
Reactions (i) and (iii) account for the formation of soluble products at peaks I and II, respectively, while reaction (ii) describes the growth of Cu<sub>2</sub>O which eventually passivates the surface and results in a decrease in current at peak I. The Cu<sub>2</sub>O formed at peak I is envisaged to undergo two reactions at peak II. Initially, the Cu<sub>2</sub>O is oxidized to produce a soluble CuO<sub>2</sub><sup>2-</sup> species according to reaction (iii), resulting in the partial removal of the Cu<sub>2</sub>O barrier to dissolution of the underlying metal. Consequently, if the sweep is reversed in this region the anodic current for the reverse sweep will be greater than that for the forward sweep, as observed (Fig. 3). Two further charge-transfer reactions are postulated to occur in the peak II region; viz., reactions (iv) and (v). Both reactions can account for passivation in this region where the passivating film is considered to consist mainly of CuO. Reaction (v) also accounts for the greater charge passed at peak II than at peak I. On the reverse sweep, part of the CuO formed at peak II is reduced to Cu<sub>2</sub>O at peak V according to reaction (vi). Further reduction of CuO and Cu<sub>2</sub>O to copper metal occurs at peak VI as described by reactions (vii) and (viii). This two-stage reduction of CuO at both peaks V and VI accounts for the greater charge passed at the latter, i.e., reduction of CuO to Cu<sub>2</sub>O is incomplete at peak V. This may result in the formation of a duplex oxide film on the metal surface consisting of an inner layer of Cu<sub>2</sub>O and an outer layer of CuO. The Cu<sub>2</sub>O formed in this region of potential and the unreduced outer layer of CuO are then reduced to the metal at peak VI.

The curves plotted in Fig. 1-4 show that the ratios  $Q(I)/Q(II)$  and  $Q(V)/Q(VI)$ , where  $Q(Y)$  is the charge passed under peak Y, increase markedly with temperature between 25° and 125°C, but remain fairly constant thereafter. This suggests that an increase in temperature from 25° to 125°C favors the initial formation of Cu<sub>2</sub>O as the potential of the metal is swept anodically. Likewise, this initial increase in temperature favors the reduction of CuO to Cu<sub>2</sub>O at peak V over the reduction of this product to Cu at peak VI. It should also be pointed out that part of the increase in the charge ratio  $Q(I)/Q(II)$  may be due to the influence of temperature upon the dissolution processes described by reactions (i) and (iii). This uncertainty cannot be resolved in the present study but will require detailed study by rotating-disk or ring-disk techniques of the type recently carried out by Ambrose *et al.* (9) for this system at 25°C.

**Thermodynamic relationships.**—In the present study for  $T \neq 25^\circ\text{C}$ , the working and reference electrodes were maintained at different temperatures and pressures. Therefore, the measured potentials contain two irreversible contributions, viz., a streaming potential due to the pressure gradient and a thermal junction potential due to the temperature gradient. For the low pressures employed (<4 MPa) the streaming potential is probably less than a few millivolts and will be ignored. The electromotive force of a cell containing a thermal junction in its initial state (i.e., before significant thermal diffusion) is the result of three contribu-

tions (18); (i) the metallic thermocouple effect which is usually small and neglected (18); (ii) the electrode temperature effect; and (iii) the thermal liquid junction potential.

The reference electrode assembly used in this study may be formally represented as follows, where SHE designates the standard hydrogen electrode at the temperature of interest



$E_{\text{ext}}$  is the potential with respect to the external SCE at 25°C,  $E_{21}$  is the potential difference for the thermal cell containing a 1 mole kg<sup>-1</sup> LiOH salt bridge, and  $E_T$  is the potential of the working electrode (WE) with respect to the SHE at the same temperature. It is this latter quantity which is calculated in a thermodynamic analysis of the system. Thus, in the absence of isothermal liquid junction potentials, the potential of the WE with respect to the external reference electrode ( $E_{\text{ext}}$ ) is related to the thermodynamic potential  $E_T$  by Eq. [3]

$$E_{\text{ext}} = E_T + E_{21} - 0.244\text{V}(\text{SCE}, 25^\circ\text{C}) \quad [3]$$

Now, the potential  $E_{21}$  is given by (i) and (ii) above, i.e.

$$E_{21} = \int_{T_1}^{T_2} \left( \frac{\partial E}{\partial T} \right)_{\text{Th,SHE}} dT + \int_{T_1}^{T_2} \left( \frac{\partial E}{\partial T} \right)_{\text{TJ}} dT \quad [4]$$

where  $(\partial E/\partial T)_{\text{Th,SHE}}$  is the thermal temperature coefficient for the cell SHE( $T_1$ )/SHE( $T_2$ ) and  $(\partial E/\partial T)_{\text{TJ}}$  is the thermal junction potential coefficient for the LiOH salt bridge. Studies by Seys and Van Haute (19) suggest that the thermal junction potential coefficient is not strongly dependent upon temperature. Thus, we write

$$\int_{T_1}^{T_2} \left( \frac{\partial E}{\partial T} \right)_{\text{TJ}} dT = 0.5 \times 10^{-3}(T - 25)\text{V} \quad [5]$$

where  $(\partial E/\partial T)_{\text{TJ}}$  has been taken as 0.5 mV/°C<sup>-1</sup> (18). The thermal temperature coefficient for the SHE at 25°C has been estimated to be 0.871 mV/°C<sup>-1</sup> at 25°C (18). If we assume that this coefficient also is not strongly dependent upon temperature then

$$\int_{T_1}^{T_2} \left( \frac{\partial E}{\partial T} \right)_{\text{Th,SHE}} dT = 0.871 \times 10^{-3}(T - 25)\text{V} \quad [6]$$

The potential of the working electrode with respect to the SCE at 25°C is therefore

$$E_{\text{ext}} = E_T + 1.371 \times 10^{-3}(T - 25) - 0.244\text{V}(\text{SCE}, 25^\circ\text{C}) \quad [7]$$

and the corrections to  $E_T$  are calculated to be -0.244, -0.17, 0, and 0.06V at 25°, 125°, 200°, and 250°C, respectively. The calculated  $E_{21}$  corrections are large, although it must be remembered that the thermal junction potential coefficient used is an estimated value and does not specifically apply to 1 mole kg<sup>-1</sup> LiOH. Thermal junction potentials vary considerably from study to study (18, 19) and the corrections calculated above should be regarded as tentative estimates only.

Macdonald *et al.* (15) have recently published detailed thermodynamic calculations on the copper water system at temperatures to 300°C. Calculated equilibrium potentials for reactions (i) to (v) referred to the SHE at the temperatures of interest together with values corrected for reference to the SCE at 25°C (i.e.,  $E_{o,\text{ext}}$ ) using Eq. [7] ( $E_o = E_T$ ) are listed in Table I.

Table I. Equilibrium potentials\* for reactions in the copper water systems at elevated temperatures

$E_o$ (V vs. SHE at T)				
Reaction	25°C	125°C**	200°C	250°C
(i)	-0.327	-0.51	-0.64	-0.74
(ii)	-0.355	-0.53	-0.66	-0.77
(iii)	-0.298	-0.49	-0.62	-0.71
(iv)	-0.186	-0.32	-0.46	-0.56
(v)	-0.271	-0.43	-0.56	-0.66

$E_{o,ext}$ (V vs. SCE at 25°C)				
Reaction	25°C	125°C	200°C	250°C
(i)	-0.571	-0.52	-0.64	-0.68
(ii)	-0.599	-0.64	-0.65	-0.71
(iii)	-0.542	-0.60	-0.62	-0.65
(iv)	-0.430	-0.43	-0.46	-0.50
(v)	-0.515	-0.54	-0.56	-0.60

\*  $[OH^-] = 1 \text{ mole kg}^{-1}$ ,  $pK_w$  values were taken from Ref. (20). The interfacial concentration of  $CuO_2^{2-}$  has been arbitrarily set at  $10^{-6} \text{ mole kg}^{-1}$ . No activity coefficient corrections were applied.

\*\* Interpolated from plots of  $E_o$  vs. temperature.

The thermodynamic consistency of the reactions proposed to account for the redox behavior of copper in high-temperature alkali solution can be judged by application of the following restrictions (13, 14): (i) for conjugate oxidation/reduction peaks on cyclic sweeping then  $E_a > E_o > E_c$  where  $E_a$  and  $E_c$  are the anodic and cathodic peak potentials and  $E_o$  is the equilibrium potential for the process responsible for the peaks, and (ii)  $E_{diss} > E_{o,diss}$  is the potential at which the proposed dissolution process with equilibrium potential  $E_{o,diss}$  begins to pass significant current. Both restrictions (i) and (ii) are, of course, equivalent to the statement that the overpotentials for anodic and cathodic processes are positive and negative, respectively. Comparison of the equilibrium potentials listed in Table I with the peak potentials shown in Fig. 1-4 show that the relationships discussed above are obeyed. Therefore, the reactions proposed are consistent with the thermodynamics of the copper water systems over the temperature range studied.

Manuscript submitted May 31, 1973; revised manuscript received Nov. 10, 1973.

Any discussion of this paper will appear in a Discussion Section to be published in the December 1974 JOURNAL. All discussions for the December 1974 Discussion Section should be submitted by Aug. 1, 1974.

#### REFERENCES

1. E. Muller, *Z. Elektrochem.*, **13**, 133 (1907).
2. W. Feitknecht and H. W. Linel, *Helv. Chim. Acta*, **27**, 775 (1944).
3. A. Hickling and D. Taylor, *Trans. Faraday Soc.*, **44**, 262 (1948).
4. S. E. S. El Wakkad and S. H. Emara, *J. Chem. Soc.*, 3508 (1953).
5. J. S. Halliday, *Trans. Faraday Soc.*, **50**, 171 (1954).
6. F. Bouillon, J. Piron, and J. Stevens, *Bull. Soc. Chim. Belges*, **67**, 643 (1958).
7. A. M. Shams El Din and F. M. Abd El Wahab, *Electrochim. Acta*, **9**, 113 (1964).
8. J. Ambrose, R. G. Barradas, and D. Shoesmith, *J. Electroanal. Interfacial Electrochem.*, In press.
9. J. Ambrose, R. G. Barradas, and D. Shoesmith, *ibid.*, In press.
10. J. Ambrose, R. G. Barradas, and K. Belinko, *ibid.*, **42**, 176 (1973).
11. B. Miller, *This Journal*, **116**, 1675 (1969).
12. M. W. Lister, *Can. J. Chem.*, **31**, 638 (1953).
13. D. D. Macdonald and D. Owen, *This Journal*, **120**, 317 (1973).
14. D. D. Macdonald and D. Owen, Paper presented at the conference on "High Temperature High Pressure Electrochemistry in Aqueous Solutions," University of Surrey, England, January 1973.
15. D. D. Macdonald, G. R. Shierman, and P. Butler, Atomic Energy of Canada Ltd., Report AEC1-4136 (1972).
16. A. Capon and R. Parsons, *Electroanal. Chem. Interfacial Electrochem.*, **39**, 275 (1962).
17. P. Stonehart, H. A. Kozlowska, and B. E. Conway, *Proc. Roy. Soc. A*, **310**, 451 (1969).
18. A. J. de Bethune, T. S. Licht, and N. Swedeman, *This Journal*, **106**, 616 (1959).
19. A. A. Seys and A. A. Van Haute, Paper presented at the conference on "High Temperature High Pressure Electrochemistry in Aqueous Solutions," University of Surrey, England, January 1973.
20. J. R. Fisher and H. L. Barnes, *J. Phys. Chem.*, **76**, 90 (1972).

## The Cathodic Behavior of CuS, MoO<sub>3</sub>, and MnO<sub>2</sub> in Lithium Cells

Fred W. Dampier\*

ESB Incorporated, C. F. Norberg Technology Center, Yardley, Pennsylvania 19067

#### ABSTRACT

The cathodic behavior of CuS and MoO<sub>3</sub> was studied in lithium cells discharged at current densities in the neighborhood of 2 mA/cm<sup>2</sup>. Two electrolytes, 1M LiClO<sub>4</sub>/propylene carbonate (PC) and 1M LiClO<sub>4</sub>/70% tetrahydrofuran (THF)-30% 1,2 dimethoxyethane (DME) were investigated for both of the cathodes, and it was found that the THF-DME electrolyte greatly increased the coulombic efficiency. The Li-MoO<sub>3</sub> cells that were discharged after one year of storage showed a 19% loss of capacity which has been attributed to trace impurities. A study of the rechargeability of the Li-MnO<sub>2</sub> cell was also undertaken, and for the fifth cycle an ampere-hour charging efficiency of 45.2% was obtained.

In recent years a number of new cathode materials (1, 2) have been found for nonaqueous batteries which give outstanding electrochemical performance, even

after one year of activated storage. Previously, most of the cathode materials investigated, for example, CuF<sub>2</sub> and CuCl<sub>2</sub>, were sufficiently soluble in organic electrolytes that self-discharge and dendrite formation were serious problems limiting the storage life to a month or less.

\* Electrochemical Society Active Member.

Key words: batteries, primary; propylene carbonate; tetrahydrofuran; lithium.

All the cathode materials that were selected for the present study are essentially insoluble in organic electrolytes and discharge results for  $\text{MoO}_3$  and  $\text{CuS}$  show minimal losses after one year of activated storage. The theoretical specific energies for lithium cells with  $\text{CuS}$ ,  $\text{MoO}_3$ , and  $\text{MnO}_2$  cathodes are 436, 442, and 845 Whr/lb, respectively. Although the  $\text{CuS}$  cathode has been described by Gabano (2, 3) and the  $\text{MoO}_3$  cathode has been investigated by Knapp (4) and Campanella (1), much more needs to be known concerning the electrochemistry of these new systems if their full potential is to be realized.

In the present research, studies were conducted to more fully characterize the cathodic behavior of  $\text{CuS}$  and  $\text{MoO}_3$  in lithium cells. Information was gained concerning the performance of the  $\text{MoO}_3$  cathode in two electrolytes not previously used in lithium cells with this cathode: 1M  $\text{LiClO}_4$ /propylene carbonate (PC) and 1M  $\text{LiClO}_4$ /70% tetrahydrofuran (THF)-30% 1,2 dimethoxyethane (DME).  $\text{MnO}_2$ , which has previously (4, 5) been used as a cathode in lithium batteries, was also studied in the  $\text{LiClO}_4$ /THF-DME electrolyte. Although  $\text{MnO}_2$  was found to have a lower specific energy than  $\text{MoO}_3$ , the results of cycling experiments have shown that the Li- $\text{MnO}_2$  cell is rechargeable.

### Experimental

**Cell construction.**—The preparation of solutions and all electrochemical measurements were performed in a recirculating argon atmosphere glove box (Vacuum Atmospheres Corporation). The experimental cells consisted of two lithium anodes (1 $\frac{3}{8}$  in. sq, 0.015 in. thick) on either side of a 1-in. sq cathode (0.035 in. thick) separated by one layer of 15-mil glass fiber filter paper (No. 934AH, Reeve-Angel).

The cathodes were prepared by pressing a blend of 85% active material, 10% graphite (No. 1651, Southwestern Graphite Company), and 5% polyethylene powder (Microthene FN-500, U. S. Industrial Chemicals) onto a 5-mil nickel 10-3/0 grid (Exmit Corporation). The active material and polyethylene powder were sieved through a 200 mesh screen, and the material that passed was mixed thoroughly with the graphite for 16-20 hr on a Fisher-Kendal mixer. A 0.015 in. diameter copper terminal wire was spot welded to the 1.0 in. sq nickel grid and the grid positioned in a steel pressing die lined with release paper. Next, approximately 1.5g of the cathode mixture was evenly spread in the cavity, a second sheet of release paper added, and the assembly compacted at 6400 psi for 3 min at 225°F. The active materials used to prepare the cathodes were  $\text{MoO}_3$  (Baker analyzed reagent),  $\text{CuS}$  (Fisher certified reagent), chemically formed  $\text{MnO}_2$  (Type "M," Diamond Shamrock Chemical Company), and electrolytic  $\text{MnO}_2$  (E. J. Lavino and Company).

Cells were assembled by wrapping one cathode in a "U" fold of one thickness of glass fiber filter paper, then sandwiching the wrapped cathode between two lithium anodes. The element was then inserted into a polypropylene cell case, using polyethylene shims to insure a snug fit, and electrolyte was added.

**Electrolyte.**—The propylene carbonate (Jefferson Chemical Company), 1,2 dimethoxyethane (yellow label, Eastman Kodak Company), and tetrahydrofuran (E. I. du Pont Company, Electrochemicals Department) used to prepare electrolytes were all dried with 5A molecular sieves (Linde Division, Union Carbide Corporation) prior to distillation. Dry argon was then bubbled through each solvent for 24 hr to remove dissolved oxygen and  $\text{CO}_2$  and the solvent distilled with a Nester/Faust NF-276 spinning band distillation apparatus (Nester/Faust Manufacturing Corporation, Newark, Delaware). The distillation column (ID 1.0 cm, length 95 cm) was equipped with a Monel spiral band which was rotated at  $1170 \pm 6$  rpm by a motor. The receiver system, in order to maintain vacuum and

avoid contamination with stopcock grease, was designed with glass drip tips, Teflon standard taper sleeves, and Teflon needle valve stopcocks. The THF and DME distillations were carried out at atmospheric pressure, but to avoid decomposition, PC was distilled at  $2.0 \pm 0.3$  Torr while the column head temperature was kept between 73° and 79°C. The reflux ratio was regulated at 15:1 by an electric timer and the first 10% and last 20% of the solvent were discarded. Analysis of the distilled PC with an F & M Model 200 gas chromatograph (W filaments, 2-ft Poropak Q column) showed the water concentration was about  $170 \pm 30$  ppm. Details concerning the gas chromatographic techniques used have been reported elsewhere (6).

Reagent grade  $\text{LiClO}_4$  (G. F. Smith Chemical Company) was twice recrystallized from water and dried at temperatures up to 220°C in a stream of dry argon at pressures from 200 to 1  $\mu\text{m}$  for 24 hr (approximately 4 hr at 220°C). The drying tube was equipped with ground glass joints and stopcocks so that the dry salt could be transferred under vacuum from the manifold to the glove box. Attempts to analyze the electrolyte using gas chromatography gave spurious results due to thermal decomposition in the injector port and other problems described by Butler (16).

**Linear sweep voltammetry.**—The voltammetric scans were performed using a Tacussel PIT-20 potentiostat programmed from a Tacussel GSTP function generator and the current-potential curves were recorded on a Tektronix 564 storage oscilloscope. The reference and counterelectrodes were 40  $\times$  8 mm strips of 0.015 in. thick lithium foil (Foote Mineral Company) of 99.9% purity. The working electrode was a 0.256 in. diameter disk of bright platinum inlaid in glass (Beckman Instruments).

### Results and Discussion

**Discharge behavior.**—The cathodic behavior of  $\text{MoO}_3$ ,  $\text{CuS}$ , and  $\text{MnO}_2$  during 2 mA/cm<sup>2</sup> constant current discharge is compared in Fig. 1 for cells using a 1.0M  $\text{LiClO}_4$ /70% THF-30% DME electrolyte. The complete discharge curve for  $\text{MoO}_3$  in Fig. 2 shows that 70.5% of the theoretical capacity based on 2 electrons/mole can be obtained to a 2.00V cutoff at 2 mA/cm<sup>2</sup>. By comparison only 31.8% of the theoretical capacity was obtained during discharge of  $\text{CuS}$  on the basis of a 1.52V instead of the regular 2.00V cutoff. Thus,  $\text{MoO}_3$  has the highest specific energy of the three cathodes by a considerable margin.

The low voltage obtained during the discharge of the Li-CuS cell generally agrees with the results of Gabano and co-workers (2, 3) who were the first to investigate this cell using the THF-DME electrolyte. When Li-CuS cells were discharged using a 1M  $\text{LiClO}_4$ /PC electrolyte,  $\text{CuS}$  utilizations of only 4.3%

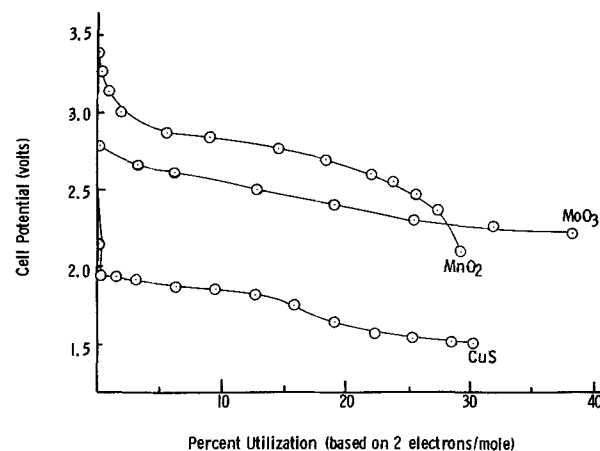


Fig. 1. Cathodic behavior of  $\text{CuS}$ ,  $\text{MoO}_3$ , and  $\text{MnO}_2$  in lithium cells. Electrolyte: 1M  $\text{LiClO}_4$ /70% THF-30% 1,2 DME. Current density: 2 mA/cm<sup>2</sup>.

were obtained in the best case. A similar reduction in capacity was also observed for the  $\text{MoO}_3$  cathode when THF-DME was replaced by PC and will be attributed to reduced  $\text{LiClO}_4$  diffusion in PC, in a later discussion of mass transfer processes.

The results given in Fig. 1 for the discharge of  $\text{MnO}_2$  were obtained using cathodes that contained 87.7% chemically formed  $\text{MnO}_2$  (200 mesh). Electrolytic  $\text{MnO}_2$  (80 mesh) was tested under similar conditions to a 2.11V cutoff and was found to yield only 17% of theoretical capacity compared to 29% obtained with chemical  $\text{MnO}_2$ .

Figure 2 shows a series of discharge curves at various current densities for Li-MoO<sub>3</sub> cells using a 1M  $\text{LiClO}_4$ /THF-DME electrolyte. The rapid polarization and low utilization obtained for the 8 mA/cm<sup>2</sup> discharge appears to be largely due to concentration polarization since the cell was found to have considerable unused capacity even though discharged to a 0.76V cutoff. The open-circuit voltage of the cell rose to 2.71V within an hour after the discharge was terminated, and the cell yielded an additional 46.7% of theoretical capacity (2.00V cutoff) when discharged through a 78 ohm resistor (2.05 mA/cm<sup>2</sup> at 2.02V).

When the discharge results of the Li-MoO<sub>3</sub> cells using the THF-DME electrolyte were obtained, calculations were carried out which showed that this system could be the basis of a high energy battery. Several D-size cells (1-11/32 in. diameter, 2-1/4 in. height) were therefore constructed with spiral wound electrodes, and it was found that they operated with a 27 ohm load for 85 hr above 2.0V. Since the cells weighed 82g, the specific energy corresponds to 105 Whr/lb.

The main limitation of the  $\text{LiClO}_4$ /THF-DME electrolyte is the loss in capacity that occurs during low temperature discharge. At -18°C only 24.2% of the theoretical capacity (based on 2 electrons/mole) of  $\text{MoO}_3$  discharged at 2 mA/cm<sup>2</sup> was obtained compared to 70.5% (to a 2.00V cutoff) at 25°C. The 72% loss in capacity that was observed is unusually large when compared with the minimal losses obtained when more volatile, less viscous solvents such as methyl formate are used in Li-MoO<sub>3</sub> cells. The choice of  $\text{LiClO}_4$  as the solute may also be a contributing factor (8) because solubility limitations can lead to problems with concentration polarization. In particular, if the accumulation of  $\text{LiClO}_4$  in the diffusion layer at the lithium electrode exceeds the solubility, film formation may occur.

In Fig. 3 the discharge characteristics for Li-MoO<sub>3</sub>/ $\text{LiClO}_4$ -PC cells stored 6 and 12 months are compared with cells discharged immediately after being filled. To a 2.00V cutoff, the utilization dropped from 32.1% of theoretical for the immediate discharge to 25% after

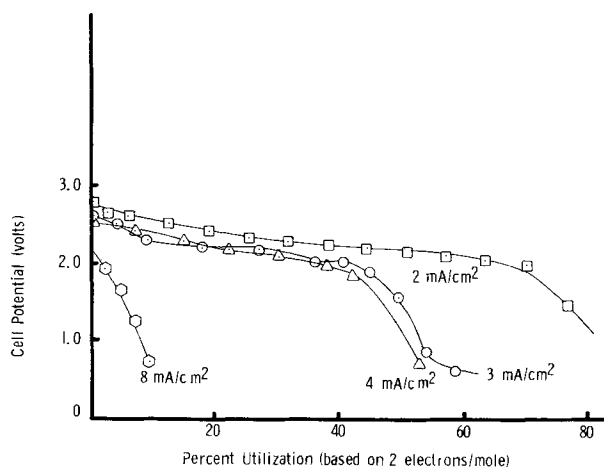


Fig. 2. Discharge characteristics of Li-MoO<sub>3</sub> cells at various current densities. Electrolyte: 1M  $\text{LiClO}_4$ /70% THF-30% 1,2 DME.

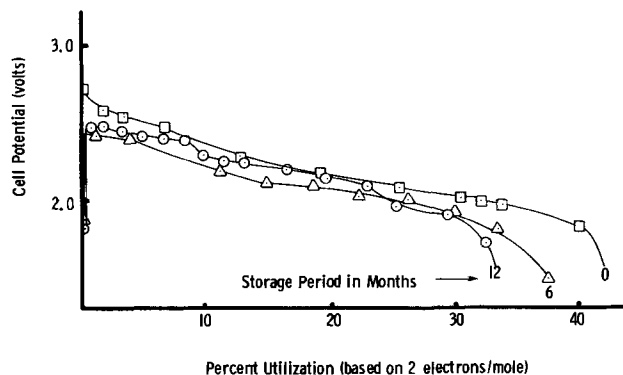


Fig. 3. Discharge characteristics of Li-MoO<sub>3</sub> cells after 6 and 12 months of storage. Electrolyte: 1M  $\text{LiClO}_4$ /PC. Current density: 2 mA/cm<sup>2</sup>.

a one year stand. Since the PC used to prepare the electrolyte contained at least 170 ppm water, it may be possible to further reduce storage losses by using an even more highly purified electrolyte. The discharge results in Fig. 3 are for cells stored under argon in sealed Mason jars with several pieces of lithium foil and fresh potassium beside the open cell inside, to act as an oxygen and water vapor getter. It was found that cells stored six months with only a lithium getter showed a 50% greater loss in capacity than cells stored with a potassium getter. Thus it appears that the water concentration must be maintained considerably lower than 170 ppm if storage losses are to be kept to a minimum.

A transient voltage delay occurred during the first minutes of discharge for the Li-MoO<sub>3</sub>/PC cells stored 6 and 12 months. For the cell stored 6 months (OCV 2.87V) a minimum voltage of 1.84V was observed after approximately 2 sec of discharge at 2 mA/cm<sup>2</sup>. The voltage then recovered to 2.18V after 30 sec and to 2.33V after 1 min. The transient delay effect is most likely due to a thin film formed on the lithium anode and probably could be eliminated by reducing the amount of water and other impurities in the electrolyte and the cathode. Since no voltage minima were observed for cells containing either PC or THF-DME in the electrolyte when the cells were discharged after 45 days' storage, the transient delay effect may be both solvent and time dependent.

An examination of the lithium anodes of the Li-MoO<sub>3</sub> cell which had been stored one year, after the cell had been discharged, revealed a border of black film about 3 mm wide outlining the portion of the lithium anode that was adjacent to the outer edge of the cathode in the assembled cell. The lithium outside this border was bright and untarnished even though it was exposed to the  $\text{LiClO}_4$ /PC electrolyte for one year. It thus appears that the black film was formed by material that diffused out of the cathode during stand. If the film was formed in this way, then the area within the border was probably filled in with film before discharge, and the film was stripped off by the dissolution of lithium during the period when the transient voltage delay was observed. Since no serious attempt, other than vacuum drying at room temperature, was made to purify either the  $\text{MoO}_3$  or graphite used to prepare the cathode, the use of more highly purified materials might further reduce the capacity losses during storage.

The exact cause of the large increase in capacity observed for both  $\text{MoO}_3$  and  $\text{CuS}$  cathodes when THF-DME rather than PC was used to prepare electrolyte is of interest for both theoretical and practical reasons if even more effective electrolytes are to be developed. At 2 mA/cm<sup>2</sup>, the capacities of Li-MoO<sub>3</sub> cells using  $\text{LiClO}_4$ /PC and  $\text{LiClO}_4$ /THF-DME electrolytes were 32 and 70% of theoretical, respectively, to a 2.00V cutoff. The 120% increase in capacity cannot be ac-

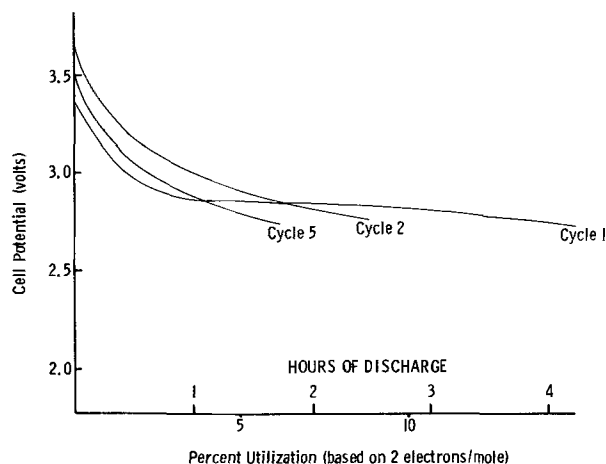


Fig. 4. Discharge characteristics of the Li-MnO<sub>2</sub> cell. Electrolyte: 1M LiClO<sub>4</sub>/70% THF-30% 1,2 DME. Current density: 2 mA/cm<sup>2</sup>.

counted for by the electrical conductance because the 1.0M LiClO<sub>4</sub>/PC electrolyte [ $\kappa = 5.3 \cdot 10^{-3} \text{ ohm}^{-1} \text{ cm}^{-1}$  (7) at 25°C] is 34% more conductive than 1.0M LiClO<sub>4</sub>/70% THF-30% 1,2 DME [ $\kappa = 3.8 \cdot 10^{-3} \text{ ohm}^{-1} \text{ cm}^{-1}$  (8)]. However, the viscosities of the 1.0M LiClO<sub>4</sub> electrolytes at 25°C are 7.08 cp (7) and 0.91 cp (9) for the PC and the THF/DME electrolytes, respectively.

In order to understand the effect of the electrolyte viscosity on the coulombic efficiency of porous cathodes one requires a theoretical model (17, 18). The recently developed model by Bennion and Dunning (10, 19) is probably best suited for this purpose. In their analysis, diffusion and conductance were found to be important factors in the mass transport and conservation equations. The electrolyte viscosity does not appear directly. However, the electrolyte viscosity is related to the diffusion coefficient to a first approximation by the Einstein Stokes equation (11). Thus the superior performance of the THF-DME, compared to the PC electrolyte, can be attributed to increased diffusion of LiClO<sub>4</sub> in the pores of the cathode when the THF-DME mixture was used as the solvent.

**Cycling behavior.**—The cell potentials for a Li-MnO<sub>2</sub> cell with a 1M LiClO<sub>4</sub>/70% THF-30% 1,2 DME electrolyte during the first, third, and fifth discharges at 2 mA/cm<sup>2</sup> are shown in Fig. 4. The cutoff voltage for discharge was 2.74V and the charging current density was 0.75 mA/cm<sup>2</sup>. The ampere-hour charging efficiencies, charging times, and cutoff voltages are summarized in Table I for the first five cycles. The decline in the charging efficiency is probably partially due to electrolyte oxidation during charging at potentials above 4.00V.

The nonaqueous Li-MnO<sub>2</sub> cell was found to resemble the alkaline Zn-MnO<sub>2</sub> cell both in having a similar sloping discharge curve and exhibiting a great decrease in cycle life (12) if discharged below a cutoff voltage about 25% higher than the normal cutoff voltage due to depleted capacity. For example, a Li-MnO<sub>2</sub> cell discharged to a 2.11V cutoff yielded a utilization of only 3.66% on the second cycle to a 2.73V cutoff compared to 8.88% for the cell described in Fig. 4.

On the basis of a comparison with the discharge results for Li-MoO<sub>3</sub>, D-size cells, cycle 2 for the Li-MnO<sub>2</sub> cell shown in Fig. 4 would be expected to yield

Table I. Charging conditions for Li-MnO<sub>2</sub> cell

Charge No.	Charge time (hr)	Charging cutoff (V)	A-hr charging efficiency (%)
1	11.50	4.20	58
2	11.00	3.98	51
3	9.76	3.82	41
4	10.33	4.08	45
5	15.25	4.22	10

a specific energy of about 34 Whr/lb for a D-size cell. Therefore, the Li-MnO<sub>2</sub> secondary cell compares favorably at this early stage with the 30 to 45 Whr/lb that can be obtained from small silver-zinc cells (12). No attempt has yet been made to optimize the cathode formulation or charging conditions, thus some improvements in the charging efficiency and cycle life may be expected.

**Linear sweep voltammetry.**—Voltammetric scans are given in Fig. 5 for the oxidation of 1.0M LiClO<sub>4</sub>/THF and 1.0M LiClO<sub>4</sub>/70% THF-30% DME using a platinum working electrode. Comparison of the curves shows that the addition of 30% DME to the electrolyte has little effect on its stability to withstand oxidation. The oxidation of the electrolyte does not appear to produce a gaseous product even at potentials over +4.5V with respect to Li/Li<sup>+</sup>.

These results suggest that the charging of lithium cells using the LiClO<sub>4</sub>/THF-DME electrolyte should be stopped once the charging voltage has reached 4.0V or else electrolyte oxidation will reduce cycle life. Since the Li-MnO<sub>2</sub> cell described earlier was charged to a 4.2V cutoff on the first charge, its limited cycle life may have been caused by oxidation of the electrolyte.

A precise determination of the maximum charging voltage is complicated by the difficulty of predicting the behavior of a high surface area carbon electrode using data obtained from voltammetric scans on platinum. In addition to surface area effects, the oxidation overpotential of an electrolyte can be greatly altered by the nature of the sometimes not so inert surface at which the reaction is being studied.

Cyclic voltammetry in the region of +4.3 to -0.2V with respect to Li/Li<sup>+</sup> (scan rate 80 mV sec<sup>-1</sup>) revealed a reduction peak at about +1.2V for the THF-DME electrolyte which can be attributed to reduction of the oxidized electrolyte. As would be expected if oxidized electrolyte was the reactant, the peak increased as the scan limit was increased from +3.5 to +4.5V. Although the oxidized compounds formed from the electrolyte have not yet been identified, recent work by Dey (13) suggests the direct oxidation of THF to form THF cations. The formation of perchlorate radicals followed by reaction with the solvent (e.g., to form tetramethylene peroxide and chlorate ion) is a possible alternative mechanism which has been found (14, 15) to occur during the electrolysis of LiClO<sub>4</sub>/acetonitrile.

### Conclusion

Lithium cells with MoO<sub>3</sub> cathodes were found to give a much higher specific energy than cells using

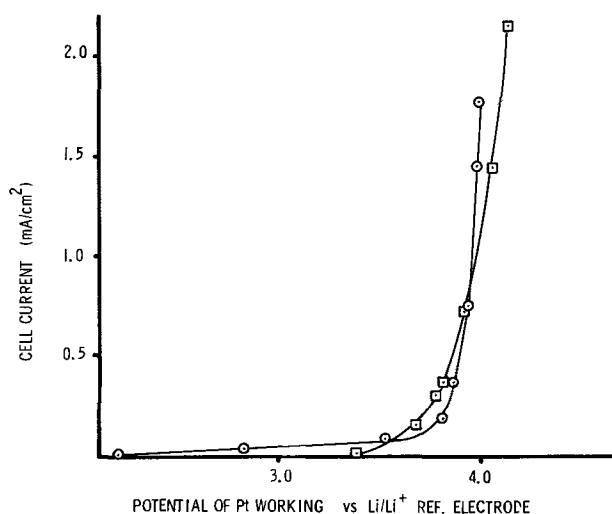


Fig. 5. Oxidation of THF and THF-DME/LiClO<sub>4</sub> electrolytes using a Pt working electrode at 25°C. □, 1.0M LiClO<sub>4</sub>/THF, scan rate 22 mV/sec.; ○, 1.0M LiClO<sub>4</sub>/70% THF-30% 1,2 DME, scan rate 10 mV/sec.



either CuS or MnO<sub>2</sub> cathodes. At 2 mA/cm<sup>2</sup>, 70.5% of the theoretical coulombic capacity of MoO<sub>3</sub> was obtained to a 2.00V cutoff for cells using a 1.0M LiClO<sub>4</sub>/THF-DME electrolyte. Although Li-MnO<sub>3</sub>/PC cells that were stored one year showed a 19% loss in coulombic capacity, substantial improvements may be possible if more highly purified materials are used.

The large increase in capacity observed for both MoO<sub>3</sub> and CuS cathodes when THF-DME rather than PC was used to prepare the electrolyte can be attributed to the increased diffusion of LiClO<sub>4</sub> in the THF-DME mixture.

Cycling experiments with the Li-MnO<sub>2</sub> cell indicate that transition metal oxides show promise as cathodes for rechargeable batteries. Oxidation reactions of the electrolyte which may occur during charging were investigated by cyclic voltammetry. The results suggest that the cycle life of the Li-MnO<sub>2</sub> cell could be improved if charging is stopped before the voltage reaches 4.0V, to prevent oxidation of the LiClO<sub>4</sub>/THF-DME electrolyte.

Manuscript submitted June 26, 1973; revised manuscript received Dec. 12, 1973. This was Paper 4 presented at the Miami Beach, Florida, Meeting of the Society, Oct. 8-13, 1972.

Any discussion of this paper will appear in a Discussion Section to be published in the December 1974 JOURNAL. All discussions for the December 1974 Discussion Section should be submitted by Aug. 1, 1974.

#### REFERENCES

1. L. Campanella and G. Pistoia, *This Journal*, **118**, 1905 (1971).
2. J. P. Gabano, G. Gerbier, and J. F. Laurent, Proc. 23rd Power Sources Conf., Atlantic City, N. J. (1969).
3. J. P. Gabano, V. Déchenaux, G. Gerbier, and J. Jammet, *This Journal*, **119**, 459 (1972).
4. H. R. Knapp, U.S. Army Electronics Command, ECOM-2632 (Oct. 1965).
5. S. G. Abens and W. F. Meyers, Livingston Electronic Corp. First Quar. Report, NASA CR-54118 (Oct. 1964).
6. R. J. Jasinski and S. Kirkland, *Anal. Chem.*, **39**, 1663 (1967).
7. R. Keller, J. N. Foster, D. C. Hanson, J. F. Hon, and J. S. Muirhead, NASA CR-1425, Rocketdyne Div., North American Rockwell Corp., (Aug. 1969).
8. Société des Accumulateurs Fixes et de Traction (S.A.F.T.), French Patent 1,579,466 (July 21, 1969).
9. J. P. Gabano, Private communication, (Sept. 1972).
10. J. S. Dunning, Ph.D. Thesis, University of California, Los Angeles, California (1972).
11. R. A. Robinson and R. A. Stokes, "Electrolyte Solutions," 2nd Ed., p. 12, Butterworths Publishers Ltd., London (1959).
12. S. Uno Falk and A. J. Salkind, "Alkaline Storage Batteries," John Wiley & Sons, Inc., New York (1969).
13. A. N. Dey and E. J. Rudd, Abstract 187, p. 465, Electrochemical Society Extended Abstracts, May 13-18, 1973.
14. A. H. Maki and D. H. Geske, *J. Chem. Phys.*, **30**, 1356 (1959).
15. H. Schmidt and J. Noack, *Z. Anorg. Allgem. Chem.*, **296**, 262 (1958).
16. J. N. Butler, Tyco Laboratories, Inc., Final Report U.S. Air Force Contract No. F19628-68-C-0056 (AD 789 109) (Sept. 1970).
17. R. Jasinski, "High Energy Batteries," Plenum Press, New York (1967).
18. R. M. Fuoss and F. Accascina, "Electrolytic Conductance," Interscience Publishers, New York (1959).
19. J. S. Dunning, D. N. Bennion, and J. Newman, *This Journal*, **120**, 906 (1973).

## Technical Note



### Measurement of Current Distribution on Wire

Aladar Tvarusko<sup>\*1</sup>

Engineering Research Center, Western Electric Company, Princeton, New Jersey 08540

The current density distribution is often not uniform even on an equipotential surface, *i.e.*, on a metal electrode of negligible electric resistance. The ohmic resistance of an electrode increases by decreasing its cross section and thus, the surface of these elongated electrodes can become nonequipotential, especially at higher current densities of practical use. The result is a nonuniform current density distribution along the electrode, such as wire (1), thin, narrow, and long metal patterns on printed circuit boards (2), etc., which leads to nonuniform electrodeposition thickness and quality, and compositional change in case of an alloy deposit (3). Another practical consequence of the nonuniform current distribution is the length of the electroplating (electrochemical) cell, *i.e.*, the length of the immersed wire or thin metal pattern. The more nonuniform the current distribution on the wire or thin

metal pattern, the shorter the cell should be (the cell length is also affected by the current carrying capability of wire and contacts).

The current density distribution can be theoretically calculated for simple geometries [see references cited in Ref. (1, 2, 4-7)] or obtained from the analysis of the final electrodeposition layer (7) or measured by analog methods (8). These methods are time consuming and do not yield *in situ* current distribution.

This paper describes an experimental setup to measure the current distribution on wire and other elongated electrodes. The efficacy of the setup is illustrated by results obtained on various wires during the electrodeposition of copper and reduction of redox species.

#### Experimental

The heart of the experimental setup, shown schematically in Fig. 1, is a clip-on milliammeter which measures through a traveling probe the magnetic field existing around the wire carrying the electrolyzing current. The clip-on d-c milliammeter is commercially

\* Electrochemical Society Active Member.

<sup>1</sup> Present address: Laboratoire Suisse de Recherches Horlogères, 2000 Neuchâtel, Switzerland.

Key words: current distribution, electrodeposition on wire, wire electrode, printed circuits, copper electrodeposition, redox system.



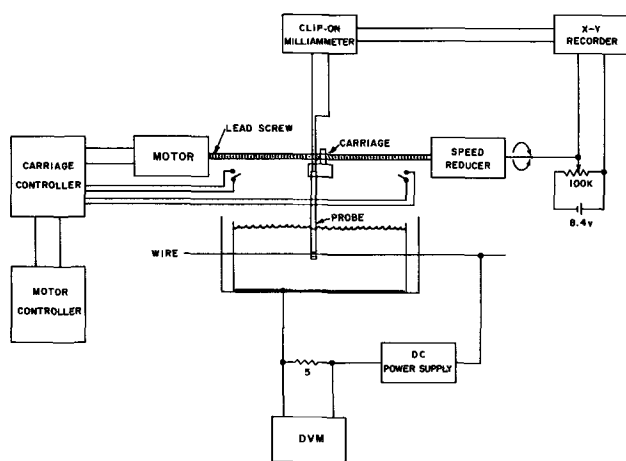


Fig. 1. Schematic of the experimental setup for the measurement of current distribution.

available (Hewlett-Packard Company, Model 428B) and its current range is 0.1 mA to 10A.

The current probe (a second harmonic flux-gate type magnetometer) is usually used in air. In order to prevent its corrosion in various electrolytes, the small current probe with a 4 mm aperture diameter (HP Model 428A-21A) was coated by a thin layer of plastic (e.g., silicone rubber); its jaws were tightly closed. The inside of the aperture was covered only by a thin continuous layer. The other, large current probe with 64 mm aperture (HP Model 3528A) was inserted into a thin polyethylene tube to prevent its contact with the solution; this probe should be used only at larger applied current,  $I_A$  values ( $>50$  mA). It should be noted that both probes measure a current which is the average current flowing through the wire within the length of the magnetic core of the probe. Therefore, the narrowest possible probe should be used, which would be advantageous also from viewpoint of hysteresis elimination to be discussed later.

The current distribution along the wire is obtained by moving the current probe parallel to the wire. The current probe is firmly held in the carriage as shown in Fig. 2. The carriage is supported and kept aligned by two stainless steel Thomson rods (59.5 cm long, 1/2 in. OD) and four stainless steel Thomson ball bushings (Type XA-B1420-SS). The two rods are anchored in the two end bearing blocks which are firmly screwed to mounting plates. The mounting plates rest on the top of the overflow cell (9) and are firmly screwed to the side rails. These features are shown in Fig. 2 and 3. Stainless steel (Type 316) was used for the construction.

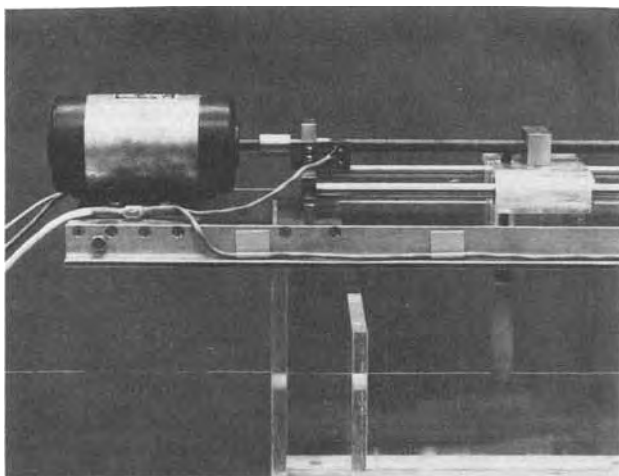


Fig. 2. Partial view of the setup. It shows the current probe in the carriage, aligning rods, lead screw, motor, and a basic switch.

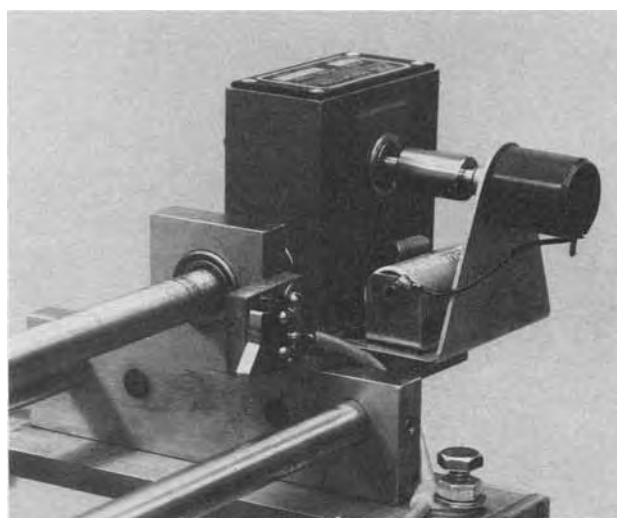


Fig. 3. View of the speed reducer and potentiometer arrangement

The brass feed screw nut is firmly screwed to the top of the carriage which is moved by the 1/2 in. rotating lead screw (20 threads per inch). The stainless steel lead screw is supported by two bearings (Hoover 77R6) which are mounted in the bearing blocks (Fig. 2, 3). The lead screw is driven through a coupler by a permanent magnet d-c motor-generator (Electro-Craft Corporation, Hopkins, Minnesota, Model E-650 with 80 oz. in. torque) which has two windings on the same armature to drive the motor and generate voltage proportional to the speed, respectively. The motor controller maintains the motor speed constant within a 3-3000 rpm range and provides dynamic braking at shutoff.

A carriage controller is inserted between the motor and its controller. The schematic diagram of the carriage controller is shown in Fig. 4. The carriage controller consists of a power supply for the relays (3PDT, 12V d-c, Potter & Brumfield, KM14D) which (i) reverse the voltage to the motor winding (RL1) and from the generator (RL4), and (ii) activate (RL2) and deactivate (RL3) the reversing relay (RL1). The signal for the relay action is obtained either from one of the subminiature basic switches (MS1, MS2, right or left side) mounted onto the bearing blocks (Fig. 2, 3) or manually from one of the push button momentary switches (4PDT, RS1, RS2, go right or left).

In automatic mode, the carriage continuously traverses the wire over a distance determined by the position of the two basic switches. The carriage can be stopped in the automatic mode at either end by switching to manual operation (SW3, off) during the last traverse. In manual mode, the carriage always stops at the other end. The carriage can be stopped at any position by interrupting (SW2) the power to the motor.

The rate of carriage traverse depends on the motor speed. Since the motor speed is maintained at a given constant rpm, the traverse rate will be linear and determined by the number of threads per unit length of lead screw.

The position of the current probe can be read off a linear scale placed near the carriage. This is cumbersome and is not suited for recording. A potential signal proportional to the position of the current probe was obtained in the following simple manner. The motor speed is reduced 50:1 by a worm and wheel assembly (PIC Design Corporation, No. DO-7) the input shaft of which is connected to the feed screw through a coupler. The output shaft of the assembly is connected by a coupler to the shaft of a 10-turn-precision wirewound, 100 kohm potentiometer (Fig. 3) which is electrically connected to an 8.4V mercury battery as shown in Fig. 1. The coupler between the

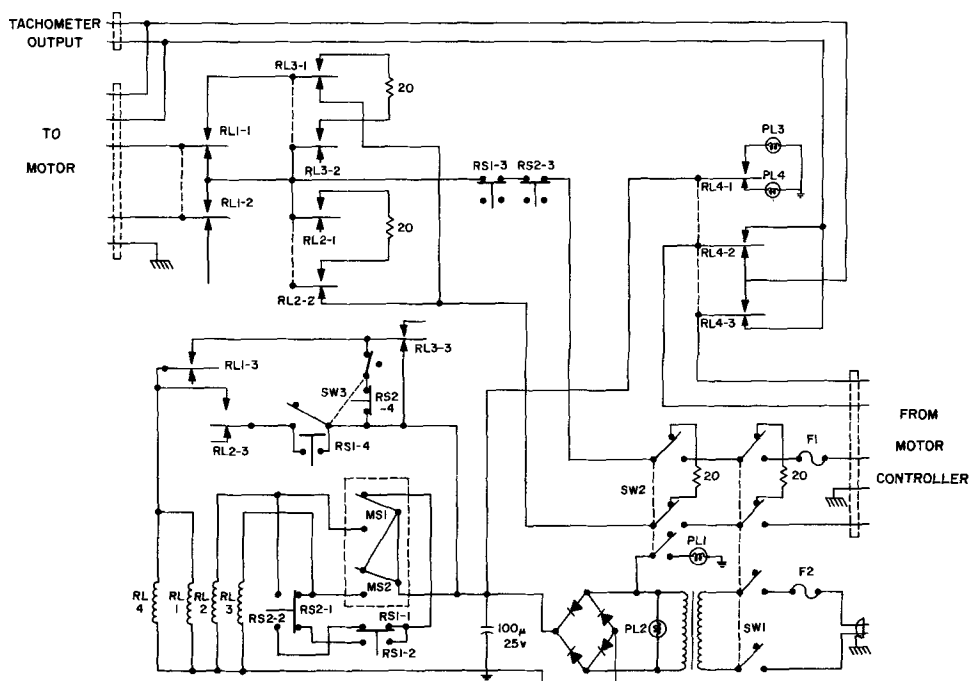


Fig. 4. Schematic diagram of the carriage controller.

worm and wheel assembly and potentiometer is tightly secured after both carriage and potentiometer are in one of their corresponding extreme positions.

Now, we have potential signals proportional to the position of the current probe and to the magnitude of the current flowing at that position. These signals can be easily recorded by an X-Y recorder (Varian Associates, Model F-80A) and thus, we obtain the current distribution curves automatically. The current can be easily differentiated by electronic means and thus, the local current density, *i.e.*, local reaction rate distribution can be obtained automatically on another X-Y recorder.

The electrolyzing current is supplied by a constant current power supply (Electronic Measurements, Model C 613). The magnitude of the applied current,  $I_A$  was measured as a voltage drop on a 5 ohm, precision resistor by a digital voltmeter (Fluke, 8100A).

Clean wires of various metals and diameters were used with a U-shaped, copper or stainless steel sheet anode. The electrodeposition of copper was studied in  $\text{CuSO}_4\text{-H}_2\text{SO}_4$  solutions of various concentrations. The

reduction of ferricyanide was investigated in a fresh, 0.04 equimolar solution of potassium ferro- and ferricyanide in 1M NaOH. The solution was not deaerated and was used in the presence of light. The measurements were made at  $24^\circ \pm 2^\circ\text{C}$ .

### Results and Discussion

The clip-on milliammeter probe is usually used in air to measure direct current flowing in a wire contacted at two points. The current measured along this wire should not change with the position of current probe. This is shown in Fig. 5 to be the case in both air and aqueous electrolytic solution; the current along such a wire remained constant in all the solutions tested. This means that the clip-on milliammeter's reading is not influenced by the ions present in large concentration around the wire and thus, this instrument can be used for the measurement of current distribution in solutions.

Figure 5 also shows the current distribution along a copper wire of 0.5 mm diameter during the electrodeposition of copper from acidified  $\text{CuSO}_4$  solution at

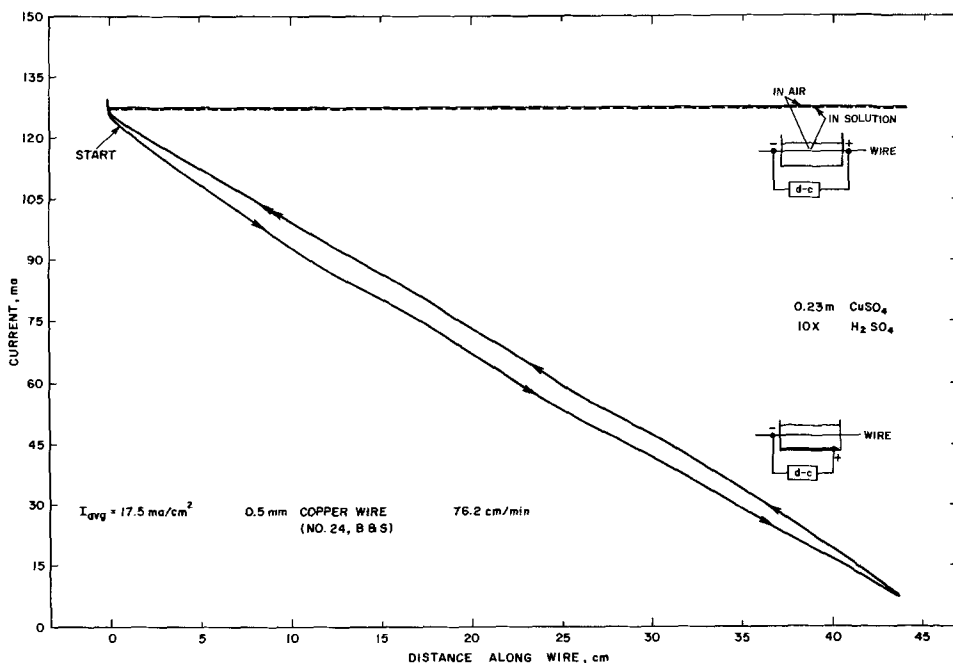


Fig. 5. Current distribution on a 0.51 mm diameter copper wire in the absence and presence of copper electrodeposition from acidified  $\text{CuSO}_4$  solution. The current probe traveled from left to right and back.

17.5 mA/cm<sup>2</sup> average current density,  $I_{avg}$  which is the applied current divided by the surface area of the wire exposed to the electrolyte in the cell. It can be seen that (i) the magnitude of the current decreases with increasing distance from the point of contact, (ii) the rate of decrease varies somewhat along the wire, (iii) a hysteresis is present, i.e., the magnitude of the current depends on the direction of the carriage sweep and is lower when the probe travels away from the contact point than toward it (indicated by the double arrow), (iv) the difference between the two curves is the greatest in the middle and decreases toward both ends, and (v) the current is not zero at the point of carriage reverse.

Before discussing the aforementioned observations, let us see the current distribution curves at other average current densities. Figure 6 shows the current distribution at low  $I_{avg}$  values, i.e., up to ca. 30% of the average limiting current density,  $\bar{I}_L$ . In addition to the aforementioned observations, it can be seen that the magnitude of the hysteresis increases with increasing current density. The current measured at the

turnaround point (Fig. 6) is 4-5% of the current measured near the wire contact. At this point, the current probe is 3-5 mm from the end wall and to a large extent, the rest current is due to the current flowing in the wire toward its end.

Figure 7 shows the current distribution at high  $I_{avg}$  values which are near and above the  $\bar{I}_L$ ; H<sub>2</sub> evolves profusely along the entire wire length at  $I_{avg} > 100$  mA/cm<sup>2</sup>. The current distribution curves are basically similar to the previously mentioned ones. The deviation between the two curves obtained during the carriage traverse, i.e., the hysteresis decreases with increasing  $I_{avg}$  values above  $\bar{I}_L$ . These and other values of deviations, expressed in percentage, are shown in Fig. 8 for an arbitrarily chosen point on the wire (20 cm). It can be clearly seen that the percentage of the deviation increases very rapidly with increasing average current density. It peaks out near the indicated average limiting current density above which it starts to decrease with increasing  $I_{avg}$  values. This behavior was also observed on other wires in all the investigated solutions and concentrations using both current

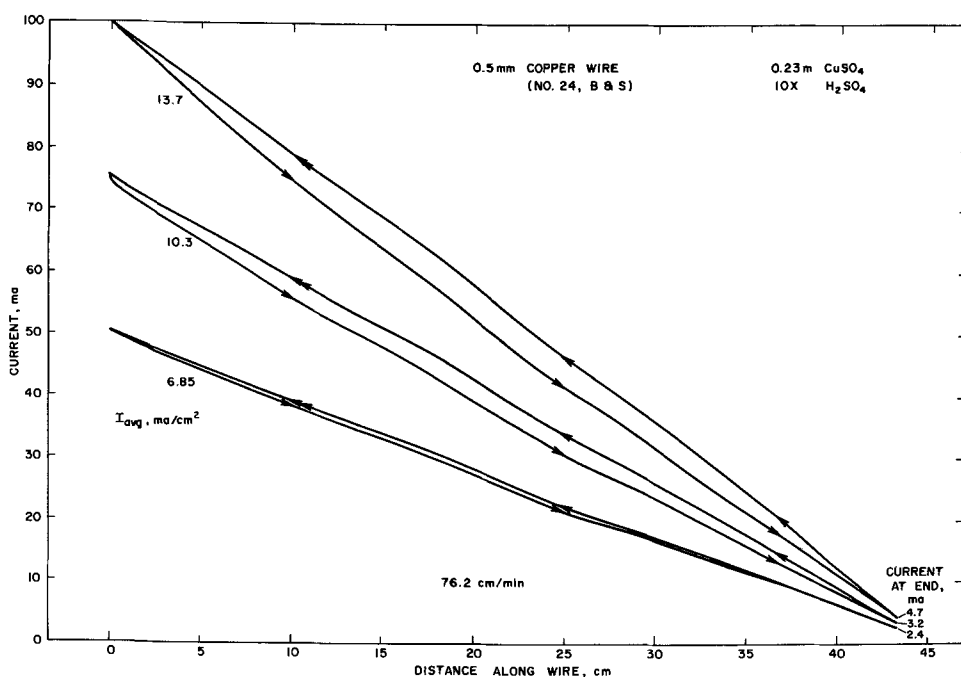


Fig. 6. Current distribution on a 0.51 mm diameter copper wire at low cathodic average current densities.

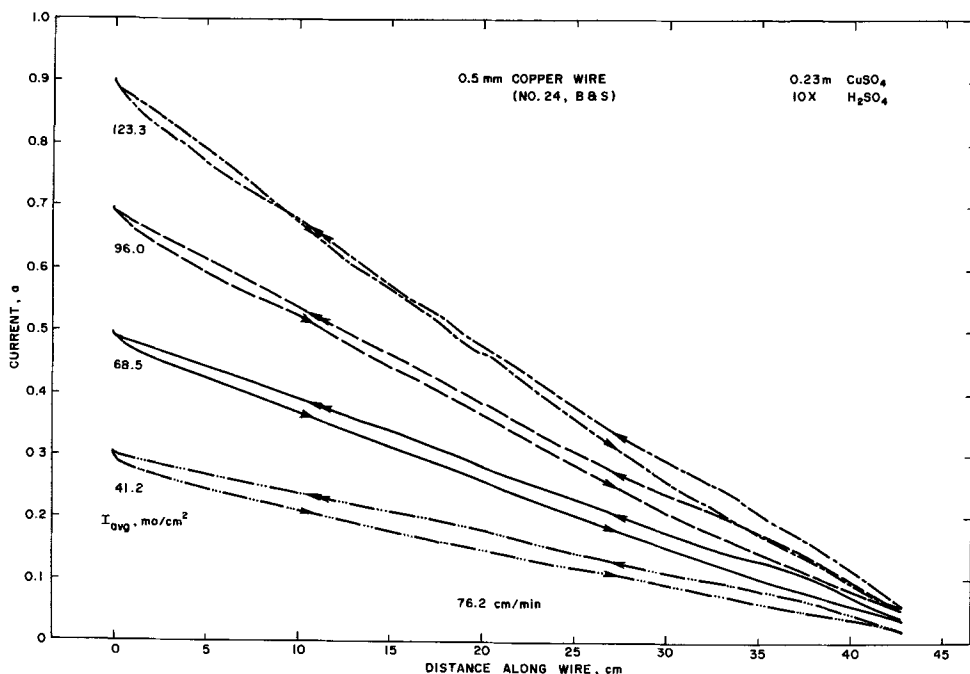


Fig. 7. Current distribution on a 0.51 mm diameter copper wire at cathodic average current densities which are near or above the average limiting current density.

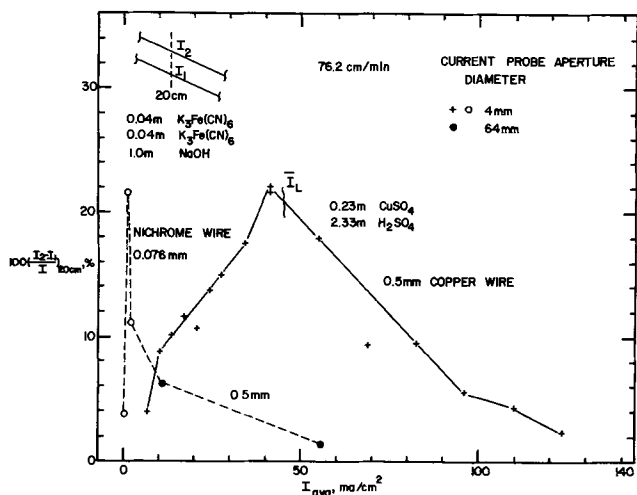


Fig. 8. Deviation between the upper and lower current distribution curves at an arbitrarily chosen point on the wire as a function of cathodic average current density in two solutions and three wires. Two current probes of different apertures were used.

probes. It should be noted that the deviation markedly decreased on a very thin Nichrome wire already at an  $I_{avg}$  value of 2  $mA/cm^2$  and  $H_2$  evolved on this highly resistive wire near its contact (its resistance is 250X that of copper wire used). This means that the hysteresis decreases even if the limiting current density is reached only over a small portion of the wire.

It is obvious from the aforementioned results that the hysteresis is not a percentage error due to the intensity of the current flowing within the wire.

The increase of the deviation up to the average limiting current density and its subsequent decrease seem to point to an enhancement of the mass transfer by the fluid flow due to the moving current probe the influence of which decreases with increasing  $H_2$  evolution. An additional evidence for the mass transfer effect can be seen in Fig. 9. The current decreases toward the lower curve when the carriage is stopped anywhere along the wire. Upon restarting the probe in the opposite direction, i.e., toward the starting point, the current decreases and the trace becomes practically the same as that of the initial full cycle.

A comparison of Fig. 9 with Fig. 5-7 reveals that the hysteresis curve is not affected by the starting

Table I. Magnitude of hysteresis at various speeds of probe traverse (4 mm aperture)

Speed, cm/min	$100 \left( \frac{I_2 - I_1}{I_1} \right)_{20 \text{ cm}}, \%$
25.4	2.8
50.8	3.4
102	5.2
127	7.8
190	13
374	12

point of the current probe traverse: the upper curve of the hysteresis loop is always obtained during the current probe's travel toward the wire contact and the lower one while the probe moves away from it. These results seem to indicate that the mass transfer rate is increased within and behind the moving small current probe (4 mm diameter) due to the increased fluid velocity and wake, respectively. The result is that less electronic current flows through the current probe during its motion away from the contact. On the other hand, during the probe's motion toward the contact point more electronic current will flow through the probe to accommodate the larger mass transfer rate within and behind the probe.

The aforementioned results were obtained at one carriage speed, 76.2 cm/min. In view of the results, it is expected that the probe (carriage) traverse speed will be an important factor in determining the magnitude of the hysteresis. Table I clearly shows this influence for a 0.5 mm diameter copper wire in 0.23M  $CuSO_4$ -10X  $H_2SO_4$  solution at  $I_{avg} = 10$   $mA/cm^2$  (0.22  $\bar{I}_L$ ). The deviation increased with increasing probe speed up to 190 cm/min above which it remained practically constant. The rate of increase of the deviation doubles above approximately 90 cm/min which seems to give the impression of the presence of laminar or turbulent fluid flow around the wire, respectively. The probe speed should be kept small to minimize the magnitude of the hysteresis. On the other hand, a higher probe speed is desired to shorten the duration of the experiment which is important especially in experiments where the resistance of the substrate changes due to the electrodeposited metal layer or other processes taking place. The probe speed (76.2 cm/min) chosen for these experiments represents a compromise between these two criteria.

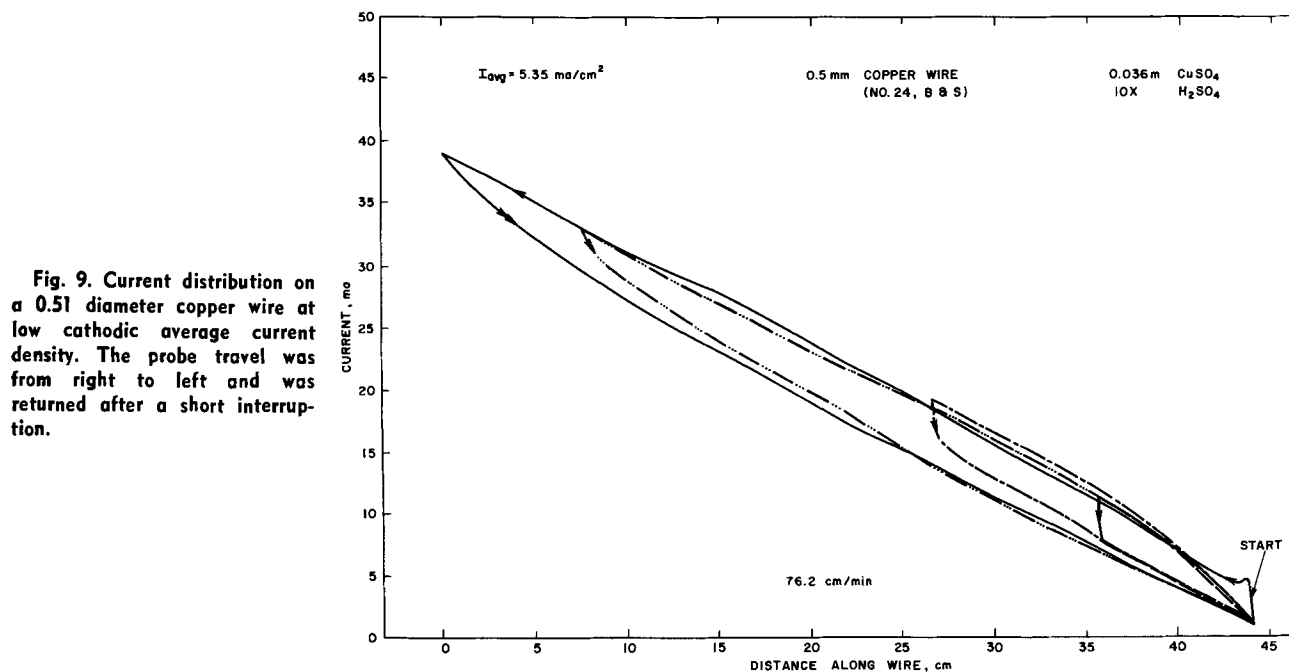


Fig. 9. Current distribution on a 0.51 diameter copper wire at low cathodic average current density. The probe travel was from right to left and was returned after a short interruption.

The presence of hysteresis is a limitation of this technique which measures the current distribution *in situ* by measuring the magnetic field existing around elongated electrodes, such as wire, thin, narrow, and long printed circuit patterns. The magnitude of the hysteresis can be markedly decreased (to ca. maximum 10% near the limiting current density) by making the measurement at slow probe traverse speed. Further improvement can be obtained by using probes of larger apertures which are limited, however, to higher average current values. The current probes commercially available are really designed to measure current flowing through a conductor in air at a certain position. In electrochemical systems, the current distribution on the electrode in solution is of interest and therefore, a narrow, ca. 1 cm diameter current probe should be used which is designed on the basis of hydrodynamic considerations; it could greatly improve or completely eliminate the undesirable hysteresis. Unfortunately, such a probe was not available for evaluation in this first attempt to measure the current distribution *in situ*.

### Acknowledgments

The author wishes to thank Mr. W. E. Wilson, Jr. for the construction of the carriage controller and his valuable assistance in the preliminary experiments.

Manuscript submitted June 12, 1973; revised manuscript received Nov. 30, 1973. This was Paper 134 presented at the Boston, Massachusetts, Meeting of the Society, Oct. 7-11, 1973.

Any discussion of this paper will appear in a Discussion Section to be published in the December 1974 JOURNAL. All discussions for the December 1974 Discussion Section should be submitted by Aug. 1, 1974.

### REFERENCES

1. R. C. Alkire and A. Tvarusko, *This Journal*, **119**, 340 (1972).
2. R. Alkire, *ibid.*, **118**, 1935 (1971).
3. A. Tvarusko, *Plating*, **58**, 983 (1971).
4. C. W. Tobias and R. Wijnsman, *This Journal*, **100**, 459 (1953).
5. C. Wagner, *Electrochim. Acta*, **12**, 131 (1967).
6. J. Newman, *Ind. Eng. Chem.*, **60**, 12 (1968).
7. A. Böhnlein, *Metalloberfläche*, **24**, 210 (1970).
8. R. H. Rousselot, Proc. Internat. Conf. "Surface 66," Basel, p. 39-47, Forster Verlag, Zürich (1967).
9. A. Tvarusko, *This Journal*, **119**, 43 (1972).

## Brief Communications



### A Preliminary Investigation of High Temperature Lithium/Iron Sulfide Secondary Cells

D. R. Vissers, Z. Tomczuk, and R. K. Steunenberg\*

Argonne National Laboratory, Chemical Engineering Division, Argonne, Illinois 60439

High-specific-energy (>200 W-hr/kg) lithium/sulfur cells are under development for off-peak energy storage in electric utility networks and for electric automobiles (1-5). Such cells have a molten-salt electrolyte such as the LiCl-KCl eutectic (mp, 352°C) and operate at temperatures between approximately 375° and 425°C. When sulfur alone is used as the active material in the positive electrode, it tends to escape from the electrode both through vaporization and through the solubility of certain sulfur-bearing species, e.g.,  $S_2^-$ ,  $S_2^{2-}$  (6-10) in the electrolyte. Although both of these effects can be suppressed by additives such as arsenic or selenium (1-5), which lower the activity of the sulfur, it is questionable whether they are sufficiently effective to permit long cell lifetimes (>1000 hr). The sulfur activity can be decreased further by the use of sulfur compounds rather than sulfur, in the positive electrode. Iron sulfides were investigated in this study on the premise that their free energies of formation are sufficient to eliminate sulfur losses by vaporization or solubility, but not large enough to cause an undue decrease in the cell voltage. Calculated values for the free energies of formation of FeS and FeS<sub>2</sub> at 400°C are 24.1 and 35.1 kcal/mole, respectively, based on data in the literature (11, 12). From a practical standpoint, iron pyrite (FeS<sub>2</sub>), in particular, has the desirable characteristics of reasonably low equivalent weight, low cost, abundance, and lack of toxicity.

### Experimental

Six cells of the general design shown in Fig. 1 were operated during the course of this investigation. The

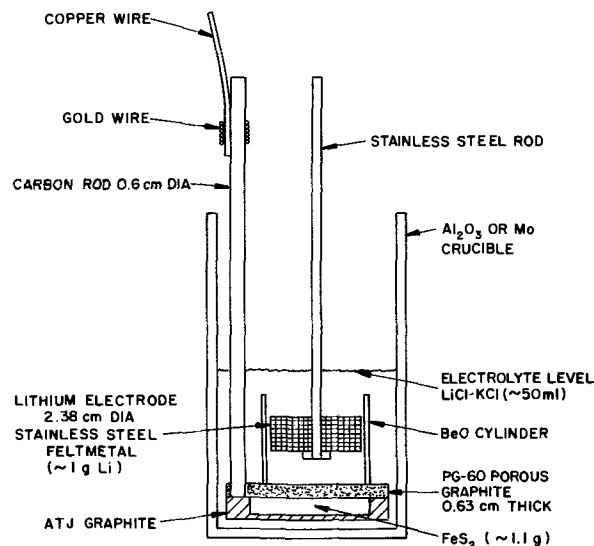


Fig. 1. Typical cell design

negative electrode in all of the cells consisted of a disk of Type 302 stainless steel Feltmetal<sup>1</sup> (90% porosity, 27  $\mu$ m avg pore diam) that was filled with ~1g of liquid lithium. The 59 mole per cent (m/o) LiCl-41 m/o KCl eutectic was used as the electrolyte. The LiCl-KCl eutectic was obtained from the Anderson Physics Laboratories, Incorporated, Champaign, Illinois, where it was prepared and purified by the method outlined by Laitinen, Tischer, and Roe (13). Commercial-grade

<sup>1</sup> A product of the Brunswick Corporation.

\* Electrochemical Society Active Member.

Key words: Li-FeS<sub>2</sub> cell, high-temperature cell, iron pyrite, iron sulfide, molten salt, secondary cell.

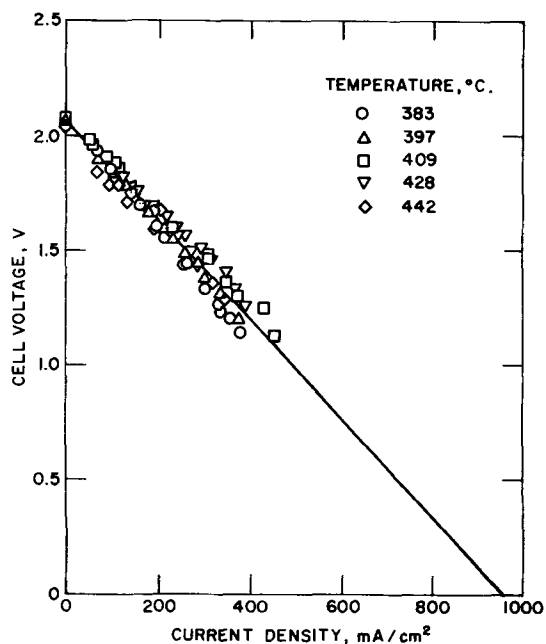


Fig. 2. Short-time voltage-current density data for a Li/FeS<sub>2</sub> cell.

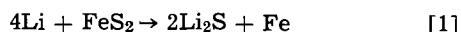
FeS<sub>2</sub><sup>2</sup> (iron pyrite) from Sargent-Welch was the active material in the positive electrode in five of the cells. In the other cell, the active material was a mixture of FeS and Li<sub>2</sub>S. The Li<sub>2</sub>S, from Foote Mineral, had a stated purity of 97% and the FeS, from Fisher Scientific, was of unspecified purity.

The cells were unsealed and were operated in a furnace well located in the floor of a high-purity (~3 ppm O<sub>2</sub>, ~1 ppm H<sub>2</sub>O) helium-atmosphere glove box. Four of the Li/FeS<sub>2</sub> cells had a positive electrode of the design shown in Fig. 1, in which the active material was contained in an ATJ graphite cup and was confined to the cup by a PG-60 porous graphite diffusion barrier, 0.63 cm thick. In the fifth Li/FeS<sub>2</sub> cell and in the sixth cell, which was a Li/FeS cell, the active material was contained in a molybdenum crucible that was covered with expanded molybdenum mesh<sup>3</sup> (~0.2 mm thick, ~50 openings/cm<sup>2</sup>), which served as a diffusion barrier. The geometric surface area of all the positive electrodes was ~5 cm<sup>2</sup>.

### Results and Discussion

Short-time voltage vs. current density data<sup>4</sup> that were obtained for a fully charged Li/FeS<sub>2</sub> cell over a temperature range of 383°-442°C are presented in Fig. 2. The results show no significant effect of temperature on the cell performance. The open-circuit voltage averaged 2.06V and the short-circuit current density was approximately 1000 mA/cm<sup>2</sup>. The maximum power density was about 0.5 W/cm<sup>2</sup> and the cell had a resistance of 0.43 ohm. The relatively high resistance, which was not unexpected, should be reduced markedly by appropriate modifications of the cell design.

Typical charge and discharge data for a Li/FeS<sub>2</sub> cell are given in Fig. 3, where the cell voltage (*IR*-included) is shown as a function of capacity density and per cent of theoretical capacity. The *IR* voltage during both charge and discharge was about 0.1V. The theoretical capacity is based on the over-all reaction



The charge and discharge curves each show two plateaus, which suggest that the cell reaction may be occurring as a two-step process, possibly involving

<sup>2</sup> This material was found to contain about 10 wt % SiO<sub>2</sub>, which was removed by a sink-float separation with tetrabromoethane.

<sup>3</sup> Obtained from Climax-Molybdenum Company of Michigan.

<sup>4</sup> Individual measurements made by closing the circuit momentarily for a period of 10-15 sec.

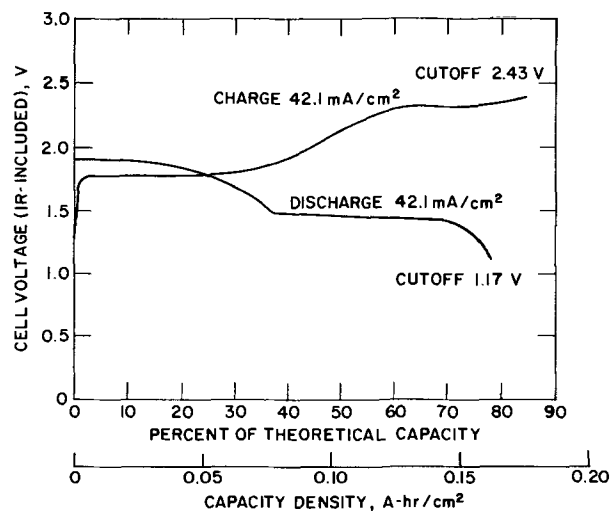
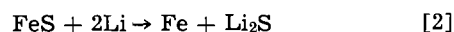


Fig. 3. Typical charge and discharge data for a Li/FeS<sub>2</sub> cell

FeS as an intermediate. At 400°C the emf's for the Li/FeS<sub>2</sub> and Li/FeS couples are estimated to be 1.96 and 1.66V, respectively. These emf values are based on free-energy data from the literature (11, 12, 14) and are in fairly good agreement with the observed *IR*-free voltage plateaus of about 2.05 and 1.6V, respectively. Although the two plateaus may suggest FeS as a simple intermediate, metallographic examination of FeS<sub>2</sub> electrodes taken from cells that had been cycled several times and whose operation had been terminated at various stages of charge, revealed, in addition to the apparent phases FeS<sub>2</sub> and FeS, the presence of several additional phases which are complex and unidentified at this time. These phases appear to be complex compounds formed by the interaction of Li<sub>2</sub>S with iron-sulfur compounds.

One experimental cell was operated over 28 discharge cycles (>200 hr) with no loss in capacity and no observable sulfur loss. With an *IR*-free charge cutoff of 2.15V, the average FeS<sub>2</sub> utilization, based on the reaction described by Eq. [1], was 49%. This behavior is generally consistent with the charge curve shown in Fig. 3. This value increased to an average of 82% when the charge cutoff was raised to 2.43V. However, the inability to convert the active material completely to FeS<sub>2</sub> suggests that it may be possible to achieve near theoretical capacities with the Li/FeS<sub>2</sub> cell if a higher charge cutoff potential is employed, and if sufficiently effective current collection is provided throughout the FeS<sub>2</sub> electrode to produce a more uniform reaction product when the cell is charged.

Operating characteristics of the Li/FeS cell were initially investigated by cycling, using an *IR*-free charge cutoff of 2.15V. The cell was operated for 14 days (28 cycles) at current densities of 30-40 mA/cm<sup>2</sup> with no observable loss in capacity. The average FeS utilization based on the reaction described by Eq. [2] was 87%, with an average coulombic efficiency of 89%



The open-circuit voltage remained nearly steady at 1.7V during charge and 1.6V during discharge. The open-circuit potential of 1.7V corresponds very closely to the calculated emf of 1.66V for a Li/FeS cell.

### Conclusions

1. The Li/LiCl-KCl/FeS<sub>2</sub> system can be operated as a secondary cell at temperatures of about 380°-440°C for periods of at least 200 hr with no significant deterioration in electrical performance.

2. The capacities of the Li/FeS<sub>2</sub> cells were in the vicinity of 80% of the theoretical value based on the oxidation of four lithium atoms per FeS<sub>2</sub> molecule during discharge.

3. The coulombic efficiencies ranged generally between 89 and 100%.

4. The open-circuit voltage was about 2.06V, with a short-circuit current density of  $\sim 1$  A/cm<sup>2</sup> for the fully charged Li/FeS<sub>2</sub> cell.

5. The Li/FeS<sub>2</sub> cell performance appears to be essentially unaffected by changes in temperature between about 380° and 440°C.

6. The cells that were tested had a relatively high internal resistance, (0.3-0.5 ohm); however, no attempt was made to minimize the resistance by improving the cell design through the use of current collectors, favorable geometry, etc.

7. The Li/LiCl-KCl/FeS system can also be operated as a secondary cell, with the capacities corresponding roughly to the oxidation of two lithium atoms per FeS molecule during discharge.

8. The chemistry of the Li/FeS<sub>2</sub> cell reactions is not yet well characterized.

#### Acknowledgments

The authors wish to express their appreciation to L. Burris, D. S. Webster, and P. A. Nelson for their guidance and encouragement. Thanks are also extended to J. Birk, A. E. Martin, B. Tani, and M. Homa for their scientific assistance. This work was performed under the auspices of the U.S. Atomic Energy Commission.

Manuscript submitted Dec. 10, 1973; revised manuscript received Jan. 28, 1974.

Any discussion of this paper will appear in a Discussion Section to be published in the December 1974

JOURNAL. All discussions for the December 1974 Discussion Section should be submitted by Aug. 1, 1974.

#### REFERENCES

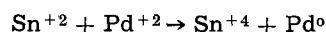
1. H. Shimotake, M. L. Kyle, V. A. Maroni, and E. J. Cairns, "Proc. 1st Intern. Electric Vehicle Symp.," p. 392, Electric Vehicle Council, New York (1969).
2. M. L. Kyle, H. Shimotake, R. K. Steunenber, F. J. Martino, R. Rubischko, and E. J. Cairns, "6th IECEC Proc.," p. 80, SAE, New York (1971).
3. W. J. Walsh, E. J. Cairns, and J. D. Arntzen, Paper 254 presented at Electrochem. Soc. Meeting, Chicago, Illinois, May 13-18, 1973.
4. E. C. Gay, P. A. Nelson, E. J. Cairns, and F. J. Martino, Paper 5191, Presented at AIChE 75th National Meeting, Detroit, Michigan, June 3-6, 1973.
5. E. C. Gay, R. K. Steunenber, J. E. Battles, and E. J. Cairns, "8th IECEC Proc.," p. 96, AIAA, New York (1973).
6. W. Giggenbach, *Inorg. Chem.*, **10**, 1308 (1971).
7. D. M. Gruen, R. L. McBeth, and A. J. Zielen, *J. Am. Chem. Soc.*, **93**, 6691 (1971).
8. J. H. Kennedy and F. Adamo, *This Journal*, **119**, 1518 (1972).
9. J. P. Bernard, A. DeHaan, and H. Van der Poorten, *Compt. Rend. Acad. Sci., Ser. C*, **276**, 587 (1973).
10. J. R. Birk, Private communication (1973).
11. R. D. Freeman, Oklahoma State Univ., Research Report No. 60 (1962).
12. D. D. Wagman, W. H. Evans, V. B. Parker, I. Halow, S. M. Bailey, and R. H. Schumm, *Nat. Bur. Std. Technical Notes* 270-4 (May 1969).
13. H. A. Laitinen, R. P. Tischer, and D. K. Roe, *This Journal*, **107**, 546 (1960).
14. E. J. Cairns, Private communication (1973).

## On the Ultraviolet Inhibition of Electroless Plating on Glass

M. Schlesinger

Department of Physics, University of Windsor, Windsor, Ontario, Canada

The process for metal patterning of dielectric substrates by u.v. light exposure and electroless plating has been discussed by members of our research group recently (1). It was pointed out there that u.v. inhibition is possible even after the activation (PdCl<sub>2</sub>/HCl) bath. This we took as an indication that the simplistic redox reaction (2)

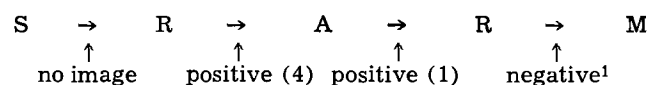


was clearly not enough to explain the chemistry of the palladium bath (3).

Since the publication of that paper we became even more interested in u.v. patterning of dielectric substrates after activation. This is so since we have found that the image definition of the photomask is much better if u.v. is applied at this stage.

The purpose of the present note is to report about the possibility of obtaining photoselective metal deposition, not only in the form of positive imaging, i.e., generation of the replica of the photomask, but also in the form of negative imaging.<sup>1</sup>

Specifically, we have found that if u.v. light is applied after activation, but before the premetallizing rinse, positive imaging results. If, on the other hand, u.v. is applied after the premetallizing rinse a negative imaging results. A summary of the effect of u.v. light at various stages is shown schematically as follows:



where S stands for the SnCl<sub>2</sub>/HCl bath, R stands for a D.I. water rinse, A stands for the PdCl<sub>2</sub>/HCl bath, and M stands for the Cu, or Ni or Co metallizing baths.

As an extension of our previous findings, we have found now that under the right conditions the growth of Cu can be also inhibited by u.v. irradiation after activation. These conditions relate mainly to rinse times between sensitization and activation and between activation and metallization.

The experiments referred to in the present note were carried out under conditions similar to those described in our previous work [Ref. (1)] except that deposition was made on glass and also that rinse times were shortened to 15 sec.

A detailed study of the foregoing effects is underway in our laboratory. This study includes the proper identification of the chemical processes accompanying the sensitization and activation steps in the conventional electroless systems.

In this connection it should be pointed out that u.v. is ineffective in the case of the catalyzing (PdCl<sub>2</sub>/SnCl<sub>2</sub>/HCl) accelerating (HCl or NaOH and similar) electroless systems.

#### Acknowledgment

The skilful technical assistance of Mr. G. Berthiaume is gratefully acknowledged.

Manuscript received Dec. 28, 1973.

Key words: electroless, imaging, plating, growth inhibition.

<sup>1</sup> Our experiments to-date have been carried out mainly on glass. Somewhat different procedures are required for different substrates.

Any discussion of this paper will appear in a Discussion Section to be published in the December 1974 JOURNAL. All discussions for the December 1974 Discussion Section should be submitted by Aug. 1, 1974.

## REFERENCES

1. S. L. Chow, N. E. Hedgecock, M. Schlesinger, and J. Rezek, *This Journal*, **119**, 1013 (1972).
2. R. L. Cohen, J. F. D'Amico, and K. West, *ibid.*, **118**, 2042 (1971).
3. C. H. de Minjer and P. F. J. v.d. Boom, *ibid.*, **120**, 1644 (1973).
4. J. F. D'Amico, M. A. DeAngelo, J. F. Henrikson, J. T. Kenney, and D. J. Sharp, *ibid.*, **118**, 1695 (1971).





## Characterization of Thermally Grown SiO<sub>2</sub> Surfaces by Contact Angle Measurements

R. G. Frieser\*

IBM System Products Division, East Fishkill Facility, Hopewell Junction, New York 12533

### ABSTRACT

This paper discusses recent advances in the study of solid surfaces by contact angle measurements which appeared promising in developing a technique to characterize different types of amorphous or polycrystalline metal and oxide surfaces. The extent to which contact angle measurements and spreading-pressure values can be used to characterize various silica surfaces is explored. A practical scheme is offered using water and an organic solvent to characterize various silica surfaces in a simple and nondestructive manner.

To study photoresist-substrate interactions successfully, it was considered desirable to first develop a scheme for characterizing the substrate surface itself. Techniques to study heterogeneous and amorphous surfaces are few. Most techniques have been developed for single-crystal studies, clearly not applicable here. Infrared and ellipsometric techniques were briefly evaluated and dropped because such techniques "see" too much of the bulk, whereas our interest is the surface proper. Recent advances in the study of surfaces by contact angle measurements, however, have made this latter technique promising (1, 2). Surface characterization by contact angle techniques usually have been avoided because they can lead to erroneous results for absolute surface energies. The difficulty, however, does not lie with the technique, or theory, but with the difficulty of obtaining pure surfaces.

To define a "clean surface" outside a very hard vacuum is actually impossible. Because this study is concerned with surfaces under normal conditions, reproducibility of surfaces rather than absolute "cleanliness" was chosen as the criterion. This means that normal gas absorption of water vapors from the atmosphere was ignored. Thermally grown silicon dioxide was chosen as a substrate, because this surface is more reproducible than any of several other possible choices.

### Surface Tension of Liquids

Several empirical attempts have been made by Zisman (3), Good and Girifalco (4) and others to derive an expression for the interfacial tension of two immiscible liquids from the surface tension of the liquids themselves. It was demonstrated by Fowkes (1) that the surface tension of a liquid is the sum of two terms, one due to dispersion forces only, and the second due to hydrogen bonding (in the case of water, for instance) or to metallic bond (in the case of mercury). For nonpolar liquids, such as saturated aliphatics, only dispersion forces are active. If we denote the surface tensions by  $\gamma$  and that portion of the surface tension due to dispersion forces by  $\gamma^d$  it follows that for satu-

rated aliphatics

$$\gamma_{al} = \gamma^d_{al}$$

for water

$$\gamma_{H_2O} = \gamma^d_{H_2O} + \gamma^{H+}_{H_2O} \quad [1]$$

for mercury

$$\gamma_{Hg} = \gamma^d_{Hg} + \gamma^M_{Hg}$$

Fowkes then postulated that the interfacial tension between two liquids is

$$\gamma_{H_2O/Hg} = \gamma_{H_2O} + \gamma_{Hg} - 2\sqrt{\gamma^d_{H_2O} \cdot \gamma^d_{Hg}} \quad [2]$$

This relationship was tested by measuring the interfacial tension between water or mercury and a series of saturated aliphatics, and  $\gamma^d$ 's for both water (21.8  $\pm$  0.7 dynes/cm) and mercury (200  $\pm$  7 dynes/cm) were obtained. These two values then were used to calculate the interfacial tension of water and mercury. Fowkes (2) obtained 424.8 dynes/cm, which agrees well with the experimental value of 426-427 dynes/cm. Therefore, the original assumption seems justified. Furthermore, Eq. [2] was derived by Fowkes (1) from a purely geometrical model. He considered the exchange of molecules at a liquid-liquid interface where the major forces between the two molecules are dispersion forces and arrived at Eq. [2]. This is the same equation as previously proposed by others except for a factor before the square root term, which Fowkes maintains is equal to one. Since this relationship can be derived from a physical model it can be claimed to have a theoretical basis as well as an empirical one.

The Young equation relates the contact angle to the surface and interfacial tensions of two immiscible liquids (Fig. 1). Combining Eq. [2] with the Young equation, Fowkes obtained the following expression for the contact angle of a liquid (l) on a solid (s)

$$\cos \theta = 2 \frac{\sqrt{\gamma^d_s \gamma^d_l}}{\gamma_l} - 1 - \frac{\pi_e}{\gamma_l} \quad [3]$$

where  $\gamma$  and  $\gamma^d$  have the same meaning noted earlier.

In Eq. [3],  $\pi_e$  is the equilibrium spreading pressure of adsorbed vapor on the solid surface, or, in other words, the lowering of the surface energy of a solid due to a very thin film or vapor of the same liquid as that forming the contact angle.

\* Electrochemical Society Active Member.

Key words: SiO<sub>2</sub> surfaces, contact angle measurements, SiO<sub>2</sub> surface contamination.



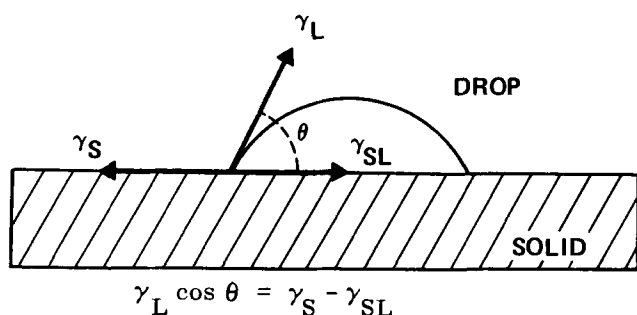


Fig. 1. In the Young equation  $\theta$  is the contact angle between the liquid and the solid.

There has been some contention that the Young equation is not thermodynamically valid in the first place (5). While the surface tensions and energy can be equated for liquids, this is not valid for solids in general. However, Fowkes stated that, since Eq. [3] can be used to calculate contact angles from independently obtained thermodynamic measurements of the surface tensions and pressure, by Eq. [3] the contact angle, too, must be a true thermodynamic quantity. Therefore the Young equations should be valid (2). Furthermore, Swalin (6) pointed out that glasses like amorphous silica are liquids thus one might equate the surface energy with the surface tensions, which for crystallized solids would not be true.

In earlier publications (1, 2), Fowkes expressed the opinion that spreading pressures could be ignored if the contact angle is greater than zero. It is obvious, therefore, that in such a situation the contact angle measurement of an appropriate liquid on the surface in question should yield the dispersion force contribution of the surface energy of the solid, when plotting  $\cos \theta$  vs.  $\sqrt{\gamma_d^d}/\gamma_l$ . Using Zisman's data (3), Fowkes has shown that this indeed is true for many low-energy liquids on low-energy solids (2). In more recent work (7), Fowkes has qualified this generalization, a position our present study will support. The equilibrium spreading pressure must be taken into account when liquids, especially polar liquids, interact with high-energy surfaces such as oxides. Making then a single contact angle measurement with appropriate liquids on the surface and knowing the surface energies of the liquids (plus the  $\pi_e$ ), the particular surface can readily be characterized.

An earlier attempt to characterize the surfaces of solids by contact angle measurement was made by Zisman and co-workers (8). Their approach was based on the concept of the "critical surface tension" of a solid. This critical surface tension is an extrapolated value on a Zisman plot for a surface tension when the cosine of the contact angle is one; i.e., under complete wetting conditions. A Zisman plot can be obtained by plotting the cosines of contact angles that a series of homologous liquids makes with a particular solid, and then extending this line (presumably a straight line) to  $\cos \theta = 1$ . While this approach is phenomenologically valid in some cases, it was not followed here for the following reasons: (i) It has no theoretical basis. (ii) In many cases, a Zisman plot is not a straight line, not even for a homologous series of liquids on a given solid, but forms a range, often curves toward lower cosine  $\theta$  values. Thus, even phenomenologically, this approach does not seem justified (9).

An improvement of the Zisman plot was obtained by Good and Girifalco (4). These investigators plotted the cosine of the contact angle that a liquid made with a particular surface against the reciprocal of the square root of the surface tension. This gave them a straight line that could be unequivocally interpreted when extrapolated to  $\cos \theta = 1$  as the critical surface tension. While it has just as little theoretical justifi-

fication as the Zisman plot, it should be pointed out that for liquids where  $\gamma_d^d$  is equal to  $\gamma_l$  and  $\pi_e = 0$ , the Good-Girifalco plot is a special case of the Fowkes plot. It is therefore obvious that Fowkes' approach is not only more general but has the virtue of having a theoretical justification.

### Experimental

**Specimens.**—Silicon wafers (10–25 ohm-cm, p type, [100]) were oxidized at 1000°C by a dry, wet, dry oxygen process in a tube furnace. Oxide film thicknesses employed were between 2000 and 3000 Å. The thickness variations ranged from 4% from front to back to 10% from top to bottom of the wafer. Oxide thickness variations were determined by ellipsometric measurements. Some of these surfaces then were hydrated by boiling in deionized water (12–14 megohms). Water distilled from a potassium permanganate solution was used to measure water contact angles. The organic solvents were purified both by distillation and by passing through an appropriate  $\text{Al}_2\text{O}_3$  absorption column. The purity of all the liquids was checked by measuring density, index of refraction, and surface tensions (and interfacial tensions between water and organics) with an automatic Fisher Tensiomat and comparing these values with those in the literature. The liquids were dispensed from a micropipette capable of delivering a drop of 0.01 mliter  $\pm 0.5\%$ .

**Measurements.**—The contact angle measurements were made on a Rame-Hart contact angle goniometer. Three Polaroid pictures were taken of each drop at equilibrium, i.e., the point the drop reached as soon as it stopped spreading. The contact angles were then determined by a conventional geometric technique. This technique proved the most reliable in a trial experiment using two investigators and gave the best precision (standard deviation  $\pm 2^\circ$ ). Other techniques for measuring contact angles which were evaluated but not used were based on reading the position of the cross hairs in the goniometer eyepiece (which proved to be the least reliable technique), cross mirrors, and tangential mirrors. All measurements of the contact angle and the surface tensions were made in laminar flow hoods of class 100 at  $24^\circ \pm 2^\circ\text{C}$  and 30% relative humidity.

To check out this technique, the  $\gamma_d^d$ 's of polyethylene and Teflon were derived using a series of organic liquids and Eq. [4] (ignoring the  $\pi_e$  term). Our results agreed within 5% of the literature values and thus the technique was considered adequate.

**Contact angle vs. time.**—Due to evaporation, the height of the drop forming the contact angle changed with time, but the diameter of the drop did not, especially for water. Since our technique of measuring the contact angle depended on the assumption that the drop is a "perfect" sphere, loss of drop height would have resulted in invalid data. After some experimentation in vapor saturated and unsaturated goniometer chambers, especially with the organic solvents, it was found undesirable to measure the contact angle of a liquid on a thin film of its own vapor. It was therefore decided not to measure contact angles in a saturated atmosphere. In general, errors due to evaporation were less severe (10–20% in 3 min) than those due to spreading (100% in 2 min) and could be avoided by taking a picture at the very moment the drop stopped spreading. As soon as the drop stopped spreading (usually within 1 or 2 sec after the drop breaks loose from the pipette), the picture was taken. With this technique, the repeatability of contact angle measurements on any given surface was  $< \pm 2^\circ$ , which is usually accepted as the best precision possible with any goniometer. The precision of contact angle measurements on comparable surfaces was  $\pm 5^\circ$ .

**Contact angle vs. size of drop.**—An almost 50% change in the contact angle as a function of drop size

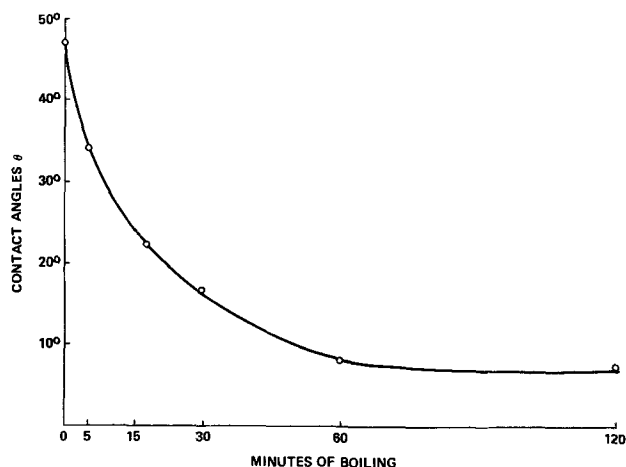


Fig. 2. Water contact angles on boiled thermal  $\text{SiO}_2$

(3-8 mm diameters) has been reported (10). Since the drop diameter of water on thermally grown silica used in this study was small, because of the geometry of our instrument and its optics, 25 measurements were made, ranging in drop size from 0.6 to 3.0 mm. While there was some scatter, the average contact angle of these measurements was  $38.2^\circ \pm 2^\circ$ . This indicates that in the range below 3 mm diameter, the contact angle was not dependent on the drop size or on the volume. Thus, in this study, the drop size used turned out to be a volume of  $2-3 \times 10^{-5}$  ml for water at  $25^\circ$ . On a silica surface this corresponds to a drop having a diameter of 1.2-1.8 mm.

### Results

**Characterization of various silica surfaces.**—For the purposes of this investigation three types of silica surfaces were differentiated. The surfaces were classified according to their wetting behavior toward water and common organic liquids. For convenience we called them "hydrophobic," "hydrophilic," and "organophilic" surfaces. The hydrophobic surface was achieved when the original oxide surface was removed from the furnace after the oxide was grown at  $1000^\circ\text{C}$  in an oxygen atmosphere. The hydrophilic surface was obtained when the hydrophobic surface was boiled in deionized water. Figure 2 shows the decrease in the contact angle of a thermally grown  $\text{SiO}_2$  surface as a function of hydration in boiling deionized water. Beyond 1 hr of boiling the contact angle changes very little, but for practical reasons  $\frac{1}{2}$  hr was chosen as our standard time of hydration for subsequent work. At this stage of the experiment only gross differences in the contact angles were of interest. Organophilic surfaces were obtained by immersing the high-temperature  $\text{SiO}_2$  surface in trichloroethylene and then drying the surface in a stream of filtered nitrogen.

Contact angles of a series of organic solvents on the various oxide surfaces were examined for their suitability to differentiate these surfaces. Both n-dodecane and n-decane spread too rapidly on  $\text{SiO}_2$  surfaces to be useful for differentiation.

The solvents used and the resulting data are summarized in Table I. The contact angles in Table I represent the average of at least three different drops per

Table I. Contact angles on various silica surfaces

Liquids	Contact angle $\theta$		
	Oxidized silicon $1000^\circ\text{C}$	Hydrated silica	Organic contamination on silica surfaces
n-Hexadecane	$13^\circ \pm 1^\circ$	$19^\circ \pm 1^\circ$	$5^\circ \pm 1^\circ$
n-Decane	$<1^\circ$	$<1^\circ$	$<1^\circ$
Decalin	$7^\circ \pm 1^\circ$	$15^\circ \pm 1^\circ$	$14^\circ \pm 1^\circ$
$\alpha$ -Bromonaphthalene	$18^\circ \pm 1^\circ$	$22^\circ \pm 2^\circ$	$22^\circ \pm 1^\circ$
Water	$48^\circ \pm 2^\circ$	$20^\circ \pm 1^\circ$	$50^\circ \pm 1^\circ$

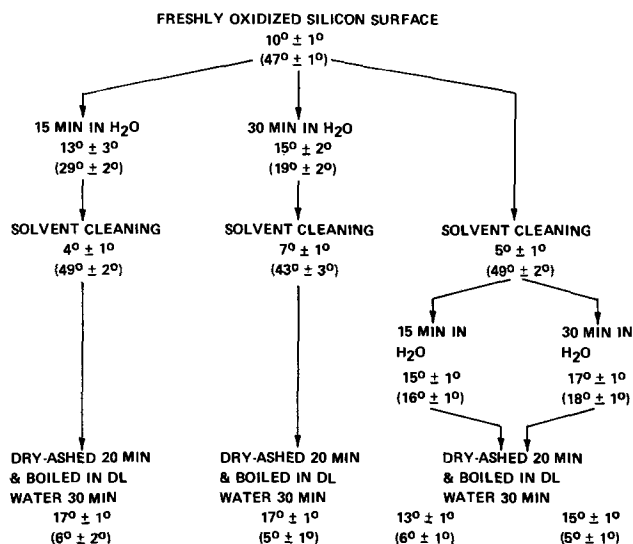


Fig. 3. Contact angles of n-hexadecane (upper line) and water (in parentheses) on surfaces given various treatments in sequence. All water treatments were at the boiling point.

surface, and at least six different surfaces for water and three different surfaces for n-hexadecane. It appears that with n-hexadecane alone, one could differentiate between the three surfaces and that these results are reproducible, but the combination of water and n-hexadecane is preferable. Figure 3 demonstrates the usefulness of differentiating between various  $\text{SiO}_2$  surfaces by measuring contact angles of both water and n-hexadecane on the same surface. This technique obviously can be applied to a study of surface cleanliness on oxides.

In this experiment, solvent cleaning means boiling twice for 5 min in trichloroethylene, followed by boiling in acetone for 5 min, boiling in deionized water for 5 min, and then blowing the sample dry in filtered nitrogen at room temperature. Dry-ashing was performed for 20 min in an atmosphere of 100 ml/min of oxygen at an operating pressure of 1 Torr with a power output of 1-2W in an rf plasma furnace.<sup>1</sup>

Thus by measuring the contact angles that water and n-hexadecane made with the surface (a simple, non-destructive technique), differentiation of the various silica surfaces is possible.

It appears from the preceding data that on high-energy surfaces the spreading pressure  $\pi_e$  cannot be ignored. In Table II the data of Fig. 3 were used to calculate from Eq. [3] the  $\gamma^d$  of silica, ignoring  $\pi_e$ . The wide spread of the values for each treatment underlines the contention that the spreading pressure cannot be ignored. Since the surfaces are different one would expect different  $\gamma^d$ s (and  $\pi_e$ ). However, each surface ought to give the same  $\gamma^d$  when measured with water and n-hexadecane. Using a value of 76 dynes/cm for the dispersion force contribution to the surface energy of silica (1) the spreading pressure was now

<sup>1</sup> Model LTA 600, manufactured by Tracer Laboratories, Incorporated.

Table II. Surface energies (ergs/square centimeter) and spreading pressures (dynes/centimeter) on various silica surfaces

Surface treatment	Water			n-Hexadecane		
	$\theta$	$\gamma^d_{\text{SiO}_2}$ <sup>(a)</sup>	$\pi_e$ <sup>(b)</sup>	$\theta$	$\gamma^d_{\text{SiO}_2}$ <sup>(a)</sup>	$\pi_e$ <sup>(b)</sup>
$1000^\circ\text{C}; \text{O}_2$	$47^\circ$	169	-39.9	$10^\circ$	27.3	36.8
15 min at $100^\circ\text{C}$ in $\text{H}_2\text{O}$	$29^\circ$	210	-53.8	$13^\circ$	27.0	37.1
30 min at $100^\circ\text{C}$ in $\text{H}_2\text{O}$	$19^\circ$	226	-58.9	$15^\circ$	26.8	37.3
Trichloroethylene	$49^\circ$	164	-38.1	$56^\circ$	27.6	36.5
Dry-ashing	$6^\circ$	237	-62.4	$16^\circ$	26.6	37.4

(a)  $\pi_e = 0$ .

(b)  $\gamma^d_{\text{SiO}_2} = 76$  ergs/cm<sup>2</sup>.

calculated and tabulated in the last columns. The values for  $\pi_e$  obtained that way for the dry-ashed surfaces followed by water boiling are of interest. While spreading pressures can be obtained from vapor absorption measurements, this is a more cumbersome technique than simply measuring contact angles or the surface tension of liquids. Fowkes proposed (6) an equation for the spreading pressure

$$\pi_e = 2 \sqrt{\gamma_s^d \gamma_l^d} - \gamma_l \quad [4]$$

Although this formula is applicable only when dispersion forces are present using 76 dynes/cm for  $\gamma_s^d$ , the following values for  $\pi_e$  were obtained for: water, -62.4 dynes/cm; and n-hexadecane, 38.9 dynes/cm. These values are almost identical (certainly in sign and order of magnitude) with those calculated from the contact angle measurements on the thermally grown SiO<sub>2</sub> and dry-ashed (Table II). It is interesting to note that the spreading pressure calculated from thermodynamic and surface tension data alone agreed well with data observed and calculated from the contact angle measurements on dry-ashed samples, not only for water but for n-hexadecane as well. It may be assumed therefore, that the dry-ashed sample was the "cleanest" surface thermodynamically that was comparable to those studied by Zisman, Fowkes, and others by absorption data of vapors and gases.

It appears obvious, therefore, that the scheme presented here permits at least an approach to the characterization of surface changes. If the "true" surface energy of a clean solid is known by some other means, such as absorption data, then the spreading pressure can be calculated from a simple contact angle measurement by use of Eq. [3] or [4]. Surface changes from this "clean" thermodynamic surface (in other words, surface contaminations) can now be determined easily by measuring the contact angle and comparing the new with the "clean" spreading pressure. Such a technique will permit an estimate of the cleanliness of the surface and the repeatability of the technique. Either the difference or the ratios of the spreading pressures may be used as a measure. On the other hand, if  $\pi_e$  is determined the  $\gamma^d$  of the solid can equally easily be determined from Eq. [3] or [4]. Since conventional  $\pi_e$ 's are not exactly easy to determine, a simple approximation would be useful. It may be assumed that as the liquid (polar or nonpolar) spreads over the polar surface an electrical double layer is set up. The atoms in the solids, of course, cannot reorient themselves but those of the liquid can. Such a liquid then may set up a zeta potential and permit a first approximation to the  $\pi_e$  values. Zeta potentials should be easier to measure than  $\pi_e$ .

If the above train of thought is valid, as a first approximation only (the actual relationship would be more sophisticated) then

$$\pi_e \text{ is proportional to a function of } \frac{\zeta}{\mu_1 + \mu_2} \quad [5]$$

where  $\zeta$  is the zeta potential in millivolts of the liquid moving across the solid and  $\mu_1$  is the dipole moment of the liquid and  $\mu_2$  the dipole moment of the solid in Debyes.

Using appropriate values in the literature or calculating the  $\mu$  from the Clausius-Masotti equation and zeta potentials from molar refractions it appears that for  $\pi_e$  values we obtained:

	Calculated from Eq. [5]	Calculated from contact angle
Water	-50 to -70	-62.4
n-Hexadecane	+20 to +30	+38.9
n-Butanol	-1.6 to -2.2	-2.1

The agreement of the numbers may be fortuitous particularly since it must be pointed out that millivolt/Debye are not equal to dynes/centimeter. However, the suggestion is here made that a more sophisticated approach in this direction may be worthwhile to pursue.

### Summary and Conclusions

Even though it is not possible to characterize high-energy surfaces unequivocally with one simple contact angle measurement, it is shown that two contact angle measurements with two different liquids can characterize the SiO<sub>2</sub> surfaces. It is further indicated that a technique can be worked out if the surface energy or the spreading pressure of the solid is known by other techniques, and for many materials used in the semiconductor industry this is possible. Changes in the surface energy can be determined easily with a simple contact angle measurement by using suitable liquids, even though polar forces do take part at the liquid-solid interfaces.

### Acknowledgment

The author is indebted to J. O'Brien and Miss B. Kriscka for the collection of the experimental data and to F. W. Anderson, Dr. M. N. Turetzky, and Dr. D. L. Klein for valuable advice and helpful discussions throughout the project.

Manuscript submitted April 2, 1973; revised manuscript received Dec. 4, 1973. This was Paper 17 presented at the Houston, Texas, Meeting of the Society, May 7-11, 1972.

Any discussion of this paper will appear in a Discussion Section to be published in the December 1974 JOURNAL. All discussions for the December 1974 Discussion Section should be submitted by Aug. 1, 1974.

### REFERENCES

1. F. M. Fowkes, in "Contact Angle, Wettability, and Adhesion," Chap. 6, in, "Advances in Chemistry Series," Vol. 43, American Chemical Society (1964).
2. F. M. Fowkes, in "Chemistry and Physics of Interfaces," pp. 1-12, (American Chemical Society, Washington, D.C. (1965)).
3. W. A. Zisman, *Ind. Eng. Chem.*, **55** (10), 19 (1963).
4. R. J. Good and L. A. Girifalco, *J. Phys. Chem.*, **61**, 944 (1957); *ibid.*, **62**, 1418 (1958); *ibid.*, **64**, 561 (1960).
5. R. E. Johnson and R. H. Dettre, *J. Colloid Interfac. Sci.*, **21**, 610 (1966).
6. R. A. Swalin, "Thermodynamics of Solids," p. 184, John Wiley & Sons, Inc., New York (1962).
7. F. M. Fowkes, in "Surfaces and Interfaces I," J. J. Burke, N. L. Reed, and V. Weiss, Editors, pp. 197-224, Syracuse University Press (1967).
8. W. A. Zisman, "A Decade of Basic and Applied Sciences in the Navy," pp. 30-41, Washington, D. C. (1957).
9. H. E. Garrett, in "Aspects of Adhesion," D. J. Alner, Editor, pp. 18-41, University of London Press, Ltd. (1966).
10. G. Koranyi, "Surface Properties of Silicate Glasses," p. 59, Hungarian Academy of Sciences (1963).

# Investigation of Surface Oxide Layers by X-Ray Appearance Potential Spectroscopy

K. N. Ramachandran and C. D. Cox

Semco Instruments Company, Ottawa, Ontario, Canada

## ABSTRACT

X-ray appearance potential spectroscopy using low energy electron excitation is a simple method for surface analysis sensitive to light elements. The spectra obtained from many elements show considerable structure which is presumably related to the valence band distribution. The apparatus consisted of a tungsten filament electron source and a large area, windowless, soft x-ray detector based on the photoelectric yield of a gold surface. The specimen, electron source, and detector were located in an all metal, bakeable vacuum system having demountable, gold wire sealed flanges. Facilities were provided for surface cleaning by ion bombardment and heating the specimen *in situ*. A 10Å layer of oxygen on nickel was readily detected using an electron current of 2 mA. The  $L_{3,2}$  structure of iron in pure and known oxide forms was obtained by performing *in situ* oxidation of a pure iron specimen. Slight but reproducible changes in the structure were observed, indicating the potential capability of the technique to distinguish between different valence states of an element. The oxygen K spectrum also showed a multiple peaked structure.

During the past few years, soft x-ray appearance potential spectroscopy has been established as a simple but powerful tool for surface analysis. The light elements from beryllium to oxygen and a number of medium and heavy elements, when present as surface impurities, have been detected by this method (1-3). Though the detection sensitivity attained so far is low compared to that of conventional methods of micro-analysis, the simplicity of the apparatus and the ability to provide information related to the valence band structure of elements make appearance potential spectroscopy an attractive technique. Most of the analysis work performed by this method has been qualitative. No effort has been made by the other authors to establish detection sensitivities of different elements or to relate the observed fine structure in the spectrum to known surface conditions developed in a specimen. The present work deals with a few quantitative results on oxides formed on nickel and iron specimens. The detailed fine structure in the K spectrum of oxygen and the  $L_{3,2}$  spectrum of iron corresponding to different types of oxides formed *in situ* are also presented.

## Apparatus

The appearance potential spectrometer was built in an all metal vacuum system consisting of several demountable flanges sealed by gold wire. A clean vacuum was obtained using a 20 liter/sec ion pump with titanium sublimation elements, initially backed up by a turbomolecular pump. After baking to about 250°C for 12 hr, a working pressure of about  $2 \times 10^{-9}$  Torr was reached, which ensured a reasonably clean specimen environment during the experiment.

The schematic diagram of the apparatus is shown in Fig. 1. The electron source located 0.5 cm away from the flat face of the specimen consisted of a U-shaped filament made of 0.125 mm tungsten wire. For heating currents lying between 2-3A, the filament was capable of delivering electron currents up to 2 mA to the specimen at a potential of 50V or more. An emission regulator was built into the filament heating circuit in order to keep the specimen current constant during the experiment. This was achieved by sensing the current at the specimen by a high-gain amplifier and using the output to control the filament current. The filament was biased positive with respect to the grounded mesh in front of the detector in order to prevent the back-

scattered electrons from entering the detector box. The interior of the triangular-shaped box was coated with an evaporated layer of gold, and this served as the photocathode by releasing electrons under the action of the incident x-rays. These electrons were collected by a positively biased electrode which was coupled to a high-gain low-noise amplifier. The specimen potential was supplied from a motor-driven power supply, continuously variable from 50 to 1000V at rates varying from 0.5 to 5 V/sec. The derivative of the total x-ray yield was obtained by introducing a small modulation to the specimen potential and using a lock-in amplifier to detect the fundamental component of the photoelectron current, as shown in the diagram.

## Results

The initial experiments were done on specimens in the shape of a disk of 1 cm diameter. The appearance potential spectra of beryllium, boron, carbon, nitrogen,

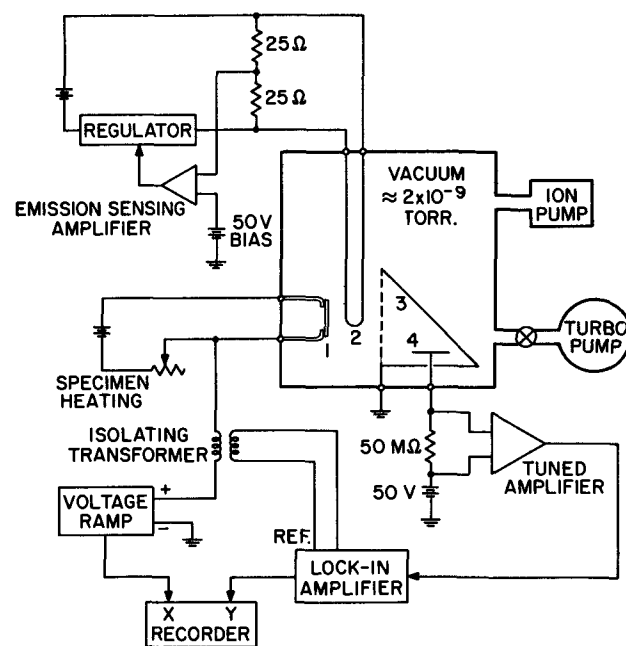


Fig. 1. Schematic diagram of the appearance potential spectrometer. 1, Specimen; 2, filament; 3, photocathode; 4, photoelectron collector.

Key words: soft x-ray shifts, oxidation.

and oxygen were obtained from such specimens (4). The results, however, were merely qualitative as there was no way of knowing the surface concentration of the different elements on the specimens used.

Oxidation of metals is a well-studied and documented process and it was therefore decided to use known oxide samples in order to establish the detection sensitivity of oxygen. A nickel specimen was prepared by vacuum deposition of a 1000-2000Å layer of nickel evaporated from a tungsten basket on to a stainless steel disk. It was then exposed to air at room temperature for a few minutes so as to oxidize the surface. This exposure is known to form a stable oxide layer of mean thickness 10Å on the surface (5). The appearance potential spectrum obtained from this sample is given in Fig. 2, showing strong  $L_{3,2}$  structure of nickel and weak but clearly discernible K structure of oxygen. The sensitivity can be improved further (by a factor of about 5) at the expense of structure resolution by increasing the modulation amplitude. Thus it seems readily possible to detect a monolayer of oxygen on nickel with a reasonable signal-to-noise ratio. To confirm that the signal was derived from the surface oxide layer, the specimen was subjected to argon ion bombardment to sputter off the oxide layer. This was performed by admitting pure argon through a leak valve and sustaining a discharge current of 1 mA through the specimen at 800V for about 15 min at an argon pressure of about  $10^{-2}$  Torr. The spectrum obtained after the above treatment showed marked reduction in the oxygen structure to the level of noise fluctuations.

**Oxidation studies on iron.**—The initial version of the apparatus using disk specimens was modified to carry out oxidation studies on iron. The specimen consisted of a high-purity iron foil (John Matthey 99.997%), 0.0125 mm thick and  $1 \times 0.5$  cm size, spot welded to two nickel supports. By passing current through the specimen, it was possible to attain temperatures up to 600°C as measured by a 0.075 mm iron-constantan thermocouple junction spot welded to the back of the specimen. The appearance potential spectrum obtained before performing any heat-treatments revealed small amounts of carbon and oxygen as shown in Fig. 3. In order to remove these contaminants, the foil was first heated to about 500°C in vacuum for several minutes so that the carbon from the bulk diffused to the surface and combined with the oxygen on the surface to form CO. After cooling to room temperature, pure oxygen was admitted at about 1 Torr for a few minutes and the pressure brought down to  $10^{-8}$  Torr. Further heating to 500°C removed more of the carbon diffusing to the surface and the cycle was repeated a few times to burn off the last traces of carbon from the specimen. Finally, the oxygen remaining on the surface was removed by heating to 300°C in pure hydrogen at  $10^{-3}$

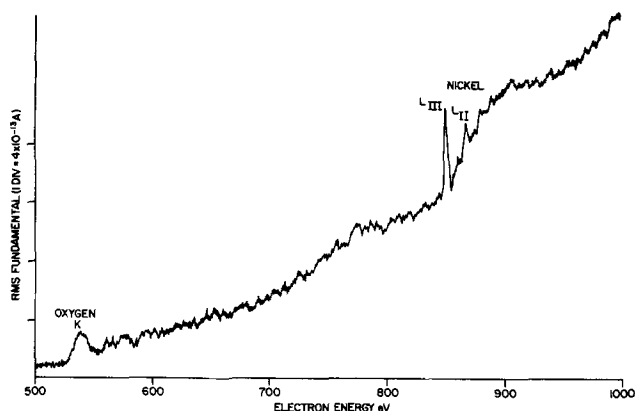


Fig. 2. Detection of oxygen ( $\approx 10\text{\AA}$ ) on nickel. Specimen current = 2 mA; modulation = 2V p-p at 500 Hz; lock-in time constant = 1 sec; residual pressure =  $2 \times 10^{-9}$  Torr.

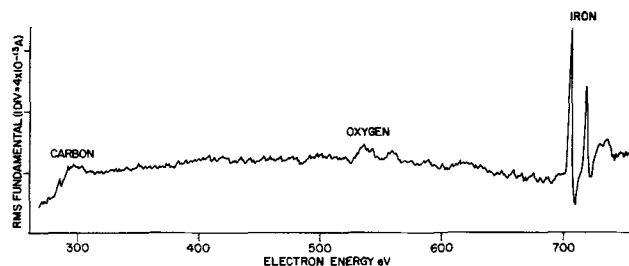


Fig. 3. Spectrum from the iron foil before surface treatments showing small amounts of carbon and oxygen. Specimen current = 2 mA; modulation = 2V p-p at 500 Hz; lock-in time constant = 1 sec; residual pressure =  $2 \times 10^{-9}$  Torr.

Torr. The technique described above is a standard procedure for the removal of carbon from the bulk of thin foils and oxygen from the surface (6).

The  $L_{3,2}$  spectrum of pure iron as obtained after the cleaning operations is shown in Fig. 4 (a). Oxygen was then admitted at about 1 Torr and the specimen heated to 200°C for 10 min to oxidize the surface. This resulted in the formation of an oxide layer of mean thickness 60Å, consisting of predominantly  $\text{Fe}_3\text{O}_4$  and some  $\gamma\text{Fe}_2\text{O}_3$  (7, 8). The spectrum of iron corresponding to this condition is given by the trace (b), Fig. 4. The specimen was then annealed in vacuum by heating

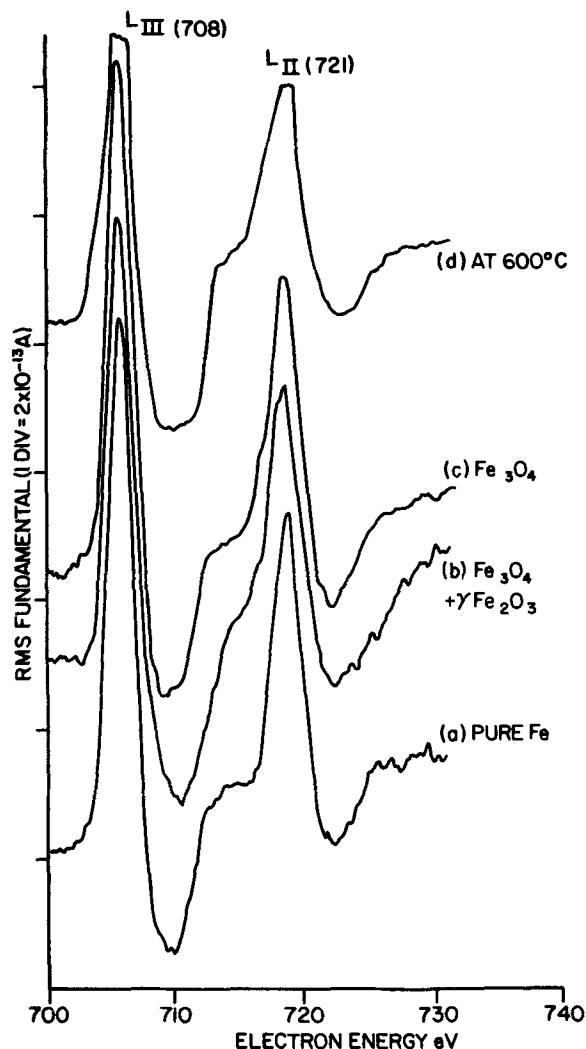


Fig. 4. L edge structure of iron in different forms. Absorption edge values from standard tables are given in brackets. The vertical shift between traces is arbitrary. Traces (a), (b), and (c) were taken at room temperature. Specimen current = 2 mA; modulation = 2V p-p at 500 Hz; lock-in time constant = 3 sec; residual pressure =  $5 \times 10^{-9}$  Torr (predominantly hydrogen).

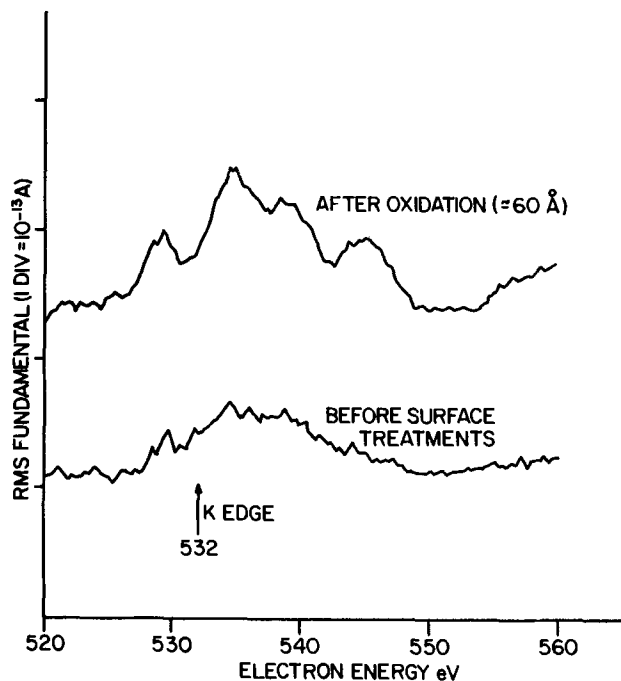


Fig. 5. K edge structure of oxygen before and after oxidation. The vertical shift between traces is arbitrary. Specimen current = 2 mA; modulation = 2V p-p at 500 Hz; lock-in time constant = 3 sec; residual pressure =  $5 \times 10^{-9}$  Torr.

to 500°C for several minutes in order to change the oxide to nearly pure  $\text{Fe}_3\text{O}_4$ . The spectrum for iron in this form is shown by trace (c), Fig. 4. The trace (d), Fig. 4, was obtained while the temperature was held constant at about 600°C which is known to transform the oxide to  $\text{FeO}$ . The oxygen K structure before surface treatment and after the first oxidation is shown in Fig. 5.

#### Discussion and Conclusion

The  $L_{3,2}$  appearance potential structure of iron in the pure and three different oxide forms is obtained using *in situ* heating and oxidation facilities. Except for the small noise fluctuations, the traces have good reproducibility. Within the energy resolution of the instrument (about 2 eV), there is no measurable energy shift between the positions of peaks in all these cases. However, there are slight but reproducible differences in the shape of the curves, especially in the region lying between the  $L_3$  and  $L_2$  peaks. The over-all structure is apparently sharpest in trace (a) in Fig. 4 corresponding to pure iron. In trace (b), Fig. 4, the peaks are broadest at the base and they almost merge into each other. Trace (d), Fig. 4, shows flattened peaks.

The changes in the iron structure are attributed to differences in the valence state of the element as it combines with oxygen. This is analogous to what is commonly known as chemical shift, which has been observed to some extent in other methods of surface

analysis such as ESCA and Auger electron spectroscopy (9). The appearance potential spectrum is directly related to the initial ionization transitions from the inner levels to the outer empty levels in the valence band and can therefore be expected to be sensitive to changes in the valence band structure (10). Though the differences observed in the present case are small, they demonstrate the potential capability of the technique to reveal the valence band structure and thereby identify the various chemical forms of an element. Much more conspicuous "shifts" have been observed in the spectra of a few alloys and compounds (3, 11). These effects, however, have to be properly characterized before practical identification of the chemical species can be made. One answer to this problem is to combine appearance potential spectroscopy with more elaborate techniques such as LEED into the same apparatus so that the results can be directly correlated.

The oxygen K spectrum in Fig. 5 shows a multi-peaked structure. Such multiple peaks are observed in the case of many other light elements, especially carbon for which the peaks have been related to plasmon effects caused by the incident electrons (12). Plasmon data on oxygen are not available at the present time in order to compare the results.

#### Acknowledgment

The authors wish to thank P. B. Sewell, National Research Council of Canada, for his advice and help in carrying out the experiment.

Manuscript submitted April 17, 1973; revised manuscript received Nov. 30, 1973.

Any discussion of this paper will appear in a Discussion Section to be published in the December 1974 JOURNAL. All discussions for the December 1974 Discussion Section should be submitted by Aug. 1, 1974.

#### REFERENCES

1. R. L. Park and J. E. Houston, *J. Vacuum Sci. Technol.*, **10**, 176 (1973).
2. P. A. Redhead and G. W. Richardson, *J. Appl. Phys.*, **43**, 2970 (1972).
3. K. N. Ramachandran, Ph.D. Thesis, University of Ottawa (1972).
4. K. N. Ramachandran and C. D. Cox, Presented at the 12th Symposium on Electron, Ion and Laser Beam Technology, May 1973; *J. Vacuum Sci. Technol.*, **10**, 1068 (1973).
5. M. J. Graham and M. Cohen, *This Journal*, **119**, 879 (1972).
6. P. B. Sewell, D. F. Mitchell, and M. Cohen, *Surface Sci.*, **33**, 535 (1972).
7. M. J. Graham, S. I. Ali, and M. Cohen, *This Journal*, **117**, 513 (1970).
8. P. B. Sewell and M. Cohen, *ibid.*, **111**, 501 (1964).
9. R. Nordberg, *Advan. X-Ray Anal.*, **13**, 390 (1970).
10. B. Dev and H. Brinkman, *Ned. Tijdschr. Vacuumtechniek*, **8**, 176 (1970).
11. J. E. Houston and R. L. Park, *J. Vacuum Sci. Technol.*, **9**, 579 (1972).
12. J. E. Houston and R. L. Park, *Solid State Commun.*, **10**, 91 (1972).

# Water Adsorption in Chemically Vapor-Deposited Borosilicate Glass Films

E. Arai and Y. Terunuma

Musashino Electrical Communication Laboratory, Nippon Telegraph and Telephone Public Corporation, Midori-cho, Musashino-shi, Tokyo, Japan

## ABSTRACT

Infrared absorption measurements have been made of physically adsorbed water and silanol in borosilicate glass films which were chemically vapor-deposited at 400°C and then exposed at room temperature to moist air of relative humidity  $50 \pm 10\%$ . Both the physically adsorbed water and silanol were found to increase with time up to about  $10^5$  min and then to decrease. The process of water adsorption was limited by the diffusion of water in CVD glass. The adsorption sites of CVD glass were suggested to decrease with the increase of time. The diffusion coefficient of water in the as-deposited glass films at room temperature was estimated to be on the order of  $10^{-15}$ – $10^{-14}$  cm<sup>2</sup>/sec and was found to decrease with the increase of B<sub>2</sub>O<sub>3</sub> content of the glass and annealing temperature prior to exposure to moist air. Heats of physical adsorption of water were 1.2 kcal/mol below 120°C and 3.3 kcal/mol above 120°C for as-deposited borosilicate glass containing 8.7 molar per cent B<sub>2</sub>O<sub>3</sub>.

Low temperature vapor-deposited silicon dioxide doped with B<sub>2</sub>O<sub>3</sub>, P<sub>2</sub>O<sub>5</sub>, As<sub>2</sub>O<sub>3</sub>, etc. is currently becoming of industrial importance as a source for diffusion into silicon substrates and for device protection, but tends to be much more porous and active for water adsorption than thermally oxidized films. Water adsorption reduces adherence of photoresist on the oxide (1, 2) and adversely affects electrical characteristics of devices (3). Although many authors have studied the infrared absorption of borosilicate glass and silica (4-8), investigations of water adsorption in low temperature vapor-deposited silicon dioxide with much internal porosity have not been reported, except for Ref. (8), where changes of B-O, B-O-H, etc. absorption bands with time for various humidity have been measured for highly boron-doped glasses. In the present work, the rate of adsorption, the heat of water adsorption, and porosity for borosilicate glass films, which were chemically vapor-deposited at 400°C, were studied, using infrared technique and electron microscopy.

## Experimental Procedure

The silicon dioxide films doped with boron oxide were deposited on substrates in an atmosphere of silane, diborane, and oxygen at 400°C, using nitrogen as a carrier gas. Growth rates of glass depend on the gas flow ratios. Typical rates were about 430 Å/min for boron-doped oxide (8.7 m/o B<sub>2</sub>O<sub>3</sub>) and 500 Å/min for nondoped oxide. Silicon or fused-silica wafers were used as substrates. The silicon wafers were 100 to 200 ohm-cm resistivity, n-type, and 0.4 mm thick with mirror polished surface. The fused-silica wafers were 0.3 mm thick with mirror polished surfaces. Infrared absorption was measured in transmission on a Model IR-27G Spectrophotometer made by Shimadzu Seisakusho, Ltd., with a bare companion wafer of approximately the same thickness of silicon or fused silica in the reference beam. The infrared transmission of silica is larger than silicon in the wave number range of 4000-2200 cm<sup>-1</sup> and is much smaller below 2200 cm<sup>-1</sup>. Moreover, infrared measurements of fused silica are not influenced by the absorption due to free carriers and curvature of the wafer due to the difference of the thermal expansion coefficient between deposited film and substrate. Fused silica was, therefore, used as a substrate to measure the absorbance of silanol at 3650 cm<sup>-1</sup> and physically adsorbed water

at 3400 cm<sup>-1</sup>. Silicon substrates were used for measurements in the range of 2000-400 cm<sup>-1</sup>, e.g., the B-O band at 1320 cm<sup>-1</sup>, the Si-O band at 1080 cm<sup>-1</sup>, and the Si-O-B band at 930 cm<sup>-1</sup>. In many cases in the present work, the adsorbed amount of water or silanol was plotted by  $\log(I_0/I)$  at 3400 or 3650 cm<sup>-1</sup>, where  $I_0/I$  is the relative intensity of transmitted infrared light. Thicknesses of the glasses were observed by interference colors in reflection with occasional checks by ellipsometer measurements. Compositions of the as-deposited films were determined by infrared absorption spectroscopy, using the published data for the infrared absorbance ratio *vs.* molar per cent B<sub>2</sub>O<sub>3</sub> obtained by chemical analysis (5, 9). Porosity of glasses was measured by an electron microscope Model JEM-T5S made by Japan Electron Optics Laboratory Company, Ltd. Heat-treatments were carried out in a nitrogen atmosphere or in a vacuum of about  $5 \times 10^{-5}$  Torr.

## Experimental Results

**Water adsorption in air.**—Changes in the time of the infrared absorption near 3 μm of boron doped and nondoped oxide exposed at room temperature to air with a relative humidity  $50 \pm 10\%$  are shown in Fig. 1 (a) and (b). Both oxides were about 1.0 μm thick. The boron content in the doped oxide was 8.7 molar per cent B<sub>2</sub>O<sub>3</sub>. It can be seen from these figures that a band at 3650 cm<sup>-1</sup> was present initially only for nondoped oxide: the broad band at about 3 μm increased with

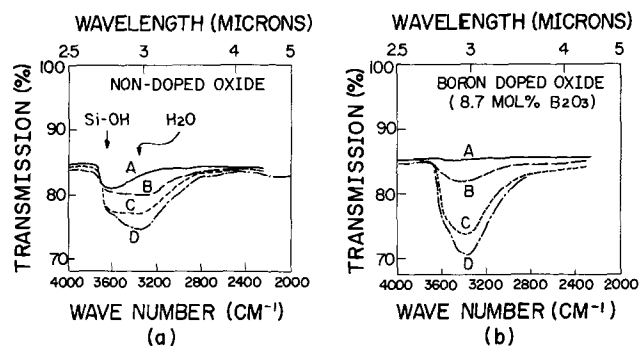


Fig. 1. Changes with time of infrared spectra of nondoped oxide and boron-doped oxide films (about 1 μm). (a) Nondoped oxide. (b) Boron-doped oxide (8.7 m/o B<sub>2</sub>O<sub>3</sub>). Curve A, Initial spectra (< 2 min exposure); curve B, 5 hr exposure; curve C, 6 days exposure; curve D, 100 days exposure.

Key words: infrared spectroscopy, physically adsorbed water, silanol, diffusion coefficient of water.



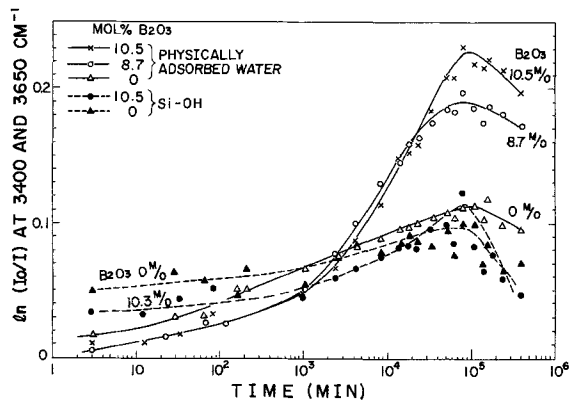


Fig. 2. Changes of  $\ln(I_0/I)$  at 3650 and 3400  $\text{cm}^{-1}$  with time for nondoped oxide and boron-doped oxide (about 1  $\mu\text{m}$ ).

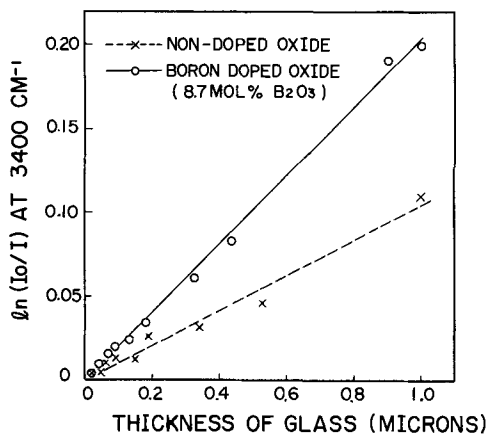


Fig. 3. Dependence of maximum values of  $\ln(I_0/I)$  at 3400  $\text{cm}^{-1}$  on thicknesses of glass.

time for both oxides. The broad band at 3  $\mu\text{m}$  can be assumed to consist of peaks at 3650  $\text{cm}^{-1}$  and at 3400  $\text{cm}^{-1}$ . The former corresponds to an oxygen-hydrogen stretching vibration of silanol groups and the latter to that of physically adsorbed water (6, 7). It is, therefore, concluded that the silanol groups adsorb on the nondoped oxide but not on the boron-doped oxide in the deposition process and the physically adsorbed water does not adsorb on both oxides in the process. Figure 2 shows the changes with time exposed to moist air of  $\ln(I_0/I)$  at 3650  $\text{cm}^{-1}$  for oxides (0 and 10.5 m/o  $\text{B}_2\text{O}_3$ ) and 3400  $\text{cm}^{-1}$  for oxides (0, 8.7, and 10.5

m/o  $\text{B}_2\text{O}_3$ ). From this figure, it is found that the adsorbed water reaches its maximum value at about  $10^5$  min and then decreases; the maximum value of physically adsorbed water increases with  $\text{B}_2\text{O}_3$  content in glass. The dependence of the maximum value of physically adsorbed water on the thickness of the glass is shown in Fig. 3, where it is found that the maximum values are nearly proportional to the glass thickness. From this figure, it is concluded that the water adsorbs uniformly on the walls of the inner porous structure. Plotting  $d^{-1} \ln(I_0/I)$  against  $t/d^2$ , it was found that  $d^{-1} \ln(I_0/I)$  lays almost on a smooth curve for samples with various thicknesses, except below about 0.2  $\mu\text{m}$  where experimental precision is poor, as shown in Fig. 4. From these facts, it is expected that the limiting process of adsorption for glass is the diffusion of water, not the adsorption itself. The diffusion coefficient of water is estimated in a later section, where these data are compared with the solution of the diffusion equation, which is shown as a solid curve in Fig. 4.

**Outflow of boron oxide from highly doped glass films.**—The infrared absorption spectrum of boron-doped oxide has B-O bands at 1320-1380, 670, and 470-520  $\text{cm}^{-1}$  and an Si-O-B band at 930  $\text{cm}^{-1}$ , in addition to the normal Si-O bands at 1070, 800, and 450  $\text{cm}^{-1}$  (4, 5, 8). Changes of these bands with time were measured for films of differing boron content. For the low doping level (<8.7 m/o  $\text{B}_2\text{O}_3$ ), the B-O and Si-O bands hardly changed with time and the bands of B-O-H at 3200, 1450, and 1197  $\text{cm}^{-1}$  did not appear (10). With higher boron content, the absorption of B-O bands and Si-O-B band decreased with time, while the absorption in the 3400-3200 region and in the 1070  $\text{cm}^{-1}$  region increased markedly, as shown in Fig. 5(a) and (b). In the spectra of Fig. 5(a), it is seen that the 3  $\mu\text{m}$  band first appears at 3250-3200  $\text{cm}^{-1}$ , and then approaches 3400  $\text{cm}^{-1}$ . The 7  $\mu\text{m}$  B-O band first has its peak at 1320  $\text{cm}^{-1}$ , then becomes broad over 1450-1320  $\text{cm}^{-1}$ , and disappears after 45 days exposure. The 9  $\mu\text{m}$  Si-O band ranges from 1200 to 1000  $\text{cm}^{-1}$  and first has its peak at 1070  $\text{cm}^{-1}$  and becomes large and sharp later. These data suggest  $\text{B}(\text{OH})_3$  is formed early and then flows out from the glass, leaving water behind it. Further, it is thought that the increase of the absorbance near 1070  $\text{cm}^{-1}$  is due to the increase of a bending vibration of B-OH but not of Si-O (4), which means that the infrared peak ratio of band at 1320  $\text{cm}^{-1}$  to that at 1070  $\text{cm}^{-1}$  is not always proportional to the  $\text{B}_2\text{O}_3$  molar ratio in glass. Figures 6(a) and (b) show the correlations of the absorbance of B-O band in

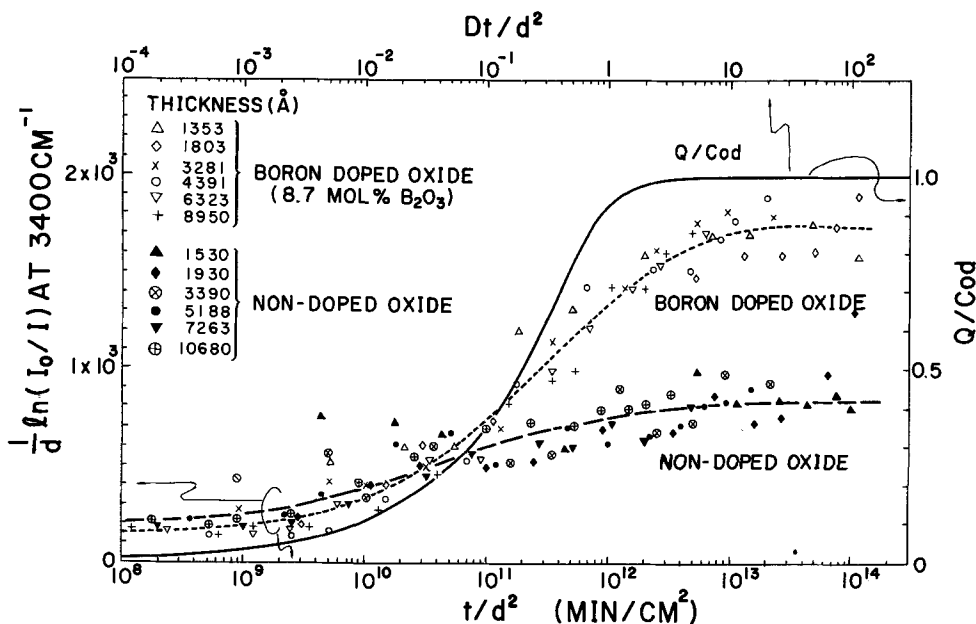


Fig. 4. Changes of  $d^{-1} \ln(I_0/I)$  at 3400  $\text{cm}^{-1}$  with  $t/d^2$  for nondoped oxide and boron-doped oxide (8.7 m/o  $\text{B}_2\text{O}_3$ ) and a calculated adsorption curve ( $Q/C_0d$  vs.  $Dt/d^2$ ).

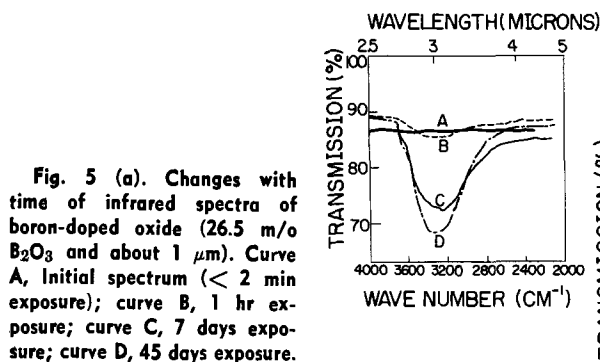


Fig. 5 (a). Changes with time of infrared spectra of boron-doped oxide (26.5 m/o B<sub>2</sub>O<sub>3</sub> and about 1  $\mu$ m). Curve A, Initial spectrum (< 2 min exposure); curve B, 1 hr exposure; curve C, 7 days exposure; curve D, 45 days exposure.

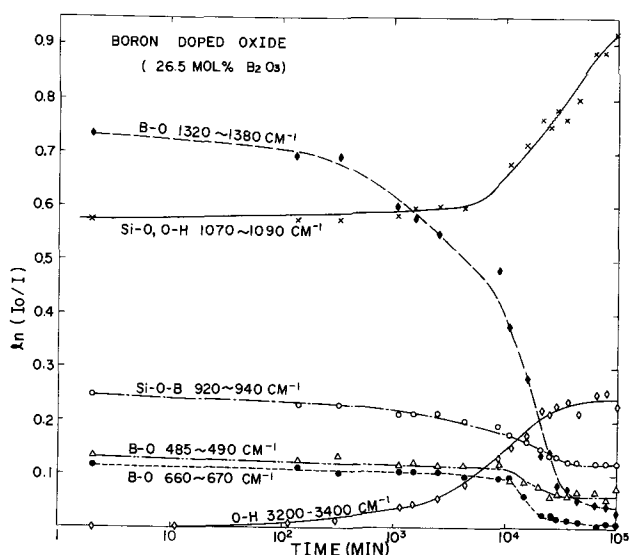
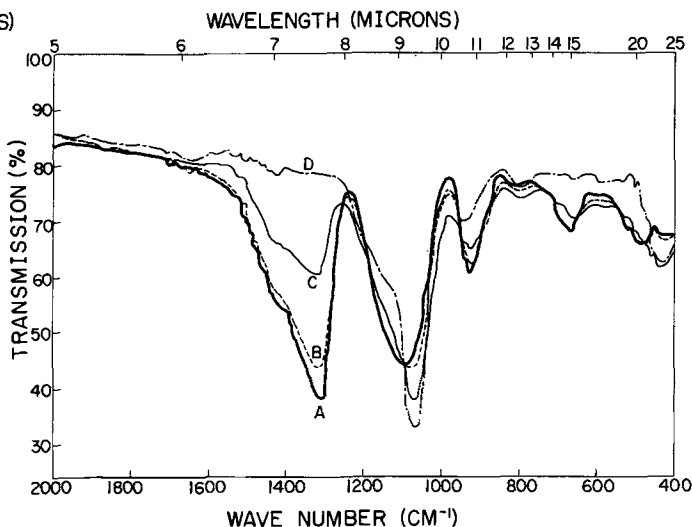


Fig. 5 (b). Changes with time of  $\ln(I_0/I)$  at various absorption bands of boron-doped oxide (26.5 m/o B<sub>2</sub>O<sub>3</sub> and about 1  $\mu$ m).

the 1320-1380 cm<sup>-1</sup> region with the band of water in the 3200-3400 cm<sup>-1</sup> region for the various B<sub>2</sub>O<sub>3</sub> contents in glass. From these figures, it is seen that the decrease of the B-O band absorbance with time corresponds with the increase of the water band absorbance for various initial boron contents in glass. From these facts, it is assumed that the adsorption sites, i.e., the internal surface area, increase with the outflow of B<sub>2</sub>O<sub>3</sub> from glass.

**Porosity and heats of adsorption.**—To study the dependence of size and density of pores in the surface of glass on B<sub>2</sub>O<sub>3</sub> content and heat-treatments, the glass surfaces were observed by electron microscopy. Figure 7 shows electron micrographs of surfaces for as-deposited glasses containing 0, 8.7, and 26.5 m/o B<sub>2</sub>O<sub>3</sub>, where the carbon-germanium replica was produced just after the deposition. From this figure, it is seen that the pore size is about 100-200 Å on an average and decreases with boron content in glass. The pore density increased with boron content in glass, for example, about 100 in a square micron for nondoped oxide, 160 and 230 for boron-doped oxides containing 8.7 and 26.5 m/o B<sub>2</sub>O<sub>3</sub>, respectively. It was also found that the pore density decreased and surface texture became smoother with the increase of the temperature of heat-treatment for boron-doped oxides containing 8.7 and 26.5 m/o B<sub>2</sub>O<sub>3</sub>. This fact corresponds with the softening of glass. Further, no changes of glass surface with exposure in air for about 10<sup>5</sup> min

were observed. To evaluate the heat of adsorption from the infrared absorption, the following treatments were carried out in vacuum. Water desorption in isochronal heat-treatment for 10 min was measured in the temperature range of 74°-243°C. A peak in the differential desorption curve of physically adsorbed water appeared at about 120°C, but silanol groups scarcely desorbed, as shown in Fig. 8. Changes in the physically adsorbed water during isothermal heat-treatments were measured in the temperature range of 76.5°-218°C after a large amount of water was initially adsorbed by immersion in water at 97°C for several hours, as shown in Fig. 9. Plotting the equilibrium values obtained at each temperature against 1/T, heats

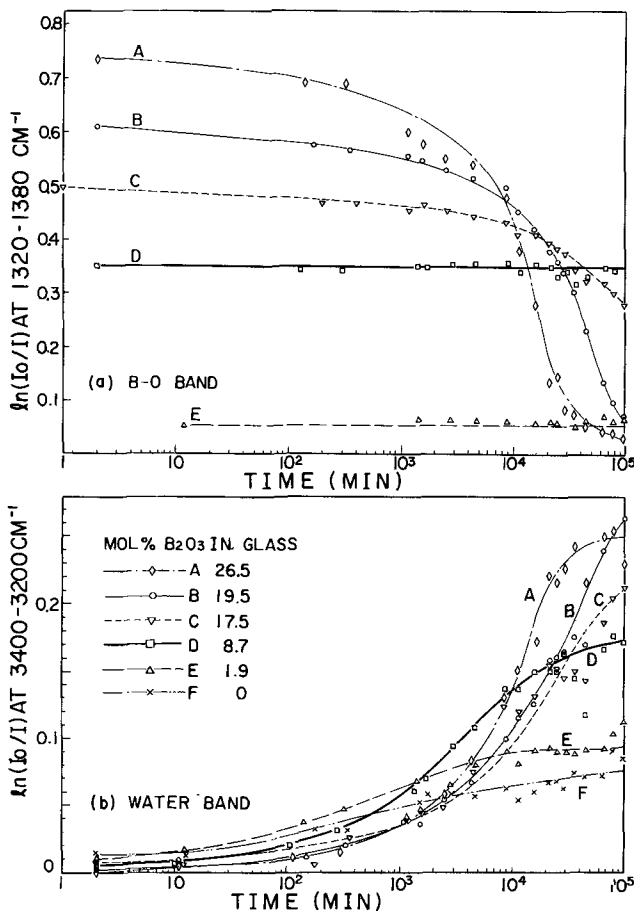


Fig. 6. Changes with time of absorbance of B-O and water band for various B<sub>2</sub>O<sub>3</sub> contents in glass (about 1  $\mu$ m). (a) B-O band at 1320-1380 cm<sup>-1</sup>. (b) Water band at 3200-3400 cm<sup>-1</sup>.

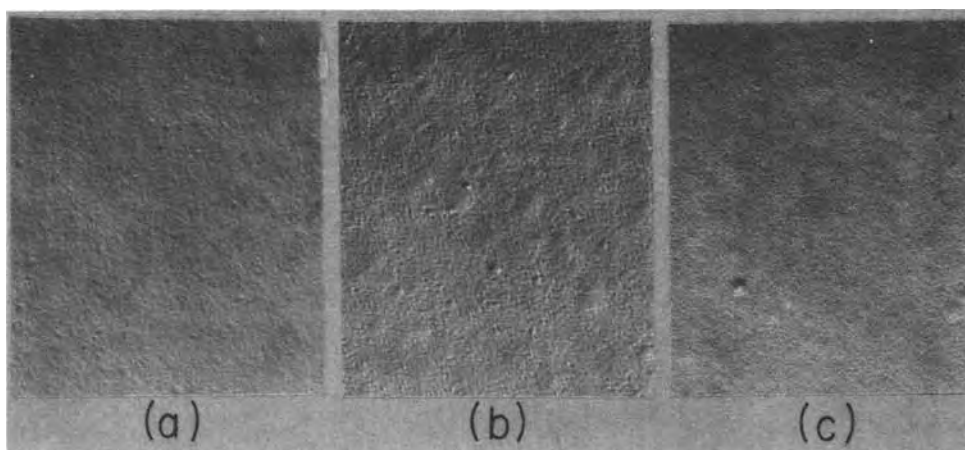


Fig. 7. Electron micrographs of surfaces of as-deposited glasses. (a) Nondoped oxide. (b) Boron-doped oxide (8.7 m/o  $B_2O_3$ ). (c) Boron-doped oxide (26.5 m/o  $B_2O_3$ ).

of physical adsorption were estimated to be 3.32 kcal/mol above 120°C and 1.15 kcal/mol below 120°C, as shown in Fig. 10. Further, the desorption in sulfuric acid was also measured. The amount of desorbed water increased with the temperature of sulfuric acid and the equilibrium values of water adsorbed in sulfuric acid were in agreement with those in vacuum above 120°C.

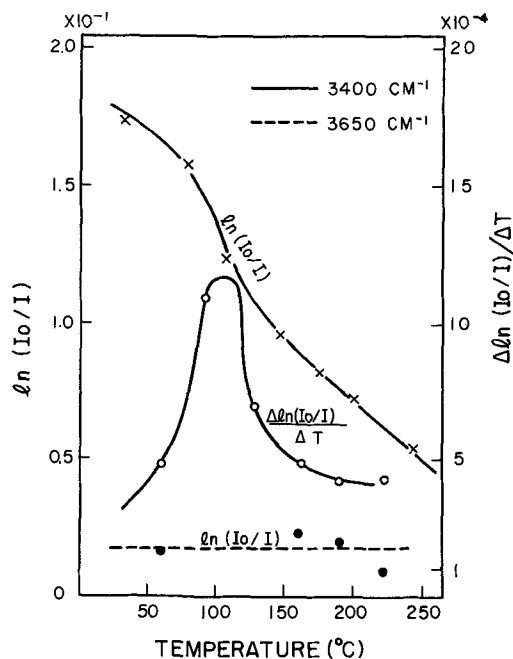


Fig. 8. Isochronal heat-treatment for 10 min in a vacuum for boron-doped oxide (8.7 m/o  $B_2O_3$  and about 1  $\mu\text{m}$ ).

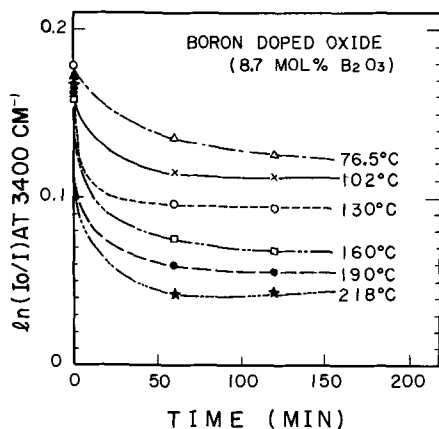


Fig. 9. Isothermal heat-treatments in vacuum for boron-doped oxide (8.7 m/o  $B_2O_3$  and about 1  $\mu\text{m}$ ).

*Water adsorption in heat-treated samples.*—Samples 1  $\mu\text{m}$  thick were heat-treated at 439°, 562°, 792°, and 1054°C for 10 min in a nitrogen atmosphere and then were exposed to moist air for various times. Figures 11(a) and (b) show changes with time of physically adsorbed water and silanol, where the latter is shown only for samples heated at 439° and 562°C to avoid confusion in the figures. From these figures, it is seen that the maximum values of physically adsorbed water appear behind those of silanol. Above 562°C, maximum values of physically adsorbed water decrease with the increase of temperature of heat-treatment, while those of samples heat-treated at 439°C are nearly the same as those of as-deposited samples. Re-adsorption of water is not observed in nondoped oxide heat-treated above 792°C for 10 min, while it is observed in boron-doped oxide (8.7 m/o  $B_2O_3$ ) even if it was heat-treated at 1054°C. The re-adsorbed amount of water for boron-doped oxide heat-treated at 1054°C for 60 min was half of that for 10 min. The reason why the maximum values of physically adsorbed water appear behind those of silanol is suggested as being due to the diffusion of water to the silanol sites. The Si-O absorption band at about 9  $\mu\text{m}$  shifted from 1060-1070  $\text{cm}^{-1}$  to 1080  $\text{cm}^{-1}$  by heat-treatment above 792°C for 1 min. On the other hand, the water contact angle of the glass surface was about 40° for nondoped oxide and about 10° for boron-doped oxide (8.7 m/o  $B_2O_3$ ) due to the heat-treatment above 792°C for 10 min, while both oxides had a water contact angle of 0° unless they were heat-treated. The Si-O absorption band of thermally oxidized  $\text{SiO}_2$  appears at 1080-1090  $\text{cm}^{-1}$  and its water contact angle is about 40° (2). These results will be reported later elsewhere in more detail. From the above results and discussion, it is suggested that the glass structure of nondoped oxide nears that of ther-

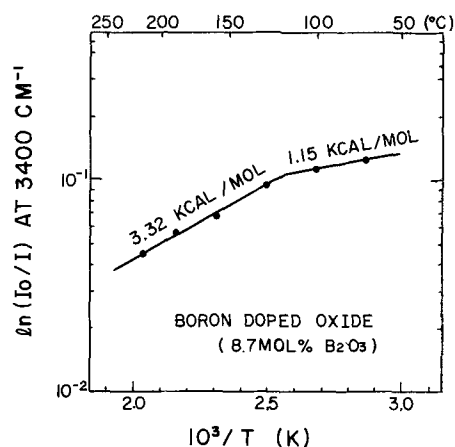


Fig. 10. Equilibrium values of  $\ln(I_0/I)$  obtained at each temperature and heats of adsorption of physically adsorbed water for boron-doped oxide (8.7 m/o  $B_2O_3$  and about 1  $\mu\text{m}$ ).

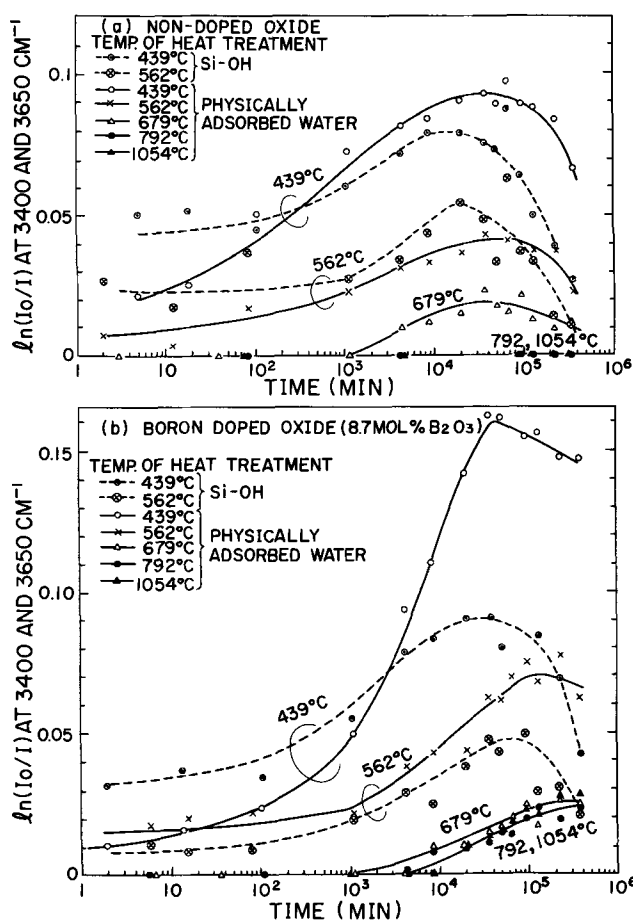


Fig. 11. Changes with time of  $\ln(I_0/I)$  at 3650 and 3400  $\text{cm}^{-1}$  for heat-treated samples (initially about 1  $\mu\text{m}$ ). (a) Nondoped oxide. (b) Boron-doped oxide (8.7 m/o  $\text{B}_2\text{O}_3$ ).

mal  $\text{SiO}_2$ , i.e., complete siloxane structure by heat-treatment above 800°C for 10 min. For boron-doped oxide, it is suggested that the B-O bond of the glass surface adsorbs the water even if it is heat-treated.

### Discussion

**Diffusion coefficient of water in glass.**—From Fig. 4, it is confirmed that the rate of water adsorption is limited by the diffusion of water in glass. In this section, the diffusion coefficient of water in glass is estimated, assuming the diffusion equation. It is certain that the glass structure changes with time slowly because the adsorbed amount of water decreased beyond approximately  $10^5$  min, as shown in Fig. 2 and 11. In other words, the internal area for adsorption decreases with time. For simplicity, it is now assumed that the diffusion coefficient is independent of time and concentration of water in glass. The diffusion equation and the initial and boundary conditions which fit the present experiment are given by

$$\frac{\partial C}{\partial t} = D \frac{\partial^2 C}{\partial x^2} \quad [1]$$

$$C = 0 \text{ at } 0 \leq x \leq d \text{ and } t = 0 \quad [2]$$

$$C = C_0 \text{ at } x = d \text{ and } t \geq 0 \quad [3]$$

$$\frac{\partial C}{\partial x} = 0 \text{ at } x = 0 \text{ and } t \geq 0 \quad [4]$$

where  $C$ ,  $D$ , and  $d$  are the concentration of water, diffusion coefficient, and glass thickness, respectively. The boundary condition of Eq. [4] expresses the fact that there is no diffusing flow across the interface between glass and substrate. The solution is given by a series of error functions, as follows (11)

$$C = C_0 \left\{ \sum_{n=0}^{\infty} (-1)^n \operatorname{erfc} \frac{(2n+1)d-x}{2\sqrt{Dt}} + \sum_{n=0}^{\infty} (-1)^n \operatorname{erfc} \frac{(2n+1)d+x}{2\sqrt{Dt}} \right\} \quad [5]$$

The total amount of water diffused into glass,  $Q$  is

$$Q = \int_0^d C(x) dx = C_0 \sqrt{Dt} \left\{ \sum_{n=0}^{\infty} (-1)^n \operatorname{ierfc} \frac{nd}{\sqrt{Dt}} - \sum_{n=0}^{\infty} (-1)^n \operatorname{ierfc} \frac{(n+1)d}{\sqrt{Dt}} \right\} \quad [6]$$

where

$$\operatorname{ierfc}(x) = \int_x^{\infty} \operatorname{erfc}(\xi) d\xi \quad [7]$$

The values of  $Q/C_0d$  calculated by digital electronic computer are shown as a solid curve in Fig. 4.  $Q/C_0d$  should be proportional to  $d^{-1} \ln(I_0/I)$  minus its initial value in the experiment. The diffusion coefficient of water is estimated, comparing  $Q/C_0d$  with the experimental values of Fig. 2, 4, and 11, as shown in Table I, where calculations of the diffusion coefficient were carried out at  $10^2$ ,  $10^3$ , and  $10^4$  min for results shown in Fig. 2 and 11, and at  $10^{10}$ ,  $10^{11}$ , and  $10^{12}$  min/cm<sup>2</sup> for results shown in Fig. 4. From this table, it is seen that the diffusion coefficient decreases with time for as-deposited and heat-treated samples, it decreases with the initial  $\text{B}_2\text{O}_3$  content in glass for as-deposited samples and with temperature of heat-treatment. The dependence of the diffusion coefficient on time, obtained above, may be explained in terms of the decrease of the internal area for adsorption. The dependence of diffusion coefficient on  $\text{B}_2\text{O}_3$  content in glass is consistent with the fact that the pore size decreases with  $\text{B}_2\text{O}_3$  content. The dependence on heat-treatment temperature corresponds with the decrease of pore size and density.

### Conclusions

The process of water adsorption in CVD glass is limited by the diffusion of water in glass. The diffusion coefficient of water in glass at room temperature is estimated to be on the order of  $10^{-15}$ – $10^{-14}$   $\text{cm}^2/\text{sec}$  for as-deposited glasses. From the changes in the amount of adsorbed water with time, it is suggested that the adsorption sites decrease with time for as-de-

Table I. Dependences of diffusion coefficient of water in glass on boron content and heat-treatment

	Diffusion coefficient ( $\text{cm}^2/\text{sec}$ )		
	Time (min)		
	$10^2$	$10^3$	$10^4$
As-deposited samples			
$\text{B}_2\text{O}_3$ content (m/o)			
0	$2.5 \times 10^{-14*}$	$2.5 \times 10^{-14**}$	$9.5 \times 10^{-14***}$
8.7	$3.3 \times 10^{-14*}$	$1.9 \times 10^{-14**}$	$1.0 \times 10^{-14***}$
17.5	—	$3.8 \times 10^{-15}$	$3.5 \times 10^{-15}$
19.5	—	$2.5 \times 10^{-15}$	$2.3 \times 10^{-15}$
26.5	—	$2.7 \times 10^{-15}$	$2.3 \times 10^{-15}$
Heat-treated samples of nondoped oxide†			
Temperature of treatment (°C)			
439	$9.5 \times 10^{-14}$	$6.7 \times 10^{-14}$	$7.7 \times 10^{-15}$
562	$3.7 \times 10^{-14}$	$2.5 \times 10^{-14}$	$1.2 \times 10^{-14}$
679	—	—	$7.8 \times 10^{-15}$
Heat-treated samples of boron-doped oxide (8.7 m/o $\text{B}_2\text{O}_3$ )†			
Temperature of treatment (°C)			
439	$8.3 \times 10^{-15}$	$8.0 \times 10^{-15}$	$6.7 \times 10^{-15}$
562	$5.0 \times 10^{-15}$	$3.3 \times 10^{-15}$	$3.8 \times 10^{-15}$
679	—	$2.0 \times 10^{-15}$	$1.4 \times 10^{-15}$
792, 1054	—	$5.5 \times 10^{-15}$	$1.2 \times 10^{-16}$

\* Calculated at  $10^{10}$  min/cm<sup>2</sup> in Fig. 4.

\*\* Calculated at  $10^{11}$  min/cm<sup>2</sup> in Fig. 4.

\*\*\* Calculated at  $10^{12}$  min/cm<sup>2</sup> in Fig. 4.

† Samples were heat-treated for 10 min at each temperature.

posited glasses, and it is probable that dangling bonds in glass, which are available for water adsorption, decrease with time. The adsorption sites for nondoped oxide decrease with the temperature and time of heat-treatment. On the other hand, the adsorption sites for boron-doped decrease by heat-treatment temporarily, but the new adsorption sites are made by exposure in air after heat-treatment.

#### Acknowledgments

The authors gratefully acknowledge discussions with Dr. M. Yoshida and Mr. H. Nakamura on diffusion and adsorption. The authors are also deeply indebted to Mr. T. Asaoka for his considerable assistance with the computations. Comments on electron microscope photographs by Dr. K. Ono and Mr. S. Hirota were extremely helpful.

Manuscript submitted June 4, 1973; revised manuscript received Nov. 16, 1973.

Any discussion of this paper will appear in a Discussion Section to be published in the December 1974 JOURNAL. All discussions for the December 1974 Discussion Section should be submitted by Aug. 1, 1974.

#### REFERENCES

1. R. O. Lussow, *This Journal*, **115**, 660 (1968).
2. A. A. Bergh, *ibid.*, **112**, 457 (1965).
3. S. R. Hofstein, *IEEE Trans. Electron. Devices*, **ED-13**, 749 (1967).
4. J. L. Parsons and M. E. Milberg, *J. Am. Ceram. Soc.*, **43**, 326 (1960).
5. V. R. Bückner and J. Fernandez, *Glastech. Ber.*, **39**, 283 (1966).
6. G. J. Young, *J. Colloid Sci.*, **13**, 67 (1958).
7. W. A. Pliskin, *This Solid Films*, **2**, 1 (1968).
8. W. A. Taft, *This Journal*, **118**, 1985 (1971).
9. D. M. Brown and P. R. Kennicott, *ibid.*, **118**, 293 (1971).
10. D. E. Bethell and N. Sheppard, *Trans. Faraday Soc.*, **51**, 9 (1955).
11. J. Crank, "The Mathematics of Diffusion," Oxford Univ. Press, London (1956).

## Deformation Occurring during the Deposition of Polycrystalline-Silicon Films

T. I. Kamins

Research and Development Laboratory, Fairchild Camera and Instrument Corporation, Palo Alto, California 94304

#### ABSTRACT

The deformation sometimes observed during the deposition of thick polycrystalline-silicon films for dielectrically isolated integrated circuits has been investigated. The degradation of films deposited by the decomposition of dichlorosilane, silane, or silicon tetrachloride in a hydrogen carrier gas has been observed to occur during the deposition rather than during the cooling cycle and to be more severe at lower deposition temperatures. This degradation has been related to the inclusion of trace quantities of gaseous contaminants, especially oxygen, in the structure of the film. The elimination of these contaminants from the deposition chamber allows the reproducible fabrication of high quality films.

Most techniques for fabricating dielectrically isolated, silicon integrated circuits involve the deposition of a thick layer of polycrystalline silicon, which serves as the mechanical support of the structure (1). This layer is generally deposited by chemical vapor deposition (1) although rapid vacuum evaporation has also been used (2). Severe wafer deformation, which may preclude further processing, sometimes occurs during the polycrystalline-silicon deposition. This degradation has been briefly investigated during a study of thin, single-crystal, silicon films which are defined by an electrochemical etching process (3) and supported by thick layers of polycrystalline silicon (4). This paper reports the results of the investigation and shows that the deformation is related to the inclusion of gaseous contaminants, especially oxygen, in the film structure. The marked change in grain structure seen in degraded films is also described.

#### Experimental Method and Observations

The polycrystalline-silicon films were deposited in a standard, horizontal, rf-heated epitaxial reactor using a hydrogen carrier gas. The deposition temperature was generally 1100°C (corrected temperature), and the final film thickness was about 250  $\mu\text{m}$ . While most of the films used in this study were deposited from dichlorosilane, silane and silicon tetrachloride have also

been employed with similar results. In most cases the films were deposited directly onto oxidized, 2 in. diameter, silicon wafers.

Visual observation during the deposition cycle showed that the deformation occurred during the deposition, while the entire system was at constant temperature, and not during the cooling cycle. The degradation cannot, therefore, be attributed to differences in the thermal coefficients of expansion between the various materials in the structure but must rather be related to stresses built into the growing layer of polycrystalline silicon. In addition, since the incidence of degradation was sporadic, it cannot be caused by an intrinsic property of the materials system under investigation.

Several observations indicated that the presence of gaseous contaminant atoms in the reactor gas stream during the deposition was of prime importance in causing degradation. For example, severe degradation was encountered when a cylinder of silane containing gaseous impurity atoms was used to deposit polycrystalline-silicon films. Severe degradation has also been observed when small quantities of air were able to enter the reaction chamber through a poorly seated end plate. Furthermore, small amounts of deformation were usually reduced by eliminating any small leaks in the reactor. Therefore, we may conclude that gaseous contaminants, including some constituent of air, lead to the degradation.

Key words: dichlorosilane, chemical vapor deposition, oxygen contamination, neutron activation analysis.

Further observation indicates that the structure of the polycrystalline silicon is especially sensitive to the presence of gaseous contaminant atoms. Even when slight deformation was observed during the deposition of thick, polycrystalline-silicon layers, high quality epitaxial films could subsequently be grown in the same reactor. When severe deformation was observed during the deposition of thick polycrystalline layers, the sense of warping was opposite for simultaneously deposited epitaxial layers. The polycrystalline films were concave upward while the epitaxial layers were convex upward, and the deformation of the epitaxial layers was less severe.

Controlled experiments indicated that the degradation is not related to the type of wafer used. No difference in the severity of degradation was seen with heavily arsenic-doped wafers with either high or low dislocation density or with lightly boron-doped wafers. Thick polycrystalline-silicon films nucleated on thin layers of low-temperature, silane polycrystalline silicon deposited directly on single-crystal silicon also showed similar amounts of deformation, indicating that the degradation is not related to the presence of the silicon dioxide layer.

The effect of temperature is significant, however. Appreciably less degradation was seen at higher deposition temperatures when the same magnitude of contamination was present. This increase in film quality with increasing deposition temperature has been seen in different reactors and with silane and silicon tetrachloride as well as with dichlorosilane.

In order to determine the constituent of air which could cause the degradation, experiments were con-

ducted in which controlled amounts of either nitrogen or oxygen were added to the hydrogen/dichlorosilane gas stream during the deposition of 250  $\mu\text{m}$  thick, polycrystalline-silicon films at 1100°C (corrected temperature) and a rate of 4  $\mu\text{m}/\text{min}$ . The addition of about 30 ppm of nitrogen did not induce any degradation, while the addition of about 20 and 44 ppm of oxygen caused moderate and severe degradation, respectively.

Photomicrographs of a high quality polycrystalline film together with photomicrographs of the moderately and severely degraded films are shown in Fig. 1-3. These photomicrographs illustrate the structure close to the outer edge of the 2 in. diameter wafer (a) and  $\frac{1}{8}$  in. from the outer edge (b). The high quality film is also shown  $\frac{1}{4}$  in. from the outer edge (c) and near the center of the wafer (d). The location of the wafer on the susceptor was the same in each case. The control sample (Fig. 1) has a large-grained structure near the center of the wafer with a gradual decrease in grain size toward the edge. This decrease probably results from the outer edge of the wafer's being cooler than the center since the wafer sits on a raised pedestal. The moderately degraded wafer (Fig. 2) shows the same large-grained structure as the control sample near the center of the wafer with a decrease in grain size toward the edge. Immediately adjacent to the edge, however, a markedly different structure is seen [Fig. 2(a)]. As the wafer deformed during the deposition, the edges lifted from the susceptor and became cooler. Therefore, the different structure may be related to a markedly lower temperature near the edges of the wafer as well as to the greater oxygen inclusion in the lower temperature portions of the wafer.

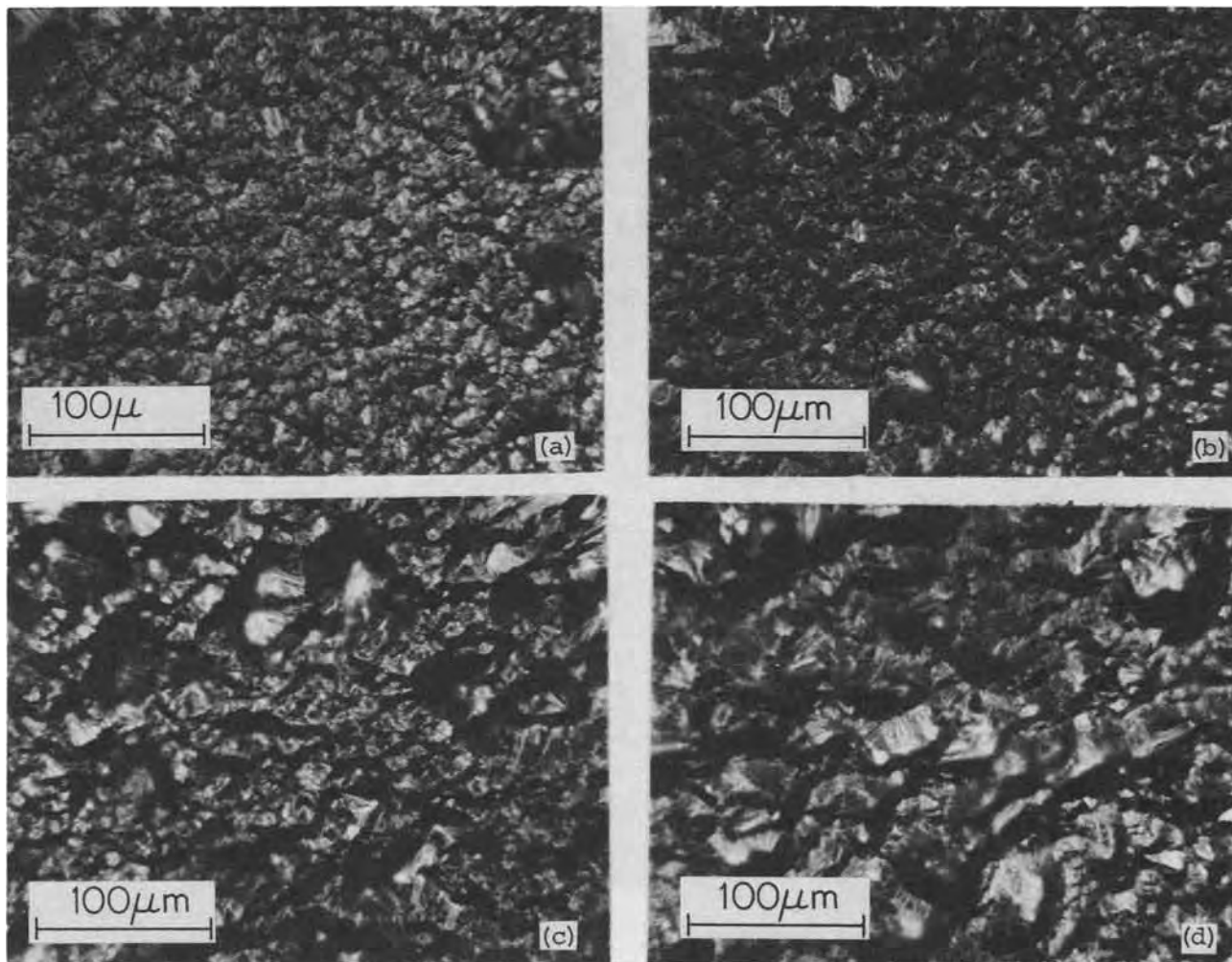


Fig. 1. Photomicrographs of high quality polycrystalline-silicon film with no oxygen added during deposition. (a) Near edge; (b)  $\frac{1}{8}$  in. from edge; (c)  $\frac{1}{4}$  in. from edge; (d) near center of wafer.



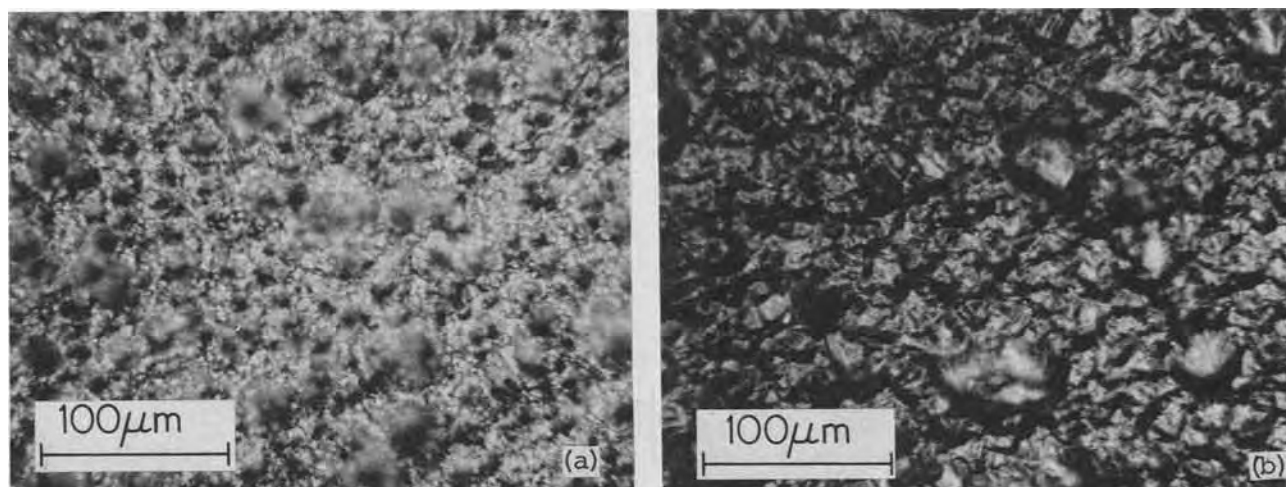


Fig. 2. Photomicrographs of moderately degraded polycrystalline-silicon film deposited with  $[O_2]/[H_2] = 20$  ppm. (a) Near edge; (b)  $\frac{1}{8}$  in. from edge.

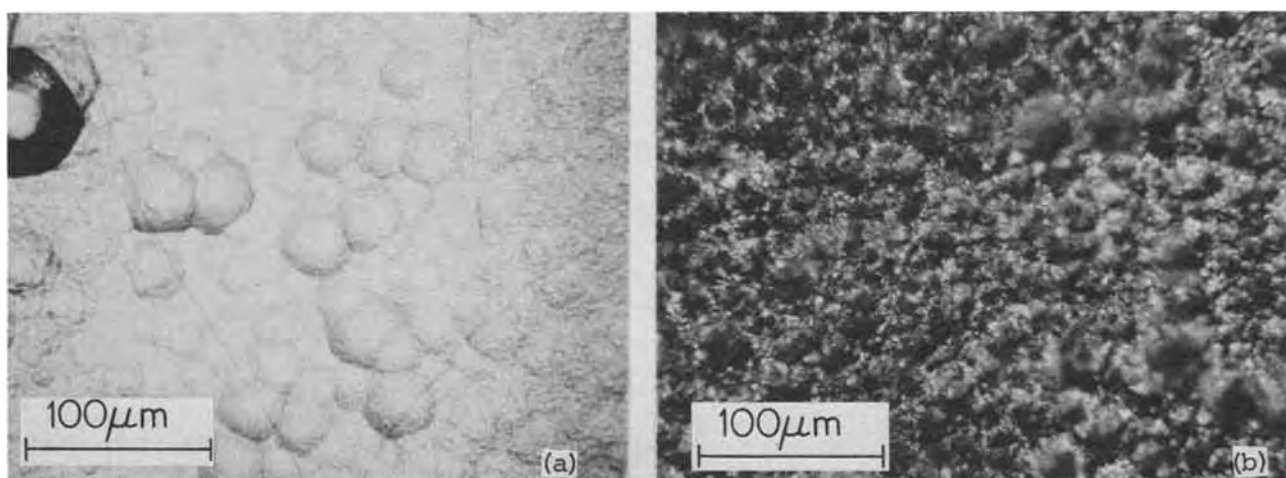


Fig. 3. Photomicrographs of severely degraded polycrystalline-silicon film deposited with  $[O_2]/[H_2] = 44$  ppm. (a) Near edge; (b)  $\frac{1}{8}$  in. from edge.

The severely degraded wafer (Fig. 3) again shows the same large-grained structure near the center, but the grain size diminishes more rapidly toward the edge of the wafer. [Compare position (b) of the severely degraded wafer with position (a) of the moderately degraded wafer.] Near the edge of the wafer, the structure appears to change completely. The faceted structure disappears and is replaced by a moundlike structure. Cracks are also seen in the silicon, probably indicating the inclusion of appreciable quantities of oxygen into the structure. The film is also much thinner near the edge than at the center because of the lower temperature near the edge during much of the deposition.

In order to determine if oxygen was actually included into the degraded polycrystalline-silicon films, wafers from the depositions shown in Fig. 1-3 were subjected to neutron activation analysis.<sup>1</sup> A total sample mass of approximately 3g was available for each analysis. The average oxygen concentrations indicated were approximately 370 ppm in the severely degraded sample (Fig. 3), 140 ppm in the moderately degraded sample (Fig. 2), and less in the control sample (Fig. 1), clearly showing that oxygen was incorporated into the structure of the degraded polycrystalline-silicon films during the deposition.

Although the oxygen concentration in the films increased monotonically with increasing oxygen addition

to the reactor gas stream, the increase did not appear to be linear. The amount of degradation did not appear to be a linear function of the oxygen flow either, indicating that the degradation process accelerated once it started. Once the edges of the wafer started lifting from the susceptor and cooling, increasing quantities of oxygen were probably included into these areas of the film. On the other hand, the oxygen concentration indicated by the neutron activation analysis was an average over the entire sample.

A further series of depositions was performed in order to determine the relative importance of the deposition rate and the oxygen-to-silicon ratio in the deposition chamber. The conditions and results of these depositions are summarized in Table I. Some films were deposited at the normal rate of  $4 \mu\text{m}/\text{min}$  (depositions 26 and 27) while others were deposited at half this rate (depositions 29, 30, and 31). A control deposition at each rate produced films of good quality (deposi-

Table I. Deposition conditions and results

Deposition No.	Deposition rate ( $\mu\text{m}/\text{min}$ )	$[O_2]/[H_2]$ (ppm)	$[O_2]$		Degradation
			$[H_2] \times \text{Dep. rate}$ ( $10^{-6} \text{ min}/\mu\text{m}$ )		
26	4.0	0.0	0.0		None
27	4.0	18.3	4.6		<No. 29
29	2.0	18.3	9.2		Severe
30	2.0	9.6	4.8		<No. 27
31	2.0	0.0	0.0		None

<sup>1</sup> Analysis performed by Gulf Radiation Technology, San Diego, California 92100.

tions 26 and 31). The same oxygen flow was used for depositions at the two rates (depositions 27 and 29) so that the oxygen-to-silicon ratio was doubled for the lower deposition rate (deposition 29). Markedly less degradation was observed for the higher deposition rate (deposition 27), indicating that the oxygen-to-silicon ratio is more significant than is the oxygen partial pressure in the deposition chamber. The oxygen flow was halved in an additional deposition at the lower rate (deposition 30) so that a comparison of different deposition rates could be made for a similar oxygen-to-silicon ratio (depositions 27 and 30). Noticeably less degradation was observed in the film deposited at the lower rate (deposition 30), indicating the importance of the deposition rate, as well as the oxygen-to-silicon ratio, in determining the film quality.

Large quantities of nitrogen have also been found to induce severe degradation. Colored regions, probably indicating the presence of silicon nitride, as well as cracking of the wafers, were seen. Since moderate quantities of nitrogen do not induce marked degradation, and since both oxygen and nitrogen (as the principal constituents of air) will probably be present at the same time, oxygen is felt to be the contaminant of greater concern.

### Discussion

In the previous section we have shown that the stress in the deposited films is related to the amount of gaseous contamination present in the system, the deposition temperature, and the deposition rate, that the stress is tensile rather than compressive, and that oxygen can be included into the growing film.

The origin of the stress may probably best be understood on the basis of the model proposed by Klokholm and Berry for the case of polycrystalline metal films (5). They argue that the tensile stress results from the internal rearrangement of deposited atoms beneath the growing surface of the film. The deposited material may be considered initially to have a disordered structure and a density less than that of the crystalline material. Consequently, any annealing which produces a more nearly perfect crystalline arrangement results in a tendency for the deposited layer to contract.

The necessity for internal rearrangement in the present case is probably related to the ease of surface diffusion of the depositing silicon atoms and the disorder present in the surface layer when it becomes buried by subsequently arriving atoms. If the surface atoms can reach low energy positions before they are buried, little internal rearrangement will be necessary, and little stress will be developed. However, a small quantity of adsorbed impurity atoms, such as oxygen, may severely impede surface diffusion of the deposited silicon atoms. The silicon atoms must then continue to rearrange after they have been covered by subsequently arriving atoms, resulting in the incorporation of a highly stressed layer in the depositing film.

At a given temperature and a given ratio of oxygen-to-silicon atoms arriving at the surface, the surface atoms will have a longer time to rearrange at lower deposition rates. Consequently, less internal rearrangement will be necessary, and less deformation will develop, as observed. However, more severe degradation was seen when the deposition rate was halved and the oxygen-to-silicon ratio was doubled, indicating that the number of adsorbed contaminant atoms is more significant than is the deposition rate.

As the temperature increases, several effects will occur. Surface diffusion will increase since it is a ther-

mally activated process. The number of adsorbed oxygen atoms will decrease since they can re-evaporate more easily, either as oxygen or as SiO. Therefore, surface diffusion can proceed more easily and less stress will develop. On the other hand, the yield strength of the substrate will probably decrease as the temperature increases. This decrease must be less rapid than the decrease in the bending force since less deformation is observed at higher deposition temperatures.

At a first glance, the detrimental effect of only a few parts per million (about  $10^{-3}$  Torr) of oxygen in the reaction chamber may seem unlikely. However, Adamsky (6) and Khan (7) have found that the presence of even  $10^{-8}$  Torr of oxygen may severely affect the deposition of germanium films; so the influence of several orders of magnitude greater concentrations of oxygen in the present case is not unlikely.

Murbach and Wilman (8) have investigated the effect of oxygen on the stress in evaporated aluminum films and have found large stresses resulting from the formation of oxides at the grain boundaries. These stresses were compressive, however, unlike those in the present case, indicating that the presence of silicon oxide at the grain boundaries of the polycrystalline-silicon films is not dominant.

The less severe deformation in the simultaneously deposited epitaxial films indicates that the atoms can reach low energy positions in these films more easily since less surface diffusion is necessary. Then the major factor influencing the deformation is the inclusion of oxygen into the films. This can cause compressive stress and curvature in the opposite sense from that in the polycrystalline-silicon films.

### Summary

The degradation sometimes observed during the deposition of thick polycrystalline-silicon films for dielectrically isolated integrated circuits has been related to the inclusion of trace quantities of oxygen into the structure of the films. The elimination of this contaminant from the deposition chamber allows the reproducible fabrication of high quality films.

### Acknowledgments

This research was supported by the Advanced Research Projects Agency under Contract DAHC 15-72-C-0171.

The author would like to thank L. Field and S. Sekigahama for assistance with the experimental investigation.

Manuscript submitted June 6, 1973; revised manuscript received Dec. 10, 1973.

Any discussion of this paper will appear in a Discussion Section to be published in the December 1974 JOURNAL. All discussions for the December 1974 Discussion section should be submitted by Aug. 1, 1974.

### REFERENCES

1. U. S. Davidsohn, *Proc. IEEE*, **57**, 1532 (1969).
2. J. J. A. Ploos van Amstel, *Philips Tech. Rev.*, **28**, 57 (1967).
3. H. J. A. van Dijk and J. de Jonge, *This Journal*, **117**, 553 (1970).
4. T. I. Kamins, *Proc. IEEE (Letters)*, **60**, 915 (1972).
5. E. Klokholm and B. S. Berry, *This Journal*, **115**, 823 (1968).
6. R. F. Adamsky, *J. Appl. Phys.*, **40**, 4301 (1969).
7. I. H. Khan, *ibid.*, **44**, 14 (1973).
8. H. P. Murbach and H. Wilman, *Proc. Phys. Soc. (London)*, **B66**, 905 (1953).



# Vacuum Deposited Silicon Devices on Fused Silica Substrates

Charles Feldman and Richard Plachy

*Applied Physics Laboratory, The Johns Hopkins University, Silver Spring, Maryland 20910*

## ABSTRACT

A technique is described for fabricating diodes and MOS devices from vacuum deposited polycrystalline silicon films on insulating substrates. Extremely pure vacuum deposited amorphous silicon films on fused silica substrates were converted into the crystalline phase during device processing. The samples could be converted either during gaseous diffusion of boron or phosphorus at 850°-950°C to form n- or p-type layers or during the initial oxidation step at 1000°C in the device definition stage. Film purity was checked by sputter-ion source mass spectrometry. Gaseous diffusion and oxide masking procedures were similar to those used in silicon integrated circuit technology. The quality of the initial resulting planar devices indicates that the process has the potential for producing a variety of silicon devices.

A goal for many years in the field of microelectronics has been the achievement of active devices from vacuum deposited films on amorphous insulating substrates (1). All of the currently successful thin film devices, in contrast, are formed epitaxially onto single-crystal substrates (2, 3). Thin film majority carrier field-effect transistors were produced some time ago from vacuum deposited germanium (4), tellurium (5), and various chalcogenides (6, 7) onto glassy substrates. These devices, however, lacked the stability and versatility to compete with silicon devices and integrated circuits. Field effect devices have recently been fabricated with some success from polycrystalline silicon deposited by thermal decomposition of silane onto oxidized single-crystal silicon substrates (8). The amorphous oxide layers on these substrates are similar in some respects to the fused silica substrates used here.

It was believed that both the polycrystalline structure and the impurities in vacuum deposited semiconducting films prevented their use in practical devices. The formation of controlled n-type and p-type material in the films was considered extremely difficult. Vacuum deposited germanium and silicon are amorphous when condensed on ambient temperature or unheated substrates. Crystalline films must be formed by deposition onto hot substrates or by heating to a "crystallization temperature" after deposition. The crystalline films were, however, always p-type. There is controversy over whether intrinsic surface states and defects or impurities kept the film p-type (9, 10). There is a strong possibility that silicon films vacuum heated using Pyrex bell jars are p-type due to the presence of boron (11). It has been shown that impurities in germanium (and presumably also silicon) films could be reduced, however, if proper purification techniques in the vacuum were employed (12).

Most of the problems in producing pure films lay in the difficulty of determining the impurities present. The thickness of the samples and small amount of total material made analysis practically impossible. Recently a sputter-ion source mass spectrometry study of amorphous and crystallized silicon films was carried out in this laboratory (13). It was found that with proper precautions pure amorphous films could be produced in the vacuum and that if these films were heated in a pure inert atmosphere, they could be crystallized without the further introduction of impurities.

In this paper, the conversion of these pure amorphous films to n-type and p-type crystalline films is described. It was found possible to process the amorphous films directly into crystalline devices using standard silicon integrated circuit techniques, and details of this work are presented. It is believed that this

study represents the first time that vacuum deposited polycrystalline silicon films on insulating substrates have been successfully processed into practical devices.

## Preparation of Amorphous Silicon Films

The samples were deposited by electron beam heating of silicon contained in a well-cooled stainless steel crucible with a molybdenum liner onto fused silica substrates held at temperatures from 300° to 500°C. The initial pressure was approximately  $5 \times 10^{-9}$  Torr, and the pressure during deposition was approximately  $5 \times 10^{-6}$  Torr. This pressure rise appears to be largely due to CO<sub>2</sub> from the silicon melt. Details of the deposition technique and the sputter-ion source mass spectrometer study were given in a previous report (13). The impurities present in the amorphous films 82B and 97A used here are approximately those listed in the previous report as 82C, Table II, and 93C, Table III, respectively. The substrates were high purity semiconductor grade fused silica which were polished by the manufacturer.<sup>1</sup> They were cleaned ultrasonically in detergent and deionized-filtered 18 megohm-cm water.

## Conversion to n- and p-Type Polycrystalline Films

The amorphous layers were converted to the crystalline phase and their electrical properties studied in order to assay the qualities of the layers for device application. The transition from amorphous to crystalline silicon films is a function of both time and temperature (14). During the conversion the short-range order of the amorphous phase with a coordination number of 4 is converted into the crystalline phase having the same coordination number, but with longer range order. A separate nucleation step was not observed in the silicon films crystallized here. Figure 1 shows a plot of time to crystallize vs. 1/T. Note that the extrapolated portion of the curve gives a crystallization time of 3 sec at 850°C. Times and temperatures considerably greater than necessary for crystallization were employed in the device processing described here and considerable grain growth probably took place. The grain size in devices processed according to the steps listed in the next section was estimated by microscopic examination and found to be between 0.5 and 1 $\mu$  in diameter.

In order to produce n- or p-type samples, the amorphous films were crystallized directly in a diffusion furnace where either phosphorus or boron dopants could be introduced into the film at the same time. Standard diffusion techniques using diborane and phosphene gases were employed. Both n- and p-type layers with smooth, uncrazed surfaces and with controllable resistivity were achieved. Because of the

Key words: silicon films, thin film devices, thin film device processing, thin film p-n junctions, thin film transistors.

<sup>1</sup> U.S. Fused Quartz Company, Fairfield, New Jersey.

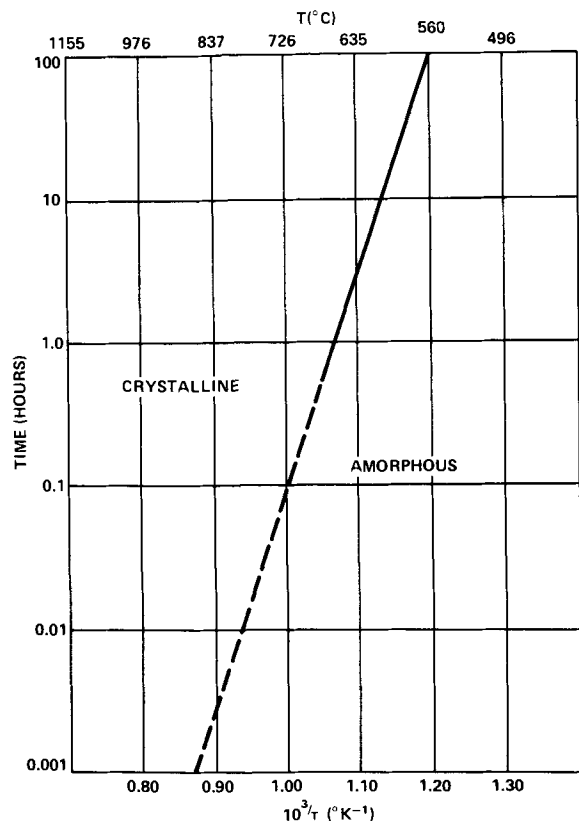


Fig. 1. Crystallization time vs. temperature in silicon films

thickness and polycrystalline structure of the films, diffusions were carried out at 850°–950°C instead of the 1000°–1200°C usually used in crystalline material. The sheet resistances resulting from doped and undoped crystallizations are given in Table I.

Conductivity type was checked with a thermoelectric probe and in every case there was agreement with the expected dopant type. In a typical doping experiment (sample 73B), phosphorus diffusion for 13 min at 950°C produced a surface layer having a sheet resistance of 450 ohms/□, while the undoped film, fired at the same temperature, had a sheet resistance of  $2.6 \times 10^{10}$  ohms/□. Note that the undoped crystallized sample (Si 73C-2) exhibited a higher sheet resistance than the companion unheated amorphous sample (Si 73C-1). Some of this resistance may be due to grain boundaries. In films less pure, however, crystallized samples have a lower resistivity than their corresponding amorphous phase.

In another set of controlled diffusions (sample 82B), a crystal wafer of opposite conductivity to the dopant was placed alongside the thin films in the diffusion furnace. The phosphorus-doped film and the wafer showed approximately the same sheet resistance. The boron-doped film, however, exhibited a sheet resist-

Table I. Diffusions in thin silicon films

Sample	Thickness, Å	Dopant type	Temperature (°C)	Time (min)	Sheet resistance ohm/□
Si 73B	4400	n(phosphorus)	950	13	$4.5 \times 10^2$
Si 73A-1	4400	n(phosphorus)	850	8	$2.3 \times 10^5$
Si 73A-2	4400	p(boron)	850	8	$1.6 \times 10^5$
Si 73C-1	4400	Untreated (amorphous)	—	—	$4.5 \times 10^9$
Si 73C-2	4400	Argon	950	13	$2.6 \times 10^{10}$
Si 82B	4270	n(phosphorus)	850	8	$1.4 \times 10^3$
p Wafer	—	n(phosphorus)	850	8	$1.5 \times 10^3$
Si 82B	4270	p(boron)	850	8	$2.8 \times 10^4$
n Wafer	—	p(boron)	850	8	$2.3 \times 10^3$
Si 97A	7000	p(boron)	850	13	$6.0 \times 10^{3*}$
Si 97A	7000	n(phosphorus)	850	15	$2.4 \times 10^{3*}$
Si 97A	7000	Undoped	—	—	$1.4 \times 10^{7*}$

\* After complete device processing.

ance an order of magnitude higher than the corresponding wafer. The reason for this discrepancy is not clear. A quantitative comparison of film and wafer resistance is, of course, fraught with difficulties. A preliminary correlation of diffusion constants in the films was not possible because the diffusion times were of the same order of magnitude as the time to come to temperature equilibrium in the furnace. Note that the last three items listed in Table I concerning sample Si 97A were measurements made from the test pattern (Fig. 2) after the complete device processing which is described in the next section.

### Device Formation

The amorphous films were processed into active test devices using techniques similar to those employed in standard silicon wafer processing for monolithic integrated circuits (15). The initial steps in the processing consisted of oxidation in dry oxygen for several hours. During this step, the film was converted to its crystalline state, thus the conversion was completed before diffusion began. This is a slight variation in procedure over the samples described in the previous section which were converted during diffusion. Diborane and phosphene were used as gaseous diffusion sources. The films were subjected to the following steps: (i) oxidation at 1000°C in dry O<sub>2</sub> for 3 hr; (ii) photolithography; (iii) p-diffusion at 850°C for 13 min (deposition); (iv) p-diffusion at 1000°C in O<sub>2</sub> for 2 hr and argon anneal 20 hr at 1000°C; (v) photolithography; (vi) n-diffusion at 850°C for 15 min (deposition); (vii) n-diffusion, 1000°C in O<sub>2</sub> for 1 hr (drive-in); (viii) aluminum deposition; (ix) photolithography; (x) sintering at 450°C.

As in the simple doping experiments, the times and temperatures were less than those usually used since higher diffusion coefficients were expected for the films (16). The oxidation steps were designed to result in less than the normal oxide thickness so that the silicon films would not be consumed in the formation of the various required oxide layers. The films were annealed in argon during the lightly doped p-type drive-in diffusion (step iv). The processing sequence for active devices was intended to result in a lightly doped p-diffusion in order to obtain both a high breakdown voltage on the diodes and a substrate region for n-channel enhancement mode MOSFET's. A thin high concentration n-type region was used in order to simplify the processing yet have nonrectifying contacts with the aluminum metallization. The shallow depth was intended to be utilized when this diffusion was used for the gate of the junction field effect devices in the test array.

### Device Characteristics

Three successful device runs using a special mask set were made following the techniques described above. A photomicrograph of a test pattern with the devices indicated by letters is shown in Fig. 2. The test mask included: junction FET's (A), n-channel enhancement mode MOSFET's (B), two types of p-channel depletion mode MOSFET's (C), four-point probe test devices for each diffusion and the substrate (D), two large diodes (E), and two types of Hall mobility test structures (F). With the exception of the junction FET's, all devices operated to some extent. The n-channel enhancement mode MOSFET's and p-n double diffused diode exhibited characteristics useful for normal circuit operation. Typical electrical test data taken from the diodes and n-channel MOSFET's and small Hall configuration are compared with estimated equivalent bulk data in Table II. The "bulk" data from the devices are considered typical of those devices fabricated in the same laboratory starting with single-crystal silicon wafers. The threshold voltage range for the films was determined at drain current 1 μA and was checked by a plot of the square root of the drain

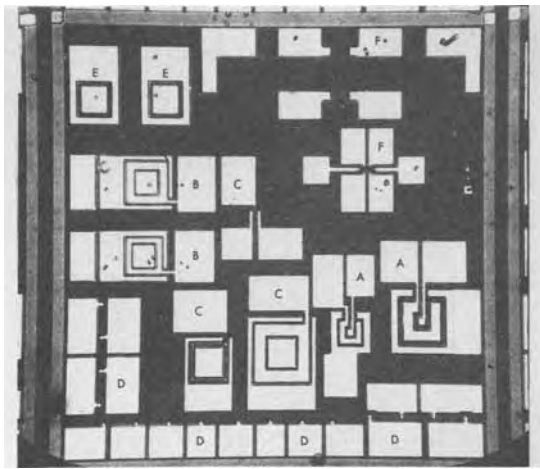


Fig. 2. Test pattern on silicon film (80x80 mil). Letters identify devices in the text.

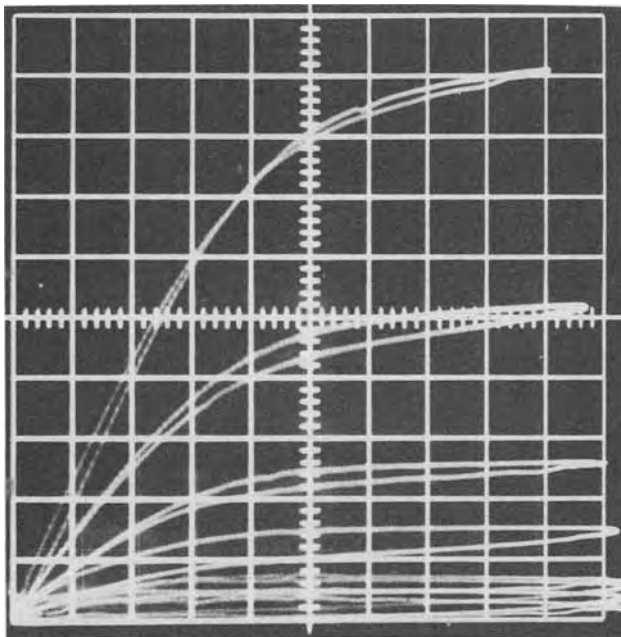


Fig. 3. n-channel MOSFET. Horizontal, 1 V/div; vertical, 1 μA/div; steps, 0.8V.

current vs. gate voltage in the manner suggested by Richman (17).

The junction FET's required a very shallow n<sup>+</sup> diffusion in order to leave a p-doped channel under the n<sup>+</sup> gate. In the runs where this device could have been fabricated, the n<sup>+</sup> diffusion was too deep.

The electrical characteristics of the n-channel MOSFET's are shown in Fig. 3, and the cross section of the device is shown in Fig. 4. The transconductance of these initial devices is lower than would be expected in single-crystal silicon. The capacitance is also low in this structure, however, and device operating speeds may be acceptable.

The p-channel depletion mode devices were a useful test vehicle. To fabricate a good p-channel deple-

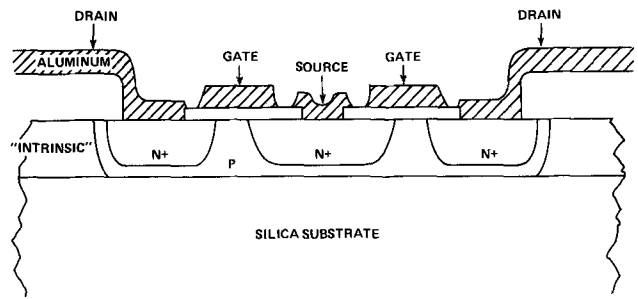


Fig. 4. Cross section of MOSFET

tion mode device, it is necessary to perform an extremely shallow and light impurity diffusion. Such a diffusion was not attempted, and these devices therefore showed the extremely low transconductance that one would expect from a thicker and more heavily doped channel region. The transconductance for these devices was approximately 0.1 μmho.

The Hall effect test structures were only used for p-diffusions. The data (Table II) indicate that the sample mobility is somewhat less than expected in bulk samples. The "bulk" Hall mobility was estimated from that expected for an equivalent thickness single-crystal semiconductor taking into account size and carrier concentration effects (18). The Hall effect device also provided data showing that the average concentration in the p-type layer was about  $5 \times 10^{17}$  carriers/cm<sup>3</sup>.

The four-point probe test devices made it possible to evaluate the effect of each diffusion into the samples. The results of these measurements on sample Si-97A are listed in Table I. Measurements of the sheet resistance coupled with measurements of film thickness yielded the average resistivity in the diffused layer. This resistivity was used to calculate the Hall mobility for the p-type layer listed in Table II.

The junction diodes appeared to be excellent and compared well with similar junctions made in single-crystal films. The forward and reverse diode characteristics are shown in Fig. 5.

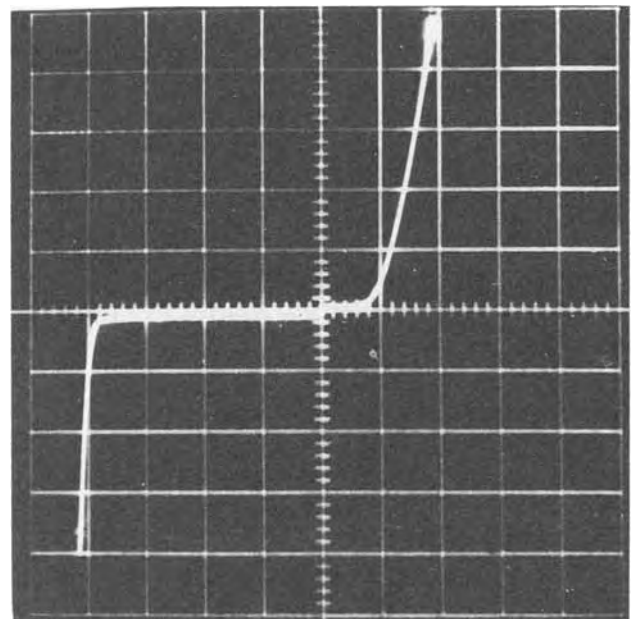


Fig. 5. p-n junction characteristics

Table II. Electrical test data

	Film	Bulk
Junction breakdown voltage	8V	8V
$g_m$ (n-channel FET)	2-25 μmhos	50-200 μmhos
Diode reverse recovery time	20-60 nsec	20-50 nsec
Threshold voltage	1-6V	0.5-1V
Gate breakdown voltage	15V	80V
(p-layer) Hall mobility	20-35 cm <sup>2</sup> /V-sec	80-90 cm <sup>2</sup> /V-sec

	Forward	Reverse
Vertical	0.05 mA/div	0.01 mA/div
Horizontal	0.5 V/div	2 V/div

### Discussion

It has been demonstrated that vacuum deposited silicon amorphous films 0.5-0.8 $\mu$  thick on fused silica substrates can be successfully converted into n- or p-type crystalline films. The amorphous layers may be directly processed by standard microelectronic techniques, and polycrystalline devices with useful characteristics fabricated. Considerable study remains to be done, however, in order to maximize device quality. It is probable that both the high purity achieved in the amorphous films and the larger grain size developed during the processing contribute to the success in forming devices.

It is interesting to compare the properties of the polycrystalline films formed here by vacuum deposition and subsequent heat-treatment with those formed by decomposition of silane onto oxidized silicon wafers by Kamins (8, 19). Kamins measured a Hall mobility in 5 $\mu$  thick p-type films with  $5 \times 10^{17}$  carriers/cm<sup>3</sup> of approximately 38 cm<sup>2</sup>/V-sec, and his data indicate a far lower mobility for films 0.5-0.7 $\mu$  thick. The films formed here with the same carrier concentration and approximately one-tenth the thickness have a mobility of 32 cm<sup>2</sup>/V-sec. Kamins observed in p-channel MOS-FET's a rather high threshold voltage which he attributed to defects and concluded that the polycrystalline films formed by him may not be generally useful. While defects and impurities generally behave differently in n-channel devices, the threshold voltages observed appear similar to those formed in crystalline devices. One may conclude that the vacuum formed layers contain fewer defects, impurities, and/or larger grains than the chemically deposited polycrystalline layers.

Since the presentation of this work, King *et al.* (20) have reported studying vacuum deposited silicon films on oxidized silicon wafers for resistor applications. They were able to dope and process their amorphous deposited layers directly into polycrystalline resistors in a process somewhat similar to that described here. The mobilities achieved, however, do not appear adequate for device formation and impurities which generally plague vacuum deposited films may be present in these films. The influence on layer properties of the oxidized silicon substrates used by King *et al.*, and Kamins, compared to the fused silica substrates used here, should be further explored. The SiO<sub>2</sub> surfaces differ in density, surface structure, and impurities, all of which affect the quality of the deposited silicon film.

### Acknowledgments

The authors greatly appreciate the aid of K. G. Hogarth in the thin film deposition and of R. N. Neuwiller

in the diffusion and photolithographic processing. The project was supported by Naval Ordnance Systems Command Contract No. N00017-72-C-4401, Task A13B.

A brief report of this work was presented at the IEEE 1973 Conference on Electron Device Techniques, New York, May 1, 1973.

Manuscript submitted June 12, 1973; revised manuscript received Nov. 20, 1973.

Any discussion of this paper will appear in a Discussion Section to be published in the December 1974 JOURNAL. All discussions for the December 1974 Discussion Section should be submitted by Aug. 1, 1974.

### REFERENCES

1. C. Feldman, *Electronics*, **37**, No. 4, 23 (1964); D. A. McLean, *Thin Solid Films*, **8**, 1 (1971).
2. J. Shewchun and F. D. King, *Solid State Electron.*, **15**, 776 (1972).
3. J. F. Allison, D. J. Dumin, F. P. Heiman, G. W. Mueller, and P. H. Robinson, *Proc. IEEE*, **57**, 1490 (1969).
4. H. L. Wilson, W. T. Layton, W. A. Gutierrez, and C. Feldman, Abstract 93, p. 104, Electrochemical Society Extended Abstracts, Pittsburgh, Pennsylvania, April 15-18, 1963.
5. P. K. Weimer, *Proc. IEEE*, **52**, 608 (1964).
6. P. K. Weimer, *ibid.*, **50**, 1462 (1962).
7. H. L. Wilson and W. A. Gutierrez, *This Journal*, **112**, 85 (1965).
8. T. I. Kamins, *Solid State Electron.*, **15**, 789 (1972).
9. R. R. Humphris and A. Catlin, *ibid.*, **8**, 957 (1965).
10. J. E. Davey, R. T. Tiernan, T. Pankey, and M. D. Montgomery, *ibid.*, **6**, 205 (1963).
11. F. G. Allen, T. M. Buck, and J. T. Law, *J. Appl. Phys.*, **31**, 979 (1960).
12. E. G. Bylander, J. R. Piedmont, L. D. Shubin, and R. C. Smith, *ibid.*, **34**, 3407 (1963).
13. C. Feldman and F. G. Satkiewicz, *This Journal*, **120**, 1111 (1973).
14. N. A. Blum and C. Feldman, *J. Non-Crystalline Solids*, **11**, 242 (1972).
15. R. M. Burger and R. P. Donovan "Fundamentals of Silicon Integrated Technology," Vol. 1, Prentice-Hall, Inc. Englewood Cliffs, N. J. (1967).
16. T. I. Kamins, J. Manoliu, and R. N. Tucker, *J. Appl. Phys.*, **43**, 83 (1972).
17. P. Richman, "Characteristics and Operation of MOS Field-Effect Devices," p. 142, McGraw-Hill Book Co., New York (1967).
18. See, for example: H. F. Wolf, "Semiconductors," p. 284, Wiley-Interscience, New York (1971).
19. T. I. Kamins, *J. Appl. Phys.*, **42**, 4357 (1971).
20. F. D. King, J. Shewchun, D. A. Thompson, H. D. Barber, and W. A. Pieczonka, *Solid State Electron.*, **16**, 701 (1973).

# Silicon Slice Analyzer Using a He-Ne Laser

H. J. Ruiz, C. S. Williams, and F. A. Padovani\*

Texas Instruments Incorporated, Dallas, Texas 75222

## ABSTRACT

Design criteria and performance characteristics are presented of an optical system capable of detecting imperfections (fractures, scratches, etc.) on the polished surfaces of semiconductor materials. This instrument is also capable of providing fast and accurate defect counting and distribution on polished, etched semiconductor surfaces. The principle involved is that of scanning a He-Ne laser beam which is focused on the surface of the slice, and analyzing the reflected and scattered light via polarizers and photomultipliers.

It would be very desirable in a production environment to have a device which could automatically analyze the surface quality of polished semiconductor surfaces. Such a device would provide a consistent and more objective scrutiny of slices than that obtained visually by an operator who has to make a value judgment on the appearance of the polished surface under strong light illumination. This device should be designed to be accurate, fast, and nondestructive, such that the tolerated surface imperfections meet today's strict requirements of polished substrates.

Minor modifications can make this device into an important tool in a research laboratory. Defects such as swirls, which exhibit a particular distribution on polished slices after preferential etching, have been shown to be correlated to impurities and/or vacancies which have been incorporated into the material during growth (1). A given distribution may be correlated to crystal-pull rate, rotation, or to the thermal profile of the crystal-puller environment. An accurate knowledge of the distribution of these defects will be extremely helpful in acquiring an understanding of the kinetics of impurity incorporation during crystal growth. This report describes below the modifications necessary for the instrument to provide accurate defect counts and their distribution over the surface of the slice. The focused spot size can be varied from about  $50\mu$  up to the beam diameter size which is 1 mm. The size of the focused spot is determined by the size of defects to be analyzed. The time required to obtain a defect count along the diameter of a 2 in. slice (see Fig. 7) is 3 min. The time required to assess surface quality on a 2 in. slice is estimated to be 10-15 sec. Here, surface quality assessment refers to the inspection of a slice for scratches, film, fractures, etc., with a predetermined amount of scattered light chosen as the criteria for accepting or rejecting a slice.

## System for Surface Quality Inspection

A schematic diagram of the system used for surface quality inspection is shown in Fig. 1. The main optical element is a bispherical condenser (BC) which is a modification of a standard optical element often used in dark field illuminators of microscopes. In the slice inspection device, the BC becomes a collector of scattered light rather than a condenser of illuminating light. The two reflecting surfaces are aluminized and protective overcoated with MgF; the two transmitting surfaces are antireflection coated. The illuminating light is incident on the slice almost normally by passing through a hole that is centered on the BC optic axis. The collecting focusing optical system comprising the BC and the positive lens was computer designed to give an on-axis image of the illuminated spot on the slice. In the configuration shown, light scattered, as from a small surface defect, into the solid angle between the cones of half angles of approximately  $32^\circ$  and  $62^\circ$  is collected by the BC and subsequently en-

ters the field stop. Specularly reflected laser light, as from a mirrorlike silicon surface, is outside the collection solid angle and, hence, will not pass through the optical system. A long wavelength pass optical filter (a Corning glass filter HR2-61) is used at the field stop. The cuton of the filter and the cutoff of the photomultiplier tube spectral response (110 or S-20) effectively form a bandpass filter centered approximately at 0.6328  $\mu$ m. Thus light passing through the field stop is restricted to only laser light scattered from the slice surface. The polished silicon slice is mounted on a spinning vacuum chuck such that the polished surface lies in the object plane of the optical system and also at the focus of the laser beam. The laser beam undergoes scattering whenever it encounters a defect on the silicon surface. The scattered light is collected by the BC, focused, and passed through a field stop, and then detected by the photomultiplier. The laser used was a Spectra Physics Model 132. Figure 2(b) is a photograph of an oscilloscope trace for signals produced by a clean, defect-free silicon slice. The slice is being rotated so that the laser beam is scanning a circle about the center of rotation. Figure 2(a) is a similar picture for a slice exhibiting film (*i.e.*, surface roughness) and a scratch. The scans for Fig. 2(a) and (b) were done at a fixed radius from the axis of spin. In another mode of scan, the He-Ne laser is translated such that the beam moves out toward the edge of the slice as it is spun, thus scanning a spiral pattern over the surface. The scanning of the light is accomplished by translating the entire optical system, *i.e.*, optics and the laser together, which is mounted in a rigid single structure. To measure the total light scattered during one spiral scan, the electronic signal of the photomultiplier was inte-

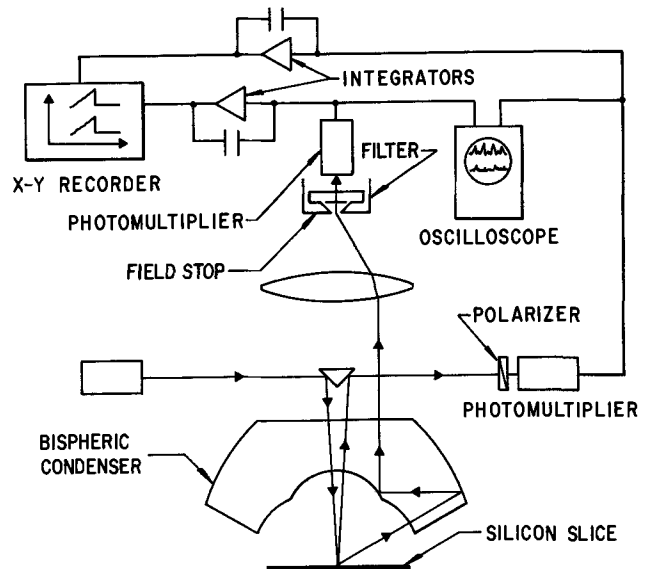


Fig. 1. Schematic diagram of slice inspector

\* Electrochemical Society Active Member.  
Key words: surface defects, defect counting, slice inspection, laser analyzer.

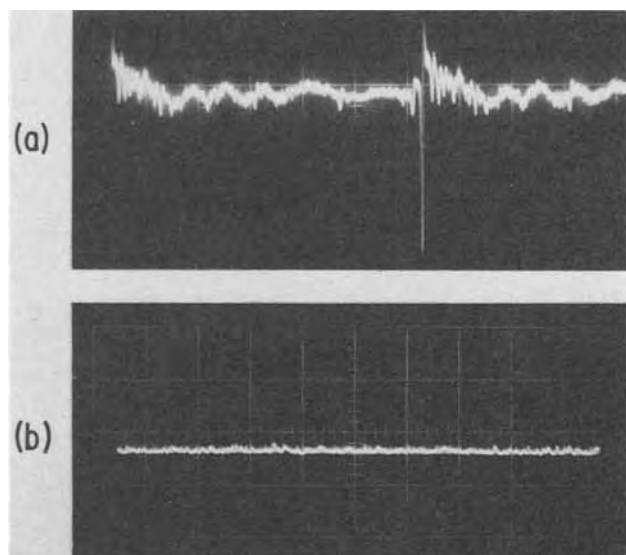


Fig. 2. Oscilloscope trace of signal obtained using (a) a slice with uniform film and a scratch, and (b) a clean defect-free slice.

grated (see Fig. 1). The output of the integrators, which is a summation of all the light scattered during a scan, provides information concerning the surface quality of the material. Figure 3 illustrates three different integrator outputs: Fig. 3(a) corresponds to a clean, defect-free slice; Fig. 3(b) corresponds to a slice with uniform film over the surface; and Fig. 3(c) corresponds to a slice exhibiting a number of defects. The shape of the electronic signal from the integrators is an indication of the surface condition, and the total integrated signal (the intensity of the electronic signal at the end of the scan) indicates the extent of surface imperfections.

By elliptically polarizing the incident beam and introducing an analyzer at the input to the photomultiplier detecting the reflected light (see Fig. 4), one is able to distinguish scratches from fractures. In the language of silicon material science, the word "fracture" refers to a special type of defect that appears too often on silicon slices. A furrow cut into a slice surface might be a scratch or a fracture, but a fracture in contrast with a scratch might be forked and the slice surface would slope gradually toward the fracture. Thus the polarization of a beam is different when reflected from the surface near a fracture whereas when re-

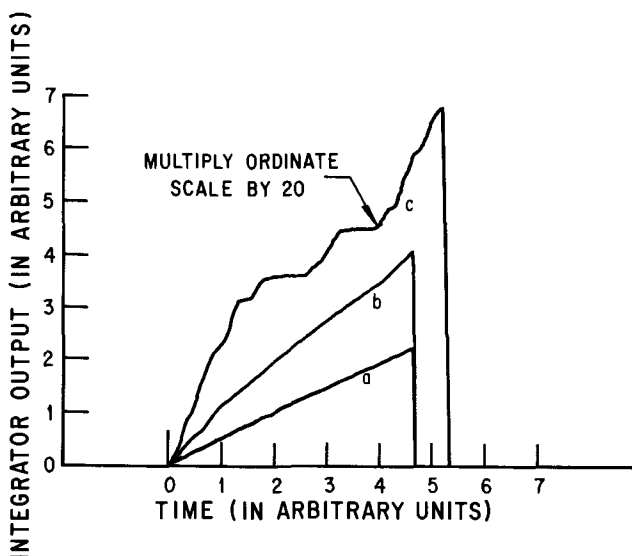


Fig. 3. Integrated scattered light from (a) a clean defect-free slice, (b) a slice with uniform film over the surface, and (c) a slice exhibiting a number of defects.

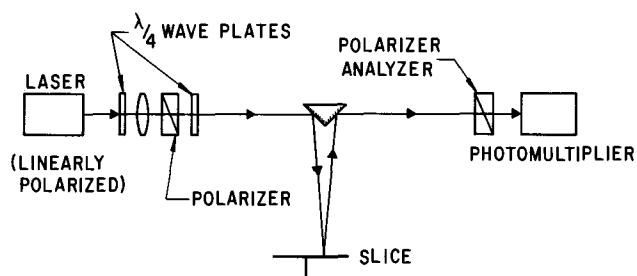


Fig. 4. Polarizing arrangement to differentiate scratches from fractures.

flected from a point near a scratch the beam is polarized just as it would be from a defect-free surface. The polarization ellipse and direction of its major axis can be adjusted by rotating the first analyzer and the quarter-wave plate. The ellipticity of the beam was chosen such that after reflection on a clean, defect-free, polished silicon slice, the beam would become linearly polarized, and thus be rejected by the linear analyzer. Because of surface slopes near fractures (see Fig. 5) these defects will cause the beam to retain some ellipticity thus allowing a second photomultiplier to detect this signal. The beam is shown in Fig. 4 to be incident at almost normal incidence; however, the polarization effects could be increased by increasing the beam angle of incidence.

#### System for Quantitative Analysis of Surface Defects

The instrument described in the previous section has been slightly modified to provide the capability for accurate defect counting and defect distribution evaluation on a silicon slice. The slice is no longer mounted on a spinner, but rather on a translational stage, and the He-Ne laser is fixed. The schematic diagram of the optics is similar to that shown in Fig. 1. The laser beam enters from the left, passes through a 30 cm focal length lens, and after being reflected off an aluminized prism it is focused on the surface of a silicon slice. If the slice is "perfectly" flat and defect-free (an ideal mirror) the laser radiation will be specularly reflected onto the other side of the prism and exit to the right out of the system. (The photomultiplier which detects reflected light is removed.) However, if the laser beam encounters imperfections on the surface of the slice, i.e., defects such as pits, dislocations, faults, etc., the radiation will then be scattered and collected by the BC. The collected scattered light is focused by a lens into a diffuser screen placed in front of the photomultiplier tube as shown in Fig. 1. The output of the photomultiplier tube is terminated by a 1 kohm resistor, and the voltage developed across this resistor is



Fig. 5. Microscopic photograph (32 $\times$ ) of a fracture illuminated by polarized light and viewed through a polarizer (analyzer).



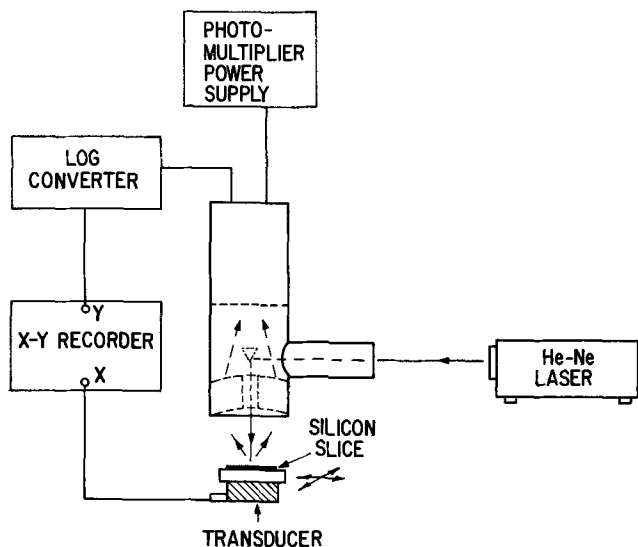


Fig. 6. System setup for defect counting and distribution evaluation.

fed into an electronic logarithmic amplifier (see Fig. 6). The output of the logarithmic converter drives the Y input to an X-Y recorder while the X input is driven by the output of a linear transducer which is coupled to a translatable stage that allows the slice to be scanned along a diameter. One thus obtains an output of linear distance (horizontal) *vs.* the logarithm of the defect density.

The performance of the instrument is based on the assumption that the defects one is trying to count scatter the light in a well-defined statistical distribution. Thus, let  $I_S$  be the average light scattered by a defect of a particular type, let  $N$  be the number of defects present in the sampled area, and  $K$  be a constant which relates the photomultiplier current  $I_{PM}$  to the amount of light received by the tube. Then

$$I_{PM} = KN I_S$$

Since  $I_S$  is constant for a given defect, and since the sampled area remains unchanged, the photomultiplier current is proportional to the defect density. Since  $I_S$

has a different value for every kind of defect, the instrument must be calibrated for each particular defect one wants to study. If the slice under inspection contains two types of defects, then one of the defects must have a uniform density across the slice such that an accurate count and distribution can be obtained on the other defect. If two defects, however, show marked variation in the distribution on a slice, then the apparatus can neither differentiate the two nor be offset so that only one defect can be studied. We have found this situation rarely present.

Some typical results obtained with this instrument are shown in Fig. 7. Upon Sirtl etching, a boron-doped silicon slice, about 15 ohm-cm, exhibited a distribution of shallow etch pits which formed a swirl pattern. The laser analyzer was used to scan the slice along a diameter, and the results are shown in Fig. 7, which illustrates the shallow etch pit density variations across the slice. A macrophotograph of the slice used is shown on the upper right-hand corner of the figure with the laser path marked.

#### Possible Extensions of the System

Coupling the system, as described here, with a cathode-ray tube display would prove very useful from the production standpoint of surface quality inspection. The spinner and/or translation position could be used to map out on the cathode-ray tube screen a picture of the slice (3). The photomultiplier output which detects the scattered light could then be used to control the intensity of the cathode-ray tube display, thus obtaining a picture of the slice with bright spots appearing at all scattering centers. The operator could then either count the bright spots (which could also be done electronically), or if all the defects are on the edge of the slice, make a judgment as to whether the slice would pass a given quality control test.

The He-Ne laser in this system could also be replaced by a combination of He-Ne and He-Cd lasers, such that the rastering beam will contain two different frequencies. Analyzers and/or filtering schemes could then be used to allow the photomultiplier to detect either wavelength separately. The relative intensity of the light scattered at the two wavelengths will provide information as to the relative size of different defects so long as the defect size is not larger than about 0.1  $\mu\text{m}$ . This arises from the fact that the intensity of Ray-

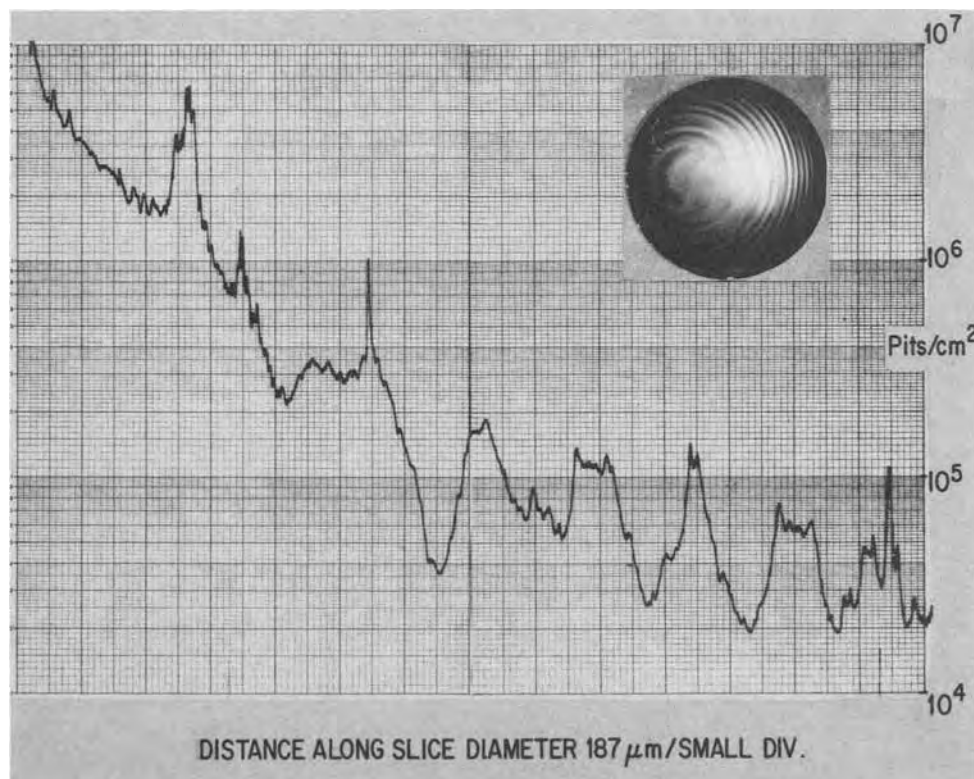


Fig. 7. Variations of shallow etch pits across a slice diameter as determined with the slice analyzer.

leigh scattering is proportional to the fourth power of the frequency of the incident radiation for scattering objects not larger than the wavelength of the incident light. The detection and differentiation of such small defects, however, might be below the range of present practical application.

### Conclusions

This instrument is capable of providing an easy, accurate, fast, and objective method for assessing surface quality on polished silicon slices in production environment. In a research laboratory, it also provides an accurate and fast method for the counting and distribution determination of defects on polished surfaces of semiconductor materials. Except for isolated cases where two different defects show markedly different distributions, one can offset and/or calibrate the instrument such that only the defects of interest are counted.

Manuscript submitted May 31, 1973; revised manuscript received Nov. 29, 1973.

Any discussion of this paper will appear in a Discussion Section to be published in the December 1974 JOURNAL. All discussions for the December 1974 Discussion Section should be submitted by Aug. 1, 1974.

### REFERENCES

1. A. J. R. de Kock, *This Journal*, **118**, 1851 (1971); *Appl. Phys. Letters*, **16**, 100 (1970).
2. F. A. Padovani and C. S. Williams, Paper M2 presented at the Topical Meeting of the Optical Society of America, Las Vegas, Nevada, January 25-26, 1971.
3. C. N. Potter and D. E. Sawyer, *Proc. 1966 Symp. on Physics of Failure in Electronics*, Vol. 5, p. 37, Air Force Cato Show Printing Co., Columbus, Ohio (1967).

## Scanning Electron Microscope Studies of Premature Breakdown Sites in GaAs IMPATT Testers

R. B. Marcus, S. E. Haszko, S. P. Murarka, and J. C. Irvin

Bell Laboratories, Murray Hill, New Jersey 07974

### ABSTRACT

Premature breakdown sites in Pt-GaAs IMPATT test diodes were examined with the scanning electron microscope operating in the electron beam induced current mode. Studies were made on mesa and planar structures, with and without air aging up to 350°C. The main conclusions of these studies are that (i) premature breakdown occurs primarily at sites of metallization defects and roughness around the periphery of the diodes; (ii) diode degradation and the lowering of the breakdown voltage following air aging is manifested at sites at the edge of the metallization; and (iii) very small sites of missing metallization ("pinholes") are sites of diode breakdown.

The reverse breakdown voltage in Schottky barrier diodes is thought to be in part limited by premature breakdown at the periphery of the metal where high field gradients are created (1). An identification of breakdown sites and a correlation of such sites with textural features of Schottky barriers has not yet been made. This paper reports on such a correlation made on Pt-GaAs IMPATT test diode structures using the scanning electron microscope (SEM) in the electron beam induced current (EBIC) mode. Experiments were made on both planar and mesa structures, some of which were aged at temperatures up to 350°C.

### Experimental

**Scanning electron microscopy.**—The SEM used for this study was a Cambridge Stereoscan S-4 equipped with specimen current amplifier capable of covering a current range of  $10^{-4}$ - $10^{-11}$ A. An EDAX x-ray detector with a Northern 707 analyzer was used for x-ray analysis of selected regions. Bias was applied from a battery powered d-c source, current limited, covering the range 0-90V and 0-300  $\mu$ A. Probes were constructed with X-Y motion and with vertical motion adjusted with a screw. The probes were mounted on standard 1¼ in. diameter specimen holders, and the probe tip consisted of electropolished 0.010 in. tungsten wire, gold plated.

In this study the Schottky barrier is made a part of a circuit which includes a battery and the input to an amplifier (Fig. 1). The sample is oriented in the SEM so that the incident beam strikes the active surface; the metal must be thin to allow sufficient penetration of the electron beam (see below). The minority

carriers generated by the rastering SEM beam and swept across the depletion region constitute a signal which is amplified and used to modulate either the intensity or the Y-deflection of the CRT beam. Since both beams are traveling in synchronism the CRT beam displays a map of the two-dimensional distribution of reverse current at the Schottky barrier. The SEM beam current is typically  $\sim 10^{-9}$ A, and with one electron-hole pair produced per 3.5 eV incident electron beam energy (2) the total current generated by a 20 keV beam is of the order of  $10^{-6}$ A, which is larger

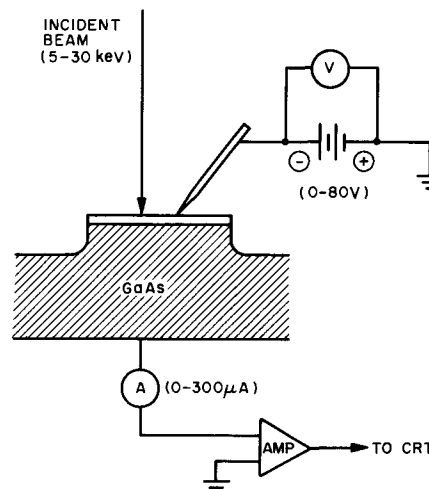


Fig. 1. Schematic diagram of circuit for obtaining EBIC signal from GaAs IMPATT tester structure.



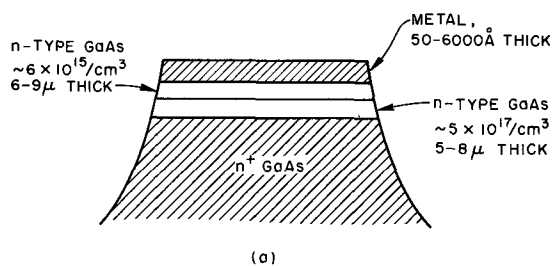
than the zero-bias leakage currents of most diodes. Since the specimen current amplifier is capable of detecting less than  $10^{-9}$ A current, the electron-beam induced current (EBIC) is more than sufficient to create a measurable signal at zero volts applied bias. As the reverse bias is increased a point is reached where the current begins to rise rapidly with increasing reverse bias. It is at this point that breakdown regions are first observed in the EBIC mode. These regions are sites of avalanche breakdown or sites of current enhancement due to other causes, such as tunneling; in either case the sites represent a limit to the nearly linear response of a diode under reverse bias. Since no distinction is made in this paper between diodes exhibiting "soft" and "hard"  $I$ - $V$  character, these regions will be called "premature breakdown" (PB) regions. When breakdown sites are examined at sufficient bias to create currents in excess of  $1 \mu\text{A}$ , well into the steeply ascending region of the  $I$ - $V$  curve, the EBIC signal due to lower bias leakage is completely masked by the PB site current.

The signal created when the incident beam strikes a PB site under avalanche conditions is due in part to avalanche multiplication of the minority carrier cloud generated by the incident beam, and in part to an incremental increase in negative potential at that site. The multiplication factor is given by  $M = I(W)/I(O)$ , where  $I(W)$  and  $I(O)$  are the minority carrier currents at the end and beginning of the depletion regions, respectively.  $M$  is essentially infinite at the avalanche breakdown voltage (3), and this fact alone would permit a PB avalanche site to be imaged. The evidence for an incremental increase of negative potential at the site of the surface bombarded by the electron beam comes from two sources. In an earlier work (4) on an SEM study of silicon bipolar transistors it was found that a 20 keV electron beam directed on a highly doped n-type emitter region produced a "pinch off" of an emitter-collector short equivalent to biasing the base by  $\sim 1\text{V}$  negative. In the present work, as will be described below, directing a 20 keV beam on platinum at a PB site caused an apparent lowering of the breakdown voltage by  $\sim 2\text{V}$ . Both these observations indicate an increase in local potential of  $\sim 1\text{V}$  due to electron beam bombardment, which would have the effect of adding a significant increase to the measured PB current at a given reverse bias setting.

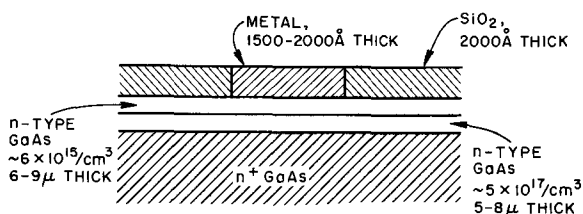
The beam "penetration" can be defined as the extrapolated value of electron transmission against film thickness to zero transmission and is expressed by the

function (5)  $R_Z = kE_0^n$ . The incident electron beam energy is  $E_0$ . For Au the constants  $k$  and  $n$  have the values 45 and 1.5, respectively, over the energy range 5 to 15 keV (9), and the extrapolated range  $R_Z$  is 2600Å. The extrapolated range is expected to be slightly higher at 20 keV, which is the beam energy used in these experiments. Thus, a 2600Å thick Pt film is a conservative upper limit for these experiments. It was found that a 2000Å Pt film is sufficiently thin to permit an EBIC signal to be generated at a PB site under the film (see Fig. 11).

*Material.*—All GaAs IMPATT testers studied and reported here were made with Au/Pt and Pt metallization. Two types of structures were examined. One is a mesa structure, with the active region on the surface of the mesa as shown in Fig. 2a. The other is a planar



(a)



(b)

Fig. 2. GaAs IMPATT tester structures used in this study. (a) Mesa structure, and (b) planar structure.

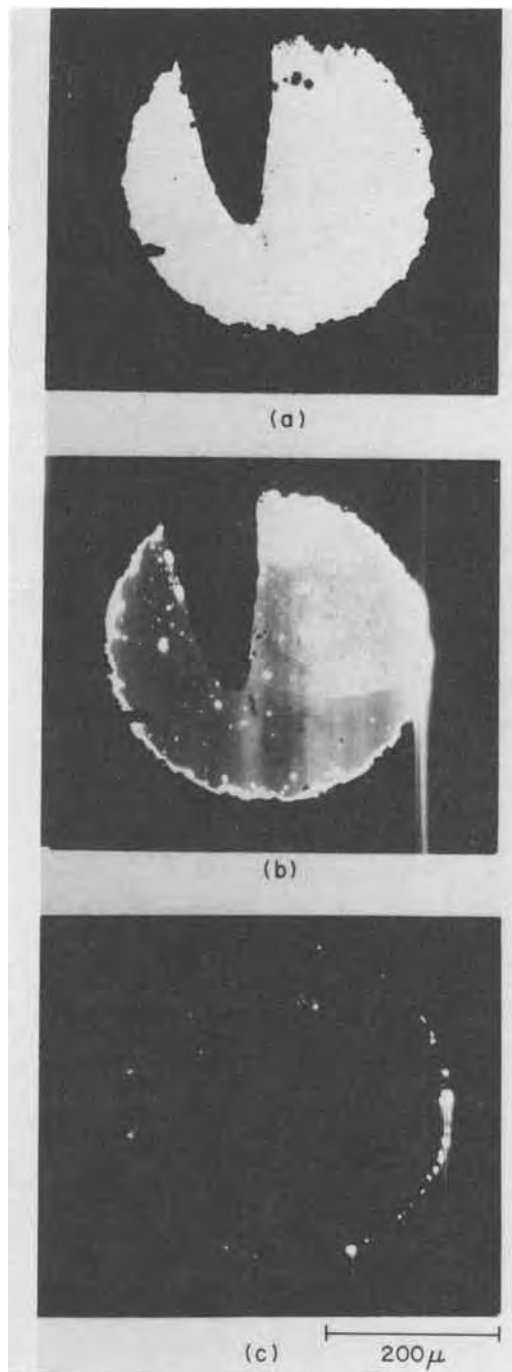


Fig. 3. Effect of bias on EBIC image of Pt planar structure. (a) Leakage pattern at 1V; (b) stronger leakage pattern at 5V; (c) PB sites imaged at 15V (30  $\mu\text{A}$ ). Aged in air 29 hr, 350°C. Sample 7, diode C-5.

Table I. Mesa structures

Metal thickness (Å)	Aging*			Remove Au ?	Diode number	PB sites		
	Au	T (°C)	Time (hr)			Number	Location	Correlation†
3000	Yes	290	216	No	1	2	Edge	1-metal overlay
6000	Yes	345	5	No	2	2	Edge	Metal overlay
				Yes	3	4	Edge	3-metal overlay
50	No	—	—	—	1	16	Edge	
				—	3	12	Center	Missing Pt
1000	Yes	350	1½	Yes	3	2	Edge	1-metal overlay
	Yes	350	1½	Yes	5	2	Edge	
	Yes	350	1½	Yes	8	2	Edge	None obvious
	Yes	350	1½	Yes	12	1	Edge	Metal overlay
	No	350	1½	—	14	1	Edge	Metal overlay
	No	350	1½	—	15	2	Edge	1-metal overlay
50	No	—	—	—	1	3	Center	Missing Pt

\* Aging of all mesa structures was performed in air.

† The textural feature which correlates with a PB site is indicated: "None obvious" means no obvious feature was found at a PB site. No entry means that no study of correlation was made. The number preceding the correlation is the number of PB sites to which that correlation applies.

structure. All diodes were fabricated from vapor-phase epitaxial GaAs grown at 900°C. A Te, Se, S, or Si doped  $1-3 \times 10^{18}/\text{cm}^3$  n-type GaAs crystal was the substrate material. An n-type  $4-7 \times 10^{17}/\text{cm}^3$  S-doped "buffer" layer of 5-8 $\mu$  thickness was grown on the substrate, and then an additional n-type  $6-9 \times 10^{15}/\text{cm}^3$  Si-doped layer was grown with a thickness of 6-9 $\mu$ .

The mesa structures were formed by sputter deposition of 50-6000Å Pt followed by Au plating. Photolithography was used to form an array of dots of diameter ranging from 0.010 to 0.050 in. Mesa structures were formed on the substrate, and then the gold was dissolved in I<sub>2</sub> solution leaving the structure described in Fig. 2a.

The planar structures were formed by deposition of ~2000 SiO<sub>2</sub> at ~275°C, followed by the formation of photolithography of an array of holes in the oxide of diameters 0.010-0.050 in. Platinum was sputter deposited to a thickness of 1000-2000Å, and tape was used to remove the Pt selectively from SiO<sub>2</sub> where it adheres poorly; the Pt adheres well to the GaAs and an array of planar diode structures is produced as shown in Fig. 2b.

The depletion depth of this material ranges from 2 to 3.5 $\mu$  over the reverse bias range 0-90V, which is the expected breakdown voltage for  $8 \times 10^{15}/\text{cm}^3$  n-type GaAs (7). The minority carriers are generated by the 20 keV electron beam well within the space charge region. Breakdown voltage is defined arbitrarily in this paper as the reverse voltage at 50  $\mu$ A current. For all diodes examined in this study the I-V curves at 50  $\mu$ A were nonlinear, and PB sites were first imaged at bias values less than or equal to the reputed "breakdown

voltages." As mentioned earlier no distinction is made between soft and hard I-V characteristics, and the definition of breakdown voltage is therefore arbitrary

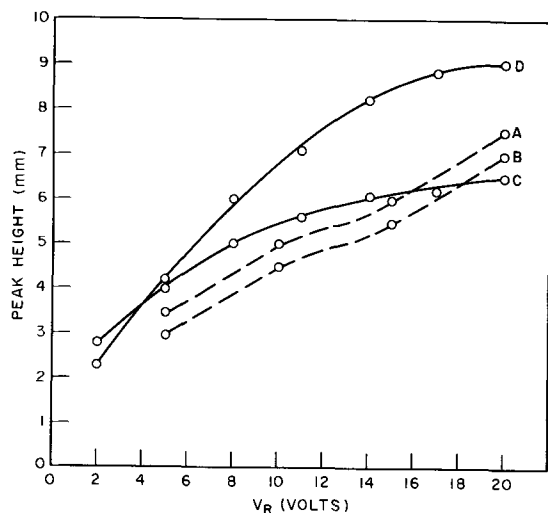


Fig. 4. Effect of bias on amplitude of Y-modulation EBIC image in leakage region of Pt planar structure. Annealed 350°C 1 hr in air; V<sub>B</sub> = 34V. Four sites were measured. Sample 7, diode A-11.

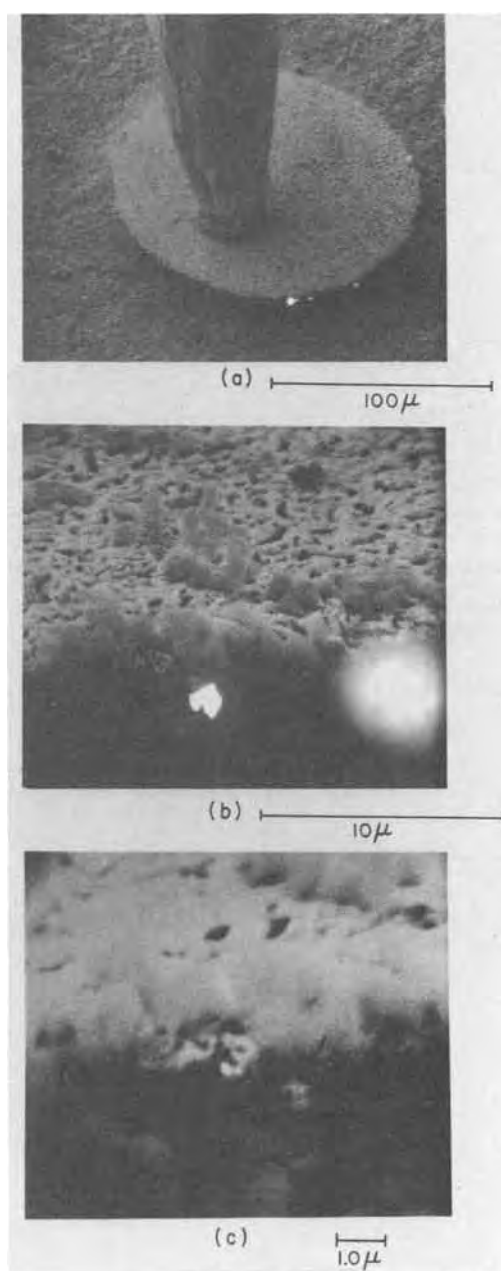


Fig. 5. PB sites at edge of Pt mesa structure. (a) Superimposed SEE and EBIC images showing location of PB sites; (b) same at higher magnification; (c) SEE image showing metallization overhang (arrow) responsible for PB site on the left in (b). Sample 2, diode 3.

Table II. Breakdown voltage data  
(Samples without Au)

	Sample number	Diode number	$V_{R,B}^*$ before aging	350°C aging		$V_{R,B}^*$ after aging
				Time (hr)	Medium	
Planar structures	7	A-11	38	1	Air	34
			—	2	Air	28
			—	11	Air	26
			—	29	Air	21
			—	1	Air	34
		B-2	—	2	Air	38
			—	11	Air	22
			—	1	Air	30
		B-6	—	29	Air	20
			—	29	Air	20
	C-5	A-8	32	1	Air	31
			—	2	Air	26
	8	C-1	67	2	Vacuum	63
			—	18	Vacuum	80
	—		84	Vacuum	68	
	9	C-6	45	24	Air	40
	10	B-2	50	24	Air	40
		B-6	50	24	Air	35
	11	B-3	35	24	Air	35
	12	F-8	40	4	Air	40
B-6		45	4	Air	37	
13	A-4	50	4	Air	48	
	B-3	55	4	Air	52	
14	1	24	133	Air	16	
	2	23	133	Air	15	
15	1	~60	—	—	—	

\* Reverse breakdown voltage is defined as the reverse voltage at 50  $\mu$ A current.

and is not to be considered a well-defined parameter for a particular diode.

Samples were aged in air over a temperature range of 290°-400°C for times ranging from 1½ to 216 hr;

one planar structure was aged in vacuum for times up to 84 hr.

### Results

*General response of SEM.*— The effect of the applied bias on the EBIC image for a given diode is illus-

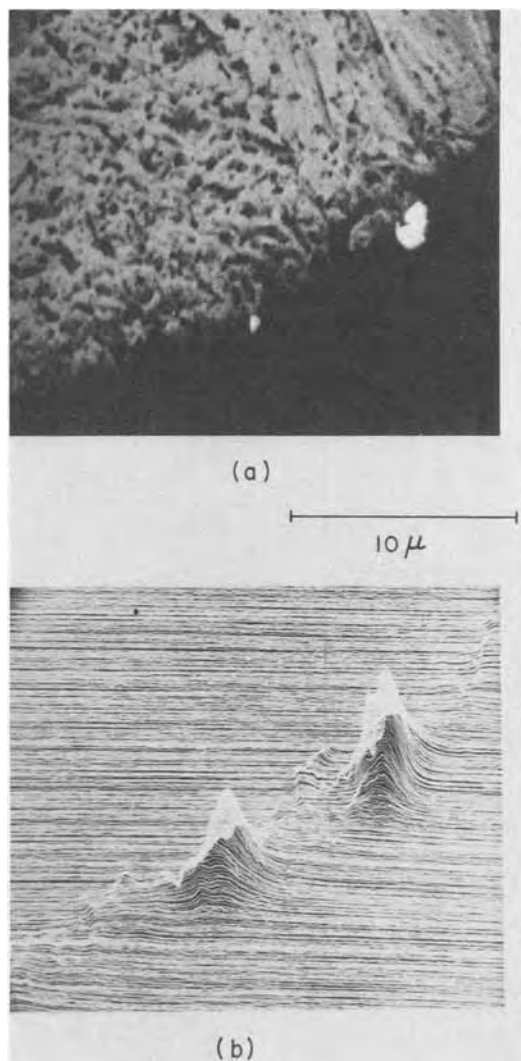


Fig. 6. PB sites at edge of Pt mesa structure. (a) Superimposed SEE and EBIC images showing location of two PB sites; (b) Y-modulation EBIC image of same area. Both images taken at 30V, 3.5  $\mu$ A. Sample 2, diode 2.

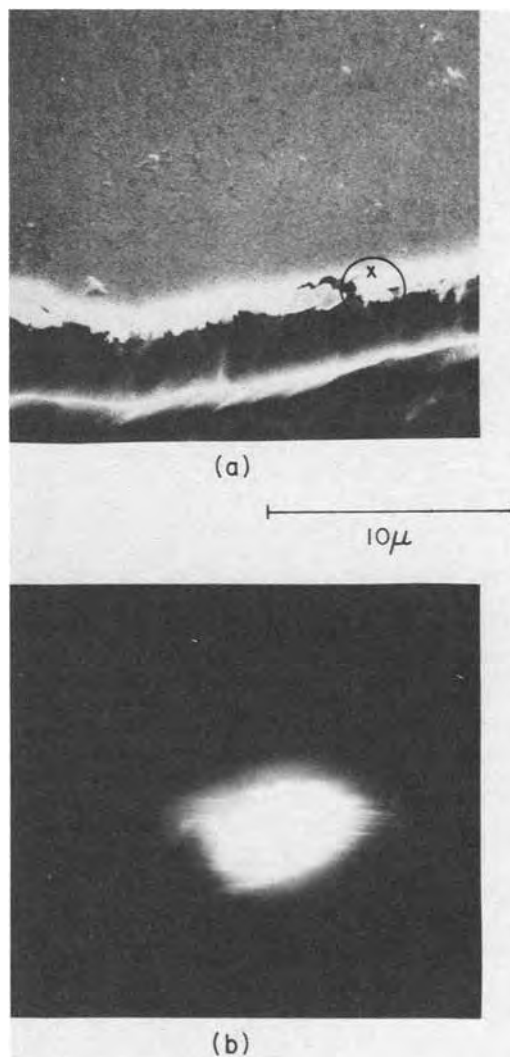


Fig. 7. PB sites at edge of Pt mesa structure. (a) SEE image showing metallization overhang; (b) EBIC image of same area showing PB site at overhang. Sample 4, diode 12.

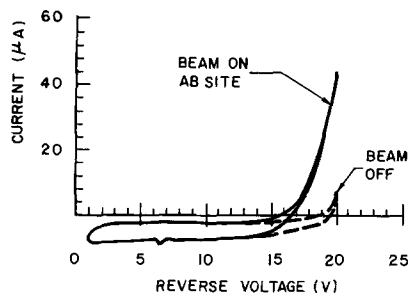


Fig. 8.  $I$ - $V$  response to electron beam striking PB site at overhang shown in Fig. 7.

trated in Fig. 3. The planar structure analyzed in Fig. 3 was made with 2000Å Pt, annealed in air at 29 hr 350°C, and has a breakdown voltage of 20V. At zero bias leakage is typically uniform across a diode (Fig. 3a), but distinct leakage areas appear upon application of bias (Fig. 3b). Premature breakdown sites are imaged when more than  $\sim 2 \mu\text{A}$  current is drawn and can first be imaged at bias voltages from 1 to  $\sim 15\text{V}$  below breakdown depending on the sharpness of the  $I$ - $V$  curve. The PB sites shown at the edge of the diode in Fig. 3c were imaged at  $30 \mu\text{A}$  current, 15V reverse bias. The large current response of PB sites with incremental increase of applied bias (under EBIC conditions) and the first appearance of PB sites at bias values near breakdown, both demonstrate that these are in fact sites of breakdown and not sites of diode leakage.

The change in intensity of the EBIC image at a leakage area for a constant gain setting is not a simple function of applied bias. Y-modulation EBIC images of diode A-11 on sample No. 7 were photographed at a number of bias settings over the range 2-20V; the sample was aged 1 hr in air at 350°C and breakdown was at 34V. The peak heights were measured at four sites and are plotted in Fig. 4. It can be seen that the EBIC signal is not linear with applied bias at any one site, and different sites show different responses. It was also found that the EBIC signal from regions between the visible leakage areas was at all times low and usually negligible compared with the signal from the leakage areas.

**Mesa structures.**—Five preparations of mesa structures were examined. These samples contained Pt metallization of thickness 50-6000Å. Details on the structure of these samples and results of the SEM studies are shown in Table I. Aspects of avalanche behavior in the mesa structures are described in Fig. 5-9.

Figure 5a shows a superimposed secondary electron emission (SEE) and EBIC image of sample 2, diode 3 after 345°C 5 hr air anneal. The EBIC image was recorded under avalanche conditions and shows PB sites at the diode edge. This is a typical observation on annealed and unannealed Pt mesa structures. Figure 5b shows a higher magnification of two of the PB sites; the PB site on the left is correlated with the Pt overhang shown in Fig. 5c (arrow). The behavior of diode 2 on the same sample is shown in Fig. 6. A superposition of SEE and EBIC images (Fig. 6a) shows metal overhang at PB sites. The Y-modulation EBIC image in Fig. 6b shows the fine structure of these sites; the fine structure is caused in part by the shape of the Pt over these regions.

The effect of electron beam bombardment of a PB site on the  $I$ - $V$  characteristics was examined on sample 4, diode 12 (Fig. 7 and 8). This sample had been heated with Au for 1½ hr at 350°C; the Au was then removed before SEM study. The EBIC image of the PB site (Fig. 7b) corresponds spatially to part of the metal overhang shown in Fig. 7a (circle). A more exact identification of the location of the PB site was possible when the electron beam was used as a probe, while monitoring the  $I$ - $V$  curve of the diode (Fig. 8). This

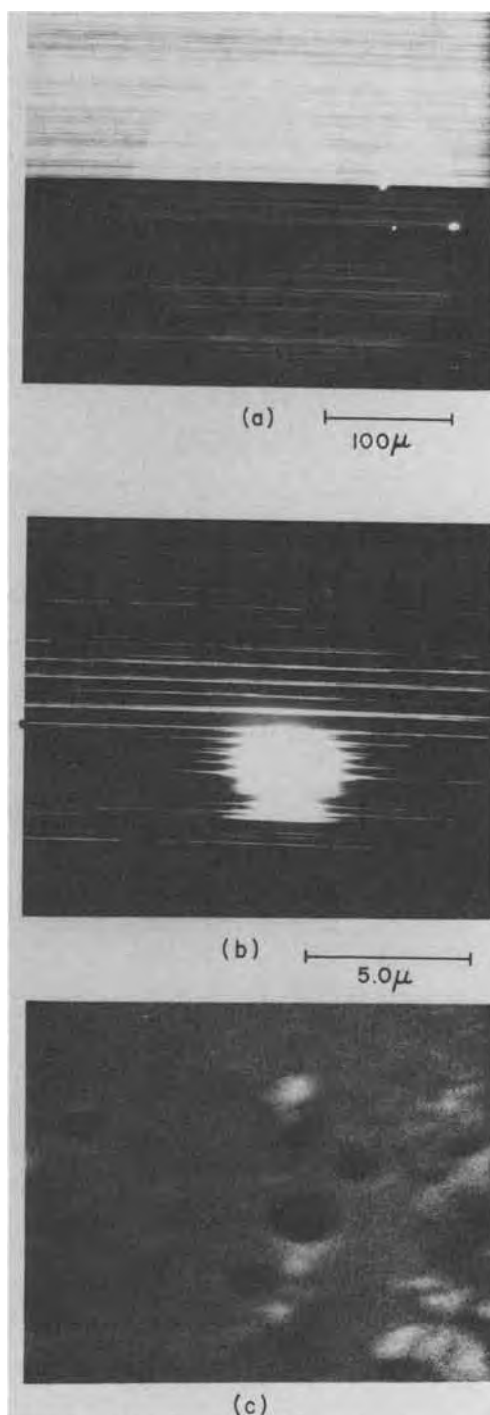


Fig. 9. PB sites away from edge of Pt mesa structure. (a) EBIC image at 30V, 230  $\mu\text{A}$  showing three PB sites; (b) EBIC image of lower left PB site at higher magnification; (c) SEE image of same area as (b) showing missing Pt region corresponding to PB site. Sample 5, diode 1.

position is marked by a cross in Fig. 7a, and the effect of the beam on the diode  $I$ - $V$  curve is easily seen (Fig. 8). This more careful analysis showed that the PB site was located along a sharp, well-defined crack in the overhanging metal film.

As shown in Table I, most PB sites occurred at the edge, and a comparatively small number of cases was observed where PB sites were found on the diode surface away from the edge. In all mesa structures these examined off-edge sites could be correlated with local regions of missing Pt or with other metallization defects.

Three off-edge PB sites from sample 5, diode 1 are shown in Fig. 9a. The higher magnification EBIC image

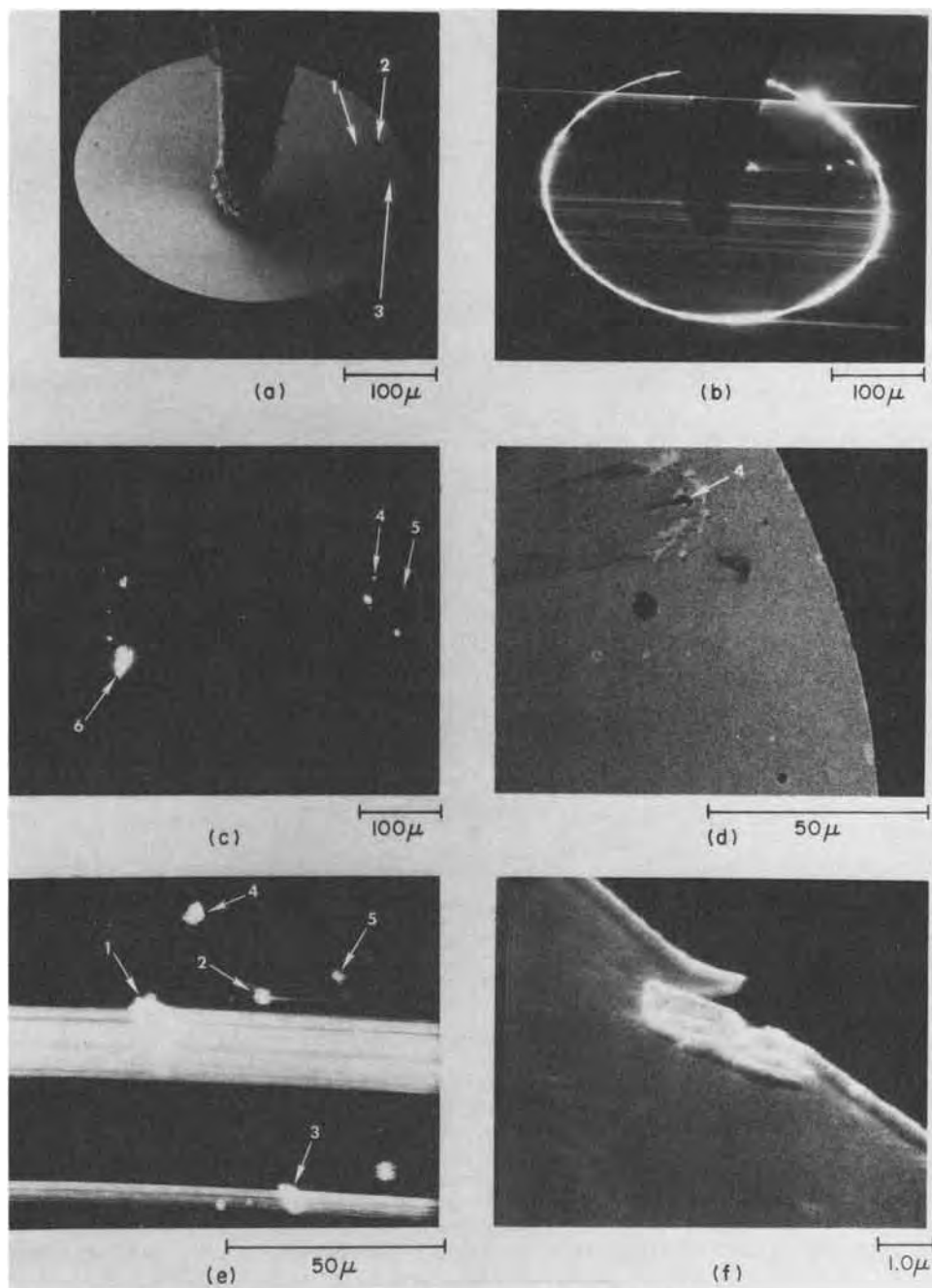


Fig. 10. PB sites at edge and away from edge of Pt planar structure. (a) SEE image showing Pt-missing regions 1, 2, and 3; (b) EBIC image at 30V, 10  $\mu$ A showing PB sites at defects 1, 2, and 3; (c) EBIC image at 15V, 30  $\mu$ A after aging 29 hr, 350°C in air showing additional PB sites (defect 3 is not visible at the low gain setting used); (d) enlarged SEE image showing additional defect 4 resulting from probe scratch; (e) EBIC image of same region as (d) showing edge location of additional PB site 5; (f) SEE image showing metallization defect at 5. Sample 7, diode A-11.

of the lower left PB site shown in Fig. 9b corresponds spatially with the large circular black area near the center of the SEE image in Fig. 9c. X-ray probe examination showed that the black areas are regions of missing Pt; no other element was detected in these regions. The same three PB sites shown in Fig. 9a were seen as microplasmas under an optical microscope. The microplasmas were seen only at higher current levels, above 500  $\mu$ A. This observation shows that these PB sites are sites of avalanche. It is not known whether avalanche breakdown occurs because of high field gradients at the edge of the Pt, or if the same bulk or surface defect which led to loss of Pt also caused avalanche breakdown.

It is obvious from the above data on the Pt samples that avalanche tends to occur at the edge of metallization for samples aged with and without Au. Breakdown degradation for mesa structures with less than 6000Å Pt occurs faster when Au is present; this point is illustrated by the data for sample 4 in Table II. Thus, we concluded that the lowering of breakdown due to the presence of Au during aging is manifested first at the weakest point in the structure, namely, at the sites

of metallization overhang around the edge of the diode. Other EBIC studies on unaged Pt mesa structures confirm that PB sites are located at metal overhang positions; *i.e.*, aging is not needed to create the Pt metal overhang sites responsible for breakdown.

*Planar structures.*—Nine preparations of planar structures were examined. The diodes of eight of the samples (samples 7-14) had the configuration shown in Fig. 2b; the metallization of the remaining sample (sample 15) was grown by electron beam deposition through a mechanical mask; this structure contained no deliberate surface oxide. Details on the structures of these samples are shown in Table III; avalanche behavior is described with the aid of Fig. 10-11.

Diode A-11 of sample 7 contained a number of PB sites that are present on the diode as formed, plus additional sites that occurred after aging in air at 350°C for 29 hr. These data are illustrated in Fig. 10 and 11. Figure 10a shows three missing Pt regions on the diode which serve as PB sites (Fig. 10b). It is known that these are PB sites rather than simply sites of increased EBIC signal due to missing metallization because these sites give a significantly stronger sig-

Table III. Planar structures

Sample number	Metal thickness (Å)	Aging			Diode No.	PB sites		Correlation*
		T (°C)	Time (hr)	Medium		No.	Location	
7	2000	—	—	—	A-11	Many	Edge Center	1-metal defect Missing Pt
		350	1	Air	A-11			
		350	2	Air	A-11			
		350	11	Air	A-11	3	Edge Center Center	1-metal defect Missing Pt None obvious
		350	29	Air	A-11			
		—	—	—	—			
		350	1	Air	B-2	Many	Edge Center	Missing Pt
		350	2	Air	B-2			
		350	11	Air	B-2			
		350	29	Air	B-6	Many	Edge Edge Center	None obvious
		350	29	Air	B-6			
		350	29	Air	C-5			
		350	1	Air	A-8	Many	Edge Center	Missing Pt
		350	2	Air	A-8			
		350	2	Air	C-1			
8	2000	350	2	Vacuum	C-1	~25	Edge	
		350	18	Vacuum	C-1			
		350	84	Vacuum	C-1			
9	2000	350	24	Air	C-6	Many	Edge	
		350	24	Air	B-2			
10	2000	350	24	Air	B-6	Many	Edge	3-metal defects Many—none obvious
		350	24	Air	B-6			
11	2000	350	24	Air	B-3	Many	Edge	Some-metal defects
		350	24	Air	F-8			
12	2000	350	4	Air	F-8	Many	Edge	1-metal defect
		350	4	Air	B-6			
13	2000	350	4	Air	B-6	Many	Edge	
		350	4	Air	A-4			
14	1000	350	4	Air	A-4	Many	Edge	
		350	133	Air	B-3			
15	2000	350	4	Air	B-3	Many	Edge	Metal defects Metal defects
		350	133	Air	1			
					2			
					1			
					6			

\* See † footnote for Table I.

nal than the EBIC signal immediately surrounding the perimeter of the Pt; the latter signal, in general, is due only to increased current generated by the electron beam in the semiconductor because of missing Pt. In addition, Fig. 10b shows a very high linear density of PB sites around the edge of the Pt. After aging additional sites were noted at 4 and 6, and a group at 6 (Fig. 10c). PB site 4 was due to a probe scratch (Fig. 10d), and PB site 5 was correlated with a metallization defect (shown in Fig. 10f). The group of PB sites at region 6 are better resolved in Fig. 11, particularly in the Y-modulation EBIC image of Fig. 11b. The SEM studies of the surface of this region showed no discernible surface features, and it is concluded that the high density of discrete sites is due to contamination or defects at the Pt/GaAs interface or in the GaAs.

### Discussion

Premature breakdown of unaged Au/Pt mesa, Pt mesa, and Pt planar structures occurs mostly at the edge of the metallization. Both methods of forming diodes leave edges which are rough. The calculated effect of junction curvature on the breakdown voltage for GaAs one-sided abrupt junctions (8) is listed below, for the case of an impurity level of  $8 \times 10^{15}/\text{cm}^3$  and for spherical curvature of radius  $r$

$r$ ( $\mu$ )	$V_B$ (V)
$\infty$	85
10	60
1	30
0.1	9

The radius of curvature of metallization overhang correlated with PB sites is of the order of  $0.1\mu$  and less; these regions of high curvature may cause premature avalanche with an expected drop in breakdown voltage of  $\sim 90\%$ . This may partially explain the generally low breakdown voltages found on the unannealed planar structures (theoretical value  $\sim 85\text{V}$ ) compared with the mesa diodes, since the former structures had

a significantly higher linear density of PB sites around the edge of the Pt than did the mesa structures. Whether premature breakdown sites imaged by EBIC in this study are due to avalanche, field emission, or tunneling is not known.

Although air aging degraded both the mesa and planar diodes, breakdown after aging still occurred primarily at the edge of the metallization. Careful examination of the SEE image of some of these regions shows that edge regions appear in different contrast compared with the rest of the Pt, including a possible preferred metallurgical interaction at the edge as in diode A-11, sample 7, after 29 hr,  $350^\circ\text{C}$  aging (see Fig. 10d). Although dislocation generation sources at the metal/GaAs interface have been noted in sample 1 using transmission electron microscopy, dislocations have not been found (9) in TEM samples prepared from GaAs just below the edge of Pt metallization in another diode of sample 7. We therefore tentatively conclude that the lowering of breakdown voltage in air-annealed mesa and planar Pt structures is due to a change in the properties of the diode which is first manifested at the weakest point, namely, at those sites at the edge of metallization where metal defects and metal overhang produce the high field gradients.

A few cases have been observed of breakdown in Pt structures away from the edge in regions not correlated with visible surface features (as diode A-11 of sample 7, Fig. 11). It is felt that important information on breakdown behavior of GaAs Schottky diodes would result from EBIC study under conditions where edge effects could be made negligible. This could be achieved by electrically isolating the edge from the rest of the diode, and has been done for Si by use of a  $p^+$  guard ring (1) and metallization overlap of oxide (10, 11), and for GaAs using a high resistivity guard ring produced by proton bombardment (12). The experiments reported in this paper are being continued with the use of proton bombardment to electrically isolate the edge.

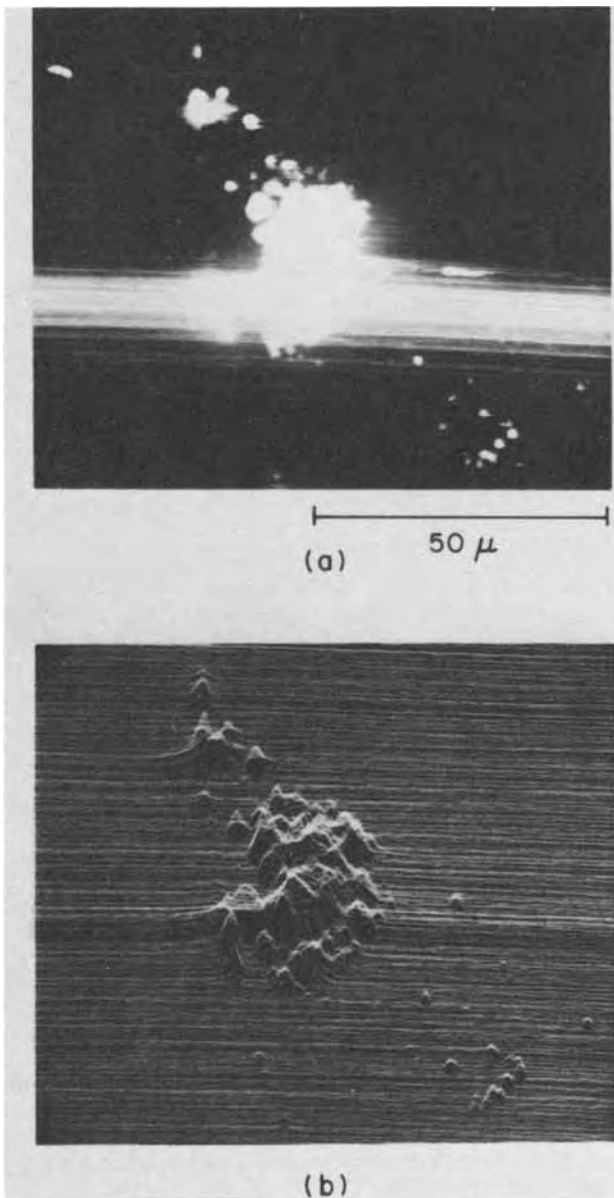


Fig. 11. High density of PB sites away from edge of Pt planar structure. Defect region 6 of Fig. 10c. (a) EBIC image at 17V, 50  $\mu$ A; (b) Y-modulation EBIC image of same area showing the discrete nature of the PB sites.

Regions of missing Pt serve as sites for premature breakdown (diode 1 of sample 5, Fig. 9; diode A-11 of sample 7, Fig. 10). The appearance of these regions of missing Pt or pinholes is due to particle contamination on the GaAs surface prior to metallization.

#### Summary

The intent of this work was to obtain information on the origin and location of breakdown sites in Pt mesa

and planar GaAs IMPATT tester diodes as a function of heat-treatment. The main results of this study are:

1. Breakdown sites have been identified using the SEM operating in the EBIC mode. These sites have been correlated with certain textural features of the diodes.

2. Premature breakdown in unaged and aged Au/Pt mesa, Pt mesa, and Pt planar structures occurs primarily at sites of metallization defects and metallization roughness around the periphery of the diodes. In the case of planar structures some of the roughness may have been due to metallurgical interaction between the Pt and GaAs after aging. These regions of high curvature produce high field gradients under bias and may cause premature avalanche. It is not known, however, whether breakdown results from avalanche, field emission, or tunneling.

3. The degradation of Pt diodes and the lowering of the breakdown voltage caused by air aging are manifested at PB sites at the edge of the metallization.

4. Very small sites of missing metallization ("pinholes") have been found to be sites of diode breakdown.

5. Leakage occurs in irregular patches across a diode. The  $I$ - $V$  characteristics of these patches are different, indicating nonuniform properties of the interfacial region with respect to leakage.

#### Acknowledgments

All epitaxial material was grown by L. Luther and electron beam deposited Pt films were grown by A. Sinha. Their cooperation is appreciated.

Manuscript submitted Aug. 2, 1973; revised manuscript received Nov. 19, 1973. This was Paper 304RNP presented at the Chicago, Illinois, Meeting of the Society, May 13-18, 1973.

Any discussion of this paper will appear in a Discussion Section to be published in the December 1974 JOURNAL. All discussions for the December 1974 Discussion Section should be submitted by Aug. 1, 1974.

#### REFERENCES

1. M. P. Lepselter and S. M. Sze, *Bell System Tech. J.*, **47**, 195 (1968).
2. E. I. Gordon and M. H. Crowell, *ibid.*, **47**, 1855 (1968).
3. S. M. Sze, "Physics of Semiconductor Devices," p. 113, John Wiley & Sons, Inc., New York (1969).
4. S. E. Haszko and R. B. Marcus, Unpublished work.
5. P. R. Thornton, "Scanning Electron Microscopy," pp. 77-78, Chapman and Hall, Ltd., London (1968).
6. V. E. Cosslett and R. N. Thomas, *Brit. J. Appl. Phys.*, **15**, 1283 (1964).
7. S. M. Sze, M. Lepselter, and R. W. MacDonald, Private communication.
8. S. M. Sze and C. Gibbons, *Solid-State Electron.*, **9**, 381 (1966).
9. P. Petroff, To be published.
10. A. Y. C. Yu and C. A. Mead, *Solid-State Electron.*, **13**, 97 (1970).
11. N. G. Anatha and K. G. Ashar, *IBM J. Res. Develop.*, **15**, 442 (1971).
12. A. G. Foyt, W. T. Lindley, C. M. Wolfe, and J. P. Donnelly, *Solid-State Electron.*, **12**, 209 (1969).



# Polarization and Charge Motion in Metal- $\text{Al}_2\text{O}_3$ - $\text{SiO}_2$ -Si Structures

A. P. Gnadinger and W. Rosenzweig

Bell Laboratories, Allentown, Pennsylvania 18103

## ABSTRACT

An investigation of the flatband voltage shifts of double insulator ( $\text{Al}_2\text{O}_3$ - $\text{SiO}_2$ ) MIS capacitors under bias temperature stress has been performed in order to assess and characterize the stability of double insulator IGFET's. These shifts were opposite to the applied bias voltage ("ionic" direction), and it was found that they are composed of two components: (a) A "fast" component which is linear with gate bias voltage and symmetric with bias polarity. Most of the shift occurs in less than 1 min at all temperatures used in this work (65°-260°C). Its magnitude is temperature activated (0.15 eV). This part of the flatband voltage shift is explained by a bulk polarization of the  $\text{Al}_2\text{O}_3$  layer with a polarizability that is independent of  $\text{Al}_2\text{O}_3$  thickness. (b) A "slow" component which is observed under positive bias. It is characterized by a linear dependence of flatband voltage shift on the logarithm of stress time for times larger than a delay time, which is thermally activated (1.2 eV). This component is interpreted to be due to motion of mobile, ionic charge, such as sodium, across the  $\text{Al}_2\text{O}_3$  and  $\text{SiO}_2$  layers. This charge motion is greatly reduced by increasing the  $\text{Al}_2\text{O}_3$  thickness.

A low threshold voltage p-channel MIS (metal-insulator-semiconductor) technology in which a double dielectric sandwich of 1000Å of  $\text{SiO}_2$  and 500Å of  $\text{Al}_2\text{O}_3$  is used as the gate insulator (1, 2) has received considerable interest in the past. Devices made with this gate structure and a Ti-Pd-Au metallization (3, 4) have a nominal threshold voltage of  $-1.0\text{V}$  if a 10 ohm-cm,  $\langle 100 \rangle$ , n-type silicon substrate is used.

One of the advantages of this technology is the excellent threshold voltage control and the inherently good stability of the threshold voltage under bias-temperature (BT) stress conditions.

A discussion of control of the initial threshold voltage is given by Clemens and Labuda (5). The question whether the inherently stable devices show any residual threshold voltage shifts during their operating life has been treated by Lampi and Labuda (6) who performed a reliability study by bias temperature aging discrete MIS transistors. They found that under negative gate bias two apparently independent types of drifts can cause small threshold voltage shifts. One is a rapid drift which shifts the threshold voltage to more positive values, and the other one is a long term drift which shifts the threshold voltage to more negative values. The latter type, referred to as "slow trapping," was shown because of its large activation energy to be negligible at normal operating temperatures and biases and can be neglected for most applications. The first type is potentially more important because it occurs at lower temperatures and in shorter times. On the basis of experimental evidence it can be interpreted to be due to polarization of the  $\text{Al}_2\text{O}_3$  layer and charge motion across the insulator structure (7). The purpose of this work is to investigate and characterize this rapid initial threshold voltage shift for both negative and positive bias and to evaluate its effect on device reliability.

As test vehicles, MIS capacitors with insulator structures identical to those in MIS transistors were used. Capacitors instead of transistors were chosen because (a) they are simple to fabricate, (b) interface states which can be introduced by bias-temperature aging (8) can easily be detected, and (c) they are geometry independent so that a one-dimensional theory can be applied. MIS transistors with short channel length very often show geometry effects due to the fringing fields

in the proximity of p-n junctions (9), obscuring the results of bias-temperature aging. By observing the flatband voltage shifts of MIS capacitors it is possible to characterize the physical mechanisms leading to the rapid initial shifts in the transistor-threshold voltage mentioned above.

## Experimental Structures and Techniques

The double insulator MIS structure used in this work consists of a thermal  $\text{SiO}_2$  layer grown on  $\langle 100 \rangle$  n-type silicon of nominal 10 ohm-cm resistivity. The  $\text{SiO}_2$  is grown in a wet oxidation at 1100°C with an  $\text{O}_2$  ambient bubbled through 80°C water, followed by an 1100°C 30-min anneal in  $\text{N}_2$ . The second insulator is a layer of  $\text{Al}_2\text{O}_3$  deposited pyrolytically at 900°C on top of the  $\text{SiO}_2$  (1, 2). Right after  $\text{Al}_2\text{O}_3$  deposition the structures are hydrogen annealed at 900°C for approximately 30 min. The metallization consists of 1000 and 2000Å of filament evaporated titanium and palladium, patterned into  $20 \times 20$  mil square dots.

The polarization and charge transport effects were investigated by observing the flatband voltage shifts of these capacitors after bias-temperature treatment. This was done by making capacitance vs. voltage (C-V) measurements before and after stressing. The stressing was done by heating the sample under bias up to the stress temperature, keeping it at that temperature for the duration of the stress time, and then cooling it down rapidly to room temperature under bias. The slice was not removed from the stress apparatus for making C-V measurements. A stress apparatus similar to the one described by Goetzberger and Lopez (8) was used. Most of the bias temperature stress experiments were performed in air. It was found that the ambient had very little influence on the results. Capacitors stressed in a nitrogen or argon ambient showed essentially identical flatband voltage shifts.

The stress temperatures were between 65° and 260°C. The upper limit of 260°C was chosen to minimize competing effects such as carrier trapping at the Si- $\text{SiO}_2$  interface (slow trapping) as mentioned above. Below 65°C it was difficult to obtain measurable flatband voltage shifts in reasonable time. The bias voltages used were always less than the values corresponding to an electric field in the  $\text{SiO}_2$  of about  $1.5 \times 10^6$  V/cm (20V for a standard structure of 500Å  $\text{Al}_2\text{O}_3$  and 1000Å  $\text{SiO}_2$ ). This was done to avoid injection of

Key words: MIS devices, aluminum oxide, sodium contamination.



electronic charge from the metal contact (10, 11). The stress times were in the range of 20 sec to 4000 min with most of the points between 1 and 1000 min. This range was found to be adequate to investigate the fast initial shifts in flatband voltage.

All the flatband voltage shifts measured after bias-temperature treatment were small, typically less than 100 mV for a standard structure of 1000Å SiO<sub>2</sub> and 500Å Al<sub>2</sub>O<sub>3</sub> stressed at 150°C with -10V gate bias. The shifts if any, resulting from room temperature stressing were less than the resolution of the measurement system which was about 10 mV.

**Experimental Results and Discussion**

All flatband voltage shifts ΔV<sub>FB</sub> reported in this work are opposite in sign to the applied stress bias. That means ΔV<sub>FB</sub> is negative for positive bias and vice versa. Figure 1 shows the absolute magnitude of ΔV<sub>FB</sub> as a function of the logarithm of time with temperature as a parameter. This is a typical plot for a standard insulator structure (500Å Al<sub>2</sub>O<sub>3</sub>/1000Å SiO<sub>2</sub>). The solid lines are for +10V bias and the broken lines for -10V. The salient characteristics of these curves are as follows: under negative bias there is an "immediate" shift, i.e., a shift in a time shorter than 20 sec, followed by a small additional shift. This immediate component increases slowly with temperature. Under positive bias, particularly at the lower temperatures, one can observe an immediate shift nearly equal to that obtained under identical negative bias, followed by a "delayed" shift which increases nearly linearly with the logarithm of time. A delayed shift can also be seen under negative bias but is much smaller than the one observed under positive bias. Lampi and Labuda (6) also observe this behavior under negative bias at 100°C and find that the shift saturates at a value which is approximately twice the value of the initial shift. It is shown below that the negative bias shift is primarily produced by a single mechanism.

The delayed component under positive bias is seen to have a delay time of about 10 min at 125°C. At higher temperatures and positive bias, the observed shifts are already increasing functions with the logarithm of time even for the shortest times. This leads one to assume that the delay time is temperature activated and shorter than 20 sec (the shortest experimental cycling time) at 155°C. On the basis of the 125°C results it is also reasonable to assume that the immediate component is also present for positive bias at the higher temperatures, in magnitude equal to the negative bias shifts.

The above interpretation at the flatband voltage shifts can be represented in idealized form as shown in Fig. 2, which is a plot of the magnitude of the shift vs. logarithm of time. Under negative gate bias there is a single component of flatband voltage shift: the im-

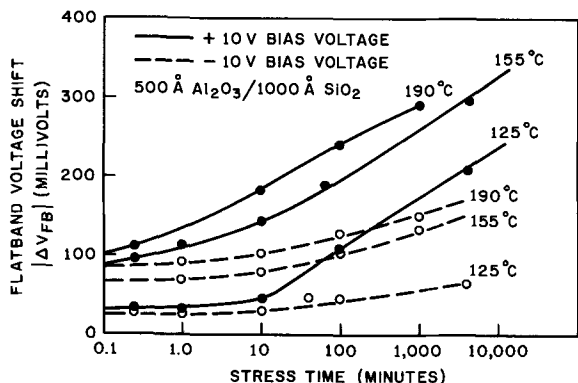


Fig. 1. Dependence of flatband voltage shift on stress time for standard double insulator structure (500Å Al<sub>2</sub>O<sub>3</sub> on 1000Å SiO<sub>2</sub>) with stress temperature and bias polarity as parameters.

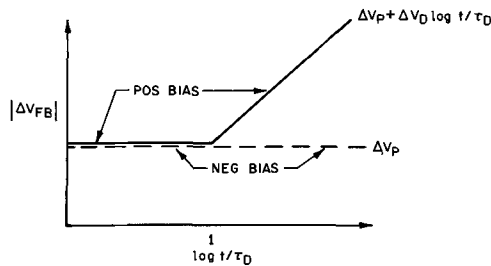


Fig. 2. Idealized representation of flatband voltage shift as a function of stress time.

mediate component. Under positive bias there are two components: the immediate component with equal magnitude as under negative bias and a delayed component increasing logarithmically with time. Mathematically they are given as follows

$$V_B < 0: \Delta V_{FB} = -\Delta V_P \quad [1]$$

$$V_B > 0: \Delta V_{FB} = -\Delta V_P \quad t \leq \tau_D$$

$$\Delta V_{FB} = -\Delta V_P - \Delta V_D \log t/\tau_D \quad t > \tau_D \quad [2]$$

It must be stressed that this model is intended to take into account only the salient features of flatband shift under bias-temperature aging. In the remainder of this section, experimental results are presented which show how ΔV<sub>P</sub>, ΔV<sub>D</sub>, and τ<sub>D</sub> vary with bias magnitude, temperature, and insulator structure. On the basis of these results the immediate component is ascribed to polarization of the Al<sub>2</sub>O<sub>3</sub> layer, and the delayed component to charge transport across the insulator.

Experimentally the immediate and delayed components under positive bias shown in Fig. 2 can only be separated readily at lower temperatures (≲ 125°C) on the basis of shift vs. log (time) plots because the delay times are too short at higher temperatures. This is evident from Fig. 1. However, they are readily separable on the basis of their bias dependence. Figure 3 is a plot of the shift (ΔV<sub>FB</sub>) as a function of positive applied bias (V<sub>B</sub>) at 190°C with time as parameter. It may be seen that the shift is a linear function of bias voltage and that the slope of this function is established even at the earliest time and remains nearly constant thereafter. This behavior suggests that the immediate component is responsible for the slope, and the magnitude of the shift attributable to it is directly proportional to the applied bias. In addition, the ΔV<sub>FB</sub> vs. V<sub>B</sub> curves have intercepts with the vertical axis which vary nearly linearly with the logarithm of time. This suggests that the delayed component is responsible for the intercept and that it is nearly bias independent, requiring only a small positive bias to produce it. A similar experiment under negative bias shows only the immediate component but no intercepts, consistent with the interpretation of Fig. 1. It

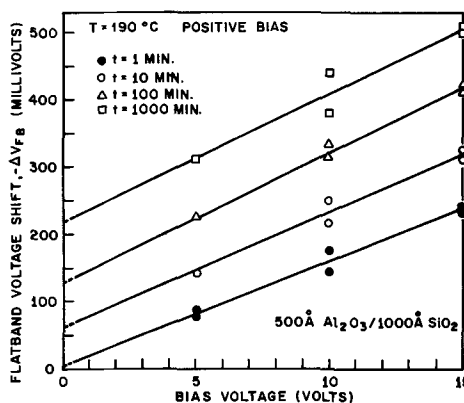


Fig. 3. Dependence of flatband voltage shift on positive-bias voltage with stress time as parameter (constant temperature).

must be noted that experimentally no discontinuity exists in  $\Delta V_{FB}$  vs.  $V_B$  as  $V_B$  goes from positive to negative. It has been observed that under positive bias,  $\Delta V_{FB}$  follows the linear variation with  $V_B$  down to about 0.5V. Below that value  $\Delta V_{FB}$  rapidly decreases to zero as  $V_B$  is reduced to zero.

The temperature activation of the two components can also be seen more clearly on  $\Delta V_{FB}$  vs.  $V_B$  plots. Figure 4 shows such plots for a stress time of 60 min with temperature as a parameter. Within experimental error and variability among devices the curves under negative bias have essentially zero intercepts, thus showing only the immediate component, represented by the slope, which increases slowly with temperature. More extensive experimental results, presented below, yield an activation energy of 0.15 eV. The positive bias curves contain both components. Since  $\Delta V_{FB}$  resulting from the immediate component is the same for both positive and negative bias (of equal magnitude and at equal temperature), one can subtract the negative bias  $\Delta V_{FB}$  from the corresponding points at positive bias and be left with only the delayed component. When this is done, nearly level lines remain, showing the field independence of the delayed component. Repeating this procedure for different stress times results in a different set of nearly level lines for each stress time. These nearly bias independent flat-band voltage shifts can now be plotted as a function of the logarithm of stress time resulting in plots similar to the one shown in Fig. 1 but containing only the delayed component and not the immediate component. Figure 5 shows a plot of the logarithm of the delay times of these curves vs. reciprocal absolute temperature. It may be seen that the points closely follow a straight line indicating a thermally activated process. The activation energy calculated from the slope is 1.2 eV. This value is close to those reported for mobile ion transport across an insulator if the process is dominated by trap release (12).

The results presented thus far can be related to a physical model. The immediate component, which varies linearly with applied bias and which is present both under positive and negative stress is indicative of a polarization mechanism. The delayed component, observed only under positive bias, which is strongly thermally activated and independent of bias voltage, can be explained by a trap-release limited charge transport of positive charge moving toward the Si-SiO<sub>2</sub> interface or negative charge moving away from it. Additional experimental evidence is presented below which shows that it is the Al<sub>2</sub>O<sub>3</sub> layer which is polarized and that the charge transport component is, most likely, the result of ionic contaminants penetrating the 500Å Al<sub>2</sub>O<sub>3</sub> layer.

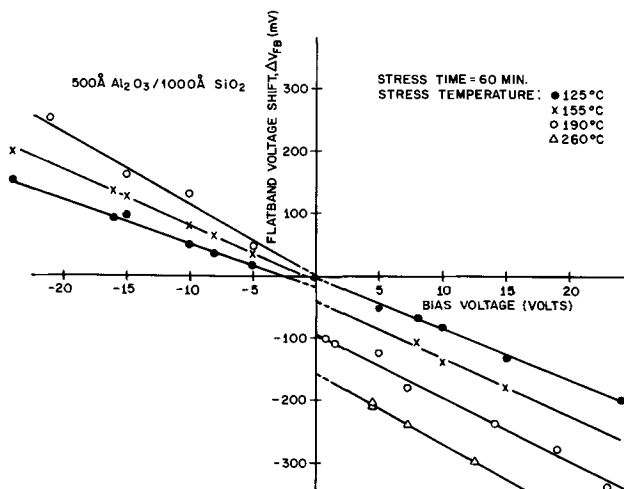


Fig. 4. Dependence of flatband voltage shift on bias voltage with stress temperature as parameter (constant stress time).

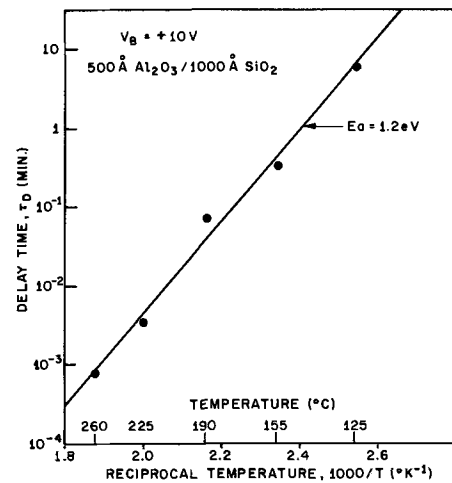


Fig. 5. Dependence of the logarithm of the delay time,  $\tau_D$ , on the reciprocal of the stress temperature.

It is extremely unlikely that the SiO<sub>2</sub> layer is polarized because this effect has not been observed in single-layer MIS structures. The polarization model has been proposed for a phosphosilicate glass film by Snow and Deal (13) and for Al<sub>2</sub>O<sub>3</sub> by Nigh<sup>1</sup> and Walden *et al.* (11). Snow and Deal have shown that

$$\Delta V_{FB} = - \frac{K_0 x_A x_P V_B}{K_A [(K_A + x_P) x_0 + K_0 x_A]} \quad [3]$$

where  $K_0$ ,  $x_0$  and  $K_A$ ,  $x_A$  are the relative dielectric constants and the thicknesses of the SiO<sub>2</sub> and the alumina layers, respectively, and  $x_P$  is the polarizability of the alumina layer. Equation [3] predicts a linear dependence of  $\Delta V_{FB}$  on the bias voltage  $V_B$  as was observed above.

Equation [3] can be rewritten in terms of electric field (13) in the alumina layer, and for  $x_P \ll K_A$  simplifies to

$$\Delta V_{FB} = - \frac{x_A x_P E_A}{K_A} \quad [4]$$

Equation [4] predicts that with constant electric field in the alumina,  $\Delta V_{FB}$  increases directly with the alumina thickness and is independent of SiO<sub>2</sub> thickness. Both of these variations were observed experimentally with Al<sub>2</sub>O<sub>3</sub> thicknesses ranging between 500 and 2400Å, and SiO<sub>2</sub> thicknesses between 1000 and 4000Å. Because of the proportionality of  $\Delta V_{FB}$  with alumina thickness, interfacial polarization at the SiO<sub>2</sub>-Al<sub>2</sub>O<sub>3</sub> interface, as described by Iida *et al.* (15), can be ruled out as a possible mechanism in our devices. (As an example see the results in Fig. 10 for 1100Å of Al<sub>2</sub>O<sub>3</sub> as compared to those in Fig. 3 and 4 for 500Å of Al<sub>2</sub>O<sub>3</sub>.) The absence of Iida's instability mechanism in our samples was probably due to the 900°C hydrogen anneal. The average polarizability,  $x_P$ , at 225°C obtained on 25 samples subjected to positive and negative bias was  $0.86 \pm 0.25$ .

All the  $\Delta V_{FB}$  vs.  $V_B$  curves at different temperatures were also analyzed to yield the activation energy for polarizability. The results are shown in Fig. 6 which is a plot of  $\log x_P$  vs.  $1/T$ . The best straight line fit gives an activation energy of 0.15 eV.

It is thus concluded that bulk polarization of the Al<sub>2</sub>O<sub>3</sub> layer is primarily responsible for the negative bias instability and partially responsible for the positive bias instability which also has a charge transport component. The experimental evidence presented below elucidates the nature and location of this charge.

In order to determine in which insulator the charge motion occurs, a BT aging experiment was conducted using structures with varying SiO<sub>2</sub> thicknesses and

<sup>1</sup> The dipolar polarization model as proposed by H. E. Nigh will be treated in detail in Ref. (14).

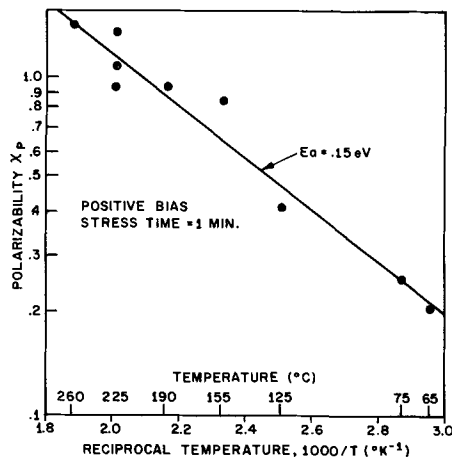


Fig. 6. Dependence of the polarizability,  $\chi_p$ , on the reciprocal of the stress temperature for constant stress time and positive bias.

constant alumina thickness,  $x_A$ . Again, the flatband voltage shifts  $\Delta V_{FB}$  were measured as a function of positive bias voltage  $V_B$  with temperature held constant and a fixed stress time larger than the delay time  $\tau_D$ . From  $\Delta V_{FB}$  vs.  $V_B$  plots similar to Fig. 3, the intercepts  $\Delta V_{FB}(i)$  are extracted and plotted in Fig. 7 as a function of  $SiO_2$  thickness. It was found that  $\Delta V_{FB}(i)$  increases linearly with increasing  $x_0$ . This means that the charge is moving across the  $SiO_2$  layer. From the slopes in Fig. 7, values for  $Q_i/q$  of  $1.9 \times 10^{10} \text{ cm}^{-2}$  and  $3.06 \times 10^{10} \text{ cm}^{-2}$  for two different slices from the same processing lot were obtained. A substantial slice to slice variation of the amount of mobile charge in the insulator structure is to be expected if this charge is due to some kind of contamination, such as sodium. The variability of the data plotted in Fig. 7 is too great to allow a determination of whether the charge moves through the  $Al_2O_3$  as well as through the  $SiO_2$ . To clarify this point a bias-temperature stress experiment was conducted in which the bias voltage was cycled between positive and negative bias polarity starting with unstressed samples. The results of this experiment are shown in Fig. 8 which is a plot of the intercepts of  $\Delta V_{FB}$  vs.  $V_B$  plots as a function of time within the indicated stress cycle. In the first cycle, the intercept is seen to rise relatively slowly, reaching about 210 mV after 3900 min. (On a plot against log time it is actually a delayed linear function as in Fig. 1 and 2.) With reversal of bias, in the second cycle, the intercept rapidly relaxes back, settling toward 40 mV. With reapplication of positive bias (third cycle) it now rises

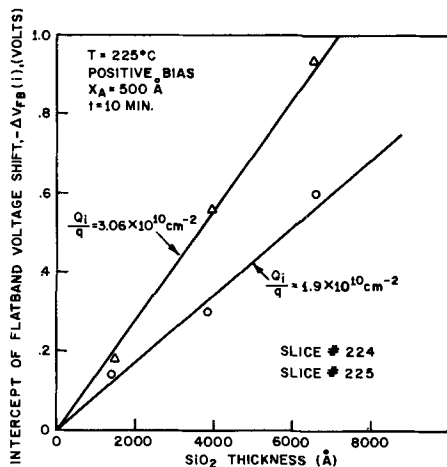


Fig. 7. Dependence of the intercept of the flatband voltage shift,  $\Delta V_{FB}(i)$ , of a  $\Delta V_{FB}$  vs.  $V_B$  curve on  $SiO_2$  thickness for two different samples.

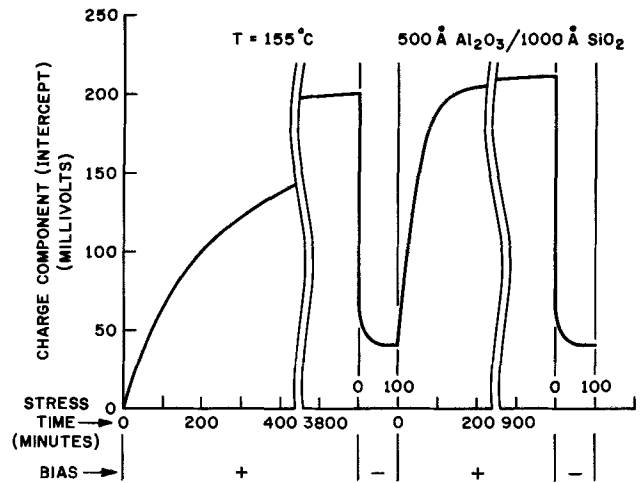


Fig. 8. Dependence of the intercept (charge motion) of a  $\Delta V_{FB}$  vs.  $V_B$  curve on stress time for  $T = 155^\circ C$ , with two complete cycles of positive followed by negative bias voltage.

much more rapidly, requiring only about 200 min to reach 210 mV. On reversal (fourth cycle) it rapidly relaxes back to about 40 mV.

The results of the cycling experiments may be explained as follows: during the first cycle, positive charge slowly moves from the metal- $Al_2O_3$  interface through the  $Al_2O_3$  by a trap-release process that is thermally activated by a 1.2 eV activation energy. Once it is through the  $Al_2O_3$  it is rapidly swept to the  $SiO_2$ -Si interface. This charge remains mobile so that on bias reversal (second cycle) it is rapidly swept back to the  $SiO_2$ - $Al_2O_3$  interface where it is retrapped. This retrapped charge must be trapped much more weakly than initially since it can be moved back to the Si- $SiO_2$  interface much more rapidly than initially (third cycle). Not only is the time varying behavior consistent with this model but the magnitudes of the shifts are also consistent. For the given structure, 1000Å  $SiO_2$  and 500Å  $Al_2O_3$ , one expects the recovered shift to be 1/5 the stressed shift if the charge originates at the metal- $Al_2O_3$  interface, moves to the Si- $SiO_2$  interface, and then returns to the  $Al_2O_3$ - $SiO_2$  interface. This is consistent with the observed values of 210 mV for the stressed shift and 40 mV for the recovered shift. A similar model was previously proposed by Snow and Dumesnil (16) in order to explain long-term drift effects caused by Na migration in metal-glass-oxide-semiconductor double-layer capacitors.

The influence of  $Al_2O_3$  thickness on the charge transport component was also studied. Figure 9 shows a plot of  $\Delta V_{FB}$  vs.  $V_B$  for different stress times and fixed temperature ( $225^\circ C$ ) for a slice with a standard  $SiO_2$  thickness ( $\approx 1000\text{Å}$ ) but an  $Al_2O_3$  thickness of about twice the standard thickness (1110Å). It may be noted that these curves show essentially no intercepts. This means that if there is mobile charge in the insulator system it has not penetrated the  $Al_2O_3$  to any significant extent. In addition, it may be seen, consistent with previous discussion, that the polarization is nearly symmetrical with positive/negative bias, increases directly with  $Al_2O_3$  thickness (by comparison with Fig. 2 and 3), and increases slightly with time.

Preliminary data on samples with  $Al_2O_3$  thicknesses of 1100 and 2400Å show that intercepts do develop after long periods of stressing with delay times increased by a factor of 50 times at 1100Å and 1300 times at 2400Å when compared to the standard 500Å  $Al_2O_3$  thickness. The effectiveness of the  $Al_2O_3$  as a barrier to ionic contamination is seen to increase nearly exponentially with thickness.

An etchback experiment was carried out to see whether the quality of the  $Al_2O_3$  layer varied with thickness. The results are shown in Fig. 10. The  $Al_2O_3$

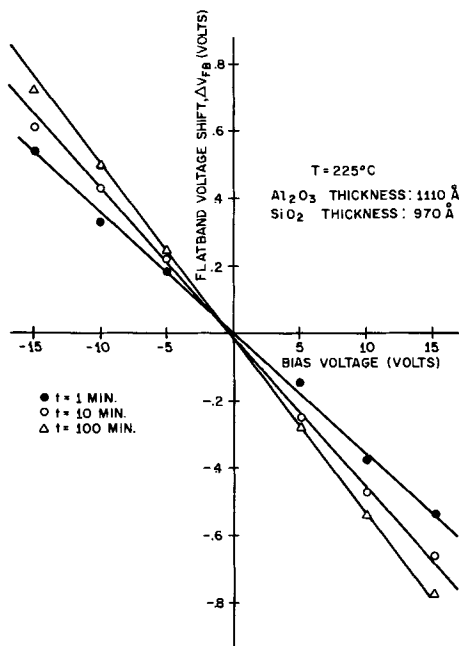


Fig. 9. Dependence of flatband voltage shift on bias voltage for thick  $\text{Al}_2\text{O}_3$  sample (1100Å) with constant temperature and stress time as parameters.

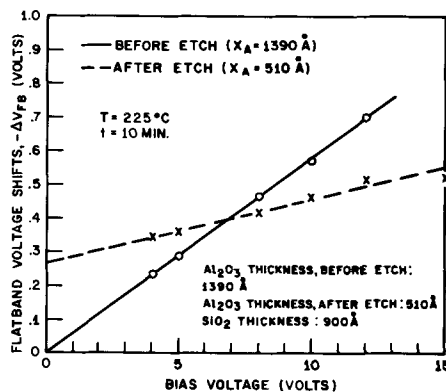


Fig. 10. Dependence of flatband voltage shift on bias voltage for constant temperature and stress time of a sample before and after etching the  $\text{Al}_2\text{O}_3$  from  $\approx 1400$  to  $\approx 500$ Å.

layer as originally grown (1390Å) shows only polarization. When the same layer is etched back to 500Å it shows both components (polarization as well as charge motion) just as a sample which was initially grown only to 500Å. This suggests that the ionic penetration properties of the  $\text{Al}_2\text{O}_3$  layer depend primarily on its thickness and not on the way in which it was produced.

It has previously been suggested (17) that the stress gradient in  $\text{Al}_2\text{O}_3$  on  $\text{SiO}_2$  is responsible for the inhibition of sodium penetration in the double insulator structure. The experimental results presented here suggest that the stress, which is an increasing function of  $\text{Al}_2\text{O}_3$  thickness, is still the controlling parameter and that trap depth is correlated with it. Thus, as the stress was relieved in the etchback experiment, the ions became more weakly trapped and the delay times shortened.

### Summary and Conclusions

A study was made of the flatband voltage shifts of double insulator MIS capacitors after bias-temperature treatment. The shifts were opposite to the bias voltage and larger in magnitude for positive than negative bias. The delay times of the shifts under positive bias were thermally activated with an activation energy of 1.2 eV. The flatband voltage shifts were found to be

linearly dependent on bias voltage with a time-varying offset for positive bias. This offset increases with increasing  $\text{SiO}_2$  thickness, stress time, and temperature. It decreases strongly with increasing alumina thickness.

The flatband voltage shifts encountered under negative bias can be explained by a bulk polarization of the alumina layer under the influence of an electric field and elevated temperature. The exact nature of this polarization cannot be established from the present data but it can be characterized by a polarizability,  $\chi_P = 0.86 \pm 0.25$  at 225°C, which was found to be independent of alumina and  $\text{SiO}_2$  thickness, but which increases slightly with increasing stress temperature (activation energy = 0.15 eV) and stress time. Most of the polarization occurs after a very short stress time (<1 min).

The flatband voltage shifts encountered under positive bias can only be explained if in addition to polarization in the  $\text{Al}_2\text{O}_3$  layer a charge motion through the insulator structure is assumed. This mobile charge is probably ionized sodium. The positively charged ions are initially located close to the metal- $\text{Al}_2\text{O}_3$  interface and are transported to the  $\text{Al}_2\text{O}_3$ - $\text{SiO}_2$  interface with an activation energy of about 1.2 eV. Subsequently they enter the  $\text{SiO}_2$  and are swept rapidly to the  $\text{SiO}_2$ -Si interface where they are locked in during the cool down under bias. Heating the sample up again with reversed bias results in a strong reduction of the flatband voltage shift. This means the mobile ions are swept back toward the  $\text{SiO}_2$ - $\text{Al}_2\text{O}_3$  interface. This cycle can be repeated several times. The amount of mobile charge was found to be slice dependent with typical values around  $2 \times 10^{10} \text{ cm}^{-2}$  depending on stress time and temperature. The charge motion through the  $\text{Al}_2\text{O}_3$  and the  $\text{Al}_2\text{O}_3$ - $\text{SiO}_2$  interface was found to be relatively slow, the relaxation of the charge from the Si- $\text{SiO}_2$  to the  $\text{SiO}_2$ - $\text{Al}_2\text{O}_3$  interface was found to be very fast (<1 min at 200°C). For  $\text{Al}_2\text{O}_3$  thicknesses larger than 500Å the amount of mobile charge penetrating the  $\text{Al}_2\text{O}_3$  in the time frame of the experiment decreases sharply. It is estimated that the delay time increases over an order of magnitude for each additional 500Å of  $\text{Al}_2\text{O}_3$ . An etchback experiment showed that charge penetration at 500Å is insensitive to the way in which the thickness is obtained. It is suggested that the ionic trapping energy is correlated to the average stress in the  $\text{Al}_2\text{O}_3$  layer which, in turn, increases with the  $\text{Al}_2\text{O}_3$  thickness. In samples with 1390Å of  $\text{Al}_2\text{O}_3$  the amount of mobile charge was unmeasurably small ( $<10^9 \text{ cm}^{-2}$ ).

The implications of these findings on the stability of MIS transistors using the standard double insulator structures are as follows: replacing threshold voltage shift for flatband voltage shift, and including explicitly the linear voltage dependence of the polarization component, one can rewrite Eq. [1] and [2] as follows

$$V_B < 0: \quad \Delta V_{TN} = -K_P V_B \quad [5]$$

$$V_B > 0: \quad \Delta V_{TP} = -K_P V_B \quad \text{for } t \leq \tau_D$$

$$\Delta V_{TP} = -K_P V_B - V_D \log(t/\tau_D) \quad \text{for } t > \tau_D \quad [6]$$

where  $\Delta V_{TN}$  and  $\Delta V_{TP}$  are the threshold voltage shifts under negative and positive bias, respectively.  $K_P$  is given by

$$K_P = \frac{K_O \alpha \chi_P}{K_A [(K_A + \chi_P) x_0 + K_O \alpha_A]} \quad [7]$$

as introduced in Eq. [3].  $V_D$  is assumed to be a constant independent of temperature and materials parameters and  $\tau_D$  is the delay time introduced in Fig. 2, which is temperature activated with an activation energy of 1.2 eV and increases sharply with  $\text{Al}_2\text{O}_3$  thickness. At the highest operating temperature assumed to be 85°C the following average numerical values apply

to a standard structure (500Å Al<sub>2</sub>O<sub>3</sub>/1000Å SiO<sub>2</sub>):  $K_P = 0.006$ ,  $V_D \cong 65$  mV/decade, and  $\tau_D \cong 200$  min.

For p-channel MOS transistors (negative bias) the expected shift after 40 years at 85°C with -10V bias is approximately 0.06V using the above values. For n-channel devices the threshold voltage shift under identical conditions (40 years, 85°C, +10V) is expected to be about -0.35V. The p-channel devices are, therefore, more stable than the n-channel devices, if 500Å of Al<sub>2</sub>O<sub>3</sub> and 1000Å of SiO<sub>2</sub> are used as gate insulators. Since the polarization shift increases linearly with Al<sub>2</sub>O<sub>3</sub> thickness but the charge transport delay time increases exponentially, stability under positive bias (n-channel) can be improved by increasing the Al<sub>2</sub>O<sub>3</sub> thickness. The optimum occurs when  $\tau_D$  is equal to end of life. Limited data suggest that this occurs at a thickness of 1400Å. Such an Al<sub>2</sub>O<sub>3</sub> thickness is probably undesirable both from a processing and circuit performance point of view. If one asks, instead, for an average end-of-life shift of 0.2V, then the data suggest an Al<sub>2</sub>O<sub>3</sub> thickness of about 700Å which is much more reasonable from both points of view and which gives adequate stability to both n- and p-channel devices.

#### Acknowledgments

The authors would like to thank E. F. Labuda for initiating this project and for many helpful discussions.

Manuscript submitted Sept. 7, 1973; revised manuscript received Nov. 27, 1973. This was Paper 89 presented at the Chicago, Illinois, Meeting of the Society, May 13-18, 1973.

Any discussion of this paper will appear in a Discussion Section to be published in the December 1974 JOURNAL. All discussions for the December 1974 Discussion Section should be submitted by Aug. 1, 1974.

#### REFERENCES

1. S. K. Tung and R. E. Caffrey, *Trans. Met. Soc. AIME*, **233**, 572 (1965).
2. H. E. Nigh, Colloque International sur les Propriétés et l'utilisation des Structures MIS, Grenoble, 1969, p. 77.
3. M. P. Lepselter, *Bell System Tech. J.*, **45**, 233 (1966).
4. R. H. Dudley and E. F. Labuda, IEEE International Electron Devices Meeting, Washington, D. C., 1969.
5. J. T. Clemens and E. F. Labuda, Paper 76 presented at Electrochemical Society Meeting, Washington, D. C., May 9-13, 1971; J. T. Clemens and E. F. Labuda, Paper 164 presented at Electrochemical Society Meeting, Chicago, Illinois, May 13-18, 1973.
6. E. E. Lampi and E. F. Labuda, 10th Proceedings, Reliability Physics, 1972, p. 112.
7. A. P. Gnadinger, Paper 164 presented at Electrochemical Society Meeting, Cleveland, Ohio, Oct. 3-7, 1971.
8. A. Goetzberger and A. D. Lopex, *This Journal*, **120**, 90 (1973).
9. E. S. Schlegel, *J. Appl. Phys.*, **42**, 425 (1971).
10. J. J. Curry and H. E. Nigh, 8th Annual Proceedings, Reliability Physics, 1970, p. 29.
11. R. A. Walden and R. J. Strain, *ibid.*, p. 23.
12. S. R. Hofstein, *IEEE Trans., Electron. Devices*, **ED-13**, 22 (1966).
13. E. H. Snow and B. E. Deal, *This Journal*, **113**, 263 (1966).
14. J. J. Curry and H. E. Nigh, To be published.
15. K. K. Iida, T. Tsujide, and M. Nakagiri, *Japan. J. Appl. Phys.*, **11**, 1153 (1972).
16. E. H. Snow and M. E. Dumesnil, *J. Appl. Phys.*, **37**, 2123 (1966).
17. C. M. Drum, R. N. Tauber, J. D. Ashner, and P. F. Schmidt, Paper 23 presented at Electrochemical Society Meeting, Washington, D. C., May 9-13, 1971.

## Diffusion of Boron from Implanted Sources under Oxidizing Conditions

J. L. Prince and F. N. Schwettmann\*

Semiconductor Research and Development Laboratories, Texas Instruments Incorporated, Dallas, Texas 75222

#### ABSTRACT

Diffusion of boron from sources implanted at 80 keV was investigated experimentally and mathematically over the range 1000°-1200°C for boron doses of  $1 \times 10^{14}$  cm<sup>-2</sup>,  $5 \times 10^{14}$  cm<sup>-2</sup>, and  $2 \times 10^{15}$  cm<sup>-2</sup>. Diffusion was in steam ambient and oxide thickness grown ranged from 0.2 to 1.2 μm. The boron diffusion coefficient was determined over the range of temperatures investigated. The segregation coefficient of boron in the Si-SiO<sub>2</sub> system was found to range from 1.8 at 1200°C to 10 at 1000°C. "Normal" diffusion was observed in all cases except that of diffusion at 1000°C for short times.

Redistribution in silicon of a predeposited boron source during thermal oxidation is of technological importance in the fabrication of bipolar and MOS devices and circuits. During such a redistribution, boron is preferentially segregated into the growing oxide, in addition to diffusing into the bulk silicon material (1). The subject has been investigated for steam and dry oxygen oxidation for the cases of initially uniform boron concentration (1), predeposition from a B<sub>2</sub>O<sub>3</sub> source (2), and predeposition from a boron nitride source (3). Diffusion from implanted, preannealed sources has been recently investigated for oxidation in a "purified argon" atmosphere (4). Oxide thicknesses

grown in this last investigation were of the order of 100Å (e.g., 200Å for oxidation at 1100°C for 2 hr). The segregation coefficient of boron in the Si-SiO<sub>2</sub> system, defined as the ratio of boron concentration in the oxide at the Si-SiO<sub>2</sub> interface to the boron concentration in silicon at the interface, was variously determined to be 3 (1), 9 (2,3), and  $16 \pm 5$  (4). In a recent work (5) on boron diffusion in SiO<sub>2</sub>, the segregation coefficient was found to be in the neighborhood of 10, with some temperature dependence. The diffusion coefficient determined by these investigators varied, but was in the neighborhood of previous work on boron diffusion in silicon by Kurtz and Yee (6a) and Fuller and Ditzemberger (6b).

This report describes experimental and mathematical investigation of diffusion of boron from implanted, but

\* Electrochemical Society Active Member.

Key words: boron, segregation, coefficient, diffusion, ion implantation.

not preannealed, sources under conditions of steam oxidation during diffusion. The temperature range of investigation was 1000°-1200°C. Under these conditions, segregation and diffusion coefficients of boron were determined by comparison of experimental profiles (obtained by incremental sheet resistance) to calculated profiles obtained by computer solution of the diffusion equation and by comparison of experimental and calculated sheet resistance of the boron layer.

### Experimental

Substrate slices were Czochralski-grown phosphorus-doped, (111) orientation, and had initial resistivity of 5-7 ohm-cm. Implanted ions were B<sup>11</sup>, obtained from an rf source using BF<sub>3</sub> as the source gas. The ion beam was focused and electrostatically scanned over the substrate surface. Implantation energy was 80 keV and implanted doses used were  $1 \times 10^{14}$  cm<sup>-2</sup>,  $5 \times 10^{14}$  cm<sup>-2</sup>, and  $2 \times 10^{15}$  cm<sup>-2</sup>. Slices were misaligned 7° during implantation to minimize channeling. After implantation and immediately before diffusion, slices were cleaned in an rf glow discharge with oxygen ambient and then in a mixture of sulfuric acid and hydrogen peroxide.

Each slice was oxidized in steam atmosphere at a temperature in the range 1000°-1200°C. The oxidation cycle consisted of a 5-min heat-up in dry O<sub>2</sub> and subsequent oxidation in steam ambient for times ranging from 15 to 180 min. Resultant oxide thickness and refractive index were measured by ellipsometry. The refractive index of the oxide was found to be independent of the implanted dose and the diffusion time to within experimental error. Oxide thickness vs. steam oxidation time is shown in Fig. 1 for the five temperatures used. These curves were calculated using the growth kinetics discussed by Grove (7) and using values for the oxidation rate parameters which provided the best fit to oxide thicknesses observed in the experiment. The curves of Fig. 1 replicate experimental oxide thickness observations to within a few per cent. The oxidation rate parameters used in Fig. 1 were 10-20% higher than those given by Grove (7).

Oxide layers were stripped in dilute HF and slices were rinsed in flowing deionized water. The sheet resistance was read using a four-point probe with light probe pressure. The depth distribution of boron was obtained for some slices by profiling using the incremental sheet resistance method (8). Some slices diffused at 1100°, 1150°, and 1200°C were analyzed using the ionic probe technique.

Resistivity data from the incremental sheet resistance analysis were converted to boron concentration through use of recent mobility data (4,9) which in-

dicates higher hole mobility for high boron concentrations than has been indicated previously (10). Accuracy of the more recent mobility data has been independently corroborated to a certain degree by the authors using incremental sheet resistance analysis on slices having low implanted boron doses. In the case of the low dose boron implants annealed at 900°C with no oxidation, use of the previously accepted hole mobilities to reduce the incremental sheet resistivity data consistently resulted in calculated integrated doses 10-20% higher than the actual dose, whereas use of the more recent values for hole mobilities resulted in calculated integrated doses within 5% of the actual dose.

### Analysis

The coordinate system used in formulating the diffusion equation and boundary conditions is shown in Fig. 2. Origin of coordinates is taken at the Si-SiO<sub>2</sub> interface. In this coordinate system, the diffusion of the boron atoms is governed by

$$\frac{\partial N}{\partial t} = \frac{\partial}{\partial y} \left( D \frac{\partial N}{\partial y} \right) + m \frac{dX_o}{dt} \frac{\partial N}{\partial y} \quad [1]$$

where  $N(y,t)$  = boron concentration;  $D$  = boron diffusion coefficient in silicon;  $m$  = thickness of silicon consumed in growing unit thickness of SiO<sub>2</sub>, assumed to be 0.44; and  $X_o(t)$  = SiO<sub>2</sub> thickness.

The initial condition is

$$N(y,0) = f(y,0) \quad [2]$$

where  $f(y,0)$  is presumed known through LSS theory or experiment. Boundary conditions are

$$N(\infty,t) = 0 \quad [3]$$

$$D \frac{\partial N}{\partial y} = (k - m) N(0,t) \frac{dX_o}{dt} \quad [4]$$

where  $k$  is the segregation coefficient of boron in the Si-SiO<sub>2</sub> system,  $k = [N(0^-,t)]/[N(0^+,t)]$ . This last boundary condition is derived from the requirement of conservation of boron atoms and under the assumption that boron diffusion in the oxide is slow relative to the oxidation rate ( $dX_o/dt$ ). This last condition is met for steam oxidation.

The boron diffusion coefficient was assumed to be the low-concentration value  $D_1$  enhanced by the local electric field effect (11). In addition, possible increase of the diffusion coefficient due to vacancy solubility enhancement (12) caused by heavy doping was accounted for by including a multiplicative factor  $[1 + (AN)/(n_i)]$ , where  $A$  is a constant between 0 and 1,  $N$  is boron concentration, and  $n_i$  is the intrinsic carrier concentration at the diffusion temperature. Uncer-

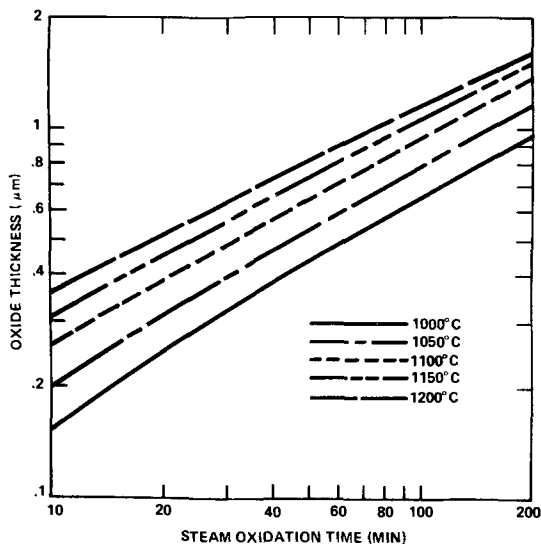


Fig. 1. Oxide thickness vs. steam oxidation time

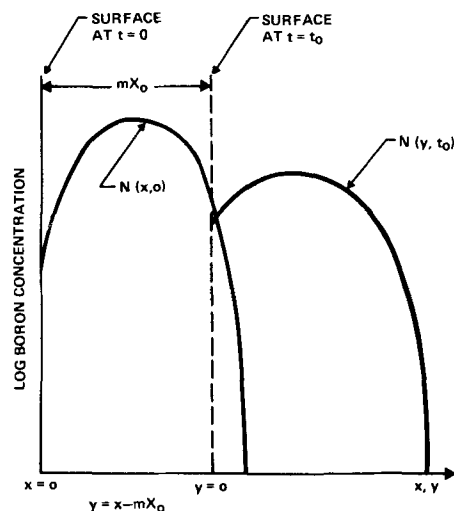


Fig. 2. Coordinate system for solution of diffusion equation

tainties in energy band and defect parameters at diffusion temperatures prevent accurate calculation of  $A$ . However, estimates (12, 13) range from  $10^{-1}$  to  $2 \times 10^{-2}$  depending on temperature. The total expression used for the diffusion constant was thus

$$D = D_1 \left( 1 + \frac{AN}{n_1} \right) \left[ 1 + \frac{1}{\sqrt{1 + 4 \left( \frac{n_1}{N} \right)^2}} \right] \quad [5]$$

Implicit in this formulation is the assumption of total activation of boron atoms. This total activation has been verified by the authors for the range of doses used in the experiment and for anneal temperatures in excess of  $900^\circ\text{C}$ .

Oxide thickness was taken to be (7)

$$X_o = \frac{k_p}{2k_1} \left\{ \left[ \frac{4(t + t^*)k_1^2}{k_p} + 1 \right]^{1/2} - 1 \right\} \quad [6]$$

where  $k_p$  and  $k_1$  are, respectively, the parabolic and linear oxidation rate coefficients,  $t$  is the oxidation time, and  $t^*$  is a parameter related to the oxide thickness which exists prior to the beginning of an oxidation cycle.

The system of Eq. [1] through [4] was solved on a computer by finite difference techniques using a Crank-Nicolson type approach (14). The nonlinearity engendered by the concentration dependence of  $D$  required use of a two-step (iterative) solution algorithm. Truncation error of the solution algorithm was found to be on the order of 0.01% for the concentration levels examined. The output of the computer solution was boron concentration vs. depth into the silicon, and sheet resistance of the boron layer. Sheet resistance was calculated using the recent hole mobility data (4, 9) discussed earlier.

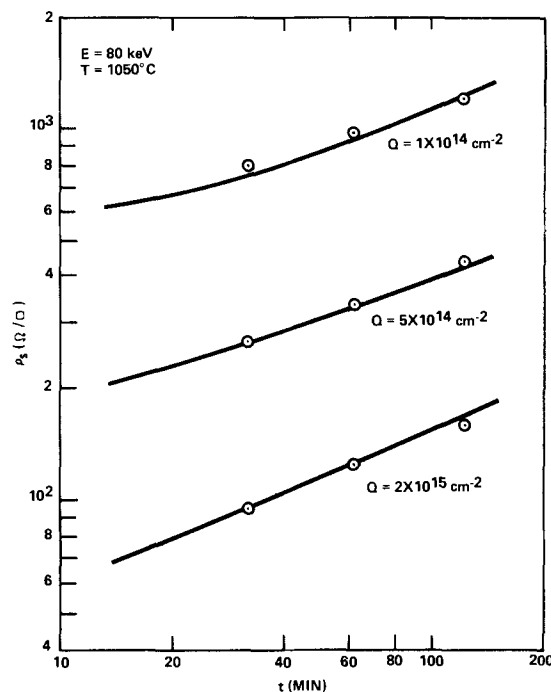
**Results and Discussion**

Figures 3 through 7 show experimental values of sheet resistance as a function of steam oxidation time for three boron doses and five diffusion temperatures. The maximum error is  $\pm 10\%$  in sheet resistance for this data. Figures 8, 9, and 10 show boron profiles ob-

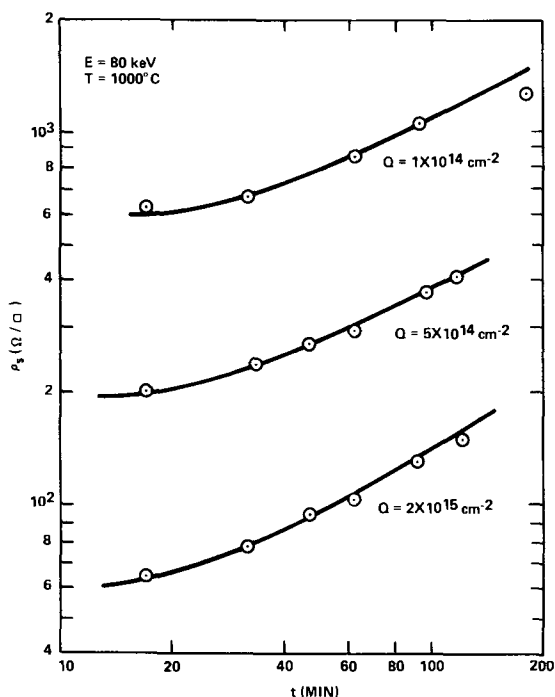
**Table I. Boron peak concentration to surface concentration ratio, from ion probe data (15)**

Diffusion temp ( $^\circ\text{C}$ )	Peak to surface concentration ratio
1000	2.7
1100	1.8
1200	1.3

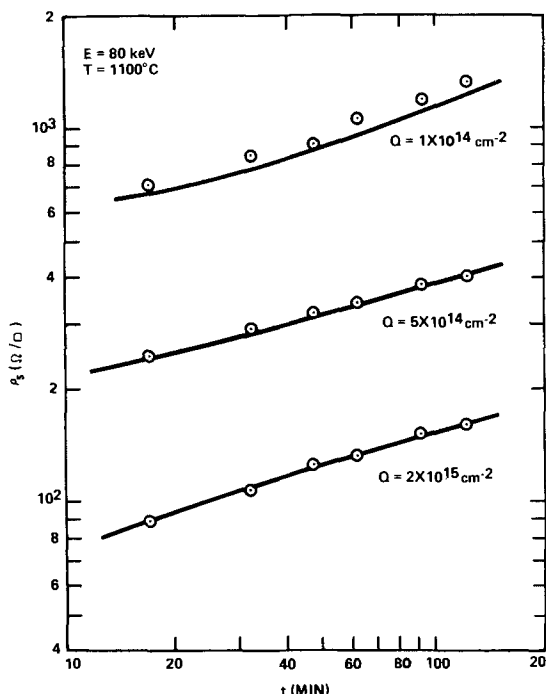
tained by incremental sheet resistance profiling. Accuracy of this data is estimated to be  $\pm 5\%$  for the distance scale and  $\pm 20\%$  for concentration. Table I gives average values of surface-to-peak boron concentration



**Fig. 4. Sheet resistance of boron layer vs. steam oxidation time,  $T = 1050^\circ\text{C}$ .**



**Fig. 3. Sheet resistance of boron layer vs. steam oxidation time,  $T = 1000^\circ\text{C}$ .**



**Fig. 5. Sheet resistance of boron layer vs. steam oxidation time,  $T = 1100^\circ\text{C}$ .**

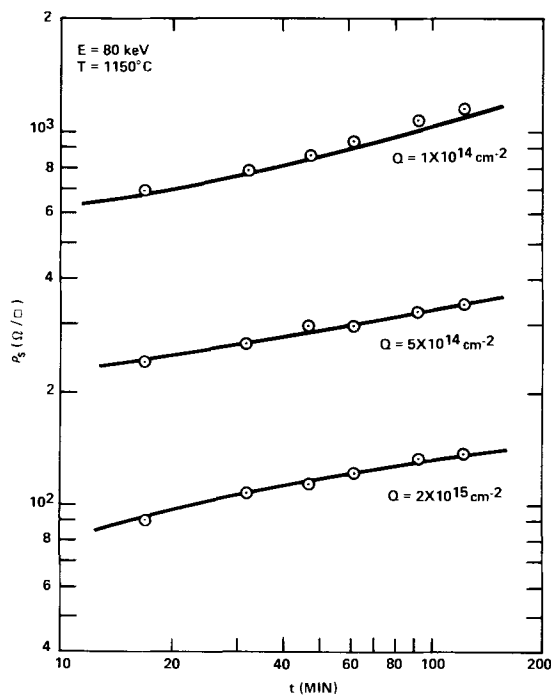


Fig. 6. Sheet resistance of boron layer vs. steam oxidation time,  $T = 1150^\circ\text{C}$ .

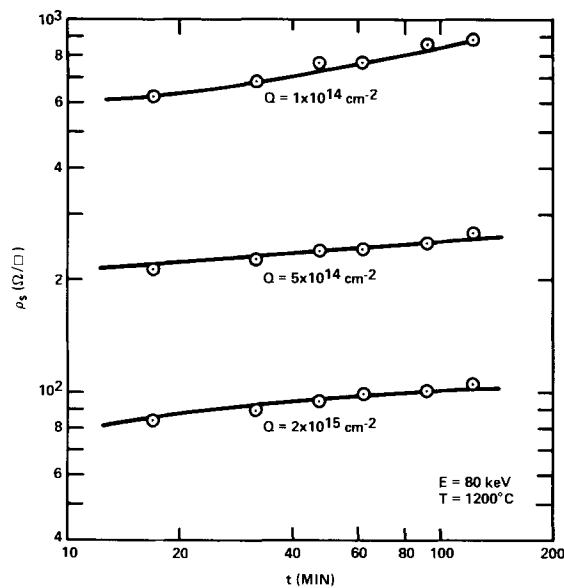


Fig. 7. Sheet resistance of boron layer vs. steam oxidation time,  $T = 1200^\circ\text{C}$ .

ratios from ion-probe data (15). Accuracy of the ratios is estimated to be  $\pm 5\%$ .

Boron diffusion coefficients at  $1000^\circ$ ,  $1100^\circ$ , and  $1200^\circ\text{C}$  were determined by iterating the computer calculation and comparing the part of the calculated boron profile past the peak concentration point to the experimental boron profiles shown in Fig. 8 through 10. The initial boron profile was taken to be of gaussian form with range  $0.285 \mu\text{m}$  and range straggling  $0.075 \mu\text{m}$  for these calculations. These values for range and range straggling are different from the theoretical values (16). However, it has been determined through compilation of results in the literature and independent experiments that these values best characterize an 80 keV boron profile, which is in fact not gaussian (17). No explicit account was taken in the numerical solution of annealing of implantation damage. This annealing was assumed to occur in times short in comparison with the diffusion times. Within wide bounds, the value of

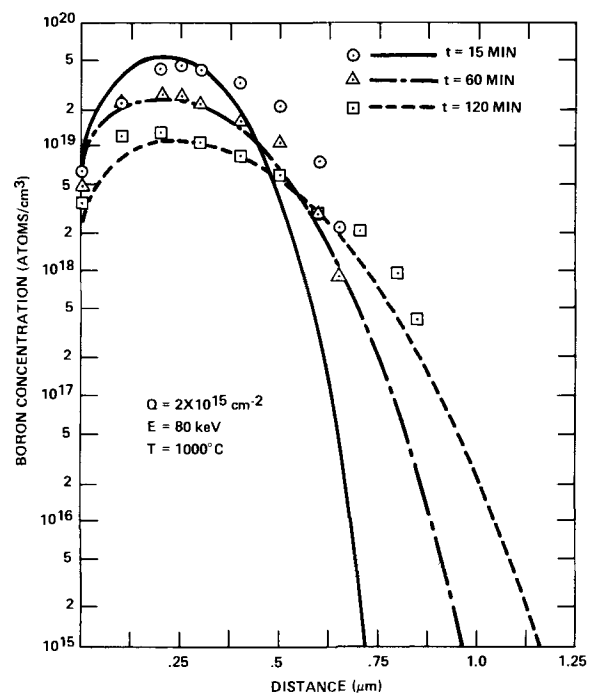


Fig. 8. Calculated and actual boron concentration profiles for oxidation at  $1000^\circ\text{C}$ .

segregation coefficient used in this comparison does not affect the calculated profile past the peak concentration point.

Various values for the constant  $A$  were used in making the above comparison. No values for  $A$  within the limits of  $10^{-1}$  to  $2 \times 10^{-2}$  gave profiles significantly different from those obtained for  $A = 0$  for the dose levels used in the experiment. Figure 11 shows the boron diffusion coefficient as a function of inverse temperature, as determined by the comparison. For diffusion at  $1000^\circ\text{C}$ , heavier weight was given to matching experimental profiles at longer times. For this temperature, experimental profiles exhibited apparent enhanced diffusion for short (e.g., 15 min) diffusion times. Also shown in Fig. 11 are examples of the boron

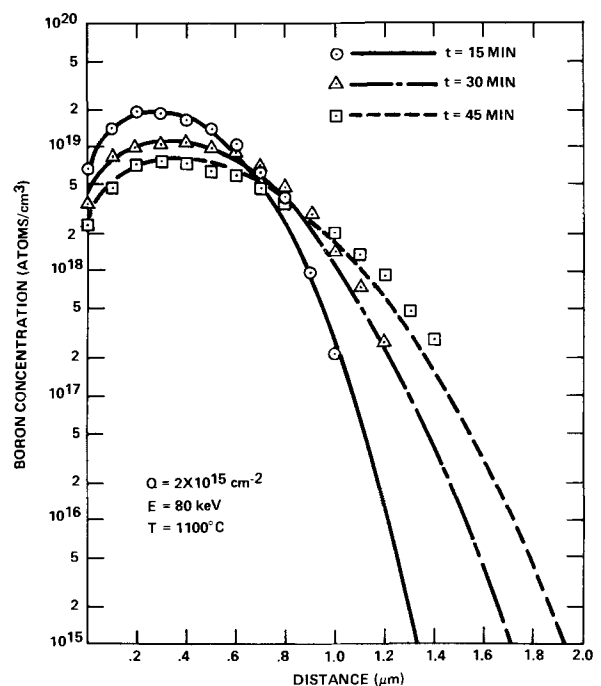


Fig. 9a. Calculated and actual boron concentration profiles for oxidation at  $1100^\circ\text{C}$ .



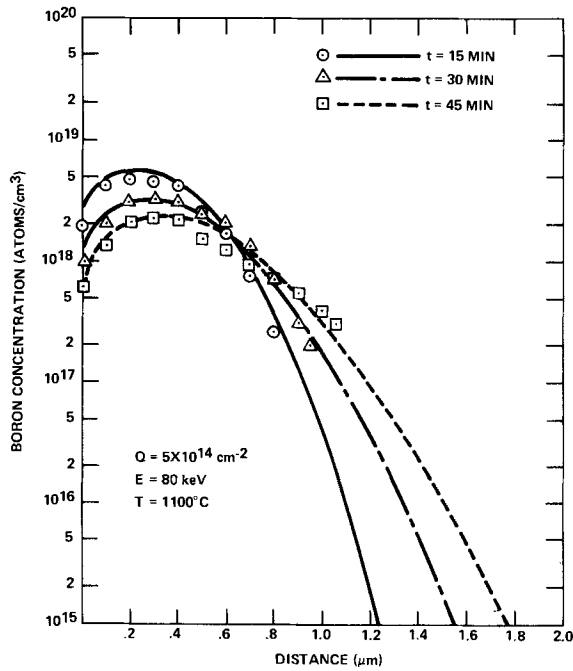


Fig. 9b. Calculated and actual boron concentration profiles for oxidation at 1100°C.

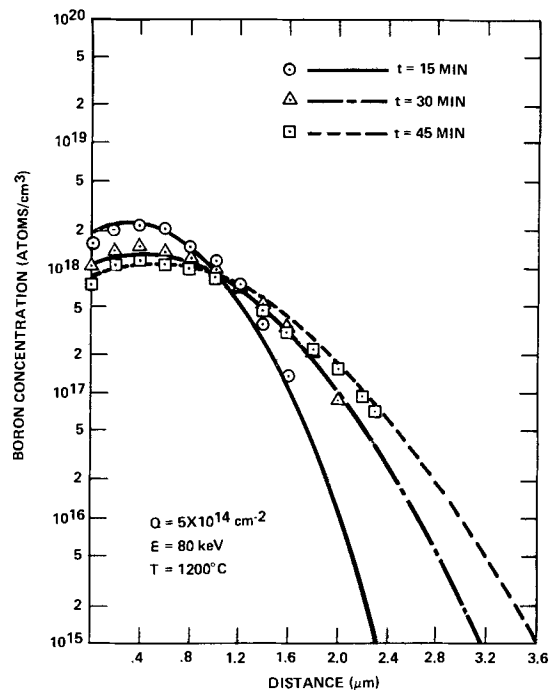


Fig. 10b. Calculated and actual boron concentration profiles for oxidation at 1200°C.

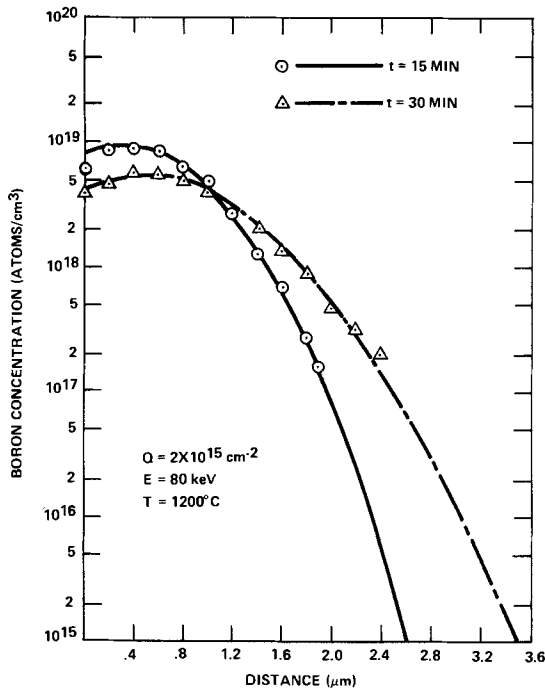


Fig. 10a. Calculated and actual boron concentration profiles for oxidation at 1200°C.

diffusion coefficient as determined by other workers. It is seen that results of this work are in general agreement with previous results over the range of common diffusion temperatures. The diffusion coefficient shown in Fig. 11 is approximated by

$$D_1 = 0.0322 \exp(-3.02/kT) \quad [7]$$

Segregation coefficient  $k$  was determined by iteration of the computer solution, using values for the diffusion coefficient calculated from Eq. [7]. Boron concentration profiles and values of sheet resistance calculated in the iteration process were compared to experimental profiles and experimental values of sheet resistance. Sensitivity of the calculated results to variations in value of the segregation coefficient is illustrated in

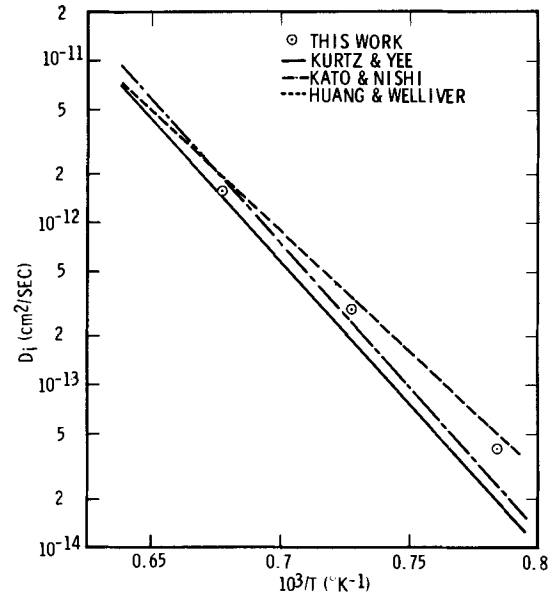


Fig. 11. Intrinsic boron diffusion coefficient vs. inverse temperature.

Fig. 12 and 13. This comparison was made for diffusion at 1200°C and for boron dose equal to  $2 \times 10^{15} \text{ cm}^{-2}$ . Results calculated for temperatures lower than 1200°C show reduced sensitivity to  $k$ . This is due to the increase in the ratio of the parabolic oxidation rate coefficient to the boron diffusion coefficient, with decreasing temperature.

Figure 14 shows the segregation coefficient determined in this work as a function of inverse temperature. The "error bars" in Fig. 14 indicate the range of values of  $k$  for which satisfactory fit to experimental data was obtained. The value of  $k$  was found to range from 1.8 to approximately 10 over the range 1200°-1000°C. The relative sizes of the boron diffusion coefficient and the parabolic oxidation rate coefficient at 1000°C are such that the comparison of experiment and calculation is insensitive to the value of the segre-

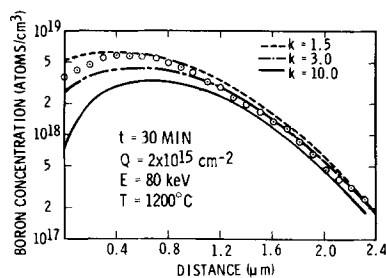


Fig. 12. Actual boron concentration profile and calculated profile for three values of segregation coefficient.

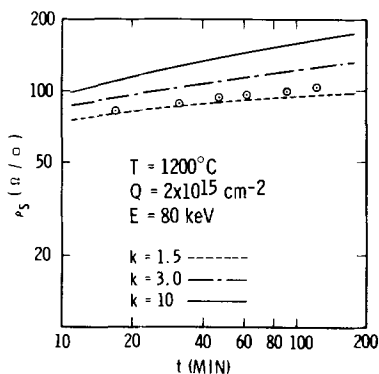


Fig. 13. Actual sheet resistance of boron layer and calculated behavior for three values of segregation coefficient.

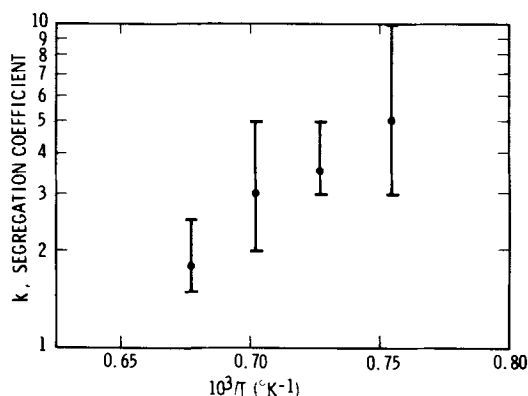


Fig. 14. Segregation coefficient vs. inverse temperature

gation coefficient. Thus, the value  $k = 10$  at  $1000^\circ\text{C}$  is an estimation and is not shown in Fig. 14. It could be in error by a factor of two in either direction. The segregation coefficient of Fig. 14 is best fit by the expression

$$k = 2.33 \times 10^{-4} \exp(1.135/kT) \quad [8]$$

The best-fit calculated boron concentration profiles and sheet resistance of the boron layers are superimposed on the experimental data of Fig. 3 through 10. These calculated quantities were obtained assuming  $A = 0$ , using the diffusion coefficient of Fig. 11, and using values of the segregation coefficient shown as experimental points in Fig. 14. Note that in the iteration process and in the calculated curves of Fig. 3 through 10, the segregation coefficient was allowed to vary with temperature but was assumed to be independent of surface concentration.

In comparing the best fit calculated boron profiles and experimental profiles, it is seen that agreement is

good for all cases but diffusion for short times at low temperatures (e.g., 15 min at  $1000^\circ\text{C}$ ). The discrepancy evident in Fig. 8 may be due to the annealing of implantation-related damage, which at  $1000^\circ\text{C}$  could take an amount of time appreciable compared to 15 min. Investigations by the authors of  $8 \times 10^{14} \text{ cm}^{-2} \text{ B}^{11}$  implantations annealed without oxidation at  $900^\circ\text{C}$  indicate a value for the boron diffusion coefficient at  $900^\circ\text{C}$  in agreement with Eq. [7].

### Conclusion

Diffusion from ion-implanted boron layers in an oxidizing atmosphere can be successfully predicted by numerical solution of the diffusion equation. Concentration enhancement of diffusion beyond the field-aiding effect was not found to be necessary to predict profiles for doses used in this work. The boron diffusion coefficient determined in the course of this work is near that found by previous workers. The boron segregation coefficient was found to be in the range 1.8 to 10 depending on temperature.

### Acknowledgments

The authors wish to acknowledge contributions of support and advice from their colleagues G. D. Cumming, W. H. Schroen, and J. G. Aiken. Careful experimental work by Alice Guffey and Pat Hass is also acknowledged.

Manuscript submitted Oct. 4, 1973; revised manuscript received Dec. 18, 1973. This was Paper 311RNP presented at the Chicago, Illinois, Meeting of the Society, May 13-18, 1973.

Any discussion of this paper will appear in a Discussion Section to be published in the December 1974 JOURNAL. All discussions for the December 1974 Discussion Section should be submitted by Aug. 1, 1974.

### REFERENCES

- (a) A. Grove, O. Leistiko, Jr., and C. T. Sah, *J. Appl. Phys.*, **35**, 2695 (1964);  
(b) B. Deal, A. Grove, E. Snow, and C. T. Sah, *This Journal*, **112**, 308 (1965).
- T. Kato and Y. Nishi, *Japan. J. Appl. Phys.*, **3**, 377 (1964).
- J. S. T. Huang and L. C. Welliver, *This Journal*, **117**, 1577 (1970).
- S. Wagner, *ibid.*, **119**, 1570 (1972).
- P. R. Wilson, *Solid-State Electron.*, **15**, 961 (1972).
- (a) A. D. Kurtz and R. Yee, *J. Appl. Phys.*, **31**, 303 (1960);  
(b) C. S. Fuller and J. A. Ditzenberger, *ibid.*, **27**, 544 (1956).
- A. Grove, "Physics and Technology of Semiconductor Devices," John Wiley & Sons, Inc., New York (1967).
- E. Tannenbaum, *Solid-State Electron.*, **2**, 123 (1961).
- B. L. Crowder, *This Journal*, **118**, 943 (1971).
- J. C. Irvin, *Bell System Tech. J.*, **41**, 387 (1962).
- K. Lehovc and A. Slobodskoy, *Solid-State Electron.*, **3**, 45 (1961).
- S. M. Hu and S. Schmidt, *J. Appl. Phys.*, **39**, 4272 (1968).
- J. Borel, G. Merckel, J. Monnier, P. Saintot, D. VanDorpe, M. Stern, and M. Maffei, 1973 IEEE International Solid State Circuits Conference, Philadelphia, Pa., February 14-16, 1973.
- D. U. Von Rosenberg, "Methods for the Numerical Solution of Partial Differential Equations," American Elsevier Publishing Co., Inc., New York (1969).
- R. Dobrott, Private communication.
- W. S. Johnson and J. F. Gibbons, "Projected Range Statistics in Semiconductors," Distributed by Stanford University Bookstore (1969).
- J. F. Gibbons and S. Mylroie, *Appl. Phys. Letters*, **22**, 568 (1973).

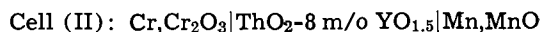
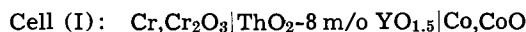
# Standard Free Energy of Formation of Cr<sub>2</sub>O<sub>3</sub>

F. N. Mazandarany\*<sup>1</sup> and R. D. Pehlke

Materials and Metallurgical Engineering, The University of Michigan, Ann Arbor, Michigan 48104

## ABSTRACT

The standard Gibbs free energy of formation of Cr<sub>2</sub>O<sub>3</sub>,  $\Delta G^\circ_f(\text{Cr}_2\text{O}_3)$ , was measured using an electrochemical technique incorporating a ThO<sub>2</sub>-Y<sub>2</sub>O<sub>3</sub> electrolyte. The following two cells were investigated



$\Delta G^\circ_f(\text{Cr}_2\text{O}_3)$  calculated from emf results for the above two cells are in good agreement, also in close agreement with a previous study of the Cr-Cr<sub>2</sub>O<sub>3</sub> equilibrium by the gas equilibration technique. The results of the present investigation lead to the following expression for the standard Gibbs free energy of formation of Cr<sub>2</sub>O<sub>3</sub>

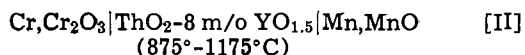
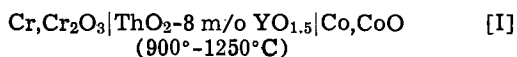
$$\Delta G^\circ_f(\text{Cr}_2\text{O}_3) = -266,600 + 59.78T \pm 350 \text{ cal} \\ (1150^\circ\text{-}1540^\circ\text{K})$$

The thermodynamics of the Cr-Cr<sub>2</sub>O<sub>3</sub> equilibrium has been the subject of numerous previous investigations. However, the results obtained by various techniques and investigators are in poor agreement.

Jeannin *et al.* (1) equilibrated Cr, Cr<sub>2</sub>O<sub>3</sub> samples with H<sub>2</sub>/H<sub>2</sub>O mixtures between 1040° and 1300°C to determine the standard Gibbs free energy of formation of Cr<sub>2</sub>O<sub>3</sub>. The results of Jeannin *et al.* were in poor agreement with previous investigations of the system (2-4) using a similar technique. However, the study of Jeannin *et al.* was in agreement with those calculated from calorimetric data within experimental error (1).

Both Tretjakow and Schmalzried (5), and Pugliese and Fitterer (6) measured the free energy of formation of Cr<sub>2</sub>O<sub>3</sub> between 800° and 1200°C using the solid oxide electrolyte technique. These investigators used a calcia-stabilized zirconia tube as the electrolyte with air as the reference electrode and a Cr, Cr<sub>2</sub>O<sub>3</sub> mixture as the "unknown" electrode. While the results of these investigations agree well at 800°C, there is as much as 15 mV difference between the measured cell potentials at 1175°C, indicating a large difference in the temperature dependence of the free energy. The results of both of these investigations are in disagreement with those of Jeannin *et al.*

The purpose of the present investigation was to measure the standard Gibbs free energy of formation of Cr<sub>2</sub>O<sub>3</sub> using the solid oxide electrolyte technique incorporating a ThO<sub>2</sub>-Y<sub>2</sub>O<sub>3</sub> solid electrolyte. The following two cells were investigated



## Experimental Technique

**Equipment.**—The galvanic cell arrangement used in the present study is shown schematically in Fig. 1. The cell consisted of a ThO<sub>2</sub>-Y<sub>2</sub>O<sub>3</sub> electrolyte pellet, 11, sandwiched between two electrodes, 10. A mullite tube, 13, pressed against the upper surface of electrolyte, 11, helped to minimize oxygen transport in the gas phase from one electrode to another. A Pt O-ring was placed between tube, 13, and the electrolyte, 11, in runs involving cell [I] to improve the separation of the gas phases in equilibrium with the two electrodes.

\* Electrochemical Society Student Member.

<sup>1</sup> Present address: General Atomic Company, La Jolla, California 92037.

Key words: free energy of formation, Cr<sub>2</sub>O<sub>3</sub>, chromium oxide, solid oxide electrolyte.

The cell was fixed at the end of the mullite tube, 9, by the compression of springs, 15, transmitted through tube 13, and push rod 12. This alumina push rod was a four-hole insulator; two holes of which accommodated a Pt/Pt-10% Rh thermocouple. A third hole accommodated the lead wire for the inner electrode, 10. Both electrode lead wires were Pt-10% Rh, gauge 26. The photograph of Fig. 2 shows the cell as it was fixed at the bottom of the mullite tube, 9, of Fig. 1.

The cell potentials were measured with a high impedance (10<sup>7</sup> ohms) potentiometric voltmeter (Keithley Model 660). The temperature voltages were measured with a Model K-2 L&N potentiometer. Both instruments were checked periodically against a known voltage source. The instruments are rated to measure voltages with an accuracy level of  $\pm 0.02\%$  of the reading.

**Materials.**—ThO<sub>2</sub>-8 mole per cent (m/o) YO<sub>1.5</sub> electrolyte pellets were obtained from the Zirconium Corporation of America. These pellets were prepared from high purity starting materials (99.9% Y<sub>2</sub>O<sub>3</sub> and 99.5% ThO<sub>2</sub>) and were sintered at temperatures exceeding 1950°C for 24 hr in an Ar/H<sub>2</sub> atmosphere to give maximum density and homogeneity. The electrolyte pellets were 2 mm high with a diameter of 12 mm. Before use in a cell, the electrolyte pellets were heated to 1000°C for 24 hr in a dry argon atmosphere with Cr chips present. Then they were polished on a 50 $\mu$  wheel before use in a cell. The electrolyte pellets were white in color before and after use in a cell.

The Cr<sub>2</sub>O<sub>3</sub> electrodes were prepared by mixing high purity Cr powder (99.5%) with analytical grade

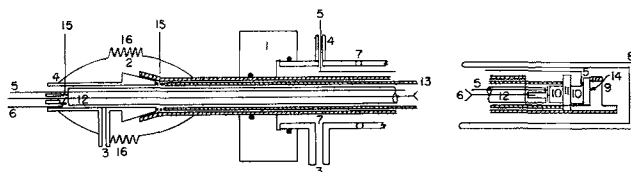


Fig. 1. Schematic drawing of cell arrangement. 1, O-ring joint assembly; 2, ground glass joint; 3, gas inlet and outlet; 4, wax seal; 5, electrode lead wire (Pt-10% Rh); 6, thermocouple (Pt/Pt-10% Rh); 7, glass-mullite seal; 8, mullite tube; 9, mullite support tube; 10, electrode; 11, electrolyte; 12, alumina push rod; 13, mullite tube; 14, zirconia support pellet; 15, compression spring; 16, tension spring.

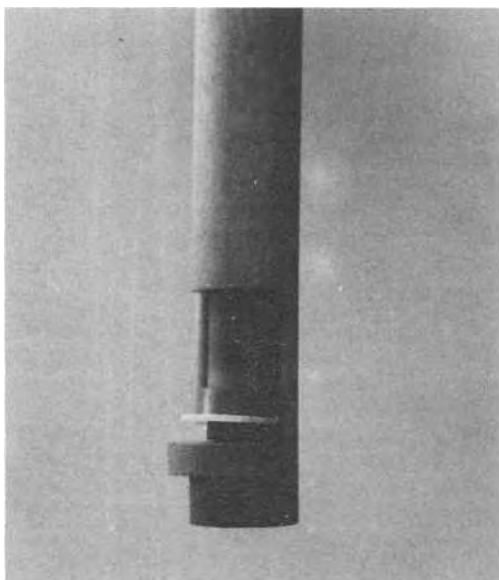


Fig. 2. View of assembled cell

Cr<sub>2</sub>O<sub>3</sub> in a 10/1 weight ratio, and compressing in a steel die at about 60,000 psi to obtain pellets with the dimensions: 6 mm diameter by 2 mm high. The pressed pellets were sintered in a dry argon atmosphere for 24 hr at 1000°C. The sintered pellets were polished on a 50 $\mu$  wheel before use in a cell.

The Mn<sub>2</sub>MnO electrodes were prepared by first pulverizing electrolytic grade Mn flakes (99.8%) to obtain relatively fine Mn powders. The Mn powders then were mixed with analytical grade MnO<sub>2</sub> in a 10/1 weight ratio and pelletized at about 100,000 psi. The pellets were placed in a Vycor tube which was evacuated to 10<sup>-5</sup> atm and sealed. The sealed capsule was heated to 900°C for 24 hr to ensure complete conversion of MnO<sub>2</sub> to MnO.

The Co<sub>2</sub>Co electrodes were prepared by mixing high purity Co powder (99.9%) with analytical grade CoO and pressing at 100,000 psi. No sintering was necessary for the Co<sub>2</sub>Co electrodes after pressing.

**Procedure.**—The assembled cell was placed vertically in the hot zone of a Pt resistance furnace. The furnace temperature was controlled by a Pt/Pt-10% Rh thermocouple that activated a proportionating controller. Temperature fluctuations in the hot zone were approximately  $\pm 0.5^\circ\text{C}$ . The temperature gradient in the hot zone of the furnace was about 1°C/in. over a distance of about 1½ in.

Before the furnace power was turned on, the cell atmosphere was evacuated several times and filled with purified argon. This prepurified grade argon gas was purified further before entering the cell tube by passing over anhydrous Mg(ClO<sub>4</sub>)<sub>2</sub>, over activated CuO (BTS catalyst), over activated Cu (reduced BTS catalyst), and finally over anhydrous P<sub>2</sub>O<sub>5</sub> and ascarite.

After the cell was completely degassed and finally filled with argon, the furnace power was turned on to heat the cell to an intermediate temperature (1100°C for cell [I] and 950°C for cell [II]). After thermal equilibration the cell was allowed to come to thermodynamic equilibrium over the next 5-12 hr. The criteria for the attainment of thermodynamic equilibrium was adopted such that at constant temperature the cell potential should not vary by more than  $\pm 0.5$  mV over a period of 1 hr and that such variation be random and not systematic.

Upon the attainment of equilibrium at the first temperature the furnace temperature was either raised or lowered by 50°C and the cell was allowed to equilibrate at the new temperature. This procedure was repeated until an equilibrium measurement had been

made at every 25°C interval over the temperature range as a minimum. In this manner, the cell was cycled through the reported temperature range at least twice before the furnace power was shut off to terminate the run. A typical run lasted for 3-6 days.

Reversibility in the cells was generally inferred from the high stability of measured potentials and high linearity of cell potential-temperature relationships which were unaffected by temperature cycling and reproducible from run to run. A further check of the reversibility was made by the following procedure. Once cell [I] had equilibrated at 1250°C, the cell was perturbed by connecting a 1.5V dry battery across the leads for 15 sec. The perturbed cell was then allowed to re-equilibrate overnight. The steady measured potential the next morning was within  $\pm 1$  mV of the value before the cell was perturbed. This procedure was repeated over the next night passing current in the opposite direction with similar results.

### Results and Discussions

The results of this study from cell [I] obtained from the cumulative data of three independent runs are listed in Table I. The data are represented by the following least squares line

$$\text{cell I: } E(\text{mV}) = 706.6 - 0.0640T \pm 1.7 \text{ mV} \\ (1173^\circ - 1523^\circ\text{K})$$

The standard errors of estimate of the coefficients in this equation are, respectively,  $\pm 2.8$  mV and  $\pm 0.0015$  mV/°K.

Similarly, the cumulative data of two independent runs on cell [II] are given in Table I. These data may be represented by the following line

$$\text{cell [II]: } E(\text{mV}) = 90.67 - 0.0347T \pm 0.8 \text{ mV} \\ (1148^\circ - 1430^\circ\text{K})$$

The standard errors of estimate of the coefficients in this equation are, respectively,  $\pm 1.7$  mV and  $\pm 0.0008$

Table I. Summary of experimental data

	Cell [I]		Cell [II]		
	Cr, Cr <sub>2</sub> O <sub>3</sub>   ThO <sub>2</sub> -YO <sub>1.5</sub>   Co, CoO		Cr, Cr <sub>2</sub> O <sub>3</sub>   ThO <sub>2</sub> -YO <sub>1.5</sub>   Mn <sub>2</sub> MnO		
	T, °C	emf, mV	T, °C	emf, mV	
Run 26	1244.9	610.0	Run 29	1100.5	139.6
	1265.8	609.2		1144.2	140.4
	1250.9	608.6		1126.2	139.6
	1249.3	611.5		1100.1	138.5
	1247.1	611.7		1072.8	137.6
	1179.2	615.5		1046.2	136.7
	1181.7	614.7		1046.2	136.7
	1131.6	616.6		1015.5	135.7
	1130.7	618.0		1015.1	135.7
	1079.0	619.8		983.3	134.8
	1084.1	618.6		979.1	134.8
	1034.5	625.7		941.8	133.9
	1038.1	623.5		903.2	132.9
	941.0	628.7		912.6	131.4
	994.5	622.2		867.9	135.1
989.3	627.5	1019.9	136.4		
1035.6	624.2				
Run 27*	1186.0	613.5	Run 30	1074.7	138.0
	1185.7	613.7		1101.3	138.9
	1146.9	614.6		1102.7	138.9
	1052.9	620.5		1145.1	140.1
	1217.5	608.4		1166.2	140.5
	1251.8	606.8		1139.2	139.5
	1272.5	611.1		1115.4	138.4
	1203.3	613.7		1110.3	138.2
	1151.2	614.5		1087.3	137.1
	1151.0	615.9		1058.4	136.0
	1151.2	615.7		1057.9	136.0
		1022.5	134.5		
		1022.5	134.5		
Run 28	1278.4	604.4			
	1210.0	611.1			
	1208.5	610.5			
	1158.1	618.5			
	1157.0	615.5			
	1158.8	613.5			
	1111.8	618.3			
	1112.3	615.3			
	906.1	627.8			
	906.5	631.8			
	904.7	633.5			
	974.4	629.2			
	1019.1	623.7			
1121.3	617.3				
1159.5	615.2				

\* Run 27 had to be terminated before any more measurements were made because one electrode lead wire broke.

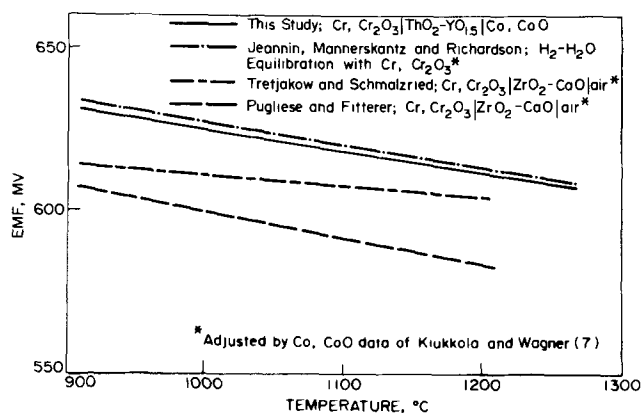


Fig. 3. Cell potential-temperature relationship for cell [I]: Cr, Cr<sub>2</sub>O<sub>3</sub> | ThO<sub>2</sub>-YO<sub>1.5</sub> | Co, CoO.

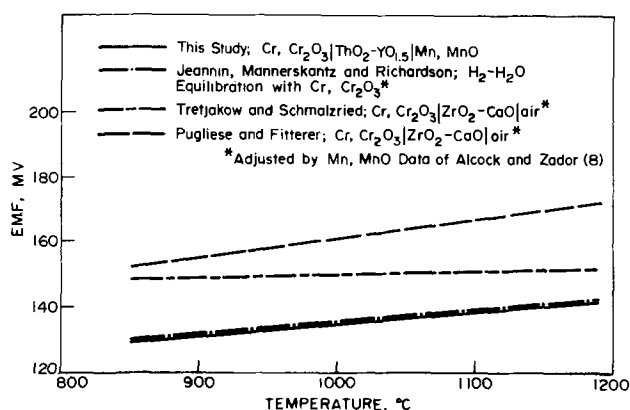


Fig. 4. Cell potential-temperature relationship for cell [II]: Cr, Cr<sub>2</sub>O<sub>3</sub> | ThO<sub>2</sub>-YO<sub>1.5</sub> | Mn, MnO.

mV/°K. The above two lines are shown in Fig. 3 and 4, respectively, along with those calculated from previously published data in the literature. In calculating the lines for the previous investigations, their reported results for the Cr, Cr<sub>2</sub>O<sub>3</sub> equilibrium were combined with the data of Kiukkola and Wagner (7) for the Co-CoO equilibrium and those of Alcock and Zador (8) for the Mn-MnO equilibrium.

Figures 3 and 4 indicate that the results of this study are consistent and in close agreement with the data of Jeannin *et al.* (1). The disagreement between the results of this study and those of Pugliese and Fitterer (6), and Tretjakow and Schmalzried (5) may have resulted from the use of a calcia-stabilized zirconia electrolyte by these investigators. A small amount of electronic conduction in calcia-stabilized zirconia at the very low oxygen potentials associated with the Cr-Cr<sub>2</sub>O<sub>3</sub> equilibrium ( $\sim 10^{-22}$  atm at 1000°C) could result in a continuous transport of oxygen ions from the high potential electrode (air in these cases) to the Cr, Cr<sub>2</sub>O<sub>3</sub> electrode-electrolyte interface. This continuous short-circuiting of the cell can polarize the Cr metal at the interface substantially to give rise to non-

equilibrium cell potentials that are below the equilibrium potentials (Fig. 3). The calculated lines from the data of these investigators appear too high in Fig. 4 for the same reason. Since the equilibrium potential of the Mn, MnO electrode is higher than that of the Cr, Cr<sub>2</sub>O<sub>3</sub> electrode, the low values reported by these investigators when subtracted from the appropriate Mn, MnO potential gives rise to cell potentials that appear too high (Fig. 4).

The measured cell potentials of this study from cells [I] and [II] are related to the standard Gibbs free energy of formation of Cr<sub>2</sub>O<sub>3</sub> by the expression

$$\Delta G^{\circ}_f(\text{Cr}_2\text{O}_3) = 3[-2EF + \Delta G^{\circ}_f(\text{MO})] \quad [1]$$

where  $E$  is the measured cell potential in mV,  $F$  is Faraday's constant, 23,066 cal/mV gram equivalent, and  $\Delta G^{\circ}_f(\text{MO})$  is the standard Gibbs free energy of formation of CoO or MnO for cells [I] and [II], respectively.

Equation [1] was used in conjunction with the measured potentials from cells [I] and [II] to calculate  $\Delta G^{\circ}_f(\text{Cr}_2\text{O}_3)$ . The data of Kiukkola and Wagner (7) for  $\Delta G^{\circ}_f(\text{CoO})$  and those of Alcock and Zador (8) for  $\Delta G^{\circ}_f(\text{MnO})$  were used in this calculation. The results are as follows

from cell [I]

$$\Delta G^{\circ}_f(\text{Cr}_2\text{O}_3) = -266,990 + 60.15T \pm 250 \text{ cal} \quad (1173^{\circ}\text{-}1540^{\circ}\text{K})$$

where  $\Delta H^{\circ}_f = -266,990 \pm 400$  cal and  $\Delta S^{\circ}_f = -60.15 \pm 0.21$  cal/°K

from cell [II]

$$\Delta G^{\circ}_f(\text{Cr}_2\text{O}_3) = -266,270 + 59.55T \pm 100 \text{ cal} \quad (1148^{\circ}\text{-}1460^{\circ}\text{K})$$

where  $\Delta H^{\circ}_f = -266,270 \pm 240$  cal and  $\Delta S^{\circ}_f = -59.55 \pm 0.11$  cal/°K. Considering the uncertainty in the Co, CoO data ( $\pm 100$  cal) and in the Mn, MnO data ( $\pm 150$  cal) the agreement between the  $\Delta G^{\circ}_f(\text{Cr}_2\text{O}_3)$  calculated from the two cells ( $\pm 200$  cal) is good. The following expression determined by the average of the results of cells [I] and [II] is recommended to represent the standard Gibbs free energy of formation of Cr<sub>2</sub>O<sub>3</sub> based on the results of this study

$$\Delta G^{\circ}_f(\text{Cr}_2\text{O}_3) = -266,600 + 59.78T \pm 350 \text{ cal} \quad (1150^{\circ}\text{-}1540^{\circ}\text{K})$$

where  $\Delta H^{\circ}_f = -266,600 \pm 640$  cal and  $\Delta S^{\circ}_f = -59.78 \pm 0.32$  cal/°K. Table II shows a comparison of standard Gibbs free energy of formation of Cr<sub>2</sub>O<sub>3</sub> as reported by various investigators. The agreement between the results of this study and those of Jeannin *et al.* is excellent.

### Summary and Conclusions

The standard Gibbs free energy of formation of Cr<sub>2</sub>O<sub>3</sub> has been measured using the solid oxide electrolyte technique incorporating a ThO<sub>2</sub>-Y<sub>2</sub>O<sub>3</sub> electrolyte with reference to the Co-CoO and Mn-MnO equilibria. The two separate measurements are consistent and are in excellent agreement with the gas equilibration results of Jeannin *et al.*

Table II. Standard Gibbs free energy of formation of Cr<sub>2</sub>O<sub>3</sub> as reported by various investigators

T (°K)	$\Delta G^{\circ}$ (cal)				
	This study -266,600 + 59.78T (1173°-1523°K)	Jeannin <i>et al.</i> (1) -266,700 + 59.95T (1313°-1573°K)	Tretjakow & Schmalzried (5) -258,600 + 55.2T (1000°-1500°K)	Pugliese & Fitterer (6) (1000°-1500°K)	Coughlin (9) -271,300 + 61.82T (298°-1823°K)
1173	-196,500	-196,400	-193,800	-193,800	-198,800
1273	-180,500	-180,400	-188,300	-186,900	-192,600
1373	-184,500	-184,400	-182,800	-180,800	-186,400
1448	-180,000	-179,900	-178,700	-175,000	-181,800

### Acknowledgment

This work was supported in part by the United States Atomic Energy Commission under Contract No. AT(11-1)-1791. This paper is based on a portion of a thesis submitted by one of the authors (F.N.M.) in partial fulfillment of the requirements for the degree of Doctor of Philosophy at The University of Michigan.

Manuscript submitted Jan. 22, 1973; revised manuscript received Nov. 8, 1973.

Any discussion of this paper will appear in a Discussion Section to be published in the December 1974 JOURNAL. All discussions for the December 1974 Discussion Section should be submitted by Aug. 1, 1974.

### REFERENCES

1. Y. Jeannin, C. Mannerskantz, and F. D. Richardson, *Trans. Met. Soc. AIME*, **227**, 300 (1963).
2. G. Grube and M. Flad, *Z. Elektrochem.*, **45**, 835 (1939).
3. Y. Granat, *Metallurgia*, **11**, 35 (1936).
4. J. N. Ramsey, D. Capalan, and A. A. Burr, *This Journal*, **103**, 135 (1956).
5. V. J. D. Tretjakow and H. Schmalzried, *Z. Elektrochem.*, **69**, 396 (1965).
6. L. A. Pugliese and G. R. Fitterer, *Met. Trans.*, **1**, 1997 (1970).
7. K. Kiukkola and C. Wagner, *This Journal*, **104**, 379 (1957).
8. C. B. Alcock and S. Zador, *Electrochim. Acta*, **12**, 673 (1967).
9. J. P. Coughlin, *U.S. Bur. Mines Bull.* **542**, 68 (1954).

## Fibrous Growth of Tantalum Carbide by A-C Discharge Method

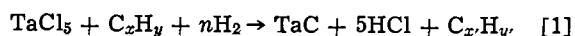
Takehiko Takahashi\* and Kohzoh Sugiyama

Department of Applied Chemistry, Faculty of Engineering, Nagoya University, Nagoya, Japan

### ABSTRACT

The growth of tantalum carbide fiber by an a-c discharge method was studied. Maximum growth rates of up to 40 mm/min were obtained under the following conditions: the discharge current (60 Hz) was 0.4-0.6 mA; the concentrations of hydrogen, argon, tantalum pentachloride, and propylene were 4.9, 94.4, 0.2, and 0.5%, respectively; and the reactant gas temperature was 400°-600°C. The minimum diameter of the grown fiber was 3.5 $\mu$ . By x-ray diffraction, the structure of the grown fiber was identified as tantalum carbide (Fm3m). The tensile strength was a relatively low value of 2.7 kg/mm<sup>2</sup>.

Tantalum carbide is characteristic of high temperature materials (mp, 3880°C). From considering the complexity of the Ta-C phase diagram (1), the phase reversion of tantalum carbide grown at high temperature is also interesting. Fibrous or filamentous growth of carbides, nitrides, and borides of the IVa group elements has been investigated by means of the a-c discharge method by the present authors (2-4). In this method, the growing tip of the fiber can easily be heated to or near its melting point even in a gas mixture of the reactants heated at 300°-600°C. The formation reaction of tantalum carbide is expressed by



where  $n$  is an arbitrary number,  $x$  and  $y$  are three and six in the case of propylene, and  $\text{C}_x\text{H}_y$  represents various hydrocarbon residuals. A rapid growth rate up to 40 mm/min can be obtained.

Some investigators have reported the deposition rate of tantalum carbide by the van Arkel method and the carburization rate of tantalum metal (5). However, no papers have dealt with fibrous growth of this compound. In this paper, the growth conditions of tantalum carbide fiber by the a-c discharge method are described.

### Apparatus and Experimental Procedure

The outline of the apparatus is shown in Fig. 1. A vertical quartz tube, the inner diameter of which was 27 mm, was used as the reaction tube. The upper half had an inner tube into which a gas mixture of hydrogen and 99.3% propylene was introduced. A gas mixture of chlorine and deoxygenated argon was introduced into the outer zone of the double tube, where chlorine reacted with the packed tantalum ribbon to form tantalum pentachloride. This gas mixture met at the middle of the tube. Two electrodes were inserted

from the upper and lower ends of the tube via syringe-type fine quartz tubes and a high a-c voltage was applied across them. The electrodes were molybdenum wires of 0.1 mm diameter. The a-c source, 60 Hz commercial power, was fed to a high voltage transformer regulating a source voltage with a Slidac (transformer). One to thirty megohm resistance was added in series in the discharge circuit to stabilize the current. Within a temperature range of 250°-650°C and a discharge current of 75  $\mu$ A-2 mA, tantalum carbide

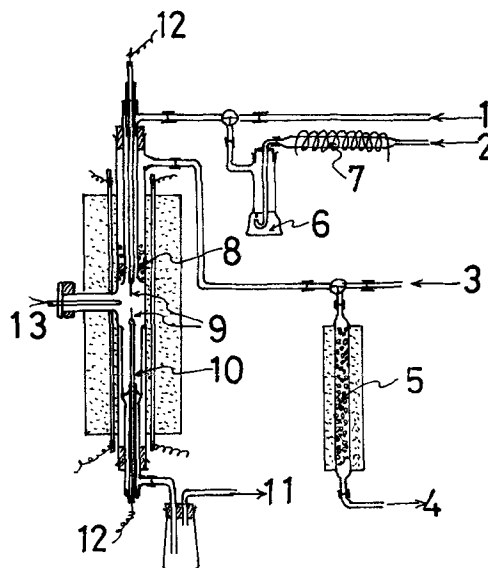


Fig. 1. Apparatus for tantalum carbide fiber growth. 1, propylene inlet; 2, hydrogen inlet; 3, chlorine inlet; 4, argon inlet; 5, titanium sponge; 6, sulfuric acid; 7, copper wire; 8, tantalum ribbon; 9, molybdenum electrode; 10, receiver; 11, outlet; 12, a-c high voltage; 13, thermocouple (C.A.)

\* Electrochemical Society Active Member.  
Key words: tantalum carbide, fibrous growth, chemical vapor deposition.

fiber grew on the tips of the electrodes. The inter-electrode distance was kept constant at 1-5 mm by moving one of the electrodes upward or downward. As the fiber length reached 30 or 50 mm, spontaneous fluctuation occurred due to gas convection. Thus grown fibers were broken off by giving a shock to each electrode and were gathered in a quartz receiver. The growth rate of fibers under a given condition was evaluated by measuring half of the moving rate of one electrode relative to the other, since the growth rates of fibers on the upper and lower electrodes were approximately equal.

### Results and Discussion

**Relation between the temperature of gases and the growth rate.**—The temperature of the reactant gases had to be held high enough to keep the tantalum chloride in the gaseous phase. Figure 2 shows the growth rate dependence of the temperature of the reactant gases between 250° and 650°C. The reaction of chlorine with tantalum ribbon began to take place above 230°C, and the amount of tantalum chloride transported by the argon carrier to the discharge zone increased gradually as the temperature ascended to 400°C, at which point a maximum growth rate of 40 mm/min was obtained. The decrease in growth rate above 400°C may be attributed to a deficiency of carbon produced in the reactant gases by pyrolysis of propylene. The diameter of the grown fiber was in the range of 3.5-12 $\mu$ . As shown in Fig. 2, the diameter was slightly affected by the gas temperature having a minimum value at 400°C. In these experiments, since the fiber grown at higher temperatures exhibited a smooth appearance microscopically, most of the experiments thereafter were performed at 500°C.

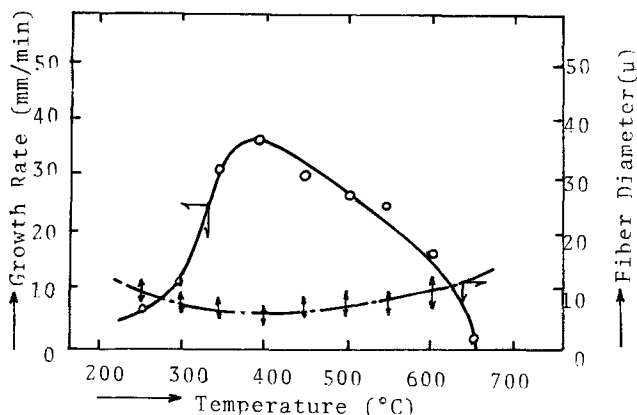


Fig. 2. Variation of growth rate and fiber diameter with reactant gas temperature. The growth conditions were: discharge current 0.15 mA; flow rate of argon, hydrogen, chlorine, and propylene 3.8, 0.2, 0.008, and 0.01 cm<sup>3</sup>/sec, respectively; added resistance in discharge circuit 30 megohms; and interelectrode distance 2 mm.

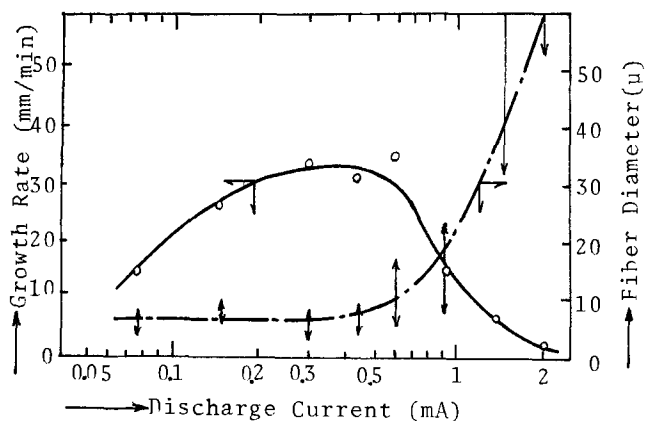


Fig. 3. Effect of the discharge current. The reactant gas temperature was 500°C, other conditions were the same as for Fig. 2.

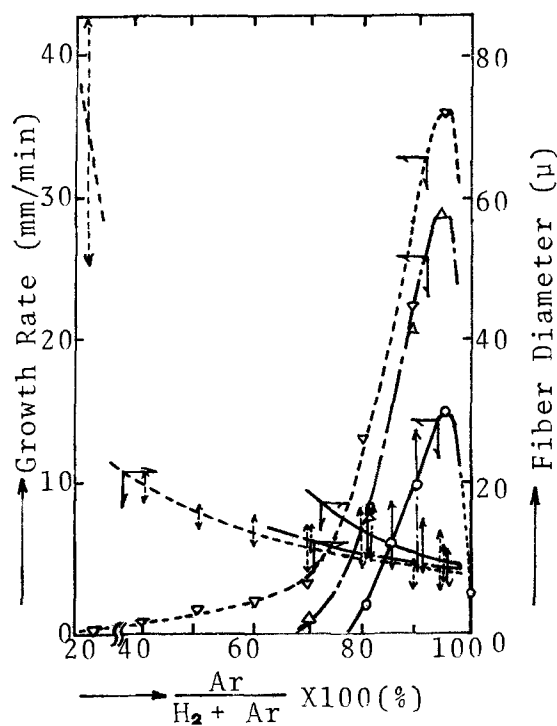


Fig. 4. Effect of the argon concentration. The reactant gas temperature was 500°C; the discharge currents were 0.15 mA (○), 0.30 mA (Δ), and 0.45 mA (▽); and the total, chlorine, and propylene flow rates were 4, 0.005, and 0.1 cm<sup>3</sup>/sec, respectively.

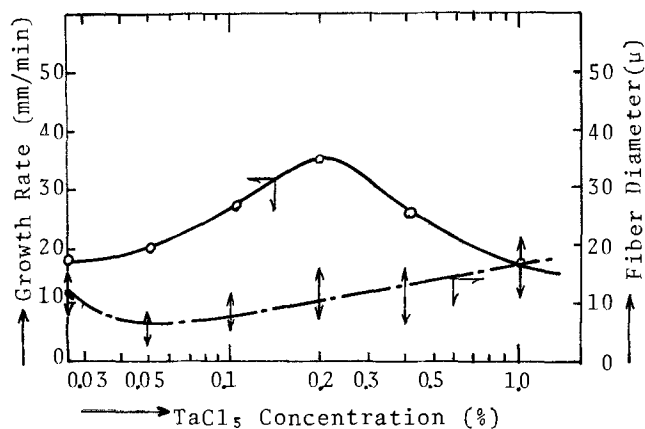


Fig. 5. Effect of tantalum pentachloride concentration. The reactant gas temperature was 500°C; the discharge current was 0.15 mA; the flow rates of argon, hydrogen, and propylene were 3.8, 0.2, and 0.01 cm<sup>3</sup>/sec, respectively; the inserted series resistance was 20 megohms; and interelectrode distance was 1 mm.

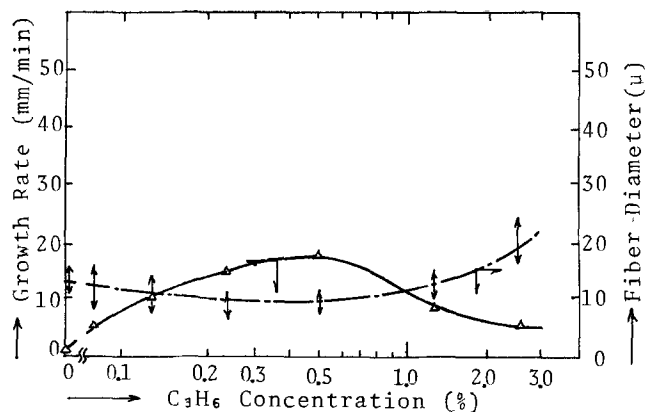


Fig. 6. Effect of propylene concentration. The conditions were the same as for Fig. 5, except that the chlorine flow rate was 0.005 cm<sup>3</sup>/sec.

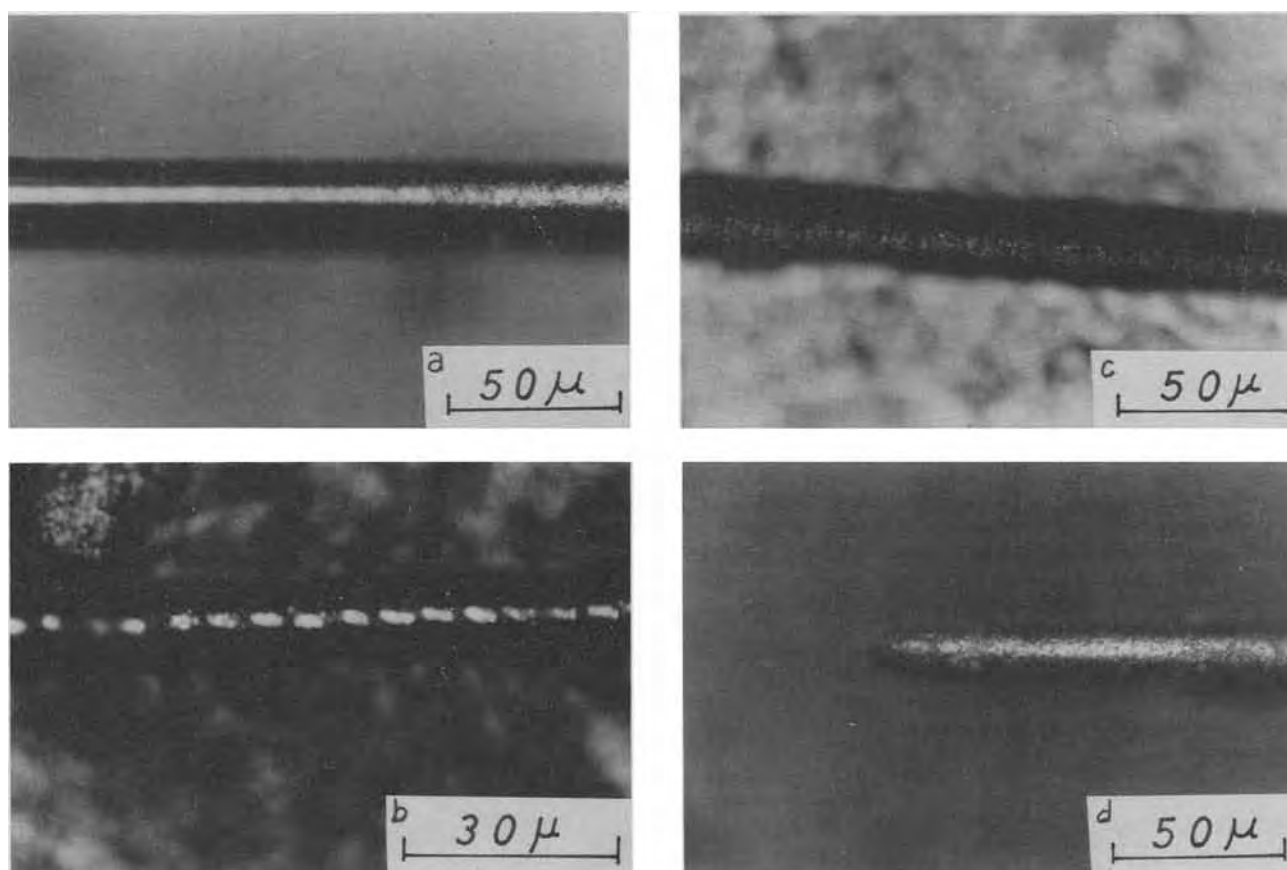


Fig. 7. Microscopic appearance. The samples were grown under the following conditions with reactant gas temperature of 500°C:

No.	Discharge current (mA)	Flow rate (cm <sup>3</sup> /sec)				Series resistance (megohm)	Inter-electrode distance (mm)
		H <sub>2</sub>	Ar	Cl <sub>2</sub>	C <sub>3</sub> H <sub>6</sub>		
a	0.15	0.2	3.8	0.005	0.0025	20	1-2
b	0.15	0.2	3.8	0.005	0.005	20	1-2
c	0.6	0.2	3.8	0.008	0.01	30	3-5
d	0.45	2.4 (60%)	1.6	0.005	0.01	30	5-8

**Effect of discharge current.**—The most important factor affecting growth rate and fiber diameter was the discharge current as shown in Fig. 3. The maximum growth rate is found at 0.4–0.6 mA. With lower discharge currents, heating of the fiber tips to promote fiber growth might be insufficient to overcome the heat loss away from the fiber by conduction, radiation, and convection. With higher currents, however, partial melting and radial growth accompanied growth along the fiber axis. These were the conditions above 0.9 mA, where the growth rate began to decrease, while the diameter of the fibers increased markedly. The power corresponding to 30–45 mW was 75  $\mu$ A discharge and to 360–540 mW was 0.9 mA discharge. The heat loss via radiation is only a trivial portion and was roughly estimated by the Stefan-Boltzmann equation to be  $10^{-3}$  mW. This estimation was obtained assuming the average temperature to be 3000°K, the fiber diameter to be 10 $\mu$ , the effective length of fiber for radiation to be 30 $\mu$ , and the emissivity of tantalum carbide to be 0.3. Accordingly, most of the heat loss is considered to arise from conduction and convection.

**Mixing ratio of hydrogen and argon.**—In Fig. 4, the effect of the mixing ratio of hydrogen and argon under a constant gas flow of 4 cm<sup>3</sup>/sec (STP) and constant propylene concentration of 2.5% is indicated. The growth rate for various discharge currents increases

with argon concentration up to 95%, and the growth rate increases with discharge current. The fiber diameter tends to be thinner as the argon concentration is higher. At an argon concentration near 100%, where the propylene concentration was nearly zero, the product was not tantalum carbide but metallic tantalum.

The appearance of the fiber was metallic when grown at low argon concentration and was dull and rough at high argon concentration. The effects of argon concentration would arise from low thermal conductivity of argon compared with hydrogen. At higher argon concentration, therefore, the growing tip is more easily heated to higher temperature than at lower argon concentration.

**Effect of concentrations of tantalum pentachloride and propylene.**—The relation between the growth rate and the tantalum chloride concentration, which is calculated from the flow rate of the inlet chlorine, is shown in Fig. 5. The maximum growth rate is found at 0.2% tantalum pentachloride, while the minimum diameter of grown fiber is found at 0.05%. The degradation of growth rate at a tantalum pentachloride concentration higher than 0.2% could be attributed to the collision loss of arc-electrons with the tantalum chloride molecule.

Figure 6 shows the effects of propylene concentration on growth rate. With a reactant gas temperature of 500°C and a discharge of 0.15 mA, the maximum growth rate of 18 mm/min was obtained at 0.5% propylene concentration. In the previous paper (6), the effect of hydrocarbon concentration in the van Arkel method was discussed and it was concluded that the concentration range below that corresponding to maximum growth rate was a carbon deficient range, while the concentration range above that corresponding to the maximum growth rate was a carbon excess range where the carbon deposit interfered with the carbide growth. By microscopic observation of a fiber grown at propylene concentration above 0.5%, however, the carbon deposition on the surface of the fiber could not be



found explicitly in this experiment. Although the carbide growth rate in the van Arkel method depends on the structure and carbon number of the hydrocarbon (7), the predominant factor may be heat stability of the hydrocarbon. As the most important factor is the high reaction temperature under the conditions of this experiment (i.e., at relatively low temperature of the reactant gases and sufficiently high temperature at the growing tips), the influence of the kind or structure of hydrocarbons would be a minor factor.

**Microscopic appearance and x-ray diffraction.**—The micrographs of the grown fiber are shown in Fig. 7. Figure 7a shows a fiber of  $12\mu$  diameter grown at a discharge current of 0.15 mA, and Fig. 7b is a fiber of about  $10\mu$  grown with the same discharge current but at a higher propylene concentration. In Fig. 7b, a number of gaps can be seen, and the distance from one gap to the next one was determined to be about  $5-7\mu$ . The growth rate of the fiber shown in Fig. 7b was about 20 mm/min, which corresponds to a growth rate of  $5.6 \mu/\text{Hz}$ . From these results, it is considered that fiber growth took place during the half cycle, either cathodically or anodically. A fiber grown with a higher discharge current and a growth rate of 36 mm/min was found to show gaps about  $10\mu$  apart as shown in Fig. 7c, and the above calculation can be applied again with good agreement. Figure 7d shows a growing tip with a taper indicating that growth along the fiber axis is followed by radial growth.

The x-ray diffraction samples were prepared by pasting some tens of fibers on a glass plate with their axes parallel to the surface. Metallic tantalum was identified only at zero propylene concentration, and tantalum carbide, designated as Fm3m, was detected at a propylene concentration of 0.12% accompanied by weak peaks of metallic tantalum. At propylene concentrations above 0.25%, only tantalum carbide was detected, and higher propylene concentrations gave broader peaks as shown in Fig. 8. The diffraction peak intensities were in agreement with the values of the ASTM card (7). In the figure, no structural orientation was found that could be attributed to the successive nucleus formation of carbide on deposited carbon which occurred at high temperature and at high concentration of hydrocarbon. This tendency is different from the results obtained in the previous papers on zirconium boride and titanium nitride where their respective peaks of (001) and (111) were weaker than ASTM values. Ramqvist (8) reported on the variation of lattice parameter of tantalum carbide with carbon concentration indicating that the lattice parameter increased linearly with the carbon content, from  $4.420\text{\AA}$  when C/Ta was 0.75 to  $4.455\text{\AA}$  when C/Ta was 1.0. The precise lattice constants, however, were not obtained in this experiment because the quantity of the grown sample examined was small. Sometimes the diffraction peaks  $\delta$ -TaO were detected. The oxide might be formed by the hydrolysis of tantalum chloride with atmospheric moisture when the TaC fibers were taken from the receiver. The relation between the discharge current and the structure of the product was studied, and it was found that the former had a minor influence on the tantalum carbide structure.

**Tensile strength and diameter of the fiber.**—The tensile strength of the grown fiber was measured at room temperature with a spring balance. A fiber was held by epoxy resin between two plates, one of which was suspended from a spring. The spring hanger was gradually moved upward until the sample fiber snapped and the breaking load was determined from a calibration curve. The diameter of the broken fiber section was measured microscopically. The strength vs. diameter relation is plotted on log-log scale in Fig. 9. The highest strength observed is  $27 \text{ kg/mm}^2$ , which is very low compared with zirconium diboride and zirconium carbide fibers grown by the same method, the strengths of which were 210 and  $50 \text{ kg/mm}^2$ , respectively.

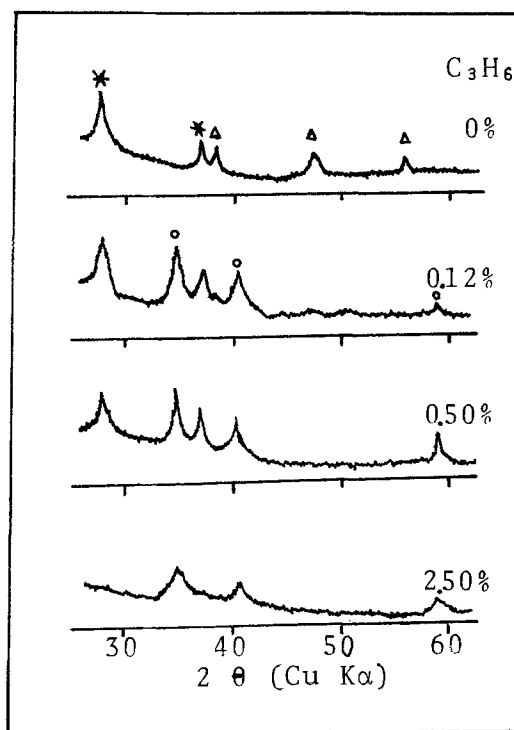


Fig. 8. X-ray diffraction diagrams. The samples were grown under the following conditions: the reactant gas temperature was  $500^\circ\text{C}$ ; the discharge current was 0.45 mA; the flow rates of argon, hydrogen, and chlorine were 3.8, 0.2, and  $0.02 \text{ cm}^3/\text{sec}$ , respectively. Legend: \* TaO, ○ TaC, and  $\Delta$  Ta.

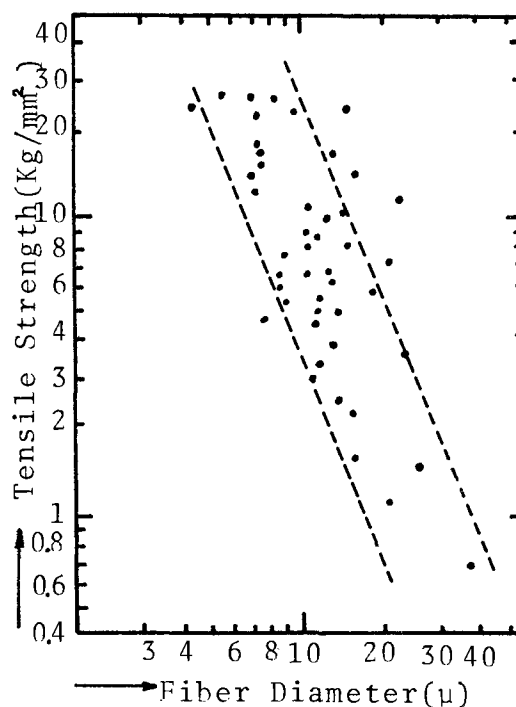


Fig. 9. Relation between the fiber diameter and tensile strength at room temperature.

### Summary

Data were obtained on growth of tantalum carbide fibers by a weak a-c discharge method. The results obtained were as follows:

1. To obtain a growth rate of 40 mm/min, the temperature of the reactant gases must be between  $400^\circ$  and  $500^\circ\text{C}$ .

2. The mixing ratio of hydrogen and argon had a strong effect on growth rate and appearance of the product. Maximum growth rate was obtained at 95% argon.

3. A discharge current of 75-600  $\mu\text{A}$  was favorable for obtaining a thin fiber.

4. Some of the fibers produced were identified as tantalum carbide with a Fm3m structure. Fibers made with low propylene concentration were found to contain metallic tantalum.

5. Crystal growth took place in the half-cycle of a.c., and growth along the fiber axis was followed by radial growth.

6. The highest tensile strength of the fibers produced was 27 kg/mm<sup>2</sup> and less.

Manuscript submitted Feb. 8, 1971; revised manuscript received Sept. 7, 1973.

Any discussion of this paper will appear in a Discussion Section to be published in the December 1974 JOURNAL. All discussions for the December 1974 Discussion Section should be submitted by Aug. 1, 1974.

#### REFERENCES

1. W. F. Bizes and J. M. Tobin, *J. Am. Ceram. Soc.*, **50**, 115 (1967).
2. T. Takahashi, K. Sugiyama, H. Itoh, and Y. Suzuki, *Kogyo Kagaku Zasshi*, **73**, 498 (1970).
3. K. Sugiyama and T. Takahashi, *ibid.*, **73**, 1959 (1970).
4. K. Sugiyama and T. Takahashi, *ibid.*, **73**, 2105 (1970).
5. C. F. Powell, J. H. Oxley, and J. M. Blocher, Jr., "Vapor Deposition," pp. 308, 364, John Wiley & Sons, Inc., New York (1966).
6. T. Takahashi, K. Sugiyama, and K. Kitagawa, *J. Metal Finishing Japan*, **19**, 513 (1968).
7. Joint Committee on Powder Diffraction Standards, "Quick Guide to the Powder Diffraction File," American Society for Testing and Materials, Philadelphia (1969), p. 333, Card No. 19-1292.
8. Lars Ramqvist, *Jernkontorets Ann.*, **152**, 465 (1968).

## Technical Notes



### The Oxidation of Two-Phase Aluminum-Copper Alloys

A. F. Beck, A. J. Brock,\* and M. J. Pryor\*

Metal Research Laboratories, Olin Corporation, New Haven, Connecticut 06504

Despite considerable past study of the oxidation behavior of aluminum and its alloys (1-4), much of the work has been conducted on solid solutions with only incidental impurities. Accordingly, the influence, if any, of second phase intermetallic compounds on oxidation behavior has not been clearly defined.

The aluminum-copper system provides a good opportunity for studying the effect of the tetragonal  $\theta$  phase ( $\text{CuAl}_2$ ) on oxidation behavior. The aluminum-rich end of the aluminum-copper equilibrium diagram is shown in Fig. 1. Oxidation kinetics were determined on two solid solution alloys, Al-1% Cu (A) at 365°C and Al-4% Cu (C) at 500°C. At these temperatures the respective alloy compositions are very close to the  $\alpha - \alpha + \theta$  phase boundary. Two additional alloys were provided, Al-2% Cu (B) which was examined at 365°C and Al-5% Cu (D) which was examined at 500°C. The alloys (B) and (D) contain 1% by weight excess copper at the appropriate oxidation temperature. This is equivalent to 1.85 weight per cent (w/o) of the  $\theta$  phase and 1.15 volume per cent (v/o) of this intermetallic compound. Detailed compositions of the alloys are contained in Table I.

Ingots of the four alloys measuring  $7.6 \times 15.2 \times 91.5$  cm were cast after being chlorine fluxed to remove dissolved hydrogen. They were subsequently homogenized at 550°C for 8 hr. After cooling to room temperature, the ingot faces were machined to remove 0.32 cm per side. The slabs were reheated to 800°F and hot rolled to a thickness of 0.51 cm. The hot-rolled slab was etched in 1.0N NaOH solution at room temperature

for 5 min, rinsed, and dipped in 50% nitric acid at 70°C for 10 sec. All alloys were cold rolled to a thickness of 0.37 mm. Specimens of alloys (C) and (D) were held at 500°C for 72 hr in order to obtain complete dissolution of  $\theta$  phase in alloy (C) and in order to stabilize the distribution of  $\theta$  phase in alloy (D). The alloys

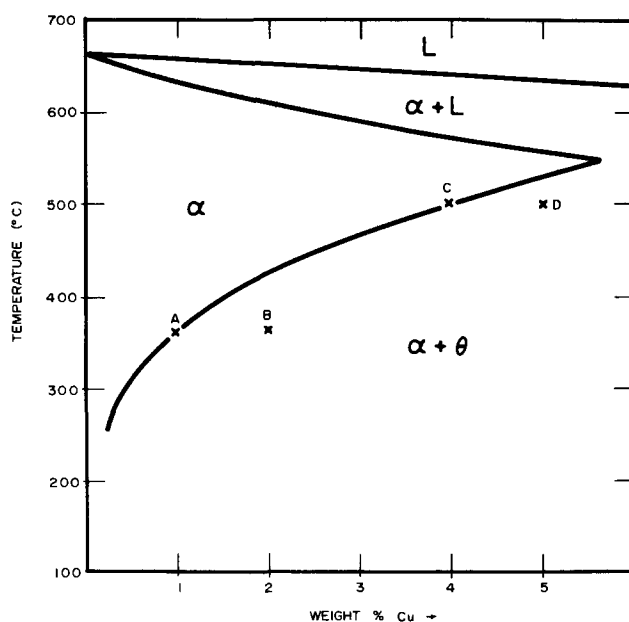


Fig. 1. Aluminum-rich end of the Al-Cu equilibrium diagram.

\* Electrochemical Society Active Member.

Key words: oxidation, aluminum-copper alloys, microstructure.

Table I. Composition of Al-Cu alloys (w/o)

Alloy	Cu	Fe	Si
A	0.97	0.002	0.001
B	2.02	0.003	0.001
C	3.92	0.003	0.001
D	5.07	0.003	0.001

were water quenched after this treatment. Alloys (A) and (B) were held at 365°C for 72 hr and water quenched. These two alloys were then cold rolled to a thickness of 0.06 mm so as to provide larger areas for oxidation at 365°C where the total weight gains are quite small. After the foregoing thermal treatments the specimens were etched in 0.5N NaOH solution at 70°C for 4 sec followed by a dip in 50% nitric acid at 85°C. This procedure was repeated 5 times.

For oxidation at 500°C specimens measuring  $1 \times 4 \times 0.037$  cm were used. For oxidation at 365°C foil specimens measuring  $4 \times 12 \times 0.006$  cm were used. These specimens were wound around a glass rod; on removing the rod spirals with suitably large surface areas and low masses were obtained. Oxidation temperatures of 365° and 500°C were selected because at the lower temperature only gamma alumina with poorly developed long range order forms as an oxidation product. At 500°C, in addition to the formation of the gamma alumina with poorly defined long range order, well developed crystalline  $\gamma$ -Al<sub>2</sub>O<sub>3</sub> nucleates at the amorphous oxide interface and grows as a series of expanding cylinders. The oxidation behavior of aluminum-copper alloys solid solutions up to and including 4% has been described earlier (4).

In this work, oxidation studies were conducted using the same experimental method as described previously (4). The oxygen pressure used was 76 Torr. Figure 2 shows the results obtained at 365°C for an Al-1% Cu solid solution (A) and for an Al-1% solid solution containing 1.15 v/o of  $\theta$  phase (B). It may be seen that the kinetic results are indistinguishable between the two alloys. The gravimetric results obtained at 500°C for the Al-4% solid solution (C) and for the Al-4% Cu solid solution containing 1.85 w/o of  $\theta$  phase were also indistinguishable within the limits of experimental error and were also identical to the results reported in our earlier publication for the same alloy (4). Clearly, the presence of a modest volume fraction (1.15%) of  $\theta$  phase has no detectable effect on over-all oxidation kinetics.

It was found previously that the presence of increasing copper contents in solid solution results in an increase in the rate of formation of the amorphous film and its thickness albeit at somewhat higher tempera-

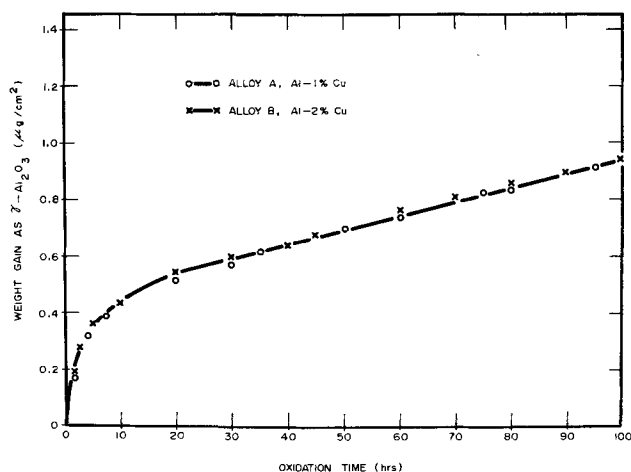


Fig. 2. Relationships between weight of  $\gamma$ -Al<sub>2</sub>O<sub>3</sub> and time for Al-1% Cu (A) and Al-2% Cu (B) at 365°C in oxygen at a pressure of 76 Torr.

tures than the 365°C used in this study. Accordingly, the film formed on alloy (B) after oxidation for 100 hr was stripped in 10% mercuric chloride dissolved in methanol and examined by transmission electron microscopy (AEI EM6G at 100 kV). The areas of amorphous film formed over the  $\theta$  phase are relatively easy to detect because this phase is subject to somewhat more chemical roughening during the specimen cleaning (Fig. 5). Electron opacity measurements made on the amorphous film formed on the  $\theta$  phase suggested that the film was no thinner and probably somewhat thicker than that formed on the solid solution matrix. Further, there were no discontinuities in the oxide film associated with the  $\theta$  phase particles.

The film formed on the Al-5% Cu alloy (D) in 16 hr at 500°C is shown in Fig. 3. The crystal density in the Al-4% matrix is characteristic of that found in earlier work (4). However, the crystals formed on the  $\theta$  phase are extremely small. Since in the solid solution regime crystal density decreases and crystal size increases with increasing copper content, the oxidation

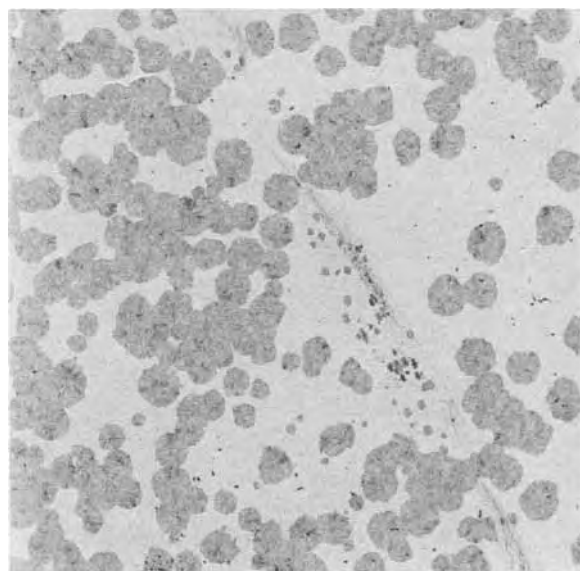


Fig. 3. Transmission electron micrograph of oxide film formed over a two-phase region of Al-5% Cu alloy (D) after oxidation for 16 hr at 500°C. Magnification 1500 $\times$ .

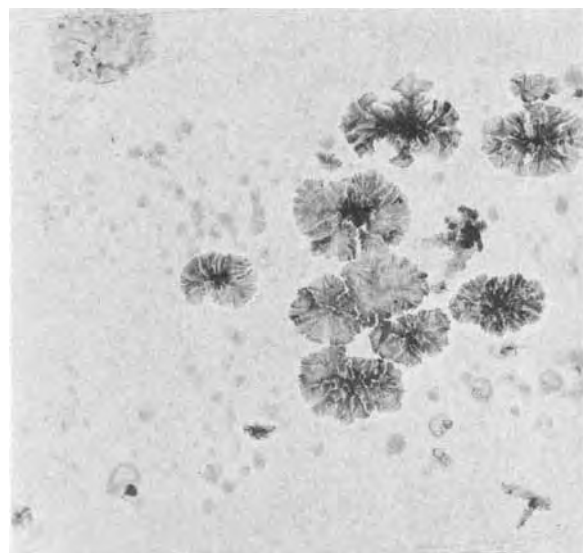


Fig. 4. Transmission electron micrograph of oxide film formed on  $\theta$  phase after oxidation for 16 hr at 500°C. Magnification 16,000 $\times$ .

behavior of the  $\theta$  phase is not characteristic of this relationship. The thickness of the gamma alumina crystals formed on the  $\alpha$  matrix is around 170Å. The thickness of crystals formed on the  $\theta$  phase is only around 90Å. Some of the crystals formed on the  $\theta$  phase have more contrast than those formed on the matrix (Fig. 4). Since they are substantially thinner, this suggests the crystalline oxide has a substantially higher copper content than that formed over the matrix.

Electron opacity measurements were made on the amorphous oxide between the crystals formed on the  $\theta$  phase. The results were somewhat variable from one  $\theta$  phase particle to another presumably because of some roughening of this phase in the specimen cleaning. This is shown in Fig. 5, a backside replica of the oxide film stripped from alloy (D) after 16 hr oxidation at 500°C. However, the electron opacities measured

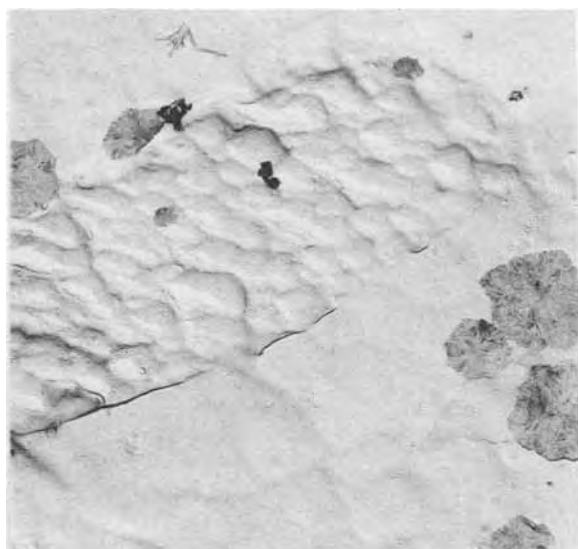


Fig. 5. Electron micrograph of underside of oxide film formed on two phase region of Al-5% Cu alloy (D) after oxidation for 16 hr at 500°C. Magnification 6000 $\times$ .

at different locations ranged from being approximately equal to that measured on the matrix to some 50% higher. Selected area diffraction confirmed that the film formed over the  $\theta$  phase was a composite of gamma alumina with poorly developed long range order and well defined  $\gamma$ -Al<sub>2</sub>O<sub>3</sub> crystals. Accordingly, the amorphous film formed over the  $\theta$  phase at 500°C is no thinner than that formed on the Al-4% Cu matrix and is probably somewhat thicker. Again, no evidence of film discontinuity associated with  $\theta$  phase particles could be found.

In summary, the presence of 1.85 w/o (1.15 v/o) of  $\theta$  phase has no detectable influence on the bulk oxidation kinetics of Al-Cu alloys at 365° and 500°C. Local examination of the films formed over the  $\theta$  phase suggests that the amorphous film is no thinner and is probably thicker than that formed over the matrix. Crystalline  $\gamma$ -Al<sub>2</sub>O<sub>3</sub> nucleation and growth at the base of the amorphous film is radically modified when there is a  $\theta$  phase substrate. Lateral growth rate of the crystals is substantially retarded and their terminal thickness is only around 50% of those formed on the matrix. Crystal nucleation on the  $\theta$  phase appears to be strongly orientation dependent although the details of this dependency have not been determined in this work.

#### Acknowledgments

The authors acknowledge the support of this work by the Aluminum Group of the Olin Corporation.

Manuscript submitted Oct. 1, 1973; revised manuscript received Dec. 21, 1973.

Any discussion of this paper will appear in a Discussion Section to be published in the December 1974 JOURNAL. All discussions for the December 1974 Discussion Section should be submitted by Aug. 1, 1974.

#### REFERENCES

1. M. J. Dignam, *This Journal*, **109**, 184, 192 (1962).
2. A. F. Beck, M. A. Heine, E. J. Caule, and M. J. Pryor, *Corrosion Sci.*, **7**, 1 (1967).
3. A. J. Brock, *This Journal*, **117**, 549 (1970).
4. A. J. Brock and M. J. Pryor, *Corrosion Sci.*, **13**, 199 (1973).

## A Method for Determining the Optimum Thickness of Graphitic Coatings Used in Electron Devices

Joseph D. Reardon

GTE Sylvania Incorporated, Electronic Components Group,  
Electronic Tube Division, Seneca Falls, New York 03148

In the manufacture of CRT devices, evacuated glass envelopes are exposed to high-energy electrons. Bombardment of glass with 15-20 keV electrons causes the evolution of O<sub>2</sub>, CO, H<sub>2</sub> (1, 2), and CO<sub>2</sub> (2). When certain glasses are thermally heated in vacuum, chlorine (2, 5) and fluorine (2) compounds are evolved which then may cause cathode poisoning during subsequent electron bombardment (8). Oxygen (3, 4), carbon dioxide (4), fluorine (5-8), and chlorine (2-7) have long been recognized as being harmful to the thermionic emission of oxide cathodes.

It is common practice, especially in the manufacture of color television picture tubes, to cover some portion of the exposed glass with an internal conductive coating, usually a graphite-silicate mixture. Although the

**Key words:** electron penetration, graphite-silicate coating, cathode ray tubes.

primary purpose of the internal coating is to provide a conductive path for electrons, the coating can also help to preserve the cathodic emission, providing that the coating thickness is sufficient to shield the glass envelope from high-energy primary electrons. This investigation was undertaken to determine the optimum coating thickness necessary to completely shield a glass surface from 25 keV electrons, the energy of electrons in an operating color TV picture tube.

#### Experimental

**Apparatus.**—A schematic diagram of the demountable plaque-scanning apparatus is shown in Fig. 1. A standard pumping arrangement consisting of a mechanical fore pump and an oil diffusion pump operating with liquid nitrogen trapping was used. The apparatus itself consists of a glass envelope fitted with a

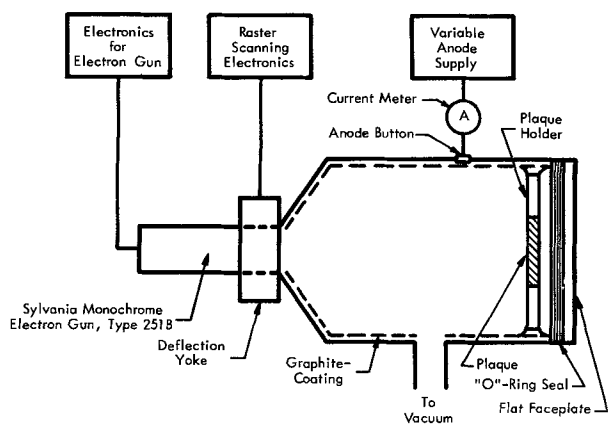


Fig. 1. Schematic diagram of the demountable electron penetration apparatus.

monochrome electron gun (Sylvania Type 251B) and a detachable faceplate. A stainless steel plaque holder was positioned in the faceplate and held in place with spring snubbers.

The glass envelope was equipped with an anode button to allow a positive potential to be applied to the plaque. Electrical continuity between the plaque and anode supply was achieved by means of a graphite coating.

The associated electronics include (i) a variable anode supply and current meter, (ii) the deflection yoke and scanning electronics, and (iii) the electron gun cathode heater and grid supplies.

**Procedure.**—Clean 2 in.  $\times$  2 in. glass plaques were masked so as to leave exposed an area of approximately one inch square in the center. Using a hand spray gun, a commercially available graphite-silicate coating (Dixon 217 coating, Joseph Dixon Crucible Company) was deposited on the plaques. By increasing the number of spray passes from one plaque to the next, the plaques were coated in varying degrees of thickness from 30,000 to 185,000Å. After the coating was allowed to air dry, the masking was removed and the plaques were fired in air at 430°C for ½ hr to set the coating.

The coating thickness of each plaque was determined using a Sloan surface profilometer. In all cases, the thickness measurements were taken at several places on the coated square. Since considerable peak-to-valley variation was observed on the thin plaques, the average minimum thickness was assumed to be the effective coating thickness.

The coated plaques were then individually placed in the demountable unit. In all cases, the vacuum system was allowed to pump down to the low  $10^{-5}$  Torr region before measurement was begun. At this point the room was darkened and a blue fluorescence was observed when the electron beam was allowed to strike the uncoated glass. With approximately 5.0 keV anode potential on the plaque, the raster and biasing controls were adjusted so as to give an anode current of 8  $\mu$ A and a surface area of approximately 0.5 cm<sup>2</sup>.

When the electron beam was positioned on the coated portion of the plaque, no fluorescence was noted. The anode potential then was gradually increased. Periodically, the raster size was adjusted to maintain the beam area of 0.5 cm<sup>2</sup>. When the blue fluorescence was just visible, the raster size was again checked and the voltage recorded. The threshold voltage (the voltage at which fluorescence is first noted) was determined for each plaque.

Using uncoated plaques, the onset of fluorescence was observed at 500 eV. Each of the threshold voltages was corrected for the so-called "dead voltage."

### Results and Discussion

Range-energy data for graphite-silicate coatings are shown graphically in Fig. 2. The electron range,  $R$ , is

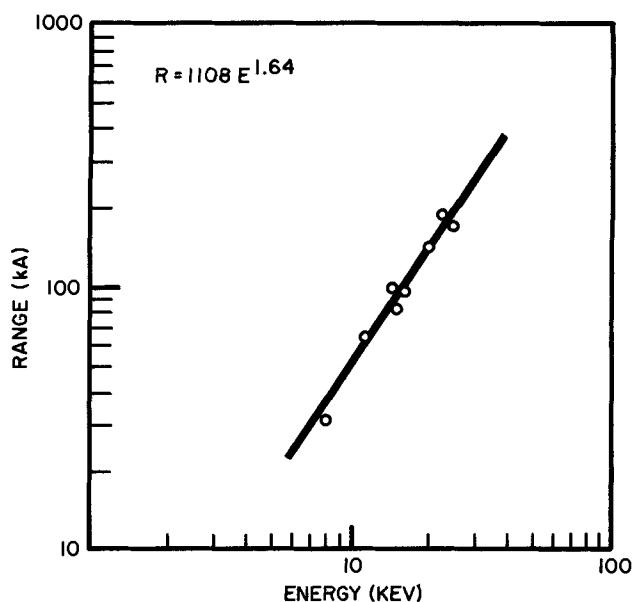


Fig. 2. Range-energy data for graphite-silicate coatings

the measured effective coating thickness. The energy,  $E$ , is the primary electron energy corresponding to the initial electron penetration for each coating sample. On a logarithmic scale the relation between  $R$  and  $E$  is linear for film thicknesses between 30,000 and 185,000Å. A computer least squares curve fit has determined that the data obeys the empirical relation

$$R = 1108 E^{1.64} \quad [1]$$

where  $R$  is expressed in angstroms and  $E$  in keV.

The optimum coating thickness for any electron device may be calculated by simply substituting the appropriate operating voltage into Eq. [1]. For the case of color TV picture tubes operating at 25 keV, a coating thickness of 220,000Å is necessary to completely shield the glass envelope from high energy electrons. Covering the glass envelope of electronic devices with graphite-silicate films in excess of this value should help to preserve the thermionic emission of oxide cathodes by reducing the level of harmful gaseous residuals.

The visual detection method used in the investigation for determining the electron range was chosen because of the experimental difficulties involved in handling graphite-silicate coatings of the type normally used in electron tubes. Kanter and Sternglass (11) have shown that range determinations using luminescent detectors give higher threshold energy values for electron penetration (smaller effective range) than can be expected by either theoretical calculations or absorption techniques. Calculations based upon the Bethe theory of energy loss (9) and the integration method of Lane and Zaffarano (10) show the calculated integrated path length,  $I$ , to be smaller than the experimental range (Fig. 3). That is, the experimental range is considerably larger than would be expected.

Sprayed coatings of the type considered here would be expected to have a porous structure. This is supported by the relatively low bulk density of the graphite-silicate coating (1.4 g/cm<sup>3</sup> compared to 2.2 g/cm<sup>3</sup> for crystalline graphite). Since it is likely that electrons should penetrate porous materials more easily than dense substances, the observed high experimental ranges may be attributed to the high void content of the graphitic coating.

Because of the probable dependence of the experimental range data on the void characteristics of the coating material, caution should be exercised in applying the electron penetration results obtained for graphite-silicate coatings to other systems. However, for

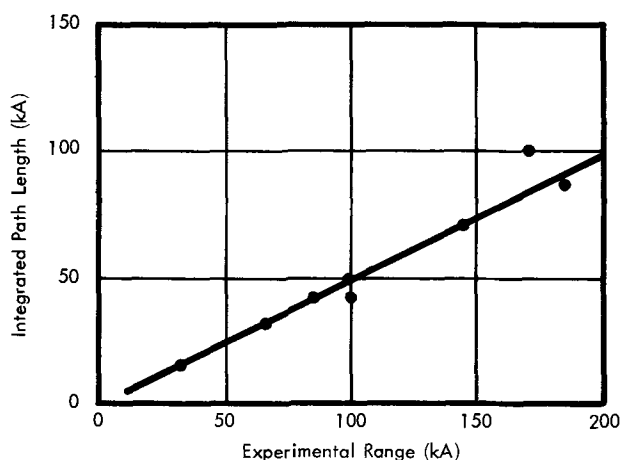


Fig. 3. Comparison of calculated and experimental ranges of electrons in graphite-silicate coatings.

films which have a high void content and do not readily lend themselves to evaluation by absorption techniques, the visual range determination employed for this investigation should give a reasonable approximation of the electron penetration.

#### Acknowledgment

The author wishes to thank Mr. Charles Rehkopf, Mr. David Benda, and Mr. Robert Donofrio for many

helpful discussions during the preparation of this manuscript. The technical assistance of Mr. Jacob Kerr and Mr. Ronald Saunders is gratefully acknowledged.

Manuscript submitted June 12, 1973; revised manuscript received Jan. 15, 1974.

Any discussion of this paper will appear in a Discussion Section to be published in the December 1974 JOURNAL. All discussions for the December 1974 Discussion Section should be submitted by Aug. 1, 1974.

#### REFERENCES

1. B. J. Todd, J. L. Lineweaver, and J. T. Kerr, *J. Appl. Phys.*, **31**, 51 (1960).
2. P. della Porta, "Residual Gases in Electron Tubes," T. A. Giorgi and P. Della Porta, Editors, Academic Press, New York (1972).
3. H. Jacobs, *J. Appl. Phys.*, **17**, 596 (1946).
4. W. J. Rudy, "Advances in Electron Tube Techniques," D. Slater, Editor, Pergamon Press (1961).
5. H. C. Hamaker, H. Bruining, and A. H. W. Aten, *Philips Res. Rept.*, **2**, 171 (1947).
6. G. C. Feaster, *J. Appl. Phys.*, **20**, 415 (1949).
7. J. R. Young, *ibid.*, **31**, 921 (1960).
8. J. Kai, M. Koitabashi, K. Watanabe, and Y. Morihiro, *J. Vacuum Sci. Technol.*, **8**, 363 (1971).
9. H. A. Bethe, *Handb. d. Phys.*, **24**, 519 (1933).
10. R. O. Lane and D. J. Zaffarano, *Phys. Rev.*, **94**, 1960 (1954).
11. H. Kanter and E. J. Sternglass, *ibid.*, **126**, 620 (1962).

## Brief Communications



### Anomalous Boron Diffusion in Silicon from Planar Boron Nitride Sources

Joseph Stach\* and Alfred Turley

Solid State Device Laboratory, Department of Electrical Engineering,  
The Pennsylvania State University, University Park, Pennsylvania 16802

This communication describes experimental results of boron diffusions using boron nitride wafers as the boron source. High surface concentrations are generated by the boron nitride diffusion system (1-3). As such, nonideal effects are introduced into the diffusion process, the most notable being anomalous diffusion profiles which exhibit dependence on the inert diffusion gas ambient.

#### Experimental

The silicon wafers used throughout the investigation were polished, <111> oriented, and 1.5 in. in diameter with a 3-7 ohm-cm arsenic doped 10-30  $\mu\text{m}$  thick epitaxial layer. Prior to diffusion, the silicon was cleaned by accepted techniques (4) and stored in covered polypropylene containers. The procedures for preparing the boron nitride sources were those developed in previous investigations (1, 2).

Extensive use was made of linear four-point probe sheet resistance measurements in the evaluation of the diffused layers. The unit used consisted of an A&M

Fell four-point probe head with wear resistant tungsten carbide probes of a  $0.04 \text{ mm} \pm 10\%$  tip radius loaded in ruby bearings and spaced  $1.00 \pm 0.01 \text{ mm}$  apart with  $200 \text{ g} \pm 2\%$  applied pressure when fully depressed; an A&M Fell four-point probe head mount; and a K&S Pacific Model 192 resistivity tester consisting of a  $0.001\text{-}10 \text{ mA} \pm 0.1\%$  full scale current source and a  $0\text{-}20 \text{ mV} \pm 0.5\%$  full scale digital voltmeter.

Boron diffusion profiles were obtained from incremental sheet resistance measurements (5, 6). Layer sectioning of silicon was performed by anodic oxidation (7) and a computer program adapted to the work of Donovan (8) and Irvin (9) was used in calculating profiles from the incremental sheet resistance data.

All diffusions were performed in a Thermco-Spartan 60 mm inside diameter furnace with a flat zone of 15 in. ( $\pm 1/2^\circ\text{C}$ ). Diffusions were performed in helium, argon, and nitrogen ambients and the effects of these ambients were studied in terms of sheet resistance, diffusion profiles, and deposition of surface films during the diffusion process.

\* Electrochemical Society Active Member.

Key words: boron nitride, boron diffusion, planar sources.

Figure 1 shows actual diffused profiles for the three ambients. Notice the surface concentrations and junction depths.

$$N_{\text{SHe}} > N_{\text{SAr}} > N_{\text{SN}_2} \quad [1]$$

and

$$X_{\text{JHe}} < X_{\text{JAr}} < X_{\text{JN}_2} \quad [2]$$

One cannot be sure of the validity of the surface concentrations due to the uncertainty in the measurement technique; however, the junction depths are significant and are supported by Fig. 2 which shows sheet resistance vs. time with gas ambient and temperature as parameters. The sheet resistance is consistent with junction depth measurements in that

$$\rho_{\text{SHe}} > \rho_{\text{SAr}} > \rho_{\text{SN}_2} \quad [3]$$

The following argument is proposed to explain these results. At very high surface concentrations, "excess" boron above solid solubility reacts with the silicon to form a new phase on the surface. Such a phase was visually observed and remained on the silicon surface after conventional borosilicate glass removal. The thickness of the phase,  $t_{\text{ph}}$ , varied with diffusion ambient as follows

$$t_{\text{phHe}} > t_{\text{phAr}} > t_{\text{phN}_2} \quad [4]$$

The relative thicknesses of the phase layers were determined by comparison of the numbers of interference minima observed on an ultraviolet-visible spectrophotometer. The experimentally determined diffused layer profiles show that diffusions which formed a heavy borosilicate glass and Si-B phase resulted in shallower junctions and higher sheet resistances for constant times and temperature. This can be explained by making the following plausible assumptions: (i) the formation of surface films (glass and phase) consumes silicon; (ii) only "excess" boron above solid solubility combines with the silicon to form a new phase on the surface; and (iii) the diffusion coefficient of boron in the surface phase is greater than boron's diffusivity in silicon. Assumption (iii) was based on the observation that for long diffusion times, the surface concentration of boron was not reduced as

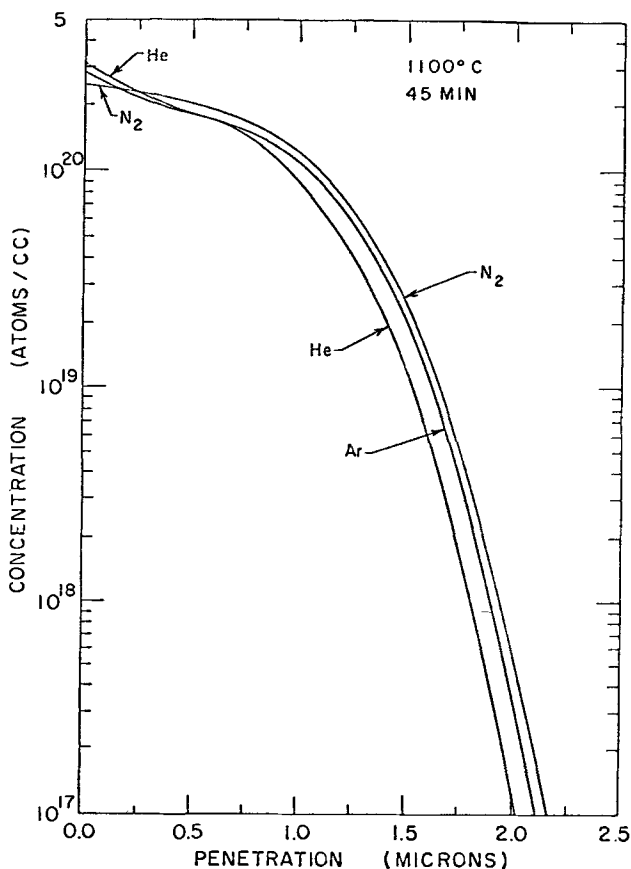


Fig. 1. Diffused impurity profile showing the effects of inert gas ambient.

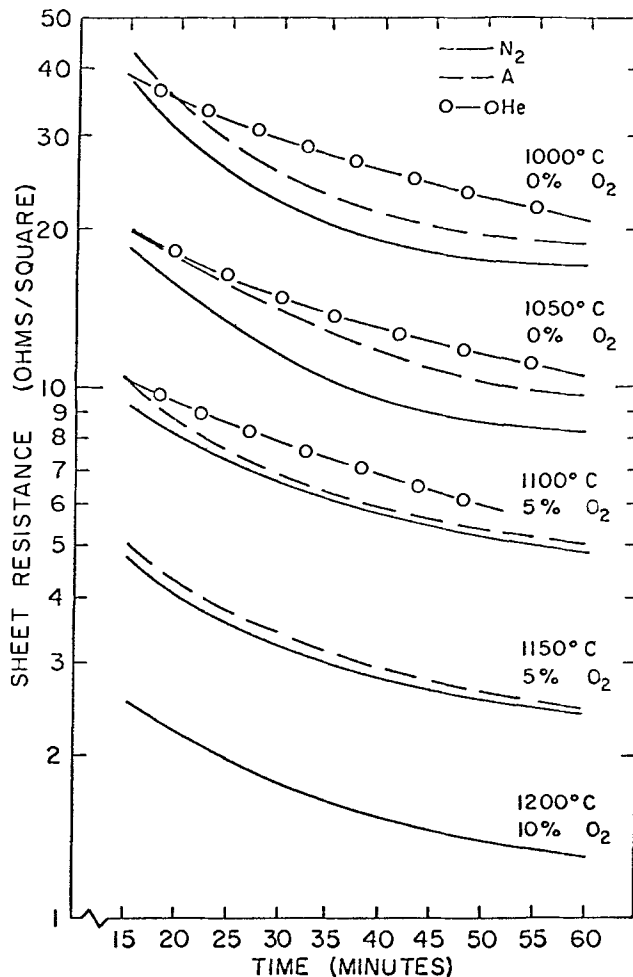


Fig. 2. Sheet resistance as a function of time with temperature and gas ambient as parameters.

would occur if the phase layer acted as a diffusion barrier. Busen *et al.* (10) have also observed such a phase following boron diffusions. They report that the phase is highly porous, with pore sizes as large as  $0.75\mu$ .

Before profiling or sheet resistance measurements were performed, the surface films were removed. This amount of silicon removed might account for the observed differences in junction depth and sheet resistance if the three assumptions presented are true.

Ideally, diffusions of this type should follow a complementary error function profile. Diffusions in the nitrogen ambient showed little or no surface phase formation. Two profiles of  $\text{N}_2$  ambient diffusions along with an erfc profile as shown in Fig. 3. One sees that the real profile differs considerably from the erfc distribution. Deeper penetration in the high concentration area suggests a concentration dependent diffusivity giving enhanced diffusion at high concentrations; however, the concentration gradient near the surface indicates that the diffusivity probably reaches a maximum value and then begins to decrease with higher concentrations. A similar type of diffusivity concentration dependence for arsenic has been reported by Kennedy and Murley (11). Concentration dependence of boron diffusion coefficient has been previously reported in the literature; but no quantitative data have yet been presented (12-14).

**Summary**

Diffusion profiles which indicate concentration dependent diffusivity and inert gas ambient dependence have been experimentally observed when boron diffusions were performed using boron nitride wafers as the boron source at temperatures between  $1100^\circ$  and  $1200^\circ\text{C}$ . Actual profiles show steeper junctions than predicted from an erfc profile.

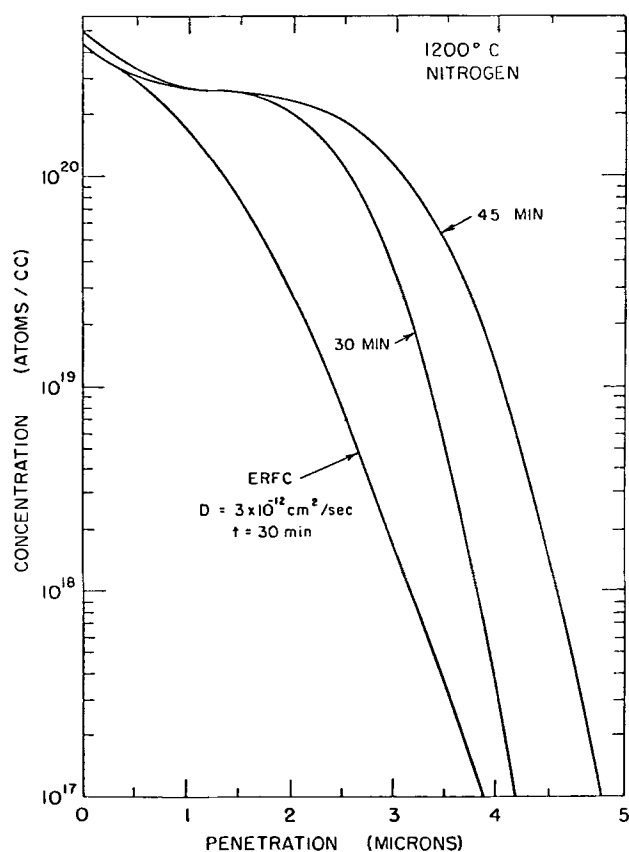


Fig. 3. Diffused impurity profiles indicating anomalous diffusion at 1200°C.

Manuscript submitted Feb. 6, 1973; revised manuscript received Nov. 30, 1973. This was Paper 77 presented at the Chicago, Illinois, Meeting of the Society, May 13-18, 1973.

Any discussion of this paper will appear in a Discussion Section to be published in the December 1974 JOURNAL. All discussions for the December 1974 Discussion Section should be submitted by Aug. 1, 1974.

#### REFERENCES

1. D. Rupprecht and J. Stach, Paper 176 presented at Electrochemical Society Meeting, Cleveland, Ohio, Oct. 3-7, 1971.
2. D. Rupprecht, J. Stach, and A. Turley, Paper 31 presented at Electrochemical Society Meeting, Houston, Texas, May 7-11, 1972.
3. D. Rupprecht and J. Stach, Paper 56 presented at Electrochemical Society Meeting, Houston, Texas, May 7-11, 1972.
4. R. P. Donovan, "Fundamentals of Silicon Integrated Device Technology," Vol. 1, p. 309, Prentice-Hall, Inc., Englewood Cliffs, N. J. (1967).
5. M. Tannenbaum and D. F. Thomas, *Bell System Tech. J.*, **35**, 1 (1956).
6. E. Tannenbaum, *Solid-State Electron.*, **2**, 123 (1961).
7. E. F. Duffek, E. A. Benjamini, and C. Mylroie, *Electrochem. Technol.*, **3**, 75 (1965).
8. R. P. Donovan, *Solid-State Electron.*, **10**, 155 (N) (1967).
9. J. C. Irvin, *Bell System Tech. J.*, **41**, 387 (1962).
10. K. M. Busen, W. A. FitzGibbons, and T. Kloffenstein, *Electrochem. Technol.*, **6**, 256 (1968).
11. D. P. Kennedy and P. C. Murley, *Proc. IEEE*, **59**, 335 (1971).
12. J. J. Chang, *IEEE Trans. Electron Devices*, **101**, 357 (1963).
13. E. L. Williams, *This Journal*, **108**, 795 (1961).
14. N. D. Thai, *Solid-State Electron.*, **13**, 165 (1970).

## Complete Removal of Sodium from Silicon Dioxide Films by Formation of Phosphosilicate Glass

Daniel V. McCaughan, Richard A. Kushner, and Sigurd Wagner

Bell Laboratories, Murray Hill, New Jersey 07974

Alkali ion contamination of thermally grown SiO<sub>2</sub> films on silicon is a serious problem in semiconductor technology. One technique which has been used with some success in alleviating this difficulty is the formation of a layer of phosphosilicate glass over either gate dielectric or passivating oxide. Phosphosilicate films are known to getter mobile ionic impurities (1,2). Most investigations of mobile charge have been carried out with capacitance-voltage methods (3) whose sensitivity to charged impurities depends strongly on their location in the insulator and is highest for charges at the SiO<sub>2</sub>/Si interface. The ionic drift techniques (4-6) on the other hand do not determine the location of charge. A drawback common to all electrical methods is that they measure either the total or the time derivative of the dielectric displacement and cannot, therefore, distinguish between ionic migration and dielectric polarization on an atomic scale. An experimentally independent but less widely used approach is afforded by the measurement of the distribution of radioactive tracers. Using <sup>24</sup>Na tracers, Yon, Ko, and Kuper (7), Kuper (8), and Buck *et al.* (9) have obtained results which show that sodium, initially distributed throughout the SiO<sub>2</sub>, is partially gettered,

**Key words:** gettering, mobile charge, ionic charge, device processing.

during the growth of a phosphosilicate glass layer, into the PSG layer. The area density of sodium, in the experiments of Kuper and co-workers (7, 8),  $6.4 \times 10^{14}/\text{cm}^2$ , and of Buck and co-workers (9),  $>1 \times 10^{14}/\text{cm}^2$ , was unrealistically high. Here we present evidence that sodium initially present only near the SiO<sub>2</sub>/Si interface in amounts comparable to those found in contaminated gate oxides ( $\leq 10^{12}/\text{cm}^2$  Na) is removed to less than detection limits during phosphorus diffusions of short duration.

About  $1 \times 10^{13} \text{ cm}^{-2}$  NaCl containing 1% radioactive sodium-22 as a tracer was evaporated onto 5000Å thick SiO<sub>2</sub> layers thermally grown on  $\sim 5 \text{ ohm-cm}$  n-type (100) silicon wafers (9, 10). <sup>22</sup>Na is a positron emitter whose radioactivity was measured by counting the coincident gamma rays resulting from positron annihilation. The samples were then bombarded with  $1 \times 10^{14} \text{ cm}^{-2}$  Ar<sup>+</sup> ions at 500 eV. This procedure drives sodium from the vacuum/oxide interface to the oxide/silicon interface (10-13).

The apparatus (13) consists of a glow discharge ion source with a 2 keV accelerator, a 60° sector mass analyzing magnet, and deflection plates for scanning the beam. The target is surrounded by a secondary electron suppressor, and the target current is measured. The energy spread at the sample is a few electron



volts. No radioactive sodium was lost during the ion bombardment. After bombardment, 1000Å were etched off the silicon dioxide. This procedure removes all sodium not drifted to the SiO<sub>2</sub>/Si interface, and counting of the <sup>22</sup>Na tracer showed that  $1 \times 10^{12}$  cm<sup>-2</sup> total sodium remained in the oxide. [Prior experiments (10-13) have shown that virtually all of this sodium resides in the SiO<sub>2</sub>, within about 200Å of the SiO<sub>2</sub>/Si interface.] Phosphorus was then diffused into the oxide for 4 min at 925°C in an atmosphere of 0.01% PBr<sub>3</sub> and 0.8% O<sub>2</sub> in nitrogen at a flux of 23 cm · sec<sup>-1</sup>. As determined by etch rate, this procedure converts approximately the top 200Å of SiO<sub>2</sub> to a phosphosilicate glass. The samples were again counted for <sup>22</sup>Na. It was

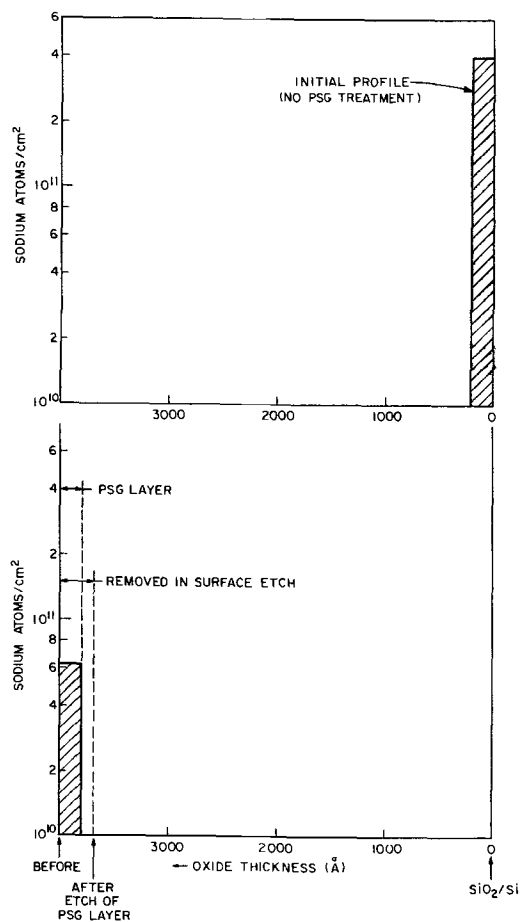


Fig. 1 (a, top). Profile of sodium in SiO<sub>2</sub> after ion bombardment and the top 1000Å removed by etching, leaving a profile of sodium at the SiO<sub>2</sub> interface only. (b, bottom) Profile of sodium in SiO<sub>2</sub> after the phosphorus diffusion step. No sodium remains at the SiO<sub>2</sub>/Si interface; etching of the top 300Å (including the phosphorus glass layer) removes all remaining sodium.

observed that  $\approx 80\%$  of the sodium had been removed during the phosphorus diffusion. [We believe that the bromine gas resulting from the oxidation of PBr<sub>3</sub> forms the very stable but volatile NaBr which then evaporates from the SiO<sub>2</sub> into the furnace atmosphere. At 925°C the vapor pressure of NaBr is 6.8 Torr (14).] Removal of the top 350Å of the oxide in 15:1 = H<sub>2</sub>O:HF, which removes SiO<sub>2</sub> at a rate of 200Å min<sup>-1</sup> showed that all the remaining sodium was contained in this top 350Å of the oxide, which included the phosphosilicate film.

The remaining oxide was devoid of any radioactive sodium to within the sensitivity limits of the measurement ( $4 \times 10^9$  total sodium/cm<sup>2</sup>). Figure 1 illustrates the concentration profiles of sodium in this sequence of experiments.

Thus, we have shown that sodium ions mobilized in device-type structures by ion bombardment can be completely eliminated by a phosphorus gettering step followed by an etchoff of the phosphosilicate layer. From past experience we know that sodium, once it is made mobile by ion bombardment, is equivalent to mobile sodium introduced by any other method. We therefore conclude that mobile sodium in SiO<sub>2</sub>/Si structures in the  $10^{11}$ - $10^{12}$  Na · cm<sup>-2</sup> range can be completely removed by the described procedure regardless of its origin or its location.

Manuscript submitted Dec. 17, 1973; revised manuscript received Jan. 17, 1974.

Any discussion of this paper will appear in a Discussion Section to be published in the December 1974 JOURNAL. All discussions for the December 1974 Discussion Section should be submitted by Aug. 1, 1974.

#### REFERENCES

1. J. M. Eldridge and P. Balk, *Trans. Met. Soc. AIME*, **242**, 539 (1968).
2. L. H. Kaplan and M. E. Lowe, *This Journal*, **118**, 1649 (1971).
3. E. H. Snow, A. S. Grove, B. E. Deal, and C. T. Sah, *J. Appl. Phys.*, **36**, 1664 (1965).
4. S. Hofstein, *IEEE Trans. Electron Devices*, **ED-13**, 222 (1966).
5. N. J. Chou, *This Journal*, **118**, 601 (1971).
6. M. Kuhn and D. J. Silversmith, *ibid.*, **118**, 966 (1971).
7. E. Yon, W. H. Ko, and A. B. Kuper, *IEEE Trans. Electron Devices*, **ED-13**, 276 (1966).
8. A. B. Kuper, *Surface Sci.*, **13**, 182 (1969).
9. T. M. Buck, F. G. Allen, J. V. Dalton, and J. D. Struthers, *This Journal*, **114**, 862 (1967).
10. D. V. McCaughan, R. A. Kushner, and V. T. Murphy, Abstracts 28 and 29, 7th Natl. Conf. on Electron Microprobes, San Francisco (1971).
11. R. A. Kushner, D. V. McCaughan, V. T. Murphy, and J. A. Heilig, *Phys. Rev. B*, In press.
12. D. V. McCaughan and V. T. Murphy, *IEEE Trans. Nucl. Sci.*, **NS-19**, 249 (1972).
13. D. V. McCaughan, R. A. Kushner, and V. T. Murphy, *Phys. Rev. Letters*, **30**, 614 (1973).
14. D. V. McCaughan and V. T. Murphy, *J. Appl. Phys.*, **44**, 2008 (1973).



## Reduction of the Silver Oxide Electrode in CsOH Solutions

Charles P. Wales

*Electrochemistry Branch, Naval Research Laboratory, Washington, D. C. 20375*

*The publication costs of this article have been assisted by the Naval Research Laboratory.*

### ABSTRACT

The electrical characteristics and changes in structure when sintered Ag electrodes were cycled in 8.4M or 3.6M CsOH solutions were compared with results for similar electrodes cycled in KOH solutions. The products of reduction were the same in the two electrolytes. Solutions of CsOH gave a better capacity when the Ag electrodes were cycled repeatedly using slow discharges, because the Ag which formed during reduction had a smaller average particle size in CsOH than in KOH as a result of lower ionic mobility in the CsOH. But polarization was higher in CsOH, so KOH was preferable to CsOH at moderate and high rates of discharge.

Reduction of the silver oxide electrode has usually been studied in aqueous KOH solutions [(1-7) and references in (8)]. Since the ionic radius and atomic weight of Cs are larger than those of K, the use of CsOH instead of KOH should indicate if the cation of the electrolyte has a strong effect on the Ag electrode. In addition, CsOH and KOH solutions having the same molar concentration contain different amounts of water. It is of interest, therefore, to determine some of the characteristics of Ag electrodes in aqueous CsOH solutions, because results may differ significantly from those obtained in KOH solutions.

A previous paper has described the oxidation of sintered silver electrodes in CsOH solutions (9). The present work is concerned with reduction or discharge of these electrodes and gives the effect of CsOH on electrical characteristics and on electrode structure.

### Experimental

Only a brief description of experimental procedure is given here, since details have already been presented (9). Test cells contained sintered silver electrodes whose average dimensions were 43.7 mm wide, 36.0 mm high, and 0.87 mm thick. Particle size distribution in an unused electrode was given earlier (7). Cells contained an excess of electrolyte. Two other sintered Ag electrodes served as counterelectrodes. All electrodes were wrapped with five layers of either cellulosic separator or crosslinked polyethylene separator. Each cell also contained a Ag/Ag<sub>2</sub>O reference electrode. Electrodes were always charged (anodically oxidized) to oxygen evolution before beginning a discharge. The 20-hr constant current charge rate was used except where otherwise stated. Temperature was 24° ± 1°C. Discharges began immediately after the end of a charge, without any stand period. Some electrodes were always discharged (reduced) using the 20-hr rate of constant current, and others were always discharged at the 1-hr rate. Discharges were ended when potential dropped about 200-250 mV below the observed Ag/Ag<sub>2</sub>O potential plateau. One or more samples were

cut from most of the electrodes and cross sections were prepared for optical microscopic examination.

### Results

*Capacity changes with cycling.*—Figure 1 gives the general trend of discharge capacity for the first 15 cycles, the period of greatest change. Each curve given in Fig. 1 is a smoothed composite of measurements from two or three electrodes, except only one electrode was cycled at the 1-hr rate in 3.6M CsOH. During the first cycle of a new electrode the largest capacity was obtained in 3.6M CsOH. Capacity in this electrolyte dropped rapidly in the first few cycles.

The rate of capacity loss decreased after a few cycles. Rates of loss given in Table I for slow discharges were measured starting at cycle 1, except for

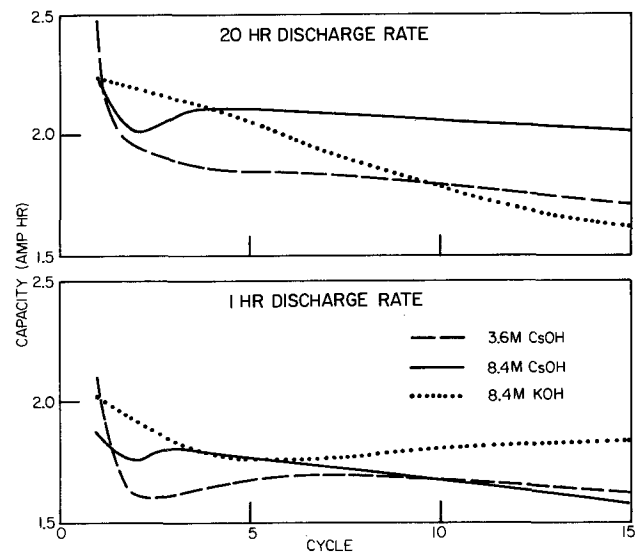


Fig. 1. Effects of cycling and of discharge rate on capacity of Ag electrodes in aqueous CsOH and KOH. All charges were done at the 20-hr rate.

Key words: silver oxide, electrolyte, electrode structure, reduction.

Table I. Rates of capacity loss per cycle when using the 20-hr discharge rate

Electrolyte	20-Hr charge rate, %		Various charge rates from 0.7 to 50 hr, %	
	To cycle 15	To cycle 30	To cycle 15	To cycle 30
3.6M CsOH	2.1	—	2.1	1.4
8.4M CsOH	0.7	—	0.9	0.5
5.5M KOH	2.3	1.4	2.7	1.4
8.4M KOH	1.9	1.0	1.3	0.8
11.6M KOH	1.7	1.2	1.4	0.9

the rare occasions when maximum capacity occurred at cycle 2 instead of 1. The results given in Table I were calculated from data taken from Ref. (7) and (9) and the present work. Rates of loss tended to be highest in the most dilute solutions. The loss in 3.6M CsOH became low after the initial sharp drop in capacity between cycle 1 and 2 (Fig. 1). The rates of loss beginning at cycle 2 were 0.9, 0.6, and 1.1% per cycle in 3.6M CsOH, in contrast to the 2.1, 2.1, and 1.4%, respectively, given in Table I.

**Electrode potentials during discharge.**—A few discharges are shown in Fig. 2 for electrodes cycled under the conditions of Fig. 1. All potentials reported in this paper are given with respect to the Ag/Ag<sub>2</sub>O reference electrode. Shapes of discharge curves at cycle 4 can be regarded as typical for later cycles, since there was little change between cycle 4 and 15 except for the total length of discharge. The greatest capacity was obtained at cycle 1 in 3.6M CsOH. Capacity at cycle 4 had dropped more rapidly in 3.6M CsOH than in 8.4M CsOH. Results at the 1-hr rate in 3.6M CsOH were not included because potentials during most of cycle 1 and 4 discharge were close to those already shown and would make Fig. 2 hard to decipher. These discharges in 3.6M CsOH resembled cycle 4 in 8.4M KOH, and at cycle 1 lacked the high initial potential shown for 8.4M CsOH. The length of the discharges differed, however, according to the trend indicated in Fig. 1.

The Ag electrodes in Fig. 1 and 2 were always charged at the 20-hr rate of constant current. Charge acceptance in CsOH decreased when charges were done at a higher current (9). Figure 3 gives examples of discharges that followed three rates of charge. The charges lasting approximately 0.8, 4, and 43 hr were done at currents that were 16, 4, and 0.5 times the 20-hr rate, respectively. Capacity that an electrode delivered was changed by a factor of two over this current range.

**Discharge at the AgO/Ag<sub>2</sub>O potential.**—Most of the active material is converted to AgO during the charge of a sintered Ag electrode to oxygen evolution. The remainder of the active material consists of Ag<sub>2</sub>O and Ag in varying amounts depending on electrode structure, electrolyte, and cycling conditions (7, 9-11). Re-

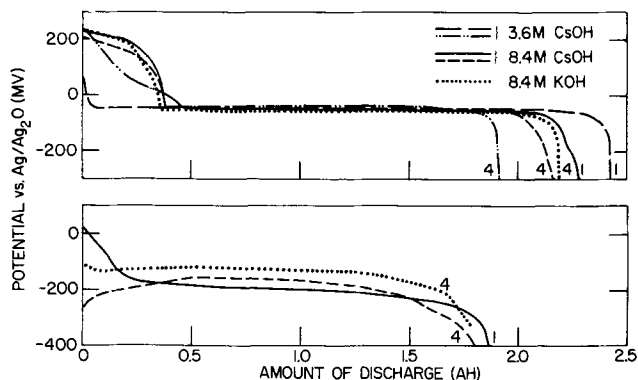


Fig. 2. Potentials of Ag electrodes when discharged at the 20-hr rate (upper half of figure) and at the 1-hr rate (lower half of figure). Cycle numbers are given beside the curves. All charges were done at the 20-hr rate.

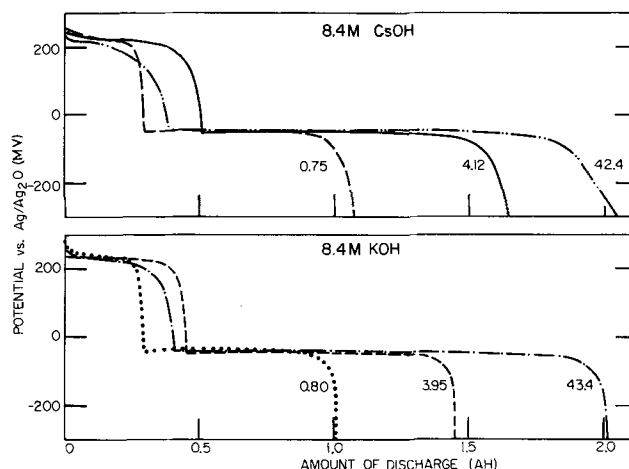


Fig. 3. Discharges at the 20-hr rate following charges at various rates. Numbers on curves give length of preceding charge in hours.

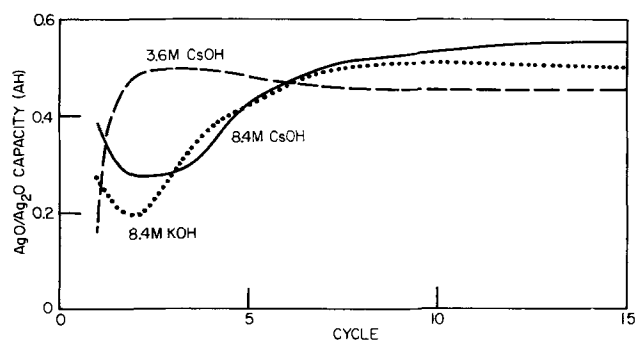


Fig. 4. Effect of cycling on the upper or AgO/Ag<sub>2</sub>O discharge potential plateau. Discharges and charges were done at the 20-hr rate.

duction of this AgO gives the familiar potential plateau usually found at the beginning of a discharge, except when current is high enough to polarize the electrode down to the Ag<sub>2</sub>O/Ag potential during the entire discharge. The AgO/Ag<sub>2</sub>O potential can be seen at the beginning of most of the discharges in Fig. 2 and 3.

Figure 4 shows the variation in discharge capacity at the AgO/Ag<sub>2</sub>O potential plateau when electrodes were cycled in three solutions. Since capacity was changing rapidly during the first few cycles, as indicated in Fig. 1, the proportion of a discharge that took place at the AgO potential did not change in exactly the same way as in Fig. 4. Table II gives the per cent of discharge that took place before potential fell to the lower or Ag<sub>2</sub>O/Ag plateau. Percentages in Table II are averages of three electrodes in each electrolyte. The AgO/Ag<sub>2</sub>O length reached a minimum at cycle 1 or 2.

Another factor affecting the length of the AgO/Ag<sub>2</sub>O potential was the rate at which an electrode was charged (Fig. 5). The proportion of a discharge that took place at this higher potential usually reached a maximum when a sintered Ag electrode was charged at the 5- to 10-hr rate. The curve for 8.4M KOH is repeated in both sections of Fig. 5. Since there was some scattering of individual measurements, small differ-

Table II. Variation in length of AgO/Ag<sub>2</sub>O potential when electrodes were cycled using the 20-hr discharge rate

Cycle	AgO length (per cent of total discharge length)				
	3.6M CsOH	8.4M CsOH	5.5M KOH	8.4M KOH	11.6M KOH
1	7	17	23	13	21
2	24	13	22	10	16
5	27	20	29	21	26
10	26	27	30	28	32
15	26	28	31	29	33

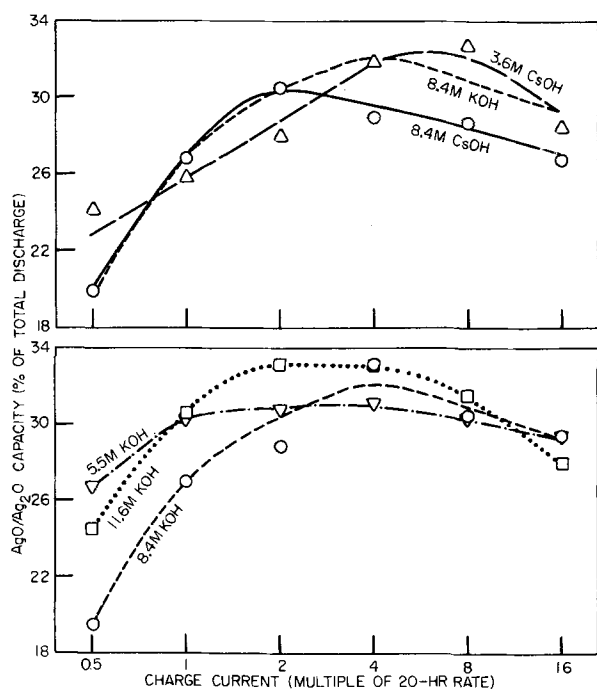


Fig. 5. Dependence of the upper (AgO/Ag<sub>2</sub>O) discharge potential plateau on the current used for the preceding charge. All discharges were done at the 20-hr rate. Points are averages of three measurements.

ences between the various curves may not be significant.

**Structural changes during a discharge.**—Structure was relatively uniform throughout electrodes that were always discharged at the 20-hr rate. Figure 6 shows a low magnification view of an electrode discharged until 32% of the total capacity had been removed. The Ag<sub>2</sub>O/Ag plateau had been reached when the discharge was 22% completed, so 44% of the AgO had been reduced to Ag<sub>2</sub>O before formation of Ag began. Then, after the potential fell to the Ag<sub>2</sub>O/Ag plateau, Ag<sub>2</sub>O was reduced to Ag and simultaneously some of the

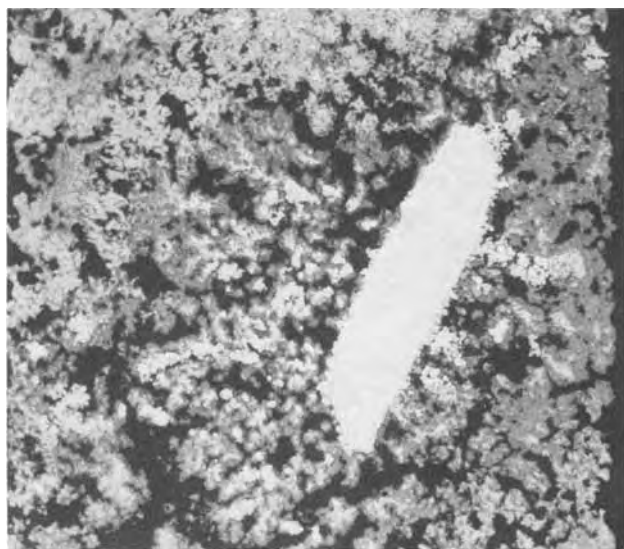


Fig. 6. Photomicrograph of electrode in 8.4M CsOH at cycle 6 after a partial discharge at the 20-hr rate had removed 32% of capacity. Potential had been at the Ag<sub>2</sub>O/Ag plateau for 2 hr when discharge was interrupted. In this cross section metallic Ag is white, Ag<sub>2</sub>O is dark gray, AgO is light gray, and empty areas (formerly filled with electrolyte) are black. Large white object is part of the Ag grid. Electrode thickness (from left to right in photograph) was 0.87 mm.

remaining AgO was reduced to Ag<sub>2</sub>O. A visual estimate of the entire cross section indicated that approximately 65% of the active material was Ag<sub>2</sub>O. The highest Ag<sub>2</sub>O concentration was near grid members, although all areas of the electrode had some Ag<sub>2</sub>O. Initial formation of metallic Ag occurred most often near the grid (Fig. 6).

Figure 7 gives a higher magnification view of another electrode that had been discharged until 10% of total capacity was removed while at the Ag<sub>2</sub>O/Ag potential plateau. All photographs are of cross sections through the electrode and, therefore, show cross sections through individual particles and crystals. The surface of AgO was reduced to Ag<sub>2</sub>O during the early part of the discharge. Porosity increased as Ag formed. Some AgO usually remained near the newly formed Ag in partly discharged electrodes, as in Fig. 7. The Ag had formed in the vicinity of the grid members and near the surfaces of the electrode, although seldom actually on the surface when the 20-hr discharge rate was used. The metallic Ag (white) that was entirely surrounded by Ag<sub>2</sub>O in Fig. 7 was residual from the preceding charge. The rest of the Ag had formed during the discharge and had rounded, convoluted shapes typical of most Ag particles after several slow discharges.

After a complete discharge at the 20-hr rate almost all oxide had been reduced to Ag (Fig. 8). About 10% of a discharged electrode consisted of small Ag particles. These small Ag particles resulted from the reduction of areas that had contained closely packed AgO with little or no Ag present. Large Ag particles, the most common form, tended to have smoother surfaces at the end of a discharge than when partly discharged (compare top of Fig. 8 with Fig. 7). Some crevices in the Ag had been filled in during the additional discharge.

**Dependence of structure on discharge rate.**—In contrast to a discharge at the 20-hr rate, during a discharge at the 1-hr rate only a small amount of Ag<sub>2</sub>O formed before reduction to Ag began taking place (Fig. 9). It was typical to have a region 50–100 μm wide where Ag<sub>2</sub>O was forming from AgO. The amount of Ag<sub>2</sub>O that formed reached a more or less constant value, and then the Ag formation rate became equal to

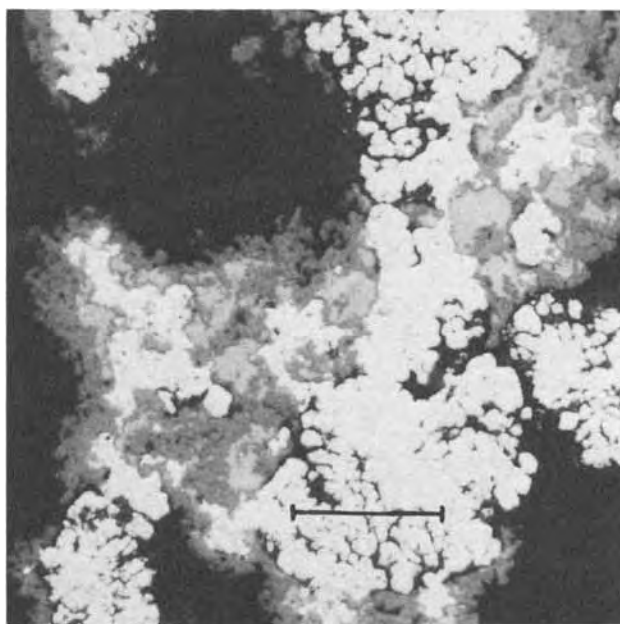


Fig. 7. Electrode that was discharged 37% in 8.4M CsOH at cycle 15. Discharge at the 20-hr rate was ended after potential had been at the Ag<sub>2</sub>O/Ag plateau for 2 hr. Surface of electrode is at the left. Most of the Ag<sub>2</sub>O and Ag shown here had formed from AgO during the partial discharge. Marker indicates 25 μm.

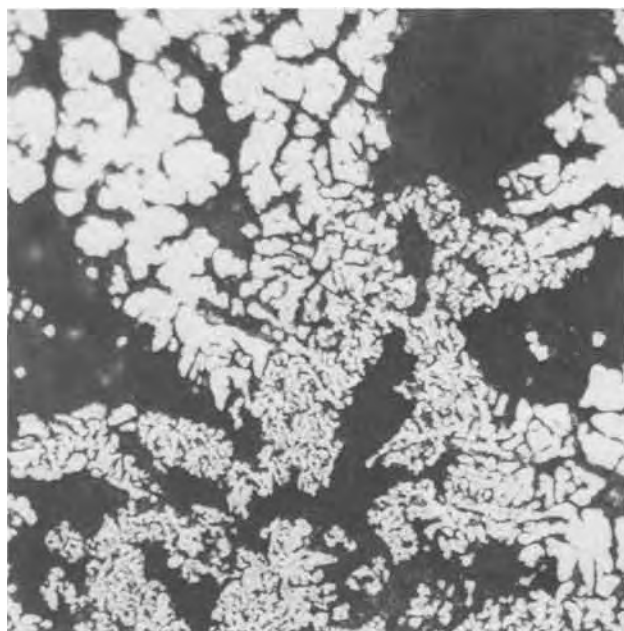


Fig. 8. Cross section of Ag particles at the end of cycle 6 discharge at the 20-hr rate in 8.4M CsOH. Approximately 7% of the volume of this electrode contained small particles such as those at the bottom of this photograph, and the rest contained larger particles as shown at the top. Same magnification as Fig. 7.

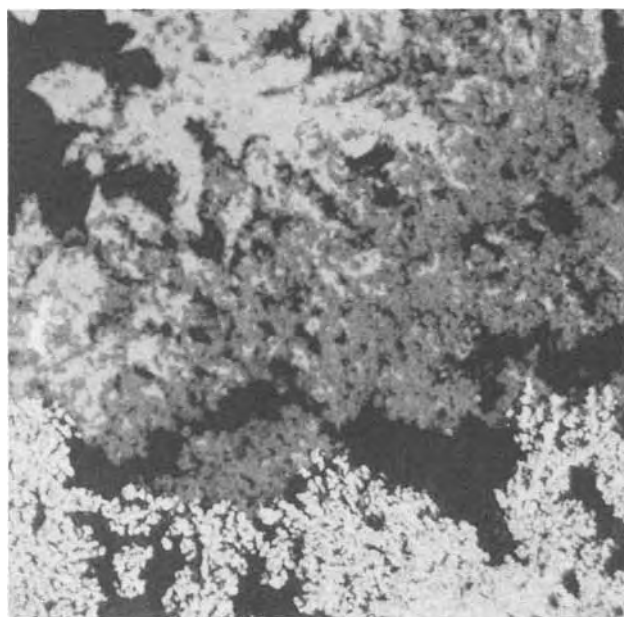


Fig. 9. Active material of electrode discharged 45% at the 1-hr rate at cycle 6 in 8.4M CsOH. Under these conditions partial reduction of AgO to Ag<sub>2</sub>O was followed by reduction to Ag in preference to formation of thick Ag<sub>2</sub>O layers. Active material is predominately AgO at the top of this photograph, Ag<sub>2</sub>O in the middle, and Ag at the bottom. To see the effect of discharge rate compare with Fig. 7 at the same magnification.

the rate of Ag<sub>2</sub>O formation. The Ag formed into smaller particles at the 1-hr rate than at the 20-hr rate (Fig. 7).

The active material near a grid was almost entirely AgO at the end of a charge. After electrodes had been discharged 10% at the 1-hr rate both Ag<sub>2</sub>O and Ag had formed in a narrow area near the grid. Also Ag had formed at the surface of the electrodes in areas that had been mainly Ag + Ag<sub>2</sub>O at the beginning of the discharge, nucleating from Ag that remained within the Ag<sub>2</sub>O. The surface of an electrode dis-

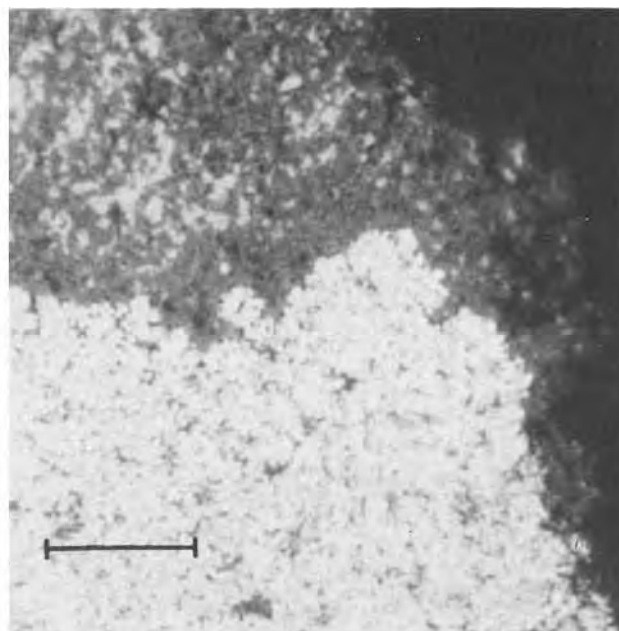


Fig. 10. Electrode discharged 50% at the 1-hr rate at cycle 30 in 8.4M CsOH, showing border between silver oxides and newly formed small particles of granular Ag. One surface of the electrode was at the right. Marker indicates 10  $\mu\text{m}$ .

charged at the 1-hr rate is included in Fig. 10. In this area the Ag particles were smaller than those shown at lower magnification in Fig. 9. After electrodes had been discharged 35-50% their surfaces were mostly the white color of Ag when the 1-hr was used, and largely the color of Ag<sub>2</sub>O when the 20-hr rate was used.

Particles of Ag that formed at the 20-hr rate are shown in Fig. 11. The Ag particles that formed during the slow discharge usually had 2  $\mu\text{m}$  as a smallest dimension, while many particles that formed during the 1-hr discharge were about 0.5  $\mu\text{m}$  in diameter and were more uniform in size and spacing. Since typical Ag particles were about four times larger after a 20-hr

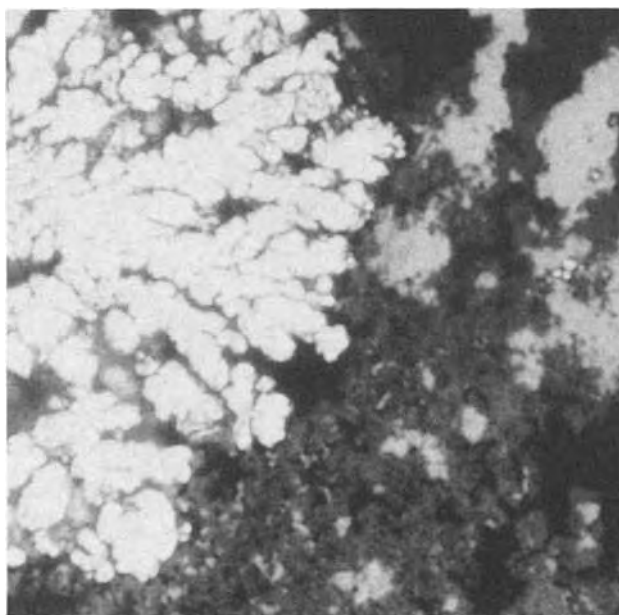


Fig. 11. Appearance of reduction products in electrode discharged 32% at the 10-hr rate in 8.4M CsOH at cycle 6. This is a high magnification view of another area of the electrode shown in Fig. 6. Compare with Fig. 10 at the same magnification to see the effect of different discharge rates.

discharge, they contained on the order of 64 times as much Ag, if a spherical shape is assumed for ease in calculation. The  $\text{Ag}_2\text{O}$  also formed into smaller particles when using the 1-hr discharge rate than when using the 20-hr rate, although the differences were not as great as for Ag.

Several cross sections that included half the width of an electrode were divided into 25 to 30 equal viewing areas the size of Fig. 6 and examined at  $108\times$  magnification. The percentage of AgO,  $\text{Ag}_2\text{O}$ , and metallic Ag was estimated for electrodes discharged at the 20-hr rate until potential had been at the  $\text{Ag}_2\text{O}/\text{Ag}$  plateau for 2 hr. Estimates were also made for electrodes 45% discharged at the 1-hr rate. Here the small particle size made it impractical to give separate estimates for  $\text{Ag}_2\text{O}$  and AgO, but high magnification indicated that half of the oxide was AgO.

Figure 12 shows the composition of horizontal cross sections that reach the center of two electrodes. The left side of Fig. 12 gives the composition at one edge of the electrodes and the right side gives the composition at the centers. When the 20-hr discharge rate had been used (upper part of Fig. 12)  $\text{Ag}_2\text{O}$  had formed in most areas of the electrode, with a slight preference for the grid of expanded sheet Ag. The right-hand grid member in the upper part of Fig. 12 is also shown in Fig. 6. Formation of metallic Ag had a definite preference for grid members and for the electrode surface during a discharge at the 20-hr rate. Concentrations of AgO had become lower at the grid than elsewhere.

When a partial discharge was done at the 1-hr rate a much higher proportion of active material was reduced to Ag (lower part of Fig. 12). Initial formation of Ag had taken place preferentially at the grid, but then formation spread rapidly to more distant areas at or near the surface of the electrode. Metallic Ag concentration was high at the edges of both partly discharged electrodes (left side of Fig. 12).

**Structural changes that occur with cycling.**— When an electrode was charged and discharged at the 20-hr rate in 8.4M CsOH the most noticeable difference was that particles had dendritic shapes at the end of cycle 1 discharge (Fig. 13) in place of the irregular shapes present in the unused electrode (7, 10). The average size of Ag particles gradually increased as an electrode was cycled using the 20-hr discharge rate. The change between cycles 1 and 6 can be seen by comparing Fig. 13 with Fig. 8 at the same magnification. There was little additional increase in average size

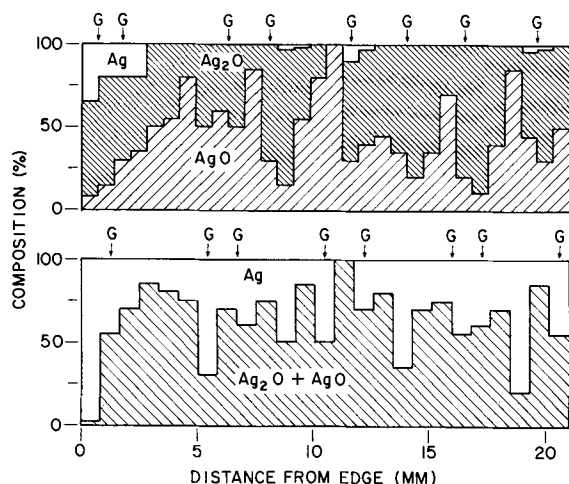


Fig. 12. Composition of active material in partly discharged electrodes at cycle 6 in 8.4M CsOH. Upper half is based on a cross section of an electrode that had been discharged 32% at the 20-hr rate (Fig. 6 and 11). Lower half refers to an electrode discharged 45% at the 1-hr rate (Fig. 9). Letter G indicates location of the grid members.

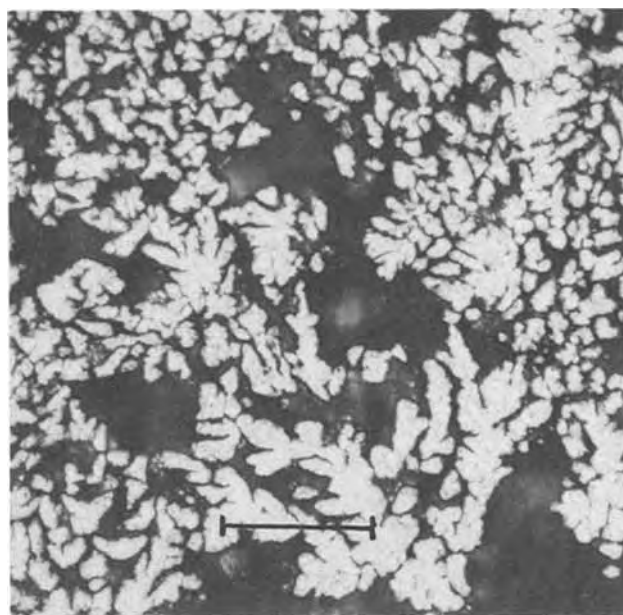


Fig. 13. Cross section through typical Ag particles that formed at the end of cycle 1 discharge at the 20-hr rate in 8.4M CsOH. Some larger particles had also formed but were less common. Marker indicates 25  $\mu\text{m}$ .

between cycle 6 and 15, but Ag particles became more rounded. Large areas of small particles developed in some places during the first few cycles, but then the size and amount of small particles decreased with additional cycling. As for the oxides, the size of  $\text{Ag}_2\text{O}$  clumps increased between cycle 6 and 15, and  $\text{Ag}_2\text{O}$  layers on AgO became thicker.

When the 1-hr discharge rate was used particle sizes had less variety with the greatest structural change being the decrease in average particle size after the first discharge. In addition, a moderately large proportion of the Ag had assumed thin dendritic shapes during the discharge at the 1-hr rate (Fig. 14). The

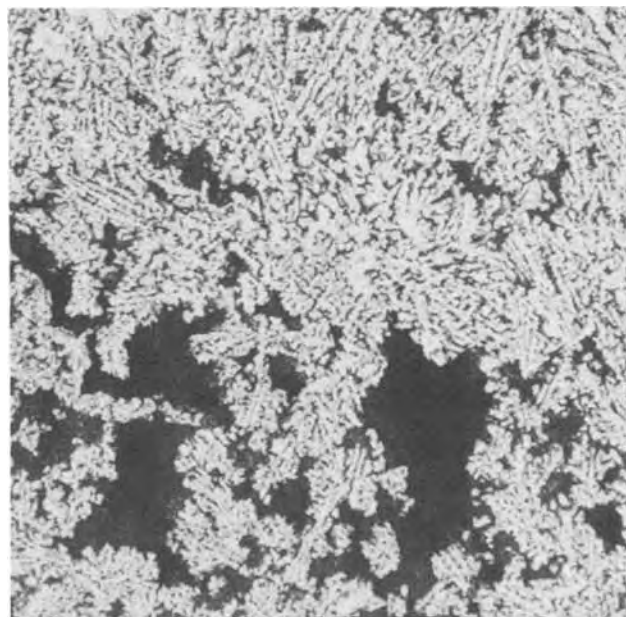


Fig. 14. Partially oriented Ag particles were fairly common after cycle 1 discharge at the 1-hr rate in 8.4M CsOH, but most of the Ag was in small granular particles such as those shown at the center and lower left. Compare with Fig. 13 at the same magnification to see the effect of a single discharge at different rates. Both electrodes had the same original structure.



proportion of thin Ag particles gradually decreased as an electrode was cycled. Thin shapes became rare by cycle 15. Areas of very closely packed small particles were not found at cycle 1 but developed with cycling in 8.4M CsOH (Fig. 10 and 15). Thin Ag particles were uncommon after a discharge at the 20-hr rate.

**Effect of electrolyte on electrode structure.**—The main difference between structures in KOH and CsOH solutions was that Ag particles tended to be smaller in CsOH. Although structural differences were not great, a smaller average particle size in CsOH was noted at both discharge rates. At the 20-hr discharge rate the size difference was greatest in the first few cycles. Another difference was that smaller and more porous  $\text{Ag}_2\text{O}$  formed in CsOH than in KOH during a discharge at the 1-hr rate.

The Ag particle sizes in discharged electrodes at cycles 6 and 15 were probably not significantly different between 3.6M and 8.4M CsOH when the 20-hr discharge rate was used, although Ag often tended to form into larger particles and in bigger clumps near the surface of an electrode cycled repeatedly in 3.6M CsOH. When the 1-hr discharge rate was used the average particle size was about twice as large in 3.6M CsOH as in 8.4M CsOH. Typical particle sizes after discharges at the 1-hr rate were 0.3–1  $\mu\text{m}$  in 8.4M CsOH, while in 3.6M CsOH 50–65% of an electrode consisted of particles 1–2  $\mu\text{m}$  in their smaller dimension with most of the remainder 0.4–1  $\mu\text{m}$ .

During a charge in 3.6M CsOH the  $\text{AgO}$  had a tendency to form into elongated shapes (9). During a discharge at the 1-hr rate the elongated  $\text{AgO}$  was reduced to many small Ag particles that remained in groups having shapes similar to the  $\text{AgO}$  (Fig. 16). When similar elongated  $\text{AgO}$  crystals were discharged at the 20-hr rate the Ag formed into larger particles which usually were not in noticeably elongated groups.

Some of the active material developed an alignment when electrodes were discharged at the 1-hr rate in 3.6M CsOH. These aligned groups of particles often, but not always, pointed at a grid member or at large Ag particles in the active material. The aligned particles did not actually touch the grid or large particles. Aligned Ag particles were not found in 8.4M CsOH or

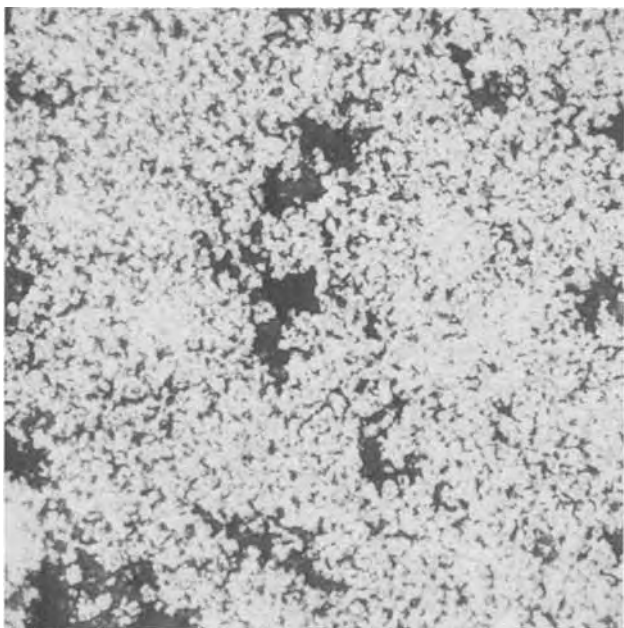


Fig. 15. Small Ag granules typical of the active material at the end of cycle 30 discharge at the 1-hr rate in 8.4M CsOH. Compare with Fig. 14 at the same magnification to see the effect of cycling. The partially oriented Ag particles of Fig. 14 had become scarce by cycle 15.

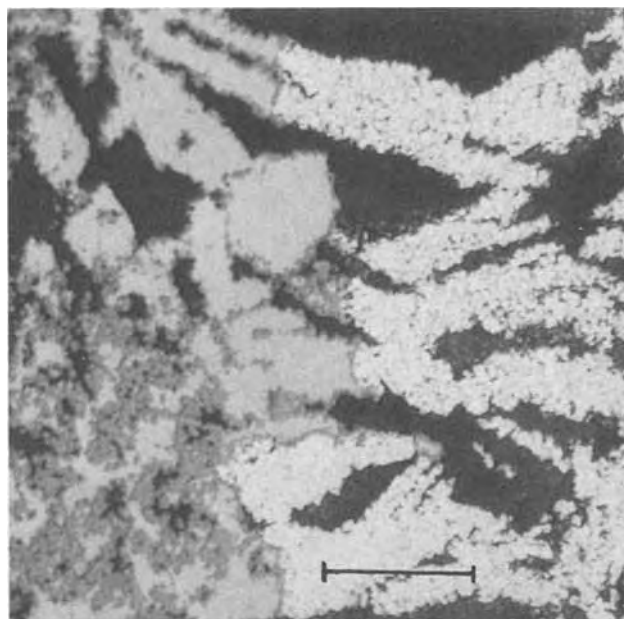


Fig. 16. An electrode discharged at the 1-hr rate at cycle 6 in 3.6M CsOH showing  $\text{Ag}_2\text{O}$  that formed on the surface of  $\text{AgO}$  (left side) and reduction of oxides to Ag (right side). The smallest Ag particles that formed at the 1-hr rate in 3.6M CsOH often were in groups that retained the shapes of the  $\text{AgO}$  particles. About two-thirds of the electrode consisted of Ag particles two to four times larger than those shown here. Marker indicates 20  $\mu\text{m}$ .

in KOH, except for a slight alignment in 5.5M KOH, the lowest KOH concentration used.

### Discussion

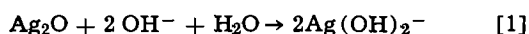
Comparison of discharge potentials and of electrode structures indicated that the products of reduction were the same in CsOH solutions as in KOH. Discharge potentials in KOH were more nearly level during both plateaus and then fell more rapidly (Fig. 3), indicating that reduction in KOH took place under conditions that were closer to equilibrium. Earlier work showed that oxidation of Ag also occurred closer to equilibrium in KOH than in CsOH (9). This difference probably occurred because conductivity in 8.4M CsOH was lower and viscosity was higher than in 8.4M KOH.

A gradual decrease in capacity following slow discharges is a general finding. The rate of capacity decrease appears to be relatively unaffected by charge rates. For example, from Fig. 10 of Ref. (12) one can calculate that a sealed Ag-Zn battery had capacity loss rates of about 1.2 and 0.9% per cycle to cycle 15 and 30, respectively. This battery was discharged at about the 15-hr rate and charges were done at the 26–34-hr rate followed by a float for 2 days at 1.95V per cell. These rates of loss are in the middle of the range of those in Table I despite the differences in cell construction and in cycling conditions.

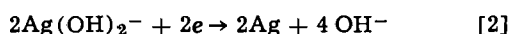
**Reduction of  $\text{AgO}$  to  $\text{Ag}_2\text{O}$ .**—Cycle 1 in 3.6M CsOH always gave a shorter  $\text{AgO}$  plateau than later cycles or the other electrolytes when the 20-hr discharge rate was used (Table II and upper part of Fig. 2). At cycle 1 a new sintered Ag electrode always accepted more capacity in 3.6M CsOH than in 8.4M CsOH (9). It was concluded that formation of an unusually large amount of  $\text{AgO}$  resulted in a smoother  $\text{AgO}$  having a smaller surface area, since oxygen evolution potentials were about 80 mV higher than in other electrolytes, although formation of  $\text{Ag}_2\text{O}$  and  $\text{AgO}$  had taken place at normal potentials. Less  $\text{Ag}_2\text{O}$  formed on the surface of this smoother  $\text{AgO}$  during discharge before  $\text{Ag}_2\text{O}$  became sufficiently thick that polarization caused electrode potential to reach the  $\text{Ag}_2\text{O}/\text{Ag}$  plateau. Electrode capacity dropped rapidly during the first few cycles in

3.6M CsOH (Fig. 1) and the differences between the AgO discharge plateau in 3.6M and 8.4M CsOH had largely disappeared by cycle 3 or 4, except for the tendency of potentials at the AgO/Ag<sub>2</sub>O plateau to have a fairly linear decrease in 3.6M CsOH rather than the curved form usually found (upper part of Fig. 2). Slow charges promoted formation of AgO having a smaller surface area. In both CsOH and KOH the proportion of a discharge that took place at the AgO/Ag<sub>2</sub>O potential was smallest following a charge at the lowest current (Fig. 5) although this low current gave maximum total discharge capacity.

**Formation of Ag.**—Supersaturation of dissolved Ag(I) was produced from the beginning of a discharge and continued until near the final fall in potential (3). The dissolved species is usually considered to be Ag(OH)<sub>2</sub><sup>-</sup>. This forms according to Eq. [1]

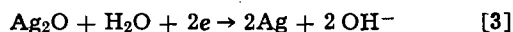


Reduction of the dissolved species gives metallic Ag



The structure of Ag that formed during reduction was greatly different than the structure of the Ag<sub>2</sub>O, because of the dissolution-precipitation mechanism given in Eq. [1] and [2]. Important factors in determining the form of Ag were differences between the solubility of Ag<sub>2</sub>O in CsOH and KOH, the degree of supersaturation, and the rate of reduction.

The over-all reaction for the formation of Ag from Ag<sub>2</sub>O is obtained by combining Eq. [1] and [2]



As a result of this reaction the hydroxyl ion concentration tended to increase in the interior of the electrode.

During a discharge at the 1-hr rate groups of small Ag particles took the shape of the AgO (Fig. 9 and 16). During a discharge at the 20-hr rate sufficient time was available for greater diffusion of Ag(OH)<sub>2</sub><sup>-</sup>, allowing Ag to grow larger and to deposit in an orientation that differed from the AgO (Fig. 11) although groups of Ag particles still kept shapes much the same as the AgO. A small space was often noted between Ag that formed during a slow discharge and adjacent oxide (Fig. 7). This space indicated that the soluble Ag species had diffused from Ag<sub>2</sub>O to nearby Ag before being reduced. During a fast discharge time was insufficient for much diffusion of Ag(OH)<sub>2</sub><sup>-</sup>, so Eq. [2] followed rapidly after Eq. [1]. As a result, Ag formed at the site of the Ag<sub>2</sub>O in small particles during a fast discharge and the variety of particle sizes was more limited.

Results of both the oxidation of Ag in CsOH (9) and the reduction of silver oxides indicated that concentration gradients were higher in CsOH than in KOH of the same molarity. An 8.4M CsOH solution has a lower conductivity and higher viscosity than 8.4M KOH. The lower conductivity indicated a lower ionic mobility, as one would expect since the Cs<sup>+</sup> ion is larger than the K<sup>+</sup> ion. Mobility decreased in concentrated solutions, probably because of the formation of ion pairs in the electrolyte, with KOH mainly in the form of water-bridged ion pairs and Cs<sup>+</sup> associated directly with the hydroxyl ion. The formation of ion pairs may also have lowered the Ag(OH)<sub>2</sub><sup>-</sup> mobility in concentrated solutions, and this would make it more difficult for large Ag particles to form, particularly in concentrated CsOH solutions. Therefore Ag did not grow into large particles as readily in CsOH as in KOH.

After initial Ag formation at the 1-hr rate took place near the grid and close to the surface, Ag formation then occurred at the electrode surface at a distance from the grid. Most of the active material near a grid had been oxidized to AgO by the time that a charge

ended, but in areas more than 1 or 2 mm from a grid the active material was mainly Ag<sub>2</sub>O + Ag in electrodes always discharged at the 1-hr rate (9). The lack of AgO formation at a distance from the grid during a charge was the result of a lowered internal conductivity and was only found when two conditions were met: (a) the original sintered Ag electrode contained a low proportion of large Ag particles; and (b) the electrode was discharged at a sufficiently high rate that average particle size decreased (7, 9). When an electrode was discharged 50% at the 1-hr rate no reduction had occurred in most areas near the center, except within about 0.05-0.1 mm of the grid, and Ag had mainly formed in areas near the electrode surface that were not close to a grid.

A discharge at the highest rate caused the greatest hydroxyl ion concentration gradients between the interior of the electrode and the bulk of the electrolyte, from the reaction of Eq. [3]. Because of these concentration gradients, reduction tended to spread along the surface of an electrode during a discharge at the 1-hr rate, in preference to spreading inward. Under these conditions the reduction of AgO was much more difficult than reduction of regions largely Ag<sub>2</sub>O. As a result, most active material in regions close to the grid remained AgO during the first half of the discharge and one or both of the silver oxides almost always remained at the surface of the electrode near a grid even though large areas further away had been converted to Ag. The preferred locations for reduction to Ag were controlled by both diffusion in the electrolyte and conductivity in the electrode.

The development of aligned groups of particles, with the alignment often pointing at the grid members and at large Ag particles, was believed to be the result of Ag precipitating from Ag(OH)<sub>2</sub><sup>-</sup> on sites where current density was highest during a discharge at the 1-hr rate. Grid members distributed the current throughout the electrode, with the largest Ag particles in the active material forming important supplementary low resistance current paths. Internal resistance had less of an effect when discharging at the 20-hr rate, so current distribution was more even and alignment of active material did not develop. The fact that alignment was only found in the more dilute CsOH or KOH solutions indicated that mobility of Ag(OH)<sub>2</sub><sup>-</sup> was also a factor. Evidence for mobility of Ag(OH)<sub>2</sub><sup>-</sup> being higher in 3.6M CsOH than in 8.4M CsOH was that Ag particles grew to a larger average size in 3.6M CsOH during a discharge at the 1-hr rate.

### Conclusions

Capacity declined more slowly in CsOH solutions than in KOH when Ag electrodes were cycled using slow discharges. At high rates of discharge KOH was the preferable electrolyte, because polarization was lower as a result of higher ionic mobility in KOH. An additional disadvantage to the use of CsOH was its higher cost. Thus CsOH is not a practical replacement for KOH under many conditions. However, the electrolyte cost is but a small proportion of the total cost of a Ag-Zn or Ag-Cd storage battery. The preferred electrolyte can be CsOH when it is necessary to obtain the best possible capacity while using slow discharges.

Metallic Ag began to form in both electrolytes while large amounts of AgO remained, because reduction of AgO to form large amounts of Ag<sub>2</sub>O was more difficult than reduction of Ag<sub>2</sub>O to Ag. The Ag did not have the same structure as Ag<sub>2</sub>O, since the formation mechanism involved a soluble intermediate. The most important factor in determining the form of Ag was the reduction rate. Preferred sites for reduction to Ag in a partly discharged electrode were controlled by a combination of diffusion in the electrolyte and electrode conductivity.

Size of Ag particles tended to be smaller in CsOH solutions than in KOH, although differences were not



great. The retention of smaller particle sizes during cycling was the reason for capacity not decreasing as rapidly in CsOH as in KOH when an electrode was given a series of slow discharges. Since large Ag particles were not completely oxidized during a charge. The Ag particles that formed during reduction at the 1-hr rate were smaller in 8.4M CsOH than in 3.6M CsOH. These size differences indicated that mobility of dissolved  $\text{Ag}_2\text{O}$  was lower in 8.4M CsOH than in 3.6M CsOH, and lower in CsOH than in KOH of the same concentration.

Manuscript submitted Sept. 19, 1973; revised manuscript received Jan. 28, 1974.

Any discussion of this paper will appear in a Discussion Section to be published in the December 1974 JOURNAL. All discussions for the December 1974 Discussion Section should be submitted by Aug. 1, 1974.

## REFERENCES

1. C. P. Wales, *This Journal*, **116**, 729 (1969).
2. C. P. Wales, *ibid.*, **116**, 1633 (1969).
3. B. Miller, *ibid.*, **117**, 491 (1970).
4. T. I. Dunaeva, G. P. Ereiskaya, and M. F. Skalozubov, *Elektrokhimiya*, **7**, 56 (1971).
5. E. G. Gagnon and L. G. Austin, *This Journal*, **118**, 497 (1971).
6. V. Tilak, R. S. Perkins, H. A. Kozłowska, and B. E. Conway, *Electrochim. Acta*, **17**, 1447 (1972).
7. C. P. Wales, "Power Sources," D. H. Collins, Editor, Vol. 4, p. 163, Oriel Press Ltd., Newcastle-upon-Tyne (1973).
8. G. D. Nagy and E. J. Casey, "Zinc-Silver Oxide Batteries," A. Fleischer and J. J. Lander, Editors, p. 133, John Wiley & Sons, Inc., New York (1971).
9. C. P. Wales, *This Journal*, **121**, 17 (1974).
10. C. P. Wales and A. C. Simon, *ibid.*, **115**, 1228 (1968).
11. C. P. Wales, *ibid.*, **118**, 1021 (1971).
12. G. M. Wylie, *Proc. 19th Annual Power Sources Conference*, p. 73 (1965).

## Lithium-Magnesium Electrodes in Propylene Carbonate

M. M. Nicholson\*

Atomics International Division, Rockwell International Corporation, Canoga Park, California 91304

The publication costs of this article have been assisted by Atomics International.

## ABSTRACT

Lithium was cathodically deposited on magnesium from 1M  $\text{LiClO}_4$  in propylene carbonate. Anodic stripping measurements by constant-current and linear potential-scan techniques indicated the presence of both alloyed and unalloyed lithium on the plated surfaces. The alloying energy was approximately 7 kcal/mole of lithium. The anodic recovery of lithium was limited by its diffusion into the underlying metal. Potential-time curves recorded on open circuit revealed two penetration stages, with  $D_1 = 1.3 \times 10^{-11}$  and  $D_2 = 3.9 \times 10^{-14}$   $\text{cm}^2/\text{sec}$ . The faster process was attributed to the transport of lithium along the grain boundaries, and the slower, to penetration of the magnesium grains. The plated electrodes were insensitive to added water at concentrations from 0.01 to 0.1M.

Dey has reported that a lithium-magnesium alloy is formed by cathodic deposition of lithium from a solution of lithium perchlorate in propylene carbonate (PC) onto a magnesium substrate at potentials differing only slightly from that of pure lithium (1). Chemical analysis of the alloy indicated 100% current efficiency for the deposition process. In the present investigation, the anodic behavior of thin alloy layers prepared in this manner was examined in dry 1M  $\text{LiClO}_4$ -PC and in this electrolyte containing added water at concentrations from 0.01 to 1M. The conclusions from this work will be of interest in organic battery applications requiring long-term storage of non-reserve cells under humid conditions. A further result was the determination of diffusion coefficients for lithium in magnesium at room temperature.

## Experimental

The magnesium electrodes were polished cross sections of 1.55-mm diameter wire which was insulated on the sides with heat-shrinkable Teflon tubing. The exposed surface was renewed between measurements, when desired, by polishing with Grade 600A silicon carbide paper, followed by buffing on dry filter paper. Contact of the electrode to the external circuit was made through a copper wire attached to the upper end of the magnesium by low-melting indium solder. The magnesium was high-purity material from Gal-

lard-Schlesinger Chemical Manufacturing Corporation, with seven specified impurities totaling less than 0.1%. Lithium perchlorate and propylene carbonate were purified by procedures that were described in detail elsewhere (2). Gas chromatographic analysis indicated 10 ppm water in the dried solvent, while the dried salt contained  $\leq 100$  ppm water. From these data, the total water content of the dry 1M  $\text{LiClO}_4$  solution was estimated to be  $\leq 1$  mM. Solutions containing 0.01-1M  $\text{H}_2\text{O}$  were prepared by volumetric additions of water to the dry electrolyte.

The cell was of a conventional H design, with a fritted glass disk separating the working and counter-electrode compartments. The reference and counter-electrodes were both of high-purity lithium metal. The cell was assembled and housed during the electrochemical measurements in an argon-atmosphere dry box at room temperature. Data were obtained under open-circuit, constant-current, and linear potential-scan conditions on a Princeton Applied Research Model 170 Electrochemistry System. The equivalent thickness of the plated lithium ranged from 0 to 1.6 $\mu$ .

## Results and Discussion

*Anodic behavior of lithium-plated surfaces.*—Two active-lithium phases were distinguishable on the plated surfaces. This is evident in the curves of Fig. 1, which were obtained by depositing lithium at  $-0.05\text{V}^1$

\* Electrochemical Society Active Member.

Key words: alloys, battery anodes, intermetallic diffusion.

<sup>1</sup> All potentials are reported with respect to the lithium electrode in the electrolyte used.

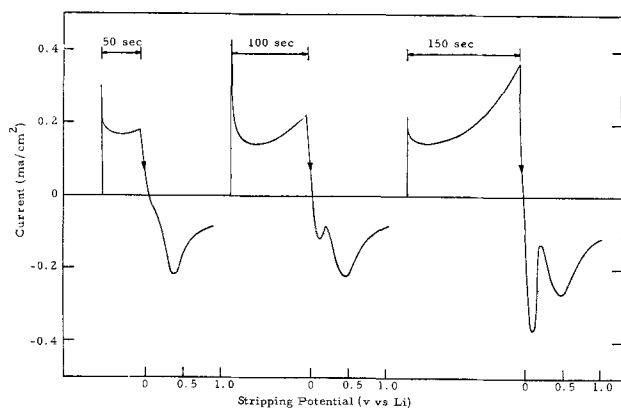


Fig. 1. Plating at  $-0.05V$ , followed by stripping at  $10\text{ mV/sec}$ . Plating times indicated above curves.

for different times and stripping immediately thereafter with a potential scan at  $10\text{ mV/sec}$ . The first anodic peak may be identified by its position near  $0.1V$  as that due to the oxidation of unalloyed lithium. This peak was sharply intensified by a threefold increase in the plating time. The second peak, at  $0.4-0.5V$ , would correspond to an alloying energy of  $\sim 8\text{ kcal/mole}$  of lithium, if rapid charge transfer is assumed for the electrode reaction. This value is comparable to the free energy of formation of  $-8.9\text{ kcal/mole}$  for the compound  $LiAl$ , which was estimated by extrapolating the high-temperature data of Yao, Heredy, and Saunders to  $25^\circ C$  (3). The height of the second peak increased only slightly with the plating time; apparently part of the alloyed lithium became inactive or was lost by penetration to the interior of the substrate.

Two anodic processes are also apparent in the constant-current stripping curves of Fig. 2, where  $Q_p$  represents the plating charge density,  $i_p$  and  $i_s$  are the plating and stripping current densities, and the corresponding transition times are designated as  $\tau_1$  and  $\tau_2$ . A complete glossary of symbols is provided at the end of this paper. At the current densities applied in Fig. 2, the unalloyed lithium was oxidized near  $0.03V$ . Most of the alloyed lithium was stripped with an additional  $0.25V$ , i.e., with the expenditure of  $\leq 6\text{ kcal/mole}$  beyond that required for the unalloyed metal. The total lithium recovery in the curves of Fig. 2 was 16-18% of the amount plated.

The loss of lithium from a freshly plated surface persisted in experiments covering a wide range of conditions. Table I gives the results of immediate and delayed stripping from surfaces that had been renewed by polishing before the deposition step. Figure 2 is

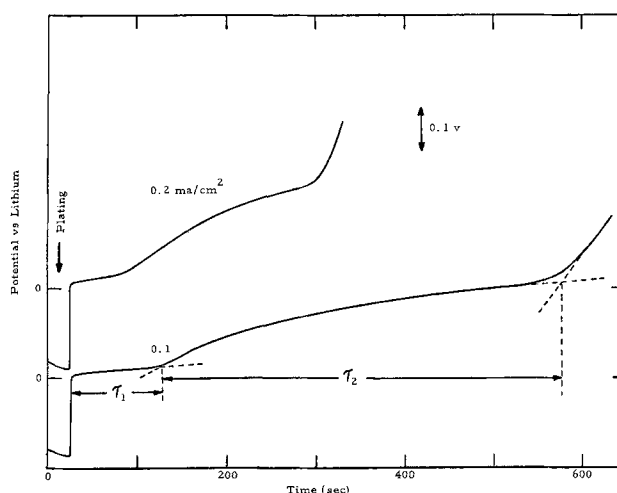


Fig. 2. Potential-time curves for immediate stripping at different rates.  $Q_p = 250\text{ mcoulombs/cm}^2$ ;  $i_p = 10\text{ mA/cm}^2$ ;  $i_s$  indicated on curves.

representative of the two-stage, undelayed stripping curves. When the standing time was long enough for the open-circuit potential to rise above  $0.05V$ , only the second oxidation stage for alloyed lithium was observed. The recovery charge  $Q_2$  for the second stripping stage was low compared to the plating charge  $Q_p$ , in all of the measurements reported in Table I. The  $Q_2$  deficiency could not have been due to a bound monolayer, however, as described by Fried and Barak in the stripping of lithium from platinum (4), since a monolayer would correspond to  $\sim 0.2\text{ mcoulomb/cm}^2$ , assuming a roughness factor of unity, while  $Q_p$  was 10-1200 mcoulombs/cm<sup>2</sup> in the present study. The open-circuit transients provided a clue to the loss of lithium from the magnesium surfaces. These results are interpreted in the section on penetration rates.

The effect of repeated plating and stripping without mechanical renewal of the surface was also examined. It was found that the cyclic curves eventually reached a steady state, as in Fig. 3, with unalloyed lithium as the predominant phase during immediate stripping. These curves and others were unaffected by stirring. It may be inferred from this fact that the disappearance of lithium was a solid-state phenomenon, rather than an interaction with impurities in the solution. The delayed recovery of lithium from an electrode which had been conditioned by cycling at  $0.2\text{ mA/cm}^2$  is shown in Fig. 4. The recovery charge for alloyed lithium,  $Q_2$ , then increased with the standing time,

Table I. Lithium recovery from fresh electrode under varied conditions

$C_{H_2O}$ (moles/liter)	Plating data		Open-circuit data		Stripping data		
	$Q_p$ (mcoulombs/ cm <sup>2</sup> )	$i_p$ (mA/cm <sup>2</sup> )	Time <sup>a</sup> (sec)	Final potential, <sup>b</sup> V vs. Li	$i_s$ (mA/cm <sup>2</sup> )	$Q_1$ (mcoulombs/cm <sup>2</sup> )	$Q_2$ (mcoulombs/cm <sup>2</sup> )
$\leq 0.001$	10	2	245	0.85	0.2	— <sup>c</sup>	0
	30	2	500	0.07	0.2	— <sup>c</sup>	3
	40	2	800	0.07	0.2	— <sup>c</sup>	2
	125	5	240	0.12	0.2	— <sup>c</sup>	13
	132	5.29	50	0.06	0.4	— <sup>c</sup>	53
	210	2	750	0.12	0.2	— <sup>c</sup>	13
	250	10	0	—	0.1	11	45
	250	10	0	—	0.2	13	44
	250	10	0	—	0.4	33	40
	250	10	75	0.00	0.2	9	43
	250	10	184	0.07	0.2	— <sup>c</sup>	38
	530	26.4	435	0.06	0.2	— <sup>c</sup>	53
	660	26.4	650	0.04	0.2	— <sup>c</sup>	74
	1160	52.9	1920	0.06	0.2	— <sup>c</sup>	67
	0.1	530	26.4	574	0.08	0.2	— <sup>c</sup>
1160		52.9	1340	0.06	0.2	— <sup>c</sup>	66
1160		52.9	0	—	0.2	0	0
1	1160	52.9	10	0.09	0.2	0	0

<sup>a</sup> After plating.

<sup>b</sup> Immediately before stripping.

<sup>c</sup> Absent with delayed stripping.

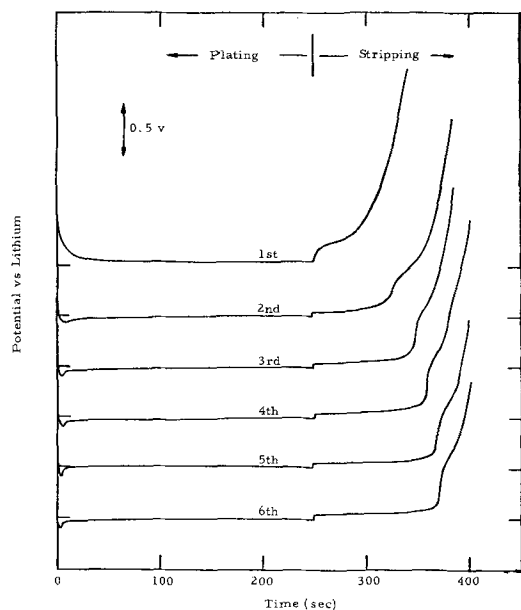


Fig. 3. Repeated plating and stripping in dry 1M LiClO<sub>4</sub>-PC.  $Q_p = 50$  mcoulombs/cm<sup>2</sup>;  $i_p = 0.2$  mA/cm<sup>2</sup>;  $i_s = 0.2$  mA/cm<sup>2</sup>; zero volt position indicated for each curve.

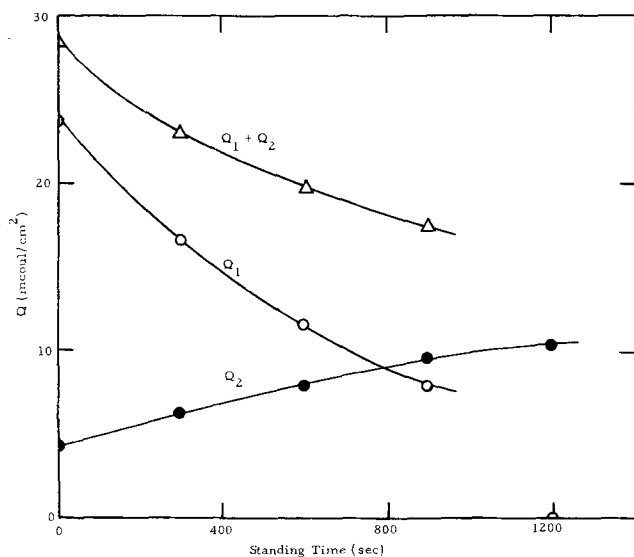


Fig. 4. Lithium recovery from conditioned electrode with delayed stripping.  $Q_p = 50$  mcoulombs/cm<sup>2</sup>;  $i_s = i_p = 0.2$  mA/cm<sup>2</sup>.

while  $Q_1$ , for unalloyed lithium, decreased. The percentage recovery per cycle, based on  $Q_2$ , was also much improved on the conditioned electrode compared to that on a fresh electrode (Table I). Furthermore, when an electrode was conditioned at 2 mA/cm<sup>2</sup> and stripped immediately at this higher current density ( $20 \leq Q_p \leq 50$  mcoulombs/cm<sup>2</sup>),  $Q_2$  was essentially zero and  $Q_1$  then accounted for 70% recovery.

**Lithium penetration rates.**—The open-circuit potential-time curves exhibited two transitions similar to those observed under anodic current. By the proper selection of  $Q_p$ , it was possible to obtain a measurable  $\tau_1$ , or to observe  $\tau_2$  with an essentially negligible  $\tau_1$ . This resolution of the transition times permitted treatment of the lithium loss in two stages, as discussed below. It was found that  $\sqrt{\tau_1}$  and  $\sqrt{\tau_2}$  were both linear functions of  $Q_p$ , passing near the origin, as shown in Fig. 5 and 6, respectively. The corresponding least squares equations are

$$\sqrt{\tau_1} = 1.11 + 0.03285Q_p \quad [1]$$

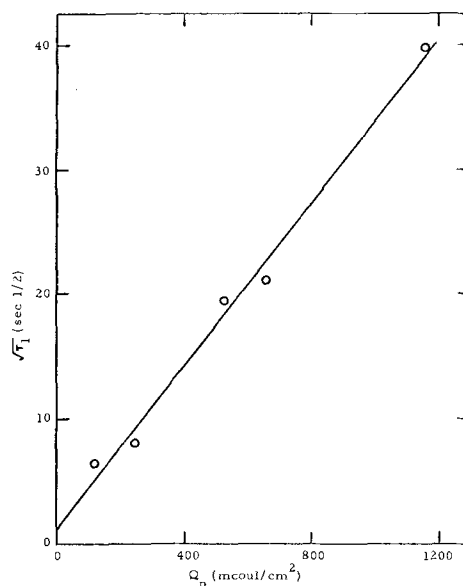


Fig. 5. First-stage penetration of lithium into magnesium

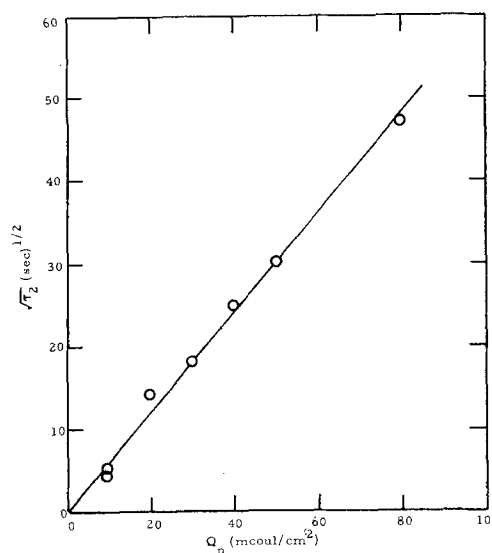


Fig. 6. Second-stage penetration of lithium into magnesium

$$\sqrt{\tau_2} = -0.07 + 0.6067Q_p \quad [2]$$

where the  $\tau$ 's are expressed in seconds and the  $Q$ 's in millicoulombs per square centimeter.

Several investigators have reported evidence of film formation on lithium in propylene carbonate solutions (5-8). Although such films can have a pronounced effect on electrode kinetics and double layer properties (5, 6), it is very unlikely that filming reactions accounted for a substantial part of the lithium loss observed in the present study. In well-purified LiClO<sub>4</sub>-PC solutions, the film thickness apparently ranges from submonolayers to several molecular layers (5, 7), and little or no corrosion has been observed visually in some tests lasting hundreds of hours (7). In contrast, the Li-Mg electrodes lost the equivalent of 50-5000 molecular layers in less than 0.5 hr. These results may be interpreted on the basis of a solid-state diffusion model by means of the following analysis:

Let  $C^0$  represent the concentration of lithium in a plated layer that is adjacent to pure magnesium at the beginning of the penetration process. As the lithium diffuses, a concentration gradient is established within the magnesium, but the boundary concentration remains at  $C^0$  until the layer of pure metal is suddenly depleted. A transition then occurs in the potential-time curve. The concentration variable is expressed as  $C^0 -$

C, where C is the lithium concentration in the magnesium as a function of time  $t$  and distance from the surface. This problem is equivalent to that involved in the Cottrell method for determination of diffusion coefficients by electrolysis at constant potential (9). The flux of lithium across the lithium-magnesium boundary on open circuit is then

$$\frac{dM}{dt} = -C^0 \sqrt{\frac{D}{\pi t}} \quad [3]$$

where  $M$  is the weight of lithium per unit area and  $D$  is its diffusion coefficient. The weight  $M^0$  of lithium corresponding to the plating charge  $Q_p$  will have disappeared in a time  $\tau$  which is found by integrating Eq. [3]

$$\int_{M^0}^0 dM = -C^0 \sqrt{\frac{D}{\pi}} \int_0^\tau \frac{dt}{\sqrt{t}} \quad [4]$$

The result may be expressed by Eq. [5]

$$\sqrt{\tau} = \frac{1}{2} \sqrt{\frac{\pi}{D}} \cdot \frac{M^0}{C^0} \quad [5]$$

which predicts direct proportionality between  $\sqrt{\tau}$  and  $Q_p$ .

From the slope of the line in Fig. 5, Eq [5] leads to a diffusion coefficient  $D_1 = 1.3 \times 10^{-11}$  cm<sup>2</sup>/sec for the first penetration process, if  $C^0$  is taken as the density of pure lithium. This value may be compared with  $4 \times 10^{-11}$  cm<sup>2</sup>/sec for sodium in lead at 20°, computed from a potentiostatic transient in aqueous NaOH (10), and  $5 \times 10^{-12}$  cm<sup>2</sup>/sec for potassium in zinc, determined in a membrane cell (11). For self-diffusion at grain boundaries in zinc,  $D$  is estimated to be  $7 \times 10^{-12}$  cm<sup>2</sup>/sec (11). It is probable, therefore, that the first-stage penetration of lithium into magnesium occurs along the grain boundaries.

Formally, the same analysis can be applied to the data in Fig. 6 for the second-stage penetration process. If  $C^0$  is again taken as the density of pure lithium, Eq. [5] yields  $D_2 = 3.9 \times 10^{-14}$  cm<sup>2</sup>/sec. This slower process may be plausibly interpreted as diffusion within the magnesium grains. It must be realized that the effective interfacial area for the second process will be larger than the projected area of the electrode if the grain boundaries have been penetrated, as visualized, before the second stage begins. If the true area were taken into account, the second diffusion coefficient would be several orders of magnitude lower than that reported. For comparison, the self-diffusion coefficient in monocrystalline zinc is  $\sim 10^{-18}$  cm<sup>2</sup>/sec at room temperature (11).

Kiseleva *et al.* evaluated penetration coefficients for the cathodic injection of sodium into cadmium from aqueous NaOH on the basis of a reactive diffusion model (12). In that system, the intermetallic layer grew periodically, reaching an incremental thickness  $a$ , which was equated to the grain diameter, in a time  $t$ . From the relation

$$\sqrt{t} = \frac{a}{\sqrt{P}} \quad [6]$$

the penetration coefficient  $P$  was found to be  $5 \times 10^{-10}$  cm<sup>2</sup>/sec for fine-grained cadmium and  $1.4 \times 10^{-9}$  cm<sup>2</sup>/sec for coarse-grained. Equation [5] resembles Eq. [6] in that the ratio  $M^0/C^0$  represents a layer thickness, and the quantity  $\sqrt{\pi}/2$  is not very different from unity. Thus, the linear diffusion model and the parabolic growth law for reactive diffusion give similar values for  $D$  and  $P$  when the thicknesses  $a$  and  $M^0/C^0$  are about the same.

The anodic behavior described in the preceding section can be explained on the basis of the three penetration processes: (i) The unalloyed lithium was exterior lithium that had not yet penetrated the grain

boundaries. (ii) Most of the alloyed lithium which was recovered anodically was grain-boundary material that had become bonded to magnesium. (iii) The unrecovered lithium in the longer experiments was lithium that had penetrated further into the magnesium grains.

*Effects of water.*—The lithium-plated electrodes showed little sensitivity to water at concentrations below 1M. Lithium-magnesium alloys have even been recommended for use in aqueous batteries (13). It is known, however, that water decreases the exchange current on a freshly cut lithium surface in LiClO<sub>4</sub>-PC (6). The recovery of lithium from magnesium electrodes that had been replated before plating in the water solutions is recorded in Tables I and II. The charge densities  $Q_1$  and  $Q_2$  were essentially independent of the water content until the latter reached the 1M level where no recovery was obtained with  $Q_p = 250$  mcoulombs/cm<sup>2</sup>. An electrode freshly plated at 1160 mcoulombs/cm<sup>2</sup> retained enough of the alloy to be detectable on open circuit for approximately 4 min. A transition occurring at that time apparently was due to the chemical reaction of lithium with water.

Repeated plating and stripping at constant current in solutions containing 0.01-0.1M H<sub>2</sub>O produced results very similar to Fig. 3 for the dry electrolyte. The curves for this conditioning sequence in 1M H<sub>2</sub>O were significantly different. The cathodic process, which may have included hydrogen evolution, then occurred at potentials as much as 0.5V below that of the reference electrode. Table III indicates the lithium recovery from conditioned electrodes at various water concentrations. Both  $Q_1$  and  $Q_2$  were measurable in this series and there was, again, no obvious trend due to the water content through the level of 0.1M. Even at 1M H<sub>2</sub>O, some of the plating charge was recovered, apparently as alloyed lithium, on the conditioned electrode.

### Conclusions

1. Two types of anodically active lithium were produced on a magnesium surface by electrodeposition from a lithium perchlorate-propylene carbonate solution. The active material appeared to consist of unalloyed lithium and of alloyed lithium that had undergone a free energy decrease of 6-8 kcal/mole.

Table II. Lithium recovery from fresh electrode in water solutions with constant plating charge and immediate stripping<sup>a</sup>

CH <sub>2</sub> O (moles/liter)	Q <sub>1</sub> (mcoulombs/cm <sup>2</sup> )	Q <sub>2</sub> (mcoulombs/cm <sup>2</sup> )	Q <sub>1</sub> + Q <sub>2</sub> (mcoulombs/cm <sup>2</sup> )
≤0.001	33	40	73
0.01	46	27	73
0.01	31	33	64
0.05	33	29	62
0.05 <sup>b</sup>	34	27	61
0.1	32	27	59
0.1 <sup>c</sup>	33	27	60
1	0	0	0

<sup>a</sup>  $Q_p = 250$  mcoulombs/cm<sup>2</sup>;  $i_p = 10$  mA/cm<sup>2</sup>;  $i_s = 0.4$  mA/cm<sup>2</sup>.

<sup>b</sup> Stirred during plating and stripping.

<sup>c</sup> Stirred during stripping.

Table III. Lithium recovery from conditioned electrode in water solutions with constant plating charge and immediate stripping<sup>a</sup>

CH <sub>2</sub> O (moles/liter)	Q <sub>1</sub> (mcoulombs/cm <sup>2</sup> )	Q <sub>2</sub> (mcoulombs/cm <sup>2</sup> )	Q <sub>1</sub> + Q <sub>2</sub> (mcoulombs/cm <sup>2</sup> )
≤0.001	24.0	4.1	28.1
≤0.001 <sup>b</sup>	25.0	3.8	28.8
0.01	23.0	2.7	25.7
0.01 <sup>b</sup>	28.0	3.7	31.7
0.05	14.3	11.5	25.8
0.05 <sup>b</sup>	15.3	9.5	25.1
0.1	22.0	5.0	27.1
0.1 <sup>b</sup>	21.2	4.9	26.1
1	0	12.0	12.0

<sup>a</sup>  $Q_p = 50$  mcoulombs/cm<sup>2</sup>;  $i_p = 0.2$  mA/cm<sup>2</sup>;  $i_s = 0.2$  mA/cm<sup>2</sup>;  $Q_1$  and  $Q_2$  (unstirred) from 5th cycle.

<sup>b</sup> Later cycle, with stirring.

2. The anodic recovery of lithium was limited by diffusion into the solid metal structure, which occurred in two stages, with a diffusion coefficient of  $1.3 \times 10^{-11}$  cm<sup>2</sup>/sec for the first stage and an apparent value of  $3.9 \times 10^{-14}$  cm<sup>2</sup>/sec for the second. The faster process probably involved the transport of lithium along the grain boundaries, while the slower diffusion was attributed to penetration of the magnesium grains.

3. In experiments lasting up to 20 min, the plated electrodes showed little sensitivity to added water at concentrations as high as 0.1M; the investigation of long-term exposure to water was precluded by the diffusional loss of lithium metal. In a 1M water solution, the alloy phase was still detectable, but the recovery of lithium was low.

#### Acknowledgment

This research was sponsored by the Naval Air Systems Command under Contract N00019-72-C-0105.

Manuscript submitted June 16, 1972; revised manuscript received Jan. 29, 1974. This was Paper 2 presented at the Miami Beach, Florida, Meeting of the Society, Oct. 8-13, 1972.

Any discussion of this paper will appear in a Discussion Section to be published in the December 1974 JOURNAL. All discussions to be published in the December 1974 Discussion Section should be submitted by Aug. 1, 1974.

#### SYMBOLS

$a$	Incremental layer thickness (Kiseleva equation)
$C$	concentration of lithium in magnesium
$C^0$	initial concentration of lithium in magnesium
$D$	diffusion coefficient of lithium
$D_1$	diffusion coefficient of lithium in first penetration process
$D_2$	diffusion coefficient of lithium in second penetration process
$i_p$	plating current density

$i_s$	stripping current density
$M$	weight of lithium per unit area
$M^0$	initial weight of lithium per unit area
$P$	intermetallic penetration coefficient (Kiseleva equation)
$Q_p$	plating charge density
$Q_1$	charge density in first stripping process
$Q_2$	charge density in second stripping process
$t$	time
$\tau$	transition time
$\tau_1$	transition time for first anodic or open-circuit process (unalloyed lithium)
$\tau_2$	transition time for second anodic or open-circuit process (alloyed lithium)

#### REFERENCES

1. A. N. Dey, *This Journal*, **118**, 1547 (1971).
2. M. M. Nicholson, *ibid.*, **118**, 1047 (1971).
3. N. P. Yao, L. A. Heredy, and R. C. Saunders, *ibid.*, **118**, 1039 (1971).
4. I. Fried and H. Barak, *J. Electroanal. Chem.*, **30**, 279 (1971).
5. R. F. Scarr, *This Journal*, **117**, 295 (1970).
6. J. N. Butler, D. R. Cogley, and J. C. Synnott, *J. Phys. Chem.*, **73**, 4026 (1969).
7. R. Jasinski, in "Advances in Electrochemistry and Electrochemical Engineering," Vol. 8, P. Delahay and C. W. Tobias, Editors, John Wiley & Sons, Inc., New York (1971).
8. A. N. Dey, Paper 62 presented at Electrochemical Society Meeting, Atlantic City, N. J., Oct. 4-8, 1970.
9. I. M. Kolthoff and J. J. Lingane, "Polarography," 2nd Ed., Vol. 1, Interscience Publishers, Inc., New York (1952).
10. N. N. Tomashova, I. G. Kiseleva, I. I. Astakhov, and B. N. Kabanov, *Soviet Electrochem.*, **4**, 419 (1968).
11. I. I. Astakhov and B. N. Kabanov, *ibid.*, **5**, 700 (1969).
12. I. G. Kiseleva, B. N. Kabanov, and D. N. Machavariani, *ibid.*, **6**, 880 (1970).
13. R. S. Dean, U.S. Pat. 2,605,297 (July 29, 1952).

## Electron Microscope Investigation of Mixed Stannous Chloride/Palladium Chloride Catalysts for Plating Dielectric Substrates

N. Feldstein\*

Surface Technology, Inc., Princeton, New Jersey 08540

and M. Schlesinger, N. E. Hedgecock, and S. L. Chow

Department of Physics, University of Windsor, Windsor, Ontario, Canada N9B 3P4

The publication costs of this article have been assisted by the University of Windsor.

#### ABSTRACT

The present investigation represents a detailed study involving transmission electron microscopy and electron diffraction of surfaces treated by the catalyzing system (SnCl<sub>2</sub>/PdCl<sub>2</sub>/HCl) in conjunction with various accelerating solutions and in some cases a subsequent electroless copper bath. Results give additional information demonstrating the proper procedure(s) necessary in the preparation of the catalytic system. In addition it was found the best plating results are obtained whenever Pd<sub>3</sub>Sn is present on the treated surface prior to the metallization step.

In the art of electroless plating of dielectric substrates, a number of catalytic chemical systems are used prior to the deposition step. To date, all practical systems are based on the combination of tin and palladium. The various available processes can be classi-

fied into two systems as follows: (i) sensitization step (SnCl<sub>2</sub>/HCl) followed by an activation step (PdCl<sub>2</sub>/HCl) and (ii) catalyzation step (PdCl<sub>2</sub>/SnCl<sub>2</sub>/HCl) followed by acceleration (HCl or NaOH and similar).

With the increased interest of commercial applications, several investigators have examined the me-

\* Electrochemical Society Active Member.

Key words: electroless, electron microscopy, plating, catalysts.

Table I. Catalyzer and accelerator solutions

	A	B	C	D <sup>b</sup>
Catalyzer solution	Shipley <sup>a</sup> 9F	Stock solution I: SnCl <sub>2</sub> 0.81M HCl 11.2M Stock solution II: PdCl <sub>2</sub> 0.113M HCl 3.36M Working solution: 80 ml DI water 40 ml stock solution I 20 ml stock solution II	Stock solution: SnCl <sub>2</sub> 0.65M HCl 10.4M PdCl <sub>2</sub> 0.045M Aged three weeks Working solution: 2 parts DI water 1 part stock solution	SnCl <sub>2</sub> 0.18M SnCl <sub>4</sub> 0.018M HCl 5.4M PdCl <sub>2</sub> 0.039M
Accelerator solution	(Fig. 1a, 2a; with aged SnCl <sub>4</sub> , Fig. 5a, 6a) Shipley 19F (Fig. 1b, 2b, 5b, 6b) or NH <sub>4</sub> F · HF 2M (Fig. 3a, 4a)	NaOH or 1.2M NH <sub>4</sub> F · HF 2M or Shipley 19F	NaOH 1.2M	NH <sub>4</sub> F · HF 2M or Shipley 19F (Fig. 3b, 4b)
Summary	Worm-like clusters (do not form if aged SnCl <sub>4</sub> is added to catalyzer) Pb <sub>3</sub> Sn present	Results similar to A, when catalyzer aged — Pd <sub>3</sub> Sn present (Copper deposit Fig. 7a, 8a; with aged catalyzer Fig. 7b, 8b)	Results similar to B, also with regard to aging	No evidence of either Pd metal (20) or Pd <sub>3</sub> Sn

<sup>a</sup> Shipley Company, Newton, Mass.

<sup>b</sup> Appendix I of Ref. (20).

chanisms of the above systems leading to the following basic conclusions.

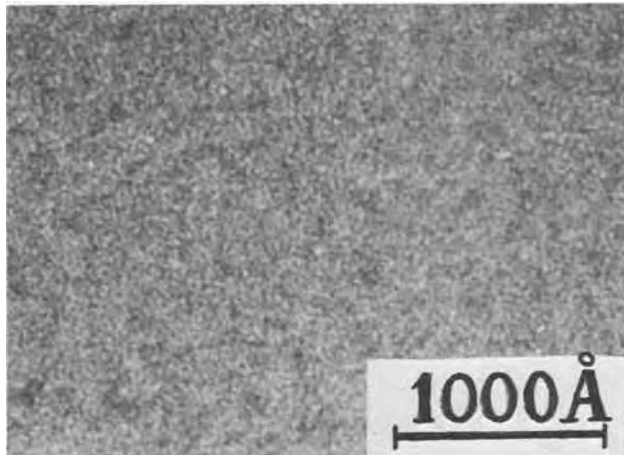
1. The redox reaction (1-3) between tin(II) and palladium(II) is not a prerequisite for the successful results of system (i). The substrate used also plays a significant role in the chemistry of the catalyzation process.

2. In the system based upon tin(II), palladium(II), and HCl, an ionic complex is formed (4-11) rather than a colloid based on elemental palladium (12).

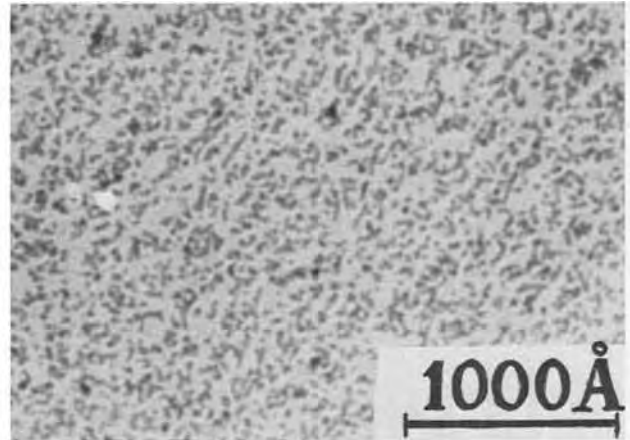
More recently significant improvements in the performance of system (i) were reported (13-15). These

improvements were especially noted with respect to the successful plating of hydrophobic surfaces as well as increasing the density of catalytic sites (15, 16) of hydrophilic surfaces.

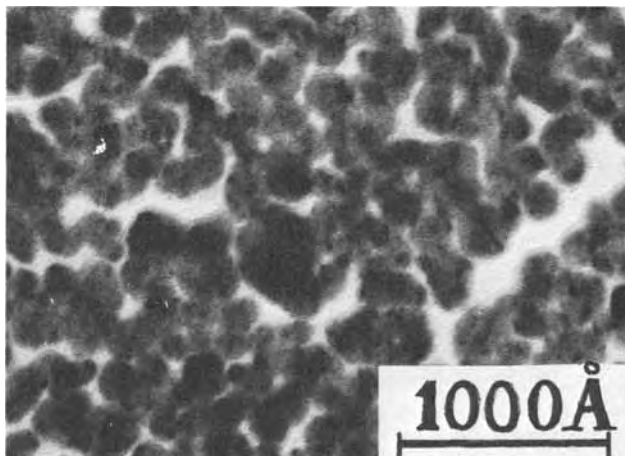
In the plating of dielectric substrates, several investigators (16-19) have examined the nature of the treated surfaces as well as the nucleation and growth of thin metallic films (cobalt, nickel, and copper). It has been generally demonstrated that the nucleation and growth of the electroless thin film is initiated at catalytic sites. In the microscopic examination of the treated surfaces, investigators (1, 16-19) de-



(a) After 2 min immersion in catalytic solution A.

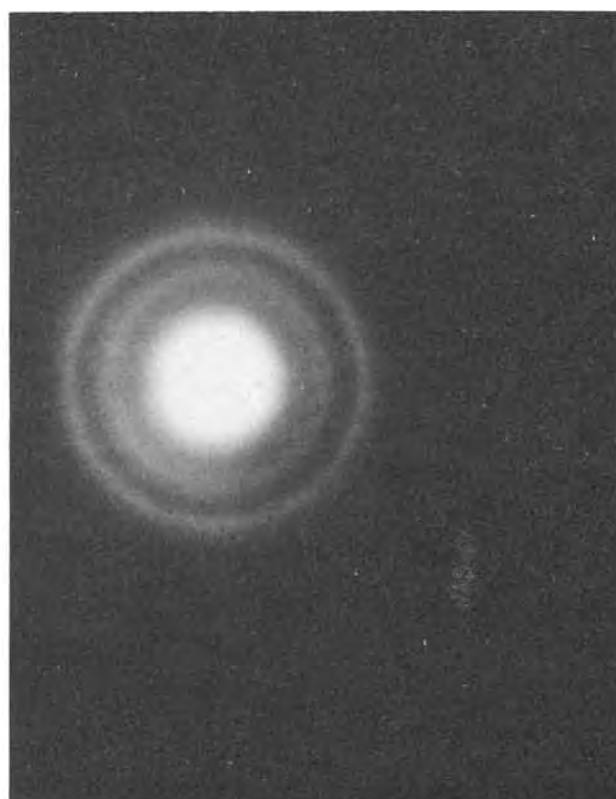


(b) Same as (a), with subsequent 1 min rinse in deionized water and 2 min immersion in accelerator solution A.

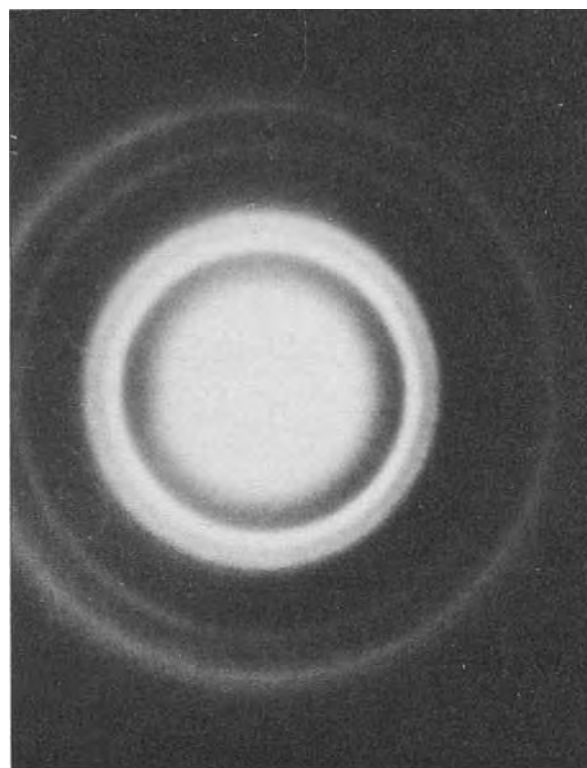


(c) Same as (b), with subsequent 1 min rinse in deionized water and 10 sec immersion in the electroless copper solution.

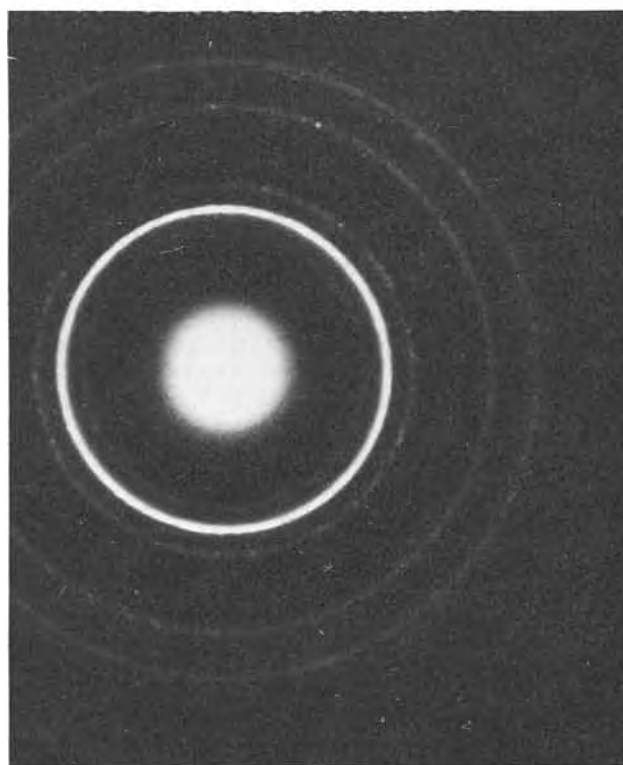
Fig. 1. Electron micrographs of a Formvar surface at various stages of the electroless deposition process.



(a)



(c)



(b)

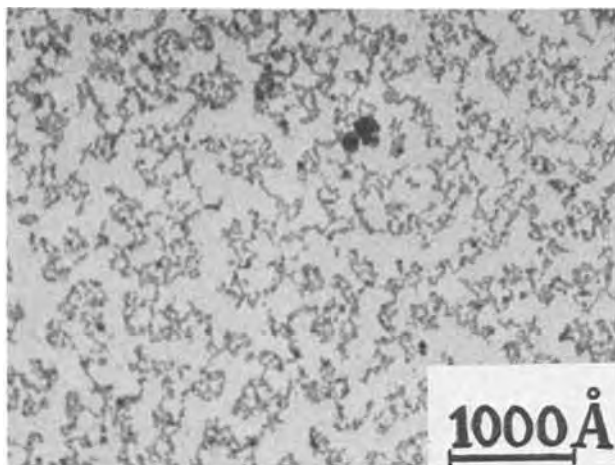
Fig. 2. Electron diffraction patterns corresponding to Fig. 1

voted special attention to the system (i) with complete omission of system (ii). Only recently (20) was an attempt made to elucidate the mechanism of activation of system (ii).

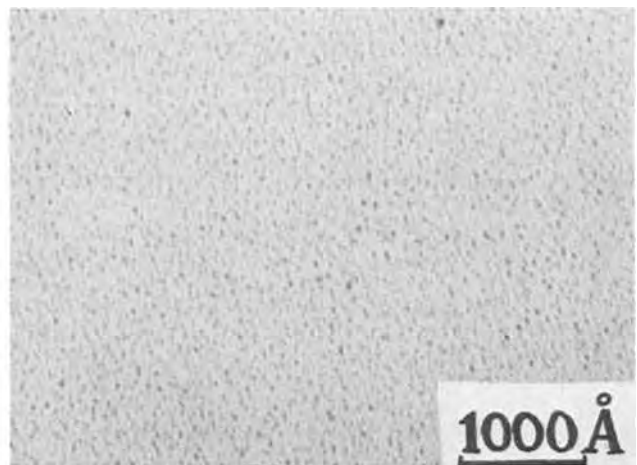
In the current investigation it was decided to examine the dielectric surface at the different stages of pretreatment, including the early stages of nucleation and growth. This investigation is especially in-

tended to provide further insight into various debated aspects of this system. Specifically: (i) the makeup of the solution; whether it is a palladium colloid or rather a tin(II) and palladium(II) ionic complex; (ii) preferred technique(s) in the preparation of such solutions; (iii) the role of the accelerator solution and its chemical nature; and (iv) the chemical nature of the catalytic surface prior to plating.



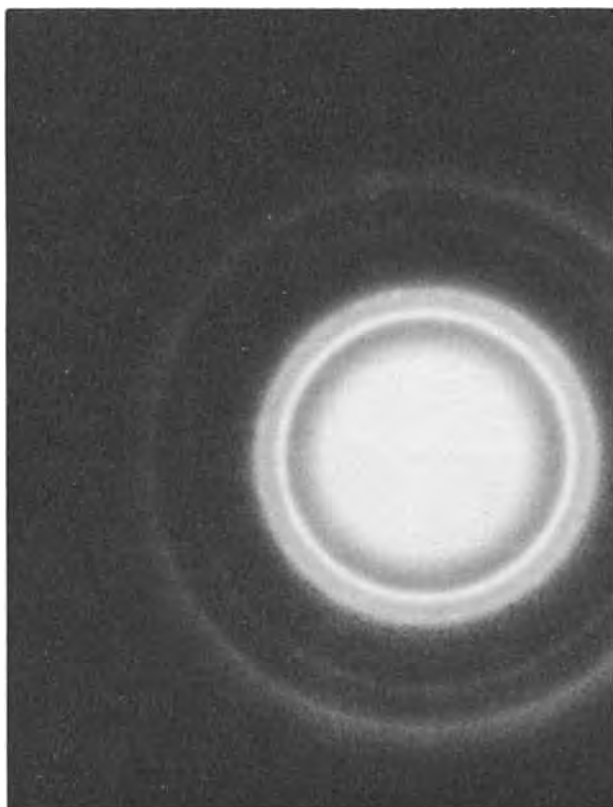


(a) After catalytic solution A



(b) After catalytic solution D

Fig. 3. Electron micrographs of the deposits obtained using ammonium bifluoride accelerator.



(a)



(b)

Fig. 4. Electron diffraction patterns corresponding to Fig. 3

### Experimental

In the present study, four distinct solutions of  $\text{SnCl}_2/\text{PdCl}_2$  and  $\text{HCl}$  were employed. They are given in Table I. Immersion time was 2 min in both steps, with a 1 min rinse in deionized water between the steps.

For the purpose of evaluating the electroless product from the surface treatment, an electroless copper bath was chosen. The compositions were bath A,  $\text{CuSO}_4$ ,  $5\text{H}_2\text{O}$  40 g/liter,  $\text{KNaC}_4\text{H}_4\text{O}_6$  100 g/liter, and  $\text{KOH}$  40 g/liter; bath B,  $\text{HCHO}$  130 g/liter and  $\text{KOH}$  120 g/liter. Fresh solutions were made for each run and they were mixed in the ratio of 1 part B to 2 parts A. Depositions were carried out at room temperature.

In some of the experiments, aged stannic solutions were added to the catalyzer (16). This was done for the purpose of comparing the influence of aged stannic solutions on the present system.

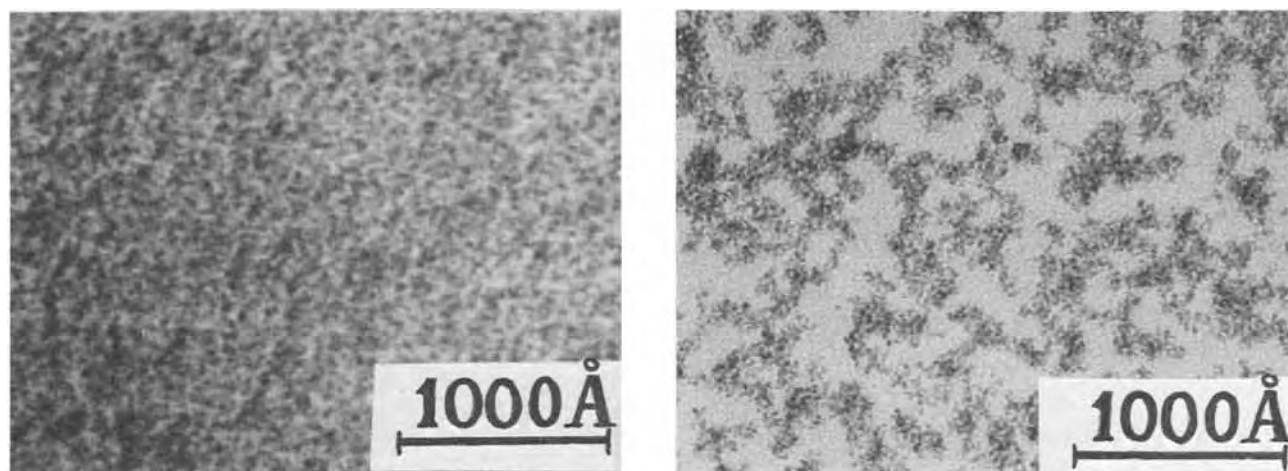
Transmission electron micrographs and electron diffraction patterns were obtained from a Hitachi HU-12 electron microscope operated at 100 kV.

Formvar coated surfaces were floated off in distilled water from the glass base and were mounted in the sample holder of the electron microscope. (The Formvar solution consisted of 4g polyvinylformal in 1 liter ethylene dichloride.)

### Results and Discussion

In Fig. 1 we present in succession transmission electron micrographs of Formvar coated surfaces obtained, using catalytic solution A, with Fig. 1a taken after catalyzation, Fig. 1b after acceleration, and Fig. 1c after 10 sec immersion in electroless copper plating bath. Figure 2 shows the corresponding diffraction patterns. From Fig. 1a and 1b it should be noted that





(a) Before the acceleration step

(b) After the acceleration (solution A) step

Fig. 5. Electron micrographs of the deposit obtained on a Formvar surface using catalytic solution A with additional aged 0.5M  $\text{SnCl}_4$

the distribution of active components(s) is rather homogeneous. Comparison of this distribution to that obtained using a conventional sensitizer ( $\text{SnCl}_2/\text{HCl}$ ) shows a marked difference [see Ref. (18), Fig. 1a]. Inspection of Fig. 1a shows a density of sites of approximately  $10^{12}$  centers/cm<sup>2</sup>. These centers are composed of particles of approximately 20Å in size. After acceleration (Fig. 1b), a tendency for cluster formation is evident. By contrast to the cluster formation in conventional sensitizer [see Ref. (18), Fig. 2a and 2b], in the current system, the clusters seem to form in a wormlike fashion. This tendency seems to be preserved as well in the early stages of the metallic end product as seen in Fig. 1c.

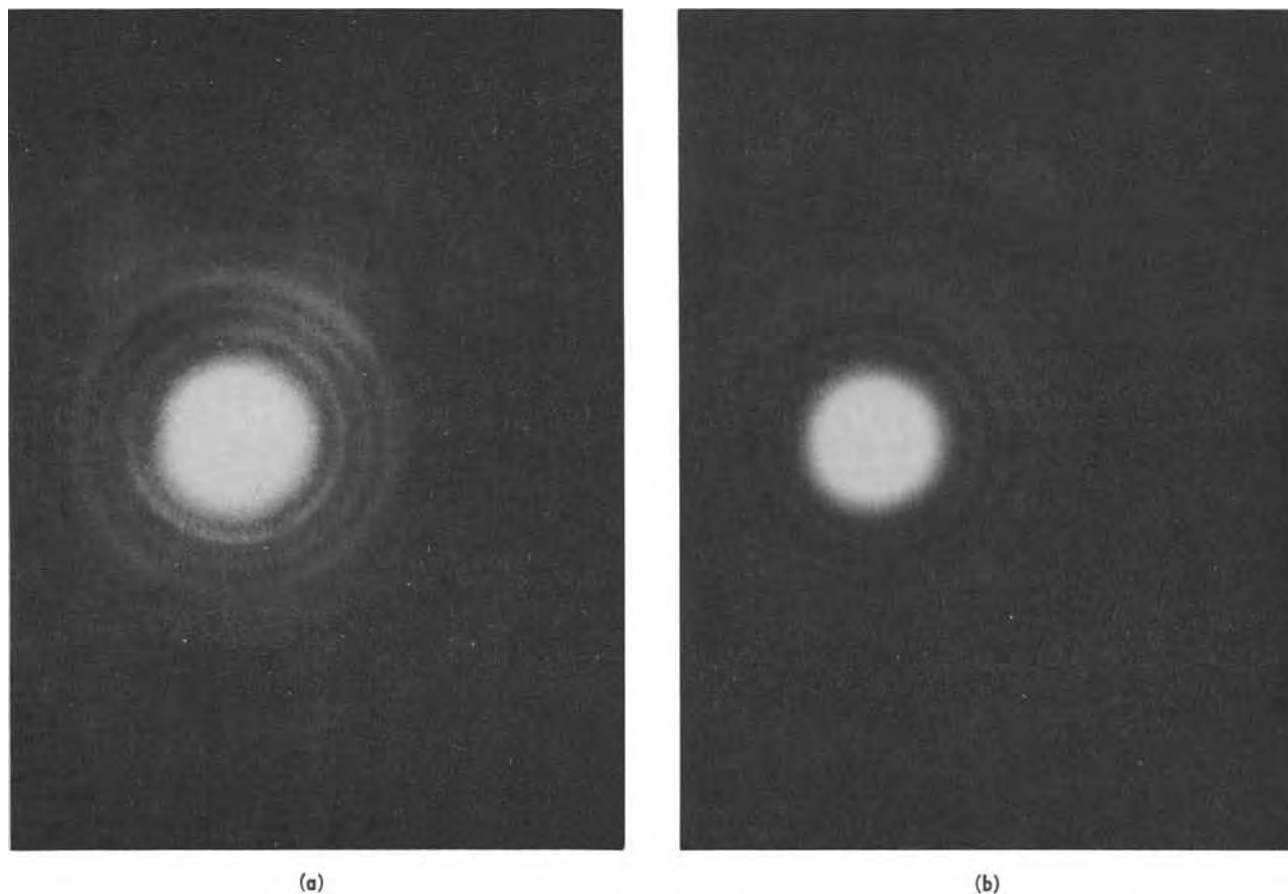
From the diffraction patterns (Fig. 2a and 2b) the following conclusions can be drawn: (i) The end

product after the catalyzing stage is amorphous. (ii) The product after the acceleration step is face-centered cubic with lattice parameters closely matching those of  $\text{Pd}_3\text{Sn}$ .

It should be noted that  $\text{Pd}_3\text{Sn}$  is the only Pd-Sn compound known to crystallize in fcc form (21).

Table II summarizes the derived lattice parameters corresponding to Fig. 2b.

Comparison of the current experimental results to those derived from the literature (21) for  $\text{Pd}_3\text{Sn}$ , offers a convincing proof that the noted deviations of the order of 1% could be best accounted for by the size of the crystallites present affecting the definition of the diffraction rings. The present finding is also in agreement with conclusions made by Cohen *et al.* (10), using Mössbauer spectroscopy. However, these



(a)

(b)

Fig. 6. Electron diffraction patterns corresponding to Fig. 5

Table II. Lattice parameters in angstroms corresponding to Fig. 2b

hkl	Experimental values	Derived from Ref. (21)
111	2.288	2.295
200	2.010	1.985
220	1.400	1.404
311	1.207	1.198
222	1.150	1.147
331	0.903	0.912

$\text{Pd}_3\text{Sn}$ : fcc with  $a = 3.97$  (21).

conclusions are not in agreement with recent results by Rantell *et al.* (20). In their work, it was concluded that metallic palladium is present at the conclusion of the acceleration step, suggesting that the redox reaction between Sn(II) and Pd(II) does take place. This lack of agreement was initially conceived as being due to possible differences in experimental conditions.

Rantell used etched ABS as substrate, while we have used Formvar deposited on glass. Secondly, the chemical composition of both the catalyzer and the accelerator solutions was different.

The following additional experiments were therefore carried out. Samples were prepared using all four possible combinations of the two catalyzers and accelerators referred to in Table I as A and D. The results obtained with the ammonium bifluoride accelerator are illustrated in Fig. 3a and 4a for catalyzer A and Fig. 3b and 4b for catalyzer D. Figure 4a shows that the post-accelerator product in this case has fcc structure with the same lattice constant as for the deposit shown in Fig. 2b. It appears that although the distribution of particles in the deposit is affected by the nature of the accelerator its chemical composition is not. In Fig. 4b no evidence of metallic palladium can be seen; indeed the nature of the deposit cannot be inferred from the electron diffraction pattern. Essentially the same results were obtained using Rantell's catalyzer with the 19F accelerator. It is possible that the deposits obtained with Rantell's catalyzer contain insufficient amounts of Pd to be observable by electron diffraction. It is also conceivable that the chemical nature of the substrate plays a role in the Sn(II) Pd(II) interaction as suggested previously by Feldstein (2).

Figures 5 and 6 show the effects on (a) the post-catalyzer deposit and (b) the post-accelerator deposit of the addition of 0.5M  $\text{SnCl}_4$ , aged for one week, to the 9F catalyzer. (About 1 ml of aged  $\text{SnCl}_4$  to 10 ml of the catalyzer was used.)

In Fig. 5b, it should be noted that the wormlike microstructure has disappeared and instead the char-

Table III. Lattice parameter comparisons corresponding to Fig. 5b

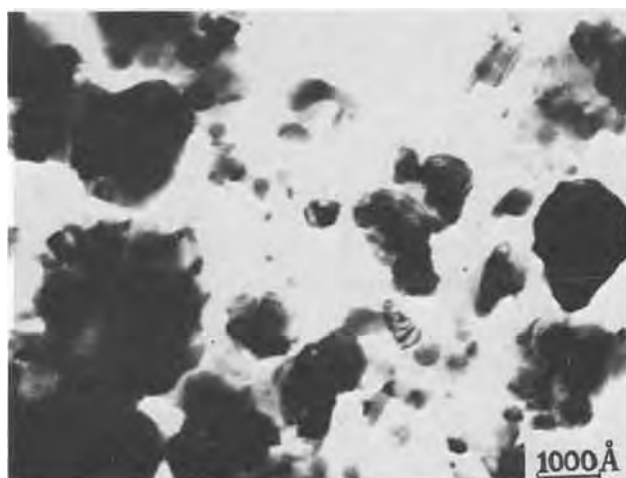
hkl	Experimental $d_{\text{calc}}$ (Å)	$d(a/a_0, c/c_0)$ <sup>(a)</sup>	$d_{\text{SnO}_2}$ (Å) <sup>(b)</sup>
110	3.250	3.200	3.350
101	2.608	2.620	2.644
200	2.245	2.275	2.369
211	1.762	1.740	1.785
310	1.442	1.440	1.498

<sup>(a)</sup> Data from Ref. (22) with  $a/a_0 = 0.962$  and  $c/c_0 = 1.006$ .

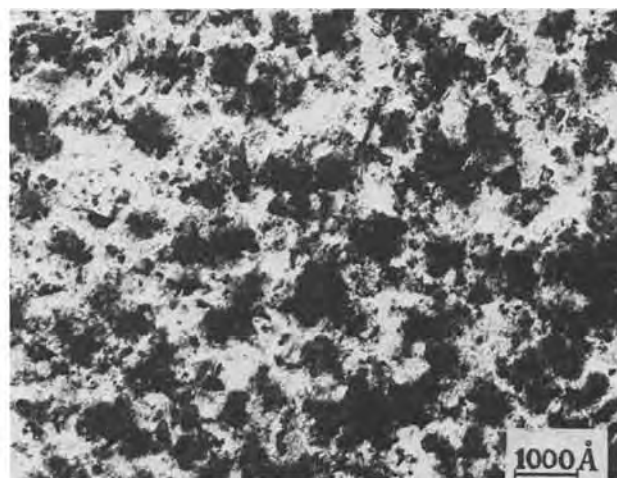
<sup>(b)</sup> Calculated using lattice constant given in Ref. (23) with  $a_0 = 4.737$  and  $c_0 = 3.186\text{Å}$ .

acteristics of an improved conventional sensitizer ( $\text{SnCl}_2/\text{HCl}$ ) have resulted [see Ref. (16), Fig. 2b]. Table III represents the lattice parameters corresponding to the surface used in Fig. 5b. It would appear that the presence of an aged  $\text{SnCl}_4$  component nullified the characteristics of the present system, with respect to the presence of  $\text{Pd}_3\text{Sn}$  and characteristic microstructure. Further work is in progress to clarify this point.

In the next phase of this investigation Formvar surfaces treated by catalytic solutions B and C were examined. In general, surfaces treated by the catalytic solution B with and without the accelerating solution step showed a diffused microstructure in the electron micrographs. The corresponding diffraction pattern also exhibits an amorphous characteristic. However, aging the working solution (solution B) for approximately two weeks was sufficient to result in a major change. Specifically, the aged solution B exhibited results similar to Fig. 1 and 2, *i.e.*, the presence of  $\text{Pd}_3\text{Sn}$  in the post-acceleration deposit is evident. In both cases, good metal distribution was obtained following the plating step. Employing unaged catalytic solution C has provided results similar to those obtained using unaged catalytic solution B, except that the diffraction pattern revealed the presence of  $\text{SnO}_2$  at the conclusion of the acceleration step. Aged solution C exhibits plating characteristics similar to aged solution B. Figure 7 shows Cu deposits obtained with the use of (a) fresh catalytic solution B followed by an accelerating solution of 1.2M NaOH and (b) same as (a) except that the catalytic solution was aged prior to use for 7 days. Figures 8a and b are the corresponding diffraction patterns. Note the marked difference between the deposits in Fig. 7a and b; whereas in Fig. 7a, there are large islands and a relatively poor coverage, in Fig. 7b a good coverage is obtained with small islands. This is also seen in Fig. 8a and b, where the difference in crystallite size is evident. Comparison of Fig. 7b with Fig. 1c, and of the corresponding diffraction patterns (Fig. 8b and



(a) Using fresh catalytic solution B



(b) Using catalytic solution B aged for 1 week

Fig. 7. Electron micrographs of the electroless copper deposit. In each case the accelerator solution was 1.2M NaOH.

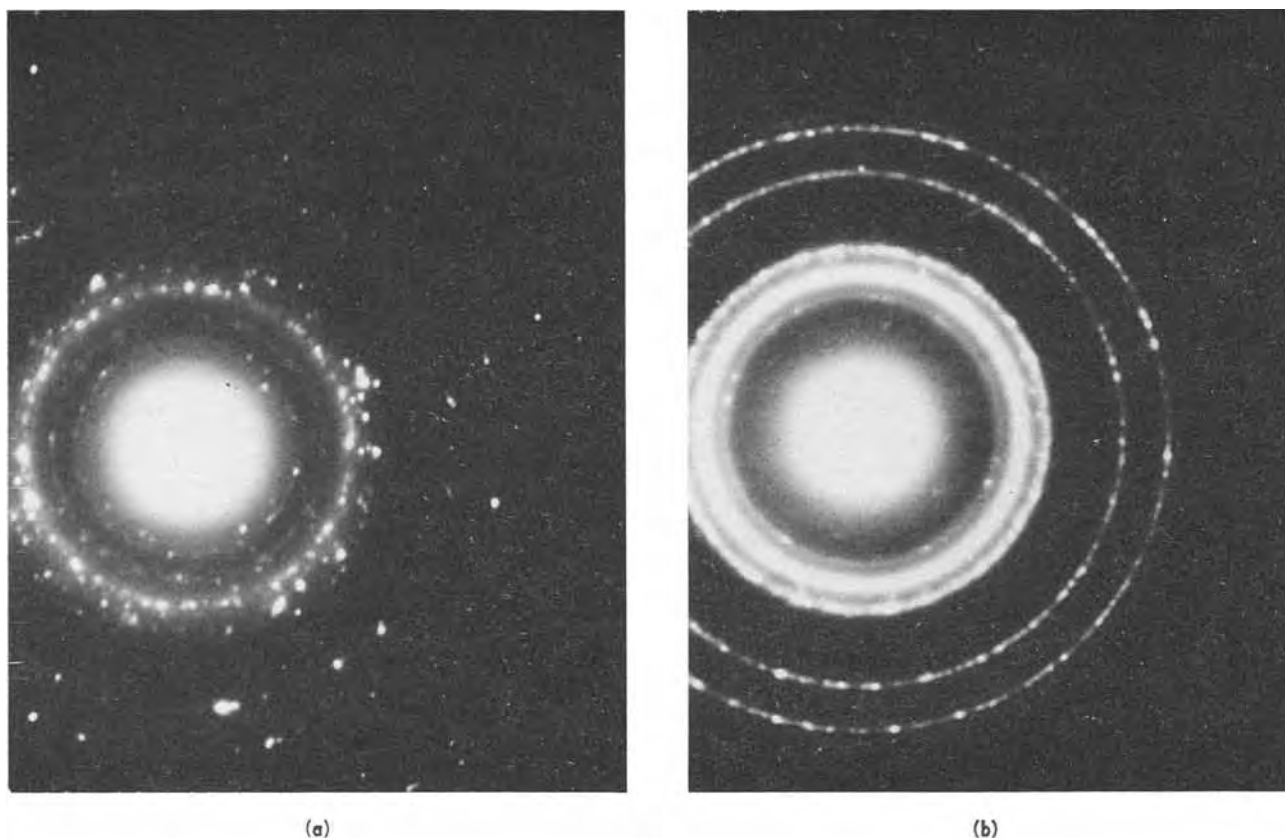


Fig. 8. Electron diffraction patterns corresponding to Fig. 7

2c) reveals a similarity in terms of surface coverage, in contrast to that seen in Fig. 7a.

Finally, it is interesting to note that the effect of aging the catalyzer on the copper deposit is also to render the product similar to that employing an improved conventional sensitizer [see Ref. (16), Fig. 3b].

#### Acknowledgment

Experimental work was carried out in the Department of Physics, University of Windsor, Windsor, Ontario, Canada. Some of the solutions used in this investigation were prepared at the RCA Corporation, David Sarnoff Research Center.

Manuscript submitted Nov. 9, 1973; revised manuscript received Jan. 31, 1974. Some aspects of this work were discussed in Paper 125 presented at the Boston, Massachusetts, Meeting of the Society, Oct. 7-11, 1973.

Any discussion of this paper will appear in a Discussion Section to be published in the December 1974 JOURNAL. All discussions for the December 1974 Discussion Section should be submitted by Aug. 1, 1974.

#### REFERENCES

1. S. L. Chow, N. E. Hedgecock, M. Schlesinger, and J. Rezek, *This Journal*, **119**, 1013 (1972).
2. N. Feldstein and J. W. Weiner, *ibid.*, **120**, 475 (1973).
3. P. F. J. v. d. Boom and C. H. DeMinjer, *ibid.*, **120**, 1644 (1973).
4. C. H. Ayres and J. A. Alsop, *J. Anal. Chem.*, **31**, 1135 (1959).
5. M. A. Khattak and R. J. Magee, *Chem. Communication*, **17**, 400 (1965).
6. E. D. D'Ottavio, U.S. Pat. 3,532,518 (Oct. 6, 1970).
7. M. Tsukahara, *J. Metal Finishing (Japan)*, **23**, 83 (1972).
8. R. J. Zeblicky, U.S. Pat. 3,672,920 (June 27, 1972).
9. R. J. Zeblicky, U.S. Pat. 3,682,671 (Aug. 8, 1972).
10. R. L. Cohen and K. W. West, *This Journal*, **120**, 502 (1973).
11. V. I. Shlenskaya, A. A. Biryukiv, and L. N. Moryakova, *J. Inorg. Chem. (Russ)*, **14**, 255 (1969).
12. C. R. Shipley, U.S. Pat. 3,011,920 (Dec. 5, 1961).
13. N. Feldstein and J. W. Weiner, *Plating*, **59**, 140 (1972).
14. N. Feldstein and J. A. Weiner, *This Journal*, **119**, 668 (1972).
15. N. Feldstein, Proc. AES Fourth Plating in the Electronics Industry Symposium, Indianapolis, Indiana, Jan. 31, 1973; and *Plating*, **60**, 611 (1973).
16. N. Feldstein, S. L. Chow, and M. Schlesinger, *This Journal*, **120**, 875 (1973).
17. A. S. Frieze, R. Sard, and R. Weil, Sixth International Conference for Electron Microscopy, Kyoto (1966), p. 533; and *This Journal*, **115**, 587 (1968).
18. J. P. Marton and M. Schlesinger, *This Journal*, **115**, 16 (1968).
19. R. Sard, *ibid.*, **117**, 864 (1970).
20. A. Rantell and A. Holtzman, *Trans. Inst. Metal Finishing*, **51**, (6), 62 (1973).
21. R. P. Elliott, "Constitution of Binary Alloys," Suppl. 1, p. 734, McGraw-Hill Book Co., New York (1965).
22. H. G. Drickemer, R. W. Lynch, R. L. Clendenen, and E. A. Perez-Albuerno, *Solid State Phys.*, **19**, 212 (1966).
23. R. W. G. Wyckoff, "Crystal Structures," Vol. 1, p. 251, John Wiley & Sons, Inc., New York (1963).

# The Electro-Oxidative Coupling of N,N-Dimethylaniline: A Rotating Ring-Disk Electrode Study

G. Neubert and K. B. Prater\*

Department of Chemistry, University of Texas at El Paso, El Paso, Texas 79968

The publication costs of this article have been assisted by the Petroleum Research Fund and the Robert A. Welch Foundation.

## ABSTRACT

The electro-oxidation of N,N-dimethylaniline (DMA) has been studied in strongly acidic aqueous media by cyclic voltammetry and rotating ring-disk electrode voltammetry coupled with digital simulation. The ring-disk data are inconsistent with the simulation of a mechanism involving coupling between two DMA cation radicals to produce N,N,N',N'-tetramethylbenzidine. The results are qualitatively consistent with a mechanism involving deprotonation of the DMA cation radical and subsequent coupling between neutral radicals.

The electro-oxidation of N,N-dimethylaniline (DMA) in aqueous media has been studied in some detail by Adams *et al.* (1-3). They found that in acidic media the product was N,N,N',N'-tetramethylbenzidine (TMB). Two mechanisms were proposed for the reaction. One involved the initial production of the dication of DMA at the electrode followed by an attack of this dication on a parent molecule to produce, with loss of two protons, TMB. The second mechanism suggested that the DMA cation radical (DMA<sup>•+</sup>) is formed at the electrode and that two such cation radicals couple with loss of two protons to form TMB. Based on later work on triphenylamines (4, 5) and the work of Nelson (6) on DMA in acetonitrile, it is now felt that the cation radical is the species which is first produced at the electrode. There is little data, however, to indicate the mechanism by which TMB eventually arises from DMA<sup>•+</sup>. This paper reports the results of cyclic voltammetry and ring-disk electrode voltammetry studies of the electro-oxidation of DMA in strongly acidic aqueous media. The results are inconsistent with a radical cation-radical cation coupling mechanism but may be consistent with a mechanism involving deprotonation of the cation radical and subsequent reaction between neutral radicals.

## Experimental

The N,N-dimethylaniline (J. T. Baker) was distilled from 85% formic acid solution (10 ml acid/100 ml DMA) using the procedure of Ritter (14). The N,N,N',N'-tetramethylbenzidine (Eastman-Kodak) was recrystallized from ethanol and acetone. All other chemicals were reagent grade and were used without further purification. The water was deionized.

The fabrication of the ring-disk electrode (15), the method of its calibration (16), and the compounding of the carbon paste (17) have previously been described. The simulation representation of the electrode used in this study is given by IR1 = 80, IR2 = 92, and IR3 = 158. The electrode was rotated with a motor-matic E-550 motor with feedback controller which was obtained from Electro Craft, Hopkins, Minnesota. All potentials are reported with respect to the SCE.

A Wenking Model 66TS10 potentiostat was used with a Hewlett Packard 7004A X-Y recorder with 17171A d-c preamp plug-ins for cyclic voltammetry, for obtaining limiting disk currents, and for obtaining ring voltamograms for collection efficiency measurements. In making collection measurements, a constant current obtained from two paralleled 90V batteries in series

with a large variable resistor was applied to the disk. This current was measured with a Keithly Digital Multimeter, Model 160. All experiments were carried out in a constant temperature bath at 25.0° ± 0.1°C.

## Cyclic Voltammetry Results and Discussion

The cyclic voltamogram in Fig. 1 is typical of those obtained for DMA at a carbon paste electrode in 1-6M H<sub>2</sub>SO<sub>4</sub> over a range of DMA concentrations from 0.5 to 5.0 mM. This cyclic is consistent with those obtained by Adams (1) in less acidic media. Peak 1 corresponds to the primary oxidation of DMA. The work of Adams *et al.* (4) leads one to conclude that the cation radical, DMA<sup>•+</sup>, is the species which is initially produced at the electrode. At the potential of peak 1, any TMB that is formed will be further oxidized to the TMB dication, TMB<sup>2+</sup>. Peak 5 corresponds to the reduction of TMB<sup>2+</sup> to TMB and peak 6 corresponds to the oxidation of TMB to TMB<sup>2+</sup>. In less acidic media, Adams (1) observed no net cathodic current in the region of peak 4, the region in which DMA<sup>•+</sup> would be expected to be reduced. It is found that in the strongly acidic media studied here, net cathodic current is observed in this region, suggesting an increased stability of DMA<sup>•+</sup> in more acidic media.

It has been suggested that peak 4 might result from the presence of either *ortho-para* or *ortho-ortho* TMB<sup>2+</sup> rather than DMA<sup>•+</sup>. In an attempt to eliminate this possibility a bulk electrolysis of a 1 mM solution

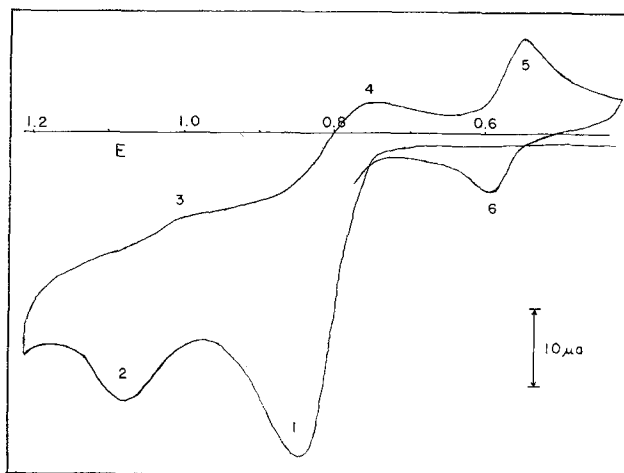


Fig. 1. Cyclic voltamogram of 1.15 mM DMA in 3M H<sub>2</sub>SO<sub>4</sub> at a carbon paste electrode and at a scan rate of 2.4 V/min.

\* Electrochemical Society Active Member.  
Key words: N,N-dimethylaniline, rotating ring-disk electrode, mechanism, digital simulation.

of DMA in 1M H<sub>2</sub>SO<sub>4</sub> was carried out at a carbon paste electrode in an H-cell. The potential of the working electrode was 0.9V vs. SCE. Halfway through the electrolysis, a slow potential scan was made on the stationary working electrode in the stirred solution. A steady-state anodic current was observed in the region of peak 1, indicating the presence in the bulk of the solution of unoxidized DMA. A steady-state cathodic current was observed in the region of peak 5, indicating the presence of TMB<sub>ox</sub> in the bulk solution. No steady-state current was observed in the region of peak 4. The stirring was then stopped and a cyclic voltamogram obtained, which was quite similar to Fig. 1 except for an enhancement in peaks 5 and 6. The significant point, however, is that peak 4 was present in the cyclic voltamogram. These results indicate that the species giving rise to peak 4 is not a stable bulk species but is present only in the diffusion layer.

The remaining DMA was electrolyzed and the resulting solution was reduced at 0.0V vs. SCE to convert the TMB<sub>ox</sub> to TMB. The solution was then neutralized with Na<sub>2</sub>CO<sub>3</sub> and the products extracted with ether. The ether solution was then evaporated to dryness. The residue was extracted with benzene and the benzene solution was chromatographed on silica gel TLC plates using benzene, acetone, and methanol as solvents. Only a single spot was observed for each of these solvents. That spot corresponded to the *para*-*para* TMB. There was no indication of any other product being formed. As a result, it is felt that peak 4 is probably due to the reduction of DMA<sup>+</sup>.

Finally, mention should be made of peaks 2 and 3 in the cyclic voltamogram. These peaks were not reported in less acidic media. They are definitely not background phenomena (as had been suggested) but appear to be due to the production of DMA<sup>+2</sup> and its subsequent reduction. This possibility is being further studied.

With this background, a further study of the nature of the coupling reaction to produce TMB was undertaken. It was felt that a ring-disk electrode study of the rate of disappearance of DMA<sup>+</sup> would be the most informative approach.

### Ring-Disk Electrode Results

A rotating ring-disk electrode (RRDE) (7-9) study was carried out on solutions which were 0.62, 1.15, and 4.49 mM in DMA and 3M in H<sub>2</sub>SO<sub>4</sub>. A voltamogram typical of those observed at the disk electrode is shown in Fig. 2. Two plateau regions are observed, one corresponding to peak 1 in Fig. 1 and the other corresponding to peak 2. The experimental procedure which was followed involved obtaining such a voltamogram for each rotation rate on a given solution and then applying a constant current to the disk electrode equal to the limiting current for peak 1 (production of DMA<sup>+</sup>). A voltamogram was then obtained for the ring electrode under these conditions. A second ring voltamogram was obtained with no current being passed at the disk electrode. Figure 3 shows typical ring voltamograms for a DMA solution as well as a voltamogram for a solution of TMB. Note that there are two plateaus for the DMA solution and only one for the TMB solution. The plateau which corresponds to peak 4 in Fig. 1 thus reflects the presence of DMA<sup>+</sup>. But, the actual current in this region is the difference between the cathodic current due to reduction of DMA<sup>+</sup> and the anodic current due to the oxidation of any TMB present.

The important parameter in the RRDE experiment is the kinetic collection efficiency,  $N_k$ , which is defined in Eq. [1]

$$N_k = -i_r/i_d \quad [1]$$

where  $i_r$  is the limiting current at the ring electrode due to the current  $i_d$  at the disk electrode. The collection efficiencies in region 4 were determined for the

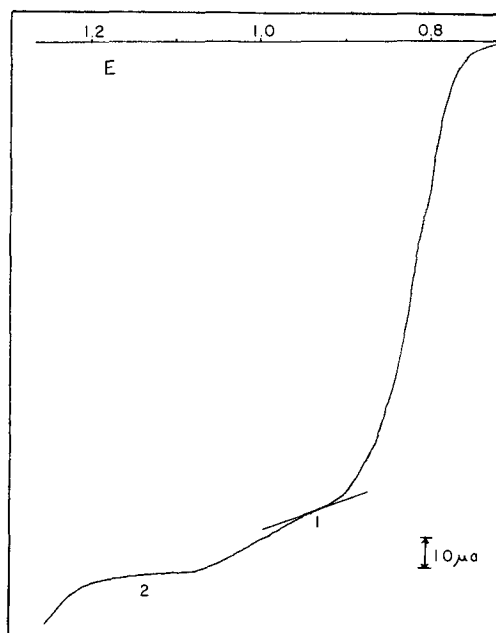


Fig. 2. Disk electrode voltamogram of 1.15 mM DMA in 3M H<sub>2</sub>SO<sub>4</sub> at a rotation rate of 2500 rpm. Point A is the limiting current for region 1.

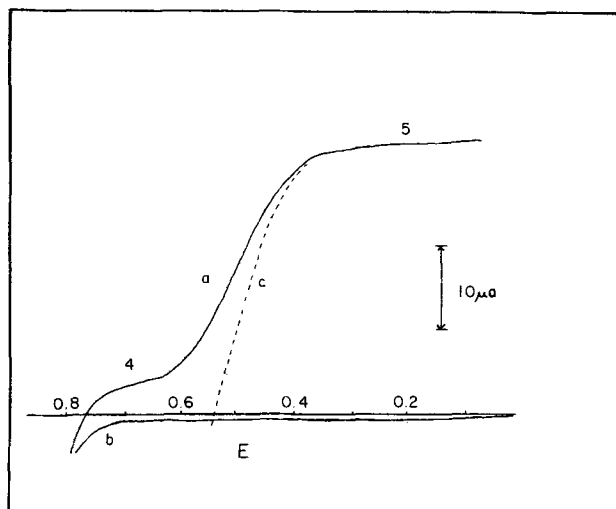


Fig. 3. Ring electrode voltamograms at a rotation rate of 2500 rpm. Curve a, 1.15 mM DMA in 3M H<sub>2</sub>SO<sub>4</sub>. Applied disk current equal to limiting disk current for region 1. Curve b, 1.15 mM DMA in 3M H<sub>2</sub>SO<sub>4</sub>. No disk current. Curve c, ca. 1 mM TMB in 3M H<sub>2</sub>SO<sub>4</sub>. Limiting current applied at disk electrode.

three solutions above over a range of rotation rates from 200 to 8000 rpm. The results are presented in Fig. 4. Each point is the average of from five to ten separate determinations. Due to electrode filming and other problems associated with carbon paste in 3M H<sub>2</sub>SO<sub>4</sub>, the uncertainty in the points is about  $\pm 10\%$ . In the 4.49 mM solution, filming became an even greater problem. It is felt that this may have resulted in curve c not coinciding with curve a and b.

### Digital Simulation Results and Discussion

A technique for the digital simulation of the RRDE has been presented previously (10-13). This technique permits the calculation of the collection efficiency as a function of various dimensionless parameters for essentially any imaginable mechanism. This technique with the modifications mentioned below has been used to calculate the collection efficiency behavior of two possible mechanisms for the oxidation and coupling of DMA.

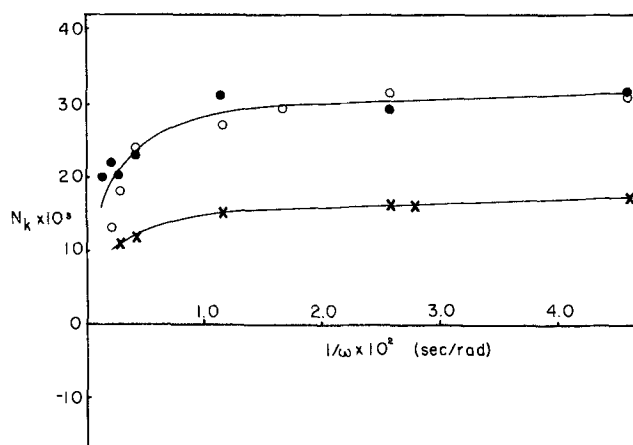
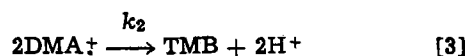
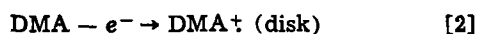


Fig. 4. Experimental collection efficiencies for peak 4 as a function of  $1/\omega$ . ● 0.625 mM DMA, 3M  $H_2SO_4$ ; ○ 1.151 mM DMA, 3M  $H_2SO_4$ ; X 4.49 mM DMA, 3M  $H_2SO_4$ .

#### Mechanism I

The first mechanism which was considered involves coupling between two  $DMA^\ddagger$  species and is given below



The TMB thus produced is subject to further oxidation at the disk



and is also subject to chemical oxidation by  $DMA^\ddagger$



At the ring electrode,  $DMA^\ddagger$  and TMB are both electroactive



Following the procedures outlined in Ref. (10) and (13), the collection efficiency,  $N_k$ , was calculated for the electrode in question and Mechanism I for various values of two dimensionless rate parameters, XKTC2 and XKTC3, which are defined by

$$XKTC2 = (0.51)^{-2/3} k_2 \omega^{-1} \nu^{1/3} D_A^{-1/3} C^{\circ A} \quad [8]$$

and

$$XKTC3 = (0.51)^{-2/3} k_3 \omega^{-1} \nu^{1/3} D_A^{-1/3} (C^{\circ A})^2 \quad [9]$$

where  $\omega$  is the rotation rate (radians/second),  $\nu$  is the kinematic viscosity ( $cm^2/sec$ ),  $D_A$  is the diffusion coefficient of, in this case, DMA ( $cm^2/sec$ ).  $C^{\circ A}$  is the bulk concentration of DMA (moles/liter) and the rate constants refer to Eq. [3] and [5].

Note that

$$XKTC3/XKTC2 = (k_3/k_2) C^{\circ A} \quad [10]$$

or, since  $k_3$  and  $k_2$  are constants, the ratio of XKTC3 to XKTC2 is directly proportional to the bulk concentration of DMA. Similarly

$$(XKTC2)^2/XKTC3 = (0.51)^{-2/3} (k_2/k_3) \omega^{-1} \nu^{1/3} D_A^{-1/3} \quad [11]$$

Since all terms in Eq. [11] except the rotation rate are constant for a given experiment, Eq. [11] reduces to

$$(XKTC2)^2/XKTC3 = K\omega^{-1} \quad [12]$$

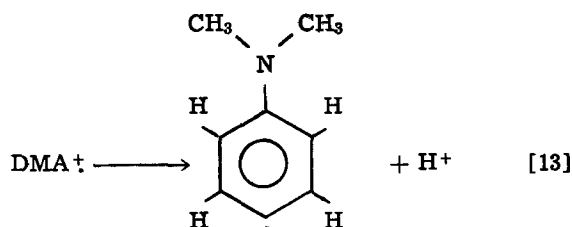
Thus, a plot of the simulated values of  $N_k$  for a constant value of  $XKTC3/XKTC2$  as a function of  $(XKTC2)^2/XKTC3$  is in fact a plot of the expected values of  $N_k$  for a fixed concentration of DMA as a

function of  $1/\omega$ . This is the same format in which the experimental data were presented (Fig. 4). The results of the simulation of Mechanism I are presented in Fig. 5 for three values of the concentration parameter.

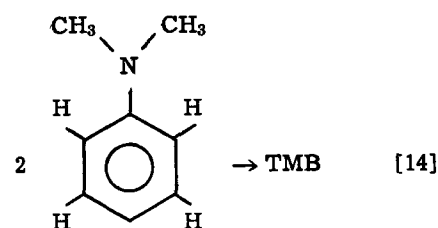
Note that while the simulated values of  $N_k$  are in the same range as those observed experimentally, the shapes of the simulated curves are distinctly different from those obtained experimentally. Furthermore, the simulation predicts a distinct concentration dependence which was not observed experimentally at the lower concentrations. This lack of agreement casts serious doubts on the acceptability of Mechanism I under the experimental conditions.

#### Mechanism II

The second mechanism which was considered took account of the apparent increased stability of  $DMA^\ddagger$  in strongly acidic media and the apparent first-order nature of its disappearance (little if any concentration dependence). This mechanism differs from Mechanism I in one respect only. In lieu of Eq. [3], the reaction is proposed to proceed in two steps. The initial step consists of the deprotonation of the cation radical, a first-order process, to yield the free radical as shown



The free radical then dimerizes very rapidly (at an infinite rate, compared to  $k_1$ ) by the second-order reaction



The net reaction is thus pseudo first order



The collection efficiency was calculated for Mechanism II for various values of the first-order rate parameter XKTC1, where

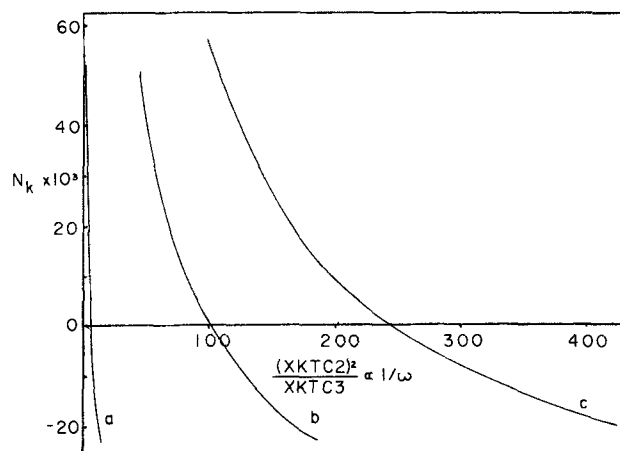


Fig. 5. Simulated collection efficiency as a function of  $1/\omega$  for Mechanism I. Curve a,  $XKTC3/XKTC2 = 1.0$ ; curve b,  $XKTC3/XKTC2 = 0.05$ ; curve c,  $XKTC3/XKTC2 = 0.02$ .

$$\text{XKT1} = (0.51)^{-2/3} k_1 \omega^{-1} \nu^{1/3} D_A^{-1/3} \quad [16]$$

and XKT3 as defined in Eq. [9]. Note that

$$\text{XKTC3}/\text{XKT1} = (k_3/k_1) (C^\circ_A)^2 \quad [17]$$

while XKT1 is a function only of rotation rate for a given experiment. Thus, a plot of the simulated values of  $N_k$  vs. XKT1 for a constant value of XKTC3/XKT1 is a plot of  $N_k$  vs.  $1/\omega$  at constant concentration. The simulation results for Mechanism II are presented in Fig. 6 for three concentrations differing by up to a factor of 10. The curves show no concentration dependence over this range. Furthermore, for XKT1 greater than about 3, the simulated curve has the same shape as the experimental curve. Quantitatively, however, the simulation predicts a net anodic current while the experimentally observed current is cathodic.

This discrepancy may be explained by considering that if the neutral radical were formed by deprotonation of DMA<sup>+</sup>, it would seem that reprotonation would be more probable than coupling especially in these media. This suggests that the irreversible deprotonation step in Mechanism II should be replaced by a fast acid-base equilibrium in which DMA<sup>+</sup> is considered to be a very weak acid. This would be consistent with the apparent increased stability of DMA<sup>+</sup> in acidic media and would result in a simulated prediction of a greater cathodic contribution to the current in region 4.

A second weakness in Mechanism II is the assumption that the oxidation of TMB at the ring electrode is diffusion controlled at the potential at which the measurements were made (about 0.7V). A glance at Fig. 3 would suggest that this is probably not the case. Taking this into account in the simulation would decrease the anodic contribution to the current in region 4.

Each of the above modifications to Mechanism II would result in a simulation which would better fit the experimental data. However, such a simulation would have at least four independently variable parameters and even then would involve some simplifying assumptions. Such a simulation is certainly feasible but it should be remembered that there are only two meaningful experimental variables, i.e., rotation rate and concentration of DMA.

It is strongly felt by the authors that there are limits beyond which it is fruitless to carry the simulation of a proposed mechanism. These limits are dictated by both practical and philosophical considerations. On the practical side, as the complexity of the mechanism increases so does the time required to simulate all of the possible permutations of values of the independent variables. As there are limits on

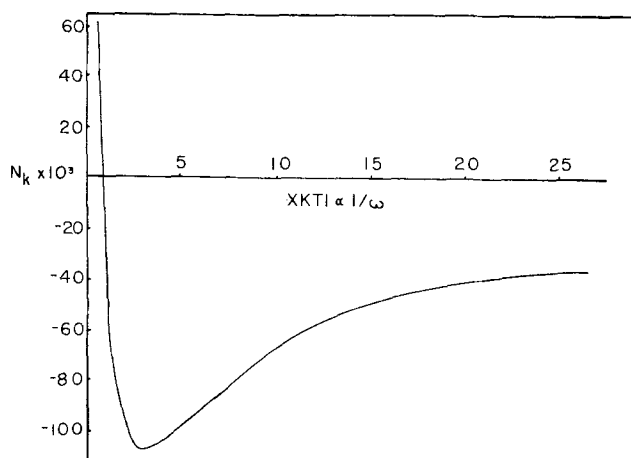


Fig. 6. Simulated collection efficiency as a function of  $1/\omega$  for Mechanism II. Results identical for  $\text{XKTC3}/\text{XKT1} = 1.0, 0.1,$  and  $0.01$ .

the availability of both computer and investigator time, the potential gain from the simulation of a mechanism must be considered. This potential gain, however, is subject to philosophical limitations.

It is clear that one can never prove that a given mechanism is correct: that is, there is no reason to contend that, because the predictions based on a specific mechanism are in agreement with experiment, the mechanism is unique in that respect. We are prone to feel that, if a mechanism consisting of two parameters adequately predicts the behavior of a system with two observables, the mechanism is probably correct, at least in its significant features. If a mechanism containing four or more parameters is needed to adequately fit a system with two observables, we should feel much less confident of its uniqueness.

It is in this latter situation that the authors find themselves. It is felt that one can safely conclude from the results presented here that the data are inconsistent with the mechanism involving cation radical-cation radical coupling but that the data are not necessarily inconsistent with a mechanism involving deprotonation of the cation radical before coupling. It is further felt that even if a more complex mechanism were simulated and found to fit the data, one should not make any stronger statement than that above without additional evidence. It would seem reasonable then, to consider whether there is any other evidence for the deprotonation mechanism and what other experiments might yield such evidence.

Carrington, Dravnieks, and Symons (18) have argued that "in sufficiently basic medium, hydrocarbon positive ions could lose ring protons." Osa, Yildiz, and Kuwana (19) proposed such a mechanism to explain results obtained in the electro-oxidation of benzene in acetonitrile. Drews and Jones (20), in a study of the stabilities of the cation radicals of the *p*-tert-butyl-, *p*-trimethylsilyl-, and *p*-trimethylgermyl-*N,N*-dimethylanilines, proposed the loss of the *para* substituent and production of the neutral DMA radical in order to explain their results.

While the fact that a similar mechanism has been proposed by others for similar systems is encouraging, additional information on the DMA system itself would be desirable. To this end, isotope effect studies on this reaction will soon begin. The possibility of substituting DMA in the 3 and 5 positions with groups which would be sufficiently bulky as to prevent coupling at the *para* position is being considered. Meanwhile, a mass spectrometer study of what may be an analogous loss of hydrogen from gas phase cation radicals is underway.

### Summary

Rotating ring-disk electrode studies of the anodic oxidation of *N,N*-dimethylaniline (DMA) in strongly acidic media are inconsistent with digital simulation results for a mechanism involving the direct coupling of the corresponding cation radicals to produce *N,N,N',N'*-tetramethylbenzidine (TMB). The experimental results are qualitative consistent with a mechanism involving deprotonation of the DMA cation radical and subsequent coupling of the neutral radicals thus produced.

### Acknowledgment

Acknowledgment is made to the donors of the Petroleum Research Fund, administered by the American Chemical Society, and to the Robert A. Welch Foundation for support of this research.

Manuscript submitted July 8, 1972; revised manuscript received Aug. 3, 1973.

Any discussion of this paper will appear in a Discussion Section to be published in the December 1974



JOURNAL. All discussions for the December 1974 Discussion Section should be submitted by Aug. 1, 1974.

## REFERENCES

1. T. Mizoguchi and R. N. Adams, *J. Am. Chem. Soc.*, **84**, 2058 (1962).
2. Z. Galus and R. N. Adams, *ibid.*, **84**, 2061 (1962).
3. Z. Galus, R. M. White, F. S. Rowland, and R. N. Adams, *ibid.*, **84**, 2065 (1962).
4. E. T. Seo, R. F. Nelson, J. M. Fritsch, L. S. Marcoux, D. W. Leedy, and R. N. Adams, *ibid.*, **88**, 3498 (1966).
5. R. F. Nelson and R. N. Adams, *ibid.*, **90**, 3925 (1968).
6. R. Hank and R. F. Nelson, *This Journal*, **117**, 1353 (1970).
7. A. N. Frumkin and L. N. Nekrasov, *Dokl. Akad. Nauk SSSR*, **126**, 115 (1959).
8. V. G. Levich, "Physicochemical Hydrodynamics," Prentice-Hall, Inc., Englewood Cliffs, N.J. (1962).
9. W. J. Albery and M. L. Hitchman, "Ring-Disc Electrodes," Oxford University Press, London (1971).
10. K. B. Prater and A. J. Bard, *This Journal*, **117**, 207 (1970).
11. K. B. Prater and A. J. Bard, *ibid.*, **117**, 335 (1970).
12. K. B. Prater and A. J. Bard, *ibid.*, **117**, 1517 (1970).
13. K. B. Prater, in "Electrochemistry: Calculations, Simulations and Instrumentation," Ch. 8, H. B. Mark, Editor, Marcel Dekker, Inc., New York (1972).
14. F. O. Ritter, *Ind. Eng. Chem.*, **28**, 33 (1936).
15. K. B. Prater, Ph.D. Dissertation, the University of Texas at Austin, Austin, Texas (1969).
16. G. Neubert, E. Gorman, R. Van Reet, and K. B. Prater, *This Journal*, **119**, 677 (1972).
17. R. N. Adams, *Anal. Chem.*, **30**, 1576 (1958).
18. A. Carrington, F. Dravniers, and M. C. R. Symons, *J. Chem. Soc.*, **1959**, 947.
19. T. Osa, A. Yildiz, and T. Kuwana, *J. Am. Chem. Soc.*, **91**, 3994 (1969).
20. M. J. Drews and P. R. Jones, *J. Organometal. Chem.*, **44**, 253 (1972).

## Chlorine and Oxygen Electrode Processes on Glasslike Carbon, Pyrolytic Graphite, and Conventional Graphite Anodes

F. Hine,\* M. Yasuda, and M. Iwata

Nagoya Institute of Technology, Nagoya 466, Japan

The publication costs of this article have been assisted by F. Hine.

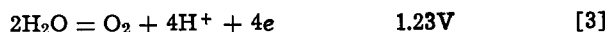
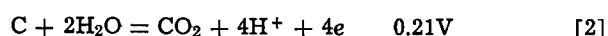
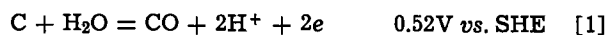
## ABSTRACT

The polarization behavior of glasslike carbon, pyrolytic graphite, and conventional graphite electrodes, in acidic solutions with and without  $\text{Cl}^-$ , has been studied. The electrode surface is covered by carbon oxides of two types depending on the electrode potential. Formation of these oxides is also affected by the  $\text{Cl}^-$  concentration, temperature, electrode material and its preparation. Electrode processes involving  $\text{O}_2$ ,  $\text{CO}$ , and  $\text{CO}_2$  were found to occur at high current densities. Transition from the chlorine evolution process to the over-all oxygen electrode process is irreversible because of irreversible exchange between adsorbed chlorine and oxygen on the working electrode. The Tafel line for the chlorine formation reaction on a fresh carbon and/or graphite anode has the slope of 130-150 mV/decade, and the reaction order with respect to  $\text{Cl}^-$  is unity.

The main reaction on graphite anodes in chlorine cells (both diaphragm and amalgam types) is, of course, evolution of chlorine gas, at more than 99% of current efficiency. Formation of some  $\text{CO}$ ,  $\text{CO}_2$ , and  $\text{O}_2$  may take place as a side reaction, and the latter is a controlling factor in consumption or corrosion of the graphite anode during electrolysis. This is one of the serious problems in the chlor-alkali industry (1, 2).

It is believed that the charge-transfer reaction of  $\text{H}_2\text{O}$  and/or  $\text{OH}^-$  takes place on the surface of the graphite anode, followed by formation of an oxide layer. Subsequent processes, i.e., formation of  $\text{CO}$  and  $\text{CO}_2$  (which consumes graphite), occur (2). On the other hand, adsorption of  $\text{Cl}^-$  and/or  $\text{Cl}$ -adatoms on the surface of graphite anodes immersed in aqueous solution containing  $\text{Cl}^-$  is significant. This retards the formation of the oxide layer and reduces consumption of the anode.

Possible electrode processes and their standard potentials ( $E^\circ$  in volts at 25°C) in acidic solution containing  $\text{Cl}^-$  are as follows



The standard potential for the chlorine evolution reaction is the highest. But the overvoltage for reactions [1], [2], and [3] is high compared to that of reaction [4], so that the graphite anode is useful in chlor-alkali cells.

In solutions free of  $\text{Cl}^-$ , formation of  $\text{CO}$ ,  $\text{CO}_2$ , and  $\text{O}_2$  occurs after adsorption of oxygen atoms by the graphite anodes, or after formation of a carbon oxide layer, or both (3-6). Very few papers concerning the characteristics of the oxide layer can be found (3, 7, 8).

Experiments with the linear potential sweep (LPS) method and the galvanostatic cathodic transient (GCT) method can be used for studying the properties of the oxide layer and of the process of its formation. On the other hand, formation of the surface oxide is limited in concentrated  $\text{Cl}^-$  solution because  $\text{Cl}^-$  and/or  $\text{Cl}$ -adatoms cover the graphite surface. Exchange between the surface oxide and chlorine is an irreversible process, and hence separate observation of these processes can best be made by means of the nonsteady-state method.

The electrochemical process may take place not only on the external surface of a commercial graphite anode, but in the pores a few millimeters deep (9).

\* Electrochemical Society Active Member.

Key words:  $\text{Cl}_2$  electrode,  $\text{O}_2$  electrode, surface oxide, glasslike carbon, pyrolytic graphite, graphite.



Such an electrode is unsuitable for studying the processes of adsorption and desorption of species on the working electrode by means of the LPS method. Due to the large area of effective surface of the porous electrode, a large amount of polarizing current may be consumed for charging of the double layer capacity (10, 11). We can avoid this difficulty by using glasslike or glassy carbon (designated GC hereafter), having a smooth surface like glass, as the working electrode. Pyrolytic graphite (PG) was also examined. Physicochemical properties of these materials can be found elsewhere (12).

### Experimental Procedure

A GC electrode (0.196 cm<sup>2</sup>) and a PG electrode (0.2 cm<sup>2</sup>) were used. Since the electrical resistance of PG was very dependent on the direction (12), the surface perpendicular to the deposited layer was used as the working electrode. A platinum wire counter-electrode, 0.5 mm diam and 3 cm long, was placed in a compartment separated by a sintered glass diaphragm from the compartment of the working electrode.

The working electrode was oxidized at a noble potential (+2.5V vs. SCE) for a few seconds, then reduced cathodically at about -2.0V prior to the measurements to eliminate any contaminants on the surface. When the galvanostatic anodic transient (GAT) method was used, the electrode was polarized cathodically (at -2.0V) before every run.

The electrode potential was measured with a Luggin probe connected to a saturated calomel electrode (+235 mV vs. SHE at 25°C).

The potential scanning rate for the LPS method (with conventional equipment) was usually 200 mV/sec. For the galvanostatic transient method, both anodic and cathodic, a high voltage dry cell (90V) with a high variable resistance (10 megohms) in series was employed as the power source. A sensitive mercury relay was of great use for switching from potentiostatic to galvanostatic polarization.

The electrolyte used was either 1M HClO<sub>4</sub>, or mixtures of HClO<sub>4</sub> and NaClO<sub>4</sub> (ionic strength = 1M). NaCl and HCl were added if necessary to examine the influence of Cl<sup>-</sup> on the formation of carbon oxide. The temperature was 50° ± 0.5°C. The electrolyte was deoxygenated prior to the experiments.

### Results

*Formation and reduction of carbon oxide and adsorption and desorption of hydrogen atoms in HClO<sub>4</sub> solutions.*—We present potential sweep diagrams for the GC in Fig. 1-3, and one for the PG in Fig. 4. The

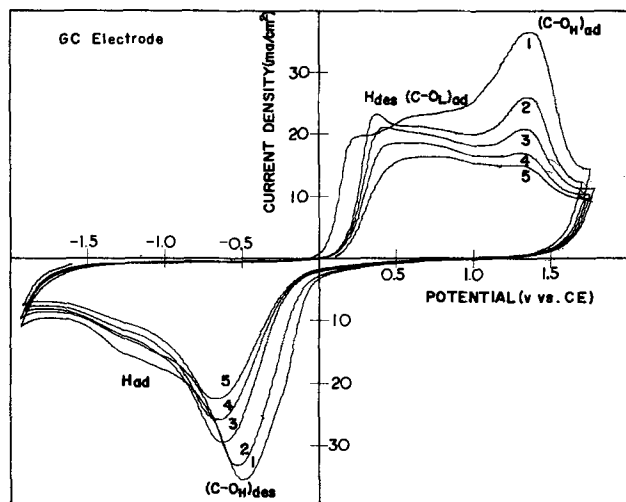


Fig. 1. Potential sweep diagrams with a glasslike carbon electrode in 1M HClO<sub>4</sub> at 50°C. Sweep rate 200 mV/sec. Curves are numbered in order of runs.

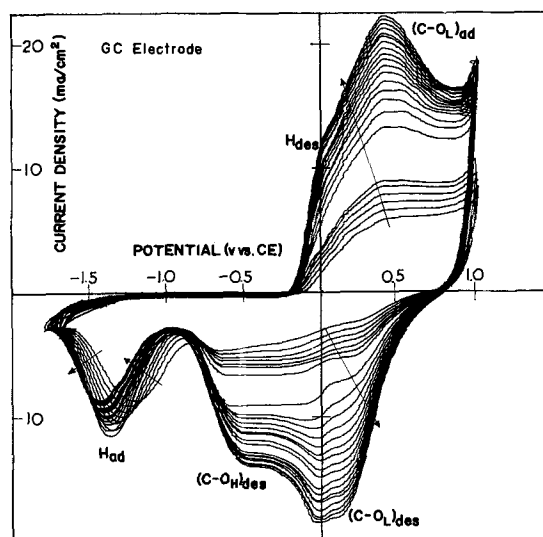


Fig. 2. Potential sweep diagrams with a glasslike carbon electrode in 1M HClO<sub>4</sub>. Sweep rate 200 mV/sec.

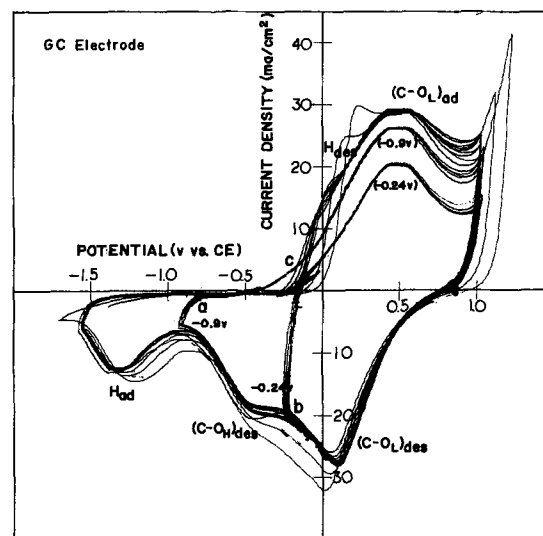


Fig. 3. Potential sweep diagrams with a glasslike carbon electrode in 1M HClO<sub>4</sub>. Sweep rate 200 mV/sec.

electrolyte was 1M HClO<sub>4</sub> and the temperature 50°C in all four sets. The sets differ only in the limits of the polarization voltage applied, as shown in Table I.

Note that evolution of CO, CO<sub>2</sub>, and O<sub>2</sub> occurs at potentials above ca. +1.7V (13, 14), and that evolution of H<sub>2</sub> occurs at potentials below ca. -1.9V. Thus, in Fig. 1 and 4, the electrodes are completely oxidized and reduced, while in Fig. 2 and 3, the effect of partial oxidation or reduction is observed.

In these figures, the sequenced order of sweeps is indicated by numbers or by arrows. Thus, in Fig. 1, the areas enclosed by successive sweeps decrease, while in Fig. 2, they increase.

The processes that occur are identified as follows: H<sub>ad</sub> and H<sub>des</sub> represent adsorption and desorption of H atoms, respectively. Also, (C-O<sub>H</sub>) and (C-O<sub>L</sub>) represent the higher and lower oxides of carbon, re-

Table I. Limits of polarization voltage in potential sweep

Figure No.	Electrode	Limits of sweep (V vs. SCE)	
		Anode	Cathodic
1	GC	+1.8	-1.9
2	GC	+1.0	-1.8
3a	GC	+1.0	-0.9
b		+1.0	-0.24
4	PG	+1.8	-1.8

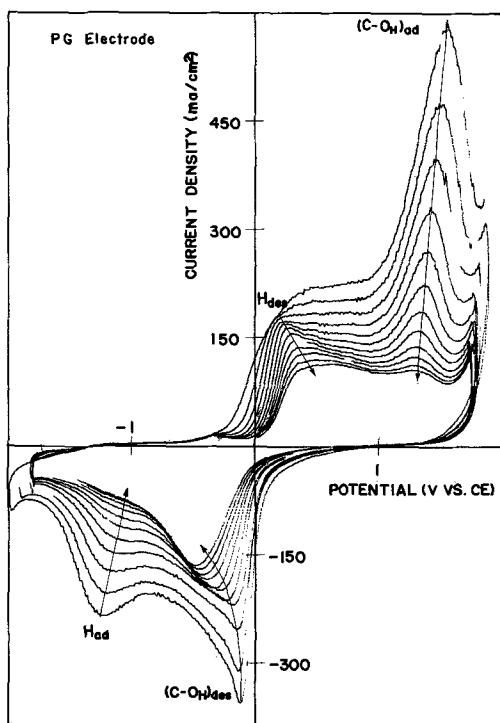


Fig. 4. Potential sweep curve with pyrolytic graphite electrode in 1M  $\text{HClO}_4$  at 50°C. Sweep rate 200 mV/sec. The curve tends to the direction shown by the arrows when the electrode is polarized repeatedly.

spectively, and the subscripts ad and des refer to formation or reduction of these species.

The results for the PG electrode, Fig. 4, are essentially the same as for the GC electrode, Fig. 1, although the current density is surprisingly larger for the PG. The surface became rough after repeated scanning over a wide voltage range.

In Fig. 1, the +0.5 and +1.3V peaks of the anodic scan correspond to the -1.3 and the -0.5V peaks of the cathodic scan, respectively. The oxide layer on the working electrode appears to be renewed if the electrode is polarized at +1.7V or more, where oxygen evolution takes place. The potential sweep curve becomes stable under such a condition.

As seen in Fig. 2, the adsorption and desorption of  $(\text{C}-\text{O}_\text{H})$  does not take place if the anodic scan is limited to +1.0V. The peak current at -0.5V during cathodic scan decreases but not to zero, and the new peak at ca. +0.1V appears. It corresponds to the +0.5V peak of the anodic scan. The curves in Fig. 2 stabilized after several hundreds of scans. It is also significant that new peaks at ca. +0.5V (anodic scan) and +0.1V (cathodic scan) appear.

In Fig. 3, the hump of the anodic scan  $\text{H}_{\text{des}}$  at ca. +0.1V disappears, provided the start of the sweep, marked "a," is more positive than -0.9V. The +0.5V peak for  $(\text{C}-\text{O}_\text{L})$  diminishes, but is still prominent when the anodic scan starts at -0.24V, marked "b."

At anodic potentials corresponding to evolution of oxidic gases, as in Fig. 1, the anodic scan peak at +1.3V and its corresponding cathodic scan peak at -0.6V indicate the formation and reduction of a surface complex which we identify as a higher oxide of carbon  $(\text{C}-\text{O}_\text{H})$ . When the anodic scan potential is only +1.0V, as in Fig. 2 and 3, a different anodic scan peak at about +0.5V and its corresponding cathodic scan peak at +0.1V are observed. We attribute this to the formation and reduction of a lower oxide of carbon  $(\text{C}-\text{O}_\text{L})$ .

The great range of 1.9V for the formation and reduction of  $(\text{C}-\text{O}_\text{H})$  indicates that this is quite an irreversible process. On the contrary, the range for the formation and reduction of  $(\text{C}-\text{O}_\text{L})$  is only about 0.4V,

which indicates that it is an unstable intermediate and that the process approaches reversibility. Figure 3 shows both  $(\text{C}-\text{O}_\text{L})_{\text{des}}$  and  $(\text{C}-\text{O}_\text{H})_{\text{des}}$ , showing that some  $(\text{C}-\text{O}_\text{H})$  may form even if the polarization is limited to +1.0V.

The results of several hundreds of experiments are summarized in Fig. 5. The circles represent peak potentials. The heavy lines represent data for GC, and the light lines for PG electrodes.

Adsorption and desorption of hydrogen seem to be irreversible on graphite and carbon, while they are quite reversible on noble metal such as Pt (15).

The peak potentials,  $E_p$ , vs. pH in the mixed solutions are shown in Fig. 6. The curves for  $(\text{C}-\text{O}_\text{L})_{\text{ad}}$  and  $\text{H}_{\text{des}}$  overlap as shown above. The potential for  $(\text{C}-\text{O}_\text{H})_{\text{ad}}$  is almost independent of pH, while that for  $(\text{C}-\text{O}_\text{H})_{\text{des}}$  is a small function of pH. On the other hand,  $\text{H}_{\text{ad}}$  depends much on pH, and the slope of the potential vs. pH curve is -0.146 V/pH. The potential for  $\text{H}_{\text{des}}$  is not affected by pH.

This is quite reasonable if  $\text{H}^+ + e \rightleftharpoons \text{H}_{\text{ad}}$  is assumed. For example, Böld and Breiter (16) have described the pH dependency of the adsorption and desorption of hydrogen and oxygen on Pt. We have also studied with carbon and graphite electrodes in alkaline solutions, where  $\text{H}_2\text{O} + e \rightleftharpoons \text{H}_{\text{ad}} + \text{OH}^-$  is proposed (17).

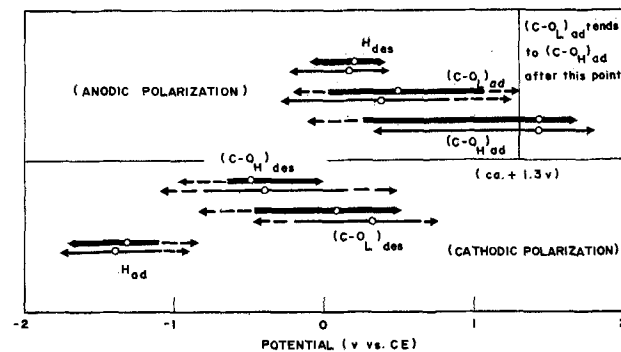


Fig. 5. Potential ranges for existing adatoms and intermediates in 1M  $\text{HClO}_4$  at 50°C. Heavy lines, glassy carbon; light lines, pyrolytic graphite.

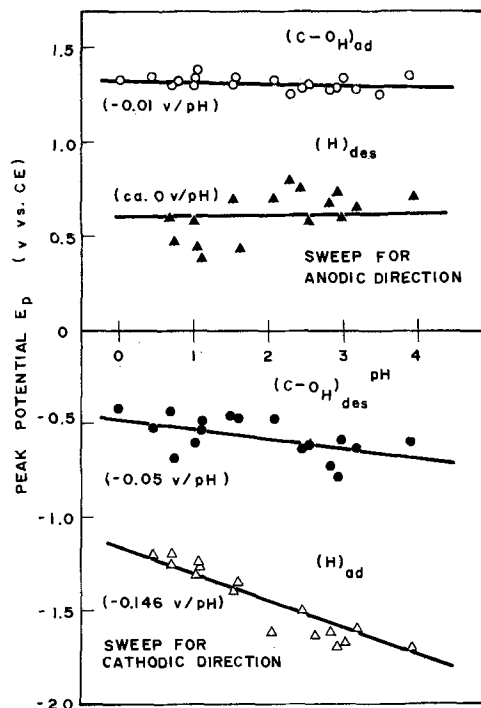


Fig. 6. Peak potential  $E_p$  vs. pH curves with glassy carbon electrode in mixed solutions of  $\text{NaClO}_4$  and  $\text{HClO}_4$  ( $\text{ClO}_4^- = 1\text{M}$ ) at 50°C. Potential sweep rate 200 mV/sec.

The +0.1V peak of the cathodic scan diminishes when the electrode is polarized at more than +1.3V. Therefore, we consider that (C-O<sub>H</sub>) is not reduced to (C-O<sub>L</sub>), or only insignificantly.

The surface of the working electrode becomes rough and the potential sweep diagram shrinks when polarization is repeated between +1.7 and -1.9V. However, the curve is stable if anodic polarization is limited up to the potential for (C-O<sub>L</sub>)<sub>ad</sub>.

**Determination of carbon oxide and hydrogen adatoms.**—Since the specific peaks for H, (C-O<sub>L</sub>), and (C-O<sub>H</sub>) overlap as described above, the GCT method was employed.

The test electrode was treated at +2.5V for 5 sec, then reduced at ca. -2.0V for 10 sec prior to the measurements. The electrolysis was carried out at a given potential,  $E_{st}$ , for about 15 sec to maintain a steady state. Then, the circuit was changed by the mercury relay to give the GCT measurement.

Figure 7 shows an example of the oscilloscope trace obtained. Coexistence of (C-O<sub>L</sub>) with (C-O<sub>H</sub>) on the electrode pretreated at +1.0V is evident, and its reduction potential in this photograph agrees with Fig. 5.  $\tau_H$  and  $\tau_O$  are the transition times for adsorption of hydrogen atom and reduction of carbon oxide, respectively. The amount of charge,  $Q_O$ , for reduction of carbon oxides was represented as follows

$$Q_O = Q_{(C-O_L)} + Q_{(C-O_H)} = i_c \tau_O \quad [5]$$

If adsorption and desorption are electrochemical processes

$$Q = i_c \tau = n \Gamma F \quad [6]$$

where  $\Gamma$  is the amount of adsorption (moles/square centimeter), and  $Q$  the amount of charge (coulombs/square centimeter) (18, 19). Figure 8 shows that  $Q$  is independent of  $i_c$ . The  $Q$ 's for the reduction of carbon oxide and for the adsorption of hydrogen depend much on the "set" potential,  $E_{st}$ .

The  $Q_O$  and  $Q_H$  on both GC and PG electrodes, as functions of  $E_{st}$ , are shown in Fig. 9. When  $E_{st}$  is less than +1.0V,  $Q_O$  and  $Q_H$  increase, and hence the oxide and hydrogen adatoms on the electrode both increase. The charges diminish suddenly at  $E_{st} > +1.3V$ , where (C-O<sub>L</sub>) converts into (C-O<sub>H</sub>) as described above. Since (C-O<sub>H</sub>) is reduced hardly at all during cathodic polarization, its reduction potential shifts to less noble, and overlaps the peak for H<sub>ad</sub>. These results agree well with Fig. 1-4. The oscilloscope trace from a noble potential is unsuitable for this discussion because  $\tau_O$  and  $\tau_H$  cannot be determined.

Adsorption of hydrogen atoms may take place at the active sites on the working electrode after O<sub>ad</sub> leaves, and vice versa. The ratio  $Q_O/Q_H$  reaches about 2 at noble potentials as shown in Fig. 10, and hence all the surface would be covered by O<sub>ad</sub>, this is, one adatom of oxygen would be bound with an active site on the carbon electrode as either (C-O<sub>L</sub>) or (C-O<sub>H</sub>). Since only higher oxide forms above +1.3V, complete reduction is difficult by cathodic polarization, thus it causes decrease in both  $Q_O$  and  $Q_H$ .

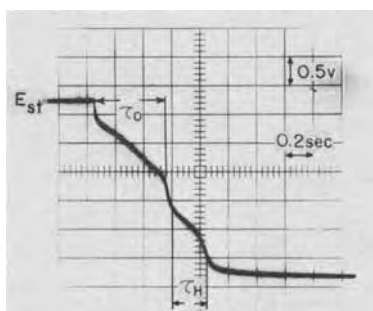


Fig. 7. Oscilloscope trace with glassy carbon electrode in 1M HClO<sub>4</sub>.  $E_{st} = 1.0V$  vs. SCE.  $i_c = 10.5 \text{ mA/cm}^2$ .

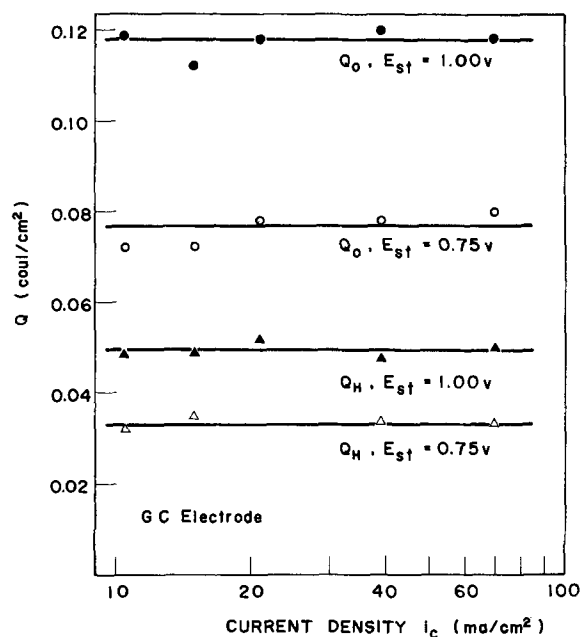


Fig. 8. Coulombs vs. current density. 1M HClO<sub>4</sub> at 50°C. Glassy carbon electrode.

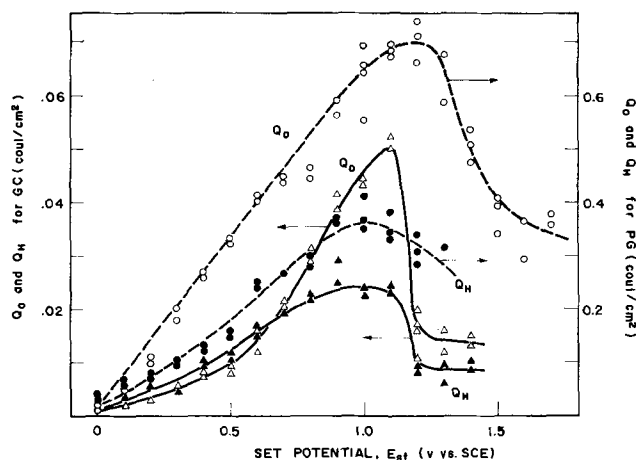


Fig. 9.  $Q_O$  and  $Q_H$  as functions of set potential. Solid lines, glassy carbon electrode; dotted lines, pyrolytic graphite electrode.

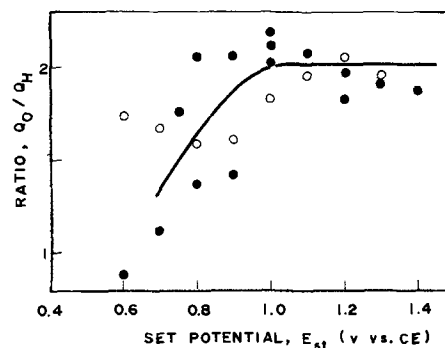


Fig. 10. Coulombs vs. set potential in 1M HClO<sub>4</sub> at 50°C. Solid points, glassy carbon electrode; open points, pyrolytic graphite electrode.

From Fig. 9, the maximum  $Q_O$  is  $5 \times 10^{-2}$  and  $7 \times 10^{-1}$  coulombs/cm<sup>2</sup> for the GC and PG electrodes, respectively. Therefore, the number of the active sites per unit area on PG electrode is about 14 times larger than for GC.

Since the electrode potential was scanned many times (sweep rate 200 mV/sec) until the polarization curve was stabilized, the working surface of the elec-

trode became rough. The roughness factor of GC electrode after such treatment was estimated to be about 200. It agrees with the SEM observation (20). It would be a major reason for the large coulombs/square centimeter described above.

**Effect of  $Cl^-$  on formation of carbon oxide.**—It is known that halide ions easily adsorb on the surface of noble metals such as Pt, if the potential is greater than the potential of zero charge (pzc). This disturbs formation of the oxide layer on the electrode surface to an extent that depends much on the electrode material, composition of solution, potential, and temperature (21, 22).

Examples of the potential sweep curves with a GC electrode in 1M  $HClO_4$  containing HCl are shown in Fig. 11. The peak current for  $(C-OH)_{ad}$  at ca. +1.4V decreases with increase in the HCl concentration, the potential for  $Cl_2$  evolution shifts toward the less noble and becomes less than the potentials for oxidic gas evolution (i.e.,  $O_2$ ,  $CO$ , and  $CO_2$ ). For the cathodic scan, the height of the peak for  $(C-OH)_{des}$  becomes lower with increase in the  $Cl^-$  concentration. The +0.5V peak appears on the cathodic scan if electrolysis is carried out for a long time at potentials higher than needed for chlorine evolution, in concentrated  $Cl^-$  solutions. This peak represents the reduction of  $Cl_2$  and it is controlled by diffusion.

Figure 12 shows  $Q$  vs.  $E_{st}$  in both 1M  $HClO_4$  and a mixed solution (1M  $HClO_4$  + 1M NaCl). Both  $Q_0$  and  $Q_H$  decrease with addition of  $Cl^-$  and depend on the  $Cl^-$  concentration (Fig. 13).

**Chlorine electrode vs. oxygen electrode.**—It is well known that when concentrated aqueous chloride solutions are electrolyzed, the main reaction at the anode is the evolution of chlorine gas. In a competitive reaction, some oxygen is also evolved. If the anode is some form of carbon or graphite, the oxidic gases are mainly  $CO_2$ , with some  $CO$  and  $O_2$ .

Figure 14 shows the potentiostatic polarization curves for PG anode in 1M  $HClO_4$  (broken line) and in 1M  $HClO_4$  + 3M NaCl (solid line). The oxygen electrode process has a Tafel slope of 210-240 mV/decade.

The chlorine electrode process with a fresh anode (cathodically reduced at -2.0V before the anodic polarization) shows a Tafel line with the slope of 135 mV/decade, but the curve deviates at noble potentials more than +1.3V, and the electrode potential tends to

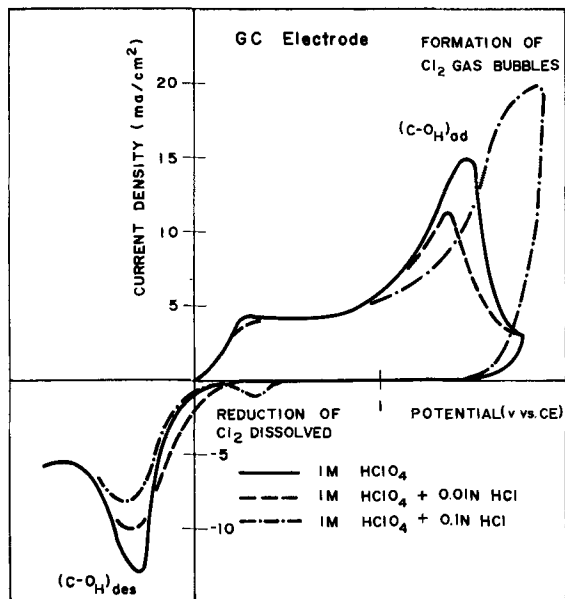


Fig. 11. Potential sweep curves of glassy carbon electrode in various solutions at 50°C. Sweep rate 200 mV/sec.

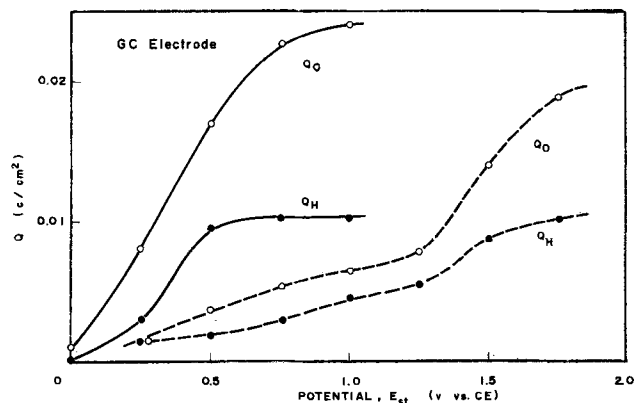


Fig. 12. Coulombs vs. set potential curves in 1M  $HClO_4$  (solid lines) and mixed solution of 1M  $HClO_4$  and 1M NaCl (broken lines) at 50°C.

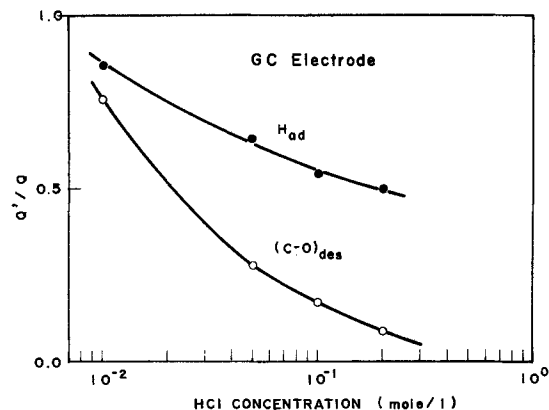


Fig. 13. Effect of  $Cl^-$  on amount of electricity for  $H_{ad}$  and  $(C-O)_{des}$  in 1M  $HClO_4$  at 50°C.  $E_{st} = 1.0V$  vs. calomel. Current density = 47.5 mA/cm<sup>2</sup>.  $Q$  = coulombs in 1M  $HClO_4$ .  $Q'$  = coulombs in solutions containing  $Cl^-$ .

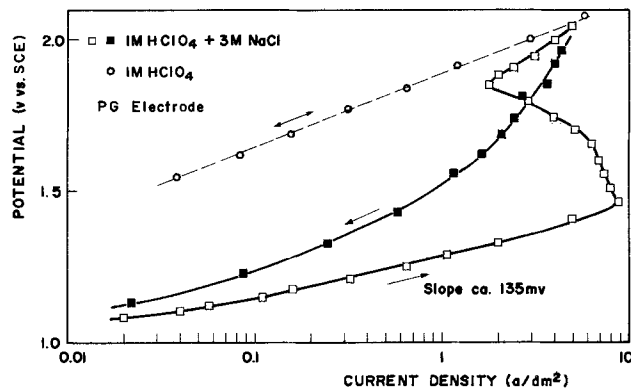


Fig. 14. Polarization curves of pyrolytic graphite anode at 50°C (potentiostatic method). Broken line shows the polarization curve of oxygen evolution reaction in 1M  $HClO_4$ .

that of the oxygen electrode process. A large hysteresis of the polarization curve of PG and GC electrodes with increase and decrease of the current was obtained. On the other hand, a graphite anode (not shown) did not show such a phenomenon, but the Tafel slope was larger than the predicted value ( $2RT/F$ ). A large area of porous surface of graphite anode would be a reason.

Figures 15-17 are the oscilloscope traces obtained by the GAT method. In  $HClO_4$  (Fig. 15), charge-up of the double layer capacity is followed by charge-up of the pseudocapacitance due to formation of carbon oxide layer as well as oxidation of  $H_{ad}$ , then the plateau for the over-all oxygen electrode process (B)

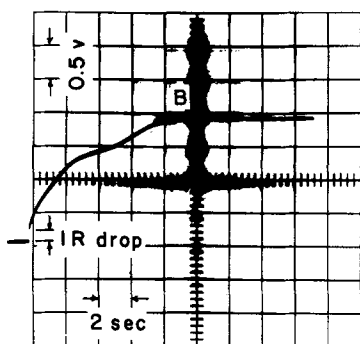


Fig. 15

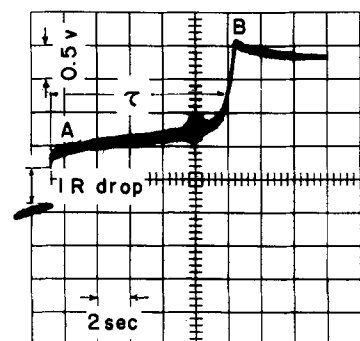


Fig. 17

appears. In solutions containing  $\text{Cl}^-$ , the potential plateau for the chlorine electrode (A) appears after charge-up of the double layer capacitance and the pseudocapacitance due to oxidation of  $\text{H}_{\text{ad}}$  and formation of  $\text{Cl}_{\text{ad}}$ . At low current densities, only plateau A appeared (Fig. 16), but plateau B was observed after few seconds at high current densities (Fig. 17).

The transition time,  $\tau$ , depends on agitation of the electrolyte, thus the process at high current densities would be controlled by diffusion of  $\text{Cl}^-$ . The  $\log i$  vs.  $\log \tau$  curves are straight with a slope of ca.  $-0.5$  at high current densities (Fig. 18). Figure 19 shows the polarization curves of the GC electrode obtained by points A and B in Fig. 16 and 17. Only oxygen evolution takes place in  $\text{HClO}_4$  containing a small amount of  $\text{Cl}^-$  (e.g., less than  $0.1\text{M}$ ), but the chlorine evolution reaction takes place easily in concentrated  $\text{Cl}^-$  solutions, at relatively low current densities. It is also important that the potential for the over-all oxygen electrode process in concentrated  $\text{Cl}^-$  solution is noble in comparison with that in  $\text{HClO}_4$ . Similar results with PG and graphite anode have also been obtained.

### Discussion

Evolution of mixed gas containing  $\text{O}_2$ ,  $\text{CO}$ , and  $\text{CO}_2$  may take place at the surface of carbon and/or graphite anode in solutions free of halide ions (13, 14). While

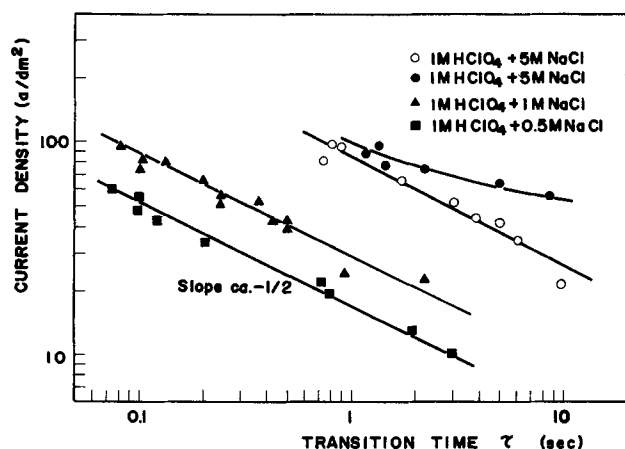


Fig. 18. Current density vs. transition time curves at  $50^\circ\text{C}$ . Open circle, glassy carbon electrode; solid symbols, pyrolytic graphite electrode.

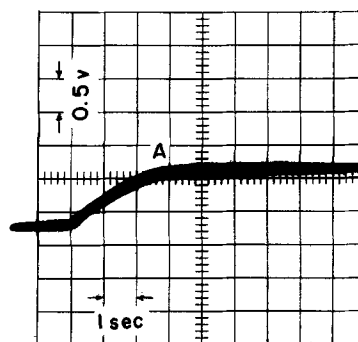


Fig. 16

Fig. 15-17. Galvanostatic anodic transient curves

Fig. No.	Electrode	Current density ( $\text{mA}/\text{cm}^2$ )	Solution
15	PG	52.0	$1\text{M HClO}_4$
16	PG	25.4	$1\text{M HClO}_4 + 5\text{M NaCl}$
17	GC	200	$1\text{M HClO}_4 + 5\text{M NaCl}$

Center line =  $0.5\text{V}$  vs. SCE. Temperature =  $50^\circ\text{C}$ .

the mechanism of formation of these gaseous substances has not been clarified yet in detail, the intermediate, probably carbon oxide or adatom of oxygen, may form on the electrode surface in aqueous solutions through the anodic charge transfer of  $\text{H}_2\text{O}$  or  $\text{OH}^-$  prior to gas evolution (14, 23, 24).

Two peaks at ca.  $+0.5\text{V}$  for  $(\text{C}-\text{O}_\text{L})$  and  $+1.4\text{V}$  for  $(\text{C}-\text{O}_\text{H})$  are observed in  $1\text{M HClO}_4$ . The surface of the working electrode becomes exceedingly rough when potential scanning is repeated at noble potentials such as  $+1.7\text{V}$ . Thus, we suppose that  $\text{CO}$  and/or  $\text{CO}_2$  may form at high potentials through the higher oxide  $(\text{C}-\text{O}_\text{H})$ . On the contrary, the strength of the bond between C- and O-atoms as the lower oxide  $(\text{C}-\text{O}_\text{L})$  would be weak, because the process of adsorption and desorption is relatively reversible. Therefore, oxygen adatoms can be reduced cathodically.

$(\text{C}-\text{O}_\text{L})$  converts into  $(\text{C}-\text{O}_\text{H})$  at noble potentials more than  $+1.3\text{V}$ , and  $(\text{C}-\text{O}_\text{H})$  is hardly reduced by cathodic polarization.

The ratio  $Q_\text{O}/Q_\text{H}$  tends to 2 at noble potentials. It becomes larger than 2 if the anode is polarized at high potentials for several minutes instead of few seconds, probably due to penetration of oxide in the porous surface. It can be recognized that the adsorption and de-

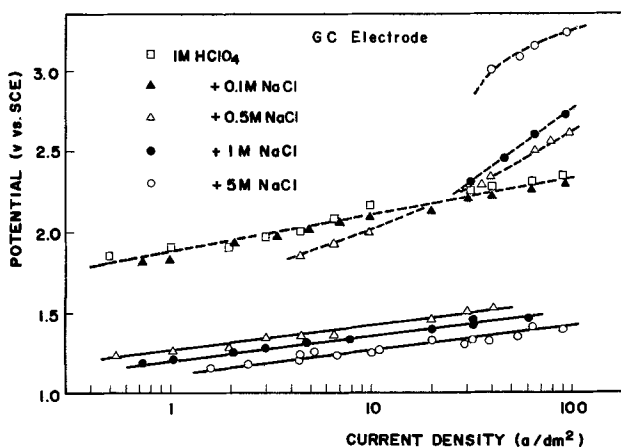
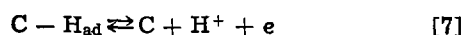
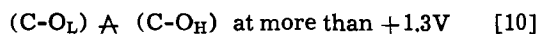


Fig. 19. Polarization curves of glassy carbon anode by means of the galvanostatic anodic transient method at  $50^\circ\text{C}$ . Solid line, chlorine electrode process; broken line, over-all anodic (oxygen) process.

sorption of H-adatom and the formation and reduction of carbon oxide take place at the active sites on the electrode by the following processes



and



The differential capacitance of the double layer on the GC electrode by the galvanostatic method is about  $3.8 \text{ mF/cm}^2$ , thus the roughness factor is estimated to be about 200. With the assumption of existence of ca.  $10^{15}$  atoms of carbon for  $1 \text{ cm}^2$  of the true surface (25), the amount of electric charge per unit area for adsorption of hydrogen atom with carbon is calculated to be

$$(10^{15} \text{ F/6} \times 10^{23}) (2 \times 10^2) = \text{ca. } 33 \text{ mcoulombs/cm}^2$$

and it is in good agreement with the maximum value of  $Q_H$  in Fig. 9 (ca.  $25 \text{ mcoulombs/cm}^2$ ).

An unstable oxide layer of carbon which can be reduced at the potential of few millivolts more noble than of hydrogen evolution is called the "oxidic layer," and is clearly divided from the "oxide layer" which is stable at the same potential (3, 5, 6).

We suppose that so-called "lower oxide" may correspond to the "oxidic layer," on the other hand, the "higher oxide" would be the "oxide layer." These two oxides are stable in solutions free of any reducing agent. They form on the electrode surface immersed in solutions for a long time. The oxide layer can be reduced easily by HCOOH and hydrogen. But any specific profile does not appear on the open-circuit potential vs. time curve obtained in solutions containing reducing agent, and its mechanism is not discussed.

The oxide layer of the electrode formed in solutions containing chloride ions reduces exceedingly slowly, and the exchange process between adatoms of oxygen and chlorine is very irreversible with respect to the electrode potential. Displacement of the higher oxide *in situ* on the carbon electrode would be difficult. The higher oxide is displaced as CO and/or CO<sub>2</sub> at potentials of +2.5V and then chlorine adatoms can form.

The specific adsorption of Cl<sup>-</sup> can take place at noble potential above the potential of zero charge, if the surface oxide does not already exist on the electrode. The pzc for carbon electrode varies from -0.13 to +0.25V vs. SHE depending on electrolyte and other conditions (26). The differential capacitance on the stress-annealed PG in NaF solution (pH ca. 6) has the minimum at ca. 0V vs. SHE (27).

Therefore, formation of the surface oxide is a squeeze process on the carbon electrode occupied already by chlorine. Transition from chlorine evolution to the over-all oxygen electrode process occurs in acidic solution containing Cl<sup>-</sup> at high current densities, but in alkaline solution the opposite transition (from oxygen to chlorine) takes place (17). The chlorine electrode and the over-all oxygen electrode processes in acidic solution are independent of pH (14, 23, 24). But the oxygen electrode process is affected by pH in alkaline solution. The chlorine electrode process is still independent of pH in this range.

The plateau A in Fig. 16 and 17 is the chlorine electrode potential because the oxide does not exist yet on the electrode. The Tafel slope of the polarization curve for the chlorine electrode process is 130-150 mV/decade (Fig. 19) and the reaction order with respect to Cl<sup>-</sup> is about unity (Fig. 20).

The "super polarization" phenomena (28) is found after plateau A, then the second plateau B appears (Fig. 17). The slope of the log *i* vs. log  $\tau$  curve is about -0.5 (Fig. 18). Therefore, the process would be controlled by diffusion (29). For the diffusion controlled

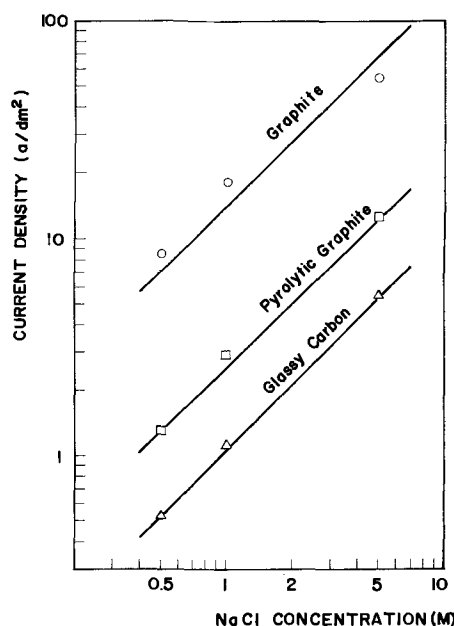


Fig. 20. Current density vs. Cl<sup>-</sup> concentration curves at 1.2V vs. SCE.

process

$$i\sqrt{\tau} = nF C^0 \sqrt{\pi D/2} \quad [11]$$

where  $C^0$  is the concentration in the bulk of solution. The Cl<sup>-</sup> concentration near the electrode decreases with increase in time after switch-on due to slow diffusion. The chlorine overvoltage and the formation of the oxide layer on the PG and GC electrodes increase. Any slow diffusion process is not observed up to 100 A/dm<sup>2</sup> of the superficial current density on the graphite anode because of its rough surface.

The Tafel slope of the polarization curve for the over-all oxygen electrode process in 1M HClO<sub>4</sub> is 210-240 mV/decade and is independent of the anode material and the method of polarization measurement. It agrees with reference data obtained in the phosphate buffer solution (14, 24). The potential for the over-all oxygen electrode process in the solution containing Cl<sup>-</sup> is significantly noble compared to that in HClO<sub>4</sub>, probably due to preferential adsorption of Cl on the working electrode.

The PG electrode polarized in a concentrated NaCl solution shows the Tafel line with the slope of ca. 135 mV/decade (Fig. 14), because the anode surface under the steady-state polarization is covered by a small amount of the lower oxide at the potential range not exceeding +1.3V, and the chlorine electrode process takes place sufficiently. At more noble potentials, on the other hand, all the surface would be covered by the higher oxide, and hence the potential moves to that for the over-all oxygen electrode process. Since its surface oxide is removed slowly with decrease in the polarizing current, the potential comes down with a large hysteresis.

The rate of the chlorine electrode process is represented as follows

$$i = k(\text{Cl}^-) \exp(\alpha FE/RT) \quad [12]$$

where *i* is the apparent current density, *k* the rate constant, and  $\alpha$  the transfer coefficient. When the active sites for the chlorine electrode process are covered by surface oxide, Eq. [12] should be corrected (30)

$$i' = k(\text{Cl}^-) (1 - \theta_o) \exp(\alpha FE/RT) \exp(-(1 - \alpha)f\theta_o) \quad [13]$$

where *i'* is the current density at the covered surface,  $\theta_o$  is the coverage, and  $fRT$  is "Temkin's parameter." From Eq. [12] and [13]

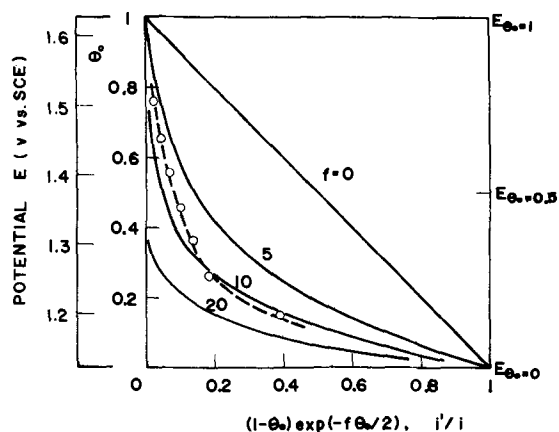


Fig. 21.  $\theta_0$  vs.  $(1 - \theta_0) \cdot \exp(-f\theta_0/2)$  curves. Broken line,  $E$  vs.  $(i'/i)$  under assumption of  $\theta_0 \sim E$ .

$$i'/i = (1 - \theta_0) \exp(-f\theta_0/2) \quad [14]$$

We assume that the line with the closed points in Fig. 14 shows the  $E$  vs.  $i'$ , whereas the straight line with the open points represents the  $E$  vs.  $i$  curve. Since  $\theta_0$  is a function of  $E$ ,  $i'/i$  varies with  $E$  as shown by the dotted line in Fig. 21, which is evaluated from Fig. 14.

Suppose that  $\theta_0$  is a linear function of  $E$  in a small range of potential, and  $E_{\theta_0=1} = 1.62\text{V}$  and  $E_{\theta_0=0} = 1.125\text{V}$ . Figure 21 also shows  $\theta_0$  vs.  $i'/i$  curves under given  $f$ 's (solid lines). Note that  $f$  is positive, thus, it is considered that the apparent activation energy of the chlorine electrode process increases with  $\theta_0$  and/or  $E$  with formation of the surface oxide, and mutual retardation between  $\text{O}_{\text{ad}}$  and  $\text{Cl}_{\text{ad}}$  may occur. This will be described in detail in a separate paper (17).

#### Acknowledgment

This work has been conducted as a part of the PhD thesis of M. Yasuda, at Kyoto University. Graphite and carbon were supplied by Nippon Carbon Company, Tokyo, and Tokai Denkyoku Manufacturing Company, Nagoya. The authors wish to express many thanks for support of Olin Corporation, New Haven, Connecticut. We also thank Dr. W. C. Gardiner, Stratford, Connecticut, Dr. R. B. MacMullin, R. B. MacMullin Associates, Niagara Falls, New York, and Dr. H. Kita of Hokkaido University for their kind suggestions and advice.

Manuscript submitted Aug. 30, 1973; revised manuscript received Dec. 26, 1973.

Any discussion of this paper will appear in a Discussion Section to be published in the December 1974 JOURNAL. All discussions for the December 1974 Discussion Section should be submitted by Aug. 1, 1974.

#### REFERENCES

1. L. E. Vaaler, *Electrochem. Technol.*, **5**, 170 (1967).
2. F. Hine and M. Yasuda, *Denki Kagaku*, **39**, 530 (1971).
3. H. Binder, A. Köhling, K. Richter, and G. Sandstede, *Electrochim. Acta*, **9**, 255 (1964).
4. P. Drossbach and P. Schmittinger, *ibid.*, **9**, 1391 (1964).
5. L. I. Krishtalik and Z. A. Rotenberg, *Zh. Fiz. Khim.*, **39**, 168 (1965).
6. L. J. J. Jansen and J. G. Hoogland, *Electrochim. Acta*, **14**, 1097 (1969).
7. K. F. Blurton, *ibid.*, **18**, 869 (1973).
8. G. Mamantov, D. B. Freeman, F. J. Miller, and H. E. Zittel, *J. Electroanal. Chem.*, **9**, 305 (1965).
9. O. S. Ksenzhek and V. V. Stender, *Soviet Electrochem.*, **3**, 197 (1967).
10. C. A. Knorr and F. G. Will, *Z. Elektrochem.*, **64**, 258, 270 (1960).
11. P. Delahay, "New Instrumental Methods in Electrochemistry," p. 130, Interscience Publishers, Inc., New York (1954).
12. "Atarashii Kogyo-Zairyo no Kagaku (Chemistry of New Industrial Materials)," T. Takei and C. Kawashima, Editors, A-8 "Tanso to Kokuen Seihin (Products of Carbon and Graphite)," p. 177, 265, Kanehara Publishing Co., Tokyo (1967).
13. P. Drossbach and H. Hoff, *Electrochim. Acta*, **14**, 101 (1969).
14. G. N. Kokhanov and N. G. Milova, *Soviet Electrochem.*, **6**, 64 (1970).
15. S. Gilman, in "Electroanalytical Chemistry," Vol. 2, p. 111, A. J. Bard, Editor, Marcel Dekker, New York (1967).
16. W. Böld and M. Breiter, *Electrochim. Acta*, **5**, 145 (1961).
17. F. Hine and M. Yasuda, Unpublished data.
18. W. Lorenz, *Z. Elektrochem.*, **59**, 730 (1955).
19. H. A. Laitinen and L. M. Chambers, *Anal. Chem.*, **36**, 5 (1964).
20. F. Hine and M. Yasuda, *Soda and Chlorine*, **24**, 316 (1973).
21. N. A. Balashova and V. E. Kazarinov, in "Electroanalytical Chemistry," A. J. Bard, Editors, Vol. 3, p. 135, Marcel Dekker, New York (1969).
22. J. P. Hoare, "The Electrochemistry of Oxygen," p. 81, Interscience Publishers, Inc., New York (1968).
23. L. I. Krishtalik and Z. A. Rotenberg, *Elektrokhimiya*, **2**, 351 (1966).
24. G. N. Kokhanov and N. G. Milova, *ibid.*, **5**, 93 (1969).
25. D. O. Hayward and B. M. W. Trapnell, "Chemisorption," 2nd ed., p. 18, Butterworths, London (1964).
26. R. S. Persins and T. N. Anderson, in "Modern Aspects of Electrochemistry," J. O'M. Bockris and B. E. Conway, Editors, No. 5, p. 203, Plenum Press, Inc., New York (1969).
27. J. P. Rodin and E. Yeager, *This Journal*, **118**, 711 (1971).
28. H. Kita and T. Yamazaki, *J. Res. Inst. Catalysis, Hokkaido Univ.*, **11**, 10 (1963).
29. P. Delahay, "New Instrumental Methods in Electrochemistry," p. 184, Interscience Publishers, Inc., New York (1954).
30. B. E. Conway, "Theory and Principles of Electrode Processes," p. 118, Ronald Press, New York (1965).

# Silver/Silver Chloride Electrodes: Surface Morphology on Charging and Discharging

T. Katan\*

*Materials and Structures, Lockheed Palo Alto Research Laboratory, Palo Alto, California 94304*

and S. Szpak

*Electronic Materials Sciences Division, Naval Electronics Laboratory Center, San Diego, California 92152*

and Douglas N. Bennion\*

*Energy and Kinetics Department, School of Engineering and Applied Science,  
University of California at Los Angeles, Los Angeles, California 90024*

*The publication costs of this article have been assisted by the Lockheed Corporation.*

## ABSTRACT

Transport modes were determined from examinations of morphology for electrochemical oxidation and reduction within electrodes consisting of beds of silver spheres  $37.2 \mu\text{m}$  in diameter in  $1\text{N KCl}$  and subjected to  $5.0 \text{ mA cm}^{-2}$  applied current density. Oxidation proceeded via silver dissolution, probably at dislocation sites, followed by diffusion and, then, deposition of  $\text{AgCl}$  in characteristic, bulbed mounds which grow together to form layers of approximately uniform thickness.  $\text{AgCl}$  film thickness, for the case of partially covered underlying silver, was about  $3500 \text{ \AA}$  and distance from silver dissolution pits to  $\text{AgCl}$  deposition sites was found to be increased from  $4,000$  to  $40,000 \text{ \AA}$  as the local transfer current density became larger within the sphere bed. Reduction of anodically formed  $\text{AgCl}$  on partially covered silver proceeded by an opposite path: solution and diffusion of  $\text{AgCl}$ , and deposition of silver on preferred sites of surrounding bare silver surface.

The mechanism of  $\text{AgCl}$  formation and reduction at silver electrodes in  $\text{KCl}$  electrolyte has been the subject of numerous publications (1-9). The work of Jaenicke *et al.* did much to clarify modes of reduction in thick films of  $\text{AgCl}$ , and Briggs and Thirsk (2) contributed valuable evidence which clarified the anodic growth of films thicker than  $1\text{-}2 \mu\text{m}$ . Little has been done, however, to gain an understanding of the mechanism of growth and reduction of  $\text{AgCl}$  that partially covers silver surfaces before films of  $\text{AgCl}$  start to become appreciably thick.

Thin films of silver chloride, which partially cover the surface of an underlying silver substrate, were first studied by Kurtz (3) who observed anodic growth of patches of  $\text{AgCl}$  with an optical microscope and noted that complete surface coverage appeared after passage of some  $8 \text{ mA min cm}^{-2}$  in  $0.1\text{N KCl}$ . More recently, Giles (4) suggested that anodic growth of the  $\text{AgCl}$  phase proceeds by progressive nucleation of three-dimensional centers of unspecified geometry and that diffusion contributes to the over-all processes. In our previous communication (5), we indicated that the reduction mechanism occurs via solution diffusion and surface diffusion to growth sites on the silver surface and that  $\text{AgCl}$  dissolution becomes rate limiting when silver chloride crystallites become small. Although these studies have contributed to establishing the over-all mechanisms involved, they have not presented a clear connection between the electrochemical reactions and the morphological changes. Direct observations of the type of Kurtz (3) were needed to elucidate the phenomenon of film formation and growth if critical distances required by modeling theory were to be determined experimentally (10, 11).

Recent theoretical work has shown that many secondary electrodes, including the  $\text{Ag/AgCl}$  electrode, may be described by a "solution-diffusion" model con-

sisting of a set of elementary processes occurring in series (10, 11). To apply such theories it is necessary to establish the effects of surface morphology on electrode performance through isolation of morphologically dependent, rate-determining steps from among a series of elementary steps and associated changes as the electrode undergoes discharge or charge.

A direct approach was used in this work by employing a scanning electron microscope to examine inner surfaces of a porous silver electrode structure after anodic and cathodic treatment. The electrode consisted of a bed of loose silver spheres so that it could be dismantled easily and the spheres examined individually after charging and discharging. The spheres were all the same size so that local current densities and associated morphological transformations could be related to depth within the sectioned electrode. This technique extends the usefulness of scanning electron microscopy (SEM) which has recently become popular in electrode studies (12-16).

## Experimental

**Electrode construction and structure.**—The porous electrode used in this investigation is shown in Fig. 1. It was constructed in the following manner. A disk-shaped silver stage,  $1.41 \text{ cm}$  in diameter and  $0.30 \text{ cm}$  in thickness, was slip-fitted inside a truncated,  $10 \text{ cm}^3$ , tubular, hypodermic syringe housing. A silver strip, spot-welded to the stage and passing through a rubber gasket below the stage, served as the electrical connection to the external circuit. A bed of silver spheres,  $37.2 \pm 4.2 \mu\text{m}$  in diameter, was placed on top of the stage, completing construction of the porous structure. Specific resistance of these beds was measured as *ca.*  $1.0 \text{ ohm-cm}$ . A micrometer shaft attached to the stage permitted microtoming of the porous structure into sections with an accuracy of  $\pm 0.0005 \text{ cm}$ .

**External circuit of electrolytic cell.**—An Electronics Model C 612 galvanostat was used to control the im-

Electrochemical Society Active Member.  
Key words: surface morphology, silver/silver chloride electrode, anodic oxidation of silver.



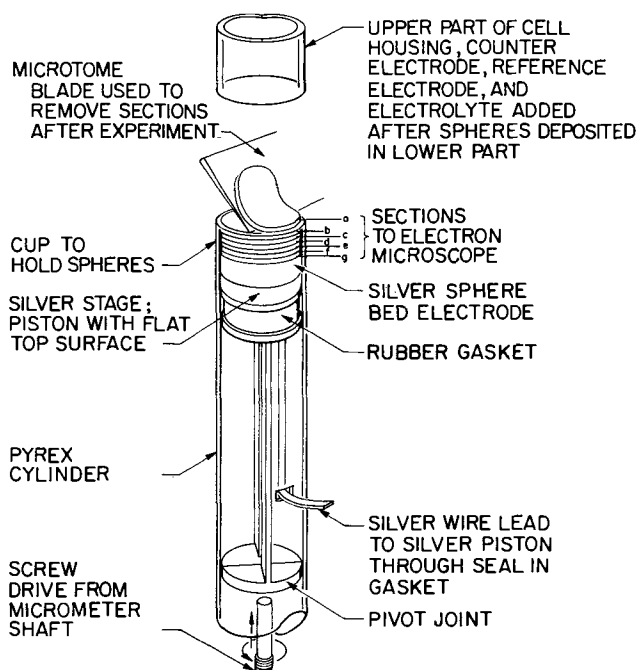


Fig. 1. View of the sphere bed electrode assemblage. (Section a, 0.0050 cm thick; subsequent sections, 0.0100 cm thick.)

posed current, which was measured with a Greibach Model 500 milliammeter. The electrode potential *vs.* that of an Ag/AgCl reference electrode, 4 cm above the bed, was recorded continuously using a Sargent MR recorder.

The electrolytic cell consisted of two parts as indicated in Fig. 1. The lower part contained the porous electrode and the upper part housed the counter and reference electrodes. These parts were joined together in a flush fit using Teflon pipe-thread sealant tape wrapped around both parts. The counterelectrode consisted of a porous silver matrix which was charged in a separate cell containing 1N KCl to form AgCl in excess of the expected total coulombs passed. The electrolyte was 1N KCl dissolved in triply distilled water which was deaerated prior to assembly.

**Experimental procedure.**—Prior to assembly of the working electrode, the silver spheres were immersed in concentrated ammonium hydroxide solution, rinsed thoroughly in distilled water, and air dried at 105°C for about 30 min. Just before use, the silver spheres were placed in 1N KCl and added as a slurry with a spatula onto the lowered stage to form the experimental structure that comprised the electrode. After filling, the silver stage was raised until the spheres protruded above the flat-cut edge of the tubular glass housing, and the excess was sliced off with the straight edge of a large stainless steel spatula. After a bed thickness of 1.00 cm was secured, assembly of the electrolytic cell was completed by attaching the upper part of the cell, placing the counter and reference electrodes, and adding electrolyte slowly so as not to disturb the sphere bed.

Upon completion of a prescribed mode of charging and discharging at room temperature ( $23^\circ \pm 1^\circ\text{C}$ ) the electrolyte was removed from the cell with the aid of a small diameter Teflon tube, and the upper part of the cell was detached. The electrode sections were removed (microtoming) and, after being washed in distilled water and air dried at 105°C for about 20 min, were examined using electron scan microscopy. The first section removed was 0.0050 cm thick, and all subsequent sections were 0.0100 cm.

Surface morphology was examined using a Cambridge Stereoscan Model Mark II. For the given re-

sults, electrodes were either charged for 11.0 min or charged for 11.0 min and then discharged for 4.0 min, all at rates of  $5.0 \text{ mA cm}^{-2}$  applied current density, *i.e.*, experiments were conducted galvanostatically. Polarization during these cycles was between 2 and 10 mV, measured with respect to the frontal surface.

**Properties of spheres constituting sphere-bed electrode.**—Regularity in sphere size and shape can be seen from the hundreds of silver spheres shown in Fig. 2. About 20 million of such spheres are estimated to constitute the electrode 1 cm thick, assuming 39% porosity. The uniformity shown here serves to confirm consistent sphere-module surface area throughout each sliced section of the electrode. Changes in surface morphology can thus be interpreted in terms of perpendicular distance of any parallel planar section from the bed's frontal plane without the usual unknown variations in specific surface area which obscure overall relations between morphology and perpendicular distance when microscopic examinations are made at high magnifications.

Additionally, each sphere has good sphericity and appears to have no appreciable surface roughness, aside from naturally occurring grain boundaries, even when viewed at 10,000X. A typical sphere is shown in Fig. 3; deviations from this general shape accounted for less than 1% of the particles. Spheres are prepared commercially by air quenching of atomized liquid silver of 99.9% purity, so that a degree of surface smoothness can develop before the droplets solidify.<sup>1</sup>

Average sphere diameter was determined to be  $37.2 \mu\text{m}$  with an average deviation of  $\pm 4.2 \mu\text{m}$ .

After the single anodizing of the spheres and the cycle of anodizing and subsequent cathodizing, an exploratory series of scanning electron microscope (SEM) photographs were made of sections taken from the electrode. Representative photographs of this series taken from the single charging and the cycle of charge with about one-quarter discharge are shown in Fig. 3-10a and 10b-12, respectively. In these photographs, silver chloride appears as a white growth upon the darker silver surface.

Decomposition of the AgCl deposit takes place in the electron microscope if observations are longer than about 15 min at 20 kV or 60 min at 10 kV. The smooth,

<sup>1</sup> Spheres were purchased from Metz Refining Company, South Plainfield, New Jersey.

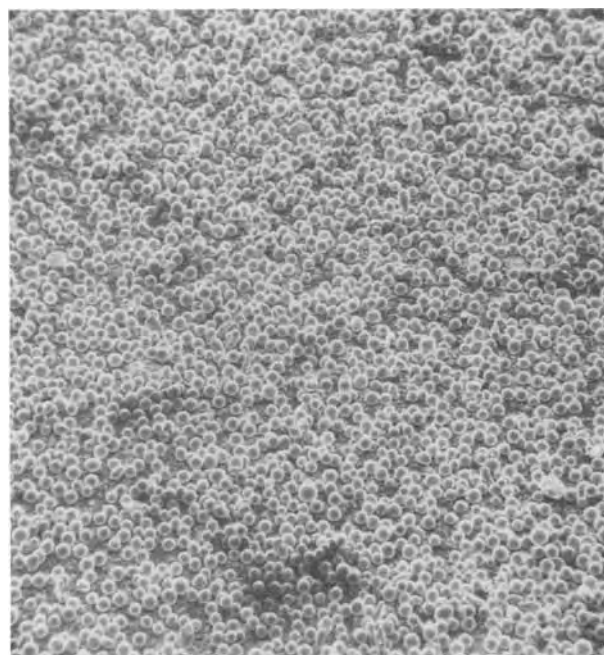


Fig. 2. Electrode structure, silver spheres  $37 \mu\text{m}$  in diameter

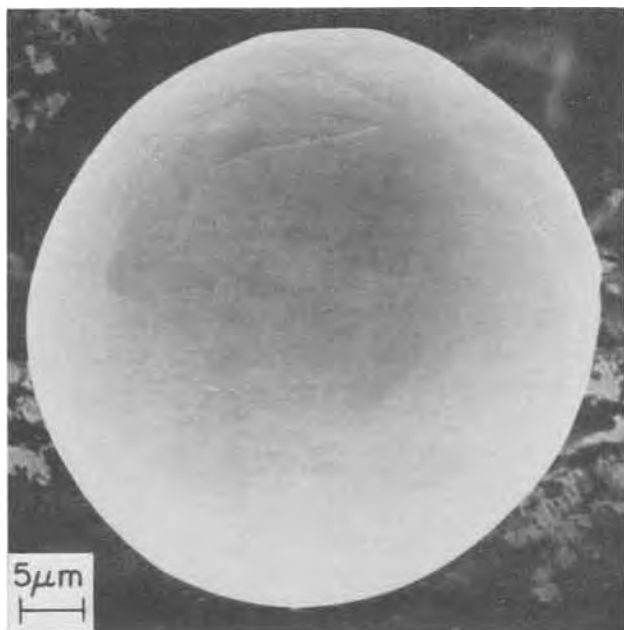
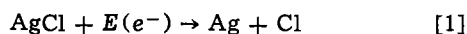


Fig. 3. Typical silver sphere used in the electrode assemblage

white AgCl is then observed to be gradually converted into a dark spongy mass which could only be metallic silver formed by a disproportionating reaction, initiated by the electron beam,  $E(e^-)$ .



This spongy Ag deposit should not be confused with the Ag formed by the electrochemical reduction of AgCl. The disproportionation is easily avoided by limiting SEM observations to 10 min or less.

### Results

Representative photographs, selected from the over one hundred viewed, are shown in Fig. 3-12. The first series, Fig. 3-10a, illustrates changes in surface coverage and morphology upon charging the sphere bed electrode for 11 min at a rate corresponding to an applied current density of  $5.0 \text{ mA cm}^{-2}$ . Figures 10b-12

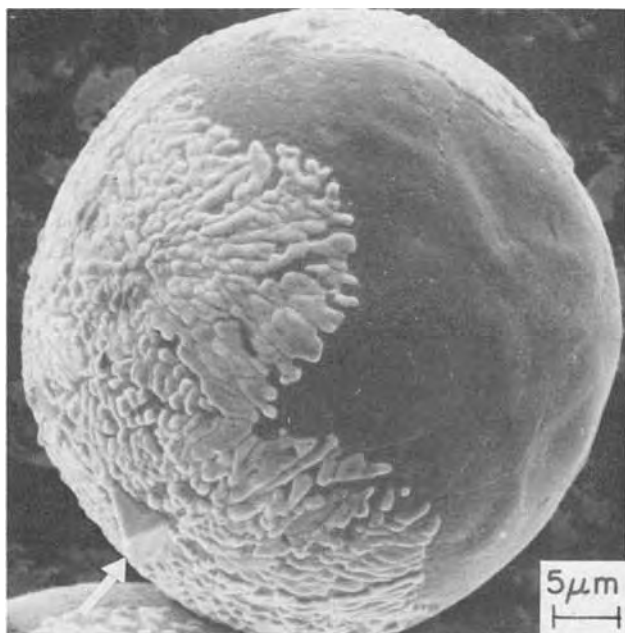


Fig. 4. Silver sphere with partially reacted surface, taken at a depth of 0.035 cm. Rare appearance of well-defined crystal planes (arrow).

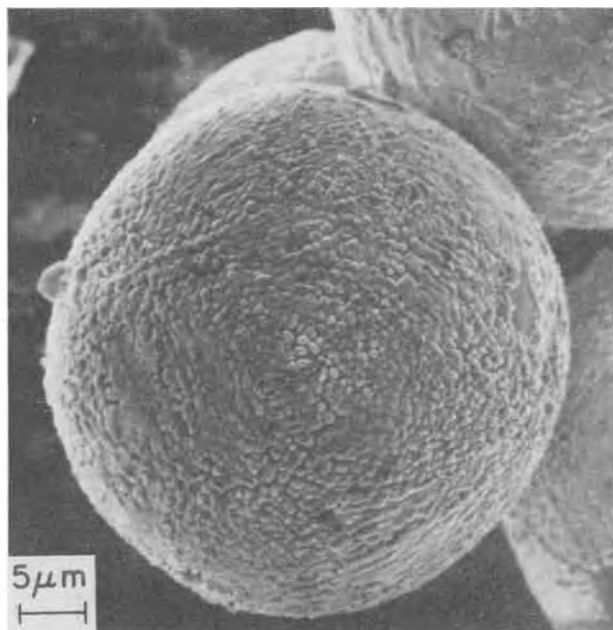


Fig. 5. Silver sphere with nearly totally reacted surface, taken at the electrode's front surface.

are assembled to illustrate the effect of subsequent discharge at the same applied current density for a period of 4.0 min.

*Reaction profile.*—After anodizing, surface coverage by AgCl was observed to be increased for spheres taken from sections closer to the electrode/bulk-electrolyte interface, i.e., closer to the frontal plane of the electrode. For example, surface coverage of spheres by AgCl was less than 10% in the seventh section taken 0.065 cm from the frontal plane, 30% in the fourth section 0.035 cm from the front, and it increased to 90-95% in the first section (0.005 cm thick). The reaction zone penetrated to a depth of approximately 0.07 cm, as evidenced by the disappearance of substantial amounts of AgCl at depths greater than 0.065 cm in the remainder of the electrode. Figures 3-5 show typical spheres taken from a depth greater than 0.065 cm, from the fourth and first sections, respectively. The manner of change in coverage by AgCl is seen by comparing these figures.

*Morphology of AgCl growth.*—The AgCl deposits appear without manifestations of crystal planes, ex-

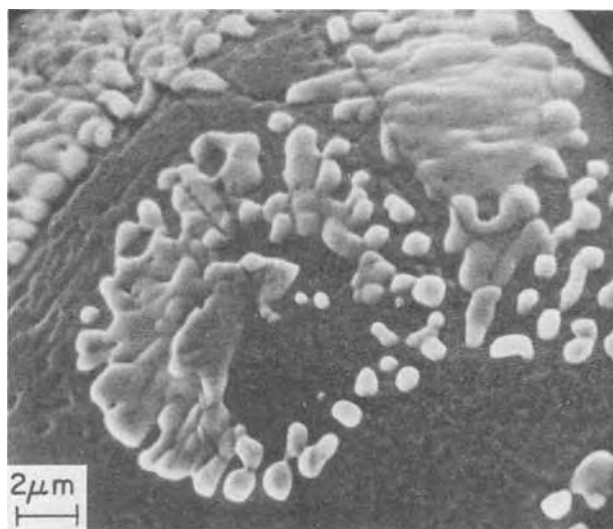


Fig. 6. Example of AgCl growth at a depth of 0.015 cm



Fig. 7. Glancing view, note the characteristic overhang

hibiting rounded, smooth surfaces (Fig. 4 and 5). Occasional exceptions are seen as in the lower left part of the sphere in Fig. 4 where a cubic crystal has formed. Only three such AgCl crystallites were observed in examinations of hundreds of spheres in the photographs for the given conditions.

A change in the form of the AgCl deposit occurs along the electrode's thickness. In the electrode, at depths greater than about 0.025 cm, the AgCl coating is more continuous, sometimes branchlike in appearance, and usually with interconnection of branches. The over-all breadth of continuity of the deposit then depends on the surface area covered, and this breadth may extend to at least 60  $\mu\text{m}$ , half or more of the sphere's circumference as shown in Fig. 4. Toward the front, the AgCl assumes the form of relatively small, discrete bulbed mounds, each about 7000 $\text{\AA}$  in effective diameter, as shown in Fig. 5. The surface density of the AgCl mounds is then  $1.1 \times 10^8$  mounds  $\text{cm}^{-2}$ . A gradual transition from the continuous form to the bulbed form is noted in the sphere bed as samples are taken toward the frontal plane. In Fig. 6, bulbed mounds were formed along with the continuous patches of film at a 0.015 cm depth within the electrode, showing an intermixing frequently seen at this depth.

Glancing views of the AgCl layers showed that the thickness remained fairly constant, always less than about 5000 $\text{\AA}$ , and the AgCl deposits usually formed an overhanging structure at their perimeter as shown in Fig. 7. The extent of overhang of the upper portions of the AgCl deposit beyond the lower AgCl/Ag perimeter varied, being always less by about 1000 $\text{\AA}$ .

**Morphology of pit growth.**—Holes or pits could be seen in the silver after anodic treatment at a surface density of about  $1.0 \times 10^8$  pits  $\text{cm}^{-2}$ . Their surface density remained fairly constant, increasing somewhat at silver grain boundaries (e.g., see upper part of

sphere, Fig. 4) and tended to decrease sharply beyond zones of pitting on the surface which surrounds the AgCl layers (e.g., see Fig. 8a). The area adjacent to the AgCl layer marked with pits extended farther from the deposit in sections taken closer to the electrode's frontal surface. The observed variation in this extension of pitting is 4,000–40,000 $\text{\AA}$ . Consequently, the bare silver patches, less than about 10,000 $\text{\AA}$  across, were pitted uniformly throughout at depths less than 0.005 cm measured from the front of the electrode. Characteristically, pits were angular in shape; sometimes perfect triangles were observed. The pits were typically 3000 $\text{\AA}$  across, on the average, but varied in size from 1000 up to 6000 $\text{\AA}$ .

Exploratory examinations were made at high magnification (10,000X) of very low AgCl coverage to locate the inception of the anodic processes. Then the pits were more rounded, sometimes circular, and usually smaller, ca. 2000 $\text{\AA}$  or less across (Fig. 9). Together with these pits, small deposits of AgCl could be seen around the mouths of the pits and as irregular deposits nearby, varying in average over-all size from 1000 to 8000 $\text{\AA}$  across. The surface densities of the initially formed silver chloride deposits and pits were determined as  $1.1 \times 10^8$  and  $1.0 \times 10^8$   $\text{cm}^{-2}$ , respectively, remaining independent of depth into the sphere bed.

**Morphology of AgCl reduction.**—The morphology of AgCl reduction was examined after a partial, rather than complete, reduction of the anodically produced films had taken place. This was done to identify the progress of reduction and to describe the cathodic process. The respective times of anodic and cathodic processes at 5 mA  $\text{cm}^{-2}$  were 11 and 4 min.

After the partial electrochemical reduction of the AgCl coatings, no darkening or structural change in the AgCl was found as evidence for metallic silver formation in the remaining AgCl layer as observed after the electron beam disproportionation in the SEM. Instead, a trend toward the formation of isolated AgCl mounds could be discerned, and a "smoothing out" of the sharp, angular edges of the pits occurred (e.g., compare Fig. 10a and 10b).

Glancing views of the AgCl deposits indicated a general loss of overhang or loss of undercutting of the amorphous AgCl. A typical view after partial reduction is shown in Fig. 11. Figures 7 and 11 may be compared for the appearance before and after cathodic treatment of the anodically formed AgCl, respectively.

Spheres taken from the same section depth, before and after cathodic treatment, revealed that the extent of the area covered with pits around each AgCl deposit increased after the cathodic process. Figures 8a

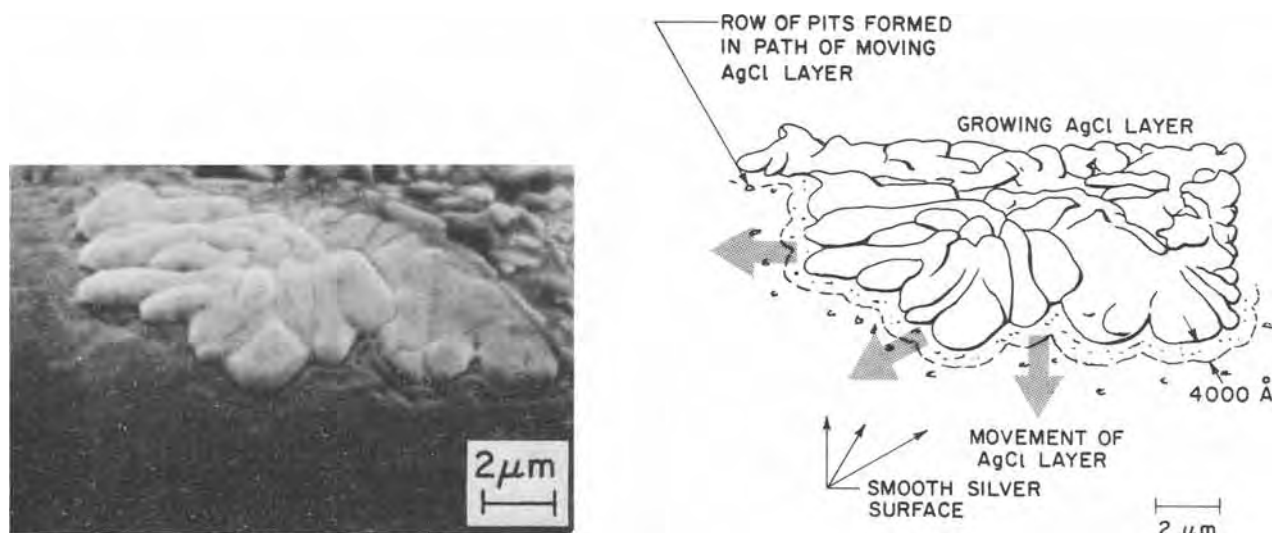


Fig. 8. Location of pits with respect to advancing silver chloride deposit. a (left), SEM photograph; b (right), graphical representation

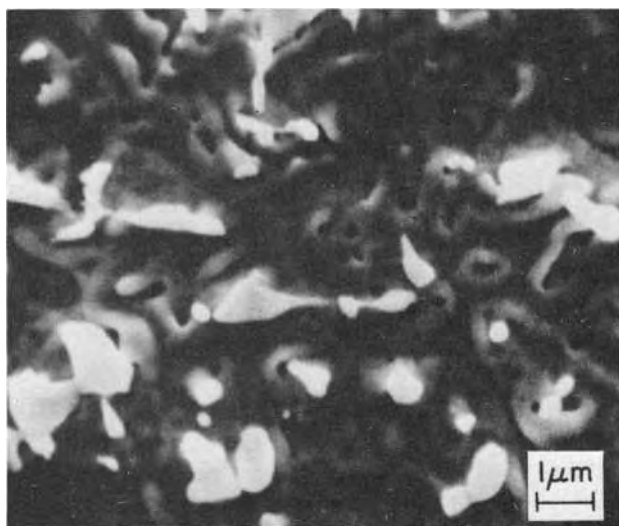


Fig. 9. SEM of initial stage of anodic process

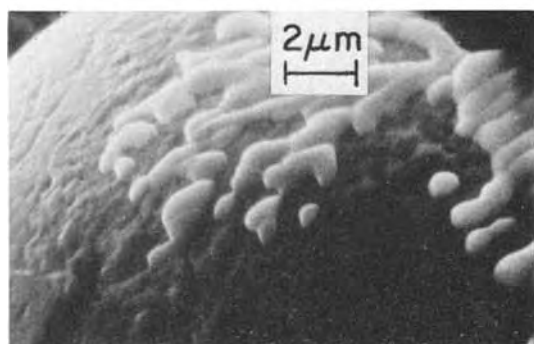
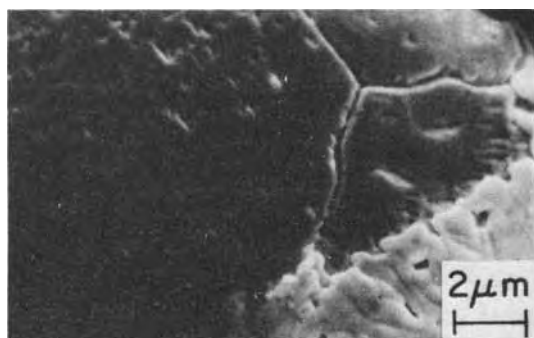


Fig. 10. Morphological changes of the silver surface. a (top), After the anodic process; b (bottom), after the anodic and subsequent cathodic treatment.

and 12a, for example, can be directly compared to show this effect. Here, for a depth of 0.065 cm into the sphere bed, *i.e.*, for the seventh section, the zone of pitting was extended from 4,000 to 14,000 Å after the 4 min treatment at a galvanostatically held 5 mA cm<sup>-2</sup> external current density.

#### Discussion

**Anodic process.**—The appearance of pits in the silver with AgCl mounds nearby indicates that silver is transported from the pits to AgCl sites where it deposits as AgCl. No other morphological change on the surface is evident that could account for this displacement. Silver could not be appreciably lost to bulk

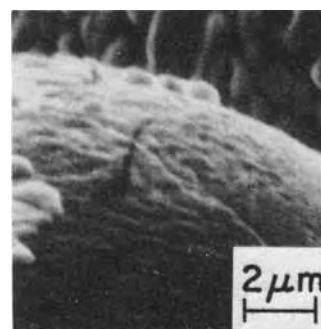


Fig. 11. Glancing view showing clearing of overhang (cf. Fig. 7)

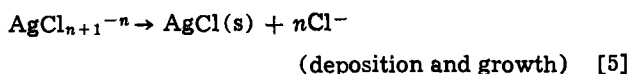
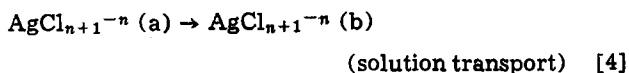
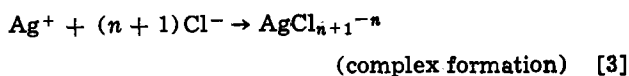
solution; complete coulombic reversibility of porous Ag/AgCl electrodes was repeatedly obtained for the given conditions. The volume of AgCl deposited appears to be larger than the pit volume in accord with the ratio of the respective molar volumes, 2.51 to 1.

Transport of silver is believed to involve bulk diffusion. The known soluble species have the formula AgCl<sub>n+1</sub><sup>-n</sup>, 0 ≤ n ≤ 3 (17), which are in mutual equilibrium in aqueous KCl solutions and which can be precursors to AgCl nucleation and subsequent precipitation. For silver dissolution to occur, silver must first be oxidized to a stable, singly charged state, and then the necessary chloride ions must combine with Ag<sup>+</sup>, forming species of the type AgCl<sub>n+1</sub><sup>-n</sup>.

The nearly constant thickness of the AgCl layers suggests that AgCl growth occurs along growing edges of the layers. This concurs with the concept of AgCl<sub>n+1</sub><sup>-n</sup> transport from the dissolution pits around the layers. Deposition of AgCl from AgCl<sub>n+1</sub><sup>-n</sup> species would take place primarily at AgCl which is closest to the dissolution pits.

Typical overhang of AgCl shown in Fig. 7 indicates that AgCl<sub>n+1</sub><sup>-n</sup> species arrive from bulk solution from above the silver surface at the edge of the AgCl. This is the strongest evidence for bulk diffusion offered here. For both surface diffusion, acting exclusively, and ion transport through the AgCl product, there should be no overhang of AgCl. For bulk diffusion, a lag in growth or retardation at the three-phase junction is anticipated in view of relative difficulties in nucleation of AgCl at the silver surface compared to the AgCl surface. The observations above are in accord with those of Giles (4) who used an independent method to postulate the existence of an intermediate diffusion transport step to a growing AgCl edge.

On the basis of these observations the anodic processes are summarized as follows



Other steps, such as embryo and swarm formation (18), are considered irrelevant to the present discussion and have been omitted. Transport of the silver bearing species is represented by Eq. [4] which is believed to constitute the principal characteristics of the anodic process. No evidence for surface diffusion could be found although its existence cannot be ruled out because of limitations of the technique used here. The relative concentrations of silver-bearing species in mutual equilibrium have been calculated for 1N KCl (5) and would be expected to change somewhat

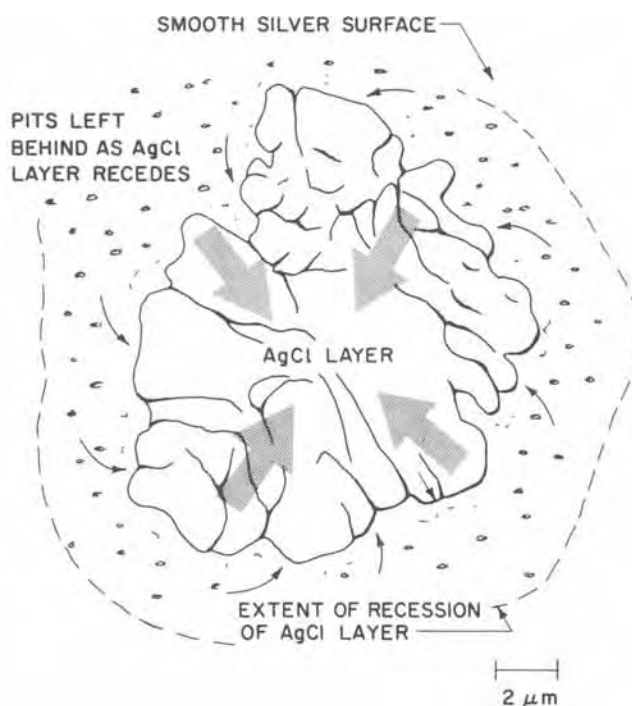


Fig. 12. Location of pits with respect to receding silver chloride deposit. a (left), SEM photograph; b (right), graphical representation

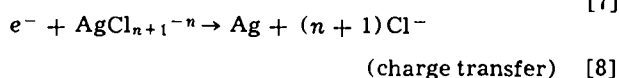
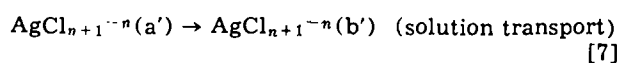
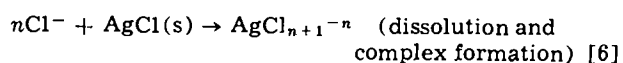
during transport to accommodate driving concentration gradients. Equilibrium constants for equilibrium between the species are established (17).

**Cathodic process.**—The absence of darkening, porosity, or structural change in layers of AgCl after partial electrochemical reduction suggests a corresponding absence of extensive cathodic reduction within the AgCl. On the other hand, the typical change everywhere in pit shape by smoothing and buildup on the previously sharp edges shows that deposition by reduction of silver species occurred at some distance from the AgCl. A transport of silver from AgCl to the surrounding surface is thus strongly indicated. This mode also has been given as the interpretation of potentiostatic current-time curves obtained during reduction of AgCl films in an earlier study by the present authors (5).

The increase in extension of the zone containing the pits surrounding the AgCl layers occurs when pits previously covered by the AgCl layers are exposed. This process is shown in Fig. 12a and 12b; AgCl located along the perimeter is being preferentially removed where the adjacent bare-silver surface is depleting the dissolved species. The typical disappearance of the overhanging AgCl upon reduction (Fig. 11) shows that dissolution occurs with transport toward the bulk region of the electrolyte. Other steps tend to increase the extent of overhang. For example, if dissolution was immediately followed by surface diffusion away from the AgCl along the silver surface, the AgCl would be preferentially dissolved at the three-phase junction. Similarly, if direct reduction of solid AgCl took place at the three-phase junction, the overhang would increase.

Examinations of the bare-silver surface indicate areas of silver deposition at small nodules and at the edges of the pits (Fig. 10b). Apparently, electroreduction of  $\text{AgCl}_{n+1}^{-n}$  occurs at preferred sites removed by some distance from the dissolution sites in accord with theory (18). The solubility of AgCl is increased by complexing from ca.  $10^{-5}$  to  $10^{-4}$ M in the presence of 1N KCl (20).

The above leads to the following set of events comprising the reduction process



Steps such as surface diffusion following solution transport have been omitted, and it could not be determined from which silver bearing species electroreduction occurs (Eq. [8]).

**Dissolution and deposition.**—It has been shown that dissolution and deposition occur in both the anodic and cathodic processes. It is interesting to examine these steps with reference to changes in local transfer current density which is known to increase from the rear toward the front of the electrode in accord with the corresponding increase in AgCl coverage (Fig. 3-5).

The presence of discrete pits in the silver after anodic dissolution (Fig. 10a) shows that only certain sites are attacked. The nearly constant pit surface density, even with strongly varying external conditions of transfer current density, indicates that the sites are determined by properties specifically connected with the solid. Similarly, the tendency previously noted for increased pitting at silver grain boundaries (Fig. 4) persists throughout the reaction zone (0.07 cm depth of penetration). We conclude that the silver surface contains preferred sites at a nearly constant density. These are most likely dislocation sites. The observed pit surface density of ca.  $10^8 \text{ cm}^{-2}$  is in fair accord with previously reported dislocation site surface density of  $1 \times 10^{-8} \text{ cm}^{-2}$  for silver (21).

The observed increase in pitted area with increase in local transfer current under anodic conditions in an outward direction from the AgCl deposits shows that all pit sites are not exactly the same energetically with reference to their distance from the deposits. It may be assumed that at the high anodic transfer currents local surface, concentration, and resistance overpotentials act to spread the area of pitting. Local transfer current density gradients are formed relative to the AgCl deposits and exist together with the over-all transfer current density profile through the electrode.

At the higher anodic transfer current densities, i.e., in sections near the electrode's frontal plane, a larger number of AgCl nucleation sites are formed with a sub-



sequent increase in number of discrete, bulbed mounds (Fig. 5). At increased reaction rates, the increased concentration of silver bearing species must favor nucleation of AgCl in accord with developed theories of nucleation (18).

Separation of pits from discrete AgCl deposition sites (Fig. 6, 9, and 10a) indicates that discrete centers for nucleation of AgCl on the silver surface must exist just as dislocation sites are postulated to exist for pit formation. At the lowest transfer current densities, before discrete AgCl particles grow together, the number of AgCl particles are counted as  $0.9 \times 10^8 \pm 0.2 \times 10^8$  centers/cm<sup>2</sup> according to photographs of the type shown in Fig. 9. At the highest transfer current density, counting the discrete, bulbed mounds of AgCl, we obtain  $1.3 \times 10^8 \pm 0.3 \times 10^8$  centers/cm<sup>2</sup> (Fig. 5). The number of AgCl nucleation centers on the surface thus remains essentially constant despite widely varying external conditions, as with the pits. The correspondence in surface densities of pit sites and AgCl deposition centers suggests a corresponding periodic occurrence of associated surface states on the silver.

During the cathodic process, the sites of AgCl dissolution are favored where curvature is sharpest (22), as evidenced by loss of overhang (Fig. 11) where concentrations of dissolved silver-bearing species is lowest, and where chloride ion concentration is highest, as evidenced by perimeter loss (Fig. 8). Both geometrical position and shape together with electrolyte concentrations influence dissolution. For electrodeposition, the formation of separated nodules of silver indicates the presence of discrete metal nucleation sites (18).

As seen, when deposition and dissolution act as the principal processes, a range of interactions is possible depending on locations, densities, and distances of separation of respective sites on the pore walls of a porous electrode.

**Modes of transport.**—The series of transport steps during anodic treatment is reconstructed as follows. Originally, sites of high potential energy, such as dislocation sites or grain boundaries, are attacked electrochemically to form rounded pits by silver dissolution, e.g., Eq. [1] and Fig. 9. The slightly soluble AgCl is deposited at nucleation sites around the pit as discrete nuclei which subsequently grow into bulbed mounds (Fig. 6). The mounds continue to grow and coalesce by diffusion of silver-bearing species through bulk electrolyte to eventually form a continuous layer (Fig. 8a) which also grows along its perimeter. Finally, cubic crystals of AgCl are formed when the deposits grow to substantial proportions (Fig. 4). At the same time, the pits become angular in shape. Generally, the transport modes can be simply represented as shown in Fig. 13.

Cathodic treatment involves retraction of the AgCl layer, as indicated, along the perimeter of the layer (Fig. 12). There is evidence for diffusion through bulk electrolyte from the AgCl deposits (Fig. 11). A surface diffusion step could not be distinguished from the SEM photographs, but definite nucleation sites for silver deposition were identified (Fig. 10b). Cathodic transport modes are simply represented by Fig. 14.

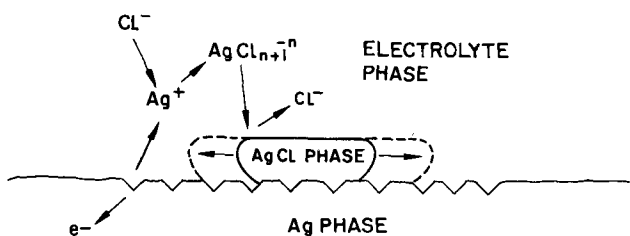


Fig. 13. Graphical representation of transport during anodic treatment.

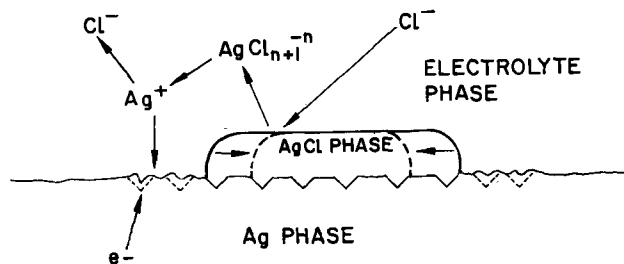
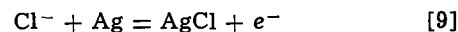


Fig. 14. Graphical representation of transport during cathodic treatment.

**Parameters affecting reaction profile.**—Observations reported here provide a basis for establishing numerical values of physical parameters for modeling theories of electrodes having sparingly soluble reactant or product in a conductive matrix (10, 11). Parameters for the tested electrode are summarized in Table I. For the determined depth of penetration by AgCl into the sphere bed, 0.07 cm, and from the calculated specific surface area of the spheres in the electrode, 986 cm<sup>2</sup>/cm<sup>3</sup>, an average transfer current density of 80  $\mu$ A cm<sup>-2</sup> could be calculated.

The chloride content of the electrolyte within the pores of the reaction zone can be calculated as being depleted in about 8 min at the imposed 5 mA cm<sup>-2</sup> superficial current density by formation of AgCl (Table I)



However, diffusion rates of chloride ion into the pores can be estimated to be able to accommodate the Cl<sup>-</sup> loss, taking Fick's first law and assuming zero Cl<sup>-</sup> in the pores (see Table I). Values for diffusion coefficients of silver bearing species in 2 and 4N KCl have been reported (5), and the solubility of AgCl in KCl solutions is known (20).

Thickness of the anodically formed AgCl remained remarkably constant for the regime of partial silver coverage by AgCl, varying from 3000 to 5000 Å and being about 3500 Å on the average. This finding suggests a limit on the initial minimum pore size and makeup particle size for porous silver electrodes. For a structure used as a secondary Ag/AgCl electrode, the smallest pores should be larger than at least twice the AgCl layer thickness to prevent pore blockage, or larger than about  $2 \times 5000 \text{ \AA}$  or 1.0  $\mu$ m. If the porous silver elec-

Table I. Physical parameters of silver sphere-bed electrode after anodizing in 1N KCl at 5.0 mA cm<sup>-2</sup> for 11.0 min

Parameter	Value
Diameter of spheres	37.2 $\mu$ m
Smallest pore diameter fitting through sphere bed	5.75 $\mu$ m
Sphere-bed porosity	38.8%
Sphere-bed specific surface area	986 cm <sup>2</sup> /cm <sup>3</sup>
Electrode thickness	1.00 cm
Electrode diameter	1.41 cm
Depth of penetration by AgCl deposits into electrode	0.07 cm
Surface area in region of penetration depth	97.3 cm <sup>2</sup>
Average transfer current density in region of penetration depth	80.2 $\mu$ A cm <sup>-2</sup>
Equivalents of anodic current passed	53.3 $\mu$ equiv.
Equivalents of Cl <sup>-</sup> in pores in penetration depth region	38.3 $\mu$ equiv.
Equivalents of Cl <sup>-</sup> diffused into pores*	71.2 $\mu$ equiv.
AgCl deposit thickness, bulbed mounds and patches	3,500 Å
Diameter of bulbed mounds of AgCl	7,000 Å
Maximum distance of pits to advancing AgCl	4,000-40,000 Å
Surface density of pit nuclei	$1.0 \times 10^8$ cm <sup>-2</sup>
Surface density of AgCl nuclei	$1.1 \times 10^8$ cm <sup>-2</sup>

\* This is a limit based on the following expression:

$$N = \frac{\epsilon^{1.5} D_0 (C_b - C_p)}{\Delta}$$

where  $N$  = flux of Cl<sup>-</sup>;  $\epsilon$  = porosity; the 1.5 power is based on the paper of De La Rue and Tobias (23);  $D_0$  is the bulk diffusion coefficient, assumed to be  $10^{-5}$  cm<sup>2</sup> sec<sup>-1</sup>;  $C_b$  is the bulk KCl concentration,  $10^{-3}$  moles/cm<sup>3</sup>;  $C_p$  is the concentration at the center of the region of penetration depth, assumed to be zero; and  $\Delta$  is half the penetration depth, 0.035 cm.

trode is thus made of spherical particles or particles resembling spheres which are pressed or sintered together, the average minimum sphere diameters can be calculated to be about  $6.5 \mu\text{m}$ , if one considers that the smallest pore diameter for a sphere bed is determined by the diameter fitting between three mutually touching spheres.

### Conclusions

Anodic oxidation of porous silver electrodes in 1N KCl progresses within the pores by pitting at dissolution sites of silver, probably at dislocation sites, and by deposition of AgCl at some distance from the pits at nucleation sites. For the regime of partial coverage of the silver by AgCl, the distance from pit formation to AgCl deposition varies from 4000 to 40,000 Å, being increased with increased local transfer current density. The deposited AgCl forms bulbed mounds, about 3500 Å high and 7000 Å in diameter, which appear to grow together to form a coating of more or less uniform thickness, 3500 Å. For silver electrodes consisting of a bed of silver spheres  $37 \mu\text{m}$  in diameter, the reaction zone characterized by the presence of AgCl is about 0.07 cm for a superficial anodic current density of  $5.0 \text{ mA cm}^{-2}$  applied for 11 min.

Cathodic reduction of the anodically formed AgCl in these electrodes proceeds via dissolution of the deposits of AgCl, mostly along their boundaries, and by electrochemical reduction to silver on the bare-silver surface.

### Acknowledgment

This work was supported in part by the Office of Naval Research. The work is a continuation of an earlier effort sponsored by Naval Air Systems Command Contract No. N00019-71-C-0369.

Manuscript submitted Sept. 17, 1973; revised manuscript received Jan. 28, 1974. This was Paper 243 presented at the Chicago, Illinois, Meeting of the Society, May 13-18, 1973.

Any discussion of this paper will appear in a Discussion Section to be published in the December 1974 JOURNAL. All discussions for the December 1974 Discussion Section should be submitted by Aug. 1, 1974.

### REFERENCES

1. W. Jaenicke, R. P. Tischer, and H. Gerischer, *Z. Elektrochem.*, **59**, 448 (1955).
2. G. W. D. Briggs and H. R. Thirsk, *Trans. Faraday Soc.*, **48**, 1171 (1952).
3. L. J. Kurtz, *Compt. Rend. URSS*, **11**, 283 (1935).
4. R. D. Giles, *J. Electroanal. Chem.*, **27**, 11 (1970).
5. T. Katan, S. Szpak, and D. N. Bennion, *This Journal*, **120**, 883 (1973).
6. W. Jaenicke, *Z. Elektrochem.*, **55**, 186 (1951); *ibid.*, **56**, 728 (1952).
7. A. R. Despic and J. O'M. Bockris, *J. Chem. Phys.*, **32**, 389 (1960).
8. T. P. Gorosh and V. P. Galushko, *Ukr. Khim. Zh.*, **28**, 66 (1962).
9. V. B. Aleskovskii, E. V. Bairashnyi, E. G. Ivanov, and V. A. Nikoshii, *Sb. Rab. Khim. Istochnikam*, **4**, 241 (1969).
10. J. S. Dunning, D. N. Bennion, and J. Newman, *This Journal*, **118**, 1251 (1971).
11. J. S. Dunning, Ph.D. Thesis (Report UCLA-ENG-7228), University of California, Los Angeles (1972).
12. F. G. Will and H. J. Hess, *This Journal*, **120**, 1 (1973).
13. D. Chua and R. J. Diefendorf, *Proc. 25th Power Sources Symp.*, Atlantic City, N. J., May 1972, p. 52.
14. C. F. Yarnell, M. C. Weeks, R. V. Biagetti, and G. W. Kammlott, Abstract 18, p. 47, Electrochemical Society Extended Abstracts, Fall Meeting, Cleveland, Ohio, Oct. 3-7, 1971.
15. Z. Nagy and J. O'M. Bockris, *This Journal*, **119**, 1129 (1972).
16. Douglas N. Bennion, Hiram Gu, and Ranna K. Hebbar, Final Report from Univ. of Calif. to Naval Air Systems Command, Contract No. N00019-72-C-0256, UCLA-ENG-7347, May 1973.
17. L. G. Sillen and A. E. Martell, "Stability Constants," Spec. Publ. No. 17, The Chemical Society, London (1964).
18. A. Ziabicki, *J. Chem. Phys.*, **48**, 4368 (1968).
19. J. O'M. Bockris and R. Despic, "Physical Chemistry," Vol. IX B, Chapter 7, p. 691, Academic Press, New York (1970).
20. W. F. Kinke, "Solubilities (Seidell)," 4th ed., Vol. 1, p. 67, D. Van Nostrand Co., Inc., New York (1958).
21. A. A. Hendrickson and E. S. Machlin, *Acta Met.*, **3**, 64 (1955).
22. W. Ostwald, *Z. Physik. Chem.*, **34**, 503 (1900).
23. R. E. De La Rue and C. W. Tobias, *This Journal*, **106**, 827 (1959).

## An Electrochemical Surface Area Meter

Y. L. Sandler\*

Physical and Inorganic Chemistry, Westinghouse Research Laboratories, Pittsburgh, Pennsylvania 15235

The publication costs of this article have been assisted by the Westinghouse Electric Corporation.

### ABSTRACT

A relatively simple, fast, and reliable electrical method for determining the surface area of powders is described. The oxygen loss from a flowing oxygen-helium mixture, caused by adsorption on the sample at liquid nitrogen temperatures, is sensed by a high-temperature galvanic cell. Operating conditions are chosen so as to conform to the one-point BET method. The method is absolute and a direct readout in terms of surface area can be obtained.

The surface area of a powder is usually determined by adsorbing an inert gas like nitrogen or krypton on the specimen cooled to liquid nitrogen temperature. By volumetric measurements giving the amount of gas physically adsorbed as a function of gas pressure, the amount of gas required to produce a surface coverage

of one monolayer and hence the surface area itself can be calculated. The theory made use of is the BET theory (1). The method is accurate but is very time consuming, even when a computer is available to handle the data.

The ultimate accuracy is usually not required; the surface area may then be determined from a single adsorption measurement (2). In our method, oxygen serves as the adsorbate, and an electrochemical cell is

\* Electrochemical Society Active Member.  
Key words: surface, galvanic cell, particle size, instrument, adsorption.

used to convert the changes in gas concentration by adsorption into an electric signal. Oxygen-ion-conducting high temperature cells are particularly suited because their response is fast and accurate; the transference number for oxygen ions is very close to one over a wide temperature range (3). In the present method, oxygen is adsorbed from a flowing oxygen-helium gas mixture by cooling the adsorbent to liquid nitrogen temperature. The oxygen content of the mixture after passing the sample is monitored continuously by means of the electrochemical cell which is used as an oxygen pump (4). A suitable voltage is applied so as to obtain the limiting current corresponding to the total removal of the oxygen from the gas stream. The time integral over the decrease in current due to adsorption gives the charge equivalent of the oxygen physically adsorbed on the sample at low temperatures. The charge in turn is a measure of the surface area if the proper conditions are chosen.

A rough calculation showed that for inert gas-oxygen mixtures containing 2-6% oxygen, as required by the method, a tubular solid electrolyte cell of the dimensions generally used in this laboratory will pump enough oxygen to allow a surface area measurement to be carried out within a few minutes. Flow rates of a few cubic centimeters per minute can be employed that do not present the sealing problems that are encountered with the electrolyte tubes at very low flow rates or in static systems.

### Theoretical

**The BET theory.**—In the derivation of the BET theory, as originally given (1, 5), the multilayer adsorption equilibrium is derived by considering the detailed balancing between the part of the surface not covered ( $S_0$ ) with the part covered once ( $S_1$ ), then the latter with the part covered twofold ( $S_2$ ), etc. For each pair, the rate of adsorption is equal to the rate of desorption

$$a_i p S_{i-1} = b_i S_i e^{-E_i/RT} \quad [1]$$

where  $E_i$  is the heat of adsorption in the layer covered  $i$ -fold,  $a_i$  and  $b_i$  are constants, and  $p$  is the gas pressure.

If  $V$  is the adsorbed gas volume and  $V_m$  is the volume required to cover a monolayer, then

$$\frac{V}{V_m} = \frac{\sum_i S_i}{\sum S_i} \quad [2]$$

The simplifying assumptions are made that, for all surface fractions covered twice or more

$$E_2 = E_3 = \dots = E_i \\ b_2/a_2 = b_3/a_3 = \dots = b_i/a_i$$

The summation (5) of Eq. [2] then leads to the form of the BET equation

$$\frac{x}{V(1-x)} = \frac{1}{V_m c} + \frac{(c-1)}{V_m c} x \quad [3]$$

where  $x = p/p^0$  is the relative pressure of the gas ( $p^0$  is the equilibrium vapor pressure of the condensed gas at the temperature of adsorption).  $c$  is a constant  $= a_1 b_2 / a_2 b_1 e^{(E_1 - E_L)/RT}$ , where  $E_L$  is the heat of liquefaction of the gas. In a "BET plot" the function  $x/V(1-x)$  is plotted vs.  $x$ , usually giving a straight line for the range  $0.05 < x < 0.3$  (see, for example, Fig. 6). According to Eq. [3], the slope of the line is  $(c-1)/V_m c$ , the intercept with the ordinate is  $1/V_m c$ . The sum of the two then is  $1/V_m$ . Thus,  $V_m$ , the gas volume in cubic centimeters (STP) required to cover the surface with one monolayer, is obtained.

**The one-point approximation.**—The value of the constant  $c$  usually is of the order  $10^2$ . Thus, in Eq. [3],  $1/V_m c \approx 0$ . This amounts to drawing the straight line from one measured point in the BET plot through the

origin. The larger the value of  $x$  chosen within the range of validity of the BET equation, the smaller the error in the slope will be. The range of validity usually is from  $x = 0.05$  to  $x = 0.30$ . With  $(c-1)/c \approx 1$ , Eq. [3] assumes the simple form

$$V_m = V(1-x) \quad [4]$$

In terms of the surface area  $S$ , Eq. [4] may be written as

$$S = NA(1-x) \quad [5]$$

where  $N$  is the number of adsorbed molecules and  $A$  is the cross-sectional area of the adsorbed molecule.

In our method  $N$  is substituted by a measured amount of electric charge  $q$  which is found by integration of the loss in pumping current due to adsorption of oxygen on the sample. From Faraday's law and a value of  $A$  of  $1.40 \times 10^{-15}$  cm<sup>2</sup> for oxygen, a charge  $q$  of 1 A-sec corresponds to a covered area ( $NA$  in Eq. [5]), of 0.218 m<sup>2</sup>. Equation [5] then becomes

$$S \text{ (in m}^2\text{)} = 0.218 (1-x) q \text{ (in A-sec)} \quad [6]$$

Two different mixtures were used in the experiments. With a liquid nitrogen bath at an average atmospheric pressure (in Pittsburgh) of 730 Torr,  $p^0$  for oxygen is 160 Torr. With 3.23% O<sub>2</sub> in helium,  $(1-x) \approx 0.85$ , therefore

$$S \text{ (in m}^2\text{)} = 0.186q \text{ (in A-sec)} \quad [6a]$$

With 6.7% O<sub>2</sub> in helium,  $(1-x) = 0.67$ , therefore

$$S \text{ (in m}^2\text{)} = 0.146q \text{ (in A-sec)} \quad [6b]$$

### Apparatus and Procedure

Figure 1 illustrates the setup of the apparatus. The oxygen-inert gas mixture, contained in cylinder C, passes through a flow regulator F and a flowmeter M over the sample S contained in a U-shaped sample holder and then passes through the electrochemical cell P in furnace E.

The cell consists of a tubular solid electrolyte made of calcia-doped zirconia which is heated by the furnace. The temperature must be chosen high enough that the current is not limited by the resistance of the electrolyte, but only by the amount of oxygen in the mixture passing the cell. An additional volume V and a capillary at the end prevent the air from entering the cell when the sample is cooled. A constant voltage  $E$  is applied to the electrodes on the inside and the outside of the electrolyte tube (the + pole is connected to the outside which is exposed to air). The current through the cell is monitored by a recorder R.

The experimental procedure is best illustrated by a typical example. Experimental details and a close examination of the method will follow. One hundred seventy-four milligrams of a cobalt oxide (Co<sub>3</sub>O<sub>4</sub>) powder were placed at the bottom of the U-shaped sample holder. A mixture of 6.7% oxygen in helium was passed over the sample, and the latter was heated to 150°C to drive off adsorbed gases. The heater was taken off and the flow was adjusted to give a certain current. This results in the initial portion of the recorder trace shown in Fig. 2 giving a plot of current vs. time. Choice of a suitable voltage and current is discussed below. When the sample holder was dipped

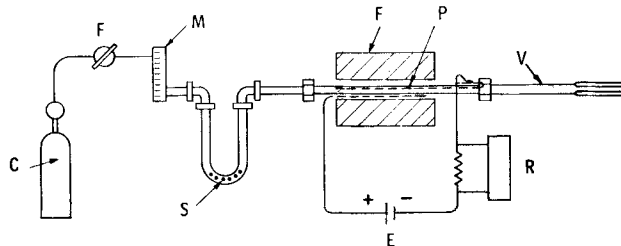


Fig. 1. Schematic of complete apparatus



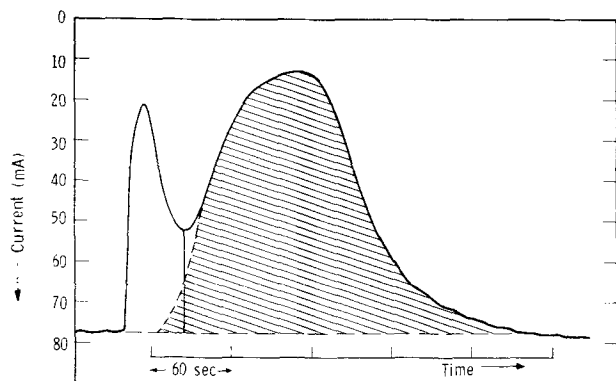


Fig. 2. Current through oxygen pump on cooling 174 mg  $\text{Co}_3\text{O}_4$ . Shaded area under second current minimum is proportional to surface area. Solid vertical line indicates point at which integrator is started (Exp. No. 15 in Table II).

in a liquid nitrogen bath, two current minima were observed as may be seen in Fig. 2. The first portion of the curve containing the first minimum is due to contraction of the gas in the cooled portion of the sample holder. The pure helium in the ballast volume  $V$  at the exit of the cell is here drawn back into the electrochemical pump. When the cooling is almost completed, adsorption of the oxygen on the sample causes the second decrease in current, a second minimum, and the return to the initial constant current. The shaded area under the curve corresponds to an electric charge  $q = 10.6$  A-sec. With the 6.7%  $\text{O}_2$  used in this experiment, according to Eq. [6b], surface area  $S = 0.146 q = 1.55 \text{ m}^2$  for the 174 mg used, or  $8.9 \text{ m}^2/\text{g}$ .

Instead of integrating the area under the curve (by weighing the paper or by planimeter), an electronic integrating device was also used. It is zeroed with respect to the base current and is started at the first maximum as indicated by the vertical line in Fig. 2. The device can be calibrated directly in terms of surface area and is read when the indicated area no longer increases.

The drawing back of pure helium into the electrochemical pump during the cooling period eliminates the need of a numerical correction for the change in gas volume on cooling the adsorption vessel and makes it possible to measure a signal directly proportional to the surface area.

### Experimental

Two gas mixtures were used in the experiments, first 3.23%  $\text{O}_2$  in He, then 6.7%  $\text{O}_2$  in He. The flowmeter was a Matheson No. 610 flowmeter (0-100  $\text{cm}^3/\text{min}$ ) which was calibrated against a bubble flowmeter. (It was required for the tests described below, but it is not required for the area measurement since the cell current itself provides a more accurate measure of oxygen flow.) Beckman Teflon connectors were used throughout and provided a satisfactory seal. The sample holder was a  $\frac{1}{4}$  in. OD U-shaped tube of 15 cm length. Only the bottom of the tube was filled with the sample. Solid electrolyte tubes, made of "pure" calcia-stabilized zirconia, were obtained from Zircoa Incorporated, and were about 4 mm ID, 5 mm OD, and 18 cm long. Inside and outside electrodes consisted of silver paste (Engelhard Industries) fired on at  $800^\circ\text{C}$  in two applications. A  $\frac{1}{4}$  in. nickel bellows was attached to the far end of the electrolyte tube to avoid damage to the latter by stress or shock.

A temperature regulator kept the temperature constant to about  $1^\circ\text{C}$ . Too large temperature fluctuations must be avoided because they induce changes in the cell current. Cell temperatures varied from  $750^\circ$  to  $850^\circ\text{C}$  with  $830^\circ$  later used as the preferred temperature. To extend the life of the silver electrodes  $650^\circ\text{C}$  was chosen as a "standby" temperature. A Tacussel potentiostat provided initially the constant voltage be-

Table I. Current-voltage characteristic of cell II,  $800^\circ\text{C}$ ,  $5.5 \text{ cm}^3/\text{min}$ , 3.23%  $\text{O}_2$

Applied voltage $E$ , mV	Current $i$ , mA
200	15.0
400	34.5
500	44.5
600	53.0
700	62.0
800	64.0
900	64.0
1000	64.5

tween the electrodes. Later we used a homemade potentiostat which was built into the current integrator. The preferred voltage chosen in the later experiments was 750 mV. A Moseley recorder connected across a 10 ohm standard resistor was used as a current monitor.

### Results and Discussion

The first results were obtained with a 3.23%  $\text{O}_2$  in He mixture, corresponding to a  $p/p^\circ = 0.15$ . In the later experiments, another electrolyte tube was used (requiring a slightly higher temperature and voltage of operation) and a 6.7%  $\text{O}_2$  mixture, corresponding to a  $p/p^\circ = 0.33$ . It is important that the cells are operated at a high enough temperature and voltage and a low enough flow rate so that the entire oxygen content of the mixture is removed on pumping the cell. When choosing too high a voltage, the measured current may become too high due to incipient electronic conduction of the electrolyte. As an example, in Table I, the current-voltage characteristic of the second cell used is given for a flow of  $5.5 \text{ cm}^3/\text{min}$  of the 3.23%  $\text{O}_2$  mixture with a cell temperature of  $800^\circ\text{C}$ .

It may be seen that up to 700 mV, the current increases rapidly. In this range, the current is determined by the cell resistance and, to a lesser extent, by cell polarization due to the difference in oxygen potential at the two electrodes. At about 800 mV, the current has reached a constant value corresponding to complete removal of the oxygen. This is the minimum voltage at which the cell must be operated if the cell temperature of  $800^\circ\text{C}$  is chosen.

Figure 3 shows a plot for the same cell at  $830^\circ\text{C}$  obtained at a constant voltage of 750 mV with the 6.7% oxygen mixture. Here the current is given as a function of flow rate. The latter was measured by means of a bubble flowmeter attached to the end of the cell. At low flow rates, the current is equal to the faradaic current calculated for the total amount of oxygen passing, as represented by the straight line through the origin. The small deviation of the experimental points, increasing with decreasing flow rates, is probably due to loss of helium in the rubber hose connection to the flowmeter and does not affect the reliability of the electrical measurements. Up to about  $5 \text{ cm}^3/\text{min}$ ,

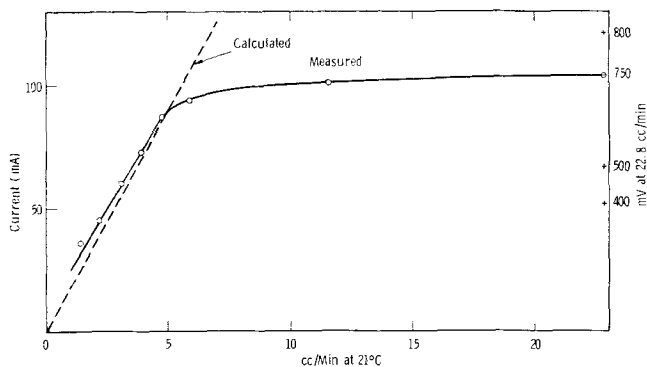


Fig. 3. Plot of cell current vs. flow rate, as determined by a bubble flowmeter, at 750 mV for 6.7%  $\text{O}_2$  in He. Cell temperature  $820^\circ\text{C}$ . Maximum currents at other voltages are given at  $22.8 \text{ cm}^3/\text{min}$  flow. Dashed line is calculated faradaic current.

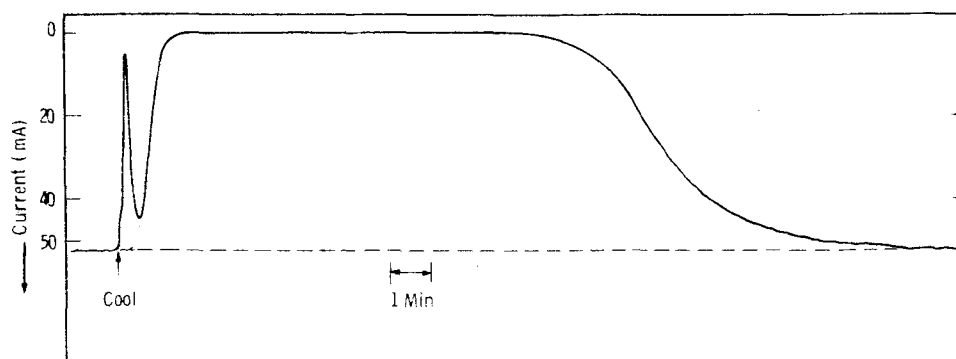


Fig. 4. Current-time recording for 7.5 mg Nuchar charcoal (7.38 m<sup>2</sup>, 980 m<sup>2</sup>/g, 3.23% O<sub>2</sub>, Exp. No. 9 in Table II).

the current represents the true flow rate under the given conditions. This is the region in which the cell should be operated. In the surface area determinations, the flow rate was generally adjusted so as to give a current about 25% below the maximum current at the chosen voltage.

At the right hand margin of Fig. 3, the voltage-current relationship is indicated for the constant flow rate of 22.8 cm<sup>3</sup>/min. At this high flow rate, the current appears to be limited essentially by the electrolyte resistance, about 7-8 ohms at 830°C, decreasing somewhat with current due to heating at the electrolyte-electrode contacts. There is no appreciable limitation of the oxygen diffusion in the gas phase or in the electrode, as may also be concluded from the sudden changes in slope from the oxygen limited to the resistance limited region. This is probably helped by the choice of helium as a diluent for the oxygen and of silver as an electrode material.

Some of the results of surface area determinations are presented in Table II. In the first series, up to Exp. No. 11, experiments were performed with the first cell at 800°C, with 3.23% oxygen, and at a voltage of 0.6V. In the subsequent experiments, the voltage and temperature had to be raised, as already discussed, due to a larger electrolyte resistance connected with poorer silver coverage of the electrolyte tube. The higher oxygen concentration (6.7%) used here helps to decrease the error involved in the one-point approximation (see section below). In columns 1 to 10, results with the present method are given. In columns 11 to 13, results with the complete BET method are presented, as obtained by Kr-adsorption (except for Co<sub>3</sub>O<sub>4</sub> which was also measured with oxygen, Exp. No. 15). The base current is given in column 7. With the 3.23% O<sub>2</sub> mixture, the flow rate at room temperature is 0.119

cm<sup>3</sup>/min per milliampere base current, and with the 6.7% O<sub>2</sub>, it is 0.056 cm<sup>3</sup> min<sup>-1</sup> mA<sup>-1</sup> (cf. Fig. 3). The charge given in column 8 is obtained by integration of the area between the second current minimum and the base current (the shaded area in Fig. 2); it was carried out in the earlier experiments by marking the recording on a cellophane film and weighing the cut-out. The electronic integrator used in the last experiments typically yielded surface area values in agreement with those obtained by weighing to better than 2%.

In the first experiments, different powders were measured ranging in specific surface area from 0.6 to 1100 m<sup>2</sup>/g. The weight of the samples used in the measurements varied from 7.5 to 250 mg, and the actual surface areas varied from 0.06 to 7.4 m<sup>2</sup>. It may be seen from the table that throughout the wide range of surface areas, there is agreement between the results obtained by the two methods (columns 10 and 13) to within about 15-30%, except for the smallest area where our measured value is about 50% higher. As will be shown, the largest part of the (generally not serious) discrepancy is due to the difference in pretreatment of the samples before the measurements, stated in columns 5, 6, 11, and 12 and not due to the methods themselves.

Figures 4 and 5 show the current recording for two extremes of surface area. In Fig. 4, 7.5 mg of "Nuchar" charcoal was measured (Exp. No. 9 in Table II). The integrated area represents a charge of 39.7 A-sec and a calculated area of 7.38 m<sup>2</sup>/g. The separation of the two minima is obviously no problem here and also for smaller areas. A similar recording for 104 mg Co<sub>3</sub>O<sub>4</sub> I is shown in Fig. 5 (Exp. No. 7 in Table II). The integrated area gives a charge of 0.03 A-sec, which corresponds to an area of only 0.06 m<sup>2</sup>. The overlap between the two minima is here considerable, and the area cor-

Table II. Surface area measurements

Exp. No.	Material	Amount, g	O <sub>2</sub> Conc., %	Furnace temp., °C	Pretreatment Temp., °C	Time, min	Base-current, mA	Charge q, A-sec	Area, m <sup>2</sup>	Spec. area, m <sup>2</sup> /g	Kr-BET area		
											Pretreated in vacuo °C	Spec. area, m <sup>2</sup> /g	
Cell I 0.60V													
4	CoFe <sub>2</sub> O <sub>4</sub>	0.254	3.23	800	60	5	60	1.17	0.218	0.86	140	2340	1.17
7	Co <sub>3</sub> O <sub>4</sub> I	0.104	3.23	800	65	1000	54	0.33	0.06	0.6	140	900	0.40
8	Co <sub>3</sub> O <sub>4</sub> II	0.175	3.23	800	80	60	53	7.30	1.36	7.75	140	2340	10.5
9	Nuchar charcoal C-115N	0.0075	3.23	800	180	60	73	39.7	7.38	980	?	?	~1100
11a	Bone char	0.050	3.23	800	200	60	67	16.5	3.06	61.2	?	?	70
11b		0.050	3.23	800	25	60	33	15.2	2.84	56.8			
11c		0.050	3.23	850	~50	10	80	18.0	2.98	59.5			
Cell II 0.75V													
12a	CoFe <sub>2</sub> O <sub>4</sub>	0.415	3.23	830	~25		55	1.84	0.304	0.73	140	2340	1.17
12b		0.415	6.7	830	~25		55	2.20	0.322	0.77			
15	Co <sub>3</sub> O <sub>4</sub> II	0.174	6.7	830	150	60	78	10.6	1.55	8.9	With O <sub>2</sub> : 150	90	10.4
16a	Bone char	0.0497	6.7	830	25	900	72	18.2	2.68	54.0	25	15	9.05
16b					190	120		18.5*					
16c					340	25		20.3	2.96	59.7		?	70
17	CoFe <sub>2</sub> O <sub>4</sub>	0.347	6.7	830	250	900	74	23.1	3.48	68.0	140	2340	1.17
								2.34	0.339	0.98			
								2.30*					

\* Values obtained by weighing cut-out area and by integrating device respectively.

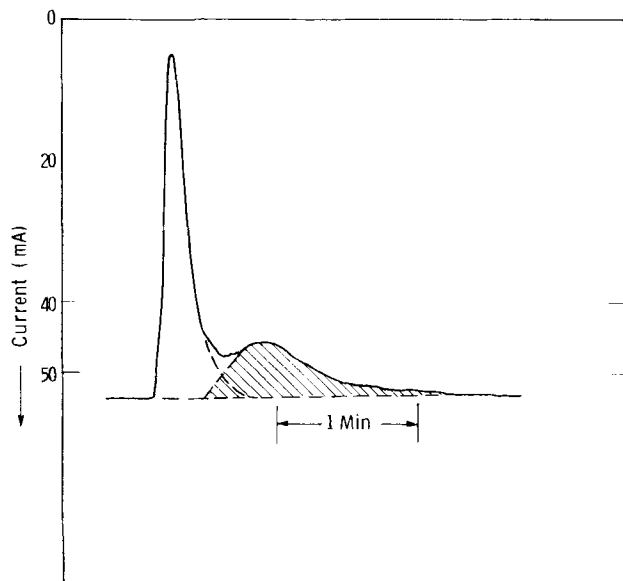


Fig. 5. Current-time recording for 104 mg  $\text{Co}_3\text{O}_4$  ( $0.06 \text{ m}^2$ , 3.23%  $\text{O}_2$ , Exp. No. 7 in Table II).

responding to oxygen adsorption is therefore relatively uncertain. The calculated value appears too high by about 50%. Nevertheless, if one is only concerned with the correct order of magnitude of the area, it is possible to estimate areas of the order of  $0.01 \text{ m}^2$ . It is important that the cooled volume be kept small, about  $1 \text{ cm}^3$  or less, otherwise the first minimum becomes too broad and covers up the second minimum.

It may be possible to narrow down further the first minimum by redesigning the reaction vessel and using a thinner glass to improve the rate of heat transfer. Optimization of the design may lead to improvement of the accuracy of measurement of low surface areas, but also to an extension of the range of measurement to below  $100 \text{ cm}^2$ . This would surpass the conventional BET method in range of applicability. Measurement of low areas of this order of magnitude have been claimed; but the reliability is open to doubt. The reason is that in a conventional adsorption experiment the amount adsorbed on a small surface is the small difference between two larger quantities, *viz.*, (gas volume plus adsorbed volume) minus gas volume. The significance of the calculated difference is not easy to judge. In the present method inspection of the curve gives an immediate idea of the significance of the measurement.

**Effect of pretreatment.**—Most of the discrepancy in the surface areas obtained by the two methods (cf. columns 10 and 13 in Table II) is due to the difference in pretreatment of the samples before measurement.

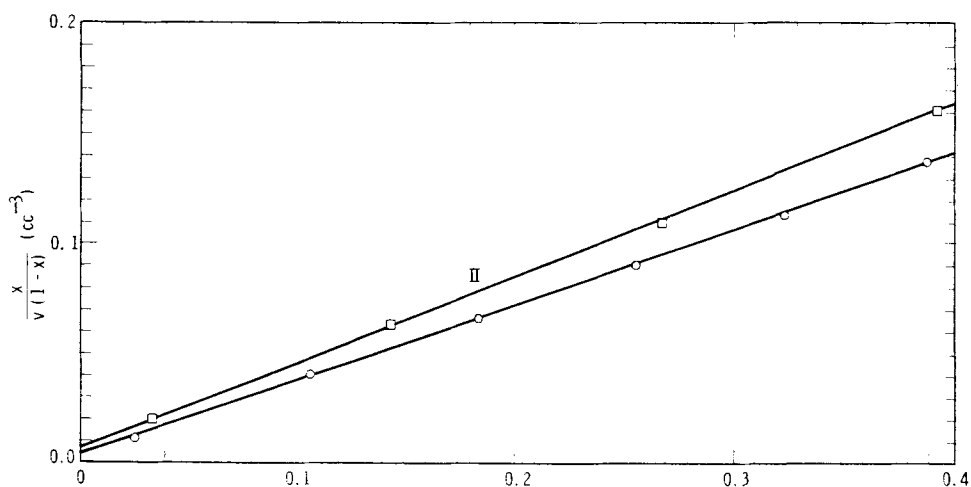
The values in column 13 were obtained by the complete BET method with krypton after pumping, mostly for prolonged periods (15–40 hr) and at an elevated temperature ( $\sim 140^\circ\text{C}$ ). This is a much more rigorous degassing treatment than was applied with our samples in the first experiments. Even when applied for the same temperature and time, removal of vapor from the pores of solids in a gas stream is not as rigorous as in a vacuum. A considerably higher temperature would have to be applied to obtain the same cleaning effect. The values obtained after prolonged degassing at a high temperature are not necessarily more meaningful than those obtained after milder degassing. The surface of the micropores bared by the rigorous degassing usually is of no interest, except when the powders are to be used as adsorbents.

The increase in apparent surface area on increasing the pretreatment temperature of the cobalt ferrite may be seen on comparing the results in Exp. No. 12 ( $25^\circ$ ), No. 4 ( $60^\circ$ ), and No. 17 ( $250^\circ$ ). Similarly, in Exp. No. 16, a bonechar was tested after pretreatment at increasingly higher temperatures. It was supplied by the Micromeritics Company as a standard having a surface area of  $70 \text{ m}^2/\text{g}$ . The pretreatment temperature used by the company is not known. As may be seen, the value of  $68 \text{ m}^2/\text{g}$  is reached after degassing in the 6.7%  $\text{O}_2$ -He mixture for 15 hr at  $340^\circ\text{C}$ ; this is in agreement with the given value to within 3%.

With  $\text{Co}_3\text{O}_4$  II (cf. Exp. No. 15), the complete isotherm was also determined with oxygen as the adsorbate and after two different pretreatments in a vacuum. The BET plots, in accordance with Eq. [3], are shown in Fig. 6. Two good straight lines were obtained, the lower one after degassing 90 min at  $150^\circ$ , the upper one after exposure to air overnight and evacuation at room temperature for 15 min. The respective surface areas were  $10.4 \text{ m}^2/\text{g}$  (in good agreement with the value obtained with krypton as adsorbate, cf. Exp. No. 8) and  $9.05 \text{ m}^2/\text{g}$ . The lower value is in good agreement with the  $8.9 \text{ m}^2/\text{g}$  obtained by our method after pretreatment in a gas stream at  $150^\circ\text{C}$  for 60 min.

**Error involved in the one-point method.**—The error involved in using the one-point approximation (cf. theoretical section) depends on the value of  $c$ , which is a measure of the strength of interaction of the oxygen with the substrate, as well as on the chosen value of  $x$ . For the two lines in Fig. 6, the  $c$  values are 120 for the larger surface area (lower line) and 80 for the smaller area. By comparing the expressions for the monolayer gas volume  $V_m$  in Eq. [3] and [4], one finds that the fractional error involved in the approximation is  $(1-x)/(1-x+cx)$ . For  $c$  values of 100, use of the 3.2% oxygen mixture ( $x = 0.15$ ) gives an error of

Fig. 6. BET plots for oxygen on  $\text{Co}_3\text{O}_4$  (Exp. No. 15, Table II). I: after degassing at  $150^\circ\text{C}$ , 90 min in vacuo; II: after evacuating at room temperature for 15 min.



5.4%, while for the 6.7% oxygen ( $x = 0.33$ ), as used in the later experiments, the error is only 2.0%.

The  $c$  values of about 100 are in the range usually encountered. The higher the value of  $c$ , the less the error involved in the approximation. It is not known what the lowest  $c$  value could be, but it probably will not be so low as to cause a considerable error in the method. With rare gases like krypton, low values have occasionally been observed (6), but this is not likely to occur with oxygen.

The experience with oxygen as an adsorbate is so far limited, but we do not foresee any difficulties. The agreement for  $\text{Co}_3\text{O}_4$  (Exp. No. 15 and 8, Table II) with the krypton value for equal pretreatment is excellent.

Conventional BET adsorption measurements are usually not made with oxygen because of the possibility of additional oxygen uptake at liquid nitrogen temperature due to chemisorption after pretreatment of the sample in a vacuum. This difficulty does not arise in the present case because, if chemisorption is possible, it will occur at the higher temperatures before cooling and will not interfere with the physical adsorption at liquid nitrogen temperature.

The accuracy to within a few per cent attainable by the described method is amply adequate for most practical purposes.

### Acknowledgment

The author is indebted to R. M. Garretson for carrying out the surface area measurements by the conventional BET method.

Manuscript submitted Aug. 27, 1973; revised manuscript received Feb. 6, 1974.

Any discussion of this paper will appear in a Discussion Section to be published in the December 1974 JOURNAL. All discussions for the December 1974 Discussion Section should be submitted by Aug. 1, 1974.

### REFERENCES

1. cf. P. H. Emmett, "Catalysis," Vol. I, p. 31, Reinhold Publishing Corp., New York (1954).
2. P. H. Emmett, "Catalysis," Vol. I, p. 39, Reinhold Publishing Corp., New York (1954).
3. J. Weissbart and R. Ruka, *Rev. Sci. Instr.*, **32**, 593 (1961).
4. D. Yuan and F. A. Kroger, *This Journal*, **116**, 594 (1969).
5. S. Brunauer, P. H. Emmett, and E. Teller, *J. Am. Chem. Soc.*, **60**, 309 (1938).
6. G. L. Gaines, Jr. and P. Cannon, *J. Phys. Chem.*, **64**, 1000 (1960).

## Application of Current-Reversal Chronopotentiometry to the Study of Electrolytic Reductive Coupling

Steven C. Rifkin and Dennis H. Evans

Department of Chemistry, University of Wisconsin, Madison, Wisconsin 53706

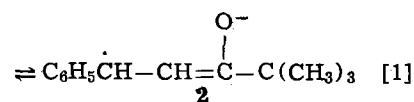
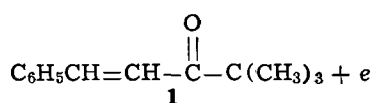
The publication costs of this article have been assisted by the National Science Foundation.

### ABSTRACT

A current-reversal chronopotentiometric technique has been developed to facilitate the determination of the reaction pathway of radical anions generated during electrolytic reductive coupling reactions. The technique permits discrimination between dimerization of the anion radicals and a reaction scheme involving reaction of a radical anion with unreduced starting material followed by one-electron reduction. The reduction of *trans*-4,4-dimethyl-1-phenyl-1-penten-3-one was studied at mercury cathodes in dimethylsulfoxide with a tetra-*n*-butylammonium perchlorate as supporting electrolyte. In the presence of 0.05M water, the reaction proceeds by dimerization of the anion radicals. At higher water concentrations a parallel pseudo first-order reaction of the radical anions was detected.

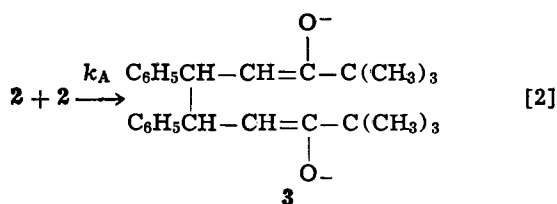
In an earlier study of the electrolytic reductive coupling of various  $\alpha,\beta$ -unsaturated ketones (1), conditions were established under which the reduction proceeded in an over-all one-electron process giving good yields of the  $\beta$ - $\beta$  coupled dimers. In particular, it was found that *tert*-butylstyrylketone, 1 (*trans*-4,4-dimethyl-1-phenyl-1-penten-3-one) formed good yields of dimer when reduced in dimethylsulfoxide (DMSO) and was less susceptible to polymerization side reactions than were less hindered enones. Therefore, the reduction of 1 was thoroughly studied using cyclic voltammetry. Though these studies demonstrated clearly that the primary electrode reaction was the reversible, one-electron reduction of 1 to its radical anion, 2, the

exact pathway for the subsequent reactions of 2 could not be determined (1)

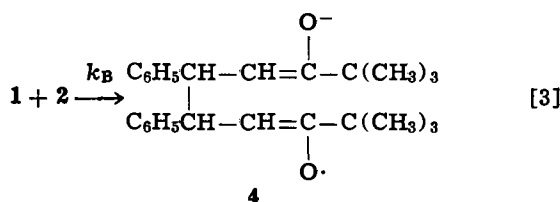


Two schemes were envisioned for the reactions of the radical species 2. The first, referred to in this paper as scheme A, involved the direct dimerization of 2 to form product, 3

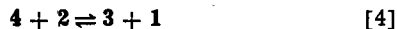
Key words: reductive coupling, electrohydrodimerization,  $\alpha,\beta$ -unsaturated ketones, current-reversal chronopotentiometry.



The second scheme (scheme B) envisioned the reaction of the radical anion, 2, with a molecule of the parent, 1, to give the dimeric radical anion, 4.



Since species 4 is assumed to be reducible at a more positive potential than 1, it immediately gains an electron at the electrode surface thereby decreasing the portion of the total flux utilized for the reduction of 1 by the amount necessary to maintain the surface concentration of 4 at zero. It is also possible instead, that species 4 gains the electron in the solution via electron transfer from 2



Peak current ratios in cyclic voltammetry or double potential step chronoamperometric data (2) are very similar for schemes A and B making experimental discrimination between the two very difficult.

Petrovich, Baizer, and Ort (3) favored scheme B as the predominant pathway in the reductive coupling of activated olefins. However, most of their cyclic voltammetric data can be explained by direct dimerization as in scheme A (1).

Recently Bard and Puglisi (4) published results of their studies of the reductive coupling of several activated olefins. They employed a rotating ring-disk electrode and concluded scheme A was much more important than scheme B. The same conclusion was reached by Lamy, Nadjo, and Saveant (5) in their studies of the reduction of various olefinic nitriles, esters, and ketones using linear sweep voltammetry. These workers based their conclusions on the observed dependence of the peak potentials upon the scan rate and substrate concentration.

The present study examines the electrohydrodimerization of 1 using a still different technique, current-reversal chronopotentiometry.

### Experimental

**Reagents.**—Dimethylsulfoxide (Matheson Coleman and Bell, Spectroquality) was usually used as received. When lower water content was desired, it was dried over molecular sieves (Matheson Coleman and Bell, Type 4A, 4-8 mesh) for several days before use. Tetra-*n*-butylammonium perchlorate, TBAP (Matheson Coleman and Bell) was used as received. Occasional inferior batches were reprecipitated from ethanol-water. Pre-purified nitrogen (Airco, Inc.) was used for solution deaeration.

The compound 1 was prepared by condensation of benzaldehyde with 3,3-dimethyl-2-butanone followed by recrystallization from ethanol-water.

**Apparatus.**—The electrochemical cell was similar in design to the Type 1 Polarographic Cell available from Princeton Applied Research Corporation (PAR). A hanging mercury drop electrode utilizing a mercury-coated platinum wire support (6) was used as the working electrode. The electrode area was 0.047 cm<sup>2</sup>. For this electrode the spherical correction to the transition time (7) will be less than 5% for times less

than 4 sec. The diffusion coefficient of 1 used in this calculation was  $3.6 \times 10^{-6}$  cm<sup>2</sup>/sec (1). In the work reported herein, the total electrolysis times did not exceed 2 sec.

A PAR Model 170 Electrochemistry System was the constant current source. Timing circuits within the instrument were used to control the time of current reversal. Since the procedure for initializing the PAR 170 programmer to accomplish this is not given in the manufacturer's instructions, it will be described here. With the programmer set for pulse excitation, the length of the forward electrolysis is given by the pulse duration. The final full scale current control gives the current for the forward electrolysis period and the initial full scale current control gives the current after the reversal. The experiment is initiated by switching the control keyboard from initial to final. This means that anodic current is flowing before the experiment is initiated. This anodic current was exactly compensated by a variable d-c power supply attached directly to the cell in parallel to the output of the PAR 170. The external power supply was varied until the initial potential was about 200 mV positive of the chronopotentiometric wave. This power supply was manually switched out of the circuit just prior to initiating the chronopotentiometric experiment.

The potential-time transients were recorded on a Tektronix Type 564 storage oscilloscope using a Model C-12 camera. Electrochemical measurements were made at  $23^\circ \pm 2^\circ\text{C}$ . In separate experiments where the temperature was varied over the range of 25°-40°C, the apparent rate constant increased by almost a factor of two for the 15°C increase in temperature. This corresponds to a temperature coefficient of only about 5% per degree centigrade and justifies the lack of precise temperature control for the major part of the work.

Gas chromatography was employed to determine the water concentration in the DMSO. A Perkin Elmer Model F11 Gas Chromatograph with thermal conductivity detector and a 6 ft Porapak Q column at 125°C was used. Methanol was employed as an internal standard in the water determination.

### Results and Discussion

The reversal of current direction during a controlled current experiment is a useful technique for probing the rate of chemical reactions following electron transfer. A common way to conduct this current-reversal chronopotentiometric experiment is to allow the forward electrolysis to proceed to the transition time before the current direction is changed. If the product of the electron transfer can be reconverted to reactant at the electrode surface, a reverse transition time,  $\tau_r$ , will be observed. Furthermore, if the product is stable, the ratio of the reverse transition time to the forward electrolysis time,  $t_1$ , is always 1/3 when forward and reverse currents are of equal magnitude (8). The  $\tau_r/t_1$  ratio is independent of  $t_1$ , where  $t_1$  is less than or equal to  $\tau_f$ , the forward transition time.

The rigorous solution for the case of a first-order following reaction producing electro-inactive product (9,10) demonstrates a dependence of  $\tau_r/t_1$  on  $k_1 t_1$  where  $k_1$  is the first-order rate constant. However, at constant  $k_1 t_1$ , the ratio is independent of  $t_1/\tau_f$ . Although no rigorous solution is available for second-order following reactions such as reactions [2] and [3], qualitative considerations lead one to suspect a dependence of  $\tau_r/t_1$  on  $t_1/\tau_f$  (at constant  $k_2 C^* \tau_f t_1$ , where  $k_2$  is the second-order rate constant and  $C^*_0$  is the bulk concentration of the starting material). Furthermore, a distinctly different dependence is anticipated for schemes A and B.

Control of the time of reversal affects the concentration profiles of the various species. During experiments with reversals made at low  $t_1/\tau_f$  values, concentrations of the parent species, 1, in the vicinity of the electrode remain relatively high whereas the con-

centrations of the radical anion, 2, are still quite small. If scheme B is followed, the shortening of the reverse transition time should be greater than if scheme A occurs. Mechanism B requires parent, 1, to react with the electrochemically produced radical anion, 2. Early in the electrolysis, abundant 1 is present with which 2 can react. As  $t_1/\tau_f$  approaches one, the opposite is true. Scheme A will have a greater effect on  $\tau_r/t_1$  than scheme B since the concentration of 2 is greater than the concentration of 1.

To test these assumptions, digital simulations were undertaken for each mechanism. The technique of Feldberg (11) was used to obtain theoretical curves of  $\tau_r/t_1$  vs.  $t_1/\tau_f$  at different values of  $k_A C^*_{ot1}$  and  $k_B C^*_{ot1}$ . In these simulations, diffusion coefficients were assumed equal, electrode geometry was planar, and the ratio of reverse to forward current densities was taken as 1/2. This value was chosen as a compromise between two competing effects. While a lower value of the reverse current enhances the relative difference in  $\tau_r/t_1$  between schemes A and B, it also leads to distorted potential-time curves during the reverse electrolysis due to the fact that a relatively large fraction of the current is being used to charge the electrical double layer. The former effect is useful but the latter aggravates the already difficult task of accurately measuring  $\tau_r$ .

The rate law for reaction [2] was defined as  $d[2]/dt = -2k_A[2]^2$  while that of reaction [3] was  $d[2]/dt = d[1]/dt = -k_B[2][1]$ . Some of the theoretical curves are shown in Fig. 1 and 2.

The most dramatic difference between the two sets of curves is the opposite sign of the slopes. For scheme A,  $\tau_r/t_1$  tends to decrease as  $t_1/\tau_f$  increases whereas for scheme B the opposite tendency is predicted. This very distinct difference simplifies the experimental determination of which scheme is operative.

The simulations of scheme B did not include solution reaction [4], the "ECE nuance" (12). When reaction [4] was included as a rapid reaction always in equilibrium, only minor differences were observed,  $\tau_r/t_1$  changing a few per cent. Small variations were also obtained when the diffusion coefficients of dimeric species in scheme B were set equal to half the diffusion coefficients of monomeric species.

A second difference between the two sets of curves is the steepness at low  $t_1/\tau_f$ . Those for scheme A drop rapidly, while those for scheme B maintain almost

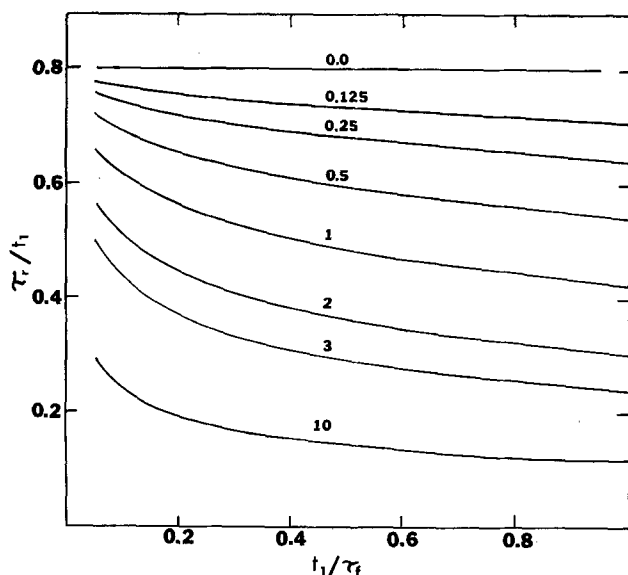


Fig. 1. Digital simulation for scheme A. Ratio of reverse transition time to forward electrolysis time as a function of the ratio of forward electrolysis time to forward transition time for various values of  $k_A C^*_{ot1}$  (numbers on curves). Ratio of reverse to forward current densities was 1/2.

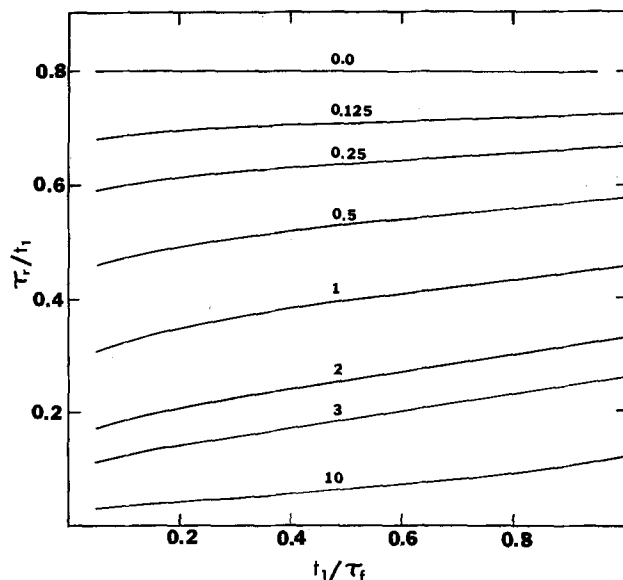


Fig. 2. Digital simulation for scheme B. See Fig. 1 for definition of terms. Numbers on curves are  $k_B C^*_{ot1}$ .

the same slope throughout. In both sets, the calculated  $\tau_r/t_1$  ratio becomes smaller at  $k C t_1$  increases. As the reaction becomes faster, the concentration higher, or the forward electrolysis time longer, the extent of the following reaction increases and  $\tau_r/t_1$  decreases.

The upper curve in Fig. 3 shows how the determinations of  $t_1$  and  $\tau_r$  were made from an experimental potential-time curve. Lines A and B were drawn along the steep portions of the curve. These regions correspond to almost all of the applied current being used to charge the double layer. Lines C and D were drawn along the two electrolysis regions of the curve. Line E was constructed perpendicular to the time axis and through the point of current reversal. Finally, line F was drawn to pass through the point of reversal and have a slope equal to  $-1/2$  of the slope of line A. The horizontal distance between the intersection of lines A and C and line E was taken to be  $t_1$ . The horizontal distance between the intersection of lines B and D and line F was taken as  $\tau_r$ .

Separate experiments were performed to determine  $\tau_f$ . The data analysis illustrated in the lower curve of Fig. 3 is that of Reinmuth (13) where  $\tau_f$  is taken as the horizontal distance between line G and the intersection of lines H and I. Several determinations of  $\tau_f$  were made at differing current densities. From these

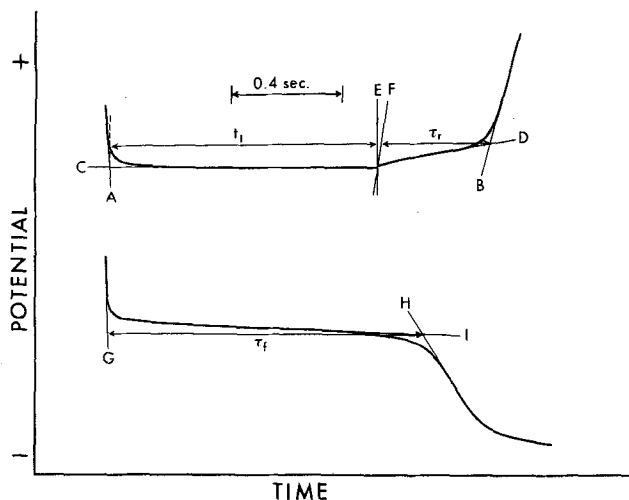


Fig. 3. Top, determination of  $t_1$  and  $\tau_r$ . Current:  $6.32 \mu A$  in forward direction,  $3.16 \mu A$  in reverse direction. Bottom, determination of  $\tau_f$ . Current:  $11.90 \mu A$ . Concentration of 1:  $1.63 \text{ mM}$  (both curves).

an average value of  $i\tau_f^{1/2}$  was computed. The standard deviation of this number was always less than 5%. This average was then used to calculate the  $\tau_f$  for the current densities used in the current-reversal experiments. Using the  $t_1$  and  $\tau_f$  values obtained as in Fig. 3, a point on the  $\tau_f/t_1$  vs.  $t_1/\tau_f$  curve could be plotted. The experimental points shown in this paper are averages of at least two and usually three or more determinations of  $\tau_f/t_1$ .

The experimental data shown in Fig. 4 were obtained using a 1.63 mM solution of 1 and a nominal  $t_1$  of 1 sec. The curve is theoretical for scheme A with  $k_{AC}^*ot_1$  equal to 2.24. For the conditions of the experiment, this corresponds to a second-order rate constant of  $1.4 \times 10^3$  liter  $\cdot$  mole $^{-1} \cdot$  sec $^{-1}$ . The general trend of the data in Fig. 4 can leave little doubt that scheme A rather than scheme B is the principal pathway. The value of the rate constant agrees with that found by cyclic voltammetry,  $1.3 \times 10^3$  liter  $\cdot$  mole $^{-1} \cdot$  sec $^{-1}$  (1). [Due to a different form of the rate law used in the theoretical paper (14), the value given in Ref. (1) must be divided by two to be equivalent to the rate constants reported in this paper.]

Strictly speaking, it can only be reported that the data fit a model in which 2 reacts by an irreversible reaction which is second order in 2. This reaction could be dimerization [2] or any other reaction scheme whose over-all rate law was second order in 2. For example, reaction 2 could enter into a rapid equilibrium with a small amount of 3 which in turn underwent irreversible protonation. This scheme also has a rate law which is second order in reaction 2.

It was found earlier (1) that addition of water caused moderate increases in the apparent value of  $k_A$ . Similar results were obtained in the present work. Current-reversal chronopotentiometric studies of 2.88 mM 1 under the conditions of Fig. 4 again gave  $k_A = 1.4 \pm 0.1 \times 10^3$  liter  $\cdot$  mole $^{-1} \cdot$  sec $^{-1}$ . Addition of 0.05M water caused the apparent  $k_A$  to increase to  $2.2 \times 10^3$  and addition of another 0.05M water gave  $k_A = 2.7 \times 10^3$  liter  $\cdot$  mole $^{-1} \cdot$  sec $^{-1}$ .

Some interesting information concerning the manner in which water affects the reaction is provided by the data presented in Fig. 5. These experiments were performed with a water concentration of 0.10M using three different concentrations of 1 and two different values of  $t_1$ . If the effect of water is one of increasing the apparent rate constant without modifying the order of the rate equation, a single value of  $k_A$  should provide an adequate fit for all the data. This was not found to be the case. This may be seen most clearly

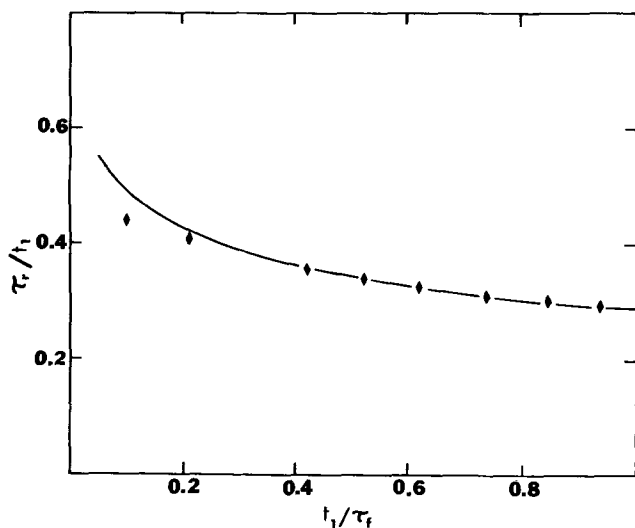


Fig. 4. Current-reversal chronopotentiometric data for reduction of 1.63 mM 1.  $t_1 = 1$  sec. Ratio of reverse to forward current densities was 1/2. Water concentration: 0.05M. Curve is theoretical for  $k_{AC}^*ot_1 = 2.24$ .

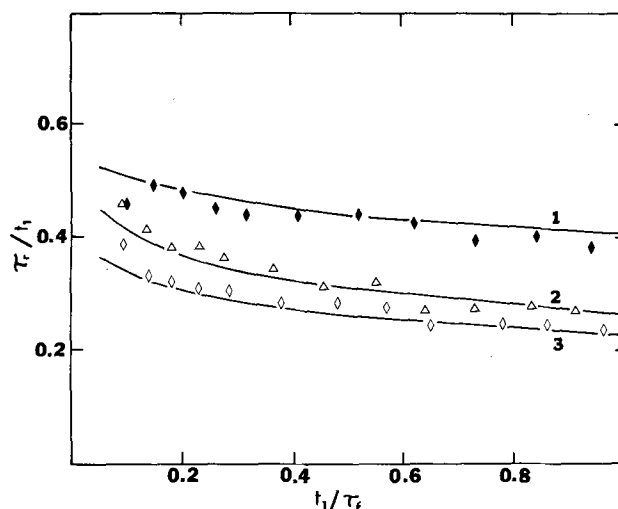


Fig. 5. Current-reversal chronopotentiometric data for reduction of 1 with 0.10M water. Curves are theoretical for  $k_A = 1.35 \times 10^3$  liter  $\cdot$  mole $^{-1} \cdot$  sec $^{-1}$  and a rate constant for parallel first-order reaction of 0.6 sec $^{-1}$ . Curve 1: 1.01 mM 1,  $t_1 = 0.50$  sec; curve 2: 3.03 mM 1,  $t_1 = 0.50$  sec; curve 3: 1.61 mM 1,  $t_1 = 1.00$  sec.

for curves 2 and 3 of Fig. 5 which have almost the same value of  $C^*ot_1$  and which should be almost coincident if the reaction is still simply second order.

To fit the data of Fig. 5, inclusion of an irreversible, first-order chemical reaction of 2 occurring simultaneously with dimerization was required. The curves in Fig. 5 are simulated curves corresponding to a dimerization rate constant of  $1.35 \times 10^3$  liter  $\cdot$  mole $^{-1} \cdot$  sec $^{-1}$  and a first-order rate constant of 0.6 sec $^{-1}$ .

Thus, at moderate water concentrations (about 0.05M as in Fig. 4) the data for various  $C^*o$ ,  $t_1$ , and  $t_1/\tau_f$  indicate that 2 reacts by a second-order process. However, at water concentrations greater than or equal to about 0.10M, some pseudo first-order reaction of 2 must be included. (Inclusion of some scheme B in parallel with scheme A was not successful in fitting the data.)

The nature of the parallel first-order reaction is not known. Water at higher concentrations may affect the reaction by protonating the radical 2 to form a neutral radical which may dimerize quickly. Further reduction of the neutral radical to form a two-electron reduction product does not seem to be prevalent because the value of  $i\tau_f^{1/2}/AC^*o$  does not increase under conditions where the first-order process is dominant. It was also found earlier (1) that reduction of 1 in DMSO containing 6% water was one of the best conditions for obtaining high yields of dimer.

The principal goal of the project was to assess the relative importance of schemes A and B in the reduction of 1. In agreement with studies of the reductive coupling of other activated olefins (4, 5), scheme A was found to be dominant.

#### Acknowledgment

This research was supported by the National Science Foundation, Grant Number GP-19579, and by the Wisconsin Alumni Research Foundation.

Manuscript submitted Oct. 30, 1973; revised manuscript received Jan. 28, 1974.

Any discussion of this paper will appear in a Discussion Section to be published in the December 1974 JOURNAL. All discussions for the December 1974 Discussion Section should be submitted by Aug. 1, 1974.

#### REFERENCES

1. J. P. Zimmer, J. A. Richards, J. C. Turner, and D. H. Evans, *Anal. Chem.*, **43**, 1000 (1971).
2. W. V. Childs, J. T. Maloy, C. P. Keszthelyi, and A. J. Bard, *This Journal*, **118**, 874 (1971).
3. J. P. Petrovich, M. M. Baizer, and M. R. Ort, *ibid.*, **116**, 743 (1969).

4. V. J. Puglisi and A. J. Bard, *ibid.*, **119**, 829 (1972).
5. E. Lamy, L. Nadj, and J. M. Saveant, *J. Electroanal. Chem.*, **42**, 189 (1973).
6. J. W. Ross, R. D. DeMars, and I. Shain, *Anal. Chem.*, **28**, 1768 (1956).
7. P. Delahay, C. C. Mattax, and T. Berzins, *J. Am. Chem. Soc.*, **76**, 5319 (1954).
8. T. Berzins and P. Delahay, *ibid.*, **75**, 4205 (1953).
9. O. Dracka, *Collection Czech. Chem. Commun.*, **25**, 338 (1960).
10. A. C. Testa and W. H. Reinmuth, *Anal. Chem.*, **32**, 1512 (1960).
11. S. W. Feldberg, in "Electroanalytical Chemistry," Vol. 3, A. J. Bard, Editor, pp. 199-296, Marcel Dekker, Inc., New York (1969).
12. S. W. Feldberg and M. D. Hawley, *J. Phys. Chem.*, **70**, 3459 (1966).
13. W. H. Reinmuth, *Anal. Chem.*, **33**, 485 (1961).
14. M. L. Olmstead, R. G. Hamilton, and R. S. Nicholson, *ibid.*, **41**, 260 (1969).

## Chronopotentiometric Investigation of the Oxidation of Aluminum in Chloroaluminate Melts

B. Gilbert,<sup>1</sup> D. L. Brotherton, and G. Mamantov\*

*Department of Chemistry, University of Tennessee, Knoxville, Tennessee 37916*

### ABSTRACT

Oxidation of an aluminum electrode in molten  $\text{AlCl}_3\text{-MCl}$  (63-37 mole per cent, M = Na or Li) has been investigated by chronopotentiometry. Well-defined and reproducible transition times, caused by the formation of a poorly conducting  $\text{Al}_2\text{Cl}_6$  layer at the electrode surface and the depletion of current-carrying alkali metal ions, were observed. The observations are in very good agreement with the theoretical predictions similar to those of Braunstein and co-workers. In the range of current densities employed (up to 300 mA/cm<sup>2</sup> at 140°C), the aluminum electrode behaves reversibly.

It has been very recently shown by Braunstein and co-workers (1) that in molten alkali metal fluoride-beryllium fluoride mixtures, the chronopotentiometric oxidation of a beryllium anode results in a layer of nearly pure, almost nonconductive  $\text{BeF}_2$  as the mobile alkali metal ions are swept away, and, as the result, the potential of the beryllium anode rises sharply.

The important feature of this phenomena is that the boundary conditions of the diffusion law are not determined by depletion of an electroactive constituent but by migration of the mobile nonelectroactive alkali metal ion. A theoretical treatment based on the concentration cell principle was developed to explain the observed chronopotentiograms.

An aluminum electrode in molten  $\text{AlCl}_3\text{-MCl}$  (M-alkali metal ion) melts should exhibit similar behavior. Holleck and Giner (2) have observed passivation phenomena in the anodic oxidation of an Al electrode in  $\text{AlCl}_3\text{-KCl-NaCl}$  melts between 100° and 160°C. The phenomena were attributed to the formation of a solid salt layer at the electrode surface, resulting from concentration changes upon current flow.

We were interested in exploring quantitatively the anodization of an Al electrode by applying the theory developed by Braunstein (1). Besides being of fundamental interest, the results of such a study are clearly of importance to the use of Al anodes in chloroaluminate melts, for example, in battery applications (3).

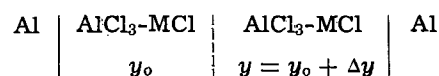
### Experimental

The electrochemical cell, instrumentation, and procedure have been described previously (4, 5). An aluminum wire (m5N from Alfa Inorganics) immersed in molten  $\text{AlCl}_3\text{-MCl}$  [63-37 mole per cent (m/o)] was used as the working electrode (surface area  $\approx 0.1$  cm<sup>2</sup>). The reference electrode was an aluminum wire (m5N) immersed in the same melt composition and separated from the main compartment by a thin Pyrex membrane. A platinum wire electrode was used to check the purity of the melt by cyclic voltammetry.

Each melt was clear and waterlike at the beginning of each experiment. After several days, the melt became slightly brown and frequently the Al electrode was covered with a black deposit, possibly a layer of aluminum metal-rich alumina caused by oxyanions coming from the Pyrex glass (6). At this point, the measurements were no longer reproducible and were not included.

### Basic Relationships

The controlled current oxidation of an Al electrode increases the concentration of  $\text{AlCl}_3$  (more correctly  $\text{Al}_2\text{Cl}_6$ ) in the vicinity of the electrode and the reversible emf should correspond to the resulting concentration cell



Such a cell should exhibit an emf corresponding to (1, 7)

$$E = \frac{1}{3F} \int_{y_0}^y (1 - t_{\text{Al}^{3+}}) \left( \frac{1 + 2y}{1 - y} \right) \frac{d\mu_{\text{AlCl}_3}}{dy} dy \quad [1]$$

where  $y$  and  $\mu$  are the stoichiometric mole fraction and chemical potential of  $\text{AlCl}_3$ , respectively,  $y_0$  is the initial stoichiometric mole fraction of  $\text{AlCl}_3$ , and  $t_{\text{Al}^{3+}}$  is the transference number of  $\text{Al}^{3+}$ .

If we assume that the transference number of  $\text{Al}^{3+}$  is essentially zero, the only current carrying species (relative to chloride) is the alkali metal cation and the emf becomes

$$E = \frac{RT}{3F} \left[ \ln \frac{y}{(1 - y)^3} - \ln \frac{y_0}{(1 - y_0)^3} + \int_{y_0}^y \left( \frac{1 + 2y}{1 - y} \right) \frac{d \ln \gamma_{\text{AlCl}_3}}{dy} dy \right] \quad [2]$$

where  $\gamma$  is the activity coefficient of  $\text{AlCl}_3$  corresponding to above concentration units. The standard state in this case is similar to that employed by Hitch and Baes (8) and corresponds to pure molten  $\text{AlCl}_3$ .

\* Electrochemical Society Active Member.

<sup>1</sup> Permanent address: University of Liege, Belgium.

Key words: molten halides, molten chloroaluminates, chronopotentiometry, aluminum oxidation in melts.



The first two terms in Eq. [2] give the ideal emf; the third term corresponds to the "excess" emf which may be calculated if the variation of the activity coefficient with stoichiometric mole fraction is known.

Similar equations can be developed for other systems, and, in general, for a system  $M + nX^- \rightleftharpoons MX_n$ , the emf is given by

$$E = \frac{1}{nF} \int_{y_0}^y (1 - t_{Mn+}) \left[ \frac{1 + (n-1)y}{1-y} \right] \frac{d\mu_{MX_n}}{dy} dy \quad [3]$$

which gives, if  $t_{Mn+} = 0$

$$E = \frac{RT}{nF} \left\{ \ln \frac{y}{(1-y)^n} - \ln \frac{y_0}{(1-y_0)^n} + \int_{y_0}^y \left[ \frac{1 + (n-1)y}{1-y} \right] \frac{d \ln \gamma_{MX_n}}{dy} dy \right\} \quad [4]$$

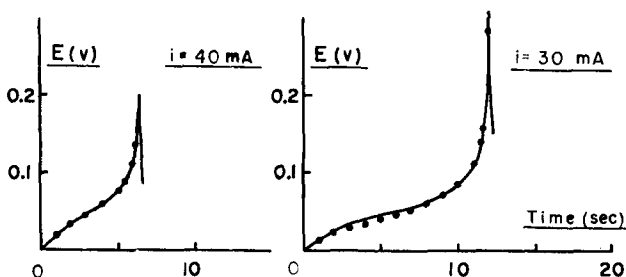
Thus, the emf of the cell does not follow the usual Nernst type behavior. However, as shown previously (1), it is possible to obtain the variation of concentrations of  $MCl$  and  $AlCl_3$  at the electrode surface with time from the solution of the diffusion equation for ordinary chronopotentiometry. These quantities can be substituted into Eq. [2], as shown below, to obtain the variation of cell emf with time, and, thus, the chronopotentiogram. Sand's equation (9) should be applicable (1).

### Results

To obtain well-defined and reproducible chronopotentiograms it was necessary to set the potential of the aluminum electrode to the initial equilibrium potential after each chronopotentiogram. In order to get reasonable transition times, high ( $\sim 200^\circ C$ ) and low ( $\sim 120^\circ C$ ) temperatures must be avoided. At these temperature extremes the transition times are either much too long (several minutes) or too short (the passivating layer forms very quickly), respectively. If the above conditions are followed, the reproducibility of transition times is better than 5%.

Typical chronopotentiograms are shown in Fig. 1. The potential of the aluminum electrode was corrected for the initial  $IR$  drop. The applicability of Sand's equation is shown in Fig. 2. Each point is an average of 5-8 measurements. The constancy of the product  $it^{1/2}$  shows clearly that in the range investigated, the oxidation process is controlled by diffusion. This conclusion supports the results of Holleck, obtained from measurements of the anodic limiting current of a rotating aluminum electrode (2).

The "ideal" emf in Eq. [2] expressed in terms of equivalent concentrations, becomes



$t = 140^\circ C$   
 $A = 0.2 \text{ cm}^2$   
 $AlCl_3\text{-}NaCl (63\text{-}37 \text{ mole } \%)$

Fig. 1. Typical chronopotentiograms obtained in molten  $AlCl_3\text{-}NaCl$  (63-37 m/o) at  $140^\circ C$ . The points correspond to the calculated curve based on an ideal behavior (Eq. [5]). The experimental curves were corrected for the  $IR$  drop. The applied currents are 40 and 30 mA, respectively;  $A = 0.2 \text{ cm}^2$ ;  $t = 140^\circ C$ .

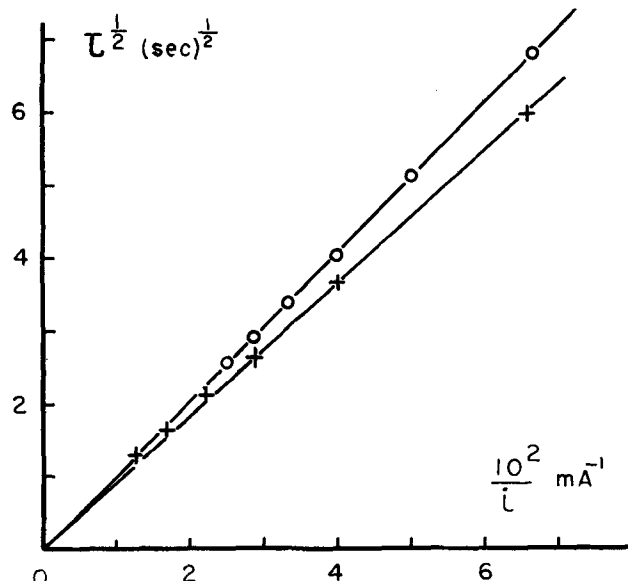


Fig. 2. Plot of  $\tau^{1/2}$  vs.  $1/i$  for the system  $AlCl_3\text{-}NaCl$  (63-37 m/o).  $\circ$ ,  $t = 140^\circ C$ ;  $\times$ ,  $t = 130^\circ C$ .

$$\frac{3FE^{ideal}}{RT} = \ln \left\{ \frac{[1 - C_{NaCl} \bar{V}_{NaCl}][1 + (\bar{V}_{AlCl_3} - \bar{V}_{NaCl}) C_{NaCl}]^2}{[\bar{V}_{AlCl_3} C_{NaCl}]^3} \right\} - \ln \left\{ \frac{[1 - C^0_{NaCl} \bar{V}_{NaCl}][1 + (\bar{V}_{AlCl_3} - \bar{V}_{NaCl}) C^0_{NaCl}]^2}{[\bar{V}_{AlCl_3} C^0_{NaCl}]^3} \right\} \quad [5]$$

where  $C^0$  and  $C$  are the initial and instantaneous concentrations (expressed in equivalents/cm<sup>3</sup>) (1) and  $\bar{V}$  is the partial molal volume.

The above equation can be solved knowing that at any time we must have

$$C_{Na+} = C^0_{Na+} - \alpha t^{1/2} \quad [6]$$

where

$$\alpha = \frac{2i}{\pi^{1/2} D^{1/2} A n F} \quad [7]$$

and

$$C_{Na+} = C_{NaCl}$$

For  $t = \tau$ , we have a pure layer of  $AlCl_3$  ( $Al_2Cl_6$ ) at the electrode surface and  $C_{NaCl} = 0$ , so  $\alpha \tau^{1/2} = C^0_{NaCl}$ .  $C^0_{NaCl}$  is estimated from the densities of the melt at the investigated temperatures and the stoichiometric mole fractions of  $NaCl$  and  $AlCl_3$ . The densities of the melt were extrapolated from the work of Boston (10).

For  $AlCl_3\text{-}NaCl$  (63-37 m/o),  $C^0_{NaCl}$  is 0.00585 equiv/cm<sup>3</sup> at  $140^\circ C$ . From this value and Fig. 2, we can determine  $\alpha$  and the average interdiffusion coefficient  $D$ .  $D$  was found to be  $1 \times 10^{-6} \text{ cm}^2/\text{sec}$  at  $140^\circ C$ . A value of  $D$  of this order of magnitude is not unreasonable considering that the transport process involves the diffusion of  $Na^+$  ions in  $AlCl_3$ -rich melts; the composition of the melt at the electrode changes continuously during the chronopotentiogram from the initial composition (63 m/o  $AlCl_3$ ) to essentially pure  $Al_2Cl_6$ . We have previously reported (11) the diffusion coefficient for  $Ti(II)$  in  $AlCl_3\text{-}NaCl$  (65-35 m/o) to be in the range  $2.5\text{-}6 \times 10^{-6} \text{ cm}^2/\text{sec}$  at temperatures  $185^\circ\text{-}260^\circ$ . The diffusion coefficient for  $Ti(III)$  in  $LiF\text{-}BeF_2\text{-}ZrF_4$  (65.6-29.4-5.0 m/o) at  $500^\circ C$  was found to be  $1.0 \times 10^{-6} \text{ cm}^2/\text{sec}$  (12). Lower values of  $D$  would be expected in viscous  $BeF_2$ -rich mixtures. From the above comparison, a higher value of  $D$  for  $Na^+$  in acidic chloroaluminates used in this work would be expected compared to the value of  $D$  of  $3 \times 10^{-7}$

cm<sup>2</sup>/sec obtained by Braunstein *et al* (1) for the diffusion of Na<sup>+</sup> in BeF<sub>2</sub>-NaF (75-25 m/o) at 520°C.

If we make the assumption that the diffusion coefficient is constant as the concentration changes, we can calculate  $C_{\text{NaCl}}$  as a function of time from Eq. [6] and from that the ideal emf. It was assumed in this calculation that the partial molal volumes are additive; this assumption is only approximately correct for this system (10).

Calculated points are also given in Fig. 1. The "ideal" curve is in reasonable agreement with the experimental curve; however, the calculated points lie slightly below the experimental values except in the final part of the curve. It can also be seen that the calculated curve fits the experimental curve better if the transition time is short.

In our calculation,  $D$  was assumed to remain constant as the composition changes (not a correct assumption). Furthermore, for the system AlCl<sub>3</sub>-NaCl it has been observed (13-15) that above 80 m/o of AlCl<sub>3</sub> and above 193°C, two liquid phases occur, of which one is probably almost pure Al<sub>2</sub>Cl<sub>6</sub>. Hence the point where a pure layer of Al<sub>2</sub>Cl<sub>6</sub> is formed at the electrode should occur sooner than in the absence of two liquid phases. The time for which  $y = 0.80$  can be easily calculated from Eq. [6] and one obtains in general that  $t_{y=0.80} = 0.26\tau$ . Thus, if the observed transition time corresponds to the immiscibility, the true transition time is about four times longer. For this condition, the calculated curve exhibits a very flat region with a sudden potential increase when the immiscibility occurs. At this point the concentration of Na<sup>+</sup> ions at the electrode surface is zero. The shape of the calculated chronopotentiogram would be different from what we observed. Nevertheless, in the range of our working temperatures, the pure Al<sub>2</sub>Cl<sub>6</sub> produced at the end of the chronopotentiogram, or in the region of immiscibility, should be a solid. Such a solid layer can be easily observed on the electrode for temperatures lower than 120°C and also at very long transition times. If this is the case, the measurements are no longer reproducible. For temperatures between 130°

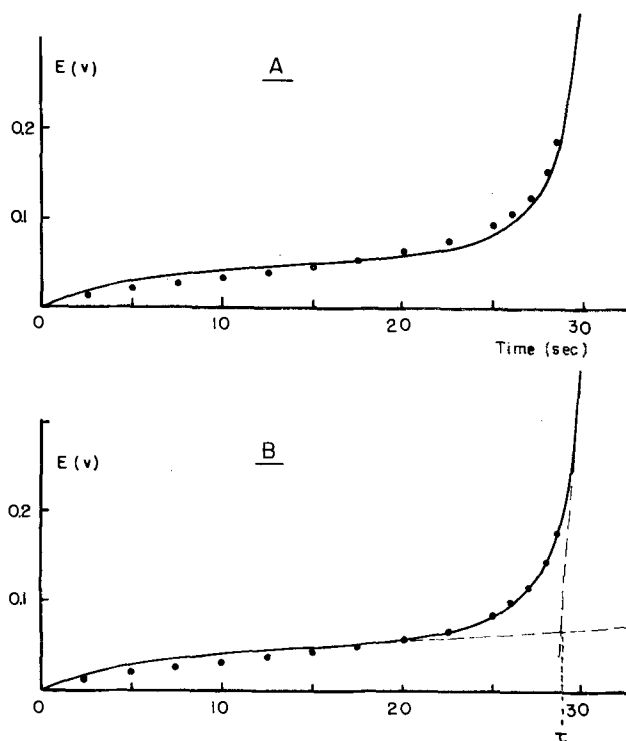


Fig. 3. Chronopotentiogram obtained in molten AlCl<sub>3</sub>-LiCl (63-37 m/o);  $t = 150^\circ\text{C}$ ;  $i = 25$  mA;  $A = 0.13$  cm<sup>2</sup>. The points are calculated from Eq. [5] for curve A and from Eq. [5] + [11] for curve B.

and 160°C, the solid phase is not observed except if the transition time exceeds several minutes. Under these conditions, the results suggest that the melt is supersaturated with Al<sub>2</sub>Cl<sub>6</sub> in the vicinity of the electrode, as also noted by Holleck and Giner (2).

In the case of AlCl<sub>3</sub>-LiCl, no immiscibility has been reported in the literature, although the only paper reporting the phase diagram of this system is rather old (13). The experimental and calculated chronopotentiograms for AlCl<sub>3</sub>-LiCl (63-37 m/o) are given in Fig. 3.

A negative deviation in the first part of the theoretical curve and a slight positive deviation for the second half of the curve are observed. The latter observation depends mostly on the chosen value of the transition time  $\tau$ .  $\tau$  was determined by the method of Reinmuth (16). The corresponding average interdiffusion coefficient is  $4.5 \times 10^{-6}$  cm<sup>2</sup> sec<sup>-1</sup>, higher than for the NaCl system as might be expected from the smaller size of the lithium cation.

Over-all, the shape of the experimental curve is only slightly different than for the AlCl<sub>3</sub>-NaCl system and also fits the theoretically calculated curve. This indicates that the immiscibility did not have time to develop in the case of AlCl<sub>3</sub>-NaCl.

The preceding calculations deal only with ideal emf. In order to calculate the effect of the "excess" emf, the variation of the activity coefficients with composition must be known. Fannin and co-workers (7) have proposed a least squares empirical polynomial for  $d \ln \gamma / dy$  in which the activity coefficients are calculated from vapor pressure measurements. In this case, the excess function becomes

$$E_{\text{excess}} = \frac{RT}{3F} \int_{y_0}^y (1 - t_{\text{Al}^{3+}}) \left( \frac{1 + 2y}{1 - y} \right) (C_1 + 2C_2y + 3C_3y^2) dy \quad [8]$$

However, the values of the coefficients  $C_1$ ,  $C_2$ , and  $C_3$  are not given; in any case, this polynomial was determined only in the range 0.55-0.75 mole fraction of AlCl<sub>3</sub>. In view of the fact that no experimental data are available for the very acidic melts, we have used a very simple function based on the assumption that the melt behaves as a regular solution (17). This assumption is not correct due to strong interactions between the melt constituents; however, it is interesting to know in what way a correction for the activity coefficients will affect the ideal function even if this correction is very approximate. Thus the activity coefficients were estimated from (17)

$$RT \ln \gamma = w(1 - y)^2 \quad [9]$$

where  $w$  is a constant.

The excess emf then becomes

$$E_{\text{excess}} = \frac{w}{3F} \int_{y_0}^y (1 - t_{\text{Al}^{3+}}) \left( \frac{1 + 2y}{1 - y} \right) (2y - 2) dy \quad [10]$$

This equation contains only one adjustable parameter,  $w$ . Comparison of Eq. [10] with Eq. [8] shows that the third term in Eq. [8] ( $3C_3y^2$ ) has been neglected and the constants are related by  $C_2 = -C_1/2 = w/RT$ ; however, there are no basic differences between the two equations.

After integration of Eq. [10] and expressing  $y$  as a function of  $C_{\text{NaCl}}$ , we obtain

$$E_{\text{excess}} = \frac{2w}{3F} \left\{ \frac{(1 - C_{\text{NaCl}}\bar{V}_{\text{NaCl}})[2 + (\bar{V}_{\text{AlCl}_3} - 2\bar{V}_{\text{NaCl}})C_{\text{NaCl}}]}{[1 + (\bar{V}_{\text{AlCl}_3} - \bar{V}_{\text{NaCl}})C_{\text{NaCl}}]^2} + \frac{(1 - C_{\text{NaCl}}^0\bar{V}_{\text{NaCl}})[2 + (\bar{V}_{\text{AlCl}_3} - 2\bar{V}_{\text{NaCl}})C_{\text{NaCl}}^0]}{[1 + (\bar{V}_{\text{AlCl}_3} - \bar{V}_{\text{NaCl}})C_{\text{NaCl}}^0]^2} \right\} \quad [11]$$

Since the absolute value of the first term in the parenthesis is always larger than that of the second, the value of the parenthesis is negative and the sign of the excess function is thus opposite to the sign of the constant  $w$ . It is also worth noting that this approximate function giving  $E^{\text{excess}}$  affects mostly the end of the chronopotentiogram; this result is similar to that obtained by Braunstein *et al.* (1) An average value of  $w \approx 7 \times 10^2$  j-mole<sup>-1</sup> has been calculated to fit the experimental curve for the system AlCl<sub>3</sub>-LiCl. The final result is given in curve B of Fig. 3 for which the agreement between the calculated and experimental values is quite good, particularly considering the approximations involved.

### Conclusions

Excellent agreement between theory and experiment has been obtained for the anodic oxidation of Al in AlCl<sub>3</sub>-NaCl (63-37 m/o) and in AlCl<sub>3</sub>-LiCl (63-37 m/o). It is clear that the mechanism resulting in the chronopotentiogram (formation of a poorly conducting Al<sub>2</sub>Cl<sub>6</sub> layer at the electrode surface and the depletion of current carrying alkali metal ions) is analogous to that observed for MF-BeF<sub>2</sub> mixtures (1). Since the calculated curves are obtained from assuming a reversible concentration cell, the observed agreement shows that the Al electrode behaves reversibly in the range of current densities employed. Furthermore, the applicability of Sand's equation requires that the oxidation process is diffusion controlled.

### Acknowledgments

This work was supported by the National Science Foundation under Contract NSF GP 32433X. A grant-in-aid from ALCOA Foundation is also gratefully acknowledged. The authors are pleased to acknowledge useful discussions with Drs. Jerry Braunstein and Catherine Vallet.

Dr. Gilbert has received partial support from the Fonds National de la Recherche Scientifique of Belgium.

Manuscript submitted Oct. 26, 1973; revised manuscript received Feb. 5, 1974.

Any discussion of this paper will appear in a Discussion Section to be published in the December 1974 JOURNAL. All discussions for the December 1974 Discussion Section should be submitted by Aug. 1, 1974.

### REFERENCES

1. J. Braunstein, H. R. Bronstein, and J. Truitt, *J. Electroanal. Chem.*, **44**, 463 (1973).
2. G. L. Holleck and J. Giner, *This Journal*, **119**, 1161 (1972).
3. G. D. Brabson, A. A. Fannin, Jr., L. A. King, and D. W. Seegmiller, Abstract 26, p. 61, Electrochemical Society Extended Abstracts, Spring Meeting, Chicago, Illinois, May 13-18, 1973.
4. G. Torsi, K. W. Fung, G. M. Begun, and G. Mamantov, *Inorg. Chem.*, **10**, 2285 (1971).
5. G. Torsi and G. Mamantov, *J. Electroanal. Chem.*, **30**, 193 (1971).
6. G. F. Uhlig, Dissertation, University of Utah, 1973.
7. A. A. Fannin, Jr., L. A. King, and D. W. Seegmiller, *This Journal*, **119**, 801 (1972).
8. B. F. Hitch and C. F. Baes, Jr., *Inorg. Chem.*, **8**, 201 (1969).
9. P. Delahay, "New Instrumental Methods in Electrochemistry," p. 184, Interscience Publishers, New York (1954).
10. C. R. Boston, *J. Chem. Eng. Data*, **11**, 262 (1966).
11. K. W. Fung and G. Mamantov, *J. Electroanal. Chem.*, **35**, 27 (1972).
12. F. R. Clayton, G. Mamantov, and D. L. Manning, *This Journal*, **120**, 1193 (1973).
13. J. Kendall, E. D. Crittenden, and H. K. Miller, *J. Am. Chem. Soc.*, **45**, 963 (1923).
14. U. I. Shvartsman, *J. Phys. Chem. (USSR)*, **14**, 253 (1940).
15. V. W. Fischer and A.-L. Simon, *Z. Anorg. Allgem. Chem.*, **306**, 1 (1960).
16. W. H. Reinmuth, *Anal. Chem.*, **33**, 485 (1961).
17. L. G. Boxall, H. L. Jones, and R. A. Osteryoung, *This Journal*, **120**, 223 (1973).

## Brief Communication



## Electrodeposition of an Amorphous Cobalt Rhenium Alloy

P. J. Cote, G. P. Capsimalis, and V. P. Greco

Waterliet Arsenal, Waterliet, New York 12189

The publication costs of this article have been assisted by the Department of the Army.

We are reporting on the formation of a cobalt-44 atomic per cent (a/o) rhenium amorphous alloy by electrodeposition from a bath developed by Netherton and Holt (1). The bath composition used to obtain the amorphous phase is given in Table I.

Our fabrication of a new amorphous metal is significant in view of the current interest in these materials and the fact that relatively few amorphous alloys have been electrodeposited.

Both x-ray and electron diffraction patterns show the diffuse rings which are characteristic of these materials (see Fig. 1).

Electrodeposition studies were made using the Beckman "Electroscan 30." Current density vs. cathode po-

tential scans were obtained in the potentiostatic mode and these revealed a break at around -850 mV as shown in Fig. 2. These data were taken in a quiescent bath. The break is far less pronounced in the stirred baths in which the specimens were prepared. Deposits made above the break generally result in the amor-

Table I.

Bath formula	Concentration (g/liter)
CoSO <sub>4</sub> · 7H <sub>2</sub> O	60
Citric acid	66
NH <sub>4</sub> ReO <sub>4</sub>	4
pH	7.8

Key words: amorphous, electrodeposition, cobalt-rhenium alloy.

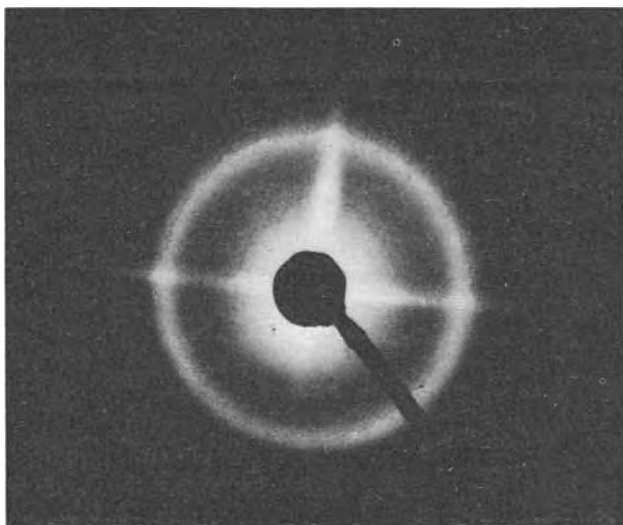


Fig. 1. This is a typical electron diffraction pattern obtained from the amorphous phase. X-ray diffraction gives essentially the same pattern. The first peak position occurs at  $\frac{4\pi \sin\theta}{\lambda} = 3.0\text{\AA}^{-1}$ .

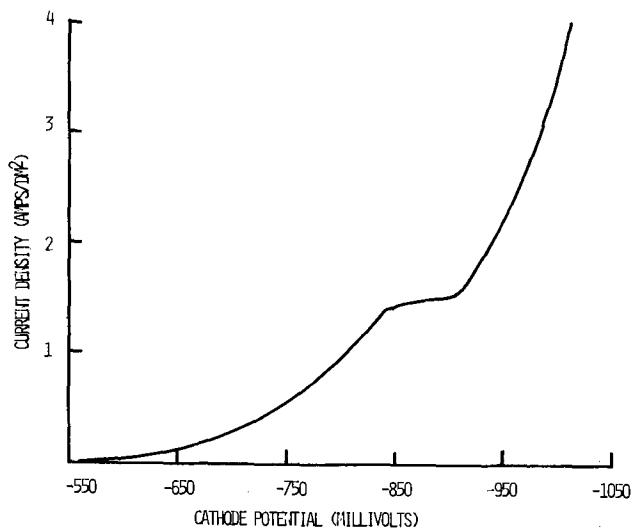


Fig. 2. The current density vs. cathode potential (SCE) shows a break which appears to correspond to the deposition of the amorphous phase under suitable bath conditions.

phous phase, and those made below the break result in a mixture of amorphous and crystalline phases. Similar behavior was reported by Omi *et al.* (2) in the

electrodeposition of a Co-25 a/o W alloy. They found two breaks which appear to correspond exactly to the transitions from amorphous to crystalline deposits. Although we see a similar correspondence under the proper bath conditions, we also observe this break with no rhenium in the bath. An explanation for the above is that the break represents the limiting current density for metal deposition. The subsequent sharp increase in slope corresponds to increased hydrogen discharge at the cathode. Making the assumption that the amorphous phase is a result of codeposited hydrogen, we can then understand the relationship between crystalline structure and cathode potential. Approaching the vicinity of the break, there is an increasing percentage of hydrogen codeposited. This corresponds to an increasing percentage of the amorphous phase in the deposit as the cathode potential is made more negative. It is worth noting here that according to (1), the Co-Re alloy composition is relatively insensitive to cathode potential over a wide range.

At the lower current densities, the crystalline phase (hcp) is present in an unusual form appearing as crystalline cones or columns imbedded in an amorphous matrix. All the columns appear to be oriented with the fiber axis parallel to the surface normal, with the  $\langle 100 \rangle$  crystallographic direction along the fiber axis. This is based in part on the appearance of only the  $\{100\}$  and  $\{200\}$  peaks in the diffraction patterns. Similar observations were reported by Cargill (3) for some of the NiP glasses produced by both electrodeposition and electroless deposition. In his case the fcc crystallites had the  $\langle 111 \rangle$  direction parallel to the surface normal.

Annealing this alloy for 1 hr at  $300^\circ\text{C}$  results in substantial crystallization directly to the stable hcp solid solution determined by x-ray and electron diffraction. Electron microscopy and diffraction from the deposit edges show the presence of some fcc crystallites and whiskers after annealing. The lattice parameter of these crystallites is about  $3.9\text{\AA}$ . This is consistent with  $\text{ReN}_{0.45}$  ( $a_0 = 3.92\text{\AA}$ ) and with a metastable solid solution of cobalt and rhenium. We note that metastable intermediate phases are commonly seen in annealed glassy metals.

Manuscript submitted Dec. 4, 1973, revised manuscript received Feb. 1, 1974.

Any discussion of this paper will appear in a Discussion Section to be published in the December 1974 JOURNAL. All discussions for the December 1974 Discussion Section should be submitted by Aug. 1, 1974.

#### REFERENCES

1. L. E. Netherton and M. L. Holt, *This Journal*, **99**, 44 (1952).
2. T. Omi, H. Yamamoto, and H. L. Glass, *ibid.*, **119**, 168 (1972).
3. G. S. Cargill, *J. Appl. Phys.*, **41**, 1 (1970).

# DISCUSSION SECTION



This Discussion Section includes discussion of papers appearing in the *Journal of The Electrochemical Society*, Vol. 120, No. 2, 4, and 6; February, April, and June 1973.

## Monolayer Formation in the Reduction of Nickel and Silver Ions from the LiCl-KCl Eutectic

G. J. Hills, D. J. Schiffrin, and J. Thompson  
(pp. 157-164, Vol. 120, No. 2)

**D. Inman<sup>1</sup> and D. G. Lovering:<sup>2</sup>** In our opinion, the results given in the paper under discussion could equally well be explained in terms of the discharge of a layer of adsorbed nickel ion containing species prior to the discharge of the ions diffusing from the bulk of the solution.

As the authors of the paper being discussed state themselves, the presence of peaks in the potentiostatic step response would have been expected on the basis of their model. Furthermore, Fig. 4 of the above-mentioned paper is a much scaled-down version of an original figure in a thesis<sup>3</sup> by one of the authors (J. T.). In the latter it is possible to discern finite intercepts in the  $\tau^{1/2}$  vs.  $i^{-1}$  plots. This behavior is typical, and often diagnostic, of an adsorption process. Again, the linear dependence of the peak current on the sweep rate in the "monolayer formation" region (cyclic voltammetry) is also indicative of an adsorption process.

Thus, as a first approximation, an AR, SR type of discharge mechanism<sup>4</sup> would seem appropriate on the basis of these results. The discharge of adsorbed layers of ions in molten salt systems has been indicated on several previous occasions<sup>5</sup> and it is therefore all the more surprising that the authors have not considered this attractive alternative explanation.

The test applied by one of us in a previous study<sup>6</sup> [increasing the sweep rate of repetitive (cyclic) linear-sweep voltammograms until the supposed adsorption-controlled current peak disappeared] could usefully be applied in the present case. Also, since an AR, SR type of discharge mechanism seems appropriate, it would be possible to move the start potential to a value more negative than the supposed AR prepeak, and confirm pure, diffusion-controlled behavior of the remaining (SR) current peak.

Finally, the results for  $\text{Ag}^I$  may also be influenced by adsorption processes. The separation between the two reduction modes could not be discerned in the chronopotentiograms which may depend on both processes. Thus the high values of the diffusion coefficients, calculated on the basis of these chronopotentiograms, may reflect the adsorption contribution to the transition time.

**G. J. Hills, D. J. Schiffrin, and J. Thompson:** We are grateful to Drs. Inman and Lovering for their discussion of an alternative explanation for the predeposition phenomena and we should have given references to their several papers which are based on the adsorption mechanism.

However, our belief is unaltered that the results presented in our paper are indicative of a monolayer

intermediate of adatoms. We certainly do not deny that this process may be preceded by a kinetically important adsorption step but only that we could not separate them except using exceptionally high sweep rates.

The involvement of a monolayer is based primarily on the charge equivalent of the predeposition step which is close to that corresponding to a close packed monolayer of metal atoms covering an area equal to the apparent or formal area of the electrodes. Given that the real surface area is somewhat larger than this, it would still require an unusually high surface charge density of adsorbed nickel ion species to account for the observed cathodic charge (extremes of  $z\text{FT} \pm$  are typically  $\pm 20 \mu\text{coulombs/cm}^2$ , cf. the present value of  $600 \mu\text{coulombs/cm}^2$ ). Then there is the evidence from other systems in which metal monolayers have been observed<sup>7,8</sup> and from the analogous studies of the adsorption of atomic hydrogen on platinum. More recent still is the direct evidence of predeposited metal monolayers obtained from measurements of the specular reflection of electrode surfaces as a function of overpotential or, as in this case, underpotential.<sup>9,10</sup>

It is, of course, not correct, as Inman and Lovering assert, that the absence of a maximum in the potentiostatic pulse transients is incompatible with a precursor metal monolayer. What we tried to say was that where the number of deposition or nucleation sites is not restricted, then lateral growth from preferred sites (which would give rise to a maximum) is not to be expected.

On the other hand, we accept Inman and Lovering's criticism of Fig. 4 in the paper being discussed. The  $\tau^{1/2}$  scale is ten times too great and there was an intercept in the original thesis figure.<sup>3</sup> However, this was small, and, in our opinion, within experimental error. Even so, we do not deny that the intercept may be real and that it may well be evidence for an adsorption process.

We hope to re-examine these systems using an electroreflectance technique and it may be that we shall be able to confirm in these systems also the existence of a metal monolayer. Whether or not it is formed solely from an adsorbed layer of metal ions might also be evident.

## On Accelerated Pitting and Crevice Corrosion Tests

J. Degerbeck (pp. 175-182, Vol. 120, No. 2)

**M. Grassiani:<sup>11</sup>** Referring to the author's conclusions in the paper under discussion concerning the uncertainty of electrochemical tests in evaluation of localized corrosion resistance in calm natural seawater, we should like to quote his own discussion: "the electrochemical specimen having the lowest pitting potential value ought to correspond better to the crevice surfaces attacked in the field test . . ." Since most of field test exposure led to crevice corrosion (either occurring under fouling or artificially achieved), it should be expected that crevice corrosion occurs at lower potentials than the mean pitting potential<sup>12</sup> and

<sup>1</sup> Department of Metallurgy and Materials Science, Imperial College of Science and Technology, London SW7, United Kingdom.

<sup>2</sup> Department of Chemistry and Metallurgy, The Royal Military College of Science, Shrivenham, Swindon, Wilts, United Kingdom.

<sup>3</sup> J. Thompson, Ph.D. Thesis, University of Southampton (1973).

<sup>4</sup> R. W. Murray and D. J. Gross, *Anal. Chem.*, **38**, 392 (1966).

<sup>5</sup> For example, R. Narayan, D. G. Lovering, and D. Inman, *Chem. Commun.*, 386 (1966); D. Inman, D. G. Lovering, and R. Narayan, *Trans. Faraday Soc.*, **64**, 2487 (1968); D. Inman, R. Sethi, and R. Spencer, *J. Electroanal. Chem.*, **29**, 137 (1971).

<sup>6</sup> D. G. Lovering, *Trans. Faraday Soc.*, **67**, 2659 (1971).

<sup>7</sup> E. Schmidt and H. R. Gygas, *J. Electroanal. Chem.*, **12**, 300 (1966).

<sup>8</sup> G. W. Tindall and S. Bruckenstein, *Anal. Chem.*, **40**, 1051 (1968).

<sup>9</sup> D. M. Kolb, The Chemical Society, Faraday Division, General Discussion on "Intermediates in Electrochemical Reactions," Oxford, England, September 1973.

<sup>10</sup> J. D. E. McIntyre and D. M. Kolb, *Symp. Faraday Soc.*, **4**, 99 (1970).

<sup>11</sup> Chemical Engineering Department, University of the Negev, Beer-Sheva, Israel.

<sup>12</sup> M. Grassiani, *Tribune du CEBEDEAU*, **25**, 515 (1972).

thus, the whole basis for comparison between the two types of tests becomes unreal. Furthermore, it should be emphasized that besides the possible contribution of  $M_nS$  surface inclusions to the lower pitting potentials observed on some specimens it is more likely that environmental factor variation (like variation of oxygen content even under  $N_2$  bubbling, or variation of stirring by that bubbling) could affect the results. Our experience<sup>13</sup> showed that full deaeration is difficult to achieve or control; on the other hand, one cannot expect to reach the "true" anodic behavior there, where oxygen still cathodically reacts resulting in more noble (and apparent) pitting potentials.

Finally, potentiodynamic polarization techniques should be more cautiously used in order to achieve the best reproducibility with the appropriate potential scan rate.

**J. Degerbeck:** The purpose of the study in the paper under discussion was to investigate the validity of different tests in predicting the relative corrosion resistance of stainless steels in a specific seawater environment. Among other things we found rather a good correlation between the minimum value of pitting potential and number of crevice attacks in the seawater; correlation coefficient was  $-0.83$  for one of the tests.

Dr. Grassiani's opinion in the above discussion is that it is unrealistic to compare the resistance to initiation of pitting to that of crevice corrosion, since crevice corrosion occurs at lower potentials than pitting. Against this I would raise the following objection:

As there seem to be certain similarities between the mechanism of formation of pitting and crevice corrosion,<sup>14,15</sup> and as practical experience and the main impression from the literature indicate that it is not quite unrealistic to assume that the relative resistance of different steels to initiation of pitting is the same as their relative resistance to initiation of crevice corrosion, I cannot see why it is unrealistic to correlate crevice corrosion from field tests with pitting from laboratory tests. That crevice corrosion occurs at potentials lower than the pitting potential is irrelevant. Further, my opinion is that from a practical point of view, it does not matter what results you compare or correlate as long as the correlation is of value in predicting the corrosion resistance in the actual environment.

In regard to the environmental factors mentioned I agree that they could affect pitting potential results. However, in our investigation we performed every trial in each of the tests exactly under the same conditions.

I am fully aware that the potentiodynamic pitting potential tests used in the present investigation are not the "best" ones. What you gain in accuracy you normally lose in time. We preferred to make use of rather fast tests.

### Diffusion Coefficients and Kinetic Parameters in Copper Sulfate Electrolytes and in Copper Fluoroborate Electrolytes Containing Organic Addition Agents

C. J. Milora, J. F. Henrickson, and W. C. Hahn  
(pp. 488-492, Vol. 120, No. 4)

**L. Grambow and W. Vielstich:**<sup>16</sup> We have recently studied the accurate determination of trace diffusion coefficients via the use of rotating electrodes (disk or

ring).<sup>17</sup> In determining the  $Cu^{++}$  diffusion coefficients in a sulfuric acid electrolyte and in a fluoboric acid electrolyte the investigations of C. J. Milora, J. F. Henrickson, and W. C. Hahn in the paper under discussion suffer from difficulties in the experimental procedure and a misleading assumption of the experimental upper limit of the speed of rotation. Moreover, an inadequate formula was used in the above-mentioned work, which results in an error of calculation of about 4-5%.

The plot of the obtained data for the limiting current  $i_L$  vs.  $\omega^{1/2}$  cannot be extrapolated to zero for either electrolyte (Fig. 3 in the paper under discussion):  $i_L = a + b\omega^{1/2}$ . Limiting currents for rotation rates  $>2500$  rpm have not been evaluated. In the afore-mentioned paper, authors explain a nonzero value by "anomalous" Adams Riddiford effects, claiming that the Pine Instrument rotating disk does not possess efficient dimensions in the isolating part of the disk. The deviations for  $f > 2500$  rpm are assumed to be due to turbulent flow of the electrolyte. However, from the data presented, a maximum Reynolds number of about 2000 can be calculated; the critical value is  $Re_{crit} \geq 1.5 \cdot 10^5$ . We assume that this anomalous experimental behavior is caused by the very high current density (up to about  $200 \text{ mA/cm}^2$ ) used. At a scan of  $2500 \text{ mV/min}$ , more than  $2 \times 10^4$  copper atom layers are formed during one period. This is a thickness of about  $1 \cdot 10^{-3} \text{ cm}$ . On the other hand, at  $2500 \text{ rpm}$  the diffusion layer  $\delta_N$  also falls in the range of  $1 \cdot 10^{-3} \text{ cm}$ . Therefore realistic data cannot be expected.

From the slope of the curve in Fig. 2 in the work being discussed the authors have calculated the  $D_{Cu^{++}}$  values using the Levich formula<sup>18</sup> (Eq. [1]). It is well known that this is a first approximation only; one should use the Gregory-Riddiford equation<sup>19</sup>

$$i_L = n \cdot F \cdot D^{2/3} \cdot c_\infty \cdot \nu^{-1/6} \cdot \omega^{1/2} \cdot \left( 1.6126 + 0.5704 \left( \frac{D}{\nu} \right)^{0.36} \right)^{-1} \quad [1]$$

This results in an increase of the evaluated data of about 5%. Thus one obtains from curve A (Fig. 2 of the paper under discussion)

$$D_{Cu^{++}} = 5.41 \cdot 10^{-6} \text{ cm}^2/\text{sec} \quad [2]$$

instead of  $5.23 \cdot 10^{-6} \text{ cm}^2/\text{sec}$  as given in the paper being discussed for the sulfuric acid electrolyte, and from curve B we get

$$D_{Cu^{++}} = 10.34 \cdot 10^{-6} \text{ cm}^2/\text{sec} \quad [3]$$

instead of  $9.88 \cdot 10^{-6} \text{ cm}^2/\text{sec}$  which the authors in the above-mentioned work have given for the fluoboric solution.

As proof we have measured in our laboratory the respective diffusion coefficients by using a much lower concentration of  $Cu^{++}$  [ $0.011N \text{ CuSO}_4/1.0N \text{ H}_2\text{SO}_4$  and  $0.0058N \text{ Cu}(\text{BF}_4)_2/1.0N \text{ HBF}_4$ , respectively] and a faster scan ( $6000 \text{ mV/min}$ ), so that the diffusion layer is much larger than the rough copper layer deposited. Figure 1 of this discussion shows the limiting current for the  $\text{H}_2\text{SO}_4$  electrolyte at a rotating copper disk electrode ( $A = 0.5027 \text{ cm}^2$ ); the speed of rotation varied from  $13.7$  to  $139.3 \text{ sec}^{-1}$  at a temperature of  $19^\circ\text{C}$ . The respective plots  $i_L$  vs.  $\omega^{1/2}$  for five different temperatures are given in Fig. 2. The experimental data points lie mostly on a straight line, and the extrapolation at any temperature goes through zero. According to the Gregory-Riddiford equation, the following data are obtained at  $25^\circ\text{C}$

$$D_{Cu^{++}} = 5.41 \cdot 10^{-6} \text{ cm}^2/\text{sec} \quad [4]$$

for the  $\text{CuSO}_4$  solution and

<sup>17</sup> B. Gostisa-Mihelcic and W. Vielstich, *Ber. Bunsenges. Physik. Chem.*, **76**, 19 (1972).

<sup>14</sup> M. Grassiani, Thesis, University of Liege, Belgium (1972).  
<sup>15</sup> J. M. DeFranoux, Paper No. 3, Marine Corrosion Conference in Conjunction with The Sea Horse Institute of Harbor Island, Biarritz (1969).

<sup>16</sup> I. L. Rosenfeld and I. S. Danilov, *Z. Phys. Chem.*, **226**, 257 (1964).

<sup>17</sup> Institut für Physikalische Chemie der Universität Bonn, 53 Bonn, Germany.

<sup>18</sup> V. G. Levich, "Physicochemical Hydrodynamics," p. 296, Prentice-Hall, Inc., Englewood Cliffs, New Jersey (1962).

<sup>19</sup> D. F. Gregory and A. C. Riddiford, *J. Chem. Soc.*, 3756 (1956).

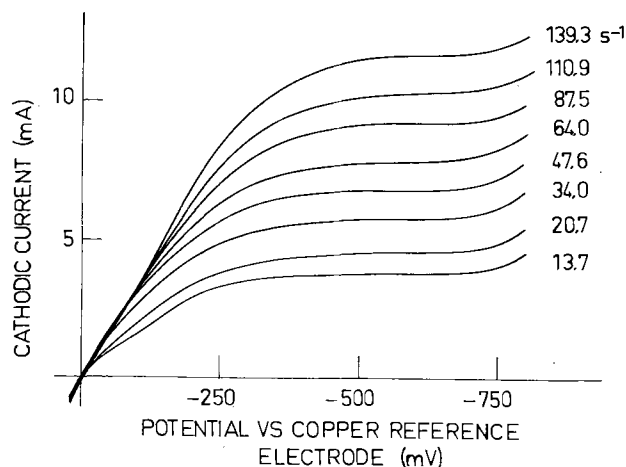


Fig. 1. Limiting currents for a 0.011N  $\text{CuSO}_4/1\text{N H}_2\text{SO}_4$  electrolyte with a copper rotating disk electrode at a scan of 6000 mV/min.

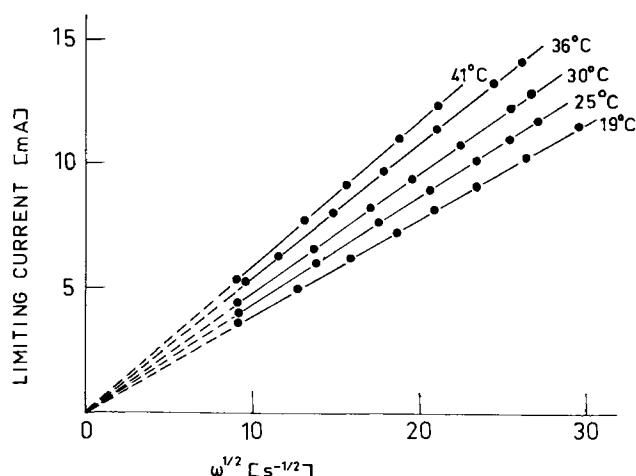


Fig. 2.  $i_L$  vs.  $\omega^{1/2}$  for the copper sulfate solution at a copper rotating disk electrode at various temperatures.

$$D_{\text{Cu}^{++}} = 9.46 \cdot 10^{-6} \text{ cm}^2/\text{sec} \quad [5]$$

for the  $\text{Cu}(\text{BF}_4)_2$  solution.

In the case of the sulfuric acid electrolyte, the authors of the work being discussed arrive at the same result as we do. For the fluoboric acid electrolyte, however, we found a difference of almost 10%.

To explain the varying conductivities in the two solutions we propose the following working hypothesis. The  $\text{Cu}^{++}$  cation is bound in different complexes in both solutions. The tetrafluoroboric anion does not come into consideration for the formation of the complex; we can assume the existence of aquocomplexes in the fluoboric acid solution. More probable is the formation of sulfato complexes in the sulfuric acid electrolyte. This assumption would explain the reduced mobility of the  $\text{Cu}^{++}$  ions in the sulfuric acid solution, since such complexes have a larger diameter than pure aquocomplexes.

### Origin of Activation Effects of Acetonitrile and Mercury in Electrocatalytic Oxidation of Formic Acid

H. Angerstein-Kozłowska, B. MacDougall, and B. E. Conway  
(pp. 756-766, Vol. 120, No. 6)

**A. Capon and R. Parsons:**<sup>20</sup> The paper under discussion brings some interesting new information to bear on the problem of formic acid oxidation. At the same time it neglects some of the information already avail-

<sup>20</sup> School of Chemistry, University of Bristol, Bristol BS8 1TS, England.

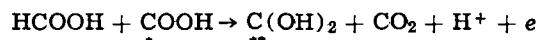
able in the literature<sup>21</sup> and it seems to us to rule out the possibility of formic anhydride playing the role of the strongly adsorbed intermediate (P) which poisons the faster oxidation process. Although the properties of P are subject to some dispute there does seem to be agreement<sup>21,22</sup> on the facts that two to three electrons are removed to produce each  $\text{CO}_2$  molecule from P and that slightly more than one electron per site (eps) is removed in its oxidation to  $\text{CO}_2$ , the site being measured in terms of hydrogen adsorption. Formic anhydride requires two electrons to be removed for its oxidation to produce two molecules of  $\text{CO}_2$ , i.e., one electron per  $\text{CO}_2$ . From the model shown in Fig. 9(a) of the paper under discussion it appears that formic anhydride should occupy six sites so that oxidation would require removal of one-third electron per site. Both these predictions are in disagreement with the experimental observations.

A  $\text{COH}$  species bonded to three Pt atoms in the surface would require removal of one electron per site and three electrons per  $\text{CO}_2$ ; this is in substantially better agreement with the experiment, though the discrepancies are still sufficiently large that it seems likely that another species may be present, but in smaller amount. The formation of  $\text{COH}$  as a predomi-

nant component of P appears to account qualitatively for the observed behavior if it is formed by two mechanisms,<sup>22</sup> (i) when adsorbed hydrogen is present by reaction of adsorbed carboxyl radicals with adsorbed hydrogen, and (ii) in the absence of adsorbed hydrogen, by a slow "disproportionation" mechanism between adsorbed carboxyl radicals and formic acid molecules. The observations reported in Fig. 8 of the paper under discussion also seem to fit this proposal satisfactorily. The observed effects of adsorption of mercury on acetonitrile would seem equally easy to interpret on this model as on the hypothesis of formic anhydride as intermediate P.

It should also be emphasized that the existence of P on the surface cannot account for the observation of the first peak for formic acid oxidation ( $\text{FA}_1$ ). If experiments are performed under conditions where the concentration of P is constant (Fig. 20 of Footnote 22) the peak remains well defined and the current is independent of the direction of the sweep. Thus the rate is determined by a surface reaction, which is in fact the fast route for oxidation of formic acid. A peak of this type cannot be accounted for in terms of a two-step reaction involving a single intermediate  $\text{COOH}$ . It therefore seems necessary to postulate the existence of at least one subsequent intermediate occupying two sites. We have suggested<sup>22</sup> that this may be  $\text{C}(\text{OH})_2$

which could be produced in the reaction



although this identification is tentative. An explanation of this type also accounts for the single peak in formic acid oxidation<sup>23</sup> on palladium where no inhibiting species P is found.

**H. Angerstein-Kozłowska, B. MacDougall, and B. E. Conway:** Drs. Capon and Parsons direct attention to the question of the number of electrons per site (eps) required for the oxidation of the poisoning intermediate P that arises spontaneously in formic acid oxidation at Pt. We had ourselves in the paper under discussion also referred to this problem in relation to the previously published<sup>24,25</sup> estimates of this quantity and to possible chemical identities<sup>24</sup> of this species.

<sup>21</sup> A. Capon and R. Parsons, *J. Electroanal. Chem.*, **44**, 1 (1973).

<sup>22</sup> A. Capon and R. Parsons, *ibid.*, **45**, 205 (1973).

<sup>23</sup> A. Capon and R. Parsons, *ibid.*, **44**, 239 (1973).

<sup>24</sup> S. B. Brummer and A. Makrides, *J. Phys. Chem.*, **68**, 1448 (1964); S. B. Brummer, *ibid.*, **69**, 1363 (1965); *Elektrokhimiya*, **4**, 243 (1968); *J. Phys. Chem.*, **69**, 562 (1965).

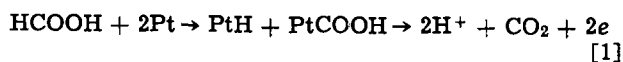
<sup>25</sup> M. Breiter, *Electrochim. Acta*, **8**, 447 (1963); *ibid.*, **10**, 503 (1965).

The generality of the activating effect of added strongly adsorbed substances on the so-called FA<sub>1</sub> oxidation current for formic acid (as stated in the paper under discussion) requires that a competitive poisoning effect is involved which diminishes the rate and extent of formation of P in the formic acid oxidation reaction, yet does not block the main reaction process. In the paper being discussed we gave evidence that added competitive poisons must act by a "third-body" effect, interfering in the production of P by preventing close approach of whatever intermediates are required for its formation. In the paper under discussion, we proposed the possibility that P was formic anhydride, stabilized by two-site adsorption, that arose from dimerization of adsorbed COOH (I), the principal intermediate in the main reaction sequence of HCOOH oxidation. Formation of such a poison would be retarded by the "third-body" effect. In the light of Capon and Parsons's comments, it is useful first to re-examine the H-blocking and surface-site requirements of formic anhydride species (II). Inspection of molecular models of a Pt (III) surface lattice and of formic anhydride indicates the possibility that the latter species is adsorbed with bonding of the two C atoms on top of two adjacent Pt atoms. This then blocks chemisorption of H only on the two Pt atoms involved so that the eps could be near one or at the least be two-thirds, i.e., close to the figure Capon and Parsons find, and quote from the literature.<sup>22</sup> The only rearrangement required in relation to our previous picture in the paper being discussed is that bonding of C to Pt occurs to the top of Pt atoms, rather than through electrons in trigonal interstitial locations, e.g., in the case of the (111) surface. In fact, it can be argued that this alternative representation of the bonding of II to Pt is more consistent with current ideas<sup>26</sup> about the disposition of d-orbitals at transition metal surfaces, e.g., the orientation of d<sub>yz</sub> and d<sub>z<sup>2</sup></sub> orbitals.

The fact that P can be oxidized, like the species formed in methanol oxidation, in the PtOH region is probably not, however, diagnostic of the nature of P, since many organic substances, and impurities, are also oxidized over the same potential range.

While the "third-body" effect associated with activation of formic acid oxidation receives a simple and direct explanation in terms of blocking of a dimerization type of reaction, a similar effect of a competitive, monofunctionally adsorbed poison could arise in a reaction such as PtX + Pt → Pt<sub>2</sub>Y where Y is a species requiring two sites for adsorption compared with only one for the reactant species from which it originates.

Further investigations in progress on the activating effect of Hg indicate that the reaction pathway corresponding to the FA<sub>1</sub> current (as in the paper under discussion) must be more complex than the chemically most direct pathway



commonly considered in the literature, and must involve a second intermediate adsorbed on at least two sites (see below), produced from -COOH. Competitive poisoning lifts the inhibition of pathway [1] by preventing [third-body effect (as in the paper being discussed)] formation of the second intermediate and the main poison (which Capon and Parsons suggest is C-OH) and allows an increase of current through pathway [1].

A schematic reaction sequence which could tentatively provide a basis for some of the features of the oxidation of formic acid and the activating effect of competitive poisons is shown below (Fig. 1).

The main pathway of the reaction must proceed through intermediates I and II; intermediate II is

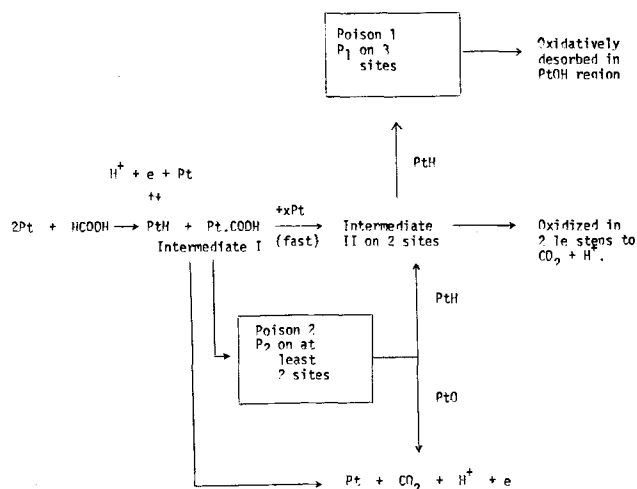


Fig. 1. Schematic reaction sequence

formed from intermediate I by reaction with H and participation of at least one further Pt site. It is then possible that the pathway through II from I could give rise to a current peak without the necessity of invoking<sup>21-23</sup> oxide blocking species, improbable<sup>27</sup> over the potential range of the FA<sub>1</sub> peak. The peak current could arise since  $\theta_H$  decreases with potential, while the oxidation of II increases with potential. The kinetics of the main pathway are modified by the presence of at least two other side products, P<sub>1</sub> (probably the species C-OH discussed by Capon and Parsons

and in their papers<sup>21-23</sup>), which originates in the H adsorption region and P<sub>2</sub> which must be invoked to explain time-dependent diminishing currents in the cathodic sweep after reduction of the surface oxide.

We thus agree with Capon and Parsons that at least two types of poison species, accumulated in the side reactions, are required if the experimental behavior is to be more fully accounted for.

Capon and Parsons<sup>21-23</sup> have suggested that the second poison is  $\begin{matrix} \text{C} \\ \text{OH} \\ \text{OH} \end{matrix}$  formed by a disproportionation reaction between COOH and HCOOH.

The disproportionation mechanism proposed by Capon and Parsons in the above discussion (cf. Footnote 21) ( $\text{HCOOH} + \text{COOH} \rightarrow \text{C}(\text{OH})_2 + \text{CO}_2 + \text{H}^+ + e$ ) for  $\text{C}(\text{OH})_2$  and that<sup>21-23</sup> for formation of  $\begin{matrix} \text{C} \\ \text{OH} \\ \text{OH} \end{matrix}$  must themselves be complex and may involve other intermediates [ $\text{C}(\text{OH})_2$  in the case of  $\begin{matrix} \text{C} \\ \text{OH} \\ \text{OH} \end{matrix}$ ], as well as acid catalyzed dehydration in the latter case. As written, the reaction schemes of Capon and Parsons<sup>21-23</sup> are purely formal and would not be easily rationalized in terms of organic reaction mechanisms.

We believe the use of formal reaction schemes, especially for heterogeneous reactions, can be misleading, as the site occupancy and geometry of the adsorbate in relation to that of the lattice must always be carefully considered, as we stressed in the paper which is being discussed.

We feel that it is more likely that  $\begin{matrix} \text{C} \\ \text{OH} \\ \text{OH} \end{matrix}$  is formed by reduction of COOH by the H dissociated from HCOOH and that



<sup>20</sup> See, for example, O. Johnson, *J. Res. Inst. Catalysis, Hokkaido Univ.*, 21, 1 (1973).

<sup>27</sup> H. Angerstein-Kozłowska, B. E. Conway, and W. B. A. Sharp, *J. Electroanal. Chem.*, 43, 9 (1973).



is a second intermediate in the main reaction path (see Fig. 1 above).

The possibility of relatively rapid production of intermediate II from  $\text{COOH} + \text{H}_{\text{ads}}$  follows from consideration of molecular models insofar as  $\text{H}_{\text{ads}}$  will be located close to the  $=\text{O}$  function in  $\text{COOH}$  at completion of the  $\text{HCOOH}$  dissociative chemisorption step. Reaction of this H with  $=\text{O}$  will be competitive with ionization of H but the proximity of H to  $=\text{O}$  and the shielding effect of  $\text{COOH}$  will enhance the possibility of reaction to form  $\overset{\cdot}{\text{C}}(\text{OH})_2$ . Formation of  $\overset{\cdot\cdot}{\text{C}}\text{OH}$  ( $\text{P}_1$ ) will naturally be a slower reaction, since extra H is required other than that provided directly by the dissociation step, and further geometrical rearrangement is required.

We suggest that outside the H region, the dissociation of the formic acid oxidation current with time is due to formation of  $\text{P}_2$  (see Fig. 1 above), e.g., a dimer such as formic anhydride.

The question of accounting for the first anodic current peak ( $\text{FA}_1$  in the paper under discussion) which Capon and Parsons mentioned<sup>21</sup> was considered by Gilroy and Conway,<sup>28</sup> who first showed in a general way how auto-inhibition effects could also cause current peaks without involvement of the potential-dependent traces of oxide species which Capon and Parsons invoke. The essential requirement was<sup>28</sup> that a step involving an adsorbed intermediate requires at least one extra site for the production of the next intermediate.

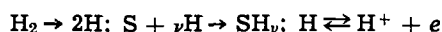
The remarks in the last paragraph of the above discussion seem to be based on a misunderstanding. Nowhere in the paper being discussed have we stated or implied that the formation of the  $\text{FA}_1$  peak is associated with accumulation of  $\text{P}_1$ . On the contrary,  $\text{FA}_1$  is a faradaic current peak for formic acid oxidation which we have shown can be modified by additives which change the quantity of P, adsorbed on the surface.

During the course of further work on activating effects in the formic acid oxidation, we have accumulated evidence for the essential features of the reaction scheme shown above, especially with regard to the effects of electrodeposited Hg. This work will be reported in more detail at a future date.

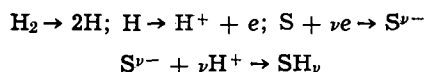
### The Anodic Oxidation of Hydrogen on Platinized Tungsten Oxides. II. Mechanism of $\text{H}_2$ Oxidation on Platinized $\text{WO}_3$ Electrodes

B. S. Hobbs and A. C. C. Tseung (pp. 766-769, Vol. 120, No. 6)

G. Vértes and G. Horányi:<sup>29</sup> In the paper under discussion the authors claim that  $\text{WO}_3$  is an active support in the catalytic oxidation of hydrogen and a mechanism of  $\text{H}_2$  oxidation is proposed. These studies are very similar to our catalytic work concerning the behavior of platinized WC and  $\text{WO}_3$  powders in liquid-phase catalytic hydrogenation. We found, however, that  $\text{WO}_3$  cannot be regarded as an active support in these processes. It is known from the literature that two fundamental types of mechanisms in liquid-phase hydrogenation may be distinguished. The first one is the atomic or radical mechanism, given by the following scheme



The second one is the ionic mechanism



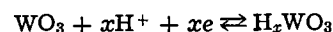
<sup>28</sup> D. Gilroy and B. E. Conway, *J. Phys. Chem.*, **69**, 1259 (1965).

<sup>29</sup> Central Research Institute for Chemistry, Hungarian Academy of Sciences, Budapest, Hungary.

Accepting the mechanism proposed by Benson *et al.*<sup>30,31</sup> and by Hobbs and Tseung a support effect may be expected in the case of hydrogenation via ionic mechanism.

As mentioned above this effect has not been observed. The rate of hydrogenation of nitrocompounds on platinum without support and with  $\text{Al}_2\text{O}_3$  or  $\text{WO}_3$  supports was the same.

The mechanistic consideration of Hobbs and Tseung is based upon the results of Benson *et al.*<sup>30,31</sup> who found that the reduction of  $\text{WO}_3$  was possible only if  $\text{WO}_3$  was mixed with platinum black and if water was pre-adsorbed on the mixture prior to admitting hydrogen to the system. If either one of these conditions was not satisfied, reduction did not take place at all at room temperature. According to Benson *et al.*,  $\text{WO}_3$  is reduced by H atoms produced by platinum splitting  $\text{H}_2$  molecules. The rapid transport of hydrogen atoms takes place in an adsorbed layer of water. This explanation does not take into consideration the possibility of the existence of electrochemical processes. The existence of the process



however, cannot be questioned.<sup>32,33</sup>

Thus the treatment of the problem in Benson's papers is inadequate, and the conclusions drawn on the mechanism of the reduction cannot be accepted. In our judgment there is no experimental evidence in the literature which provides the role of H atoms on this reduction. On the contrary, there exist several experimental facts attesting to the possibility of the electrochemical reduction of  $\text{WO}_3$  (reduction by  $\text{Zn} + \text{HCl}$ ,  $\text{Sn}^{2+}$ , etc. as has been stated in Glemser's work cited above<sup>32</sup>).

In Part I of the paper under discussion<sup>33</sup> the authors' opinion seemed to be similar to that outlined above. Thus, the conclusions drawn in Part II (i.e., the paper presently under discussion) rather contradict the previous assertions.

In addition, it should be noted that the experimental results reflected in Fig. 2 of the work under discussion do not prove the existence of the chemical pathway of reduction (by H atoms) and the support effect.

This type of curve is well known from catalytical literature. Similar experimental results have been obtained for different reactions on varying the concentration of the catalyst on an inactive support. These problems have been treated extensively, for example, in the theory elaborated by Kobozev which gives a mathematical formulation of the phenomenon.<sup>34,35</sup> From this theory it follows that an increase in the specific catalytic activity at low catalyst concentrations on the support cannot be regarded as a proof of a support effect.

B. S. Hobbs<sup>36</sup> and A. C. C. Tseung: In the above discussion G. Veres and G. Horanyi did not find any difference between the rate of hydrogenation of nitrocompounds on unsupported platinum and on platinum supported on  $\text{Al}_2\text{O}_3$  or  $\text{WO}_3$ . They therefore suggested that  $\text{WO}_3$  cannot be an active support for hydrogenation reactions and in turn implied that our results are invalid. This is a rather surprising deduction. It is important to note that Veres and Horanyi did not state the exact experimental conditions of their study, i.e., whether the size of the platinum crystallites on each of the three samples was the same or whether the

<sup>30</sup> J. E. Benson, H. W. Kohn, and M. Boudart, *J. Catalysis*, **5**, 307 (1966).

<sup>31</sup> M. Boudart, M. A. Vannice, and J. E. Benson, *Z. Physik. Chem. N.F.*, **64**, 171 (1969).

<sup>32</sup> O. Glemser and C. Naumann, *Z. Anorg. Allgem. Chem.*, **265**, 288 (1951).

<sup>33</sup> B. S. Hobbs and A. C. C. Tseung, *This Journal*, **119**, 580 (1972).

<sup>34</sup> J. G. Tolpin, G. S. John, and E. Field, "Advances in Catalysis," Vol. 5, p. 217, Academic Press, New York (1953).

<sup>35</sup> J. M. Thomas and W. J. Thomas, "Introduction to the Principles of Heterogeneous Catalysis," Academic Press, New York (1967).

<sup>36</sup> Electrical Research Association, Leatherhead, Surrey, England.

is a second intermediate in the main reaction path (see Fig. 1 above).

The possibility of relatively rapid production of intermediate II from  $\text{COOH} + \text{H}_{\text{ads}}$  follows from consideration of molecular models insofar as  $\text{H}_{\text{ads}}$  will be located close to the  $=\text{O}$  function in  $\text{COOH}$  at completion of the  $\text{HCOOH}$  dissociative chemisorption step. Reaction of this H with  $=\text{O}$  will be competitive with ionization of H but the proximity of H to  $=\text{O}$  and the shielding effect of  $\text{COOH}$  will enhance the possibility of reaction to form  $\overset{\cdot}{\text{C}}(\text{OH})_2$ . Formation of  $\overset{\cdot}{\text{C}}\text{OH}$  ( $\text{P}_1$ ) will naturally be a slower reaction, since extra H is required other than that provided directly by the dissociation step, and further geometrical rearrangement is required.

We suggest that outside the H region, the dissociation of the formic acid oxidation current with time is due to formation of  $\text{P}_2$  (see Fig. 1 above), e.g., a dimer such as formic anhydride.

The question of accounting for the first anodic current peak ( $\text{FA}_1$  in the paper under discussion) which Capon and Parsons mentioned<sup>21</sup> was considered by Gilroy and Conway,<sup>28</sup> who first showed in a general way how auto-inhibition effects could also cause current peaks without involvement of the potential-dependent traces of oxide species which Capon and Parsons invoke. The essential requirement was<sup>28</sup> that a step involving an adsorbed intermediate requires at least one extra site for the production of the next intermediate.

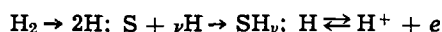
The remarks in the last paragraph of the above discussion seem to be based on a misunderstanding. Nowhere in the paper being discussed have we stated or implied that the formation of the  $\text{FA}_1$  peak is associated with accumulation of  $\text{P}_1$ . On the contrary,  $\text{FA}_1$  is a faradaic current peak for formic acid oxidation which we have shown can be modified by additives which change the quantity of P, adsorbed on the surface.

During the course of further work on activating effects in the formic acid oxidation, we have accumulated evidence for the essential features of the reaction scheme shown above, especially with regard to the effects of electrodeposited Hg. This work will be reported in more detail at a future date.

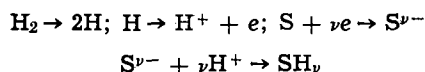
### The Anodic Oxidation of Hydrogen on Platinized Tungsten Oxides. II. Mechanism of $\text{H}_2$ Oxidation on Platinized $\text{WO}_3$ Electrodes

B. S. Hobbs and A. C. C. Tseung (pp. 766-769, Vol. 120, No. 6)

G. Vértes and G. Horányi:<sup>29</sup> In the paper under discussion the authors claim that  $\text{WO}_3$  is an active support in the catalytic oxidation of hydrogen and a mechanism of  $\text{H}_2$  oxidation is proposed. These studies are very similar to our catalytic work concerning the behavior of platinized WC and  $\text{WO}_3$  powders in liquid-phase catalytic hydrogenation. We found, however, that  $\text{WO}_3$  cannot be regarded as an active support in these processes. It is known from the literature that two fundamental types of mechanisms in liquid-phase hydrogenation may be distinguished. The first one is the atomic or radical mechanism, given by the following scheme



The second one is the ionic mechanism



<sup>28</sup> D. Gilroy and B. E. Conway, *J. Phys. Chem.*, **69**, 1259 (1965).

<sup>29</sup> Central Research Institute for Chemistry, Hungarian Academy of Sciences, Budapest, Hungary.

Accepting the mechanism proposed by Benson *et al.*<sup>30,31</sup> and by Hobbs and Tseung a support effect may be expected in the case of hydrogenation via ionic mechanism.

As mentioned above this effect has not been observed. The rate of hydrogenation of nitrocompounds on platinum without support and with  $\text{Al}_2\text{O}_3$  or  $\text{WO}_3$  supports was the same.

The mechanistic consideration of Hobbs and Tseung is based upon the results of Benson *et al.*<sup>30,31</sup> who found that the reduction of  $\text{WO}_3$  was possible only if  $\text{WO}_3$  was mixed with platinum black and if water was pre-adsorbed on the mixture prior to admitting hydrogen to the system. If either one of these conditions was not satisfied, reduction did not take place at all at room temperature. According to Benson *et al.*,  $\text{WO}_3$  is reduced by H atoms produced by platinum splitting  $\text{H}_2$  molecules. The rapid transport of hydrogen atoms takes place in an adsorbed layer of water. This explanation does not take into consideration the possibility of the existence of electrochemical processes. The existence of the process



however, cannot be questioned.<sup>32,33</sup>

Thus the treatment of the problem in Benson's papers is inadequate, and the conclusions drawn on the mechanism of the reduction cannot be accepted. In our judgment there is no experimental evidence in the literature which provides the role of H atoms on this reduction. On the contrary, there exist several experimental facts attesting to the possibility of the electrochemical reduction of  $\text{WO}_3$  (reduction by  $\text{Zn} + \text{HCl}$ ,  $\text{Sn}^{2+}$ , etc. as has been stated in Glemser's work cited above<sup>32</sup>).

In Part I of the paper under discussion<sup>33</sup> the authors' opinion seemed to be similar to that outlined above. Thus, the conclusions drawn in Part II (i.e., the paper presently under discussion) rather contradict the previous assertions.

In addition, it should be noted that the experimental results reflected in Fig. 2 of the work under discussion do not prove the existence of the chemical pathway of reduction (by H atoms) and the support effect.

This type of curve is well known from catalytical literature. Similar experimental results have been obtained for different reactions on varying the concentration of the catalyst on an inactive support. These problems have been treated extensively, for example, in the theory elaborated by Kobozev which gives a mathematical formulation of the phenomenon.<sup>34,35</sup> From this theory it follows that an increase in the specific catalytic activity at low catalyst concentrations on the support cannot be regarded as a proof of a support effect.

B. S. Hobbs<sup>36</sup> and A. C. C. Tseung: In the above discussion G. Vertes and G. Horanyi did not find any difference between the rate of hydrogenation of nitrocompounds on unsupported platinum and on platinum supported on  $\text{Al}_2\text{O}_3$  or  $\text{WO}_3$ . They therefore suggested that  $\text{WO}_3$  cannot be an active support for hydrogenation reactions and in turn implied that our results are invalid. This is a rather surprising deduction. It is important to note that Vertes and Horanyi did not state the exact experimental conditions of their study, i.e., whether the size of the platinum crystallites on each of the three samples was the same or whether the

<sup>30</sup> J. E. Benson, H. W. Kohn, and M. Boudart, *J. Catalysis*, **5**, 307 (1966).

<sup>31</sup> M. Boudart, M. A. Vannice, and J. E. Benson, *Z. Physik. Chem. N.F.*, **64**, 171 (1969).

<sup>32</sup> O. Glemser and C. Naumann, *Z. Anorg. Allgem. Chem.*, **265**, 288 (1951).

<sup>33</sup> B. S. Hobbs and A. C. C. Tseung, *This Journal*, **119**, 580 (1972).

<sup>34</sup> J. G. Tolpin, G. S. John, and E. Field, "Advances in Catalysis," Vol. 5, p. 217, Academic Press, New York (1953).

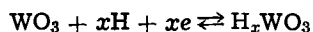
<sup>35</sup> J. M. Thomas and W. J. Thomas, "Introduction to the Principles of Heterogeneous Catalysis," Academic Press, New York (1967).

<sup>36</sup> Electrical Research Association, Leatherhead, Surrey, England.

hydrogenation results were normalized to unit Pt surface area or unit Pt weight. Unless these points are clarified, it is rather pointless to quote the results as scientific evidence at all. In addition, our tests were done on Teflon bonded electrodes. The pores of our catalysts were basically dry and hence permitted the rapid diffusion of H<sub>2</sub>; whereas liquid-phase hydrogenation could well be limited by the rate of H<sub>2</sub> diffusion through the pores of the catalyst since they are filled with liquid. Thus, it is important to know whether the hydrogenation reaction in their case was mainly limited by the mass transfer of the reactants.

We prepared the supported catalysts by mixing a stock preparation of platinized WO<sub>3</sub> with varying percentages of WO<sub>3</sub> and then plotting activity/unit weight of Pt black *vs.* Pt loading (see Fig. 2 in the paper under discussion). The results clearly showed that a synergistic effect was in operation. On the other hand, no such effect was found in the case of platinized B<sub>4</sub>C, *i.e.*, regardless of Pt loading (0.01-0.12 mg Pt/cm<sup>2</sup>), the activity/unit weight of Pt loading remained unchanged for the platinized B<sub>4</sub>C electrodes (Fig. 5 of the paper under discussion).

Furthermore, Vertes and Horanyi suggested that the formation of H<sub>x</sub>WO<sub>3</sub> could be via an electrochemical process



If this mechanism is the main process, then it is impossible to reconcile it with the greatly enhanced activity of platinized WO<sub>3</sub> for the oxidation of hydro-

gen, since if  $x\text{H}^+$  is required to form H<sub>x</sub>WO<sub>3</sub>, then the support cannot speed up the rate of H<sub>2</sub> oxidation. Benson *et al.*<sup>30</sup> gas-phase studies on the formation of H<sub>x</sub>WO<sub>3</sub> only involved the adsorption of one monolayer of H<sub>2</sub>O and hence the electrochemical mechanism is rather unlikely. Furthermore, the formation of H<sub>x</sub>WO<sub>3</sub> by the Zn + HCl reduction process<sup>32</sup> is likely to involve the formation of a H atom which could then diffuse to the WO<sub>3</sub> surface, resulting in the formation of H<sub>x</sub>WO<sub>3</sub>. Moreover, Polterak<sup>37</sup> showed that a WO<sub>3</sub> crystal can be reduced to tungsten blue (H<sub>x</sub>WO<sub>3</sub>) when it is placed near but not touching a cathode undergoing H<sub>2</sub> evolution, thus confirming the validity of our proposed mechanism.

Finally, Kobozev's mathematical formulations<sup>34</sup> tend to agree rather than disagree with our results, since we have shown that the increase in specific activity with decreased Pt loading reached a maximum value when the number of Pt particles to WO<sub>3</sub> particles is about 1:1 and the activity decreases thereafter. In the case of the normal supported catalyst the increase in specific activity is usually associated with decreased Pt crystallite size as the platinum concentration on the supported catalyst is reduced. In our work, we have carefully avoided this pitfall; the catalyst samples were prepared by mixing a stock preparation of platinized WO<sub>3</sub> with varying percentages of WO<sub>3</sub>, thus ensuring that the platinum crystallite size remained unchanged.

<sup>37</sup> G. Polterak, *Zh. Fiz. Khim.*, **27**, 599 (1953).



## Contributions of Oxygen, Silicon, and Hydrogen to the Interface States of an Si-SiO<sub>2</sub> Interface

W. Fahrner<sup>1</sup>

*Institut für Angewandte Festkörperphysik der Fraunhofer-Gesellschaft,  
D-7800 Freiburg i.Br., Eckerstrasse 4, West Germany*

*The publication costs of this article have been assisted by the  
Institut für Angewandte Festkörperphysik der Fraunhofer-Gesellschaft.*

### ABSTRACT

Oxygen, silicon, and hydrogen ions are implanted with doses of  $10^{10}$ - $10^{15}/\text{cm}^2$  through the oxide of a MOS structure. The development of induced levels in Si can be observed. Annealing experiments from room temperature to  $800^\circ\text{C}$  show the transition from the nonequilibrium incorporation to the initial (nonimplanted) state. Hydrogen implantation hinders the restoration of a Si-SiO<sub>2</sub> interface under H<sub>2</sub> annealing.

In a previous paper (1) we showed that implantation of oxygen at a Si-SiO<sub>2</sub> interface creates two deep-lying levels in Si ( $E_c - E = 0.51$  and  $0.71$  eV). When we measured the oxygen implanted sample three months later, we observed a broad spectrum of surface states, but not a trace of the deep lying levels. Furthermore, it was shown (2) that SiH implantation produces a level  $E_c - E$  at  $0.58$  eV. These results led us to the well-known suggestion that interface states could be explained as the result of nonstoichiometry, i.e., a local abundance of either oxygen or silicon, or a disorder at the interface.

Models corresponding to such an assumption were given for example by Revesz and Zaininger (3) or Kooi (4). According to Kooi's model, hydrogen should interact with the unsaturated dangling bonds and therefore reduce the number of surface states. Thus we included in our studies an investigation involving hydrogen implantation to test this hypothesis.

### Experimental

The experimental procedure was as follows:  $\langle 100 \rangle$  epitaxial n and p samples of about  $1$  ohm-cm resistivity were cleaned and oxidized in dry oxygen. The lifetime of the minority carriers was better than  $80$   $\mu\text{sec}$ . The oxide thickness was in the range of  $500$ - $1000\text{\AA}$ . The samples were then implanted, annealed, and  $0.50$  mm diameter aluminum dots were evaporated onto the oxide. The accelerator energy was chosen to make the implantation range equal to the oxide thickness. (We used an accelerator energy of  $95$  keV in order to implant Si through  $1000\text{\AA}$  SiO<sub>2</sub> f.e.). For this purpose we used the range tables of Johnson and Gibbons (5). We made two experimental series for each implanted ion species. In one series the annealing temperature was kept constant at  $500^\circ\text{C}$ , and the ion dose was varied from  $10^{10}$ - $10^{15}/\text{cm}^2$  in steps of a factor of  $10$ . In the other series the annealing temperature

was varied from room temperature to  $800^\circ\text{C}$  in steps of  $100^\circ\text{C}$  while maintaining the ion dose. In this second series we used the results of the first series to choose a dose where the induced levels could be seen most clearly.

To determine surface state density  $N_{ss}$  and, to a rough approximation, the fixed charge density, we used the slow ramp technique (6) in connection with a  $71$  AR-Boonton  $1$  MHz bridge. For the higher  $N_{ss}$  values we had to measure the sample capacitance at a frequency of  $30$ - $50$  MHz in order to get a dispersion-free C-V curve. This was done point-by-point with a  $33$  B Boonton bridge.

For each series a nonimplanted control sample was measured in order to determine the original surface-state density ( $< 10^{10}/\text{cm}^2$   $\text{eV}^{-1}$ ). Because the C-V

curves give more information than just the deduced  $N_{ss}$  ( $\psi_{CB}$ ) plots, we rather present the former ones ( $\psi_{CB}$  = energy measured with respect to the conduction band).

### Results

An implantation of oxygen caused the appearance of the two deep lying levels (Fig. 1a-e). The lowest dose used of  $10^{10}/\text{cm}^2$  was low enough to have no measurable effect on the surface states compared to the control sample. [Radiation damage was removed in this series by annealing at  $500^\circ\text{C}$  in H<sub>2</sub> for  $2$  hr (7).] The number of states in the levels grew with increasing ion dose. For an oxygen dose of  $10^{13}/\text{cm}^2$ , only the upper level at  $0.51$  eV could be seen; the  $0.71$  eV level disappeared under the low energy tail of the  $0.51$  eV level. At a dose of  $10^{14}/\text{cm}^2$ , the  $0.51$  eV level was close to the upper detection limit of  $N_{ss}$  by the slow ramp technique. Stability of the samples was excellent, neither leakage currents nor flatband shifts could be observed. Up to the dose of  $10^{13}/\text{cm}^2$  flatband voltage was above  $-1\text{V}$ . For the  $10^{14}/\text{cm}^2$  sample we observed a considerable downward shift to  $\approx -7\text{V}$  and a donorlike doping effect.

<sup>1</sup> Present address: IBM Corporation, East Fishkill Facility, Hopewell Junction, New York 12533.

Key words: surface states, nonequilibrium state of impurities, implantation in a MOS structure.

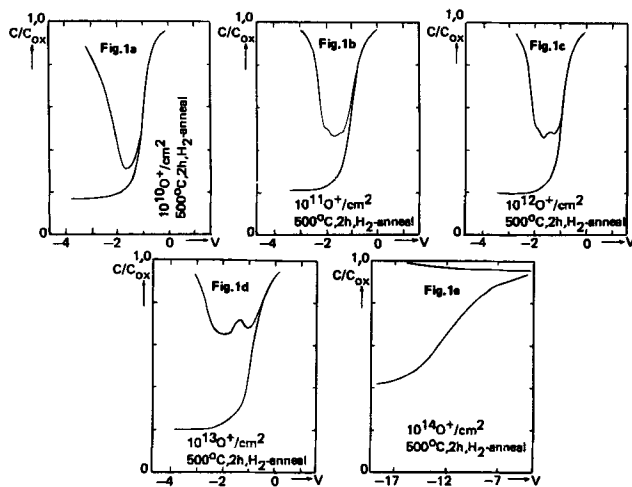


Fig. 1a-e. n-type samples, oxygen implantation through  $\approx 500\text{\AA}$  SiO<sub>2</sub>.

In the second experimental series for oxygen, the results of the annealing experiments are given in Fig. 1f-j. With a fixed ion dose of  $10^{13}/\text{cm}^2$ , which gave a good resolution of the peaks, we started with an annealing temperature of  $400^\circ\text{C}$ . The two levels can be seen clearly at the relative values of  $C/C_{\text{ox}} = 0.775$  and  $0.805$ , respectively. The  $500^\circ\text{C}$  experiment was already done in the first series. On comparison, one sees that the ion doses were not exactly the same because the  $0.71\text{ eV}$  level is still slightly visible. The  $0.51\text{ eV}$  level did not decrease very much, but the  $0.71\text{ eV}$  level is reduced to  $C/C_{\text{ox}} = 0.74$ . Annealing at  $600^\circ\text{C}$  makes both levels disappear; we see only a broad spectrum of surface states. The shape of these curves is identical to that obtained for a  $10^{12}\text{O}/\text{cm}^2$  implanted sample, annealed at  $500^\circ\text{C}$ , but measured after an aging period of 3 months. Compared to this aged sample, the stability of the  $600^\circ\text{C}$  annealed sample is relatively poor.

For each new measuring cycle, these C-V curves were displaced to the right, as indicated by the arrows. The  $N_{\text{ss}}$  values of the control sample were nearly attained for the  $700^\circ\text{C}$  sample even though the same drifting behavior was observed. Finally, at  $800^\circ\text{C}$  the  $N_{\text{ss}}$  values, stability, and flatband voltage of the control sample were reached. A summary of the oxygen results is given in Fig. 2a and b, where the values of  $N_{\text{ss}}$  vs. dose and annealing temperature are plotted.

The same experiments were repeated with  $^{30}\text{Si}$ . (This isotope was used instead of  $^{28}\text{Si}$  or  $^{29}\text{Si}$  in order to

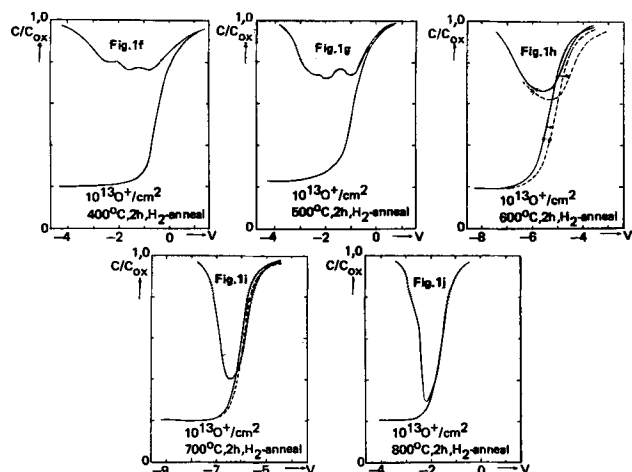


Fig. 1f-j. The same kind of samples as before implanted with  $10^{13}\text{O}/\text{cm}^2$ . The annealing temperature was in the range of  $400^\circ\text{C}$  -  $800^\circ\text{C}$ .

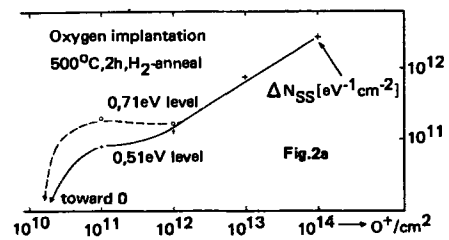


Fig. 2a. Induced  $N_{\text{ss}}$  values vs. oxygen dose, taken either for both oxygen levels or at the  $0.51\text{ eV}$  level.

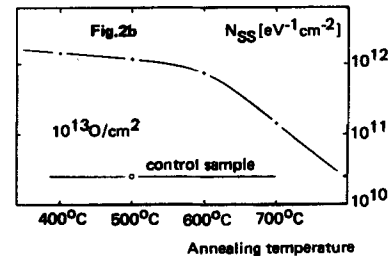


Fig. 2b. Reduction of  $N_{\text{ss}}$  under annealing. The implantation dose was  $10^{13}\text{O}/\text{cm}^2$ . The original surface-state density is reached at  $800^\circ\text{C}$ .

block out the CO and N<sub>2</sub> impurities on the  $^{28}\text{Si}$  line and the  $^{28}\text{SiH}$  impurity on the  $^{29}\text{Si}$  line). With varying Si dose (Fig. 3a-d) we see again that a dose of  $10^{10}/\text{cm}^2$  does not measurably change the number of surface states found in the control sample. At a dose of  $10^{11}/\text{cm}^2$ , the first hint of a level was visible. (The overshoot effect and the capacitance hook of the low-frequency and high-frequency curve, respectively, are caused by the well-understood effects of a elevated surface-state density and the formation of a depletion edge region around the Al dot which acts as a barrier against the n channel.)

Figure 3c shows that the level barely seen in Fig. 3b actually contains three levels of  $E_c - E = 0.93$ ,  $0.63$ , and  $0.34\text{ eV}$ , respectively, (Fig. 4). A significant change in the curves similar to that seen in the transition from  $10^{13}$  to  $10^{14}/\text{cm}^2$  for oxygen was already observed, when we increased the dose from  $10^{12}$  to  $10^{13}/$

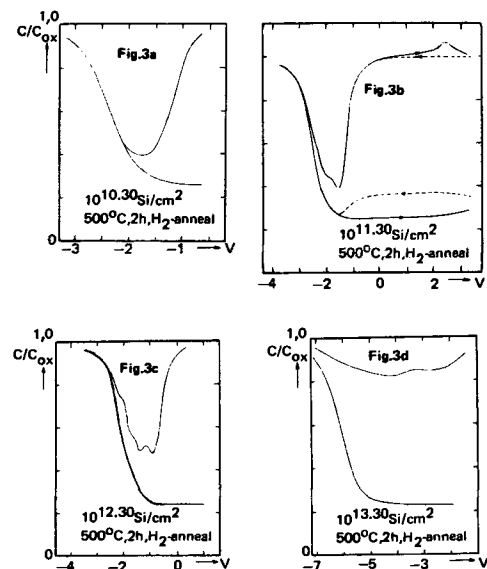


Fig. 3a-d. p-type samples, silicon implantation through  $\approx 500\text{\AA}$  SiO<sub>2</sub>. The dose was in the range of  $10^{10}$ - $10^{13}/\text{cm}^2$ , the annealing temperature was  $500^\circ\text{C}$ . C-V curves were plotted from accumulation to inversion (full line) and back (dashed line; not shown for every plot). When full and dashed line coincide, only the full line is shown. The dose was in the range of  $10^{10}$ - $10^{14}\text{O}/\text{cm}^2$ , the annealing temperature was  $500^\circ\text{C}$ .

SSST

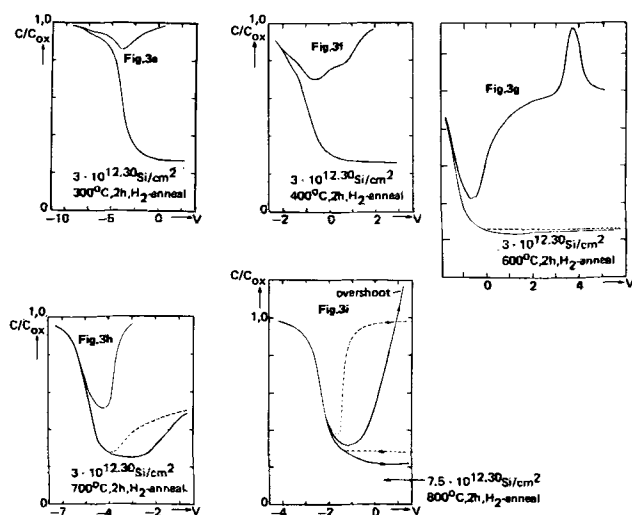


Fig. 3e-i. p-type samples, implanted with  $3 \cdot 10^{12}$   $^{30}\text{Si}/\text{cm}^2$  through  $\approx 800\text{\AA}$   $\text{SiO}_2$ . The annealing temperature was in the range of  $300^\circ\text{--}800^\circ\text{C}$ .

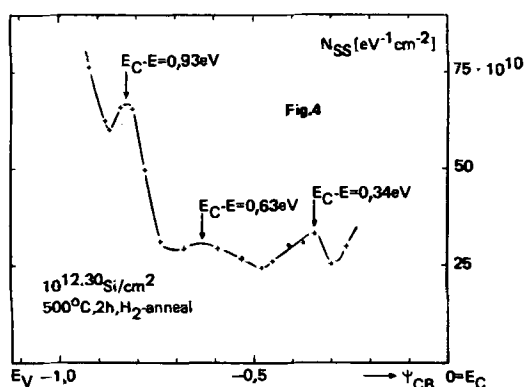


Fig. 4.  $N_{ss}(\Psi_{CB})$  deduced from Fig. 3c

$\text{cm}^2$  for silicon. The minimum surface-state density is now  $1.8 \cdot 10^{12} \text{ eV}^{-1} \text{ cm}^{-2}$ , the flatband voltage  $\approx -7\text{V}$ . For our highest dose of  $10^{14}/\text{cm}^2$  we obtained a straight line in the low-frequency meaning that  $N_{ss}$  was always  $> 5 \cdot 10^{13} \text{ eV}^{-1} \text{ cm}^{-2}$ . From these results it

is clear that any information about an induced level must be accompanied by a statement of the implantation and annealing conditions.

We will not discuss the reduction of  $N_{ss}$ ,  $V_{FB}$ , and of the drift by annealing for implanted silicon because the effects were very similar to those already described for oxygen. This can be seen in Fig. 3e-i.

Finally, we want to report on the results of hydrogen implantation. Up to a dose of  $10^{15}/\text{cm}^2$  we did not see any change in the C-V plots (not shown) compared to the control sample. This indicates that the hydrogen is either distributed over the whole sample volume, or it has diffused out. These assumptions are further supported by two facts. First, hydrogen has a very high diffusion constant of  $D = 10^{-5} \text{ cm}^2/\text{sec}$  at  $500^\circ\text{C}$  (8) which is comparable to the lithium diffusion constant of  $D = 1.8 \cdot 10^{-5} \text{ cm}^2/\text{sec}$  at  $1200^\circ\text{C}$ . Second, experimental evidence found by Card and Kao (9) showed that for a proton bombardment at 25 MeV an annealing temperature of  $300^\circ\text{C}$  was sufficient to restore the initial high-frequency curves. With a better resolution, however, one finds that this annealing temperature limit must be increased to  $500^\circ\text{C}$ . At temperatures equal to or below  $200^\circ\text{C}$ , a level  $E_c - E = 0.78 \text{ eV}$  for hydrogen is found (Fig. 5). At  $300^\circ$  and  $400^\circ\text{C}$  this level disappeared, while another level at  $E_c - E = 0.25 (\pm 0.05) \text{ eV}$  appeared (Fig. 6). Only above

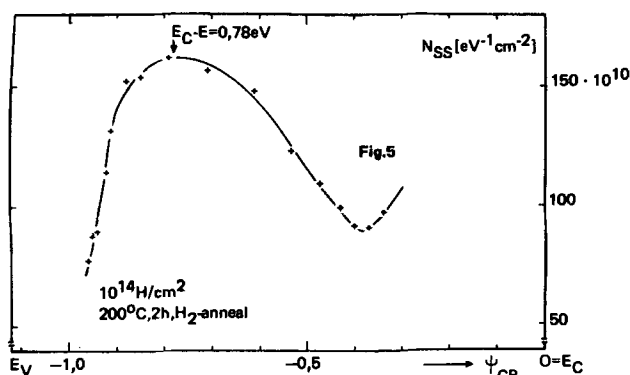


Fig. 5.  $N_{ss}(\Psi_{CB})$  for an H implantation of  $10^{14}/\text{cm}^2$  and  $200^\circ\text{C}$  annealing temperature.

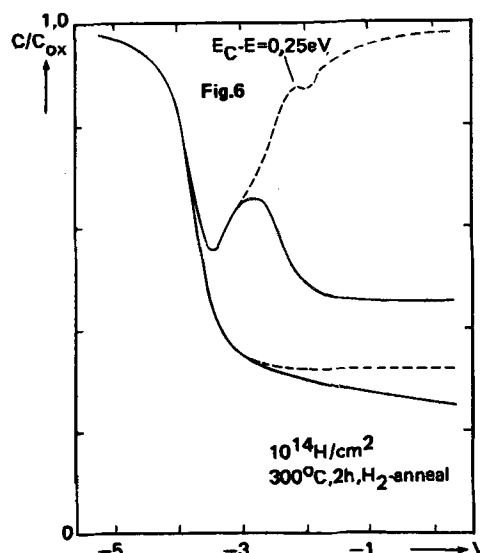


Fig. 6. C-V plot for a  $10^{14} \text{ H}/\text{cm}^2$  implanted sample annealed at  $300^\circ\text{C}$ . A level at  $E_c - E = 0.25 \pm 0.05 \text{ eV}$  is seen.

$500^\circ\text{C}$  was no influence of hydrogen on the surface states and fixed charge density observed.

### Discussion

The main results of these experiments are the following. First, surface states cannot be explained as a nonstoichiometry effect of oxygen or silicon. The oxidation temperature is at about  $1000^\circ\text{C}$ , but any nonstoichiometry or at least the surface states due to a nonstoichiometry disappear before  $800^\circ\text{C}$  are reached. Thus we can only speculate what the actual source of the surface states might be. The cleanliness of the sample preparation obviously influences the number of surface states. It cannot be excluded that surface states are just the product of a small amount of impurities which can never be avoided. The second, and surprising, result is that implanted H does not accelerate the restoration of the interface, but hinders it. (For a sample implanted with "inert" ions, i.e., N, Ar, etc., an annealing temperature of  $300^\circ\text{C}$  in  $\text{H}_2$  is sufficient to restore the interface). Therefore, it is not possible to reach lower device processing temperatures by H implantation. These two results together show that the suggested models do not correctly describe the influence of oxygen, silicon, and hydrogen on an Si-SiO<sub>2</sub> interface.

### Acknowledgment

We are grateful to K. Eisele, A. Goetzberger, E. Klausmann, F. Pohl, J. Schaub, and T. Scheffer for critical reading of the manuscript, discussions, drawing of the figures, and performing of the ion implantation.

Manuscript submitted Aug. 7, 1973; revised manuscript received Nov. 2, 1973.

Any discussion of this paper will appear in a Discussion Section to be published in the December 1974 JOURNAL. All discussions for the December 1974 Discussion Section should be submitted by Aug. 1, 1974.

#### REFERENCES

1. W. Fahrner and A. Goetzberger, *Appl. Phys. Letters*, **21**, 329 (1972).
2. W. Fahrner, Thesis, Universität Freiburg, p. 55 (1972).
3. A. G. Revesz and R. H. Zaininger, *IEEE Trans. Electron Devices*, **ED-13**, 246 (1966).
4. E. Kooi, *Philips Res. Rept.*, **21**, 477 (1966).
5. W. S. Johnson and J. F. Gibbons, "Projected Range Statistics in Semiconductors," Stanford Univ. Bookstore, Stanford, Calif. (1969).
6. R. Castagné, *Compt. Rend. Acad. Sci. Paris*, **267**, série B, 866 (1968).
7. W. Fahrner and A. Goetzberger, in "Second International Conference on Ion Implantation," I. Ruge and J. Graul, Editors, p. 307, Springer-Verlag, Berlin, New York (1971).
8. H. Reiss and C. S. Fuller, in "Semiconductors," N. B. Hannay, Editor, p. 234, Reinhold Publishing Corp., New York (1959).
9. H. C. Card and K. C. Kao, *Electron. Letters*, **6**, 749 (1970).

## Application of Interface Demarcation to the Study of Facet Growth and Segregation: Germanium

A. F. Witt,\* M. Lichtensteiger, and H. C. Gatos\*

Department of Metallurgy and Materials Science and Center for Materials Science and Engineering, Massachusetts Institute of Technology, Cambridge, Massachusetts 02139

The publication costs of this article have been assisted by the Massachusetts Institute of Technology.

#### ABSTRACT

It has been demonstrated that interface demarcation, achieved by transmitting current pulses across the growth interface, combined with spreading resistance measurements, is uniquely suited for the quantitative investigation of facet growth and associated dopant segregation behavior. Interface demarcation lines (intercepts of the periodically delineated interface with a plane parallel to the growth axis) were used (i) as "rate striations" for the determination of microscopic growth rates, (ii) as "locators" for the identification of simultaneously grown areas in the core and off-core regions, and (iii) as "time reference markers" for the in-time correlation of growth and segregation behavior. Applying this technique to Czochralski-type growth of Ga-doped Ge it was found that facet growth and segregation are more complex phenomena than assumed in the accepted theoretical models.

The dopant segregation associated with facet growth has been extensively investigated in semiconductor crystals since the discovery of the coring effect (1).<sup>1</sup> These studies, based on macroscopic data, have led to the following main conclusions: (i) The tendency of growth facet formation during crystal pulling by the Czochralski technique depends on the growth direction; it decreases according to the sequence:  $\langle 111 \rangle > \langle 100 \rangle > \langle 110 \rangle$  (2). (ii) For a given system the ratio of  $k_{\text{eff}}$  (facet) to  $k_{\text{eff}}$  (off-facet) is constant and greater than one (3); the only reported exception is the system Ge-Ga where this ratio is smaller than one (4). (iii) The vertical facet growth rate remains virtually constant (under constant pulling rate) irrespective of growth rate variations in the off-facet region (5). (iv) The appearance of rotational segregation inhomogeneities in the core region depends on the facet inclination relative to the horizontal and on the thermal asymmetry (5). (v) Nonrotational dopant inhomogeneities exhibit no discontinuities from the core to the off-core regions (5).

Investigations comparing the segregation behavior in core and off-core regions have been based primarily on compositional information obtained from transverse resistivity scans across these regions. Because of the

curvature of the off-facet growth interface, such results are of limited value since they do not correspond to identical growth interfaces.

Theoretical treatments of the coring effect are based on the concept of intermittent, rapid, lateral layer growth on kinetically supercooled facets (6); the specificity of coring (the variation of the ratio  $k_{\text{eff}}$  (facet) to  $k_{\text{eff}}$  (off-facet) with regard to the nature of the dopant and the host crystal is attributed to chemisorption at the growth interface.

The present communication reports on the successful application of a recently developed experimental approach (7) to the quantitative investigation of facet growth and segregation on a microscale and to the comparison of the simultaneous facet and off-facet segregation behavior; this approach combines the interface demarcation with spreading resistance measurements. Emphasis is placed on the demonstration of the usefulness and potential of this approach rather than on the analysis or interpretation of specific facet growth effects.

#### Experimental Procedure

The segment of the germanium single crystal employed in this study was pulled at a rate of 3.2 cm/hr under seed rotation (3.1 rpm) from a melt doped with gallium ( $2 \times 10^{20}$  atoms/cm<sup>3</sup>). Interface demarcation during growth (8) was accomplished by transmitting current pulses (20A) of 0.03 sec duration at a repetition rate of 0.5 sec across the growth interface. A 2 mm thick section was obtained by cutting the crystal along the rotational axis. The plane containing the rotational axis was chemically polished (Syton HT-30)

\* Electrochemical Society Active Member.

Key words: germanium, facet growth, impurity segregation, interface demarcation, crystal growth.

<sup>1</sup> The term core in semiconductor crystals refers to the part of the crystal associated with interface-facet growth and exhibits a higher dopant concentration than the rest of the crystal (with one reported exception pointed out in text); this behavior is referred to as coring effect; a core region is not necessarily located in the central part of the crystal. In this paper the term core is broadly used for the part of the crystal associated with facet growth without consideration of dopant segregation behavior.

and etched in  $1\text{HF} + 1\text{H}_2\text{O}_2 + 1\text{CH}_3\text{COOH}$  for 6 sec to reveal the interface demarcation lines (intercepts of the periodically delineated growth interface with the plane) and the inherent segregation inhomogeneities. The microscopic dopant concentration profile in the crystal section was then determined through spreading resistance scans; a detailed description of this technique has been reported elsewhere (7).

### Experimental Results

The present experimental approach is applied to the determination of: (i) the microscopic vertical growth rate; (ii) the dopant concentration profile; and (iii) the dependence of dopant segregation on the vertical growth rate. The growth and segregation behavior in the facet region is then contrasted with that of the corresponding off-facet region.

Figure 1 is a photomicrograph of the germanium segment studied showing the areas analyzed designated as A, B, C, and D. The core and off-core regions as well as the rotational segregation inhomogeneities are clearly visible. Interface demarcation lines are not visible at this magnification. It should be noted that interface demarcation in no way interferes with the basic growth and segregation behavior (8).

Fig. 1. Differentially etched segment of a Ga-doped Ge single crystal pulled with seed rotation. The areas analyzed, designated as A, B, C, and D, are 0.086 cm long and correspond to a growth period of 64 sec. Traces of the spreading resistance measurements in some instances extend beyond the areas analyzed. Interface demarcation lines are not visible at this magnification. Areas A and D are shown under high magnification in Fig. 2.

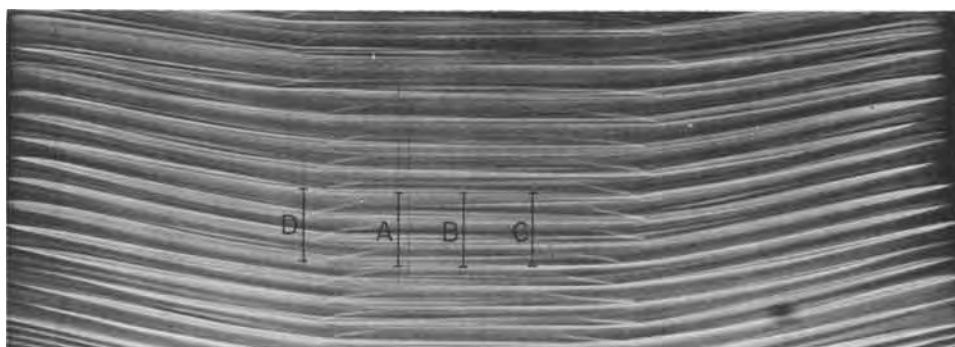
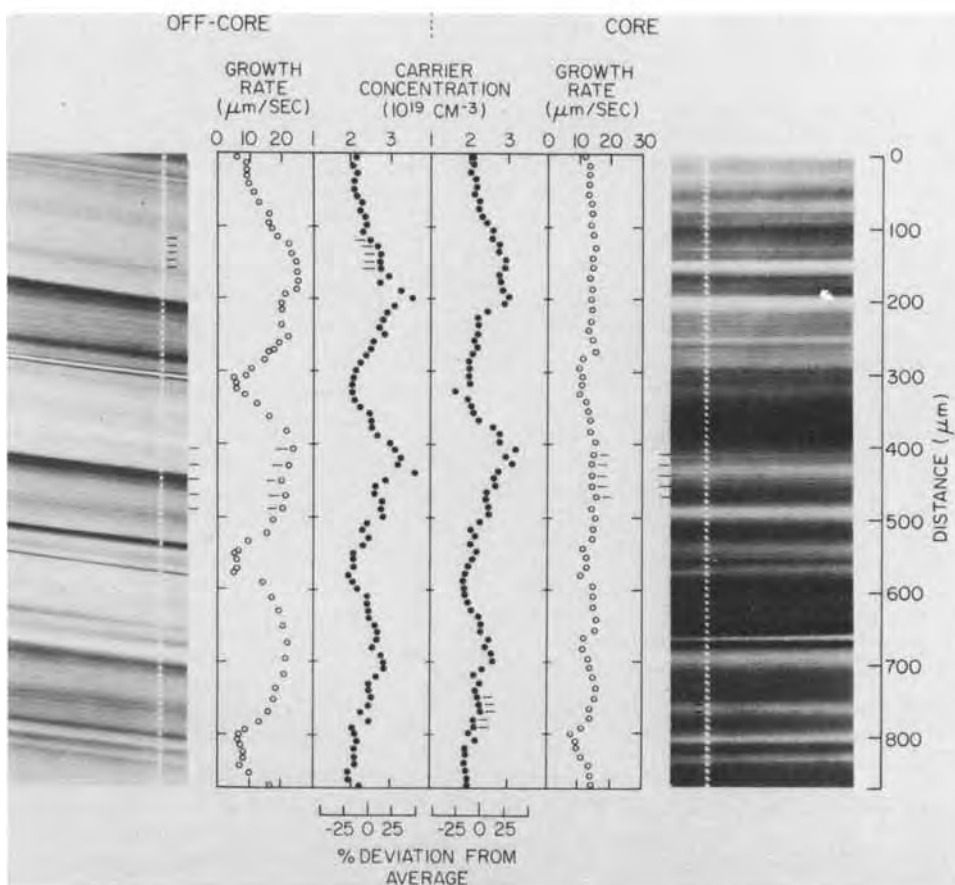


Fig. 2. Differentially etched core area (right-hand side) and a corresponding off-core area (left-hand side) of a Ga-doped Ge single crystal. The core and off-core areas shown here under high magnification are the A and D areas in Fig. 1. The impact traces of the spreading resistance measurements are visible on both crystal growth rates and the carrier (dopant) concentrations are plotted as a function of distance. For convenience the correspondence between individual impact traces and the carrier concentration and microscopic rate points is indicated for five points in each plot.



**Growth rate analysis.**—Using the interface demarcation lines (introduced in the present case at 0.5-sec intervals) as time markers, the average macroscopic growth rate,  $V_{\text{avg-mac}}$ , of the core region area A (right-hand side of Fig. 2) is directly determined from the number of demarcation lines in this area (0.086 cm long).  $V_{\text{avg-mac}}$  is, thus, found to be  $13.4 \mu\text{m/sec}$  ( $4.8 \text{ cm/hr}$ ) which corresponds to the sum of the pulling rate ( $8.6 \mu\text{m/sec}$ ) and the simultaneous lowering rate of the melt level ( $4.8 \mu\text{m/sec}$ ). The vertical microscopic facet growth rate, obtained from the spacing of successive demarcation lines (Fig. 2), varies between 7 and  $16 \mu\text{m/sec}$ ; the average microscopic growth rate,  $V_{\text{avg-mic}}$ , is found to be identical with  $V_{\text{avg-mac}}$ . The small, random growth rate variations observed in the core region cannot be correlated with rotational growth-rate variations in the off-core region (right-hand side of Fig. 2).

The quantitative agreement between  $V_{\text{avg-mac}}$  and  $V_{\text{avg-mic}}$  indicates the absence of backmelting since backmelting would result in  $V_{\text{avg-mic}} > V_{\text{avg-mac}}$  (9). Microscopic growth rate measurements made in three different areas within the core (A, B, and C) show that the random growth rate variations are identical in magnitude and take place at exactly the same time



throughout the core region. Thus, it is apparent that the facet advances, at all times, parallel to the established growth interface; off-facet growth rate variations are completely accommodated in the off-facet region adjacent to the facet.

**Dopant concentration analysis.**—The microscopic dopant distribution in the core region (with a linear resolution of  $10\ \mu\text{m}$ ) is obtained from spreading resistance scans, the impact traces of which can be seen in the photomicrographs of Fig. 2. The dopant concentration profile of the core area A is given on the right-hand side of Fig. 2. Each point on the graph corresponds to an identifiable impact trace on the crystal; for convenience this correspondence is indicated for five points in the lower segment of the plot by short horizontal lines.

The dopant concentration plot shows segregation inhomogeneities with deviations exceeding  $\pm 25\%$  from the average concentration. The inhomogeneities reflect unambiguously the rotational periodicity, consistent with the etching behavior observed on the photomicrograph in Fig. 1. The dopant profile in the core area B, not shown here, exhibited essentially the same periodic inhomogeneities as area A, but with a slight displacement of the dopant concentration maxima and minima in the downward direction. Transverse scans across the core indicated only very small compositional variations in quantitative agreement with the vertical displacements of the concentration maxima and minima.

**Analysis of the vertical growth rate dependence of core segregation.**—The outstanding feature of the present approach is that it allows an exact analysis of the growth rate dependence of segregation since both the composition and the corresponding growth rate can be determined at any point in the crystal.

An inspection of the dopant concentration and vertical growth rate profiles of the core area A, in Fig. 2, indicates that the Burton, Prim, and Slichter (BPS) analysis (10) is not applicable to core segregation since significant segregation changes are observed under conditions of virtually constant vertical growth rate; in some instances even an increase in dopant concentration is observed under conditions of decreasing vertical growth rate. These results are consistent with the established theoretical models which assume that core segregation depends on the horizontal rather than on the vertical growth rates.

**Comparison of the core segregation to the off-core segregation behavior.**—The off-core area D (left-hand side of Fig. 2) corresponding to the core area A (right-hand side of Fig. 2) is identified by following the uppermost demarcation line in area A to the off-core area D. Starting with this demarcation line, which represents the growth interface across the core and off-core areas at the same instant in time, the dopant concentration and growth rate for the off-core area are plotted in Fig. 2 as a function of distance.

In contrast to the core segregation, the segregation behavior in the corresponding off-core area D is in quantitative agreement with the BPS theory for steady-state growth conditions; i.e., a plot of  $\ln(1/k_{\text{eff}} - 1)$  vs. growth (from the data of Fig. 2) exhibited a constant slope over the entire area; the value of the corresponding boundary layer thickness ( $\delta$ ) was found to be  $320\ \mu\text{m}$ , which is smaller than the value of  $580\ \mu\text{m}$  calculated from the Cochran analysis. Irregular small variations in segregation, not associated with growth rate fluctuations are attributed to convection-induced boundary layer perturbations; they do not affect the BPS analysis.

The dopant concentration and its variation in the corresponding core and off-core areas, plotted in Fig. 2 as a function of distance, are virtually identical. This result indicates that the ratio of  $k_{\text{eff}}$  (facet) to  $k_{\text{eff}}$

(off-facet) is equal to one under the present growth conditions, rather than less than one as reported previously (3).

Although this result may be valid only for the present experimental conditions, it is, nevertheless, most interesting since the dopant concentration variations in the off-core region are controlled by the vertical microscopic growth rate while in the adjacent core region these variations are presumably controlled by the horizontal growth rate.

The direct comparison of the segregation behavior in the corresponding areas as presented in Fig. 2 is of interest as a spatial dopant distribution analysis. The exact comparison of the segregation behavior in the corresponding core and off-core regions must be based, however, on an analysis of the dopant concentration vs. time (as determined from the number of time markers); such analysis takes into account independently fluctuating growth rates in the two regions, causing changes in the curvature of the growth interface. The conversion of the concentration vs. distance plots of Fig. 2 to concentration vs. time plots is given in Fig. 3. This plot indicates virtually identical segregation behavior in the corresponding regions and, thus, no detectable coring effect.

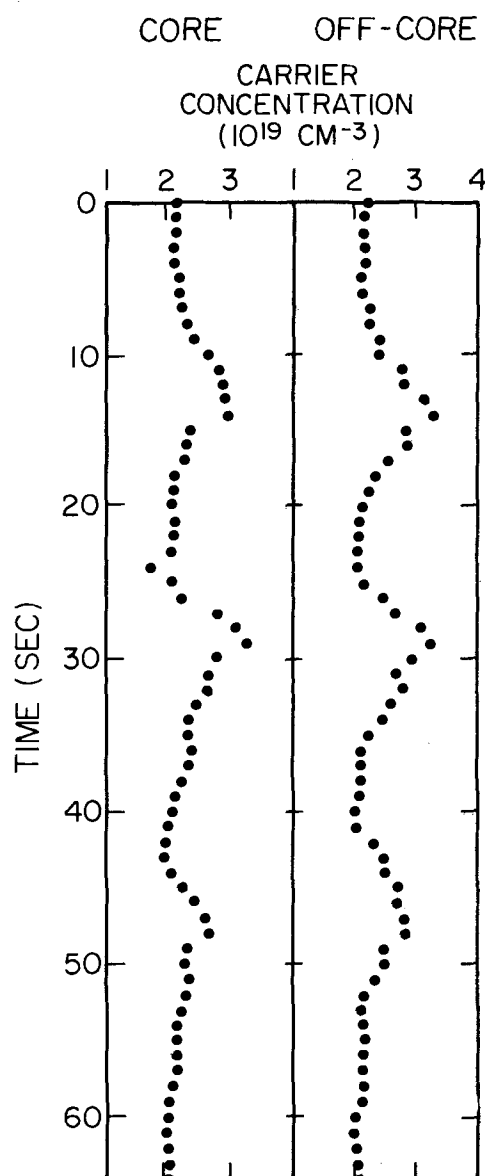


Fig. 3. Carrier (dopant) concentration in the core and off-core areas of Fig. 2 plotted as function of time (as determined from the number of time markers).

### Summary

It is shown that the growth interface demarcation technique in combination with spreading resistance measurements constitutes a unique experimental approach for the quantitative investigation of growth and segregation behavior associated with the presence of an interface facet (coring effect).

While the present communication is primarily intended to demonstrate the applicability and scope of the above experimental approach, the limited amount of results presented shows clearly the complexity of these phenomena. Thus, segregation inhomogeneities can appear in the core region with the same periodicity (corresponding to the rate of rotation) and equal in magnitude to those in the adjacent off-core region, although the vertical growth rate of the core remains virtually constant. Furthermore, these inhomogeneities appear in phase in the two regions and exhibit identical dopant concentrations under the experimental conditions reported in this study. The absence of a coring effect [ $k_{\text{eff}}(\text{facet}) = k_{\text{eff}}(\text{off-facet})$ ] in the present case, is in contrast to earlier results showing [ $k_{\text{eff}}(\text{facet}) > k_{\text{eff}}(\text{off-facet})$ ]. In the light of experiments now in progress in our laboratory the present data should not be taken as representative of Czochralski-type growth behavior but rather as an indication that, for a given system, segregation at growth facets is a complex function of the growth parameters and particularly sensitive to boundary layer characteristics and the thermohydrodynamic behavior of the melt; furthermore, it was observed that the nature of the dopant affects not only the magnitude of coring but also the extent and stability of faceting.

### Acknowledgments

The authors are indebted to the National Science Foundation for financial support and continued encouragement. The authors also express their deep appreciation to Mr. B. Chin, Mr. J. T. Floe, and Miss N. A. Gatos for their competent assistance.

Manuscript received Aug. 21, 1973.

Any discussion of this paper will appear in a Discussion Section to be published in the December 1974 JOURNAL. All discussions for the December 1974 Discussion Section should be submitted by Aug. 1, 1974.

### REFERENCES

1. K. F. Hulme and J. B. Mullin, *Phil. Mag.*, **4**, 1286 (1954); J. A. M. Dickhoff, *Solid-State Electron.*, **1**, 202 (1960).
2. A. J. Strauss, *Solid-State Electron.*, **5**, 97 (1962); W. A. Tiller, in "The Art and Science of Growing Crystals," J. J. Gilman, Editor, p. 276, John Wiley & Sons, Inc., New York (1963).
3. J. B. Mullin, in "Compound Semiconductors," R. K. Willardson and H. L. Goering, Editors, p. 378, Reinhold Publishing Corp., New York (1962).
4. J. A. M. Dickhoff, *Philips Tech. Rev.*, **25**, 195 (1963-1964).
5. K. Morizane, A. F. Witt, and H. C. Gatos, *This Journal*, **115**, 747 (1968).
6. A. Trainor and B. E. Bartlett, *Solid-State Electron.*, **2**, 106 (1961); P. J. Holmes, *J. Phys. Chem. Solids*, **24**, 1239 (1963).
7. A. F. Witt, M. Lichtensteiger, and H. C. Gatos, *This Journal*, **120**, 1119 (1973).
8. M. Lichtensteiger, A. F. Witt, and H. C. Gatos, *ibid.*, **118**, 1013 (1971).
9. A. F. Witt and H. C. Gatos, *ibid.*, **115**, 70 (1968).
10. J. A. Burton, R. C. Prim, and W. P. Slichter, *J. Chem. Phys.*, **21**, 1987 (1953).

## The Retention of Fluorine by Silicon Surfaces: Interaction with Gold-Refractory Transistor Metallizations

H. Day, A. Christou, and D. J. Bressan

Naval Research Laboratory, Washington, D. C. 20375

The publication costs of this article have been assisted by the Naval Research Laboratory.

### ABSTRACT

The interaction of gold-tantalum transistor metallizations with silicon substrates has been studied as a function of fluorine ion contamination. An  $\text{NH}_4\text{F}$  buffered etch solution tagged with 118-min half life  $^{18}\text{F}$  was used to quantitatively establish the fluorine contamination as a function of water rinse time and evacuation time before metal deposition. Pinhole formation in the refractory layer due to fluorine ion contamination with a subsequent rapid interdiffusion of gold and silicon during a 300°C anneal was shown to be a probable failure mechanism for transistors.

Efforts to increase the reliability of microwave power transistors have led to the investigation of metallization systems which adhere well and effectively withstand high temperature and high current density without degradation or failure due to (i) alloying, (ii) interdiffusion of silicon and contact metal (1), (iii) interaction of metal and  $\text{SiO}_2$  or other passivating layers (2), or to (iv) electromigration (3). Metallization systems which have been extensively investigated and are in present use are (i) pure aluminum or aluminum with small percentages of other metals added and (ii) gold which is usually deposited on a refractory layer in direct contact with silicon or platinum silicide. The purpose of the refractory layer is to

Key words: surfaces, metallizations, ion contamination, reliability, transistors.

provide adherence and to serve as a diffusion barrier between the gold and silicon which form a eutectic melt at 370°C. In the present paper we report some observations on the retention of fluorine by chemically processed silicon surfaces and its interaction at 300°-400°C with subsequently deposited contact metals. These observations lead to the conclusion that absorbed fluorine is directly responsible for the interdiffusion of the gold and silicon through the tantalum layer at elevated temperatures.

### Experimental

In preparing silicon substrates for ohmic contact formation,  $\text{SiO}_2$  is generally removed by etching in hydrofluoric acid buffered with  $\text{NH}_4\text{F}$  to moderate the etch rate. The solution may also contain a chelating

agent to prevent metal ions from plating out on the silicon. As pointed out by several authors (4-6) such a procedure leaves fluorine on the silicon with a concentration which varies with the rinsing agent and the duration and mechanics of the rinse cycle. Due to the strength of the F-Si bond (136 kcal/mole) it was suggested (4) that the fluorine was chemically adsorbed with a surface concentration of the order of one atomic layer. In this experiment it was necessary to measure the concentration without disturbing the distribution and without desorption in order to correlate metallization defects with the fluorine concentration. For this reason, the radiochemical technique was chosen and the etch solution was tagged with the  $^{18}\text{F}$  isotope.

Radioactive  $^{18}\text{F}$  was prepared according to the reaction  $^{18}\text{O}(\alpha, p\text{n})^{18}\text{F}$  from  $\text{Li}_2\text{O}$  by  $\alpha$ -particle irradiation in the Naval Research Laboratory cyclotron. Following procedures worked out by Eisele *et al.* (7) the fluorine was extracted in the form of  $\text{H}^{18}\text{F}$  within 1 hr following irradiation and added directly to the etch solution. The specific activity of the resulting solution was 47,300 cpm/ $\mu\text{g}$  of fluorine.

Prior to metallization the silicon wafers were dipped in the etch solution for 10 sec, rinsed, and then counted at various intervals for verification of fluorine contamination, its concentration, and the absence of other radioactive contaminants such as Na. One sample received a tantalum deposition after the first count in order to determine the amount of fluorine desorption in the evacuation and subsequent rf plasma discharge.

Following counting the samples were stored in ambient for approximately 16 hr after which they were all placed in a rf sputter deposition unit along with the fluorine-free control wafer for tantalum-gold deposition. The gold and tantalum were deposited using an argon pressure of  $5\mu$  and a rf power of 200W. This resulted in a substrate maximum temperature of about  $100^\circ\text{C}$ . The thickness of the tantalum layer was 2000Å while that of the gold layer was 3000Å. After metallization the wafers were annealed in vacuum at  $300^\circ\text{C}$  for 8 hr.

In addition to the radiochemical technique, scanning electron microscopy with dispersive x-ray analysis and the electron microprobe analysis were used for correlation of contamination with the physical properties of the layers. Etch pits with associated hillocks were also counted.

### Results and Discussion

The raw counting data as a function of time after the first wafer was etched is shown in Fig. 1 with rinse duration as the parameter. The slope of the curves indicate a half life of approximately 118 min which is

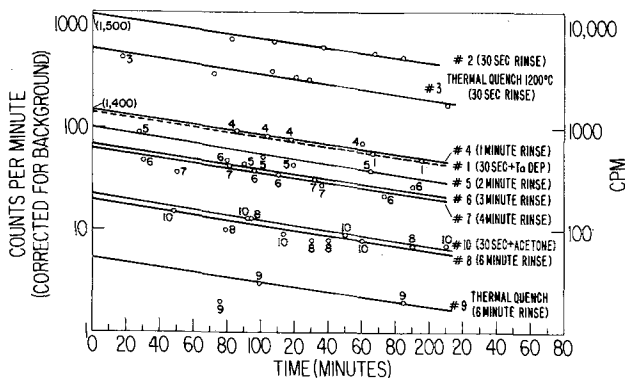


Fig. 1. Radioactivity count vs. time after etching wafer No. 1. Rinse duration is the parameter. A thermal quench (No. 3 and 6), an acetone rinse (No. 10), and rf sputter deposition of tantalum (No. 1) are processing variations. No. 1 is referred to the right-hand scale.

that of  $^{18}\text{F}$ . Therefore, no other radioactive species was involved. The variation of the fluorine ion concentration as a function of rinse duration is shown in Fig. 2. Previous investigations of the effectiveness of the acetone rinse (4, 5) are in general agreement with the results shown here. The value measured for the Ta-metallized sample also indicates that no desorption took place in the sputter deposition procedure. A scanning electron microgram of etch pit and hillock formation with associated energy dispersive x-ray spectra is shown in Fig. 3. This type of fault rather than a general penetration along all grain boundaries is typical of the gold-tantalum system in the presence of fluorine. The x-ray spectra (one taken by scanning the etch pit and the other taken by scanning the surrounding area) show the change in the relative

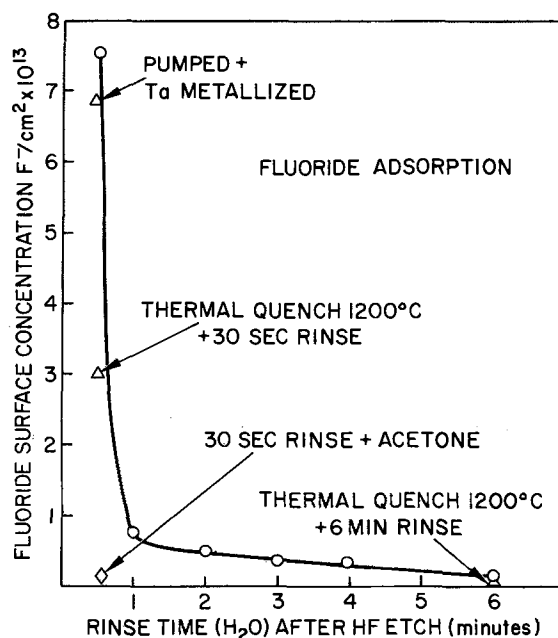


Fig. 2. Fluoride surface concentration vs. rinse time after etching in HF tagged with  $^{18}\text{F}$ .

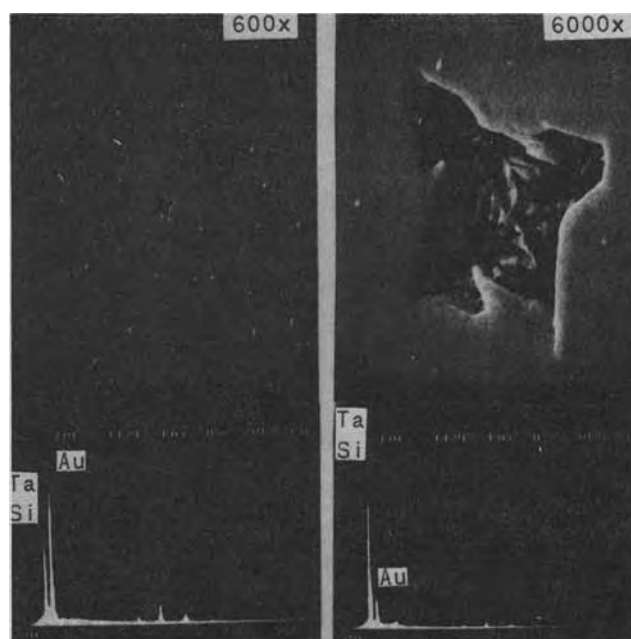


Fig. 3. Energy dispersive x-ray analysis of a typical etch pit (and surrounding area) in a gold-tantalum metallization on a silicon wafer contaminated with fluorine (1 min rinse) and annealed at  $300^\circ\text{C}$  for 8 hr.

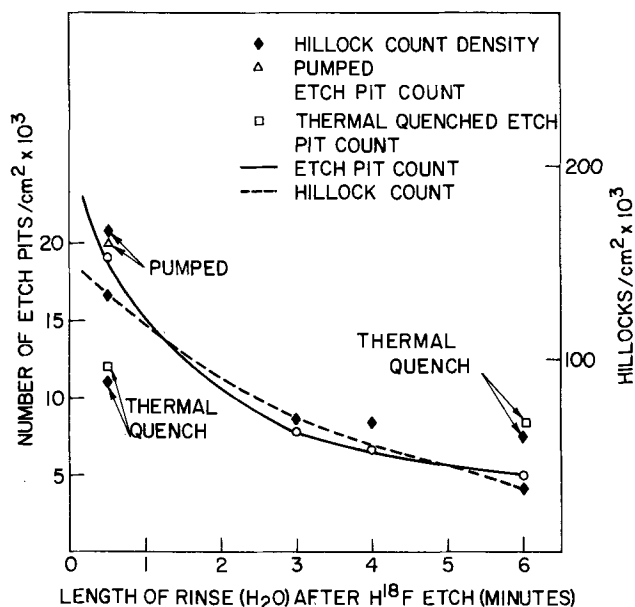


Fig. 4. Etch pit and hillock counts vs. rinse duration with thermal quenching and rf sputter deposition of tantalum as variations in processing.

amounts of Au, Ta, and Si. Fluorine or other contaminant peaks are not evident in the spectra since the concentrations are generally below the sensitivity of this technique. Similarly, x-ray spectra of the hillocks show them to consist solely of Au and Si. Figure 4 shows etch pit and hillock counts in the metallization as a function of rinse time in correlation with the contamination data. The control wafer etch pit count was  $10/\text{cm}^2$ , several orders of magnitude below that of the contaminated wafers. However, the fact that the etch pit count in this case was not zero was surprising since the diffusion was being attributed to the effects of fluorine. This will be discussed later in connection with annealing in ambient and the tantalum reaction with  $\text{SiO}_2$ .

The reaction of the gold-tantalum film with silicon substrates of 1.0 and 0.008 ohm-cm resistivity was also correlated with fluorine contamination. When annealed at  $350^\circ\text{C}$ , metallizations on high resistivity contaminated samples degraded to greater than  $1000$  etch pits/ $\text{cm}^2$  in 72 hr while low resistivity contaminated samples degraded to the same level in only 24 hr. It is known that (9,10) surface defects can serve as nucleation centers for the formation of precipitates of foreign atoms. From the present investigation it is believed that fluorine will precipitate at silicon surface defects, the density of which is greater in the low resistivity silicon. Therefore, subsequent annealing at  $350^\circ\text{C}$  results in enhanced diffusion at silicon defects (10) and the subsequent formation of pinholes in the metallization.

In many cases gold-tantalum metallizations deposited on clean silicon wafers from which the native oxide was not removed have withstood vacuum anneals at  $350^\circ\text{C}$  for as much as 800 hr without etch pit formation. Furthermore, samples identical to the fluorine-free control wafer mentioned previously showed no etch pit formation when annealed in ambient at  $350^\circ\text{C}$  for 8 hr. This is in agreement with Schaible and Maissel (8) who found that gold would not diffuse through tantalum if oxygen or  $\text{SiO}_2$  were present to react with tantalum. This and the foregoing results lead us to the conclusion that the absence of oxygen in the tantalum grain boundaries or the presence of fluorine which is available to react with the oxidized grain boundary leaves the gold free to diffuse through the tantalum and react with the silicon thus causing the etch pit or void and hillock formation. Since fluorine normally etches tantalum the reaction is not necessarily confined to the grain boundary. However, the rate of reaction is expected to be much greater at the grain boundary. The fact that this takes place only at discrete points along the grain boundaries is being investigated further.

#### Acknowledgments

The authors wish to acknowledge the assistance of Dr. Peter Wilkness of the Ocean Sciences Division, NRL, and the members of the staff of the NRL Cyclotron Facility, Nuclear Sciences Division. This work is sponsored by the Office of Naval Research.

Manuscript submitted Aug. 6, 1973; revised manuscript received Nov. 2, 1973. This was Paper 162 presented at the Boston, Massachusetts, Meeting of the Society, Oct. 7-11, 1973.

Any discussion of this paper will appear in a Discussion Section to be published in the December 1974 JOURNAL. All discussions for the December 1974 Discussion Section should be submitted by Aug. 1, 1974.

#### REFERENCES

1. R. S. Keen, L. R. Loewenstern, and G. L. Schnable, Proc. Sixth Annual Reliability Physics Symposium, Los Angeles, Calif., Nov. 6-7, 1967, pp. 216-233.
2. J. McCarthy, *Microelectronics and Reliability*, **9**, 187 (1970).
3. H. B. Huntington and A. R. Grone, *J. Phys. Chem. Solids*, **20**, No. 1/2, 76 (1961).
4. G. B. Larrabee, K. G. Heinen, and S. A. Harrell, *This Journal*, **114**, 867 (1967).
5. Werner Kern, *RCA Rev.*, **31**, No. 2, 287.
6. Song-Jay Wey and G. Lewis, *J. Vacuum Sci. Technol.*, **10**, No. 2, 413 (1973).
7. J. A. Eisele, R. E. Larson, and P. E. Wilkness, *Intern. J. Appl. Radiation Isotopes*, **21**, 219 (1970).
8. P. M. Schaible and L. I. Maissel, *Trans. Ninth National Vacuum Symp., AVS*, pp. 190-193 (1962).
9. H. J. Queisser, K. Hubner, and W. Shockley, *Phys. Rev.*, **123**, 1245 (1961).
10. G. H. Schuttke, *This Journal*, **108**, 163 (1961).

# Solid-State Coulometric Titration: Critical Analysis and Application to Wüstite

Robert A. Giddings<sup>1</sup> and Ronald S. Gordon

Division of Materials Science and Engineering, University of Utah, Salt Lake City, Utah 84112

## ABSTRACT

A critical analysis was performed on galvanic cell techniques which employ calcia-stabilized zirconia electrolytes. The presence of low-level electron or hole conduction in the ionic conducting range of the electrolyte was found to be responsible for oxygen permeation through the electrolyte which can either oxidize or reduce a single-phase oxide and, hence, lead to drift in the open-circuit emf with time. Taking oxygen permeation into account quantitatively, a series of isothermal titration experiments in wüstite was performed in which the cell emf was found to be linear with composition (i.e., oxygen-iron molal ratio). These results are in excellent agreement with a recent composite analysis of all thermodynamic data in the Fe-O system. Previous cell studies in which deviant behavior has been reported are probably due to improper galvanic cell techniques. No evidence was found to support the existence of more than one-phase or second-order transitions within the wüstite phase.

Recently, considerable interest has been generated on the use of solid-state galvanic cells which employ oxide electrolytes (e.g. CaO-ZrO<sub>2</sub>, Y<sub>2</sub>O<sub>3</sub>-ThO<sub>2</sub>) to study the thermodynamic properties of nonstoichiometric oxide systems. Since voltages may be measured with high precision emf measurements should lead to a direct evaluation of oxygen activities with much greater accuracy than is normally possible with conventional gas equilibration techniques. The precision of measurement in combination with the possibility of coulometric titration, which allows the composition of an oxide to be changed *in situ*, permits not only a continuous determination of oxygen activity as a function of composition, but also the composition limits of the phase itself. In spite of the potential advantages, the use of oxide electrolytes has not always led to increased accuracy in the measurement of oxygen activities. Several workers (1-4) have reported difficulties in operating cells which were stable with time, thereby necessitating the use of empirical correction factors to determine absolute compositions.

Several emf measurements (1, 3, 5-8) of oxygen activities and phase boundary composition limits for wüstite exhibit rather poor agreement with each other and do not agree with a recent composite analysis of the Fe-O system by the authors (9). Included in this composite were seven independent studies, using either CO<sub>2</sub>/CO gas equilibration (10-13) or galvanic cell (3, 8) techniques. The composite possessed the following properties: (i) the partial molal free energy of oxygen ( $\Delta\bar{G}_o$ ) in wüstite varied linearly with composition (O/Fe)<sup>2</sup> and temperature;<sup>3</sup> (ii) the partial molal enthalpy ( $\Delta\bar{H}_o$ ) and entropy ( $\Delta\bar{S}_o$ ) of oxygen varied linearly with composition and were independent of temperature. EMF or gravimetric data which deviated from this linear behavior were rejected for experimental reasons (9).

In the present paper, a critical analysis of galvanic cell techniques, which employ calcia-stabilized-zirconia (CSZ) electrolytes, is given to determine the cause for nonlinear behavior (e.g.,  $\Delta\bar{G}_o$ ,  $\Delta\bar{H}_o$ ,  $\Delta\bar{S}_o$  vs.

O/Fe) which has been reported in several emf studies on wüstite (1, 6, 7). Consideration is given to the manner in which the low-level electronic conduction (hole or electron) present in CSZ causes cell instabilities due to oxygen permeation through the electrolyte. Electronic conductivity and oxygen permeation measurements in CSZ are described and assessed as to their bearing on the proper design and operation of a cell for the study of single-phase wüstite. Results from such a properly designed cell are also reported. Finally, a critical analysis of all galvanic cell data (this and previous studies) for wüstite is given which shows that the conflicting results now in the literature can be related to experimental techniques in which cell instabilities were either ignored or improperly taken into account.

## Experimental Procedure

Conductivities, oxygen permeation rates, and oxygen activities were determined using galvanic cells which employed calcia-stabilized zirconia electrolytes. The cell geometry employed in the present study is given in Fig. 1. Electrolyte pellets were fabricated from Wah Chang reactor grade ZrO<sub>2</sub> and reagent grade CaCO<sub>3</sub> to yield an over-all composition of 0.85 ZrO<sub>2</sub>-0.15 CaO. The powders were dry mixed, calcined at 1000°C, hydrated [to form Ca(OH)<sub>2</sub>], pressed in a 1/2 in. steel die, and fired in an oxygen atmosphere at 1700°C to yield

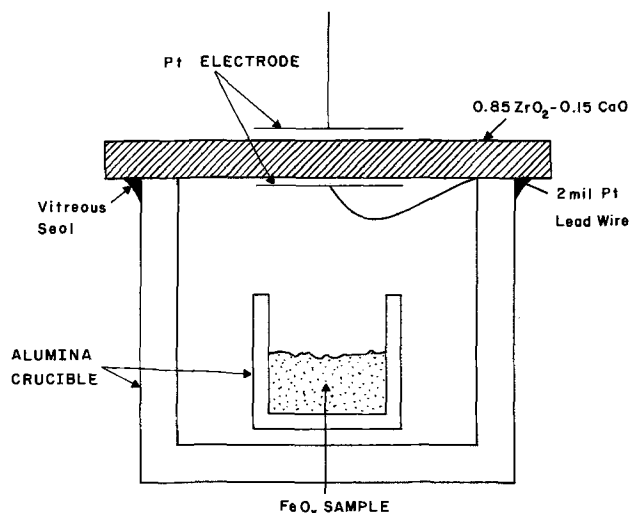


Fig. 1. Schematic of galvanic cell

<sup>1</sup> Present address: Metallurgy and Ceramics Laboratory, General Electric Research and Development Center, Schenectady, New York 12301.

Key words: calcia-stabilized zirconia; oxygen permeation; electron, hole, ionic conduction.

<sup>2</sup> O/Fe, the ratio of the number of moles of oxygen to the number of moles of iron in the wüstite phase, will be the variable to describe composition in this study.

<sup>3</sup> In Ref. (9) it is stated incorrectly that  $\Delta\bar{G}_o$  was linear with  $1/T$  for the composite. Actually  $\Delta\bar{G}_o$  is linear with  $T$  and  $\log P_{O_2}$  is linear with  $1/T$ .

pieces approximately 98% of theoretical density. The vitreous seal was prepared from a standard 0080 composition glass ground to -325 mesh. The powdered glass was painted on the crucible-electrolyte joint and, as the cell was raised to temperature, the seal formed *in situ*. Sintered Pt electrodes were used and the inner lead was brought out of the cell between the crucible and the electrolyte, through the glass seal. The electrodes were prepared from unfluxed Pt paste. The foregoing procedure permitted the production of a gas-tight cell chamber with an internal volume of approximately 0.5 cm<sup>3</sup> and an electrolyte area of approximately 0.4 cm<sup>2</sup>.

Isothermal, coulometric titration experiments were performed between 965° and 1112°C using samples of loosely packed powdered iron (GAF HP carbonyl 99.6-99.9%). Sample sizes were approximately 0.08g. Cell potentials and titration currents (0.5-0.8 mA) were monitored with a Keithley 610B electrometer and measured with a L&N potentiometer (14).

### Results

Due to repeated unsuccessful attempts (14) to produce cells which exhibited (timewise stable) emf's for single-phase wüstite, a thorough characterization of the conduction properties of the electrolyte was deemed necessary prior to undertaking coulometric titration studies. Characterization of the electrolyte was initiated by first determining the reversibility of the electrodes over the range of temperatures and potentials to be used in the study. Then a polarization cell was constructed to determine the magnitude of the low-level hole conductivity. Finally, the rate of oxygen permeation through the electrolyte was measured and correlated with previously determined hole conductivities. After the rate of oxygen permeation (under open-circuit conditions) was found to be of sufficient magnitude to warrant consideration, isothermal, coulometric titrations were performed on a cell containing a sample of wüstite. Corrections were made to the titration data to account for oxygen permeation; then the data were analyzed to give emf vs. composition relations.

**Conductivity studies.—D-C ionic conductivity.**—Recently, Brook, Pelzmann, and Kroger (15) reported nonohmic behavior for the cell



when operated at 520°C. They observed the current-voltage relationships to be dependent upon the preparation technique for the Pt electrodes. It was expected that electrodes prepared from unfluxed Pt paste would behave in a reversible manner if the cell was operated at temperatures over 900°C. D-C conductivity studies were performed to check the reversibility of the sintered platinum electrodes. At all temperatures between 785° and 1234°C, ohmic (*i.e.* reversible electrode) behavior was observed (14). The activation energy for the conduction process was 31 kcal/mole, a value which is in good agreement with oxygen ion transport as measured by a-c (16, 17) and tracer (18) techniques.

**Hole conductivity.**—Patterson, Bogren, and Rapp (19) have shown that the steady-state polarization current density in an anionic conductor (*i.e.*, CSZ) is

$$J_{ss} = K\sigma_n[\exp U - 1] + K\sigma_p[1 - \exp - U] \quad [1]$$

in which

$$K = RT/LF \quad [2]$$

and

$$U = EF/RT \quad [3]$$

$E$  is the thermodynamic emf of the cell,  $L$  is the thickness of the electrolyte,  $F$  is the Faraday constant,  $\sigma_n$  and  $\sigma_p$  are the electron and hole conductivities for the electrolyte equilibrated with the oxygen pressure of the reversible electrode, and  $RT$  has its usual meaning.

In order to perform polarization measurements, a blocking electrode must be established. A blocking (or rectifying) electrode is one which allows current of some species to pass in only one direction. The blocking nature can be accomplished in two ways. Generally, electrodes of the polarizing type are constructed from materials which are impervious to the species for which blocking is desired (*i.e.*, O<sup>2-</sup> in CSZ); if the polarized interface is covered by the electrode, there can be no supply of the species to the interface. Patterson *et al.* (19) employed the impervious electrode technique in their use of a 2.5 mm thick Pt pellet to cover a CSZ electrolyte surface. An alternative method of accomplishing the polarizing effect is to encapsulate a reversible electrode in an environment which contains no supply of the blocked species, thereby preventing that species from entering the electrolyte.

It was decided to construct the polarization cell based on the method of encapsulation. If proper polarization behavior was obtained, it would allow calculation of the electronic conductivity as well as provide strong evidence for the integrity of the encapsulation method. If leaks were present, oxygen from the surrounding air could enter the polarized chamber and result in ohmic behavior for the current-voltage relationships. The cell used for the polarization measurements is given as



Converted data, according to the method of Patterson *et al.* (19), are presented in Fig. 2 for temperatures between 932° and 1155°C. Linearity was observed between the converted current density and  $\exp U$ , indicating proper polarization behavior. Values of  $\log \sigma_p$ , calculated from the intercepts in Fig. 2 are presented as a function of the reciprocal temperature in Fig. 3 and result in an activation energy of 52.4 kcal/mole for hole conduction. Reasonably good agreement exists between the polarization data of the present study and other reported hole conductivities (19-22). In addition, these measurements indicate the technique for cell encapsulation was sufficient to provide an environment which does not suffer from mechanical leaks to an ambient air atmosphere.

Some comments should be made about potential problems which could be encountered when hot glass sealing techniques are used in cell measurements. Due to high alkali ion mobilities in glasses a possibility exists for the glass to act as a medium for direct oxygen transfer into the sample chamber. At or near the inner platinum electrode (Fig. 1) lead, oxygen ions can be oxidized and released as molecules into the sample chamber. Alkali ions would then diffuse to the high oxygen activity side (outside the cell) and the liberated electrons would pass through the short-circuiting lead wire to the outside of the cell where they would reduce other oxygen gas molecules to oxygen

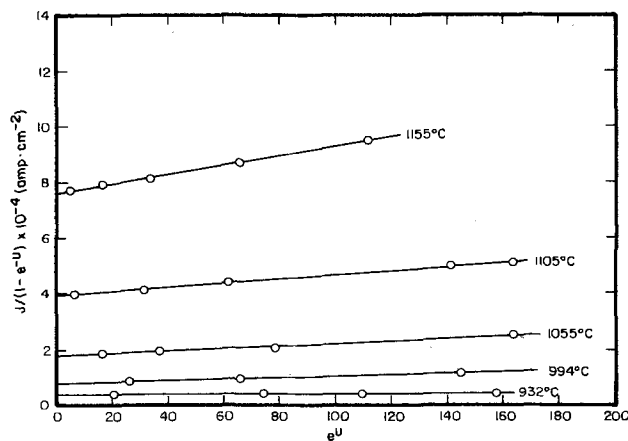


Fig. 2. Converted data for the polarization studies

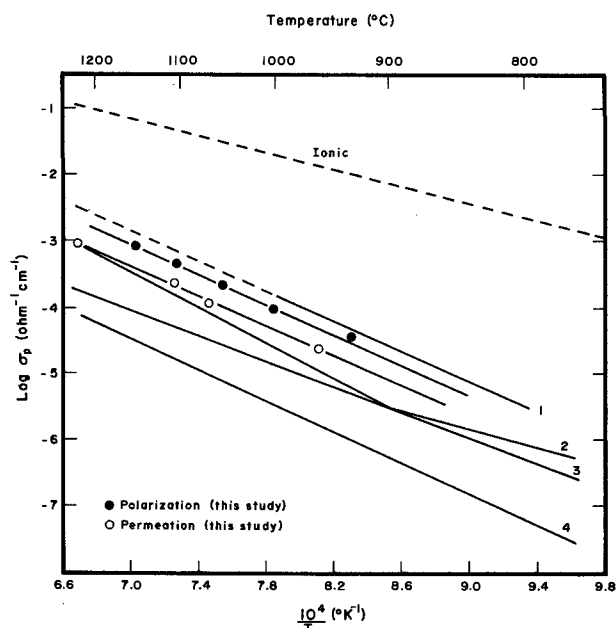


Fig. 3. Hole conductivities in calcia-stabilized zirconia: 1, Patterson, Bogren, and Rapp (19); 2, Kitazawa (22); 3, Heyne and Beekmans (21); 4, Smith, Mesaros, and Amoto (20).

ions. This process would then allow for a continuous passage of oxygen into the sample chamber at a rate controlled by alkali diffusion in the glass. In addition, if the platinum lead wire contacts the CSZ electrolyte, then a similar process would occur with the transfer of oxygen ions from the glass into the CSZ tablet and eventually oxygen molecules would be liberated at the inner electrode. The rate of this process could be governed by either alkali diffusion in the glass or oxygen ion transport in the electrolyte. Finally the type of glass which is used for the seal is also important. A glass containing only aliovalent ions should be used. Variable valent impurities (e.g., Fe) should be avoided since they are easily reduced and may lead to some bulk electronic conductivity in the glass and, hence, to an internal short-circuit.

It is difficult to estimate the exact magnitude of oxygen transfer into the cell by means of the glass seal. However, some comments can be made as to the nature of the results which would be observed if oxygen permeation through the glass or through the CSZ pellet because of a lead wire short-circuit were significantly greater than direct oxygen permeation through the electrolyte. Both of these short-circuiting mechanisms should result in permeation rates with fairly low activation energies (i.e., those corresponding to alkali conduction in glasses (15-18 kcal/mole) or ionic conduction in CSZ (31 kcal/mole)). Since the observed permeation rate (Fig. 3) possessed a much higher activation energy (~52 kcal/mole), these short-circuiting, oxygen transport mechanisms can be discounted in the present study. Furthermore if oxygen were permeating into the cell by these processes one would expect to see ohmic behavior in the polarization measurements and not the blocking electrode behavior observed in the present study (Fig. 2).

Thus in galvanic cell studies, in which an encapsulated electrode is used, a polarization measurement is an important quality control check which will not only test for mechanical leaks and lead wire short-circuits, but it will also test the stability of the sealing medium (glass in this study).

**Oxygen permeability studies.**—The presence of a finite electronic conductivity in CSZ will allow oxygen to permeate through the electrolyte under open-circuit conditions. The rate of oxygen permeation will be controlled by the migration of electronic defects,

either holes accompanying oxygen ion migration or electrons flowing in the opposite direction. The permeation rate ( $P$ ) may be expressed in terms of the steady-state polarization current density (refer to Eq. [1])

$$P \left( \frac{gO_2}{\text{cm}^2 \text{ sec}} \right) = \frac{8}{F} (J_{ss}) \quad [4]$$

When the electrolyte is being operated at oxygen activities which make holes the predominant electronic species, and when cell emf's are large ( $\geq 0.5V$ ) the rate of oxygen permeation becomes a function of temperature only

$$P = \frac{8K\sigma_p}{F} \quad [5]$$

Experiments (960°-1222°C) were designed to measure oxygen permeation through a zirconia electrolyte. A known amount of iron was encapsulated in a cell and an open-circuit emf was measured as a function of time. Air was used as the reference potential in order to make  $\sigma_p \gg \sigma_n$ . For all compositions of  $FeO_y$  within the wüstite phase field, the emf was large so that Eq. 5 was applicable. The permeation rate was determined from a decay of emf with time as the sample oxidized from an over-all composition of  $Fe-Fe_xO$  to  $Fe_2O-Fe_3O_4$ . By knowing the width of the phase field in terms of oxygen content and having measured the time necessary for the sample to oxidize across the field, a permeation rate and, hence, a hole conductivity were calculated. A typical permeation experiment at 1222°C is given in Fig. 4. Hole conductivities, which were calculated from these permeation studies, are presented in Fig. 3 and are in good agreement with those calculated from other permeation measurements (20) and with the measured hole conductivities (19, 21, 22). The high activation energy (approximately 52 kcal) for the permeation rate supports the hypothesis that the source of cell instability is an inherent electrolyte property related to electronic (hole) conductivity.

When  $\sigma_n \gg \sigma_p$  the rate of oxygen permeation may be taken from Eq. [4] to be

$$P = \frac{8K}{F} \sigma_n [\exp U - 1] \quad [6]$$

As such, it is expected that an instability in the reverse direction (e.g., the reduction of a wüstite sample by oxygen permeation controlled by electron conduction) would be present in a cell with an  $Fe-Fe_xO$  reference electrode. Rizzo *et al.* (1, 5, 23) have reported instabilities in the reducing direction in studies of wüstite using cells with  $Fe-Fe_xO$  reference electrodes. Electron conductivities calculated from their reported instabilities in both titration (1, 23) and open-circuit permeation (5, 23) experiments are plotted in Fig. 5. Electron conductivities reported by Patterson *et al.* (19) and by Heyne and Beekmans (21) are included

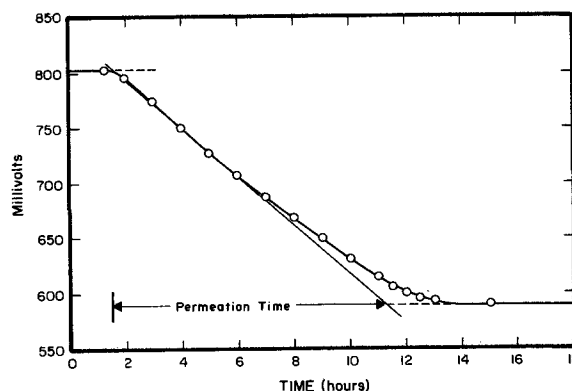


Fig. 4. EMF decay due to oxygen permeation (1222°C)



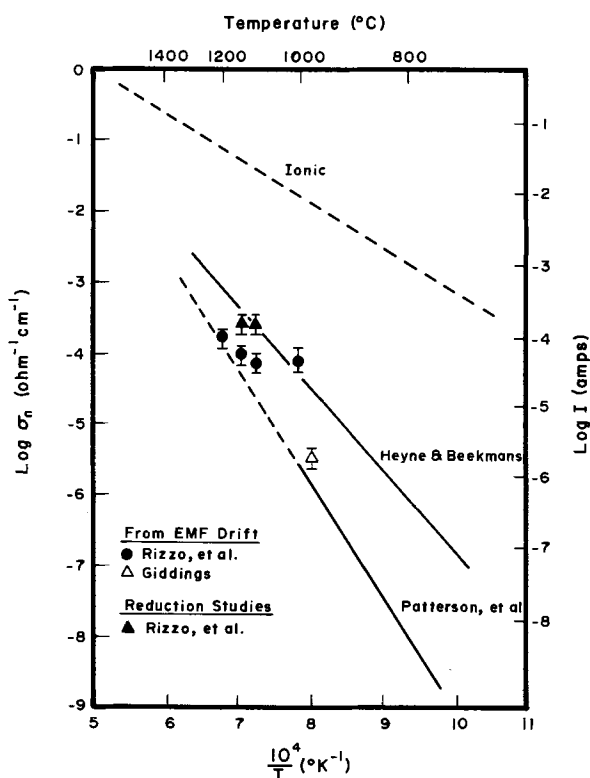


Fig. 5. Electron conductivities in calcia-stabilized zirconia for Fe- $\text{Fe}_x\text{O}$  potentials.

in Fig. 5. Also included in Fig. 5 is one conductivity calculated from instabilities observed in preliminary work (14) for the present study using a cell similar to that employed by either Rizzo and Smith (8) or Fender and Riley (7). The good agreement between the measured electron conductivities and those calculated from cell instabilities strongly suggests that oxygen permeation in a CSZ cell with a Fe- $\text{Fe}_x\text{O}$  reference potential is controlled by low-level electron conduction in the electrolyte.

**Factors important in cell design.**—In view of the foregoing results, it is now possible to make some definitive conclusions concerning the proper design and operation of galvanic cells which employ CSZ electrolytes. A standard criterion for the validity of galvanic cell operation is that the emf be stable with time. However, since electronic conductivities in CSZ are significant in magnitude, at temperatures over 900°C, continuous oxygen transfer is expected and, as such, the emf generated by a single-phase specimen would be expected to decay continuously with time. Therefore, the proper criterion for the operation of a cell should be that the magnitude and the temperature dependence of the cell instability be consistent with electronic conduction in the electrolyte.

The design of a galvanic cell for studies in single-phase, nonstoichiometric oxide systems should minimize the area of the electrolyte which is used to separate environments of differing oxygen partial pressures. Control of the maximum temperature of experimentation is another method of controlling the maximum observed oxygen permeation rate. However, temperature limitations are not always satisfactory since phenomena of interest may not occur at temperatures where permeation is insignificant.

The oxygen potential gradient (and thereby the cell potential) can be minimized by choosing a suitable reference; however, a limited number of metal-metal oxide systems exist that behave in such a manner as to allow their use as reference for galvanic cell measurements. It should be noted that a relatively small oxygen potential gradient does not always ensure small

permeation rates. The rate of cell drift expected when the electronic conductivity is due primarily to electron conduction (e.g., Fe- $\text{Fe}_x\text{O}$  reference potentials) was given by Eq. [6]. The exponential dependence of the drift rate with oxygen potential gradient (i.e.,  $E$ ) can give significant rates of transfer even at relatively low cell voltages. An alternative scale is presented in Fig. 5 to illustrate the expected electron drift currents for a cell potential of 100 mV. (The assumed geometry was 1 cm<sup>2</sup> of electrolyte area and an electrolyte thickness of 0.3 cm.) Drift currents in the milliamp range can be expected at temperatures over 1200°C for a 100 mV cell potential.

The final method by which errors due to oxygen permeation through the electrolyte can be minimized is by increasing sample sizes. If the size of the sample is doubled, the compositional error per unit time is halved. Increasing sample sizes has its limitations; as the sample size increases, generally so does the time necessary for the attainment of equilibrium after a coulometric titration step. Thus, the total compositional error encountered is not halved, but hopefully reduced.

Some comment should be made as to the type of experiments that can be conducted with a CSZ electrolyte in the determination of oxygen activities in single-phase systems. Isothermal titration most readily allows for the characterization of experimental error due to compositional changes encountered through oxygen permeation. If the reference potential is chosen to make hole conductivity the predominant electronic process, and if the potential gradient is sufficiently large, then only the time necessary for completion of the experiment is needed in order to define the compositional error. As the cell potential drops, the oxygen transfer rate becomes dependent upon the potential, and, as such, the time spent at any incremental cell voltage needs to be measured. EMF *vs.* temperature measurements for supposedly isocomposition conditions are, in a strict sense, impossible to perform. At low temperatures and with sufficiently large sample sizes, the condition of isocomposition can be nicely approximated. As the temperature is raised, the potential across the cell will change as will the magnitude of the electronic conductivity. In order to calculate the necessary compositional corrections, the time spent at any temperature and potential will have to be defined. Corrections of this sort are, at best, difficult to make, and as such, emf *vs.* temperature experiments becomes very poorly defined at high temperatures.

In order to calculate valid thermodynamic properties from galvanic cell measurements, the system of interest should be at equilibrium. Rigorously, a single-phase system contained in a galvanic cell which employs a calcia-stabilized zirconia electrolyte can never be at equilibrium in that oxygen is continually transferred through the electrolyte either into or out of the system. The condition of equilibrium can be approximated by having mass transport in the sample be much faster than the rate of oxygen transport into or out of the sample chamber. The requirements that transport processes in the sample be much faster than permeation processes in the electrolyte places stringent restrictions on the choice of single-phase materials which can be satisfactorily studied by galvanic cell techniques.

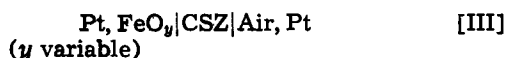
One advantage of coulometric titration experiments is the ability to change *in situ* the composition of a single phase by very small increments; thereby allowing isothermal emf measurements to be made across phases with narrow ranges of composition. However, in a phase with a narrow range of composition, even a small amount of oxygen permeation through the electrolyte can result in compositional changes that are a large percentage of the total range of nonstoichiometry.

Besides problems which can occur due to oxygen permeation, one must also consider the stoichiometric



stability of the materials which are used for the cell chamber. If a significant amount of oxygen can be taken up or released by the chamber wall, and the electrolyte, then compositional errors can be introduced during coulometric titration experiments. Problems of stoichiometric stability would most probably occur when studying phases of very narrow compositional ranges (i.e., those in which the emf changes rapidly with small changes in composition) or when very small samples (i.e., either sputtered or vapor-deposited, thin films which might be employed to help promote equilibration) are used. The double layer capacitance of the CSZ electrolyte has been found to be approximately  $4 \mu\text{f}/\text{cm}^2$  at  $400^\circ\text{C}$  (24). If not taken into account, such a capacitance would introduce an error of  $\sim 4 \times 10^{-6}$  coulombs for a total emf change of 1V in a cell of  $1 \text{ cm}^2$  electrolyte area. This error is insignificant for the conditions of the present study.

**Isothermal coulometric titration.**—Based on the criteria for satisfactory cell design developed in the previous section, a cell was designed with the intention of performing isothermal coulometric titration studies on single-phase wüstite



Air was used as the reference potential to insure that the electronic conductivity in the electrolyte was due primarily to hole conduction. The use of air as a reference also made the expected cell voltages sufficiently large ( $\cong 0.5\text{V}$ ) so as to readily allow calculation of corrections due to oxygen permeation through the electrolyte.

Isothermal coulometric titrations were performed at six temperatures:  $980^\circ$ ,  $1015^\circ$ ,  $1023^\circ$ ,  $1055^\circ$ ,  $1075^\circ$ , and  $1112^\circ\text{C}$ . Titrations were conducted by oxidizing the sample from the Fe-Fe<sub>x</sub>O phase boundary to the Fe<sub>2</sub>O-Fe<sub>3</sub>O<sub>4</sub> phase boundary (i.e., titration of oxygen into the sample). One isothermal experiment was conducted under both titration "in" and titration "out" conditions to check reversibility.

The oxygen permeation rate through the electrolyte was determined by measuring the rate of emf decay with time at  $1118^\circ\text{C}$ , and at an over-all sample composition near the iron-rich boundary. The decay was measured for 12 hr resulting in a 38 mV potential drop. The measured permeation rate corresponded to a hole conductivity in the calcia-stabilized zirconia electrolyte of  $6.48 \times 10^{-4} (\text{ohm cm})^{-1}$  at  $1118^\circ\text{C}$  in good agreement with the previous hole conductivity and permeation experiments (Fig. 3). All corrections to titration data were based on conductivities calculated from this singular drift rate measurement. Conductivities at other temperatures were calculated using an activation energy of 52.4 kcal/mole.

Data for the  $1112^\circ\text{C}$  titration are presented in Fig. 6. (An adjustable coulomb scale has been used in order to organize the curves on a single figure.) Included in the figure are the data for emf vs. coulombs taken from the measurements before and after corrections were made to compensate for the oxygen permeation through the electrolyte. Corrections made on the oxidizing titration data were based on the total time of the experiment. During a reducing titration, a potential is applied to the cell which reverses the oxygen potential gradient across the electrolyte; and as such, corrections made on the reducing titration data were based only on the time the cell was either at or coming to equilibration after a titration step. Good agreement existed between the slopes of the two corrected emf vs. coulomb curves, indicating the measurements were reversible and reproducible. The width of the single-phase field determined from the oxidizing titration is 29.02 coulombs which gives the reported boundary composition of 1.1575. The reducing titration indicates the width of the phase field to be 29.05 coulombs, which

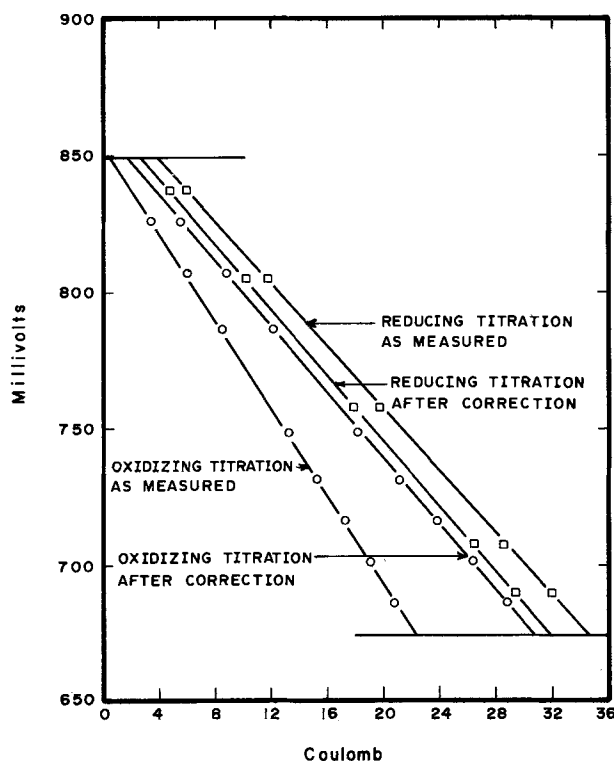


Fig. 6. Isothermal titration at  $1112^\circ\text{C}$  showing composition corrections.

corresponds to a composition of 1.1576 for the oxygen-rich phase boundary.

During titrations performed for this study, difficulty was encountered in precisely establishing the single-phase boundaries.<sup>4</sup> In order to determine compositions from the coulometric titrations, it was decided to extrapolate the observed, reproducible linear behavior for single-phase wüstite to the potentials corresponding to the Fe-Fe<sub>x</sub>O and Fe<sub>2</sub>O-Fe<sub>3</sub>O<sub>4</sub> two-phase equilibria. From the intersection of the lines, the coulombs needed to cross the phase field could be determined, and assuming a composition for the iron-rich boundary, compositions could be calculated for the single-phase regions as well as for the oxygen-rich boundary.

Boundary potentials were taken from the composite analysis (9) described earlier. They may be expressed as follows<sup>5</sup>

$$\text{Fe-Fe}_x\text{O} \quad E (\text{mV}) = 1354 - 0.3649 T (^\circ\text{K}) \quad [7]$$

$$\text{Fe}_2\text{O-Fe}_3\text{O}_4 \quad E (\text{mV}) = 1462 \\ + T(0.4838 - 0.3349 \log T) \quad [8]$$

The emf vs. composition data generated in this study for single-phase wüstite were analyzed in terms of a linear expression,  $E = M(\text{O}/\text{Fe}) + B (T \text{ constant})$ .<sup>6</sup> A listing of the coefficients for the emf vs. composition relations is presented in Table I. The lines described in Table I are shown graphically in Fig. 7. Data from other galvanic cell measurements are included in the figure and will be discussed in the next section. Included in Table I is a summary of the compositions corresponding to the wüstite oxygen-rich phase boundary as determined by extrapolating the linear single-phase behavior to the oxygen-rich potential. These compositions are in excellent agreement with the com-

<sup>4</sup> This problem is not uncommon in this system and has been reported in several studies (1, 10, 12). Similar problems were encountered in the permeation studies. Reference is made to the nonlinear emf time behavior at the boundaries as shown in Fig. 4.

<sup>5</sup> These emf's are for  $P_{\text{O}_2} = 0.18 \text{ atm}$ . (Partial pressure of oxygen in air at Salt Lake City.)

<sup>6</sup> This behavior is consistent with a linear relation between  $\Delta G_0$  and  $\text{O}/\text{Fe}$ , which is characteristic of the composite data analysis for this system (9).

Table I. Equations describing emf vs. composition behavior

T °C	*EMF = M(O/Fe) + B (Volts)		Oxygen-rich boundary	
	M	B	Compo- sition	Potential* volts
980	-1.429	2.400	1.1424	0.768
1015	-1.549	2.514	1.1429	0.743
1023	-1.561	2.523	1.1438	0.738
1055	-1.647	2.601	1.1453	0.715
1075	-1.651	2.598	1.1489	0.701
1112	-1.636	2.569	1.1575	0.675
1112	-1.635	2.567	1.1576	0.675

\* Potentials are for a 0.18 atm reference potential.

posite boundary (9) (see Fig. 8) and Darken and Gurry's original diagram (10).

### Discussion of Reported Cell Measurements

Several workers (1, 3, 5-8) have studied single-phase wüstite by using galvanic cells with CSZ electrolytes to

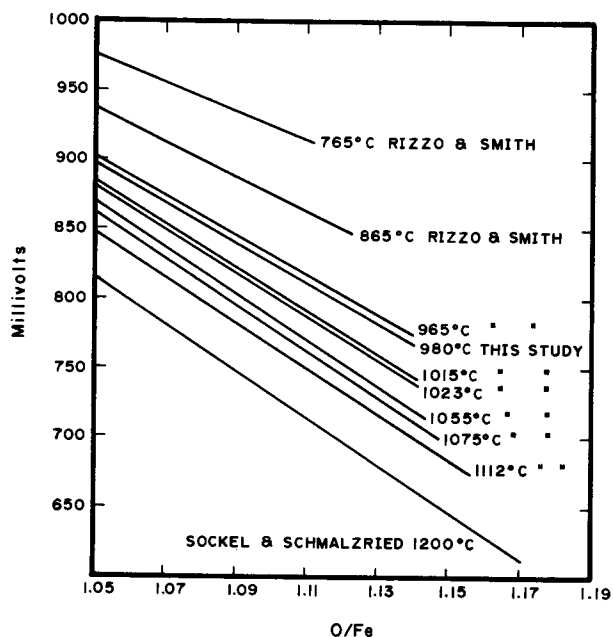


Fig. 7. Linear behavior—cell potential vs. composition

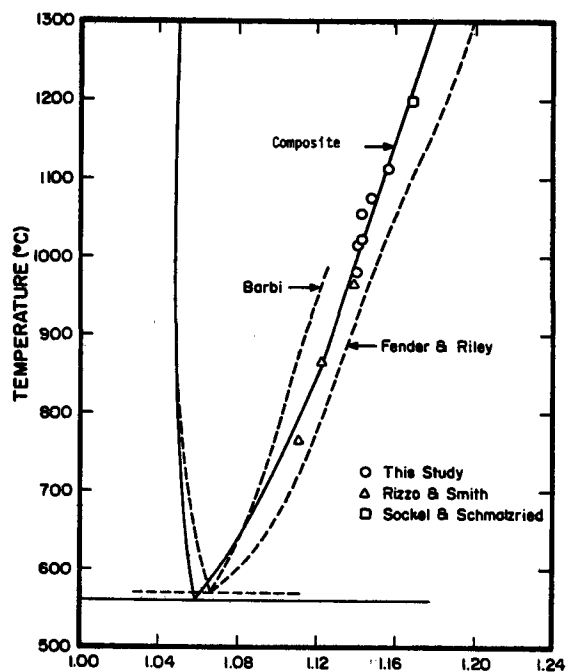


Fig. 8. Wüstite phase diagram

measure oxygen activities as a function of temperature and composition. Considerable disagreement exists between the general functional dependencies observed by some of the workers (1, 6, 7) and those reported in the composite analysis (9) and in the present study. In the present study some general criteria have been identified which must be considered when a galvanic cell with a CSZ electrolyte is used to measure oxygen activities in a single-phase, binary oxide. All of the existing oxygen activity data obtained by emf techniques will be examined critically to determine if the experimental methods employed by the various workers can account for the apparent discrepancies in the data.

Barbi (6) conducted measurements with the cell



He employed an experimental technique similar to that of Kiukkola and Wagner (25) in that three pellets were contained in a common sample chamber through which argon was passed in order to control the oxygen environment. EMF vs. temperature studies were performed, and Barbi extrapolated the single-phase, isothermal behavior to the potential corresponding to the oxygen-rich phase boundary to determine the boundary composition. A marked discrepancy exists between Barbi's oxygen potentials and oxygen-rich phase boundary compositions and those reported in the composite (9). The oxygen potentials are higher and the phase boundary (which is given in Fig. 8) is oxygen deficient.

The temperatures employed in Barbi's study ( $T \leq 1000^\circ\text{C}$ ) are too low for oxygen permeation to be important and as such, an explanation for the anomalous activities and boundary compositions most probably lies in the use of the flowing gas around the wüstite sample. Due to the low equilibrium oxygen pressures encountered in the iron-oxygen system (for the  $\text{Fe}_2\text{O}-\text{Fe}_3\text{O}_4$  equilibrium,  $P_{\text{O}_2} = 10^{-24}$  atm at  $600^\circ\text{C}$  and  $P_{\text{O}_2} = 10^{-13}$  atm at  $1000^\circ\text{C}$ ) it is doubtful whether the purity of the argon was sufficient to establish a true equilibrium between the sample and the gas phase. It is expected that the measured single-phase potentials are high due to a local oxidation of the sample by the flowing gas phase. If the measured single-phase potentials are high, then an isothermal extrapolation to a correct boundary potential will result in the boundary composition appearing oxygen-deficient relative to the correct composition.

Rizzo (23) and Rizzo *et al.* (1, 5) determined oxygen activities in single-phase wüstite as a function of temperature ( $1057^\circ\text{C}$ - $1200^\circ\text{C}$ ) by employing Cell [III] and [IV]. Titration data taken by Rizzo using an air reference cell required no compositional corrections in that the observed emf's were stable with time, an unexpected occurrence in view of the results of the present study. An explanation for the stability can be found by examining the experimental cell geometry employed by Rizzo. Placed within the sample chamber was a zirconium metal shield which was used as an electrical ground as well as an oxygen getter to control the partial pressure of the oxygen in the argon gas flowing through the sample chamber. Stable emf's were generated by adjusting the flow rate of the argon. It is postulated that the result of the above experimental technique was a dynamic equilibrium for the wüstite sample which was not representative of a true static equilibrium condition. By adjusting the argon flow rate to give a stable emf, the sample was made to lose oxygen to the environment at a rate equal to the rate at which oxygen permeated through the electrolyte, thereby generating a steady-state situation, not a true equilibrium condition. In all of these measurements, oxygen activities higher than those in the composite were generated for compositions within single-phase wüstite.

All of the studies by Rizzo *et al.* which employed a cell of Type [IV] (where no zirconium getter was present) exhibited an instability in a reducing direction. The preceding discussion has shown the instability to be consistent with oxygen permeation (refer to Fig. 5). However, the use of a flowing gas through the sample chamber probably led to the generation of metastable results in that all of the reported activities appear to be abnormally high.

Rizzo and Smith (8) employed a cell of Type [IV] to determine the oxygen activity of wüstite as a function of composition at 765°, 865°, and 965°C. They used a cell design which encapsulated the wüstite sample in a zirconia electrolyte tube with a static vacuum environment. Due to the low temperatures employed, the massive sample sizes (approximately 10 times larger than the samples used in the present study), and the low magnitude of the electron conductivity in the electrolyte when Fe-Fe<sub>3</sub>O<sub>4</sub> is used as a reference at these temperatures cell emf's would be expected to be stable with time. The linearity in the emf *vs.* composition reported by Rizzo and Smith is consistent with the behavior observed in the present study and the composite analysis. The oxygen-rich phase boundary compositions for wüstite, which are shown in Fig. 8, are in good agreement with those calculated from the composite.

Using a cell similar to that of Rizzo and Smith, Fender and Riley (7) measured oxygen activities in single-phase wüstite. They reported nonlinearity in their isocomposition, emf *vs.* temperature data. The nonlinearity was interpreted in terms of linearity over limited temperature ranges, each separated by a definite break in the slope of the emf-temperature curve. The breaks in slope were attributed to second or higher order phase changes occurring within wüstite and similar to those reported by Kleman (26). Boundary compositions for the oxygen-rich boundary of wüstite were determined by extrapolating the single-phase, isothermal behavior to the boundary potentials. These compositions, which are plotted in Fig. 8, are in marked disagreement with the compositions reported in the composite and in other cell studies (3, 8), and are a direct result of the breaks in the emf *vs.* temperature data. These breaks to lower cell emf's as the temperature increases are consistent with data that would be generated by a cell instability in the reducing direction.

Fender and Riley reported that their cell was cycled over a temperature range between 700° and 1300°C for several days with a reproducibility of better than  $\pm 1$  mV. The extreme precision claimed by these workers is difficult to comprehend. At the higher temperatures (> 900°-1000°C), one would expect substantial drift currents due to electron conduction in the electrolyte. (The reader is referred to Fig. 5 for an indication of the expected magnitude of such currents.) It should be noted that the curvature in the emf *vs.* temperature data of Fender and Riley was more pronounced both as the temperature and the cell potential were increased. Both of these effects are consistent with an increased oxygen permeation rate through the CSZ electrolyte which is controlled by low-level electron conduction, and, hence, a reduction of the sample. Fender and Riley report that no drift in cell emf was observed at temperatures up to 1350°C, a remarkable result when compared with the results of the present study and those of Sockel and Schmalzried (3).

Sockel and Schmalzried (3) measured the oxygen activity of wüstite as a function of composition by performing an isothermal titration at 1200°C using a cell of Type [III]. Their experiment was conducted by equilibrating the sample via the gas phase in a static N<sub>2</sub> environment (a procedure similar to the method employed in the present study). Compositional corrections were made on the raw data to account for cell instability (*i.e.*, drift), although no explanation was

offered as to the source of the drift. After compositional corrections were made, the emf was found to be linear with composition. The data of Sockel and Schmalzried are presented in Fig. 7, and the composition of the oxygen-rich phase boundary, determined from their measurement, is shown in Fig. 8. Excellent agreement exists between these data and the composite, both with respect to single-phase activities and the composition of the oxygen-rich boundary.

### Conclusions

The problem of cell instability is one which has arisen frequently in the application of galvanic cells to the study of oxygen activities in single-phase oxide systems. Even where careful consideration was given to experimental procedures to ensure an equilibrium environment, galvanic cells have generated emf's which were unstable with time. A cause of cell instability has been identified to be oxygen permeation through the electrolyte (*i.e.*, 0.85 ZrO<sub>2</sub>-0.15 CaO). The rate of permeation is controlled by low-level hole or electron conduction which is present in the ionic conducting range of the electrolyte.

The identification of oxygen permeation as a source of cell instability provides an important insight into the application of galvanic cells for the study of single-phase compounds. In order to perform reliable measurements of oxygen activities, the effect of oxygen permeation through the electrolyte must be minimized (*i.e.*, low temperatures and large sample sizes) or else the rate of oxygen permeation must be characterized quantitatively so that the composition of the single-phase compound can be determined accurately.

Galvanic cell measurements of oxygen activities in single-phase wüstite (for which the oxygen permeation rate through the CSZ electrolyte was characterized) indicate that the cell emf was a linear function of composition between 980° and 1112°C. A critical analysis of all the reported galvanic cell work in wüstite also revealed the cell emf was a linear function of composition between 765° and 1200°C. The oxygen-rich phase boundary compositions of wüstite which were determined by galvanic cell measurements are essentially those reported in a recent composite analysis and reported originally by Darken and Gurry (10). Those galvanic cell studies in which nonlinear behavior was observed or phase boundary compositions differed markedly from those of the composite are those in which either a static environment was not provided in the sample chamber or else the effect of oxygen permeation through the electrolyte was not properly taken into account. No evidence was found in the present study to support the existence of more than one-phase or second-order transitions within the wüstite phase, as reported by Kleman and Fender and Riley.

### Acknowledgments

Robert A. Giddings is grateful for the partial support of a National Science Foundation Traineeship. He is also very grateful for the financial support extended by the Division of Materials Science and Engineering at the University of Utah.

This paper is based in part on a thesis submitted by Robert A. Giddings for the Ph.D. degree in Materials Science and Engineering at the University of Utah (1972).

Manuscript submitted July 17, 1973; revised manuscript received Nov. 26, 1973. This was Paper 187 presented at the Houston, Texas, Meeting of the Society, May 7-11, 1972.

Any discussion of this paper will appear in a Discussion Section to be published in the December 1974 JOURNAL. All discussion for the December 1974 Discussion Section should be submitted by Aug. 1, 1974.

### REFERENCES

1. H. F. Rizzo, R. S. Gordon, and I. B. Cutler, Proc. Natl. Bureau of Standards Symp. on Mass Trans-

- port in Oxides, October 1967, NBS Special Publication 296, pp. 129-142 (August 1968).
2. B. C. H. Steele, *ibid.*, pp. 165-172.
  3. H. G. Sockel and H. Schmalzried, *Ber Bunsenges Phys. Chem.*, **72**, 745 (1968).
  4. Y. D. Tretyakov and R. A. Rapp, *Trans. AIME*, **245**, 1235 (1969).
  5. H. F. Rizzo, R. S. Gordon, and I. B. Cutler, *This Journal*, **116**, 226 (1969).
  6. G. B. Barbi, *J. Phys. Chem.*, **68**, 2912 (1964).
  7. B. E. F. Fender and F. D. Riley, *J. Phys. Chem. Solids*, **30**, 793 (1969).
  8. F. E. Rizzo and J. V. Smith, *J. Phys. Chem.*, **72**, 485 (1968).
  9. Robert A. Giddings and Ronald S. Gordon, *J. Am. Ceram. Soc.*, **56**, 111 (1973).
  10. L. S. Darken and R. W. Gurry, *J. Am. Chem. Soc.*, **67**, 1398 (1945).
  11. Pierre Vallet and Paul Raccach, *Mem. Sci. Rev. Met.*, **62**, 1 (1965).
  12. R. J. Ackerman and R. W. Sandford, Jr., Tech. Rept. ANL-7250, Sept. 1966.
  13. B. Swaroop and J. B. Wagner, Jr., *Trans. AIME*, **239**, 1215 (1967).
  14. R. A. Giddings, Ph.D. Thesis, University of Utah, Salt Lake City, Utah (1972).
  15. R. J. Brook, W. L. Pelzmann, and F. A. Kroger, *This Journal*, **118**, 185 (1971).
  16. T. H. Etsell and S. N. Flengas, *Chem. Rev.*, **70**, 339 (1970).
  17. W. D. Kingery, J. Pappis, M. E. Doty, and S. C. Hill, *J. Am. Ceram. Soc.*, **42**, 393 (1959).
  18. L. A. Simpson and R. E. Carter, *ibid.*, **49**, 139 (1966).
  19. John W. Patterson, E. C. Bogren, and Robert A. Rapp, *This Journal*, **114**, 752 (1967).
  20. A. W. Smith, F. W. Mesaros, and C. D. Amoto, *J. Am. Ceram. Soc.*, **49**, 249 (1966).
  21. L. Heyne and N. M. Beekmans, *Proc. Brit. Ceram. Soc.*, **19**, 229 (1971).
  22. K. Kitazawa, ScD. Thesis, Massachusetts Institute of Technology, Cambridge, Massachusetts (1972).
  23. H. F. Rizzo, Ph.D. Thesis, University of Utah, Salt Lake City, Utah (1968).
  24. J. Bruce Wagner, in "Fast Ion Transport in Solids," W. Van Gool, Editor, pp. 489-502, North Holland/American Elsevier Publishing Company, New York (1973).
  25. K. Kiukkola and C. Wagner, *This Journal*, **104**, 308 (1957); *ibid.*, **104**, 379 (1957).
  26. M. Kleman, *Mem. Sci. Rev. Met.*, **62**, 457 (1965).

## Effects of Diffusion on Aluminum Depletion and Degradation of NiAl Coatings

James L. Smialek and Carl E. Lowell

National Aeronautics and Space Administration, Lewis Research Center, Cleveland, Ohio 44135

The publication costs of this article have been assisted by the National Aeronautics and Space Administration.

### ABSTRACT

Experiments were performed to critically demonstrate the effects of diffusion on the aluminum depletion and degradation of NiAl coatings on superalloys. Pack aluminized IN 100 and Mar-M200 were diffusion annealed in  $5 \times 10^{-3}$  Torr vacuum at 1100°C for 300 hr. Aluminum losses due to oxidation and vaporization were minimal. Metallographic and electron microprobe analyses showed considerable interdiffusion of the coating with the substrate, which caused a large decrease in the original aluminum level of the coating. Subsequent cyclic furnace oxidation tests were performed at 1100°C using 1 hr cycles on prediffused and as-coated specimens. The prediffusion treatment decreased the oxidation protection for both alloys, but more dramatically for IN 100. Identical oxidation tests of bulk NiAl, where such diffusion effects are precluded, showed no signs of degradation at twice the time needed to degrade the coated superalloys. These results, plus limited tests showing the reduced oxidation resistance of aluminum-poor NiAl, suggest a degradation model whereby the coating is first depleted of aluminum by diffusion, as opposed to  $Al_2O_3$  spalling, then rapidly degraded by the formation of spall-prone oxides.

As aircraft gas turbine inlet temperatures have increased, blade materials have been coated to reduce the adverse effects of oxidation. Recent advances in directionally solidified eutectics will allow even higher blade temperatures ( $\sim 1100^\circ\text{C}$ ) and require greater protection from coatings. It has been shown, however, that current NiAl coatings fail during cyclic oxidation at 1100°C in times less than  $\sim 1000$  hr (1, 2).

The failure of the coating is generally assumed to result from the alternate formation and spalling of an  $Al_2O_3$  film during cyclic oxidation (3-7). Repetition of these processes leads to aluminum depletion and a resultant acceleration of oxidation. That aluminum is removed from the coating is an often demonstrated fact. But that this is a result of the initial oxidation and  $Al_2O_3$  spalling has not been conclusively proven. An alternative process is possible: the aluminum concentration of the coating may first be diluted by inter-

diffusion with the substrate. This possibility is raised because bulk NiAl does not appear to suffer from cyclic oxidation as severely as NiAl coatings on superalloys (8).

It is important to determine which mechanism controls coating breakdown if improvements are to be sought. If spalling of  $Al_2O_3$  controls, then coatings research should endeavor to reduce the growth rate of  $Al_2O_3$  and improve scale adherence. If, on the other hand, diffusion is the predominant mechanism, then coatings research should be directed toward minimizing diffusion.

The purpose of this investigation was to determine the relative importance of diffusion and  $Al_2O_3$  scale spallation to coating breakdown. To achieve this goal, pack aluminized IN 100<sup>1</sup> and Mar-M200<sup>2</sup> were vacuum annealed at 1100°C to allow diffusion to proceed inde-

Key words: coatings, superalloys, oxidation, spalling.

<sup>1</sup> 0.18 C, 10 Cr, 15 Co, 3 Mo, 5 Ti, 5.5 Al, 1 V, balance Ni.  
<sup>2</sup> 0.15 C, 9 Cr, 10 Co, 12.5 W, 1 Nb, 2 Ti, 5 Al, balance Ni.

pendently of oxidation. As-coated and as-diffused coatings were compared before and after cyclic furnace oxidation at 1100°C. The as-coated specimens were also compared to thin samples of bulk NiAl in 1100°C oxidation. The extent of degradation was judged by specific weight change, metallography, and electron microprobe analyses.

#### Materials and Procedure

Cast coupons of IN 100 were cut into  $1.3 \times 2.5 \times 0.25$  cm test specimens. A directionally solidified bar of Mar-M200 was cut into  $0.6 \times 2.5 \times 0.25$  cm test specimens. Holes 0.3 cm diam were spark cut in one end of the specimens for subsequent hanging in furnace oxidation tests. The specimens were prepared for coating by vapor-blasting with alumina grit and rinsing in trichloroethylene, then in ethyl alcohol.

Bulk NiAl alloys ranging from 35 to 50 atom per cent (a/o) aluminum were arc-melted into 50g buttons from high purity (99.99%) nickel and aluminum. Thin ( $\sim 200\mu$ ) oxidation specimens of stoichiometric NiAl were produced by mounting and hand grinding slices of the button. Specimens of various hypostoichiometric compositions were sectioned into 0.25 cm thick slices.

Coating of the superalloys was accomplished by a pack aluminizing process described elsewhere (9). Briefly, the pack process consists of heating the specimens to 1100°C for 16 hr in a pack of 98 weight per cent (w/o)  $\text{Al}_2\text{O}_3$  filler, 1 w/o Al, and 1 w/o NaCl activator. Flushing the pack with argon at 0.5 liter/min prevented oxidation during aluminizing. Variations in the coating weight occurred from specimen to specimen. The limits for IN 100 specimens were 15.9-19.5 mg/cm<sup>2</sup> of aluminum; and the limits for Mar-M200 specimens were 19.8-23.3 mg/cm<sup>2</sup>.

Diffusion annealing of the coated specimens was performed in a vacuum tube furnace at 1100°C for 300 hr. The coated specimens were first preoxidized in 1100°C air for 2 hr in order to form an  $\text{Al}_2\text{O}_3$  film. This was needed to prevent vaporization of the coating during vacuum annealing. A moderate vacuum of  $5 \times 10^{-3}$  Torr also prevented gross aluminum depletion of the coating by curtailing both vaporization and oxida-

tion. A weight gain often occurred for both the pre-oxidation and vacuum annealing treatments (0.8 mg/cm<sup>2</sup> total max). Since primarily  $\text{Al}_2\text{O}_3$  was formed, a mass balance calculation could be performed to determine the actual amount of aluminum lost. This loss was found to be 0.9 mg/cm<sup>2</sup> or only 4% of the aluminum deposited during aluminizing.

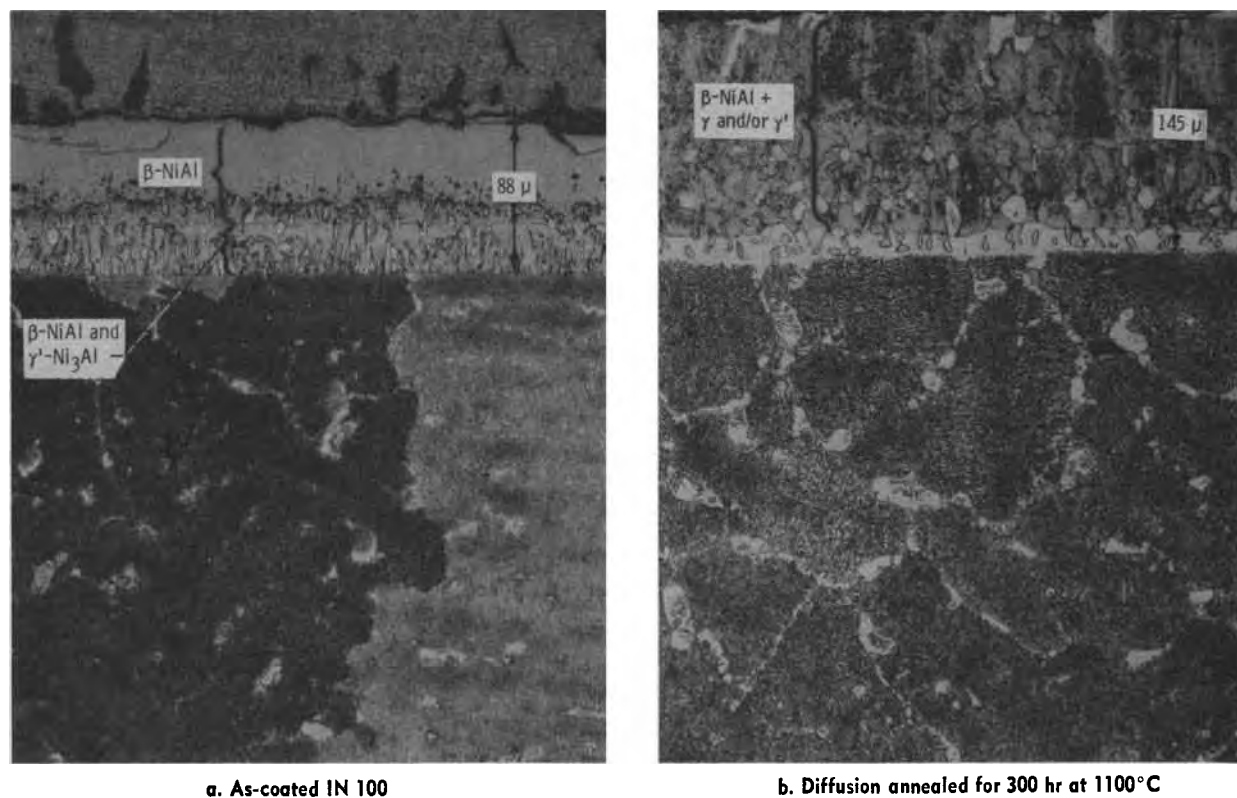
The possibility of vaporization losses through the  $\text{Al}_2\text{O}_3$  film during annealing was also considered. The major gaseous species over alumina at these conditions would be  $\text{AlO}_2$ , with a vapor pressure less than  $10^{-18}$  atm and an aluminum loss rate less than  $10^{-14}$  mg/(cm<sup>2</sup>-sec), ( $10^{-8}$  mg/cm<sup>2</sup> for a 300-hr anneal).

Cyclic oxidation testing was performed at 1100° and 1200°C in vertical-tube resistance furnaces with a hot zone of 30 cm. Specimens were suspended by platinum wire hangers attached to a pneumatic cylinder. They were automatically lowered into and raised out of the furnaces by means of an electronic timer/solenoid switch/pneumatic pump arrangement as described in Ref. (8). For 1100°C tests one cycle consisted of 1 hr in the hot zone followed by 1/3 hr in room air. For 1200°C tests one cycle consisted of 1/10 hr in the hot zone followed by 1/6 hr in room air. Nominal heating and cooling rates were 20°C/sec and 10°C/sec, respectively. Specimens were weighed every 15 hr on an analytical balance accurate to 0.2 mg.

Post-test analyses consisted of surface x-ray diffraction, metallography, and electron microprobe. *In situ* surface scales were identified by diffractometer scans using  $\text{Cu K}\alpha$  radiation with a LiF monochromator. Metallographic specimens were copper-plated before standard mounting and polishing. Etching was accomplished by immersion in a 33%  $\text{H}_2\text{O}$ -33%  $\text{CH}_3\text{OOH}$ -33%  $\text{HNO}_3$ -1%  $\text{HF}$  solution. Microprobe analyses of the polished cross sections were performed with a 15 kV, 30 nA electron beam integrated over a  $40\mu$  wide path.

#### Results and Discussion

*Pack aluminized IN 100.*—Diffusion annealing of pack-coated IN 100 at 1100°C for 300 hr produced some very definite effects. Figure 1 shows a striking change



a. As-coated IN 100

b. Diffusion annealed for 300 hr at 1100°C

Fig. 1. Effect of diffusion on coating structure of aluminized IN 100. X250.

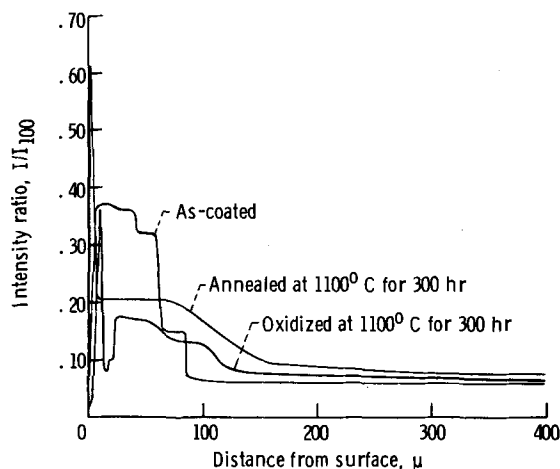


Fig. 2. Aluminum microprobe profiles for pack aluminized IN 100.

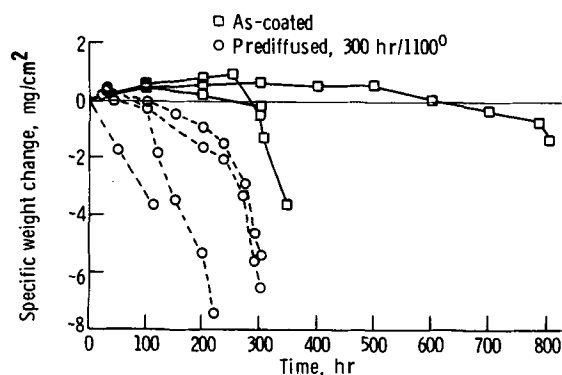


Fig. 3. Effect of diffusion on the oxidation of pack aluminized IN 100. (1100°C, 1 hr cycle furnace tests.)

in coating structure and an increase in over-all coating thickness of 65%. X-ray diffractometer scans identified  $\beta$ -NiAl as the major coating phase for both as-coated and as-annealed coatings. Other phases in the annealed coating were identified as  $\gamma$ -Ni and/or  $\gamma'$ -Ni<sub>3</sub>Al. These phases probably corresponded to the light-etching phases and fine precipitates in the coat-

ing, as shown in Fig. 1b. Annealing also formed  $\alpha$ -Al<sub>2</sub>O<sub>3</sub> plus some TiO<sub>2</sub> (rutile) surface scales.

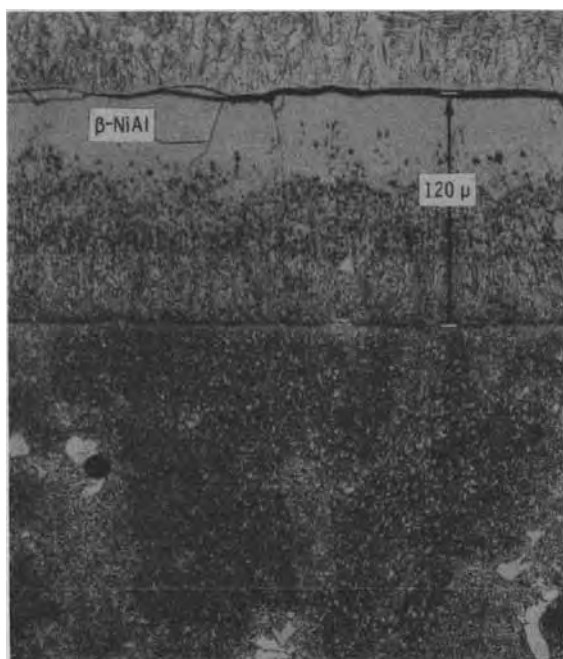
Microprobe profiles for aluminum (Fig. 2) showed that the diffusion annealing treatment decreased the maximum aluminum intensity level in the coating by 40% of the as-coated value and increased the coating thickness by ~60%. (An Al<sub>2</sub>O<sub>3</sub> film is indicated by the sharp peaks at the surface.) Similar effects occurred for the specimen cyclicly oxidized (1 hr cycles) at the same temperature for the same amount of time. Here the maximum aluminum intensity level was decreased by 54% of the as-coated value, and a 10 $\mu$  surface depletion zone occurred due to oxidation. This implies that depletion of aluminum, the accepted cause of failure for NiAl coatings, occurs to a large extent by interdiffusion with the substrate, in addition to the repeated spalling and formation of an oxide film.

The cyclic oxidation behavior of the diffusion annealed specimens was markedly poorer than that of the as-coated specimens (Fig. 3). On the average, diffusion annealed specimens showed a negative weight change (an indication of spalling) at 50 hr, compared to 380 hr for specimens with no preannealing treatment. While considerable scatter in the data exists, the two scatter bands are separable to a significant extent.

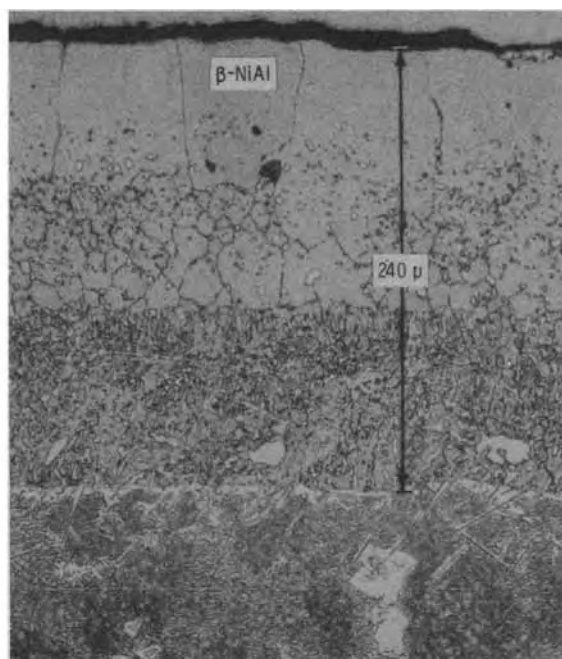
*Pack aluminized Mar-M200.*—Diffusion also affected NiAl coatings on Mar-M200, though not so adversely in oxidation testing. The microstructures in Fig. 4 show that the 1100°C/300 hr diffusion annealing actually doubled the coating thickness. X-ray diffractometer scans showed that  $\beta$ -NiAl was still the only coating surface phase after annealing.

The microprobe profiles in Fig. 5 show that 1100°C/300 hr diffusion annealing reduced the maximum aluminum intensity level by 48% of the as-coated value and indeed doubled the coating thickness. Cyclic oxidation (1 hr cycles) at the same temperature for 700 hr had the same effect on the aluminum profile. No additional effects of oxidation, such as a surface depletion zone, were apparent.

The gravimetric data in Fig. 6 shows that diffusion annealing was not so degrading for coated Mar-M200 oxidation behavior as it was for IN 100. The average oxidation time needed to produce a negative weight change was 270 hr for diffusion annealed specimens compared to 520 hr for as-coated specimens. Thus,



a. As-coated Mar-M200



b. Diffusion annealed for 300 hr at 1100°C

Fig. 4. Effect of diffusion on coating structure of aluminized Mar-M200; X250.



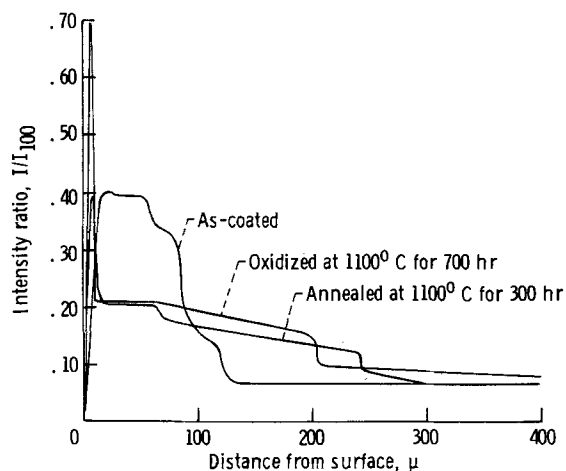


Fig. 5. Aluminum microprobe profiles for pack aluminized Mar-M200.

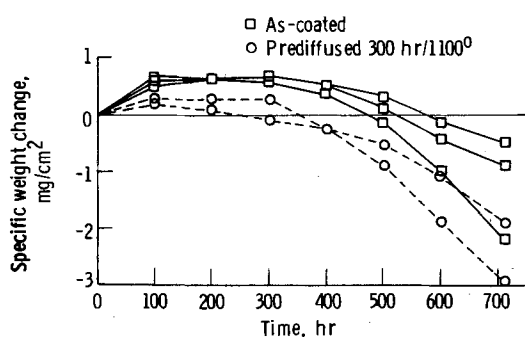


Fig. 6. Effect of diffusion on the oxidation of pack aluminized Mar-M200. (1100°C, 1 hr cycle furnace tests.)

while acknowledging the scatter, the effect of pre-annealing was apparent. The improved behavior of annealed IN 100 coatings was due to the 36% heavier coatings originally deposited (or 66% thicker coatings after annealing). The result was that the coated Mar-M200 was more protective, on the average, than coated IN 100. Thus the 300 hr preannealing treatment repre-

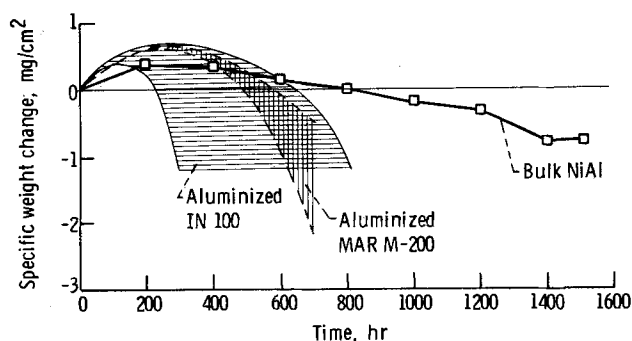


Fig. 7. Comparison of NiAl-coated superalloys with bulk NiAl. (1100°C, 1 hr cycle furnace tests.)

sented a smaller fraction of the coating "lifetime," and was therefore less harmful, for Mar-M200 than for IN 100.

**Comparison of bulk NiAl with coated superalloys.**—Two thin specimens of bulk stoichiometric NiAl were oxidized under the same conditions as IN 100 and Mar-M200. The thickness used (200 $\mu$ ) was intended to contain no more aluminum per exposed area than the NiAl coatings on the superalloys; *i.e.*, it approximated two coatings back-to-back. Yet the cyclic oxidation resistance was markedly better than either coated IN 100 or Mar-M200, as shown in Fig. 7. The average time for a negative weight change was 800 hr for NiAl compared to 380 and 520 hr for the coated superalloys. Even after 1500 hr of oxidation the bulk NiAl had not yet lost 1 mg/cm<sup>2</sup>. More importantly, the rate of spalling, as indicated by these curves, was only half that for the coated superalloys even at twice the oxidation time.

X-ray diffractometer scans of the bulk NiAl surface identified only  $\beta$ -NiAl and Al<sub>2</sub>O<sub>3</sub>. However, on coated IN 100 the identified surface phases were Al<sub>2</sub>O<sub>3</sub>, spinel ( $a_0 = 8.10\text{\AA}$ ), TiO<sub>2</sub>, and  $\gamma$  and/or  $\gamma'$ ; and coated Mar-M200 surface phases were Al<sub>2</sub>O<sub>3</sub>,  $\gamma$  and/or  $\gamma'$ , and some NiAl (800 and 700 hr data for the least spalling specimens of IN 100 and Mar-M200, respectively).

No surface depletion or secondary phases were observed metallographically for bulk NiAl, despite considerable efforts at etching (Fig. 8). However the most

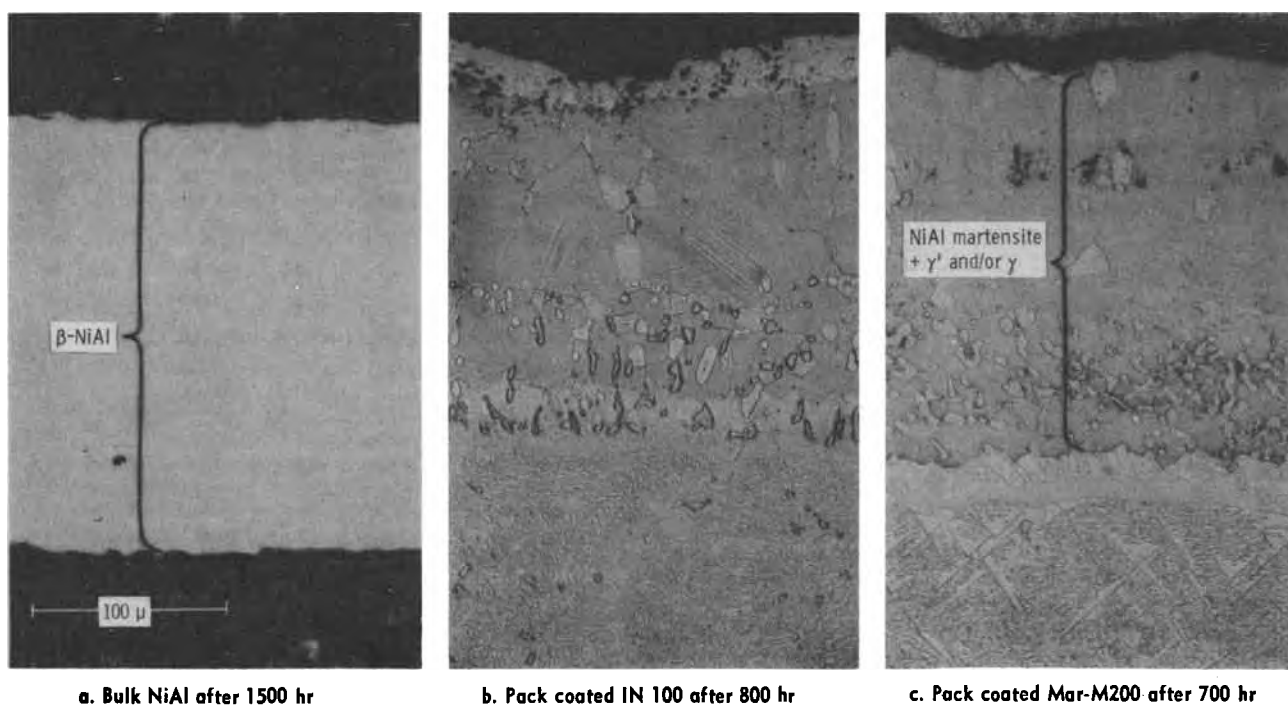


Fig. 8. Comparative degradation of bulk NiAl and aluminized superalloys, oxidized in 1100°C furnace tests, 1 hr cycles. Etched. X250

spall-resistant coated IN 100 and Mar-M200 specimens exhibited martensitic NiAl and  $\gamma$  or  $\gamma'$ , indicating a decrease in the aluminum content of the coating from about 50 a/o to at least 37 a/o (6, 10).

Microprobe data on these specimens also bears this out (Fig. 9): virtually no depletion zone was apparent for the pure NiAl specimen, and the over-all aluminum intensity level was reduced by only  $\sim 16\%$  of its original value. In comparison the aluminum intensity level for the coated superalloys was reduced by  $\sim 49\%$  of the original value.

Since the thin NiAl specimens can be considered simply as a coating without the interdiffusional effects of a substrate, it is apparent that significant gains in coating oxidation life could be obtained by limiting interdiffusion with the superalloy substrates. This harmful interdiffusion may involve both the inward diffusion of aluminum and outward diffusion of nickel as well as the "contamination" of the coating by the substrate alloying elements.

**Degradation model.**—At this point it was clear that diffusion processes were effective mechanisms in initiating coating breakdown. The data also suggest that complete conversion to  $\text{Ni}_3\text{Al}$  is not necessary for rapid oxidation and spalling to occur, i.e., accelerated oxidation was noted for aluminum-depleted  $\beta$ -NiAl. In order to confirm this behavior, supplementary oxidation tests were performed on aluminum-poor compositions of bulk NiAl. An accelerated  $1200^\circ\text{C}$  test with a high cycle frequency (0.10 hr) was used to provide easy differentiation between alloys. The gravimetric data in Fig. 10 show that, indeed, spalling was more pronounced for compositions having less than  $\sim 40$  a/o aluminum. No gradual trend with composition was observed, rather the gravimetric curves fell into two bands. Metallographic and x-ray diffraction analyses showed that only  $\text{Al}_2\text{O}_3$  was formed and no depletion zone occurred for the low-spalling alloys, while  $\text{Al}_2\text{O}_3$  and spinel oxides formed and a  $50\mu$   $\gamma/\gamma'$  depletion zone occurred for the high-spalling alloys. Similar compositional effects can probably be expected for  $1100^\circ\text{C}/1$  hr cycle testing, but the test times needed would be much longer. [These data are consistent with isothermal work in the Ni-Al system (11). The experiments in this work indicated that the critical amount of aluminum needed for exclusive  $\text{Al}_2\text{O}_3$  formation lies between 30 and 40 a/o at this temperature.]

Taking the above data into account along with the previously discussed effects of diffusion, it appears that aluminide coating degradation at  $1100^\circ\text{C}$  follows this sequence. First the aluminum level is significantly decreased due to diffusion and to a lesser extent by repeated  $\text{Al}_2\text{O}_3$  spalling. Only after the aluminum content of  $\beta$ -NiAl decreases to where spinel oxides form does oxide spalling become the predominant cause of aluminum loss. Surface depletion zones of  $\gamma/\gamma'$  soon follow, with the final stages of degradation being the same as for previously reported models. Thus, while diffusion may not account for most of the alu-

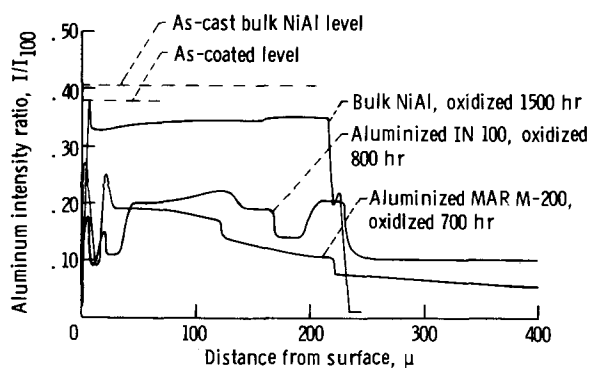


Fig. 9. Comparison of aluminum depletion for bulk NiAl and coated superalloys after cyclic oxidation at  $1100^\circ\text{C}$ .

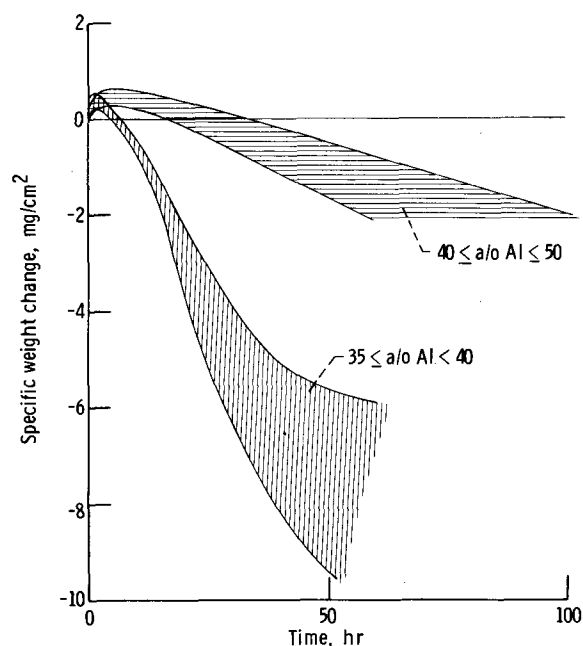


Fig. 10. Effect of composition on cyclic oxidation behavior of bulk NiAl. ( $1200^\circ\text{C}$ , 1/10 hr cycle furnace tests.)

minum lost in a severely degraded coating, it is responsible for the initiation of the coating degradation process.

Admittedly diffusion may play a less important role at temperatures below  $1100^\circ\text{C}$ . The activation energy for  $\text{Al}_2\text{O}_3$  growth was calculated to be about 30 kcal/mole from Arrhenius plots of the parabolic rate constant for Ni-42 a/o Al (11). This is less than the 55 kcal/mole for self-diffusion in Ni-38 a/o Al (12). This implies that diffusion will become less significant relative to  $\text{Al}_2\text{O}_3$  growth at lower temperatures. However it is difficult to predict the actual temperature at which diffusion is no longer the controlling mechanism for aluminum loss.

### Concluding Remarks

Based on a comparison of bulk NiAl and diffusion annealed coatings with as-coated superalloys in  $1100^\circ\text{C}$  cyclic oxidation, the following conclusions appear justified: (i) loss of aluminum in the coating by diffusion with the substrate triggers coating degradation rather than spallation of  $\text{Al}_2\text{O}_3$  alone; and (ii) this loss of aluminum allows oxides other than  $\text{Al}_2\text{O}_3$  to form with an increased rate of spalling, which leads to rapid coating failure. Thus the long-time use of NiAl coatings at  $1100^\circ\text{C}$  will require a reduction of coating/substrate interdiffusion, possibly by the use of diffusion barriers.

Manuscript submitted Sept. 19, 1973; revised manuscript received Dec. 13, 1973. This was Paper 88 presented at the Boston, Massachusetts, Meeting of the Society, Oct. 7-11, 1973.

Any discussion of this paper will appear in a Discussion Section to be published in the December 1974 JOURNAL. All discussions for the December 1974 Discussion Section should be submitted by Aug. 1, 1974.

### REFERENCES

1. V. S. Moore, W. D. Brentnall, and A. R. Stetson, NASA CR-72714, Solar Div., International Harvester Co. (1970).
2. S. R. Levine, NASA TM X-2370 (1971).
3. G. W. Goward, D. H. Boone, and C. S. Giggins, *ASM Trans. Quart.*, **60**, 228 (1967).
4. T. K. Reddin, *Trans. AIME*, **242**, 1695 (1968).
5. G. W. Goward, *J. Metals*, **22** (10), 31 (1970).
6. J. L. Smialek, *Met. Trans.*, **2**, 913 (1971).



7. W. A. Sanders, C. A. Barrett, and H. B. Probst, NASA TN D-6400 (1971).  
 8. G. J. Santoro, D. L. Deadmore, and C. E. Lowell, NASA TN D-6414 (1971).  
 9. S. R. Levine, NASA TM X-71423 (1973).  
 10. J. L. Smialek, *Met. Trans.*, **4**, 1571 (1973).  
 11. F. S. Pettit, *Trans. AIME*, **239**, 1296 (1967).  
 12. M. M. P. Janssen, *Met. Trans.*, **4**, 1623 (1973).

## Ellipsometric Measurements of the Plasma Oxidation of Nb and Ta and Their Interpretation

K. Knorr<sup>1</sup>

*Institut Max Von Laue-Paul Langevin, Grenoble, France*

and J. D. Leslie<sup>2</sup>

*Centre de Recherches sur les Très Basses Températures, Grenoble, France*

*The publication costs of this article have been assisted by the National Research Council of Canada.*

### ABSTRACT

Ellipsometric results presented in this paper show that it is possible to grow a uniform Nb oxide film by plasma oxidation, and the index of refraction of this Nb oxide is 2.30. Similarly, in a previous paper we showed that plasma oxidation of Ta produced a uniform Ta oxide film with a refractive index of 2.21. These results are in contrast to the earlier work of Lee *et al.*, who fitted their ellipsometric measurements on the plasma oxidation of Nb and Ta with two-layer models. It is shown that the Nb and Ta oxides in the work of Lee *et al.* were not grown to a sufficient thickness to prove definitively that the oxides were composed of two layers, and that their data can be fitted equally well with one-layer models.

In this paper we would like to report on an ellipsometric study of the plasma oxidation of niobium. In a previous paper (1) we reported on a similar study on tantalum. In these studies we have found that it is possible to grow uniform oxides on niobium and tantalum by plasma oxidation. In contrast, Lee *et al.* (2), in the only previous ellipsometric study of the plasma oxidation of tantalum and niobium, reported that their data were consistent with two-layer oxides. In order to investigate this difference in interpretation, we have performed two-layer calculations on ellipsometric data. It is shown that the Nb and Ta oxides in the work of Lee *et al.* were not grown to a sufficient thickness to prove definitively that the oxides were composed of two layers, and it is also shown that their data can be fitted equally well with one-layer models.

### Experimental Procedures

Since the experimental arrangement and procedures have been described in detail in the earlier article on the plasma oxidation of Ta (1), only a brief description will be given here.

The plasma oxidation is carried out in a metal high vacuum chamber which can be evacuated to  $10^{-7}$  Torr during sample cleaning or held at a pressure of 0.05 Torr of oxygen under flow conditions while the sample is being oxidized. The vacuum chamber has two optical windows located so that *in situ* ellipsometric measurements can be carried out during the plasma oxidation. The ellipsometer (3) used is automated and is capable of taking a reading per second. It utilizes a He-Ne laser ( $\lambda = 6328\text{\AA}$ ) as a light source, the angle of incidence is  $59.5^\circ$ , and the angular resolution of the polarizer null, P, or analyzer null, A, is  $0.01^\circ$ .

With the ellipsometer it was possible to test various treatments of the surface of the sample to find the one that gave the cleanest surface possible prior to growth

of the plasma oxide. The criterion used was that the best surface treatment should produce the highest P value possible and a stable A value, since a dirty surface layer would act primarily to reduce the P reading from its true clean surface value and by a much smaller amount lower or raise the A reading depending on whether the surface layer was absorbing or non-absorbing, respectively. As in the case of Ta (1), the best treatment was found to consist of heating the sample to a white heat in vacuum. This was accomplished by having the sample in the form of a foil, 0.1 mm thick, and passing a large current through it while it was in the high vacuum chamber at a pressure of  $10^{-7}$  Torr. Typically this heat-treatment gave P,A readings of  $30.0^\circ$  and  $34.7^\circ$ , respectively.

The cleaned sample had a wire spotwelded to it for supplying the drive current for the plasma oxidation and then the sample was mounted in place for the optical measurements with mica sheets. The top mica sheet had a hole,  $9 \times 18$  mm, which defined the active area of the sample on which the oxide was formed. The glow discharge cathode, which is a  $10 \times 4 \times 0.5$  cm piece of Al covered with 0.1 mm Ta foil, is located 8 cm away from the sample with its  $40 \text{ cm}^2$  front surface facing the sample. A Au probe located close to the sample was used to measure the voltage of the plasma adjacent to the sample.

With the sample mounted, the system was pumped down and then argon gas was admitted to a pressure of 0.05 Torr and a short glow cleaning was employed, by putting  $-400\text{V}$  on the glow discharge cathode. This ensured that no water or dust particles were in the sample, and changed the P,A readings by only  $0.1^\circ$ . The argon gas was then pumped out of the chamber, and the system was flushed several times with oxygen to ensure that all the argon was removed. A pressure of 0.05 Torr of oxygen under flow conditions was established,  $-1000\text{V}$  were applied to the glow discharge cathode, and a constant drive current of 10 mA was injected into the sample to initiate the plasma oxidation.

<sup>1</sup> Present address: Physikalisches Institut, Robert-Mayer-Str. 2-4, 6 Frankfurt, Main, Germany.

<sup>2</sup> Present address: Department of Physics, University of Waterloo, Waterloo, Ontario, Canada.

Key words: ellipsometry, refractive index.

During the plasma oxidation the P,A readings were displayed digitally by the automatic ellipsometer and were recorded. In addition, the digital P,A readings were converted to analog signals so that the curve in the P,A plane could be plotted directly on an X-Y recorder during the experimental run. The voltage of the sample and the voltage of the nearby Au probe in the plasma were measured and recorded during a run. The output of a digital clock, together with the constant value of the drive current being supplied to the sample, allowed the total charge  $q$  passed through the sample to be measured. Normally P,A readings were taken for a period of 20,000 sec to grow 1500Å of oxide, and with a time of approximately 5 sec to take a P and A reading we ended with 4000 P,A points to characterize a run.

### Nb Results and Discussion

The quarter-wave plate used in the phase delay section of the ellipsometer was measured and found to have a phase delay of  $89.6^\circ$  and a fast-slow axis transmission ratio of 1. These values were used to convert the P,A readings into the standard quantities  $\Delta$  and  $\psi$ . [If the phase delay had been exactly  $90^\circ$ , the conversion would be  $\Delta = 2P + 90^\circ$  and  $\psi = A$ , but the slightly different value of the phase delay modifies this conversion very slightly, but in a well-known way (4). The quantities  $\Delta$  and  $\psi$  are defined by  $\Delta = \arg R_p/R_s$  and  $\tan \psi = |R_p/R_s|$  (5), where  $R_p$  and  $R_s$  are the complex reflectivities for the light in and perpendicular to the plane of incidence, respectively.] In Fig. 1, we present our ellipsometric results on the plasma oxidation of Nb in the form of a plot of  $\Delta$  vs.  $\psi$ . Our experimental data are presented as a solid line through the approximately 4000 data points defining the curve. The scatter of the data is within the thickness of the solid line. The dashed line near the maximum in  $\psi$  denotes the experimental region where the P nulls are so broad that the  $\Delta$  values are not well defined, but the A nulls remain quite sharp so that the  $\psi$  values are accurately known.

To get the best fit to our ellipsometric data on the plasma oxidation of Nb shown in Fig. 1, we had to shift our bare surface P value from the experimentally measured value of  $30.0^\circ$  to  $30.8^\circ$  while leaving our bare surface A value at the experimentally measured

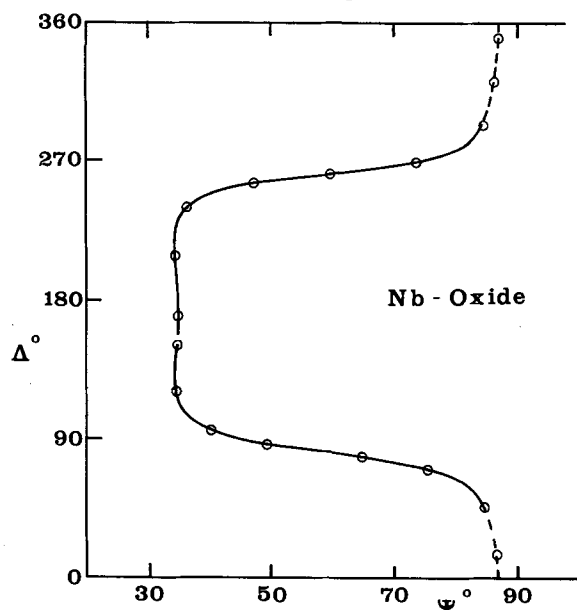


Fig. 1. Ellipsometric results for the plasma oxidation of Nb. The solid curve is the experimental results and the open circles denote the theoretical fit obtained using a refractive index of 2.30 for the Nb oxide. Experimental conditions: sample area 162 mm<sup>2</sup>, constant drive current 10 mA, oxygen pressure 0.05 Torr, cathode voltage -1000V, wavelength 6328Å, and angle of incidence 59.5°. Bare-surface values:  $\Delta_0 = 151.60^\circ$  and  $\psi_0 = 34.64^\circ$ .

value of  $34.7^\circ$ . This shift in the bare surface value of P by  $0.8^\circ$  corresponds to assuming that our surface treatment of the Nb sample left a 12Å layer of Nb oxide, which is certainly reasonable since a thin layer of thermal oxide would form spontaneously as soon as the heated-out foil was first exposed to oxygen. Using initial P,A values of  $30.8^\circ$  and  $34.7^\circ$ , respectively, the index of refraction of Nb at 6328Å is found to be  $3.0 - i3.6$ .

The data of Fig. 1 could be fitted with an oxide of constant, real index of refraction of 2.30 growing on the bare Nb surface with initial  $\Delta, \psi$  values of  $151.60^\circ$  and  $34.64^\circ$ , respectively. The theoretical fit obtained with this index is shown in Fig. 1 as a series of open circles. This fit was obtained two ways. First, theoretical P,A curves were generated by varying the index of refraction of the oxide in a standard ellipsometer program (4) while keeping all other parameters fixed, and a visual fit was determined by superimposing these theoretical P,A curves plotted on one sheet of paper on the experimental P,A curve plotted on another sheet of paper. The visual fitting procedure was checked later by an automatic nonlinear least squares fitting ellipsometer program which obtained the best fit between the experimental and theoretical curves by adjusting the real and imaginary parts of the index of refraction of the oxide film to minimize the least squares deviation between the experimental and theoretical values of P and A for a selected set of points on the experimental curve. Using this program, we found almost the same index of refraction for the Nb oxide

film, i.e.,  $\hat{n} = n - ik$ , with  $n = 2.29 \pm 0.01$  and  $k = 0.003 \pm 0.003$ . The rms deviation in A was found to be  $0.25^\circ$ . Since the error in  $k$  is as large as its value, we suggest that it is valid to take  $k$  to be zero within experimental error and use the value of 2.30 for the Nb oxide refractive index which gives an almost perfect visual fit between the experimental and theoretical curves.

The only previous ellipsometric study of the plasma oxidation of Nb is that of Lee *et al.* (2). Our Fig. 1 should be compared with their Fig. 4. Their experimental data consist of 15 points that were taken with a manual ellipsometer, operating at 5461Å and an angle of incidence of  $65^\circ$ , and their experimental points were probably taken by stopping the oxidation process at particular points to make ellipsometric measurements, although this is not stated. Our experimental data were obtained with an automated ellipsometer, operating at 6328Å and an angle of  $59.5^\circ$ , that took data points at least every 5 sec while the oxidation process was proceeding at constant sample driving current. Our experimental data are presented in Fig. 1 as a solid line through the approximately 4000 data points defining our curve.

Lee *et al.* fitted their ellipsometric data on the plasma oxidation of Nb with a two-layer model for the oxide, i.e., an outer layer with an index of 2.15 and an inner layer with an index of 2.37, with the outer layer comprising 40% of the total thickness of the two layers at any stage of the growth. Their fit is presented as a solid curve with the experimental data as superimposed points. As discussed earlier, we have been able to fit our ellipsometric data on the plasma oxidation of Nb by a single uniform Nb oxide layer with an index of refraction of 2.30. This difference in interpretation of the ellipsometry data by Lee *et al.* and ourselves is discussed fully in the next section of this paper.

In Fig. 2 we present our electrical measurements during the growth of the Nb oxide in the form of plots of time, total charge passed  $q$ , and sample voltage  $V$  vs. oxide thickness. As can be seen in Fig. 2, the time or total charge passed  $q$  vs. oxide thickness plot is well represented by a straight line passing almost through the starting point. The voltage  $V$  of the sample with respect to a Au probe nearby in the plasma increases

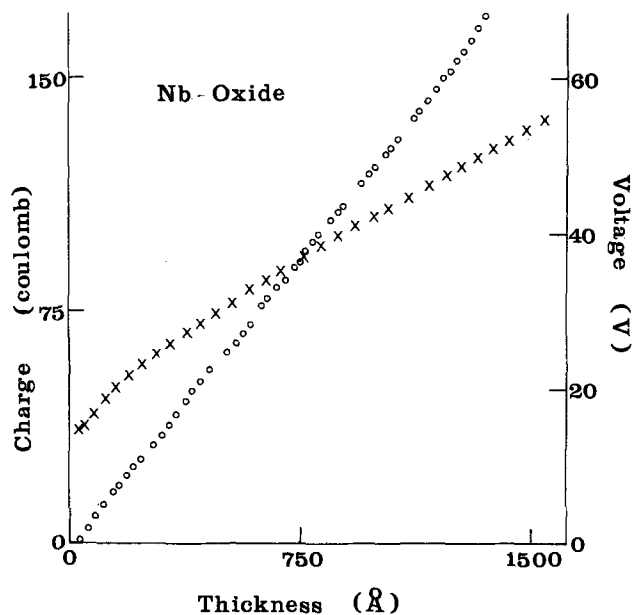


Fig. 2. Electrical measurements for the plasma oxidation of Nb. The open circles denote the total charge passed through the sample vs. the oxide thickness. The crosses denote the voltage of the sample with respect to a Au probe nearby in the plasma vs. the oxide thickness.

fairly quickly to a certain value at low thickness and then increases linearly with thickness thereafter. The electrical behavior reported here for the plasma oxide on Nb is similar to what was found for the plasma oxide on Ta (1). From Fig. 2, it can be seen that the plasma oxide on Nb is growing at an approximately constant rate of 7.5Å per 100 sec. The current efficiency,  $\eta$ , was calculated from  $\eta = (GA\nu F\rho)M^{-1}$ , where  $G$  is the oxide growth rate,  $A$  is the sample area,  $\nu$  is the valency of the metal ion,  $F$  is the Faraday constant,  $\rho$  is the oxide density, and  $M$  is the molecular weight of the oxide, assuming that the oxide being formed is  $Nb_2O_5$  with a molecular weight of 266 and a density of 4.4 g/cm<sup>3</sup> (6). A value of  $\eta = 0.2\%$  was found and this is in the same range as the value of 0.4% found for the plasma oxide on Ta (1).

#### Interpretation of Ellipsometric Measurements of the Plasma Oxidation of Nb and Ta

In this paper for Nb, and in a previous paper (1) for Ta, we have found that our ellipsometric measurements are consistent with a single uniform layer of oxide, with a purely real index of refraction, being formed by the plasma oxidation process. In contrast, Lee *et al.* (2) state that their ellipsometric measurements on the plasma oxidation of Ta and Nb indicate that the oxide being formed consists of two layers, with different indices, that grow simultaneously so that each layer remains a certain fraction of the total thickness. In a situation such as this, some questions naturally arise. Are the two groups seeing different physical behavior? Is the apparent difference in physical behavior just due to differences in interpretation? How valid is a given interpretation? In this section we would like to address ourselves to answering these questions about our experiments and those of Lee *et al.* on the plasma oxidation of Nb and Ta.

It must be clearly understood that ellipsometric experiments do not measure directly the number of layers in an oxide, the indices of refraction of the layers, etc. In an ellipsometric experiment of the type used to follow the growth of films, the state of polarization of light reflected from the investigated surface is determined and expressed by  $\Delta$  and  $\psi$ . Starting from a point  $\Delta_0, \psi_0$  in the  $\Delta, \psi$  plane, characterizing the bare, oxide-free surface,  $\Delta$  and  $\psi$  change while the oxide film

is formed generating an ellipsometric curve. To deduce information from the ellipsometric curve, a model of the structure of the film has to be assumed and then the free parameters of the model can be determined by curve fitting.

The simplest possible model is that the film is a single uniform layer, characterized by an index of

refraction  $\hat{n} = n - ik$ . This is a two parameter model if the fitting procedure involves varying both  $n$  and  $k$ , otherwise if  $k$  is taken to be zero it reduces to a one parameter model. All the other parameters involved in the calculations, i.e., the angle of incidence  $\theta$ , the wavelength of the light  $\lambda$ , the refractive index of the surrounding medium  $\hat{n}_m$ , and the refractive index of the substrate material  $\hat{n}_s$  should be known. The starting point  $\Delta_0, \psi_0$ , if it is truly characteristic of the bare, oxide-free surface, determines the value of  $\hat{n}_s$  directly.

The next more complicated model is that the film is composed of two layers. This can be a five parameter model, since each film is characterized by an  $n$  and a  $k$ , and there has to be an additional parameter to characterize the division of the total thickness between the two films. If it is assumed that the two films have purely real indices, i.e., both  $k$ 's are zero, then the two-layer model has only three free parameters.

Now, while a limited portion of an ellipsometric curve cannot determine directly parameter values for models, if the ellipsometric data have been taken over a sufficient thickness range certain general features of the ellipsometric curve can distinguish clearly between various possibilities. For example, in the open type of ellipsometric curve, as shown in Fig. 1 for the plasma oxidation of Nb, a periodicity of 360° in  $\Delta$  of the ellipsometric curve indicates that the oxide film is a single uniform layer with a purely real index. A two-layer model cannot produce such a periodicity of 360° in  $\Delta$ , although for certain values of indices (purely equal) and ratios of thicknesses of the two films, the resulting ellipsometric curves can be periodic in  $\Delta$ , where the period is a particular integral multiple of 360°. General features, such as the periodicity in  $\Delta$ , are more powerful in discriminating between various models than comparing the accuracy of fitting, since a model with more free parameters can usually be made to give a better fit over a limited portion of a curve.

Now with the preceding discussion on ellipsometric curve fitting as background, let us examine the ellipsometric data. There are distinct differences in the general features of the data between our experiments and those of Lee *et al.* As shown in Fig. 1 for Nb and in Fig. 3 of a previous paper (1) for Ta, our ellipsometric data on the plasma oxidation of Nb and Ta shows an almost perfect 360° periodicity in  $\Delta$ , since  $\psi$  is coming back almost exactly to its original value after  $\Delta$  has changed by 360°. As we have stated earlier, this general behavior is consistent only with a model involving a single uniform layer with a purely real index, and consequently we have used such a model in fitting our data. In contrast, the ellipsometric data of Lee *et al.* (2) on the plasma oxidation of Nb and Ta have the general feature that  $\psi$  is significantly lower than its original value as the change in  $\Delta$  from its original value approaches 360°. Lee *et al.* used a two-layer model to fit their data, but we would like to show in the following that this is not the only model that will reproduce their experimental results since a one-layer absorbing film (nonzero  $k$  value) has the same general behavior over the thickness range studied.

We concentrate first on their results on Ta. Lee *et al.* have taken 10 ellipsometer readings during the growth of the oxide. Since a reconstruction of the experimental points from their Fig. 3 would be inexact, we calculated their theoretical two-layer ellipsometric curve and picked out 10 points of this curve which have

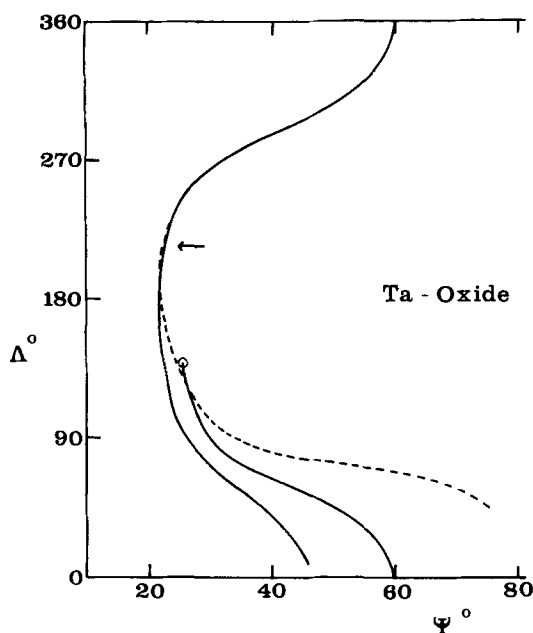


Fig. 3. Comparison of two fitting models for the ellipsometric data of Lee *et al.* on the plasma oxidation of Ta. The solid curve represents a single-layer model with index  $2.02 - i0.049$ . The dashed curve represents the two-layer model used by Lee *et al.* Where the dashed curve is not shown it is superimposed on the solid curve within the resolution of the figure. The open circle denotes the bare Ta surface value of the optical parameters, and the growth of the oxide corresponds to moving down the solid or dashed curves. The arrow indicates the final thickness to which the oxide was grown by Lee *et al.* In the model of Lee *et al.*, this final oxide thickness is  $1100\text{\AA}$ , composed of an outer layer of  $473\text{\AA}$  with an index of  $1.89$  and an inner layer of  $627\text{\AA}$  with an index of  $2.22$ . In the single-layer model with index  $2.02 - i0.049$  this final oxide thickness is  $1150\text{\AA}$ .

about the same positions as the experimental ones. Since the starting point  $\Delta_0, \psi_0$  of the ellipsometric curve is not given, we had to read it from their Fig. 3. Now we fitted a one-layer model to the selected points using a nonlinear least squares fit computer program.

This yields a refractive index of the oxide of  $\hat{n} = (2.02 \pm 0.01) - i(0.049 \pm 0.003)$ . All the other parameters were held constant, in particular we used the same  $\Delta_0, \psi_0$  as for the two-layer model.

The results of this comparison are shown in Fig. 3. The solid line shows the one-layer fit and the dashed line shows the two-layer model. The feature to note is that the two curves superimpose from the starting point (denoted by an open circle) to within  $20^\circ$  in  $\Delta$  of the last experimental point (located by the arrow). Obviously, the one-layer fit and the two-layer model deviate drastically from one another as the oxide thickness is increased beyond the experimental range published by Lee *et al.* Indeed, the dashed line on the second cycle crossing its counterpart on the first cycle and rising toward a higher maximum is characteristic of such a two-layer model, and the observation of such behavior would have been very strong evidence that their oxide film was composed of two distinct layers. (Certainly, no combination of  $n$  and  $k$  in a one-layer model would be able to produce such an effect.) However, their published data stop at the point indicated by the arrow.

Over the experimentally measured thickness range, the rms deviation between the one-layer and two-layer curves in Fig. 3 is  $0.35^\circ$  in  $\psi$ , i.e., assuming that the error occurs completely in  $\psi$ . This deviation is probably no larger than that between the experimental points and the two-layer curve. (Lee *et al.* do not give a numerical value for the deviation for the case of Ta, but from the value given for the case of Nb, and from comparing the two diagrams for Nb and Ta, we conclude that a deviation larger than  $0.3^\circ$  in  $\psi$  is very likely in the Lee *et al.* experiment on Ta.)

A similar comparison between a one-layer fit and the two-layer model of Lee *et al.* was carried out for the case of Nb. The least squares fit computer program gives a single layer with the index  $\hat{n} = (2.27 \pm 0.01) - i(0.016 \pm 0.004)$ . Over the experimentally measured thickness range, the rms deviation between the single-layer ellipsometry curve and the two-layer model of Lee *et al.* is  $0.25^\circ$  in  $\psi$ . This deviation is possibly a little higher than that between the experimental points and the two-layer curve, but which fit is actually better depends on the exact positions of the experimental values. Once again, the experimental values do not extend into the thickness range where the one-layer fit and the two-layer model deviate widely, and where experimental points falling on the two-layer curve would have ruled out our alternative interpretation.

In conclusion, the almost perfect  $360^\circ$  periodicity in  $\Delta$  exhibited by our ellipsometric data on the plasma oxidation of Nb and Ta confirms our interpretation that the oxide being formed consists of a uniform single layer with a zero (or almost vanishing) absorption. The indices of refraction found for these plasma produced oxides are  $2.30$  in the case of Nb and  $2.21$  in the case of Ta. In contrast, we have shown that the data of Lee *et al.* on the plasma oxidation of Nb and Ta do not have a unique interpretation. In addition to their interpretation in terms of a two-layer model, a one-layer model involving a uniform but absorbing oxide fits their experimental data equally well over the experimentally measured thickness range. In order for Lee *et al.* to have tested whether their oxide films really consisted of two layers, their ellipsometric measurements should have been carried out to greater oxide thickness where the difference between a two-layer model and an absorbing single layer is readily apparent.

Manuscript submitted July 27, 1973; revised manuscript received *ca.* Dec. 1, 1973.

Any discussion of this paper will appear in a Discussion Section to be published in the December 1974 JOURNAL. All discussions for the December 1974 Discussion Section should be submitted by Aug. 1, 1974.

#### REFERENCES

1. J. D. Leslie and K. Knorr, To be published.
2. W. L. Lee, G. Olive, D. L. Pulfrey, and L. Young, *This Journal*, **117**, 1172 (1970).
3. Similar to the ellipsometer described by J. L. Ord, *Surface Sci.*, **16**, 155 (1969).
4. F. L. McCrackin, E. Passaglia, R. R. Stromberg, and H. L. Steinberg, *J. Res. Natl. Bur. Std.*, **67A**, 363 (1963).
5. M. Born and E. Wolf, "Principles of Optics," 3rd ed., Pergamon Press, New York (1965).
6. L. Young, "Anodic Oxide Films," p. 188, Academic Press, New York (1961).

# Dielectric Breakdown Properties of SiO<sub>2</sub> Films Grown in Halogen and Hydrogen-Containing Environments

C. M. Osburn\*

IBM Thomas J. Watson Research Center, Yorktown Heights, New York 10598

The publication costs of this article have been assisted by the IBM Corporation.

## ABSTRACT

Thermal oxidation of silicon, in the presence of chlorine or bromine compounds, effectively improved the dielectric breakdown characteristics (as measured with a voltage ramp) of the resulting SiO<sub>2</sub> films. At high halogen concentrations the oxidation rate was erratic; the optimal initial breakdown properties were attained by oxidizing with about one-half of the halogen-containing additive that would cause etching of the Si. Oxidation in the presence of halides increased the resistance of SiO<sub>2</sub> films to dielectric breakdown under accelerated bias-temperature stressing. The maximum time to failure varied semilogarithmically with HCl concentration and increased by 0.3 to 0.65 decade per per cent of HCl (0-3% HCl range) for applied fields from 2 to 7 MV/cm, respectively. Higher oxidation temperatures further improved the resistance of HCl oxides to dielectric wear-out. The longer wear-out times were attributed to hydrogen rather than the halogen and could be achieved by oxidation in small concentrations of H<sub>2</sub>O, annealing in H<sub>2</sub>, or implantation of H<sub>2</sub> or H<sub>2</sub>O.

Thermal oxidation of silicon in environments containing small concentrations of halogens and halides improves properties of the resultant SiO<sub>2</sub> films (1-8) and underlying silicon (9-12). This procedure effectively reduces fixed oxide charge (1, 3, 5, 7), interface state (1, 8), and mobile charge (1-5, 7) densities. At higher temperatures ( $\approx 1150^\circ\text{C}$ ), SiO<sub>2</sub> films prepared with HCl additions seem to neutralize Na<sup>+</sup> ion contamination effects, often introduced during later processing (2-4).

Superior SiO<sub>2</sub> dielectric breakdown distributions have also been achieved by oxidation in HCl-O<sub>2</sub> atmospheres at high temperatures or even by HCl cleaning the quartz oxidation tube (13). These oxide films were also considerably more resistant to failure as a result of electrochemical degradation under accelerated bias-temperature aging (6). Substantial reductions in the Si minority carrier generation rates have been noted after HCl oxidation (9, 12) or Cl<sub>2</sub> gettering (12, 14) of metallic impurities from the Si.

Gettering is generally believed to be partially responsible, at least, for these beneficial effects, wherein metal contaminants are removed (as volatile halides) from the oxide or underlying silicon. Presumably, Na removal gives a lower mobile oxide charge, while the elimination of recombination centers like Cu, Fe, or Ag from the silicon results in a lower minority carrier generation rate. This gettering model for the transport of impurities, however, does not explain all properties of halogen-grown oxides, particularly the Na neutralization (2-5) effect and flatband voltage instabilities (15) in which incorporated chlorine (5, 15-17) probably plays a role.

This study was undertaken to more completely establish the influence of hydrogen and halogens on the dielectric breakdown properties of SiO<sub>2</sub> films. Both initial breakdown voltage characteristics and time to failure under accelerated stressing were measured.

## Experimental

Metal-oxide-semiconductor capacitor structures were fabricated from moderately doped n- or p-type, (100) silicon wafers. Silicon dioxide layers were grown at 850°-1150°C in atmospheres containing small concen-

trations of HCl, Cl<sub>2</sub>, HBr, CCl<sub>4</sub>, C<sub>2</sub>HCl<sub>3</sub>, or H<sub>2</sub>O. Oxidation times were adjusted because of the enhanced oxidation rate in the presence of halogens (15, 19); final oxide thicknesses were measured ellipsometrically. Halogen gas concentrations were limited ( $\lesssim 10\%$  HCl, 10% HBr, or 2% Cl<sub>2</sub>) to prevent silicon corrosion; even so, considerable care had to be taken to ensure uniform oxide growth without localized Si pitting. The problem was more severe with other gases; for example visibly nonuniform oxide films often resulted from oxidation in 1% CCl<sub>4</sub> or 3% C<sub>2</sub>HCl<sub>3</sub> at 1000°C. The test structures were completed by depositing through a mask, an array of 100 aluminum dots from an E-gun source and annealing to remove radiation damage incurred during metallization.

Statistical distributions of the breakdown voltages of identically prepared capacitors were determined with an applied ramp voltage by detecting the first breakdown event [see Ref. (20)]; these results constitute an initial or "time-zero" measure of oxide quality. In addition, the times to failure were also determined using accelerated bias-temperature conditions (6). Past work has shown that the initial breakdown distributions provided a quantitative measure of the oxide defect density (13), while the accelerated testing data gave information about the rate at which the dielectric strength decreased (6).

## Results and Discussion

*Statistical breakdown voltages.*—Silicon dioxide films that are thermally oxidized in the presence of halogens show improved time-zero distributions. The results in Fig. 1 show the improvements obtained with 3% HCl or 2% Cl<sub>2</sub> at an oxidation temperature of 1000°C compared with the standard SiO<sub>2</sub> for 450Å films. The maximum dielectric strength remains constant under all oxidation conditions, but the average breakdown voltage is increased and the statistical spread is reduced for the halogen-oxidized films. The defect density was calculated as described in Ref. (20) by associating low-field breakdowns (i.e., those capacitors exhibiting less than 80% of the maximum dielectric strength) with oxide film defects; the standard films had 100 defects/cm<sup>2</sup> compared to 40 for HCl- and 12 for Cl<sub>2</sub>-grown films, respectively. It should be emphasized that the defect density varied with wafer lot and source, cleaning, and cleanliness of the oxidation fur-

\* Electrochemical Society Active Member.  
Key words: dielectric breakdown, silicon dioxide, reliability, HCl oxidation.

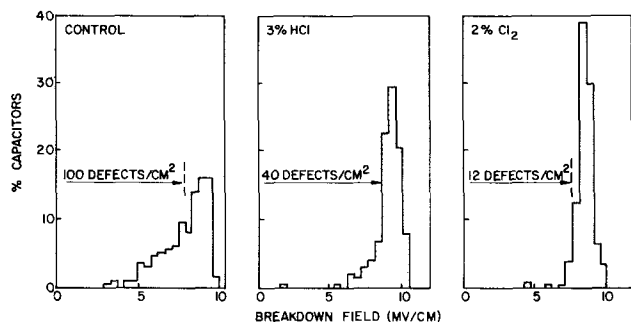


Fig. 1. HCl and Cl<sub>2</sub> effects on the statistical distributions of breakdown strength for SiO<sub>2</sub> films grown at 1000°C.

nance, and this variation could be very large. Over a three-year period with hundreds of oxidation runs, the standard defect density has varied from 16 to over 300. Therefore the absolute values of the defect density were not as meaningful as the relative fluctuations during a single oxidation since the uniformity within any given run was usually better than 20%.

The influence of HCl, Cl<sub>2</sub>, CCl<sub>4</sub>, C<sub>2</sub>HCl<sub>3</sub>, and HBr concentrations during oxidation on the defect density is portrayed in Fig. 2. For HCl oxides, the defect density was lowest when about 3% HCl was added during oxidation. The most substantial improvement appeared between 0 and 1% HCl. The 0% defect density plotted here was typical of what could be consistently achieved with careful preparation. Oxides grown in 6% and 9% HCl did not show visible corrosion even though breakdown measurements revealed that they were inferior to films grown with lower HCl concentrations. Apparently, breakdown distributions reflect corrosion effects more sensitively than visual observations do. Moreover, wafer corrosion could be observed occasionally under these conditions if careful procedures were not followed: the oxidation tube needed to be equilibrated with the temperature and gas concentration of interest for a considerable period of time (~1 day) to minimize corrosive effects (18). The use of longer oxidation times (to produce much thicker SiO<sub>2</sub> layers) revealed substrate attack and nonuniform oxidation effects (18) that were not apparent with the thin films used in this study. With all the halogen additives tested, lowest defect densities were attained at concentrations of about half those necessary to pro-

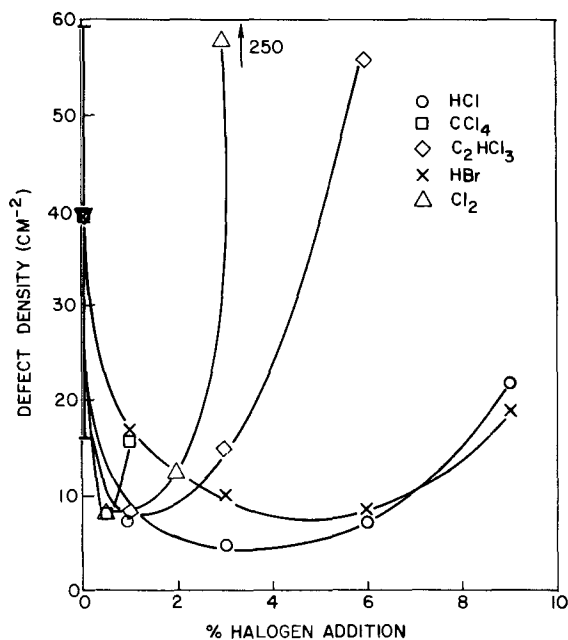


Fig. 2. Effect of halogen added during oxidation on the breakdown defect density.

duce nonuniform films. Films grown in 4% H<sub>2</sub>O-96% O<sub>2</sub> did not show any improvement in time zero breakdown characteristics; apparently the improvement is a result of the presence of the halogen and not hydrogen or water vapor.

As with conventional oxidation, the defect density increases with oxidation temperature in HCl-grown oxides (Fig. 3). Higher oxidation temperatures for HCl oxides do, however, cause a relatively greater degradation so that the beneficial effects of HCl are no longer significant for an oxidation temperature of 1150°C.

Previous studies have considered various origins of the breakdown voltage improvement seen here. For this purpose, low field breakdowns can be roughly attributed to two types of defects (13), electrical and physical. The former depend both on the presence of electrically charged impurities which enhance the internal electric field and on the presence of interface states which increase oxide conduction levels and result in low field breakdowns. Physical defects reduce oxide uniformity and planarity and consist of substrate bumps or spikes, and oxide pinholes, crystalline regions, and particulate inclusions. The influence of halogen (especially Cl) oxidation, on removing, reducing, or neutralizing electrical disorder is well established (1-5, 7, 8, 10-12, 19). Recent work (21) has shown that the majority of defects are probably physical since proper wafer cleaning procedures before oxidation can almost completely eliminate these defects. It can also be postulated that the halogen might reduce the level of physical defects. Impurities or particulates forming protrusions of the silicon surface may be gettered or dislodged by the action of Cl. Likewise airborne particulate matter may react and be diminished in size, if not removed entirely from the system.

*Accelerated breakdown.—Effect of halogens.*—Dielectric degradation was generally measured under higher temperatures and fields than those normally encountered by the gate insulator in typical FET use, in order to reduce the wear-out time to manageable values of no more than a few hundred hours. Figure 4 displays the distributions of failure times observed on testing 700Å films at 5 MV/cm and 300°C. This figure reveals an increase in failure times of up to two orders of magnitude for films grown in 2% HCl over those grown in pure O<sub>2</sub> at 1000°C. Two reliability features of HCl-grown oxide films should be noted: the longer time for 100% failure, and the smaller spread in failure times. The time required for 100% failure (see Fig. 4) was defined as  $t_{max}$  and was previously shown (6) to be a measure of the wear-out of a film that is free of significant defects. Thus, the addition of HCl during oxidation apparently retards the electrochemical-type degradation (6) that normally occurs under accelerated bias-temperature stressing. The narrowing of the distribution of failure times is believed to reflect a

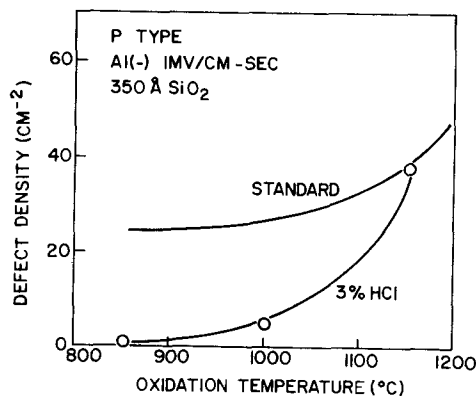


Fig. 3. Effect of oxidation temperature on defect density for standard and HCl oxides.

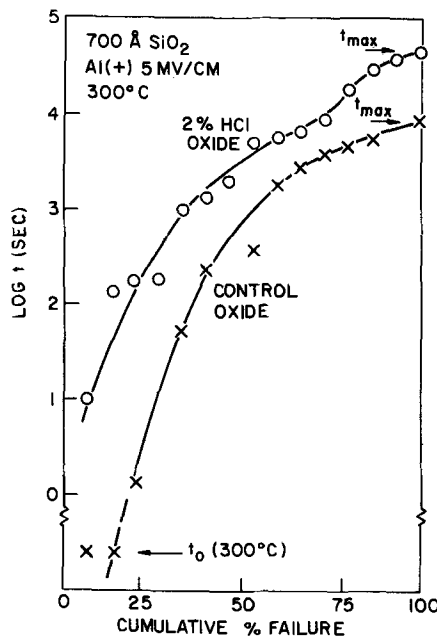


Fig. 4. Statistical failure times for HCl and standard oxides. Both oxides were grown at 1000°C.

tightening of the initial breakdown voltage distribution since HCl-oxides are more uniform and defect-free to begin with; thus, their wear-out times should be less scattered.

A detailed study was made of the effects of HCl concentration and oxidation temperature on the accelerated wear-out process. Using  $t_{max}$  as the measure of oxide quality, this parameter is shown in Fig. 5 as a function of applied field and HCl concentration for SiO<sub>2</sub> films grown at 1000°C. Note that for a given field, the wear-out time increases with HCl concentration up to at least 6% HCl. Between 0 and 3% HCl, log  $t_{max}$  varied almost linearly with the HCl concentration with slopes ranging from 0.3 decades/% HCl at 2 MV/cm to 0.65 decade/% HCl at 7 MV/cm. The improvement

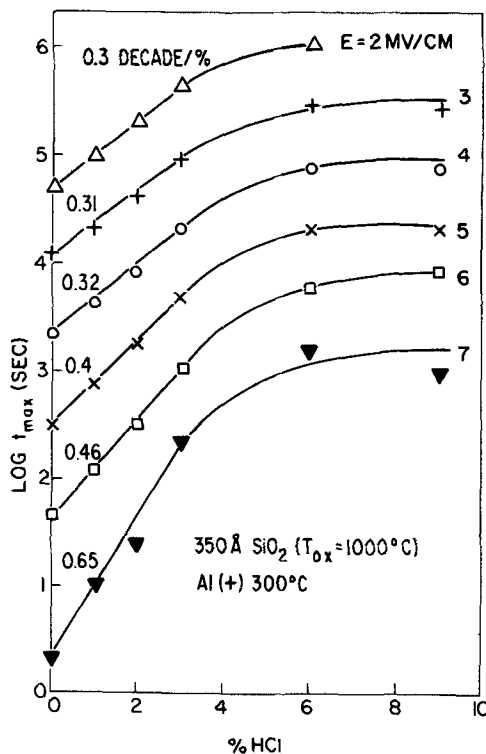


Fig. 5. Effect of HCl concentration on maximum time to breakdown.

in wear-out time seems to saturate above 6% HCl. On the other hand, the initial defect density increases when more than 6% HCl is used (Fig. 2), and other experiments have shown that the average failure time for 9% HCl was indeed even shorter than that with 3% HCl. These experiments clearly show that over-all component reliability depends on both the initial defect density and the rate of wear-out; the enhanced wear-out time for 9% as compared to 3% HCl oxides is overshadowed by the higher defect density.

The influence of oxidation temperature on wear-out in HCl oxides is shown in Fig. 6 where it is seen that higher temperatures give longer failure times. The oxidation temperature does not affect wear-out times in standard oxides. At 850°C, HCl oxidation gives no improvement in wear-out characteristics compared to the standard SiO<sub>2</sub>, even though Fig. 3 shows that this oxidation procedure yields excellent initial breakdown characteristics. With an 1150°C oxidation, however, the initial breakdown characteristics are poor while accelerated breakdown times are the longest observed here. This result further demonstrates that time-zero and accelerated breakdown mechanisms are influenced differently by the presence of HCl in the oxidation atmosphere. Nevertheless, both measures of oxide integrity are involved in the over-all reliability of the dielectric film.

Identical failure times were measured on oxide films grown on both n-type and p-type silicon substrates. Since HCl oxidation markedly reduces minority carrier generation in the underlying silicon (9-12), measurements made with the silicon surface inverted could be suspect. The results shown in Fig. 7 verify the fact that the effects are real and not due to a loss of field in the depleted silicon surface. Note the improved failure times for both electrode polarities. A negative bias on the aluminum electrodes gives the longer wear-out times for standard oxides; with HCl oxidation, the relative advantage of Al(-) over Al(+) is even greater. For Al(+),  $t_{max}$  was determined to be thermally activated with  $\Delta H = 1.4$  eV for temperatures

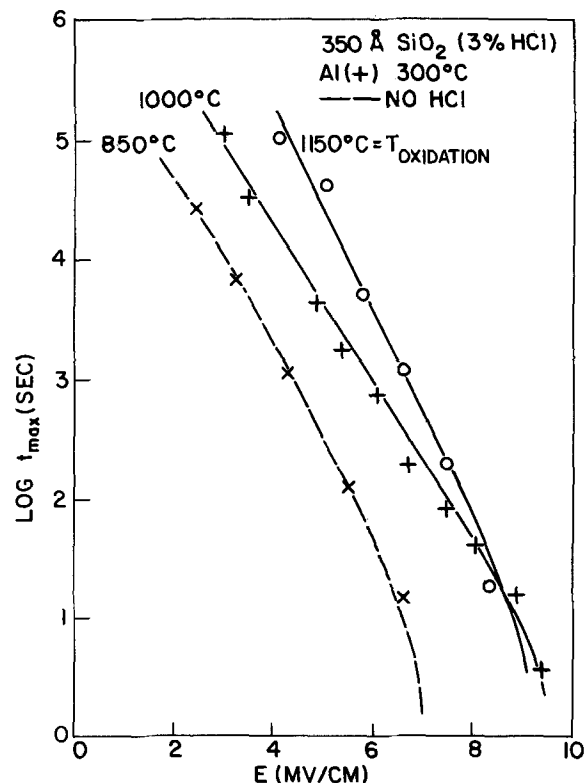


Fig. 6. Effect of oxidation temperature on accelerated breakdown time as a function of applied field. The dashed line represents a control oxidation and is valid in the range 850°-1150°C.

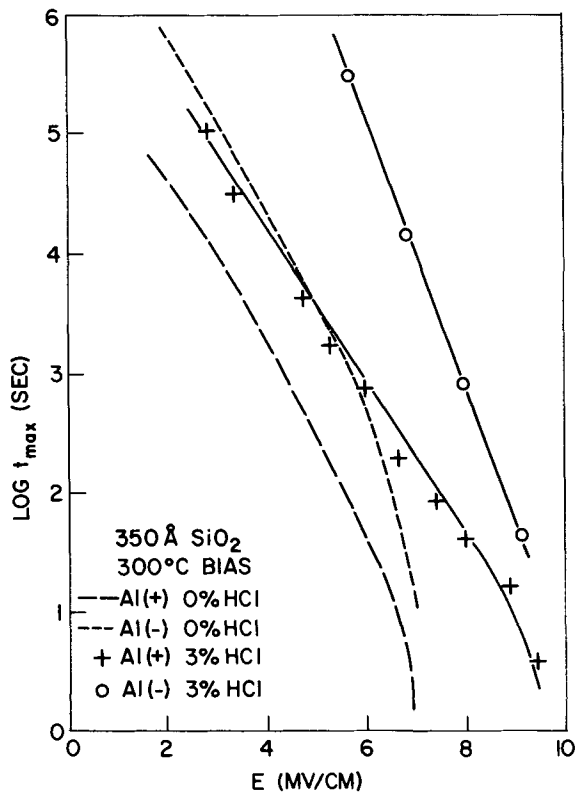


Fig. 7. Influence of bias polarity on accelerated breakdown in HCl oxides.

between 250° and 400°C. This activation energy agrees well with that obtained earlier for the wear-out of pure SiO<sub>2</sub> films under similar conditions (6).

In contrast to the above HCl oxide results, SiO<sub>2</sub> films grown at 1000°C in the presence of Cl<sub>2</sub> exhibit shorter failure times than the standard oxides (Fig. 8).

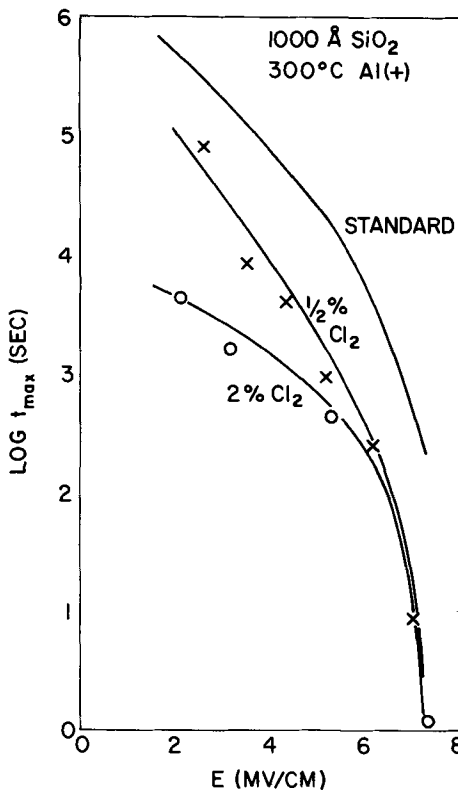


Fig. 8.  $t_{max}$  vs. applied field for different Cl<sub>2</sub> concentrations for oxidation at 1000°C.

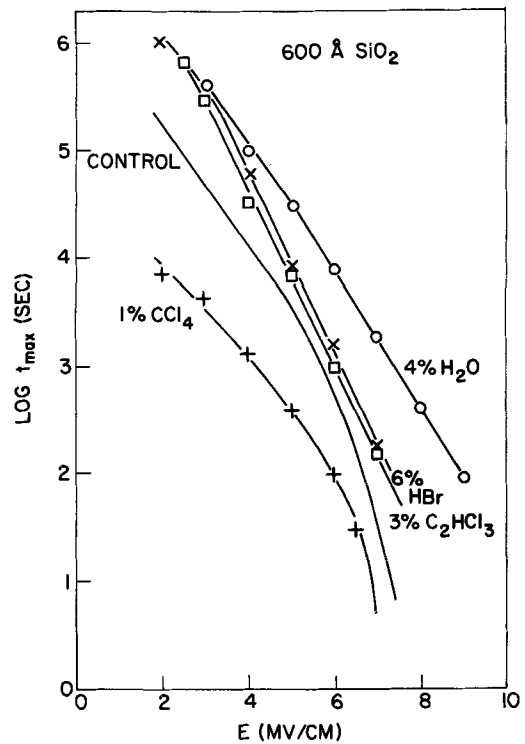


Fig. 9. Maximum time to failure for CCl<sub>4</sub>, C<sub>2</sub>HCl<sub>3</sub>, HBr, and H<sub>2</sub>O oxides.

This finding is surprising considering that Cl<sub>2</sub> additions are superior to HCl for improving  $t_0$  breakdown characteristics (recall Fig. 1). Thus, this study shows that HCl and Cl<sub>2</sub> oxidation additives lead to markedly divergent accelerated breakdown characteristics in addition to giving different incorporated Cl profiles in SiO<sub>2</sub> (15, 17), oxide polarizability behavior (15), and oxidation kinetics (18, 19). However, both additives effectively enhance ramp breakdown voltage distributions and minority carrier generation (12).

The effects of the other additives on wear-out is portrayed in Fig. 9. Improvements can be noted for C<sub>2</sub>HCl<sub>3</sub>, HBr, and H<sub>2</sub>O grown films, but CCl<sub>4</sub> gave poorer than normal characteristics. Table I summarizes several properties of MOS structures fabricated using various oxidation ambients. It is seen that Cl can be associated with minority carrier lifetime improvements while both Cl and Br enhance  $t_0$  or ramp breakdown characteristics. Nevertheless, only the hydrogen-containing compounds promote SiO<sub>2</sub> integrity under the accelerated bias-temperature stressing used here. Chlorine, either as Cl<sub>2</sub> or in CCl<sub>4</sub>, is indeed detrimental to long term SiO<sub>2</sub> reliability.

**Effects of hydrogen.**—Annealing studies of standard and H<sub>2</sub>O grown oxides give additional information on the hydrogen effects. Films grown in 4% H<sub>2</sub>O at 1000°C remain highly resistant to wear-out even after a ½-hr anneal in N<sub>2</sub>, although annealing at higher temperatures (1100°-1200°C) eliminates the hydrogen improvement effect (see Fig. 10). Since one might ascribe this enhancement of wear-out resistance to the incor-

Table I. Effect of oxidation addition on minority carrier lifetime,  $t_0$  breakdown, and dielectric wear-out

Oxidation addition	Improves lifetime (12)	Contains Cl	Improves $t_0$ breakdown	Contains halogen	Improves dielectric wear-out	Contains H
CCl <sub>4</sub>	Yes	Yes	Yes	Yes	No	No
Cl <sub>2</sub>	Yes	Yes	Yes	Yes	No	No
HCl	Yes	Yes	Yes	Yes	Yes	Yes
C <sub>2</sub> HCl <sub>3</sub>	Yes	Yes	Yes	Yes	Yes	Yes
HBr	No	No	Yes	Yes	Yes	Yes
H <sub>2</sub> O	No	No	No	No	Yes	Yes



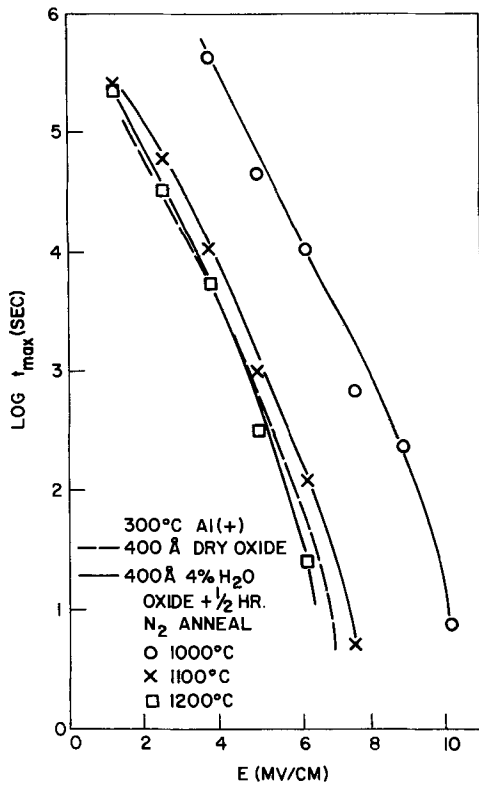


Fig. 10. Effect of nitrogen annealing temperature on  $t_{max}$  for oxides grown in 4% H<sub>2</sub>O.

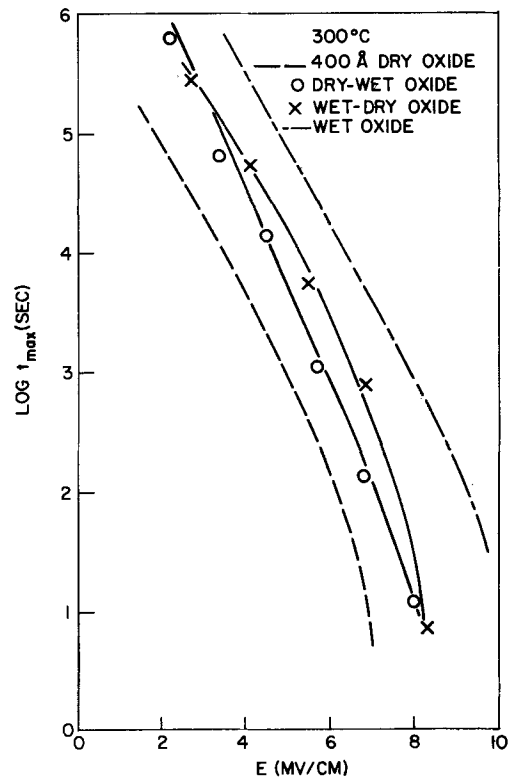


Fig. 11. Effect of sequential oxidation of 200 Å in dry O<sub>2</sub> and in O<sub>2</sub> + 4% H<sub>2</sub>O. ○, dry oxide followed by H<sub>2</sub>O oxide; x, H<sub>2</sub>O oxide followed by dry oxide.

poration of hydroxyl groups into the oxide, it should be pointed out that infrared spectroscopy studies (22) have demonstrated that a brief anneal (< ½ hr) at 1000°C in O<sub>2</sub> is sufficient to remove almost all these species. Composite films made of SiO<sub>2</sub> films grown in pure O<sub>2</sub> and 96% O<sub>2</sub>-4% H<sub>2</sub>O ambients are more reliable than standard films, regardless of the order of the oxidation steps, although they are not as reliable as films completely grown in 4% H<sub>2</sub>O (see Fig. 11). Silicon dioxide films annealed in forming gas (20% H<sub>2</sub>-80% N<sub>2</sub>) also exhibit somewhat better wear-out characteristics provided the annealing temperature was high enough (see Fig. 12). With 900°C annealing, breakdown times are perceptively lengthened at low applied fields while 1050°C annealing results in a 2- to 5-fold change. Ion implantation of either H<sub>2</sub><sup>+</sup> or H<sub>2</sub>O<sup>+</sup> appears to lead to higher dielectric wear-out integrity (Fig. 12) but time-zero characteristics of implanted oxides were below standard.

**Model.**—An earlier study (6) proposed a model to account for dielectric degradation and failure in SiO<sub>2</sub> films: energy states in the SiO<sub>2</sub> bandgap are created at the injecting electrode during accelerated bias-temperature stressing. When charged, these trap states cause a dipole lowering of the injecting barrier and allow excessive current to promote failure by a localized thermal runaway.

The mechanism responsible for interface state generation is still unresolved. Transport of a chemical species (either foreign or intrinsic to SiO<sub>2</sub>) through the film or an electrochemical reaction of the electrode metal could contribute to this generation of trap states, albeit in different ways.

Oxides grown in the presence of hydrogen or halogens show the same general electrical deterioration prior to breakdown as do films grown in 100% O<sub>2</sub>. About the only difference between the two types of oxides is the time lapse before the observation of degradation. Large flatband voltage shifts appear in Cl<sub>2</sub> oxides (15) stressed at room temperature so that it is not surprising that such films exhibit early failure

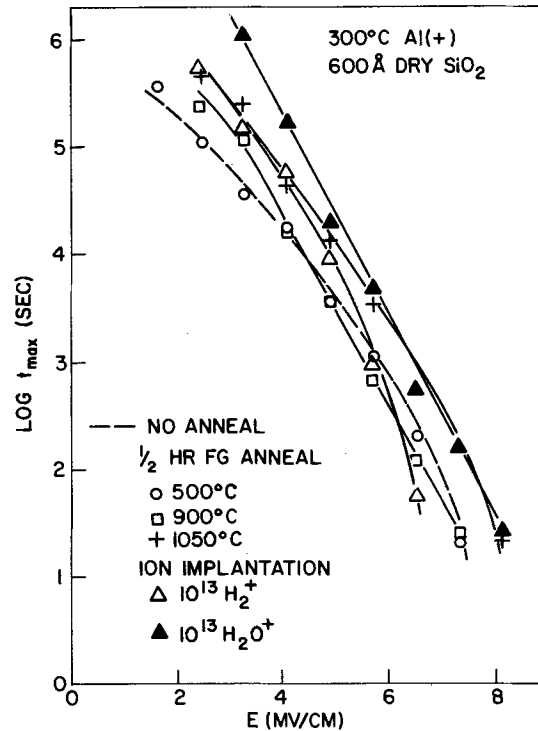


Fig. 12. Improvement in  $t_{max}$  as a result of annealing dry oxides in forming gas (20% H<sub>2</sub>) at high temperature (○, 500°C; □, 900°C; +, 1050°C) and as a result of ion implantation (△, 10<sup>13</sup>H<sub>2</sub><sup>+</sup>; ▲, 10<sup>13</sup>H<sub>2</sub>O<sup>+</sup>).

times. On the basis of our earlier model, it appears that dielectric lifetime improvements can be attributed to a slower generation rate of the localized trap states responsible for barrier lowering, and a hydrogen species is associated with a net reduction in the generation rate. There is some other evidence to support this model. For example, the importance of hydrogen

for annealing out (at  $\sim 500^\circ\text{C}$ ) surface states in MOS structures is well established (23). In addition, the introduction of atomic hydrogen at room temperature has been shown to greatly reduce the enhanced conduction that resulted from accelerated stressing of MOS capacitors (6). Annealing studies repeated here have shown that the hydrogen can be introduced either during or after oxidation although it is most effective when added during oxidation, and it also can be implanted.

**Field enhancement breakdown.**—Electric field enhancement (24-25) due to the presence of mobile ions (particularly sodium) has been shown to be one time-dependent dielectric breakdown mechanism in  $\text{SiO}_2$  films. Experiments were conducted as part of this study to verify that this sodium neutralization (2-5) could lead to a reliability improvement in intentionally contaminated films. Oxides 1000Å thick were grown at  $1150^\circ\text{C}$  in oxygen containing 0, 3, or 9% HCl; sodium levels of  $6 \times 10^{12}$  and  $10^{14} \text{ Na}^+/\text{cm}^2$  were evaporated onto the film before metal capacitor dots were deposited.

The current through a Na contaminated film was previously (25) shown to reflect the amount of field enhancement (and hence decrease of the effective Fowler-Nordheim tunneling distance) near the injecting silicon. As the electrically uncompensated sodium was drifted through the oxide, the current increased to a maximum and then decayed provided the sample did not break down during the drift (see insert Fig. 13). As can be readily seen, the maximum current through the HCl oxides below 7 MV/cm was at least 2-4 orders of magnitude lower than in the standard oxide. This measurement is taken as direct evidence that the internal electric field due to the Na space charge can be greatly reduced because of Na neutralization.

### Summary

Oxidation of silicon in  $\text{O}_2$  with HCl,  $\text{Cl}_2$ ,  $\text{CCl}_4$ ,  $\text{C}_2\text{HCl}_3$ , or HBr additions increased the average  $\text{SiO}_2$  breakdown voltage and reduced the statistical data spread. The amount of improvement observed varied with the additive species and its concentration during oxidation. The best characteristics were obtained using about half the amount of halogen that would cause visual nonuniformity in the  $\text{SiO}_2$  films and Si etching. The breakdown defect density increased more rapidly with oxidation temperature for HCl oxides than for standard oxides. The improvements were tentatively attributed to the removal of heavy metal impurities. The time to breakdown under accelerated bias stressing depended on the species used. Chlorine and  $\text{CCl}_4$  oxides had reduced failure times; HCl, HBr,  $\text{C}_2\text{HCl}_3$ , and  $\text{H}_2\text{O}$  oxides had vastly improved dielectric integrity. In the range 0-3% HCl during oxidation, the failure times increased by 0.3-0.65 decades/% HCl for applied fields of 2-7 MV/cm, respectively. The improvement due to HCl seemed to saturate near 6-9% HCl when oxidation occurred at  $1000^\circ\text{C}$ , but increasing oxidation temperature gave longer failure times. The measurements indicate that the basic degradation in all the tested oxides was the same as in standard films. The improved wear-out reliability was attributed to the presence of hydrogen rather than halogens, since an improvement was observed in oxides grown in 4%  $\text{H}_2\text{O}/\text{O}_2$  or annealed at high temperature in hydrogen. It was observed that Na neutralization (2-5) could lower the internal electric field due to the Na-ion space charge and hence provide another basis for obtaining highly reliable silicon dioxide films.

### Acknowledgments

Helpful conversations with Y. van der Meulen, N. Chou, J. Eldridge, and J. Ziegler are gratefully acknowledged. Ion implantation of hydrogen was suggested by A. Fowler and performed by B. Crowder and N. Penebre. The author would also like to express

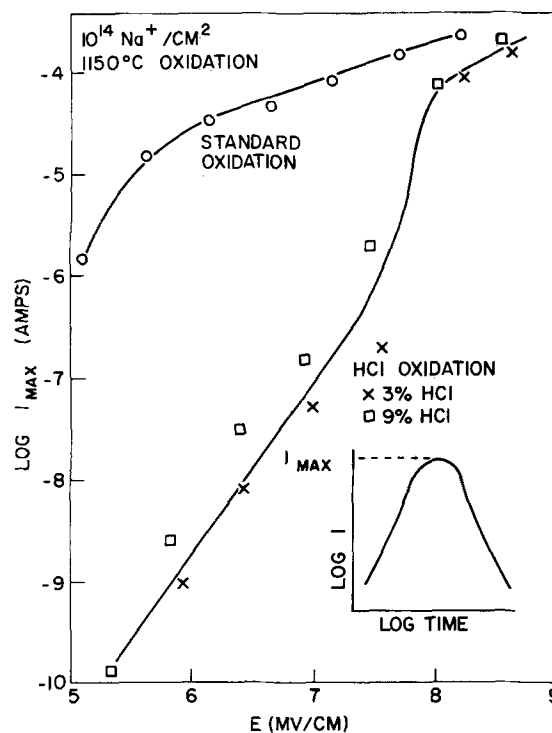


Fig. 13. Current maxima in Na-contaminated HCl oxides. Insert shows time dependence of current through  $\text{SiO}_2$ .

gratitude to D. Ormond for assistance in sample preparation and measurement. Other samples and encouragement were also provided by T. Fennell, G. Schmidt, E. Terner, and R. Troutman.

Manuscript submitted Sept. 14, 1973; revised manuscript received Dec. 28, 1973.

Any discussion of this paper will appear in a Discussion Section to be published in the December 1974 JOURNAL. All discussions for the December 1974 Discussion Section should be submitted by Aug. 1, 1974.

### REFERENCES

1. R. J. Kriegler, Y. C. Cheng, and D. R. Colton, *This Journal*, **119**, 388 (1972).
2. R. J. Kriegler, *Appl. Phys. Letters*, **20**, 449 (1972).
3. R. J. Kriegler, J. D. Morris, and D. R. Colton, *This Journal*, **119**, 241C (1972).
4. R. J. Kriegler, *Thin Solid Films*, **13**, 11 (1972).
5. R. J. Kriegler, in "Semiconductor Silicon," Howard R. Huff and Ronald R. Burgess, Editors, p. 363, The Electrochemical Society Softbound Symposium Series, Princeton, N. J. (1973).
6. C. M. Osburn and N. J. Chou, *This Journal*, **120**, 1377 (1973).
7. M. Chen and J. W. Hile, *ibid.*, **119**, 223 (1972).
8. M. Severi and G. Soncini, *Electron. Letters*, **8**, 402 (1972).
9. S. Brojdo, J. V. Dalton, W. J. Palito, and H. A. Waggener, *This Journal*, **119**, 237C (1972).
10. P. H. Robinson and F. P. Heiman, *ibid.*, **118**, 141 (1971).
11. R. S. Ronen and P. H. Robinson, *ibid.*, **119**, 747 (1972).
12. D. R. Young and C. M. Osburn, *ibid.*, **120**, 1578 (1973).
13. C. M. Osburn and D. W. Ormond, *ibid.*, **119**, 597 (1972).
14. M. Waldner and I. Sivo, *ibid.*, **107**, 298 (1960).
15. Y. J. van der Meulen, C. M. Osburn, and J. F. Ziegler, *ibid.*, **120**, 88C (1973).
16. R. L. Meek, *This Journal*, **120**, 308 (1973).
17. N. J. Chou, C. M. Osburn, Y. J. van der Meulen, and R. Hammer, *Appl. Phys. Letters*, **22**, 380 (1973).
18. Y. J. van der Meulen and J. G. Cahill, Paper C2, Electronic Materials Conf. of AIME, Las Vegas, Nev., Aug. 1973.
19. K. Hirabayashi and J. Iwamura, *This Journal*, **120**, 1595 (1973).

20. C. M. Osburn and D. W. Ormond, *ibid.*, **119**, 591 (1972).
21. J. M. Green, C. M. Osburn, and T. O. Sedgwick, Paper C4 Electronic Materials Conf. of AIME, Las Vegas, Nev., Aug. 1973.
22. W. A. Pliskin, in "Semiconductor Silicon," Howard R. Huff and Ronald R. Burgess, Editors, p. 506, The Electrochemical Society Softbound Symposium Series, Princeton, N. J. (1973).
23. P. Balk, Paper 111 presented at Electrochemical Society Meeting, Buffalo, N. Y., Oct. 10-14, 1965.
24. S. I. Raider, *Appl. Phys. Letters*, **23**, 34 (1973).
25. C. M. Osburn and S. I. Raider, *This Journal*, **120**, 1369 (1973).

## Synthesis of Photochromic and Cathodochromic Sodalite

I. F. Chang\*

IBM Thomas J. Watson Research Center, Yorktown Heights, New York 10598

The publication costs of this article have been assisted by the IBM Corporation.

### ABSTRACT

An efficient and reliable technique for synthesizing sodalite is described. This new synthesis is termed "structure conversion method." It converts a complex sodium-aluminosilicate structure into a sodalite structure while at the same time incorporating the alkali halide and activator compounds to form cathodochromic (CC) or photochromic (PC) sodalite in one step without requiring additional sensitizing procedure. Both PC and CC sodalites of high quality have been synthesized by this method. The results of structural analysis, optical measurements, and electron beam excitation of these materials are presented.

Materials which exhibit a photochromic (PC) effect (1) are of considerable technical interest. They have applications in many areas, such as, filter optics (2), holography (3), information storage (4, 5), and display (6-13). In the field of high density information displays, a storage cathode-ray tube (CRT) requiring no refreshing is particularly advantageous. The storage CRT screen calls for sensitive cathodochromic (CC) materials. The alkali halide family with color centers (14), which is a well-known system exhibiting both PC and CC properties, has been used in some of the applications mentioned above (4-7).

Recently, a series of studies (15-28) has been focused on another material group, i.e., the sodalites. Sodalite, Na<sub>8</sub>Al<sub>6</sub>Si<sub>6</sub>O<sub>24</sub>·Na<sub>2</sub>X, is a general name for a group of materials or minerals in which X is Cl<sub>2</sub>, Br<sub>2</sub>, I<sub>2</sub>, (OH)<sub>2</sub>, S, etc. Rigorously, one distinguishes them as chlorosodalite, bromosodalite, etc. When X takes the form of SO<sub>4</sub>, CO<sub>3</sub>, WO<sub>4</sub>, MoO<sub>4</sub>, CrO<sub>4</sub>, etc. they are generally referred to as noselites. There have been natural sodalites [known as hackmanites (29, 30) which exhibit the PC property] found on many parts of the earth (16, 18, 30-33). However, synthetic sodalites generally show more sensitivity with respect to the PC and CC properties (27, 26). In fact, they possess certain characteristics which are superior to the alkali halides, such as material stability (nonhygroscopic, higher melting temperature), more effective coloration and bleaching behavior (higher efficiency), and less fatigue (i.e., the probability of forming a complex center is smaller). Therefore, methods of synthesizing both PC sodalite and CC sodalite have become technically important.

It is generally believed that the color absorption in sodalites is due to an F-center type impurity, i.e., an electron trapped at a negative ion vacancy, for example, a chlorine vacancy in chlorosodalite. In synthesizing PC sodalites, in addition to negative ion vacancies, an impurity activator is necessary since it acts as an electron donor which, upon u.v. excitation, gives an electron to the F-center trap via the conduction band. Activators such as Fe (21) and OH (34) have been reported to play a role in the PC process in sodalite;

however, the sulfur-doped sodalite seems to be most efficient (27) in exhibiting tenebrescence (photochromism). In synthesizing efficient CC sodalites, no activators are necessary, since the high energy electron bombardment can directly fill the F-center trap.

Single-crystal sodalite has been synthesized (35-37), but most work on PC sodalite has been on powder material. This is because the PC sodalite powder is easier to make and is particularly useful for storage display applications. Several processes for synthesizing sodalites have been developed in the past (15-19, 38-48). These can be classified into four major categories: (i) hydrothermal growth (38-40, 15, 16, 19, 22, 23, 41, 42); (ii) solid-state reaction or sintering (43, 17, 18, 44, 42); (iii) diffusion in zeolite (19, 45); and (iv) aluminosilicate gel reaction (42, 46-48). However, most of these methods have disadvantages, such as incomplete reaction, low efficiency, high cost, and long processing time. They are, therefore, not very suitable for large quantity industrial processing (see Discussions and Summary section below).

In the present work, a simple, efficient, and economical method of synthesizing PC and CC sodalites is described. This new synthesis is termed "structure conversion method." It converts a commercially available molecular sieve material (complex sodium aluminosilicate), an alkali halide, and a sulfur compound (used as activator for PC but not necessary for CC material) into sodalite in one step without requiring further sensitizing procedures. Both PC and CC sodalites of high quality have been synthesized by this method. Also discussed in this paper are the results of structural analyses, optical measurements, and electron beam excitation of these materials.

### Synthesis Procedure

The structure conversion method (SCM) is different from hydrothermal growth, solid-state sintering, and aluminosilicate gel reaction in that it is not a synthesis from the oxide and salt components. It is also different from the diffusion method (19) which diffuses a gaseous sulfur compound and an alkali halide into a zeolite structure [3(Na<sub>2</sub>O·Al<sub>2</sub>O<sub>3</sub>·2SiO<sub>2</sub>)]. The procedure of the diffusion method is that the mixture of zeolite and sodium chloride is dried at low temperature and low

\*Electrochemical Society Active Member.

Key words: photochromics, cathodochromics, synthesis, sodalite, display.

pressure of 0.05-0.01 mm for 24 hr. The evacuated sample is then slowly opened to H<sub>2</sub>S or SO<sub>2</sub> and allowed to come to atmospheric pressure. The diffusion is preferably carried out at 250°C to prevent aggregation and pore blocking. At this temperature, there is no structure change or conversion occurring. However, the basic mechanism of SCM is the conversion of complex sodium-aluminosilicate structure into a sodalite structure while at the same time incorporating the alkali halide (and activator compound) to form CC(PC) sodalite. The complex Na-Al-silicate chosen to be the starting material is the type that contains a basic building block in the form of a tetrahedron with four oxygen ions surrounding a smaller silicon or aluminum ion. These tetrahedra are identical to those in the sodalite structure, thus the starting material, in essence, has a "distorted sodalite structure" or has the same basic structural units as sodalite. Due to this structural distortion, the material can have very large "apertures" and "pores" so that the incorporation of dopants (alkali halide) and activators (sulfur compound) becomes very efficient. There are several different groups of material that have this property. The readily available one is the commercial molecular sieve material.<sup>1</sup> Our experiments indicate that these molecular sieves can easily be converted to sodalite.

Figure 1 describes the synthesis procedure of the structure conversion method. The process of synthesizing PC sodalites is shown in Fig. 1a. The commercial Linde molecular sieve<sup>1</sup> is used as the starting Na-Al-silicate. The alkali halide and the sulfur compound used are reagent grade. These starting materials (all in powder form) are mixed in a quartz boat which is then placed in a furnace under reducing atmosphere. The sulfur compound used can be sodium sulfide, sulfite, or sulfate. Excess sodium halide is always used since the excess salt can be leached out after the heating process. We have experimented with several different kinds of sieve material, namely, sieves with different sizes of pores (Linde 3A, 4A, 5A, 10X, and 13X type which have channel sizes, 3, 4, 5, 8, and 10Å, respectively). Our results indicate that the Linde 13X molecular sieve, (Na<sub>86</sub>[(AlO<sub>2</sub>)<sub>86</sub>(SiO<sub>2</sub>)<sub>106</sub>])·XH<sub>2</sub>O, gives the best PC sodalite and Type 4A, (Na<sub>12</sub>(AlO<sub>2</sub>(SiO<sub>2</sub>)<sub>12</sub>)·XH<sub>2</sub>O, the next best. The Linde 3A, 5A, and 10X sieves which contain potassium and calcium ions do not result in very sensitive PC material by the SCM synthesis. Therefore, in describing the physical properties of the synthesized sodalites below, we shall restrict our discussions to sodalites prepared from the Linde 13X and 4A sieves only.

In the synthesis of sodalites by the structure conversion method, there are three basic processing parameters, namely the furnace temperature, the re-

<sup>1</sup> Molecular sieve materials are synthetic sodium-aluminosilicate (often referred to as zeolites). There are several companies which produce them (e.g., Zeolite Chemical Company, Hungerford and Terry Inc., Metalene Chemical Company, etc). Materials used in this work are from Linde Division, Union Carbide Corporation.

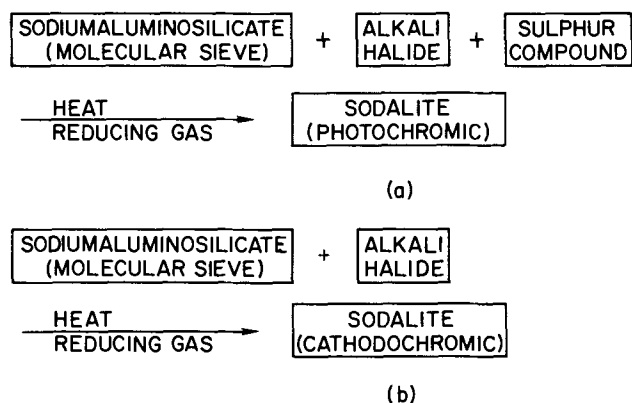


Fig. 1. The synthesis procedure of the structure conversion method (a) for photochromic sodalites and (b) for cathodochromic sodalites.

ducing gas flow rate, and the reaction time. Although sensitive PC sodalites have been made by the SCM over a broad range of temperature (650°-1100°C), with either forming gas or hydrogen as reducing agent and with a variable length of heating cycle (6-16 hr), we find that there is an optimal set of conditions which gives the most consistent results. It is: temperature = 850°C; flow rate = 3 liter/min forming gas (for a 2½ in. furnace tube); and reaction time = 8 hr. The resulting materials are very sensitive PC sodalites; that is, no separate sensitizing step is required. After washing and leaching, the material is checked by x-ray diffraction which confirms that it has a sodalite structure. The x-ray and optical measurements of the PC sodalite will be discussed below.

The synthesis of CC sodalite is essentially identical to that for the PC sodalite. Figure 1b illustrates the procedure. Again we use molecular sieve material as the starting Na-Al-silicate. However, in the synthesis of CC sodalites, the sulfur compound is found to be unnecessary, as has also been pointed out by others (25, 26). Comparing various nonsulfur-doped CC sodalites prepared by the SCM, we find that the Linde 4A type of molecular sieve is best suited for CC sodalite synthesis.

### Physical Properties

**X-ray diffraction.**—The x-ray diffraction of both the molecular sieves (the starting material) and the resulting material were measured with a Debye-Scherrer powder diffraction camera. The source was CuK<sub>α</sub> radiation. The results indeed confirm that the structure conversion is complete. Table I shows the x-ray data for the Linde 13X sieve and the PC chlorosodalite prepared from it by the SCM. The left side of the table also lists the National Bureau of Standards (NBS) diffraction data (33) for a single-crystal chlorosodalite which was taken from Ice River, British Columbia (33). Comparing the result of the synthesized sodalite powder in the center column of Table I with the single-crystal data, one notes that the agreement is indeed very good. It shows not only a matching set of

Table I. X-ray diffraction data of natural, single-crystal sodalite and synthetic sodalite by SCM using Linde 13X and Linde molecular sieve 13X

JCPDS 20-1070 (33)			IBM SC-13X			13X, (NaAl) <sub>86</sub> Si <sub>106</sub> O <sub>384</sub> ·XH <sub>2</sub> O		
hkl	d, Å	I/I <sub>1</sub>	d, Å	I/I <sub>1</sub>	hkl	d, Å	I/I <sub>1</sub>	
110	6.3	80	6.29	81	111	14.4	100	
200	4.45	40	4.442	30	320	8.823	50	
			3.992	9.5	311	7.515	39	
211	3.63	100	3.631	100	331	5.713	51	
310	2.81	50	2.81	45	333, 511	4.792	17	
222	2.57	70	2.563	66	440	4.404	31	
321	2.38	70	2.373	73	531	4.20	vw	
400	2.22	10	2.22	14	620	3.936	13	
330, 411	2.10	80	2.094	90	533	3.796	62	
420	1.99	30	1.986	30	444	3.60	vw	
332	1.896	30	1.894	29	711, 551	3.50	vw	
422	1.814	30	1.814	20	642	3.33	54	
431	1.743	30	1.741	20	731, 553	3.25	vw	
521	1.621	30	1.621	19	733	3.044	20	
440	1.569	60	1.570	53	822, 660	2.938	35	
433, 530	1.523	40	1.523	32	751, 555	2.878	61	
442, 600	1.48	60	1.480	49	840	2.787	32	
532, 611	1.441	60	1.441	50	911, 753	2.731	14	
620	1.404	5			664	2.657	34	
541	1.371	30	1.370	22	931	2.616	18	
622	1.339	30	1.339	23	844	2.54	w	
631	1.310	30	1.309	25	882, 1020	2.45	vw	
444	1.281	30	1.282	19	666, 1022	2.399	19	
640	1.231	5			775, 1111	2.25	vw	
552, 633	1.209	60	1.209	46	880	2.198	15	
642	1.189	5			935, 1131 +	2.179	14	
730	1.167	20	1.167	9.8	873, 1133	2.117	13	
651, 732	1.129	40	1.128	25	984, 1200	2.08	vw	
800	1.110	5			991	1.948	12	
554, 741 +	1.093	20	1.094	13	1086, 10100 +	1.763	14	
644, 820	1.078	20	1.078	19	997, 1193	1.716	18	
662	1.019	20	1.017	9.7	+ 7 lines to 1.309			
752	1.007	20						
840	0.994	30	0.994	21				
833, 910	0.982	10						
842	0.969	10						
655, 761 +	0.958	30	0.959	11				
754, 851 +	0.936	10						
763, 932	0.917	20	0.915	12				
844	0.906	20	0.906	9.3				
+ 9 lines to 0.7847					+ 4 lines to 0.7913			

lines but also a set of comparable relative intensities. Furthermore, the indices of the observed lines ( $hkl$ ) obey the "even" rule ( $h + k + l = 2N$ ) pointed out by Tomisaka *et al.* (40). However, one may point out that there is one extra line exhibited by the synthetic PC sodalite at 3.992Å with relatively weak intensity which is not observed in the single-crystal sample. But this line has been reported by Tomisaka *et al.* on a natural sodalite powder sample from the Princers Mine, Canada. A similar line has also been observed by Williams *et al.* (19) in their synthetic sodalites which were prepared by solid-state sintering, or hydrothermal growth, using  $\text{Na}_2\text{SO}_4$  as activator or by diffusing  $\text{SO}_2$  into a zeolite structure. Thus, one may suggest that this extra line is related to the sulfur activator incorporated in the powder sodalite. The Linde 13X molecular sieve material has a set of diffraction lines entirely different from those of the sodalite. This is shown in the last column of Table I which agrees with the data of Broussard and Shoemaker (49).

The x-ray diffraction results for PC Cl-sodalite prepared from Linde 4A molecular sieve are shown in Table II. Again the synthetic sodalite powder shows a set of interplanar spacings which matches very well with the single-crystal data. One also notes an extra diffraction line. This line corresponds to slightly larger interplanar spacing (4.234Å) and intensity than the extra line which appeared in the sodalite prepared from Linde 13X. Although there is no obvious explanation for this difference, one may point out that Williams *et al.* (19) have also observed similar lines corresponding to 4.23, 4.24, and 4.29Å spacings in their sintered, hydrothermally grown, and  $\text{H}_2\text{S}$  activated sodalites, respectively.

**Photochromic behavior.**—The best way to calibrate the sensitivity of a PC sodalite is to measure its photo-induced absorption. We have made optical absorption measurements for various sodalites using a Cary 14 spectrometer. The sodalite powder is immersed in a liquid with matching index of refraction. Only sulfur-doped samples show u.v. induced coloration. Figure 2

Table II. X-ray diffraction data of natural single-crystal sodalite and synthetic sodalite by SCM using Linde 4A and Linde molecular sieve 4A

JCPDS 20-1070 (33)			IMB SC-4A			4A, $(\text{NaAlSi})_{12}\text{O}_{40} \cdot \text{SH}_2\text{O}$		
$hkl$	$d, \text{Å}$	$I/I_1$	$d, \text{Å}$	$I/I_1$	$hkl$	$d, \text{Å}$	$I/I_1$	
110	6.3	80	6.3	81	100	12.33	100	
200	4.45	40	4.452	29	110	8.703	87	
—	—	—	4.234	21	111	7.101	56	
211	3.36	100	3.635	100	210	5.507	45	
310	2.81	50	2.813	39	211	5.0	w	
222	2.57	70	2.57	68	220	4.341	16	
321	2.38	70	2.377	70	300, 221	4.101	59	
400	2.22	10	2.22	w	310	3.894	w	
330, 411	2.10	80	2.097	86	311	3.709	74	
420	1.99	30	1.989	23	222	3.54	w	
332	1.896	30	1.897	21	320	3.414	29	
422	1.814	30	1.816	18	321	3.289	63	
431	1.743	30	1.744	20	400	3.075	w	
521	1.621	30	1.625	28	322, 410	2.984	71	
440	1.569	60	1.573	49	330, 411	2.899	20	
433, 530	1.523	40	1.526	28	331	2.82	w	
442, 600	1.48	60	1.483	44	420	2.752	26	
532, 611	1.441	60	1.444	47	421	2.688	18	
620	1.404	5	1.409	10	332	2.622	57	
541	1.371	30	1.373	17	422	2.51	10	
622	1.339	30	1.343	19	430, 500	2.44	w	
631	1.310	30	1.313	19	431, 510	2.413	w	
444	1.281	30	1.285	16	333, 511	2.361	30	
640	1.231	5	1.231	v/w	432, 520	2.288	w	
552, 633	1.209	60	1.212	39	521	2.23	w	
642	1.189	5	—	—	440	2.173	14	
730	1.167	20	—	—	441, 522	2.13	w	
651, 732	1.129	40	1.131	21	433, 530	2.103	w	
800	1.110	5	—	—	531	2.07	w	
554, 741 +	1.093	20	1.096	11	442, 600	2.049	27	
644, 820	1.078	20	1.079	10	610	2.023	w	
662	1.019	20	1.021	11	443, 540 +	1.920	16	
752	1.007	20	—	—	541	1.892	w	
840	0.994	30	0.996	16	550, 543 +	1.739	29	
833, 910	0.982	10	+1 line	—	720, 641	1.689	19	
842	0.969	10	at 0.849	—	+8 lines	—	—	
655, 761 +	0.958	30	—	—	to 1.220	—	—	
754, 851 +	0.936	10	—	—	—	—	—	
763, 932	0.917	20	—	—	—	—	—	
844	0.906	20	—	—	—	—	—	
+9 lines	—	—	—	—	—	—	—	
to 0.7847	—	—	—	—	—	—	—	

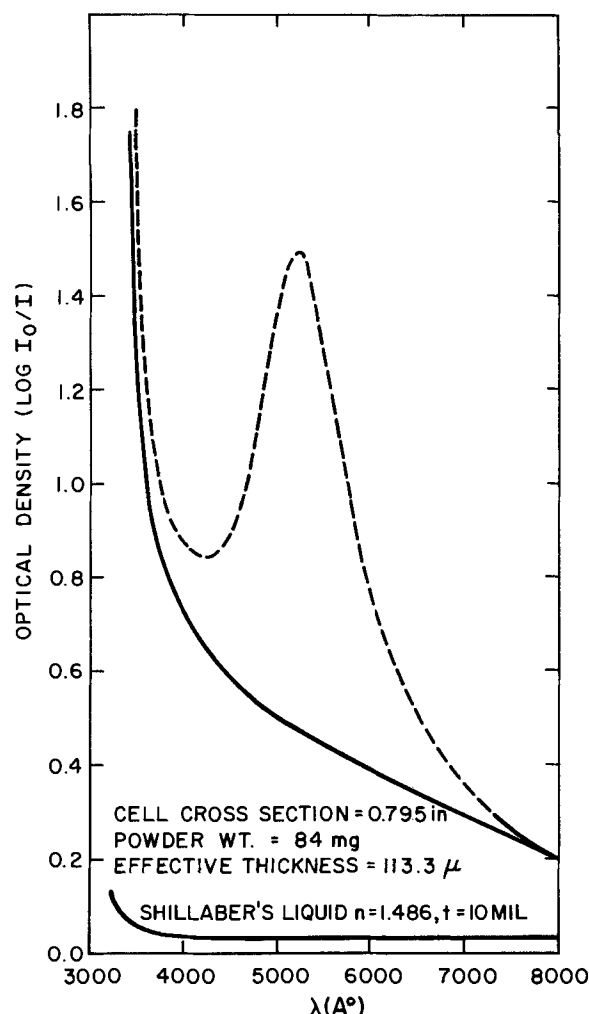


Fig. 2. Ultraviolet induced color absorption in sulfur-doped photochromic chlorosodalite.

shows an example of u.v. induced color absorption in a Cl-sodalite. The solid line is the absorption before u.v. excitation and the dotted line is the u.v. induced absorption. The absorption of the background liquid with matching index of refraction (1.486) is also shown in Fig. 2. The absorption coefficient derived from the change in the optical density exceeds  $200 \text{ cm}^{-1}$  which is by far the highest ever reported for Cl-sodalite. Using this value in the Smakula formula (50, 14), one can obtain an estimate of the switchable color center density which is shown in Table III along with results for Br- and I-sodalites. One notes that the absorption peaks of Cl-, Br-, and I-sodalite (Table III) shift progressively towards longer wavelengths, which correspond to the progressive increase of their lattice constants. This correlation (a linear curve for the relation of peak wavelength *vs.* lattice constant when plotted in log-log coordinates) which is an analog of Ivey's relation (14) for color center absorption in alkali halides, has also been noted by others (22, 23, 25). The typical density of switchable centers of PC

Table III. Lattice constant, absorption peak, absorption coefficient, and switchable color center density of various synthetic sodalites

Type	Cl	Br	I
Lattice constant, Å	8.89	8.93	9.02
Absorption peak, Å	5250	5450	5950
Absorption coefficient at 300°K, $\text{cm}^{-1}$	206	114	147
Density of switchable center, $\text{cm}^{-3}$	$2.3 \times 10^{18}$	$1.1 \times 10^{18}$	$1.5 \times 10^{18}$

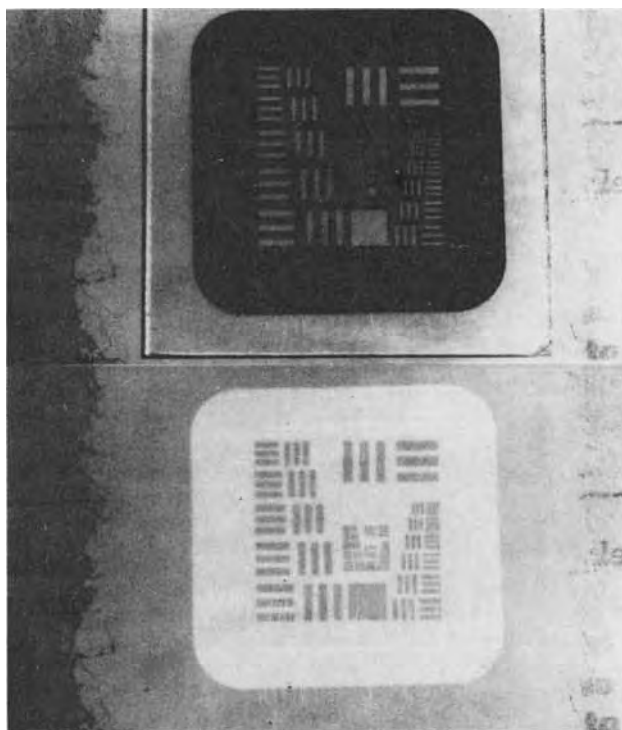


Fig. 3. An image produced on the sulfur-doped photochromic chlorosodalite: the contrast equals 4:1.

sodalite synthesized by the SCM is of the order of  $10^{18}/\text{cm}^3$ . For that density, the material shows a reflective contrast ratio of somewhat better than 4:1. An example of the contrast and resolution capabilities of SCM sodalite is shown in Fig. 3 for a Cl-sodalite. The powder sample was sandwiched between two sheets of plastic (3 mils thick) and was exposed to a u.v. light source [Black Light,<sup>2</sup> broad-band peaked at 3650Å and ~15W input power] placed 5 cm above for 5 sec through a glass mask (2.5 mm thick). The two Polaroid pictures (Fig. 3) were taken with the mask covering the sodalites (top) and with the mask removed (bottom). The image has a contrast of about 4:1, and is purple on a white background.

**Cathodochromic behavior.**—The electron beam coloration experiments were performed in a demountable cathode-ray system. Sodalite powders were sprayed onto NES<sup>3</sup> glass plates and were tested with electrons of 10–20 kV. Both sulfur-doped and nonsulfur-doped sodalites can be colored by an electron beam but to different degrees. In general the sulfur-doped samples show lower sensitivity in terms of maximum contrast (<10:1) but higher sensitivity to photobleaching. Therefore, they are more suitable for photo-erasable cathodochromic screen applications. The nonsulfur-doped samples are more sensitive in terms of both maximum contrast (20:1 to 40:1) and cathodochromic efficiency but are less sensitive to photobleaching. Thus, they are suitable for high contrast thermal erasable cathodochromic screen applications. Comparing various CC sodalites (nonsulfur-doped) prepared by the SCM, we find that Br-sodalites give the best sensitivity in terms of coloration for a given e-beam charge density. We also find that the 4A type molecular sieve material is better suited for CC sodalite synthesis, i.e., better sodalites can be obtained. Figure 4 shows the cathodochromic characteristic measured for some typical nonsulfur-doped CC sodalites. The powder layer was 1.5 mils thick. The electron beam energy used was 20 kV. The contrast (in transmission) was measured with a brightness spotmeter (Photoresearch Corporation) without optical filter. One notes that the Br-

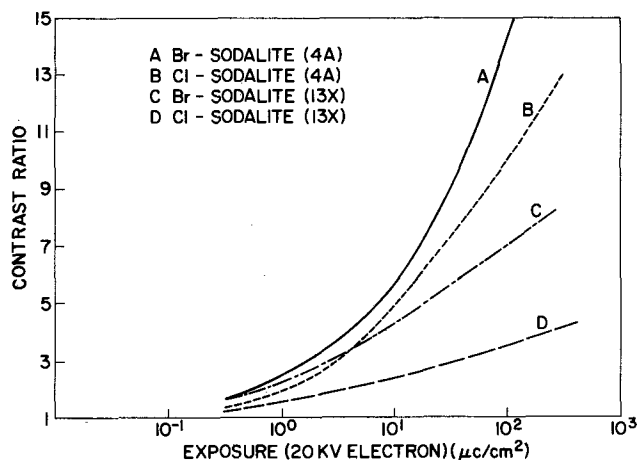


Fig. 4. Cathodochromic characteristics of several nonsulfur-doped sodalites.

sodalite is more sensitive particularly at lower charge density than the Cl-sodalite. One notes also that the sensitivity of the sodalite prepared from Linde 4A molecular sieve is superior to that made from Linde 13X molecular sieve. The Br-sodalite (4A) is most sensitive and can be colored to saturation with a transmission contrast greater than 40:1. This sensitivity is better than most synthetic sodalites reported in the literature.

#### Discussions and Summary

The earliest work on sodalite synthesis was reported by Friedel and Friedel (38) who had synthesized sodalite by the hydrothermal growth method (HTG). Subsequently, the HTG method has been used by many people (15, 16, 19, 22, 23, 39–42) with various minor modifications or variations. Basically, one starts with a mixture of  $\text{Al}_2\text{O}_3$ ,  $\text{SiO}_2$ ,  $\text{NaCl}$ ,  $\text{NaOH}$  (or  $\text{Na}_2\text{SO}_4$ ), and water. The mixture is first heated at low temperature to adjust for a proper amount of water and is then sealed in a gold or platinum tube which is placed in an autoclave under high pressure (~1000 bars) and at a temperature of 350°–460°C for several days. Noble metal tubes have to be used because of the corrosion problem. The result obtained at this stage is not PC (sulfur-doped) or CC (nonsulfur-doped). A sensitization step, heating the material at 900°C in an inert atmosphere or in a reducing atmosphere for some hours, is required to activate the material. Although sensitive sodalites (25, 26) have been produced by the HTG method, it is obviously an expensive and inefficient technique.

The other commonly used method is solid-state sintering (SSS), which is a dry method. It starts with a stoichiometric mixture of aluminum oxide, silicon dioxide alkali halide, and alkali hydroxide or sulfate according to the sodalite formula. This mixture is dry milled and then fired at 750°C in silica dishes. Firing and grinding are repeated many times to insure more complete reaction. A final firing at 900°C under reducing atmosphere is required to activate the sodalite. The inherent disadvantages of this technique are the lengthy procedures required and the problem of incomplete reaction. Sodalites synthesized via aluminosilicate gel (42) also have a similar drawback.

In comparison with the techniques discussed above, the structure conversion method (SCM) is much simpler. It converts a molecular sieve material (complex sodium aluminosilicate) with dopants and activators into a CC or PC sodalite in a single step. This conversion may be described more explicitly as follows. The molecular sieve materials have the basic building blocks of silicon-oxygen and aluminum-oxygen tetrahedra for the sodalite framework. The silicon ion and the aluminum ion both have a coordination number of four; specifically, they are surrounded by four oxygen

<sup>2</sup> Black Light, trade name of Spectronics Corporation.

<sup>3</sup> Conductive coating, trade name of PPG Industries.

ions forming tetrahedra. These tetrahedra are connected together to form a strong framework. The framework, while strong, is not rigid. Within the framework, there are cavities and pores which can be occupied by other ions and molecules. When the proper amounts of sodium and ionic halogen have been incorporated into the cavities, the framework collapses to the sodalite structure. The process of collapse involves the tetrahedra rotating about the twofold axes until the oxygen ions come into contact with the sodium ions which themselves are in contact with the halogen ions. This partial collapse of the framework reduces the edge of the cubic unit from its maximum value of about 9.4 to 8.87Å for chlorosodalite. The chlorine ion in chlorosodalite can easily be exchanged by iodine, bromine, sulfur, etc. However, if the substituted group is larger than  $\text{Cl}^-$ , then the collapse of the framework is less pronounced. This effect is illustrated (28) by the changes of lattice constant (cubic edge) among various sodalites shown in Table III.

In synthesizing PC sodalite, sulfur ions acting as electron donors in the material are necessary. The sulfur activator is incorporated in the form of  $\text{Na}_2\text{SO}_4$ ,  $\text{Na}_2\text{SO}_3$ , or  $\text{Na}_2\text{S}$ . These sulfur oxide molecules or ions have to diffuse into the aluminosilicate framework and become reduced (except in the sulfide case) to sulfur ions,  $\text{S}^{2-}$ , during the structure conversion. Since the structure conversion is carried out in a reducing atmosphere which prevents the sulfur ions from being oxidized to disulfur ions (27, 42) (and perhaps also prevents the oxygen ion from replacing the sulfur ion), very sensitive PC sodalites can be obtained in this single processing step without requiring any additional sensitizing procedure. These sulfur oxide ions are relatively large in size (in comparison with  $\text{Cl}^-$ ); therefore, it is not surprising that the larger pore size (cavities and channels) molecular sieves, like the 10Å pore 13X sieve, are better suited for PC sodalite synthesis where sulfur is required.

In the case of CC sodalite synthesis, the sulfur activator is not required. Therefore, the channel size of the sieve material is not as important an issue as in the case of PC sodalite. In fact, our experimental results show that the Linde 4A sieve (4Å pore size) is best suited to CC sodalite synthesis. For sensitive CC behavior it is essential to have a halogen deficiency (halogen vacancies) in the sodalite structure. Therefore, it is conceivable that when using a 4Å sieve rather than a 10Å sieve as a starting material, a proper amount of halogen deficiency may result, in that the halogen atom, having a radius about twice that of the sodium atom, is more restricted by the 4Å channel relative to the 10Å channel. Furthermore, the CC characteristics of sodalite are somewhat sensitive to the perfection of its structure. This has also been experienced by Schipper *et al.* (42) in their sodalites synthesized by the aluminum silicate gel reaction. The structural perfection of the synthetic sodalite can be characterized by the Al/Si ratio which should be 1 for a perfect sodalite. The Linde 4A sieve has an Al/Si ratio equal to 1 whereas the 13X sieve has an Al/Si ratio less than 1. This may be the reason that the 4A sieve can be consistently converted to better CC sodalites than the 13X sieve, even though quite sensitive CC sodalites have been synthesized from the latter.

In summary, an efficient and reliable technique for synthesizing sodalites has been developed, which we have termed the structure conversion method. For both PC and CC sodalite synthesis, it is a single-step process requiring no additional sensitization procedure. The structure conversion method would be particularly advantageous for industrial processing. It uses commercially available molecular sieves as starting material. The mechanism is one in which the incorporation (through diffusion) of alkali halides and sulfur compounds (required for PC sodalite) is accomplished at the same high temperature at which the structure

change or conversion (distorted sodalite to sodalite) takes place. No additional sensitizing procedure is required. Molecular sieve material with larger pore size (Linde 13X) is better suited for the synthesis of PC sodalite since it allows more efficient diffusion of relatively large sulfur oxide ions, whereas molecular sieve material with Al/Si ratio the same as that in sodalite (Linde 4A) is best suited for the synthesis of CC sodalite. Using this technique, PC sodalites having switchable color center densities  $>10^{18}/\text{cm}^3$  and very sensitive nonsulfur-doped CC sodalites can be obtained routinely.

#### Acknowledgment

The author expresses his sincere appreciation for many useful discussions with R. Dreyfus, H. Taub, K. Pennington, and A. V. Brown. The assistance of J. Karasinski and D. Paul on the x-ray diffraction measurements, of P. Wraight on some of the cathodochromic characteristic data, and of C. X. Duncombe on sodalite synthesis is gratefully acknowledged. He also thanks Y. J. Doerr and R. Shendo of Union Carbide who have provided him with some technical information and data on Linde molecular sieves.

Manuscript received Sept. 21, 1973. This was Paper 33 presented at the Chicago, Illinois, Meeting of the Society, May 13-18, 1973.

Any discussion of this paper will appear in a Discussion Section to be published in the December 1974 JOURNAL. All discussions for the December 1974 Discussion Section should be submitted by Aug. 1, 1974.

#### REFERENCES

1. G. H. Brown, Editor, "Photochromism," John Wiley and Sons, Inc., New York (1971).
2. A. J. Cohen and H. L. Smith, *Science*, **137**, 981 (1962).
3. D. R. Bosomworth and H. J. Gerritsen, *Appl. Opt.*, **7**, 95 (1968).
4. R. G. Bessent and W. A. Runciman, *Brit. J. Appl. Phys.*, **17**, 991 (1966).
5. M. R. Tubbs and D. K. Wright, *Phys. Stat. Sol. (a)*, **7**, 155 (1971).
6. A. H. Rosenthal, *Proc. I.R.E.*, **28**, 203 (1940).
7. P. G. R. King, *J. IEE (London) Proc.*, **93A**, 171 (1946).
8. H. F. Ivey, U.S. Pat. 2,752,521 (1956); also *Proc. IEEE*, **57**, 853 (1969).
9. H. C. A. Hankins and I. S. Torsun, *Electron. Letters*, **6**, 137 (1970).
10. I. Gorog, *Appl. Opt.*, **9**, 2243 (1970).
11. P. H. Heyman, I. Gorog, and B. Faughnan, *IEEE Trans. Electron Devices*, **ED-18**, 685 (1971).
12. Y. Uno and H. Maeda, *SID Intern. Symp. Digest*, **III**, 76 (1972).
13. P. T. Bolwijn and R. A. van Doorn, *J. Phys. D.*, **5**, 896 (1972).
14. J. H. Schulman and W. D. Compton, "Color Centers in Solids," Pergamon Press, Elmsford, N. Y. (1962).
15. D. B. Medved, *J. Chem. Phys.*, **21**, 1309 (1953).
16. D. B. Medved, *Am. Mineralogist*, **39**, 615 (1954).
17. R. D. Kirk, *This Journal*, **101**, 461 (1954).
18. R. D. Kirk, *Am. Mineralogist*, **40**, 22 (1955).
19. E. F. Williams, W. G. Hodgson, and J. S. Brinen, *J. Am. Ceram. Soc.*, **52**, 139 (1969).
20. W. Phillips and Z. J. Kiss, *Proc. IEEE*, **56**, 2072 (1968).
21. W. Phillips, *This Journal*, **117**, 1557 (1970).
22. M. J. Taylor, D. J. Marshall, P. A. Forrester, and S. D. McLaughlan, *Radio Electron. Eng.*, **40**, 17 (1970).
23. P. A. Forrester, D. J. Marshall, S. D. McLaughlan, and M. J. Taylor, NATO AGARD Proc. No. 5 (1970).
24. C. Z. van Doorn, D. J. Schipper, and P. T. Bolwijn, *This Journal*, **119**, 85 (1972).
25. P. T. Bolwijn, D. J. Schipper, and C. Z. van Doorn, *J. Appl. Phys.*, **43**, 132 (1972).
26. B. W. Faughnan and I. Shidlovsky, *RCA Rev.*, **33**, 273 (1972).
27. I. F. Chang and A. Onton, *J. Mater. Electron.*, **2**, 17 (1973).



28. D. Paul and I. F. Chang, AIME 15th Conf. Electronic Materials, Las Vegas, Aug. 27-29, To be published.
29. L. H. Borgström, *Geol. Foren. Stockholm, Forh.*, **23**, 563 (1901).
30. O. I. Lee, *Am. Mineralogist*, **21**, 764 (1936).
31. Ei-ichi Iwase, *Z. Krist.*, **99**, 314 (1938).
32. L. I. Anikina, T. S. Dobrolyubskaya, and A. V. Karyakin, *Geokhimiya*, **2**, 256 (1967).
33. Berrett, NBS Report No. JCPDS-20-1070, Thesis, University of Manitoba, Winnipeg, Canada (1968).
34. D. W. G. Ballentyne and K. L. Bye, *J. Phys. D.*, **3**, 1438 (1970).
35. U. K. Mel'nikov and B. N. Litvin, *Sov. Phys.-Cryst.*, **10**, 216 (1965).
36. K. L. Bye and E. A. D. White, *J. Crystal Growth*, **6**, 335 (1970).
37. B. N. Litvin and N. S. Triodina, *Sov. Phys.-Cryst.*, **15**, 1116 (1971).
38. C. Friedel and G. Friedel, *Bull. Soc. Franc. Mineral.*, **13**, 183 (1890).
39. L. P. Ni, O. B. Khalyapina, and G. L. Perckrest, *Zh. Prikl. Khim.*, **39**, 2639 (1966).
40. T. Tomisaka and H. P. Eügster, *Mineralogical J.*, **5**, 249 (1968).
41. I. Shidlovsky, B. W. Faughnan, P. M. Heyman, and I. Gorog, Paper 158 presented at Electrochemical Society Meeting, Cleveland, Ohio, Oct. 3-7, 1971.
42. D. J. Schipper, C. Z. van Doorn, and P. T. Bolwijn, *J. Am. Ceram. Soc.*, **55**, 256 (1972).
43. J. S. Prener and R. Ward, *J. Am. Chem. Soc.*, **72**, 2780 (1950).
44. R. Radler, Inorg. Phototropic Material for High Density Computer Memory, Clearing House for Federal Scientific and Technical Information, U.S. Dept. of Commerce, AD-407796 (1963), AD-608426 (1964).
45. R. W. Dreyfus and W. P. Hornberger, Unpublished work.
46. R. M. Barrer and E. A. D. White, *J. Chem. Soc.*, 1561 (1952).
47. R. M. Barrer, J. W. Baynham, F. W. Bultitude, and W. M. Meier, *J. Chem. Soc.*, 195 (1959).
48. R. M. Carr, P. W. Larking, and G. L. Lyon, *Australian J. Chem.*, **21**, 2555 (1968).
49. L. Broussard and D. P. Shoemaker, *J. Am. Chem. Soc.*, **82**, 1041 (1960).
50. A. Smakula, *Z. Physik*, **59**, 603 (1960).

## Native Oxide Mask for Zinc Diffusion in Gallium Arsenide

S. M. Spitzer,\* B. Schwartz,\* and G. D. Weigle

Bell Laboratories, Murray Hill, New Jersey 07974

The publication costs of this article have been assisted by Bell Laboratories.

### ABSTRACT

This paper reports the first use of an amorphous native oxide on gallium arsenide to mask against zinc diffusion. Anodic oxides were grown at low temperature ( $\leq 100^\circ\text{C}$ ), and stripes were defined in this oxide using standard photolithographic processing. These samples were diffused, after an appropriate annealing cycle, in a closed system using a zinc source ( $\text{Zn}_3\text{As}_2 + \text{GaAs}$ ) at  $612^\circ\text{C}$  for times up to 2 hr. Diffusion depths were measured using a lap and stain procedure, and the results showed the oxide to be effective as a zinc barrier. Furthermore, no anomalous lateral underdiffusion was observed indicative of a high integrity interface between the oxide and semiconductor.

The planar process, used to advantage in silicon device technology, has not been so fully exploited in the gallium arsenide technology because no similar native oxide had been available. Requirements of an oxide in a typical planar process are that the oxide: (i) must be compatible with photolithography, (ii) act as a pinhole-free, high breakdown, field strength insulator exhibiting good adherence, and (iii) serve as a mask for the controlled diffusion of dopants.

Previous attempts (1, 2) at growing a native oxide on GaAs have produced only brittle, crystalline forms of  $\beta\text{-Ga}_2\text{O}_3$  or  $\text{GaAsO}_4$ , which are extremely porous to Zn. Deposited insulators (3-5) such as  $\text{SiO}_2$  or  $\text{Si}_3\text{N}_4$  are not optimum Zn masks because of a large thermal coefficient of expansion mismatch resulting in cracking and lifting of such films at relatively high diffusion temperatures. The use of PSG films as a Zn diffusion mask has been reported (6, 7); however, considerable lateral diffusion is observed indicating a poor quality insulator-semiconductor interface. Deposited aluminum oxide (8) has been used successfully, although the lateral diffusion is a factor of up to 2 times the vertical diffusion depth which is unsatisfactory for precise line definition.

The use of a native oxide film to mask against Zn diffusion is reported for the first time in this paper. Sample preparation including oxidation, annealing and diffusion procedures critical to proper utilization

of the oxide as a diffusion mask, and results and conclusions thereof are discussed below.

### Sample Preparation

N-type gallium arsenide wafers of {111} orientation and Se-doped in the  $10^{17}$ - $10^{18}/\text{cm}^3$  range were polished by lapping with  $0.3\ \mu\text{m}$  alumina and etching  $75\ \mu\text{m}$  from the arsenic face with a bromine methanol solution for a final wafer thickness of  $0.3\ \text{mm}$ .

The wafers were thoroughly degreased in a trichloroethylene, acetone, water, methanol rinse cycle prior to anodization. The slices were then placed in a 30%  $\text{H}_2\text{O}_2$  aqueous solution with pH adjusted to 2 using  $\text{H}_3\text{PO}_4$  (9), and anodized at voltages ranging from 100-180V d-c at room temperature and at  $100^\circ\text{C}$  (10). Following anodization, the samples were baked in a nitrogen ambient for 2 hr at  $250^\circ\text{C}$ . A  $0.34\ \text{mm}$  stripe pattern on  $0.63\ \text{mm}$  centers was defined using a Shipley AZ-111 photoresist (11).

### Annealing and Diffusion

A closed system, routinely used for GaAs laser processing, was utilized for Zn diffusion in this experiment. The Zn dopant is derived from a source of powdered  $\text{Zn}_3\text{As}_2$  and GaAs, which is also designed to maintain a partial pressure of As over the GaAs wafer during diffusion. A typical diffusion cycle is 25 min at  $612^\circ\text{C}$  to obtain a sheet resistivity of 45 ohms/ $\square$  on a  $1\text{-}4 \times 10^{18}/\text{cm}^3$  p-layer equivalent to a surface concentration of  $10^{20}/\text{cm}^3$  to a depth of  $0.33\ \mu\text{m}$ .

\*Electrochemical Society Active Member.  
Key words: anodic oxidation, electro-optical device technology, compound semiconductors.



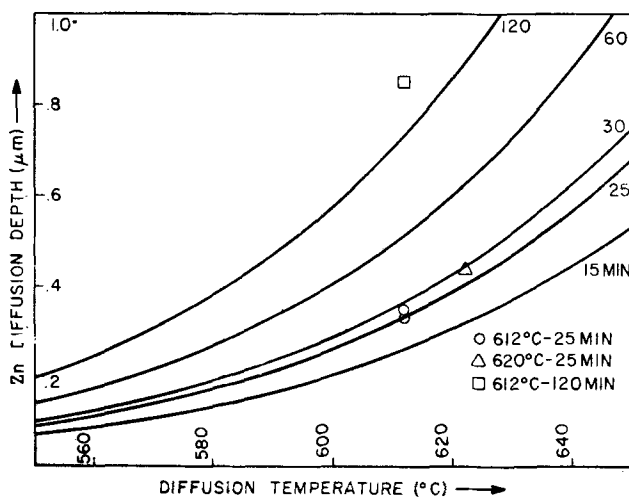


Fig. 1. Calculation of junction depth for Zn diffusion from a 5/50/45 (Ga,As,Zn) source as a function of time and temperature for an ideal closed system. Data points show experimental values determined on a less than ideal closed diffusion system.

When anodized samples were Zn diffused subsequent to the 250°C drying cycle, the oxide took on a mottled, discolored appearance. At this relatively high temperature, the oxide film was not completely stable and it reacted with the Zn. It was found that by annealing the oxide at 600°C for 30 min in dry nitrogen this problem could be eliminated. This annealing step serves to densify the oxide as evidenced by a decrease in thickness ranging from 25-50% indicated in Table I and increases its chemical stability (10). Following the annealing step, the oxide remained visibly unchanged after Zn diffusion at 650°C for times up to 2 hr.

Diffusion depth was measured by lapping the sample with a 0.25 μm diamond suspended in methyl ethyl ketone on a cylindrical drum (12) and then staining with a 30% HNO<sub>3</sub> aqueous solution to delineate the p-n junction. Cylinder lapped sections showed the "standard" Zn diffusion (612°C for 25 min) to penetrate 0.33 ± 0.5 μm, and showed that oxides 1300Å or greater effectively masked the "standard" diffusion, while thinner oxides only attenuated the diffusion depth.

### Discussion

The variation of junction depth with time and temperature for a closed system Zn diffusion in several III-V compounds may be written as (13)

$$x_j = X\sqrt{t} \exp(-E/kT) \quad [1]$$

where  $t$  is the diffusion time in hours. Casey and Panish (14) have determined  $X = 1930 \text{ cm/hr}^{1/2}$  and  $E = 1.33 \text{ eV}$  for Zn diffusion in GaAs at temperatures below 744°C. The theoretical junction depth vs. diffusion temperature relation is plotted with time as a parameter in Fig. 1. Experimental points are plotted on the same figure showing good agreement between theory and experiment.

Table I summarizes the oxide thickness, diffusion cycle, and junction depth data for the various samples used in this experiment. Note that while thicker oxides were grown and used, only a 1300Å thick oxide after an appropriate annealing cycle was required to

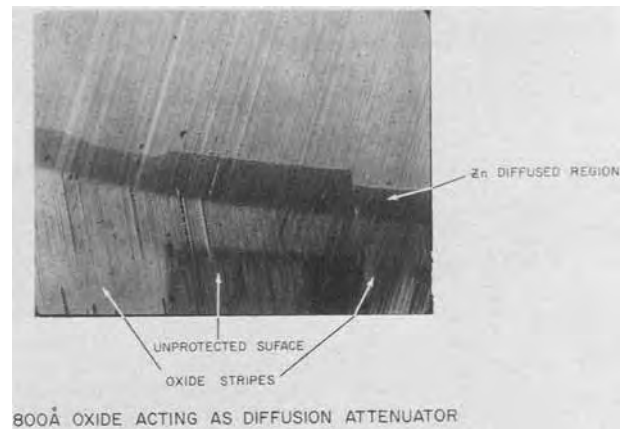


Fig. 2. Cylinder lapped section of 800Å thick oxide stripe geometry on GaAs substrate. Zn junction depth as indicated by chemical staining is 0.85 μm under the unprotected surface and 0.55 μm under the oxide stripe.

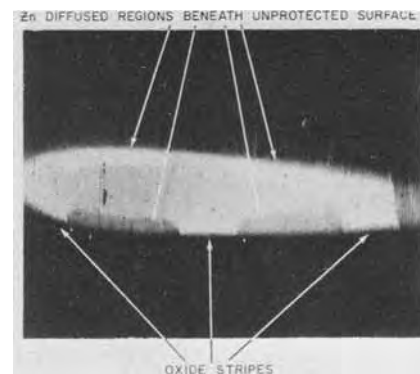


Fig. 3. Cylinder lapped section of 3600Å thick oxide stripe geometry on GaAs substrate. Zn junction depth under the unprotected surface is 0.44 μm and diffusion is masked under the oxide stripe.

mask against a 3300Å Zn diffusion. Figure 2 shows a cylinder lapped section of an 800Å thick oxide. Note that after diffusing a 0.85 μm layer of Zn into the unprotected GaAs surface, a 0.55 μm layer of Zn penetrates under the oxide. With thicker oxides ( $\geq 1300\text{Å}$ ), however, no Zn penetration through the oxide is observed. In Fig. 3 a cylinder lapped section shows 3600Å of oxide acting as a Zn barrier. In both cases sharp boundaries are observed between diffusion under the protected (oxidized) and unprotected stripes on the semiconductor, i.e., no observable anomalous lateral diffusion within resolvable limits occurs indicative of a high bond strength, low defect density interface between the oxide and semiconductor.

An estimate of the diffusion coefficient of Zn in the native oxide can be made using the model described by Baliga and Ghandi (7). If for a given diffusion cycle two different oxide thicknesses are used, the relative diffusion coefficient of Zn in the oxide as compared with GaAs can be written as

$$D_{\text{oxide}}/D_{\text{GaAs}} = \left( \frac{d' - d}{x'_j - x_j} \right)^2 \quad [2]$$

Table I.

Sample	$t_{\text{ox}}$ as-grown (Å)	Annealing cycle	$t_{\text{ox}}$ after anneal (Å)	Diffusion cycle	Zn depth	
					GaAs (μm)	Oxide (μm)
Gas-011-1	—	600°C for 30 min	800	612°C for 25 min	0.33	0.20
Gas-020-4	1700	650°C for 15 min	800	612°C for 120 min	0.85	0.55
Gas-035-3	2880	600°C for 30 min	1600	612°C for 25 min	0.35	—
Gas-040-3	2375	600°C for 30 min	1300	612°C for 25 min	0.33	—
Gas-040-4	4875	600°C for 30 min	3600	620°C for 25 min	0.44	—

where  $d'$  and  $d$  are the oxide thicknesses, and  $x'_j$  and  $x_j$  are the Zn diffusion depths under the respective oxides. For samples where the oxide acted as a Zn barrier,  $x_j = 0$ . The calculation yields an upper bound on  $D_{\text{oxide}}/D_{\text{GaAs}}$

$$D_{\text{oxide}}/D_{\text{GaAs}}|_{\text{upper bound}} = \left( \frac{d' - d}{x'_j} \right)^2 \quad [3]$$

and for  $d' = 1300\text{\AA}$ ,  $d = 800\text{\AA}$ , and  $x'_j = 2000\text{\AA}$

$$D_{\text{oxide}}/D_{\text{GaAs}}|_{\text{upper bound}} = 0.06 \quad [4]$$

Thus the diffusion coefficient of Zn in the native oxide is less than one-sixteenth of the diffusion coefficient of Zn in GaAs. In comparison, the diffusion coefficient of phosphorous in  $\text{SiO}_2$  is one-tenth that of phosphorous in silicon and the diffusion coefficient of boron in  $\text{SiO}_2$  is one-thirtieth that of boron in silicon (15) (for a closed system at  $1150^\circ\text{C}$ ). These values indicate that the diffusion coefficient of Zn in the native oxide on GaAs falls into the realm of usable values for diffused device fabrication. It should be pointed out that this calculation is of a qualitative nature, used here to illustrate the Zn mask potential of the native oxide.

### Conclusions

It has been shown that the anodic native oxide, after an appropriate annealing cycle, can be used as a mask for Zn diffusion in GaAs. Such oxides are grown either at room temperature or at  $100^\circ\text{C}$ ; they are readily compatible with standard photolithographic processing, and are easily etched in dilute HCl (before annealing at  $650^\circ\text{C}$  for 30 min) which does not attack the GaAs surface.

Since Zn can be diffused through the thinner oxides, such thin oxides can be used as diffusion buffers to prevent semiconductor surface damage from reaction with the diffusant. Thus a combination of thick and thin oxides will permit well-controlled selective area diffusion and protect the GaAs surface from damage as well as contamination from the ambient.

No gross strain was found to be present after oxide growth, following a  $250^\circ\text{C}$  dry cycle and after annealing at  $600^\circ\text{C}$  for 1 hr, as evidenced by viewing the sample through crossed polarizers (10) in an infrared microscope. This, along with the absence of any observable anomalous lateral diffusion, indicates a high integrity oxide-semiconductor interface.

These results suggest a potential GaAs planar technology based on a native oxide. Work is continuing at present to extend the high temperature/time operating limits of the native oxides for use as a diffusion mask to other dopants, and potentially as a restricted area epitaxy mask.

### Acknowledgments

We wish to thank R. E. Albano for his assistance with sample diffusion, and Mrs. D. R. Ketchow for her expertise with the cylinder lap technique. We give particular thanks to L. R. Dawson for his help with the lapping and staining procedure and many useful discussions on this experiment.

Manuscript submitted Sept. 11, 1973; revised manuscript received Nov. 29, 1973. This was Paper 301RNP presented at the Boston, Massachusetts, Meeting of the Society, Oct. 7-11, 1973.

Any discussion of this paper will appear in a Discussion Section to be published in the December 1974 JOURNAL. All discussions for the December 1974 Discussion Section should be submitted by Aug. 1, 1974.

### REFERENCES

1. M. Rubenstein, *This Journal*, **113**, 540 (1966).
2. H. T. Minden, *ibid.*, **109**, 733 (1962).
3. S. W. Ing and W. Davern, *ibid.*, **111**, 120 (1964).
4. W. von Muench, *IBM J. Res. Develop.*, **10**, 438 (1966).
5. S. R. Shortes, J. A. Kanz, and E. C. Wurst, Jr., *TMS-AIME*, **230**, 300 (1964).
6. D. Flatley, N. Goldsmith, and J. Scott, *This Journal*, **111**, 61C (1964).
7. B. J. Baliga and S. K. Ghandi, *IEEE Trans. Electron. Devices*, **ED-19**, 761 (1972).
8. K. Saito, E. Adachi, and N. Sakurai, *Japan. J. Appl. Phys.*, **41** (Suppl., Proc. 3rd Conf. Solid State Devices), 237 (1972).
9. R. A. Logan, B. Schwartz, and W. J. Sundburg, *This Journal*, **120**, 1385 (1973).
10. S. M. Spitzer, B. Schwartz, and G. D. Weigle, To be published.
11. R. L. Field, Internal communication.
12. B. McDonald and A. Goetzberger, *This Journal*, **109**, 141 (1962).
13. L. L. Chang, *Solid-State Electron.*, **7**, 853 (1964).
14. H. C. Casey, Jr. and M. B. Panish, *TMS-AIME*, **242**, 406 (1968).
15. R. M. Burger and R. P. Donovan, "Fundamentals of Silicon Integrated Device Technology," Vol. I, Oxidation, Diffusion and Epitaxy, Prentice-Hall, Inc., Englewood Cliffs, N. J. (1967).

## X-Ray Imaging Technique for Observing Liquid Encapsulation Czochralski Crystal Growth

H. D. Pruett<sup>1</sup> and S. Y. Lien

Western Electric, Engineering Research Center, Princeton, New Jersey 08540

The publication costs of this article have been assisted by the Western Electric Company.

### ABSTRACT

An imaging technique has been developed to facilitate growth of uniform diameter crystals by the liquid encapsulation Czochralski method. A point source of x-rays is used to produce a shadow image of the growing crystal on a scintillation screen. A high-sensitivity TV camera converts the shadow image into a real-time display on a TV monitor. System components are described, and results obtained from growing GaP crystals are presented.

In processing semiconductor wafers into electronic devices such as light-emitting diodes, it is desirable to

<sup>1</sup> Temporary address: Western Electric, Montgomery Plant, Aurora, Illinois 60507.

Key words: crystal growth, x-ray imaging, gallium phosphide.

have uniformly sized wafers. This allows the use of standard size masks and fixtures. Uniformly sized wafers can be produced by growing crystals of uniform diameter, or by centerless grinding of oversized crys-

tals having nonuniform diameters. For silicon, equipment is commercially available to automatically control the crystal diameter during growth. Furthermore, the raw material costs are low enough that centerless grinding is an economically viable process. For gallium phosphide (GaP), none of the above is true; commercial equipment is not available and material costs are substantial. In addition, pulled GaP crystals tend to be strained and break easily when subjected to centerless grinding. Because of the above considerations, a program to develop a better method of producing GaP crystals of uniform diameter was undertaken. This paper describes the system which was developed to meet this objective.

At present, large GaP ingots are grown by using the liquid encapsulation Czochralski (LEC) method.<sup>2</sup> The growth procedure starts by placing polycrystalline GaP in a quartz crucible, placing a precast slug of  $B_2O_3$  on top of the powdered GaP, and heating the crucible in a graphite susceptor in a chamber pressurized to about 800 psi with an inert gas. At 400°-500°C the  $B_2O_3$  melts, covers the GaP, and thereafter inhibits the evolution of phosphorus whose vapor pressure is about 35 atm at the melting point of GaP. The remaining steps in the growth procedure are similar to those used in normal Czochralski growth, namely, seeding, shouldering, and growth of a uniform diameter body.

As an ingot is being grown, a process which requires several hours, some phosphorus escapes from the melt and condenses on cold surfaces in the chamber, such as, the optical windows used for viewing the growth process. After a few hours at the GaP melting temperature, the normally transparent encapsulant gradually becomes clouded with fine particles of P and/or GaP. Furthermore, thermal gradients in the ambient gas introduce optical distortions. Together, these factors compound the difficulty of accurately determining the size and shape of the growing crystal by visual observation, which is normally done using a closed-circuit TV system. This requirement for more reliable, more quantitative information on which to base control decisions was the primary incentive for developing a better method of sensing the diameter of the growing crystal.

Several techniques were examined (2-4) but none appeared to offer an adequate solution to the diameter sensing problem. It appeared that an x-ray shadow-imaging technique would, however, eliminate the visibility limitations caused by the buildup of phosphorus deposits on the optical windows, clouding of the encapsulant, and thermal gradients in the ambient. This paper describes such an x-ray imaging technique based on a closed-circuit TV system. Although developed for GaP, it can be also applied to the growth of other materials.

Basically, the technique utilizes a small x-ray source to cast a shadow image of the growing crystal onto a fluorescent screen. An intensified TV camera is used to convert the x-ray shadow image into a corresponding visible image which is displayed on a TV monitor. This approach not only eliminates the above visibility problems, but the image produced also provides an excellent indication of the melt temperature. This is because the viewpoint is perpendicular to the axis of rotation of the growing crystal, and, consequently, the shape of the meniscus at the liquid-solid interface is clearly visible. The meniscus shape has proved to give a better indication of the melt temperature in the growth area than can be obtained from any other temperature-sensing apparatus known to us.<sup>3</sup> As is common knowledge, melt temperature is a critical parameter for both the initial seeding operation and the

growth of the uniform diameter portion of the crystal. Within a few seconds after the seed is first dipped into the melt, an experienced observer can tell from the meniscus shape whether or not the melt temperature is proper for seeding. The shape continues to be an invaluable indicator of melt temperature during subsequent phases of crystal growth.

### X-Ray Imaging System

A schematic of the over-all x-ray imaging system is shown in Fig. 1. Beryllium entrance and exit windows are used to maximize the x-ray transmission of the system. These windows are supported by stainless steel flanges which have elliptically shaped openings. In Fig. 2, which is a cross-sectional view of the crucible assembly, the area enclosed by the dotted line indicates the approximate field of view provided by the elliptical opening at the exit port.

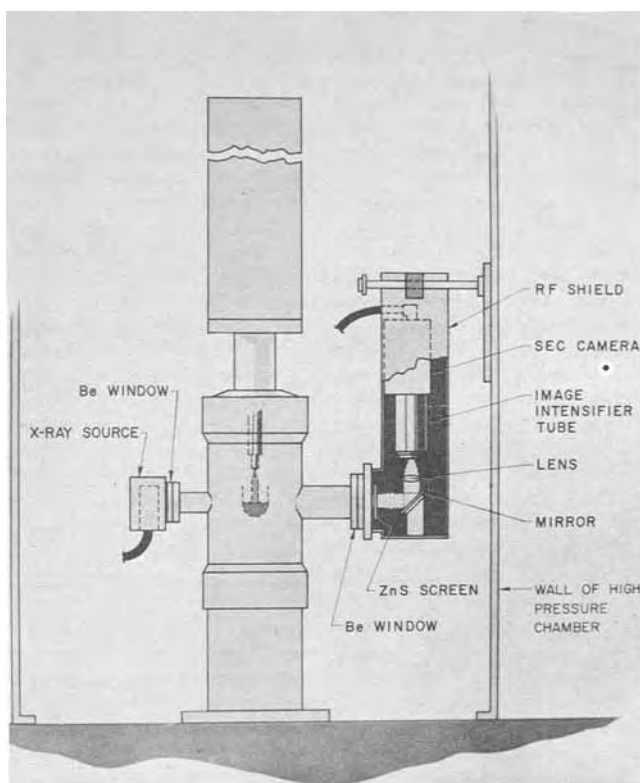


Fig. 1. Drawing of the x-ray imaging system showing location of various components.

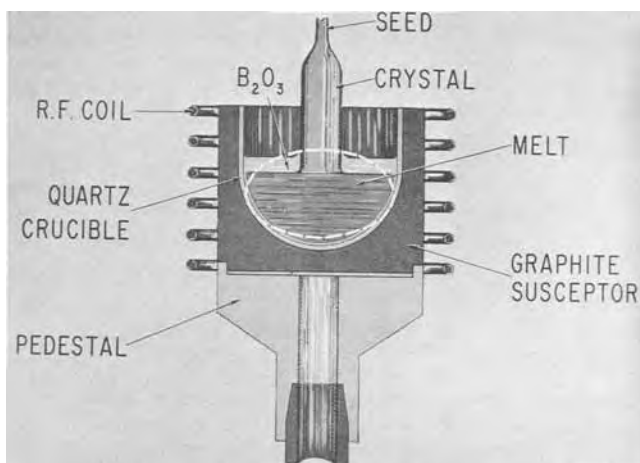


Fig. 2. Cross-sectional view of the crucible assembly. Objects within the area enclosed by the elliptically shaped dotted line are visible in the TV monitor picture.

<sup>2</sup> Recently, a Bridgman technique for growing large GaP crystals has been disclosed by Blum and Chicotka (1). Material produced by this technique has not yet been evaluated for manufacturing light-emitting diodes.

<sup>3</sup> A qualitative discussion of meniscus shape is given in a related paper (5).

The x-ray source used in the present system has a tungsten target tube with a focal spot size of 0.5 mm. Output capability of the system is 8 mA at 100 kV. Focal spot size is important in fluoroscopic imaging because it affects edge resolution; this is illustrated in Fig. 3. Assuming that the tube emits radiation uniformly over the focal spot area, the extent of the x-ray penumbra is proportional to both the focal spot size and the object-to-screen distance, but is inversely proportional to the source-to-object distance. In our system, the growing crystal is approximately midway between the source and the screen, resulting in a penumbra of about 0.5 mm at the plane of the fluorescent screen.

A tungsten target x-ray tube was chosen for the present application after studying two interrelated factors. For fluoroscopic imaging, the image contrast should be as high as possible and the total transmitted flux should be the largest value which is consistent with acceptable image contrast. An indication of image contrast can be obtained from a plot of mass absorption coefficient vs. x-ray energy. In Fig. 4 such a plot is shown for the materials used in the present crystal

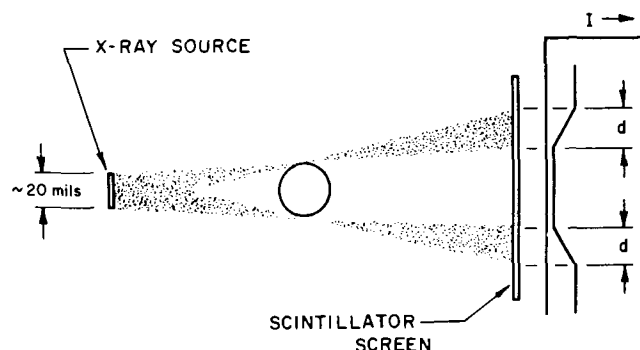


Fig. 3. Drawing which illustrates degradation of edge definition of a shadow image when using a finite sized source of radiation.

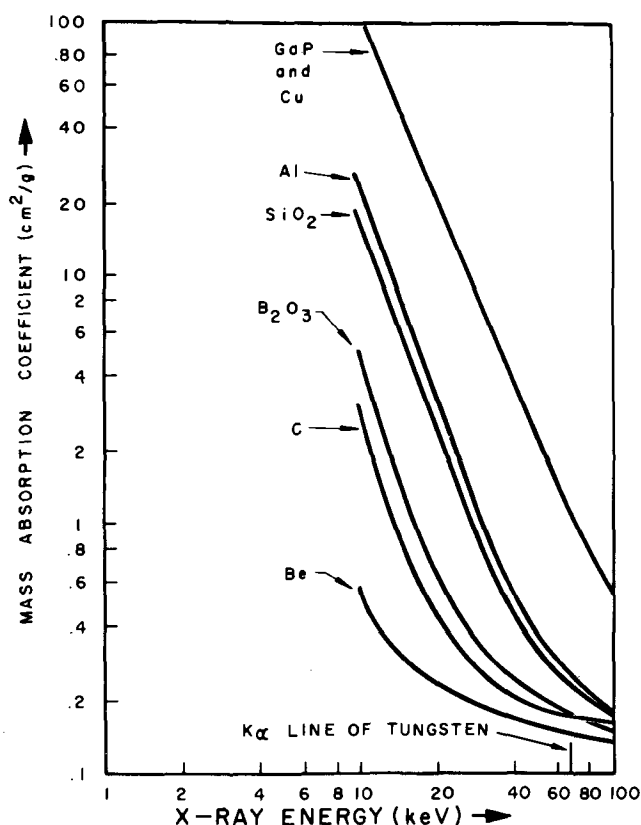


Fig. 4. Log-log plot of mass absorption coefficients vs. wavelength for materials in the x-ray path in the crystal puller.

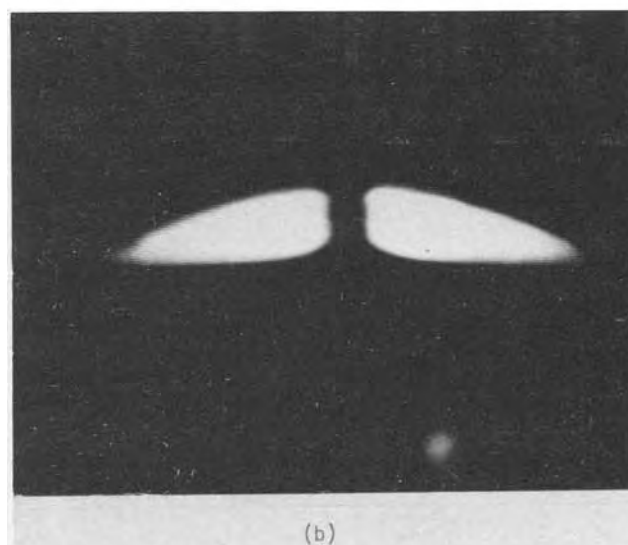
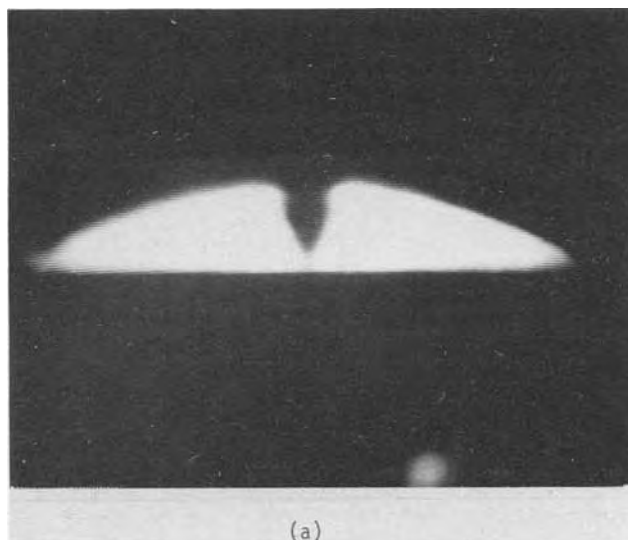


Fig. 5. TV monitor image during seeding operation: (a) Just prior to dipping seed into melt; (b) immediately after seed has contacted melt. Ordinarily the seed is blunt tipped rather than pointed as in (a). Seed has square cross section with  $\frac{1}{8}$  in. sides.

puller. At a given energy, the vertical distance between the curves for two materials is a measure of the contrast that can be obtained in a fluoroscopic image involving those two materials. This contrast is relatively independent of x-ray energy in the low energy region, but rapidly decreases for energies at and beyond the onset of Compton scattering. At very high energies, image contrast is mostly dependent on relative absorber thickness rather than on the types of material involved. For the  $K_{\alpha}$  emission of tungsten, image contrast is nearly optimum between GaP and the various

Table I. X-ray transmission of apparatus

Item	Transmission (%)
SiO <sub>2</sub> liner (two $\frac{1}{4}$ in. walls)	68
Carbon susceptor (two $\frac{1}{4}$ in. walls)	63
SiO <sub>2</sub> crucible (two $\frac{1}{16}$ in. walls)	83
RF coil (four $\frac{1}{32}$ in. Cu walls)	1.4
(four $\frac{1}{32}$ in. Al walls)	78
Be windows (one $\frac{1}{8}$ in. thick and one $\frac{1}{4}$ in. thick)	71.2
B <sub>2</sub> O <sub>3</sub> encapsulant (3 in. thick layer)	9.2
Total	0.033% Cu rf coil
Transmission	1.82% Al rf coil

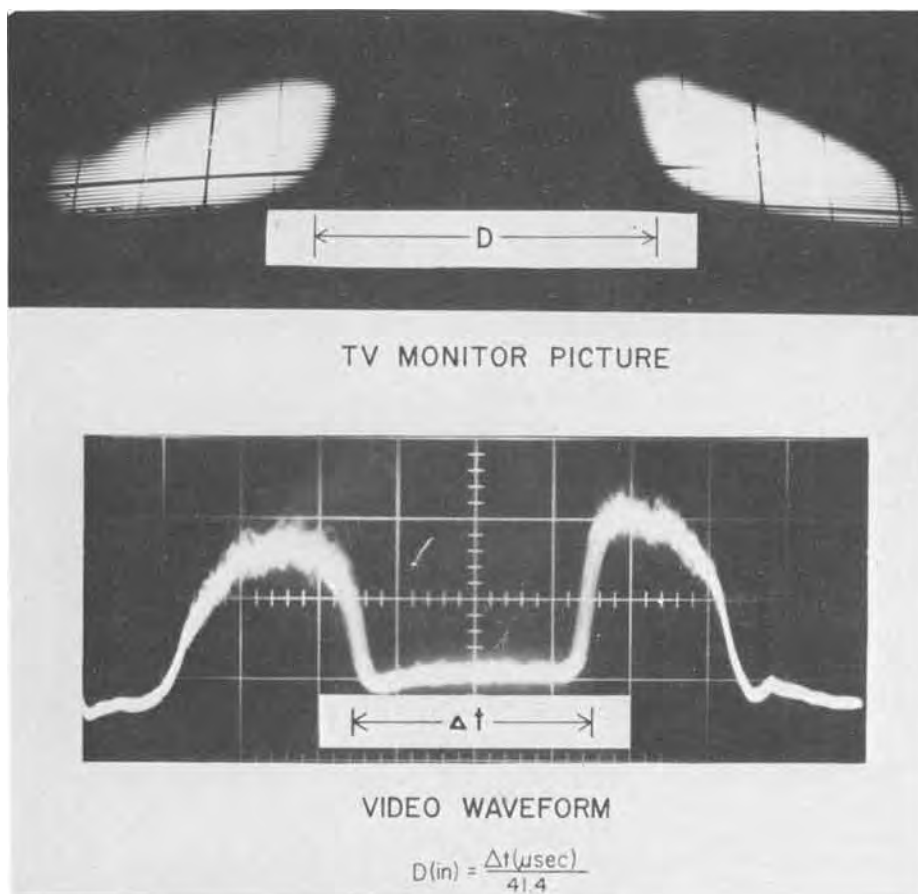


Fig. 6. (a) TV monitor photograph taken approximately 40 min after the seeding operation shown in Fig. 5b. A gradually tapered shoulder was being grown in this picture. (b) Video waveform of the darkened horizontal line segment parallel to melt level in Fig. 6a.



Fig. 7. Photograph of a crystal typical of those which can be grown by means of the x-ray imaging system.

other materials in the crystal puller. At the same time, the over-all x-ray transmission for tungsten radiation is higher than that of any other anode material commonly available in commercial x-ray tubes.

In Table I, the calculated x-ray transmission of the components in the crystal puller is given. Because of its high absorption, the original rf heating coil was replaced with one made of Al. Because of lower conductivity, the calculated joule heating losses are approximately 25% higher than in the original coil, but

this was considered a small penalty for the substantial improvement in image quality which was obtained.

An important link in the imaging system is the fluorescent screen used for converting the x-ray shadow image to a visible image. The over-all conversion efficiency of the screen is dependent on its thickness and quantum conversion efficiency. Because of the compromise that must be made between spatial resolution and over-all conversion efficiency, relatively thin screens must be used. Such screens absorb only a few

per cent of the incident x-ray beam. For the present application, a brief study indicated that the best compromise is produced by a ZnCdS screen, Type PFG-4.<sup>4</sup>

An intensified TV camera is used to view the shadow image on the fluorescent screen. The image intensifier tube is a Type WE-30677 and the camera tube is a Type WX-31792, both manufactured by Westinghouse Electric. This combination of components has provided adequate sensitivity for viewing the low level image of the growing crystal.

To maximize the signal-to-noise ratio of the image, the video bandwidth was tailored to meet the spatial resolution inherent in the image. As shown in Fig. 3, the edge definition of a shadow image depends on the source dimensions. A diffuse edge requires less video bandwidth for faithful reproduction than does a perfectly sharp edge. This means that, for a diffuse image, the video bandwidth can be reduced accordingly, thereby reducing the Johnson noise of the circuit. This noise is proportional to the square root of the bandwidth.

### Results

Some typical images seen on the TV monitor during the seeding operation are shown in Fig. 5a and 5b. In the lower figure, the shape of the meniscus is clearly visible. As mentioned earlier, this shape is the best indicator of melt temperature available. The TV monitor image and associated video waveform of a selected horizontal scan line are shown in Fig. 6a and 6b. In the upper photograph, the melt level is above the major axis of the elliptical viewing area. At a later date, a crucible lift assembly was added to the crystal puller to allow the melt level to be maintained coincident with this axis. The dark vertical lines in Fig. 6a are due to a calibrated grid attached to the face of the TV monitor and used for visually determining the crystal diameter. By electronically measuring and appropriately converting the time interval  $\Delta t$  shown in Fig. 6, the crystal diameter can be read directly on a digital display. Also, the binary-coded decimal (BCD) input to the digital display can be used to implement a closed-loop system for automatically controlling the diameter of the growing crystal. At the present time, we have implemented the visual display but not the closed-loop control system.

In Fig. 7 and 8 some recently grown crystals are shown. Necking of the seed to reduce dislocation density is an operation which can be readily observed and controlled with the x-ray imaging system. This is illustrated in Fig. 7 where the seed is still attached to the crystal. Through the excellent diameter information presented in the TV monitor picture and associated digital readout, the crystal puller operator has all the information necessary to make control decisions. A reasonably experienced operator can control crystal diameter to 1/16 in. or better, as illustrated in Fig. 7. With closed-loop control, it should be possible to produce crystals similar to the one shown in Fig. 8 whose diameter of 1.56 in. was controlled to  $\pm 20$  mils by manual operation of the crystal puller.

### Summary and Conclusions

In this paper an alternative method of observing LEC crystal growth has been presented. The configuration of the system used to implement this x-ray imaging system has been given and some of the performance requirements of the system components have been discussed. Photographs of typical TV monitor images were shown in which the meniscus shape used for deriving temperature information is clearly visible. Photographs of crystals grown solely by observation

<sup>4</sup> Manufactured by U.S. Radium Corporation, Cedar Knolls, New Jersey 07927.



Fig. 8. Photograph of crystal whose diameter of 1.56 in. was controlled to within 20 mils.

of the fluoroscopic image were shown to illustrate the diameter control that can be achieved manually. On the basis of our experience and the evidence presented in this paper, we conclude that x-ray imaging permits a substantial improvement in viewing and controlling LEC crystal growth.

Manuscript submitted Oct. 10, 1973; revised manuscript received Jan. 17, 1974. This was Paper 47 presented at the Chicago, Illinois, Meeting of the Society, May 13-18, 1974.

Any discussion of this paper will appear in a Discussion Section to be published in the December 1974 JOURNAL. All discussions for the December 1974 Discussion Section should be submitted by Aug. 1, 1974.

### REFERENCES

1. S. E. Blum and R. J. Chicotka, *This Journal*, **120**, 588 (1973).
2. K. J. Bachmann, H. J. Kirsch, and K. J. Vetter, *J. Crystal Growth*, **7**, 290 (1970).
3. A. E. Zinnes, B. E. Nevis, and C. D. Brandle, Jr., Second National Conference on Crystal Growth, Princeton, N. J., July 1972. To be published in *J. Crystal Growth*.
4. R. G. Dessauer, E. J. Patzner, and M. R. Poponiak, U.S. Pat. 3,493,770 (1970).
5. S. Y. Lien and H. D. Pruetz, International Conference on Crystal Growth, Tokyo, Japan, March 1974.



# Auger Electron Spectroscopy Determination of the Oxygen/Silicon Ratio in Spin-On Glass Films

J. N. Smith, S. Thomas, and K. Ritchie

Materials Research Laboratory, Motorola Semiconductor Division, Phoenix, Arizona 85008

The publication costs of this article have been assisted by Motorola Incorporated.

## ABSTRACT

Instrumental parameters for the determination of the oxygen/silicon ratio in SiO<sub>2</sub> films using Auger electron spectroscopy have been studied and optimized. In the case of a binary system such as this, the ratio of the Auger peak heights from the two components is a measure of their relative abundance and can yield meaningful results when compared with a standard. This method has been utilized to determine the oxygen/silicon ratio in spin-on glass films densified at various temperatures. The oxygen/silicon ratios of nondoped spin-on glass films show a general trend to increase and approach 2 as densification temperatures increase. The structural re-arrangement of the silica network at ~400°C is also reflected by the oxygen/silicon ratios. The oxygen/silicon ratio for other commonly used oxide films produced from steam, oxygen, and CVD was also determined. The techniques and results of this study are discussed.

Auger electron spectroscopy (AES) is a technique increasingly being used for the unambiguous identification of the elemental constitution of a solid surface (1-3). In this relatively new technique, a beam of electrons (typically 1-5 keV) is used to bombard the surface of the solid specimen, giving rise to ionization of the atomic levels. The atom subsequently relaxes either by the emission of x-ray photons or more probably (in the energy range 0-2000 eV) by the emission of Auger electrons. In AES, these Auger electrons which are characteristic of the surface species are detected, thus enabling the positive identification of the surface elements present. Since the mean free paths of these relatively low energy Auger electrons are rather short, they can escape without any significant energy loss only from a region very close to the surface. Typically their escape depth is ~5-10Å and this is why AES is a truly surface technique.

Besides unambiguously identifying the surface elemental constitution, AES yields a wealth of information regarding the chemical nature of the surface species. The differences in the chemical environment are manifest in the Auger spectra in a variety of forms, such as, a shift in the energy of the Auger electrons, changes in the shape and intensity of the Auger peaks, changes in the fine structure, etc. These chemical effects in AES have been discussed in detail by Haas, Grant, and Dooley (4). The chemical effects observed in the Auger spectra thus offer valuable information regarding the chemical nature of the constituents which supplement the knowledge of the elemental constitution. In the case of SiO<sub>2</sub>, these effects are very pronounced and are discussed below.

The present Auger spectroscopy investigation of nondoped spin-on glass has been primarily directed at a quantitative evaluation of the oxygen/silicon atomic ratio as a function of the heat-treatment. SiO<sub>2</sub> films produced from the oxidation of silicon by oxygen and steam, as well as chemical vapor deposition (CVD), were also studied for comparison. Although AES is widely used and the characteristic features in the Auger spectra from all the elements are well established, the technique is still mostly qualitative or at best semiquantitative. At the present time, there are no quantitative data available which enable one to translate the number of Auger electrons detected, or more commonly, the Auger peak-to-peak height, to

an absolute value of the surface concentration. However, it should be possible to make meaningful measurements of the surface concentration by comparing the Auger peak height with that from a standard. Quartz was used as a standard in this work. In the case of a binary system the ratio of the Auger peak heights from the two components is a measure of their relative abundance. It is this method which has been adopted in the present studies on the oxygen/silicon ratio in spin-on glass.

## Experimental

The experimental techniques employed in AES are well established (2, 3) and are not discussed here. The Auger analysis was made in a standard ultrahigh vacuum with a cylindrical mirror analyzer (CMA) incorporating an integral electron gun (Physical Electronics Industries). The ambient pressure during the experiment was typically  $1-2 \times 10^{-10}$  Torr, readily achieved without baking the system. Twelve samples were mounted on the carousel and each sample could be rotated in turn to face the integral electron gun for Auger analysis. The beam energy,  $E_p = 3$  keV, beam current  $I_p = 5 \mu\text{A}$ , and the modulating signal of 3 eV peak-to-peak, were kept constant throughout the experiment. The necessity for the use of the moderately low beam current is discussed in the following paragraph. As is generally the practice, the derivative of the energy distribution,  $dN(E)/dE$  is plotted as a function of the electron energy,  $E$ . The Auger spectra were plotted after removing ~20Å from the surface by Xe-ion sputtering. The sputter removal is essential in order to remove the impurities absorbed on the surface. It is assumed that the elemental constitution of the glass at 20Å below the surface is typically characteristic of the "bulk."

Before presenting the results, some of the problems encountered in the Auger analysis of SiO<sub>2</sub> and the assumptions made in the measurement of oxygen/silicon peak height ratios are mentioned. The first major problem encountered in the AES study of SiO<sub>2</sub> is the effect the primary electron beam has on the surface. It is generally recognized that the AES is a non-destructive technique. However, the beam parameters usually employed (typically  $E_p = 1-5$  keV,  $I_p = 10-100 \mu\text{A}$ ) do have a profound adverse effect on the SiO<sub>2</sub> surface. Extreme care has to be taken to minimize this effect. The primary effect of the high primary current density is to dissociate the SiO<sub>2</sub> into elemental

Key words: densification of SiO<sub>2</sub>, surface analysis, stoichiometry of SiO<sub>2</sub> films.

silicon and oxygen. Under prolonged electron bombardment of the sample, the oxygen is desorbed leaving the surface enriched in "elemental silicon" as evidenced by the growth of the Auger peak characteristic of elemental silicon and the reduction in the oxygen Auger peak. The assumption is made, although presumptuous, that two separate species, namely, elemental silicon and  $\text{SiO}_2$ , coexist at the surface. Of course, it is quite likely that the surface is composed of  $\text{SiO}_x$  where  $x < 2$ . In a separate investigation, we established the optimum beam parameters required to minimize the dissociation effect. A beam current of  $5 \mu\text{A}$  (or lower) is found to be adequate for the analysis without causing any noticeable dissociation effect in the time required for plotting the spectrum ( $\sim 30$  sec).

The method of measuring the ratio of the oxygen/silicon Auger peak heights requires that there is no marked change in the shape of the silicon or oxygen Auger peaks (in  $\text{SiO}_2$ ) due to the chemical effects. For  $\text{SiO}_x$  samples where  $x \approx 2$ , no difference in the silicon or oxygen Auger peak shapes was observed. This was established after studying  $\text{SiO}_2$  samples prepared by a variety of techniques, e.g., oxidation in oxygen at  $1100^\circ\text{C}$ , oxidation in steam at  $1100^\circ\text{C}$ , chemical vapor deposition, and spin-on. Hence, it is valid to measure the oxygen/silicon Auger peak heights ratio in order to make a comparison of the oxygen/silicon content.

All nondoped spin-on glass films on silicon wafers were prepared by flooding the wafer with solution and spinning for 10 sec at 4000 rpm on a Headway Photoresist spinner. The film was then densified for 30 min at temperatures varying from  $200^\circ$  to  $1100^\circ\text{C}$  in  $100^\circ\text{C}$  increments. These densification cycles were carried out in oxygen and nitrogen ambients, with a 1 liter/min flow rate. The film thickness of spin-on glasses is known to be a function of densification temperature (5). A typical value of film thickness after densification at  $1100^\circ\text{C}$  in nitrogen was  $\sim 4000\text{\AA}$ .  $\text{SiO}_2$  films were also prepared by other methods commonly used, e.g., steam grown films at  $1100^\circ\text{C}$ , oxygen grown films at  $1100^\circ\text{C}$ , and from the chemical vapor reaction of silane and oxygen at  $450^\circ\text{C}$ .

### Results and Discussion

Figure 1 is a typical Auger spectrum from a  $\text{SiO}_2$  sample. For purposes of comparison, the low energy Auger spectrum from a clean elemental silicon surface is also shown. It is worthwhile discussing briefly the main features in the Auger spectra from Si and  $\text{SiO}_2$  for a better understanding of the similarities and differences between the two. The principal Auger peak from elemental silicon appears at 92 eV (measured at the maximum negative deflection in the  $dN(E)/dE$  curve and has its origin from the  $L_{2,3}VV$  transition. In

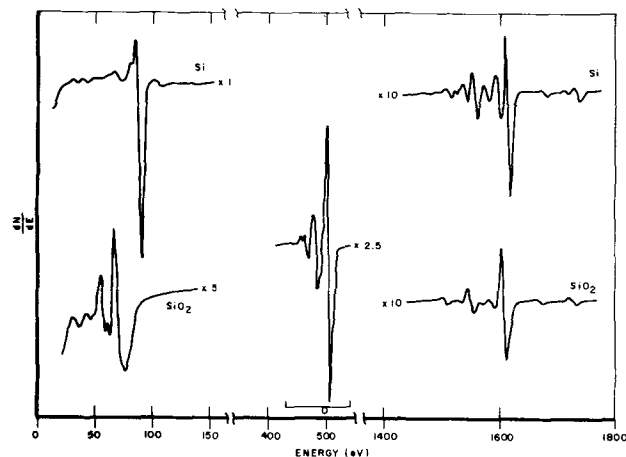


Fig. 1. Typical Auger spectrum of elemental silicon and  $\text{SiO}_2$

the case of  $\text{SiO}_2$ , the peak "shifts" to 75 eV. Both these peaks originate in silicon following the  $L_{2,3}VV$  transition, the only difference being the chemical nature of silicon in the two cases, one in the form of elemental silicon and the other as  $\text{SiO}_2$ . The above "chemical shift" is not primarily due to a shift in the binding energies in silicon, but rather has its origin in the change in the density of states in the valence band (strictly, changes in the transition density). There is a group of high energy Auger peaks originating from the KLL type transitions, the strongest peak appearing at about 1620 eV in elemental silicon (Fig. 1). In  $\text{SiO}_2$  the strongest peak occurs at about 1617 eV following a general shift of all the KLL Auger peaks by  $\sim 3$  eV. It is not implied that this measured shift in energy is the true chemical shift due to the changes in the binding energies. The measurement of the absolute chemical shift in the case of insulating surfaces is complicated by the possible changes in the surface potential. In the case of elemental silicon, each KLL Auger peak has two very prominent plasmon loss peaks associated with it. These plasmon loss features are very weak in the KLL Auger spectrum from a  $\text{SiO}_2$  surface. The large chemical shift in the low energy Auger spectrum and the plasmon loss features in the KLL spectrum are exploited in distinguishing the presence of the two species, elemental silicon and  $\text{SiO}_2$ . In the present study, the ratio of the main oxygen, 508 eV Auger peak height (Fig. 1) to the silicon, 75 eV (in  $\text{SiO}_2$ ) peak height is measured as characteristic of the oxygen/silicon ratio of the surface. The ratio of the peak heights was determined at twenty different areas on each sample and the mean value taken. Although one could measure the oxygen, 508 eV/silicon, 1617 eV peak heights, the relatively low intensity of the latter introduces a much larger error.

The oxygen/silicon ratios measured from the Auger spectra are tabulated in Table I for the films studied. The numbers in parentheses represent the oxygen/silicon ratio of the respective films normalized to a value of 2.0 for quartz. It is of interest to note that the oxygen/silicon ratio for the CVD, steam, and  $\text{O}_2$  films are close to 2.0. The higher value for the steam-grown oxide (2.05) is in line with the general view that surplus  $\text{H}_2\text{O}$  and/or OH species are incorporated in steam-grown oxide films.

From Fig 2 it is evident that the oxygen/silicon ratio for the nondoped spin-on glass shows a general trend to increase and approach 2 as the densification temperature approaches  $1100^\circ\text{C}$ . This behavior is most likely due to the loss of organic solvents at lower temperatures with oxidation and subsequent loss of organic species at higher temperatures. This is supported, in part, by the lower oxygen/silicon ratio for the same films densified under  $\text{N}_2$ . While the solvent loss at lower temperatures would be similar, the lack of sufficient oxygen for complete oxidation of the organic species produces a lower oxygen/silicon ratio at higher temperatures. The abrupt rise in the oxygen/silicon ratio at  $\sim 400^\circ\text{C}$  is due to a structural re-arrangement

Table I. Oxygen/silicon Auger peak height ratios

Temp., $^\circ\text{C}$	Nitrogen		Temp., $^\circ\text{C}$	Oxygen	
	O/Si ratio	$\sigma^*$		O/Si ratio	$\sigma^*$
25	3.41 (1.73)**	0.05	25	3.54 (1.81)**	0.08
200	3.43 (1.74)	0.04	200	3.51 (1.80)	0.08
300	3.60 (1.84)	0.06	300	3.61 (1.84)	0.04
400	3.71 (1.90)	0.05	400	3.73 (1.90)	0.03
500	3.67 (1.87)	0.04	500	3.66 (1.87)	0.05
600	3.60 (1.84)	0.04	600	3.70 (1.89)	0.05
800	3.72 (1.89)	0.02	800	3.83 (1.95)	0.04
900	3.77 (1.92)	0.03	900	3.76 (1.92)	0.04
1000	3.71 (1.89)	0.04	1000	3.88 (1.98)	0.03
1100	3.78 (1.93)	0.03	1100	3.88 (1.98)	0.04

Quartz 3.92, (2.00),  $\sigma = 0.06$ ; steam 4.01, (2.05),  $\sigma = 0.06$ ; oxygen 3.85, (1.96),  $\sigma = 0.03$ ; CVD 3.83, (1.95),  $\sigma = 0.03$ .

\*  $\sigma$ , Standard deviation at twenty different areas per sample.

\*\* ( ), O/Si ratio normalized to quartz = 2.00.



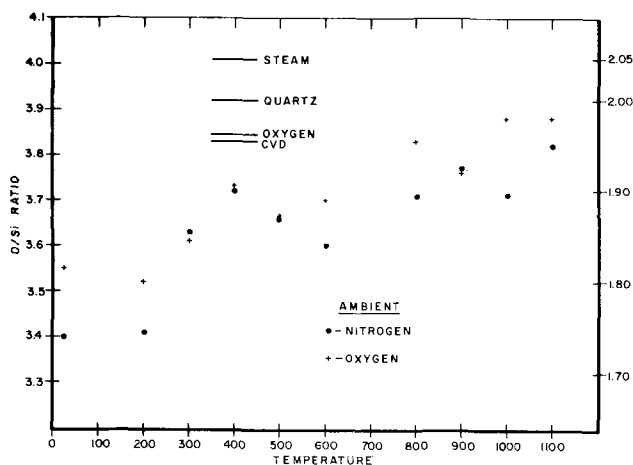


Fig. 2. Oxygen/silicon ratio vs. densification temperature in oxygen and nitrogen ambients. Values on right ordinate represent the O/Si ratio normalized to a value of 2.00 for quartz.

of the silica network. This is supported by changes that occur in the infrared spectra, etch rate, differential scanning calorimetry, and thermal gravimetric analysis

data reported in an earlier study which are characteristic of structural re-arrangement (5) in the silica network. The slight decrease observed in the oxygen/silicon ratio between 900° and 1000°C may also be due to structural re-arrangements, but no additional supporting evidence is available at this time.

Manuscript submitted Oct. 1, 1973; revised manuscript received Jan. 14, 1974. This was Paper 307RNP presented at the Chicago, Illinois, Meeting of the Society, May 13-18, 1973.

Any discussion of this paper will appear in a Discussion Section to be published in the December 1974 JOURNAL. All discussions for the December 1974 Discussion Section should be submitted by Aug. 1, 1974.

#### REFERENCES

1. L. A. Harris, *J. Appl. Phys.*, **39**, 1419 (1968).
2. C. C. Chang, *Surface Sci.*, **25**, 53 (1971).
3. P. W. Palmberg, in "Electron Spectroscopy," D. A. Shirley, Editor, p. 835, North-Holland Publishing Co., Inc., Amsterdam (1972).
4. T. W. Haas, J. T. Grant, and G. J. Dooley, *J. Appl. Phys.*, **43**, 1853 (1972).
5. K. Ritchie and J. N. Smith, Submitted to *This Journal*.

## The Syntheses, Electrical and Optical Properties of Doped and Undoped $\text{CuAlS}_2$

P. C. Donohue, J. D. Bierlein, J. E. Hanlon,<sup>1</sup> and H. S. Jarrett

Central Research Department, E. I. du Pont de Nemours and Company, Wilmington, Delaware 19898

The publication costs of this article have been assisted by E. I. du Pont de Nemours and Company.

#### ABSTRACT

Colorless  $\text{CuAlS}_2$  was prepared by using either a small excess of Al or a deficiency of S or Cu. A stoichiometric ratio of the reactants or deficiency of Al yielded a green color product. These crystals showed ESR and optical absorption similar to iron-doped crystals indicating that trace amounts of  $\text{Fe}^{+3}$  are responsible for the color. Crystals heated in the presence of elements such as Si or Cd lose their color and ESR spectrum, indicative of a reduction of  $\text{Fe}^{+3}$  to  $\text{Fe}^{+2}$ . All as-grown and most doped crystals were p-type, while most crystals doped with a combination of Cd/Al were n-type. Colorless  $\text{CuAlS}_2$  fluoresces with a broad peak at about 600 nm. The fluorescence may be stimulated by infrared after exposure to u.v. Mn-doped crystals exhibit red-orange fluorescence.

$\text{CuAlS}_2$  (1) is of interest since it has a related structure and comparable bandgap to  $\text{ZnS}$ . Thus it might have useful fluorescent or semiconducting properties.

Honeyman (2) reports an optical bandgap of 3.35 eV for  $\text{CuAlS}_2$  measured on black or deep-green crystals prepared by chemical transport. Optical absorption studies show major peaks at ~900 and 625 nm. Optical studies by Bhar and Smith (3) suggest an indirect gap at 1.84 eV.

Reports of the electrical properties are also in conflict. Honeyman reports n-type conduction with  $\rho_{298\text{K}} \sim 10^6\text{-}10^7$  ohm-cm while Tell *et al.* (4) report p-type conduction ( $\rho_{298\text{K}} = 10^2\text{-}10^3$  ohm-cm) on melt-grown crystals.

To gain a better understanding of  $\text{CuAlS}_2$ , we have studied the optical and electrical properties as functions of stoichiometry and dopants.

<sup>1</sup> Deceased.

Key words: doping,  $\text{CuAlS}_2$ , electrical optical properties.

#### Experimental

Syntheses were carried out in a manner similar to that described by Honeyman (2). Elemental reagents were weighed in desired proportions and sealed in dried evacuated silica tubing (15 mm OD, 13 mm ID, 15 cm long) with enough iodine to produce a pressure of ~1 atm during reaction. Instead of using powdered metals as Honeyman did, Al and Cu wire of 5N purity were used. The use of wires instead of powders reduces the contamination by surface oxide. We found commercially obtained 5N Al powder to be highly impure, containing primarily Fe and Si impurities. Also, the commercially obtained 5N Cu and Al wires were not as pure as specified. Our emission spectroscopy showed Cu: 2-25 ppm Mg, 0.5-2 ppm Si, and 1-5 ppm Fe; Al: 100-500 ppm Mg, 20-150 ppm Cr, 10-50 ppm Si, and 10-50 ppm Fe.

Reactions were carried out in natural gradient tube furnaces. The ends of the silica tubes containing the reactants were furthest in the furnaces while the other

ends were at the outer extremities. The temperature of the center regions was raised to about 800°C. After about 48 hr, the tubes were cooled, removed, and shaken to remove sulfide crusts which had formed on the Al wire and to break up copper sulfide. The tubes were refired at about 800°–1000°C in the reactant ends and at 400°–600°C in the cooler ends until all the S was taken up. The tubes were then heated at about 1000°C with no gradient for several days. Crystals generally grew as blades out of the crystalline mass.

Some doped crystals were prepared by heating previously prepared crystals in the presence of the dopant elements, Zn, Cd, Si, Ge, Sn, and Al, in evacuated silica tubes at 400°–800°C for from 1 to 24 hr followed by a quench in cold water. Crystals doped with Fe, Cr, and Mn were prepared by starting with the dopant in the reactants and proceeding with syntheses as described.

Crystals were characterized by chemical analyses, emission spectroscopy, and x-ray powder diffraction. Lattice constants were refined by least squares technique from Guinier camera data. Electrical resistivities and Seebeck coefficients were obtained using a two-probe, hot-probe method with silver paste contacts.

Optical transmission data were obtained on polished crystals using a Cary 14 spectrophotometer. Absorption coefficients were calculated employing dielectric constant data of Honeyman (2).

Fluorescent emission spectra of CuAlS<sub>2</sub> and Mn-doped CuAlS<sub>2</sub> excited by 253.7 nm Hg light were measured on powders between 300 and 750 nm using a ½m Bausch and Lomb monochromator fitted with an EMI extended S-20 response photomultiplier tube. The monochromator detector system was calibrated against an Eppy quartz-iodine standard lamp.

ESR was measured on powdered samples at X band using a Varian spectrometer.

## Results and Discussion

**Color as a function of stoichiometry.**—The color of CuAlS<sub>2</sub> is primarily the result of impurities. The valence state of the impurities and the resulting sample color can be controlled by adjusting the stoichiometry. It can be made colorless or pale-green depending on the reactant ratio. Colorless material results from using a small stoichiometric excess of Al or deficiency of Cu or S. Pale-green crystals form when either a stoichiometric proportion of reactants is used or one with a small excess of oxidizing power is used, i.e., deficiency of Al or excess S.

Black crystals formed when stoichiometric ratios of Al and Cu powders (found to contain Fe and Cr impurities) were used. This may account for the black crystals obtained by Honeyman. Use of excess Al powder, even with these impurities, produced colorless material.

It was not possible to distinguish among colorless, green, or black crystals by chemical analyses or x-ray diffraction. The cell dimensions and ranges refined from Guinier camera data from four colorless and four green samples are: colorless,  $a = 5.333 \pm 0.002\text{Å}$ ,  $c = 10.428 \pm 0.005\text{Å}$ ; green,  $a = 5.333 \pm 0.0001\text{Å}$ ,  $c = 10.433 \pm 0.002\text{Å}$ . Reported cell dimensions are smaller (1,2). We observed smaller cells on samples prepared above 1100°C perhaps indicating loss of S.

Emission spectroscopy of green and colorless crystals showed little difference. The major contaminants were Si (~500 ppm) and Fe (~30 ppm); all other elements totaled ~20 ppm.

The nature of the color-producing species was determined by comparing optical absorption data and ESR of colorless and pale-green crystals with data from iron- and chromium-doped crystals.

Crystals were doped with Fe and Cr by incorporating the dopant in the starting ratio. Compositions were prepared of starting formulas CuAl<sub>0.99</sub>M<sub>0.01</sub>S<sub>2</sub> and Cu<sub>0.99</sub>M<sub>0.01</sub>AlS<sub>2</sub> when M = Fe and Cr. The colors of the

products differed greatly. Substitution for Al produced black crystals when M = Fe and dark-green crystals when M = Cr. Substitution for Cu yielded orange crystals when M = Fe and pink crystals when M = Cr.

The ESR spectrum of the black, iron-doped crystals was identical to but stronger than the spectrum obtained from the pale-green CuAlS<sub>2</sub>. The ESR of the orange, Fe-doped crystals was much weaker and different from the black Fe-doped crystals. No ESR was observed in the colorless, undoped crystals.

We believe that the iron on the Al site is trivalent. Thus the pale-green color of the undoped CuAlS<sub>2</sub> is due to Fe<sup>+3</sup>. The color can be bleached by reduction of Fe<sup>+3</sup> to Fe<sup>+2</sup> when excess Al is used in the preparation.

The evidence for Fe<sup>+3</sup> as the cause of the color is further substantiated by the optical absorption data in Fig. 1.

The spectrum for the Fe<sup>+3</sup> doped crystals is qualitatively similar to but much stronger than the spectrum of the pale-green crystals. It is also similar to the spectrum reported by Honeyman (2) indicating that his material probably contained Fe. The absorption peaks near 11,000 and 16,000 cm<sup>-1</sup> correspond to the Fe<sup>3+</sup> transitions <sup>6</sup>A<sub>1</sub>(<sup>6</sup>S) to <sup>4</sup>T<sub>1</sub>(<sup>4</sup>G) and <sup>4</sup>T<sub>2</sub>(<sup>4</sup>G), respectively, observed in ZnS and other compounds doped with Fe<sup>+3</sup> (5).

The colorless CuAlS<sub>2</sub> showed no absorption due to Fe<sup>+3</sup> and a sharper cutoff at the band edge. The absence of color can be attributed to the reduction of the valence state of iron due to the reactant ratio containing greater reducing strength in the form of excess Al.

The optical transmission data for the Cr-doped CuAlS<sub>2</sub> are shown in Fig. 2. The dark-green and pink crystals show very different spectra. The green crystals have absorption bands near those of Fe<sup>+3</sup> and could account for the pale-green color in the undoped crystals. The ESR observed for the dark-green, Cr<sup>+3</sup>-doped crystals, however, was different from the spectra of the pale-green undoped crystals, again suggesting that Fe<sup>+3</sup> is the major cause of the color in the undoped crystals. This result is substantiated by Brandt *et al.* (6).

**Electrical properties and doping.**—Two-probe resistivity measurements<sup>2</sup> at room temperature and Seebeck coefficients are: colorless crystals  $\rho = 10^2$ – $10^4$  ohm-cm, 20–50  $\mu\text{V}/^\circ\text{C}$ ; green crystals  $10^4$ – $10^6$  ohm-cm, 20–200  $\mu\text{V}/^\circ\text{C}$ ; black crystals  $10^6$ – $10^8$  ohm-cm, 200  $\mu\text{V}/^\circ\text{C}$ . The resistivity of the black crystals is in the range found by Honeyman (2). The resistivity and p-type character of the colorless crystals agree with Tell *et al.* (4). The

<sup>2</sup> Four-probe resistivities are generally an order of magnitude lower, e.g., a green crystal showed  $\rho_{298\text{K}} = 2 \times 10^2$  ohm-cm;  $E_a = 0.004$  eV, 18  $\mu\text{V}/^\circ\text{C}$ .

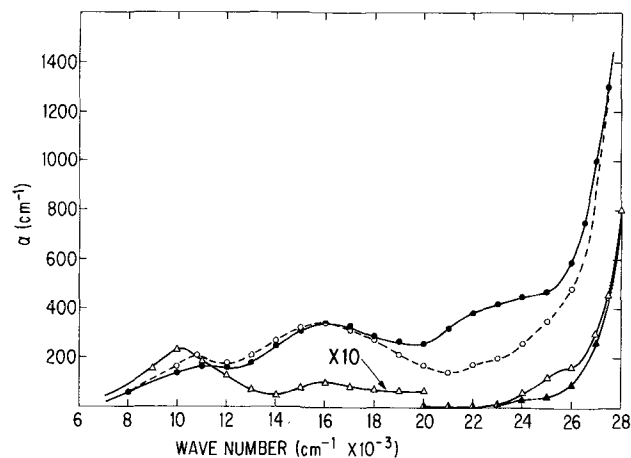


Fig. 1. Absorption coefficients vs. wave number for CuAlS<sub>2</sub>. ● = Honeyman (2); ○ = Fe doped; △ = green undoped; ▲ = colorless undoped.

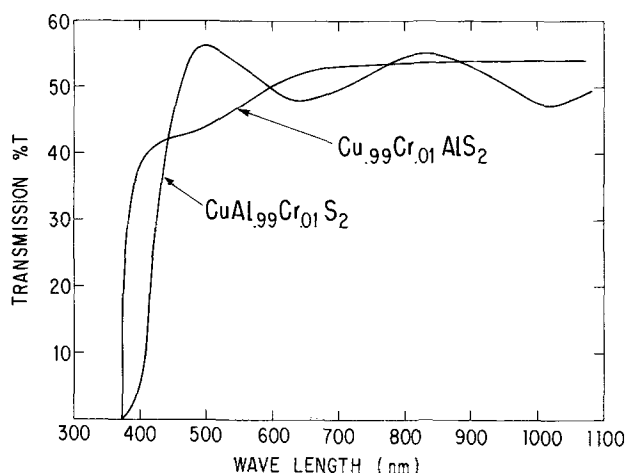


Fig. 2. Optical transmission of Cr-doped- $\text{CuAlS}_2$  vs. wavelength. The crystal thickness is  $85\mu$ .

high resistivity of the black crystals suggests that the Fe levels act as hole traps.

Many attempts were made to dope the crystals in order to produce n-type conductivity. Most crystals doped with Cd or combinations of Cd/Al showed n-type conductivity, with two-probe resistivities at room temperature in the range  $\rho = 10^1$ - $10^4$  ohm-cm and Seebeck coefficients in the range  $-100$  to  $-200 \mu\text{V}/^\circ\text{C}$ . Crystals doped with Cu, Al, and Si were p-type with generally lowered room-temperature resistivities in the range  $10^1$ - $10^3$  ohm-cm and Seebeck coefficients in the range  $5$ - $50 \mu\text{V}/^\circ\text{C}$ .

Crystals either black, green, or colorless, when heated in the presence of any one of the dopant elements Al, Cu, Zn, Cd, Ga, In, Si, Ge, Sn, etc., became pale-yellow. The loss of green color was accompanied by a disappearance of ESR, indicative of a reduction of  $\text{Fe}^{+3}$  to its divalent state. Green crystals from the same batch were doped with Al, Si, and a combination of Cd/Al, respectively. Absorption coefficients (Fig. 3) show a greater degree of transmission at  $25,000 \text{ cm}^{-1}$  than the green material and a complete absence of the peak at  $16,100 \text{ cm}^{-1}$ . The Si- and Al-doped crystals show a peak at  $25,640 \text{ cm}^{-1}$ . This peak is absent in the crystal doped with the combination of Cd/Al.

The optical and electrical data suggest that the level at  $25,640 \text{ cm}^{-1}$  may be associated with an acceptor level since it is present in the best p-type conductors and absent when Cd, the n-type dopant, is present.

It is suspected that Cd may substitute for Cu since the ionic radii of  $\text{Cu}^{+1}$  and  $\text{Cd}^{+2}$  are comparable. The use of Al in combination with Cd should help to keep Cd from the Al sites where it may act as an acceptor.

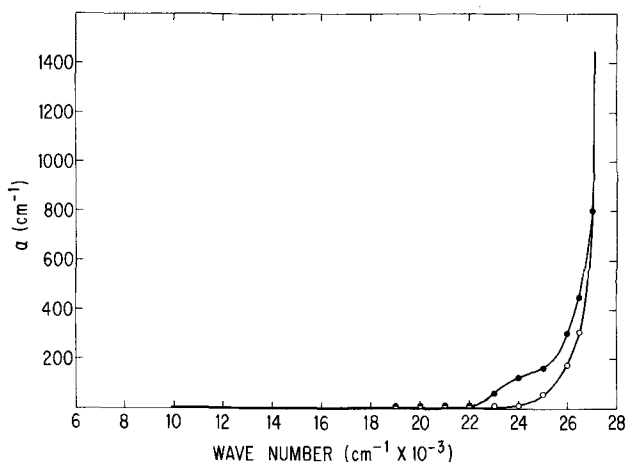


Fig. 3. Absorption coefficients vs. wave number for  $\text{CuAlS}_2$ .  $\circ$  = Cd/Al doped;  $\bullet$  = Si and Al doped.

Green or colorless crystals when heated in air between  $400^\circ$  and  $600^\circ\text{C}$  become nearly black and the ESR characteristic of  $\text{Fe}^{+3}$  is enhanced.

Resistivity measurements on crystals heated in air show lowered p-type resistivity in the range  $10^0$ - $10^1$  ohm-cm. This is in contrast to black, as-prepared crystals and may be the result of  $\text{Cu}^{+2}$  formation on the surface.

**Fluorescent properties and Mn doping.**—Colorless crystals of  $\text{CuAlS}_2$  exhibit weak orange fluorescence as shown in Fig. 4. This fluorescence may be stimulated by infrared radiation after prior exposure to ultraviolet radiation. The stimulated and excitation spectra are shown in Fig. 5. We believe that the infrared-stimulated luminescence is due to the energy exchange between the  $\text{Fe}^{+2}$  and  $\text{Fe}^{+3}$  states. This is supported by the observation that the green crystals have a higher stimulated luminescence output than the colorless crystals.

Crystals doped with Mn by addition of Mn into the starting ratio were nearly colorless and exhibited bright orange-red fluorescence (Fig. 6). The infrared-stimulated fluorescence was not seen in these compositions.

**Bonding and conduction.**— $\text{CuAlS}_2$  has a wide bandgap, can be doped p- and n-type, and allows incorporation of many dopants. It may be compared to ZnS which has a wide bandgap (3.7 eV) and is iso-electronic with a related "tetrahedral" structure. In contrast to ZnS which is a poor n-type conductor, it is a good p-type conductor. It has been speculated that the cause of the p-type conduction is the ease of formation of Cu vacancies due to the lesser contribution of Cu to the covalent bonding (4). We wish to offer an alterna-

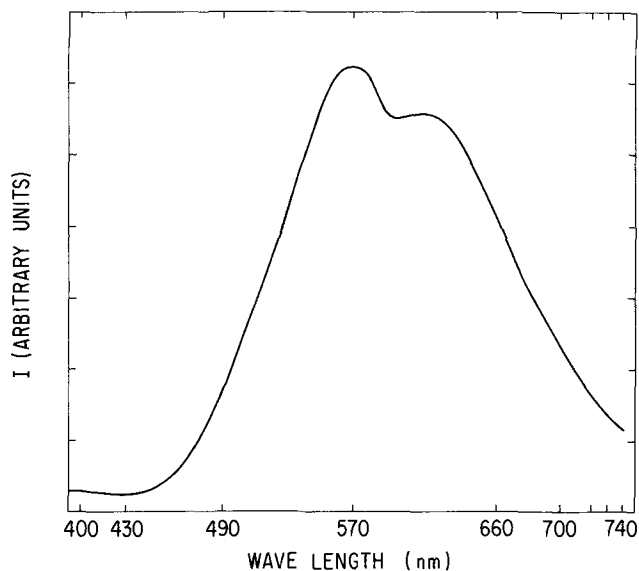


Fig. 4. Fluorescence emission of  $\text{CuAlS}_2$

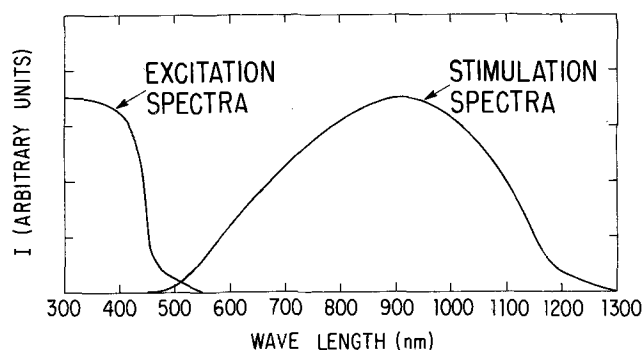


Fig. 5. Stimulation and excitation spectra of  $\text{CuAlS}_2$

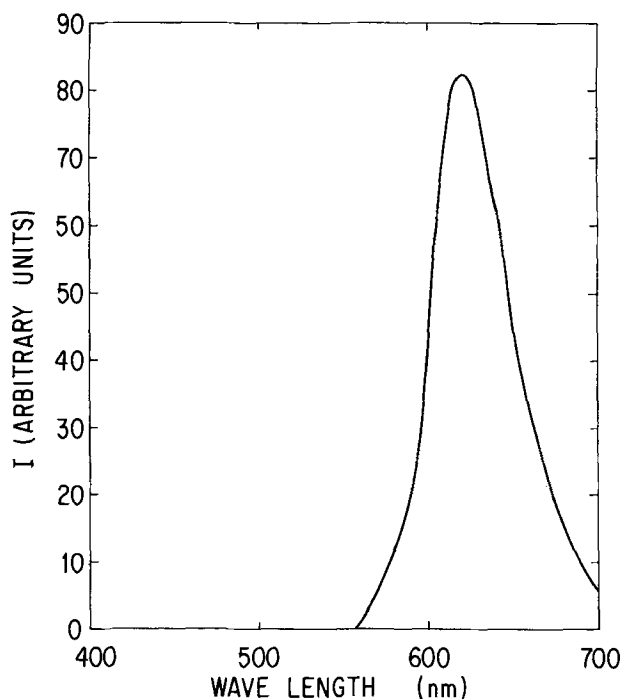


Fig. 6. Fluorescence emission of Mn-doped  $\text{CuAlS}_2$

tive mechanism. Since Cu d-orbitals have been shown to be close to the valence band in this compound (7) it would seem that if a trace of  $\text{Cu}^{+2}$  were present, the  $d^9$  level could act as an acceptor state. In contrast, the  $d^{10}$  level of Zn in ZnS is very stable.

When attempts are made to dope ZnS p-type, such as, by incorporation of Zn vacancies, the lattice compensates by loss of S. In contrast,  $\text{CuAlS}_2$  with cation vacancies can compensate by formation of  $\text{Cu}^{+2}$ .

It would seem from electronegativity differences, a rough measure of covalent character, that the Cu-S bonds having the smaller electronegativity difference

should be more covalent than the Al-S bonds. Thus the valence and conduction band edges would be primarily composed of Cu-S states since the splitting of the more ionic Al-S bonds would be greater. The major conduction would occur in the Cu-S bonds where a small amount of  $\text{Cu}^{+2}$  could act as an acceptor. For similar reasons,  $\text{Cu}_2\text{S}$  is a good p-type conductor while  $\text{Al}_2\text{S}_3$  is a wide bandgap, practically insulating, semiconductor.

It follows from this limited study that since  $\text{CuAlS}_2$  is greatly affected by impurities and stoichiometry, further study will require preparation of extremely pure material with more carefully controlled impurity concentrations.

#### Acknowledgments

Mr. D. W. Reutter is thanked for assistance in sample preparation. Mr. B. F. Gordon performed the electrical measurements. Mr. G. A. Wint assisted in obtaining the optical data. Dr. P. E. Bierstedt is thanked for helpful discussion.

Manuscript submitted Sept. 18, 1973; revised manuscript received Dec. 4, 1973.

Any discussion of this paper will appear in a Discussion Section to be published in the December 1974 JOURNAL. All discussions for the December 1974 Discussion Section should be submitted by Aug. 1, 1974.

#### REFERENCES

1. H. Hahn, G. Frank, W. Klingler, A. D. Meyer, and G. Storger, *Z. Anorg. Allgem. Chem.*, **271**, 153 (1953).
2. W. N. Honeyman, *J. Phys. Chem. Solids*, **30**, 1935 (1969).
3. G. C. Bhar and R. C. Smith, *Phys. Status Solidi*, **A13**, 157 (1972).
4. B. Tell, J. L. Shay, and H. M. Kasper, *J. Appl. Phys.*, **43**, 2469 (1972).
5. P. M. Jaffe and E. Banks, *This Journal*, **111**, 52 (1964).
6. G. Brandt, A. Rauber, and J. Schneider, *Solid State Commun.*, **12**, 481 (1973).
7. J. L. Shay, B. Tell, H. M. Kasper, and L. M. Schiavone, *Phys. Rev.*, **B5**, 5003 (1972).

## The Vapor Pressure of Iron Pentacarbonyl

A. G. Gilbert and K. G. P. Sulzmann

*Institute for Pure and Applied Physical Sciences and Department of Applied Mechanics and Engineering Sciences, University of California, San Diego, La Jolla, California 92037*

*The publication costs of this article have been assisted by the University of California.*

#### ABSTRACT

Vapor pressure measurements have been made on pure iron pentacarbonyl between  $+31^\circ$  and  $-19^\circ\text{C}$ . The experimental results may be expressed in the form

$$\log_{10} p \text{ (mm Hg)} = -(2096.7^\circ\text{K}/T) + 8.4959$$

which corresponds to a heat of vaporization for the liquid carbonyl of  $\Delta H = (9.588 \pm 0.12)$  kcal/mole. This result confirms and extends the earlier measurements made by Trautz and Badstübner (2) between  $0^\circ$  and  $140^\circ\text{C}$ . The need for careful purification of commercially available iron pentacarbonyl is emphasized, particularly for establishing the correct vapor pressure below  $45^\circ\text{C}$ .

Vapor pressure measurements for the liquid-gas equilibrium of  $\text{Fe}(\text{CO})_5$  were reported originally by Dewar and Jones (1) for temperatures down to  $-17^\circ\text{C}$ , and by Trautz and Badstübner (2) for temperatures down to  $0^\circ\text{C}$ . These data agree only at temperatures above about  $45^\circ\text{C}$ . At decreasingly lower temperatures,

Key words: iron pentacarbonyl, vapor pressure.

the measurements in Ref. (1) are increasingly larger than those reported in Ref. (2), and at  $-7^\circ\text{C}$  they deviate by more than a factor of three from the extrapolated data in Ref. (2). Unfortunately, these differing results have been quoted independently, without explanation for the discrepancy, by incorporating the data of Ref. (2) in data collections (3) and those of

Ref. (1) in specification sheets for the carbonyl (4). Since, in the course of absolute line-intensity measurements on Fe-atoms produced by shock-heating trace amounts of  $\text{Fe}(\text{CO})_5$  in argon, we required accurate vapor-pressure data below  $0^\circ\text{C}$ , we have made additional measurements on the purified carbonyl at temperatures between  $+31^\circ$  and  $-19^\circ\text{C}$ , which allowed us to resolve the discrepancy in favor of the data reported in Ref. (2).

### Experimental Procedure

The equilibrium vapor pressure of  $\text{Fe}(\text{CO})_5$  was measured by using a precision bourdon-tube gauge with a fused quartz spiral (Texas Instruments, Model 140A), which has a minimum resolution of  $3 \times 10^{-3}$  Torr and a measurement repeatability of  $6 \times 10^{-3}$  Torr [see Ref. (5)]. The gauge was connected to a removable glass sample-reservoir and to a high-vacuum pumping station by an all-glass system. Backstreaming of diffusion-pump oil was prevented by a liquid nitrogen trap, which was separated from the system during vapor-pressure measurements in order to avoid condensation of the iron pentacarbonyl vapor. The entire apparatus was evacuated routinely to pressures below about  $5 \times 10^{-6}$  Torr and exhibited a leak rate of less than  $1 \times 10^{-9}$  scc/sec helium.

The iron pentacarbonyl used for vapor pressure measurements was obtained by purifying technical grade samples of an assayed purity of better than 99.5% (Matheson, Coleman, and Bell); the major contaminants were iron nonacarbonyl and iron oxide (4). The test sample was transferred into the sample reservoir in a dry nitrogen environment in order to prevent oxidation by atmospheric oxygen and by water vapor (1). The measurement apparatus was evacuated, filled and flushed with dry nitrogen before connecting the sample-reservoir, which contained about  $40 \text{ cm}^3$  of carbonyl under nitrogen atmosphere. Decomposition of the carbonyl by photon absorption (1) was avoided by shielding the entire apparatus against room-light with cloth-bound tape.

After attaching the sample-reservoir to the system, the iron pentacarbonyl was solidified at liquid nitrogen temperature, and the whole system was evacuated to a pressure of less than  $5 \times 10^{-6}$  Torr. Then the measurement system was isolated from the pump station and its liquid nitrogen cold-trap; without further purification, the sample temperature was raised by suspending the reservoir in different temperature baths which consisted of alcohol-ice mixtures and/or water. Uniform composition of the bath was assured by continued stirring. The bath temperature was measured by an iron-constantan thermocouple gauge with an accuracy of  $0.1^\circ\text{C}$ . Vapor pressure measurements for the impure carbonyl were obtained at constant temperatures between about  $-10^\circ$  and  $+50^\circ\text{C}$  and are shown in Fig. 1, together with the data reported in Ref. (1). From these data, it is apparent that the impure liquid iron pentacarbonyl is contaminated by a substance with a gas-phase pressure which becomes increasingly important for temperatures below about  $45^\circ\text{C}$ . It is interesting to note that our data for the impure carbonyl agree with those reported in Ref. (1).

A possible contaminant with a gas-phase pressure larger than that of the pentacarbonyl below about  $+20^\circ\text{C}$  could be carbon monoxide, which is adsorbed in the liquid and which is formed (6) whenever the pentacarbonyl is decomposed under the influence of light or heat to form the solid nonacarbonyl,  $\text{Fe}_2(\text{CO})_9$ . Formation of solid iron oxide will also free CO. Both processes can occur during packing and storage of the pentacarbonyl. The presence of adsorbed carbon monoxide appears reasonable since (i) all of the other known and stable decomposition products are solids at the temperatures of interest and (ii) the impurity could be removed by distilling some of the carbonyl to waste (see below). In order to remove the impurity

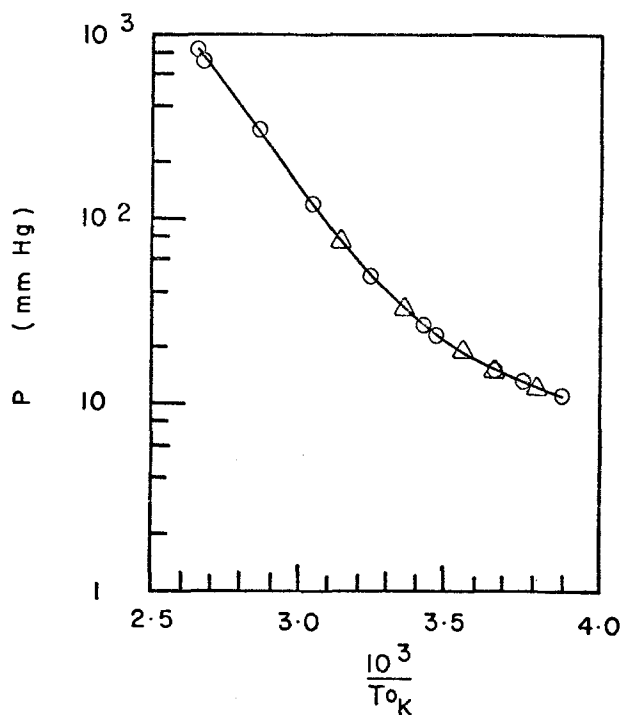


Fig. 1. Measured vapor pressure of  $\text{Fe}(\text{CO})_5$  before purification ( $\Delta$ ) and Jones (1906) data ( $\circ$ ).

before measuring the actual vapor pressure of iron pentacarbonyl for temperatures below about  $+31^\circ\text{C}$ , a part of the sample ( $\sim 3 \text{ cm}^3$ ) was distilled to waste before each measurement. The distillation was accomplished by keeping the sample at a temperature of about  $-12^\circ\text{C}$  and by pumping the noncondensables into a separate cold trap at liquid-nitrogen temperature. The trap was excluded from the system before each measurement.

### Results

The experimental data obtained for the purified iron pentacarbonyl are presented in Table I and are plotted in Fig. 2. The results may be represented by an Arrhenius plot of the form

$$4.573 \log_{10} p = -\Delta H/T + B \quad [1]$$

which corresponds to the integrated Clausius-Clapeyron equation for equilibrium between the liquid and the vapor phase. A least squares fit to the data shown in Table I results in the expression

$$\log_{10} p (\text{mm Hg}) = -(2096.7/T) + 8.4959 \quad [2]$$

where  $T$  is in  $^\circ\text{K}$ . Thus, we obtain for the heat of vaporization,  $\Delta H$ , of the liquid pentacarbonyl the value  $(9588 \pm 120)$  cal/mole. These results may be compared with those given in Ref. (2). It turns out that our expression [2] agrees within  $+1.3\%$  and  $-0.1\%$  with a least squares fit to the data of Trautz and Badstübner

Table I. Vapor pressures of pure iron pentacarbonyl

Temperature $^\circ\text{K}$	Pressure mm Hg	$(\log p)_{\text{obs}}$ $-(\log p)_c^*$
254.16	1.728	-0.009
	1.717	-0.011
266.16	4.359	+0.021
	4.370	+0.022
273.16	6.565	-0.003
	6.526	-0.005
283.16	12.063	-0.009
	11.995	-0.012
286.76	15.413	+0.004
	15.390	+0.003
304.16	40.489	+0.004
	39.025	-0.011

\* Calculated from Eq. [2].

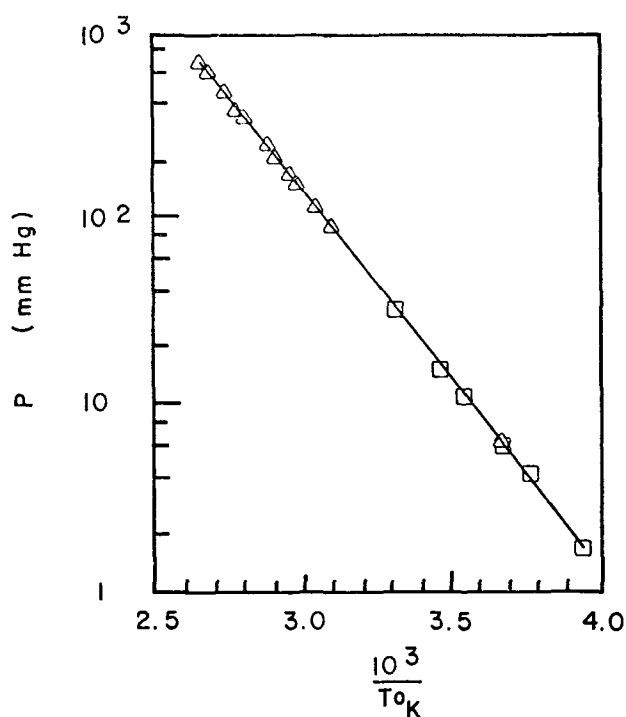


Fig. 2. Measured vapor pressure of  $\text{Fe}(\text{CO})_5$  after purification ( $\square$ ) and Trautz (1929) data ( $\triangle$ ).

(2) over the temperature range  $0^\circ\text{C} \leq t \leq 59.9^\circ\text{C}$  and which results in a heat of vaporization of 9487 cal/mole. Because of the excellent agreement between our

low-temperature data and those of Ref. (2) over a larger temperature range for pure iron pentacarbonyl, we have to reject the data shown in Ref. (1) and quoted in Ref. (4). By comparing the data obtained for the pure and the impure carbonyl, we estimate a heat for desorption of carbon monoxide from the liquid pentacarbonyl of less than 900 cal/mole, if adsorbed CO is the cause of the increased vapor pressure at low temperatures for the impure carbonyl.

#### Acknowledgment

This research was supported in part by the Advanced Research Projects Agency of the Department of Defense and monitored by the U.S. Army Research Office-Durham under Contract DAHC04-72-C-0037, and in part by the National Aeronautics and Space Administration under grant NGR-05-009-226.

Manuscript received April 17, 1973.

Any discussion of this paper will appear in a Discussion Section to be published in the December 1974 JOURNAL. All discussions for the December 1974 Discussion Section should be submitted by Aug. 1, 1974.

#### REFERENCES

1. J. Dewar and H. O. Jones, *Proc. Roy. Soc.*, **76**, 558 (1905).
2. M. Trautz and W. Badstübner, *Z. Elektrochem.*, **35**, 799 (1929).
3. K. K. Kelley, *U. S. Bur. Mines, Bull.*, 383 (1935); reprinted, *U. S. Bur. Mines, Bull.*, 601 (1962).
4. See, for example, Data for Iron Pentacarbonyl as published by Matheson, Coleman and Bell Manufacturing Chemists, Bull. M-5-62, Milwaukee, Wisconsin (1972).
5. A. A. Boni, *This Journal*, **113**, 1089 (1966).
6. W. E. Trout, Jr., *J. Chem. Educ.*, **14**, 575 (1937).

# Phase Equilibria and Vapor Pressures of Pure Phosphorus and of the Indium/Phosphorus System and Their Implications Regarding Crystal Growth of InP

K. J. Bachmann\* and E. Buehler

Bell Laboratories, Murray Hill, New Jersey 07974

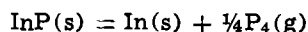
The publication costs of this article have been assisted by Bell Laboratories.

## ABSTRACT

The vapor pressure as a function of temperature of several commercial grades of red phosphorus and a specially prepared crystalline sample has been measured. For crystalline red P we obtain a heat of sublimation,  $\Delta H_s = 31.9 \pm 1$  kcal/mole. The commercial grades yield vapor pressures, which above 450°C are described by the equation  $\ln p = -(10.8 \pm 0.4) \times 10^3/T + (16.5 \pm 0.6)$ . The sublimation equilibrium of red P can be utilized for controlling phosphorus pressures,  $p > 10$  atm, with a reproducibility of 10% if commercial P of at least 5N purity is used. Measurements of the pVT relation of phosphorus vapor in the regimes  $800^\circ\text{K} \leq T \leq 1400^\circ\text{K}$  and  $3 \text{ atm} \leq p \leq 35 \text{ atm}$  reveal deviations up to 10% from ideal gas behavior. Excellent accuracy in describing the behavior of phosphorus vapor is obtained when van der Waals equation is used in conjunction with the critical data of Marckwald and Helmholtz and a critical coefficient of 0.375 for calculation of both the co-volume and the interaction parameter. Consideration of the pressure dependence of the equilibrium constant  $K_p$  for the reaction  $P_4 = 2P_2$  yielded approximate values for the fugacity constant at 1000° and 1100°C. The pTx relation at the liquidus in the vicinity of stoichiometric InP for indium-rich and phosphorus-rich compositions were established by simultaneous vapor pressure and DTA measurements. The melting point of stoichiometric InP is  $1335^\circ \pm 1^\circ\text{K}$  and the corresponding equilibrium phosphorus pressure is  $27.5 \pm 1$  atm. T-x liquidus data calculated with the assumption of ideal behavior of the liquid are in good agreement with our experimental data. Interpretation of the liquidus pressure data yields values of the standard enthalpies and entropies at 298°K

$$\Delta H^\circ_{298} = 22.1 \text{ kcal/mole}, \Delta S^\circ_{298} = 15.78 \text{ e.u.}$$

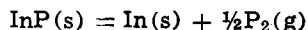
for the reaction



and

$$\Delta H^\circ_{298} = 36.0 \text{ kcal/mole}, \Delta S^\circ_{298} = 25.28 \text{ e.u.}$$

for the reaction



These results are in excellent accord with the standard enthalpies reported by Panish and Arthur and agree within 3% with literature data on the standard entropies of the reactants. The growth of n- and p-type InP crystals via the gradient freeze technique is discussed and the degree of control of the liquidus concentration is evaluated for various conditions of crystal growth.

Recently we have reported on the performance of several CdSnP<sub>2</sub>/InP heterodiodes and of heavily compensated InP homodiodes prepared by LPE from Sn-solution, and the results of this early work suggest that future developmental work might lead to new practical light sources and detectors in the near infrared (1). As a result of this work it was necessary to obtain accurate data on phase equilibria and vapor pressures of the indium/phosphorus system, which are essential for properly controlling the growth of large homogeneously doped p-type InP crystals required as substrate material.

For a summary of the earlier literature on the properties of InP we refer the reader to the review articles of Folberth (2) and Renner (3). Various techniques for growing InP single crystals have been evaluated by Weisberg *et al.* and by Richman (4), who considered the gradient-freeze method as the most suitable technique, since it provides optimum control of the thermal decomposition equilibrium of InP during the process of crystal growth. Though the gradient-freeze technique,

as designed by Weisberg *et al.*, offers an excellent choice for growing n-type InP crystals, modifications become necessary for preparing Zn- or Cd-doped p-type InP crystals, because of vapor transport of the dopants in a temperature gradient. A modified gradient-freeze technique was utilized by us for preparing Zn-doped InP crystals and will be briefly described below.

From the work of van den Boomgaard and Schol (5) on the In/P phase diagram, it is known that the liquidus composition is a strong function of vapor pressure, and preliminary experiments (6) on the stoichiometry of InP prepared at different phosphorus pressures suggest that, similar to the Ga/As (7) and Ga/P systems (8), a small homogeneity range exists in the solid state around the stoichiometric InP composition. Maintaining a constant phosphorus vapor pressure is, therefore, a necessary condition for preparing crystals of uniform stoichiometry.

Two methods have been employed in the past for controlling the phosphorus vapor pressure in a closed reaction volume: (i) Utilizing the sublimation equilibrium of red phosphorus, *i.e.*, controlling pressure via the temperature at which excess solid red phosphorus

\* Electrochemical Society Active Member.  
Key words: In/P phase diagram, phosphorus vapor, sublimation equilibrium of P, III-V compounds.

is held. (ii) Keeping all the phosphorus in the vapor phase and controlling pressure via the temperature and the density of the phosphorus vapor. The first method suffers from the fact that it is possible for part of the vapor to condense, forming metastable yellow phosphorus, which has a much higher vapor pressure at the same temperature. Also, the variation in the vapor pressure curves of commercially available phosphorus, which presumably deviate more or less from an equilibrium state, is unknown. In order to establish some confidence in the reproducibility and accuracy of control via method (i), we report in the next section our vapor pressure measurements of several commercial red phosphorus samples in the range 650°-850°K and, for comparison, our measurements of yellow P and a specially prepared sample of monoclinic red P.

Method (ii) is utilized where the entire closed off reaction volume has to be kept above the critical temperature of phosphorus. Then all of the phosphorus is inevitably in the vapor state and its pressure can only be controlled by the quantity of phosphorus initially loaded into the capsule and the temperature at which it is maintained.

Preuner and Brockmüller (9) determined the  $pVT$  relation for phosphorus vapor. They utilized a quartz spiral manometer. Stock, Gibson, and Stamm (10) used a quartz membrane manometer of similar sensitivity for their study. Both investigations were restricted to very low gas densities [Ref. (9):  $0.05 \leq d \leq 1.3$  mg/cm<sup>3</sup>; Ref. (10):  $0.16 \leq d \leq 1.0$  mg/cm<sup>3</sup>], where the assumption of ideal behavior appears to be reasonable. The results of the vapor pressure measurements of Ref. (9) and (10) differ by as much as 10-20%, especially for the higher vapor densities. The controversy as to whether the vapor pressure data must be interpreted in the light of the two-step reaction



as assumed in Ref. (9), or reaction [1] only (Ref. 10), was resolved by Stevenson and Yost (11), who calculated the equilibrium constant  $K_p'$  of reaction [2] from spectroscopic data and showed that reaction [2] does indeed not contribute in a measurable way to the vapor pressure at  $T < 1500^\circ\text{K}$ . Utilizing the data of Ref. (10), a fairly constant value of  $\Delta H^\circ_0$  for reaction [1] was obtained from  $K_p$  at various temperatures, while the same test of consistency fails for the data of Ref. (9). Thus, the results of Stock *et al.* have been henceforth accepted as a basis for numerous thermochemical calculations and have been incorporated without further experimental check into the most recent literature on the thermodynamic properties of phosphorus [see, for example, the well-known book of Stull and Sinke (12), the JANAF thermochemical tables (13), and the report of Farr (14)]. However, considering the many possible sources of error in the work of Ref. (10), the constancy of  $\Delta H^\circ_0$  is perhaps less significant than assumed by Stevenson and Yost (11). Though we do not doubt the validity of their thermodynamic calculations, an independent check of at least some of the data of Stock *et al.* seemed to be in order. In addition, knowledge of the deviation of phosphorus vapor from ideal behavior at elevated pressures would be desirable. This is of interest in crystal growth work and for thermochemical calculations concerning the III-V and II-IV-V<sub>2</sub> phosphides, which exhibit decomposition pressures typically several tens of atmospheres at their melting points. Thus, a new determination was made of the  $pVT$  relation for phosphorus vapor in the regimes  $800^\circ\text{K} \leq T \leq 1400^\circ\text{K}$  and  $3 \text{ atm} \leq p \leq 35 \text{ atm}$ . This work is presented below in a later section.

The liquidus line of the indium/phosphorus  $T$ - $x$  phase diagram has been determined in the indium-rich

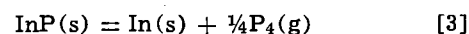
Table I. Literature values of the melting point of InP and of the corresponding equilibrium phosphorus pressure

$T_m(\text{InP})$ [°C]	$p_m(\text{InP})$ [atm]	Reference
1070	—	Köster and Ulrich (16)
1068 ± 2	—	Panish and Arthur (26)
1045	5	Schafer and Weiser (15), Weiser (25)
1062 ± 7	60	Van den Boomgaard and Schol (5)
1070	9-45	Nashelski, Ostrovskaya, Yakobson (19)
1070	15.5	Folberth (3, 20)
1058 ± 3	21 ± 5	Richman (21)
1055 ± 1.5	25 ± 2	Ugal, Bityutskaya, and Popova (40)
1062 ± 1	25.7 ± 1	This work

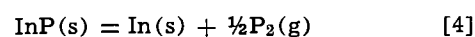
regime by several authors (15-19, 26), but considerable discrepancies exist between their results. Various values of the melting point of InP have been reported in the literature and they are listed in Table I.

Doubt regarding the equilibrium dissociation pressure of stoichiometric InP also exists. For example, by use of In-rich  $pTx$  data, van den Boomgaard and Schol (5) estimated that the equilibrium phosphorus pressure  $p_m(\text{InP})$  was 60 atm at the melting point of stoichiometric indium phosphide ( $T_m(\text{InP}) = 1062^\circ \pm 7^\circ\text{C}$ ). Richman (4) and Folberth (20) state that stoichiometric InP is obtained in crystal growth experiments when the phosphorus pressure is between 15-25 atm. However, no reliable conclusions regarding  $p_m(\text{InP})$  can be drawn from this observation, since the vapor pressure varies drastically with composition and the homogeneity range of InP is very small, so that crystals grown from slightly indium-rich melts may still appear to be single-phase material of stoichiometric composition. The formation of voids, observed by Richman (14), in InP ingots grown at  $p \geq 30$  atm, is a kinetic phenomenon and as such not suitable for pinpointing  $p_m(\text{InP})$ . From a measurement of the thermal decomposition pressure of InP in a confined volume, Richman (21) concluded that the equilibrium phosphorus pressure is 21 atm at the melting point of InP. However, his arguments are based on a single experiment and the extrapolation to 21 atm at 1058°C is strictly a matter of choice. [Compare Fig. 4, Ref. (21) and the discussion in the section on the  $pTx$  Diagram of the Indium/Phosphorus System below in this paper.]

Thermodynamic data for the thermal decomposition reactions



and



have been computed by various authors (22-26) in the In-rich region from data obtained at low total pressures. For a review of this work we refer to the paper by Panish and Arthur (26), who determined the heats of formation,  $\Delta H^\circ_{298} = 22.1 \text{ kcal mol}^{-1}$  and  $\Delta H^\circ_{298} = 36.0 \text{ kcal mol}^{-1}$ , for reactions [3] and [4], respectively. An attempt was made by Panish and Arthur at testing the compatibility of the total vapor pressure data of Ref. (5) and (21) by calculating the corresponding partial pressures of P<sub>4</sub> and P<sub>2</sub> and relating their temperature dependence to reactions [3] and [4]. Utilizing  $K_p$  values for reaction [1] taken from Ref. (13), the data of Ref. (21) were found to be compatible with the low pressure data, while the results of Ref. (5) were not.

Decomposition pressure curves in the vicinity of the melting point of InP and above will be presented later in this paper, and the relation of these measurements to the results of Ref. (5), (21), and (26) will be discussed. Also, new data on the  $pTx$  relation in the vicinity of  $T_m(\text{InP})$  are presented, which include liquidus compositions on the phosphorus-rich side of the phase diagram, resulting in reliable values of both  $T_m(\text{InP})$  and  $p_m(\text{InP})$ .

#### Vapor Pressure of Solid Red Phosphorus

The vapor pressure of red phosphorus was determined in the arrangement schematically shown in Fig.



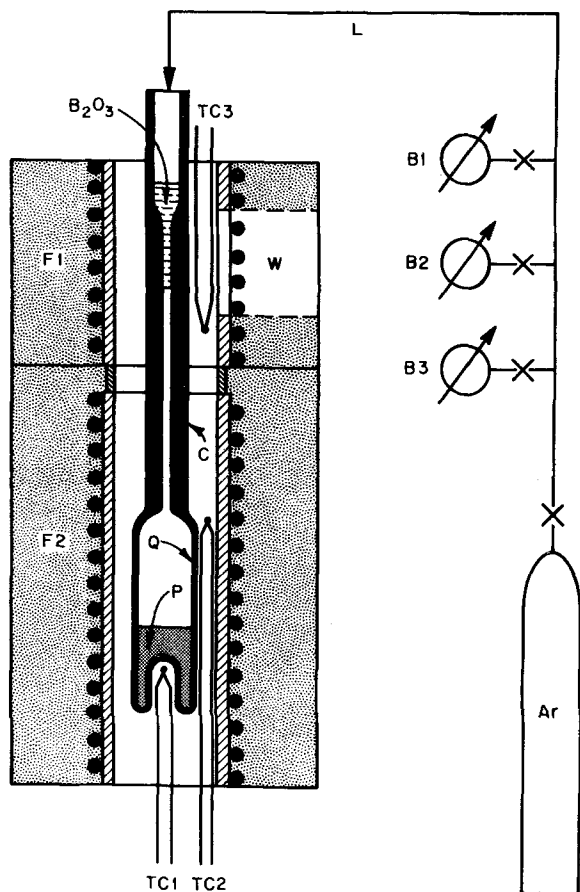


Fig. 1. Arrangement for measuring the vapor pressure of solid red phosphorus. F1, F2 furnaces; W, window in F1; Q, quartz capsule containing the phosphorus; C, capillary tube containing a column of liquid  $B_2O_3$ ; L, argon feed line attached to C by a double O-ring seal; B1 to B3, Bourdon gauges (−15 to 15 psi, 0 to 200 psi, 0 to 600 psi); TC, thermocouple.

1. The furnace F1 was used to establish a column of molten  $B_2O_3$  in capillary C which closes off the quartz capsule Q containing  $\sim 1$ g of solid red phosphorus. The latter is slowly heated by means of furnace F2. The vapor pressure inside the closed-off volume ( $v \approx 4$

$cm^3$ ) was balanced by a corresponding argon pressure, thus keeping the meniscus of liquid  $B_2O_3$  in C at a stationary position. The pressure was read on a set of Bourdon gauges, B1 to B3, connected to the argon feed line L and the corresponding temperatures were measured with thermocouple TC located in the recessed portion of capsule Q.

Compared to a quartz Bourdon gauge used as a null indicator in similar work (9, 10, 21, 27), our arrangement has the advantage that at better sensitivity to a pressure differential the  $B_2O_3$  layer can be maintained at a temperature  $> 900^\circ C$ . This is not possible for a quartz Bourdon gauge indicator because of the inability to control drift at  $t > 800^\circ C$  due to changes in the elasticity of quartz at such elevated temperatures (9, 10). The capability of keeping the indicator section at high temperature, and of minimizing its volume fraction compared to the total closed off volume, is of importance for two reasons:

1. It permits simulating in the vapor pressure measurements of red phosphorus the conditions encountered during growth of InP crystals via the gradient-freeze technique in a two-temperature zone arrangement as described in Ref. (3) and in a later section of this paper.

2. Isothermal conditions can be established in the measurements of phosphorus vapor densities at high temperatures and pressures (described below). Otherwise, interpretation of the experimental data becomes hopelessly confused because of complications due to nonideal behavior and dissociation.

The results of experiments to determine the vapor pressure of several grades of red phosphorus, each of at least 5N purity, as a function of temperature, and the relation of these data to the results of other (27), are shown in Fig. 2. At temperatures above  $700^\circ K$  the vapor pressures of the commercial grade starting materials are almost identical and the data deviate very little from a straight line, corresponding to an average heat of sublimation  $\overline{\Delta H}_s = 21.4 \pm 0.8$  kcal/mole; valid between  $700^\circ$  and  $950^\circ K$ . For clarity only 2 sets of our data for commercial red P are plotted in Fig. 2 and a complete list of the vapor pressure equations observed in the various individual experiments is provided in Table II.

The data represented by full circles in Fig. 2 were obtained when pure white P was the starting material

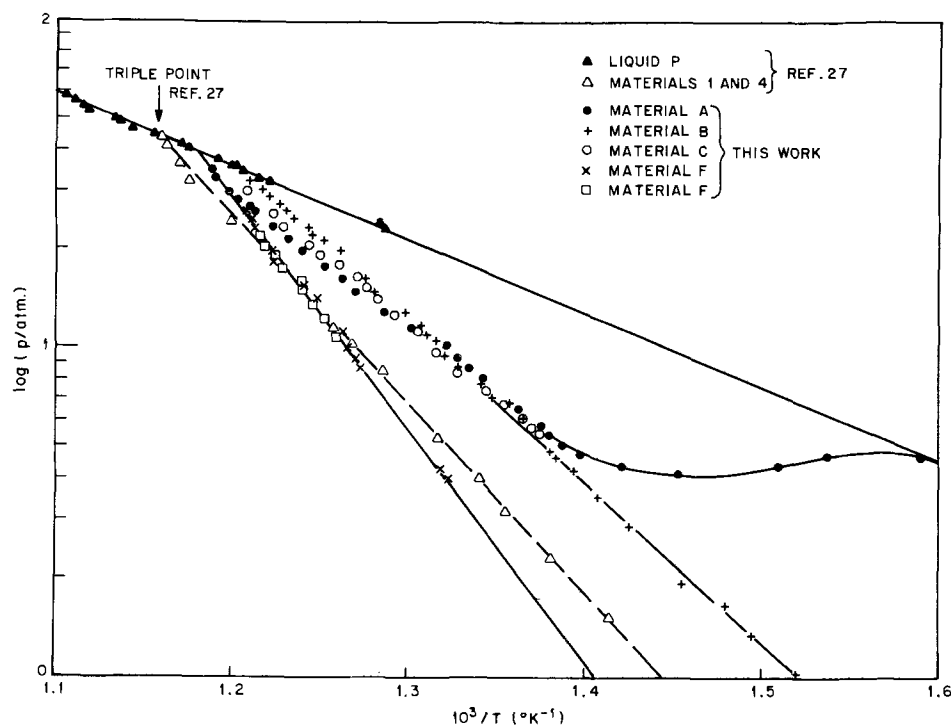


Fig. 2. Vapor pressure  $p$  of various commercial grades of red phosphorus and specially prepared monoclinic phosphorus as a function of temperature  $T$ ,  $\ln p = -\Delta H_s/RT + \text{const.}$

Table II. Sublimation pressure of red phosphorus  $\ln p = -\Delta H_s/RT + K, p$  [atm]

$\Delta H_s$ [kcal/ mole]	K	Range of T [°C]	Reference	Material
25.9	18.9	505-570		1
20.0	14.8	290-456	Smith and Bokhorst (27)	2
22.8	16.7	308.5-474.5		3
25.5	18.4	308.5-486.5		4
19.7	14.8	320-500		I
24.0	17.5	310-500	Farr (14)	II
28.0	20	380-560		IV
28.8	20.6	320-510		V
18.2	14.0	450-570		A
22.2	17.0	380-554		B
20.3	16.1	450-559	This work	C
20.7	17.1	430-554		D
22.2	15.8	450-500		E
31.9	22.7	450-575		F

(material A, Table II), which converts above 350°C into amorphous red P at a rate such that the pressure drops temporarily with increasing  $T$  and then merges with the vapor pressure curve of red P. The heating rate in this experiment varied from 3°/min below 500°C to 1.5°/min at higher  $T$ . The vapor pressure curve obtained in this manner corresponds to the vapor pressure curve of amorphous red P, material I, reported by Farr (14).

Four experiments with commercial red P were also performed: (i) material B = 5N, spongy red P supplied by a commercial vendor; (ii) material C = 6N, dense purple P, and (iii) material D labeled by the supplier as "black" 5N P, both supplied by a second vendor; (iv) material E, which is another batch of material C. The individual vapor pressure curves of these materials correspond to those of material II of Farr (14) and material 3 of Smits and Bokhorst (27). The state of the investigated commercial red P is in between the amorphous and the monoclinic crystalline state.

At  $T > 450^\circ\text{C}$  the reproducibility of vapor pressures of red P from different commercial sources is  $\sim 10\%$ . In our opinion, utilizing the sublimation equilibrium of red phosphorus for controlling vapor pressure is advantageous, compared to other techniques, when the temperature distribution over the closed-off reaction volume is nonuniform, the numerical value of  $v$  is difficult to assess and when pressures  $\geq 10$  atm are desired. For  $T < 450^\circ\text{C}$  considerable deviations from the average straight line in the  $\ln p$  vs.  $1/T$  plot occur and large differences exist between the vapor pressures of different batches of commercial red P. Because of this uncertainty in vapor pressure, utilization of the sublimation equilibrium appears to us not suitable for controlling phosphorus pressures below 5 atm, unless specially prepared crystalline material is used.

For evaluating the vapor pressure curve of monoclinic red P, 18g of material B were distilled into an evacuated quartz ampul. The resulting white P condensate was sealed-off and then heated for 31 days at 520°C. After this time interval the phosphorus had been converted into a crystalline red material comparable to materials 1 and 4 of Smits and Bokhorst<sup>1</sup> and V of Farr. The vapor pressure curve for this material (material F, Table II) is described by the relation

$$\ln p = - (16.1 \pm 0.5) \times 10^3/T + 22.7 \pm 0.7$$

corresponding to a heat of sublimation  $\Delta H_s = 31.9 \pm 1$  kcal/mole, which is somewhat larger than the values of Ref. (14) and (27). However, considering the extremely slow evaporation kinetics of monoclinic red P<sup>2</sup>

<sup>1</sup> Nesmejanov (28) considers the results of Ref. (27) as the best data for the vapor pressure of red P. Note that the data listed in Table 233, of Ref. (28) are not the measured experimental data of Ref. (27) but were calculated with an average value of  $\Delta H_s$  deduced from their experiments with materials 1 and 4.

<sup>2</sup> In our experiments with material F the temperature was changed in steps yielding initial heating rates of 20°C/hr. During the first hour after each temperature change, considerable deviations toward lower pressure readings occurred and these data were rejected. The data plotted in Fig. 2 correspond to heating rates  $\leq 5^\circ\text{C/hr}$  typically encountered 1½ hr after initiating each temperature change.

and taking into account that there is presently no reliable technique available for determining small residues of amorphous red P in the crystalline matrix, the observed difference in  $\Delta H_s$  is only significant insofar as it indicates that the materials presently looked at, including our material F, may not truly represent an equilibrium state.

### Density of Phosphorus Vapor in the Regions $800^\circ\text{K} \leq T \leq 1400^\circ\text{K}$ and $3 \text{ atm} \leq p \leq 35 \text{ atm}$

The pressure/temperature relationship for phosphorus vapor of various densities was measured in the apparatus shown in Fig. 3. Pressure measurements were made, as in the afore-described vapor pressure determination of red P, by balancing the phosphorus pressure inside quartz ampul Q by an equivalent argon pressure using a column of liquid  $\text{B}_2\text{O}_3$  inside C as indicator.

The density of the phosphorus vapor was varied between 5.6 and 39 mg/cm<sup>3</sup> by evaporating known weights of P inside Q. The volume of Q varied slightly from experiment-to-experiment ( $v_Q \approx 44 \text{ cm}^3$ ) while the volume of C could be kept constant (capillary length to the meniscus 22 cm,  $v_C = 0.57 \text{ cm}^3$ ). The error in determining the total closed-off volume is

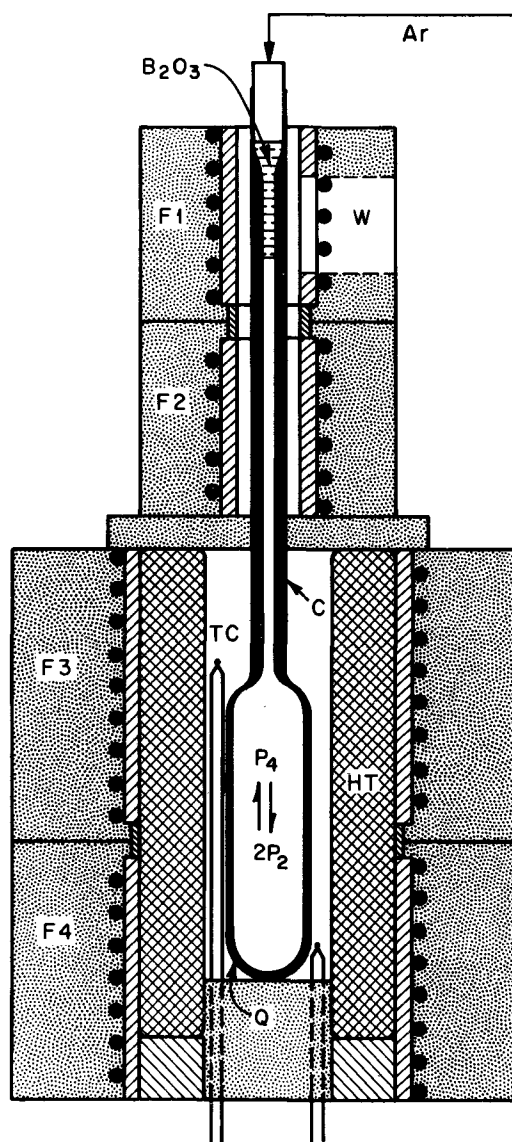


Fig. 3. Apparatus for measuring the  $pVT$  relation for phosphorus vapor in the range  $800^\circ\text{K} \leq T \leq 1400^\circ\text{K}$  and  $3 \text{ atm} \leq p \leq \text{atm}$ . Q, quartz ampul; C, capillary containing a column of liquid  $\text{B}_2\text{O}_3$ ; F1 to F4, furnaces; HT, 18 in. long sodium-filled heat tube (Dynatherm Corporation); W, window in F1.

estimated to be  $< 0.5\%$ . Measurements of  $v_0$  prior to and after performing the experiment were reproducible within  $0.2\%$ , so that volume changes due to plastic flow of the quartz tubes at the higher  $T$  can be neglected.

For establishing isothermal conditions a vertical arrangement of four independently heated furnaces F1 to F4 were used (Fig. 3). Q and part of C are located in an 18 in. long sodium-filled isothermal furnace liner HT (Dynatherm Corporation) heated by F3 and F4. The temperature distribution in this section is uniform within  $2^\circ\text{C}$  for all temperatures  $T > 750^\circ\text{K}$ . F2 is used to extend the isothermal zone as far as possible towards the  $\text{B}_2\text{O}_3$  section heated by F1. Since the  $\text{B}_2\text{O}_3$  was kept at  $T \cong 1150^\circ\text{K}$  to provide sufficiently low viscosity, a temperature gradient is necessarily introduced between F1 and F2 when Q is at  $T < 1150^\circ\text{K}$ . However, the volume fraction of phosphorus vapor near the  $\text{B}_2\text{O}_3$  layer, which is then at a different temperature, can always be kept below  $0.5\%$  of the total volume. This corresponds to a maximum error in average temperature of  $\lesssim 2^\circ$  when Q is at  $800^\circ\text{K}$ .

Temperature measurements were made using Pt/Pt-10% Rh thermocouples, calibrated in the same arrangement against the melting points of Ag, Au, and Cu, and are correct within  $\pm 1^\circ$ .

The accuracy of the Bourdon gauges used in this work is  $\pm 1\%$  which is the limiting factor in the accuracy of our experiments. Before closing-off by the liquid  $\text{B}_2\text{O}_3$ , some Ar was always trapped in  $v$  which expands linearly with  $T$  and a small correction in the phosphorus pressure readings for this Ar background was made. The error introduced by the background correction is neglectable for the high vapor density experiments ( $\leq 0.1\%$ ), but becomes substantial ( $1\%$ ) in the lowest vapor density experiments.

Figure 4 shows a family of experimentally determined curves

$$p = p(\rho, T) \quad [5]$$

for various phosphorus vapor densities  $\rho = n/v$  as parameter, where  $n$  is the number of moles  $\text{P}_4$  in the absence of dissociation. For comparison, also, dashed lines, given by the relation

$$p = (1 + \alpha)\rho RT \quad [6]$$

are plotted in Fig. 4 and represent the corresponding vapor pressures for ideal behavior of phosphorus vapor of different density. The degree of dissociation  $\alpha = \alpha(\rho, T)$  of  $\text{P}_4$  molecules, which are predominant at low temperatures, into  $\text{P}_2$  molecules, was deduced from values of the equilibrium constant for the dissociation of  $\text{P}_4$

$$K_p = \frac{p^2_{\text{P}_2}}{p_{\text{P}_4}} = \frac{4\alpha^2}{1 - \alpha} \cdot p_0 \quad [7]$$

The values of  $K_p$  are tabulated in Ref. (13).<sup>3</sup> The deviation of the experimental points from the dashed line corresponds to the error of conventional vapor pressure calculations based on the assumption of ideal behavior.

Comparison of the experimentally determined vapor pressure curves with the corresponding ideal gas curves yields the following general observations:

1. In the temperature and vapor density regimes considered here, sizable errors can be made in calculating phosphorus vapor pressures assuming ideal behavior in the vapor phase (see Table III).

2. All experimental curves rise at a faster rate with temperature than the corresponding ideal gas curves and they are shifted at the lower temperatures to lower pressures as expected from van der Waals equation

$$p = \frac{nR}{v - nb} \cdot T - \frac{n^2a}{v^2} \quad [8]$$

<sup>3</sup> Note that actually the reciprocals of  $K_p$ , as defined by Eq. [7], are listed in Ref. (13), because  $\text{P}_2$  is taken as standard state of phosphorus vapor.

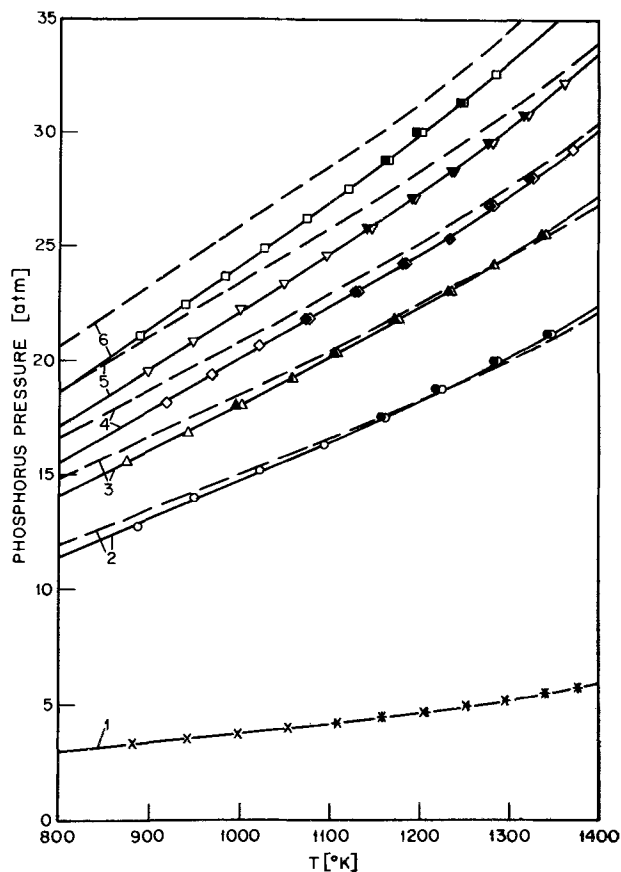


Fig. 4. Phosphorus vapor pressure as a function of temperature  $T$  for various vapor densities as parameter.

Curve No.	1	2	3	4	5	6
$\rho$ [mole/liter]	0.045	0.181	0.225	0.254	0.284	0.314

Open symbols and x represent data obtained on heating, full symbols and + represent data obtained on cooling. The dashed lines are the corresponding vapor pressure curves for ideal gas behavior, calculated with  $K_p$  taken from Ref. (13). For the lowest vapor density, curve 1, the calculated ideal gas values agree within the limits of accuracy with the experimental data.

$b$  is the co-volume of the phosphorus molecules and  $a$  is an interaction parameter.

Calculations of  $a$  and  $b$  from experimentally determined values of the critical temperature  $T_k$  and of the critical pressure  $p_k$ , assuming a critical coefficient  $s = 0.375$ ,<sup>4</sup> yields  $a = 32.4$  atm liter<sup>2</sup>/mole<sup>2</sup>,  $b = 0.121$  liters/mole for  $T_k = 968^\circ\text{K}$ ,  $p_k = 82.2$  atm (27) and  $a = 30.1$  atm liter<sup>2</sup>/mole<sup>2</sup>,  $b = 0.109$  liters/mole for  $T_k = 993.8^\circ\text{K}$ ,  $p_k = 93.3$  atm (29), respectively. At the higher vapor densities and at moderate

$$^4 s \equiv \frac{p_k V_k}{RT_k}, \text{ where } V_k \text{ is the critical volume.}$$

Table III. RMS deviation of vapor pressure curves calculated by ideal gas law, van der Waals equation, Eq. [9] and [10], and Redlich-Kwong equation, respectively, from experimentally determined vapor pressure curves in the regimes  $800^\circ\text{K} \leq T \leq 1400^\circ\text{K}$  and  $3 \text{ atm} \leq p \leq 35 \text{ atm}$

(Curve No. Fig. 4)	Ideal gas	van der Waals	Eq. [9] & [10]	Redlich's Eq.
1	1.1	1.0	1.0	1.3
2	2.6	2.8	1.6	8.5
3	2.7	3.5	1.2	9.4
4	3.8	2.8	0.8	12.4
5	5.3	2.0	1.9	15.3
6	7.1	3.4	1.0	18.8

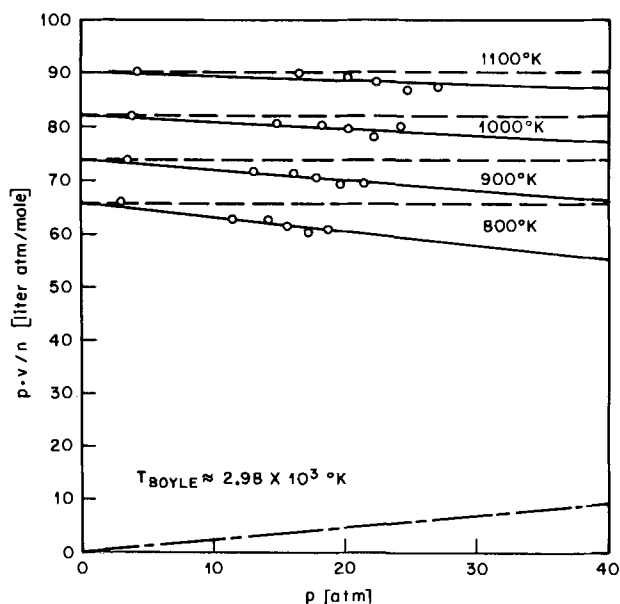


Fig. 5.  $p \cdot V/p$  diagram constructed from the data Fig. 4. --- Isotherms  $p \cdot V = RT$ , — smooth average  $p \cdot V = RT + Bp$ , - - - Boyle curve calculated with critical data of Ref. (29).

$T$ , considerable better fit of the experimental data is obtained with Eq. [8] than with Eq. [6] and the critical data of Ref. (29) yield better results than those of Ref. (27).

Figure 5 shows a  $p \cdot V/p$  diagram constructed from the data shown in Fig. 4. The dashed lines parallel to the abscissa represent ideal behavior, i.e.,  $p \cdot V = RT$ , for various isotherms taken in intervals of  $100^\circ\text{K}$  between  $800^\circ$  and  $1100^\circ\text{K}$ , where dissociation is negligible. The dash-dot line, lower part of Fig. 5, represents the Boyle curve calculated from the critical data given in Ref. (20), i.e., all experimental values of  $p \cdot V$  should be below the corresponding ideal gas values. The solid lines through the experimental points correspond to the equation

$$p \cdot V = RT + Bp \quad [9]$$

Taking the slopes  $B$  and using the parameters  $a$  and  $b$  calculated from the critical data of Ref. (29), one obtains the empirical relation

$$B = b - \frac{a}{RT^\chi} \quad [10]$$

where  $1.03 \leq \chi \leq 1.06$  for  $800^\circ \leq T \leq 1100^\circ\text{K}$ .

A comparison of the root-mean-square deviation of the experimentally determined vapor pressures from vapor pressure curves calculated by Eq. [6], [8], [9], and [10], respectively, is given in Table III. Our data were also compared with vapor pressure calculations according to the equations of Redlich and Kwong (30) and Berthelot. Taking the critical data of Ref. (29) for calculating the second virial coefficients  $B = b - a/RT^{3/2}$  with  $s = 0.3335$  (Redlich) and  $B = b - a/RT^2$  with  $s = 0.281$  (Berthelot), it was found that these equations are not suitable for describing the behavior of phosphorus vapor in the considered regimes of  $p$  and  $T$ , as expected from the experimental result  $\chi \approx 1$ . Considering the usually large deviations of experimentally determined critical coefficients from 0.375, the data of Ref. (29) provide a surprisingly accurate basis for the calculation of phosphorus vapor pressures according to Eq. [9] and [10].

In discussing the behavior of phosphorus vapor at  $T > 1200^\circ\text{K}$ , where sizable deviations from linearity become apparent in the  $p$  vs.  $T$  plot (Fig. 4), the following interrelated phenomena have to be taken into account:

1. The increase in pressure at  $T \geq 1200^\circ\text{K}$  due to dissociation of  $\text{P}_4$  molecules according to Eq. [1] becomes larger than the error limits in the vapor pressure determination.

2. The creation of  $\text{P}_2$  species in the vapor phase causes changes in the virial coefficients.

3.  $K_p$  becomes a function of pressure due to nonideal behavior of phosphorus vapor.

Figure 6 shows a plot of  $\log K_p$  vs.  $p$  for two isotherms at  $1273^\circ$  and  $1373^\circ\text{K}$ , respectively. For comparison, the data of  $K_p$  obtained at the highest pressure considered in Ref. (9) and (10), respectively, are also plotted.<sup>5</sup> The straight lines through the data points correspond to the equation

$$\log K_p = k_1 + k_2 p \quad [11]$$

where  $k_1$  and  $k_2$  are constants. Let

$$K_f = \frac{f_{\text{P}_2}^2}{f_{\text{P}_4}} = \frac{\gamma_{\text{P}_2}^2}{\gamma_{\text{P}_4}} \cdot K_p \quad [12]$$

where  $f_{\text{P}_4}$  and  $f_{\text{P}_2}$  are the fugacities of  $\text{P}_4$  and  $\text{P}_2$ , respectively, and  $\gamma_i = f_i/p_i$  are the corresponding fugacity coefficients. Since, by definition,  $\lim_{p \rightarrow 0} \gamma_i = 1$ , the fu-

gacity constant  $K_f$  becomes identical with  $K_p$  at the limit  $p \rightarrow 0$ . Neglecting the interaction between different molecular species,  $\gamma_i$  may be related to the second virial coefficients,  $B_i$ , of the corresponding component gases by

$$\gamma_i = \exp(B_i p / RT)$$

and

$$\ln K_p = \ln K_f + \frac{B_{\text{P}_4} - 2B_{\text{P}_2}}{RT} \cdot p \quad [14]$$

which corresponds to Eq. [11]. However, since several simplifying assumptions are made in deriving Eq. [14] and the accuracy of  $K_p$  is poor ( $\sim 20\%$ ),<sup>6</sup> it is presently not clear as to whether or not Eq. [14] provides a valid description of the pressure dependence of  $K_p$ .

The values of  $\log K_f$  obtained by extrapolating the straight lines (Fig. 6) to  $p = 0$  are tabulated in Table

<sup>5</sup> The values of  $K_p$  obtained for the very low  $p$  in Ref. (9) and (10) are generally somewhat smaller, but no conclusions regarding the pressure dependence of  $K_p$  may be drawn from this observation, since the interpretation of their experimental data depends entirely on the assumption of ideal behavior, which is most likely satisfied, so that the variation of  $K_p$  with  $p$  must be related to some systematic error in their work.

<sup>6</sup> In our work the limitation in the accuracy of  $K_p$  results from a large relative error in  $\alpha$  due to the suppression of dissociation at high  $p$ . Though at a given  $T$  larger values of  $\alpha$  are obtained at the lower densities considered in Ref. (9) and (10), the accuracy of their vapor density calculations is severely limited due to several sources of error related to the considerably nonuniform temperature distribution in their apparatus, which is not a factor in our work. A consideration of the propagation of error in calculating  $K_p$  from the experimental  $pVT$  relation reported in Ref. (9) and (10) reveals, therefore, a similar error level of  $K_p$  as encountered in our work at comparatively high pressure.

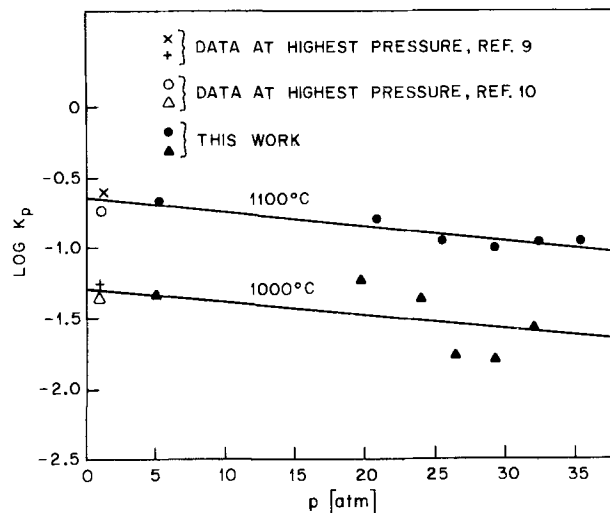


Fig. 6. Pressure dependence of the equilibrium constant  $K_p$  for the reaction  $\text{P}_4 = 2\text{P}_2$ .

Table IV. Values of the equilibrium constant of the reaction  
 $P_4 = 2P_2$  at 1000° and 1100°C

T [°K]	Log $K_f$	Log $\bar{K}_p$	Log $\bar{K}_p^*$	Log $\bar{K}_p^{**}$
1273	-1.30	-1.46	-1.41	-1.45
1373	-0.65	-0.82	-0.79	-0.78

$\bar{K}_p$  = average value of  $K_p$ .  
 \* Ref. (9).  
 \*\* Ref. (10).

IV and compared to the average values of  $K_p$  deduced from the data in Ref. (9) and (10). They are 10-20% smaller than the corresponding data of Ref. (9) and (10), while averaging our data, i.e., neglecting any pressure dependence of  $K_p$ , leads to values  $|\log \bar{K}_p|$  which are ~5% larger than the data of Ref. (9) and (10). For a definitive evaluation of the fugacity constant of phosphorus vapor, new accurate measurements at low total pressure are required. An experiment of this nature is presently being set up and the results of this work will be reported in a future publication.

### $p$ - $T$ - $x$ Diagram of the Indium/Phosphorus System in the Vicinity of the Melting Point of InP

The  $p$ - $T$ - $x$  relation of the indium/phosphorus system at liquidus compositions near stoichiometric InP was evaluated in a slightly modified version of the previously described apparatus shown in Fig. 3. For performing DTA measurements simultaneously with the vapor pressure determination, an indentation was provided in the bottom of Q, into which two thermocouples were inserted; one for monitoring the sample temperature  $T$  and the other for determining the temperature differential  $\Delta T$  between the sample and an outside thermocouple which measures the environmental temperature inside the heat tube HT. Both  $T$  and  $\Delta T$  were recorded on a Leeds and Northrup Ser. 600 two-pen recorder, which was calibrated by means of a Leeds and Northrup Cat. No. 8686 potentiometer. Most of the voltage, generated by the T-measuring thermocouple, was compensated by means of Leeds and Northrup Model C set point unit to permit sensitive recording in the vicinity of the melting point of InP.

Vapor pressure curves obtained during thermal decomposition of pure InP are shown in Fig. 7. Undoped n-type InP, prepared by gradient-freeze technique from 6N indium at 25 atm phosphorus pressure, was used. Preliminary analytical results indicated an excess of  $\sim 10^{19}$  indium atoms/cm<sup>3</sup>. In the course of the thermal decomposition reaction the surface of the InP is further depleted of phosphorus, so that an equilibrium between the solid and a liquid solution of InP in In is established, the composition of which varies with  $T$  according to the liquidus line of the In/P system. The ratio of the amount of liquid and solid depends on the amount of indium phosphide  $m_{\text{InP}}$  put into Q, on the free volume  $v$  filled with phosphorus vapor, and on temperature. For a given  $v/m_{\text{InP}}$  there exists a temperature  $T_m$ , at which all InP is dissolved, characterized by a discontinuity in the decomposition pressure vs.  $T$  curve. The composition of the liquid at  $T_m$  can be calculated from  $v$  and  $m_{\text{InP}}$  utilizing the vapor density data of the previous paragraph.

Since the same pressure values are obtained in liquid state on heating as well as on cooling we are sure that the melt is always in equilibrium with the vapor phase and a calculation of the composition  $x_{\text{In}}$  of the liquid at the melting point  $T_m$  from  $m_{\text{InP}}$ ,  $v$ , and  $p_m$  appears to be reasonable. Although the heating and cooling rates in the vicinity of the melting point were reduced from 1°/min to 0.2°/min, the realization of equilibrium in solid state is less clear. Considerable supercooling of the melt was observed and no data for solid material were taken on cooling in the preliminary experiments with pure InP. The consistency of our data and the absence of a steep pressure rise at the

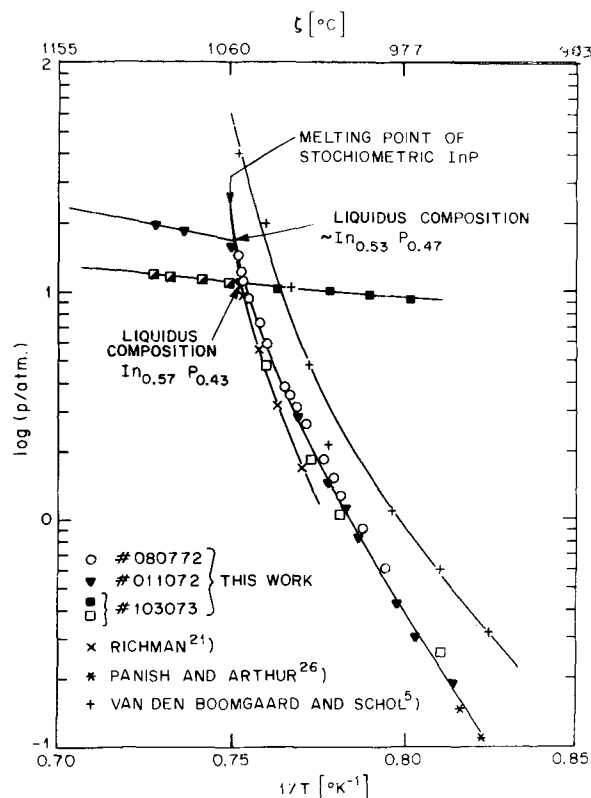


Fig. 7. Thermal decomposition pressure of indium phosphide. +, data of Ref. (5); x, data of Ref. (21); \*, data of Ref. (26). □, This work, large free volume of phosphorus vapor, increasing  $T$ ; ■, same experiment, decreasing  $T$ ; ▽, ○, this work, small free volume of phosphorus vapor, increasing  $T$ .

melting point indicate, however, that the solid material was near to equilibrium during the heating cycle.

For comparison we have plotted the vapor pressure curves of Ref. (5) and Ref. (21) in Fig. 7. The data of Ref. (5) are not compatible with our results. The vapor pressure curve of Richman deviates somewhat from our curve towards lower pressures, but the two curves join near the melting point and extrapolate to  $p \approx 24$  atm at 1062°C<sup>7</sup> which may be regarded as a lower limit of  $p_m$ (InP). Clearly, the values of  $p_m$ (InP) given in Ref. (15) and (20) are much too low. Our vapor pressure curve joins smoothly to the low pressure data of Ref. (22) to (26). The two highest total pressure points, taken from the work of Panish and Arthur (26), which overlap in pressure range with our measurements, are in excellent agreement with our data.

In order to extend our measurements to more phosphorus-rich compositions, a set of experiments were performed with additions of phosphorus to the InP. The vapor pressure curves obtained in these experiments are shown in Fig. 8. After evaporation of the added red P the vapor pressure increases linearly with temperature up to the melting point with a slope corresponding to the expansion of the generated phosphorus vapor. Note that no deviation from linearity due to dissociation is observed at  $T \geq 1200^\circ\text{K}$ , i.e., some of the phosphorus vapor diffuses at these higher  $T$  into the solid InP particles, which have much lower equilibrium vapor pressure up to  $T$  near to  $T_m$  (compare Fig. 7). At  $T_m = 1335^\circ\text{K}$  discontinuities occur in all vapor pressure curves, which are identified as being approximately  $T_m$ (InP).<sup>8</sup> In case the phosphorus pres-

<sup>7</sup> At 1058°C, taken as  $T_m$ (InP) in Ref. (21), both curves would extrapolate to a pressure  $< 20$  atm.

<sup>8</sup> The fact that, regardless of the amount of P added, the same melting point is observed on heating, indicates, that either no equilibrium between the solid and the vapor is reached via solid-state diffusion, i.e., that the major parts of the InP grains remain at nearly stoichiometric composition, or the liquidus is extremely flat.

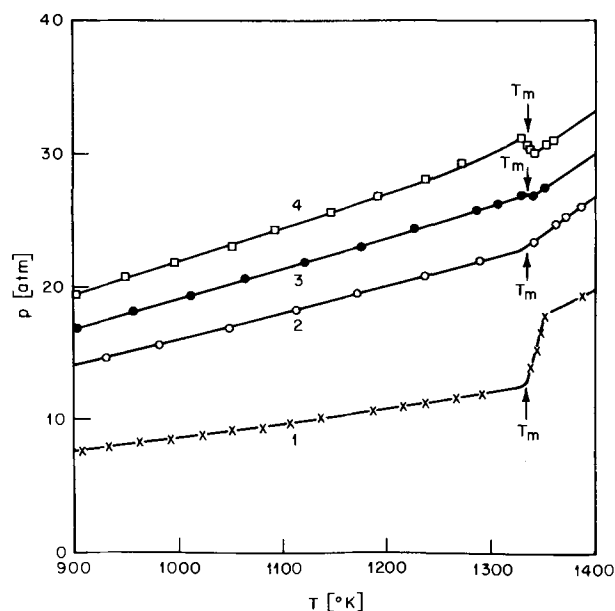


Fig. 8. Vapor pressure of mixtures of InP and red P. x, 10g InP + 0.5g P; o, 10g InP + 1.0g P; ●, 10g InP + 1.2g P; □, 10g InP + 1.5g P.

sure at  $T_m$  is much smaller than  $p_m(\text{InP})$ , phosphorus is released from the melt, resulting in a sudden rise in pressure, until its composition corresponds to equilibrium with the vapor phase. On the other hand, a pressure drop is observed due to condensation of P into the melt, when the phosphorus pressure at  $T_m$  exceeds  $p_m(\text{InP})$ . The former is clearly the case for curve 1 (Fig. 8) while the latter applies for curve 4. Thus, within the range of our experiments, the liquidus compositions are established on both the indium-rich and phosphorus-rich sides of InP.

In the two experiments with highest phosphorus additions, (curves 3 and 4) DTA measurements were performed simultaneously with the vapor pressure determinations. Figure 9 shows thermocouple voltage vs. time traces, monitored during melting in Expt. 3, which correspond to the sample temperature  $T_s$  and to the ambient temperature  $T_a$ , respectively. While the temperature  $T_a$  of the heat tube HT (Fig. 3) increases

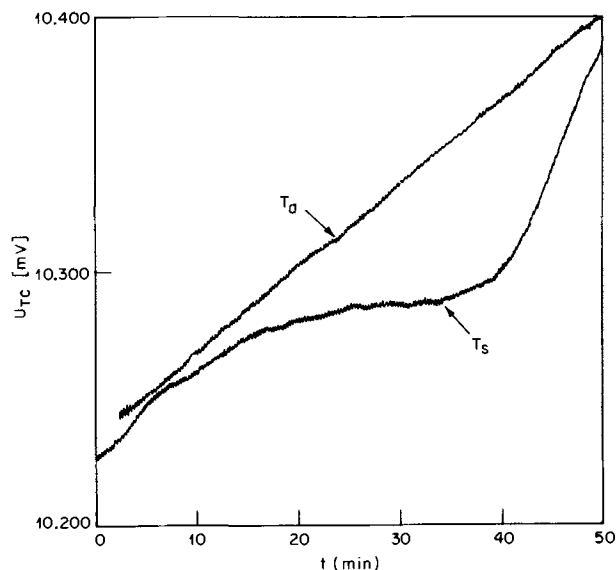


Fig. 9. Pt/Pt 10% Rh-thermocouple voltage vs. time curves monitored during melting in Expt. 3, performed in a modified version of the apparatus Fig. 3. Linear trace corresponds to ambient temperature  $T_a$  provided by HT, the other curve represents the changes in the InP-sample temperature  $T_s$ .

linearly with a rate of  $0.2^\circ/\text{min}$ , a distinct plateau is observed in the sample temperature at  $1334.8^\circ\text{K}$ . Since the pressure during the entire melting period remains constant at 26.9 atm we conclude that these values of  $T_m$  and  $p_m$  must be very close to the liquidus temperature and pressure of a stoichiometric InP melt. The liquidus composition calculated for Expt. 3 from  $m_{\text{InP}}$ ,  $m_p$ , and  $v$ , utilizing the vapor pressure information of a previous section of this paper, amounts to  $x_{\text{In}} = 0.51 \pm 0.01$ .

A plot  $\Delta T = T_a - T_s$  vs.  $T_s$  obtained during melting for Expt. 4 is shown in Fig. 10. Also, the variation of vapor pressure in this interval of  $T_s$  is shown as dashed curves. The thermocouple voltage vs. time recording, corresponding to  $T_s$ , is shown in the inset to provide some information on the kinetics of melting. After heating the melt at a rate of  $0.2^\circ/\text{min}$  up to  $\sim 1100^\circ\text{C}$ , it was cooled at the same rate through the melting temperature without any sign of solidification.

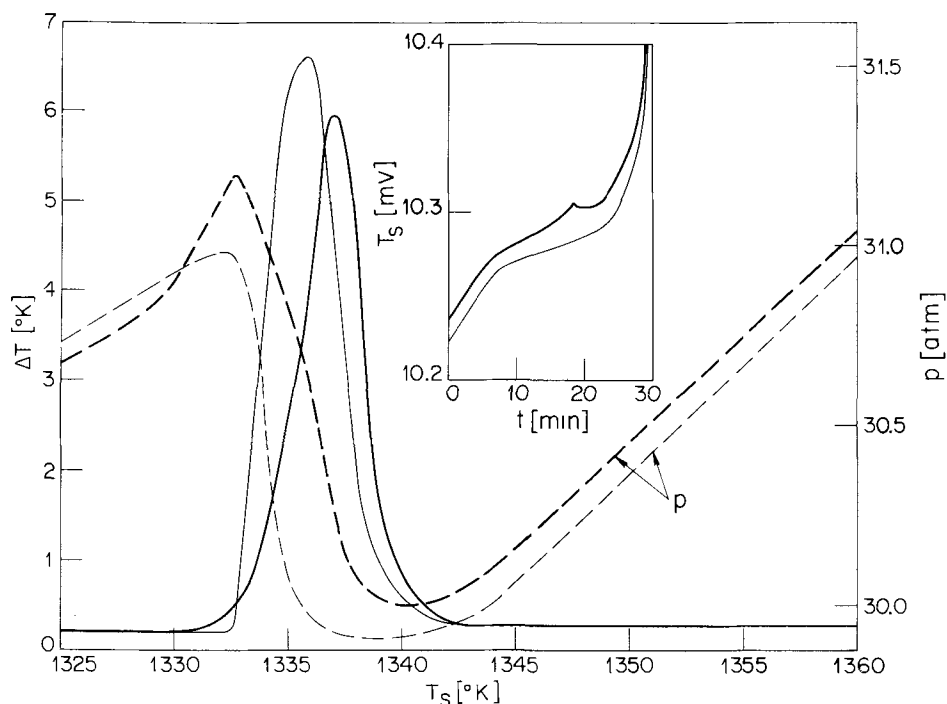


Fig. 10. Simultaneous plot  $\Delta T$  and  $p$  vs.  $T_s$  obtained during melting in Expt. 4, —  $\Delta T$ ; - - -  $p$ ; Inset: Thermocouple voltage traces corresponding to  $T_s$  vs. time  $t$ ; thick lines first heating cycle, thin lines third heating cycle.

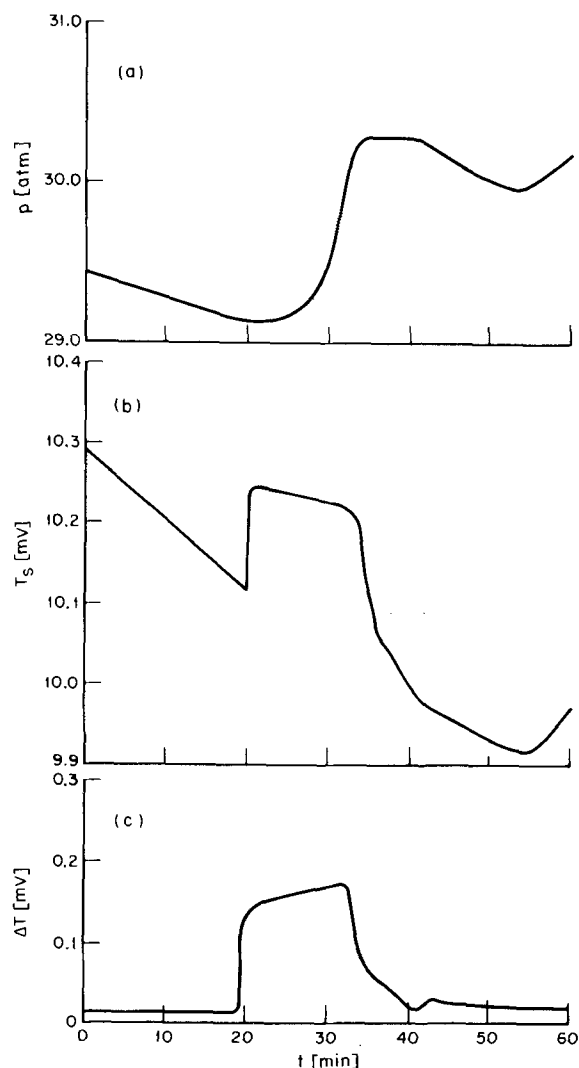


Fig. 11. Plots of (a)  $p$ , (b)  $T_s$ , and (c)  $\Delta T$  vs. time obtained during solidification from the supercooled melt in Expt. 4 during the first cooling cycle.

However, a sudden rise in temperature was observed upon supercooling by  $\sim 10^\circ$ , accompanied with an increase in phosphorus pressure.<sup>9</sup>

Figure 11 shows recordings of  $T_s$  and  $\Delta T$  vs. time obtained in Expt. 4 (Fig. 8) during solidification from the supercooled melt. Also, in Fig. 11, the behavior of vapor pressure is shown, which, after complete solidification of the melt, exhibited a value similar to that obtained prior to melting. A closed hysteresis loop in vapor pressure is thus obtained on cycling between  $1310^\circ$  and  $1350^\circ\text{K}$ . The supercooling temperature  $1325^\circ\text{K}$  and the value of the highest plateau temperature  $T_p = 1331^\circ$  are reproducible within  $1^\circ$  but a time lag exists between the temperature and pressure vs. time curves<sup>10</sup> so that the pressure at  $T_p$  differs from the equilibrium vapor pressure at the liquidus temperature  $T_m \approx T_p$ . The release of phosphorus during solidification is most revealing since it indicates that the solid formed by crystallization is more indium rich than the melt, which supports our conclusion that in Expt. 4 a liquid at the phosphorus-rich side of the In/P phase diagram has been attained. The liquidus composition calculated from  $m_{\text{InP}}$ ,  $m_p$ , and  $v$  for Expt. 4 amounts to  $x_{\text{In}} = 0.50 \pm 0.01$ , while from the pressure drop at the melting point one obtains a liquidus composition of  $x_{\text{In}} = 0.494$ .

<sup>9</sup> Richman (4) reported supercooling by as much as  $50^\circ\text{C}$  in crystal growth experiments at  $\sim 25$  atm. This was confirmed in Expt. No. 3 where a much larger supercooling of  $55^\circ\text{C}$  was observed.

<sup>10</sup> Note that the maximum  $\Delta T$  occurs at a later time than the first steep increase in  $T$ .

Both the  $\Delta T$  vs.  $T$  and  $T_s$  vs.  $t$  curves shown in Fig. 10 indicate a wider temperature range of melting in the first melting process (thick lines) than after several successive melting/freezing cycles (thin lines). An explanation for this observation can be given by assuming that a phosphorus-rich layer is formed during the first heating cycle via solid-state diffusion of P into the initially stoichiometric InP. This material starts melting at  $1332^\circ\text{K}$ , which is accompanied by a release of phosphorus, so that the vapor pressure curve bends upward. After melting of the outermost P-rich layer of the InP the still stoichiometric part melts and phosphorus is simultaneously condensed into the melt leading to a rapid decrease in pressure. In the subsequent solidification cycle a more homogeneous solid is formed, which is slightly less indium rich than the original material if a finite homogeneity range is assumed for the solid. The temperature range of melting thus decreases and the melting point of  $1334.7^\circ\text{K}$ , indicated by the  $\Delta T$  vs.  $T$  and  $T$  vs.  $t$  curves for the third melting cycle shown as thin lines in Fig. 10, is lower than the melting point of stoichiometric InP.

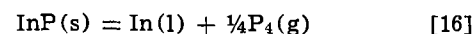
From the above-described vapor pressure behavior and temperature characteristics, observed in Expt. 3 and 4, we conclude, that the melting point of stoichiometric InP is  $T_m(\text{InP}) = 1335^\circ \pm 1^\circ\text{K}$  and that the corresponding liquidus equilibrium pressure is  $p_m(\text{InP}) = 27.5 \pm 1$  atm. Knowing the melting point of InP and taking the estimated entropy of fusion  $\Delta S^F$  from the work of Panish and Ilegems (31) the liquidus of the In/P system may be calculated by the equation

$$T(x_p) = T_m(\text{InP})/\Phi(x_p) \quad [15]$$

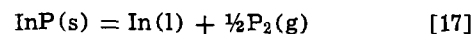
$$\Phi(x_p) = 1 + \frac{1}{2} \frac{R}{\Delta S^F} \ln 4x_p(1-x_p)$$

which was derived by Wagner (32) and has been successfully applied for calculating the liquidus line of the Ga/Sb system by Schottky and Bever (33). The application of Eq. [15] relies on the assumption of ideal behavior of the liquid, which seems to be satisfied for the In/P system as indicated by the results of Ref. (26) and (31). Table V shows a comparison of our experimental  $pTx$  results with calculated liquidus data, which supports the conclusions of Ref. (26) and (31).

In Table VI the liquidus total pressure data are separated into partial pressures of  $P_2$  and  $P_4$ . Assuming the activity coefficients of In in the liquid being  $\approx 1$ , these data may be combined with the results of Eq. [15] for calculating free energy changes for the reactions



and



according to

$$\Delta G^\circ(16) = -RT \ln (x_{\text{In}}[p_{P_4}/\text{atm}]^{1/4}) \quad [18]$$

and

$$\Delta G^\circ(17) = -RT \ln (x_{\text{In}}[p_{P_2}/\text{atm}]^{1/2}) \quad [19]$$

The free energy changes Eq. [18] and [19] can be related to the free energy changes of reactions [3] and [4] at  $298^\circ\text{K}$  by calculating the "Sigma" functions (34)

Table V. Calculated liquidus temperatures\* and experimental liquidus temperatures and pressures\*\* of the In/P system in the vicinity of stoichiometric InP

$x_p$	$T_m^{\text{calc}} [^\circ\text{K}]$	$T_m^{\text{exp}} [^\circ\text{K}]$	$p_m$ [atm]
0.43	1331.2	$1331.0 \pm 1$	11
0.46	1333.8	$1334.0 \pm 1$	18
0.47	1334.3	$1334.0 \pm 1$	23
0.49	1334.9	$1334.8 \pm 1$	26.6
0.51	1334.9	$1334.7 \pm 1$	29.9

\* Assuming ideal behavior of the melt, Eq. [15].

\*\* Experiments Fig. 7 and 8, except highest  $T_m$  of Fig. 7, since calculation of  $x_p$  from  $v$  and  $m_{\text{InP}}$  is uncertain for small  $v$ .

Table VI. Partial pressures of P<sub>2</sub> and P<sub>4</sub> at the liquidus of the In/P-system in the vicinity of stoichiometric InP and the heat of dissociation of InP according to Eq. [3] and [4] at 298°K

T <sub>m</sub> [°K]	p <sub>P<sub>4</sub></sub> [atm]	p <sub>P<sub>2</sub></sub> [atm]	Σ <sup>(3)</sup> (T) [cal/°K mole]	Σ <sup>(4)</sup> (T) [cal/°K mole]	ΔH <sub>298</sub> (3) [cal/mole]	ΔH <sub>298</sub> (4) [cal/mole]
1303.0	2.60	0.39	-1.207	-2.412	22134	36083
1327.0	10.01	0.99	-0.912	-1.772	22150	35897
1331.2	10.01	0.99	-0.951	-1.871	22272	36142
1333.8	16.72	1.28	-0.804	-1.724	22120	36018
1334.3	21.53	1.47	-0.716	-1.623	22011	35897
1334.9	25.03	1.57	-0.719	-1.633	22025	35926
1335.0	25.90	1.60	-0.741	-1.654	22055	35957
1334.9	28.21	1.69	-0.722	-1.623	22029	35913

$$\Delta S_{298}^{(3)} = 15.78 \text{ e.u.}, \overline{\Delta H}_{298}^{(3)} = (22,100 \pm 83) \text{ cal/mole.}$$

$$\Delta S_{298}^{(4)} = 25.28 \text{ e.u.}, \overline{\Delta H}_{298}^{(4)} = (35,979 \pm 87) \text{ cal/mole.}$$

$$\begin{aligned} \Sigma^{(3)}(T) &= -\frac{\Delta G^{\circ}(16)}{T} + \frac{1}{T} \int_{298}^{429} \Delta C_p(3) dT \\ &\quad - \int_{298}^{429} \Delta C_p(3) d \ln T + \frac{1}{T} \int_{429}^T \Delta C_p(16) dT \\ &\quad - \int_{429}^T \Delta C_p(16) d \ln T + \frac{\Delta H_{\text{In}}^{\text{F}}}{T} - \Delta S_{\text{In}}^{\text{F}} \\ &= -\frac{\Delta H_{298}^{\circ}(3)}{T} + \Delta S_{298}^{\circ}(3) \quad [20] \end{aligned}$$

and

$$\begin{aligned} \Sigma^{(4)}(T) &= -\frac{\Delta G^{\circ}(17)}{T} + \frac{1}{T} \int_{298}^{429} \Delta C_p(4) dT \\ &\quad - \int_{298}^{429} \Delta C_p(4) d \ln T + \frac{1}{T} \int_{429}^T \Delta C_p(17) dT \\ &\quad - \int_{429}^T \Delta C_p(17) d \ln T + \frac{\Delta H_{\text{In}}^{\text{F}}}{T} - \Delta S_{\text{In}}^{\text{F}} \\ &= -\frac{\Delta H_{298}^{\circ}(4)}{T} + \Delta S_{298}^{\circ}(4) \quad [21] \end{aligned}$$

where  $\Delta H_{\text{In}}^{\text{F}} = 780 \text{ cal/g-atom}$  and  $\Delta S_{\text{In}}^{\text{F}} = 1.817 \text{ e.u.}$  are the heat and entropy of fusion, respectively, for In at its melting point 429.32°K (12) and  $\Delta C_p(i)$  is the

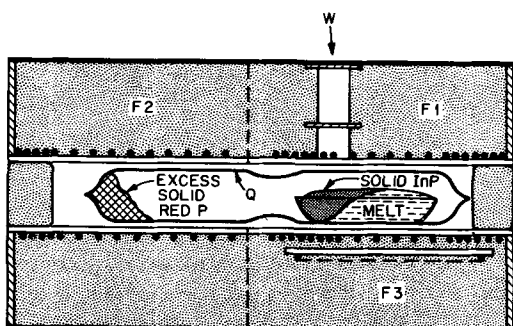
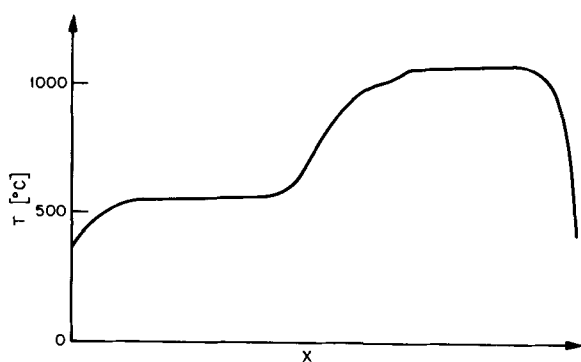


Fig. 12. Arrangement for preparing n-type InP crystals F1 to F3, furnaces; Q, evacuated quartz ampul containing a boat with the melt and excess red P; W, window in F1.

change of heat capacity for reaction  $i$  ( $i = 3, 4, 16, 17$ ), for example  $\Delta C_p(16) = C_p[\text{In}(l)] + \frac{1}{4}C_p[\text{P}_4(g)] - C_p[\text{InP}(s)]$ . The values of  $\Sigma^{(3)}(T)$  and  $\Sigma^{(4)}(T)$  listed in Table VI were calculated using heat capacity data given in Ref. (13) for P<sub>4</sub>(g) and P<sub>2</sub>(g), data given by Hultgren *et al.* (35) for In, and the data of Pankratz (36) for InP. Columns 7 and 8 of Table VI show  $\Delta H_{298}^{\circ}$  values for reactions [3] and [4], respectively, calculated from the  $\Sigma(T)$  values with  $\Delta S_{298}^{\circ}(3) = 15.78 \text{ e.u.}$  and  $\Delta S_{298}^{\circ}(4) = 25.28 \text{ e.u.}$ , respectively, which provide the best fit of the experimental data. Assuming that the standard entropies of In(s) and P<sub>2</sub>(g) and P<sub>4</sub>(g) are known correctly [Ref. (12) and (13)], we obtain from the above given  $\Delta S_{298}^{\circ}$  values for reactions [3] and [4] a standard entropy of InP  $S_{298}^{\circ}(\text{InP}) = 14.76 \text{ e.u.}$  and  $S_{298}^{\circ}(\text{InP}) = 14.60 \text{ e.u.}$ , respectively. The average of these two numbers  $\Delta S_{298}^{\circ}(\text{InP}) = 14.68 \text{ e.u.}$  is about 3% higher than the value of Piesbergen (37),  $S_{298}^{\circ}(\text{InP}) = 14.28 \text{ e.u.}$ , but within the error limits of our evaluation. The average values of  $\Delta H_{298}^{\circ}(3)$  and  $\Delta H_{298}^{\circ}(4)$  are virtually identical with the values of Panish and Arthur (26).<sup>11</sup>

### Growth of InP Crystal from the Melt

With the information acquired on vapor pressures and the  $pT_x$  relation in the indium/phosphorus system near to the melting point of stoichiometric indium phosphide, the degree of control of the liquidus composition under the conditions of crystal growth may be evaluated. Figure 12 shows an arrangement utilized by us for gradient-freeze crystal growth of n-type InP. Furnace F1 was used to bring a boron nitride boat containing indium to a temperature of 1065°C and the excess red phosphorus in the other section of the evacuated quartz tube Q was then heated slowly by means of F2 to maintain finally a phosphorus pressure of 27.5 atm. After synthesis of the InP, the temperature of F1 was lowered at a linear rate 15°C/day until the melt was solidified. A window W was provided in F1 to facilitate proper remelting for seeding purposes as described by Richman (4). In order to minimize heterogeneous nucleation at the bottom of the boat, a third furnace F3 was used to set up a vertical temperature gradient of  $\sim 4^\circ\text{C/cm}$ .

Considering the slope of the vapor pressure curve of solid red P at 27.5 atm and assuming that the temperature of the excess phosphorus is controlled to within  $\pm 1^\circ$ , the pressure during this crystal growth procedure is constant to  $\pm 0.65 \text{ atm}$  and reproducible

<sup>11</sup>Note added in proof: We would like to note that the above agreement of our data with those derived by others may be fortuitous and does not prove the In/P solutions are, in fact, ideal solutions. The experimental data of this paper meanwhile have been used by M. B. Panish (41) in a simple solution calculation assuming that the excess free energy of mixing  $G_{\text{InP}}^{\text{E}}$  of the binary solution is of the form  $G_{\text{InP}}^{\text{E}} = \alpha X(1-X)$  where X is the mole fraction of one component and  $\alpha = \alpha(T, p)$  is an interaction parameter. A disagreement results between values of  $\alpha$  calculated from vapor pressure data and from liquidus data, respectively, when existing thermodynamic data for the standard reference state pressure of liquid P are used. The work of Panish shows that this disagreement can be removed by appropriate modifications in the reference state pressure and that our data and the data of others are also consistent with the simple solution model. However, there exists no measured value for  $\Delta S_{\text{InP}}^{\text{F}}$  for InP.  $\alpha$  is close to zero over a wide range of T and both models yield a calculated liquidus line within the error limits of the experimental data. Therefore, at the present time, the distinction between the ideal solution model and the simple solution model for the In/P system is, in our opinion, a matter of choice.



to within  $\sim 3$  atm if commercial P is used. The change of the liquidus composition with pressure implied by our  $xp$ -data is  $\partial x/\partial p = 4.5 \times 10^{-3} \text{ atm}^{-1}$ . With the above-described technique for pressure control, the liquidus composition is constant within  $\pm 3 \times 10^{-3}$  and may vary from one experiment to another within  $1.35 \times 10^{-2}$ . Because of the variability in commercial sources of red P, Richman (4) held the entire quartz ampul above the critical temperature of P, thus controlling pressure via the temperature of F2. In this mode of operation, the reproducibility of phosphorus pressure depends on the reproducibility of the free volume of Q, which requires standardization of the glass blowing procedures, and on a careful determination of the amounts of P used up for synthesis and for establishing 27.5 atm pressure. The nonuniform temperature distribution of the assembly, which changes during crystal growth, makes reliable vapor pressure calculations difficult and we feel, therefore, that utilization of the sublimation equilibrium is the more reliable technique for vapor pressure control, especially if a material exhibiting a well-characterized vapor pressure, as for example our material F, is used.

However, utilization of the sublimation equilibrium of red P for pressure control and optical observation of the seeding process is inadequate for preparing Zn- or Cd-doped p-type InP crystals under conditions of relatively large temperature gradients. Continuous loss of  $\text{ZnP}_2$  from the melt via vapor transport to the colder parts of Q leads to a nonuniform dopant distribution in the InP ingot and increases the danger of explosions, since  $\text{ZnP}_2$  crystals sticking to the inner walls of Q create strains and often cause cracking of Q during the cooling down procedure.

Zn-doped p-type InP crystals were, therefore, grown under almost isothermal conditions for the entire quartz ampul containing prereacted InP plus the required amounts of P and  $\text{ZnP}_2$  to establish at the melting point a phosphorus pressure of 27.5 atm and the desired dopant concentration in the melt. In order to accomplish crystal growth with a reasonable rate, a compromise has to be made between the applied cooling rate of the furnace and the temperature gradient, which were in our experiments  $6^\circ\text{C}/\text{day}$  and  $0.2^\circ\text{C}/\text{cm}$ , respectively. Since boats of 12.5 cm length were used, the average temperature of the quartz ampul at the time the solidification process is complete is about  $2.5^\circ\text{C}$  lower than at the time of seeding. This corresponds to a change of the liquidus composition of  $2 \times 10^{-4}$ . Crystals were grown by this technique which exhibited resistivities typically 0.07 ohm-cm, corresponding to  $10^{18}$  holes/cm<sup>3</sup> and Hall mobilities of 92 cm<sup>2</sup>/Vsec. A similar degree of control of the liquidus composition may be attained during zone melting of InP in an arrangement as described by Folberth and Weiss (38). Further details of the preparation of InP crystals, characterization of their purity and defect structure, and a discussion of kinetic effects during InP crystal growth, will be presented elsewhere (39).

### Summary

The vapor pressure curves of solid red phosphorus have been measured for various commercially available products and a specially prepared monoclinic material. The heat of sublimation of monoclinic red P was calculated to be  $\Delta H_s = 31.9 \pm 1$  kcal/mole. The commercial products yield vapor pressures which, above  $450^\circ\text{C}$ , are described by the equation  $\ln p = -(10.8 \pm 0.4) \times 10^3/T + (16.5 \pm 0.6)$ . The sublimation equilibrium of red P can be utilized for controlling phosphorus pressures  $p > 10$  atm with a reproducibility of 10% if commercial P of at least 5N purity is used.

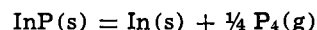
Measurements of the  $pVT$  relation of phosphorus vapor in the regimes  $800^\circ\text{K} \leq T \leq 1400^\circ\text{K}$  and  $3 \text{ atm} \leq p \leq 35 \text{ atm}$  reveal deviations up to 10% from ideal gas behavior. Excellent accuracy in describing the behavior of phosphorus vapor is attained by use of van

der Waals equation, the critical data of Marckwald and Helmholtz, and a critical coefficient of 0.375 for calculating both the co-volume and the interaction parameter. Consideration of the pressure dependence of  $K_p$  results in approximate values for the fugacity constant at  $1000^\circ$  and  $1100^\circ\text{C}$ .

The  $pT_x$  relation at the liquidus in the vicinity of stoichiometric InP for indium-rich and phosphorus-rich compositions was established by simultaneous vapor pressure and DTA measurements. The melting point of stoichiometric InP is  $1335^\circ \pm 1^\circ\text{K}$  and the corresponding equilibrium phosphorus pressure is  $27.5 \pm 1$  atm. The  $T-x$  liquidus calculated on the assumption of ideal behavior of the liquid is in good agreement with our experimental data. Interpretation of the liquidus pressure data yields values of the standard enthalpies and entropies at  $298^\circ\text{K}$

$$\Delta H^\circ_{298} = 22.1 \text{ kcal/mole}, \Delta S^\circ_{298} = 15.78 \text{ e.u.}$$

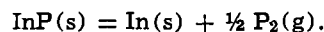
for the reaction



and

$$\Delta H^\circ_{298} = 36.0 \text{ kcal/mole}, \Delta S^\circ_{298} = 25.28 \text{ e.u.}$$

for the reaction



These results are in excellent accord with the standard enthalpies reported by Panish and Arthur and agree within 3% with literature data on the standard entropies of the reactants.

The growth of n- and p-type InP crystals via the gradient-freeze technique is discussed and the degree of control of the liquidus concentration is evaluated for various conditions of crystal growth.

### Acknowledgments

We would like to thank M. Ilegems for discussion and J. H. Wernick and M. B. Panish for reviewing the manuscript. Also, we thank J. L. Shay for evaluating the electrical properties of our InP crystals.

Manuscript received July 19, 1973.

Any discussion of this paper will appear in a Discussion Section to be published in the December 1974 JOURNAL. All discussions for the December 1974 Discussion Section should be submitted by Aug. 1, 1974.

### REFERENCES

1. J. Shay, K. J. Bachmann, E. Buehler, and J. H. Wernick, *Appl. Physics Letters*, **23**, 226 (1973); *ibid.*, **24**, 192 (1974).
2. O. G. Folberth, *Halbleiterprobleme*, **V**, 40 (1960).
3. Th. Renner, *Solid-State Electron.*, **1**, 39 (1960).
4. L. R. Weisberg, F. D. Rosi, and P. G. Herkart, in "Properties of Elemental and Compound Semiconductors," H. C. Gatos, Editor, Vol. 5, p. 25, Interscience Publishers, New York (1959); D. Richman, in "Compound Semiconductors," R. K. Willardson and H. L. Goering, Editors, Vol. 1, p. 214, Reinhold Publishing Corp., New York (1962).
5. J. Van den Boomgaard and K. Schol, *Philips Res. Rept.*, **12**, 127 (1957).
6. C. K. Kim, K. J. Bachmann, and E. Buehler, Unpublished work.
7. R. M. Logan and D. T. J. Hurle, *J. Phys. Chem. Solids*, **32**, 1739 (1971).
8. A. S. Jordan, A. R. Von Neida, R. Caruso, and C. K. Kim, *This Journal*, **121**, 153 (1974).
9. G. Preuner and I. Brockmüller, *Z. Physik. Chem.*, **81**, 129 (1913).
10. A. Stock, G. E. Gibson, and E. Stamm, *Ber.*, **45**, 3527 (1912).
11. D. P. Stevenson and D. M. Yost, *J. Chem. Phys.*, **9**, 403 (1941).
12. D. R. Stull and G. C. Sinke, "Thermodynamic Properties of the Elements," Washington, D. C. (1956).
13. JANAF Thermochemical Tables, D. R. Stull and H. Prophet, Editors, NSRDS-NBS37, Washington, D. C. (1971).

14. T. D. Farr, Tennessee Valley Authority, Chem. Eng. Rep. No. 8, Muscle Shoals, Alabama (1950).
15. M. Schafer and K. Weiser, *J. Phys. Chem.*, **61**, 1424 (1957).
16. W. Köster and W. Ulrich, *Z. Metallk.*, **49**, 365 (1958).
17. R. N. Hall, *This Journal*, **110**, 385 (1963).
18. N. A. Goryunova, Thesis, Leningrad (1958).
19. A. Ya. Nashelskii, V. Z. Ostrovskaya, and S. V. Yakobson, *Zh. Fiz. Khim.*, **38**, 891 (1964).
20. O. G. Folberth, *J. Phys. Chem. Solids*, **7**, 295 (1958).
21. D. Richman, *ibid.*, **24**, 1134 (1963).
22. J. Drowart and P. Goldfinger, *J. Chim. Phys.*, **55**, 721 (1958).
23. P. Goldfinger and M. Jeunehomme, in "Advances in Mass Spectrometry," J. D. Waldron, Editor, p. 534, Pergamon Press, New York (1959).
24. H. Gutbier, *Z. Naturforsch.* **16a**, 268 (1961).
25. K. Weiser, *J. Phys. Chem.*, **61**, 513 (1957).
26. M. B. Panish and J. R. Arthur, *J. Thermodyn.*, **2**, 299 (1970).
27. A. Smits and S. C. Bokhorst, *Z. Physik. Chem.*, **91**, 249 (1916).
28. A. N. Nesmeyanov, "Vapour Pressures of the Elements," Academic Press, New York (1963).
29. W. Marckwald and K. Helmholtz, *Z. Anorg. Allgem. Chem.*, **124**, 81 (1923).
30. O. Redlich and J. N. S. Kwong, *Chem. Rev.*, **44**, 233 (1949).
31. M. D. Panish and M. Illegems, in "Progress in Solid State Chemistry," H. Reiss, Editor, Vol. 7, p. 39, Pergamon Press, New York (1973).
32. C. Wagner, *Acta Met.*, **6**, 309 (1958).
33. W. F. Schottky and M. Bever, *ibid.*, **6**, 320 (1958).
34. C. D. Thurmond and C. J. Frosch, *This Journal*, **111**, 184 (1964).
35. R. Hultgren, R. L. Orr, P. D. Anderson, and K. K. Kelley, "Selected Values of Thermodynamic Properties of Metals and Alloys," John Wiley & Sons, Inc., New York, Suppl. pages (1971).
36. L. B. Pankratz, Report 6592, U.S. Dept. of the Interior, Bureau of Mines (1965).
37. U. Piesbergen, *Z. Naturforsch.* **18a**, 141 (1963).
38. O. G. Folberth and H. Weiss, *ibid.*, **10a**, 615 (1955).
39. K. J. Bachmann and E. Buehler, *J. Electron. Mat.*, **3**, 279 (1974); *J. Appl. Phys.*, To be published.
40. Ya. A. Ugai, L. A. Bityutskaya, and A. D. Popova, *Izv. Akad. Nauk SSSR, Neorganicheskie Materialy*, **3**, 1988 (1967).
41. M. B. Panish, *J. Crystal Growth*, To be published.

## Brief Communication



# Crystal Chemical Relations Between the Nonmetal Borides $B_{48}B_2C_2$ and $B_{48}B_2N_2$ and the Hypothetical "I-Tetragonal Boron"

Klaus Ploog

Mineralogisches Institut der Universität Bonn in KFA-Jülich, D-517 Jülich, Germany and  
Max-Planck-Institut für Festkörperforschung, D-7 Stuttgart, Germany

The publication costs of this article have been assisted by  
the Max-Planck-Institut für Festkörperforschung.

Since the crystal structure determination of a tetragonal modification of elementary boron by Hoard *et al.* in 1958 (1) several other authors (2-4) have recently reported the preparation of this tetragonal boron "polymorph" by chemical vapor deposition on carbon substrates. In our own systematic investigations of the vapor deposition of elementary boron (5) however, we have shown that it is impossible to prepare this so-called "I-tetragonal boron"  $B_{48}B_2$  in a pure form and that it can therefore no longer be considered a true polymorph of elementary boron. We suggest that the formation of this boron "modification" in the reported experiments (2-4) was induced in such a way that the deposited boron picked up some carbon from the substrate and reacted on the surface. This resulted in the nucleation and growth of crystals, which actually were tetragonal boron carbide and not pure tetragonal boron. The purpose of this note is to give a critical review of the crystal structure of the hypothetical "I-tetragonal boron" and its relations to the two nonmetal borides  $B_{48}B_2C_2$  and  $B_{48}B_2N_2$ .

In order to produce the basic icosahedral framework of the lattice of Hoard *et al.* in a reproducible manner we have developed a new preparative method (6). Pyrolysis of  $BBr_3-CH_4-H_2$  mixtures on Ta substrates at 1200°C yields the boron-rich tetragonal boron carbide  $B_{48}B_2C_2$  (lattice constants:  $a = 8.722$

and  $c = 5.080\text{Å}$ ; density: 2.43 g/ml), while pyrolysis of  $BBr_3-N_2-H_2$  mixtures on BN substrates at 1400°C yields a boron-rich boron nitride  $B_{48}B_2N_2$  (lattice constants:  $a = 8.646$  and  $c = 5.127\text{Å}$ ; density: 2.46 g/ml).

By single-crystal structure analysis of both the B-C and B-N phases (space group:  $P4_2/nmm$ ) including very precise intensity measurements (6) we determined the absolute electron densities in the holes of the icosahedral framework by Fourier sections and by least squares techniques. This gave an R factor of 5.8% for  $B_{48}B_2C_2$  and 5.5% for  $B_{48}B_2N_2$ . In this way it was possible to localize the carbon and nitrogen atoms and the single boron atoms and to attach them to definite interstitial icosahedral holes. As a result we found that in  $B_{48}B_2C_2$  and  $B_{48}B_2N_2$  the unstable  $B_{48}B_2$  lattice is stabilized by carbon or nitrogen atoms forming bridges between the  $B_{12}$  icosahedra.

The unit cells of the tetragonal nonmetal borides (Fig. 1) contain a total of fifty boron and two carbon or nitrogen atoms. Forty-eight boron atoms form four  $B_{12}$  icosahedra, centered in the position  $4e \left( \frac{111}{444}, \frac{133}{444}, \frac{313}{444} \right)$ , which is in agreement with the  $B_{48}B_2$  structure of Hoard *et al.* The remaining boron and the respective carbon and nitrogen atoms occupy the positions 2a, 2b, 8i, and 8h between the icosahedra

Key words: boron modifications, structure of elemental boron, chemical vapor deposition, nonmetal borides.

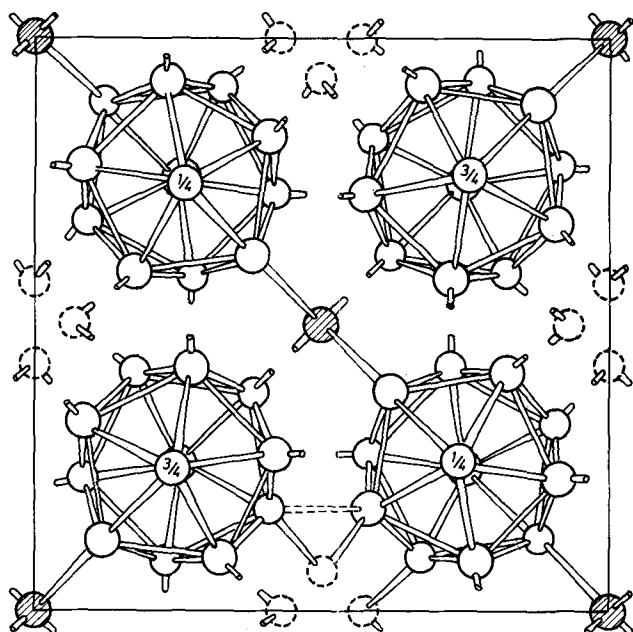


Fig. 1. Unit cell of tetragonal  $B_{48}B_2C_2$  and  $B_{48}B_2N_2$  projected along the  $c$ -axis direction and including the bonding possibilities of the single boron atoms (dashed circles) distributed statistically around  $4b$ . For clarity the borons in  $2a$  and  $8h$  are omitted here. The carbon and nitrogen atoms respectively are represented by hatched circles.

(see Table 1). Within the icosahedra we found boron-boron distances ranging from 1.774 to 1.859 Å in  $B_{48}B_2C_2$  and from 1.777 to 1.885 Å in  $B_{48}B_2N_2$ , with an average B-B distance of 1.809 and 1.808 Å for  $B_{48}B_2C_2$  and  $B_{48}B_2N_2$ , respectively, which are very similar to the values found in elementary boron. Of the twelve icosahedral boron atoms, six have bonds to neighboring icosahedra, among them four with B-B distances of 1.670 Å ( $B_{48}B_2C_2$ ) and 1.660 Å ( $B_{48}B_2N_2$ ), respectively, and two with B-B distances of 1.686 Å ( $B_{48}B_2C_2$ ) and 1.710 Å ( $B_{48}B_2N_2$ ), respectively. Of the remaining six icosahedral boron atoms two are bonded to carbon and nitrogen atoms, respectively, in the position  $2b$   $\left(00 \frac{1}{2}, \frac{11}{22}, 0\right)$  with a B-C distance of 1.629 Å and a B-N distance of 1.589 Å, and four are statistically bonded to two single boron atoms in the statistically occupied positions  $8i$  and  $8h$ . The B-B distances to the atoms in  $8i$  and  $8h$  are respectively 1.622 and 1.728 Å for  $B_{48}B_2C_2$  and 1.611 and 1.703 Å for  $B_{48}B_2N_2$ .

The boron atoms in the position  $2a$  merely fill interstitial holes and have no bonding functions, whereas the positions  $2b$  deserve special attention. They act as bridges with covalent bondings between four icosahedra. In contrast to the proposal of Hoard *et al.* (1) the positions  $2b$  are, however, occupied by carbon or nitrogen and not by boron atoms. The four icosahedra

surrounding the C and N atoms form flattened tetrahedra due to a tetragonal  $c/a$  ratio of 0.58 and 0.59, respectively.

A further difference relative to the former structure proposal was found in the two single boron atoms per unit cell, which are statistically distributed over 16 positions, namely  $8i$  and  $8h$  around the positions  $4c$   $\left(0 \frac{1}{2}, 0, \frac{1}{2}, 0, 0, \frac{11}{22}, \frac{1}{2}, 0, \frac{1}{2}\right)$  (see Table I). The holes around  $4c$ , which are surrounded by four icosahedra, measure approximately 3.5 Å in diameter. Therefore they are too large to accept just one bonding boron atom in a fixed central position as a link between all four icosahedra. The boron atoms are thus found to be displaced toward every two of the four surrounding icosahedra shown in Fig. 1, which finally yields the statistical distribution. The displacement from the center of the tetrahedral holes is about 0.6 Å. It arises from the geometric bonding conditions in the rigid icosahedral framework, in which the  $B_{12}$  icosahedra are to be linked by strongly directed covalent bondings.

The instability of the basic  $B_{48}$  framework itself and the necessity of incorporating additional foreign atoms into the tetragonal lattice to stabilize it, results from geometric as well as from electronic requirements. The geometric problems arise from the characteristic packing difficulties in three-dimensional network of icosahedral structures. In the tetragonal  $B_{48}$  framework, only six of the twelve external intericosahedral bonds, formed by each icosahedron, are radially directed along the quasi-fivefold axis. These six, whilst directed outward, would deviate by more than  $25^\circ$  from the favorable pentagonal axis producing a strain sufficiently large to preclude them from the preferred geometry. To alleviate these packing difficulties, at least two interposed single atoms per cell are required, each of which should possess four valence electrons and should be able to form four bonds directed along the quasi-fivefold axes of four icosahedra located at the vertices of a flattened tetrahedron around the position  $2b$ . Suitable foreign atoms to stabilize the tetragonal framework are carbon and nitrogen, as the covalent radii (B, 0.82 and C, 0.77 Å) and electronegativities (B, 2.07 and C, 2.50 Pauling Units) of B and C are similar. Since the electron deficiency of  $B_{12}$  icosahedra (cf. below) is counterbalanced by the great electronegativity of N (3.07 Pauling Units), the smaller covalent radius of N (0.74 Å) may be compensated in part by contracting the cell in the  $a$ -axis direction and by withdrawing the electron density from the boron framework. A further improvement of the packing difficulties in the icosahedral framework is achieved by further interposed single boron atoms located around the position  $4c$ , which, however, can link only two icosahedra, as the spatial separation of the four icosahedra around  $4c$  allows only two at a time to come together close enough for bonding.

To describe the electronic structure of the tetragonal framework we use the concept of closed-shell configuration of  $B_{12}$  icosahedra, postulated by Longuet-Higgins and Roberts (7). According to this approximate theory, the hypothetical  $B_{48}B_2$  cannot be of a closed-shell type, since there would be a deficit of several electrons per unit cell relative to that of a closed shell. Each boron atom possesses one  $s$ - and three  $p$ -orbitals. The unhybridized set of 48 atomic orbitals of one  $B_{12}$  icosahedron can be combined into twelve equivalent outward-pointing  $s-p$  hybrid orbitals and 13 bonding and 17 antibonding molecular orbitals, which lie mainly within the icosahedron and are separated by a substantial energy gap. As the outward-pointing hybrids interact only slightly within the icosahedron, these twelve orbitals provide a single radial  $s-p$  hybrid orbital at each vertex of the icosahedron, which can form a strong  $\sigma$ -bond between the

Table I. Occupation of the intericosahedral sites in  $B_{48}B_2C_2$  and  $B_{48}B_2N_2$

Atom		Equivalent position and number of electrons per site		Coordinates		
				$\frac{x}{a}$	$\frac{y}{b}$	$\frac{z}{c}$
B (5)	(in $B_{48}B_2C_2$ )	2a	0.64	0	0	0
	(in $B_{48}B_2N_2$ )		0.07	0	0	0
B (6)	(in $B_{48}B_2C_2$ )	8i	0.49	0.4330	0	0
	(in $B_{48}B_2N_2$ )		1.15	0.4306	0	0
B (7)	(in $B_{48}B_2C_2$ )	8h	0.56	0	0.5	0.8557
	(in $B_{48}B_2N_2$ )		0.13	0	0.5	0.8655
C	(in $B_{48}B_2C_2$ )	2b	5.45	0	0	0.5
N	(in $B_{48}B_2N_2$ )		6.55	0	0	0.5

icosahedron and any external group. In order to achieve internally a closed-shell configuration while forming simultaneously twelve externally directed  $\sigma$ -bonds, a regular  $B_{12}$  icosahedron requires 38 valence electrons, two more than can be supplied by the twelve boron atoms. Twelve of the electrons are used to form the external bonds whilst the remaining 26 are delocalized in the thirteen bonding orbitals inside the icosahedron. At least part of the deficit of two electrons per  $B_{12}$  icosahedron should be transferred from additional intericosahedral atoms.

To perform a count of the electrons per unit cell for  $B_{48}B_2C_2$  and  $B_{48}B_2N_2$  we used the occupancy numbers in Table I, which were derived for the occupation of the intericosahedral sites by the two boron and the two carbon or nitrogen atoms, respectively. The occupancy numbers were calculated by systematic variation and least squares analysis. Since we were working on a relative scale the figures refer to fully occupied icosahedral position, i.e., five electrons per site. As can be seen from Table I, in  $B_{48}B_2C_2$  the total number of electrons for the four intericosahedral atoms per cell is 20.6, giving a calculated electron deficit of 1.4 electrons per unit cell which is possibly transferred to the  $B_{12}$  icosahedra. In  $B_{48}B_2N_2$  however, this transfer is much lower i.e., only 0.6 electrons per cell. Although conclusions regarding transfer of charge as derived from even the best x-ray data must be regarded with reserve,  $B_{48}B_2C_2$  and even more  $B_{48}B_2N_2$  do not seem to completely provide conditions necessary for the proposed closed-shell configuration of  $B_{12}$  icosahedra.

Nevertheless, the nonmetal borides  $B_{48}B_2C_2$  and  $B_{48}B_2N_2$  are, in addition to  $BeB_{12}$  (8) and  $AlBe(B_{12})_2$  (9), two stable phases with the lattice of the hypothetical "I-tetragonal boron," which can be prepared in a reproducible manner and in which the tetragonal icosahedral framework is stabilized by suitable foreign atoms. For the  $BeB_{12}$  and the  $AlBe(B_{12})_2$ , however, unequivocal attachments of the foreign atoms to definite interstitial icosahedral sites are lacking, as yet there exists no accurate determination of the absolute electron densities in the icosahedral holes.

The existence of the so-called "I-tetragonal boron"  $B_{48}B_2$  as a true polymorph of elementary boron, postulated by Hoard *et al.* (1), must be definitely excluded. In a paper published in 1967 (10), Hoard and Hughes expressed some doubts on the existence of this phase but were unable to establish the presence of impurities or further improve their structure determination. It seems that the reliable determination of such stabilizing atoms failed because of the ineradicable inaccuracy of the available x-ray data (R-index 11.4%)

rather than by the proposed variable degree of internal disorder.

Finally there is the question of the actual analytical composition of the crystals, on which Hoard *et al.* carried out their structure investigations. In the original paper from 1958 the shortness of the bond between the 2b and an icosahedral boron atom was first related to a possible replacement of the 2b boron atom by carbon, nitrogen, or even oxygen impurities. However, in the following sentence they emphasized the absence of carbon and oxygen in the preparation of their crystals and nitrogen was excluded as an "unlikely" impurity, also without direct analysis. Merely on the basis of a total analysis for boron the replacement of "no more than one-fourth, more probably, no significant fraction" of the 2b boron atoms by other impurities was admitted. In order to retain the interpretation for the occupancy of the 2b sites by boron, Hoard *et al.* explained an observed excess electron density in the position 2b by an additional partial occupation of the positions 2a or 4b. The only impurity taken into consideration for this occupation was tantalum arising from the filament. The maximum degree of filling of 2a sites should correspond to an atomic tantalum to boron ratio of about 1/1400 in the crystal. These conclusions were, however, not verified by direct analysis.

Manuscript received Nov. 2, 1973.

Any discussion of this paper will appear in a Discussion Section to be published in the December 1974 JOURNAL. All discussions for the December 1974 Discussion Section should be submitted by Aug. 1, 1974.

#### REFERENCES

1. J. L. Hoard, R. E. Hughes, and D. E. Sands, *J. Am. Chem. Soc.*, **80**, 4507 (1958).
2. I. Ahmad and W. J. Heffernan, *This Journal*, **118**, 1670 (1971).
3. A. Luque, *Compt. Rend. (Série C)*, **274**, 286 (1972).
4. T. Sugaya, Y. Takeuchi, and O. Watanabe, *Phys. Status Solidi (a)*, **15**, K5 (1973).
5. K. Ploog, *J. Less-Common Metals*, **31**, 15 (1973).
6. K. Ploog, H. Schmidt, E. Amberger, G. Will, and K. H. Kossobutzki, *ibid.*, **29**, 161 (1972).
7. H. C. Longuet-Higgins and M. de V. Roberts, *Proc. Roy. Soc. (London)*, Ser. A, **230**, 110 (1955).
8. H. J. Becher, *Z. Anorg. Allgem. Chem.*, **306**, 266 (1960).
9. H. J. Becher and H. Neidhard, *Acta Cryst.*, **B24**, 280 (1968).
10. J. L. Hoard and R. E. Hughes, in "The Chemistry of Boron and its Compounds," E. L. Muetterties, Editor, p. 25, John Wiley and Sons, Inc., New York (1967).

## DISCUSSION SECTION



This Discussion Section includes discussion of papers appearing in the *Journal of The Electrochemical Society*, Vol. 119, No. 10; October 1972; and Vol. 120, No. 11; November 1973.

### Chlorine Adsorption at a Titanium Surface

T. Smith (pp. 1398-1406, Vol. 119, No. 10)

I. H. Khan<sup>1</sup> and Y. Rajapakse:<sup>2</sup> We wish to make the following comments on the recent calculations by

<sup>1</sup>NASA-Ames Research Center, Moffett Field, California 94035.  
<sup>2</sup>Stanford University, Stanford, California 94305.

Smith in the paper under discussion of the diffusion and segregation coefficients and activation energies for chlorine on titanium.

First, examination of the equations in the Appendix of the paper being discussed shows that a factor  $K/l$  has been omitted from the expressions for  $C(x, t)$  (Eq. [A-14]),  $C_s(t)$  (Eq. [A-15]), and  $C_s(\infty) - C_s(t)$  (Eq. [A-17]).<sup>3</sup> The correct expressions are

<sup>3</sup>In Eq. [A-14] of the work being discussed the coefficient of  $\exp(-k_n^2 D t / l^2)$  should be the residue as  $s = s_n$ . However, the coefficient given in the paper under discussion differs from the residue by a factor of  $K/l$ .

$$\frac{C(x, t)}{C_0} = \frac{l}{l+K} \left[ 1 - 2 \frac{K}{l} \sum_{n=1}^{\infty} \frac{\cos(\kappa_n x/l) \exp(-\kappa_n^2 D t/l^2)}{\left[ 1 + \frac{K^2 \kappa_n^2}{l(l+K)} \right] \cos \kappa_n} \right] \quad [1]$$

$$C_s(t) = l K C_0 / (l + K) \left[ 1 - 2 \frac{K}{l} \sum_{n=1}^{\infty} e^{-\kappa_n^2 D t/l^2} / (1 + K^2 \kappa_n^2 / l(l + K)) \right] \quad [2]$$

$$C_s(\infty) - C_s(t) = 2 C_0 l K^2 e^{-t/\tau_1} / [l(l + K) + K^2 \kappa_1^2] - \dots \quad [3]$$

It is to be noted that the first term in the series in Eq. [2] gives the one-term approximation for  $C_s(\infty) - C_s(t)$  valid for large values of  $t$ .

Second, we will consider the solutions of Eq. [3]-[5] in the paper under discussion for the three unknowns  $K$ ,  $C_0$ , and  $\kappa_1$

$$2lK^2C_0/[l(l + K) + K^2\kappa_1^2] = a$$

$$lK C_0 / (l + K) = b$$

$$\kappa_1 K / l = -\tan \kappa_1$$

where  $a$  is the coefficient of  $\exp(-t/\tau_1)$  and  $b$  is  $C(\infty)$  and they are determined experimentally. Eliminating  $C_0$  between the first two equations, we obtain

$$(\kappa_1^2 - 2d)y^2 + (1 - 2d)y + 1 = 0 \quad [4]$$

where  $y = K/l$  and  $d = b/a$ .

For this quadratic equation to have real roots, the discriminant must be positive. Since  $d$  is positive and  $\kappa_1$  lies between  $\pi/2$  and  $\pi$ , a necessary condition for real roots is

$$d \geq \kappa_1 - 1/2 \quad [5]$$

For the experiments in the work being discussed the value of  $d$  is 0.57. The condition for real roots is obviously violated. Hence, it is not possible to calculate the values of the diffusion and segregation coefficients and activation energies.

Third, we have attempted to calculate the diffusion and segregation coefficients for sulfur on the surface of Ti. Our experimental data yield a value of about 1. Condition [5] is again violated, and our attempts were unsuccessful. The failure to calculate the diffusion and segregation coefficients, using our experimental data as well as those in the paper under discussion, based on corrected Eq. [1]-[3] suggests that the assumptions made in the above-mentioned work for the mathematical model may not be valid.

Last, the solution of Eq. [4] depends on the value of  $d$ , which in turn depends on  $C(\infty)$ . It should be pointed out that  $C(\infty)$  may not necessarily be determined by Auger peak height. Initially the Auger peak height increases with time and hence with surface impurity concentration. Subsequently, the peak attains its maximum height and does not increase any further with time. This maximum does not necessarily mean that the surface concentration has reached its equilibrium. This may instead be due to the fact that the Auger peak height is insensitive to surface coverage greater than a few atomic layers.

In view of the considerations mentioned above, it is apparent that it is not possible to calculate the diffusion and segregation coefficients as well as the activation energies for surface diffusion and segregation, using the method described in the paper under discussion. Hence, the mathematical model as well as the method of analysis, calculated results, and conclusions in the above-mentioned paper need reconsideration.

### Minority Carrier Generation Studies in MOS Capacitors on N-Type Silicon

D. R. Young and C. M. Osburn (pp. 1578-1581, Vol. 120, No. 11)

W. Zechnall;<sup>4</sup> In the paper under discussion values of the surface generation velocity are reported which were determined from the intercept of the Zerbst plot<sup>5</sup> with  $C_{inv}/C - 1 = 0$ . However, a theoretical calculation carried out in our laboratories shows that such an intercept can be obtained even without assuming any influence of surface generation. In our calculation we used the exact expression of the volume generation rate which is given by the theory of Shockley, Read, and Hall<sup>6,7</sup>

$$U_{vol} = (p \cdot n - n_1)^2 / (\tau_{no}(p + n_1) + \tau_{po}(n + n_1)) \quad [1]$$

$n$  and  $p$  are the densities of electrons and holes in the space charge region, and  $\tau_{no}$  and  $\tau_{po}$  the low-level lifetimes of electrons and holes. To describe the time behavior of a MOS capacitor during the whole transient this equation must be applied instead of the following simple approximation

$$U_{vol} = n_1 / (\tau_{no} + \tau_{po}) \quad [2]$$

which was used both by Zerbst and the author in the above-mentioned work.

This approximation is valid for the transient behavior of a MOS capacitor in the case of large deviations from thermal equilibrium only. Applying the Zerbst analysis resulting from Eq. [2] to our numerical results which were calculated without any influence of surface generation, we obtain the Zerbst plots drawn in Fig. 1.

The Zerbst plots show an intercept with  $C_{inv}/C - 1 = 0$ , whose magnitude is inversely proportional to the generation lifetime  $\tau_{gen} = \tau_{no} + \tau_{po}$ . Applying the method of Zerbst to determine the surface generation velocity from the intercepts, we obtain a value of 1.3 cm/sec from curve a (Fig. 1) and a value of 0.13 cm/sec from curve b. These values are virtual ones, because the calculation was carried out for volume generation only. Thus, the very small values of surface generation velocity reported in the paper under discussion are a consequence of the large values of generation lifetime measured. The calculation shows that a reasonable value of surface generation velocity cannot be obtained from the intercept of the Zerbst plot.

<sup>4</sup> Institut für Theoretische Elektrotechnik, Technische Hochschule Aachen, 51 Aachen, West Germany.

<sup>5</sup> M. Zerbst, *Z. Angew. Phys.*, **22**, 30 (1966).

<sup>6</sup> W. Shockley and W. T. Read, *Phys. Rev.*, **87**, 835 (1952).

<sup>7</sup> R. N. Hall, *ibid.*, **87**, 387 (1952).

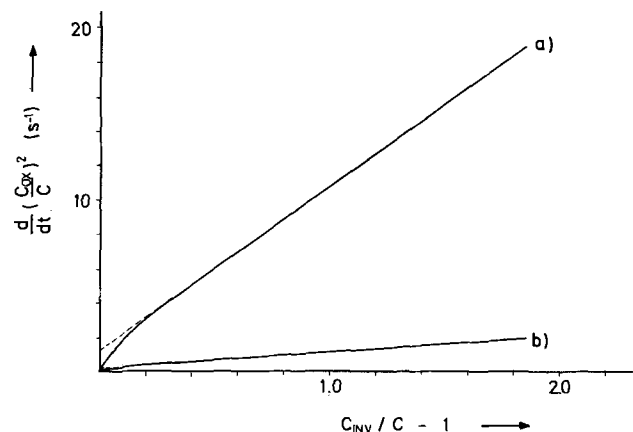


Fig. 1. Zerbst plots obtained from the results of a theoretical calculation. Substrate impurity concentration  $10^{15} \text{ cm}^{-3}$  (n-type), oxide thickness 1200Å, voltage step from 0 to -10V. Values of generation lifetime: a,  $\tau_{gen} = 11 \mu\text{sec}$ ; b,  $\tau_{gen} = 110 \mu\text{sec}$ .

**D. R. Young and C. M. Osburn:** The authors would like to thank W. Zechall as well as T. W. Collins<sup>8</sup> for their more complete Shockley, Read, Hall analysis of minority carrier generation. Clearly the use of

<sup>8</sup> T. W. Collins, Ph.D. Dissertation, University of California, Davis, California (1973); *IEDM Technical Digest*, p. 342 (1973).

Zerbst plots to obtain a surface generation velocity is in error since other mechanisms give the appearance of surface generation. To correctly interpret lifetime and surface generation from pulsed capacitance relaxation curves, it is necessary to use the exact solution.



## A Secondary Battery Based on the Copper(II)-(I) and (I)-(0) Couples in Acetonitrile

B. Kratochvil and K. R. Betty

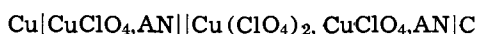
*Department of Chemistry, University of Alberta, Edmonton, Alberta, Canada*

*The publication costs of this article have been assisted by the University of Alberta.*

### ABSTRACT

A secondary cell based on the copper(II)-(I) and (I)-(0) couples in acetonitrile has been constructed and studied at room and low temperatures. The over-all cell reaction is  $\text{Cu}^{++} + \text{Cu(s)} \rightleftharpoons 2\text{Cu}^+$ . A positive compartment consisting of a graphite sheet in contact with an acetonitrile solution of copper(II) perchlorate was separated by an anionic ion-exchange membrane from a negative electrode of copper metal in acetonitrile. Lithium or sodium perchlorate was added to the negative compartment to decrease internal resistance. The cell develops an open-circuit potential of 1.35V and is reversible at coulombic efficiencies of close to 100%. A test unit was carried through more than 45 charge and discharge cycles at room temperature. Discharge characteristics are poorer at  $-14^\circ\text{C}$  than at room temperature. The anionic ion-exchange membrane used as a separator was stable to the solvent, chemicals, and potentials used, and effectively blocked transport of copper(II) species. About 90% of full charge was retained after a wet stand of 2 months.

The electrochemical stability, low viscosity, and low freezing point ( $-45^\circ\text{C}$ ) of acetonitrile,  $\text{CH}_3\text{CN}$ , suggest its usefulness as a solvent for batteries designed to operate at low ambient temperatures (1-3). In this solvent the copper(II)-(I) couple has been found to be reversible (4); Bialozor (5) found that, although electrodeposition of copper(I) on platinum from acetonitrile solution is irreversible, the overpotential is relatively low. Owing to appreciable stabilization of copper(I) by acetonitrile (AN), the standard potentials of the copper(II)-(I) and copper(I)-(0) couples differ by 1.283V (6). Cells of the type



in which the electrode reactions on discharge are  $\text{Cu}^{++} + e \rightarrow \text{Cu}^+$  and  $\text{Cu(s)} \rightarrow \text{Cu}^+ + e$ , were assembled and tested at two temperatures.

### Experimental

**Materials.**—Technical-grade acetonitrile (Matheson, Coleman, and Bell) was purified by method D1 described by Coetzee and co-workers (7), with some modifications. The commercial product was refluxed with  $\text{CaH}_2$  (Ventron) at a ratio of 10 g/liter. Because no hydrogen evolution was observed, stirring was continued for only 3 hr instead of the recommended 2 days. After addition of 5g of  $\text{P}_4\text{O}_{10}$  (British Drug House) to each liter of decanted material, the mixture was distilled in an all-glass still under high reflux ratio. The first 5% and last 20% of the still output were discarded. The resulting product was refluxed over  $\text{CaH}_2$  (5 g/liter) for 1 hr, then distilled slowly under a high reflux ratio. Again the first 5% and last 20% of the still output were discarded. The collected product

was placed in a tightly stoppered glass bottle and transferred to a dry box until needed. All flasks were oven dried at least 2 hr at  $110^\circ\text{C}$  before use. The water content, determined by Karl Fischer titration, was less than  $5 \times 10^{-4}\text{M}$ .

The preparation of  $\text{Cu}(\text{ClO}_4)_2 \cdot 4\text{CH}_3\text{CN}$  was as described in Ref. (6); the material had a purity of 99.6% on the basis of analysis for copper by aqueous EDTA titration.

$\text{NaClO}_4$  (anhydrous, G. F. Smith Chemical Company) was dried for 20 hr under vacuum, transferred to a dry box, and then used immediately.

$\text{LiClO}_4 \cdot 3\text{H}_2\text{O}$  (G. F. Smith Chemical Company) was recrystallized from water and dried under vacuum, first at  $80^\circ\text{C}$  for 24 hr, and then at  $100^\circ\text{C}$  for 48 hr. The salt was stored in a dry box in a tightly closed oven-dried reagent bottle.

The negative electrode of the battery was 20 gauge electrolytic copper wire wound on a polyethylene frame. The wire was cleaned by immersion in concentrated  $\text{HCl}$  for 2 min, then rinsed with distilled water. The wire and frame were dried immediately under vacuum overnight and placed in a dry box for final assembly of the cell. Visual inspection of the wire just before assembly showed no evidence of a surface film.

The positive electrode was an 8 by 8 cm sheet of 0.32 or 0.63 cm pressed graphite. Each sheet was rinsed in distilled water and dried under vacuum 8-10 hr at room temperature before use.

Migration of copper(II) to the negative electrode of the charged cell would result in self-discharge. Therefore an Amfion A-60 anionic ion-exchange membrane, consisting of a polyethylene backbone containing quaternary ammonium anion-exchange sites, was employed as a permselective separator. The membrane was converted from the original chloride form to the

**Key words:** batteries, acetonitrile, copper.

EST

perchlorate by soaking it in aqueous 1M NaClO<sub>4</sub> for 1 hr, then was stored in a fresh portion of 1M NaClO<sub>4</sub> until needed. When a cell was to be constructed, a 12 by 12 cm section of membrane was soaked several hours in technical-grade acetonitrile. Upon soaking, the lateral dimensions increased about 10% over the water-wet form, the thickness decreased, and the flexibility increased markedly. The wet membrane was cut to a final size of 10 by 10 cm, and bolt holes were punched along the edges; it was then dried under vacuum overnight and transferred to a dry box immediately before final assembly of the cell.

**Apparatus.**—Experiments were performed in a nitrogen atmosphere in a Kewaunee Scientific Equipment glove box, with P<sub>4</sub>O<sub>10</sub> as desiccant.

The test cell is shown in Fig. 1. The geometric cross-sectional area was 64 cm<sup>2</sup>. Contact with the graphite electrode was made by a platinum wire press fitted into a hole drilled through the polyethylene case into the graphite.

Voltages were measured with a Heath EU-805 Universal Digital Instrument (UDI) and an Orion Model 701 Digital pH meter coupled with Heath EUW-20A and EU-20B chart recorders. The controlled-potential charging source, two Burgess No. 6 1.5V heavy-duty dry cells in parallel, was placed in series with a 20 ohm current limiting resistor. Galvanostatic charging and discharging were accomplished with a Sargent Model IV Constant-Current Coulometer. Control circuitry was breadboarded with a Heath EU-801A Analog-Digital Designer (ADD).

Cells were assembled in the dry box in the fully charged state. By means of a syringe, a solution of Cu(ClO<sub>4</sub>)<sub>2</sub> in acetonitrile was introduced into the cathodic compartment, and a solution of LiClO<sub>4</sub> or NaClO<sub>4</sub> in acetonitrile into the anodic compartment. Theoretical capacity was varied by changing the concentration of copper(II) salt introduced. The LiClO<sub>4</sub> and NaClO<sub>4</sub> solutions were about 0.9M, which is near the solubility limits of these salts. In all the cells studied, the quantity of copper metal present in the negative electrode was in excess of that required for complete reduction of the copper(II) added to the positive compartment. The cells were cycled either by discharge through a constant resistance followed by recharge at controlled potential or by galvanostatic discharge and recharge. Discharges through constant resistance were to varying depths, whereas controlled-potential recharge was to full charge as indicated by a final charging current of less than 0.5 mA. Discharges at constant current were to exhaustion as indicated by a cell voltage of 0, whereas constant-current recharges were terminated when 1.60V was reached. After termination of the first recharge process, cells were allowed to stand overnight; then recharge was continued, usually at a lower current level, until acceptance of only a small increment of charge at the lowest current level of 4.65 mA indicated full charge. The overnight stand

reduced the effects of concentration polarization caused by the relatively low solubility of copper(I) perchlorate in acetonitrile.

Low-temperature studies were conducted in a dry box by immersing a cell in a bath of dry ice and ethylene glycol at -14°C.

## Results and Discussion

**Cell tests.**—A series of galvanostatic discharges and charges were made at various levels of current, and the voltage was recorded as a function of time. A typical discharge cycle is shown in Fig. 2 for a current level of 9.65 mA. The early part of the discharge occurs at about 1.2V and is followed by a long shoulder before a sharp break downward at about 0.5V. On the same figure is plotted the voltage of the copper(II)-(I) positive electrode against an Ag|0.01M AgNO<sub>3</sub> reference electrode, connected to the positive compartment by a Luggin capillary and a bridge of LiClO<sub>4</sub> in acetonitrile. As expected, polarization occurs principally at the positive electrode. Lithium and sodium perchlorate performed equally well as inert electrolyte; essentially no difference was observed between them.

Voltage-time curves were extrapolated to zero time on the basis of readings obtained 30 and 60 sec after commencement of discharge, and the resulting potential was plotted against current level (Fig. 3). A least squares treatment yielded an intercept of 1.352 ± 0.007V, which is taken to be the open-circuit voltage.

Deliverable capacity to 0.65V cutoff under load is plotted against current drain in Fig. 4. Data were obtained under conditions of continuous discharge after full charge.

Coulombic efficiencies (charge/discharge) were in the range of 1.11-0.92 for eleven galvanostatic cycles. The mean coulombic efficiency was 1.021 ± 0.054. After lengthy discharge the cell tended to accept less than 100% recharge. This tendency is attributed to polarization during the necessarily long recharge that caused early termination of the recharge process at the 1.60V cutoff.

**Cycle tests.**—A series of discharges to varying depths through constant resistance, followed by recharge at controlled potential, were made. Current-time curves for discharge and recharge are shown in Fig. 5 and 6 for the twenty-third cycle of one cell, a cycle carried to extreme depth. Most of the cycling was by automatic

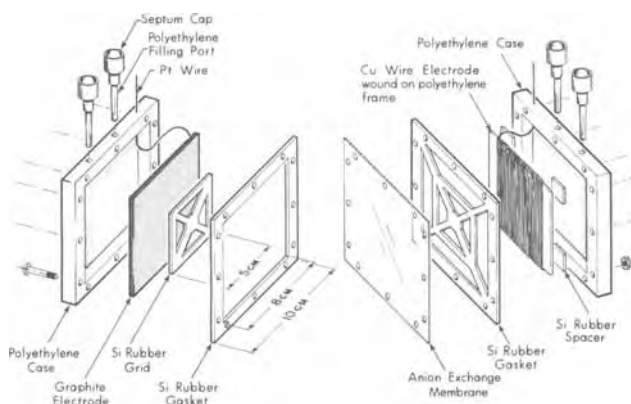


Fig. 1. Sketch of disassembled cell

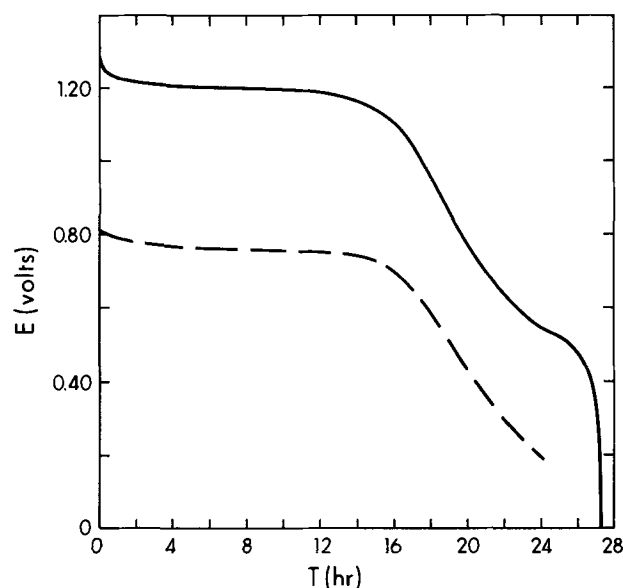


Fig. 2. Constant-current discharge at 9.65 mA for Cu|CuClO<sub>4</sub>|Cu(ClO<sub>4</sub>)<sub>2</sub>,CuClO<sub>4</sub>|C in acetonitrile as solvent. Geometric area ≈ 64 cm<sup>2</sup>. Solid line represents E<sub>cell</sub>. Dotted line represents the potential of the positive electrode relative to an Ag|0.01M AgNO<sub>3</sub> in a reference electrode.



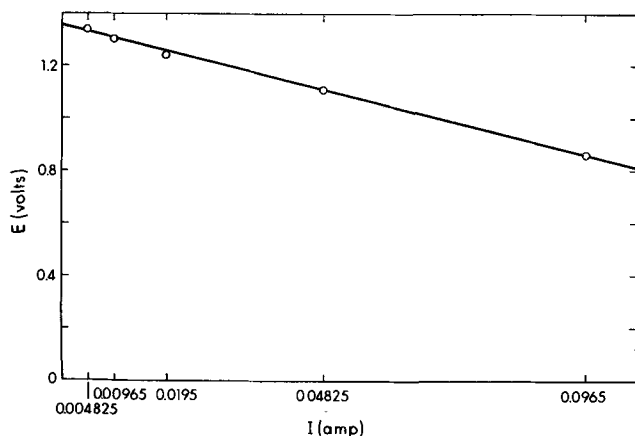


Fig. 3. Voltage at zero time as a function of current drain. Voltages were determined by extrapolation to zero of readings obtained 30 and 60 sec from commencement of discharge. Each point is the mean of two discharge runs.

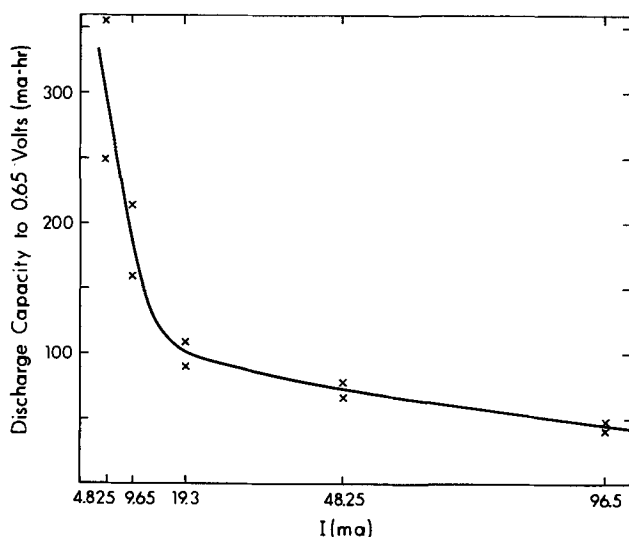


Fig. 4. Discharge capacity to 0.65V under load for  $\text{Cu}|\text{CuClO}_4||\text{Cu}(\text{ClO}_4)_2,\text{CuClO}_4|\text{C}$  in acetonitrile as solvent. Constant-current discharge from full charge. Geometric area  $\approx 64 \text{ cm}^2$ ; theoretical capacity = 402 mA-hr.

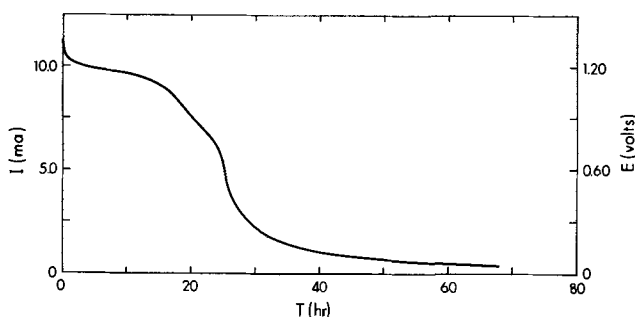


Fig. 5. Discharge through 120 ohm load for  $\text{Cu}|\text{CuClO}_4||\text{Cu}(\text{ClO}_4)_2,\text{CuClO}_4|\text{C}$  in acetonitrile as solvent. Twenty-third cycle.

switching from discharge to charge when the cell voltage fell to 0.9V, followed by a switch back to discharge when the charging current fell to 0.5 mA. No deterioration in cell performance was noted after 45 cycles. Current-time curves for the first eleven cycles were integrated with an Ott planimeter to yield coulombic efficiencies; values of 1.00-1.12 were obtained, with a mean of  $1.031 \pm 0.036$ . The cell has good shelf-life properties. A fully charged cell lost only 12% of charge after a wet stand of 2 months, and full recharge was accepted.

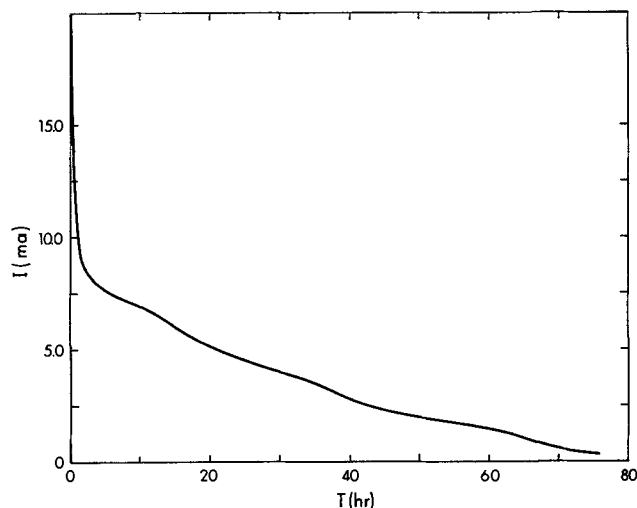


Fig. 6. Controlled-potential recharge for  $\text{Cu}|\text{CuClO}_4||\text{Cu}(\text{ClO}_4)_2,\text{CuClO}_4|\text{C}$  in acetonitrile solvent. Twenty-third cycle. Cell heavily polarized by discharge at commencement of recharge. Initial current  $> 35 \text{ mA}$ ; charging voltage = 1.55V; series resistance = 20 ohms.

Disassembly of cells that had been extensively cycled revealed that, during recharge, copper(I) tended to replate onto the copper wire as loosely adherent nodules, many of which fell to the bottom of the cell, thereby removing the copper from further reaction. Also, the anion-exchange membrane was considerably distended by osmotic pressure in the positive compartment as a result of exclusion of copper(II) species from the negative compartment. Both the copper electrode and the membrane showed yellow discoloration, probably from copper oxide and hydroxide species formed by reaction with water. The graphite electrodes were clean and showed no sign of deterioration.

*Low-temperature studies.*—Discharge performance at  $-14^\circ\text{C}$  was distinctly below that at room temperature. A discharge at 4.65 mA delivered only 94 mA-hr to 0.65V cutoff at  $-14^\circ\text{C}$ , whereas 356 and 248 mA-hr were obtained at the same current level at room temperature. The discharge curve was similar to that shown in Fig. 2. Cell impedance at 1000 Hz at full charge increased from 5 ohms at room temperature to about 20 ohms at  $-14^\circ\text{C}$ . The marked drop in cell capacity and the increase in internal resistance are attributed to mass-transport limitations at the lower temperature.

### Summary

A secondary cell consisting of the copper(II)-(I) and (I)-(0) couples in acetonitrile is reversible, is capable of repeated cycling, and holds charge well over extended periods. Cell performance is appreciably diminished at lower temperatures. Electrodeposited copper metal is loosely adherent under the conditions studied and is poor in quality. The use of an anionic ion-exchange membrane as a separator provides low resistance to current flow. The membrane studied was stable to the solvent, chemicals, and potentials used, and it effectively blocked transport of copper(II) species. The cell may be discharged to great depth without apparent effect on subsequent performance.

### Acknowledgments

The authors gratefully acknowledge preliminary cell design and fabrication by Mr. Gary McCue. They also thank Professor G. S. H. Lock of the University of Alberta, Department of Mechanical Engineering, for several stimulating discussions and for part of the financial support of Mr. McCue.

Work supported in part by the National Research Council of Canada.

Manuscript submitted Nov. 27, 1973; revised manuscript received Feb. 26, 1974.

Any discussion of this paper will appear in a Discussion Section to be published in the June 1975 JOURNAL. All discussions for the June 1975 Discussion Section should be submitted by Feb. 1, 1975.

#### REFERENCES

1. G. V. Lago, J. P. Karnes, J. B. Jennings, and R. L. Smith, Final Report, Contract DA-36-039-SC-74994 (PB 143899) (March 1959).
2. M. Arcand, Final Report, Contract DA-36-039-SC-72363 (PB 135749) (July 1957).
3. F. Solomon, *Proc. Ann. Battery Res. Develop. Conf.*, **12**, 94 (1958).
4. I. M. Kolthoff and J. F. Coetzee, *J. Am. Chem. Soc.*, **79**, 1852 (1957).
5. S. G. Biallozor, *Electrochim. Acta*, **17**, 1243 (1972).
6. J. K. Senne and B. Kratochvil, *Anal. Chem.*, **44**, 585 (1972).
7. J. F. Coetzee, G. P. Cunningham, D. K. McGuire, and G. R. Padmanabhan, *ibid.*, **34**, 1139 (1962).

## Formation Processes of the Lead-Acid Battery Negative Plates

D. Pavlov, V. Iliev, G. Papazov, and E. Bashtavelova

*Bulgarian Academy of Sciences, Institute of Physical Chemistry,  
Division of Electrochemical Power Sources, Sofia 13, Bulgaria*

#### ABSTRACT

The advance of the processes within the bulk of the negative plate upon formation in sulfuric acid was studied by electron-microprobe and x-ray diffraction experiments and by microscopic observations. It was found that besides the electrochemical reaction of the formation of sponge lead there were also chemical reactions of the formation of lead sulfate which remain included in the lead network of crystals. The electrochemical reduction of lead sulfate takes place after the consumption of lead oxide and tribasic lead sulfate present in the paste. The elementary chemical and electrochemical reactions as well as their mutual relationships are determined as the basis of these measurements.

The change in total porosity and pore size distribution during formation of the lead-acid battery negative plate was studied. Upon formation, both the pore radii and the porosity of the active mass increase. The electrocrystallization processes of lead during formation are also discussed. Upon reduction of  $3\text{PbO} \cdot \text{PbSO}_4 \cdot \text{H}_2\text{O}$  and  $\text{PbO}$  a lead crystal network is formed in the first stage. During the second stage, lead, obtained by reduction of lead sulfate, is deposited on the network.

The technology of lead-acid battery plates includes the following stages. By the mixing of a partially oxidized lead powder with a sulfuric acid solution a paste is obtained which consists of lead hydrate, lead monoxide, and basic lead sulfates. Besides these compounds the negative plate paste also contains barium sulfate and an expander. After pasting on a grid and curing, the paste is subjected to formation. During formation, the lead monoxide and the basic sulfates are transformed by electrochemical reactions into active material, i.e., lead at the negative plate and lead dioxide at the positive one.

The influence of barium sulfate, of the expander, and of the conditions of formation on the properties of the negative plate have been studied previously (1-11). The microstructure of the lead crystals obtained upon formation, as well as the way in which these crystals grow, has already been investigated (12-15). The chemical and electrochemical reactions which take place upon formation have been presented by Pavlov (15).

The aim of the present paper is to establish the elementary chemical, electrochemical, and crystallization processes which occur during the formation process and to elucidate their mutual relationships.

#### Experimental

Traction battery plates with dimensions of  $285 \times 180 \times 4$  mm were formed. They were produced with a paste containing 4.5% sulfuric acid, barium sulfate, and expander. The formation was effected in two cells, each

constituting two positive and one negative plate. A sulfuric acid solution of density 1.05 was used in a volume of  $3000 \text{ cm}^3$ . For every gram of paste there was  $1.89 \text{ cm}^3$  of sulfuric acid solution. Immediately after pouring the solution in the cells, a current density of  $10.00 \text{ mA/cm}^2$  was applied. The following parameters were checked during formation at 2 hr intervals: (i) density and temperature of the sulfuric acid solution; (ii) distribution of lead over the cross section of the plate; (iii) distribution of lead sulfate over the cross section of the plate; (iv) phase composition at the surfaces and in the bulk of the plate; (v) total porosity and pore size distribution at the surfaces and in the bulk of the plate.

Samples were taken of the negative plates for determinations (ii)-(v). In order to eliminate differences along the height and width of the plates, material was taken from three different locations of the plates. The samples were collected in the following manner. At 2 hr intervals the formation process was stopped. The negative plates were removed from the cells and washed with water. Three portions were removed from each plate, each containing four grid rectangles. The plates were then returned into the cells, the current was corrected, and the formation process was resumed. The six samples were abundantly washed with water and dried in a nitrogen atmosphere. The samples taken from one of the negative plates were used for observing the distribution of lead along the cross section of the plate and for determining the distribution of lead sulfate across the cross section of the plate. The samples from the second negative plate were used for phase composition and porosity studies.

**Key words:** lead-acid battery, lead-acid battery technology, lead electrode, formation of the lead electrode, reactions in porous masses.

### Determination of the Elementary Chemical and Electrochemical Reactions

*Change in the sulfuric acid concentration in the bulk of the electrolyte during formation.*—The formation of the battery plates takes place in a sulfuric acid solution. Lead monoxide and the basic sulfates are unstable in sulfuric acid. This is why chemical sulfatization reactions of the lead monoxide and of the basic sulfates take place parallel with the electrochemical reactions. The participation of the sulfuric acid in the chemical reactions leads to a change in its concentration within the bulk of the electrolyte. The density changes of sulfuric acid within the bulk of the electrolyte during formation are represented in Fig. 1. Two stages can be observed on this curve. During the first stage sulfuric acid penetrates into the plates and reacts with the paste, and hence its concentration in the bulk of the electrolyte decreases. During the second stage the sulfate products obtained during the first stage are formed. Sulfuric acid is evolved as a result of these reactions. It leaves the plates thus increasing the sulfuric acid concentration in the bulk of the electrolyte.

*Advance of the reactions of formation of lead across the cross section of the plate.*—The samples were enclosed in aluminum molds and soaked under vacuum with polyester resin. After hardening of the resin, the samples were machined until the cross section of the plate appeared clearly. After dry polishing the cross section was observed under a microscope and photographed on color and black-and-white films. Such micrographs are illustrated in Fig. 2. It is easily seen that the formation of lead begins first at those portions of the member grid that are closest to the solution. Lead forms zones which advance at the surface of the plates (Fig. 2b). In those portions of the plate surface not already occupied by the lead zones the paste reacts with sulfuric acid and white lead sulfate zones originate (Fig. 2b). After the lead zones have covered the surface of the plate they advance into the paste (Fig. 2c-e). From the photographs it is seen that a thin layer of white crystals occurs at the boundary between the lead zone and the unformed paste. Between the sixth and the eighth hour of formation the entire cross section of the plate is occupied by the lead zone. The formation process ends at the fourteenth hour, when the lead mass has become dark-gray in color.

*Determination of the distribution of lead sulfate across the cross section of the plate.*—The samples selected for these studies were placed in cylindrical aluminum molds which were filled with epoxy resin. After hardening of the resin the mold was cut so that the sample was divided into two identical halves. After

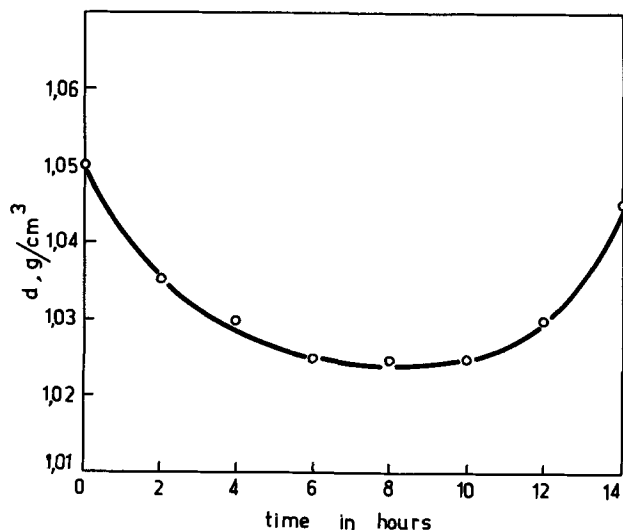


Fig. 1. Change in the electrolyte density within the bulk of the electrolyte during formation.

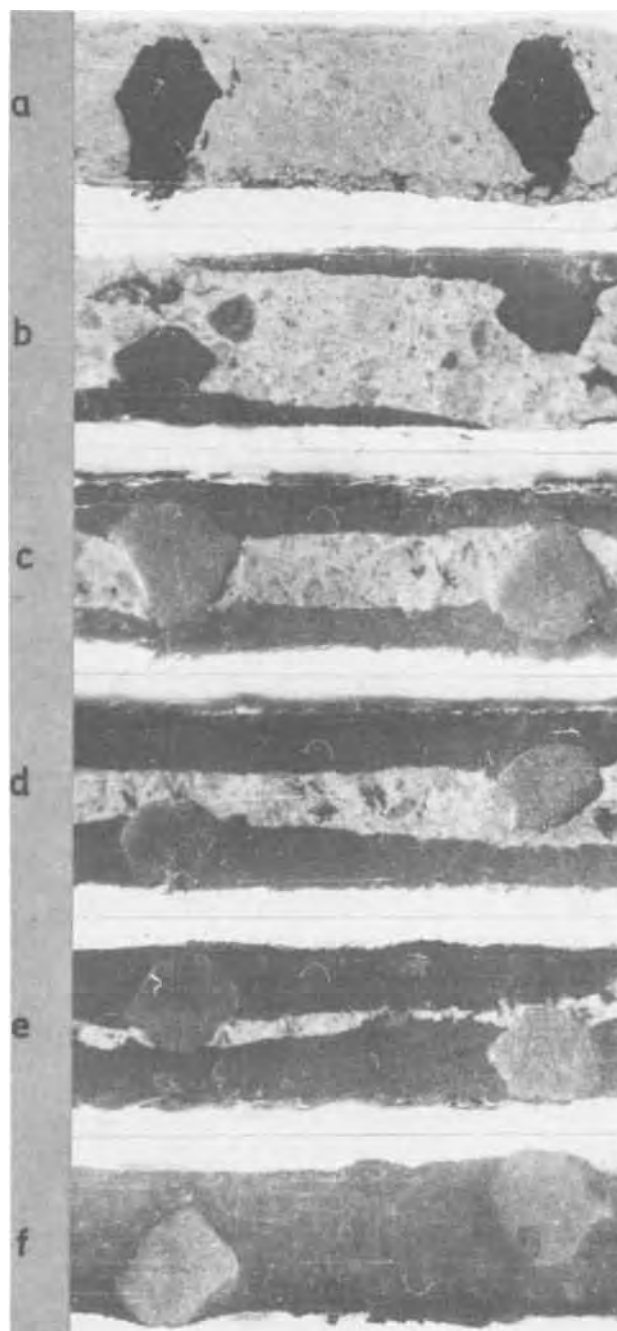


Fig. 2. Micrograph of the cross section of the negative plate during formation. a, Prior to formation; b-e, plates during formation (the dark patches are the lead zone); f, fully formed plate.

dry polishing, a conductive 100-150Å thick carbon layer was deposited on the cross section. The determination of the sulfur distribution across the cross section of the plate was carried out with a Hitachi XMA-5 electron microprobe. The electron beam was scanned repeatedly across a  $240 \times 240 \mu$  area and the intensity of the sulfur line was recorded. In this way the average sulfur content over the scanned areas was determined. The electron beam was then scanned on the following point. These measurements made it possible to establish the distribution of lead sulfate along the cross section perpendicular to the plate surface.

Figure 3 represents the results of the measured relative amounts of lead sulfate (free and bonded in basic sulfate). The thickness of the plate is plotted in relative units on the abscissas axis. From the figure it can be seen that lead sulfate is first formed at the surface of the plate. Then it advances slowly into the inner parts of the paste. At the eighth hour of formation lead

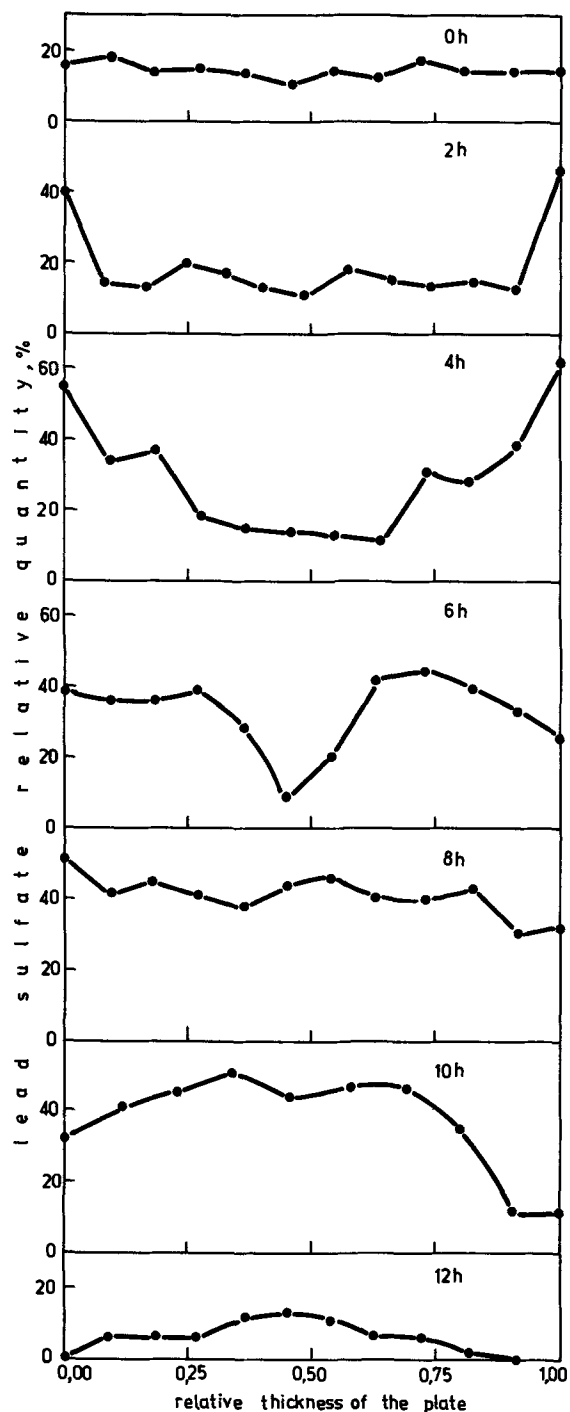


Fig. 3. Change in the distribution of the total amount of lead sulfate along the cross section of the plate during formation.

sulfate is almost uniformly distributed across the entire cross section of the plate. The reduction of lead sulfate takes place after the eighth hour along the entire cross section of the plate. However, this process is most rapid at the surface of the plate (Fig. 3).

The results of these measurements indicate that the processes of sulfatization of lead oxide and of tribasic lead sulfate take place from the surface toward the interior of the plate. From Fig. 2 it is seen that the advance of the lead zone follows a similar path. The end of the sulfatization of the paste occurs at about the same time when the lead zone occupies the entire plate. This indicates that a relationship exists between the processes of formation of lead and lead sulfate. After that, the reduction of lead sulfate occurs in the whole lead zone but most rapidly in the surface portions of the plate.

*Phase composition studies of the paste during formation.*—The samples were divided across the cross section into three portions: two at the surfaces and one in the bulk. The surface portions were joined together. After grinding, the samples were x-rayed with a TuR M-61 diffractometer with filtered copper radiation.

The quantitative x-ray phase analysis is based on the equation

$$I_1 = K \frac{x_1}{\rho_1 \sum x_j m_j} = K \frac{x_1}{\rho_1 m}$$

where  $I_1$  is the intensity of the analytical x-ray reflection of the phase we wish to determine,  $K$  is an apparatus constant,  $x_1$  the weight percentage of the  $i$ th phase in the mixture,  $\rho_1$  is the density of the  $i$ th phase,  $m_j$  is the specific absorption coefficient of x-rays by the  $j$ th phase, and  $m$  is the average absorption coefficient of the sample.

In a three-component system, when the intensity of the analytical reflection of a given phase is referred to the sum of the intensities of the analytical reflections of the three phases, the average absorption coefficient,  $m$ , and the apparatus constant,  $K$ , are eliminated from the equation. For the first phase the relative intensity is given by the expression

$$\frac{I_1}{I_1 + I_2 + I_3} = \frac{x_1}{\rho_1 \left( \frac{x_1}{\rho_1} + \frac{x_2}{\rho_2} + \frac{x_3}{\rho_3} \right)}$$

For a given sample the term included in brackets remains constant in the expressions referring to the three phases.

The aim of the present investigation is to establish the elementary reactions which take place during formation of the plate. It is therefore sufficient to find the changes in the amounts of the individual phases present in the paste during formation, and it is not necessary to determine their absolute contents. In this case the x-ray diffraction method may be used only for determining the changes in the relative intensities of the reflections. The error introduced in this determination depends on the densities of the components.

The analysis of the x-ray diffraction patterns indicates that the cured paste of the negative plate consists of considerable amounts of tet.  $\text{PbO}$  and tribasic lead sulfate and minor amounts of lead. The following x-ray reflections were used in the study of the change in the amounts of each phase:  $d = 3.26\text{\AA}$  for  $3\text{PbO} \cdot \text{PbSO}_4 \cdot \text{H}_2\text{O}$ ,  $d = 3.00\text{\AA}$  for  $\text{PbSO}_4$ . The reflection with  $d = 3.12\text{\AA}$  corresponds to tet.  $\text{PbO}$  (the strongest reflection in the pattern) and overlaps with the  $3.13\text{\AA}$  reflection of  $3\text{PbO} \cdot \text{PbSO}_4 \cdot \text{H}_2\text{O}$  ( $I = 35$ ). The  $2.86\text{\AA}$  reflection corresponds to lead ( $I = 90$  of the pattern) and overlaps with the  $2.84\text{\AA}$  reflection ( $I = 10$ ) of  $3\text{PbO} \cdot \text{PbSO}_4 \cdot \text{H}_2\text{O}$ .

Figure 4 illustrates the change in the relative intensities of the reflections of the individual phases at the surface and in the bulk of the plate during formation. It should be noted that the numerical values of the relative intensities do not reflect the relative amounts of the phases in the mixture. It is seen that during formation, lead oxide and tribasic sulfate react with sulfuric acid thus leaving lead sulfate in the paste adjacent to the surfaces. The formation of lead in the first 4 hr occurs only at the surface parts of the plate by electrochemical reduction of lead oxide and tribasic sulfate. After the eighth hour, the reduction of the lead sulfate formed during formation begins. This reduction begins first at the surface, and at the fourteenth hour the negative plate is entirely formed.

*Elementary chemical and electrochemical reactions and their mutual relationships.*—From the results of Fig. 2-4 a model can be suggested for the elementary chemical and electrochemical reactions and for the elucidation of their mutual relationships. This model

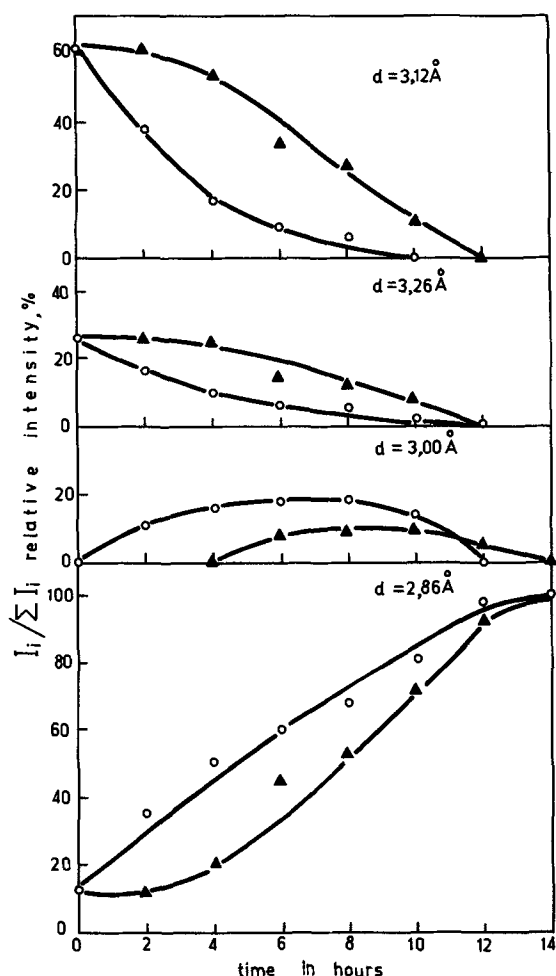


Fig. 4. Change in the phase composition of the negative plate during formation.  $d = 3.12\text{Å}$ , tet.  $\text{PbO} + 3\text{PbO} \cdot \text{PbSO}_4 \cdot \text{H}_2\text{O}$ .  $d = 3.26\text{Å}$ ,  $3\text{PbO} \cdot \text{PbSO}_4 \cdot \text{H}_2\text{O}$ .  $d = 3.00\text{Å}$ ,  $\text{PbSO}_4$ .  $d = 2.86\text{Å}$ ,  $\text{Pb} + 3\text{PbO} \cdot \text{PbSO}_4 \cdot \text{H}_2\text{O}$ . ○, At the surface of the plate; ▲, in the bulk of the plate.

should include the elementary reactions which occur from the two starting compounds of the paste, lead oxide and tribasic lead sulfate.

Figure 5a diagrammatically shows the reactions when lead oxide is the starting compound. Divalent lead ions and  $\text{OH}^-$  ions are formed upon dissolution of the oxide (reaction [A]). The lead ions may participate

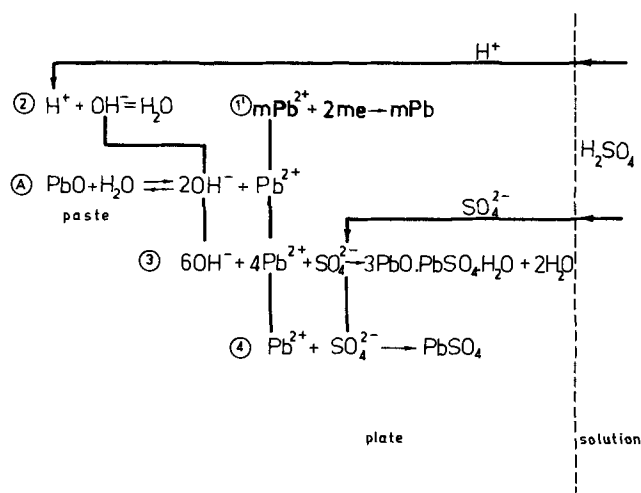


Fig. 5a. Diagram of the elementary chemical and electrochemical reactions with  $\text{PbO}$  as starting material.

in the electrochemical reaction [1'] in which lead is formed, and in the chemical reactions [3] and [4], which are conducive to tribasic lead sulfate and lead sulfate. The hydroxyl ions participate not only in reaction [3] but also in the neutralization reaction [2]. On the one hand reaction [2] influences the dissolution rate of  $\text{PbO}$  (reaction [A]), and on the other, controls the pH of the pore solution at the considered place in the paste. It should be stressed that the nature of the lead ions which are in equilibrium with lead oxide, tribasic sulfate, and lead sulfate, and which participate in the electrochemical reaction [1'], depends on the pH of the solution. At low pH the lead ions are free  $\text{Pb}^{2+}$  ions; at  $\text{pH} > 6$  they are bonded in complexes such as  $\text{Pb}(\text{OH})^+$ ,  $\text{Pb}(\text{OH})_2$ ,  $\text{Pb}(\text{OH})_3^-$ , and  $\text{HPbO}_2^-$ . For simplicity let us assume that only  $\text{Pb}^{2+}$  ions originate in the pores. This means that the rate of the decomposition reactions of the complexes are infinitely large.

If the flow of sulfuric acid arriving from the bulk of the electrolyte toward a given location of the plate which contains lead oxide is smaller than the dissolution rate of lead oxide (reaction [A]), the pH of the pore solution will be close to neutral. As a result reaction [3] occurs in the paste, and tribasic lead sulfate crystals will grow. If the sulfuric acid flow from the bulk of the electrolyte to the given location is larger than the dissolution rate of lead oxide (reaction [A]), the pH of the solution will be low, reaction [4] will take place, and lead sulfate will form. In the presence of an electrode surface (lead mass) close to the location, the electrochemical reaction [1'] takes place. This reaction is the electrochemical reduction of lead oxide to lead. The equilibrium potential of this reaction is given by Eq. [1'a]

$$\text{PbO} + 2e + 2\text{H}^+ = \text{Pb} + \text{H}_2\text{O} \quad [1'a]$$

$$E = 0.248 - 0.059 \text{pH}$$

Figure 5b gives the diagram of the elementary chemical and electrochemical reactions which occur when  $3\text{PbO} \cdot \text{PbSO}_4 \cdot \text{H}_2\text{O}$  is the starting material. As a result of the dissolution of tribasic lead sulfate (reaction [B]) the pore solution contains  $\text{Pb}^{2+}$ ,  $\text{OH}^-$ , and  $\text{SO}_4^{2-}$  ions. The  $\text{Pb}^{2+}$  ions may participate both in the electrochemical reaction 1'' and in the chemical reaction [4]. Whether reaction [4] will occur or not depends on the accession of sulfuric acid from the bulk of the electrolyte. If this flow is larger than the dissolution rate of  $3\text{PbO} \cdot \text{PbSO}_4 \cdot \text{H}_2\text{O}$  the pH of the pore solution will be low. Reaction [4] will then take place, yielding lead sulfate. The lead ions which are generated upon dissolution of  $3\text{PbO} \cdot \text{PbSO}_4 \cdot \text{H}_2\text{O}$  participate in the electrochemical reaction [1'']. The equilibrium potential of the  $\text{Pb}/3\text{PbO} \cdot \text{PbSO}_4 \cdot \text{H}_2\text{O}$  electrode is given by the equation

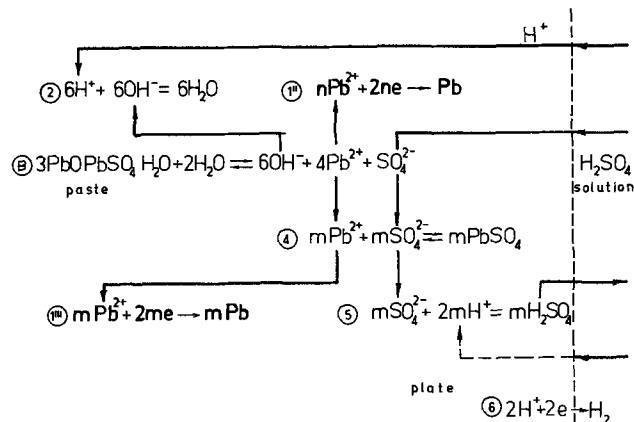
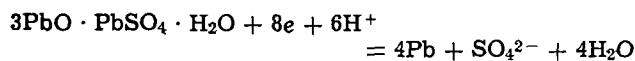
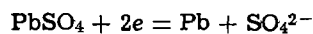


Fig. 5b. Diagram of the elementary chemical and electrochemical reactions with  $3\text{PbO} \cdot \text{PbSO}_4 \cdot \text{H}_2\text{O}$  as starting material.



$$E = 0.030 - 0.044 \text{ pH} - 0.007 \log a_{\text{SO}_4^{2-}} \quad [1''\text{a}]$$

When lead oxide and tribasic sulfate are consumed in the paste or are located at a distance which does not ensure a flow of  $\text{Pb}^{2+}$  ions toward the electrode surface and which could participate in the electrochemical reactions [1'] and [1''], reduction of the lead sulfate begins. This process may take place provided the electrode potential is more negative than the equilibrium potential of the  $\text{Pb}/\text{PbSO}_4$  electrode



$$E = -0.356 - 0.029 \log a_{\text{SO}_4^{2-}} \quad [1'''\text{a}]$$

Sulfuric acid originates as a result of the reduction of lead sulfate and diffuses back into the bulk of the electrolyte.

The electrochemical reaction takes place at those locations of the lead zone which are in contact with lead compounds forming with lead electrodes with the most positive equilibrium potentials. These are the electrochemical reactions [1'a] and [1''a] which take place until the eighth hour of formation. When  $\text{PbO}$  and  $3\text{PbO} \cdot \text{PbSO}_4 \cdot \text{H}_2\text{O}$  are consumed, reaction [1'''\text{a}] will take place and lead sulfate will be reduced.

Lead ions are consumed when the electrochemical reaction takes place in the solution layer at the boundary with the lead crystals. In order to maintain the electroneutrality of the solution in the pores of the plate, in this layer the consumption of the positive charges of the  $\text{Pb}^{2+}$  ions must be compensated. This may be achieved by migration of  $\text{H}^+$  ions from the bulk of the solution toward this layer and of sulfate ions in the opposite direction. These flows control the advance of the lead zone along the thickness of the plate. If the migration flows are hindered at a given place in the plate, the pore solution there is charged negatively by  $\text{SO}_4^{2-}$  and  $\text{OH}^-$  ions. This decreases the rate of the electrochemical reaction  $\text{Pb}^{2+} + 2e = \text{Pb}$  since the number of negative ions at this place increases. This decreases the rate at which the lead zone advances along the cross section of the plate. The migration flows are largest at the surface of the plate. Hence, the lead zone advances first along the two surfaces of the plate, and only after having covered them continues toward the bulk of the plate.

### Evolution of the Pore Structure of the Plate during Formation

By following the changes in phase composition during formation one can determine the way in which the volume fraction of the plate occupied by matter is built up. The plate shows good working parameters when there is a maximum access of sulfuric acid to lead. This is achieved when the active mass is very porous. Such a structure originates during plate formation. It is therefore desirable to determine the influence of the formation processes on the building up of the porous structure of the active mass. Table I gives the densities and the molar volumes of lead and of the lead compounds present in the plate (16). From Table I it can be seen that there is a considerable difference in the molar volumes of lead and lead compounds.

Table II gives the changes in the molar volume during certain chemical and electrochemical reactions. The

Table II.

Reactions		Relative volume change with respect to the initial product, %
Starting product	End product	
PbO	Pb	-23
	$3\text{PbO} \cdot \text{PbSO}_4 \cdot \text{H}_2\text{O}$	+60
	$\text{PbSO}_4$	+100
$3\text{PbO} \cdot \text{PbSO}_4 \cdot \text{H}_2\text{O}$	Pb	-52
	$\text{PbSO}_4$	+23
$\text{PbSO}_4$	Pb	-60

molar volume increases during all reactions of sulfatization of lead oxide and tribasic sulfate. In all electrochemical reduction reactions the same volume decreases.

The porosity of the active mass is expressed by two parameters: total porosity and pore size distribution. The changes in these parameters in the surface and bulk portions of the plates were followed during formation. The samples for these measurements were taken and dried together with the samples for the phase composition studies.

The measurements of total porosity and pore size distribution were carried out with a Carlo Erba 65 AG mercury porosimeter. The formation of lead amalgam was avoided by creating a thin stearic acid film (17). The samples from the surface and bulk portions were soaked in a 1% stearic acid solution in chloroform for 6 hr. They were then transferred to watch glasses and dried at  $105^\circ\text{C}$ . A determined amount of material was weighed and introduced in the glass cell of the porosimeter. The results obtained are given in Fig. 6. The curves of the surface and internal portions of the plates are plotted and compared with that of the unformed plate.

These measurements show that upon formation of the negative plate the pore radii and the total porosity increase. Prior to formation the pore radii range between 0.1 and  $0.3\mu$ . After formation, the pore radii vary between 0.6 and  $8\mu$ , with a predomination of 1-4  $\mu$  pores. The active mass has a porosity about 15% larger than that of the unformed plate. However, if we take into account the data of Table II, it becomes clear that this value is too low. This discrepancy is caused by the fragmentation of the samples during preparation. The fragments break down at the locations of the largest pores where the active mass is most brittle. These pores are thus lost in the measurement.

Two stages may be recognized in the evolution of total porosity. During the first one (until the sixth hour) the total porosity of the surface decreases. This indicates that the chemical reaction products predominate over the electrochemical reaction products. During this stage the porosity in the interior of the plate remains constant. This shows that the effect of the sulfatization reactions is compensated for by the effect of lead formation. During the second stage the total porosity both of the surfaces and of the inner parts increases. This is connected with the reduction of lead sulfate.

From Fig. 6 it can be seen that at the beginning of formation, part of the pores decreases in radius. These pores are located at those points of the paste where only chemical sulfatization reactions have taken place. From Table I it is seen that the molecular volume of the products (lead sulfate and tribasic lead sulfate) is larger than that of the starting compounds (lead oxide). On the other hand, at the exterior of the plate, where a lead zone has formed, the pore radius has increased (Fig. 2h). With the advance of formation the lead zone increases, as does the pore radius. Until the sixth hour, this effect is larger at the surface parts than

Table I.

Compound	Density, g/cm <sup>3</sup>	Molar volume, cm <sup>3</sup> /mole
Pb	11.34	12.28
$\text{PbSO}_4$	6.23	47.96
PbO ort.	9.64	29.15
PbO tet.	9.36	23.88
$3\text{PbO} \cdot \text{PbSO}_4 \cdot \text{H}_2\text{O}$	6.50	152.00

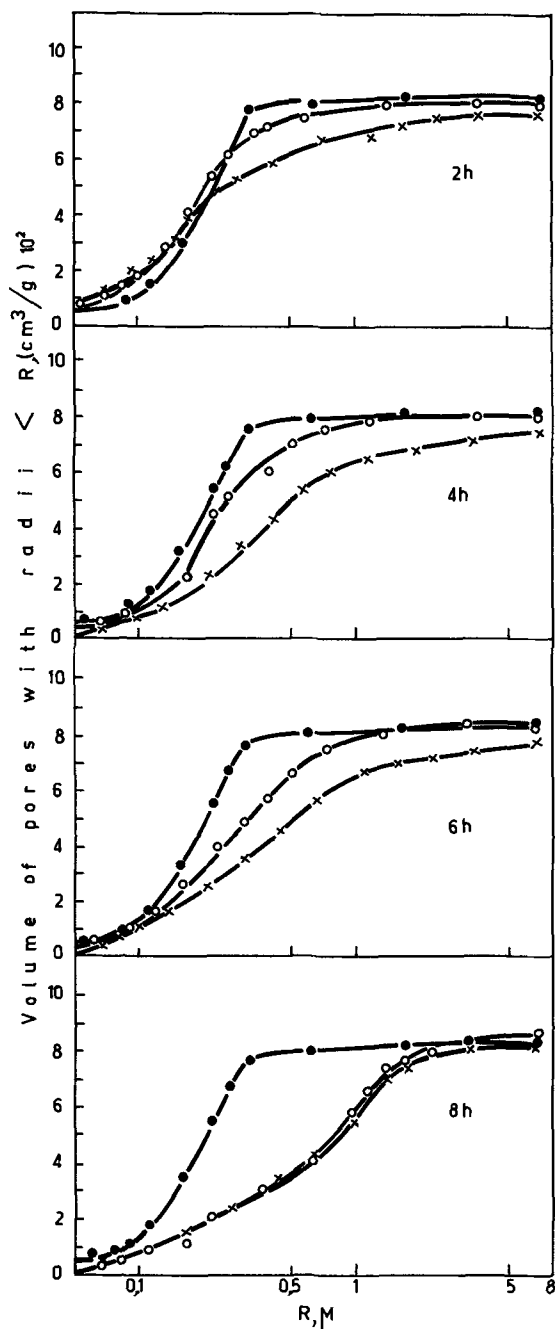


Fig. 6a. Change in pore size distribution and volume porosity until the eighth hour of formation.

in the bulk. This is in good accord with the results of the phase composition studies.

From Fig. 6 it is seen that at the eighth hour of formation the pore size distribution in the interior of the plate becomes identical with that of the surface parts. It can be assumed that after this moment the reaction of formation of lead at the surface and in the bulk takes place at the same rate. Hence, the pore size distribution curves after the eighth hour have the same shape.

#### Electrocrystallization Processes during Formation of the Negative Plate

From the consideration of the elementary chemical and electrochemical reaction mechanism it becomes apparent that the evolution of the lead active mass takes place in two stages. During the first stage the lead crystals are formed at the expense of dissolution of lead oxide and tribasic sulfate. The crystallization

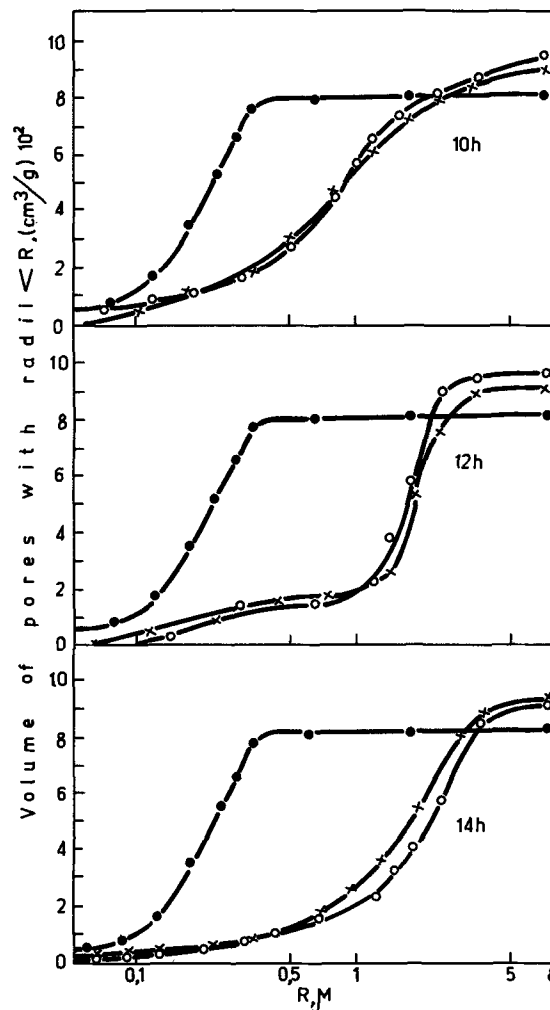


Fig. 6b. Continuation of Fig. 6a. Subsequent change in the pore size distribution and volume porosity after the eighth hour of formation. ●, Unformed plate; ○, at the surface of the plate; ×, in the bulk of the plate.

process occurs at a pH of the pore solution higher than that of the bulk solution but lower than 6 (the upper limit of stability of lead sulfate). During this stage a network of lead crystals is built up. This network begins from the grid members, grows first at the surface, and then in the interior of the plate. This lead network includes lead sulfate crystals. The growth of the lead crystals is controlled by the flow of lead ions which arrive from the lead oxide and tribasic sulfate which are being dissolved. At a defined thickness of the plate, paste density, and manufacturing technology conditions can be created which could ensure a directed growth of the lead crystals from the surface towards the center of the plate. Such a microstructure of the active mass has been observed (14).

During the second stage the lead sulfate crystals are reduced. They are dissolved and  $\text{Pb}^{2+}$  ions lose their charge on the primary network of lead crystals. This process occurs at a pH of the pore solution smaller than that of the bulk solution. This gives rise to the secondary structure of the active mass. It may be concluded that the buildup of the active mass of the negative plate depends on current and paste density, sulfuric acid concentration in the electrolyte, and temperature. The determination of the effect of each of these individual parameters is of particular interest since it will widen and increase our knowledge of the elementary processes which take place upon formation of the negative plate.

Manuscript received Jan. 22, 1974.

Any discussion of this paper will appear in a Discussion Section to be published in the June 1975 JOURNAL. All discussions for the June 1975 Discussion Section should be submitted by Feb. 1, 1975.

## REFERENCES

1. E. Willihnganz, National Lead Company Research Laboratory Report, May 1940 Meeting of National Battery Manufacturers Association.
2. E. Willihnganz, *Trans. Electrochem. Soc.*, **92**, 281 (1947).
3. T. I. Popova and B. N. Kabanov, *Zh. Prikl. Khim.*, **32**, 326 (1959).
4. Ja. B. Kasporov, E. G. Yampol'skaya, and B. N. Kabanov, *ibid.*, **32**, 326 (1959).
5. E. G. Jampol'skaya, M. I. Ershova, I. I. Astakhov, and B. N. Kabanov, *Electrokhimiya*, **2**, 1327 (1966).
6. S. C. Barnes, *Proc. Intern. Conf. Lead*, 2nd, *Arnhem.*, Oct. 4-7, 1965.
7. W. Simon, *Bosch. Techn. Ber.*, **1**, 234 (1966).
8. I. A. Agouf, M. A. Dasoyan, L. A. Ivanenko, E. V. Parshikova, and K. M. Solov'eva, *Pap. Electrochem. Power Sources*, **5**, 21, (1970). (Published by Energia, Leningrad.)
9. V. V. Novodershkin and G. I. Manoim, *ibid.*, **1**, 36 (1966).
10. J. R. Pierson, P. Gurlusky, A. C. Simon, and S. M. Caulder, *This Journal*, **117**, 1463 (1970).
11. E. F. Bordt, G. A. Kolinova, V. V. Novodershkin, and M. A. Dasojan, *Pap. Electrochem. Power Sources*, **7**, 55 (1972). (Published by Energia, Leningrad.)
12. A. C. Simon and E. L. Jones, *This Journal*, **109**, 760 (1962).
13. N. E. Bagshaw and K. P. Wilson, *Electrochim. Acta*, **10**, 867 (1963).
14. A. C. Simon, in *Power Sources 2, 1968*, Proc. Sixth Intern. Symp., Brighton, D. H. Collins, Editor, p. 33, Pergamon Press, New York (1970).
15. D. Pavlov, Proc. Symp. Batteries for Traction and Propulsion, p. 135, Columbus Section of The Electrochemical Society (1972).
16. J. Burbank, *This Journal*, **113**, 10 (1966).
17. M. Svata, "Porosimetrie a jeji pouziti," *Czech. Acad. Sci.*, p. 94, Praha (1969).

## Impurity Effects in the Dissolution of Anodic Tantalum Oxide

J. P. S. Pringle\*

Chalk River Nuclear Laboratories, Atomic Energy of Canada Limited, Chalk River, Ontario, Canada

The publication costs of this article have been assisted by Atomic Energy of Canada Limited.

## ABSTRACT

Anodic tantalum oxide dissolves slowly and uniformly in hydrogen fluoride almost saturated with ammonium fluoride. When the oxide is implanted with heavy ions at fluences of around  $10^{16}/\text{cm}^2$ , the dissolution accelerates; implanted with the same fluence of hydrogen, it decelerates. Similar effects have been reported in the literature for impurities incorporated from the electrolyte during anodization, and so the changes in the dissolution rate can be ascribed to the physical presence of the impurities themselves. Accelerated dissolution can be correlated with the concentration profiles of implanted atoms. This provides a new method for measuring the latter, and one that is particularly useful for elements, such as neon, which have no long-lived radioisotopes. The nature of the accelerating process could not be determined owing to limitations in data and analysis.

Anodic tantalum oxide dissolves slowly and very uniformly in concentrated mixtures of hydrofluoric acid and ammonium fluoride. Thin uniform layers can therefore be removed in succession, and this forms the basis of a sectioning technique (1) for measuring the range profiles of implanted radioactive ions (2). Implantation, however, is accompanied by radiation damage, and the latter is known to change the properties of materials. To ensure the precision of the measurements, therefore, it was necessary to find out whether implantation affected the oxide dissolution. Experiments with stable isotopes, performed at fluences of  $10^{16}$ - $10^{17}/\text{cm}^2$ , showed that indeed it did (3). The implantation of hydrogen slowed the dissolution, but the implantation of other elements accelerated it.

This difference between hydrogen and other implants indicated that radiation damage was not responsible for the changes in dissolution rate. Further confirmation was supplied by reanodizing implanted samples to greater thickness. The anodizing current is thought to flow through the oxide by the simultaneous rearrangement of a number of atoms, both tantalum and oxygen, to new positions (4, 5), so that any structural changes due to radiation damage should anneal out. If the change in dissolution rate remains, therefore, it must be attributed to the continued presence of the implanted species. Experiments with implanted radio-

active krypton and copper show that this is precisely what happens; on reanodization, the krypton stays in the oxide and the accelerated dissolution effect stays with it, while the copper migrates out of the oxide entirely, and no accelerated dissolution is observed (3). Impurities incorporated from the solution during anodization, should therefore behave similarly, and this is indeed observed.

### Effect of Impurities Incorporated during Anodization

Radioactive  $^{32}\text{P}$  and  $^{35}\text{S}$  are found in the outer layers of films formed in phosphate and sulfate electrolytes containing  $^{32}\text{PO}_4^{---}$  and  $^{35}\text{SO}_4^{--}$  (6, 7), and nuclear microanalysis has shown that nitrogen is incorporated from nitric acid electrolytes (8). Though there is no definite proof that these impurities are present as the oxyanions, this seems probable in view of the oxygen analyses by Amsel *et al.* (8). Naturally, the amount of impurity incorporated varies with the experimental conditions and is very small in the dilute aqueous electrolytes normally used (6, 1). In concentrated electrolytes, however, it can be large. Anodic films formed in these electrolytes are scarcely oxides, and their properties are indeed significantly different. The difference is, however, restricted to the outer layers of the film containing the impurity, since the inner layers appear to be similar in all respects with films formed in dilute electrolytes (6, 9, 10).

Accelerated dissolution of these outer layers in HF reagents has been observed for films formed in con-

\* Electrochemical Society Active Member.

Key words: tantalum, anodic oxidation, ion implantation, oxide dissolution, impurity effects.



centrated  $\text{H}_2\text{SO}_4$  (8, 9),  $\text{HCOOH}$  (11), and  $\text{Na}_2\text{B}_4\text{O}_7$  in ethylene glycol (9). The acceleration increases with electrolyte concentration (8, 9), and hence presumably with the impurity concentration in the film. Nuclear microanalysis indicates that the  $\text{SO}_4^{--}:\text{Ta}$  ratio in the outer layer of films formed in 95%  $\text{H}_2\text{SO}_4$  is about 0.75:1, and it is found that such layers dissolve at about eight times the normal rate (8). For comparison, the  $10^{16}$   $^{84}\text{Kr}^+/\text{cm}^2$  illustrated in Fig. 2 of Ref. (3) are mostly present in the first 300Å of oxide, to give an average Kr:Ta ratio of 0.15:1; and the accelerated stripping that results is, on average, about twice the normal rate. The effects observed with incorporated sulfate and implanted krypton are therefore approximately in proportion.

Not all incorporated impurities accelerate the dissolution, however, as examination of the films formed in 85%  $\text{H}_3\text{PO}_4$  will show. A report (6) that the outer layers of these films show accelerated stripping is in error, because the film thicknesses were determined by reciprocal capacity measurements. Similar measurements on films formed in concentrated formic acid did not tally with thicknesses obtained by optical and weight gain methods (11). If the corrections indicated in Ref. (11) are applied to the measurements reported in Ref. (6), the latter will agree with (9) and (11) that the outer layer of films formed in 85%  $\text{H}_3\text{PO}_4$  dissolve at about two thirds the normal rate. Phosphate impurity therefore decelerates the dissolution. Decelerated dissolution has also been observed with implanted hydrogen atoms (3), where it was attributed to the formation of hydrogen bonds. A similar chemical reason may well be responsible for the effect with phosphate.

Studies with phosphate- $^{32}\text{P}$  electrolytes have shown that the  $^{32}\text{P}$  is incorporated uniformly throughout the outer layer of the oxide (6, 7), and further experiments (6, 9) show that this layer dissolves at a constant rate. The deceleration thus appears to be related to the concentration profile of the presumed phosphate- $^{32}\text{P}$ , and a similar comment is probably true for sulfate- $^{35}\text{S}$  (6, 9). It should be noted, however, that recent measurements with an ion microprobe mass spectrometer (12) suggest that the phosphorus is not incorporated uniformly, but is concentrated toward the outer edge of the outer layer. Obviously, further work is needed to resolve this discrepancy.

The dissolution of anodic tantalum oxide is thus affected by impurities, however these are incorporated. It is then reasonable to suppose that any change in the dissolution rate will be proportional to the local concentration of the impurity atoms, and hence that the variation in the dissolution rate will be related to their concentration profile. The present paper shows that this variation can indeed be used to measure the concentration profiles of implanted atoms.

### Experimental Procedure

Chemically polished tantalum foils,  $3.5 \times 1.0 \times 0.037$  cm (0.015 in.), were anodized to the required thickness at 1 mA/cm<sup>2</sup> and 25°C in 0.1M  $\text{H}_2\text{SO}_4$ . A small area,  $0.5 \times 0.8$  cm, in the middle of one face was then implanted with the appropriate fluence, usually  $10^{16}/\text{cm}^2$ , of noble gas ions in a mass separator. The fluence was monitored by determining the amount of charge deposited on the foil. Oxide thicknesses on the implanted and nonimplanted areas were then measured by means of a spectrophotometric method (1). Though calibrated for nonimplanted oxide, the method can be applied, with reasonable confidence, to oxides implanted with up to  $10^{16}$  ions/cm<sup>2</sup> (3). The anodic film was then sectioned by dissolution in HF almost saturated with  $\text{NH}_4\text{F}$  (1), and the thicknesses on both areas measured after the removal of each oxide layer. More complete details can be found in Ref. (3), where the identical procedure was used.

The implanted atoms came to rest only in the surface layer of the anodic film. When sectioning began, therefore, this surface layer dissolved more rapidly than usual, and so the oxide thickness,  $X$ , on the implanted area decreased faster than that,  $X_n$ , on the nonimplanted area. Once the surface layer had been removed, the remaining oxide on the implanted area was oxide that had not been implanted at all. It therefore dissolved at the same rate as the oxide on the nonimplanted area, so that the film thickness on both areas now decreased at the same rate. The heavy lines in the top part of Fig. 1 illustrate this process schematically. An alternative and more convenient method (3) of presenting the results is given in the bottom part of the figure, where the implantation differential, which is defined as the oxide thickness remaining on the implanted area less that remaining on the nonimplanted area, is plotted against the oxide thickness dissolved from the latter; i.e.,  $(X - X_n)$  vs.  $(X_n(1) - X_n)$ , where  $X_n(1)$  is the initial thickness on the nonimplanted area.

The experimental measurements were in the form of a series  $I = 1, 2, \dots, N$  of oxide thicknesses,  $X(I)$ , remaining on the implanted area as a function of the corresponding thicknesses,  $X_n(I)$ , remaining on the

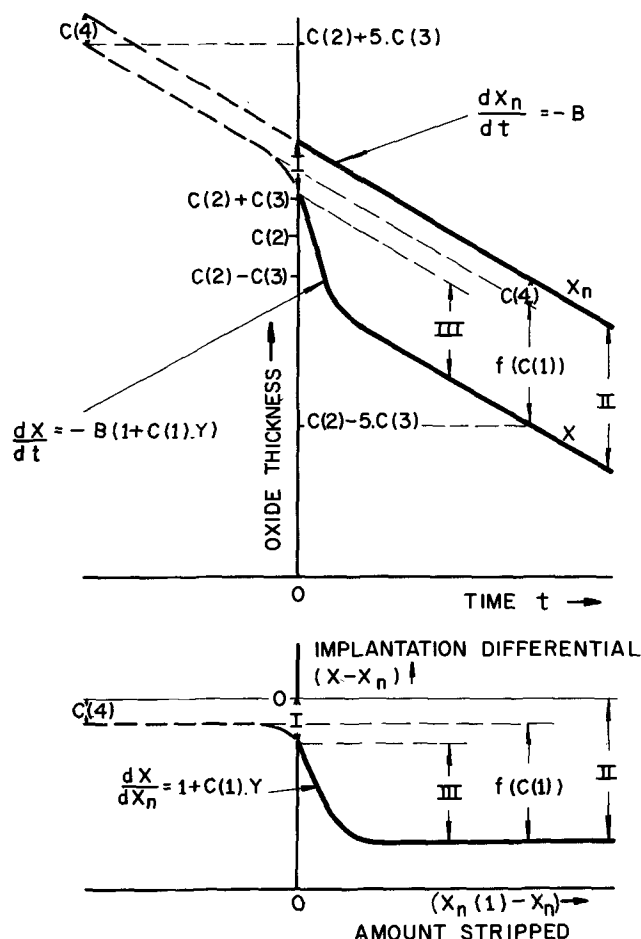


Fig. 1. Schematic diagrams to illustrate the relation between the various parameters discussed in the text. The experimentally measurable quantities defined in Ref. (3) are the initial implantation differential (I), the final implantation differential (II), and the magnitude of the accelerated stripping (III). The upper diagram shows how the thicknesses on the implanted area,  $X$ , and the nonimplanted area,  $X_n$ , vary with time, while the lower illustrates the corresponding variation in the implantation differential,  $X - X_n$ , as a function of the oxide thickness dissolved from the nonimplanted area,  $X_n(1) - X_n$ . All experimental results, both here and in (3), are presented in the format of the lower illustration. The constant of integration,  $C(4)$ , has been drawn as a negative quantity in these diagrams; experimentally it was found to be positive.

nonimplanted area. The standard errors in each measurement,  $EX(I)$  and  $EX_n(I)$ , were calculated as described in (1). The problem was, therefore, to correlate the variation in  $X$  with the concentration profile of the implanted atoms.

### Mathematical Analysis

Range profiles for ions implanted in anodic tantalum oxide are normally distributed within experimental error (2). Using the nomenclature of previous papers, these profiles can be described by

$$Y = \frac{F}{\sqrt{2\pi} \cdot C(3)} \cdot \exp \left[ - \left( \frac{X - C(2)}{\sqrt{2} \cdot C(3)} \right)^2 \right] \quad [1]$$

where  $Y$  is the local concentration of implanted ions in units of number/cubic angstrom;  $X$  is the distance in angstroms from the metal/oxide interface;  $F$  is the fluence of implanted ions in units of number/angstrom, equivalent to  $10^{-16}$  times the number/square centimeter;  $C(2)$  is the distance in angstroms between the profile mode and the metal/oxide interface; and  $C(3)$  is the standard deviation, also in angstroms, of the range profile.

Since the concentration profile remains close to a normal distribution on further anodization (4), Eq. [1] can be applied with little error to reanodized samples as well.

As a first attempt, the accelerated dissolution of the oxide may be attributed to the instantaneous dissolution of a certain volume,  $C(1) \text{ \AA}^3$ , in the immediate vicinity of each implanted ion. When one cubic angstrom of implanted oxide is dissolved at the normal rate, therefore, it will be accompanied by an additional  $C(1) \cdot YA^3$  dissolved instantaneously. If the dissolution rate for the nonimplanted oxide is given by

$$dX_n/dt = -B \quad [2]$$

that for the implanted oxide will be

$$dX/dt = -B(1 + C(1) \cdot Y) \quad [3]$$

where the negative signs occur because the sectioning decreases both  $X$  and  $X_n$ . The simultaneous integration of Eq. [2] and [3] then describes the relationship between  $X$  and  $X_n$ , as illustrated in the upper part of Fig. 1.

It is, however, much more convenient to eliminate the time variable. Dividing Eq. [2] and [3] by  $dt/dX_n = -1/B$  gives

$$dX_n/dX_n = 1 \quad [4]$$

and

$$dX/dX_n = 1 + C(1) \cdot Y \quad [5]$$

as indicated in the lower part of Fig. 1. The simultaneous integration of Eq. [4] and [5] is now taken with respect to  $X_n$ , and can be performed numerically by means of a Runge-Kutta procedure (13) on a computer. The integration is, of course, taken in the direction of decreasing  $X$  and  $X_n$ .

Figure 1 shows the connection between the parameters  $C(1)$ ,  $C(2)$ , and  $C(3)$ , and the quantities previously defined (3). Range profiles in anodic tantalum oxide are not complete normal distributions, because they are truncated by the oxide surface (2). The Runge-Kutta procedure must therefore be started well beyond the oxide surface. In the present analyses it was started at an oxide thickness equivalent to  $C(2) + 5C(3)$ ; that is, five standard deviations before the mode. A constant of integration,  $C(4)$ , is necessary; as illustrated in Fig. 1, this is simply the difference between  $X$  and  $X_n$  at the start of the procedure, not at the start of the experimental measurements themselves. Though actually drawn as a negative quantity,  $C(4)$  may be positive; its physical significance is discussed later.

Best estimates for the four parameters were obtained by applying the least squares fitting procedure described in (2). The independent variable was  $X_n$ , and

the dependent variable  $X$ . To make the fit,  $X$  was computed for the  $N$  values of  $X_n$  and the values of the four parameters adjusted until the sum of the squares of the differences between observed and calculated values for both  $X$  and  $X_n$  was minimized. Besides giving best estimates for the parameters, the procedure also provided standard errors in these estimates, and a chi-square probability measurement or fitting probability,  $p(X^2)_{N-4}$ , for the goodness-of-fit.

The least squares fitting procedure has, however, certain limitations, and these became effective in the course of this work. Since they have not been studied to any extent, either here or elsewhere, a detailed discussion is impossible; a few qualitative comments are all that can be presented.

The fewer the experimental points, and the more inaccurate they are, the less the information that can be extracted from them in a least squares fit; that is, the fewer the parameters that can be characterized, the more inaccurate they are, and the greater the difficulty of distinguishing between alternative expressions of fit. It has been recommended that the number of experimental points should be at least three times the number of parameters to be fitted (14), so that at least twelve points were required here. With twelve to sixteen points per sample, the modal values,  $C(2)$ , were generally reasonable but the standard deviations,  $C(3)$ , were frequently not. This recommendation is, however, only a rule of thumb, and so it is not very surprising that there should be occasions on which it does not apply. When the number of points was raised to more than six times the number of parameters to be fitted, that is, to twenty-four or more points, reasonable results were always obtained with both parameters, as is demonstrated later.

One criterion for the satisfactory fit of a number of samples is that the fitting probabilities should be scattered about 0.5; that is, some should be better than average and some should be worse. The fits made here with twenty-four or more points all gave fitting probabilities of better than 0.908, which is rather too good to be true. Too good a fit will be obtained if the error in each experimental point has been overestimated; this does not seem likely here, since the magnitude of these errors is well established (1, 2). Alternatively, too many parameters could have been used in the fitting; again this does not seem likely, because the system can hardly be described with less. The obverse of this argument is that the experimental data are insufficient to characterize the number of parameters used, and this explanation is believed correct.

The least squares fitting procedure is thus being pushed rather close to its limit in the present work, and so there is some additional uncertainty in the figures quoted. The mathematical significance of any comparisons is therefore less reliable than usual.

### Testing the Proposed Correlation

For test purposes, samples with known concentration profiles were required. These were prepared by implanting  $^{84}\text{Kr}^+$  and  $^{85}\text{Kr}^+$  jointly at 40 keV to a total fluence of  $10^{16}$  ions/cm<sup>2</sup>; the stable  $^{84}\text{Kr}^+$  provided the fluence required for the dissolution measurements, while the radioactive  $^{85}\text{Kr}^+$  acted as the tracer needed for the measurement of the concentration profile. Two such samples were used, one as implanted, while the other was reanodized by 2308Å; the results have been illustrated in Fig. 2 of Ref. (3). The test of the correlation, then, was whether the parameters  $C(2)$  and  $C(3)$  determined from the dissolution analysis would agree with those obtained from the radioactive measurements within their combined experimental errors.

The range profile in the implanted sample gave

$$C(2) = 1708 \pm 2\text{ \AA}; \quad C(3) = 84 \pm 2\text{ \AA}$$

by  $^{85}\text{Kr}$  analysis, and

$$C(2) = 1712 \pm 9\text{ \AA}; \quad C(3) = 100 \pm 15\text{ \AA}$$

by dissolution analysis. Similarly, the specimen implanted and then reanodized gave

$$C(2) = 2432 \pm 13\text{\AA}; \quad C(3) = 102 \pm 9\text{\AA}$$

by  $^{85}\text{Kr}$  analysis, and

$$C(2) = 2433 \pm 2\text{\AA}; \quad C(3) = 88 \pm 4\text{\AA}$$

by dissolution analysis. Since the difference between any pair of measurements is less than twice the root mean square of the component standard errors, the results apparently agree.

In reaching this conclusion, however, several other factors must be taken into account, besides the uncertainty in the least squares fitting procedure described previously.

(i) It has been assumed that the range profile for  $^{84}\text{Kr}^+$  ( $^{85}\text{Kr}^+$ ) implanted to  $10^{16}$  ions/cm $^2$  at 40 keV is normally distributed.—This assumption is certainly justified for krypton ions implanted at fluences up to  $10^{15}$  ions/cm $^2$ , as demonstrated previously (2). The present sample shows that it is justified for  $10^{16}$  ions/cm $^2$  as well, since the fitting probability,  $p(\chi^2)_{23}$ , obtained with the  $^{85}\text{Kr}$  analysis was 0.863, well above the acceptance limit of 0.025 (2).

(ii) It has been assumed that the  $^{84}\text{Kr}$  concentration profile remains normally distributed on further anodization.—As discussed elsewhere (4), reanodization has the effect of folding a normal distribution into the original profile. If the latter is a complete normal distribution, the final profile will also be normally distributed, and its standard deviation will be equal to the square root of the sum of the squares of the component standard deviations. When the initial profile is a truncated normal distribution, however, the final profile cannot be normally distributed. The departure from normality will depend on the degree of truncation and on the relative magnitudes of the component standard deviations. If the truncation is small and the standard deviation of the folding distribution large, the departure from normality will be negligible, as demonstrated by the 5 keV  $^{125}\text{Xe}$  samples reanodized in previous work (4).

In the present work, however, the krypton ions were implanted at 40 keV. Though the degree of truncation is much the same for both 5 and 40 keV (2), the relative magnitude of the standard deviation folded in will be much less for a broad 40 keV profile than for a narrow 5 keV one. It is not surprising, therefore, that the normal distribution should give a poor fit ( $p(\chi^2)_{10} < 0.001$ ) to the reanodized sample by  $^{85}\text{Kr}$  analysis. By contrast, the fit obtained with the dissolution analysis ( $p(\chi^2)_{10} = 0.958$ ) was excellent.

(iii) Equation [5] contains the assumption that  $C(1)$  is a constant independent of the stripping rate [1].—Three oxide specimens were implanted with  $10^{16}$  39

keV  $^{40}\text{Ar}^+$ /cm $^2$  in the same series of implantations to ensure reproducibility (3), and then analyzed in three different samples of the HF-NH $_4$ F stripping agent. The proportions of HF and NH $_4$ F were adjusted (1) to obtain stripping rates in a ratio of approximately 1:2:4, and the samples were maintained at 26°C by means of a water bath. Average stripping rates were calculated by dividing the total stripping time into the total thickness removed from the nonimplanted area. The results are given in Table I, from which it will be seen that the three  $C(1)$  values are indeed similar.

(iv) Equation [5] also requires that  $C(1)$  be independent of the implantation fluence  $F$ .—In this same series of implantations, an anodic oxide was implanted with  $2 \times 10^{16}$  39 keV  $^{40}\text{Ar}^+$ /cm $^2$ . Table I shows that the value of  $C(1)$  was again similar to those obtained at  $10^{16}$  ions/cm $^2$ .

(v) The proposed correlation must give acceptable ( $p(\chi^2)_{N-4} > 0.025$ ) fits to the experimental data.—The initial implantation differential,  $I$ , is always negative with these heavy ions, and may be taken as a first estimate for  $C(4)$ . As indicated in Fig. 1, it must be corrected for that portion of the normal distribution extending beyond the oxide surface, and since this correction is positive, the effects tend to cancel. The initial implantation differentials for the three  $10^{16}$   $^{40}\text{Ar}^+$ /cm $^2$  samples in Table I averaged  $-16\text{\AA}$ , while  $C(4)$  averaged  $+10\text{\AA}$ ; the truncation correction was therefore  $+26\text{\AA}$ . This positive result with  $C(4)$  may perhaps be interpreted as a swelling of the oxide structure due to the implantation of the argon ions. Such an effect would normally be masked by the sputtering responsible for the observed negative implantation differential. When  $2 \times 10^{16}$   $^{40}\text{Ar}^+$ /cm $^2$  were implanted,  $C(4)$  was twice as large, exactly as expected from this interpretation.

(vi) The proposed correlation must give reasonable estimates for  $C(1)$ .—The crude hypothesis, that each implanted ion is embedded in a volume  $C(1)\text{\AA}^3$  which dissolves instantaneously, thus accounts rather well for the observations considered so far. It but remains to examine  $C(1)$ , which for the sample implanted with  $2 \times 10^{16}$   $^{40}\text{Ar}^+$ /cm $^2$  was found to be  $337\text{\AA}^3$  (Table I). An estimate for  $C(1)$  may readily be obtained from the magnitude of the accelerated stripping (labeled III in Fig. 1) corrected for the truncation effect; the result is  $322\text{\AA}$ . That is, the implantation of  $2 \times 10^{16}$   $^{40}\text{Ar}^+$ /cm $^2$  of surface gives rise, on average, to the removal of  $322\text{\AA}^3$  by accelerated stripping, so that each implanted  $^{40}\text{Ar}^+$  gives rise to the removal of  $161\text{\AA}^3$ . This figure is just less than half the computed one, and so the latter must be in error.

(vii) Correction for  $C(1)$ .—The fault is, however, readily corrected. For every cubic angstrom removed from the implanted area by ordinary dissolution, an additional  $C(1) \cdot Y\text{\AA}^3$  will be removed by accelerated

Table I. Parameters for 39 keV  $^{40}\text{Ar}^+$  range profiles determined from dissolution analyses

Standard errors have been quoted. Interpolation of the range data in (2) suggests that the modal range should be about 230Å and the standard deviation 150Å

Average stripping rate, Å/min	Implantation fluence, $F$ ions/Å $^2$	Volume per ion, $C(1)$ , Å $^3$	Modal range, $(X(1) - C(2))$ , Å	Standard deviation, $C(3)$ , Å	Integration constant, $C(4)$ , Å	Number of experimental points, $N$	$p(\chi^2)_{N-4}$
$dX/dX_n = 1 + C(1) \cdot Y = 1 + C(1)/(\sqrt{2\pi} \cdot C(3)) \cdot \exp(-((X - C(2))/(\sqrt{2} \cdot C(3)))^2)$ [5]							
21.0	1	392 ± 6	216 ± 3	148 ± 4	11 ± 4	34	0.986
50.2	1	386 ± 6	213 ± 3	147 ± 4	12 ± 4	35	0.974
116.7	1	366 ± 6	225 ± 3	145 ± 4	7 ± 4	32	0.999
50.1	2	337 ± 8	224 ± 4	150 ± 6	22.5 ± 8	31	0.908
$dX/dX_n = \exp(C(1) \cdot Y) = 1 + C(1) \cdot Y + \frac{(C(1) \cdot Y)^2}{2!} + \dots + \frac{(C(1) \cdot Y)^m}{m!} + \dots$ [6]							
50.1	2	224 ± 5	223.5 ± 4	168.5 ± 6	24 ± 7	31	0.928
$dX/dX_n = 1/(1 - C(1) \cdot Y) = 1 + C(1) \cdot Y + (C(1) \cdot Y)^2 + \dots + (C(1) \cdot Y)^m + \dots$ [7]							
50.1	2	161 ± 4	223 ± 4	191.5 ± 6	25.5 ± 6	31	0.858

stripping due to the implanted ions it contains. This additional volume will itself contain implanted ions, and these will give rise to the removal of a further  $(C(1) \cdot Y)^2 A^3$  by accelerated stripping. The argument repeats in such a way that Eq. [5] becomes

$$\frac{dX}{dX_n} = 1 + C(1) \cdot Y + (C(1) \cdot Y)^2 + \dots + (C(1) \cdot Y)^m + \dots \quad [6]$$

Since this argument assumes that there is no overlap between adjacent  $C(1)$  cells,  $C(1) \cdot Y < 1$ ; hence [6] may be written

$$\frac{dX}{dX_n} = \frac{1}{(1 - C(1) \cdot Y)} \quad [7]$$

A least squares fit of Eq. [7] gave  $C(1)$  as  $161 \text{ \AA}^3$ , exactly as required; that is, the quantity labeled  $f(C(1))$  in Fig. 1 is now just  $2 \cdot C(1)$ . Table I shows, however, that though  $C(2)$  and  $C(4)$  remained the same as before,  $C(3)$  ballooned from the expected  $150 \text{ \AA}$  to  $192 \text{ \AA}$ ; Eq. [7] is not, therefore, satisfactory either.

(viii) *A second correction.*—But it is not realistic to suppose there will be no overlap between adjacent  $C(1)$  cells. The ions are implanted at random, and so some will come sufficiently close to cause overlap. The proportion that do so will obviously increase with increasing fluence. Some relatively straightforward mathematics, based on the fraction of the over-all volume present in the  $C(1)$  cells, showed that Eq. [7] would convert to

$$\frac{dX}{dX_n} = \exp(C(1) \cdot Y) \quad [8]$$

when overlap was taken into account. The least squares fit of Eq. [8] gave results intermediate to those from Eq. [5] and [7], for reasons that are obvious from the series expansions in Table I.

(ix) *Further corrections.*—Even with these corrections applied, therefore, the correlation is still not realistic. The second correction permits adjacent  $C(1)$  cells to overlap completely, which would mean that two  $^{40}\text{Ar}^+$  ions come to rest in exactly the same place to form  $^{80}\text{Kr}^{++}$ ! Furthermore, it is unreasonable that the individual  $C(1)$  cells should dissolve instantaneously at an infinite rate; they would dissolve at some multiple of the normal rate. Again, the boundary between the  $C(1)$  cells and the rest of the oxide is unlikely to be sharp. The rate of dissolution will decrease with distance from the implanted ion and may also vary with direction. Almost certainly, the rate would change once the implanted atom itself had been dissolved.

These several factors can only be described with the aid of additional parameters. Previous discussion has shown that the available measurements are barely adequate to characterize the four parameters that must be used; they would therefore be quite incapable of resolving more. The conclusion must be, then, that it is impossible to determine the mechanism of the accelerating process from the available data, and hence that it is impossible to determine the true correlation between the concentration profile and the accelerated dissolution.

Nevertheless, the fit of Eq. [5] has given good values for the mode and standard deviation of the krypton and argon profiles studied. Provided sufficient experimental points are taken, therefore, this accelerated dissolution may be used to measure range profiles at fluences of  $10^{16}/\text{cm}^2$ .

#### Concentration Profiles Measured by Accelerated Dissolution

When Eq. [5] was fitted to the samples reported in the previous paper (3), reasonable results were ob-

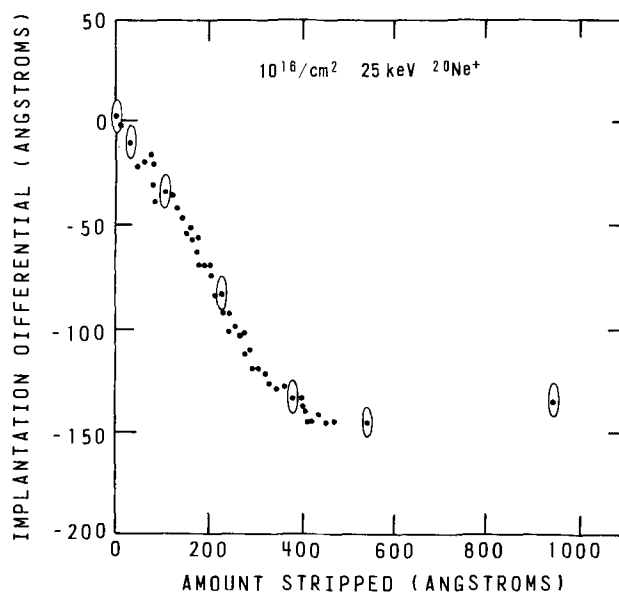


Fig. 2. Accelerated stripping observed with  $10^{16} \text{ }^{20}\text{Ne}^+/\text{cm}^2$ , implanted at 25 keV. Error ellipses have been drawn around some of the points at radii equal to twice the standard errors to indicate the magnitude of the 95% confidence limits around each point.

tained for the modes and poor results for the standard deviations. These samples had not, however, been intended for least squares fit analysis, and so relatively few points had been taken. The use of accelerated dissolution for range profile measurements may be illustrated by reference to the 25 keV  $^{20}\text{Ne}^+$  sample of Fig. 2; the modal range was found to be  $257 \pm 11 \text{ \AA}$ , and the standard deviation  $183 \pm 25 \text{ \AA}$ . For comparison, range parameters obtained with various radioisotopes (2) may be extrapolated to 25 keV  $^{20}\text{Ne}^+$ , and give a modal range of about  $280 \text{ \AA}$  and a standard deviation of about  $180 \text{ \AA}$ ; the two estimates are thus in reasonable agreement.

This accelerated dissolution method for measuring range profiles is particularly useful with elements, such as the neon discussed above, for which no long-lived isotopes exist.

#### Conclusions

1. Implantation of impurities changes the dissolution rate of anodic tantalum oxide in buffered HF, and these changes are very similar to those reported with impurities incorporated from the electrolyte during anodization.
2. This observation provides additional evidence that the radiation damage accompanying ion implantation is not responsible for the observed effects.
3. The implantation of heavy ions accelerates the dissolution, and this acceleration can be correlated empirically with the range profile.
4. The mechanism of the acceleration is, however, so complex that it cannot be elucidated from the available experimental evidence.
5. If the ions are implanted at a fluence of about  $10^{16}/\text{cm}^2$ , an empirical correlation can be used to measure their concentration profiles.

#### Acknowledgments

It is a pleasure, once again, to acknowledge the assistance of D. Phillips, who performed the experimental measurements. J. A. Davies and D. C. Santry kindly reviewed the manuscript and made valuable suggestions for improvement.

Manuscript submitted Nov. 7, 1973; revised manuscript received Feb. 11, 1974.

Any discussion of this paper will appear in a Discussion Section to be published in the June 1975 JOURNAL.

All discussions for the June 1975 Discussion Section should be submitted by Feb. 1, 1975.

## REFERENCES

1. J. P. S. Pringle, *This Journal*, **119**, 482 (1972).
2. J. P. S. Pringle, *ibid.*, **121**, 45 (1974).
3. J. P. S. Pringle, *ibid.*, **121**, 195 (1974).
4. J. P. S. Pringle, *ibid.*, **120**, 398 (1973).
5. J. P. S. Pringle, *ibid.*, **120**, 1391 (1973).
6. J. J. Randall, Jr., W. J. Bernard, and R. R. Wilkinson, *Electrochim. Acta*, **10**, 183 (1965).
7. D. M. Smyth, *This Journal*, **113**, 1271 (1966).
8. G. Amsel, C. Cherki, G. Feuillede, and J. P. Nadai, *J. Phys. Chem. Solids*, **30**, 2117 (1969).
9. D. A. Vermilyea, *Acta Met.*, **2**, 482 (1954).
10. C. J. Dell'Oca and L. Young, *This Journal*, **117**, 1545 (1970).
11. D. M. Cheseldine, *ibid.*, **111**, 1128 (1964).
12. R. E. Pawel, J. P. Pemsler, and C. A. Evans, Jr., *ibid.*, **119**, 24 (1972).
13. F. E. Lane, in Atomic Energy of Canada Limited Report Number 1744 (Part A) Addendum II, p. 38, Chalk River, Ontario (1969).
14. A. J. Ferguson, "Angular Correlation Methods in Gamma Ray Spectroscopy," North Holland, Amsterdam (1965).

## Further Observations on the Marker Behavior of Noble Gases during the Anodic Oxidation of Tantalum

J. P. S. Pringle\*

Chalk River Nuclear Laboratories, Atomic Energy of Canada Limited, Chalk River, Ontario, Canada

The publication costs of this article have been assisted by Atomic Energy of Canada Limited.

## ABSTRACT

Argon, krypton, xenon, and radon have been used as markers for measuring the transport numbers of metal and oxygen during the anodic oxidation of tantalum. Within experimental error, the results are independent of marker concentration over five orders of magnitude, and so the markers do not influence the transport mechanism by their presence, or by any radiation damage accompanying their implantation. Neon behaves in the same way as the heavier gases and is thus also suitable as a marker.

An oxide film on a metal surface will thicken only if metal atoms, or oxygen atoms, or both migrate across it. The actual mechanism can be identified by labeling a thin layer in the oxide with a suitable marker. On further oxidation, the metal atoms migrating outward through the marked layer give rise to new oxide between it and the oxide/environment interface. Similarly, oxygen atoms migrating inward form new oxide between it and the metal/oxide interface. The final position of the marker is thus determined by its position in the initial oxide, as modified by the subsequent metal and/or oxygen migrations to either side. By measuring the position of the marker before and after the oxidation event, therefore, the relative migration of metal and oxygen may be determined.

Though this concept is simple enough in theory, it presents one very formidable difficulty in practice. This is the difficulty of establishing that the chosen marker really is behaving as a marker. Two requirements must be met: the marker must not itself migrate during the oxidation event, and it must not interfere with the oxidation process; that is, it must be both immobile and inert.

These questions have been discussed at length in a recent report on the anodic oxidation of tantalum (1). Because the metal and oxygen migrations in this system are associated with the passage of an electric current, their relative magnitude can be specified in terms of transport numbers. Atoms of the heavier noble gases were used as markers, and their immobility tested against the following argument. If one of the noble gases is immobile, they all will be, and hence the transport numbers measured with the different gases should be exactly the same. Very precise measurements, using a sectioning technique (2) to measure the concentration profiles of radioactive noble gas isotopes (3), showed, however, that they were not

exactly the same. The transport numbers measured with  $^{41}\text{Ar}$ ,  $^{79}\text{Kr}$ , and  $^{125}\text{Xe}$  were all slightly different from one another, and the differences were significant at the 2.5% probability level. Furthermore, the measurements were in the correct order for a real effect, since  $^{79}\text{Kr}$  gave the intermediate result. The small mobility revealed was interpreted as a nonrandom Brownian motion, and an appropriate correction was made to obtain best estimates for the transport numbers. Noble gas markers must therefore be regarded as almost, but not quite, immobile.

No changes in the anodizing behavior had been detected with the markers present, and so they were presumed to be inert. These experiments had, however, been conducted with radioisotopes of the noble gases, and so the implanted concentrations were very low; not more than about 260 atoms per million matrix tantalum and oxygen atoms in fact. [Due to an unfortunate miscalculation, the concentrations quoted in the previous paper (1) are ten times too large.]

### Experimental Procedure

A further test for the marker behavior of the noble gases was to implant them at much higher fluence, so that their effect on the transport mechanism, if any, would be enhanced. The maximum fluence obtained in the previous experiments with radioisotopes had been about  $10^{13}/\text{cm}^2$ ; by implanting stable isotopes as well, the total fluence could easily be raised to  $10^{16}/\text{cm}^2$  or more. Radioactive ( $\sim 10^{13}$   $^{85}\text{Kr}/\text{cm}^2$ ) and stable isotopes ( $10^{16}$   $^{84}\text{Kr}/\text{cm}^2$ ) were therefore implanted at the same time into a small area,  $0.5 \times 0.8$  cm, on the face of a  $3.5 \times 1.0$  cm anodized tantalum foil, according to the procedure described elsewhere (4). Under these circumstances, the radioisotope acted as a tracer for the much larger quantity of stable isotope, and so the concentration profile of both isotopes together could be determined by the usual sectioning technique (2). Within experimental error, these profiles were found to

\* Electrochemical Society Active Member.

Key words: tantalum, anodic oxidation, ion implantation, markers.

be normally distributed (5), both before and after further anodization, and so their modes could be used as measures of marker position. Transport numbers were then calculated from the formula derived in Ref. (1), viz.

$$\begin{aligned} t_m &= (h_f - C(2) - \tau)/(h_f - h_i) \\ t_o &= (C(2) + \tau - h_i)/(h_f - h_i) \end{aligned} \quad [1]$$

where  $t_m$  and  $t_o$  are the transport numbers of the metal and oxygen, respectively,  $h_i$  is the initial oxide thickness,  $h_f$  the oxide thickness after further anodization,  $C(2)$  the modal position of the gas in the final oxide, and  $\tau$  the modal range of the gas as implanted.

Implantation fluences of  $10^{16}/\text{cm}^2$  give rise to noble gas concentrations of several atom per cent in the surface layers of the oxide. Not surprisingly, such massive concentrations of impurity alter the properties of the anodic film. Thus oxide loaded with noble gas dissolves more rapidly in the  $\text{HF-NH}_4\text{F}$  reagent used for sectioning (2), and so the film thickness on the  $0.5 \times 0.8$  cm implanted area thins faster. The difference (film thickness on the implanted area less that on the surrounding nonimplanted area) has been defined as the implantation differential (4), and it varies as sectioning proceeds. A typical (not best) result is illustrated in Fig. 1. The rate of change in the implantation differential is determined by the accelerated stripping rate on the implanted area, and this in turn can be related to the local concentration of noble gas impurity. It is therefore possible to use this variation in the implantation differential to measure the noble gas concentration profile (5). Accelerated stripping thus provides an alternative method for measuring transport numbers at high gas concentrations, and the  $10^{16}$   $^{84}\text{Kr} + ^{85}\text{Kr}/\text{cm}^2$  sample in Table I shows that the results agree, within experimental error, with those obtained from the radioisotope measurements.

Pilot measurements with an ellipsometer indicate that a high concentration of noble gas impurity alters

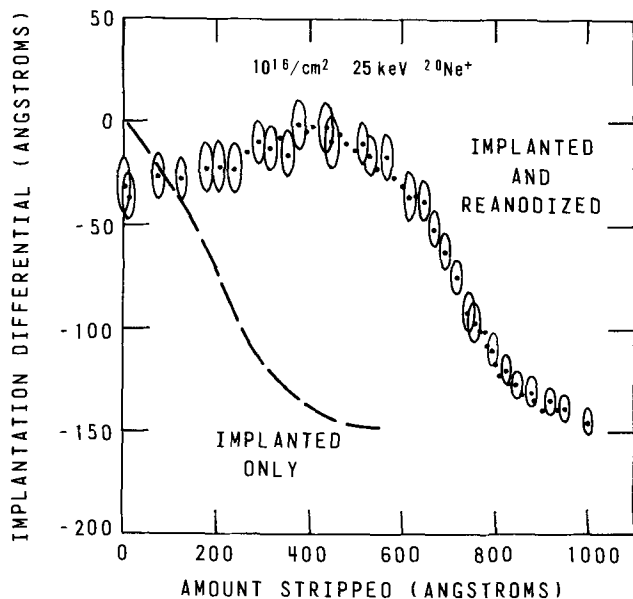


Fig. 1. Variation of the implantation differential for anodic tantalum oxide implanted with  $10^{16}$  25 keV  $^{20}\text{Ne}^+/\text{cm}^2$ , and reanodized from an initial thickness of 913Å to a final thickness of 3048Å. The amount stripped is the total oxide thickness removed from the nonimplanted area during the sectioning process (2); the implantation differential is the film thickness remaining on the implanted area less that remaining on the nonimplanted area. Error ellipses have been drawn at radii of twice the standard errors around some points to indicate the magnitude of the 95% confidence limits around each point. The dashed line indicates the result for a sample, in the same series of implantations (4), that had not been reanodized. The original results are given in Fig. 2 of Ref. (5).

Table I. Comparison of transport numbers for oxygen in the anodic oxidation of tantalum, as determined by radioisotope and accelerated stripping methods and Eq. [1]

Errors quoted are least squares errors of fit, calculated according to Eq. [11] in Ref. (1); the measurements at  $10^{10}$  ions/ $\text{cm}^2$  may well be subject to additional error owing to changes in the optical characteristics of the oxide (4). Anodizing conditions: 1 mA/ $\text{cm}^2$ , 0.1M  $\text{H}_2\text{SO}_4$ , 25°C, with approximately 2000Å of oxide added.

Noble gas	At a fluence of	The transport number measured by radioactivity was	The transport number measured by accelerated stripping was	At a fluence of
$^{222}\text{Rn}$	$10^{11}/\text{cm}^2$ <sup>(a)</sup>	$0.749 \pm 0.002$		
$^{136}\text{Xe}$	$10^{12}/\text{cm}^2$ <sup>(a)</sup>	$0.746 \pm 0.003$		
$^{78}\text{Kr}$	$10^{13}/\text{cm}^2$ <sup>(a)</sup>	$0.743 \pm 0.003$		
$^{84}\text{Kr} + ^{85}\text{Kr}$	$10^{16}/\text{cm}^2$ <sup>(b)</sup>	$0.744 \pm 0.007$	$0.744 \pm 0.006$	$10^{16}/\text{cm}^2$
$^{41}\text{Ar}$	$10^{13}/\text{cm}^2$ <sup>(a)</sup>	$0.741 \pm 0.003$		
$^{40}\text{Ar}$			$0.760 \pm 0.010$	$10^{16}/\text{cm}^2$
$^{20}\text{Ne}$			$0.761 \pm 0.006$	$10^{16}/\text{cm}^2$

<sup>(a)</sup> Data from Ref. (1).

<sup>(b)</sup> Illustrated in Fig. 2 of Ref. (4).

the optical properties of the anodic film, particularly after further anodization (4). A change in the optical properties will introduce systematic errors into oxide thicknesses measured by the spectrophotometric method (2), and hence into all the quantities appearing on the right-hand side of Eq. [1]. Transport numbers measured with high concentrations of noble gas are therefore inherently less accurate than those measured at low concentrations.

### Discussion

Table I shows that the transport numbers are independent of fluence over the five orders of magnitude studied. The radon atoms implanted at a fluence of  $10^{11}/\text{cm}^2$  will come to rest approximately 100 matrix atoms apart, and so there will, in effect, be large stretches of unimplanted oxide between them. Any interference with the transport mechanism in the natural oxide should therefore be very slight. By contrast, the implantation of  $10^{16}$   $^{84}\text{Kr}^+$  and  $^{85}\text{Kr}^+/\text{cm}^2$  puts the krypton atoms in almost nearest neighbor positions to one another. The similarity of the transport numbers under these extreme conditions then strongly suggests that noble gas markers do not affect the transport process by their presence, or by any radiation damage accompanying their insertion. The implication, therefore, is that the noble gas atoms present in high concentrations must be as mobile, or more correctly, as immobile, as those implanted at low concentration.

High concentrations of noble gas impurity could also affect the over-all kinetics of the anodization process. Since anodization normally gives rise to oxide film of uniform thickness (2), any change in the kinetics on the implanted area during further anodization may be expected to give a final oxide thickness different from usual. This would be manifest as a nonzero implantation differential. Reference to Fig. 1, and the corresponding Fig. 2 of Ref. (4) for krypton, will show that the implantation differential was negative immediately after reanodization, so that the final thickness on the implanted area was less. This observation was generally true of reanodized samples containing  $10^{16}$  noble gas atoms/ $\text{cm}^2$  and suggested that the anodization was slightly inhibited by this quantity of noble gas. Such interpretation must be viewed with caution, however, in view of the uncertainty attaching to film thickness measurements at high concentrations of impurity. Nevertheless, from the magnitude of the effect observed at  $10^{16}/\text{cm}^2$ , it is quite clear that the effect at  $10^{13}/\text{cm}^2$  would be negligible, and hence that the noble gas markers would indeed be effectively inert at the lower fluence.

Because accelerated stripping does not depend on the nuclear properties of the implanted atoms, it could be

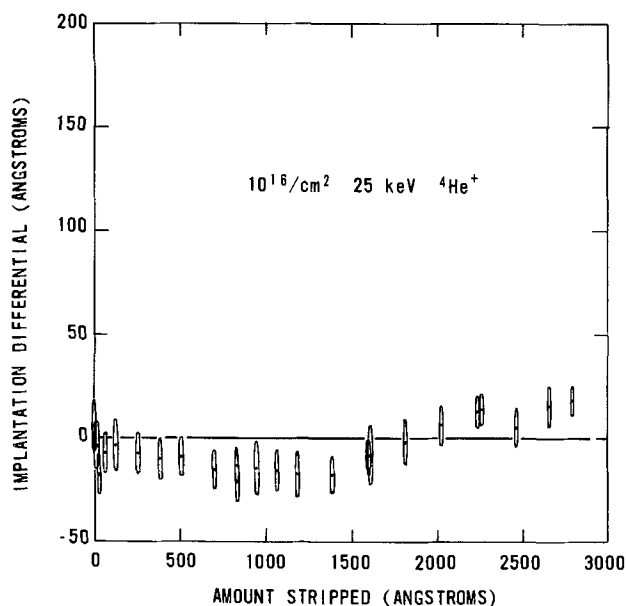


Fig. 2. Accelerated stripping, or lack of it, observed with implanted helium. Similar results were obtained with implantations at 40 and 55 keV.

used to extend the transport number measurements to neon, for which no long-lived radioisotopes exist. The result, as indicated in Fig. 1 and Table I, was the same within experimental error as those obtained with the heavier noble gases, and so neon is also suitable as a marker species. A further extension to helium proved impossible, since no accelerated dissolution was observed with this element (Fig. 2). Either helium does not accelerate the stripping, or it was not present,

having diffused out again immediately after implantation. The latter seems quite possible, since it diffuses rapidly in vitreous  $\text{SiO}_2$  and  $\text{GeO}_2$  (6).

### Conclusions

1. Up to  $10^{16}/\text{cm}^2$ , the implantation fluence of a noble gas marker has no effect on the measurement of transport numbers.

2. Noble gas markers do not, therefore, influence the transport mechanism during anodization, either by their presence or by any radiation damage accompanying their implantation.

3. Implanted in trace amounts,  $10^{13}/\text{cm}^2$  or less, noble gas markers have no effect on the kinetics of the anodization process and are therefore effectively inert.

4. Neon behaves in the same way as the heavier noble gases and is thus also suitable as a marker.

### Acknowledgments

The author is indebted to D. Phillips for performing many of the experimental measurements, and to J. A. Davies for reviewing the manuscript. Especial thanks are due to one of the JOURNAL reviewers, for valuable suggestions on how to improve the presentation.

Manuscript submitted Nov. 7, 1973; revised manuscript received Feb. 11, 1974.

Any discussion of this paper will appear in a Discussion Section to be published in the June 1975 JOURNAL. All discussions for the June 1975 Discussion Section should be submitted by Feb. 1, 1975.

### REFERENCES

1. J. P. S. Pringle, *This Journal*, **120**, 398 (1973).
2. J. P. S. Pringle, *ibid.*, **119**, 482 (1972).
3. J. P. S. Pringle, *ibid.*, **121**, 45 (1974).
4. J. P. S. Pringle, *ibid.*, **121**, 195 (1974).
5. J. P. S. Pringle, *ibid.*, **121**, 860 (1974).
6. J. E. Shelby, *J. Appl. Phys.*, **43**, 3068 (1972).

## Measurement of Cathode Mass Transfer Coefficients in Electrowinning Cells

V. A. Ettel, B. V. Tilak,<sup>1</sup> and A. S. Gendron

*The International Nickel Company of Canada, Limited,  
J. Roy Gordon Research Laboratory, Sheridan Park, Mississauga, Ontario, Canada*

*The publication costs of this article have been assisted by The International Nickel Company of Canada, Limited.*

### ABSTRACT

A recently developed, simple technique for determining cathode mass transfer coefficients in full scale electrowinning cells is discussed. The approach involves the determination of the limiting current for mass transfer controlled codeposition of silver in the cathode deposit. A rotating disk electrode was used to establish the validity of the method. Examples demonstrate the usefulness of the method for mapping local values of the mass transfer coefficient on the cathode under typical natural and forced convection flow regimes in electrowinning cells.

Recent attempts to develop pollution-free metallurgical technology have led to renewed effort in electrochemical research [see for example (1-3)]. A major effort has been directed towards operation of electrowinning cells at increased current densities either by optimizing cell design or by employing forced convection. For example, by employing a current redistributing anode (4, 5), smooth, compact, and uniform cop-

per was electrowon at current densities 15% higher than those obtainable in conventional cells using the identical electrolyte. Other approaches utilize forced agitation in the electrolytic cell by sparging with gas (6, 8) or by electrolyte recirculation (7). In order to assess the potential of alternative cell designs resulting from such developments, it is desirable to have a rapid, convenient method of determining local values of the cathode mass transfer coefficient ( $k$ ) *in situ* in full scale electrowinning cells.

<sup>1</sup> Present address: Hooker Chemical Corporation, Niagara Falls, New York 14300.

Key words: natural convection, forced convection, model cells.



The mass transfer coefficient ( $k$ ), defined as  $D/\delta$  (see Eq. [1]), has previously been determined by measurement of limiting current (9-11, 20), interferometric methods (12, 13) and by Brenner's freezing method (14)

$$i_{\text{Cu}+2} = 2F k_{\text{Cu}+2} (C_{\text{Cu}+2, \text{bulk}} - C_{\text{Cu}+2, \text{surf}}) \\ = 2F \frac{D_{\text{Cu}+2}}{\delta_{\text{Cu}+2}} (C_{\text{Cu}+2, \text{bulk}} - C_{\text{Cu}+2, \text{surf}}) \quad [1]$$

In the first method, the local limiting current density ( $i_L$ ) values are obtained by measuring  $i_L$  at various points on the surface of a vertical plate, which contains small cathodes that are insulated from one another and provided with potential probes. Dilute electrolytes are usually used in these measurements to minimize the limiting current. For measuring  $k$  in concentrated electrolytes used in practice, a modified approach has been used. Limiting current measurements are recorded using a movable probe electrode (5) placed in close proximity to the working electrode. This technique has been used to gather information on the degree of electrolyte agitation at the cathode in conventional electro-winning cells. However, the hydrodynamics at the probe are not the same as at the cathode surface and hence these measurements are of only limited value. Furthermore, evaluation of the extent of mass transfer from  $i_L$  is made uncertain by the area changes at the electrode since the deposits are powdery at the limiting current density.

It should also be pointed out that the value of the mass transfer coefficient measured under limiting current density conditions is not necessarily the same value as that prevalent under normal operating conditions (cf. Eq. [1]) since  $k$  depends on the current density itself.

Interferometric methods are based on differing refractive indices of the electrolyte in the diffusion layer and the bulk solution, arising from the concentration changes near the cathode during electrolysis. In Brenner's freezing method, the electrolyte near the cathode is suddenly frozen, and a thin section of the solid is shaved off for analysis of the composition of the layer.

While these techniques are very useful, particularly for bench top systems, they require complicated experimental arrangements. As such they cannot be readily used to determine mass transfer coefficients in large scale cells using concentrated electrolytes.

### Principles of the Present Method

The tediousness of the earlier methods for measuring mass transfer coefficients is largely overcome in the present method. This involves determination of limiting current density for the deposition of an ion which is codeposited at its maximum or mass transfer controlled rate. This can be achieved by selecting an ion which is reduced at more positive potentials than that of the major reducible species. Thus, in the case of either copper or nickel electro-winning using sulfate electrolytes, silver can be used. Since the standard potential of silver is  $\sim 460$  mV more noble than that of copper,  $\text{Ag}^+$  (at low concentrations) should plate at its mass transfer controlled (limiting) current density ( $i_{L, \text{Ag}^+}$ ) at the normal operating cathode potential ( $\sim -100$  mV vs.  $\text{Cu}/\text{CuSO}_4$  sat'd). From an analysis of the Ag content in the cathode deposit,  $i_{L, \text{Ag}^+}$  can be calculated. From this value and the bulk concentration of  $\text{Ag}^+$  in the electrolyte, the mass transfer coefficient for  $\text{Ag}^+$  deposition can be calculated from Eq. [2]

$$k_{\text{Ag}^+} = \frac{i_{L, \text{Ag}^+}}{FC_{\text{Ag}^+}} \quad [2]$$

This value reflects the actual operating conditions at the cathode and does not suffer the usual limitations of a measurement made at the limiting current for copper.

The assumption that the codeposition of Ag was mass transfer controlled was verified using a rotating disk electrode.

### Experimental

Cu and Ni electro-winning electrolytes for the rotating disk electrode studies were prepared from Analar grade chemicals using distilled water. The copper electrolyte was used without purification. However, the nickel electrolyte was initially purified by activated charcoal and  $\text{H}_2\text{O}_2$  treatment to reduce pitting of nickel deposits. Copper was deposited at a temperature of 25° and 55°C from the electrolyte containing a few ppm  $\text{Ag}^+$  (added as  $\text{Ag}_2\text{SO}_4$ ) under galvanostatic conditions at a current density of 3.5 A/dm<sup>2</sup>, using a stainless steel rotating disk electrode (rde) at various angular velocities. The rotating disk assembly was made by Pine Instrument Company. The electrode surface was polished to a mirror finish with 0.05 $\mu$  alumina on Buehler microcloth prior to each experiment. After each run the deposited copper was stripped for analysis. The Ag concentration in the metal and electrolyte was determined by atomic absorption spectrophotometry. A similar approach was used for the nickel rde studies except that a titanium cathode was used. Kinematic viscosity measurements of the electrolytes were made using an Ostwald viscosimeter.

A model electro-winning cell constructed of Plexiglas was used to obtain information on the mass transfer profiles in a full height cell. The rectangular cell was 110 cm high with a cross section of 6.5  $\times$  50 cm and was in fact a 50 cm wide section of a full-size industrial cell. The cell contained two Pb-6% Sb anodes and a stainless steel cathode, (electrode gap 2.6 cm). Electrolyte recirculating through the cell at 4.6 liters/min was initially generated and continuously replenished by leaching electrolytic grade copper drillings in the presence of air. The electrolyte contained 25 g/liter Cu and 100 g/liter  $\text{H}_2\text{SO}_4$  and the cell was operated at 25°C. Under steady-state conditions the copper concentration in the electrolyte could be maintained within  $\pm 2$  g/liter by controlling the air flow rate to the leaching tank. When operating with electrolyte jetting to provide agitation, the cell contained only a single anode and cathode (spacing 5 cm gap).

The chloride level in the original electrolyte was reduced to a negligible value (1 ppm) by precipitation with  $\text{Ag}_2\text{SO}_4$ , and the silver concentration in the electrolyte was adjusted to about 10 ppm prior to starting the plating run. During the run the silver level in the cell was slightly depleted ( $\sim 10\%$ ) so that an average of initial and final values was used for the calculations.

An additional series of tests using air sparging at 55°C with electrolyte containing 60 g/liter Cu, 140 g/liter  $\text{H}_2\text{SO}_4$ , 5 g/liter Fe and small concentrations of Ni, Co, and As were completed in a modified model cell measuring 110  $\times$  6  $\times$  15 cm.

### Results of Rotating Disk Experiments

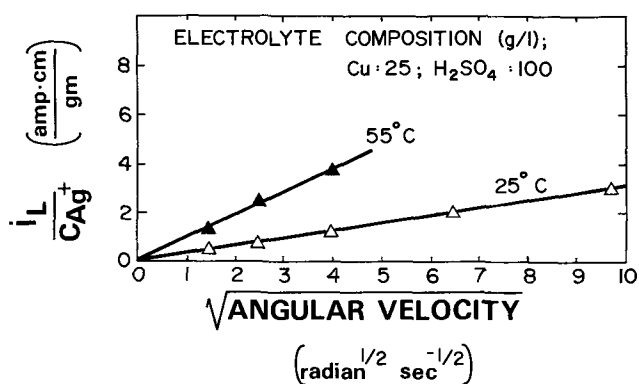
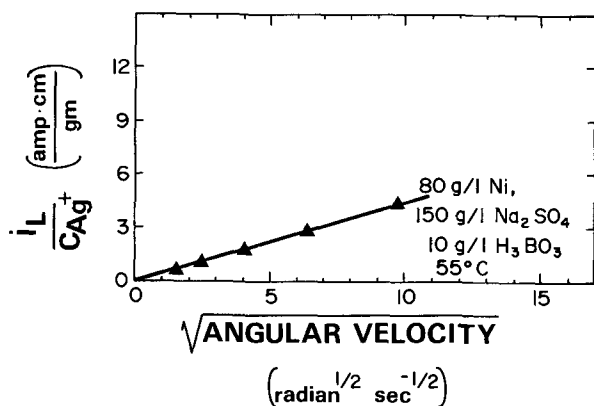
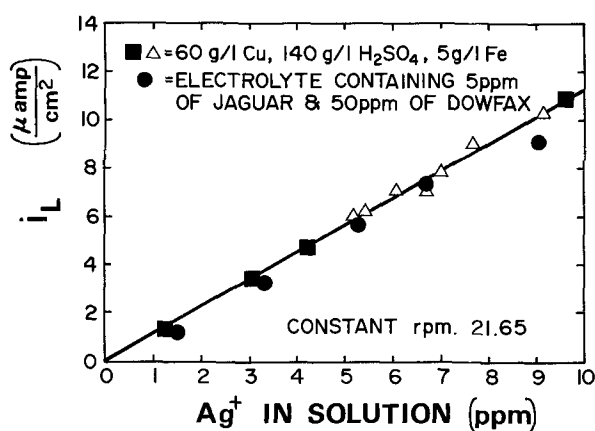
According to Levich's theory for mass transport by convective diffusion to a rotating disk electrode the limiting current density is given by (18)

$$i_{L, \text{Ag}^+} = 0.62 nFD_{\text{Ag}^+}^{2/3} \nu^{-1/6} \omega^{1/2} C_{\text{Ag}^+} \quad [3]$$

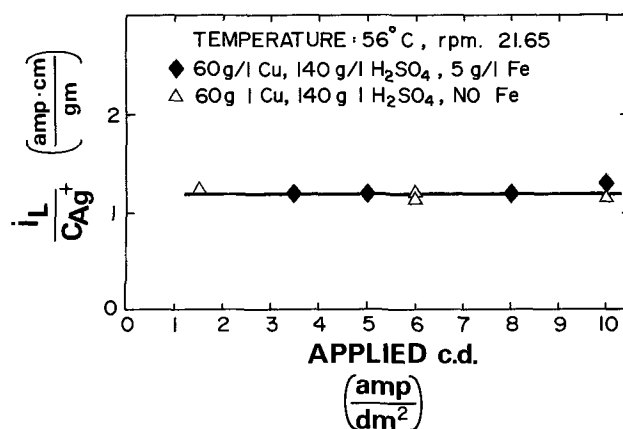
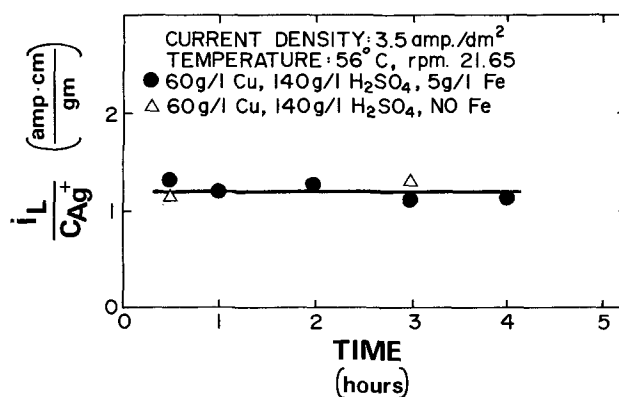
where  $D$  is the diffusion coefficient of the ion,  $\nu$  is the kinematic viscosity of the electrolyte,  $\omega$  is the angular velocity of the rotating disk electrode, and  $C_{\text{Ag}^+}$  is the bulk concentration of  $\text{Ag}^+$  ion. It follows from this equation that: (i)  $i_L/C_{\text{Ag}^+}$  is proportional to  $\omega^{1/2}$  and (ii) at constant  $\omega$ ,  $i_L$  is proportional to the bulk concentration of  $\text{Ag}^+$  ion.

The experimental curves plotted in Fig. 1 and 2 show that  $i_L/C_{\text{Ag}^+}$  was proportional to  $\omega^{1/2}$  in both copper and nickel electro-winning electrolyte. At constant angular velocity of the rotating disk electrode,  $i_L$  was directly proportional to  $C_{\text{Ag}^+}$  (see Fig. 3). These results are in accordance with theory and showed that Ag codeposition was diffusion controlled.



Fig. 1.  $i_L/C_{Ag^+}$  curves obtained for  $Ag^+$  in copper electrolyteFig. 2.  $i_L/C_{Ag^+}$  curve obtained for  $Ag^+$  in nickel electrolyteFig. 3. Dependence of limiting current density for  $Ag^+$  on concentration of  $Ag^+$  in solution.

Electrowinning electrolytes usually contain frothing agents to prevent acid misting and addition agents to improve the quality of the deposit. In the present

Fig. 4. Dependence of  $i_L/C_{Ag^+}$  on applied current densityFig. 5. Dependence of  $i_L/C_{Ag^+}$  on duration of electrolysis

studies, Dowfax 2AO was added as a frothing agent and Jaguar + as an addition agent. The influence of these additives on Levich plots was examined, and it was found that the linearity and slope of  $i_L/C_{Ag^+}$  plot with  $\omega^{1/2}$  was unaffected by the additives. With no additives the slope in Fig. 3 was 1.171 (standard error 0.344) and with the additives the slope was 1.106 (standard error 0.339). Varying the applied current density also had no effect on the results (see Fig. 4), which were also independent of the duration of electrolysis (Fig. 5). The presence of iron (5 g/liter) in the electrolyte did not affect the measurements (see Fig. 4).

Uniform distribution of silver in copper was confirmed by electron probe and chemical analysis of 0.185 mm thick copper deposits.

The diffusion coefficient of  $Ag^+$  ion in various Cu electrowinning electrolytes at 25° and 55°C calculated from these and other Levich plots is presented in Table I along with  $D_{Ag^+}$  values reported in the literature. It is seen that the present values are in close agreement with  $D_{Ag^+}$  values obtained by transient techniques. The diffusion coefficient of  $Ag^+$  ion in Cu

Table I. Diffusion coefficient of  $Ag^+$  ion

Method used	Electrolyte (g/liter)	Temp. (°C)	$D_{Ag^+}$ (cm <sup>2</sup> /sec)	Kinematic viscosity (centistokes)	Reference
1 Present results	Cu: 60 H <sub>2</sub> SO <sub>4</sub> : 140	55	$1.487 \times 10^{-5}$	0.825	$i_L$ vs. $\sqrt{rpm}$ plot
2 Present results	Cu: 60 H <sub>2</sub> SO <sub>4</sub> : 140	55	$1.610 \times 10^{-5}$	0.825	$i_L$ vs. $C_{Ag^+}$ plot
3 Present results	Cu: 25 H <sub>2</sub> SO <sub>4</sub> : 100	55	$1.962 \times 10^{-5}$	0.6060	$i_L$ vs. $\sqrt{rpm}$ plot
4 Present results	Cu: 25 H <sub>2</sub> SO <sub>4</sub> : 100	25	$4.291 \times 10^{-6}$	1.1108	$i_L$ vs. $\sqrt{rpm}$ plot
5 $i^{1/2}$ analysis	Ag in 0.1M KNO <sub>3</sub>	25	$1.55 \times 10^{-5}$	—	(15)
6 $i^{1/2}$ analysis	Ag in 0.1M KNO <sub>3</sub>	25	$1.73 \times 10^{-5}$	—	(16)
7 $i^{1/2}$ analysis	Ag in 0.2M KNO <sub>3</sub>	25	$1.536 \times 10^{-5}$	—	(17)
8 Present results	Ni: 80 Na <sub>2</sub> SO <sub>4</sub> : 150 H <sub>2</sub> BO <sub>3</sub> : 10 (pH = 3.2)	55	$0.701 \times 10^{-5}$	1.059	$i_L$ vs. $\sqrt{rpm}$ plot

electrowinning electrolytes containing 60 g/liter Cu and 140 g/liter  $H_2SO_4$  is  $1.55 \pm 0.06 \times 10^{-5}$  cm<sup>2</sup>/sec, at 55°C. In less concentrated electrolytes (Cu: 25 g/liter), the diffusion coefficient of  $Ag^+$  ion was  $1.96 \times 10^{-5}$  cm<sup>2</sup>/sec at 55°C and  $4.29 \times 10^{-6}$  cm<sup>2</sup>/sec at 25°C.

### Results and Discussion of Model Cell Experiments

In order to optimize the design of electrowinning cells it is important to know the local values of the cathode mass transfer coefficient since the maximum current density used during electrowinning is determined largely by the area of the cathode characterized by the lowest mass transfer coefficient (i.e., having the poorest agitation). For example, if the current density in a given copper electrowinning system were gradually increased, the cathode deposit would first become rough and impure in this region of poor agitation. The most desirable conditions for improved electrowinning operations therefore require large mass transfer coefficients that are uniform over the entire cathode. The usefulness of the present method in design and optimization of electrodeposition systems can be illustrated by typical examples from our model cell investigations of copper electrowinning cell performance.

Since the present experimental work was performed with the primary objective of developing a method to assess the performance of various electrolytic cells, no attempt has been made to discuss in detail the hydrodynamic patterns in conventional and forced convection cells which has been reported elsewhere (19). All the results are reported in terms of  $k_{Ag^+}$  rather than  $k_{Cu^{2+}}$  for reasons discussed later.

In a conventional copper electrowinning cell there are two different hydrodynamic regimes acting on the cathode surface. The electrolyte flow pattern induced by bubbles of anodic oxygen is shown schematically in Fig. 6. The upward flow of electrolyte along the anode is driven by the pump action of anodic gas. The electrolyte near the cathode is characterized by random turbulent flow in the top 5-10 cm. Below that a downward flow is developed over the face of the cathode, with the downward velocity decreasing toward the bottom of the cell. In the lower part of the cell the flow regime is essentially natural convection resulting from density differences caused by electrodeposition.

The vertical mapping of the cathode mass transfer coefficient ( $k_{Ag^+}$ ) for such copper electrowinning conditions in the model cell is also shown in Fig. 6. These results refer to a vertical mapping along the center line of the cathode.

At the top of the cathode the agitation caused by the anode gas results in a fairly high mass transfer coefficient  $k_{Ag^+} = 51 \times 10^{-5}$  cm/sec, compared to the value of  $k_{Ag^+} = 28 \times 10^{-5}$  cm/sec at the cathode bottom where natural hydrodynamic conditions predominate.

The electrolyte agitation in an electrowinning cell can be enhanced by employing forced convection, which

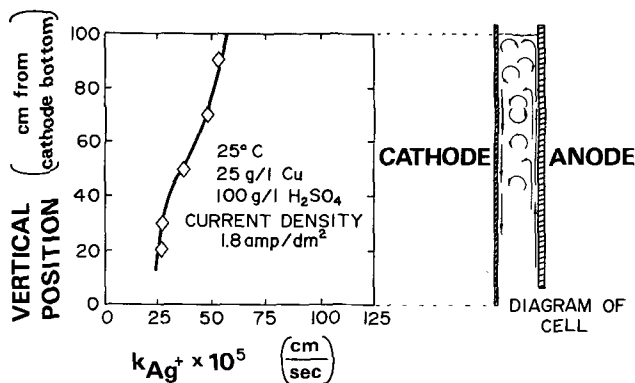


Fig. 6. Vertical distribution of  $k_{Ag^+}$  in conventional copper electrowinning cell.

results in significantly improved mass transport (i.e., increased  $k$ ) at the cathode surface. A series of tests were carried out to measure the vertical distribution of the mass transfer coefficient for both electrolyte jetted and air sparged systems.

In the electrolyte recirculation system the electrolyte was jetted upwards over the cathode surface from a position near the cell bottom (see Fig. 7). Air sparging was provided by means of a perforated PVC tube sparger with 40 mil vertical holes set at 5 cm spacing.

In the electrolyte jetted system  $k_{Ag^+}$  at the bottom of the cathode was  $150 \times 10^{-5}$  cm/sec and only  $72 \times 10^{-5}$  cm/sec at the top (see Fig. 8) indicating significant mass transport enhancement occurred only at the bottom of the cell. Although  $k_{Ag^+}$  at the top of the jetted cell was about 40% higher than the value at the top of the natural convected cell, this can be attributed to the higher current density used in the jetted run (i.e., increased agitation from anode gas). The air sparged results on the other hand (see Fig. 8) indicate that the mass transfer coefficient ( $k_{Ag^+}$ ) was essentially uniform at  $300 \times 10^{-5}$  cm/sec over the entire cathode.

The results presented in Fig. 9 show the effect of the air sparging rate on the cathode mass transfer coefficient. For example, at a low air sparging rate (specific air flow 3.7 cm/min)  $k_{Ag^+}$  was  $100 \times 10^{-5}$  cm/sec while at the higher flow (specific air flow 46 cm/min) the mass transfer coefficient  $k_{Ag^+}$  was  $300 \times 10^{-5}$  cm/sec. The specific air flow rate is defined as the air flow rate per horizontal cross section between electrodes. The effect of anodic oxygen evolution was not noticeable during these tests simply because the amount of  $O_2$  evolved was small relative to the quantity of air sparged. Similar results were obtained at a more normal electrowinning operating temperature of 55°C as shown in Fig. 10.

### Conversion of Mass Transfer Coefficients

In real electrowinning systems, the flow regime consists either of mixed laminar/turbulent flow as in the

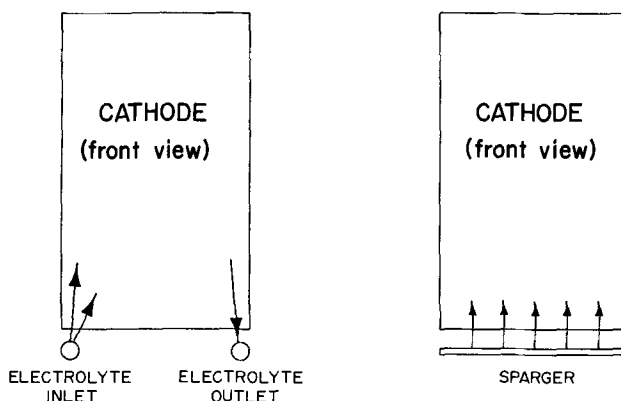


Fig. 7. Diagram of electrolyte jetted and air sparged operation

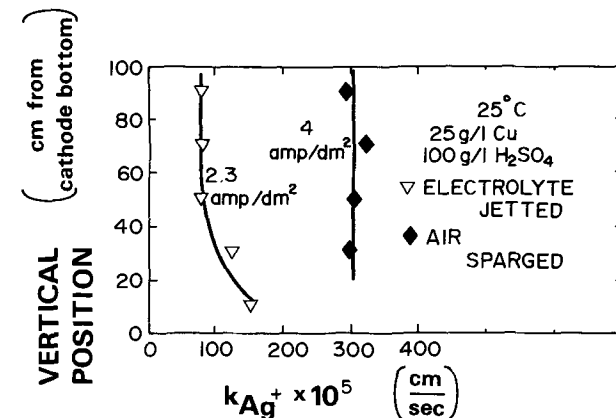
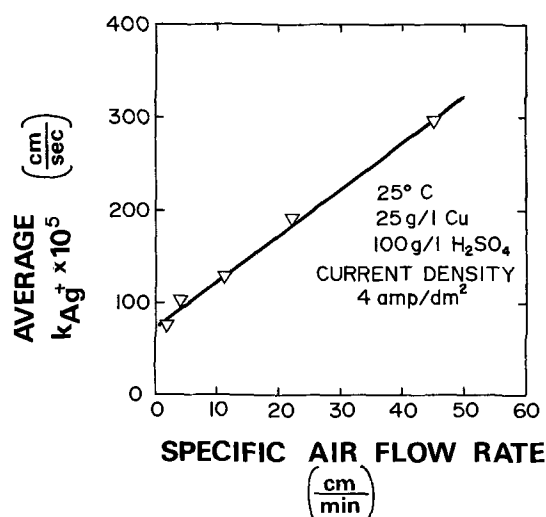
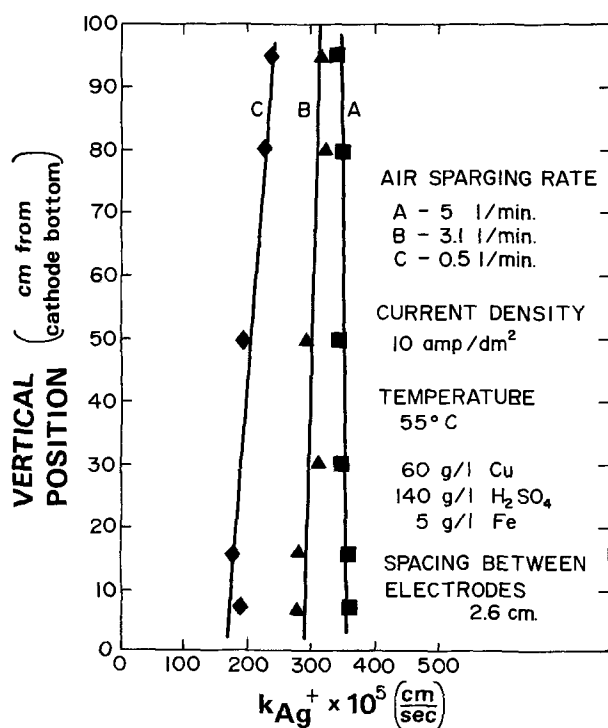


Fig. 8. Vertical distribution of  $k_{Ag^+}$  in electrolyte jetted and air sparged copper electrowinning cell.

Fig. 9. Dependence of  $k_{Ag^+}$  on specific air flow rateFig. 10. Effect of air sparging rate on  $k_{Ag^+}$  in copper electro-winning.

case of conventional copper or zinc cells, or essentially turbulent flow as in the case of forced convection systems.

The calculation of  $k_{Cu+2}$  from  $k_{Ag^+}$  tracer data depends on the particular flow regime acting on the cathode. Thus, for electrodeposition in all flow regimes except laminar natural convection the copper mass transfer coefficient can be calculated using Eq. [4] (18, 22)

$$k_{Cu+2} = k_{Ag^+} \left( \frac{D_{Cu+2}}{D_{Ag^+}} \right)^{2/3} \quad [4]$$

For natural convection in laminar regime  $k_{Cu+2}$  can be calculated using Eq. [5] (23)

$$k_{Cu+2} = k_{Ag^+} \left( \frac{D_{Cu+2}}{D_{Ag^+}} \right)^{3/4} \quad [5]$$

If experimental values of  $D_{Cu+2}$  are not available for the particular electrolyte systems under study, the desired values can be estimated from the correlation pub-

lished by Hannaert (21)

$$D_{Cu+2}^{18^\circ C} = \frac{47 \times 10^{-6}}{5.0 + \Gamma} \text{ cm}^2/\text{sec} \quad [6]$$

$$D_{Cu+2}^{60^\circ C} = \frac{118 \times 10^{-6}}{5.0 + \Gamma} \quad [7]$$

where  $\Gamma = \text{ionic strength} = \sum z_i^2 C_i$  (moles/liter).

While the calculations of the  $k_{Cu+2}$  from either equation are straightforward, the correct form of the equation required for the transitional flow regime encountered in most currently operating cells (i.e., non-agitated) is not evident. While this may cause some theoretical discrepancy, the  $k_{Cu+2}$  values calculated for real copper electrolytes using Eq. [3] and [4] are in agreement within a few per cent as shown by the following example.

For the 60 g/liter Cu, 140 g/liter  $H_2SO_4$ , 5 g/liter Fe electrolyte, at  $55^\circ C$ ,  $D_{Ag^+} = 1.55 \times 10^{-5}$  cm/sec. Using the generalized correlation (21)  $D_{Cu+2}$  for this electrolyte was estimated at  $1.0 \times 10^{-5}$  cm/sec. Therefore using Eq. [2] and [3] to calculate  $k_{Ag^+}$  gives the following results:  $k_{Cu+2} = 0.75 k_{Ag^+}$  and  $k_{Cu+2} = 0.73 k_{Ag^+}$ . This small difference is within the experimental error involved in applying the silver method to full size cells ( $\sim \pm 5\%$ ) since the results achieved in the full height model cell cannot be as reproducible as those obtained with the rde. This is not due to any failing of the method but rather for example, difficulty in maintaining uniform spacing between electrodes, analysis for small quantities of silver, etc.

The calculated  $k_{Cu+2}$  values are slightly lower than the corresponding  $k_{Ag^+}$  values, and limiting current densities calculated using  $k_{Cu+2}$  are also slightly lower than values based on  $k_{Ag^+}$ .

Since the proposed method can be readily used to provide routine measurement of cathode mass transfer coefficients in electro-winning operations, it provides a means of removing guess work from cell optimization and development studies.

### Conclusion

The mass transfer controlled codeposition method has been shown to provide a convenient means of obtaining quantitative information useful in optimizing electro-winning cell design. The experimental error involved in applying the silver method to full size cells is about 5%. Such studies are of considerable importance since the maximum current density used during copper electro-winning is determined by the area of the cathode having the poorest agitation (or characterized by the lowest mass transfer coefficient).

### Acknowledgment

The authors thank The International Nickel Company of Canada, Ltd. for permission to publish the information contained in this paper.

Manuscript submitted July 30, 1973; revised manuscript received Dec. 7, 1973. This was Paper 249 presented at the Chicago, Illinois Meeting of the Society, May 13-18, 1973.

Any discussion of this paper will appear in a Discussion Section to be published in the June 1975 JOURNAL. All discussions for the June 1975 Discussion Section should be submitted by Feb. 1, 1975.

### LIST OF SYMBOLS

C	concentration in bulk of electrolyte (mole/cm <sup>3</sup> )
D	diffusion coefficient (cm <sup>2</sup> /sec)
F	Faraday constant (coulomb/equiv)
$i_L$	limiting current density (A/cm <sup>2</sup> )
k	cathode mass transfer coefficient (cm/sec)
z	charge of ion
$\delta$	diffusion layer thickness (cm) = $zFD C/i_L$
$\nu$	kinematic viscosity (cm <sup>2</sup> /sec)
$\omega$	angular velocity (radians/sec)
$\Gamma$	$\sum z_i^2 C_i$ (moles/liter) See Ref. (21).

## REFERENCES

1. *Eng. Mining J.*, **173**(6), 173 (1972).
2. P. R. Kruesi, U.S. Pat., 3,673,061 (1972).
3. SEC Corporation, South African Pat., 717102 (1972).
4. V. A. Ettel, Belgian Pat. 772,115 (1972).
5. V. A. Ettel, Paper presented at 100th AIME Meeting, New York, 1971.
6. V. A. Ettel, A. S. Gendron, and B. V. Tilak, Paper presented at 102nd AIME Meeting, Chicago, 1973.
7. P. Strub and E. J. Clugston, Paper presented at 101st AIME Meeting, San Francisco, 1972.
8. W. W. Harvey, M. R. Randlett, and K. I. Bangerskis, Paper presented at 102nd AIME Meeting, Chicago, 1973.
9. J. R. Lloyd, E. M. Sparrow, and E. R. G. Eckert, *This Journal*, **119**, 702 (1972).
10. A. A. Wragg, *Electrochim. Acta.*, **16**, 373 (1971).
11. G. Wranglen and O. Nilson, *ibid.*, **7**, 121 (1962).
12. A. Tvarusko and L. S. Watkins, *ibid.*, **14**, 1109 (1969).
13. A. Tvarusko and L. S. Watkins, *This Journal*, **118**, 580 (1971).
14. A. Brenner, *Proc. Am. Electroplaters' Soc.*, **95**, 4 (1940).
15. M. von Stackelberg, M. Pilgram, and V. Toome, *Z. Electrochem.*, **57**, 342 (1953).
16. H. A. Laitinen, I. M. Kolthoff, and V. Toome, *J. Am. Chem. Soc.*, **61**, 3344 (1939).
17. J. F. Zimmerman, Ph.D. Thesis, Univ. of Kansas, Lawrence, Kansas (1964).
18. V. Levich, *Disc. Faraday Soc.*, **1**, 37 (1947).
19. A. S. Gendron and V. A. Ettel, Paper presented at Joint American Institute of Chemical Engineers/Canadian Society of Chemical Engineers Meeting, Vancouver, Sept. 1973.
20. N. Ibl, *Chemie. Ing. Tech.*, **43**, 202 (1971).
21. P. Hannaert, *Ind. Chim. Belge*, **32**, 223 (1967).
22. K. J. Vetter, "Electrochemical Kinetics," Academic Press, New York (1967).
23. A. J. Arvia and S. L. Marchiano, *Mod. Aspects Electrochem.*, **6**, 159 (1971).

## The Effect of Oxygen Dissolved in Pt on the Potential of a Pt/O<sub>2</sub> Electrode at Rest

James P. Hoare\*

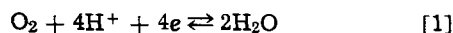
*Electrochemistry Department, Research Laboratories, General Motors Corporation, Warren, Michigan 48090*

*The publication costs of this article have been assisted by the General Motors Corporation.*

### ABSTRACT

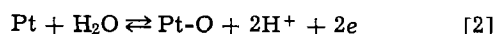
The rest potential of the front side of a Pt foil diaphragm in O<sub>2</sub>-saturated acid solution was recorded while the back side of the foil was anodized at a constant current. The rest potential of the front side rose to a value of 0.05V less noble than the reversible value of 1.229V. This behavior is caused by the increase of dissolved oxygen in Pt produced by anodization which affects the rate of the local cell on the front side. From the effects of foil thickness on the rest potential, a value for the diffusion of oxygen along the grain boundaries in Pt was estimated at  $1.56 \times 10^{-12}$  cm<sup>2</sup>/sec.

The rest potential of a prerduced, bright Pt electrode in O<sub>2</sub>-saturated acid solution is never observed to be much more noble than about 1.06V. If, however, a Pt electrode is strongly preoxidized, the reversible O<sub>2</sub> potential, 1.23V, is observed (1-7) on such a Pt electrode in O<sub>2</sub>-saturated solutions. At one time, considerable controversy existed (8) over the reasons why the rest potential on prerduced bright Pt does not reach the theoretical reversible value of 1.23V. In more recent times, there is significant agreement on the point (1, 9-16) that the 1.06V potential is a mixed potential (17) and the Pt/O<sub>2</sub> system is a polyelectrode (18). However, disagreement arises concerning the nature of the oxidation reaction of the local cell. It is generally agreed that the reduction reaction is the 4-electron O<sub>2</sub>/H<sub>2</sub>O reaction



Those mechanisms which involve a peroxide couple are discounted because either the potential relationships do not correspond to experimental observation or a source of H<sub>2</sub>O<sub>2</sub> is required since H<sub>2</sub>O<sub>2</sub> is consumed rather than generated.

It was proposed (12) that the oxidation reaction of the local cell mechanism is the Pt/Pt-O reaction



because Pt is not inert and Eq. [2] can take place under the driving force of the local cell. Because the way in which the local cell is set up, a layer of ad-

sorbed oxygen, Pt-O, is formed on the Pt surface. Wroblawa and co-workers (14) rejected Eq. [2] for the reason that a complete layer of Pt-O would be formed in a few hours with the appearance of a 1.23V rest potential, a situation which, of course is contrary to observation. On the prerduced Pt, Wroblawa and co-workers (14) suggested instead that the oxidation reaction is the oxidation of impurities. Such a mechanism appears to be highly unlikely because it is improbable that not only the same amount but also the same kind of impurities would be present in the great variety of systems in which a value of about 1.05V has been reported (11-14, 16, 19, 20).

If a steady-state removal of Pt-O could take place so that the Pt-O coverage would remain at  $\theta \sim 0.3$  at a rest potential of 1.06V as observed experimentally (21), the local cell mechanism involving Eq. [2] could be considered favorably once more. There is ample evidence in the literature (21-31) that oxygen can be dissolved in Pt although some workers (32-35) reject this concept in preference to surface or so-called phase oxide layers. It is suggested here that when a prerduced Pt electrode is placed in O<sub>2</sub>-saturated acid solution oxygen is adsorbed on the Pt surface until a potential in the vicinity of 1V is reached after which oxygen may be dermasorbed into the surface of the metal. When the rate of formation of Pt-O by local cell action equals the rate at which oxygen is dissolved in the Pt metal, a steady-state coverage is reached at  $\theta \sim 0.3$  and the rest potential is about 1.05V (21).

Suppose one were able to charge the Pt metal with dissolved oxygen to the point of saturation. At this point, no more oxygen could be dissolved, and the sur-

\* Electrochemical Society Active Member.

Key words: oxygen electrode, platinum, rest potential, dissolved oxygen.

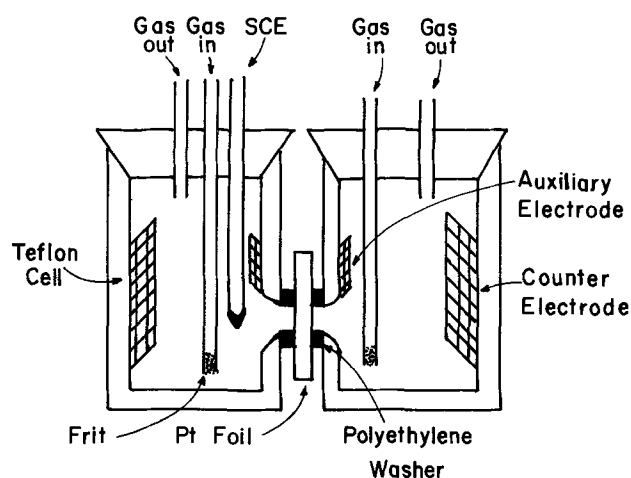


Fig. 1. Diagram of two-compartment cell

face would become covered with a layer of electronically conducting Pt-O. Since the local cell could no longer exist, the potential-determining reaction would become Eq. [1] and the observed potential would be the reversible oxygen potential.

In this report, evidence, obtained from monitoring the potential on the front side of a Pt diaphragm while the back side is anodized,<sup>1</sup> is presented as strong support for the  $O_2/H_2O$ ,  $H^+$ , Pt-O/Pt mechanism of the Pt/ $O_2$  rest potential.

### Experimental

All measurements were made on Pt (99.9+ % pure) foil (0.00127, 0.00254, and 0.00508 cm thick) in 2N  $H_2SO_4$  made with triply distilled  $H_2O$  from an all quartz still. The Pt foils to which Pt lead wires were spot welded were cleaned by successively soaking in concentrated  $HNO_3$  followed by flaming in a burning  $H_2$  jet. This procedure was repeated until all coloration of the  $H_2$  flame disappeared. A two-compartment cell made of Teflon (see Fig. 1) was cleaned by soaking in aqua regia, then concentrated  $HNO_3$ , and finally by leaching in triply distilled  $H_2O$  for at least a week with frequent changes of water. The cleaned Pt foil was clamped between two halves of the leached cell using polyethylene washers as shown in Fig. 1. If no leaks were found around the washers, the cell was filled with 2N  $H_2SO_4$  solution, and the cell tops sealed with molten polyethylene. By observing the foils with a bright light behind them, it was possible to reject them if any pinholes were present. The cell electrodes were then preelectrolyzed anodically for at least 16 hr against removable Pt wire cathodes.

After the preelectrolysis procedure,  $H_2$  was bubbled through both sides of the cell until the potential of the foil became zero with respect to the Pt gauze counter and auxiliary electrodes in each compartment. These steps were taken to ensure that all adsorbed and dissolved oxygen in the Pt as well as any peroxides generated by the preelectrolysis were removed from the system. All gases used were prepurified by passing them through a multicomponent purification train before entering the cell. A probe-type saturated calomel reference electrode (SCE) was inserted through the cell top into the left hand compartment, and the potential of a Pt/ $H_2$  electrode vs. SCE was determined. Finally, purified oxygen was bubbled through the left hand compartment, purified nitrogen through the right, and the rest potential (vs. SCE) of the front side of the foil was followed with a General Radio Electrometer Model 1230A. All potentials in this report are recorded with respect to the normal hydrogen electrode unless stated otherwise.

<sup>1</sup> One of the reviewers noted that this metal foil diaphragm technique was used by Frumkin and Aladzhilova (40) and by Kobosev and Monblanova (41). It might also be noted that Schuldiner and Hoare (42) used this same technique to study the Pd- $H_2$  system.

Anodization at constant current of the back side of the foil against a large Pt gauze counterelectrode was begun when the rest potential of the front side of the foil reached about 1V. In a couple of cases as shown in Fig. 2, the potential was permitted to come to a steady state,  $1.04V < E < 1.06V$  (requiring 19 to 24 hr) before anodization was begun. If there were no pinholes in the foil or no leaks between the cell compartments, the potential on the front side of the cell was not affected when anodization of the back side was begun; otherwise, the potential of the front side shifted immediately towards more noble values. The potential of the back side during anodization had values between 2.040 and 2.090V ( $i = 6.1 \text{ mA/cm}^2$ ). At the end of the run,  $H_2$  was bubbled again in the left hand compartment, and the value of the SCE vs. Pt/ $H_2$  was rechecked. Values of SCE before and after agreed within 2 or 3 mV. The temperature of all experiments was ambient ( $24^\circ \pm 1^\circ C$ ).

### Results

The rest potential of a Pt foil 0.00127 cm thick is plotted as a function of time in Fig. 2 (circles) and the point when anodization of the back side of the Pt diaphragm was begun is indicated by the arrows. Also included in Fig. 2 is the rest potential (triangles) of a Pt gauze auxiliary electrode in the left hand compartment. The data shown in Fig. 2 were repeated at least three times on different samples of Pt foil with similar results being obtained in each case. Before anodization was begun, the potential of both the foil and auxiliary gauze rose with time to a virtual steady value (1.045V, foil; 1.040V gauze). When the anodization of the back side of the foil was begun, no changes were observed in the potential for about 2 hr, after which the potential of the foil began to shift towards more noble values. Eventually, a steady value of 1.180V was reached after about 2 days whereas the Pt gauze auxiliary oxygen electrode reached the steady value of 1.055V.

To be certain that a good seal was formed between the two cell compartments, the foil area ( $2.81 \text{ cm}^2$ ) was made much larger than the area exposed to the electrolyte ( $0.786 \text{ cm}^2$ ). Since the rest potential reached a steady value of about 50 mV less noble than the reversible value, it was suspected that an area effect may be operative. To check this, three sizes of Pt foil were used. In Fig. 3, the data obtained on 0.00127 cm thick Pt foils of two different total (one side) areas ( $2.81$  and  $5.28 \text{ cm}^2$ ) are presented. The origin of these plots is the time when anodization of the back side was begun. The rest potential of the larger area foil came to a steady value of 1.121V. When a foil with an area of  $1.15 \text{ cm}^2$  was used, leaks developed in every case (4 attempts), and the desired data could not be obtained.

Plots of the rest potential obtained on Pt foils of three different thicknesses, 0.00127 cm (area =  $2.81$

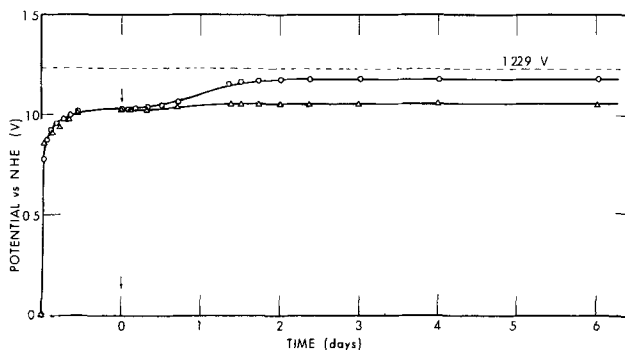


Fig. 2. A plot of the rest potential of the front side of a Pt diaphragm (0.00127 cm thick,  $2.81 \text{ cm}^2$  in area) as a function of the time for which the back side was anodized ( $6.1 \text{ mA/cm}^2$ ) (circles). Arrows indicate when anodization was begun. Triangles represent data for auxiliary Pt gauze electrode.

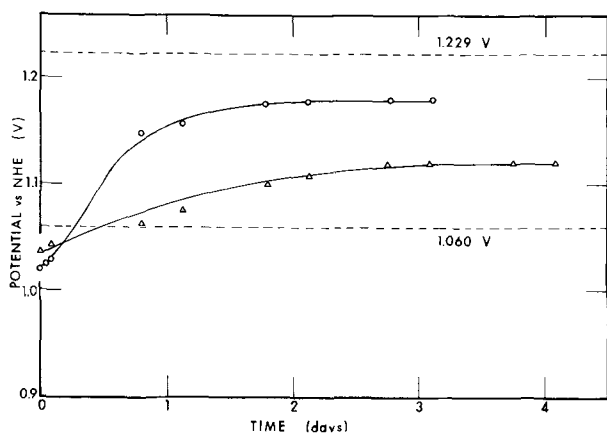


Fig. 3. A plot of rest potential of 0.00127 cm thick Pt foil with areas of 2.81 cm<sup>2</sup> (circles) and 5.88 cm<sup>2</sup> (triangles) as a function of time for which the back side was anodized.

cm<sup>2</sup>), 0.00254 (area = 2.88 cm<sup>2</sup>), and 0.00508 cm (area = 3.01 cm<sup>2</sup>) are given in Fig. 4 where the origin is the time when anodization of the back side was begun. In these instances, the front side had not come to a steady value before anodization was begun because it was found that the final result was not affected by the time when anodization was begun. Of course, the initial delay or induction period observed in Fig. 2 is masked by the drifting potential in Fig. 3 and 4. After about 3 days, the potential on the thicker foils reached a steady rate of increase equal to about 4 mV/day. If it can be assumed that this rate is maintained until a value of 1.180V (the potential reached by foils with an area of about 2.9 cm<sup>2</sup>) is obtained, it can be determined that the required time for 0.00254 cm foil would be 9.5 days and for 0.00508 cm foil, 25.0 days.

### Discussion

When the prerduced Pt electrode is placed in O<sub>2</sub>-saturated acid solution, the rest potential,  $E$ , drifts to more noble values and the coverage,  $\theta$ , of the metal surface with Pt-O, increases. It has been shown by a number of workers [e.g., (3, 21, 36, 37)] that  $E$  rises linearly with  $\theta$ . At steady state,  $dE/dt = 0$  and  $E$  has a constant value lying in the potential range between 1.04 and 1.06V. Also,  $d\theta/dt = 0$ , and  $\theta$  has a constant value in the range lying between 0.25 and 0.30. Under these conditions, Pt-O is formed by the local cell current density,  $i_{loc}$ , as fast as it is dissolved in the Pt metal. Therefore, the rate of disappearance of Pt-O,  $-dx/dt$ , must be equal to  $i_{loc}$ . The Pt metal acts as a vast reservoir for dissolved O. If, for example, one assumes that in the saturated state one O atom is associated with each unit cell of the face centered cubic lattice, there would be, on the average, one O atom

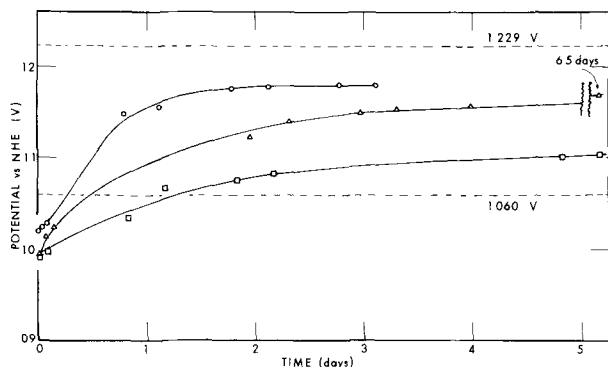


Fig. 4. A plot of the rest potential of Pt foils (area  $\sim 2.9$  cm<sup>2</sup>) of three thicknesses (0.00127 cm, circles; 0.00254 cm, triangles; 0.00508 cm, squares) as a function of the time for which the back side of the Pt diaphragm was anodized.

for every 4 Pt atoms. From the density of Pt (21.45 g/cm<sup>3</sup>), the charge in forming an O atom ( $3.2 \times 10^{-19}$ C) and the value of  $i_{loc}$  ( $3.2 \times 10^{-7}$  A/cm<sup>2</sup>) (38), it would require about 190,000 days to saturate a cubic centimeter of Pt with dissolved oxygen for one side exposed to the local cell current. For this reason this steady-state rest potential seems to remain indefinitely.

It has been found (21) that anodization at high potentials,  $\sim 2$ V, causes large amounts of O to be dissolved in Pt metal. As the back side of the Pt foil diaphragm is anodized, the concentration of dissolved O,  $C_a$ , increases to a point where it becomes more difficult to dissolve the Pt-O on the front side. Consequently,  $-dx/dt$  or  $i_{loc}$  will fall. Then  $-di_{loc}/dt = K(dC_a/dt)$  where  $K$  is a proportionality constant. To increase the driving force for Pt-O dissolution, the chemical potential of the Pt-O layer must increase by an increase in  $\theta$ ; as a result,  $E$  increases (3) in agreement with the data in Fig. 2-4.

If  $C_a$  reaches the saturation value,  $C_o$ ,  $dC_a/dt = 0$  and  $i_{loc} = 0$  because no more Pt-O can dissolve. In this case,  $\theta$  reaches a value of unity and  $E$  assumes the value of the reversible oxygen potential 1.229V (3) since the only potential determining process available is the O<sub>2</sub>/H<sub>2</sub>O reaction, Eq. [1].<sup>2</sup> However, dissolved oxygen can escape from the Pt foil which is outside of the polyethylene washers and which is not in contact with the solution. Here O atoms can diffuse to the surface where they combine and escape to the environment as O<sub>2</sub> molecules. Although the rate of oxygen penetration at escape from the metal lattice may be smaller than the rate of migration within the lattice, there is a leakage of oxygen to the atmosphere, and hence, an area effect because oxygen can exit at all sites to the Pt surface. At those sites exposed to air, the Pt-O film is less stable than at those sites exposed to the O<sub>2</sub>-saturated electrolyte. This rate of loss of  $C_a$  increases with increasing values of  $C_a$  (chemical potential of dissolved oxygen) until the rate of increase due to anodization of the back side equals the rate of loss due to escape from the solution-free Pt surface. At this point,  $dC_a/dt = 0$  and  $C_a$  equals the steady-state value,  $C_{ss}$ . In this situation,  $i_{loc}$ ,  $\theta$ , and  $E$  reach steady-state values. The area data, in Fig. 3, show that the rest potential in the steady state,  $E_{ss}$ , depends on the area of the Pt foil exposed to the external atmosphere.

The discussion so far suggests that as  $C_a$  increases and both  $\theta$  and  $E$  increase,  $i_{loc}$  should decrease. To check on this, polarization measurements on the front side were made at very low currents after the anodizing current on the back side of the foil was discontinued. The measuring technique using a high resistor made from a pencil line drawn on a strip of Mylar film and placed in the constant current circuit has been described before (38). These data were difficult to obtain because only a few points could be made before the polarization of the electrode caused changes in the system which shifted the rest potential. A sample of the data from which  $i_{loc}$  was estimated is shown in Fig. 5 for two different runs made on foils exhibiting an  $E$  of 1.155V. The summary of data in Table I shows one other value of  $i_{loc}$  obtained at  $E = 1.180$ V. Indeed,  $i_{loc}$  decreases as  $C_a$ ,  $\theta$ , and  $E$  increase.

The data in Fig. 2 show an induction period after anodization was begun. Such behavior is to be expected because at  $E = 1.06$ V,  $C_a$  is very small, and time is required to increase  $C_a$  to the point where it affects  $i_{loc}$ . Also, this behavior predicts that an effect of foil thickness on the rest potential should be found in agreement with the data of Fig. 4. Foils of the same area but of

<sup>2</sup> It was pointed out by one of the reviewers that a value of  $\theta = 0.65$  was found by Laitinen and Enke (43) on Pt at 1.23V in N<sub>2</sub> and a value of  $\theta = 0.71$  by Schuldiner et al. (44) on Pt at 1.23V in H<sub>2</sub>. Both of these groups of researchers obtained  $\theta$  at Pt electrodes which were polarized to 1.23V whereas Hoare et al. (3) obtained  $\theta$  at Pt electrodes which exhibited 1.23V at rest. This difference in experimental conditions may account for the differences in reported values of  $\theta$  at 1.23V.

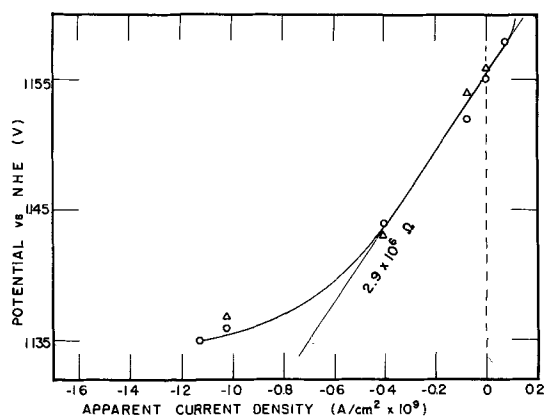


Fig. 5. Constant current polarization curve at low current density obtained on the front side of a Pt diaphragm exhibiting a rest potential of 1.155V after the back side had been anodized for two different runs, circles and triangles.

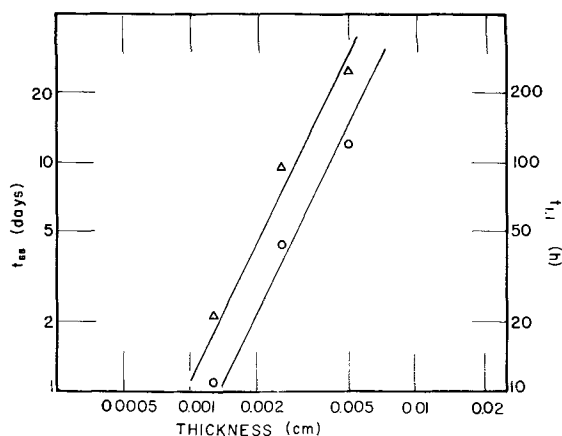


Fig. 6. Plots of  $t_{1.1}$  (circles) and  $t_{ss}$  (triangles) as a function of the thickness of the Pt diaphragm.

increasing thickness require a longer time at constant current to reach a value of  $C_a$  which affects  $i_{loc}$  because of the increased volume of metal. If we may assume the relationship

$$t = kd^n \quad [3]$$

where  $t$  is the time to reach a given value of  $E$ ;  $k$ , a constant;  $d$ , the foil thickness; and  $n$ , an exponent, the slope of a plot of  $\log t$  vs.  $\log d$  yields a value for  $n$ . Such a plot for the times to reach 1.1V,  $t_{1.1}$ , and steady state,  $t_{ss}$ , is given in Fig. 6. Lines with a slope of 2 are drawn through the points and thus a likely value for  $n$  is 2. Equation [3] is similar to the time lag relationship.

$$D = d^2/6t_{lag} \quad [4]$$

where  $D$  is the diffusion constant and  $t_{lag}$  is time required to reach steady state. In this case,  $k = 1/6D$ ,  $n = 2$ , and  $t_{lag} = t_{ss}$ . If the data from Fig. 4 are substituted into Eq. [4], a value of  $D$  can be obtained as tabulated in Table II. This average value of  $D$  ( $1.56 \times 10^{-12}$  cm<sup>2</sup>/sec) is in fair agreement with that ( $4.4 \times 10^{-11}$  cm<sup>2</sup>/sec) obtained before (26). This value of  $D$  seems to be large for the diffusion of the relatively large

Table I. Values of the local cell current density at various rest potentials

$E$ (V)	$\theta$	Slope = $dE/di$ (ohm $\times 10^7$ )	$i_{loc} = \frac{di}{\theta E} \left( \frac{RT}{F} \right)$ (A/cm <sup>2</sup> $\times 10^6$ ) (38)
1.060	0.28	8000	320
1.155	0.80	29	8.84
1.180	0.95	1.4	1.80
1.229	1	—	0

Table II. Determination of diffusion constant of O through Pt metal

$t_{ss}$ (days)	$d$ (cm $\times 10^3$ )	$d^2$ (cm <sup>2</sup> $\times 10^6$ )	$D$ (cm <sup>2</sup> / sec $\times 10^{12}$ )
2.3	1.27	1.61	1.36
9.5	2.54	6.45	1.32
25.0	5.08	25.9	2.0
Average			1.56

O atom through the Pt lattice (39) and indicates that the oxygen diffuses through the Pt along grain boundaries.

Unfortunately, it is not possible to estimate a value for  $C_{ss}$  since it is not known what fraction of the anodic current is consumed in the process producing dissolved oxygen,  $C_a$ . Consequently,  $dC_a/dt$  cannot be determined.

In summary, these data support the conclusions that oxygen can be dissolved in Pt, that the rest potential is made up of the O<sub>2</sub>/H<sub>2</sub>O and the Pt/Pt-O reactions, that a steady rest potential is reached when the rate of Pt-O formation equals the rate of its disappearance by dissolution in the metal, and that the reversible oxygen potential can be observed if a conducting complete layer ( $\theta = 1$ ) of adsorbed oxygen can be maintained on the Pt surface.

Manuscript submitted Nov. 7, 1973; revised manuscript received Feb. 14, 1974.

Any discussion of this paper will appear in a Discussion Section to be published in the June 1975 JOURNAL. All discussions for the June 1975 Discussion Section should be submitted by Feb. 1, 1975.

#### REFERENCES

- R. Kh. Burshtein, M. R. Tarasevich, and V. A. Bogdanovskaya, *Elektrokhim.*, **8**, 1542 (1972).
- J. P. Hoare, *This Journal*, **110**, 1019 (1963); **112**, 849 (1965).
- J. P. Hoare, R. Thacker, and C. R. Wiese, *J. Electroanal. Chem.*, **30**, 15 (1971).
- J. O'M Bockris and A. K. M. S. Huq, *Proc. Roy. Soc.*, **A237**, 277 (1956).
- W. Visscher and M. A. V. Devanathan, *J. Electroanal. Chem.*, **8**, 127 (1964).
- N. Watanabe and M. A. V. Devanathan, *This Journal*, **111**, 615 (1964).
- G. Bianchi, F. Mazza, and T. Mussini, *Electrochim. Acta*, **11**, 1509 (1966).
- J. P. Hoare, "The Electrochemistry of Oxygen," pp. 15-46, Interscience, New York (1968).
- T. P. Hoar, *Proc. Roy. Soc.*, **A142**, 628 (1933).
- J. Giner, *Z. Elektrochem.*, **63**, 386 (1959).
- D. S. Ganamuthu and J. V. Petrocilli, *This Journal*, **114**, 1036 (1967).
- J. P. Hoare, *ibid.*, **109**, 858 (1962).
- D. Winkelmann, *Z. Elektrochem.*, **60**, 731 (1956).
- H. Wroblawa, J. L. B. Rao, A. Damjanovic, and J. O'M. Bockris, *J. Electroanal. Chem.*, **15**, 139 (1967).
- V. I. Nesterova and A. N. Frumkin, *Zh. Fiz. Khim.*, **26**, 1178 (1952).
- A. J. Appleby, *This Journal*, **117**, 328, 641 (1970).
- C. Wagner and W. Traud, *Z. Elektrochem.*, **44**, 391 (1938).
- E. Lange and P. Van Rysselberghe, *This Journal*, **105**, 420 (1958).
- M. B. Clark, W. G. Dorland, and K. V. Kordesch, *Electrochem. Technol.*, **3**, 166 (1965).
- F. J. Smale, *Z. Physik. Chem.*, **14**, 577 (1894).
- R. Thacker and J. P. Hoare, *J. Electroanal. Chem.*, **30**, 1 (1971).
- A. Hickling, *Trans. Faraday Soc.*, **41**, 333 (1945).
- T. V. Kalish and R. Kh. Burshtein, *Dokl. Akad. Nauk SSSR*, **81**, 1093 (1951); **88**, 863 (1953).
- V. I. Luk'yanycheva and V. S. Bagotskii, *ibid.*, **155**, 160 (1964).
- A. D. Obrucheva, *Zh. Fiz. Khim.*, **26**, 1448 (1952).
- J. P. Hoare, *This Journal*, **116**, 612, 1390 (1969).
- J. Balej and O. Spalek, *Czech. Chem. Comm.*, **37**, 499 (1972); **38**, 29 (1973).
- P. R. Nadebaum and T. Z. Fahidy, *Electrochim. Acta*, **17**, 1659 (1972).

29. R. Parsons and W. H. M. Visscher, *J. Electroanal. Chem.*, **36**, 329 (1972).
30. S. Schuldiner, T. B. Warner, and B. J. Piersma, *This Journal*, **112**, 212, 853 (1965); **113**, 573 (1966); **114**, 343 (1967).
31. H. Shimizu, *Electrochim. Acta*, **14**, 55 (1969).
32. D. Gilroy and B. E. Conway, *Can. J. Chem.*, **46**, 875 (1968).
33. H. Angerstein-Kozłowska, B. E. Conway, and W. B. A. Sharp, *J. Electroanal. Chem.*, **43**, 9 (1973).
34. S. Shibata and M. P. Sumino, *Electrochim. Acta*, **16**, 1089 (1971).
35. S. Shibata, *ibid.*, **17**, 395 (1972).
36. W. Bold and M. W. Breiter, *ibid.*, **5**, 145 (1961).
37. K. J. Vetter and D. Berndt, *Z. Elektrochem.*, **62**, 378 (1958).
38. J. P. Hoare, *This Journal*, **112**, 602 (1965).
39. R. J. Brook, W. L. Pelzmann, and F. A. Kröger, *ibid.*, **118**, 185 (1971).
40. A. N. Frumkin and N. A. Aladzhalova, *Zh. Fiz. Khim. SSSR*, **18**, 493 (1944).
41. N. I. Kobosev and V. V. Monblanova, *ibid.*, **6**, 308 (1935); **7**, 645 (1936).
42. S. Schuldiner and J. P. Hoare, *This Journal*, **103**, 178 (1956); **103**, 237 (1956); **104**, 564 (1957); **105**, 278 (1958).
43. H. A. Laitinen and C. G. Enke, *ibid.*, **107**, 773 (1960).
44. S. Schuldiner, M. Rosen, D. R. Flinn, and C. H. Presbrey, *Electrochim. Acta*, **17**, 1637 (1972).

## Technical Notes



### Film Formation on Anodically Polarized Lead

H. Vaidyanathan,\* Ram A. Narasagoudar, T. J. O'Keefe, W. J. James,\* and J. W. Johnson\*

Graduate Center for Materials Research, University of Missouri-Rolla, Rolla, Missouri 65401

The publication costs of this article have been assisted by the University of Missouri.

A complexity of processes occurs when lead is anodically polarized in aqueous electrolytes. Anodic disintegration (1), formation of oxides  $\text{PbO}$ ,  $\beta\text{-PbO}_2$ ,  $\alpha\text{-PbO}_2$  (2-6), and the formation of oxysalts (7) have been postulated in addition to the simple generation of  $\text{Pb}^{2+}$  ions. Most of the work to date concerns the formation of these oxides and oxysalts when Pb is polarized in  $\text{H}_2\text{SO}_4$ . However, there are other electrolyte systems where the polarization behavior is more definable, and an understanding of these processes would contribute considerably to solving some unanswered questions of behavior of the common lead-acid cell. In the present study, Pb dissolution was investigated in aqueous  $\text{HNO}_3$  solution with a view of relating the polarization characteristics to surface oxidation steps in a typical nonprecipitating medium.

Oxidation steps and subsequent film formation have been characterized by a systematic study of the current ( $i$ )-potential ( $E$ ) relation followed by analysis of the polarized electrodes by x-ray diffraction and scanning electron microscopy (SEM). The  $i$ - $E$  relationship was obtained by potential sweep voltammetry (PSV) which has been widely used in studies on the dissolution and deposition of metals (8-11).

Lead wires with a diameter of 1.5-5 mm and 99.9999% purity,<sup>1</sup> supplied by Electronic Space Products, Incorporated, Los Angeles, California, were used for this study. Several potential sweep experiments were carried out, and the  $i$ - $E$  curves obtained were reproducible at sweep rates of 1-100 mV/sec. Figure 1 shows one of the typical  $i$ - $E$  curves obtained. Two distinct waves with broad maxima, one at  $\approx 0.65\text{V}$  and the other at  $\approx 1.35\text{V}$ , were obtained during the forward (anodic) sweep. The black film began to form on the electrode surface at  $\approx 0.6\text{V}$  and remained visible until the potential reached  $\approx 0.25\text{V}$  during the reverse (cathodic) sweep. Some spalling of the electrode occurred during the potential sweep. The effect of changes in sweep rates on the nature of the  $i$ - $E$  be-

havior is given in Fig. 2. Curve a, which was obtained at 1.0 mV/sec, shows a prominent wave with a broad maximum at  $\approx 1.2\text{V}$ . Curve b, which was obtained at 91 mV/sec, showed no waves during the anodic sweep; however, two waves were obtained with maxima at  $\approx 0.6\text{V}$  and  $\approx 1.3\text{V}$  during the reverse sweep. Curve c shows the  $i$ - $E$  behavior at a sweep rate of 200 mV/sec

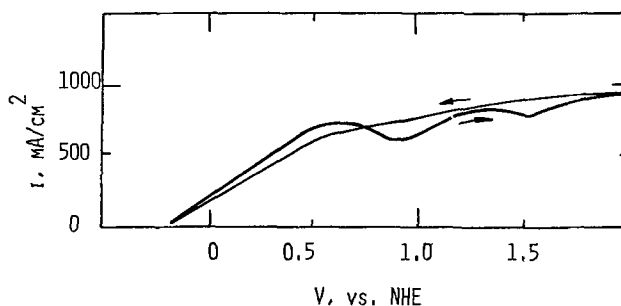


Fig. 1.  $i$ - $E$  relation obtained for Pb in 1.0M  $\text{HNO}_3$  at a sweep rate of 9 mV/sec.

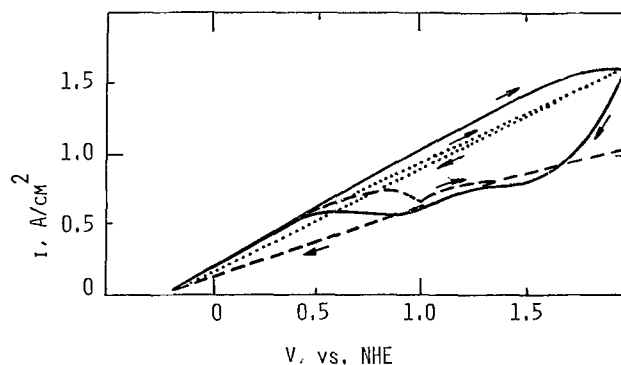


Fig. 2.  $i$ - $E$  relation obtained for Pb in 1.0M  $\text{HNO}_3$  at various sweep rates. Curve a (dashed line), 1 mV/sec; curve b (solid line), 91 mV/sec; curve c (dotted line), 200 mV/sec.

\* Electrochemical Society Active Member.

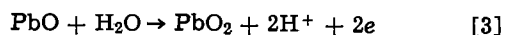
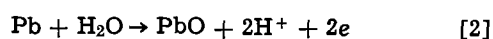
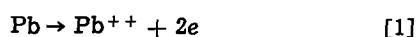
Key words: electron microscopy, potential sweep voltammetry.

<sup>1</sup> Typical impurities in ppm are Fe < 0.1, Ce 0.1, and Mg 0.1.



in which oxidation waves are totally absent. Current density values showed only a slight increase when the sweep rate is increased from 1 to 9 mV/sec, but the increase was appreciable at 90 mV/sec. However, when C.D. values are considered for the reverse sweep alone, they show little response to changes in sweep rate, particularly at high sweep rates.

The *i-E* behavior of Pb in NaOH has been reported earlier, and two oxidation waves were also found (12). In HNO<sub>3</sub>, the oxidation waves appear only at low sweep rates, which suggests that convective conditions in the electrolyte play a positive role in the configuration of the *i-E* curves. Mass transfer by diffusion also influences the *i-E* behavior, as reflected by the high C.D. values at 90 mV/sec (curve b). The appearance of oxidation waves at low sweep rates for Pb in HNO<sub>3</sub> is similar to that reported for Zn in alkaline solutions by Powers and Breiter (13). The oxidation waves indicate that more than two oxidation steps are involved when Pb is polarized. The two waves can be associated with the formation of different oxides with different structures and solubilities. The first wave obtained at  $\approx 0.7V$  may correspond to the formation of PbO and the second wave at  $\approx 1.35V$  to that of PbO<sub>2</sub>. The oxidation steps involved are



The indications obtained for the formation of PbO and PbO<sub>2</sub> are preliminary. Hence, a detailed analysis of the electrode surface after potentiostating, at various potentials from 0.5 to 1.66V was carried out by x-ray diffraction and SEM in order to substantiate our proposition. Very rapid dissolution occurs when an anodic potential is impressed on the electrode. In addition, the electrode surface gradually turns black due to the accumulation of minute dark particles. The particles do not appear to originate as a result of chemical or electrochemical reaction in solution, but rather as a result of electrochemical reaction at the electrode surface producing disintegrated Pb and/or oxides. The polarized anodes were rinsed with distilled water and acetone and dried carefully in a desiccator in a manner which would not disturb any film present on the surface. X-ray diffraction and SEM studies were done immediately after each potentiostatic experiment. For the SEM studies, the entire electrode was scanned. The lead wires were of proper diameter and length to allow them to be mounted directly in a Debye-Scherrer camera. Table I lists the results of the x-ray analyses. PbO (orthorhombic) is obtained on the surface from 0.5 to 1.78V while indications of  $\beta$ -PbO<sub>2</sub> are obtained only at potentials approximately 1.5V or greater. X-ray identification was largely based on direct comparison with diffraction patterns for pure PbO (yellow) and  $\beta$ -PbO<sub>2</sub>. Since only very small amounts of the oxide formed on the electrode, only the major lines of the x-ray pattern were visible, thus making the identification rather difficult. It may be noted that x-ray analyses of cycled electrodes also give evidence for the formation of PbO and  $\beta$ -PbO<sub>2</sub>.

Figure 3 shows an SEM micrograph of a Pb anode which was polarized at 0.6V for 20 min. There is no

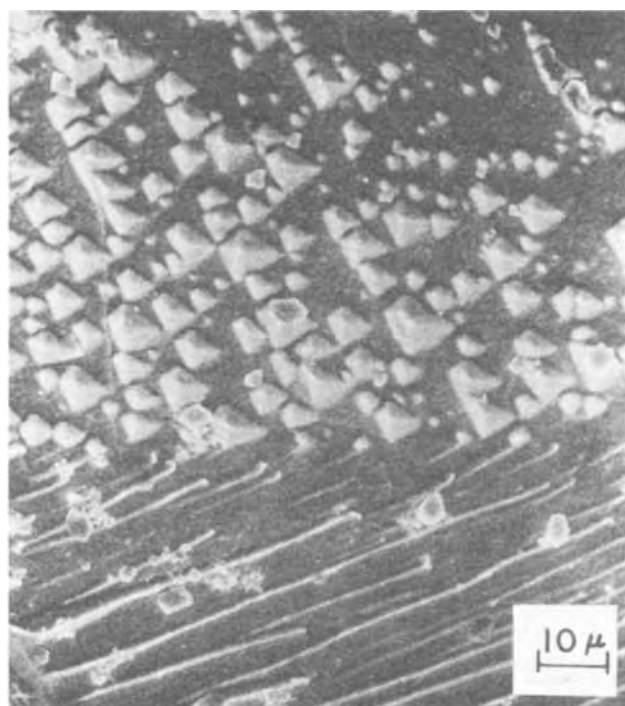


Fig. 3. Scanning electron micrograph of an anodically polarized Pb electrode showing faceted surface structure. Magnification 1000 $\times$ .

evidence of pitting, and, in fact, there is pronounced faceting, the nature of which is dependent on the individual grain orientation. The pyramids are probably formed by (111) planes, but due to their elongated nature, the surface orientation is more probably (211) rather than (100). It may also be assumed from this that the (111) faces are less active for anodic dissolution in HNO<sub>3</sub> solutions. Faceted surface textures are quite common and have been reported during the anodic dissolution of Cu (16), electrodeposition of Fe (17) and Ni (18), and chlorination of Mo and W (19).

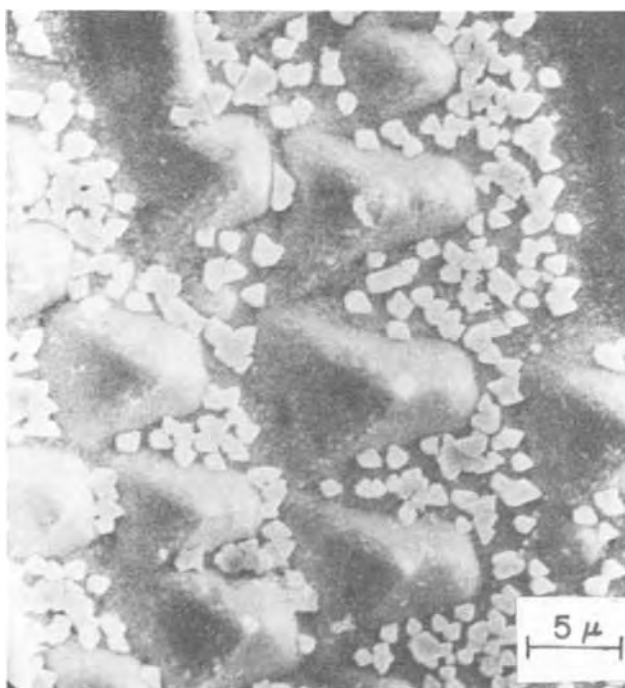


Fig. 4. Scanning electron micrograph of an anodically polarized Pb electrode showing faceted surface structure and oxide particles. Magnification 3000 $\times$ .

Table I. X-ray diffraction data

Potential (V)	Electrolyte	d (experimental)	d (ASTM)	Substance
0.5	0.2M HNO <sub>3</sub>	3.06	3.07	PbO (orthorhombic)
		2.96	2.95	PbO (orthorhombic)
0.72	1.0M HNO <sub>3</sub>	3.06	3.07	PbO (orthorhombic)
		2.96	2.96	PbO (orthorhombic)
1.22	1.0M HNO <sub>3</sub>	3.06	3.07	PbO (orthorhombic)
		2.96	2.96	PbO (orthorhombic)
1.5	1.0M HNO <sub>3</sub>	3.8	—	Unidentifiable
		3.45	3.50	$\beta$ -PbO <sub>2</sub>

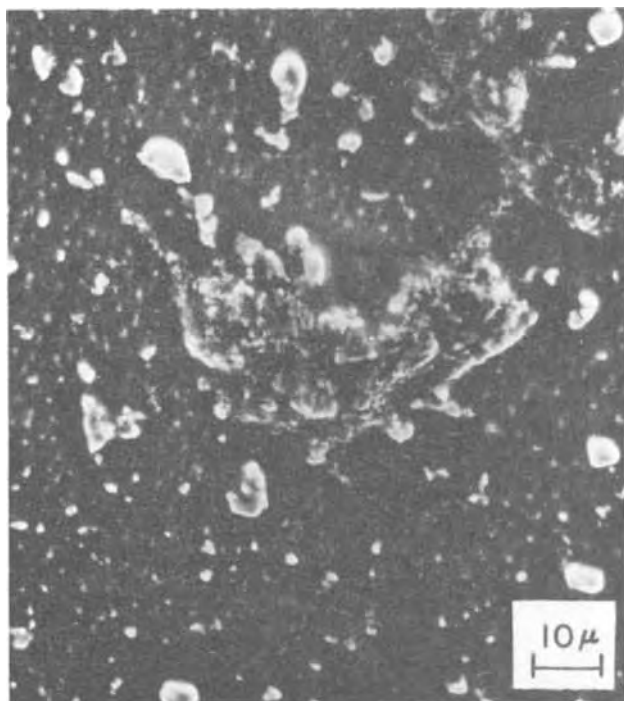


Fig. 5. Scanning electron micrograph of an anodically polarized Pb electrode showing very minute particles of disintegrated Pb and a lump of  $\beta$ -PbO<sub>2</sub>. Magnification 1000 $\times$ .

Figure 4 shows an SEM micrograph of a Pb anode which has been polarized at 0.3V for 40 min. Besides the protruding parts of lead crystals, some other crystalline material is seen on the surface. It occurs mainly in the spaces dividing the individual crystals of Pb, and from x-ray analysis it appears that the material is PbO (orthorhombic). This potential may correspond to the onset of nucleation of the PbO.

Figure 5 shows the SEM micrograph of Pb which has been anodically polarized at 1.3V. The SEM was taken after rinsing the electrode in distilled water and dilute ammonium acetate solution, which dissolves all other oxidation products except PbO<sub>2</sub>. The surface contained numerous minute particles. It was felt that this morphology may represent the various stages of uneven dissolution which eventually resulted in disintegration. The single large particle shown appears to have a different morphology and is thought to be  $\beta$ -PbO<sub>2</sub>, as shown by x-ray analysis. The visible evidence of spalling of the electrode in Fig. 4 shows that disintegration of the anode is probably occurring. Therefore, the black film obtained during polarization may be due to the finely divided particles of Pb produced as a result of disintegration as well as of oxides.

Anodic film formation of Pb has been discussed at length by several authors (20). We have shown the formation of disintegrated Pb, PbO (yellow), and  $\beta$ -PbO<sub>2</sub>, and faceting when Pb is polarized in HNO<sub>3</sub>. The voltammetric curves and their strange dependence on sweep rate indicate that oxide film formation is a function of the hydrodynamic conditions in the electrolysis cell, and for the formation of PbO and PbO<sub>2</sub> that current must be supplied for a certain minimum amount of time. In a fast sweep rate study, most of the current is utilized in the discharge of Pb<sup>++</sup> ions. Mass-transfer effects of Pb<sup>++</sup> ions thus produced impede the transport of H<sub>2</sub>O molecules to the electrode surface. As is evident from Eq. [2] and [3], H<sub>2</sub>O is crucial in the formation of PbO and PbO<sub>2</sub>.

Manuscript submitted Jan. 28, 1974; revised manuscript received March 15, 1974.

Any discussion of this paper will appear in a Discussion Section to be published in the June 1975 JOURNAL. All discussions for the June 1975 Discussion Section should be submitted by Feb. 1, 1975.

#### REFERENCES

1. J. W. Johnson, C. K. Wu, and W. J. James, *Corrosion Sci.*, **8**, 309 (1968).
2. J. J. Lander, *This Journal*, **98**, 213 (1951); *ibid.*, **98**, 220 (1951).
3. J. Burbank, *ibid.*, **103**, 87 (1956); *ibid.*, **104**, 693 (1957); *ibid.*, **106**, 369 (1959).
4. P. Ruetschi, J. Sklarchuk, and R. T. Angstadt, *Electrochim. Acta*, **8**, 333 (1963).
5. P. Ruetschi and B. D. Cahan, *This Journal*, **104**, 406 (1957); *ibid.*, **105**, 369 (1958).
6. T. Akewo Chiku and Koichi Nakajima, *ibid.*, **118**, 1395 (1971).
7. D. Pavlov and N. Iordanov, *ibid.*, **117**, 1103 (1970).
8. D. Pavlov, *Electrochim. Acta*, **13**, 2051 (1968).
9. H. Vaidyanathan, M. E. Straumanis, and W. J. James, *This Journal*, **121**, 7 (1974).
10. J. L. Weininger and M. W. Breiter, *ibid.*, **110**, 484 (1963).
11. N. White and F. Lawson, *J. Electroanal. Chem.*, **25**, 409 (1970).
12. J. P. Carr and N. A. Hampson, *This Journal*, **118**, 1262 (1971).
13. R. W. Powers and M. W. Breiter, *ibid.*, **116**, 719 (1969).
14. P. Delahay, Editor "New Instrumental Methods in Electrochemistry," Chap. 6, Wiley-Interscience, New York (1966).
15. Ralph N. Adams, "Electrochemistry at Solid Electrodes," Marcel Dekker, Inc., New York (1969).
16. D. Landolt, R. H. Muller, and C. H. Tobias, *This Journal*, **118**, 36 (1971).
17. K. E. Heusler and R. Knoedler, *Electrochim. Acta*, **15**, 243 (1970).
18. A. K. N. Reddy, *J. Electroanal. Chem.*, **6**, 141 (1963).
19. A. Landsberg, C. L. Hoatsen, and F. E. Block, *This Journal*, **118**, 1331 (1971).
20. James P. Hoar, Editor, "The Electrochemistry of Oxygen," Chap. VII, Wiley-Interscience, New York (1968).

# Hafnium Electrowinning Studies

D. R. Spink\*

Department of Chemical Engineering, University of Waterloo, Waterloo, Ontario Canada

and C. P. Vijayan\*\*

Département de Génie Métallurgique, École Polytechnique, Montréal, Québec, Canada

The publication costs of this article have been assisted by the University of Waterloo.

Hafnium, an electropositive metal, is not deposited from aqueous electrolytes because of the decomposition of water at lower potentials. Therefore, other solvents must be considered for electrowinning of hafnium.

Fused salt media are known as excellent solvents for  $\text{HfCl}_4$ . One of the problems associated with electrowinning of hafnium from fused salts relates to the apparent absence of a significant amount of a reduced state of hafnium in the bulk of the fused salt. Therefore, when  $\text{HfCl}_4$  is used as the source of hafnium added to the electrolyte, it becomes necessary to provide a suitable complexing agent to stabilize the melt; i.e., to retain the  $\text{HfCl}_4$  in the melt at the operating temperature. The presence of reduced states of hafnium in the immediate vicinity of the cathode does not ameliorate this situation.

Most electrowinning research has been confined to low  $\text{HfCl}_4$  concentrations (<10%  $\text{HfCl}_4$ ) in fused salt melts and operating temperatures of about 800°C (1-4). The vapor pressure of  $\text{HfCl}_4$  over most such melts at this temperature is significant so that a gradual loss of  $\text{HfCl}_4$  from the melt occurs. In cells used for electrowinning hafnium, it is quite difficult to operate with a "hot-top" design to prevent condensation of  $\text{HfCl}_4$  emanating from the melt; thus the concentration of  $\text{HfCl}_4$  in the melt is gradually depleted as  $\text{HfCl}_4$  condenses and deposits in exit ports, seals, etc. Such condensation of  $\text{HfCl}_4$  in the upper portions of the cell, for example, in the cathode removal chamber, inevitably leads to the further problem of cell contamination resulting from subsequent and unavoidable exposure to moisture (air).  $\text{HfCl}_4$  may also escape from the cell through the anode (chlorine) off-gas vent and in fact may be of sufficient quantity to plug this vent when a significant vapor pressure of  $\text{HfCl}_4$  over the salt melt develops at the operating temperature of the cell.

Thus, one of the objectives of the present work was to determine whether more suitable fused salt electrolytes could be found for the electrowinning process.

The problem of solubility of the vapor,  $\text{HfCl}_4$ , in molten alkali and alkaline earth chlorides is directly related to the phase diagrams of the binary systems  $\text{MCl} = \text{XCl}_4$  (Fig. 1). Any desired composition may be obtained by exposing the melt to the reactive  $\text{HfCl}_4$  vapor, providing that the pressure is maintained at the value required by the composition and temperature. However, to be considered as potential electrolytes for electrowinning hafnium, the solutions must have decomposition pressures which are negligibly small so that the bath will retain its metal tetrachloride content under normal operating conditions in an inert gas atmosphere but otherwise in an open electrolytic cell. According to Flengas *et al.* this condition restricts the useful composition of the chloride solutions to ranges representing the  $\text{MCl}-\text{M}_2\text{XCl}_6$  subsystem, and to salt components that produce complex  $\text{M}_2\text{XCl}_6$  compounds of maximum thermodynamic stability (8).

Flengas *et al.* have stressed the fact that solutions containing  $\text{XCl}_4$  in excess of the amount required to

form the  $\text{M}_2\text{XCl}_6$  species are thermally unstable and cannot be considered as potential electrolytes.

Howell *et al.* (5) conducted studies on the properties of the low temperature eutectic region, as well as of the high temperature eutectic region of the binary systems  $\text{MCl}-\text{XCl}_4$ . According to the phase diagram and vapor pressure results obtained by these investigators, the range of liquid composition for melts with vapor pressures below 100 mm Hg is reasonably wide for practical use as an electrolyte in the regions of both eutectics.

The objective of the present work, then, was to conduct comparative studies of the electrolysis of melts in the system  $\text{MCl}-\text{HfCl}_4$  corresponding to the lower melting eutectic and the higher melting eutectic to qualitatively determine which was the better system for further study. As far as we could determine, no experimental electrolytic work has been performed over the range of  $\text{HfCl}_4$  contemplated herein.

## Investigation

It should be made clear at the outset that the immediate goal of this work was not to produce pure metal, but only to define the most promising areas with respect to  $\text{HfCl}_4$  concentration in molten salt baths where stability of the bath coupled with the ability to produce metallic hafnium were of paramount importance.

*Materials.*—Sodium chloride and potassium chloride were of Analar purity. Pure hafnium tetrachloride was supplied by Teledyne Wah Chang, Albany, Oregon, and by Amax Speciality Metals, Incorporated, Akron, New York. Both companies purified the  $\text{HfCl}_4$  by special treatments. The only element of interest in the  $\text{HfCl}_4$

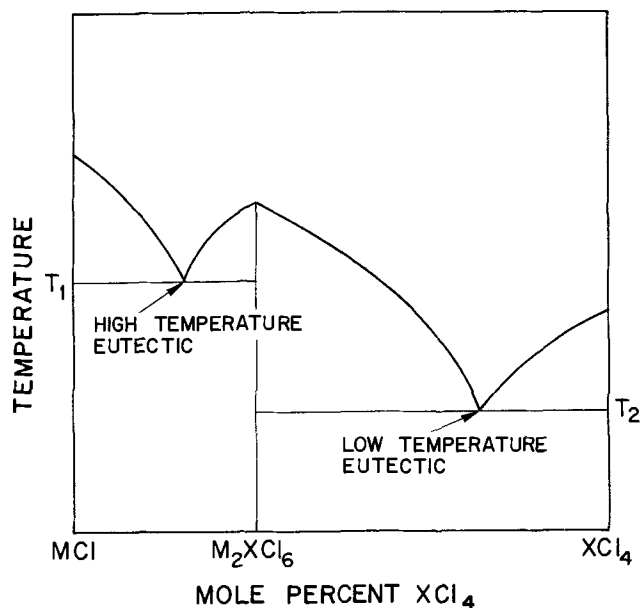


Fig. 1. Generalized phase diagram of the system  $\text{MCl}-\text{XCl}_4$ . M stands for Li, Na, or K; X stands for Zr or Hf.

\* Electrochemical Society Active Member.

\*\* Electrochemical Society Student Member.

Key words: fused salts, eutectics, reactive metals.

was the oxygen content which cannot easily be determined directly. Carefully conducted sublimation tests indicated that the material supplied was completely volatile thus indicating the absence of  $\text{HfO}_2$  per se; however, there exist strong suspicions that  $\text{HfOCl}_2$  (anhydrous) is volatile so we have assumed that, regardless of any precautions taken, a small quantity of oxygen would probably be present in all baths made. The presence of large amounts of oxygen in the bath was known to preclude the development of massive crystalline deposits of metallic hafnium; nevertheless, the black, powderlike deposits expected would show characteristic metallic crystalline structure under proper magnification, and further, would indicate the presence of metallic hafnium by the brilliance of the sparks produced by the burning of a small sample in an open flame. While it is accepted that these analytical methods were crude, it was shown that they were satisfactory for the specific evaluation required. Emission spectroscopy and oxygen analysis were employed primarily to verify the acceptability of the above-described techniques.

**Equipment.**—Two different types of cells were used. For the low melting eutectic, glass cells were used which afforded visual observations of the anode and cathode during the electrolysis experiments. (The heating furnaces were designed with windows such that visual observation of the melt could be made.) All of the low melting runs formed water-clear melts of low viscosity at temperatures below  $300^\circ\text{C}$  so that visual observation was an exceedingly simple matter.

For the higher melting eutectic, a glass-lined steel cell was found to be the most practical. Initially, graphite rod (1/4 in.  $\phi$ ) was used as the anode in both types of cell. Later, as explained below, 1/4 in.  $\phi$ -nickel rod was used in the glass cells with the low temperature eutectic melts. Various metallic rods were used for cathodes; e.g., 1/16 in. Type 304 stainless steel, 1/4 in. mild steel, and, for the higher temperature melts, 1/8 in. nickel rods. All appeared to perform well.

In most cases, the eutectic was first made in a special melter. The  $\text{HfCl}_4$  and salts were weighed and added to the melter vessel in a dry box. After appropriate evacuation and argon backfill steps, the melter vessel was placed in a furnace and slowly heated to about  $100^\circ\text{C}$  above the melting point of the mix and held there, usually overnight. The melter vessel was constructed to withstand considerable pressure. After cooling, the solidified melt was removed from the melter in a dry box and broken to  $\sim 1/8$  in. size pieces which were stored in sealed containers. "Black" salt found at the bottom of the melting vessel was removed since it was known to contain most of the oxygen-containing species of hafnium (11).

**Procedure.**—For the low temperature melts, a new glass cell was made for each experiment. The anode and cathode were first cemented into the openings provided with a Saureisen cement<sup>1</sup> and allowed to set in a drying oven. The premelted salt was added to the cell and the feed port was sealed. The cell was now evacuated several times, backfilling as required with argon. The cell was placed in its special furnace and slowly heated until complete melting was observed. The temperature was fixed at  $310^\circ\text{C}$  for most of the low temperature runs; composition of hafnium tetrachloride in the  $\text{NaCl-KCl}$  (1:1M)- $\text{HfCl}_4$  was 63 mole per cent (m/o). The experiments were conducted at cell voltages ranging from 5 to 20V which gave anode and cathode current densities ranging from 19 to 77 A/dm<sup>2</sup>. Electrolysis was maintained as long as reasonable voltages could maintain the current flow but rarely longer than a few hours. During these relatively short runs, any attack of the glass container by a reduced state of the hafnium was felt to be negligible.

<sup>1</sup> Saureisen Sealing Cement (No. 33, Powder), Saureisen Cement Company, Pittsburgh, Pennsylvania.

For the high temperature eutectic experiments, a glass-lined steel cell was used. The anode and cathode were cemented into the cell top and ceramic sleeves were employed to obtain suitable electrical insulation. Since the melt could not be observed, somewhat longer periods of heating were provided to assure that a homogeneous melt had been obtained (electrical conductivity of the melt was no measure of the homogeneity of the melt). A temperature of  $565^\circ\text{C}$  was used for most of the high temperature experiments. The system used consisted of 27 m/o  $\text{HfCl}_4$  and 73 m/o salts ( $\text{NaCl/KCl}$ ). The cell voltage ranged from 2.5 to 7.0V, and anode and cathode current densities varied from 9 to 59 A/dm<sup>2</sup> and from 19 to 115 A/dm<sup>2</sup>, respectively.

### Discussion

The crude experiments strongly indicated that the low temperature eutectic was unsuitable for electrolysis of hafnium. Of concern was the observed instability of the melt resulting in profuse loss of tetrachloride vapor. Without special precautions, the gaseous tetrachloride condensed in, and would consequently plug, the chlorine off-gas line. Perhaps of even greater concern was an observed inability to produce metallic hafnium deposits from the low melting eutectic bath. This was unexpected since the electrolysis could be visually observed. In most cases observed, the cathodic deposit built up readily in a typically dendritic form of growth. The ready evolution of chlorine from the anode was also easily observed and verified by the wet KI test. However, after water leaching, much of the deposit appeared to have been dissolved and that which remained was decidedly not hafnium metal. During leaching, no unusual reactions were observed nor was there any evidence of hydrogen formation or evolution.

One final interesting observation that has been unexplained so far was the disintegration of graphite anodes within the melt during electrolysis of only the low melting hafnium eutectic. (No such degradation occurred in the very similar  $\text{ZrCl}_4$  eutectic.) The graphite rods swelled and disintegrated below the melt. It is of interest to note that graphite held up satisfactorily in the high temperature eutectic melts containing either  $\text{HfCl}_4$  or  $\text{ZrCl}_4$ . Nickel anodes were subsequently used for all of the low temperature eutectic experiments and these held up well.

The high temperature eutectics appeared to be much more stable as evidenced by the lack of copious quantities of tetrachloride vapor fumes emanating from the chlorine purge port. Some fuming was observed which would indicate that further testing might evaluate  $\text{RbCl}$  or  $\text{CsCl}$  along with  $\text{KCl}$  as recommended by Flengas (8).

Adherence of the deposit to the cathode gave no problem in any of the baths tested. All cathodes were cleaned well before each run which, according to Lebedeva (10), is a basic requirement for an adherent deposit.

Small metallic crystallites of hafnium were readily produced from the high temperature melts. Current efficiency was estimated to be about 70% in the high temperature experiments. Since no attempt was made in these tests to produce material of high purity, only one sample was analyzed for oxygen; it indicated approximately 1% oxygen. Several of the metallic samples were converted to the oxide for analysis by emission spectroscopy. The resulting hafnium oxide spectra were very clean, indicating only trace quantities<sup>2</sup> of any impurity. These analyses confirmed our belief that for the short reduction periods employed, attack of the glass containers by reduced states of hafnium was not important.

<sup>2</sup> Less than the lower limit for which a specific analytical concentration can normally be determined.

### Conclusions

In the series of preliminary screening tests, it was not possible to produce metallic hafnium from the low melting eutectic; furthermore, the instability of this melt makes it unattractive for use as a commercial electrolyte.

The high temperature eutectic not only appeared to be much more stable, but it consistently gave crystalline metallic deposits of hafnium.

### Acknowledgment

The support rendered by the National Research Council of Canada is gratefully acknowledged.

Manuscript submitted Nov. 2, 1973; revised manuscript received Feb. 25, 1974.

Any discussion of this paper will appear in a Discussion Section to be published in the June 1975 JOURNAL. All discussions for the June 1975 Discussion Section should be submitted by Feb. 1, 1975.

### REFERENCES

1. J. R. Nettle, J. M. Hiegel, and D. H. Baker, Jr., U.S. Bureau of Mines, Report of Investigation 5851, Washington, D. C. (1961).
2. D. R. Spink, Internal Reports, Carborundum Metals Company, Incorporated, (1958 and 1969).
3. C. A. Hampel, Editor, "Encyclopedia of Electrochemistry," pp. 692-693 and 1188-1191, Reinhold Publishing Corporation, New York (1964).
4. G. M. Martinez, M. M. Wong, and D. E. Couch, *TMS-AIME*, **245**, 2237 (1969).
5. L. J. Howell, R. C. Sommer, and H. H. Kellogg, *J. Metals*, **209**, 193 (1957).
6. D. R. Spink, Personal research.
7. L. J. Howell and H. H. Kellogg, *TMS-AIME*, **215**, 143 (1959).
8. S. N. Flengas and P. Pint, *Can. Met. Quart.*, **8**, 151 (1969).
9. J. E. Dutrizac and S. N. Flengas, Advances in Extractive Metallurgy, Proc. of Symp., April 17-20, 1967, Institute of Mining and Metallurgy, London, England (1968).
10. K. P. Lebedeva and A. M. Baraboshkin, *Electrochem. Molten Solid Electrolytes*, **3**, 83 (1966).
11. D. R. Spink, *TMS-AIME*, **224**, 965 (1962).

## Effect of Sodium Ions on the Electrochemical Reduction of Diethyl Fumarate in Dimethylsulfoxide and Acetonitrile

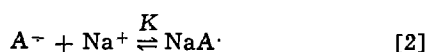
Michael D. Ryan and Dennis H. Evans

Department of Chemistry, University of Wisconsin-Madison, Madison, Wisconsin 53706

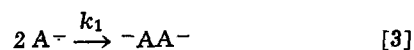
The publication costs of this article have been assisted by the National Science Foundation.

Childs *et al.* (1) studied the electrochemical reductive coupling of diethyl fumarate (*trans*-C<sub>2</sub>H<sub>5</sub>O<sub>2</sub>CCH = CHCO<sub>2</sub>C<sub>2</sub>H<sub>5</sub>), **1**, in *N,N*-dimethylformamide (DMF). Their attention was focused on the dimerization mechanism with tetra-*n*-butylammonium iodide as supporting electrolyte. Using double potential step chronoamperometry, these workers showed that the initially formed radical anions reacted by a second-order, irreversible, dimerization reaction in contrast to more complex schemes which had been proposed earlier. This conclusion was confirmed for **1** and other activated olefins by later studies using rotating ring-disk electrode voltammetry (2), linear sweep voltammetry (3), and current-reversal chronopotentiometry (4).

Childs *et al.* (1) noted that the addition of sodium or lithium ions to the supporting electrolyte caused a substantial increase in the rate of dimerization of the radical anions of diethyl fumarate. Lithium also had the effect of decreasing the importance of polymerization side reactions as evidenced by an increase of the coulometric *n*-value to unity. An analogous effect of sodium and lithium has been reported for the reduction of some  $\alpha,\beta$ -unsaturated ketones in dimethylsulfoxide (5). The increased rate of dimerization was ascribed to ion pair formation between the radical anions and the metal cations with the neutral ion pairs reacting more rapidly than the anion radicals. A quantitative study of the effect of sodium on the reduction of phthalaldehyde in *N,N*-dimethylformamide has been reported by Lasia (6) who treated his data in terms of the following reactions (*A* = phthalaldehyde)



Key words: electrohydrodimerization, cyclic voltammetry, ion pairs.



If the rate of the ion pairing reaction [2] is rapid enough so that the reaction can be assumed to be at equilibrium, and if sodium is present in excess, the observed dimerization rate constant,  $k_{obs}$ , may be related to  $K$ ,  $k_1$ ,  $k_2$ ,  $k_3$ , and  $C_{Na}$  by the equation

$$k_{obs} = (k_1 + k_2KC_{Na} + k_3K^2C_{Na}^2) / (1 + KC_{Na})^2 \quad [6]$$

where  $K$  is the formation constant for the ion pair ( $M^{-1}$ ) and  $C_{Na}$  is the molar concentration of sodium.

This paper presents results for the reduction of **1** in the presence of sodium in dimethylsulfoxide (DMSO) and acetonitrile (AN). Though these solvents have similar dielectric constants, the tendency for ion pair formation is much greater in AN than in DMSO. Fujinaga *et al.* (7) noted that formation constants for the ion pairs of the radical anions of naphthoquinones and metal ions are greater in AN than in DMSO. As pointed out by Krygowski (8), this is consistent with the concept of donicity ( $DN$ ) defined by Gutmann (9). A high donicity solvent such as DMSO ( $DN = 29.8$ ) stabilizes the unpaired metal ions by solvation in contrast to a lower donicity solvent such as AN ( $DN = 14.1$ ) in which solvation of metal ions is weak and ion pair formation is favored.

### Experimental

**Materials.**—Dimethylsulfoxide (DMSO) and acetonitrile (AN) were Matheson Coleman and Bell Spectroquality solvents. Water content as determined by gas chromatography was about 30 mM for each solvent. Tetra-*n*-butylammonium perchlorate (Matheson

Coleman and Bell) was recrystallized from acetone-water and vacuum dried at room temperature. Anhydrous sodium perchlorate (Matheson Coleman and Bell) was found to contain less than 1 mole per cent (m/o) water by determining loss of weight after vacuum drying at 200°C (10). Diethyl fumarate (Aldrich) was used as received.

**Apparatus.**—The voltammetric cell has been described elsewhere (11) as has the digital data acquisition system and procedures for analysis of cyclic voltammetric data (12). A silver reference electrode (SRE) comprising a silver wire in contact with 0.10M tetra-*n*-butylammonium perchlorate and 0.010M silver nitrate in DMSO was used for the DMSO studies and an aqueous saturated calomel electrode (SCE) was used in AN. The hanging mercury drop electrode area was 0.029 cm<sup>2</sup>.

**Experimental procedures.**—Experiments were performed at a temperature of 24° ± 1°C. For sodium perchlorate concentrations less than 0.10M, sufficient tetra-*n*-butylammonium perchlorate was added to assure an ionic strength of 0.1M.

Rate constants were determined using the method described by Olmstead, Hamilton, and Nicholson (13) where the anodic peak current,  $i'_a$ , is measured from zero current rather than from an extension of the cathodic peak. The theoretical results were extended to switching potentials necessary for this research but not encompassed in the work of Olmstead *et al.* by applying digital simulation techniques (14). The rate law for dimerization of the radicals,  $R$ , was written as  $-dC_R/dt = 2kC_R^2$  where  $k$  is the second-order dimerization rate constant. Olmstead *et al.* omitted the 2 in their formulation of the rate law.

### Results and Discussion

Peak potentials and observed rate constants,  $k_{obs}$ , as a function of sodium concentration for DMSO as solvent are presented in Table I. The rate constants are averages of individual values obtained from at least three different scan rates in the range of 0.5-50 V/sec. The shapes of the voltammetric peaks, the peak current ratios, and the dependence of the cathodic peak potential on scan rate were all consistent with an irreversible dimerization following reversible electron transfer (13).

There are several constants which must be evaluated in Eq. [6]. The dimerization rate constant for the radical anions,  $k_1$ , was taken as  $k_{obs}$  in the absence of sodium ions. The value found was  $1.4 \times 10^3$  liter·mole<sup>-1</sup>sec<sup>-1</sup>. The evaluation of  $K$  is based on the dependence of the peak potential on sodium concentration. Two factors cause the peak potential to move in the positive direction as the sodium concentration increases. First, the ion pair formation (reaction [2]) causes a positive shift in the potential. This would

Table I. Dependence of peak potential and  $k_{obs}$  on sodium concentration for the reduction of diethyl fumarate in DMSO<sup>a</sup>

$C_{Na}, M$	$E_p^b$	$k_{obs} \times 10^{-3}$ , liter·mole <sup>-1</sup> sec <sup>-1</sup>
0.0	-1.728	1.4
0.004	-1.724	3.4
0.0063	-1.724	4.7
0.010	-1.717	6.6
0.016	-1.711	11
0.025	-1.705	17
0.040	-1.699	24
0.064	-1.692	35
0.10	-1.692	38
0.16	-1.684	60
0.25	-1.674	97
0.40	-1.659	170
0.63	-1.645	445

<sup>a</sup> 0.96 mM diethyl fumarate; 24°C; tetra-*n*-butylammonium perchlorate added to solutions containing low sodium concentrations to bring total ionic strength to about 0.1M.

<sup>b</sup> V vs. SRE; 0.050 V/sec.

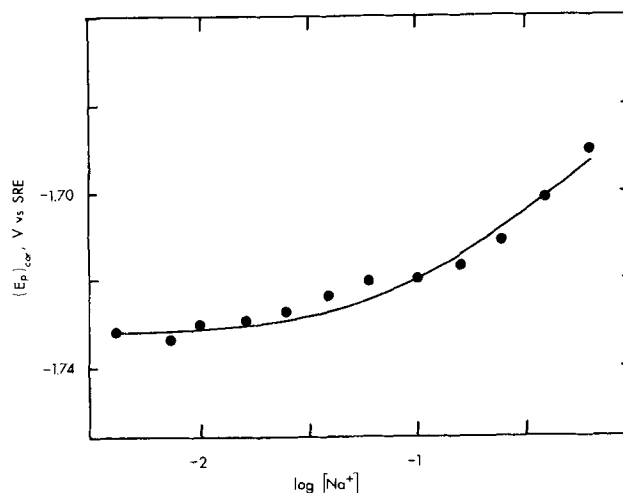


Fig. 1. Corrected peak potentials for reduction of diethyl fumarate in DMSO as a function of sodium concentration. Concentration of diethyl fumarate, 0.96 mM; scan rate, 0.050 V/sec. Peak potentials corrected for effect of chemical reactions following the initial electron transfer (see text).

be observed even if the radicals did not dimerize. Second, the chemical reactions of the anion radicals, reactions [3]-[5], also cause a positive shift in the peak potential. Since the two effects are additive, we may correct the observed peak potentials for the effects of the second factor by applying the theory for an irreversible dimerization reaction following a reversible electron transfer reaction (13) to the observed peak potentials and rate constants in Table I.<sup>1</sup>

Peak potentials corrected in this manner are presented in Fig. 1. The residual dependence of peak potential on sodium concentration should be due only to the first factor (ion pair formation) and the data should be interpretable in terms of the equation (15)

$$(E_p)_{cor.} = E_{1/2} - 0.0285 + 0.0592 \log(1 + KC_{Na}) \quad [7]$$

where  $E_{1/2}$  is the half-wave potential for reaction [1]. The curve in Fig. 1 is that predicted by Eq. [7] with  $E_{1/2} = -1.704$  V vs. SRE and  $K = 5.8 M^{-1}$ .

The final two rate constants,  $k_2$  and  $k_3$ , can be obtained by finding the values which best fit Eq. [6] using the experimental values of  $k_{obs}$  and the  $k_1$  and  $K$  which were evaluated above. Figure 2 shows the curve predicted by Eq. [6] for  $K = 5.8 M^{-1}$ ,  $k_1 = 1.4 \times 10^3$ ,  $k_2 = 5.0 \times 10^4$ , and  $k_3 = 3.1 \times 10^5$  liter·mole<sup>-1</sup>sec<sup>-1</sup>. The ionic strength was substantially greater for the four highest sodium concentrations than it was for those of 0.1M and below. This could have affected the rate constants though the important reactions in this region of concentration (reactions [4] and [5]) are not ion-ion reactions and should not be highly dependent on ionic strength. An alternative fit for sodium concentrations of 0.10M and below gives  $k_2 = 6.8 \times 10^4$  and  $k_3 = 2.0 \times 10^5$  liter·mole<sup>-1</sup>sec<sup>-1</sup>. The model assumes that the rate of ion pairing is much greater than the dimerization reactions. Ion pairing rate constants are known to be large. For example, the over-all rate constant for sodium exchange in the 2,5-di-*tert*-butyl-1,4-benzoquinone radical anion-sodium ion pair is about  $10^8$  liter·mole<sup>-1</sup>sec<sup>-1</sup> (16). In summary, for DMSO as solvent, ion pairing is weak but the rate

<sup>1</sup> This procedure is based on the fact that the boundary value problem comprising reactions [1]-[5] is of the same form as that solved by Olmstead *et al.* (13) when it is assumed that reaction [2] is fast and that the diffusion coefficients of the radical anion and ion pair are identical. The formulation treats the sum of the radical anion and ion pair concentrations as a new variable. The rate constant in the formulation is  $k_{obs}$  from Eq. [6] and the standard potential includes the effect of reaction [2], i.e., it is given by  $E^\circ + 0.0592 \log(1 + KC_{Na})$ . Hence, the theoretical data of Ref. (13) may be used to evaluate  $k_{obs}$ . Furthermore, the shifts in peak potential as the sodium concentration is changed are due to both the kinetic effect and the shift in the formal potential. The two effects are additive.

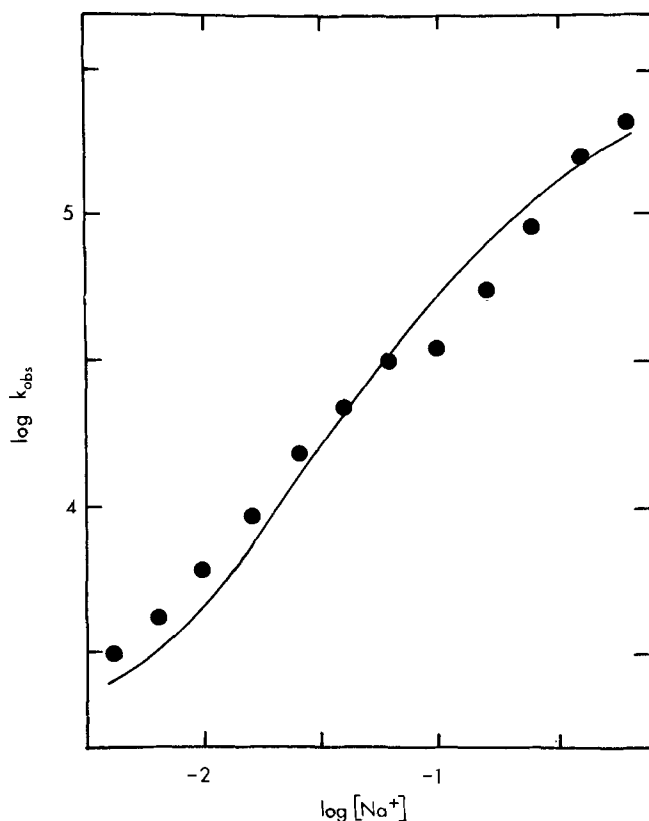


Fig. 2. Observed rate constants for dimerization of radical anions of diethyl fumarate in DMSO as a function of sodium concentration. Concentration of diethyl fumarate, 0.96 mM. Curve is Eq. [6] with  $K = 5.8 \text{ M}^{-1}$ ,  $k_1 = 1.4 \times 10^3$ ,  $k_2 = 5.0 \times 10^4$ , and  $k_3 = 3.1 \times 10^5 \text{ liter} \cdot \text{mole}^{-1} \text{sec}^{-1}$ .

of dimerization of the ion pairs is about two orders of magnitude greater than that of the free radical anions. At low sodium concentrations, the dimerization proceeds by reactions [3] and [4], and as the sodium concentration is increased, reaction [5] becomes important while reaction [3] wanes.

When AN was used as solvent, the dimerization reactions were extremely rapid in the presence of sodium ions. With as little as 2 mM sodium, no oxidation peak was obtained for a cyclic voltammogram of 0.29 mM **1** at 50 V/sec. This means that  $k_{\text{obs}}$  is greater than about  $10^6 \text{ liter} \cdot \text{mole}^{-1} \text{sec}^{-1}$ . This greatly enhanced rate is due to the greater tendency for ion pair formation in AN as compared to DMSO. Even at low sodium concentrations, the ion pair is the predominant form of the anion radical, i.e.,  $K_{\text{Na}} \gg 1$ . Under this condition (and  $k_3 > k_2 > k_1$  as was observed in DMSO) Eq. [6] reduces to  $k_{\text{obs}} = k_3$  and the observed rate constant is no longer a function of sodium concentration. As a result, the kinetic effect on the peak potential for the reduction of **1** in AN will be a constant and any shift in peak potential as the sodium concentration is varied must be attributed to the ion pairing (reaction [2]). The effect is described by Eq. [7] which predicts that the peak potential should shift 59 mV for a tenfold change in sodium concentration when the ion pair is the predominant species ( $K_{\text{Na}} \gg 1$ ).

Peak potentials for the reduction of **1** in AN are presented in Fig. 3 along with a line of the theoretical 59 mV slope. These data are consistent with a reaction scheme in which most of the radical anions exist as ion pairs, and the dimerization proceeds by reaction between these ion pairs (reaction [5]).

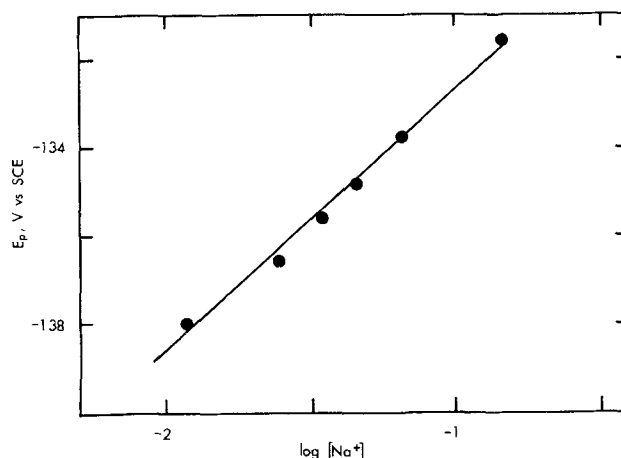


Fig. 3. Peak potentials for reduction of diethyl fumarate in AN as a function of sodium concentration. Concentration of diethyl fumarate, 0.29 mM; scan rate, 0.100 V/sec.

In conclusion, it has been possible to correlate the data for the reduction of **1** in DMSO containing sodium to the mechanism given by reactions [1]-[5]. The ion pair formation constant and the three rate constants were evaluated. In AN, the same mechanism is probably active but the formation constant of the ion pair is large enough that only the pathway involving dimerization of ion pairs is observed.

#### Acknowledgment

This research was supported by the National Science Foundation, Grant Number GP-19579. Acknowledgment is also made to the donors of the Petroleum Research Fund, administered by the American Chemical Society, for partial support of this work. Most of the computer equipment was obtained through National Science Foundation Grant Number GP-12221.

Manuscript submitted Jan. 2, 1974; revised manuscript received Feb. 28, 1974.

Any discussion of this paper will appear in a Discussion Section to be published in the June 1975 JOURNAL. All discussions for the June 1975 Discussion Section should be submitted by Feb. 1, 1975.

#### REFERENCES

- W. V. Childs, J. T. Maloy, C. P. Keszthelyi, and A. J. Bard, *This Journal*, **118**, 874 (1971).
- V. J. Puglisi and A. J. Bard, *ibid.*, **119**, 829 (1972).
- E. Lamy, L. Nadjo, and J. M. Saveant, *J. Electroanal. Chem.*, **42**, 189 (1973).
- S. C. Rifkin and D. H. Evans, *This Journal*, In press.
- J. P. Zimmer, J. A. Richards, J. C. Turner, and D. H. Evans, *Anal. Chem.*, **43**, 1000 (1971).
- A. Lasia, *J. Electroanal. Chem.*, **42**, 253 (1973).
- T. Fujinaga, K. Izutsu, and T. Nomura, *ibid.*, **29**, 203 (1971).
- T. M. Krygowski, *ibid.*, **35**, 436 (1972).
- V. Gutmann, *Chem. Brit.*, **7**, 102 (1971).
- R. L. Kay, B. J. Hales, and G. P. Cunningham, *J. Phys. Chem.*, **71**, 3925 (1967).
- R. C. Buchta and D. H. Evans, *Anal. Chem.*, **40**, 2181 (1968).
- P. E. Whitson, H. W. VandenBorn, and D. H. Evans, *ibid.*, **45**, 1298 (1973).
- M. L. Olmstead, R. G. Hamilton, and R. S. Nicholson, *ibid.*, **41**, 260 (1969).
- S. W. Feldberg, in "Electroanalytical Chemistry," Vol. 3, A. J. Bard, Editor, pp. 199-296, Marcel Dekker, Inc., New York (1969).
- R. S. Nicholson and I. Shain, *Anal. Chem.*, **36**, 706 (1964).
- A. W. Rutter and E. Warhurst, *Trans. Faraday Soc.*, **66**, 1866 (1970).



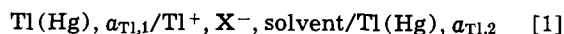
# Electrochemical Measurements of Dilute Thallium Amalgams

Mark Salomon\*

Power Sources Technical Area, U. S. Army Electronics Technology and Devices Laboratory,  
Fort Monmouth, New Jersey 07703

The publication costs of this article have been assisted by the U. S. Army.

In 1919 Richards and Daniels published their detailed work on concentrated thallium amalgams (1). These results were used by Lewis and Randall in their classical thermodynamic treatment of concentrated solutions (2). Richards and Daniels made very precise emf measurements ( $\pm 2 \mu\text{V}$ ) on the concentration cell



In cell [1],  $a_{\text{Tl},1}$  and  $a_{\text{Tl},2}$  are the activities of Tl in the amalgams and  $\text{X}^-$  is the anion. Richards and Daniels also made some measurements on the cell



but refer to these measurements as being "only approximate." It is noted that the emf's of cells [1] and [2] are independent of the nature of  $\text{X}^-$  and of the solvent. Cowperthwaite *et al.* (3) made very precise emf measurements ( $\pm 0.02 \text{ mV}$ ) on cell [2] using a 5% Tl amalgam. The Nernst relation for cell [2] is

$$E_2 = E^{\circ}_2 - (2 \cdot 3RT/F) \log(N_2 f_2) \quad [3]$$

where  $N_2$  and  $f_2$  are, respectively, the mole fraction and rational activity coefficient of Tl in the amalgam.  $E^{\circ}_2$  is defined by

$$E^{\circ}_2 = E^{\circ}_{\text{Tl(Hg)}} - E^{\circ}_{\text{Tl}} \quad [4]$$

where  $E^{\circ}_{\text{Tl(Hg)}}$  is the standard potential of the Tl amalgam [the reference state is infinite dilution (2)] and  $E^{\circ}_{\text{Tl}}$  is the standard potential of solid thallium.  $E^{\circ}_2$  is evaluated by plotting the function  $E'$  against  $N_2$  and extrapolating to  $N_2 = 0$ .  $E'$  is defined by

$$E' = E_2 + (2 \cdot 3RT/F) \log N_2 \quad [5]$$

A problem arises in the evaluation of  $E^{\circ}_2$  because the  $E_2$  values of Richards and Daniels are, supposedly, based on approximate values for the solid Tl electrode. Cowperthwaite's values for cell [2] using a 5% Tl amalgam can be combined with Richards's and Daniels's data for cell [1] to obtain  $E_2$  values as a function of  $N_2$ , but Cowperthwaite *et al.* do not state the accuracy of the concentration of the 5% amalgam. This latter method was used by the present author (4, 5) but it was pointed out by Singh *et al.* (6) that these  $E_2$  values differ by as much as 23 mV (positive) from those values based on Richards's and Daniels's approximate measurements. Since the  $E_2$  data of Richards and Daniels are widely quoted, particularly in recent works in nonaqueous solvents (4-8), it is important to have accurate values, and this then is the purpose of this communication.

## Experimental

$\text{TlNO}_3$  and 1/8 in. Tl wire (Apache Chemicals, 99.999% pure) were treated as follows. The Tl wire was rinsed in dilute  $\text{H}_2\text{SO}_4$  and distilled water and dried for 12 hr at  $60^\circ\text{C}$  in a vacuum oven. The as-received  $\text{TlNO}_3$  was dried under identical conditions. Reagent grade (Fisher Chemicals) dimethylsulfoxide (DMSO) was used as the solvent and was treated for 2-4 weeks with Type 4A molecular sieves. These chemicals were transferred to an argon-filled VAC dry box in which the oxygen content was less than 1 ppm.

\* Electrochemical Society Active Member.

Key words: thallium amalgams, standard potentials, activity coefficients.

An oxide film did form on the Tl wire during the transfer but was scraped off and the Tl would remain clean and bright for several weeks in the dry box. A stock Tl amalgam of  $\sim 10\%$  Tl by weight was prepared with triply distilled Hg. More dilute amalgams were prepared by adding Hg to this stock amalgam. A Mettler H15 balance was used for all weighings inside the dry box. The electrolyte used was  $\sim 0.1\text{M}$   $\text{TlNO}_3$  in DMSO.

The electrochemical cell consisted of five compartments, three of which contained Tl amalgam and the remaining contained Tl wire. The cell was filled in the dry box, sealed by wetting the ground joints with electrolyte, removed to the laboratory, and placed in a water bath. Four temperatures of  $15^\circ$ ,  $20^\circ$ ,  $25^\circ$ , and  $35^\circ\text{C}$  were employed; regulation was  $\pm 0.02^\circ\text{C}$ .

A Keithley 610C electrometer was used for the emf measurements of cell [2]. The output of the electrometer was measured with a Systron Donner 1103 counter with a Model 1936 integrating DVM plug in. Using a calibrated Weston cell as a standard, the accuracy of the emf readings was  $\pm 0.03 \text{ mV}$ .

## Results and Discussion

All emf readings were stable to within the accuracy limits of the instrumentation ( $\pm 0.03 \text{ mV}$ ). The bias potential between the two Tl electrodes was, within the stated accuracy, zero for all measurements. Some problems did arise with several measurements at  $15^\circ\text{C}$ . DMSO freezes at  $18.5^\circ\text{C}$  but can be supercooled in the presence of an electrolyte if the cooling is carried out slowly. During the measurements on 0.038, 0.081, and 6.005% Tl in Hg, the temperature was cooled rapidly from  $35^\circ$  to  $15^\circ\text{C}$  and the solution froze. Warming and recooling resulted in erratic readings and bias potentials of  $\sim 0.5 \text{ mV}$ . The emf data for these amalgams were not recorded at  $15^\circ\text{C}$  but were obtained by extrapolation as explained below.

The results of the measurements are given in Table I. Over the temperature range studied, it was found that the temperature coefficient,  $dE/dT$ , for any given amalgam is constant within the limits of the experimental error. This result is in agreement with those of Richards and Daniels. Because  $dE/dT$  is constant, the emf values for the three discarded points at  $15^\circ\text{C}$  could be evaluated by simple extrapolation to within

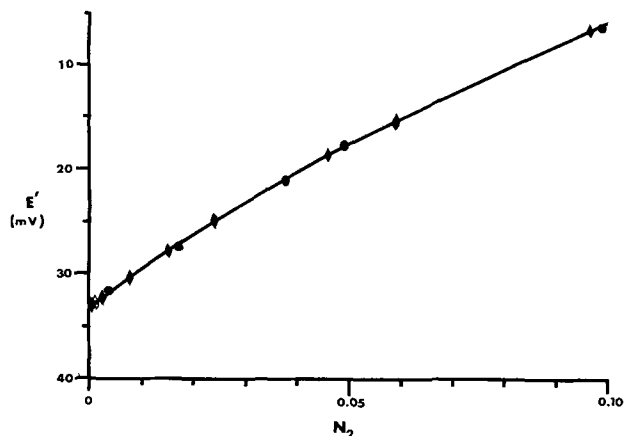


Fig. 1. Plot of  $E'$  (Eq. [5]) vs.  $N_2$  (mole fraction of Tl)



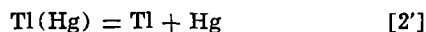
Table I. Experimental results for cell [2]

Weight per cent Tl	N <sub>2</sub>	E <sub>2</sub> (mV)				log f <sub>2</sub>			
		15°C	20°C	25°C	35°C	15°C	20°C	25°C	35°C
0.038	0.000375	(228.71)**	232.17	235.67	242.63	0.00245	0.00258	0.00254	0.000245
0.081	0.000792	(209.96)	213.14	216.33	222.64	0.00612	0.00533	0.00507	0.00507
0.260	0.002547	180.31	182.90	185.56	190.90	0.01732	0.01788	0.01775	0.01685
0.332*	0.003254	173.93	176.38	178.86	183.81	0.02239	0.02355	0.02464	0.02633
0.790	0.00759	151.06	153.09	155.27	159.64	0.04573	0.04659	0.04598	0.04432
1.526	0.01498	132.08	133.93	135.82	139.62	0.09130	0.09026	0.08904	0.08603
2.477	0.02432	117.24	118.83	120.52	123.96	0.14045	0.13943	0.13726	0.13166
4.670	0.04588	95.03	96.42	97.86	100.69	0.25309	0.24895	0.24443	0.23650
6.005	0.05900	(86.24)	87.23	88.43	90.81	0.29769	0.29777	0.29481	0.28900
9.799	0.08635	64.90	65.98	67.16	69.52	0.45868	0.45010	0.44137	0.42427

\* The data for this amalgam is taken from Ref. (1).

\*\* Values in parentheses are extrapolated (see text); error is  $\pm 0.05$  mV.

$\pm 0.05$  mV. These extrapolated  $E_2$  values are given in parentheses in Table I. The plot of  $E'$  (Eq. [5]) against  $N_2$  at 20.0°C is shown in Fig. 1. In this figure, the diamond points refer to the present results and the circles refer to the data of Richards and Daniels. It is seen that Richards's and Daniels's values lie within 0.03 mV of the line drawn through the diamond shaped points (this is within the accuracy of the present emf measurements). The extrapolation of  $E'$  to  $N_2 = 0$  for the present data is simpler than with Richards's and Daniels's original data because  $E'$  vs.  $N_2$  becomes linear below the point for  $N_2 = 0.003254$  (the 0.332% Tl amalgam). Above this point, the plot is nonlinear which results in a slightly less accurate value for  $E_2$  (see below). Table II gives the present values of  $E_2$  as a function of temperature. Also included in Table II is the standard free energy change,  $\Delta G_2^\circ$ , for the reaction of cell [2], i.e., for



A least squares analysis was performed on the data in Table II and the resulting values for the standard enthalpy and entropy (both are assumed to be independent of temperature) are, respectively,  $\Delta H_2^\circ = 646.1 \pm 4.9$  cal mole<sup>-1</sup> and  $\Delta S_2^\circ = -0.398 \pm 0.016$  eu. These errors are the statistical standard deviations of the least squares slope and intercept, respectively. A more realistic estimate of these standard deviations can be obtained by combining the variances of the statistical analysis and the experimental error. This then gives

Table II. Standard potentials and free energies for reaction [2]

°C	E <sub>2</sub> (mV)	ΔG <sub>2</sub> <sup>°</sup> (cal mole <sup>-1</sup> )
15.0	32.99	760.8
20.0	33.06	762.4
25.0	33.16	764.7
35.0	33.33	768.6

$$\Delta H_2^\circ = 646.1 \pm 5.0 \text{ cal mole}^{-1}$$

$$\Delta S_2^\circ = -0.40 \pm 0.22 \text{ eu}$$

The rational activity coefficients were calculated from Eq. [3] and are given in Table I. The values of  $f_2$  at 20.0°C are ~2% higher than those calculated by Lewis and Randall<sup>1</sup> who evaluated  $f_2$  from Richards's and Daniels's data and are therefore based on the non-linear extrapolation. If Lewis's and Randall's data for  $f_2$  are used in Eq. [3] to calculate  $E_2$  at 20.0°C, an average value of 32.78 mV is obtained. The difference between this and the present value for  $E_2$  is much greater than the experimental error and is therefore significant. Values for the activities of Hg in the amalgams were calculated from the Gibbs-Duhem equation and the results are, essentially, identical to those of Lewis and Randall. It is evident therefore that if Richards's and Daniels's statement on the approximate nature of their  $E_2$  values is taken literally, errors can result. This by no means vitiates previous results (4, 5) but rather requires slight adjustments as suggested by Singh *et al.* (6).

Manuscript received Jan. 25, 1974.

Any discussion of this paper will appear in a Discussion Section to be published in the June 1975 JOURNAL. All discussions for the June 1975 Discussion Section should be submitted by Feb. 1, 1975.

<sup>1</sup> Lewis and Randall (2) calculated the  $f_2$  data only for 20.0°C.

#### REFERENCES

1. T. W. Richards and F. Daniels, *J. Am. Chem. Soc.*, **41**, 1732 (1919).
2. G. N. Lewis and M. Randall, *ibid.*, **43**, 233 (1921).
3. I. A. Cowperthwaite, V. K. La Mer, and J. Barksdale, *ibid.*, **56**, 544 (1934).
4. M. Salomon, *This Journal*, **116**, 1392 (1969); *ibid.*, **117**, 325 (1970).
5. M. Salomon, *J. Phys. Chem.*, **73**, 3299 (1969).
6. G. Singh, J. C. Hall, and P. A. Rock, *J. Chem. Phys.*, **56**, 1855 (1972).
7. D. Cogley and J. N. Butler, *This Journal*, **113**, 1074 (1966).
8. W. H. Smyrl and C. W. Tobias, *ibid.*, **115**, 33 (1968).

## The Stability of Carbonate Ion in Fused Nitrate

A. G. Keenan, Carlos G. Fernandez,\* and Thomas R. Williamson\*

Department of Chemistry, University of Miami, Coral Gables, Florida 33124

The publication costs of this article have been assisted by the University of Miami.

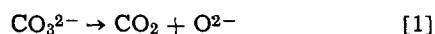
Numerous methods for adding oxide ion to nitrate melts for use in electrochemical studies have appeared

\* Electrochemical Society Student Member.

Key words: fused nitrates, carbonate ion, oxide ion, electromotive force, oxygen electrode.

in the literature (1). No really convenient source appears yet to be available. In recent publications (2, 3) Fredericks and Temple, in studying the platinum-oxygen electrode in fused nitrates, have used carbonate ion as a source of oxide ion. Between 250° and 350°C

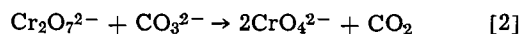
they give the reaction



This is based on earlier work of Kust (4-6) who first proposed the reaction. In the presence of a platinum-oxygen electrode, the oxygen flow was considered to drive the reaction to completion by sweeping out the carbon dioxide. The reaction was also assumed to proceed in the absence of the oxygen although in some cases an unspecified amount of dichromate was added "to enhance the evolution of  $\text{CO}_2$ " (4).

In contrast to the above, Zambonin (7) has reported that carbonate ion is stable in nitrate melts from 230° to 330°C.

In none of the above references was the system investigated sufficiently thoroughly to allow an unequivocal conclusion regarding the reaction. While pursuing our previous electrochemical studies in nitrate melts (8-10), we have found it necessary to study the matter further. As a result, it has been established that carbonate ion is stable in fused  $\text{KNO}_3$  at 350°C up to 100 hr. Purging with oxygen or nitrogen has no effect. If dichromate is added, it reacts stoichiometrically according to the equation



This reaction has also been proposed by others (11).

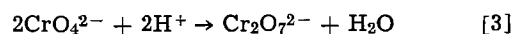
### Experimental

Reagent grade chemicals were utilized throughout this work. The  $\text{KNO}_3$  was dried in a vacuum desiccator at 130°C for 24 hr and then stored at 110°C.  $\text{K}_2\text{Cr}_2\text{O}_7$  and  $\text{K}_2\text{CO}_3$  were dried at 110°C for at least 24 hr. The melt consisted of 10g  $\text{KNO}_3$  at 350°C maintained in a fused salt bath.  $\text{K}_2\text{CO}_3$  was added as pellets formed in a laboratory press. The melt was allowed to stand at 350°C for various times up to 100 hr undisturbed or while being purged with either oxygen or nitrogen gas. It was then frozen, dissolved in boiled distilled water, and titrated with standardized HCl.

The colorimetric indicators methyl red and phenolphthalein were used with boiling in some titrations. In others, a Corning Series 500 Combination Electrode was used to monitor the pH curve. This was used in conjunction with a Sargent Constant Rate Buret (Model C) and a Model SR Recorder with a pH recording adapter. In all cases a very pronounced classical weak-base titration curve with two end points, one in the region of pH 9 and the other at 5.5, was obtained. Blank runs showed that any salt error due to the  $\text{KNO}_3$  was negligible. The volume of titrant to the first end point was equal to that from the first to the

second. The titration errors were less than 1%. Thus, within this accuracy carbonate is stable and the only base present for the given conditions.

To study the effect of dichromate, known amounts were added to a  $\text{KNO}_3$  melt at 350°C containing a known amount of carbonate in various mole ratios up to 1:1. Upon addition of the dichromate, a vigorous evolution of gas was observed and the orange color of the dichromate changed to the easily distinguishable yellow of chromate. Titrations as described above showed, that after the reaction, carbonate was present in the melt in an amount equal to the initial less the number of moles which would have been used up by reaction [2]. When dichromate was added in an amount stoichiometrically equivalent to the carbonate, no carbonate end points were found on titration. Instead, an inflection point was observed at pH 3.5 accompanied by a visually observable change from the yellow of chromate to the orange of dichromate. The volume of HCl consumed corresponded to the amount of dichromate originally added according to the known stoichiometry



### Acknowledgment

This work was supported by a contract from the Office of Naval Research, Material Sciences Division, Power Program.

Manuscript received Aug. 14, 1973.

Any discussion of this paper will appear in a Discussion Section to be published in the June 1975 JOURNAL. All discussions for the June 1975 Discussion Section should be submitted by Feb. 1, 1975.

### REFERENCES

1. A. G. Keenan and Carlos G. Fernandez, *This Journal*, **120**, 1697 (1973).
2. M. Fredericks and R. B. Temple, *Inorg. Chem.*, **11**, 968 (1972).
3. M. Fredericks, R. B. Temple, and G. W. Thickett, *J. Electroanal. Chem.*, **38**, App. 5 (1972).
4. R. N. Kust, *Inorg. Chem.*, **3**, 1035 (1964).
5. R. N. Kust, *J. Phys. Chem.*, **69**, 3662 (1965).
6. R. N. Kust, *This Journal*, **116**, 1137 (1969).
7. P. G. Zambonin, *Anal. Chem.*, **44**, 763 (1972).
8. K. Notz and A. G. Keenan, *J. Phys. Chem.*, **70**, 662 (1966).
9. A. G. Keenan, K. Notz, and F. L. Wilcox, *ibid.*, **72**, 1085 (1968).
10. A. G. Keenan and W. H. Duerwer, *ibid.*, **73**, 212 (1969).
11. J. D. VanNorman and R. A. Osteryoung, *Anal. Chem.*, **32**, 398 (1960).



## Computation of Standard Specific Rate Constants of Partial Processes in Mixed Potential Systems

Francis M. Donahue\*

Department of Chemical Engineering, The University of Michigan, Ann Arbor, Michigan 48104

In a recent paper the author proposed a method of determining the respective rate laws for partial processes in mixed potential systems (1). This method has recently been applied to electroless copper plating systems (2). The emphasis in that work (2) and subsequent publications (3, 4) was toward a determination of the reaction orders in order to elucidate the reaction mechanism. However, the resulting reaction orders made an exact elucidation impossible: it was possible only to make general remarks concerning possible mechanisms (3, 4). One may question the validity of an indirect analysis particularly when nonintegral reaction orders are obtained and an atomistic mechanism cannot be proposed (2-4). This note will provide a means of testing the analysis further and will indicate how additional information associated with the rate law can be obtained.

Since only selective pieces of data are used in the determination of the reaction orders for the partial processes (1, 2), it is possible that an incorrect analysis and/or poor data could lead to incorrect rate laws. A typical test of the validity of a rate law in chemical kinetics is the determination of the specific rate constant using all of the rate data. At a fixed temperature the computed rate constant should be reasonably constant. Therefore, the computation of the rate constants for the partial processes provides a means of testing both the theoretical analysis and the quality of the data. Furthermore, computation of the standard specific rate constants for the partial processes leads directly to a complete numerical representation of the rate laws.

Casting Eq. [15] and [16] of Ref. (2) in the form of Eq. [4a] and [4b] of Ref. (1), respectively, and rearranging yields

$$k^{\circ}_a = \frac{(-r_a) \exp\left(\frac{\phi^{\circ}_a - \psi_o}{\beta_a}\right)}{[\text{HCHO}]^{0.18} [\text{OH}^-]^{0.18}} \quad [1]$$

and

\* Electrochemical Society Active Member.

Key words: copper, corrosion, electrode kinetics, electroless plating, mixed potentials, partial processes, standard specific rate constants.

$$k^{\circ}_c = \frac{(-r_c) [\text{HCHO}]^{0.23} \exp\left(\frac{\psi_o - \phi^{\circ}_c}{\beta_c}\right)}{[\text{Cu}^{2+}]^{1.7} [\text{OH}^-]^{0.18}} \quad [2]$$

where  $k^{\circ}_c$  includes the ligand concentration and reaction order (2). The data used in the analysis are given in Table I. The plating solutions and plating rates are from recent work (5) while the mixed potentials were given elsewhere (2). The Tafel slopes were those of Paunovic (6) with an appropriate correction for temperature. The standard electrode potential of the formaldehyde reaction was computed in the manner described previously (3, 4) using data from Pourbaix (7). The standard electrode potential of the copper-cupric ion reaction was found in Pourbaix (7). The standard potentials were not corrected for the change in temperature since the values of the temperature coefficients were not known for both partial processes.

The values of the standard specific rate constants computed from Eq. [1] and [2] are given in Table I. The mean value of the anodic constant at 40°C was  $9.40 \times 10^{-3} \mu\text{m/hr M}^{0.36}$  with a standard deviation of  $1.9 \times 10^{-3} \mu\text{m/hr M}^{0.36}$ ; the mean cathodic constant at 40°C was  $1.38 \times 10^{-4} \mu\text{m/hr M}^{1.65}$  with a standard deviation of  $0.53 \times 10^{-4} \mu\text{m/hr M}^{1.65}$ . The precision of the computed values of the rate constants is a significant corroboration of both the theoretical analysis (1) and the experimental data (2, 5).

A question which often arises in analyses of this type is, What is the effect of the temperature coefficient of the standard potential on such computations? Since the temperature coefficient of the copper-cupric ion system is known (8), this effect will be ascertained for the cathodic partial process. Since the mixed potential,  $\psi_o$ , is measured with respect to a saturated calomel electrode (SCE) in the same solution, the standard potential of the copper-cupric ion system, i.e.,  $\phi^{\circ}_c$  of Eq. [2], must also be measured with respect to SCE. The hypothetical cell for that combination is



with a potential

Table I. Data for electroless copper plating solutions

CuSO <sub>4</sub> , M	NaOH, M	HCHO, M	Temp, °C	Plating rate, $\mu\text{m/hr}$	Mixed potential, mV vs. SCE	$k^{\circ}_a \times 10^8$ , $\mu\text{m/hr M}^{0.36}$	$k^{\circ}_c \times 10^4$ , $\mu\text{m/hr M}^{1.65}$
0.05	0.25	0.33	31	2.28	-700	7.02	0.31
0.01	0.25	0.33	40	1.68	-780	10.8	1.31
0.025	0.25	0.33	40	2.57	-725	7.18	1.08
0.05	0.25	0.33	40	3.56	-685	7.50	1.02
0.10	0.25	0.33	40	4.77	-640	7.32	1.03
0.05	0.125	0.33	40	3.35	-650	9.80	2.18
0.05	0.375	0.33	40	3.90	-645	9.03	2.30
0.05	0.25	0.16	40	3.55	-670	12.0	1.16
0.05	0.25	0.65	40	3.80	-690	11.5	1.15
0.05	0.25	0.33	50	8.10	-675	30.9	4.55
0.05	0.25	0.33	60	11.2	-665	46.9	11.8

$$\phi^{\circ}_{\text{Cu}/\text{Cu}^{2+}} \text{ (vs. SCE)} = \phi^{\circ}_{\text{Cu}/\text{Cu}^{2+},\text{H}} - \phi_{\text{SCE,H}} \quad [4]$$

The temperature coefficient of the cell is

$$\frac{d\phi^{\circ}_{\text{Cu}/\text{Cu}^{2+}}}{dt} \text{ (vs. SCE)} = \frac{d\phi^{\circ}_{\text{Cu}/\text{Cu}^{2+},\text{H}}}{dt} - \frac{d\phi_{\text{SCE,H}}}{dt} \quad [5]$$

where the "isothermal" temperature coefficients on the right-hand side of Eq. [5] can be computed according to de Bethune *et al.* (8). The exponent in Eq. [2] becomes

$$\frac{1}{\beta_c} \left[ \psi_{0T} - \phi^{\circ}_{\text{Cu}/\text{Cu}^{2+},\text{H},25} + \phi_{\text{SCE,H},25} - \frac{d\phi^{\circ}_{\text{Cu}/\text{Cu}^{2+}}}{dt} \text{ (vs. SCE)} (t - 25) \right] \quad [6]$$

If Eq. [6] replaces the exponent in Eq. [2], a new set of standard specific rate constants may be computed. This substitution was performed and the results are shown in Table II. In all cases the resulting rate constant was from 10 to 40% lower than that computed "ignoring" the temperature coefficient. The mean rate constant at 40°C was  $1.11 \times 10^{-4} \mu\text{m/hr M}^{1.65}$  with a standard deviation of  $0.43 \times 10^{-4} \mu\text{m/hr M}^{1.65}$ . While the rate constants computed using the temperature coefficient correction are more correct than those computed ignoring it, the improvement probably does not justify the additional computations, particularly when the temperature coefficient is unknown and must be computed from the standard reaction entropy [see Ref. (8)]. However, in some mixed potential systems the effect could be more dramatic. In the present work, the differences between the mixed and standard potentials were on the order of 800 mV. Therefore, the temperature correction represented only a small fraction of the exponential term. In corrosion systems, for example, where this difference might only be a few hundred millivolts, even a small temperature correction could lead to big differences in the computed rate constants.

The present work indicates that the theoretical analysis (1) is self-consistent and offers a means for the determination of the complete rate laws for partial processes in mixed potential systems. Further, the procedure for effecting these determinations is outlined here and elsewhere (1, 2).

### Acknowledgments

The author wishes to express his gratitude to Professor N. Ibl of ETH Zurich for his stimulation and courtesies during a sabbatical leave from the University of Michigan and to Mrs. C. Lacy of the University of Michigan for technical assistance.

Manuscript submitted Sept. 25, 1973; revised manuscript received Feb. 4, 1974.

Table II. Comparison between calculations ignoring and considering the temperature coefficient of the standard electrode potential

$k^{\circ}_c \times 10^4 \mu\text{m/hr M}^{1.65}$	
Ignored	Considered
0.31	0.28
1.12	0.90
1.08	0.87
1.02	0.82
1.03	0.83
2.18	1.75
2.30	1.85
1.16	0.93
1.15	0.93
4.55	3.22
11.8	7.42

Any discussion of this paper will appear in a Discussion Section to be published in the June 1975 JOURNAL. All discussion for the June 1975 Discussion Section should be submitted by Feb. 1, 1975.

### SYMBOLS

$d$	differential operator
$k^{\circ}$	standard specific rate constant, units dependent on reaction orders
$M$	concentration, moles/liter
$-r$	plating rate, $\mu\text{m/hr}$
$t$	temperature, °C
$\beta$	Tafel slope (base "e"), V
$\phi^{\circ}$	standard electrode potential, V
$\psi_0$	mixed potential, V
$[x]$	concentration of species "x", M

### Subscripts

a	pertaining to anodic partial process
c	pertaining to cathodic partial process
Cu/Cu <sup>2+</sup>	pertaining to copper-cupric ion electrode
H	with respect to the standard hydrogen electrode
SCE	with respect to the saturated calomel electrode
T	at temperature "T," °C
25	at 25°C

### REFERENCES

1. F. M. Donahue, *This Journal*, **119**, 72 (1972).
2. F. M. Donahue and F. L. Shippey, *Plating*, **60**, 135 (1973).
3. F. M. Donahue, *Oberfläche-Surface*, **13**, 301 (1972).
4. F. M. Donahue, "Proceedings of the 8th Congress of the International Union for Electrodeposition and Surface Finishing," pp. 193-201, Forster-Verlag AG, Zurich (1973).
5. F. L. Shippey and F. M. Donahue, *Plating*, **60**, 43 (1973).
6. M. Paunovic, *ibid.*, **55**, 1161 (1968).
7. M. Pourbaix, "Atlas of Electrochemical Equilibria in Aqueous Solutions," Pergamon Press, Oxford (1966).
8. A. J. de Bethune, T. S. Licht, and N. Swendeman, *This Journal*, **106**, 616 (1959).



## The Sulfidation Properties of Cobalt-Iron Alloys in Hydrogen Sulfide-Hydrogen Atmospheres at 700°C

D. J. Young,\* P. Mayer,<sup>1</sup> and W. W. Smeltzer\*

Department of Metallurgy and Materials Science, McMaster University, Hamilton, Ontario, Canada

The publication costs of this article have been assisted by McMaster University.

### ABSTRACT

Cobalt and Co-Fe alloys containing from 1 to 90 weight per cent (w/o) Fe sulfidize according to a parabolic rate relation at 700°C in H<sub>2</sub>/H<sub>2</sub>S atmospheres corresponding to  $p_{S_2} = 6 \times 10^{-6}$  and  $8 \times 10^{-8}$  atm. Austenitic alloys (0-13 w/o Fe) sulfidize less rapidly than ferritic alloys (25-100 w/o Fe), minimum values of the parabolic rate constant being found at ~4 w/o Fe for both values of  $p_{S_2}$ . The scale on austenitic alloys is (CoFe)<sub>9</sub>S<sub>8</sub> at  $p_{S_2} = 8 \times 10^{-8}$  atm and at  $p_{S_2} = 6 \times 10^{-6}$  atm this sulfide is partially overlaid by (CoFe)<sub>1-x</sub>S. This latter sulfide decomposes on cooling to form a two-phase mixture of (CoFe)<sub>9</sub>S<sub>8</sub> and (CoFe)<sub>3</sub>S<sub>4</sub>. Ferritic alloys form a mixed (CoFe)<sub>1-x</sub>S monosulfide at both sulfur pressures. The high sulfidation rates of the ferritic alloys are ascribed to the high concentration of defects in the cation lattice of the monosulfide whereas the lower sulfidation rates of the austenitic alloys are controlled by the relatively low diffusivity of metal in almost stoichiometric (CoFe)<sub>9</sub>S<sub>8</sub>.

Commercially available cobalt-base alloys frequently contain minority amounts of iron (1). The well-known susceptibility of iron to sulfur corrosion (2) suggests that its presence in these alloys may be detrimental to their performance at high temperatures. This paper reports the effects of alloy iron content on the sulfidation rates of Co-Fe alloys in H<sub>2</sub>/H<sub>2</sub>S atmospheres.

The sulfidation of pure cobalt has been investigated under a number of conditions. Parabolic kinetics have been found for the scaling reaction in the temperature range 400°-750°C at sulfur pressures of 100-400 mm Hg by Davin (3) and at a pressure of 1 atm by Mrowec *et al.* (4). The former demonstrated that the parabolic rate constant,  $k_p$ , was proportional to  $p_{S_2}^{1/2}$  at 700°C. In both cases a duplex sulfide scale was produced. This scale has been identified (5) as consisting of Co<sub>1-x</sub>S in the outer layer and Co<sub>9</sub>S<sub>8</sub> in the inner layer.

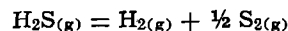
Studies (6) of the sulfidation of pure cobalt in H<sub>2</sub>/H<sub>2</sub>S atmospheres have produced similar results although the  $p_{S_2}$  dependence of the rate has not been determined. For corrosion by sulfur vapor and by H<sub>2</sub>S, marker experiments indicated that cobalt was the mobile species within the scale.

The sulfidation properties of iron have been reviewed by Haycock (2). Quite different phenomena are observed according to whether the environment consists of sulfur or of H<sub>2</sub>S. In the former case, parabolic kinetics are found and quantitative agreement with Wagner's theory is obtained (7). In the latter case, linear kinetics are found, the resultant scale being highly porous in nature. The reasons for this difference in behavior are not understood.

### Experimental

Alloys were prepared by vacuum melting the required proportions of cobalt (>99.997 w/o pure) and iron (>99.975 w/o pure). The actual iron contents of the alloys were 0.93, 4.1, 9.6, 49.9, and 90.0 w/o. Alloy rods were annealed in an argon atmosphere at 1200°C for ten days, machined to a uniform diameter (~10 mm), and cut into disks with a wire saw. The disks were metallographically polished to 1μ diamond abrasive and stored under acetone prior to use.

Sulfidation kinetics were determined gravimetrically using a McBain balance assembly. The apparatus has been described elsewhere (8). The reaction was investigated at  $T = 700 \pm 5^\circ\text{C}$  and  $p_{S_2}$  equal to  $8 \times 10^{-8}$  atm and  $6 \times 10^{-6}$  atm. The sulfur partial pressures were controlled by mixing H<sub>2</sub> and H<sub>2</sub>S in known proportions, the required H<sub>2</sub>/H<sub>2</sub>S ratio being obtained from the known standard free energy change of the reaction (9)



Cross sections of the sulfidized samples were examined metallographically. Phases present in the scale were determined by electron microprobe analyses. Point counts obtained from the probe were analyzed with respect to Co and Fe standards. Systematic corrections were applied to the data for atomic number and mass absorption (10).

### Results

**Kinetics.**—The reaction kinetics were invariably parabolic, as shown in Fig. 1 and 2, although induction periods were occasionally found. As can be seen from the plots, the initial reaction stages were not observed. The time taken for the balance to reach mechanical equilibrium was the reason for this delay. It was al-

\* Electrochemical Society Active Member.

<sup>1</sup> Present address: Ontario Research Foundation, Sheridan Park, Mississauga, Ontario, Canada.

Key words: parabolic kinetics, (CoFe)<sub>9</sub>S<sub>8</sub>, (CoFe)<sub>3</sub>S<sub>4</sub>.

15555

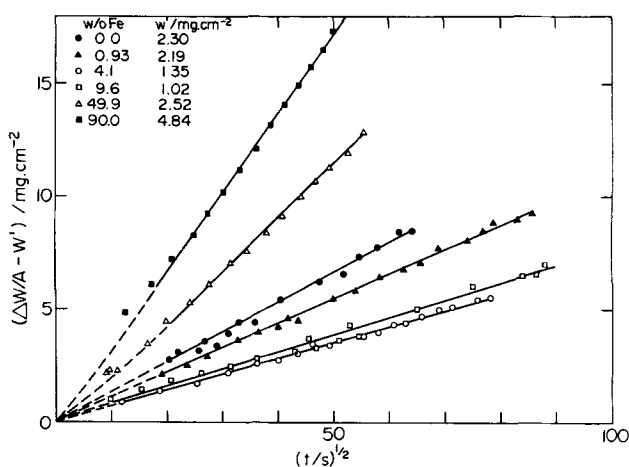


Fig. 1. Parabolic plots for sulfidation of Co-Fe alloys at  $T = 700^\circ\text{C}$  and  $p_{S_2} = 8 \times 10^{-8}$  atm.

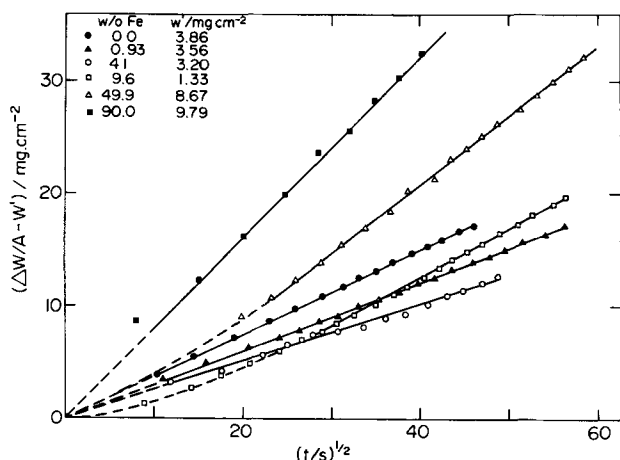


Fig. 2. Parabolic plots for sulfidation of Co-Fe alloys at  $T = 700^\circ\text{C}$  and  $p_{S_2} = 6 \times 10^{-6}$  atm.

lowed for by fitting the data by linear regression to the equation

$$\Delta W/A + W' = (k_p t)^{1/2}$$

where  $\Delta W/A$  is the weight change per unit area found after time,  $t$ . It is this equation which has been employed in plotting Fig. 1 and 2. Values for  $W'$  are shown on the figures.

Variation of the parabolic rate constant with iron alloy content is shown in Fig. 3. A minimum in the rate at about 4 w/o Fe is apparent for both  $p_{S_2}$  values. This figure shows that at all alloy compositions a higher reaction rate is associated with the higher  $p_{S_2}$  value.

**Scale morphologies and constitutions.**—In all cases the sulfide scales were tightly adherent to the metal and remarkably compact and pore free. Representative examples are shown in Fig. 4, 5, and 6. Apart from the case of pure cobalt, all alloys developed scales of large grain size. Additional, smaller grains were found at the scale-metal interface on the ferritic alloys.

At  $p_{S_2} = 8 \times 10^{-8}$  atm a single layer scale is always formed; at  $p_{S_2} = 6 \times 10^{-6}$  atm regions of an additional, two-phase scale are found at the sulfide-gas interface. The extent to which this additional layer covers the inner layer is variable within the utilized exposure periods, but in general increases with increasing alloy iron content up to 49.9 w/o Fe when total coverage is achieved. A single-phase scale was found, however, on the 90.0 w/o Fe alloy.

The constitutions of the sulfide layers within the scales, as determined by microprobe analyses, are summarized in Table I. Only in the case of the 49.9 w/o Fe alloy was it possible to analyze separately the

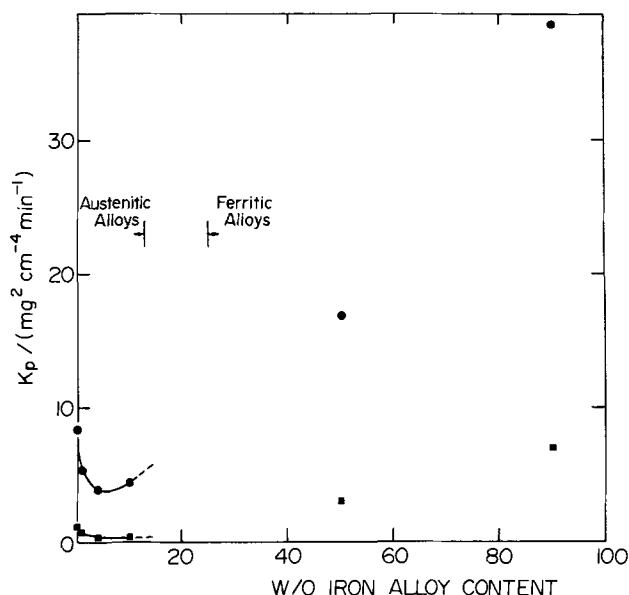


Fig. 3. Variation of parabolic rate constant,  $k_p$ , with iron alloy content:  $\bullet$ — $p_{S_2} = 6 \times 10^{-6}$  atm;  $\blacksquare$ — $p_{S_2} = 8 \times 10^{-8}$  atm.

two phases in an outer sulfide layer. They proved to be  $(\text{CoFe})_9\text{S}_8$  and  $(\text{CoFe})_3\text{S}_4$ . For the other alloys, the regions of the two phases were of a size comparable to the probe beam and consequently only an average composition could be measured.

Concentration profiles in the scale constituents were also measured. Results for the scales formed on 4.1, 9.6, and 49.9 w/o Fe alloys at  $p_{S_2} = 6 \times 10^{-6}$  atm are shown in Fig. 7, 8, and 9.

## Discussion

The fact that all the alloys sulfidized according to parabolic kinetics, together with the observation that the resultant scales were compact, implies that the reactions are diffusion controlled. It is then reasonable to assume that the alloy-scale system can be described with the aid of a thermodynamic framework since local equilibrium conditions would prevail.

As a first step, we employ the concentration profiles illustrated in Fig. 7-9 and those from the other sulfidized alloys to construct the  $700^\circ\text{C}$  section of the Fe-Co-S phase diagram shown in Fig. 10. It is apparent from this diagram that the sulfidation properties of the austenitic alloys (0-13 w/o Fe) and of the ferritic alloys (25-100 w/o Fe) may conveniently be distinguished.

The similarity in appearance of the two-phase sulfide scales (Fig. 4-6) suggests that the identification of

Table I. Microprobe identifications of sulfidation products\*

Alloy	$p_{S_2}$ /atm	Inner layer	Outer layer
Co	$8 \times 10^{-8}$ $6 \times 10^{-6}$	$\text{Co}_9\text{S}_8$ $\text{Co}_3\text{S}_4$	— Two phase; average composition $\text{CoS}$
Co-4.1 w/o Fe	$8 \times 10^{-8}$ $6 \times 10^{-6}$	$\text{Co}_{62}\text{Fe}_8\text{S}_{45}$ $\text{Co}_{33}\text{Fe}_2\text{S}_{45}$	— Two phase; average composition $\text{Co}_{48}\text{Fe}_8\text{S}_{50}$
Co-9.6 w/o Fe	$8 \times 10^{-8}$ $6 \times 10^{-6}$	$\text{Co}_{50}\text{Fe}_5\text{S}_{45}$ $\text{Co}_{52}\text{Fe}_4\text{S}_{44}$	— Two phase; average composition $\text{Co}_{48}\text{Fe}_8\text{S}_{51}$
Co-49.9 w/o Fe	$8 \times 10^{-8}$ $6 \times 10^{-6}$	$(\text{FeCo})_{50}\text{S}_{50}$ $(\text{FeCo})_{50}\text{S}_{50}$ (see Fig. 9)	— Two phase; $\text{Co}_{35}\text{Fe}_{10}\text{S}_{56}$ + $\text{Co}_{45}\text{Fe}_9\text{S}_{45}$
Co-90 w/o Fe	$8 \times 10^{-8}$ $6 \times 10^{-6}$	$\text{Fe}_{45}\text{Co}_5\text{S}_{50}$ $\text{Fe}_{42}\text{Co}_6\text{S}_{52}$	— —

\* Maximum random errors are estimated at 4% at the 60% level, 3% at the 35% level, 2% at the 20% level, and 0.5% at the 1% level.

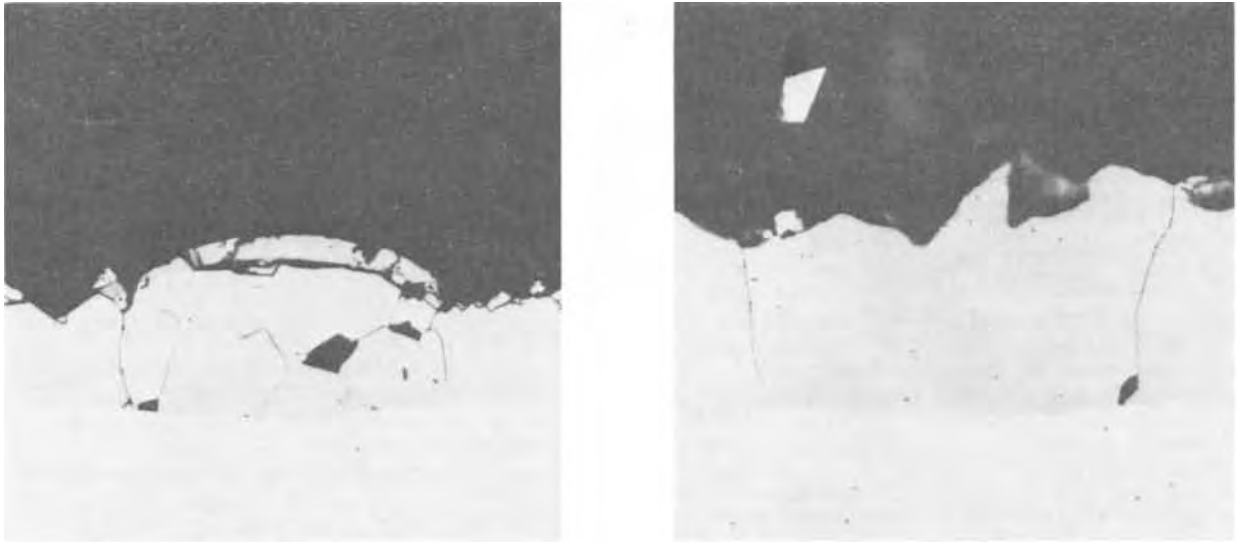


Fig. 4. Cross sections of sulfidized Co-4.1 w/o Fe alloy. Lefthand micrograph ( $\times 216$ )  $p_{S_2} = 6 \times 10^{-6}$  atm,  $t = 40$  min; righthand micrograph ( $\times 620$ )  $p_{S_2} = 8 \times 10^{-8}$  atm,  $t = 140$  min.

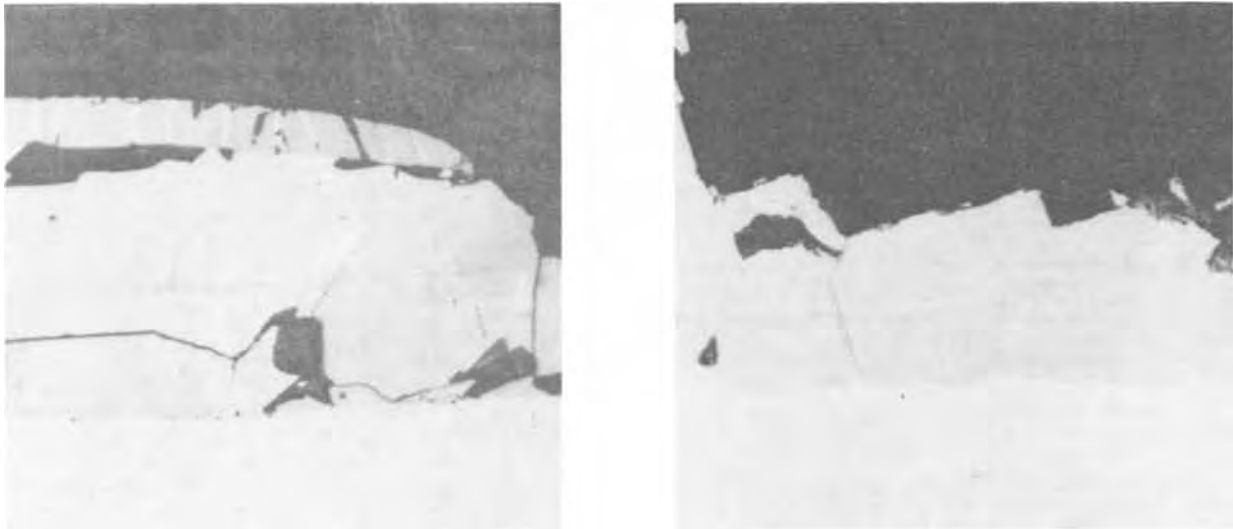


Fig. 5. Cross sections of sulfidized Co-9.6 w/o Fe alloy. Lefthand micrograph ( $\times 620$ )  $p_{S_2} = 6 \times 10^{-6}$  atm,  $t = 35$  min, righthand micrograph ( $\times 1000$ )  $p_{S_2} = 8 \times 10^{-8}$  atm,  $t = 150$  min.

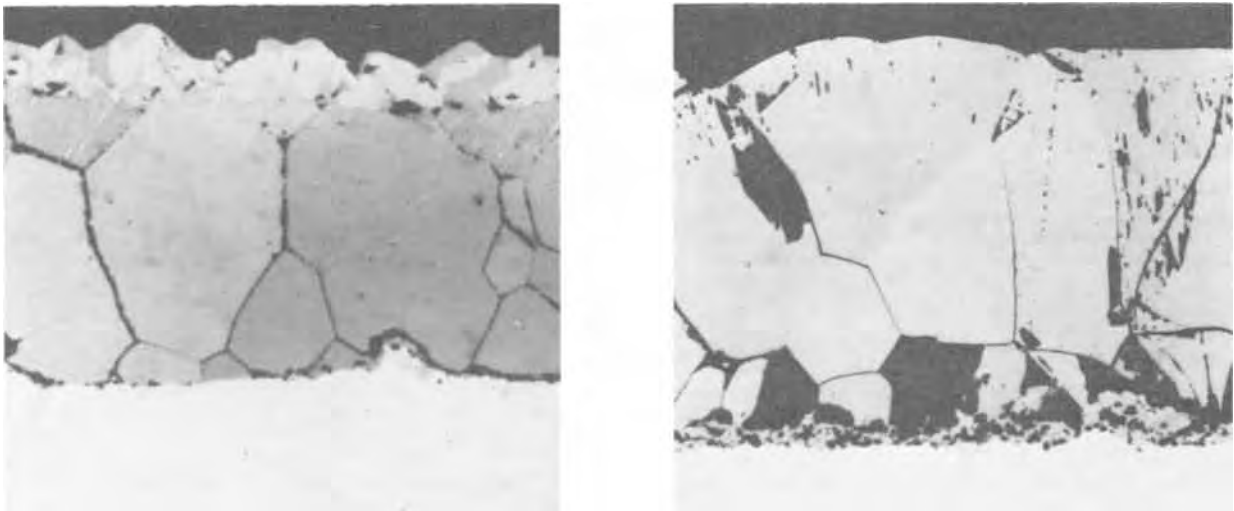


Fig. 6. Cross sections of sulfidized Co-49.9 w/o Fe alloy. Lefthand micrograph ( $\times 500$ )  $p_{S_2} = 6 \times 10^{-6}$  atm,  $t = 60$  min; righthand micrograph ( $\times 620$ )  $p_{S_2} = 8 \times 10^{-8}$  atm,  $t = 50$  min.

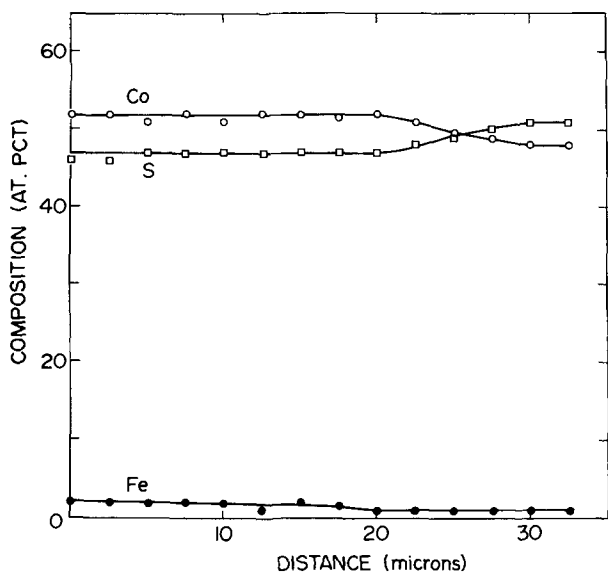


Fig. 7. Concentration profiles in scale shown in the lefthand micrograph of Fig. 4. Distance measured from scale-alloy interface.

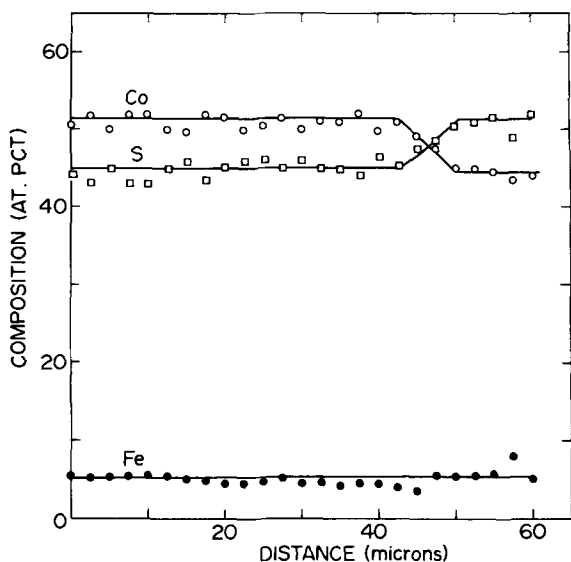


Fig. 8. Concentration profiles in scale shown in the lefthand micrograph of Fig. 5. Distance measured from scale-alloy interface.

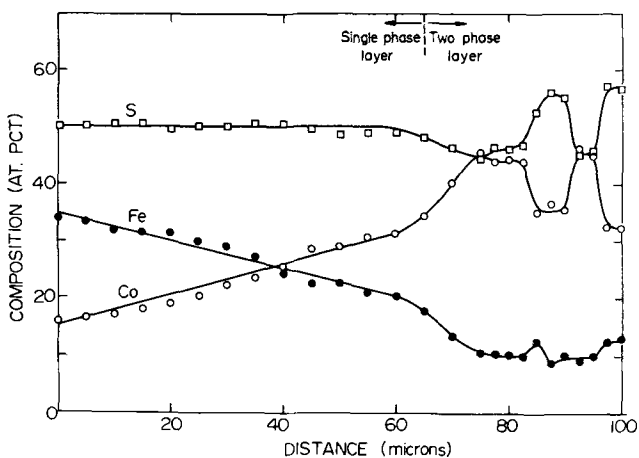


Fig. 9. Concentration profiles in scale shown in the lefthand micrograph of Fig. 6. Distance measured from scale-alloy interface.

these phases achieved for the 49.9 w/o Fe alloy applies as well to the other alloys. Assuming that this is the case, the sulfidation products of the various alloys can

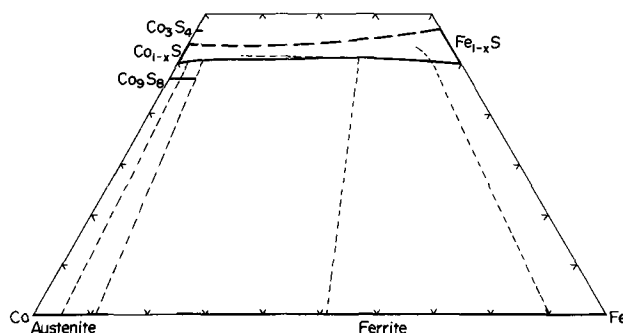


Fig. 10. Partial 700°C isotherm of the Co-Fe-S system as deduced from the composition paths found in the sulfidized alloy samples. Composition paths are shown as dotted lines.

be summarized as in Table II. A common pattern, accordingly, is apparent in the morphological development of sulfides on austenitic alloys. This pattern may be explained in terms of the thermodynamics of the binary Co-S system.

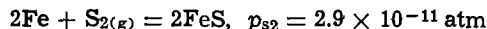
From the data of Rosenqvist (11), the following equilibrium  $p_{S_2}$  values at  $T = 700^\circ\text{C}$  are estimated



Thus at the experimental  $p_{S_2}$  values of  $8 \times 10^{-8}$  and  $6 \times 10^{-6}$  atm, pure cobalt is expected to form a  $\text{Co}_9\text{S}_8$  scale at the low sulfur pressure and a duplex scale of  $\text{Co}_9\text{S}_8$  overlaid by  $\text{CoS}$  at the high pressure. Since  $\text{CoS}$  undergoes a eutectoid decomposition at  $460^\circ\text{C}$  to  $\text{Co}_9\text{S}_8$  and  $\text{Co}_3\text{S}_4$  which is not suppressed by quenching (11), it is to be expected that  $\text{Co}_{1-x}\text{S}$  will appear at room temperature as a two-phase layer if it is a stable product layer at the reaction temperature.

The pattern of sulfide products predicted for pure cobalt is precisely that found for the austenitic alloys. The formation of  $(\text{CoFe})_9\text{S}_8$  and  $(\text{CoFe})_{1-x}\text{S}$  is not surprising in view of the similarities in size, polarizability, and ionization potential of  $\text{Co}^{2+}$  and  $\text{Fe}^{2+}$ . For the same reasons, the thermodynamics of the mixed sulfides are closely similar to those of the cobalt sulfides. Since  $\text{Co}_{1-x}\text{S}$  and  $\text{Fe}_{1-x}\text{S}$  are isotypic, the two sulfides are mutually soluble in all proportions (Fig. 10). The highly ordered  $\text{Co}_9\text{S}_8$  structure (12), however, has a limited solubility capacity for substitutional cations. Consequently, the  $(\text{CoFe})_9\text{S}_8$  phase field extends into the ternary Co-Fe-S isotherm over a finite compositional range.

Turning now to the ferritic alloys, we note from Rosenqvist (11) that at  $700^\circ\text{C}$



and that no lower sulfides exist. The formation of  $(\text{CoFe})_{1-x}\text{S}$  on these alloys is therefore readily explicable on the same grounds as enumerated above for the austenitic alloys.  $\text{Fe}_{1-x}\text{S}$  is stable at room temperature and, therefore, a two-phase layer structure is not to be expected in the quenched scales formed on the iron-rich alloys. The appearance of such a product near the gas interface of the scale on the 49.9 w/o Fe alloy indicates that  $(\text{CoFe})_{1-x}\text{S}$  in this region of the scale

Table II. Phase identification of sulfide scales

	$p_{S_2} = 8 \times 10^{-9} \text{ atm}$		$p_{S_2} = 6 \times 10^{-6} \text{ atm}$	
	Inner layer	Outer layer	Inner layer	Outer layer
Austenite	$(\text{CoFe})_9\text{S}_8$	—	$(\text{CoFe})_9\text{S}_8$	$(\text{CoFe})_9\text{S}_8 + (\text{CoFe})_3\text{S}_4$
Ferrite				
49.9 w/o Fe	$(\text{CoFe})_{1-x}\text{S}$	—	$(\text{CoFe})_{1-x}\text{S}$	$(\text{CoFe})_9\text{S}_8 + (\text{CoFe})_3\text{S}_4$
90.0 w/o Fe	$(\text{CoFe})_{1-x}\text{S}$	—	$(\text{CoFe})_{1-x}\text{S}$	—



was essentially  $\text{Co}_{1-x}\text{S}$  while the sulfide nearer the metal was essentially  $\text{Fe}_{1-x}\text{S}$ . Reference to the concentration profile of Fig. 9 shows that indeed the fraction of  $\text{Co}_{1-x}\text{S}$  in the mixed sulfide increases with increasing sulfur activity. If the behavior of this solid solution is nearly ideal, this observation is consistent with the fact that  $\text{Co}_{1-x}\text{S}$  coexists with sulfur at a higher pressure than does  $\text{Fe}_{1-x}\text{S}$ . A similar effect is found, although to a lesser degree, for the  $(\text{CoFe})_{1-x}\text{S}$  scale formed on the 90.0 w/o Fe alloy.

The influence of alloy iron content and sulfur pressure on the sulfidation kinetics can be explained qualitatively in terms of the defect structures of the sulfides. While  $\text{Co}_9\text{S}_8$  is practically stoichiometric, and hence exhibits relatively low cation diffusivity, the monosulfides exhibit large degrees of nonstoichiometry (11).  $\text{Fe}_{1-x}\text{S}$  exhibits at  $T = 700^\circ\text{C}$  a wider existence range (50-57 a/o S) than  $\text{Co}_{1-x}\text{S}$  (50-54 a/o S). Nonstoichiometry in the monosulfides is known to arise through cation vacancy formation, the vacancy concentration increasing with sulfur pressure. Thus  $(\text{CoFe})_{1-x}\text{S}$  is expected to possess a high cation diffusivity, the diffusivity increasing both with iron content and sulfur pressure.

The sulfidation properties of the alloys are now explicable. In the case of the ferritic alloys, faster reaction rates are found at the higher sulfur pressure employed and the 90.0 w/o Fe alloy sulfidizes more rapidly than the 49.9 w/o Fe alloy at both sulfur pressures because  $(\text{CoFe})_{1-x}\text{S}$  of increasing iron content is the sole reaction product. Sulfidation of the austenitic alloys is presumably controlled largely by diffusion through the  $(\text{CoFe})_9\text{S}_8$  scale and is consequently slower than in the case of the ferrite alloys. The localized appearance of  $(\text{CoFe})_{1-x}\text{S}$  to ultimately form an outer scale layer is presumably due to the difficulty of nucleating this phase. The nucleation and rate of growth of  $(\text{CoFe})_{1-x}\text{S}$  on the  $(\text{CoFe})_9\text{S}_8$  layer of sulfidized austenite is apparently related to iron content. The more widespread nucleation and rapid growth of the former sulfide with increasing alloy iron content is consistent with the fact that  $\text{Fe}_{1-x}\text{S}$  is more stable than  $\text{Co}_{1-x}\text{S}$ .

A detailed description cannot presently be given for the minima found in the parabolic sulfidation rates at ~4 w/o Fe (Fig. 3) since the defect structure and diffusion mechanism for  $\text{Co}_9\text{S}_8$  are unknown. However, we may surmise that the  $(\text{CoFe})_9\text{S}_8$  phase field narrows as the iron content increases. Such an effect will lead to a diminution of the growth rate. Simultaneously, at the higher sulfur pressure, the amount of  $(\text{CoFe})_{1-x}\text{S}$  formed increases with iron content. The superposition of these two effects leads to a minimum in the rate constant as the alloy iron content increases. At the lower experimental value of  $p_{\text{S}_2}$  the monosulfide is not stable for alloys of small iron content, and hence none is formed on the austenitic alloys. Consequently, only a decrease in the parabolic rate constant was observed with increasing iron content in the austenitic alloys. The rate increases, however, for the ferritic al-

loys where the iron content is so high that the stable reaction product is the monosulfide,  $(\text{CoFe})_{1-x}\text{S}$ .

### Summary

The sulfidation of cobalt-iron alloys at  $700^\circ\text{C}$  in hydrogen sulfide-hydrogen atmospheres is controlled by cation diffusion through the sulfide scale and parabolic kinetics result. Ferritic alloys sulfidize faster than do austenitic alloys because the scale on the former is composed entirely of high diffusivity  $(\text{CoFe})_{1-x}\text{S}$  whereas on the latter it is composed largely of the low diffusivity  $(\text{CoFe})_9\text{S}_8$ . A minimum in the sulfidation rate is found in the austenitic alloy range at ~4 w/o Fe alloy content. This effect is thought to result from the simultaneous decrease in diffusivity of  $(\text{CoFe})_9\text{S}_8$ , and increase in ease of  $(\text{CoFe})_{1-x}\text{S}$  formation with increasing iron content.

The morphology of the sulfide scales on austenitic alloys is the same as that of the scales on pure cobalt. Similarly, the ferrite alloys sulfidize so as to produce the same morphology as that found for pure iron. This close similarity between, respectively, cobalt-rich mixed sulfides and pure cobalt sulfides and between iron-rich mixed sulfide and pure iron sulfide is a consequence of the very similar chemistry of cobalt and iron.

### Acknowledgment

This research was sponsored by the National Research Council of Canada.

Manuscript submitted Oct. 23, 1973; revised manuscript received Jan. 28, 1974.

Any discussion of this paper will appear in a Discussion Section to be published in the June 1975 JOURNAL. All discussions for the June 1975 Discussion Section should be submitted by Feb. 1, 1975.

### REFERENCES

1. "Metals Handbook," 8th ed., p. 467, ASM, Metals Park, Ohio (1961).
2. E. W. Haycock, in "High Temperature Metallic Corrosion of Sulfur and Its Compounds," Z. A. Foroulis, Editor, p. 110, The Electrochemical Society Softbound Symposium Series, New York (1970).
3. A. Davin, *Cobalt*, **30**, 19 (1966).
4. S. Mrowec and T. Werber, *Chem. Anal.*, **7**, 605 (1962).
5. V. I. Arkarov and E. B. Blankova, *Fiz. Metal. Metalloved.*, **8**, 452 (1959).
6. A. Davin and D. Coutsouradis, *Cobalt*, **17**, 23 (1962).
7. K. Hauffe, "Oxidation of Metals," p. 385, Plenum Press, New York (1965).
8. G. Romeo, W. W. Smeltzer, and J. S. Kirkaldy, *This Journal*, **118**, 740 (1971).
9. G. N. Lewis and M. Randall, "Thermodynamics," p. 173, McGraw-Hill Book Co., New York (1961).
10. J. Philibert, "Proc. 3rd Int. Symp. X-Ray Optics and X-Ray Microanalysis," Academic Press, New York (1963).
11. T. Rosenqvist, *J. Iron Steel Inst.*, **176**, 37 (1954).
12. D. Lundqvist, *Arkiv Kemi, Mineralogi Geologi*, **24A**, Paper 22 (1947).

# Optimum Arrangement of Phosphor Particles in Cathode-Ray Picture Tube Screens

Lyuji Ozawa\* and Herbert N. Hersh\*

Zenith Radio Corporation, Chicago, Illinois 60639

The publication costs of this article have been assisted by the Zenith Radio Corporation.

## ABSTRACT

The geometry and optical properties of the phosphor screen in a cathode-ray picture tube have been studied in connection with the phosphor particle size distribution. The specific surface area,  $S_w$  ( $\text{cm}^2/\text{g}$  phosphor), which determines the amount of light scattering in the screen, is equal to  $(k/\rho)(\bar{\phi}_2)^{-1}$ , where  $\rho$  is specific gravity of phosphor,  $\bar{\phi}_2$  is the mean surface particle size, and  $k$  is constant. Geometry shows that the total surface area of phosphor particles densely arranged in a single layer on the faceplate is independent of the particle size and is constant. The total surface area of the phosphor particles in the screen, therefore, depends on the number,  $L$ , of particle layers, rather than on the gross thickness.  $L$  is equal to  $1.65w(\rho\bar{\phi}_2)^{-1}$ , where  $w$  is the screening weight ( $\text{g}/\text{cm}^2$ ). The usefulness of  $L$  as a determinant of the brightness of a phosphor screen has been demonstrated. It was found experimentally that the optimum number of the particle layers producing maximum luminescence with minimum scattering is about 1.4.

In cathode-ray picture tubes, phosphors are used as electron-to-visible light transducers. The phosphor is a powder containing a wide distribution of sizes, usually between 1 and 30  $\mu\text{m}$ . Layers of these phosphor particles make up the screen of the cathode-ray picture tube.

The calcium tungstate screen used in x-ray image intensifiers has been studied by Coltman, Ebbighausen, and Altar (1) with the view to determining the energy conversion efficiency from x-rays to light (5%) and the optical properties of the screen to optimize screen thickness. The optical properties of the screen of calcium halophosphate phosphor used in fluorescent lamps have been studied by Butler and Homer (2) and by Bo and Takeyama (3) in order to determine the optimum screen thickness for the absorption and scattering of the exciting ultraviolet light and of the emitted light.

The cathode-ray picture tube screen differs somewhat from the screens for x-ray image intensifiers and fluorescent lamps in the excitation mechanism, the kind of phosphors used, and the method of making the screen. In the case of the picture tube screen, the amount of the emitted light depends on the electron beam accelerating voltage and beam density; the penetration range of the electron beam into the phosphor crystal is determined by the accelerating voltage, and the amount of the emitted light at a given voltage depends on the beam density (4). When the phosphor particle size is larger than the electron penetration range, the light is produced in the particles arranged on the first, gun-side layer of the phosphor screen and must travel through the phosphor screen to reach the observer. Minimization of the absorption and scattering of the emitted light by the phosphor particles must be considered in determining the optimum thickness of a phosphor screen in a cathode-ray picture tube.

This report describes an optical and geometrical analysis of the phosphor screen in a cathode-ray picture tube. In the first part of the paper the optical properties of the turbid screen are discussed in order to determine the contribution of scattering and absorption by the phosphor particles. Then the number of particle layers in a screen is discussed. The optimum number is determined experimentally in the final section,

where it is demonstrated to be a useful parameter in the construction of phosphor screens.

## Optical Properties of the Turbid Screen

Although the individual phosphor particles are more or less transparent, the resulting screen is translucent or turbid. The absorption and scattering of this assembly of phosphor particles must be considered in determining the total optical properties of the viewing screen. It is difficult to estimate exactly the contribution of each individual phosphor particle; therefore, the macroscopic contribution of all the phosphor particles taken together are considered in this paper.

The optical properties of the turbid phosphor screen can be evaluated by Kubelka's model (5) which is illustrated in Fig. 1. The light is considered to be generated at  $x = 0$ . The light intensity at  $x$  can be expressed by the following differential equations

$$\frac{di}{dx} = -(\alpha + \beta)i + \beta j \quad [1]$$

$$-\frac{dj}{dx} = -(\alpha + \beta)j + \beta i \quad [2]$$

where  $i$  and  $j$  are light intensities for the directions indicated in Fig. 1, and  $\alpha$  and  $\beta$  are respectively absorption and scattering coefficients of the screen. The  $\alpha$  and  $\beta$  differ essentially from the absorption coefficient

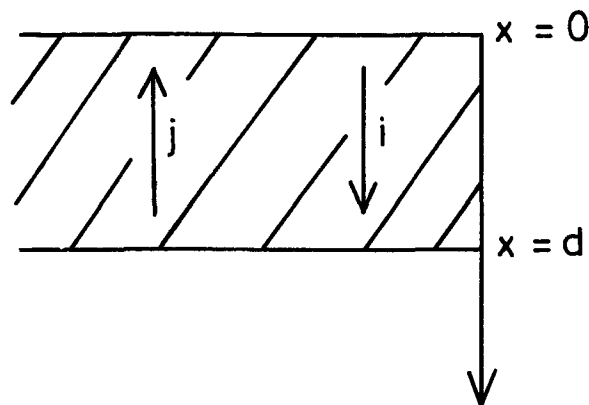


Fig. 1. Optical model of a turbid screen

\* Electrochemical Society Active Member.

Key words: phosphor screen, particle size distribution, television, cathodoluminescence.

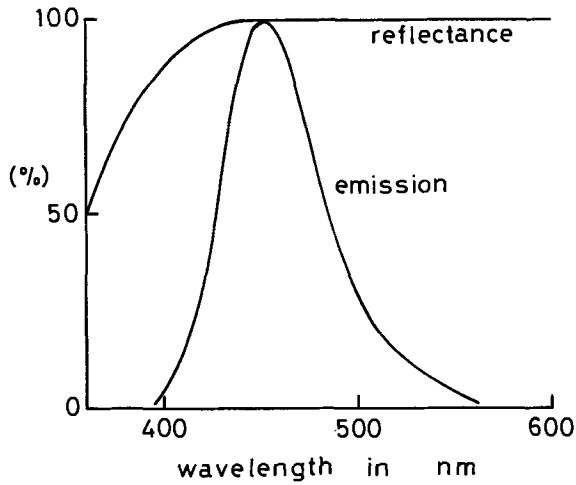


Fig. 2. Emission and reflectance spectra of ZnS:Ag:Cl blue phosphor. Reflectance spectrum was obtained with phosphor screen of 2 mm thickness that gives  $R_\infty$ .

defined in the Lambert-Beer law and are determined with the phosphor screen. With the boundary conditions,  $i = i_0$  at  $x = 0$  and  $j = 0$  at  $x = d$ , the solutions of Eq. [1] and [2] are hyperbolic functions, and the reflectance  $R(x)$  and transmittance  $T(x)$  of the screen of thickness  $x$  are expressed by the equations

$$R(x) = \frac{\sinh \gamma x}{a \sinh \gamma x + b \cosh \gamma x} \quad [3]$$

$$T(x) = \frac{b}{a \sinh \gamma x + b \cosh \gamma x} \quad [4]$$

where  $a = 1 + \alpha/\beta$ ,  $b = (a^2 - 1)^{1/2}$ ,  $\gamma = \beta b = (\alpha + 2\alpha\beta)^{1/2}$ . Then,  $R_\infty$  and  $T_\infty$  as  $x \rightarrow \infty$  are given by

$$R_\infty = 1/(a + b), T_\infty = 0$$

Therefore

$$a = \frac{1}{2} \left( \frac{1}{R_\infty} + R_\infty \right), \quad b = \frac{1}{2} \left( \frac{1}{R_\infty} - R_\infty \right) \quad [5]$$

The ratio of the absorption to the scattering of the screen ( $c = \alpha/\beta$ ) is given by

$$c = \frac{1 + R_\infty^2}{2R_\infty} - 1 \quad [6]$$

Thus,  $a$ ,  $b$ , and  $c$  are calculated from Eq. [5] and [6] using  $R_\infty$  which is obtained by measurement of a thick phosphor screen.

Figure 2 shows the emission and reflectance spectra of a commercial ZnS:Ag:Cl blue phosphor used for color TV picture tube screen. The spectra were obtained using a thick screen (2 mm) which gives  $R_\infty$ . As listed in Table I, the  $c$ -values calculated in the spectral region of the emission are small enough to neglect the  $(\alpha/\beta)^2$  term for the optical properties of the phosphor screen. Similar results are obtained for green and red TV phosphors. Since, in the region of interest,  $c \approx 0.00005 = \alpha/\beta$ ,  $\beta \gg \alpha$ , and the solution of Eq. [1] and

[2], integrated from 0 to  $d$  is

$$T(d) = (1 + \beta d)^{-1} \quad [7]$$

Equation [7] indicates that the optical properties of the cathode-ray picture tube screen in the spectral region of cathodoluminescence depend on the scattering coefficient of the screen.

Figure 3 shows a photograph of the particles of the commercial blue ZnS:Ag:Cl phosphor. The photograph was obtained with a scanning electron microscope at magnification of 10,000. Light scattering at the boundary surface of the particles can be assumed to be the source of the light scattering of the phosphor screen. In general, light scattering is a complex function of particle shape, roughness, and refractive index, and for our simple shapes it may be a simple function of the total surface area of the particles involved. The calculation of the total surface area of the phosphor powder is complicated by the fact that the particles are not of equal size, but, rather, are distributed in size. Estimation of the total surface area of the phosphor particles involved, therefore, must be made statistically in accordance with the particle size distribution.

Experimentally, several methods of determining particle size are available. It was found in all cases that the particle size distribution was not a normal (Gaussian) distribution but followed a log-normal distribution (6). Figure 4 shows the particle size distributions of the blue ZnS:Ag:Cl and the red  $Y_2O_3$ :Eu phosphors on log-normal probability graph paper. The frequency (probability) of the distribution for each phosphor was calculated from sedimentation and microscopic data falling in a specified size interval. In the microscopic method it was required to count 200 particles, at least, to get a good reproducibility,  $\pm 5\%$  error.

**Geometric Arrangement of Particles in the Screen**

*Specific surface area of particles.*—The total surface area,  $S$ , and the total weight,  $W$ , of the phosphor powder in a screen are calculated from the following equations (7, 8)

$$S = \int_0^\infty k_s n \phi^2 d\phi; \quad W = \int_0^\infty k_v \rho n \phi^3 d\phi \quad [8]$$

The specific surface area  $S_w (= S/W)$ , therefore is given by

$$S_w = S/W = \frac{k_s}{k_v \rho} \frac{\int_0^\infty n \phi^2 d\phi}{\int_0^\infty n \phi^3 d\phi} \text{ (cm}^2/\text{g)} \quad [9]$$

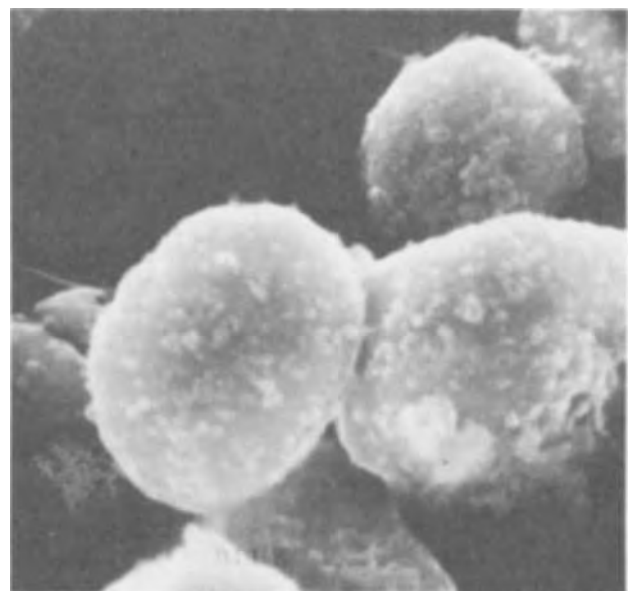


Fig. 3. Scanning electron micrograph of particles of ZnS:Ag:Cl blue phosphor under  $\times 10,000$  magnification.

Table I.  $R_\infty$ ,  $c$ , and  $\theta$  values for ZnS:Ag:Cl blue phosphor

Wavelength (nm)	$R_\infty$	$c$ values	$\theta$ values
360	0.50	0.2500	0.707
370	0.63	0.1087	0.466
380	0.74	0.0457	0.302
390	0.82	0.0196	0.198
400	0.89	0.0068	0.117
410	0.93	0.0026	0.072
420	0.96	0.008	0.040
430	0.98	0.0002	0.020
440	0.99	0.00005	0.010
450	0.99	0.00005	0.010

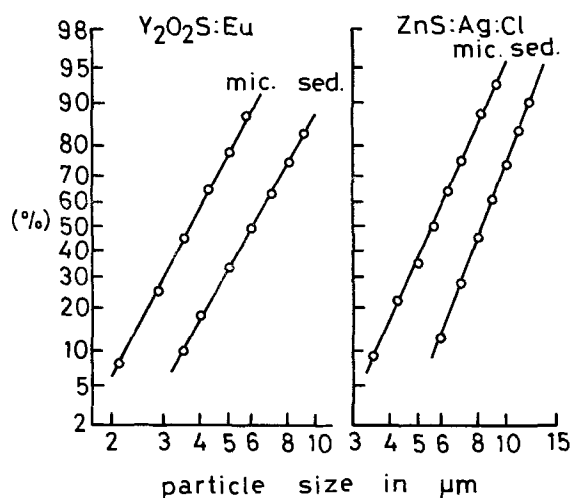


Fig. 4. Particle size distribution of  $Y_2O_2S:Eu$  and  $ZnS:Ag:Cl$  phosphors plotted on log-normal probability paper. Distribution for each phosphor was obtained by calculation from weight sedimentation (sed.) and microscopic (mic.) data.

$$S_w = \frac{k}{\rho} (\bar{\phi}_2)^{-1} \text{ (cm}^2/\text{g)} \quad [10]$$

where

$$\bar{\phi}_2 = \frac{\int_0^\infty n\phi^3 d\phi}{\int_0^\infty n\phi^2 d\phi} \text{ (cm)} \quad [11]$$

$\rho$  is density,  $\phi$  is particle size, and  $k = k_s/k_v$ . Thus, the specific surface area of the phosphor powder,  $S_w$ , is calculated by the mean surface particle size  $\bar{\phi}_2$ . The light scattering in the phosphor screen is connected directly to the mean particle size  $\bar{\phi}_2$  by the relation  $\beta \sim S_w \sim (\bar{\phi}_2)^{-1}$ . Consequently, it is reasonable to use the mean surface particle size  $\bar{\phi}_2$  in discussing the geometry and optical properties of the phosphor screen, as will be verified by Fig. 9.

**The number of phosphor layers.**—The total number of phosphor particles ( $N$ ) in a screen of screening weight ( $w$ ) on a unit screening area is given by

$$N = 6w / \left( \pi \rho \int_0^\infty n\phi^3 d\phi \right) \text{ (cm)} \quad [12]$$

The number of the particles which are densely arranged in a single layer on unit screening plate is given by

$$\frac{N}{L} = 2/\sqrt{3} \int_0^\infty n\phi^2 d\phi \text{ (cm}^{-2}\text{)} \quad [13]$$

Therefore, the number of phosphor layers ( $L$ ) in a screen of the screening weight  $w$  (g phosphor/cm<sup>2</sup>) is calculated to be

$$L = 1.65 w / (\rho \bar{\phi}_2) \quad [14]$$

If the shape factor varies, the factor 1.65 would be different from 1.65. It is important to note that  $L$  is a statistical number defined in terms of  $\bar{\phi}_2$  and is not easily related to a physical description of the actual physical arrangement in a real screen. It is nonetheless a useful concept in describing the optical properties of the phosphor screen.

Now we consider the total surface area of the phosphor particles densely arranged in a single layer on the faceplate of the cathode-ray tube. The area of the faceplate is fixed. When the phosphor particles of number  $n$  having particle size ( $\bar{\phi}_2$ ) are densely arranged in a single layer on the faceplate, the total surface area ( $S_1$ ) of the  $n$  particles is expressed by

$$S_1 = \pi n (\bar{\phi}_2)^2 \quad [15]$$

The total surface area for other sizes,  $\bar{\phi}_2'$ , which are  $g$

times  $\bar{\phi}_2$  (bigger or smaller), i.e.,  $\bar{\phi}_2' = g\bar{\phi}_2$ , can be calculated. The number of particles of size  $g\bar{\phi}_2$  required to arrange a single-layer screen on the faceplate is  $g^{-2}n$ . Then, the total surface area,  $S_1'$ , for particle size  $g\bar{\phi}_2$  is seen to be

$$S_1' = g^2 n \pi \bar{\phi}_2^2 g^{-2} = \pi n (\bar{\phi}_2)^2 = S_1 \quad [16]$$

Thus, the surface area per phosphor layer is not only a constant, but is independent of particle size.

**Light out from a multilayered screen.**—When the light scattering in the phosphor screen is proportional to the total surface area of the phosphor particles, Eq. [7] can be rewritten as

$$T(L) = \frac{1}{1 + \beta L} \quad [17]$$

When the cathodoluminescence  $B_0$  is produced in the particles arranged on the first, gun-side layer of the phosphor screen, the observed screen brightness is defined relatively as  $\frac{B}{B_0}(L)$  in order to be consistent with the relation  $T(L) = i/i_0$  where  $i$  is defined as in Eq. [1]. Then, the screen brightness  $\frac{B}{B_0}(L)$  can be expressed as

$$\frac{B}{B_0}(L) = \frac{1}{1 + \beta L} \quad [18]$$

Equation [18] shows the dependence of the screen brightness on the number of phosphor layers. A screen brightness function,  $(1 - B_0/B)$ , can be defined as

$$1 - \frac{B_0}{B} = -\beta L \quad [19]$$

Note that  $B_0$  used in this report is a different arbitrary constant for each screen series because of different particle size distributions and excitation conditions and  $B$  and  $B_0$  are never measured in absolute units but in terms of photomultiplier readings.

### Experimental

**Phosphors and screening preparation.**—In the study of phosphor screens of different particle size, the phosphors should be similar in the dispersion of their size distribution and in crystal form in order to avoid variances due to the packing of the phosphor particles in the screen. A yellow emitting  $(Zn,Cd)S:Ag:Cl$  phosphor was selected in this study because it was relatively easy to control both the dispersion and crystal form of the powder. Phosphors having four different mean particle sizes ( $\bar{\phi}_2 = 6, 10, 15,$  and  $25 \mu\text{m}$ ) were prepared by firing the mixture of  $ZnS$  and  $CdS$  (1:1 ratio) at various temperatures. X-ray diffraction analysis shows that all of the phosphors were of the hexagonal crystal form (zinc wurtzite). The particle size distribution of the phosphors was determined by the weight sedimentation method. The mean particle size,  $\bar{\phi}_2$ , was calculated from these sedimentation data. Table II gives the statistical parameters of the phosphor particles. All of the dispersions,  $\sigma^2$ , of the particle size distribution were about the same.

Table II. Statistical parameters of particle size distribution of  $(Zn,Cd)S:Ag:Cl$  phosphors used to screen study

Sample No.	1	2	3	4
$\bar{\phi}_2$ ( $\mu\text{m}$ )	6	10	15	25
$\bar{\phi}_3$ ( $\mu\text{m}$ )	7	11	19	29
$\sigma$	0.37	0.35	0.37	0.35

$\bar{\phi}_3$  is the mean weight particle size determined from weight sedimentation data.  $\sigma$  is standard deviation of log-normal distribution.

The phosphor screen was prepared as follows. The phosphor powder was suspended in 1% potassium silicate solution (Kasil No. 1). Then the phosphor suspension was poured into 0.5% barium nitrate solution having glass plates on the bottom of the container. The heights of barium nitrate solution were 10 cm for 6 and 10  $\mu\text{m}$  powders and were 20 cm for 15 and 25  $\mu\text{m}$  powders. The screening weight of the phosphor was determined by weighing the glass plate before and after screening.

**Measurements.**—The phosphor screens of different screening weights were mounted in a demountable cathode-ray apparatus in which eight screens could be mounted at one time. The screen brightness,  $B$ , in relative units, under excitations of 10, 17.5, and 25 kV electron beams, were measured at the glass side (transmitted light) with a Spectraspot Brightness-Photometer. The purpose of the measurements was to determine the dependence on  $w$  and  $L$ . Since the raster size and electron beam current were not under control, the relationship between the brightness,  $B$ , and accelerating voltage cannot be seen in the following results.

**Results and Discussion**

**Particle size and electron penetration range.**—Figures 5 and 6 show the results of the screen brightness tests under 10, 17.5, and 25 kV electron beam excitation for phosphor particle sizes  $\bar{\phi}_2 = 6$  and 10  $\mu\text{m}$ . When the screen was made with 6  $\mu\text{m}$  phosphor powder, the optimum screen thickness ( $\text{mg}/\text{cm}^2$ ) shifted to high screening weight with increase in the accelerating voltage (Fig. 5). With phosphor powders above 10  $\mu\text{m}$ , however, the optimum thickness did not change with accelerating beam voltage (Fig. 6).

These results indicate decidedly that the electrons of energy less than 25 kV do not penetrate through the first particle layer of the phosphor screen (gun side) when the screens are composed of particles larger than 10  $\mu\text{m}$  (Fig. 7a). If the phosphor particle size is smaller than the electron penetration depth, the electron beams penetrate the second particle layer through the first particle layer, resulting in a shift of the optimum

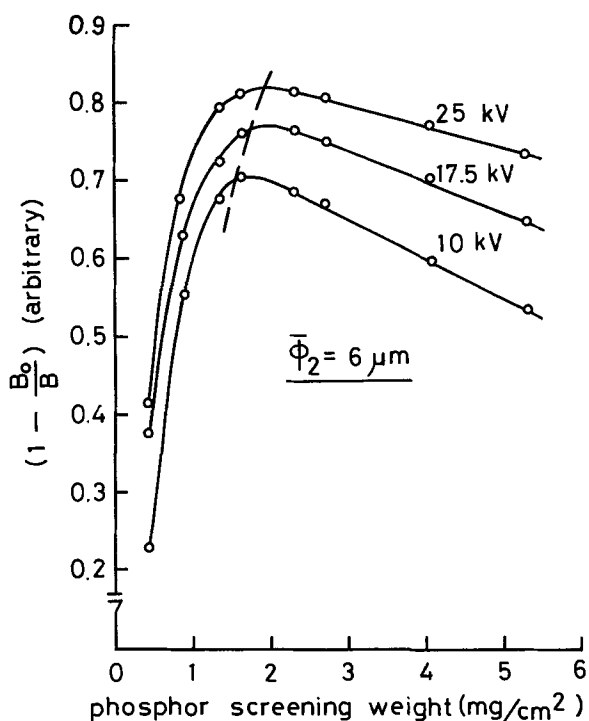


Fig. 5. Screen brightness function  $(1 - B_0/B)$ , in arbitrary units, of phosphor screens of 6  $\mu\text{m}$  powder as a function of screening weight.  $B_0$  is an arbitrary constant which is different for each beam accelerating voltage. Variable is accelerating voltage.

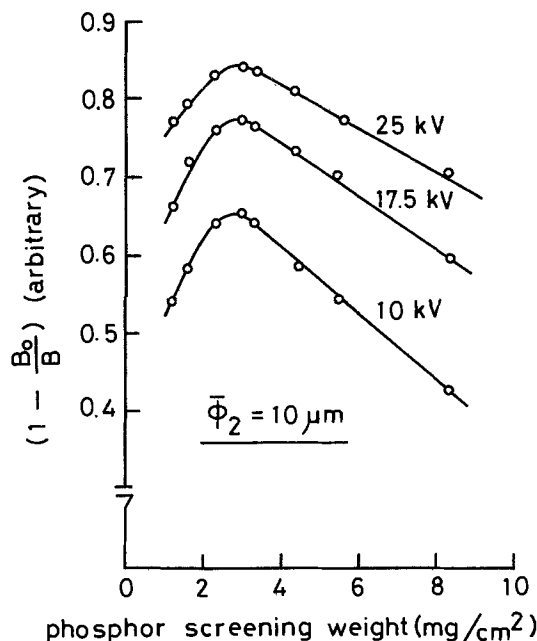


Fig. 6. Screen brightness function,  $(1 - B_0/B)$ , of phosphor screens of 10  $\mu\text{m}$  powder as a function of screening weight.  $B_0$  is arbitrary constant which is different for each beam accelerating voltage. The screens were excited by electron beams of 10, 17.5, and 25 kV.

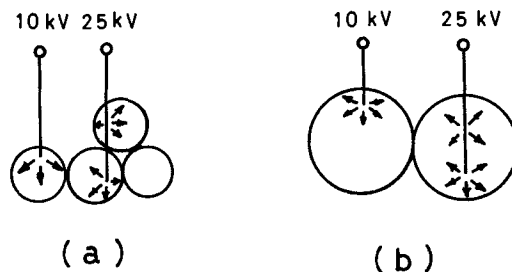


Fig. 7. Penetration model of 10 and 25 kV electron beams into small phosphor particles (a) and into large phosphor particles (b).

screening weight with the beam accelerating voltage (Fig. 7b). It can be said that the penetration depth of 25 kV electron beams into (Zn,Cd)S:Ag:Cl phosphor is about 10  $\mu\text{m}$ , which coincides with the penetration range estimated by extrapolation of Feldman's results (9).

**Optimum number of phosphor particle layers.**—Figure 8 shows the normalized relative screen brightness

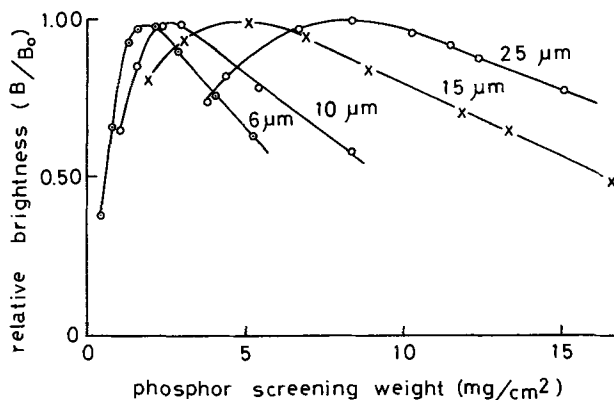


Fig. 8. Normalized relative brightness,  $(B/B_0)$ , of phosphor screens for various particle size powders as a function of the screening weight. (Each curve is normalized at its maximum brightness  $B_0$ .)

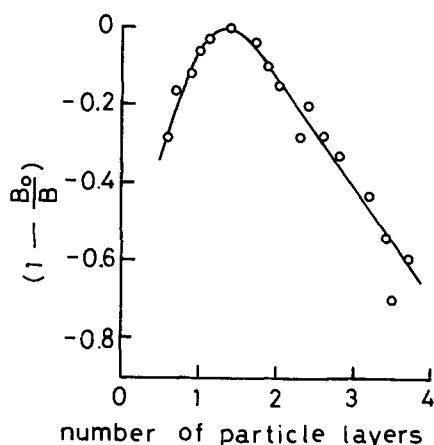


Fig. 9. Brightness function,  $(1 - B_0/B)$ , of phosphor screens for various particle size powders as a function of  $L$ , the calculated number of particle layers.  $B_0$  is a different constant for each particle size powder screen and is assumed to be unity for  $L = 1.4$ .

for different phosphor particle sizes. It can be seen that the optimum screening weight varies with phosphor particle size as follows: 2.0 mg/cm<sup>2</sup> for 6  $\mu$ m, 2.8 mg/cm<sup>2</sup> for 10  $\mu$ m, 4.3 mg/cm<sup>2</sup> for 15  $\mu$ m, and 8 mg/cm<sup>2</sup> for 25  $\mu$ m. If an optimum phosphor screen requires a certain number of phosphor particle layers, higher screening weight is required for large particle size. Figure 9 shows the same data of Fig. 8 but the abscissa is expressed in terms of  $L$ , the number of particle layers, instead of the screening weight. All of the data fit one curve from which the optimum value of  $L$  is calculated to be 1.4. For screens having more than 1.4 layers, the brightness decreases with the increase in  $L$  in accordance with Eq. [19]. The scattering coefficient per phosphor layer ( $\beta$ ) is determined from the slope to be 0.28.

**Demonstration of the significance of  $L$ .**—In order to see the meaning of the optimum number of phosphor particle layers, a screen containing a P4 phosphor (used in B&W television) was studied. A P4 phosphor is a white-emitting mixture of a blue ZnS:Ag:Cl (455 nm peak) and a yellow (Zn,Cd):Ag:Cl (550 nm peak) phosphor. Since the absorption band of the yellow phosphor extends to the spectral region of the blue phosphor luminescence (Fig. 10), yellow phosphor particles laid down under the blue emitting particles in the screen should absorb the blue luminescence, resulting in a color shift to yellow; Fig. 11 shows the screen brightness function,  $(1 - B_0/B)$ , at 455 and 550 nm of P4 phosphor screens of various  $L$ -values.  $B_0$  is normalized at maximum intensity for each curve. The mean surface particle size of the phosphor powder was 9  $\mu$ m. This result can be interpreted as follows. When the screening weight is increased to a value

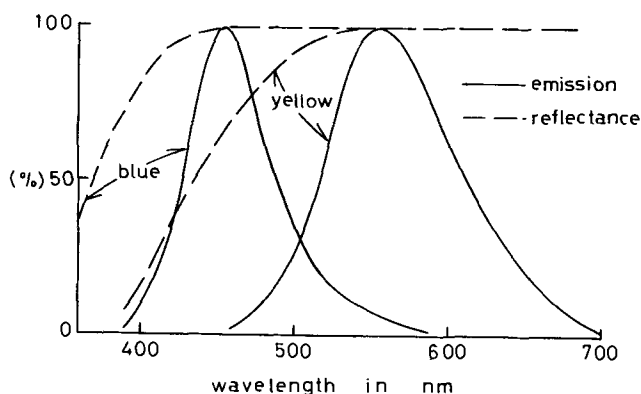


Fig. 10. Emission and reflectance spectra of the P4 blue and yellow sulfide phosphors used in black and white television screen.

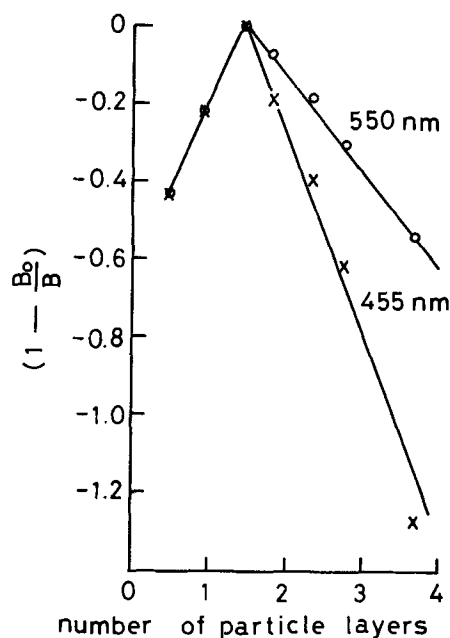


Fig. 11. Screen brightness function,  $(1 - B_0/B)$ , at 455 and 550 nm of P4-phosphor screens as a function of the number of particle layers,  $L$ .  $B_0$  is a different constant for each color brightness and is assumed to be unity for  $L = 1.4$ .

corresponding to  $L = 1.4$  layers, the luminescent color of the screen does not change, indicating that both the blue and yellow phosphor particles just fill in the uncovered spaces on the screen plate; consequently the points for  $L < 1.4$  fall on one line in Fig. 11. Above the optimum 1.4 layers, excess yellow-emitting particles on the viewing side of the screen absorb the blue luminescence, giving rise to two lines in Fig. 11 for 550 and 455 nm emission. Since neither phosphor absorbs yellow luminescence, the 550 nm intensity decreases with the slope determined from the curve in Fig. 9. The steeper slope of the 455 nm curve in Fig. 11 is due to absorption of the blue light, plus scattering.

These results (Fig. 9 and 11) definitely indicate that the extra particles in the screens with more than 1.4 layers are not involved in the cathodoluminescence and merely contribute to the scattering and absorption of the emitted light. The optimum number of particle layers, therefore, is the maximum number of particle layers to cover the faceplate with minimum scattering.

The fact that continuum model appears to apply to the slopes of the curves having more than 1.4 particle layers in Fig. 9 and 11 indicates that there is multiple scattering of the generated light even though there are only a few particle layers.

The optimum number of particle layers may vary slightly with the change in the shape factor of the phosphor particles (crystal form), differences in the dispersion of the particle size distribution, and in the screening method especially when one includes an aluminum reflecting layer. In a practical phosphor screen, therefore, a more accurate value of  $L$  (optimum) should be determined experimentally in each case.

### Summary

It has been shown that the optical properties of the screen of a cathode-ray picture tube are mainly governed by scattering by the phosphor particles. It has been shown that the total surface area of particles arranged in a multilayered screen depends only on the number of layers of the phosphor particles and not on the particle size. The light output is shown theoretically and experimentally to depend on a statistically defined number of layers,  $L$ . Approximately 1.4 particle layers represent the optimum screen construc-

tion; the optimum particle size is equal to the electron penetration depth, 10  $\mu\text{m}$  at 25 kV.

#### Acknowledgment

The authors wish to thank Ms. H. Stanczyk for preparation of the screens and Mr. D. Stupegia for measurement of screen brightness under cathode-ray excitation.

Manuscript submitted June 11, 1973; revised manuscript received Feb. 18, 1974.

Any discussion of this paper will appear in a Discussion Section to be published in the June 1975 JOURNAL. All discussions for the June 1975 Discussion Section should be submitted by Feb. 1, 1975.

#### REFERENCES

1. J. W. Coltman, E. G. Ebbighausen, and W. Altar, *J. Appl. Phys.*, **18**, 530 (1947).
2. K. H. Butler and H. H. Homer, *Illum. Engng.*, **55**, 396 (1960).
3. H. Bo and S. Takeyama, *Illum. Engng. Japan*, **44**, 227 (1960).
4. G. F. F. Garlick, "Luminescence of Inorganic Solids," p. 685, Academic Press, Inc., New York (1966).
5. P. Kubelka, *J. Opt. Soc. Am.*, **38**, 448 (1948).
6. M. J. Bergin and K. H. Butler, *This Journal*, **101**, 149 (1954).
7. J. M. Dalla Valle, "Micromeritics," Pitman Publishing Co., New York (1951).
8. G. Herdan, "Small Particle Statistics," Elsevier Publishing Co., New York (1953).
9. C. Feldman, *Phys. Rev.*, **117**, 455 (1960).

# The Kinetics of Silicon Deposition on Silicon by Pyrolysis of Silane

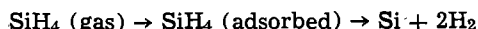
## A Mass Spectrometric Investigation by Molecular Beam Sampling

R. F. C. Farrow

Ministry of Defence, Royal Radar Establishment, Malvern, Worcestershire, England

#### ABSTRACT

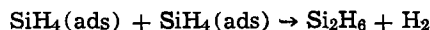
The kinetics of silane pyrolysis on a silicon (111) surface has been investigated mass spectrometrically by molecular beam sampling over the silane pressure range  $1 \times 10^{-5}$  to  $4 \times 10^{-1}$  Torr and specimen temperature range 20°-1200°C. Silane decomposition was found to occur by the mechanism



where both the amount of adsorbed silane and decomposition rate depend linearly on silane pressure. The activation energy for decomposition was  $17 \pm 2$  kcal mole<sup>-1</sup> and the surface reaction efficiency ( $\alpha$ ) was found to obey the equation

$$\alpha = 5.45 \exp(-17 \times 10^3/RT)$$

At silane pressures  $P_{\text{S}} > 5 \times 10^{-3}$  Torr, small quantities of disilane formed by the bimolecular surface reaction



were detected with an activation energy for production of  $56 \pm 6$  kcal mole<sup>-1</sup>.

Measurements of silicon growth rate as a function of silane pressure supported the first-order mechanism for decomposition. The condensation coefficient ( $\sigma$ ) of silicon adatoms, determined from measurements of the silicon growth rate as a function of temperature and the surface reaction efficiency, was found to be less than 0.3 over the entire temperature range 700°-1200°C, indicating that the majority of silicon adatoms were desorbed. This behavior was accounted for on the basis of a step flow model for silicon growth and an activation energy for surface diffusion of  $36 \pm 6$  kcal mole<sup>-1</sup> derived. Addition of arsine to the silane was found to inhibit silane pyrolysis. The measurements suggest an activation energy of  $18 \pm 3$  kcal mole<sup>-1</sup> for desorption of arsenic adsorbed on the silicon (111) surface. Additions of more than 1% diborane to the silane, on the other hand, resulted in a significant increase in silane reaction efficiency.

The pyrolysis of silane ( $\text{SiH}_4$ ) on silicon is a reaction widely used in the electronics industry in the production of homoepitaxial silicon layers. Several investigations have been reported (1-4) on the vacuum deposition of silicon on silicon by silane pyrolysis but the conclusions of the various investigators concerning the kinetics of the decomposition reaction and the pressure dependence of silicon growth rate differ widely. Thus, activation energies for silane decomposition ranging from 10 kcal mole<sup>-1</sup> (3) to 37 kcal mole<sup>-1</sup> (1) have been reported. Moreover, there is considerable disagreement as to the mechanism and order of the decomposition reaction. Joyce and Bradley

(1) found the growth rate to vary as silane pressure  $P_{\text{S}}^{1.3}$  whilst more recent investigations (3, 4) have revealed a linear dependence of growth rate on pressure suggesting a first-order decomposition reaction.

No investigations have been reported in which the gas phase products of silane pyrolysis, as a function of specimen temperature and silane pressure, have been detected, identified, and recorded. The aim of the present work was to carry out such an investigation, including a study of the influence of arsine and diborane on silane pyrolysis, and to correlate reaction kinetic data with silicon growth rate measurements in an attempt to resolve the existing disagreements mentioned above.

Key words: silicon, silane, reaction kinetics.

### Experimental Procedure

The pyrolysis of silane was studied using the molecular beam sampling system shown schematically in Fig. 1. The system incorporated three apertures, a  $0.12 \times 10$  mm sampling slit ( $A_1$ ) and two  $1 \times 10$  mm beam collimating slits ( $A_2$  and  $A_3$ ). High speed differential pumping of the two collimating chambers and the detection chamber was provided by three 1500 liter  $\text{sec}^{-1}$  oil diffusion pumps ( $P_1, P_2, P_3$ ), each fitted with molecular sieve traps, and a thermoelectrically cooled chevron baffle to prevent back diffusion of the silicone (Type 705) oil. Base pressures in the low  $10^{-10}$  Torr pressure range, with negligible contribution from hydrocarbon species, were achieved in all four chambers after system bakeout at  $300^\circ\text{C}$ . Valve V was closed after bakeout.

The molecular beam of products was detected by an Electronic Associates, Inc. Model 250A quadrupole mass spectrometer (ion source M). Two methods of discriminating the molecular beam of products from the isotropic background were used. In the first, used for all product species except those of disilane which were at a very low concentration, the molecular beam was modulated at 10 Hz by a 12-blade chopper wheel (C) rotated by a magnetic rotary drive. The modulated ion currents of molecular beam species were then monitored by phase-sensitive detection (psd). Pressures of products in the reaction chamber down to  $10^{-5}$  Torr could be conveniently detected by this method. For the detection of the very weak disilane species (pressures in the reaction chamber ranging from  $10^{-5}$  to  $10^{-7}$  Torr), the molecular beam ion currents could be measured with greater statistical accuracy, than by continuous psd, by recording the ion currents of the species with the chopper in the open and closed positions and taking the difference as the molecular beam contribution.

Initial silane pressures in the reaction chamber in the range  $10^{-3}$  to 1 Torr were measured using a capacitance manometer. Silane and dopant gas pressures below  $10^{-3}$  Torr were derived from an ion gauge reading of pressure in the first collimating chamber, the relation between the reaction chamber pressure and that in the collimating chamber having been established from a previous calibration experiment. This method eliminated the need for ion gauge filaments in the reaction chamber which would have been undesirable from the point of view of pyrolysis on the filament and other possible side reactions. The gases used in these experiments were supplied by the Mattheson Company, Inc. The silane was of semiconductor grade ( $>50$  ohm-cm deposited material) used undiluted; the arsine and diborane were also of semiconductor grade, diluted to 5% in helium.

The silicon specimens used in this work were bars,  $20 \times 3 \times 0.4$  mm, of 10 ohm-cm, P-type material with the  $20 \times 3$  mm faces parallel to the (111) plane to within  $\pm 3^\circ$ . They were supplied by Chisso, Inc. Both major faces of the bar were polished using the Mon-

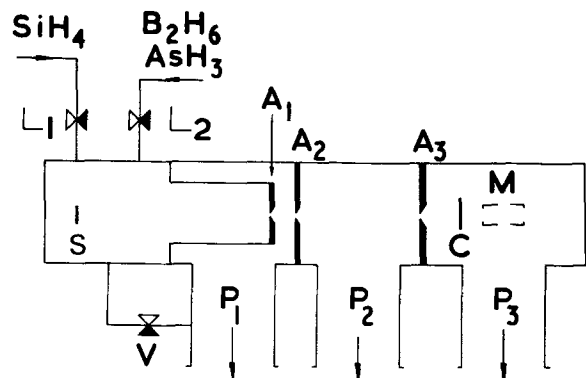


Fig. 1. Schematic diagram of molecular beam sampling system

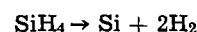
santo method. The chemical precleaning treatment before loading consisted of ultrasonic cleaning in a solvent followed by several cycles of a nitric acid/ethanol/HF cleaning procedure (6). The specimens were held in thick, high-purity tantalum clips and heated resistively. Specimen temperatures were measured using a partial radiation optical pyrometer and were corrected for emissivity using the data of Allen (7).

The specimen was heated to  $1250^\circ\text{C}$  in a background pressure of less than  $10^{-9}$  Torr for a few minutes before each run to remove initial oxide and carbon contamination of the silicon surface (5).

The thickness of deposited epitaxial silicon layers was determined using three independent methods: (i) measurement of the thickness of the specimen before and after deposition, (ii) measurement of the dimensions of stacking fault defects which originated at the substrate-layer interface, and (iii) the bevel-stain technique. Agreement between the three methods was well within experimental errors.

### Results and Analysis of Data

**Molecular beam sampling of silane pyrolysis.**—The pyrolysis of silane was monitored over the specimen temperature ( $T_S$ ) range  $20^\circ$ – $1200^\circ\text{C}$  and at silane (reactant) pressures in the range  $10^{-5}$  to  $4 \times 10^{-1}$  Torr. The temperature dependence of product species for an initial silane pressure at  $20^\circ\text{C}$  of  $P_S^0 = 10^{-4}$  Torr is shown in Fig. 2. The onset of pyrolysis is marked by a rise in the molecular hydrogen signal and a simultaneous fall in each of the Si,  $\text{SiH}_n$  ( $n = 1$  to 4), and H signals. The relative ratios between the Si,  $\text{SiH}_n$ , and H signals did not change significantly with temperature, indicating that unreacted silane and molecular hydrogen were the only detectable products in the reaction chamber for this value of  $P_S^0$  and that the Si,  $\text{SiH}_n$ , and H signals could be attributed to the fragmentation of silane in the mass spectrometer ion source. The observation of molecular hydrogen as a pyrolysis product was consistent with the over-all decomposition reaction



Surface reaction efficiencies were derived both from the  $\text{H}_2$  product signal and the decrease in the unreacted silane signal on the basis of the following arguments.

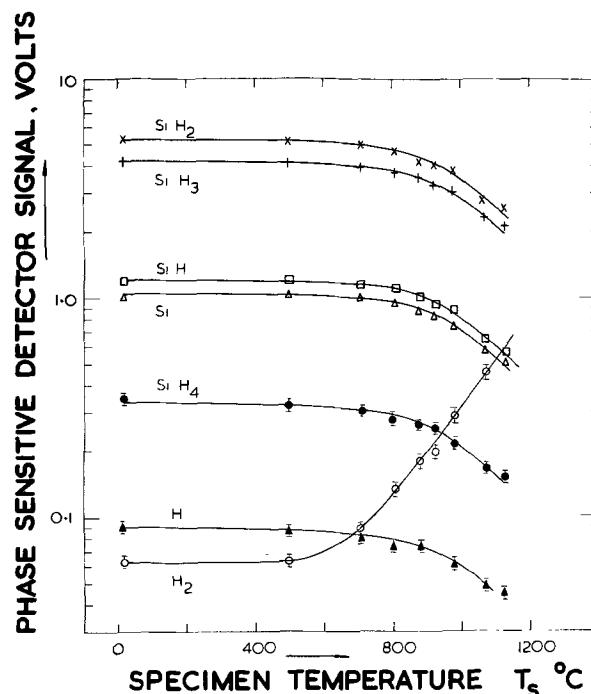


Fig. 2. Temperature dependence of molecular beam products at  $P_S^0 = 10^{-4}$  Torr.



We define the surface reaction efficiency  $\alpha$  as the probability that a silane molecule decomposes on striking the silicon surface. Furthermore, let

$P_S^T$ ,  $P_H^T$  be the partial pressure of silane and hydrogen, respectively, in the reaction chamber at a specimen temperature  $T_S$ .

$R_i$  the inlet rate of silane into the reaction chamber in molecules per unit time.

$n_S$ ,  $n_H$  the rate of collisions of silane and hydrogen molecules, respectively, with the specimen in molecules per unit area per unit time per unit pressure.

$A_S$  the total effective reaction surface area (0.8 cm<sup>2</sup> in the present case).

$A_0$  the effective area (including conductance factor) of the sampling slit (1.2 × 10<sup>-2</sup> cm<sup>2</sup> in the present case).

$S_S$ ,  $S_H$  the speed of the sampling slit in molecules per unit time per unit pressure for silane and hydrogen, respectively.

Then, after steady-state conditions are attained in the reaction chamber, for silane

$$R_i - \alpha n_S P_S^T A_S - S_S P_S^T = 0 \quad [1]$$

and for hydrogen

$$2\alpha n_S P_S^T A_S - S_H P_H^T = 0 \quad [2]$$

Now with pressures  $P_S^T$ ,  $P_H^T$  sufficiently low (i.e., <10<sup>-3</sup> Torr) that the mean free path  $\lambda$  in the reaction chamber is much greater than the chamber dimensions (~5 cm), interaction between molecules can be neglected and molecules striking a surface in the reaction chamber are directionally randomized. Under these conditions,  $n_S P_S^T$ ,  $n_H P_H^T$ ,  $S_S P_S^T$ , and  $S_H P_H^T$  can be replaced by

$$\frac{P_S^T}{\sqrt{2\pi m_S kT}}, \frac{P_H^T}{\sqrt{2\pi m_H kT}}, \frac{P_S^T A_0}{\sqrt{2\pi m_S kT}}, \frac{P_H^T A_0}{\sqrt{2\pi m_H kT}}$$

respectively, where  $m_S$  and  $m_H$  are the molecular masses of silane and hydrogen, respectively. Furthermore, since  $R_i$  remained at a steady value determined by the initial setting of the leak value for a particular initial silane pressure  $P_S^0$

$$R_i = \frac{P_S^0 A_0}{\sqrt{2\pi m_S kT}} \quad [3]$$

Hence from Eq. [1] and [3]

$$\alpha = \frac{A_0}{A_S} \left( \frac{P_S^0}{P_S^T} - 1 \right) \quad [4]$$

and from Eq. [2]

$$\alpha = \frac{2A_0}{A_S} \left( \frac{P_H^T}{P_S^T} \right) \quad [5]$$

Equations [4] and [5] were used to derive  $\alpha$  as a function of temperature and pressure from the sampled H<sub>2</sub> and SiH<sub>4</sub> species. The relationship between the (sampled) molecular beam intensities of these species and the partial pressures of H<sub>2</sub> and SiH<sub>4</sub> in the reaction chamber was established from a previous calibration experiment. Significant departure from linearity in the relationship occurred only at  $P_S^T$ ,  $P_H^T > 2 \times 10^{-2}$  Torr. Derivation of  $\alpha$  from Eq. [5] involved a determination of the relative sensitivity of the mass spectrometer for H<sub>2</sub> and SiH<sub>4</sub>. A known 3% SiH<sub>4</sub>-97% H<sub>2</sub> gas mixture was used in this determination.

Values of  $\alpha$ , calculated using Eq. [4], are plotted as a function of silane pressure at three different temperatures in Fig. 3. It is seen that for  $P_S^T < 10^{-3}$  Torr,  $\alpha$  is independent of pressure but apparently decreases with  $P_S^T$  for  $P_S^T > 10^{-3}$  Torr. Values of  $\alpha$  calculated using Eq. [5] agreed well at all pressures with those calculated using Eq. [4] and showed an identical pressure dependence to that shown in Fig. 3. We believe that this pressure dependence is due to a breakdown in

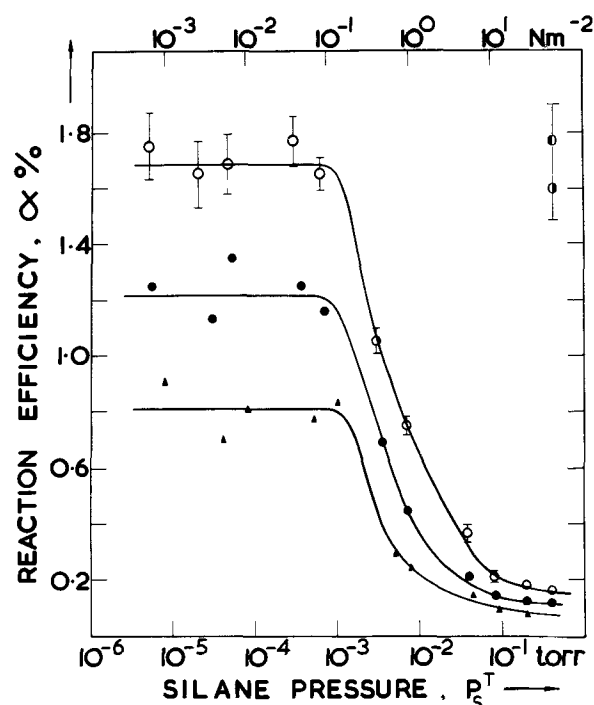


Fig. 3. Surface reaction efficiency,  $\alpha$ , for silane pyrolysis as a function of pressure.  $\circ$ , Calculated from Eq. [4],  $T_S = 1156^\circ\text{C}$ ;  $\bullet$ , calculated from Eq. [6],  $T_S = 1156^\circ\text{C}$ ;  $\ominus$ , calculated from Eq. [8],  $T_S = 1156^\circ\text{C}$ ;  $\bullet$ , calculated from Eq. [4],  $T_S = 1076^\circ\text{C}$ ;  $\blacktriangle$ , calculated from Eq. [4],  $T_S = 987^\circ\text{C}$ .

validity of Eq. [4] and [5] rather than to a genuine departure from the first-order reaction mechanism indicated by the pressure independent reaction efficiency below  $P_S^T = 10^{-3}$  Torr. Equations [4] and [5] were derived on the basis of molecular flow conditions in the reaction chamber. However, at pressures  $P_S^T > 10^{-3}$  Torr in the reaction chamber, the mean free path for silane will become less than the diameter (~5 cm) of the pipework forming the walls of the reaction chamber. Thus, over the pressure range 10<sup>-3</sup> Torr (Knudsen number  $\lambda/d = 1$ ) to 10<sup>-1</sup> Torr ( $\lambda/d = 10^{-2}$ ), there will be a transition from molecular to streamline flow of molecules between the silane entry port and sampling slit (18). The existence of streamline flow in the reaction chamber is supported by the observation that, at pressures  $P_S^T > 10^{-3}$  Torr, silicon deposition occurred not only on the specimen but on one of the specimen clips, the one further down line in the direction of streamline flow between the silane entry port and the sampling slit. As suggested in the discussion, this observation can be explained by transport of silicon from the specimen down the streamlines to the clip.

Under streamline flow conditions, it is expected that only silane molecules within the boundary layer of flow over the specimen will be able to diffuse to the specimen surface and that a considerable fraction of silane molecules entering the reaction chamber will bypass the specimen on streamlines outside the boundary layer. The fractional decrease in silane signal observed when the specimen is heated to a given temperature will thus be less than in the molecular flow regime since the flow of silane molecules outside the boundary layer will remain unaffected by the specimen temperature but will contribute to the sampled silane signal. For the same reason, the ratio of the H<sub>2</sub> to silane signals at a given temperature will be less than in the molecular flow regime. Thus the transition from molecular to streamline flow would account for the apparent systematic decrease in  $\alpha$  with pressure shown in Fig. 3.

A quantitative estimate of the effect of streamline flow in the reaction chamber on the reaction efficiency

derived from the sampled species was made in the following way: let

$A_T$  be the cross-sectional area of streamline flow over the specimen ( $A_T = \pi D^2/4 = 19.6 \text{ cm}^2$  in the present case, since silane was carried to and from the specimen in 5-cm diameter pipework).

$A_B$  the cross-sectional area of flow within the specimen boundary layer.

$I_{H^T}$  the mass spectrometer signal for the  $H_2$  pyrolysis product at a specimen temperature  $T_S$ .

$I_{S^T}$  the mass spectrometer silane signal at a specimen temperature  $T_S$ .

$I_{S^0}$  the mass spectrometer silane signal at ambient temperature.

$Q_H/Q_S$  the mass spectrometer sensitivity ratio for  $H_2$  and silane molecules.

Then

$$\frac{I_{S^0}}{I_{S^T}} = \frac{R_1}{R_1 - \frac{A_B}{A_T} \alpha' R_1} = \frac{1}{1 - \frac{A_B}{A_T} \alpha'} \quad [6]$$

where  $\alpha'$  is the proportion of silane flow in the boundary layer region which is decomposed and is given by

$$\alpha' = \frac{\alpha n_S P_S^T}{S_S P_S^T + \alpha n_S P_S^T} = \frac{\alpha A_S}{A_0 + \alpha A_S} \quad [7]$$

where  $P_S^T$  is the silane pressure in the boundary layer and can safely be assumed equal to that outside the layer for the low volumetric flow rates and reaction efficiencies in the present experiments. In deriving Eq. [7], silane molecules in the boundary layer were assumed to diffuse randomly to the specimen surface. In addition, the conductance of the source slit at silane pressures of  $P_S^T \sim 1$  Torr was assumed to be the same ( $0.14 \text{ liter sec}^{-1}$ ) as in the molecular flow regime. The validity of this latter assumption was confirmed by molecular beam intensity measurements which showed that the source slit conductance was constant up to  $P_S^T \sim 2$  Torr. Equation [6] becomes equivalent to Eq. [4] in the limit when all molecules entering the reaction chamber may take part in random diffusion to the specimen surface, i.e., for  $A_B/A_T = 1$ .

In the case of the  $H_2$  pyrolysis product we have

$$\frac{I_{H^T}}{I_{S^T}} = \left( \frac{2\alpha' R_1 A_B/A_T}{R_1 - \frac{A_B}{A_T} \alpha' R_1} \right) \frac{Q_H}{Q_S} = \frac{2}{\frac{A_T}{A_B \alpha'} - 1} \cdot \frac{Q_H}{Q_S} \quad [8]$$

which becomes equivalent to Eq. [5] in the case of  $A_B/A_T = 1$ . An estimate of  $A_B/A_T$  in the streamline flow regime at  $P_S^T \sim 1$  Torr was made on the basis of the expected boundary layer width, given by (14)

$$\delta \sim \sqrt{\frac{l\nu}{U}} \approx 2.2 \text{ cm} \quad [9]$$

where  $l$  was taken as the distance ( $0.9 \text{ cm}$ ) from the leading edge of the specimen clip to the center of the specimen;  $\nu$  the kinematic viscosity for silane at 1 Torr,  $20^\circ\text{C}$ , was  $59 \text{ cm}^2 \text{ sec}^{-1}$ ; and  $U$  the flow velocity was  $10.7 \text{ cm sec}^{-1}$  at the specimen position for the  $0.14 \text{ liter sec}^{-1}$  silane flow.

Assuming the boundary layer cross section to be circular with a diameter of  $2\delta$ , a value of  $A_B/A_T = 0.77$  would be expected. However, this value can be considered only as an order of magnitude estimate since Eq. [9] is strictly applicable only to flow over an infinitely wide flat plate and takes no account of edge or end effects which are likely in the case of a finite specimen. It is possible, for example, that  $A_B/A_T = 0.77$  is an overestimate as a result of "pinch-in" of the boundary layer over the specimen which was both thinner and less wide than the leading specimen clip. Moreover, since both the specimen and clips were rectangular in cross section, the assumption of a circular

cross-section boundary layer might also be expected to lead to an overestimate of  $A_B/A_T$ . We have found, in fact, that reaction efficiencies derived from sampling data in the streamline flow regime using Eq. [6] and [8] with  $A_B/A_T = 0.25$  (see the two half-shaded points in Fig. 3) agree well with values calculated using Eq. [4] and [5].

It may be concluded from the molecular beam sampling data that the invariance of reaction efficiency over the silane pressure range  $10^{-5}$  to  $10^{-3}$  Torr is consistent both with a linear variation of adsorbed silane with pressure and with the first-order, unimolecular surface reaction



Furthermore, the preceding calculations of reaction efficiency in the streamline flow regime show that the sampling data at pressures above  $P_S^T = 10^{-3}$  Torr are not necessarily inconsistent with the view that this mechanism is valid up to  $P_S^T \sim 1$  Torr.

The broad line in Fig. 4 shows the temperature dependence of silane reaction efficiency measured at various initial silane pressures  $P_S^0$  and plotted on an Arrhenius scale. The line shown was the best fit (within 5%) to the  $\alpha$  values derived using Eq. [4] and [5] and represents the equation

$$\alpha = 5.45 \exp \left[ \frac{-17 \times 10^3}{RT_S} \right] \quad [10]$$

where  $R$  is the molar gas constant,  $1.98 \text{ cal mole}^{-1} \text{ deg}^{-1}$ . Moreover, values of  $\alpha$  (calculated using Eq. [6] and [8] with  $A_B/A_T = 0.25$ ) derived from sampling data in the streamline flow region at  $P_S^0 = 4.10^{-1}$  Torr were also well represented by Eq. [10]. The temperature dependence of the apparent reaction efficiencies at  $P_S^0 = 2.10^{-1}$  Torr calculated using Eq. [4] are also shown in Fig. 4 for the purpose of comparison with the corrected reaction efficiencies represented by the broad line. It is seen that whilst the effects of streamline flow lead to an apparent reduction in reaction efficiency, they have no effect on the slope of the Arrhenius plot.

Disilane ( $\text{SiH}_3$ )<sub>2</sub> was detected as a pyrolysis product at silane pressures  $P_S^0 > 5 \times 10^{-3}$  Torr. The molecular beam ion currents of disilane species detected at  $P_S^0 = 1.05 \times 10^{-1}$  Torr as a function of specimen temperature are summarized in Table Ia and the total molecular beam ion currents for silane and disilane recorded at  $T_S = 1123^\circ\text{C}$  at four initial silane pressures are given in Table Ib. The tabulated ion currents have been cor-

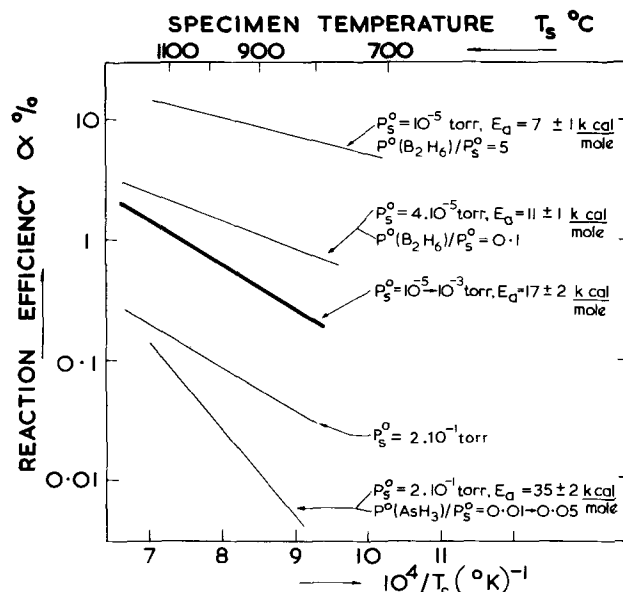


Fig. 4. Surface reaction efficiency,  $\alpha$ , for silane pyrolysis as a function of temperature.

Table Ia. Disilane species detected at  $P_S^0 = 1.05 \times 10^{-1}$  Torr; electron energy 90 eV

$T_S$ (°C)	Ion currents $\times 10^{11}$ A at $m/e$									Disilane TIC* $\times 10^{11}$ A	Silane TIC $\times 10^7$ A
	56	57	58	59	60	61	62	63	64	56 $\rightarrow$ 64	28 $\rightarrow$ 32
20	0	0	0	0	0	0	0	0	0	0	35.4
884	0.4	0.7	0.4	0	0	0	0.3	0.2	0	2	35.2
910	1.4	1.9	1.5	0	1.6	0.8	1.3	0.6	0.2	9.3	35.0
1010	2.4	3.7	5.5	1.0	8.8	3.5	4.3	1.0	0.4	30.6	34.3
1059	5.9	9.9	16.6	5.5	27.5	10.3	13.2	2.6	0.9	82.4	33.3
1123	8.7	14.5	26.0	8.3	40.0	15.7	20.3	3.4	0.8	137.7	31.7
1123	22	36	65	21	100	39	51	8.5	2.0		
1123†	30	41	64	21	100	31	51	—	—		

\* TIC = total ion current.  
† Ref. (8).

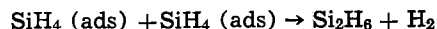
Table Ib. Total ion currents for disilane and silane species recorded at  $T_S = 1123^\circ\text{C}$ ; electron energy 90 eV

$P_S^0$ (Torr)	TIC silane $T_S = 20^\circ\text{C}$ $\times 10^7$ A	TIC silane $T_S = 1123^\circ\text{C}$ $\times 10^7$ A	TIC disilane $T_S = 1123^\circ\text{C}$ $\times 10^{11}$ A	TIC silane (corrected) $T_S = 1123^\circ\text{C}$ $\times 10^7$ A	TIC disilane (corrected) $T_S = 1123^\circ\text{C}$ $\times 10^{11}$ A
$5 \times 10^{-8}$	3.0	1.73	1.7	1.5	1.7
$19 \times 10^{-8}$	10.6	6.94	20.5	3.2	24
$5 \times 10^{-2}$	24.3	21.6	66.0	6.65	106
$1.05 \times 10^{-1}$	35.4	31.7	137.7	13.0	507

rected for background ion currents recorded at  $T_S = 20^\circ\text{C}$ .

The relative intensities of disilane species observed at  $T_S = 1123^\circ\text{C}$  are compared with Potzinger and Lampe's (8) disilane mass spectrum in the last two lines of Table Ia. The agreement is generally good, considering that errors in the very small disilane ion currents recorded in this work are expected to be about 5%. The disilane species at 63 and 64 amu, not recorded by Potzinger and Lampe, can be assigned to combinations of disilane species containing  $\text{Si}^{29}$  and  $\text{Si}^{30}$ .

In order to extract reaction kinetic information from the pressure dependence of the detected disilane species, two main correction factors had to be taken into account. Firstly, at the values of  $P_S^0$  ( $>5 \times 10^{-3}$  Torr) at which disilane was detected, significant attenuation of the sampled molecular beam species occurred as a result of collisions between the beam molecules and background gas (predominantly silane) in the first collimating chamber. Moreover, since the molecular diameter for disilane is greater than for silane, this attenuation will result in a preferential elimination of disilane from the sampled beam. The detected silane and disilane total ion currents have therefore been corrected (to a first approximation) for this attenuation effect assuming the mutual cross section for collision between disilane beam molecules and silane background molecules to be  $\pi(1.5 \sigma_S)^2$  compared with  $\pi\sigma_S^2$  for silane-silane collisions, where  $\sigma_S$  is the silane molecular diameter. The disilane total ion currents (TIC) at  $T_S = 1123^\circ\text{C}$  corrected for this effect are given in the last column of Table Ib. Secondly, in the case of the silane TIC a further correction was necessary since the pressure range of the observations coincided with the transition from molecular to streamline flow in the reaction chamber. Over the pressure range of this transition, the proportion ( $A_B/A_T$ ) of the silane TIC due to silane which had interacted with the specimen decreased from unity in the molecular flow regime to 0.25 in the streamline flow regime. The effective values of  $A_B/A_T$  over the transition range were calculated, using Eq. [6], from the values of  $I_S^0/I_S^T$  measured over this range. The values of silane TIC corrected for this effect and for attenuation due to scattering are listed in column 4 of Table Ib. A log-log plot of corrected disilane TIC against corrected silane TIC gave a straight line of slope  $2.1 \pm 0.1$ . This result is consistent with the expected bimolecular surface reaction for production of disilane



where the silane molecules are adsorbed on adjacent surface sites.

The activation energy for disilane production at  $P_S^0 = 1.05 \times 10^{-1}$  Torr was derived from an Arrhenius plot of the ratio of disilane TIC to silane TIC (see Table Ia). This plot gave a straight line with a slope corresponding to an activation energy of  $56 \pm 6$  kcal mole $^{-1}$ . The two correction factors discussed in the preceding paragraph had no effect on the temperature dependence of silane or disilane TIC.

*Silicon growth rate measurements.*—Silicon growth rates were measured over the silane pressure range  $P_S^T = 10^{-3}$  to 1 Torr and at temperatures from  $700^\circ$  to  $1200^\circ\text{C}$ . Silicon layers grown above  $800^\circ\text{C}$  were epitaxial with low stacking fault densities (see Discussion). The silicon growth rate was taken as the thickness of deposited silicon divided by the deposition time. Continuous monitoring of the pyrolysis products during deposition confirmed that the rate of silane decomposition was constant over the period of deposition.

The pressure dependence of the growth rate at  $T_S = 987^\circ\text{C}$  is shown in Fig. 5. It is seen that the observed growth rates all lie within experimental error on a straight line of slope unity. This result, taken together with the pressure independent reaction efficiency indicated by the molecular beam sampling data, provides strong evidence for first-order, unimolecular decomposition of silane over the entire pressure range covered.

The temperature dependence of the silicon growth rate,  $R$ , measured at  $P_S^T = 10^{-1}$  Torr is shown by the closed circles in Fig. 6. Up to  $T_S = 1070^\circ\text{C}$ , the growth rate follows an exponential rate dependence with an activation energy of  $10 \pm 1$  kcal mole $^{-1}$ . The fall in growth rate at  $T_S > 1100^\circ\text{C}$  can be attributed to the onset of appreciable silicon evaporation.

From the measured values of silicon growth rate and surface reaction efficiency (see crosses in Fig. 6), the silicon condensation coefficient,  $\sigma$ , defined as the fraction of silicon atoms produced by the pyrolysis of silane which are incorporated into the silicon layer, was calculated in the following way:

On the silicon (111) surface, a growth rate of  $R$  micrometers per minute ( $\mu\text{m}/\text{min}$ ) corresponds to a condensation rate of  $8.34 \times 10^{16}R$  atoms  $\text{cm}^{-2} \text{sec}^{-1}$ . Furthermore, the rate of production of free silicon atoms per unit area of specimen surface at  $P_S^T = 10^{-1}$  Torr is

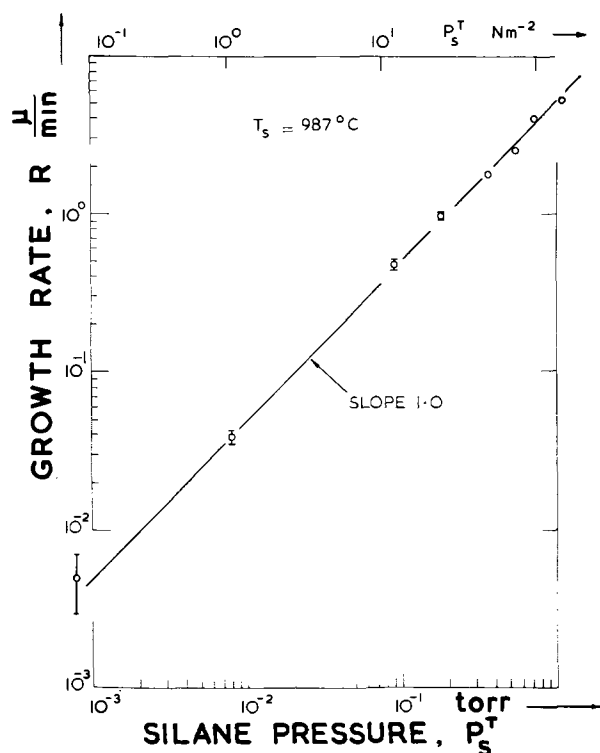


Fig. 5. Pressure dependence of silicon growth rate,  $R$ , at  $T_s = 987^\circ\text{C}$ .

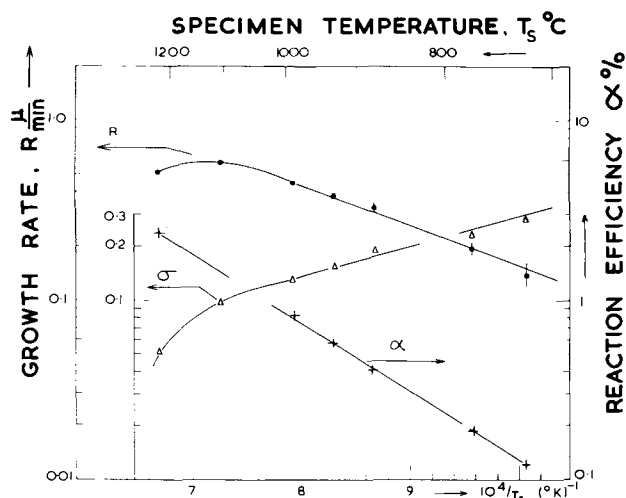


Fig. 6. Temperature dependence of silicon growth rate,  $\kappa$ , at  $P_S T = 10^{-1}$  Torr, surface reaction efficiency,  $\alpha$ , given by Eq. [10], and silicon condensation coefficient,  $\sigma$ .

$$\alpha P_S T n_S = 3.6 \times 10^{19} \alpha \text{ atoms cm}^{-2} \text{ sec}^{-1}$$

hence

$$\sigma = 0.232 \times 10^{-2} R/\alpha \quad [11]$$

The values of  $\sigma$  calculated using Eq. [11] are indicated by triangles in Fig. 6. It can be seen that  $\sigma$  is less than 0.3 over the entire temperature range covered. This result is in agreement with the conclusion of Henderson and Helm (4) that the majority of silicon adatoms are desorbed from the growth surface and is considered further in the Discussion section.

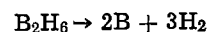
**Effect of arsine on silane pyrolysis.**—The effect of arsine on silane pyrolysis was investigated by adding controlled concentrations of arsine to the silane entering the reaction chamber whilst continuously monitoring the pyrolysis products. It was found that the addition of arsine led to a progressive decrease in the efficiency of silane pyrolysis with time. At  $T_s = 932^\circ\text{C}$  and  $P_S^0 = 2 \times 10^{-1}$  Torr, for example, the silane reaction

efficiency fell to 50% of the initial value about 9 sec after a concentration of  $P^0(\text{AsH}_3)/P_S^0 = 1\%$  arsine was added to the silane. The silane reaction efficiency under these conditions asymptotically approached a lower limit of 20% of the initial value. Similar experiments at higher arsine concentrations showed that the time constant for the fall in silane reaction efficiency decreased with increasing arsine concentration but that the lower limit to the silane reaction efficiency remained unchanged. The temperature dependence of this limiting reaction efficiency measured at  $P_S^0 = 2 \times 10^{-1}$  Torr is shown in Fig. 4. The values shown were calculated using Eq. [4] and may be compared with the  $\alpha$  values also shown in Fig. 4 for  $P_S^0 = 2 \times 10^{-1}$  Torr measured in the absence of arsine. It can be seen that the activation energy for silane pyrolysis has been increased by 18 kcal mole $^{-1}$ .

**Effect of diborane on silane pyrolysis.**—The effect of diborane on the silane pyrolysis was investigated both in the same way as for arsine and by monitoring the pyrolysis of silane on an initially boron-covered surface.

The addition of less than 1% diborane to the silane had no detectable effect on the efficiency of silane pyrolysis. At concentrations above 1%, however, the efficiency of silane pyrolysis was measurably increased. For example, at  $T_s = 850^\circ\text{C}$  and  $P_S^0 = 4 \times 10^{-5}$  Torr, the silane reaction efficiency increased from  $\alpha = 0.3$  to 0.9% over a period of several minutes after the addition of 10% diborane to the silane. Simultaneous measurements of the diborane pressure in the reaction chamber showed that the diborane reaction efficiency (calculated from the fall in diborane pressure using an equation analogous to Eq. [4]) increased from 0.3 to 0.8% over the same period. The temperature dependence of the enhanced silane reaction efficiency under steady-state conditions is shown in Fig. 4. This shows that the activation energy for silane pyrolysis in the presence of 10% diborane has been reduced to  $11 \pm 1$  kcal mole $^{-1}$ . The corresponding reduction in the activation energy for diborane pyrolysis was from  $16 \pm 2$  kcal mole $^{-1}$  to  $12 \pm 1$  kcal mole $^{-1}$ . Further increase of the diborane concentration led to an even greater enhancement of both silane and diborane reaction efficiencies. In Fig. 4 it can be seen that the activation energy of silane pyrolysis has been further reduced to  $7 \pm 1$  kcal mole $^{-1}$  for  $P^0(\text{B}_2\text{H}_6)/P_S^0 = 5$ . The activation energy of diborane pyrolysis under these conditions was  $11 \pm 1$  kcal mole $^{-1}$ .

The catalytic effect of diborane on silane pyrolysis was investigated further by monitoring silane pyrolysis on an initially boron-covered surface. A clean silicon (111) surface was exposed to diborane at a pressure  $P^0(\text{B}_2\text{H}_6) = 0.76 \times 10^{-3}$  Torr at  $T_s = 1035^\circ\text{C}$  for 300 sec whilst the diborane pyrolysis was continuously monitored. Apart from unreacted diborane, only molecular hydrogen was detected as a pyrolysis product suggesting the over-all decomposition



The diborane reaction efficiency (calculated using an equation analogous to Eq. [4]) increased from an initial value of 0.8 to 45% after about 30 sec, remaining at this value for the remaining 270 sec. This suggests that complete boron coverage of the silicon surface was attained after 30 sec. After 300 sec, the specimen temperature was reduced to  $20^\circ\text{C}$ , the diborane leak valve closed and the diborane pumped away. Silane was then admitted to a pressure  $P_S^0 = 1.2 \times 10^{-5}$  Torr and the specimen temperature rapidly increased to  $1035^\circ\text{C}$  whilst the silane pyrolysis was continuously monitored. The time dependence of silane reaction efficiency is shown in Table II where the time zero corresponds to the time at which the specimen temperature reached a stable value of  $T_s = 1035^\circ\text{C}$ . The initial silane reaction efficiency was 100% and the time dependence of  $\alpha$

Table II. Time dependence of silane reaction efficiency,  $\alpha$ , measured on an initially boron-covered surface for  $P_S^\circ = 1.2 \times 10^{-5}$  Torr,  $T_S = 1035^\circ\text{C}$

Time (sec)	0	130	250	370	480	630	760	1000	1330
$\alpha$ (%)	100	27	8	5.5	4.3	3.3	2.7	2.1	1.8

over the first 250 sec is well represented by

$$\alpha = \exp(-10^2 \alpha t) \quad [12]$$

Assuming that the initial rate of fall of  $\alpha$  is the same as the initial rate of coverage of the surface with silicon, a value of  $\sigma = 0.25$  for the initial condensation coefficient of silicon on the boron-covered surface at  $T_S = 1035^\circ\text{C}$  was estimated on the basis of the known impingement rate ( $n_S P_S^\circ$ ) of silane on the surface at  $\alpha = 100\%$ . Even after 1330 sec (after which time the boron layer should have been buried by many silicon layers), the silane reaction efficiency (1.8%) was still considerably higher than the value (0.85%) measured on a clean silicon (111) surface. This difference cannot be attributed to the polycrystallinity of the deposited silicon (see Discussion) and may have been due to boron diffusing to the reaction surface from the buried boron layer.

### Discussion

Although *in situ* analysis by Auger spectroscopy or reflection high energy electron diffraction (RHEED) to establish the level of contamination of the silicon (111) surface in the present work has not been possible, we believe the surfaces on which our study of silane pyrolysis and silicon deposition (in the absence of arsine and diborane) is based to be at least as impurity free as the "clean" ( $<10^{13}$  impurity atoms  $\text{cm}^{-2}$ ) silicon surfaces attained recently by Henderson and Helm (4) by argon ion cleaning. This belief is supported by several experimental results. Firstly, the absence of both three-dimensional nucleation and an induction period, when silicon layers ranging in thickness from a monolayer to several microns were deposited on the initially "flashed" specimen, implies (5) the lack both of surface carbon contamination and of carbon-containing species in the reaction chamber. Secondly, whilst it is conceivable that "flashing" may bring Ni to the specimen surface and change the surface concentration of silicon dopant, this initial surface was rapidly covered with a freshly deposited epitaxial silicon layer during the silane reaction kinetic measurements. In fact, no difference in reaction rates measured on the initially "flashed" and freshly deposited surface could be detected. Finally, electron microscopic and optical examination of layers several micrometers thick, deposited at  $T_S > 800^\circ\text{C}$  in the reaction chamber, revealed that the surfaces of the layers were essentially featureless except for a low density ( $10^2$ - $10^3$   $\text{cm}^{-2}$ ) of stacking faults. No pits or growth pyramids were detected. This suggests that our layers were of similar quality to those deposited by Henderson and Helm under "clean" conditions. Below  $800^\circ\text{C}$ , the quality of the silicon layers progressively decreased and below  $750^\circ\text{C}$  the layers became polycrystalline, probably as a result both of the decreasing surface mobility of silicon adatoms and the correspondingly increasing effect of trace impurities in the silane and from the specimen environment.

The molecular beam sampling data and growth rate measurements provide strong evidence that, on a clean silicon (111) surface, silane decomposition occurs by the reaction



where both the amount of adsorbed silane and the decomposition rate depend linearly on silane pressure. The first-order dependence of adsorbed silane on pressure is typical (9) of Langmuir adsorption behavior

where the surface is only sparsely covered by a weakly adsorbed reactant, in this case silane. Further evidence for weak adsorption of silane on silicon is provided by the fact that only a small fraction of the molecules impinging on the specimen surface decomposed and that adsorption of silane molecules on adjacent sites, leading to disilane production, was a rare event for all specimen temperatures and silane pressures covered in the present work.

As recently pointed out (4), both the low value and temperature dependence of the silicon condensation coefficient can be adequately accounted for on the basis of a step-flow model for silicon growth. In this model, it is assumed that silicon adatoms are incorporated into an atomic step if they diffuse to the step edge before desorbing. The mean distance,  $d$ , which an adatom may diffuse before desorbing is  $\sqrt{D\tau}$ , where  $\tau$  is the mean stay time for adatoms given by

$$\tau \approx 1/\nu \exp(\Delta G_{\text{des}}/RT_S) \quad [13]$$

where  $\nu$  is an atomic frequency and  $\Delta G_{\text{des}}$  is the free energy of activation for adatom desorption.  $D$  is the surface diffusion coefficient given by

$$D \approx a^2 \nu \exp(-\Delta G_{\text{sd}}/RT_S) \quad [14]$$

where  $a$  is the distance of an adatom jump and  $\Delta G_{\text{sd}}$  the free energy of activation for surface diffusion. Then

$$d = \sqrt{D\tau} \approx a \exp[(\Delta G_{\text{des}} - \Delta G_{\text{sd}})/2RT_S] \quad [15]$$

Now, in the presence of step sources such as dislocations, the mean step separation is not expected to be an exponential function of temperature and the temperature dependence of the condensation coefficient will be primarily controlled by  $d$ . Under these conditions, the slope of the  $\ln \sigma$  vs.  $1/T_S$  plot will correspond to  $(\Delta G_{\text{des}} - \Delta G_{\text{sd}})/2R$ . From the data in Fig. 6, we obtain  $\Delta G_{\text{des}} - \Delta G_{\text{sd}} = 14 \pm 5$  kcal mole $^{-1}$  and, assuming that  $\Delta G_{\text{des}}$  equals the Si-Si bond energy (50 kcal mole $^{-1}$ ) (10), then  $\Delta G_{\text{sd}} = 36$  kcal mole with a standard deviation of at least 6 kcal mole $^{-1}$ ; a value intermediate between previous estimates which range from 4.2 kcal mole $^{-1}$  (11) to 58 kcal mole $^{-1}$  (2) and compares reasonably well with Henderson and Helm's (4) recent value of 26 kcal mole $^{-1}$ .

Hirth and Pound (12) have shown that with decreasing temperature the separation between monatomic steps on a close-packed crystal surface approaches a steady-state value of  $d \approx 6\sqrt{D\tau}$ , which corresponds to a low temperature limit of  $\sigma = 1/3$  for the condensation coefficient. From Fig. 6 it is seen that the measured values of  $\sigma$  show no departure from exponential rate behavior with decreasing temperature at  $\sigma \sim 1/3$  and would approach a low temperature limit of unity if this behavior continued at temperatures below  $700^\circ\text{C}$ . This is not inconsistent with the predictions of Hirth and Pound, since as they have pointed out, if the spacing between monatomic ledges, macroscopic steps, or crystal edges becomes smaller than  $\sqrt{D\tau}$ , then the condensation coefficient will tend to unity. This is to be expected in the present case in view of the increasing polycrystallinity of silicon layers grown at  $T_S < 700^\circ\text{C}$ .

Silicon layers deposited under arsenic inhibited growth conditions and those deposited in the presence of more than 0.2% diborane were polycrystalline at all growth temperatures. The possibility that the considerable changes in silane decomposition rate, observed on the addition of arsine or diborane, may not have been due to arsine or diborane directly but to polycrystallinity of the reaction surface can be discounted, however, since no significant (*i.e.*,  $> 5\%$ ) reproducible difference between silane decomposition rate on an epitaxial silicon (111) surface and that on a polycrystalline surface, measured at the same temperature in the absence of arsine or diborane, could be detected.

The inhibition of silane decomposition in the presence of arsine was also observed (3) in an earlier series of investigations by the present author. Moreover, Gupta (15) and Eversteyn and Put (13) have recently observed this effect in conventional atmospheric pressure reactors. The small number  $[\text{As}(\text{solid})/\text{Si}(\text{solid}) < 10^{-3}]$  of arsenic atoms incorporated into silicon layers grown under growth-inhibited conditions in both of these investigations suggests that only a small fraction of the silicon surface is covered with adsorbed arsenic adatoms. Since the silicon surface is sparsely covered with silane, one is led to the conclusion that, for a low coverage of arsenic to produce such a drastic effect on the rate of silane decomposition, either the arsenic atoms block off certain sites on the silicon surface which are active in inducing silane pyrolysis or that adsorbed silane molecules are strongly attracted to adsorbed arsenic atoms and that decomposition is then strongly hindered by strong bonding between the arsenic atom and the activated silane complex. Further studies of the arsenic-influenced silicon surface using RHEED/Auger techniques would be necessary to throw further light on the mechanism involved. Whichever mechanism is appropriate, one may assume that, under inhibited growth conditions, desorption of an arsenic adatom from the surface is the rate-limiting step for silane decomposition. Thus the 18 kcal mole<sup>-1</sup> increase in activation energy for silane decomposition on the addition of arsine may be identified with the activation energy for desorption of arsenic adsorbed on the silicon (111) surface.

The catalytic effect of boron on silane pyrolysis suggests that silane molecules are attracted to boron adatoms on the silicon surface and that decomposition of the silane is not hindered by a strong bond between the activated silane complex and the boron adatom. One possible reason for a weaker bond between boron and the activated silane complex than between arsenic and the complex is that boron (Group 3) is electron deficient compared with arsenic (Group 5). This suggestion is consistent with the fact that phosphine as well as arsine has been found (13) to inhibit silane pyrolysis, whilst diborane has the opposite effect.

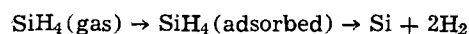
Our conclusions on the mechanism, reaction order, and activation energy for silane pyrolysis on a clean silicon (111) surface are in agreement with those of Henderson and Helm (4). The values of surface reaction efficiency given by Eq. [10], however, are some 40 to 50% higher than those derived from Henderson and Helm's published values [see Table I of Ref. (4)] of the rate constant for silane decomposition. This discrepancy is, however, not surprising in view of the large standard deviations in the values ( $\pm 10\%$  for our own values and at least  $\pm 30\%$  for Henderson and Helm's). Care was taken in the present work to minimize errors in this quantity from possible pyrolysis on the Ta specimen clips and uncertainties in effective reaction surface area. Thus, very thick (2 mm) Ta clips were used which remained cold ( $< 150^\circ\text{C}$ ) even during specimen heating at  $1150^\circ\text{C}$ . The silicon specimen was thin (0.4 mm) so that the ends of the specimen near the clips remained cold and a very sharp temperature gradient existed over only a short length of specimen between the clips and the 80% of specimen surface area over which the temperature was uniform to  $\pm 10^\circ\text{C}$ . The effective reaction surface area was determined from the dimensions of the uniformly deposited silicon layer examined after unloading. It is interesting that noticeable deposition of silicon occurred on only one of the specimen clips, the one furthest down line in the direction of streamline flow between the silane inlet port and sampling slit. This suggests that the deposition resulted not from pyrolysis on the clip but from condensation of silicon desorbed from the specimen and carried down line to the cold Ta clip. This observation supports the conclusion that

the majority of silicon adatoms are desorbed from the growth surface. Direct mass spectrometric detection of the collision-free beam of silicon desorbed from the specimen was not possible in the present work because of the very small solid angle subtended by the specimen at the detector and the large  $m/e = 28$  peak due to fragmentation of silane in the ion source.

In view of the excellent agreement between the present work and that of Henderson and Helm (4), where in both investigations care was taken to establish and maintain clean specimen surface conditions using ultra high vacuum techniques, it seems likely that previously reported (1, 2) departures from first-order kinetics of silane decomposition resulted at least in part from specimen surface contamination. Joyce *et al.* (5) have, for example, shown that even small fractions of a monolayer of carbon contamination can result in considerable changes in silicon growth morphology and have demonstrated that the silicon surfaces on which Joyce *et al.* (2) carried out silane reaction kinetic studies were contaminated by carbon and possibly  $\text{SiO}_2$ . Furthermore, we have found that deliberate carbon contamination of the silicon (111) surface by pyrolysis of ethylene can lead to a reduction in silane pyrolysis rate compared with that on a clean silicon (111) surface. Moreover, in the early work of Joyce and Bradley (1), the silicon growth experiments were carried out in a poor background ( $P_B > 10^{-6}$  Torr) vacuum environment with likely specimen contamination from pump oils and residual gases. In the more recent preliminary molecular beam study (3) of silane pyrolysis involving the present author, first-order reaction kinetics were found but an activation energy for silane decomposition of only  $10 \pm 1$  kcal mole<sup>-1</sup> was reported. We now believe that this value was systematically low by several kcal mole<sup>-1</sup> as a result of contamination of the silicon (111) surface with boron (resulting from an immediately preceding experiment involving heavy boron doping) released from the system walls during specimen heating.

### Conclusions

The pyrolysis of silane on a silicon (111) surface has been investigated mass spectrometrically by molecular beam sampling over a wide silane pressure  $P_S^T = 10^{-5}$  to  $4 \times 10^{-1}$  Torr and specimen temperature ( $T_S = 20^\circ$  to  $1200^\circ\text{C}$ ) range. The results are consistent with the mechanism



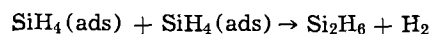
where both the amount of adsorbed silane and decomposition rate depend linearly on silane pressure, indicating sparse coverage of the silicon surface with silane over the pressure and temperature ranges covered.

Values of the surface reaction efficiency,  $\alpha$ , for silane decomposition have been calculated both from the fall in silane pressure in the reaction chamber and from the production of molecular hydrogen. Good agreement between values derived by the two methods was obtained and the reaction efficiency was found to obey the equation

$$\alpha = 5.45 \exp(-17 \times 10^3/RT)$$

An apparent dependence of  $\alpha$  on silane pressure above  $P_S^T = 10^{-3}$  Torr was attributed to the effects of streamline flow in the reaction chamber.

Small quantities of disilane were detected at silane pressures above  $5 \times 10^{-3}$  Torr and were attributed to the bimolecular reaction



where the silane molecules are adsorbed on adjacent surface sites.

Measurements of silicon growth rate as a function of silane pressure up to  $P_S^T = 1$  Torr supported the first-order mechanism for silane decomposition. The condensation coefficient,  $\sigma$ , of silicon adatoms, determined

from measurements of the silicon growth rate as a function of temperature and the surface reaction efficiency, was found to be less than 0.3 over the entire temperature range 700°-1200°C, indicating that the majority of silicon adatoms were desorbed. This behavior was accounted for on the basis of a step-flow model for silicon growth and an activation energy for surface diffusion of  $36 \pm 6$  kcal mole<sup>-1</sup> derived therefrom.

Addition of arsine to the silane was found to inhibit silane pyrolysis whilst, in contrast, addition of more than 1% diborane to the silane considerably enhanced the silane pyrolysis rate.

The results of the present investigation are in excellent agreement with those of Henderson and Helm (4) whose measurements were made on silicon (111) surfaces with  $<10^{13}$  impurity atoms cm<sup>-2</sup>. Previously reported departures, both from first-order silane pyrolysis and from the present activation energy of  $17 \pm 2$  kcal mole<sup>-1</sup>, are attributed, at least in part, to specimen surface contamination.

#### Acknowledgments

The author wishes to acknowledge with thanks the assistance of Dr. W. Bardsley and Dr. J. D. Filby in initiating the present work and is grateful for helpful discussions with Dr. R. M. Logan. The assistance of W. C. Hopper and C. N. Horsfall in the design and construction of the molecular beam chopping mechanism is also acknowledged with thanks. This paper is published with the permission of the Director, Royal Radar Establishment and Copyright Controller HBM Stationery Office.

Manuscript submitted Oct. 24, 1972; revised manuscript received Nov. 19, 1973.

Any discussion of this paper will appear in a Discussion Section to be published in the June 1975 JOURNAL.

All discussions for the June 1975 Discussion Section should be submitted by Feb. 1, 1975.

#### REFERENCES

1. B. A. Joyce and R. R. Bradley, *This Journal*, **110**, 1235 (1963).
2. B. A. Joyce, R. R. Bradley, and G. R. Booker, *Phil. Mag.*, **15**, 1167 (1967).
3. R. F. C. Farrow and J. D. Filby, *This Journal*, **118**, 149 (1971).
4. R. C. Henderson and R. F. Helm, *Surface Sci.*, **30**, 310 (1972).
5. B. A. Joyce, J. H. Neave, and B. E. Watts, *ibid.*, **15**, 1 (1969).
6. K. Fairhurst and G. J. Rich, *Microelectronics and Reliability*, **5**, 15 (1966).
7. F. J. Allen, *J. Appl. Phys.*, **28**, 1510 (1957).
8. P. Potzinger and F. W. Lampe, *J. Phys. Chem.*, **73**, 3912 (1969).
9. A. W. Adamson, "Physical Chemistry of Surfaces," 1st ed., p. 546, Interscience Publishers, Inc. New York (1967).
10. J. Kleinberg, W. Argersinger, and E. Griswald, "Inorganic Chemistry," p. 104, Heath, Boston (1960).
11. E. C. Abbink, R. M. Broudy, and G. P. McCarthy, *J. Appl. Phys.*, **39**, 4673 (1968).
12. J. P. Hirth and G. M. Pound, in "Condensation and Evaporation, Progress in Materials Science," Vol. 11, B. Chalmers, Editor, Macmillan, New York (1963).
13. F. C. Eversteyn and B. H. Put, *This Journal*, **120**, 106 (1973).
14. L. D. Landau and E. M. Lifshitz, "Fluid Mechanics," p. 148, Pergamon, New York (1959).
15. D. C. Gupta, *J. Electron. Mater.*, **1**, 371 (1972).
16. D. Richman and R. H. Arlett, *This Journal*, **116**, 872 (1969).
17. D. T. J. Hurle, R. M. Logan, and R. F. C. Farrow, *J. Crystal Growth*, **12**, 73 (1972).
18. T. E. Lucas, in "Handbook of Vacuum Physics," Vol. 1., p. 131, A. H. Beck, Editor, Pergamon, New York (1964).

## Insulator Charge and $V_{FB}$ Stability of SNOS Capacitors

C. A. Barile, R. C. Dockerty, and A. Nagarajan

IBM System Products Division, East Fishkill Facility, Hopewell Junction, New York 12533

The publication costs of this article have been assisted by the IBM Corporation.

#### ABSTRACT

SNOS capacitors, which have a polycrystalline silicon gate and a nitride-oxide gate insulator, are fabricated using a wide range of insulator thicknesses and high temperature anneals. The insulator charge depends on the oxide and nitride thickness, and the charge level is most sensitive to the final annealing step before metallization. A premetal anneal in H<sub>2</sub> is required to produce a low fast state density.  $V_{FB}$  shifts under bias-temperature stress result from charge accumulation at the nitride-oxide interface.

The metal-insulator-silicon capacitor is a convenient tool for studying the oxidized silicon surface (1-4). This paper describes the characterization of SNOS capacitors which have a polycrystalline silicon gate electrode and a silicon nitride-silicon dioxide gate dielectric. The gate insulator charge,  $Q_{eff}$ , and fast surface-state density,  $N_{fs}$ , depend on the particular process used to fabricate the capacitor. The flatband voltage shift,  $\Delta V_{FB}$ , under bias-temperature stress depends on the fabrication process, stress voltage, stress temperature, and stress time. This shift is caused by the difference in nitride and oxide conductivity (5).

Key words: silicon gate, nitride-oxide dielectric,  $V_{FB}$  stability, fast surface states.

#### Sample Preparation

SNOS capacitors were prepared on 1¼ and 2¼ in. silicon substrates. Capacitors with a boron-doped Si gate were made on n-type substrates while p-type substrates were used to make samples with a phosphorous-doped Si gate. A variety of annealing cycles, film thicknesses, and diffusion processes were studied. Table I outlines the process sequence for capacitors with a B-doped Si gate. The process steps appropriate for a P-doped Si gate are shown in parentheses.

#### Experimental Techniques

The high frequency (1 MHz) MOS C-V technique was used to measure  $t_{eq}$  the equivalent gate dielectric



Table I. Process sequence

1. 2 ohm-cm, n-type substrate (p-type substrate)
2. Gate oxide, 970°C, O<sub>2</sub>
3. Gate nitride, 800°C, NH<sub>3</sub> + SiH<sub>4</sub> + N<sub>2</sub>
4. Nitride anneal
5. Silicon gate, 800°C, SiH<sub>4</sub> + H<sub>2</sub>
6. BBr<sub>3</sub> deposition, 905°C (POCl<sub>3</sub> deposition, 870°C)
7. BBr<sub>3</sub> drive in and reoxidation, 1050°C, O<sub>2</sub> (POCl<sub>3</sub>, 1000°C, steam)
8. Premetal anneal
9. Etch silicon gate pattern (20 mil dots)
10. Backside Al
11. Sinter 400°C, 1 hr, N<sub>2</sub>

thickness, and  $Q_{eff}$ . The equivalent thickness was calculated using Eq. [1]

$$t_{eq} = t_{ox} + t_n \frac{K_{ox}}{K_n} = \frac{K_{ox}\epsilon_0 A_g}{C_{max}} \quad [1]$$

$Q_{eff}$  was obtained from Eq. [2]

$$Q_{eff} = -\frac{C_{max}}{A_g} [V_{FB} - \phi_{ms}] \quad [2]$$

The following values were used for the gate to substrate work function:  $\phi_{ms} = +0.83$  (n substrate, B-doped Si gate) and  $\phi_{ms} = -0.80$  (p substrate, P-doped Si gate).

The fast surface-state density was measured by the quasi-static technique (6). Data was obtained by sweeping from inversion to accumulation at a sweep rate of 0.05 V/sec. The value quoted for the fast state density is the number of states per cm<sup>2</sup> between  $\psi_s = 0$  and  $\psi_s = 2\phi_F$ .

All wafers used for  $V_{FB}$  stability studies were first checked for mobile ion contamination by the high temperature quasistatic C-V technique (7). In this technique, the capacitor is heated to 200°C and a ramp voltage ( $f = 0.02$  Hz) is applied. As the ramp voltage decreases from +5 to -5V, the current through the capacitor,  $I = A_g C_{mos} dv/dt$ , and the gate voltage are recorded on an x-y plotter. Curve 1 of Fig. 1 shows a typical trace. When the ramp voltage reaches -5V a +10V (for  $t_{eq} = 500A$ ) fixed bias is applied to the gate as the ramp voltage is removed. After the sample is stressed for 75-175 sec the fixed bias is removed and the ramp voltage, which is then +5V, is reapplied. The current-voltage curve is again recorded as the ramp sweeps from +5 to -5V. The presence of mobile ions is revealed by the bump on the post-stress curve (curve 2). The mobile ion density per cm<sup>2</sup>,  $N_i$ , is

$$N_i = \frac{AK_1 K_t}{qA_g} \left[ 1 + \frac{t_n K_{ox}}{t_{ox} K_n} \right] \quad [3]$$

In Eq. [3]  $K_1$  is the vertical scale of Fig. 1 in amperes/inch,  $K_t$  is the number of seconds/inch for the hori-

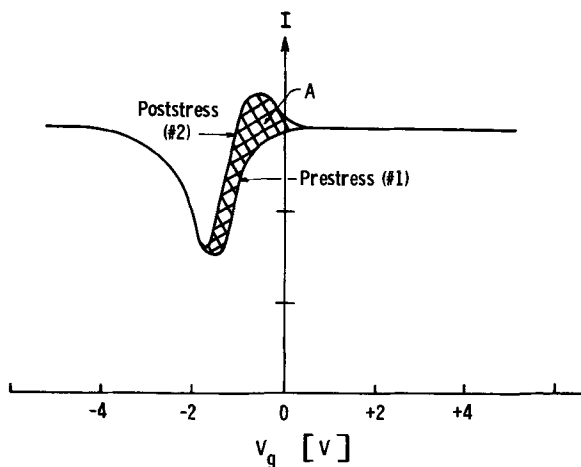


Fig. 1. Mobile ionic charge measurement at 200°C

zontal scale, and  $A$  is the cross-hatched area in square inches. The factor  $[1 + t_n K_{ox}/t_{ox} K_n]$  appears in Eq. [3] because the mobile ions move only in the SiO<sub>2</sub> layer.

After the mobile ion density was checked to be less than  $5 \times 10^{10}$  cm<sup>-2</sup>,  $V_{FB}$  shifts were measured by the following procedure. A high frequency C-V was measured before the sample was stressed in the dark at elevated temperature. After the stress was completed the sample was rapidly cooled to room temperature under bias and a second C-V trace was made.

### Experimental Results

$Q_{eff}$  and  $N_{fs}$  were measured for a variety of annealing cycles as well as for several oxide and nitride thicknesses. All nitride and premetal anneals were done for 0.5 hr.

The following nitride anneals were used: no anneal, H<sub>2</sub> at 900°C, N<sub>2</sub> at 1050°C, and N<sub>2</sub> at 1100°C. These anneals had no significant effect on either  $Q_{eff}$  or  $N_{fs}$ . This step was therefore eliminated from the process sequence and the remainder of the data in this paper was obtained from devices processed with no nitride anneal.

The premetal anneal greatly influences  $Q_{eff}$  and  $N_{fs}$ . Table II shows  $Q_{eff}$  and  $N_{fs}$  for various premetal anneals. Several conclusions are evident from this table: (i) A N<sub>2</sub> anneal produces a low or negative  $Q_{eff}$  and a high  $N_{fs}$ . The H<sub>2</sub> anneal results in a low  $N_{fs}$ . (ii) The capacitor with a P-doped Si gate has a lower  $Q_{eff}$  than the corresponding sample with a B-doped Si gate. (iii) For samples with a B-doped Si gate, the 900/300 dielectric has a lower  $Q_{eff}$  than the 300/300 insulator.

Table III contains additional data on the  $t_{ox}$  and  $t_n$  dependence of  $Q_{eff}$ . This table shows the same trend as Table II, that is,  $Q_{eff}$  decreases as  $t_{ox}$  increased, and  $t_n$  is held constant. (The devices represented in this table had a 800°C premetal anneal in H<sub>2</sub>.) All data in the remainder of the paper, with the exception of Table V, were obtained from capacitors processed with the 800°C premetal anneal in H<sub>2</sub>.

Figures 2 and 3 show that  $Q_{eff}$  is a function of the silicon gate thickness and diffusion junction depth for devices with a B-doped Si gate.  $Q_{eff}$  increases as  $X_j$  increases or  $t_{polySi}$  decreases. The value of  $X_j$  is the junction depth in a single-crystal silicon monitor wafer. Except for these two figures, all data in the paper were obtained from capacitors with a silicon gate thickness of 0.7 μm and  $X_j = 1.25$  μm.

Table II.  $Q_{eff}$  and  $N_{fs}$  for various premetal anneals

Gate dopant	Oxide thickness (Å)	Nitride thickness (Å)	$Q_{eff}/q$ (cm <sup>-2</sup> )	$N_{fs}$ (cm <sup>-2</sup> )	Premetal anneal* (°C)
B	300	300	$3.7 \times 10^{11}$	$0.5 \times 10^{11}$	H <sub>2</sub> , 800
B	300	300	3.3	0.5	H <sub>2</sub> , 900
B	300	300	0.1	5.0	N <sub>2</sub> , 900
B	300	300	-1.3	7.0	N <sub>2</sub> , 1050
B	900	300	3.1	none	none
B	900	300	2.5		H <sub>2</sub> , 800
B	900	300	2.3		H <sub>2</sub> , 900
P	300	300	1.3	0.5	H <sub>2</sub> , 800

\* All anneals are 0.5 hr.

Table III.  $Q_{eff}$  for units with a B-doped Si gate\*

Oxide thickness (Å)	Nitride thickness (Å)	$Q_{eff}/q$ (cm <sup>-2</sup> )	$N_{fs}$ (cm <sup>-2</sup> )
400	100	$4.3 \times 10^{11}$	$< 0.5 \times 10^{11}$
400	200	3.1	$< 0.5$
300	300	3.7	$< 0.5$
400	300	3.4	$< 0.5$
600	300	3.1	$< 0.5$
900	300	2.5	$< 0.5$

\* 800°C premetal anneal in H<sub>2</sub> and no nitride anneal.



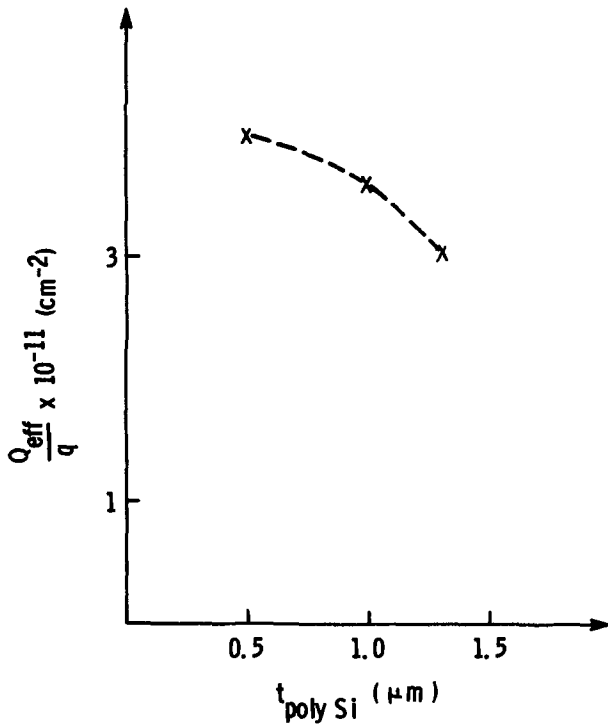


Fig. 2. Insulator charge vs. polycrystalline silicon thickness

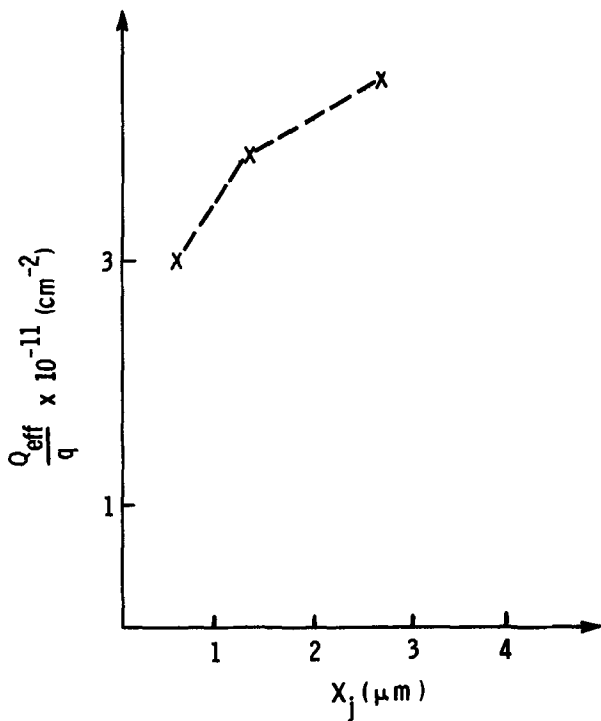


Fig. 3. Insulator charge vs. junction depth

The  $V_{FB}$  stability of SNOS capacitors with a boron-doped Si gate was measured for a wide range of bias temperature stress conditions. Figures 4, 5, and 6 show the time, temperature, and voltage dependence of  $\Delta V_{FB}$  for capacitors with a 300/300 gate insulator. These devices had a 800°C premetal anneal in  $H_2$  and no nitride anneal. Figure 7 shows  $\Delta V_{FB}$  vs.  $t$  for a similar device which had a P-doped Si gate. Note that  $\Delta V_{FB}$  (+ stress)  $>$   $\Delta V_{FB}$  (- stress) for capacitors with a B-doped Si gate whereas the reverse is true for a P-doped gate electrode.

The data in Fig. 4-7 can be described by the following equation

$$\Delta V_{FB} = C \exp(-\beta \Delta H) (V_G)^m (t)^n \quad [4]$$

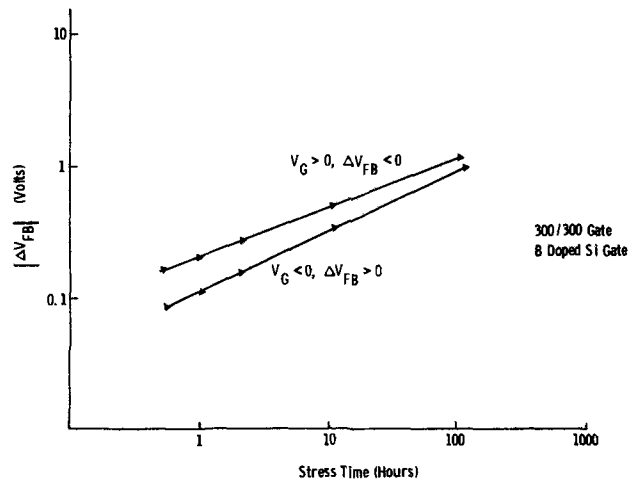


Fig. 4.  $V_{FB}$  shift for stress at 200°C,  $\pm 10V$

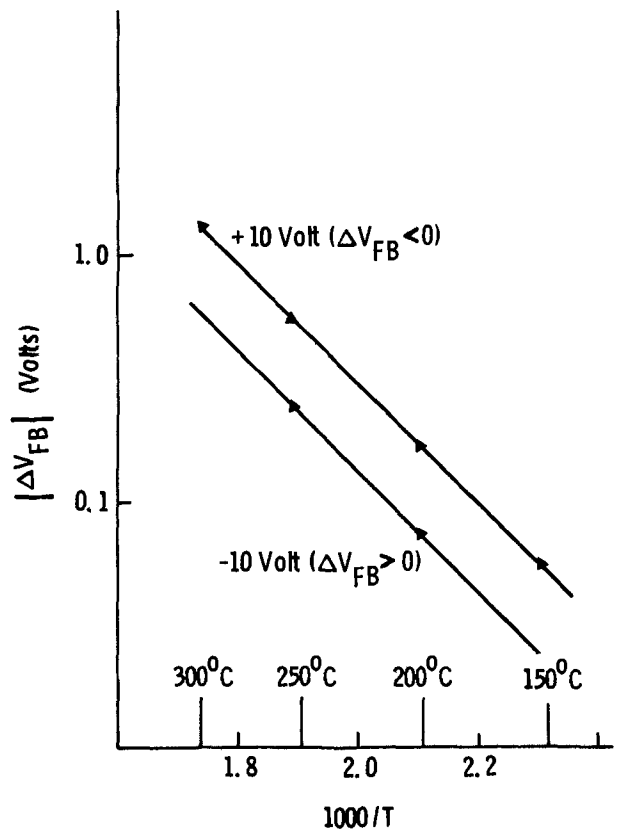


Fig. 5.  $\Delta V_{FB}$  temperature dependence for a 30 min stress

This equation gives a good fit to the experimental data over the following range of stress conditions:  $V_G$ , 8-20V (for the 300/300 gate);  $t$ , 0.5-500 hr;  $T$ , 85°-250°C. The parameters calculated from capacitors with a 300/300 gate dielectric are:  $\Delta H$ , 0.35-0.45 eV;  $m$ , 3.5-4.0 eV;  $n$ , 0.35-0.5 eV.

Table IV shows the dependence of  $\Delta V_{FB}$  on the  $NH_3$ : $SiH_4$  ratio used to deposit the silicon nitride. The data indicates that improved stability is achieved by using a higher  $NH_3$ : $SiH_4$  ratio. With the exception of the devices represented in Table IV, all capacitors were fabricated with  $NH_3$ : $SiH_4 = 133:1$ .

Table V shows the effect of various nitride and premetal anneals on the  $V_{FB}$  stability. The nitride anneals have little impact on  $\Delta V_{FB}$ , whereas the premetal anneal in  $N_2$  greatly increases the  $V_{FB}$  shift for positive stress. Table VI contains the results of  $V_{FB}$  stability measured on capacitors with various oxide and nitride thicknesses. An improvement in  $V_{FB}$  stability is achieved by reducing  $t_n$ .  $V_{FB}$  stability is discussed in

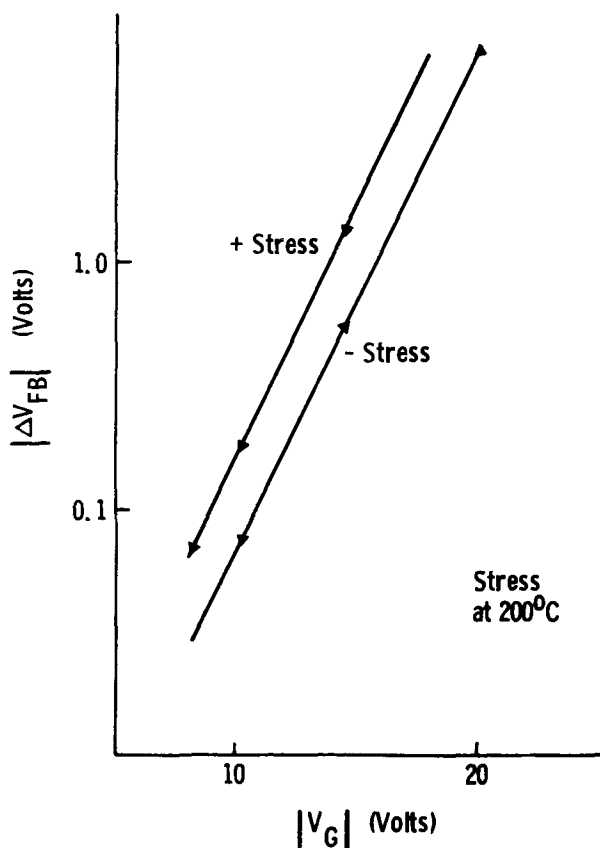


Fig. 6.  $\Delta V_{FB}$  voltage dependence for a 30 min stress

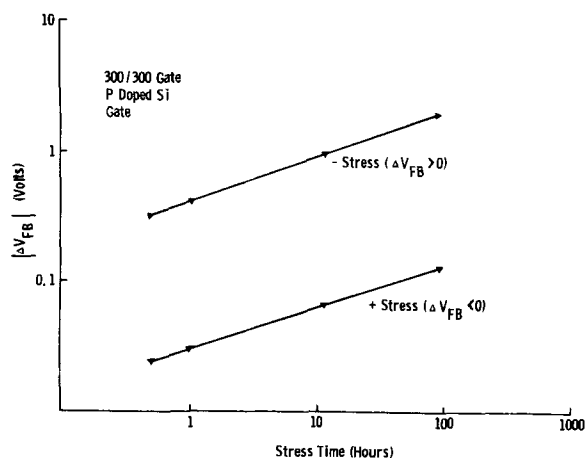


Fig. 7.  $V_{FB}$  shift for a stress at 200°C,  $\pm 10V$

the next section, and  $V_{FB}$  shifts will be shown to result from the dual dielectric instability.

**Discussion**

Several process parameters affect  $Q_{eff}$  of the SNOS capacitors which have a B-doped Si gate. A nitride anneal in  $H_2$  or  $N_2$  has little impact on  $Q_{eff}$ . It is felt that this anneal does not influence  $Q_{eff}$  because the devices are exposed to subsequent high temperature processing during the diffusion and these process steps wash out any effects of the nitride anneal.

The premetal anneal, which is the last high temperature process step, has a significant effect on  $Q_{eff}$  and  $N_{fs}$  (see Table II). A premetal anneal in  $N_2$  produces a low or negative  $Q_{eff}$  but a high  $N_{fs}$ . The low or negative  $Q_{eff}$  is produced by negative charges trapped in the acceptor-like surface states which are located near the Si conduction band edge. A low  $N_{fs}$  results if a premetal anneal in  $H_2$  is used. Creation and reduc-

Table IV.

a.  $\Delta V_{FB}$  for a +10V stress at 200°C

$NH_3/SiH_4$	$\Delta V_{FB}$ (0.5 hr) (V)	$\Delta V_{FB}$ (40 hr) (V)
2/1	-0.95	-
133/1	-0.17	-0.80
10,000/1	-0.30	-0.66

b.  $\Delta V_{FB}$  for a -10V stress at 200°C

$NH_3/SiH_4$	$\Delta V_{FB}$ (0.5 hr) (V)	$\Delta V_{FB}$ (40 hr) (V)
2/1	+0.90	-
133/1	+0.8	+0.64
10,000/1	+0.28	+0.39

Table V.

a.  $\Delta V_{FB}$  for a 12.5V 17 hr, 200°C stress

Nitride anneal	$\Delta V_{FB}$ (+ stress) (V)	$\Delta V_{FB}$ (- stress) (V)
None	-1.15	+0.92
900°C, hydrogen	-1.30	+0.90
1050°C, nitrogen	-1.40	+0.93
1100°C, nitrogen	-1.20	+0.93

b.  $\Delta V_{FB}$  for a 10V, 17 hr, 200°C stress

Premetalization anneal	$\Delta V_{FB}$ (+ stress) (V)	$\Delta V_{FB}$ (- stress) (V)
800°C, hydrogen	-0.6	+0.45
900°C, nitrogen	-4.2	+0.50

Table VI.  $\Delta V_{FB}$  for a stress at  $E_{ox} = 2 \times 10^6$  V/cm, 200°C, 30 min

Oxide thickness (Å)	Nitride thickness (Å)	$\Delta V_{FB}$ (+ stress) (V)	$\Delta V_{FB}$ (- stress) (V)
300	300	-0.17	+0.08
400	200	-0.13	+0.03
400	100	-0.085	+0.025

$$E_{ox} = \frac{V_G}{t_{ox}}$$

$$t_{eq} = t_{ox} + t_n \frac{K_{ox}}{K_n}$$

$$\Delta V_{FB} = \frac{\Delta Q_{no}}{K_{no}} t_n$$

tion of fast states by  $N_2$  and  $H_2$  annealing has been reported by Deal *et al.* for MNOS capacitors (8).

An increase in the polysilicon gate thickness or a reduction in  $X_j$  reduces  $Q_{eff}$  of SNOS capacitors with a B-doped Si gate (see Fig. 2 and 3). A similar effect was reported by Fujimoto *et al.* for SNOS capacitors with a P-doped Si gate (9). The reduction in  $Q_{eff}$  is achieved by minimizing the boron penetration into the  $Si_3N_4$ .

The dependence of  $Q_{eff}$  on  $t_{ox}$  and  $t_n$  indicates that the charge at the nitride-oxide interface,  $Q_{no}$ , makes a major contribution to  $Q_{eff}$ . Equation [5] relates  $Q_{no}$  to  $Q_{eff}$  assuming that  $Q_{no}$  is the only charge in the gate dielectric

$$Q_{eff} = \frac{t_n}{t_{eq}} \frac{K_{ox}}{K_n} Q_{no} \quad [5]$$

The trend of data from Table III (except for  $t_{ox} = 400\text{Å}$ ,  $t_n = 100\text{Å}$ ) agrees with Eq. [5], i.e., an increase in  $t_{ox}$  or a reduction in  $t_n$  reduces  $Q_{eff}$ .

The  $V_{FB}$  stability data cannot be explained by mobile ion motion or by slow surface state trapping. The mobile ion density is less than  $5 \times 10^{10} \text{ cm}^{-2}$ . This density can produce a maximum  $V_{FB}$  of 75 mV for the capacitors with a 300/300 gate dielectric.  $V_{FB}$  shifts are observed in the 300/300 gate which are much larger than 75 mV. The absence of hysteresis in the room temperature C-V curves is indicative of a small slow surface-state density. Slow surface-state trapping produces a positive  $V_{FB}$  shift under positive stress and a negative  $V_{FB}$  shift for negative stress. However, the

experimental data is of the opposite polarity, i.e.,  $\Delta V_{FB} > 0$  for negative stress, and therefore slow-state trapping cannot produce the observed  $V_{FB}$  shifts.

The dual dielectric instability model predicts that charge accumulates at the nitride-oxide interface when the capacitor is biased because  $J_n \neq J_{ox}$ . For our samples  $J_n \gg J_{ox}$  when the bias is first applied. In this case a positive stress produces a negative  $\Delta V_{FB}$  and conversely. As charge accumulates at the interface,  $E_{ox}$  is increased and  $E_n$  is reduced until  $J_{ox} = J_n$ . If the initial current densities are substantially different, a large amount of charge will accumulate at the nitride-oxide interface before the  $V_{FB}$  shift saturates.

The dual dielectric instability model predicts a  $V_{FB}$  shift which is a function of the stress temperature, time, and voltage (5, 10, 11). This behavior is observed in the SNOS capacitors. The model predicts a reduction in  $\Delta V_{FB}$  if the nitride resistivity is increased. This increase has been accomplished in three ways: by using a high  $NH_3:SiH_4$  ratio during the nitride deposition (12), by using a thick polysilicon gate, and by using a shallow B diffusion to dope the gate electrode. The last two methods minimize the reduction in nitride resistivity due to boron penetration into the  $Si_3N_4$ . Improved  $V_{FB}$  stability was also achieved by reducing the nitride thickness. This improvement is expected according to Eq. [6] which relates  $\Delta V_{FB}$  to  $\Delta Q_{no}$

$$\Delta V_{FB} = - \frac{t_n}{K_n \epsilon_0} \Delta Q_{no} \quad [6]$$

A detailed knowledge of the oxide and nitride conductivity vs. field curves, the various barrier heights and the trap distributions throughout the nitride-oxide insulator is necessary to predict the time, temperature, and voltage dependence of the  $V_{FB}$  shift. No such attempt was made in this study. However, the qualitative agreement between the experimental data and the model gives good evidence that the dual dielectric instability is the cause of the  $V_{FB}$  shifts in our SNOS capacitors.

#### Acknowledgments

The authors wish to acknowledge the support of the East Fishkill facility, especially P. Stern and R. Holmwood, for processing the wafers and the technical assistance of N. Anantha, D. Fouts, P. Lin, and E. Zachos. Many of the measurements were made by J. Nodich and R. Smith.

Manuscript submitted June 19, 1973; revised manuscript received ca. Dec. 10, 1973.

Any discussion of this paper will appear in a Discussion Section to be published in the June 1975 JOURNAL. All discussions for the June 1975 Discussion Section should be submitted by Feb. 1, 1975.

#### LIST OF SYMBOLS

$A_g$	gate electrode area ( $cm^2$ )
$C_{max}$	maximum capacitance (farads)
$C_{mos}$	MOS capacitance per unit area (farads/ $cm^2$ )
$E_{ox}, E_n$	oxide, nitride electric field (V/cm)
$J_{ox}, J_n$	oxide, nitride current per unit area (A/ $cm^2$ )
$K_{ox}, K_n$	oxide, nitride relative dielectric constant
$q$	$1.6 \times 10^{-19}$ (coulombs)
$\Delta Q_{no}$	change in $Q_{no}$ (coulombs/ $cm^2$ )
$t_{ox}, t_n$	oxide, nitride thickness (cm)
$t_{polySi}$	silicon gate electrode thickness (cm)
$t$	stress time (hr)
$T$	temperature ( $^{\circ}K$ )
$V_{FB}$	flat band voltage (volts)
$V_G$	gate to substrate voltage (volts)
$\beta$	$q/kT$
$\epsilon_0$	$8.85 \times 10^{-14}$ (farads/cm)
$\phi_F$	$kT/q \ln Na/ni$
$\psi_s$	band bending (volts)

#### REFERENCES

1. A. S. Grove, B. E. Deal, E. H. Snow, and C. T. Sah, *Solid-State Electron.*, **8**, 145 (1965).
2. P. V. Gray, *Proc. IEEE*, **57**, 1543 (1969).
3. B. E. Deal, A. S. Grove, and E. H. Snow, *This Journal*, **114**, 266 (1967).
4. B. E. Deal, P. J. Fleming, and P. L. Castro, *ibid.*, **115**, 300 (1968).
5. D. Frohman-Bentchkowsky and M. Lenzlinger, *J. Appl. Phys.*, **40**, 3307 (1969).
6. M. Kuhn, *Solid-State Electron.*, **13**, 873 (1970).
7. D. Kerr, Proc. of the Int. Conf. on Prop. and Use of M.I.S. Structures, Grenoble (1969).
8. B. Deal, E. Mackenna, and P. Castro, *This Journal*, **116**, 997 (1969).
9. S. Fujimoto, M. Mackawa, Y. Inoue, and Y. Haneta, Extended Abstracts, Electrochem. Society Meeting, Washington (1971).
10. F. A. Sewell, H. A. R. Wegener, and E. T. Lewis, *Appl. Phys. Letters*, **14**, 45 (1969).
11. E. Ward, R. Wakefield, and J. Cunningham, IEEE Int. Electron Dev. Conf., late paper 17.6, Washington (1970).
12. V. Y. Doo, D. R. Kerr, and D. R. Nichols, *This Journal*, **115**, 61 (1968).

# Preparation and Performance of Dendritic Heat Sinks

S. Oktay and A. F. Schmeckenbecher

IBM System Products Division, East Fishkill Facility, Hopewell Junction, New York 12533

The publication costs of this article have been assisted by the IBM Corporation.

## ABSTRACT

A new heat-transfer surface, i.e., a "dendritic" heat sink, is presented. The preparation of the dendrites by forming a "brush" of nickel powder on a surface with a magnet and plating them in place with electroless nickel to form a dendritic finned surface is described. It is shown that, in addition to increased heat-transfer rates due to the compact heat-transfer area, the unique characteristics of the cavities on a dendritic surface improve the boiling mode of heat-transfer. Despite their small size, dendritic heat sinks in a FC88 cooling liquid can dissipate about 6W from the surface (about  $0.1 \times 0.1$  in. or  $2.54 \times 2.54$  mm) of a silicon chip at 45°C. The thermal performance of the dendritic structure and the reliability of the dendritic heat sinks are discussed.

A new heat-transfer surface, called a "dendritic" heat sink, is presented and analyzed. The dendritic structure is prepared by forming a "brush" of nickel powder on a surface with a magnet and plating the needles of the brush with electroless nickel to form a dendritic finned surface. Dendritic structures are found to be especially useful for providing heat sinks on small components such as integrated circuit chips (Fig. 1).

In addition to the increased heat-transfer rates due to the extended heat-transfer area that the dendritic heat sinks provide, it is found that the unique characteristics of the cavities on a dendritic surface improve the boiling mode of heat-transfer. The nature of these cavities and the associated surface roughness are analyzed. The dendritic structure forms "reentrant" type cavities (Fig. 2), which heretofore have not been possible to manufacture on a large scale, and which remain active even in the absence of noncondensable gases. Consequently, the dendritic cavities provide numerous nucleation sites continuously, thereby allowing boiling at lower wall superheat than that possible with conventional engineering surfaces. The performance of these cavities is analyzed from theoretical considerations and related to experimental observations.

Thermal tests show that the cooling efficiency of the dendritic structure in "FC-88" (trademark of Minnesota Mining and Manufacturing Company) cooling liquid is as good or better than that of a solid molybdenum<sup>1</sup> stud which has up to 20 times the weight of the dendritic structure.

It is also noted in Fig. 3 that the bubble nucleation on the dendrites is initiated close to the heated surface while in a stud or in a thick chip the heat must be conducted through a relatively large metal mass before it can be dissipated by boiling.

The reliability aspects of the dendritic heat sinks are also discussed. For example, it is shown that due to the light weight of the dendrites, the projected reliability of flip-chip solder joints to the chip package ("C-4" joint) (1) is improved by 17% over the conventional copper heat sink. The reliability of dendrites is discussed with respect to the results of various environmental tests. Mechanical tests indicated that as much as 1300g are required to shear dendrites from the back of a 2.125 mm (85 mil) chip.

**Key words:** boiling heat-transfer, electrolessly plated heat sink, electronic components cooling, nucleation sites.

<sup>1</sup>Moly heat sinks were used because of their better thermal expansion characteristics to match that of silicon. While a better match is expected to yield better mechanical (hence, thermal) integrity at the metal-metal interface, it should also be noted that even a better heat conductor such as a copper heat sink with the same surface characteristics as moly is expected to give comparable boiling heat-transfer coefficients at the metal-liquid interface, which is the primary regime with which we are concerned. Also no attempt was made to compare conduction across the plated interface to other type bonded interfaces.

## Preparation of Dendritic Heat Sinks

A "skeleton" structure is formed by aligning magnetic powder such as low expansion NiFe alloys in a magnetic field, followed by a plating step which fixes the powder in position and joins the structure to the chip.

To assure good adhesion of the electroless nickel plate to the silicon of the chip, the back of the chip is roughened by sandblasting, plated with a flash of palladium by a dip in 0.1% palladium chloride solution, and annealed at 125°-350°C. Initially the device side of the chip is covered by a layer of a resist material for protection against sensitizing and the subsequent plating steps.

A diverging magnetic field is then generated in the area above the chip by placing the pointed pole of a bar magnet underneath the chip. A small amount of a ferromagnetic powder is placed on the chip. In the diverging field the powder particles are attracted toward the chip. An attracted particle becomes a magnet by itself, attracting more particles. Strings of particles result, which stand up away from the surface of the chip. Adjacent strings repel each other since they are magnetized with their north and south poles in the same direction (Fig. 4). Near the pole of the bar magnet, the strings of particles are forced closer to each other by the stronger field at the pole. A brushlike structure results. The height and width of the structure can be controlled by the amount and the size of the powder particles, by mechanically holding the particles in a mold (Fig. 5), and by the shape and spacing of the magnet.

After the "skeleton" brush has been formed, the assembly is immersed into an electroless plating bath and plated with a 10-25  $\mu\text{m}$  ( $\frac{1}{2}$ -1 mil) thick coat of metal, e.g., nickel. The chemical reducing agent in the electroless bath supplies the electrons for the reduction of the metal salt at the catalytic surface. No electrodes are required and the bath has a "throwing power," i.e., the ability to plate in recesses, cavities, etc. which is limited only by the necessity to resupply the ions of the metal and the reducing agent. Convection and diffusion in the plating bath usually are sufficient to supply the surfaces of the ferromagnetic particles and of the semiconductor chips with the metal ions and reducing agent, resulting in a metal deposit of uniform thickness, even in recesses between the powder particles. Consequently, mechanically strong and well-bodied needles ("dendrites") are formed by a relatively thin metal layer. The plating metal layer closely duplicates the roughness of the ferromagnetic particles as well as cavities formed by the particles. The powder particles, before being put on the chip, are activated for electroless plating by the usual procedures, such as a dip in a palladium chloride solution.

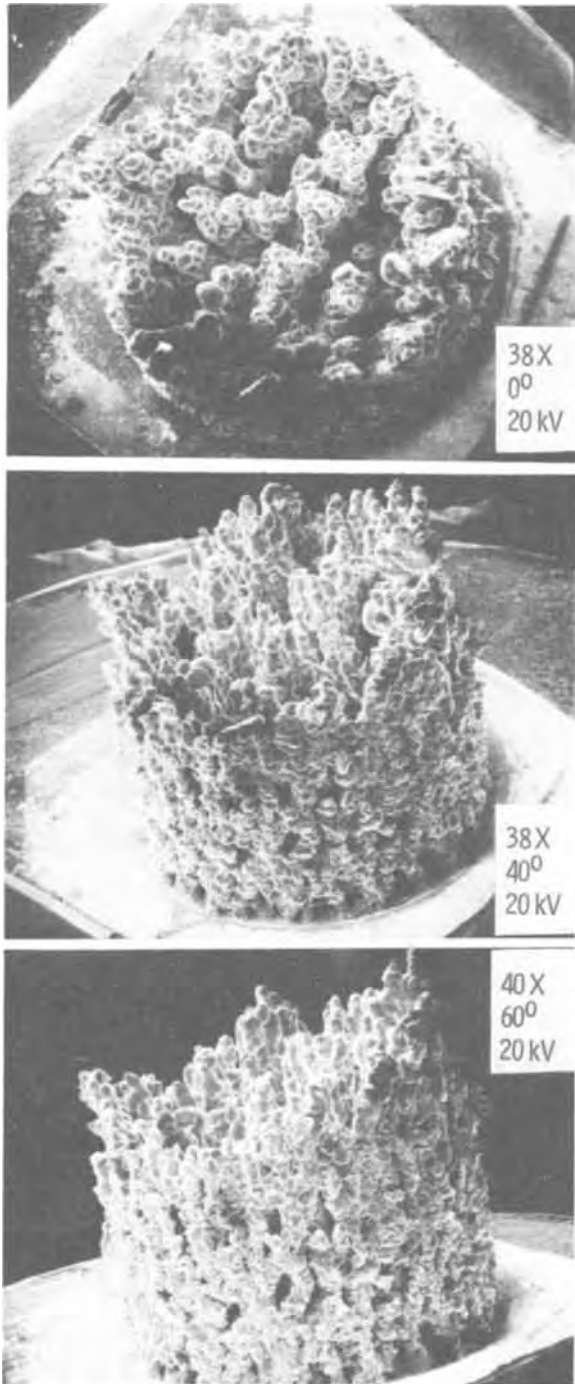


Fig. 1. SEM micrograph of dendritic heat sink

The plating fixes the strings of powder particles in position and joins them to the surface of the chip.

Heat sinks have been formed on integrated circuits by using nickel powder of different particle sizes [carbonyl nickel powder of 2-4  $\mu\text{m}$  diameter, reduced nickel powder of irregular particle size and shape from Fisher Scientific Company, or from Baker and Adamson Chemical Company, "Kovar" (low expansion Fe, Ni, Co alloy) powder from B.S.A. Metals Powders Limited, Birmingham, England, and others].

Figures 6-8 give a scanning electron microscope picture and a microsection of a typical heat sink on a chip formed by the above method.<sup>2</sup>

Many dendritic heat sinks can be formed simultaneously on a wafer before dicing if an electromagnet is used with a pole piece which is somewhat larger than the wafer and which has a small individual pole at

<sup>2</sup> Scanning electron microscope pictures were taken by E. K. Brandis, IBM Corporation, Hopewell Junction, New York 12533.

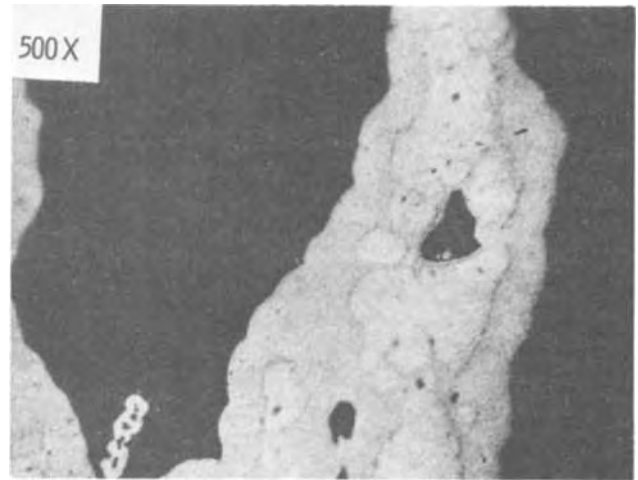


Fig. 2. Microsectioning of a dendrite with a "reentrant" cavity (500X).

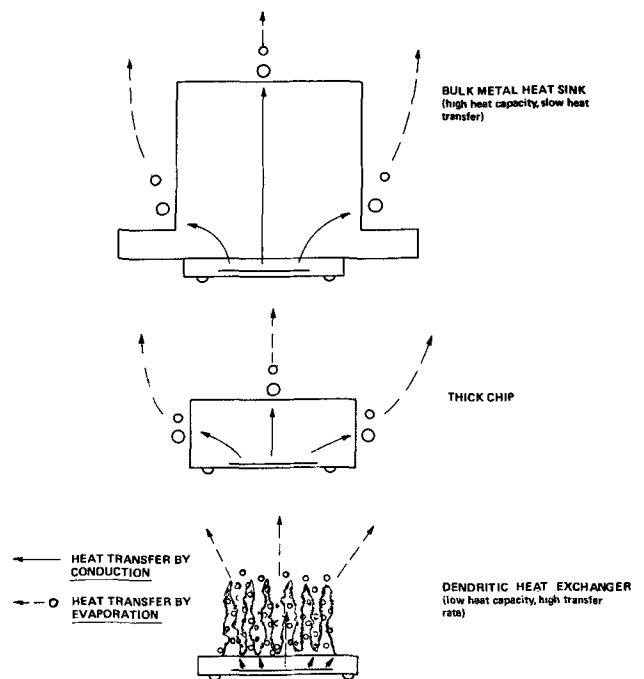


Fig. 3. Bubble nucleation sites on different heat sinks

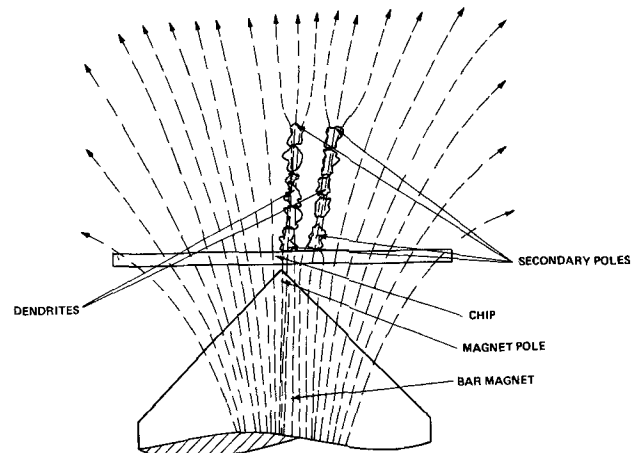


Fig. 4. Magnetic alignment of ferromagnetic particles

each chip site on the wafer (Fig. 9). With the magnet turned off, a layer of nickel powder of uniform thickness is deposited on the wafer by forming a suspension

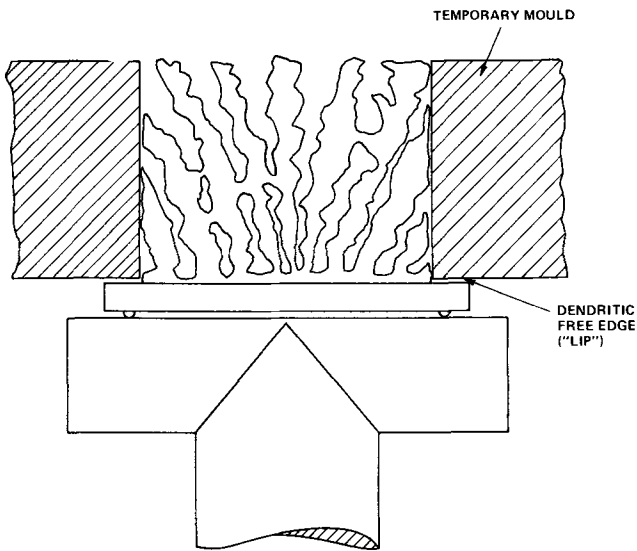


Fig. 5. Preparation of dendritic heat sinks

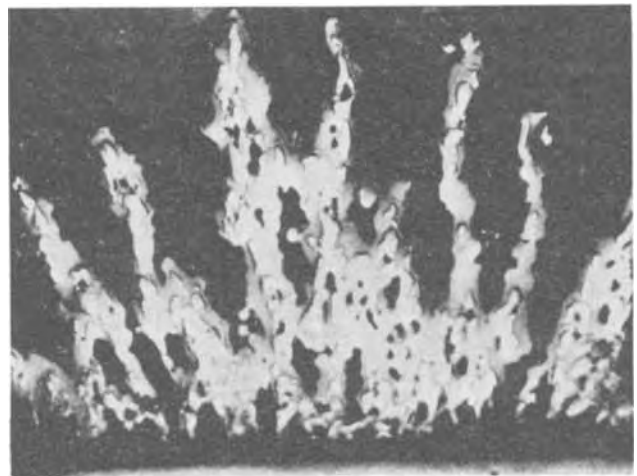


Fig. 8. Microspeciation of a dendritic heat sink 100X SEM photograph.

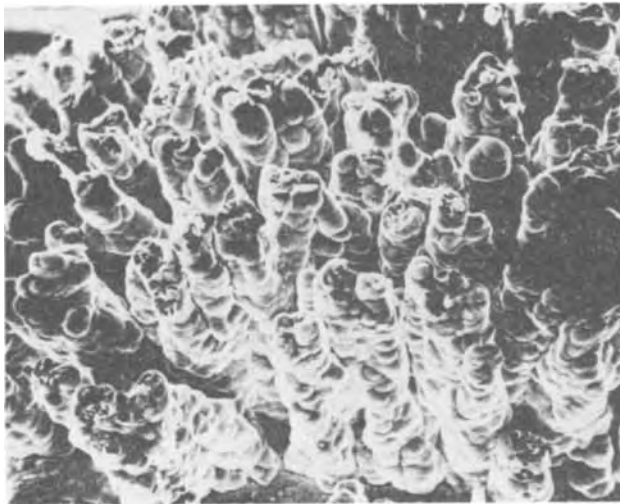


Fig. 6. Dendritic heat sink 81X SEM photograph

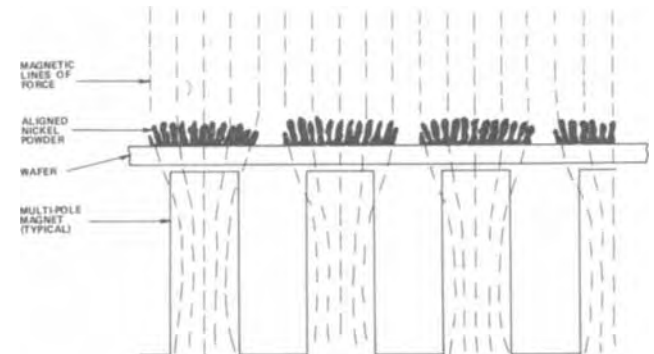


Fig. 9. Multiple plating of dendritic heat sinks

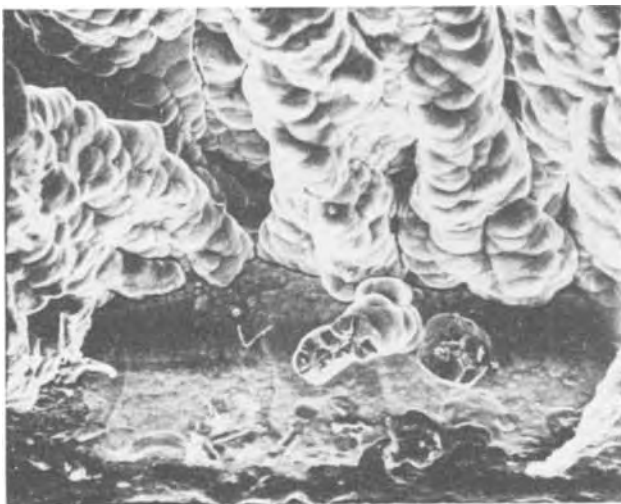


Fig. 7. Dendritic heat sink 100X SEM photograph

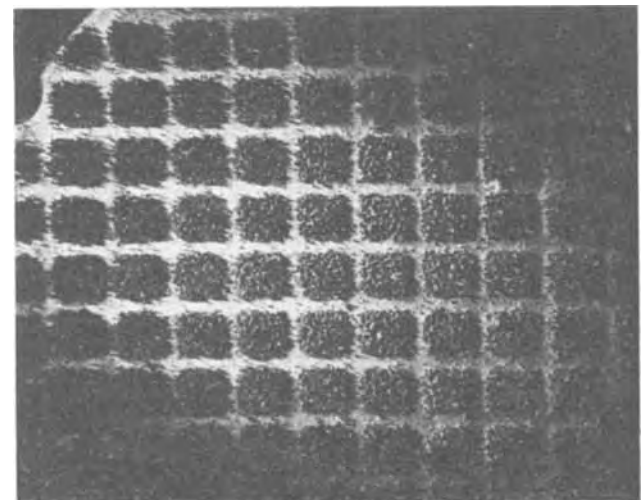


Fig. 10. Dendritic heat sink formed on a wafer

of the powder in a liquid and allowing the powder to settle on the wafer. When the magnet is turned on, the powder particles are attracted to the individual poles and can be plated as described to form a heat sink on each chip site. Figure 10 shows a wafer with dendritic heat sinks formed by this procedure.

Wafers with dendritic heat sinks have been diced by the standard procedure of slurry dicing. The cuts were clean with no damage to the dendrites (Fig. 11).

**Thermal Evaluation of Dendritic Heat Sinks and Analysis of Dendritic Structures**

Thermal evaluation of dendritic heat sinks was performed on chips of various sizes which are noted below. The dendrites were approximately 0.75 mm (30 mils) high and made out of nickel powder. The chips were C-4 (1) joined and powered, and the chip temperatures were obtained from measurements made of the  $V_{BE}$  of the diodes in the chips. The diodes were first calibrated.

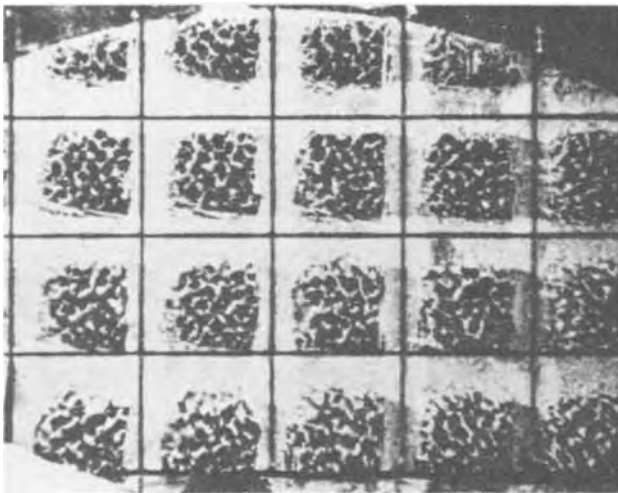


Fig. 11. Wafers with dendritic heat sink after dicing

A series of thermal tests on dendritic heat sinks, as well as on slotted solid moly studs for comparison, was made under identical conditions. The reference temperature of the underside of the substrate directly below the chip was monitored with a thermocouple.

Figure 12a shows that the chip temperature on the dendrite was about 2°C lower than the moly stud. Substrate temperatures were the same for both modules. Initial boiling of the dendrite and stud were 0.25 and 0.50W, respectively. Both modules were boiling throughout at 1W. The "sawtooth" effect (described later) was only 1°-2°C in each case.

Although the dendrites are 1/10 and 1/20 the weight of the stud, there is approximately 3X the surface area.<sup>3</sup> The large surface area, cavities, and crevices contribute to the thermal efficiency of this heat sink. The geometry of the cavities is also important for heat dissipation when FC-88 becomes contaminated.

Thermal studies made in a multiliquid (2) system ("Coolanol 45" trademark of Monsanto Chemical Company over "FC-88" trademark of Minnesota Mining and Manufacturing Company) have led to some interesting cooling characteristics. Figure 12b shows a thermal comparison of a moly stud with a dendritic heat sink. A large "sawtooth effect" (large drop in temperature when boiling starts) is observed only with the moly stud. It was found that the secondary coolant (Cool-

\*Surface profile measurements made by Micromeritics Instruments Corporation, Norcross, Georgia, yielded the following results on the dendritic heat sinks: specific surface area/weight, 219 cm<sup>2</sup>/g; specific surface area/unit, 2.19 cm<sup>2</sup>/dendrite. These numbers should be compared with those for the stud: 2.55 cm<sup>2</sup>/g and 0.57 cm<sup>2</sup>/stud, respectively. Also the porosity measurements using mercury under pressure indicate that reentrant cavities exist in the surface of the dendrites. These surface studies were conducted by S. P. Carbone, IBM Corporation, Hopewell Junction, New York 12533.

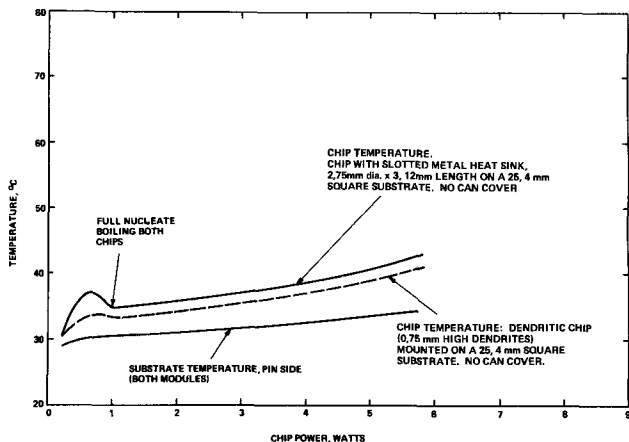


Fig. 12a. Chip temperature vs. chip power (dendritic, stud) in FC88.

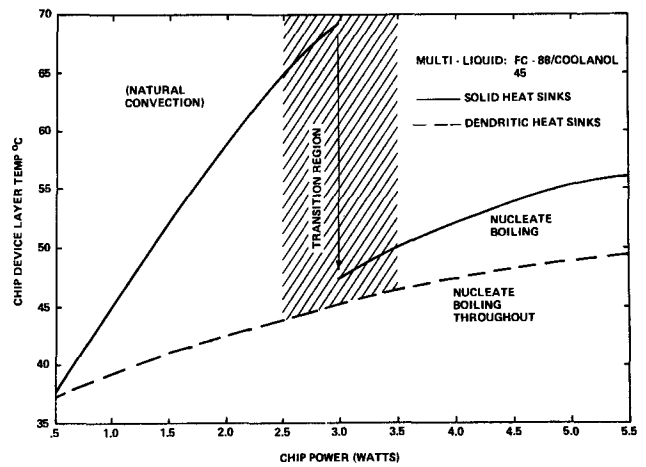


Fig. 12b. Chip temperature vs. chip power (dendritic, stud) in FC88 with a layer of Coolanol 45 on top.

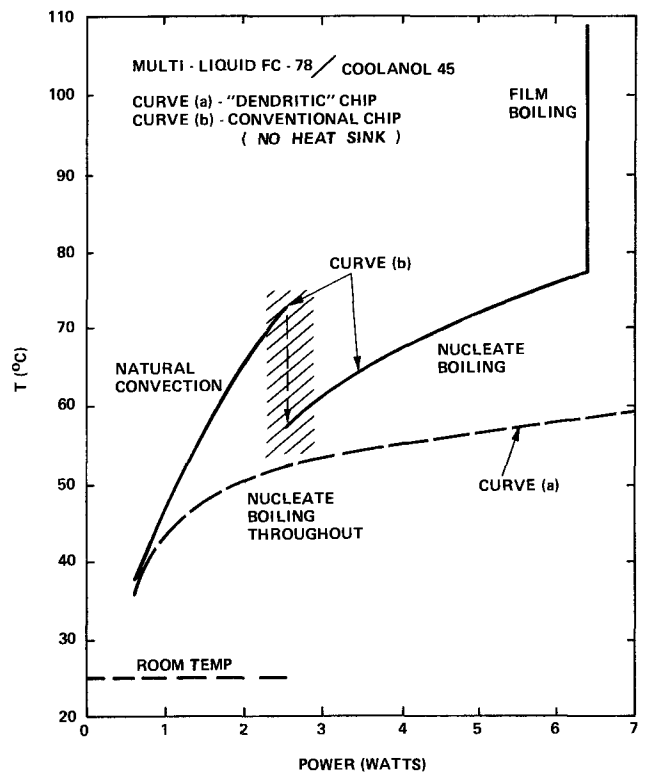


Fig. 12c. Chip temperature vs. chip power (dendritic, plain) in FC88 with a layer of Coolanol 45 on top.

anol 45) was  $\approx 0.1\%$  soluble in FC-88. This contaminant preferentially wets the heat sink to form a film.

The Coolanol 45 film acts as a thermal insulator on the stud and bubbles do not nucleate on this smooth surface ("hot area boiling"). Boiling starts when the temperature becomes high ( $>70^\circ\text{C}$ ). Once boiling starts, it is vigorous and strips the film. Then heat is conducted away rapidly and the stud approaches its normal cooling curve. If the power is left below 3W (natural convection), the chip temperature can remain above  $70^\circ\text{C}$ . This is much higher than the  $62^\circ\text{C}$  chip temperature at 5.5W. The dendritic curve exhibits nucleate boiling from 0.5W power with a small "sawtooth" ( $1^\circ\text{-}2^\circ\text{C}$ ).

The "fouling" problem can be critical in computers not only if contamination is allowed to accumulate over some period, but also if the parts are not thoroughly cleaned initially.

Figure 13a, shows the chip temperatures obtained with solid heat sink mounted chips. The "sawtooth" effect seen in the figure represents a  $30^\circ\text{C}$  jump which



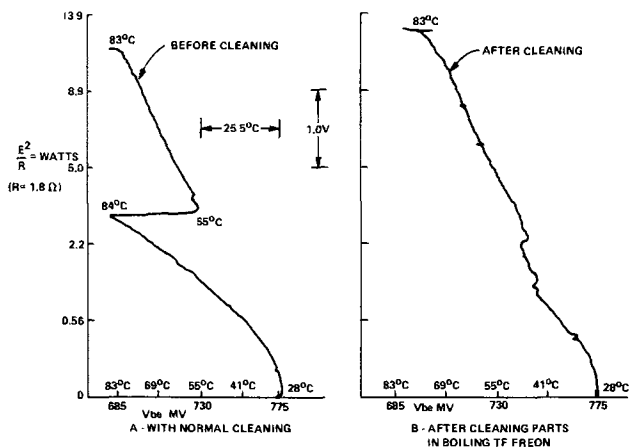


Fig. 13. Chip temperatures vs. chip power with solid heat sink mounted chip (heat sink dimensions given in Fig. 12a).

results in 83°C at approximately 3W. However, soon after the initiation of boiling, the temperature drops down to a normal level and at approximately 6W reaches an average chip temperature of 72°C.<sup>4</sup> After cleaning the part in boiling TF Freon, the "sawtooth" was reduced to a few degrees as seen in Fig. 13b. Note, however, that the cleaning did not change the temperature in the boiling regime. The effect of cleanliness is to initiate boiling at lower power levels.

In the case of dendritic heat sinks, the contamination caused a rise in chip temperature of only 3°C, and thereafter the temperature remained constant for 5700 hr. These dendritic chips have been operating in a cooling loop for 6400 hr. The slight effect of contamination on boiling from the dendrites and the better thermal performance of dendritic heat sinks can be attributed to the surface characteristics of the dendritic structures.

It is known that surface condition is an important variable in boiling heat-transfer. Many types of commercially available surfaces (machined, rolled, or drawn) have been investigated and studies in this area have been published (3). It has been found that a substantial decrease in the nucleate-boiling wall superheat can be obtained by artificially changing the size and distribution of cavities on the surface.

What is perhaps more important is the nature of the cavities which influence the bubble nucleation process. Bubbles form at a heated surface from cavities which already have some gas or vapor present, i.e., so-called active cavities (see Fig. 14a). As the wall surrounding the active cavity is heated, heat is transmitted to the liquid-vapor interface where evaporation takes place, thereby causing the bubble to grow. The bubble continues to grow until an equilibrium condition is reached which is governed by the relationship

$$\Delta p = p_b - p_l = \frac{2\delta}{r} \quad [1]$$

where  $p_b$  is the pressure inside the bubble;  $p_l$  is the

<sup>4</sup> To obtain the junction temperature, usually 6°C is added which yields 78°C at approximately 6W.

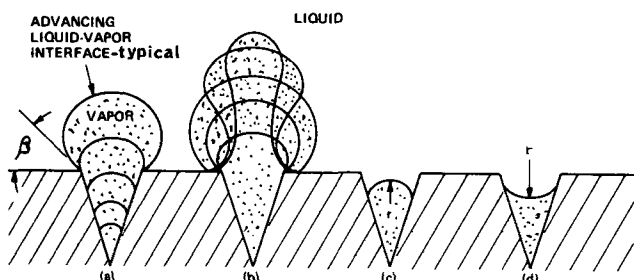


Fig. 14. Nucleation from cavities [from Ref. (5)]

pressure inside the liquid;  $\delta$  is the surface tension of the liquid; and  $r$  is the radius of the spherical bubble.

Then, as the bubble detaches from the surface, a portion of the vapor is trapped inside the cavity as shown in Fig. 14b. This trapped vapor becomes the nuclei for the next bubble. Depending upon the bubble size and the proximity of other cavities, this vapor-trapping process can induce neighboring inactive cavities filled with pure liquid into activity.

The amount of wall superheat needed to grow and detach a bubble of a given size compatible with the liquid properties may be computed from Eq. [1] after relating the temperature ( $T$ ) to the pressure ( $p$ ) with the perfect gas approximation in the Clausius-Clapeyron equation (4). Thus

$$T_v - T_{sat} \approx \frac{R_v T_{sat}^2}{L p_l} \left( \frac{2\delta}{r} - p_g \right) \quad [2]$$

where  $T_v$  is the temperature of the pure vapor and hence that of the wall, approximately;  $T_{sat}$  is the saturation temperature of the liquid;  $R_v$  is the gas constant of the vapor;  $L$  is the latent heat of vaporization;  $p_g$  is the partial pressure of any inert gases present in the cavity; and  $(T_v - T_{sat}) \equiv \Delta T$  is the wall superheat. Note that Eq. [2] is obtained from Eq. [1] by letting  $p_b = p_v + p_g$  where  $p_v$  and  $p_g$  are, respectively, the partial pressures of pure vapor of the liquid and any other gases that may be present in the bubble.

It is seen from Eq. [2] that less superheat is required when noncondensable gases are present in the bubble which can be verified easily by experiments. It is also suggested by Eq. [2] that at relatively high gas pressures ( $p_g$ ), it is possible to form bubbles at wall temperature below the saturation temperature of the liquid, i.e., in subcooled liquid. (An extreme example is the forced flow of air through a tube submerged in a body of liquid.) It is sometimes possible to form bubbles in subcooled liquids even in the absence of inert gases in the cavities in the wall surface. Some cavities can contain pure vapor even at highly subcooled temperatures. To explain this, Rohsenow (5) considers two cases of different contact angle  $\beta$  and opposite curvature of the interface:  $p_v > p_l$  in Fig. 14c and  $p_v < p_l$  in Fig. 14d. As the surface is allowed to cool below the saturation temperature of the liquid, if the cavity in Fig. 14c contains pure vapor only, the liquid-vapor interface collapses and the cavity becomes filled with liquid, i.e., becomes inactive. "As cavity (d) cools down, however, the interface recedes into the cavity, decreasing the radius of curvature and reducing  $p_v$ . Since  $p_v$  decreases,  $T_{sat}$  of the vapor decreases; the interface does not collapse and the cavity with vapor already in it is ready as an active bubble nucleation site when the wall surface is subsequently heated" (5).

It is clear from the discussion above that if cavities which behave as shown in Fig. 14d can be found, boiling can be initiated at these cavities at all times at a given constant temperature. It can be shown that one such cavity, called a "reentrant" cavity, is that which has a small opening at the surface with a larger diameter cavity below it (see Fig. 15).

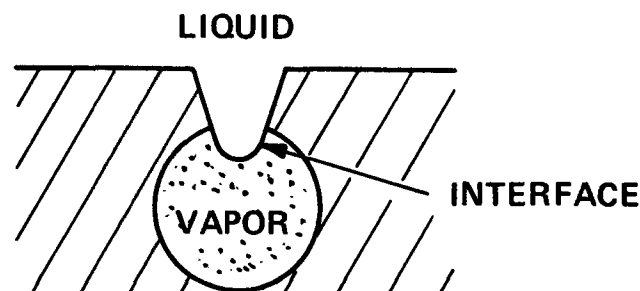


Fig. 15. Idealized "reentrant" cavity



Experiments indicate that with the surface cavities such as shown in Fig. 2, boiling does indeed commence repeatedly at the same wall temperature. On conventional surfaces, on the other hand, the commencement of boiling is not always consistent with a given wall temperature.

In boiling experiments with dendritic heat sinks, the liquid was boiled for long periods of time to drive off the noncondensable gases such as air. Furthermore, the experiments were conducted in a multifluid boiling setup. In this scheme two immiscible liquids are used, where the heavier primary liquid (e.g., FC-78) is in contact with the heat sink. Once the gases are forced out from the primary coolant the secondary coolant (Coolanol 45) on top of the primary coolant forms a barrier between the boiling liquid and the ambient, thus forming a "sealant" against air. In this manner, it was assured to the extent of the solubility of air in the liquids, that the bubbles were not activated by the presence of noncondensable gases, but rather by pure vapor in active cavities.

It was also found, as mentioned before, that boiling on a dendritic surface commences at a lower temperature than that measured on an ordinary surface. For example, it is clear in Fig. 12c that nucleation is prevalent at much lower power levels on "dendritic chips" than on plain chips. This leads to the important result that, since at low power dissipation the corresponding surface temperatures are small, any finite temperature "jump" in transition from natural convective mode to boiling is negligible. In comparison, on surfaces where boiling does not start until high power levels are reached, the unpredictable "jump" in the transition region may be high as seen in Fig. 13a.

The early boiling, i.e., at low wall superheat, on dendritic surfaces may be explained by the fact that the expected distribution of active cavities is much larger with dendrites than with ordinary roughness. In addition, it is known that, aside from the shape of the cavities, roughness alone has an effect on the stability of a bubble. For example, a surface roughness parameter can be related to the contact angle that a bubble forms with the surface which in turn is associated with wettability (6). The stability of the contact angle can then be determined as a function of the surface roughness parameter. Since the roughness of dendritic surfaces is very irregular, it is expected that the probability of finding unstable bubbles, i.e., early detaching bubbles, is high. The boiling process need not wait until a particular nucleation condition for some particular surface is reached. Boiling commences at the lowest wall temperature governing the thermal behavior of any one of the many dendritic cavities.

The irregularity or randomness of these cavities goes down to a very small scale, as evidenced by Fig. 16, which shows a variety of surface structures even at 5000X.

The configuration of the dendritic cavities promote boiling as well as convective cooling since the irregularities provide large surface area. Due to the large area per unit volume, a dendritic finned surface is expected to be advantageous in air cooling also.

### Reliability Tests on Dendritic Heat Sinks

The reliability aspects related to dendritic heat sinks can be addressed from two perspectives. One is the reliability of the dendrites themselves, and the second is the influence of the dendrites on the reliability of the total system.

On the latter perspective we placed four chips with dendritic heat sinks in two board cooling loop systems in order to determine if the dendrites do come loose after long periods of operation in a boiling medium and contaminate the system. The results showed that after 6400 hr of operation, no contamination attributable to the dendrites was detected. In order to assess the reliability risk in an accelerated manner, we

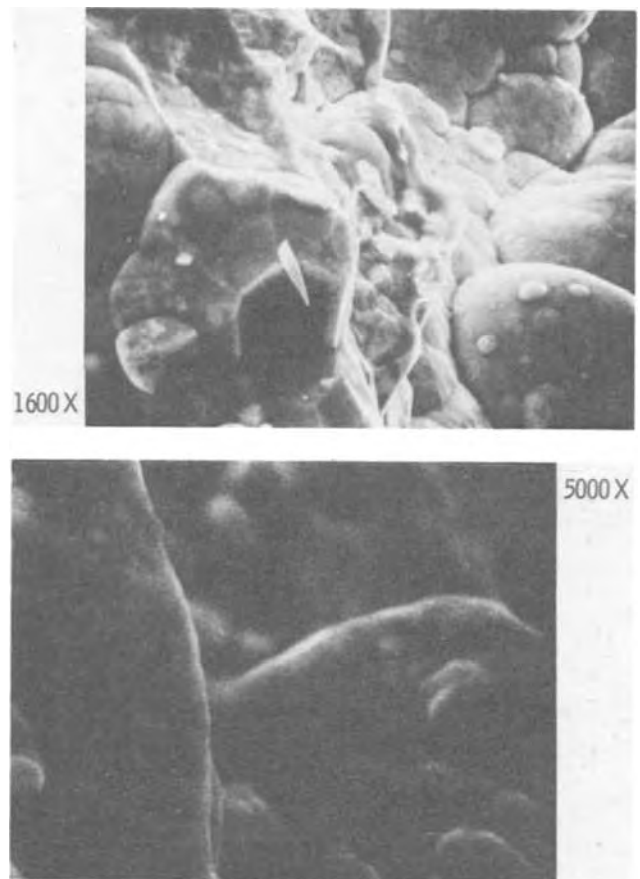


Fig. 16. Dendritic cavities and surface irregularities to 1600X and 5000X.

have also done shear tests on dendrites. A dendritic structure can withstand up to 1300g in shear. This should be compared with a shear failure of the C-4 solder connection (1) of the chip with the package at about 1000g. In relation to the solder joint itself, the light weight of the dendritic heat sinks contributes to the improved reliability of the C-4 joints in fatigue. For example, assuming an ellipsoidal model for the C-4 configuration, and a solder volume of  $0.001 \text{ mm}^3$  (70 mils<sup>3</sup>) it was shown (7) that the C-4 pad height reaches 0.081 mm (3.23 mils) for the 12 mg dendritic heat sink.

As a comparison, calculations project a delta reliability of +17% relative to the 180 mg molybdenum heat sink due to the increased height of the solder

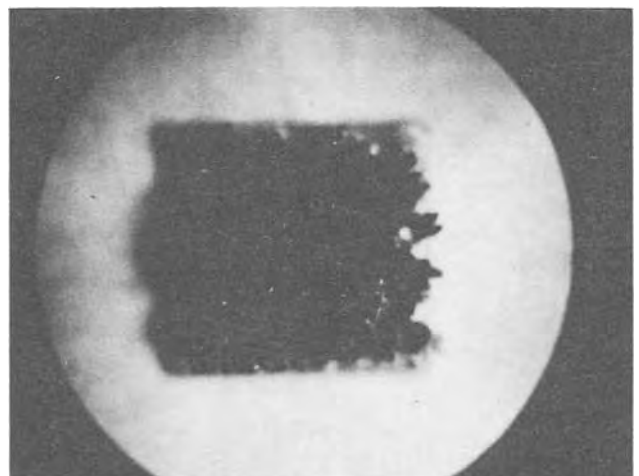


Fig. 17. Honeycomb-like dendritic heat sink made from 2-4 $\mu$  nickel powder.

pad. Inertial effects due to a higher mass of the stud heat sink have not been considered in this calculation.

Another concern was the possibility of the plating solution being trapped in the porous surface of the dendrites. Such inclusions, if present, might affect the mechanical strength, corrosion resistance, etc. of the heat sinks.

Ultraviolet spectrographic analysis shows that the plating bath contains more than 10% each of nickel, phosphorus, and sodium. Dendrites made from various nickel powders and annealed in nitrogen to 350°C also contain more than 10% nickel, and between 1 and 10% phosphorus, but the sodium content is below the sensitivity of the analysis, i.e., <0.1%. These results seem to indicate that very little of the plating bath is trapped permanently in the heat sinks during plating.

Still another concern was that since the heat sinks consist of a ferromagnetic material, high frequency a-c currents in the circuits on the other side of the chips might be affected. Three chips were a-c tested prior to growing dendrites on them. The a-c test results indicated no change of the a-c characteristics of the chips.

Several dendritic heat sinks on chips of different types have been subjected to various environmental tests. No measurable degradation has been detected.

Two chips of  $2.85 \times 2.70$  mm ( $0.112 \times 0.106$  in.) with nickel dendrites were heated to 330°C in nitrogen for 2 min and cooled to room temperature. The heat cycle was repeated 10 times. No cracks were observed under the microscope (50X) on the dendrites or between the dendrites and the silicon chips after this treatment. A shock test involved ten impact blows, each in two directions, with a peak acceleration of  $4500g \pm 10\%$  and a pulse duration of  $200 \pm 5$   $\mu$ sec. The shock direction was both parallel and perpendicular to the plane of the chip. None of the four samples tested was visibly affected or damaged by the shock test.

The two chips with dendrites which had been heat-treated as described were vibration tested. The chips were vibrated in three planes, vibration in each plane as follows: (i) sweep from 20 to 2000 Hz and return for 20 min; (ii) between 20 and 28 Hz, constant amplitude of 0.35 in. peak; and (iii) between 28 and 2000 Hz, constant acceleration of 15g peak. None of the samples were visibly affected or damaged by the vibration test.

Other chips with dendritic heat sinks were subjected to 85°C/85% RH test for 504 hr. The two chips without the dendrites were used as controls. Fifty standard electrical tests on all modules showed no failure. There was no visible corrosion.

Three chips were also subjected to 50 cycles of wet thermal shock from 0° to 100°C in FC 40 fluorochemical liquid. Two chips had dendritic heat sinks on them while the third, without dendrites, was used as control. Fifty standard electrical tests on all modules showed no failures.

### Conclusions

The dendritic structure brings together on a single surface many different types of roughness, such as might be generated artificially by subsequently drawing, filing, sandblasting, etc. the single surface. As discussed above, on such surfaces, the boiling process need

not wait until a particular nucleation condition for some particular surface roughness is reached, but a whole "spectrum" of suitable roughnesses is available, yielding always some nuclei for boiling at the lowest wall temperature. Experiments discussed above have shown that on such surfaces superheating (boiling delay) becomes negligible. Consequently, a maximum cooling effect for liquid cooling is achieved. Air cooling with dendritic heat sinks is also possible. This together with the large surface area, low weight, and high mechanical strength makes the dendrites suitable for use as an excellent heat sink in the cooling of integrated circuit chips. The reliability of the dendritic heat sink and of the plated chip itself also seem to be excellent, though these results are based on a relatively small number of samples. The preparation of dendritic heat sinks is simple and inexpensive.

### Acknowledgment

The authors wish to thank Messrs. S. Carbone and V. B. Jagirdar for their help in formulating and conducting some of the experiments. The authors also thank Messrs. R. E. Mascitelli, E. D. Renner, and G. Slayton for their competent work in the preparation and testing of the dendritic heat sinks and Mr. H. D. Kaiser for his constant encouragement of our work.

Manuscript submitted Aug. 14, 1973; revised manuscript received Jan. 21, 1974. This was Paper 81 presented at the San Francisco, California, Meeting of the Society, May 12-17, 1974.

Any discussion of this paper will appear in a Discussion Section to be published in the June 1975 JOURNAL. All discussions for the June 1975 Discussion Section should be submitted by Feb. 1, 1975.

### LIST OF SYMBOLS

$L$	latent heat of vaporization
$p_b$	pressure inside the bubble
$p_g$	partial pressure of any inert gases present in the cavity
$p_l$	pressure inside the liquid
$p_v$	partial pressure of pure vapor of the liquid
$r'$	radius of the spherical bubble
$R$	gas constant
$R_v$	gas constant of the vapor
$T_{sat}$	saturation temperature of the liquid
$T_v$	temperature of the pure vapor and hence that of the wall, approximately
$\Delta T$	wall superheat
$\delta$	surface tension of the liquid

### REFERENCES

1. L. F. Miller, *IBM J. Res. Develop.*, **13**, 239 (1969).
2. S. Oktay, *ibid.*, **15**, 342 (1971).
3. R. H. Young and R. L. Hummel, A.I.Ch.E. Seventh National Heat Transfer Conference, August 1964.
4. K. Denbigh, "The Principles of Chemical Equilibrium," The Syndics of the Cambridge University Press, London (1964).
5. W. M. Rohsenow and H. Choi, "Heat, Mass and Momentum Transfer," p. 219, Prentice-Hall, Inc., Englewood Cliffs, N. J. (1961).
6. R. F. Gould, Editor, "Contact Angle Wettability and Adhesion," American Chemical Society, Washington, D.C. (1964).
7. K. C. Norris. Private communication.

# High Temperature Reactions in the Silicon-Hydrogen-Chlorine System

E. Sirtl,<sup>\*1</sup> L. P. Hunt,<sup>\*</sup> and D. H. Sawyer

Dow Corning Corporation, Solid State Research and Development, Hemlock, Michigan 48626

The publication costs of this article have been assisted by Dow Corning Corporation.

## ABSTRACT

The partial pressures of the gaseous species in equilibrium with solid silicon in the Si-H-Cl system are presented as a function of temperature for different Cl/H ratios and total pressures. Computations were performed using our recently determined value of  $\Delta H_f^\circ_{298}$  (SiHCl<sub>3,g</sub>) = -116.9 kcal/mol. Experimental data concerning the deposition and dissolution of silicon over a temperature range of 1200°-1700°K are compared to the equilibrium data and general conclusions drawn about the probable reaction mechanisms involved, especially for decomposition of the compounds SiCl<sub>4</sub> and SiHCl<sub>3</sub>. Particular emphasis is put on attempting to integrate the diverse body of experimental data that exists for silicon deposition from SiCl<sub>4</sub>-H<sub>2</sub> and SiHCl<sub>3</sub>-H<sub>2</sub> mixtures at high temperatures.

A previous article (1) presented a thorough thermodynamic evaluation of the Si-H-Cl system in terms of the increase or decrease of the amount of silicon in the gaseous phase as a function of temperature and Cl/H ratio. One of the purposes of this work is to present the partial pressure of the various species in equilibrium with solid-phase silicon as computed using the same thermodynamic data published in that paper. It is also intended to present a general discussion to assist in understanding the complexity of reaction mechanisms that can be involved during high temperature processing of semiconductor silicon. Comparisons are made, where possible, between well characterized experimental data and that of the computed equilibrium situation.

## Equilibrium Concentration of Individual Species

Calculations based on earlier reported thermodynamic data (1) considered fourteen gaseous species to be in equilibrium with solid silicon. The gas phase composition based on these data is shown as a function of temperature for different Cl/H ratios in Fig. 1a-c. The gaseous species Si, Cl<sub>2</sub>, and Si<sub>2</sub>Cl<sub>6</sub> do not appear on the graphs due to their low equilibrium partial pressures, while SiH<sub>4</sub>, SiCl, SiCl<sub>3</sub>, and Cl appear in only some of the plots. All the aforementioned species can be ignored when describing the equilibrium state of the system under the conditions indicated while maintaining  $\approx 99\%$  accuracy. At temperatures higher than 1700°K or Cl/H ratios lower than 0.01 it becomes necessary to consider some of these species. An example of the calculated partial pressures of the minor constituents at conditions of 1600°K and 1 atm is shown in Table I for various Cl/H ratios. The partial pressure of hexachlorodisilane exhibits a maximum in the temperature range of 1200°-1400°K for a given Cl/H ratio.

The three Cl/H ratios chosen have a particular significance with respect to experimental conditions. The lowest value, 0.01, is typical of conditions used for epitaxial deposition and vapor etching of silicon, while 0.1 represents typical conditions for high temperature polycrystalline silicon deposition. The highest value, 1.0, is common to conditions for silicon dissolution (chlorosilane synthesis) or for chlorosilane disproportionation reactions.

The effect of pressure on the equilibrium composition of the gas phase is seen by comparing Fig. 1b and 2. At reduced total pressure, SiCl<sub>4</sub> and SiCl<sub>2</sub> become somewhat more predominant at the expense of the hydrogen containing species. From a thermochemical standpoint, inert gas dilution has a similar effect on the Si-H-Cl system as does reduction of total pressure; i.e., an initial system containing a chlorosilane in hydrogen will reach the same equilibrium point, with respect to all species except H<sub>2</sub> and the inert gas, under comparable conditions such as  $P_T = 0.1$  atm and 0% inert gas as opposed to  $P_T = 1.0$  atm and 90% inert gas as long as the sum of partial pressures of the silicon containing species is considerably lower than the total pressure. These systems are expected to differ substantially in practice, however, due to changes in gas kinetics.

## General Trends in Experimental Data

All experimental data available in the literature can be categorized into two different graphical systems using the following terms:  $\eta$  = fractional silicon yield from a chlorosilane,  $R$  = silicon deposition rate, and  $x$  = mole fraction of chlorosilane in hydrogen.

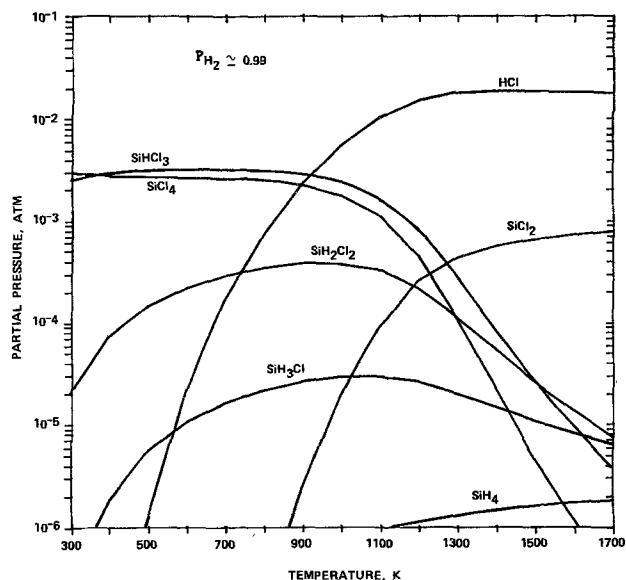


Fig. 1a. Temperature variation of the equilibrium gas phase composition at 1 atm total pressure and Cl/H = 0.01.

<sup>\*</sup> Electrochemical Society Active Member.  
<sup>1</sup> Present address: Consortium für Electrochemische Industrie G.M.B.H., 8 München 70, Zielstattstr. 20, West Germany.  
Key words: decomposition, deposition, kinetics, reduction, silicon, thermochemical equilibrium.

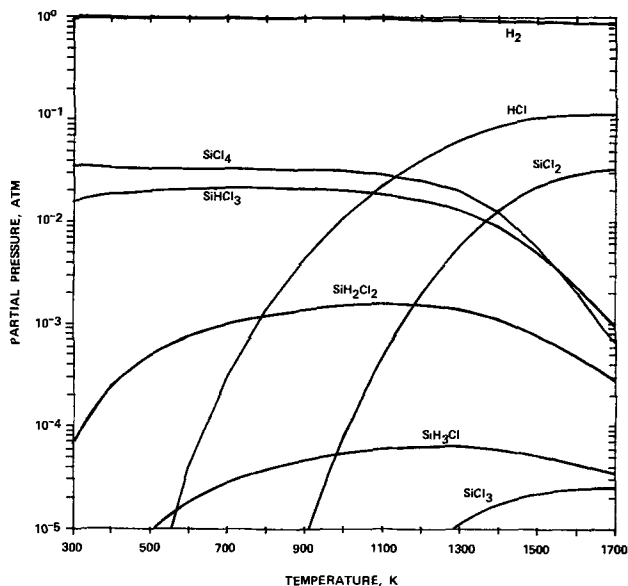


Fig. 1b. Temperature variation of the equilibrium gas phase composition at 1 atm total pressure and Cl/H = 0.10.

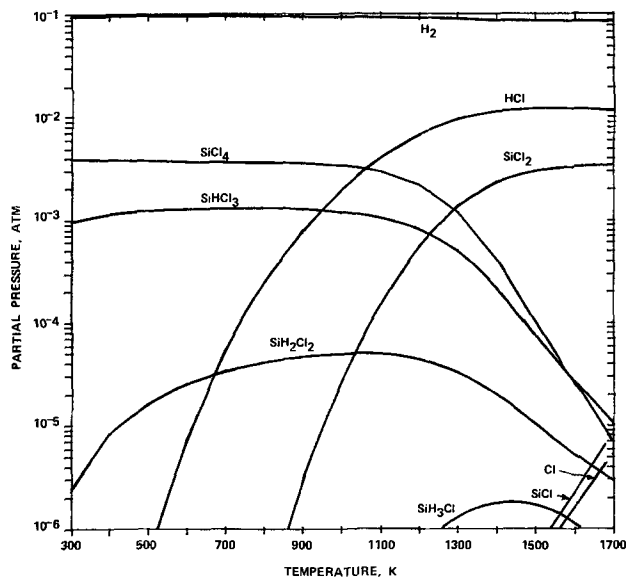


Fig. 2. Temperature variation of the equilibrium gas phase composition at 0.1 atm total pressure and Cl/H = 0.10.

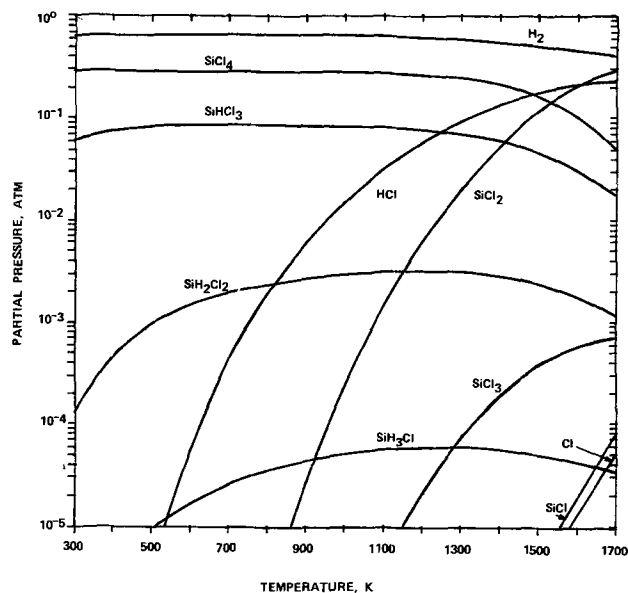


Fig. 1c. Temperature variation of the equilibrium gas phase composition at 1 atm total pressure and Cl/H = 1.0.

The first system indicates the temperature function of  $\eta$  (Fig. 3a) or of  $R$  at a constant value of  $x$ . The second one portrays the correlation of  $\eta$  or the product  $x \cdot \eta$  (Fig. 3b) to the mole fraction  $x$  at a fixed temperature. The entity  $x \cdot \eta$  is a measure of the potential silicon yield per volume of gas mixture and can be related to the deposition rate  $R$  in grams/hour or microns/minute via the absolute or linear flow rate, depending on the geometry of the reactor system. For the first system, the nature of the temperature function is similar, irrespective of whether  $\eta$  or  $R$  is used as the parameter. In the case of variable composition, however, the shapes of the curves are different for  $\eta$  as

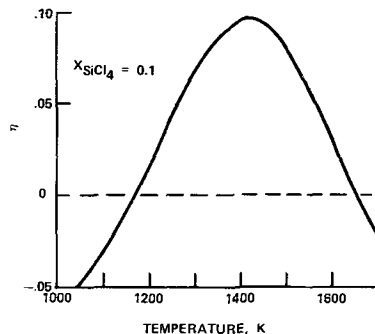


Fig. 3a. Variation of silicon yield with temperature

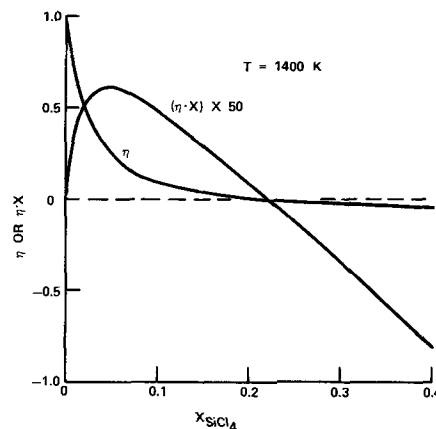


Fig. 3b. Variation of  $\eta$  and  $\eta \cdot x$  with mole fraction of  $\text{SiCl}_4$

compared to  $x \cdot \eta$  (or  $R$ ). This is shown by schematic drawings in Fig. 3a and b.

If the yield or growth rate of silicon is plotted vs. temperature, a maximum generally occurs both experi-

Table I. Equilibrium partial pressures of minor components for various Cl/H ratios at 1600°K and 1 atm total pressure

Cl/H	Partial pressure, atm					
	Si	SiCl	SiCl <sub>2</sub>	Si <sub>2</sub> Cl <sub>6</sub>	Cl	Cl <sub>2</sub>
0.01	$8 \times 10^{-8}$	$1 \times 10^{-9}$	$1 \times 10^{-7}$	$9 \times 10^{-14}$	$8 \times 10^{-7}$	$5 \times 10^{-11}$
0.10	$8 \times 10^{-8}$	$7 \times 10^{-6}$	$3 \times 10^{-5}$	$6 \times 10^{-9}$	$5 \times 10^{-9}$	$2 \times 10^{-9}$
1.00	$8 \times 10^{-8}$	$2 \times 10^{-5}$	$6 \times 10^{-4}$	$2 \times 10^{-9}$	$1 \times 10^{-5}$	$2 \times 10^{-9}$

mentally and theoretically somewhere between 1000° and 1700°K showing a shift toward lower temperature with increasing mole fraction of the chlorosilane. The fit of the experimental data with theory varies widely depending on reactor geometry and flow rate. Within a given system, the experimental yield curve shows a peak that is more narrow than that of the corresponding theoretical curve, but which coincides fairly well in terms of its maximum. This is demonstrated in Fig. 4, where conversion rates experimentally determined during the growth of polycrystalline silicon are compared with calculated data. In the case of the curves given by Wolf and Teichmann (2), there exists appreciable difference between the  $\eta$  values at low and high flow rates. In contrast to the yield gradients on both sides of the peak, the maxima are nearly unchanged in magnitude.

Plots of yield or growth rate vs. mole fraction can be particularly informative in the  $\text{SiCl}_4\text{-H}_2$  system where the dissolution of elemental silicon is observed at relatively low chlorosilane concentrations. The diagram in Fig. 5 indicates that the experimental output of silicon per unit volume is less than the calculated value at low mole fractions as expected. However, at higher mole fractions, the experimental curve gen-

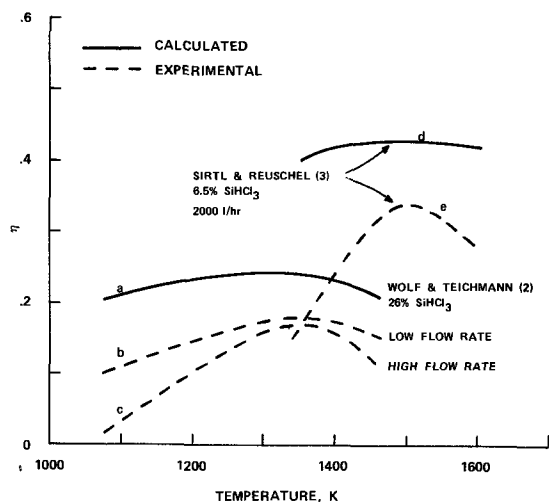


Fig. 4. Temperature comparison of polycrystalline silicon deposition yields from  $\text{SiHCl}_3\text{-H}_2$  mixtures.

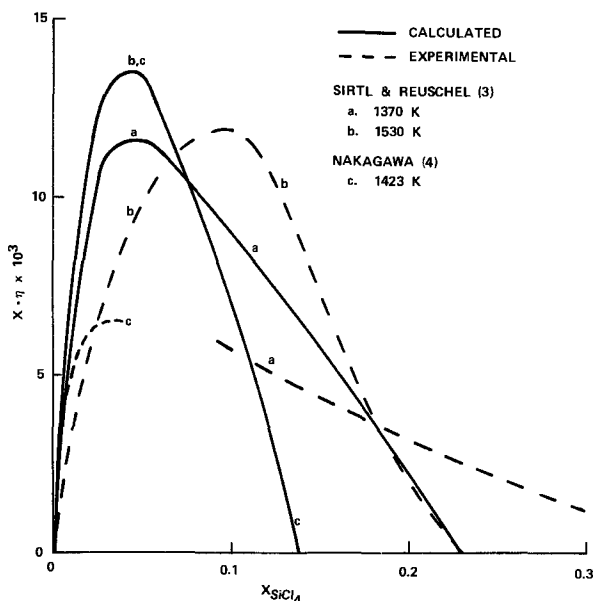


Fig. 5. Comparison of calculated and experimental relative weights of deposited silicon as a function of the mole fraction of  $\text{SiCl}_4$ .

erally intersects the corresponding theoretical curve before it reaches the  $\eta = 0$  line (threshold line). Similar results are obtained (see Fig. 6) when the linear growth rate of silicon is plotted vs. the mole fraction of trichlorosilane.

When sufficient information about the linear flow rate in a vertical reactor is available, quantitative comparisons can be made between theory and experiment based on the simplified model of a gas stream impinging perpendicularly on a target. In this case the maximum theoretical deposition rate, assuming that all impinging molecules react at the surface, is

$$R = (\eta f_1 \rho_g / \rho_s) \cdot 10^4 \text{ } (\mu/\text{min}) \quad [1]$$

where  $\rho_g$  and  $\rho_s$  are the corresponding silicon densities of the input gas and the substrate, and  $f_1$  is the linear flow rate in centimeters/minute. The latter term is obtained from the relation

$$f_1 = f_v / A \quad [2]$$

where  $f_v$  is the volumetric flow rate (cubic centimeters/minute) and  $A$  is the cross-sectional area (square centimeters) of the reactor at the position of the substrate. The theoretically calculated growth rates expressed in microns/minute are mathematically independent of the gas flowing past the substrate in contrast to rates expressed in grams/minute which require a correction term (6).

Figure 6 demonstrates an effect similar to that in Fig. 5 with the basic difference being the ratio of gas flow to silicon surface area due to use of an epitaxy reactor. This diagram also shows the shift of the theoretical threshold<sup>2</sup> value by reducing the total pressure. The deviation of experimental threshold points from calculated ones is due to kinetic effects as shown by plots of our experimental data (see Appendix) in Fig. 7a and b. The measurement of an equilibrium system by extrapolation of data to zero growth rate and zero flow rate indicates that the approach to equilibrium is highly sensitive to the flow rate, especially at its low values.

A compilation of threshold data in the chlorosilane-hydrogen system is given in Table IIa. Even though some of the theoretical values seem to be closely approached, and in one case even exceeded, lack of sufficient experimental details makes it difficult to examine these data thoroughly. It is clear, however, that measured threshold values occur at higher mole fraction than calculated values. If the threshold point is approached from the region of silicon dissolution (by intentionally adding and changing the hydrogen chloride partial pressure), the situation described in Table IIb is found. It can be seen that just the inverse effect

<sup>2</sup> Threshold is defined here as the conditions of experimental parameters that allow neither a net deposition nor net etching of solid silicon, i.e., conditions that allow no net transfer of silicon to or from the gas phase.

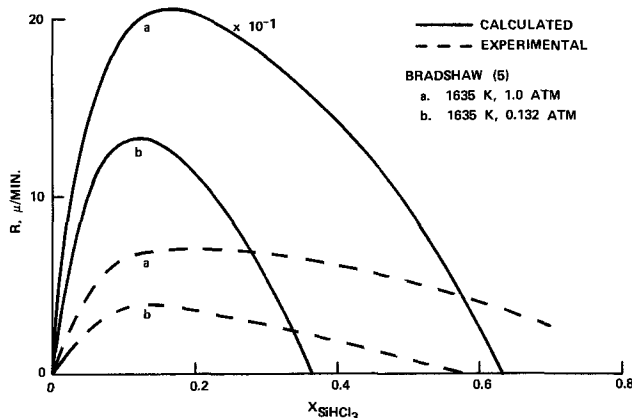


Fig. 6. Theoretical and experimental deposition rate data as a function of  $\text{SiHCl}_3$  mole fraction at different total pressures.

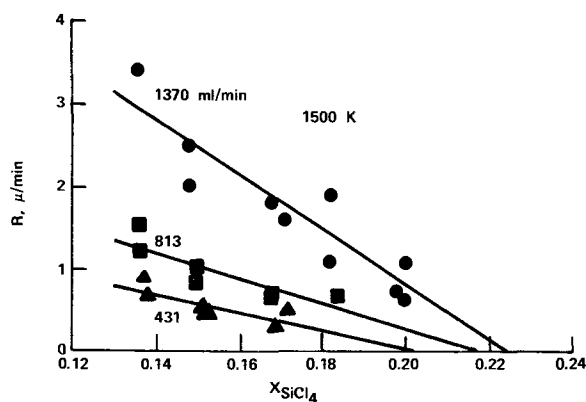


Fig. 7a. Silicon deposition rates (extrapolated to zero) as a function of  $\text{SiCl}_4$  mole fraction for various total gas flow rates.

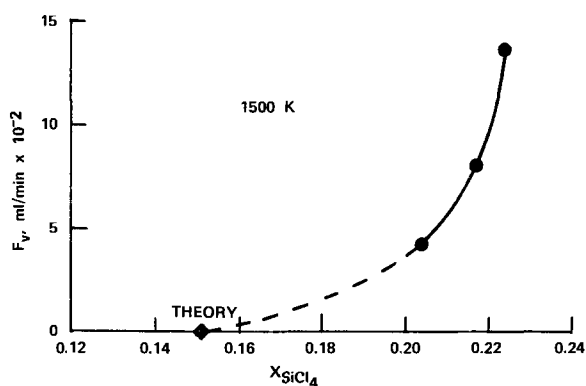


Fig. 7b. Threshold values at different flow rates as a function of  $\text{SiCl}_4$  mole fraction.

of the above-mentioned phenomenon appears; the experimental threshold values show a shift toward lower Cl/H ratios.

### Discussion of Experimental Data

This section does not aim at a thorough mathematical treatment of complex diffusion effects as has been done by others (5, 11, 12, 15-19). It attempts to correlate our theoretical equilibrium curves, which we feel are very accurate, with experimental facts and to explain deviations on the basis of different kinetic models.

If a gaseous compound is decomposed on a heated substrate, surface reactions will be the limiting factor in cases of high flow rates, supported by high concentrations and lower temperatures. Each one of these parameters alone can be of sufficient influence to establish a surface controlled mechanism. The number of active sites at the phase boundary is another critical factor that may be used to determine the character of a heterogeneous reaction.

**Kinetically controlled deposition.**—As long as the situation in a reactor is completely controlled by surface kinetics, a direct correlation of experimental deposition rates with the corresponding equilibrium situation calculated for given substrate temperatures is impossible. For silicon, this was demonstrated by the work of Theuerer (9) and Bracken (14) where a linear function could be found in a  $\log R$  vs.  $1/T$  plot for both  $\text{SiCl}_4/\text{H}_2$  and  $\text{SiHCl}_3/\text{H}_2$  mixtures on single-crystal substrates at temperatures up to  $1350^\circ\text{C}$ . Of course, the experimental data have to be lower than the equilibrium values, but the slope of such a curve is indicative only of the activation energy of the rate-limiting step in surface kinetics. Different substrate orientations and their influence on silicon deposition rates have been studied (14, 20, 21) elsewhere. Similar investigations on germanium (22) supported the opinion that significant differences in growth rates occur only in surface re-

Table IIa. Threshold values of chlorosilane-hydrogen mixtures

Reference <sup>(a)</sup>	Temperature, °K	Mole fraction		$x_e - x_0$
		Exper.	Calc.	
(7)	1630	0.08	0.11	-0.03
(8)	1523	0.15	0.14	0.01
(7)	1470	0.18	0.17	0.01
(b)	1500	0.22	0.15	0.07
(8)	1523	0.26	0.14	0.12
(9)	1543	0.28	0.13	0.15
(3)	1530	0.30	0.14	0.16
(10)	1473	0.38	0.17	0.21
(3)	1370	0.40	0.23	0.17
(5)	1635	0.55	0.36	0.19

<sup>(a)</sup> Silicon tetrachloride was used in all cases at a total pressure of 1 atm except for trichlorosilane in Ref. (5) at 0.132 atm.

<sup>(b)</sup> This work (see Appendix).

Table IIb. Threshold values of chlorosilane- $\text{H}_2$ -HCl mixtures

Reference	Temperature, °K	Cl/H ratio		$\frac{\text{Cl}}{\text{H}}_e - \frac{\text{Cl}}{\text{H}}_0$	Comments
		Exper.	Calc.		
(11)	1403	0.008	0.52	-0.51	$x_{\text{SiH}_4} = 0.001$
(12)	1573	0.021	0.28	-0.26	$x_{\text{SiCl}_4} = 0.040$
(13)	1503	0.031	0.38	-0.35	$x_{\text{SiCl}_4} = 0.023$
(13)	1503	0.041	0.38	-0.34	$x_{\text{SiCl}_4} = 0.024$
(13)	1503	0.070	0.38	-0.31	$x_{\text{SiCl}_4} = 0.031$
(14)	1488	0.111	0.113	-0.002	$x_{\text{SiHCl}_3} = 0.040$

action-limited systems, with (11) being the least reactive crystal face. The contrary situations, reported by Sheftal' and Givargizov (23) for the  $\text{GeCl}_4\text{-H}_2$  system, can be interpreted in terms of reactants being considerably contaminated with oxygen. In this case, the impurity is able to block active sites but may favor the formation of two-dimensional growth on a (111) plane. When the surface reaction rate becomes comparable with or greater than the diffusion rate of the different gaseous compounds in the diffusion layer, a discussion of the real equilibrium situation is much more meaningful.

**Diffusion-controlled deposition.**—The nearly proportional displacement of experimental and theoretical low flow rate data, as shown by curve b in Fig. 4, can be described as resulting from mass transport limitation based on Sedgwick's (6) approach for calculating deposition rate data according to Eq. [3]

$$R = J \cdot \eta \cdot \beta \quad [3]$$

Here, the silicon deposition rate in grams/minute is simply formulated as the product of the flux ( $J$ , grams/minute) of silicon into the reactor, the fractional thermodynamic efficiency ( $\eta$ ) under isothermal conditions, and the fractional part ( $\beta$ ) of the gas stream that actually reaches equilibrium conditions at the phase boundary. Since equilibrium can be assumed to be established in the vicinity of the phase boundary at low flow rates and high temperatures ( $1200^\circ\text{-}1700^\circ\text{K}$ ), the result of inefficient contact ( $\beta < 1.0$ ) of the gas stream with the substrate is schematically shown in Fig. 8 where  $\beta$  is assumed to have a constant value. A similar mass transport limited reaction has been reported by Silvestri (22) in the  $\text{Ge-H-Cl}$  system and could also be found in Shepherd's paper (12) after comparison with our theoretical data.

The introduction of the factor  $\beta$  certainly is a way to describe and understand a number of experimental curves on a generalized basis and seems to work well in many cases where the process is more or less controlled by diffusion. This is favored by low flow rates,<sup>3</sup> high temperatures, and a large number of active surface sites. In particular, it applies to the growth of

<sup>3</sup> The experimental approach of zero flow conditions in Fig. 7b, for instance, may never reach the theoretical value for the same reason.

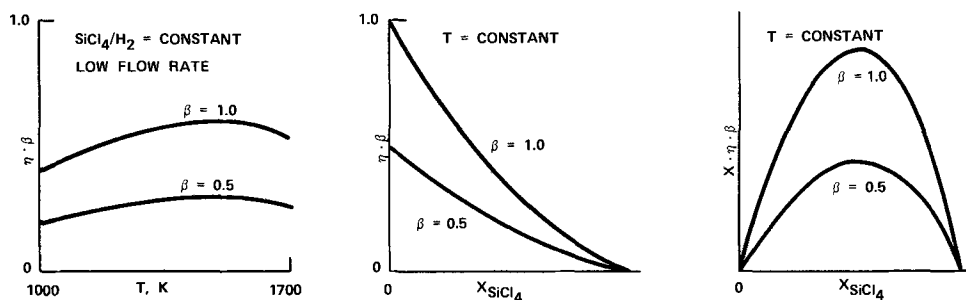
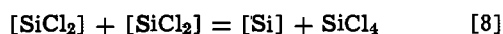
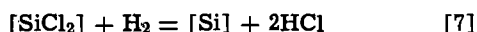
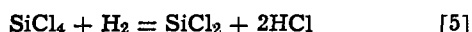


Fig. 8a-c. Effect of contact efficiency,  $\beta$ , of the gas stream on the deposition parameters of silicon from  $\text{SiCl}_4\text{-H}_2$  mixtures.

polycrystalline material as such or to epitaxial deposition processes where polycrystalline material is simultaneously formed as a by-product on the susceptor. The temperature function of  $\eta$  during growth of polycrystalline silicon is shown in Fig. 4. Whereas curve b seems to fit Sedgwick's approach, curves c and e show considerable deviations from such a model in both high and low temperature regions. Before we try to explain this phenomenon, the basic reversible reactions in the  $\text{SiHCl}_3/\text{H}_2$  and  $\text{SiCl}_4/\text{H}_2$  systems shall be pointed out<sup>4</sup>



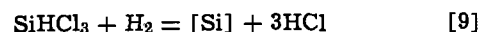
High flow rates at low temperatures favor a surface reaction like [7] as the rate-controlling step. Support is given to this assumption by kinetic investigations in the system B-H-Cl (24, 25) where the reduction of adsorbed boron-chlorine compounds to elemental boron is claimed to be reaction controlling. Occasionally, concurrent blocking of active centers by traces of oxygen may also contribute to the slope of curves c and e. A similar reason has been suggested by Silvestri (22) in his investigation of germanium deposition from  $\text{GeCl}_4\text{-H}_2$  mixtures.

At high temperatures, however, low surface mobility of the reactants cannot be the reason for increased deviation from the calculated values. The high equilibrium partial pressures of silicon dichloride and hydrogen chloride in this temperature region (see Fig. 1b and c) certainly play a major role in the reaction mechanism responsible for the strongly negative yield gradient. As the reactive diffusion layer markedly increases in thickness at higher temperature, homogeneous reactions of type [4] and [5] can take place there to a larger extent. Since addition of hydrogen chloride to the reaction mixture has been reported to suppress silicon growth more than expected as compared to equilibrium conditions (see Table IIb), it can be assumed that HCl being preformed in the diffusion layer will exert the same influence on silicon deposition in such a case.

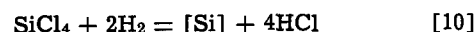
**Transitionally controlled deposition.**—The analysis of epitaxial silicon deposition rates as a function of the mole fraction of chlorosilanes (Fig. 5 and 6) calls for an explanation as to why the theoretical curves reach the threshold point at a lower chlorosilane concentration. A different kinetic model must be used since control by an uninhibited heterogeneous reaction over the entire range of the mole fraction of the chlorosilane would result in the experimental curves being forced to remain within the envelope of the calculated ones, as shown by the idealized situation in Fig. 8b and c. Data by Runyan *et al.* (7), in the case of  $\text{SiCl}_4\text{-H}_2$  and  $\text{GeCl}_4\text{-H}_2$  mixtures, indicate a transition between two different deposition mechanisms since both depressions and protrusions on a (111)

surface were enhanced at lower chloride concentrations while they disappeared at higher concentrations. This means that at higher excess of hydrogen the chlorosilane molecules impinging upon the surface are immediately reduced to silicon at or near the point where they hit the surface. At higher chlorosilane concentrations the original molecules or their first reaction product,  $\text{SiCl}_2$ , are forced to travel along the surface until they reach an active site (growth step) where elemental silicon can be formed. Normally, the concentration of hydrogen chloride generated by reactions of type [4] or [5] would be high enough here to suppress silicon deposition according to reaction [7] (see Fig. 1c). As the  $\text{SiCl}_2$  molecules, however, are strongly concentrated along the edge of a growth lamella (reaction [6]), conditions are ideal for a reaction of type [8] where no HCl is generated to counteract silicon deposition. Presently, however, we are unable to exclude another model according to which an incomplete reaction to form  $\text{SiCl}_2$  is followed by a more efficient reaction of type [7] near the threshold region. Similar thoughts already were developed in an earlier paper (3).

At a first glance it is surprising to see the threshold value in Fig. 6 shifted to lower mole fractions by applying reduced pressure. As the summary reactions



and



show an increase in gaseous compounds by one mole each, the contrary case might be expected. A more thorough examination, however, reveals that the partial reactions [4] and [5] are of the same character. When a temperature region is discussed where the partial pressure of  $\text{SiCl}_2$  is no longer negligible, reactions producing this molecular species are thermodynamically favored because the reaction entropies of reactions [4] and [5] simply are higher by 4-5 eu as compared to reactions [9] and [10].

Irrespective of most different types of equipment and experimental conditions general outlines can be given as to what extent either surface-controlled or diffusion-controlled reactions are expected to play the predominant role. In Table III the contribution of the

Table III. Influence of experimental conditions on kinetics of silicon deposition from  $\text{SiHCl}_3\text{-H}_2$  and  $\text{SiCl}_4\text{-H}_2$  mixtures

Variables	Diffusion controlled	Surface controlled	Surface controlled
Linear flow rate	Low <sup>6a</sup>	Medium	High <sup>5b</sup>
Mole fraction chlorosilane	Low <sup>6a</sup>	Medium	High <sup>6b</sup>
Substrate temperature	High <sup>7a</sup>	Medium	Low <sup>7b</sup>
Temperature gradient (near surface)	Low	Medium	High
Surface site density	High	Medium	Low
Silicon surface per reaction volume	High	Medium	Low

<sup>6a</sup> <0.3 cm/sec; <sup>6b</sup> >3 cm/sec.

<sup>6a</sup> <0.01; <sup>6b</sup> >0.1

<sup>7a</sup> <1300°K; <sup>7b</sup> >1550°K.

\* Brackets indicate nongaseous species.

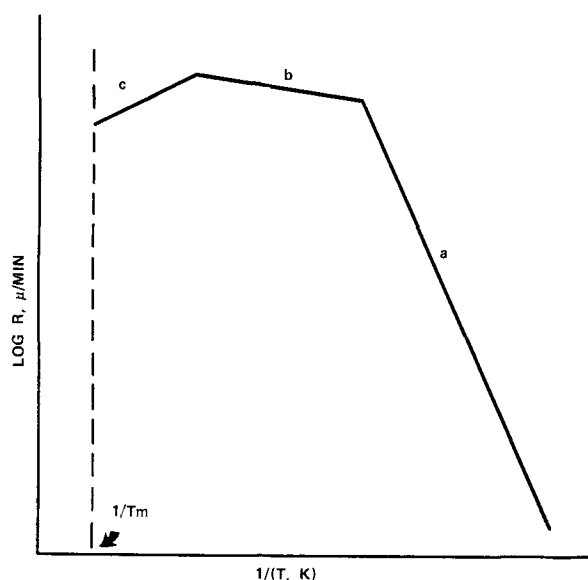


Fig. 9. Schematic plot of deposition rate vs. temperature based on different kinetic regimes.

most influential parameters is demonstrated in form of a chart. A fairly reliable prediction can be made about the most probable kinetic regime of a particular reaction system from the six different choices depending on whether the balance of checked conditions lies to the left or right of center.

**The Arrhenius equation.**—Basically, the shape of the  $\log R$  vs.  $1/T$  curve (Fig. 9) arises due to the existence of three different kinetic regimes. At lower temperatures, curve a characterizes the activation energy of the rate-limiting reaction at the silicon surface. At medium temperatures curve b describes a slightly increasing efficiency due to the conditions of diffusion-limited mass transport. The subsequent decrease in growth rate at the highest temperatures (curve c), besides the thermodynamic aspects, can be explained by reactions in the diffusion layer leading to enhanced etching effects on the silicon surface, as stated above. In the case of monosilane, the same phenomenon (26) is attributed to homogeneous nucleation.

Depending on the temperature range being investigated, as well as the concentration and nature of the silicon compound, one or two out of these three principal stages have not been revealed in most of the published experimental curves. Evidently, one has to be cautious in calculating activation energies within a temperature range where an overlapping of surface-controlled and diffusion-controlled reactions on the background of the theoretical maximum yield curve does not allow a simple application of the convenient Arrhenius equation (33).

Thus, different activation energies of the silicon deposition reaction have been reported for different compounds under various experimental conditions (Table IV). However, a family of curves recently obtained for different chlorosilanes at concentrations of 0.1% each (34) seems to indicate the same activation

Table IV. Literature data on activation energies of silicon deposition reactions

Reaction mixture	Activation energy (kcal/mol)	Reference
SiH <sub>2</sub> Cl <sub>2</sub> -H <sub>2</sub>	6	(27, 28)
	13	(29)
SiHCl <sub>3</sub> -H <sub>2</sub>	18	(14)
	22	(30, 31)
SiCl <sub>4</sub> -H <sub>2</sub>	37	(9)
	40-46	(8)
	44	(16)
	50	(32)

energy at lower temperatures. This is interpreted, at least in the concentration range mentioned, as the migration of silicon ad-atoms being the rate-limiting step. Additional experiments would be welcome to test the validity of this model in different concentration ranges and to further characterize its atomic nature.

### Summary

A thorough thermodynamic analysis of the Si-H-Cl system was made to assist in understanding what gas phase species can be involved in the high temperature reactions occurring during silicon deposition under various conditions. Experimental data from the literature were then processed to point out existing trends. Attempts to clarify these trends were made by considering the probable reactions occurring under both diffusion-controlled and kinetically controlled regimes. Mixed regimes were considered and a method was offered to tabularly determine the probable controlling regime. The limitations of applying the Arrhenius equation to deposition rate data were discussed.

Manuscript submitted April 13, 1972; revised manuscript received Oct. 22, 1973.

Any discussion of this paper will appear in a Discussion Section to be published in the June 1975 JOURNAL. All discussions for the June 1975 Discussion Section should be submitted by Feb. 1, 1975.

### APPENDIX

#### Threshold Experiments

The epitaxial deposition unit consisted of a metered supply of pure hydrogen (accurate to better than  $\pm 10\%$  volume flow), a thermostatically controlled SiCl<sub>4</sub> saturator capable of maintaining a H<sub>2</sub>/SiCl<sub>4</sub> gas phase ratio within an accuracy of  $< \pm 0.1\%$  independent of the H<sub>2</sub> flow, and a pedestal reactor. The reactor was such that the feed entered from the bottom and exited at the top. The surface of the silicon wafer substrate to be deposited upon was pointed downward (see Fig. 10). This configuration was used to reduce errors due to thermal convection. Substrate temperatures were measured with a  $0.65\mu$  disappearing fila-

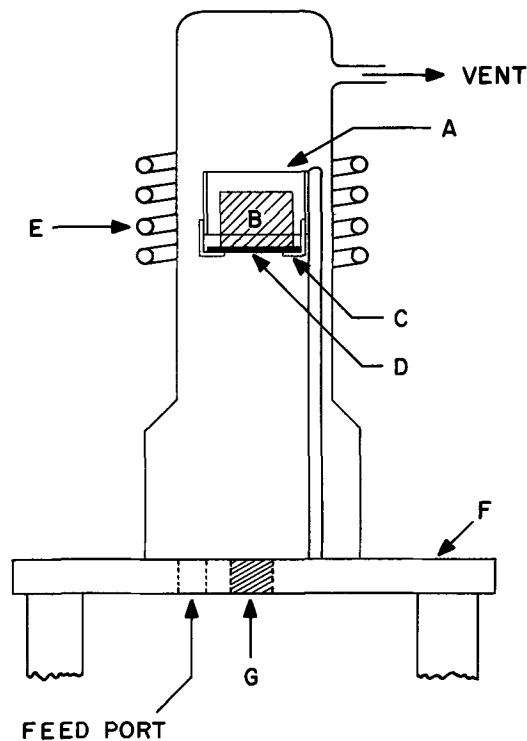


Fig. 10. Bottom feed epitaxial reactor. A, Quartz substrate-susceptor cylinder; B, SiC coated graphite susceptor; C, quartz support hooks; D, silicon wafer substrate; E, induction coil; F, stainless steel baseplate; G, quartz window.



ment pyrometer and corrected for emissivity using a standard curve obtained by prior calibration. Substrate temperature measurement accuracy was better than  $\pm 10^\circ\text{C}$ . The thickness of the deposited silicon layer was determined by conventional measurements on stacking faults and is considered precise to within 5-10%.

The substrates were 8 mils thick by 28 mm diameter polished, float-zoned silicon wafers of [111] orientation. Prior to mounting in the reactor, substrates were sequentially cleaned ultrasonically in trichloroethylene, acetone, and methanol followed by drying under a heat lamp.

Conventional silicon epitaxial procedure was used except the pre-cleaning in  $\text{H}_2$  at  $> 1200^\circ\text{C}$  was carried out for 2-5 min instead of the usual 15-30 min. This procedure left a sufficient amount of oxide on the surface such that surface originated stacking faults could easily be generated. Deposition was performed at a corrected temperature of  $1225^\circ \pm 6^\circ\text{C}$ .

#### REFERENCES

1. L. P. Hunt and E. Sirtl, *This Journal*, **119**, 1741 (1972).
2. E. Wolf and R. Teichmann, in "Reinststoffprobleme. I. Reinststoffdarstellung," Akademie-Verlag, Berlin (1966).
3. E. Sirtl and K. Reuschel, *Z. Anorg. Allgem. Chem.*, **332**, 113 (1964).
4. M. Nakagawa, *Kogyo Kagaku Zasshi*, **62**, 177 (1959).
5. S. E. Bradshaw, *Int. J. Electron.*, **23**, 381 (1967).
6. T. O. Sedgwick, *This Journal*, **111**, 1381 (1964).
7. W. R. Runyan, E. G. Alexander, and S. E. Craig, Jr., *ibid.*, **114**, 1154 (1967).
8. E. G. Bylander, *ibid.*, **109**, 1171 (1962).
9. H. C. Theuerer, *ibid.*, **108**, 649 (1961).
10. W. Steinmaier, *Philips Res. Repts.*, **18**, 75 (1963).
11. J. Bloem, *This Journal*, **117**, 1397 (1970).
12. W. H. Shepherd, *ibid.*, **112**, 988 (1965).
13. I. M. Skvortsov and V. V. Nikolaeva, *Izv. Akad. Nauk SSSR, Ser. Neorg. Mat.*, **6**, 1000 (1970).
14. R. C. Bracken, in "Chemical Vapor Deposition," p. 731, 2nd Intern. Conf., J. M. Blocher, Jr. and J. C. Withers, Editors, The Electrochemical Society Softbound Symposium Series, New York (1970).
15. P. C. Rundle, *Int. J. Electron.*, **24**, 405 (1968).
16. F. C. Eversteyn, P. J. W. Severin, C. H. J. v. d. Brekel, and H. L. Peek, *This Journal*, **117**, 925 (1970).
17. F. A. Kuznetsov and V. I. Belyi, *ibid.*, **117**, 785 (1970).
18. F. C. Eversteyn, *Philips Res. Repts.*, **26**, 134 (1971).
19. P. C. Rundle, *J. Cryst. Growth*, **11**, 6 (1971).
20. S. K. Tung, *This Journal*, **112**, 436 (1965).
21. S. Mendelson, in "Single Crystal Films," M. H. Francombe and H. Sato, Editors, MacMillan Co., New York (1964).
22. V. J. Silvestri, *This Journal*, **116**, 81 (1969).
23. N. N. Sheftal' and E. I. Givargizov, *Soviet Phys.-Cryst.*, **9**, 576 (1965).
24. P. E. Gruber, in "Chemical Vapor Deposition," p. 25, 2nd Intern. Conf., J. M. Blocher, Jr. and J. C. Withers, Editors, The Electrochemical Society Softbound Symposium Series, New York (1970).
25. H. E. Carlton, J. H. Oxley, E. H. Hall, and J. M. Blocher, Jr., *ibid.*, p. 209.
26. K. J. Sladek, *This Journal*, **118**, 654 (1971).
27. W. C. Benzing, A. E. Ozias, and I. M. Helmer, "The Rate of Epitaxial Film Growth from Dichlorosilane," Applied Materials Technical Report.
28. M. Van Hoy, "Dichlorosilane Epitaxial Layers for Integrated Circuits," presented at the 71st National Meeting of the American Institute of Chemical Engineers, Feb. 20-23, 1972.
29. A. Lekholm, *This Journal*, **119**, 1122 (1972).
30. J. M. Charig and B. A. Joyce, *This Journal*, **109**, 957 (1962).
31. J. Burmeister, *J. Cryst. Growth*, **11**, 131 (1971).
32. J. Nishizawa, T. Terasaki, and M. Shimbo, *J. Cryst. Growth*, **12**, 241 (1972).
33. V. S. Kravchenko, Yu. M. Rumiantsev, and F. A. Kuznetsov, in "The Third Intern. Conf. on Chem. Vapor Deposition," p. 122, F. A. Glaski, Editor, Am. Nuclear Soc., Hinsdale, Ill. (1972).
34. J. Bloem, in "Semiconductor Silicon 1973," p. 180, H. R. Huff and R. R. Burgess, Editors, The Electrochemical Society Softbound Symposium Series, Princeton, N. J. (1973).

## Iron Oxide—An Inorganic Photoresist and Mask Material

W. Robert Sinclair,\* D. L. Rousseau, and J. J. Stancavish

Bell Laboratories, Murray Hill, New Jersey 07974

The publication costs of this article have been assisted by Bell Laboratories.

#### ABSTRACT

The etching rate in dilute acids of iron oxide thin films prepared either by sputtering in  $\text{CO}/\text{CO}_2$  mixtures or by low temperature chemical vapor deposition techniques, may be modified by irradiation with an argon-ion cw laser. Depending on the exposure time and power levels used, laser irradiation may (i) leave the film unaffected, (ii) greatly reduce its solubility, or (iii) completely remove the film. For exposures ranging from several seconds to a few minutes, the power level necessary to produce low solubility is several hundred milliwatts per square millimeter. Film evaporation begins at a few watts per square millimeter. By rapidly translating the film through the focal point of a laser beam, regions of reduced solubility in the form of a line as narrow as  $1\ \mu\text{m}$  have been obtained at writing velocities of 2000 cm/sec. It is proposed that with these techniques, iron oxide "see through" masks for use in integrated circuit technology may be written directly.

It has recently been shown that iron oxide films are suitable as "see through" masks for use in integrated circuit technology. These films may be made by chemical vapor deposition (CVD) using  $\text{Fe}(\text{CO})_5$  (1) or by rf sputtering of Fe or  $\text{Fe}_2\text{O}_3$  electrodes in a  $\text{CO}-\text{CO}_2$  atmosphere (2). Chemical analysis (3, 4) in-

dicates the films are a mixture of  $\text{Fe}_2\text{O}_3$  and  $\text{Fe}_2(\text{CO})_9$ . An essential attribute of these films is their rapid rate of solution in 6M HCl. In this report we investigate the possibility of changing the etching rate of these films using a cw laser beam as a heating agent.

Clearly the etching rate of iron oxide films and ways of modifying it are of great importance in the use of iron oxide as a mask material. In particular,

\* Electrochemical Society Active Member.

Key words: photomasks, laser irradiation, thin films.

MacChesney *et al.* have shown that the etching rate in 6M HCl of CVD iron oxide films is quite dependent on the substrate temperature during deposition. Films prepared at about 200°C dissolve very slowly ( $t \sim 1$  hr) in 6M HCl, whereas films prepared at 160°C or lower dissolve in less than 1 min. Sullivan (3) has also shown that heat-treatments can convert a "soluble" film to an "insoluble" film. These results suggested that localized heating might be used to produce insoluble patterns of iron oxide in a soluble iron oxide film. Electron beam heating of iron oxide films has been studied and is discussed in the accompanying article (5). There have been a few reports in the literature of inorganic materials in which the rate of solubility has been modified by electron beam irradiation (6, 7) and a report by Fitzgibbons and Hartwig (8) in which the solubility of an amorphous film of  $\text{TiO}_2$  was modified both by electron beam irradiation and by exposure to ultraviolet radiation. In the present work we have found that by controlling the intensity of an incident laser beam the films may be made to behave either as positive or as negative resists. Linewidths as small as 1  $\mu\text{m}$  have been obtained at laser beam scanning velocities of 2000 cm/sec.

### Experimental

Two sources of  $\sim 2500\text{\AA}$  thick iron oxide films were used in this investigation. Some were prepared by sputtering from an Fe electrode in an 80% CO-20%  $\text{CO}_2$  plasma and the others, which were prepared commercially by the CVD method, were purchased from Towne Laboratories in Somerville, New Jersey. The samples were irradiated with a Coherent Radiation Model 53 Argon-Ion Laser. In general the 5145Å output was used. A few irradiations were carried out at 4880Å but these showed no observable differences in the resulting changes to the iron oxide film. The output power of the 1.5 mm diameter beam at 5145Å was held constant at either 1.5 or 2.5W.

Two series of experiments were performed. In the first, for various exposure times, the average power threshold required to reduce the solubility of the iron oxide film was determined. The measurements were made by operating the laser at constant power and then controlling the power density at the film by focusing the beam and varying the position of the sample in the divergent cone of light, as shown in Fig. 1a. The samples were irradiated for a constant time ranging from 10 sec to 5 min. Lenses with focal lengths ranging from 5 to 9 cm were used. The resulting thresholds were determined by calculating the average power density over the appropriate cross-sectional area. In these experiments the most consistent results were obtained from the CVD films possibly because they had a very homogeneous thickness range, and the results quoted are those obtained from these films.

In a second series of experiments, iron oxide samples were attached to a 6 in. diameter turntable as shown in Fig. 1b. By using synchronous motors, rotation speeds ranging from about 0.1 to 2000 rpm were obtained giving sample velocities of about 0.1-2000 cm/

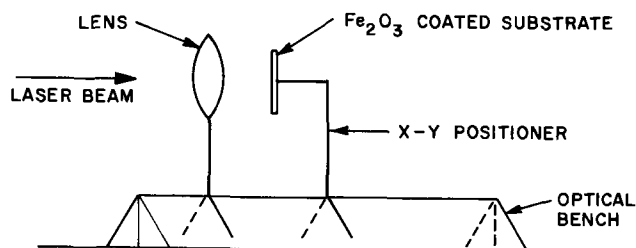


Fig. 1a. Schematic drawing of experimental arrangement for static sample irradiations.

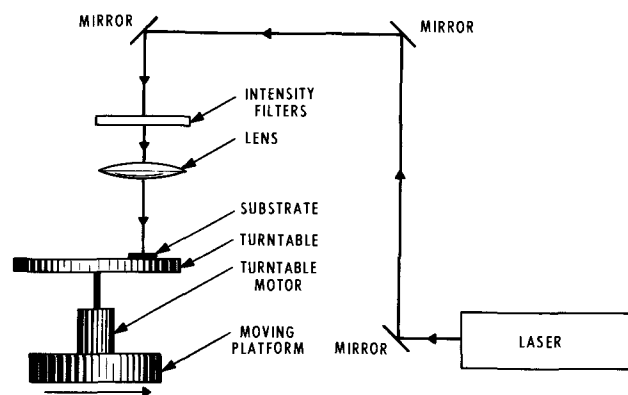


Fig. 1b. Schematic drawing of experimental arrangement for moving sample irradiation.

sec. The turntable motor was attached to a platform which was laterally translated so that the laser beam interacted with the substrate in a series of quasi-parallel arcs. Samples were placed at the focal point of a lens with a 6 mm focal distance and the beam intensity was attenuated by insertion of neutral density filters. With this system, measurements of the minimum linewidths and the feasibility of high speed writing were determined. In these experiments only sputtered films (1000 and 2500Å thick) were studied. In the following discussion only results for the 2500Å thick films are presented. The thinner films behaved in a similar fashion except that smaller linewidths were obtained in general.

Although most measurements were made on samples deposited on glass or fused silica substrates, films deposited on sapphire substrates were also studied to explore the importance of thermal conductivity, and to verify that the observed solubility changes were not strongly substrate sensitive. After irradiation and microscopic inspection, the films were treated with 6M HCl for about 2 min to see if any insoluble material had been produced. Any resulting insoluble material could be left in a 6M HCl bath for 1 hr without apparent change, establishing a ratio of greater than 25 for the etch rate difference before and after irradiation. Exposure of this material for a few minutes to a reducing solution containing powdered iron in 6M HCl would dissolve the irradiated samples (9).

### Results and Discussion

The effect of laser irradiation on soluble iron oxide films is a critical function of the laser power density and of exposure time. At insufficient exposure the irradiated section will dissolve in 6M HCl in about the same time as the unexposed films and there is no visual evidence of change. At more powerful exposures the film is made insoluble and there is a noticeable darkening of the film where exposed. The optical absorption spectrum of an exposed film is compared with that of a typical unexposed CVD film in Fig. 2. The results are similar to those obtained on heating iron oxide films in an oven to about 475°C (10). Because of the strong absorption at 589 nm by this insolubilized film one would probably prefer to use a light source of longer wavelength than the often used sodium d-line if one wishes to make use of the irradiated film as a see through mask. It should be pointed out that spectra intermediate between the extremes presented in Fig. 2 should be obtainable at slightly lower laser powers. In these experiments in which the laser beam was incident on the sample for times between 10 sec and 5 min, the threshold flux sufficient to yield an insoluble residue after etching in 6M HCl was determined. The limits for several exposure times are indicated in Table I. It is seen that there is a wide range of power densities in which the solubility is reduced, but there are problems in determining precise limits for the range

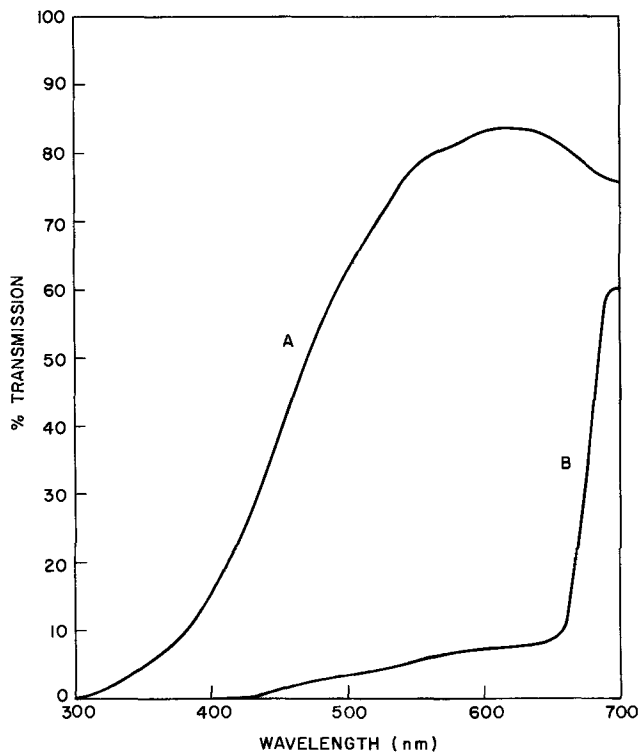


Fig. 2. Optical absorption spectra for iron oxide films. a, Not laser irradiated; b, laser irradiated.

of conditions. At low power densities fogging occurs as the lateral heat conduction becomes increasingly important. Furthermore, at this end, the degree of etch rate varies fairly continuously, approaching the un-irradiated value at lower power densities. At the high power density end, the film cracks and bubbles, with occasional breakage of the glass substrate. As the power is increased, the iron oxide is completely removed from the substrate so that the process effectively leads to a positive resist. Qualitatively similar results were obtained with iron oxide deposited on a sapphire substrate but the thresholds were about 50% higher.

To study in greater detail the exposure needed to modify the solubility of iron oxide films upon laser irradiation, and to determine the minimum linewidths readily obtainable, samples were placed on the rotating table and passed through the focal point of the laser beam. As with the static experiments, several different stages of change in the film could be identified, depending on the incident laser intensity. At the highest intensities, the laser beam left a completely transparent path with insoluble iron oxide boundaries (Fig. 3a). At lesser intensities some globules of insoluble material remained in an otherwise transparent path (Fig. 3b). At still lower intensities the laser beam left a darkened path which was found to be insoluble in 6M HCl (Fig. 3c). Finally at the lowest intensities there was no effect on the appearance or solubility of the film. The velocities in these experiments ranged from 0.5 to 2000 cm/sec. At low scan speeds, low laser powers and long focal length lenses were used. The long focal length lenses gave rather large ( $\sim 100 \mu\text{m}$ ) diffraction limited spots, so that the resulting lines were correspondingly wide. At high scanning speeds, higher laser powers

Table I. Power density requirements for negative resist formation in iron oxide in static experiments

Exposure time (sec)	Minimum power density ( $\text{mW}/\text{mm}^2$ )	Maximum power density ( $\text{mW}/\text{mm}^2$ )
10	1000	3000
30	800	2000
300	500	1500

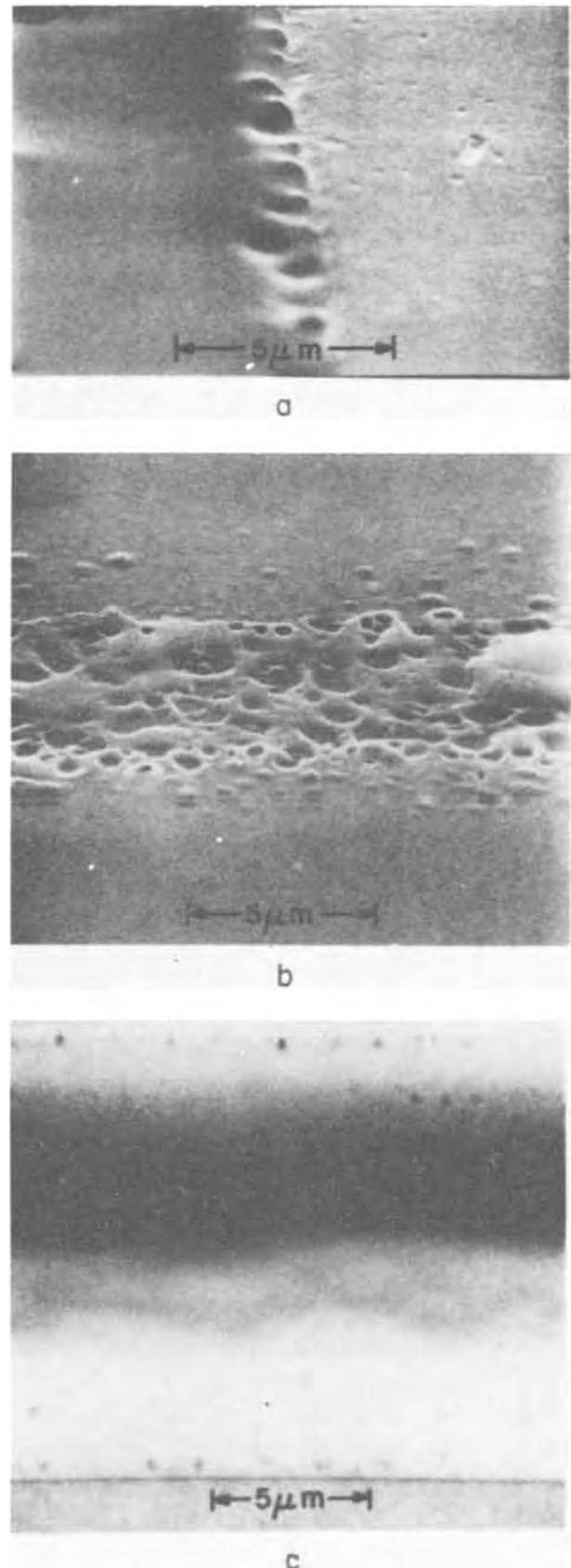


Fig. 3. Scanning electron microscope view of laser irradiated iron oxide films from kinetic experiments. a, Edge between completely evaporated iron oxide line on right and unreacted iron oxide film on left. Total width of line was  $36 \mu\text{m}$ . b, Line of insoluble iron oxide globules and voids. Iron oxide in areas above and below this line has been removed by dissolving in acid. c, Line of insoluble iron oxide. Iron oxide in areas above and below this line has not been removed by dissolving in acid as yet. After dissolving in acid a small amount of granularity will be noted at the edges of the line.

Table II. Linewidths of iron oxide films (ca. 2500Å thick) on fused silica made insoluble by laser action as a function of scan speed and power density

Scan speed (cm/sec)	Power density (W/mm <sup>2</sup> )	Linewidth (μm)
3	$3 \times 10^2$	70
30	$3 \times 10^4$	7
2000	$10^5$	1

were used along with short focal length lenses to obtain a high flux density. Therefore, the widths of the lines we obtained were, in some cases, as small as 1 μm. In Table II some typical scan speeds, linewidths, and power densities are listed for conditions under which the iron oxide films were reduced in solubility (i.e., the formation of a negative resist). Since near the focal point the cross section varies rapidly, accurate power density measurements were not made. The values reported in the table correspond to the approximate center of the power range for negative resist formation. It should be pointed out that at the limit of the range studied, lines as narrow as 1 μm were obtained at writing speeds as high as 2000 cm/sec.

The ultimate limit to the resolution obtainable and maximum writing speed with which solubility changes may be effected no doubt may be extended beyond the limits obtained in this investigation. The purpose of this study was only to demonstrate the general feasibility of laser induced solubility changes. Narrower lines should be obtainable by reducing the focal length of the lens. Similarly, faster writing speeds should be possible by increasing the power density at the sample surface.

The details of the structure of both the sputtered and the CVD films are not yet well understood, nor are the changes which occur upon selective heating. Initially it was felt that the presence of carbon in the films had little effect on the etch rate and it was crystalline size that dominated solubility properties (1). However, chemical analyses (3, 4) have now shown that the films typically contain ~25% Fe<sub>2</sub>(CO<sub>3</sub>)<sub>3</sub> in Fe<sub>2</sub>O<sub>3</sub>, and infrared spectra have confirmed the presence of carbonate in the films. Furthermore, in CVD films deposited on substrates held at 200°C, and found to be insoluble, chemical analysis indicated there was no carbon present. Although it is not known which effect is dominant it is now felt that both crystalline size and also the presence of iron carbonate may influence the solubility. In this study, in addition to the before-mentioned visible absorption measurements, a few preliminary reflection electron diffraction measurements have been made in an effort to determine the differences between the laser exposed insoluble films and unexposed films. Diffraction patterns of the laser treated films were sharper than the patterns obtained from untreated films, corresponding to a substantial increase in crystallite size. From the d-spacings the irradiated films were identified as α-Fe<sub>2</sub>O<sub>3</sub>. This is consistent with other studies in which air annealed films give Fe<sub>2</sub>O<sub>3</sub> and vacuum annealed films give Fe<sub>3</sub>O<sub>4</sub> and Fe<sub>2</sub>O<sub>3</sub> (5).

From the results presented here it is clear that laser induced changes in the solubility of iron oxide films may have application in the production of integrated circuits. The usefulness of iron oxide films as photoresist material with high temperature stability is worth exploring. At relatively low laser intensities the film becomes insoluble and thus acts as a negative resist, whereas at high laser intensities the film may be completely vaporized giving a positive resist. It was observed that the edge definition surrounding this vaporized area was substantially sharper than that obtainable from metallic films and other oxide films that lack such crystallinity changes. This is possibly due to a higher power threshold for removal of the crystallized border material than for removal of the amorphous material (11). Exposure could be carried out by placing a conventional mask over the sample. However, in view of the short exposure times shown to be needed in the present study, the mask step may be completely eliminated, and, with a programmed laser beam, a pattern might be written directly on the photoresist material. (At a scanning speed of 2000 cm/sec a 1 μm wide path will cover a 1 by 1 cm area in about 5 sec assuming no overlap and no time loss at the beginning and end of a pass.) Such a technique would also be particularly appropriate for making iron oxide masks for thin-film circuits on ceramic where minimum linewidths are ~50μ.

#### Acknowledgment

We thank M. V. Sullivan and P. A. Turner for several helpful discussions. The reflection electron diffraction determinations were done by G. W. Kammlott and the visible absorption spectrum was measured by Mrs. G. A. Pasteur. Assistance in microscopy by Mrs. I. M. Payne was also very helpful.

Manuscript submitted Oct. 11, 1973; revised manuscript received Jan. 28, 1974.

Any discussion of this paper will appear in a Discussion Section to be published in the June 1975 JOURNAL. All discussions for the June 1975 Discussion Section should be submitted by Feb. 1, 1975.

#### REFERENCES

1. J. B. MacChesney, P. B. O'Connor, and M. V. Sullivan, *This Journal*, **118**, 776 (1971).
2. F. G. Peters, W. Robert Sinclair, and M. V. Sullivan, *ibid.*, **119**, 305 (1972).
3. M. V. Sullivan, *ibid.*, **120**, 545 (1973).
4. P. K. Gallagher, W. Robert Sinclair, R. A. Fastnacht, and J. P. Luongo, *Thermochim. Acta*, **8**, 141 (1974).
5. G. W. Kammlott and W. Robert Sinclair, *This Journal*, **121**, 929 (1974).
6. T. W. O'Keeffe and R. M. Handy, *Solid-State Electron.*, **11**, 261 (1968).
7. B. H. Hill, *This Journal*, **115**, 668 (1969).
8. E. T. Fitzgibbons and W. H. Hartwig, NASA, JSEP Tech. Rep. AFSOR 69-1972, April 5, 1970; also Abstract 12, p. 38, Electrochemical Society Extended Abstracts, Spring Meeting, May 9-13, 1971.
9. M. V. Sullivan, Personal communication.
10. R. B. Elo and R. N. Tauber, Personal communication.
11. M. Feldman, D. L. Rousseau, W. Robert Sinclair, W. W. Weick, Unpublished results.

# Fe<sub>2</sub>O<sub>3</sub>—An Inorganic Electron Resist Material

G. W. Kammlott and W. Robert Sinclair\*

Bell Laboratories, Murray Hill, New Jersey 07974

The publication costs of this article have been assisted by Bell Laboratories.

## ABSTRACT

Fe<sub>2</sub>O<sub>3</sub> films of the type used for see-through masks dissolve much more slowly in 6M HCl after irradiation with the electron beam of a scanning electron microscope. The ratio of the time to dissolve irradiated material to the time to dissolve unirradiated material is 25 or greater. The films behave, therefore, as negative resists. Irradiation studies were conducted over a voltage range of 5-30 kV, a current range of  $5 \times 10^{-8}$ - $7 \times 10^{-7}$ A, and scanning rates in the range 1-500 mm/sec. On glass substrates at room temperature a minimum current of  $1 \times 10^{-7}$ A is required at a beam diameter of approximately 1  $\mu$ m. At  $7 \times 10^{-7}$ A, Fe<sub>2</sub>O<sub>3</sub> flakes from the substrate thus establishing a practical maximum current for the process. In general, the line width of the Fe<sub>2</sub>O<sub>3</sub> made insoluble increases with increasing voltage and decreases with increasing scanning rate. For a scanning rate of 500 mm/sec and a beam current of  $4 \times 10^{-7}$ A at 10 kV, a line width of 0.8  $\mu$ m is obtained. Edge definition is excellent. Transmission electron microscopy shows the irradiated, insoluble part of the film to be a mixture of Fe<sub>3</sub>O<sub>4</sub> and  $\alpha$ -Fe<sub>2</sub>O<sub>3</sub>. Similar results are obtained for Fe<sub>2</sub>O<sub>3</sub> films deposited onto oxidized silicon and silicon, although the latter requires a somewhat higher threshold current. Use of this process is suggested for direct construction of see-through masks without intermediate steps involving organic resists. Because of their dimensional and thermal stability, Fe<sub>2</sub>O<sub>3</sub> resist films should also be useful as masks for processes involving high temperatures. These include ion implantation, sputtering, and possibly dopant diffusion.

Fe<sub>2</sub>O<sub>3</sub> films prepared by reacting Fe(CO)<sub>5</sub> and O<sub>2</sub> at temperatures below 165°C dissolve within a few minutes in 6M HCl (1) at room temperature. Due to this ease of etching, coupled with desirable optical and mechanical properties, the so-called soluble Fe<sub>2</sub>O<sub>3</sub> films have been used recently for see-through masks (2) in integrated circuit manufacture. In contrast, Fe<sub>2</sub>O<sub>3</sub> films prepared at temperatures of 200°C and higher by the same reaction are relatively insoluble. A film of the high temperature form of the same thickness (ca. 2500Å) requires 50 min or more to dissolve in the same solvent. MacChesney *et al.* (1) have attributed this difference in rate of dissolution to differences in grain size in the deposited films. This led to speculation that techniques could be developed for changing the crystallite size in selected areas and, using the consequent large change in rate of dissolution, the Fe<sub>2</sub>O<sub>3</sub> film would then behave as a resist material. As we shall show later, the chemistry involved in these reactions is not as simple as initially thought. Nevertheless, electron beam irradiation and laser irradiation (3) have been used successfully to change the rate of dissolution of Fe<sub>2</sub>O<sub>3</sub> films. The use of localized electron beam irradiation to decrease the dissolution rate of soluble Fe<sub>2</sub>O<sub>3</sub> films in selected areas is the topic of this paper.

Inorganic materials are not usually thought of as resist materials. We are aware of three other studies of inorganic systems, however, where substantial changes in the rate of dissolution as a result of electron beam irradiation have been reported. O'Keeffe and Handy (4) found that electron beam irradiation of SiO<sub>2</sub> could increase the etch rate by a factor of 3. Hill (5) studied the electron irradiation of Al<sub>2</sub>O<sub>3</sub> and Ta<sub>2</sub>O<sub>5</sub> films and noted a decrease in the rate of dissolution. Fitzgibbons and Hartwig (6) irradiated a gel-like film of TiO<sub>2</sub> and obtained an insoluble film.

## Experimental

**Material.**—Amorphous Fe<sub>2</sub>O<sub>3</sub> films which dissolve quickly in 6M HCl can be prepared either by chemical vapor deposition (CVD) (1) or by sputtering (8). Al-

though patterns have been written on films prepared either way, only the results on CVD films will be presented since results on the sputtered films showed greater spread in results possibly because they were less homogeneous in thickness. The CVD films used (2500Å thick) were from a commercial source (Towne Laboratories, Somerville, New Jersey). For transmission electron microscopy (TEM), films of Fe<sub>2</sub>O<sub>3</sub> deposited on carbon coated glass substrates were obtained from the same source.

**Instrumentation.**—All electron beam exposures were carried out with a Cambridge Stereoscan Mk IIa scanning electron microscope (SEM) equipped with a beam blanking unit, a specimen current amplifier, and a 400 $\mu$  final aperture. Accelerating voltages of 5-30 kV were used and specimen currents ranged from  $5 \times 10^{-8}$  to  $1 \times 10^{-6}$ A. The electron beam was approximately 1  $\mu$ m in diameter or less with a current density of up to 50 A/cm<sup>2</sup>. The focused beam scanned the Fe<sub>2</sub>O<sub>3</sub> film in two perpendicular directions to yield grid patterns of various sizes. Most patterns measured 1 mm  $\times$  1 mm and were written at beam speeds up to 500 mm/sec. The SEM was also used for subsequent evaluation of the patterns, and transmission electron microscopy (TEM) was carried out with a Siemens Elmiskop 1A.

## Experimental Procedures

Since Fe<sub>2</sub>O<sub>3</sub> films are sufficiently conductive all current measurements were obtained by grounding them via a current amplifier. Condenser lens currents were varied to yield various sample currents, and the beam was then focused. The size of scanned area and the line speed determined the beam speed and the frame speed was set to yield between 100 and 250 lines per frame.

All exposures were evaluated visually (most of the patterns were readily seen with the unaided eye) as well as with a low power light microscope. Subsequent immersion in 6M HCl for approximately 2 min dissolved the unexposed areas. Some of the remaining grid patterns were then evaluated with the SEM.

For TEM, an Fe<sub>2</sub>O<sub>3</sub> film (~1000Å) deposited on carbon coated glass was floated onto a water surface and

\* Electrochemical Society Active Member.

Key words: photomasks, electron irradiation, thin films.

mounted on a copper grid. Patterns were then written with the SEM in a similar fashion but no etching treatment was given in this case.

### Results

At 5 kV some patterns written at  $3 \times 10^{-7}$ A and at beam speeds of 0.1 and 0.25 mm/sec were observable during the first period of the etching process. These patterns were removed from the substrate by 6M HCl along with the unexposed film. This is not surprising since calculation indicates that most of the energy loss in the  $\text{Fe}_2\text{O}_3$  film occurs above the film-substrate interface for these conditions (8). Thus a layer of acid-soluble film remains between the irradiated film and the substrate.

At 10 kV all patterns remained after etching. However, a minimum current of  $1 \times 10^{-7}$ A is required to form an insoluble film. The maximum effective beam speed changed drastically with current increase. At  $1 \times 10^{-7}$ A the maximum effective beam speed was 1 mm/sec, at  $2 \times 10^{-7}$ A 50 mm/sec, and at  $3 \times 10^{-7}$ A up to 500 mm/sec. At the latter two currents the resulting line width was  $0.8\mu$  (cf. Fig. 1) leading to a calculated current density of 40 A/cm<sup>2</sup>. When the beam speed at  $3 \times 10^{-7}$ A was slowed down the line width broadened to  $1.2\mu$  at 250 mm/sec and  $1.5\mu$  at 100-25 mm/sec. One of the remarkable features of these lines is the excellent edge definition as indicated in Fig. 1. Similarly, at  $4 \times 10^{-7}$ A and 250 mm/sec the line width was  $1.5\mu$  and at 25 mm/sec  $2\mu$ . Further slowing down of the beam resulted in flaking of the written path leaving a bare central area with a wall of unetched material on either side of the path (cf. Fig. 2).

Similar results were obtained at 20 and 30 kV with increases in line width by approximately a factor of 2 at comparable beam speed and current levels.

The electron irradiated films that remain on the glass substrate after etching are quite difficult to dissolve in 6M HCl. They are not noticeably attacked in less than an hour. This leads to a ratio of dissolution times for the irradiated material to the unirradiated material of at least 25.

Measurements of a less thorough nature have been made with  $\text{Fe}_2\text{O}_3$  on an oxidized (2000Å) silicon slice and also on an unoxidized silicon slice. With the oxidized silicon the electron beam and writing parameters are essentially the same as for the glass substrate. With the unoxidized silicon much slower scanning rates are required indicating perhaps that the greater ther-

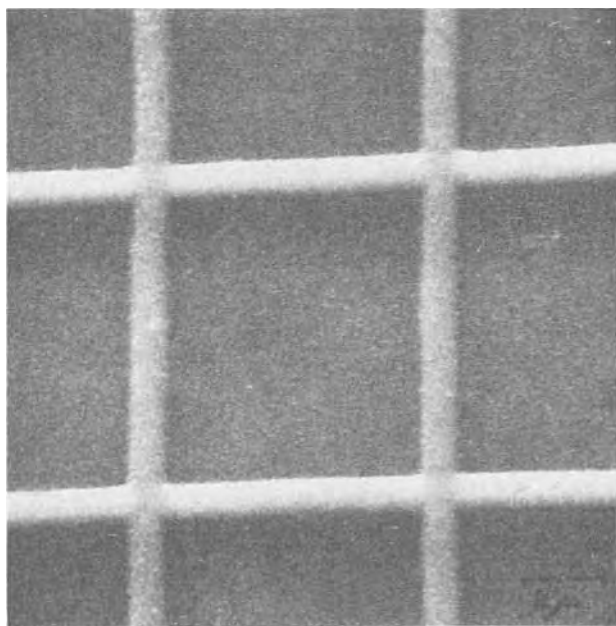


Fig. 1. Pattern written at 10 kV  $3 \times 10^{-7}$  and 500 mm/sec beam speed.

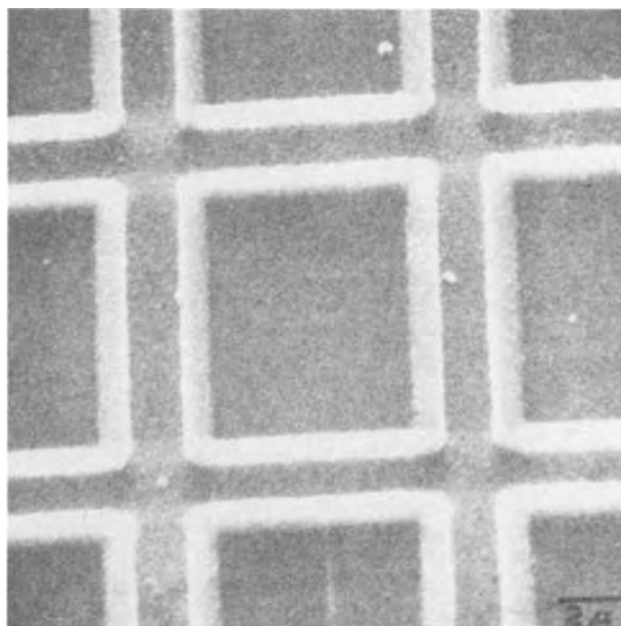


Fig. 2. Pattern written at 10 kV  $4 \times 10^{-7}$  and 10 mm/sec beam speed.

mal conductivity of silicon as compared with glasses affects the process.

Transmission electron micrographs clearly show the pattern written by the electron beam as a matrix of crystallized material with crystallite sizes up to  $0.5\mu\text{m}$ . Selected area diffraction of the unexposed squares and exposed line support this observation. While the unexposed areas yield rather broad ring patterns because of crystallite sizes well below 100Å, the exposed areas show a number of superimposed single-crystal patterns (cf. Fig. 3). For more detailed identification of the materials involved in the reaction process, samples were prepared by annealing films in air and in vacuum as well as by beam exposure with the lines closely spaced to yield large areas of totally exposed material. Several large area electron diffraction patterns were obtained. The unexposed film, as well as films annealed in vacuum at  $300^\circ\text{C}$  for 2 hr and in air at  $450^\circ\text{C}$  for 1-5 hr yield similar broad diffuse ring patterns, although changes in color and rate of solution in 6M HCl are clearly obtained. Sharp ring patterns were obtained for these films when exposed in the TEM at high current levels for less than 1 min. A square exposed in the SEM at 10 kV and  $3 \times 10^{-7}$ A, and also films annealed at  $450^\circ\text{C}$  for 15 hr in air and in vacuum gave rise to sharp ring patterns. The d-spacings were determined using densitometer tracings and an Au standard diffraction pattern and compared to data in the ASTM powder diffraction file. The film annealed in air was identified as  $\alpha\text{-Fe}_2\text{O}_3$ . The vacuum-annealed film was  $\text{Fe}_3\text{O}_4$ , and the material exposed to the electron beam a mixture of the two iron oxides.

### Discussion

The original hypothesis on which this work was based was that we could heat an  $\text{Fe}_2\text{O}_3$  film with an electron beam to obtain larger crystallites and that these larger crystallites, following MacChesney's surmise, would have a much slower rate of solution in 6M HCl. The results tend to confirm these ideas but the sinter-mechanism of grain growth involved is not yet resolved. At the outset, one might expect some correlation between the product of the maximum scanning speed and the current. However, as indicated earlier, this does not hold as the scanning rate increases. In this discussion no reference has been made to the heat of crystallization which should become increasingly significant as the scanning rate increases.



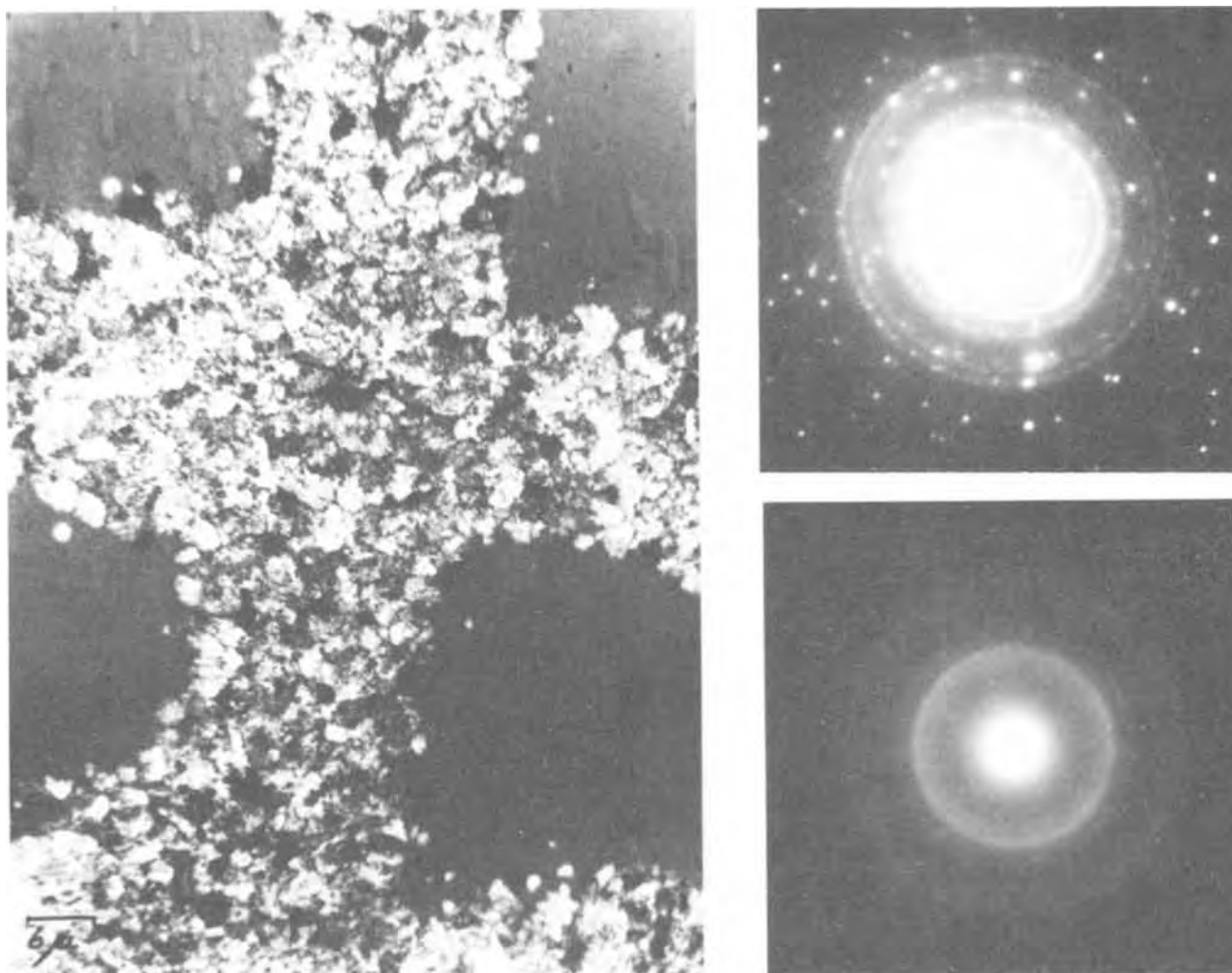


Fig. 3. Transmission electron micrograph of pattern written into  $\text{Fe}_2\text{O}_3$  film at  $3 \times 10^{-7}$  10 kV and 100 mm/sec beam speed. Selected area diffraction patterns from unexposed and exposed area show crystallization due to beam exposure.

Before any meaningful discussion of the kinetics of this crystallization process can be made, the heat of reaction and activation energy of the process must be determined. In addition, it is now known that there is a significant amount of carbonate in the film (9,10) and the slowing down of the dissolution process in acid might be explained, with our present meager knowledge of the system, simply in terms of the loss of an acid soluble carbonate on heating. These are probably not the only approaches available to an understanding of this interesting process. However, more experimental information is needed to characterize the reaction(s) involved. Since inorganic resist materials could have advantages over organic resists in some processes, better understanding of the chemistry and physics of this system may enable a more efficient search to be made for other inorganic resists. It would be surprising if  $\text{Fe}_2\text{O}_3$  were unique in its properties.

From the results obtained it is evident that one should be able to "write" contact or projection  $\text{Fe}_2\text{O}_3$  masks using a programmed electron beam. Writing machines have already been built and used in various laboratories using organic resists. Here, the  $\text{Fe}_2\text{O}_3$  will be both the mask material and the resist material. The fact that the ratio of dissolution time of the exposed  $\text{Fe}_2\text{O}_3$  to dissolution time of the unexposed  $\text{Fe}_2\text{O}_3$  is so large means that the solution process need not be closely controlled. The danger of undercutting, present when organic resists are used, is eliminated. We anticipate that the consequent cut in processing steps will result in masks with fewer defects and concomitant savings.

### Summary

The rate of solution in 6M HCl of  $\text{Fe}_2\text{O}_3$  films of the soluble type used in making see-through masks has been made drastically slower by a factor of 25 or greater by irradiation with electrons in a SEM. For 2500Å films on a glass substrate a minimum current of  $1 \times 10^{-7}$ A at 10 kV is required. At higher than  $7 \times 10^{-7}$ A at 10 kV the films distort and may detach from their substrates. The total voltage range studied was 5-30 kV. Scanning rates from 1 to 500 mm/sec were used. In general, the line width of insolubilized  $\text{Fe}_2\text{O}_3$  increased with increasing voltage and with decreasing scanning rate. Similar results were obtained on silicon substrates with 2000Å of thermal  $\text{SiO}_2$ . One can also write on unoxidized silicon substrates using different experimental parameters.

The films before electron irradiation are amorphous. After writing in the SEM, the films are a crystalline mixture of  $\alpha$ - $\text{Fe}_2\text{O}_3$  and  $\text{Fe}_3\text{O}_4$ .

### Acknowledgments

The authors are pleased to acknowledge technical assistance and advice from conversations with R. D. Heidenreich, M. V. Sullivan, L. F. Thompson, and P. A. Turner.

Manuscript submitted Oct. 11, 1973; revised manuscript received Jan. 28, 1974.

Any discussion of this paper will appear in a Discussion Section to be published in the June 1975 JOURNAL. All discussions for the June 1975 Discussion Section should be submitted by Feb. 1, 1975.

## REFERENCES

1. J. B. MacChesney, P. B. O'Connor, and M. V. Sullivan, *This Journal*, **118**, 776 (1971).
2. W. Robert Sinclair, Miles V. Sullivan, and R. A. Fastnacht, *ibid.*, **118**, 341 (1971).
3. W. Robert Sinclair, D. L. Rousseau, and J. Stan-cavish, *ibid.*, **121**, 925 (1974).
4. T. W. O'Keeffe and R. M. Handy, *Solid-State Elec-tron.*, **11**, 261 (1968).
5. B. H. Hill, *This Journal*, **115**, 668 (1969).
6. E. T. Fitzgibbons and W. H. Hartwig, NASA, JSEP Tech. Rep. AFSOR 69-1972, April 5, 1970; Ab-stract 12, p. 38, Electrochemical Society Extended Abstracts, Spring Meeting, Washington, D.C., May 9-13, 1971.
7. F. G. Peters, W. Robert Sinclair, and M. V. Sulli- van, *This Journal*, **119**, 305 (1972).
8. T. E. Everhart and P. H. Hoff, *J. Appl. Phys.*, **42**, 5837 (1971).
9. M. V. Sullivan, *This Journal*, **120**, 545 (1973).
10. P. K. Gallagher, W. Robert Sinclair, R. A. Fast- nacht, and J. P. Luongo, *Thermochim. Acta*, **8**, 141 (1974).

## A Systematic Investigation of Quantitative Fits to III-V Pseudobinaries Using the Quasiregular Model and Its Special Cases

R. F. Brebrick\* and R. J. Panlener

*Metallurgy and Materials Science, Mechanical Engineering Department,  
Marquette University, Milwaukee, Wisconsin 53233*

*The publication costs of this article have been assisted by Marquette University.*

### ABSTRACT

Previous analyses of the liquidus and solidus lines in III-V pseudobinary systems are combined and extended. (i) The ideal, strictly regular, athermal, and quasiregular models are investigated for each phase. (ii) A quantitative measure,  $\sigma$  ( $^{\circ}\text{C}$ ) of a fit is defined and determined. (iii) All sets of values for the parameters of a model giving a value of  $\sigma$  less than a critical value ( $7^{\circ}$ - $16^{\circ}\text{C}$ ) characterizing the experimental accuracy are determined and treated on an equal footing. It is found that the strictly regular liquid-quasiregular solid model is the simplest model giving satisfactory fits for all of the seven systems chosen as the best defined experimentally. Moreover these fits are obtained over a range of values of the three model parameters. As a consequence, thermodynamic properties of the liquid are not closely specified by the analysis. In contrast, for the solid at one temperature,  $T = m$ , we find  $\Delta G_{\text{M}}^{\text{xs}} = (b \pm 200)y_1y_2$ , where the  $y$ 's are mole fractions and  $m$  and  $b$  are determined from the fits:  $m$  and  $b$  are correlated to the properties of the III-V components, and  $m$  is  $0.98 \pm 0.03$  of the average of their melting points while, within  $\pm 250$  cal,  $b$  is proportional to the sixth power of the fractional difference in their lattice parameters. Three of four other systems with data satisfy these correlations. Seven others with no data are discussed. The stability of a quasiregular phase is discussed and the conditions for the formation of normal and "inverted" miscibility gaps established.

The nine III-V binary systems containing either Al, Ga, or In on the one hand and P, As, or Sb on the other, all show a single, zinc-blende structure compound at 50 atom per cent (a/o). The eighteen ternary systems formed by taking at least one element from each of the above two groups all have a single pseudobinary section between two III-V compounds. Considerable, though by no means complete, data is available for the pseudobinary sections. Foster and Scardefield (1, 2) and Foster, Scardefield, and Woods (3, 4) have recently determined solidus points for four of these in which a complete range of solid solutions is formed. A thermodynamic analysis by Foster and Woods (5, 6, 3, 4) indicates that six pseudobinary sections can be satisfactorily fit on the assumption that the liquid phase is essentially ideal while the solid phase is athermal (zero enthalpy of mixing, nonzero excess entropy of mixing). Panish and Ilegems (7) obtain what they consider somewhat poorer fits on the assumption that both liquid and solid phases are strictly regular (nonzero enthalpy of mixing, zero excess entropy of mixing). The latter authors were in general not primarily

concerned with an optimum fit in the pseudobinary section, but rather with acceptable over-all fits in both the ternary proper and in the pseudobinary section.

For eleven pseudobinary sections Stringfellow (8) has obtained qualitative agreement using a strictly regular model in which the adjustable parameters are fixed by considerations independent of the experimental liquidus and solidus lines. Subsequently he has recalculated (9) the interaction parameters for the solid solutions. A proportionality constant occurring in his calculation is chosen so that the interaction parameters agree as closely as possible with those obtained by Panish and Ilegems (7). Steininger (10) has shown for a number of binary and pseudobinary systems that, given either the liquidus line or the solidus line, the other can be calculated accurately assuming ideal solutions. Moreover, this is the case even when an ideal solution model does not fit the individual liquidus and solidus lines well.

In this paper we present the results of computer fits to those seven, III-V, pseudobinary sections for which the data seem most reliable. Our working premise, which proved correct, was that the quasiregular liquid-quasiregular solid model, containing a maximum of

\* Electrochemical Society Active Member.

Key words: inverted miscibility gap, Gibbs free energy of mixing, lattice parameter, miscibility gap.



four adjustable parameters, two for each phase, is sufficiently flexible to lead to satisfactory fits. The objectives are to combine and extend the previous analyses by:

1. Obtaining, hitherto unavailable, quantitative measures of all fits obtained. This measure, denoted by  $\sigma$ , is defined in the next section.
2. Establishing the simplest variants of the general model (those with the maximum number of zero values for the four adjustable parameters) that give satisfactory fits for all the systems.
3. Determining the sensitivity of  $\sigma$  to the exact values of the adjustable parameters. Thus an essential part of our investigation is not only to determine the minimum  $\sigma$  attainable, but also to fix the range over which the adjustable parameters can be changed without significantly increasing  $\sigma$  above this minimum value.

After defining a quantitative measure of fit,  $\sigma$ , a critical value is adopted for each system below which  $\sigma$  must fall if a fit is to be considered satisfactory. Then all sets of values for the adjustable parameters giving a value of  $\sigma$  less than the critical value are to be considered on equal terms with that parameter set that gives the minimum value. Admittedly, an element of arbitrariness in the specification of a critical value for  $\sigma$  cannot be avoided in practice. Nevertheless, this is preferable to a procedure in which no specification is made and the best fit obtained is taken as unique. Among the specific interesting results obtained within the general objectives, are answers to the following questions: (a) Does the ideal liquid-athermal solid model, proposed by Foster and Woods, describe the III-V pseudobinaries better than an ideal liquid-strictly regular solid model? (b) Is the two parameter, ideal liquid-quasiregular solid model better than the two parameter, strictly regular liquid-strictly regular solid model? (c) Which, if any, thermodynamic properties are most closely and reliably fixed as a result of the fits to the liquidus and solidus lines?

We find that ideal liquid-athermal solid and ideal liquid-strictly regular solid models give essentially the same fits except for GaAs-GaSb. However, the computer fits show there is no basis for choosing either of these models over the more general ideal liquid-quasiregular solid model, since satisfactory fits are obtained for a significant range in the adjustable parameters of the solid phase. The ideal liquid-quasiregular solid model gives satisfactory fits for five of the seven systems and appears slightly inferior to the strictly regular liquid and solid model, which gives satisfactory fits for six systems. The simplest variant of the full quasiregular model that fits all seven systems with the presently available data is the three parameter, strictly regular liquid-quasiregular solid model. For each system, satisfactory fits are obtained along a line segment in the plane of the two adjustable parameters for the solid phase. Thus although the thermodynamic properties of the pseudobinary liquid phase are not closely defined, the excess Gibbs free energy of mixing of the solid phase is defined at one temperature,  $T = m$ , to within  $\pm 200$  cal in terms of a parameter,  $b$ . Correlations are found between these parameters and the properties of the III-V compounds defining a pseudobinary section. The parameter,  $m$ , is  $0.98 \pm 0.03$  of the average of the melting points. The parameter,  $b$ , is proportional to the sixth power of the fractional difference in the room temperature lattice parameters. Analysis of four additional III-V pseudobinary sections shows these correlations hold well for two systems, fair for the third, and not at all for the fourth. The discrepancy in the last case is most likely due to significant errors in the experimental solidus points and a calculated solidus line, believed to be more accurate, is given. The seven remaining pseudobinaries for which there are no data are also discussed in view of the empirical correlations found.

The plots of only a few phase diagrams are given in this paper. The disposition of the experimental points can be seen in plots already given in Ref. (1-6) or, for all the III-V pseudobinaries, in Ref. (7). Moreover, on page size graphs the agreement between experimental points and the calculated phase diagrams would look near perfect when the fits are within  $16^\circ\text{C}$  or, as in most cases here, within  $10^\circ\text{C}$ .

Before presenting the results, the necessary thermodynamic background is outlined in the next section along with a discussion of some relevant, general properties of a quasiregular phase that have not been given previously.

### Thermodynamic Background

A binary phase is called a simple solution (11) if the excess Gibbs free energy of mixing can be represented in terms of a composition-independent parameter,  $\Omega$ , as

$$\Delta G_M^{xs} = \Omega x_1 x_2 \quad [1]$$

where  $x_1$  and  $x_2$  are the mole fractions of components 1 and 2, respectively. We assume throughout that  $\Omega$  depends linearly on the temperature,  $T$ , i.e.

$$\Omega = W - VT \quad [2]$$

Solutions described by Eq. [1] and [2] have been called quasiregular in the past and, although objections (7) have been made against this terminology, we use it in favor of the lengthy phrase "linear temperature dependence, simple solution." It follows immediately that the enthalpy and excess entropy of mixing are given by

$$\Delta H_M = W x_1 x_2 \quad [3]$$

and

$$\Delta S_M^{xs} = V x_1 x_2 \quad [4]$$

so that Eq. [2] is tantamount to the assuming that  $\Delta H_M$  and  $\Delta S_M^{xs}$  are independent of  $T$ . Special cases of the quasiregular model of a phase include the ideal model ( $W = V = 0$ ), the strictly regular model ( $W \neq 0, V = 0$ ), and the athermal model ( $W = 0, V \neq 0$ ).

A quasiregular solution described by Eq. [1] and [2] can become unstable relative to internal decomposition, i.e., a miscibility gap can form. The behavior of this phenomenon can be elucidated by determining the zeros of the first and second composition-derivatives of the Gibbs free energy of mixing. Since the argument follows that widely given (11, 12) for strictly regular solutions, it is not repeated here. However, the main results and how they differ from those for the strictly regular solution have not been previously discussed and so are summarized. A miscibility gap, whose extremes at any  $T$  are symmetric about  $x = 1/2$ , is present whenever  $\Omega \cong 2RT$ , where  $R$  is the gas constant. In view of Eq. [2] this condition can be written as

$$W \cong (V + 2R)T \quad [5]$$

The critical temperature at which the miscibility gap disappears,  $T_c$ , is determined by taking the equality sign in Eq. [5], i.e.

$$T_c = W/(2R + V) \quad [6]$$

Thus for the special case of an athermal solution,  $W = 0$ , the critical temperature is zero. In contrast to the situation for strictly regular solutions, there are two kinds of miscibility gaps possible: the normal type that disappears for  $T > T_c$  and an inverted miscibility gap that appears for  $T \cong T_c$  and becomes wider as the temperature is increased. The former type is possible for strictly regular solutions, but not the latter. The situation can be summarized by reference to Fig. 1 in which the  $W$ - $V$  plane is divided into four quadrants by the lines  $W = 0$  and  $V = -2R$ . No miscibility gap occurs for values of  $W$  and  $V$  in quadrant I,  $\Omega$  is negative at all temperatures, and  $T_c$  from Eq. [6] is negative. In quadrant II a normal miscibility gap oc-

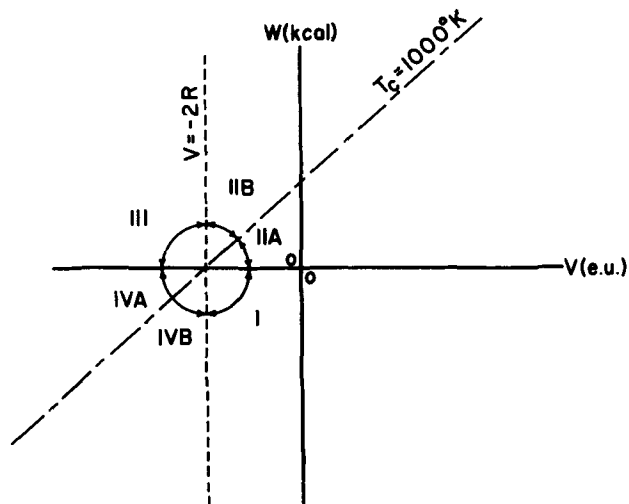


Fig. 1. Structure of the  $W$ - $V$  parameter plane for a quasiregular solution.

curs for temperatures between  $0^\circ$  and  $\infty^\circ\text{K}$ . From Eq. [6] the critical temperature,  $T_c$ , is the same for all values of  $W$  and  $V$  lying on a straight line through the point,  $W = 0$ ,  $V = -2R$ , and ranges in value from  $0^\circ\text{K}$  along the line  $W = 0$  to infinity along the line  $V = -2R$ . The line labeled  $T_c = 1000^\circ\text{K}$  is obtained by substituting  $1000^\circ\text{K}$  for  $T_c$  in Eq. [6]. Thus below this line and above the line,  $W = 0$ , (in region IIA)  $T_c$  lies between  $0$  and  $1000^\circ\text{K}$ . In region III an inverted miscibility gap occurs at all temperatures,  $\Omega$  is positive at all temperatures, and  $T_c$  is negative. In region IV inverted miscibility gaps occur above a critical temperature that ranges from zero along the line,  $W = 0$ , to infinity along the line,  $V = -2R$ . Thus, in region IVB an inverted miscibility gap occurs only for temperatures above a critical temperature which lies above  $1000^\circ\text{K}$ . It can be appreciated that these general properties of a quasiregular solution are a useful guide in fitting phase diagrams. Thus, if a continuous range of solid solutions are formed at  $1000^\circ\text{K}$ , only those values of  $W$  and  $V$  in the contiguous regions IIA, I, and IVB need be considered.

Although we are unaware of the existence of inverted miscibility gaps in any inorganic system, they have been observed in the triethylamine-water (13) and ethyl ether-ethyl acetate (14) systems. Closed miscibility gaps, terminating at an upper and lower consolute temperature, have been observed for a number of systems (14) including nicotine-water,  $\beta$ -picoline-water, etc., but this more complex behavior is not describable in terms of the quasiregular model with temperature and composition-independent parameters,  $W$  and  $V$ .

For a quasiregular solution the chemical potentials of the two components are determined by Eq. [1] and the definition of the Gibbs free energy of mixing

$$\Delta G_m = \Delta G_{M^{xs}} + RT(x_1 \ln x_1 + x_2 \ln x_2) \quad [7]$$

$$= x_1 \mu_1 + x_2 \mu_2 \quad [8]$$

and are given by

$$\mu_1 = RT \ln x_1 + \Omega x_2^2 + \mu_1^\circ \quad [9]$$

$$\mu_2 = RT \ln x_2 + \Omega x_1^2 + \mu_2^\circ \quad [10]$$

where  $\mu_1^\circ$  and  $\mu_2^\circ$  are the chemical potentials of pure 1 and pure 2, respectively, and are for the pure solids when Eq. [1] is applied to a solid solution. When Eq. [1] is applied to a liquid solution then  $\mu_1^\circ$  and  $\mu_2^\circ$  are taken as the chemical potentials of, respectively, pure liquid 1 and pure liquid 2. The assumption that any one of Eq. [1], [9], or [10] holds over the entire composition range leads to the other two, provided  $\Omega$  does not depend on composition. (If the chemical potential is known for one component, that for the

other can be obtained by an integration of the Gibbs-Duhem relation.) On the other hand, the assumption that  $\mu_1$  is given by Eq. [9] with a parameter  $\Omega$  that depends on composition, leads to equations for  $\Delta G_{M^{xs}}$  and  $\mu_2$  that are different than Eq. [1] and [10].

The phase lines describing the coexistence of two phases in a binary system are determined from the condition that the chemical potential of each component be the same in both phases. For a coexisting liquid and solid these are

$$\mu_1(L) = \mu_1(S) \quad [11]$$

$$\mu_2(L) = \mu_2(S) \quad [12]$$

where L and S identify, respectively, the liquid and solid phases. Utilizing Eq. [9] and [10] and (with the conventional definitions for  $\mu_1^\circ(L)$ ,  $\mu_1^\circ(S)$ , etc., cited after Eq. [10]) assuming  $\Delta C_p = 0$  between the liquid and solid phases of both pure 1 and pure 2 leads to the two equations

$$RT \ln x_1 + \Omega_L x_2^2 = RT \ln y_1 + \Omega_S y_2^2 + \Delta H_1(T/T_1 - 1) \quad [13]$$

$$RT \ln x_2 + \Omega_L x_1^2 = RT \ln y_2 + \Omega_S y_1^2 + \Delta H_2(T/T_2 - 1) \quad [14]$$

where  $y_1$  and  $y_2$  are the mole fractions in the solid solution,  $R$  is the gas constant,  $\Delta H_1$  and  $T_1$  are the heat of fusion per mole and melting temperature of pure 1, and  $\Delta H_2$  and  $T_2$  are the analogous quantities for pure component 2.

Since we are attempting quantitative fits of phase diagrams it seems appropriate to comment on the "approximation" that led to the last terms in Eq. [13] and [14]. For simplicity these comments are made with reference to Eq. [13], and hence component 1, alone. Completely analogous comments hold for Eq. [14] and component 2. The last term in Eq. [13],  $\Delta H_1(T/T_1 - 1)$ , is commonly identified as an approximation for the difference between the chemical potential of pure solid 1 and that of pure liquid 1. The approximation is admittedly correct in the near vicinity of the melting point,  $T_1$ , but is somewhat in doubt for the wide temperature ranges over which it must often be used, e.g., for III-V pseudobinaries involving GaSb the extreme temperature ranges are  $712^\circ$ - $525^\circ\text{C}$  for the pseudobinary with InSb and  $712^\circ$ - $1485^\circ\text{C}$  for that with GaP. An accurate expression for the desired chemical potential difference depends on obtaining the heat capacity difference between solid and liquid over temperature ranges where one of these phases is unstable or, at best, metastable. Experiments at elevated pressures would generally extend the temperature range of one phase so that its heat capacity at normal pressure could be obtained by extrapolation. Obtaining the heat capacity of the other phase outside its normal temperature range would depend on the ability of preparing a supercooled liquid, possible in some instances, or on the unlikely possibility of preparing a superheated solid over a wide temperature range. Alternatively, the measured heat capacities for each phase in the neighborhood of the melting point can be extrapolated outside the normal temperature range for each phase and the correction term calculated and added to  $\Delta H_1(T/T_1 - 1)$ . Following this course with the measurements of Lichter and Sommelet (15) we arrive at a  $\Delta C_p$  for GaSb given by

$$\Delta C_p(\text{cal}/^\circ\text{K-mole}) = C_p(L) - C_p(S) = 1.4 - 3(10^{-3})(T - 985) \quad [15]$$

This leads to correction terms that are 1.4% or less of the main term for all temperatures between  $525^\circ$  and  $1500^\circ\text{C}$  and therefore negligible. However, the validity of the extrapolation for  $\Delta C_p$  can be questioned for temperatures increasingly removed from the melting point. Thus from a fundamental point of view,

Table I. Properties of III-V compounds

Compound	AlP	AlAs	AlSb	GaP	GaAs	GaSb	InP	InAs	InSb
$T_{mp}$ (°C)	2530	1770	1057	1485	1240	712	1070	942	525
$\Delta H$ fusion (kcal/mole)	40.92*	34.0*	19.53	26.37*	25.18	15.8	19.7*	18.4	11.41
$a_0$ (Å)**	5.451	5.662	6.136	5.451	5.653	6.096	5.869	6.058	6.479

\* Estimated values from Foster and Woods.  
\*\* Ref. (17).

the entire discussion above seems operationally meaningless. Therefore we redefine the chemical potentials of the pure components. At and above the melting point,  $T_1$ ,  $\mu_1^\circ(L)$  is the chemical potential of the stable phase, pure liquid 1. At and below the melting point,  $\mu_1^\circ(S)$  is the chemical potential of the stable phase, pure solid 1. Below  $T_1$ ,  $\mu_1^\circ(L)$  is the chemical potential of a hypothetical liquid phase, which coincides with real liquid phase at  $T_1$ , but otherwise is defined by the equation

$$\mu_1^\circ(L) = \mu_1^\circ(S) - \Delta H_1(T/T_1 - 1); T < T_1 \quad [16]$$

Above  $T_1$ ,  $\mu_1^\circ(S)$  is the chemical potential of a hypothetical solid phase defined in terms of that of the real liquid phase by

$$\mu_1^\circ(S) = \mu_1^\circ(L) + \Delta H_1(T/T_1 - 1); T > T_1 \quad [17]$$

Similar definitions are adopted for component 2. With these definitions the last terms in Eq. [13] and [14] are exact by definition and the assumption that  $\Delta C_p = 0$  for each pure component is unnecessary.

### Computational Procedure

The experimental liquidus points,  $(T_{j,\text{expt}}, x_j)$ , and the experimental solidus points,  $(T_{k,\text{expt}}, y_k)$  were taken from tabulations, or more often, scaled from graphs. The basic equations are [13] and [14] with  $\Omega_S$  and  $\Omega_L$  depending linearly on temperature as shown in Eq. [2]. The computer calculation starts with initial guesses for the solid parameters,  $W_S$  and  $V_S$ , and the liquid parameters,  $W_L$  and  $V_L$ . (In a given calculation some or all of these may be fixed throughout the calculation at any desired value including zero. The latter situation corresponds to one of simple variants of the general quasiregular liquid-quasiregular solid model. Thus, if all four parameters are fixed at zero, one has the ideal liquid-ideal solid model.) The first experimental liquidus composition is then inserted into Eq. [13] and [14] along with the initial values for  $W_S$ ,  $V_S$ ,  $W_L$ , and  $V_L$ , and these two simultaneous equations are solved for the liquidus temperature for  $x_1$ ,  $T_{1,\text{calc}}$ , and the composition of the coexisting solid. This procedure is repeated for each of the  $N$  liquidus points. The  $M$  experimental solidus compositions,  $y_k$ , are then inserted one at a time into Eq. [13] and [14] and these solved simultaneously for the solidus temperature for  $y_k$ ,  $T_{k,\text{calc}}$ , and the composition of the coexisting liquid. A residual function, or standard deviation,  $\sigma$ , is calculated using the equations

$$\sigma^2 = \sigma_{\text{LIQ}}^2 + \sigma_{\text{SOL}}^2 \quad [18]$$

and

$$\sigma_{\text{LIQ}}^2 = \sum_{j=1}^N (T_{j,\text{calc}} - T_{j,\text{expt}})^2/N \quad [19]$$

$$\sigma_{\text{SOL}}^2 = \sum_{k=1}^M (T_{k,\text{calc}} - T_{k,\text{expt}})^2/M \quad [20]$$

The values of the adjustable parameters are then changed in a systematic "trial-and-error" manner based on the simplex minimization technique of Nelder and Mead (16). For each set of values of  $W_S$ ,  $V_S$ ,  $W_L$ , and  $V_L$  a value of  $\sigma$  is calculated. The cyclic calculation continues until a minimum value is found. It should

be noted that the over-all residual function  $\sigma$  is constructed from those for the solid and liquid with equal weight given to each, regardless of the relative numbers of liquidus and solidus points. Thus the calculated liquidus and solidus lines must individually fit the data well if a low  $\sigma$  is to be attained, and a very good fit to a large number of solidus points cannot offset a poor fit to a few liquidus points.

### Experimental Data

The III-V compounds along with their melting points, heats of fusion, and lattice parameters (17) are given in Table I. Estimated values are indicated by an asterisk. The values for melting points and heats of fusion, both estimated and weighted experimental values, are the same as those used by Foster and Woods (1-6). Their papers should be consulted for the literature references. Panish and Ilegems (7) used estimated values for the heats of fusion of GaP, InP, and AlAs that are 1-3 kcal different. The pseudobinaries analyzed and the number of liquidus points and solidus points used are listed in Table II. Critical values of  $\sigma$  were assigned on the assumption that ordinarily an accuracy of 7°C can be expected for the liquidus and solidus points. Using Eq. [18], [19], and [20] this gives a value of 10° when both liquidus and solidus points are available. For GaP-InP the four liquidus points were obtained by extrapolation of a fit to the ternary liquidus using a strictly regular model (18). We still assume an accuracy of 7° for these points but recognize this may bias the situation in favor of models assuming a strictly regular liquid. For GaAs-GaSb the four solidus points are confined to a narrow composition range near pure GaAs and the solidus line drops very sharply with temperature. Consequently, the critical value of  $\sigma_{\text{SOL}}$  was doubled to 14°C, giving a critical value of 16°C for  $\sigma$ . For InAs-InSb there is significant scatter among independent data sets in certain composition intervals along both the liquidus and solidus. Consequently, we have increased the critical value to 11°C for both phase lines to give a critical value of 16°C for  $\sigma$ .

### Results

*Ideal liquid-quasiregular solid model.*—The general type of result obtained is shown in Fig. 2 for GaAs-GaP where labeled contours of constant  $\sigma$  are shown in the  $W_S$ - $V_S$  plane. Contours for the lower values of interest are of the same elongated shape but too closely spaced to be presented clearly. Therefore they are omitted in favor of a "best-fit line segment" with a table giving the variation of  $\sigma$  for a few values of  $V_S$  along the best-

Table II. (a) Pseudobinary systems analyzed, (b) percentage difference in lattice parameters, (c) numbers of liquidus and solidus points used, and (d) critical values adopted for  $\sigma$

a	b		c	d
	200 $\Delta a_0$			
	$a_0(1)$	$+ a_0(2)$		
AlAs-GaAs	0.1		0-8	7
GaP-InP	7.5		4-8	10
GaAs-InAs	6.9		2-8	10
GaSb-InSb	6.1		9-15	10
GaP-GaAs	3.6		0-7	7
GaAs-GaSb	7.5		7-4	18
InAs-InSb	6.7		18-15	16

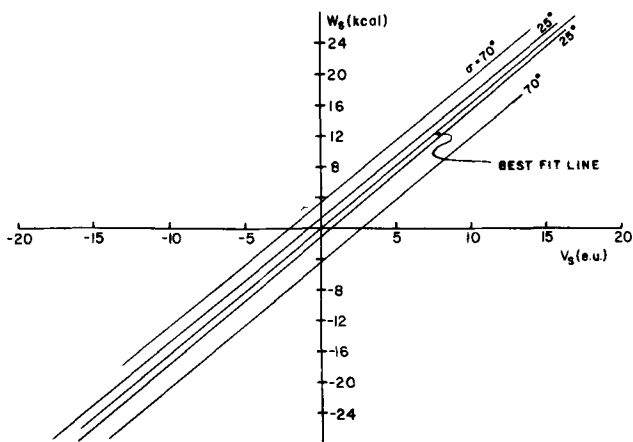


Fig. 2. Contours of constant  $\sigma$  and the best-fit line in the  $W_S$ - $V_S$  plane obtained with the ideal liquid-quasiregular solid model for the GaAs-GaP pseudobinary. Variation of  $\sigma$  along the best-fit line:

$V_S$	-15.6	-6	0	+8.0	+14.7
$\sigma$	10.0	5.0	1.8	5.0	10.0

fit line. The best-fit line segment was obtained by fixing  $V_S$ , finding the lowest possible value of  $\sigma$  and the value of  $W_S$  associated with it, then connecting all such points in the  $W_S$ - $V_S$  plane. It is seen that  $\sigma$  varies slowly along the best-fit line but rapidly at right angles to it. Thus although the smallest value attained for  $\sigma$  is 1.2°C at  $W_S = 1.8$  kcal and  $V_S = 2.0$  eu, the value of  $\sigma$  does not reach 10°C until one moves along the best-fit line to  $V_S = 14.7$  eu or to  $V_S = -15.6$  eu. Even if the critical value of  $\sigma$  is revised downward to 5°C, all of the  $W_S$ - $V_S$  values for  $-6 \leq V_S \leq +8$  are to be considered equally good on the basis of the currently available experimental data for the pseudobinary. A similar result is shown in Fig. 3 for GaSb-InSb. However, for clarity, no contours are shown, only the best-fit line segment. Instead, the upper half of the line corresponding to a critical temperature of 798°K, as calculated using Eq. [6], and the lower half of the line corresponding to a critical temperature of 985°K for an inverted miscibility gap are shown. It can be anticipated that if the best-fit line segment were extended to intersect these lines of constant critical temperature that the value of  $\sigma$  would increase rapidly since the experimental data show no miscibility gap in the 798°-985°K interval.

All of the systems analyzed show the same behavior as seen in Fig. 2 and 3, differing only in the position of the best-fit line, the lowest value of  $\sigma$  attained on it, and the rate of change of  $\sigma$  along it. The data can be summarized by giving the slope and intercept of the best-fit line along with Fig. 4, showing the variation of  $\sigma$  along the best-fit line in a plot of  $\sigma$  against  $V_S$ . However, to avoid the incorrect assumption that  $\sigma$  increases infinitely rapidly in a direction perpendicular to the best-fit line, the best-fit line is written as

$$W_S = mV_S + b \pm \delta \quad [21]$$

Here  $m$  and  $b$  are the slope and intercept, respectively,

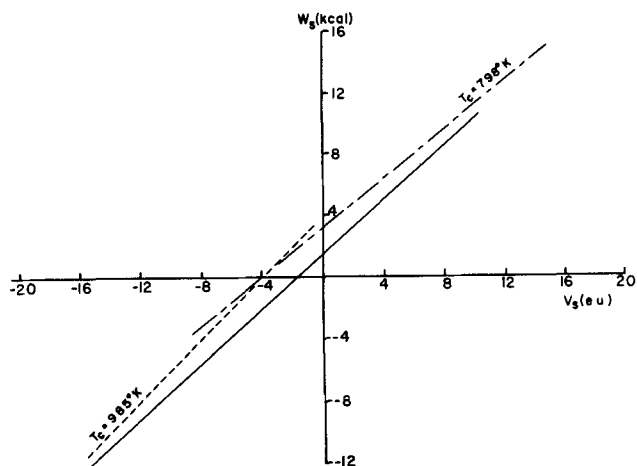


Fig. 3. Best-fit line and lines of constant critical temperature,  $T_c = 798^\circ$  and  $985^\circ$ K obtained with the ideal liquid-quasiregular solid model for the GaSb-InSb pseudobinary. See Fig. 4 for the variation of  $\sigma$  along the best-fit line.

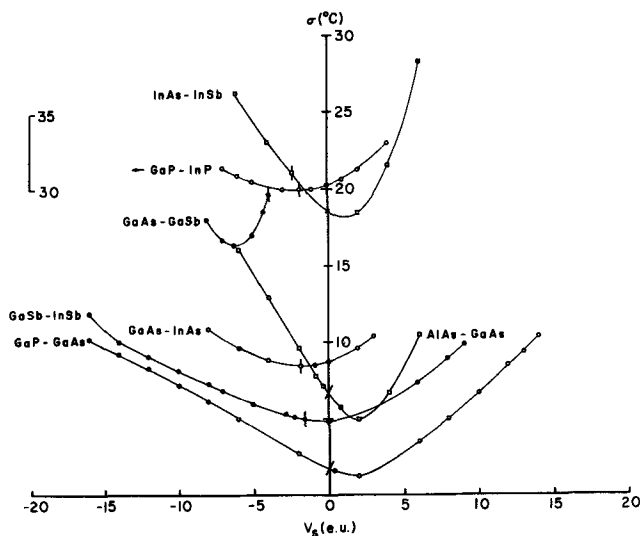


Fig. 4. Ideal liquid-quasiregular solid model. Variation of  $\sigma$  with  $V_S$  along the best-fit line in the  $W_S$ - $V_S$  plane. For InP-GaP the values of  $\sigma$  are given at the left-hand side of the figure.

of the best-fit line, while  $\delta$  is the amount  $W_S$  can be moved from its best-fit position in a direction perpendicular to the best-fit line before  $\sigma$  increases by 5°C. Then Eq. [21] along with Fig. 4 can be used to delineate a long rectangular area in the  $W_S$ - $V_S$  plane that includes and somewhat exceeds the elongated oval-like area for which  $\sigma$  is less or equal to  $\sigma_{MIN} + 5$ . These parameters are listed in Table III for the various systems. Also given are the minimum value of  $\sigma$  and the values of  $W_S$  and  $V_S$  for which  $\sigma$  reaches the listed cutoff value. The cutoff value of  $\sigma$  is identical to the critical value assigned in Table II if a good fit is obtained. Finally the value of  $\sigma$  is given for the ideal

Table III. Summary of results for the ideal liquid-quasiregular solid model

	$m, ^\circ\text{K}$	$b, \text{cal}$	$\delta, \text{cal}$	$\sigma_{MIN}, ^\circ\text{C}$	Fit	Cutoff in $\sigma, ^\circ\text{C}$	Values at cutoff				Ideal liquid and solid		
							Low		High		$\sigma$	$\sigma_{SOL}$	$\sigma_{LIQ}$
							$W_S(\text{cal})$	$V_S(\text{eu})$	$W_S(\text{cal})$	$V_S(\text{eu})$			
AlAs-GaAs	1800	0.0	300	5.0	Good	7	-360	-0.2	7560	4.2	6.8	6.8	0
GaP-InP	1491	2900		30.0	Bad	32	-7556	-7.5	8363	3.0	86	85	10
GaAs-InAs	1342	2550	200	8.3	Good	10	-6308	-6.6	5905	2.5	55	53	16
GaSb-InSb	872.7	1418	300	4.9	Good	10	-10,800	-14.0	9534	9.3	32	16	28
GaP-GaAs	1649.5	31	200	1.2	Good	7	-16,247	-9.8	+16,666	+10.3	1.7	1.7	0
GaAs-GaSb	1194	4650	200	16.2	Good	18	-4902	-8.0	-723	-4.5	199	199	13
InAs-InSb	930	2300		18.4	Bad	21	68	-2.4	5741	3.7	95	93	17

liquid-ideal solid model, which is seen to be satisfactory for only two systems.

It is seen that five of the seven pseudobinaries are fit satisfactorily and three of these are fit very well. The fit for InAs-InSb is unsatisfactory but close enough to be considered doubtful. The fit for GaP-InP is bad. In both of these cases the lowest value attained for  $\sigma$  corresponds to a high value for  $\sigma_{LIQ}$  and a satisfactory value for  $\sigma_{SOL}$ , i.e., the model does not fit the liquidus points well. At the cutoff values listed in Table III for these two systems the value of  $\sigma_{SOL}$  has increased by  $5^\circ$  over the minimum value attained. If the estimated liquidus points for GaP-InP are excluded, a satisfactory best fit of  $7^\circ\text{C}$  is obtained while the best-fit line is essentially unchanged.

The InSb-InAs pseudobinary seems the best defined experimentally of all those considered. Therefore, we conclude the liquid in this pseudobinary is not adequately described as ideal. This is perhaps not surprising in view of the complicated nature of the Sb-As binary system in which the liquidus shows a minimum. However, one would also expect some difficulty in fitting the liquidus for the GaSb-GaAs system. That this does not occur may be due to the fact that the Sb-As interactions are reduced in significance at the higher temperatures encountered in the GaSb-GaAs pseudobinary.

The values of  $V_S$  giving the lowest  $\sigma$  when  $W_S = 0$  (indicated by the short vertical bar on each curve of Fig. 4) are what would be calculated from the values of  $V_S/RT$  given by Foster and Woods (3-6). Therefore, our results include theirs and yield a quantitative measure of the fits possible with the ideal liquid-athermal solid model. More importantly, by comparison with the value of  $\sigma$  for  $V_S = 0$ , strictly regular solid, it is seen that the ideal liquid-athermal solid model is not significantly better than the ideal liquid-strictly regular solid model except for GaAs-GaSb. Furthermore, there is no basis for categorizing the solid solutions more specifically than as quasiregular.

In view of the generally wide ranges of values for  $W_S$  and  $V_S$  that lead to satisfactory fits, especially for those systems for which the smallest values of  $\sigma$  are attained, the values calculated for the enthalpy and excess entropy of mixing of the solid solutions are subject to such a wide uncertainty as to be meaningless. In contrast, the values calculated for the excess Gibbs free energy of mixing, as well as those for the chemical potentials are more closely defined at one temperature between the melting points of the pure compounds. This can be seen by inserting the value of  $W_S$  from Eq. [21] for the best-fit line segment into Eq. [1], [9], and [10]. One obtains

$$\Delta G_M^{xs}(S) = \{(m - T)V_S + b \pm \delta\}y_1y_2 \quad [22]$$

$$\mu_1^{xs}(S) = \{(m - T)V_S + b \pm \delta\}y_2^2 \quad [23]$$

$$\mu_2^{xs}(S) = \{(m - T)V_S + b \pm \delta\}y_1^2 \quad [24]$$

As a concrete illustration, fits with  $\sigma \leq 7^\circ\text{C}$  are obtained for GaP-GaAs along a best-fit line segment for all values of  $V_S$  between  $-9.8$  and  $+10.3$  eu. Equally acceptable values for the excess entropy of mixing of the 50 mole per cent (m/o) solid therefore range from  $-2.5$  to  $+2.5$  eu while those for the enthalpy of mixing range from  $-1.0$  to  $+1.0$  kcal/mole. In contrast, the value calculated for  $\Delta G_M^{xs}(S)$  for 50 m/o is  $b = -200 \pm 200$  cal/mole at  $T = m = 1637^\circ\text{K}$  (about halfway between the melting points of GaAs and GaP). Therefore for each system analyzed, the most significant thermochemical quantities following from a fit of the phase lines are the excess Gibbs free energy of mixing and the chemical potentials of the solid phase at a temperature  $T = m$ . In other words, the interaction parameter for the solid,  $\Omega_S$ , is closely defined as a result of a fit of the phase diagram only near one temperature,  $T = m$ , where it is equal to  $b$ .

Finally, the GaAs-GaSb system is unique among those analyzed in that the experimental solidus points are not distributed well across the composition range, but are concentrated in the 85-100 m/o GaAs interval due to difficulty in obtained equilibrated samples. This provides an opportunity to illustrate an element of flexibility possessed by the quasiregular model of the solid which is not shared by a strictly regular model. In Fig. 5 three different calculations of the phase lines using the ideal liquid-quasiregular solid model are shown. The temperature scale is magnified to show the desired detail and as a consequence only the low-temperature portion containing no experimental points is seen. For all three calculations the liquidus line is essentially the same and fits the experimental points well with  $\sigma_{LIQ} = 6^\circ\text{C}$ . The values used for  $W_S$  and  $V_S$  are listed in the figure caption and all fall along the best-fit line segment given in Table III for GaAs-GaSb. The best fit of the solidus points is obtained with curve 1 and is somewhat better than those obtained with curves 2 and 3. Note that curves 1 and 3 are within  $15^\circ\text{C}$  of one another and curves 2 and 3 are within  $3^\circ\text{C}$  of one another. However, curves 1 and 2 correspond to a complete range of solid solutions from  $0^\circ\text{K}$  to the respective solidus lines. In contrast, curve 3 shows a narrow miscibility gap in the solid solution that extends from 45 to 55 m/o GaAs at a peritectic temperature of  $734.5^\circ\text{C}$ . An optimum fit using a strictly regular model for the solid is significantly poorer as can be inferred from Fig. 4. Moreover, the values required for  $W_S$  are near 4300 cal so that the sole option is a miscibility gap in the solid solution from  $0^\circ\text{K}$  to over  $712^\circ\text{C}$ .

*Strictly regular liquid and solid.*—Contours of constant  $\sigma$  plotted on the plane of the two adjustable parameters,  $W_S$  and  $W_L$  show the same elongated form as for the previous model. The results can again be presented by listing the parameters of the best-fit line segment

$$W_S = sW_L + i \pm \delta \quad [25]$$

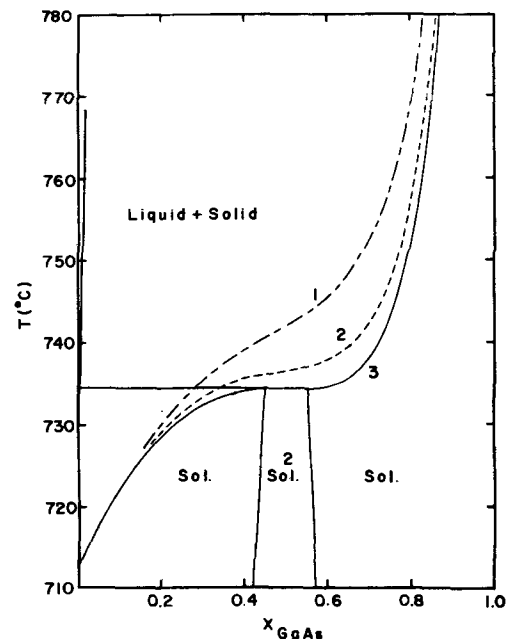


Fig. 5. Detail in low-temperature range of GaAs-GaSb phase diagram calculated using ideal liquid-quasiregular solid model. Liquidus lines coincide for all three calculations. The peritectic shown is for curve 3 only.

Solidus	$W_S(\text{cal})$	$V_S(\text{eu})$	$\sigma_{SOL}(^\circ\text{C})$
1	-2514.	-6.0	15.6
2	0.0	-3.385	18.6
3	+608.2	-3.854	20.4

Table IV. Summary of results for the strictly regular liquid-strictly regular solid model

s	i, cal	$\delta$ , cal	$\sigma_{\text{MIN}}$ , °C	Fit	Cutoff in $\sigma$ , °C	Values at cutoff				Stringfellow's parameters				
						Low		High		$W_L$ (cal)	$W_S$ (cal)	$\sigma$ (°C)	$\sigma_{\text{LIQ}}$	
						$W_L$ (cal)	$W_S$ (cal)	$W_L$ (cal)	$W_S$ (cal)					
	*0.342	-8												
AlAs-GaAs	0.475	-60	270	6.2	Good	7	-250	-179	1600	539	1270	0	12	—
GaP-InP	0.424	2960	150	8.5	Good	10	+1200	3496	+1700	3681	2695	3630	33	29
GaAs-InAs	0.509	2509		7.8	Good	10	-1060	1970	220	2621	2695	2815	39	32
GaSb-InSb	0.620	1400		4.1	Good	10	-1320	582	500	1710	2695	1846	52	49
	**0.804	50												
GaP-GaAs	0.708	50	160	1.1	Good	2.8	-2500	-1720	+2500	+2060	1252	985	1	—
GaAs-GaSb	0.175	4270		31	Bad	33	-1500	4270	-430	4457	467	3355	185	20
InAs-InSb	0.240	2200		13	Good	16	+170	2241	660	2358	467	2289	14	10

\* Upper values for  $s$  and  $i$  apply for  $W_L > 400$ .

\*\* Upper values for  $s$  and  $i$  apply for  $W_L > 0$ .

and by showing the variation of  $\sigma$  along this line segment in a plot of  $\sigma$  against  $W_L$ . The slope,  $s$ , and intercept,  $i$ , of the best-fit line are listed in Table IV along with the parameter  $\delta$  which has the same definition as previously. For two systems the best-fit line consists of two segments. Also shown are the lowest value of  $\sigma$  and the values of  $W_L$  and  $W_S$  for specified cutoff values of  $\sigma$ .

For comparison the values (8) of  $W_L$  and the revised values (9) of  $W_S$  given by Stringfellow and the associated values of  $\sigma$  and  $\sigma_{\text{LIQ}}$  calculated by us are given in the last four columns. (The associated values of  $\sigma_{\text{SOL}}$  can be calculated using Eq. [18].) With the exceptions of the AlAs-GaAs, GaP-GaAs, and InAs-InSb systems, the values of  $\sigma$  are more than 20°C over the 10°-16°C critical values chosen by us as characterizing a good fit. With the exception of the GaAs-GaSb system,  $\sigma_{\text{LIQ}}$  is one to two times as large as  $\sigma_{\text{SOL}}$  for the five systems with liquidus points, while  $\sigma_{\text{SOL}}$  is 23°C or less.

The variation of  $\sigma$  along the best-fit line is shown in Fig. 6 for the various systems. Using the same critical values of  $\sigma$  as before, the fits for six of the systems are satisfactory. Comparison of the fits in Fig. 6 for the strictly regular model with those in Fig. 4 shows that four pseudobinaries are fit to better than 10°C with both models. The strictly regular model fits the GaP-InP system much better with  $\sigma_{\text{MIN}} = 8.5^\circ$  as opposed to 30°; the InAs-InSb system slightly better with  $\sigma_{\text{MIN}} = 13^\circ$  as opposed to 18.4°; and the GaAs-GaSb system significantly worse with  $\sigma_{\text{MIN}} = 31^\circ$  as opposed to 13.9°. On the basis of fits to the phase lines we would judge the strictly regular model to be slightly superior at present and, when it is remembered that there is a general paucity of liquidus points, to be

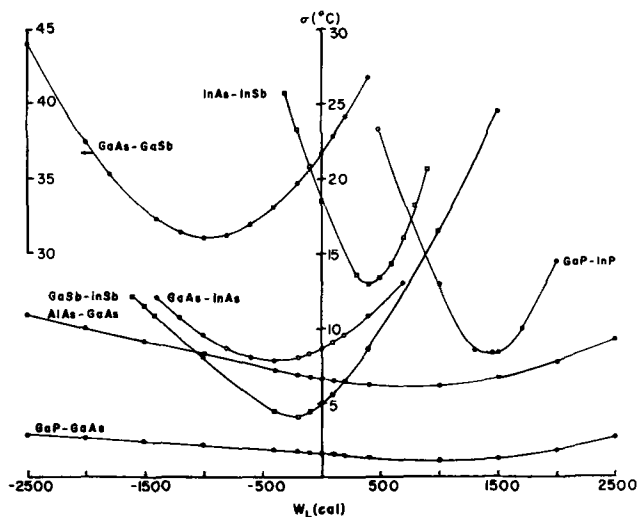


Fig. 6. Strictly regular liquid and solid model. Variation of  $\sigma$  with  $W_L$  along the best-fit line in the  $W_S$ - $W_L$  plane. For GaSb-GaAs the values of  $\sigma$  are given along the left-hand side of the figure.

potentially superior when more liquidus points are obtained.

Table IV shows that, except for GaP-InP, there is a wide percentage spread in the values of  $W_L$  associated with  $\sigma$ -values less than the cutoff value. Therefore, the enthalpy of mixing of the liquid phase does not emerge from an analysis of the phase lines as a sharply defined quantity. In contrast the variation in  $W_S$  is considerably less for three systems, so that the enthalpy of mixing of the solid phase is defined to within  $\pm 100$  cal out of a total of 2000-4000 cal for GaP-InP, GaAs-GaSb, and InAs-InSb. For all systems except GaP-InP the range obtained for the enthalpy of mixing of the solid includes the value obtained from the ideal liquid-quasiregular solid model for the excess Gibbs free energy of mixing of the solid at the intermediate temperature  $T = m$  ( $b$  in Table III).

*Quasiregular liquid-ideal solid.*—The minimum value of  $\sigma_{\text{SOL}}$ , obtainable with the quasiregular liquid-ideal solid model will be close to that obtained with the ideal liquid-ideal solid model shown in the next to last column of Table III. The minimum value obtainable for  $\sigma$  must be no smaller than this, and therefore the quasiregular liquid-ideal solid model will give unsatisfactory fits for at least five of the seven systems considered. This model is not pursued further.

*Strictly regular liquid-quasiregular solid.*—The liquidus and solidus lines for all seven systems are satisfactorily fit by one, if not both, of the two parameter models discussed in the sections on Ideal liquid-quasiregular solid model and Strictly regular liquid and solid. Therefore it has already been established in principle that the strictly regular liquid-quasiregular solid model, which contains these simpler models as special cases, will give a satisfactory fit for all seven systems. It therefore is the simplest variant of the full quasiregular model that will satisfactorily fit all seven systems. It has been applied here only to those four systems for which there are more than two liquidus points. For each of these systems it was found that for a fixed value of the liquid parameter,  $W_L$ , that satisfactory fits were obtained along a best-fit line in the  $W_S$ - $V_S$  plane, similar to the situation with the ideal liquid-quasiregular solid model for which  $W_L = 0$ . Enough different values of  $W_L$  were used to establish the absolute minimum in  $\sigma$ . The results are summarized in Table V which lists several values of  $W_L$  for each system, including  $W_L = 0$  for comparison, the slope,  $m$ , and intercept on the  $W_S$  axis,  $b$ , of the best-fit line (Eq. [21]), the minimum value of  $\sigma$  obtained for the fixed value of  $W_L$ , and the value of  $V_S$  at which the minimum occurred. Similar to the situation for  $W_L = 0$ , which is discussed in the section on Ideal liquid-quasiregular solid model and summarized in Table III, the value of  $\sigma$  varies slowly along the best-fit line and generally there is a wide range of  $W_S$  or  $V_S$  values along this line for all of which  $\sigma$  is less than the critical value characterizing a satisfactory fit.

Table V. Summary of results for the strictly regular liquid-quasiregular solid model

Asterisk entry indicates best fit

	$W_L$ , cal	$W_S = mV_S + b$		Best fit	
		$m$ (°C)	$b$ (cal)	$\sigma_{MIN}$ (°C)	$V_S$ (eu)
GaP-InP	2000	1482	3808	14	-1.5
	1500*	1482	3616	8.1	-1.0
	1000	1482	3397	12.8	-1.0
	0	1491	2900	30	-2.0
GaSb-InSb	300	874	1686	7.5	-1.0
	0	875	1418	4.9	0
	-250*	863	1338	4.0	0
	-500	868	1115	4.6	0
GaAs-GaSb	-800	876	868.6	6.4	-0.5
	0	1194	4650	16.2	-6.2
	-500*	1194	4550	15.2	-5.5
	-1000	1194	4500	17.0	-5.0
InAs-InSb	-1500	1210	4200	25.6	-4.0
	0	930	2300	18.4	+1.0
	450*	987	2180	12.6	+1.0
	900	987	2250	20.5	+1.0

The general features of Table V are: (i) a satisfactory fit is obtained with some value of  $W_L$  for each system; (ii) the lowest value of  $\sigma$  is not much lower than that obtained with one of the simpler models when the simpler model gives a satisfactory fit; (iii) the parameter  $m$ , defining the slope of the best-fit line does not vary much over the range of  $W_L$  shown; and (iv) the parameter  $b$  defining the intercept of the best-fit line on the  $W_S$  axis does not vary much with  $W_L$  except for the GaP-InP system, where large values of  $W_L$  are required to obtain a satisfactory fit.

For the GaP-InP system  $\sigma$  values less than the adopted critical value of 10°C are obtained only for values of  $W_L$  between 1000 and 2000 cal. By interpolation of the data in Table V this range can be narrowed to about 1300-1700 cal. For the GaSb-InSb system a range of  $W_L$  values even wider than the +300 to -800 cal range shown allows values of  $\sigma$  less than the 10°C critical value, the very slow variation of  $\sigma$  along a best-fit  $W_S$ - $V_S$  line (see Fig. 4) being accompanied by a similar slow variation with  $W_L$ . Values of  $\sigma$  less than 6°C are obtained for values of  $W_L$  between -700 and +150 cal. For the GaSb-GaAs system the value of  $W_L$  must lie between 0 and about -600 cal in order to attain a value of  $\sigma$  below 16°C. For the InAs-InSb system the value of  $W_L$  must lie by interpolation between about +200 and +650 cal in order to attain a  $\sigma$  below 16°C.

It appears that when a system is fit well by the ideal liquid-quasiregular solid model, that analysis using the strictly regular liquid-quasiregular solid model will improve the fit but will not greatly change the parameters  $m$  and  $b$  of the best-fit line along which the values of  $W_S$  and  $V_S$  giving satisfactory fits lie. Therefore, we infer that the values of  $m$  and  $b$  given in Table III for the three systems not analyzed with the strictly regular liquid-quasiregular solid model (because of a paucity of liquidus points) can be grouped with the values of  $m$  and  $b$  in Table V for those systems that were analyzed.

### Discussion

From Table IV and V it can be seen that the liquid parameter,  $W_L$ , is not closely fixed as a result of fitting the liquidus and solidus lines and no clear regularities are apparent. For this reason and because there are only three systems for which more than four liquidus points have been measured (the four points of the GaP-InP system are estimated), the quasiregular liquid-quasiregular solid has not been used. At present it appears that this model will be capable of providing a satisfactory fit when more liquidus points are available, indeed the strictly regular liquid-quasiregular solid model may also. More important, we infer from the calculations discussed thus far that the full quasiregular model will still yield a best-fit line in the  $W_S$ - $V_S$  plane that is close to those given in Table V and III. In other words, a fit of the liquidus and solidus

Table VI. Solid solution parameters  $m$  and  $b$  from computer fits of pseudobinary sections

	$2m/(T_1 + T_2)$	$b$ , cal	$b$ (calc), cal
AlAs-GaAs	1.01	$0.0 \pm 300$	0.0
GaP-InP	0.98	$3616 \pm 200$	3948
GaAs-InAs	0.98	$2550 \pm 200$	2589
GaSb-InSb	0.97	$1338 \pm 400$	1233
GaP-GaAs	1.01	$31 \pm 200$	55
GaAs-GaSb	0.96	$4550 \pm 200$	4299
InAs-InSb	0.98	$2180 \pm 150$	2180

lines by the models discussed has afforded a characterization of the thermodynamic properties of the solid phase that most likely will not be basically changed by application of the quasiregular model to both phases. This characterization is shaped by the choice of the quasiregular model of a phase as a general framework. But it is also influenced by the procedure of adopting a critical value of  $\sigma$  and accepting on equal terms all fits with  $\sigma$  values less than this, rather than simply taking the one fit with the minimum value of  $\sigma$ . The latter would lead to a unique value of  $W_S$  and  $V_S$  and a definite enthalpy and excess entropy of mixing of the solid. The former leads to the result that for the solid phase at one temperature,  $T = m$ , the excess Gibbs free energy of mixing is equal to  $b$  with an uncertainty of about  $\pm 200$  cal. We wish now to discuss these parameters.

Table VI shows the ratio of  $m$  to the average melting point (in °K) of the two III-V compounds defining a pseudobinary section, the value of  $b$  obtained from the computer fits, and a calculated value,  $b$  (calc), obtained from the equation

$$b(\text{calc}) = 237.5(10^8) \left\{ \frac{2(a_1 - a_2)}{(a_1 + a_2)} \right\}^6 \quad [26]$$

where  $a_1$  and  $a_2$  are the room temperature lattice parameters of the III-V compounds. It can be seen that  $m$  is  $0.98 \pm 0.03$  of the average melting points of the III-V components in all cases and that  $b$  (calc) is within 250 cal of the center of the range in  $b$  determined from the computer fits. The case of GaP-InP is interesting in that the value of  $b$  for  $W_L = 0$  does not fit the empirical correlation given by Eq. [26]. However, as  $W_L$  is changed toward 1500 cal in order to obtain a fit better than the critical value of 10°C, the value of  $b$  increases sufficiently to agree with  $b$  (calc) to within 232 cal. The correlation of  $b$  with fractional lattice parameter difference is also shown in Fig. 7 where  $b$  is plotted against the sixth power of this variable. Based on the premise that the III-V solid solutions can be described as strictly regular, Stringfellow (9) has presented arguments that the interaction energy ought to vary as the square of the lattice parameter difference and the negative 4.5th power of the average lattice parameter of the two pure III-V compounds. If the values of  $b$  given in Table VI are plotted against this variable and a best straight line drawn, the fit is decidedly inferior to that afforded by Eq. [26].

The values of  $b$  given in Table VI are within 500 cal of the values for the solid parameter,  $W_S$  obtained by Panish and Ilegems (7) using a strictly regular model for both the liquid and solid phases. However, the thermodynamic interpretation of the two quantities is different as discussed previously. Moreover it is not clear how closely the value of  $W_S$  in the strictly regular model is defined using the available pseudobinary and ternary data. As indicated in the section on Strictly regular liquid and solid, the pseudobinary data alone does not always suffice to yield a closely defined value for  $W_S$ .

Encouraged by the remarkable correlation established for  $m$  and  $b$  in Table VI, we postulate that for all eighteen III-V pseudobinary sections that: (i) the strictly regular liquid-quasiregular solid model will



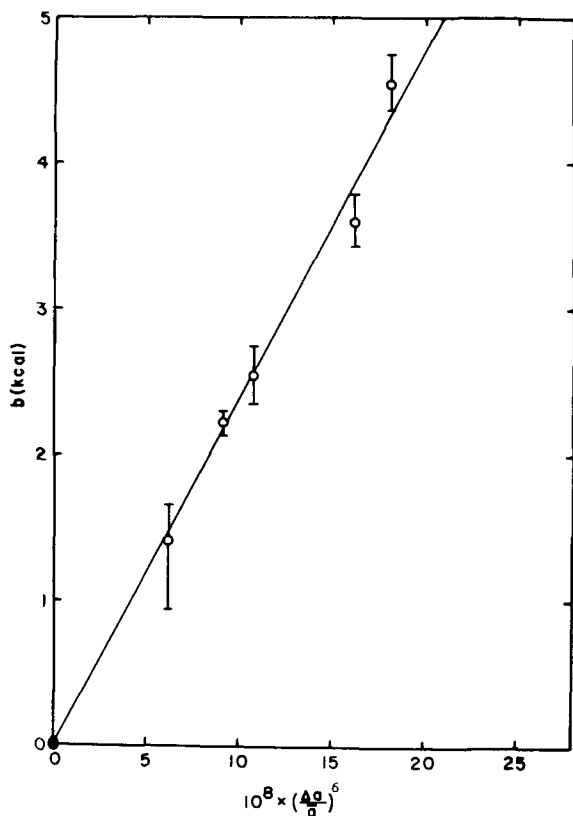


Fig. 7. Intercept  $b$  of the best-fit line in the  $W_S$ - $V_S$  plane for various pseudobinary systems (from Tables III and V), plotted against the sixth power of fractional difference in room temperature lattice parameters of III-V components.  $\Delta a = |a_1 - a_2|$ ,  $a = (1/2)(a_1 + a_2)$

give a satisfactory fit of the liquidus and solidus lines as more liquidus and solidus points are obtained, and (ii) the excess Gibbs free energy of mixing will be given by

$$\Delta G_M^{xs}(S) = by_1y_2$$

$$= 237.5(10^8) \left[ \frac{2(a_1 - a_2)}{(a_1 + a_2)} \right]^6 y_1y_2 \text{ cal/mole} \quad [27a]$$

at

$$T = m = 0.495(T_1 + T_2) \quad [27b]$$

We are aware of no experimental thermochemical data to check this correlation. Unfortunately, its application to pseudobinary phase diagram calculations is somewhat restricted because in effect it only predicts the best-fit line in the  $W_S$ - $V_S$  plane along which the values of  $W_S$  and  $V_S$  giving a minimum  $\sigma$  must lie. The range of, say  $V_S$ -values giving satisfactory fits, or the value of  $V_S$  giving the best fit, are unknown. The value that ought to be used for the liquid parameter,  $W_L$ , is also left unspecified. However, it would appear from the systems analyzed that the  $V_S$ -values ought to be generally small, between about +2 and -5 eu. Moreover

for the systems analyzed there is a measure of independence between the liquidus and solidus lines so that the assumption of an ideal liquid does not greatly affect the position of the calculated solidus line although it may well lead to a poor fit of the liquidus. With these facts in mind some comments can be made about those pseudobinary sections for which there is no data, while for four pseudobinaries, for which there is data, the applicability of the empirical correlation can be checked.

If the lattice parameters differ by no more than 4% from their average value for a particular pair of III-V compounds forming a ternary system, then  $G_M^{xs}$  for the solid solution in the pseudobinary section will be 200 cal/mole or less. In this case the solid solution can be fairly well described as ideal in the temperature interval between the melting points of the pure compounds. (Of the remaining seven ternary systems with no data, AlP-GaP, AlP-AlAs, and AlAs-GaAs fall in this category.)

On the other hand when this difference is 9.9% or greater, as is the case of AlP-AlSb, GaP-GaSb, and InP-InSb, then  $b$  is 22,000 cal/mole or greater. The possibility of a miscibility gap in the solid solution can be examined by constructing a best-fit line according to Eq. [21] on a plot such as Fig. 1 with  $m$  and  $b$  given by Eq. [27b] and [26], respectively. The following common conclusion is reached. Unless the values of  $V_S$  giving satisfactory fits are either larger than 36 eu or smaller than -80 eu, all three systems will show a miscibility gap in a temperature range between the higher melting point and at least as low as the lower melting point. Specifically, either a normal miscibility gap with  $T_c$  greater than the higher melting point ( $-3.97 < V_S < 36$ ), or an inverted miscibility gap with  $T_c$  less than the lower melting point will form ( $-80 < V_S < -3.97$ ). The large magnitudes required of  $V_S$  to avoid a miscibility gap seem unlikely to be encountered.

For the AlAs-AlSb system, for which the lattice parameters differ by an amount that is 8.08% of the average parameter, the calculated value of  $b$  is 6340 cal/mole and the situation is intermediate. Except for a short segment, the predicted best-fit line in the  $W_S$ - $V_S$  plane lies between the line of constant critical temperature equal to 2043°K, the melting point of AlSb, and that of constant critical temperature equal to 1330°K, the melting point of AlAs. Values of  $V_S$  greater than -3.7 are associated with a normal miscibility gap with  $1330^\circ\text{K} \leq T_c \leq 2043^\circ\text{K}$ . Values of  $V_S$  less than -4.2 are associated with an inverted miscibility gap with  $T_c$  in the same range. Only for  $-4.2 < V_S < -3.7$  is there complete solid solution in the 1330°-2043°K interval.

There are four remaining pseudobinary sections for which there is experimental data but which were not discussed in the main section of this paper. They were analyzed using the ideal liquid-quasiregular solid model and again a best-fit line was found in the  $W_S$ - $V_S$  plane. The results are summarized in Table VII. In the case of the first two systems there is excellent agreement between the parameters of the best-fit line,  $m$  and  $b$ , as obtained from the computer fits and the values calculated for these parameters from the corre-

Table VII. Results from ideal liquid-quasiregular solid model for four additional systems

	No. of liquidus and solidus points	Ref.	Best fit		Best-fit line		From Eq. [26] and [27b]	
			$\sigma_{MIN}$ (°C)	$V_S$ (eu)	$m$ (°K)	$b$ (cal)	$m$	$b$
AlAs-InAs	0-6	2	6.6	-1.5	1610	2050	1564	2268
AlSb-GaSb	10-6	*19, 20, 21	26	0	1150	0	1111	0
AlSb-InSb	13-13	*19, 22, 23	28.7	+4	1012	180.5	1064	625
**	4-13		19.4	+2	990	159	1064	625
InP-InAs	3-3	24	17	> +12	1261	970	1228	25

\* Solidus points from cooling curves are discarded.

\*\* Eliminate liquidus points of Ref. (23).



lations represented by Eq. [27b] and [26]. The fact that  $\sigma_{\text{MIN}}$  for the AlSb-GaSb system is no lower than 26°C can be attributed in large part to the scatter of the experimental data and in part to the fact that the two liquidus points between 55 and 100 m/o GaSb are about 40° below the calculated liquidus.

The poor fit obtained for the AlSb-InSb system is essentially all due to the scatter in the data. The liquidus points of Goryunova (23) are some 35°C higher than those of Koster and Thoma (19) in the 20-45 m/o AlSb interval. The solidus points of Goryunova (23) show a scatter of about  $\pm 12^\circ\text{C}$  between 0 and 60 m/o AlSb and are about 20°C higher than the point of Wooley and Smith (22) at 15 m/o AlSb. In spite of this, the agreement of the value of  $m$  obtained from the computer analysis with that calculated from Eq. [27b] is within 5%. The value of  $b$  is about 450 cal below the value of 625 cal calculated from Eq. [26], somewhat more than the  $\pm 250$  cal deviation expected. If the liquidus points of Goryunova are eliminated, the results shown in the asterisk entry of Table VII are obtained. The value of  $\sigma_{\text{MIN}}$  is lowered to about the limit set by the scatter of the solidus data, but the values of  $m$  and  $b$  obtained are in poorer agreement with the predicted values. When the liquidus points of Goryunova *et al.* are used, and those of Koster and Thoma eliminated, a value of 28.6°C is obtained for  $\sigma_{\text{MIN}}$  ( $\sigma_{\text{LIQ}}$  being 22.6°C) even with the strictly regular liquid-quasiregular solid model. Therefore we conclude the liquidus points of Goryunova *et al.* are seriously in error, especially in the 25-45 m/o AlSb interval. The phase lines have been calculated using the ideal liquid-quasiregular solid model and are shown along with experimental points in Fig. 8. The lower solidus line was obtained using  $W_s = 625$  cal,  $V_s = 0$  eu, a point on the predicted best-fit line. Decreasing  $W_s$  by 200 cal to 425 cal, the uncertainty in the intercept,  $b$ , of the best-fit line, yields the upper solidus line. Both calculated solidus lines are within 5°-10°C of one another and are 15°-20°C below the experimental points between 25 and 50 m/o of AlSb. We would conjecture the actual solidus line lies closer to those calculated than to the experimental points.

For the InP-InAs system the value of  $m$  agrees with that calculated from Eq. [27b] but the value of  $b$  is significantly larger than the calculated value of 25 cal. The poor fit is almost entirely due to the three solidus points being significantly below the calculated line. In view of the poor agreement with our correlation and because the solidus points (24) appear to have been determined from cooling curves, we conclude the solidus points are significantly in error. Therefore possible solidus lines were calculated in the following manner. The liquidus points were fit alone using the strictly regular liquid-quasiregular solid model with fixed values of  $W_s$  and  $V_s$  satisfying the theoretical best-fit line equation ( $m = 1228$ ,  $b = 25$ ). For  $W_s = 1253$  cal,  $V_s = 1.0$  eu, a best value of 3°C is obtained for  $\sigma_{\text{LIQ}}$  with  $W_L = 30$  cal. For  $W_s = 25$  cal,  $V_s = 0.0$  eu, we find  $\sigma_{\text{LIQ}} = 3^\circ\text{C}$  at  $W_L = 70$  cal. The solidus lines generated with either set of parameters are within 2°C of each other, as are the liquidus lines. The calculated lines are shown in Fig. 9 along with the experimental

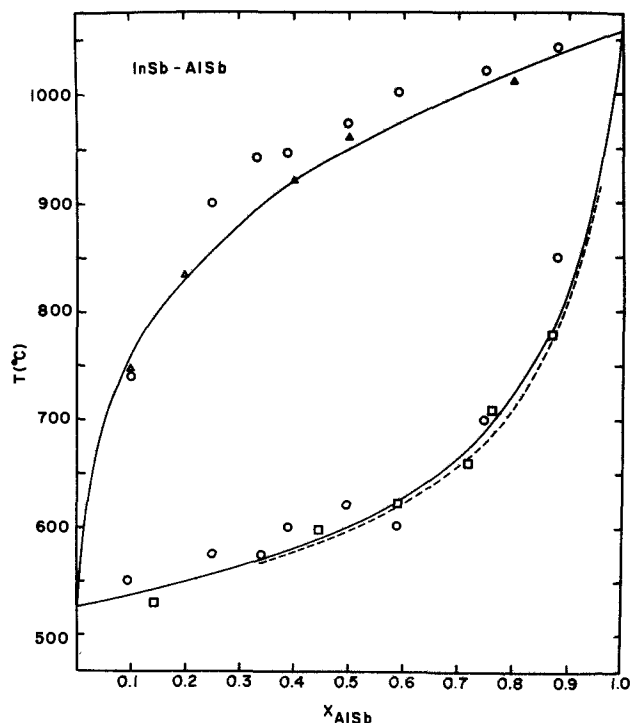


Fig. 8. Pseudobinary section for AlSb-InSb. The lines are calculated using ideal liquid-quasiregular solid model with points on predicted best-fit line,  $W_s = 625$  cal,  $V_s = 0$  eu (lower, dashed solidus), and with  $W_s = 425$  cal,  $V_s = 0$  eu (upper solidus). Experimental data are shown as points. Circles, Goryunova *et al.* (23); triangles, Koster and Thoma (19); squares, Wooley and Smith (22).

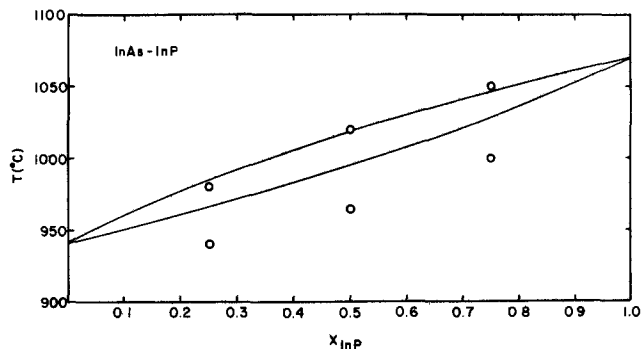


Fig. 9. Pseudobinary section for InP-InAs. Solid lines calculated using strictly regular liquid-quasiregular solid model and predicted values for  $W_s$  and  $V_s$ . Circles represent experimental points of Koster and Ulrich (24).

points. The small separation of the calculated lines is in qualitative agreement with the experimental results of Wagner and Thompson (25).

Finally, calculated liquidus and solidus points are given in Table VIII for six of the seven systems considered in the main part of the paper. The GaAs-GaSb

Table VIII. Calculated liquidus and solidus temperatures,  $T(l)$  and  $T(c)$ , in °C

AB-CD	$X_{\text{CD}}$ or $Y_{\text{CD}}$	0	0.05	0.1	0.2	0.3	0.4	0.5	0.6	0.7	0.8	0.9	0.95	1.0
AlAs-GaAs	$T(l)$	1770		1748	1724	1697	1668	1634	1596	1549	1489	1404		1240
	$T(c)$	1770	1692	1625	1522	1450	1397	1357	1326	1300	1277	1257	1248.6	1240
GaP-InP	$T(l)$	1485		1464	1442	1420	1396	1370	1339	1301	1250	1171		1070
	$T(c)$	1485	1373	1292	1207	1167	1144	1129	1118	1107	1096	1084	1077	1070
GaAs-InAs	$T(l)$	1240		1223	1204	1184	1162	1136	1107	1073	1031	982		942
	$T(c)$	1240	1166	1118	1062	1031	1010	995	984	973	963	952	947.3	942
GaSb-InSb	$T(l)$	712		701	688	674	659	641	622	599	573	546		525
	$T(c)$	712	673	645	609	587	572	561	553	545	538	532	528	525
GaP-GaAs	$T(l)$	1485		1469	1452	1433	1413	1391	1367	1340	1310	1276		1240
	$T(c)$	1485	1462	1440	1402	1370	1343	1320	1282	1267	1253	1246	1246	1240
InAs-InSb	$T(l)$	942		926.4	910	892	873	851	828	794	753	688		525
	$T(c)$	942	787	695	617	587	572	563	556	550	543	535	530	525

system, discussed in connection with Fig. 5, is omitted. The ideal liquid-quasiregular solid model was used for the AlAs-GaAs and GaP-GaAs systems having no experimental liquidus points. The strictly regular liquid-quasiregular solid model was used for the others. In every case the values of the model parameters giving the best fit were used as given in Table V or Table III and Fig. 4. We believe the calculated points in Table VIII are the best present estimates and are especially helpful for those systems like GaSb-InSb and InSb-InAs where there is noticeable scatter in the experimental solidus points.

#### Acknowledgments

The authors wish to acknowledge the support of Marquette University, particularly in providing computer time, and of partial support by the National Science Foundation through GH-33009. The first author also wishes to acknowledge helpful discussions with the late Dr. J. F. Woods and Dr. L. M. Foster of IBM, and the IBM Corporation for a Summer Consultantship in 1972.

Manuscript submitted Aug. 14, 1973; revised manuscript received Jan. 15, 1974.

Any discussion of this paper will appear in a Discussion Section to be published in the June 1975 JOURNAL.

All discussions for the June 1975 Discussion Section should be submitted by Feb. 1, 1975.

#### ADDENDUM

After submission of this paper for publication a re-determination of the solidus line in the GaAs-GaSb system appeared in print (26). Five solidus points are given, which extend as low as 30 m/o GaAs. Moreover a peritectic temperature of 745°C with a miscibility gap from 38 to 61 m/o GaAs is estimated. A fit of 13°C can be obtained to the liquid and solidus points with  $W_L = -500$  cal,  $W_S = 5566$  cal, and  $V_S = 1.5$  eu. However although the calculated miscibility gap extends from near 40 to near 60 m/o, the calculated peritectic temperature is only 733°C. Using the quasiregular model for both liquid and solid one can obtain a peritectic temperature of 740°C and a 45-55 m/o miscibility gap only if it is assumed that: (i) the value of 712°C for the melting point of GaSb is low by at least 4°C, or (ii) the value of 15.8 kcal/mole for the heat of fusion of GaSb is high by 2.2 kcal. The required errors are greater to account for the reported peritectic temperature of 745°C and miscibility gap extending from 40 to 60 m/o. We feel these assumptions are unlikely. Therefore either the experimental peritectic temperature and miscibility gap are considerably in error or the quasiregular model is inadequate for GaAs-GaSb and most likely for all III-V pseudobinaries in which the lattice parameters of the components differ by more than 7%

of their average value. It is apparent that more data on the miscibility gap in GaAs-GaSb solid solutions are highly desirable.

#### REFERENCES

1. L. M. Foster and J. E. Scardefield, *This Journal*, **117**, 534 (1970).
2. L. M. Foster and J. E. Scardefield, *ibid.*, **118**, 495 (1971).
3. L. M. Foster, J. E. Scardefield, and J. F. Woods, *ibid.*, **119**, 765 (1972).
4. L. M. Foster, J. E. Scardefield, and J. F. Woods, *ibid.*, **119**, 1426 (1972).
5. L. M. Foster and J. F. Woods, *ibid.*, **118**, 1175 (1971).
6. L. M. Foster and J. F. Woods, *ibid.*, **119**, 504 (1972).
7. M. B. Panish and M. Ilegems, in "Progress in Solid State Chemistry," H. Reiss and J. O. McCaldin, Editors, Vol. 7, Chap. 2, p. 39, Pergamon Press, Oxford (1972).
8. G. B. Stringfellow, *J. Phys. Chem. Solids*, **33**, 665 (1972).
9. G. B. Stringfellow, *ibid.*, **34**, 1749 (1973).
10. J. Steininger, *J. Appl. Phys.*, **41**, 2713 (1970).
11. E. A. Guggenheim, "Thermodynamics," 5th Edition, p. 197, North Holland Publishing Co., Amsterdam (1967).
12. R. A. Swalin, "Thermodynamics of Solids," p. 163, John Wiley & Sons, Inc., New York (1962).
13. A. Findlay, in "The Phase Rule and Its Applications," A. N. Campbell and N. O. Smith, Editors, 9th Edition, p. 98, Dover Publications, Inc. New York (1951).
14. S. Glasstone, "Textbook of Physical Chemistry," 2nd Edition, p. 728, D. Van Nostrand Co., Inc., New York (1946).
15. B. D. Lichter and P. Sommelet, *Trans. TMS-AIME*, **245**, 99 (1969).
16. J. A. Nelder and R. Mead, *Computer J.*, **7**, 308 (1965).
17. H. E. Casey Jr., and F. A. Trumbore, *Mat. Sci. Eng.*, **6**, 69 (1970).
18. M. B. Panish, *J. Chem. Thermo.*, **2**, 319 (1970).
19. W. Koster and B. Thoma, *Z. Metallk.*, **46**, 293 (1955).
20. J. F. Miller, H. L. Goering, and R. C. Himes, *This Journal*, **107**, 527 (1960).
21. A. S. Borschevski, I. I. Burdiyan, E. Yu Lubenskaya, and E. V. Sokolova, *Russ. J. Inorg. Chem.*, **4**, 1306 (1959).
22. J. C. Wooley and B. A. Smith, *Proc. Phys. Soc.*, **72**, 214 (1958).
23. N. A. Goryunova, "The Chemistry of Diamond Like Semiconductors," MIT Press, Cambridge, Mass. (1965).
24. W. Koster and W. Ulrich, *Z. Metallk.*, **49**, 365 (1958).
25. J. W. Wagner and A. G. Thompson, Private communication, published in Ref. (7).
26. M. F. Gratton and J. C. Wooley, *J. Electron. Mat.*, **2**, 455 (1973).

# Thermal Nitridation of Magnesium at Lower Temperatures and Pressures of the Nitrogen Atmosphere

J. Kodymová-Turková, L. Láska, and V. Krejčí

*Institute of Physics, Czechoslovak Academy of Sciences, Na Slovance 2, Praha 8, Czechoslovakia*

## ABSTRACT

The dependence of the thermal nitridation of polycrystalline magnesium specimens, located in pure nitrogen, on time, temperature, and pressure has been investigated. Parameters of the experiments were chosen with regard to the conditions of nitridation in a d-c and rf discharge plasma. The temperature dependence was measured up to 500°C and was not detectable below 300°C. The long term kinetic plot at intermediate temperature 450°C, following the initial period, can be approximated by a logarithmic dependence, and the best explanation of the nitridation mechanism seems to be Fehlner and Mott's conception based on boundary diffusion. The value of the activation energy of the process calculated from the linear parts of the nitridation curves at different temperatures was 19.2 kcal/mole. The pressure dependence of the nitridation was measured in the range of 0.2-400 Torr and could best be described by a  $p^{1/4}$  dependence.

Although definite analogies exist between oxidation and nitridation, much less attention has been given to nitride systems and the theoretical approach to gas-solid reactions is concerned with oxidation only.

The present paper describes the thermal growth of magnesium nitride on polycrystalline magnesium in  $N_2$  under the same conditions (pressure and temperature) as we used for experiments in d-c and rf glow discharges (1). The results allow us to distinguish between thermal effects and those effects due to the plasma, in the nitridation process. The authors of existing publications on this subject generally aimed at finding the most effective methods of producing the nitride and therefore investigated the thermal process at higher temperatures and higher gas pressures than occur in a discharge plasma [summarized in Ref. (2, 3)]. A few studies on kinetics under widely varying conditions have been reported: these include linear, parabolic, and logarithmic laws of nitridation and 5-50 kcal/mole activation energy for this process (4-11).

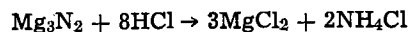
## Experimental Arrangement and Procedure

The metallic samples were used in the form of round specimens (diameter 10 mm, thickness 0.45-0.7 mm) cut from a magnesium sheet which contained the following amounts of impurities: Mn, 1.41%; Zn, < 0.003%; Fe, < 0.001%; Cu, 0.0005%; Pb, Ni, Si, Al, < 0.0005%; and Ag, < 0.0002%. Although there was a relatively high content of Mn compared with the samples used in Ref. (5), the agreement of our results indicates that it has no significant effect on the magnesium nitridation.

The surface of the specimens was cleaned by a chemical treatment: they were immersed in dilute nitric acid, washed in distilled water and ethyl alcohol, and dried. The specimens prepared in this way were placed into molybdenum glass ampoules whose volumes (30 ml-2 liters) were large enough to ensure that the  $N_2$  pressure decrease due to the chemical reaction would not exceed 5%. Outgassing of the ampoules and specimens was achieved by heating them to 200°C while pumping continuously with an oil diffusion pump to a pressure of  $10^{-6}$  Torr. Finally, the ampoules were filled with spectroscopically pure nitrogen to the appropriate pressure (measured by an oil manometer) and sealed. The thermal treatment was accomplished in an oven of 0.75 m<sup>3</sup> volume whose temperature was measured by a thermocouple and maintained automatically at a constant value.

**Key words:** magnesium thermal nitridation, kinetics.

The concentration of the magnesium nitride produced during the nitridation period was determined immediately after opening the ampoule by the following chemical method: the nitride was dissolved in 1N hydrochloric acid so that the nitrogen bound in the nitride changed into ammonium ions according to



The quantitative determination of  $NH_4^+$  after the reaction with the Nessler agent (alkaline solution of mercury(II)-potassium iodide) was carried out by a colorimetric method. The sensitivity of the chemical analysis was  $5 \times 10^{-3}$  mg  $NH_4^+$ /liter. The average error of the whole analytical determination, including the colorimetric measurements, was about 6%. The film thickness was calculated using the factor  $1 \mu g N_2/cm^2 = 130\text{\AA}$ . Each point plotted on the graphs is an average value taken from at least four measurements.

## Results and Discussion

The process of magnesium nitridation was investigated in a temperature range from 200° to 500°C and pressure range from about 0.2 to 400 Torr. The results are summarized in Fig. 1-4.

We have found the first signs of measurable nitridation at a temperature of about 300°C, in agreement with Ref. (5, 9). Higher values given, e.g., in Ref. (4, 6) may probably be ascribed to a lower sensitivity of the methods used for the nitride determination. At temperatures higher than 500°C the investigation became difficult due to the relatively high vapor pressure of magnesium (12) and the film formation was then influenced by magnesium sublimation (1, 5, 6, 8, 9). The dependence of the extent of nitridation on temperature has an exponential character, as expected.

In most of our measurements, the specimens were exposed to nitrogen for a time comparable with the analogous plasma experiments. In addition, we have also investigated the kinetics of the magnesium nitridation at the intermediate temperature 450°C for 10 hr (Fig. 1). During this long period a film thickness of about 1300Å was achieved. To interpret the course of the nitridation curve in Fig. 1, some of the theories and models which have been proposed to explain intermediate temperature oxidation (13-15) might be applied. After an initial period, which lasted about 20 min, the average film thickness was about 75Å. The sensitivity of the chemical method of analysis was sufficient to yield a measure of the nitridation after 10 min from the beginning of the experiment. After this

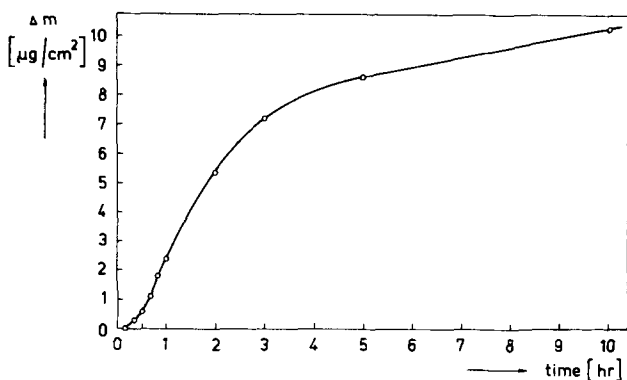


Fig. 1. Time dependence of nitridation of magnesium at 450°C and  $p = 1.2$  Torr ( $\Delta m$  is weight of nitrogen uptake per unit surface area).

time we have always observed an increase of the nitridation rate. It seems that the process of successive heating of the ampoules, gas, and specimens, and the associated transient thermal phenomena, was the rate-determining process in the initial stages of reaction.

The long term kinetic plot is approximately logarithmic in form. Such a kinetic form is predicted by the Cabrera-Mott model (16) of high field ionic transport and also by the Fehlner-Mott model (17) of grain boundary diffusion coupled with a bimolecular process for grain growth. Perrow *et al.* (18) employed transmission electron microscopy to study the structure of thin nickel oxide films (thicknesses comparable with those of our magnesium films) formed on polycrystalline metal substrate and found that the main defects inside the films were the boundaries between the small oxide crystallites which acted as low resistance diffusion paths especially at intermediate temperatures. The character of the boundaries among various oriented grains of the metal substrate is often transmitted to the growing film and anomalous structures can arise as Finch and Quarell (19) found for magnesium oxide films formed on magnesium. It is quite likely that nitridation of magnesium involves a complex heterogeneous multistage process since existing oxidation theories cannot unequivocally describe the details of the present results.

In Fig. 2 parts of the nitridation curves (without the initial periods) are plotted for specimens exposed to nitridation at different temperatures for 1 hr only, the time important for our plasma experiments. A pressure of about 1 Torr was chosen for the same reason. For the small film thickness of about 300 Å a phase boundary reaction determines the growth rate resulting in a

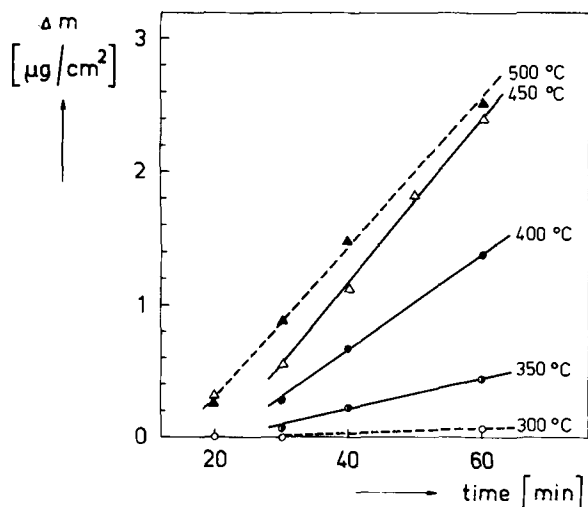


Fig. 2. Linear parts of nitridation curves at different temperatures ( $p = 1.2$  Torr).

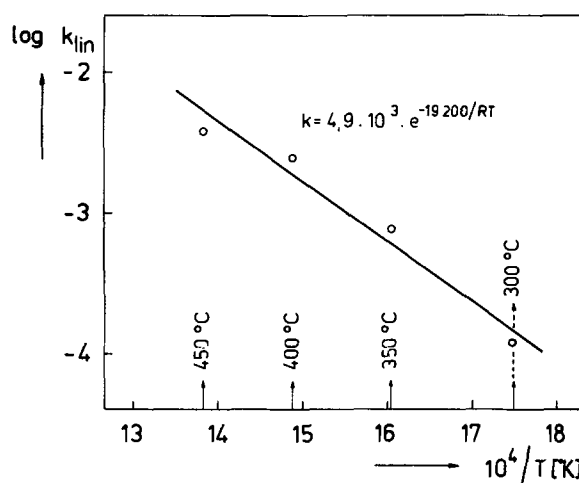


Fig. 3. Plot of logarithm of linear rate constant vs.  $1/T$

linear relation between weight gains and time. The linear dependence in this period is understandable and can be explained by the fast growth of nitride crystallites at the beginning of the gas-solid reaction.

The value of the rate constant at 450°C calculated from the curve in Fig. 2 is equal to  $3.8 \times 10^{-3}$  mg/cm<sup>2</sup> hr and is in good agreement with the value  $4.0 \times 10^{-3}$  mg/cm<sup>2</sup> hr, given by Sthapitanonda and Margrave (5). Their published results and those in Ref. (11) are only suitable for a comparison with our data from the point of view of the similar experimental conditions. A plot of  $\log k_{lin}$  vs.  $1/T$  is shown in Fig. 3. The value of the activation energy of the process calculated from this dependence is 19.2 kcal/mole [22.3 kcal/mole in Ref. (5)]. In Ref. (6, 7) values of 49.9 and 31.7 kcal/mole were found for very thick films where lattice diffusion is the rate-controlling process and the magnesium nitridation has a parabolic time dependence. The relatively low value of  $Q$  obtained in our case supports the suggested mechanism of nitridation. The value 5.8 kcal/mole reported by Belin (8) for the domain of exponential dependence of nitridation, when the nitride film grew on well outgassed Mg, shows that the purity of the surface of the specimens plays an important role in the whole process.

The dependence of the nitridation rate on the gas pressure at 450°C and after 30 min reaction is shown in Fig. 4. We can state that the influence of gas pressure for the very short exposure periods is relatively small and that it can be best approximated by a fourth root dependence. It appears to be consistent with the assumption of a boundary diffusion mechanism rather than with the porous model adopted in Ref. (5) on the

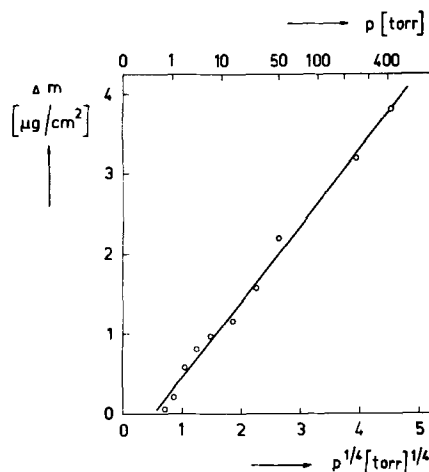


Fig. 4. Extent of reaction after 30 min at 450°C at different pressures.

basis of the fact that the ratio of molar volumes of magnesium to magnesium nitride is smaller than unity.

#### Acknowledgment

The authors are indebted to Dr. J. Hejduk and Dr. V. Hermoch for valuable remarks concerning the manuscript.

Manuscript submitted March 9, 1973; revised manuscript received Aug. 20, 1973.

Any discussion of this paper will appear in a Discussion Section to be published in the June 1975 JOURNAL. All discussions for the June 1975 Discussion Section should be submitted by Feb. 1, 1975.

#### REFERENCES

1. J. Turková, L. Láška, and V. Krejčí, Vorträge der Arbeitstagung in Suhl Oct. 23-26, 1972, Teil III, p. 197, Physikalische Gesellschaft der DDR, Berlin (1973).
2. G. V. Samsonov, "Nitridy," AN Ukr.SSR, Kiev (1969).
3. G. V. Samsonov, "Nemetalicheskie nitridy," AN SSSR, Moscow (1969).
4. H. N. Terem, *Rev. Fac. Sci. Univ. Istanbul*, **16A**, 81 (1951), or in Ref. (5).
5. P. Sthapitanonda and J. L. Margrave, *J. Phys. Chem.*, **60**, 1628 (1956).
6. I. A. Makolkin, I. I. Vernibud, J. N. Zhvanko, and V. T. Karpov, *Zh. Prikl. Khimii*, **33**, 824 (1960).
7. J. G. Murgulescu and D. Cismaru, *Rev. Chim. Acad. Populaire Roumaine*, **4**, 251 (1960).
8. P. Belin, *Compt. Rend. Acad. Sci. Paris*, **255**, 3164 (1962); **258**, 4715 (1964).
9. T. V. Dubovik, V. S. Polichuk, and G. V. Samsonov, *Zh. Prikl. Khimii*, **37**, 1828 (1964).
10. R. Sifferlen, *Compt. Rend. Acad. Sci. Paris*, **259**, 1520 (1964).
11. J. Oudar and J. Paidussi, in "Oxidation des Métaux," J. Bénard, Editor, Vol. II, Gauthier-Villars, Paris (1964).
12. L. Brewer, in "The Chemistry and Metallurgy of Miscellaneous Materials: Thermodynamics," L. L. Quill, Editor, McGraw-Hill Book Co., New York (1950), or in Ref. (5).
13. M. Matyáš, Surface Oxidation of Metals and Alloys in a Gaseous Environment," (in Czech), CSAV, Prague (1958).
14. O. Kubashevski and B. E. Hopkins, "Okislenie metalov i splavov," Moscow (1955); (Translation from English, London (1953)).
15. R. C. Logani and W. W. Smeltzer, *Can. Met. Quart.*, **10**, 149 (1971).
16. N. Cabrera and N. F. Mott, *Rep. Progr. Phys.*, **12**, 163 (1948-1949).
17. F. P. Fehlner and N. F. Mott, *Oxidation of Metals*, **2**, 59 (1970).
18. J. M. Perrow, W. W. Smeltzer, and J. D. Embury, *Acta Met.*, **16**, 1209 (1968).
19. G. I. Finch and A. G. Quarell, *Proc. Roy. Soc.*, **A 141**, 389 (1933).

## Oxidative Vaporization Kinetics of $\text{Cr}_2\text{O}_3$ in Oxygen from 1000° to 1300°C

Carl A. Stearns, Fred J. Kohl, and George C. Fryburg

NASA Lewis Research Center, Cleveland, Ohio 44135

The publication costs of this article have been assisted by the National Aeronautics and Space Administration.

#### ABSTRACT

Rates of oxidative vaporization of  $\text{Cr}_2\text{O}_3$  on preoxidized resistively heated chromium were determined in flowing oxygen at a pressure of 0.115 Torr for temperatures from 1000° to 1300°C. Reaction controlled rates were obtained from experimental rates by a gold calibration technique, and these rates were shown to agree with those predicted by thermochemical analysis. The activation energy obtained for the oxidative vaporization reaction corresponded numerically with the thermochemical enthalpy of the reaction. A theoretical equation is given for calculating the rate from thermodynamic data using boundary-layer theory.

Numerous investigators have studied the kinetics of chromium(III) oxide ( $\text{Cr}_2\text{O}_3$ ) scale formation on chromium and chromium-containing alloys heated in oxidizing environments (1-8). Gravimetric measurements above 1000°C yield a net weight loss which has been shown to be due to the loss of the gaseous species chromium(VI) oxide ( $\text{CrO}_3$ ) formed from the reaction of the  $\text{Cr}_2\text{O}_3$  protective scale with oxygen (3). The volatilization of  $\text{CrO}_3$  has been incorporated into the analyses of the kinetics of oxidation of materials with  $\text{Cr}_2\text{O}_3$  scales (7, 9). However, Caplan and Cohen (5), Hagel (3), and Graham and Davis (10) appear to be the only investigators to have measured explicitly the oxidative vaporization of  $\text{Cr}_2\text{O}_3$ .

Caplan and Cohen (5) established that  $\text{CrO}_3$  was the species which accounted for the evaporation of chromium oxide when  $\text{Cr}_2\text{O}_3$  was heated in oxygen, although they did not identify  $\text{CrO}_3$  in the vapor phase. Grimley *et al.* (11) subsequently identified this mole-

cule in the vapor phase by mass spectrometry. Hagel (3) measured the rate of weight loss of  $\text{Cr}_2\text{O}_3$  heated in oxygen and obtained a vaporization-temperature relationship which he used to correct his scale formation data. Hagel's vaporization corrections may be valid for his data obtained in a single experimental arrangement. However, his vaporization data cannot be considered as valid for other experimental arrangements (6, 9) because the volatilization reaction was undoubtedly gas diffusion controlled under the conditions of his experiments (furnace tests with static oxygen pressure of 76 Torr). The danger in using furnaces to study reactions that yield volatile products has been explained by Fryburg (12). Experimental techniques required to obtain meaningful data for such reactions have been described by Fryburg and Petrus (13, 14) for the oxidation of platinum. They showed that above a certain gas pressure (dependent on sample size and geometry) oxidative vaporization reactions become limited by mass transport through a boundary layer. Bartlett (15) has developed mass transport equations

Key words: oxidation, vaporization, kinetics, chromium, thermodynamics, activation energy.

which adequately explain experimental results over a wide range of temperature, pressure, and flow rate for the oxidation of both platinum and tungsten. Considerations such as these must be applied when studying the oxidative vaporization of  $\text{Cr}_2\text{O}_3$ .

Recently Graham and Davis (10) investigated the oxidative vaporization of hot-pressed and sintered samples of  $\text{Cr}_2\text{O}_3$  in free and forced convection in the pressure range from  $10^{-3}$  to 1 atm. They properly treated the mass transport problem and showed that the total pressure and flow dependencies were consistent with the assumption that the rate controlling step was the diffusion of  $\text{CrO}_3(\text{g})$  through a stagnant boundary layer. However, this study was made only at  $1200^\circ\text{C}$  and rates were not measured in the reaction controlled regime.

The work reported here was undertaken to determine the rate of oxidative vaporization of  $\text{Cr}_2\text{O}_3(\text{s})$  in molecular oxygen and its dependence on temperature. The work was part of a study of the enhanced oxidation of  $\text{Cr}_2\text{O}_3$  and chromium produced by exposure to oxygen atoms [see following paper (16)]. The experimental arrangement used in the program was dictated by requirements of the oxygen atom study. While this arrangement did not lend itself to a simple theoretical mass transport analysis, meaningful rate data were obtained by the use of a gold calibration technique.

### Experimental

**Samples.**—Test samples (12 cm long by 0.3 cm wide and 0.04 cm thick) were prepared from a chromium-0.1 weight per cent (w/o) yttrium alloy made from iodide chromium by arc melting and drop casting into a water-cooled copper mold. The small yttrium addition improves oxide adherence. Samples were diamond sawed from hot rolled sheet of the alloy. Sample surfaces were cleaned with a dental abrasive unit (using 50  $\mu\text{m}$  alumina powder and nitrogen gas) and anodically electropolished in a 2% sodium hydroxide solution for from 1 to 3 min with a current density of 0.3  $\text{A}\cdot\text{cm}^{-2}$ . Prior to testing, samples were washed with hot water and rinsed in ethanol.

Emission spectrographic and chemical analysis of samples yielded the following typical impurity analysis in parts per million: 230 iron, 10 aluminum, 8 copper, 5 calcium, 2 magnesium, 60 carbon, 50 oxygen, 5 nitrogen, and 5 hydrogen.

**Apparatus.**—A schematic diagram of the experimental arrangement is shown in Fig. 1. The sample was supported vertically by a fixed clamp at the top and a movable clamp at the bottom to allow for thermal expansion when the sample was heated. The bottom clamp was mounted in a linear ball bushing in such a fashion that it was free to move vertically but constrained from rotating.

The test chamber was evacuated with two 425 liters- $\text{min}^{-1}$  mechanical pumps. A 400 liters- $\text{sec}^{-1}$  oil diffusion pump was also available for high vacuum pumping. Gases were admitted into the system through a Pyrex tube (1.4 cm OD) connected to a flow control and a mixing manifold. The glass tube was arranged so that incoming gas impinged directly onto the flat side of the sample. Research Grade gases were used in all experiments.

Gas pressures in the test chamber were measured with a vacuum thermocouple gauge; the filament was heated by a 30.00 mA current from a regulated d-c power supply. Thermocouple voltages were read to the third decimal place with a digital voltmeter. The thermocouple gauge was calibrated for oxygen against a McLeod gauge. For other gases and gas mixtures, calibration was against a fused quartz precision pressure gauge.

Temperature control for the resistively heated sample was facilitated by a Pt-Pt13%Rh thermocouple (0.127 mm diameter wire) spot welded to the back face of the sample at its midpoint. This thermocouple was

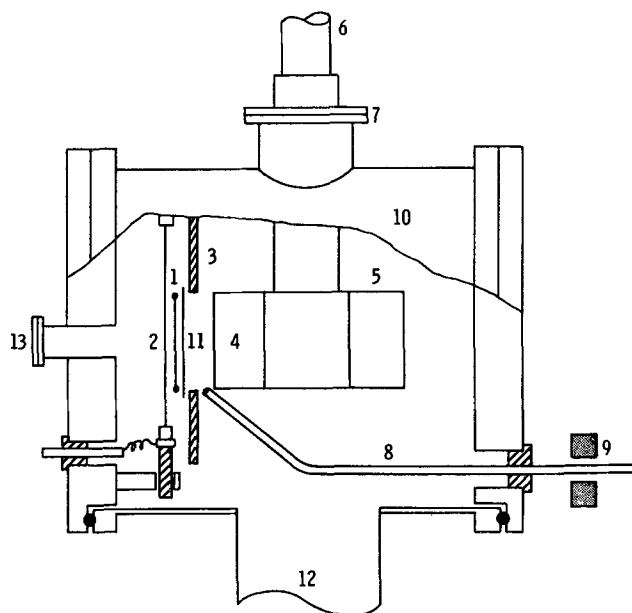


Fig. 1. Schematic of apparatus: 1, movable platinum resistance thermometer; 2, chromium sample filament; 3, shield; 4, platinum target; 5, eight sided rotatable target holder; 6, cooling reservoir; 7, rotatable seal; 8, gas inlet; 9, microwave discharge cavity; 10, vacuum chamber; 11, shutter; 12, vacuum pump; 13, window.

the primary element for a precision set-point, proportional controller-indicator. The output of the controller was used to drive a voltage controlled 100A d-c power supply. The power supply output was fed to the sample through insulated, water-cooled feed-throughs and flexible copper braid.

For all experimental conditions the sample temperature was held constant with time to at least  $\pm 0.5^\circ\text{C}$ . Temperatures were also measured with a micro-optical brightness pyrometer ( $\lambda = 650 \text{ nm}$ ) to supplement the thermocouple. The pyrometer was sighted through a shutterable window onto the back surface of the sample and the pyrometer-read temperatures were corrected for window absorption and sample emissivity. Corrected pyrometer temperatures measured next to the thermocouple junction were found to be in agreement with the thermocouple-indicated temperatures if a value of 0.7 was used for the sample emissivity. This value is consistent with literature values (17) for the emissivity of oxidized chromium.

The pyrometer was used mainly to survey the length of a sample for temperature gradients. Samples were discarded if the central portion opposite the opening to the collection target was not uniform in temperature to within  $\pm 5^\circ\text{C}$ .

Products vaporizing from the sample passed through an opening (2.6 cm on a side) in a water-cooled copper shield and were condensed on a cooled platinum target. Eight targets (5.1 cm on a side and 0.125 mm thick) were clamped against an eight-sided copper mounting block by copper frames screwed to the block. The block in turn was attached to a cylindrical copper reservoir through which coolant was circulated. The whole assembly could be externally rotated relative to the sample so that a designated target could be brought into position opposite the sample. Targets not directly in front of the sample were masked from the sample by the copper shield. In addition, the opening in the shield could be closed with an externally controllable water-cooled shutter. Target to sample distance was approximately 1.8 cm.

Ethanol was used as the coolant for the target assembly. It was cooled in a dry ice-alcohol bath. Tests were made prior to actual experiments to determine target temperature as a function of sample temperature and time. For these tests a thermocouple was at-

tached to the face of a target facing the sample. These tests demonstrated that the target temperature could be held below  $70^\circ\text{C}$  for indefinite periods of time when the sample temperature was  $1300^\circ\text{C}$ . Lower sample temperatures yielded proportionately lower target temperatures.

**Procedure for  $\text{Cr}_2\text{O}_3(\text{s})$  oxidations.**—Cleaned chromium samples were preoxidized *in situ* before an oxidation experiment by heating to the desired oxidation temperature for one-half hour in 0.115 Torr of flowing oxygen. For the temperatures of the experiments ( $1000^\circ\text{--}1300^\circ\text{C}$ ) approximately 0.01 mm (0.4 mil) oxide scales were formed as shown in Fig. 2.

Oxidation runs at each pressure and temperature were started by opening the shutter and collecting effusate on a target for a measured length of time. At  $1000^\circ\text{C}$  runs extended for 8–10 hr per target, but at  $1250^\circ\text{C}$  runs were only of the order of 10 min in length. Generally between 5–25  $\mu\text{g}$  of chromium were collected on a given target. After a series of runs (one for each of the eight targets) was completed, the sample was cooled and the block and targets were warmed to room temperature. Clean dry air was admitted to the system and the targets were removed for condensate analysis. The condensate was dissolved from each target with a stream of distilled water and the resulting solution was diluted to a measured volume. Each solution was quantitatively analyzed for chromium content by atomic absorption spectroscopy. The spectrometer was calibrated with solutions prepared from a purchased standard potassium dichromate solution. The analysis method had a sensitivity of 0.02 ppm chromium; sample solutions were usually held in the range from 0.2 to 2 ppm.

**Procedure for gold calibrations.**—In order to obtain "reaction controlled" rates from our experimental rates, it is obvious that we must determine the fraction of the  $\text{CrO}_3$  formed that is actually condensed on the target. This is the "collection fraction" of the apparatus. In addition, the oxidative vaporization may be diffusion limited (12, 13, 18). If so, we must determine the fraction of  $\text{CrO}_3$  volatilizing from the specimen surface that diffuses through the boundary layer to the target. This is called the "escape fraction."

These two fractions were determined by measuring the rate of evaporation of gold ribbons in the apparatus. The gold was 99.99% pure with silver and silicon being the major metallic impurities. The gold samples were made the same length and width as the chromium samples but the thickness was only 0.025 cm. Gold samples were cleaned in aqua regia and rinsed with water and ethanol.

The gold samples were mounted and heated in an identical manner to the chromium samples. Because of

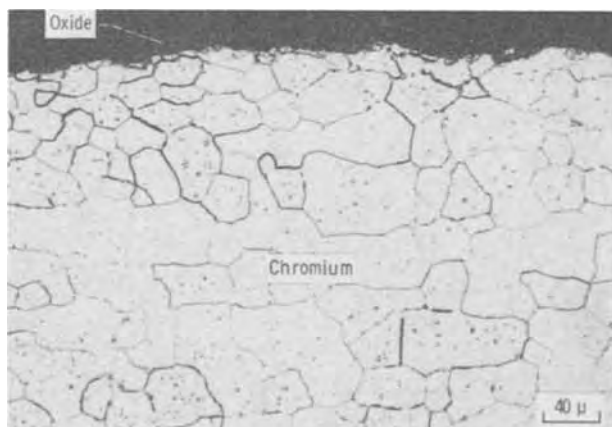


Fig. 2. Microstructure of typical oxidized specimen of Cr-0.1% Y showing oxide scale. Etchant: 10% sulfuric acid/chromic acid.

the high thermal conductivity of gold, temperature gradients were unavoidable: usually a temperature drop of about  $20^\circ\text{C}$  existed over the length from the midpoint to the top or bottom edge of the collection opening. Temperatures were measured with the optical pyrometer at 0.5 cm intervals over the 2.6 cm collection opening. Rates of evaporation were calculated and summed for 0.5 cm increments along the sample using the average temperature of each increment.

Experimental runs were performed at temperatures around  $1000^\circ\text{C}$  both under good vacuum conditions ( $<5 \times 10^{-6}$  Torr) and under the conditions of the oxidation experiments: with flowing oxygen at 5 liters- $\text{hr}^{-1}$  (STP) and 0.115 Torr pressure. Between 25 and 50  $\mu\text{g}$  of gold were collected on each platinum target. The quantity of gold on each target was determined by dissolving the gold in a stream of concentrated nitric acid, diluting with water to a measured volume, and analyzing the solution by atomic absorption spectroscopy. The sensitivity of the gold analysis was 0.1 ppm.

### Thermochemical Predictions

Fryburg and Petrus (13) showed that kinetic data, obtained from a study of the oxidative vaporization of platinum, could be correlated with equilibrium thermodynamic data. It is useful to reverse this process and to predict kinetic behavior from thermodynamic data. Kellogg type (19) equilibrium thermochemical diagrams aid in such predictions, as demonstrated by Gulbransen and Jansson (20–23) for the chromium-oxygen system. Gulbransen and Jansson employed the free energy of formation ( $\Delta G^\circ_f$ ) and equilibrium constant ( $\log K_p$ ) data for the gaseous chromium-oxygen molecules  $\text{CrO}$ ,  $\text{CrO}_2$ , and  $\text{CrO}_3$  as compiled by Schick (24) from the original mass spectrometric studies of Grimley *et al.* (11). The diagrams show that the important molecular species in equilibrium with  $\text{Cr}_2\text{O}_3(\text{s})$  and  $\text{O}_2(\text{g})$  should be  $\text{CrO}_3(\text{g})$  and  $\text{CrO}_2(\text{g})$  in the temperature range  $1000^\circ\text{--}2000^\circ\text{K}$  and at oxygen pressures greater than  $10^{-6}$  atm. The results of a recent transpiration study of the  $\text{Cr}_2\text{O}_3\text{--O}_2$  system by Kim and Belton (25) which apparently yielded more reliable data for  $\text{CrO}_3(\text{g})$  were employed by Kohl and Stearns (26) to construct revised diagrams which showed that the  $\text{CrO}_3$  molecules should be greater than an order of magnitude more abundant than indicated by Gulbransen and Jansson. Recent mass spectrometric studies on the vaporization of  $\text{CrO}_3(\text{c})$  by Schafer and Rinke (27), McDonald and Margrave (28), and Washburn (29) have established the existence of several "new" chromium oxide vapor species:  $(\text{CrO}_3)_3$ ,  $(\text{CrO}_3)_4$ ,  $(\text{CrO}_3)_5$ ,  $\text{Cr}_3\text{O}_7$ ,  $\text{Cr}_4\text{O}_{10}$ , and  $\text{Cr}_5\text{O}_{13}$ . In addition,  $\text{Cr}_2(\text{g})$  has been identified by Kant and Strauss (30). Therefore we have recalculated diagrams for the chromium-oxygen system and included the new vapor species.<sup>1</sup>

A thermochemical diagram at  $1500^\circ\text{K}$  is shown in Fig. 3. The diagram was constructed by the methods outlined by Gulbransen and Jansson (20). For  $\text{O}_2$  pressures greater than  $10^{-8}$  atm,  $\text{CrO}_3(\text{g})$  is still the predominant vapor species above  $\text{Cr}_2\text{O}_3(\text{s})$  but the new species  $\text{Cr}_3\text{O}_7(\text{g})$  becomes more important than  $\text{CrO}_2(\text{g})$  for  $\text{O}_2$  pressures greater than  $10^{-1}$  atm. The slope of the  $\text{CrO}_3(\text{g})$  line in the  $\text{Cr}_2\text{O}_3(\text{s})$  phase region is  $\frac{3}{4}$  and can be expected to describe the dependence of  $\text{CrO}_3(\text{g})$  pressure on oxygen pressure [as shown by Graham and Davis (10)].

From the respective diagrams at different temperatures one can obtain the vapor pressures of each species as a function of temperature for any given oxygen pressure. Thus, in Fig. 4 we have plotted the vapor pressure of the major species over the  $\text{Cr}_2\text{O}_3(\text{s})$  phase, for an oxygen pressure of  $1.51 \times 10^{-4}$  atm (0.115

<sup>1</sup> Thermodynamic data for  $\text{Cr}(\text{g})$ ,  $\text{CrO}(\text{g})$ , and  $\text{CrO}_2(\text{g})$  were taken from Schick (24). Data for  $\text{Cr}_2\text{O}_3(\text{s})$  were calculated from  $\Delta G^\circ_f$  values given by Wicks and Block (31). Thermodynamic data for  $\text{CrO}_3(\text{g})$  and the "new" chromium-oxygen molecules are given in the following paper (16).



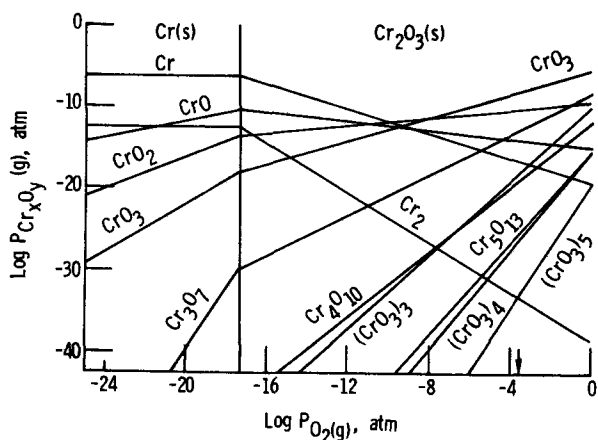


Fig. 3. Equilibrium thermochemical diagram for the chromium-oxygen system at 1500°K. Arrow indicates experimental oxygen pressure ( $1.51 \times 10^{-4}$  atm).

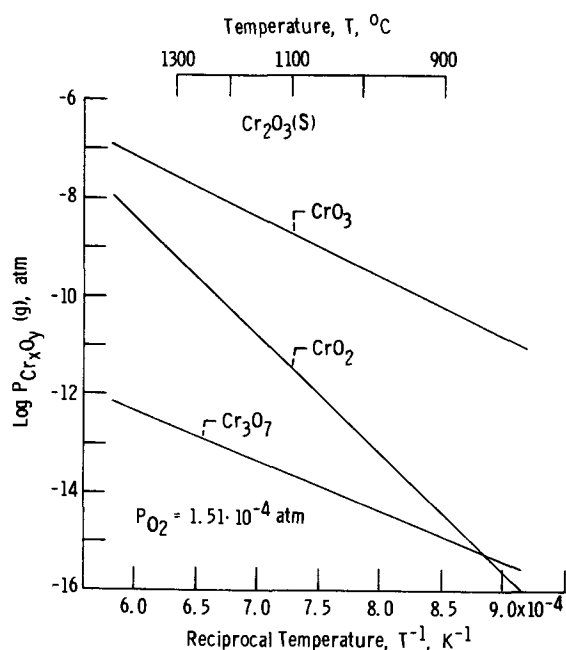
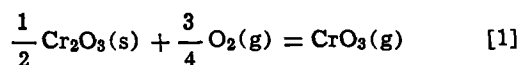


Fig. 4. Equilibrium vapor pressures of various oxide species of the chromium-oxygen system over  $\text{Cr}_2\text{O}_3(\text{s})$  vs.  $(1/T)$  under an oxygen pressure of  $1.51 \times 10^{-4}$  atm.

Torr), against reciprocal temperature. From this figure it is obvious that  $\text{CrO}_3(\text{g})$  will be the major vapor product in the oxidative vaporization of  $\text{Cr}_2\text{O}_3(\text{s})$  under our experimental conditions over the entire temperature range of this study. The slope of the  $\text{CrO}_3(\text{g})$  line in Fig. 4 is related to the enthalpy change for the reaction



In the case of the oxidative vaporization of platinum, the enthalpy change was shown to be equivalent to the energy of activation for the reaction (13) and thus it is not unreasonable to expect the same kind of correlation in the present studies.

The vapor pressure of  $\text{CrO}_3(\text{g})$  can be expressed analytically as

$$\log P_{\text{CrO}_3(\text{g})} (\text{atm}) = \frac{-1.247 \times 10^4}{T} + 3.20 + \frac{3}{4} \log P_{\text{O}_2(\text{g})} (\text{atm}) \quad [2]$$

over the temperature range 1270°-1570°K where the

thermodynamic data<sup>2</sup> have been taken from the work of Kim and Belton (25). Using the Hertz-Langmuir equation and the vapor pressure of  $\text{CrO}_3(\text{g})$  from Eq. [2] one can calculate the rate of vaporization of  $\text{CrO}_3(\text{g})$  and/or the rate of loss of chromium due to vaporization of the oxide. The rate of loss of chromium is given by

$$\begin{aligned} \dot{m}_{\text{Cr}} (\text{g-cm}^{-2}\text{-sec}^{-1}) &= P_{\text{CrO}_3(\text{g})} (2\pi RT M_{\text{CrO}_3})^{-1/2} M_{\text{Cr}} \\ &= 44.35 P_{\text{CrO}_3(\text{g})} (\text{atm}) \frac{M_{\text{Cr}}}{M_{\text{CrO}_3}^{1/2} T^{1/2}} \quad [3] \end{aligned}$$

where  $M$  is the appropriate molecular weight. We have used this equation<sup>3</sup> to calculate the predicted maximum rate of oxidative vaporizations of  $\text{Cr}_2\text{O}_3(\text{s})$ . This rate corresponds to "reaction controlled" conditions uninhibited by mass transport through a boundary layer.

## Results and Discussion

**Preliminary calibrations.**—Oxidative vaporization reactions obey linear kinetics, that is, the rates are time independent. Preliminary experiments validated the time independence of the rates for the oxidative vaporization of  $\text{Cr}_2\text{O}_3$ . In addition, oxidative vaporization reactions may be diffusion limited (12, 13, 18). Experiments at different oxygen pressures and experiments with inert gas additives (14) indicated that the oxidation was slightly diffusion limited for our experimental arrangement. The experimental conditions were dictated by the fast-flow, intermediate-pressure requirements of our oxygen-atom oxidation studies described in the following paper (16). The oxygen-atom output optimized at an oxygen pressure of 0.115 Torr with a flow rate of 5 liters-hr<sup>-1</sup>(STP). Consequently, all the results reported in this paper were obtained at one pressure and one flow rate; namely, 0.115 Torr and 5 liters-hr<sup>-1</sup>(STP).

To obtain reaction controlled rates it was necessary to correct the measured rates. This was done by determining the "escape fraction" of the  $\text{CrO}_3(\text{g})$  formed in the oxidation reaction. In addition, the geometrical collection fraction for the apparatus was required. This fraction allowed correction for the fact that even in the absence of a boundary layer not all of the vapor product reaches the collection target (due to finite size of target, shield, etc.). Both the escape fraction and the geometrical collection fraction were determined experimentally using gold samples of the same width as the Cr-0.1Y samples.

The geometrical collection fraction was obtained by comparing the measured rate of evaporation of gold in a vacuum of  $<10^{-5}$  Torr with the rate calculated from the vapor pressure data of Hultgren *et al.* (33). Two gold samples were used and measurements were made at temperatures between 1000° and 1012°C. An average value of  $0.455 \pm 0.05$  was obtained for the geometrical collection fraction.

The escape fraction was obtained by comparing the measured rate of evaporation of gold in a vacuum of  $<10^{-5}$  Torr with the rate measured under the conditions of the oxidation experiments; namely, 0.115 Torr of oxygen flowing at 5 liters-hr<sup>-1</sup>(STP). Numerous experiments yielded an average value of  $0.335 \pm 0.04$  for the escape fraction.

Reaction controlled rates were calculated from our experimentally measured rate by dividing the measured rate by the product of the escape fraction and geometrical collection fraction, namely  $0.153 \pm 0.03$ . The error we have associated with this product arises from the precision of our experiments and does not include errors arising from inaccuracies in the vapor

<sup>2</sup> The results of Kim and Belton (25) were obtained in a temperature range of 1600°-1860°K. We have adjusted their vapor pressure expression to our temperature range by use of the heat contents of  $\text{CrO}_3(\text{g})$ ,  $\text{O}_2(\text{g})$ , and  $\text{Cr}_2\text{O}_3(\text{s})$ .

<sup>3</sup> Note that this equation is slightly different from that given previously by Kohl and Stearns (26) and Rapp (32). The previous equation was not dimensionally correct and yielded results about 40% too high.



pressure of gold. We estimate this inaccuracy to be as much as  $\pm 50\%$ . Because of the magnitude of this possible error we have not corrected our escape fraction for the fact that the atomic weight and other atomic parameters of gold are different from those of  $\text{CrO}_3(\text{g})$ . Calculations indicate that the diffusivity of  $\text{CrO}_3(\text{g})$  is about 10% greater than the diffusivity of gold. In addition, we have assumed that the escape fraction is independent of the temperature of the sample. This assumption is based on the fact that for the oxidative vaporization of platinum the escape fraction was shown to be independent of sample temperature (14).

**Analysis of oxide scale and identification of oxide condensate.**—Numerous samples of our oxide scales were subjected to x-ray diffraction. The analyses always confirmed that the scale was  $\text{Cr}_2\text{O}_3$ .

Two samples were subjected to ion microprobe mass analysis:<sup>4</sup> one was unoxidized starting material and the other was a sample which had undergone several oxidative vaporization experiments. Yttrium was detected in the oxide layer of the reacted sample at a concentration approximately four times that detected in the bulk unoxidized sample. Samplings in different regions of the oxidized sample showed the yttrium content to vary by a factor of five, while comparable data taken from the unoxidized sample showed yttrium to be constant. The spectrum obtained from the oxidized layer also revealed increases in the levels of all metallic contaminants, especially Fe, Al, Ca, and Mg. In addition, the elements Si, Mn, Na, and Co were identified as low-level metallic impurities. From these results it is concluded that the nonvolatile oxide forming metallic impurities tend to concentrate in the surface oxide layer on the oxidized chromium where chromium has been lost by vaporization. However, because our oxide scales were generally removed between experiments, this effect should not have been cumulative and should not have affected our results.

The oxide condensate obtained in these experiments formed a reddish brown deposit on the platinum targets. When collected on polished platinum targets the condensates were always readily soluble in water, forming yellow-colored solutions. If the platinum became etched (from cleaning in aqua regia) the deposits were often only partly soluble in water and required 1:1 HCl or fusion with  $\text{K}_2\text{S}_2\text{O}_8$ . For all the experiments reported here only polished platinum targets were used, and the targets were cleaned with  $\text{K}_2\text{S}_2\text{O}_8$ . In addition, the oxide deposits were always dissolved as soon as feasible after a series of experiments.

Attempts to identify the deposits by electron diffraction were unsuccessful and only  $\text{Cr}_2\text{O}_3$  was identified. Apparently, the hydrocarbon background in the electron diffraction unit reduced the  $\text{CrO}_3$  to  $\text{Cr}_2\text{O}_3$ . We have assumed that the deposits were  $\text{CrO}_3(\text{s})$  based on their reddish-brown color, their water solubility ( $\text{Cr}_2\text{O}_3$  is insoluble in  $\text{H}_2\text{O}$ ), the yellow color of the water solutions, the thermochemical predictions, and the findings of Caplan and Cohen (5) and of Grimley *et al.* (11).

**Pressure dependence.**—Experiments were performed to determine the order of the reaction with respect to the pressure of oxygen. Thermodynamic analysis indicates that the rate should depend on the  $3/4$  power of the oxygen pressure. Runs were made at a given temperature in which the total pressure and gas flow rate were maintained constant, and the oxygen partial pressure was varied by dilution with nitrogen gas. The oxygen pressures were varied from 0.115 to 0.070 Torr. Greater dilution with nitrogen seemed to produce a permanent decrease in the rate of oxidation and resulted in an hysteresis effect with changing pressure. Nitrogen was used as the dilution gas because its mo-

lecular weight, collision cross section, and collision integral are nearly the same as those of oxygen. Thus, by keeping the total pressure of  $\text{O}_2\text{-N}_2$  mixture constant, the escape fraction should also remain constant. A log-log plot of our rates of oxidation vs. the partial pressure of oxygen for a temperature of  $1200^\circ\text{C}$  is presented in Fig. 5. A line of slope =  $3/4$  has been drawn through the points. It is evident that the rate obeys a  $3/4$  dependency on oxygen pressure within experimental precision.

**Temperature dependence.**—The effect of temperature on the rate of oxidative vaporization was measured over the range from  $1000^\circ$  to  $1300^\circ\text{C}$  at a constant oxygen pressure of 0.115 Torr. Measurements at lower temperatures were impractical because of the unreasonably long times involved in collecting a measurable condensate. A typical set of results is shown in Fig. 6 in the form of an Arrhenius plot. The experimental rates, corrected for geometrical and diffusion-limitation factors, are represented by the circled points. The solid line through these points was derived from a least squares fit of the data, and yields an activation energy of  $61.5 \pm 5 \text{ kcal-mole}^{-1}$  for the oxidation process.

We have extensively investigated the effect of varying several experimental parameters on the value obtained for the activation energy. Parameters varied included sample, oxygen pressure (0.050, 0.075, and 0.115

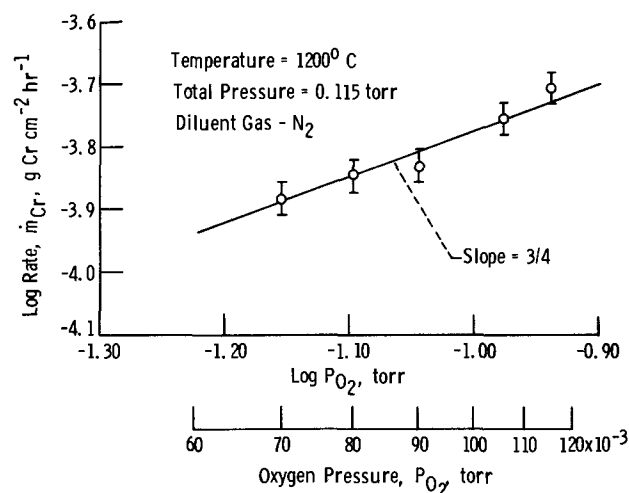


Fig. 5. Pressure dependence of oxidative vaporization of  $\text{Cr}_2\text{O}_3$

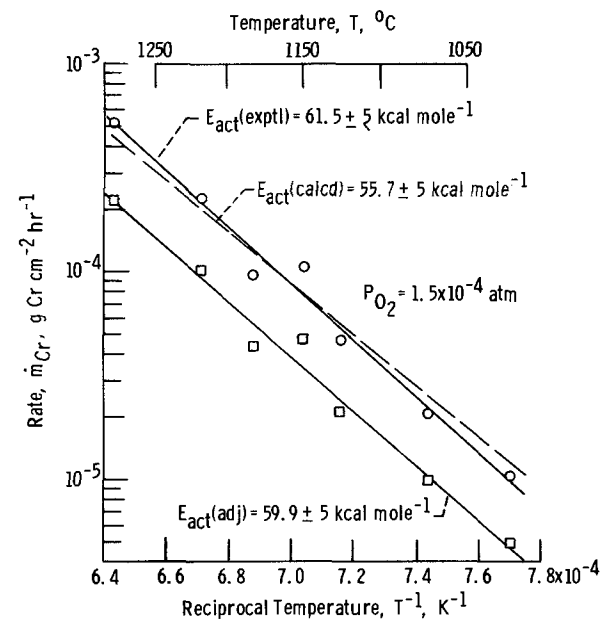


Fig. 6. Temperature dependence of oxidative vaporization of  $\text{Cr}_2\text{O}_3$ .

<sup>4</sup>We wish to thank Applied Research Laboratories, Sunland, California, for providing the ion microprobe analyses.

Torr), flow rate (2 and 5 liters-hr<sup>-1</sup>), sample-target separation (1.8 to 3.0 cm), and sample composition (Cr-0.1Y and Ni-40Cr). Although the actual rates varied with some of these parameters, the temperature dependence did not and the energy of activation was found to be the same within experimental precision of  $\pm 5$  kcal-mole<sup>-1</sup>.

Included in Fig. 6, as the dashed line, are the predicted rates calculated from Eq. [3] for a pressure of 0.115 Torr. As noted earlier, the experimental energy of activation and the enthalpy of reaction may be expected to be numerically equal for oxidative vaporization reactions of the type being considered. Actually the two quantities are different by a small amount due to a temperature term that arises from the Hertz-Langmuir equation. The energy of activation can be calculated from the enthalpy of the reaction by the relationship (34)

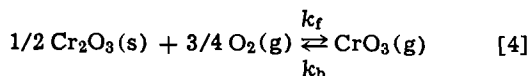
$$E_{\text{act}}/R = \Delta H^\circ_T/R - T/2 \quad [4]$$

The enthalpy in this temperature range is  $\Delta H^\circ_{1400} = 57.1$  kcal-mole<sup>-1</sup>. Thus the calculated energy of activation is 55.7 kcal-mole<sup>-1</sup> as given in Fig. 6.

The experimental rates are not exactly comparable to the rates calculated from thermodynamic data because the temperature of the oxygen in our experiments is not at the temperature of the specimen, in fact, it is probably closer to room temperature.<sup>5</sup> To facilitate comparison we have adjusted our experimental rates by multiplying by the factor<sup>6</sup>  $(300/T)^{1/2}$ , where room temperature has been taken as 300°K. These adjusted results are given as the squared points in Fig. 6. The line through these points was derived from a least squares fit and yields an "adjusted" energy of activation of  $59.9 \pm 5$  kcal-mole<sup>-1</sup>. This value may be compared with our calculated value of  $55.7 \pm 2$  kcal-mole<sup>-1</sup> and is found to be in agreement within experimental error. The rates represented by the squared points may be compared with the calculated rates and are seen to be roughly one-half of the calculated rates. This is probably within the experimental error of our measurements which depend directly on the accuracy with which we could measure the vaporization rate of gold in our apparatus. In addition, we have probably underestimated the temperature of the gas in the boundary layer.<sup>5</sup> If so, the "adjusted" rates may have been reduced too much and a value closer to the experimental rates may be more accurate. In any case, the agreement is quite good for this type of measurement.

**Theoretical rate equation.**—We have shown that the kinetics of the oxidative vaporization of Cr<sub>2</sub>O<sub>3</sub>(s) in the reaction controlled region can be adequately described by the equilibrium thermodynamic data. It is, therefore, possible to derive an equation for the rate of oxidative vaporization in any pressure region under various flow conditions, requiring only the equilibrium constant of the reaction and the Nusselt number obtained from dimensionless fluid correlations. The development parallels that of Bartlett (15).

The oxidation process is represented by the reaction



<sup>5</sup> The quantity of importance in experiments involving gas-solid reactions is the collision flux of the gas with the solid. This depends on the pressure and the temperature of the gas. When a small diameter filament is heated in a bulb containing gas at a pressure low enough that the mean-free path is comparable to the diameter of the bulb (Knudsen region), all the gas molecules striking the wire have a temperature equal to that of the bulb. As the pressure is increased and/or the diameter of the wire is increased, the gas molecules striking the wire will have temperatures approaching the wire temperature. In the viscoelastic pressure region one usually takes the gas temperature in the boundary layer as the average of the wire and bulb temperature. In our experiments the ratio of the mean-free path to the ribbon width was about 0.2. While this is not in the Knudsen region, it is fairly close and for the sake of simplicity we have assumed that the gas striking the chromium ribbon is at room temperature.

<sup>6</sup> The collision flux,  $Z$ , varies as  $T^{-1/2}$  as indicated by the well-known kinetic theory equation  $Z = p/(2\pi MRT)^{-1/2}$ .

At pressures where the mean free path ( $\lambda$ ) of the CrO<sub>3</sub>(g) is large compared with the width ( $L$ ) of the chromium ribbon, all the CrO<sub>3</sub>(g) formed escapes from the ribbon and the rate is reaction controlled. At higher pressures where  $\lambda/L < 1$ , some of the volatilizing CrO<sub>3</sub>(g) will be back reflected to the chromium ribbon where it will decompose and the rate will be diffusion limited. In this case the rate will be determined by the rate of mass transport of CrO<sub>3</sub>(g) through a stagnant boundary layer of oxygen (because  $P_{\text{CrO}_3} \ll P_{\text{O}_2}$ ). The mass flux of CrO<sub>3</sub>(g) across the boundary layer is given by

$$\dot{m}_D = \frac{k_m M_{\text{CrO}_3} (P_{\text{CrO}_3,s} - P_{\text{CrO}_3,\delta})}{P_t} \quad [5]$$

where  $\dot{m}_D$  is in g-cm<sup>-2</sup>-sec<sup>-1</sup>;  $k_m$  is the mass transfer coefficient which can be calculated from boundary layer theory (mole-cm<sup>-2</sup>-sec<sup>-1</sup>);  $P_{\text{CrO}_3,s}$  and  $P_{\text{CrO}_3,\delta}$  are the steady-state values of the partial pressures of CrO<sub>3</sub>(g) at the surface of the chromium ribbon and at the outer edge of the boundary layer, respectively; and  $P_t$  is the total pressure or the stagnation pressure in a flowing system.

Generally,  $P_{\text{CrO}_3,\delta} = 0$  and Eq. [5] reduces to

$$\dot{m}_D = k_m M_{\text{CrO}_3} P_{\text{CrO}_3,s} / P_t \quad [6]$$

The rate of formation of CrO<sub>3</sub>(g) by chemical reaction is given by

$$\dot{m}_R = M_{\text{CrO}_3} (k_f P_{\text{O}_2,s}^{3/4} - k_b P_{\text{CrO}_3,s}) \quad [7]$$

where  $k_f$  and  $k_b$  are the forward and backward rate constants of the reaction, respectively.  $P_{\text{O}_2,s}$  is the partial pressure of oxygen at the surface of the chromium ribbon.

However, because  $P_{\text{CrO}_3(g)} \ll P_{\text{O}_2}$ ,  $P_{\text{O}_2,s}$  can be taken equal to the pressure in the system:  $P_{\text{O}_2}$ . We have tacitly assumed in Eq. [7] that the condensation coefficient of CrO<sub>3</sub>(g) on the chromium is one.

The exact value of  $P_{\text{CrO}_3,s}$  is unknown. However, it can be eliminated from Eq. [6] and [7]. In addition, from consideration of the mass balance,  $\dot{m}_D = \dot{m}_R$ ; and by definition,  $K_e = k_f/k_b$ . Performing these operations and substitutions, we obtain

$$\dot{m}_D = \frac{M_{\text{CrO}_3} k_b K_e P_{\text{O}_2}^{3/4}}{1 + k_b P_t / k_m} \quad [8]$$

The backward rate constant  $k_b$  is simply the surface collision frequency of CrO<sub>3</sub>(g) molecules in mole-cm<sup>-2</sup>-sec<sup>-1</sup> per unit pressure, and is given by the kinetic theory expression

$$k_b = (2\pi M_{\text{CrO}_3} RT)^{-1/2} \quad [9]$$

Inserting this expression into Eq. [8], we obtain

$$\dot{m}_D = \frac{(2\pi M_{\text{CrO}_3} RT)^{-1/2} M_{\text{CrO}_3} K_e P_{\text{O}_2}^{3/4}}{1 + (2\pi M_{\text{CrO}_3} RT)^{-1/2} P_t / k_m} \quad [10]$$

where  $R$  is in erg-mole<sup>-1</sup>-K<sup>-1</sup> and  $P$  is in dyne-cm<sup>-2</sup>.

Equation [10] is valid at all pressures and at temperatures for which reaction [4] occurs. At low pressures where  $1 \gg (2\pi M_{\text{CrO}_3} RT)^{-1/2} P_t / k_m$ , Eq. [10] reduces to

$$\dot{m}_D = (2\pi M_{\text{CrO}_3} RT)^{-1/2} M_{\text{CrO}_3} K_e P_{\text{O}_2}^{3/4} \quad [11]$$

which is analogous to Eq. [3] except it is in units of grams CrO<sub>3</sub>(g) rather than grams Cr. The rate of oxidation is proportional to  $P_{\text{O}_2}^{3/4}$  and is reaction controlled. At high pressures where  $1 \ll (2\pi M_{\text{CrO}_3} RT)^{-1/2} P_t / k_m$ , Eq. [10] reduces to

$$\dot{m}_D = M_{\text{CrO}_3} k_m K_e P_{\text{O}_2}^{3/4} / P_t \quad [12]$$

The mass transfer coefficient,  $k_m$ , is related to the Nusselt number ( $\text{Nu}_m$ ) for mass transfer by the relation

$$k_m = \frac{Nu_m P_t D_{CrO_3}}{LRT_g} \quad [13]$$

where  $D_{CrO_3}$  is the diffusion coefficient of CrO<sub>3</sub> in cm<sup>2</sup>-sec<sup>-1</sup> and  $L$  is a characteristic dimension of the sample, i.e., the ribbon width.

All of the quantities in these two equations ([12] and [13]) are known except the diffusion coefficient and the Nusselt number. The former can be calculated from the Chapman-Enskog equation and the Nusselt number is obtained from semiempirical correlations used extensively in engineering analyses (35).

### Summary of Results

Experimental rates for the oxidative vaporization of Cr<sub>2</sub>O<sub>3</sub> in low pressure, flowing oxygen, when corrected for geometrical and diffusion-limiting factors, agree within experimental error with rates calculated from equilibrium thermodynamic data.

The experimentally determined pressure and temperature dependencies also agree within experimental error with the dependencies predicted from equilibrium thermodynamic data. Both experiment and thermodynamic data show that the reaction varies as the 3/4 power of the oxygen pressure. The experimental energy of activation, adjusted for the fact that the oxygen is not at the temperature of the specimen, was  $59.9 \pm 5$  kcal-mole<sup>-1</sup> and the enthalpy calculated for the reaction was  $55.7 \pm 2$  kcal-mole<sup>-1</sup>.

Predicted on these findings one can conclude that the rate of oxidative vaporization of Cr<sub>2</sub>O<sub>3</sub> in oxygen can be calculated realistically from equilibrium thermodynamic data. An equation is derived for calculating the rate under any conditions of temperature, pressure, and flow condition using thermodynamic data and the Nusselt number obtained from dimensionless fluid correlations

### Acknowledgments

It is a pleasure to thank J. R. Stephens for supplying us with the chromium used in this study. We also wish to thank J. W. Graab and W. F. Davis for carrying out the chemical analyses. We gratefully acknowledge helpful discussions with C. E. Lowell on the nature of the oxide scales on chromium and chromium alloys.

Manuscript submitted Nov. 30, 1973; revised manuscript received Feb. 11, 1974. This paper was presented in part as Paper 105 at the Boston, Massachusetts, Meeting of the Society, Oct. 7-11, 1973.

Any discussion of this paper will appear in a Discussion Section to be published in the June 1975 JOURNAL. All discussions for the June 1975 Discussion Section should be submitted by Feb. 1, 1975.

### REFERENCES

- G. R. Wallwork and A. Z. Hed, *Oxidation of Metals*, **3**, 229 (1971).
- C. E. Lowell, D. L. Deadmore, S. J. Grisaffe, and I. L. Drell, NASA TN D-6290 (1971).
- W. C. Hagel, *Trans. Am. Soc. Metals*, **56**, 583 (1963).
- M. S. Seltzer, B. A. Wilcox, and J. Stringer, *Met. Trans.*, **3**, 2391 (1972).
- B. Caplan and M. Cohen, *This Journal*, **108**, 438 (1961).
- L. Cadiou and J. Paidassi, *Mem. Sci. Rev. Met.*, **66**, 217 (1969).
- J. Stringer, *Oxidation of Metals*, **5**, 49 (1972).
- C. S. Giggins and F. S. Pettit, *Met. Trans.*, **2**, 1071 (1971).
- C. S. Tedmon, Jr., *This Journal*, **113**, 766 (1966).
- H. C. Graham and H. H. Davis, *J. Am. Ceram. Soc.*, **54**, 89 (1971).
- R. T. Grimley, R. P. Burns, and M. G. Inghram, *J. Chem. Phys.*, **34**, 664 (1961).
- G. C. Fryburg and H. M. Murphy, *Trans. Met. Soc. AIME*, **212**, 660 (1958).
- G. C. Fryburg and H. M. Petrus, *This Journal*, **108**, 496 (1961).
- G. C. Fryburg, *Trans. Met. Soc. AIME*, **233**, 1986 (1965).
- R. W. Bartlett, *This Journal*, **114**, 547 (1967); *Trans. Met. Soc. AIME*, **230**, 1097 (1964).
- G. C. Fryburg, F. J. Kohl, and C. A. Stearns, *This Journal*, **121**, 952 (1974).
- C. J. Smithells, "Metal Reference Book," Butterworths Scientific Publishers, London (1949).
- D. E. Rosner, *Ann. Rev. Materials Sci.*, **2**, 573 (1972).
- H. H. Kellogg, *Trans. Met. Soc. AIME*, **236**, 602 (1966).
- S. A. Jansson and E. A. Gulbransen, 4th International Congress on Metallic Corrosion, Amsterdam, Netherlands, Sept. 7-14, 1969, p. 77.
- E. A. Gulbransen and S. A. Jansson, in "Heterogeneous Kinetics at Elevated Temperatures," G. R. Belton and W. L. Worrell, Editors, pp. 181-208, Plenum Press, New York (1970).
- S. A. Jansson, *J. Vacuum Sci. Technol.*, **7**, S5 (1970).
- E. A. Gulbransen and S. A. Jansson, in "Oxidation of Metals and Alloys," pp. 63-86, American Society for Metals (1971).
- H. L. Schick, Editor, "Thermodynamics of Certain Refractory Compounds," Academic Press, New York (1966).
- Y. Kim, Ph.D. Thesis, University of Pennsylvania (1969).
- F. J. Kohl and C. A. Stearns, NASA TMX-52879 (1970); NASA TMX-67980 (1971).
- H. Schafer and K. Rinke, *Z. Naturforsch.*, **20b**, 702 (1965).
- J. D. McDonald and J. L. Margrave, *J. Inorg. Nucl. Chem.*, **30**, 665 (1968).
- C. A. Washburn, Ph.D. Thesis, University of California (1969), UCRL-18685, PB-183562.
- A. Kant and B. Strauss, *J. Chem. Phys.*, **45**, 3161 (1966).
- C. E. Wicks and F. E. Block, *U.S. Bur. Mines Bull.*, **605** (1963).
- R. A. Rapp, in "High Temperature Corrosion of Aerospace Alloys," pp. 147-154, AGARD-CP-120 (1972).
- R. Hultgren, R. L. Orr, P. D. Anderson, and K. K. Kelley, Selected Values of Thermodynamic Properties of Metals and Alloys, Univ. California, Dept. Mineral Tech., Supplements, issue dated Aug. 1969.
- E. Rutner, in "Condensation and Evaporation of Solids," E. Rutner, P. Goldfinger, and J. P. Hirth, Editors, p. 149, Gordon and Breach, New York (1964).
- R. B. Bird, W. E. Stewart, and E. L. Lightfoot, "Transport Phenomena," Chap. 21, John Wiley & Sons, Inc., New York (1960).

# Enhanced Oxidative Vaporization of $\text{Cr}_2\text{O}_3$ and Chromium by Oxygen Atoms

George C. Fryburg, Fred J. Kohl, and Carl A. Stearns

NASA Lewis Research Center, Cleveland, Ohio 44135

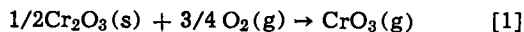
The publication costs of this article have been assisted by the National Aeronautics and Space Administration.

## ABSTRACT

Rates of oxidative vaporization of  $\text{Cr}_2\text{O}_3$  have been found to be markedly enhanced in the presence of oxygen atoms. Investigations were conducted over the temperature range 200°-1250°C. For  $\text{Cr}_2\text{O}_3$  the enhancement was about  $10^9$  at 550°C in oxygen containing 2.5% atoms. Rapid oxidative vaporization of bare chromium was observed below 800°C, the rate being about one-half that of  $\text{Cr}_2\text{O}_3$ . Results are interpreted in terms of thermochemical analysis.

Some years ago one of us demonstrated that oxygen atoms caused a marked enhancement in the rate of oxidation of platinum (1, 2). Subsequently, Rosner and Allendorf (3) extended these studies to molybdenum and tungsten obtaining similar enhancements in the rates of oxidation. Madix (4), using atomic beam techniques, found an enhanced oxidation of germanium and silicon with oxygen atoms. All of these metals form volatile oxides in the temperature range in which the enhanced oxidation was discovered.

This paper reports on the enhancement, by oxygen atoms, of the oxidative vaporization of an oxide; namely,  $\text{Cr}_2\text{O}_3$ . The normal oxidation reaction is represented by the equation



In oxygen, at reduced pressures, this oxidative vaporization is detectable above roughly 900°C [see preceding paper (5)]. In partially atomic oxygen, the rate is enhanced so markedly that oxidation is readily measured down to 200°C. We have determined the rate of oxidative vaporization of  $\text{Cr}_2\text{O}_3$  in partially atomic flowing oxygen at a total pressure of 0.115 Torr<sup>1</sup> from 200° to 1250°C. The experimental rates were corrected by the method given in the preceding paper (5) to give "reaction controlled" rates. Oxidative vaporization rates were also calculated from the equilibrium thermodynamic data for comparison.

During the course of this investigation we observed, below 800°C, a direct oxidative vaporization of chromium metal by the oxygen atoms. This has also been noted by Sutcliffe (6). As a result, measurements were also made of the rate of oxidative vaporization of electropolished chromium in partially atomic oxygen.

## Experimental Procedure

The main features of the experimental arrangement and the procedures used in this investigation were described in the preceding paper (5). As before, samples were prepared from a chromium-0.1 weight per cent (w/o) yttrium alloy. In the present experiments the oxygen was dissociated by a 100W, 2450 MHz microwave power supply with a slotted wave guide [item 9, Fig. 1 of Ref. (5)]. The amount of dissociation in the region of the oxidation sample was determined with a platinum resistance thermometer [item 1, Fig. 1 of Ref. (5)], similar to one used previously (1), that could be moved directly in front of the specimen in the flow stream of oxygen. The sensing element of this thermometer was made from platinum ribbon 0.025 mm thick, 0.25 mm wide, and 3 cm long. The central 2 cm was tapped off with 0.025 mm diameter wires for po-

tentiometric readings. The platinum ribbon was operated at 900°C, a temperature at which the recombination coefficient for oxygen atoms is close to one (7, 8). The percentage of oxygen atoms in the oxygen can be obtained from the measured joule heating resulting from the recombination of the atoms, knowing the heat of recombination and the pressure of the oxygen [see Ref. (1) for details]. Corrections<sup>2</sup> were made for the heating resulting from  $\text{O}_2$  (<sup>1</sup> $\Delta_g$ ) molecules that are also formed in the discharge (9, 11).

Research Grade oxygen was used. This gas contained less than 1 ppm of water vapor so it was necessary to add 5% of nitrogen (also Research Grade) to the oxygen in order to produce a more useful concentration of oxygen atoms.<sup>3</sup> With the nitrogen added we obtained about 2.5% oxygen atoms at the sample, and with the pure oxygen we obtained about 1.2%.

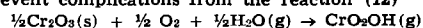
The procedure for conducting experiments was similar to that described in the preceding paper (5). For  $\text{Cr}_2\text{O}_3$  oxidations the chromium ribbons were all pre-oxidized at a high temperature: 1100°-1300°C. This was done, as before, *in situ* for one-half hour in the flowing oxygen at 0.115 Torr, and the thickness of  $\text{Cr}_2\text{O}_3$  scale formed was 0.01 mm (0.4 mil) or greater. The temperature of the specimens was obtained from the reading of the thermocouple spot welded onto the back. This was checked with the micro-optical pyrometer at the higher temperatures.

In addition, it was necessary to stabilize the discharge before the oxidations could be performed. The first stabilization of the day required 30 min run-in time to obtain constant oxygen atom output. If the arc was shut off during the day, 5 to 10 min run-in was sufficient. During these arc stabilizations the shutter was kept closed so that the specimen was not exposed to any atoms. The oxygen atom output was very stable after the initial run-in and was reproducible from day to day as long as the oxygen inlet tube remained clean. Over long periods of time the output dropped slowly. Periodically, the inlet tube was removed and cleaned in 5% HF followed by copious rinsing with distilled water.

The oxide condensate formed in these experiments was always readily soluble in water, and we have as-

<sup>2</sup> Auxiliary experiments were run in which a long silver ribbon was placed in the gas inlet tube, just downstream from the discharge. This effectively removed all the oxygen atoms as indicated by blackening of only the upstream end of the silver (9). The blackening results from formation of AgO (10) by the oxygen atoms. The residual heating caused by the  $\text{O}_2$  (<sup>1</sup> $\Delta_g$ ) in the gas was found to be 10% of heating obtained without the silver ribbon. This percentage remained the same with or without the nitrogen addition to the oxygen.

<sup>3</sup> The water vapor in the oxygen was maintained as low as possible to prevent complications from the reaction (12)



The added  $\text{N}_2$  is dissociated in the discharge and the nitrogen atoms react very rapidly with  $\text{O}_2$  and/or NO to form oxygen atoms. No nitrogen atoms reach the sample.

Key words: oxidation, vaporization, kinetics, chromium, thermodynamics, oxygen atoms, activation energy.

<sup>1</sup> This pressure was the optimum for oxygen atom production.

sumed it was CrO<sub>3</sub> based on the reasoning used in the preceding paper (5). As before, the water solutions were analyzed for chromium by atomic absorption spectroscopy.

**Thermochemical Predictions**

Equilibrium thermochemical diagrams have proven useful in describing the chemistry of oxidation and vaporization for many metal-metal oxide-oxygen systems (13-18). The preceding paper (5) demonstrated that the thermodynamic description could also be correlated with the kinetic behavior for the oxidative vaporization of a condensed phase metal oxide, Cr<sub>2</sub>O<sub>3</sub>, reacting with molecular oxygen. Here we extend the use of thermochemical diagrams to provide a description of the oxidative vaporization of condensed phase chromium and Cr<sub>2</sub>O<sub>3</sub> reacting with atomic oxygen. The effect of adding atomic oxygen is equivalent to increasing the chemical potential of oxygen.

Thermochemical diagrams for the chromium-atomic oxygen system at 800° and 1500°K are given in Fig. 1 and 2, respectively. (Details of the method of construction and sources of thermodynamic data are given in the Appendix.) For comparison we give a diagram for the chromium-molecular oxygen system at 800°K in Fig. 3. A similar diagram at 1500°K was given in Fig. 3 of the preceding paper (5).

The atomic oxygen thermochemical diagrams differ markedly from the molecular oxygen ones in several respects. In addition to Cr and Cr<sub>2</sub>O<sub>3</sub> condensed phases, a CrO<sub>3</sub> condensed phase is present at high oxygen atom pressures. Whereas the complex chromium-oxygen molecules are relatively unimportant in the molecular

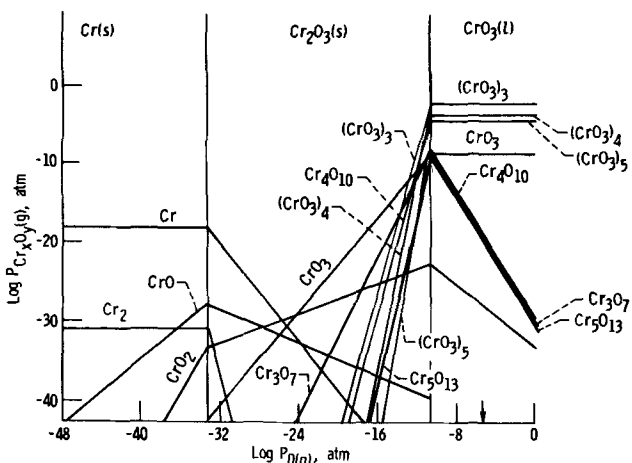


Fig. 1. Equilibrium thermochemical diagram for the chromium-atomic oxygen system at 800°K. Arrow indicates experimental oxygen atom partial pressure ( $3.8 \times 10^{-6}$  atm).

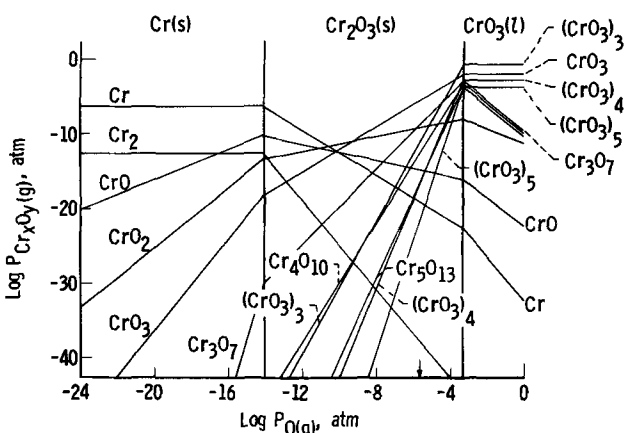


Fig. 2. Equilibrium thermochemical diagram for the chromium-atomic oxygen system at 1500°K. Arrow indicates experimental oxygen atom partial pressure ( $3.8 \times 10^{-6}$  atm).

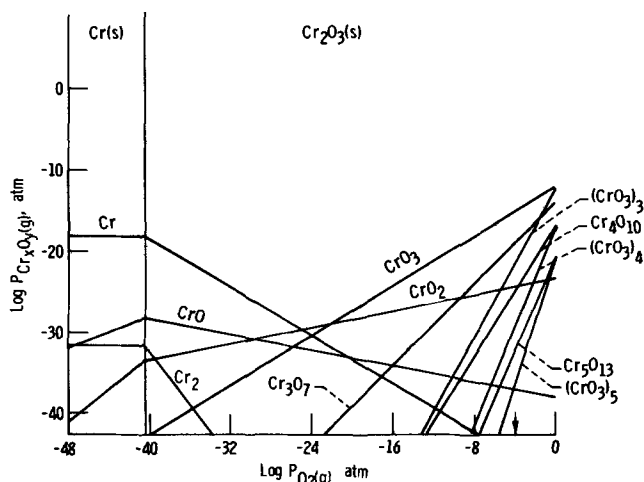


Fig. 3. Equilibrium thermochemical diagram for the chromium-oxygen system at 800°K. Arrow indicates experimental oxygen pressure ( $1.51 \times 10^{-4}$  atm).

oxygen case, the polymeric (CrO<sub>3</sub>)<sub>n</sub> and Cr<sub>n</sub>O<sub>3n-2</sub> molecules ( $n = 3, 4,$  and  $5$ ) are the predominant species in the vapor phase at high oxygen atom pressures, particularly over the CrO<sub>3</sub> phase. In addition, the actual vapor pressures of the oxides are markedly higher in the atomic oxygen case. At 800°K comparison of the vapor pressure of (CrO<sub>3</sub>)<sub>3</sub> under our oxygen atom partial pressure of  $3.8 \times 10^{-6}$  atm (denoted by arrow in Fig. 1) with the vapor pressure of CrO<sub>3</sub> under our molecular oxygen partial pressure of  $1.5 \times 10^{-4}$  atm (denoted by arrow in Fig. 3) indicates an enhancement in oxide vapor pressure of about  $10^{13}$ . The oxidative vaporization rate should be enhanced by a similar factor. At 1500°K the situation is a little different. Under our oxygen atom concentration (denoted by arrow in Fig. 2), the polymers of CrO<sub>3</sub> are not stabilized at this higher temperature and the main oxide product is again the monomer, CrO<sub>3</sub>. Comparison of the vapor pressure of CrO<sub>3</sub> from Fig. 2 at  $P_O = 3.8 \times 10^{-6}$  atm with the vapor pressure from Fig. 3 of the preceding paper (5) at  $P_{O_2} = 1.51 \times 10^{-4}$  atm, indicates an enhancement of about  $10^2$ .

It is instructive to plot the vapor pressures of the various oxide species against  $T^{-1}$  for our oxygen atom partial pressure,  $P_O = 3.8 \times 10^{-6}$  atm, as presented in Fig. 4. The polymers of CrO<sub>3</sub> are stabilized over

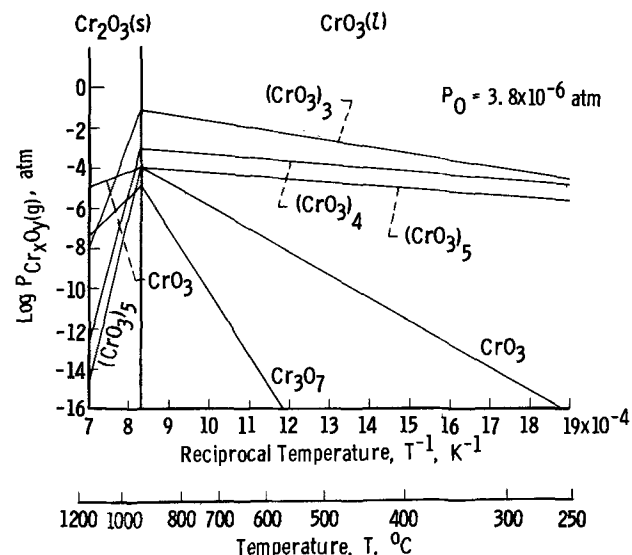


Fig. 4. Equilibrium vapor pressures of various oxide species of the chromium-atomic oxygen system vs. reciprocal temperature under an oxygen atom partial pressure of  $3.8 \times 10^{-6}$  atm.

$\text{CrO}_3(\text{l})$  and are the principal vapor species up to the  $\text{Cr}_2\text{O}_3$ - $\text{CrO}_3$  phase boundary at a temperature around  $950^\circ\text{C}$ . At temperatures above this, the pressure of the polymers decreases dramatically and the monomer of  $\text{CrO}_3$  becomes the most abundant oxide species as in molecular oxygen. Because the rate of oxidative vaporization should vary with the vapor pressures, we conclude that the rate in oxygen atoms should increase with temperature to  $950^\circ\text{C}$  and then fall abruptly with increasing temperature.

For comparison with our corrected experimental rates of oxidative vaporization of  $\text{Cr}_2\text{O}_3$ , rates have been calculated from the oxide vapor pressures obtained from the thermochemical diagrams using the Hertz-Langmuir equation, as in the preceding paper (5). However, in this case more than one oxide species were significant. Therefore rates were calculated for each species and the individual rates summed to give the total rate of oxidation.

## Results and Discussion

### General

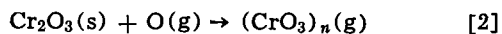
The rates of oxidation presented in this paper have been corrected for a "geometrical factor" and a "diffusion-limitation factor" (escape fraction) as described in the preceding paper (5). No corrections have been made for the fact that the diffusing  $\text{CrO}_3$  moiety may change with temperature, exhibiting slightly different diffusivities. This would be a secondary effect. All rates reported here were obtained with an oxygen flow rate of 5 liters- $\text{hr}^{-1}$  (STP) and a pressure of 0.115 Torr in the main chamber. Turning on the microwave discharge to produce atoms had negligible effect on the pressure.

The rates of oxidation of  $\text{Cr}_2\text{O}_3$  measured at different temperatures in oxygen containing 2.5% O atoms are shown in Fig. 5 (upper solid curve). Also shown for comparison are rates of oxidation of  $\text{Cr}_2\text{O}_3$  in molecular oxygen (dashed curve), which vary from  $0.5 \text{ mg}\cdot\text{cm}^{-2}\cdot\text{hr}^{-1}$  at  $1300^\circ\text{C}$  to  $0.005 \text{ mg}\cdot\text{cm}^{-2}\cdot\text{hr}^{-1}$  at  $1000^\circ\text{C}$ . Obviously, the rate of oxidation of  $\text{Cr}_2\text{O}_3$  has been greatly enhanced by the small concentration of oxygen atoms. Rapid oxidation rates, nearly  $10 \text{ mg}\cdot\text{cm}^{-2}\cdot\text{hr}^{-1}$ , were observed in the region around  $550^\circ\text{C}$ .

Unexpectedly, a rapid, direct oxidative vaporization of chromium metal was observed below about  $800^\circ\text{C}$ . This occurs partly because of the rapid removal of the  $\text{Cr}_2\text{O}_3$  by the oxygen atoms at temperatures at which  $\text{Cr}_2\text{O}_3$  can reform only slowly. Consequently, rates of oxidation of electropolished chromium were also determined and these results are shown in the lower solid curve of Fig. 5.

It is informative to express the oxidation results in terms of the "oxidation probability"<sup>4</sup> of the oxygen atoms,  $\epsilon_0$ . These have been calculated from the rates and the measured flux of oxygen atoms, and are presented in Fig. 5 along the right-hand ordinate. The maximum values, which occur at  $550^\circ\text{C}$ , are  $\epsilon_0 = 3 \times 10^{-2}$  for  $\text{Cr}_2\text{O}_3$  oxidation and  $\epsilon_0 = 1.4 \times 10^{-2}$  for the Cr oxidation. In the high temperature region ( $950$ - $1250^\circ\text{C}$ ),  $\epsilon_0 = 2 \times 10^{-3}$  for the  $\text{Cr}_2\text{O}_3$  oxidation.

The peculiar temperature dependence of the  $\text{Cr}_2\text{O}_3$  rates displayed in Fig. 5 is similar to that predicted from thermochemical diagrams. We believe it arises from the fact that the oxygen atoms stabilize the polymers of  $\text{CrO}_3$  at the lower temperatures and the oxidative vaporization reaction proceeds via the reaction



where  $n = 3, 4, \text{ and } 5$ . That is, the  $\text{CrO}_3$  evaporates as fast as it is formed by the oxidation reaction, and in polymeric form. However, at  $550^\circ\text{C}$  the polymers apparently become unstable on the surface of the speci-

<sup>4</sup> The "oxidation probability" as used by Rosner (3) is a dimensionless reaction probability defined as the ratio of the flux of metal atoms (regardless of their chemical state of aggregation) away from the reacting surface to the collision flux of  $\text{O}(\text{g})$  with the surface.

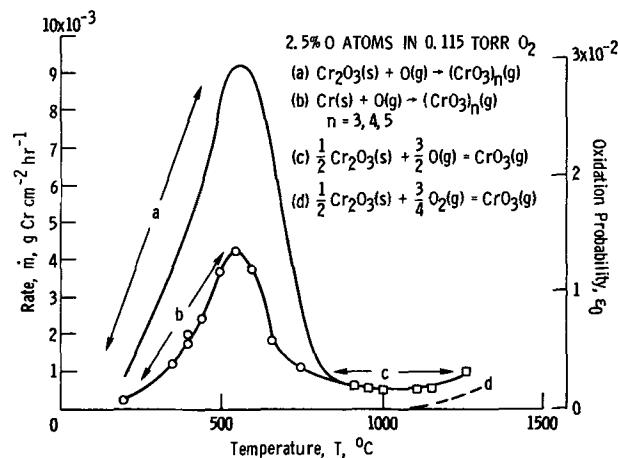
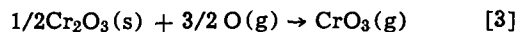


Fig. 5. Oxidative vaporization of  $\text{Cr}_2\text{O}_3$  and chromium in partially atomic oxygen.

men and have difficulty forming. As the temperature increases, the probability of formation decreases. The rate drops because the monomer cannot evaporate at this low temperature. Evaporation of the monomer becomes significant only above  $800^\circ\text{C}$ , and above this temperature the oxidative vaporization proceeds via reaction



The rates for chromium (lower solid curve) display the same type of temperature dependence (from  $200^\circ$  to  $800^\circ\text{C}$ ), and the same explanation would apply to these data. The oxidation, in this region, is represented by the reaction



where  $n = 3, 4, \text{ and } 5$ .

### Oxidation of $\text{Cr}_2\text{O}_3$

**Results in temperature range  $200$ - $800^\circ\text{C}$ .**—The rapid removal of the  $\text{Cr}_2\text{O}_3$  from the preoxidized chromium observed in this temperature region resulted in rates that were time dependent even though one would expect time-independent rates for this type of reaction that should follow linear kinetics. This was especially noticeable around  $550^\circ\text{C}$ . A series of 1-min runs at this temperature yielded a rapidly decreasing rate that leveled off at a value equal to that of the electropolished chromium (lower solid curve). Therefore, individual experimental values have not been given for the rates of oxidation of  $\text{Cr}_2\text{O}_3$  in the range  $200$ - $800^\circ\text{C}$ . The curve represents the maximum values observed and should correspond to the rate for a thick layer of  $\text{Cr}_2\text{O}_3$  on the chromium substrate. The oxidation process occurring in this temperature region is represented by reaction [2]; namely,  $\text{Cr}_2\text{O}_3(\text{s}) + \text{O}(\text{g}) \rightarrow (\text{CrO}_3)_n(\text{g})$ , where  $n = 3, 4, \text{ and } 5$ .

Because of the semiquantitative nature of the  $\text{Cr}_2\text{O}_3$  results in this lower temperature region, it was not possible to determine the order of this reaction with respect to oxygen atoms. However, an Arrhenius plot of the results in the region  $200$ - $550^\circ\text{C}$ , presented in Fig. 6, indicates that the reaction is occurring with a small activation energy. The points have been taken from the smoothed curve presented in Fig. 5 (upper solid curve), and obviously do not give a linear curve on the Arrhenius plot. We have drawn two straight lines through the data merely for the purpose of calculating the activation energies. The lower temperature value,  $8.4 \text{ kcal}\cdot\text{mole}^{-1}$ , was probably less affected by the rapid removal of  $\text{Cr}_2\text{O}_3$  and is probably the more reliable value. In any event both values are small and in the range observed for metal-oxygen atom reactions (2, 3).

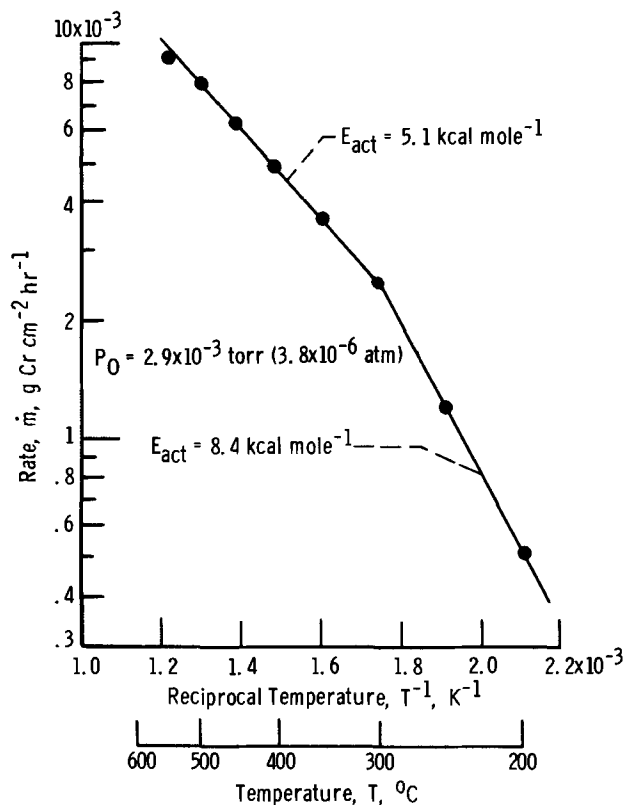


Fig. 6. Arrhenius plot of the oxidative vaporization of  $\text{Cr}_2\text{O}_3$  in partially atomic oxygen from 200° to 550°C.

**Results in temperature range 900°-1250°C.**—Above 900°C the reported rates of oxidation of  $\text{Cr}_2\text{O}_3$  in oxygen atoms were time independent and not complicated by removal of  $\text{Cr}_2\text{O}_3$ ; the rate of removal of  $\text{Cr}_2\text{O}_3$  was less in this region and the rate of formation by oxidation of the underlying chromium by normal oxygen was greater. We did, however, observe a temperature hysteresis effect in this temperature regime; runs repeated at a given temperature were higher than previously if the specimen had been oxidized at a higher temperature in the time intervening. The effect appeared to be caused by a greatly increased roughening of the oxide surface which occurred around 1200°C, and/or by a greater thickness of oxide scale that formed at the higher temperatures. In any event, the rates in this temperature regime were obtained from specimens that were all preoxidized at 1300°C. This procedure eliminated the temperature-hysteresis effect.

The oxidation process in this temperature region is represented by reaction [3]; namely,  $1/2\text{Cr}_2\text{O}_3(\text{s}) + 3/2\text{O}(\text{g}) \rightarrow \text{CrO}_3(\text{g})$ . The rates of this reaction appear to be independent of temperature from 950° to 1250°C (see Fig. 5); they are nearly constant up to 1100°C above which they increase due to the addition of oxide from the oxidation by oxygen molecules. The two simultaneous reactions seem to be additive and independent of each other.

Results of detailed studies of the rates in this region are shown in Fig. 7, where we have plotted the rate arising from only the oxygen atoms against the temperature. The rate arising from the oxygen molecules has been subtracted from the total rate; below 1100°C this correction is insignificant and at 1250°C it is roughly 33% of the total rate. It is evident from Fig. 7 that indeed there is little activation energy required for the reaction of oxygen atoms with  $\text{Cr}_2\text{O}_3$  in this temperature regime. A linear least squares analysis of an Arrhenius plot of this data yielded an  $E_{\text{act}} = 0.57$  kcal-mole<sup>-1</sup>. This low activation energy for the oxygen atom reaction is similar to the results obtained with the metals platinum (2) and molybdenum and tungsten (3).

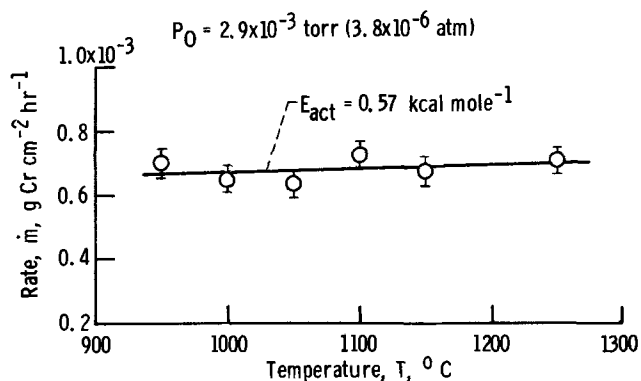
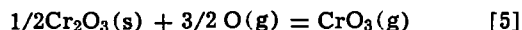


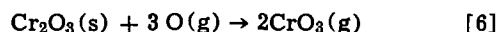
Fig. 7. Oxidative vaporization of  $\text{Cr}_2\text{O}_3$  by oxygen atoms from 950° to 1250°C.

We have investigated the effect of varying the oxygen atom concentration on the rate in this temperature regime. The concentration of oxygen atoms was lowered by removing the 5%  $\text{N}_2$  from the oxygen stream. While only two concentrations were available by this technique, the runs could be cycled readily between the two oxygen atom concentrations and the points presented represent the average of several runs.<sup>5</sup> In addition, the origin represents a bona fide point.

The results at a temperature of 1050°C are presented in Fig. 8, where the rate is plotted against the three-halves power of the partial pressure and of the collision flux of the oxygen atoms. The results indicate that the reaction is 3/2 order with respect to oxygen atoms. The 3/2 order is unusual because the reaction of oxygen atoms with metals always exhibits first-order kinetics (2, 3). In addition, oxygen atom recombination on solid surfaces usually follows first-order kinetics (6). However, in this case the 3/2 order is predicted by the stoichiometry of the oxidative reaction



It appears, therefore, that the rate-determining step must be quite complicated, involving the formation of an activated complex on the surface consisting of three oxygen atoms and a  $\text{Cr}_2\text{O}_3$  moiety



It is surprising that the activation energy for such a complex reaction should be as low as 0.5 kcal-mole<sup>-1</sup>.

**Comparison with thermodynamic predictions.**—As in the reaction of  $\text{Cr}_2\text{O}_3$  with molecular oxygen [see preceding paper (5)] the rate data can be compared with rates predicted from thermodynamic data. This comparison is presented in Fig. 9 where we have plotted

<sup>5</sup> The standard deviation of the mean of the individual runs was  $\pm 4\%$ .

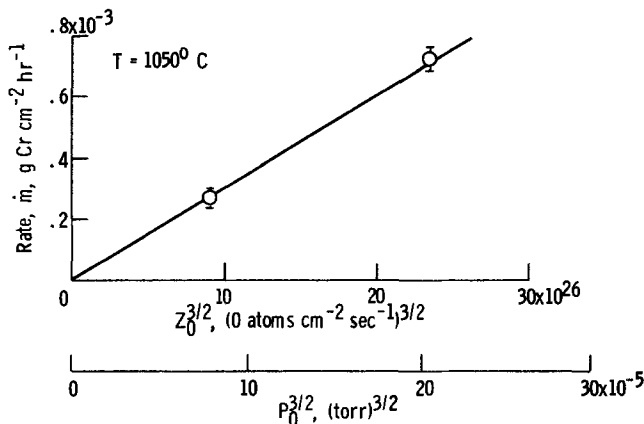


Fig. 8. Oxidative vaporization of  $\text{Cr}_2\text{O}_3$  vs. the 3/2 power of the oxygen atom collision flux at 1050°C.



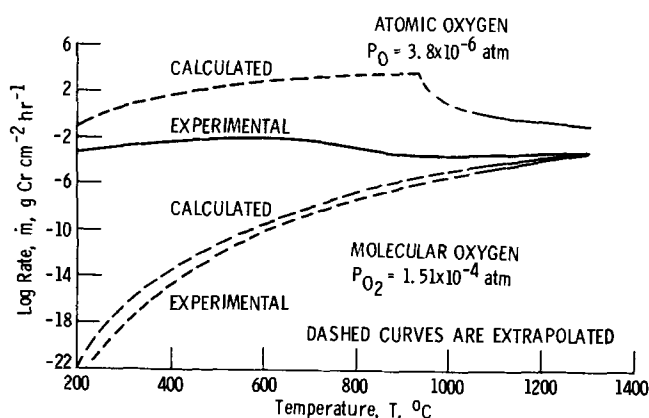


Fig. 9. Experimental and calculated rates of oxidative vaporization of  $\text{Cr}_2\text{O}_3$  in partially atomic and molecular oxygen.

the logarithm of the rate against the temperature. We have also included the comparison in molecular oxygen from our preceding paper and have extrapolated these to 200°C using a linear extrapolation of log rate vs.  $T^{-1}$ . The calculated and experimental rates in partially atomic oxygen are in qualitative agreement; both indicate a marked enhancement in the oxidation rate and exhibit a maximum in the rate at intermediate temperatures. Nevertheless, there is a large difference in the values of the rates<sup>6</sup> and in the temperature at which the maximum occurs. Both of these factors are dependent on the concentration of oxygen atoms on the surface of the  $\text{Cr}_2\text{O}_3$ . We believe the disparity arises from the fact that the concentration of oxygen atoms on the surface is much less than the equilibrium value corresponding to the gaseous partial pressure. This results from rapid recombination of the adsorbed oxygen atoms on the hot surface. While it has been shown that  $\text{Cr}_2\text{O}_3$  at room temperature has a very low recombination coefficient for oxygen atoms (6, 19), the recombination coefficient increases rapidly with increasing temperature (6).<sup>7</sup> This might offer an explanation for the drop in rate at 550°C. However, we feel that destabilization of the  $\text{CrO}_3$  polymers is a more plausible explanation because of the thermodynamic data presented in the section on Thermodynamic Predictions.

**Enhancement in the oxidation rate.**—It is interesting to consider the enhancement in the rate of oxidation of  $\text{Cr}_2\text{O}_3$  effected by this small concentration of oxygen atoms in the gas phase. The enhancements have been calculated at different temperatures from the results given in Fig. 9, and are presented in Fig. 10. We have given here the enhancement calculated from both the experimental and the calculated rates. The enhancements are truly enormous at the lower temperatures, the experimental values being  $10^{20}$  at 200°C and  $10^9$  at 550°C. At 1000°C the enhancement is 100. Of course, with larger concentrations of oxygen atoms, the enhancements would be even greater. In this respect, more valid values for the enhancements can be obtained by comparing the "oxidation probabilities" of the oxygen atoms and of the  $\text{O}_2$  molecules in the oxida-

<sup>6</sup> It should be noted that these experimental rate data in oxygen atoms have not been corrected [as was done in preceding paper (5)] for the fact that the temperature of the oxygen was not the same as the sample. The correction is insignificant in comparison to the discrepancy between the experimental and calculated rates.

<sup>7</sup> It should be noted that an oxygen atom recombination coefficient changing with temperature would affect the value of the energy of activation obtained from the data that we have presented in Fig. 6 and 7. In fact, this may account for lack of linearity throughout the entire temperature range displayed by the data for reaction [2] presented in Fig. 6. Certainly the recombination coefficient on  $\text{Cr}_2\text{O}_3$  is increasing in this temperature range (6). This would have the effect of depressing the higher temperature data and may also indicate that the value of 8 kcal-mole<sup>-1</sup> should be the preferred value for the energy of activation for reaction [2].

The data for reaction [3] presented in Fig. 7 fall nicely on a straight line and yield a very reasonable value for the energy of activation. It appears that the oxygen-atom recombination coefficient on  $\text{Cr}_2\text{O}_3$  in this temperature range is either constant or changes little.

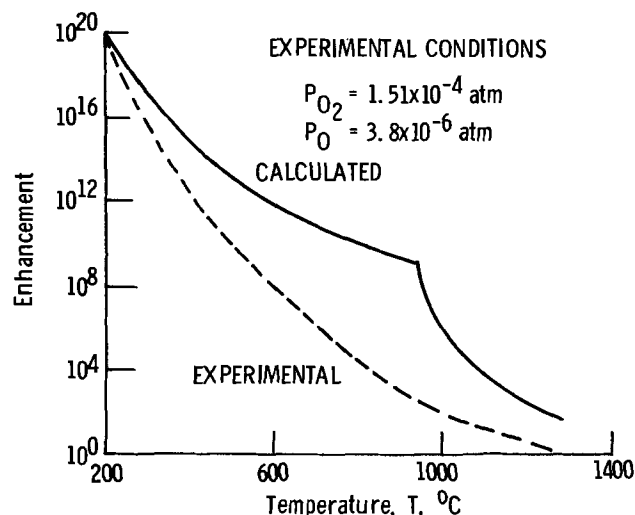


Fig. 10. Enhancement of oxidative vaporization of  $\text{Cr}_2\text{O}_3$  in partially atomic oxygen.

tive vaporization of  $\text{Cr}_2\text{O}_3$ . Table I illustrates such a comparison for the temperature range 1000°-1300°C where the analogous reactions [1] and [3] are occurring; that is, oxidation to the  $\text{CrO}_3(\text{g})$  monomer is taking place. The  $\epsilon_0$  for the oxygen atoms is constant and is given in column 2. The  $\epsilon_{\text{O}_2}$  have been calculated from the smoothed data of the preceding paper (5) and are given in column 3. The enhancement is given in column 4 and varies from  $10^4$  at 1000°C to 40 at 1300°C.

#### Oxidation of Chromium

A very interesting discovery of this work was the occurrence of the rapid, direct oxidative vaporization of chromium metal by oxygen atoms in the region below 800°C. The rates of oxidation of electropolished chromium in oxygen atoms (lower solid curve of Fig. 5) were time independent, as one would expect for such a reaction. Below about 800°C the chromium ribbons remained bright and shiny after a series of oxidations wherever they had been exposed to the oxygen atoms, though some bright green  $\text{Cr}_2\text{O}_3$  was formed toward the ends of the ribbons near 800°C. The rates were fairly reproducible and were generally about one-half the rates observed for  $\text{Cr}_2\text{O}_3$ , based on the amount of product. The rates displayed the same peculiar dependence on temperature that the  $\text{Cr}_2\text{O}_3$  rates did, and we explain this behavior on the same basis. The reaction occurring is represented by reaction [4]; namely,  $\text{Cr}(\text{s}) + \text{O}(\text{g}) \rightarrow (\text{CrO}_3)_n(\text{g})$ , where  $n = 3, 4, \text{ and } 5$ .

We have investigated the order of this reaction at a temperature of 450°C. The results are given in Fig. 11 where the rate of oxidative vaporization of chromium is plotted against the partial pressure and the collision flux of oxygen atoms. The results follow first-order kinetics quite nicely. The oxygen atom concentration was varied as described above. The points represent the average of several runs and the origin again represents a bona fide point. The first-order kinetics for the reaction of chromium with oxygen atoms is in agreement with the results found for the other metals. The rate-determining step is probably similar to that postulated by one of us for platinum, molybdenum, and tungsten (2); namely

Table I. Comparison of oxidation probabilities of O atoms and  $\text{O}_2$  molecules in the oxidative vaporization of  $\text{Cr}_2\text{O}_3$

Temp, °C	$\epsilon_0$	$\epsilon_{\text{O}_2}$	$\epsilon_0/\epsilon_{\text{O}_2}$
1000	$2 \times 10^{-3}$	$2.4 \times 10^{-7}$	$8.5 \times 10^3$
1100	$2 \times 10^{-3}$	$2.9 \times 10^{-6}$	$6.9 \times 10^2$
1200	$2 \times 10^{-3}$	$1.3 \times 10^{-5}$	$1.5 \times 10^2$
1300	$2 \times 10^{-3}$	$5.3 \times 10^{-5}$	$3.8 \times 10^1$



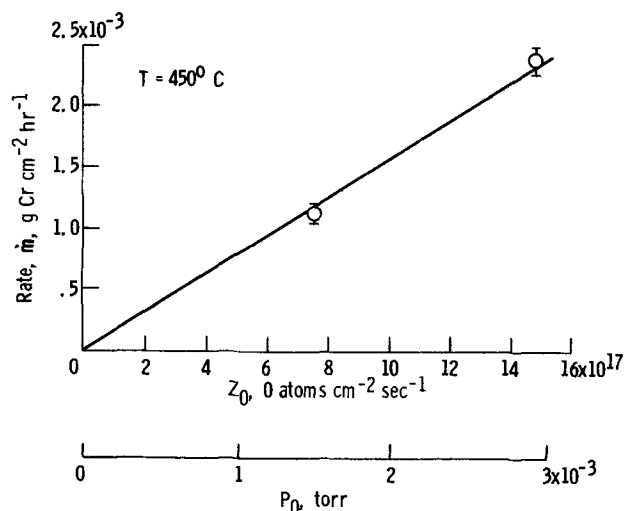
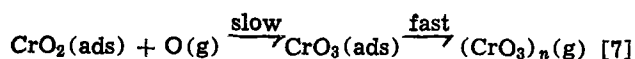


Fig. 11. Oxidative vaporization of chromium vs. oxygen atom collision flux at 450°C.



The "oxidation probabilities" of the oxygen atoms in this reaction have been calculated and are presented in Fig. 5. Because the reaction is first-order, the "oxidation probability" is equivalent to the "collision efficiency" which is defined as the fraction of oxygen atoms striking the surface that react. The maximum value of the "collision efficiency" occurs at 550°C and is  $\epsilon_0 \approx 0.014$ , i.e., one oxygen atom reacts in every 70 atoms that strike the chromium metal. This may be compared with the "collision efficiency" of oxygen atoms in the platinum metal oxidation (2),  $\epsilon_0 = 5 \times 10^{-6}$ , and with the "oxidation probability" reported for molybdenum and tungsten (3) which vary from about 0.1 to 0.5 depending on the temperature. It should be noted, however, that the chromium-oxygen atom reaction occurs at noticeably lower temperatures than the reaction of the other metals. This results partly from the high volatility of  $\text{CrO}_3$  down to 200°C, but it also indicates that the activation energy for the reaction must be low, as observed with the other metals. An Arrhenius plot of our rate data for electro-polished chromium in the temperature range 200°–550°C is presented in Fig. 12. A least squares analysis of this data yields an activation energy of 7.2 kcal-mole<sup>-1</sup>. This is in good agreement with the values found by Rosner (3) for similar reactions of molybdenum and tungsten with oxygen atoms; namely 6 kcal-mole<sup>-1</sup> and 4 kcal-mole<sup>-1</sup>, respectively. These results emphasize the fact that these metal-oxygen atom reactions can occur at any temperature above which the oxide product is volatile. We have also shown in this paper that the same is probably true for oxide-oxygen atom reactions, in which a lower valent oxide can be oxidized to a higher valent, volatile oxide.

### Summary and Implications

We have shown that the oxidative vaporization of  $\text{Cr}_2\text{O}_3$  is markedly enhanced by oxygen atoms over the entire temperature range of this study: 200°–1250°C. A rapid direct oxidative vaporization of chromium metal also occurs in the presence of oxygen atoms from 200° to 800°C. The kinetic parameters for the reactions studied are summarized in Table II.

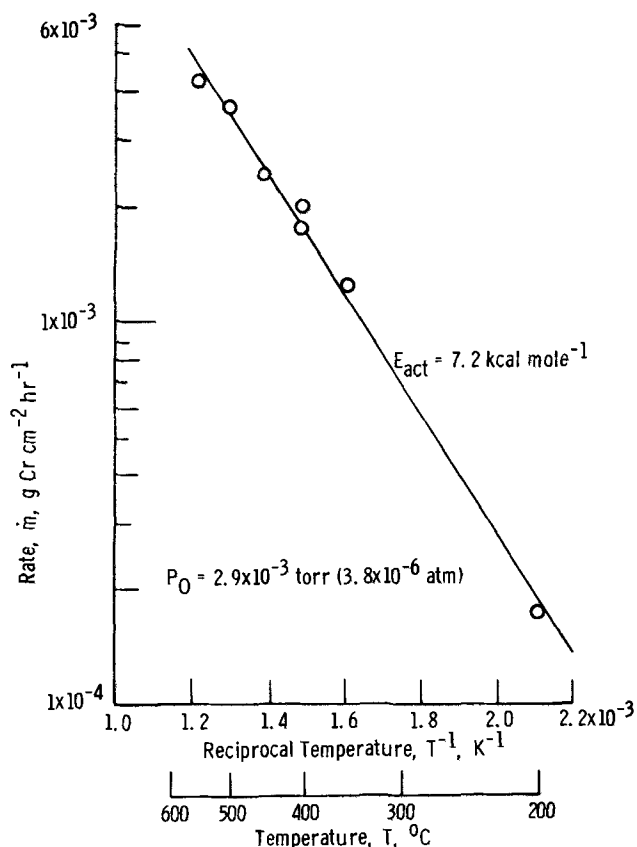
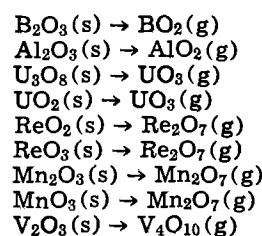


Fig. 12. Arrhenius plot of oxidative vaporization of chromium in partially atomic oxygen from 200° to 550°C.

Based on the high reactivity of oxygen atoms and the low activation energy found for the oxidative vaporization of  $\text{Cr}_2\text{O}_3$ , we predict that an enhanced oxidation in oxygen atoms should be exhibited by any oxide for which there exists a stable, gaseous oxide of high volatility with the metal in a higher valence state. Of course the enhancement would occur only in the temperature and pressure range where the higher valent oxide was volatile and abundant. The following systems fulfill these criteria



It is evident from this study that the high rate of removal of the so-called protective oxide  $\text{Cr}_2\text{O}_3$  and the subsequent high rate of removal of underlying chromium metal by oxygen atoms poses a serious problem in the selection of materials for reentry vehicles which experience high heating rates under conditions such that high oxygen atom concentrations are present.

Our measurements on the chromium-atomic oxygen system have revealed some interesting phenomena and raised some interesting questions. More sophisticated methods, such as high pressure mass spectrometry and

Table II. Summary of kinetic parameters

Reaction	Temperature range, °C	Order	$E_{\text{act}}$ , kcal-mole <sup>-1</sup>	$\epsilon_0$
$\text{Cr}_2\text{O}_3 + \text{O} \rightarrow (\text{CrO}_3)_n(\text{g})$	200 → 550	—	8	$0.2 \times 10^{-2} \rightarrow 3 \times 10^{-2}$
$\frac{1}{2}\text{Cr}_2\text{O}_3 + \frac{3}{2}\text{O} \rightarrow \text{CrO}_3(\text{g})$	800 → 1250	3/2	<1	$2 \times 10^{-3}$
$\text{Cr} + \text{O} \rightarrow (\text{CrO}_3)_n(\text{g})$	200 → 550	1	7	$0.1 \times 10^{-2} \rightarrow 1.4 \times 10^{-2}$

Table A-1. Equilibrium constants for the chromium-oxygen system

Temp., °K	log $K_p$ for formation of species from reference state Cr(s) and O <sub>2</sub> (g)													
	O(g)	Cr <sub>2</sub> O <sub>3</sub> (s)	CrO <sub>3</sub> (l)	Cr(g)	Cr <sub>2</sub> (g)	CrO(g)	CrO <sub>2</sub> (g)	CrO <sub>3</sub> (g)	(CrO <sub>3</sub> ) <sub>2</sub> (g)	(CrO <sub>3</sub> ) <sub>3</sub> (g)	(CrO <sub>3</sub> ) <sub>4</sub> (g)	(CrO <sub>3</sub> ) <sub>5</sub> (g)	Cr <sub>3</sub> O <sub>7</sub> (g)	Cr <sub>4</sub> O <sub>10</sub> (g)
500	-22.939	105.04	48.704	-33.610	-56.595	-16.090	9.821	31.03	140.51	188.84	236.57	135.57	184.87	232.64
600	-18.547	85.253	38.893	-26.723	-45.490	-12.472	9.403	25.23	112.56	150.71	188.70	109.21	148.66	186.79
700	-15.449	71.138	31.943	-31.813	-37.582	-9.896	7.382	21.10	92.78	123.71	154.80	90.64	123.03	154.34
800	-13.101	60.566	26.772	-18.137	-31.669	-7.973	6.809	18.01	77.82	103.30	129.18	76.59	103.65	129.80
900	-11.272	52.343	22.75	-15.284	-27.086	-6.483	6.002	15.60	66.21	87.47	109.30	65.69	88.62	110.76
1000	-9.806	45.775	19.53	-13.006	-23.434	-5.296	5.512	13.68	56.93	74.80	93.40	56.98	76.59	95.53
1100	-8.606	40.382	16.90	-11.147	-20.459	-4.331	5.105	12.10	49.34	64.44	80.39	49.85	66.75	83.07
1200	-7.604	35.915	14.71	-9.604	-17.990	-3.532	4.762	10.80	43.01	55.80	69.55	43.90	58.55	72.69
1300	-6.755	32.118	12.85	-8.302	-15.914	-2.862	4.466	9.689	37.65	48.49	60.37	38.87	51.61	63.90
1400	-6.027	28.888	11.26	-7.191	-14.143	-2.292	4.208	8.750	33.06	42.23	52.51	34.56	45.67	56.37
1500	-5.395	26.044	9.88	-6.233	-12.620	-1.803	3.980	7.912	29.08	36.80	45.69	30.83	40.51	49.85
1600	-4.842	23.603	8.67	-5.398	-11.296	-1.380	3.776	7.204	25.60	32.05	39.73	27.56	36.00	44.14

high temperature ESCA are required to pursue this study and should yield valuable information.

### Acknowledgments

It is a pleasure to thank J. R. Stephens for supplying us with the chromium used in this study. We also wish to thank J. W. Graab and W. F. Davis for carrying out the chemical analyses.

Manuscript submitted Nov. 30, 1973; revised manuscript received Feb. 11, 1974. This paper was presented in part as Paper 105 at the Boston, Massachusetts, Meeting of the Society, Oct. 7-11, 1973.

Any discussion of this paper will appear in a Discussion Section to be published in the June 1975 JOURNAL. All discussions for the June 1975 Discussion Section should be submitted by Feb. 1, 1975.

### APPENDIX

Thermochemical diagrams were constructed following the method outlined by Gulbransen and Jansson (14-18). Thermodynamic data for O(g), Cr(g), CrO(g), and CrO<sub>2</sub>(g) were taken directly from Schick (20); the log  $K_p$  values for Cr<sub>2</sub>O<sub>3</sub>(s) were calculated from  $\Delta G_f^\circ$  values given by Wicks and Block (21). Thermodynamic data for Cr<sub>2</sub>(g) were taken from Kant and Strauss (22). The data for the condensed phase of CrO<sub>3</sub> (mp = 470°K) are given by Schick to 800°K. The values of log  $K_p$  to 1600°K were obtained by linearly extrapolating the low temperature values given in Schick vs. reciprocal temperature up to 1600°K. For CrO<sub>3</sub>(g), the values of log  $K_p$  were obtained by use of the relationship:  $\log K_{p, CrO_3(g)} = \log P_{CrO_3(g)} + \frac{1}{2} \log K_{p, Cr_2O_3(s)} - \frac{3}{4} \log P_{O_2(g)}$ . The values of log  $P_{CrO_3(g)}$  as a function of temperature and oxygen pressure were taken from the work of Kim and Belton (12) for the temperature range 1500°-1800°K. The values of log  $K_{p, CrO_3(g)}$  at lower temperatures were obtained by linear extrapolation of the high temperature values vs. reciprocal temperature down to 500°K.

The mass spectrometrically determined vapor pressure data of Washburn (23) for the (CrO<sub>3</sub>)<sub>3</sub>, (CrO<sub>3</sub>)<sub>4</sub>, (CrO<sub>3</sub>)<sub>5</sub>, Cr<sub>3</sub>O<sub>7</sub>, Cr<sub>4</sub>O<sub>10</sub>, and Cr<sub>5</sub>O<sub>13</sub> molecules over CrO<sub>3</sub>(s) were used to obtain the necessary thermodynamic data for these molecules. The reliability of thermodynamic data derived from Washburn's measurements are based on the assumption that the complex chromium-oxygen molecules observed in the mass spectrometer were in equilibrium with the condensed phase CrO<sub>3</sub> and with each other in the Knudsen cell source. Washburn's vapor pressure measurements covered the temperature range of 415°-568°K. By combining his vapor pressures and heats of sublimation with our selected value<sup>9</sup> of 4.0 kcal-mole<sup>-1</sup> for the heat of melting of CrO<sub>3</sub>(s), values were obtained for the heats of vaporization and for the vapor pressures of the chromium-oxygen molecules over CrO<sub>3</sub>(l) at temperatures above 470°K. These vapor pressures were extrapolated linearly vs. reciprocal temperature to 1600°K. The log  $K_p$  values for the molecules were ob-

<sup>9</sup> Log  $K_p$  stands for the logarithm (to the base 10) of the equilibrium constant for the reaction of forming the given compound from its elements in their standard states.

<sup>10</sup> The selected value of  $\Delta H_m(CrO_3)$  of 4.0 kcal-mole<sup>-1</sup> is obtained by consideration of the values listed by Coughlin (24) of 3.77 kcal-mole<sup>-1</sup>, Schick's (20) estimate of 5.36 kcal-mole<sup>-1</sup>, and the experimental value of 3.9 kcal-mole<sup>-1</sup> recalculated from the data given by McDonald and Margrave (25).

tained by use of expressions of the type

$$\log K_{p, (CrO_3)_3(g)} = \log P_{(CrO_3)_3(g)} + 3 \log K_{p, CrO_3(l)}$$

and

$$\log K_{p, Cr_3O_7(g)} = \log P_{Cr_3O_7(g)} + \log P_{O_2(g)} - \log P_{(CrO_3)_3(g)} + \log K_{p, (CrO_3)_3(g)}$$

from 500° to 1600°K. Washburn found that the oxygen partial pressures in his Knudsen cell were a factor of 10<sup>-10</sup> less than that expected from thermodynamic calculations. Therefore in order to calculate the equilibrium O<sub>2</sub> partial pressures at the various temperatures it is assumed that CrO<sub>3</sub> vaporizes congruently and that the sum of the number of moles of Cr<sub>3</sub>O<sub>7</sub>, Cr<sub>4</sub>O<sub>10</sub>, and Cr<sub>5</sub>O<sub>13</sub> equals the number of moles of O<sub>2</sub>(g). The values of log  $K_p$  for all of the species under consideration are given from 500° to 1600°K in Table A-1. The not-well characterized CrO<sub>2</sub>(c) phase was not considered in the present treatment because calculations showed that even higher oxygen pressures were needed to stabilize this phase than were needed to stabilize CrO<sub>3</sub>.

The partial vapor pressures of the molecular species were calculated by consideration of the expression for the equilibrium constant in terms of the activities of reactants and products for the appropriate chemical reactions, and use of the relationship

$$\log K_{\text{reaction}} = \sum \log K_{p, \text{products}} - \sum \log K_{p, \text{reactants}}$$

### REFERENCES

- G. C. Fryburg, *J. Chem. Phys.*, **24**, 175 (1956).
- G. C. Fryburg, *J. Phys. Chem.*, **69**, 3660 (1965).
- D. E. Rosner and H. D. Allendorf, *This Journal*, **114**, 304 (1967).
- R. J. Madix and A. A. Susu, *Surface Sci.*, **20**, 377 (1970).
- C. A. Stearns, F. J. Kohl, and G. C. Fryburg, *This Journal*, **121**, 945 (1974).
- P. G. Dickens and M. S. Sutcliffe, *Trans. Faraday Soc.*, **60**, 1272 (1964).
- G. C. Fryburg and H. M. Petrus, *J. Chem. Phys.*, **32**, 622 (1960).
- G. Erlich, *ibid.*, **31**, 1111 (1959).
- L. Elias, E. A. Ogyzlo, and H. I. Schiff, *Can. J. Chem.*, **37**, 1680 (1959).
- D. G. H. Marsden and J. W. Linnett, in "Fifth Combustion Symposium," p. 685, Reinhold Publishing Co., New York (1955).
- S. N. Foner and R. L. Hudson, *J. Chem. Phys.*, **25**, 601 (1956).
- Y. Kim, Ph.D. Thesis, University of Pennsylvania (1969).
- H. H. Kellogg, *Trans. Met. Soc. AIME*, **236**, 602 (1966).
- S. A. Jansson and E. A. Gulbransen, 4th International Congress on Metallic Corrosion, Amsterdam, Netherlands, Sept. 7-14, 1969, p. 77.
- E. A. Gulbransen and S. A. Jansson, in "Heterogeneous Kinetics at Elevated Temperatures," G. R. Belton and W. L. Worrell, Editors, pp. 181-208, Plenum Press, New York (1970).
- E. A. Gulbransen, *Corrosion-NACE*, **26**, 19 (1970).
- S. A. Jansson, *J. Vacuum Sci. Technol.*, **7**, S5 (1970).
- E. A. Gulbransen and S. A. Jansson, in "Oxidation of Metals and Alloys," pp. 63-89, American Society for Metals (1971).

19. C. D. Scott, NASA TN D-7113 (March 1973).  
 20. H. L. Schick, Editor, "Thermodynamics of Certain Refractory Compounds," Academic Press, New York (1966).  
 21. C. E. Wicks and F. E. Block, *U.S. Bur. Mines Bull.* 605 (1963).  
 22. A. Kant and B. Strauss, *J. Chem. Phys.*, **45**, 3161 (1966).  
 23. C. A. Washburn, Ph.D. Thesis, University of California (1969); UCRL-18685, PB 183562.  
 24. J. P. Coughlin, *U.S. Bur Mines Bull.* 542 (1954).  
 25. J. D. McDonald and J. L. Margrave, *J. Inorg. Nucl. Chem.*, **30**, 665 (1968).

## Thermodynamic Properties, Transference Numbers, and Ionic Mobilities in Molten Lithium Chloride-Cadmium Chloride Mixtures from EMF Measurements

Wishvender K. Behl\*<sup>1</sup>

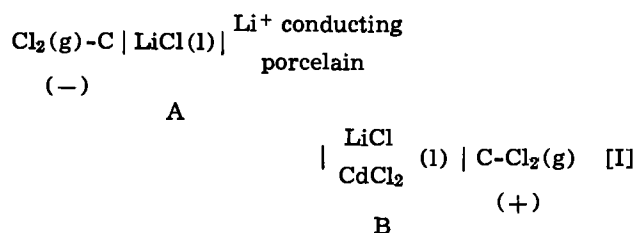
Brookhaven National Laboratory, Upton, New York 11973

The publication costs of this article have been assisted by Brookhaven National Laboratory.

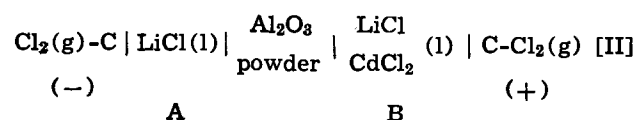
### ABSTRACT

Thermodynamic and transference properties of the system LiCl-CdCl<sub>2</sub> were investigated at 650°C by emf measurements. For a study of thermodynamic properties, a cell using a porcelain conductive only to lithium ions was employed to separate the two salt compartments, whereas for the study of transference properties a liquid junction between the two salt compartments was established through a coiled quartz tube filled with alumina powder. Results are presented for the relative Gibbs partial molar free energies of both components and transference numbers and mobilities of cations relative to chloride ion over the entire composition range of the system.

Porcelains or glasses conductive only to alkali ions have been recently used (1-5) as membranes in concentration cells to determine the thermodynamic properties of molten alkali halide-metal halide mixtures from emf measurements. A potassium ion conducting glass has also been used (6) as a membrane in solid-state cells to determine the free energy of formation of double salts of KCl with MgCl<sub>2</sub>, CaCl<sub>2</sub>, SrCl<sub>2</sub>, and BaCl<sub>2</sub>. In the present studies, a porcelain conductive only to lithium ions (1) was used as a membrane to study the thermodynamic properties of lithium chloride-cadmium chloride mixtures at 650°C from emf measurements on concentration cells of the type



The transference numbers of the cations relative to the chloride ion in mixtures of lithium chloride-cadmium chloride were also determined in the present studies from emf measurements on concentration cells with transference of the type



The liquid junction between the two salt compartments

was established (7, 8) through a coiled quartz tube filled with alumina powder. The transference numbers determined in the present studies were combined with the equivalent conductance data of Bloom *et al.* (9) to calculate the cation mobilities relative to the chloride ion in lithium chloride-cadmium chloride mixtures. The emf method has been previously used by several workers to determine the transference numbers of cations relative to the common anion in mixtures of molten chlorides (7, 8), fluorides (10), and nitrates (11).

### Experimental Procedure

Reagent grade lithium chloride and cadmium chloride (Fisher Scientific Company) were purified by the standard treatment (1, 7, 8) with hydrogen chloride gas. The cell designs for cells [I] (1, 6) and [II] (7) have been described in detail elsewhere. For emf measurements on cell [I], lithium chloride was contained in a porcelain tube (McDaniel Refractory) made of mullite, SiO<sub>2</sub>, and containing approximately 1% Li<sub>2</sub>O. The porcelain tube was placed in a Vycor container (57 mm diameter) containing the lithium chloride-cadmium chloride mixture. The mole fraction of lithium chloride in the mixture was varied from 0.1 to 0.9 by addition of weighed amounts of purified lithium chloride. For emf measurements on cell [II], the porcelain tube was replaced by a Vycor tube connected to the outer Vycor container by a coiled quartz tubing filled with predried alumina powder (Grade T-61, 120 mesh, Aluminum Company of America). The liquid junction between lithium chloride and the lithium chloride-cadmium chloride mixture was established through the alumina powder in the coiled quartz tube. The powdered alumina was found ideal for these experiments since it not only prevented any gravitational flow from one side to the other but was also inert to any cation exchange that usually occurs (7) between the lithium chloride and quartz frit membranes.

Spectrochemical grade graphite rods (Ultra Carbon Company) were used as electrodes. Chlorine and hy-

\* Electrochemical Society Active Member.

<sup>1</sup> Present address: Power Sources Technical Area, Electronics Technology and Devices Laboratory (ECOM), Fort Monmouth, New Jersey 07703.

Key words: concentration cell with transference, emf measurements, Gibbs free energies of mixing, ionic mobilities, transference numbers, lithium chloride-cadmium chloride mixtures.

Table I. Cell potentials as a function of lithium chloride mole fraction in lithium chloride-cadmium chloride mixtures at 650°C

$x_{LiCl}$	$E_{Cell},^* V$	$E_{Cell},\dagger V$
0.1	0.222	0.0385
0.2	0.159	0.0346
0.3	0.121	0.0311
0.4	0.090	0.0270
0.5	0.068	0.0213
0.6	0.047	0.0168
0.7	0.030	0.0115
0.8	0.017	0.0064
0.9	0.0085	0.0034

\* Cell [I]: (g)  $Cl_2$ -C | LiCl(l) |  $Li^+$  conducting porcelain | LiCl-CdCl<sub>2</sub>(l) | C-Cl<sub>2</sub>(g) (-) (+)

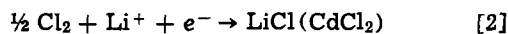
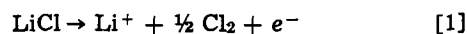
† Cell [II]: (g)  $Cl_2$ -C | LiCl(l) |  $Al_2O_3$  powder | LiCl-CdCl<sub>2</sub>(l) | C-Cl<sub>2</sub>(g) (-) (+)

drogen chloride gases (Matheson Company) were used directly from the cylinders. A wire-wound furnace was used to heat the cell assembly and the temperature was controlled at 650°C within  $\pm 2^\circ C$  with a Honeywell Brown Pyrovane temperature controller.

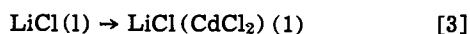
### Results and Discussion

The emf measurements on cells [I] and [II] were carried out at 650°C over the entire composition range of the LiCl-CdCl<sub>2</sub> mixtures. The emf values were extremely stable and reproducible within  $\pm 0.5$  mV. The emf data, mean values of two separate experiments for both cells [I] and [II], are summarized in Table I.

The electrode reactions at the negative and positive electrodes in cell [I] are, respectively, given by



with the porcelain conducting only  $Li^+$  ions from the left- to right-hand compartment. The over-all cell reaction for cell [I] is thus given by



Thus, on passage of 1 faraday of electricity, 1 mole of lithium chloride is transported from the left-hand compartment of cell [I] to the right-hand compartment. The relative partial free energy of lithium chloride ( $G_{LiCl}^M$ ) is, therefore, given by

$$G_{LiCl}^M = -FE_{Cell} \quad [4]$$

where  $F$  is the Faraday constant. The relative partial free energy of lithium chloride ( $G_{LiCl}^M$ ) was calculated by use of Eq. [4] and the data over the whole composition range of the mixtures are presented in Table II. The activities ( $a_{LiCl}$ ) and partial excess free energies of lithium chloride ( $G_{LiCl}^E$ ) in the mixtures were then determined by use of equations

$$G_{LiCl}^M = 2.303 RT \log a_{LiCl} \quad [5]$$

$$G_{LiCl}^E = G_{LiCl}^M - 2.303 RT \log x_{LiCl} \quad [6]$$

The activities ( $a_{LiCl}$ ) and partial excess free energies of lithium chloride ( $G_{LiCl}^E$ ), so obtained, are also sum-

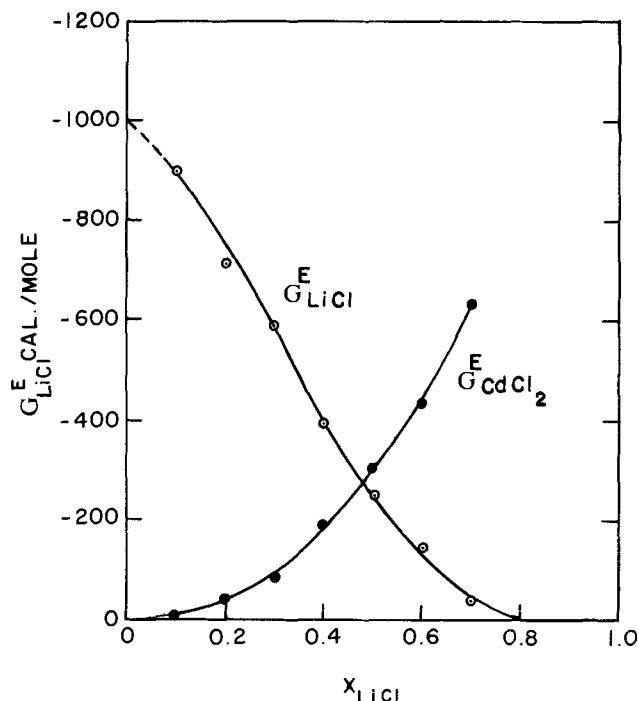


Fig. 1. Excess partial molar free energies of lithium chloride and cadmium chloride as a function of lithium chloride mole fraction in LiCl-CdCl<sub>2</sub> mixtures at 650°C.

marized in Table II. A plot of  $G_{LiCl}^E$  vs. lithium chloride mole fraction is shown in Fig. 1.

The excess partial molar free energy of cadmium chloride in the mixtures was obtained by graphical integration of the Gibbs-Duhem equation

$$G_{CdCl_2}^E = \int_0^{x_{LiCl}} \frac{G_{LiCl}^E}{(1-x_{LiCl})^2} dx_{LiCl} - \frac{x_{LiCl} G_{LiCl}^E}{1-x_{LiCl}} \quad [7]$$

For the purpose of integration of Eq. [7], the limiting value of  $G_{LiCl}^E$  was obtained by extrapolating the  $G_{LiCl}^E$  vs.  $x_{LiCl}$  plot presented in Fig. 1 to zero mole fraction of lithium chloride.

The relative partial molar free energies ( $G_{CdCl_2}^M$ ) and activities ( $a_{CdCl_2}$ ) of cadmium chloride in the mixtures were then obtained by use of the relations

$$G_{CdCl_2}^M = 2.303 RT \log a_{CdCl_2} \quad [8]$$

$$= 2.303 RT \log x_{CdCl_2} + G_{CdCl_2}^E$$

These data are also summarized in Table II.

The excess integral molar free energy of mixing,  $g^E$ , in mixtures of lithium chloride-cadmium chloride was calculated from the excess thermodynamic quantities presented in Table II by use of the equation

$$g^E = x_{LiCl} G_{LiCl}^E + x_{CdCl_2} G_{CdCl_2}^E \quad [9]$$

The excess integral molar free energies ( $g^E$ ) as a function of lithium chloride mole fraction are summarized in Table II.

Table II. Thermodynamic quantities of lithium chloride and cadmium chloride in mixtures of lithium chloride-cadmium chloride at 650°C

$x_{LiCl}$	$G_{LiCl}^M$ (cal/mole)	$G_{LiCl}^E$ (cal/mole)	$a_{LiCl}$	$G_{CdCl_2}^M$ (cal/mole)	$G_{CdCl_2}^E$ (cal/mole)	$a_{CdCl_2}$	$g^E$ (cal/mole)
0.1	-5120	-897	0.061	-199	-6	0.897	-95
0.2	-3667	-715	0.135	-449	-40	0.783	-175
0.3	-2791	-593	0.218	-739	-84	0.668	-237
0.4	-2076	-395	0.323	-1127	-190	0.541	-272
0.5	-1522	-251	0.436	-1578	-307	0.423	-279
0.6	-1084	-147	0.554	-2114	-434	0.318	-262
0.7	-692	-38	0.686	-2841	-633	0.212	-217
0.8	-392	0	0.800	-	-	-	-
0.9	-186	0	0.900	-	-	-	-

From the data presented in Table II, it is seen that the mixtures of lithium chloride and cadmium chloride show a slight negative deviation from Raoult's law over most of the composition range.

In contrast to cell [I], the current in cell [II] is conducted by the cadmium and chloride ions as well as by the lithium ions. The emf of cell [II] is, therefore, given by (12)

$$E_{\text{Cell}} = -\frac{1}{F} \int_A^B t_{13} d\mu_{\text{LiCl}} - \frac{1}{2F} \int_A^B t_{23} d\mu_{\text{CdCl}_2} \quad [10]$$

where  $F$  is the Faraday constant and  $t_{13}$  and  $t_{23}$  are, respectively, the transference numbers of the lithium ion (cation 1) and cadmium ion (cation 2) relative to the chloride ion (anion 3);  $\mu_{\text{LiCl}}$  and  $\mu_{\text{CdCl}_2}$  are the chemical potentials of lithium chloride and cadmium chloride in the mixture, respectively. The derivation of Eq. [10] has been discussed in detail by Wagner (12). Now, making use of the Gibbs-Duhem equation

$$d\mu_{\text{CdCl}_2} = -\frac{x_{\text{LiCl}}}{1-x_{\text{LiCl}}} d\mu_{\text{LiCl}} \quad [11]$$

and the following other relations

$$d\mu_{\text{LiCl}} = 2.303RT \log a_{\text{LiCl}} \quad [12]$$

$$t_{13} + t_{23} = 1 \quad [13]$$

$$x_{\text{LiCl}} = \frac{2x'_{\text{LiCl}}}{1+x'_{\text{LiCl}}} \quad [14]$$

Equation [10] can be rewritten as

$$E_{\text{Cell}} = -\frac{2.303 RT}{F} \int_A^B \frac{t_{13} - x'_{\text{LiCl}}}{1-x'_{\text{LiCl}}} d \log a_{\text{LiCl}} \quad [15]$$

where  $x_{\text{LiCl}}$ ,  $x'_{\text{LiCl}}$ , and  $a_{\text{LiCl}}$  are, respectively, the mole fraction, equivalent fraction, and activity of lithium chloride in the LiCl-CdCl<sub>2</sub> mixture. Partially differentiating Eq. [15] with respect to  $\log a_{\text{LiCl}}$ , we have

$$\left( \frac{\partial E_{\text{Cell}}}{\partial \log a_{\text{LiCl}}} \right)_B = -\frac{2.303 RT}{F} \left( \frac{t_{13} - x'_{\text{LiCl}}}{1-x'_{\text{LiCl}}} \right)_B \quad [16]$$

Using the activity values of lithium chloride in the lithium chloride-cadmium chloride mixtures determined from emf measurements on cell [I], the term on the left side of Eq. [16] can be obtained by graphical differentiation of the  $E_{\text{Cell}}$  vs.  $\log a_{\text{LiCl}}$  plot presented in Fig. 2.

The transference numbers of the lithium ion ( $t_{13}$ ) and the cadmium ion ( $t_{23}$ ) relative to the chloride ion are then determined by use of Eq. [16] and [13], respectively. The transference number data, so obtained, are summarized in Table III.

The mobilities of the lithium ion ( $b_{13}$ ) and cadmium ion ( $b_{23}$ ) relative to the chloride ion are related (7,13)

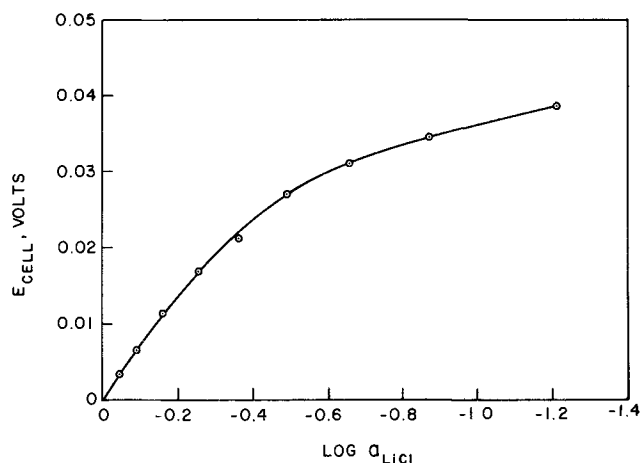
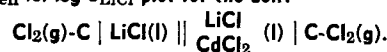


Fig. 2.  $E_{\text{Cell}}$  vs.  $\log a_{\text{LiCl}}$  plot for the cell:



to the cation transference number ( $t_{13}$  and  $t_{23}$ ) and equivalent conductance ( $\lambda$ ) of the lithium chloride-cadmium chloride mixture by the equations

$$b_{13} = \frac{t_{13}\lambda}{x'_{\text{LiCl}}F} \quad [17]$$

and

$$b_{23} = \frac{t_{23}\lambda}{x'_{\text{CdCl}_2}F} \quad [18]$$

The equivalent conductance ( $\lambda$ ) of lithium chloride-cadmium chloride mixtures at 650°C was obtained from the specific conductance and density data of Bloom *et al.* (9) and combined with the experimentally determined cation transference numbers ( $t_{13}$  and  $t_{23}$ ) to obtain the cation mobilities relative to the chloride ion by use of Eq. [17] and [18]. These data are also summarized in Table III. The cation mobilities are also plotted in Fig. 3 as a function of the lithium chloride mole fraction. The alkali ion was found to have relatively larger mobility as compared to the cadmium ion over the whole composition range of the mixtures. This behavior is similar to the behavior in systems LiCl-PbCl<sub>2</sub> (7,14), LiCl-CeCl<sub>3</sub> (8), NaCl-CeCl<sub>3</sub> (8), KCl-PbCl<sub>2</sub> (15), KCl-CaCl<sub>2</sub> (7), KCl-MgCl<sub>2</sub> (7), and KCl-CeCl<sub>3</sub> (8) where the alkali ion has been found to have a relatively larger mobility than the mobilities of the second cation in the mixture over most of the composition range.

### Summary and Conclusions

Thermodynamic properties, cation transference numbers, and cationic mobilities in lithium chloride-cadmium chloride mixtures at 650°C were determined

Table III. Transference numbers and mobilities of lithium ions ( $t_{13}$ ,  $b_{13}$ ) and cadmium ions ( $t_{23}$ ,  $b_{23}$ ) relative to the chloride ion in mixtures of lithium chloride-cadmium chloride at 650°C

$x_{\text{LiCl}}$	$x'_{\text{LiCl}}^*$	$\frac{\partial E}{\partial \log a_{\text{LiCl}}}$	$t_{13}$	$t_{23}$	$\lambda^\dagger$ (cm <sup>2</sup> ohm <sup>-1</sup> equiv <sup>-1</sup> )	$b_{13} \times 10^8$ (cm <sup>2</sup> sec <sup>-1</sup> V <sup>-1</sup> )	$b_{23} \times 10^8$ (cm <sup>2</sup> sec <sup>-1</sup> V <sup>-1</sup> )
0.0	0.0	—	—	1.000	57.58	—	0.80
0.1	0.053	-0.0080	0.094	0.906	63	1.16	0.82
0.2	0.111	-0.0155	0.186	0.814	69	1.20	0.86
0.3	0.176	-0.0210	0.271	0.729	75	1.20	0.89
0.4	0.250	-0.0335	0.387	0.613	80	1.28	0.88
0.5	0.333	-0.0430	0.489	0.511	88	1.34	0.70
0.6	0.429	-0.0515	0.590	0.410	98	1.40	0.73
0.7	0.538	-0.0600	0.690	0.310	109	1.45	0.76
0.8	0.667	-0.0700	0.791	0.209	125	1.54	0.81
0.9	0.818	-0.0770	0.895	0.105	148	1.65	0.87
1.0	1.0	—	1.000	—	173.48	1.80	—

$$* x'_{\text{LiCl}} = \frac{x_{\text{LiCl}}}{2 - x_{\text{LiCl}}}$$

† H. Bloom, I. W. Knaggs, J. J. Molloy, and D. Welch (9).

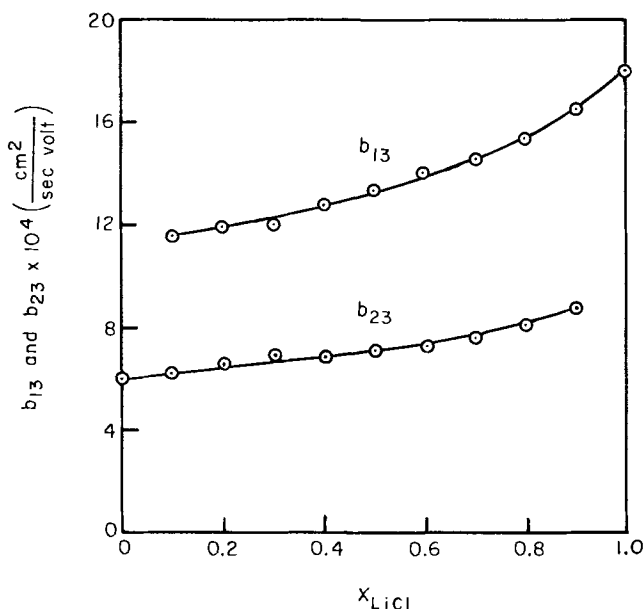


Fig. 3. Mobilities of  $Li^+$  ( $b_{13}$ ) and  $Cd^{++}$  ( $b_{23}$ ) ions relative to the chloride ion as a function of lithium chloride mole fraction in  $LiCl$ - $CdCl_2$  mixtures at  $650^\circ C$ .

from emf measurements on concentration cells with transference. The system showed slight negative deviation from Raoult's law and lithium ion was observed to possess relatively larger mobility than the cadmium ion over the entire composition range of the lithium chloride-cadmium chloride mixtures.

#### Acknowledgments

The author is grateful to Dr. J. J. Egan for suggesting this research problem and for many helpful discussions. This work was performed under the auspices of the

U.S. Atomic Energy Commission and supported in part by the U.S. Army Electronics Command, Fort Monmouth, New Jersey 07703.

Manuscript submitted Dec. 18, 1973; revised manuscript received Feb. 15, 1974.

Any discussion of this paper will appear in a Discussion Section to be published in the June 1975 JOURNAL. All discussions for the June 1975 Discussion Section should be submitted by Feb. 1, 1975.

#### REFERENCES

1. J. J. Egan, Brookhaven National Laboratory Report BNL-799 (S-64), 1963; *ibid.*, BNL-841 (S-66), 1963; *ibid.*, BNL-954 (S-68), 1965; *ibid.*, BNL-50023 (S-69), 1966; J. J. Egan and J. Bracker, *J. Chem. Thermodynamics*, **6**, 9 (1974).
2. T. Ostvold, *Acta Chim. Scand.*, **20**, 2187 (1966); **20**, 2320 (1966); **26**, 2788 (1972).
3. G. D. Robbins, T. Forland, and T. Ostvold, *ibid.*, **22**, 3002 (1968).
4. Y. Dutt and T. Ostvold, *ibid.*, **26**, 2743 (1972).
5. V. Sabet and T. Ostvold, *ibid.*, **27**, 396 (1973).
6. J. J. Egan, in "Thermodynamics," Vol. I, p. 157, IAEA, Vienna (1965).
7. W. K. Behl and J. J. Egan, *J. Phys. Chem.*, **71**, 1764 (1967).
8. W. K. Behl, *This Journal*, In press.
9. H. Bloom, I. W. Knaggs, J. J. Molloy, and D. Welch, *Trans. Faraday Soc.*, **49**, 1458 (1953).
10. K. A. Romberger and J. Braunstein, *Inorg. Chem.*, **9**, 1273 (1970).
11. M. Okada and K. Kawamura, *Electrochim. Acta*, **15**, 1 (1970).
12. C. Wagner, "Advances in Electrochemistry and Electrochemical Engineering," Vol. 4, p.1, Wiley-Interscience, New York (1966).
13. A. Klemm, in "Molten Salt Chemistry," M. Blander, Editor, Wiley-Interscience, New York (1964).
14. A. Klemm and E. V. Monse, *Z. Naturforsch.*, **12a**, 319 (1957).
15. F. R. Duke and R. A. Fleming, *This Journal*, **106**, 130 (1957).

## Technical Notes



### Nitrogen Doping Behavior in GaP Using $NH_3$ as the Dopant Source

D. D. Roccasecca, R. H. Saul,\* and O. G. Lorimor

Bell Laboratories, Murray Hill, New Jersey 07974

The publication costs of this article have been assisted by Bell Laboratories.

Efficient green luminescence in GaP arises from the decay of excitons bound to nitrogen atoms which occupy phosphorus sites (1). The most efficient green LED's have utilized liquid phase epitaxy (LPE) layers where ammonia was the source of nitrogen (2-5). Using this approach, efficiencies as high as 0.33% have been achieved for encapsulated  $15 \times 15$  mil die operated at 10 mA (6). Nitrogen incorporation as a function of ammonia partial pressure  $p_{NH_3}$  (in a  $\sim 1$  atm  $H_2$

carrier) has been reported by several workers (2, 7) for doping levels in the  $10^{18}$  atoms/cm<sup>3</sup> range<sup>1</sup> where the highest efficiencies are obtained. Basically, it has been found that the N concentration increases linearly with  $p_{NH_3}$  until  $p_{NH_3} \approx 10^{-3}$  atm, at which time the N concentration reaches a constant value. The morphology of the LPE becomes disturbed at this and higher values of  $p_{NH_3}$ . The initial linear behavior is consistent with the isoelectronic behavior of N in GaP while the limiting value corresponds to the  $p_{NH_3}$  over liquid Ga in

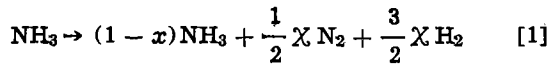
\* Electrochemical Society Active Member.

Key words: light emitting diodes, liquid phase epitaxy, impurity incorporation.

<sup>1</sup> The nitrogen concentrations have been corrected in accordance with the recent work of Lightowlers *et al.* (8).

equilibrium with solid GaN,  $p^*_{\text{NH}_3}$  (9). Using a model due to Phillips and Van Vechten (10), Stringfellow (11) has computed the temperature dependence of N and the corresponding limiting values of  $p^*_{\text{NH}_3}$ . These calculations and those of Thurmond and Logan (9) assume that  $\text{NH}_3$  does not dissociate under the high temperature conditions of LPE. In the experimental phase of the latter work, this condition could be met provided a new quartz furnace tube and a low oxygen (and water vapor) ambient was used.

Although  $\text{NH}_3$  is thermodynamically unstable at elevated temperatures, catalysts [e.g., Pt and W (12)] are generally required to promote  $\text{NH}_3$  decomposition, which can be described by the following equation



where  $x$  is the mole fraction of consumed  $\text{NH}_3$ . This reaction has been studied by Ban (13) using a time-of-flight mass spectrometer. His results, using an  $\text{H}_2$  carrier gas, indicate that over the temperature range  $700^\circ\text{--}950^\circ\text{C}$ ,  $x \leq 0.03$  for quartz and graphite catalysts. The relatively high  $\text{NH}_3$  stability under these conditions suggests that both quartz and graphite are suitable structural materials for growth reactors which utilize  $\text{NH}_3$ . However, during the course of developing a multislice LPE system for GaP green LED's (5), we observed, as shown in Fig. 1, that the incorporated N level was substantially lower than previously reported (2,7). Moreover, for this system which utilized a quartz reactor and graphite boat, the incorporated N level was found to be sublinear with the inlet  $\text{NH}_3$  pressure for low flow rates (50  $\text{cm}^3/\text{min}$ ). (All flow rates are the room temperature flow rates.) Further, for a given  $p_{\text{NH}_3}$ , the incorporated N level increased with the total gas flow rate. These results suggested that N incorporation was kinetically controlled, perhaps as a result of  $\text{NH}_3$  decomposition. The work described here was undertaken to determine the extent of  $\text{NH}_3$  decomposition for typical LPE conditions which are appropriate for green LED's and to study the (catalytic) effect of graphite and quartz on  $\text{NH}_3$  stability. While the quantitative results are specific to the operation of our LPE system (5), the results are thought to be generally applicable to other systems (including vapor epitaxy systems) which utilize  $\text{NH}_3$  and the same construction materials, viz., quartz and graphite.

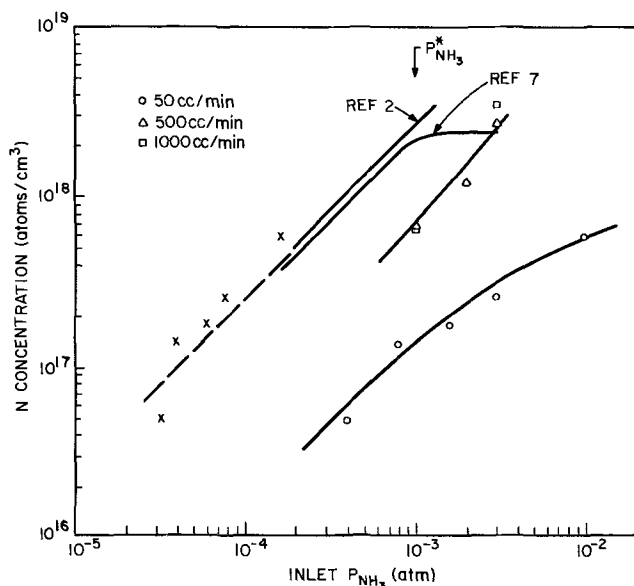


Fig. 1. Incorporated nitrogen concentration for crystals grown from an initial temperature of  $1015^\circ\text{C}$  as a function of inlet  $\text{NH}_3$  partial pressure. The crosses are corrected values as discussed in the text.

Returning to Fig. 1, we note that if  $\text{NH}_3$  decomposition were significant, the value of  $p_{\text{NH}_3}$  over the growth solution could be substantially lower than the values deduced from the relative inlet  $\text{NH}_3$  and  $\text{H}_2$  flow rates. The actual values of  $p_{\text{NH}_3}$  were therefore determined by titrating the exit gas with a solution of known pH (9). Since these values were time invariant, the outlet pressure should nearly equal the  $\text{NH}_3$  pressure over the melt. At room temperature, where  $\text{NH}_3$  is stable, the inlet and outlet pressures were determined to be equal by the titration method and agreed within 10% of the value calculated from the inlet flow rates. At typical LPE temperatures ( $\sim 1000^\circ\text{C}$ ) however, the outlet pressure was generally found to be lower than the inlet pressure. This behavior is illustrated in Fig. 2, where it is shown that for a total flow rate of 50  $\text{cm}^3/\text{min}$  (the volume of the reactor tube is  $\sim 5$  liters with a diameter of 7 cm at the location of the graphite boat), the ratio of outlet to inlet values of  $p_{\text{NH}_3}$  decreases monotonically with increasing inlet  $p_{\text{NH}_3}$ ; that is, the higher the inlet  $p_{\text{NH}_3}$  for a given flow rate, the greater the amount of  $\text{NH}_3$  consumed within the reactor. Note also that when He is substituted for  $\text{H}_2$  as the carrier gas, the  $\text{NH}_3$  consumption is substantially increased. This result is qualitatively consistent with the decomposition reaction given by Eq. [1]. Using the curve in Fig. 2, one can approximate the outlet  $p_{\text{NH}_3}$  values corresponding to the data in Fig. 1. The corrected values given by the crosses in Fig. 1, lie reasonably well on a linear extrapolation of published data for higher doping levels. This agreement clearly demonstrates that the actual  $p_{\text{NH}_3}$  in the system controlling the incorporation is more accurately measured at the outlet rather than at the inlet due to  $\text{NH}_3$  decomposition. As one might infer from Fig. 1, for higher flow rates (shorter residence time)  $\text{NH}_3$  stability is enhanced, which is borne out by the increased outlet  $p_{\text{NH}_3}$  values for a given inlet  $p_{\text{NH}_3}$ .

The results of Ban (13) and of Thurmond and Logan (9) indicate that for graphite-quartz systems, negligible  $\text{NH}_3$  decomposition occurs, although the latter suggest that under certain conditions quartz can behave as a catalyst. To identify the structural material catalyzing or reacting with  $\text{NH}_3$ , measurements were made at room temperature and at  $1026^\circ\text{C}$ , with and without the graphite boat, using a high  $p_{\text{NH}_3}$  value ( $3 \times 10^{-3}$  atm) to provide a worst case situation. The

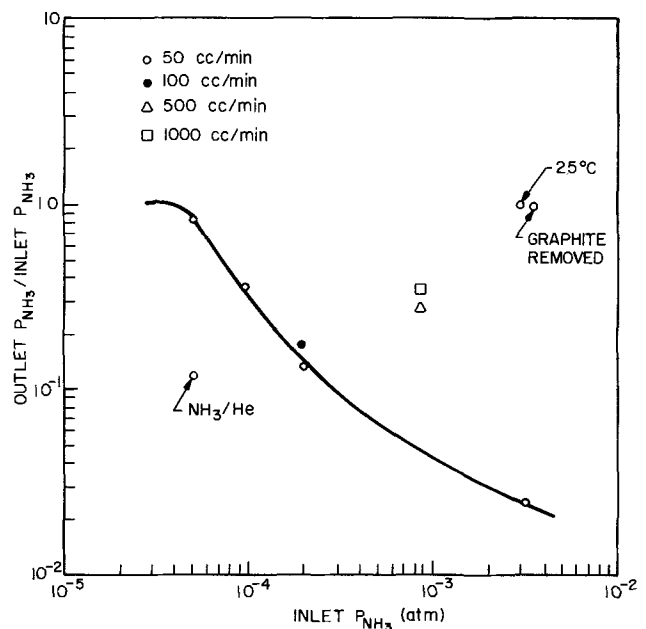


Fig. 2. The variation of the ratio of effluent to inlet values of  $\text{NH}_3$  partial pressure at  $\sim 1000^\circ\text{C}$  for various conditions. The values refer to typical LPE conditions except where indicated (see text).

results shown in Fig. 2 clearly show that the graphite boat and not the quartz reactor is causing the  $\text{NH}_3$  consumption. Additionally, we find that the type and surface area of the graphite effects  $\text{NH}_3$  stability, although this was not extensively studied. From a practical standpoint, viz., the growth of N-doped LPE material, we believe that the influence of graphite on the stability of  $\text{NH}_3$  is a general effect whose magnitude will depend upon the specific system geometry. However, as shown in Fig. 1, the use of high flow rates (500-1000  $\text{cm}^3/\text{min}$ ) makes it possible to controllably achieve high N levels, appropriate for green LED's under conditions approaching those where  $\text{NH}_3$  is stable.

During the latter stages of this work, gas chromatography was used to identify and monitor some of the major gas species present in the reactor at various temperatures and under actual LPE conditions. A GOW-MAC gas chromatograph, Model 69-570, was used. This unit permits continuous flow of the reactor effluent gas through a sampling coil, with a bypass to flush the sample gas into the appropriate column. The purest available grade of He was used as the carrier gas. Three columns were employed in this work. A 5A Molecular Sieve ( $\frac{1}{4}$  in. OD  $\times$  4 ft) column was used to detect  $\text{O}_2$  and  $\text{N}_2$  with detection limits of 10 and 0.5 ppm, respectively. The high detection limit for  $\text{O}_2$  results from  $\text{H}_2$  interference (the major constituent of the effluent gas). However, this could be lowered to  $\sim 0.1$  ppm by using a He ambient within the reactor. A Porapak "Q" ( $\frac{1}{4}$  in. OD  $\times$  4 ft) column was used for detecting  $\text{CH}_4$  with a detection limit of 0.5 ppm and a Chromasorb 103 ( $\frac{1}{4}$  in. OD  $\times$  3 ft) column was used for  $\text{NH}_3$  detection to  $\sim 3$  ppm. All columns were maintained at room temperature except the latter which was maintained at  $70^\circ\text{C}$ . Since the sensitivity improves with decreasing detector (thermistor bridge) temperatures, the chromatograph was modified so that the Chromasorb column was thermally isolated from the detector, thus permitting the column to be operated at elevated temperatures while maintaining the detector at room temperature.

Gas calibration was accomplished with an exponential dilution flask (EDF) (14), using He as the carrier. Each gas at 100% concentration was injected into the EDF with a syringe, and the detector cell output was measured at known time intervals. The peak and integrated output signals,  $c_0$ , corresponding to the initially injected and thus known gas concentration was determined from the following equation

$$c = c_0 \exp - ft/v \quad [2]$$

where  $c$  is the detector output (proportional to the gas concentration) at time  $t$ ,  $f$  is the flow rate through the EDF, and  $v$  is the EDF volume. Generally, the value of  $c_0$  was chosen to be in the range where measurements were to be made. Finally, the delay time (after injection into the appropriate column) for detecting the output signal serves as a signature for the specific gas involved.

Since oxygen is deleterious to the efficiency of GaP green LED's and, as suggested previously (9), may contribute to  $\text{NH}_3$  dissociation, the reactor effluent at room temperature was analyzed for  $\text{O}_2$  and  $\text{N}_2$  using a He ambient for increased sensitivity. As indicated elsewhere (5), the loading end of the reactor is enclosed in an  $\text{N}_2$  filled enclosure to minimize entrance of air into the reactor. This was just one of many precautions to minimize  $\text{O}_2$  contamination. The present results indicate that such enclosures are quite effective. For example, 50 min after loading and using a reactor flow rate of  $\sim 500$   $\text{cm}^3/\text{min}$ , the  $\text{O}_2$  level in the exit gas was reduced to 6 ppm compared to 55 ppm for  $\text{N}_2$ ; after 150 min, these values dropped to  $<2$  and 34 ppm, respectively. After overnight flushing these values fell to  $\sim 1$  and  $\sim 5$  ppm and correspond to a background level of air resulting from leaks in the extensive gas panel used for vapor doping the LPE layers (5).

Table I. Concentration of  $\text{N}_2$  and  $\text{CH}_4$  in reactor exit gas for various reactor temperatures using a flow rate of 500  $\text{cm}^3/\text{min}$

	Concentration (ppm)				
	25°C	700°C	850°C	925°C	1015°C
$\text{N}_2$	5-10	14	16	32	50 (230)*
$\text{CH}_4$	$<0.5$	$<0.5$	2	22	200 (2000)*

\* Parentheses denote 50  $\text{cm}^3/\text{min}$  flow rate.

For a 500  $\text{cm}^3/\text{min}$  flow rate,  $p_{\text{NH}_3}$  (inlet)  $\approx 10^{-3}$  atm, and a  $\text{H}_2$  carrier gas, the determined  $\text{CH}_4$  and  $\text{N}_2$  concentrations for various temperatures are given in Table I. The conditions at  $1015^\circ\text{C}$  are those which correspond to actual LPE conditions for green LED's. First, these results indicate that substantial levels of  $\text{CH}_4$  are generated within the reactor at elevated temperatures; additional experiments deleting  $\text{NH}_3$  from the gas stream show that most of this results from the direct reaction of graphite with the  $\text{H}_2$  carrier. Decreasing the flow rate to 50  $\text{cm}^3/\text{min}$ , increases the  $\text{CH}_4$  level to  $\sim 2000$  ppm at  $1015^\circ\text{C}$ . The presence of such high levels of  $\text{CH}_4$  may affect the gaseous reactions in vapor epitaxy systems but does not appear to be of consequence for LPE. These results also show that the  $\text{N}_2$  level increases monotonically with reactor temperature, reaching  $\sim 50$  ppm at  $1015^\circ\text{C}$ . This increasing decomposition of  $\text{NH}_3$  with increasing temperature has the effect of displacing the curve in Fig. 2 downward with increasing temperature. Decreasing the flow rate to 50  $\text{cm}^3/\text{min}$ , increases the  $\text{N}_2$  level to  $\sim 230$  ppm, with a corresponding decrease in the effluent  $p_{\text{NH}_3}$  value. As expected, when one deletes the  $\text{NH}_3$  or the graphite boat, the initial ( $25^\circ\text{C}$ )  $\text{N}_2$  value for all reactor temperatures is measured. Using the measured  $\text{N}_2$  levels, the corresponding concentrations of consumed  $\text{NH}_3$  according to Eq. [1] are twice the  $\text{N}_2$  values. The values deduced from the titration and chromatographic measurements of  $p_{\text{NH}_3}$  indicate that at least half of the consumed  $\text{NH}_3$  is decomposed into its elemental constituents.

The  $\text{NH}_3$  dissociation behavior described above essentially relates to the doping of the growth solution. We find that under identical growth and doping conditions, the incorporated N concentration also depends on substrate orientation. The results shown in Fig. 1 are for {111}P (or B-face) oriented substrates. The N concentration for {100} and {111}Ga (or A-face) oriented crystals are respectively 50 and 75% lower than for {111}P crystals grown simultaneously in the same melt. Orientation dependence of the distribution coefficient has been explained in terms of surface band bending (15); however, it is not clear how this model is applicable to isoelectronic impurities such as N. We note that the present results are consistent with the "available site" model (16), wherein impurities which substitute on a Group V site (P site for N) are incorporated more readily on the corresponding Group V face. Further work is needed to fully understand these effects; however, it is clear that the higher N concentration for the {111}P orientation is desirable for efficient green LED's.

In conclusion, we find that contrary to previous work (9,13),  $\text{NH}_3$  can rapidly dissociate at elevated temperatures in the presence of graphite. The decomposition is undesirable not only for N incorporation in GaP but also, for example, halogen transport methods for growing GaN, InN, etc. In experimental systems where the mass of graphite is small, this problem will not be serious. However, for large capacity, commercial-type systems, such as the one studied in this work, as much as 95% of the available  $\text{NH}_3$  can be decomposed. (We note that in Ban's reactor, the surface area of the graphite liner was 25  $\text{cm}^2$ , while the LPE boat we use has an area of  $\sim 400$   $\text{cm}^2$ .) Consequently, for



systems where graphite is the only practical structural material, values of flow rate, inlet  $p_{\text{NH}_3}$ , etc., must be found to give the desired  $p_{\text{NH}_3}$  values appropriate to the reaction zone. In our case, monitoring the  $\text{NH}_3$  concentration in the effluent gas, determined by either titration or chromatography, was extremely useful for establishing optimum doping conditions. We note that reduction of the effective surface area of graphite components, e.g., by applying pyrolytic coatings, is a means of minimizing catalytic  $\text{NH}_3$  decomposition; this was not found necessary, however, for reproducibly achieving high efficiency LED's. Finally, preliminary data on the orientation dependence of N incorporation suggests that the {111}P orientation is preferable for efficient LED's.

Manuscript submitted Oct. 29, 1973; revised manuscript received Feb. 24, 1974.

Any discussion of this paper will appear in a Discussion Section to be published in the June 1975 JOURNAL. All discussions for the June 1975 Discussion Section should be submitted by Feb. 1, 1975.

#### REFERENCES

1. D. G. Thomas, J. J. Hopfield, and C. J. Frosch, *Phys. Rev. Letters*, **15**, 857 (1965).
2. R. A. Logan, H. G. White, and W. Wiegmann, *Solid-State Electron.*, **14**, 55 (1971).
3. I. Ladany and H. Kressel, *Proc. IEEE*, **60**, 1101 (1972).
4. O. G. Lorimor, H. W. Hackett, Jr., and R. Z. Bachrach, *This Journal*, **120**, 1424 (1973).
5. R. H. Saul and D. D. Roccasecca, *ibid.*, **120**, 1128 (1973).
6. R. H. Saul and D. D. Roccasecca, Work in progress.
7. O. G. Lorimor and L. R. Dawson, *This Journal*, **118**, 292C (1971).
8. E. C. Lightowers, J. C. North, and O. G. Lorimor, Submitted to *J. Appl. Phys.*
9. C. D. Thurmond and R. A. Logan, *This Journal*, **119**, 622 (1972).
10. J. C. Phillips and J. A. Van Vechten, *Phys. Rev.*, **B2**, 2147 (1970).
11. G. B. Stringfellow, *This Journal*, **119**, 1780 (1972).
12. C. N. Hinshelwood, "The Kinetics of Chemical Change," Clarendon Press, Oxford, England (1940).
13. V. S. Ban, *J. Cryst. Growth*, **17**, 19 (1972).
14. C. H. Hartmann and K. P. Kimick, Pittsburgh Conference on Analytical Chemistry and Applied Spectroscopy, March 1965.
15. K. Zschauer and A. Vogel, Proc. 1970 International Symp. on GaAs, The Institute of Physics, London (1971); H. C. Casey, M. B. Panish, and K. B. Wolfstirn, *J. Phys. Chem. Solids*, **32**, 571 (1971).
16. J. V. DiLorenzo, *J. Cryst. Growth*, **17**, 189 (1972).

## Vapor-Phase Epitaxial Growth of CdSe on Sapphire and CdS

W. M. Yim\* and E. J. Stofko

RCA Laboratories, Princeton, New Jersey 08540

The publication costs of this article have been assisted by the RCA Corporation.

Epitaxial growth of CdSe on sapphire has been reported previously by using an organometallic CVD process (1) and also, very recently, by using a vacuum evaporation technique (2). In general, CVD methods are often preferable since they provide a greater degree of flexibility and control as one could adjust the input vapor concentrations to achieve precise stoichiometry. In a previous work (3) we demonstrated the single-crystal epitaxy of ZnSe and CdS on sapphire by reaction of the Group II metal vapors with the Group VI hydride gases in an open-flow system. We have now extended this technique to the preparation of CdSe.

We report in this paper the epitaxial growth of high purity, single-crystal CdSe on sapphire, as well as on CdS, by using the hydride CVD technique. Also included are some electrical data obtained on the epitaxial layers.

The CVD apparatus is similar to that previously used for epitaxial growth of other II-VI compounds (3), but with one important modification to be described shortly. The cadmium was transported as vapor by passing 100 cm<sup>3</sup>/min H<sub>2</sub> over molten Cd at ~500°C; the selenium was introduced from a separate inlet as gaseous hydride, 20 cm<sup>3</sup>/min H<sub>2</sub>Se; and an additional 500 cm<sup>3</sup>/min H<sub>2</sub> was used as carrier gas. The cadmium and H<sub>2</sub>Se vapors were carried downstream and reacted to form CdSe on a substrate at ~700°C.

Two substrate materials were used almost exclusively; these were single-crystal wafers of sapphire with (0001) orientation and CdS single-crystal wafers of both (0001) and (000 $\bar{1}$ ) orientations. The sapphire substrates, ~10 mil thick and ~1 cm<sup>2</sup> in surface area, were supplied with a mirror-smooth finish by Insaco (Quakertown, Pennsylvania), and were used with no

further surface polishing prior to the epitaxial growth. The CdS substrates (~20 mil thick and ~1 cm<sup>2</sup>) were cut from melt-grown boules obtained from Eagle-Picher (Miami, Oklahoma), and were chemically polished with a 30% HCl solution in water.

In order to achieve epitaxy consistently and reproducibly, we found it important to preheat all substrates in ~100 cm<sup>3</sup>/min H<sub>2</sub> for several minutes until the temperature reached to about 600°C before inserting them in the deposition zone.<sup>1</sup> Perhaps more important, we found it necessary to separate the cadmium and H<sub>2</sub>Se vapors until they meet and react very near the substrate. This was accomplished by extending the Cd vapor inlet tube to a location as close as 1 cm from the substrate, while keeping the H<sub>2</sub>Se inlet tube at about 10 cm upstream from the Cd inlet. Without separating the reactant gases and placing one of the gas inlets in close proximity of the substrate, many whiskers and platelets were found to form inside the CVD apparatus ahead of the deposition zone. When this occurred, the deposited layers on various substrates, particularly on sapphire, were nearly always polycrystalline.

With the above growth conditions, we have obtained relatively high deposition rates: the average value is 3 μ/min on sapphire, 2 μ/min on (000 $\bar{1}$ ) CdS, and 1 μ/min on (0001) CdS. Emission spectrographic analysis showed the deposited layers to be high purity with the major metallic impurities of <1 ppm Cu, 3 ppm Si, and 3 ppm Mg.

Typical microstructure of as-grown epitaxial layers on sapphire is shown in Fig. 1(a). The hexagonal growth features shown here, as well as in Fig. 2(a) and Fig. 2(b) for CdSe on (0001) and (000 $\bar{1}$ ) CdS substrates, respectively, are characteristic of epitaxy of a wurt-

\* Electrochemical Society Active Member.

Key words: chemical vapor deposition, heteroepitaxy, CdSe, resistivity, photosensitivity.

<sup>1</sup> While detailed examinations are lacking, there appeared no deleterious thermal etching of the substrates after the preheating.

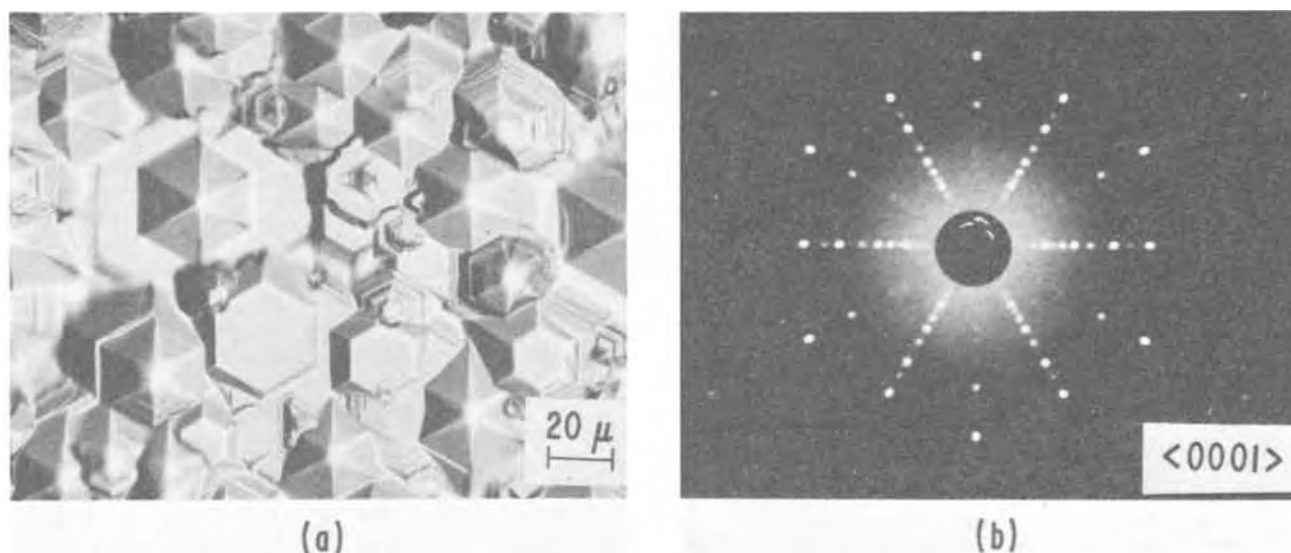


Fig. 1. As-deposited CdSe epitaxial layer on (0001) sapphire: (a) microstructure, (b) x-ray Laue pattern. The  $\langle 0001 \rangle$  axis of CdSe is perpendicular to the plane of the paper.

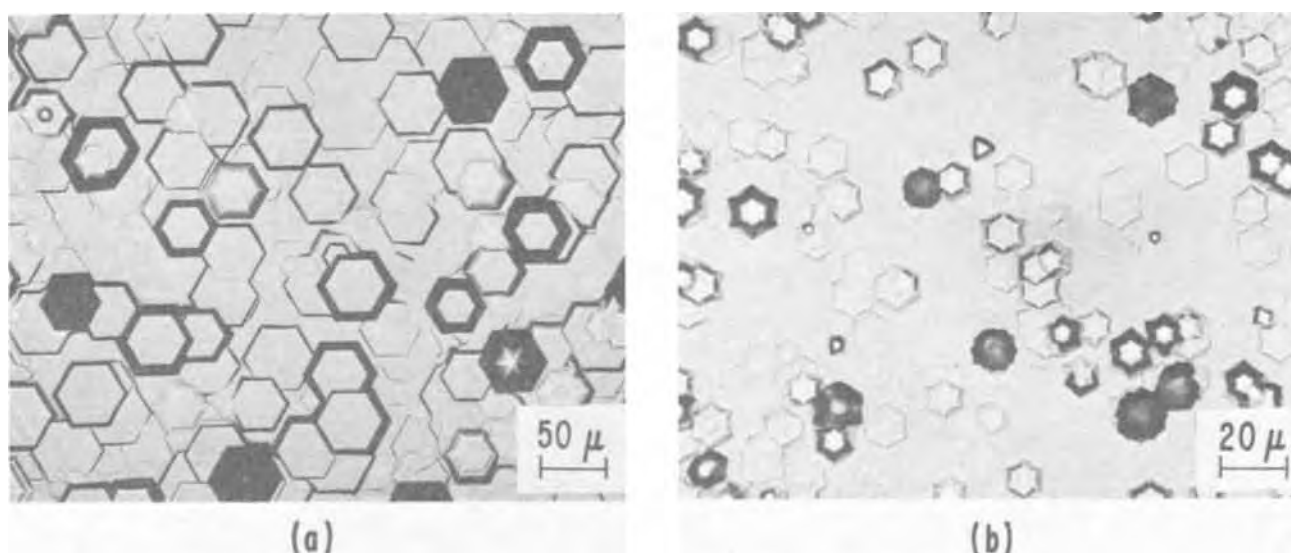


Fig. 2. Microstructure of as-deposited CdSe epitaxial layer on (a) (0001) CdS and (b) (0001) CdS. The x-ray Laue patterns for these CdSe layers are very similar to that shown in Fig. 1(b).

zite structure material grown with the  $c$ -axis perpendicular to the surface. The x-ray Laue pattern of Fig. 1(b) proves this, and that the well-resolved sharp diffraction spots indicate a high degree of single crystallinity. In the present work only the hexagonal structure was observed for CdSe deposited in the substrate temperature range investigated of  $550^{\circ}$ - $750^{\circ}\text{C}$ , although the cubic form is known and is frequently obtained, mixed with the hexagonal form, in vacuum-evaporated CdSe on various substrates heated up to about  $400^{\circ}\text{C}$  (4).

All the epitaxial CdSe layers grown without intentional doping showed high resistivity<sup>2</sup> and photosensitivity. Dark resistivity values measured at room temperature for the undoped CdSe were between  $5 \times 10^6$  and  $1 \times 10^7 \text{ ohm} \cdot \text{cm}$  and, with As doping by introducing a small flow of  $\text{AsH}_3$  during epitaxial growth, a resistivity value as high as  $1.2 \times 10^9 \text{ ohm} \cdot \text{cm}$  was obtained. Because of the high resistivity we were unable to determine the free carrier concentration by conventional Hall-effect measurements. However, assuming a Hall mobility of  $65\text{-}650 \text{ cm}^2/\text{V}\cdot\text{sec}$ , the latter being a value reported for melt-grown CdSe crystals (5), we arrive at a free carrier concentration of  $10^9\text{-}$

<sup>2</sup> All were  $n$ -type, doped or undoped, consistent with the well-known difficulty of obtaining  $p$ -type CdSe.

$10^{10}/\text{cm}^3$  for the  $10^7 \text{ ohm} \cdot \text{cm}$  material at room temperature. The CdSe can easily be made more conductive, if desired, either by increasing the Cd vapor flow or by decreasing the  $\text{H}_2\text{Se}$  flow; for instance, by using  $2.5 \text{ cm}^3/\text{min}$   $\text{H}_2\text{Se}$  which is only a tenth of the flow rate described above, we obtained CdSe of  $\sim 10^2 \text{ ohm} \cdot \text{cm}$ .

The ratio of two resistance values (one measured in the dark and the other obtained by illuminating the same specimen with a microscope lamp), which was taken arbitrarily as a measure of the photosensitivity, was 3000 for the  $10^7 \text{ ohm} \cdot \text{cm}$  material. This single-crystal layer had a low electron trap density at room temperature of  $\leq 10^{14}/\text{cm}^3$ , as measured with the "dark current doubling" method of Rose (6). By contrast, a vacuum-deposited polycrystalline CdSe film (4) with a dark resistivity and a resistance ratio similar to that of the  $10^7 \text{ ohm} \cdot \text{cm}$  layer mentioned above, had one order of magnitude larger trap density of  $1.4 \times 10^{15}/\text{cm}^3$ . It might well be that the lower trap density is related to improved crystallinity of the epitaxial layer.

#### Acknowledgments

We are grateful to Dr. H. Kiess of RCA, Zurich for making the trap density measurements, and to Dr. A. Rose for valuable discussions.

Manuscript submitted Nov. 7, 1973; revised manuscript received Feb. 13, 1974.

Any discussion of this paper will appear in a Discussion Section to be published in the June 1975 JOURNAL. All discussions for the June 1975 Discussion Section should be submitted by Feb. 1, 1975.

## REFERENCES

1. H. M. Manasevit and W. I. Simpson, *This Journal*, **118**, 644 (1971).
2. T. M. Ratcheva-Stambolieva, Yu. D. Tchistyakov, G. A. Krasulin, A. V. Vanyukov, and D. H. Djoglev, *Phys. Status Solidi (a)*, **16**, 315 (1973).
3. W. M. Yim and E. J. Stofko, *This Journal*, **119**, 381 (1972).
4. W. M. Yim and E. J. Stofko, Unpublished work.
5. S. S. Devlin, in "Physics and Chemistry of II-VI Compounds," M. Aven and J. S. Prener, Editors, p. 603, North-Holland Publishing Co., Amsterdam (1967).
6. A. Rose, Private communication. For general understanding of photoconductivity, see A. Rose, "Concepts in Photoconductivity and Allied Problems," Interscience Publishers, New York (1963).

## Trimethylstibine as a Source of Sb for Doping Epitaxial Si Layers

H. M. Manasevit,\* W. I. Simpson, and F. M. Erdmann

Rockwell International, Electronics Research Division, Anaheim, California 92803

The publication costs of this article have been assisted by Rockwell International.

A suitable source of Sb has not been developed for doping epitaxial Si layers even though Sb would be preferable to As or P because of its lower diffusivity. Stibine ( $\text{SbH}_3$ ) might be a possible source of Sb, but its instability at ambient temperatures could offer problems in dopant control.

Previously trimethylstibine (TMSb) had been successfully used in our laboratories as a source of Sb in forming alloys of  $\text{GaAs}_{1-x}\text{Sb}_x$  (1), and Gittler and Porter (2) have prepared Sb-doped  $\text{SiO}_2$  from a mixture of TMSb,  $\text{SiH}_4$ , and  $\text{O}_2$ . It was of interest to determine if TMSb could also be used to introduce Sb into a growing layer of Si at the relatively high growth temperature.

The apparatus used in these studies is shown schematically in Fig. 1. The TMSb (bp =  $80.6^\circ\text{C}$ ) was kept in a stainless steel reservoir with the tip of the inlet tube above the surface of the liquid. The Si source was  $\text{SiH}_4$  in a carrier gas of Pd-purified  $\text{H}_2$  (total flow = 6

liters/min). Chemically polished (111) p-type Si and mechanically polished (10 $\bar{1}$ 4)- and (01 $\bar{1}$ 2)-oriented  $\text{Al}_2\text{O}_3$  were used as substrates. The latter  $\text{Al}_2\text{O}_3$  orientation leads to (100)Si overgrowth; the former to (111)Si overgrowth (3). A 15-min  $\text{H}_2$  etch of the substrates at  $\sim 1250^\circ\text{C}$  preceded Si deposition. The films on Si substrates were nominally 10 and 25  $\mu\text{m}$  thick and grown at  $1050^\circ\text{C}$  at a rate of  $\sim 0.6 \mu\text{m}/\text{min}$ ; those on  $\text{Al}_2\text{O}_3$ , 1.5-1.85  $\mu\text{m}$  thick, and grown at  $\sim 1075^\circ\text{C}$  at about the same rate.

Only resistivity (4-point probe) measurements were made on the as-grown Sb-doped films on Si substrates, while Hall-effect measurements were made on the Si-on-sapphire (SOS) films after their properties were stabilized by annealing in dry  $\text{O}_2$  at  $1100^\circ\text{C}$  for 1 hr.

The initial depositions were performed with the TMSb maintained at  $-45^\circ\text{C}$  by means of a chlorobenzene slush; but it was found that the TMSb vapor would require excessive dilution in order to produce films with doping levels in the  $10^{16}$ - $10^{18} \text{ cm}^{-3}$  range. The TMSb vapor pressure was, therefore, reduced by

\* Electrochemical Society Active Member.

Key words: epitaxy, silicon, doping, antimony, metalorganics, sapphire.

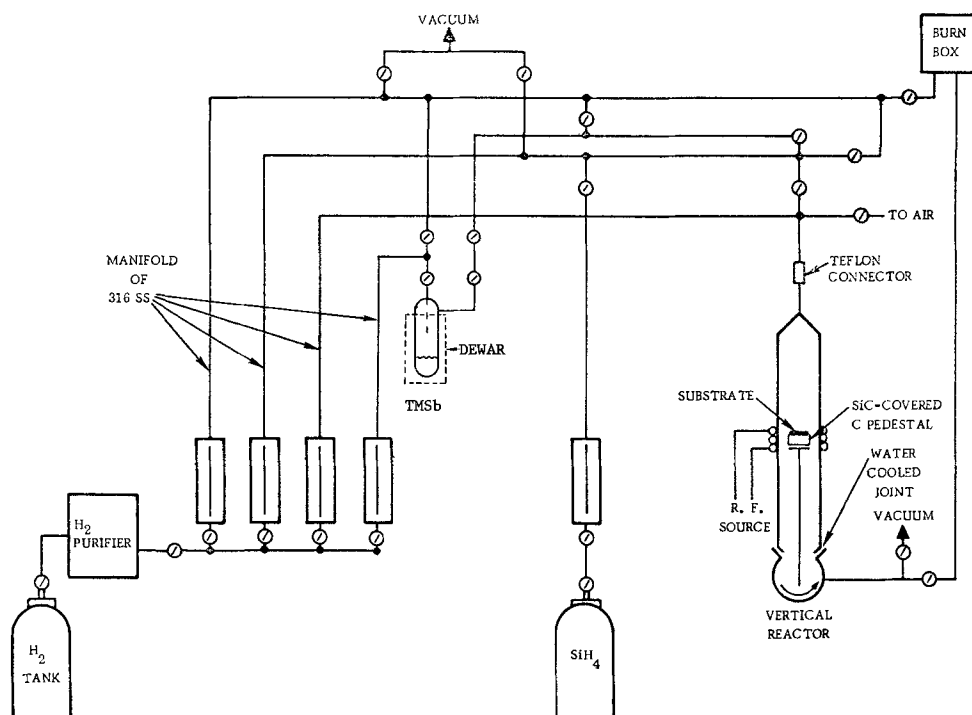


Fig. 1. Schematic diagram of chemical vapor deposition apparatus.

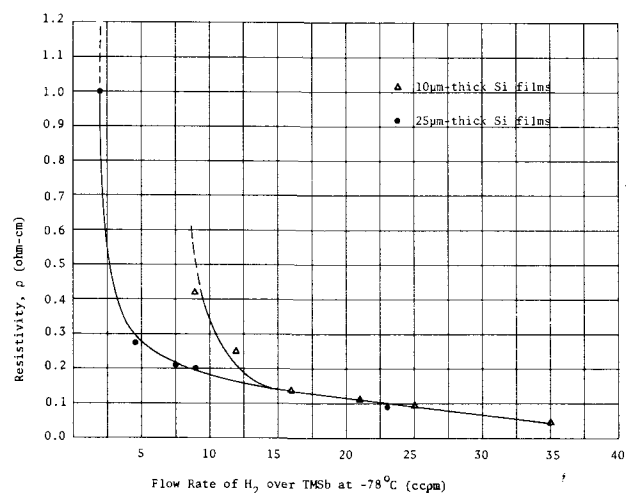


Fig. 2. Resistivity of Si homoepitaxial films vs. flow rate of  $H_2$  over TMSb at  $-78^\circ C$ .

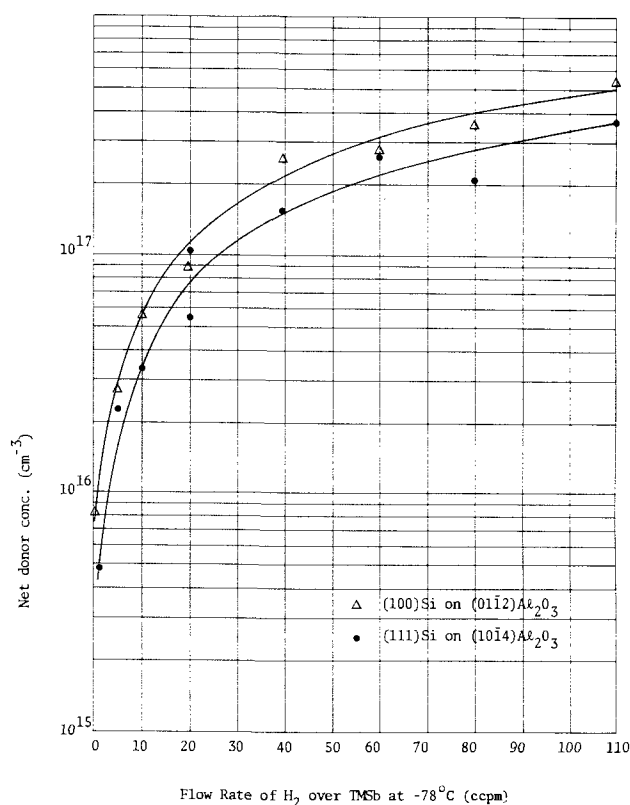


Fig. 3. Net donor concentration in Si-on- $Al_2O_3$  films vs. flow rate of  $H_2$  over TMSb at  $-78^\circ C$ .

using a dry ice-acetone slush to lower the TMSb bath temperature to  $-78^\circ C$ . The results of these preliminary studies are recorded in Fig. 2 and 3, in which the elec-

trical properties of the films are plotted vs. the flow rate of  $H_2$  over TMSb at  $-78^\circ C$ .

Figure 2 depicts the resistivity data obtained for the homoepitaxial growth of relatively thick Sb-doped Si films on (111)Si. At resistivities less than about 0.15 ohm-cm, i.e., for carrier concentrations greater than  $5 \times 10^{16} \text{ cm}^{-3}$  (4), the resistivity vs. flow rate curves for the 10 and the 25  $\mu\text{m}$  thick films are in good agreement, but at higher resistivities the curves do not coincide. This deviation, which occurs at flow rates less than about 15 ccpm, is not believed to indicate that there is a systematic dependence of resistivity on thickness or a limitation on the use of TMSb as a source for low concentrations of Sb. It was probably the result of the very limited number of experiments made during this preliminary study and inefficient equilibration of the relatively low  $H_2$ -TMSb flows with the  $SiH_4$  and much higher  $H_2$  flows before these components were introduced into the reactor.

Figure 3 shows that TMSb is an effective source of Sb dopant for both (111)Si and (100)Si thin films grown on  $Al_2O_3$ . It is also of interest that the donor concentrations in (100)Si films grown on (0112) $Al_2O_3$  tend to be consistently higher than in (111)Si films grown simultaneously on (1014) $Al_2O_3$ .

The plots in Fig. 2 and 3 do indicate that the higher  $H_2$  flow rates and, therefore, increased concentrations of TMSb produce decreases in resistivity and increases in donor concentration in Si epitaxial films, as expected.

In summary, these preliminary studies have demonstrated the feasibility of using TMSb as a source of Sb for doping epitaxial Si layers. Further studies are required in order to (i) learn how to control the doping better, (ii) establish the doping limits possible using TMSb, and (iii) determine if carbon is a contaminant. A preferable process for producing homogeneously doped layers would involve the use of prepared cylinders of carrier gases containing controlled amounts of TMSb.

#### Acknowledgments

The authors wish to acknowledge the assistance of J. P. Wendt in carrying out many of the electrical measurements, and Drs. R. P. Ruth and A. C. Thorsen in reviewing the manuscript.

Manuscript submitted July 17, 1973; revised manuscript received Jan. 24, 1974. This was Paper 312RNP presented at the Chicago, Illinois, Meeting of the Society, May 13-18, 1973.

Any discussion of this paper will appear in a Discussion Section to be published in the June 1975 JOURNAL. All discussions for the June 1975 Discussion Section should be submitted by Feb. 1, 1975.

#### REFERENCES

1. H. M. Manasevit and W. I. Simpson, *This Journal*, **116**, 1725 (1969).
2. F. L. Gittler and R. A. Porter, *ibid.*, **117**, 1551 (1970).
3. H. M. Manasevit, R. L. Nolder, and L. A. Moudy, *Trans. Met. Soc. AIME*, **242**, 465 (1968).
4. S. M. Sze and J. C. Irvin, *Solid-State Electron.*, **11**, 599 (1966).

# Relationship Between Process-Induced Defects and Soft P-N Junctions in Silicon Devices

L. E. Katz

Bell Laboratories, Allentown, Pennsylvania 18103

The publication costs of this article have been assisted by Bell Laboratories.

Soft reverse-breakdown characteristics in Si devices have been a recurring problem for the semiconductor industry. Extensive literature (1-8) has been published concerning causes and mechanisms for soft junctions. The undesired electrical characteristics have been attributed to both defects and impurities. Precipitates, dislocations, stacking faults, and other unspecified defects have been proposed as culprits.

The aim of this study was to make a large number of diodes and transistors by using a simple processing scheme and then to investigate the correlation between degraded electrical characteristics and any defects revealed by etching.

## Experimental Procedure

Polished (100)-oriented, Czochralski low-dislocation wafers, P-doped with 0.7-1.2 ohm-cm resistivity, were obtained from various suppliers. A ring-dot type structure was used for the devices. The base and emitter windows were respectively 125 and 75  $\mu\text{m}$  in diameter. Approximately 3000 devices were made on each wafer. The processing steps are listed in Table I.

Electrical evaluation was accomplished by measuring the collector-base and collector-emitter reverse breakdown voltages,  $BV_{CB}$  and  $BV_{CEO}$ , on a curve tracer, generally at 10  $\mu\text{A}$ , although on occasion 1 or 5  $\mu\text{A}$  were used. Defects were revealed by Sirtl etching (9) for short times (20 to 120 sec).

## Defects Produced by Oxidation and Reoxidation

Several groups of wafers were processed through the procedure outlined in Table I. Following base reoxidation, the diodes were evaluated by measuring  $BV_{CB}$ . Depending on several variables, the most important being the ambient during the high temperature operations, yields for various wafers ranged from about 50 to more than 90%. A  $BV_{CB}$  value of  $\sim 60\text{V}$  was expected based on the resistivity and procedure employed, and any value substantially below this was

Key words: defects, silicon, soft junctions.

Table I. Device processing sequence

	Temperature ( $^{\circ}\text{C}$ )
Initial clean	
Initial oxidation-steam	1050
Photoresist	
Base (B) predeposition (BN)	870
Drive-in (1% oxygen)	1150
Reoxidation-steam ( $x_j \sim 2.1 \mu\text{m}$ )	1050
Photoresist	
Emitter (P) diffusion ( $\text{POCl}_3$ ) ( $x_j \sim 1.1 \mu\text{m}$ )	1000

considered to represent a loss in yield, as was a "rounded knee" in the  $I$ - $V$  curve. Upon processing through the emitter cycle, a further reduction in yield was usually observed.

Since in some cases reduced yields were measured after base reoxidation, a number of wafers processed to this point were etched to determine if defects were present that could be responsible for the leakage. Two types of defects were revealed by etching, as shown in Fig. 1. One type (Fig. 1a), which is bow-shaped, has been identified by transmission electron microscopy (TEM) as an extrinsic stacking fault bounded by Frank partial dislocations. Other authors have made similar determinations (10). The depth of the stacking fault is thought to be  $\sim 1/5$  to  $1/10$  of its length (11), indicating a depth of  $\sim 1$  to  $2 \mu\text{m}$  for the stacking fault present following reoxidation. Such defects are fairly common in (100) steam-oxidized Si wafers containing non-homogeneities. The other defect (Fig. 1b), which is kite-shaped upon etching, is observed only within diode regions. Preliminary TEM analysis (12) shows the defect to be a rod-shaped precipitate extending into the Si.<sup>1</sup> The densities of both defects vary widely, but observations of many samples give a general density of stacking faults in the mid- $10^4$  to mid- $10^5/\text{cm}^2$  range averaged over the regions between diodes. The stacking faults are generally observed outside the diode regions, but apparent traces of stacking faults are

<sup>1</sup> The defect will be referred to as a rod in this paper.

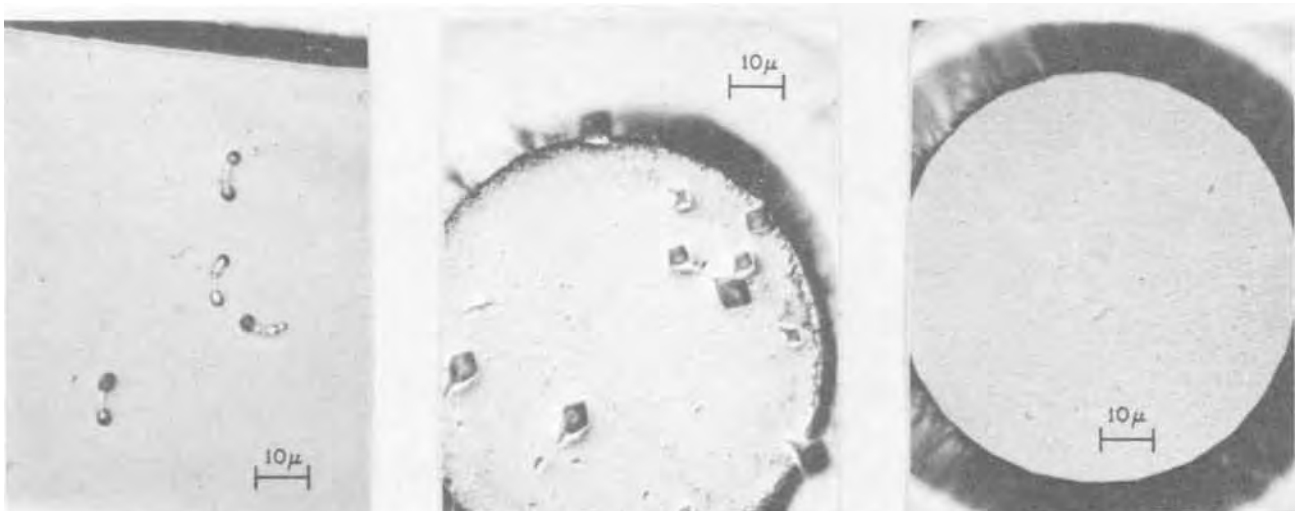


Fig. 1. Etching defects following base reoxidation: (a, left) region between diodes; (b, center) degraded reverse characteristic, and (c, right) good reverse characteristics.

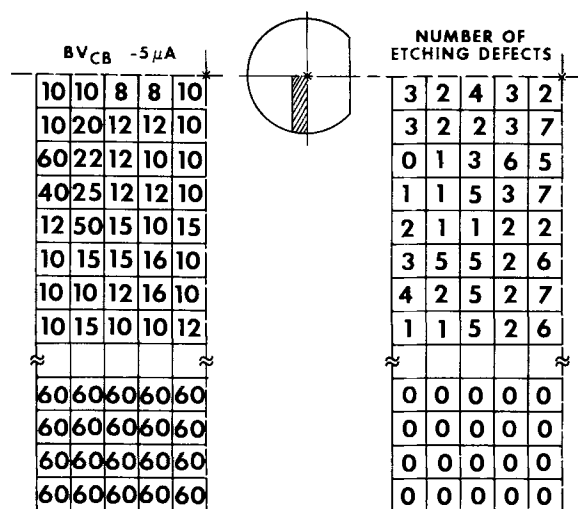


Fig. 2. Correlation between electrical characteristics (BV<sub>CB</sub> at 5 μA) and rod defects after base reoxidation.

sometimes present within the diode regions. The rod defect has a density of  $\sim 2 \times 10^5/\text{cm}^2$  averaged over the diode regions, a value comparable to the stacking fault density. It is noted that many diodes are free of these defects (Fig. 1c). They appear to form most frequently in areas of the wafers that have stacking faults between the diodes.

The stacking faults revealed by etching are oriented in the  $\langle 110 \rangle$  directions. This is characteristic of stacking faults in Si, since they form on (111) planes which intersect with a (100) surface in the  $\langle 110 \rangle$  directions.

Since defects were detected after the base reoxidation step, wafers were etched sequentially following each of the previous high temperature operations to determine the step at which defects are introduced. Stacking faults were observed in wafers which had been subjected to the initial oxidation and remained the only defects revealed by etching after boron pre-deposition and drive-in. It was only after the base reoxidation step that rods were observed. It was found that the formation of these defects during reoxidation

could generally be avoided by using a highly oxidizing ambient at the drive-in stage.

The etching experiments suggested that the rods might be responsible for the observed degradation of the base-collector characteristics. Two studies were carried out to determine whether this was the case. The first of these studies was based on the correlation that previous authors have established between light emission from microplasmas and electrical breakdown (13, 14). Diodes (on several wafers) that exhibited poor breakdown characteristics following the base reoxidation step were biased to a voltage where light emission could be observed. The light levels were generally low. Photographs were taken of light emission patterns, the diodes were then Sirtl etched, and the etch patterns were photographed. Comparison of many light emission photographs with the corresponding etching photographs showed that every light emission spot corresponded to a rod defect, indicating that the defects are responsible for breakdown. Every etch defect could not be correlated with a light spot, but this is probably a consequence of the difficulty in observing and photographing the light spots.

Direct evidence that the rod defects are responsible for degrading the collector-base reverse characteristics is provided by the second study, in which a large number of diodes on one wafer were first probed electrically and then etched to reveal the defects present. The results are shown in Fig. 2. For each of the diodes, the left side of the figure gives the value of BV<sub>CB</sub> measured at 5 μA, and the right side gives the number of defects observed after etching. The figure also includes a sketch of the wafer, on which the area where data were taken is indicated by cross-hatching. It is seen that the maximum voltage, 60V, was obtained for every diode that was free of defects—even one located in an area where all the other diodes were degraded. On the other hand, a significantly lower voltage was obtained for every diode that contained even one defect. This correlation strongly supports the conclusion that the reduction in device yield observed after the base reoxidation step is due to the formation of rod defects.

In view of the adverse effect of the rods on device yield, it is of considerable interest to know the nuclea-

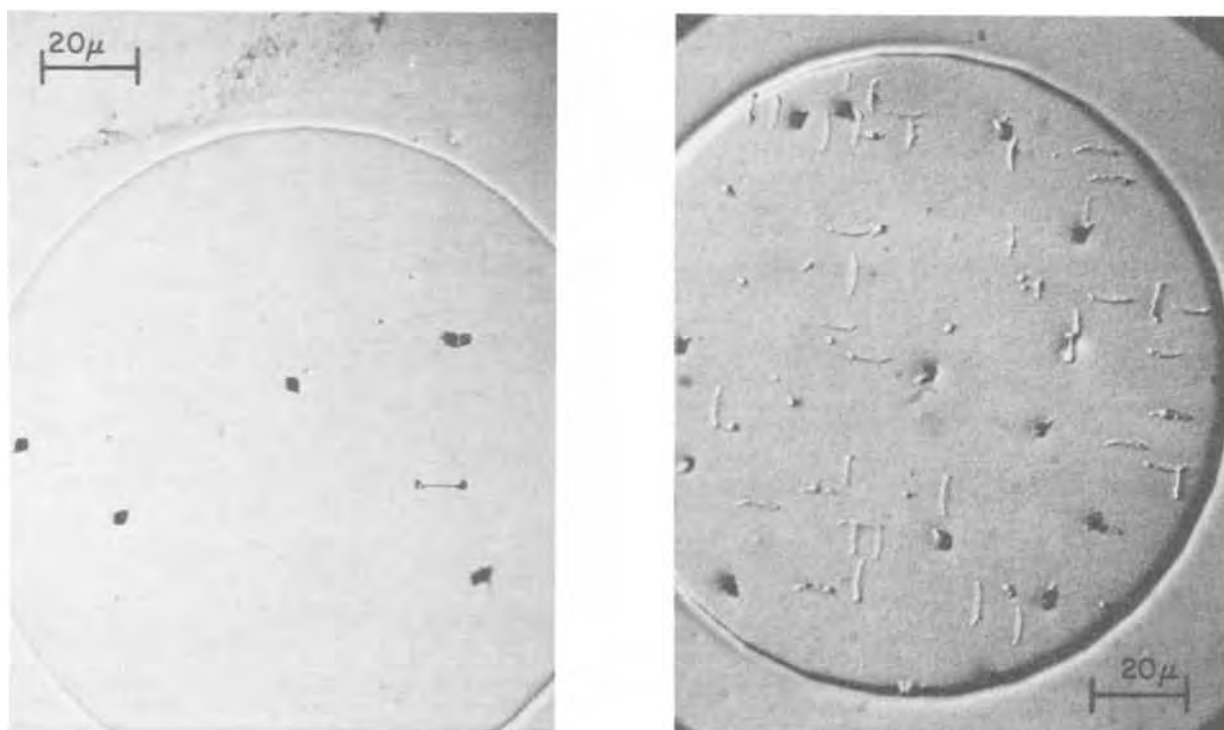


Fig. 3. Relationship of rods to stacking faults: (a, left) formation of rods on stacking faults and (b, right) rods and stacking faults

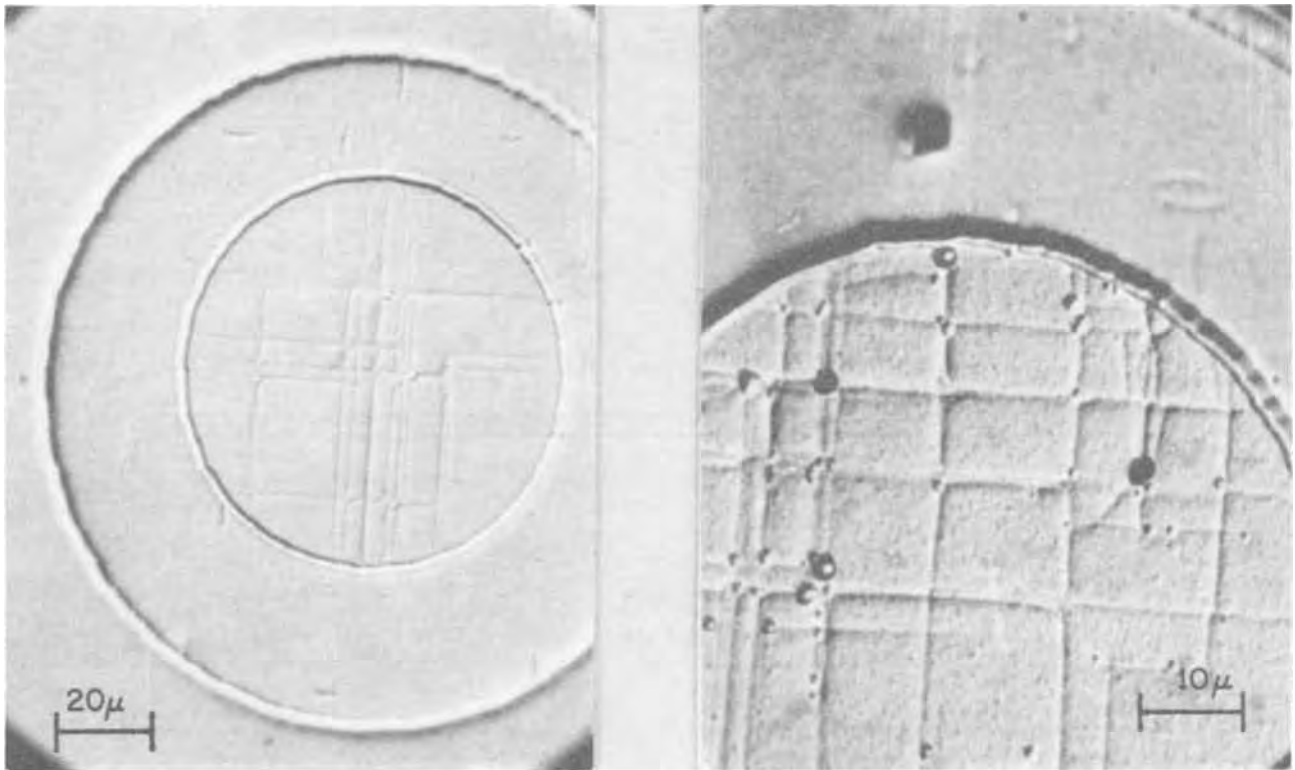


Fig. 4. Etching defects following emitter diffusion: (a, left) small defects and linear defects in emitter, good reverse characteristic and (b, right) small and large defects in emitter, degraded reverse characteristic.

tion mechanism, whether they are precipitates and if so, their chemical composition, and especially how to formulate the processing sequence to either prevent their formation or render them harmless.

With regard to the nucleation of the rods, an obvious question is whether the stacking faults are the nucleation sites. Some information concerning this question is provided by Fig. 3. The photograph on the left shows several rod defects. In one case the defect formation on the Frank partial dislocations at the end of the stacking fault is observed. A similar development, more fully matured, appears on the same photograph. Another diode with a poor reverse characteristic is shown in the photograph on the right. Based on these etching studies, it appears that in some instances the rods are nucleated by Frank partial dislocations associated with stacking faults, but that in general this is not the case.

**Defects Produced by Emitter Diffusion**

Let us go one step further and examine etching behavior following emitter diffusion. Linear etch defects associated with the high concentration phosphorus diffusion are evident with the emitter region (inner circle in Fig. 4a and b). Two other types of etching defects are also observed within emitter regions: (i) small defects without an apparent preferred orientation; (Fig. 4a and b) (ii) larger defects, oval in shape, with apparent <100> orientations, which are probably traces of the rod defect previously observed (Fig. 4b). In order to determine whether either type of defect causes degradation of the emitter-collector reverse characteristics, a large number of diodes on one wafer were first probed electrically and then etched to reveal defects, the same procedure used to investigate the defects formed in base reoxidation. The results are summarized in Fig. 5. The electrical data, which are given on the left side of the figure, show that for each diode either  $BV_{CEO}$  was greater than 40V, or the emitter and collector were shorted or showed poor electrical characteristics. The measurements were made on two areas of the wafer, one with high device yield and the other with low

yield. It was found that the small, unoriented defects do not degrade the junctions, since many diodes containing several of these defects exhibited hard breakdown. On the other hand, the large (100)-oriented defects are clearly associated with collector-emitter shorting. The number of these defects observed in each diode is given on the right side of Fig. 5. It is seen that every diode containing one or more defects exhibits shorting or poor electrical characteristics, while every diode without defects exhibits hard breakdown. Thus, the only shorted diode in the high yield region is also the only one containing a defect, and the three

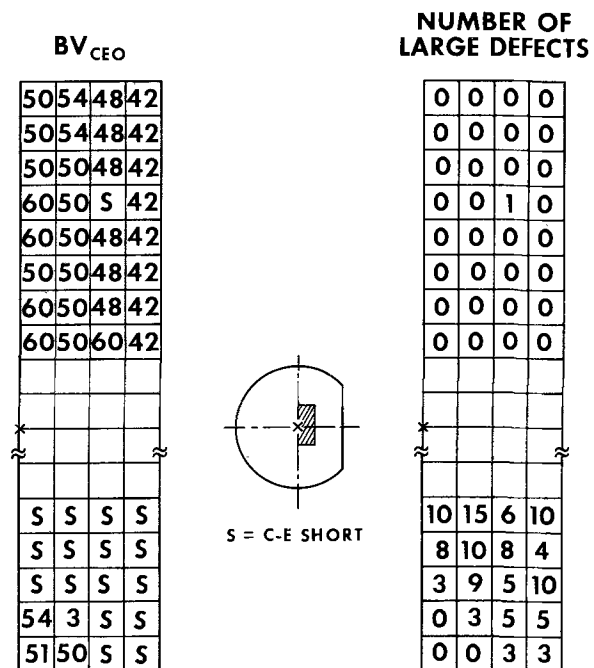


Fig. 5. Correlation between electrical characteristics ( $BV_{CEO}$ ) and large etching defects after emitter diffusion.



hard breakdown diodes in the low yield region are the only ones without defects. Use of an oxidizing ambient during the base drive-in cycle reduced the number of defects produced during emitter diffusion.

### Conclusions

A simple processing scheme has been examined to determine the nature of defects which form, the steps during which they form, and their effect on yield. Oxidation induced stacking faults were observed following the first high temperature operation. A rod defect formed during the base reoxidation step and correlated with light emission spots as well as soft and low breakdown on a one-to-one basis. Upon processing through the emitter cycle, another defect—presumably resulting from the rod defect—formed and correlated on a one-to-one basis with collector-emitter shorts.

In some cases the partial dislocations associated with the extrinsic stacking faults were the nucleation sites for the rods. In other cases, rods were observed to be separate from stacking faults. Use of a strongly oxidizing ambient during base drive-in tended to suppress the formation of defects during subsequent processing.

Manuscript submitted Sept. 6, 1973; revised manuscript received Jan. 10, 1974. This was Paper 67 presented at the Chicago, Illinois, Meeting of the Society, May 13-18, 1973.

Any discussion of this paper will appear in a Discussion Section to be published in the June 1975 JOURNAL.

All discussions for the June 1975 Discussion Section should be submitted by Feb. 1, 1975.

### REFERENCES

1. A. Goetzberger and W. Shockley, *J. Appl. Phys.*, **31**, 1821 (1960).
2. F. Barson, W. J. Armstrong, and W. E. Mutter, *This Journal*, **111**, 1263 (1964).
3. E. D. Jungbluth and P. Wang, *J. Appl. Phys.*, **36**, 1967 (1965).
4. J. M. Fairfield and G. H. Schwuttke, *This Journal*, **113**, 1229 (1966).
5. J. E. Lawrence, *ibid.*, **112**, 796 (1965).
6. J. E. Lawrence, in "Semiconductor Silicon," R. R. Haberecht and E. L. Kern, Editors, p. 596, The Electrochemical Society Softbound Symposium Series, New York (1969).
7. K. V. Ravi, C. J. Varker, and C. E. Volk, *This Journal*, **120**, 533 (1973).
8. J. E. Lawrence, in "Semiconductor Silicon," H. R. Huff and R. Burgess, Editors, p. 17, The Electrochemical Society Softbound Symposium Series, Princeton, N. J. (1973).
9. E. Sirtl and A. Adler, *Z. Metallk.*, **52**, 529 (1961).
10. R. J. Jaccodine and C. M. Drum, *Appl. Phys. Letters*, **8**, 29 (1966).
11. A. W. Fisher and J. A. Amich, *This Journal*, **113**, 1054 (1966).
12. A. G. Cullis and L. E. Katz, Paper 28 presented at Electrochemical Society Meeting, San Francisco, California, May 12-17, 1974.
13. R. Newman, W. C. Dash, R. N. Hall, and W. E. Burch, *Phys. Rev.*, **98**, 1536 (1955).
14. R. Newman, *ibid.*, **100**, 700 (1955).

## Analytical Determination of Boron in Chemically Deposited Polycrystalline Silicon

M. Briska and A. Kiofsky

IBM Laboratories, D-703 Boeblingen, West Germany

The publication costs of this article have been assisted by IBM Corporation.

Polycrystalline silicon has become increasingly interesting in semiconductor technology, i.e., for self-aligned MOS devices. It can be formed by chemical vapor deposition (CVD) in the way described by Eversteyn and Put (1).

Doping of the films is achieved by conventional impurity diffusion into the deposited layer or by codeposition of the dopant out of the gas phase.

A first correlation between resistivity and doping concentration for phosphorous and boron-doped polycrystalline films was established recently by Fripp and Slack (2) for a doping range from  $5 \times 10^{15}$  to  $7 \times 10^{17}$  B atoms/cm<sup>3</sup>.

For the doping concentrations of the polycrystalline layers these authors took the values which they found for simultaneously deposited poly and single crystalline epitaxial layers via resistivity measurement and Irvin's curves (4).

For many purposes higher p-doping levels ( $10^{17}$ - $10^{20}$  atoms/cm<sup>3</sup>) are used which correspond to boron amounts in the microgram range, which is, as shown in the following, accessible to quantitative chemical analysis. The analytically determined values are compared with the sheet resistivity of the polycrystalline silicon layers.

### Experimental Procedure

**Preparation of the polycrystalline Si film.**—The B-doped polycrystalline Si films (0.6  $\mu$  thick) were prepared by the pyrolytic decomposition of SiH<sub>4</sub>-H<sub>2</sub> and B<sub>2</sub>H<sub>6</sub>-Ar gas mixtures in a conventional induction heated reactor. The decomposition temperature was

920°C. By variation of the B<sub>2</sub>H<sub>6</sub>-Ar partial pressure one is able to produce p-doping levels of the polycrystalline Si films in the range of  $10^{17}$ - $10^{20}$  B atoms/cm<sup>3</sup>. All these films were grown over a thin Si<sub>3</sub>N<sub>4</sub> film on silicon wafers.

**Performance of the chemical analysis and the sheet resistivity measurements.**—For the chemical analysis the back side of a wafer was covered (by evaporation) with a Cr-Cu-Au film of 2000Å. This is to protect the back side of the Si wafer from the NaOH attack when dissolving the polycrystalline Si film on the front side. The Si film is dissolved in 25-50 ml 0.4% NaOH at 100°C. The complete dissolution is achieved when the brown-blue color of the Si<sub>3</sub>N<sub>4</sub> underlayer appears. The amount of silicon dissolved is determined by weight difference.

The NaOH solution is concentrated and transferred into a 20 ml volumetric quartz flask. Corresponding to the expected B concentration, 2-4 ml of the solution, containing 20 mg NaOH, are pipetted into a Pt crucible and evaporated to dryness at 110°C. The residue is moistened with 0.1 ml H<sub>2</sub>O and 1 ml 0.1% curcumin solution in CH<sub>3</sub>COOH is added. The solution remains for 7-8 min at room temperature. Then 1 ml H<sub>2</sub>SO<sub>4</sub>/CH<sub>3</sub>COOH 1:1 is added and the whole mixture is kept for another 25 min at room temperature. After that the mixture together with 25 ml water is transferred into a quartz separation funnel. The B-curcumin complex is extracted with 6 ml cyclohexanone containing 1% phenol, adjusted with acetone to a total of 10 ml. The absorbance of the solution is measured against water at 555 nm and compared with those of a boron standard

Key words: boron determination, silicon films, sheet resistivity.



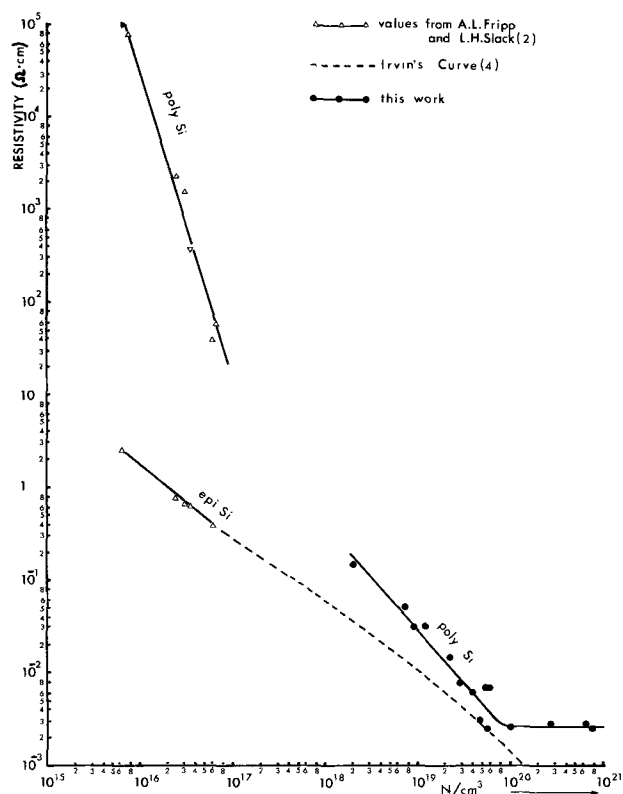


Figure 1

solution. The optical pathlength is 5 cm. The detection limit of the method is 10 ng.

The sheet resistivity measurements were performed by four-point probe measurement and thickness measurements by infrared spectrometry.

### Results

In Fig. 1 the results are graphically exhibited. The number of boron atoms/cm<sup>3</sup> found by chemical analy-

sis are plotted on the abscissa and the corresponding sheet resistivity on the ordinate. We included into this graph values found by Fripp and Slack (2). For their values, the abscissa does not represent boron concentration but electrically determined carrier concentration.

The experimental error both in sheet resistivity measurements and chemical boron concentration cannot account for the fairly high spread of the single measurements. Also variation in thickness, which affects the resistivity of polycrystalline films (3) is believed not to be responsible for the effect as all films had constant thickness of 0.6 $\mu$  with a variation of less than  $\pm 3\%$ . Traps at grain boundaries leading to inconsistent resistivity measurements are used as explanation. It is shown that at higher boron concentrations the resistivity of the polycrystalline film approaches that of single crystalline films of the same carrier concentration.

The fairly constant level in resistivity of  $3 \times 10^{-3}$  ohm-cm for dopant concentrations  $> 5 \times 10^{19}$  atoms/cm<sup>3</sup> is explained by the solid solubility of boron in silicon at the film preparation temperature of 920°C, which results in a calculated resistivity limit of  $2.5-3 \times 10^{-3}$  ohm-cm (1).

### Acknowledgment

We gratefully acknowledge the assistance and valuable discussions from E. Ebert and W. Hoffmeister.

Manuscript submitted Sept. 10, 1973; revised manuscript received Feb. 12, 1974.

Any discussion of this paper will appear in a Discussion Section to be published in the June 1975 JOURNAL. All discussions for the June 1975 Discussion Section should be submitted by Feb. 1, 1975.

### REFERENCES

1. F. C. Eversteyn and B. H. Put, *This Journal*, **120**, 106 (1973).
2. A. L. Fripp and L. H. Slack, *ibid.*, **120**, 145 (1973).
3. T. I. Kamins, *J. Appl. Phys.*, **42**, 4357 (1971).
4. J. C. Irvin, *Bell System Tech. J.*, **41**, 387 (1962).

## Surface Photovoltage Method Extended to Silicon Solar Cell Junction

E. Y. Wang

Electrical Engineering Department, Wayne State University, Detroit, Michigan 48202

and C. R. Baraona and H. W. Brandhorst, Jr.

NASA Lewis Research Center, Cleveland, Ohio 44135

The publication costs of this article have been assisted by Wayne State University.

Previous investigators (1-4) have shown that the surface photovoltage (SPV) method can be used to measure the minority carrier diffusion length in semiconductor materials. The conventional SPV method uses the surface junction formed in bulk materials due to the existence of surface states. The SPV method associated with lifetime gradient or resistivity gradient in semiconductor by electron irradiation has been reported previously (5). More recently, the SPV method has been applied to epitaxial semiconductor layers (6). In the present work we extend the conventional

Key words: surface photovoltage method, silicon solar cell, minority carrier diffusion length.

SPV method to a diffused junction such as that found in the silicon solar cell. The purpose of this paper is to show that the minority carrier diffusion lengths measured with the diffused junction and with a surface junction are identical. This extended SPV method provides a means to nondestructively measure minority carrier diffusion lengths before and after diffusion processing, using the same measurement technique. In addition, the SPV method uses capacitive contacts to eliminate contamination to the devices. This contact contamination would interfere with subsequent device fabrication processes and with the diffusion length measurement itself.

### Theory

The theory of the SPV method has been studied previously (3-9); however, the theory is briefly outlined here for completeness. The induced surface photovoltage ( $V_{sp}$ ) in p-type material is a function of excess minority carriers ( $\Delta n$ ) at the surface. The minority carriers are injected by illumination through the front surface of the specimen.  $\Delta n$  depends on the incident photon flux density ( $\phi$ ), the optical absorption coefficient ( $\alpha$ ), and the minority carrier diffusion length ( $L$ ). For the one dimensional case, Moss (7) has shown that

$$\Delta n = \frac{\gamma\phi(1-R)\alpha L}{(D/L + S)(1 + \alpha L)}$$

where  $\gamma$  is the quantum efficiency,  $R$  is the reflection coefficient,  $D$  is the minority diffusion coefficient, and  $S$  is the surface recombination velocity. In the extended SPV method, it is more appropriate to consider  $S$  as the junction recombination velocity. The assumptions in obtaining the above relationship are

- I.  $\alpha d_1 \ll 1$
- II.  $d \gg L$
- III.  $p \gg \Delta n$
- IV.  $d_1 \ll L$
- V.  $\alpha d > 1$

where  $d$  is the specimen thickness,  $d_1$  is the depth of the surface junction, and  $p$  is the majority carrier concentration.

$V_{sp}$  is some function of  $\Delta n$  at the depth of the junction, but its exact dependence need not be known. The incident monochromatic photon flux is adjusted as the wavelength is varied to make  $V_{sp}$  constant. In the 0.8 and 1.03  $\mu\text{m}$  wavelength range used in the measurement,  $\gamma$ ,  $R$ , and  $S$  are essentially constant. Hence  $\phi$  will be a linear function of  $1/\alpha$ . The diffusion length is determined from the intercept of this straight line at  $\phi = 0$  on the  $\phi$  vs.  $1/\alpha$  plot.

It is important to examine whether each of the basic assumptions of the SPV method is still valid when extended to silicon solar cell diffused junctions.

I.  $\alpha d_1 \ll 1$ . The depth of a solar cell diffused junction ( $d_1$ ), obtained from theoretical error function calculations or from experimental results (10), is about 0.25  $\mu\text{m}$ . The internal electric field in the  $n$  region is estimated to be  $10^4$  V/cm, using impurity gradient data derived from Hall and resistivity measurements. The field-free region is estimated to begin at a depth of 0.7  $\mu\text{m}$  beneath the illuminated surface for 10 ohm-cm cells and even less for a 0.7 ohm-cm cell. The wavelength region used in the SPV measurement is from 0.8 to 1.03  $\mu\text{m}$ . The corresponding  $\alpha$  values are 890 and 33.0  $\text{cm}^{-1}$ , respectively (11). The maximum product of  $\alpha d_1$  in the study is therefore about  $6.23 \times 10^{-2}$ , and the condition  $\alpha d_1 \ll 1$  is amply satisfied.

II.  $d \gg L$ . The thickness of the solar cell diodes ( $d$ ) was about 300-400  $\mu\text{m}$ . The measured minority carrier diffusion lengths shown in Fig. 1-4 are 170 and 70  $\mu\text{m}$  for the 10 and 0.7 ohm-cm material, respectively.  $d$  is only about a factor of two larger than measured  $L$  for 10 ohm-cm cells. Philips (6) has shown, however, that the  $d \gg L$  condition can be relaxed and  $\phi$  vs.  $\alpha^{-1}$  will maintain a linear relationship. In fact, Bullis and Baroddy (12) have concluded from their experimental results that as long as  $d > 1.2L$ , the  $L$  values obtained in the SPV method are relatively independent of  $d$ .

III.  $p \gg \Delta n$ . Solar cells were made using the same material and processes as for the junction devices used for SPV measurements. The short circuit current of the solar cells was measured over a range of illumination intensity which included the light level used in the SPV measurements. The short circuit current was linear with intensity, indicating the excess minority carrier density,  $\Delta n$ , was much less than the majority

carrier concentration  $p$  in the base region of the diode. Hence, the condition  $p \gg \Delta n$  is also fulfilled.

IV.  $d_1 < L$ . Since  $d_1 = 0.25 \mu\text{m}$  and  $L = 70 \mu\text{m}$  for 0.7 ohm-cm cells, and 170  $\mu\text{m}$  for 10 ohm-cm cells, the condition  $d_1 < L$  is always met.

V.  $\alpha d > 1$ . The cell thickness is about  $3-4 \times 10^{-2}$  cm and values of  $\alpha$  range from 890  $\text{cm}^{-1}$  at wavelength of 0.80  $\mu\text{m}$  to 33  $\text{cm}^{-1}$  at 1.03  $\mu\text{m}$ .  $\alpha d > 1$  is generally satisfied except at longer wavelengths ( $> 1.03 \mu\text{m}$ ).

### Experimental Arrangement

The experimental arrangement is similar to that reported elsewhere (1-3). A small area of the specimen is illuminated by a mechanically chopped light beam from a monochromator. The illuminated area is held constant. The intensity is controlled by varying the voltage of the light source, so that the relative photon flux density is only proportional to the product of the thermopile reading and the wavelength. The photovoltage is coupled through a dielectric to a conducting glass contact on the front surface and through a metallic pressure type back contact to a phase sensitive detector. The detector is tuned to the chopper frequency. The relative photon flux density is measured by a thermopile. The samples measured were of typical solar cell configuration, although they had no evaporated metal contacts. The phosphorous diffused n-type junctions were about 0.25  $\mu\text{m}$  deep. p-type base materials of two different resistivities were used: 10 and 0.7 ohm-cm.

Typical results are shown in Fig. 1 and 2. Measurements were made on each diode for differing values of  $V_{sp}$ . All the results show a linear dependence of  $K\phi$  on  $1/\alpha$  with a constant intercept at  $K\phi = 0$ , where  $K$  is arbitrary normalized constant. The minority carrier diffusion length obtained by the SPV method is 170  $\mu\text{m}$  for the 10 ohm-cm cells, and 70  $\mu\text{m}$  for the 0.7 ohm-cm cell. Cells were then etched in a solution of 2 parts acetic, 3 parts nitric, and 1 part hydrofluoric acid for a time sufficient to remove the n layers, while still maintaining  $d > L$ . The etched specimens were then measured by the conventional SPV technique. The results are shown in Fig. 3 and 4. The minority carrier diffusion lengths are in good agreement with the values obtained from the measurements of the diffused junction diodes. The minority carrier diffusion lengths measured by the x-ray method (13) on the solar cells also agree with the values obtained by the SPV method.

### Discussion and Conclusion

Experimental errors mainly originate from two sources, energy flux density calibration of the thermo-

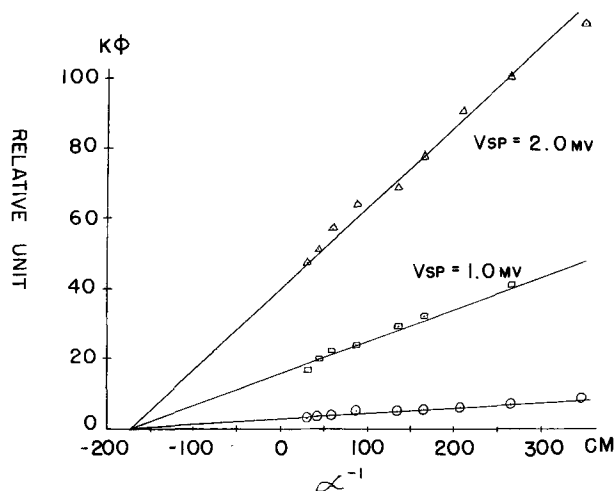


Fig. 1. Relative photon flux density ( $K\phi$ ) vs. the inverse of the optical absorption coefficient ( $\alpha$ ) for typical 10 ohm-cm silicon solar cell.

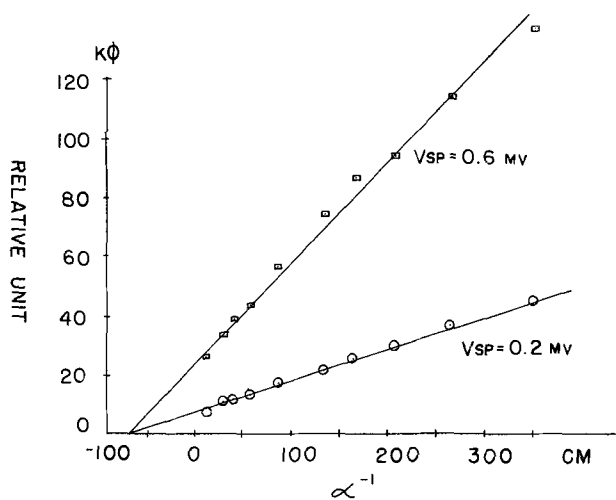


Fig. 2. Relative photon flux density ( $K\phi$ ) vs. the inverse of the optical absorption coefficient ( $\alpha$ ) for a typical 0.7 ohm-cm silicon solar cell.

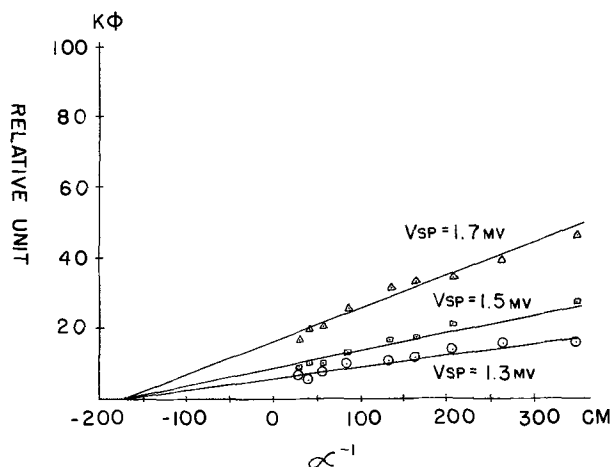


Fig. 3. Relative photon flux density ( $K\phi$ ) vs. the inverse of the optical absorption coefficient ( $\alpha$ ) for the 10 ohm-cm silicon base material.

pile readings and uncertainty in  $\alpha^{-1}$  value because of the wavelength resolution of the spectrometer. From the estimate of the sensitivity of the microvoltmeter ( $\pm 1.0 \mu\text{V}$ ), the thermopile reading error could be  $\pm 10\%$  at low  $K\phi$  values and  $\pm 2\%$  at high  $K\phi$  values. Because of the nature of the variation of  $\alpha^{-1}$  with wavelength, the uncertainty in  $\alpha^{-1}$  is  $\pm 2\%$  at short wavelength and  $\pm 4\%$  at longer wavelengths.

In conclusion, our results show that the minority carrier diffusion lengths obtained from solar cell diffused junctions, and from the same bulk material with the n-regions removed by etching, are identical within experimental error by using the SPV method. The minority carrier diffusion values obtained here also agree with those obtained by the x-ray method. These

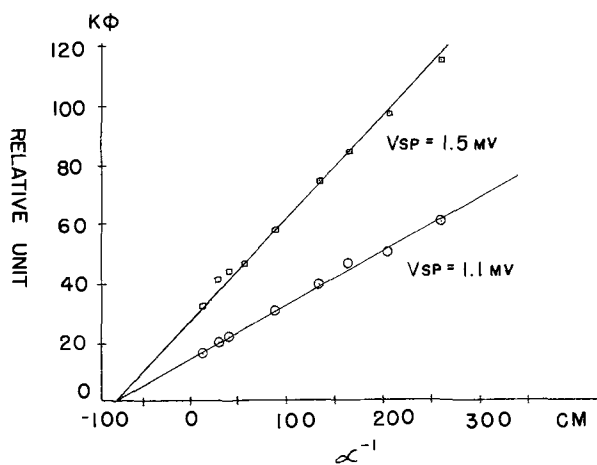


Fig. 4. Relative photon flux density ( $K\phi$ ) vs. the inverse of the optical absorption coefficient ( $\alpha$ ) for the 0.7 ohm-cm silicon base material.

results indicate that the basic assumptions of the SPV method are indeed still valid for diffused junctions, as well as for surface junctions. The results further suggest that the influence of energy band bending on the n-region of solar cells is negligible. This is to be expected since the solar cell n-region is heavily doped (almost degenerate), and since the surface of n- or p-type bulk silicon material usually exhibits n-type behavior (14). If this were not the case, the minority carrier diffusion lengths obtained would not have been identical.

Manuscript submitted Sept. 28, 1973; revised manuscript received Feb. 25, 1974. This was Paper 211 presented at the Chicago, Illinois, Meeting of the Society, May 13-18, 1973.

Any discussion of this paper will appear in a Discussion Section to be published in the June 1975 JOURNAL. All discussions for the June 1975 Discussion Section should be submitted by Feb. 1, 1975.

#### REFERENCES

1. E. O. Johnson, *J. Appl. Phys.*, **28**, 1349 (1957).
2. A. Quilliet and P. Gosar, *J. Physics Radium*, **21**, 575 (1960).
3. A. M. Goodman, *J. Appl. Phys.*, **32**, 2550 (1961).
4. J. Vilm and W. E. Spicer, *ibid.*, **36**, 2815 (1965).
5. R. M. Esposito, J. J. Lofferski, and H. Flicker, *ibid.*, **38**, 825 (1967).
6. W. E. Philips, *Solid-State Electron.*, **15**, 1097 (1972).
7. T. S. Moss, *J. Electron. Control*, **1**, 126 (1955).
8. E. O. Johnson, *Phys. Rev.*, **111**, 153 (1958).
9. S. C. Choo and A. C. Sanderson, *Solid-State Electron.*, **13**, 609 (1970).
10. D. M. Harris, Private communication.
11. W. R. Runyan, Final Report NASA Grant 44-007-016.
12. W. M. Bullis and T. J. Baroddy, Jr., MBS Tech. Notes 555, p. 9 (1970).
13. W. Rosenzweig, *Bell System Tech. J.*, **41**, 1573 (1962).
14. A. S. Grove, "Physics and Technology of Semiconductor Devices," p. 307, John Wiley and Sons, Inc., New York (1961).



# Conductance-Viscosity Studies on Some Moderately Concentrated Nonaqueous Electrolyte Solutions from $-50^{\circ}$ to $125^{\circ}\text{C}$

## I. Solutions of $\text{Bu}_4\text{NI}$ , $\text{KSCN}$ , and $\text{NH}_4\text{Br}$ in $\text{N,N}$ -Dimethylformamide

T. V. Rebagay,<sup>1</sup> J. F. Casteel, and P. G. Sears\*

Department of Chemistry, University of Kentucky, Lexington, Kentucky 40506

The publication costs of this article have been assisted by the University of Kentucky.

### ABSTRACT

Conductances, viscosities, and densities have been determined at  $25^{\circ}$  intervals between  $-50^{\circ}$  and  $125^{\circ}\text{C}$  for moderately concentrated solutions of  $\text{Bu}_4\text{NI}$ ,  $\text{KSCN}$ , and  $\text{NH}_4\text{Br}$  in  $\text{N,N}$ -dimethylformamide. Results are summarized for the fitting of the experimental data as functions of temperature and molality to appropriate equations by computer least squares procedures. Activation energies of viscous flow and conductance, molar conductance-viscosity products, and specific conductance maxima also are discussed.

$\text{N,N}$ -dimethylformamide, hereafter designated DMF, has several advantageous physical properties such as a convenient and broad liquid range ( $-61^{\circ}$  to  $153^{\circ}\text{C}$ ), a medium dielectric constant (36.7 at  $25^{\circ}\text{C}$ ), and low viscosity (0.796 cP at  $25^{\circ}\text{C}$ ). Previous typical studies (1-4) dealing mostly with dilute solutions at one or more temperatures between  $15^{\circ}$  and  $50^{\circ}\text{C}$  have shown DMF to be an excellent electrolytic solvent. The principal objective of the research reported herein has been to extend the existing knowledge about DMF as an electrolytic solvent by obtaining and discussing matching conductance and viscosity data for moderately concentrated solutions of three salts in DMF at eight temperatures over an unusually broad  $175^{\circ}$  range. Concentrations of salts ranged up to 6, 8, and 30% by weight (approximate upper limits of solubility at  $-50^{\circ}\text{C}$ ) for  $\text{NH}_4\text{Br}$ ,  $\text{KSCN}$ , and  $\text{Bu}_4\text{NI}$ , respectively.

### Experimental

DMF (Fisher Certified) was rendered anhydrous by refluxing over freshly ignited calcium oxide and then fractionated at 10 mm using a 1m distillation column packed with 6-mm porcelain saddles. A 60% middle fraction was retained for use in preparation of solutions. The values for the conductance, viscosity, and density of the solvent at  $25^{\circ}$  were in good agreement with those previously reported (1).

Eastman Grade  $\text{Bu}_4\text{NI}$ , Mallinckrodt Analytical Reagent  $\text{NH}_4\text{Br}$ , and Baker Analyzed Reagent  $\text{KSCN}$  were dried for several days in a desiccator over anhydrous barium perchlorate and used without further purification. Subsequent Karl Fischer analyses on similarly dried compounds gave a maximum water content of 0.01%.

Solutions in glass-stoppered flasks were prepared on a weight basis using calibrated weights and applying

appropriate buoyancy corrections. Sufficient amounts of the solutions were prepared to permit separate portions of a solution to be used for the determinations of conductance, viscosity, and density. All measurements on each solution were completed within 18 hr after its preparation.

Each conductance cell was U-shaped with the two arms connected with smaller tubing which primarily controlled the magnitude of the cell constant. Standard tapered glass connections with marked positions made possible the reproducible placement of electrode inlet tubes in the cells. Platinum electrodes, 15 mm in diameter and welded to nickel lead wires, protruded from firm mountings in the ends of the inlet tubes into the solution. The electrodes were platinized (6 coulombs- $\text{cm}^{-2}$ ) following the recommendation of Jones and Bollinger (5). Cell constants at  $25^{\circ}$ , ranging from 6.301 to  $41.47\text{ cm}^{-1}$ , were based on resistances of several aqueous potassium chloride solutions of known molarities and on the corresponding conductance data of Lind, Zwolenik, and Fuoss (6). The values for the constant of a cell at temperatures other than  $25^{\circ}$  were calculated from the value at  $25^{\circ}$  and the cell dimensions by the method of Washburn (7).

Resistances of the solutions contained in the conductance cells were measured with a Dike-Jones bridge assembly manufactured by the Leeds and Northrup Company. For resistances exceeding 30,000 ohms, the cell was shunted in parallel with 30,000 ohms and the series cell resistance was computed from the measured parallel resistance. Resistances of solutions measured at 50, 1000, and 2000 Hz were found to have negligible frequency dependence. No solvent corrections were applied to the conductances of the nonaqueous solutions since the conductance of the solvent in each case was  $<0.01\%$  that of the solution.

The equipment and procedures which were used in the determination of viscosities and densities have been discussed thoroughly in previous articles (8,9). Densities were necessary for calculating absolute vis-

\* Electrochemical Society Active Member.  
<sup>1</sup> Present address: College of Pharmacy, University of Kentucky, Lexington, Kentucky 40506.  
Key words: conductance, viscosity, density, electrolyte,  $\text{N,N}$ -dimethylformamide, activation energy.

EST

Table I. Molar conductances, viscosities, and densities of solutions of Bu<sub>4</sub>NI, KSCN, and NH<sub>4</sub>Br in N,N-dimethylformamide from -50° to 125°C

Molality	-50°	-25°	0°	25°	50°	75°	100°	125°
Molar conductances, ohm <sup>-1</sup> -cm <sup>2</sup> -mole <sup>-1</sup>								
Bu <sub>4</sub> NI								
0.0729	9.80	20.4	33.0	47.1	61.8	77.0	92.4	108.8
0.1522	7.62	16.41	27.0	38.8	51.3	64.0	77.0	90.7
0.240	6.01	13.57	22.8	33.2	44.2	55.6	67.0	78.2
0.306	5.20	11.98	20.5	30.1	40.3	51.0	61.7	72.7
0.376	4.45	10.59	18.37	27.3	37.0	46.9	57.0	67.5
0.491	3.47	8.82	15.75	23.9	32.8	42.1	51.7	61.5
0.563	2.99	7.85	14.31	21.9	30.3	39.1	48.0	57.3
0.692	2.32	6.47	12.21	19.16	26.9	35.0	43.3	52.0
0.798	1.856	5.56	10.84	17.23	24.5	32.1	40.0	48.4
0.908	1.497	4.76	9.55	15.56	22.3	29.6	37.3	45.3
1.015	1.227	4.14	8.55	14.19	20.6	27.6	34.9	42.6
1.157	(a)	(a)	7.40	12.54	18.57	25.2	32.0	39.5
KSCN								
0.1026	13.18	26.6	42.2	58.9	76.3	93.7	110.4	128.5
0.214	10.83	22.6	36.1	50.8	65.5	80.2	94.3	109.1
0.317	9.37	19.90	32.2	45.4	58.9	72.1	84.7	97.2
0.429	8.02	17.57	28.8	41.0	53.4	65.5	76.9	88.0
0.542	6.92	15.59	26.0	37.4	48.8	60.0	70.7	81.3
0.732	5.39	12.81	22.0	32.1	42.4	52.6	62.3	72.0
0.782	4.97	12.21	21.1	30.9	41.0	51.0	60.5	69.6
0.905	4.27	10.87	19.45	28.5	38.2	48.2	56.8	65.8
NH <sub>4</sub> Br								
0.1041	7.97	14.93	22.1	29.3	36.2	42.6	48.3	53.0
0.229	5.68	10.83	16.12	21.4	26.4	31.0	35.2	39.0
0.351	4.50	8.81	13.29	17.75	22.0	25.8	29.4	32.6
0.488	3.65	7.31	11.22	15.21	18.93	22.4	25.5	28.5
0.628	3.05	6.32	9.89	13.47	16.87	20.0	22.9	25.8
0.778	2.52	5.49	8.74	12.05	15.27	18.20	20.9	23.5
Viscosities, centipoises								
Bu <sub>4</sub> NI								
0.0729	4.06	1.984	1.230	0.860	0.643	0.504	0.409	0.336
0.1522	4.66	2.19	1.333	0.910	0.677	0.528	0.425	0.349
0.240	5.46	2.44	1.441	0.988	0.726	0.562	0.452	0.370
0.306	6.13	2.68	1.562	1.042	0.762	0.587	0.469	0.384
0.376	6.95	2.91	1.663	1.107	0.799	0.613	0.489	0.400
0.491	8.67	3.38	1.868	1.216	0.869	0.659	0.523	0.424
0.563	9.82	3.67	1.988	1.281	0.909	0.685	0.542	0.439
0.692	12.48	4.32	2.25	1.412	0.984	0.739	0.582	0.471
0.798	15.48	4.95	2.50	1.535	1.057	0.786	0.615	0.496
0.908	19.23	5.71	2.77	1.670	1.137	0.838	0.650	0.521
1.015	23.63	6.57	3.08	1.815	1.222	0.890	0.687	0.548
1.157	(a)	(a)	3.51	2.02	1.332	0.959	0.736	0.584
KSCN								
0.1026	4.09	1.998	1.240	0.870	0.650	0.509	0.412	0.340
0.214	4.72	2.22	1.354	0.933	0.697	0.544	0.437	0.359
0.317	5.39	2.46	1.473	1.005	0.742	0.574	0.462	0.378
0.429	6.22	2.75	1.612	1.082	0.790	0.609	0.487	0.397
0.542	7.26	3.06	1.744	1.163	0.843	0.645	0.515	0.420
0.732	9.47	3.68	2.04	1.322	0.943	0.711	0.564	0.455
0.782	10.30	3.88	2.11	1.368	0.967	0.731	0.575	0.466
0.905	12.23	4.42	2.33	1.492	1.038	0.778	0.609	0.490
NH <sub>4</sub> Br								
0.1041	4.24	2.07	1.257	0.875	0.653	0.509	0.411	0.338
0.229	4.82	2.25	1.361	0.937	0.698	0.541	0.434	0.356
0.351	5.50	2.47	1.472	1.002	0.737	0.571	0.458	0.374
0.488	6.33	2.77	1.615	1.079	0.789	0.606	0.484	0.395
0.628	7.31	3.06	1.751	1.160	0.842	0.643	0.512	0.416
0.778	8.71	3.45	1.927	1.268	0.910	0.688	0.547	0.450
Densities, gram-cm <sup>-3</sup> , × 10 <sup>4</sup>								
Bu <sub>4</sub> NI								
0.0729	10204	9964	9727	9495	9254	9014	8771	8515
0.1522	10258	10019	9784	9553	9313	9076	8834	8579
0.240	10313	10072	9839	9611	9374	9137	8904	8647
0.306	10362	10115	9883	9652	9414	9170	8942	8694
0.376	10388	10147	9920	9695	9459	9225	8989	8741
0.491	10458	10219	9990	9764	9530	9298	9066	8821
0.563	10480	10255	10025	9800	9567	9331	9106	8863
0.692	10551	10316	10092	9865	9631	9404	9177	8936
0.798	10601	10363	10138	9919	9686	9459	9236	8995
0.908	10651	10413	10186	9966	9739	9512	9288	9050
1.015	10690	10452	10230	10013	9788	9558	9340	9104
1.157	(a)	(a)	10290	10071	9844	9617	9406	9168
KSCN								
0.1026	10208	9967	9734	9503	9260	9020	8777	8521
0.214	10264	10024	9794	9563	9325	9086	8846	8593
0.317	10316	10080	9849	9620	9380	9144	8906	8654
0.429	10371	10134	9907	9678	9440	9205	8971	8721
0.542	10429	10191	9962	9735	9498	9264	9035	8790
0.732	10517	10279	10055	9823	9591	9359	9128	8892
0.782	10543	10304	10076	9851	9620	9389	9157	8915
0.905	10599	10364	10136	9914	9681	9450	9221	8981
NH <sub>4</sub> Br								
0.1041	10231	9986	9753	9519	9279	9037	8791	8537
0.229	10303	10061	9827	9596	9356	9115	8871	8616
0.351	10376	10133	9898	9669	9430	9196	8949	8694
0.488	10456	10215	9984	9751	9514	9273	9032	8780
0.628	10534	10295	10061	9826	9590	9353	9118	8865
0.778	10619	10376	10144	9914	9676	9440	9203	8952

(a) Solubility exceeded.

cosities and converting concentrations from a weight to a volume basis.

The temperature was controlled within 0.05° at 25° and higher temperatures with a Model H-1 high temperature bath (Cannon Instrument Company) and within 0.2° at 0°C and lower temperatures with a manually controlled low-temperature bath which also has been described elsewhere (10).

All determinations were made in duplicate with very good precision except in about five cases at the lowest temperatures where differences as great as 0.5% were observed. Mean values for the experimental data were fitted to various equations by least squares analyses performed with an IBM 360/65 computer using double precision Fortran IV programming.

### Results and Discussion

The experimental data are presented in tabular form in Table I. Also any part or all of the data can be calculated within specified limits through the use of equations and constants provided in this article.

The molar conductance for each of the three electrolytes in DMF increases with increasing temperature and decreasing concentration in a typical manner. For corresponding concentrations and temperatures, the molar conductance of NH<sub>4</sub>Br is significantly less than those of KSCN and Bu<sub>4</sub>NI indicating that NH<sub>4</sub>Br is less dissociated than the other two electrolytes in DMF.

The viscosities of solutions of each salt in DMF increase with increasing concentration and decreasing temperature as expected. Two other trends observed from the viscosity data for each system were that the temperature coefficient of solution viscosity increases with increasing electrolyte concentration and that the relative viscosity ( $\eta/\eta_0$ ) decreases with increasing temperature.

The nonlinear nature of plots of  $\ln \eta$  vs.  $1/T$  and  $\ln \Lambda$  vs.  $1/T$  clearly indicates that simple Arrhenius expressions for describing the temperature dependence of viscosities and conductances, in which  $E_{vis}$  or  $E_{con}$  is a constant, are not applicable. Moreover, Girifalco equations such as  $\log \eta = A + B/T + D/T^2$  and  $\log \Lambda = A' + B'/T + D'/T^2$ , which previously had been found to describe very well the behavior of other non-aqueous salt solutions of comparable concentrations

over a 75° range (11), were not satisfactorily applicable to the data for the DMF-salt solutions over the broader 175° range in this study.

Taking into account theoretical considerations, computational advantages, and agreement between observed and calculated values, viscosity and molar conductance data as functions of temperature were fitted finally to the following equations, respectively

$$\eta = \exp(\alpha + \beta/T + \gamma/T^2 + \delta/T^3 + \epsilon/T^4) \quad [1]$$

$$\Lambda = \exp(-(\alpha' + \beta'/T + \gamma'/T^2 + \delta'/T^3 + \epsilon'/T^4)) \quad [2]$$

Equivalent forms of Eq. [1] and [2] are expanded Arrhenius expressions such as  $\eta = A \exp(E_{vis}/RT)$  and  $\Lambda = A' \exp(-E_{con}/RT)$  in which  $E_{vis}$  and  $E_{con}$  are not constants but functions of temperature. Also, the common logarithm forms of Eq. [1] and [2] are related to expanded Girifalco equations (11, 12). The above equations may be changed to common logarithmic form by dividing each constant listed in Table II and Table III by 2.30258.

The parameters obtained through fitting mean experimental values of  $\eta$  and  $\Lambda$  to Eq. [1] and [2], using a nonlinear least squares program of the type described by Wentworth (13), are compiled in Tables II and III, respectively. The deviation data in these tables confirm that the equations apply excellently to the experimental data over the entire 175° range. Specifically, the mean and maximum deviations respectively between calculated and observed values are  $\leq 0.27\%$  and  $\leq 0.62\%$  for viscosities and  $\leq 0.35\%$  and  $\leq 0.56\%$  for molar conductances.

Viewing viscous flow and conductance as rate processes, activation energies of viscous flow and conductance for the DMF-salt solutions were calculated using Eq. [3] and [4] which were obtained by taking the natural logarithm expressions for Eq [1] and [2] and, in each case, differentiating with respect to  $1/T$  and multiplying the result by  $R$

$$E_{vis} = R d(\ln \eta) / d(1/T) \\ = R(\beta + 2\gamma/T + 3\delta/T^2 + 4\epsilon/T^3) \quad [3]$$

$$E_{con} = -R d(\ln \Lambda) / d(1/T) \\ = -R(\beta' + 2\gamma'/T + 3\delta'/T^2 + 4\epsilon'/T^3) \quad [4]$$

Table II. Parameters for viscosity data fitted to Eq. [1]

Molality	$\alpha$	$\beta \times 10^{-5}$	$\gamma \times 10^{-5}$	$\delta \times 10^{-5}$	$\epsilon \times 10^{-10}$	% Deviation	
						Mean	Max
Bu <sub>4</sub> NI							
0.0729	-6.67979	3.93703	-0.94299	1.04163	—	0.19	0.33
0.1522	-6.57489	3.87787	-0.93257	1.05150	—	0.20	0.54
0.240	-7.05236	4.39228	-1.09955	1.23844	—	0.24	0.52
0.306	-6.51537	3.92317	-0.96158	1.11743	—	0.17	0.53
0.376	-2.62177	-0.81575	1.19418	-3.19129	3.21214	0.12	0.23
0.491	-3.24929	-0.14065	0.95764	-2.86289	3.11727	0.18	0.28
0.563	-1.99624	-1.65988	1.65715	-4.28396	4.21352	0.15	0.27
0.692	-1.95899	-1.51280	1.54545	-4.00784	4.04009	0.24	0.47
0.798	-0.24693	-3.63962	2.54860	-6.09231	5.68834	0.27	0.62
0.908	-0.71064	-3.19408	2.42636	-6.01732	5.80355	0.20	0.46
1.015	-0.28967	-3.69144	2.66584	-6.52854	6.25122	0.21	0.49
1.157 <sup>(a)</sup>	-5.73477	3.60121	-0.93291	1.26618	—	0.12	0.20
KSCN							
0.1026	-6.62288	3.89224	-0.92875	1.02647	—	0.19	0.49
0.214	-7.02664	4.31806	-1.06279	1.17449	—	0.14	0.36
0.317	-6.76901	4.12704	-1.01026	1.13836	—	0.21	0.55
0.429	-6.67089	4.07384	-0.99767	1.14185	—	0.20	0.50
0.542	-6.78765	4.26466	-1.07132	1.24122	—	0.21	0.47
0.732	-2.73731	-0.74589	1.25131	-3.46193	3.55898	0.25	0.44
0.782	-1.52721	-2.23084	1.94159	-4.88339	4.68479	0.10	0.22
0.905	-1.53852	-2.21234	1.94695	-4.90874	4.71961	0.20	0.53
NH <sub>4</sub> Br							
0.1041	-6.51090	3.77465	-0.89328	0.99793	—	0.15	0.33
0.229	-7.10271	4.36206	-1.07207	1.18404	—	0.15	0.31
0.351	-4.95708	1.82308	0.06531	-1.05978	1.66561	0.16	0.28
0.488	-5.09779	2.14634	-0.12743	-0.58292	1.27185	0.14	0.30
0.628	-4.54121	1.41057	0.25742	-1.45362	2.01365	0.14	0.26
0.778 <sup>(b)</sup>	3.07716	-7.59030	4.23382	-9.18443	7.62064	0.10	0.19

<sup>(a)</sup> For 0° to 125°C only.

<sup>(b)</sup> For -50° to 100°C only.

Table III. Parameters for molar conductance data fitted to Eq. [2]

Molality	$\alpha'$	$\beta' \times 10^{-3}$	$\gamma' \times 10^{-6}$	$\delta' \times 10^{-8}$	$\epsilon' \times 10^{-10}$	% Deviation	
						Mean	Max
<b>Bu<sub>4</sub>NI</b>							
0.0729	-8.32474	2.33964	-0.50130	0.52711	0.21833	0.16	0.33
0.1522	-7.72966	1.82593	-0.26312	0.02933	0.62895	0.16	0.32
0.240	-2.79076	-3.83966	2.21576	-4.74978	4.07944	0.06	0.15
0.306	-5.23386	-0.92125	0.95793	-2.36085	2.41081	0.06	0.13
0.376	-5.60280	-0.41944	0.74239	-1.95017	2.13994	0.18	0.37
0.491	-3.57716	-2.91577	1.91897	-4.36575	4.00476	0.14	0.35
0.563	-3.79676	-2.55974	1.75680	-4.05099	3.80564	0.18	0.33
0.692	-4.63305	-1.45158	1.26171	-3.08219	3.14785	0.22	0.48
0.798	-4.57179	-1.66310	1.45639	-3.67086	3.76724	0.24	0.45
0.908	-3.37465	-3.16124	2.17327	-5.15866	4.93877	0.16	0.40
1.015	-2.83439	-3.78326	2.46618	-5.76868	5.44788	0.21	0.52
1.157 <sup>(a)</sup>	-25.30201	25.96365	-12.17285	26.04913	20.27341	0.11	0.21
<b>KSCN</b>							
0.1026	-8.23446	2.28513	-0.55854	0.73166	0.01156	0.23	0.37
0.214	-7.61868	1.80197	-0.35324	0.30170	0.38149	0.22	0.47
0.317	-5.01662	-1.03852	0.84785	-1.94275	1.95624	0.14	0.26
0.429	-3.88732	-2.20522	1.33952	-2.87135	2.63502	0.16	0.34
0.542	-5.97288	0.33508	0.23886	-0.78988	1.20201	0.15	0.36
0.732	-5.35378	-0.35407	0.58063	-1.52751	1.82042	0.14	0.29
0.782	-1.78965	-4.64481	2.51306	-5.35911	4.65215	0.12	0.27
0.905	-1.64330	-4.77686	2.58138	-5.52058	4.82065	0.35	0.56
<b>NH<sub>4</sub>Br</b>							
0.1041	1.76140	-7.87552	3.66932	-7.26734	5.59581	0.04	0.10
0.229	-1.85282	-3.34385	1.77170	-3.68889	3.14916	0.12	0.28
0.351	-2.28834	-2.63240	1.47104	-3.14519	2.81267	0.14	0.30
0.488	-4.35162	29.41617	0.27200	-0.77098	1.09092	0.19	0.46
0.628	-6.23888	2.23322	-0.62549	0.81643	0.08145	0.19	0.41
0.778	-3.14582	-1.38116	0.98414	-2.33969	2.40549	0.24	0.53

<sup>(a)</sup> For 0° to 125°C only.

Table IV. Energies of activation of viscous flow and conductance,\* and their ratios, for selected solutions and temperatures

Molality	-25°			25°			75°		
	$E_{vis}$	$E_{con}$	$E_{vis}/E_{con}$	$E_{vis}$	$E_{con}$	$E_{vis}/E_{con}$	$E_{vis}$	$E_{con}$	$E_{vis}/E_{con}$
<b>Bu<sub>4</sub>NI</b>									
0.0729	2805	2858	0.981	2239	2156	1.038	2182	1930	1.130
0.491	3557	3506	1.015	2635	2518	1.046	2443	2183	1.119
1.015	4673	4471	1.045	3165	3008	1.052	2762	2524	1.094
<b>KSCN</b>									
0.1026	2797	2739	1.021	2238	2037	1.099	2181	1785	1.222
0.542	3333	3097	1.076	2518	2157	1.167	2350	1772	1.326
0.905	3813	3480	1.096	2791	2352	1.187	2576	1903	1.383
<b>NH<sub>4</sub>Br</b>									
0.1041	2855	2349	1.215	2286	1707	1.339	2212	1376	1.608
0.488	3196	2625	1.218	2471	1785	1.384	2339	1426	1.640
0.778	3450	2879	1.198	2614	1897	1.377	2430	1513	1.606

\* In calories.

Table V. Parameters for density data fitted to Eq. [5]

Molality	$a$	$-b \times 10^7$	$-c \times 10^6$	% Deviation	
				Mean	Max
<b>Bu<sub>4</sub>NI</b>					
0.0729	1.2174	8420	191	0.03	0.05
0.1522	1.2216	8372	189	0.03	0.05
0.240	1.2283	8521	150	0.04	0.09
0.306	1.2366	8800	105	0.03	0.06
0.376	1.2329	8370	158	0.04	0.07
0.491	1.2448	8734	91	0.04	0.05
0.563	1.2494	8841	68	0.03	0.06
0.692	1.2543	8799	63	0.03	0.06
0.798	1.2592	8851	43	0.04	0.07
0.908	1.2664	9021	11	0.04	0.06
1.015	1.2676	8888	18	0.05	0.07
1.157	1.2639	8356	89	0.03	0.09
<b>KSCN</b>					
0.1026	1.2152	8250	216	0.03	0.05
0.214	1.2212	8327	189	0.03	0.05
0.317	1.2257	8293	188	0.03	0.05
0.429	1.2306	8302	174	0.03	0.06
0.542	1.2433	8311	83	0.03	0.06
0.732	1.2493	8636	106	0.03	0.06
0.782	1.2531	8758	79	0.04	0.06
0.905	1.2581	8724	78	0.03	0.04
<b>NH<sub>4</sub>Br</b>					
0.1041	1.2200	8415	195	0.03	0.06
0.229	1.2251	8282	210	0.04	0.05
0.351	1.2324	8322	196	0.05	0.08
0.488	1.2412	8367	188	0.03	0.05
0.628	1.2250	8804	110	0.03	0.07
0.778	1.2621	8727	120	0.04	0.06

Values of  $E_{vis}$  and  $E_{con}$  at -25°, 25°, and 75° calculated using Eq. [3] and [4] are presented in Table IV for a few typical solutions of the three salts in DMF. Generally, the values of  $E_{vis}$  and  $E_{con}$  increase with increasing salt concentration and decreasing temperature. Except for the most dilute Bu<sub>4</sub>NI-DMF solutions at the lowest temperatures,  $E_{vis} > E_{con}$ . Values of  $E_{vis}/E_{con}$  (also included in Table IV) in some cases are close to unity and for all solutions increase with increasing temperature.

Values of the molar conductance-viscosity product,  $\Lambda\eta$ , have ranges of 23.0-40.6, 32.2-53.9, and 10.7-33.8 ohm<sup>-1</sup>-cm<sup>2</sup>-mole<sup>-1</sup> cP for DMF solutions of Bu<sub>4</sub>NI, KSCN, and NH<sub>4</sub>Br, respectively. For the four most dilute Bu<sub>4</sub>NI-DMF solutions, the  $\Lambda\eta$  product exhibits a maximum near -25° or 0°; for all other solutions of the three salts, the  $\Lambda\eta$  product decreases with increasing temperature and increasing salt concentration. The relatively low products for the NH<sub>4</sub>Br-DMF solutions are attributed primarily to the low values of  $\Lambda$  for NH<sub>4</sub>Br.

The results for both activation energies and  $\Lambda\eta$  products generally reflect closer correlation between conductance and viscosity behavior for the Bu<sub>4</sub>NI-DMF system than for the KSCN-DMF and NH<sub>4</sub>Br-DMF systems.

Table VI. Parameters for viscosity data fitted to Eq. [6]

Temp. °C	c <sub>1</sub>	c <sub>2</sub>	c <sub>3</sub>	c <sub>4</sub>	c <sub>5</sub>	% Deviation	
						Mean	Max
<b>Bu<sub>4</sub>NI</b>							
-50 <sup>(a)</sup>	6.41064	-26.46795	95.47505	-131.11560	78.57181	0.34	1.10
-25 <sup>(a)</sup>	2.55284	-6.41797	21.91092	-25.75996	14.15160	0.23	0.58
0	1.30619	-1.37847	5.26508	-5.27606	3.11139	0.29	0.86
25	0.97528	-1.32846	4.29308	-4.09208	1.94320	0.15	0.28
50	0.67858	-0.56305	2.00400	-1.76582	0.85188	0.20	0.45
75	0.50383	-0.19283	0.84151	-0.57095	0.29931	0.16	0.32
100	0.43238	-0.31328	1.02566	-0.79959	0.33578	0.12	0.37
125	0.34375	-0.16783	0.60869	-0.41139	0.17083	0.18	0.43
<b>KSCN</b>							
-50	4.38290	-7.71205	3.20801	-42.96557	28.28358	0.20	0.64
-25	2.91676	-8.55493	25.42371	-28.20817	13.33046	0.08	0.18
0	1.27800	-1.12263	4.24967	-4.24634	2.35721	0.21	0.51
25	1.08323	-2.04301	6.02563	-6.30015	2.83674	0.07	0.13
50	0.55492	0.36107	-0.41385	0.69732	-0.10536	0.09	0.20
75	0.43671	0.26701	-0.25043	0.36682	-0.02320	0.05	0.10
100	0.39150	-0.02378	0.30461	-0.12483	0.08768	0.10	0.19
125	0.32420	-0.00651	0.16848	0.01569	0.00735	0.11	0.25
<b>NH<sub>4</sub>Br</b>							
-50	7.84156	-31.73239	93.66864	-109.19230	51.06860	0.06	0.12
-25	2.95857	-7.41657	20.08976	-20.31220	8.82221	0.22	0.44
0	1.55737	-2.64313	8.25324	-8.38331	3.64842	0.16	0.32
25	1.11844	-2.29168	6.89750	-7.73695	0.34922	0.06	0.13
50	0.56027	0.35277	-0.32016	0.33634	0.09432	0.10	0.21
75	0.50652	-0.22447	1.01540	-1.10020	0.56905	0.03	0.05
100	0.49392	-0.79717	2.41538	-2.67844	1.18139	0.00	0.00
125 <sup>(b)</sup>	0.32918	-0.03527	0.20221	-0.02443	—	0.02	0.04

<sup>(a)</sup> Does not include datum for 1.157 molal solution.<sup>(b)</sup> Does not include datum for 0.778 molal solution.

Table VII. Parameters for molar conductance data fitted to Eq. [6]

Temp. °C	c <sub>1</sub>	c <sub>2</sub>	c <sub>3</sub>	c <sub>4</sub>	c <sub>5</sub>	% Deviation	
						Mean	Max
<b>Bu<sub>4</sub>NI</b>							
-50 <sup>(a)</sup>	16.550	-30.577	23.817	-12.456	3.927	0.30	0.65
-25 <sup>(a)</sup>	32.942	-58.072	50.968	-31.780	10.160	0.11	0.33
0	51.623	-85.835	72.721	-41.547	11.710	0.14	0.24
25	73.873	-127.018	121.486	-74.869	20.859	0.16	0.46
50	99.047	-185.180	212.635	-151.046	45.329	0.13	0.45
75	124.253	-240.096	294.455	-217.258	66.429	0.17	0.57
100	148.772	-286.487	349.128	-249.881	73.560	0.26	0.95
125	183.038	-391.824	534.685	-406.414	123.350	0.32	0.94
<b>KSCN</b>							
-50	21.652	-39.060	54.890	-55.467	21.794	0.26	0.72
-25	38.066	-44.887	39.268	-39.294	16.544	0.05	0.12
0	66.620	-119.211	189.558	-198.228	79.779	0.11	0.25
25	86.425	-118.740	139.092	-139.748	49.863	0.16	0.35
50	120.922	-216.048	329.506	-319.245	121.420	0.05	0.12
75	155.534	-314.123	524.653	-524.951	202.732	0.08	0.14
100	171.670	-277.589	356.680	-307.477	111.254	0.05	0.11
125	198.700	-299.722	318.203	-230.281	76.258	0.23	0.40
<b>NH<sub>4</sub>Br</b>							
-50	16.352	-35.558	33.823	-12.798	—	0.07	0.16
-25	29.654	-62.097	57.594	-20.692	—	0.17	0.37
0	44.593	-96.737	95.136	-35.762	—	0.19	0.40
25	57.467	-132.527	134.591	-51.761	—	0.16	0.36
50	73.700	-163.125	164.712	-62.229	—	0.23	0.52
75	88.176	-200.067	207.100	-79.637	—	0.24	0.43
100	99.662	-225.220	232.329	-88.705	—	0.21	0.48
125	110.702	-225.718	272.978	-107.871	—	0.02	0.05

<sup>(a)</sup> Does not include datum for 1.157 molal solution.

The densities for the DMF-salt solutions as a function of temperature are described excellently by the following quadratic equation

$$\rho = a + bT + cT^2 \quad [5]$$

Parameters for fitting the density data to Eq. [5] along with deviation data are compiled in Table V.

The viscosity, molar conductance, and density data as similar functions of molality can be described excellently by the following general polynomial equation in which  $Y = \eta$  or  $\Lambda$  or  $\rho$

$$Y = c_1 + c_2m^{1/2} + c_3m + c_4m^{3/2} + \dots \quad [6]$$

Results for fitting the experimental data by normal least squares analyses to Eq. [6], together with corresponding deviation data, are summarized in Tables VI-VIII, respectively.

Equations are not provided for calculating the specific conductances ( $\kappa$ ) of the salts in DMF as functions of temperature and molality; however,  $\kappa$  can be calculated from molar conductance and other data as follows

$$\kappa = \Lambda C/1000 = \Lambda \rho m / (1000 + mM_2) \quad [7]$$

in which  $C$  is the molarity (moles of solute per liter of solution) and  $m$  is the molality (moles of solute per 1000g of solvent). For the NH<sub>4</sub>Br-DMF system,  $\kappa$  exhibits a maximum for the 0.732 molal solution at -50° and otherwise increases continuously with increasing concentration at all other temperatures. For the Bu<sub>4</sub>NI-DMF system,  $\kappa$  exhibits maximum values for 0.376, 0.563, 0.692, 0.908, and 1.015 molal solutions at -50°, -25°, 0°, 25°, and 50°, respectively, whereas  $\kappa$  increases with increasing concentration at 75° and higher temperatures. This type of behavior for the Bu<sub>4</sub>NI-



Table VIII. Parameters for density data fitted to Eq. [6]

Temp, °C	c <sub>1</sub>	c <sub>2</sub> × 10 <sup>3</sup>	c <sub>3</sub> × 10 <sup>2</sup>	c <sub>4</sub> × 10 <sup>2</sup>	% Deviation	
					Mean	Max
Bu <sub>4</sub> NI						
-50	1.01514	-0.551	8.205	-2.807	0.01	0.04
-25	0.99193	-5.839	9.256	-3.390	0.02	0.06
0	0.96674	2.080	8.163	-2.783	0.02	0.03
25	0.94350	1.568	8.430	-2.866	0.01	0.03
50	0.91902	3.126	8.341	-2.762	0.01	0.04
75	0.89621	-4.498	9.808	-3.460	0.03	0.10
100	0.86942	8.454	8.077	-2.526	0.02	0.05
125	0.84518	-1.501	10.178	-3.581	0.01	0.04
KSCN						
-50	1.01702	-9.261	7.012	-1.368	0.01	0.02
-25	0.99108	-0.007	5.704	-7.514	0.01	0.02
0	0.96764	-0.669	6.162	-1.076	0.01	0.02
25	0.94322	6.772	4.848	-0.281	0.02	0.05
50	0.91692	1.722	3.280	0.589	0.01	0.02
75	0.89337	13.368	4.202	0.099	0.01	0.03
100	0.87031	3.462	6.504	-1.227	0.02	0.04
125	0.84416	5.324	6.425	-1.104	0.02	0.07
NH <sub>4</sub> Br						
-50	1.01967	-16.743	9.147	-2.074	0.01	0.01
-25	0.99516	-18.374	9.842	-2.606	0.00	0.01
0	0.97352	-27.604	11.356	-3.371	0.01	0.02
25	0.94458	3.660	6.061	-0.535	0.01	0.03
50	0.92303	-11.387	8.889	-2.131	0.01	0.02
75	0.89720	-3.461	7.825	-1.626	0.02	0.04
100	0.87405	-11.751	9.197	-2.171	0.01	0.01
125	0.85032	-21.021	10.698	-2.885	0.00	0.00

DMF system has been observed previously for other nonaqueous systems (14) but differs from that reported for solutions of electrolytes in water and ethanol for which a maximum in  $\kappa$  tends to occur at approximately the same concentration at each temperature (15, 16). For any electrolyte solution in which  $\kappa$  exhibits a maximum as a function of concentration at some temperature, it is noteworthy that  $\kappa$  decreases with increasing concentration for concentrations above the maximum. In such a case, the effect of introducing additional conducting particles or ions is more than counterbalanced by the effect of an increase in viscosity and a concomitant decrease in ionic mobilities, or by the effect of increased ionic association, or both, resulting in a net decrease in the specific conductance of the system.

Related conductance-viscosity studies on moderately concentrated solutions of electrolytes in other pure and mixed nonaqueous solvents over the same 175° range will be presented in subsequent articles in this series.

#### Acknowledgment

This work was supported in major part by Themis Contract DAA-69-C-0366.

Manuscript submitted July 23, 1973; revised manuscript received March 11, 1974.

Any discussion of this paper will appear in a Discussion Section to be published in the June 1975 JOURNAL. All discussions for the June 1975 Discussion Section should be submitted by Feb. 1, 1975.

#### SYMBOLS

$\Lambda$	molar conductance, $\text{ohm}^{-1}\text{-cm}^2\text{-mole}^{-1}$
$\eta$	absolute viscosity of solution, cP
$\eta_0$	absolute viscosity of solvent, cP
$T$	temperature, °K
$R$	molar gas constant, $\text{cal-mole}^{-1}\text{-deg}^{-1}$
$E_{\text{vis}}$	activation energy of viscous flow, cal
$E_{\text{con}}$	activation energy of conductance, cal
$\rho$	density, $\text{g-mliter}^{-1}$
$Y$	general variable in Eq. [6]
$m$	molality, $\text{mole-kg}^{-1}$
$C$	molarity, $\text{mole-liter}^{-1}$
$\kappa$	specific conductance, $\text{ohm}^{-1}\text{-cm}^{-1}$
$M_2$	molecular weight of salt, $\text{g-mole}^{-1}$
$\ln$	logarithm to base $e$
$\log$	logarithm to base 10
$\alpha, \beta, \gamma, \delta, \epsilon$	constants in Eq. [1] and [3]
$\alpha', \beta', \gamma', \delta', \epsilon'$	constants in Eq. [2] and [4]
$a, b, c$	constants in Eq. [5]
$c_1, c_2, c_3, c_4$	constants in Eq. [6]

#### REFERENCES

- D. P. Ames and P. G. Sears, *J. Phys. Chem.*, **59**, 16 (1955).
- L. R. Dawson and W. W. Wharton, *This Journal*, **107**, 710 (1960).
- C. M. French and K. H. Glover, *Trans. Faraday Soc.*, **51**, 1418 (1955).
- J. E. Prue and P. J. Sherrington, *ibid.*, **57**, 1795 (1961).
- G. Jones and D. M. Bollinger, *J. Am. Chem. Soc.*, **57**, 280 (1935).
- J. E. Lind, Jr., J. J. Zwolenik, and R. M. Fuoss, *ibid.*, **81**, 1557 (1959).
- E. W. Washburn, *ibid.*, **38**, 2431 (1916).
- P. G. Sears and W. C. O'Brien, *J. Chem. Eng. Data*, **13**, 112 (1968).
- P. G. Sears, W. D. Siegfried, and D. E. Sands, *ibid.*, **9**, 261 (1964).
- P. G. Sears, R. R. Holmes, and L. R. Dawson, *This Journal*, **102**, 145 (1955).
- P. G. Sears and L. R. Dawson, *J. Chem. Eng. Data*, **13**, 124 (1968).
- L. A. Girifalco, *J. Chem. Phys.*, **23**, 2446 (1955).
- W. E. Wentworth, *J. Chem. Educ.*, **42**, 96, 162 (1965).
- P. G. Sears, W. W. Wharton, and L. R. Dawson, *This Journal*, **102**, 430 (1955).
- A. N. Campbell and W. G. Paterson, *Can J. Chem.*, **36**, 1004 (1958).
- A. Than and E. S. Amis, *J. Inorg. Nucl. Chem.*, **31**, 1685 (1969).

# Investigation of Subvalent Ion Effects During Aluminum Anodization in Molten NaCl-AlCl<sub>3</sub> Solvents

R. J. Gale and R. A. Osteryoung\*

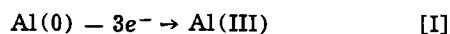
Department of Chemistry, Colorado State University, Fort Collins, Colorado 80521

The publication costs of this article have been partially assisted by the Colorado State University.

## ABSTRACT

Anode current yield variations with current density have been measured in the nominal 1:1 and 1:2 molar NaCl-AlCl<sub>3</sub> molten electrolytes by an anodic stripping procedure. In the range of apparent current densities 0.03-6.30 mA cm<sup>-2</sup>, the *brutto* electrode reaction was found to be a faradaic three-electron oxidation. Subvalent ion effects could not be positively established. Experimental difficulties in removing final traces of impurities limit the precision of coulometric determinations in these systems; however, the anodic stripping procedure does provide a sensitive means of detecting corrosion losses of aluminum.

It has recently been reported (1, 2) that the anode current yields for aluminum dissolution in molten NaCl-AlCl<sub>3</sub> solvents are appreciably higher at low current densities than required for the three-electron oxidation reaction



As early as 1857 (3), high current yields for the anodic dissolution of aluminum were recorded, and they have since been observed for a variety of electrolytes; aqueous (4, 5), organic (6-8), and nonaqueous (1, 2, 9). In general, the alternative explanations to account for these deviations from a faradaic three-electron oxidation are (i) the formation of subvalent aluminum ions, (ii) spallation or electrophoretic removal of colloidal aluminum particles, and (iii) chemical corrosion, i.e., direct electrolyte or impurity attack on the anode surface.

Delimarskii *et al.* (1) found that the anode current yields in the NaCl-AlCl<sub>3</sub> (1:2M) electrolyte at 160°C were dependent on the anodic current densities for the range 10-150 mA cm<sup>-2</sup> and, for all experiments, the anode current efficiencies were usually >100% and exceeded the cathode current efficiencies (weight losses corresponding to faradaic three-electron oxidation of aluminum are 100%). From studies in the equimolar NaCl-AlCl<sub>3</sub> melt at 300°C, Storozhenko (2) determined current yields >100% for the anodic dissolution of annealed aluminum anodes and, similarly, the current yields increased with decreasing anodic current densities, to reach a value 230% at the minimum investigated current density of 0.11 mA cm<sup>-2</sup>. Delimarskii and co-workers considered that chemical corrosion or losses from spallation were unable to explain the magnitude of their anode current yields, whereas the results of Storozhenko are stated to have been corrected for losses due to chemical corrosion. Accordingly, both sets of data were interpreted by the assumption that considerable quantities of univalent aluminum ion are formed under the conditions of anodization, especially at current densities of 10 mA cm<sup>-2</sup> and lower.

It was of interest to examine this phenomenon in more detail as the presence of free or complex univalent aluminum ion in larger than trace quantities might have significant consequences in many of the chemical or electrochemical studies, in particular

chloroaluminate solvents, e.g., materials corrosion in aluminum deposition or battery electrolyte applications. The introduction of univalent aluminum would arise from commonly used melt purification procedures, which involve either equilibration with metallic aluminum (10) or preelectrolyses between aluminum electrodes (2, 11). In addition, on the basis of the above experimental findings (1, 2), potentiometric techniques which involve anodization to determine melt pCl<sup>-</sup> and alkali metal chloride-AlCl<sub>3</sub> equilibrium compositions, such as the one adopted in this laboratory (12), would be susceptible to the anode current yield variations with current density. In order to reexamine the dependence of the anode current yields on current densities, a coulometric procedure was chosen in which a constant quantity of aluminum was electrodeposited on an inert electrode substrate and then stripped from the electrode. This method enabled precise *in situ* measurements, whereas the precision of gravimetric methods is limited by the presence on the electrodes of solidified salt which has to be removed before weighing or accounted for quantitatively.

## Experimental

*Melt purification.*—Preelectrolyses were carried out in a cell, similar in all essential details to one previously described (11), and under a purified nitrogen atmosphere (Vacuum/Atmospheres Company dry box with HE-493 Dri-Train). To the cell, containing an aluminum anode rod (6.35 mm diameter, Johnson Matthey Specpure grade) and an Al wire spiral cathode (23 mil, Alfa Inorganics, m5N purity), were added 2 g-mole quantities of aluminum chloride (Fluka A.G., iron-free) and sodium chloride (Fisher Scientific Company) and the temperature was raised to between 175° and 200°C. Before electrolysis was commenced, dark coatings formed on both electrodes in the molten electrolyte; Uhlig (13) noted that similar coatings were formed for the 40-60 mole per cent (m/o) NaCl-AlCl<sub>3</sub> system. The impure, straw colored melt was then electrolyzed for 10 days with an anodic current density of ~0.25 mA cm<sup>-2</sup>, to produce a clear, colorless melt. At the end of the electrolysis, the anode surface was dark and pulverulent. No dark coating appeared on a clean Al anode rod introduced into the purified melt, nor did one occur with subsequent anodization of this rod. Attempts to analyze these dark coatings are described in a later section of this paper.

\* Electrochemical Society Active Member.  
Key words: fused salts, NaCl-AlCl<sub>3</sub> melt, aluminum electrode, subvalent aluminum, Al(I) ion.

**Gravimetric coulometry.**—The current efficiency for Al deposition was determined with a Sargent coulometric current source. Aluminum foil samples (10 mil, Alfa Inorganics, m5N purity) were weighed and used as cathodes at a current density of  $1.4 \text{ mA cm}^{-2}$  (geometrical area) for 20,000 sec ( $i = 48.25 \text{ mA}$ ). The aluminum electrocrystallized from this purified melt in a fine, dendritic form, cf. (14). Samples were carefully removed from the melt and placed in a fritted-glass sintered crucible, initially washed in dried dimethyl sulfoxide, thoroughly washed with distilled water, and finally dried *in vacuo* and reweighed. The cathodic deposition efficiency calculated on the basis of three electrons was  $100.0 \pm 0.4\%$  (standard deviation  $\sigma$ , five experiments).

**Anodic stripping.**—Preliminary deposition and stripping experiments were made in the purification cell, at  $175^\circ \pm 2^\circ\text{C}$ , with a PAR Model 170 electrochemistry system (Princeton Applied Research Corporation) in the constant current mode. A multipurpose instrument (15) coupled to a Houston Instruments X-Y recorder, Model 2000, was used to record cyclic voltammograms. The reference electrode comprised a spiral of Al wire (Alfa Inorganics, m5N purity) contained in a fine fritted-glass sintered compartment; the auxiliary electrode was an Al wire spiral immersed in the bulk solution. Two types of solid working electrodes have been used: (i) a  $\frac{1}{8}$  in. diameter tungsten rod electrode (Alfa Inorganics, m3N8 purity), and (ii) a 3 mm diameter vitreous carbon rod electrode (Atomergic Chemetals Company, Type V 25-52). The tungsten rod was sealed into a Pyrex glass tube using a bead of uranium glass, ground flat on an emery wheel, and polished with 600 grit silicon carbide powder. Final treatment consisted of lapping on a polishing wheel to a mirror-bright finish with Type B Alumina powder (Fisher Scientific Company), thoroughly rinsing with distilled water, and drying at  $110^\circ\text{C}$  *in vacuo*. The vitreous carbon electrode was sealed into a Pyrex glass tube with the procedure described by Gupta (16), and its surface was prepared in an identical manner to that of the tungsten electrode. These electrodes were immersed into the molten electrolyte at least 2 hr before commencement of experiments, and, immediately prior to each experiment, they were treated by cyclic potential sweeps from  $+0.40$  to  $+1.80\text{V}$  vs. Al reference in similar melt composition, for a few minutes, to minimize effects from electroactive impurities. Cyclic voltammograms shown in Fig. 1 indicate the extent to which the background currents vary when these

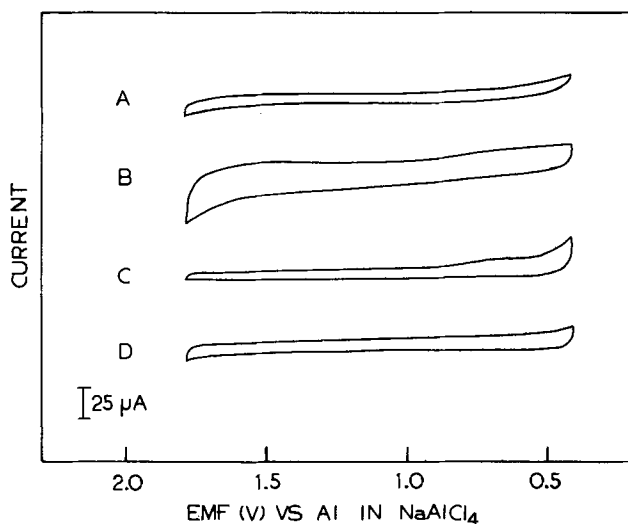


Fig. 1. Cyclic voltammetry of melt background; sweep rate  $\nu = 444 \text{ mV sec}^{-1}$ ; (A) C electrode,  $t = 0$ ; (B) C electrode,  $t = 24$  hr; (C) W electrode,  $t = 0$ ; (D) W electrode,  $t = 24$  hr; C electrode area,  $0.071 \text{ cm}^2$ ; W electrode area,  $0.079 \text{ cm}^2$ .

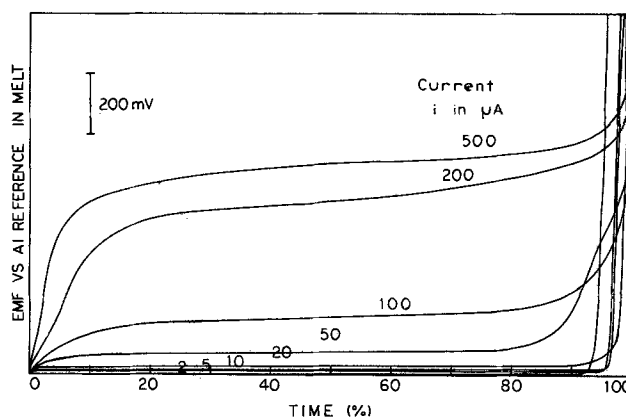


Fig. 2. Anodic stripping curves at various current densities in melt A, W electrode.

electrodes were immersed for 24 hr. The results of the preliminary experiments are illustrated in Fig. 2 and summarized in Table I. Cathodic depositions were made at  $100 \mu\text{A}$  currents for 100 sec and the aluminum was immediately stripped at 2, 5, 10, 20, 50, 100, 200, and  $500 \mu\text{A}$  anodic currents with appropriate recorder time base settings. The transition time,  $\tau$ , was determined from the emf/time curves by extrapolation of the maximum gradient values at the completion of stripping. The precision of the technique is estimated to be of the order  $\pm 1\%$  for all current densities used; however reproducibility was slightly better for the tungsten electrode than for the carbon electrode, which may have a higher content of electroactive impurities. The composition of the melt used for preliminary experiments, melt A, was calculated to have a  $p\text{Cl}^-$  of 1.31 by the potentiometric-anodization procedure of Boxall *et al.* (12), using an assembly program for a PDP-12 digital computer.

**Corrosion experiments.**—It was of importance to investigate whether or not the deviations from 100% relative efficiencies in Table I at the lower current densities represented a dependence of the current yield on the anodic current density because of a greater contribution from subvalent ion formation to the net dissolution mechanism, or indeed, if the relative efficiency loss could be ascribed to side reactions or corrosion processes. Aluminum was deposited on the tungsten electrode at  $100 \mu\text{A}$  for 100 sec and the electrode was left on open circuit for 1000 and 5000 sec before stripping at an anodic current of  $100 \mu\text{A}$ . The measured relative efficiencies were  $97.6 \pm 0.5\%$  ( $\sigma$ , five experiments) and  $91.1 \pm 0.8\%$  ( $\sigma$ , five experiments) for 1000 and 5000 sec, respectively, which indicated

Table I. Anodic stripping efficiency variation with current density as percentage of the cathodic deposition charge at  $175^\circ\text{C}$

Apparent current density* ( $\text{mA cm}^{-2}$ )	W electrode $\tau$ (%)	C electrode $\tau$ (%)
0.03	95.8	89.5
0.06	97.8	95.7
0.13	99.2	97.2
0.25	99.0	98.8
0.63	99.8	98.6
1.26	100.0	100.0
2.52	100.0	99.8
6.30	100.0	98.6

\* Calculated for the geometrical area of the W electrode,  $\frac{1}{8}$  in. diameter.

that under these conditions corrosion losses of the freshly deposited aluminum were occurring. The sources of oxidizing agents in a "purified" melt are either (i) the cell and its component parts, (ii) the electrode substrates or their insulation sheaths, (iii) the dry box atmosphere, or (iv) residual impurities in the chemicals. Certain of these variables could be excluded by redesign and Fig. 3 is a schematic of a revised cell. Experiments with melt compositions B, C, D, and E were made in this cell. The melt compositions were varied by the addition of solid  $\text{AlCl}_3$ , followed by preelectrolyses.

**Analyses of dark coatings.**—There have been reports that a dark deposit forms on the surfaces of aluminum anodes (1, 2) in alkali metal chloride- $\text{AlCl}_3$  electrolytes. Delimarskii *et al.* have suggested that this is in good agreement with the hypothesis of disproportionation of monovalent aluminum during anodization, according to reaction [V], to produce finely dispersed aluminum metal. Correspondingly, Storozhenko suggested that, at current densities  $<60\text{--}80 \text{ mA cm}^{-2}$ , the fraction of univalent aluminum ions became greater than the equilibrium value and that aluminum powder appeared in the anolyte region and on the anode. As no dark coatings were observed to form on aluminum surfaces after melts had been purified by sufficient periods of preelectrolyses, it is possible that the coatings are associated with an impurity in the system which diffuses or is electrophoretically attracted toward the anode. To obtain samples for analyses, the dark coating was scraped from an anode and extracted from the solidified salt with liquid  $\text{SO}_2$  (17). A qualitative emission spectrographic determination showed

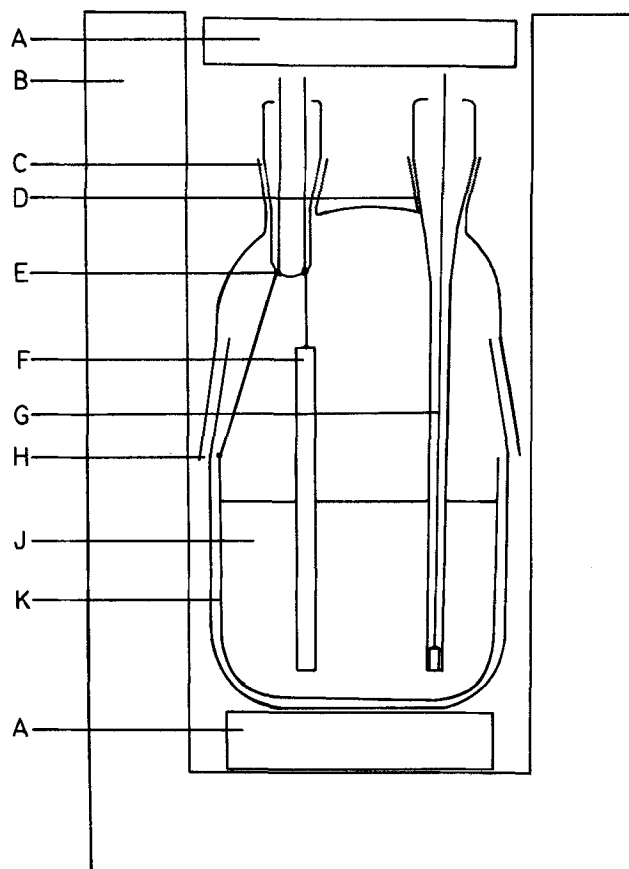


Fig. 3. Revised electrochemical cell. A, Asbestos heat insulation; B, furnace; C, 14/20 ground joint for reference and counterelectrodes; D, 14/20 ground joint for working electrode; E, uranium glass-tungsten seals; F, Al reference electrode (unshathed); G, W rod working electrode sealed into Pyrex tube with uranium glass; compartment for thermocouple (not shown); H, 45/50 ground joint; J, melt; K, Al lining for cell, 10 mil (Alfa Inorganics; m5N purity).

the major metallic constituents in the residue to be Si, B, Sn, Mn, and Al, in agreement with the results of Fung, Mamantov, and Young (10) for analyses of dark-brown deposits found in  $\text{NaCl-AlCl}_3$  melts with elemental aluminum.

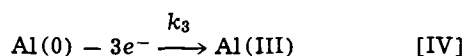
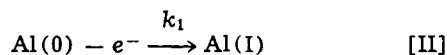
## Results and Discussion

The data in Tables I and II indicate that there is no dependence of the anode current yield on the current density, within the experimental accuracy of these results, if the variations from 100% relative anode dissolution efficiencies are ascribed as due entirely to corrosion losses. As the cathodic current yield was determined to be  $100.0 \pm 0.4\%$  at  $175^\circ\text{C}$  on the basis of three electrons, the anode dissolution for the current density range  $0.03\text{--}6.30 \text{ mA cm}^{-2}$  may be described by the reverse of this reaction. The magnitude of the mean corrosion rate found in melt A at  $175^\circ\text{C}$  ( $\sim 10\%$  in 5000 sec) represents an aluminum loss of  $9 \times 10^{-12} \text{ mole cm}^{-2} \text{ sec}^{-1}$  and compares to a minimum corrosion value quoted by Delimarskii *et al.* (1) of  $1 \times 10^{-9} \text{ mole cm}^{-2} \text{ sec}^{-1}$ . Skala (18) has reported a corrosion rate for iron in a ternary  $\text{KCl-NaCl-AlCl}_3$  melt (14-22-64 m/o) of  $2 \times 10^{-10} \text{ mole cm}^{-2} \text{ sec}^{-1}$  and has suggested that the most active impurities to cause the oxidative losses are hydrogen compounds. Del Duca (19) found anode current efficiencies of  $100 \pm 1\%$  and  $98 \pm 2\%$  at current densities 0.3 and  $0.5 \text{ mA cm}^{-2}$ , respectively, for aluminum dissolution in an equimolar  $\text{NaCl-AlCl}_3$  melt. Figure 2 illustrates that the anodic polarization increases to higher potential values *vs.* Al reference with increase in the anodic stripping current density. In melt A, the dissolution of aluminum from a charge of  $\sim 1 \text{ mcoulomb}$  polarized the Al electrode about  $+600 \text{ mV}$  at  $6.30 \text{ mA cm}^{-2}$ , which very approximately represents the emf difference between an Al electrode in  $\text{NaCl}$  saturated  $\text{NaCl-AlCl}_3$  and one in the 1:2M melt composition. The corresponding polarization increase found in the nominal 1:2M melt E was of the order  $+50 \text{ mV}$  at  $500 \mu\text{A}$ . Holleck and Giner (20) have reported similar passivation phenomena of the Al electrode in a ternary  $\text{KCl-NaCl-AlCl}_3$  melt.

Table II. Anodic stripping efficiency variation with current density as percentage of the cathodic deposition charge; aluminum-lined cell, W electrode

Apparent current density* ( $\text{mA cm}^{-2}$ )	Melt B $\tau$ (%)	Melt C $\tau$ (%)	Melt D $\tau$ (%)	Melt E $\tau$ (%)
0.03	99.8	94.2	99.5	98.2
0.06	98.6	92.3	98.7	97.5
0.13	99.5	98.0	97.7	98.2
0.25	99.5	98.9	99.2	98.0
0.63	100.0	97.6	99.8	97.6
1.26	100.0	96.7	98.6	97.6
2.52	99.4	98.8	97.8	97.5
6.30	99.0	99.4	98.7	97.5
Emf <i>vs.</i> satd. reference, $175^\circ\text{C}$ (mV)	+39.5	+39.5	+433	+610
Approx. p Cl-, $175^\circ\text{C}$	1.31	1.31	4.75	6.25
Temp, $^\circ\text{C}$	175	300	175	165
Relative yield after corrosion	Not determined	$93 \pm 5$ (5000 sec)	$98 \pm 1$ (1000 sec)	$98 \pm 1$ (1000 sec)

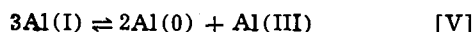
Several factors may contribute to the discrepancy between the current yields determined by this study and the results obtained earlier (1, 2); in previous studies higher contents of impurities may have been present and the corrosion rates at open circuit may have been smaller than those experienced under conditions of anodic polarization. In addition, it is feasible that the systems may not have achieved an equilibrium state with respect to subvalent aluminum formation. Wagner (21) has derived illustrative equations to determine current yields from electrolyses of solutions containing an electroactive metal present in several cationic valency states. Following this example, and disregarding all reactions of the divalent aluminum state to simplify discussion, the reactions at the anode can be written



where  $k_1$ ,  $k_2$ , and  $k_3$  are the net rates of the reactions in mole unit area<sup>-1</sup> sec<sup>-1</sup>. Then, within the restrictions imposed by Nernstian behavior, diffusion, transference, and ionic charge balance of the Wagner steady-state model, the number of moles,  $\epsilon$ , of aluminum dissolved at the anode per faraday of electricity passed is given by the expression

$$\epsilon = \frac{k_1 + k_3}{k_1 + 2k_2 + 3k_3}$$

The limitations implicit from a consideration of the electrode kinetics in this manner should be recognized. (i) If  $k_2 = k_3 = 0$ , Al(I) ions will be formed in accordance with reaction II, and  $\epsilon = 1$ . (ii) If  $k_1 = k_2 = 0$ , then Al(III) ions will be formed by reaction [IV] only, and  $\epsilon = 1/3$ . (iii) If  $k_1 \sim 0$  and  $k_3 > 0$ , the diffusion of Al(I) ions from the bulk electrolyte to react at the anode according to reaction [III] would give  $\epsilon < 1/3$ . (iv) A value of  $\epsilon = 1/3$  is not unique to (ii). If  $k_1 = k_2$  and  $k_3 \cong 0$ ,  $\epsilon = 1/3$ , and without a knowledge of all the rate constants for each discrete reaction step involved, the steady-state concentration of Al(I) ions at the electrode surface cannot be calculated. The occurrence of the homogeneous disproportionation reaction, if sufficiently high concentrations of Al(I) ions are able to accumulate in the vicinity of the anode



could further complicate analyses of the causes underlying the anode current yield values.

For the reverse of reaction [V] as written, Storozhenko (2) has determined from the solubilities of aluminum in tetrachloroaluminate melt equilibrium constants of  $24.7 \times 10^{-6}$  (200°C),  $33.8 \times 10^{-6}$  (300°C), and  $59.1 \times 10^{-6}$  (400°C). These values may be compared to the thermodynamic functions calculated by Foster *et al.* (22) for the gaseous phase equilibria; for the reverse of reaction [V], the equilibrium constants are  $10^{-26.2}$  (227°C) and  $10^{-14.0}$  (427°C). Univalent aluminum compounds have been studied fairly extensively in the vapor phase at high temperatures, *q.v.* the compilation of thermochemical data for AlCl (23) (references therein) and Ref. (24, 25). However, scant information is available with regard to the stability of subvalent species of aluminum in either liquid or solid phases.<sup>1</sup> *A priori* no correlation between the relative stabilities in the vapor and the solution phases is possible, as the changes of the free energy and entropy

<sup>1</sup> Despite varied experimental approaches (26-29) no compound of subvalent aluminum, stable at room temperatures, has yet been characterized unequivocally; Kinsella (29) was unsuccessful both with solid-state preparative methods, which seemed to be most promising from a thermodynamical standpoint, and electrolytic techniques involving anodization.

accompanying dissolution of a molecule, such as aluminum monochloride in a molten salt, depend on properties specific to the solute and the solvent phase. Lower oxidation states of certain metals are known to be stabilized in chloroaluminate melts with high aluminum chloride contents, *e.g.*, Cd<sub>2</sub><sup>2+</sup>, Pb<sup>+</sup> Sn<sub>2</sub><sup>+</sup> (30), and Hg<sub>3</sub><sup>2+</sup> (31). Possible reasons for this stabilization have been discussed by Anders (32), Skala (18), and Mamantov (33). These include, firstly, steric factors and charge densities of anions which affect the stability of low valent cations and, secondly, increased stabilization is expected to occur as the solvent media are made increasingly acidic in the Lewis sense. This is because low valence state cations are generally less acidic than those in higher valence states. Nevertheless, the equilibrium constants for the reverse of reaction [V] in an equimolar melt composition as derived by Storozhenko would necessitate a considerable increase in stabilization of univalent aluminum species in comparison with the respective gaseous phase equilibria. Until the impurities that cause aluminum loss can be eliminated, or at least their effects quantitatively monitored, the aluminum solubility studies are liable to the same indeterminate errors as would be nonequilibrium anodic current yield measurements.

### Acknowledgments

This work was supported by the Air Force Office of Scientific Research under Grant No. AFOSR-71-1995G. We are grateful to Mr. D. L. Dick, Department of Chemistry, Colorado State University, for the emission spectrographic results.

A grant-in-aid from the ALCOA Foundation is also gratefully acknowledged.

Manuscript submitted Dec. 4, 1973; revised manuscript received March 25, 1974.

Any discussion of this paper will appear in a Discussion Section to be published in the June 1975 JOURNAL. All discussions for the June 1975 Discussion Section should be submitted by Feb. 1, 1975.

### REFERENCES

1. Yu. K. Delimarskii, V. F. Makogon, and A. Ya. Zhigailo, *Sov. Electrochem.*, **5**, 98 (1969).
2. V. N. Storozhenko, *ibid.*, **8**, 942 (1972).
3. F. Wohler and H. Buff, *Justus Liebig's Ann. Chem.*, **103**, 218 (1857).
4. E. Rajjola and A. W. Davidson, *J. Am. Chem. Soc.*, **78**, 556 (1956).
5. M. Straumanis and K. Poush, *This Journal*, **112**, 1185 (1965); L. Rédey, *ibid.*, **113**, 1345 (1966).
6. A. W. Davidson and F. Jirik, *J. Am. Chem. Soc.*, **72**, 1700 (1950).
7. M. Garreau and I. Epelboin, *J. Chim. Phys.*, **63**, 1515 (1966).
8. L. Kiss, M. L. Varsnyi, and E. Dudas, *Magy. Kem. Folyoirat*, **79**, 216 (1973).
9. W. E. Bennett, A. W. Davidson, and J. Kleinberg, *J. Am. Chem. Soc.*, **74**, 732 (1952).
10. K. W. Fung, G. Mamantov, and J. P. Young, *Inorg. Nucl. Chem. Letters*, **8**, 219 (1972).
11. L. G. Boxall, H. L. Jones, and R. A. Osteryoung, *This Journal*, in press.
12. L. G. Boxall, H. L. Jones, and R. A. Osteryoung, *ibid.*, **120**, 223 (1973).
13. G. F. Uhlrig, Ph.D. Thesis, University of Utah (1973).
14. R. C. Howie and D. W. Macmillan, *J. Appl. Electrochem.*, **2**, 217 (1972).
15. E. P. Parry and R. A. Osteryoung, *Anal. Chem.*, **36**, 1366 (1964).
16. N. K. Gupta, *Rev. Sci. Instr.*, **42**, 1368 (1971).
17. H. Kuehnl and U. Geffarth, *Z. Anorg. Allgem. Chem.*, **391**, 280 (1972).
18. M. Skala, Ph.D. Thesis, University of Alberta (1973).
19. B. S. Del Duca, *This Journal*, **118**, 405 (1971).
20. G. L. Holleck and J. Giner, *ibid.*, **119**, 1161 (1972).
21. C. Wagner, *Electrochim. Acta*, **14**, 971 (1969).
22. L. M. Foster, A. S. Russell, and C. N. Cochran, *J. Am. Chem. Soc.*, **72**, 2580 (1950).
23. JANAF Thermochemical Tables, 2nd ed. (1971).

24. J. S. Bandarawalla and V. A. Altekar, *Trans. Indian Inst. Metals*, **21**, 68 (1968); *Chem. Abstr.*, **71**:64915a.
25. T. Kikuchi, T. Kurosawa, and T. Yagihashi, *Nippon Kinzoku Gakkaishi*, **33**, 305 (1969); *Chem. Abstr.*, **70**:117248y.
26. W. C. Schumb and H. H. Rogers, *J. Am. Chem. Soc.*, **73**, 5806 (1951).
27. S. Herzog, K. Geisler, and H. Präkel, *Angew. Chem. Intern. Ed. Engl.*, **2**, 47 (1963).
28. J. J. Eisch and J. L. Considine, *J. Am. Chem. Soc.*, **90**, 6257 (1968).
29. E. Kinsella, Ph.D. Thesis, University of London (1968).
30. T. C. F. Munday and J. D. Corbett, *Inorg. Chem.*, **5**, 1263 (1966).
31. G. Torsi, K. W. Fung, G. M. Begun, and G. Mamantov, *ibid.*, **10**, 2285 (1971).
32. U. Anders, Ph.D. Thesis, University of Alberta (1969).
33. K. W. Fung and G. Mamantov, in "Advances in Molten Salt Chemistry," Vol. 2, J. Braunstein, G. Mamantov, and G. P. Smith, Editors, Chap. 4, Plenum Publishing Corp., New York (1973).

## A New Electrolyte for Hydrocarbon Air Fuel Cells

A. A. Adams\*

Department of Chemistry, The American University, Washington, D. C. 20016

and H. J. Barger, Jr.\*

U.S. Army Mobility Equipment Research and Development Center, Fort Belvoir, Virginia 22060

The publication costs of this article have been assisted by the U.S. Army.

### ABSTRACT

The purpose of this work was to find an electrolyte which increased the rate of propane electro-oxidation over that observed in phosphoric acid. The monohydrate of trifluoromethanesulfonic acid has been demonstrated to have a positive effect. The limiting current at 135°C was more than 1000% greater than that observed in phosphoric acid under comparable conditions. Hydrogen oxidation was shown to be more facile in  $\text{CF}_3\text{SO}_3\text{H} \cdot \text{H}_2\text{O}$ . Experiments are described which provide some insight into the nature of the electrochemical oxidation process.

Direct oxidation hydrocarbon air fuel cells have been the goal of many investigators since Grubb and Niedrach (1) reported the electro-oxidation of saturated hydrocarbons. The rates for the oxidation of hydrocarbons were very low and could not be considered for a practical fuel cell system. Since that time, numerous attempts have been made to develop electrocatalysts which exhibit superior activity for hydrocarbon oxidation. This approach did not develop a material which demonstrated a performance and economy which warranted the advanced development of hydrocarbon air fuel cell systems. Another approach toward the improvement of the electro-oxidation of hydrocarbons is to investigate other electrolytes, the subject of the present paper.

It was demonstrated by Cairns (2, 3) in the mid 1960's that the electrolyte had a considerable effect on the rate of oxidation of alkanes. The highest current densities were supported in hydrofluoric acid. Hydrofluoric acid could not be considered suitable due to the great chemical activity of the system. Though other acid electrolytes have been examined, phosphoric acid is the electrolyte most commonly used in hydrocarbon air fuel cells (4, 5).

An analysis of the problem indicates that certain specifications are necessary for the ideal (hypothetical) electrolyte. These specific properties include:

(i) The electrolyte should be a good medium for the efficient reactions of hydrocarbons and air.

(ii) The electrolyte must be a good medium for ionic charge transport.

(iii) The electrolyte should be a good solvent for the reactants, the hydrocarbon and air.

(iv) The electrolyte must act as a suitable medium for mass transport for the diffusion of materials to catalytic surfaces and removal of products of the reaction.

(v) The electrolyte must be physically, chemically, and electrochemically stable over the operating temperature and potential range.

(vi) The electrolyte should not interfere with the catalytic reactions.

(viii) The electrolyte should not be strongly reactive with the cell construction materials or matrix.

Based on these specifications, the literature was examined for possible acid electrolytes (6). A promising system of compounds is the perfluoroalkane sulfonic acids. These acids have high acid strengths and are excellent ionic conductors (7). The simplest acid, trifluoromethanesulfonic acid, forms a stable monohydrate which melts at 34°C and boils at 96°C/1 mm Hg. The objective of this research was to investigate the electrochemical oxidation of propane in trifluoromethanesulfonic acid monohydrate and compare the results with those for the reaction of propane in 85% phosphoric acid.

### Experimental

*Apparatus.*—Electrochemical measurements were conducted in a three-compartment glass cell of approximately 30 ml capacity in which the working and countercompartments were separated by a medium glass frit. A Luggin capillary provided contact between the working electrode and the dynamic hydrogen electrode system (8). All potentials given will be with reference to the DHE. The working electrode assembly was removable so different electrode materials could be investigated. In the development of the current potential curves a platinum mesh (99.99%) of approximately 4 cm<sup>2</sup> "real" surface area was utilized. A

\* Electrochemical Society Active Member.

Key words: electrolyte, performance enhancement, anion adsorption, reaction mechanism, limiting current, propane oxidation,  $\text{CF}_3\text{SO}_3\text{H} \cdot \text{H}_2\text{O}$ .

smooth platinum wire (99.99%) of approximately 0.5 cm<sup>2</sup> "real" surface area was used in the experiments determining the adsorption of propane on the electrode. The counterelectrode was a platinized platinum mesh connected to a Pt wire lead. Potentials were controlled by a Wenking Potentiostat (Model 66TS3). Pretreatment steps were effected by switching potentiometers into the input circuit of the potentiostat using mercury-wetted relays fired at times from 1 msec to 10 sec regulated by a bank of wave form generators (all wave form generators were Tektronix Model 162). A digital panel meter (Electronic Research Company, Model 4000) was used to read all voltage and cell current values in the development of the current density-potential curves. The cell current values were obtained using the digital panel meter in parallel with a known resistance. Charging curves were displayed on a dual beam oscilloscope (Tektronix Type 555 with a Type 1A7 vertical plug in) and photographed with a Polaroid camera (Tektronix 75 mm/lens, Series 125). All experiments were repetitive runs to establish the reproducibility of results. An air oven maintained cell temperature to  $\pm 0.5^\circ\text{C}$  of the desired value.

**Materials.**—Trifluoromethanesulfonic acid was obtained from 3M Company, Minneapolis, Minnesota. The acid monohydrate was prepared by the method of Gramsted and Hazeldine (7) and redistilled 3 times at atmospheric pressure, collecting the fraction between 184°-186°C. The resultant product is a white, needlelike, crystalline product (mp 33.8°C). Fisher reagent grade phosphoric acid was purified by refluxing 1 volume 30% H<sub>2</sub>O<sub>2</sub> with 2 volumes of 85% H<sub>3</sub>PO<sub>4</sub> and reconcentrated to 85% H<sub>3</sub>PO<sub>4</sub> (9). High purity helium 99.995% and instrument grade propane 99.5% minimum purity were obtained from the Matheson Company. The helium used for purging was deoxygenated by passing over a bed of copper turnings at 400°C. The helium was appropriately humidified to maintain the H<sub>3</sub>PO<sub>4</sub> concentration at 85% regardless of cell temperature.

**Experimental techniques.**—The surface area of the electrode was determined by using a cathodic galvanostatic pulse after a series of potential pretreatment steps. This "real" electrode area was calculated assuming a value of 210  $\mu\text{C}/\text{cm}^2$  as the maximum cathodic galvanostatic charge associated with the deposition of a monolayer of hydrogen on the electrode surface (10). The potential pretreatment step provided a reproducible electrode surface for charge measurements as previously described by Brummer *et al.* (11) and Gilman (12).

Current density ("real" area)-potential diagrams were constructed at several temperatures from 55° to 135°C for the background (using helium), for hydrogen, and for propane. In performing the current *vs.* potential runs, a potential value was set and the system allowed to equilibrate for 5 min before the current value was recorded. The potential was scanned in the anodic direction and back toward the open-circuit potential to establish the hysteresis in the system and electrolyte stability.

Work was begun on the adsorption characteristics of propane in CF<sub>3</sub>SO<sub>3</sub>H·H<sub>2</sub>O using the galvanostatic method of Brummer *et al.* (11). A series of potential steps are imposed on the electrode followed by a galvanostatic pulse. The potential was raised from open circuit to 2.00V for 10 sec in CF<sub>3</sub>SO<sub>3</sub>H·H<sub>2</sub>O. It was found that the 2.00V step *vs.* 1.35V step used for phosphoric acid was necessary to obtain a reproducible surface area determination. All other steps used were the same for CF<sub>3</sub>SO<sub>3</sub>H·H<sub>2</sub>O and for 85% H<sub>3</sub>PO<sub>4</sub>. The 2.00V step was followed by a 0.1 msec step at 0.05V. This was followed by an adsorption step at a selected potential and time. The difference between the potential time curves of helium run in the electrolyte (background) *vs.* propane in the electrolyte gives a measure of the charge due to adsorption of propane on the electrode.

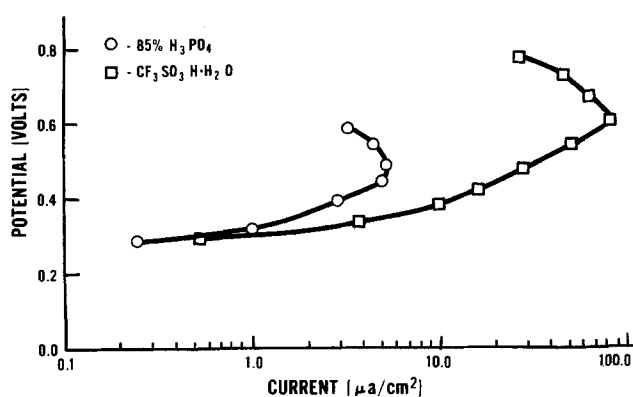


Fig. 1. Current density-potential diagram comparing the electrochemical oxidation of propane on smooth platinum at 135°C in CF<sub>3</sub>SO<sub>3</sub>H·H<sub>2</sub>O and in 85% H<sub>3</sub>PO<sub>4</sub>.

Several experiments were performed using the multipulse potentiodynamic method (13). After the pretreatment potential steps and an adsorption potential step a voltage ramp was imposed on the electrode. The current changes and the potential ramp on the electrode were followed using an oscilloscope.

### Results and Discussion

The principal objective of this effort was to determine if the subject electrolyte enhanced the electrochemical oxidation of propane compared to that observed in 85% H<sub>3</sub>PO<sub>4</sub>. In order to have a direct basis for comparison with our cell, a number of the experiments performed by Brummer *et al.* (11) in H<sub>3</sub>PO<sub>4</sub> were repeated. Our results were generally in good agreement with those reported earlier where the limiting currents at 135°C occurred between 0.5 and 0.6V. The accumulation of charge on the electrode surface was found to be very potential dependent with the greatest adsorption occurring at about 0.3V. A significant portion of the reaction intermediates on the electrode desorbed when the working electrode was cathodically pulsed. The remaining intermediates could only be removed when the potential was raised to a highly oxidizing level.

The first experiments were to examine the electrochemical oxidation of propane in CF<sub>3</sub>SO<sub>3</sub>H·H<sub>2</sub>O and compare these results with those in 85% H<sub>3</sub>PO<sub>4</sub> at 135°C. This comparison is presented in Fig. 1. At all potentials, the current density values are higher for the reaction in CF<sub>3</sub>SO<sub>3</sub>H·H<sub>2</sub>O than in 85% H<sub>3</sub>PO<sub>4</sub>. The limiting current density value in CF<sub>3</sub>SO<sub>3</sub>H·H<sub>2</sub>O is approximately 82  $\mu\text{A}/\text{cm}^2$  and in 85% H<sub>3</sub>PO<sub>4</sub> the limiting current density is approximately 5.5  $\mu\text{A}/\text{cm}^2$ . Thus, on a strictly comparative basis, the oxidation of propane was enhanced by a factor of 15 in the acid monohydrate.

Table I shows the temperature dependence of the propane reaction in the acid monohydrate. The data for the reaction of propane in 85% H<sub>3</sub>PO<sub>4</sub> at 135°C are also shown for comparison purposes.

The effect of temperature can be observed on the reaction of propane in CF<sub>3</sub>SO<sub>3</sub>H·H<sub>2</sub>O compared to the reaction of propane in 85% H<sub>3</sub>PO<sub>4</sub> in Table I. The current density values, at a set potential, increase with temperature in CF<sub>3</sub>SO<sub>3</sub>H·H<sub>2</sub>O, which is as expected.

Table I. Summary of propane current density data for 85% H<sub>3</sub>PO<sub>4</sub> and CF<sub>3</sub>SO<sub>3</sub>H·H<sub>2</sub>O at several potentials

Potential <i>vs.</i> DHE, V	85% H <sub>3</sub> PO <sub>4</sub> at 135°C, $\mu\text{A}/\text{cm}^2$	CF <sub>3</sub> SO <sub>3</sub> H·H <sub>2</sub> O at 95°C, $\mu\text{A}/\text{cm}^2$	CF <sub>3</sub> SO <sub>3</sub> H·H <sub>2</sub> O at 115°C, $\mu\text{A}/\text{cm}^2$	CF <sub>3</sub> SO <sub>3</sub> H·H <sub>2</sub> O at 135°C, $\mu\text{A}/\text{cm}^2$
0.4	1.4	0.68	1.3	25.0
0.5	5.3	2.8	4.5	53.0
0.6	4.7	7.2	9.4	66.0
Limiting current	5.5	24.0	16.0	82.0

At all temperatures, the limiting current values for  $\text{CF}_3\text{SO}_3\text{H}\cdot\text{H}_2\text{O}$  are higher than the limiting current value for 85%  $\text{H}_3\text{PO}_4$  at 135°C. At 115°C, the limiting current density value for the reaction of propane in the acid monohydrate appears to go through a minimum value. It is felt that there is insufficient data to state at this time that this is a true minimum. The limiting current density value at 115°C is, however, a reproducible value. The implication that a minimum exists in the limiting current density at 115°C awaits further testing at 110° and 120°C. Some experiments were run at 55°C where the system exhibited anomalous behavior on a day to day basis indicating a lower temperature limit for cell operation.

The temperature dependence of current density at 0.50V is shown in the Arrhenius-type plot of Fig. 2. This potential was chosen so as to compare the activation energy calculated for  $\text{CF}_3\text{SO}_3\text{H}\cdot\text{H}_2\text{O}$  with those calculated by Cairns (2) for several inorganic acids. The value calculated for the oxidation of propane in  $\text{CF}_3\text{SO}_3\text{H}\cdot\text{H}_2\text{O}$  is 13 kcal/mole as opposed to a value of approximately 16 kcal/mole for the oxidation of propane in such electrolytes as  $\text{H}_2\text{SO}_4$ , HF,  $\text{H}_3\text{PO}_4$ , and  $\text{CsCO}_2$ . The reasons for the decrease in activation energy are not apparent from this data; however, one of the implications of this lower activation energy is that to achieve a reaction rate of propane equivalent to that observed in  $\text{CF}_3\text{SO}_3\text{H}\cdot\text{H}_2\text{O}$  at 135°C, it would be necessary to operate at a much higher temperature in 85%  $\text{H}_3\text{PO}_4$ .

Previous results in  $\text{HClO}_4$ ,  $\text{H}_2\text{SO}_4$ , and  $\text{H}_3\text{PO}_4$  indicate that two general classes of intermediates are formed on the electrode, one which desorbs on cathodic pulse and another which does not (2, 10). The former consists of hydrocarbon radicals or fragments. The nondesorbable class consists of a highly oxidized species, considered to be a carbon bonded to at least 1 oxygen atom, and a polymeric carbon material. Using the galvanostatic method in  $\text{CF}_3\text{SO}_3\text{H}\cdot\text{H}_2\text{O}$ , the anodic charging curve with propane was observed to have a single wave instead of the characteristic double wave observed in  $\text{H}_3\text{PO}_4$ . Furthermore, the total charge due to adsorbed intermediates was very low, often barely distinguishable from a charging curve under helium.

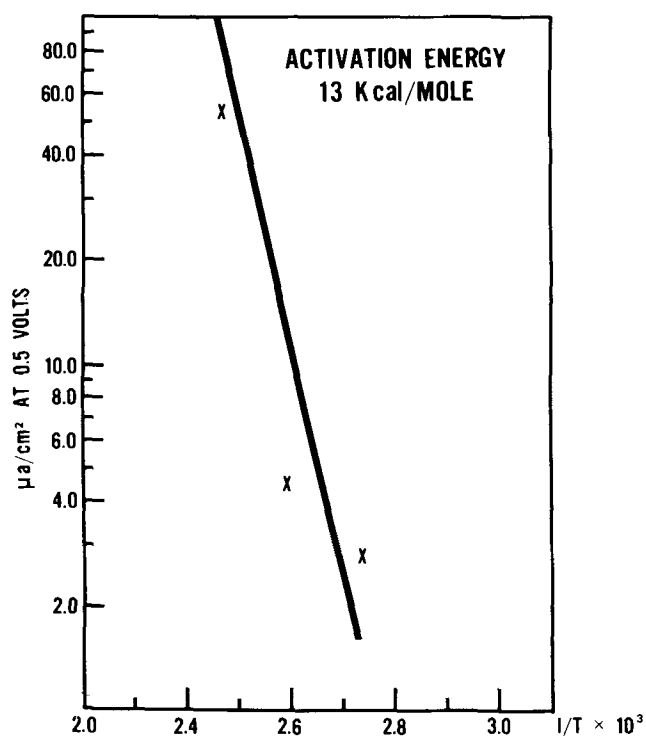


Fig. 2. Log of the current density (at an anode potential of 0.5V) as a function of reciprocal absolute temperature for the oxidation of propane on smooth platinum in  $\text{CF}_3\text{SO}_3\text{H}\cdot\text{H}_2\text{O}$ .

In order to determine whether the highly oxidized species could be formed on the electrode, experiments were performed using carbon dioxide as the reactant. Following potential pretreatment steps as described above,  $\text{CO}_2$  is adsorbed on the electrode at 0.15V. The intermediate thus formed is considered to be the same as the highly oxidized species formed in the anodic oxidation of hydrocarbons in inorganic acids (14). The anodic charging curve for "reduced"  $\text{CO}_2$  in  $\text{CF}_3\text{SO}_3\text{H}\cdot\text{H}_2\text{O}$  was similar to those obtained using propane and helium. All anodic charging curves obtained in  $\text{CF}_3\text{SO}_3\text{H}\cdot\text{H}_2\text{O}$  were analogous to the "reduced"  $\text{CO}_2$  anodic charging curve in  $\text{H}_3\text{PO}_4$  (15). These results indicate that the adsorbed polymeric carbon material formed during the oxidation of propane in  $\text{H}_3\text{PO}_4$  is not present in the acid monohydrate. The formation of the polymeric material is considered to be an undesirable side reaction. The oxidation of propane in the acid monohydrate would appear to proceed by a more straightforward reaction path.

A single oxidation peak for propane in the acid monohydrate is indicated from results obtained from the multipulse potentiodynamic method. Whereas these results are preliminary they are reproducible. It is obvious that additional work must be performed on the adsorption of propane on smooth platinum to elucidate the mechanism of the oxidation process in the electrolyte. However, all of the results to this point suggest that the mechanism is different from that observed for propane in  $\text{H}_3\text{PO}_4$ .

An investigation of the current-potential behavior of hydrogen in  $\text{CF}_3\text{SO}_3\text{H}\cdot\text{H}_2\text{O}$  could offer an additional insight into the behavior of the electrolyte. It has been previously demonstrated that higher oxidation rates are supported in acid electrolytes with lower tendencies of acid anion adsorption on platinum (4). Assuming more active sites are available for reaction, enhanced oxidation of hydrogen would be observed in the acid monohydrate. The current density-potential curves for hydrogen at a platinum electrode in phosphoric acid and at two temperatures of  $\text{CF}_3\text{SO}_3\text{H}\cdot\text{H}_2\text{O}$  are shown in Fig. 3. The limiting current value in 85%  $\text{H}_3\text{PO}_4$  at 135°C is approximately 20  $\mu\text{A}/\text{cm}^2$ . The limiting current values for  $\text{CF}_3\text{SO}_3\text{H}\cdot\text{H}_2\text{O}$  at 95° and 115°C are approximately 75 and 118  $\mu\text{A}/\text{cm}^2$ . At a 20°C lower temperature, the oxidation of hydrogen in  $\text{CF}_3\text{SO}_3\text{H}\cdot\text{H}_2\text{O}$  is almost 6 times more rapid than the reaction of hydrogen in 85%  $\text{H}_3\text{PO}_4$  at 135°C. As is clear from the graph, at all potentials the current densities are higher at a given potential in  $\text{CF}_3\text{SO}_3\text{H}\cdot\text{H}_2\text{O}$  at 115°C than in 85%  $\text{H}_3\text{PO}_4$  at 135°C. It is significant that enhancement of the oxidation of both hydrogen and propane oxidation in  $\text{CF}_3\text{SO}_3\text{H}\cdot\text{H}_2\text{O}$  as compared to 85%  $\text{H}_3\text{PO}_4$  was observed. A possible factor in the enhancement is the reduced amount of acid anion adsorption resulting in additional active sites on the electrode as a result of a reduced amount of electrolyte adsorbed on the electrode.

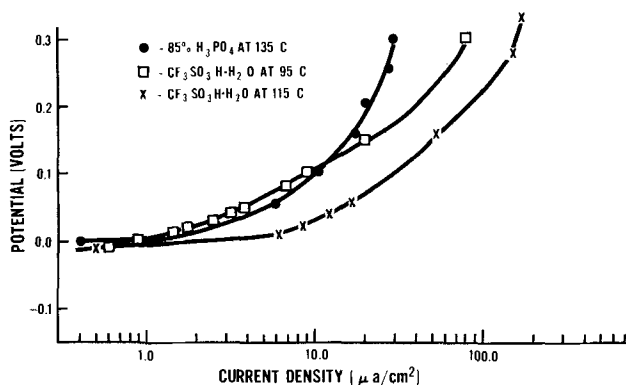


Fig. 3. Current density-potential diagram for the oxidation of hydrogen on smooth platinum in 85%  $\text{H}_3\text{PO}_4$  at 135°C and in  $\text{CF}_3\text{SO}_3\text{H}\cdot\text{H}_2\text{O}$  at 95° and 115°C.



One important consideration is the stability of the acid monohydrate, at elevated temperatures, over several weeks or months. Experiments were conducted over a 6 week period in which the limiting current density values were compared with values in freshly prepared acid monohydrate. Over the 5 week period, at 135°C, the limiting current density declined to 78  $\mu\text{A}/\text{cm}^2$ , which is close to the value of 82  $\mu\text{A}/\text{cm}^2$  in freshly prepared acid monohydrate. Although over time the electrolyte developed a slightly darker appearance, it must be emphasized that there was no significant decrease in the electrochemical performance of the reaction of propane in  $\text{CF}_3\text{SO}_3\text{H}\cdot\text{H}_2\text{O}$  over 6 weeks.

Vapor pressure data available indicates the electrolyte would be unsuitable for use at 150°C or above (7). By altering the chain length of the alkane group this problem may be alleviated. Increase in chain length decreases the vapor pressure. If no loss in the activity of the reaction of propane occurs, the lowering of the vapor pressure would be desirable. Fuel cell construction materials specifically designed for phosphoric acid fuel cells may not be useful in the  $\text{CF}_3\text{SO}_3\text{H}\cdot\text{H}_2\text{O}$ . In that case new cell materials would have to be developed.

### Conclusion

Trifluoromethanesulfonic acid monohydrate increases the performance of a platinum wire electrode in the electro-oxidation of propane and hydrogen. Results with propane in  $\text{CF}_3\text{SO}_3\text{H}\cdot\text{H}_2\text{O}$  indicate a different over-all process as compared to that observed in 85%  $\text{H}_3\text{PO}_4$ . Much needs to be learned about the physical characteristics, such as vapor pressure and gas solubilities, in  $\text{CF}_3\text{SO}_3\text{H}\cdot\text{H}_2\text{O}$  before it can be used as an electrolyte in a practical fuel cell. However, the enhancement observed with trifluoromethanesulfonic acid monohydrate indicates that the perfluoroalkanesulfonic acids as a class of compounds are worthy of further experimentation for hydrocarbon air fuel cell use.

### Acknowledgment

This work was supported by the U.S. Army Mobility Equipment Research and Development Center, Fort Belvoir, Virginia, under Contract DAAK02-72-C-0084.

Helpful discussions with Dr. R. T. Foley are gratefully acknowledged.

Manuscript received Dec. 17, 1973. This was Paper 22 presented at the Boston, Massachusetts, Meeting of the Society, Oct. 7-11, 1973.

Any discussion of this paper will appear in a Discussion Section to be published in the June 1975 JOURNAL. All discussions for the June 1975 Discussion Section should be submitted by Feb. 1, 1975.

### REFERENCES

1. W. T. Grubb and L. W. Niedrach, *This Journal*, **110**, 1086 (1963); W. T. Grubb and L. W. Niedrach, *Proc. Ann. Power Sources Conf.*, **17**, 71 (1963).
2. E. J. Cairns, Paper 140 presented at Electrochemical Society Meeting, San Francisco, California, May 9-13, 1965; see also, *ibid.*, Extended Abstracts of Electro-Organic Division.
3. E. J. Cairns, in "Hydrocarbon Fuel Cell Technology," B. S. Baker, Editor, Academic Press, New York (1965).
4. E. J. Cairns, in "Advances in Electrochemistry and Electrochemical Engineering," Vol. 8, Charles W. Tobias, Editor, Wiley-Interscience, New York (1971).
5. N. Palmer, U.S. Pat. 3,592,696 (assigned to Leesona Corp.) (1971).
6. A. A. Adams and R. T. Foley, in Interim Technical Report No. 2, Contract No. DAAK02-72-C-0084, U.S. Army MERDC, Fort Belvoir, Va., February 1973.
7. T. Gramsted and R. N. Hazeldine, *J. Chem. Soc.*, 173 (1956).
8. J. Giner, *This Journal*, **111**, 376 (1964).
9. M. L. Savitz, R. L. Januszkeski, and G. R. Fry-singer, in "Hydrocarbon Fuel Cell Technology," B. S. Baker, Editor, p. 443, Academic Press, New York (1965).
10. W. T. Grubb and C. J. Michalske, *This Journal*, **111**, 1015 (1964).
11. S. B. Brummer, J. I. Ford, and M. J. Turner, *J. Phys. Chem.*, **69**, 3424 (1965).
12. S. Gilman, *J. Phys. Chem.*, **67**, 78 (1963).
13. S. Gilman, *Trans. Faraday Soc.*, **61**, 2561 (1965).
14. J. Giner, *Electrochim. Acta*, **8**, 857 (1963).
15. J. Giner, in First Technical Report, Contract No. DAAE15-67C-0048, U.S. Army MERDC, Fort Belvoir, Va., August 1967.

# Transference Numbers in Molten Mixtures of Alkali Chloride-Cerium Chloride from EMF Measurements

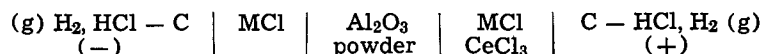
Wishvender K. Behl\*

Power Sources Technical Area, U.S. Army Electronics Technology and Devices Laboratory (ECOM), Fort Monmouth, New Jersey 07703

The publication costs of this article have been assisted by the U.S. Government.

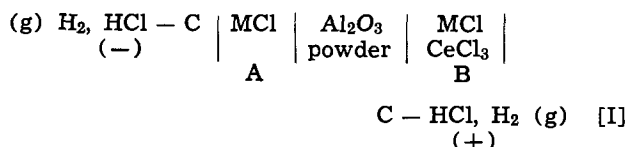
## ABSTRACT

Transference numbers of the cations relative to the chloride ion in molten mixtures of alkali chloride-cerium chloride were determined from emf measurements on concentration cells with transference of the type



where M is Li, Na, or K. The cells were operated with a mixture of hydrogen and hydrogen chloride gases instead of chlorine gas to minimize the possibility, if any, of the oxidation of cerous chloride to ceric chloride. The emf measurements were carried out at 850°C, and results are presented over the entire composition range of the systems studied. It was also shown that, in these mixtures, the alkali ions possess a relatively larger mobility than the cerous ion.

Transference properties of molten salt mixtures have been extensively studied (1, 2) in the past. However, even though a large number of these studies have been devoted to molten halide mixtures, data on the transference properties of molten alkali chloride-cerium chloride mixtures are nonexistent. In the present studies, transference numbers of cations relative to the chloride ion in molten mixtures of LiCl-CeCl<sub>3</sub>, NaCl-CeCl<sub>3</sub>, and KCl-CeCl<sub>3</sub> were determined from emf measurements on concentration cells with transference of the type



where M is Li, Na, or K. These cells were operated with a mixture of hydrogen and hydrogen chloride gases instead of chlorine gas to minimize the possibility, if any, of the oxidation of cerous chloride to ceric chloride. The emf method has been employed by several workers to determine the transference numbers of cations relative to common anion in mixtures of molten chlorides (3, 4), fluorides (5), and nitrates (6).

## Experimental Procedure

Reagent grade chemicals (Fisher Scientific Company) were used in these experiments. Sodium and potassium chlorides were melted under vacuum, re-solidified, and stored in an argon atmosphere. Lithium chloride and cerous chloride heptahydrate (CeCl<sub>3</sub>·7H<sub>2</sub>O) were dehydrated by heating at 110°-120°C for 24 hr under a flowing atmosphere of hydrogen chloride (HCl) gas. The temperature was then raised to about 50° above the melting points of lithium chloride (610°C) and cerous chloride (822°C) and the hydrogen chloride gas bubbled for another 3-4 hr. In case of lithium chloride, the treatment with hydrogen chloride gas was followed by bubbling chlorine gas for 2-3 hr to remove the black organic impurities. The temperature was then lowered and anhydrous lithium and

cerous chlorides, so obtained, were stored in an atmosphere of argon gas.

The cell design used for the emf measurements and other experimental details have been described earlier (3). Briefly stated, a 5-in. long quartz tube (25 mm diam) closed at the bottom and containing the pure alkali chloride was placed in an outer Vycor container (57 mm diam) containing the alkali chloride-cerous chloride mixture. The liquid junction between the alkali chloride and alkali chloride-cerous chloride mixture was established through a coiled quartz tubing (6 mm diam) filled with predried powdered alumina (Grade T-61, 120 mesh, Aluminum Company of America). The mole fraction of the alkali chloride in the mixture was varied from 0 to 0.9 by the addition of weighed amounts of purified alkali chloride. The powdered alumina was found ideal for these experiments since it not only prevented any gravitational flow from one side to the other but also was inert to any cation exchange that usually occurs (3) between the alkali chlorides and the commonly employed quartz frit membranes.

Spectrochemical grade carbon rods (Ultra Carbon Company) were used as the electrodes. The hydrogen and hydrogen chloride gases were used directly from the cylinders. A wire-wound cylindrical furnace was used to heat the cell assembly and the temperature of the cell controlled within ±2°C with a Guardsman-West temperature controller. The emf measurements were made with a Leeds and Northrup K-5 potentiometer.

## Results and Discussion

Designating the alkali ion (M<sup>+</sup>), cerous ion (Ce<sup>+++</sup>), and chloride ion (Cl<sup>-</sup>) as ions 1, 2, 3, respectively, the emf of cell I is given by (3, 7)

$$E_{\text{cell}} = -\frac{1}{F} \int_A^B t_{13} d\mu_{\text{MCl}} - \frac{1}{3F} \int_A^B t_{23} d\mu_{\text{CeCl}_3} \quad [1]$$

where F is the Faraday constant and  $\mu_{\text{MCl}}$  and  $\mu_{\text{CeCl}_3}$  are, respectively, the chemical potentials of alkali chloride and cerous chloride. The transference numbers ( $t_{13}$  and  $t_{23}$ ) of the alkali ion (cation 1) and cerous ion (cation 2) are defined relative to the chloride ion (anion 3) and are related to each other by the equation

\* Electrochemical Society Active Member.  
Key words: alkali chloride-cerium chloride mixtures, concentration cells with transference, emf measurements, molten salt mixtures, transference numbers.

$$t_{13} + t_{23} = 1 \quad [2]$$

Equation [1] can be simplified (4) and rewritten as

$$E_{\text{cell}} = - \frac{2.303 RT}{F} \int_A^B \frac{t_{13} - x'_{13}}{1 - x'_{13}} d \log a_{\text{MCl}} \quad [3]$$

where  $x'_{13}$  and  $a_{\text{MCl}}$  are, respectively, the equivalent fraction and activity of the alkali chloride in the mixture;  $R$  and  $T$  have their usual thermodynamic significance. The equivalent fraction ( $x'_{13}$ ) is related to the mole fraction ( $x_{13}$ ) by the equation

$$x'_{13} = \frac{x_{13}}{3 - 2x_{13}} \quad [4]$$

Partially differentiating Eq. [3] with respect to  $\log a_{\text{MCl}}$ , we have

$$\left( \frac{\partial E_{\text{cell}}}{\partial \log a_{\text{MCl}}} \right)_B = - \frac{2.303 RT}{F} \left( \frac{t_{13} - x'_{13}}{1 - x'_{13}} \right)_B \quad [5]$$

Since the activities of alkali chlorides in molten mixtures of alkali chloride-cerium chloride are known (8), the term on the left side of Eq. [5] can be obtained by graphical differentiation of  $E_{\text{cell}}$  vs.  $\log a_{\text{MCl}}$  plots. The transference number of the alkali ion ( $t_{13}$ ) relative to the chloride ion can then be obtained by use of Eq. [5]. The transference number of the cerous ion ( $t_{23}$ ) relative to the chloride ion, by definition, is given by Eq. [2].

At a given composition of the molten salt mixture, the transference numbers of the cations ( $t_{13}$  and  $t_{23}$ ) relative to the chloride ion are related (2) to their respective mobilities by the equations

$$b_{13} = \frac{t_{13} \lambda}{x'_{13} F} \quad [6]$$

and

$$b_{23} = \frac{t_{23} \lambda}{x'_{23} F} \quad [7]$$

where  $b_{13}$  and  $b_{23}$  are, respectively, the mobilities of the alkali ion ( $M^+$ ) and cerous ion ( $Ce^{++}$ ) relative to the chloride ion;  $x'_{13}$  and  $x'_{23}$  are the corresponding equivalent fractions of the alkali chloride and cerium chloride in the mixture; and  $\lambda$  is the equivalent conductance of the molten salt mixture. Since no conductivity measurements have been reported in the literature for the alkali chloride-cerium chloride mixtures, the cation mobilities ( $b_{13}$  and  $b_{23}$ ) cannot be calculated from the transference number data alone. It is, however, possible to calculate cation mobility ratios from the transference numbers. Thus, combining Eq. [6] and [7], we have

$$\frac{b_{13}}{b_{23}} = \frac{t_{13} x'_{23}}{t_{23} x'_{13}} \quad [8]$$

The mobility of the alkali ion relative to the cerous ion ( $b_{12}$ ) is similarly obtained by combining Eq. [6] and [7]. Thus

$$b_{12} = b_{13} - b_{23} = \left( \frac{t_{13}}{x'_{13}} - \frac{t_{23}}{x'_{23}} \right) \frac{\lambda}{F} \quad [9]$$

Since by definition,  $t_{23} = 1 - t_{13}$  and  $x'_{23} = 1 - x'_{13}$ , Eq. [9] can be simplified as

$$b_{12} = b_{13} - b_{23} = \left( \frac{t_{13} - x'_{13}}{x'_{13} x'_{23}} \right) \frac{\lambda}{F} \quad [10]$$

The emf measurements on the molten salt mixtures LiCl-CeCl<sub>3</sub>, NaCl-CeCl<sub>3</sub>, and KCl-CeCl<sub>3</sub> were carried out at 850°C over the entire composition range of the

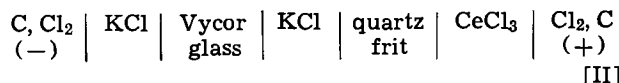
Table I. Cell<sup>†</sup> potentials as a function of alkali chloride mole fraction in the alkali chloride-cerium chloride mixtures at 850°C

$x$ , alkali chloride	LiCl-CeCl <sub>3</sub>		NaCl-CeCl <sub>3</sub>		KCl-CeCl <sub>3</sub>	
	$a_{\text{LiCl}}^*$	$E_{\text{cell}}$ , V	$a_{\text{NaCl}}^*$	$E_{\text{cell}}$ , V	$a_{\text{KCl}}^*$	$E_{\text{cell}}$ , V
0.00	—	0.1425	—	0.1720	—	0.2364
0.10	0.048	0.1213	0.012	0.1611	0.0026	0.2280
0.20	0.100	0.1100	0.031	0.1493	0.008	0.2160
0.25	0.135	0.1026	0.043	0.1370	—	—
0.30	0.168	0.0972	0.058	0.1355	0.017	0.2006
0.35	0.200	0.0890	0.081	—	0.025	0.1927
0.40	0.243	0.0824	0.107	0.1186	0.037	0.1810
0.45	0.285	0.0738	0.133	0.1090	—	—
0.475	—	—	—	—	0.060	0.1654
0.50	0.346	0.0680	0.173	0.0981	—	—
0.52	—	—	—	—	0.090	0.1510
0.55	0.390	0.0589	0.223	0.0875	—	—
0.60	0.448	0.0523	0.284	0.0765	0.163	0.1272
0.65	0.535	0.0434	0.359	0.0630	—	—
0.67	—	—	—	—	0.290	0.1018
0.70	0.611	0.0380	0.445	0.0498	—	—
0.733	—	—	—	—	0.350	0.0732
0.75	0.680	0.0286	0.544	0.0363	0.465	0.0678
0.80	0.754	0.0238	0.653	0.0308	0.604	0.0470
0.85	—	—	0.761	0.0183	0.710	0.0300
0.873	0.865	0.0152	—	—	—	—
0.884	—	—	0.830	0.0110	—	—
0.89	—	—	—	—	0.805	0.0190

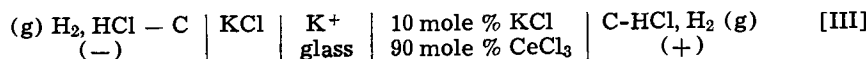
† Cell: (g) H<sub>2</sub>, HCl - C | MCl | Al<sub>2</sub>O<sub>3</sub> powder | MCl | CeCl<sub>3</sub> | C - HCl, H<sub>2</sub> (g) (+)  
where M is Li, Na or K.  
\* From Ref. (8).

mixtures. These data are summarized in Table I. The activities of the alkali chlorides in these mixtures are known (8) at 825°C. Assuming that the excess free energies of mixing remain constant as the temperature is increased from 825° to 850°C, the activities were recalculated at 850°C and are also summarized in Table I.

In an effort to determine the magnitude of "liquid junction potential" between pure molten potassium chloride and cerium chloride, Bronstein (9) measured the emf of the cell



At 850°C, the emf of cell [II] was found to be 0.600V. This value is considerably higher than the value of 0.236V obtained in the present studies employing cell [I] where MCl now refers to KCl and mole fraction of KCl in the right-hand half-cell is zero. The higher emf in cell [II] may be due to exchange of K<sup>+</sup> from the melt with the quartz frit so that over a period of time, the quartz frit would behave as a K<sup>+</sup> conductive membrane. This explanation seems plausible in view of the value of 0.572V obtained by Egan (8) for cell [III] at 825°C.



Behl and Egan (3) noticed a similar exchange of Li<sup>+</sup> from the melt with a quartz frit in their experiments with the system LiCl-PbCl<sub>2</sub>. The alumina powder used to establish the liquid junction in cell [I] was found to be inert (3) toward any exchange with alkali ions from the melt.

The plots of  $E_{\text{cell}}$  vs.  $\log a_{\text{MCl}}$  based on data presented in Table I for the molten salt mixtures LiCl-CeCl<sub>3</sub>, NaCl-CeCl<sub>3</sub>, and KCl-CeCl<sub>3</sub> are, respectively, shown in Fig. 1-3. From these plots, the term  $(\partial E_{\text{cell}} / \partial \log a_{\text{MCl}})$  was determined at various mole fractions by graphical differentiation and substituted in Eq. [5] to obtain the transference numbers of the alkali ions ( $t_{13}$ ) relative to the chloride ion. The transference numbers of the cerous ions ( $t_{23}$ ) were then determined by use of Eq. [2]. These data are summarized in Table II.

The transference numbers ( $t_{13}$ ) of alkali ions relative to the chloride ion in mixtures of molten alkali

Table II. Cation transference numbers and mobility ratios in the alkali chloride-cerium chloride mixtures at 850°C

Alkali chloride concentration*		LiCl-CeCl <sub>3</sub>			NaCl-CeCl <sub>3</sub>			KCl-CeCl <sub>3</sub>		
$x_{13}$	$x'_{13}$	$t_{13}$	$t_{23}$	$b_{13}/b_{23}$	$t_{13}$	$t_{23}$	$b_{13}/b_{23}$	$t_{13}$	$t_{23}$	$b_{13}/b_{23}$
0.1	0.0357	0.114	0.886	3.48	0.103	0.897	3.10	0.096	0.904	2.87
0.2	0.0769	0.284	0.716	4.76	0.218	0.782	3.35	0.226	0.774	3.51
0.3	0.1250	0.415	0.585	4.97	0.333	0.667	3.50	0.321	0.679	3.31
0.4	0.1818	0.516	0.484	4.80	0.461	0.539	3.85	0.413	0.587	3.17
0.5	0.2500	0.613	0.387	4.75	0.573	0.427	4.04	0.502	0.498	3.02
0.6	0.3333	0.701	0.229	4.69	0.692	0.308	4.49	0.635	0.365	3.48
0.7	0.4375	0.796	0.204	5.02	0.783	0.217	4.64	0.837	0.163	6.60
0.8	0.5714	0.881	0.119	5.55	0.846	0.154	4.14	0.952	0.048	14.88
0.9	0.7500	0.965	0.035	9.19	0.914	0.086	3.54	0.980	0.020	16.33

\*  $x_{13}$  = mole fraction;  $x'_{13}$  = equivalent fraction.

chloride-cerium chloride were found to be greater than the equivalent fraction ( $x'_{13}$ ) of the alkali chloride in the mixture over the entire composition range. If  $t_{13} = x'_{13}$  over the whole composition range of the mixture, it can be seen from Eq. [3] that the emf of cell [I] would be zero over the whole composition range of mixtures. Examples of such behavior have been reported in literature for the systems AgNO<sub>3</sub>-NaNO<sub>3</sub> (10) and NaCl-KCl (3). Further, in such cases, Eq. [10] predicts that the cation mobilities  $b_{13}$  and  $b_{23}$  would be identical over the whole composition range.

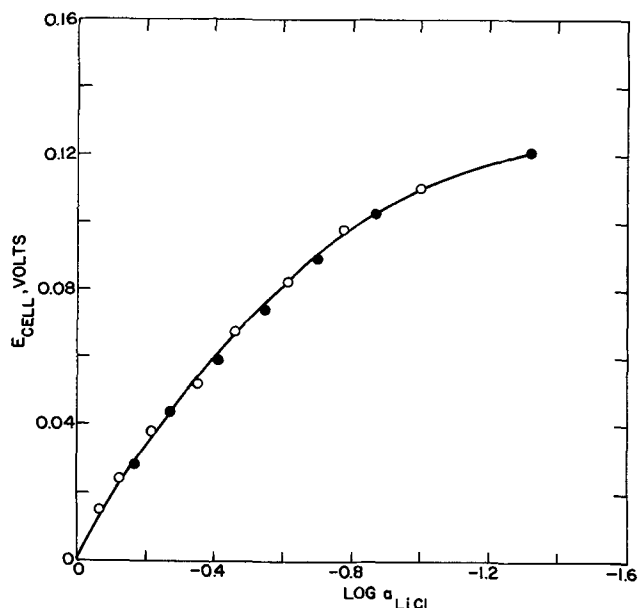


Fig. 1.  $E_{\text{cell}}$  vs.  $\log a_{\text{LiCl}}$  plot for the system LiCl-CeCl<sub>3</sub>. Open and closed circles represent data of two separate experiments.

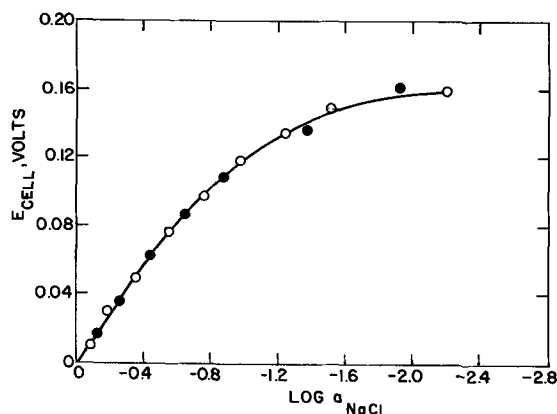


Fig. 2.  $E_{\text{cell}}$  vs.  $\log a_{\text{NaCl}}$  plot for the system NaCl-CeCl<sub>3</sub>. Open and closed circles represent data of two separate experiments.

This has been experimentally demonstrated in the case of the system AgNO<sub>3</sub>-NaNO<sub>3</sub> (11). Since  $t_{13} > x'_{13}$  over the whole composition range of the alkali chloride-cerium chloride mixtures, it can be seen from Eq. [10] that the alkali ions possess relatively higher mobilities than the cerous ion over the entire range of composition of these mixtures. Plots of the term ( $t_{13} - x'_{13}$ ) vs.  $x'_{13}$  for the systems LiCl-CeCl<sub>3</sub>, NaCl-CeCl<sub>3</sub>, and KCl-CeCl<sub>3</sub> are presented in Fig. 4. There is close similarity in behavior of the three systems. The cation mobility ratio ( $b_{13}/b_{23}$ ) in alkali chloride-cerium chloride mixtures was also determined by use of Eq. [8] over the whole composition range, and the data are summarized in Table II. The mobility ( $b_{13}$ ) of the alkali ion relative to the chloride ion was found to be much greater than the mobility ( $b_{23}$ ) of the cerous ion relative to the chloride ion. These results are not surprising in view of the smaller equivalent conductance (12) of pure cerium chloride as compared to the equivalent conductances (12) of pure alkali chlorides. The mobilities of the alkali ions in the systems KCl-PbCl<sub>2</sub> (13), LiCl-PbCl<sub>2</sub> (14), KCl-CaCl<sub>2</sub> (3), KCl-MgCl<sub>2</sub> (3), and LiCl-CdCl<sub>2</sub> (4) have also been found to be greater than the mobilities of the second cation in the mixture by a similar order of magnitude over most of the composition range of the mixtures.

### Summary and Conclusions

The emf method was employed to determine the transference numbers of the cations relative to the chloride ion in molten mixtures of LiCl-CeCl<sub>3</sub>, NaCl-CeCl<sub>3</sub>, and KCl-CeCl<sub>3</sub> at 850°C. Even though the individual cation mobilities relative to the chloride ion in these mixtures could not be calculated due to the absence of any conductance data, it was possible to

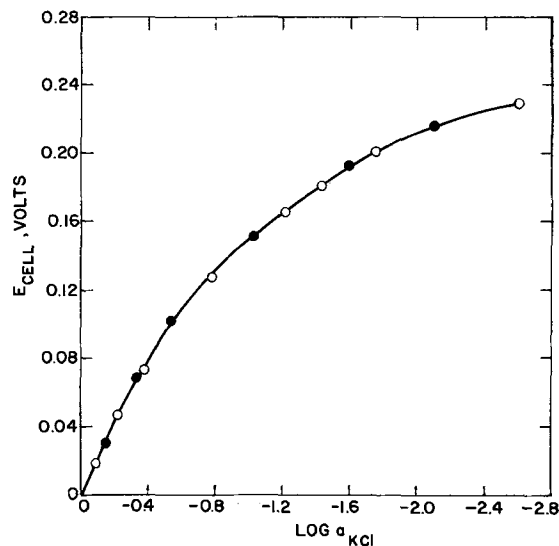


Fig. 3.  $E_{\text{cell}}$  vs.  $\log a_{\text{KCl}}$  plot for the system KCl-CeCl<sub>3</sub>. Open and closed circles represent data of two separate experiments.

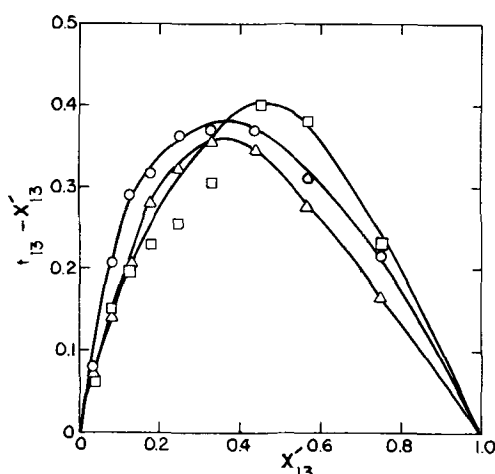


Fig. 4.  $(t_{13} - x'_{13})$  vs.  $x'_{13}$  plots for the systems  $\text{LiCl-CeCl}_3$  ( $\circ$ ),  $\text{NaCl-CeCl}_3$  ( $\triangle$ ), and  $\text{KCl-CeCl}_3$  ( $\square$ ).

show that the alkali ions possessed relatively larger mobility than the cerous ion over the whole composition range of the mixtures.

#### Acknowledgment

The author would like to thank Dr. J. J. Egan, Brookhaven National Laboratory, Upton, New York, for making available the thermodynamic data on alkali chloride-cerium chloride mixtures and for many helpful suggestions.

Manuscript submitted Oct. 25, 1973; revised manuscript received March 6, 1974. This was Paper 269 presented at the Chicago, Illinois, Meeting of the Society, May 13-18, 1973.

Any discussion of this paper will appear in a Discussion Section to be published in the June 1975 JOURNAL. All discussions for the June 1975 Discussion Section should be submitted by Feb. 1, 1975.

#### REFERENCES

1. B. R. Sundheim, "Fused Salts," B. R. Sundheim, Editor, McGraw-Hill Book Co., New York (1964).
2. A. Klemm, "Molten Salt Chemistry," M. Blander, Editor, Interscience Publishers, Inc., New York (1964).
3. W. K. Behl and J. J. Egan, *J. Phys. Chem.*, **71**, 1764 (1967).
4. W. K. Behl, *This Journal*, **121**, 959 (1974).
5. K. A. Romberger and J. Braunstein, *Inorg. Chem.*, **9**, 1273 (1970).
6. M. Okada and K. Kawamura, *Electrochim. Acta.*, **15**, 1 (1970).
7. C. Wagner, "Advances in Electrochemistry and Electrochemical Engineering," Vol. 4, pp. 1-46, P. Delahay, Editor, Interscience Publishers, Inc., New York (1966).
8. J. J. Egan and J. Bracker, *J. Chem. Thermodynamics*, **6**, 9 (1974).
9. H. R. Bronstein, *J. Phys. Chem.*, **73**, 1320 (1969).
10. R. W. Laity, *J. Am. Chem. Soc.*, **79**, 1849 (1957).
11. F. R. Duke, R. W. Laity, and B. Owens, *This Journal*, **104**, 299 (1957).
12. G. J. Janz, "Molten Salt Handbook," Academic Press, New York (1967).
13. F. R. Duke and R. A. Fleming, *This Journal*, **106**, 130 (1959).
14. A. Klemm and E. V. Monse, *Z. Naturforsch.*, **12a**, 319 (1957).

## Electrode Kinetics of the Alkali Metals in $\text{AlCl}_3$ -Propylene Carbonate Solution

Jacob Jorné\*<sup>1</sup> and Charles W. Tobias\*

Inorganic Materials Research Division, Lawrence Berkeley Laboratory, and Department of Chemical Engineering, University of California, Berkeley, California 94720

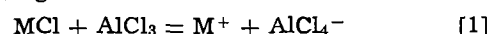
The publication costs of this article have been assisted by the University of California.

#### ABSTRACT

Kinetic parameters of the deposition-dissolution process for solid alkali metals in alkali metal chloride- $\text{AlCl}_3$ -propylene carbonate solution were evaluated using micropolarization measurements at 25°C. The exchange current densities were evaluated at different molalities of the alkali metal chlorides, and the cathodic transfer coefficients were calculated from the concentration dependence.

Interest in nonaqueous high energy batteries is reflected in an increasing number of investigations concerning the electrochemical behavior of active metals in nonaqueous solvents. So far very few investigations have reached the stage of evaluating kinetic parameters of the charge transfer process. The feasibility of electrodeposition of all the alkali metals from the corresponding solutions of the alkali metal chlorides in  $\text{AlCl}_3$ -propylene carbonate has been demonstrated (1). Lithium, sodium, potassium, rubidium, and cesium were deposited at ambient temperature, showing stable and reversible behavior. The alkali metal chlorides are practically insoluble in PC, however in the presence of

$\text{AlCl}_3$ , a complex is formed between the chloride and  $\text{AlCl}_3$  according to the reaction



where M represents the alkali metal. This reaction is responsible for high solubility and conductivity of all the alkali metal halides in PC; it allows the study of the electrochemical behavior of alkali metals with a common anion species.

In the present work, kinetic parameters of the deposition-dissolution process for solid alkali metals in alkali metal chloride- $\text{AlCl}_3$ -PC solutions have been evaluated using micropolarization measurements at 25°C. The micropolarization experiments were conducted over a range of alkali metal chloride molalities (0.01-1.0M) in constant unit molality solutions of  $\text{AlCl}_3$  in PC.

\* Electrochemical Society Active Member.

<sup>1</sup> Present address: Department of Chemical Engineering and Material Sciences, Wayne State University, Detroit, Michigan 48202.

Key words: electrode kinetics, alkali metals, propylene carbonate, exchange current density, transfer coefficient.

### Previous Work

Despite the increasing interest in dissolution-deposition processes in nonaqueous solutions, few investigations dealt directly with the kinetics of the electrode process. Moreover, most of the literature dealt exclusively with lithium systems. Although the work of Harris and Tobias (2) included deposition tests of active metals from cyclic esters, these were mostly qualitative in nature and did not reach the stage of systematic kinetic measurements.

The electron transfer kinetics of  $\text{Li}/\text{Li}^+$  reaction in PC was studied by several laboratories. Burrows and Jasinski (3) measured the exchange current density of  $\text{Li}(s)$  in 1M  $\text{LiClO}_4$ -PC at 28°C, using micropolarization measurements. However, the reported exchange current density appears too low (0.0275 mA/cm<sup>2</sup>), probably due to the inclusion of an ohmic drop in the potential measurements. Meibuhr (4) measured the exchange currents of lithium in different  $\text{LiClO}_4$  concentrations in PC, at temperatures up to 70°C. At 28°C, for 1M  $\text{LiClO}_4$ -PC solution, the exchange current,  $i_0 = 0.95$  mA/cm<sup>2</sup>, and the transfer coefficient,  $\alpha = 0.67$ , were calculated from the linear polarization curves and from the concentration dependence of the exchange current. The solution was stirred by bubbling argon, and the ohmic drop was excluded using a pulse technique. The Nernstian behavior of the lithium electrode was confirmed by concentration cells. The enthalpy of solvation at zero polarization was estimated as 8.5 kcal/mole, and the reaction order was one, which reaffirmed the assumption that the charge transfer was the rate-determining step. In a second article, Meibuhr (5) studied the anion effect on the electrode kinetics of  $\text{Li}/\text{Li}^+$  in PC. The exchange currents for unit molarity solutions of  $\text{LiAlCl}_4$ ,  $\text{LiPF}_6$ , and  $\text{LiBF}_4$  are 0.40, 0.29, and 0.5 mA/cm<sup>2</sup>, respectively. The transfer coefficient for  $\text{LiAlCl}_4$  was  $\alpha = 0.8$ . The water content of the solutions had a major influence on the electrode performance. Scarr (6) measured the kinetics of lithium electrode in different concentrations of  $\text{LiClO}_4$  in PC. Film formation and two levels of activity were observed, depending on the pretreatment of the electrode. The film was broken at high currents. The exchange current density of a film-free electrode in 1M  $\text{LiClO}_4$  PC solution is  $1.78 \pm 0.33$  mA/cm<sup>2</sup>. Generally, good agreement was found between Meibuhr's and Scarr's results, which are complementary, since Scarr worked at moderately high currents, while Meibuhr's work is restricted to the zone of linear current-potential dependence. Butler, Cogley, and Synnot (7) studied the aging effect on the kinetics of lithium in  $\text{LiClO}_4$  solution in PC. Even when the solvent was quite "dry" (<0.001M  $\text{H}_2\text{O}$ ), the exchange current dropped from 10.2 mA/cm<sup>2</sup> at 1 sec after the exposure of the freshly cut lithium surface, to 1.6 mA/cm<sup>2</sup> after 1 hr. The effect of water was also dramatic; the presence of 0.02M  $\text{H}_2\text{O}$  reduced the exchange current to 0.026 mA/cm<sup>2</sup> after 1 hr. It seems that most measurements were taken on aged surfaces; the exchange currents of fresh surfaces may have no practical meaning. The effect of water content on the behavior of lithium electrodes in  $\text{LiClO}_4$  (8,9) showed that  $\text{LiOH}$  was formed on the electrode during the deposition of lithium from  $\text{LiClO}_4$  solution in PC.

The anodic polarization of lithium in 1.0M  $\text{AlCl}_3$  PC solution was investigated by Jackson and Blomgren (10), using an interrupter and a constant load pulse technique. Severe polarization of the concentration type was observed, which could be caused by the formation of  $\text{LiCl}$  layer during the anodic discharge. Sufficient stirring removed the product which dissolved in  $\text{AlCl}_3$  solution and eliminated the concentration polarization.

In a study of the anodic behavior of sodium in  $\text{NaClO}_4$  PC solution, Meibuhr (11) reports that the exchange current depends strongly on the  $\text{Na}^+$  concentration. At 1M  $\text{NaClO}_4$  and at 19°C, the exchange current was 0.21 mA/cm<sup>2</sup>.

The behavior of lithium in related solvents is reported in several papers. The electrochemical behavior of  $\text{Li}$  in solutions of  $\text{LiClO}_4$ ,  $\text{KPF}_6$ , and of  $\text{KCNS}$  in ethylene carbonate was reported by Pistoia *et al.* (12,13). Ethylene carbonate was proposed as a superior solvent for high energy batteries due to its higher conductance and lower viscosity, and due to the better anodic polarization characteristics found for  $\text{Li}$  in  $\text{LiClO}_4$ -EC solution.

The kinetics of  $\text{Li}(\text{Hg})$  in  $\text{LiCl}$  solution in DMSO was reported by Cogley and Butler (14,15). The Tafel equation with cathodic transfer coefficient  $\alpha = 0.75$  was obeyed over the current density range of  $10^{-5}$  to  $3 \times 10^{-3}$  A/cm<sup>2</sup>. The exchange currents were in the order of 0.1-1.0 mA/cm<sup>2</sup>.

Tiedemann and Bennion (22) compared their kinetic measurements of  $\text{Li}$  in dimethyl sulfoxide to similar measurements in PC, however it should be kept in mind that their measurements were performed in different solvent, and medium effects must be considered as partly responsible for the higher exchange currents in dimethyl sulfoxide; the effect of the medium on the electrode kinetics is discussed in detail by Journé (1).

### Experimental

The micropolarization measurements of the alkali metals were performed in the same six-compartment cell where the cell potentials were measured (1,16). The galvanostatic experiments were conducted between two alkali metal electrodes where the central one served as the working electrode. The central working electrode was prepared in the glove box by sealing an approximately 5 cm long portion of a bright alkali metal wire in epoxy resin. The end of the wire, not sealed in epoxy resin, was used for an electrical contact by attaching it to an alligator clip. The other end of the coated wire was cut at a right angle to the wire to expose the bright alkali metal surface with an area equal to the cross-sectional area of the wire. The other alkali metal electrodes were simply the original bright wires. Alkali metals react slowly with epoxy resin. The polarization experiments were performed within a few hours after the exposure and no signs of reaction between the metals and the resin were observed throughout the measurements. In addition, the small bias potentials between the coated and uncoated electrodes (1) indicate this effect to be negligible. In the case of rubidium and cesium, the working electrodes, as well as the counterelectrodes, were prepared by pouring the molten metals into the cup electrodes (1,16). The solutions were stirred during the micropolarization experiments by a small magnetic stirrer at the bottom of the central cell, just under the electrode's surface. The stirring was somewhat less efficient in the cases of Rb and Cs because the stirrer was underneath the cup, while the active surface of the electrode was facing upward. The small currents employed insured that concentration overpotentials were negligible, even in the cases of Rb and Cs.

Preanodization was found necessary to obtain reproducible results. The standard procedure was to anodize the working electrode for 10 min at a current density of 0.1 mA/cm<sup>2</sup> prior to each micropolarization cycle. The potential was measured between the central working electrode and one of the two  $\text{Tl}(\text{Hg})/\text{TlCl}$  reference electrodes. The current was increased first in the anodic direction, then back toward the cathodic direction, then back to the equilibrium state. The current was applied by a constant current power supply, Model C 612 Electronic Measurements, and was measured by a Keithley 601 Electrometer. The potential was measured by an AC/DC Differential Voltmeter (John Fluke Model 887-A). The cells were suspended in constant temperature baths at 25° and 35°C  $\pm$  0.01°C. The preparation of the electrodes and the assembly of the cells have been described previously (1,16). Propylene carbonate (Jefferson Chemical Company, Hous-

ton, Texas) was distilled in a low pressure distillation column packed with stainless steel helices; the reflux ratio was 60 to 100; and the head temperature was 65°C. The solutions were treated with molecular sieves 4A. This treatment increased the stability of the alkali metals in the solutions. Gas chromatographic analysis showed the water content to be always below 50 ppm. All operations were conducted inside the argon glove box (1, 16). Addition of  $\text{AlCl}_3$  to PC results in violent reaction, accompanied by high heat of solution and darkening of the solution. This was avoided by adding the alkali metal chloride first, then adding the  $\text{AlCl}_3$  very slowly while cooling the solution with a cooling mixture of chloroform-carbon tetrachloride-dry  $\text{CO}_2$  (1). Solutions prepared in this way were almost colorless. The stability of the solutions increased as the ratio of the alkali metal chloride to  $\text{AlCl}_3$  molalities approached unity.

Because of the relatively low conductivity of the solutions ( $10^{-3}$ - $10^{-2}$  ohm $^{-1}$ -cm $^{-1}$ ), it was necessary to correct the overpotentials for ohmic drop between the working electrode and the tip of the reference electrode's connection. The ohmic drop was determined by a rapid current interrupter technique, in which the constant current was interrupted, and the potential was traced on a fast oscilloscope. The immediate drop in the potential was the  $IR$  drop, and the ohmic resistance was calculated by dividing it by the total current. The ohmic drop was then subtracted from the total overpotential. Rectangular wave form pulses were derived from an E. M. Test Pulser, Lawrence Berkeley Laboratory. The potentials were observed on a Tektronix Oscilloscope, and the potential trace was analyzed from the polaroid prints. The oscilloscope was operating at 0.01-1.0 msec/cm and 50-200 mV/cm. The ohmic drop was determined at four different currents for each cell, both in anodic and cathodic directions. The currents employed during the pulse measurements were higher than the currents employed during the micropolarization experiments, and it has been assumed that the current distribution remained unchanged. Typical oscilloscope traces of the potential during current interruptions both in the cathodic and the anodic directions, are presented in Fig. 1. Currents were in the order of 0.1-1.0 mA, and the calculated ohmic resistances were in the order of 100-300 ohms. The calculated resistance from the four measurements agreed within 10%.

The polarization experiments were conducted at different alkali metal chloride molalities in  $\text{AlCl}_3$  (1M)-PC solution and 25°C.

### Results

**Micropolarization of the alkali metals in their chloride solutions in  $\text{AlCl}_3$  (1M)-PC.**—Micropolarizations of the alkali metals in different molalities of alkali metal chlorides in  $\text{AlCl}_3$  (1M)-PC solution are presented in Fig. 2-6. The temperature was held constant at  $25 \pm 0.01^\circ\text{C}$ . The overpotentials are  $IR$  free, and the ohmic drop was estimated from the current interrupter technique. At low overpotentials, linear behavior was observed for all the metals; deviation from linearity was observed at potentials above approximately 50 mV, where the nonlinear Tafel behavior became appreciable.

The exchange current densities were calculated from the slopes of the linear polarizations, assuming single electron charge transfer controlled mechanism according to the equation

$$i_a^0 = \frac{1}{A} \frac{RT}{F} \frac{\partial i}{\partial \eta_{i=0}} \quad [2]$$

and the results are presented in each figure (Fig. 2-6).

**Enthalpy of activation at zero polarization.**—Micropolarizations of the lithium electrode in different LiCl concentrations in  $\text{AlCl}_3$  (1M)-PC were performed at three different temperatures: 25°, 30°, and 35°C. Fig-

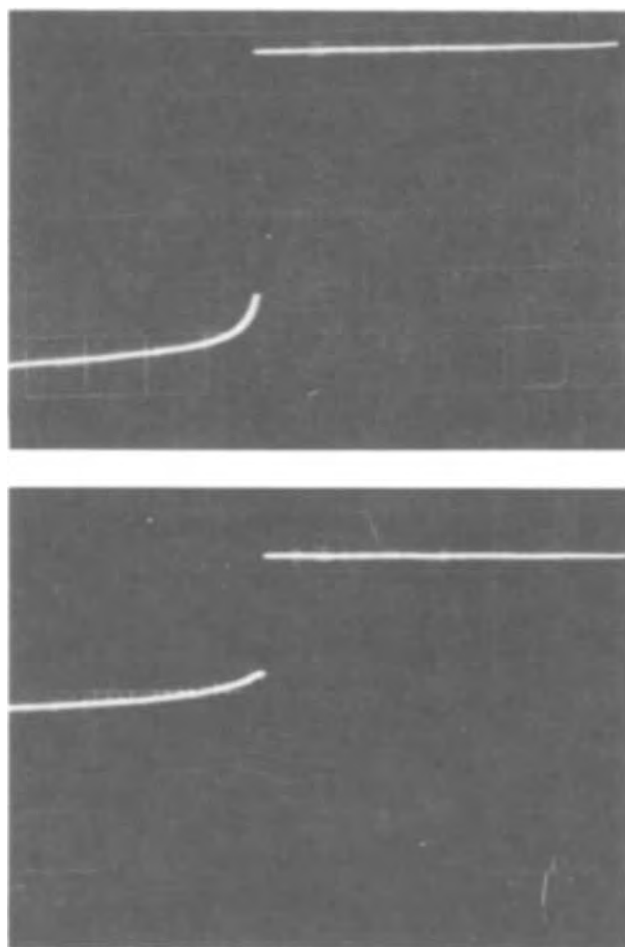


Fig. 1.  $IR$  drop determination in the six-compartment cell using a current interrupter technique.  $\text{Rb/RbCl}(0.10M)$  in  $\text{AlCl}_3(1.0M)$ -PC at 25°C. Top, cathodic current,  $i = 1.0$  mA; bottom, anodic current,  $i = 0.5$  mA. Vertical scale, 50 mV/cm; horizontal scale, 1 msec/cm.

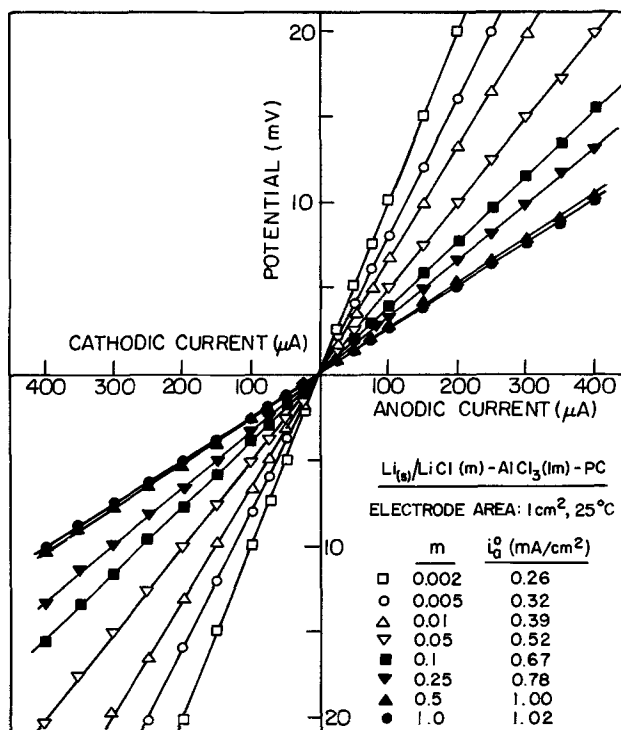


Fig. 2. Micropolarization of  $\text{Li}(s)/\text{LiCl}(M)$  in  $\text{AlCl}_3(1M)$ -PC solution.

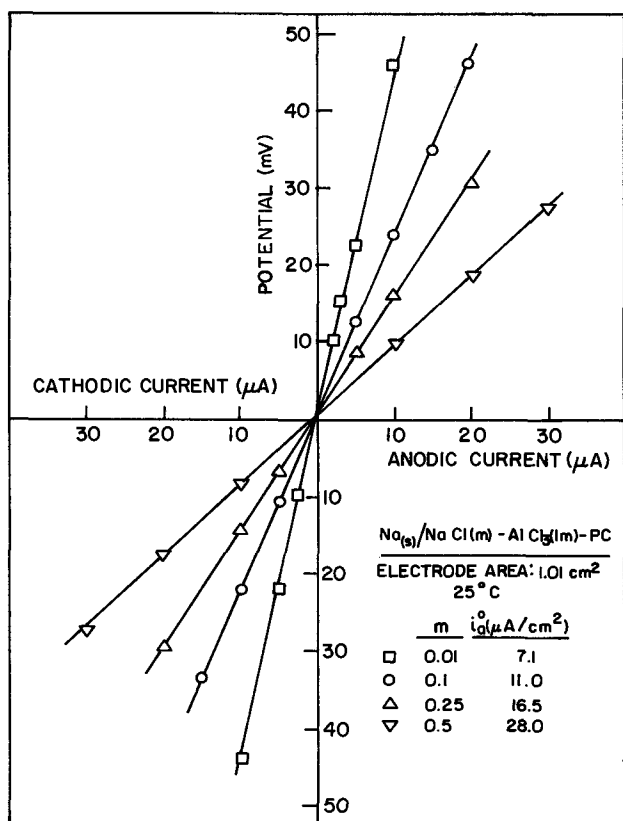


Fig. 3. Micropolarization of  $\text{Na}(s)/\text{NaCl}(M)$  in  $\text{AlCl}_3(1M)$ -PC solution.

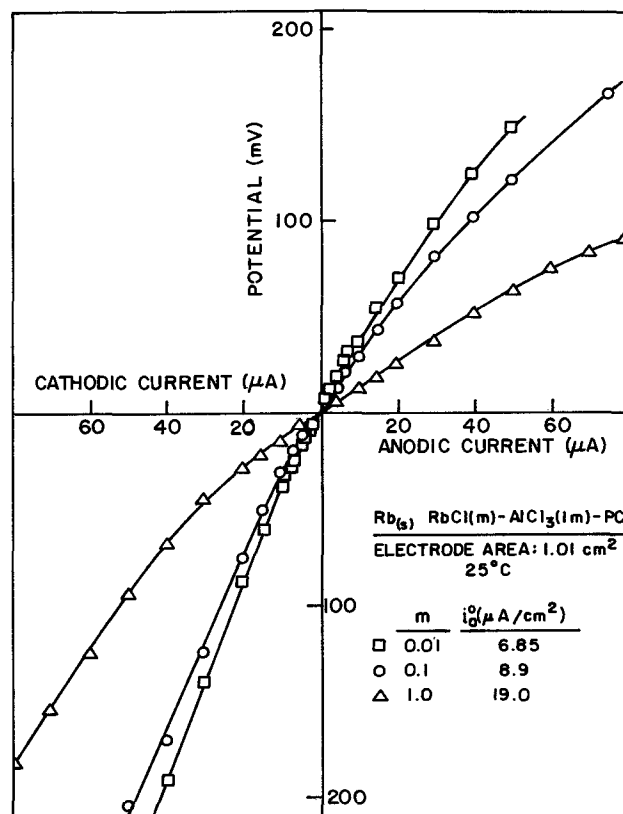


Fig. 5. Micropolarization of  $\text{Rb}(s)/\text{RbCl}(M)$  in  $\text{AlCl}_3(1M)$ -PC solution.

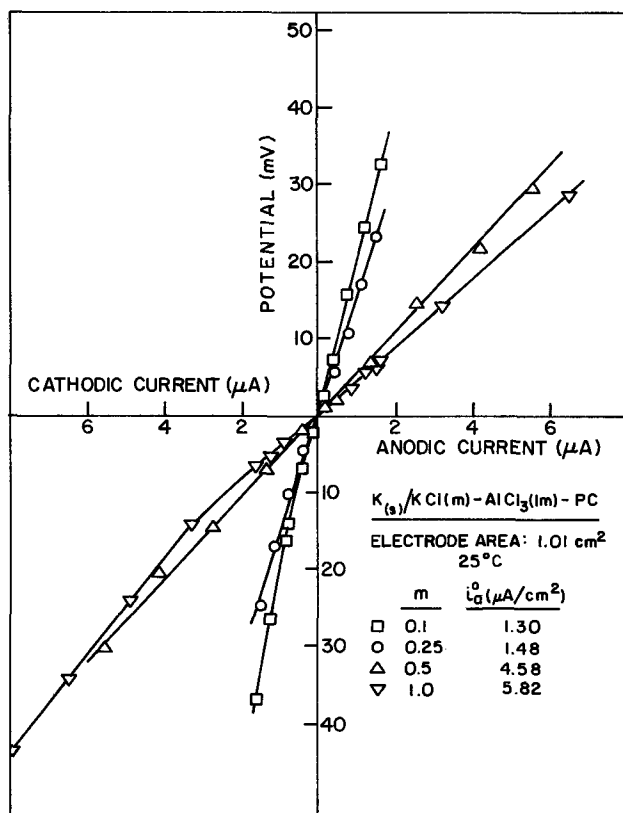


Fig. 4. Micropolarization of  $\text{K}(s)/\text{KCl}(M)$  in  $\text{AlCl}_3(1M)$ -PC solution.

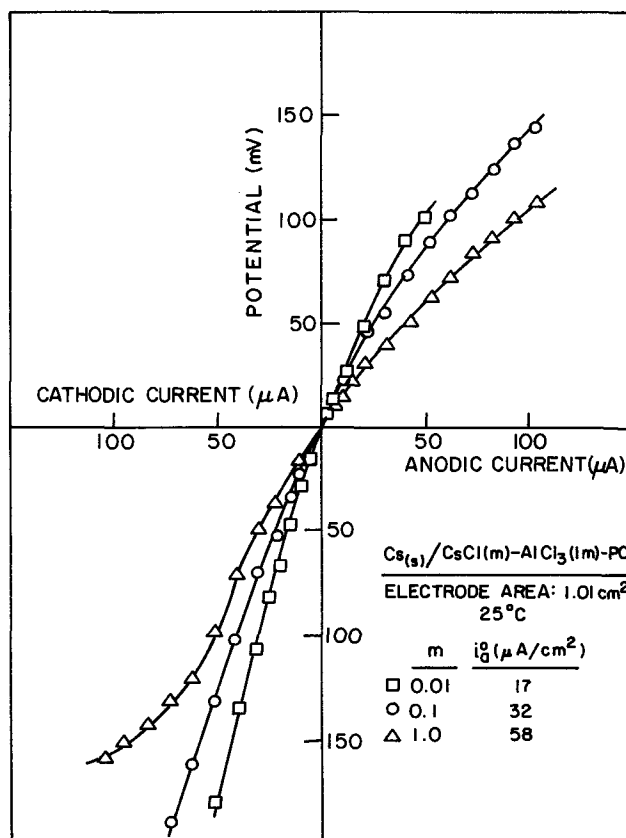


Fig. 6. Micropolarization of  $\text{Cs}(s)/\text{CsCl}(M)$  in  $\text{AlCl}_3(1M)$ -PC solution.

ure 7 presents the plot of the apparent exchange current densities,  $i_a^0$ , vs.  $1/T$  for the various  $\text{LiCl}$  molalities. The slopes of the lines are about equal, and the average enthalpy of activation at zero polarization was

calculated as

$$\Delta H_o^* = -R \frac{\partial \ln i_a^0}{\partial (1/T)} = 8.6 \text{ kcal/mole} \quad [3]$$



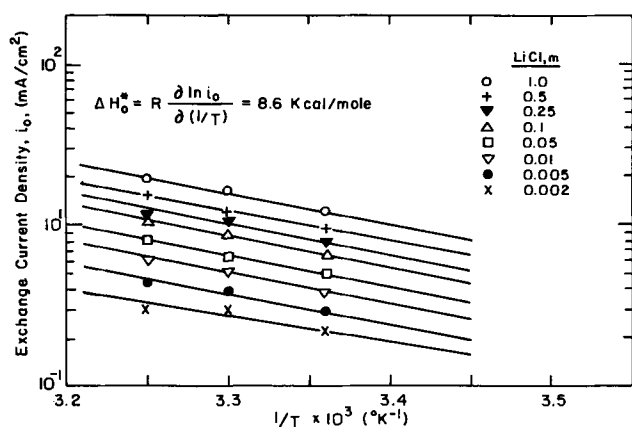


Fig. 7. Determination of the enthalpy of activation at zero polarization for Li/LiCl(M) in  $\text{AlCl}_3(1M)$ -PC solution.

The value of  $\Delta H_0^*$  is within the order of magnitude expected for soft metals. A similar value of 7.1 kcal/mole was obtained for the sodium electrode in  $\text{NaClO}_4$  solution in PC (1).

The micropolarization behavior of a cesium electrode in  $\text{CsAlCl}_4$  (0.25M) solution in PC is presented in Fig. 8. The plot of  $i_a^0$  vs.  $1/T$  is presented in Fig. 9, from which the enthalpy of activation at zero polarization is 10.4 kcal/mole. A somewhat lower exchange current density was obtained for the Cs electrode at 23.5°C. At this temperature cesium is solid, while the other temperatures employed are above the melting point of cesium, i.e., 28.5°C.

### Discussion

Micropolarizations of the alkali metals in alkali metal chloride solutions in  $\text{AlCl}_3$  (1M)-PC were presented in Fig. 2-6. The apparent exchange current densities were calculated from the slopes at the point of zero current. A linear behavior can be observed for all

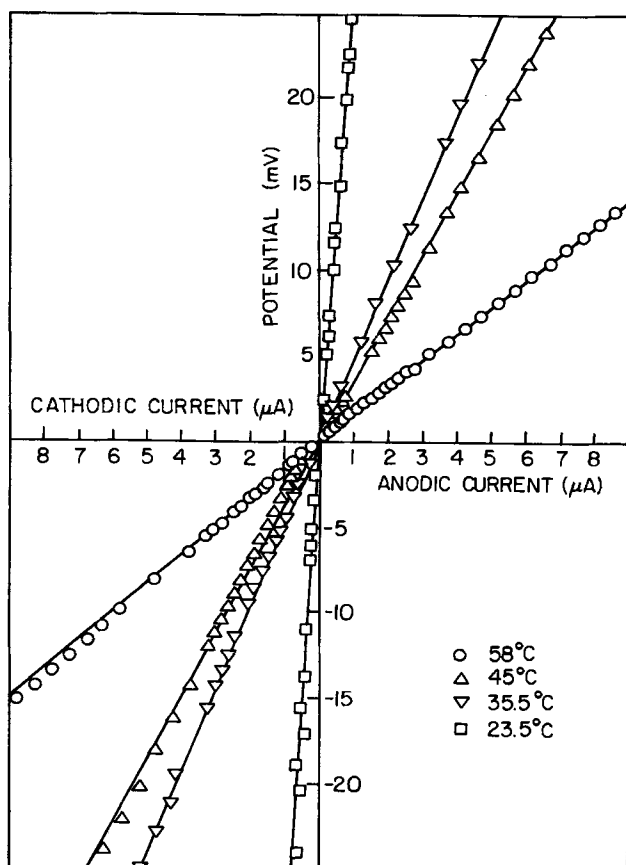


Fig. 8. Micropolarization of Cs(s)/ $\text{CsAlCl}_4(0.25M)$  in PC

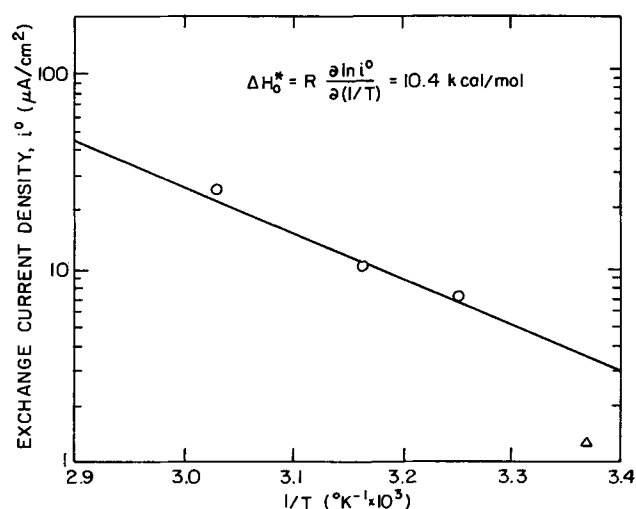


Fig. 9. Determination of the enthalpy of activation at zero polarization of Cs(s)/ $\text{CsAlCl}_4(0.25M)$ , PC.  $\circ$ , Liquid Cs;  $\Delta$ , solid Cs.

the alkali metals over a wide range of alkali metal chloride concentrations. Using a low current and moderate stirring ensured the elimination of concentration overpotential. The apparent exchange current densities were not corrected for the nonuniform current densities across the surface of the electrodes. The influence of the nonuniformity of the current across the electrode is discussed in the Appendix, where it is shown that, despite relatively low conductivities, this correction is negligible for the present case, because of low exchange current densities.

The comparison of the magnitude of the exchange currents to corresponding values in the literature is restricted to the lithium system, because no information is available for the rest of the alkali metals. The exchange current density of Li in  $\text{LiAlCl}_4$  (1M), according to the present results, is 1.02, 1.5, and 2.0  $\text{mA/cm}^2$  at 25°, 30°, and 35°C, respectively. These values are in general agreement with the exchange currents of 0.40, 1.05, 1.49, and 2.35  $\text{mA/cm}^2$  reported by Meibuhr (5) for  $\text{LiAlCl}_4$  (1M) at 19°, 35°, 46°, and 55°C, respectively. A plot of the exchange current densities vs.  $1/T$  is presented in Fig. 7, and the calculated enthalpy of activation at zero polarization,  $\Delta H_0^* = 8.6$  kcal/mole, is in agreement with an enthalpy of 6.4 kcal/mole, reported by Meibuhr (5). Kinetic measurements of Li in  $\text{LiClO}_4$  solutions in PC were performed by Meibuhr (4) and Scarr (6). The exchange current densities in  $\text{LiClO}_4$  (1M) solution were 0.95, 1.8, 3.4, and 5.25  $\text{mA/cm}^2$  at 28°, 43°, 58°, and 67.5°C, respectively (4), and 1.78  $\text{mA/cm}^2$  at 23°C (6). The  $i_0$  values for  $\text{LiClO}_4$  solution in PC are of the same order of magnitude as those obtained here for  $\text{LiAlCl}_4$ . Butler *et al.* (7) found that the current density changes significantly during the first few minutes after the preparation of a clean fresh Li surface. However, all earlier experiments, as well as the present ones, were performed on aged surfaces, which is a more practical condition. Preanodization of the surface was necessary to obtain reproducible results. It is not clear whether this procedure removes adsorbed impurities or breaks an insulating film on the electrode. Scarr (6) reports two levels of activities of Li electrode in  $\text{LiClO}_4$  solution in PC, depending on the pretreatment of the surface, and the lower level of activity was associated with film formation.

The exchange current densities for the rest of the alkali metals are lower than those for Li. The wide differences in the exchange currents in the alkali metal series are discussed in detail elsewhere (1), where the medium effect and the influence of the individual ionic energetics on the electrode kinetics is discussed with regard to the behavior of the alkali metal amalgams.

The free energies of transfer of the alkali metal ions from water to  $\text{AlCl}_3$ -PC solution are:  $-0.6$ ,  $-4.2$ ,  $-4.7$ ,  $-3.1$ , and  $-5.0$  kcal/mole for  $\text{Li}^+$ ,  $\text{Na}^+$ ,  $\text{K}^+$ ,  $\text{Rb}^+$ , and  $\text{Cs}^+$ , respectively (1). A large negative free energy of transfer means that the ion is on a low energy level, strongly solvated, and as a result, the exchange current density is low. The low exchange current densities of some of the alkali metals might also be the result of their reactivity toward impurities, water traces, and possibly the solvent itself. This is especially true for potassium, which showed reactivity toward PC solutions which had not been treated with molecular sieves.

The exchange current density of a Na electrode in  $\text{NaCl}$  (0.5M) solution in  $\text{AlCl}_3$  (1M)-PC is  $28 \mu\text{A}/\text{cm}^2$  at  $25^\circ\text{C}$ , which can be compared qualitatively to a value of  $12 \mu\text{A}/\text{cm}^2$  for a Na electrode in  $\text{NaClO}_4$  (0.5M) solution in PC at  $19^\circ\text{C}$  (11).

The reported exchange current densities are subjected to the influence of the films formed due to the inherent reactivity of the alkali metals with PC. Film formation was observed on Li electrodes in PC (6, 23).

The transfer coefficients of the electrochemical reaction at the alkali metal electrode interface can be calculated from the dependence of the exchange current density on the concentration of the reduced ion (19, 20)

$$1 - \alpha_c = \frac{\partial \log i_a^0}{\partial \log m_{M^+}} \quad [4]$$

where  $\alpha_c$  is the cathodic transfer coefficient. Figure 10 presents the plot of  $\log i_a^0$  vs.  $\log m_{\text{MCl}}$  for all the alkali metals, as well as the calculated  $\alpha_c$ . The cathodic transfer coefficient for Li is  $\alpha_c = 0.75$ , in agreement with  $\alpha_c = 0.8$  reported for  $\text{LiAlCl}_4$  in PC, and  $\alpha_c = 0.62$ - $0.72$  for  $\text{LiClO}_4$  in PC (4-6). The lithium system was further investigated at three different temperatures,  $25^\circ$ ,  $30^\circ$ , and  $35^\circ\text{C}$ . The plots of  $\log i_a^0$  vs.  $\log m_{\text{LiCl}}$  at the three temperatures are presented in Fig. 11, and the parallel lines show that the transfer coefficient does not change over this temperature range. An average  $\alpha_c = 0.75 \pm 0.05$  was calculated for the three temperatures.

The behavior of the alkali metals in the Tafel region should be investigated in the future. Cyclic polarizations were obtained for K, Rb, and Cs and are covering the Tafel region (1). Although the polariza-

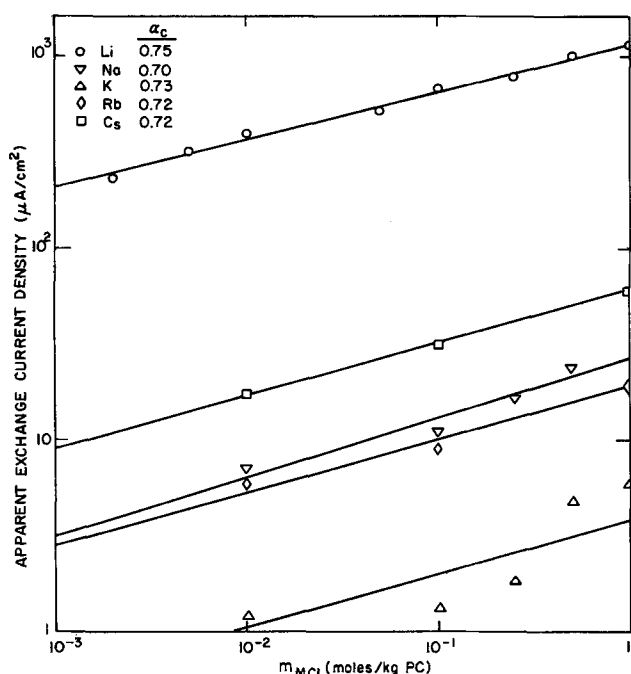


Fig. 10. Determination of the cathodic transfer coefficients of the alkali metals in  $\text{AlCl}_3$ (1M)-PC.

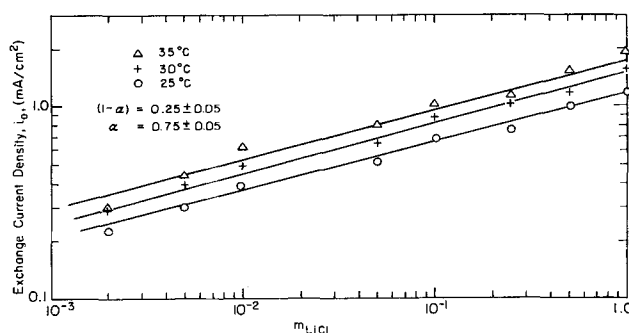


Fig. 11. Determination of the cathodic transfer coefficients of Li in  $\text{AlCl}_3$ (1M)-PC at  $25^\circ$ ,  $30^\circ$ , and  $35^\circ\text{C}$ .

tions include the ohmic drop between the working and the reference electrode, Tafel behavior can nevertheless be observed qualitatively in some of these figures. It is believed that the exchange currents in this region are higher than the values obtained in the micropolarization experiments because of continuous renewal of the active surface and the breakage of possible film formation at high deposition or dissolution rates.

### Acknowledgment

This work was conducted under the auspices of the U.S. Atomic Energy Commission.

Manuscript submitted Jan. 28, 1974; revised manuscript received March 21, 1974. This was Paper 277 presented at the Chicago, Illinois, Meeting of the Society, May 13-18, 1973.

Any discussion of this paper will appear in a Discussion Section to be published in the June 1975 JOURNAL. All discussions for the June 1975 Discussion Section should be submitted by Feb. 1, 1975.

### APPENDIX

#### Nonuniform Current Distribution and Ohmic Drop Effects in Micropolarization Measurements

Under nonuniform current density conditions, the exchange current,  $i^0$ , determined from the linear polarization, depends on the location of the reference electrode, because the measured overpotential is related to the local current density which differs from the average current density. The correction can be obtained by solving the secondary current distribution subjected to a boundary condition of linear polarization. The present analysis follows the treatment of Tiedemann, Newman, and Bennion (21) concerning the error in measurements of electrode kinetics caused by nonuniform ohmic potential drop to a disk electrode.

The correction for the apparent exchange current  $i^0/i^0_{\text{apparent}}$  was solved for the general arbitrary location of the reference electrode (21), and is plotted against  $J$

$$J = (\alpha_a + \alpha_c) \frac{Fr_0 i^0}{RT\kappa_a}$$

$J$  represents, in a way, the throwing power of the system.

The exchange current densities reported in the present work are the apparent ones; however, the corrections are negligible. Considering the extreme conditions,  $r = 0.5$  cm,  $\kappa_a = 5 \times 10^{-3}$  ohm $^{-1}$ -cm $^{-1}$ ,  $i^0 = 1.0$  mA/cm $^2$ , and assuming  $(\alpha_c + \alpha_a) = 1$ , we can estimate the largest possible  $J$  for the present systems to be

$$J = 4$$

Since the reference electrodes were located far away from the disk electrode, the correction, according to curve B in Fig. 1 (21) is about  $i^0/i^0_{\text{apparent}} = 1.1$ , which

is negligible, especially since the errors in the exchange current values are probably more than 10%. It should be mentioned here that the extreme conditions given above were realistic only for the lithium system. For the rest of the alkali metals the exchange current densities are ten times lower, and the conductivities are somewhat higher, both resulting in lower  $J$ , and the correction is probably in the order of 1%.

## REFERENCES

- Jacob Jorné, Ph.D. Thesis, LBL 1111, University of California, Berkeley, California (1972).
- William S. Harris, Ph.D. Thesis, UCRL 8381, University of California (1958).
- B. Burrows and R. Jasinski, *This Journal*, **115**, 365 (1968).
- Stuart G. Meibuhr, *ibid.*, **117**, 56 (1970).
- Stuart G. Meibuhr, *ibid.*, **118**, 1320 (1971).
- Robert F. Scarr, *ibid.*, **117**, 295 (1970).
- J. N. Butler, D. R. Cogley, and J. C. Synnott, *J. Phys. Chem.*, **73**, 4026 (1969).
- B. Burrows and S. Kirkland, *This Journal*, **115**, 1164 (1968).
- A. N. Dey, *ibid.*, **114**, 823 (1967).
- G. W. Jackson and G. E. Blomgren, *ibid.*, **116**, 1483 (1969).
- Stuart G. Meibuhr, *ibid.*, **118**, 709 (1971).
- Gianfranco Pistoia, *ibid.*, **118**, 153 (1971).
- G. Pistoia, M. DeRoss, and B. Scrosati, *ibid.*, **117**, 500 (1970).
- D. R. Cogley and J. N. Butler, *ibid.*, **113**, 1074 (1966).
- D. R. Cogley and J. N. Butler, *J. Phys. Chem.*, **72**, 4568 (1968).
- Jacob Jorné and Charles W. Tobias, Submitted to *This Journal*.
- John Newman, *ibid.*, **113**, 501 (1966).
- L. Hsueh, M.S. Thesis UCRL 16607, University of California (1966).
- Paul Delahay, "Double Layer and Electrode Kinetics," Interscience Publishers, Inc., New York (1965).
- Terrell, N. Andersen, and Henry Eyring, in "Physical Chemistry, An Advanced Treatise," Henry Eyring, Editor, Academic Press, New York (1970). Vol. IXA/Electrochemistry.
- William H. Tiedemann, John Newman, and Douglas N. Bennion, *This Journal*, **120**, 256 (1973).
- William H. Tiedemann and Douglas N. Bennion, *ibid.*, **120**, 1624 (1973).
- A. N. Dey, Abstract 62, p. 154, Electrochemical Society Extended Abstracts, Fall Meeting, Atlantic City, N. J., Oct. 4-8, 1970.

## Mass Transfer of Minor Components in a Propagating Crack

William H. Smyrl\*

Sandia Laboratories, Albuquerque, New Mexico 87115

and John Newman\*

Inorganic Materials Research Division, Lawrence Berkeley Laboratory, and  
Department of Chemical Engineering, University of California, Berkeley, California 94700

The publication costs of this article have been assisted by the U.S. Atomic Energy Commission.

### ABSTRACT

The mass transfer of a dilute species in a liquid in a propagating crack is treated. The analysis includes the effect of convective flow of the liquid. The results of the calculations show that the crack tip is devoid of the minor species, and that the mass flux of this component is also negligible in this region. Therefore, minor components could not behave as "critical" species in such systems. Calculation of the flux distribution allowed the determination of the potential distribution in the crack.

The failure of structural materials such as metals and their alloys by stress corrosion cracking is a complex phenomenon which involves the interplay of metallurgical, mechanical, and environmental influences. For an alloy of a particular metallurgical condition in a constant environment, the crack propagation may be investigated as a function of stress intensity,<sup>1</sup> a mechanical variable. It is generally found for titanium and aluminum alloys (1-3) that the rate of crack extension is dependent on the stress intensity at low stress levels but becomes independent of the stress intensity at higher levels. Several workers (4-6) have suggested that the process limiting the crack growth rate at high stress intensities is related to mass transfer of components in the environment. "Cavitation"

caused by limitations on the fluid flow in a propagating crack could also limit the cracking rate, as discussed recently (7).

The alloy titanium-8% aluminum-1% molybdenum-1% vanadium has been found to be susceptible to stress corrosion cracking in molten LiCl-KCl eutectic (8). A plateau velocity of 1 cm/sec was observed at high stress intensities, and the crack extension rates were a function of stress intensity at lower stress intensities. The presence of the plateau velocity could not be explained by cavitation (7), so the possible role of mass transfer has been investigated. Possible species which could limit the rate of crack extension in the molten salt environment are Li<sup>+</sup>, K<sup>+</sup>, or some impurity such as H<sub>2</sub>O (or OH<sup>-</sup>). The first two are ruled out by the dependence of the cracking rate on electrical potential (8, 9). Water was present in the commercial eutectic material at about 1 ppm (reported as OH<sup>-</sup>), and the SCC tests were carried out under potential conditions

\* Electrochemical Society Active Member.

Key words: stress corrosion cracking, molten salt, corrosion, convective diffusion.

<sup>1</sup> The stress intensity is related to the stress, flaw size, and specimen geometry for materials which obey the laws of linear elastic fracture mechanics (1, 2).

where water was reacting at mass transfer limited rates. However, when additional water was deliberately added to the melt, the crack velocity was unchanged. The water concentration could not be varied over wide limits because of limited solubility, so the tests were not as conclusive as one would like. Therefore, the mathematical treatment of the mass transfer of dissolved water to a crack tip was studied, and the present contribution presents the results of that study.

The rate of electrode reactions in electrolytic systems is influenced by activation, ohmic, and concentration effects. The activation and ohmic influences are dominant at low currents and high concentrations of reacting species, and the interplay between the two determine the distribution of current in the system. In situations where the concentration of the reacting species becomes depleted at the electrode, the rate of reaction and current distribution on the electrode are determined by the relative accessibility of various parts of the surface to mass transfer of the reacting component. Even if the surface is uniformly accessible to mass transfer, the potential distribution near the electrode may be nonuniform. Variations in the electrical potential along the surface may lead to discharge of other species besides the one under mass transfer control. Nonuniform potential distributions would be important in systems where the electrode is large and where there are two or more electroactive species in solution. Of particular interest in the present study is the potential distribution associated with the mass transfer behavior in the crack and its possible role in determining the distribution of other (anodic dissolution) reactions within the crack.

### Model

The physical model to be treated here is sketched in Fig. 1. The crack is wedge shaped, with a geometrically sharp tip, and extends through the thickness of the material. The coordinate system moves with the crack tip, so that the sides of the crack appear to move with the velocity  $V$  (1 cm/sec for LiCl-KCl) away from the tip. The flow pattern of the liquid has been determined from a treatment of the fluid mechanics of the system (7) and is shown also in this figure. The assumption is adopted here that these velocity profiles are not changed by the mass transfer processes which we are considering. This is justified by the small concentration of the species of interest and may be checked by using the results which are obtained below. This inclusion of convective effects on mass transfer has not been considered previously for stress corrosion calculations.

The steady-state velocity profiles in the liquid were found to be (7), for a small crack angle,  $2\theta_w$

$$v_r = -\frac{V}{2} \left\{ 1 - 3 \frac{\theta^2}{\theta_w^2} \right\} \quad (\text{radial component}) \quad [1]$$

$$v_\theta = \frac{V\theta}{2} \left\{ 1 - \frac{\theta^2}{\theta_w^2} \right\} \quad (\text{angular component}) \quad [2]$$

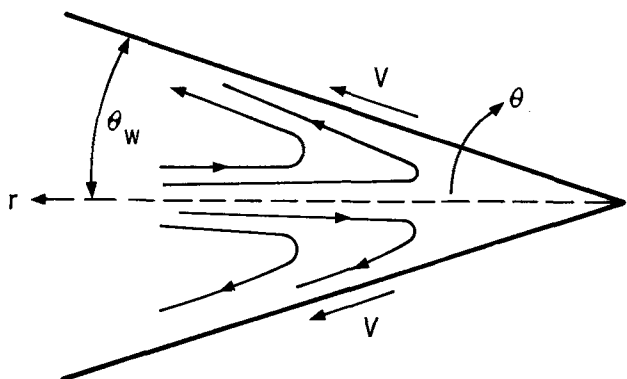


Fig. 1. Fluid flow in a propagating crack

These relationships are valid near the crack tip and out to distances from the crack tip of

$$r = O \left( 47 \frac{\nu}{\theta_w^2 V} \right)$$

where the notation  $O(\ )$  denotes "order of magnitude of." With the physical properties of molten LiCl-KCl<sup>2</sup> and a crack angle,  $2\theta_w$ , of  $10^{-2}$  radians, this amounts to

$$r = O(10^{+3} \text{ cm})$$

At greater distances from the crack tip, inertial and pressure forces determine the fluid flow characteristics, except near the crack walls where viscous forces are also important. We shall not be interested in such large distances from the crack tip except for completeness. Also, seepage of liquid in from the sides of the crack for plates of finite thickness becomes important at distances from the crack tip where the thickness is of the same order as  $\theta_w r$ .

The equation of convective diffusion for this system is, at steady state

$$v_r \frac{\partial c}{\partial r} + \frac{v_\theta}{r} \frac{\partial c}{\partial \theta} = D \left( \frac{\partial^2 c}{\partial r^2} + \frac{1}{r} \frac{\partial c}{\partial r} + \frac{1}{r^2} \frac{\partial^2 c}{\partial \theta^2} \right) \quad [3]$$

where  $c$  = concentration,  $D$  = diffusion coefficient, and  $v_r$ ,  $v_\theta$  are given in Ref. (1) and (2).

The boundary conditions are

$$c = 0 \text{ at crack wall} \quad [4]$$

$$c \rightarrow c_\infty \text{ at } \theta = 0, r \rightarrow \infty \quad [5]$$

An auxiliary condition is

$$\frac{\partial c}{\partial \theta} = 0 \text{ at } \theta = 0 \quad [6]$$

since by symmetry there is no transfer of material across the crack center line. Equation [3] is valid for uncharged species, or for charged species where migration effects are not important. Migration makes no substantial contribution to Eq. [3] for our case because the concentration of any minor species is small as compared to that of  $K^+$ ,  $Li^+$ , and  $Cl^-$ . The boundary conditions are appropriate when the species,  $H_2O$ , is being consumed (reduced) at limiting current. Since most of the stress corrosion tests have been carried out under potentiostatic conditions, almost to the lithium deposition potential, this is justified. We are also assuming that the discharge of water does not introduce a passive film on the surface which would change the discharge characteristics. Titanium displays no passivation characteristics in the molten salt, so this assumption may be reasonable.

### Mathematical Treatment

For cracks of small angle, the  $\theta$ -dimension can be scaled accordingly, and the distance from the crack tip can be made dimensionless in such a way that different regions of mass transfer are revealed.

Introduction of the new variables

$$\theta^* = (\theta/\theta_w) \\ r^* = \frac{rV}{D} (\theta_w)^2$$

into Eq. [3] yields

$$-\frac{1}{2} (1 - 3\theta^{*2}) \frac{\partial c}{\partial r^*} + \frac{1}{2} \theta^* \frac{(1 - \theta^{*2})}{r^*} \frac{\partial c}{\partial \theta^*} \\ = \frac{1}{r^{*2}} \frac{\partial^2 c}{\partial \theta^{*2}} + \theta_w^2 \left( \frac{\partial^2 c}{\partial r^{*2}} + \frac{1}{r^*} \frac{\partial c}{\partial r^*} \right) \quad [7]$$

The last two terms, which contain the contribution of radial diffusion, may be discarded except for very small

<sup>2</sup>The viscosity,  $\nu$ , of molten LiCl-KCl at 375°C is  $1.33 \times 10^3$  cm<sup>2</sup>/sec. The velocity,  $v$ , of cracking in the plateau is 1 cm/sec.

values of  $r^*$ . All the other terms are of order unity, but these two terms are of order  $\theta_w^2$  or  $10^{-4}$  for  $r^*$  of order unity. Since appreciable mass transfer occurs only at larger values of  $r^*$ , we neglect these radial diffusion terms in the remainder of this work.

The radial convection term (first term on the left) and the angular diffusion term (first term on the right) are the most important terms for  $r^*$  of order unity. The second term on the left (angular convection) will become important at larger values of  $r^*$ . Attempting a separation of variables on the two dominant terms leads one to expect a solution of the form

$$c \sim \frac{e^{-K/r^*}}{r^{*s}} f(\theta^*)$$

where  $K$  is the separation constant and  $f$  is a function to be determined. The expectation that the angular convection term would become important at larger values of  $r^*$  suggests that additional terms could be added to this solution in the form

$$c \sim \frac{e^{-K/r^*}}{r^{*s}} f_0(\theta^*) + r^* \frac{e^{-K/r^*}}{r^{*s}} f_1(\theta^*) + r^{*2} \frac{e^{-K/r^*}}{r^{*s}} f_2(\theta^*) + \dots$$

The equation for the concentration can be recognized as an ordinary perturbation expansion for the solution of Eq. [7]. We are finally led to adopt the form

$$c = \frac{e^{-K/r^*}}{r^{*1/2}} \sum_{n=0}^{\infty} (r^*)^n f_n(\theta^*) \quad [8]$$

where  $K$  is a constant and the  $f_n$ 's are functions to be determined. Substitution into the equation of convective diffusion gives

$$f_0'' + \frac{1}{2} (1 - 3\theta^{*2}) K f_0 = 0$$

$$f_0 = 0 \text{ at } \theta^* = 1, f_0' = 0 \text{ at } \theta^* = 0 \quad [9]$$

$K$  is an eigenvalue and  $f_0$  is arbitrarily set equal to 1 at  $\theta^* = 0$ . For  $n = 1, 2, 3, \dots$

$$f_n'' + \frac{1}{2} (1 - 3\theta^{*2}) K f_n = \frac{1}{2} \theta^* (1 - \theta^{*2}) f_{n-1}' - \frac{1}{2} (1 - 3\theta^{*2}) (n - 3/2) f_{n-1} = g_n \quad [10]$$

With this form for  $c$ , the neglected radial diffusion terms become of the same order as the retained terms when  $r^*$  is of order  $\theta_w$ . The solution to Eq. [9] is

$$f_0 = a_0 \left[ \left( \frac{3K}{2} \right)^{1/8} e^{-\frac{1}{2} \sqrt{\frac{3K}{2}} \theta^{*2}} {}_1F_1 \left( \frac{\sqrt{\frac{3K}{2}} - \frac{K}{2}}{4 \sqrt{\frac{3K}{2}}}, \frac{1}{2}, \sqrt{\frac{3K}{2}} \theta^{*2} \right) \right] \quad [11]$$

where  ${}_1F_1(b, d, x)$  is the confluent hypergeometric function. The function has a series form (10)

$${}_1F_1(b, d, x) = 1 + \frac{b}{d} x + \frac{b(b+1)}{2!d(d+1)} x^2 + \dots \quad [12]$$

$K$  is chosen such that

$$f_0 = 0 \text{ at } \theta^* = 1$$

(i.e.,  ${}_1F_1 = 0$  at  $\theta^* = 1$ ) [13]

Also,  $a_0$  is chosen arbitrarily so that

$$f_0 = 1 \text{ at } \theta^* = 0$$

The solution will be renormalized by "matching" with the outer diffusion layer solution (see below).

For the solution to the nonhomogeneous equation

$$f_n'' + \frac{1}{2} (1 - 3\theta^{*2}) K f_n = g_n$$

we try<sup>3</sup>

$$f_n = h_0(\theta^*) \int_0^{\theta^*} g_n f_0(\theta^*) d\theta - f_0(\theta^*) \int_0^{\theta^*} g_n h_0(\theta^*) d\theta + B_n f_0(\theta^*) \quad [14]$$

Since  $f_0$  is an eigensolution of the homogeneous equation, a solution is possible only if

$$\int_0^1 g_n f_0 d\theta = 0$$

This is true for  $n = 1$ , and it is this requirement that dictates the power  $s$  of  $r^*$  in the leading term of the solution in Eq. [8]. The value of  $B_n$  in the above solution must be selected to meet the requirement

$$\int_0^1 g_{n+1} f_0 d\theta = 0$$

Although Eq. [12] provides an analytic solution to Eq. [9] for each eigenvalue  $K$ , it is not in a convenient form for the calculation of the higher  $f_n$ 's. From Eq. [13] it is also difficult to determine the eigenvalues accurately, but it does allow one to estimate the eigenvalues. Therefore, a numerical technique discussed by Newman (11) was used for the calculation of eigenvalues and eigenfunctions. This then allowed the numerical integration of the ordinary, inhomogeneous, linear, second order differential Eq. [10] for the  $f_n$ 's. The eigenvalues so obtained were checked by using condition of Eq. [13].

The equation for  $f_0$ , Eq. [9], is an ordinary, homogeneous, second order differential equation. It is nonlinear, however, since  $K$  is unknown. A second differential equation is introduced

$$\frac{dK}{d\theta^*} = 0 \quad [15]$$

and both  $f_0$  and  $K$  are unknowns. Equations [9] and [15] are a nonlinear system of two, coupled, ordinary differential equations with boundary conditions

$$f_0 = 0 \text{ at } \theta^* = 1$$

$$f_0 = 1 \text{ at } \theta^* = 0$$

$$f_0' = 0 \text{ at } \theta^* = 0$$

The equations can be linearized about a trial solution, producing a series of coupled, linear differential equations. In finite difference form these give coupled, tri-diagonal matrices which can be solved on a high speed, digital computer. The nonlinear problem can then be solved by iteration [see Newman (12)].

The solution for  $f_n$  is then determined numerically by evaluating the integrals in Eq. [14]. The linearly independent solution for the homogeneous Eq. [9] was actually determined by finite difference methods but with different boundary conditions from those used for  $f_0$ .

The mass flux to the walls is determined from the derivatives of the  $f$ 's at the wall.

The results of these calculations are shown on Fig. 2 and Table I. In Fig. 2, only the first three  $f$ 's are plotted although the first nine were used to calculate the concentration profiles.  $f_0$  has a rather simple behavior,

<sup>3</sup> Here  $h_0 = f_0(\theta^*) \int_0^{\theta^*} \frac{d\theta^*}{f_0^2(\theta^*)}$  is a second solution of the homogeneous equation.

Table I. Derivates of the  $f_n$ 's at the wall ( $\theta = 1$ )

$f_0' = -1.0830$
$f_1' = -0.07550$
$f_2' = -8.866 \times 10^{-4}$
$f_3' = +1.744 \times 10^{-5}$
$f_4' = -3.297 \times 10^{-7}$
$f_5' = +1.335 \times 10^{-8}$
$f_6' = -6.893 \times 10^{-10}$
$f_7' = +4.501 \times 10^{-11}$
$f_8' = -3.455 \times 10^{-12}$

beginning at the value of 1 at the crack centerline and decreasing to 0 at the wall. The higher terms have a more complicated behavior. For small values of  $r^*$ , the first term in the series (Eq. [8]) is dominant and involves only  $f_0$ . For larger  $r^*$ , the higher terms become important and serve to give a concentration profile which shows the greatest change near the wall. This is shown in Fig. 3 for two different values of  $r^*$ . At the largest value of  $r^*$  ( $r^* = 20$ ), the concentration profile is compared to that calculated from the boundary layer results (next section) to demonstrate how well the two agree. More is said about this later.

In Fig. 4 is shown the concentration profile down the crack centerline. From these results it is seen that at  $r^* = 0(1)$  the concentration is already very small, and by the time  $r^*$  becomes of the order of  $\theta_w$ , where the radial diffusion terms become important in Eq. [7],  $c/c_\infty$  is of the order of  $10^{-347}$ .

These calculations were made for the first eigenvalue,  $K_0$ , where

$$K_0 = 7.65902$$

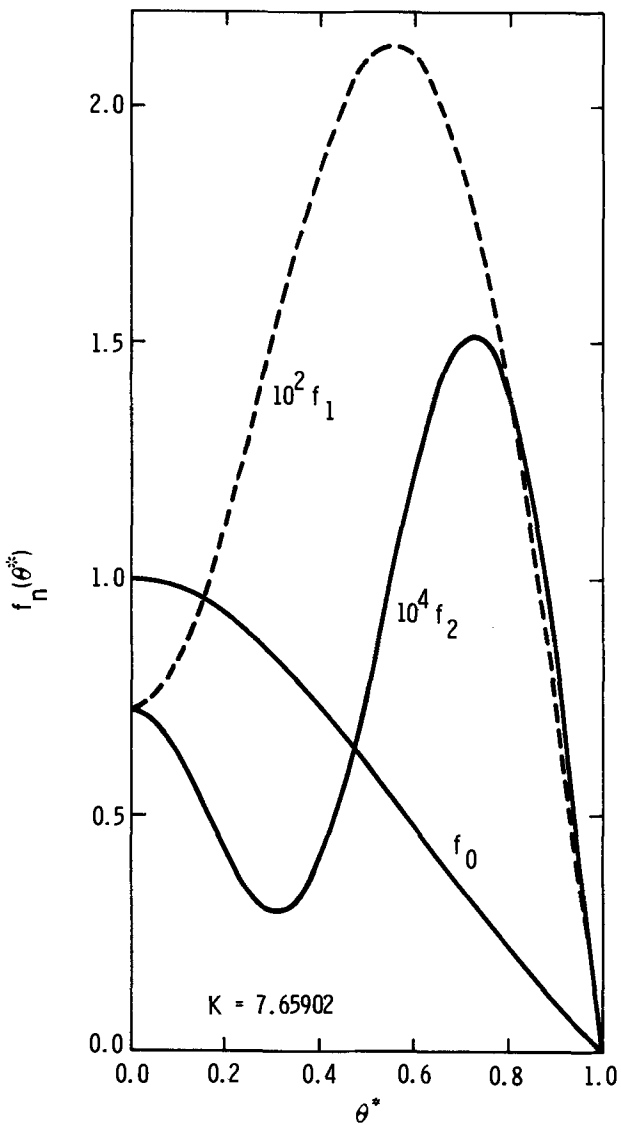


Fig. 2.  $f_n(\theta^*)$  for first eigenvalue

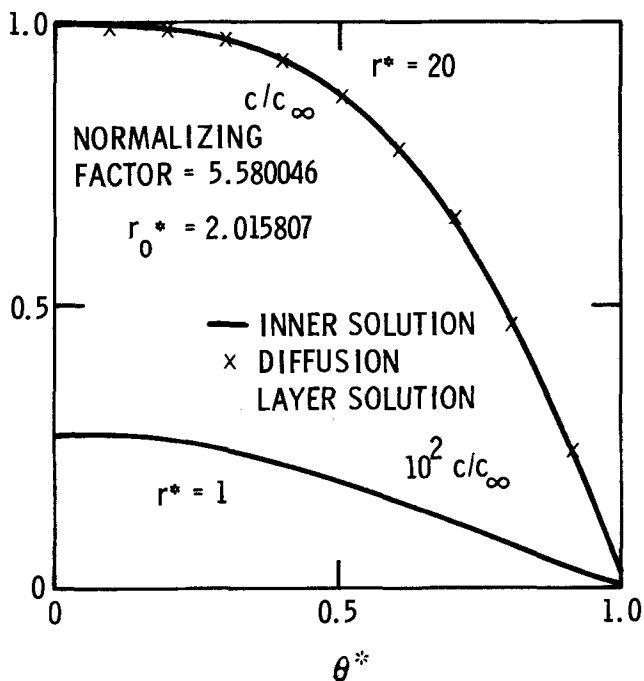


Fig. 3. Concentration profiles across crack

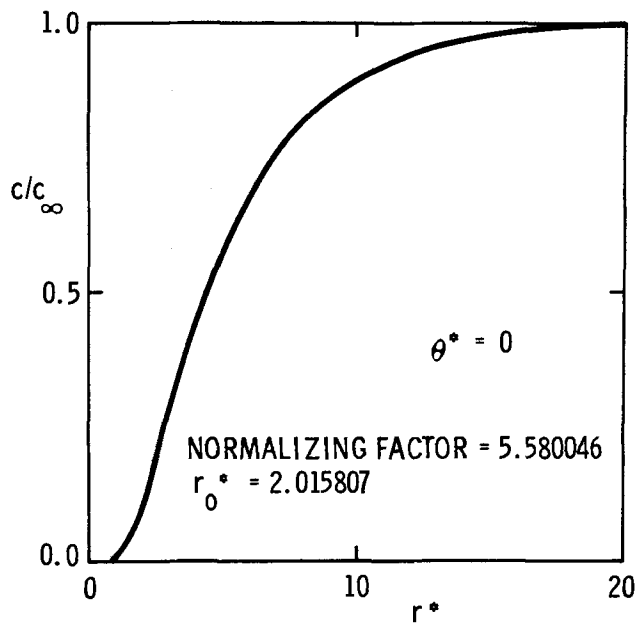


Fig. 4. Concentration profile along crack centerline

The next higher eigenvalue was found to be

$$K_1 = 150.03633$$

The complete solution would be expected to be a linear combination of the eigensolutions with the associated eigenvalues. Since the solution for  $K_1$  could not be matched with the boundary layer region, and the associated concentration profiles across the crack showed an oscillatory behavior, with the concentration even becoming negative, the contribution of this solution to the complete solution must be negligible. Higher eigenvalues and eigensolutions were expected to show similar behavior and therefore were ignored. The lowest solution was judged to be quite adequate for matching all the boundary conditions.

*Diffusion layer region.*—For large values of  $r^*$ , the concentration profile showed the greatest variation near the crack wall, and the concentration approached a constant value near the crack centerline. The boundary layer type behavior leads one to search for such

a region which would describe the asymptotic characteristics of the region just examined for large values of  $r^*$ .

Adopt the variables

$$\begin{aligned} r^* &= r^* \\ y &= r^*(1 - \theta^*) \end{aligned}$$

Introducing these variables into Eq. [7] and ignoring the radial diffusion terms, we have

$$\begin{aligned} -\frac{1}{2} \left\{ -2 + \frac{6y}{r^*} - 3 \left( \frac{y}{r^*} \right)^2 \right\} \frac{\partial c}{\partial r^*} \\ -\frac{1}{2} \left\{ 3 \left( \frac{y}{r^*} \right)^2 - 2 \left( \frac{y}{r^*} \right)^3 \right\} \frac{\partial c}{\partial y} = \frac{\partial^2 c}{\partial y^2} \quad [16] \end{aligned}$$

Now, terms of order  $y/r^*$  and higher are neglected to yield

$$\frac{\partial c}{\partial r^*} = \frac{\partial^2 c}{\partial y^2} \quad [17]$$

with boundary conditions

$$\begin{aligned} c &= 0 \text{ at } y = 0 \\ c &= c_\infty \text{ as } y \rightarrow \infty \end{aligned}$$

Implicit in these assumptions is the expectation that most of the concentration variation will occur near the wall in this region. Also, the second boundary condition above expresses that the concentration approaches a constant far from the crack wall, and that this constant is the bulk concentration.

Since this is a diffusion layer region, we try a similarity transformation of Eq. [17]. The similarity variable is

$$\eta = \frac{y}{g(r^*)}$$

and Eq. [17] is transformed into two ordinary differential equations

$$\frac{d^2 c}{d\eta^2} + 2\eta \frac{dc}{d\eta} = 0 \quad [18]$$

$$g \frac{dg}{dr^*} = 2 \quad [19]$$

The solutions to these equations are

$$c = \frac{2c_\infty}{\sqrt{\pi}} \int_0^\eta e^{-x^2} dx = c_\infty \operatorname{erf}(\eta) \quad [20]$$

$$g = (4r^* + 4r_0^*)^{1/2} \quad [21]$$

Equation [20] is the error function solution which is commonly encountered in diffusion layer problems and is tabulated by Abramowitz and Stegun (13). The constant  $r_0^*$  in Eq. [21] may be arbitrarily chosen to give the best "match" with the solution from the region where  $r^* = 0(1)$  [see, for example, Van Dyke (14)].

The concentration profile given by Eq. [20] has been shown already in Fig. 3. The comparison there indicates that the diffusion layer solution provides a good description of the asymptotic behavior of Eq. [8] for values of  $r^*$  of about 20 and above.

In Fig. 5 the flux to the wall is plotted as a function of  $r^*$ . The solid line was calculated from the solution obtained in the  $r^* = 0(1)$  region. The dotted line was calculated from the diffusion layer results. There is a good match for values of  $r^*$  greater than about 10. This could be viewed as the inner limit of validity of the diffusion layer results. One also notes that for  $r^* = 0(1)$ , the flux has decreased markedly to near zero. For  $r^* = 0(\theta_w)$ , the flux is so small as to be insignificant.

*Matching of results.*—Figures 3 and 5 indicate that the results from the two regions agree and may be "matched." The procedure for doing this was as fol-

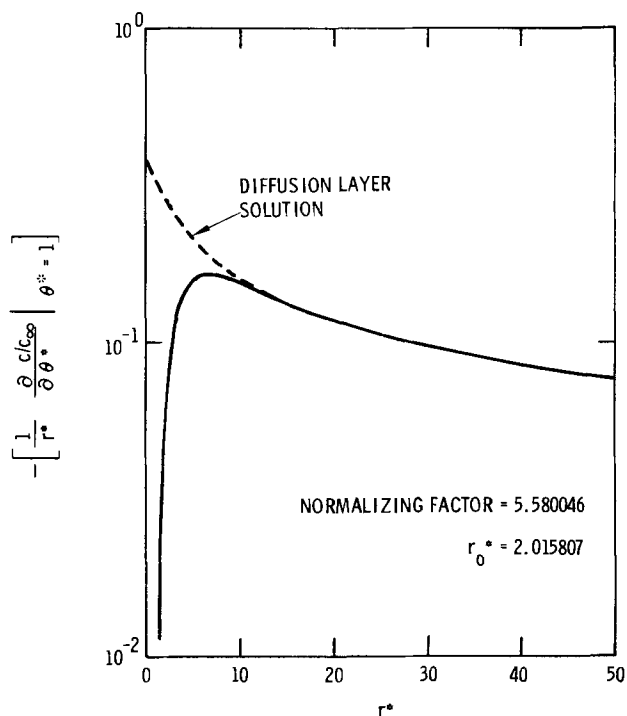


Fig. 5. Flux to the wall

lows. It was noted that the concentration along the crack centerline approached an asymptotic value as  $r^*$  approached 20 (see Fig. 4), which was the bulk concentration,  $c_\infty$ . Both sides of Eq. [8] were divided by  $c_\infty$  to produce a dimensionless equation. Using  $c/c_\infty \rightarrow 1$  as  $r^* \rightarrow 20$  ( $\theta^* = 0$ ), one may renormalize the equation (essentially renormalize  $f_0$  at  $\theta^* = 0$ ). The normalization factor was found to be 5.580046. The renormalized Eq. [8] is then

$$c/c_\infty = \frac{e^{-K_0/r^*}}{r^{*1/2}} N \sum_{n=0}^{\infty} (r^*)^n f_n(\theta^*) \quad [22]$$

where  $N = 5.580046$ . Equation [22] was then used to calculate the concentration profile across the crack. The agreement between the inner region and the diffusion layer region was good at large  $r^*$ . It was found that the match could be improved, however, by choosing a value of  $r_0^*$  (see Eq. [21]) of

$$r_0^* = 2.015807$$

The results have been given in Fig. 3 and 5. The justification for choosing  $r_0^*$  to give the best match has been discussed by Van Dyke (14). Thus, Eq. [8] gives an adequate description of the results for  $\theta_w < r^* \leq 20$ . The diffusion layer solution should be used for larger values of  $r^*$ .

*Other regions.*—Far from the crack tip, outside the diffusion layer, the concentration is constant and is identical to the bulk concentration. That is, there is no effect of diffusion in this region and no other mechanism to create concentration differences.

For values of  $r^*$  of the order of  $\theta_w$ , all terms in Eq. [7] are important. The concentration and flux to the wall have already decreased to such a low level that one can ignore them for the purposes of this paper. For  $r^* = O(\theta_w)$

$$r = O\left(\frac{D}{\theta_w V}\right) = O(10^{-3} \text{ cm})$$

At still smaller values of  $r^*$ , i.e.,  $r^* = O(\theta_w^2)$  or  $r^* \approx 10^{-5}$  cm, only the diffusion terms are important in Eq. [7]. Here again, the exceedingly small values of concentration and flux make this region unimportant for the present treatment.

### Potential Distribution in the Crack

The results of the flux distribution calculation can be used to evaluate the potential distribution in the system. We start with the equation for the divergence of the current

$$\frac{\partial}{\partial r} (r i_r) + \frac{\partial}{\partial \theta} (i_\theta) = 0 \quad [23]$$

since there is no buildup of charge anywhere. Integration of this equation with respect to  $\theta$ , from 0 to  $\theta_w$ , yields

$$\int_0^{\theta_w} \left[ \frac{\partial}{\partial r} (r i_r) \right] d\theta + i_\theta \Big|_{\theta=0}^{\theta=\theta_w} = 0$$

If we introduce

$$-\kappa \frac{\partial \phi}{\partial r} = \kappa i_r$$

where  $\kappa$  is the conductivity, and assume that variations of potential are predominantly radial

$$-\frac{\partial}{\partial r} \left( r \frac{\partial \phi}{\partial r} \right) \kappa \theta_w + i_\theta \Big|_{\theta=0}^{\theta=\theta_w} = 0 \quad [24]$$

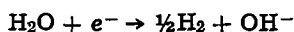
The current and flux to the wall are related by

$$i_\theta \Big|_{\theta=\theta_w} = -\frac{nFD}{r} \frac{\partial c}{\partial \theta} \Big|_{\theta=\theta_w}$$

This is appropriate for either of the reactions



or



Equation [24] becomes

$$-\frac{\partial}{\partial r} \left( r \frac{\partial \phi}{\partial r} \right) \kappa \theta_w - \frac{nFD}{r} \frac{\partial c}{\partial \theta} \Big|_{\theta=\theta_w} = 0 \quad [25]$$

The potential may now be calculated from the flux

distribution by determining  $\frac{\partial c}{\partial \theta} \Big|_{\theta=\theta_w}$  from Eq. [22]

or [20]. Since both equations are written in terms of  $r^*$  and  $\theta^*$ , we write Eq. [25] as

$$-\frac{\partial}{\partial r^*} \left( r^* \frac{\partial \phi}{\partial r^*} \right) \kappa \theta_w - \frac{nFDc_\infty}{r^* \theta_w} \frac{\partial (c/c_\infty)}{\partial \theta^*} \Big|_{\theta^*=1} = 0$$

Integration twice with respect to  $r^*$  yields

$$\phi_{r^*} - \phi_0 = \frac{nFDc_\infty}{\kappa \theta_w^2} \int_0^{r^*} \frac{1}{r^*} \int_0^{r^*} \frac{1}{r^*} \frac{\partial (c/c_\infty)}{\partial \theta^*} \Big|_{\theta^*=1} dr^* dr^* \quad [26]$$

Introduction of Eq. [22] into [26] gives

$$\phi_{r^*} - \phi_0 = -\frac{nFDc_\infty N}{\kappa \theta_w^2} \sum_{n=0}^{\infty} \int_0^{r^*} \frac{1}{r^*} \int_0^{r^*} \frac{e^{-K_n/r^*}}{4^{*3/2}} (r^*)^2 f_n'(\theta^*=1) dr^* dr^* \quad [27]$$

A similar equation may be written for the potential variation in the diffusion layer region.

The potential variation in the solution for  $1 \leq r^* < 20$  was calculated from Eq. [27] by numerical Simpson integration. For the diffusion layer region, the integration could be carried out directly to obtain an analytic result. The results of these calculations are shown in Fig. 6. In the region between the crack tip and  $r^* \approx 1$ , there is negligible current flow and therefore a negligible potential variation. Larger current flow in the outer regions of the crack cause larger po-

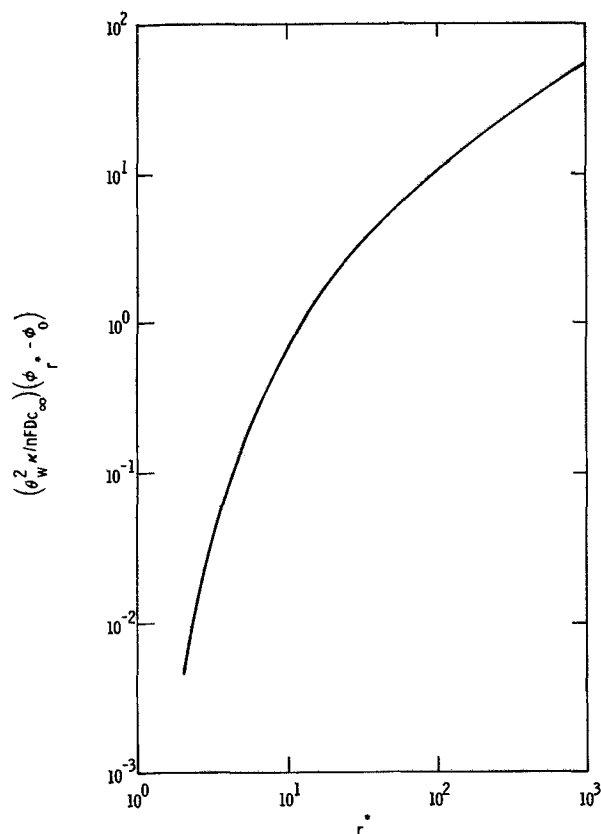


Fig. 6. Potential as a function of distance from the crack tip

tential differences in the solution. The potential difference between two points would be directly proportional to the bulk concentration of the reactant and inversely proportional to the square of the crack angle.

The calculation of the potential drop down a crack for a specific system may be helpful. We shall calculate the total potential drop down the crack. The outer limit of the validity of the model is where seepage of liquid in from the sides becomes important. For a specimen 1 cm thick, seepage becomes important where the thickness is of the same order as  $\theta_w r$ . Therefore

$$r = 1/\theta_w = 2 \times 10^2 \text{ cm}$$

where  $2\theta_w$  is  $10^{-2}$  radians. Since

$$r^* = r \left( \frac{V}{D} \theta_w^2 \right)$$

then introduction of the velocity of cracking (1 cm/sec) and a diffusion coefficient of  $10^{-5}$  cm<sup>2</sup>/sec, yields

$$r^* = 500$$

The total potential difference between this point and the crack tip is

$$(\phi_{500} - \phi_0) \frac{\kappa \theta_w^2}{nFDc_\infty} = 33.9$$

For  $c_\infty = 8.2 \times 10^{-8}$  moles/cm<sup>3</sup> (i.e., 1, ppm weight);  $\kappa = 1.2$  mho/cm [ref. (15)];  $F = 9.65 \times 10^4$  coulombs/equiv;  $n = 1$ ;  $D = 10^{-5}$  cm<sup>2</sup>/sec;  $\theta_w^2 = 0.25 \times 10^{-4}$ ; and  $\phi_{500} - \phi_0 = 890$  mV. In order to have a potential drop of this magnitude over a crack length of 1 cm, the concentration would have to be larger by about 200, or the crack angle would have to be smaller by an order of magnitude.

### Summary

As a summary, Fig. 7 indicates the different regions that have been revealed in this investigation and the different modes of mass transfer in them. Again, for



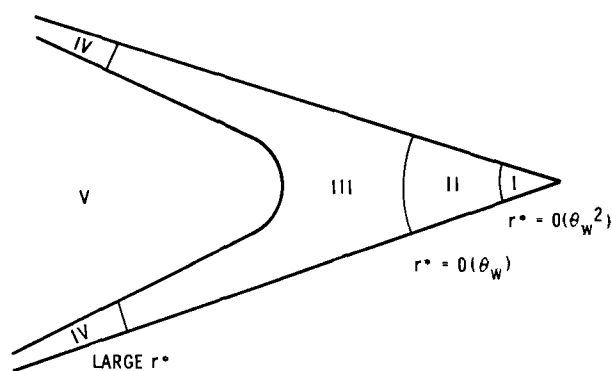


Fig. 7. Regions of mass transfer. Region I, diffusion only; region II, all terms important; region III, radial diffusion negligible; region IV, radial convection, angular diffusion; region V, concentration constant.

distances nearer the crack tip than  $10^{-3}$  cm, the solution is essentially devoid of the reactive species, and their flux is also negligible.

### Conclusions

From the results of this study, it may be concluded that minor components being consumed in a crack at rates limited by mass transfer have vanishingly small concentrations near the crack tip. In addition, the flux of minor components is extremely small in the crack tip region. It is unlikely that such species would be important as critical species in crack extension processes. More specifically, small amounts of  $\text{OH}^-$ ,  $\text{H}_2\text{O}$ , or  $\text{O}_2$  dissolved in molten  $\text{LiCl-KCl}$  cannot be critical species in the cracking of Ti 8-1-1.

Figure 7 contains information which should be useful for other systems. For example, Ti 8-1-1 is susceptible to cracking in aqueous halide solutions (1) with crack velocities which range from  $10^{-3}$  to  $10^{-1}$  cm/sec. Aluminum alloys crack in aqueous solutions (2) with velocities between  $10^{-8}$  and  $10^{-3}$  cm/sec. Beck and Grens (5) have presented a model for SCC in aqueous solutions which neglects convective effects. The Beck-Grens model would therefore be appropriate for describing events in the crack tip region only (region I in Fig. 7). The size of region I for aqueous solutions would be (i) for titanium alloys

$$r_{I1} = O(\theta_w^2) = \frac{\tau V \theta_w^2}{D}$$

and

$$r_{I1} = O\left(\frac{D}{V}\right)$$

or

$$10^{-4} \text{ cm} < r_{I1} < 10^{-2} \text{ cm}$$

for the range of velocities given above, and (ii) for the velocities given for aluminum alloys

$$10^{-2} \text{ cm} < r_{I1} < 10^3 \text{ cm}$$

These estimates should be regarded as the outer limits of distance from the crack tip for which the Beck-Grens (5) type treatment could be used. Other comparisons with the Beck-Grens model are difficult to make because of the different assumptions involved in their treatment as compared to ours.

The present results are useful in assessing the importance of minor components in controlling the potential drop down cracks. For the molten salt system, it appears that the concentration of  $\text{H}_2\text{O}$  would have to be larger than 1 ppm before a sizable potential drop would be expected. The full treatment of the superposition of anodic processes on the mass transfer limited processes of minor components will be presented in a subsequent paper. It should be noted from Fig. 6, however, that the tip of the crack is less cathodic than the mouth of the crack, with the present

assumption of a cathodic process occurring at a mass transfer limited rate. This could permit a different process to occur anodically at the crack tip even though the external surface is cathodically polarized.

It is tempting to extrapolate the results to solutions of higher concentration. One would be led to conclude that none of the reactive species could get to the crack tip, no matter what the bulk concentration. However, this conclusion is probably not justified, because it is doubtful if the same analysis could be used for more concentrated solutions. One could expect in such solutions that the mass transfer processes could change the fluid flow characteristics, with results which might be quite different than those found here.

Manuscript submitted Sept. 6, 1973; revised manuscript received March 15, 1974. This was Paper 244 presented at the Chicago, Illinois, Meeting of the Society, May 13-18, 1974.

Any discussion of this paper will appear in a Discussion Section to be published in the June 1975 JOURNAL. All discussions for the June 1975 Discussion Section should be submitted by Feb. 1, 1975.

### LIST OF SYMBOLS

$c$	concentration (moles/cm <sup>3</sup> )
$D$	diffusion coefficient (cm <sup>2</sup> /sec)
$f_n(\theta^*)$	functions defined in Eq. [8]
${}_1F_1$	confluent hypergeometric function
$g_n(\theta^*)$	functions defined in Eq. [10]
$h_o$	function defined in Footnote 3.
$K$	constant defined in Eq. [8]
$N$	normalization factor
$r$	radial dimension (cm)
$r^*$	dimensionless variable
$v_r$	radial component of liquid velocity in crack (cm/sec)
$v_\theta$	angular component of liquid velocity in crack (cm/sec)
$V$	velocity of crack propagation (cm/sec)
$y$	dimensionless variable
$\eta$	similarity variable
$\theta$	angular dimension
$\theta_w$	crack angle
$\theta^*$	reduced variable
$\kappa$	conductivity (mho/cm)
$\nu$	fluid kinematic viscosity (cm <sup>2</sup> /sec)
$\phi$	potential (V)

### REFERENCES

1. M. J. Blackburn, J. A. Feeney, and T. R. Beck, in "Advances in Corrosion Science and Corrosion Engineering," Vol. 3, M. G. Fontana and R. W. Staehle, Editors, Plenum Publishing Corp., New York (1973).
2. Markus O. Speidel and Michael V. Hyatt, in "Advances in Corrosion Science and Corrosion Engineering," Vol. 2, M. G. Fontana and R. W. Staehle, Editors, Plenum Publishing Corp., New York (1972).
3. M. J. Blackburn, W. H. Smyrl, and J. A. Feeney, in "State of the Art: Stress Corrosion Cracking," B. F. Brown, Editor, U.S. Government Printing Office, Washington, D.C. (1972).
4. S. M. Wiederhorn, *J. Am. Ceram. Soc.*, **50**, 407 (1967).
5. T. R. Beck and E. A. Grens, *This Journal*, **116**, 177 (1969).
6. T. R. Beck, in "The Theory of Stress Corrosion Cracking in Alloys," J. C. Scully, Editor, NATO, Brussels (1971).
7. John Newman and W. H. Smyrl, *Met. Trans.*, To be published.
8. W. H. Smyrl and M. J. Blackburn, *Proc. Intern. Symp. Stress Corrosion Mechanisms in Titanium Alloys*, Atlanta, Georgia, January 1971, To be published.
9. W. H. Smyrl and M. J. Blackburn, Unpublished data.
10. P. M. Morse and H. Feshbach, "Methods of Theoretical Physics, Part I," p. 604, McGraw-Hill Book Co., New York (1953).
11. John Newman, in "Electroanalytical Chemistry," Vol. 6, A. J. Bard, Editor, pp. 187-352, Marcel Dekker, Inc., New York (1973).

12. John Newman, *Ind. Eng. Chem. Fundamentals*, **7**, 514 (1968).
13. M. Abramowitz and I. A. Stegun, "Handbook of Mathematical Functions," Dover Publications, Inc., New York (1965).
14. M. Van Dyke, "Perturbation Methods in Fluid Mechanics," Academic Press, New York (1964).
15. E. R. Van Artsdalen and I. S. Yaffe, *J. Phys. Chem.*, **S9**, 118 (1955).

## Electrochemical Behavior of Iron Within Crevices in Nearly Neutral Chloride Solutions

E. McCafferty\*

Naval Research Laboratory, Washington, D. C. 20375

The publication costs of this paper have been assisted by the Naval Research Laboratory.

### ABSTRACT

In crevices where the internal iron is not short-circuited to external metal, the corrosion rate is determined by the limiting cathodic current for oxygen reduction. This limiting current, and accordingly the corrosion rate, is independent of pH and  $\text{Cl}^-$  concentration but is suppressed to a constant value when the height of the crevice is less than the thickness of the oxygen diffusion layer. When iron in the crevice is short-circuited to external, open platinum, the initial crevice corrosion rate is independent of crevice height but increases with increasing  $\text{Cl}^-$  concentration and area of external electrode. At constant  $\text{Cl}^-$  concentration, the crevice corrosion rate of internal iron short-circuited to open external iron decreases with increasing chromate ion concentration. At a constant chromate ion concentration which does not give protection, the crevice corrosion rate is greater the greater the chloride ion concentration for short times, but at longer times the rates are essentially independent of bulk chloride concentration.

Rosenfeld and Marshakov (1) have shown that crevice corrosion usually proceeds in two main stages: (i) initiation by differential aeration and (ii) propagation by crevice acidification. Initially, the sheltered metal in contact with a restricted oxygen supply becomes anodic relative to the open metal to which it is connected. At longer times, the presence of the crevice plays a different role, that of causing corrosion products to accumulate within the crevice so as to change the local solution composition and pH.

Reports that not only crevices (1, 2) but also stress-corrosion cracks (3, 4) and pits (5, 6) acidify locally has led to the view that all three forms of localized corrosion share the unifying feature of being "occluded corrosion cells" (7) having restricted exchange with bulk electrolyte and thus common solution chemistries. Thus, most recent studies have utilized the thermodynamic, rather than kinetic, approach, with emphasis on factors such as resultant crevice solution chemistry, pH, and electrode potential (8-11). Little recent work has been done on the polarization kinetics of metals under crevices. One exception has been the correlation between the shape of cyclic anodic polarization curves for various engineering alloys in 3½% NaCl with their longer range performances in natural seawater (12). Polarization curves have been reported in some well-defined but synthetic, generalized "occluded corrosion cells" *sans* crevices, in which the "internal" metal was activated by anodic polarization (13) or by deaeration (14). Other investigators have reported current-time (15) and potential-time (10, 16), but not current-potential relationships.

The purpose of this study was to take up the systematic approach of Rosenfeld and Marshakov (1) in order to investigate in an organized manner kinetic aspects of a fairly simple crevice system. Iron was chosen, partly because of the attention given this metal in a wide variety of open systems. The effect of vari-

able crevice height, chloride ion concentration, and chromate inhibitor is considered.

### Experimental

**Electrode.**—Ferrovac E high purity iron with the following impurities was used in this study: 0.007 C, 0.01 Mn, 0.002 P, 0.007 S, 0.006 Si, 0.025 Ni, 0.007 Cr. An iron electrode (1¼ in. diameter) was encased in a Teflon holder by pressing the cylindrical iron bar through an undersized opening in the Teflon. The uppermost rim of Teflon was machined away, and the electrode edge masked with alkyd varnish, a material found suitable in preventing the formation of unintentional, microscopic crevices (17). Before use, the exposed iron face (7.9 cm<sup>2</sup> projected area) was dry-polished through 3/0 emery papers and washed with ethanol.

**Crevice assembly.**—The electrode holder was machined to fit into the cell as shown in Fig. 1. A central feature of the assembly is the provision for an adjustable crevice height. The crevice was formed by positioning the optically polished bottom surface of a glass disk a measured distance from the iron surface by means of a micrometer attached to the disk top. Two small holes (<1 mm diameter) through the glass disk led to Ag/AgCl reference electrodes, prepared by chlorodizing silver wire (18). These Luggin capillaries enabled measurement of the electrode potential at the center and near the edge of the crevice. Thus, electrochemical processes within the crevice could be monitored. The solution in the capillary section was the same as the bulk electrolyte and was kept from draining into the crevice by filter-paper plugs packed into the capillary bottom. Electrode potentials were thus measured *vs.* Ag/AgCl in the test solution but were converted to potentials *vs.* a commercial Ag/AgCl standard electrode.

**Solutions.**—Sodium chloride solutions were used: (i) with sodium chromate inhibitor (pH = 8.4), to study the initiation of crevice corrosion on passive iron, and (ii) without inhibitor (pH = 5.5), to study active

\* Electrochemical Society Active Member.

Key words: corrosion, crevices, iron, electrochemical polarization, chloride ion, chromate ion, oxygen reduction.

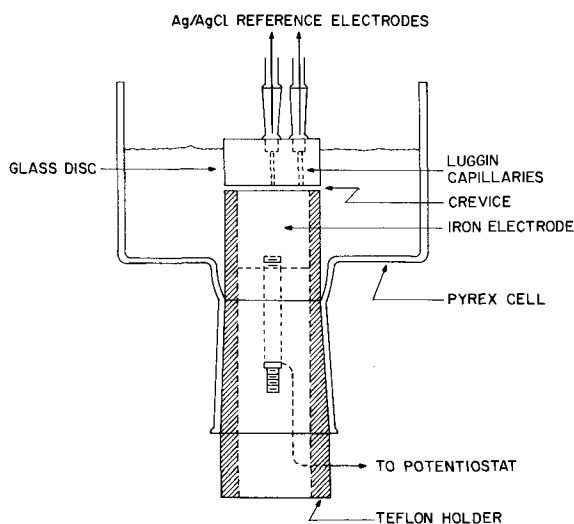


Fig. 1. The crevice corrosion cell. (Micrometer assembly and auxiliary electrode not shown.)

crevices. The 3½% NaCl solution (wt/vol) was of particular interest because the chloride ion concentration (0.6*N*) is the same as in natural seawater. All solutions were prepared from reagent grade chemicals and double-distilled water prepared in a quartz still. During all experiments, the cell electrolyte was open to the air and quiescent.

**Procedures.**—For the  $\text{CrO}_4^{2-}/\text{Cl}^-$  solutions, a ring-shaped piece of iron (area  $\cong 50 \text{ cm}^2$ ) cut from the same bar as the crevice iron was used as the external open electrode. This split-electrode arrangement allowed measurement of current between active internal and passive external electrodes. After 15 min immersion in a given solution, the two parts were short-circuited through a Wenking potentiostat used in a two-electrode configuration (19), which essentially uses the potentiostat as a zero resistance ammeter. Electrode potentials of internal and external iron and crevice corrosion current were recorded for approximately 48 hr of coupling. Chromate ion and chloride ion concentrations were varied, but the crevice height was fixed at 10 mils (0.25 mm) for this set of experiments.

Two types of crevices were investigated for the chromate-free solutions: (i) "isolated" crevices, in which internal iron was not connected to external metal, and (ii) "coupled" crevices, in which internal iron was short-circuited to external metal.

The former configuration allowed study of local cell activity within a crevice, and the latter simulated the more practical case in an overlapping joint, for example, where metal within the crevice is in electrical contact with metal outside the crevice.

The effect of crevice width, pH, and  $\text{Cl}^-$  ion concentration was studied for the "isolated" crevice. The narrower "isolated" crevices were polarized galvanostatically using a series of variable resistors in series with a 45V battery ( $R_{\text{ext}} \gg R_{\text{cell}}$ ). (Use of the potentiostat in the normal three-electrode configuration yielded oscillations in current for the narrower crevices, but there were no problems with thicker crevices or with the two-electrode configuration for "coupled" crevices.)

For "coupled" crevices in the chromate-free solutions, a platinum gauze electrode was used as the open, external electrode in order to confine corrosion to the internal iron. Crevice iron and external platinum were immersed (uncoupled) for 24 hr to reach steady-state potentials prior to coupling through the potentiostat in the two-electrode configuration. Evans polarization diagrams were determined for different crevice heights,  $\text{Cl}^-$  concentrations, and external areas,

## Results and Discussion

### Inhibitor-Free Solutions

**Isolated crevices.**—Polarization curves were determined after 24 hr immersion in 0.6*N* and 0.06*N* NaCl solutions. Steady-state open-circuit potentials were established in about 10 hr, as shown in Fig. 2. In all cases, open-circuit potentials measured at the crevice center were identical with potentials measured near the crevice edge.

Figure 3 shows typical polarization curves in 0.6*N* NaCl for both the open sample and for "isolated" crevices, i.e., crevice metal not coupled to open external metal. In all cases, the cathodic branch was determined first, open circuit was reestablished, and the anodic branch then determined. For cathodic polarization, electrode potentials measured via the Luggin capillary at the crevice center were the same as those near the edge. For anodic polarization, there were slight differences between the two locations (5–20 mV) in a few cases, but only at high anodic overvoltages.

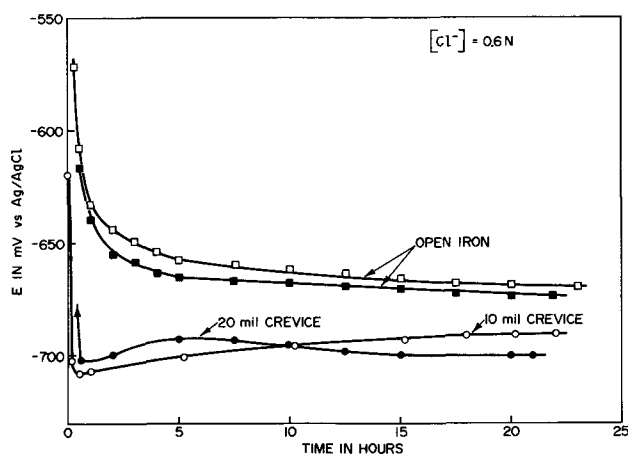


Fig. 2. Establishment of steady-state open-circuit potentials for open and crevice iron in 0.6*N* NaCl.

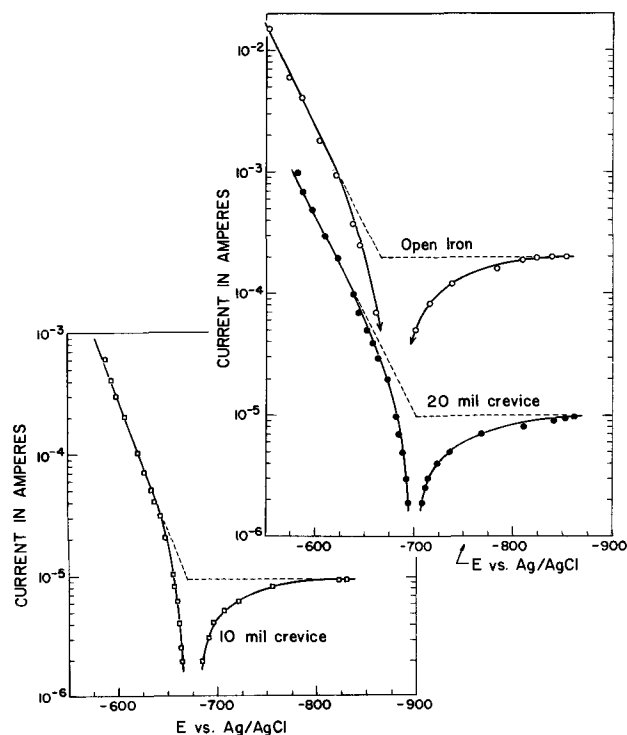
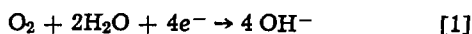


Fig. 3. Polarization curves for open iron and iron in "isolated" crevices in 0.6*N* NaCl after 24 hr immersion.

The shape of the cathodic curves in Fig. 3 is characteristic of a diffusion controlled process. The over-all cathodic reaction in nearly neutral solutions is the reduction of oxygen (20)



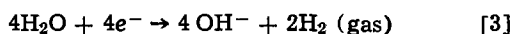
The anodic branches are activation controlled, with Tafel slopes of 40-60 mV/decade. All anodic curves were well behaved, and none displayed the peculiar property observed by Rosenfeld and Marshakov (1), in which some anodic curves started out in the direction of more negative potentials before turning back toward more positive potentials.

For both the crevices and open sample, the corrosion rate at open-circuit potential is equal to the limiting cathodic current for oxygen reduction, according to

$$i_{\text{net}} = i_{\text{Fe}} + i_{\text{O}_2} = 0 \quad [2]$$

With these "isolated" crevices, the limiting cathodic current density for oxygen reduction is less than that for the open sample, and correspondingly so is the iron corrosion rate, as shown in Fig. 3. This same effect has been seen by Rosenfeld and Marshakov (1).

At higher negative potentials than in Fig. 3, the predominant cathodic reaction is hydrogen evolution (21)



( $E^\circ = -0.83\text{V vs. NHE} = -1.03\text{V vs. Ag/AgCl}$ ), rather than oxygen reduction. With extensive cathodic polarization, the shape of the polarization curve changed from diffusion control to activation control, and exhibited a Tafel slope of 120 mV/decade, characteristic of hydrogen evolution (22). In the oxygen reduction region, the polarization behavior was independent of pH and  $\text{Cl}^-$  ion concentration, as required by Eq. [1] and shown in Fig. 4 for a 10 mil crevice.

The effect of the "isolated" crevice is thus to stifle the oxygen reduction reaction, even for a relatively wide opening of 125 mils (3.19 mm), as seen in Fig. 5 for 0.06N NaCl. The limiting cathodic rate is further suppressed to a constant value for crevice heights between 5 and 20 mils (0.13-0.51 mm). The crevice height of 20 mils (0.51 mm) is significant in that it is approximately the thickness  $\delta$  of the oxygen diffusion layer near the electrode surface calculated from (23)

$$i_{l,c} = nF \frac{D}{\delta} C \quad [4]$$

where  $i_{l,c}$  is the mass-transfer limited cathodic current density for the open sample (0.20 mA/7.9 cm<sup>2</sup>),  $n = 4$  electrons transferred per mole  $\text{O}_2$  according to Eq. [1], and  $C$  and  $D$  are the diffusion coefficients and concentration, respectively, of oxygen. With  $D = 1.65 \times 10^{-5}$

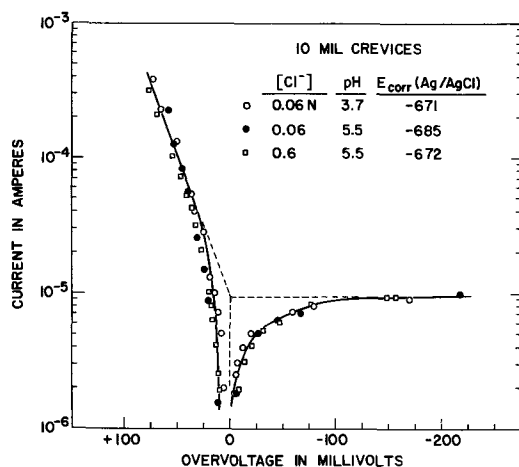


Fig. 4. Effect of pH and  $\text{Cl}^-$  ion concentration on the polarization of iron in 10 mil (0.25 mm) "isolated" crevices.

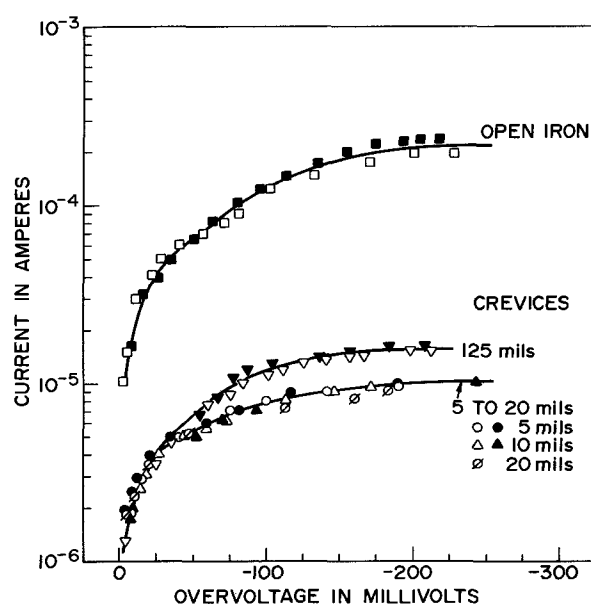


Fig. 5. Effect of crevice height on the cathodic polarization of iron in 0.06N NaCl.

cm<sup>2</sup>/sec (24) for 0.05N NaCl at 25°C, and  $C = 8.2$  mg/liter (25), Eq. [4] gives:  $\delta = 0.063$  cm, or 25 mils. This value agrees with that of Rosenfeld and Vashkov (26) who calculated the thickness of the diffusion layer to be 0.50 mm (20 mils) for iron in 0.5N NaCl. Experiments by Rosenfeld and Marshakov (1b) with variable crevices gave  $\delta = 0.25$ -0.50 mm.

Thus in crevices not coupled to outside open metal, when the crevice height is comparable to the thickness of the oxygen diffusion layer, diffusion of oxygen into the crevice is impeded and hence the corrosion rate is reduced, according to Eq. [2].

All polarization curves reported were steady-state curves. Figure 6 shows potential-time dependence for the galvanostatic cathodic polarization of a 20 mil crevice in 0.06N NaCl. For the lowest applied currents, only a few minutes were necessary to establish a steady-state potential, but several hours were necessary to reach a steady potential near the limiting cathodic current for oxygen reduction.

**Coupled crevices.**—The effect of activating the crevice iron was studied by coupling it to external, open platinum. This arrangement simulates practical cases, as in an overlapping joint, for example, where metal within the crevice is in electrical contact with metal outside the crevice. The iron in the crevice was con-

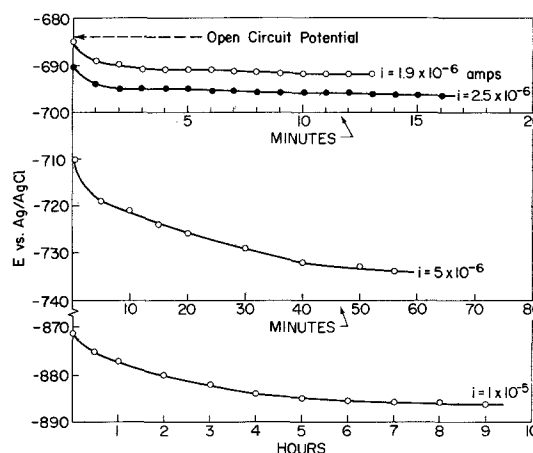


Fig. 6. Establishment of equilibrium potentials during the galvanostatic polarization of iron in a 20 mil (0.50 mm) crevice in 0.06N NaCl.

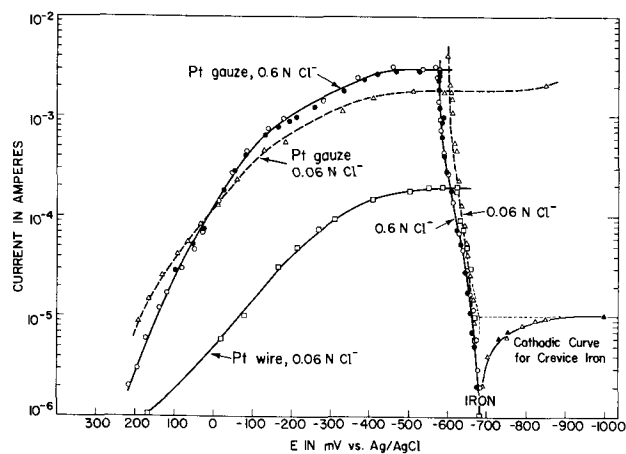


Fig. 7. Effect of  $\text{Cl}^-$  ion concentration and area of external platinum on the polarization behavior of the couple: iron (10 mil crevice)/platinum (open).

connected to the external platinum gauze using the potentiostat in the two-electrode configuration (19). This arrangement forces the cathodic reaction (oxygen reduction) to continue outside the crevice at the platinum surface after the oxygen within the crevice has been consumed, and the anodic reaction (iron dissolution) is confined to the crevice. Typical Evans polarization diagrams are shown in Fig. 7. Initially, the iron and platinum were uncoupled for 24 hr, so that each electrode reached its own steady-state potential. These open-circuit potentials for uncoupled iron and uncoupled platinum (zero current flow) tend toward the bottom of the diagram. With increased current flow, these two potentials approach each other and nearly coincide except for a moderate IR drop (at most 50 mV). The current at the intersection of the iron and platinum polarization curves is the short-circuit corrosion current for that couple.

As with the "isolated" crevices, the electrode potentials of iron at the crevice center and near the crevice edge were either identical or displayed but small differences (5-15 mV).

Figure 7 also compares the crevice corrosion current for the "isolated" (uncoupled) crevices to that for the iron/platinum couples. In the former case, the crevice corrosion current is only  $1 \times 10^{-5}$  A (Fig. 4), and is determined by the rate of oxygen reduction within the crevice. As seen in Fig. 7, the corrosion rate of the coupled crevices is also under cathodic control but is determined by the rate of oxygen reduction at the open electrode outside the crevice.

Table I summarizes the results of various experiments which investigated the effect of crevice height, chloride ion concentration, and area of external platinum on the corrosion rate of the couple: iron (crevice)/platinum (external).

Table I shows that the presence of the crevice increases but slightly the corrosion current compared to the open sample (e.g., 1.8-2.1 mA for crevices coupled to platinum gauze in 0.06N NaCl vs. 1.5 mA for the open iron coupled to the same platinum gauze). Thus even a crevice as narrow as 3-10 mils does not hinder the corrosion of iron in the crevice once the iron has been activated by coupling to an external

cathode. However, the crevice does restrict the attack to the metal near the crevice edge, as was also the case for the  $\text{CrO}_4^{2-}/\text{Cl}^-$  solutions.

Figure 7 shows that for a given crevice height and chloride content, a decrease in area of the external cathode causes a decrease in crevice corrosion current. The ratio of open to sheltered metal has been shown to be important in longer range, more practical immersion tests. For example, Ellis and LaQue (27) have reported a linear increase in weight loss with increasing external area for stainless steel in flowing seawater.

Table I shows that increasing the bulk chloride ion increased the corrosion current, for a given external area and crevice height. However, a change in crevice height for a given external area and chloride content (either 0.06N or 0.6N) had no effect on the crevice corrosion rate. The explanation may be that the concentration of chloride ions entering the crevice is not strongly dependent on the crevice height. Work by Ulanovskii and Korovin (28), has shown that the increase in  $\text{Cl}^-$  ion concentration during the anodic polarization of graphite is about the same for 0.2 mm (i.e., 10 mil) as for 0.6 mm (24 mil) crevices.

Table I also shows that the measured crevice corrosion current was not affected by nuances in the experimental procedure. With 0.6N NaCl, the short-circuit current was the same for galvanostatic polarization as for potentiostatic polarization. Also, it made no difference if the platinum external electrode was positioned horizontally or vertically (same area in each case). In some cases, the short-circuit current measured by the potentiostatic method was checked with a simple zero-resistance ammeter (29). The two values always agreed within 5%.

The average pH within the crevice was measured after each run for the 0.06N NaCl solutions. The bulk electrolyte was slowly pipetted off below the crevice level; and the crevice was opened. The average crevice pH was  $4.7 \pm 0.3$ , as measured both by narrow range pH papers and the micro-pH electrode. This same value was recently measured for iron in 3½% NaCl in another study in this laboratory by Bogar and Fujii (9), who sampled crevice electrolytes with a microcapillary and touched the extracted drops to narrow-range pH papers.

An accumulation of ferrous ions within the crevice has been found (2, 12) to accompany the low pH. Possible equilibrium reactions leading to an increase locally in  $\text{H}^+$  ions involve the hydrolysis of ferrous ions entrapped within the crevice, and have been summarized by Peterson (2). Detailed step-by-step mechanisms for dissolution within crevices have not been determined. However, Fig. 7 does show that in the early stages of the corrosion process, the  $\text{Cl}^-$  ion does not stimulate the anodic reaction. At constant potential (and constant pH = 4.5, in view of the above), the anodic rate is lower for the higher  $\text{Cl}^-$  ion concentration, in agreement with result for open iron in deaerated systems (30, 31).

#### Chromate Solutions

*Effect of coupling.*—Results for a typical experiment in which iron within the crevice (7.9  $\text{cm}^2$  area) was coupled to open, external iron (~50  $\text{cm}^2$  area) are shown in Fig. 8. The time axis is logarithmic for illus-

Table I. Short-circuit current for iron coupled to platinum

Cl <sup>-</sup> conc.	External cathode		Short-circuit current in mA			
	Type	Approx. area	3 mils	10 mils	20 mils	Open
0.06N	Wires	3 $\text{cm}^2$	—	0.20	—	0.17
	Gauze	175 $\text{cm}^2$	2.1	1.8, 2.1	—	1.5
0.6N	Gauze	175 $\text{cm}^2$	—	2.9, 2.8, 2.5 <sup>(a)</sup>	3.2, <sup>(b)</sup> 3.0	—

<sup>(a)</sup> Horizontally positioned platinum cathode.

<sup>(b)</sup> Galvanostatic run.

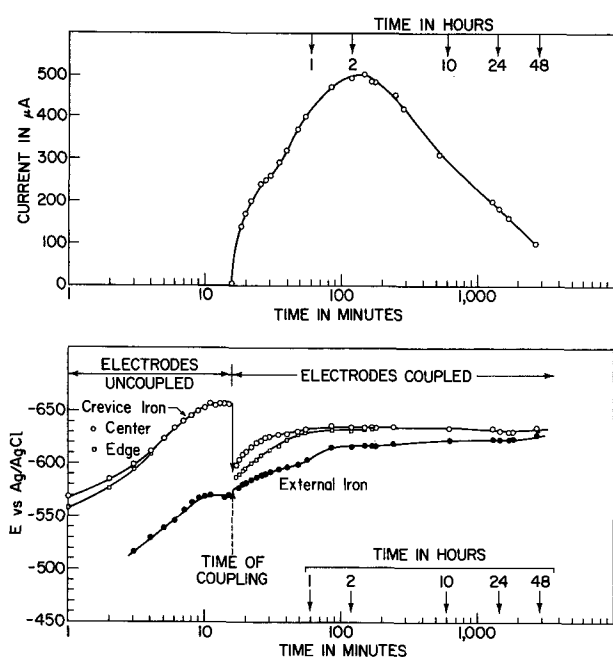


Fig. 8. Effect of coupling iron within a 10 mil (0.25 mm) crevice in  $0.006N$   $Na_2CrO_4$  +  $0.6N$   $NaCl$  to open external iron. (Area of crevice iron =  $7.9$   $cm^2$ , area of external iron =  $50$   $cm^2$ ).

tration purposes only. For the first 15 min of the experiment, the crevice iron and external iron were uncoupled, i.e., each at its own open-circuit potential. At 15 min time, the electrodes were short-circuited using the potentiostat in the two-electrode configuration. Upon coupling, the potentials of the crevice iron and external iron shifted toward each other but were not identical due to an  $IR$  drop between the crevice interior and outer electrode. In all experiments, the initial shift in potential upon coupling was larger for the crevice iron than for external iron. At the end (48 hr) of the experiment shown in Fig. 8, the potential difference between crevice iron (laden with corrosion products) and passive external iron was only 7 mV. The maximum potential difference for this experiment was 34 mV at 0.5 hr time.

Figure 8 shows that there was no difference in electrode potential between the crevice center and crevice edge before coupling. After coupling, the potential of the crevice edge was usually intermediate between that of the crevice center and external iron, as seen in Fig. 8. But at the end of every experiment, there again was no difference in potential between the two locations in the crevice. This suggests that at long times the occluded internal electrolyte develops a uniform composition throughout the crevice.

Figure 8 also shows the current between inner and outer iron surfaces when coupled. The current reached a maximum at about 2 hr, and then gradually decreased with time.

This decrease in current can be attributed to two related effects. First, as the crevice iron becomes active, the accumulation of ferrous ions within the crevice causes a decrease in local pH, as discussed earlier. (For all cases except  $0.6N$   $Cl^-/0.6N$   $CrO_4^{2-}$ , where there was little crevice corrosion, the measured crevice pH after 48 hr was in the range 4.5-6.0, as compared to the bulk pH of 8.4) In going from neutral to acidic solutions, the anodic polarization curve for active iron is shifted to lower current density values at constant potential for open iron in deaerated  $1N$  chloride (32, 33). Using open iron in bulk solutions deaerated by intentional degassing as a "scaled-up model" for crevice iron in small volumes deaerated by oxygen consumption, then the anodic partial curve for crevice iron will intersect the cathodic curve for open iron at a decreased current. As shown in Fig. 8, and was typi-

cal, the electrode potential of the crevice iron was essentially constant after the maximum in crevice corrosion current had been reached.

If there is an increase in  $Cl^-$  content within the crevice, as predicted (5b) or observed with artificial crevices (8, 13, 34, 35), this will also cause a decrease in anodic current according to the "halide-inhibited" mechanism of iron dissolution (30). Only if there is a drastic increase in chloride concentration (approximately 3-6M) coupled with an intense acidity ( $pH < 0$ ) will there be acceleration of the anodic reaction caused by the conjoint action of  $Cl^-$  and  $H^+$  ions (31, 36).

Secondly, insoluble corrosion products which accumulate within the crevice form a resistive barrier. For the experiment in Fig. 8, gross bleeding of rust out of the crevice was first noticed at about 10 hr time. All crevices which underwent corrosion were heavily laden with corrosion products after termination of the 48 hr runs.

The effect of the chromate ion is seen in Fig. 9 which shows the crevice corrosion current at a constant chloride ion concentration of  $0.6N$ . The crevice corrosion current decreases with increasing amounts of chromate inhibitor. Duplicate runs in Fig. 9 show that the trends are clear although the exact shapes of the curves are not identically reproducible.

The effect of the chloride ion is shown in Fig. 10, which plots the crevice corrosion current for a constant chromate ion concentration of  $0.006N$ . In the early stages of the process, the corrosion current is greater the greater the  $Cl^-$  ion concentration. However, at longer times, all the crevices exhibit essentially the same rate. This suggests that the long-term

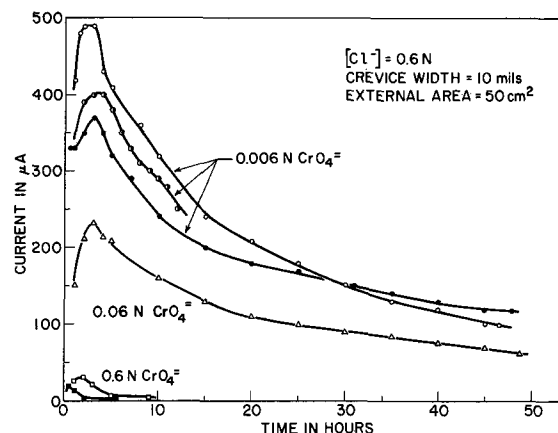


Fig. 9. Effect of chromate ion concentration on the crevice corrosion of iron at constant chloride ion concentration.

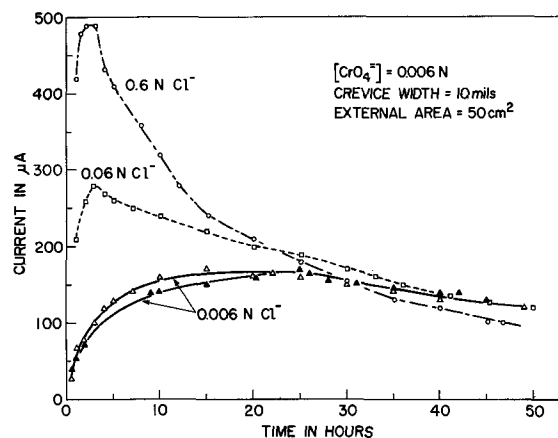


Fig. 10. Effect of chloride ion concentration on the crevice corrosion of iron at constant chromate ion concentration.

Table II. Comparison of electrode potentials for crevice iron and external iron coupled in  $\text{CrO}_4^{2-}/\text{Cl}^-$  solutions

[CrO <sub>4</sub> <sup>2-</sup> ]	[Cl <sup>-</sup> ]	(E <sub>external</sub> - E <sub>crevice, center</sub> ) in mV		
		Max. ΔE	24 hr	48 hr
0.006N	0.6N	34 (0.5 hr)	9	7
		21 (1.5 hr)	14	17
0.06	0.6	24 (4.5 hr)	12	15
		14 (1 hr)	5	—
		5 (2 hr)	—	—
0.006N	0.006N	99 (14 hr)	71	58
		106 (24 hr)	106	87
0.006	0.06	73 (1 hr)	44	57
0.006	0.6	34 (0.5 hr)	9	7
		21 (1.5 hr)	14	17

crevice corrosion rate is controlled by the common local chemistry set up in each of the occluded cavities. In each case, the band of rust around the crevice mouth serves to restrict exchange of the local and bulk electrolytes.

**Potential difference between inner and outer surfaces.**—Table II compares the electrode potentials between the internal active iron and the external passive iron when coupled in  $\text{CrO}_4^{2-}/\text{Cl}^-$  solutions. The potential of the crevice edge was measured with the reference electrode located within the crevice top, as shown in Fig. 1. The potential of the open, external iron was measured with a similar reference electrode located outside the crevice. The electrode potential of the crevice was more negative than that of the open metal due to a restricted oxygen supply to the crevice (1, 5, 37), but the potential difference between the two was fairly small, i.e., 10–100 mV for the active crevices (i.e., excluding the 0.6N  $\text{Cl}^-/0.6\text{N}$   $\text{CrO}_4^{2-}$  solution, which showed little crevice corrosion). Data for duplicate runs in Table II show the maximum potential difference between the crevice center, and the open iron was reproducible to within 15 mV.

Steady-state potential differences between inner and outer stainless steel surfaces in 3½% NaCl have been recently reported to be 50–150 mV (10, 16). According to Korovin and Ulanovskii (37), when the oxygen concentration in seawater is lowered from 9 to 1 mg/liter, the change in potential of a 13% chromium steel coupled to platinum is shifted but 85 mV in the negative direction. This information as well as the data reported here shows that neither the initiation nor continuation of crevice corrosion requires a large potential difference between inner and outer metal surfaces. As noted by Karlberg and Wranglen (10), the concept that there is a large potential difference between the crevice and external metal is based upon potential measurements of uncoupled, unpolarized components in solutions of differing oxygen content. As shown in Fig. 8, the potential difference between the inner and outer surface is much larger before coupling than after.

**Distribution of crevice attack.**—Attack in the crevice was not uniform. In all cases, attack was most severe around the edges of the iron surface near the crevice opening. This observation is consistent with that of Karlberg and Wranglen (10) who noted that attack with 13 and 17% chromium steels always started near the mouth of the crevice.

A mathematical analysis of current distribution in a system similar to but not identical with an active crevice has been given by Waber (38). Current flow between a coplanar anode and cathode in contact and both under a thin film of electrolyte was concentrated at the anode/cathode juncture. It was shown that the zone of attack would spread inward with increasing thickness of the electrolyte layer and with increasing conductivity.

### Summary

For isolated crevices (internal iron not short-circuited to external iron):

1. The anodic corrosion rate was determined by the limiting current for oxygen reduction.

2. The limiting cathodic current, and hence the corrosion rate, was less than that for the open sample.

3. For crevice heights less than the thickness of the oxygen diffusion layer, the limiting cathodic current, and hence the corrosion rate, was suppressed to a constant value.

4. The limiting cathodic current for oxygen reduction was not dependent on pH nor  $\text{Cl}^-$  concentration.

For coupled crevices (internal iron short-circuited to external iron or platinum):

1. The initial current depended on the chloride ion concentration and area of external electrode but not on the crevice height.

2. In the  $\text{CrO}_4^{2-}/\text{Cl}^-$  solutions, the crevice corrosion currents increased with time to maxima but then decreased.

3. At constant chloride ion concentration, the crevice corrosion current decreased with increasing chromate ion concentration.

4. At constant chromate ion concentration, the crevice corrosion current was greater the greater the  $\text{Cl}^-$  ion concentration for the early stages of the process, but at longer times the corrosion rates were the same.

5. Attack within the crevice was not uniform and was most severe near the crevice mouth.

Manuscript submitted July 2, 1973; revised manuscript received March 26, 1974.

Any discussion of this paper will appear in a Discussion Section to be published in the June 1975 JOURNAL. All discussions for the June 1975 Discussion Section should be submitted by Feb. 1, 1975.

### REFERENCES

- (a) I. L. Rosenfeld and I. K. Marshakov, *Corrosion*, **20**, 115t (1964); (b) I. L. Rosenfeld and I. K. Marshakov, *Zh. Fiz. Khim.*, **30**, 2724 (1956).
- M. H. Peterson, T. J. Lennox, Jr., and R. E. Groover, *Materials Protection*, **9** (1), 23 (1970).
- B. F. Brown, C. T. Fujii, and E. P. Dahlberg, *This Journal*, **116**, 218 (1969).
- J. A. Smith, M. H. Peterson, and B. F. Brown, *Corrosion*, **26**, 539 (1970).
- (a) M. Pourbaix, *ibid.*, **26**, 431 (1970); (b) M. Pourbaix, in "The Theory of Stress Corrosion Cracking in Alloys," J. C. Scully, Editor, p. 17, NATO, Brussels (1971).
- G. Butler, P. Stretton, and J. G. Beynon, *Brit. Corrosion J.*, **7**, 1968 (1972).
- B. F. Brown, *Corrosion*, **26**, 249 (1970).
- T. Suzuki, M. Yamabe, and Y. Kitamura, *ibid.*, **29**, 18 (1972).
- F. D. Bogar and C. T. Fujii, Abstract 64, p. 160, Electrochemical Society Extended Abstracts, Fall Meeting, Miami Beach, Florida, Oct. 8–13, 1972.
- G. Karlberg and G. Wranglen, *Corrosion Sci.*, **11**, 499 (1971).
- M. H. Peterson and T. J. Lennox, Jr., *Corrosion*, **29**, 406 (1973).
- B. E. Wilde and E. Williams, *Electrochim. Acta*, **16**, 1971 (1971).
- Y. Kitamura and T. Suzuki, "Proceedings of the 4th International Congress on Metallic Corrosion, Amsterdam, 1969," p. 716, published by NACE (1972).
- A. Pourbaix, *Corrosion*, **27**, 449 (1971).
- E. A. Lizlovs, *This Journal*, **117**, 1335 (1970).
- J. F. Bates, *Corrosion*, **29**, 28 (1973).
- N. D. Greene, W. D. France, Jr., and B. E. Wilde, *ibid.*, **21**, 275 (1965).
- D. J. G. Ives and G. J. Janz, "Reference Electrodes," p. 205, Academic Press, New York (1951).
- J. Dévay, B. Lengyel, Jr., and L. Meszáros, *Acta Chim. Acad. Sci. Hung.*, **62**, 157 (1969).
- Z. A. Iofa and M. A. Makhuba, *Protection of Metals USSR*, **3**, 329 (1967).
- G. Kar, I. Cornet, and D. W. Fuerstenau, *This Journal*, **119**, 33 (1972).
- E. J. Kelly, *ibid.*, **112**, 124 (1965).
- J. J. Lingane, "Electroanalytical Chemistry," p. 227, Interscience Publishers, New York (1958).

24. "International Critical Tables," Vol. V, p. 64 (1929).
25. "Standard Methods for the Examination of Water and Wastewater," 13th ed., p. 480, American Public Health Association, Washington, D. C. (1971).
26. I. L. Rosenfeld and O. I. Vashkov, *Protection of Metals USSR*, **1**, 56 (1965).
27. O. B. Ellis and F. L. LaQue, *Corrosion*, **7**, 362 (1951).
28. I. B. Ulanovskii and Yu. M. Korovin, *J. Appl. Chem., USSR*, **35**, 1683 (1961); also, I. B. Ulanovskii, *ibid.*, **39**, 768 (1966) [English translations of *Z. Prikl. Khim.*].
29. J. M. Fouts and C. W. Bergerson, *Corrosion*, **13**, 12t (1957).
30. W. J. Lorenz, *Corrosion Sci.*, **5**, 121 (1965).
31. E. McCafferty and N. Hackerman, *This Journal*, **119**, 999 (1972).
32. S. Asakura and K. Nobe, *ibid.*, **118**, 13 (1971).
33. R. J. Chin and K. Nobe, *ibid.*, **119**, 1457 (1972).
34. E. D. Parsons, H. H. Cudd, and H. L. Lochte, *J. Phys. Chem.*, **45**, 1339 (1941).
35. M. J. Pryor, *Corrosion*, **9**, 467 (1953).
36. N. A. Darwish, F. Hilbert, W. J. Lorenz, and H. Rosswag, *Electrochim. Acta*, **18**, 421 (1973).
37. Yu. M. Korovin and I. B. Ulanovskii, *Corrosion*, **22**, 16 (1966).
38. J. T. Waber, *This Journal*, **103**, 64 (1956).

## The Effect of Chelating Agents on the Transient Behavior of Passivated Iron under Cathodic Potential Pulsing

Kotaro Ogura\*<sup>1</sup> and Norman Hackerman\*

Department of Chemistry, Rice University, Houston, Texas 77001

The publication costs of this article have been assisted by the Robert A. Welch Foundation.

### ABSTRACT

The passive layer was formed potentiostatically on iron in basic solution containing various chelating agents: o-phenanthroline, malonic acid, 8-hydroxyquinoline. 0.15N borate-0.15N boric acid solution was also used for comparison. A cathodic potential pulse was applied to the passivated iron in the same solution, and cathodic reduction was then carried out galvanostatically in basic solution without chelating agents. The cathodic pulse reduced adsorbed oxygen on passive iron, and the coverage by adsorbed oxygen decreased depending upon the properties of the chelating agents. o-Phenanthroline did not influence the coverage of adsorbed oxygen since it diffused away in the form of the ferrous-o-phenanthroline from the metal surface. The coverage by adsorbed oxygen in the solution containing malonic acid and 8-hydroxyquinoline was low, and the cause was attributed to the replacement of adsorbed oxygen by oxalic acid or metallic chelate. The thicker passive layer was produced in the borate-boric acid solution, and the adsorbed oxygen was replaced by the ring polymer which exists predominantly in the mixed solution and acts as a corrosion inhibitor.

Experimental conditions necessary to achieve the passivity of iron are well known; however, there are few papers (1-3) which treat the effects of chelating agents or other organic compounds on passivated iron. Passivation should be influenced by chelating agents in solution since the sorbed layer on the passive film plays an important role in passivation as previously reported (1, 2).

In this paper, the effect of chelating agents on the transient behavior of passivated iron was studied under the same conditions as those described previously (4).

### Experimental

Iron samples were the same as those used before (4). 0.01M sodium borate was used for pretreatment and for cathodic reduction. The solution was deaerated with purified nitrogen and preelectrolyzed at 80  $\mu\text{A}/\text{cm}^2$  for 48 hr. The 0.01M sodium borate solutions used for anodization contained 0.002M of the following analytical grade chelating agents: o-phenanthroline, malonic acid, and 8-hydroxyquinoline. A solution of 0.15N borate and 0.15N boric acid was used for comparison. All were deaerated with purified nitrogen for 48 hr, but not preelectrolyzed.

The experimental techniques were the same as those described previously (4). Passivation was performed

potentiostatically for 20 min and the specimen was then subjected to a single cathodic potential pulse. The specimen was then washed twice with 0.01M sodium borate solution and cathodic reduction was carried out in 0.01M sodium borate at 20.9  $\mu\text{A}/\text{cm}^2$ . The change in potential with time was followed by an X-Y recorder equipped with a preamplifier having an input impedance of more than  $10^{13}$  ohms.

### Results

**Current-time curves.**—A cathodic potential pulse was applied to the passivated iron which had been preanodized in solutions containing chelating agents. The response current of the pulse at 1460 mV is shown in Fig. 1 and 2 for 0.01M borate solution containing 0.002M o-phenanthroline and 0.002M malonic acid, respectively. 0.002M 8-hydroxyquinoline and 0.15N boric acid-0.15N borate solution were also used as chelating agents.

For the preanodizing potential of 1460 mV, the response current depended upon the chelating agent and the pulse amplitude, except with 0.002M 8-hydroxyquinoline (not shown). With less noble preanodizing potentials such as 900 mV, the response currents were appreciable for all chelating agents studied.

**Logarithmic current-time curves.**—The log of response current of various pulses at 1000 mV is shown in Fig. 3 and 4 for 0.01M borate solution containing 0.005M o-phenanthroline, and 0.002M 8-hydroxyquino-

\* Electrochemical Society Active Member.

<sup>1</sup> Present address, Department of Applied Chemistry, Yamaguchi University, Ube, Yamaguchi-Ken, Japan.

Key words: chelating agents, passivated iron, coverage.



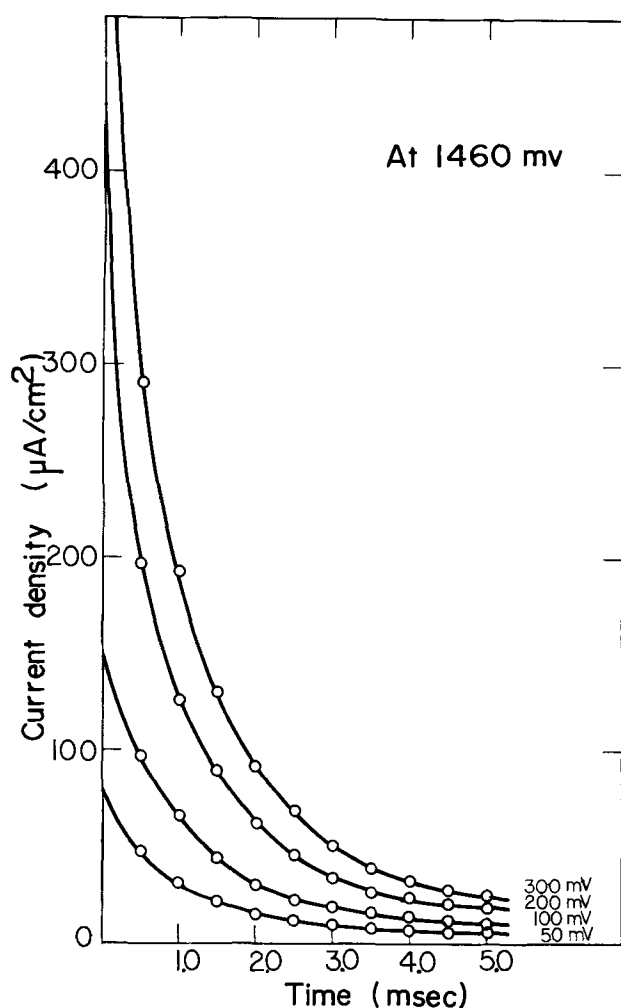


Fig. 1. Response current density of various cathodic potential pulses during preanodizing at 1460 mV in 0.01M  $\text{Na}_2\text{B}_4\text{O}_7$  containing 0.002M o-phenanthroline.

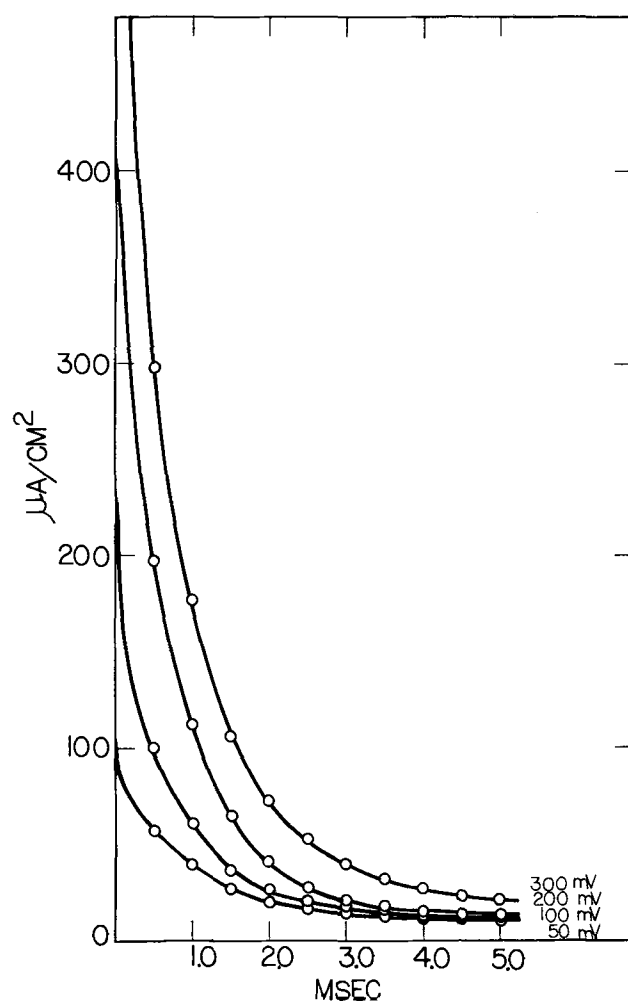


Fig. 2. Response current density of various cathodic potential pulses during preanodizing at 1460 mV in 0.01M  $\text{Na}_2\text{B}_4\text{O}_7$  containing 0.002M malonic acid.

line. In the initial stage of pulsing, the logarithmic current is linearly related with time. This was also true in all solutions, but the slope of the straight line depended upon the solution used.

**Current-preanodizing potential curves.**—The response current of the 300 mV pulse at 5.0 msec was plotted against preanodizing potential for various solutions in Fig. 5. In each solution, a minimum current density was observed near the oxygen evolution potential. The current increased with decreasing preanodizing potential and passed through a maximum. Generally, if the solution contained a chelating agent, the response current of a cathodic potential pulse became lower than that in solutions without chelating agents. At potentials more noble than 800 mV the response current in 0.15N borate-0.15N boric acid solution was the same as in solutions containing chelating agents.

**Cathodic reduction.**—After the solution had been subjected to a pulse, the solution was replaced by a 0.01M borate solution containing no chelating agent. Typical reduction curves are shown in Fig. 6. The cathodic decay curves were similar in each case, i.e., they decayed through two plateaus. The passive layer which had been formed anodically in each experimental solution was reduced at first plateau, i.e., around  $-200$  mV (RHE). Hydrogen evolved at the second plateau, i.e., around  $-270$  mV (RHE). The latter potential depended upon the solution in which the specimen had been anodized. These potentials corresponded to  $-920$  mV (SCE) for the complete re-

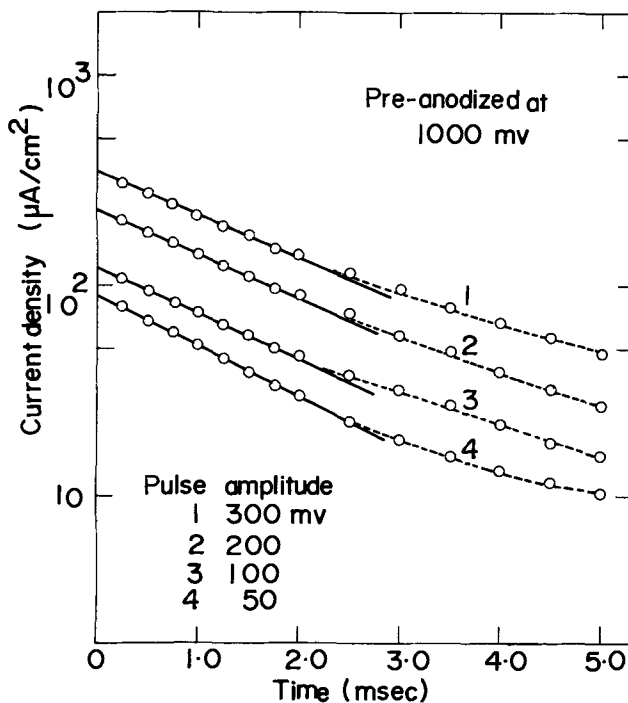


Fig. 3. Logarithmic dependence of response current on time during preanodizing at 1000 mV in 0.01M  $\text{Na}_2\text{B}_4\text{O}_7$  containing 0.005M o-phenanthroline.

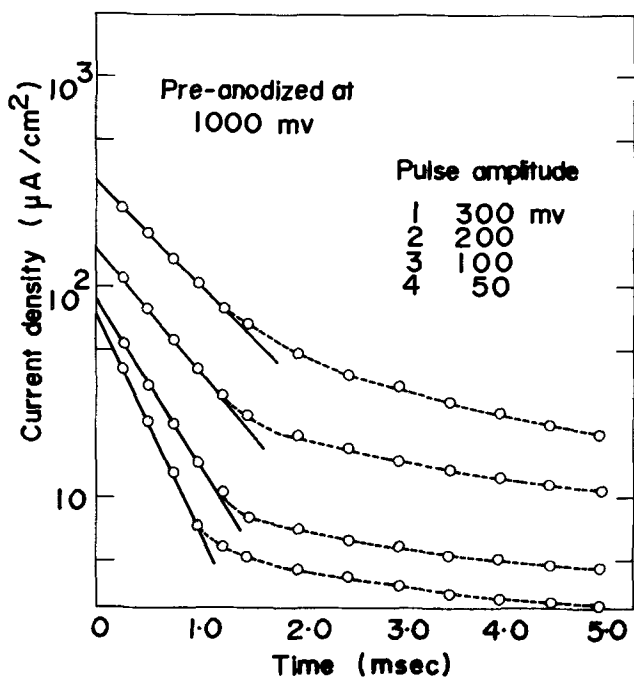


Fig. 4. Logarithmic dependence of response current on time during preanodizing at 1000 mV in 0.01M Na<sub>2</sub>B<sub>4</sub>O<sub>7</sub> containing 0.002M 8-hydroxyquinoline.

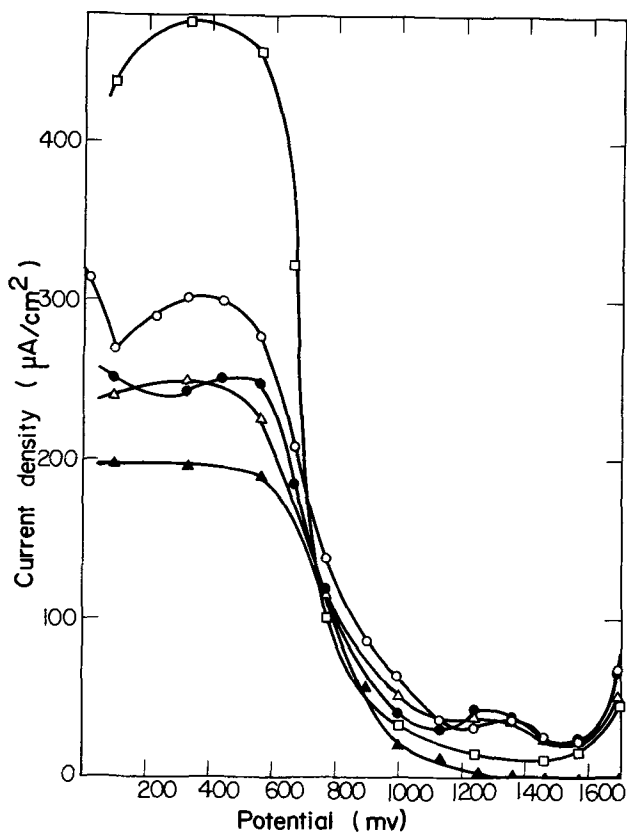


Fig. 5. Response current density at pulses duration of 5.0 msec vs. preanodizing potential in various solutions. —○—, 0.001M Na<sub>2</sub>B<sub>4</sub>O<sub>7</sub> without chelating agent; —△—, with 0.002M o-phenanthroline; —●—, with 0.002M malonic acid; —▲—, with 0.002M 8-hydroxyquinoline; —□—, 0.15N borate-0.15N boric acid.

duction of the passive layer and to -1000 mV (SCE) for the hydrogen evolution, respectively (5).

The amount of charge needed for reduction of the passive layer can be estimated from Fig. 6 and is plotted vs. preanodizing potentials in Fig. 7. There is

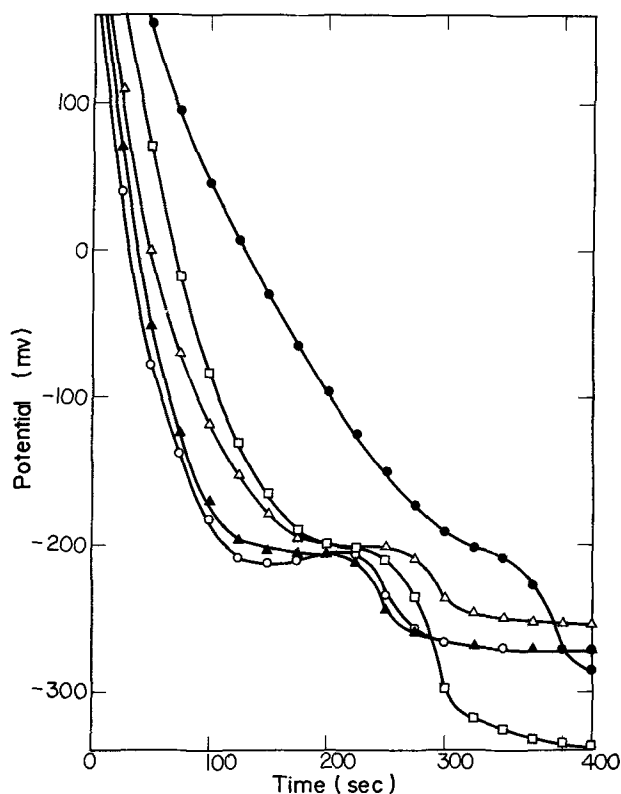
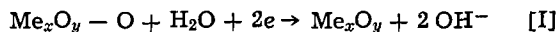


Fig. 6. Cathodic reduction curves. Anodized first in (—●—) 0.01M Na<sub>2</sub>B<sub>4</sub>O<sub>7</sub> containing 0.002M malonic acid; (—△—) 0.15N borate-0.15N boric acid; (—□—) 0.01M Na<sub>2</sub>B<sub>4</sub>O<sub>7</sub> containing 0.002M 8-hydroxyquinoline; (—▲—) 0.01M Na<sub>2</sub>B<sub>4</sub>O<sub>7</sub> containing 0.002M o-phenanthroline; (—○—) 0.01M Na<sub>2</sub>B<sub>4</sub>O<sub>7</sub> at 1220 mV. All specimens were reduced in 0.01M Na<sub>2</sub>B<sub>4</sub>O<sub>7</sub> without chelating agent at 20.9 µA/cm<sup>2</sup>.

approximately a linear relationship between preanodizing potential and the amount of charge in agreement with Nagayama's and Cohen's result (5). As shown in Fig. 7, the iron passivated in 0.002M malonic acid, 0.002M 8-hydroxyquinoline, or 0.15N borate-0.15N boric acid needs more charge to reduce the passive film than that formed in pure 0.01M borate solution. In the solution with o-phenanthroline, however, the amount of charge needed was smaller and decreased with increasing o-phenanthroline concentrations.

### Discussion

From many experimental facts, it was suggested previously (4) that cathodic potential pulsing did not affect the constitution of so-called bulk oxide, but only the sorbed layer on the surface of passivated iron, and that the reaction [I] occurred under pulsing



where Me<sub>x</sub>O<sub>y</sub> is the passive film and -O is the adsorbed oxygen on passive film. The response current of the pulse was explained by the cathodic reduction of the adsorbed oxygen, since the transient current caused by discharging the electric double layer could be neglected in a potentiostatic experiment using a high response potentiostat.

In Fig. 8, the current at zero time is plotted on a logarithmic scale as a function of electrode potential for various preanodizing potentials. The electrode potential was obtained by subtracting the pulse amplitude from the preanodizing potential as done before (4). The linear relationship between *i*<sub>t=0</sub> and the electrode potential holds in 0.01M borate solution containing 0.005M o-phenanthroline. This relationship was not influenced by the presence of the chelating agents added in 0.01M borate, and also held in 0.15N borate-0.15N boric acid solution, as shown in Fig. 9.

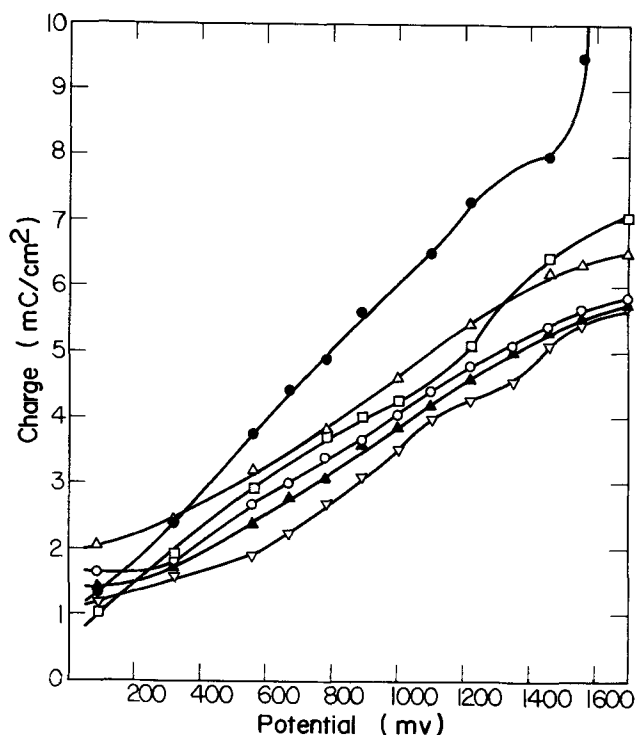


Fig. 7. Amount of charge needed for cathodic reduction vs. pre-anodizing potential. Anodized first in (—●—) 0.001M Na<sub>2</sub>B<sub>4</sub>O<sub>7</sub> containing 0.002M malonic acid; (—△—) 0.15N borate-0.15N boric acid; (—□—) 0.01M Na<sub>2</sub>B<sub>4</sub>O<sub>7</sub> containing 0.002M 8-hydroxyquinoline; (—○—) 0.01M Na<sub>2</sub>B<sub>4</sub>O<sub>7</sub>; (—▲—) 0.01M Na<sub>2</sub>B<sub>4</sub>O<sub>7</sub> containing 0.002M o-phenanthroline; (—▽—) 0.01M Na<sub>2</sub>B<sub>4</sub>O<sub>7</sub> containing 0.006M o-phenanthroline. All specimens were reduced in 0.01M Na<sub>2</sub>B<sub>4</sub>O<sub>7</sub> without chelating agent at 20.9 μA/cm<sup>2</sup>.

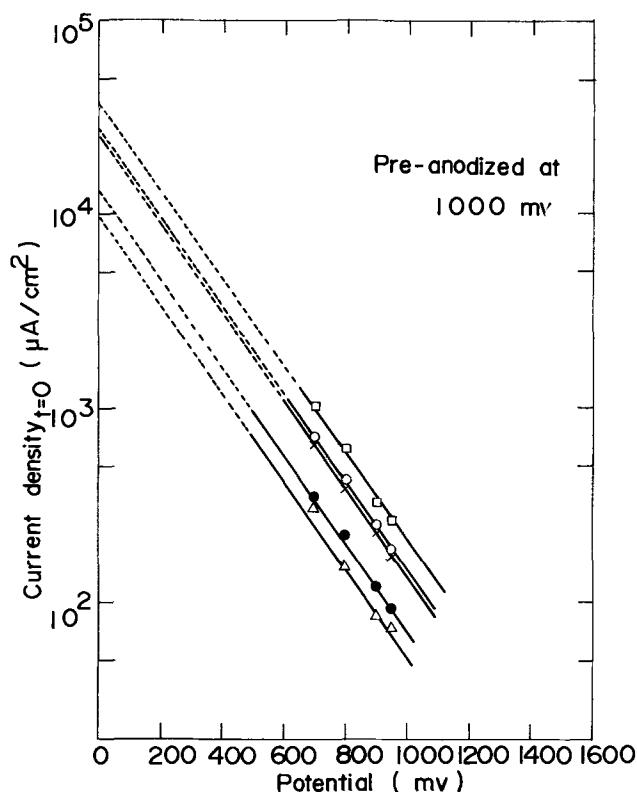


Fig. 9. The response current at the time of zero vs. the electrode potential for the specimens pre-anodized at various potentials in various solutions. —□—, Borate-boric acid (pH, 8.41); and —○—, 0.01M Na<sub>2</sub>B<sub>4</sub>O<sub>7</sub> with no chelating agent; —×—, with 0.002M malonic acid; —●—, with 0.005M o-phenanthroline; and —△—, with 0.002M 8-hydroxyquinoline.

As discussed previously (4), the slope in Fig. 9 corresponds to the left-hand side of the following equation

$$\left(\frac{\partial \log i}{\partial V}\right)_{t=0} = -\frac{\alpha nF}{2.303 \times RT}$$

From this result,  $\alpha$  was estimated to be 0.1. This value was constant, independent of the presence of the chelating agent.

The intercept at the electrode potential of zero in Fig. 9 gives the current density,  $i^*_{t=0}$  given by Eq. [7]

in Ref. (4).  $i^*$  for various pre-anodizing potentials in various solutions is indicated in Table I. If the value of  $k_o$  is known, the concentration of adsorbed oxygen on passivated iron can be calculated.

$k_o$  was estimated by the same method as that discussed before (4). That is, if the logarithm of the left-hand side of Eq. [5] in Ref. (4) is plotted vs. the electrode potential, the intercept at the electrode potential of zero should give  $k_o/2.303$ . Based upon such consideration, Fig. 10 was constructed. The logarithm of the left-hand side of Eq. [5] is linearly related with the electrode potential in each solution. Also, the slope of the straight line is always constant.  $k_o$  was calculated from the value of the intercept which depended upon the solution used, and the result is indicated in Table I.

Finally, the concentration of adsorbed oxygen on passivated iron was calculated by using Eq. [7] in Ref. (4) and  $k_o$  obtained above. The result is shown in Table I. In each solution, the concentration of adsorbed oxygen increased with increasing pre-anodizing potential. This behavior is discussed below by considering the coverage of passive iron by adsorbed oxygen.

The coverage  $\theta$  was obtained under the assumption that the coverage  $\theta^*$  at 1360 mV in the solution without the chelating agent is equal to 1.0. The result is plotted

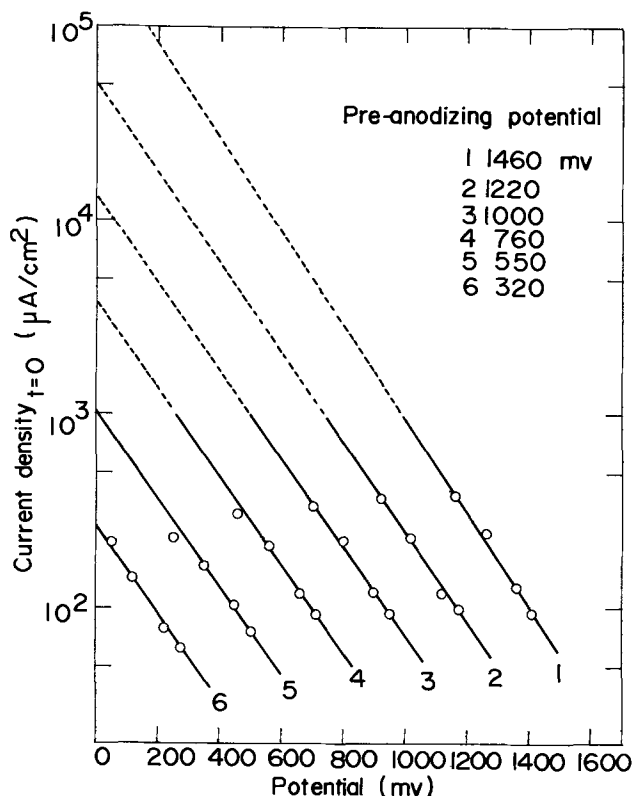


Fig. 8. The response current at the time of zero vs. the electrode potential for the specimens pre-anodized at various potentials in 0.01M Na<sub>2</sub>B<sub>4</sub>O<sub>7</sub> containing 0.005M o-phenanthroline.

Table I. The concentration of adsorbed oxygen on passivated iron before applying cathodic potential pulse at various preanodizing potentials

	Preanodizing potential (mV)	$i^*$ (mA/cm <sup>2</sup> )	$C^*$ (10 <sup>-10</sup> mole/cm <sup>2</sup> )
In 0.005M <i>o</i> -phenanthroline $k_o = 1.94 \times 10^2$ (sec <sup>-1</sup> )	1220	51.0	1.36
	1100	26.2	0.70
	900	13.5	0.36
	760	7.11	0.19
	550	1.05	0.03
320	0.27	0.01	
In 0.002M malonic acid $k_o = 3.57 \times 10^2$ (sec <sup>-1</sup> )	1350	68.9	1.00
	1240	27.6	0.55
	1200	27.6	0.40
	1100	17.9	0.26
	1000	12.4	0.18
	780	4.82	0.07
560	2.50	0.00	
In 0.002M 8-hydroxyquinoline $k_o = 5.29 \times 10^2$ (sec <sup>-1</sup> )	1350	75.6	0.74
	1250	42.9	0.42
	1000	9.80	0.10
	780	5.90	0.06
	560	1.95	0.02
In borate-boric acid (pH 8.41) $k_o = 6.90 \times 10^2$ (sec <sup>-1</sup> )	1350	206	1.55
	1220	127	0.95
	1100	74.6	0.56
	1000	38.0	0.29
	780	15.6	0.12
	550	6.90	0.05
	320	2.20	0.02

against preanodizing potential in Fig. 11. At each preanodizing potential, the concentration of adsorbed oxygen decreased by the addition of the chelating agent in solution. Especially, with malonic acid and 8-hydroxyquinoline, the coverage was low. Each chelating agent used is discussed below.

*o*-Phenanthroline.—When the iron was anodized in solutions containing *o*-phenanthroline, the iron surface became intensely red. This color disappeared on further anodization.

Ferrous iron forms a red complex with *o*-phenanthroline according to the following (6)

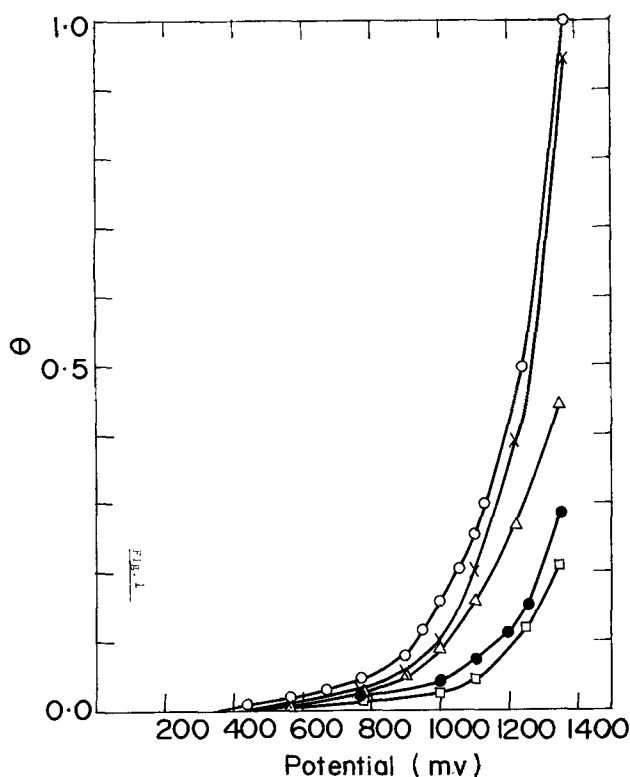
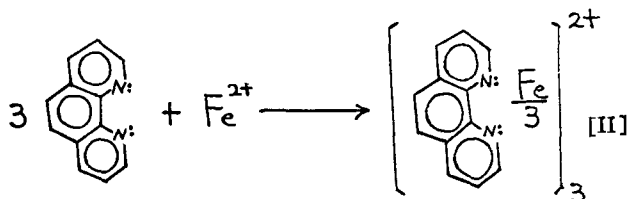


Fig. 11. The coverage  $\theta$  vs. the anodizing potential. —○—, 0.01M Na<sub>2</sub>B<sub>4</sub>O<sub>7</sub> without chelating agent; and —×—, with 0.005M *o*-phenanthroline; and —△—, borate-boric acid (8.41, pH); —●—, 0.01M Na<sub>2</sub>B<sub>4</sub>O<sub>7</sub> with 0.002M malonic acid; and —□—, with 0.002M 8-hydroxyquinoline.

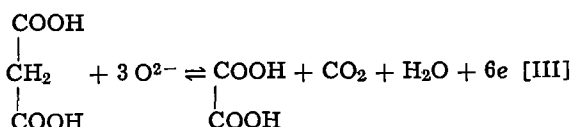


This is also a ferric-*o*-phenanthroline complex, but its color is light blue.

The appearance of the red color and its subsequent disappearance indicates the formation of the complex on the surface and its consequent diffusion to the bulk of the solution. Obviously, another possibility is the conversion of the "compound" on the surface to a less intensely colored state.

Given the former explanation, adsorbed oxygen exists on the passivated iron without being disturbed by *o*-phenanthroline. This is supported by the deduced observation that coverage by adsorbed oxygen was comparable in the solution with or without a chelating agent.

*Malonic acid*.—As shown in Fig. 7, the amount of charge needed for reduction of the passive film formed in solutions containing malonic acid was very large compared with the other solutions. The interpretation of this large amount of required charge is as follows. Malonic acid is known to be oxidized anodically according to the following reaction (7)



The standard potential for reaction [III] has not yet been measured exactly. However, it is known that this reaction can occur without accompanying oxygen evo-

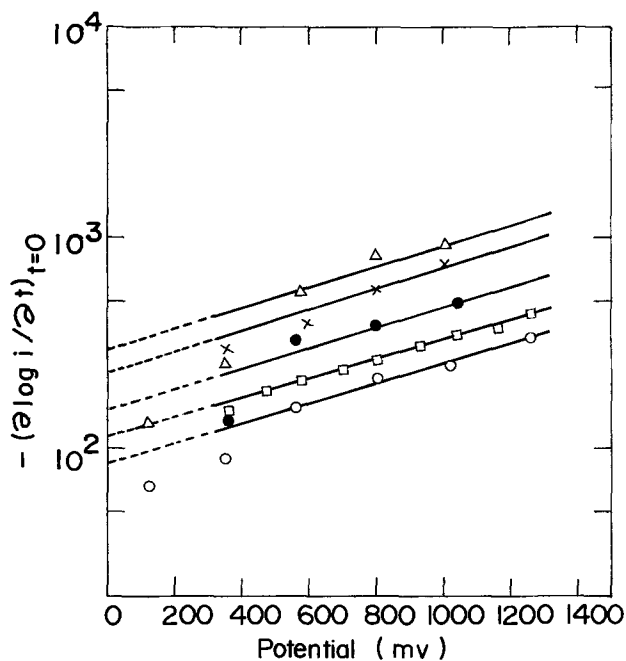
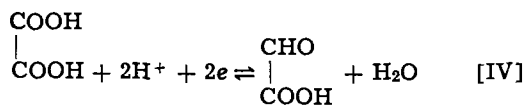


Fig. 10. —  $(\partial \log i / \partial t)_{t=0}$  vs. the electrode potential. —△—, Borate-boric acid (pH, 8.41); and —×—, 0.01M Na<sub>2</sub>B<sub>4</sub>O<sub>7</sub> with 8-hydroxyquinoline (0.002M); —●—, with malonic acid (0.002M); —□—, with no chelating agent; and —○—, with *o*-phenanthroline (0.005M).

lution on platinum (7). If iron is anodized in the solution containing malonic acid, reaction [III] may occur simultaneously with the oxidation of iron.

The reduction curve may involve reduction of anodically produced oxalic acid as well as the passive film. The following mechanism should be considered (7)

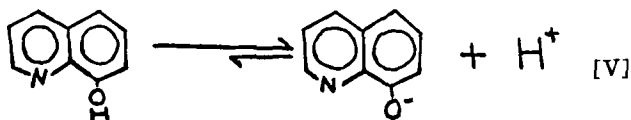


The aldehyde produced can be further reduced to alcohol depending upon the reduction conditions. The bulk solution used for reduction did not contain any chelating agent, but oxalic acid may still be adsorbed on passive iron after replacing the solution with one without the chelating agent.

Figure 11 shows that the coverage of adsorbed oxygen in the solution with malonic acid is lower than that without the chelating agent. The lower coverage in this solution can be explained by the adsorption of oxalic acid.

**8-Hydroxyquinoline.**—In the solution containing 0.002M 8-hydroxyquinoline, a small response current was observed for the whole range of preanodizing potentials, as shown in Fig. 5. In the cathodic reduction, 8-hydroxyquinoline affected the hydrogen overpotential, as indicated in Fig. 6. The amount of charge needed for reduction was approximately the same as that in the solution without chelating agent.

The solution pH in this experiment was always 9.2. At this pH, 8-hydroxyquinoline should be dissociated as shown below



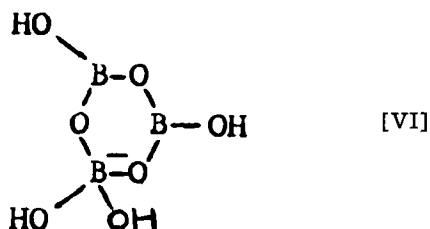
8-Hydroxyquinoline is known to be a corrosion inhibitor for aluminum, and an aluminum chelate on the metal surface has been postulated (8) because the surface loses its metallic luster.

In the case of iron, a metal chelate is believed to form on the surface since the response current was very small. Iron has six electrons in d-orbitals. In the excited state, these electrons can be arranged in such a way that two electrons with opposite spin direction occupy each of three d-orbitals (9). Therefore, there are two unfilled d-orbitals. These orbitals may be occupied by the lone paired electrons of nitrogen and oxygen in 8-hydroxyquinoline.

The lowest coverage was observed with 8-hydroxyquinoline, as shown in Fig. 11. An iron chelate on passive iron could account for this experimental fact. That is, a part of the adsorbed oxygen would be replaced by the produced metallic chelates, and hence the coverage of adsorbed oxygen should decrease, as indicated in Fig. 11.

**0.15N borate-0.15N boric acid.**—This solution has been used for the study of the passivity of iron (5, 10-12), and its buffer property is the focus of attention. However, borate is a corrosion inhibitor (13).

An equivolume mixture of 0.15N borate-0.15N boric acid has a pH of 8.41, and there is the evidence that polymers are present in the mixed solution (9). The predominant species appears to be the ring polymer as shown below



The coverage of adsorbed oxygen on iron passivated in this solution was lower than in 0.01M borate. This may be due to the displacement of adsorbed oxygen by this polymer.

It was found that the passive layer produced in this solution was thicker than that in 0.01M borate. This can be seen from the observation shown in Fig. 7 where the amount of charge for the reduction of the passive layer in this solution was larger than that formed in 0.01M borate. The polymer shown above appears to act as a corrosion inhibitor which causes a thicker film and a smaller coverage of adsorbed oxygen in this solution than has been seen previously.

## Conclusions

The passive layer was formed on iron in solutions containing various chelating agents, and a cathodic potential pulse was applied to the specimen. Adsorbed oxygen on passive iron was reduced by the cathodic pulse, and the coverage by adsorbed oxygen decreased depending upon the properties of the chelating agents. o-Phenanthroline reacted with iron to form the ferrous-o-phenanthroline complex which diffused away from the metal surface after passivation. This agent did not influence the existence of adsorbed oxygen. The coverage by adsorbed oxygen in the solution with malonic acid and 8-hydroxyquinoline was lower than that without the chelating agent. The lower coverage was attributed to the replacement of adsorbed oxygen by oxalic acid or metallic chelate. The thicker passive layer was produced in the borate-boric acid solution, and the adsorbed oxygen was replaced by the ring polymer which exists predominantly in the mixed solution.

## Acknowledgments

The authors thank Dr. Shiro Haruyama of Tokyo Institute of Technology for helpful discussions. The financial support by the Robert A. Welch Foundation of Houston, Texas, is gratefully acknowledged. They are also indebted to the Battelle Memorial Institute of Columbus, Ohio, for the generous supply of zone-refined iron.

Manuscript submitted Oct. 15, 1973; revised manuscript received Feb. 22, 1974.

Any discussion of this paper will appear in a Discussion Section to be published in the June 1975 JOURNAL. All discussions for the June 1975 Discussion Section should be submitted by Feb. 1, 1975.

## LIST OF SYMBOLS

$V$	electrode potential (vs. RHE)
RHE	reversible hydrogen electrode
$i$	current density ( $\mu\text{A}/\text{cm}^2$ )
$t$	time (sec)
$n$	number of electrons
$F$	Faraday constant
$\alpha$	transfer coefficient
$T$	absolute temperature
$i^*_{t=0, V=0}$	current density at $t = 0$ and $V = 0$
$k_0$	rate constant at 0V vs. RHE
$\theta$	surface coverage by adsorbed oxygen
$\theta^*$	surface coverage by adsorbed oxygen at 1360 mV

## REFERENCES

1. E. S. Snavely and N. Hackerman, *Can. J. Chem.*, **37**, 268 (1959).
2. K. C. Tsai and N. Hackerman, *This Journal*, **118**, 28 (1971).
3. D. Posadas, A. J. Arvia, and J. J. Podesta, *Electrochim. Acta*, **16**, 1041 (1971).
4. K. Ogura and N. Hackerman, *This Journal*, **120**, 1638 (1973).
5. M. Nagayama and M. Cohen, *ibid.*, **109**, 781 (1962).
6. C. R. Noller, "Chemistry of Organic Compound," W. B. Saunders Company, Philadelphia (1965); R. A. Day and A. L. Underwood, "Quantitative Analysis," 2nd ed., p. 154, Prentice-Hall, Inc., Englewood Cliffs, N. J. (1967).
7. M. J. Allen, "Organic Electrode Process," p. 109,

- Chapman Publishers, London (1958).
8. Y. Hayakawa, T. Mitamura, and T. Kaneko, *J. Electrochem. Soc. Japan*, **29**, 41 (1961).
  9. F. A. Cotton and G. Wilkinson, "Advanced Inorganic Chemistry," Interscience Publishers, New York (1966).
  10. J. Kruger and J. P. Calvert, *This Journal*, **113**, 1258 (1966).
  11. H. Wroblowa, V. Brusica, and J. O'M Bockris, *J. Phys. Chem.*, **75**, 2823 (1971).
  12. K. Ogura, S. Haruyama, and K. Magasaki, *J. Electrochem. Soc. Japan*, **37**, 102 (1969).
  13. J. Dulat, *Proc. Intern. Congr. Metall. Corros.*, **2nd.**, p. 135, New York (1963).

## An Investigation of Composite Aluminum Oxide Films by Radiotracer and Gravimetric Methods

Robert S. Alwitt\*<sup>1</sup> and Walter J. Bernard\*

*Sprague Electric Company, North Adams, Massachusetts 01247*

*The publication costs of this article have been assisted by the Sprague Electric Company.*

### ABSTRACT

Composite oxide films on aluminum were produced by reaction with boiling water followed by anodic oxidation in a phosphate electrolyte tagged with  $P^{32}$  tracer. The amount of phosphorus remaining in the film was followed during stepwise dissolution. It was found that the phosphorus concentration in the barrier portion of this film was two orders of magnitude lower than in a conventional anodic oxide. The amounts of hydrous oxide and barrier oxide in the composite film were determined using a combination of film stripping and metal dissolution procedures. The weight of barrier oxide was only 75% of the weight of a conventional anodic oxide, while the dielectric constants of the two films were about the same. Some important properties of the hydrous oxide were inferred from the behavior observed in these experiments.

When aluminum is first reacted with hot water and then anodically oxidized, the resulting film consists of a barrier oxide layer next to the metal and a layer of pseudoboehmite, a hydrous oxide, at the outer surface. The barrier portion consists of both anodic oxide and dehydrated hydrous oxide. The unusual anodization kinetics and special properties of these composite oxides have been discussed in previous papers (1, 2). In those studies it was possible only to estimate the individual amounts of barrier oxide and hydrous oxide in the final film since no technique was available for direct measurement of these quantities. One estimate indicated that about 25% less barrier oxide was needed to support a particular voltage during anodization than was the case for a conventional anodic oxide (2). This higher field strength did not appear to be accompanied by any significant change in dielectric constant. We have now investigated this more rigorously and find that this earlier estimate was essentially correct. These results are presented here.

A mechanism has been proposed by Vedder and Vermilyea (3) for the growth of the pseudoboehmite layer during reaction with water. They have proposed that growth of the film occurs by transport of hydrolyzed Al species through the liquid phase to deposition sites, and that sufficient film porosity is maintained to support this mechanism, even after long reaction times. On the other hand, a mechanism proposed for the growth of the composite oxide barrier layer stipulates the presence of an inner region of the pseudoboehmite layer that is impermeable to the anodizing electrolyte (2). There is circumstantial evidence for such a region, based on dielectric measurements (4). To help resolve this issue, composite oxides were

anodized in a phosphate electrolyte tagged with  $P^{32}$ , and the activity of the film was measured after successive thinning in a conventional  $H_3PO_4$ - $CrO_3$  stripping solution. Phosphate anions are strongly adsorbed onto aluminum oxides (5), thus assuring a high  $P^{32}$  content in the composite film. The results presented here are interpreted as supporting the existence of an inner region that is impermeable to solvated anions.

### Experimental

**General.**—Specimens with an area of 100 cm<sup>2</sup> were cut from 99.99% Al foil, electropolished in a perchloric acid-acetic anhydride bath, rinsed, and then reacted with boiling distilled water for 5 min. Anodic oxidation was done at a constant current to 175V in an electrolyte of either 0.01M  $NaH_2PO_4$  or 100 g/liter  $H_3BO_3$  at 90°C.

The outer portion of the film, which is the hydrous oxide layer, was dissolved in a stirred solution of 5%  $H_3PO_4$  + 2%  $CrO_3$  at 85° ± 0.1°C. Dissolution was done in a stepwise manner with a measurement of specimen weight after each step, the weight change being assumed as due to loss of hydrous oxide alone. However, it was recognized that some nonuniform attack on the film can occur, causing a slight dissolution of the barrier portion as well. Therefore, an individual specimen was occasionally removed from this sequence and re-anodized to 175V in order to replace such barrier oxide, and the weight gain, which is entirely barrier film, was used as a correction on the stripping weight loss. Specimen weights after stripping and after re-anodization were measured with an accuracy of ±10 μg. In some instances, the capacitance at 120 Hz was measured in a neutral ammonium borate solution.

After stripping, the remaining oxide was recovered by dissolving the Al metal in warm 10%  $Br_2$ -methanol, then rinsing the oxide in warm methanol, and drying.

\* Electrochemical Society Active Member.

<sup>1</sup> Present address: United Chemi-Con, Inc., R&D Laboratory, West Springfield, Massachusetts 01089.

Key words: anodic oxide, hydrous aluminum oxide, pseudoboehmite film, phosphorus distribution.

The oxide was weighed before and after heating for 2 hr at 900°C to remove any structural water.

**$P^{32}$  tracer measurements.**—Radioactive  $P^{32}$  was added to the formation electrolyte as chloride-free phosphoric acid (obtained from New England Nuclear Corporation). The small additional quantity of radioactive material had no appreciable effect on the solution concentration or its pH. The amount of tracer used resulted in an initial counting rate of several thousand counts per minute; this necessitated a fairly large coincidence correction during the first periods of film stripping, but had the advantage of permitting an appreciable counting rate as the boundary of the phosphorus-containing film was approached. The counting rate was also corrected for isotopic decay of the tracer (half-life of  $P^{32}$  is 14.3 days).

Absolute values of the phosphorus content of the films were determined by comparison with the activity of standard volumes of the anodizing solution. Aliquot portions of the electrolyte in the form of fine droplets were distributed uniformly over the surface of a sheet of nonanodized aluminum with the same counting geometry as the anodized specimens. (The effective area of the anodized specimen, however, is twice that of the geometric area presented to the Geiger-Mueller tube, since both sides of the foil contribute to the counting rate. This is because the foil used is only 0.075 mm thick and thus essentially transparent to the  $\beta$ -particles emitted by  $P^{32}$  [ $E_{max} = 1.7$  Mev].) The aluminum foil was then dried at 50°C and counted; no corrections for self-absorption were necessary.

A 0.01M  $NaH_2PO_4$  solution was used to anodize three specimens each at constant currents of 1.0 and 0.3 mA/cm<sup>2</sup>. These were rinsed in distilled water for 1 hr to remove superficial phosphate ion, then washed with acetone, and air dried before measuring the activity, weight, and capacitance, in that order. The films were stripped in 30 sec steps, rinsed for 10 min after each step, and the sequence of measurements repeated. Single specimens were removed after 1, 2, 2½, and 4 min stripping times and reanodized in nontracer electrolyte to get a correction for barrier film attack. Activity measurements were stopped after a total of 3 min stripping, but weight and capacitance measurements were continued with two specimens for a total stripping time of 9 min. The oxide remaining on the four specimens removed early from the stripping sequence was quantitatively recovered after dissolving the metal substrate in bromine-methanol solution.

### Results

The weight losses obtained during stripping of the tracer specimens are shown in Fig. 1. The open circles

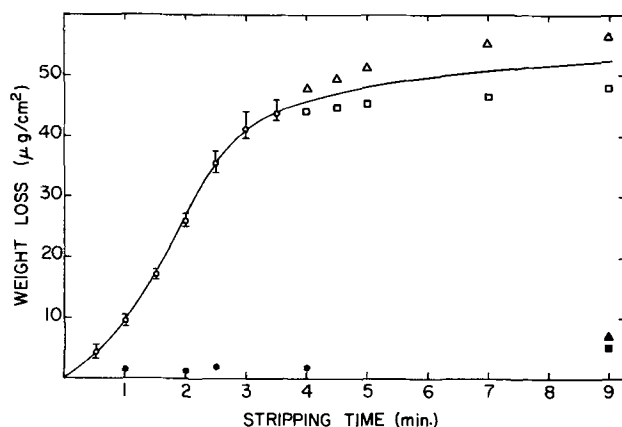


Fig. 1. Weight loss of composite oxides in 5%  $H_3PO_4$  + 2%  $CrO_3$  solution at 85°C. Symbols represent average for all specimens (○) and results with single specimens anodized at 0.3 mA/cm<sup>2</sup> (□) and at 1.0 mA/cm<sup>2</sup> (△). Filled symbols represent weight gain during reanodization of single specimens.

represent the average for all specimens at that time. There was no significant difference between the averages of the specimens anodized at 1 mA/cm<sup>2</sup> and at 0.3 mA/cm<sup>2</sup>. For times of 4 min and longer, only one specimen from each current density was still being stripped. The filled circles represent the weight gain of single specimens during reanodization after the indicated stripping time. Initially, it had been hoped that capacitance measurements could be used as a measure of barrier film dissolution during stripping, but the capacitance increase was always much larger than predicted from the weight gain. This indicates that the small amount of barrier attack was localized, rather than uniform across the film. After correcting for barrier film loss, it was found that the weight of the 0.3 mA/cm<sup>2</sup> sample remained constant between 4 and 9 min stripping times, while the 1.0 mA/cm<sup>2</sup> sample lost only an additional 3.50 μg/cm<sup>2</sup> over this time interval. After 9 min stripping, the average corrected weight loss was 46.4 μg/cm<sup>2</sup>. This represents the weight of hydrous oxide in the composite film.

The average weight of a pseudoboehmite film produced during a 5 min reaction with boiling water is 63.5 μg/cm<sup>2</sup> (4). The difference between this figure and 46.5 μg/cm<sup>2</sup> (17.0 μg/cm<sup>2</sup>) represents the hydrous oxide converted to barrier film, 26.8% of the initial amount.

The oxide remaining on each of the four samples that had been stripped for times of 4 min or less before reanodization was recovered after dissolving the metal in bromine-methanol solution. Adding the corrected stripping weight loss to this weight gave the total composite oxide weight. The average for the four samples was 102.4 μg/cm<sup>2</sup>, with a range of 97.1–110.8 μg/cm<sup>2</sup>. The average weight of barrier oxide was found to be 55.9 μg/cm<sup>2</sup>, obtained by subtracting the 46.5 μg/cm<sup>2</sup> of hydrous oxide from the total weight.

Because of the similarity of experimental conditions to those used previously (1), it was expected that current efficiency of anodic oxidation would be 100%, as in the earlier case. Rather than make this assumption, the weight of anodic oxide was calculated by subtracting from the weight of barrier oxide the contribution from converted hydrous oxide. That is, remembering that the pseudoboehmite contains about 27% water (1, 6), the weight of  $Al_2O_3$  from converted hydrous oxide is  $0.73 \times 17.0 \mu\text{g}/\text{cm}^2$  which, when subtracted from the total barrier weight gives an average weight of anodic oxide of 43.5 μg/cm<sup>2</sup>. The average charge for anodic oxidation was equivalent to 44.9 μg/cm<sup>2</sup>, for an average current efficiency of 96.6%. Within the accuracy of this experiment, this is not significantly different from 100%.

A summary of these film weights is presented graphically in Fig. 2. It should be pointed out here that there is no intention to claim that the anodic oxide and converted hydrous oxide exist as distinct layers, an inference that might be drawn from the bar graph in

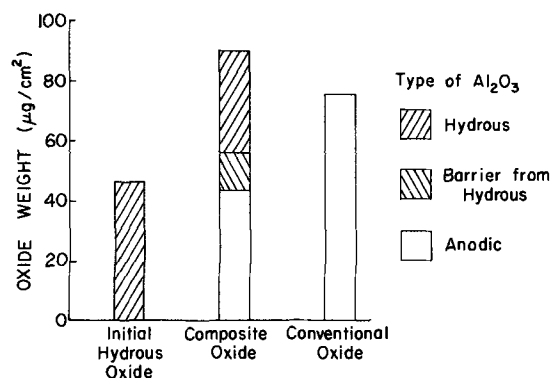


Fig. 2. Weight and distribution of oxide films produced by anodic oxidation to 175V. Note that weights are only for  $Al_2O_3$ , the weight of water in each oxide has been subtracted.

Fig. 2. The distribution of the oxide from the two sources is not known at this time. Shown for comparison is the weight of a conventional 175V anodic barrier oxide formed in an identical phosphate electrolyte at 1 mA/cm<sup>2</sup> and a temperature of 98°C (7). The composite oxide is able to support this voltage with 25% less barrier film. This is in agreement with previous results arrived at by less rigorous methods (1, 2).

The reciprocal capacitance of the conventional film was 31.7 cm<sup>2</sup>/μf compared with 22.2 cm<sup>2</sup>/μf for the composite oxide anodized at 1 mA/cm<sup>2</sup>. The reciprocal capacitances are almost in the same proportion as the barrier film weights, indicating that the dielectric constants of the two films are about the same.

In this experiment, there seemed to be no effect of current density on the amount of hydrous oxide converted to barrier film. To verify this, some measurements were made at essentially the same conditions, but using 100 g/liter H<sub>3</sub>BO<sub>3</sub> in place of the phosphate electrolyte and covering a range of current densities from 0.1 to 10 mA/cm<sup>2</sup>. The average corrected stripping weight loss was 47.0 μg/cm<sup>2</sup> and varied by only ± 3% over the full range of current density. Moreover, this figure differed by only 0.5 μg/cm<sup>2</sup> from the corresponding value obtained in the phosphate electrolyte. Thus, neither current density nor electrolyte had any effect on the conversion of pseudoboehmite to barrier oxide.

In this experiment, it was found that the charge required to reach 175V decreased by 7% for a tenfold increase in current density (0.256 coulomb/cm<sup>2</sup> at 0.1 mA/cm<sup>2</sup> and 0.238 coulomb/cm<sup>2</sup> at 1.0 mA/cm<sup>2</sup>). This is the same dependence as found for conventional barrier oxides (8).

**Phosphorus distribution.**—The activity of each specimen decreased sharply as the hydrous oxide was removed by stripping. From the relationship between P<sup>32</sup> activity and weight of total phosphorus, the average phosphorus remaining in the film after each strip was found to be as shown in Fig. 3. There was very little variation among samples, and no dependence on the current density used during anodization. For example, for each of the first four strips the range of activity was less than ± 5%, while for the last two strips this increased to about ± 10%. Activity measurements were stopped when the measured activity dropped to the

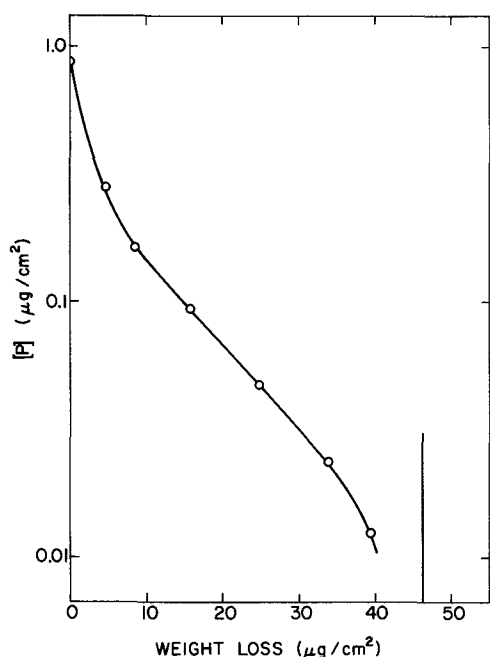


Fig. 3. Phosphorus content of composite oxide during stepwise dissolution. The vertical line represents weight of hydrous oxide determined by extended stripping.

magnitude of the background correction. This occurred before all the hydrous oxide was dissolved. The vertical line in Fig. 3 represents the weight of hydrous oxide in these composite films.

The curve in Fig. 3 should not be considered a profile of the phosphorus distribution through the pseudoboehmite because the highly porous nature of the film makes it likely that dissolution occurred preferentially along pores and channels most accessible to the solution. These same regions would presumably be the places where phosphate anions were initially specifically absorbed, although additional inward diffusion may have occurred under the driving force of the anodization field. The fact that the same phosphorus distribution was obtained at both 0.3 and 1.0 mA/cm<sup>2</sup>, with their corresponding immersion times in the anodizing solution of about 830 and 245 sec, indicates that this is a steady-state distribution governed by the porosity gradient in the film.

After stripping 39.5 μg/cm<sup>2</sup> of hydrous oxide all but 0.0127 μg/cm<sup>2</sup> phosphorus, about 1% of the initial phosphorus, had been removed. The remaining phosphorus was in the small amount of hydrous oxide still on the surface and in the barrier film. Only 2 μg/cm<sup>2</sup> of barrier film had been dissolved at this time. These figures can be analyzed in two ways. First, since the initial weight of pseudoboehmite was 63.5 μg/cm<sup>2</sup>, the remaining phosphorus could be considered to have been distributed in 24.0 μg/cm<sup>2</sup> of hydrous oxide, for an average concentration of  $5.3 \times 10^{-4}$  μg P/μg oxide. In the second calculation, the remaining phosphorus could be treated as being wholly in the barrier film. Since the weight of barrier film was found to be 55.9 μg/cm<sup>2</sup>, this is equivalent to an average concentration of  $2.3 \times 10^{-4}$  μg P/μg oxide. These concentrations can be compared with the phosphorus in a conventional 175V anodic oxide formed in the tagged phosphate electrolyte at 1 mA/cm<sup>2</sup> and 98°C. In that case, the average concentration was found to be  $2.3 \times 10^{-2}$  μg P/μg oxide (7), or about 100 times the level in the composite oxide barrier film.

### Discussion

The very low concentration of phosphorus in the portion of the pseudoboehmite film incorporated into the barrier layer indicates that this inner portion of the hydrous oxide was essentially impermeable to phosphate anions. There does not appear to be a sharp boundary defining this region, but rather a porosity gradient through the film, so that other ions might be excluded from a greater or lesser thickness depending on their size and penetrating ability. In the present case, the 17.0 μg/cm<sup>2</sup> of pseudoboehmite incorporated into the barrier film represents a thickness of 710Å, using a density of 2.44 g/cc (6) for the pseudoboehmite. The over-all thickness of the initial hydrous oxide layer was about 4000Å (4).

According to the model proposed by Vedder and Vermilyea (3) for the growth of hydrous oxide, hydrolyzed aluminum species are produced at the base of the film and are then transported, through solution that has penetrated the film, to deposition sites. This picture is not compatible with our finding that the inner portion of the film is impermeable to solvated species. An alternate model for the growth of hydrous oxide has been proposed (9).

The dissolution rates in 5% H<sub>3</sub>PO<sub>4</sub>-2% CrO<sub>3</sub> of the hydrous and composite films, as calculated from the slopes of the plot of weight loss vs. time in Fig. 1, are about 0.3 and 0.015 μg/cm<sup>2</sup>-sec, respectively. The rate of dissolution of a conventional barrier oxide formed in phosphate electrolyte is reported to be 0.29 μg/cm<sup>2</sup>-sec (7); this is just about the same as the stripping rate of hydrous oxide. This was very surprising, since it was expected that the porosity and large specific surface area of the hydrous film (4) would promote much more rapid dissolution than for a compact barrier oxide. Perhaps the internal surfaces on which N<sub>2</sub>



adsorbs during a BET measurement are not accessible to solvated species. It is also possible that the macroscopic porosity observed in electron micrographs (3, 10) is a property of the dry state only, and that water is imbibed into the structure to produce swelling and a reduction in porosity when the film is wet.

The very low stripping rate of the composite oxide barrier film may be due to the presence of  $\gamma$ -alumina, which, when produced by thermal oxidation, has been observed to be only very slowly dissolved, if at all, by the stripping solution (11). Jackson and Waddell (12) have reported that the surface of the barrier film of a composite oxide formed in a boric acid electrolyte is  $\gamma$ - $\text{Al}_2\text{O}_3$ , with a small amount of amorphous oxide distributed in the crystalline oxide. Our own electron diffraction studies confirmed the presence of a  $\gamma$ -alumina surface, for films formed in both borate and phosphate electrolytes. The phosphate film had a higher degree of crystallinity and showed a (511) preferred orientation.

The usual product of the dehydration of boehmite is  $\gamma$ -alumina (13). The  $\gamma$ -alumina in the composite oxide might be the result of field-assisted dehydration. The (511) orientation found in one sample could result from slippage of the oriented pseudoboehmite layer during dehydration. On the other hand,  $\gamma$ -alumina has been found in conventional anodic oxides (1) so the origin of this phase is not certain.

We have no ready explanation for the higher field sustained by the composite oxide during anodic oxidation. There are examples in the literature of systems where the field strength of the oxide has been increased, for example, by incorporation of anions (14), but this has been accompanied by a decrease in dielectric constant. This coupling is not present in the composite oxides, for which the dielectric constant appears to be about the same as for a conventional film. The  $\gamma$ -alumina phase is not known to be a particularly good insulator or dielectric so the mere presence of this phase cannot explain the effect. It was thought that the unusual electrical properties might arise from a particular orientation of the  $\gamma$ -oxide on the surface, but although a phosphate-formed film showed a preferred orientation that was missing from the borate-formed specimen, they had identical field strengths. It has been suggested that the special properties of this film may be due to the presence of a hydrogen aluminum spinel structure (2). The information obtained in the present experiments was not of a nature to test this hypothesis.

Since current density had no effect on the amount of pseudoboehmite converted to barrier oxide, but the amount of anodic oxide deposited decreased with current density in the expected fashion, the net result is that the weight of composite barrier film showed a lesser dependence on current density than in the case of a conventional anodic oxide.

The same anodization kinetics and film properties were obtained using borate or phosphate electrolyte. Shimura (15) also found only a small effect of electrolyte type on anodization kinetics of composite oxides. These observations are in accord with the idea that film growth by cation transport does not occur at a surface in contact with electrolyte, but rather at the

barrier oxide/hydrous oxide interface (2). New barrier film is produced by a reaction between Al cations and pseudoboehmite (e.g.,  $\text{Al}^{+3} + \text{AlOOH} + \text{H}_2\text{O} \rightarrow \text{Al}_2\text{O}_3 + 3\text{H}^+$ ) and/or by a reaction between cations and water released from the pseudoboehmite by a prior dehydration step.

### Conclusions

1. The innermost region of the pseudoboehmite film produced in boiling water is essentially impermeable to phosphate anions and presumably other solvated species of similar size.
2. From the relatively slow stripping rate of the hydrous oxide it is inferred that the large internal area measured by nitrogen adsorption is not accessible to aqueous solution at ordinary temperatures and pressure.
3. Previous estimates of hydrous oxide conversion and reduced barrier film weight in the composite oxide have been confirmed by direct gravimetric analysis.
4. The amount of pseudoboehmite transformed to barrier film is independent of the current density used during anodic oxidation.

### Acknowledgment

We appreciate the assistance of Mrs. E. Vigna and Mr. S. Szpak in obtaining the results presented here.

Manuscript submitted Jan. 28, 1974; revised manuscript received March 22, 1974.

Any discussion of this paper will appear in a Discussion Section to be published in the June 1975 JOURNAL. All discussions for the June 1975 Discussion Section should be submitted by Feb. 1, 1975.

### REFERENCES

1. R. S. Alwitt, *This Journal*, **114**, 843 (1967).
2. R. S. Alwitt, A. J. Breen, and J. S. L. Leach, in "Proceedings of the Symposium on Oxide-Electrolyte Interfaces," R. S. Alwitt, Editor, The Electrochemical Society Softbound Symposium Series, Princeton, N. J. (1973).
3. W. Vedder and D. A. Vermilyea, *Trans. Faraday Soc.*, **65**, 561 (1969).
4. R. S. Alwitt, *This Journal*, **118**, 1730 (1971).
5. Y. R. Chen, J. N. Butler, and W. Stumm, *J. Colloid Sci.*, **43**, 421 (1973).
6. W. J. Bernard and J. J. Randall, Jr., *This Journal*, **107**, 483 (1960).
7. J. J. Randall, Jr. and W. J. Bernard, Submitted to *Electrochim. Acta*.
8. W. J. Bernard and J. W. Cook, *This Journal*, **106**, 643 (1959).
9. R. S. Alwitt, Submitted to *This Journal*.
10. R. S. Alwitt, in "Anodic Properties of Metals and Semiconductors," Vol. 4, J. S. Diggle and A. K. Vijh, Editors, Marcel Dekker, New York (To be published in 1974).
11. J. J. Randall, Jr., Unpublished results.
12. N. F. Jackson and P. D. S. Waddell, *J. Appl. Electrochem.*, **2**, 345 (1972).
13. B. C. Lippens and J. H. deBoer, *Acta Cryst.*, **17**, 1312 (1964).
14. J. J. Randall, Jr., W. J. Bernard, and R. R. Wilkinson, *Electrochim. Acta*, **10**, 183 (1965).
15. M. Shimura, *J. Electrochem. Soc. Japan*, **40**, 55 (1972).

# Electroless Cobalt Deposition from Acid Baths

F. Pearlstein and R. F. Weightman

*Pitman-Dunn Laboratory, Frankford Arsenal, Philadelphia, Pennsylvania 19137*

*The publication costs of this article have been assisted by the Department of the Army.*

## ABSTRACT

An acid electroless cobalt plating bath was developed which utilizes dimethylamine borane (DMAB) as the reducing agent and which provides bright deposits at over 13  $\mu\text{m/hr}$  at 70°C. The bath, slightly modified, is also usable at room temperature for deposition on palladium-activated nonconductors. Additions of even small quantities of hypophosphite to the DMAB bath resulted in failure to achieve deposition; the effect of hypophosphite additions on the single electrode potentials was determined and the results discussed. Electroless cobalt-boron deposits were found superior, in some respects, to electroless nickel-phosphorus for providing protection for steel against corrosive attack. A double layer deposit of electroless nickel plus electroless cobalt topcoat provided more effective protection for steel than either deposit, alone, of the same total thickness. Chromating treatments were found effective for retarding the tendency for tarnishing of cobalt during salt exposure. The magnetic properties of some electroless cobalt-boron deposits were determined; the coercivity was considerably lower than that of electroless cobalt-phosphorus deposits.

Electroless cobalt deposition was first described by Brenner and Riddell (1). Since that time, a great deal of interest has been shown in the electroless cobalt deposits because of their ability to be readily plated upon suitably activated plastic (2) and because of the wide variety of magnetic properties attainable. Electroless cobalt deposits have been employed for high quality, high density recordings and for computer storage elements in high speed switching devices (3). The magnetic deposits are produced from hypophosphite-based baths and consist of cobalt-phosphorus (4-10) or ternary alloys of cobalt and phosphorus plus an additional metal element (11-18).

It is well known that from baths containing hypophosphite reducing agent, electroless cobalt deposits can be produced only from alkaline-type baths whereas nickel deposits are produced from both alkaline and acid baths (19). The acid-type electroless nickel baths have enjoyed the greater commercial acceptance because of higher deposition rates and elimination of unpleasant ammonia fumes. In the desire to develop a useful acid-type electroless cobalt plating bath, attention was directed to the use of other reducing agents. Dimethylamine borane (DMAB), for example, is a more powerful reducing agent than hypophosphite and is capable of providing electroless cobalt deposits from both acid and alkaline baths (20, 21).

The studies reported herein were conducted to develop acid electroless cobalt plating baths and to determine some characteristics of the baths and properties of deposits.

## Experimental

Preliminary studies involved preparation of acid-type electroless cobalt plating baths containing cobalt sulfate, dimethylamine borane (DMAB), and an organic radical (to function as buffer, exaltant, and/or chelate) such as acetate, lactate, citrate, succinate, or glycolate. Succinate was indicated from these experiments to be the most effective additive of the group for providing sound deposits at high rates.

Experimental electroless cobalt plating baths were prepared with reagent grade chemicals except for DMAB<sup>1</sup> which was 99+ % purity. A thermostatically controlled water bath was used to heat and maintain solutions within 1.0°C of the desired temperature.

**Key words:** electroless plating, cobalt, nickel, amine borane, hypophosphite.

<sup>1</sup> Callery Chemical Company, Callery, Pennsylvania 16024.

Copper panels (2 × 2.5 cm) were alkaline cleaned, chemically polished, and palladium activated [30 sec in a solution of 0.1 g/liter PdCl<sub>2</sub> and 0.1 ml/liter HCl (38%) at 25°C], thoroughly rinsed, dried, and reweighed. Deposition tests were conducted for a 1 hr period with an area to volume ratio of 1:20.

The effect of bath constituent concentration, bath pH, and bath temperature on electroless cobalt deposition rate was determined.

The effect of hypophosphite additions to an acid-type electroless cobalt plating bath (utilizing DMAB reducing agent) on deposition rate was determined. The steady-state potential of 13  $\mu\text{m}$  electroless cobalt-boron plated specimen in the baths of mixed DMAB-hypophosphite was also determined. The specimen was successively immersed for 5 min periods into baths (at 70°C) containing 0, 0.25, 0.5, 1.0, 2.0, 4.0, 6.0, and 8.0 g/liter sodium hypophosphite monohydrate. The potential of the specimen was measured at the end of each 5 min immersion period vs. a saturated calomel electrode immersed into the bath for 5 sec. A Hewlett Packard 410C Vacuum Tube Voltmeter, with input resistance of 10<sup>8</sup> ohms was used for taking the potential measurements. Similar tests were conducted with an alkaline cobalt bath<sup>2</sup> containing various proportions of DMAB and hypophosphite and with the acid and alkaline bath in which the cobalt salt was replaced with the molar equivalent of nickel sulfate.

The ability for clean, nonactivated copper to spontaneously initiate deposition of cobalt from the acid-type electroless plating bath at 70°C was determined as a function of DMAB concentration. Potential measurements were also made. Deposition tests were conducted on other substrates including steel, electroless nickel, platinum, and palladium-activated plastic.

A heavy (about 200  $\mu\text{m}$ ) deposit of electroless cobalt was applied to steel and hardness measurements made perpendicular to the surface using a Vickers indenter with 50g load applied. The deposit hardness was also determined after heat-treatment at 250°C in an air oven.

Electroless cobalt deposits were analyzed for composition, i.e., cobalt (electrodeposition method), boron (atomic absorption method), carbon (Leco Automatic Carbon Determinator), and nitrogen (Kjeldahl distillation-titration method).

<sup>2</sup> 35 g/liter CoSO<sub>4</sub> · 7 H<sub>2</sub>O, 80 g/liter Na<sub>2</sub>CO<sub>3</sub> · 2H<sub>2</sub>O, 50 g/liter NH<sub>4</sub>Cl, 60 ml/liter NH<sub>4</sub>OH (28% NH<sub>3</sub>); 80°C.

Electroless cobalt deposits were applied to steel Hull Cell panels<sup>3</sup> ( $6.7 \times 10$  cm) from the acid-DMAB bath in nominal thicknesses of 2.5, 5, and 10  $\mu\text{m}$  and tested for corrosion resistance during exposure to 5% neutral salt spray. For comparative purposes, tests were also conducted with conventional electroless nickel-phosphorus<sup>4</sup> plated steel panels. A set of panels was also prepared with a double layer deposit consisting of approximately 7.5  $\mu\text{m}$  electroless nickel followed by a topcoat of 2.5  $\mu\text{m}$  electroless cobalt and subjected to the salt spray test. Triplicate panels were prepared for each type and thickness of deposit was tested. The steel panels were prepared for electroless plating as follows: (i) 1 min in 50% (volume) hydrochloric acid (38%) at 25°C (to remove protective zinc coating), cold water rinse (CWR); (ii) 5 min in orthosilicate soak alkaline cleaning bath at 85°C and soft bristle brushing, CWR; (iii) 1 min in 50% (volume) hydrochloric acid (38%) at 25°C, CWR.

Chromating treatments were applied to electroless cobalt, freshly deposited on steel, by immersion for 10 sec in 200 g/liter  $\text{Na}_2\text{Cr}_2\text{O}_7 \cdot 2\text{H}_2\text{O}$  — 6 ml/liter  $\text{H}_2\text{SO}_4$  (sp. gr. 1.84) or in Alodine 1200S<sup>5</sup> (7.5 g/liter, pH 2.1) at 25°C, rinsed, and dried. The specimens were evaluated for tarnish resistance during salt spray exposure.

Cobalt deposits were applied to chemically polished and palladium-activated copper panels from the following baths:

Bath constituent	Co-B (acid)	Co-B (alk)	Co-P (alk)
Cobalt sulfate, $\text{CoSO}_4 \cdot 7\text{H}_2\text{O}$ (g/liter)	25	30	30
DMAB, $(\text{CH}_3)_2\text{HNBH}_3$	4	4	—
Sodium hypophosphite, $\text{NaH}_2\text{PO}_2 \cdot \text{H}_2\text{O}$ (g/liter)	—	—	20
Sodium succinate, $\text{C}_4\text{H}_4\text{Na}_2\text{O}_4 \cdot 6\text{H}_2\text{O}$ (g/liter)	25	—	—
Sodium citrate, $\text{Na}_3\text{C}_6\text{H}_5\text{O}_7 \cdot 2\text{H}_2\text{O}$ (g/liter)	—	80	80
Ammonium chloride, $\text{NH}_4\text{Cl}$ (g/liter)	—	50	50
Ammonium hydroxide (28% $\text{NH}_3$ ), $\text{NH}_4\text{OH}$ (ml/liter)	—	60	60
Temperature, °C	70	80	80
pH	5.0	9.0	9.0

The coercive force of various thicknesses of the deposits was determined using a vibrating sample magnetometer.<sup>6</sup>

### Results and Discussion

The effect of dimethylamine borane (DMAB) concentration on deposition rate was determined from solutions containing 25 g/liter cobalt sulfate heptahydrate and 15 g/liter sodium succinate hexahydrate. Results are shown in Fig. 1. The baths were adjusted to pH 5.0 with sulfuric acid solution and were operated at 80°C. Deposition rates increased essentially linearly with DMAB concentration to a maximum at about 4 g/liter. At above this DMAB concentration, catalytic particles formed in the solution which tended to settle to the beaker bottom and resulted in rapid bath decomposition.

The effect of succinate concentration on deposition rate was determined from solutions containing 25 g/liter cobalt sulfate heptahydrate and 4 g/liter DMAB at pH 5.0 and at 80°C (see Fig. 2). When no succinate was present, spongy cobalt formed within the solution accompanied by rapid bath decomposition, and virtually no deposition was produced on the palladium-activated copper specimen. Satisfactory bath stability was provided by the presence of 10 g/liter or more of the succinate in the bath. Succinate also provided buffering action, i.e., prevented rapid change in bath pH during deposition. Deposition rates were highest and essentially constant at sodium succinate hexahydrate concentration of 15–30 g/liter. A 25 g/liter concentration was adopted for additional studies.

The effect of bath pH (measured at 25°C) on deposition rates was determined. Both initial pH and the pH after completion of deposition test are shown in Fig. 3.

<sup>3</sup> R. O. Hull Company, Incorporated, Cleveland, Ohio 44102.  
<sup>4</sup> Bath: 25 g/liter  $\text{NiSO}_4 \cdot 6\text{H}_2\text{O}$ , 9 g/liter  $\text{NaC}_2\text{H}_3\text{O}_2$ , 22.5 g/liter  $\text{NaH}_2\text{PO}_2 \cdot \text{H}_2\text{O}$ , 0.001 g/liter  $\text{Pb}(\text{C}_2\text{H}_3\text{O}_2)_2 \cdot 3\text{H}_2\text{O}$ ; pH 4.6; 85°C.  
<sup>5</sup> Amchem Products, Incorporated, Ambler, Pennsylvania 19002.  
<sup>6</sup> Princeton Applied Research Corporation, Princeton, New Jersey 08540.

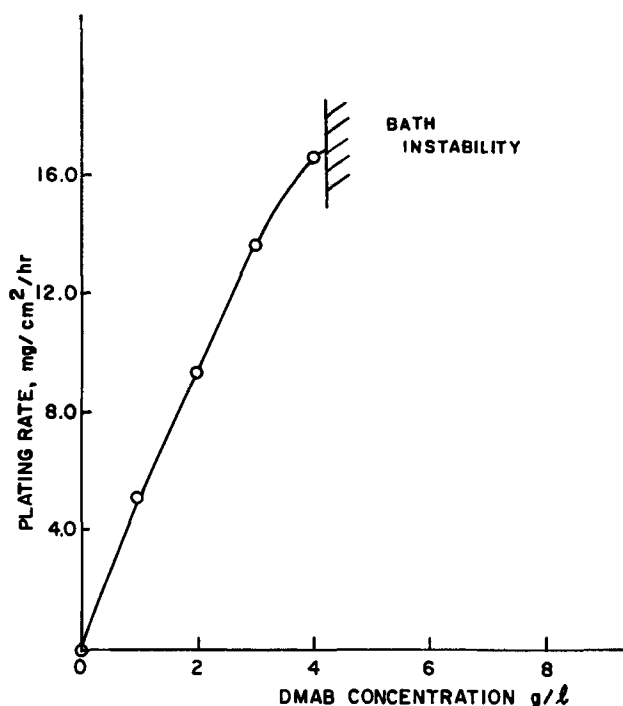


Fig. 1. Effect of DMAB concentration on electroless cobalt plating rate. Bath: 25 g/liter  $\text{CoSO}_4 \cdot 7\text{H}_2\text{O}$ , 15 g/liter  $\text{C}_4\text{H}_4\text{Na}_2\text{O}_4 \cdot 6\text{H}_2\text{O}$ ; pH 5.0; temp. 80°C.

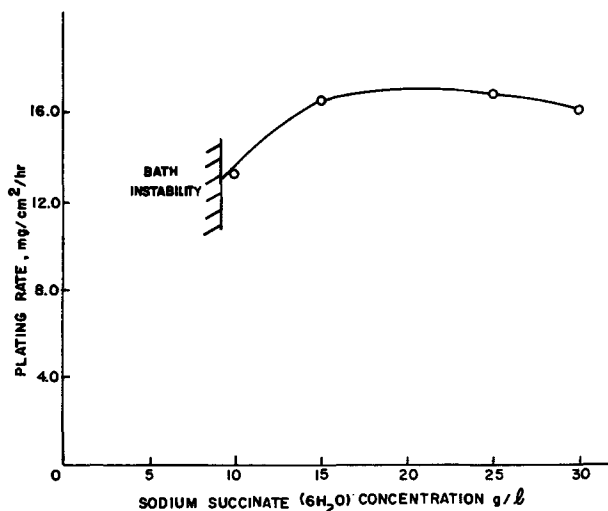
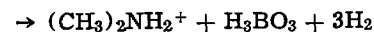


Fig. 2. Effect of succinate concentration on electroless cobalt plating rate. Bath: 25 g/liter  $\text{CoSO}_4 \cdot 7\text{H}_2\text{O}$ , 4 g/liter DMAB; pH 5.0; temp. 80°C.

The deposition rate increased markedly with bath pH. Baths of pH above about 5.5 tended to be unstable and deposits formed on beaker walls and bottom.

It is interesting to note that baths at pH 4.5 or lower increased in pH during the deposition test, while baths at pH 5.5 or above decreased. Normally, electroless plating baths decrease in pH during use because hydrogen ions are a product of the reaction (19, 22). However, DMAB is subject to acid catalyzed hydrolysis (24) leading to consumption of  $\text{H}^+$



Indeed, it was found that even when no electroless plating was occurring, baths (80°C) at pH 4.5 or below increased in pH with time, and that gassing was evident within the solutions. At bath pH of 5.0, little

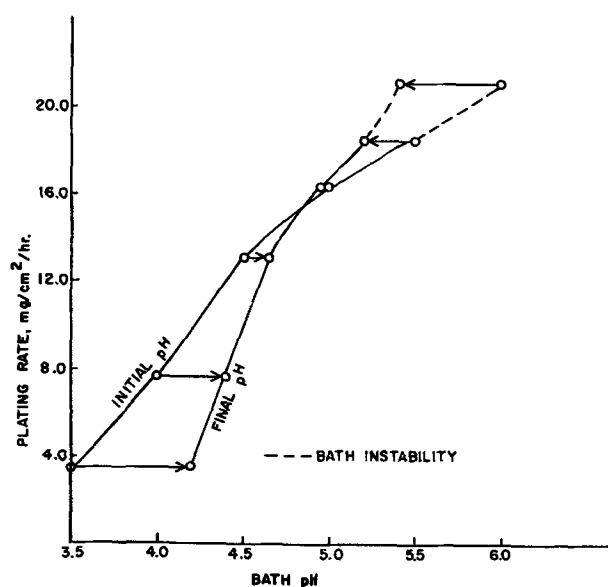


Fig. 3. Effect of bath pH on electroless cobalt plating rate. Bath: 25 g/liter  $\text{CoSO}_4 \cdot 7\text{H}_2\text{O}$ , 25 g/liter  $\text{C}_4\text{H}_4\text{Na}_2\text{O}_4 \cdot 6\text{H}_2\text{O}$ , 4 g/liter DMAB; temp. 80°C.

change in pH resulted during (or without) deposition and subsequent tests were conducted with baths at this pH unless otherwise noted.

Electroless cobalt deposition rates were little affected by cobalt salt concentration within the range of 15-45 g/liter and tests were continued with baths containing 25 g/liter cobalt sulfate heptahydrate.

The rate of cobalt deposition increased with increasing bath temperature in a manner typical of most electroless plating baths (24-26) (see Fig. 4). At 90°C, the bath was subject to spontaneous production of cobalt particles and rapid decomposition. At 80°C, the bath was stable during the 1 hr plating tests but there was a tendency for catalytic particles to form in the bath during more extended plating periods thereby causing bath decomposition. The bath can be made much less susceptible to such decomposition by introducing trace amounts of a catalytic poison (e.g., 1-2 mg/liter lead acetate trihydrate or thiourea). However, at bath temperatures of 80°C or above, wasteful consumption of DMAB by hydrolysis is probably significant (23) and it is thus advisable, from a practical standpoint, to operate the bath at lower temperatures except where very high deposition rates are

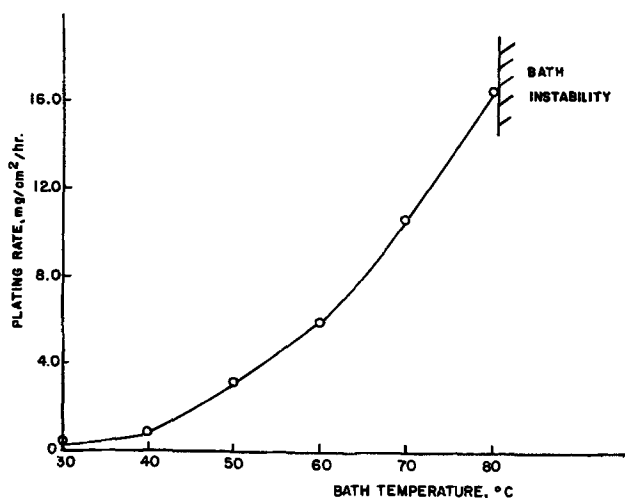


Fig. 4. Effect of bath temperature on electroless cobalt plating rate. Bath: 25 g/liter  $\text{CoSO}_4 \cdot 7\text{H}_2\text{O}$ , 25 g/liter  $\text{C}_4\text{H}_4\text{Na}_2\text{O}_4 \cdot 6\text{H}_2\text{O}$ , 4 g/liter DMAB; pH 5.0.

of primary importance. At 70°C, the bath is operable without the necessity of addition of catalytic poison stabilizers, and hydrolysis losses are minimized.

Deposition rates are quite low at a bath temperature of 40°C or lower. However, the baths can be used even at room temperatures (22°-27°C) for applying thin, conductive deposits to palladium-activated nonconductors, provided the bath pH is increased to about 6.3.

There was a tendency for gas pits to form on the electroless cobalt deposits. Workpiece movement was helpful in alleviating this condition, but addition to the bath of about 15 g/liter or more sodium sulfate also reduced the tendency for pitting to occur. The presence of sodium sulfate in the bath had no apparent deleterious effects and did not affect deposition rate.

The electroless plating bath of preferred composition is 25 g/liter cobalt sulfate ( $\text{CoSO}_4 \cdot 7\text{H}_2\text{O}$ ), 25 g/liter sodium succinate ( $\text{C}_4\text{H}_4\text{Na}_2\text{O}_4 \cdot 6\text{H}_2\text{O}$ ), 15 g/liter sodium sulfate ( $\text{Na}_2\text{SO}_4$ ), and 4 g/liter dimethylamine borane [ $(\text{CH}_3)_2\text{HNBH}_3$ ]. The bath at pH 5.0 and at a temperature of 70°C produces bright electroless cobalt deposits at a rate of about 13  $\mu\text{m/hr}$ .

*Baths of mixed DMAB-hypophosphite.*—The effect of hypophosphite additions to the electroless cobalt plating bath on deposition rate at 70°C is shown in Fig. 5. As little as 1 g/liter sodium hypophosphite monohydrate substantially reduced the deposition rate; 4 g/liter or more prevented deposition entirely. It was thus demonstrated that, not only is hypophosphite reducing agent unable to provide electroless cobalt deposition from acid solutions, but its presence prevents deposition from a DMAB bath. The steady-state mixed potentials of an electroless cobalt specimen in the baths of increasing hypophosphite concentrations are also shown in Fig. 5. The curve of potentials *vs.* hypophosphite concentration closely paralleled that of deposition rate.

The deposition potential for cobalt in the electroless plating bath (70°C, pH 5.0), but from which the reducing agents were excluded, was determined by applying increasing cathodic current in very small increments to a gold electrode. The cathode potential at which the first signs of cobalt deposition appeared was about -0.67V (SCE).<sup>7</sup>

<sup>7</sup> Similar tests were conducted in the same bath but with 23.4 g/liter  $\text{NiSO}_4 \cdot 6\text{H}_2\text{O}$  present instead of the cobalt salt. The deposition potential for nickel was determined to be about -0.59V (SCE).

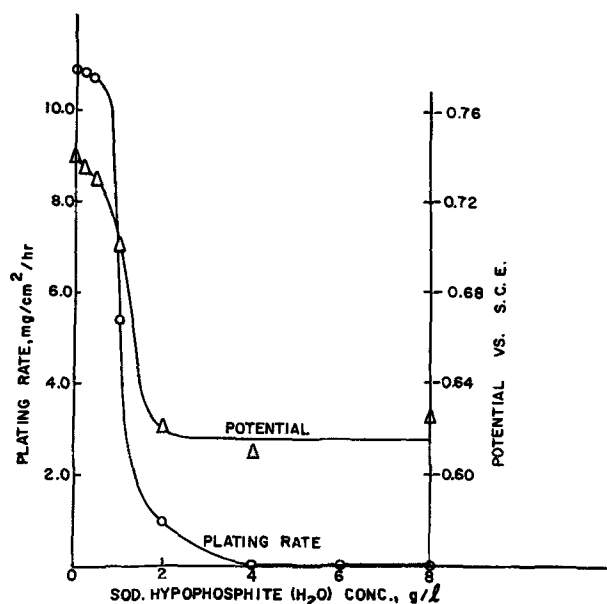


Fig. 5. Effect of hypophosphite additions to bath on electroless cobalt plating rate and potential. Bath: 25 g/liter  $\text{CoSO}_4 \cdot 7\text{H}_2\text{O}$ , 25 g/liter  $\text{C}_4\text{H}_4\text{Na}_2\text{O}_4 \cdot 6\text{H}_2\text{O}$ , 15 g/liter  $\text{Na}_2\text{SO}_4$ , 4 g/liter DMAB; pH 5.0; temp. 70°C.

It can be seen from Fig. 5 that when about 2 g/liter or more of the hypophosphite is present in the bath, the steady-state mixed potential of the catalytic surface is not attained at which cobalt can be deposited and is at a level characteristic for baths containing hypophosphite alone. Gassing at the palladium-activated specimens was observed in all solutions, though the rate was considerably decreased in the baths from which deposition was not obtained. The action of hypophosphite may be considered analogous to lowering the hydrogen overvoltage of a surface and thus preventing the metal deposition from occurring.

The effect of hypophosphite-DMAB combinations in alkaline electroless cobalt plating baths, from which deposits are produced when either reducing agent is present alone, on deposition rate and potential are shown in Fig. 6. Marked antagonism is indicated between the hypophosphite and DMAB from the deposition rate measurements, and solutions with relatively little hypophosphite behave more like baths containing only hypophosphite. The hypophosphite might be considered as preferentially adsorbing or dehydrogenating on the surface thereby nullifying the presence of DMAB. The decrease in steady-state mixed potential of electroless cobalt is most pronounced in the solutions containing little hypophosphite and it decreases more gradually with further increases in hypophosphite.

Similar studies of nickel deposition rate in mixed hypophosphite-DMAB baths were conducted from both acid and alkaline solutions. Marked antagonism was not exhibited for the nickel plating baths (see Fig. 7). Nickel deposition rates from the alkaline baths were not greatly affected by the relative proportions of hypophosphite and DMAB (see Fig. 8). It is evident that the metal ions also provide some interaction with one or both of the reducing agents as witnessed by the differences in behavior of the cobalt and nickel baths.

*Deposition on various substrates.*—Substrates that are sufficiently catalytically active to spontaneously initiate deposition by immersion in the (25-25-15-4) electroless cobalt plating bath (pH 5.0, 70°C) are steel, electroless nickel, palladium, or gold. Aluminum is spontaneously plated, presumably by first providing a displacement deposit of cobalt. A thin immersion zinc

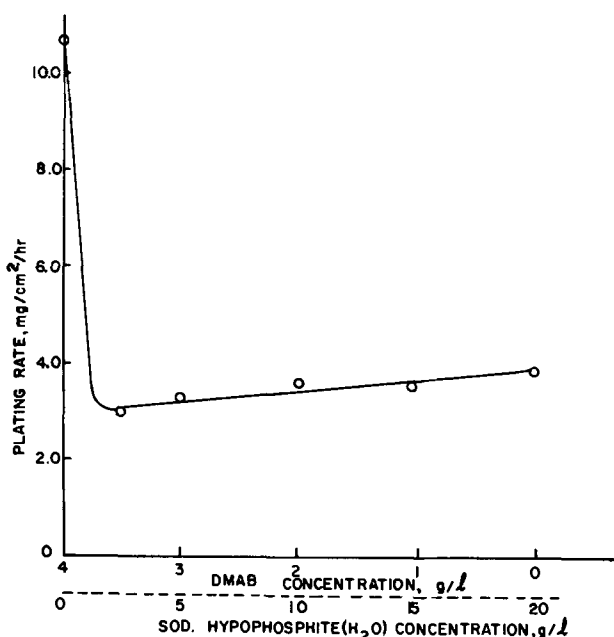


Fig. 6. Effect of DMAB-hypophosphite combinations on electroless cobalt plating rate from alkaline bath. Bath: 35 g/liter  $\text{CoSO}_4 \cdot 7\text{H}_2\text{O}$ , 80 g/liter  $\text{Na}_3\text{C}_6\text{H}_5\text{O}_7 \cdot 2\text{H}_2\text{O}$ , 50 g/liter  $\text{NH}_4\text{Cl}$ , 60 ml/liter  $\text{NH}_4\text{OH}$  (28%  $\text{NH}_3$ ); temp. 80°C.

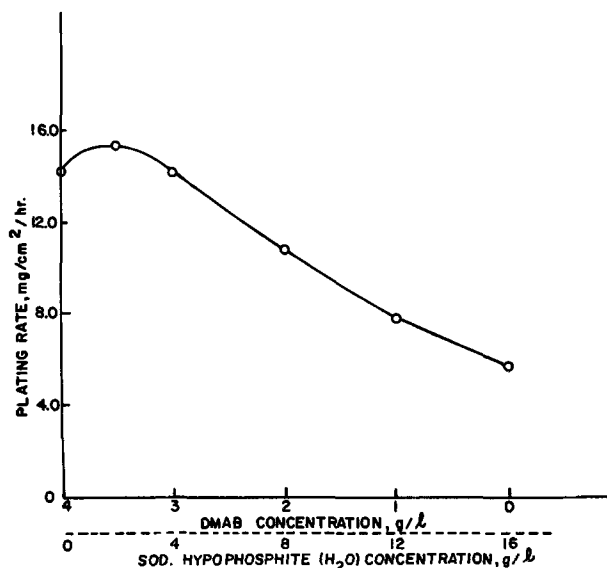


Fig. 7. Effect of DMAB-hypophosphite combinations on electroless nickel plating rate. Bath: 23.4 g/liter  $\text{NiSO}_4 \cdot 6\text{H}_2\text{O}$ , 25 g/liter  $\text{C}_4\text{H}_4\text{Na}_2\text{O}_4 \cdot 6\text{H}_2\text{O}$ , 15 g/liter  $\text{Na}_2\text{SO}_4$ ; pH 5.0; temp. 70°C.

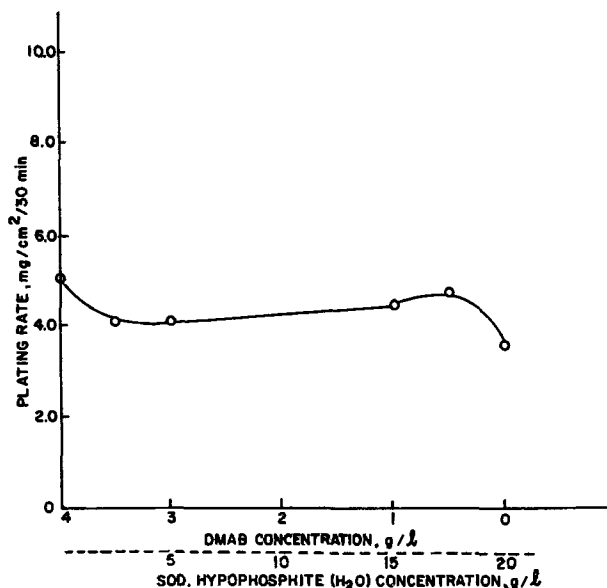


Fig. 8. Effect of DMAB-hypophosphite combinations on electroless nickel plating rate from alkaline bath. Bath: 32 g/liter  $\text{NiSO}_4 \cdot 6\text{H}_2\text{O}$ , 80 g/liter  $\text{Na}_3\text{C}_6\text{H}_5\text{O}_7 \cdot 2\text{H}_2\text{O}$ , 50 g/liter  $\text{NH}_4\text{Cl}$ , 60 ml/liter  $\text{NH}_4\text{OH}$  (28%  $\text{NH}_3$ ); temp. 80°C.

deposit on aluminum, by treatment in zincate solution, is desirable for rapid, uniform coverage with cobalt.

Copper, brass, silver, platinum, titanium, or stainless steels usually do not initiate electroless cobalt deposition unless one of the following steps are taken: (i) activation of the surface by nucleation with a catalytically active metal such as palladium; (ii) contact in the solution with an actively plating metal; (iii) momentary application of sufficient cathodic current to apply a thin cobalt film electrolytically. Nonconductors are readily plated after palladium activation (27).

The effect of DMAB concentration on the potential of electrolytic copper (99.9% purity) in the cobalt plating bath is shown in Fig. 9. The potential became more negative with increased DMAB concentration, and though gassing was visible in all baths containing DMAB, deposition was usually not initiated. However, occasionally spontaneous initiation occurred as illustrated by the dotted line in Fig. 9 and has even occurred in the baths containing only 4 g/liter DMAB.

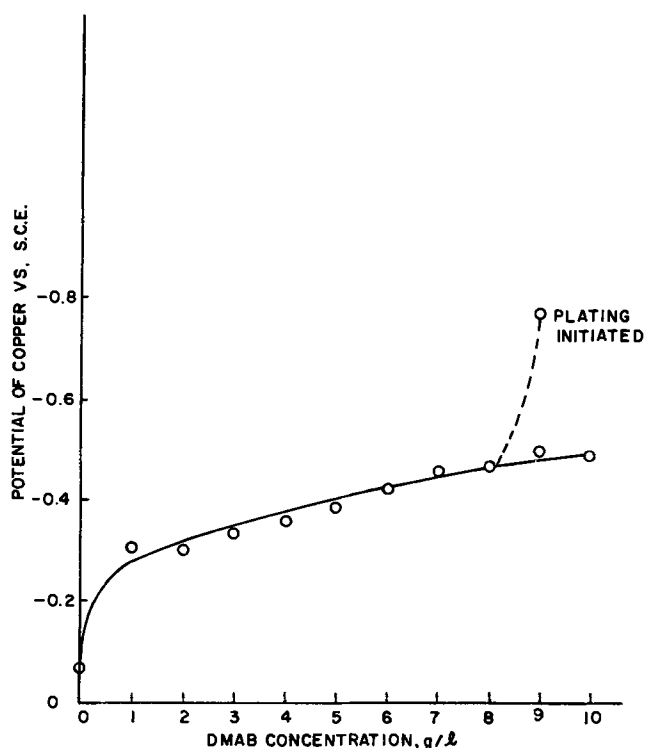


Fig. 9. Effect of DMAB concentration on the steady-state potential of copper in electroless cobalt plating bath. Bath: 25 g/liter  $\text{CoSO}_4 \cdot 7\text{H}_2\text{O}$ , 25 g/liter  $\text{C}_4\text{H}_4\text{N}_2\text{O}_4 \cdot 6\text{H}_2\text{O}$ , 15 g/liter  $\text{Na}_2\text{SO}_4$ ; pH 5.0; temp. 70°C.

The explanation for this phenomena is not known, but catalytic particles that enter the bath may provide the initiating influence by chance contact. Platinum is more catalytically active than copper, acquiring a potential of  $-0.54\text{V}$  in the 4 g/liter DMAB baths, but, as mentioned earlier, did not initiate cobalt deposition.

It was found that when the succinate of the electroless cobalt plating bath of preferred composition was substituted by the equivalent molar quantity of sodium malonate, deposition was more likely to be spontaneously initiated on copper, and deposition rates were unaffected by the substitution. It thus appears that the succinate has an inhibiting effect on the catalytic initiation of cobalt deposition on copper and that malonate can be used in place of succinate in the bath if spontaneous deposit initiation on copper is desired.

**Deposit properties.**—*Composition*—The composition of electroless cobalt deposits from the preferred (25-25-15-4) bath (pH 5.0, 70°C) was determined to be: cobalt, 96.0% by weight; boron, 1.7% by weight; carbon, 0.97% by weight; and nitrogen, 0.05% by weight. The presence of carbon and nitrogen indicates organic or organometallic compounds in the deposit.

**Hardness.**—Electroless cobalt-boron deposits were found to have a hardness of 270 kg/mm<sup>2</sup> (Vickers) in the as-plated condition. After heating 24 hr at 250°C,

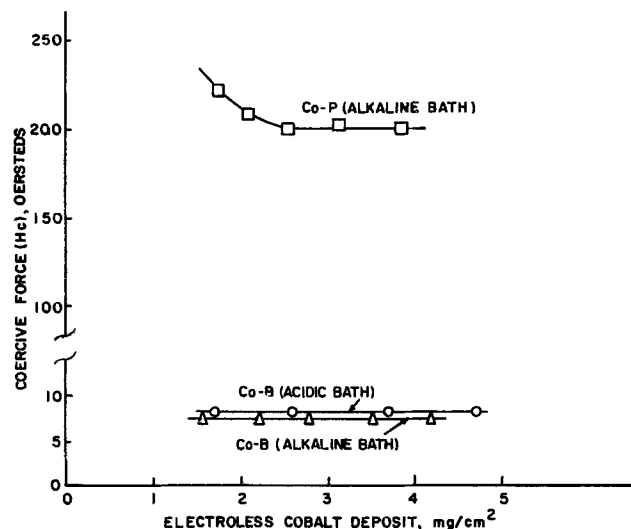


Fig. 10. Coercive force of electroless cobalt deposits produced from various baths.

the hardness increased to 480 kg/mm<sup>2</sup>. Additional heating at 250°C further increased the hardness to a maximum of about 640 kg/mm<sup>2</sup> after a total heating time of 4 days.

**Magnetic properties.**—The coercive force of electroless cobalt deposits produced from three baths are shown in Fig. 10. The coercive force of the cobalt-boron deposits was constant, over the range of thickness tested, at about 8 oersteds. The coercive force of cobalt-phosphorus deposits was considerably higher and increased with decreasing deposit thickness.

**Corrosion prevention.**—The results of salt spray exposure tests on electroless cobalt and nickel plated steel panels are shown in Table I. All of the electroless cobalt or electroless nickel deposits were quite protective to steel for up to 48 hr salt spray exposure. With longer exposure times, the protective value of the coatings increased with thickness. The electroless nickel deposits were somewhat more protective of steel than cobalt deposits. However, edge corrosion was very pronounced with electroless nickel coated specimens while the electroless cobalt plated steel was resistant to edge corrosion.

The corrosion potential of electroless cobalt-boron deposits, immersed in 50 g/liter sodium chloride solution for 24 hr, was  $-0.60\text{V}$  (SCE). Steel and electroless nickel in the salt solution have corrosion potentials of  $-0.63$  and  $-0.35\text{V}$ , respectively. The pronounced edge corrosion encountered with electroless nickel plated steel is undoubtedly the result of the adverse electrochemical relationship of the couple. The potentials would indicate cobalt and steel to be much more galvanically compatible in salt solution than nickel and steel.

From the corrosion potentials it can be predicted that a double layer deposit of electroless nickel-phosphorus followed by a topcoat of electroless cobalt-

Table I. Corrosion resistance of electroless cobalt or nickel plated steel

Deposit	Deposit thickness, $\mu\text{m}$	Corrosion rating* after exposures to salt spray, avg of 3				
		24 hr	48 hr	72 hr	96 hr	168 hr
Electroless cobalt	3	5	4	3+	3 (sl. E)	2 (E)
Electroless cobalt	5	5	5	4	3+	3 (sl. E)
Electroless cobalt	10	5	5	5	5	3+ (sl. E)
Electroless nickel	3	4 (E)	4 (E)	4 (E)	3+ (E)	2+ (E)
Electroless nickel	6	5 (E)	5 (E)	5 (E)	5 (E)	5 (E)
Electroless nickel	12	5	5 (E)	5 (E)	5 (E)	5 (E)

\* Ratings (excluding edges): 5 = no basis metal attack; 4 = traces of basis metal attack; 3 = slight basis metal attack; 2 = moderate basis metal attack; 1 = considerable basis metal attack. E = edge corrosion; sl. E = slight edge corrosion.

boron would probably provide synergistic protection because of the ability of the cobalt to sacrificially protect the nickel layer from corrosive penetration. This relationship with the synergistic protection of electro-deposited nickel double layers has been well established (28-30). Double layer deposits (7.5  $\mu\text{m}$  electroless nickel-2.5  $\mu\text{m}$  electroless cobalt) on steel were found capable of preventing basis metal attack (even at edges) during 168 hr salt spray exposure and were superior to the same total thickness of either layer alone.

**Tarnish resistance.**—Electroless cobalt-boron deposits tarnish rapidly during salt spray exposure to produce a tenacious, unattractive, mottled, blue-brown film.

Consideration was given to blackening the electroless cobalt deposits in order to avoid the tarnishing during salt spray exposure and also to provide a non-reflective surface often desired for military equipment. Some success was achieved in providing a blackened surface by immersion for 10 min in 10 g/liter potassium persulfate solution at 25°C.

Immersion of electroless cobalt deposits in a dichromate-sulfuric acid solution greatly improved the resistance of the surface to tarnishing; the surface remained bright and untarnished after 72 hr salt spray exposure. The solution was mildly corrosive to the cobalt-boron, removing about 0.1  $\mu\text{m}$  during the 10 sec immersion. No visible film was produced by the treatment.

The proprietary chromating solution was noncorrosive to the electroless cobalt and also substantially improved resistance to tarnishing though not quite as effectively as the other solution. Longer immersion times (e.g., 30 sec or more) in the proprietary solution resulted in the imparting of a visible iridescent film that provided improvement of the deposit in resistance to basis metal corrosion during salt spray exposure.

The chromate treatments described above may be valuable for application to thin, magnetic, electroless cobalt deposits since even slight atmospheric corrosion can significantly alter the magnetic properties (9).

### Conclusions

An acid electroless cobalt plating bath at pH 5.0 of the following composition is capable of producing bright deposits (96.0% Co, 1.7% B, 0.97% C, 0.05% N) at a rate of about 13  $\mu\text{m/hr}$  at 70°C: 25 g/liter cobalt sulfate ( $\text{CoSO}_4 \cdot 7\text{H}_2\text{O}$ ), 25 g/liter sodium succinate ( $\text{C}_4\text{H}_4\text{Na}_2\text{O}_4 \cdot 6\text{H}_2\text{O}$ ), 15 g/liter sodium sulfate ( $\text{Na}_2\text{SO}_4$ ), and 4 g/liter dimethylamine borane [ $(\text{CH}_3)_2\text{HNBH}_3$ ].

Steel, electroless nickel, gold, aluminum (zincate treated), or palladium-activated nonconductors spontaneously initiate electroless cobalt deposition from the acid bath; copper, silver, brass, or platinum usually do not initiate deposition.

The hardness of as-plated electroless cobalt deposits is 270 kg/mm<sup>2</sup> (Vickers) and can be increased to 640 kg/mm<sup>2</sup> by heating at 250°C. The coercive force of cobalt-boron deposits are relatively low at about 8 oersteds.

Electroless cobalt deposits can provide effective protection for steel against corrosive attack. Synergistic protection is provided by a double layer deposit consisting of electroless nickel-phosphorus and electroless

cobalt topcoat. A chromating treatment improves resistance of the cobalt to tarnishing.

The presence of even small quantities of hypophosphite in electroless cobalt plating baths with DMAB results in marked reduction of deposition rate or cessation of deposition.

### Acknowledgment

The authors gratefully acknowledge the participation of Dr. A. Tauber, U.S. Army Electronics Command, Fort Monmouth, New Jersey, in conducting the experimental work involving magnetic measurements of deposits.

Manuscript submitted Oct. 29, 1973; revised manuscript received March 30, 1974. This was Paper 222 presented at the Miami Beach, Florida, Meeting of the Society, Oct. 8-13, 1972.

Any discussion of this paper will appear in a Discussion Section to be published in the June 1975 JOURNAL. All discussions for the June 1975 Discussion Section should be submitted by Feb. 1, 1975.

### REFERENCES

1. A. Brenner and G. E. Riddell, *J. Res. Natl. Bur. Std.*, **37**, 31 (1946); *Proc. Am. Electroplaters' Soc.*, **33**, 23 (1946).
2. J. S. Sallo, *Plating*, **54**, 257 (1967).
3. F. R. Morrall, *ibid.*, **59**, 131 (1972).
4. R. D. Fisher and W. H. Chilton, *This Journal*, **109**, 485 (1962).
5. Y. Moradzadeh, *ibid.*, **112**, 891 (1965).
6. L. D. Ranson and V. Zentner, *ibid.*, **111**, 1423 (1964).
7. J. G. Miksic, R. Travieso, A. Arcus, and R. H. Wright, *This Journal*, **113**, 360 (1966).
8. J. S. Judge, J. R. Morrison, and D. E. Speliotis, *ibid.*, **113**, 547 (1966).
9. J. S. Judge, J. R. Morrison, D. E. Speliotis, and G. Bate, *ibid.*, **112**, 681 (1965).
10. R. D. Fisher and W. H. Chilton, *Plating*, **54**, 537 (1967).
11. F. Pearlstein and R. F. Weightman, *ibid.*, **54**, 714 (1967).
12. J. R. DePew and D. E. Speliotis, *ibid.*, **54**, 705 (1967).
13. R. D. Fisher, *IEEE Trans. Magnetics*, **2**, 681 (1966).
14. M. Soraya, *Plating*, **54**, 549 (1967).
15. R. J. Heritage and M. T. Walker, *J. Electron. Control*, **7**, 543 (1960).
16. J. Ragrowski and M. Lauriente, *This Journal*, **109**, 987 (1962).
17. J. C. Hendy, H. D. Richards, and A. W. Simpson, *J. Mater. Sci.*, **1**, 127 (1966).
18. G. W. Lawless and R. D. Fisher, *Plating*, **54**, 709 (1967).
19. A. Brenner and G. E. Riddell, *J. Res. Natl. Bur. Std.*, **39**, 385 (1947); *Proc. Am. Electroplaters' Soc.*, **34**, 156 (1947).
20. R. M. Hoke, U.S. Pat. 2,990,296 (1961).
21. T. Berzins, U.S. Pat. 3,338,726 (1967).
22. R. M. Lukes, *Plating*, **51**, 969 (1964).
23. G. O. Mallory, *ibid.*, **58**, 319 (1971).
24. K. M. Gorbunova and A. A. Nikiforova, *J. Phys. Chem., USSR*, **28**, 883 (1954).
25. M. Schwartz, *Proc. Am. Electroplaters' Soc.*, **47**, 176 (1960).
26. F. Pearlstein and R. F. Weightman, *Plating*, **56**, 1158 (1969).
27. F. Pearlstein, *Metal Finishing*, **53**, 59 (1955).
28. M. M. Beckwith, *Plating*, **47**, 402 (1960).
29. A. H. DuRose, *Proc. Am. Electroplaters' Soc.*, **47**, 83 (1960).
30. A. H. DuRose and W. J. Pierce, *Metal Finishing*, **57**, 44 (1959).

# The Electroreduction of Oxygen and Hydrogen Peroxide on Sodium-Tungsten Bronzes

Jean-Paul Randin\*

*Hydro-Quebec Institute of Research, Varennes, Quebec, Canada*

*The publication costs of this article have been assisted by the Hydro-Quebec Institute of Research.*

## ABSTRACT

Sodium-tungsten bronzes of the general formula  $\text{Na}_x\text{WO}_3$  ( $0.34 < x \leq 0.89$ ), with high and low platinum contents, were investigated regarding their electrocatalytic activity towards the reduction of oxygen and hydrogen peroxide in sulfuric acid solutions. Contrary to the findings of some other workers  $\text{Na}_x\text{WO}_3$  are found to be poor catalysts for the cathodic reduction of oxygen. The presence of platinum in the bronze at concentrations in the 1000 ppm range does not increase significantly the catalytic properties of the bronze electrode. Sodium tungsten bronzes are relatively good catalysts for the cathodic reduction of hydrogen peroxide in acid solutions. The reaction is first-order with respect to the  $\text{H}_2\text{O}_2$  concentration and zero-order with respect to the  $\text{H}^+$  concentration. The steady-state current-potential curve exhibits a slope of  $2 RT/F$  and, at more cathodic potentials, a characteristic inhibition inflection. In contrast to other electrodes the cathodic reduction of  $\text{H}_2\text{O}_2$  on  $\text{Na}_x\text{WO}_3$  occurs at potentials less cathodic than those required for the reduction of oxygen.

Sodium-tungsten bronzes containing traces of platinum have been reported to exhibit good electrocatalytic activity for the oxygen reduction reaction (1-6). These findings stimulated considerable interest but other reports (7-10) failed to confirm the exceptionally good catalytic behavior reported by Bockris *et al.* (1-6). In the present study bronzes of the general formula  $\text{Na}_x\text{WO}_3$  ( $0.34 < x \leq 0.89$ ), with high and low platinum contents, were investigated regarding their electrocatalytic activity towards the oxygen reduction in 1N  $\text{H}_2\text{SO}_4$ . Since hydrogen peroxide is in some cases an intermediate in the reduction of oxygen to water, the irreversibility of the over-all reduction of oxygen in these cases can perhaps be due to the reduction of  $\text{H}_2\text{O}_2$  to  $\text{H}_2\text{O}$ . Because this problem had not been explicitly considered previously on sodium-tungsten bronzes, it was also investigated in the present work.

## Experimental

Sodium-tungsten bronze samples with an  $x$  value between 0.34 and 0.89, and platinum content from 1 up to 1200 ppm were investigated. The preparation and analysis of these samples were described recently (11).

A three-compartment cell was used with a rotating disk electrode system. Steady-state current-potential curves were automatically recorded with the system described recently by Bélanger (12). Some runs were performed with a conventional galvanostatic setup and the results were found to be the same both with the potentiostatic and the galvanostatic methods. For the reduction of oxygen long times were necessary to reach the steady-state values, especially in the low current region and during the first scan. Polarization times up to 8 hr were used with the galvanostatic method with potential variations corresponding to about 40 mV. Reproducible results were usually obtained with the potentiostatic method using 10 mV potential step per 5 min. The rotating disk technique was used to eliminate diffusion effects although there was no significant increase of current with increasing rotating speeds in the linear sections of the current-potential curves. Unless otherwise noted, the measurements were carried out at a rotation speed of 900 rpm. The instruments and the cells employed, as well as the details on the electrode mounting and gas purification,

were similar to those used in our previous work (13-15).

All solutions were made from sulfuric acid (ULTREX, J. T. Baker Chemical Company), sodium sulfate (J. T. Baker Chemical Company, certified), unstabilized hydrogen peroxide (Fisher Scientific Company, certified), and conductivity water. The peroxide concentration was determined by titration with potassium permanganate after the completion of a set of measurements. Great care was taken to eliminate impurity effects by working under carefully controlled conditions. No preelectrolysis was conducted in the present work, however, since it was previously noted that preelectrolysis tends to produce impurities, especially from the anode (13).

The oxygen gas (99.99%) and the mixtures oxygen-helium (1 and 10%  $\text{O}_2$ ) used in the present study were passed through a gas train which included in order, silica gel, active carbon, silica gel, ascarite and a glass wool filter to remove water, organics, and  $\text{CO}_2$ .

A hydrogen reference electrode in the same solution or a  $\text{Hg}/\text{Hg}_2\text{SO}_4$  (1N  $\text{H}_2\text{SO}_4$ ) electrode was used as reference electrode. All electrode potentials are given with respect to a standard hydrogen electrode.

Experiments were carried out at room temperature unless otherwise specified.

## Results

*The electrocatalytic reduction of oxygen.*—Open circuit potentials were poorly reproducible, and it took a long time to reach a stable value. After 1 hr of stabilization, the rest potential was usually around 0.4V, with extreme values from 0 to 0.6V. The open-circuit potential did not vary significantly whether oxygen, helium, or hydrogen was bubbled into the electrolyte.

A Tafel relationship for the cathodic reduction of oxygen was obtained only over a short range of potentials, *i.e.*, from about 0.1 to  $-0.2\text{V}$  (Fig. 1). In this potential range the current-potential curve is free of hysteresis between the ascending (potentials acquiring more negative values) and descending curves. When the potential is increased cathodically, interference from the hydrogen evolution reaction seriously affects the results and pronounced hysteresis was observed between the ascending and descending curves. Tafel slopes ranging between 120 and 280 mV/decade were obtained, most of them exhibiting a value around 200 mV/decade.

\* Electrochemical Society Active Member.

Key words: electrocatalysis, platinum-traces, inhibition, hydrogen tungsten bronze.



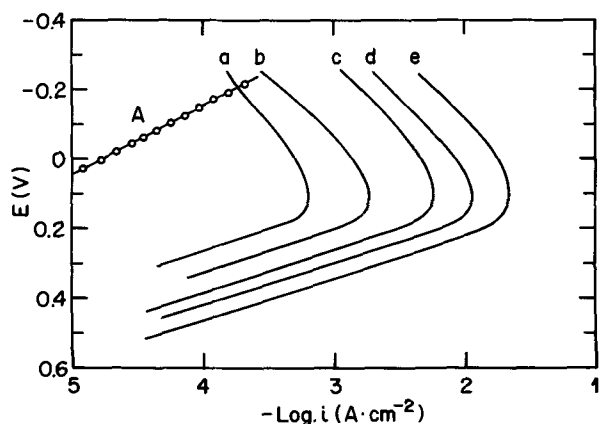


Fig. 1. Potentiostatic, steady-state (point-by-point) current-potential relationships on  $\text{Na}_{0.65}\text{WO}_3$  at 900 rpm. Curve A: for the reduction of oxygen (in  $\text{O}_2$ -saturated  $1\text{N H}_2\text{SO}_4$ ). Curves a-e: for the reduction of  $\text{H}_2\text{O}_2$  in He-saturated  $1\text{N H}_2\text{SO}_4$  solutions containing (a) 0.0046, (b) 0.0094, (c) 0.046, (d) 0.093, and (e) 0.18M  $\text{H}_2\text{O}_2$ .

The addition of platinum in the bronze sample increases the rate of the oxygen reduction reaction by a very small amount only (Table I). The composition of the bronze samples devoid of platinum has no significant effect on the catalytic behavior of this material for the oxygen reduction reaction (Table II).

**The electroreduction of hydrogen peroxide.**—Open-circuit potentials of sodium-tungsten bronze electrodes in  $1\text{N H}_2\text{SO}_4$  solutions in the presence and absence of hydrogen peroxide are shown in Fig. 2 as a function of pH. The various pH values were obtained by adding small amount of solid NaOH to the electrolyte. The measurements were carried out only at  $\text{pH} \leq 3$  since at greater pH values the sodium-tungsten bronze is attacked and catalytic decomposition of  $\text{H}_2\text{O}_2$  occurs. The open-circuit potential has low reproducibility, and long times (at least 24 hr) were needed to reach a stable value. At a given pH, the mixed potential depends on the  $\text{H}_2\text{O}_2$  concentration but no clear relationship was found. At a given  $\text{H}_2\text{O}_2$  concentration the open-circuit potential depends linearly on pH with a slope of about 80 mV/pH (Fig. 2). The results did not depend significantly on whether the solution was saturated with oxygen or helium. An open-circuit potential vs. pH curve with a slope of about 30 mV/pH was found in the absence of  $\text{H}_2\text{O}_2$  and  $\text{O}_2$  (Fig. 2).

Table I. Effect of platinum on the rate of the oxygen reduction reaction on  $\text{Na}_{0.6}\text{WO}_3$

Pt content (ppm)	Current density at $E = -0.17\text{V}$ ( $\text{mA} \cdot \text{cm}^{-2}$ )
2	0.07-0.15
100	0.12-0.19
200	0.19
500	0.20
1200	0.26

Table II. Effect of the x value in  $\text{Na}_x\text{WO}_3$  on the rate of the oxygen reduction reaction

(Samples with platinum content in the ppm range)

x value	Current density at $E = -0.17\text{V}$ ( $\text{mA} \cdot \text{cm}^{-2}$ )
0.34	0.07-0.19
0.58	0.07-0.15
0.64	0.08-0.15
0.82	0.12
0.89	0.11

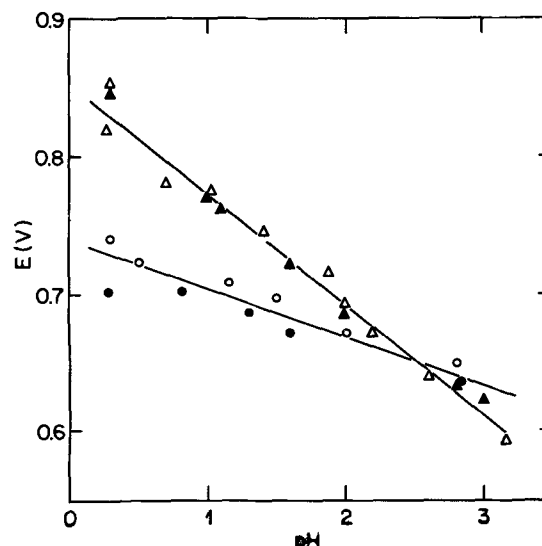


Fig. 2. Rest potential vs. pH for a  $\text{Na}_{0.65}\text{WO}_3$  electrode in the presence and absence of  $\text{H}_2\text{O}_2$  in  $1\text{N H}_2\text{SO}_4$  + small amount of solid NaOH. He-saturated  $0.1\text{M H}_2\text{O}_2$  ( $\Delta$ ),  $\text{O}_2$ -saturated  $0.1\text{M H}_2\text{O}_2$  ( $\blacktriangle$ ), He-saturated ( $\circ$ ),  $\text{O}_2$ -saturated ( $\bullet$ ).

**Steady-state current-potential relationships.**—No detectable spontaneous decomposition of  $\text{H}_2\text{O}_2$  was observed on  $\text{Na}_x\text{WO}_3$  in acidic media. The reduction current can, therefore, be attributed only to the reduction of  $\text{H}_2\text{O}_2$ . Steady-state current-potential curves for several concentrations of  $\text{H}_2\text{O}_2$  are presented in Fig. 1. At potentials anodic enough to avoid interference from the hydrogen evolution reaction, the current-potential relationships present no hysteresis between the ascending and descending curves. A Tafel region is observed between 0.5 and 0.2V with a slope of about 120 mV/decade, i.e.,  $2 \times 2.3 \text{ RT/F}$ . At potentials more cathodic than about 0.2V a characteristic inhibition inflection of the type discussed by Gilroy and Conway (16) is observed. The dependence of the current density in the inflection region on the rotation speed (Fig. 3) indicates that the reduction of  $\text{H}_2\text{O}_2$  is first-order with respect to hydrogen peroxide concentration and that the process is under combined diffusion and kinetic control.

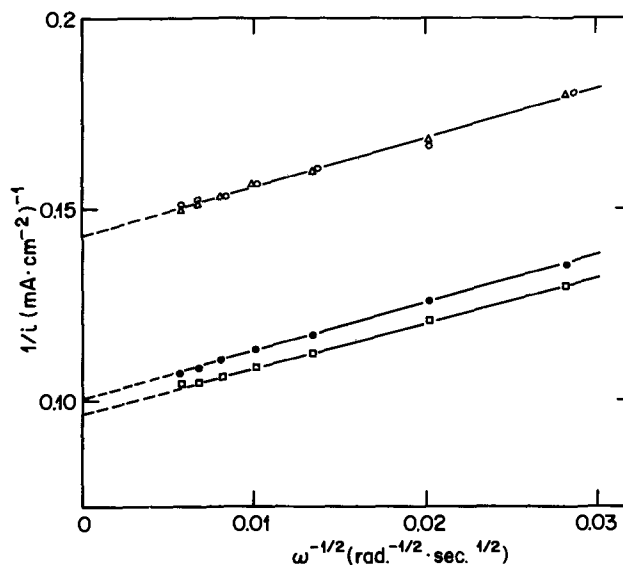


Fig. 3. Plots of  $1/i$  in the inhibition inflection region vs.  $\omega^{-1/2}$  for the reduction of  $\text{H}_2\text{O}_2$  in He-saturated  $1\text{N H}_2\text{SO}_4$  +  $0.052\text{M H}_2\text{O}_2$  on  $\text{Na}_{0.65}\text{WO}_3$ .  $E = 0.2\text{V}$  ( $\circ$ ),  $0.1\text{V}$  ( $\square$ ),  $0.0\text{V}$  ( $\bullet$ ), and  $-0.1\text{V}$  ( $\Delta$ ).

The anodic oxidation of  $\text{H}_2\text{O}_2$  was attempted on sodium-tungsten bronzes, but it was found that these electrodes show no activity for this reaction.

**Reaction orders.**—The plot of the reaction rate vs. the  $\text{H}_2\text{O}_2$  concentration (Fig. 4) indicates that a reaction mechanism first-order with respect to hydrogen peroxide takes place at constant potential. The reaction order with respect to hydrogen is close to zero between pH approximately 0 and 1.8. At pH values higher than about 2, the shape of the current-potential curve in the inhibition region is slightly different from that observed at lower pH. This behavior suggests that the electrode surface changes in this pH range. Impedance measurements carried out in solutions of pH around 3 exhibited a peak in addition to those found at lower pH (15). This peak was attributed to the dissolution of the bronze electrode. This side reaction may interfere with the hydrogen peroxide reduction reaction and prevent the determination of the true reaction order over a wide pH range.

**Apparent heat of activation.**—Arrhenius plots of the current density at constant potential vs.  $1/T$  give an apparent heat of activation equal to 8.3 kcal/mole (Fig. 5). A hydrogen electrode in 1N  $\text{H}_2\text{SO}_4$  was used as the reference electrode. The activation energy has not been corrected for the temperature coefficient of the reversible  $\text{H}_2\text{O}_2$ - $\text{H}_2\text{O}$  potential, nor for changes in  $\text{H}_2\text{O}_2$ ,  $\text{H}_2\text{O}$ , or  $\text{H}^+$  activity as a function of temperature. Neglecting the changes in activity coefficient and taking  $-0.658 \text{ mV}/(^{\circ})$  as the  $(dE_0/dT)_{\text{isoth}}$  (17) for the  $\text{H}_2\text{O}_2/\text{H}_2\text{O}$  couple, the heat of activation at constant overpotential would be about 10 kcal/mole.

**Effect of the bronze composition.**—The rate of the peroxide reduction reaction was found not to depend significantly on either the  $x$  value in  $\text{Na}_x\text{WO}_3$  (for  $x$  between 0.34 and 0.89) or the platinum content of the bronze electrode (between a few ppm up to 1200 ppm).

**The electroreduction of  $\text{O}_2 + \text{H}_2\text{O}_2$ .**—Investigations in 1N  $\text{H}_2\text{SO}_4$  solutions containing  $\text{O}_2$  and  $\text{H}_2\text{O}_2$  were carried out to detect any possible coupling of the  $\text{O}_2$  and  $\text{H}_2\text{O}_2$  reduction processes. The sum of the current-potential curves for the oxygen reduction alone (in  $\text{O}_2$ -saturated 1N  $\text{H}_2\text{SO}_4$ ) and for the hydrogen peroxide reduction alone (in He-saturated 1N  $\text{H}_2\text{SO}_4 + \text{H}_2\text{O}_2$ ) is equal to the experimental curve for the reduction of  $\text{O}_2 + \text{H}_2\text{O}_2$  carried out at once (in  $\text{O}_2$ -saturated 1N  $\text{H}_2\text{SO}_4 + \text{H}_2\text{O}_2$ ). This result indicates the absence of coupling between the two reactions.

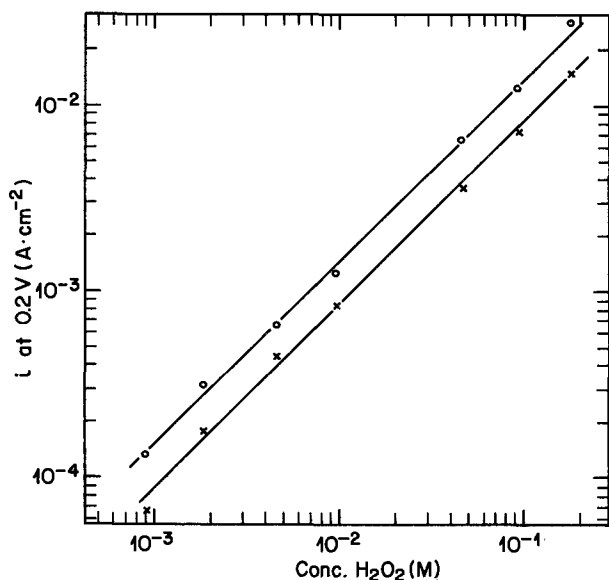


Fig. 4. A plot of the current density at 0.2V (x) and at the current maximum (O) vs. the concentration of  $\text{H}_2\text{O}_2$  in He-saturated 1N  $\text{H}_2\text{SO}_4$  on  $\text{Na}_{0.85}\text{WO}_3$  at 900 rpm.

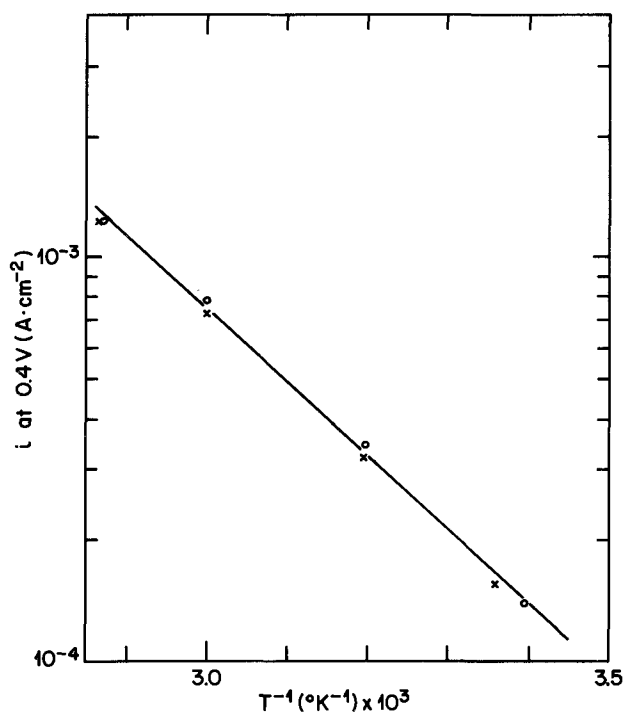


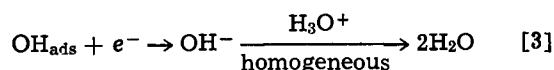
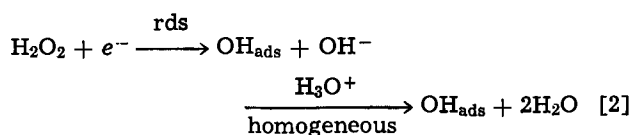
Fig. 5. Current density vs.  $T^{-1}$  plots for  $\text{Na}_{0.58}\text{WO}_3$  (x) and  $\text{Na}_{0.65}\text{WO}_3$  (O) in He-saturated 1N  $\text{H}_2\text{SO}_4 + 0.05\text{M H}_2\text{O}_2$ . The apparent heat of activation calculated from these plots is 8.3 kcal/mole.

## Discussion

**Reduction of  $\text{H}_2\text{O}_2$ .**—The reduction of  $\text{H}_2\text{O}_2$  on  $\text{Na}_x\text{WO}_3$  is found to be first-order with respect to the  $\text{H}_2\text{O}_2$  and zero-order with respect to  $\text{H}^+$  ions. The Tafel slope is close to  $2 \times 2.3 RT/F$ . The same reaction orders were found on Hg (18) and Pt (19-20), whereas a first-order reaction with respect to both  $\text{H}_2\text{O}_2$  and  $\text{H}^+$  was found on pyrolytic graphite and active charcoal (21). A Tafel slope of  $2 \times 2.3 RT/F$  was also found on pyrolytic graphite (21), whereas on platinum a very high slope yielding  $(1 - \alpha) = 0.2$  was obtained (19). The same mechanism as that advanced by Bagot-skiy *et al.* (18) for the reduction of  $\text{H}_2\text{O}_2$  on Hg is proposed for  $\text{Na}_x\text{WO}_3$ . The current-potential relation may be represented by

$$i = k [\text{H}_2\text{O}_2] \exp \left( - \frac{(1 - \alpha)\eta F}{RT} \right) \quad [1]$$

with the following mechanism



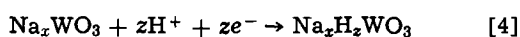
The  $\text{OH}^-$  produced by the electron transfer reactions [2] and [3], in acidic solutions, is immediately neutralized by  $\text{H}_3\text{O}^+$ . Assuming  $\alpha = 1/2$ , the observed Tafel slope is consistent with the proposed mechanism.

The current density at the maximum of the current-potential curve is proportional to the concentration of  $\text{H}_2\text{O}_2$  in the solution (Fig. 4), suggesting that the maximum may be associated with the diffusion limiting current for the reduction of peroxide. However, the plot of  $1/i$  vs.  $\omega^{-1/2}$  (Fig. 3) indicates that diffusion plays only a minor role in the reaction kinetics at, or near, the maximum of the current-potential curve. The inflection in the current-potential curve should

therefore be attributed to some kind of inhibition phenomenon.

Following earlier suggestions by Bagotskiy and Vasilev (22), inhibition and passivation in oxidation reactions were discussed quantitatively by Gilroy and Conway (16), and found to be either the result of an inhibiting species produced in a competing reaction, or of self-inhibition arising from the decomposition of adsorbed radicals. Since inhibition of the reduction of  $H_2O_2$  has not been observed on other electrodes (18-21), it may be assumed that the sodium-tungsten bronze electrode plays an important role in the inhibition process. Furthermore, it is unlikely that a parasitic oxidation reaction of the bronze itself is responsible for the negative Tafel slope, since the shape of the current-potential curves does not depend on the concentration of  $H_2O_2$ .

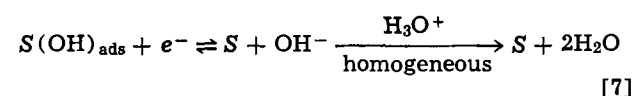
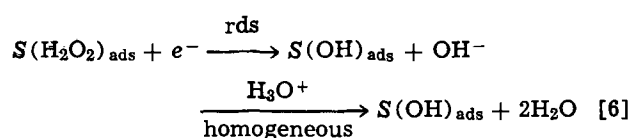
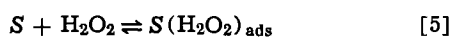
Since the position of the current-potential curves is a function of  $H_2O_2$  concentration, it is suggested that, at a given potential, the same fraction of surface sites are blocked independently of the  $H_2O_2$  concentration. This situation can arise from a parallel reaction such as the hydrogen bronze formation



This reaction has been shown to occur in the potential range in which the inhibition region begins, i.e., about 0.2V (13). The activity of  $Na_xH_zWO_3$  for the reduction of  $H_2O_2$  may be much lower than that of  $Na_xWO_3$ . If this is the case, the number of active sites decreases with the progress of reaction [4].

The inhibition of the cathodic reduction of  $H_2O_2$  on  $Na_xWO_3$  may, therefore, be described as the result of a competition for surface sites between peroxide and proton. This phenomenon is similar to that described by Gilroy and Conway (16) for the case of anodic oxidation in competition with oxide formation. In the present study, the reverse situation, i.e., cathodic reduction occurring in competition with hydride formation, has been shown to take place.

To take into account the preceding results, the reaction mechanism can be formulated as follows



where  $S$  represents an undefined surface adsorption site at the bronze electrode (see the text following Eq. [3]). As mentioned earlier, the above sequence of reactions [5] to [7] would be proceeding in competition with the parallel reaction [4] suggested here.

The mixed potential established at the bronze electrode is a complex one and does not seem to be defined primarily by the  $H_2O_2/O_2$  couple. The presence of  $H_2O_2$  seems to have more effect than that of oxygen. The behavior of  $Na_xWO_3$  differs substantially from that of the noble metals for which the mixed potentials are defined by the  $H_2O_2/H_2O$  and  $O_2/H_2O_2$  couples. It also depends on pH (about 60 mV/pH) but is independent of the hydrogen peroxide concentration (23). The poor reproducibility of the results obtained with  $Na_xWO_3$  prevent one from drawing definite conclusions from these measurements. Since sodium is leached out of the electrode (13-15, 24) it is possible that the mixed potential depends on  $Na^+$ .

*Effect of the  $x$ -value and platinum content of the  $Na_xWO_3$  electrodes on the reduction of oxygen or hydrogen peroxide.*—Frumkin *et al.* (25) have suggested that the electrocatalytic properties of an electrode de-

pend mainly on the chemical composition, i.e., electronic properties, of its surface and not on its bulk properties. Several studies (13-15, 24) have shown that sodium depletion occurs at the sodium tungsten bronze surface. Consequently, the surface composition of a polarized  $Na_xWO_3$  electrode changes little as a function of the bulk  $x$  value (15). It is therefore not surprising that the bulk  $x$  value in  $Na_xWO_3$  has no significant effect on the rate of the oxygen reduction reaction (Table II). Similar results were found for the hydrogen peroxide reduction (see above) and the hydrogen evolution reaction (26).

In Table I the rate of the oxygen reduction reaction on  $Na_xWO_3$  is found to depend only slightly on the platinum content of the electrode. This finding is in sharp contrast with the result of Bockris *et al.* (6) who found that the rate of oxygen reduction is accelerated several thousand times by the presence of 400 ppm of platinum in the bronze electrode. In the present work and other related studies (13-15) the platinum content of the  $Na_xWO_3$  electrode in the range 0-1200 ppm was found not to have a significant influence on the various electrochemical phenomena investigated. In particular, the flatband potential of the semiconducting surface layer did not change with the platinum content (15). Therefore this element does not influence the electronic structure of the catalytic surface.

The results reported by Bockris *et al.* (6) for the reduction of oxygen on platinum-free bronze samples are quite similar to those observed in the present work. The chief discrepancy between the results of Bockris *et al.* (6) and those of the present study [and of other investigations (7-10)] occurs with the samples containing platinum. It may therefore be suggested that the platinum incorporation differs substantially from one investigation to the other. However, a bronze sample containing about 1200 ppm of Pt and prepared in Bockris' laboratory<sup>1</sup> was tested by the present author and found to behave similarly to the samples investigated in the present study. This is not surprising because of the similarity of the methods of preparation (11, 24, 27). Therefore, it is unlikely that the method of preparation is the only factor responsible for the discrepancy. Experimental factors may be the cause of some of the difference, although it is not evident why results obtained with platinum-free samples do not differ substantially from one study to another.

## Conclusions

1. Sodium-tungsten bronzes are relatively good catalysts for the cathodic reduction of hydrogen peroxide in acid solutions.
2. Sodium-tungsten bronzes are poor catalysts for the oxygen reduction reaction, in agreement with previous work (7-10).
3. The presence of platinum in the bronze at concentrations in the 1000 ppm range does not increase significantly the catalytic properties of the bronze.
4. The electrocatalytic properties of the bronzes do not depend significantly on the  $x$  value in  $Na_xWO_3$ .
5. There is no coupling effect between the oxygen and hydrogen peroxide reduction reactions.

## Acknowledgments

The author thanks Mr. R. Bellemare for his assistance in the experimental work, Drs. A. K. Vijh and G. Bélanger for helpful discussions, and Dr. G. G. Cloutier, Director of Research, IREQ, for his interest and encouragement.

Manuscript submitted Dec. 17, 1973; revised manuscript received March 27, 1974.

Any discussion of this paper will appear in a Discussion Section to be published in the June 1975 JOURNAL. All discussions for the June 1975 Discussion Section should be submitted by Feb. 1, 1975.

<sup>1</sup> Samples sent by J. McHardy to A. K. Vijh in May 1969 and tested for platinum content at the N.R.C., Ottawa at our request (11).

## REFERENCES

1. D. B. Sepa, A. Damjanovic, and J. O'M. Bockris, *Electrochim. Acta*, **12**, 746 (1967).
2. A. Damjanovic, D. Sepa, and J. O'M. Bockris, *J. Res. Inst. Catalysis, Hokkaido Univ.*, **16**, 1 (1968).
3. J. O'M. Bockris, A. Damjanovic, and J. McHardy, "Proc. 3rd Int. Symp. Fuel Cells," Brussels, Belgium, June 16-20, 1969, p. 15, Press. Acad. Européennes, Brussels (1969).
4. R. A. Fredlein and J. McHardy, "24th Power Sources Symp." p. 175, P.S.C. Pub. Committee, Red Bank, N. J. (1970).
5. J. McHardy and J. O'M. Bockris, in "From Electrocatalysis to Fuel Cells," G. Sandstede, Editor, p. 109, University of Washington Press, Seattle, Washington (1972).
6. J. O'M. Bockris and J. McHardy, *This Journal*, **120**, 61 (1973).
7. B. Broyde, *J. Catalysis*, **10**, 13 (1968).
8. J. M. Fishman, J. F. Henry, and S. Tessore, *Electrochim. Acta*, **14**, 1314 (1969).
9. R. D. Armstrong, A. F. Douglas, and D. E. Williams, *Energy Conversion*, **11**, 7 (1971).
10. J. Heffler and H. Böhm, *Metaloberfläche—Angew. Electrochem.* **27**, 77 (1973).
11. J. P. Randin, *This Journal*, **120**, 1325 (1973).
12. G. Bélanger, *ibid.*, **118**, 583 (1971).
13. J. P. Randin, A. K. Vijh, and A. B. Chughtai, *ibid.*, **120**, 1174 (1973).
14. J. P. Randin, *ibid.*, **120**, 378 (1973).
15. J. P. Randin, *Electrochim. Acta*, **19**, 87 (1974).
16. D. Gilroy and B. E. Conway, *J. Phys. Chem.*, **69**, 1259 (1965).
17. A. J. de Bethune, in "The Encyclopedia of Electrochemistry," C. A. Hampel, Editor, p. 421, Reinhold Publishing Co., New York (1964).
18. V. S. Bagotskiy and I. E. Yablokova, *Zh. Fiz. Khim.*, **27**, 1663 (1953).
19. R. Gerischer and H. Gerischer, *Z. Physik. Chem. N.F.*, **6**, 178 (1956).
20. D. Winkelmann, *Z. Elektrochem.*, **60**, 731 (1956).
21. A. J. Anurova, V. S. Daniel-Bek, and A. L. Rotinyan, *Elektrokhimiya*, **4**, 815 (1968).
22. V. S. Bagotskiy and Y. B. Vasiley, *Electrochim. Acta*, **9**, 869 (1964).
23. J. O'M. Bockris and S. Srinivasan, "Fuel Cells: Their Electrochemistry," p. 423, McGraw-Hill Book Co., New York (1969).
24. J. McHardy and J. O'M. Bockris, *This Journal*, **120**, 53 (1973).
25. A. Frumkin, N. Polianovskaya, I. Bagotskaya, and N. Grigoryev, *J. Electroanal. Chem.*, **33**, 319 (1971).
26. J. P. Randin and A. K. Vijh, *Electrochim. Acta*, To be published.
27. R. A. Fredlein and A. Damjanovic, *J. Solid State Chem.*, **4**, 94 (1972).

## Electrochemical Redox Patterns for Pyridinium Species: 1-Methylnicotinamide and Nicotinamide Mononucleotide

Conrad O. Schmakel,<sup>1</sup> K. S. V. Santhanam,<sup>2</sup> and Philip J. Elving\*

The University of Michigan, Ann Arbor, Michigan 48104

### ABSTRACT

The detailed mechanisms for the electrochemical reduction in aqueous media of pyridinium species have been elucidated on the basis of the electrochemical, spectrophotometric, and chemical properties of two such species and their reduction products: 1-methyl-3-carbamoylpyridinium ion (1-methylnicotinamide; MCP<sup>+</sup>) and nicotinamide mononucleotide (NMN<sup>+</sup>). An initial reversible pH-independent one-electron (1e) addition to the pyridinium ion to produce a free radical is followed by its irreversible dimerization to an apparent 6,6' species. At more negative potential, the free radical is reduced to an apparent 1,6 dihydropyridine species (2e reduction product; NMN<sup>+</sup> may form some 1,4 isomer); the dimer is stable to reduction within the available potential range. At sufficiently positive potential, both 1e and 2e reduction products can be oxidized back to MCP<sup>+</sup> or NMN<sup>+</sup>. Rate constants for the free radical dimerization at 30° is  $6 \times 10^7$  mol<sup>-1</sup> sec<sup>-1</sup> for MCP<sup>+</sup> and  $2 \times 10^6$  mol<sup>-1</sup> sec<sup>-1</sup> for NMN<sup>+</sup>; activation energies are 4.1 kcal mol<sup>-1</sup> for MCP<sup>+</sup> and 3.6 kcal mol<sup>-1</sup> for NMN<sup>+</sup>. While MCP<sup>+</sup> is negligibly adsorbed, its dimeric and dihydropyridine products are strongly and moderately adsorbed, respectively; NMN<sup>+</sup> and its reduction products are negligibly adsorbed. Both reduction products are susceptible to acid-catalyzed hydrolysis; the rate increases with decreasing pH; at any given pH, the dimer is less stable than the dihydropyridine species.

Among the principal components in the electron transport chain in biological oxidation-reduction reactions are pyridinoproteins, which utilize pyridine nucleotides as coenzymes. A basic understanding of the electrochemical redox behavior of pyridine nucleotides should contribute to a better understanding of the electron transport chain, since the site of both biological and electrochemical redox activity in the pyridine nucleotides is the pyridine ring. Of the relevant nucleotides, nicotinamide mononucleotide (NMN<sup>+</sup>) (Fig. 1) is the simplest one structurally; its behavior would

provide the basis for understanding that of the larger pyridine nucleotides such as NAD<sup>+</sup> (nicotinamide adenine dinucleotide; also called diphosphopyridine nucleotide or DPN<sup>+</sup>) and NADP<sup>+</sup> (nicotinamide adenine dinucleotide phosphate; triphosphopyridine nucleotide or TPN<sup>+</sup>).

The polarographic behavior of many 1-substituted 3-carbamoylpyridinium ions<sup>3</sup> (1-14) has been investigated on the basis of their being model compounds for understanding the polarographic behavior of NAD<sup>+</sup>. However, only in the case of the 1-methyl-3-carbamoylpyridinium ion (1-methylnicotinamide; MCP<sup>+</sup>) (Fig. 1) have extensive data been collected. Although

\* Electrochemical Society Active Member.

<sup>1</sup> Present address: Abbott Laboratories, Scientific Divisions, North Chicago, Illinois, 60064.

<sup>2</sup> Permanent address: Tata Institute of Fundamental Research, Bombay 5, India.

Key words: dihydropyridines, dimerization, free radicals, methyl nicotinamide, nicotinamide mononucleotide.

<sup>3</sup> These have included the following where the N(1) substituent is indicated: CH<sub>3</sub> (1-10), C<sub>2</sub>H<sub>5</sub> (2), C<sub>6</sub>H<sub>7</sub> (2), C<sub>4</sub>H<sub>9</sub> (2), CH<sub>2</sub>C<sub>6</sub>H<sub>5</sub> (2, 3), CH<sub>2</sub>CH<sub>2</sub>SO<sub>4</sub><sup>-</sup> (8), CH<sub>2</sub>C<sub>6</sub>H<sub>4</sub>SO<sub>4</sub><sup>-</sup> (8), D-glucopyranosidyl (9, 10), D-glucopyranosidyltetraacetate (6, 9, 10).

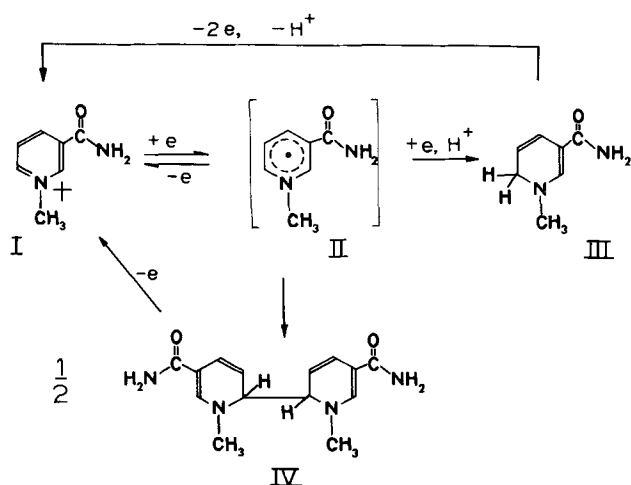


Fig. 1. Reaction paths for the electrochemical behavior of 1-methyl-3-carbamoylpyridinium ion ( $\text{MCP}^+$ ; 1-methylnicotinamide), nicotinamide mononucleotide ( $\text{NMN}^+$ ), and their reduction products. In the case of  $\text{NMN}^+$ , the  $\text{CH}_3$  group is replaced by a ribosophosphate group and some of the dihydropyridine species (III) may be present as the 1,4 isomer.

there is general agreement concerning the over-all process for  $\text{MCP}^+$ , there is considerable disagreement on specifics, *e.g.*, under similar conditions  $E_{1/2}$  for the first of the two polarographic waves seen has been reported (1-3, 7) as varying from  $-0.94$  to  $-1.11\text{V}$ . Two recent papers (15, 16) report polarographic patterns for  $\text{MCP}^+$ , which are more complex than those seen by other investigators or in the present study. Wave I is reported (7, 17, 18) to be due to a reversible  $1e$  process, but the over-all electrochemical process is irreversible due to subsequent dimerization (1, 17, 18); however, the dimerization rate constant obtained by cyclic voltammetry (18) differs by many orders of magnitude from that obtained by pulse radiolysis (19). Other inconsistencies in the literature involve potential data, presence or absence of catalytic hydrogen evolution,<sup>4</sup> chemical and electrochemical properties of the reduction products, correlation of ultraviolet spectral properties of the latter with structure, and the role of adsorption phenomena.

$\text{NMN}^+$  is in many respects a more realistic model compound for understanding  $\text{NAD}^+$  and  $\text{NADP}^+$  than  $\text{MCP}^+$ ; the electronic structure of the pyridine ring in  $\text{NMN}^+$  is more closely related to that of the coenzymes because of the similar inductive effects of the N-substituents, *e.g.*, the action of dilute base on  $\text{MCP}^+$  is different from that on  $\text{NMN}^+$  and  $\text{NAD}^+$  [the amide group of  $\text{MCP}^+$  is readily hydrolyzed, but the nucleotides cleave at the nicotinamide-ribose linkage (20)]. In addition,  $\text{NMN}^+$ , like the coenzymes, has a bulky N-substituent which presumably is effective in determining the isomeric form of the initial electrochemical reduction product, *e.g.*, a 4,4' as opposed to a 6,6' dimer.  $\text{NMN}^+$  enjoys the same freedom from the adenine moiety as does  $\text{MCP}^+$ , which simplified interpretation of ultraviolet spectra (here characteristic only of the pyridine ring) and eliminates adsorption due to the adenine moiety (21). The two previously reported electrochemical studies (15, 22) of  $\text{NMN}^+$  are fragmentary and some of the results seem questionable; interesting results obtained for  $\text{NMN}^+$  by Berg and Hanschmann (23, 24) have, unfortunately, not yet been published.

Because of the uncertainties in the reported behavior of  $\text{MCP}^+$  and the lack of information on  $\text{NMN}^+$ , the electrochemical behavior of these two compounds was systematically investigated with emphasis on the use of

<sup>4</sup> A catalytic hydrogen evolution reaction occurs when a compound is present whose protonated adduct under the experimental conditions is more easily reducible, *i.e.*, has a lower activation energy in respect to net addition of an electron to the proton, than the uncomplexed proton itself.

Table I. Buffer and background electrolyte solutions<sup>a</sup>

Buffer No.	pH range	Composition
1	0.0-1.0	HCl + KCl
2	2.0-8.0	$\text{Na}_2\text{HPO}_4 \cdot 7\text{H}_2\text{O}$ + citric acid monohydrate + KCl
3	3.9-5.9	$\text{HOAc}$ + $\text{NaOAc}$
4	9.0-10.0	$\text{K}_2\text{CO}_3$ + $\text{KHCO}_3$
5	9.0-10.0	$\text{K}_2\text{CO}_3$ + $\text{KHCO}_3$ + KCl <sup>b</sup>
6	9.0-10.0	$\text{K}_2\text{CO}_3$ + $\text{KHCO}_3$ + $\text{Et}_4\text{NCl}$ <sup>c</sup>
7	9.0-10.0	$\text{NH}_3$ + $\text{NH}_4\text{Cl}$
8	11.0-12.0	$\text{KOH}$ + KCl

<sup>a</sup> The final ionic strength of buffer solutions used in all experiments was  $0.5\text{M}$  unless otherwise stated.

<sup>b</sup> KCl concentration:  $0.4\text{M}$ .

<sup>c</sup>  $\text{Et}_4\text{NCl}$  concentration:  $0.4\text{M}$ .

rapid perturbation techniques to study intermediate species and adsorption, and on the detailed examination of final products prepared by macro-scale electrolysis.

### Experimental

Chemicals, apparatus, and procedures used have largely been described (25).

**Chemicals.**—The reported analytical data and spectrophotometric assay indicated sufficient purity for polarographic study of the following: nicotinamide mononucleotide ( $\text{NMN}^+$ ) (Sigma; P-L Biochemicals), reduced nicotinamide mononucleotide ( $\text{NMNH}$ ) (Sigma), and 1-methyl-3-carbamoylpyridinium chloride ( $\text{MCP}^+$ ) (Sigma).

The buffer solutions used, prepared from reagent grade chemicals, are listed in Table I.

### Results and Discussion

**D.-C. polarography.**—1.  $\text{MCP}^+$ .—Above pH 9,  $\text{MCP}^+$  exhibits two well-defined waves (Table II; Fig. 2A). A catalytic hydrogen wave<sup>4</sup> (Fig. 3), whose height in-

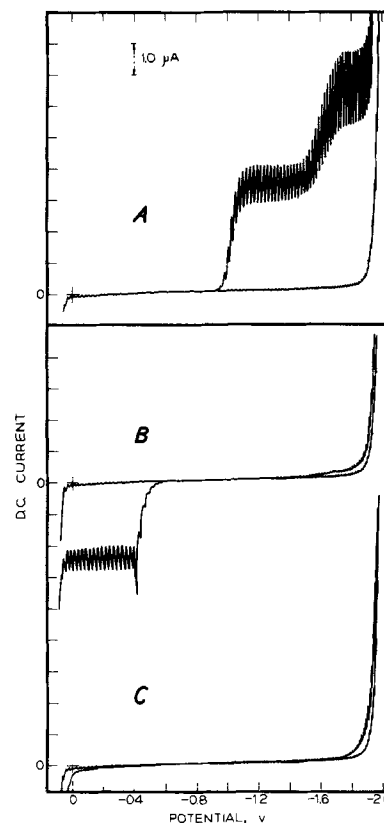


Fig. 2. Electrolysis of 1-methyl-3-carbamoylpyridinium ion ( $1.20\text{mM}$ ) in pH 10 KCl/carbonate buffer. D-C polarograms: A, before electrolysis; B, after electrolysis at  $-1.25\text{V}$ ; C, after electrolysis at  $-1.80\text{V}$ . Background polarogram shown for each case.

Table II. Variation in polarographic behavior of 1-methyl-3-carbamoylpyridinium ion with pH

Buffer No.	pH	Conc., mM	Wave I			Wave II		
			$-E_{1/2}$ , V	Wave slope, <sup>a</sup> mV	$I^b$	$-E_{1/2}$ , V	Wave slope, <sup>a</sup> mV	$I^b$
2	3.7	0.32	1.03	58	3.6 <sup>c</sup>	—	—	—
2	4.4	0.32	1.04	51	3.0 <sup>c</sup>	—	—	—
3	5.2	0.96	1.05	48	— <sup>g</sup>	—	—	—
2	5.8	0.32	1.04	60	2.11 <sup>c</sup>	—	—	—
2	7.2	0.32	1.02	54	1.85	1.55	—	13.2 <sup>c</sup>
2	7.4	0.77	1.02	50	1.78	1.55	—	10.2 <sup>c</sup>
2	7.7	0.50	1.02	52	1.78	1.56	—	6.5 <sup>c</sup>
f	7.8	0.45	1.04	50	1.98	—	—	—
2	8.0	0.32	1.02	56	1.90	1.55	—	3.8 <sup>c</sup>
4	9.2	0.90	1.05	44	1.8	1.65	— <sup>g</sup>	1.8
4	9.4	0.32	1.03	53	1.90	1.59	89	1.92
5	9.4	0.32	1.03	51	1.95	1.58	86	1.96
7	9.7	0.50	1.03	50	1.91	1.53	76	2.06
6	9.8	0.50	1.10	60	1.80	1.62	65	1.82
8	11.1	0.38	1.03	56	1.81	1.59	84	1.73
8	12.0	0.50	1.03	53	1.90	1.60	88	1.81
8	12.8	0.50	1.04	d	d	1.60	d	d

<sup>a</sup> Wave slope calculated as  $(E_{1/4} - E_{3/4})$ .<sup>b</sup> Diffusion current constant,  $I = i_d/Cm^{2/3}t^{1/6}$ .<sup>c</sup> Limiting currents of these waves exhibit partial kinetic character due to merging catalytic hydrogen wave;  $I$  values calculated for comparison.<sup>d</sup> 1-Methyl-3-carbamoylpyridinium ion is unstable in basic solutions.<sup>e</sup> Phosphate buffer, 0.3M ionic strength.<sup>f</sup> Borate buffer, 0.5M ionic strength.<sup>g</sup> Poorly defined wave.

creases with decreasing pH, begins to merge with wave II below pH 8 and with wave I below pH 3.

At pH 9.6, both waves are diffusion controlled ( $h$  and temperature variation), of equal height (diffusion current constant,  $I$ , magnitudes correspond to 1e faradaic processes), and proportional to concentration ( $I$  is  $1.94 \pm 0.05$  for both waves between 0.05 and 4.7 mM).

$E_{1/2}$  for wave I is pH-independent (average value:  $-1.03V$ ). Addition of surface-active  $Et_4N^+$  (pH 9.4 buffer 6) shifts it 70 mV more negative. Increase in ionic strength of pH 9.4 KCl/carbonate buffer from 0.1 to 2.0M shifts  $E_{1/2}$  from  $-1.02$  to  $-1.04V$ .  $E_{1/2}$  shifts with concentration at low concentration ( $-1.06V$  at 0.05 mM and  $-1.10V$  at 0.01 mM). Wave I is due to a reversible electron transfer, e.g., slopes of the wave ( $E_{1/4} - E_{3/4}$ ) and  $\log [i/(i_d - i)]$  vs.  $E$  plot are generally of the magnitude expected for a reversible 1e cathodic wave followed by an irreversible chemical reaction (26, 27); the log plot is not always strictly linear over the entire rising portion of the wave. Such deviations are probably due to the dimerization and adsorption phenomena subsequently discussed.

Above pH 9,  $E_{1/2}$  for wave II is virtually pH-independent, but depends somewhat on background electrolyte nature. Increase in ionic strength of pH 9.4

KCl/carbonate buffer from 0.1 to 2.0M shifts  $E_{1/2}$  from  $-1.64$  to  $-1.55V$ . Increase in MCP<sup>+</sup> concentration from 0.01 to 4.7 mM shifts  $E_{1/2}$  from  $-1.52$  to  $-1.63V$ . Based on its slope, wave II involves an irreversible electron transfer. Below pH 8, the wave II current depends on pH, being due to a faradaic reduction plus catalytic hydrogen evolution<sup>4</sup> due to reduction of the protonated product; the combined wave is peak-shaped (Fig. 3). At pH 7.4, the total wave II current decreases with increasing  $t$  ( $i_1$  proportional to  $h^{-0.23}$ ), suggesting that an adsorbed species is the catalyst for hydrogen evolution. At pH 6.7, an increase in phosphate buffer capacity from 0.004 to 0.04M increases the wave II height fivefold to a magnitude about 20 times that of wave I. 2. NMN<sup>+</sup>.—NMN<sup>+</sup> displays a single cathodic wave (wave I) below pH 6 (Table III). At pH 1, the wave is ill-defined ( $i_1$  has kinetic character) and occurs near background discharge. With increasing pH, wave I decreases in height to a limiting value at pH 4-5 (equivalent to a 1e reduction) and becomes diffusion controlled; the height remains constant to pH 10-11, where it begins to decrease because of hydrolysis.  $E_{1/2}$  is independent of pH up to pH 5, becomes about 80 mV more negative between pH 5.0 and 7.5, and then is constant up to pH 12; the shift is due to the secondary

Table III. Variation in polarographic behavior of NMN<sup>+</sup> with pH

Buffer No.	pH	Conc., mM	Wave I				Wave II				Background shift <sup>d</sup> , mV
			$-E_{1/2}$ , V	Wave slope, <sup>a</sup> mV	$I^b$	$x^c$	$-E_{1/2}$ , V	Wave slope, <sup>a</sup> mV	$I^b$	$x^c$	
1	1.0	0.30	0.88	89	6.0	—	—	—	—	—	260
2	2.1	0.30	0.91	81	3.7	0.20	—	—	—	—	230
2	2.9	0.28	0.91	81	2.30	0.33	—	—	—	—	280
2	4.4	0.29	0.89	63	1.59	0.45	—	—	—	—	180
3	5.0	0.28	0.90	68	1.40	0.51	—	—	—	—	250
3	5.0	0.48	0.98	50	—	—	—	—	—	—	—
3	5.4	0.29	0.80	70	1.41	—	—	—	—	—	290
2	6.1 <sup>e</sup>	0.32	0.92	66	1.36	0.50	1.58	—	11.5	-0.14	0
2	7.1 <sup>e</sup>	0.32	0.96	65	1.36	0.50	1.60	97	1.97	0.19	0
2	8.0 <sup>e</sup>	0.32	0.97	60	1.30	0.51	1.64	100	1.80	0.38	0
4	9.0	0.26	1.08	50	1.3	—	1.72	—	—	—	—
4	9.3 <sup>f</sup>	0.28	1.03	50	1.36	—	1.73	90	1.47	—	0
5	9.3	0.28	0.96	65	1.43	—	1.63	89	1.62	—	0
5	9.3 <sup>g</sup>	0.28	0.93	71	1.43	—	1.56	79	1.65	—	0
4	9.4 <sup>g</sup>	0.29	0.98	67	1.37	0.51	1.63	92	1.64	0.35	0
6	9.6	0.29	1.08	56	1.28	0.50	1.64	83	1.49	0.51	—
8	11.8 <sup>h</sup>	0.26	0.98	64	—	—	—	—	—	—	0

<sup>a</sup> Wave slope calculated as  $(E_{1/4} - E_{3/4})$ .<sup>b</sup> Diffusion current constant,  $I = i_d/Cm^{2/3}t^{1/6}$ . In order to compare relative wave heights,  $I$  values have been calculated in some cases for waves whose limiting currents are not diffusion controlled.<sup>c</sup> Power of the corrected mercury height in  $i = K \cdot h^x$ . Height dependence determined using 3-6 mercury heights.<sup>d</sup> Shift in background discharge in the presence of the electroactive species compared to that for the supporting electrolyte alone.<sup>e</sup> Triton X-100 (0.0001%) added to obtain potential data for first wave.<sup>f</sup> NMN<sup>+</sup> is unstable in basic solutions.<sup>g</sup> Ionic strength = 0.10M. Wave II ill-defined.<sup>h</sup> Ionic strength = 2.0M.

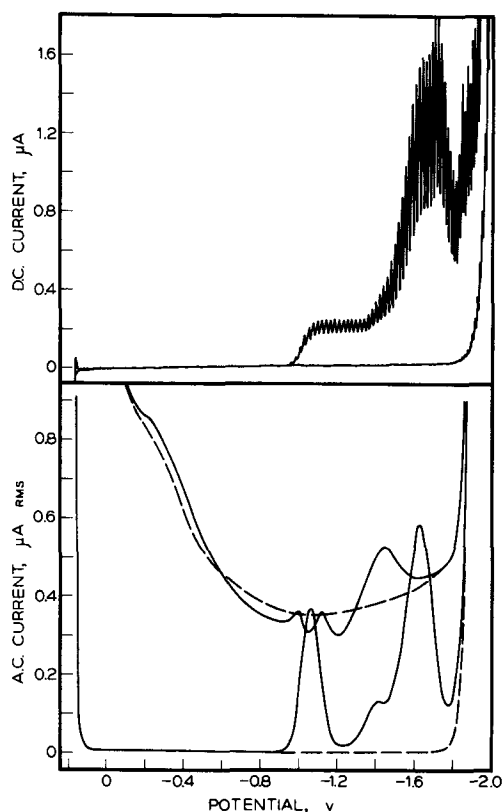


Fig. 3. D-C and a-c polarograms of 0.77 mM 1-methyl-3-carbamoylpyridinium ion in pH 7.4 McIlvaine buffer. (Cf. Fig. 4 caption for curve identification.)

phosphate dissociation of  $\text{NMN}^+$  [the corresponding  $\text{pK}_a$  for AMP is between 6.0 and 6.7 (28)].  $\text{MCP}^+$ , as expected, does not exhibit a similar  $E_{1/2}$  shift.

At pH 6, where the background discharge potential is identical to that for background alone,  $i_1$  for wave II is kinetically controlled and greater than that of wave I, since it results—similarly to  $\text{MCP}^+$ —from simultaneous formation of the  $2e$  product by a second  $1e$  addition to the pyridine ring and catalytic hydrogen evolution. Below pH 6, the wave II height increases rapidly with decreasing pH, which accounts for the positive shift in background discharge, *i.e.*, unless polarographic sensitivity is very low, the rising portion of wave II serves as discharge. Above pH 6, wave II decreases in height, reaching at pH 9 a height identical to that of wave I; above pH 10, it is obscured by reduction of nicotinamide formed by  $\text{NMN}^+$  hydrolysis.

Consequently, due to hydrogen evolution at lower pH and decomposition at higher pH, the characteristics of waves I and II can be studied thoroughly and simultaneously only between pH 9 and 10. The polarographic patterns obtained in this pH region depend on ionic strength and surfactant presence, *e.g.*,  $\text{Et}_4\text{N}^+$ . The latter is adsorbed at the interface in the potential region where faradaic processes occur. Wave II is also better defined in presence of KCl.

Increase in ionic strength (pH 9.3 KCl/carbonate buffer) from 0.1 to 2.0M shifts waves I and II positively by 100 and 170 mV, respectively (Table III). Wave II, which appears as an ill-defined shoulder on background discharge at low ionic strength (0.1M), becomes well-defined at higher ionic strength with a height about equal to that of wave I. However, with increasing  $\text{Et}_4\text{NCl}$  concentration (ionic strength held constant), wave I shifts to more negative potential and wave II appears and grows in height; the background discharge potential remains constant.

At sufficiently high  $\text{Et}_4\text{NCl}$  concentration, *e.g.*, buffer 6,  $\text{NMN}^+$  exhibits two well-defined, diffusion-controlled ( $h$  and temperature variations) waves of about

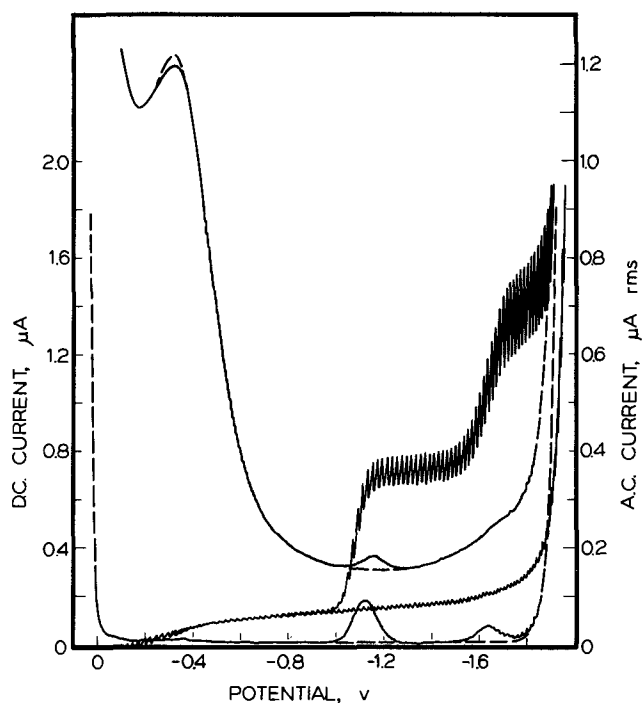


Fig. 4. D-C and a-c polarograms of 0.32 mM  $\text{NMN}^+$  in pH 9.6  $\text{Et}_4\text{NCl}$ /carbonate buffer. D-C polarograms shown with and without electroactive species present. Solid lines represent in-phase (lower curves) and quadrature (upper curves) components of total a-c current; dashed lines represent corresponding background currents.

equal height, whose  $I$  values correspond to  $1e$  processes (Fig. 4). Wave I slope varies with temperature ( $1.4^\circ$ – $36.0^\circ$ ) as expected for a reversible wave. Wave II is irreversible, based on its slope. With increasing concentration, the two waves remain of equal height, but wave I  $E_{1/2}$  shifts from  $-1.12\text{V}$  at 0.01 mM to  $-1.06\text{V}$  at 0.86 mM.

**Cyclic voltammetry.**—The results discussed were obtained at a hanging mercury drop electrode (hmde), *e.g.*, Tables IV and V, except for those in the subsection on the pyrolytic graphite electrode (pge).

1.  $\text{MCP}^+$ .—At slow scan rate ( $v = 0.1\text{V/sec}$ ), sweeps to more negative potential above pH 9 produce a cathodic peak at  $-1.13\text{V}$  (wave I process). Below pH 9, an additional cathodic peak appears at  $-1.70\text{V}$  due to the catalytic process; at pH 7.3, the rising portion of this peak serves as background discharge.

Table IV. Effect of scan rate on cyclic voltammetric behavior<sup>a</sup> of  $\text{MCP}^+$  and  $\text{NMN}^+$

Scan rate, V/sec	Cathodic peak			Anodic peak		
	$-E_{pc}$ , V	$i_{pc}$ , $\mu\text{A}$	$i_p/v^{1/2}$	$-E_{pa}$ , V	$i_{pa}$ , $\mu\text{A}$	$i_{pa}/i_{pc}$
MCP (0.90 mM)						
0.10	1.13	7.75	24.5	0.32	2.00	0.26
0.15	1.14	9.25	23.9	0.32	2.75	0.30
0.20	1.14	10.25	22.9	0.32	4.25	0.41
0.48	1.14	18.0	26.1	0.31	8.00	0.44
0.80	1.14	23.0	25.7	0.28	10.00	0.43
1.00	1.15	26.0	26.0	0.26	13.0	0.50
2.50	1.15	42.0	26.6	0.25	22.0	0.52
NMN (0.78 mM)						
0.10	1.22	5.70	18.0	0.13	2.60	0.46
0.15	1.22	7.00	18.4	0.13	3.50	0.50
0.20	1.22	7.80	17.4	0.13	3.70	0.47
0.80	1.24	13.7	15.3	0.13	6.81	0.50
1.00	1.25	14.7	14.7	0.12	7.36	0.50
2.50	1.25	24.2	15.3	0.12	12.1	0.50

<sup>a</sup> Data for first cathodic peak ( $i_c$ ) and for anodic peak corresponding to oxidation of the resulting ultimate reduction product in pH 9.0 carbonate buffer.

Table V. Effect of rapid scan rate on cyclic voltammetric reduction<sup>a</sup> of MCP<sup>+</sup> and NMN<sup>+</sup>

Scan rate, V/sec	Peak I		Peak II	
	$i_p$ , $\mu\text{A}$	$i_p/v^{1/2}$	$i_p$ , $\mu\text{A}$	$i_p/v$
MCP (0.80 mM)				
4.48	50.0	23.6	28.0	6.5
6.72	57.5	22.2	50.0	7.5
8.96	60.0	20.0	60.0	6.7
11.2	65.0	19.5	75.0	7.1
13.4	70.0	19.5	95.0	7.1
15.7	72.0	18.2	110	6.7
17.9	80.0	18.9	120	6.7
NMN (0.87 mM) <sup>b</sup>				
2.40	27.0	17.4		
4.80	38.0	18.0		
7.20	47.0	17.5		
9.60	53.0	16.8		
12.0	56.0	17.2		
14.4	63.0	16.2		

<sup>a</sup> Data for pH 9.25 KCl/carbonate buffer.

<sup>b</sup> The second NMN<sup>+</sup> cathodic peak is not well defined.

Potential sweep reversal immediately after peak Ic produces a pH-independent anodic peak ( $E_p = -0.3$  to  $-0.4\text{V}$ ), due to oxidation of the 1e reduction product to MCP<sup>+</sup>, which shifts positively with increasing  $v$  and merges with anodic background discharge above 5 V/sec (Table IV). The ratio of anodic to cathodic peak heights varies with experimental conditions from 0.5 or less to nearly one, e.g., at  $v = 0.1$  V/sec, the ratio decreases with decreasing pH due to acid catalyzed decomposition of the reduction product (cf. discussion of reduction product stability).

At pH 9.3, the peak Ic current function,  $i_p/v^{1/2}$ , is almost constant with increasing  $v$ , indicating diffusion control (Table V). The peak IIc current increases markedly with increasing  $v$ , surpassing the peak I current above 9 V/sec; the broadness of peak II and the relative constancy of its  $i_p/v$  ratio with increasing  $v$  are suggestive of an adsorption-controlled faradaic process.

An anodic peak complementary to cathodic peak Ic appears only at  $v$  exceeding 20 V/sec, where potential reversal at 40 mV or more beyond peak Ic ( $E_p = -1.26\text{V}$ ) produces an anodic peak ( $E_p = -1.20\text{V}$ ) (the peak is barely evident at 16 V/sec) (Fig. 5). The 60 mV peak potential difference suggests a reversible 1e process. Appearance of a reversible anodic peak only at high  $v$  demonstrates the presence of a chemical reaction following charge transfer. The prewave or prepeak at ca.  $-0.6\text{V}$  is due to adsorption of the reduction product. No anodic peak complementary to peak IIc appears.

2. NMN<sup>+</sup>.—The cyclic voltammetric behavior of NMN<sup>+</sup> is generally similar to that of MCP<sup>+</sup>. At  $v = 0.1$  V/sec, a single ill-defined peak Ic ( $E_p = -0.93\text{V}$ ) is produced at low pH, close to background discharge. With increasing pH, Ic becomes better defined and its current decreases to a limiting value above pH 6;  $E_p$  becomes more negative between pH 5 and 7 and then is constant (Fig. 6), similar to dme wave I. On varying  $v$  from 0.005 to 0.5 V/sec at pH 8.0, the  $i_p/v^{1/2}$  ratio remains constant, suggesting diffusion control, but  $E_p$  shifts 20 mV more negative.

In slightly alkaline solution, peak IIc ( $E_p = -1.69\text{V}$  at pH 9) appears. The fact that its current is less than 10% that of Ic, supports the ultimate wave I product not being further reduced in the wave II process. (Peak IIc may also be due in part to reduction of nicotinamide present as a minor impurity or formed by NMN<sup>+</sup> hydrolysis; cf. discussion of controlled potential electrolysis.)

Reversing the potential sweep after the appearance of either peak Ic or IIc yields a single anodic peak Ia, corresponding to oxidation of the 1e reduction product. In alkaline solution, repetitive cycling in a potential region, which includes peaks Ic and Ia, causes no

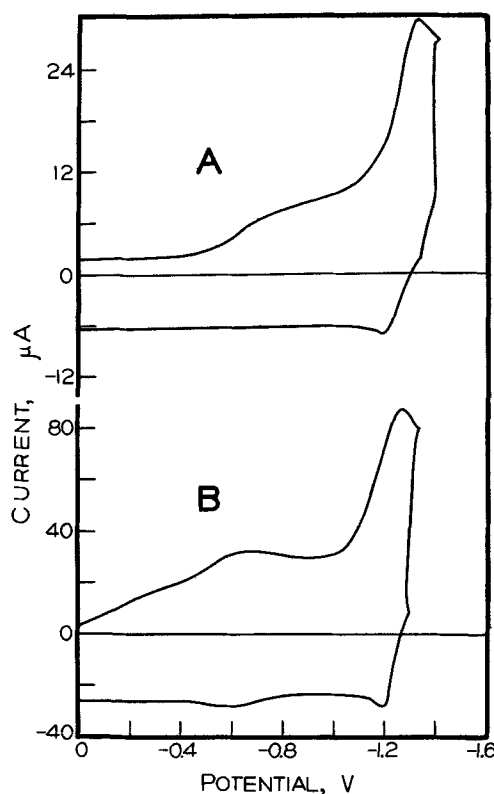


Fig. 5. Cyclic voltammograms in pH 9.0 carbonate buffer of (A) NMN<sup>+</sup> (0.48 mM; scan rate = 20 V/sec) and (B) 1-methyl-3-carbamoylpyridinium ion (1.22 mM; scan rate = 90 V/sec).

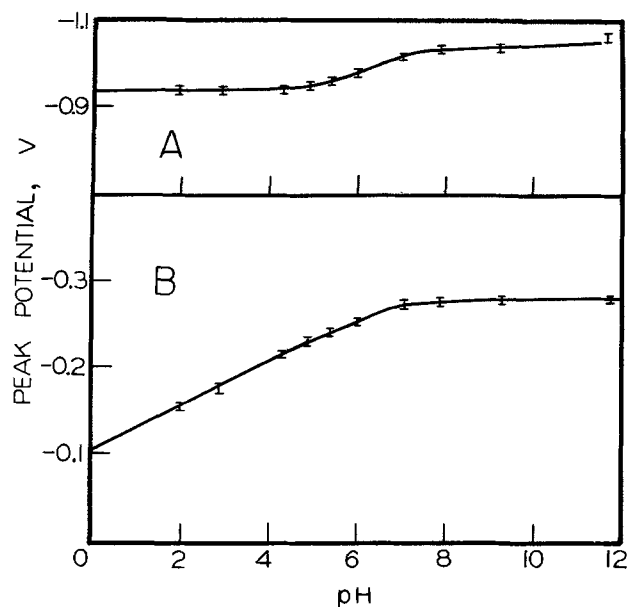


Fig. 6. Variation in potential of (A) cathodic peak Ic and (B) anodic peak Ia (oxidation of ultimate peak Ic reduction product) of NMN<sup>+</sup> with pH on cyclic voltammetry at the hanging mercury drop electrode or hmde. Scan rate = 100 mV/sec.

diminution of the cathodic peak current, indicating that the oxidation regenerates the original electroactive species. If the sweep is reversed before peak Ia is reached, the peak Ic current is about 5-10% less. Other evidence indicates the peak current ratio of 0.5 (Table IV) to be fortuitous, e.g., after controlled potential electrolysis, the anodic peak exceeds 0.5 times the original cathodic peak.

Above pH 7, peak Ia  $E_p$  is pH-independent at  $-0.27\text{V}$  (Fig. 6). Below pH 7, the oxidation becomes more dif-



ficult with decreasing pH. Below pH 6, the peak Ia current decreases rapidly with decreasing pH due to acid instability of the 1e reduction product.

NMN<sup>+</sup> exhibits a detectable anodic peak, reversible or complementary to peak Ic, at and above 6 V/sec (Fig. 5), whereas MCP<sup>+</sup> exhibits such a peak only above 16 V/sec, suggesting that the primary oxidizable product in the Ic process reacts chemically more rapidly in the case of MCP<sup>+</sup>.

**3. Cyclic Voltammetry at PGE.**—The behavior of MCP<sup>+</sup> and NMN<sup>+</sup> at the pge (Fig. 7A and 8) is essentially the same as at the hmde (differences are likely to be due to greater adsorption on the pyrolytic graphite electrode or pge). At pH 10, MCP<sup>+</sup> shows peak Ic ( $E_p = -1.16$ ); on the reverse sweep, the resulting product is oxidized at  $-0.34$ V. Similarly, NMN<sup>+</sup> at pH 9.6 shows a cathodic peak at  $-1.12$ V and an anodic peak at  $-0.04$ V.

Although oxidation of the postulated dihydropyridine product of the wave II process cannot be seen at the dme or hmde due to prior oxidation of mercury, it is readily observed at the pge (cf. section on controlled potential electrolysis). Oxidation of 1,4-NMNH, which is a possible 2e reduction product of NMN<sup>+</sup>, is shown in Fig. 8. A negative potential sweep produces no cathodic behavior other than that due to NMN<sup>+</sup>, present as an impurity; on the return sweep, an anodic peak ap-

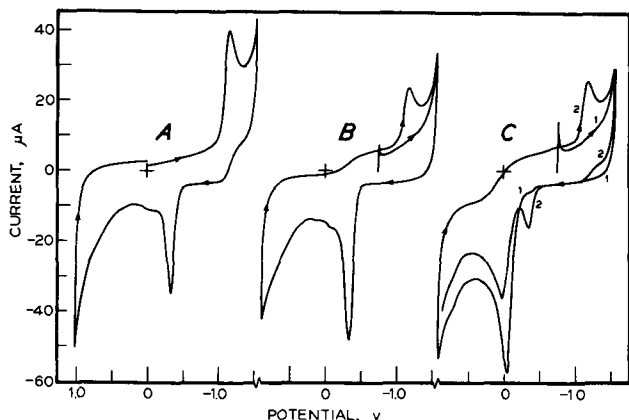


Fig. 7. Electrolysis of 1.20 mM 1-methyl-3-carbamoylpyridinium ion in pH 10 Et<sub>4</sub>NCl/carbonate buffer. Cyclic voltammograms at the pge: A, before electrolysis; B, after electrolysis at  $-1.40$ V; C, after electrolysis at  $-1.80$ V.

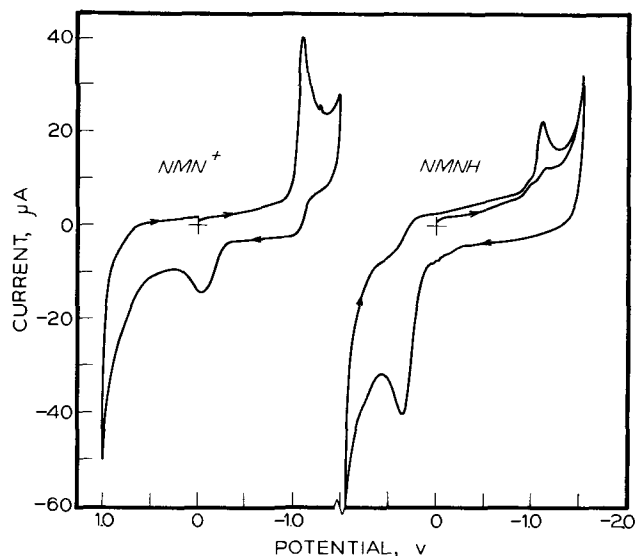


Fig. 8. Cyclic voltammograms of NMN<sup>+</sup> (1.44 mM) and 1,4-NMNH (1.30 mM) at the pge in pH 9.6 Et<sub>4</sub>NCl/carbonate buffer. Scan rate = 100 mV/sec.

pears at 0.35V due to oxidation of 1,4-NMNH. When the sweep is again reversed toward more negative potential, a cathodic peak appears at  $-1.12$ V due to reduction of NMN<sup>+</sup> produced on the anodic sweep.

**A.-C. polarography.**—In the potential region where there is no faradaic process, the quadrature (out-of-phase) a-c current component is proportional to the differential double layer (DL) capacity at the solution-electrode interface and thus provides a convenient index to adsorption at the interface of the electroactive species and its products.

The initial discussion of the behavior of MCP<sup>+</sup> is based on a-c polarography at 50 Hz with a 3.54 mV rms amplitude and a 3 sec droplife, e.g., Fig. 10A.

In the potential region prior to the first reduction step, the DL capacity is only slightly altered by even a relatively high MCP<sup>+</sup> concentration (1.2 mM). An apparent trend towards greater adsorption with increasing negative potential beyond the electrocapillary maximum (ecm) is not unexpected for a positively charged species; however, little can be said concerning the adsorbability of MCP<sup>+</sup> beyond  $-0.9$ V because of its reducibility.

The faradaic peak (in-phase component) at  $-1.07$ V corresponds to the wave I process. DL capacity changes in this potential region are due to surface-activity of the dimeric reduction product. The quadrature response is complicated by the simultaneous faradaic current increase due to the reduction and capacity current decrease due to strong adsorption of dimer. A tensammetric peak at  $-1.43$ V (due to desorption of dimer) is primarily capacitive in nature but has a resistive in-phase component at  $-1.41$ V, probably because the adsorption-desorption process is partially diffusion controlled thus introducing a resistive component to the electrode impedance (absence of a d-c polarographic wave at about  $-1.4$ V is proof that the a-c peak arises from adsorption-desorption phenomena). Increases in MCP<sup>+</sup> concentration and ionic strength decrease the DL capacity in the vicinity of  $-1.0$ V, increase the tensammetric peak height, and shift the latter to more negative potential, as the result of an increase in the surface activity of the dimer.

The faradaic peak at  $-1.62$ V corresponds to the wave II process; no quadrature component is observed. The DL capacity in this potential region is identical to that for background electrolyte alone, showing that the 2e reduction product is not adsorbed in the potential region where it is formed.

Additional evidence concerning the adsorbability of the two reduction products was obtained from the a-c polarographic behavior of solutions of the products prepared by controlled-potential electrolysis (cf. section on latter).

Replacement of KCl/carbonate buffer by Et<sub>4</sub>NCl/carbonate buffer considerably alters the pattern; adsorption effects are largely eliminated, i.e., the DL capacity is essentially identical to that for background electrolyte alone. A shoulder on the in-phase and quadrature components of wave I may indicate a shift of the tensammetric peak seen in KCl/carbonate buffer to more positive potential due to preferential adsorption of Et<sub>4</sub>N<sup>+</sup>.

In pH 7.4 McIlvaine buffer, the behavior of MCP<sup>+</sup> is essentially the same as in KCl/carbonate buffer, except that the catalytic hydrogen wave obscures the in-phase potential region beyond  $-1.4$ V (Fig. 3). The quadrature component in this potential region is relatively unaffected.

The following behavior of MCP<sup>+</sup> and NMN<sup>+</sup> was observed, using a signal of 7.1 mV rms amplitude at 50-800 Hz, and a natural droptime (Table VI).

A well-defined in-phase peak, which corresponds to wave I, is observed in pH 5.2 acetate and pH 9.0 carbonate buffers for MCP<sup>+</sup> ( $E_s = -1.10$ V) and for NMN<sup>+</sup> ( $E_s = -1.03$  and  $-1.15$ V). Peak currents are only a small fraction of those calculated for a reversible 1e process uncomplicated by accompanying chemi-

Table VI. Phase-selective a-c polarographic behavior of 1-methyl-3-carbamoylpyridinium ion (MCP<sup>+</sup>) and nicotinamide mononucleotide (NMN<sup>+</sup>)

pH <sup>a</sup>	Fre- quency, <sup>b</sup> Hz	MCP <sup>+</sup>			NMN <sup>+</sup>		
		Conc., mM	-E <sub>s</sub> , V	i <sub>s</sub> , μA	Conc., mM	-E <sub>s</sub> , V	i <sub>s</sub> , μA
5.2	50	0.96	1.08	0.80	0.48	1.02	0.11
	100		1.09	0.85		1.02	0.25
	200		1.10	0.80			
	500	1.10	0.60	1.03	0.85		
	800				1.03	1.32	
	1000				1.03	1.60	
9.0	50	3.47	1.08	1.70			
	100		1.09	1.85			
	200		1.10	1.80			
	500	1.11	1.30				
	50	0.90	1.10	0.50	0.40	1.15	0.12
	100		1.10	0.55		1.15	0.19

<sup>a</sup> Buffers No. 3 and 4 were used in these experiments.

<sup>b</sup> Blanks indicate that measurements were not made at the conditions involved.

cal reactions (29); loss of the primary electrochemical product by a chemical reaction would account for this. The variations of  $E_s$  and  $i_s$  with frequency are as expected for a chemical reaction involving the primary product.

MCP<sup>+</sup> shows additional peaks at -1.39 and -1.69, which correspond to the tensammetric process and wave II.

In both pH 9.3 KCl/carbonate and pH 9.6 Et<sub>4</sub>NCl/carbonate buffers at 50 Hz (Fig. 4), NMN<sup>+</sup> gives faradaic peaks at -1.12 and -1.64V, which correspond to the two d-c waves. Addition of NMN<sup>+</sup> causes little alteration in the DL capacity, indicating no appreciable adsorption of either NMN<sup>+</sup> or the two reduced species. Increase in ionic strength at pH 9.3 from 0.1 to 2.0M slightly increases the surface activity of NMN<sup>+</sup> but neither product is adsorbed. Similar behavior is seen in acidic solution;  $E_s$  for wave I becomes more positive below pH 6 in accord with the d-c behavior.

In Et<sub>4</sub>NCl/carbonate buffer, the a-c currents for the faradaic NMN<sup>+</sup> processes represent less than 3% of that expected for a simple reversible 1e process and are not appreciably altered on increasing the alternating voltage from 50 to 800 Hz. Thus, both a-c polarographic steps are over-all irreversible.

**Controlled potential electrolysis and coulometry.**—1. *MCP<sup>+</sup> wave I process.*—MCP<sup>+</sup> (1.20 mM) was electrolyzed in pH 10 buffer 5 at -1.25V, at which potential adsorption of the reduction product would be expected, and in pH 10 buffer 6 at -1.40V, at which potential the DL capacity is identical to that for background alone; except where subsequently indicated, the final electrolyzed solutions had nearly identical faradaic and spectral properties, thus showing little effect due to adsorption on the nature of the electrolysis products. A faradaic  $n$  of  $0.96 \pm 0.01$  was obtained. A persistent bright greenish-yellow color developed during electrolysis. Shifting of the applied potential to -1.80V, when electrolysis was complete, gave no additional current flow, confirming that the final wave I product is neither an intermediate in the formation of wave II nor further reduced to a different product.

Solutions before electrolysis had the single characteristic MCP<sup>+</sup> absorption band at 264 nm ( $\epsilon = 4600$ ) [literature (22):  $\lambda_{\max} = 264$  nm;  $\epsilon = 4600$ ] (Fig. 9A). Spectra, taken after electrolysis, had maxima at 277 nm ( $\epsilon = 12,500$ ) and 358 nm ( $\epsilon = 8300$ ) (Fig. 9B) ( $\epsilon$  values, calculated assuming a dimeric wave I product, are averages for the two backgrounds).

Polarography of the electrolyzed solution showed absence of the two MCP<sup>+</sup> cathodic waves and a diffusion controlled ( $h$  study) anodic wave ( $E_{1/2} = -0.45$ V in buffer 5) (Fig. 2B), which was 71% of the wave Ic height. On cyclic voltammetry at the pge (Fig. 7B), a sweep initiated at -0.75V showed only background behavior; on the return sweep, a large anodic peak ap-

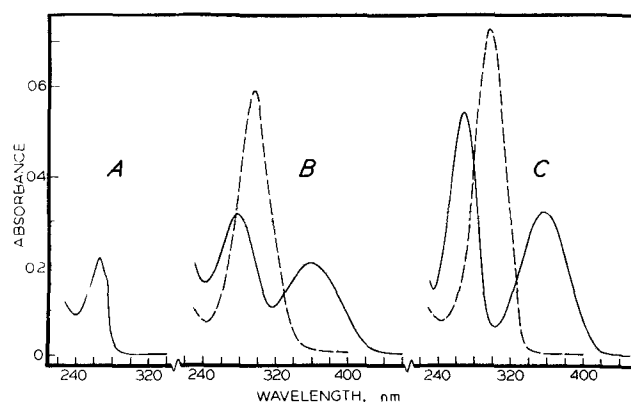


Fig. 9. Electrolysis of 1.20 mM 1-methyl-3-carbamoylpyridinium ion in pH 10 Et<sub>4</sub>NCl/carbonate buffer. Absorption spectra obtained by a 1/25 dilution of electrolysis solutions with buffers indicated. Solid line (pH 10 carbonate buffer): A, before electrolysis; B, after electrolysis at -1.40V; C, after electrolysis at -1.80V. Dashed line (McIlvaine buffer): B, acid catalyzed decomposition product of dimer (final pH = 7.4); C, acid catalyzed decomposition product of dihydropyridine species (final pH = 4.5).

peared at -0.34V. On further reversal toward more negative potential, a cathodic peak due to reduction of MCP<sup>+</sup> appeared at -1.17V. Thus, the reduction product formed under lengthy macroscale conditions is the same as that formed under the more temporal conditions of cyclic voltammetry; oxidation of this product produces the starting material.

A-C polarography of the electrolyzed solution showed the absence of faradaic peaks corresponding to MCP<sup>+</sup> reduction (Fig. 10B) and the presence of both in-phase and quadrature components of the tensammetric process involving dimer desorption at -1.4V. This is added support for the previous interpretation of the a-c polarographic pattern of MCP<sup>+</sup> (Fig. 10A). Actually, the dimer is strongly adsorbed over a rather wide potential region on both sides of the ecm. The faradaic peak at -0.30V (in-phase component) corresponds to the d-c anodic wave and exhibits a maximum of the first kind as does the d-c wave.

Electrolytic oxidation of the MCP dimer solution at -0.40V consumed less than one electron per original MCP<sup>+</sup> molecule. The resulting solution showed a well-defined polarographic wave, whose  $E_{1/2}$  of -1.05V agrees with that of MCP<sup>+</sup> and whose height agreed with the faradaic  $n$  just mentioned.

These results may be rationalized on the basis of the product of the wave I process being a dimer, which slowly decomposes. The magnitude of the anodic wave due to the dimer may be less than that of the predecessor cathodic wave due to (i) chemical decomposition of the dimer (cf. discussion of its acid-catalyzed hydrolysis) and (ii) an expected difference in diffusion coefficients between the original species and the derived dimer (if decomposition is assumed to be negligible, a ratio of 0.71 for the anodic-cathodic wave heights corresponds to a diffusion coefficient ratio of 0.50).

2. *MCP<sup>+</sup> wave II process.*—Electrolyses in both backgrounds at -1.80V gave a faradaic  $n$  of  $1.95 \pm 0.02$ , and colorless solutions of nearly identical spectral and faradaic properties, e.g., maxima at 270 nm ( $\epsilon = 11,400$ ) and 358 nm ( $\epsilon = 6600$ ) (Fig. 9C), and the absence of both original cathodic waves and no new waves corresponding to oxidation of the 2e product (Fig. 2C); a small amount of the 1e product was formed ( $2.5 \pm 0.5\%$  as estimated from the anodic wave height). Oxidation of the 2e product is readily observed at the pge (Fig. 7C). Sweep 1 to negative potential, initiated at -0.75V, shows only background cathodic behavior; on the return sweep, a large anodic peak appears at -0.04V due to oxidation of the 2e product; subsequent reversal toward more negative potential (sweep 2)

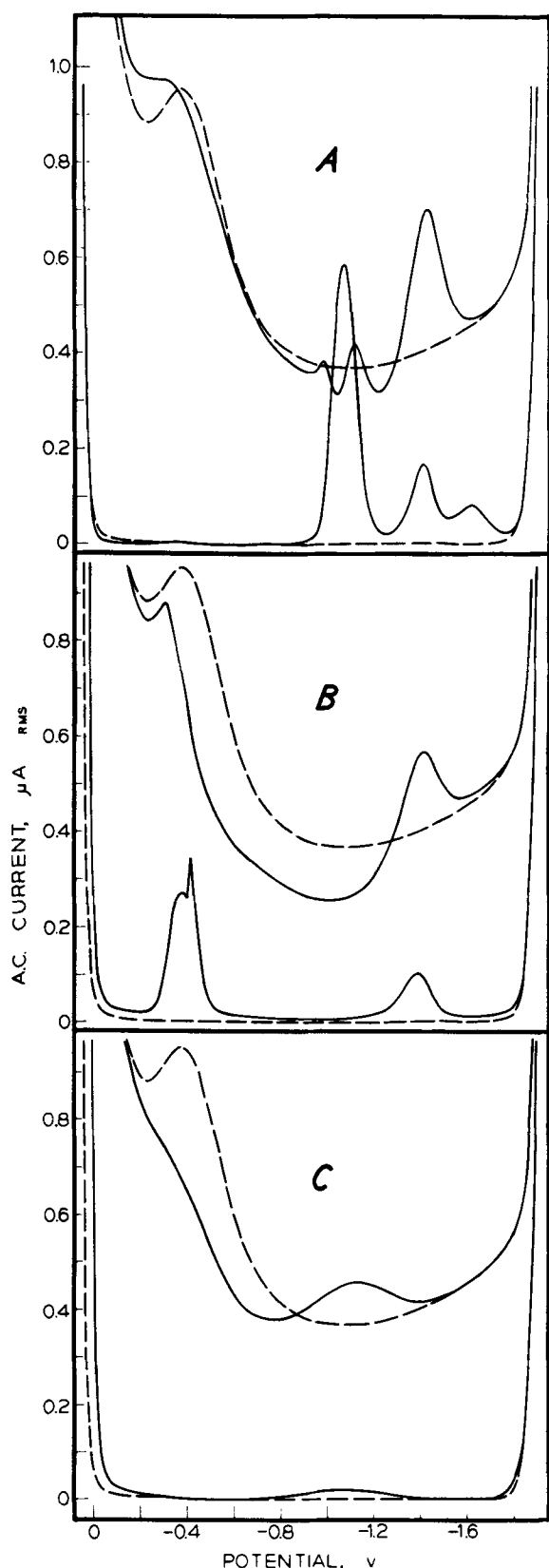


Fig. 10. Electrolysis of 1.20 mM 1-methyl-3-carbamoylpyridinium ion in pH 10 KCl/carbonate buffer. A-C polarograms: A, before electrolysis; B, after electrolysis at  $-1.25\text{V}$ ; C, after electrolysis at  $1.80\text{V}$ . The upper pair of curves represent the quadrature component; the lower pair represent the in-phase component; dashed lines correspond to background current.

produces a cathodic peak at  $-1.18\text{V}$  due to reduction of  $\text{MCP}^+$  formed during the oxidation step. Finally when the sweep is once again reversed toward more

positive potential, an anodic peak appears at  $-0.34\text{V}$  (dimer oxidation) in addition to the one at  $-0.04\text{V}$ .

A.-C polarography of the electrolyzed solution shows the expected absence of faradaic behavior (Fig. 10C). Absence of the tensammetric process at  $-1.4\text{V}$  further supports assignment of this peak to dimer desorption. The  $2e$  product, which is less strongly adsorbed than the  $1e$  product, most strongly affects the DL capacity in the potential region on either side of the ecm; it is involved in a rather broad desorption hump centering at  $-1.12\text{V}$ . Beginning at about  $-1.5\text{V}$ , the DL capacity is identical to that for background alone, confirming that the  $2e$  reduction product is not adsorbed in the potential region of its formation.

3. Stability of  $\text{MCP}^+$  reduction products.—The temporal stability was determined by keeping an aliquot of each pH 10 electrolyzed solution at  $25^\circ\text{C}$  under nitrogen for 2 hr and periodically running spectra. Based on the 358 nm adsorption, the dimer concentration decreased at a rate of 6%/hr and that of the  $2e$  product at 2%/hr. Since the time required for electrolysis was relatively short (40 min for the  $1e$  product and 60 min for the  $2e$  product), little product was lost and molar absorptivities were calculated assuming no loss.

Aliquots of each solution were also diluted (1/25) with carbonate or McIlvaine buffer (room temperature under air) to obtain solutions of pH 9.3, 7.4, and 4.5; the dimer half-life in these was 112, 5.1, and 0.1 min, respectively, emphasizing the rapid increase in decomposition rate with decreasing pH. In all cases, as the two dimer absorption bands decreased in intensity, a new band developed at 296 nm (Fig. 9B). At pH 7.4, an isosbestic point formed at 331 nm, suggesting that the dimer decomposed directly to its acid catalyzed product without going through an intermediate. At pH 4.5, the 296 nm band formed rapidly but then slowly decreased in intensity; this phenomenon was not investigated further. At pH 9.3, the final decomposed solution also had a small shoulder at 265 nm, which may be due to oxidation of a small portion of the dimer to  $\text{MCP}^+$  in the presence of air (under the experimental conditions, this reaction is slow compared to the acid catalyzed decomposition; cf. subsequent discussion).

The effect of pH on stability of the  $2e$  product is similar, except that, at any given pH, the decomposition is much slower. In pH 9.3 carbonate buffer, the half-life of the  $2e$  product was 420 min; as the absorption band due to the acid catalyzed product developed, an isosbestic point formed at 316 nm. No evidence of direct oxidation by air was found. In pH 4.5 McIlvaine buffer, the final acid catalyzed product had an absorption band at 298 nm (Fig. 9C).

In another experiment, aliquots of solutions of both reduction products were diluted (1/2) with carbonate or McIlvaine buffer to pH 9.9 and 7.7 solutions, which were examined after 24 hr (room temperature under air). Polarography of the dimer solutions revealed disappearance of the anodic wave and, at pH 9.9, the presence of a broad wave characteristic of  $\text{H}_2\text{O}_2$ , superimposed on which was the  $\text{MCP}^+$  pattern; based on the wave II height, 49% of the dimer was oxidized. This solution had peaks at 264 nm due to dimer oxidation and at 292 nm due to acid decomposition of dimer; the intensity of the latter accounted for 32% of the dimer. Thus, about 81% of the dimer could be accounted for. At pH 7.7, the spectrum indicated virtually complete decomposition of dimer; a polarogram revealed only solution discharge at ca. 0.25V more positive than for background electrolyte alone. Evidently, the decomposition product catalyzes hydrogen ion reduction under the conditions used.

The pH 9.9  $2e$  product solution also gave a  $\text{H}_2\text{O}_2$  wave, which was much smaller than that for the  $1e$  product, and the  $\text{MCP}^+$  pattern, which accounted for 12% of the  $2e$  product. Analysis at the pge indicated that 60% of the  $2e$  product still remained; absorption at 358 nm showed 57%  $2e$  product. The increased absorption in the 280-300 nm region indicated that the  $2e$

product not accounted for (approximately 30%) probably had decomposed to the acid catalyzed product. At pH 7.7, virtually all of the 2e reduction product decomposed (based on the spectrum and the absence at the pge of the 2e product anodic peak); a polarogram revealed only solution discharge at 0.12V more positive than for background electrolyte alone (the decomposition product of the 2e reduction product also catalyzes hydrogen ion reduction).

**4. NMN<sup>+</sup> wave I process.**—Electrolysis on the limiting portion of NMN<sup>+</sup> wave I at  $-1.2$  or  $-1.3$ V (generally in pH 9.6 buffer 6, where the NMN<sup>+</sup> waves are well defined and diffusion controlled) gave  $n$  values of  $1.00 \pm 0.01$ . A transient greenish-yellow color reached maximum intensity when electrolysis was 80-90% complete. When electrolysis was continued for an additional 0.5 hr after the current fell to background level, the current remained unchanged but the color diminished in intensity, yielding a clear, faintly yellow solution. A plot of log current vs. time was linear, showing that the electrolysis rate was first order and that no mechanistic complications were involved such as a slow chemical step prior to electron transfer or formation of an intermediate which could undergo a slow chemical transformation followed by further reduction.

The results (cf. also subsequent discussion) suggest that most of the NMN<sup>+</sup> is directly converted to a relatively stable dimer which does not absorb appreciably in the visible region. A small portion may be involved in formation of an unstable by-product, which produces the transient color and slowly decomposes to a compound which is not reduced at the applied potential.

The two characteristic NMN<sup>+</sup> cathodic waves were absent from polarograms of the electrolyzed solutions; two new waves appeared, one anodic ( $E_{1/2} = -0.25$ V) and a smaller cathodic wave ( $E_{1/2} = -1.6$  to  $-1.7$ V, depending on pH); the latter corresponds to reduction of free nicotinamide. The anodic wave is diffusion controlled and independent of concentration; it corresponds to oxidation of dimer to NMN<sup>+</sup> and correlates with the cyclic voltammetric anodic peak. Electrolysis on its limiting portion ( $-0.1$ V) regenerated NMN<sup>+</sup>.

Prior to electrolysis, the NMN<sup>+</sup> solution exhibits the 265 nm absorption band ( $\epsilon = 4900$ ) characteristic of the pyridinium ion (Fig. 11A). On dilution with 1M KCN, the 265 nm band is replaced by one at 327 nm ( $\epsilon = 6300$ ) (Fig. 11A) due to cyanide addition at the 4-position of the pyridine ring [literature (20, 30):  $\lambda_{\max} = 327$  nm;  $\epsilon = 5900$ ]. The 265 nm band also disappears during electrolysis, and bands with maxima at 263 nm

( $\epsilon = 7800$ ) and 339 nm ( $\epsilon = 7400$ ) appear and grow (Fig. 11B). ( $\epsilon$  values, calculated assuming a dimeric product, represent the average for two electrolyses at pH 9.6.) Reduction of the pyridine ring during electrolysis is also indicated by the fact that dilution of the electrolyzed solution with 1M KCN gave the same spectrum as dilution with carbonate buffer.

**5. NMN<sup>+</sup> wave II process.**—Electrolyses on the limiting portion of wave II at  $-1.8$ V gave an average  $n$  of 1.93. No transient color appeared; the completely electrolyzed solution was only a faint yellow. Aliquots of the latter solution, diluted with pH 9.6 carbonate buffer, had maxima at 259 nm ( $\epsilon = 4400$ ) and 339 nm ( $\epsilon = 6500$ ) (Fig. 11C). Dilution with 1M KCN gave an identical spectrum, indicating involvement of the pyridine ring in the reduction.

Polarograms of the electrolyzed solutions showed a small dimer anodic wave; based on its height, approximately 17% NMN<sup>+</sup> was converted to the 1e product. The pge voltammetric pattern was similar to that for 1,4-NMNH (Fig. 8).

**6. Stability of NMN<sup>+</sup> reduction products.**—At pH 9-10, solutions of both NMN<sup>+</sup> reduction products exhibit two ultraviolet absorption bands due to the reduced pyridine structure. Both products decompose in pH 7 phosphate solution (acid catalyzed hydrolysis). The decomposition rate increases with decreasing pH; at any given pH, the dimer is less stable than the 2e product. During hydrolysis, the two absorption bands decrease in intensity and a more intense band develops at 278 nm (Fig. 11B and 11C). In pH 2 McIlvaine buffer, the 278 nm band forms rapidly but then slowly decreases in intensity with time.

**7. Mercury adduct formation.**—Mercury adducts were formed on adding HgCl<sub>2</sub> solution (0.04M phosphate buffer; pH 6.7) to solutions of each reduction product of MCP<sup>+</sup> and NMN<sup>+</sup>; the final solutions had a pH of 9.3. On addition of excess HgCl<sub>2</sub>, the two characteristic dimer absorption bands disappeared and a new band appeared at 293 nm ( $\epsilon = 28,200$ ) for MCP<sup>+</sup> and at 281 nm ( $\epsilon = 26,200$ ) for NMN<sup>+</sup>; spectral properties of the adducts were much the same as those of the acid-catalyzed hydrolysis products. The dihydropyridine products behaved similarly; unfortunately, insufficient HgCl<sub>2</sub> was added to determine  $\lambda_{\max}$  and  $\epsilon$ .

Addition of excess HgCl<sub>2</sub> or concentrated HCl to relatively concentrated MCP dimer solutions instantaneously discharged the bright greenish yellow color due to loss of the 358 nm band; the tail of this band extends well out into the visible region and is undoubtedly responsible for the color. Although the tail of the 358 nm band of the 2e product extends almost as far out into the visible region as does that of the dimer, its solutions are colorless.

### Redox Pattern

The reaction scheme outlined in Fig. 1 seems best to fit the electrochemical, chemical, and spectral data for the redox behavior of 1-methyl-3-carbamoylpyridinium ion (MCP<sup>+</sup>), nicotinamide mononucleotide (NMN<sup>+</sup>), and their reduction products.

The electrochemical behavior of the MCP<sup>+</sup> and NMN<sup>+</sup> ions is in some ways similar to that of nicotinamide itself (25). However, as might be expected for a positively charged pyridinium nucleus, the first reduction step is independent of pH and occurs at slightly more positive potential; thus, two well defined 1e waves appear in slightly alkaline solution rather than the merging waves seen for nicotinamide (25). The initial reversible uptake of an electron to form a neutral free radical (II) (source of polarographic wave I) is followed by irreversible dimerization to an apparent 6,6' dimer (IV). At the wave II potential, the ion (I) is reduced to the dihydropyridine (III) (apparently the 1,6 species, although some 1,4 isomer may be produced in the case of NMN<sup>+</sup>); the dimer is not reduced at this potential. The dimer (IV) can be oxidized to MCP<sup>+</sup> or

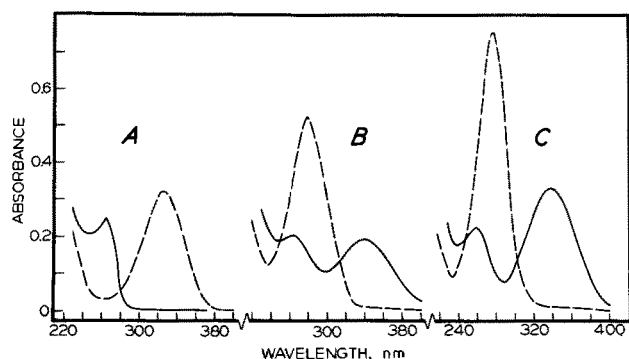


Fig. 11. Electrolysis of 1.37 mM NMN<sup>+</sup> in pH 9.6 Et<sub>3</sub>NCl/ carbonate buffer. Adsorption spectra obtained by a 1/25 dilution of electrolysis solutions with buffer indicated. Solid line (pH 9.6 carbonate buffer): A, before electrolysis; B, after electrolysis at  $-1.3$ V; C, after electrolysis at  $-1.8$ V. Dashed line: A, cyanide addition product of NMN<sup>+</sup> (1.0M KCN); B, acid catalyzed decomposition product of dimer (0.2M phosphate buffer; pH 6.7); C, acid catalyzed decomposition product of dihydropyridine species (0.1M phosphate buffer; pH 6.8).

NMN<sup>+</sup> at a potential considerably more positive than that of wave I; the dihydropyridine species (III) is oxidizable at still more positive potential.

Other details of the individual mechanistic steps and of the supporting evidence and arguments are given in the following sections.

**Characterization of reduction products.**—Although the three isomeric 1-substituted 3-carbamoyldihydropyridines can be distinguished by their nmr spectra (31-35), much more emphasis has been placed on their characteristic ultraviolet absorption spectra in the 240-400 nm region (36-41). Most 1-substituted 3-carbamoylpyridinium ions show a single absorption band at about 265 nm, which, on reduction, is replaced by a single band at about 410 nm for 1,2-dihydropyridines and at about 350 nm for 1,4-dihydropyridines, and by two bands at about 265 and 360 nm for 1,6-dihydropyridines; these patterns have also been theoretically predicted (41).

Postulation of the 6,6' dimer and the 1,6-dihydropyridine species for the two electrochemical reduction products of each compound reflects the two absorption bands observed in the 240-400 nm region, *e.g.*, Fig. 11. Although the 1,6 isomers are clearly the major products, small amounts of other isomers might be present, *e.g.*, in the case of the 2e product, the 1,4 isomer would be expected to exhibit a single absorption band at about the same wavelength as the long wavelength band of the 1,6 isomer, *e.g.*, the 1,4 isomer of reduced MCP has a single band at 360 nm ( $\epsilon = 7000$ ) (42). In the case of NMN<sup>+</sup>, particularly, the presence of some 1,4-isomer cannot be entirely excluded (compare Fig. 11C and 12), especially since the 2e electrochemical reduction product of NAD<sup>+</sup> is partially enzymatically active, indicating the presence of 1,4-NADH (43). The 1,2 isomer can be excluded in all cases, because the final electrolysis solutions were essentially colorless.

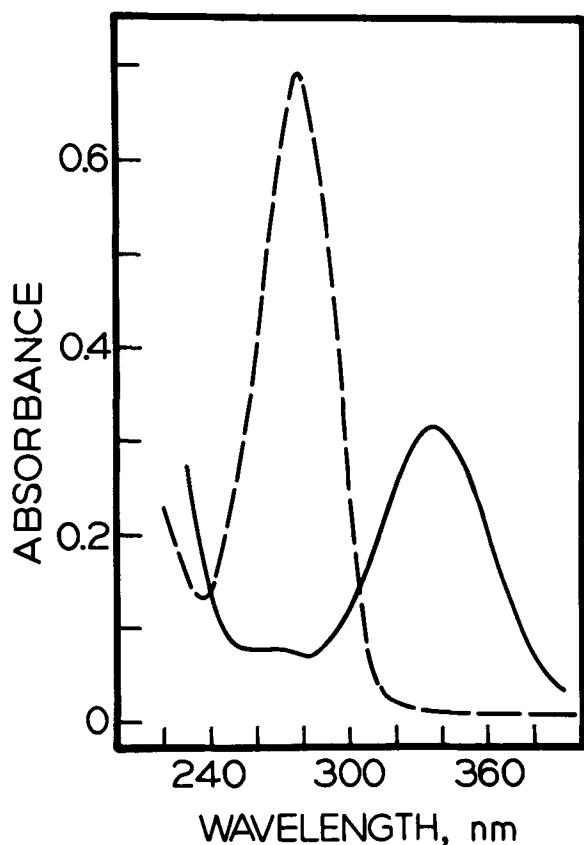


Fig. 12. Absorption spectrum of 1,4-NMNH ( $5.2 \times 10^{-5}M$ ). Solid line: pH 9.4 carbonate buffer. Dashed line: pH 6.8 phosphate buffer (0.2M) (acid catalyzed decomposition product of 1,4-NMNH).

It should be mentioned that the validity of using spectral arguments for the dihydropyridine species for assigning the position of dimerization in partially reduced pyridines has not been thoroughly tested, *e.g.*, using the criteria outlined, structures were readily assigned to dimers of nicotinamide model compounds prepared by zinc reduction (37) but others have suggested caution (44).

The results of reducing MCP<sup>+</sup> by a variety of other than electrochemical methods are generally in good accord with those recorded in the present study, *e.g.*, irradiation with x-rays results in free radical formation and a dimeric product (19, 45), whose physical and chemical properties, including even molar absorptivities, are in remarkably close agreement with those of the electrolytically prepared dimer. The same is true of the dimeric products prepared by Zn reduction (37, 46) and of the 2e reduction product prepared with borohydride (47).<sup>5</sup> Dithionite reduction, on the other hand, leads exclusively to a 1,4-dihydropyridine (31, 32, 42).

**1. Hydrolysis of reduction products.**—The two reduction products of each compound undergo acid-catalyzed decomposition even in neutral or alkaline solution containing such proton donors as H<sub>2</sub>PO<sub>4</sub><sup>-</sup>. The decomposition rate increases with decreasing pH; the dimer is less stable than the dihydropyridine species at any given pH. The decomposition, which involves hydrolysis of the 4,5 C=C bond and is an example of enamine nucleophilicity (48, 49), accounts for the loss of absorption in the 260 and 340 nm regions and the concomitant increase in absorption in the 280 nm region (Fig. 9 and 11).

Since the two MCP<sup>+</sup> reduction products are directly oxidized in alkaline solution by molecular oxygen to MCP<sup>+</sup> and H<sub>2</sub>O<sub>2</sub>, two decomposition paths are possible on exposure to air. However, both reactions occur so slowly for the 1,6-dihydropyridine species that, after 24 hr, only about 40% of the latter is lost, less than half of which is due to oxidation by O<sub>2</sub>; both reactions occur more rapidly for the dimer, all of which disappears after 24 hr with about half being oxidized to MCP<sup>+</sup>. The more ready oxidation of the dimer by oxygen is consistent with the electrochemical oxidation potentials.

The proposed structures of the reduction products are also supported by their formation of mercury adducts, probably in a manner analogous to the addition of HgCl<sub>2</sub> to NADH (50, 51).

**2. Rationalization of previous results.**—Previous electrolyses (1) of MCP<sup>+</sup> did not take into account the acid instability of the reduction products. The product, isolated after electrolyses for several hours on the wave I potential in pH 7-8.1 phosphate buffers, had a molecular weight close to that for a dimeric product and a single absorption peak at 298 nm; it was postulated to be a 6,6' dimer. The final wave I electrolysis solution gave a cathodic polarographic wave at about -1.65V (depending on pH), which was attributed to reduction of the 4,5 double bonds of the dimer; no mention was made of an anodic wave due to dimer oxidation. Electrolysis on the -1.65V wave gave a *n* of 2.11 with no change in ultraviolet absorption spectrum; this was explained on the basis that, since the 4,5 double bond was only cross conjugated with the main 298 nm chromo-

phore,  $\text{—N—C=C—C=O}$ , removal of the 4,5 double bond by reduction would leave the basic chromophore intact.

In view of the present results, the compound previously isolated was actually the acid-catalyzed decomposition product of the dimer, which, in the pH range employed, has a rather short half-life relative to the electrolysis periods used. This would account for presence of the 298 nm band and absence of the anodic

<sup>5</sup> Under certain conditions, borohydride reduction can lead to all three products (36-39, 47).

wave. The cause of the cathodic wave at  $-1.65\text{V}$  is less clear, since its characteristics were not given. In pH 7.7 McIlvaine buffer, the decomposition product of the dimer causes a catalytic hydrogen wave since background discharge is about  $0.25\text{V}$  more positive than for background electrolyte alone; at  $5\ \mu\text{A}$ , the early discharge had a potential of  $-1.67\text{V}$ . It may be that, under the conditions previously used (1), the catalytic wave exhibited a limiting portion, which might easily be taken to represent further reduction of the dimer. Electrolysis on this wave would not alter the catalyst (the dimer decomposition product) and no change in the ultraviolet spectrum would be expected. During electrolysis, the limiting current of the wave might be expected to drop due to an increase in solution pH (the capacity of the  $0.1\text{M}$  phosphate buffer used would be low around pH 8).

The present investigation has shown that the actual dimer cannot be further reduced after being prepared either at the hmde or under macroscale conditions.<sup>6</sup>

In the previous study (1), after electrolysis at potentials on MCP<sup>+</sup> wave II in pH 7.8-9.2 phosphate buffers, a product was isolated with a single band at  $360\text{ nm}$ , which was identified as the 1,4-dihydropyridine compound. Under the pH conditions and time periods employed, a significant portion of the product should have been the acid-catalyzed decomposition product of the dihydropyridine species. The 1,4- and 1,6-dihydropyridine species exhibit extreme acid lability and decompose at pH 8 and below (42).

*Characteristics of electron transfer and associated chemical reactions.*—In slightly alkaline solution,  $E_{1/2}$  values for both MCP<sup>+</sup> waves are in good agreement with those in one report (7),  $80\text{ mV}$  more positive than those in a second (1), and  $90\text{ mV}$  more negative than those of a third report (3); the last study used the iodide salt, but in the others the experimental conditions were about the same. Since  $\Delta E_{1/2}$  between the two waves is the same in all four studies, it is likely that the various reference electrodes differed in potential although all are reported to be vs. SCE; liquid junction potential effects should be small. [The potential scale used in the present investigation was frequently checked by examining a  $0.5\text{ mM}$  CdCl<sub>2</sub> solution in  $1.0\text{M}$  HCl; at all times, the latter exhibited an  $E_{1/2}$  of  $-0.642 \pm 0.002\text{V}$ , which is identical to the accepted value of  $-0.642\text{V}$  (26).]

*1. Evidence for wave I electron transfer reversibility and subsequent dimerization.*—The generally reversible characteristics of the first MCP<sup>+</sup> electron-transfer process as determined from analysis of the cyclic voltammetric and d-c polarographic waves—and to a lesser extent, those of NMN<sup>+</sup>—observed in the present study agree with previous suggestions, for which substantial proof was not offered. The essentially irreversible faradaic a-c response for wave I results from the dimerization subsequent to electron transfer; under the a-c conditions used, the reversibility of the over-all electrochemical process is tested. The basic requirement for chemical irreversibility on a-c polarography is that the period of the applied alternating voltage sufficiently exceeds the half-life associated with the chemical step that reoxidation of the initial reduction product cannot contribute significantly to the alternating current (39). The greatest applied frequency ( $800\text{ Hz}$ ) corresponds to a period of  $1.8\text{ msec}$ ; based on the dimerization rate constants found for the MCP and NMN free radicals, a free radical half-life of at most a few tenths of a msec would be predicted.

Dimerization reactions involving the primary product of electrochemical reduction can be differentiated from first order follow-up chemical reactions by the cyclic voltammetric potential difference,  $E_p - E_{p/2}$ ,

<sup>6</sup> The possible very small wave or peak at  $-1.6\text{V}$  on a polarogram of the wave I electrolysis product (Fig. 2B) is insignificant due to the fact that, when the same solution was electrolyzed at  $-1.7\text{V}$  under macroscale conditions, the current fell to the level of that of the background electrolyte alone after the first few minutes.

which should theoretically be  $39/n\text{ mV}$  for the second order reaction and  $48/n\text{ mV}$  for the first order, compared to  $57/n\text{ mV}$  in absence of a coupled chemical reaction (29). Measurement of  $E_p - E_{p/2}$  for peak Ic of MCP<sup>+</sup> and NMN<sup>+</sup> over a large number of curves ( $v < 0.2\text{ V/sec}$ ) gave an average value of  $42\text{ mV}$  for each, suggesting dimerization.

The significance of the positive shifts in wave I  $E_{1/2}$  with increasing MCP<sup>+</sup> and NMN<sup>+</sup> concentration and drop-time is somewhat obscured in the case of MCP<sup>+</sup> by the presence of adsorption phenomena involving the reduction product. In the absence of adsorption, such shifts (for a reversible electrode process) are indicative of irreversible dimerization subsequent to charge transfer (53). The shifts in  $E_{1/2}$  for MCP<sup>+</sup> wave II with concentration and ionic strength are explicable in terms of the rates of two competing reactions: dimerization of the initially produced radicals and their reduction to produce wave II, e.g., an increase in depolarizer concentration will increase the dimerization rate more rapidly than the rate of the electron-transfer process; thus, in order to obtain wave II, it is necessary to increase the rate of electrochemical reduction of the radicals, i.e., to make the electrode potential more negative (54).

The effects of ionic strength and surfactants on the polarographic pattern of NMN<sup>+</sup> appear to be related to changes in the DL structure and the two charge centers of the electroactive species. The ionic strength effect suggests existence at low ionic strength of an intramolecular complex of the ion-pair type between the negatively charged phosphate group and the positively charged pyridinium ion; such complexation could increase the electron density in the nicotinamide nucleus. With increasing ionic strength, the complex dissociates, causing wave I to become more positive and wave II to appear and grow; in the absence of tetraalkylammonium salts, wave II exhibits partial kinetic control even at  $0.5\text{M}$  ionic strength. Wave II of MCP<sup>+</sup>, which has no phosphate moiety, is well defined, even at low ionic strength. The occurrence of MCP<sup>+</sup> wave I at a more negative potential than wave I of the dissociated form of NMN<sup>+</sup>, may be due to the dimerization reaction as well as to structural features (cf. section on formal potentials).

*2. Free radical dimerization rates.*—Three approaches for calculating the dimerization rate constant,  $k_d$ , from cyclic voltammetric data are pertinent to the present situation. Nicholson (55, 56) has described two methods. One is based on the shift of peak potential,  $E_p$ , with scan rate,  $v$ ; its accuracy depends on accurate measurement of  $E_p$ , compensated for  $iR$  drop; the method can be employed to estimate  $k_d$  when no anodic peak corresponding to oxidation of the reduced species is seen provided that  $E^\circ$  is known. The other approach involves graphical correlation of the ratio of the anodic and cathodic peak heights ( $i_{pa}/i_{pc}$ ) for the oxidation and the formation of the free radical with the kinetic parameter product,  $k_d \tau C$ , where  $\tau$  is the time interval between  $E^\circ$  (generally taken to be close to  $E_{1/2}$ ) and the potential at which direction of the potential sweep is reversed, and  $C$  is the bulk solution concentration of the original electroactive species.

Saveant (57) obtained a closed form solution relating  $k_d$  to the ratio of the observed peak current,  $i_{pa}$ , to the normal diffusion peak current,  $i_{pd}$ , at the same  $v$

$$i_{pa}/i_{pd} = (2\pi k_d \tau C)^{-1/3} \quad [1]$$

A plot of the current ratio vs.  $\tau^{-1/3}$  should yield a straight line, from which  $k_d$  can be calculated; practically,  $i_{pd}$  can be replaced by  $i_{pc}$ .

The rate constant for dimerization of the MCP free radical produced in the first electron transfer process has been estimated (18) on the basis of  $E_p$  shift with  $v$  to be  $2.24 \times 10^{-2}\text{ l mol}^{-1}\text{ sec}^{-1}$ . This value is in marked contrast to the rate constant of  $6.9 \times 10^7\text{ l mol}^{-1}\text{ sec}^{-1}$  determined by pulse radiolysis (19).



In the present investigation, analysis of the  $i_{pa}/i_{pc}$  ratios for 15 measurements for  $\tau$  ranging from 2 to 8 msec at 30° gives a  $k_d$  for the MCP free radical of  $(6.1 \pm 1.1) \times 10^7 \text{ l mol}^{-1} \text{ sec}^{-1}$  (mean and standard deviation). Use of Eq. [1] gives a  $k_d$  8% higher:  $(6.6 \pm 2.2) \times 10^7 \text{ l mol}^{-1} \text{ sec}^{-1}$ . The accuracy of the  $k_d$  measurement is estimated to be  $\pm 15\text{--}20\%$ , based on measurement errors of 3–4% in  $\tau$  and 5% in the current ratio.

The good agreement of MCP dimerization rate obtained in the present study with that obtained on pulse radiolysis is of special significance since it would tend to indicate that the dimerization rate of the free radical, which is a neutral species, is not appreciably affected by the occurrence of the corresponding chemical reaction at the solution-electrode interface in the electrical double layer region. It is possible that the deviation of the earlier reported (18) electrochemically determined dimerization rate, which is stated to be probably inaccurate due to complications caused by adsorption, resulted from an error in calculation.<sup>7</sup>

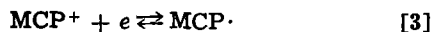
The dimerization rate constant at 30° for the free radical produced from  $\text{NMN}^+$  is  $(1.5 \pm 0.1) \times 10^6 \text{ l mol}^{-1} \text{ sec}^{-1}$  (3 measurements; calculated by peak ratio method); Eq. [1] gives a comparable figure.

Activation energies, calculated from Arrhenius plots for the range of 7°–50°, are 4.1 kcal mol<sup>-1</sup> for  $\text{MCP}^+$  and 3.6 kcal mol<sup>-1</sup> for  $\text{NMN}^+$ ; the corresponding calculated frequency factors at 25° are  $6 \times 10^{10}$  and  $8 \times 10^8 \text{ l mol}^{-1} \text{ sec}^{-1}$  compared to that of about  $10^{11} \text{ l mol}^{-1} \text{ sec}^{-1}$  expected for a reaction between neutral free radicals (58), where there are no extensive solvation differences between reactants and products. Consequently, the low experimental frequency factor for  $\text{NMN}^+$  may indicate a large solvation difference between its free radical and the corresponding dimer, and/or the presence of small residual charges on the free radicals with the accompanying electrostatic repulsion. It is possible that the negative nature of the  $\text{NMN}$  free radical, as a result of the secondary phosphate dissociation ( $\text{pK}_a$  6–7), is the cause (cf. previous discussion of the shift with pH of  $E_{1/2}$  for  $\text{NMN}^+$  wave I).

**3. Formal potentials.**—When a rapid chemical reaction follows a charge-transfer reaction, the resulting polarographic  $E_{1/2}$  is not a simple criterion for the ease of reduction of the molecule. Different compounds can be validly compared only when the potentials are corrected for the effect of the chemical reactions. This can be done, using cyclic voltammetric peak potentials and the relationship (56)

$$E_p = E_c^\circ - \frac{0.058}{3nF} \log \frac{4.78 \times 3\pi D_0}{D_R} \cdot \frac{RTk_d C^\circ}{nFv} \quad [2]$$

Using the  $k_d$  determined in the present study,  $E_c^\circ$  for the initial electron addition process (wave I)



is calculated to be  $-1.18\text{V}$ ; the corresponding  $E_c^\circ$  for  $\text{NMN}^+$  is  $-1.24\text{V}$ . However, in view of the uncertainties in  $k_d$  and in equating  $D_0$  and  $D_R$ , it would be best to round both values off to  $-1.2\text{V}$ .

**4. Adsorption and catalytic hydrogen evolution.**—The differences in adsorption at the interface between cationic  $\text{MCP}^+$  and  $\text{NMN}^+$ , and between their neutral reduction products reflect the presence of a hydrophobic substituent on N(1) of  $\text{MCP}^+$  and a hydrophilic substituent on N(1) of  $\text{NMN}^+$ . The difference in adsorption of the MCP dimeric product (strongly adsorbed) and dihydropyridine product (moderately adsorbed)

also reflects the difference in hydrophobic nature of the two compounds.

Adsorption of reduction products plays a role in the catalytic evolution of hydrogen. In the case of  $\text{MCP}^+$ , for example, additional current in wave II region below pH 8 (Fig. 3) has been ascribed to catalytic hydrogen evolution because the limiting current increases rapidly with decreasing pH, increases with increasing buffer capacity at a given pH, and exhibits partial kinetic behavior. At pH 7.4, the catalytic wave peak current occurs at  $-1.72\text{V}$ , which is near the initial limiting portion of wave II. Little adsorption of either reduction product should occur at this potential since a-c desorption peaks for both products occur at more positive potential. On the other hand, the mercury height-dependence of the catalytic wave suggests that an adsorbed species acts as catalyst, giving rise to a so-called surface catalytic wave (59). This situation is explicable on the basis that weak adsorption corresponding to a very low surface coverage occurs even at potentials more negative than those of the desorption peaks (54). Surface catalytic waves have been shown (54) to occur even with surface coverages as low as 0.5%. With increasing negative potential, the surface coverage, although small, should decrease, which would account for the peaked shape of the wave, i.e., the rate of the electrode reaction increases with increasing negative potential but less catalyst is available due to decreasing surface coverage. The increase in catalytic wave height with decreasing  $h$  is due to the greater surface coverage at longer drop-time.

#### Acknowledgments

The authors thank the National Science Foundation and the Horace H. Rackham School of Graduate Studies of the University of Michigan, which helped support the work described.

Manuscript submitted Dec. 26, 1973; revised manuscript received March 23, 1974.

Any discussion of this paper will appear in a Discussion Section to be published in the June 1975 JOURNAL. All discussions for the June 1975 Discussion Section should be submitted by Feb. 1, 1975.

#### REFERENCES

1. J. N. Burnett and A. L. Underwood, *J. Org. Chem.*, **30**, 1154 (1965).
2. W. Ciusa, P. M. Strocchi, and G. Adamo, *Gazz. Chim. Ital.*, **80**, 604 (1950).
3. S. J. Leach, J. H. Baxendale, and M. G. Evans, *Australian J. Chem.*, **6**, 395 (1953).
4. V. Moret, *Arch. Sci. Biol.*, **40**, 635 (1956).
5. V. Moret, *Giorn. Biochim.*, **5**, 51 (1956).
6. F. Sorm and Z. Sormova, *Chem. Listy*, **42**, 82 (1948).
7. P. C. Tompkins and C. L. A. Schmidt, *Univ. Calif. (Berkeley) Publ. Physiol.*, **8**, 247 (1943).
8. I. Bergmann, in "Polarography 1964," G. J. Hills, Editor, p. 985, Interscience, New York (1966).
9. M. Brezina and P. Zuman, "Polarography in Medicine, Biochemistry, and Pharmacy," Interscience, New York (1958).
10. C. Carruthers and V. Suntzeff, *Arch. Biochem. Biophys.*, **45**, 140 (1953).
11. B. Janik and P. J. Elving, *Chem. Rev.*, **68**, 295 (1968).
12. D. Thevenot and R. Buvet, *J. Electroanal. Chem.*, **39**, 429 (1972).
13. A. L. Underwood and J. N. Burnett, in "Electroanalytical Chemistry," A. J. Bard, Editor, Vol. 6, pp. 1–85, Marcel Dekker, New York (1972).
14. P. J. Elving, J. E. O'Reilly, and C. O. Schmamel, in "Methods of Biochemical Analysis," D. Glick, Editor, Vol. 21, pp. 287–465, Interscience, New York (1973).
15. D. Thevenot and G. Hammouya, *Experientia Suppl.*, **18**, 631 (1972).
16. D. Thevenot and R. Buvet, *J. Electroanal. Chem.*, **39**, 447 (1972).
17. A. J. Cunningham, Ph.D. Thesis, Emory University, Atlanta, Georgia (1966).
18. A. J. Cunningham and A. L. Underwood, *Biochemistry*, **6**, 266 (1967).

<sup>7</sup> Reference to the dissertation (17), on which the paper (18) was based, revealed that a scan rate of 57.3 V/sec had to be used in order to obtain a minimum detectable anodic peak corresponding to the free radical oxidation. However, calculation, based on Nicholson's graphical method (56), shows that, for  $k_d = 10^{-2} \text{ l mol}^{-1} \text{ sec}^{-1}$ , an  $i_{pa}/i_{pc}$  ratio of close to one would be observed even at the slow scan rate of 0.1 V/sec.

19. E. J. Land and A. J. Swallow, *Biochim. Biophys. Acta*, **162**, 327 (1968).
20. N. O. Kaplan, in "The Enzymes," Vol. III, P. D. Boyer, H. Lordy, and K. Myrböck, Editors, pp. 105-169, Academic Press, New York (1960).
21. B. Janik and P. J. Elving, *J. Am. Chem. Soc.*, **92**, 235 (1970).
22. C. Carruthers and J. Tech, *Arch. Biochem. Biophys.*, **56**, 441 (1955).
23. H. Berg, Private communication.
24. H. Hanschmann, Doctoral Dissertation, Friedrich Schiller University, Jena, DDR (1970).
25. C. O. Schmakel, K. S. V. Santhanam, and P. J. Elving, *This Journal*, **121**, 345 (1974).
26. L. Meites, "Polarographic Techniques," John Wiley and Sons, Inc., New York (1965).
27. R. Bonnaterre and G. Cauquis, *J. Electroanal. Chem.*, **32**, 199 (1971).
28. R. Phillips, *Chem. Rev.*, **66**, 501 (1966).
29. E. R. Brown and R. F. Large, in "Physical Methods of Chemistry," A. Weissberger and B. N. Rossiter, Editors, Part IIA, pp. 423-530, John Wiley and Sons, Inc., New York (1971).
30. J. M. Siegel, G. A. Montgomery, and R. M. Bock, *Arch. Biochem. Biophys.*, **82**, 288 (1959).
31. H. E. Dubb, M. Saunders, and J. H. Wang, *J. Am. Chem. Soc.*, **80**, 1767 (1958).
32. R. F. Hutton and F. H. Westheimer, *Tetrahedron*, **3**, 73 (1958).
33. W. L. Meyer, H. R. Mahler, and R. H. Baker, Jr., *Biochim. Biophys. Acta*, **64**, 353 (1962).
34. C. C. Johnston, J. L. Gardner, C. H. Suelter, and D. E. Metzler, *Biochemistry*, **2**, 689 (1963).
35. H. Sund, H. Diekmann, and K. Wallenfels, in "Advances of Enzymology," F. F. Nord, Editor, Vol. 26, p. 115, Interscience, New York (1964).
36. K. Wallenfels and H. Schüly, *Ann.*, **621**, 106 (1959).
37. K. Wallenfels, *Ciba Found. Study Group*, **2**, 10 (1959).
38. S. Chaykin and L. Meissner, *Biochem. Biophys. Res. Commun.*, **14**, 233 (1964).
39. S. Chaykin, L. King, and J. G. Watson, *Biochim. Biophys. Acta*, **124**, 13 (1966).
40. H. Sund, in "Biological Oxidations," T. P. Singer, Editor, p. 603, Interscience, New York (1967).
41. G. Maggiora, H. Johansen, and L. L. Ingraham, *Arch. Biochem. Biophys.*, **131**, 352 (1969).
42. G. W. Rafter and S. P. Colowick, *J. Biol. Chem.*, **209**, 773 (1954).
43. C. O. Schmakel, K. S. V. Santhanam, and P. J. Elving, Work in progress.
44. R. W. Burnett and A. L. Underwood, *Biochemistry*, **7**, 3328 (1968).
45. G. Stein and A. J. Swallow, *J. Chem. Soc.*, 306 (1958).
46. K. Wallenfels and N. Gellrich, *Chem. Ber.*, **92**, 1406 (1959).
47. W. Traber and P. Karrer, *Helv. Chim. Acta*, **41**, 2066 (1958).
48. E. M. Kosower, "Molecular Biochemistry," p. 166, McGraw-Hill Book Co., New York, (1962).
49. D. J. McClemens, A. K. Garrison, and A. L. Underwood, *J. Org. Chem.*, **34**, 1867 (1969).
50. A. Stock, E. Sann, and G. Pfeiderer, *Ann.*, **647**, 188 (1961).
51. T. C. Bruice and S. J. Benkovic, "Bioorganic Mechanisms," p. 301, W. A. Benjamin, New York (1966).
52. D. E. Smith and T. G. McCord, *Anal. Chem.*, **40**, 474 (1968).
53. J. Heyrovsky and J. Kuta, "Principles of Polarography," p. 396, Academic Press, New York (1966).
54. S. G. Mairanovskii, *J. Electroanal. Chem.*, **4**, 166 (1962).
55. R. S. Nicholson, *Anal. Chem.*, **37**, 667 (1965).
56. M. L. Olmstead, R. G. Hamilton, and R. S. Nicholson, *ibid.*, **41**, 260 (1969).
57. J. M. Saveant, *Electrochim. Acta*, **12**, 999 (1967).
58. K. J. Laidler, "Chemical Kinetics," p. 215, McGraw-Hill Book Co., New York (1965).
59. S. G. Mairanovskii, *J. Electroanal. Chem.*, **6**, 77 (1963).

## Technical Notes



### Determination of Water Contamination in Liquid Inorganic Oxyhalide Electrolytes

Kenneth French,\* Peter Cukor, Carmine Persiani, and James Auburn\*

GTE Laboratories Incorporated, Waltham, Massachusetts 02154

The publication costs of this article have been assisted by GTE Laboratories Incorporated.

Liquid inorganic oxyhalides have found application in at least three areas of advanced technology. Selenium oxychloride and phosphorus oxychloride were found to be desirable materials as solvent media for liquid lasers (1). These oxychlorides readily dissolve rare earth and other metallic salts and do not contain hydrogen atoms which tend to quench laser fluorescence. Solutions of rare earth salts in phosphorus oxychloride have also been used in electroluminescence studies (2). Thionyl chloride, sulfur chloride, and phosphorus oxychloride have been proposed for use as solvents in high energy density lithium batteries (3). These solvents can be rendered ionically conducting with the dissolution of lithium salts. They are compatible with strong oxidizing agents, such as

chlorine, and do not irreversibly decompose when subject to electrical potentials several times the open circuit voltage of the cells in which they are used. Although lithium metal is stable to attack in these electrolytic solutions, the solvents can be electrochemically reduced at catalytic surfaces and act as cathode depolarizers.

It is important in these applications that the solution be free from water contamination. Water reacts with these oxyhalide solvents readily, making their purification and storage a difficult task. In the course of the reaction of oxyhalides with water, a halogen atom is replaced with an OH group



Infrared spectrophotometry provides a convenient method of measuring the extent of this reaction.

\* Electrochemical Society Active Member.

Key words: lithium, oxyhalides, batteries, infrared trace analysis.



This paper reports on procedures of purification and storage of oxyhalides and on infrared spectrophotometric methods for the determination of the extent of their reaction with water.

### Experimental

Phosphorus oxychloride ( $\text{POCl}_3$ ) was purchased from Baker and Adamson, and thionyl chloride ( $\text{SOCl}_2$ ) and sulfuryl chloride ( $\text{SO}_2\text{Cl}_2$ ) were purchased from Research Organic Inorganic Chemical Corporation. These solvents were purified by stirring over lithium metal in a dry argon atmosphere for 24 hr followed by distillation from this mixture.

Lithium chloride was purchased from Foote Mineral Company and dried in vacuum at  $200^\circ\text{C}$ . Aluminum chloride (99.999%) was purchased from Rocky Mountain Research, Incorporated and used without purification. All handling of these materials was conducted inside a glove box flushed with dry argon.

Electrolytes were prepared in thionyl chloride ( $\text{SOCl}_2$ ) and sulfuryl chloride ( $\text{SO}_2\text{Cl}_2$ ) by dissolving equimolar amounts of lithium chloride and aluminum chloride in the purified solvents. The resulting solutions showed evidence of water contamination upon infrared analysis. It was determined that the contamination was introduced into these solutions by the aluminum chloride, as mixtures of lithium chloride with these solvents produced liquids without evidence of water contamination. The solutions were dried further by placing a piece of clean lithium metal in the electrolytic solution and allowing them to stand until the OH absorption band, which is the spectral evidence of water contamination, gradually diminished.

To obtain calibration curves, samples of solvents or the electrolytes were placed in dried 0.5, 1, or 10 cm cells having infrasil windows inside an argon filled glove box. These cells were fitted with ground glass joints and sealed by means of halocarbon grease so that they could be removed from the glove box to the Perkin Elmer Model 621 infrared spectrophotometer. The spectra were recorded using an empty cell as reference. After obtaining infrared absorption spectra of the dry liquids, the cells were returned to the glove box where known amounts of water were added by means of a microliter syringe. Spectra were obtained for each addition and changes in absorption bands were observed.

### Results and Discussion

The spectra of freshly prepared oxyhalides are shown in Fig. 1-3. Also shown on these figures are the spectra of these solvents after the addition of a known amount of water. The reaction of water with phosphorus oxychloride and thionyl chloride manifests itself in the spectra by the appearance of a broad hydrogen bonded OH band while the reaction with sulfuryl chloride produces sharp, free OH absorption bands (4-6).

These spectral data allow the construction of calibration curves using essentially the method of additions. The calibration curves, slopes, and intercepts, as well as the conditions under which the curves were obtained, are summarized in Table I.

The phosphorus oxychloride calibration curve departed from linearity at the low concentration range (0-10 ppm) when 1 cm cells were used. A smooth but nonlinear curve was obtained when calibration procedure was repeated with 10 cm cells. (Fig. 4).

It was possible to prepare  $\text{POCl}_3$  solution virtually free of water reaction products. Thionyl chloride and sulfuryl chloride solutions showed the presence of some residual water reaction products (about 5 ppm) even in the freshly prepared solvents. Thus calibration curves prepared using these materials did not intercept the vertical axis at zero absorption value.

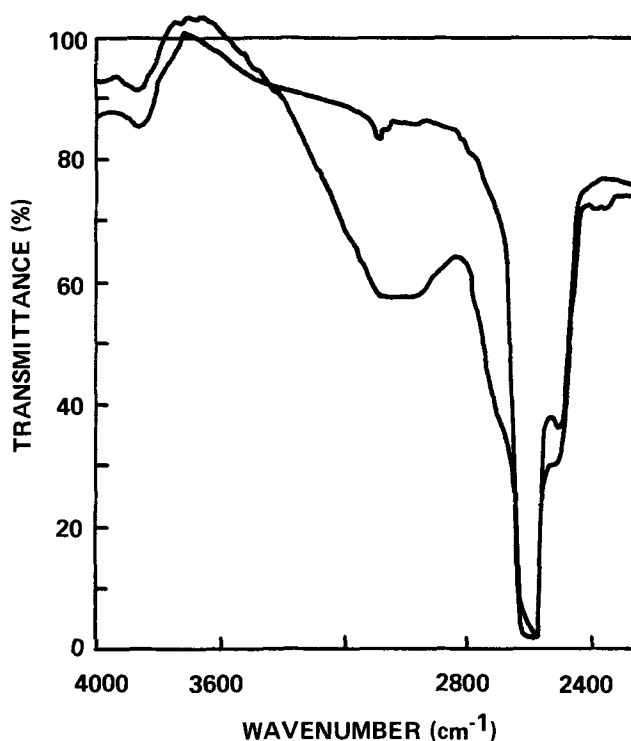


Fig. 1. Spectra of dry and water contaminated  $\text{POCl}_3$  (1 cm cell, 40 ppm).

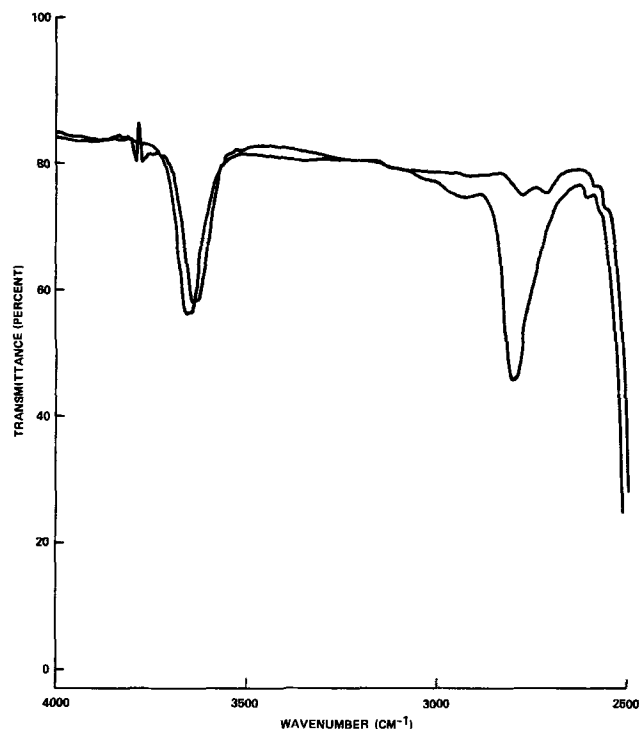


Fig. 2. Spectra of dry and water contaminated  $\text{SOCl}_2$  (0.5 cm cell, 40 ppm).

The limit of detection of the method was around 0.5 ppm water reaction product, using a 10 cm cell, and water contamination free material.

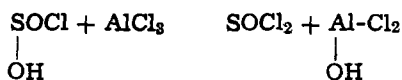
The spectra of the electrolytes exhibited a broad OH band in the  $3000\text{--}3700\text{ cm}^{-1}$  region as a result of addition of water (Fig. 5 and 6). The shape and location of this band is typical of metal hydroxides and of hydrated salts. It was also observed that the OH band originally present in the solvent disappeared upon addition of the  $\text{AlCl}_3$  suggesting that the following re-

Table I. Conditions of construction of calibration curves of solvents and electrolytes

Solvent	Calibration wavelength, cm	Base line	Cell path, cm	Absorbance slope, ppm H <sub>2</sub> O	Intercept absorbance	Background interference,* ppm H <sub>2</sub> O
POCl <sub>3</sub>	3200	Horizontal at 3600	1	0.0075	0.010	~0
POCl <sub>3</sub>	3200	Horizontal at 3600	10	(See Fig. 4)		
SOCl <sub>2</sub>	2800	Through 3200 and 2600	0.5	0.0058	0.019	3
SOCl <sub>2</sub>	2800	Horizontal at 3100	10	0.052	0.28	4
SO <sub>2</sub> Cl <sub>2</sub>	3700	Through 3800 and 3620	0.5	0.0018	0.025	10
SO <sub>2</sub> Cl <sub>2</sub>	3700	Through 3820 and 3620	10	0.060	0.45	6
	3600	Horizontal at 3620		0.038	0.18	5
SOCl <sub>2</sub> electrolyte	3380	Through 3040 and 3720	0.5	0.0053	0.14	25
SO <sub>2</sub> Cl <sub>2</sub> electrolyte	3400	Through 3600 and 3080	0.5	0.0011	0.02	10

\* This term refers to the concentration equivalent of the intercept absorbance.

action is taking place



Calibration curves were prepared to determine the amount of water that has reacted with the electrolyte (Table I). These calibration curves, constructed essentially by the method of additions, did not pass through the origin because of the presence of residual

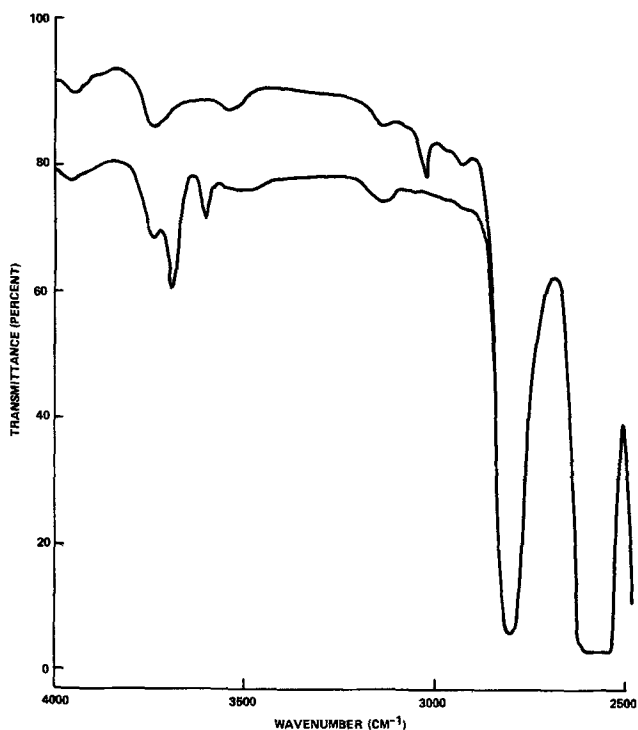


Fig. 3. Spectra of dry and water contaminated SO<sub>2</sub>Cl<sub>2</sub> (0.5 cm cell, 90 ppm).

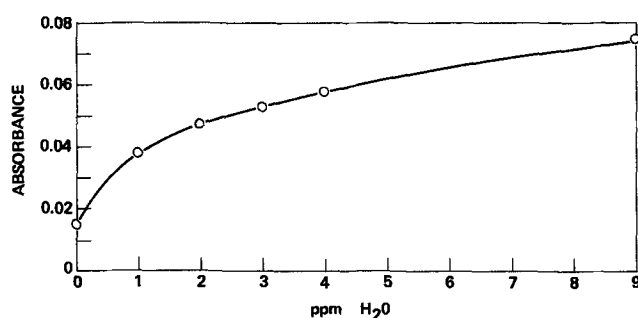


Fig. 4. Calibration curve for the determination of water contamination in POCl<sub>3</sub> using a 10 cm cell.

water contamination in the freshly purified electrolyte. The SO<sub>2</sub>Cl<sub>2</sub> electrolyte consistently showed much less water than the SOCl<sub>2</sub> electrolyte.

It was also possible to determine the moisture content of "anhydrous" AlCl<sub>3</sub>. A known amount of this substance was dissolved in dry SOCl<sub>2</sub> and aliquots of this solution were further diluted with dry solvent. A spectrum was obtained of the original solution and of each dilution. These spectra exhibited, due to the moisture content of AlCl<sub>3</sub>, a broad OH band very much similar in shape and location to the OH band present in the electrolyte. A curve of absorption vs. AlCl<sub>3</sub> concentration was constructed and was found to be parallel to the corresponding electrolyte calibration curve. Hence the electrolyte calibration curves can be used to determine the moisture content of AlCl<sub>3</sub>.

### Conclusions

Phosphorus oxychloride, thionyl chloride, and sulfuric chloride may be prepared in dry form by stirring over lithium in dry argon atmosphere followed by distillation. These solvents react with water to form OH containing species. The concentration of these contaminants may be determined by infrared spectrophotometry. POCl<sub>3</sub> and SOCl<sub>2</sub> yield upon reaction with water broad hydrogen bonded OH bands with minimums at 3200 and 2800 cm<sup>-1</sup>, respectively. SO<sub>2</sub>Cl<sub>2</sub> reacts with water and exhibits a sharp, free OH band at 3700 and at 3600 cm<sup>-1</sup>. The optimum limit of detection of the contamination products is around 0.5 ppm.

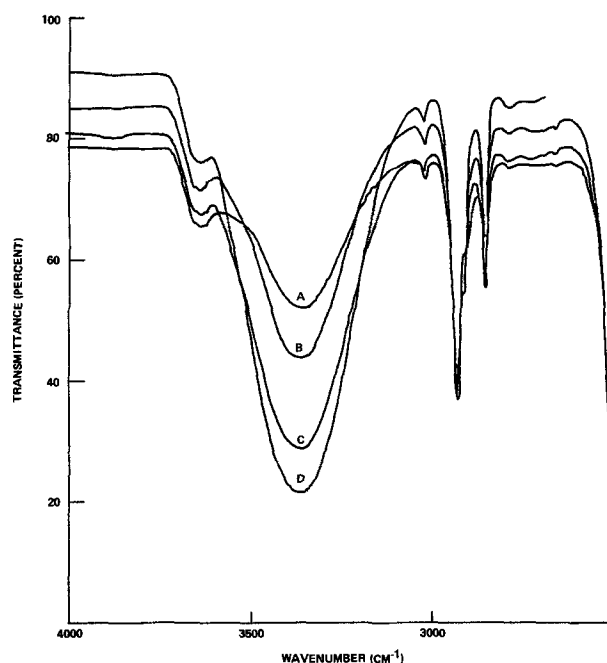


Fig. 5. Spectra of SOCl<sub>2</sub> electrolyte containing various amounts of water.

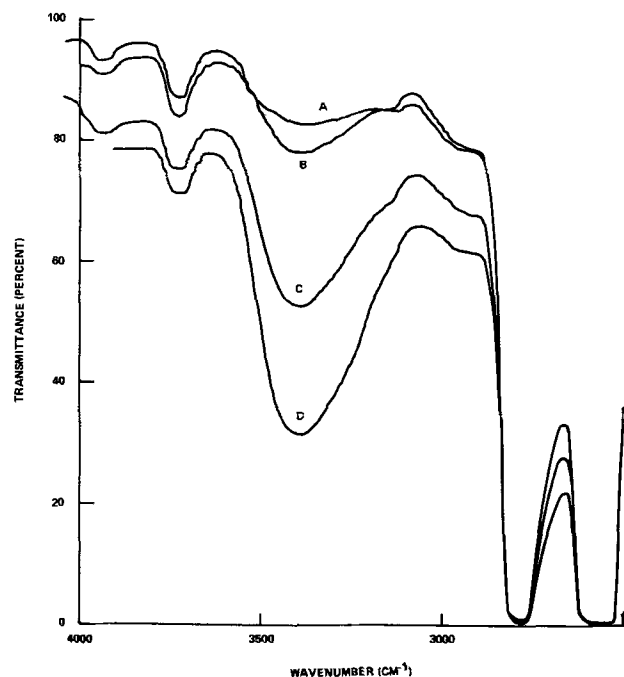


Fig. 6. Spectra of  $\text{SO}_2\text{Cl}_2$  electrolyte containing various amounts of water.

Electrolytes prepared by dissolving in these solvents a  $\text{LiCl}/\text{AlCl}_3$  mixture exhibit in their spectra a broad OH band around  $3400\text{ cm}^{-1}$  due to the presence of moisture in  $\text{AlCl}_3$ . It is possible to measure by infrared spectrophotometry both the extent of water contamination of the electrolytes and the moisture content of

the original  $\text{AlCl}_3$  crystals. Efforts to free the electrolyte from water related contamination were successful when an  $\text{SO}_2\text{Cl}_2$  solvent was used but were less fruitful for  $\text{SOCl}_2$  containing electrolytes.

#### Acknowledgment

The authors gratefully acknowledge the contributions of Mr. Edward W. Lanning to portions of this work related to the analysis of  $\text{POCl}_3$ . This work was supported in part by the U.S. Navy Office of Naval Research.

Manuscript submitted Feb. 8, 1974; revised manuscript received April 4, 1974.

Any discussion of this paper will appear in a Discussion Section to be published in the June 1975 JOURNAL. All discussions for the June 1975 Discussion Section should be submitted by Feb. 1, 1975.

#### REFERENCES

1. A. Heller, *J. Am. Chem. Soc.*, **88**, 2058 (1966); A. Heller, *Appl. Phys. Letters*, **9**, 106 (1966); A. Lempicki and A. Heller, *ibid.*, **9**, 198 (1966); V. P. Belan, V. V. Grigoryants, and M. E. Zhabotinski, IEEE Conference on Laser Engineering and Applications, Washington, D. C., 1967; N. Blumenthal, C. B. Ellis, and D. Grafstein, *J. Chem. Phys.*, **48**, 5726 (1968); E. J. Schmitschek, *J. Appl. Phys.*, **39**, 6120 (1968); C. Brecher and K. French, *J. Phys. Chem.*, **73**, 1785 (1969).
2. A. Heller, K. W. French, and P. O. Haugsjaa, *J. Chem. Phys.*, **56**, 2368 (1972).
3. J. J. Auborn, K. W. French, S. Lieberman, V. Shah, and A. Heller, *This Journal*, **120**, 1613 (1973); W. K. Behl, J. A. Christopoulos, M. Ramirez, and S. Gilman, *ibid.*, **120**, 1619 (1973).
4. R. N. Jones and C. Sandorfy, in "Technique of Organic Chemistry," A. Weissberger, Editor, Vol. IX, Chap. 4, Interscience Publishers, Inc., New York (1956).
5. M. Rand, *Anal. Chem.*, **35**, 2126 (1963).
6. L. Drasch and D. Smith, *ibid.*, **23**, 853 (1951).

## Electrochemistry in n-Hexanol.

### I. The $\text{H}_2(\text{g}, \text{Pt}) \mid \text{HCl}(\text{hex}) \mid \text{TlCl}(\text{s}) \mid \text{Tl}(\text{Hg})$ Cell

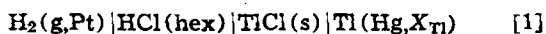
Carlos H. Contreras-Ortega and Peter A. Rock

Department of Chemistry, University of California, Davis, California 95616

The publication costs of this article have been assisted by the University of California.

n-Hexanol is a potentially useful model solvent for the electrochemical study of processes thought to occur in biological membranes. The dielectric constant of n-hexanol (13.3 at  $25^\circ\text{C}$ ) is comparable to that found for biological membranes ( $\sim 10$ ) (1), and n-hexanol is amphipathic. n-Hexanol has a wide liquid range ( $-47^\circ$ - $158^\circ\text{C}$ ), a low vapor pressure (1 Torr at  $25^\circ\text{C}$ ), and it is not difficult to prepare in a high purity, anhydrous state.

This paper reports the results of our electrochemical measurements on cells of the type



The cells were found to behave reversibly, and the standard cell voltage for cell [1] was computed as  $\mathcal{E}^\circ = -973 \pm 10\text{ mV}$  at  $296^\circ\text{K}$  [strong electrolyte standard state for  $\text{HCl}(\text{hex})$ , and a pure  $\text{Tl}(\text{s})$  standard state for  $\text{Tl}(\text{Hg})$ ].

Because of the need to exclude oxygen and water from the cell, the entire cell was set up and studied as

**Key words:** n-hexanol, hydrogen electrode, alcohols, thallium electrode.

a closed system on the vacuum line (2, 3). The  $\text{H}_2(\text{g})$  [99.999 atomic per cent (a/o)] used was purchased from the Matheson Chemical Company. The purity of the  $\text{H}_2(\text{g})$  was checked by mass spectrometry. Before use in the emf cells the  $\text{H}_2(\text{g})$  was run through a "DEOXO" hydrogen purifier (Englehard Industries), and then through  $\text{CaSO}_4$  drying towers. Thallium amalgams were prepared from weighed quantities of reagent grade Tl (precleaned with  $0.01M$   $\text{H}_2\text{SO}_4$ ) and reagent grade Hg. The amalgam was washed with dilute ( $0.001M$ )  $\text{HNO}_3$ , thoroughly dried under high vacuum, and stored in a reservoir on the vacuum line.

The n-hexanol used (98% purity) was obtained from the Aldrich Chemical Company. The n-hexanol was purified by successive distillations over  $\text{CaH}_2(\text{s})$  (Fisher Scientific Company, purified grade). The first distillation was carried out at 1 atm under helium (bp  $157^\circ\text{C}$ ). The middle 65% of the distilled n-hexanol was then transferred (without exposure to the atmosphere) to the distillation apparatus on the vacuum line. The n-hexanol was then vacuum distilled over

dry CaH<sub>2</sub>(s) at a pressure of 43–49 Torr and a head temperature of 75°–85°C. The distillation column was an 18 mm diameter Pyrex tube 120 cm in length, which was packed with 3 × 5 Raschig rings. Only the middle 75% of the distillate was used to make the cell solutions. The purity of the n-hexanol was checked by NMR, mass spectrometry, and infrared spectrometry. The anhydrous HCl(g), the TlCl(s), and the hydrogen electrodes (Pt black on Au coils) were prepared as described previously (3). The HCl(hex) solutions were prepared on the vacuum line from anhydrous HCl(g) and purified n-hexanol.

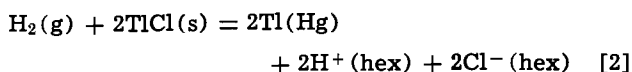
The cell construction was of the simple H-type with a central, large-bore stopcock. The cell was set up to operate as an automatically controlled, closed system on the high vacuum line. Samples of Tl(Hg), TlCl(s), and HCl(hex) were run into the cell from their respective storage compartments on the vacuum line after the cell was mounted on the line. The H<sub>2</sub>(g) was continuously recycled through the cell by means of automatic pumps (4). Pressures were measured on a differential manometer with a cathetometer; atmospheric pressure was read with a barometer. The emf measurements were made with a Leeds and Northrup Company certified 7555 Type K-5 potentiometer and a Leeds and Northrup Company 9828 electronic null detector. All cells were run at room temperature (296.0° ± 1.0°K), which was periodically recorded while the measurements were in progress.

The molalities of the HCl(hex) cell solutions were determined as follows: samples of the cell solution were obtained from the cells and weighed; the weighed samples [~15g and 15 ml of 0.1M NaClO<sub>4</sub>(aq)] were added to water and titrated potentiometrically (Beckman E-2 glass electrode vs. saturated calomel) with carbonate-free NaOH(aq). The NaOH(aq) was standardized potentiometrically against HCl(aq) obtained by dilution of constant-boiling HCl(aq). The possible interference of n-hexanol with the analysis was ruled out by titration of known quantities of HCl(aq) in the presence and absence of added n-hexanol. The mole fraction of thallium in the amalgams, X<sub>Tl</sub>, was determined by the acidimetric method of Richards and Daniels (5).

The results of our measurements on cells of the type [1] are presented in Table I. The emf, pressure, and temperature measurements were taken at 1 hr intervals during the life of the cell and the results were averaged. The period of stability of the cells ranged from 13 to 43 hr with a mean lifetime of 25 hr. The pressures reported have been corrected for the vapor pressure of the cell solutions (~1.0 Torr). Barometer location and temperature corrections have also been applied. Reversibility checks (emf vs. meter-scale position) gave no evidence of a hysteresis loop; this is strong evidence

that the cells were operating under reversible conditions.

The postulated cell reaction for the cell [1] is



Application of the Nernst equation to this cell reaction yields ( $\omega = RT/F$ )

$$\mathcal{E} = \mathcal{E}^\circ - \frac{\omega}{2} \ln \left\{ \frac{a_{\text{Tl}(\text{Hg})}^2 a_{\text{H}^+}^2 a_{\text{Cl}^-}}{a_{\text{H}_2(\text{g})} a_{\text{TlCl}(\text{s})}^2} \right\} \quad [3]$$

If we take  $a_{\text{H}_2(\text{g})} \simeq (P_{\text{H}_2}/760)$ ,  $a_{\text{Tl}(\text{Hg})} = X_{\text{Tl}}\gamma_{\text{Tl}}$ ,  $a_{\text{TlCl}(\text{s})} = 1$ , and  $a_{\text{H}^+} a_{\text{Cl}^-} = m_{\text{HCl}}^2 \gamma_{\pm}^2$  then

$$\mathcal{E} - \frac{\omega}{2} \ln \left( \frac{P_{\text{H}_2}}{760} \right) + \omega \ln X_{\text{Tl}} \gamma_{\text{Tl}} + 2\omega \ln m_{\text{HCl}} = \mathcal{E}_\text{H} \quad [4]$$

where

$$\mathcal{E}_\text{H} = \mathcal{E}^\circ - 2\omega \ln \gamma_{\pm} \quad [5]$$

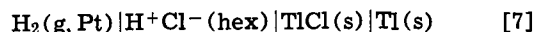
The values of  $\gamma_{\text{Tl}}$  (relative to the hypothetical, ideal, unit-mole-fraction solute standard state for Tl in Hg) at various X<sub>Tl</sub> values were obtained from the data of Richards and Daniels as described in Ref. (3). As  $m_{\text{HCl}}$  approaches zero, we expect from Debye-Hückel theory that the value of  $\ln \gamma_{\pm}$  for HCl(hex) should approach that given by the equation

$$\ln \gamma_{\pm} \simeq -15.3m^{1/2}/(1 + m^{1/2}) \quad [6]$$

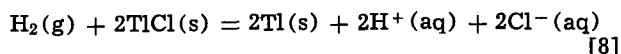
Consequently, a plot of the Hitchcock extrapolation function  $\mathcal{E}_\text{H}$  vs.  $m^{1/2}/(1 + m^{1/2})$  should have a (theoretical) slope of  $2\omega A = 2 \times 25.506 \times 15.3 = 780.5$  mV and an intercept of  $\mathcal{E}^\circ$ . A least squares analysis of a plot of  $\mathcal{E}_\text{H}$  vs.  $m^{1/2}/(1 + m^{1/2})$  using the data in Table I yielded a slope of  $517.1 \pm 43.0$  mV and an intercept of  $\mathcal{E}^\circ = -917.6 \pm 3.8$  mV.

The value of the experimental slope is significantly less than the theoretical value, but it should be noted that the Debye-Hückel limiting law slope is more difficult to reach the lower the value of the dielectric constant of the solvent. If we require that the slope of the Hitchcock plot be the Debye-Hückel theoretical value, then a least squares analysis of the data yields an intercept of  $\mathcal{E}^\circ = -940.5 \pm 10.2$  mV. If we assume that  $\ln \gamma_{\pm}$  for HCl is given by Eq. [6], then an  $\mathcal{E}^\circ$  value can be computed for each cell in Table I. The average of the eight  $\mathcal{E}^\circ$  values is  $\mathcal{E}^\circ = -940.6 \pm 4.3$  mV. Consequently, we consider our best estimate for the standard potential of cell [1] to be  $\mathcal{E}^\circ = -940 \pm 10$  mV.

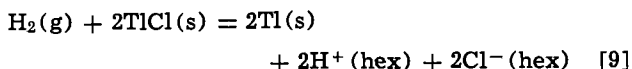
Because  $\mathcal{E}^\circ = -32.8$  mV at 296°K for the reaction  $\text{Tl}(\text{Hg}) = \text{Tl}(\text{s})$  (3), we compute a standard potential of  $\mathcal{E}^\circ = -973 \pm 10$  mV at 296°K for the cell



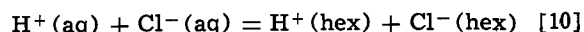
The standard potential for the reaction



is  $\mathcal{E}^\circ = -556.8$  mV at 25°C (6). Combination of this result with our value of  $\mathcal{E}^\circ = -973$  mV for the reaction



yields, for the reaction



a value of  $\Delta G^\circ \simeq 40.1$  kJ·mole<sup>-1</sup> (molality scale) or  $\Delta G^\circ = 31.6$  kJ·mole<sup>-1</sup> (mole fraction scale) for the standard Gibbs energy of transfer of HCl from water to n-hexanol. The positive value of  $\Delta G^\circ$  reflects the stronger solvation of the proton in water than in n-hexanol. The standard potential at 297°K for the re-

Table I. Results of measurements on the cell (Pt)H<sub>2</sub>(g) | HCl(m,hex) | TlCl(s) | Tl(Hg,X<sub>Tl</sub>) where T = 296.0° ± 1.0°K

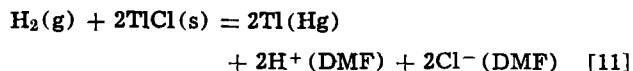
$m_{\text{HCl}}$ (mole · kg <sup>-1</sup> )	X <sub>Tl</sub>	ln γ <sub>Tl</sub>	P <sub>H<sub>2</sub></sub> , Torr	ℰ(expt.),* mV	ℰ(calc),† mV
0.00834	0.03762	0.4578	721.4	-558.7 ± 0.4	-559.7
0.01546	0.06192	0.6824	729.1	-594.9 ± 0.05	-588.5
0.01128	0.06236	0.6864	722.3	-590.1 ± 0.3	-584.2
0.008058	0.06269	0.6895	719.1	-576.0 ± 0.3	-577.9
0.005799	0.06183	0.6815	727.8	-562.9 ± 0.05	-569.5
0.01662	0.06236	0.6864	722.9	-594.6 ± 0.1	-589.7
0.008274	0.06269	0.6895	716.6	-576.6 ± 0.3	-578.5
0.004220	0.06183	0.6815	718.5	-555.9 ± 0.08	-561.1

\* The last three cells in this table were run with 99.5% D<sub>2</sub>, 99.9% DCl, and >95% n-hexanol-OD rather than H<sub>2</sub>, HCl, and n-hexanol-OH. The reported emf values for the deuterium cells were converted to hydrogen cells by subtracting 3.1 mV from the measured emf values (6).

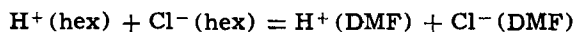
† The values of ℰ given in this column were calculated from Eq.

[5] and [6] using  $\mathcal{E}^\circ = -940.5$  mV and  $2\omega A = 780.5$  mV.

action



(where DMF is N,N-dimethylformamide) is  $-887 \text{ mV}$  (3). For the reaction



we compute  $\Delta G^\circ = +8.3 \text{ kJ}\cdot\text{mole}^{-1}$  (molality scale) or  $+6.7 \text{ kJ}\cdot\text{mole}^{-1}$  (mole fraction scale). The positive value of  $\Delta G^\circ$  reflects the fact that alcohols generally are stronger bases than amides.

Our electrochemical results show that the hydrogen electrode is a well-behaved reference electrode in anhydrous hexanol. In some of our cells the voltage was stable to better than  $50 \mu\text{V}$  for periods ranging up to 20 hr. n-Hexanol thus appears to warrant further investigations both as a low dielectric constant solvent for conventional electrochemical studies, and as a model solvent for bioelectrochemical processes.

### Acknowledgment

This research was supported by NSF Grant GP-33264.

Manuscript received March 11, 1974.

Any discussion of this paper will appear in a Discussion Section to be published in the June 1975 JOURNAL. All discussions for the June 1975 Discussion Section should be submitted by Feb. 1, 1975.

### REFERENCES

1. K. S. Cole, "Membranes, Ions and Impulses," University of California Press, Berkeley, Calif. (1968).
2. L. F. Silvester, J. J. Kim, and P. A. Rock, *J. Chem. Phys.*, **56**, 1863 (1972).
3. L. F. Silvester and P. A. Rock, *This Journal*, **121**, 518 (1974).
4. L. F. Silvester and P. A. Rock, *ibid.*, **121**, 251 (1974).
5. T. W. Richards and F. Daniels, *J. Am. Chem. Soc.*, **41**, 1732 (1919).
6. C. H. Contreras-Ortega, L. F. Silvester, and P. A. Rock, *J. Chem. Phys.*, To be submitted.
7. A. J. de Bethune and N. A. Swendeman Loud, "Standard Aqueous Electrode Potentials and Temperature Coefficients at  $25^\circ\text{C}$ ," C. A. Hampel, Skokie, Ill. (1964).



## Thermodynamics and Kinetics of Pack Aluminide Coating Formation on IN-100

S. R. Levine and R. M. Caves

National Aeronautics and Space Administration, Lewis Research Center, Cleveland, Ohio 44135

The publication costs of this article have been assisted by the National Aeronautics and Space Administration.

### ABSTRACT

The effect of variation of pack activators, compositions, temperature, and time on the thickness and structure of aluminide coatings formed on the nickel-base superalloy IN-100 was studied in one-step packs containing aluminum at unit activity. Times were varied from 4 to 24 hr and temperatures were varied from 982° to 1149°C in NaCl-activated packs. The other halides of sodium and the ammonium halides were primarily used to activate 1093°C, 16-hr packs. In addition, an analysis of the thermodynamics and kinetics of aluminizing was carried out. The mechanism of coating formation in each pack was established from agreement between observed coating weights and predictions based on a gaseous diffusion model and solid-state diffusion considerations which used published diffusion data for the Ni-Al system. Pack temperature rather than pack aluminum activity controls the principal coating phase formed. The halides ranked according to aluminum weight gain in 1 w/o (weight per cent) Al packs are  $F \cong Cl > Br > I$ . Solid-state nickel diffusion controlled the rate of coating formation in fluoride-activated packs. Gaseous diffusion controlled the rate of coating formation in bromide-, iodide-, and  $NH_4Cl$ -activated packs containing 1 w/o Al. In NaCl-activated packs containing 1 w/o Al the ability of the substrate to supply nickel appeared to be in balance with the ability of the pack to supply aluminum. However, the observed rate constant and activation energy indicated that solid-state diffusion controlled coating growth. Increasing pack aluminum content from 1 to 5 w/o shifted control of coating formation from the gas phase to the solid state in the 16-hr, 1093°C, NaBr-activated pack. Regardless of the rate-controlling step, the kinetics of coating formation were parabolic. The activation energy for coating formation controlled by solid-state diffusion was 88 kcal/mole. Similar coating microstructures and weight gains were obtained for each halogen regardless of whether its source was a sodium or ammonium halide.

Aluminide coatings are commonly used to extend the life of superalloys in the oxidation/corrosion/erosion environment encountered in gas turbines (1). Such protection is provided by aluminum oxide scales which preferentially form on the  $\beta$ -MAI phase which is analogous to NiAl in the Ni-Al binary system. Generally these intermetallic aluminide coatings are diffusion formed by exposing the blade or vane alloy surface to an aluminum-rich environment at elevated temperature. The aluminides may be applied by a number of methods including pack cementation, slurry spraying and sintering, and slurry spraying and fusing in the presence of a fluxing agent (2, 3). The pack cementation method is the most established and commonly used technique for large scale batch processing of engine components currently in commercial flight service.

Although the commercial pack aluminides are performing successfully in the 700°-1000°C metal operating temperature range of current engines, the requirements of higher operating temperatures for improved engine performance with even longer times between

overhaul will place ever more stringent demands on coating technology. Even if new coating systems come into use for these high-temperature needs, the relatively low-cost aluminide coatings will continue to be used at peak temperatures to 1100°C. One way to improve such aluminide coatings is by gaining a more thorough understanding of the pack cementation process and then using this insight to optimize pack conditions for each alloy and application.

A fairly extensive background on pack aluminizing exists in the literature, but knowledge of the effect of pack variables on coating structure and performance remains far from complete (2, 4-6). Goward and Boone (5) have summarized the formation mechanisms for aluminide coatings. They formulate two classifications: (i) the low-temperature, high-activity pack and (ii) the high-temperature, low-activity pack. Each coating class has its peculiarities and advantages. The two-step high-activity process (application followed by diffusion annealing) tends to first form  $M_2Al_3$  which reverts to MAI on annealing. Such coatings incorporate substrate constituents and microstructural features, whereas the low-activity process (which also may re-

Key words: nickel alloys, protective coatings, diffusion.

quire two steps) tends to form MAI and to incorporate only selected substrate constituents (4). In the high-activity process, aluminum is supplied at a rate much greater than it can react to form  $\beta$ -MAI. Thus  $M_2Al_3$  is formed by inward diffusion of Al. In the low-activity process the rate of supply of aluminum is less than the rate at which nickel can be supplied through  $\beta$ , and thus nickel-rich  $\beta$  is formed. The advantages derived from each pack class might be conferred upon a coating by a one-step hybrid pack in which aluminum is present at unity activity and the temperature is high enough to maintain  $\beta$ -formation.

The purpose of this study was to develop a fuller understanding of the important processing variables, transport mechanisms, and thermodynamics of the pack aluminizing process. This was done by studying the effect of several pack activators, pack compositions, temperatures, and times on the thickness and structure of pack aluminide coatings formed on nickel-base superalloy IN-100 in high-activity, high-temperature hybrid packs.

Prior exploratory studies evolved a pack consisting of 1 w/o NaCl, 1 w/o Al with the balance inert  $Al_2O_3$  filler to which the substrates are exposed for 16 hr at 1093°C under an argon atmosphere. In this study the fluorides, chlorides, bromides, and iodides of sodium and ammonium were used as activators. Pack times were varied from 3 to 24 hr, pack temperatures were varied from 982° to 1149°C, and activator and aluminum concentrations were varied over the range of 1-3 and 1-5 w/o, respectively.

The coated specimens were evaluated by weight gain, optical metallography, microhardness measurements, electron microprobe raster micrography (EMP), x-ray fluorescence (XRF), and x-ray diffraction (XRD).

### Experimental Procedures

**Coating deposition.**—Commercially cast IN-100 having a nominal composition of 5.5 w/o Al, 15.3 w/o Co, 9.6 w/o Cr, 3.2 w/o Mo, 4.3 w/o Ti, 0.9 w/o V, 0.17 w/o C, with the balance nickel and minor trace elements, was the substrate used for this study. Specimens were cast in two configurations:  $5.1 \times 2.5 \times 0.25$  cm coupons and  $10.2 \times 2.5 \times 0.64$  cm erosion bars. Specimen edges were radiused from 0.04 to 0.08 cm by abrasive tumbling or grinding on a water-wetted belt sander. Both types of specimens were then grit blasted with -100 mesh  $Al_2O_3$  to produce a uniform matte finish, rinsed, measured, vapor degreased, rinsed in distilled water, and weighed prior to placement in the pack.

The pack box consisted of an aluminized Inconel retort as shown in cross section in Fig. 1. The specimens were rested in a premixed powder consisting of Alcoa A-1 grade -100 mesh alumina powder, -100 mesh 99% pure Al, and reagent grade activator salt. The packs contained at least 1 w/o Al and 1 w/o activator. The balance was  $Al_2O_3$ . In one NaI-activated pack the activator content was raised to 3 w/o and

in one NaBr-activated pack the aluminum content was raised to 5 w/o.

The assembled pack was purged for 1 hr with high-purity argon prior to insertion into the preheated box furnace which was controlled to  $\pm 15^\circ C$ . The packs required about 1 hr to heat up to the furnace temperature. Pack times are reported as time at temperature rather than as time in the furnace. Argon flow was maintained at 0.057 m<sup>3</sup>/hr throughout the time the packs were above room temperature. Upon completion of the scheduled exposure, the pack was removed from the furnace and cooled to room temperature. The specimens were removed from the powder, brushed, rinsed in distilled water, and weighed to determine aluminum pickup.

**Additional evaluations.**—Metallographic cross sections of some specimens in the as-coated condition were examined to evaluate the effect of the various pack conditions on coating structure and thickness. In addition, microhardness measurements were made with a Knoop indenter driven by a 200g load. The EMP analyses by electron backscatter and element x-ray raster micrography were performed on some metallographic cross sections of the coated specimens to determine qualitative element distributions. Also, XRF analyses *in situ* and XRD analyses of scrapings and *in situ* were performed.

The pack materials from completed 16 and 24 hr, 1093°C, NaCl-activated packs were analyzed for Cl, Na, and Al. Three bulk samples from the 24-hr pack were leached to extract the following elements: one sample was water leached to extract Cl and Al present as soluble halide salt; another was HCl leached to extract Na and Al; and a third was given a redundant NaOH leach to check the extraction of Cl and Al. Sodium was analyzed by flame emission spectroscopy, Al was determined by atomic absorption spectroscopy, and Cl was determined by spectrophotometry using the mercuric thiocyanate procedure. Sequential leaches on single samples were used to analyze a bulk sample and a sample taken from within 0.5 cm of the specimen surface in the 16-hr pack.

### Results

The results of aluminide coating deposition on IN-100 in packs activated with the halides of sodium and ammonium are presented in Table I.

**Effect of time.**—*Chloride-activated packs.*—Coating deposition times of 4, 6, 8, 16, and 24 hr at 1093°C were used with the baseline NaCl-activated pack. As shown in Table I, the variation in coating weights and thicknesses of specimens within a pack was generally small. There was more variation in these measurements between packs as primarily observed in the 16-hr packs. This variation influenced coating composition and microstructure. A satisfactory explanation for this behavior could not be found. Variations in temperature, variable levels of residual oxygen, nitrogen, and moisture in the assembled packs, or incomplete mixing of the pack ingredients may be responsible.

The XRD analysis indicated that the coatings deposited by 1093°C, NaCl-activated packs were primarily  $\beta$ -MAI.  $M_2Al_3$  was detected *in situ* as a minor coating phase in a coating put down in 8 hr and in the heaviest coating put down in 16 hr.

Photomicrographs of coatings deposited by the NaCl-activated packs are presented in Fig. 2. The zone adjacent to the substrate which etched distinctly lighter in the 4-, 8-, and 16-hr pack coatings is of relatively constant thickness (16-30  $\mu m$ ) as a function of time compared to the growth of the outer or primary coating layer (32-77  $\mu m$ ). In all coatings a discontinuous layer of carbides similar in appearance to the substrate carbides was clearly visible in the as-polished samples. The samples coated for 4 and 8 hr have microstructures characteristic of "low-activity" pack coatings

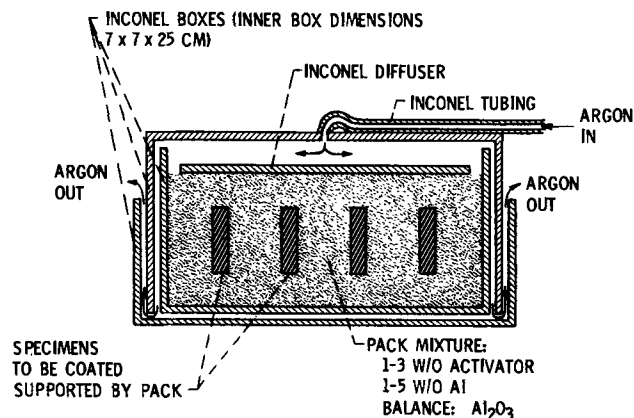


Fig. 1. Schematic cross-section view of an assembled pack box

Table I. Pack aluminide coating deposition parameters and results

Activator	Temperature, °C	Time, hr	Weight % Activator	Aluminum	Aluminum pickup, mg/cm <sup>2</sup>	Coating thickness, μm	XRF			Major phase	XRD	
							Al <sup>(a)</sup>	Ni <sup>(b)</sup>	Ti <sup>(b)</sup>		Minor phases	
NaF	1093	16	1	1	13.3 ± 1.2	108	6.0	64	1.3	MAI	Al <sub>2</sub> Cr <sub>3</sub>	Al <sub>2</sub> O <sub>3</sub>
NaCl	982	16	1	1	2.6 ± 0.1	18	8.3	72	0.2	MAI	—	—
NaCl	1038	16	1	1	6.0 ± 0.6	40	9.1	72	0.3	MAI	Al <sub>2</sub> O <sub>3</sub>	—
NaCl	1038	16	1	1	6.4 ± 0.4	46	9.4	73	0.1	MAI	—	—
NaCl	1093	4	1	1	7.4	48	—	—	—	MAI	—	—
NaCl	1093	8	1	1	7.1 ± 0.3	50	7.1	74	0.1	MAI	M <sub>2</sub> Als	—
NaCl	1093	8	1	1	7.9 ± 0.1	62	—	—	—	—	—	—
NaCl	1093	15	2	2 <sup>(c)</sup>	13.9 ± 0.5	—	—	—	—	—	—	—
NaCl	1093	15	1	1	12.2 ± 0.2	79	—	—	—	MAI	—	—
NaCl	1093	16	1	1	18.6 ± 0.3	115	7.7	69	0.1	MAI	M <sub>2</sub> Als	—
NaCl	1093	16	1	1	15.4	—	—	—	—	—	—	—
NaCl	1093	24	1	1	14.3 ± 1.3	107	6.8	71	0.2	MAI	—	—
NaCl	1093	24	1	1	17.2 ± 0.3	115	—	—	—	—	—	—
NaCl	1140	16	1	1	16.1 ± 3.0	132	8.5	67	0.5	MAI	Al <sub>2</sub> O <sub>3</sub>	—
NaBr	1093	4	1	1	3.8	35	—	—	—	MAI	—	—
NaBr	1093	8	1	1	5.5	48	—	—	—	MAI	—	—
NaBr	1093	16	1	1	6.8 ± 0.2	52	7.2	81	0.1	MAI	Al <sub>2</sub> Cr <sub>3</sub>	—
NaBr	1093	16	1	5	16.1	136	—	—	—	MAI	—	—
NaBr	1093	24	1	1	8.4	86	—	—	—	MAI	—	—
NaI	1093	16	1	1	5.1 ± 0.3	50	7.4	78	0.1	MAI	—	—
NaI	1093	16	3	1	5.9 ± 0.1	—	—	—	—	—	—	—
NH <sub>4</sub> F	1093	16	1	1	15.7 ± 2.9	115	4.3	59	4.2	MAI	NiO	TiO <sub>2</sub>
NH <sub>4</sub> Cl	1093	3	1	1	4.6 ± 0.2	42	—	—	—	MAI	—	—
NH <sub>4</sub> Cl	1093	16	1	1	10.5 ± 1.6	80	7.1	74	0.3	MAI	—	—
NH <sub>4</sub> Br	1093	16	1	1	7.6 ± 0.1	73	5.4	81	0.1	MAI	Al <sub>2</sub> O <sub>3</sub>	—
NH <sub>4</sub> I	1093	16	1	1	5.2 ± 0.2	53	5.2	80	0.1	MAI	—	—

(a) Counts relative to counts from Al × 100.

(b) Counts relative to counts from IN-100 × 100.

(c) Spacing between specimens, 3.3 cm minimum except for this pack where 1.9 cm spacing was used.

with carbides concentrated in the light etching zone adjacent to the substrate (5). In the samples aluminided for longer times the carbides also penetrate the primary layer. Some substrate carbide depletion (not shown) was noticeable after 16 hr. After 24 hr the thickness of the substrate carbide depleted zone was comparable to the coating thickness. Since the carbides

in the coating are rich in Ti, Mo, and V as were the substrate carbides, they are presumed to be of the MC type (7). Their distribution and the occurrence of carbide depletion of the substrate indicates formation of these carbides in the coating by precipitation as well as by inclusion as a result of coating growth. An additional minor coating phase, revealed as the light etch-

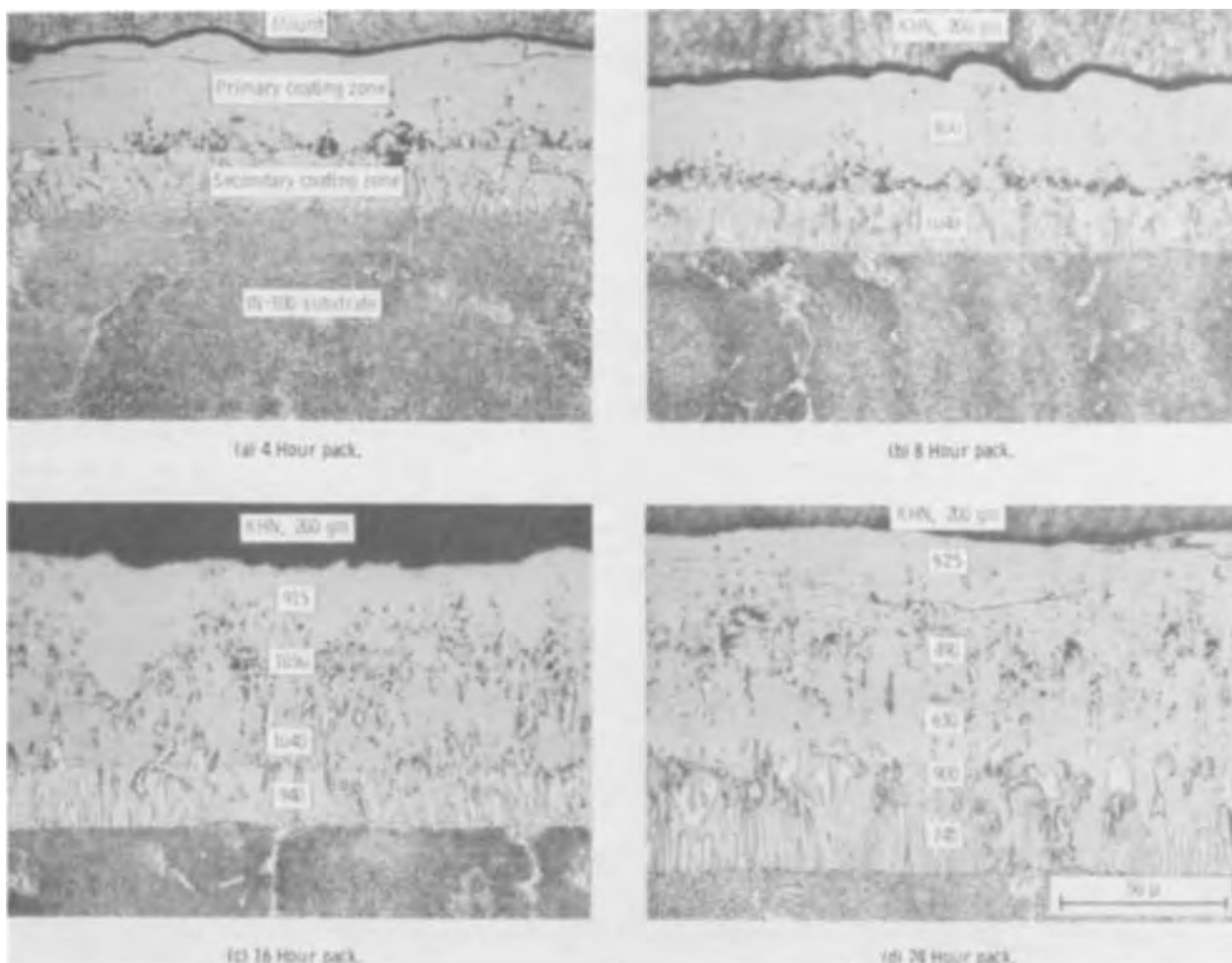


Fig. 2. Cross-sectional microstructures of aluminide coatings deposited on IN-100 in 1093°C NaCl-activated packs



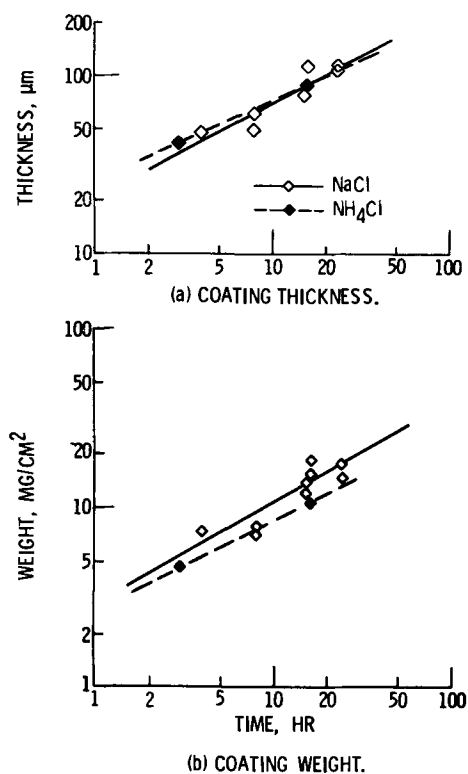


Fig. 3. Growth of aluminide coatings on IN-100 in sodium and ammonium chloride-activated 1093°C packs.

ing particles concentrated primarily in the lighter etching zone, is rich in Cr, Mo, and V and lean in Ni,

Co, and Ti. Occasional Al<sub>2</sub>O<sub>3</sub> inclusions (large dark particles) and other particles (primarily rich in Cr) are also found in the primary layer.

The coating deposition data for NaCl-activated packs, as plotted in Fig. 3, were fit to power law growth equations

$$x = (kt)^{1/n}; \quad w = (k't)^{1/n'} \quad [1]$$

appropriate for diffusion through a growing phase or depleting zone in the pack. Analysis of thickness ( $x$ ) and weight ( $w$ ) data gave  $1/n$  and standard deviation values of  $0.54 \pm 0.10$  and  $0.56 \pm 0.12$  for thickness and weight data, respectively, indicating parabolic behavior. Fitting the thickness data to a parabolic growth equation ( $n = 2$ ) gives a rate constant ( $k$ ) of  $1.6 \times 10^{-9}$  cm<sup>2</sup>/sec with a standard deviation of  $\pm 0.4 \times 10^{-9}$  cm<sup>2</sup>/sec.

The data for NH<sub>4</sub>Cl-activated packs, as plotted in Fig. 3, were fit to the power law growth equation. Using the standard deviations found for NaCl, the values of  $1/n$  and their standard deviations are  $0.46 \pm 0.10$  and  $0.49 \pm 0.12$  for thickness and weight gain data, respectively. These values suggest that parabolic kinetics prevailed in NH<sub>4</sub>Cl-activated packs. The parabolic rate constant was  $1.3 \pm 0.4 \times 10^{-9}$  cm<sup>2</sup>/sec (again using the standard deviation obtained for NaCl).

**NaBr-activated packs.**—Microstructures of coatings deposited in 4-, 8-, 16-, and 24-hr, 1 w/o aluminum NaBr-activated, 1093°C packs are presented in Fig. 4. The outer inclusion-free zone of the coatings deposited in 4-, 8-, and 16-hr packs shows a change in color as a function of depth not seen in coatings deposited in NaCl-activated packs. This is indicative of a transition from Al-rich MAI at the surface to Al-lean MAI in the

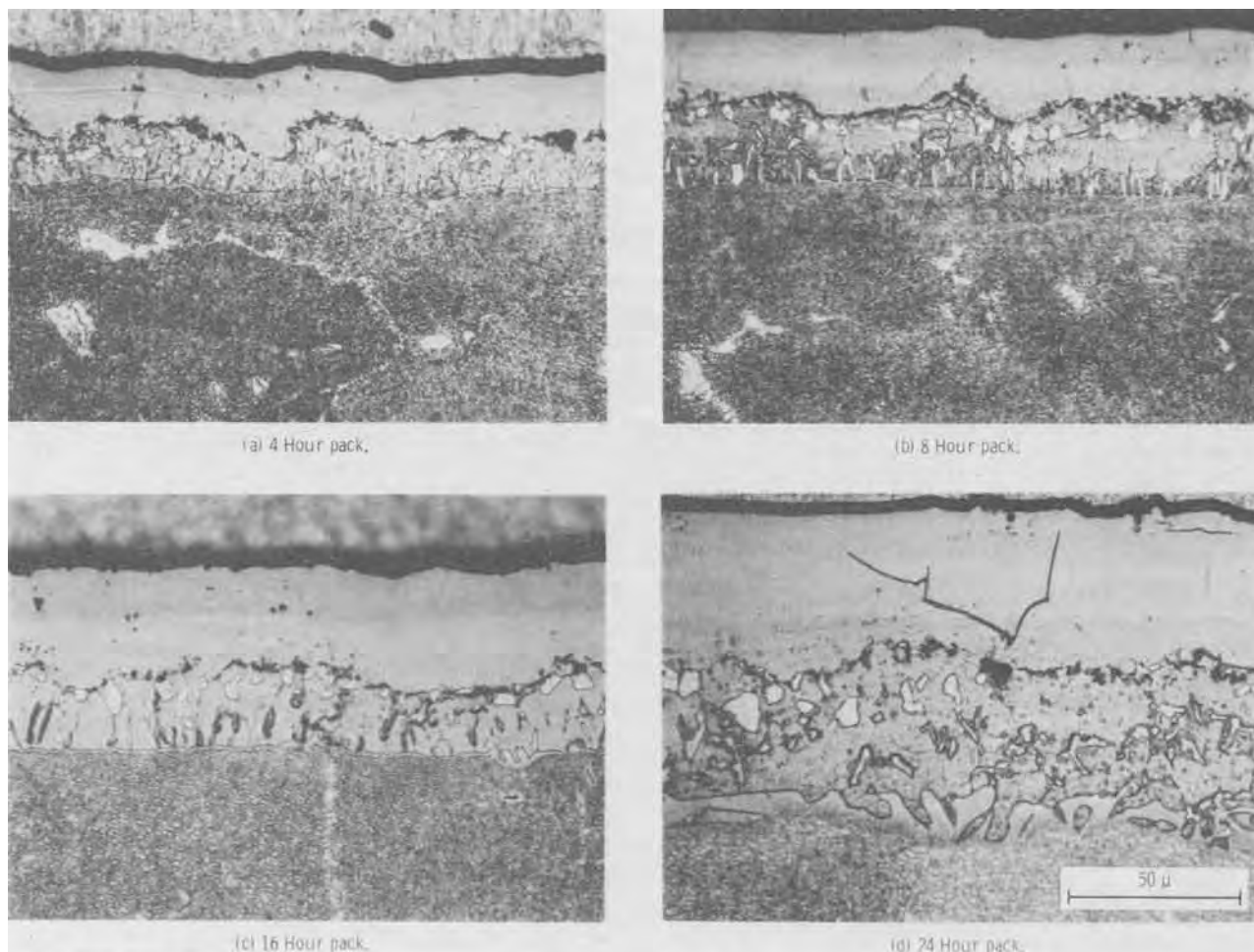


Fig. 4. Cross-sectional microstructures of aluminide coatings deposited on IN-100 in 1093°C NaBr-activated packs

coating interior (4). The interface between the inclusion-free outer zone and the inner zone is quite irregular in NaBr-activated packs when compared to the interface developed in NaCl-activated packs (Fig. 2). This irregularity is indicative of sensitivity to small local variations in pack composition as previously reported by Brill-Edwards and Epner (6).

The aluminum weight gain data are plotted against pack time in Fig. 5. When fit to the power law rate equation,  $1/n$  and standard deviation, values of  $0.44 \pm 0.13$  and  $0.44 \pm 0.04$  were obtained for thickness and weight gain data, respectively. Thus coating formation adheres fairly well to a parabolic growth law. The parabolic rate constant was  $7.9 \times 10^{-10}$  cm<sup>2</sup>/sec with a standard deviation of  $\pm 2.3 \times 10^{-10}$  cm<sup>2</sup>/sec. This is less than the parabolic rate constants calculated for coating formation in chloride-activated packs. The differences in rate constants, coating microstructures, and sensitivities to local variations in pack composition between coatings formed in chloride- and bromide-activated packs may be indicative of a difference in the rate-controlling step in coating formation in these packs.

**Effect of temperature.**—Coating deposition temperatures of 982°, 1038°, 1093°, and 1149°C were used with NaCl-activated packs run for 16 hr. Inclusion of data from 15-hr, 1093°C packs is felt to introduce a negligible error. The log of coating weight squared at constant time is, to a good approximation, a linear function of reciprocal absolute temperature as can be seen from Fig. 6. A +15°C variation in temperature gives an 18% increase in coating thickness. Regression analyses of weight gain and coating thickness data for assumed parabolic behavior gave activation energies of 88 kcal/mole. The standard deviations of the activation energy (slope) were  $\pm 11$  and  $\pm 13$  kcal/mole for the lines fit to thickness and weight data, respectively.

The XRD results confirmed that the primary coating phase was  $\beta$ . Photomicrographs of coatings deposited at each of the four pack temperatures are shown in Fig. 7. Coatings deposited at 982° through 1093°C are very similar in general microstructure. They all have the characteristic inclusion-free outer or primary  $\beta$ -layer and a distinctly defined, lighter etching zone having a high concentration of MC carbide inclusions. Second-phase inclusions are concentrated at the inner part of the primary layer in the 982° and 1038°C deposited coatings as they were in the coating applied in the 8-hr, 1093°C pack. Longer times or higher temperatures spread the distribution of these particles throughout the outer layer. The growth of the primary  $\beta$ -layer was much more sensitive to tem-

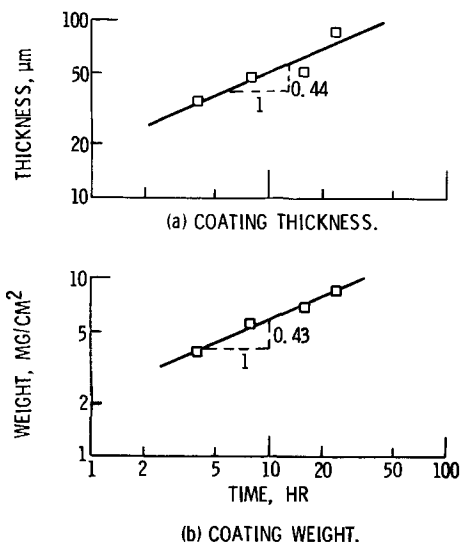


Fig. 5. Growth of aluminide coatings on IN-100 in 1 w/o aluminum sodium bromide-activated 1093°C packs.

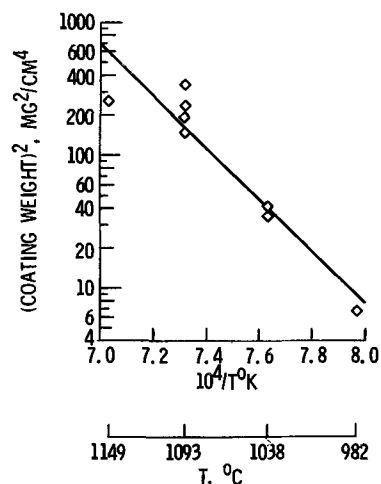


Fig. 6. Effect of temperature on the formation of aluminide coatings on IN-100 in 15- and 16-hr NaCl-activated packs.  $w^2 = k_0 t \exp(-1000 Q/RT)$ .

perature than was the growth of the secondary zone adjacent to the substrate. Carbide depletion of the substrate to a depth comparable to the coating thickness (not shown), recrystallization of the columnar secondary zone, formation of a layer of  $\gamma$  (nickel solid solution) at the coating substrate interface, and growth of a zone of large equiaxed grains essentially free of second-phase inclusions in the outer  $\beta$ -layer have all occurred in the coating deposited at 1149°C. The coating is also considerably softer than coatings deposited at lower temperatures. These features are characteristic of a partially depleted aluminide coating on IN-100 (8). In summary, coating microstructures obtained in 982° or 1038°C, 16-hr packs (Fig. 7a and b) and 1093°C, 4- and 8-hr packs (Fig. 2a and b) have microstructures characteristic of low-activity pack coatings (i.e., a single-phase  $\beta$  outer coating zone) whereas the coating microstructures obtained at higher temperatures or longer times are hybrids incorporating features found in heat-treated high-activity pack coatings and low-activity pack coatings as discussed by Goward and Boone (5).

**Effect of activators.**—The results of activator variation in 16-hr, 1093°C packs are listed in Table I and plotted as bar graphs in Fig. 8a and b. In all cases the XRD analysis of the coatings detected  $\beta$  as the major coating phase. Examination of Fig. 8a and b indicates that aluminum pickup generally increases with decreasing atomic number of the halogen. The XRF analyses of the surface (Fig. 8c and d) indicated that the trend for surface nickel content was approximately the inverse of the trend for aluminum pickup; i.e., surface nickel content generally increased with increasing atomic number of the halogen. These observations indicate that the ability of higher molecular weight halogens to deposit aluminum is less than that of lower molecular weight halogens. Thus gas phase kinetics and thermodynamics must play a significant role in aluminum deposition under some conditions.

The changes in halide and the accompanying changes in the rate of coating formation have an effect on the coating microstructure and phase distribution as can be seen in the photomicrographs in Fig. 9 and 10. The coatings formed in 16-hr, fluoride- and chloride-activated packs have microstructural features derived from both the heat-treated high-activity and the low-activity pack classifications. The bromide- and iodide-activated pack coatings (Fig. 9c and d and 10c and d) have microstructural features peculiar to low-activity pack coatings. Aluminum content in these coatings is generally lower than in lower temperature or shorter time NaCl-activated pack coatings having about the same weight (Fig. 3a and b and 7b). Consequently, the coatings formed in bromide- and iodide-activated

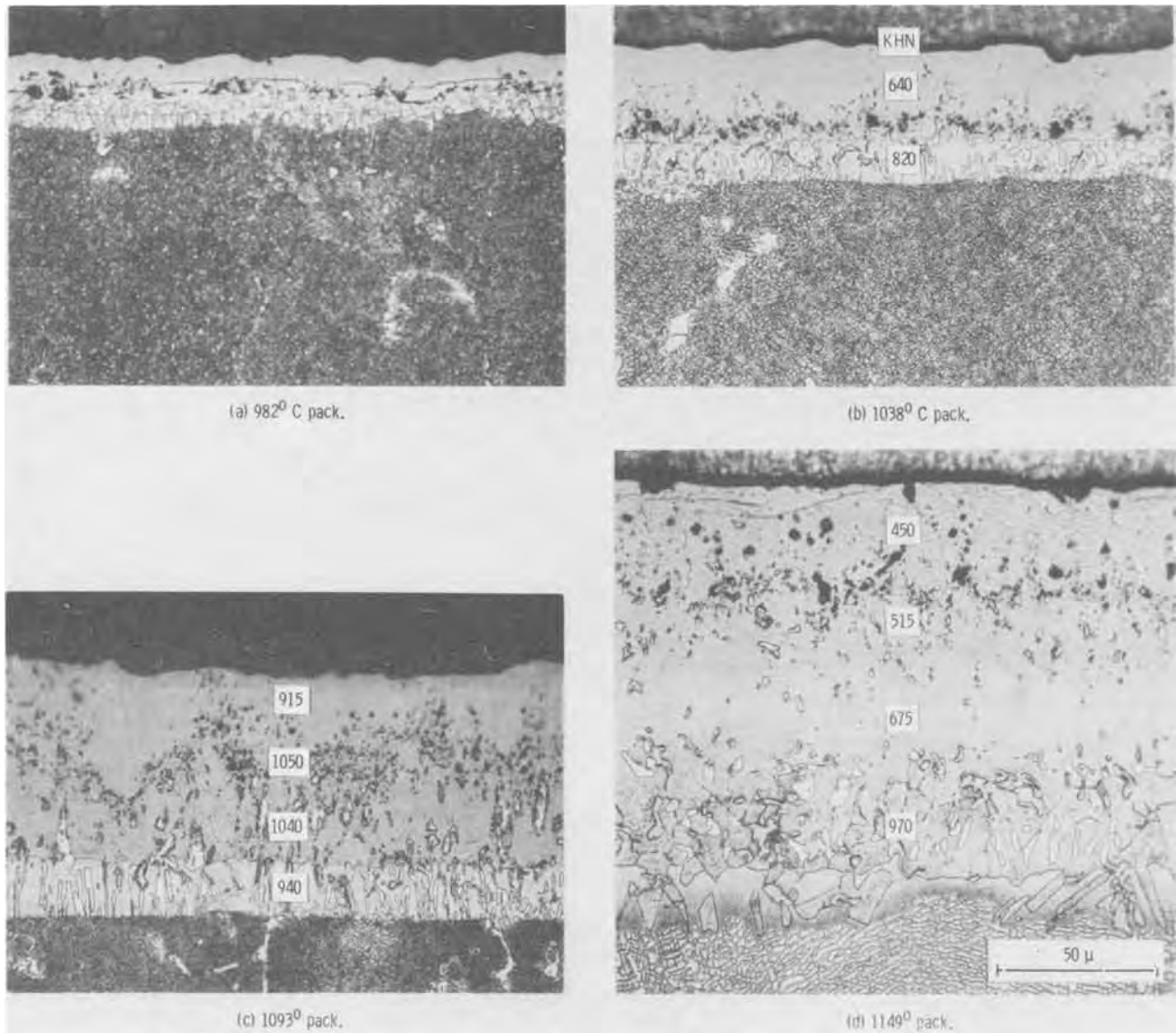


Fig. 7. Cross-sectional micrographs showing the effect of temperature on aluminide coating growth on IN-100 in NaCl-activated 16-hr packs.

packs are generally softer than coatings formed in corresponding fluoride- and chloride-activated packs.

However, they have microstructures similar to these NaCl-activated pack coatings.

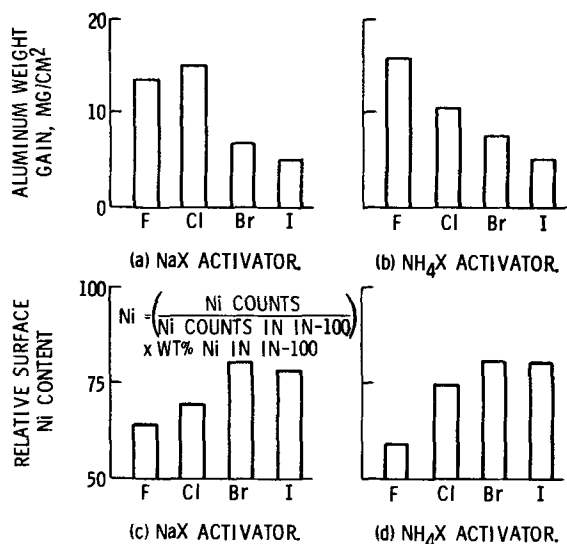


Fig. 8. Aluminum weight gain and surface nickel content in 16 hr, 1093°C packs as a function of halide activator.

*Effect of pack composition.*—An increase in pack aluminum and NaCl content from 1 to 2% had no significant impact on aluminum pickup in a 1093°C, 16-hr, 1% aluminum pack. Also, an increase in NaI content from 1 to 3% had no significant impact on aluminum deposition in a 1093°C, 16-hr, 1% aluminum pack. However, an increase of aluminum content from 1 to 5% in a 1% NaBr, 1093°C, 16-hr pack increased aluminum pickup from 6.8 to 16.1 mg/cm<sup>2</sup>. The microstructure of this coating, shown in Fig. 11, is very similar to microstructures of 16- and 24-hr NaCl-deposited coatings. This sensitivity to pack aluminum content indicates that gas phase kinetics play a significant role in the rate of aluminum deposition in NaBr-activated packs. Similar behavior could be anticipated in NH<sub>4</sub>Br- and iodide-activated packs based on the strong similarities between coatings put down by these packs and the 1 w/o Al, NaBr-activated pack.

**Discussion**

*Pack stability.*—In this study aluminide coatings were deposited on IN-100 in a semiopen system. The ability of such a system to maintain stable bulk pack aluminum deposition capability throughout an experiment is a natural first subject for discussion. For ex-

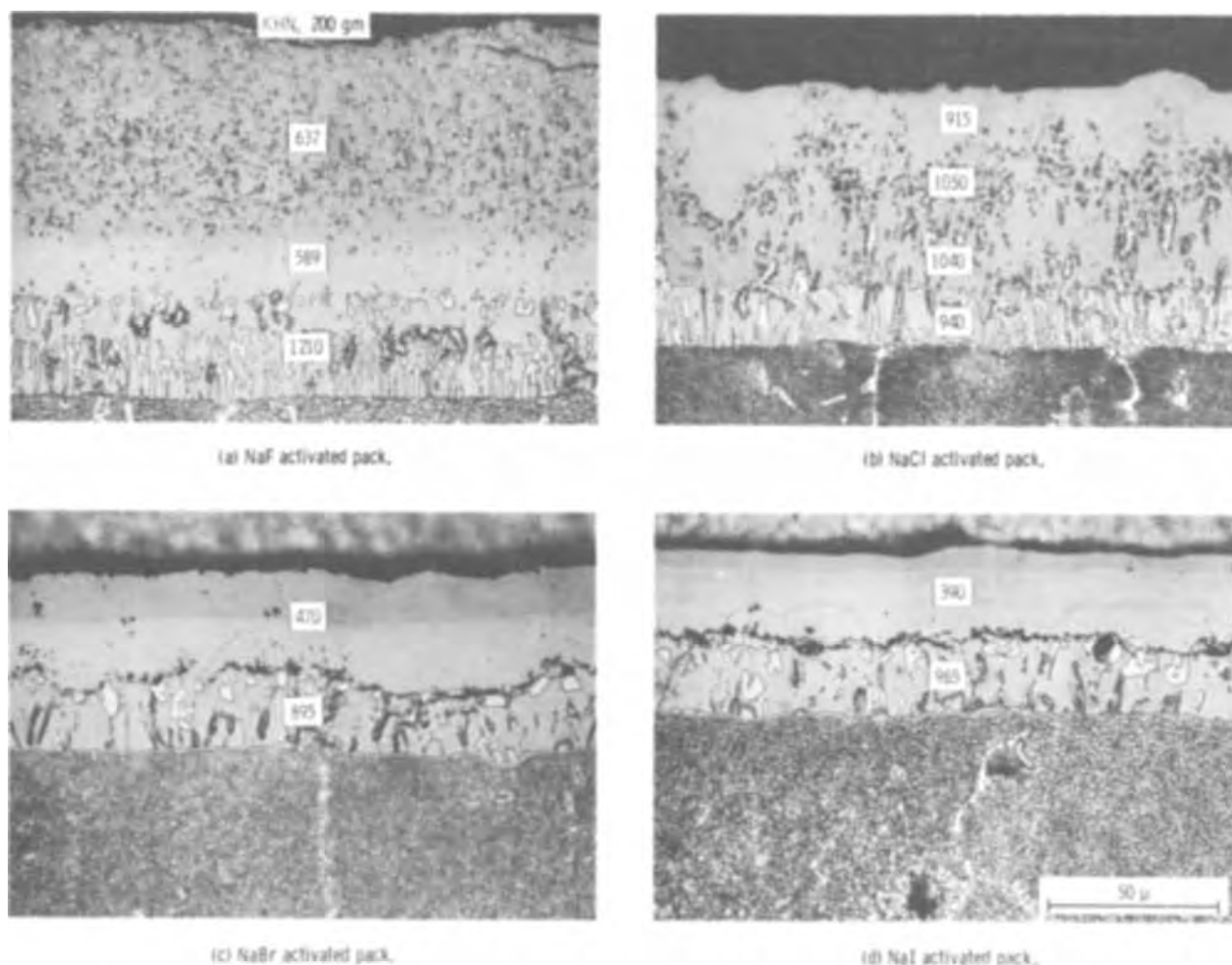


Fig. 9. Cross-sectional micrographs showing the effect of halogen variation in sodium halide-activated 1093°C, 16-hr packs.

ample, a maximum in coating microhardness was observed at 16 hr and  $M_2Al_3$  was detected as a minor phase only in 8- and 16-hr coatings deposited in 1093°C, NaCl-activated packs. These observations may be indicative of a decline in bulk pack aluminum deposition capability with time or may merely be due to the growth of a depleted zone in the pack adjacent to the specimen surface.

To obtain some feeling for the stability of the various packs and eventually permit an analysis of the kinetics of aluminum deposition, thermodynamic analyses for the initial bulk pack compositions were performed. The results of the thermodynamic analyses of the bulk pack compositions, as discussed in detail in Appendix A, are presented in Table II. On the basis of condensed phases present, the packs fall into three groups: sodium halide-activated packs with NaX(l) and Al(l) present;  $NH_4F$ -activated packs with  $AlF_3(s)$  and  $AlN(s)$  present; and  $NH_4X$  ( $X = Cl, Br, \text{ or } I$ ) activated packs with Al(l) and  $AlN(s)$  present. Based on the nature of the condensed phases present at local equilibrium in the bulk pack as listed in Table II, the sodium halide- and ammonium fluoride-activated packs should be stable as a function of time whereas the other ammonium halide-activated packs may not be stable.

The results of Cl, Na, and Al analyses of pack material from a 24-hr NaCl-activated, 1093°C pack as listed in Table III did not confirm that a significant decrease in bulk pack aluminum deposition capability occurred. Calculation of the partial pressures of reactive species in the pack at 24 hr from the results of the chemical analyses gave values equal to or greater than those calculated for the initial conditions. Thus the absence of  $M_2Al_3$  in the 24-hr pack is attributed

to formation of a depleted zone in the pack at the specimen surface. More direct evidence of depleted zone formation was obtained from the XRD and chemical analyses of samples taken from the bulk pack and from within 0.5 cm of the sample surface after completion of a 16-hr, 1093°C, NaCl-activated pack as reported in Table III. Aluminum was detected by XRD as a minor phase in the bulk pack but was not detected at the specimen surface. Conversely, NaCl was detected as a possible minor phase at the specimen surface but was not detected in the bulk pack. Chemical analyses of these samples, as listed in Table III, confirm the XRD results. The Al content of the bulk pack was considerably higher than that of the pack close to the specimen surface whereas the Na and Cl constants of the bulk pack were found to be lower than at the specimen surface. Thus a depleted zone is formed in the packs. Formation of a depleted zone in aluminizing packs was previously reported by Brill-Edwards and Epner (6). An idealized sketch of the depleted zone is shown in Fig. 12. The actual depleted zone probably does not show an abrupt transition since gaseous diffusion permits gradual depletion of aluminum over an extended transition zone.

Since no condensed halide source is present in  $NH_4X$  ( $X = Cl, Br, \text{ or } I$ ) activated packs whereas NaX(l) is present in corresponding sodium halide packs the stability of the  $NH_4X$  packs may be considerably lower than that of NaX-activated packs. Also, for example, extremely high initial deposition rates may be obtained with  $NH_4Cl$  during the early part of the coating cycle when the partial pressure of  $AlCl(g)$  is more than an order of magnitude higher than in the NaCl-activated pack. However, the coating deposition data for NaCl- and  $NH_4Cl$ -activated packs, plotted in Fig. 3, suggest

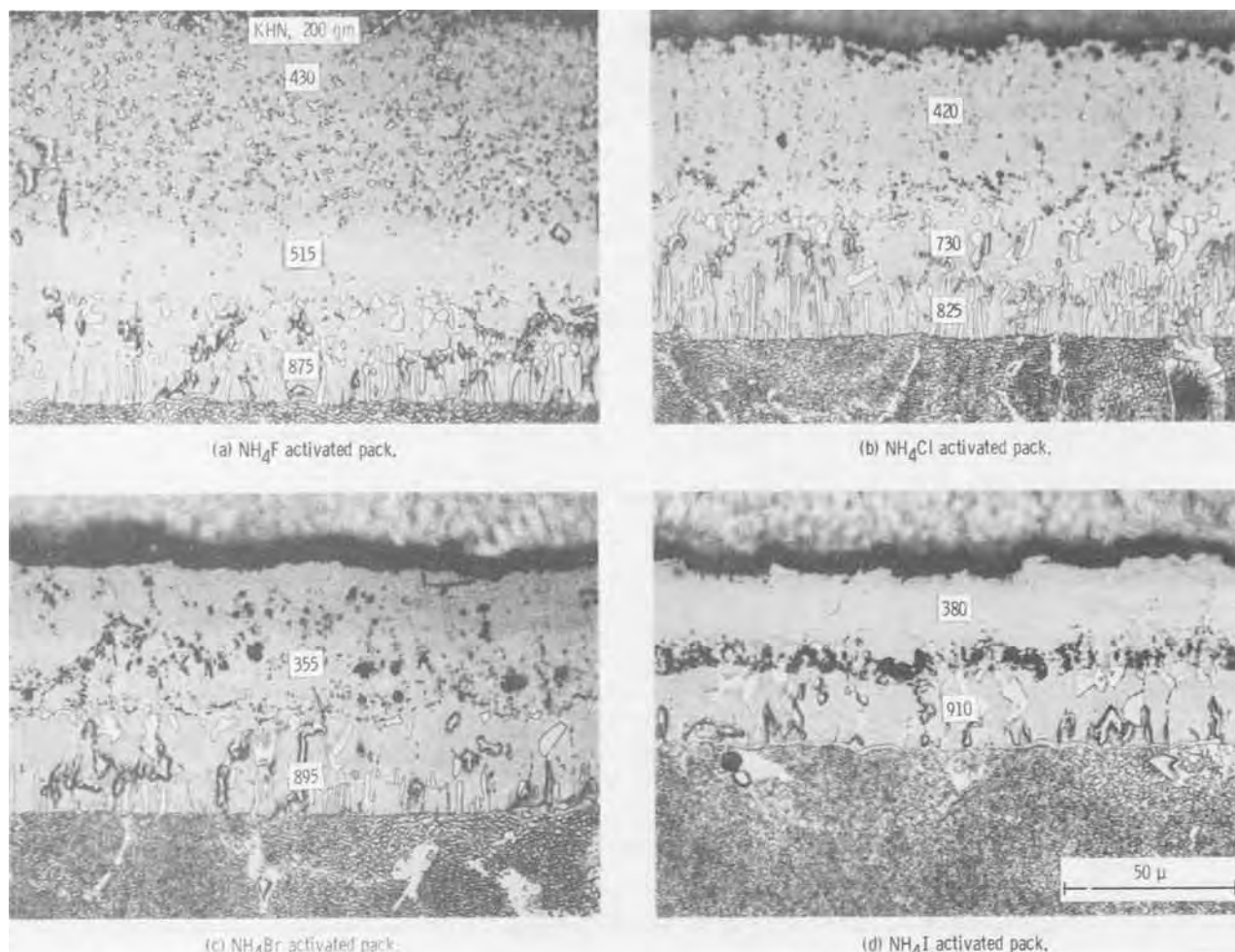


Fig. 10. Cross-sectional micrographs showing the effect of halogen variation in ammonium halide-activated 1093°C, 16-hr packs.

that the  $\text{NH}_4\text{X}$  ( $\text{X} = \text{Cl}, \text{Br}, \text{or I}$ ) activated packs behave similarly to  $\text{NaX}$ -activated packs in the sense that initial deposition rates are not significantly different and that rapid dilution of the  $\text{NH}_4\text{Cl}$ -activated pack does not occur in spite of the absence of a condensed halide phase. In addition, there is strong correspondence between the microstructures and weights of coatings applied by corresponding halides of sodium and ammonium as can be seen from Fig. 9 and 10 and Table I.

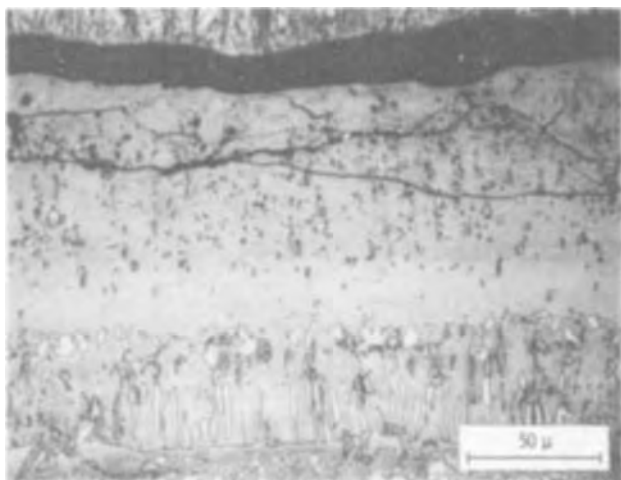


Fig. 11. Cross-sectional microstructure of an aluminide coating deposited on IN-100 in a 1 w/o NaBr, 5 w/o Al, 16-hr, 1093°C pack.

**Pack kinetics.—Experimental.**—In this study parabolic rate constants of  $1.3 \pm 0.4 \times 10^{-9} \text{ cm}^2/\text{sec}$  for  $\text{NH}_4\text{Cl}$ -activated coating deposition and  $1.6 \pm 0.4 \times 10^{-9} \text{ cm}^2/\text{sec}$  for  $\text{NaCl}$ -activated coating deposition were obtained. These values are less than rate constants reported by Janssen and Rieck (9) for growth of  $\text{NiAl}$  between  $\text{Ni}_2\text{Al}_3$  and  $\text{Ni}_3\text{Al}$  and for nonstoichiometric  $\text{NiAl}$  from  $\text{NiAl}$  and  $\text{Ni}$ . Extrapolation of their results to 1093°C gave rate constants of  $5 \times 10^{-9} \text{ cm}^2/\text{sec}$  for the former reaction and  $6 \times 10^{-9} \text{ cm}^2/\text{sec}$  for the latter. The difference between rate constants for coating formation on IN-100 and diffusion in binary couples could be due to both the effects of solutes such as Cr, Co, and Ti derived from the IN-100 substrate and to the order of magnitude variation in diffusivity between stoichiometric  $\text{NiAl}$  (in which the diffusivity of nickel is a minimum) and nickel-rich  $\text{NiAl}$  (10) (which controls layer growth as determined by Janssen and Rieck).

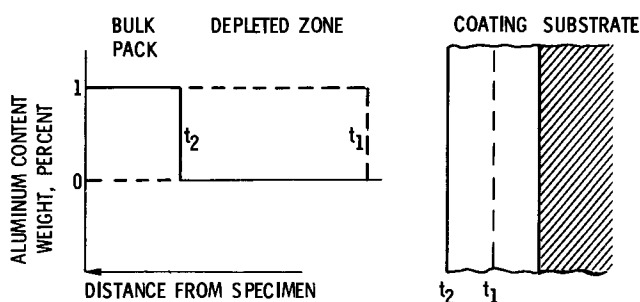


Fig. 12. Idealized depleted zone formation during pack aluminizing. Time,  $t_2 > t_1$ .



Table II. Calculated initial pressures of reactive pack species (atm)

Acti- vator	Temper- ature, °C	P <sub>Al</sub>	P <sub>AlX</sub>	P <sub>AlX<sub>2</sub></sub>	P <sub>AlX<sub>3</sub></sub>	P <sub>AlX<sub>4</sub></sub>	P <sub>Al<sub>2</sub>X<sub>3</sub></sub>	ΣP <sub>AlX<sub>i</sub></sub>	P <sub>NaX</sub>	P <sub>Na<sub>2</sub>X<sub>2</sub></sub>	P <sub>Na</sub>	P <sub>Na<sub>2</sub></sub>	ΣP <sub>Na<sub>i</sub></sub>	Initial conditions moles				
														Al (t)	AlN (s)	AlF <sub>3</sub> (s)	NaX (t)	Al <sub>2</sub> O <sub>3</sub>
NaF	1093	1.54 × 10 <sup>-4</sup>	8.19 × 10 <sup>-3</sup>	2.36 × 10 <sup>-3</sup>	3.61 × 10 <sup>-3</sup>	1.39 × 10 <sup>-5</sup>	—	8.79 × 10 <sup>-3</sup>	1.23 × 10 <sup>-3</sup>	6.20 × 10 <sup>-4</sup>	9.63 × 10 <sup>-3</sup>	6.15 × 10 <sup>-4</sup>	9.69 × 10 <sup>-3</sup>	—	—	—	—	
NaCl	982	1.41 × 10 <sup>-7</sup>	9.04 × 10 <sup>-4</sup>	8.07 × 10 <sup>-5</sup>	3.81 × 10 <sup>-7</sup>	<3 × 10 <sup>-7</sup>	—	9.85 × 10 <sup>-4</sup>	6.91 × 10 <sup>-3</sup>	2.48 × 10 <sup>-3</sup>	1.07 × 10 <sup>-3</sup>	1.42 × 10 <sup>-4</sup>	1.07 × 10 <sup>-3</sup>	—	—	—	—	
NaCl	1038	4.96 × 10 <sup>-7</sup>	2.03 × 10 <sup>-3</sup>	1.89 × 10 <sup>-4</sup>	9.09 × 10 <sup>-7</sup>	<3 × 10 <sup>-7</sup>	—	2.22 × 10 <sup>-3</sup>	1.44 × 10 <sup>-3</sup>	4.82 × 10 <sup>-3</sup>	2.41 × 10 <sup>-3</sup>	5.20 × 10 <sup>-7</sup>	2.41 × 10 <sup>-3</sup>	—	—	—	—	
NaCl	1093	1.54 × 10 <sup>-6</sup>	4.20 × 10 <sup>-3</sup>	4.03 × 10 <sup>-4</sup>	1.98 × 10 <sup>-6</sup>	<3 × 10 <sup>-7</sup>	—	4.61 × 10 <sup>-3</sup>	2.77 × 10 <sup>-2</sup>	8.67 × 10 <sup>-3</sup>	5.01 × 10 <sup>-3</sup>	1.66 × 10 <sup>-4</sup>	5.01 × 10 <sup>-3</sup>	—	—	—	—	
NaCl	1149	4.45 × 10 <sup>-6</sup>	8.27 × 10 <sup>-3</sup>	8.20 × 10 <sup>-4</sup>	4.10 × 10 <sup>-6</sup>	<3 × 10 <sup>-7</sup>	—	9.10 × 10 <sup>-3</sup>	5.10 × 10 <sup>-2</sup>	1.49 × 10 <sup>-2</sup>	9.91 × 10 <sup>-3</sup>	4.92 × 10 <sup>-4</sup>	9.91 × 10 <sup>-3</sup>	—	—	—	—	
NaBr	1093	1.54 × 10 <sup>-6</sup>	1.75 × 10 <sup>-3</sup>	—	7.73 × 10 <sup>-6</sup>	—	—	1.76 × 10 <sup>-3</sup>	5.03 × 10 <sup>-3</sup>	—	1.77 × 10 <sup>-3</sup>	2.08 × 10 <sup>-7</sup>	1.77 × 10 <sup>-3</sup>	—	—	—	—	
NaI	1093	1.54 × 10 <sup>-6</sup>	4.61 × 10 <sup>-3</sup>	—	1.23 × 10 <sup>-3</sup>	—	—	4.61 × 10 <sup>-3</sup>	1.32 × 10 <sup>-1</sup>	—	4.61 × 10 <sup>-3</sup>	1.41 × 10 <sup>-3</sup>	4.61 × 10 <sup>-3</sup>	—	—	—	—	
NH <sub>4</sub> F	1093	5.18 × 10 <sup>-3</sup>	2.06 × 10 <sup>-2</sup>	4.43 × 10 <sup>-3</sup>	5.05 × 10 <sup>-3</sup>	2.74 × 10 <sup>-3</sup>	7.91 × 10 <sup>-3</sup>	7.83 × 10 <sup>-3</sup>	—	—	—	—	—	—	—	—	—	
NH <sub>4</sub> Cl	1093	1.54 × 10 <sup>-4</sup>	7.65 × 10 <sup>-2</sup>	1.34 × 10 <sup>-1</sup>	1.20 × 10 <sup>-3</sup>	4.03 × 10 <sup>-7</sup>	2.15 × 10 <sup>-9</sup>	2.23 × 10 <sup>-1</sup>	—	—	—	—	—	—	—	—	—	
NH <sub>4</sub> Br	1093	1.54 × 10 <sup>-4</sup>	4.35 × 10 <sup>-2</sup>	—	1.19 × 10 <sup>-3</sup>	—	2.21 × 10 <sup>-9</sup>	1.63 × 10 <sup>-1</sup>	—	—	—	—	—	—	—	—	—	
NH <sub>4</sub> I	1093	1.54 × 10 <sup>-4</sup>	3.10 × 10 <sup>-1</sup>	—	3.74 × 10 <sup>-3</sup>	—	1.98 × 10 <sup>-9</sup>	3.14 × 10 <sup>-1</sup>	—	—	—	—	—	—	—	—	—	

Sample	Chemical analysis			
	Leach	Na, ppm	Cl, ppm	Al, ppm
No. 1, 24-hr, bulk	H <sub>2</sub> O	—	237	53
	HCl	113	—	2072
	NaOH	—	226	1995
No. 2, 24-hr, bulk	Average values	113	232	2034 <sup>(b)</sup>
	H <sub>2</sub> O	—	230	33
	HCl	54	—	947
16-hr, bulk	Average values	54	229	963
	H <sub>2</sub> O	31	220	0
	HCl	57	—	7540
16-hr, surface	Total values <sup>(a)</sup>	88	220	7540
	H <sub>2</sub> O	88	327	0
	HCl	55	—	360
X-Ray diffraction				
Sample	Major phase	Minor phase	Possible minor phase	
16-hr, bulk	α-Al <sub>2</sub> O <sub>3</sub>	Al	—	
16-hr, surface	α-Al <sub>2</sub> O <sub>3</sub>	—	NaCl	

(a) Leaches were successive on a single sample.  
 (b) Average Al analysis for HCl and NaOH leaches only.

Also, in this study an activation energy of 88 ± 13 kcal/mole was obtained for the deposition process in NaCl-activated packs. This value is in poor agreement with a value of 41 kcal/mole reported by Janssen and Rieck (9) for diffusion of nickel in β as determined by layer growth studies. However, the activation energy falls close to the upper end of the range of values for nickel diffusion in NiAl reported by Hancock and McDonnell (10): 73.4 ± 2.3 kcal/mole for stoichiometric NiAl to 42.5 ± 6.3 kcal/mole for the 48.3 a/o (atom per cent) Ni composition. The activation energy is also in agreement with the activation energy of 81 kcal/mole reported for Co tracer diffusion in NiAl by Berkowitz *et al.* (11). Based on the coating growth rate constants and activation energies observed in this study and their reasonable agreement with data for the NiAl system (9-11), we conclude that nickel diffusion through the coating may be the rate-controlling step in Na<sub>4</sub>Cl- and NH<sub>4</sub>Cl-activated packs run between 982° and 1149°C. Additional support comes from metallography and XRD results which indicated that the coating was primarily β and from the observed insensitivity of NaCl packs to 1% variations in aluminum and activator content.

In NaBr-activated packs high sensitivity of coating weight to pack aluminum content was observed. The kinetics of aluminum deposition in 1 w/o NaBr packs adhered reasonably well to a parabolic growth law, but the parabolic rate constant (7.9 ± 2.3 × 10<sup>-10</sup> cm<sup>2</sup>/sec) was smaller than in NaCl-activated packs (1.6 ± 0.4 × 10<sup>-9</sup> cm<sup>2</sup>/sec). Based on the sensitivity of NaBr packs to aluminum content and the lower aluminum pickup of 1 w/o Al bromide- and iodide-activated packs compared to chloride- and fluoride-activated packs, the authors conclude that gas phase kinetics was the rate-controlling step in aluminum deposition from bromide- and iodide-activated packs containing 1 w/o aluminum.

*Analytical.*—To further elucidate the role of gas phase kinetics in aluminide coating formation, analyses of aluminum transport from the bulk pack through the pack depleted zone to the surface of the coating were carried out. The starting points for the analyses were the thermodynamic calculations discussed in Appendix A and the pack depletion zone model, Fig. 12. The analyses of gas phase kinetics are discussed in Appendix B where the calculation of instantaneous fluxes of aluminum for a simplified case is outlined. The in-

stantaneous flux is given by

$$\frac{N_{Al}d}{A} = \frac{\sum_{i=1}^n D_i(P_1 - P'_i)}{RT} \quad [2]$$

where  $D_i$  and  $P_i$  are the diffusivity and partial pressure of the  $i$ th aluminum-bearing species with the prime referring to the sample surface,  $d$  is the diffusion distance and  $N_{Al}$  is the rate of transport of Al in moles/second. The computations included mass balances on H, X, and Na and allowed for condensation of NaX(l) as appropriate. In  $NH_4X$ -activated packs dilution by 9.8 moles of argon (4 hr of argon flow) was used to arrive at bulk pack compositions. In the case of  $NH_4F$  pseudoequilibrium bulk pack compositions were used since dilution with 9.8 moles of argon results in disappearance of the  $AlF_3(s)$  phase. The computations were made for an assumed surface aluminum activity of  $1 \times 10^{-2}$ . This is a reasonable choice for average aluminum activity in view of the fact that Steiner and Komarek (12) report an activity of  $1 \times 10^{-2}$  for aluminum in stoichiometric NiAl at 1000°C. Results are listed in Table IV for major diffusing species.

From the instantaneous fluxes the diffusion direction of each species in the pack depleted zone was ascertained. These are illustrated in Fig. 13 (a) for the simplified model for NaX-activated packs in which NaX(l) condensation was not considered, (b) for the complete model for NaX-activated packs where NaX(l) condensation was considered, and (c) for  $NH_4X$ -acti-

vated packs. Instantaneous fluxes of major species are compared to the net instantaneous aluminum flux in Fig. 14. Aluminum is deposited primarily by AlX. NaX(l) condensation (Fig. 14b) augments aluminum deposition by not requiring halogen removal by AlX<sub>2</sub> and AlX<sub>3</sub> diffusion (Fig. 14a). In reality, the actual fluxes for NaX-activated packs are probably bounded by the complete and simplified models. Evidence of NaX condensation in the depleted zone was obtained. However, some depletion of Na as a result of reaction with alumina and by transport out of the semiopen system does occur.

In addition to aluminum being deposited, loss of substrate species from IN-100 can contribute to observed net specimen weight change and thus cause misinterpretation of coating weight. Analyses were performed for Ni and Cr. Very small amounts of nickel are lost from the substrate as nickel and nickel halide. At 1366°K the partial pressure of nickel over the alloy is only about  $10^{-10}$  atm (13). This gives a nickel flux of about  $10^{-14}$  moles/cm<sup>2</sup>-sec from the coating surface to the bulk pack.

The estimated Cr partial pressure over IN-100 is 0.1  $P_{Cr} = 1.3 \times 10^{-7}$  atm at 1366°K (13). This gives a Cr flux of about  $1.3 \times 10^{-11}$  moles/cm<sup>2</sup>-sec. Thus, at worst, the chromium weight loss in a 16-hr, 1093°C pack was about 1% of the aluminum weight gain.

The rate of aluminum deposition  $dw/dt$  in milligrams per square centimeter-second was computed from the instantaneous fluxes according to the following equation

Table IV. Major instantaneous fluxes and net aluminum deposition rate constants and weights for gaseous diffusion from a bulk 1 w/o Al pack to a surface at aluminum activity  $1 \times 10^{-2}$

Acti- vator	Temper- ature, °K	AlX				AlX <sub>2</sub>		AlX <sub>3</sub>		X	
		$P_{1s}$	$P'_{1s}$	$\frac{D_1}{\text{cm}^2 \text{ sec}}$	$\frac{D_1 \Delta P_1}{RT \text{ moles-cm}^2 \text{ sec}}$	$D_2$	$\frac{D_2 \Delta P_2}{RT}$	$D_3$	$\frac{D_3 \Delta P_3}{RT}$	$D_4$	$\frac{D_4 \Delta P_4}{RT}$
A. Simplified model: only AlX, AlX <sub>2</sub> , AlX <sub>3</sub> , and X considered											
NaF	1366	$8.19 \times 10^{-2}$	$8.23 \times 10^{-3}$	1.57	$1.0 \times 10^{-6}$	1.32	$-2.6 \times 10^{-10}$	1.16	$-3.4 \times 10^{-7}$	2.95	$-2.7 \times 10^{-19}$
NaCl	1255	$9.04 \times 10^{-4}$	$8.15 \times 10^{-4}$	1.12	$7.5 \times 10^{-9}$	0.875	$-3.1 \times 10^{-9}$	0.739	$-3.8 \times 10^{-10}$	1.60	$-1.4 \times 10^{-15}$
NaCl	1311	$2.03 \times 10^{-3}$	$4.74 \times 10^{-4}$	1.19	$1.7 \times 10^{-8}$	0.934	$-7.2 \times 10^{-9}$	0.788	$-8.4 \times 10^{-10}$	1.71	$-7.2 \times 10^{-13}$
NaCl	1366	$4.20 \times 10^{-3}$	$8.73 \times 10^{-4}$	1.27	$3.8 \times 10^{-8}$	0.993	$-1.6 \times 10^{-8}$	0.839	$-1.8 \times 10^{-9}$	1.82	$-3.1 \times 10^{-14}$
NaCl	1422	$8.27 \times 10^{-3}$	$1.89 \times 10^{-3}$	1.35	$7.5 \times 10^{-8}$	1.05	$-3.1 \times 10^{-8}$	0.891	$-3.7 \times 10^{-9}$	1.93	$-1.3 \times 10^{-13}$
NaBr	1366	$1.75 \times 10^{-3}$	$3.66 \times 10^{-4}$	1.11	$1.4 \times 10^{-8}$	—	—	0.732	$-4.7 \times 10^{-9}$	1.41	$-5.0 \times 10^{-12}$
NaI	1366	$4.61 \times 10^{-3}$	$4.13 \times 10^{-3}$	0.981	$4.1 \times 10^{-9}$	—	—	0.636	$-5.0 \times 10^{-10}$	1.17	$-2.7 \times 10^{-9}$
B. Complete solution: all species considered											
NaF	1366	$8.19 \times 10^{-2}$	$3.00 \times 10^{-3}$	1.57	$1.1 \times 10^{-6}$	1.32	$2.4 \times 10^{-8}$	1.16	$1.9 \times 10^{-8}$	2.95	$-7.8 \times 10^{-20}$
NaCl		$4.20 \times 10^{-3}$	$1.09 \times 10^{-4}$	1.27	$4.7 \times 10^{-6}$	0.993	$3.4 \times 10^{-9}$	0.839	$1.2 \times 10^{-11}$	1.82	$-2.3 \times 10^{-15}$
NaBr		$1.75 \times 10^{-3}$	$3.94 \times 10^{-5}$	1.11	$1.7 \times 10^{-8}$	—	—	0.732	$4.4 \times 10^{-11}$	1.41	$-3.1 \times 10^{-13}$
NaI		$4.61 \times 10^{-3}$	$9.18 \times 10^{-5}$	0.981	$4.1 \times 10^{-8}$	—	—	0.636	$6.6 \times 10^{-14}$	1.17	$-3.0 \times 10^{-11}$
NH <sub>4</sub> F		$2.06 \times 10^{-2}$	$1.01 \times 10^{-3}$	1.57	$2.7 \times 10^{-7}$	1.32	$4.1 \times 10^{-8}$	1.16	$-1.0 \times 10^{-7}$	2.95	$-8.8 \times 10^{-19}$
NH <sub>4</sub> Cl		$1.27 \times 10^{-2}$	$2.27 \times 10^{-4}$	1.27	$1.4 \times 10^{-7}$	0.993	$-7.2 \times 10^{-8}$	0.839	$3.7 \times 10^{-10}$	1.82	$-3.4 \times 10^{-15}$
NH <sub>4</sub> Br		$8.34 \times 10^{-3}$	$6.82 \times 10^{-4}$	1.11	$7.5 \times 10^{-8}$	—	—	0.732	$-2.4 \times 10^{-8}$	1.41	$-8.4 \times 10^{-12}$
NH <sub>4</sub> I		$7.57 \times 10^{-3}$	$6.19 \times 10^{-3}$	0.981	$1.2 \times 10^{-8}$	—	—	0.636	$-1.7 \times 10^{-9}$	1.17	$-4.1 \times 10^{-9}$
Acti- vator	Temper- ature, °K	Na		Al <sub>2</sub> X <sub>3</sub>		HX		H <sub>2</sub>		$k_{Al}$ , mg <sup>2</sup> -sec	Predicted Al weight gain, mg/cm <sup>2</sup>
		$D_5$	$\frac{D_5 \Delta P_5}{RT}$	$D_6$	$\frac{D_6 \Delta P_6}{RT}$	$D_7$	$\frac{D_7 \Delta P_7}{RT}$	$D_8$	$\frac{D_8 \Delta P_8}{RT}$		
A. Simplified model: only AlX, AlX <sub>2</sub> , AlX <sub>3</sub> , and X considered											
NaF	1366	—	—	—	—	—	—	—	—	$5.9 \times 10^{-2}$	5.8
NaCl	1255	—	—	—	—	—	—	—	—	$3.2 \times 10^{-4}$	4.3
NaCl	1311	—	—	—	—	—	—	—	—	$7.8 \times 10^{-4}$	6.7
NaCl	1366	—	—	—	—	—	—	—	—	$1.6 \times 10^{-3}$	9.7
NaCl	1422	—	—	—	—	—	—	—	—	$3.2 \times 10^{-3}$	14
NaBr	1366	—	—	—	—	—	—	—	—	$7.8 \times 10^{-4}$	6.7
NaI	1366	—	—	—	—	—	—	—	—	$3.2 \times 10^{-4}$	4.3
B. Complete solution: all species considered											
NaF	1366	1.93	$1.2 \times 10^{-6}$	0.801	$7.5 \times 10^{-11}$	—	—	—	—	$1.0 \times 10^{-1}$	76
NaCl		1.93	$5.3 \times 10^{-8}$	0.610	$5.9 \times 10^{-20}$	—	—	—	—	$4.3 \times 10^{-3}$	16
NaBr		1.93	$1.7 \times 10^{-8}$	—	—	—	—	—	—	$1.5 \times 10^{-3}$	9.5
NaI		1.93	$4.1 \times 10^{-3}$	—	—	—	—	—	—	$3.5 \times 10^{-3}$	14
NH <sub>4</sub> F		—	—	0.801	$-8.1 \times 10^{-9}$	2.61	$-5.9 \times 10^{-9}$	8.17	$3.1 \times 10^{-9}$	$1.7 \times 10^{-2}$	31
NH <sub>4</sub> Cl		—	—	0.610	$5.0 \times 10^{-17}$	—	—	—	—	$3.5 \times 10^{-3}$	15
NH <sub>4</sub> Br		—	—	—	—	1.29	$-2.2 \times 10^{-9}$	8.17	$1.1 \times 10^{-9}$	$4.3 \times 10^{-3}$	16
NH <sub>4</sub> I		—	—	—	—	1.09	$-3.1 \times 10^{-9}$	8.17	$1.6 \times 10^{-9}$	$8.9 \times 10^{-4}$	7.2

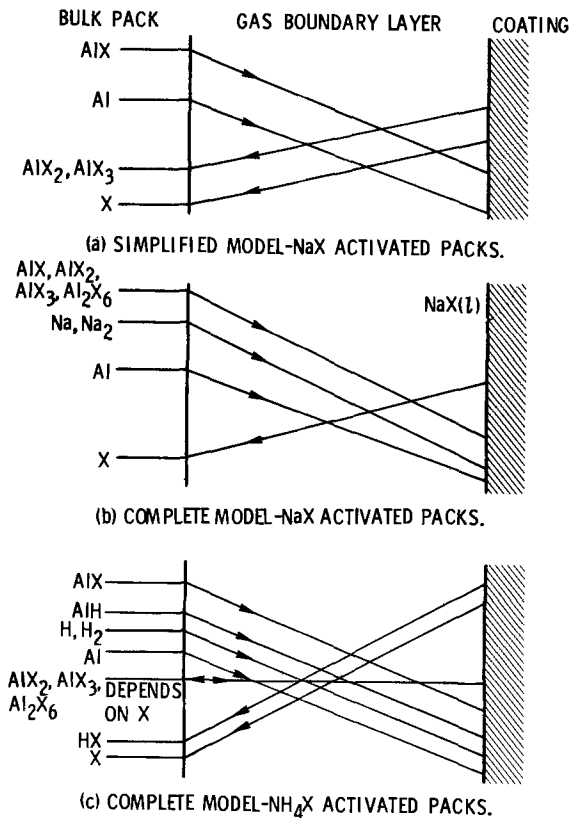


Fig. 13. Schematic showing gas diffusion directions during aluminum deposition.

$$\frac{dw}{dt} = \left(\frac{\rho}{w}\right) \left(\frac{\epsilon}{l}\right) (m_{Al}1000) \left(\frac{N_{Al}d}{A}\right) \quad [3]$$

The term  $\rho/w = 1/d$  defines the growth of the pack depleted zone in terms of coating weight  $w$  and pack aluminum content  $\rho = 8 \text{ mg/cm}^3$  in 1 w/o Al packs. The term  $\epsilon/l$  corrects for diffusion through a porous medium. The effective transport area of the pack is to a good approximation, equal to the pack porosity,  $\epsilon = 0.79$ . In addition, the transport path is nonlinear and a correction factor  $l = 4$  was arbitrarily assumed. The third term converts from moles of aluminum to milligrams. Integration gives

$$w^2 = \frac{2\rho\epsilon}{l} \left(\frac{N_{Al}d}{A}\right) 2.7 \times 10^4 t \quad [4]$$

The aluminum deposition rate constants

$$k_{Al} = \frac{2\rho\epsilon}{l} \left(\frac{N_{Al}d}{A}\right) 2.7 \times 10^4 \quad [5]$$

are listed in Table IV. Inclusion of sodium halide condensation results in a 1.7 to 11-fold increase in  $k_{Al}$  depending on the halide. The moles of NaX(l) condensed are about equal to the moles of Al deposited according to the complete solution.

Computed instantaneous fluxes were relatively insensitive to large changes in assumed surface aluminum activity. For example, a tenfold decrease in surface aluminum activity would increase the computed instantaneous flux by a factor of 2 and the coating weight by only a factor of  $\sqrt{2}$ .

Predicted aluminum weight gains for 16-hr, 1 w/o Al packs are also listed in Table IV. These predicted values are plotted against observed aluminum weight gains in Fig. 15. For NaX-activated packs an average predicted value was used. The good agreement between observed and predicted coating weights in bromide- and iodide-activated, 1 w/o Al packs confirms that deposition is controlled by gaseous diffusion. The choice of an  $l$  value of 5 would have given better

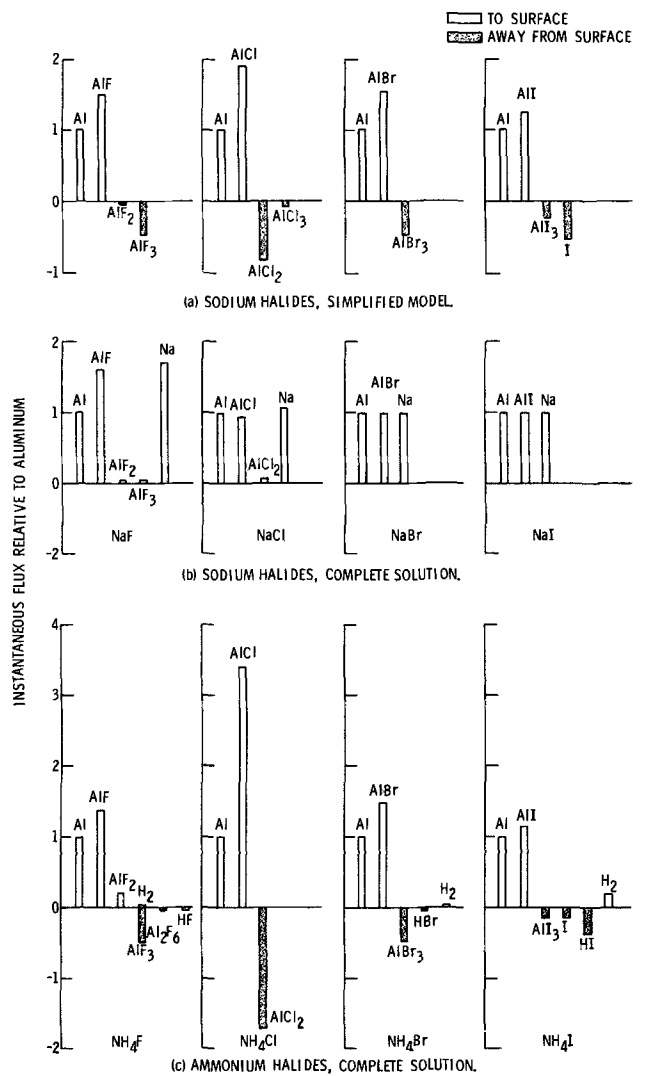


Fig. 14. Instantaneous fluxes of diffusing species relative to net instantaneous aluminum flux. Surface aluminum activity, 0.01; 1 w/o Al; 1093°C packs.

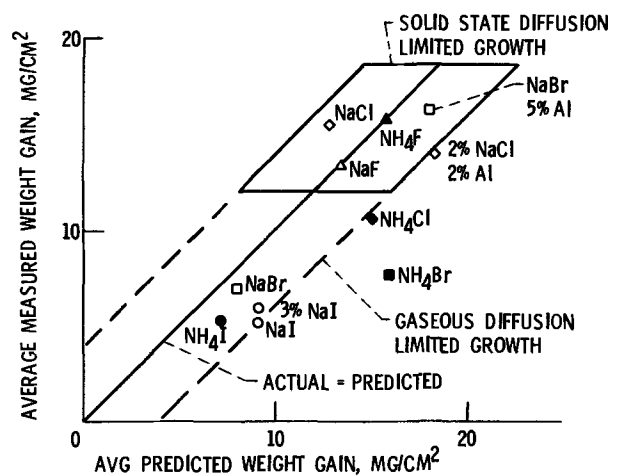


Fig. 15. Comparison of actual and predicted aluminum weight gain for 1N-100, 1093°C, 16-hr packs. 1 w/o Al and activator unless indicated otherwise.

agreement. Earlier it was stated that solid-state diffusion of nickel may be the rate-controlling step in NaCl- and NH<sub>4</sub>Cl-activated packs. However, good agreement between observed and predicted weights based on the gaseous diffusion model indicates that gaseous diffusion controls coating deposition in NH<sub>4</sub>Cl-



activated packs. There appears to be a balance between the predicted ability of the pack to supply aluminum and the observed ability of the substrate to absorb aluminum via nickel diffusion in NaCl-activated packs. However, in 1 w/o Al packs activated with NaCl, based on the observed rate constant and activation energy, the solid-state diffusion step can be considered rate controlling. If gaseous diffusion was rate controlling a pseudoactivation energy of 50 kcal/mole would have been observed rather than 88 kcal/mole. The pseudoactivation energy for gaseous diffusion was determined from the temperature dependence of  $k_{Al}$  computed for NaCl-activated packs. Although this activation energy does not take surface aluminum activity variation into account, the influence of this factor is expected to be small since  $k_{Al}$  was shown to be relatively insensitive to large changes in surface aluminum activity. Similarly, in the 5 w/o Al pack activated with NaBr the agreement between observed and predicted coating weights based on the gaseous diffusion model is good. However, based on coating weight and microstructure, the solid-state diffusion step can be considered rate controlling.

In fluoride-activated packs predicted coating weights based on gaseous diffusion models were two to five times greater than observed weights. The net aluminum deposition rate constants for assumed parabolic behavior, when put on a thickness basis (using a conversion factor of  $7.7 \times 10^{-4}$  cm/mg/cm<sup>2</sup>), were  $1.0 \times 10^{-8}$  and  $4.8 \times 10^{-8}$  cm<sup>2</sup>/sec for the NH<sub>4</sub>F and NaF activators, respectively. These rate constants are greater than rate constants for NiAl growth as determined from Janssen and Rieck (9) by more than an order of magnitude. Thus, *a posteriori*, solid-state diffusion controls the rate of coating growth when the net aluminum deposition rate constant is greater than  $5 \times 10^{-9}$  cm<sup>2</sup>/sec ( $8.4 \times 10^{-3}$  mg<sup>2</sup>/cm<sup>4</sup>-sec) at 1093°C in the Ni-Al system. Since observed coating weights were limited to  $15.3 \pm 3.3$  mg/cm<sup>2</sup>, solid-state diffusion controls deposition on IN-100 when the net aluminum deposition rate constant exceeds  $4.3 \pm 1.8 \times 10^{-3}$  mg<sup>2</sup>/cm<sup>4</sup>-sec or  $2.5 \pm 1.1 \times 10^{-9}$  cm<sup>2</sup>/sec. Predicted coating weights for fluoride-activated packs are plotted on a solid-state diffusion control basis in Fig. 15.

### Concluding Remarks

In this experimental and analytical study of high-temperature packs having aluminum present at unit activity, MAI coating formation was controlled by either solid-state or gaseous diffusion. Although the experiments were performed on IN-100, the analysis is quite general and may be applied to any nickel-base superalloy. Based on these results it appears that the classification of aluminide packs into "high-activity" and "low-activity" as proposed by Goward and Boone (5) can be extended. Coating formation can be more accurately described in terms of the ability of the pack to supply aluminum and the ability of the substrate to supply nickel. The primary variable is temperature rather than pack aluminum activity. This is illustrated in Fig. 16 where the classifications proposed by Goward and Boone are shown on the left. Coatings similar to those produced in low-activity packs can be produced in packs having aluminum present at unit activity provided that they are carried out at high temperature as illustrated on the right of Fig. 16. The coating formation process can be controlled either by diffusion in the gas phase or solid phase depending on the activator and pack aluminum content.

### Summary of Results

The effect of variation of pack activators, pack compositions, temperature, and time on the thickness and structure of aluminide coatings formed on nickel-base alloy IN-100 was studied in a series of one-step packs in which aluminum was initially present at unit activity. Times were varied from 4 to 24 hr and temperatures were varied from 982° to 1149°C in NaCl-

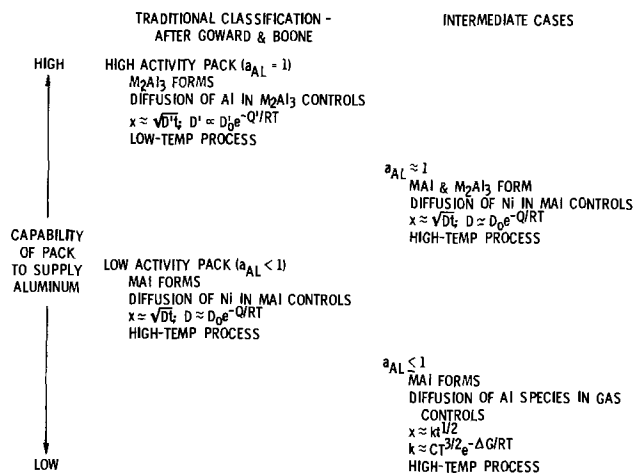


Fig. 16. Proposed expanded classification of aluminide packs

activated packs. The other halides of sodium and the ammonium halides were primarily used to activate 1093°C, 16-hr packs. Through an analysis of the thermodynamics and kinetics of reactions in the pack and comparison with published diffusion data in the Ni-Al binary system the mechanism of coating formation in each pack was established. The following are the results of this study:

1. Coating weights can be successfully predicted from analyses of pack thermodynamics and diffusion in the pack and coating.
2. Pack temperature rather than pack aluminum activity controls the principal coating phase formed.
3. The halide pack activators ranked in order of decreasing aluminum weight gain in 1 w/o aluminum packs are:  $F \approx Cl > Br > I$ .
4. Solid-state nickel diffusion was the rate-controlling step in coating formation in fluoride-activated packs. Gaseous diffusion controlled the rate of coating formation in 1 w/o Al bromide- and iodide-activated packs and NH<sub>4</sub>Cl-activated packs. In NaCl-activated packs containing 1 w/o Al the predicted ability of the pack to supply aluminum was in balance with the ability of the substrate to supply nickel. However, the observed rate constants and activation energy indicated that the solid-state diffusion step controlled coating growth.
5. An increase in pack aluminum content from 1 to 5 w/o shifted control of coating formation from gas phase diffusion to solid-state diffusion in 16-hr, 1093°C NaBr packs and resulted in a coating similar in weight, thickness, and microstructure to those formed in NaCl-activated packs.
6. Regardless of the rate-controlling step, the kinetics of coating formation were near parabolic.
7. The activation energy for coating formation controlled by solid-state diffusion was  $88 \pm 13$  kcal/mole on IN-100.
8. Similar coating microstructures and weight gains were obtained for each halogen regardless of whether its source was a sodium or ammonium salt. Coating microstructures bore greatest resemblance to "low-activity" pack coatings with some features peculiar to "high-activity" pack coatings apparent in coatings applied for longer times or at higher temperatures.

Manuscript submitted Dec. 10, 1973; revised manuscript received March 15, 1974. This was Paper 84 presented at the Boston, Massachusetts, Meeting of the Society, Oct. 7-11, 1973.

Any discussion of this paper will appear in a Discussion Section to be published in the June 1975 JOURNAL. All discussions for the June 1975 Discussion Section should be submitted by Feb. 1, 1975.

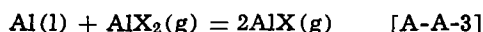
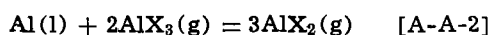
## APPENDIX A

## Thermodynamics

Calculation of bulk pack composition at equilibrium was accomplished with the aid of CEC 71, a computer program by Gordon and McBride described in NASA SP-273 (14). The thermodynamic data for the program were taken from the JANAF tables (15). Data for NaI(g), which were not available in the JANAF tables, were computed from spectrochemical data by B. J. McBride, Lewis Research Center (private communication). Pack compositions prior to establishment of equilibrium were computed from the pack starting materials.

To illustrate the calculation, the outline of an approximate hand calculation method for sodium halide-activated packs follows:

## 1. Chemical reactions



## 2. Equations

## a. Sodium balance

$$M_{\text{NaX}(g)} + M_{\text{Na}(g)} + M_{\text{NaX}(l)} = M_{\text{NaX}(s)}^0 \quad [\text{A-A-5}]$$

## b. Halogen balance

$$M_{\text{X}(g)} + M_{\text{NaX}(g)} + M_{\text{NaX}(l)} + 3M_{\text{AlX}_3(g)} + 2M_{\text{AlX}_2(g)} + M_{\text{AlX}(g)} = M_{\text{NaX}(s)}^0 \quad [\text{A-A-6}]$$

## c. Equilibrium, Eq. [A-A-1]

$$K_3 = P_{\text{Na}}^3 P_{\text{AlX}_3} \quad [\text{A-A-7}]$$

Note that  $K_3$  corresponds to  $\text{AlX}_3$ .

## d. Equilibrium, Eq. [A-A-2]

$$K_2 = \frac{P_{\text{AlX}_2}^3}{P_{\text{AlX}_3}^2} \quad [\text{A-A-8}]$$

## e. Equilibrium, Eq. [A-A-3]

$$K_1 = \frac{P_{\text{AlX}}^2}{P_{\text{AlX}_2}} \quad [\text{A-A-9}]$$

Note that  $K_1$  corresponds to  $\text{AlX}$ .

## f. Equilibrium, Eq. [A-A-4]

$$K_4 = \frac{1}{P_{\text{Na}} P_{\text{X}}} \quad [\text{A-A-10}]$$

Elimination of  $M_{\text{NaX}(c)}^0$  between Eq. [A-A-5] and [A-A-6] permits the resulting equation to be rewritten in terms of pressures. This leaves five equations in five unknowns. The solution was performed for NaF and NaCl activators. The results agreed with the computer program to within 20% for the former and 3% for the latter. The difference was primarily due to exclusion of minor species in the hand calculation. Results of the computer solutions are listed in Table II. In one case, the NaF-activated pack, the presence of  $\text{Al}_2\text{O}_3$  was included in the machine calculations. The species present at equilibrium were Al(l), Al, AlF, AlF<sub>2</sub>, AlF<sub>3</sub>, AlO, AlOF, Al<sub>2</sub>F<sub>6</sub>, Al<sub>2</sub>O, Al<sub>2</sub>O<sub>2</sub>, Al<sub>2</sub>O<sub>3</sub>(s), Ar, F, Na, NaF(l), NaF, NaO, Na<sub>2</sub>, and Na<sub>2</sub>F<sub>2</sub>. No significance difference in the partial pressures of F, AlF, AlF<sub>2</sub>, and AlF<sub>3</sub> were noted when the results were compared with the calculation made with  $\text{Al}_2\text{O}_3$  omitted. Thus  $\text{Al}_2\text{O}_3$  was omitted from all other calculations. One shortcoming of the analysis of the NaF-activated pack should be noted: cryolite formation was not considered. Since the cryolite melt is extensively dissociated (18) the impact of cryolite formation on this analysis is considered small.

## APPENDIX B

## Kinetics

Instantaneous fluxes of gaseous species from the bulk pack to the substrate surface and vice versa were

computed for 1 atm total pressure and a surface aluminum activity of  $1 \times 10^{-2}$ . The results are summarized in Table IV. Several checks on diffusion conditions were made prior to performing the calculation. First, it was established that diffusion occurs in the viscous flow regime. For molecular diffusion to occur the pack particle size would have to be reduced from about 100 $\mu$  to about 0.1 $\mu$ . Second, it was established that interchange between argon and hydrogen occurs very rapidly in the  $\text{NH}_4\text{F}$ -activated pack and therefore diffusivities were computed based on argon as the major constituent. The computation was performed for equilibrium conditions after dilution by 9.8 moles of argon in  $\text{NH}_4\text{Cl}$ , Br- and I-activated packs and pseudo-equilibrium conditions in  $\text{NH}_4\text{F}$ -activated packs. Diffusivities were estimated from the Gilliland equation (16)

$$D = \frac{0.0043 \left[ T^3 \left( \frac{1}{m_a} + \frac{1}{m_b} \right) \right]^{1/2}}{P(V^{1/3}_a + V^{1/3}_b)^2} \quad [\text{A-B-1}]$$

Molar volumes at the normal boiling point were computed from data in the literature (17) and from an estimated value of 18 cm<sup>3</sup>/g-atom for aluminum.

In making the instantaneous flux calculations the roles of Na<sub>1</sub>(g) and NaX in sodium halide-activated packs and of HX(g) and H<sub>2</sub>(g) in  $\text{NH}_4\text{X}$ -activated packs were included. Solution of this problem involving as many as ten simultaneous equations was accomplished on a digital computer. The instantaneous flux calculation in outline form for a simplified case for NaX-activated packs wherein the roles of Na<sub>1</sub>(g) and NaX are neglected follows:

## 1. Chemical reactions

## a. Bulk pack



## b. Surface

Substitute Al (Al in NiAl) for Al(l) in Eq. [A-B-2], [A-B-3], and [A-B-4].

## 2. Equilibrium equations

## a. Equation [A-B-2]

$$K_1 = \frac{P_{\text{X}(g)} a_{\text{Al}}}{P_{\text{AlX}_1(g)}} = \frac{P_4 a}{P_1} \quad [\text{A-B-5}]$$

## b. Equation [A-B-3]

$$K_2 = \frac{P_{\text{X}(g)}^2 a_{\text{Al}}}{P_{\text{AlX}_2(g)}} = \frac{P_2^2 a}{P_2} \quad [\text{A-B-6}]$$

## c. Equation [A-B-4]

$$K_3 = \frac{P_{\text{X}(g)}^3 a_{\text{Al}}}{P_{\text{AlX}_3(g)}} = \frac{P_3^3 a}{P_3} \quad [\text{A-B-7}]$$

For reactions in the bulk pack the aluminum activity is set equal to  $P_{\text{Al}(g)}/P_{\text{Al}(l)} = 1$ . For reactions at the surface, aluminum activity was set at  $1 \times 10^{-2}$  and the pressures are distinguished by primes.

## 3. Instantaneous fluxes

## a. Aluminum to the surface

$$\frac{N_{\text{Al}}}{A} = \frac{D_1}{RT} \frac{(P_1 - P'_1)}{d} + \frac{D_2}{RT} \frac{(P_2 - P'_2)}{d} + \frac{D_3}{RT} \frac{(P_3 - P'_3)}{d} \quad [\text{A-B-8}]$$

The contribution of Al(g) diffusion to the net aluminum flux is negligible.

## b. Halogen balance at the surface

$$0 = D_1(P_1 - P'_1) + 2D_2(P_2 - P'_2) + 3D_3(P_3 - P'_3) + D_4(P_4 - P'_4) \quad [\text{A-B-9}]$$

The unknowns are  $P'_1$ ,  $P'_2$ ,  $P'_3$ ,  $P'_4$ ,  $N_{\text{Al}}/A$ , and  $d$ . Multiplication of both sides of Eq. [A-B-8] by  $d$  gives the combined variable  $N_{\text{Al}}d/A$  and leaves five

equations and five unknowns. Therefore, each pressure and the instantaneous fluxes of all species can be estimated.  $P_1$  and the instantaneous fluxes are listed in Table IV. Instantaneous fluxes were found to be relatively insensitive to changes in surface aluminum activity. A tenfold decrease in aluminum activity increases the net instantaneous aluminum flux by a factor of 2.

## SYMBOLS

A	area, cm <sup>2</sup>
a	activity of aluminum at the coating surface, dimensionless
$D_i$	diffusivity of the <i>i</i> th species, cm <sup>2</sup> /sec
<i>d</i>	diffusion distance, cm
$K_j$	equilibrium constant for the <i>j</i> th reaction
<i>k, k'</i>	rate constant
<i>l</i>	path length correction factor
<i>M</i>	moles
$m_a, m_b$	molecular weight, grams/mole
$N_{Al}$	aluminum flow, moles/sec at any instant
$n, n'$	rate equation exponent
$P_i$	partial pressure of the <i>i</i> th species in the bulk pack, atm
$P_1$	partial pressure of the <i>i</i> th species at the coating surface, atm
<i>Q</i>	activation energy, kcal/mole
<i>R</i>	gas constant, cm <sup>3</sup> -atm/°K-mole or cal/°K-mole
<i>T</i>	absolute temperature, °K
<i>t</i>	time, sec
$V_a, V_b$	molar volume at the normal boiling point, cm <sup>3</sup> /mole
<i>w</i>	coating weight, mg/cm <sup>2</sup>
<i>X</i>	halogen atom, F, Cl, Br, or I
<i>x</i>	coating thickness, cm
<i>ε</i>	pack porosity
<i>ρ</i>	pack aluminum concentration, mg/cm <sup>3</sup>

## REFERENCES

1. S. J. Grisaffe, "The Superalloys," C. T. Sims and W. C. Hagel, Editors, Chap. 12, John Wiley & Sons, Inc., New York (1972).
2. J. D. Gadd, J. F. Nejedlik, and L. D. Graham, *Electrochem. Technol.*, **6**, 307 (1968).
3. A. R. Stetson, U.S. Patent 2,927,043 (1960).
4. G. W. Goward, D. H. Boone, and C. S. Giggins, *Trans. ASM*, **60**, 228 (1967).
5. G. W. Goward and D. H. Boone, *Oxidation of Metals*, **3**, 475 (1971).
6. H. Brill-Edwards and M. Epner, *Electrochem. Technol.*, **6**, 299 (1968).
7. H. E. Collins, *Trans. ASM*, **62**, 82 (1969).
8. R. M. Caves and S. J. Grisaffe, NASA TN D-6317 (1971).
9. M. M. P. Janssen and G. D. Rieck, *Trans. AIME*, **239**, 1372 (1967).
10. G. F. Hancock and B. R. McDonnell, *Phys. Status Solidi*, **4**, 143 (1971).
11. A. E. Berkowitz, F. E. Jaumot, and F. C. Nix, *Phys. Rev.*, **95**, 1185 (1954).
12. A. Steiner and K. L. Komarek, *Trans. AIME*, **230**, 786 (1964).
13. R. C. Weast, Editor, "Handbook of Chemistry and Physics," Chemical Rubber Co., Cleveland, Ohio (1971).
14. S. Gordon and B. J. McBride, NASA SP-273 (1971).
15. Anon., "JANAF Thermochemical Tables," Dow Chemical Co., Midland, Mich. (Dec. 31, 1960 to June 30, 1970).
16. E. R. Gilliland, *Ind. Eng. Chem.*, **26**, 681 (1934).
17. LeBas: "The Molecular Volumes of Liquid Chemical Compounds," Longuens, London (1915) [Referenced in A. S. Foust *et al.*, "Principles of Unit Operations," John Wiley & Sons, Inc., New York (1960)].
18. W. B. Frank, *J. Phys. Chem.*, **65**, 2081 (1961).

## Chemomechanical Polishing of CdS

Vincent Y. Pickhardt and Donald L. Smith

Perkin-Elmer Corporation, Norwalk, Connecticut 06856

The publication costs of this article have been assisted by the Perkin-Elmer Corporation.

## ABSTRACT

The chemomechanical polishing of the "A" or cadmium-rich face of cadmium sulfide has been accomplished. The etchant contained 90 mliters nitric acid, 300 mliters precipitated silica, and 10g aluminum chloride per 1000 mliters water. Best results were obtained using a poromeric polishing disk with 370 g/cm<sup>2</sup> work pressure at 240 rpm polishing wheel speed. Surfaces were completely featureless when viewed by Nomarski and Michelson interference microscopy at 155 and 400 $\times$ , and gave good LEED patterns after brief heat-cleaning under vacuum.

CdS is a desirable substrate for the epitaxial growth of semiconductor thin films for electrooptic devices. For such applications, the crystals must be flat, highly polished, and damage-free. Many etchants have been suggested in previous articles (1-3), but none of them produces all of these surface requirements simultaneously. We describe below a procedure utilizing both mechanical and chemical polishing which produces excellent results on the (0001A) face of CdS.

### Experimental Procedure

Undoped, single-crystal CdS (Eagle-Picher ultra-high purity grade) was x-ray oriented to within 2° of the (0001) plane and sawn by a continuous loop wire saw into 8 x 10 x 2 mm wafers. The "A" face was differentiated from the "B" face by a 60 sec etch in 50%<sup>1</sup>

Key words: chemomechanical polishing, cadmium sulfide, polishing.

<sup>1</sup> All concentrations of HCl and HNO<sub>3</sub> are expressed as a volume per cent of the standard 38% and 70% assay solutions respectively.

HCl (1). The oriented crystals were mounted on a 3 cm diameter titanium polishing block with the "A" face exposed. A schematic of the equipment is shown in Fig. 1. The block and its closely fitting dressing ring are held by rollers about half way out to the edge of the 10 in. diameter motor-driven polishing pad, and the block and ring rotate about their axis due to friction with the pad, providing compound motion.

The wafers were first mechanically polished on a 3 $\mu$  silicon carbide-impregnated polishing disk with water as lubricant, to remove all surface and subsurface wire saw damage. Both polishing block and dressing ring were then cleaned in a concentrated detergent to remove any particle contamination. Final chemical polishing was completed on the same apparatus. The etchant which produced best results contained 90 mliter HNO<sub>3</sub>, 300 mliter precipitated silica, 10g AlCl<sub>3</sub> (anhydrous powder), and 1 mliter concentrated detergent as an anticoagulant per 1000 mliters deionized

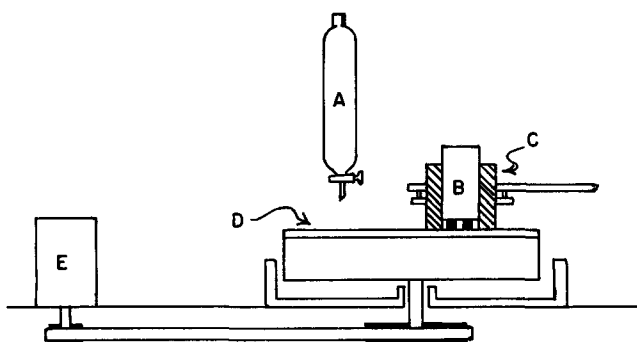


Fig. 1. Schematic of chemomechanical polishing equipment: A, separating funnel; B, polishing block containing crystals; C, dressing ring; D, polishing pad; E, motor drive.

water. This was fed to the polishing pad immediately after mixing at approximately 25 mliters/min. The crystals were weighted to 370 g/cm<sup>2</sup>. Best results were obtained using a Politex-Pix poromeric polishing pad at a speed of 240 rpm.

### Results

After approximately 30 min of polishing with the above etchant, the crystal surfaces showed a flat, highly polished, "mirror-like" finish. Surfaces were com-



Fig. 2. "B" face of polished CdS wres viewed by Nomarski microscopy at 400X magnification. The "A" face is not shown because it is featureless under the same conditions of observation.

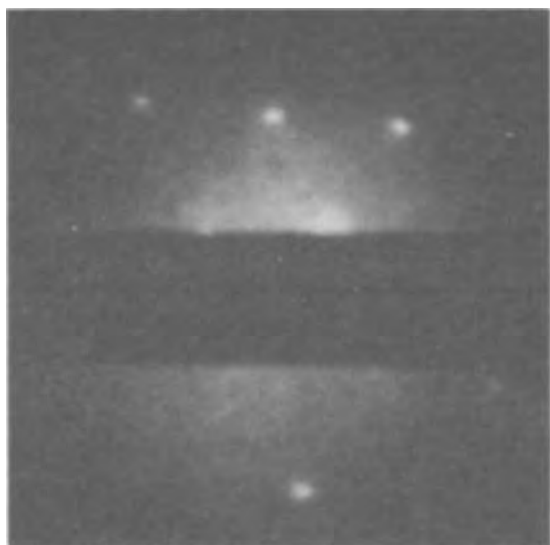


Fig. 3. LEED pattern of polished CdS after 450° flash; 92 eV

Table I. Auger spectra of CdS(0001A)

Element	Nominal eV	Auger peak strengths, $\mu$ V Before flash	Auger peak strengths, $\mu$ V After flash
S	152	78	109
Cl	181	1.0	0.4
C	272	3.6	2.4
Cd	277, 283		
Cd	321	2.1	2.7
Cd	376, 382	16.6	18.2
O	510	<0.1	<0.1

pletely featureless when viewed by Nomarski microscopy at 155 and 400X. When viewed by Michelson interference microscopy at 370X the crystals showed no defects and showed flatness to better than 300Å (resolution limit) over the 0.3 mm field.

Of utmost importance is removal of all subsurface damage from sawing and mechanical polishing operations. Although a polishing time of 30 min is suggested, in some instances this must be lengthened to remove preferential etching caused by leftover subsurface damage. Extreme care must be taken while handling crystals so as not to introduce damage between operations. The etchant composition is also important. An increase in acid concentration produces large etch pits, a decrease in concentration produces surface "scratching." Deletion of AlCl<sub>3</sub> produces preferential etching and surface "scratching." Increasing the silica content leads to the same pits encountered with higher acid concentrations, and deletion produces an orange-peel effect across the crystal face.

On the "B" face, the same etchant produces an orange-peel texture and "scratches." An etchant consisting of 150 mliters HCl and 5g AlCl<sub>3</sub> per 1000 mliters H<sub>2</sub>O, on a Pellon Pan-W polishing pad produces somewhat better results. Shallow scratches were apparent when the surface was viewed by Nomarski microscopy at 400X magnification although no preferential etching or orange-peel effect was observable (see Fig. 2).

Polished "A"-surfaces were also examined by low-energy electron diffraction (LEED) and Auger spectroscopy at 10<sup>-9</sup> Torr using a hemispherical grid apparatus. A 1-min flash to 450°C was sufficient to generate the sharp (1 x 1) LEED pattern shown in Fig. 3, whereas ion bombardment is generally required to generate any LEED pattern on CdS (4) and other semiconductors. The diffraction pattern was observable down to 20 eV, below which surface charging became a problem, and up to 180 eV, above which the diffraction features faded into the diffuse background. Table I compares Auger spectra taken before and after the 450°C flash. The only contaminants detected were C and Cl. Both of these were reduced considerably, though not completely eliminated, by the 450°C flash, with accompanying increases in the Cd and S signals. Based on the quality of the LEED pattern and on relative Auger peak strengths, residual contamination is estimated to be about 1/10 monolayer.

### Acknowledgments

The authors express their appreciation to Robert McGraw for invaluable consultations. This research was supported by the Advanced Research Projects Agency of the Department of Defense and was monitored by ONR under Contract No. N00014-73-C-0280.

The views and conclusions contained in this article are those of the authors and should not be interpreted as necessarily representing the official views or policies, either expressed or implied, of the aforementioned Agency or the United States Government.

Manuscript submitted Feb. 28, 1974; revised manuscript received March 15, 1974.

Any discussion of this paper will appear in a Discussion Section to be published in the JUNE 1975 JOURNAL. All discussions for the JUNE 1975 Discussion Section should be submitted by Feb. 1, 1975.

## REFERENCES

1. M. V. Sullivan and W. R. Bracht, *This Journal*, **114**, 295 (1967).
2. W. H. Strehlow, *J. Appl. Phys.*, **40**, 2928 (1969).
3. E. P. Warekois, M. C. Lavine, A. N. Mariano, and H. C. Gatos, *ibid.*, **33**, 690 (1962).
4. L. R. Bedell and H. E. Farnsworth, *Surface Sci.*, **41**, 165 (1974).

# Hall Effect, Schottky Barrier Capacitance, and Photoluminescence Spectra Measurements for GaAs Epitaxial Layer and Their Correlation

T. Katoda and T. Sugano

Department of Electronic Engineering, The University of Tokyo, Hongo, Bunkyo-ku, Tokyo, Japan

The publication costs of this article have been assisted by The University of Tokyo.

## ABSTRACT

The main causes of a decrease in the electron mobility of GaAs epitaxial layers grown by the vapor phase deposition system are confirmed to be due to the compensating acceptors and the space charge regions, both of which are associated with copper contamination, from a discussion on the correlation among the results of measurements (listed in the title) on the same samples. Deep traps do not play an important role in determining electron mobility because of their scattering cross section as small as  $1.04 \times 10^{-22} \text{ cm}^2$ .

GaAs space charge regions have been suggested as one of the "mobility killers" (1-4). On the other hand, deep traps in the GaAs have been detected by measurement of Schottky barrier capacitance (5-8) or by photoluminescence measurement (9-11). However the correlation between them has not been discussed and consequently the species which form space charge regions or deep traps have not been identified.

In this paper the results of independent measurements such as the Hall effect, Schottky barrier capacitance, and photoluminescence measurements on the same samples are shown, and the correlation among them and with the growth conditions are discussed. Figure 1 shows the measurements which were conducted in this work, the quantities which can be obtained from these measurements, and the correlation among them which is subsequently discussed in this paper. Here the relation of the compensation ratio of impurities, and densities of space charge regions and deep traps to contamination by copper is confirmed by independent measurements. The electron mobility in GaAs in the presence of deep traps is consistently explained from the correlation among electron mobility, density of deep traps, and their scattering cross section obtained by measuring the Schottky barrier capacitance.

## Experimental

**Sample preparation.**—N-type GaAs layers were epitaxially grown on semi-insulating Cr-doped GaAs substrates by the Ga-AsCl<sub>3</sub>-H<sub>2</sub> reaction system as shown in Fig. 2.

The purity of Ga and AsCl<sub>3</sub> were both 99.99999%. Hydrogen was purified by a Pd diffuser, all components of which were made of stainless steel to avoid contamination by copper. The reaction tubes used were high-purity, fused quartz tubes (class SSGH, Toshiba Denko) aged in pure hydrogen atmosphere at 1000°C before use. The substrates were mechanically polished and chemically etched by a mixture solution with H<sub>2</sub>O<sub>2</sub>:1, H<sub>2</sub>O:1, and H<sub>2</sub>SO<sub>4</sub>:3 before deposition. Growth parameters of the samples are listed in Table I.

**Hall measurement.**—Electron mobility and density, and their temperature dependences, were measured by

the van der Pauw method (12). Ohmic contacts were made by alloying the mixture of In and Sn to the epitaxial layer. Their ohmic property was checked from

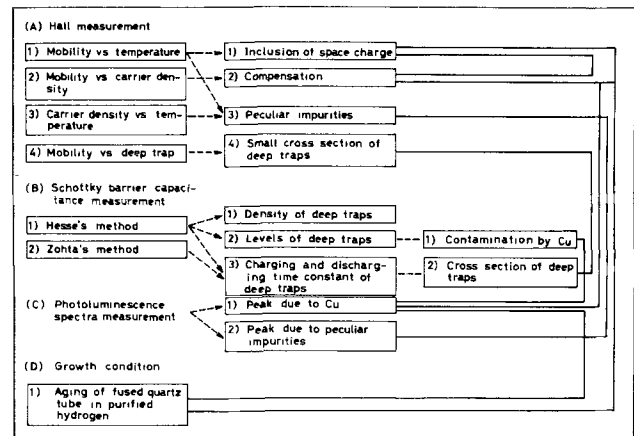


Fig. 1. Experimental results and correlation among them. --- Indicates experimental result, — indicates the correlation which affirms the results on both sides.

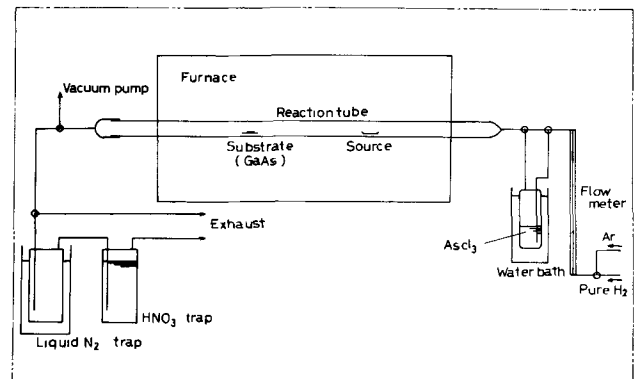


Fig. 2. Schematic diagram of the GaAs epitaxial growth system

Key words: compound semiconductor, electronic properties, epitaxial growth, mobility, defects.

Table I. Growth parameters and electrical properties of the GaAs epitaxial layers

Sample No.	Source temp (°C)	Substrate temp (°C)	AsCl <sub>3</sub> temp (°C)	H <sub>2</sub> flow rate (ml/min)	Dopant	Epitaxial layer thickness (μm)	Electron mobility (295°K) : μ (cm <sup>2</sup> /V·sec)	Carrier density (295°K) : n (cm <sup>-3</sup> )	γ*	Peak of 0.91-0.95 μm**	Type of μ - T curve
124	860	740	14	50	Te	8.4	4100	8.80 × 10 <sup>16</sup>	23.2	Yes	A
178	860	740	20	50	Undoped	5.2	5950	1.70 × 10 <sup>15</sup>	1.88	—	B
204	840	755	16	110	Undoped	45.0	7200	1.50 × 10 <sup>14</sup>	1.52	NS***	D
206	840	695	19	120	Undoped	10.3	1800	8.35 × 10 <sup>12</sup>	5.50	No	C
213	840	740	14	130	Undoped	20.4	2240	3.22 × 10 <sup>15</sup>	1.30	No	C
217	840	740	10	130	Undoped	27.2	6600	4.03 × 10 <sup>14</sup>	1.18	NS	D
219	840	725	10	110	Undoped	17.2	3500	1.20 × 10 <sup>16</sup>	1.37	No	B
230	840	740	12	110	Undoped	14.5	6100	8.72 × 10 <sup>15</sup>	1.24	—	B
233	840	740	4	124	O <sub>2</sub>	30.4	3170	6.40 × 10 <sup>15</sup>	1.60	Yes	A
235	840	675	4	120	Undoped	11.7	4800	7.28 × 10 <sup>15</sup>	1.37	Yes	A
236	840	690	4	120	Undoped	16.2	3060	2.43 × 10 <sup>15</sup>	2.74	Yes	A

\* γ : a measure of macroscopic homogeneity of epitaxial layer.  
 \*\* Peak of 0.91-0.95 μm : photoluminescence peak due to copper.  
 \*\*\* NS : negligibly small.

room temperature to the liquid nitrogen temperature and confirmed to be good.

**Measurement of frequency dependence of Schottky barrier capacitance.**—To determine the relation of frequency dependence of capacitance of Schottky barrier diodes on electron mobility in the epitaxial layer, Schottky diodes were fabricated on the same epitaxial layers as those used in mobility measurement. The configuration is shown in Fig. 3. Ohmic contacts were made on the side edges and the top surface of the epitaxial layer.

**Measurement of photoluminescence.**—Photoluminescence spectra were measured for some of the samples whose electron mobility and density as well as Schottky barrier capacitance were measured. Photoluminescence spectra were also measured for GaAs epitaxial layers grown in a fused quartz tube with and without aging in purified hydrogen. Measurements were conducted at room temperature, the liquid nitrogen temperature, and about 10°K. The excitation source was He-Ne laser and the detector was a RCA 7102 photomultiplier.

**Results of Hall and Schottky Barrier Capacitance Measurements**

**Experimental results of temperature dependence of electron mobility.**—Some of the experimental results on electron mobility vs. temperature characteristics are shown in Fig. 4. Hereinafter those curves are classified into four groups for the convenience of discussion.

In Fig. 4(a), the curves belonging to groups A and B are shown. The former is characterized by small magnitude and small temperature dependence in a range near room temperature. The carrier density of those samples at room temperature is as high as 6.40 × 10<sup>15</sup> cm<sup>-3</sup> and electron mobility is as small as 3170 cm<sup>2</sup>/V·sec (sample No. 233).

Electron mobility of the samples belonging to group B in Fig. 4(a) is fairly large: for example, 6000 cm<sup>2</sup>/V·sec at room temperature. But at the liquid nitrogen temperature, electron mobility is not increased as much as expected from the theory of polar optical mode scattering and ionized impurity scattering.

Electron mobility of the samples belonging to group C reveals a large dependence on temperature, although

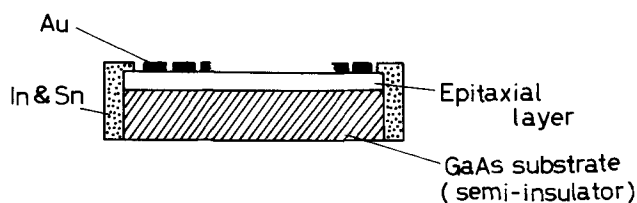


Fig. 3. Cross section of Schottky barrier diodes. The In and Sn alloy forms an ohmic contact and the Au dots form the Schottky barrier with a GaAs epitaxial layer.

the magnitude is as small as 1800 cm<sup>2</sup>/V·sec at room temperature (sample No. 206); while that of the samples belonging to group D likewise displays a large dependence on temperature, although the magnitude is as large as 7200 cm<sup>2</sup>/V·sec at room temperature (sample No. 204).

**Theoretical consideration on temperature dependence of electron mobility.**—Theoretical curves of temperature dependence of electron mobility are shown in Fig. 4(a) and 4(b) by solid-line curves. Each curve is calculated to be fitted to the curves in each group by assuming the particular magnitude of contributions caused by various scattering mechanisms. The scattering mechanisms, taken into account in this calculation

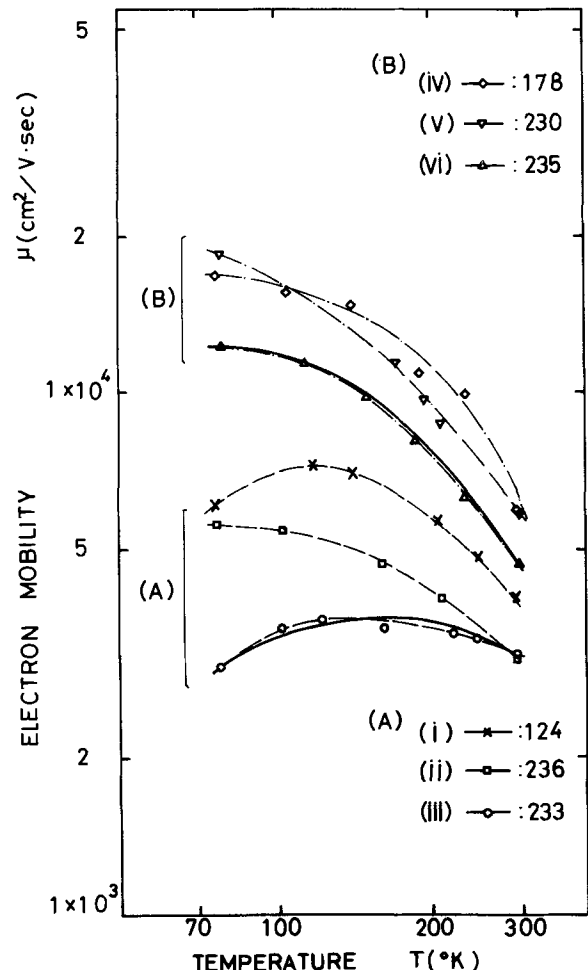


Fig. 4(a). Temperature dependence of electron mobility (I). In groups A and B, scattering by ionized impurities and space charge regions are dominant.

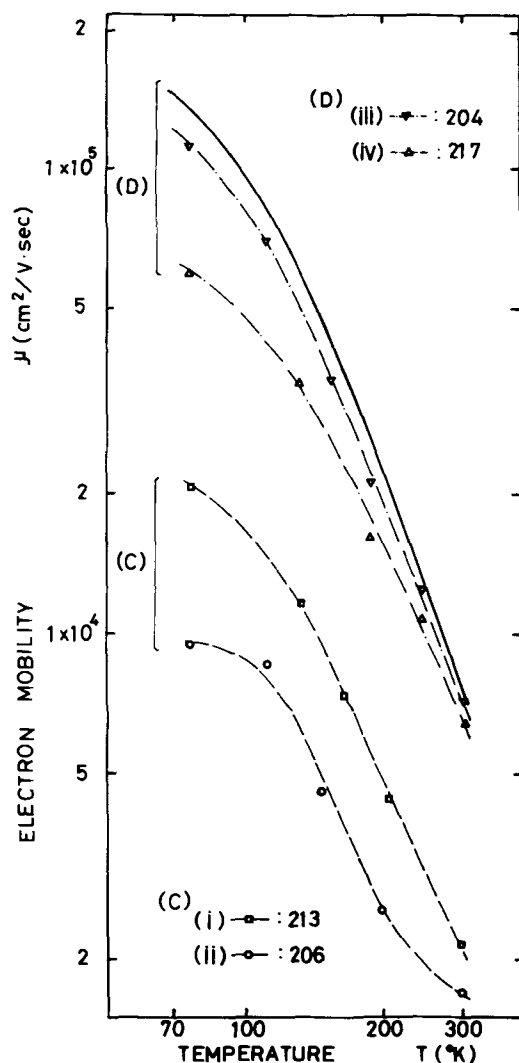


Fig. 4(b). Temperature dependence of electron mobility (II). In group C, scattering by ionized impurities, whose density changes largely with temperature, is dominant; in group D, scattering by polar optical phonon is dominant.

tion, are as follows:

(i) *Polar optical mode scattering*.— Electron mobility determined by this mechanism,  $\mu_{PO}$ , is given by

$$\mu_{PO} = 5.31 \times 10^3 \cdot x(z) (e^z - 1) z^{-1/2} \quad (\text{cm}^2/\text{V}\cdot\text{sec}) \quad [1]$$

where  $z = \theta/T$ ,  $\theta$  is the longitudinal optical phonon temperature (416°K for GaAs), and function  $x(z)$  calculated by Petritz and Scanlon (13) is used.

(ii) *Piezoelectric scattering*.— Electron mobility determined by piezoelectric scattering,  $\mu_{PE}$ , derived by Van Daal (14) and Hutson (15), is given by

$$\mu_{PE} = 3.16 \times 10^5 (300/T)^{1/2} \quad (\text{cm}^2/\text{V}\cdot\text{sec}) \quad [2]$$

(iii) *Deformation potential scattering*.— The following expression derived by Bardeen and Shockley (16) is used for electron mobility due to this mechanism,  $\mu_{DP}$

$$\mu_{DP} = 5.5 \times 10^8 T^{-3/2} \quad (\text{cm}^2/\text{V}\cdot\text{sec}) \quad [3]$$

(iv) *Ionized impurity scattering*.— The result according to the Brooks-Herring theory (17) is used for electron mobility by this scattering,  $\mu_I$

$$\mu_I = 1.87 \times 10^8 \cdot T^{-3/2}/N_I \{ \ln(1.17 \times 10^4 \cdot T^2/n') - 1 \} \quad (\text{cm}^2/\text{V}\cdot\text{sec}) \quad [4]$$

$$n' = n + (N_D - N_A - n)(n + N_A)/N_D$$

where  $n$  is the electron density,  $N_D$  is the shallow donor density,  $N_A$  is the acceptor density, and  $N_I$  is the ionized impurity density.

(v) *Space charge scattering*.— The expression of the electron mobility,  $\mu_{SC}$ , derived by Weisberg (1, 18)

$$\mu_{SC} = 2.4 \times 10^9 / N_s Q (T \cdot m/m_0)^{1/2} \quad (\text{cm}^2/\text{V}\cdot\text{sec}) \quad [5]$$

is used. In the expression,  $m_0$  is the mass of a free electron,  $m$  is the effective mass of an electron,  $N_s$  is the density of space charge regions, and  $Q$  is the scattering cross section.

For the sake of simplicity, the relation

$$1/\mu = \sum_i (1/\mu_i) \quad [6]$$

is assumed, where  $\mu$  is electron mobility and  $i$  denotes the  $i$ th kind of scattering mechanisms.

### Discussion

*Temperature dependence of electron mobility*.— Experimental curves of electron mobility vs. temperature characteristics can be explained as follows:

*Groups A and B*.— Two curves calculated by assuming that piezoelectric scattering, deformation scattering, scattering by polar optical phonon, ionized impurity, and space charge regions are predominant as shown in Fig. 4(a).

Equation [6] is a poor approximation when contributions caused by more than two types of scattering are comparable in magnitude, but good agreement between the calculated and the experimental curves still can be obtained if the ionized impurity density at 77°K and the values of the product of the space charge region density and the scattering cross section at 300°K are assumed for each curve in Fig. 4(a), as listed in Table II.

It may be concluded that scattering by ionized impurities and the space charge regions are playing an important role in determining electron mobility in the case of groups A and B.

*Groups C and D*.— The solid-line curve in Fig. 4(b) is calculated by considering polar optical phonon scattering, piezoelectric scattering, deformation potential scattering, and ionized impurity scattering. Both scattering by space charge regions and by neutral impurities has been neglected.

Table II. Carrier density, donor density, acceptor density, compensation ratio, and space charge region of the samples belonging to groups A and B

Sample No.	Carrier density (77°K) : $n$ ( $\text{cm}^{-3}$ )	Donor density : $N_D^+$ ( $\text{cm}^{-3}$ )	Acceptor density : $N_A^-$ ( $\text{cm}^{-3}$ )	Compensation ratio : $(N_D^+ + N_A^-)/n$	Space charge region : $N_s Q$
233	$5.80 \times 10^{16}$	$4.66 \times 10^{16}$	$4.08 \times 10^{16}$	15.0	$8.87 \times 10^4$
236	$1.38 \times 10^{16}$	$1.23 \times 10^{16}$	$1.09 \times 10^{16}$	18.8	$1.07 \times 10^5$
124	$8.75 \times 10^{16}$	$\sim 6.75 \times 10^{16}$	$\sim 0$	$\sim 1.0$	$6.31 \times 10^4$
235	$4.40 \times 10^{16}$	$8.20 \times 10^{16}$	$3.80 \times 10^{16}$	2.73	$4.61 \times 10^4$
230	$6.30 \times 10^{16}$	$8.60 \times 10^{16}$	$2.30 \times 10^{16}$	1.73	$2.23 \times 10^4$
178	$1.57 \times 10^{16}$	$5.19 \times 10^{16}$	$3.62 \times 10^{16}$	5.17	$2.55 \times 10^4$

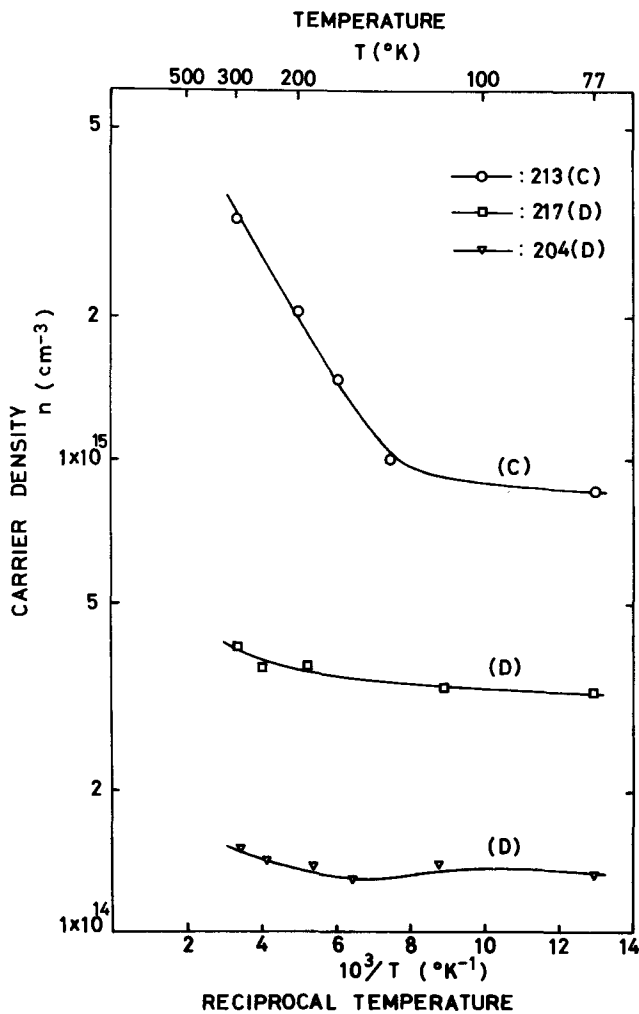


Fig. 5. Temperature dependence of carrier density of the samples classified into groups C and D in Fig. 4(b).

The density of the total impurity is assumed to be  $N_i = 4.0 \times 10^{14} \text{ cm}^{-3}$  at room temperature. Curve (iii) in Fig. 4(b) is for sample No. 204, whose carrier density is  $1.5 \times 10^{14} \text{ cm}^{-3}$  at room temperature. A small disagreement of the calculated curve with the experimental result is found, however, since sample No. 204 is assumed to be slightly compensated and contains neutral impurities, and since the approximation  $1/\mu = \sum(1/\mu_i)$  is not necessarily valid for highly pure samples, such a small difference is reasonable. The temperature dependence of electron mobility in group C can be explained by considering the presence of impurities, as discussed in the next section.

**Temperature dependence of electron density.**—The temperature dependence of carrier density of the samples belonging to group C in Fig. 4(b), obtained by the Hall measurement, is plotted as shown in Fig. 5. For comparison, characteristics of the samples belonging to group D are shown in the figure. Carrier density of the samples belonging to groups A and B revealed a temperature dependence similar to those of the samples in group D. It is evident from the figure that the samples in group C show much larger temperature dependence of carrier density above 150°K than those in group D.

The values of activation energy obtained from these curves are listed in Table III, and that of the sample in group C is 5.0 ~ 5.5 times larger than those of the samples in group D.

The temperature dependence of the ionized impurity density corresponding to the electron mobility vs. temperature characteristic curve (i) in Fig. 4(b) (sample No. 213) is shown in Fig. 6. It is much larger than temperature dependence of the carrier density shown in

Table III. Activation energy of carrier density vs. temperature characteristics shown in Fig. 5. Sample No. 213 is classified into group C and samples No. 204 and 217 are classified into group D

Sample No.	Activation energy (eV)
204	$4.88 \times 10^{-3}$
217	$4.48 \times 10^{-3}$
213	$2.46 \times 10^{-2}$

Fig. 5. This difference can be understood if the donor and acceptor levels in the forbidden gap are assumed to be as shown in Fig. 7. When the Fermi level crosses the donor level with an increase in temperature, and the acceptor level is located above the donor level, some of the donor and acceptor impurities are ionized at high temperatures while they are neutral at low temperatures. The former are positively charged and the latter are negatively charged. Then the change of the total ionized impurity (equal to the sum of ionized donors and ionized acceptors) is much larger than that of the carrier density (equal to the difference between the ionized donors and ionized acceptors).

The species which form such levels have not been clarified, however, the peak corresponding to the activation energy of the carrier density vs. the temperature characteristics of sample No. 213 is visible in the photoluminescence spectrum of the same sample, as shown in Fig. 8.

*Experimental results of frequency dependence of Schottky barrier capacitance.*—Figure 9 shows two examples of frequency vs. capacitance characteristics of

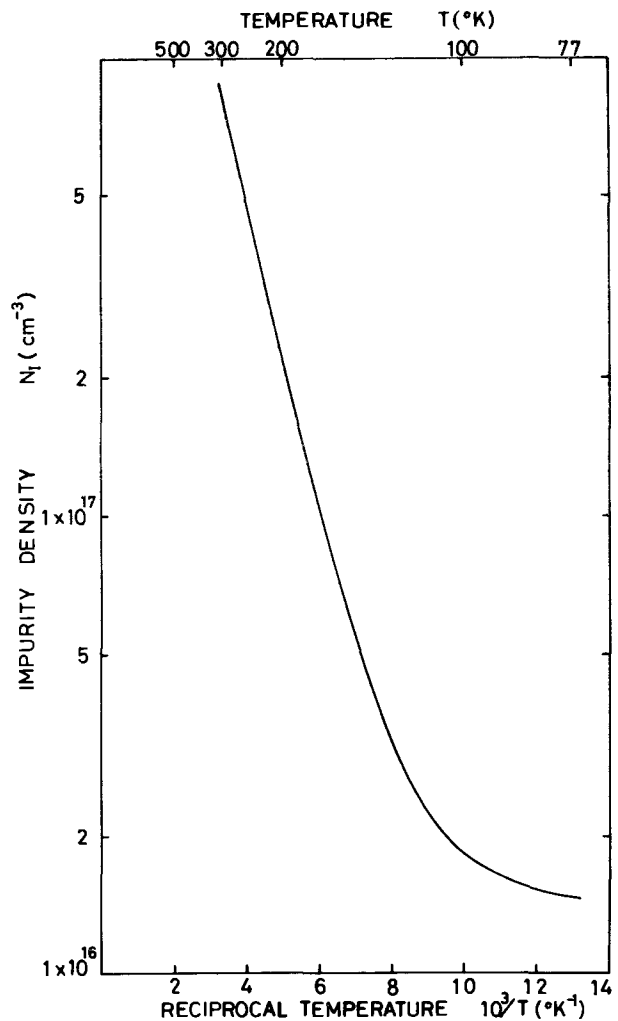
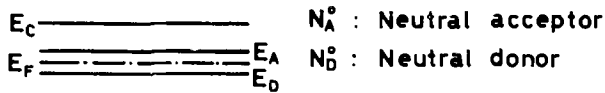


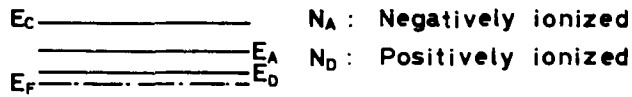
Fig. 6. Temperature dependence of the ionized impurity density corresponding to the mobility vs. temperature curve (i) in Fig. 4(b).



At low temperature



At high temperature



$E_C$  : Conduction band edge

$E_F$  : Fermi level

Fig. 7. Energy level model explaining the temperature dependence of the ionized impurity density and the carrier density for the samples in group C.

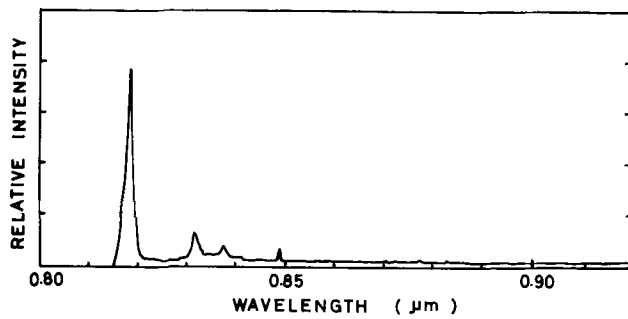


Fig. 8. Photoluminescence spectrum from sample No. 213 whose carrier density vs. temperature characteristics is shown in Fig. 5. The peak from 0.83 to 0.85  $\mu\text{m}$  corresponds to its activation energy.

Schottky barrier diodes fabricated on epitaxial layers on semi-insulating GaAs substrate. The electron mobility vs. temperature characteristics of sample No. 233 in Fig. 9(a) is shown as curve (iii), and that of sample No. 230 is shown as curve (v) in Fig. 4(a). Those samples whose frequency vs. capacitance characteristics are shown in Fig. 9(b) correspond to the samples in Fig. 4(b). The capacitance of all samples except No. 217 reveals a large dependence on frequency.

**Analysis according to the Hesse theory.**—From these data, the relation  $\Delta V/\Delta(1/C^2) - C$  is plotted, where  $V$  is voltage,  $C$  is capacitance, and  $\Delta$  denotes the difference of measured quantities. The relation  $dV/d(1/C^2) - C$  in the case of a Schottky barrier diode is given by Hesse (19) as

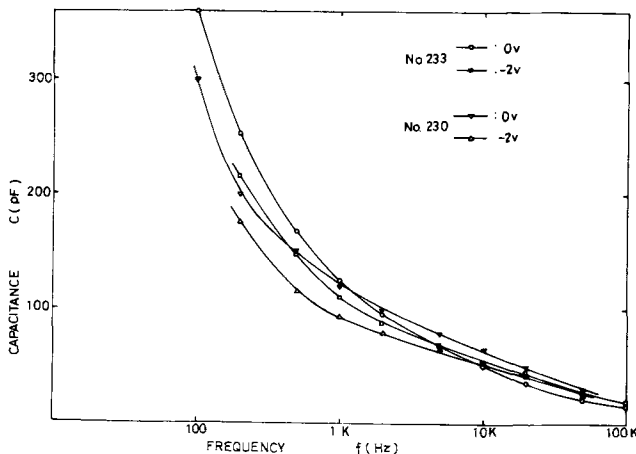


Fig. 9(a). Frequency dependence of a Schottky barrier capacitance (I) for the samples in groups A and B.

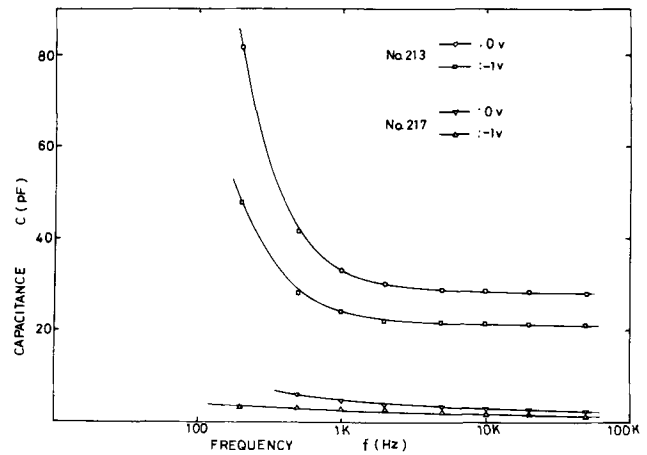


Fig. 9(b). Frequency dependence of a Schottky barrier capacitance (II) for the samples in groups C and D.

$$\frac{dV}{d(1/C^2)} = \frac{q(N_D + N_T)}{2\epsilon} \left[ 1 - \frac{C}{C_\infty} g(\omega) \right] \quad [7]$$

where  $N_D$  is the density of the shallow donor;  $N_T$ , the density of the deep donor;  $\omega$ , the signal angular frequency at measurement;  $C_\infty$ , the value of capacitance at infinite frequency;  $g(\omega)$ , the function indicating the frequency dependence of charging and discharging characteristics of deep donors;  $q$ , the electron charge; and  $\epsilon$ , the dielectric constant.

Equation [7] indicates that the relation of  $dV/d(1/C^2) - C$  is linear, and extrapolations to zero capacitance should converge at a point regardless of the measuring frequency, from which the value of  $N_D + N_T$  is calculated.

Figure 10 shows examples of the plotting of  $\Delta V/\Delta(1/C^2) - C$ . Although the lines do not necessarily converge at a point for zero capacitance, the value of  $N_D + N_T$  is approximately given as listed in Table IV. One of the reasons for this nonconvergence may be that Eq. [7] includes an effect of only a single level.

From the Hesse theory, the value of  $E_F - E_T$ , also can be obtained, where  $E_F$  is the Fermi level and  $E_T$  is the trap level. Table IV shows examples of  $N_D + N_T$ ,  $E_C - E_T$ , and  $N_T/N_D$ . The value of  $E_C - E_T$  is calculated by adding  $E_C - E_F$  to  $E_F - E_T$ , where  $E_C$  is the bottom level of the conduction band. Their levels are 0.18, 0.28, and 0.54 eV from the conduction band edge. 0.18 eV is near the level of 0.20 eV, which has been attributed to an unidentified defect (20), and 0.54 eV is near the level of 0.56 eV due to the same defect (21) or the level of 0.55 eV made by copper. These results are likely to imply that those samples, which contain such deep traps, are contaminated by copper.

The charging and discharging time constant  $\tau$  also can be approximately calculated from the following equation with Eq. [7]

$$g(\omega \rightarrow \infty) = 1 - \frac{1}{\omega\tau} \cdot \frac{N_D + N_T}{N_D} \quad [8]$$

The value of  $dV/d(1/C^2)$  at 20 kHz was used as in the calculation for sample No. 230.

**Analysis according to Zohra's theory.**—Zohra (22) showed that the variation of  $\Delta V/\Delta(1/C^2)$  with frequency can be expressed as

Table IV. Various values obtained by plotting the relation  $\Delta V/\Delta(1/C^2) - C$

Sample No.	$N_D + N_T$ (cm <sup>-3</sup> )	$N_D$ (cm <sup>-3</sup> )	$N_T$ (cm <sup>-3</sup> )	$N_T/N_D$	$E_C - E_T$ (eV)
213	$5.26 \times 10^{16}$	$3.2 \times 10^{15}$	$4.9 \times 10^{16}$	15	0.18
217	$4.44 \times 10^{14}$	$4.0 \times 10^{14}$	$4.4 \times 10^{13}$	0.11	
230	$3.63 \times 10^{17}$	$1.1 \times 10^{16}$	$3.5 \times 10^{17}$	32	0.28
233	$1.55 \times 10^{18}$	$4.7 \times 10^{16}$	$1.5 \times 10^{18}$	32	0.54

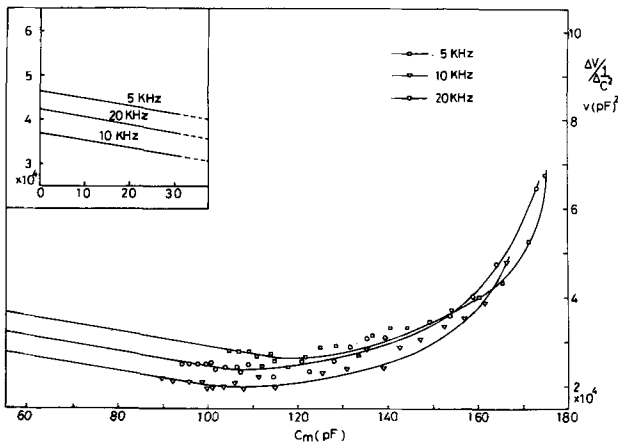


Fig. 10(a). Experimental values of  $\Delta V/\Delta(1/C^2)$  as a function of  $C_m$ .  $C_m = \sqrt{C(C + \Delta C)}$ . (Sample No. 233.)

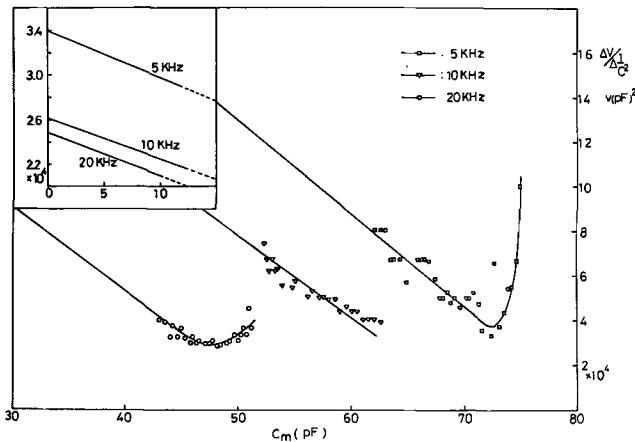


Fig. 10(b). Experimental values of  $\Delta V/\Delta(1/C^2)$  as a function of  $C_m$ .  $C_m = \sqrt{C(C + \Delta C)}$ . (Sample No. 230.)

$$[\Delta V/\Delta(1/C^2)]_\omega = \frac{1}{2} q\epsilon A^2 [(N_D - N_A) + N_T(1 - C\lambda_0/\epsilon A)(1 - j\omega\tau)(1 + \omega^2\tau^2)^{-1}] \quad [9]$$

where  $N_D$  and  $N_A$  are the shallow donor and acceptor densities respectively,  $N_T$  is the density of deep traps,  $C$  is capacitance at angular frequency  $\omega$ ,  $A$  is the area of a Schottky barrier diode,  $\tau$  is a charging and discharging time constant, and  $\lambda_0$  is the distance from the plane where the energy band starts bending to the plane, where the bulk Fermi level equals the potential of the trap level. The solid-line curve in Fig. 11 shows an example of plotting the real part of Eq. [9] for sample No. 230.  $N_D$ ,  $N_A$ , and  $N_T$  in Tables II and IV were used in the calculation. The broken line in Fig. 11 shows the relation of  $\Delta V/\Delta(1/C^2)$  vs. the frequency obtained from the experiment. Considerably good agreement is evident between the theoretical (solid) curve and the experimental (broken) curve if  $\tau = 5.76 \times 10^{-4}$  sec is assumed.

The value of  $\tau = 5.76 \times 10^{-4}$  sec is in rather good agreement with  $3.20 \times 10^{-4}$  sec obtained from the Hesse method. A slight difference exists because the value of  $\Delta V/\Delta(1/C^2)$  at 20 kHz was used as that for  $\omega \rightarrow \infty$  in the analysis according to the Hesse theory; however, 20 kHz is too low to approximate  $\omega \rightarrow \infty$ .  $\tau$  obtained to fit Eq. [9] to the experimental results is used later in calculating the scattering cross section of deep traps.

**Correlation among the experimental results, compensation ratio, and space charge scattering.**—Figure 12 shows the relation between the compensation ratio and the value of the product of the space charge region

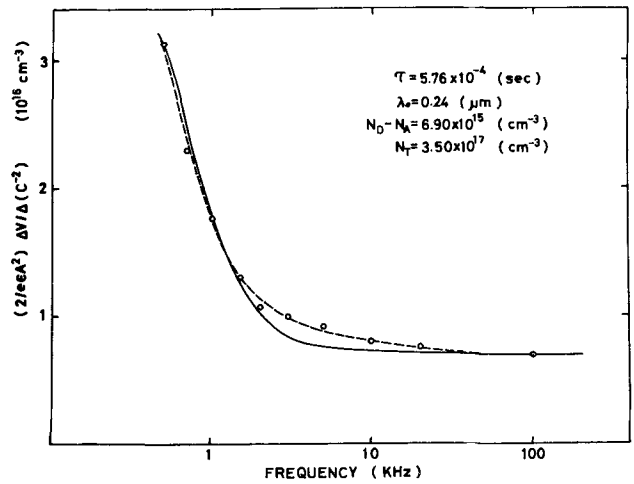


Fig. 11. Frequency dependence of  $\Delta V/\Delta(C^{-2})$ , where  $V$  is voltage and  $C$  capacitance;  $\circ$  represents an experimental value and the solid line is the theoretical one.

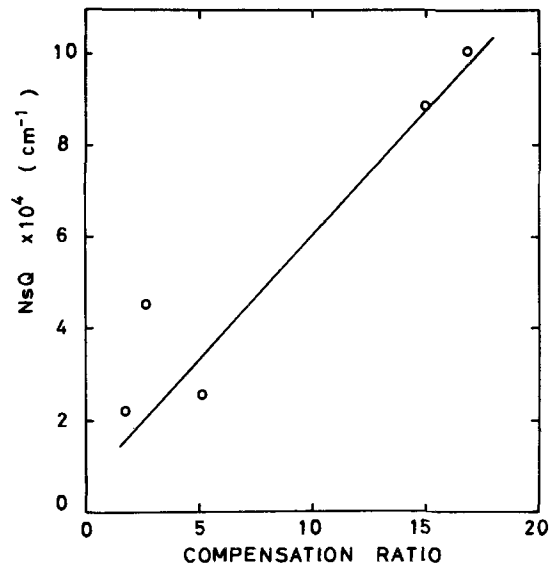


Fig. 12. Relation between the compensation ratio and the value of the product of the space charge region  $Ns$  and scattering cross section  $Q$ .

density and their scattering cross section listed in Table II for samples belonging to groups A and B. It is obvious that the value of  $NsQ$  increases with the compensation ratio (23). Correlation between the sources of compensating impurities and the space charge region has been discussed by Ikoma (2, 3) regarding heat-treated GaAs samples. He suggested that the space charge region is related to the inhomogeneity of the epitaxial layer.

The parameter  $\gamma$  which is defined by

$$\gamma = R_{AB,CD}/R_{BC,DA} \quad (R_{AB,CD} \cong R_{BC,DA})$$

$$\text{OR} \quad R_{BC,DA}/R_{AB,CD} \quad (R_{BC,DA} \cong R_{AB,CD})$$

is a measurement of macroscopic inhomogeneity of the epitaxial layer, as Ikoma proposed.  $R_{AB,CD}$  indicates resistance of the epitaxial layer; that is, it equals the voltage across contacts C and D divided by the current flowing between contacts A and B of the sample used in the van der Pauw method (12).

The  $\gamma$ -values for the samples discussed in this paper are listed in Table I;  $\gamma$  is generally small except for a few samples, which implies that the samples are macroscopically homogeneous. Thus, the source of the space charge region is not related to the macroscopic inhomogeneity of the epitaxial layer.

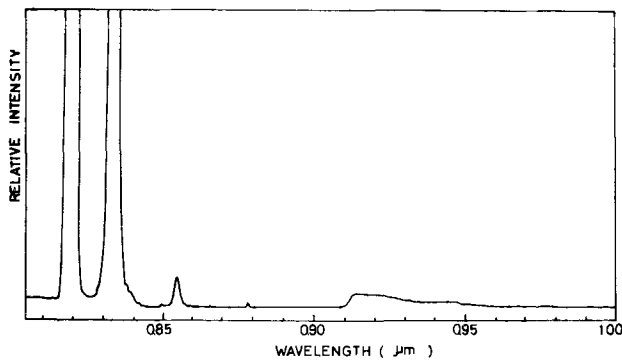


Fig. 13. Photoluminescence spectrum of sample No. 233

*Correlation among density of space charge region, compensating acceptors, and photoluminescence spectra.*—As already discussed, there is correlation between density of the space charge region and that of the compensating acceptors.

Figure 13 shows an example of the photoluminescence spectrum from GaAs epitaxial layer (sample No. 233) whose electronic properties were discussed in previous sections. As is well known, the peak in a range from 0.91 to 0.95  $\mu\text{m}$  in Fig. 13 corresponds to a level caused by copper. Existence or nonexistence of this peak for each sample is listed in Table I. This peak frequently appears in the photoluminescence spectra of samples belonging to groups A and B, whose compensation ratio is rather large. This suggests that there is correlation among density of the space charge region, the compensation ratio, and contamination by copper.

Recalling that space charge region is a model (1) for a scattering center which has a large scattering cross section, the space charge region is suggested to be formed by clusters of impurities such as copper, or copper and defect complexes in the crystal. When most of the copper atoms in the epitaxial layer form clusters, the level they make may be shifted. This is an explanation of the reason why, in the spectrum of sample No. 219 which belongs to group B of mobility vs. temperature characteristics, the peak between 0.91 and 0.95  $\mu\text{m}$  disappears.

*Correlation between the level of deep traps measured by Schottky barrier capacitance method and photoluminescence spectra.*—The level of deep traps 0.54 eV in sample No. 233 obtained by measuring the Schottky barrier capacitance vs. the frequency characteristics in Fig. 9(a) corresponds to existence of the peak between 0.91 and 0.95  $\mu\text{m}$  due to the copper (9, 11) in Fig. 13.

*Correlation among electron mobility, aging time of fused quartz tube in purified hydrogen, and photoluminescence spectra.*—The mean value of the electron mobility in the GaAs epitaxial layer grown in the vapor phase system rises with the aging time of a quartz tube at high temperature such as 1000°C in purified hydrogen, as shown in Fig. 14.

The photoluminescence peak between 0.91 and 0.95  $\mu\text{m}$  of GaAs epitaxial layers caused by copper atoms disappears after sufficient aging of a fused quartz tube. This implies that the main source of copper atoms, which are suggested to form space charge regions and compensate the donor impurities decreasing the electron mobility in GaAs epitaxial layer, is eliminated by aging of a fused quartz tube (24).

*Cross section of deep traps.*—The trap density of samples No. 230 and 233 are thirty times larger than that of the shallow donor impurity shown in Table IV, but these deep traps are electrically neutral at least at a low field. On the other hand, the mobility determined by neutral impurity scattering is derived as follows (25)

$$\mu_N = 8.36 \times 10^{19} (1/N_N) \quad (\text{cm}^2/\text{V}\cdot\text{sec}) \quad [10]$$

where  $N_N$  is the density of neutral impurity. Here neu-

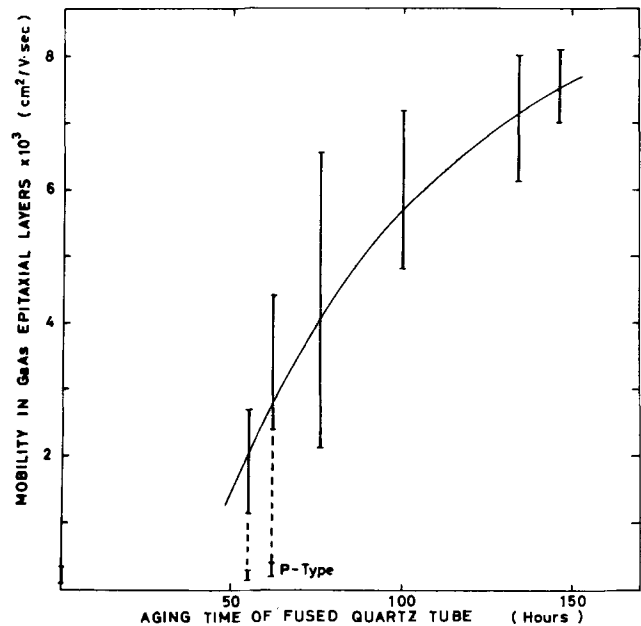


Fig. 14. Aging time of a fused quartz tube in purified hydrogen and electron mobility in GaAs epitaxial layer grown in that quartz tube.

tral impurity implies the neutral fraction of shallow donors and shallow acceptors. If mobility is calculated by substituting deep donor density into  $N_N$  in Eq. [10], too small a value is obtained as electron mobility. Furthermore, electron mobility at low field can be explained without counting the effect of these deep donors. This implies that those deep traps have very small scattering cross sections, neither assuming a significant role in determining electron mobility nor corresponding to the space charge regions.

The cross section  $\sigma$  of deep traps, on the other hand, can be calculated by using the charging and discharging time constant  $\tau = 5.76 \times 10^{-4}$  sec for sample No. 230 obtained from the analysis according to the Zohta theory, following the relation

$$1/\tau = N_T \cdot v_{th} \cdot \sigma \quad [11]$$

where  $N_T$  is the density of deep traps and  $v_{th}$  is the electron thermal velocity. If the value  $N_T = 3.50 \times 10^{17} \text{ cm}^{-3}$  listed in Table IV is substituted into Eq. [11], the small cross section  $\sigma = 1.04 \times 10^{-22} \text{ cm}^2$  is obtained as expected from the relation between electron mobility and density of the deep traps.

## Conclusions

The conclusions obtained from this work are as follows:

1. The Hall measurement of GaAs epitaxial layers grown in a vapor phase system revealed that compensating acceptors and space charge regions are two of the physical origins of decreasing electron mobility, and that both compensation and formation of the space charge region are related to contamination by copper. These results are supported by Schottky barrier capacitance measurement and by photoluminescence spectra of the same samples. In the Schottky barrier capacitance measurement deep traps whose energy level is identical to one made by copper were measured; in the photoluminescence measurement, a peak due to copper was observed.

2. Electron mobility of GaAs epitaxial layers grown in a fused quartz tube before and after aging in a hydrogen atmosphere suggested that compensating acceptors and space charge regions are mainly introduced from an unaged fused quartz tube. The photoluminescence peak attributed to copper appeared in the samples made in an unaged fused quartz tube, and disap-

peared in the samples made in an aged fused quartz tube.

3. The small scattering cross section of the deep traps obtained by Schottky barrier capacitance measurement ( $\sigma = 1.04 \times 10^{-22} \text{ cm}^2$ ) implies that those deep traps assume no significant role in determining the electron mobility in GaAs. This result supports the theory that electron mobility in GaAs epitaxial layers can be explained without considering the effect of deep traps.

4. A photoluminescence peak, corresponding to the activation energy, was found, which determines the temperature dependences of electron density and mobility.

### Acknowledgments

We express our deep appreciation to S. Akai and T. Suzuki, Research Laboratory, Sumitomo Electric Industries, for their supply of GaAs substrate and to H. Imai, Department of Electronic Engineering, the University of Tokyo, for his photoluminescence measurements in cooperation with our work.

This work has been supported by the Grant-in-Aid, for Scientific Research from the Ministry of Education, Japanese Government and also by the Electrical Communication Laboratory, Nippon Telegraph and Telephone Public Corporation. Their support is greatly appreciated.

Manuscript submitted May 21, 1973; revised manuscript received Dec. 10, 1973.

Any discussion of this paper will appear in a Discussion Section to be published in the June 1975 JOURNAL. All discussions for the June 1975 Discussion Section should be submitted by Feb. 1, 1975.

### REFERENCES

1. L. R. Weisberg, *J. Appl. Phys.*, **33**, 1817 (1962).
2. H. Ikoma, *J. Phys. Soc. Japan*, **25**, 1069 (1968).
3. M. Toyama and H. Ikoma, *Japan. J. Appl. Phys.*, **8**, 1449 (1969).
4. H. Ikoma, *ibid.*, **28**, 1474 (1970).
5. R. Williams, *J. Appl. Phys.*, **37**, 3411 (1966).
6. Y. Furukawa and Y. Ishibashi, *Japan. J. Appl. Phys.*, **6**, 503 (1967).
7. R. R. Senechal and J. Basinski, *J. Appl. Phys.*, **39**, 4581 (1968).
8. H. Okamoto, S. Sakata, and K. Sakai, *ibid.*, **44**, 1316 (1973).
9. W. J. Turner, G. D. Pettit, and N. G. Ainslie, *ibid.*, **34**, 3274 (1963).
10. K. Sugiyama, *Japan. J. Appl. Phys.*, **6**, 601 (1967).
11. N. Nakashima, *ibid.*, **10**, 1737 (1971).
12. L. J. van der Pauw, *Philips Res. Rept.*, **13**, 1 (1958).
13. R. L. Petritz and W. W. Scanlon, *Phys. Rev.*, **97**, 1620 (1955).
14. H. J. Van Daal, *Philips Res. Rept.*, **3**, 49 (1965).
15. A. R. Hutson, *J. Appl. Phys.*, **32**, 2287 (1961).
16. J. Bardeen and W. Shockley, *Phys. Rev.*, **80**, 72 (1950).
17. H. Brooks, *Advan. Electron. Electron Phys.*, **7**, 158 (1955).
18. E. M. Conwell and M. O. Vassell, *Phys. Rev.*, **166**, 797 (1968).
19. K. Hesse and H. Strack, *Solid-State Electron.*, **15**, 767 (1972).
20. J. Blanc, R. H. Bube, and L. R. Weisberg, *J. Phys. Chem. Solids*, **25**, 225 (1964).
21. R. H. Bube and H. E. MacDonald, *Phys. Rev.*, **128**, 2062, 2071 (1962).
22. Y. Zohta, *J. Appl. Phys.*, **43**, 1713 (1972).
23. R. G. Hamerly and M. W. Heller, *ibid.*, **42**, 5585 (1971).
24. J. T. Edmond, *ibid.*, **31**, 1428 (1960).
25. C. Erginsoy, *Phys. Rev.*, **79**, 1013 (1950).

## Ge-Nitride, Ge-Oxide, and Ge-Oxynitride Formation by Ion Implantation

H. J. Stein

Sandia Laboratories, Albuquerque, New Mexico 87115

The publication costs of this article have been assisted by Sandia Laboratories.

### ABSTRACT

The first formation of compounds of Ge by ion implantation into Ge has been achieved. Infrared absorption bands characteristic of four-fold coordinated  $\text{GeO}_2$  and of  $\text{Ge}_3\text{N}_4$  were observed after implantation with  $3 \times 10^{17}/\text{cm}^2$  200 keV  $\text{O}_2^+$  or  $\text{N}_2^+$  respectively, into high-resistivity Ge substrates. The absorption band for  $\text{Ge}_3\text{N}_4$  was also produced by 60 keV  $\text{N}^+$  implantation into Ge, and the band intensity increased approximately as the square root of the number of implanted nitrogen atoms. Implantation with  $2 \times 10^{17}$  200 keV  $\text{NO}^+/\text{cm}^2$  produced an absorption band with a peak position between those for  $\text{GeO}_2$  and  $\text{Ge}_3\text{N}_4$ , which is analogous to the band position for  $\text{Si}_x\text{O}_y\text{N}_z$  relative to  $\text{Si}_3\text{N}_4$  when  $y \approx z$ . Sample temperatures were  $< 200^\circ\text{C}$  during implantation, and the samples were subsequently annealed to  $500^\circ\text{C}$ . Absorption band positions for the Ge compounds formed by ion implantation were observed to shift  $20\text{-}30 \text{ cm}^{-1}$  toward higher wave numbers upon annealing. This shift is attributed to densification by an annealing of implantation-produced expansion.

Thin insulating films are an essential part of planar semiconductor-device technology. Oxide films on silicon are readily formed by thermal oxidation of the Si substrate to produce chemically stable insulating films. To obtain stable insulating films on other semiconductors, however, it is usually necessary to form the films

Key words: ion implantation, compounds, germanium, infrared absorption, annealing.

by evaporation, by sputtering, or by chemical reactions which do not incorporate substrate atoms.

Ion implantation provides another method to form thin films which incorporate substrate atoms, and a number of authors have demonstrated that silicon oxide and silicon nitride can be formed by the implantation of oxygen (1-4) or nitrogen (3-6), respectively, into silicon. There are no known previous

studies of germanium oxide ( $\text{GeO}_2$ ) or germanium nitride ( $\text{Ge}_3\text{N}_4$ ) formation by ion implantation, and relatively few studies of chemically formed  $\text{GeO}_2$  or  $\text{Ge}_3\text{N}_4$  films.

The usual methods for forming  $\text{GeO}_2$  yield either an amorphous film or a hexagonal crystalline film (7), both of which are very chemically active. Therefore, thermally produced  $\text{GeO}_2$  has not been useful in Ge device fabrication. It is of interest to determine if tetragonal  $\text{GeO}_2$ , which is more stable chemically than the hexagonal or amorphous  $\text{GeO}_2$ , will be produced by oxygen implantation into Ge. Previous studies (8) have shown that absorption due to Ge-O-Ge stretching for the fourfold coordination of Ge with oxygen in hexagonal or amorphous  $\text{GeO}_2$  occurs at about  $880\text{ cm}^{-1}$ , whereas the stretching mode for sixfold coordination of Ge with oxygen in tetragonal  $\text{GeO}_2$  occurs at about  $700\text{ cm}^{-1}$ . Thus, infrared absorption can be used to distinguish between hexagonal or amorphous and tetragonal  $\text{GeO}_2$ .

Nagai and Niimi (9) formed amorphous  $\text{Ge}_3\text{N}_4$  in films by reacting  $\text{GeCl}_4$  and  $\text{NH}_3$  on Ge substrates held between  $400^\circ$  and  $600^\circ\text{C}$ , and Bagratishvili *et al.* (10) formed amorphous  $\text{Ge}_3\text{N}_4$  films by reacting  $\text{N}_2\text{H}_4$  and Ge. Such films have dielectric characteristics (10, 11) comparable to those for  $\text{Si}_3\text{N}_4$ , and they are characterized by a broad infrared absorption band with a substrate-temperature-dependent peak between  $720$  and  $780\text{ cm}^{-1}$  (9, 10).

We report here on germanium nitride and germanium oxide formation by nitrogen and oxygen implantation into Ge. A  $3 \times 10^{17}$   $200\text{ keV O}_2^+/\text{cm}^2$  implantation was used to form Ge oxide. The formation of Ge nitride was investigated by performing an implant with each of the following fluences:  $10^{16}$   $60\text{ keV N}^+/\text{cm}^2$ ,  $10^{17}$   $60\text{ keV N}^+/\text{cm}^2$ , and  $3 \times 10^{17}$   $200\text{ keV N}_2^+/\text{cm}^2$ . In addition, an implantation with  $2 \times 10^{17}$   $200\text{ keV NO}^+/\text{cm}^2$  was performed to investigate the formation of Ge oxynitride.

### Experimental Details

Samples with optical faces of  $1.27 \times 0.63\text{ cm}$  and a thickness of  $\sim 1\text{ mm}$  were cut from high resistivity n-type Ge. The sample faces were finished with successively finer (15, 6, and  $1\text{ }\mu\text{m}$ ) diamond polishing compounds. To further minimize surface damage on the optical faces they were rubbed lightly for 15 min on a POLITEX pad in a solution of 1 part  $\text{NH}_4\text{OH}$  to 700 parts of 30%  $\text{H}_2\text{O}_2$ . The composition of the solution was adjusted to obtain a pH of 7. Differential transmittance measurements were made at room temperature in a Beckman IR-12 spectrophotometer. Unimplanted Ge samples were matched in thickness and surface preparation to samples selected for implantation, and these unimplanted samples were used in the reference beam of the spectrophotometer for the differential measurements. During implantation the samples were clamped to an Al holder by a Ta coverplate with an aperture slightly smaller than the samples. Magnetically selected and electrostatically scanned ion beams between 5 and  $20\text{ }\mu\text{A}/\text{cm}^2$  were used for the implantation. Secondary electrons were electrostatically suppressed. Isochronal annealing of the implanted samples was performed for 20 min periods in  $100^\circ\text{C}$  increments within a nitrogen atmosphere tube furnace. Oxidation of Ge was observed upon annealing at  $600^\circ\text{C}$ , therefore the annealing study was terminated at  $500^\circ\text{C}$ .

### Experimental Results

Differential transmittance spectra for Ge after implantation with  $\text{O}_2^+$ ,  $\text{NO}^+$ , and  $\text{N}_2^+$  are shown in Fig. 1. The results are arbitrarily displaced along the transmittance axis to provide separation among the spectra. Absorption bands at approximately  $860$ ,  $750$ , and  $685\text{ cm}^{-1}$  for  $\text{O}_2^+$ ,  $\text{NO}^+$ , and  $\text{N}_2^+$  implanted Ge are attributed to  $\text{GeO}_2$ ,  $\text{Ge}_x\text{O}_y\text{N}_z$  (germanium oxynitride), and  $\text{Ge}_3\text{N}_4$ , respectively. From calculated (12) ion ranges and ion profiles (peak range  $\sim 2500\text{ \AA}$ , standard

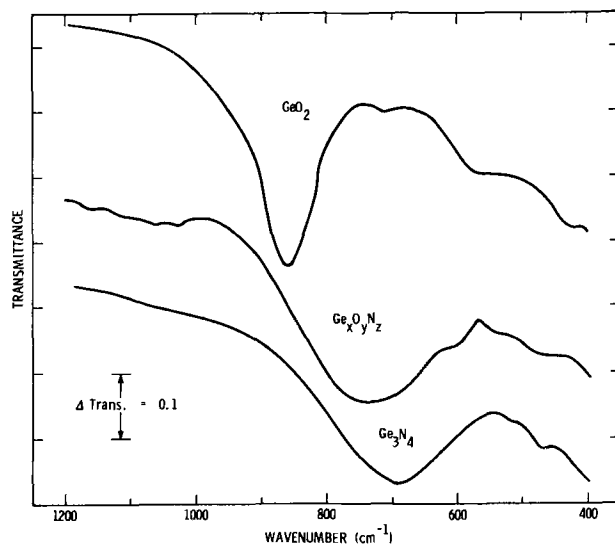


Fig. 1. Transmittance vs. wave number for  $\text{GeO}_2$ ,  $\text{Ge}_3\text{N}_4$ , and  $\text{Ge}_x\text{O}_y\text{N}_z$  films formed by  $200\text{ keV}$  implantation of Ge with  $3 \times 10^{17}\text{ O}_2^+/\text{cm}^2$ ,  $3 \times 10^{17}\text{ N}_2^+/\text{cm}^2$ , and  $2 \times 10^{17}\text{ NO}^+/\text{cm}^2$ , respectively. Spectra are arbitrarily displaced along transmittance axis to provide clarity.

deviation  $\sim 800\text{ \AA}$ ) combined with measured ion fluences, implantations with  $3 \times 10^{17}\text{ cm}^{-2}$   $200\text{ keV N}_2^+$  or  $\text{O}_2^+$  are expected to give volume concentrations of nitrogen or oxygen approximately equal to the volume concentration of Ge. Sputtering by the incident ions and a change of atomic composition during implantation will, however, tend to broaden the ion profile and reduce the volume concentration of the implanted ions. The number of nitrogen and oxygen atoms per unit area are obviously equal for the  $\text{NO}^+$  implantation, and the volume concentration of the two atoms are expected to be approximately equal.

Figure 2 shows the transmittance for the samples of Fig. 1 after annealing at  $500^\circ\text{C}$ . The major absorption bands are observed to sharpen slightly and shift toward higher frequencies upon annealing. Small changes in weak absorption bands also occur upon annealing. Some of the annealing-induced changes only make existing bands more apparent. For example, a weak band near  $600\text{ cm}^{-1}$  is readily distinguishable in the oxynitride after annealing to  $500^\circ\text{C}$ , but it is also present as a shoulder on the major absorption band before annealing. Figure 3 shows the major band posi-

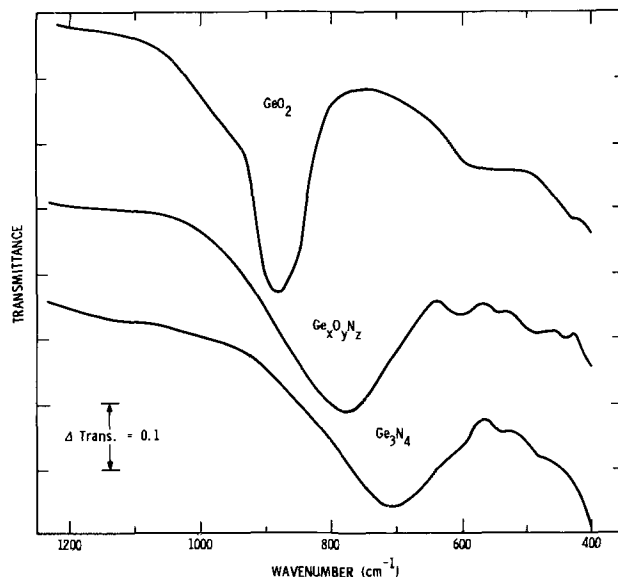


Fig. 2. Transmittance vs. wave number for the samples of Fig. 1 after annealing at  $500^\circ\text{C}$ .

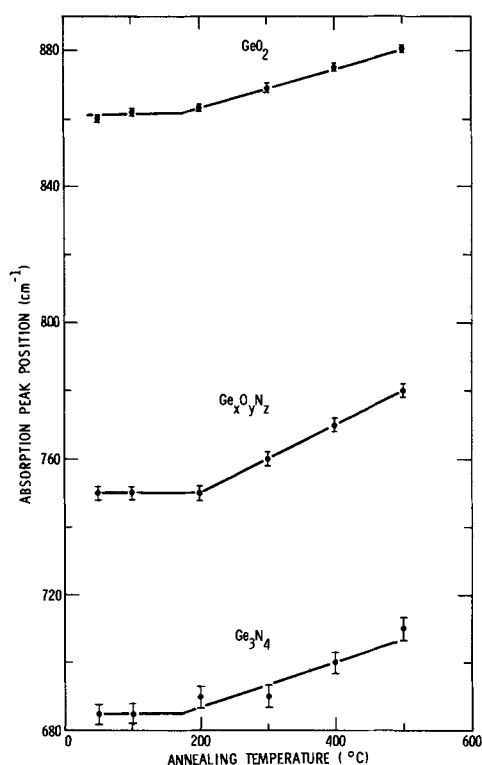


Fig. 3. Wave number positions for absorption peaks as a function of annealing temperature for the  $\text{GeO}_2$ ,  $\text{Ge}_x\text{O}_y\text{N}_z$ , and  $\text{Ge}_3\text{N}_4$  films formed by ion implantation.

tions for  $\text{GeO}_2$ ,  $\text{Ge}_x\text{O}_y\text{N}_z$ , and  $\text{Ge}_3\text{N}_4$  as a function of annealing temperature. The point of contact of the minimum in transmittance to a smoothed line parallel to the background transmittance was used to determine the peak position. Uncertainty in band position increases with band width. The onset of the 20–30  $\text{cm}^{-1}$  upward frequency shift is shown to occur at an annealing temperature near 200°C. This indicates the effective temperature during implantation of the samples was < 200°C.

Figure 4 shows the germanium nitride bands produced by  $10^{16}$  and  $10^{17}$  60 keV  $\text{N}^+/\text{cm}^2$  compared to the band produced by  $3 \times 10^{17}$  200 keV  $\text{N}_2^+/\text{cm}^2$ . Volume concentrations for nitrogen are ~ 2 and 20% of the Ge concentration within a standard deviation of the peak ion range following  $10^{16}$  and  $10^{17}$  60 keV  $\text{N}^+/\text{cm}^2$  implantations, respectively. In order to have a common annealing history for the samples, the results shown

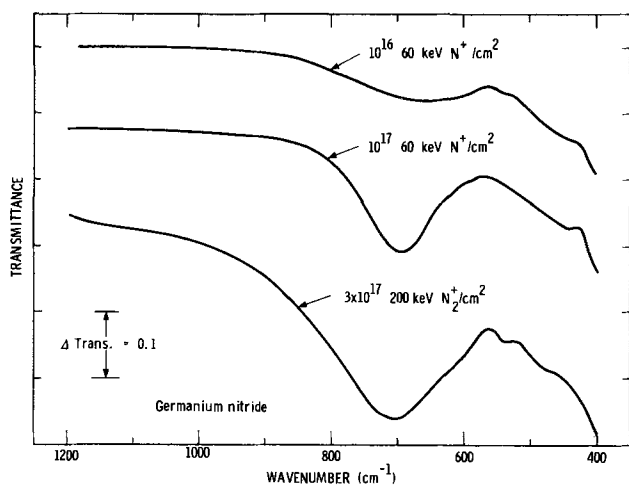


Fig. 4. Absorption bands produced by implantation of  $10^{16}$  and  $10^{17}$  60 keV  $\text{N}^+/\text{cm}^2$  into Ge compared to that produced by  $3 \times 10^{17}$  200 keV  $\text{N}_2^+/\text{cm}^2$ . All samples were annealed at 500°C prior to the measurements.

in Fig. 4 are those measured after annealing at 500°C. The area in the absorption band increases approximately with the square root of the implanted nitrogen atoms, and there is a small shift of the absorption band toward higher frequency with increasing nitrogen fluence.

### Discussion

The strong absorption band near 860  $\text{cm}^{-1}$  and the weak band near 570  $\text{cm}^{-1}$  shown in Fig. 1 for  $\text{O}_2^+$  implanted Ge suggest fourfold coordinated  $\text{GeO}_2$  formation by oxygen implantation into Ge. A second weak band near 700  $\text{cm}^{-1}$  may indicate that a small fraction of the  $\text{GeO}_2$  exists in the tetragonal phase. However, the 700  $\text{cm}^{-1}$  band anneals out between 300° and 500°C and is missing in the  $\text{GeO}_2$  results shown in Fig. 2. Therefore, the structural form for  $\text{GeO}_2$  produced by implantation with  $3 \times 10^{17}$   $\text{O}_2^+/\text{cm}^2$  is essentially the same as that formed by thermal oxidation (7, 8). Higher fluence implants, which would increase the oxygen concentration relative to Ge, may favor formation of the tetragonal phase. The Ge-O-Ge stretching mode for dispersed-interstitial oxygen (13) in Ge also occurs near 860  $\text{cm}^{-1}$  and has been observed in oxygen-implanted Ge (14). But, the solubility (13) of dispersed oxygen is  $\approx 10^{18}$   $\text{cm}^{-3}$ , and the width at half maximum for the dispersed oxygen band (13) is only 6  $\text{cm}^{-1}$  compared with a more typical  $\text{GeO}_2$  half-width of  $\approx 90$   $\text{cm}^{-1}$  observed for the oxide band in the present experiment.

An upward frequency shift and sharpening of absorption bands upon annealing was previously shown for compounds formed in Si by ion implantation (4). Studies (15) on pyrolytically grown Si-oxide films have shown that the Si-O stretching bandwidth decreases and the band position shifts to higher frequencies on decrease of porosity in the films. Since implantation causes annealable expansion of Si (16) and presumably of Ge also, the slight sharpening and the upward frequency shift of the band positions for the Ge compounds formed by ion implantation is attributed to densification associated with the annealing of implantation-produced expansion.

The broad absorption band near 700  $\text{cm}^{-1}$  following 200 keV  $\text{N}_2^+$  implantation is interpreted as evidence for amorphous  $\text{Ge}_3\text{N}_4$  formation. Absorption results in Fig. 4 indicate that  $\text{Ge}_3\text{N}_4$  is also formed by 60 keV implantation with  $10^{16}$  and  $10^{17}$   $\text{N}^+/\text{cm}^2$ . The magnitude of the absorption in the bands produced by nitrogen implantation increases approximately as the square root of the implanted nitrogen atoms, which suggests a bimolecular process for forming  $\text{Ge}_3\text{N}_4$ . This dependence may occur simply because the available uncombined Ge is being depleted. However, a previous study showed that  $\text{Ge}_3\text{N}_2$  was formed from the reaction of nitrogen with germane ( $\text{GeH}_4$ ) (17), so that Ge-N precursors may also be involved in  $\text{Ge}_3\text{N}_4$  formation by ion implantation. The absorption characteristics for  $\text{Ge}_3\text{N}_2$  are not known. The dependence of the band position on implanted nitrogen atoms suggests that nitrogen deficiency in the implanted layer causes a lowering of the Ge-N vibrational frequencies.

Etch rates in HF solution are slow for both  $\text{Si}_3\text{N}_4$  (18) and  $\text{Ge}_3\text{N}_4$  (10). Therefore, Si oxynitrides ( $\text{Si}_x\text{O}_y\text{N}_z$ ) with faster etch rates are sometimes used rather than  $\text{Si}_3\text{N}_4$  in masking applications where the layer must be removed by an etching process. The infrared absorption band for  $\text{Si}_x\text{O}_y\text{N}_z$  is shifted toward higher wave numbers relative to  $\text{Si}_3\text{N}_4$  dependent on the values of  $y$  and  $z$  (18). The same effect is apparently occurring for  $\text{Ge}_x\text{O}_y\text{N}_z$ . The band position for  $\text{Ge}_x\text{O}_y\text{N}_z$  relative to that for  $\text{Ge}_3\text{N}_4$  is in accord with that for  $\text{Si}_x\text{O}_y\text{N}_z$  relative to  $\text{Si}_3\text{N}_4$  (18) when  $y \approx z$ .

### Conclusions

Ion-induced absorption bands show that Ge oxide, Ge nitride, and Ge oxynitride can be formed by ion implantation into Ge. These compounds are expected to exist in thin layers dependent on the ion ranges in

Ge. A shift in the absorption bands toward higher wave numbers upon annealing is typical of compounds formed in Si by ion implantation and is attributed to densification of the implanted layer by annealing of displacement-produced expansion.

The absorption band formed by oxygen implantation into Ge is characteristic of fourfold coordinated  $\text{GeO}_2$ , which is the usual form produced by thermal oxidation of Ge and is not a useful dielectric film for device applications. The absorption band formed by nitrogen implantation into Ge is in reasonable accord with that for amorphous  $\text{Ge}_3\text{N}_4$ , and previous studies of amorphous  $\text{Ge}_3\text{N}_4$  have shown that it is a suitable dielectric material for device applications. Thus, ion implantation offers an alternate method for producing potentially useful dielectric films on Ge.

Implantation of  $\text{NO}^+$  into Ge produces an oxynitride with a band position between that for the nitride and the oxide, completely analogous to absorption in  $\text{Si}_x\text{O}_y\text{N}_z$  for approximately equal concentrations of oxygen and nitrogen.

#### Acknowledgment

This work was supported by the United States Atomic Energy Commission.

Manuscript submitted Dec. 17, 1973; revised manuscript received March 7, 1974.

Any discussion of this paper will appear in a Discussion Section to be published in the June 1975 JOURNAL. All discussions for the June 1975 Discussion Section should be submitted by Feb. 1, 1975.

#### REFERENCES

1. M. Watanabe and A. Tohi, *Japan. J. Appl. Phys.*, **5**, 737 (1966).
2. P. Pavlov and E. Shitova, *Sov. Phys.-Dokl.*, **12**, 11 (1967).
3. J. Freeman, G. Gard, D. Mazy, J. Stevens, and F. Whiting, European Conf. on Ion Implantation, Reading, Berkshire, England (1970), p. 74.
4. J. A. Borders and W. Beezhold, "2nd International Conference on Ion Implantation in Semiconductors," I. Ruge and J. Graul, Editors, p. 241, Springer-Verlag, New York (1971).
5. J. Stephen, B. J. Smith, G. W. Hinder, D. C. Marshall, and E. M. Wittam, *ibid.*, p. 489.
6. R. J. Dexter, S. B. Watelski and S. T. Picraux, *Appl. Phys. Letters*, To be published.
7. W. A. Albers, Jr., E. W. Valyocsik, and P. V. Mohan, *This Journal*, **113**, 196 (1966).
8. M. K. Murthy and E. M. Kirby, *Phys. Chem. Glasses*, **5**, 144 (1964); E. R. Lippincott, A. Van Valkenburg, E. E. Weir, and E. N. Bunting, *J. Res. Nat. Bur. Std.*, **61**, 61 (1958).
9. H. Nagai and T. Niimi, *This Journal*, **115**, 671 (1968).
10. G. D. Bagratishvili, R. B. Janelidze, and V. A. Chagelishvili, "Proc. International Conference on Physics and Chemistry of Semiconductor Heterojunctions and Layer Structures," Vol. V, p. 65, G. Szigeti, Chief Editor, Akademiai Kiado, Budapest (1971).
11. T. Yashiro, *Japan. J. Appl. Phys.*, **10**, 169 (1971).
12. D. K. Brice, Sandia Laboratories, RR71-0599 (1971).
13. W. Kaiser, *J. Phys. Chem. Solids*, **23**, 255 (1962); J. Bloem, C. Haas, and P. Penning, *ibid.*, **12**, 22 (1959).
14. H. J. Stein, *J. Appl. Phys.*, **44**, 2889 (1973).
15. W. A. Pliskin and H. S. Lehman, *This Journal*, **112**, 1013 (1965).
16. W. Beezhold, "2nd International Conference on Ion Implantation in Semiconductors," I. Ruge and J. Graul, Editors, p. 267, Springer-Verlag, New York (1971).
17. R. Storr, A. N. Wright, and C. A. Winkler, *Can. J. Chem.*, **40**, 1296 (1962).
18. D. M. Brown, P. V. Gray, F. K. Heumann, H. R. Philip, and E. A. Taft, *This Journal*, **115**, 311 (1968).

## Reliability of Gold/Stabilized Tantalum Metallizations for Microwave Power Transistors

Aristotelis Christou and Howard M. Day

Naval Research Laboratory, Washington, D. C. 20375

The publication costs of this article have been assisted by the Naval Research Laboratory.

#### ABSTRACT

Thin film systems based on platinum-tantalum-gold and tungsten-tantalum-gold have been investigated as metallization contacts for microwave power transistors. Platinum and tungsten deposited between layers of tantalum effectively stabilized the tantalum against grain boundary diffusion. The present investigation shows that Pt-Ta-Au and W-Ta-Au metallizations (i) are metallurgically stable, (ii) resist electrochemical corrosion, and (iii) are readily processed with existing technology.

In a previous investigation on the structure and thermal stability of rf sputtered Ta-Au films (1), the formation of TaAu above 450°C and the low-temperature grain boundary diffusion of gold resulted in an appreciable increase in sheet resistance. The growth of the TaAu layer followed a parabolic rate law and the low-temperature grain boundary diffusion occurred with an activation energy of 0.41 eV. Annealing the films up to 600°C also resulted in (i) particle growth with an activation energy of 0.5 eV for gold and 0.4 eV for tantalum, and (ii) reduction of thermal stresses and defect

density in the films. Finally, the results of Ref. (1) indicate that when modified to prevent grain boundary diffusion, Ta-Au should be suitable for applications in devices which operate at high temperatures.

In the work reported here, platinum and tungsten layers have been sputter deposited between 1000Å tantalum layers in order to stabilize the tantalum against grain boundary diffusion at gold or tantalum grain boundaries. The resulting structures were then overlaid with 2000-5000Å of sputtered gold. We report the effects of annealing on the structure of Ta-Pt-Ta-Au and Ta-W-Ta-Au films deposited on polished (111) oriented quartz and (100) silicon. The films were in-

Key words: metallizations, sputtering, microwave transistors, reliability, thermal stability, thin films.

vestigated using x-ray and electron diffraction methods, electrical resistivity measurements, and optical and scanning electron microscopy. The interdiffusion between gold, tantalum, and platinum has been studied by Auger electron spectroscopy.

This investigation is part of a larger effort to increase the reliability of microwave power transistors. One approach has been the application of metallizations which can withstand the high temperatures encountered in these devices without undergoing degradation or failure due to alloying or to interdiffusion of silicon, silicon dioxide, and metal. Aluminum and gold are the two major types of metal contacts currently in use. The aluminum contact usually incorporates small amounts of silicon and/or copper for the purpose of minimizing interdiffusion, alloying, and electromigration. In some cases, a stable silicide (i.e., platinum silicide) (3) is used with aluminum to isolate the aluminum from the silicon. The gold system generally incorporates a stable silicide as the low resistivity contact to silicon followed by a barrier layer (usually one or more refractory metals) and gold as the conductor. The barrier layer serves the purpose of isolating the gold from the silicon since that combination has a low melting point (eutectic temperature) of 377°C. The gold systems are potentially better from the standpoint of electromigration and high-temperature stability. Some of the metallization systems investigated in the literature include Mo-Au (4), W-Au (5), W:Ti-Au (6), Ti-Pt-Au (7), and more recently, Ta-Au (1) and Ta-Pt-Au (2).

### Experimental

**Film deposition.**—The metal films used in this study were rf sputter deposited using an argon pressure of  $5\mu$  and an rf power of 200W. The substrates used were polished (111) oriented quartz plates, 3 cm in diameter. For studies of Au-Si interdiffusion, (100) silicon substrates were used. The substrates were etched in buffered HF followed by a 15 min rinse in hot deionized water. Tantalum (800-1200Å thickness) was deposited first onto the substrate, followed by a 300-500Å layer of platinum or tungsten, and followed by a second layer of 1000Å of tantalum. A 2000-5000Å layer of gold was deposited as the top layer. The diffusion barrier thickness was maintained constant at 2500Å. During deposition, the cathode to substrate distance was maintained at 7.5 cm. Thin film thermocouple substrate temperature measurements indicate that the steady-state temperature during sputtering was 100°C. In all cases of sputter deposition, the substrate holder was water cooled to prevent further temperature increases.

The deposited Ta-Pt-Ta-Au and Ta-W-Ta-Au specimens were annealed in vacuum at pressure less than  $10^{-5}$  Torr. Tantalum tube furnaces with a 7 cm opening were used. The temperature variation was maintained at  $\pm 5^\circ\text{C}$ . The specimens reached temperature at a rate of  $20^\circ\text{C}/\text{min}$ . Isochronal annealing experiments were carried out by maintaining each specimen at temperature for 2400 sec. Isothermal experiments were carried out by annealing at a fixed temperature for up to 800 hr.

**X-ray diffraction and film examination.**—All x-ray data were obtained with a GE XRD-3 diffractometer using Ni filtered copper radiation as described previously (1). The calculation of stresses and strains in gold and tantalum was determined according to the method of Greenough (8). Each diffraction peak was scanned at  $0.5^\circ/\text{min}$  to determine the position of the peak. Three points which straddle the peak were then selected for intensity counting. The stress, after the necessary corrections was determined by the method described previously (1). Since the radiation penetrates the thin film and barrier layer, diffraction from the single-crystal substrate is always obtained. To eliminate overlapping, a method suggested by Walker (9) was used. The substrate was misoriented by changing  $2\theta$  at the Bragg angle. By misorienting the substrate,

the substrate peaks fall to zero since the planes parallel to the front surface are off axis. Instrumental broadening corrections were used to correct for inaccuracies in measurement of the peak position. The total change in the lattice parameter can be due to residual strain, solid solution effects, or a combination of both (9). Solid solution effects were eliminated by the independent measure of the lattice parameter using a multiple exposure technique (9).

Optical and scanning electron microscopy were used to analyze specimens in which large changes in resistivity were observed. In addition, the behavior of the Ta-Pt-Ta-Au metallization scheme at temperatures up to  $550^\circ\text{C}$  was investigated by Auger electron spectroscopy (AES). Surface composition was measured by AES while simultaneously sputter etching the specimen. In this way, a profile of the in-depth composition variations of the thin film layer was obtained (10).

The electrical resistivity measurements were carried out using a conventional in line four-point probe (2). The sheet resistance and the resistivity were obtained from the measured data using the method of Smits (11). Activation energies were obtained from isochronal and isothermal anneals. The annealing stage limits were determined on the basis of the minimum values of  $\Delta\rho/\Delta T$ , the isochronal derivative. Changes in electrical resistivity were also studied as a function of the ratio of platinum to tantalum and tungsten to tantalum (Pt/Ta, W/Ta).

In the present investigation a corrosion test similar to the one devised by Cunningham *et al.* (6) was applied. The test specimens were prepared with  $15\mu$  Ta/Au metal stripes spaced  $10\mu$  apart on glass plates. The gold-tantalum test stripes were examined for corrosion resistance by placing a drop of 0.001N phosphoric acid on the test slices and biasing the first and fourth stripes to 6V. The corrosion and electrolysis action was monitored by optical microscopy.

### Results and Discussions

**As-deposited film structure.**—The grain size of the deposited tantalum, tungsten, and gold films was in the range of 100-300Å, 200-400Å, and 300 to 600Å, respectively. Likewise, the grain size of the platinum was 200-400Å. The gold films were strongly (111) textured while the tantalum and platinum did not show any observable texture. The electrical resistivity of the gold films after deposition was measured to be 1.25 times the bulk resistivity. The sputtered tantalum films were prepared with a resistivity of 2.1 times that of bulk tantalum while the tungsten films were prepared with a resistivity of 3.0 times that of bulk tungsten. The tantalum films were deposited as bcc-Ta as verified by electron diffraction examination.

**Isochronal and isothermal anneals.**—**Resistivity.**—Isothermal and isochronal annealing of Ta-Pt-Ta-Au specimens with a variable platinum:tantalum layer thickness ratio shows that resistivity changes up to  $650^\circ\text{C}$  occur in two discrete stages and that the resistivity changes depend on the Pt:Ta thickness ratio (2). Figure 1 shows isothermal resistivity data at  $350^\circ$  and  $450^\circ\text{C}$  for various Pt:Ta ratio specimens with a barrier layer (Pt + Ta) and gold layer thickness of 2500 and 2000Å, respectively. Annealing at  $350^\circ\text{C}$  produces a decrease in resistivity which can be attributed to annealing out of vacancies and dislocations. Since electrical resistivity of the gold films after deposition was measured to be 1.25 times the bulk resistivity, isothermal annealing of the films with the absence of solid solution formation, decreases the density of structural defects quenched in during sputtering. The lowest resistivity was obtained with a Pt:Ta ratio of 0.24. Annealing at temperatures between  $450^\circ$  and  $540^\circ\text{C}$  resulted in a maximum 10% increase in resistivity for Ta-Pt-Ta-Au specimens with a Pt:Ta ratio of 0.15. Isochronal annealing of the same specimens indicates the existence of two annealing stages (stage I, between  $27^\circ$  and  $450^\circ\text{C}$  and stage II between  $450^\circ$



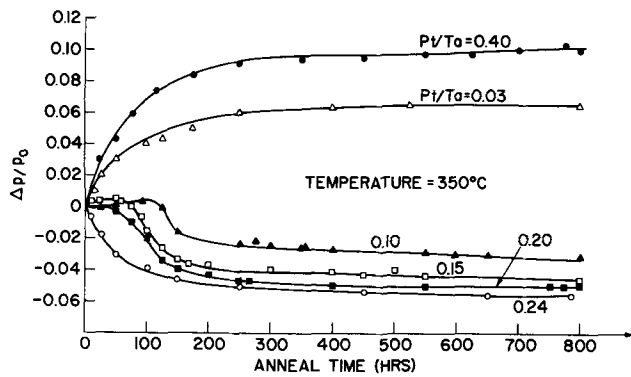


Fig. 1a. Isothermal annealing curves at 350°C for Ta-Pt-Ta-Au with various Pt/Ta ratios.

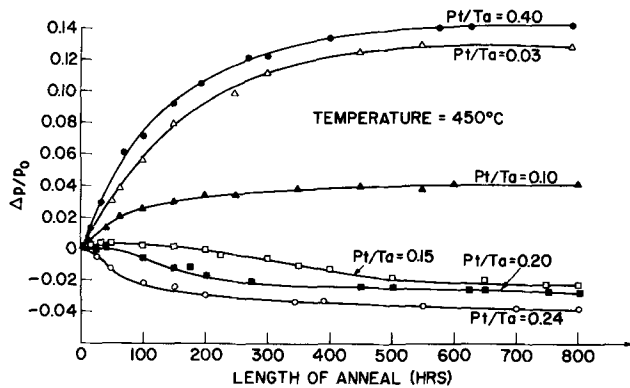


Fig. 1b. Isothermal annealing curves at 450°C for Ta-Pt-Ta-Au Ref. (2).

and 650°C). At temperatures above 450°C, the observed resistivity changes are attributed to interdiffusion between gold and tantalum at the Au-Ta interface and between tantalum and platinum at the Pt-Ta interface. This has been verified by x-ray diffraction and Auger electron spectroscopy and is discussed in the following sections.

The effect of platinum on the stage I resistivity changes is pronounced. Specimens without the platinum layer resulted in a 100% increase in  $\Delta\rho/\rho_0$  after annealing at 450°C for 600 hr, as described in Ref. (1). The addition of 300Å of platinum between the tantalum layers eliminated the increase in resistivity. In as much as the increase in resistivity for Ta-Au specimens has been attributed to gold precipitation at tantalum grain boundaries (1) the addition of platinum tends to inhibit gold grain boundary diffusion by precipitating to and passivating the tantalum grain boundaries. The interdiffusion problem is discussed in a later section. Figure 2 shows the effect of varying the thickness platinum to tantalum ratio. The lowest resistivity was obtained with a Pt:Ta ratio of 0.24, while maintaining the total thickness of the barrier layer (Pt + Ta) constant at 2500Å. Increasing the Pt:Ta ratio above 0.24 results in a rapid increase in resistivity. These specimens, qualitatively analyzed by energy dispersive x-ray analysis, show that for Pt:Ta > 0.24, the interdiffusion of gold and platinum dominates and degrades the gold film resistivity. Since the resistivity did not degrade for  $0.10 < \text{Pt:Ta} < 0.24$ , one can assume that a reliable diffusion barrier was formed with platinum effectively precipitating to the tantalum grain boundaries. In addition, as the anneal temperature is increased from 350° to 525°C, the interdiffusion between Au and Ta (1) increases, resulting in higher levels of resistivity as shown in Fig. 2.

**Interdiffusion.**—Figures 3a-c show typical depth-composition profiles for as-sputtered and annealed SiO<sub>2</sub>/Ta-Pt-Ta-Au metallizations. The as-sputtered composition profile of Fig. 3a shows no interdiffusion between the various constituents. Sharp interfaces are shown between the gold and the tantalum. The diffuse

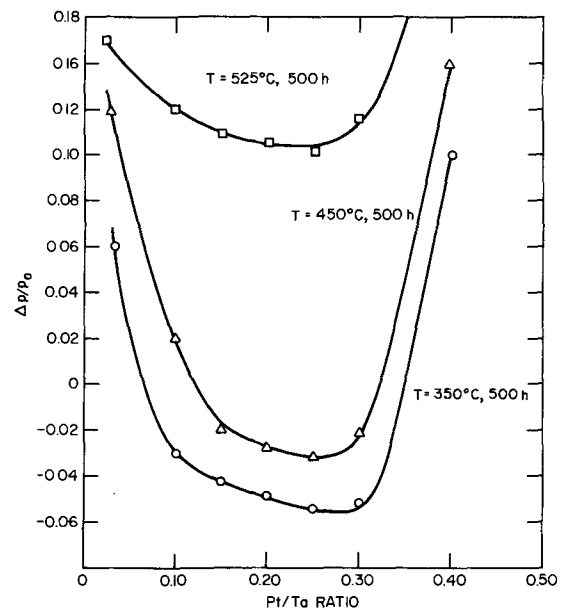


Fig. 2. Variation of  $\Delta\rho/\rho_0$  with Pt/Ta ratio at  $T = 350^\circ, 450^\circ,$  and  $525^\circ\text{C}$  Ref. (2).

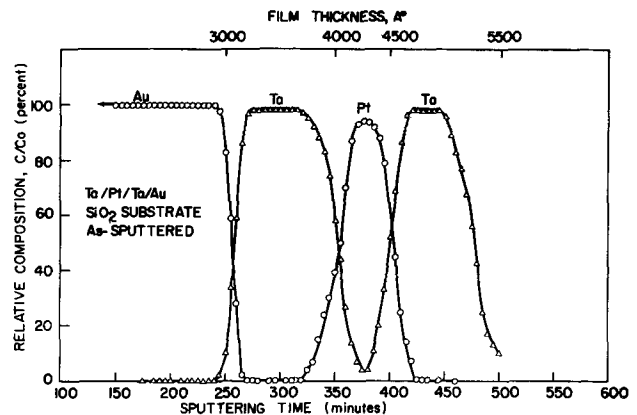


Fig. 3a. AES composition-depth profiles for as-sputtered Ta-Pt-Ta-Au films.

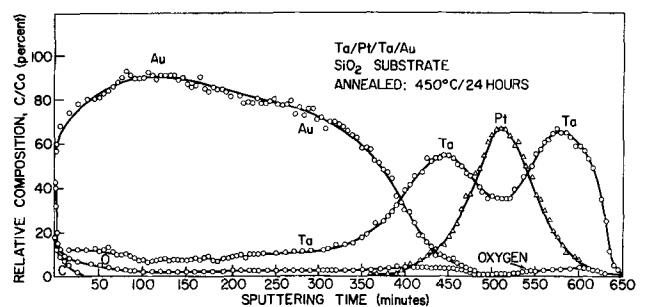


Fig. 3b. AES composition-depth profiles for Ta-Pt-Ta-Au annealed at 450°C for 24 hr.

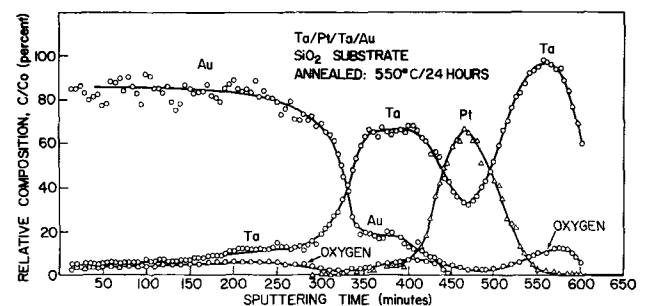


Fig. 3c. AES composition-depth profiles for Ta-Pt-Ta-Au annealed at 550°C for 24 hr.

interfaces between the platinum and tantalum may be attributed to the decreased thickness of the platinum layer (approximately 300Å) and to differential sputtering. Annealing at 450°C for 24 hr (Fig. 3b) resulted in the interdiffusion between Ta and Pt, with Pt spreading into the Ta films. The interface between the Au and Ta became diffused and was characterized by a gold tail into the Ta film. However, the Ta-Pt-Ta has remained an effective barrier to gold-SiO<sub>2</sub> interdiffusion. The Pt film has diffused into both Ta films with an enhanced diffusion toward the free surface. The Au-Ta interface composition is shown to be approximately 43% Au, 43% Ta, 8% Pt, and 4-6% O. The important observation at 450°C is the out-diffusion of Ta to the Au surface which considerably affects the conductivity characteristics of the metallization scheme (1).

The out-diffusion of Ta to the gold surface, likewise, was observed after annealing the SiO<sub>2</sub>/Ta-Pt-Ta-Au specimens at 550°C for 24 hr (Fig. 3c). The Au is shown to have diffused through the Ta. The Ta-Pt-Ta barrier, even after prolonged annealing at 550°C, has effectively prevented the interdiffusion of gold and silicon dioxide. Also shown, in the 450° and 550°C SiO<sub>2</sub>/Ta-Pt-Ta-Au specimens is the reaction between the tantalum and the oxide. From Fig. 3b and c, oxygen was always found with tantalum, probably in the form of Ta<sub>2</sub>O<sub>5</sub> as reported by others (12). It is speculated that the oxygen comes from the SiO<sub>2</sub> surface which reacts with the tantalum and out-diffuses to the gold surface. The reaction between the tantalum and the oxide at the Ta-SiO<sub>2</sub> interface may account for the increased Ta concentration adjacent to the oxide found in the 550° and 450°C specimens. The tantalum at the interface is in the form of both bcc-Ta and Ta<sub>2</sub>O<sub>5</sub>.

X-ray diffractometer traces from SiO<sub>2</sub>/Ta-Pt-Ta-Au samples annealed at 350°, 450° and 550°C are shown in Fig. 4. After a 24 hr anneal at 350°C, the compounds TaPt and Ta<sub>2</sub>Pt were formed. Annealing at 450° and 550°C the compounds TaAu, TaPt, and Ta<sub>2</sub>Pt were formed. The AES results indicate that TaAu formed at the original gold-tantalum interface at temperatures above 450°C and that the displaced tantalum is distributed through the gold layer. The XRD and AES measurements indicate that the gold-tantalum reaction has a tendency to be self-limiting. The amount of Ta distributed in the Au layer remained constant at temperatures between 350° and 550°C (apparently annealing above 450°C is necessary for TaAu formation). The AES results also indicate that the compounds Ta<sub>2</sub>Pt and TaPt form in the platinum zone and at the tantalum-platinum interfaces. The 300-500Å platinum film is distributed throughout the tantalum layers. Likewise, the tantalum at both Pt-Ta interfaces diffuses into the platinum film. The Pt-Ta reactions are self-limiting with a critical temperature of 350°C for their activation.

**Experiments with Ta-W-Ta diffusion barriers.**—Experiments with Ta-W as the diffusion barrier were conducted. Isothermal annealing produced increases of 0.10 and 0.33 in  $\Delta\rho/\rho_0$  at 350° and 420°C, respec-

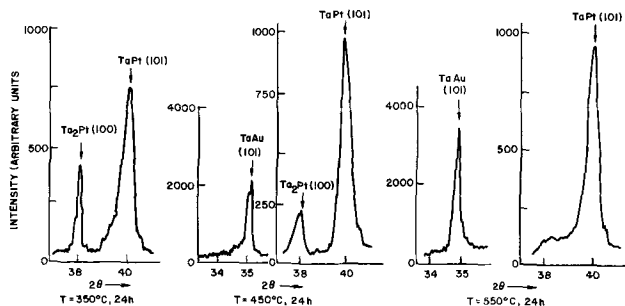


Fig. 4. XRD traces for Ta-Pt-Ta-Au annealed at 350°, 450°, and 550°C.

tively. Figure 5a shows the resistivity isothermal annealing curves for Ta-W-Ta-Au and indicates that Ta-W is not as effective as Ta-Pt in minimizing interdiffusion and compound formation between the gold and silicon. As shown in Fig. 5a, a W/Ta ratio of 0.10 was found to optimize the barrier effectiveness of the refractory layer. The Ta-W-Ta-Au (W/Ta of 0.10) when annealed at 350°C resulted in a 10% increase in resistivity, and a 25% increase in  $\Delta\rho/\rho_0$  when annealed at 420°C for 400 hr. Figure 5b shows a comparison of the Ta-Pt and Ta-W diffusion barriers with Ta and tantalum-palladium. The isothermal annealing experiments of Fig. 5b clearly indicate that metallurgical stability can be obtained with Ta-Pt diffusion barriers. In contrast to Ta-Pt, microcracks in Ta-W and Ta-Pd layers and rapid interdiffusion between Pd and Au result in resistivity increases of over 20% for Ta, Ta-W, and Ta-Pd diffusion barriers. Scanning electron microscopy investigation of the Ta-W layer showed microcracks in the tungsten, propagating to the tantalum layers as the primary reason for the increase in resistivity at 450°C. Figure 6 shows cracking of the Ta-W layer at 450°C. At temperatures of up to 525°C interdiffusion between Ta and W was not detected. Similarly, the Au-Ta interdiffusion as expected was detected at temperatures above 450°C. Cracking in the Ta-W layers prevented useful conclusions from Auger (AES) data to be obtained.

**Mechanical stability and corrosion resistance.**—*Internal stresses.*—Stress, particle size, and film adhesion are the important parameters which affect the mechanical stability of thin films on a substrate. In the present investigation, the variation of internal stresses and particle size with anneal temperature has been determined. The stresses in the gold film of the Ta-Pt-Ta-Au and Ta-W-Ta-Au structures were tensile in nature before annealing. The average stress in the sputtered gold obtained from x-ray peak shift data

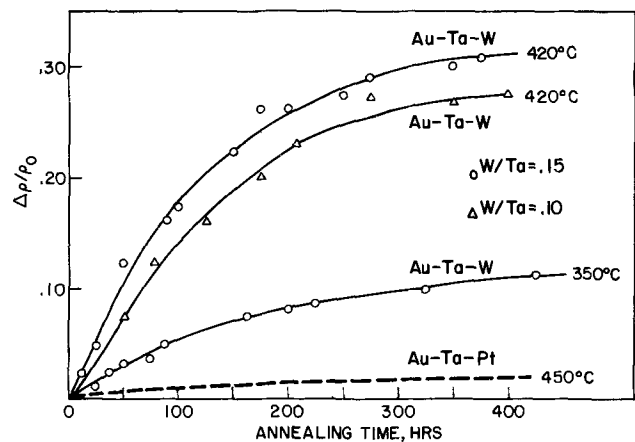


Fig. 5a. Isothermal annealing curves for Ta-W-Ta-Au thin films with W/Ta ratios of 0.10 and 0.15.

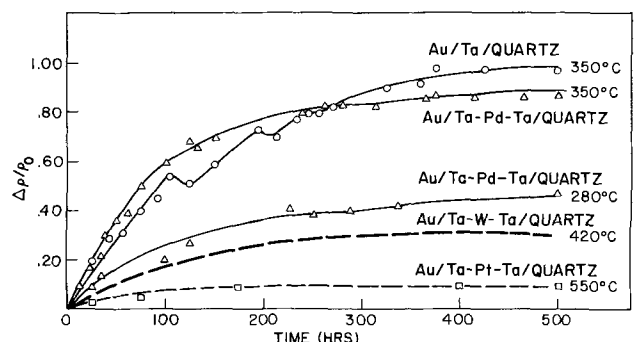


Fig. 5b. A comparison of isothermal annealing behavior of Ta-Pt, Ta-W, Ta-Pd, and Ta diffusion barriers.

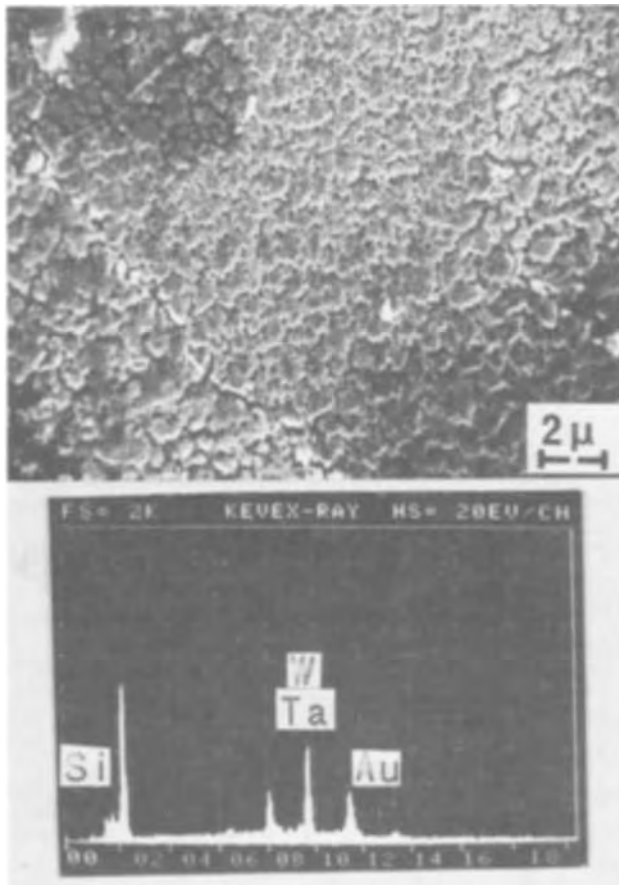


Fig. 6. Microcracks in the Ta-W layer after annealing at 470°C for 2 hr.

was  $1.8 \times 10^9$  dynes/cm<sup>2</sup>. Tensile stresses were also observed in the barrier layer. Annealing the Ta-Pt-Ta-Au and Ta-W-Ta-Au structures with 2000Å of gold at 450°C for up to 24 hr resulted in a decrease of internal stress in gold from  $1.8 \times 10^9$  dynes/cm<sup>2</sup> to  $0.1 \times 10^9$  dynes/cm<sup>2</sup>. The results summarized in Fig. 7 indicate that a significant decrease in internal stress of sputtered Ta-Pt-Ta-Au films can be obtained by annealing up to 450°C. The rapid decrease in internal stress observed in the Ta-W layer at 200°–300°C indicates the occurrence of a rapid stress relief taking place probably by film microcracks. The internal stress reduction of the magnitude shown in Fig. 7 is too large to be accounted for by dislocation and vacancy annihilation.

**Corrosion resistance and etchability.**—The Ta-Pt-Ta-Au and Ta-W-Ta-Au structures subjected to the corrosion test showed vigorous electrolysis upon application of a 6V bias. After approximately 1 min, loose Au appeared at the anode, after 10 min the anode lost its supply of Au and electrolysis continued via the unattacked Ta-Pt strip. No Ta-Pt or Ta-W dissolution was observed on any strip for the 30 min duration of the experiment. This observation is not surprising since the oxides of tantalum, platinum, and tungsten being insoluble in water will not self-bias the Ta-Pt and Ta-W systems and result in rapid corrosion. At an external bias of 6V, the Au ion is transported in the electrolyte to the nearest cathode region where it plates out. The Ta-Pt and Ta-W layers remain relatively unattacked since the amount of oxygen evolution at a 6V bias is insignificant.

An etching process has been worked out for the Ta-Pt-Ta-Au and Ta-W-Ta-Au systems using an iodine-saturated solution of KI at 90°C for the gold and a KOH:H<sub>2</sub>O<sub>2</sub>(9:1) saturated solution at 27°C for tantalum. Typical etching rates of 1000Å/60 sec were obtained with undercutting maintained to less than

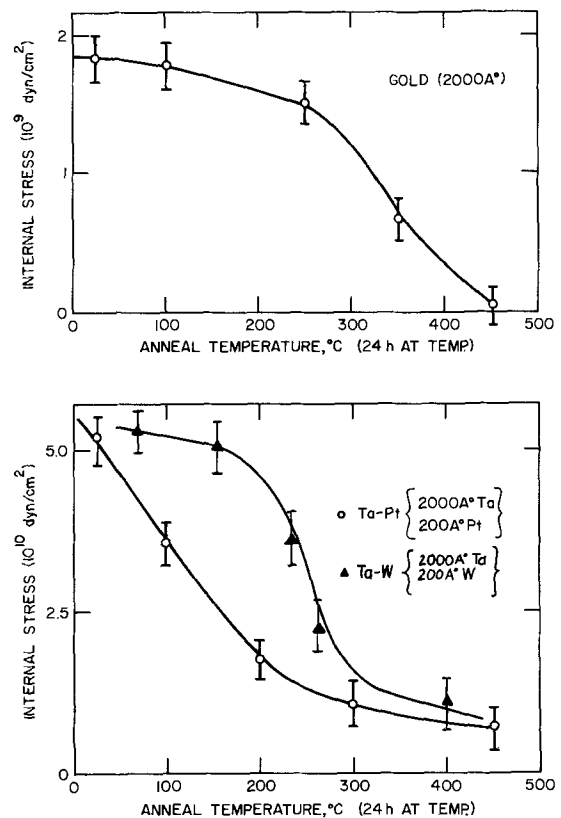


Fig. 7. Variation of internal stress with anneal temperature obtained from peak shift data in the Ta-Pt-Ta-Au and Ta-W-Ta-Au systems.

3000Å. An additional etch for the Ta-based films which also reduces undercutting is the HNO<sub>3</sub>:HC<sub>2</sub>H<sub>3</sub>O<sub>2</sub>:HF in the proportions 6:2:1 and diluted 1:1 with deionized water. Typical etching rates, obtained with HNO<sub>3</sub>:HC<sub>2</sub>H<sub>3</sub>O<sub>2</sub>:HF etch, were 1000Å/20 sec. The KOH:H<sub>2</sub>O<sub>2</sub> etch, however, was more desirable due to the reproducibility of etching rates and the elimination of damage to the underlying thermal SiO<sub>2</sub> film or the exposed Si substrate. In applying each etch, one uses standard photolithographic techniques to define a pattern on the Au film followed by etching away the excess Au. By allowing the Au pattern to act as a mask, the wafer can then be placed in the chosen etch for a period of up to 45 sec, removed, and rinsed in running DI H<sub>2</sub>O. No etching of Si occurs with both etches if 30–45 sec dips are used followed by a DI-H<sub>2</sub>O rinse.

### Summary and Conclusions

A stabilized tantalum-gold thin film system has been investigated as a metallization contact for microwave power transistors. The stabilized tantalum was used as a barrier metal in order to minimize interdiffusion and compound formation between the gold and the silicon. In the present investigation, the tantalum was stabilized against rapid diffusion of gold at tantalum grain boundaries by alloying a 200–500Å film of platinum between 1000Å layers of tantalum. The entire structure when overlaid with up to 3000Å of sputtered gold resulted in the following characteristics: (i) the resistivity decreased by 6% when annealed at 350°C for 800 hr, but increased by only 3% when annealed at 450°C, and (ii) evidence of diffusion through tantalum grain boundaries was absent. The present investigation has shown that the Ta-Pt-Ta-Au metallization (i) is metallurgically stable with no significant degradation of resistivity below 500°C, (ii) resists electrochemical corrosion, and (iii) is readily processed with existing technology. The Ta-Pt-Ta-Au system should find applications as a metalliza-

tion for microwave power transistors and in other devices where protection against corrosion and electromigration at a high current density is important. In contrast to Ta-Pt-Ta-Au, the Ta-W-Ta-Au metallization undergoes resistivity degradation of up to 15% at 450°C as a result of microcracking in the tungsten layer. The microcracks in tungsten provide diffusion paths for gold-silicon interdiffusion.

#### Acknowledgments

The authors wish to acknowledge the assistance of Mr. Marvin Bark in chemical etching. This work was sponsored by the Office of Naval Research.

Manuscript submitted Sept. 20, 1973; revised manuscript received Feb. 25, 1974. This was Paper 157 presented at the Boston, Massachusetts, Meeting of the Society, Oct. 7-14, 1973.

Any discussion of this paper will appear in a Discussion Section to be published in the June 1975 JOURNAL. All discussions for the June 1975 Discussion Section should be submitted by Feb. 1, 1975.

#### REFERENCES

1. A. Christou and H. Day, *J. Appl. Phys.*, **44**, 3386 (1973).
2. A. Christou and H. Day, *J. Elect. Mater.*, **3**, 25 (1974).
3. G. J. van Gorp, *Appl. Phys. Letters*, **19**, 476 (1971).
4. L. E. Terry and R. W. Wilson, *Proc. IEEE*, **57**, 1580 (1969).
5. G. L. Schnable and R. S. Keen, 6th Ann. Reliability Physics Symp., Los Angeles, Calif., November 1967, pp. 170-192.
6. J. A. Cunningham, C. R. Fuller, and C. T. Haywood, *IEEE Trans. on Rel.*, **R-19**, 182 (1970).
7. M. P. Lepselter, Bell Lab. Record, 289 (October/November 1966).
8. G. B. Greenough, *Prog. Metal Phys.*, **3**, 176 (1952).
9. G. A. Walker and C. C. Goldsmith, *J. Vacuum Sci. Technol.*, **7**, 569 (1970).
10. P. M. Palmberg, *ibid.*, **9**, 160 (1972).
11. F. M. Smits, *Bell System Tech. J.*, **37**, 711 (1958).
12. N. J. Maskalick, C. W. Lewis, and A. M. Reingold, "Transactions 8th National Vacuum Symposium, 1961," p. 874, Pergamon Press, Oxford (1962).

## Phosphorus Diffusion in Partially Crystallized Films of SiO<sub>2</sub>

D. R. Campbell,\* E. I. Alessandrini, K. N. Tu, and J. E. Lewis

IBM Thomas J. Watson Research Center, Yorktown Heights, New York 10598

The publication costs of this article have been assisted by the IBM Corporation.

#### ABSTRACT

The diffusion of phosphorus into thin SiO<sub>2</sub> films on Si was studied to assess the significance of an anomalous, rapid diffusion mode. Diffusions were performed over a wide range of temperature and time using neutron-activated, red phosphorus diffusion sources. It was found that diffusion anneals in P vapors catalyzed a localized amorphous-to-crystalline transformation in the initially amorphous films, creating rapid diffusion paths at the interfaces between the crystalline islands and the surrounding amorphous matrix. The shape of the penetration profiles confirmed that interfaces contributed to the flux of P through the film. Both rapid and normal diffusion coefficients were determined and are discussed. Crystallization with subsequent rapid diffusion may be a contributing factor to the failure of SiO<sub>2</sub> diffusion masks.

Although the diffusion of P in amorphous SiO<sub>2</sub> films has frequently been investigated (1-5) there is considerable discrepancy in the measured values of diffusivity and fundamental uncertainty concerning the diffusion process (3). In view of the widespread use of P in Si device technology, we felt it imperative to clarify the question of P diffusion in amorphous SiO<sub>2</sub> films by undertaking a further study. Our results provide additional data for diffusion in the amorphous matrix and identify a hitherto unrecognized diffusion process in "amorphous" films involving migration along the interface between crystallized islands and the amorphous matrix which surrounds them. The localized crystallization of the film is attributed to a catalytic influence of phosphorus.

#### Experimental

Our study employed 0.5 $\mu$  amorphous films of steam grown SiO<sub>2</sub> on (100) Si wafers (B-doped, 2 ohm-cm) and was performed over a wide range of temperature (1100°-500°C) and time (1 hr-4 days) using P<sup>32</sup> isotope. The source of the radioisotope was neutron-activated, red phosphorus powder which was encapsulated, together with the SiO<sub>2</sub>/Si samples in evacuated silica ampoules. At diffusion temperatures, the phosphorus source vaporized and provided constant surface concentration boundary conditions. Serial sectioning in

50-200Å steps was performed by timed etching of the amorphous SiO<sub>2</sub>/Si with a diluted "P"-etch (6). The etch rate was established with the aid of ellipsometry measurements of thicknesses successively removed. The activity of each section was determined by liquid scintillation methods.

#### Results and Discussion

*Evidence of crystallization.*—The extended depth of P penetration as illustrated by Fig. 1, suggested that structural defects (i.e., crystallites) were contributing to the flux of P through the SiO<sub>2</sub> films in addition to that anticipated from ordinary diffusion in the amorphous matrix. Structural defects were further suggested by the appearance of numerous, small areas of high P concentration on autoradiographs of the diffused films (7). Reflection electron diffraction from the surface of the same films showed the presence of  $\alpha$ -cristobalite, a crystalline phase which apparently resulted from a catalytic influence of P, as samples given simulated diffusion anneals without P showed no evidence of crystallization (Fig. 2). Subsequently, some diffused wafers were diced and portions with structural defects, as determined from autoradiographs, were back-etched and examined by electron transmission and diffraction microscopy techniques. It was determined that the defects were crystallized islands, surrounded by amorphous material (7). In fact, many were several microns in diameter and easily seen by optical microscopy (Fig. 3).

\* Electrochemical Society Active Member.

Key words: diffusion mask,  $\alpha$ -cristobalite, network diffusion, interface diffusion.

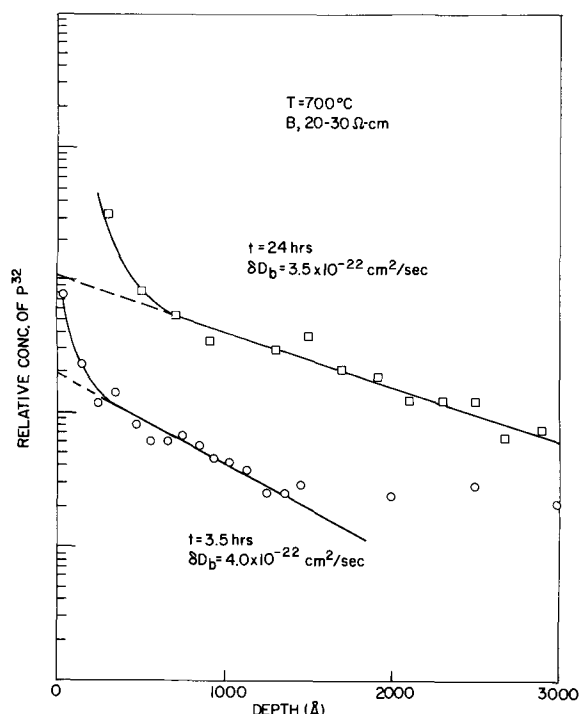


Fig. 1. Phosphorus penetration profiles due to rapid diffusion along the crystalline-amorphous boundary. The relatively close agreement between  $\delta D_b$  values for two different diffusion times substantiates the use of Fisher's boundary diffusion model.

The density of crystallites necessary to account for the level of P activity seen in the tailing regions of our profiles is approximately  $10^4/\text{cm}^2$  assuming the individual crystals are a few microns in diameter. Confirmation of the above density and size of defects by optical microscopy is possible for samples diffused at  $700^\circ\text{C}$  and above. At lower temperatures, the presumed smaller size of the crystallites (*i.e.*, submicron) precluded observation by optical means.

**Penetration profiles.**—On the basis of this experimental evidence, and with the aid of Fig. 4, we can explain our profiles as follows: In the vicinity of a

crystallized island, a rapid diffusion path exists at the interface between crystalline and amorphous regions. The diffusivity in the boundary,  $D_b$ , may be a few orders of magnitude greater than the diffusivity in the undisturbed amorphous network,  $D_n$ . Therefore, depending where on the film surface the  $\text{P}^{32}$  vapors impinge, there will occur different modes of diffusion. One mode is directly into the amorphous matrix, which gives the first portion of our profile where the concentration falls smoothly from its high initial value at the surface until it intercepts the linear portion at a depth of a few hundred angstroms. A typical experimental profile is shown in Fig. 5 where  $D_n$  has been determined by fitting the profile to a complementary error function. In Fig. 4, this diffusion is responsible for the isoconcentration contours that are parallel to the specimen surface as occur at some distance from the crystalline region. In Fig. 6, we show the values of  $D_n$  plotted against  $1/T$  together with data from two other investigations (2, 3). The second diffusion mode, as evidenced by the linear portion of the profile in Fig. 1 is due to a combination of rapid diffusion down the crystalline-amorphous boundary with eventual lateral migration into the amorphous network away from the boundary. Lateral migration into the crystallized region is neglected; it should not appreciably affect our results owing to the anticipated lower diffusivity of P in this denser phase. In analyzing these and similar profiles, we have used the expressions

$$\delta D_b = 2.8 \left( \frac{D_n}{\pi t} \right)^{1/2} \left( \frac{\partial \ln c}{\partial x} \right)^{-2} \quad [1]$$

$$\beta = \frac{\text{Cot}^2 \psi}{\pi^{-1/2}} = \frac{\delta D_b}{D_n \sqrt{D_n t}} \quad [2]$$

which are based on the well-known Fisher analysis modified to take account of the lack of lateral migration into the crystallized region (8). Here  $\delta$  is the width of the interface,  $\left( \frac{\partial \ln c}{\partial x} \right)$  the slope from the penetration profile, and  $t$  the duration of the diffusion anneal. The calculated values of  $\delta D_b$  for a set of measurements on films prepared from 2 ohm-cm, B-doped Si are shown plotted *vs.*  $1/T$  in Fig. 7. In Fig. 4, the second diffusion mode is responsible for the bending of the isoconcentration contours down at the boundary,

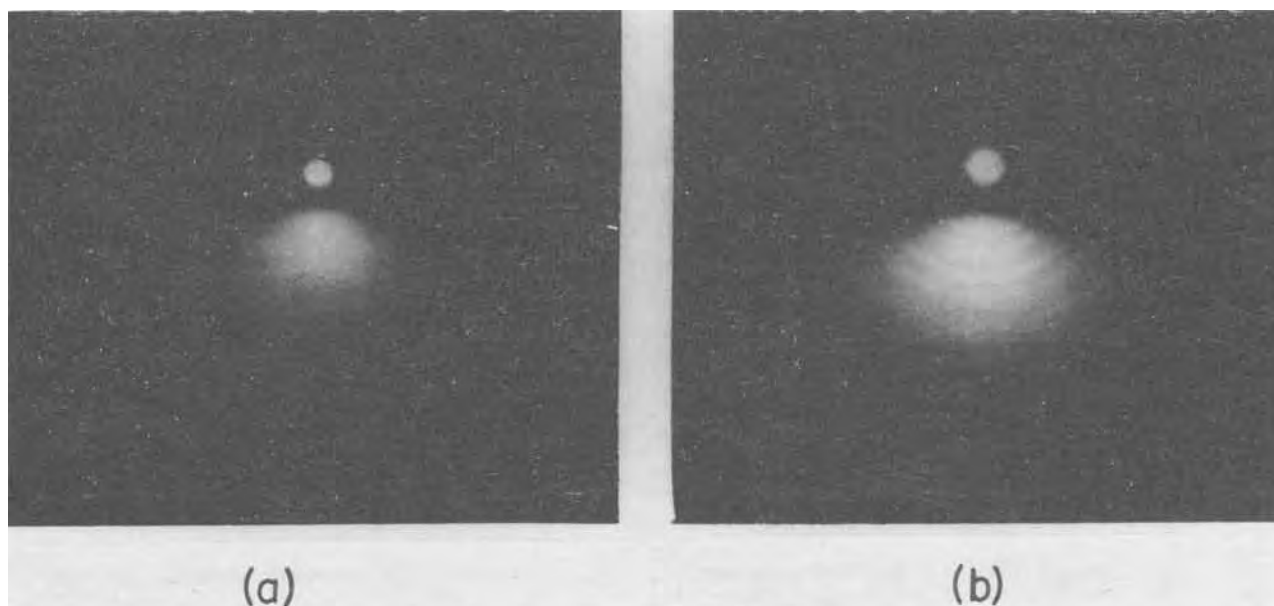


Fig. 2. Reflection electron diffraction patterns from (a)  $\text{SiO}_2$  film given a simulated diffusion anneal for 92 hr at  $700^\circ\text{C}$  without phosphorus, (b) film diffused with phosphorus for 92 hr at  $700^\circ\text{C}$ . In (a), the undiffused film stays amorphous. The presence of  $\alpha$ -crystobalite is indicated in the pattern in (b).

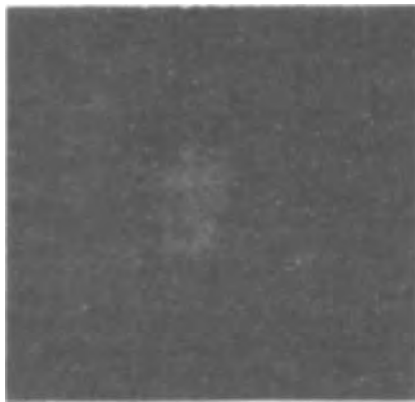


Fig. 3. Crystalline island in a P-diffused SiO<sub>2</sub> film (400X)

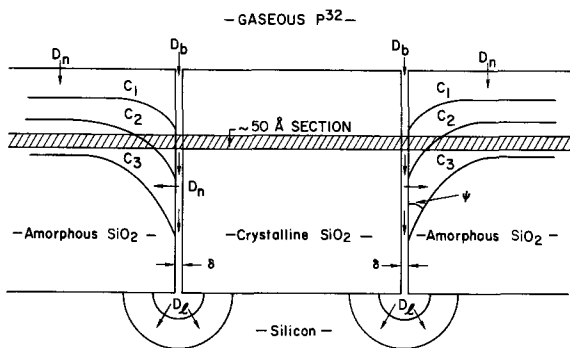


Fig. 4. Isoconcentration contours for P in an SiO<sub>2</sub> film in the vicinity of a crystallized island. The concentrations decrease with depth into the film or  $C_1 > C_2 > C_3$ . The network diffusivity is denoted by  $D_n$ , diffusivity in the crystalline-amorphous boundary by  $D_b$ , and diffusion into the underlying Si by  $D_i$ . The cross hatched portion indicates the material removed in a typical section.

which they all intercept at the same angle  $\psi$ . Some of the P atoms starting out in the boundaries penetrate completely through the film and become incorporated in the underlying Si where they enhance the exposure of autoradiographs in places corresponding to defect locations. This effect was confirmed by autoradiographs taken of wafers from which the oxide was completely removed after diffusion.

**Diffusion coefficients.**—Two distinctly different types of diffusion behavior are expected for dilute impurities in directionally bonded, amorphous materials. The first, more rapid, mechanism involves migration through the interstices of the structure while the second, slower, mechanism involves migration as part of the network structure. Examples of the former are the diffusion of inert gases (9, 10) and alkali and noble metal impurities (11, 12) in SiO<sub>2</sub> and possibly noble metal impurities (13, 14) in chalcogenide glass films. Examples of the latter are the diffusion of various network forming ions in SiO<sub>2</sub> films (15). Many of these ions are also common dopants for Si (e.g., Al, B, P, As, Sb).

We find the network diffusivity for phosphorus to be

$$D_n = D_n^\circ e^{-Q_n/kt} = 2.0 \times 10^{-10} \text{ (cm}^2/\text{sec)} e^{-1.7 \text{ eV}/kt}$$

from measurements over the range 1095°-772°C. No attempt has been made to assess the errors in  $D_n^\circ$  and  $Q_n$  which may be considerable. A clear indication of slow network diffusion as shown in Fig. 5 was difficult to obtain and analyze because of interferences from concomitant processes such as formation of phosphosilicate glass (PSG) layers on the surface and crystallization of the film. Both of these influenced our profiles significantly. The high temperature extrapolation of our data still comes reasonably close to the data of Allen, Bernstein, and Kurtz (2) shown in Fig. 6, par-

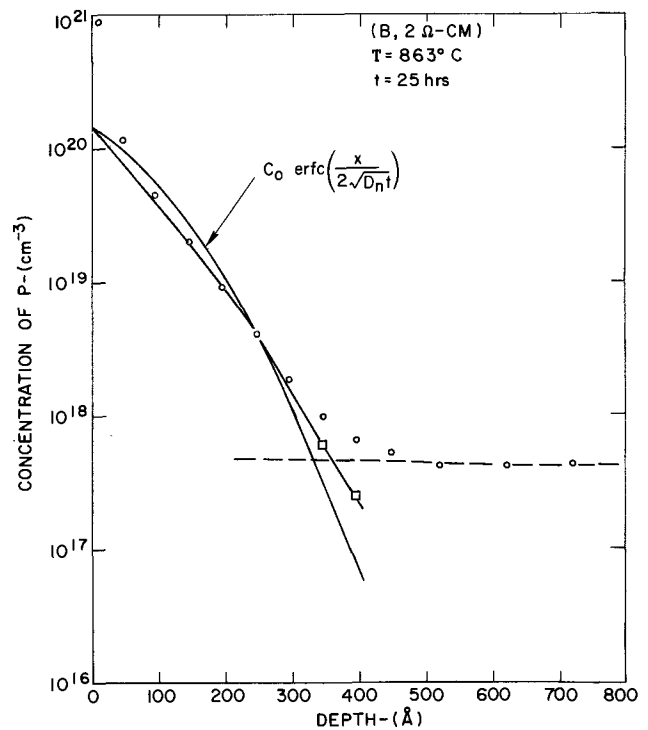


Fig. 5. Phosphorus penetration profile due to slow network diffusion. The open circles represent experimentally determined points; the open squares represent an estimated portion of the profile obtained by subtracting the background activity associated with the crystallites. The background level is represented by the horizontal, broken line. The solid line through the plotted points is the apparent shape of the experimentally determined profile. High surface concentrations are attributed to the formation of a thin PSG layer. The complimentary error function was calculated assuming  $C_0$ , the solid solubility for P in SiO<sub>2</sub>, to be  $\sim 1.4 \times 10^{20} \text{ cm}^{-3}$  and  $D_n$  as  $7.0 \times 10^{-18} \text{ cm}^2/\text{sec}$ .

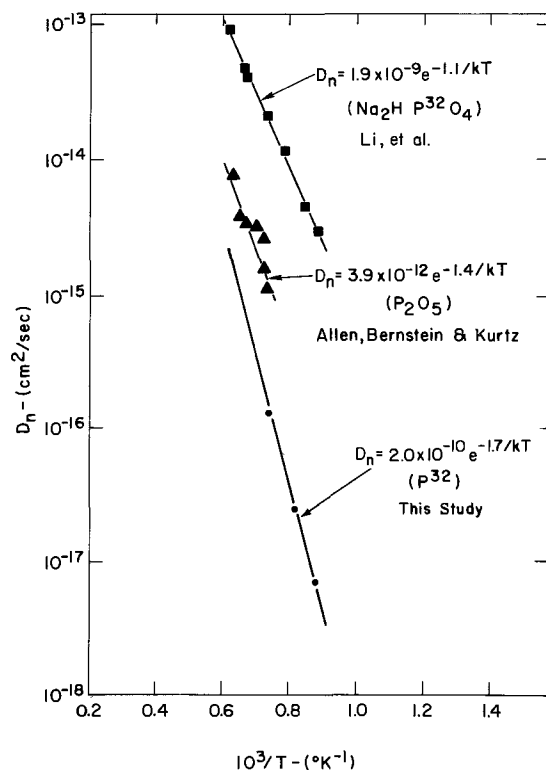


Fig. 6. Log  $D_n$  vs.  $1/T$  for diffusion of P<sup>32</sup> in SiO<sub>2</sub> film

ticularly in view of the large spread in other reported values. (15). Here the discrepancy may be related to

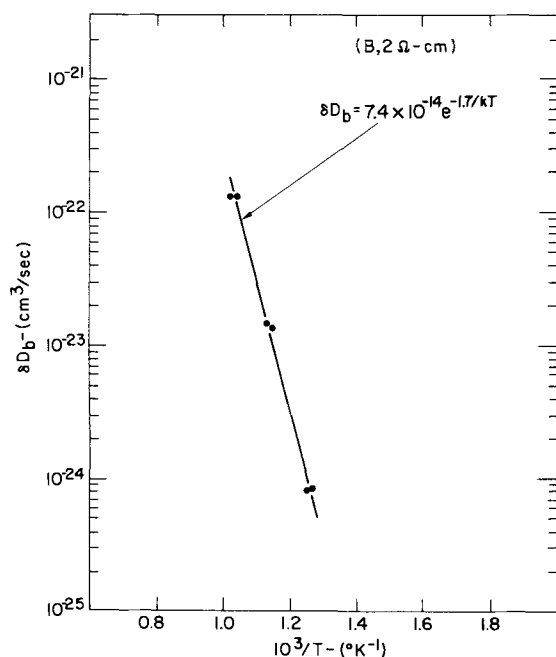


Fig. 7. Log  $\delta D_b$  vs.  $1/T$  for diffusion of  $P^{32}$  in  $SiO_2$  films. Two measurements were made at each of the temperatures,  $700^\circ$ ,  $600^\circ$ , and  $516^\circ C$ . Values of  $\delta D_b$  displaced laterally for clarity in plotting.

a difference in experimental method; our method involved direct profiling of the  $SiO_2$  while Allen *et al.* determined their values of  $D_n$  from profiling measurements of the underlying Si, using a two-phase diffusion model. A consequence of their method is that the effective concentration of P in their oxide was probably several mole per cent, considerably higher than the  $10^{20} - 5 \times 10^{18}/cm^3$  range of our measurements. Although we do not think a significant concentration effect occurs in our case, at higher P levels  $D_n$  may become strongly concentration dependent because the phase diagram (16) indicates that the melting point of PSG falls rapidly with increasing P content. Therefore, in view of their higher concentrations, higher  $D_n$  values appear reasonable. Concentration effects may not have much bearing on the very large discrepancy between our data and that of Li *et al.* (3). The introduction of network modifying  $Na^+$  ions from their disodium-phosphate source is more likely the cause. The well-known affinity of  $Na^+$  ions for P in PSG suggests that the high diffusivity they see is due to some influence of Na on the local environment of P, resulting in enhanced mobility.

The low values for  $D_n^\circ$  and  $Q_n$  we report are not easily reconciled with a specific diffusion mechanism. Diffusion mechanisms for the motion of network-forming ions are undefined in contrast to the situation for interstitial species where detailed models have been suggested (9). Also, the information obtained in this study is insufficient in itself to indicate a mechanism, as will be clear after the following discussion of possible approaches to the problem.

Well above the glass transition temperature, the diffusion of constituent ions or molecules of a fluid is traditionally thought to be directly related to viscous flow of the fluid through the Stokes-Einstein equation. Under these conditions, a free volume model (17-20) successfully accounts for the viscosity of some fluids; organic liquids are one example (21). The situation for oxide glasses is less clear, both from the point of view of viscosity mechanisms (22-25) and the connection between viscosity and the migration of individual ions or network units (26). Well below the glass transition temperature of silica, where our measurements were made, the activation energy for viscous flow (27) is  $\sim 7$  eV or 4 times larger than for P

diffusion. This suggests that an interpretation of diffusion analogous to viscosity treatments would not succeed. Another approach is to apply concepts of defect diffusion as in crystalline materials although there is yet no proof that distinct defects contribute to diffusion in silica (12).

Assuming they might, the low values of  $D_n^\circ$  and  $Q_n$  suggest a similarity to diffusion of metal ions in crystalline oxides under extrinsic conditions. The values of the preexponential terms are typically several orders of magnitude lower than in the intrinsic case because they incorporate the relative concentrations of athermal defects. For example, the concentration of Si vacancies which might exist by virtue of structural discontinuities or impurity association. Activation energies would likewise be low for they involve only migration energy of the diffusing species. Other types of defect mechanisms could also be mentioned but it seems pointless to speculate further on these or any other mechanisms without additional information. In particular, we are uncertain regarding the coordination of P in the network, the exact diffusing specie and the nature and possible influence of defects. Structural information on P coordination would be most useful here, but suitable studies such as infrared spectroscopy or radial distribution function measurements were beyond the scope of this work. Knowledge of the charge state of the diffusing specie might identify it, but our own attempts at ionic drift measurements were unsuccessful because of reactions between the metal electrode and the oxide films at the high temperatures required. A realistic test of the influence of defects on diffusion in  $SiO_2$  films is obviously important but obtaining samples with controlled defect concentrations seems to be a major problem (12).

Diffusion down the crystalline-amorphous interface is given by

$$\delta D_b = \delta D_b^\circ e^{-Q_b/kt} = 7.4 \times 10^{-14} \text{ cm}^3/\text{sec} e^{-1.7 \text{ eV}/kt}$$

The activation energy is the same as we found for the amorphous matrix. This suggests that the migration process along the interface is similar to that in the network. Estimating the boundary width,  $\delta$ , at  $10^{-7}$  cm fixes  $D_b^\circ$  at  $\sim 10^{-6}$   $cm^2/\text{sec}$ . In the defect picture of diffusion, a larger preexponential factor for interface vs. network diffusion could imply that greater defect concentrations occur in the boundaries. This correlates with the customary notion that such regions have fewer or weaker bonds than the bulk.

A considerable error may occur in  $\delta D_b$  due to scatter in the measurement and possibly to the continued nucleation and growth of crystallites during diffusion. Continued nucleation and growth would invalidate Fisher's analysis which presumes stable boundaries. However, the change in the slope of the profiles with time follows Fisher's kinetics (Fig. 7) which implies that the extent of crystallization of our films becomes stabilized in times which are short compared with the durations of the diffusions.

### Conclusions

From a practical standpoint, the formation of crystallites such as we have seen in a diffusion mask during P diffusion, or in an  $SiO_2$  layer during PSG deposition, will leave the underlying Si susceptible to P penetration in localized areas (28) where such unintentional doping may be undesirable. It seems unlikely that a network-forming ion like phosphorus should catalyze crystallization, especially in view of the results of Sugano *et al.* who did not find evidence of crystallization in P-doped oxides (29). However, analogous crystallization effects have been attributed to the presence of As which is also a network forming ion in arsinosilicate glasses (30). The reason cited was that  $As_2O_5$  was capable of forming distinct compounds with  $SiO_2$  which may have provided nuclei for the subsequent growth of crystalline  $SiO_2$ . Compounds such as  $P_2O_5 \cdot SiO_2$  or  $P_2O_5 \cdot 2 SiO_2$ ,

which are known to occur from phase segregation in PSG films (31), are possible candidates for nuclei (7). Crystalline areas in films may also act as sites for accumulation of undesirable metallic ions such as Na, but attempts to see such an effect using Na<sup>22</sup> tracer and autoradiography techniques were inconclusive due to sensitivity problems.

#### Acknowledgment

The authors are particularly indebted to R. MacInnes for diffusing and profiling the specimens and to R. Robinson for autoradiography with tagged Na. The authors wish also to extend their appreciation to Dr. E. Bassous, Mrs. D. Bauer, and Mr. J. A. Kucza for advice and assistance in sample preparation, and to Drs. D. Gupta, A. Mayadas, and R. Rosenberg for many helpful discussions.

This work is supported in part by ARPA Contract No. F19628-73-C-0006 administered by AFCRL.

Manuscript submitted Aug. 10, 1973; revised manuscript received March 12, 1974. This was Paper 252 presented at the Miami Beach, Florida, Meeting of the Society, Oct. 8-13, 1972.

Any discussion of this paper will appear in a Discussion Section to be published in the June 1975 JOURNAL. All discussions for the June 1975 Discussion Section should be submitted by Feb. 1, 1975.

#### REFERENCES

1. C. T. Sah, H. Sello, and D. A. Tremere, *J. Phys. Chem. Solids*, **11**, 288 (1959).
2. R. B. Allen, H. Bernstein, and A. D. Kurtz, *J. Appl. Phys.*, **31**, 334 (1960).
3. Li Ke-Cheng, Xue Shin-Yin, Zhu Shong-de, and Huang Yun, *Acta Physica Sinica*, **20**, 496 (1965).
4. Y. Watanabe and M. Yoshida, *Japan. J. Appl. Phys.*, **6**, 410 (1967).
5. M. L. Barry, *This Journal*, **117**, 1405 (1970).
6. After W. Pliskin, IBM, SPD, East Fishkill. The etch was prepared as follows, 15 ml HF, 10 ml HNO<sub>3</sub>, 3 liters H<sub>2</sub>O.
7. E. I. Alessandrini and D. R. Campbell, *This Journal*, **121**, 1115 (1974).
8. J. C. Fisher, *J. Appl. Phys.*, **22**, 74 (1951). Fisher's method is considered accurate provided the parameter  $\beta$  (Fig. 1) is  $\sim 100$  or greater, which was the case for our diffusions. Our expressions for  $\delta D_0$  and  $\beta$  differ by factors of 2 and  $\frac{1}{2}$ , respectively, from their usual forms since we can have leakage from the interface in only one direction, i.e., into the amorphous material. The correction factor 2.8 is taken from N. A. Gjostein, in "Techniques of Metals Research," R. A. Rapp, Editor, p. 557, Interscience, New York (1970).
9. W. G. Perkins and D. R. Begeal, *J. Chem. Phys.*, **54**, 1683 (1971).
10. K. N. Woods and R. H. Doremus, *Phys. Chem. Glasses*, **12**, 69 (1971).
11. G. H. Frischat, *J. Am. Ceram. Soc.*, **51**, 528 (1968).
12. R. H. Doremus, *Phys. Chem. Glasses*, **10**, 28 (1969).
13. L. A. Freeman, R. F. Shaw, and A. D. Yoffe, *Thin Solid Films*, **3**, 367 (1969).
14. S. Maruno, T. Yamada, M. Noda, and Y. Kondo, *Japan. J. Appl. Phys.*, **10**, 653 (1971).
15. A recent summary of diffusion in SiO<sub>2</sub> films has been given by M. Ghezzi and D. M. Brown, *This Journal*, **120**, 146 (1973).
16. R. Y. Tien and F. A. Hummel, *J. Am. Ceram. Soc.*, **45**, 422 (1962).
17. M. H. Cohen and D. Turnbull, *J. Chem. Phys.*, **31**, 1164 (1959).
18. D. Turnbull and M. H. Cohen, *ibid.*, **34**, 120 (1961).
19. D. Turnbull and M. H. Cohen, *ibid.*, **52**, 3038 (1970).
20. J. Naghizadeh, *J. Appl. Phys.*, **35**, 1162 (1964).
21. J. Cukierman, J. W. Lane, and D. R. Uhlman, *J. Chem. Phys.*, **59**, 3639 (1973).
22. P. B. Macedo and T. A. Litovitz, *ibid.*, **42**, 245 (1965).
23. L. L. Sperry and J. D. Mackenzie, *Phys. Chem. Glasses*, **9**, 91 (1968).
24. P. B. Macedo and A. Napolitano, *J. Chem. Phys.*, **49**, 1887 (1968).
25. M. Goldstein, *ibid.*, **51**, 3728 (1969).
26. H. N. Stein, C. H. Cornelisse, and J. M. Stevels, *J. Non-Crystalline Solids*, **1**, 143 (1969).
27. G. Hetherington, K. H. Jack, and J. C. Kennedy, *Phys. Chem. Glasses*, **5**, 130 (1964).
28. The inhomogeneities seen in the diffusion masking properties of SiO<sub>2</sub> films for P by Fränz and Langheinrich could well be due to crystallization. I. Fränz and W. Langheinrich, *Solid-State Electron.*, **14**, 835 (1971).
29. T. Sugano, K. Hoh, K. Kudo, and N. Hishinuma, *Japan. J. Appl. Phys.*, **7**, 715 (1968).
30. M. Ghezzi and D. M. Brown, *This Journal*, **120**, 110 (1973).
31. P. F. Schmidt, W. van Gelder, and J. Drobek, *ibid.*, **115**, 79 (1968).

## Etching Studies of Anomalous Defects in P-Type GaP Crystals

T. Iizuka<sup>1</sup>

Bell Laboratories, Murray Hill, New Jersey 07974

The publication costs of this article have been assisted by Bell Laboratories.

#### ABSTRACT

Anomalous defects in GaP crystals prepared by Czochralski, solution-growth, and vapor-growth techniques have been investigated by chemical etching, optical microscopy, and scanning electron microscopy. These defects were found in as-grown highly Zn-, Cd-, or Zn(PO<sub>3</sub>)<sub>2</sub>-doped GaP crystals with carrier concentrations ranging from  $8 \times 10^{17}/\text{cm}^3$  to  $2 \times 10^{19}/\text{cm}^3$ . Thermal oxidation (at 850°C for 5 $\frac{3}{4}$  hr in air) of vapor-grown crystals doped with Zn, or Cd, produced the same defect in the surface layers (20 $\mu$  depth) of the crystals. The anomalous defects were developed distinctly by chemical etching as characteristic deep etch pits both on P(111) and on {110} cleavage surfaces. These pits were distinguished from ordinary dislocation etch pits both by their morphology and etching behavior. The density of the pits was between  $10^2$  and  $10^6/\text{cm}^2$ . From detailed observation, it has been proposed that the anomalous defects are special dislocations modified with some impurities. It seems that the relevant impurities are zinc (or cadmium) and/or oxygen.

Zinc and oxygen are used in GaP crystals for the fabrication of red-light emitting diodes; therefore, understanding the behavior of Zn and O in the crystal is of great importance. (Zn,O)-doped, liquid encap-

sulated Czochralski (LEC) crystals are especially important from the standpoint of device production. At the present time, efforts to prepare efficient diodes by single n-tipping on LEC p-type substrates have been unsuccessful.

<sup>1</sup>Present address: Electrotechnical Laboratory, Tokyo, Japan.  
Key words: etching, defect, GaP.



The present work is concerned with anomalous etch pits (hereafter defects responsible for the formation of the anomalous etch pits are called anomalous defects) which are observed in highly Zn-, Cd-, or  $\text{Zn}(\text{PO}_3)_2$ -doped GaP crystals. Also considered are thermal oxidation-induced defects in GaP crystals which appear to be the same as the anomalous defects in as-grown crystals. As for the oxidation of GaP crystals, compositions of the thermal oxidation products have been reported by Gershenson *et al.* (1) and Rubenstein (2). Recently, aqueous oxidation of GaP and GaAs crystals has been done by Schwartz (3). No detailed studies on the oxidation mechanism, however, have been reported. It has not been demonstrated whether the oxidation takes place at the oxide-GaP interface by the inward transport of oxygen through the oxide film or at the outer surface of the film by the outward motion of Ga and P through the film. In this work, the thermal oxidation is performed and described only from the anomalous defect point of view.

### Experimental

In this work, liquid encapsulated Czochralski (LEC) crystals, solution-grown (SG) crystals, and halogen transported vapor-grown (VG) crystals were investigated. Most of these crystals were doped with Zn, Cd, or  $\text{Zn}(\text{PO}_3)_2$ , and the carrier concentrations ranged from  $8 \times 10^{17}/\text{cm}^3$  to  $2 \times 10^{19}/\text{cm}^3$ . Undoped, S-, Te-, and  $\text{Ga}_2\text{O}_3$ -doped crystals were also examined for comparison. Slices cut parallel to the  $\{111\}$  planes from these crystals were mechanically polished and inspected by transmitted visible light. The slices were then chemically etched with chlorine-saturated methanol to obtain smooth  $\text{P}(\bar{1}\bar{1}\bar{1})$  surfaces. The slices were cleaved along  $\{110\}$  surfaces and then etched with a ferricyanide etchant (4) [50 mliters  $\text{H}_2\text{O}$ , 6g KOH, 4g  $\text{K}_3\text{Fe}(\text{CN})_6$  for 5 min at the etchant's boiling temperature]. Most of the work was done on the  $\text{P}(\bar{1}\bar{1}\bar{1})$  and  $\{110\}$  surfaces. Observation of the etched surfaces was performed with an optical microscope. The detailed structure of the etch pits was investigated with a scanning electron microscope.

Thermal oxidation of GaP crystals in air in an open tube was performed at  $850^\circ\text{C}$  for 5-3/4 hr. Annealing of the samples in evacuated ( $\leq 10^{-7}$  and  $10^{-3}$  Torr) capsules was also performed at  $850^\circ\text{C}$  for 5-3/4 hr to examine the net effect of the annealing on the samples. After these treatments, the  $\text{P}(\bar{1}\bar{1}\bar{1})$  surfaces were examined with an optical microscope. The compositions of the film were analyzed by x-ray diffraction. The films were dissolved in HCl, and then the samples were etched with the ferricyanide etchant for the optical observation.

### Results

**General observations.**—Very characteristic anomalous etch pits differing from ordinary dislocation etch pits have been observed in GaP crystals doped with Zn, Cd, or  $\text{Zn}(\text{PO}_3)_2$ . Characteristics of the crystals examined are summarized in Table I.

In general, the ferricyanide etchant does not reveal distinct dislocation etch pits on either the  $\text{P}(\bar{1}\bar{1}\bar{1})$  or the  $\{110\}$  cleavage surfaces of ordinary GaP crystals. However, this etchant can reveal distinctly the anomalous etch pits on these surfaces of highly Zn-, Cd-, or  $\text{Zn}(\text{PO}_3)_2$ -doped GaP crystals. It should be emphasized that this is a notable difference in the etching behavior between the anomalous defects and ordinary grown-in dislocations. Etchants for chemical polishing, for example, chlorine-saturated methanol or warm aqua regia, do not develop the anomalous etch pits on either the  $\text{P}(\bar{1}\bar{1}\bar{1})$  or  $\{110\}$  surfaces of GaP crystals containing the anomalous defects. The shape of the anomalous etch pits revealed with the ferricyanide etchant on the  $\text{P}(\bar{1}\bar{1}\bar{1})$  surface is typically an elongated triangle with the long axes parallel to the  $\langle 211 \rangle$

Table I. Sample characteristics

Sample	Growth method	Dopant	$N_A - N_D$ ( $\text{cm}^{-3}$ )	As-grown anomalous etch pit density ( $\text{cm}^{-2}$ )
RD 47 (seed end)	LEC	$\text{Zn}(\text{PO}_3)_2$	$1.3 \times 10^{18}$	0
RD 47 (tail end)	LEC	$\text{Zn}(\text{PO}_3)_2$	$4 \times 10^{18}$	$10^4$
RD 43	LEC	$\text{Zn}(\text{PO}_3)_2$	$5 \times 10^{18}$	$10^5$
RD 124	LEC	Zn	$2.6 \times 10^{18}$	0
RD 70	LEC	Zn	$3 \times 10^{18}$	0
RD 125	LEC	Zn	$2 \times 10^{18}$	0
MS 80502	SG	Zn	$6 \times 10^{18}$	$10^6$
H 227	VG	Zn	$3 \times 10^{18}$	$10^2$
H 611	VG	Zn	$5 \times 10^{18}$	$10^6$
H 203	VG	Zn	$1.5 \times 10^{19}$	$10^4$
H 194	VG	Cd	$8 \times 10^{17}$	$10^5$
H 161	VG	Cd	$1 \times 10^{18}$	$10^6$

directions as indicated in Fig. 1. The tangent of the short curved side of the pits is parallel to  $\langle 110 \rangle$  directions. The orientations of the two long sides of the pits are not simple, low index crystallographic orientations. Occasionally equilateral triangle anomalous etch pits were found on the  $\text{P}(\bar{1}\bar{1}\bar{1})$  surfaces. Figures 2a and b are micrographs of anomalous etch pits taken with a scanning electron microscope, indicating the deep structure of the pits. It is believed that the dark appearance of the anomalous etch pits comes from their depth. On  $\text{Ga}(111)$  surfaces of these crystals, dark triangle etch pits differing from ordinary dislocation etch pits were also revealed after the ferricyanide etching. Special structures, for example, decorated dislocations with Zn, or Cd, which were expected to correspond to the anomalous defects were not detected by transmitted visible light inspection through the crystals.

**Distribution of the anomalous etch pits.**—Czochralski-grown crystals.—It was observed that large anomalous etch pits were mainly distributed in annular rings on the  $\text{P}(\bar{1}\bar{1}\bar{1})$  slices cut perpendicular to the growth axis of a highly  $\text{Zn}(\text{PO}_3)_2$ -doped LEC crystal, RD 43, as schematically shown in Fig. 3. In the central region, denoted I in the figure, the density of the anomalous etch pits was about  $1 \times 10^5/\text{cm}^2$  and the pit size was the largest, approximately  $15\mu$  along the long axis (see Fig. 1). In the surrounding region II, the density of the pits decreased to the lowest value, about  $7 \times 10^4/\text{cm}^2$  and the size was reduced to less than  $5\mu$ . In region III, the density was the largest  $2 \times 10^5/\text{cm}^2$ , and the size was about  $10\mu$ . In the outermost region, IV, there

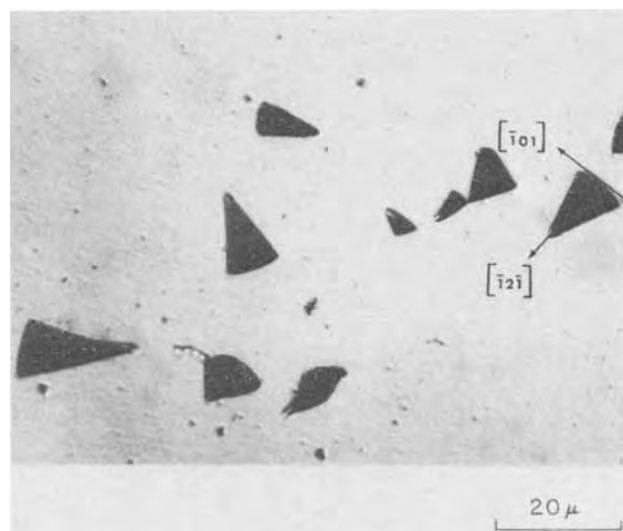


Fig. 1. Typical anomalous etch pits developed with ferricyanide etchant on a  $\text{P}(\bar{1}\bar{1}\bar{1})$  surface of a highly  $\text{Zn}(\text{PO}_3)_2$ -doped LEC crystal ( $N_A - N_D = 5 \times 10^{18}/\text{cm}^3$ ).

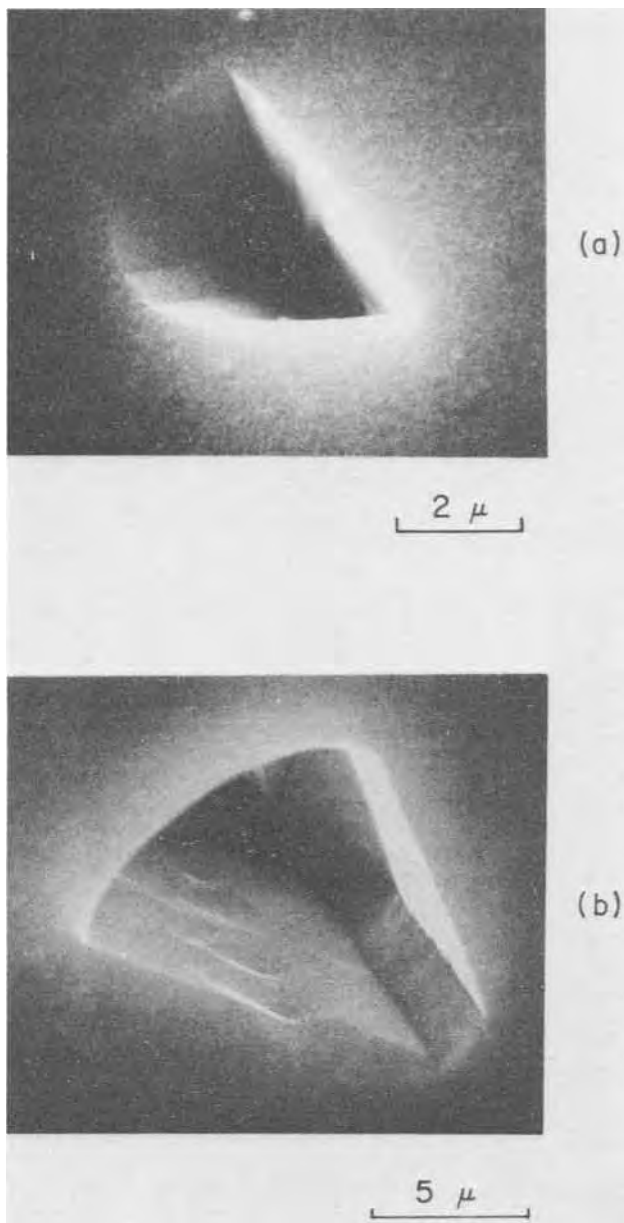


Fig. 2. Scanning electron micrographs of anomalous etch pits developed with ferricyanide etchant on  $P(\bar{1}\bar{1}\bar{1})$  surfaces of (a) the same sample as Fig. 1, and (b) a highly Zn-doped VG crystal ( $N_A - N_D = 1.5 \times 10^{19}/\text{cm}^3$ ).

were a few small ( $1\mu$ ) pits. In a region between III and IV, the anomalous etch pits were distributed as arrays along  $\langle 110 \rangle$  directions as shown in Fig. 4. It is well known that impurities are sometimes preferentially distributed in annular ring patterns in a  $\{111\}$  slice cut perpendicular to the growth axis of Czochralski crystals by the facet effect. For example, Cronin *et al.* (5) have reported the appearance of annular facets of high tellurium concentrations in Te-doped Czochralski-grown GaAs crystals. Therefore, the similar annular ring distribution of the large anomalous etch pits in a highly  $\text{Zn}(\text{PO}_3)_2$ -doped LEC crystal suggests that the anomalous defects are correlated with similarly distributed impurities incorporated during crystal growth. In a slightly less  $\text{Zn}(\text{PO}_3)_2$ -doped LEC crystal than above, the anomalous etch pits were found only on stacking faults or twin lamella grooves as shown in Fig. 5, and no anomalous etch pits were observed in other regions of this crystal. The anomalous etch pits have not been formed in the following LEC crystals: (i) three heavily Zn-doped different crystals with carrier concentrations of  $2.6 \times 10^{18}$ ,  $3 \times$

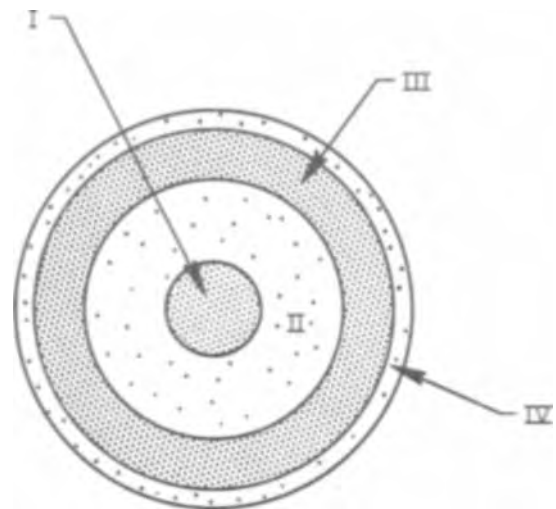


Fig. 3. Schematic annular ring distribution of large anomalous etch pits on a  $P(\bar{1}\bar{1}\bar{1})$  surface of a LEC crystal.

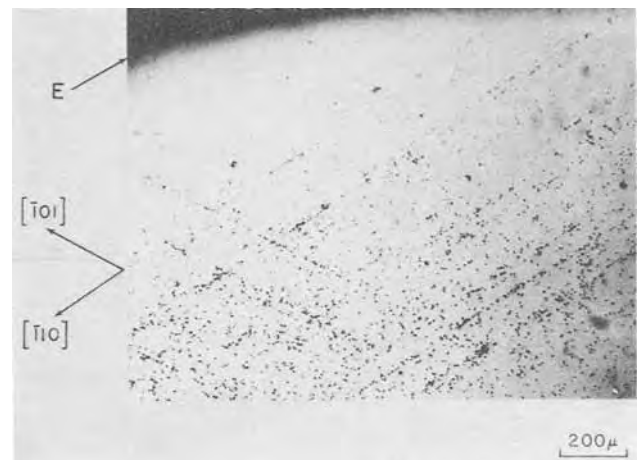


Fig. 4. Arrays of anomalous etch pits along  $\langle 110 \rangle$  directions at the edge of  $P(\bar{1}\bar{1}\bar{1})$  surface of a LEC crystal. Arrow E indicates wafer edge.

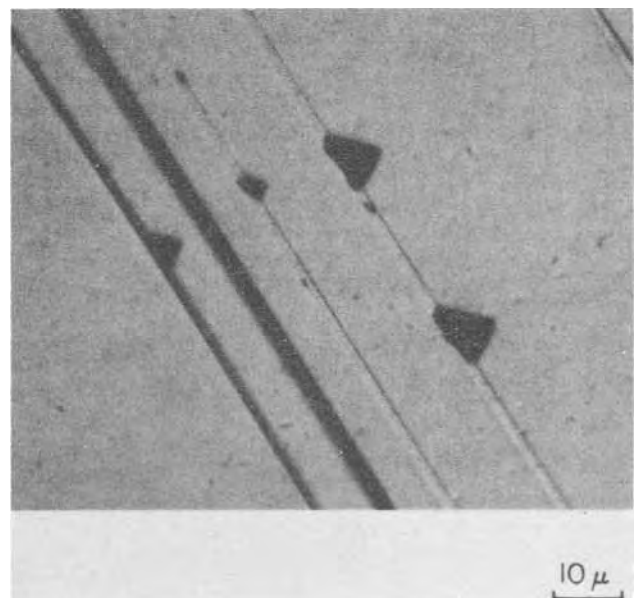


Fig. 5. Anomalous etch pits on stacking fault (or twin lamella) grooves in a tail part of a  $\text{Zn}(\text{PO}_3)_2$ -doped LEC crystal RD 47 ( $N_A - N_D = 4 \times 10^{18}/\text{cm}^3$ ).

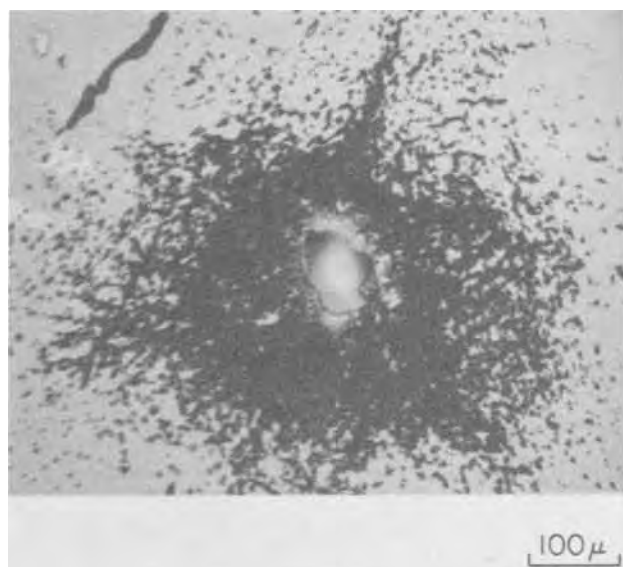


Fig. 6. A cluster of anomalous etch pits around an impurity inclusion on a  $P(\bar{1}\bar{1}\bar{1})$  surface of a highly Zn-doped SG crystal ( $N_A - N_D = 6 \times 10^{18}/\text{cm}^3$ ).

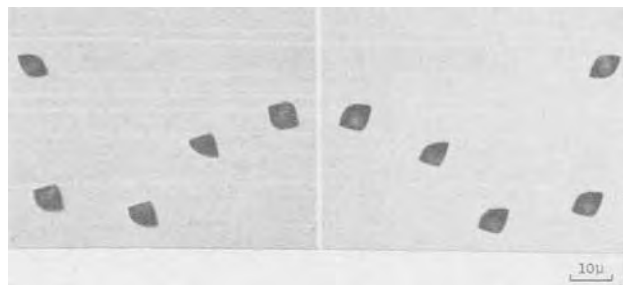


Fig. 7. Anomalous etch pits on matched  $\{110\}$  cleavage surfaces of a SG crystal. White horizontal lines are cleavage marks.

$10^{18}$ , and  $2 \times 10^{19}/\text{cm}^3$ , (ii) undoped,  $\text{Ga}_2\text{O}_3$ -, and lightly  $\text{Zn}(\text{PO}_3)_2$ -doped crystals, and (iii) highly S-doped crystals<sup>2</sup> ( $N_D - N_A \sim 9 \times 10^{17}$ ,  $3 \times 10^{18}/\text{cm}^3$ ).

**Solution-grown crystals.**—Clusters of the anomalous etch pits have been observed in a highly Zn-doped SG crystal with a carrier concentration of  $6 \times 10^{18}/\text{cm}^3$ . They were mostly distributed around impurity inclusions as shown in Fig. 6. Figure 7 shows a pair of  $\{110\}$  cleavage surfaces of the crystal etched with the ferricyanide reagent. There is a one to one correspondence between the pits on the cleaved halves. In S-, or Te-doped SG crystals with carrier concentrations of  $2 \times 10^{17}$  and  $8 \times 10^{17}/\text{cm}^3$ , the anomalous etch pits have not been observed.

**Vapor-grown crystals.**—Many anomalous etch pits have been observed in a highly Zn-doped VG crystal with a carrier concentration of  $5 \times 10^{18}/\text{cm}^3$  (Fig. 8). The density of the pits was of the order of  $10^6/\text{cm}^2$ . On the other hand, in other Zn-, or Cd-doped VG crystals with carrier concentrations ranging from  $8 \times 10^{17}/\text{cm}^3$  to  $1.5 \times 10^{19}/\text{cm}^3$ , the anomalous etch pit densities were between  $10^2/\text{cm}^2$  and  $10^4/\text{cm}^2$ . In those crystals with a low density of the anomalous etch pits, it was observed that the pits were preferentially located on stacking faults or on microtwin lamella grooves. The anomalous etch pits have not been observed in Te-doped VG crystals with carrier concentrations of  $3 \times 10^{16}$  and  $1 \times 10^{17}/\text{cm}^3$ .

**Thermal oxidation-induced anomalous defects.**—In addition to the grown-in anomalous defects, it has

<sup>2</sup> These highly S-doped LEC crystals were supplied from Sanyo Electric Company, Ltd., Osaka, Japan.

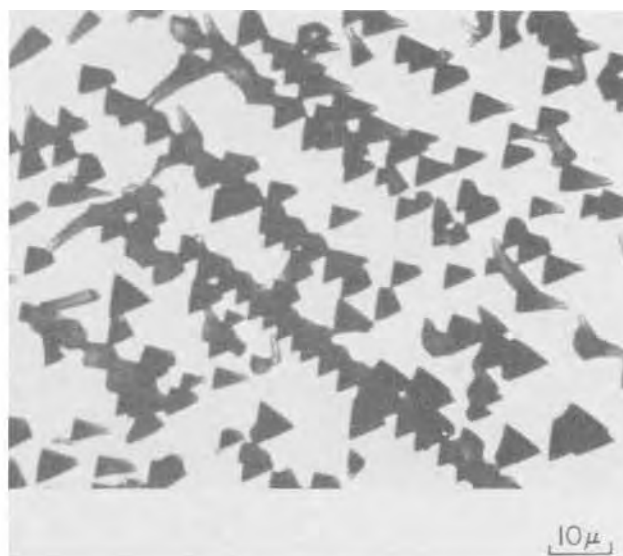


Fig. 8. Anomalous etch pits on a  $P(\bar{1}\bar{1}\bar{1})$  surface of a highly Zn-doped VG crystal.

been found that the anomalous defects were generated by thermal oxidation of GaP crystals previously doped with Zn or Cd. Interference color films were formed on the oxidized surfaces and the films were identified as being primarily  $\text{GaPO}_4$  by x-ray diffraction method. The formation of  $\text{GaPO}_4$  by the thermal oxidation of GaP crystals has previously been reported by Gershenson *et al.* (1) and Rubenstein (2). Surfaces of samples annealed in vacuum were inspected with an optical microscope, and it was found that there was no visible trace of the oxide films. Relatively few anomalous etch pits (density:  $10^2$ - $10^4/\text{cm}^2$ ) were found in some as-grown Zn-, or Cd-doped VG crystals as was described in the section on Vapor-grown crystals. However, after the thermal oxidation and subsequent etching of these crystals with the ferricyanide etchant, it was found that many more ( $10^5$ - $10^6/\text{cm}^2$ ) anomalous etch pits were newly formed on the surface (Fig. 9). It was found that some anomalous etch pits were distributed on intersections of the surface with stacking faults or on microtwin lamellae parallel to the  $\langle 110 \rangle$  directions on the  $P(\bar{1}\bar{1}\bar{1})$  surfaces. Successive polishing and etching showed that the newly formed defect is a short line defect (less than  $20\mu$  in

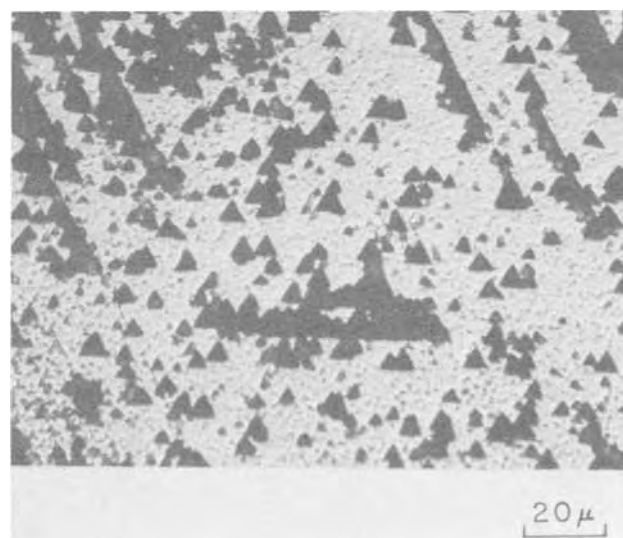


Fig. 9. Anomalous etch pits on a  $P(\bar{1}\bar{1}\bar{1})$  surface developed with ferricyanide etchant after thermal oxidation of a Cd-doped VG crystal ( $N_A - N_D = 8 \times 10^{17}/\text{cm}^3$ ).

length) and that the density is highest,  $10^5$ - $10^6/cm^2$ , on the exposed surface and gradually decreases to the original value at a certain depth ( $\sim 20\mu$  from the exposed surface). On the other hand, annealing of these crystals in high vacuum ( $\leq 10^{-7}$  Torr) at  $850^\circ C$  for  $5\frac{3}{4}$  hr, and subsequent etching did not reveal any new anomalous etch pits on the surfaces. Annealing in low vacuum ( $\leq 10^{-3}$  Torr) and etching sometimes produced new anomalous etch pits of a low density ( $10^2$ - $10^4/cm^2$ ) and sometimes did not produce the pits. These results indicate that these anomalous defects are produced by thermal oxidation and that the oxidation occurs readily even in the presence of a minute amount of residual air in the ampoule in the case of low vacuum sealing ( $\leq 10^{-3}$  Torr). When Te-doped VG crystals ( $N_D - N_A \sim 3 \times 10^{16}$ ,  $1 \times 10^{17}/cm^3$ ) were oxidized under identical conditions, no anomalous etch pits were produced on the surfaces.

### Discussion

**Correlation of the anomalous defects with dislocations.**—A good correspondence between the distributions of the anomalous etch pits on the cleaved halves (Fig. 7) indicates that the anomalous defect is a dislocation. At the periphery of the  $\{111\}$  cross-sectional slices of Czochralski-grown crystals, arrays of dislocation etch pits running parallel to  $\langle 110 \rangle$  directions are frequently observed as star patterns (6). These dislocations are attributed to slip caused by thermal stress during crystal growth (6). Therefore, the arrays of the anomalous etch pits in the  $\langle 110 \rangle$  directions at the periphery of the LEC crystal, RD 43 (Fig. 4), suggest that the anomalous etch pits are attributed to grown-in dislocations. Dislocations are frequently generated around impurity inclusions in various kinds of crystals due to the difference of thermal expansion coefficients between the inclusion and the matrix. The clusters of the anomalous etch pits around the impurity inclusions (Fig. 6) indicate that the pits are due to the dislocations. Therefore, it has been concluded that the anomalous defect is a dislocation, or rather an anomalous dislocation.

**Thermal oxidation-induced anomalous defects.**—It has been deduced that the thermal oxidation-induced defects are identical with the anomalous defects observed in as-grown crystals from the following results:

(i) The characteristic etching behavior of the oxidation-induced defects is the same as those of the grown-in anomalous defects. That is, oxidation-induced defects are revealed distinctly with the ferricyanide etchant as dark etch pits both in the  $P(111)$  and  $\{110\}$  surfaces.

(ii) The detailed structure of the thermal oxidation-induced pits as obtained with a scanning electron microscope is the same as that of the grown-in defect.

(iii) The oxidation-induced defects are formed in highly Zn-, or Cd-doped VG crystals. The grown-in anomalous defects are found in as-grown crystals doped with the same kind of impurities.

(iv) The oxidation-induced defects are preferentially located on stacking faults or on microtwin lamellae in the VG crystals. This behavior is the same as that of the anomalous defects in as-grown VG crystals.

At the present time, there is no decisive evidence that the location of the oxidation-induced anomalous defects corresponds to that of grown-in dislocation outcrops. As was described in the section on Thermal oxidation-induced anomalous defects, however, the oxidation-induced anomalous defects are line defects (less than  $20\mu$  in length) propagating from the surface into the bulk. Also, the densities of the oxidation-induced anomalous etch pits at the oxidized surfaces are nearly the same as those of grown-in dislocations. Therefore, it is believed that dislocations close to the

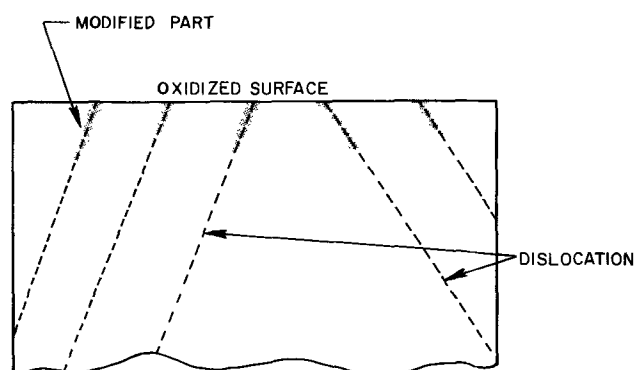


Fig. 10. A proposed structure of thermal oxidation-induced anomalous defects.

oxidized surface are partly modified to form the anomalous defect as schematically shown in Fig. 10, and that oxygen plays a role in the formation of the anomalous defect.

**Correlation of the anomalous dislocation with impurities.**—As was described in the section on Results, the anomalous dislocations were found in highly Zn( $PO_3$ )<sub>2</sub>-doped LEC crystals, but they were not detected in highly Zn-doped LEC crystals. In highly Zn (or Cd)-doped VG and SG crystals, however, they were formed. No anomalous dislocations, however, were found in S-, or Te-doped VG and SG crystals. Also, they were not found in undoped, highly S-, or Ga<sub>2</sub>O<sub>3</sub>-doped LEC crystals. On the other hand, the anomalous dislocations were newly formed by the thermal oxidation of highly Zn-, or Cd-doped VG crystals. From these results, it has been concluded that the anomalous dislocation is correlated with some impurities. It seems probable that the relevant impurities are both zinc (or cadmium) and oxygen, or zinc (or cadmium). At the present stage, however, there is no decisive proof that the impurities are both zinc (or cadmium) and oxygen, or zinc (or cadmium). A definitive identification of the impurities remains to be obtained.

The distinct development of the anomalous etch pits on the  $P(\bar{1}\bar{1}\bar{1})$  and the  $\{110\}$  surfaces with the ferricyanide etchant is probably due to such a characteristic nature of the defects. Also, for the same reason, the large anomalous etch pits are formed in the region I and III of Fig. 3 which are believed to contain higher concentrations of the impurities than the rest. Further investigation of the anomalous dislocation is in progress.

### Acknowledgments

The author is indebted to H. W. Verleur, L. C. Luther, and M. Kowalchik for preparing the samples. K. B. Wolfstirn and M. Kowalchik helped with the experiments. The author is grateful to G. W. Kammlott for the scanning electron microscope photographs and to S. E. Haszko for his analysis of the oxide films. Thanks are also due to B. Schwartz, F. A. Trumbore, L. C. Luther, and G. A. Rozgonyi for their critical reading of the manuscript and helpful comments.

Manuscript submitted Dec. 1, 1972; revised manuscript received March 19, 1974.

Any discussion of this paper will appear in a Discussion Section to be published in the June 1975 JOURNAL. All discussions for the June 1975 Discussion Section should be submitted by Feb. 1, 1975.

### REFERENCES

1. M. Gershenson and R. M. Mikulyak, *J. Appl. Phys.*, **35**, 2132 (1964).
2. M. Rubenstein, *This Journal*, **113**, 540 (1966).

3. B. Schwartz, *ibid.*, **118**, 657 (1971).

4. M. I. Val'kovskaya and Yu. S. Boyarskaya, *Sov. Phys. Solid State*, **8**, 1976 (1967).

5. G. R. Cronin, G. B. Larabee, and J. F. Osborne, *This*

*Journal*, **113**, 292 (1966).

6. For example, E. Billig, *Proc. Roy. Soc. (London)* **235A**, 37 (1956); F. D. Rosi, *RCA Rev.*, **19**, 349 (1958).

## The Heterogeneous Precipitation of Silicon Oxides in Silicon

K. V. Ravi\*<sup>1</sup>

Materials Research Laboratory, Motorola, Inc., Semiconductor Products Division, Phoenix, Arizona 85008

The publication costs of this article have been assisted by Motorola Incorporated.

### ABSTRACT

Long-time, high-temperature oxidation of dislocation-free silicon single crystals is observed to result in the precipitation of silicon oxides. Precipitation is found to occur in banded or striated distribution across the oxidized wafers. The distribution pattern assumed by the precipitates is identical to the pattern assumed by shallow, noncrystallographic etch pits observed upon etching the unoxidized wafers. By employing optical and transmission electron microscopy, the distribution, the morphology, and the structure of the precipitates have been examined. The precipitates are distributed in discrete clusters separated by precipitate-free regions. They have been identified to be a mixture of both  $\alpha$  and  $\beta$  cristobalite. The formation of precipitates results in the faceting of the crystal surfaces as a result of the diffusion and oxidation inhibiting effects of the precipitates. The heterogeneous nucleation is postulated to occur at vacancy clusters in the crystals, and models are presented for the nucleation phenomena and to account for the faceting effect of the precipitates.

The behavior of oxygen in single-crystal silicon has been a subject of great interest over the years. As is well known, oxygen can be associated with silicon in the form of a dissolved impurity incorporated into the crystal during growth. It can also be introduced into the crystal by diffusion during thermal oxidation. The solid solubility limit of oxygen in silicon has been reported to be in the range of  $10^{18}$  atoms/cm<sup>3</sup> (1). Excess oxygen above the solubility limit can precipitate. The phenomenon associated with the precipitation of oxygen in silicon has been studied by a variety of techniques. Among the principal techniques and the essential results obtained the following stand out:

(a) Perhaps the most extensively used method for detecting the presence of oxygen in silicon is the infrared absorption technique. The infrared absorption band of silicon at  $9\mu$  is found to be related to a silicon-oxygen molecular vibration. From the observation of a decrease in this absorption band when silicon containing dissolved oxygen is heat-treated at elevated temperatures ( $\sim 1000^\circ\text{C}$ ), the hypothesis of clustering and precipitation of oxygen in the form of Si-O complexes has been advanced (2-5). Corbett *et al.* (6) have proposed the existence of a number of vacancy-oxygen complexes as evidenced by the appearance and the disappearance of infrared absorption bands of different wavelengths when irradiated silicon is annealed.

(b) In recent years, careful observation of the surfaces of Sirtl (7) etched silicon crystals has revealed the presence of large densities of noncrystallographic etch pits. These etch pits, which appear roughly circular when viewed at high magnification, have been variously called anomalous etch pits, empty etch pits, and saucer pits. These pits have been related to vacancy-oxygen complexes in the crystal (8). A large concentration of vacancies are retained in crystals grown from the melt. These vacancies are then postulated to interact with dissolved oxygen during the cooling stage with the resulting complex having a

mobility less than that of either individual vacancies or oxygen atoms. With increasing size, these complexes become immobile and eventually can be observed by the etch pitting technique or by x-ray techniques following suitable decoration by a fast diffusing metal such as copper (8).

(c) X-ray diffraction methods have been used to detect the presence of small, localized, strain-producing centers by first decorating these centers with copper (9). X-ray transmission topographs of copper-decorated crystals have revealed the presence of radial distribution of strain-producing centers which have been suggested as being due to oxygen-vacancy complexes. The anomalous x-ray transmission technique was employed by Patel and Batterman (9) to detect the presence of a pre-precipitation stage in silicon. They observed a reduction in the anomalously transmitted x-ray intensity when silicon containing oxygen was heat-treated at  $1000^\circ\text{C}$ . This change in the transmitted x-ray intensity was observed to occur before the decrease in the  $9\mu$  infrared absorption band manifested itself, indicating that early stages of impurity clustering were affecting the anomalous x-ray intensity.

Other evidence for precipitation of oxygen is found in the observation that new donor states are introduced into silicon following low-temperature annealing ( $< 500^\circ\text{C}$ ) (10). These donors can be annealed out at high temperatures ( $\sim 1000^\circ\text{C}$ ) and the donor concentration is found to be related to the measured oxygen concentration in the crystal. Heat-treatment of silicon has also been observed to influence its plastic deformation characteristics and it has been proposed that silicon-oxygen clusters function as dislocation generating sites during deformation (11).

Precipitation of  $\text{SiO}_2$  has been observed to occur at dislocations when silicon is annealed at high temperatures for extensive periods of time in oxygen ambients (12). It has been suggested that  $\text{SiO}_2$  precipitation occurs when silicon containing oxygen is heat-treated at high temperatures (13).

The heterogeneous precipitation of impurities can also occur at strain-producing centers other than dis-

\* Electrochemical Society Active Member.

<sup>1</sup> Present address: Tyco Laboratories, Inc., Waltham, Massachusetts 02154.

Key words: oxygen, vacancies, clusters, cristobalite.

locations. The technique for investigating the nature and distribution of vacancy clusters in silicon uses this phenomenon of heterogeneous precipitation. Both copper (8) and lithium (14) have been found to preferentially precipitate at vacancy clusters. Batavin (15) has suggested that  $\text{SiO}_2$  precipitates nucleate at vacancy clusters.

The present work is concerned with the precipitation of the oxides of silicon in dislocation-free crystals. The effects of extended oxidation on the nature and distribution of crystalline silicon oxides in silicon are examined.

### Experimental Procedure

Single crystals grown by both the floating zone and Czochralski techniques were the vehicles for the experiments. The crystals were dislocation free and wafers cut from the crystals were chemically-mechanically polished to remove surface damage. The wafers were oxidized at  $1200^\circ\text{C}$  for periods of time ranging from 1 to 60 hr in a steam ambient. Careful precautions were taken to avoid the generation of dislocations in the wafers due to thermal, stress-induced slip. The distribution, the morphology, and the structure of the precipitates formed were investigated by optical and transmission electron microscopy. For transmission electron microscopy, thin foils were prepared by the conventional jet thinning techniques. The oxygen content of the crystals prior to oxidation varied from a high value of  $\sim 10^{18}$  atoms/cm<sup>3</sup> to below the detectability limit for the floating zone crystals.

### Experimental Results

Extended oxidation of dislocation-free wafers resulted in distinct effects when the as-grown crystal contained an inhomogeneous distribution of vacancy clusters. Considerable evidence exists in the literature that vacancy clusters frozen into the solid during crystal growth function as heterogeneous nucleation sites for metal precipitates (8, 14) as well as for the formation of extrinsic stacking faults (16, 17). Long oxidation at high temperatures ( $>>2$  hr at  $1200^\circ\text{C}$ ) resulted in the formation of discrete precipitates. These precipitates formed in regions of the wafer which contained a high density of vacancy clusters as evi-

denced by the observation of a high density or non-crystallographic etch pits upon preferential etching prior to oxidation.

*Surface structure.*—Following extended oxidation the  $\text{SiO}_2$  films formed were removed by dissolution in HF and the surfaces observed using optical microscopy. At low magnifications, the oxidized wafers were found to exhibit a banded or sometimes spiral shaped distribution of bright and dark regions. The changes in the surface brightness were related to the changes in the direction of scattered light from the surface. The patterns of differing brightness were identical to the patterns of shallow etch pits observed prior to oxidation and following preferential etching. The significant difference was that following extended oxidation the banded or "swirl" type patterns become observable without the need for preferential etching such as Sirtl etching or the equivalent. These patterns were frequently observable through the  $\text{SiO}_2$  films formed on the surface. Figures 1a and b are typical examples of wafers exhibiting this behavior. In Fig. 1a, bright bands are observable across the wafer whereas in Fig. 1b, the central portion of the wafer contains a circular bright region.

Examination of the surfaces at high magnification using interference contrast techniques revealed that the bright regions of the wafers were composed of varying densities of star shaped or square hillocks with an apparent presence of a second phase at the apices of the hillocks. Figures 2 and 3 show interference contrast optical micrographs of the surfaces of the oxidized wafers. In Fig. 2 are shown micrographs obtained at different regions of a  $\langle 111 \rangle$  oriented wafer. The star shaped hillocks vary in density from near zero to  $10^7/\text{cm}^2$  (as subsequently determined by transmission electron microscopy). The four micrographs in Fig. 2 show the typical density distribution of the hillocks in a wafer. The apparent presence of a second phase at the apices of the hillocks is also revealed in these micrographs and was subsequently confirmed by electron microscopy as discussed in the next section.

Figure 3 shows similar hillock formation on  $\langle 100 \rangle$  oriented wafers. In this case, the hillocks are in the

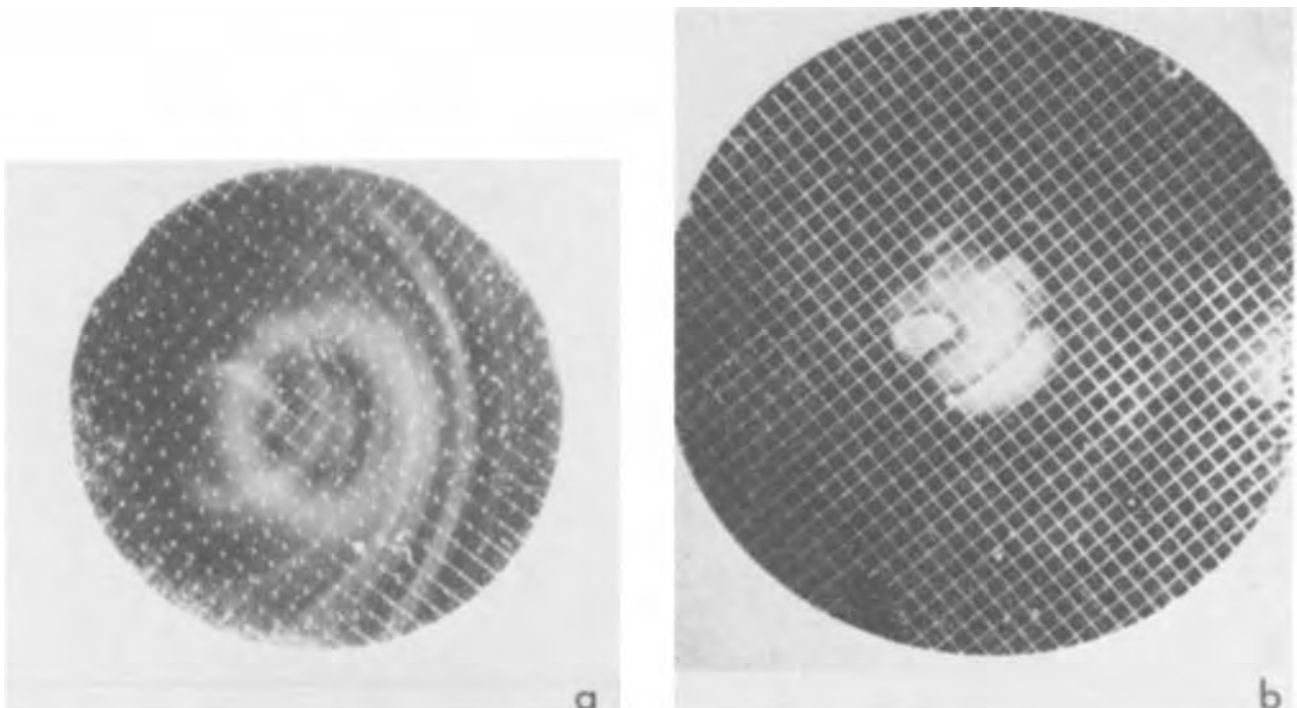
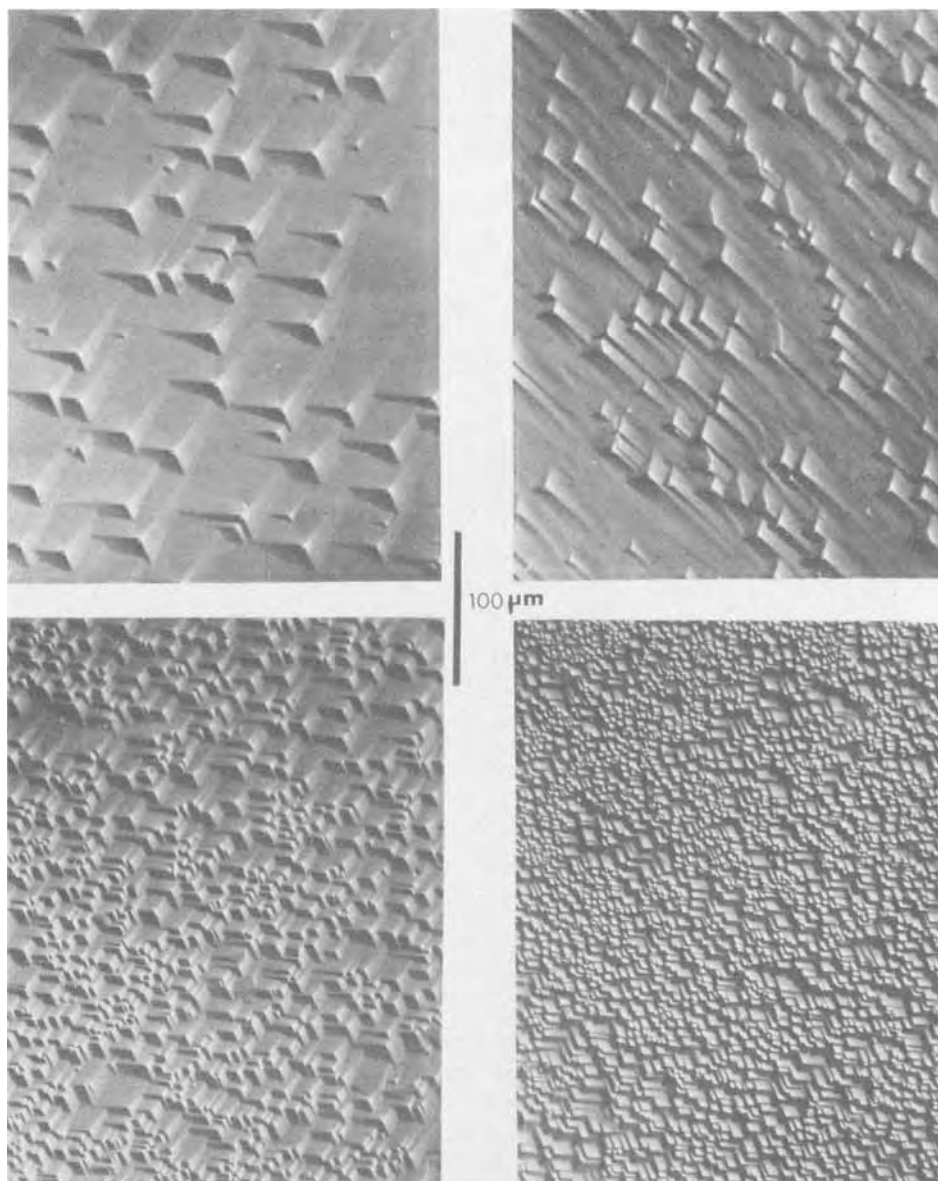


Fig. 1. Optical micrographs of oxidized dislocation-free crystals showing the hazy appearance of bands in (a) and a central circular region in (b) due to the faceting of the surface. Wafers are 2 in. in diameter and were not preferentially etched.



**Fig. 2.** Interference contrast optical micrographs from the hazy regions of the crystal surfaces showing faceting of the surface. Triangular hillocks with an apparent presence of precipitates at the apices are distributed across the wafer in varying densities. ( $\langle 111 \rangle$  orientation). Wafer surfaces are not preferentially etched.



form of squares. The hazy regions of the wafer observed when viewed at low magnification are evidently a result of faceting of the crystal surface.

**Precipitate morphology and distribution.**—Transmission electron microscopy at regions which generated surface hillocks confirmed the presence of precipitates in the crystal. A notable aspect of the precipitates was the striking nature of the precipitate distribution. Figure 4 is a transmission electron micrograph of precipitates in a  $\langle 111 \rangle$  oriented wafer. These precipitates were generated as a consequence of a  $1200^{\circ}\text{C}$  oxidation for 10 hr. The following are the significant features of the precipitate morphology and distribution:

(a) The precipitation is observed to have occurred in discrete regions with clusters of precipitates concentrated within an area of  $\sim 1 \mu\text{m}^2$ .

(b) The precipitate density within the clusters has been found to vary from a single particle to  $10^{10}$  precipitates/ $\text{cm}^2$ .

(c) The particle size within each cluster has been found to range from  $\sim 100$  to  $\sim 4000 \text{ \AA}$  with occasional large individual particles  $\sim 1 \mu\text{m}$  in size.

(d) The clusters are separated by distances of  $1 \mu\text{m}$  or more with almost completely precipitate-free regions surrounding each cluster. The density of precipitate clusters has been observed to be as high as  $10^7/\text{cm}^2$ . Although the individual precipitate particles

exhibited no characteristic shape, the clusters displayed a tendency to form in triangular patterns [on (111) surfaces] with edges aligned along equivalent  $\langle 110 \rangle$  directions.

Since the crystal surfaces were found to be non-planar with discrete hillocks at the site of each precipitate cluster, it should be expected that the non-planarity affect the observed diffraction contrast in the electron microscope. This expectation was borne out when the specimens were oriented for exact two beam diffracting conditions. Figure 5 shows the precipitate clusters imaged under two beam (Si reflections) bright field conditions. Each precipitate cluster is surrounded by triangular shaped thickness extinction contours appearing as alternate dark and bright bands. This verifies the facts that each cluster is situated at the apex of a triangular shaped hillock in the silicon. The degree of surface tilt associated with each cluster would determine the number of fringes observed around the clusters. From an examination of a large number of specimens, it was found that the number of dark and white fringes surrounding the precipitates varied. Figure 6 shows a case where the precipitate cluster is surrounded by one dark and one bright fringe. Figure 7 is a  $\{220\}$  weak beam image of a number of precipitate clusters with differing numbers of thickness extinction contours around the different clusters. A rough estimate of the tilt in-

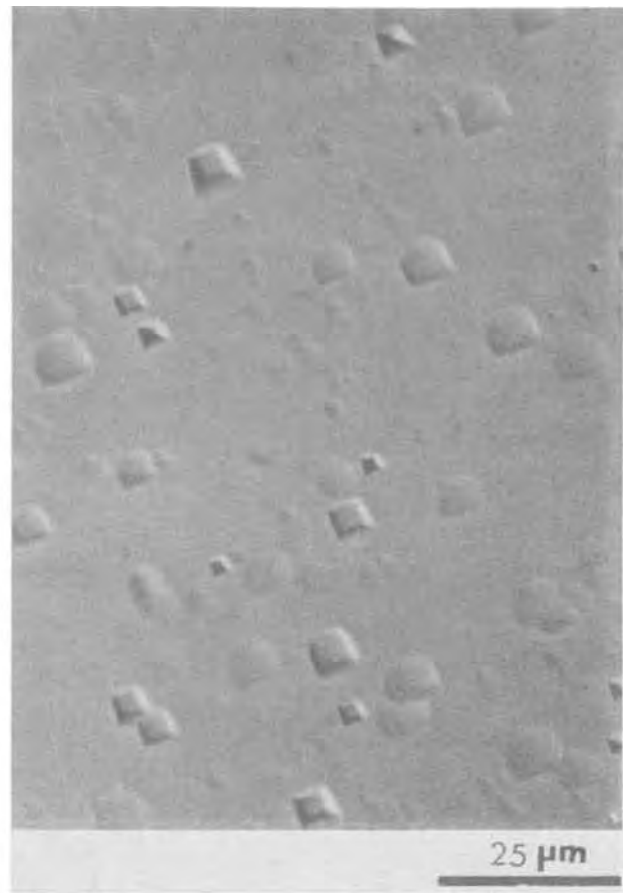
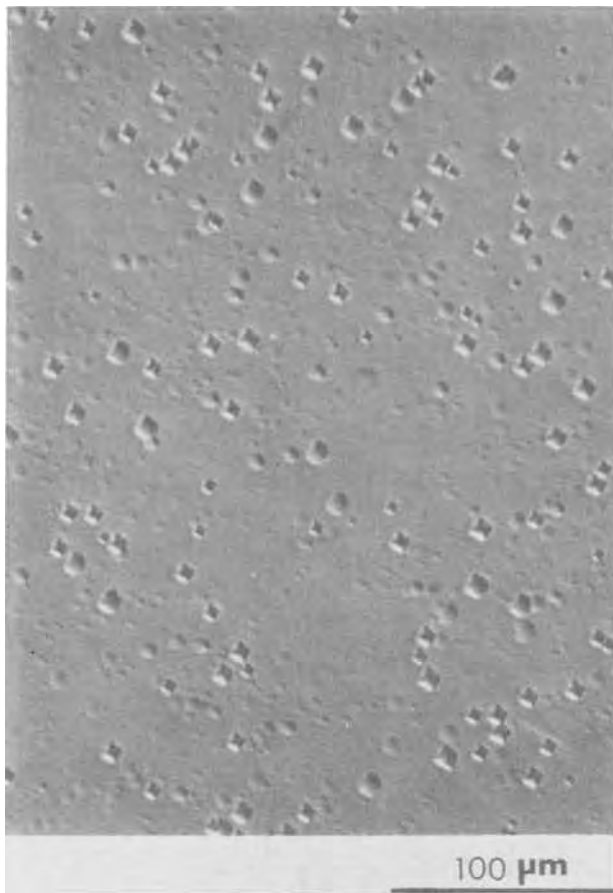


Fig. 3.  $\langle 100 \rangle$  oriented wafers showing the formation of square shaped hillocks after extended oxidation.

involved at each hillock can be made by using weak beam imaging techniques and the method described by Bicknell (18). The width of the extinction fringes around the precipitate clusters was measured in the

$\{220\}_{\text{Si}}$  weak beam image and using the formula  $1/S' \cot \theta = \text{fringe width}$ , the angle  $\theta$  was computed. Here  $S'$  is the deviation parameter (19) and  $\theta$  is the inclina-

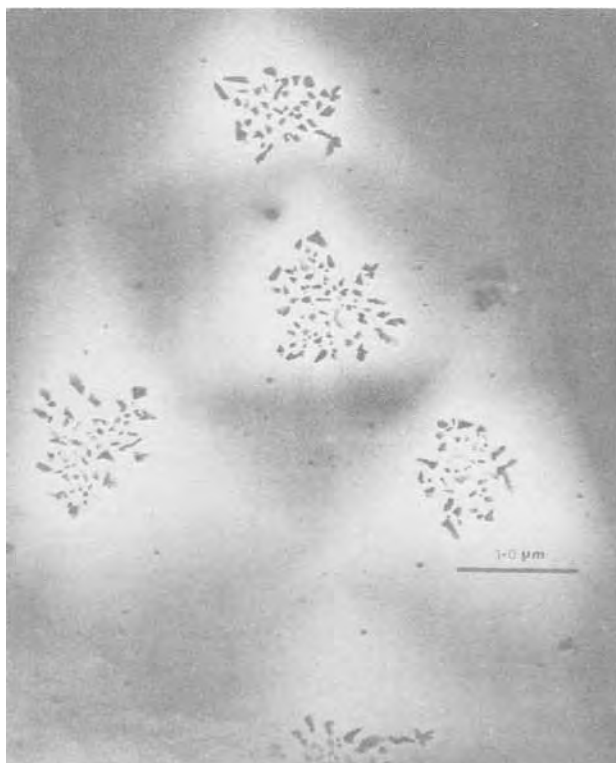


Fig. 4. Transmission electron micrographs of precipitate clusters

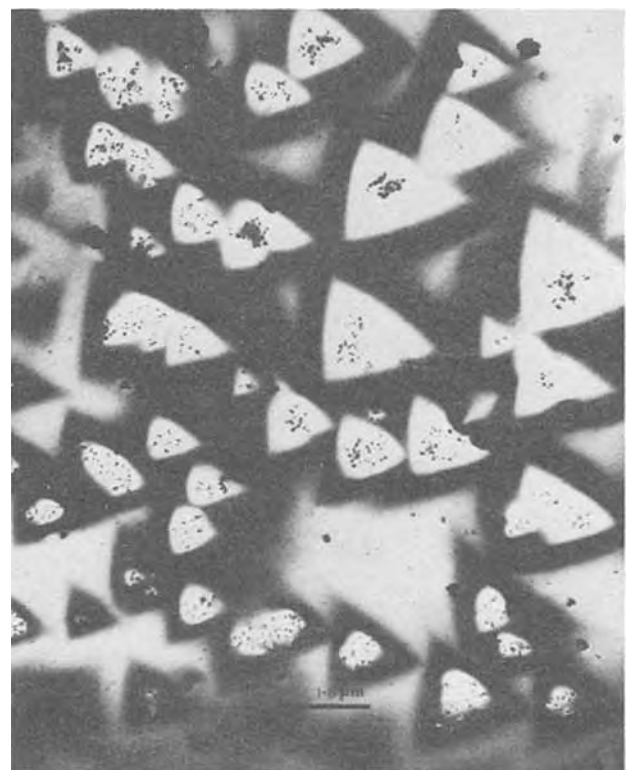


Fig. 5. Two beam bright field image demonstrating the thickness extinction fringes around the precipitate clusters.



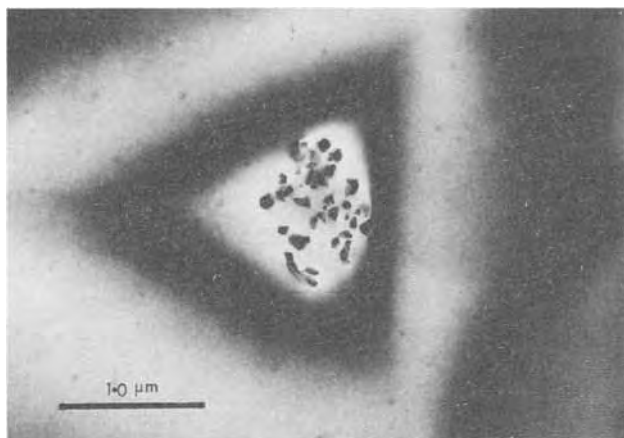


Fig. 6. Higher magnification micrograph of a single precipitate cluster surrounded by one bright and one dark extinction fringe.



Fig. 7.  $\{220\}$  weak beam image of multiple fringes around precipitate clusters.

tion of the surface at the facets (or hillocks) to the normal to the electron beam direction  $\langle 111 \rangle$  or the silicon surface. Figure 8 is a typical example of a  $\{220\}$  weak beam image of the precipitate clusters and the thickness extinction contours surrounding the clusters. From an analysis of a number of samples, it was found that the angle of tilt of the sides of the hillock with the surface of the sample varied between  $0.7^\circ$  and  $2^\circ$ .

Figure 9 shows precipitation in a  $\langle 100 \rangle$  oriented wafer. Figure 9a shows a single large precipitate located at the center of a hillock whereas Fig. 9b is a micrograph of a precipitate cluster. The thickness extinction contours again verify that the precipitates are located at the top of a hillock, in this case a square shaped hillock with the sides aligned along orthogonal  $\langle 110 \rangle$  directions.

*Precipitate structure.*—The large density of individual particles in each cluster of precipitates per-

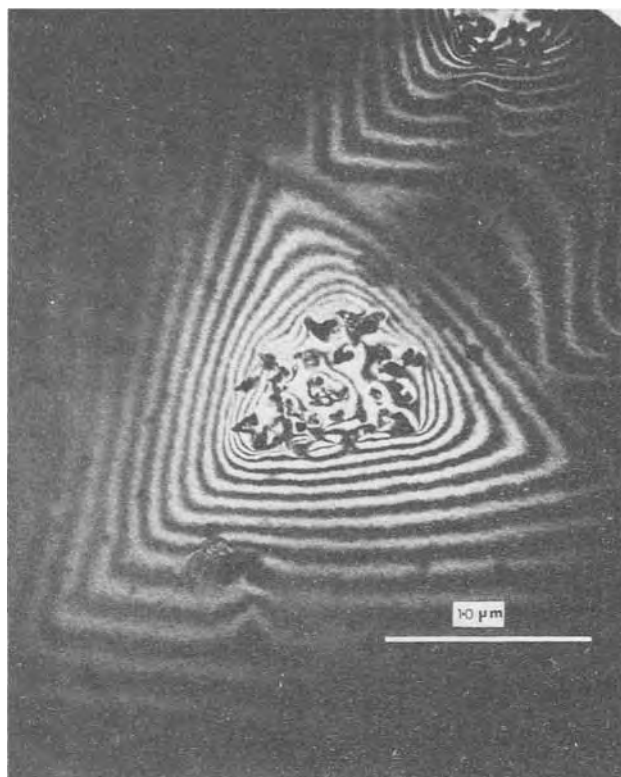


Fig. 8.  $\{220\}_{\text{Si}}$  weak beam image of precipitate cluster and surrounding extinction fringes.

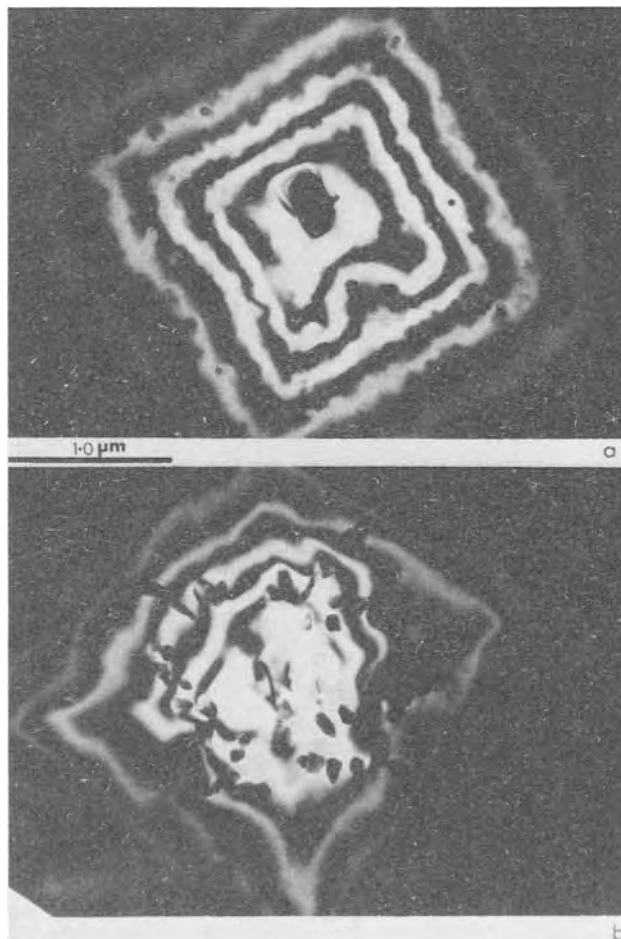


Fig. 9.  $\langle 100 \rangle$  oriented wafer showing a single precipitate in (a) and a precipitate cluster in (b) both being surrounded by thickness extinction contours. The sides of the hillock are aligned along  $\langle 110 \rangle$  directions.

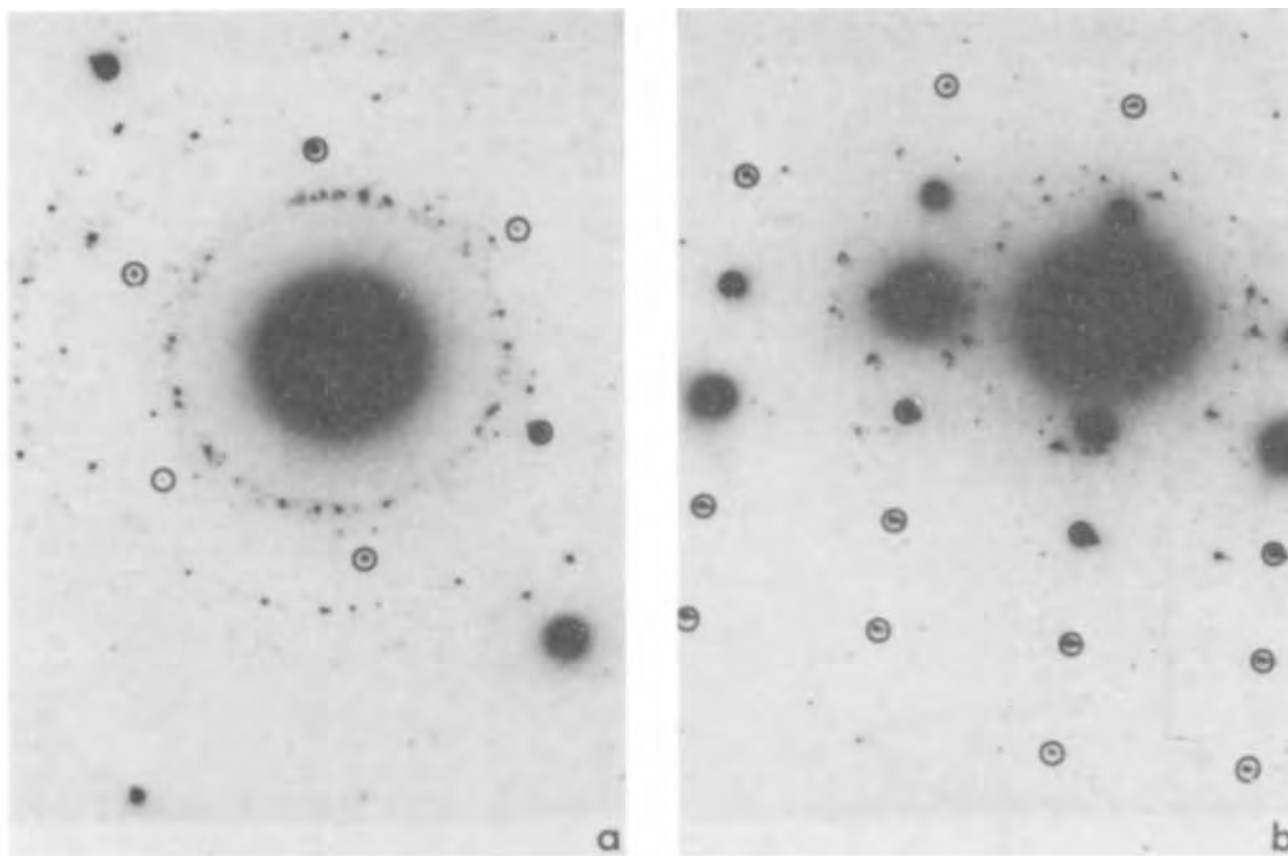


Fig. 10. Selected area diffraction patterns showing precipitate reflections and Si reflections (circled). a,  $\langle 111 \rangle_{\text{Si}}$ ; b,  $\langle 110 \rangle_{\text{Si}}$ .

mitted their identification by selected area diffraction analysis. Figure 10a and b show typical diffraction rings due to the precipitates seen in association with the silicon spots. Although each precipitate particle was a single crystal, the large particle density in any given cluster and the relatively small precipitate size resulted in discontinuous diffraction rings made up of spots. The two patterns shown in Fig. 10 were obtained from two different orientations, viz., (111) and (110).

Table I shows average interplanar spacings calculated from measured reflection spacings on the diffraction patterns. X-ray data on  $\alpha$  and  $\beta$  cristobalite are also shown. The measured interplanar spacings can be correlated with the known interplanar spacings of both  $\alpha$  and  $\beta$  cristobalite. A similar result was obtained by Bialas and Hesse (12) for precipitates nu-

cleated at dislocations. They found, however, that some precipitates exhibited moiré patterns furnishing a second means of determining the precipitate structure. From the analysis, they concluded that the precipitates are predominantly  $\beta$ -SiO<sub>2</sub>. In the present work, extensive examination did not reveal the presence of moiré fringes in any of the precipitates. This might indicate that no coherency exists between the precipitate and silicon lattices.

Although no strong displacement fringe contrast around individual precipitate particles was observed, frequently, the diffraction spots due to the precipitates were found to be streaked. Streaking or the observation of rel-rods can be attributed to either the existence of coherency strains or the presence of faulted structures. Examination of some of the larger particles exhibiting streaked diffraction spots indicated the possible existence of faulting within the precipitates. Figures 11a and b are bright and dark field images of a precipitate which gave rise to streaks at the precipitate reflections. The corresponding diffraction pattern from the precipitate is shown in Fig. 11c. The precipitate exhibits a high density of fine parallel striations. These striations are observed to lie normal to the direction of streaks in the precipitate diffraction spots. This is shown in Fig. 11c where the streaks (arrowed) are shown to be normal to the striations in the precipitate. The dark field image in Fig. 11b was obtained from the streak spots indicating that the streaking is associated with the striations in the precipitate. Similar striated structures have been shown to be a result of faulting in the structure (20). It can hence be concluded that the precipitates are faulted. The  $\beta$ -phase of crystalline SiO<sub>2</sub> is a high-temperature phase stable above 577°C and has a cubic structure ( $A_0 = 7.18\text{\AA}$ ) whereas the  $\alpha$ -phase is a low-temperature phase with a tetragonal structure ( $A_0 = 4.971\text{\AA}$  and  $C_0 = 6.918\text{\AA}$ ). Consequently, the  $\beta$ -phase which would be unstable below 577°C could transform to the  $\alpha$ -phase and if the transformation

Table I. The measured values of interplanar spacings are compared with the known spacings of  $\alpha$  and  $\beta$  cristobalite

d-Spacings in angstroms		
Average measured	$\alpha$ cristobalite*	$\beta$ cristobalite*
4.28	4.05	4.15
3.42	3.35	—
2.88	2.841	2.92
2.736	—	—
2.606	—	—
2.59	—	2.53
2.54	—	—
2.487	2.485	—
2.432	—	—
2.42	2.465	—
2.146	2.118	2.17
2.105	2.019	2.07
1.89	1.870	—
1.69	—	1.69
1.66	—	1.641
1.56	—	1.460

\* ASTM card index x-ray powder data file.

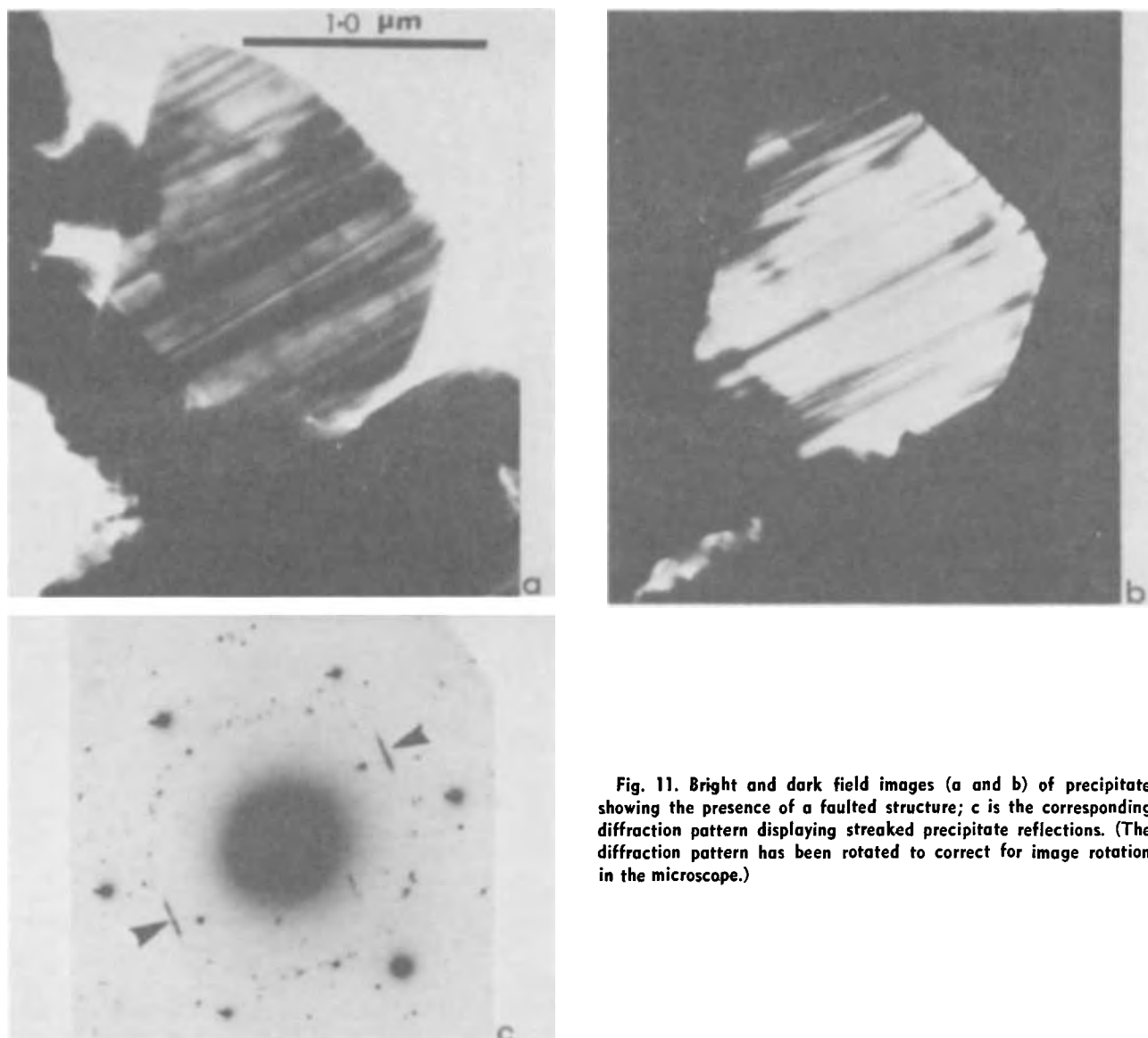


Fig. 11. Bright and dark field images (a and b) of precipitate showing the presence of a faulted structure; c is the corresponding diffraction pattern displaying streaked precipitate reflections. (The diffraction pattern has been rotated to correct for image rotation in the microscope.)

is incomplete due to thermal or strain energy considerations the structures resulting could be faulted. The classic case of faulting resulting from a phase transformation is the case of cubic austenite transforming to tetragonal martensite in ferrous alloys where the martensite phase is often found to be faulted and twinned.

### Discussion

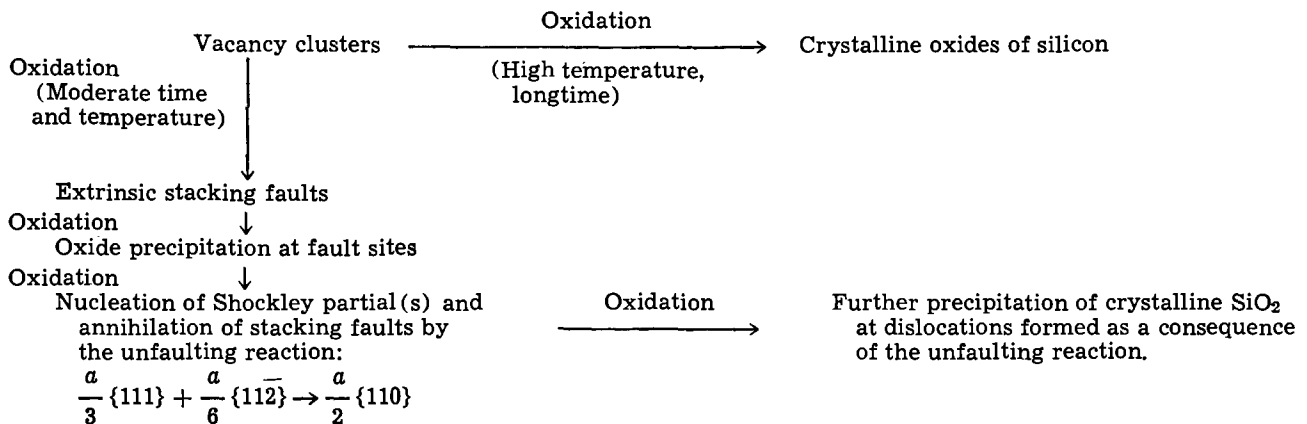
The results presented above show that oxides of silicon can heterogeneously nucleate at specific regions of a crystal, the nucleation sites not being dislocations, stacking faults, or other crystallographic defects. From the observation of the common distribution pattern of the precipitate clusters and the so-called shallow or empty etch pits observed on etched surfaces prior to oxidation, the precipitate nuclei are suggested to be vacancy clusters. These vacancy clusters or, more exactly, vacancy-solute atom clusters, are formed in the crystals during growth. The concept of vacancy-solute atom clusters functioning as nuclei for precipitation in solid solutions is not new. Hart (21) has suggested that precipitation processes are initiated by the migration of small groups of solute atoms and vacancies which gradually agglomerate to form large clusters which function as precipitate nuclei. Embury and Nicholson (22) suggest that the precipitate distribution in aluminum alloys is largely controlled by the distribution and con-

centration of vacancies. The stability of solute-vacancy clusters has been related to one of two causes. In one case, it is proposed that vacancies are integral chemical constituents of the precipitating phases which reduce the volume free energy of the system and facilitate nucleation and growth (21). An alternative proposal maintains that stable vacancy-solute atom clusters result purely from size effect considerations. If the precipitation of an equilibrium phase results in an increase in the atomic volume, the incorporation of vacancies in the precipitate nuclei will assist in the reduction of the misfit strain energy of the precipitate. It has been suggested that vacancy assisted nucleation occurs only in systems where an increase in the atomic volume takes place during precipitation (22). The high-temperature crystalline phase of  $\text{SiO}_2$  forms with an increase in the atomic volume, the specific volume of  $\text{SiO}_2$  being about 10% higher than that of silicon. Consequently, precipitation of  $\text{SiO}_2$  at sites of excess vacancy clusters is eminently feasible. The lack of evidence for any elastic or plastic strains around the precipitates indicates that the difference in atomic volume between the two phases ( $\text{SiO}_2$  and Si) is accommodated by the vacancy clusters.

The quenched in supersaturation of vacancies, *i.e.*, the vacancy clusters can either be annihilated during oxidation by forming dislocation loops or, if the binding energy between vacancies and oxygen atoms is

sufficiently high, they can form stable complexes with oxygen. The absence of dislocation loops in the structures observed and the presence of precipitates indicates that the latter mechanism prevails. However, it is known that oxidation of silicon can also generate faulted dislocation loops at the sites of vacancy clusters (16, 23). This apparent dichotomy is related to the particular thermal conditions required to generate the two defect types, viz., faulted loops or oxide precipitates.

Precipitation of crystalline oxides occurs only with extended oxidation at high temperatures as demonstrated in this work. Stacking fault nucleation, on the other hand, occurs under more moderate conditions of oxidation or in the early stages of a longtime-high temperature oxidation process. The transformation of a vacancy cluster into secondary defects can be represented as follows:



The transformations depicted indicate that a vacancy cluster can nucleate oxide precipitates either directly or indirectly through a series of transformations involving a stacking fault. A brief examination of the feasibility of these two reactions and the probability of their occurrence is worth considering.

The discussion above indicates that the direct nucleation of crystalline SiO<sub>2</sub> at vacancy clusters is possible. This is aided by strain energy considerations as well as perhaps by the reaction kinetics of the system at high temperatures. However, the second reaction involving a stacking fault is also possible. As mentioned before, extrinsic stacking faults can nucleate at vacancy clusters. With longer oxidation, the faults can function as nucleation sites for precipitates of oxides. It has been suggested by Sanders and Dobson (24) that oxide platelets observed at stacking faults by Booker and Stickler (25) after severe oxidation are likely to be a result of preferential growth of the surface oxide into the silicon where the Frank dislocation intersects the oxide-silicon interface. The next stage in the transformation involves the annihilation of the stacking fault by the nucleation of a Shockley partial which reacts with the Frank to form an undissociated dislocation of the type  $a/2 \{110\}$ . This unfauling reaction has been shown to occur in close-packed metals (26). The nucleation of a Shockley partial is stress aided, consequently misfit strains around a precipitate can initiate the unfauling reaction. Experimental evidence exists to show that stacking fault annihilation in silicon occurs by the unfauling reaction (27). The product of the unfauling reaction is a dislocation which can function as a heterogeneous nucleating agent for further SiO<sub>2</sub> precipitation.

Although both mechanisms discussed are possible, the weight of evidence in favor of the direct nucleation mechanism is perhaps greater. The annihilation of stacking faults would result in dislocations which should be evident in the structures observed. As demonstrated, the structures observed were completely devoid of dislocations or stacking faults.

Finally, since the initial indications of precipitation were evident as a result of faceting of the crystal surface, a model is proposed to account for this effect. As demonstrated, each precipitate cluster is observed to be located at the apex of a hillock or elevated region surrounded by facets in the crystal surface. The schematic sketches in Fig. 12 show the proposed model. The vacancy clusters distributed inhomogeneously through the crystal nucleate particles of crystalline silicon dioxide in the early stages of oxidation. The formation of the precipitates at the surface will inhibit further oxidation of the silicon at the precipitate sites. This can occur as a result of the oxide particles functioning as a mask to the diffusion of oxygen into the silicon as well as by preventing the silicon-oxygen reaction at the precipitate sites. Since the precipitates are closely clustered in discrete regions, oxidation of

the surrounding precipitate-free silicon can continue unimpeded. This would result in a greater consumption of the silicon surrounding the precipitates leading to the formation of raised hillocks with the precipitates on top of the hillocks. The crystallographic nature of the hillocks, i.e., triangular and square shaped on (111) and (100) surfaces is evidently a result of different oxidation rates on close-packed planes as opposed to the rates on nonclose-packed planes. The effect is the analog of the formation of triangular and

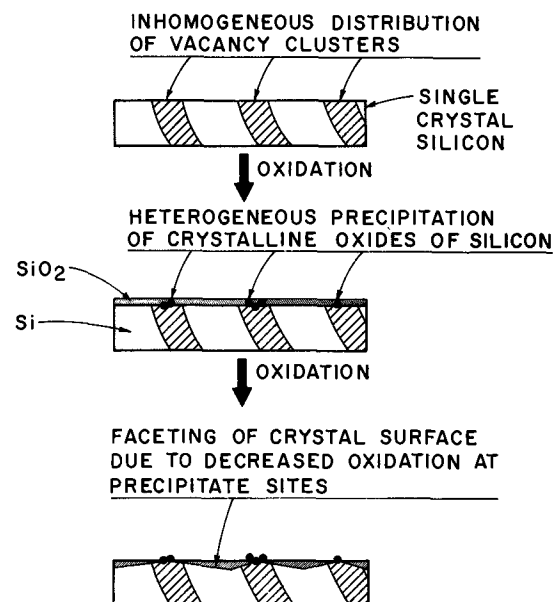


Fig. 12. Schematic sketches showing the proposed model to account for the faceting of the crystal surface as a result of precipitation.

square pits at sites of defects in crystals of the two orientations upon preferential etching.

### Summary

In summary, it has been postulated that crystalline oxides of silicon can nucleate heterogeneously at sites of vacancy clusters. Both  $\alpha$  and  $\beta$  crystal phases appear to coexist in the material. Some evidence for faulting in the precipitates is presented. The formation of clusters of oxide particles in the surface regions of the crystal leads to faceting of the surface due to the oxidation and diffusion regarding effect of the precipitates. The precipitation phenomenon is discussed with respect to models of nucleation at vacancy complexes and both direct and indirect nucleation models have been examined.

Manuscript submitted Nov. 12, 1973; revised manuscript received March 20, 1974.

Any discussion of this paper will appear in a Discussion Section to be published in the June 1975 JOURNAL. All discussions for the June 1975 Discussion Section should be submitted by Feb. 1, 1975.

### REFERENCES

1. T. Takano and M. Maki, "Semiconductor Silicon," H. R. Huff and R. R. Burgess, Editors, p. 469, The Electrochemical Society Softbound Symposium Series, Princeton, N. J. (1973).
2. W. Kaiser, P. H. Keck, and C. F. Lang, *Phys. Rev.*, **101**, 1264 (1956).
3. W. Kaiser and P. H. Keck, *Bull. Am. Phys. Soc., Ser. 11*, **1**, 321 (1956).
4. W. Kaiser, *Phys. Rev.*, **105**, 1751 (1957).
5. W. Kaiser and P. H. Keck, *J. Appl. Phys.*, **28**, 882 (1957).
6. J. W. Corbett, G. D. Watkins, and R. S. McDonald, *Phys. Rev.*, **105**, 1751 (1964).
7. E. Sirtl and A. Adler, *Z. Metallk.*, **52**, 529 (1961).
8. A. J. R. deKock, *This Journal*, **118**, 1851 (1971).
9. J. R. Patel and B. W. Batterman, *J. Appl. Phys.*, **34**, 2716 (1963).
10. C. S. Fuller and R. A. Logan, *ibid.*, **28**, 1427 (1957).
11. J. R. Patel and A. R. Chaudhuri, *ibid.*, **33**, 2223 (1962).
12. D. Bialas and J. Hesse, *J. Mater. Sci.*, **4**, 779 (1969).
13. I. L. Shul'pina, L. V. Lainer, M. G. Mil'vidskii, and E. P. Rashevskaya, *Sov. Phys.-Solid State*, **9**, 1291 (1967).
14. A. J. R. deKock and P. G. T. Booren, *J. Appl. Phys.*, **44**, 2816 (1973).
15. V. V. Batavin, *Sov. Phys.-Cryst.*, **15**, 100 (1970).
16. K. V. Ravi and C. J. Varker, *J. Appl. Phys.*, **45**, 263 (1974).
17. J. Matsui and T. Kawamura, *Japan. J. Appl. Phys.*, **11**, 197 (1972).
18. R. W. Bicknell, *Phys. Status Solidi*, **7**, K1 (1971).
19. P. B. Hirsch, A. Howie, R. B. Nicholson, D. W. Pashley, and M. J. Whelan, "Electron Microscopy of Thin Crystals," Butterworths, London (1965).
20. A. J. Baker, P. M. Kelly, and J. Nutting, "Electron Microscopy and Strengths of Crystals," G. Thomas and J. Washburne, Editors, p. 899, Interscience Publishers, Inc., New York (1963).
21. E. W. Hart, *Acta Met.*, **6**, 553 (1958).
22. J. D. Embury and R. B. Nicholson, *ibid.*, **13**, 403 (1965).
23. A. J. R. deKock, *Appl. Phys. Letters*, **16**, 100 (1970).
24. I. R. Sanders and P. S. Dobson, *Phil. Mag.*, **20**, 881 (1969).
25. G. R. Booker and R. Stickler, *ibid.*, **11**, 1303 (1965).
26. R. E. Smallman and K. W. Westmacott, *Mater. Sci. Eng.*, **9**, 249 (1972).
27. K. V. Ravi, To be published.

## Vickers Microhardness Characterization of Sintered Borosilicate Films

M. N. Turetzky\* and J. B. Jenkins

IBM System Products Division, East Fishkill Facility, Hopewell Junction, New York 12533

and H. R. Fraser, Jr.

GPD, Boulder, Colorado 80302

The publication costs of this article have been assisted by the IBM Corporation.

### ABSTRACT

The application of Vickers microhardness to glass surfaces has been reviewed, and despite differences of opinion as to its theoretical significance, it is judged useful for engineering applications. The technique has been applied to the study of sintered films of borosilicate glass on alumina substrates. The range of glaze thickness and load magnitude for which the hardness remains unchanged is defined. The effect of the degree of sintering (i.e., extent of densification), degree of phase separation, and aging of the HF etched surface on the microhardness have been measured. Hardness can also be used to detect surface stress which occurs in the region of glass-metal interfaces.

A characterization technique is desired to determine the effects of many processes and treatments on the nature of 1-5 mil thick glazed surfaces. The technique should be essentially nondestructive, able to be performed rapidly, and not be affected by inhomogeneities of the glass surface. Two alternatives for glass surface characterization are as follows:

(i) Infrared transmission spectroscopy yields considerable information about the composition of glass

films (1). Although informative, it is limited to films generally below  $\frac{1}{2}$  mil in thickness and is an averaging technique over the area of the incident beam. In addition, transmission techniques generally yield information about bulk rather than surface characteristics.

(ii) Etching and corrosion studies also yield considerable information about glass composition (2, 3). Selective etching is also useful for determining strain and density in deposited  $\text{SiO}_2$  films (4). Its destructive character is the main disadvantage of etching. Since

\* Electrochemical Society Active Member.

Key words: glass films, Vickers hardness, sintering, glass-metal stress.

there is a wide variety of glass compositions, a corresponding variety of etchants is also needed.

### Microhardness—Definition

For our purposes, we defined the hardness of a material as the resistance it offers to indentation by a much harder body. In practice, it is assumed that the indenter is so hard that it does not undergo any deformation. The hardness of the material under study is measured as the ratio of the load to the area of the permanent depression produced by that load. Hardness is therefore presented in units of pressure, most commonly kilograms per square millimeter. A very small square pyramidal diamond with  $136^\circ$  apex angle was used as the indenter in our experiments.

For 25-100g loads on hard glasses, the base diagonal of the indentation is only  $8-16\mu$  long and  $1-2\mu$  deep so the term "microhardness" is accurate. The small size of this indent makes it likely that it will be placed in a flawless area on most glass samples. For example, Ernsberger (5) has shown that in average plate glass there are about 10,000 flaws/cm<sup>2</sup>, or an average of only one per  $10^4 \mu^2$ . One should be cautioned that while it is unlikely that an indent will fall on a glass flaw, the stress fields of flaws may be close enough to interact and give some value for the hardness below the ultimate hardness of the glass, due to the high magnitude of the stress fields around the flaws according to Shand (6) and Marsh (7).

**History.**—One of the earliest applications of hardness measurements to glass was performed by Taylor (8), but the first comprehensive study was by Ainsworth (9-11). Ainsworth established the useful range of the operating parameters in the actual indenting process, contact duration of the diamond with the glass surface, and the independence of hardness and applied load. Ainsworth also demonstrated that the general Meyer equation,  $P = aD^n$ , where  $a$  and  $n$  are constants, held for diamond indentation on glass and that  $a = 1$  and  $n = 2$  within a load range of 10-140g.

Ainsworth also succeeded in showing many relationships between changes in hardness and other known properties of glass. For example, Poole (12) reported on the viscosity composition dependence of  $K_2O-SiO_2$  glasses; he noticed an inflection in the 19 and 22%  $K_2O$  regions. Ainsworth's hardness *vs.* composition data shows inflections in the same composition region. Several other investigators have clearly demonstrated the correlation of microhardness with other properties of glass [e.g., Douglas (13), Westbrook (14), Frischat (15), and Izumitani (16)].

More recent work by Prod'homme (17) takes issue with Ainsworth's contention that hardness is load independent. Some of the difference is due to the fact that Prod'homme made measurements up to a 300g load, much higher than those of other workers in the field. At this high stress, glass cracking can often be observed, as it was by us; it introduces a large variation in hardness measurements.

Prod'homme extended the hardness measurements to many soft glasses such as the selenides and antimonides, where Vickers hardness is only 10-25% of that of silica. By doing this, he was able to show a relationship between viscosity and hardness over a 25-fold range of microhardness.

The ease and precision of microhardness measurements have led to several attempts to find a basic mechanism for the formation of the indent in glass. However, there is no agreement on the physical meaning of Vickers hardness of glass. Ernsberger (18) maintains that hardness can best be interpreted through densification, while Marsh (7) claims a relationship between hardness and the elastic limit of glass. Regardless of the final resolution of this dispute there is a clearly established correlation between diamond hardness and observed strength of glasses (19).

### Sample Preparation

Our studies were restricted to a commercially available borosilicate glass.<sup>1</sup> The samples were prepared in the following manner. (i) A slurry consisting of ball-milled glass in terpineol was deposited by spraying on 99% alumina substrates; (ii) after an initial drying cycle the samples were sintered at  $810^\circ C$  during a 45 min heating and cooling cycle in a controlled atmosphere, three-stage sintering furnace; (iii) in some cases after sintering, the glass surface was lapped flat and fire polished by passing through the furnace again.

### Experimental Technique

It is extremely important to note that hardness data is only meaningful in a statistical sense. Thus, our technique was designed to minimize operator-dependent errors. A Miniload<sup>2</sup> hardness tester equipped with a Vickers diamond was used to perform these characterizations. The method consists essentially of bringing the diamond into contact with the test surface under controlled conditions with a known load and measuring the diagonal length of the resultant impression.

The diagonal length of the indent was measured with an eyepiece micrometer. The index line is first set at zero on the micrometer scale, scanned across the indent, and read only after final adjustment. In this equipment, the micrometer scale is not superimposed on the indent but is read at the bottom edge of the field of view. The operator can make successive measurements, uninfluenced by knowledge of previous diagonal lengths. Measurements were never made for periods exceeding 2 hr to avoid operator fatigue.

For the  $136^\circ$  square pyramidal diamond used the hardness can be calculated from  $V_H = 1854 P/d^2$ . When  $P$  is in grams and  $d$  is in microns, the hardness units are in kilograms per square millimeter.

To test our technique a standard steel test block was measured. Table I shows these calibration results. Four groups of ten indentations were made in the test sample. To determine the best load application range, a series of measurements was made on borosilicate glass films on alumina substrates. These results are shown in Table II and are derived from four groups of five measurements at each of the indicated loads. In our case, the glass seemed to crack at load values above 100g.

The difference between the two standard deviations given in Table II for any sample and load is due to

<sup>1</sup> 7070 Glass, Corning Glass Works, Corning, New York.  
<sup>2</sup> Registered trademark of The Leitz Corporation.

Table I. Vickers hardness (kg/mm<sup>2</sup>) calibration studies on steel test block

	15g Load	100g Load
$V_H$	579	568
$\sigma^{(a)}$	8.95	5.60
$\sigma^{(b)}$	9.52	5.30
Mfg.'s values	581	564

(a) Average standard deviation within each group of ten measurements.

(b) Standard deviation for all measurements at indicated load.

Table II. Effect of load on borosilicate glass hardness

Load, g	Sample 1			Sample 2		
	$V_H$	$\sigma^{(a)}$	$\sigma^{(b)}$	$V_H$	$\sigma^{(a)}$	$\sigma^{(b)}$
25	720	13.4	26.0	735	18.1	22.1
50	728	12.7	17.6	727	12.6	15.5
100	733	9.2	13.0	723	8.3	14.9
200	755	6.1	11.0	743	9.0	13.4

(a) Average standard deviation for four sets of five observations each.

(b) Standard deviation for all measurements at indicated load.



Table III. Effect of sintering temperatures

Firing temperatures (°C)	Just fired				Fired, lapped, and refired			
	Set 1		Set 2		Set 1		Set 2	
	V <sub>H</sub>	$\sigma$	V <sub>H</sub>	$\sigma$	V <sub>H</sub>	$\sigma$	V <sub>H</sub>	$\sigma$
770	—	—	584.9	17.50	628.1	13.09	618.9	11.32
780	—	—	—	—	653.9	12.43	—	—
790	—	—	636.1	14.71	705.6	16.53	665.0	8.30
810	—	—	710.5	14.40	730.3	10.79	723.8	9.25
830	—	—	712.4	13.70	—	—	730.3	10.79
850	—	—	717.5	16.69	742.4	14.05	753.8	10.46

two effects. One is caused by the difficulty of accurately measuring the dimensions of the indent; this is more prominent in the case of the lower loads which produce small indents in this hard glass. The second effect is due to significant differences in hardness between the very edges of a glaze film and the bulk of the surface. These two effects were reduced in subsequent experiments by making all hardness measurements at a 100g load in a relatively central area of the part.

Variations in hardness due to slurry batch-to-batch variations, origins of powder used to make the slurry, and spraying vs. doctor-blading application techniques were also studied. No statistically significant hardness variations were detected. Hardness was also found to be independent of glaze thickness in the 15-125 $\mu$  range. However, thin glazes displayed an increased tendency to crack around the indent.

**Sintering process effects on hardness.**—In some initial experiments it was observed that fired sample hardness was lower than that of samples which had been fired, lapped, and refired. This variation suggested that the singly fired parts were not fully sintered. Consequently, an experiment was conducted where a series of parts was sintered at various temperatures with the hardness measured after firing and then again after being lapped and refired. Table III lists these results and Fig. 1 displays them graphically. Each entry in Table III represents at least two samples with seven measurements per sample. In a separate experiment the role of controlled lapping on the measured hardness of refired parts was investigated and found to be without effect.

Table III shows distinct time and temperature correlation, since refired parts had higher hardness at the same firing temperature than once-fired parts. This indicates more complete sintering and more densification. The shape of the curves also reveals that even the once-fired parts were essentially sintered at temperatures above 810°C, and no further densification was to be expected. Below 810°C the linear curve shows gradual pore elimination. Note that because of the time and temperature phenomena, the refired parts appear to be completely sintered at a lower temperature. This hardness measurement technique can clearly allow monitoring of processes dependent on sintering or densification. An additional experiment described in the section on aging effects shows that repeated firings at 810°C caused no further densification.

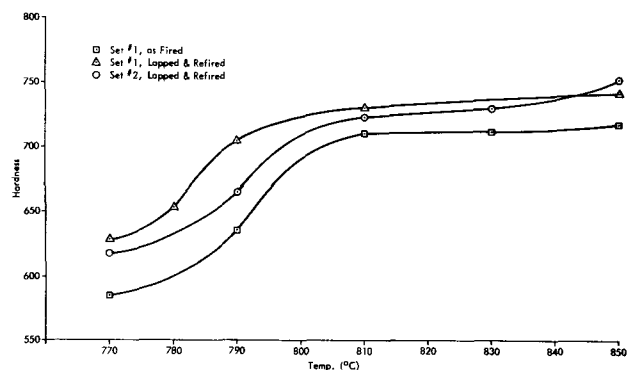


Fig. 1. Effect of firing temperature on hardness of borosilicate glass

**Phase separation role.**—Under the proper conditions, borosilicate glass tends to phase separate by two different mechanisms (20): spinodal and nucleation and growth into boron oxide and silica-rich phases. These phases may be fairly large in area, sometimes as much as 1-2 mil in diameter (21).

Since these two phases can differ markedly in hardness, measuring this characteristic should be useful for determining the extent of phase separation. Accordingly, five samples were prepared. Two were held for 24 hr at 750°C, two for 48 hr at 650°C, and the last was a control. From earlier work, it was expected that the control would be slightly phase separated and that the heat-treated samples would be extensively separated. Twenty-five hardness measurements were made on each sample and are shown as histograms in Fig. 2-6.

Figure 6, the control sample histogram, displays essentially a normal curve shape, implying a homogeneous surface with only measurement errors. On the other hand, Fig. 2-5 show a wide dispersion of hardness.

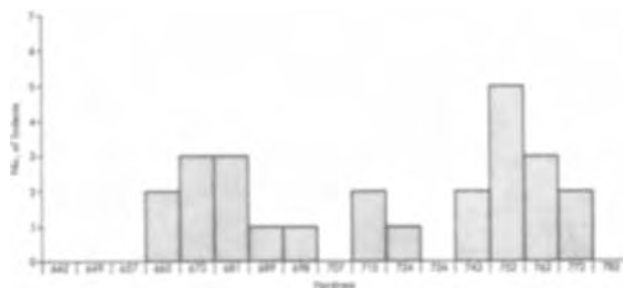


Fig. 2. Hardness distribution: 48 hr at 650°C (sample 1)

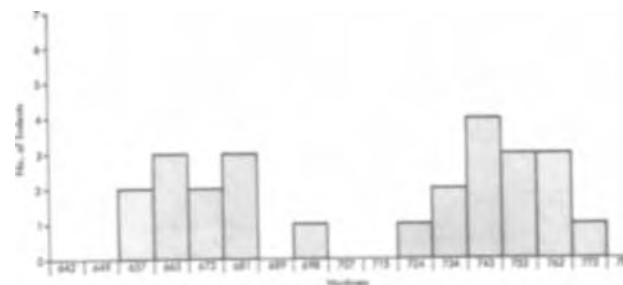


Fig. 3. Hardness distribution: 48 hr at 650°C (sample 2)

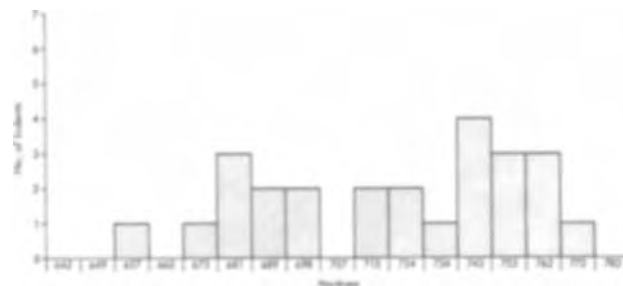


Fig. 4. Hardness distribution: 24 hr at 750°C (sample 1)

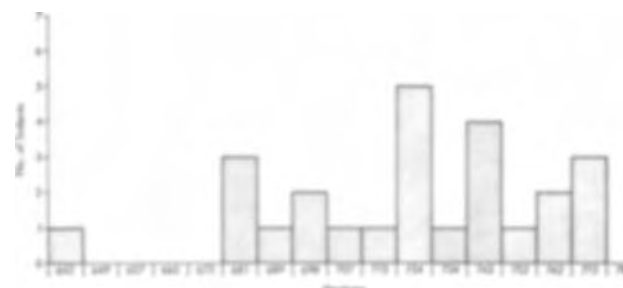


Fig. 5. Hardness distribution: 24 hr at 750°C (sample 2)

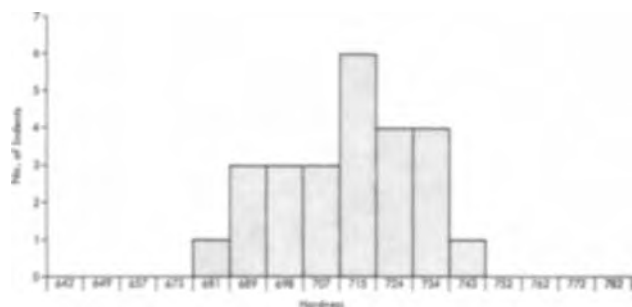


Fig. 6. Hardness distribution (control)

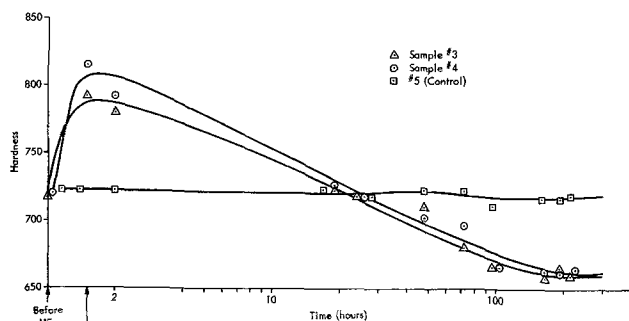


Fig. 7. Decay of hardness after HF etching

The higher values are thought to correspond to the indenter placement, primarily in a silica-rich phase, and the lower values to a boron oxide rich phase. The diamond pyramid hardness can be used to determine the extent of phase separation as long as the dimensions of the heterogeneous regions are of the same magnitude as the diamond impression. Despite this restriction, Vickers hardness measurements can be used to detect many types of surface inhomogeneities.

**Glass surface stability.**—The following experiments addressed some of the questions one might pose concerning the stability of a processed glass surface. The first experiment, as previously mentioned, examined whether repetitive firing at the critical temperature of 810°C caused the hardness to change. After eleven refrings there was no change in hardness or standard deviation. The second experiment examined surface hardness after HF<sup>3</sup> etching of the surface. Two parts were treated with HF and the third part was used as a control on the experiment. Table IV lists the hardness and standard deviation of these parts before and after treatment and until 9 days after treatment. Figure 7 shows these hardness values as a function of time. One additional part was HF etched, and immediately after etching was placed in an oven for 1 hr at 150°C. The hardness of this sample at all critical times is given in Table V.

A similar decay was observed in strength measurements on etched soda-lime glass by Ray and Stacy (22).

<sup>3</sup> One part 49% HF, seven parts DI water.

Table IV. Borosilicate aging after HF etching

Time after HF etching	V <sub>H</sub> /σ		
	No. 3	No. 4	No. 5 (control)
Before	717.0/11.31	720.8/10.23	722.4/7.89
Immediately after	792.6/24.31	815.4/13.92	722.8/11.86
1 hr after	788.2/15.56	782.2/18.98	722.8/11.86
2 hr after	780.0/16.43	792.4/12.66	722.4/7.89
19 hr after	722.8/17.40	726.4/13.43	724.4/9.50
24 hr after	719.2/17.40	717.2/17.14	718.8/7.66
2 days after	711.8/9.78	703.2/9.96	724.6/14.40
3 days after	681.4/15.77	692.8/9.96	722.4/7.89
4 days after	668.2/12.13	666.8/14.97	711.8/9.78
7 days after	658.8/17.09	662.0/16.28	717.0/7.18
8 days after	666.6/11.87	662.0/13.00	717.0/7.18
9 days after	660.4/14.21	665.0/14.97	719.0/10.32

Table V. Heating after HF etching

Time	V <sub>H</sub> /σ
Before HF etch	720.6/8.44
Immediately after etching	800.6/13.54
After 1 hr at 150°C	665.3/16.82
1 hr after cooling	670.0/16.16
1 day after HF cleaning	666.6/14.21

This decay is hypothesized to occur according to the following mechanism. Borosilicate glasses show a characteristic rise in hardness following HF surface etching, which is most likely due to rounding of flaw tips and the subsequent reduction of interaction of those flaw tips and the indenter's stress field.

The presence of phase separation permits substantially faster etching of the boron oxide rich phase than the silicon oxide rich phase. This selective etching increases the surface area. Contained on this surface area are an increasing number of phase boundaries which are probable sites for the initiation of new flaws. Another consequence of the increased surface area would be the opportunity for a higher flaw density and ultimately a hardness lower than the original hardness. Since the rate of flaw formation is expected to increase at higher temperatures, the rapid attainment of equilibrium hardness by heating is understandable.

Our final experiment examined the possibility of determining the amount of stress existing at a point on the glass surface. For this purpose, 700-800Å chromium films were vacuum evaporated on borosilicate glass surfaces heated to between 100°-250°C. These films were subsequently etched by conventional photolithographic processing into strips ¼ in. wide and a few inches long. The thought was to provide a highly stressed surface near the chrome strips to determine if this stress affected hardness. It was expected that the different substrate temperatures during evaporation would produce different stress values in the chrome. Hardness measurements were taken in five spots on and around the lines. The five spots measured were: 1, in the middle of the chrome lines; 2, at the edge of the line but on it; 3, half on the chrome and half on the glass; 4, on the glass at the edge of the line; and 5, approximately 1.0 mil away from the line in the glass. Figure 8 shows the location of the indentations. Five measurements were made for each site on each sample. Table VI lists the hardness results for each sample at each of the locations. The films had to be very thin to measure the hardness immediately adjacent to them because the very gradual slope on the diamond face would impinge upon a thick film. The hardness is quite low adjacent to the strips (positions 3 and 4); a small distance from the strip the hardness again returns to its normal value. This observation is consistent with the work of Carlson (26) on bonded laminates, from which we can infer that the residual stresses in the glass are largest near the edges of the metal film. As mentioned earlier, the indenter hardness is expected to decrease when mea-

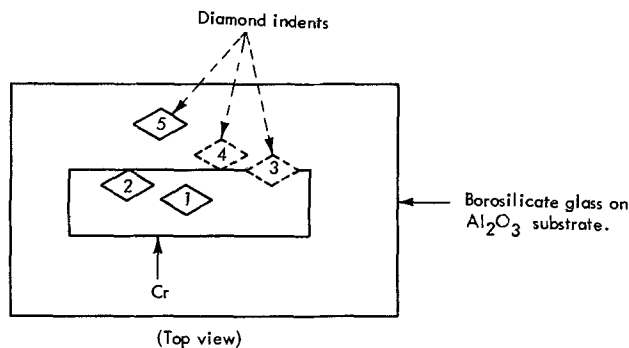


Fig. 8. Location of indentations around Cr strip



Table VI. Hardness near highly stressed chrome strips

Position (Fig. 8)	$V_H$	$\sigma$	Substrate temperature (°C)
1	728.0	17.14	100
2	714.0	11.24	
3	685.8	17.34	
4	657.2	14.70	
5	718.8	7.66	
1	724.2	6.72	150
2	703.0	11.55	
3	673.0	11.31	
4	666.6	13.15	
5	722.9	7.89	
1	722.4	7.89	250
2	710.2	13.12	
3	674.6	13.15	
4	688.4	16.18	
5	720.8	10.23	

sured in the immediate region of an existing stress field. These results tend to make us agree with Marsh (7) that the hardness measures some yield stress such as the maximum shear stress or the maximum principal stress. Thus, this tool seems to offer substantial promise as a qualitative microstress measuring device. To offer a quantitative tool, further refinements must be made experimentally and mathematically.

### Conclusions

Vickers microhardness can be used to characterize many changes in a glass surface. Unfortunately, the hardness data cannot be reduced to indicate specific physical effects. Microhardness is especially valuable for studying surface inhomogeneities, surface stress, and surface density variations, e.g., incompletely sintered glass surfaces.

Vickers microhardness has several technical advantages over standard measurements. These measurements can generally be made on actual parts rather than on special samples only. Hardness measurements can be made rapidly and are nearly nondestructive, since only a very small surface area is affected. Furthermore, microhardness is an especially valuable tool for glass surfaces because the ensuing measurements are usually flaw independent. Vickers microhardness measurements do have some limitations which should be restated: they are extremely operator dependent and are restricted to specularly reflecting surfaces.

Manuscript submitted May 14, 1973; revised manuscript received Feb. 1, 1974. This was Paper 13 pre-

sented at the Chicago, Illinois, Meeting of the Society, May 13-18, 1973.

Any discussion of this paper will appear in a Discussion Section to be published in the June 1975 JOURNAL. All discussions for the June 1975 Discussion Section should be submitted by Feb. 1, 1975.

### REFERENCES

1. W. A. Pliskin, D. R. Kerr, and J. A. Perri, "Physics of Thin Films," Vol. 4, p. 257, Academic Press, New York (1967).
2. F. R. Bacon, *Glass Ind.*, **49**, 554 (1968).
3. W. A. Pliskin, in "Measurement Techniques for Thin Films," B. Schwartz and N. Schwartz, Editors, p. 280, The Electrochemical Society Soft-bound Symposium Series, New York (1967).
4. W. A. Pliskin and H. S. Lehman, *This Journal*, **112**, 1013 (1965).
5. F. M. Ernsberger, "Advances in Glass Technology, VI International Congress on Glass," pp. 511-524, Plenum Press, New York (1962).
6. E. B. Shand, "Glass Engineering Handbook," 2nd ed., p. 47, McGraw-Hill Book Co., New York (1958).
7. D. M. Marsh, "Fracture of Solids," D. C. Drucker and J. J. Gilman, Editors, p. 143-155, Gordon and Breach, Science Publishers, Inc., New York (1963).
8. E. W. Taylor, *J. Soc. Glass Technol.*, **34**, 69T (1950).
9. L. Ainsworth, *ibid.*, **38**, 480T (1954).
10. L. Ainsworth, *ibid.*, **38**, 501T (1954).
11. L. Ainsworth, *ibid.*, **38**, 536T (1954).
12. Cited by Ainsworth, p. 515, Ref. (10).
13. R. W. Douglas, *J. Soc. Glass Technol.*, **42**, 45 (1958).
14. J. H. Westbrook, *Phys. Chem. Glasses*, **1**, 32 (1960).
15. G. H. Frischat, *J. Non-Crystalline Solids*, **3**, 407 (1970).
16. T. Izumitani, *J. Soc. Glass Technol.*, **14**, 35 (1973).
17. M. Prod'homme, *Phys. Chem. Glasses*, **9**, 101 (1958).
18. F. M. Ernsberger, Eighth International Conference on Glass, p. 123, Society of Glass Technology, London (1969).
19. W. B. Hillig, in *Advances in Materials Research*, H. Herman, Editor Vol. 2, pp. 383-411, Interscience Publishers, New York (1968).
20. O. V. Mazurin, M. V. Streltsina, and A. S. Totesh, *Phys. Chem. Glasses*, **10**, 63 (1969).
21. B. S. R. Sastry and F. A. Hummel, *J. Am. Ceram. Soc.*, **43**, 23 (1960) (especially see p. 29).
22. N. H. Ray and M. H. Stacey, *J. Mater. Sci.*, **4**, 73 (1969).
23. J. A. Carlson and L. P. Sapetta, *Adhesives Age*, **8**, 26 (1967).

# A New Method for Chemical Vapor Deposition of Silicon Dioxide

Y. Avigal, I. Beinglass, and M. Schieber<sup>\*1</sup>

School of Applied Science and Technology, Hebrew University of Jerusalem, Jerusalem, Israel

## ABSTRACT

A new method for the deposition of SiO<sub>2</sub> films prepared by the oxidation of alkyl-silane vapors is reported. It is found that the oxidation of tripropylsilane (C<sub>3</sub>H<sub>7</sub>)<sub>3</sub>SiH in oxygen at a temperature of about 650°C yields transparent adhesive and uniform films of SiO<sub>2</sub> grown on silicon substrates. The growth rate of the films as a function of various growth parameters is studied. The films have been characterized using IR absorption, spark source mass spectrometry, and emission spectroscopy. The structure of the films has been studied by optical microscopy and scanning electron microscopy and the index of refraction by ellipsometry. The applicability of these films to the planar MOS technology in microelectronics is evaluated by the following properties: etch rate, masking efficiency, flatband voltage, and electrical stability. Finally, the characteristics of MOS field effect transistors built with these oxides are given and shown to be almost comparable to those built with thermally grown SiO<sub>2</sub>.

Dielectric films of SiO<sub>2</sub> for MOS application are usually prepared by thermal oxidation which is performed at temperatures between 900° and 1200°C. The thermally grown films are used as a selective masking (1) and as a gate (2) oxide. The disadvantage of the thermally grown oxide is a relative high temperature of formation which can cause a shift of the p-n junction boundaries during the oxidation. Films of SiO<sub>2</sub> produced by the decomposition of ethyl-silanes such as tetraethoxysilane, TEOS (3), have a high porosity and high etch rates, a tendency to cracking and a high load of carbon contamination. Therefore, they cannot be used as gate dielectric films. Thin films of SiO<sub>2</sub> produced by the method of oxidation of silane (4) have a low temperature of deposition but cannot be used as gate oxide unless an extra step of annealing at high temperature is added (11). This is due to the high flatband voltage and the low electrical stability of the MOS devices produced with these unannealed films.

We have been interested in studying the possibility of growing SiO<sub>2</sub> films at a relatively low temperature of deposition. The grown films should be used as gate oxides and selective masks against doping. The proposed growth method is that of chemical vapor deposition. CVD of SiO<sub>2</sub> films obtained by the oxidation of alkyl-silicon compounds. We have proved the compatibility of SiO<sub>2</sub> films produced by this method at temperatures as low as 700°C for the various uses of SiO<sub>2</sub> films in microelectronics.

## Experimental Procedure

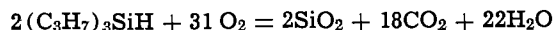
The films were deposited in an apparatus shown in Fig. 1. The source material for silicon was liquid tripropylsilane, TPS (K and K Laboratories, Incorporated) which was kept at a temperature of 30°C. The vapors of TPS were carried by a flow of N<sub>2</sub> and O<sub>2</sub> and deposited on a substrate of (100) n- or p-type Si with a resistivity of 10 ohm-cm. The Si substrate wafer is first brought to the desired temperature at a flow of 1800 cc/min pure N<sub>2</sub> in a resistance furnace. A total flow of 400-1410 cc/min O<sub>2</sub> is then introduced in the reactor and a part of the N<sub>2</sub> + O<sub>2</sub> mixture up to 240 cc/min is then passed over the TPS source material for 5-20 min. The coated SiO<sub>2</sub> wafers are then removed and the thickness measured with a Tolansky interferometer.

\* Electrochemical Society Active Member.

<sup>1</sup> Present address: EG&G, Nuclear Science & Instrumentation Laboratories, Goleta, California 93017.

Key words: thin films, SiO<sub>2</sub> films, MOS-FET devices, chemical vapor deposition, organometallic derivatives of silicon.

The reaction of deposition of SiO<sub>2</sub> in the case of complete oxidation of TPS can be written as



In fact the oxidation is not complete, as can be detected qualitatively by the smell of various organic by-products.

Figure 2 shows the variation of the rate of deposition of SiO<sub>2</sub> as a function of the substrate tempera-

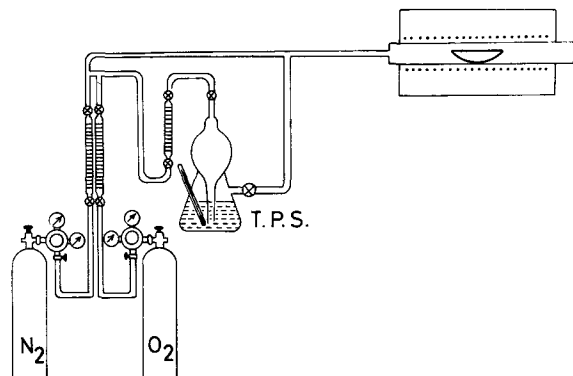


Fig. 1. Experimental setup

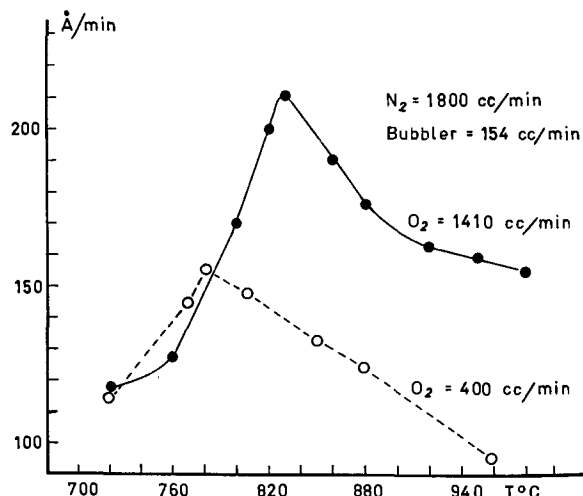


Fig. 2. The temperature variation of the rate of deposition of SiO<sub>2</sub> films on Si by oxidation of tripropylsilane (TPS).

ture, at a constant flow rate of the gas mixture through the TPS bubbler. The oxygen flow was 400 cc/min and 1410 cc/min.

Figure 3 shows the variation of  $R$  with the flow rate through the TPS at a constant substrate temperature of 770°C, a flow rate of 1000 cc/min of  $N_2$ , and at a flow rate of 925 and 1410 cc/min of  $O_2$  respectively.

Both in Fig. 2 and Fig. 3  $R$  goes through a maximum which has a different location for different oxygen on over-all flow rates. We believe that both maxima are due to variation in the distribution of the amount of deposit along the reaction tube. This distribution was inspected and found to go through a maximum.

Differences in the  $O_2$  flow rates do not seem to affect the rate of deposition *per se* but rather through its effect on the over-all flow rate, meaning, we believe, that even in the case of 400 cc/min  $O_2$ , there was an excess of  $O_2$  to allow for complete oxidation of the TPS. All three deposition parameters, i.e., temperature, over-all flow rate, and TPS concentration in the gas phase, affect the distribution of deposit along the tube. An increase in the temperature causes a higher temperature gradient in the entering gases with the result of a shift in maximum of the deposit distribution toward the inlet of the reaction tube. An increase of the flow rate causes a lower drift of the  $SiO_2$  clusters along the gas stream which also causes a shift in the maximum of deposit distribution towards the outlet of the reaction tube. An increase in the TPS concentration in the gas phase causes a higher rate of nucleation and aggregation of the  $SiO_2$ , which shifts the maximum in the deposit distribution towards the inlet of the tube.

One can conclude that for a constant location of the substrates in the reaction tube, the deposition rate across it would go through a maximum when the combination of all three parameters would locate the maximum in the deposit distribution right above the substrate.

### Characterization of the Grown Films

The TPS oxidized films have been analyzed by emission spectrography. Table I summarizes the experimental results. The only major impurities (noting the net impurities concentration) are B, Al, and Ca

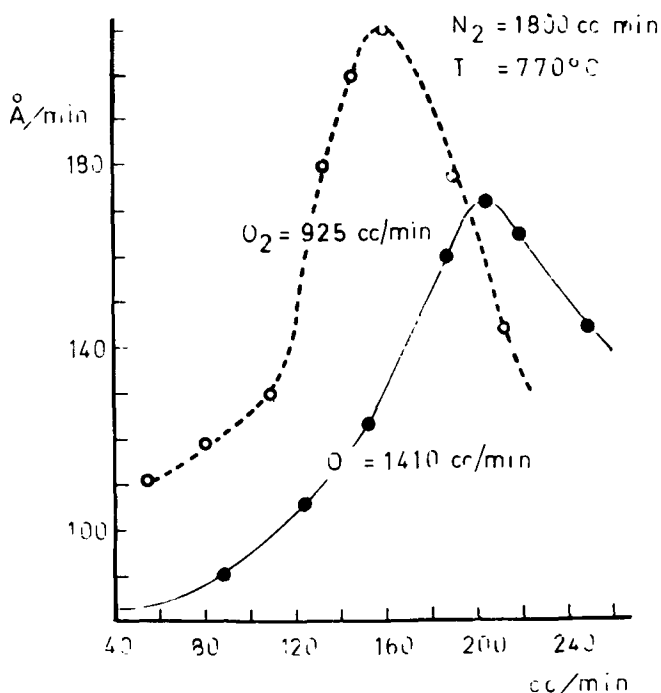


Fig. 3. The variation of the rate of deposition of  $SiO_2$  films on Si by oxidation of TPS as a function of the molar fraction of TPS in the gas phase.

Table I. Emission spectrographic analysis (in ppm) of thin films of  $SiO_2$  on Si substrate produced by the oxidation of TPS

	Blank	TPS	Net impurities in TPS
B	30-300	150-1500	120-1200
Si	6-60	30-300	23-240
Mg	5-50	30-300	25-250
Pb	30-300	20-200	—
Fe	0.6-6	10-100	10-94
Al	2-20	100-1000	100-1000
Ca	30-300	150-1500	120-1200
Tl	—	10-100	10-100
Cu	0.3-3	3-30	3-30
Na	30-300	30-300	—

which originate from the commercially available source material. No attempts have been made to purify the raw material. The procedure of the preparation of the sample on electrodes is solution of the  $SiO_2$  film by hydrofluoric acid (at this step the Si forms gases) damping the electrode in the solution and drying the electrode.

The carbon contamination of the  $SiO_2$  films has been analyzed by spark source mass spectrometry. The total amount of carbon detected in our films is below 5 ppm. The very low carbon contamination in our films relative to the higher concentration in the TEOS grown films can be explained by the much higher oxygen concentration in our system which allows for a more efficient oxidation of the organic carbon.

The microstructure of the grown films has been analyzed by scanning electron microscopy. It has been found to be an island-type growth, the diameter of which first increases with the increasing temperature of deposition, and then decreases, as shown in Fig. 4B. It is interesting to note that with each temperature, there is a variation in the island diameter which corresponds to the temperature variation in the rate of growth, and even the shape of the respective curves is also similar, as can be seen by comparing Fig. 4B and 2. The thickness of these islands must be lower than their radius (which is 700-1000Å at most), otherwise the metallic layer in some of the built capacitors would come in contact with the substrate between those islands with the result of a short circuit. Such a behavior was not found.

The index of refraction of the  $SiO_2$  films has been measured by ellipsometry. It has been found that the TPS oxidized films have a high index of refraction, 1.46-1.48 which is similar to that of the thermal oxide (5), or to the densified silane oxidized films (4) as can be seen in Table II which lists the index of refraction of  $SiO_2$  films, grown by different methods.

The infrared spectrum of the  $SiO_2$  films deposited at 750°C is shown in Fig. 5. It can be seen that there is no shift in the absorption band on annealing the deposit at 850°C.

The etch rate of the TPS oxidized  $SiO_2$  films has been determined in both P etch (15:10:300 HF:HNO<sub>3</sub>):

Table II. Refraction index  $n$ , etch rate (ER) in Å/sec in P etch and buffered HF, and the dielectric constant  $E$ , for  $SiO_2$  films produced by different methods

Film source	Refractive index, $n$	Etch rate, Å/sec		Dielectric constant, $E$
		P etch	Buffered etch	
TPS oxidation	1.46-1.48	2.5	16-18.5	4.5-5.0 (1MH)
Silane oxidation	1.43-1.46 (4)		81-87 (4)	4.30-5.73 (1KH)
Silane oxidation plus densification	1.46-1.49 (4)		18-21.3 (4)	
Pyrolytic decomposition	1.43 (6)	6-20 (6)		
Pyrolytic decomposition plus densification	1.45-1.46 (6)	2-2.9 (6)		
Thermal oxidation (steam)	1.475 (5)	2	18.1	3.83 (1KH)

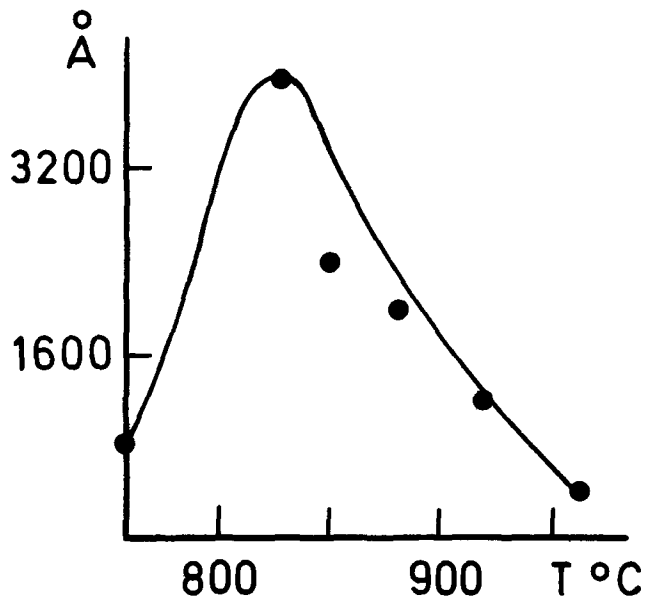
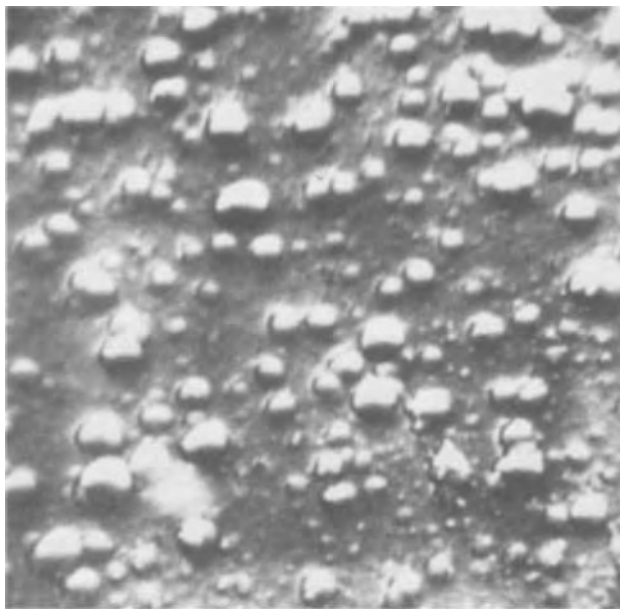


Fig. 4. The variation of the size of the growth islets of SiO<sub>2</sub> films as a function of the deposition temperature. (A, left) Scanning electron micrograph at 45° incidence and × 13,000 as a function of temperature. (B, right) Diameter in angstroms as a function of temperature.

H<sub>2</sub>O) and buffered etch (454g NH<sub>4</sub>F, 654g H<sub>2</sub>O, 163 cc HF) and is listed in Table II. It can be seen that the TPS oxidized films have a low etch rate comparable to that of the thermal (6) or the densified silane oxidized films (4).

The masking efficiency of the SiO<sub>2</sub> films has been determined by measuring the diffusion of boron through TPS oxidized and thermally grown films, deposited on 1 ohm-cm n-type (100) silicon wafers. The source of boron used for diffusion has been BN wafers which are first oxidized at 900°C to form B<sub>2</sub>O<sub>3</sub> (7). The oxidized BN wafers have been used to predeposit boron at 1150°C for 15 min in argon, followed by a drive-in process for 210 min at 1150°C. The SiO<sub>2</sub> films were

removed after the completion of the diffusion process and the depth of p-n junction, X<sub>j</sub>, was measured by the "lapping and staining" method (8), as a function of the thickness of the films, X<sub>o</sub>. There is a linear dependence of X<sub>j</sub> vs. X<sub>o</sub> as predicted by the "two boundaries" model of diffusion (9) as shown in Fig. 6, for both thermal films grown in (wet O<sub>2</sub>) at 1100°C and the oxidized TPS films deposited at 780°C. The slope of the line, r, is related to the diffusion constants of the boron in the SiO<sub>2</sub> film D<sub>1</sub> and in the silicon, D<sub>2</sub>. The constant D<sub>1</sub> is determined by knowing r and D<sub>2</sub>. Our shape of the graph of X<sub>j</sub> vs. X<sub>o</sub> is similar to that of Anand *et al.* (10). It can be seen that the D<sub>1</sub> values of the oxidized TPS films are similar to those of the thermally grown films.

The dielectric constants have been measured using a Boonton capacitance bridge. The results are summarized in Table II. The capacitance-voltage, C-V, curves of MOS capacitors produced by the oxidized TPS films, as deposited at 800°C has been measured and proved to have a high flatband voltage, V<sub>fb</sub> of about 15V.

After annealing at 800°C for 30 min in N<sub>2</sub> the V<sub>fb</sub> is reduced to -3V as shown in Fig. 7. The bias temperature, BT, stability test of the C-V curves measured at a field of ±1.5 × 10<sup>6</sup> V/cm, and a temperature of

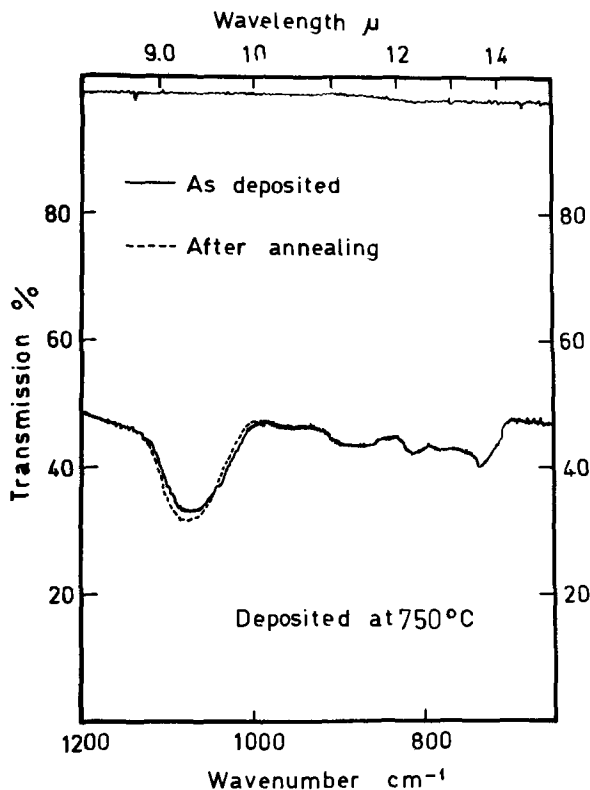


Fig. 5. Infrared spectra of the SiO<sub>2</sub> films as grown at 750°C before and after annealing at 850°C.

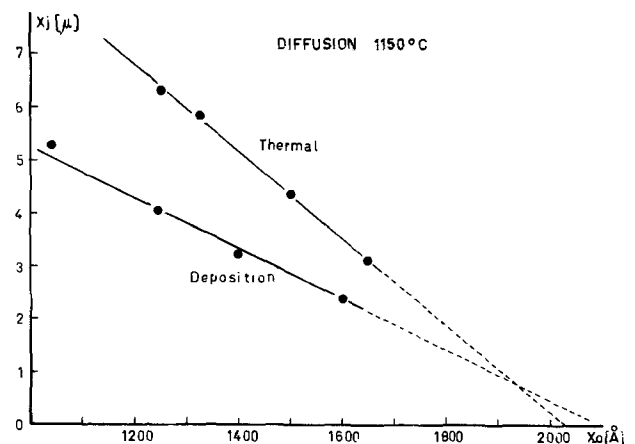


Fig. 6. Masking efficiency of the SiO<sub>2</sub> films against diffusion of boron at 1150°C for 210 min expressed in terms of X<sub>o</sub> = thickness of the films (Å) as a function of X<sub>j</sub> = depth of the p-n junction.

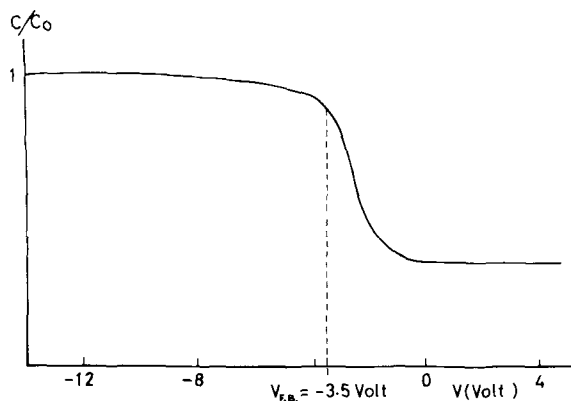


Fig. 7. Capacitance vs. voltage of the SiO<sub>2</sub> films after annealing at 800°C showing a flatband voltage of -3V.

250°C for 30 min have shifted the  $V_{fb}$  by less than 0.5V, which shows that MOS capacitors produced with the oxidized TPS films have a high electrical stability, and can be used as a gate oxide for MOS applications.

An MOS field effect transistor has been built using the oxidized TPS films of 1000Å thickness as the gate oxide. Figure 8 shows the current-voltage characteristics of the FET before and after annealing in N<sub>2</sub> for 30 min at 850°C. It can be seen that the amplification increases from 300 to 2000, for unannealed and annealed oxidized TPS films, respectively. Figure 9 shows the threshold voltage of the MOS FET produced with a gate oxide of oxidized TOS SiO<sub>2</sub> film as deposited and after annealing in N<sub>2</sub> for 850°C. It can be seen that the threshold voltage decreases with annealing from 16 to 2.97V respectively.

Table III. The diffusion constants is the SiO<sub>2</sub> films  $D_1$  (cm<sup>2</sup>/sec) and in the silicon substrate  $D_2$  (cm<sup>2</sup>/sec), and the ratio  $r = (D_1/D_2)^{1/2}$  for films of SiO<sub>2</sub> grown by thermal oxidation (wet O<sub>2</sub>) and oxidation of TPS. The diffusion temperature is 1150°C

Growth method	$r$	$D_2$ (cm <sup>2</sup> /sec)	$D_1$ (cm <sup>2</sup> /sec)
Oxidized TPS	$2.16 \times 10^{-2}$	$1.2 \times 10^{-12}$	$5.6 \times 10^{-16}$
Thermal oxidation	$1.25 \times 10^{-2}$	$1.2 \times 10^{-12}$	$1.87 \times 10^{-16}$
Thermal oxidation (9)	$1.65 \times 10^{-2}$	$4.2 \times 10^{-18}$	$1.3 \times 10^{-16}$
Pyrolytic TEOS (10)	$8.2 \times 10^{-2}$	$2.5 \times 10^{-18}$	$17 \times 10^{-16}$
Thermal oxidation	$2.3 \times 10^{-2}$	$2.5 \times 10^{-18}$	$1.3 \times 10^{-16}$

Discussion

One of the advantages of the TPS oxidized SiO<sub>2</sub> films over the thermal films is a lower temperature of deposition. The annealing temperature of these oxides for their use as a gate oxide in MOS devices might be lowered below the 850°C currently used.

The values for the etch rate and index of refraction of our TPS oxidized films before annealing are equal to those of the oxidized silane and the decomposed TEOS films after annealing as can be seen in Table II. The stretching modes of the IR spectrum of our TPS oxidized films did not change their frequency after annealing while the oxidized silane or decomposed TEOS did change their frequency. All these facts prove that the oxidized TPS films, even unannealed, have a high density and a low porosity and, therefore can compare even to the thermal oxidized films as efficient mask against diffusion of boron. The diffusion constants  $D_1$  of boron in the TPS oxidized films are only slightly higher than the thermally oxidized films and much lower than the decomposed TEOS as is seen in Table III.

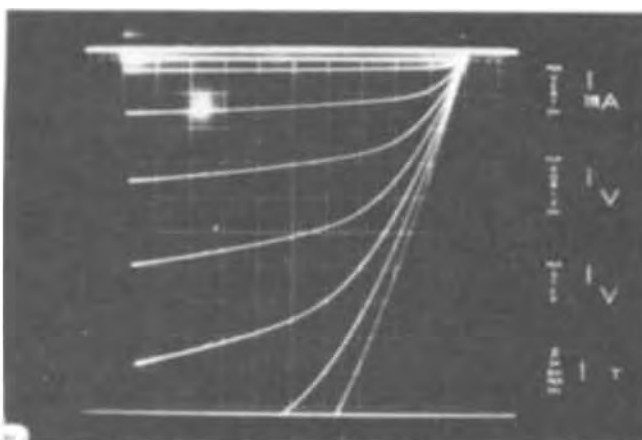
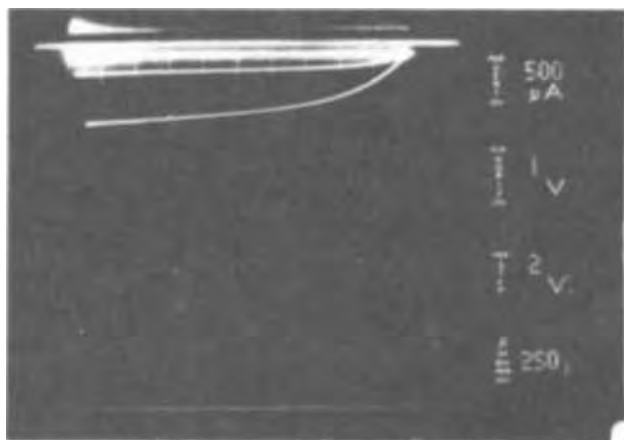


Fig. 8. Drain current  $I_D$  vs. drain voltage  $V_D$  before and after annealing of a MOS field effect transistor produced with SiO<sub>2</sub> film gate deposited from oxidized TPS before and after annealing.

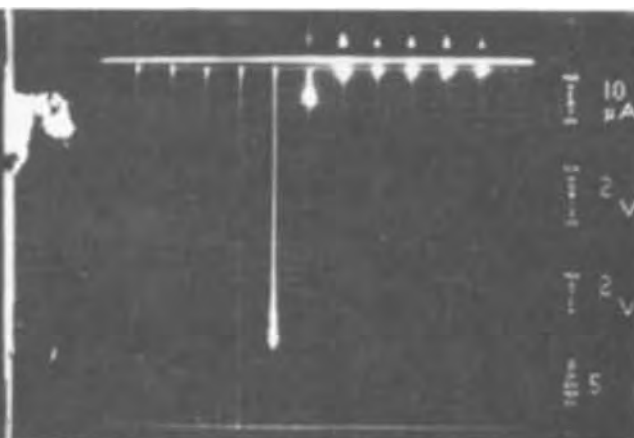
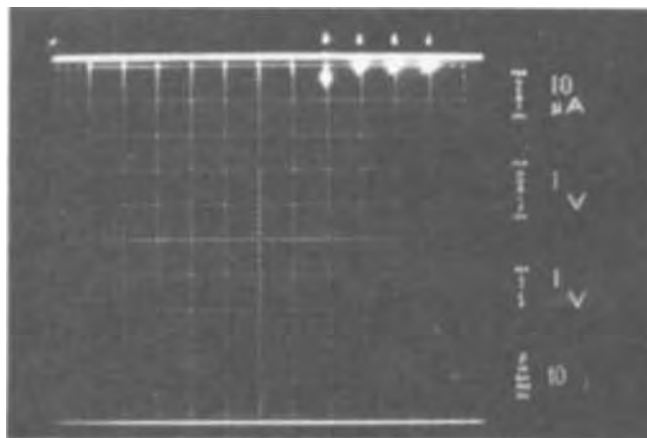


Fig. 9. Threshold voltage of the FET before and after annealing.

Only for the use as a gate oxide was it necessary to anneal the TPS oxidized films. Such an annealing process has reduced the defects and caused a reduction of the flatband voltage. The bias temperature stability of the C-V curves of the MOS structures grown by the oxidized TPS are comparable to those of the thermally oxidized films. The lower temperature of deposition of the TPS oxidized films offers a clear advantage over the thermally oxidized films since in the former case the lower temperature of deposition avoids any shift of the p-n junction boundaries, through diffusion.

### Conclusion

It has been proved that the TPS oxidized SiO<sub>2</sub> films deposited at about 750°C even in an unannealed state can be used as an efficient mask against boron diffusion and if annealed at about 850°C can be used as a gate oxide in MOS devices. The quality of the TPS oxidized SiO<sub>2</sub> films is superior to that of oxidized silane or decomposed TEOS and almost comparable to that of the thermally oxidized films. The fact that they are grown at a much lower temperature than the thermally oxidized films makes the TPS oxidized films attractive for potential use in MOS devices.

### Acknowledgments

The authors wish to thank Dr. K. H. Zaininger, Mr. J. Shaw, and Mr. F. Taft of the RCA Laboratories, Princeton, New Jersey, for their help in manufacturing the MOS FET produced with our gate oxide SiO<sub>2</sub> films prepared by the oxidation of TPS.

This work was supported in part by a grant of the National Council of Research and Development, The Prime Minister's Office, Jerusalem.

Manuscript submitted July 11, 1973; revised manuscript received March 1, 1974.

Any discussion of this paper will appear in a Discussion Section to be published in the June 1975 JOURNAL. All discussions for the June 1975 Discussion Section should be submitted by Feb. 1, 1975.

### REFERENCES

1. C. J. Frosch and L. J. Derick, *This Journal*, **104**, 547 (1957).
2. C. T. Sah, *IEEE Trans. Electron Devices*, **ED-11**, 324 (1964).
3. J. Klerer, *This Journal*, **108**, 1070 (1961).
4. N. Goldsmith and W. Kern, *RCA Rev.*, **28**, 153 (1967).
5. R. J. Archer, *J. Opt. Soc. Am.*, **52**, 970 (1962).
6. W. A. Pliskin and H. S. Lehman, *This Journal*, **112**, 1013 (1965).
7. N. Goldsmith, J. Olmstead, and J. Scott, Jr., *RCA Rev.*, **28**, 344 (1967).
8. C. S. Fuller and J. A. Ditzenberger, *J. Appl. Phys.*, **27**, 544 (1956).
9. S. Horiuchi and J. Yamaguchi, *Japan J. Appl. Phys.*, **1**, 314 (1962).
10. K. V. Anand, H. D. McKell, and D. C. Northrop, *J. Phys. D: Appl. Phys.*, **4**, 1722 (1971).
11. M. L. Barry, in "Chemical Vapor Deposition, Second International Conference," John M. Blocher, Jr. and James C. Withers, Editors, pp. 595-617, The Electrochemical Society Softbound Symposium Series, New York (1970).

## Reexamination of Some Aspects of Thermal Oxidation of Silicon

Y. Ota<sup>1</sup> and S. R. Butler

*Materials Research Center and Department of Metallurgy and Materials Science, Lehigh University, Bethlehem, Pennsylvania 18015*

*The publication costs of this article have been assisted by The National Science Foundation.*

### ABSTRACT

This paper reports a study of the water vapor pressure and low level sodium impurity dependence of the oxidation rate of silicon at 1000° and 1230°C. The oxidation studies were carried out in an rf heated cold wall oxidizer which is also described. The important aspect of the oxidizer is that the sample is placed between two closely spaced silicon blocks to give a very uniform temperature region and therefore uniform oxide properties. It is shown that the oxidation rate coefficient (in the parabolic range) increases monotonically with water vapor pressure. However, the rate also shows some dependence on the other gas phase constituents. At constant H<sub>2</sub>O partial pressure the parabolic rate constant increases, going from H<sub>2</sub>O-argon mixture to pure H<sub>2</sub>O (vacuum) or H<sub>2</sub>O-hydrogen mixture. For sodium concentrations in the range 0.4-10 ppm (atomic) in the water vapor atmosphere no changes in oxidation rate were observed at 1000° or at 1230°C.

The over-all phenomenology of thermal oxidation of silicon has been well established by many workers and is summarized by Deal and Grove (1) and Pliskin (2). More recently Revesz and Evans (3) have investigated the oxidation process with special emphasis on impurity effects. They report changes in the coefficients in the growth rate expressions due to sodium doping of the oxidizing atmosphere for certain restricted conditions. Also these authors (3) have assumed an expression to calculate the oxidant partial pressure (water vapor) in flowing systems which differs from conventional practice (4).

<sup>1</sup> Present address: Bell Laboratories, Reading, Pennsylvania 19604.  
Key words: oxidation, silicon, impurities, rf heating.

One other study (5) has investigated the effect of sodium on silicon oxidation under conditions of high sodium content. However the oxide formed was an unidentified crystalline phase. Therefore these results do not appear to be relevant to this investigation.

In the present work, we describe a cold wall oxidation apparatus which has proved useful for producing films of uniform properties, in particular, oxide thickness and electrical characteristics. We have determined the water vapor partial pressure in several chemically different flowing atmospheres, and report the effect of these variables on oxide growth rate. Finally, we will present methods and results for growth of oxide films

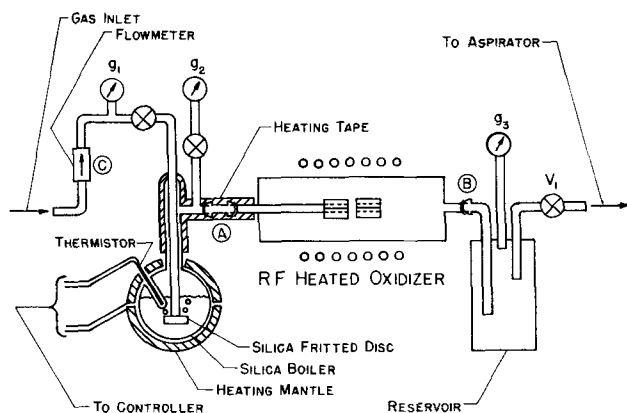


Fig. 1. Schematic diagram of the rf heated, cold wall oxidation system.

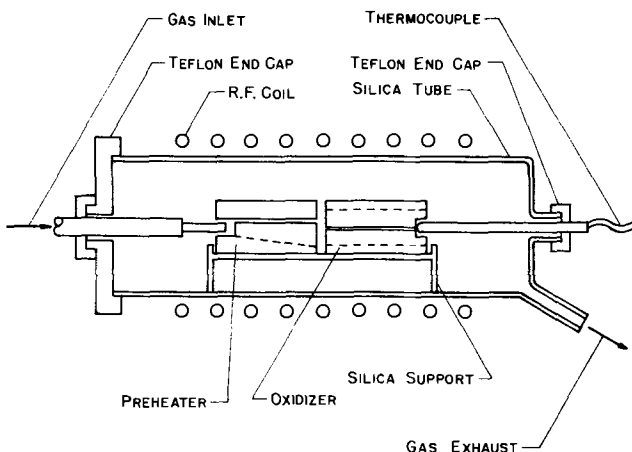


Fig. 2. Diagram of the rf heated oxidation chamber. The Teflon end caps are o-ring sealed. The large silica tube is 80 mm I.D. by 53 cm long.

in wet atmospheres of known sodium concentration in the range  $\leq 10$  ppm.

### Experimental

The cold wall oxidation system is shown schematically in Fig. 1. The entire system is maintained within a closed laminar flow clean bench. The system is cleaned by etching and washing in the usual manner with filtered ( $< 0.2 \mu\text{m}$ ) deionized water of greater

than 15 megohm-cm resistivity and sodium content  $< 1$  ppb.<sup>2</sup> All of the glass components are commercial high purity  $\text{SiO}_2$  (G.E. 204 or 510). The only other parts exposed to the ambient of the sample are fabricated from Teflon or device grade single crystal silicon (see Fig. 2). The principal difference between this system and previous ones, e.g., see Ref. (3), is in the use of a susceptor structure which completely encloses the sample. This is illustrated in Fig. 3, and contrasts with the usual practice of lying the sample on a heated substrate. In the present case the sample is in a cavity formed by a pair of nested single crystal silicon blocks,<sup>3</sup> as illustrated in Fig. 3. The temperature in the sample space has been measured by sliding the thermocouple (Pt-Pt 10% Rh), without the silica sheath that normally encloses it, along the entire length of the cavity above the surface where the sample is placed. The temperature was constant to within  $\pm 2^\circ\text{C}$ . Power was supplied by a 450 kHz-10 kW generator which was simply set at a constant power level and was stable enough to maintain the

<sup>2</sup> Analysis by R. Hunsberger, Western Electric Company, Reading, Pennsylvania.

<sup>3</sup> Supplied by D. Mehta, Western Electric Company, Allentown, Pennsylvania.

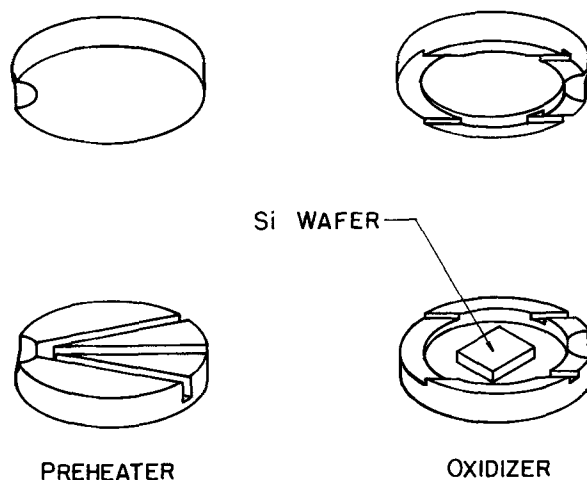


Fig. 3. Expanded diagram of the silicon susceptor for gas preheating and wafer oxidation. Dimensions of each piece are 2 in. diameter  $\times$   $\frac{1}{2}$  in. thick.

temperature constant to  $\pm 5^\circ\text{C}$  for several hours at  $1230^\circ\text{C}$ . In addition, the gas atmosphere which flows over the sample is preheated to the same temperature as the sample. As a result, there was no difference in the measured temperature in the sample space with or without the flowing atmosphere (this was tested with 50 liters/hr of argon at STP). Equilibrium thermodynamic calculations of gas phase partial pressures are meaningful under these conditions.

Ambient atmospheres used for the oxidation consisted of pure water vapor and water vapor-argon or water vapor-hydrogen mixtures. The water vapor source and saturator for gas mixtures consisted of a two liter fused silica flask covered with a heating mantle. The water temperature was maintained by a controller (Fisher Scientific Company, Model 15-177-150) with a thermistor probe immersed in a well in the flask. This system maintains the water temperature constant to  $\pm 0.2^\circ\text{C}$ . The gas was admitted to the saturator through a fritted silica disk. The degree of saturation of the argon or hydrogen was determined by disconnecting the system at point A in Fig. 1 and collecting the water by passing the gas through a condenser. This determination was made as a function of the saturator temperature for flow rates as measured at point C in Fig. 1. The flow rates used were determined by a standard wet test meter to be: argon, 51 liters/hr; hydrogen, 156 liters/hr. For these flow conditions the pressure in the system, as measured with gauges  $g_1$  and  $g_2$ , never deviated from atmospheric by as much as 5%. When the flowing atmospheres were used the system was exhausted at point B in Fig. 1. In one series of experiments, oxidation was carried out in pure water vapor at various reduced pressures. For these experiments the pressure was controlled by setting the temperature of the vapor source at some value between  $40^\circ$  and  $100^\circ\text{C}$ . The pressure, as measured on gauge  $g_3$  in Fig. 1, was then maintained at the vapor pressure of water ( $\phi$ ) corresponding to the source temperature. This was done by adjusting a needle valve ( $V_1$ ) in the line connecting the reservoir to a water aspirator.

When films were to be grown from water vapor contaminated with sodium, the following procedure was used. A two liter solution of a chosen concentration would be made up from deionized water and reagent NaOH. One liter of the solution was used as a vapor source for the oxidation. A separate fused silica boiler and oxidizer chamber, like those in Fig. 1, were used so as not to contaminate the apparatus used for normal clean steam growth. During growth, about 200 cc of the NaOH solution would be converted to steam. To determine the sodium content of this vapor, the solution in the boiler was replaced by the remaining

liter of original solution. Again about 200 cc of solution was converted to steam and collected at point A in Fig. 1. The sodium content of this solution was determined by measuring its conductivity at 60 Hz. The measurement was calibrated with standard solutions maintained at the same temperature (21°C). In all cases, the distillate naturally contained less sodium than the solution, e.g., 10 ppm (atomic) Na solution gave a 1.2 ppm distillate. The sodium content of selected samples was determined<sup>4</sup> by standard etching and flame photometry methods (7, 8, 12).

The oxide film thickness was determined by multiple beam interferometry with the standard step etching and evaporated metal coating method. A Zeiss Model WL microscope fitted with a Leitz multiple beam interferometry attachment was used for these measurements (error  $\pm 1\%$  in the range covered). Uniformity of oxide thickness over the wafer surface was determined from capacitance measurements. This was determined by a 1 MHz capacitance bridge C-V measurement (error  $\pm 1\%$ ) of many capacitors formed by evaporating aluminum "dots" (area = 2.1 mm<sup>2</sup>  $\pm 1\%$ ) through a mask over the surface of the oxidized wafer.

### Results and Discussion

The results of the determination of the water vapor pressure in argon and hydrogen flow streams as a function of the saturator temperature are given in Fig. 4. The water pressure was calculated from the expression

$$P_{\text{H}_2\text{O}} = \left[ \frac{n_{\text{H}_2\text{O}}}{n_{\text{H}_2\text{O}} + n_{\text{gas}}} \right] P_{\text{total}} \quad [1]$$

where  $P_{\text{total}}$  is essentially 1 atm. The  $n$ 's are numbers of moles of water or gas (H<sub>2</sub> or Ar) which have passed through the system in some time interval. These were determined by collecting and weighing the water and measuring the gas flow rate at room temperature. The figure also shows by the curve (Revesz-Evans), the vapor pressure of water (6) in an arbitrary gas stream as calculated via the expression given in Table 3 of Revesz and Evans (3)

$$P_{\text{H}_2\text{O}} = \left[ \frac{P_{\text{pure H}_2\text{O}}}{P_{\text{pure H}_2\text{O}} + P_{\text{gas}}} \right] P_{\text{total}} \quad [2]$$

While Eq. [2] appears to be a correct statement of Dalton's law, as it would be for a closed system, it is not applicable to a flowing system. We can see that this expression should be incorrect by going to the limit of a 100°C saturator temperature, i.e.,  $P_{\text{pure H}_2\text{O}} =$

<sup>4</sup> The authors are indebted to R. Hunsberger of Western Electric Company, Reading, Pennsylvania, for performing these analyses.

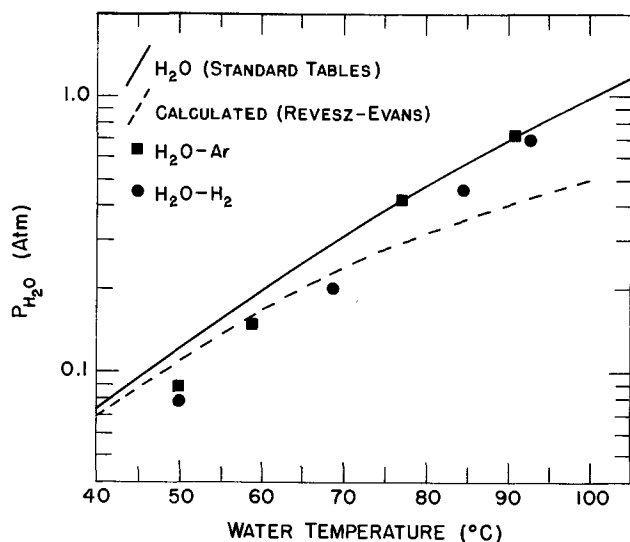


Fig. 4. Water partial pressure in flowing argon and hydrogen atmospheres as function of saturator temperature.

1 atm. In this limit even though the gas pressure at the inlet to the saturator is 1 atm no gas flows in (neglecting diffusion). Therefore the gas flowing from the outlet is pure steam, however Eq. [2] would predict a water vapor pressure of  $\frac{1}{2}$  atm instead of 1 atm. From a comparison of the calculated curve with the experimental data, it is also clear that the method of calculation given in Ref. (3) is incorrect.

The final curve in Fig. 4 is the vapor pressure of pure water (6). Comparison of this curve with the data clearly indicates that the flowing atmospheres used in the present experiments were not saturated under all conditions. Studies were not carried out as a function of flow rates even though that might have resulted in finding conditions where saturation could be achieved (4). The rationale for this was that high flow rates were required to adequately flush the oxidizer tube and thus maintain an oxidation ambient of known composition. Since the steps taken in this work to reach saturation were not fully successful we suggest that the normal practice of simply bubbling the gas through the water is not likely to produce saturation. In that case, changes in gas flow rate might result in vapor pressure changes and thus in a corresponding fluctuation of the oxidation process. In Ref. (4) independence of oxidation rate on flow rate was used to indicate a saturated flow stream. While such a condition is practical, it is not necessarily saturated, i.e., at equilibrium. It is only necessary to be in a steady state. We conclude that a flowing gas stream will not in general be saturated even if reasonable steps are taken and therefore the water pressure should be experimentally determined. This point has not been specifically established in most of the previous work (1-3).

Having established the growth conditions, the thickness of oxide grown was determined as a function of growth time. In the thickness range studied (0.1-1.5  $\mu\text{m}$ ), the thickness across a given sample, from capacitance measurements, was uniform to within  $\pm 3\%$ .

The oxide "quality" was measured by  $\frac{Q_{\text{FB}}}{q} \left( \equiv \frac{C_{\text{ox}} \Delta V_{\text{FB}}}{q} \right)$  (7) as the

oxidizer "cleaned up" by exposure to pure steam at the high temperature. Presumably this "cleaning up" is the leaching of impurities such as sodium from the silica walls of the system. This was shown to take place by Yurash and Deal (7) who measured the increased sodium content of steam as it passed through an oxidation system. Burgess and Donega (10) have also directly demonstrated the decrease in sodium content of the oxidizer atmosphere with time.

After about 50 accumulated hours at temperature, samples with  $Q_{\text{FB}}/q$  values below  $1 \times 10^{11} \text{ cm}^{-2}$  were obtained. In the time range studied, 20 to 300 min, the oxidation time at temperature is well defined ( $\pm 2\%$  for the shortest times) as a result of the rapid heating and cooling of the rf heated oxidizer. The thickness-time relation was determined within experimental reproducibility to obey  $x \propto t^{1/2}$ , where  $x$  is oxide thickness and  $t$  is oxidation time. For films in the thickness range 0.1-1.5  $\mu\text{m}$  this is to be expected, and thus values of the growth rate coefficient  $B$  of Ref. (1) were calculated [note:  $B$  is defined in the relation  $x^2 + Ax = B(t + \tau)$ ]. The results are presented in Fig. 5.

The general agreement between our results and those taken from Ref. (1), and the essentially linear dependence on water pressure, are apparent. This result implies that the wet oxygen atmosphere used in Ref. (1) was saturated.

The deviation of the pure water vapor data from linearity, at low pressures, could be the result of a small air leak in the system. This is possible because the requirement of cleanliness prevents completely vacuum sealing (e.g., by the use of grease on the joints). This would mean at low pressures the actual



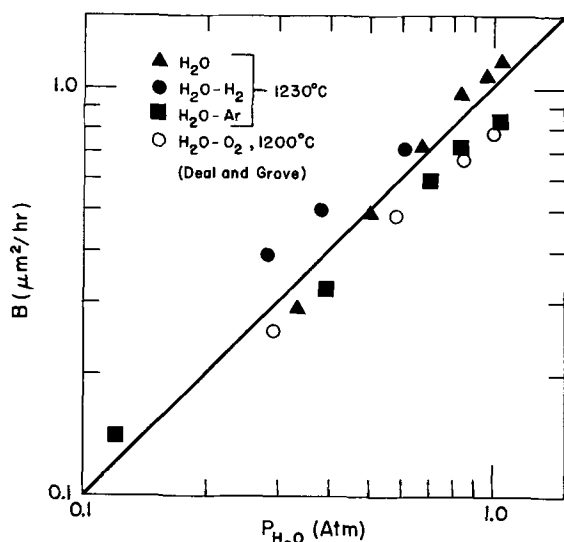


Fig. 5. Parabolic oxidation rate constant as a function of water vapor partial pressure. The 45° line on the figure is included only to indicate the form of a linear relation.

water pressure is less than that indicated so that the data points would move to lower pressure and thus nearer a linear relation. The differences for the several gas mixtures with the same water vapor pressure are outside the estimated error due to thickness and time measurements given above. However fitting the data to linear relations by a least-squares regression analysis gave the following values for the growth rate coefficients

$$\begin{aligned} \text{pure water vapor, } B (\mu\text{m}^2/\text{hr}) &= (1.13 \pm 0.13) P_{\text{H}_2\text{O}} (\text{atm}) \\ \text{hydrogen-water vapor, } B &= (1.24 \pm 0.17) P_{\text{H}_2\text{O}} \\ \text{argon-water vapor, } B &= (0.82 \pm 0.07) P_{\text{H}_2\text{O}} \end{aligned}$$

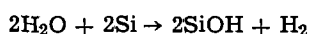
The error limits given specify the three standard deviation confidence band. Therefore we see that it is not statistically meaningful to distinguish between the pure water vapor and water vapor-hydrogen data. However there does seem to be a statistically significant difference between those data and the water vapor-argon data.

The expression for the parabolic growth rate coefficient in the phenomenological theory (1) is

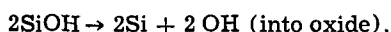
$$B = \frac{2D_{\text{eff}}C^*}{N_1}$$

The symbols have the same meanings as given by Deal and Grove (1).  $C^*$ , the concentration of oxidant in the oxide at the gas-oxide surface, must be assumed to be proportional to the oxidant partial pressure to be consistent with the observed linear pressure dependence. In fact, the coefficient  $B$  should be proportional to the concentration of the diffusing species in oxide sites from which diffusion can proceed.

Deal and Grove (1) calculated this concentration and compared it to the water solubility of Moulson and Roberts (13) with good agreement. However as pointed out by Revesz and Evans (3) since Deal and Grove found  $C \propto P_{\text{H}_2\text{O}}$  and Moulson and Roberts found  $C \propto P_{\text{H}_2\text{O}}^{1/2}$  the agreement must be considered fortuitous. Pliskin (2) has also attempted to rationalize the linear pressure dependence on the assumption that "... the surface is covered with silanol groups. . .", resulting in the following reaction equation



and



This would lead to a linear pressure dependence as can be seen by adding the equations and writing the mass action expression for the resulting equation, i.e.

$$\frac{P_{\text{H}_2} a_{\text{OH}}^2}{P_{\text{H}_2\text{O}}^2} = K$$

and therefore

$$(\gamma C_{\text{OH}}) = (K/P_{\text{H}_2})^{1/2} P_{\text{H}_2\text{O}}$$

Thus assuming the activity coefficient  $\gamma$  is constant one gets the desired expression of  $C^*$  in the notation of Deal and Grove (1)

$$C_{\text{OH}} = C^* = \left( \frac{K}{\gamma^2 P_{\text{H}_2}} \right)^{1/2} P_{\text{H}_2\text{O}}$$

However, note the dependence on hydrogen pressure,  $P_{\text{H}_2}$ . The data in Fig. 5 for  $\text{H}_2\text{O}-\text{H}_2$  mixtures does not show a dependence on hydrogen pressure.

We therefore conclude that to date there is no acceptable model for the processes going on at the gas-oxide interface. The data of Fig. 5 would indicate some role for other gas phase species at present not understood or previously reported. Some interesting complimentary effects have been observed (11) in dry oxygen oxidation, namely, several oxygen species appear to be involved in the Si-SiO<sub>2</sub> interfacial reaction in the linear oxidation region. It should be mentioned that we have carried out a limited number of oxidations in pure 100°C steam at different temperatures between 900° and 1230°C. The slope of the  $\ln B$  vs.  $1/T$  plot agrees closely with Ref. (1). The agreement of our results with those of Grove and Deal (1) when such results were obtained under comparable conditions indicates that the carrier gas effects just cited are not spurious.

Finally, Revesz and Evans (3) reported significant increases in the kinetic coefficient  $B$  [called  $k$  in Ref. (3)] due to sodium "doping" for certain wet and dry oxidation conditions. Specifically, the wet oxidation which is of relevance to our work was carried out in very low water vapor pressure ambients, 0.031 atm (assuming saturation) resulting in very slow oxidation. Since the method of doping used in Ref. (3) involved contaminating a substrate or placing sodium oxide in the tube furnace, no specific control of sodium level was possible. However the authors state the average sodium content of the oxides was  $10^{20} \text{ cm}^{-3}$ . Therefore the conditions used in Ref. (3) of low oxidation rate and rather high sodium concentration accentuated the effect on growth rate. In addition the nonmonotonic effect of doping with temperature was not explained and leads one to suggest the possibility of large variations in the actual doping levels.

In the present study we have controlled the doping to lower levels. This is demonstrated by the results of sodium analysis for our highest doping level which are presented in Fig. 6.

A graphical integration gives an average concentration of less than  $3 \times 10^{19} \text{ cm}^{-3}$ . Therefore we expect significantly less sodium in all of our samples and corresponding less effect on growth rates than in Ref. (3). Specifically with ambient doping in the range from 0.4 to 10 ppm no consistent change in  $B$  was observed. Some typical data demonstrating this point are presented in Table I. It is apparent that with low sodium levels and high oxidation rates (due to the higher water vapor pressures) typical of oxidation conditions for electronic applications, no significant sodium effect should be expected in the growth rate. This is in contrast to the electrical properties such as interfacial charge which are very sensitive to sodium content. These effects have been observed and will be reported separately.

### Conclusions

The principal conclusions from this study are:

1. An rf heated cold wall oxidizer can be constructed which produces uniform oxides over large areas.

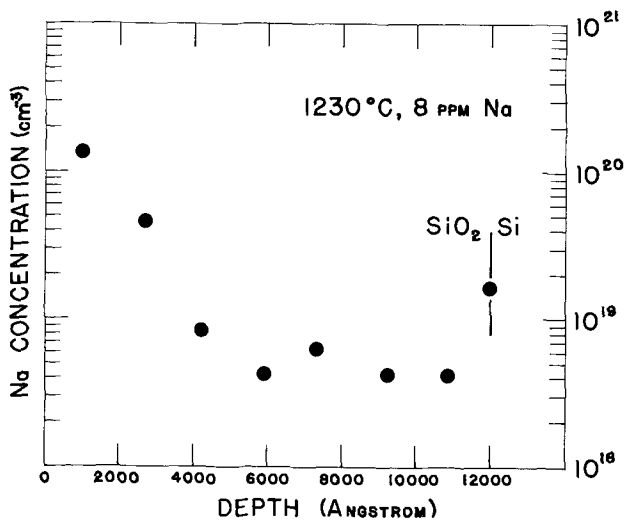


Fig. 6. Sodium distribution in thermally grown  $\text{SiO}_2$ . Oxidation condition:  $1230^\circ\text{C}$ , steam atmosphere containing 8 ppm Na.

2. Flowing gas streams used as carrier gas for wet oxidation may not be saturated. Above  $80^\circ\text{C}$  saturator temperature the effect is probably less than 20% for typical flow conditions.

3. The parabolic growth rate during wet oxidation of silicon does show some dependence on details of the gas phase composition other than simply oxidant partial pressure.

4. No effect of gas stream sodium impurities on growth rates was observed during wet oxidation of silicon for Na concentrations below 10 ppm in the oxidation atmosphere.

#### Acknowledgments

The authors wish to acknowledge many helpful discussions with F. J. Feigl, D. M. Smyth, D. A. Mehta, and W. R. Smith. Support for this work came from the National Science Foundation, Grant GK 29113 and the Materials Liaison Program of Lehigh University. Chemicals were supplied for this work as a grant from the Lehigh Valley Chemical Company of Easton, Pa.

Table I. Parabolic growth rate coefficient at  $1230^\circ\text{C}$  in steam of various sodium contents

Sodium concentration (ppm)	Growth rate coefficient B ( $\mu\text{m}^2/\text{hr}$ )
0 (~1 ppb)	$1.15 \pm 0.05^*$
0.14	1.10
1.4	1.14
4.0	1.08
8.0	1.20
10.0	1.14

\* Average of 30 determinations.

Manuscript submitted Nov. 2, 1973; revised manuscript received Feb. 25, 1974.

Any discussion of this paper will appear in a Discussion Section to be published in the June 1975 JOURNAL. All discussions for the June 1975 Discussion Section should be submitted by Feb. 1, 1975.

#### REFERENCES

- B. E. Deal and A. S. Grove, *J. Appl. Phys.*, **36**, 3770 (1965).
- W. A. Pliskin, *IBM J. Res. Develop.*, **10**, 198 (1966).
- A. G. Revesz and R. J. Evans, *J. Phys. Chem. Solids*, **30**, 551 (1969).
- M. A. Lieberman and G. Averkiou, Paper 91 presented at Electrochemical Society Meeting, San Francisco, California, May 9-13, 1965.
- O. F. Devereux, R. Y. Wang, and K-H. Chien, *This Journal*, **118**, 1147 (1971).
- Handbook of Chemistry and Physics*, 52nd ed., p. D148, The Chemical Rubber Co., Cleveland, Ohio (1972).
- B. Yurash and B. E. Deal, *This Journal*, **115**, 1191 (1968).
- W. R. Knolle and T. F. Retajczyk Jr., *ibid.*, **120**, 1106 (1973).
- S. M. Sze, "Physics of Semiconductor Devices," Part III, J. Wiley and Sons, Inc., New York (1969).
- T. E. Burgess and H. M. Donega, *This Journal*, **116**, 1313 (1969).
- R. Ghez and Y. J. van der Meulen, *ibid.*, **119**, 1100 (1972).
- J. E. Barry, H. M. Donega, and T. E. Burgess, *ibid.*, **116**, 257 (1969).
- A. J. Moulson and J. P. Roberts, *Trans. Faraday Soc.*, **57**, 1208 (1961).



## The Preparation and Properties of CVD-Silicon Tubes and Boats for Semiconductor Device Technology

W. Dietze

Siemens AG, Bereich Halbleiter, D-8000 Munchen 46, Frankfurter Ring 152, West Germany

and L. P. Hunt\* and D. H. Sawyer

Dow Corning Corporation, Solid State Research and Development, Hemlock, Michigan 48626

The publication costs of this article have been assisted by the Dow Corning Corporation.

At present quartz is the most important material for producing tubes and boats for diffusion and oxidation processes in silicon device technology. The advantage of quartz compared to other materials is its combination of purity, resistance to mechanical and temperature changes at high temperature, and good workability. But there are limits for the application of quartz. At temperatures exceeding 1200°C it becomes increasingly soft and devitrifies, especially where it contacts other materials. In this state, quartz tubes slowly sag and flatten, and also become more permeable to gases and trace impurities. High temperatures are, however, necessary to accelerate the different diffusion and oxidation processes.

Quartz can be obtained in a relatively pure quality. However, even these pure grades contain undesirably high levels of some metal impurities such as sodium, which must be excluded from various oxidation processes.

One of the most disturbing effects in silicon device processing is the generation of clusters of dislocations at contact points between the quartz boat and a silicon wafer during high temperature processing, partly caused by mechanical stress at these points of the wafer. This phenomenon is shown in Fig. 1 by a wafer that had been dislocation-free before processing. The mechanical stress that produced these dislocations was due to the difference in thermal expansion coefficients between the silicon wafers and the quartz boat.

The use of silicon tubes prepared by chemical vapor deposition (CVD) eliminates most of the difficulties encountered with quartz tubes. Polycrystalline silicon does not soften like quartz at temperatures approaching 1400°C; its resistance to cracking caused by thermal shock is excellent; its purity level is very high; and its coefficient of expansion is nearly identical with that of the silicon wafers.

Si-tubes and boats can also be made from monocrystalline or polycrystalline bulk silicon by coring, sawing, and grinding methods. This is, however, an expensive and difficult process due to the somewhat brittle material.

### Preparation of Silicon Tubes

Polycrystalline silicon tubes and other shaped hollow bodies are produced by the same basic CVD method used to deposit semiconductor-grade silicon rods: the hydrogen reduction of pure trichlorosilane. In the case of hollow bodies, however, it is necessary

\* Electrochemical Society Active Member.

Key words: semiconductor tubes and boats, silicon tubes and boats, quartz tubes and boats, vapor deposition, trichlorosilane reduction, silicon deposition.

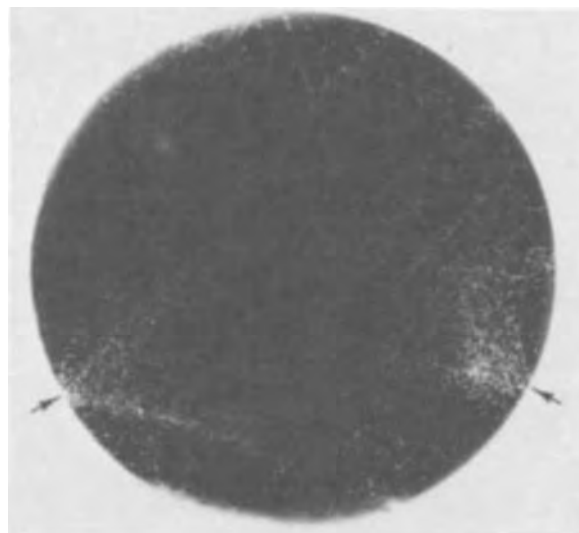
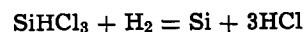


Fig. 1. Clusters of dislocations generated on a silicon wafer at its two contact points with a quartz boat used during processing.

to deposit silicon on a substrate such as pure graphite (1, 2), the outside dimensions of which become the inside dimensions of the silicon form being grown. The over-all chemical reaction taking place at temperatures exceeding 1000°C is



It is important during deposition of silicon tubes that there be no intergrowth of the silicon and graphite resulting from, for example, rough or porous surfaces. In addition, the formation of silicon carbide at the interface due to excessive temperatures must be prevented in order that silicon can be easily separated from graphite after deposition. The deposition reactors shown in Fig. 2 are modifications of the Siemens silicon deposition process for producing polycrystalline silicon rods. The tubular graphite substrates are electrically connected through the base plate via graphite chucks to a power supply. In the first case, a single test tube-shaped substrate is used for producing a closed-end silicon tube. A long graphite connecting-rod extends coaxially to the closed end of the substrate where electrical contact is made by a screw-type connection.

The other diagram in Fig. 2 shows an example for simultaneously making two open-ended silicon tubes

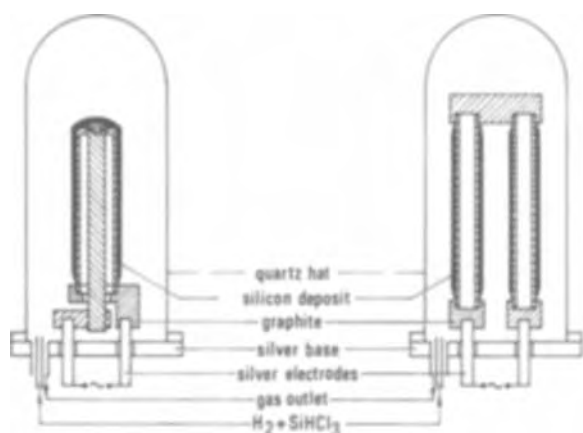


Fig. 2. Different reactor systems for the production of silicon tubes.

by connecting the tubular substrates in series by means of a conductive material such as a graphite bridge. Silicon is deposited at a substrate temperature greater than  $1000^{\circ}\text{C}$  using the appropriate flow rate (50-500 liters/min) and mole ratio (5-50%  $\text{SiHCl}_3$ ) of the trichlorosilane-hydrogen gas mixture, the exact conditions being very dependent upon the reactor configuration used, and the surface quality and the degree of crystallite size wanted. Equal deposition conditions are required over the entire surface area in order to obtain a uniform and smooth silicon layer. Silicon deposition is discontinued at a predetermined diameter and the resulting tube is removed from the deposition apparatus, cut to length, and separated from the graphite mandrel. Separation can be accomplished by burning out the graphite or, in the case of a closed-end silicon tube, by simply pulling the graphite tube out of the silicon tube.

Other shaped hollow bodies are produced in a similar manner, the main difference being the configuration of the substrate material used. Figure 3 shows the as-cut end sections of silicon tubes with circular and rectangular cross sections. These tubes are 1.6m in length.

Tube ends can be either left as-cut, or ground to form a male taper for mating with a female quartz joint (Fig. 4). They can also be joined to a Pyrex® tube of the same diameter by standard glass blowing techniques to form a vacuum-tight and mechanically stable connection.

Finally the tubes are etched in an  $\text{HF-HNO}_3$  solution to remove surface impurities and to produce a silicon tube with the equivalent purity level of normal polycrystalline silicon in rod form.

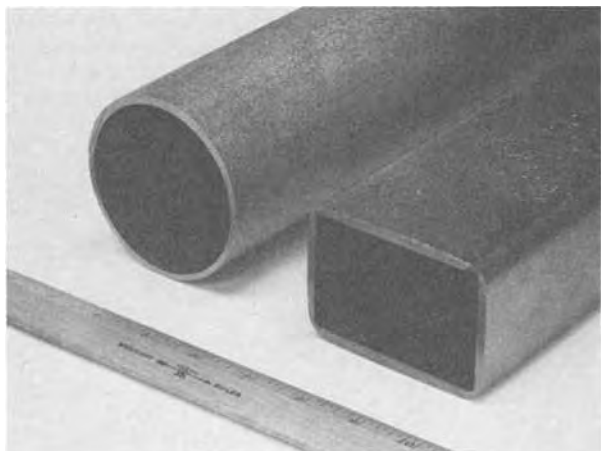


Fig. 3. Silicon tubes with circular and rectangular cross sections

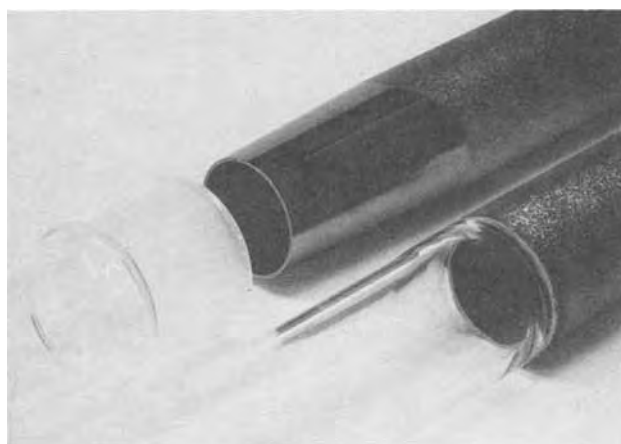


Fig. 4. Silicon tubes with ground taper and silicon-glass connections

### Preparation of Silicon Boats

In contrast to quartz, silicon is not workable by glass blowing techniques. Therefore, one must begin with silicon tubes having a suitable cross section, either circular or somewhat rectangular. Since boats are made by diamond sawing, the polycrystalline silicon material must be of a high quality, free of mechanical stresses which can cause cracks during sawing of the somewhat brittle material. It should be largely homogeneous in spite of the fact that there is a high degree of crystallite texture due to crystal growth from the gas phase. The crystal size has to be much smaller than the over-all layer thickness of the deposited silicon hollow body. This is attainable through optimized deposition parameters as indicated by the very smooth and nodular-free silicon surface seen in Fig. 5 which actually shows the outline of the machined graphite substrate surface.

Silicon boats for supporting silicon wafers are used for open tube diffusion or oxidation processes, diffusion in vacuum, and other diffusing and heat-treating techniques. These boats should consist of only one part due to their increased mechanical stability and easier handling when filled with slices. It is possible to develop such silicon boats for supporting single silicon slices (Fig. 6a) in vertical or horizontal positions in a parallel or perpendicular direction to the diffusion transport gas. On the right side of Fig. 6a is a boat which is similar to conventional quartz boats with a parallel arrangement. The third boat (in the center) with cross standing silicon slices was developed for arrangements having little space. Figure 6b presents silicon boats for supporting vertical or horizontal stacks of silicon slices. On the left side is a boat for

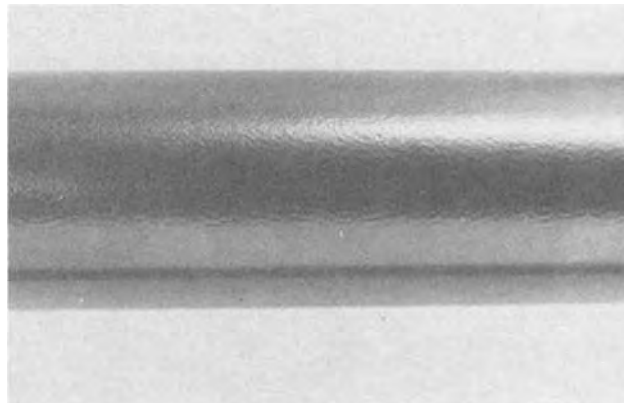


Fig. 5. Silicon tube with a smooth and highly perfect surface that shows the machining marks induced by the removed graphite substrate.

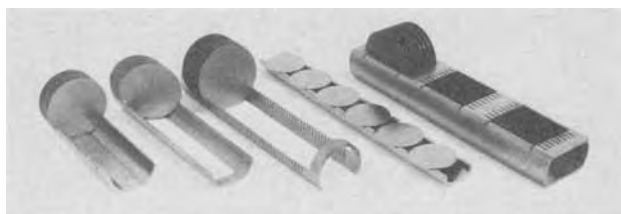


Fig. 6a. Different silicon boats supporting individual silicon slices.



Fig. 6b. Different silicon boats supporting stacks of silicon slices.

stacks of any desired magnitude held at one end with a short silicon rod, and on the right side is a both-end-open silicon tube with a small contraction for holding a stack of silicon slices in the inside.

#### Properties of Silicon Tubes and Boats

A material properties comparison must be made in order to understand why silicon can replace quartz in certain semiconductor device processes.

Silicon tubes do not lose their rigidity at high temperatures due to their polycrystalline structure. A 50 mm ID tube unsupported over a length of 1.2m visually exhibited no sagging after being exposed to a temperature of 1300°C for over 2000 hr. Even a 100 mm ID tube heated to nearly 1400°C (mp of Si 1420°C) for over 400 hr showed no evidence of changing its structural shape (3).

A closed-end silicon tube (50 mm ID) with a glass tube connection was evacuated and heated to about 1350°C at the closed end in order to test porosity and stability. It proved to be highly vacuum tight and no sagging was observed. The glass connection was stable up to 400°C. In contrast to polycrystalline material, monocrystalline silicon begins to soften at temperatures near its melting point.

Thermal shock resistance of silicon tubes was tested by repeatedly pushing a tube from room temperature into a 1150°C furnace and, then after 15 min, pulling it back into its original position. Although heating rates of up to 500°C/min and cooling rates of as high as 900°C/min were reached, the tube suffered no cracking, distortion, or other adverse effects.

The structural rigidity and stability of silicon tubes at high temperatures and in high temperature gradients results in them having much longer lifetimes than quartz and, therefore, allows development of device processes that are not temperature limited due to the sagging or devitrification of a quartz tube. For example, higher temperature diffusions than normal can result in increased device capacity due to the shorter diffusion times required. Silicon tubes have also been found to be equally stable in oxidizing or reducing atmospheres in contrast to a ceramic tube which exhibits a shorter lifetime in a reducing atmosphere due to its chemical change.

The lower heat capacity of silicon compared to quartz and mullite (70% Al<sub>2</sub>O<sub>3</sub> and 30% SiO<sub>2</sub>) allows more optimal thermal properties for furnace design and operation. When a silicon tube is used in place of both a quartz tube and ceramic liner, the lower system heat capacity of about 20% allows for more rapid heat-up and cool-down of the furnace. In addition, heat-up rates for silicon have been found to be more linear with time (3) than for quartz. The higher ther-

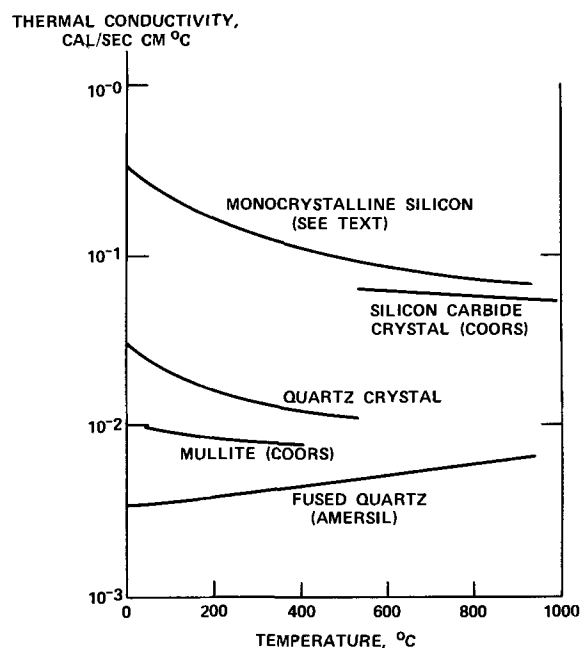


Fig. 7. Comparative thermal conductivities.

mal conductivity of silicon as compared to quartz (Fig. 7) also allows for improved thermal performance of the furnace system. It is possible at sufficiently high temperatures to obtain a longer uniform temperature zone in a silicon tube since the transport of thermal energy along the tube is more efficient. However, this effect does not result in a larger heat loss from the furnace, because normal cooling of the silicon tube extending outside the furnace results in a sharp temperature decrease. This is enhanced by the multitude of grain boundaries which impede heat conduction at low temperatures. Although the thermal conductivity of polycrystalline silicon will be less than that of the monocrystalline form at temperatures less than about 300°K, the thermal conductivities will be very nearly equivalent at typical furnace temperatures (4).

Measurement of the force required to draw a boat through a tube indicates that the coefficient of friction for silicon-on-silicon is more than an order-of-magnitude less than for quartz-on-quartz at a temperature of 1200°C (3) due to the softening of quartz at high temperatures. Softening may also result in sticking problems between the quartz boat and the quartz tube. Friction on quartz at high temperatures produces quartz powder which disturbs diffusion processes. This is avoided by using a silicon system.

In contrast to quartz, polycrystalline silicon tubes, even when evacuated, are not permeable to most trace impurities (copper being an obvious exception) at high temperatures and have been found to be a better gettering agent for these impurities than monocrystalline silicon under specific operation conditions. A re-doping effect from polycrystalline silicon tubes to silicon slices has not been observed.

The generation of slippage and clusters of dislocations at the contact points of quartz and silicon during the diffusion and oxidation processes at high temperatures has been avoided by using silicon boats to keep silicon wafers dislocation-free (5).

#### Purity of Hollow Bodies

Emission and spark-source mass spectroscopy combined with neutron activation analysis have provided a measurement of the level of impurities found in pure quartz, graphite (as a substrate) and polycrystalline silicon tubes. The results of these analyses, which are summarized in Table I, indicate that silicon is much purer than quartz in its purest available form. If a comparison is made using the activation analysis re-

Table I. Quartz, silicon tube, and graphite substrate impurities (ppba)

Element	Quartz		Silicon		Graphite (high purity) Emission spectroscopy Schunk & Ebe
	Neutron activation analysis		S.S. mass spectrosc.		
	Heraeus (1970)	Hackel (1973)	Siemens (1973)	Dow Corning	
As	—	—	0.5	—	—
Au	0.7	0.7	0.003	—	1
C	—	—	—	300	—
Ca	—	—	—	20	—
Cl	—	—	—	110	—
Co	0.2	6.0	0.007	—	—
Cr	5.0	56.0	0.4	10	—
Cu	28.0	79.0	5.0	20	42
F	—	—	—	150	—
Fe	20.0	1200.0	4.0	50	—
K	—	—	—	3	—
Mn	0.6	190.0	—	3	—
Na	260.0	1035.0	0.6	—	19
Ni	—	—	4.0	—	—
Sb	1600.0	160.0	0.22	—	40
Tl	—	—	—	6	—
Zn	2.0	2.0	0.3	—	—

sults to be consistent, the average ratios of the impurities in quartz to those in silicon can be classified as

Quartz/Silicon Ratio	Impurities
>1000	Na, Sb
100-1000	Au, Co, Cr, Fe
10-100	Cu, Zn

The low level of Na in silicon tubes is very advantageous since Na from quartz is a detrimental impurity in some oxidation processes. The low impurity level of Au, Fe, and Cu is also significant. These impurities exist at a lower level in the silicon tube due to the CVD technique, the elemental diffusivities and vapor pressures, and the final chemical etching of the silicon surface, which can getter many impurities very easily.

Silicon tube purity was also tested by resistivity measurements made on single crystals produced from polycrystalline tubes by the Czochralski and multiple-pass floating zone methods. Analyses indicated a donor level of 1.4 ppba (75 ohm-cm) with an acceptor level of 0.8 ppba (350 ohm-cm).

The foregoing analyses indicate, therefore, that the polycrystalline boats or tubes used for device processing actually have a purity comparable to that of the slices used.

### Conclusions

Silicon tubes with dimensions up to 1.8m long by 100 mm inside diameter can be prepared by chemical vapor deposition on the correspondingly shaped surface of heated graphite which can be separated from the silicon afterwards. Similarly, one can produce silicon hollow bodies with a noncircular cross section making possible the preparation of a variety of different silicon boats for supporting silicon slices during diffusion and oxidation processes. For this purpose CVD-silicon is considered superior to conventional quartz for reasons of purity, permeability to trace impurities, and mechanical stability at high temperatures.

### Acknowledgment

The authors wish to express their gratitude to Drs. K. Reuschel and E. Sirtl for helpful discussions and to thank Messrs. A. Kasper and R. Moore for their experimental assistance.

This work has been supported in parts by the technological program of the Federal Department of Education and Science of the FRG. The authors alone are responsible for the content.

Manuscript submitted Sept. 10, 1973; revised manuscript received March 18, 1974. This was Paper 154 presented at the Boston, Massachusetts, Meeting of the Society, Oct. 7-11, 1973.

Any discussion of this paper will appear in a Discussion Section to be published in the June 1975 JOURNAL. All discussions for the June 1975 Discussion Section should be submitted by Feb. 1, 1975.

### REFERENCES

- W. Keller, A. Kersting, and K. Reuschel, Ger. Offen. 1,805,970 (Sept. 17, 1970).
- W. Dietze, K. Reuschel, and H. Sandmann, U.S. Pat. 3,746,496 (July 17, 1973).
- K. C. Hartung, Private communication.
- Y. S. Touloukian, Editor, "Thermophysical Properties of Matter. Vol. 1. Thermal Conductivity, Metallic Elements and Alloys," IFI/Plenum Publishing Corp., New York (1970).
- W. Dietze and K. Reuschel, 3. Materialgüte-Kolloquium der DGF, Freiburg (1971).

## Catalyzed Crystallization in SiO<sub>2</sub> Thin Films

E. I. Alessandrini and D. R. Campbell\*

IBM Thomas J. Watson Research Center, Yorktown Heights, New York 10598

The publication costs of this article have been assisted by the IBM Corporation.

Considerable interest has been shown in thermally grown silicon oxide films from the standpoint of device-oriented properties as well as structural properties. Defects in oxide films have been reported (1-4) and are believed to be small crystallites formed at localized nucleation centers, such as impurities, during heat-treatment. However, the type of impurities and the conditions which induce crystallization in the amorphous films are not clearly understood.

This paper describes the structural aspects of phase transformations in SiO<sub>2</sub> films when P<sup>32</sup> is diffused in the amorphous oxide. The purpose of this investigation was to determine the effect of the impurity as a function of time and temperature and compare the results

with similarly treated films without phosphorus. It will be shown that the transformation from the amorphous to a crystalline phase was dependent on the catalytic behavior of the phosphorus.

### Experimental Procedure

Thin films of amorphous SiO<sub>2</sub> were prepared by dry thermal oxidation and grown to 1000Å in thickness on silicon wafers (Czochralski, p-type, boron doped, 2 ohm-cm) 1 in. in diameter with a (100) orientation. Two series of experiments were carried out: (i) phosphorus was diffused into the amorphous films using P<sup>32</sup> isotope at two different times and temperatures (525°C for 100 hr under a low P pressure followed by 25 hr at 1200°C anneal in vacuum) and (ii) undiffused films given the same heat-treatments. The source of the radioisotope was neutron activated, red phosphorus

\* Electrochemical Society Active Member.

Key words: catalyzed crystallization, SiO<sub>2</sub> films, α-quartz, α-cristobalite, phosphosilicate compounds.

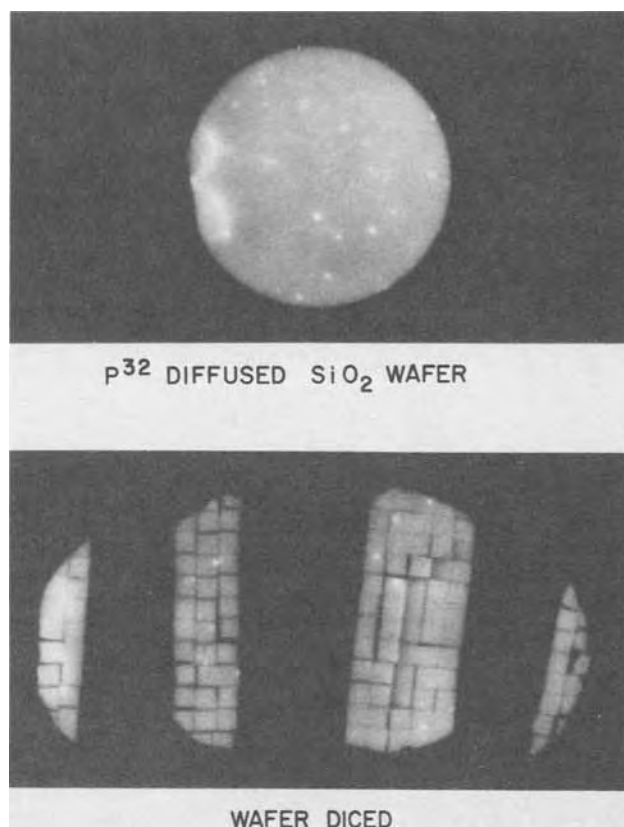


Fig. 1. Autoradiographs of  $P^{32}$  diffused  $SiO_2/Si$ . Heat-treatment 100 hr at  $525^\circ C$ . Magnification 2X.

powder which was encapsulated together with the  $SiO_2/Si$  samples in evacuated silica ampuls. At the temperatures of treatment, the phosphorus source was completely vaporized.

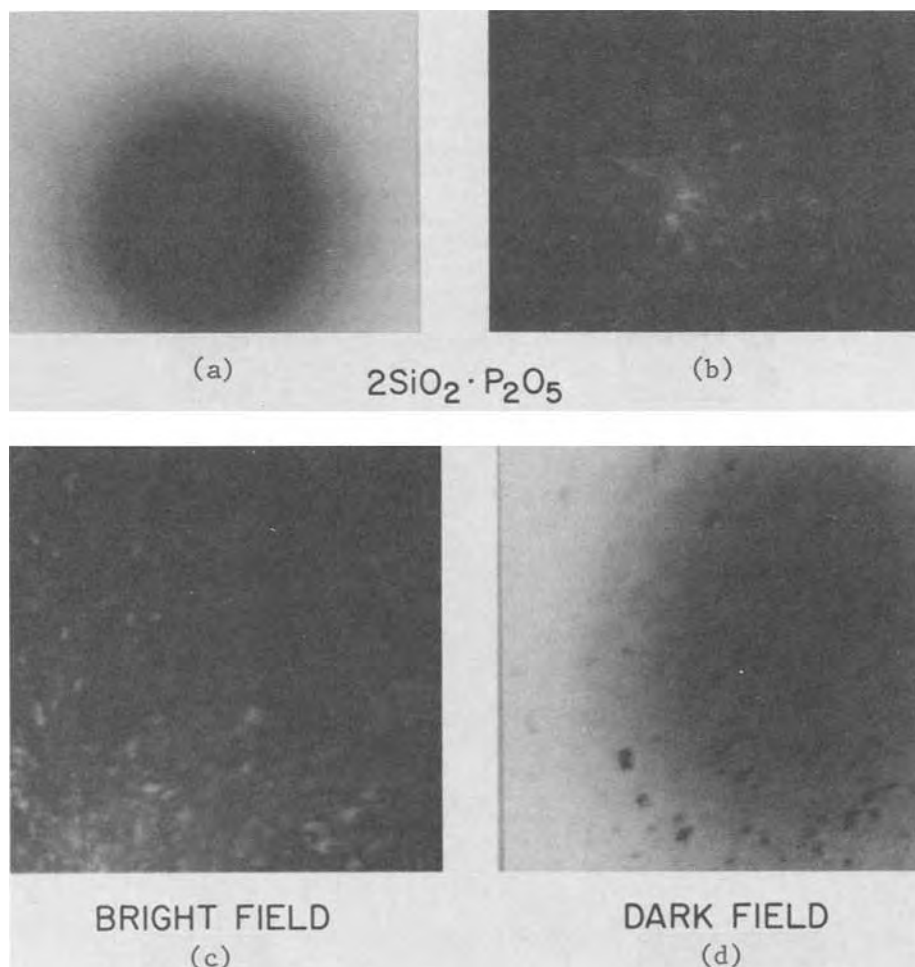
Upon completion of the heating cycles, autoradiographs were made of the  $P^{32}$  diffused samples (Fig. 1), and structural defects were suggested by the appearance of numerous small areas of high  $P^{32}$  concentration. Some of these wafers were diced and portions which showed high  $P^{32}$  concentrations as well as portions showing the least concentrations were prepared for examination in an electron microscope by back jet-etching through the Si substrates using a 9:1  $HNO_3:HF$  etchant. In addition, undiffused wafers were also prepared and examined by the same technique for comparison.

#### Experimental Results and Discussion

Prior to heat-treating the  $SiO_2/Si$  samples transmission and reflection electron diffraction patterns were obtained. The results indicated that the 1000Å  $SiO_2$  film was amorphous, and the electron micrographs confirmed this result. After  $P^{32}$  was diffused at  $525^\circ C$  for 100 hr, samples were taken, using the autoradiographs, from heavily concentrated  $P^{32}$  areas as well as from areas of the lowest concentration in the amorphous films. Electron micrographs and selected area diffraction patterns from these areas showed the onset of crystallization (Fig. 2), and the areas of heavy concentration of the radioactive isotope were found to be completely crystallized while the least concentrated areas showed scattered crystallites in an amorphous matrix. The particles, shaped as spherulites, can be seen in dark field (Fig. 2) when a reflection of the diffraction pattern is used for image formation.

The electron diffraction patterns showed random orientation of the crystallites. The data were analyzed,

Fig. 2.  $P^{32}$  diffused  $SiO_2$  films on (100) Si wafer treated  $525^\circ C$  100 hr showing presence of  $2SiO_2 \cdot P_2O_5$  in the amorphous  $SiO_2$  matrix. (a) Selected area electron diffraction pattern of  $2SiO_2 \cdot P_2O_5$ . (b) Micrograph of area in (a) magnified 36,000X. (c) Bright field of area magnified 63,000X. (d) Dark field of area magnified 63,000X obtained by using  $10\bar{1}2$  reflection for imaging.





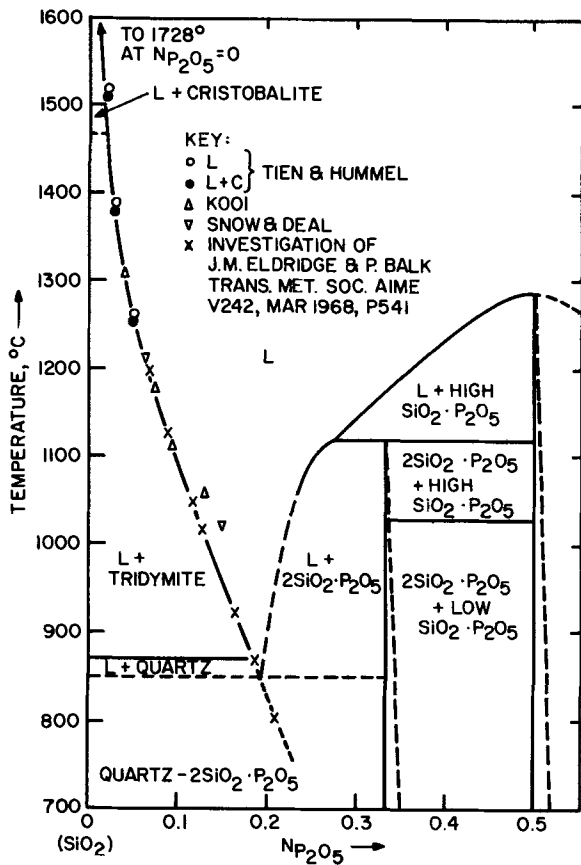


Fig. 3. Correspondence of PSG composition with the maximum solubility of crystalline SiO<sub>2</sub> in phosphosilicate liquid solution. Phase diagram from R. Y. Tien and F. A. Hummel, *J. Am. Ceram. Soc.*, 45, 422 (1962).

as shown in Table I, and the structure was identified as that of 2SiO<sub>2</sub> · P<sub>2</sub>O<sub>5</sub>. According to the phase diagram (Fig. 3) the appearance of this phase at 525°C heat-treatment seemed reasonable.

In the second portion of this investigation, these films were given an additional annealing treatment at 1200°C in evacuated silica ampuls for 25 hr. A transformation was apparent from both the electron diffraction patterns and micrographs (Fig. 4). The analysis of the diffraction data proved that two polymorphic SiO<sub>2</sub> structures were now present. They were the α-quartz form as well as the α-cristobalite form (Fig. 5). The diffraction pattern in Fig. 6 has been indexed. We have found that the major constituent was α-quartz. Since it is known that the polymorphic

Table I. Phase identification of crystallites formed after P<sup>32</sup> was diffused at 525°C for 100 hr

d (Å)	Observed	I	d (Å)	2SiO <sub>2</sub> · P <sub>2</sub> O <sub>5</sub> [Ref. (7-8)] hkl	I/I
			8.06	0.003	
			6.55	1011	34
5.905	S		5.93	1012	19
4.018	S		4.024	0006	44
3.948	VS		3.941	1015	52
			3.932	1120	
3.550	VS		3.533	1123	100
3.401	M		3.364	2021	17
			3.277	2022	6
			3.078	1017	7
2.823	M		2.812	1126	36
			2.783	2025	52
2.669	VW		2.684	0009	6
2.549	W		2.559	2131	17
			2.517	2132	9
2.430	W		2.423	2027	3
			2.367	2134	18
			2.272	2135	
2.281	S		2.270	3030	14
			2.259	2028	
			2.216	1129	17
2.188	W		2.185	3033	8
			2.090	101,11	5
2.057	W		2.063	2137	11
1.972	WM		1.977	3036	25
1.913	VVW		1.910	2243	4
			1.883	3141	3
			1.845	202,11	3
			1.792	101,13	
1.800	W		1.792	112,12	5
			1.766	2246	
1.756	W		1.761	213,10	12
			1.759	3145	
1.700	VW		1.685	4042	4
1.657	W		1.670	213,11	10

phase transformation of SiO<sub>2</sub> is very sluggish, it seems likely that continued annealing for long periods of time at 1200°C would result in the complete phase change to α-cristobalite.

The undiffused films were given heat-treatments of similar times and temperatures. Results were obtained using the identical techniques for sample preparation and examination as in the case of the diffused films. They showed that no crystalline phase developed (Fig. 6).

In summary, our primary concern in this study was the correlation between impurity and its effect on the formation of crystallites of SiO<sub>2</sub> in the amorphous film matrix. No attempt was made to analyze the steps that constitute the chemical reaction which led to

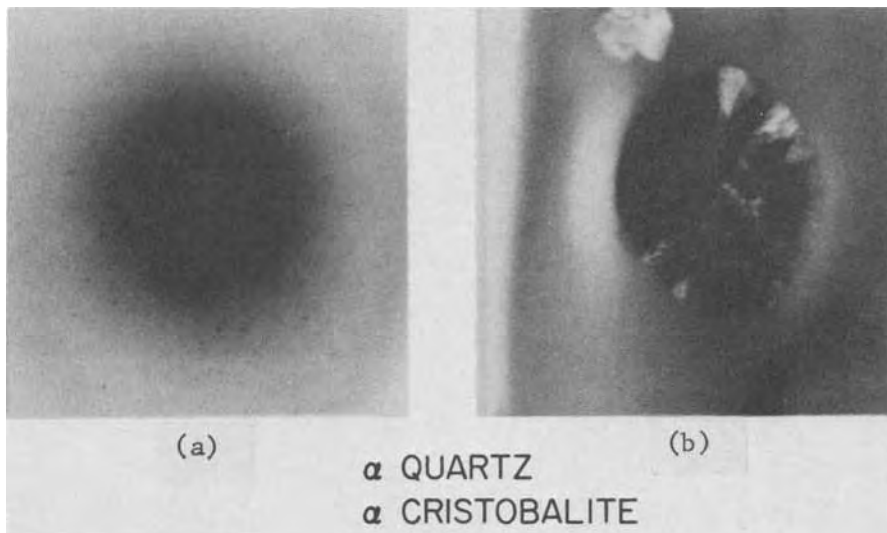


Fig. 4. P<sup>32</sup> diffused SiO<sub>2</sub> film on (100) Si wafer after 100 hr at 525°C. (a) Selected area electron diffraction pattern of α-quartz and α-cristobalite. (b) Electron micrograph of same area 100,000X.



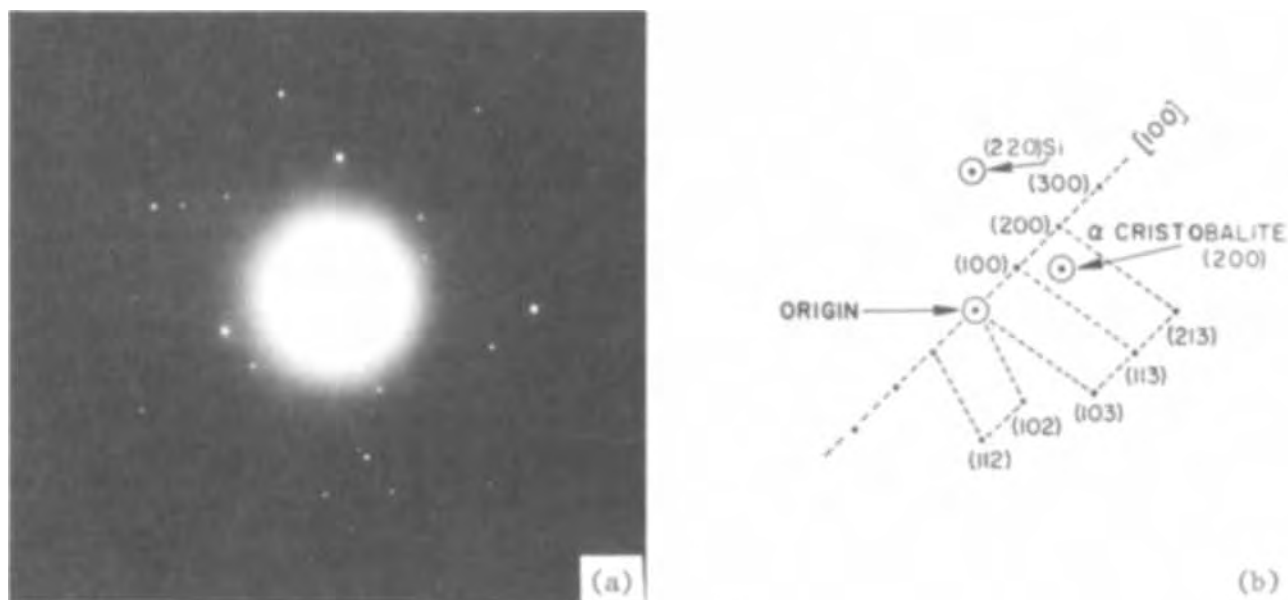
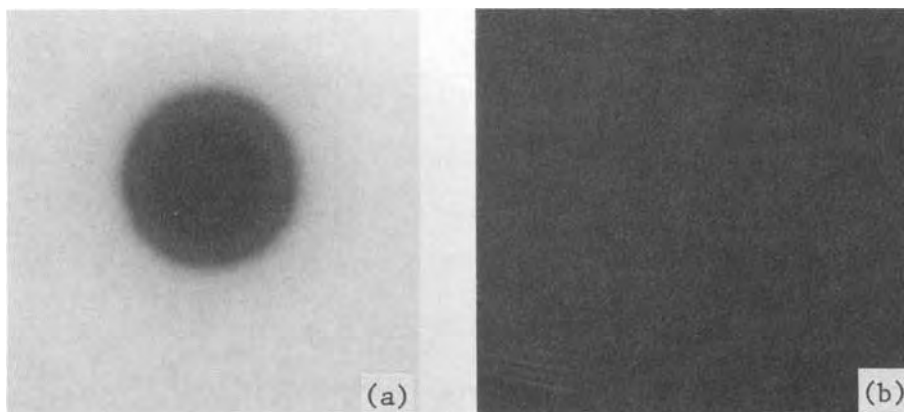


Fig. 5. Transmission electron diffraction pattern. (a) Pattern showing reflections of  $\alpha$ -quartz and  $\alpha$ -cristobalite. (b) Schematic diagram of pattern. Indexed  $\alpha$ -quartz reflections are represented by dots. Type 1121 planes 1 beam, type 1125 planes 11 and horizontal to beam, type 1010 planes 11 and vertical to beam. a and c axis tilted  $24^\circ$  to each other.

Fig. 6. Amorphous  $\text{SiO}_2$ . Undiffused  $\text{SiO}_2$  film on (100) Si wafer heat-treated  $525^\circ\text{C}$ , 100 hr plus; additional 25 hr at  $1200^\circ\text{C}$ . (a) Electron diffraction pattern. (b) Electron micrograph 63,000X.



crystalline compound formation. Rather, we simply note that the phase change after the heat-treatment at  $525^\circ\text{C}$  for 100 hr as shown by varying  $\text{P}^{32}$  concentrations in the autoradiographs and determined by electron microscopy suggests evidence of a first stage of crystallization. This stage is characterized by the appearance of phosphosilicate compounds which in turn become the nuclei for the subsequent growth of crystalline phases of  $\text{SiO}_2$ .

Our work has shown that crystallization does occur when P-rich crystallites form, and their formation is directly dependent on the sufficient transport, by diffusion, of P into localized areas of the amorphous  $\text{SiO}_2$  films. In this study, the presence of a gas phase provided for the rapid transport of  $\text{P}^{32}$  at the film surface. The formation of  $2\text{SiO}_2 \cdot \text{P}_2\text{O}_5$  in turn catalyzed the  $\text{SiO}_2$  phases. Crystallization did not occur in the uniformly P-doped samples of Sugano *et al.* (3) probably because diffusion in the solid amorphous phase is too slow to allow for the formation of suitable nuclei (5).

#### Acknowledgments

The authors are grateful to K. N. Tu for helpful discussions, E. Bassous for growing the films, and K. Grebe for technical assistance in cutting samples.

This research was partially supported by ARPA contract No. F196828-73-C-0006.

Manuscript submitted Aug. 10, 1973; revised manuscript received March 12, 1974.

Any discussion of this paper will appear in a Discussion Section to be published in the June 1975 JOURNAL. All discussions for the June 1975 Discussion Section should be submitted by Feb. 1, 1975.

#### REFERENCES

1. N. Nagasima, *Japan. J. Appl. Phys.*, **9**, 879 (1970).
2. A. N. Knopp and R. Stickler, *Electrochem. Technol.*, **2**, 298 (1964).
3. T. Sugano, K. Hou, K. Kudo, and N. Hishinuma, *Japan. J. Appl. Phys.*, **7**, 715 (1968).
4. A. N. Knopp, *Electrochem. Technol.*, **5**, 37 (1967).
5. T. Y. Tien and F. A. Hummel, *J. Am. Ceram. Soc.*, **45**, 422 (1962).

# C-MOS and Complementary Isolated Bipolar Transistor Monolithic Integration Process

Mougahed Darwish and R. Taubenest

Centre Electronique Horloger S.A., Neuchâtel, Switzerland

The publication costs of this article have been assisted by the Centre Electronique Horloger S.A.

Circuits using integrated complementary MOS and bipolar devices combine the low power consumption of MOS and the current handling capabilities of bipolar technology with optimum use of device area. In addition, the use of the silicon surface properties directly combined with the volume electrical effects have opened a new area of circuit engineering, as exemplified by the BIGFET (1). Earlier attempts of device integration are found in the literature (2, 3). The major difficulties with these earlier fabrication schemes involve a disproportionately large number of masks, a number of difficult overlapping diffusions, and a lack of electrical isolation between the bipolar structures.

In this work, by using the epi layer with the C-MOS process, the bipolar transistors can be isolated, *vs.* the nonisolated bipolar transistors provided by conventional C-MOS process. This feature has significant advantages in circuit design. Since the present work was not oriented to a particular circuit application, there was sufficient latitude in optimizing geometry and electrical parameters. It was found that the use of a vertical npn and a lateral pnp transistor design lent itself particularly well to our fabrication process.

A listing of the various structural elements and electrical parameters for C-MOS and complementary bipolar devices shows that there are a number of common features (Tables I and II). By judicious combination it is possible to reduce the complexity of an integration scheme to a minimum number of steps. It can be seen that it is possible to fabricate at the same time:

1. The n-type substrate of the MOS transistors and the n epi layer of the bipolar transistors.
2. The p<sup>-</sup> diffusion regions which may serve simultaneously as the pockets for the n-channel MOS and as the isolation for the bipolar transistors.
3. The p<sup>+</sup> diffusion regions, forming the (i) source and drain of the p-channel MOS, (ii) the base of the

Key words: monolithic integration, complementary, isolated bipolar, MOS, semiconductor devices.

npn transistors, and (iii) the emitter and collector of the pnp transistors.

In this way, three masks and three diffusions (plus one epi layer) suffice to form the primary steps. To complete the devices another three masks are necessary for: (i) thin oxide regions (source-drain-gate and contacts), (ii) contact windows, (iii) metallization.

Depending upon the application it may be necessary to use one or two additional masks due to two inherent characteristics of such fabrication schemes:

1. The lateral pnp bipolar transistor will have a comparatively low current gain, since the major part of the carriers injected by the lower (bottom) portion of the emitter will not reach the collector (4).

2. For the vertical bipolar transistor npn the depth  $X_{p+}$  of the base is larger than the emitter junction depth  $X_{n+}$ . Consequently, the p-MOS using the same p diffusion will be larger than the n-MOS using the n<sup>+</sup> emitter diffusion. This could possibly be a serious limit of the high frequency performance of the p-channel MOS.

This can be eliminated by using two additional masks to form:

1. A buried layer blocking the useless carrier injection from the bottom of the emitter. Consequently, the current gain of the pnp will be improved.

2. A supplementary p<sup>+</sup>-diffusion (called p<sup>+2</sup>) to form source and drain of the p-channel MOS independently of the p<sup>+</sup> base diffusion.

By way of comparison a set of six masks are also used for metal gate C-MOS and for conventional bipolar technology. Si-gate C-MOS needs six or seven masks (6, 8).

The choice of a six, seven, or eight mask process will depend on the circuit application. In each case the technique makes efficient use of chip area and results in electrically isolated devices. A further advantage is that only conventional masking and fabrication procedures are used. The experimental procedure and results presented here are for devices using the maximum number of eight masks.

Table I. Basic elements for complementary MOS-transistors

	Substrate n-Type	Diffusion p <sup>-</sup>	Elements Diffusion p <sup>+</sup>	Diffusion n <sup>+</sup>
Function	p-channel	n-channel	source-drain p-channel	source-drain n-channel
Properties	$C_s \approx 10^{15}$ at/cm <sup>2</sup>	$C_s \approx 8 \cdot 10^{15}$ at/cm <sup>2</sup>	$C_s > 10^{15}$ at/cm <sup>2</sup> $X_{p+} < X_{SUBSTR.}$	$C_s > 8 \cdot 10^{15}$ at/cm <sup>2</sup> $X_{n+} < X_{p+}$

Table II. Basic elements for complementary bipolar transistors

	Substrate p-type	Epitaxial layer n-type	Elements Diffusion p <sup>-</sup>	Diffusion p <sup>+</sup>	Diffusion n <sup>+</sup>
Function	Bottom isolation	Collector npn Base pnp	Sidewall isolation	Base npn Emitter collector pnp	Emitter npn
Properties	—	—	$N_{p-} > N_{epi}$ $X_{p-} > X_{epi}$	$N_{p+} \gg N_{epi}$ $X_{p+} < X_{epi}$	$N_{n+} \gg N_{p+}$ $X_{n+} < X_{p+}$

Types of bipolar transistors used; npn, vertical type; pnp, lateral type.

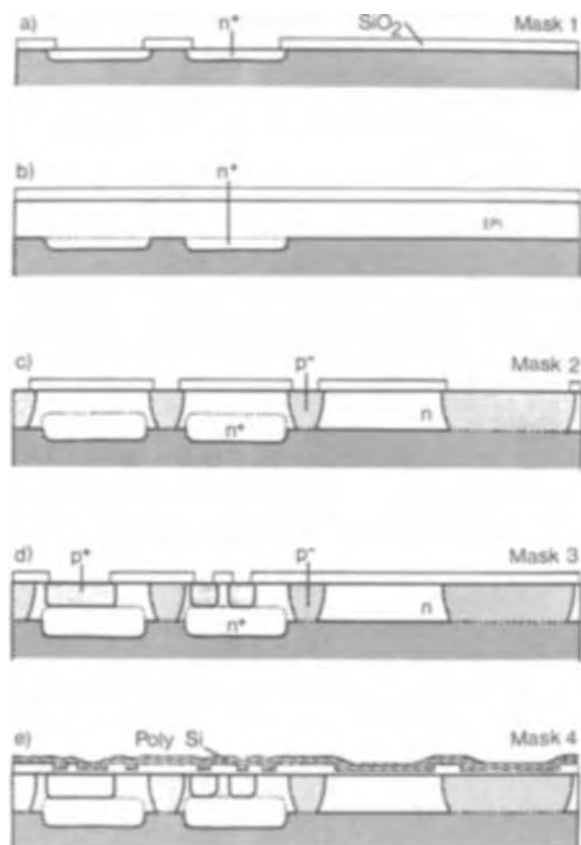


Fig. 1. (a) Window etching and buried layer diffusion. (b)  $n$  epitaxial layer deposition and oxide growth. (c) Window etching and  $p^+$  diffusion. (d)  $p^+$  diffusion. (e) Opening of  $n^{+1}$  and  $p^{+2}$  regions, gate oxidation and polycrystalline silicon deposition.

### Experimental

$p$ -type silicon wafers of the (100) orientation and 2-5 ohm-cm resistivity were cleaned using standard cleaning processes and oxidized in wet oxygen at 1200°C. The oxide layer thickness was approximately 1  $\mu$ m. Then windows were cut into the oxide layer where the buried layers were to be diffused with standard photolithographic and etching techniques (Fig. 1a). The diffusion of the buried layer was carried out using a solid-solid vacuum diffusion process (5) or, alternately, the more convenient doped oxide diffusion process (6). The junction depth and the resistivity of the antimony-doped regions were 4 $\mu$  and 130 ohms/ $\square$ , respectively.

After the appropriate etching and cleaning steps the  $n$ -type epitaxial layer was grown using the thermal decomposition of silane. The thickness of the layer was approximately 7  $\mu$ m, and the resistivity was in the range of 1.5-2.5 ohm-cm (Fig. 1b).

After a second thermal oxidation ( $SiO_2 \sim 1\mu$ ) and the appropriate photoresist work, the oxide windows for the isolation diffusion and the  $p$ -well were etched, followed by a closed-capsule diffusion at 1200°C for 10 hr. In this case the source-wafers were of  $p$ -type with a resistivity of 0.3-0.4 ohm-cm (Fig. 1c).

It should be noted that the condition  $X_{p^-} > X_{epi}$  will be attained during the following heat-treatments.

The base-diffusion ( $p^{+1}$ ) of the vertical npn transistors and the emitter and collector diffusions of the pnp's is accomplished by a boron doped oxide diffusion step, giving a penetration of 2.6 $\mu$  and a sheet resistivity of around 600 ohms/ $\square$  (Fig. 1d).

The base-diffusion is followed by a photoetching step which opens the regions where source-drain-gate of  $n$ - and  $p$ -channel MOS will be formed at the same time as the  $p^+$  and  $n^+$  regions of the bipolar elements. After the formation (7) of the gate oxide (1100Å) a 6000Å layer of polycrystalline silicon is deposited (Fig.

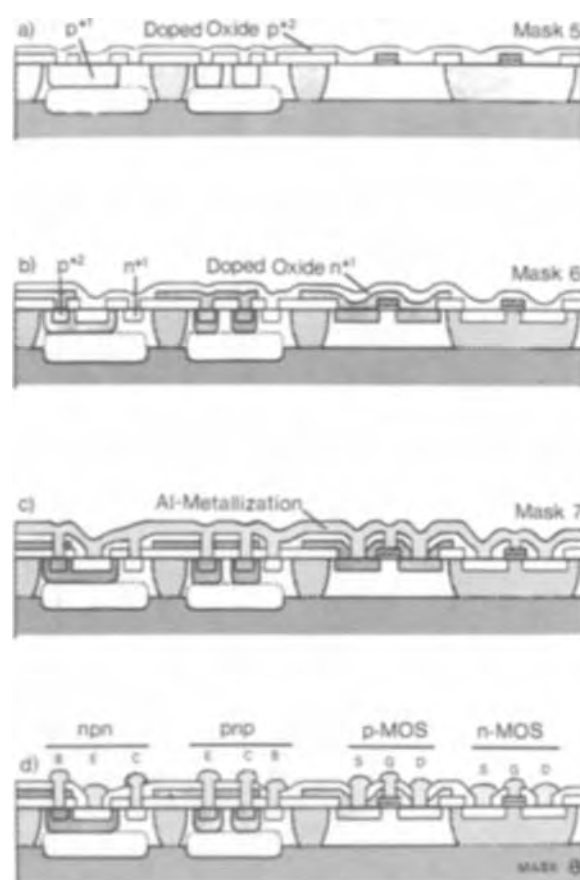


Fig. 2. (a) Poly Si delineation, window opening  $n^{+1}$  and  $p^{+2}$ . Doped oxide deposition  $p^{+2}$ . (b) Window etching for  $n^{+1}$  regions, doped oxide deposition  $n^{+1}$ , simultaneous diffusion of  $p^{+2}$  and  $n^{+1}$  regions. (c) Etching of contact windows and evaporation of Al. (d) Delineation of contacts and interconnections.

1e), the gate electrodes delineated and the remaining thin oxide on the source-drain regions is etched away. Next a boron-doped oxide layer is deposited on the entire surface (Fig. 2) and openings are etched out where the  $n^+$  regions will be diffused (source and drains and polycrystalline Si layer for gate of the  $n$ -channel MOS, emitter of the npn transistor,  $n$ -contacts). The etching process is followed by a phosphorus-doped oxide deposition. Finally the  $p^{+2}$  and the  $n^+$  regions (MOS) are diffused in a single diffusion cycle (6), giving a penetration of 1 $\mu$  and a sheet resistivity of 100 ohms/ $\square$ , both for boron and phosphorus.

An evaporated and photoetched layer of aluminum (1  $\mu$ m) provides for the necessary contacts and interconnections. A final annealing step in forming gas at 400°C reduces oxide charge (8).

### Results

As shown in Tables III and IV the electrical parameters of typical devices constructed in this manner

Table III. Characteristic properties of the MOS transistors

Type of transistor	$V_{th, extr.}$ (volts)	$\beta$
$n$ -channel	0.68	13
$p$ -channel	0.80	3.8
parasitics	>5.45	—

$$W = L = 10 \mu\text{m}.$$

$$W, \text{ gate width; } L, \text{ gate length; } \beta = 2 \left[ \left( \frac{\partial \sqrt{I_D}}{\partial V_G} \right)_{V_D} \right]^2.$$

Table IV. Characteristic properties of the bipolar transistors

Type of transistor	$h_{fe}$ at $I_B = 1 \mu A$ $V_{CE} = 1V$	$BV_{EBO}$ (V)	$BV_{BCO}$ (V)	$BV_{RCO}$ (V)
npn	150	13	10	38.5
pnp	8	38.5	35	38.5

The gain of the pnp transistors is controlled by  $\beta^*$  in the following equations:  $h_{fe} = \frac{\alpha}{1 - \alpha}$  where  $\alpha = \gamma\beta^*$  and  $\beta^* = 1/(\cosh W_p/L_p)$ . The symbols have the usual meaning.

compare favorably with the conventional discrete technology.

The properties of the npn and the pnp transistors are given in Table IV.

The  $\gamma$  may be optimized by the proper choice of the diffusion parameters of the  $p^{+1}$  diffusion and the buried layer diffusion,  $W_p$ , by adjusting the physical dimensions and  $L_p$  by choosing arsenic instead of antimony as the dopant for the buried layer because of the higher minority carrier lifetime (9).

**Conclusion**

It should be stressed that the MOS + bipolar approach also allows for a high degree of freedom in the optimization of the respective elements. The diffusions  $n^{+}$ ,  $p^{+1}$  and the buried layer are available for the optimization of the bipolar part of the circuit. The bipolar transistors are less sensitive to the surface concentration in the p-wells. This allows easy adjustment of the threshold voltage of the MOS transistors

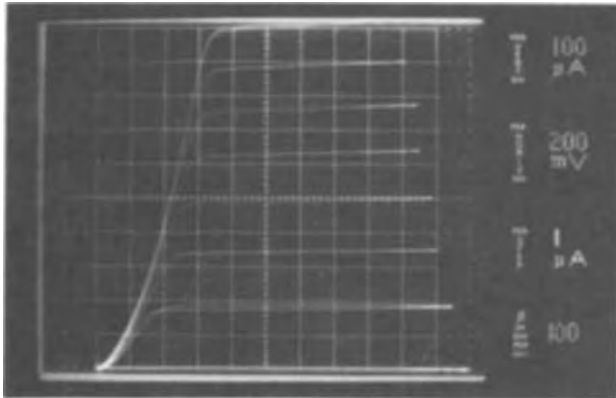


Fig. 3. Bipolar transistor npn. Curves  $I_c = f(V_{CE})$ , shown with increasing steps of  $I_B$ . Emitter surface:  $10 \times 10 \mu m^2$ ;  $BV_{CE} = 13V$ .

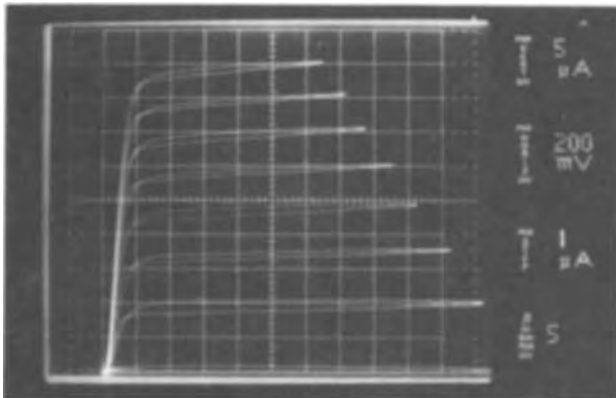


Fig. 4. Bipolar transistor pnp. Curves  $I_c = f(V_{CE})$ , shown with increasing steps of  $I_B$ . Emitter surface:  $10 \times 10 \mu m^2$ ;  $BV_{CE} = 38V$ .

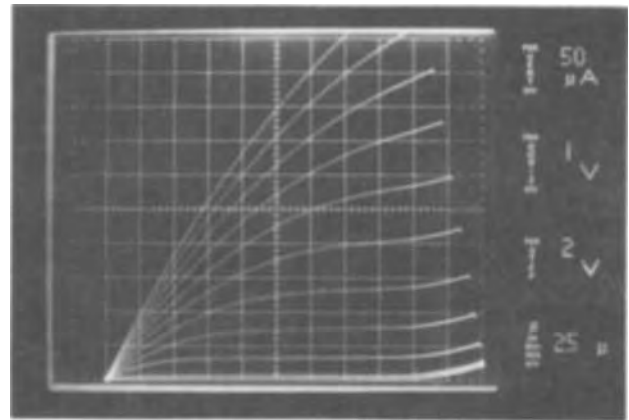


Fig. 5. P-channel MOS, silicon gate. Curves  $I_D = f(V_D)$ , shown with increasing steps of  $V_G$ . Gate surface:  $10 \times 10 \mu m^2$  (nomin.).

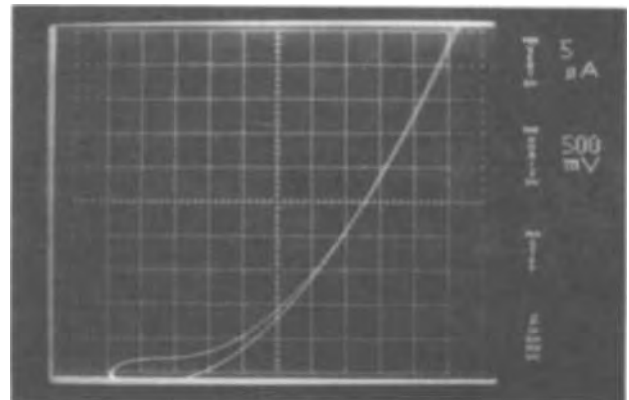


Fig. 6. P-channel MOS, silicon gate. Curve  $I_D = f(V_D)$ , at  $V_D = V_G$ .

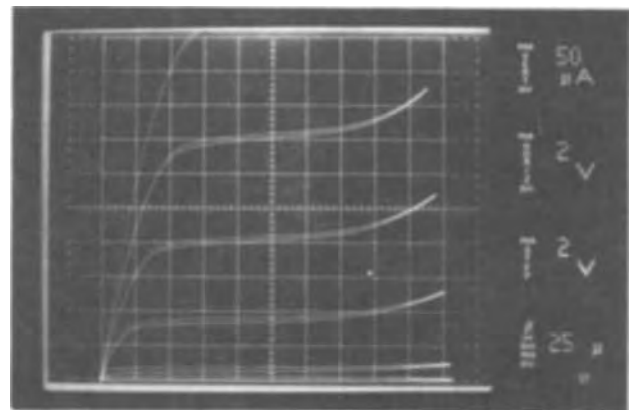


Fig. 7. N-channel MOS, silicon gate. Curve  $I_D = f(V_D)$ , shown with increasing steps of  $V_G$ . Gate surface  $10 \times 10 \mu m^2$  (nomin.).

for optimization in particular applications. Otherwise, the limitations and tolerances of the separate bipolar and C-MOS processes apply to this technology.

One immediate application of this technology is in the area of light emitting diode displays. The MOS circuits perform the appropriate logic and decoding functions and the bipolar devices provide the switching and current handling.

More generally, such a technology is useful in applications where logic and analogic functions are required simultaneously as for instance in thermocompensation circuits. The bipolar is used as an analog device while the MOS performs the digital part.

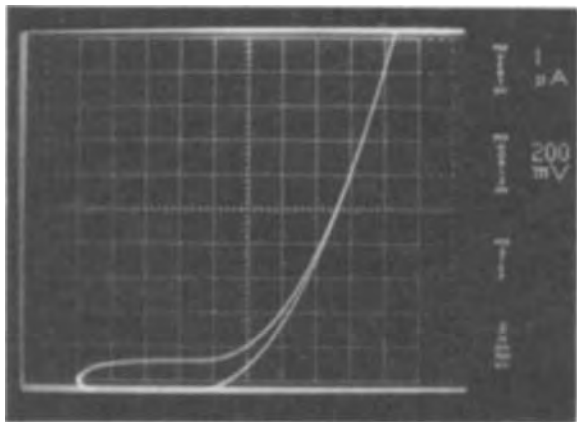


Fig. 8. N-channel MOS, silicon gate. Curve  $I_D = f(V_D)$ , at  $V_D = V_G$ .

### Acknowledgments

The authors are indebted to F. Leuenberger and R. Guye for valuable contributions, and to M. Perdrix for efficient technical assistance.

Manuscript submitted June 20, 1973; revised manuscript received Dec. 10, 1973.

Any discussion of this paper will appear in a Discussion Section to be published in the June 1975 JOURNAL. All discussions for the June 1975 Discussion Section should be submitted by Feb. 1, 1975.

### REFERENCES

1. G. Mayer, G. Cheney, E. Kings, and E. Parks, *Bell Syst. Tech. J.*, **51**, 363 (1972).
2. H. C. Lin, J. C. Ho, R. Iyer, and K. Kwong, *IEEE Trans. Electron Devices*, **ED-16**, 945 (1969).
3. F. J. Link, R. Cook, and R. J. Lesniewski, *Electronics*, **43**, 72 (1970).
4. J. Lindmayer and W. Schneider, *Solid-State Electron.*, **10**, 225 (1967).
5. R. Dahlberg, R. Gereth, A. Kostka, and K. Kreuzer, in "Semiconductor Silicon", R. R. Haberecht and E. L. Kern, Editors, p. 458, The Electrochemical Society Softbound Symposium Series, New York (1969).
6. E. Vittoz, B. Gerber, and F. Leuenberger, *IEEE Sol. St. Circuits*, **SC-7**, 100 (1972).
7. F. Leuenberger, *Electronics Letters*, **7**, 561 (1971).
8. F. Faggin and T. Klein, *Solid State Electron.*, **13**, 1125 (1970).
9. J. Simpson, R. Lieberman, R. F. Helm, and M. H. Hanes, Paper 201RNP presented at Electrochemical Society Meeting, Cleveland, Ohio, Oct. 3-7, 1971.

## Brief Communications



### Luminescence of Alkali-Alkaline Earth-Phosphates Activated with $\text{Eu}^{2+}$

M. S. Waite

*Division of Materials Science and Physics, Thames Polytechnic, London, S.E. 18, England*

*The publication costs of this article have been assisted by the Thames Polytechnic.*

Orthophosphates of formula  $\text{M}^{\text{I}}\text{M}^{\text{II}}\text{PO}_4$ , where  $\text{M}^{\text{I}} = \text{Li, Na, and K}$  and where  $\text{M}^{\text{II}} = \text{Ca, Sr, and Ba}$ , have been examined as hosts for various activators, but principally  $\text{Ce}^{3+}$ ,  $\text{Sn}^{2+}$  (1, 2), and  $\text{Cu}^+$  (3). The  $\text{Ce}^{3+}$  doped phosphors were found to possess moderate efficiencies, up to 4%, under electron beam excitation (1) and high efficiencies under 254 nm excitation, 88% (quantum efficiency) being quoted for  $\text{LiSrPO}_4:\text{Ce}$  (3). High quantum efficiencies under 254 nm excitation can also be observed with Cu as activator (3). As part of a survey of  $\text{Eu}^{2+}$  doped phosphors we have examined the effect of  $\text{Eu}^{2+}$  activation on this group of materials and the preliminary results are summarized below.

Phosphors were prepared by firing  $\text{M}_2\text{CO}_3$ ,  $\text{M}^{\text{II}}\text{CO}_3$ , and  $(\text{NH}_4)_2\text{HPO}_4$  with  $\text{Eu}_2\text{O}_3$  to a fixed dopant concentration of 2 mole per cent (m/o). The firing was carried out in two stages: an initial firing at 800°-900°C being followed by firing in 2%  $\text{H}_2/\text{N}_2$  at 1000°-1200°C. All the members of this group showed  $\text{Eu}^{2+}$  band luminescence but with considerable variation in efficiency to ultraviolet and electron beam excitation. X-ray powder photographs were taken of the powdered phosphors and the  $d$  (hkl) values compared with those reported by Wanmaker and Spier and with other lit-

erature values (4-7). The "heavier" members of this group of compounds, where  $\text{M}^{\text{I}} = \text{K, Na}$  and  $\text{M}^{\text{II}} = \text{Ba, Sr, Ca}$ , are polymorphic, the low temperature form being orthorhombic with the  $\beta$   $\text{K}_2\text{SO}_4$  structure (8). The phosphors prepared by the techniques outlined above are predominantly of this form, in agreement with the conclusions expressed by Wanmaker and Spier (3). The  $d$  (hkl) values for the lithium containing phosphors also agree with those reported by these authors.

Emission spectra under 365 nm excitation are given in Fig. 1. Estimates of the efficiencies under both 365 and 250-270 nm excitation have been made using as standards several phosphors from Levy West Laboratories:  $\text{Zn}_2\text{SiO}_4:\text{Mn}$ ,  $\text{ZnS}:\text{Ag}$ , and  $\text{ZnS}:\text{Cu}$  (Table I). Although a thorough optimization has not yet been completed it seems that the K- and Ba-containing phosphors are the most efficient. This is in contrast to the case of cerium and copper doping where the lithium-based phosphors were found to be the most efficient. Assuming a value of at least 80% for the quantum efficiency of the standard willemite sample under 254 nm excitation,<sup>1</sup> then the efficiency of  $\text{KBaPO}_4:\text{Eu}$ , which is comparable, may prove high enough for commercial application.

**Key words:** luminescence, phosphates,  $\text{Eu}^{2+}$  activation.

<sup>1</sup> Manufacturer's recommendation.

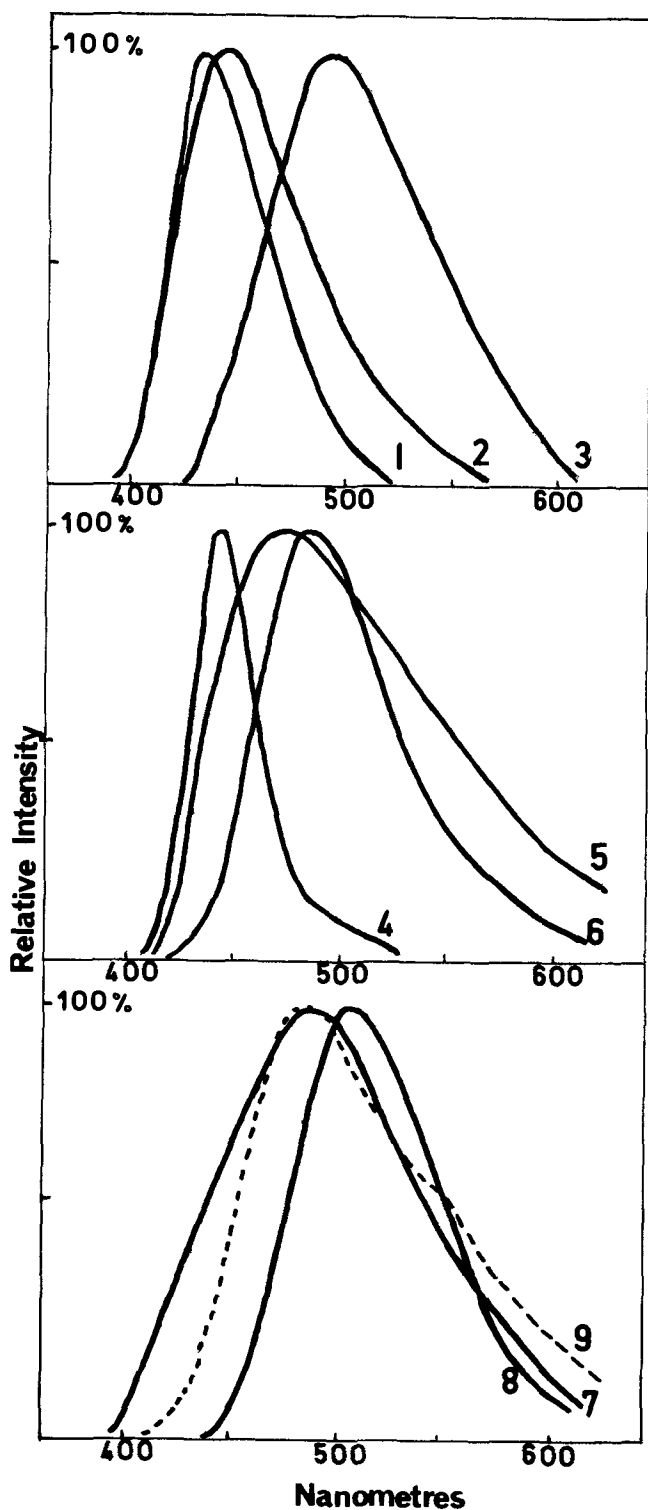


Fig. 1. Emission spectra under 365 nm (Hg) excitation. Curve 1,  $\text{KBaPO}_4$ ; curve 2,  $\text{NaBaPO}_4$ ; curve 3,  $\text{LiBaPO}_4$ ; curve 4,  $\text{KSrPO}_4$ ; curve 5,  $\text{NaSrPO}_4$ ; curve 6,  $\text{LiSrPO}_4$ ; curve 7,  $\text{KCaPO}_4$ ; curve 8,  $\text{NaCaPO}_4$ ; curve 9,  $\text{LiCaPO}_4$ .

Measurements of the CR efficiencies were made for several of these phosphors. The results are given in Table II with the response times to pulsed beam excitation as determined by Wight and Bramwell, Services Electronics Research Laboratories, Baldock, England.  $\text{KSrPO}_4$  shows the best combination of efficiency ( $\sim 5\%$ ) with fast response ( $< 200$  nsec) and narrow band width ( $< 40$  nm).

Table I. Emission characteristics with ultraviolet excitation

Phosphor	Emission max. (nm)	Band width (nm)	Band area (relative to standard)*	
			(365 nm excitation)	(250-270 nm excitation)
$\text{KBaPO}_4$ :Eu	430	50	185	105
$\text{NaBaPO}_4$ :Eu	440	70	135	80
$\text{LiBaPO}_4$ :Eu	483	85	15	15
$\text{KSrPO}_4$ :Eu	430	35	65	30
$\text{NaSrPO}_4$ :Eu	455	120	10	10
$\text{LiSrPO}_4$ :Eu	470	70	20	15
$\text{KCaPO}_4$ :Eu	485	110	35	35
$\text{NaCaPO}_4$ :Eu	505	78	40	20
$\text{LiCaPO}_4$ :Eu	485	105	60	45
ZnS:Ag (Levy West Type G231, Ni killed, Batch No. 16538C)			100	
ZnS:Cu (Levy West Type FF12, Batch No. 117)			92	
$\text{Zn}_2\text{SiO}_4$ :Mn (Levy West Type H916, Batch No. 233)				100

\* Believed correct to  $\pm 5\%$ .

Table II. Efficiencies and response times to electron beam excitation

Phosphor	Energy efficiency, %*	Response times, nsec†	
		Rise	Decay
$\text{KBaPO}_4$ :Eu	$2.4 \pm 0.3$	315	220
$\text{NaBaPO}_4$ :Eu	$2.0 \pm 0.2$	630	680
$\text{KSrPO}_4$ :Eu	$5.2 \pm 0.5$	185	170
$\text{KCaPO}_4$ :Eu	$0.2 \pm 0.03$		
$\text{NaCaPO}_4$ :Eu	$4.0 \pm 0.5$	480	560
$\text{LiCaPO}_4$ :Eu	$0.5 \pm 0.1$	460	640

\* Beam voltage, 8 kV; current density,  $0.01$ - $1.0 \mu\text{A}/\text{cm}^2$ .  
† 25 kV,  $1 \mu\text{A}$  pulses of width  $10 \mu\text{sec}$ ; response time quoted as  $1/e$  value.

Thus, the preliminary investigation indicates that several members of this group of phosphors may possess promising characteristics as lamp or CRT phosphors and a more detailed investigation of the connection between structure or composition and efficiency is being carried out.

#### Acknowledgments

We are grateful to D. R. Wight and Miss S. Bramwell for permission to publish the response time measurements and to A. Vecht of Thames Polytechnic and P. J. Dean and D. Robbins of the Royal Radar Establishment, Malvern, England, for valuable discussion.

We gratefully acknowledge the permission of the Ministry of Defence to publish this work.

Manuscript received Feb. 5, 1974.

Any discussion of this paper will appear in a Discussion Section to be published in the June 1975 JOURNAL. All discussions for the June 1975 Discussion Section should be submitted by Feb. 1, 1975.

#### REFERENCES

1. A. Brill and H. A. Klasen, *Philips Res. Rept.*, **7**, 421 (1952).
2. A. Brill, H. A. Klasen, and P. Zalm, *ibid.*, **8**, 393 (1953).
3. W. L. Wanmaker and H. L. Spier, *This Journal*, **109**, 109 (1962).
4. E. Thilo, *Naturwissenschaften*, **10**, 239 (1941).
5. R. Klement and F. Steckenreiter, *Z. Anorg. Allgem. Chem.*, **245**, 236 (1950).
6. R. Klement and P. Kresse, *ibid.*, **310**, 53 (1961).
7. M. A. Bredig, *J. Phys. Chem.*, **46**, 747 (1942).
8. R. W. G. Wyckoff, "Crystal Structures," 2nd ed., Vol. 3, Chap. VIII B, Interscience Publishers, New York (1963).

# Self-Aligned Gaps—An Alternative Technique for Closely Spaced Metallization Patterns

J. D. E. Beynon, R. A. Haken, and I. M. Baker

Department of Electronics, University of Southampton, Southampton, England

Recently much interest has been shown in producing narrow lateral gaps in metallization patterns, particularly for charge-coupled structures. A recent paper by Berglund *et al.* (1) describes a technique in which the lateral gap between electrodes can be made very small, or even eliminated, by separating adjacent electrodes by a vertical gap. The necessary discontinuity in the metallization is achieved by using a "shadowing" effect during vacuum deposition of the metal. The structure described by Berglund *et al.* relies on the formation of a ledge (or hangover) at the insulator step; this is accomplished by selectively undercutting a double-insulator system that exhibits a disjoint etching characteristic. The ledge is subsequently used to form the required "shadow" in the metallization. They did not consider using an oxide step for producing the shadow because such steps do not have vertical edges; they also envisaged difficulty in generating a well-collimated metal vapor beam during deposition.

We have found, however, that closely spaced metallization patterns can be fabricated by using oxide steps to produce a shadow in the beam of metal vapor when this is deposited obliquely to the plane of the slice. In this connection we have investigated the effect of etch temperature upon the profile of the oxide step [Haken *et al.* (2)]; we have found that a near vertical oxide edge can be obtained near the top of the step if the etch temperature is no more than 25°C (at higher temperatures the oxide edge becomes shallower). By evaporating the metal at a relatively low rate (of the order of  $10^{-3} \text{ cm}^{-3} \text{ sec}^{-1}$ ) and by employing a source-to-target distance of 20 cm, we have obtained sufficiently good resolution in the shadow to produce satisfactory self-aligned gaps.

Using this technique, we have produced CCD's with aluminum [Baker *et al.* (3)] and gold/nichrome metallization; a typical gap in a 32 bit CCD shift register with gold/nichrome metallization is shown in Fig. 1 where the oxide step height is  $0.3 \mu\text{m}$ . The interelectrode gap is  $0.5 \mu\text{m}$  and the total length of gap in one of these registers is  $0.64 \text{ cm}$ .

This technique compares favorably with others that have been proposed for producing closely spaced metallization patterns. Its main advantage is the extreme

**Key words:** charge-coupled devices, self-aligned gaps.

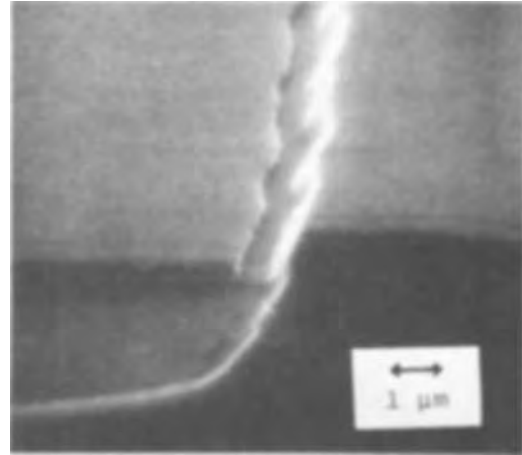


Fig. 1. Part of one of the interelectrode gaps in the CCD structure described in the text. The oxide step height is  $0.3 \mu\text{m}$  and the gap width is  $0.5 \mu\text{m}$ . (The large depth of field of the electron microscope is partly responsible for the ragged appearance of the oxide step; note, however, how the edge of the metal faithfully follows the profile of the top of the oxide step.)

simplicity with which small gaps can be fabricated; only one mask is needed to define the oxide steps which are subsequently used to form the shadows in the metal vapor beam. We intend to publish a more detailed account of CCD device fabrication using this technique shortly.

Manuscript received Dec. 17, 1973.

Any discussion of this paper will appear in a Discussion Section to be published in the June 1975 JOURNAL. All discussions for the June 1975 Discussion Section should be submitted by Feb. 1, 1975.

## REFERENCES

1. C. N. Berglund, J. T. Clemens, and E. H. Nicollian, *This Journal*, **120**, 1255 (1973).
2. R. A. Haken, I. M. Baker, and J. D. E. Beynon, *Thin Solid Films*, **18**, 53 (1973).
3. I. M. Baker, J. D. E. Beynon, and M. A. Copeland, *Electron. Letters*, **9**, 48 (1973).



## Current Developments in Electric Ground Propulsion Systems, R&D Worldwide

James D. Busi and Lawrence R. Turner\*

U.S. Army Foreign Science and Technology Center, Charlottesville, Virginia 22901

The publication costs of this article have been assisted by the Department of the Army.

In an attempt to decrease atmospheric pollution in major population centers throughout the world and to partially reduce the automotive demand on the world's limited petrochemical supply, numerous foreign and domestic research programs have been initiated to develop power sources to supplement or replace the combustion engine in ground transportation vehicles. All-electric and hybrid-electric vehicles have been proposed, designed, and developed in an attempt to save the environment and to more efficiently use existing petrochemical fuels. Although hybrid-electric vehicles have been successfully demonstrated, the major emphasis of this paper is on all-electric vehicles and their potential electrochemical power sources. To develop competitive vehicles of these types, power sources with increased thermal, electromechanical, and electrochemical energy conversion efficiencies and transfer systems must be developed. Vehicles which are efficient, cost effective, and reliable, and require very little maintenance over extended periods of time, are a primary developmental goal. The over-all advantages of a total-electric or hybrid-electric vehicle are: (i) reduction of emission and noise pollution; (ii) increase in off-road mobility for military applications through the use of electronic slip control of the vehicle's speed, acceleration, and braking; (iii) regenerative braking to regain energy in the form of momentum normally wasted in conventional braking; and (iv) relatively low maintenance requirements. Currently, the major disadvantages of an electric vehicle are limited range and speed, and high cost. Electric vehicles are initially far more expensive than conventional automobiles due to limited production (approximately 20,000/yr in the United States). Once electric vehicles become publically accepted for both urban and rural transit, the "hard-tool" production of standard vehicles will be undertaken, and their initial cost will decrease significantly.

### Foreign Developmental Programs

Currently, eight countries are conducting the majority of the active research in the area of all-electric and hybrid-electric vehicles: United States, U.S.S.R., United Kingdom (U.K.) Japan, Sweden, France, Italy, and the Federal Republic of Germany (F.R.G.). Most foreign and domestic programs include development of a variety of potential electrochemical power sources plus road testing of advanced prototype vehicles made of new lightweight plastic and composite materials.

If one were to try to rate all of these countries in the area of electric vehicle and battery/fuel cell de-

velopment, one might obtain some close variation of the following:

Vehicle development	Battery/fuel cell development
1. U.K., U.S., Japan	1. Japan
2. F.R.G.	2. U.S.
3. U.S.S.R.	3. U.K.
4. France	4. France, F.R.G.
5. Italy	5. Sweden, U.S.S.R.
6. Sweden	6. Italy

These rankings are based upon the total amount of R&D funding programmed up to 1975, the number of fundamental and applied research programs, and the actual number of successful prototype electrochemical power sources experimentally demonstrated in laboratory cells and tested vehicles.

**Federal Republic of Germany (F.R.G.).**—In the F.R.G., no national program per se exists for the development of electric vehicle systems. The government, however, does have some major influence on the direction and funding of programs that are presently being pursued since sponsorship of a majority of the effort is by industrial consortiums that are under close government control. Nine major German industrial firms, with a budget estimated to be greater than \$650,000 for battery and fuel cell development alone, are presently involved in the various phases of electric vehicle R&D.

In 1970, Dr. Helmut Meysenber, the Technical Director of the Rheineschwesfäelisches Electrizaetswerke, AG (RWE), announced the organization and financing of a group of companies to develop electric vehicles by 1972. Included in this group were Rheineschwesfäelisches Electrizaetswerke, AG, VARTA, AG (traction batteries), Robert Bosch (motors and controls), Messerschmitt Bölkow Blohm (MBB) (assembly), and Farbrenfabriken Bayer, AG (plastic body). Figure 1 shows two versions of this group's electric transport vehicle which has now been produced on an experimental basis and which was demonstrated at the 1972 Munich Olympics.

A second major program has been undertaken by Volkswagen's Wolfsburg Research and Development Center (manufacture), Robert Bosch (motors and controls), and VARTA, AG (traction batteries) for the development of a prototype vehicle, the "Electrovan," shown in Fig. 2, which is equipped with a roll-on/roll-off battery exchange rack. Further, a third group, Mercedes (Daimler-Benz Aktiengesellschaft) (design and manufacture), Robert Bosch (motors and controls), and VARGA, AG (traction batteries), has developed a hybrid-electric bus and a transport van, shown in Fig. 3-5 which in 1972 were road tested in Frankfurt and Hamburg (1-4).

\* Electrochemical Society Active Member.

Key words: fuel cell, traction batteries, sodium-sulfur battery.



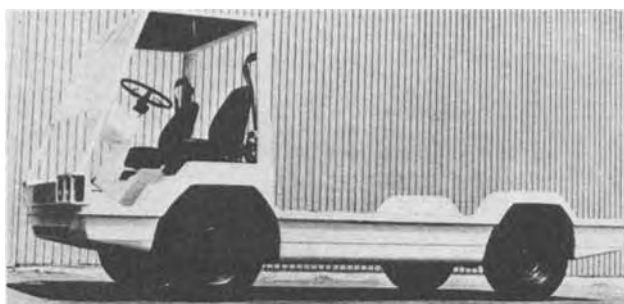


Fig. 1. The F.R.G. "marathon" van. Battery type, lead-acid; number of cells, 72; rating, 144V, 180 A-hr; maximum range, 65 miles; maximum speed, 50 mph; payload, 2200 lb.



Fig. 2. Volkswagen electric van showing battery rack. Battery type, lead-acid; maximum range, 60 miles; maximum speed, 45 mph; payload, 2000 lb.

Japan.—In 1966, the Japanese set up a program to tackle positively technical problems and to develop new technologies to keep pace with the growth momentum of their economy. A system of National Research and Development Programs was established and, in conjunction with their requirements, the Agency of Industrial Science and Technology of the Ministry of International Trade and Industry (MITI) launched a program for the development of electric vehicles with a 1971-1975 budget of \$14 million. This over-all program is illustrated in Fig. 6.

During the 1971-1975 time period, R&D efforts were initiated for the development of an over-all structure most suitable for an electric vehicle, plus an epochal improvement in component parts was initiated. The plan for the electric vehicles entails the simultaneous pursuit of a wide variety of associated R&D areas, which have been grouped into five projects: (i) es-



Fig. 3. Mercedes electric van. Battery type, lead-acid; rating, 144V, 150 A-hr; maximum range, 35 miles; maximum speed, 48 mph.



Fig. 4. Mercedes hybrid-electric bus. Battery type, lead-acid; rating, 380V, 275 A-hr; maximum range, 180 miles; maximum speed, 35 mph.

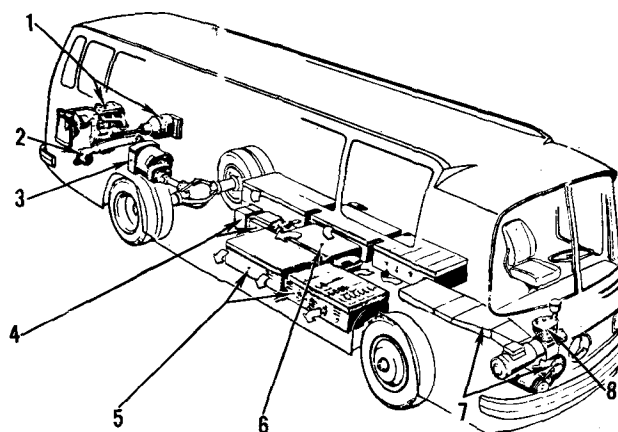


Fig. 5. Cross-sectional view of Mercedes hybrid-electric bus. 1, OM 314 motor with generator; 2, cooling blower for traction motor; 3, electric traction motor with speed reduction drive; 4, high voltage section; 5, five lead batteries; 6, electronic control; 7, blower for cooling the batteries; 8, air compressor and power steering pump.

establishment of test and evaluation criteria; (ii) development of experimental vehicles; (iii) development of components; (iv) development of charging systems; and (v) study of utilization systems.

The design objectives set forth thus far outline the development of a small- and medium-scale transport vehicle, a small- and medium-scale passenger vehicle, and a bus specified in Table I. The Japanese have recently tested a municipal transportation system designed around a lead-acid battery, electric-drive, mass-transport vehicle.

The success of past tests has led to the purchase of additional buses which use the roll-on/roll-off modu-

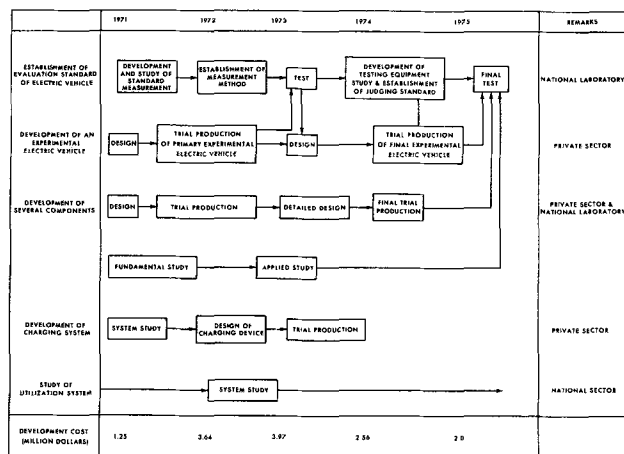


Fig. 6. The over-all Japanese development plan for electric vehicles.

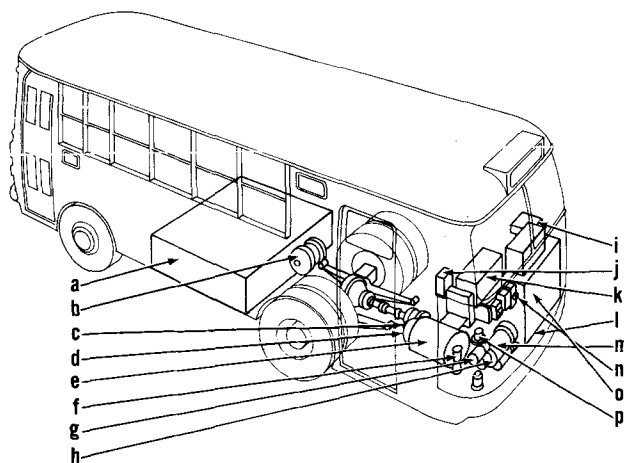


Fig. 7. Sectional view of Osaka electric bus. a, Power unit (batteries); b, air tank; c, parking brake; d, first stage reduction gear; e, main motor; f, air compressor; g, oil pump; h, auxiliary motor; i, forward/reverse transfer device; j, auxiliary battery; k, controller; l, controller; m, voltage convertor; n, no-break fuse; o, controller; p, controller.

lar battery pack concept. The construction of the Osaka electric bus and its recharging station are shown in Fig. 7 and 8; these are similar to West German all-electric buses developed by MAN, VARTA AG, and RWE. Daihatsu and Nissan Motor Company Limited have also produced commercial electric vehicles for a number of years. Recently, both companies have produced several electric vans demonstrated at EXPO-70. These are shown in Fig. 9 and 10 (5-8).

*The United Kingdom.*—The first electric vehicle appeared before a startled British public in 1837, the same year Queen Victoria came to the throne. Although a primitive form of vehicle, this electric car

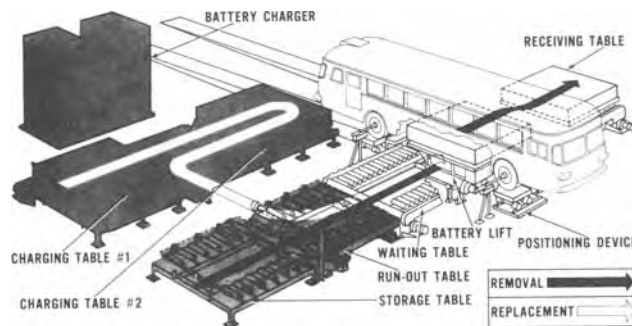


Fig. 8. Osaka electric bus battery charging replacement equipment.



Fig. 9. Daihatsu S37 V-type electric van. Battery type, improved lead-acid; capacity, 72V, 125 A-hr; no. of batteries, 7; maximum range, 42 miles; maximum speed, 42 mph; weight, 1650 lb; payload, 550 lb.

was a prototype for a new viable means of transport in the United Kingdom. Today, the electric vehicle population in the U.K. is estimated to exceed one-half million. The majority of these are industrial trucks, but a surprising number are registered road vehicles.

Although no known national program for the development of electric vehicles exists in the U.K., the government does influence the existing effort through the Electricity Council. The U.K. is one of the world's leaders in electric vehicle design, development, and application, and exports electric vehicles to a number of other nations (more than 30 companies produce electric vehicles in the U.K.). Funding for the development of electrochemical power sources this year alone is estimated to exceed \$950,000. Figure 11 points out the depth of the U.K. program, and its primacy in many developmental areas was the announcement in late 1972 of the operation of the world's first sodium-sulfur battery-powered vehicle. Even though this vehicle is in the early prototype stages, it is the

Table I. Projected specifications and performance of Japanese electric vehicles (end of 1973) (8)

Parameters	Cargo vehicle		Passenger vehicle		Bus
	Small scale	Medium scale	Small scale	Medium scale	
No. of passengers	2	2	4 or 2	5 or 3	60-80
Payload (kg)	200	1,000	100	300	—
Total weight (kg)	1,100	3,500	1,000	2,000	15,000
Maximum speed (km/hr)	70	70	80	80	60
Range (km)	130-150	180-200	130-150	180-200	230-250
Acceleration ability [0-30 km/hr (sec)]	5	5	4	3	8
Climbing ability (speed up 6° slope)	40	40	40	40	25

The weight of batteries is less than 30% of vehicle weight.  
 Energy density of lead batteries is 60 W-hr/kg.  
 Range of one charge is construed to be the distance traveled at 40 km/hr on a constant basis.



Fig. 10. Nissan short haul electric vehicle. Capacity, 96V, 125 A-hr; maximum range, 41 miles; maximum speed 32 mph; weight, 2000 lb; payload, 550 lb.



Fig. 11. Electricity Council Research Centre and British Railway sodium-sulfur powered electric vehicle.

sodium-sulfur traction battery, successfully demonstrated in this test-bed vehicle, that is receiving worldwide R&D interest. This work is detailed more fully in the section on the sodium-sulfur battery (9-14).

**U.S.S.R.**—In 1899, a Soviet electrical engineer, I. V. Romanov, demonstrated a battery-powered "electric carriage," the first Soviet all-electric vehicle, in St. Petersburg which could travel 36 miles at a speed of 18 mph. The first Soviet electric-powered "car" per se was built in 1935, and from 1948 to 1959 several prototypes were tested in the Moscow and Leningrad areas. A coordinated effort for the development of electric vehicles did not begin until 1968, when a council was set up under the direction of the Ministry of the Electrical Engineering Industry of the U.S.S.R. and the American Academy of Sciences, to tackle the scientific problems involved, which included: the Ministry of

Automobile Transportation, the Yerevan Polytechnical Institute imeni Karl Marx, and the All-Union Scientific Research Institute for Electric Transport.

Between 1969 and today, a variety of prototype vehicles have been tested, and a series of experimental vehicles were produced at the Cheboksari Motor Works shown in Fig. 12.

Armenian scientists have developed a computer model for the optimal design of electric vehicles, making it possible to swiftly and objectively assess prototype proposals. The newest Soviet prototype vehicle is shown in Fig. 13 (15-24).

#### All-Electric Vehicle Requirements

The U.S. Department of Transportation has estimated that the minimal energy and power requirements for an all-electric family car are 135 W-hr/lb and 100 W/lb, respectively. Under normal interstate highway driving conditions, this vehicle would have a range of 200 miles per charge at an average speed of 60 mph, which is adequate for urban transit in and out of most major metropolitan areas in the United States. These requirements are summarized in Table II. Minimal requirements for other types of all-electric vehicles are presented in Table III (25-27).

#### Electrochemical Power Sources

Three types of electrochemical power sources are available for all-electric vehicles: aqueous electrolyte storage batteries, organic or molten electrolyte high energy batteries, and fuel cells. The major battery systems of significant R&D interest are summarized in Table IV; presently, the lead-acid, nickel-zinc, zinc-air, sodium-sulfur, and lithium-sulfur traction



Fig. 12. Soviet prototype electric van EM-0466. Motors, two d.c.; range, 48 miles; speed, 27 mph; weight, 1700 kg; load capacity, 454 kg.



Fig. 13. New Soviet electric vehicle

Table II. Minimal requirements for an all-electric family car\* by the U.S. Department of Transportation (25, 26)

Range	200 miles per charge
Speed	60 mph
Service life	5 yr
Battery cycle life	≧3000
Operational temperatures	-29° to +50°C
Total weight (battery)	1500-2000 lb
Estimated cost	≧\$10/kW-hr with salvage value
Energy density	≧135 W-hr/lb
Power density	≧100 W-hr/lb
Charging time	15 min

\* The family car is defined as weighing approximately 4000 lb, being capable of carrying 5-6 people, having a maximum speed of 80 mph, and being able to accelerate from 0 to 60 mph in 13 sec.

Table III. Other on-road all-electric vehicle requirements (27)

Vehicle	Range (miles/charge)	Speed (mph)	Energy density (W-hr/lb)	Power density (W/lb)
Commuter car	100	60	28	31
Delivery van	80	40	33	36
City taxi	150	40	64	30
City bus	120	30	55	25

Table IV. Practical and theoretical energy densities of potential traction batteries (28)

System	Theoretical energy density (W-hr/kg)	Practical energy density (W-hr/kg)	Operational temperature (°C)
Li-S	2800	330	350-450
Li-Cl <sub>2</sub>	2200	150	400-500
Li-Se	1300	300	350-400
Zn-air	1100	60	*Low
Fe-air	940	50	Low
Na-S	785	100-250	300-400
Li-Te	650	250	400-470
Cd-air	500	50	Low
Ag-Zn	440	120	Low
Ni-Zn	330	40	Low
Ag-Cd	270	50	Low
**Ni-Fe	265	17	Low
**Ni-Cd	210	17-20	Low
**PbO <sub>2</sub>	170	17*	Low

\* Low temperatures are operational temperatures below 100°C.  
 \*\* Conventionally used storage batteries in both industrial and commercial all-electric vehicles.

batteries are very promising for application in urban transit and interstate vehicles.

**Lead-acid traction battery.**—Developed in 1852 and technically explained by Gladstone's "Double Sulfation Theory" in 1888, the lead-acid battery has become the predominant battery system used in more than 90% of the all-electric vehicles produced today because of its long service life, high reliability, and low cost (approximately \$0.30-1.00/lb, depending upon the battery's quality). Improvements in both materials and electrode designs have extended the service life of this battery from 300 to 2000+ recharge cycles. Currently, improved lead-acid batteries are being successfully tested in urban transit vehicles and buses in the F.R.G. and in Japan. The Electro Bus and the associated recharge system developed by VARTA, AG, Daimler-Benz, and Bosch, of the F.R.G., has been successfully tested and was found to require minimal maintenance and to have significantly reduced emissions (see Fig. 3-5). The Japanese have also demonstrated an all-electric bus in Osaka, and a fleet of electric delivery vans at EXPO '70 (see Fig. 7 and 8). Additional applications of lead-acid batteries in short range all-electric and hybrid-electric vehicles will increase throughout the 1970's, with improvements in the charge acceptability and capability of the battery. Specific improvements in lightweight alloys for cell connectors and in superthin, long-life separators, plus the use of bipolar or foil electrodes, are anticipated. Even with these innovations, it is rather doubtful that the lead-acid battery will meet the requirements for an all-electric vehicle capable of extended travel on

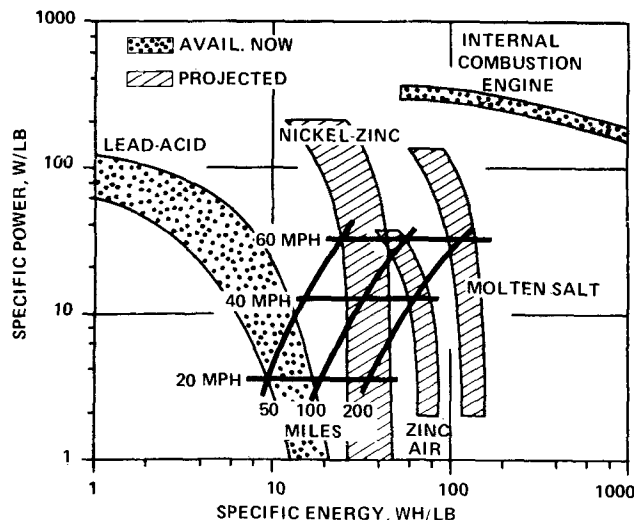


Fig. 14. Power source comparison with vehicle requirements. 200 lb vehicle (500 lb batteries).

interstate highways due to its limited energy density (see Fig. 14). For an all-electric vehicle to commercially compete with internal combustion engines, batteries having greater energy densities must be developed (29, 30).

**Nickel-zinc traction battery.**—Initially discovered in the 1800's, the nickel-zinc alkaline battery has been extensively investigated by the Soviets since the mid-1950's, and by the United States since the 1960's. Today, active research continues in the United States, U.S.S.R., F.R.G., and Japan for applications in hybrid-electric engine vehicles. The nickel-zinc battery operates according to the following electrochemical reaction, producing approximately 1.7V per cell with a theoretical energy density of 146 W-hr/kg. Currently, Furukawa Battery Company Limited of Yokohama, Japan, has developed several prototype 96V, 140 A-hr batteries with nylon and cellophane separators, achieving an energy density of 45-50 W-hr/kg, with a service life of 200 cycles. It was found that the relatively short cycle life was due to separator failure at high electrolyte temperatures generated during charging. Improved heat-resistant separators similar to those used in NASA silver-zinc batteries (sterilized separators) may double the service life of this battery. Similar U.S. research by ESB Incorporated and by Energy Research Corporation has resulted in the successful demonstration of prototypes having energy densities twice that of lead-acid batteries. Potentially, the nickel-zinc battery is the best battery for hybrid-electric vehicles because of its stable discharge voltage, wide operational temperature range, deep discharge capability (50-75% discharge), and relatively low cost. Nickel-zinc batteries having power densities of 100+ W/lb, costing approximately \$2.00/lb, will probably be a reality within the next 5 years (27-33).

**Zinc-air traction battery.**—In recent years, the zinc-air alkaline storage battery has dominated the field of metal-air batteries because of its low cost, high energy density, and favorable electrochemical reactivity. Having a theoretical energy density of 614 W-hr/lb and an open-circuit voltage of 1.65V, the zinc-air battery is promising; however, serious problems regarding zincate ion, carbonate, and zinc dendrite formation have limited cycle life. In developing a secondary zinc-air system, four basic prototype systems have been investigated (33-34): (i) the mechanically rechargeable battery (1964); (ii) the noncirculating alkaline electrolyte battery (1968); (iii) the circulating alkaline electrolyte battery (1968); and (iv) the zinc-feeding-fuel battery (1970). A 1 kW mechanically rechargeable zinc-air battery has been

developed and evaluated by General Motors Corporation in an Opel Kadett test-bed vehicle. The battery had an energy density of 42 W-hr/lb and a power density of 31 W/lb and could meet the power requirements for urban transit vehicles. This battery was shelved, however, because of practical recharge problems. Noncirculating alkaline electrolyte zinc-air batteries have also been investigated, but during charging have suffered from zincate ion and dendrite formation on the surface of the zinc anode. After a number of charges, the dendrites penetrate through the separator, short circuiting the cells. The British Electricity Council Research Centre in Capenhurst, England, has developed a hydrodynamic zinc-air cell to reduce zinc dendrite formation by bubbling argon gas over the anode's surface. Tests indicated that at a current density of 800-1500 A/m<sup>2</sup> a smooth homogeneous electrodeposition of zinc on the anode resulted (see Fig. 15 and 16).

A circulating electrolyte zinc-oxygen 27 kW battery created by Gulf General Atomic has achieved a 27 W-hr/lb energy density and a 20 W/lb power density. This system was technically encouraging, but because of its complexity, was not economically feasible for commercial vehicles.

Sony Corporation Limited of Japan has developed a new pulverized zinc fuel battery, which is externally charged by a zinc and electrolyte regeneration unit (see Fig. 17 and 18). This battery achieved an energy density of 41 W-hr/lb and a power density of 10 W/lb for a 50-100 hr operation at a cost of approximately \$100/kW. The Sony battery is very com-



Fig. 15. ECRC's electrodeposition of zinc on the anode at 600 A/m<sup>2</sup>.

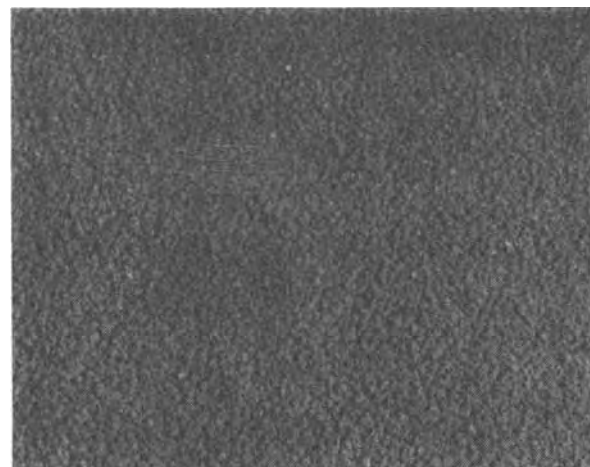


Fig. 16. ECRC's homogeneous electrodeposition of zinc on the anode at 1000 A/m<sup>2</sup>.

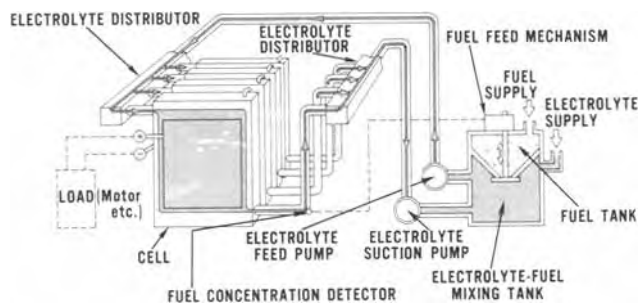


Fig. 17. Flow diagram of Sony metal fuel battery system

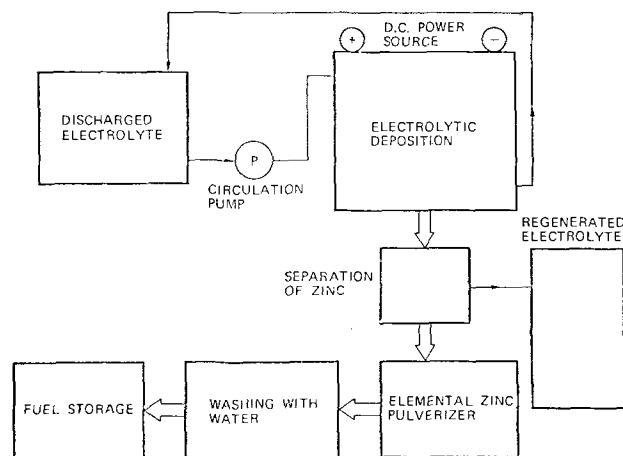


Fig. 18. Flow diagram of fuel and electrolyte regeneration process by Sony.

plex and must be simplified before serious consideration can be given to standard production of this power source (35).

**Sodium-sulfur and lithium-sulfur high energy batteries.**—The sodium-sulfur (Na-S) storage battery originally developed by Dr. Nils Weber and Dr. Joseph Kummer of Ford Motor Company Research Laboratories, Dearborn, Michigan, in 1966, appears to be the most promising electrochemical power source for long-range (200+ miles/charge at 60 mph) all-electric vehicles. This battery has a theoretical energy density of 346 W-hr/lb and an open-circuit voltage of from 1.8 to 2.1V. The battery operates at an optimal temperature of 300°C.

The over-all reaction mechanism is shown in Fig. 19, and the construction of a Japanese prototype by Yuasa Battery Company Limited and Toshiba is shown in Fig. 20. Interest in, and research on, this battery has rapidly increased since 1966 because of the battery's following advantages (36):

- (i) It has high energy and power densities due to lightweight reactant materials.
- (ii) Due to the economical abundance of reactant materials, the battery's cost/kW-hr may be smaller than that of lead-acid traction batteries.
- (iii) No self-discharge mechanism is foreseen.
- (iv) No shape changes on electrodes occur because the reactants are liquids.
- (v) No gases are generated during charging.
- (vi) There is no danger of electrolyte spillage.

The service life of this battery depends upon the life of the beta-alumina ( $\text{Na}_2\text{O} \cdot 11\text{Al}_2\text{O}_3$ ) ceramic separator which is permeable only to the sodium ion along the C-axis. Yuasa, Toshiba, and Toyota Motors Research Laboratory have conducted extensive research to increase the strength and lower the internal resistance of the ceramic. The resistivity has been reduced by the addition of impurities such as  $\text{Mg}^{+2}$ ,  $\text{Ni}^{+2}$ ,  $\text{Cu}^{+2}$ , and  $\text{MgO}$ , but the exact doping procedure is proprietary and the subject of patent



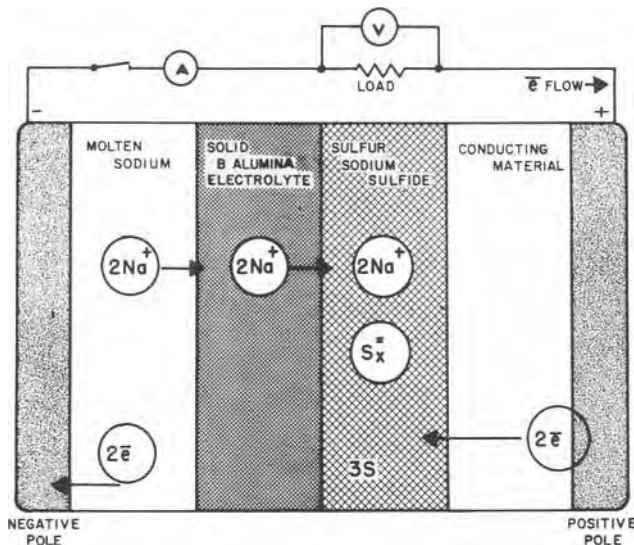


Fig. 19. Reaction mechanism for sodium-sulfur high energy traction battery.

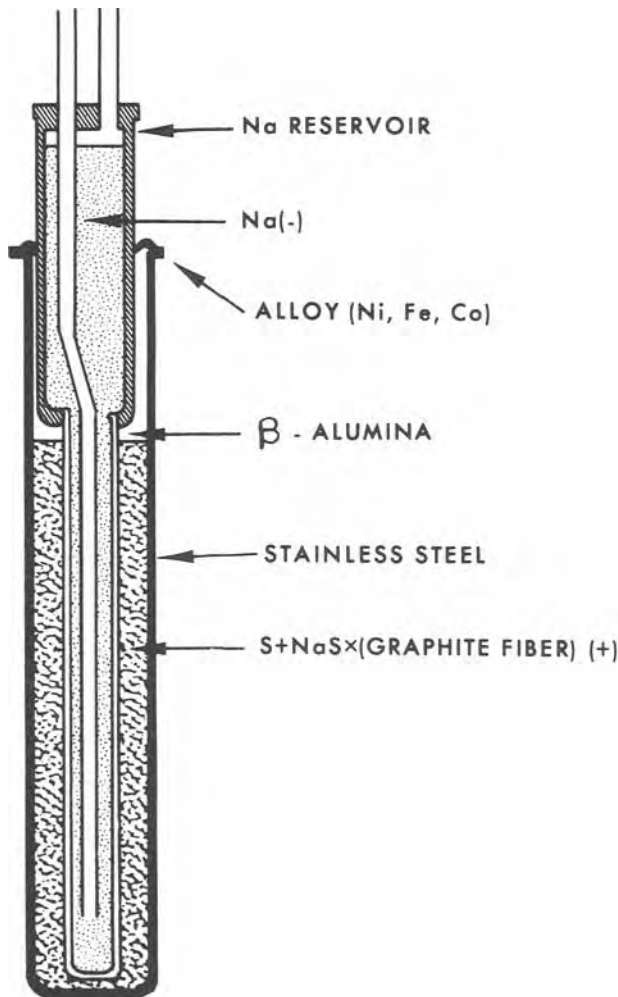


Fig. 20. Sectional view of Yuasa's sodium-sulfur battery

applications. Continued progress in developing improved ceramic materials, sealing techniques, and production methods are anticipated with limited production of sodium-sulfur battery-powered vehicles expected by 1978.

Lithium-sulfur high energy batteries have a theoretical energy density of 700 W-hr/lb and an open-circuit potential of 2.25V at operating temperatures of 300°-370C°. The electrolytes are a molten LiI-KI-LiCl

eutectic salt, with molten lithium and sulfur as the anode and cathode. This battery has a high discharge rate capability, and should be particularly useful in large power installations. Currently, the major problems of this system are high temperature corrosion and solubility, sulfur loss, and sulfur electrode inefficiencies. Application of this battery in electric vehicles appears remote (possibly by the mid-1980's) because of these material problems (32).

Other prototype batteries have been developed by Compagnie General d'Electricite (CGE) of France, the Czechoslovak Academy of Sciences in Bratislava, and British Railways of the U.K. Recently, British Railways and the Electricity Council Research Center (ECRC) have completed initial road testing of the world's first sodium-sulfur powered vehicle, an 18 cwt Bedford delivery van (see Fig. 11 and 21), employing thirty 1 kW module, sodium-sulfur cells achieving 100 miles per charge at 40 mph (37).

**Fuel Cells for Ground Propulsion Systems**

Fuel cells, which were discovered by Sir William Grove in 1839 and greatly improved through the 1950's and 1960's, have been successfully employed in electric vehicles produced by ASEA of Sweden, Shell Thornton Limited of the U.K., General Motors Corporation, Union Carbide, and several other companies in the United States. These systems, using ammonia, hydrazine, and hydrogen fuels, are reliable, pollution free, and very efficient, but because of the use of exotic noble metal catalysts, are rather expensive and complex for standard production. Even with reduced catalyst loadings and the use of substitutes, such as tungsten carbide and tungsten bronzes for platinum and palladium electrodes, costs will be greater than that for lead-acid, nickel-zinc, and possibly sodium-sulfur systems. Currently, the "Target" program involving Pratt and Whitney Aircraft Corporation and thirty utility companies, plus the EXXON-Alsthoms corporation programs, are the only two major U.S. fuel cell programs. Major breakthroughs must result from these programs to revive the fuel cell for ground propulsion systems. Only with the initiation of a "Hydrogen Economy," with economic methods of hydrogen generation by electrolysis or thermal cracking of water, hydrogen transmission via conventional gas lines, and noncryogenic or pressurized storage of hydrogen, will the fuel cell emerge as a practical propulsion source for commercial transportation. Philips Research Laboratories of the Netherlands has developed new rare earth intermetallic compounds, which store large quantities of room temperature hydrogen at 5 atm pressure

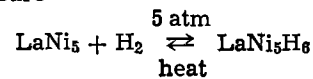
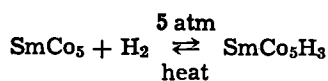


Fig. 21. British Railway's and ECRC's 30 kW sodium-sulfur powered delivery van.



These reversible hydride complexes have been developed for the Stirling engine, but fuel cell applications are evident; however, large scale production of hydrogen to meet current domestic energy demands has yet to be demonstrated (38, 39).

#### Raw Material Requirements

The materials required for the large scale production of these electrochemical power sources include elements such as lithium, sodium, sulfur, chlorine, alumina, lead, and graphite, which are economically abundant. Other elements such as nickel, cadmium, zinc, and the noble metal catalysts are not abundant in the United States and will have to be imported from Canada or the U.S.S.R. to satisfy the demands of a growing electric vehicle population. This importing activity will not improve the balance-of-payments situation abroad and, with the high demand anticipated, the price of these metals will increase rapidly. Construction materials for containers, cell connectors, and contacts which are corrosion resistant, thermally and chemically stable, and enhance electrical conductivity, such as niobium, tantalum, and tungsten, are not presently available to meet this demand; thus, substitute materials such as aluminum, stainless steel, high temperature plastics, and graphite must be used. Fuels such as hydrazine for fuel cells are also very expensive because of the high production costs. Breakthroughs in the synthesis of hydrazine, along with improvements in the distribution and availability of these fuels, must be made before the fuel cell can readily compete with the internal combustion engine and appeal to the buying public (40).

#### Conclusion

Review of the power requirements, cost and availability of materials and reactants, reliability and service, safety, and public appeal indicates a high temperature alkali metal battery system such as the sodium-sulfur and lithium-sulfur battery is most promising and offers the greatest potential for satisfying the foregoing requirements for conventional six-passenger cars. Currently, lead-acid traction batteries are adequate for powering lightweight (1500 lb) all-electric commuter cars in urban areas where the maximum driving range is less than 25 miles per day. Secondly, fuel cells offer an effective energy density, power density, and reliability; however, the cost and availability of fuels and catalysts limit their applications. Possibly, by the mid 1980's, when the availability and public acceptability of hydrogen as a fuel is a reality, fuel cells will begin to emerge as a significant power source for both propulsion and domestic power applications. Greater investment by the United States Government in R&D relating to electrochemical power sources in this crucial area is necessary. The magnitude of the technical problems involved and the significance of the potential technological achievements should be recognized in conjunction with the necessity to limit pollution in the metropolitan areas.

Manuscript submitted Aug. 3, 1973; revised manuscript received Nov. 12, 1973. This was Paper 10 presented at the Boston, Massachusetts, Meeting of the Society, Oct. 7-11, 1973.

Any discussion of this paper will appear in a Discussion Section to be published in the December 1974 JOURNAL. All discussions for the December 1974 Discussion Section should be submitted by Aug. 1, 1974.

#### REFERENCES

1. Tomasz Sobiecki, *Motor*, 26, No. 4, pp. 22-24 (1972); *ibid.*, 26, No. 5, pp. 6-11 (1972).
2. K. J. Oehms, *Duet. Elektrohandwerk*, 24, No. 22, pp. 14-16 (1971).
3. H. G. Raschblichler, *Automotive Engineering Congress, January 10-14, 1972*, No. 720187, Society of Automotive Engineers, Detroit, Mich. (1972).
4. *Electrical Review*, London, England (Dec. 3, 1971).
5. *Technocrat*, Tokyo, Japan, Vol. 5, No. 10 (1970).
6. Isamu Takooka et al., *Proc. Second Intern. Electric Vehicle Symp.*, 56, Electric Vehicle Council, New York, (1971).
7. Aikazu Watnabe, *ibid.*, 70 (1971).
8. Isamu Takooka, *Automotive Engineering Congress, January 10-14, 1972*, No. 720189, Society of Automotive Engineers, Detroit, Mich. (1972).
9. Dr. Hans-George Muller, *Proc. Second Intern. Electric Vehicle Symp.*, 83, Electric Vehicle Council, New York (1971).
10. *Electrical Review*, London, England, 19 (Nov. 9, 1972).
11. M. R. Andrew et al., *Automotive Engineering Congress, January 10-14, 1972*, No. 720192, Electric Vehicle Council, New York (1972).
12. Berkeley S. Hender, *Automotive Engineering Congress, January 10-14, 1972*, No. 720190, Electric Vehicle Council, New York (1972).
13. *Electrical Review*, London, England (July 7, 1972).
14. *Electrical Times*, London, England (June 1, 1972).
15. B. Borizov, *Za Rulem*, No. 12, p. 11, Moscow, USSR (1971).
16. *TechnoTASS*, Tokyo, Japan, No. 101 (Nov. 15, 1971).
17. *GUDOK*, USSR, (January 6, 1971).
18. *Krbsnaya Zvezda*, USSR (May 23, 1971).
19. *KOMMUNIST*, USSR, p. 2 (Oct. 23, 1971).
20. *NTO CSSR*, USSR, No. 2 (1972).
21. *TechnoTASS*, Tokyo, Japan, No. 126 (May 15, 1972).
22. *Militartechnik*, East Germany, No. 2, p. 93 (1972).
23. Lev Kolodnyy, *Moskovskaya Pravda*, Moscow, USSR, p. 4 (Sept. 27, 1972).
24. *Veda a Zivot*, USSR, No. 12, pp. 734-735 (1972).
25. Mark Salomon "Batteries for Ground Transportation Systems," U.S. Department of Transportation, Cambridge, Massachusetts (1971).
26. E. J. Cairns, "Development of High Energy Batteries for Electric Vehicles," Argonne National Laboratories, Argonne, Illinois (1972).
27. C. C. Christianson, *Proc. Second Intern. Electric Vehicle Symp.*, pp. 172-186, Electric Vehicle Council, New York (1971).
28. J. P. Gomis, J. F. Laurent, and F. Lassere, in "The International Union of Producers and Distributors of Electrical Energy Symposium," Brussels, Belgium (March 1972).
29. K. J. Oehms, in "Der Elektro Nister Deutsche Elektrohandwerk," Frankfurt, West Germany (1972).
30. Israel Borkovitch, *The Engineer*, p. 33, London, England (Sept. 2, 1971).
31. George C. Kugler, *Proc. Second Intern. Electric Vehicle Symp.*, pp. 502-505, Electric Vehicle Council, New York (1971).
32. Sidney Gross, *Proc. Symp. Batteries for Traction and Propulsion*, pp. 8-25, the Columbus Section of The Electrochemical Society, Columbus, Ohio (1972).
33. Jack R. Kettler, *Proc. Symp. Batteries for Traction and Propulsion*, pp. 213-241, the Columbus Section of The Electrochemical Society, Columbus, Ohio (1972).
34. *Electrical Review*, London, England (April 28, 1972).
35. Mideo Baba, "A New Zinc Air Fuel Battery System," Sony Corp., Tokyo, Japan (1971).
36. H. A. Christopher, *Proc. Second Intern. Electric Vehicle Symposium*, pp. 482-501, Electric Vehicle Council, New York (1971).
37. *Electrical Review*, pp. 627-629, London, England (Nov. 10, 1972).
38. C. Marchetti, *Chemical Economy & Engineering Review*, pp. 7-25 (January 1973).
39. Derek P. Gregory, in *Scientific American*, pp. 13-21 (January 1973).
40. J. H. B. George, *U.S. Department of Transportation Report DOT-TSC-OST-73-1*, Washington, D.C. (June 1972).

# Thin Oxide Films on Iron<sup>1</sup>

Morris Cohen\*

Division of Chemistry, National Research Council of Canada, Ottawa, Ontario, Canada

The first two papers (1, 2) I presented at a Meeting of the Electrochemical Society were given at Birmingham, Alabama in 1946. They were concerned with a technique for studying corrosion and an inhibitor for stopping corrosion. The next paper (3) was the first paper on inhibition by sodium nitrite. The final conclusion in that paper was as follows: "The mechanism for inhibition is probably the formation of a tight oxide layer which is formed by the combined action of nitrite and oxygen and is repaired by the nitrite." It was also proposed that the same type of mechanism was applicable to chromate inhibition. At the time this was quite contrary to the most commonly accepted dogma on passivity and inhibition. This review will deal with attempts our laboratory has made to determine the mechanisms of formation of and the properties of these thin oxide films on iron.

## Chemically Formed Films—Inhibitors

The early work on nitrite showed that the weight loss of iron in solution decreased as both the concentrations of nitrite and oxygen (4, 5) were increased. At intermediate concentrations pitting was observed. There was also some decrease in the nitrite concentration during the exposure of the iron specimen to the nitrite solution. Ammonia was shown to be a by-product of the reaction of nitrite with iron. On this basis it was postulated that the film was formed by adsorption of nitrite on the iron surface followed by a reaction to form oxide and ammonia. This is illustrated in Fig. 1. The O-O distance in the nitrite is not too far removed from the Fe-Fe distance in iron. This same type of adsorption-reaction mechanism was also proposed for other oxidizing inhibitors such as chromate and molybdate (6). In the case of the nitrite the reduction product of the inhibitor is soluble and hence a protective film containing iron and oxygen, and possibly hydrated oxide would be formed. Under sufficiently inhibiting conditions only an anhydrous cubic oxide is observed by electron diffraction (9). With chromate the reduction product is insoluble  $\text{Cr}_2\text{O}_3$  and this would be expected to be found in the film (7). Figure 2 is the electron diffraction pattern of the " $\text{Fe}_3\text{O}_4\text{-}\gamma\text{-Fe}_2\text{O}_3$ " film formed on a single crystal of iron exposed to sodium nitrite solution. This film is epitaxial with the underlying metal and about 20-30Å in thickness. In Table I the amount of  $\text{Cr}_2\text{O}_3$  in film formed in chromate solution as a function of exposure conditions, is presented.

Nonoxidizing inhibitors require the presence of oxygen to prevent corrosion. This is illustrated for sodium phosphate (10) in Fig. 3. This figure also shows the relationship between corrosion rate and potential. It can be seen that inhibition of corrosion in solutions containing the nonoxidizing phosphate ion occurs only in the presence of oxygen. The phosphate is a buffer which prevents acidity from developing and also acts to precipitate ferric phosphate in pores which may develop in the film. The amount of phosphate in the film depends on the surface preparation of the iron and the corrosivity of the solution (11). An electron micrograph of an iron specimen which had been exposed to a phosphate solution containing chloride ion showed large inclusions which gave the diffraction pattern of a hydrated  $\text{FePO}_4$ .

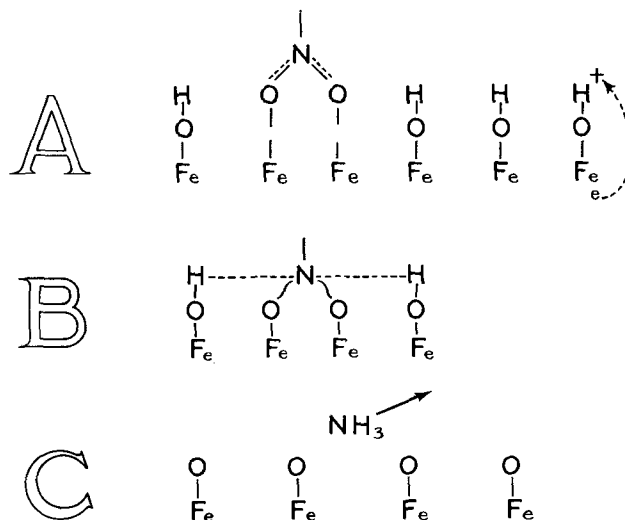


Fig. 1. Adsorption of  $\text{NO}_2^-$  on iron and reaction to form  $\text{NH}_3$ ,  $\text{H}_2$ , iron oxide film.

The behavior in both oxidizing and nonoxidizing inhibitors (6) in the presence of oxygen is shown in Fig. 4. A much higher concentration of nonoxidizing anion is required to inhibit the corrosion of iron. In all cases when the corrosion is inhibited the potential of the iron is greater than 0, (hydrogen scale) and  $< -500$  mV when corroding. The films are mainly composed of " $\text{Fe}_3\text{O}_4\text{-}\gamma\text{-Fe}_2\text{O}_3$ ." Some  $\gamma\text{-FeOOH}$  and other ferric compounds may also be present under some conditions. Phosphorus and chromium compounds in the films were determined using radio-tracer techniques (7-11).

## Electrochemically Formed Films

**Electropolishing.**—In the course of this work it was desirable to start with a clean smooth surface having a reproducible type of oxide film on it. To this end a technique was developed for electropolishing in a 5% perchloric-acetic acid mixture (12) which produced a smooth iron surface covered with a thin film of the " $\text{Fe}_3\text{O}_4\text{-}\gamma\text{-Fe}_2\text{O}_3$ " type oxide. This film, and variations thereof, were studied using reflection high energy electron diffraction (13). Lattice spacing measurements were made both immediately after electropolishing and after aging in air or vacuum. Some specimens were also first cathodically reduced in a borate buffer solution (14), and then exposed to air. The results are shown in Table II. It can be seen that the lattice parameter of the freshly electropolished specimen (8.26) is lower than that for either  $\gamma\text{-Fe}_2\text{O}_3$  (8.32) or  $\text{Fe}_3\text{O}_4$  (8.38). On annealing or aging over a period of time the lattice parameter gradually changes

Table I. Amount of chromium (as  $\text{Cr}_2\text{O}_3$ ) in film formed in chromate solution

Surface condition	Solution	$\mu\text{g Cr}_2\text{O}_3/\text{cm}^2$ *
$\text{H}_2$ -reduced wire	De-aerated	1.6
$\text{H}_2$ -reduced sheet	De-aerated	1.4
Etched sheet with air-formed film	De-aerated	0.1
Etched sheet with air-formed film	Exposed to air	0.6

\* 1  $\mu\text{g Cr}_2\text{O}_3 \approx 20\text{\AA}$ .

\* Electrochemical Society Active Member.  
<sup>1</sup> The Corrosion Division Award Address, delivered at the Boston, Massachusetts, Meeting of the Society, October 9, 1973.  
 Key words: passivity, inhibition, thin films.



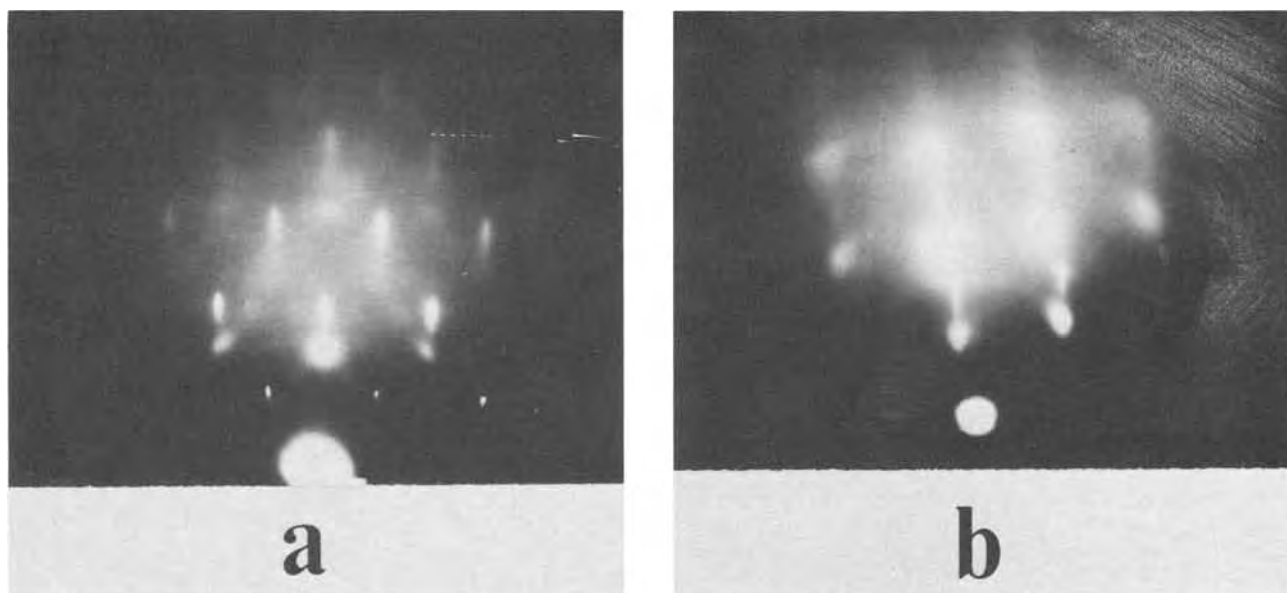


Fig. 2. Electron diffraction patterns of  $\text{Fe}_3\text{O}_4-\gamma\text{Fe}_2\text{O}_3$  on iron exposed to nitrite solutions (a), (112) Fe in N/1000 Na  $\text{NO}_2$  aerated. (b), (100) Fe in 3N Na  $\text{NO}_2$ , aerated.

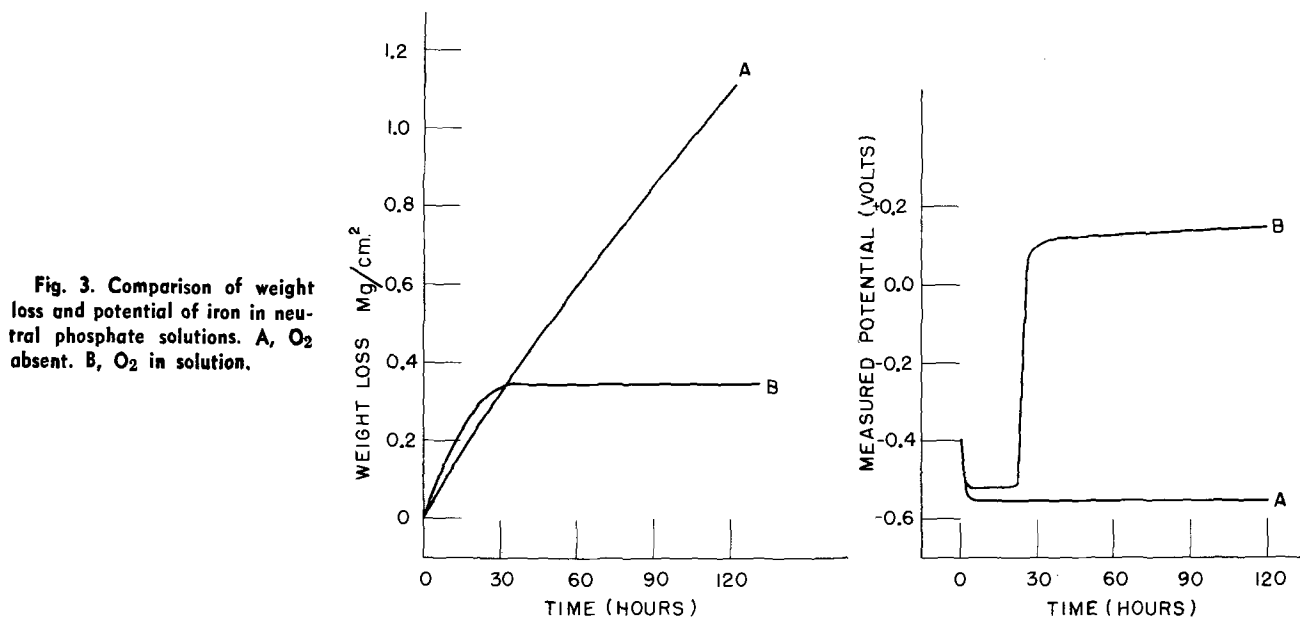


Fig. 3. Comparison of weight loss and potential of iron in neutral phosphate solutions. A,  $\text{O}_2$  absent. B,  $\text{O}_2$  in solution.

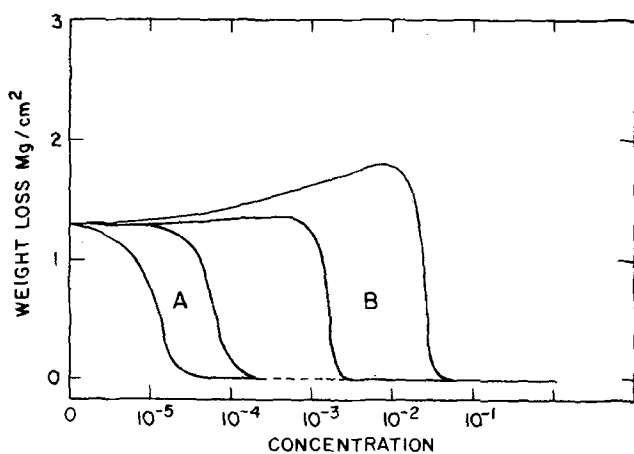


Fig. 4. Weight loss curves for iron exposed to various inhibitors in aerated solutions. A, oxidizing inhibitors such as  $\text{CrO}_4^{2-}$ ,  $\text{NO}_2^-$ , and  $\text{WO}_4^{2-}$ ; B, nonoxidizing inhibitors such as phosphate, borate, benzoate, silicate.

to a final 8.38. This would indicate that the electro-polishing (plus initial air exposure) produces a film which is cation deficient in relation to  $\gamma\text{-Fe}_2\text{O}_3$ . On aging in air or vacuum, iron diffused into the film gradually converts through  $\gamma\text{-Fe}_2\text{O}_3$  to  $\text{Fe}_3\text{O}_4$ . If the E.P. film is cathodically reduced and the specimen exposed to air the iron oxide has an average lattice parameter closer to that of  $\gamma\text{-Fe}_2\text{O}_3$ . This oxide also converts to  $\text{Fe}_3\text{O}_4$  on vacuum annealing. The diffraction patterns are similar to those shown in Fig. 2 for films formed in nitrite solution. This indicates that the film is a highly epitaxed microcrystalline cubic iron oxide with an average crystallite size of 20-30Å. The thickness of the electroplated film on this (112) surface was estimated to be 17Å by the cathodic reduction technique.

*Anodic passivity.*—Having now developed the techniques for reproducible surface preparation, analytical cathodic reduction and electron optical examination of the thin films, we felt it should be possible to do a more definitive study on films formed by anodic oxidation, that is the so-called anodically formed passive

Table II. Iron single crystal. (112) Surface variation of lattice parameter,  $a$ , of air-formed oxide\*

Surface preparation	$a$ , Å	
E.P. air exp., 5-15 min	8.26	0.03
E.P. exp. in E.D.C., 5 min	8.27	0.04
E.P. exp. in E.D.C., 30 min	8.26	0.03
E.P. exp. in E.D.C., 60 min	8.27	0.04
E.P. exp. in E.D.C., 120 min	8.32	0.04
E.P. exp. in E.D.C., 240 min	8.32	0.03
E.P. exp. in E.D.C., 22 hr	8.38	0.04
E.P., 1½ hr at 200°C, in vacuum 10 <sup>-6</sup> mm Hg	8.38	0.03
E.P. plus C.R., air exp., 10 min	8.32	0.04
E.P. and E.P. plus C.R., air exp. 17-18 hr	8.39	0.004

E.P., electropolished.  
C.R., cathodically reduced.  
E.D.C., vacuum of electron diffraction camera.

\* At room temperature, 25°C.

film. For a number of reasons, such as pH control, the solution used for cathodic reduction, i.e., a borate buffer, modified slightly to remove chloride and give a pH of 8.4 was used in these studies (15, 16). This was a solution in which it was possible to form a passive film from an originally bare surface [something which could not be done with chloride or sulfate (17)].

The typical potentiostatic polarization curve obtained in the borate buffer solution is shown on line 1 of Fig. 5. The specimens were electropolished and cathodically reduced before the anodic polarization. Essentially no dissolution of iron occurs between about -200 mV and +850 mV (SCE). Only small amounts of iron are observed between -500 mV and -250 mV. Typical potentiostatic charging curves in the passive region are shown in Fig. 6. Graphical integration of these curves gave the number of coulombs passed during polarization while analysis of the solution for Fe<sup>2+</sup> gave the number of coulombs used for iron dissolution. The difference was used in forming the film. These results are also shown in Fig. 5. As can be seen the thickness of the passive film varies from about 8 Å at -400 mV to 30 Å at 850 mV. Above this potential oxygen evolution sets in and renders the coulometric method inaccurate for the estimation of thickness. In these neutral solutions the anodically dissolved iron was always in the ferrous state. Some specimens were passivated at constant current. The number of coulombs used to reach the various passive potentials was about the same as for a short time potentiostatic oxidation. Electron diffraction patterns of the films formed by anodic oxidation of an iron single crystal were similar to those on

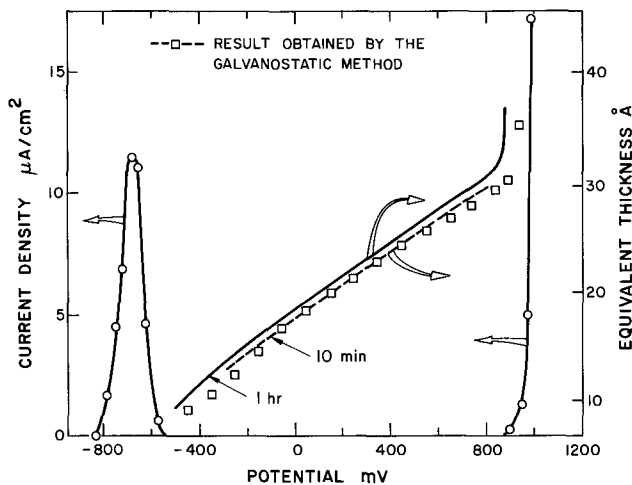


Fig. 5. Polarization curve and oxide thickness in borate-buffer solution. —○—, polarization curve; —□—, 10 min galvanostatic oxidation; —1 hr potentiostatic oxidation.

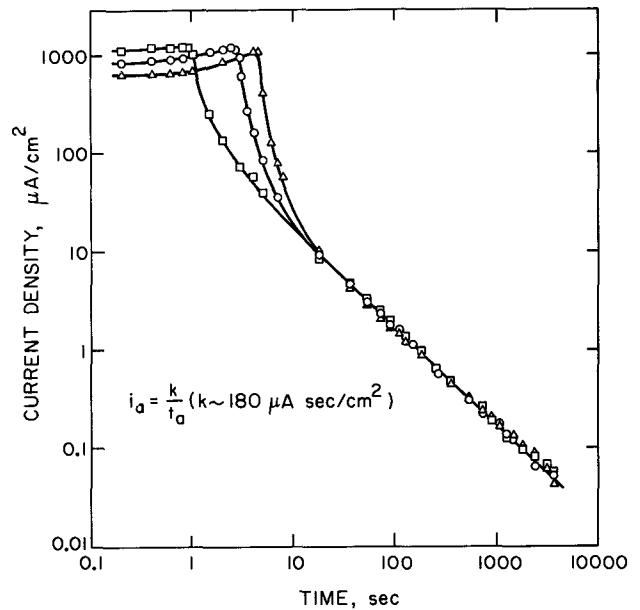


Fig. 6. Change of current with time during anodic polarization of iron in borate buffer at various potentials. —□—, -300 mV; —○—, +200 mV; —△—, +600 mV.

specimens formed by oxidation in nitrite solution or by electropolishing. The film was a highly oriented epitaxial microcrystalline cubic oxide.

A typical cathodic reduction curve for these films is shown in the top part of Fig. 7. Two waves are evident, one for the reduction of  $\gamma$ -Fe<sub>2</sub>O<sub>3</sub> (to give Fe<sup>2+</sup> in solution) and the other for the reduction of Fe<sub>3</sub>O<sub>4</sub> (to give a combination of Fe<sup>2+</sup> in solution and deposited iron). The amount of iron cathodically produced in the solution after various anodic treatments is shown in the bottom part of Fig. 7. These were done with no intermediate exposure to air or oxygen. The initial cathodic reduction current efficiency is low,

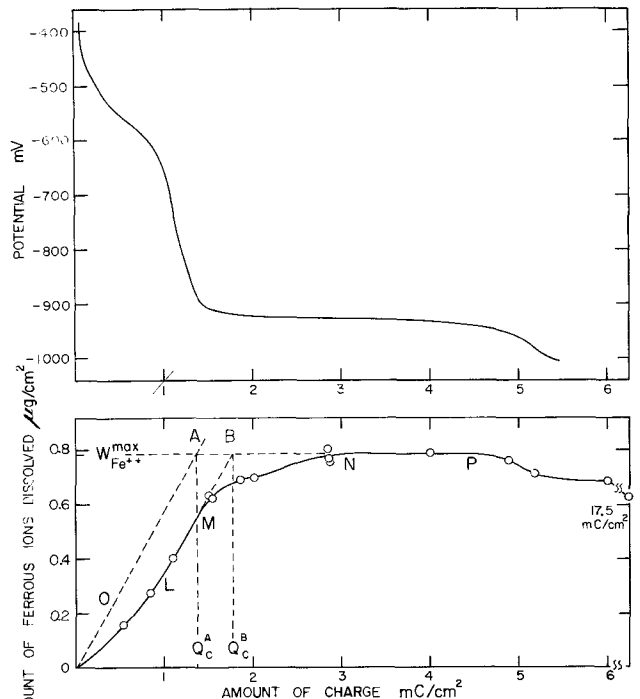


Fig. 7. Top curve: Cathodic reduction at 10 µA/cm<sup>2</sup> of anodically oxidized specimen. The two waves correspond to the reduction of  $\gamma$ -Fe<sub>2</sub>O<sub>3</sub> and Fe<sub>3</sub>O<sub>4</sub>. Bottom curve: The amount of Fe<sup>2+</sup> in solution after various times of cathodic reduction. The dotted line represents a current efficiency of 100% for the reduction of  $\gamma$ -Fe<sub>2</sub>O<sub>3</sub>.

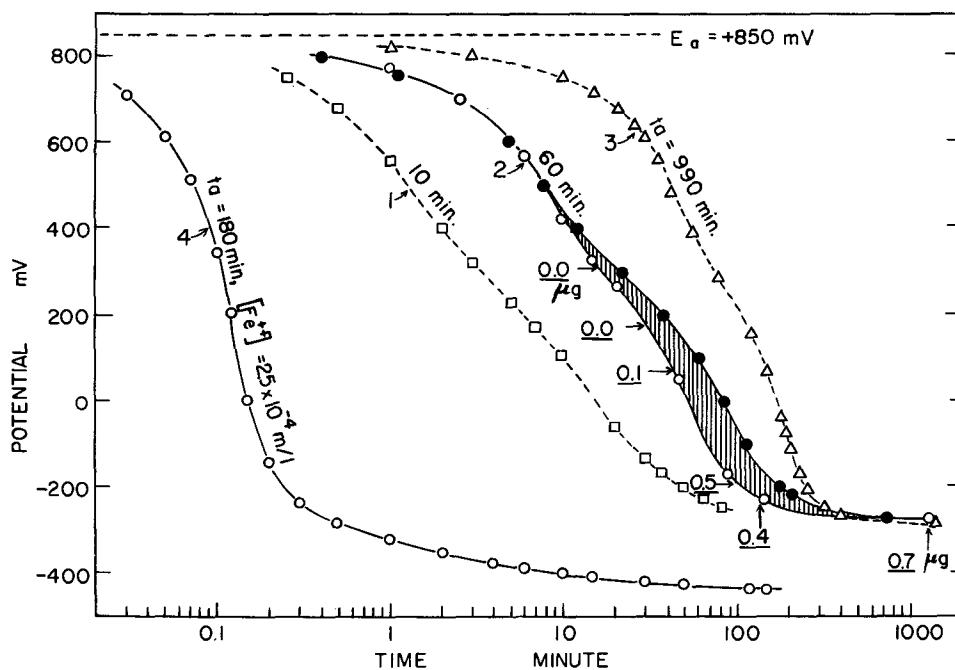
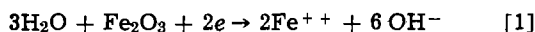


Fig. 8. Decay curves for potential of iron anodically oxidized at +850 mV for various times. Ferrous iron was added to the solution to obtain curve 4. The numbers on curve 2 correspond to the amount of iron in solution.

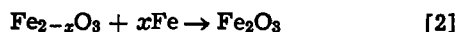
if based on the reaction



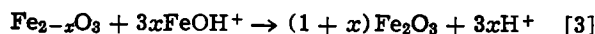
This was taken to indicate that the outer layer of the film was composed of a cation-deficient  $\gamma\text{-Fe}_2\text{O}_3$  of the general formula  $\text{Fe}_{2-x}\text{O}_3$ , the  $x$  being accounted for by the presence of a higher valent iron species in the outer layer of the film such as  $\text{Fe}^{6+}$ . This behavior was observed with films formed well below the oxygen evolution potential and hence could not be attributed to oxygen adsorption.

A series of experiments were also performed in which, after anodic polarization, the open-circuit potential of the specimen was followed with time. This type of decay curve is shown in Fig. 8. In the absence of  $\text{Fe}^{++}$  the rate of decay of the potential is very slow and depends on the time of the polarization. If ferrous iron is added the decay is very rapid and the final steady-state potential is lower. In all cases the final steady-state potential is still in the passive region. At much longer times the film finally breaks down and corrosion starts. The final steady-state potential is also dependent on the pH of the solutions.

During the decay the reaction is probably

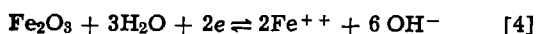


This is a solid-state reaction in which diffusing iron from the underlying metal reacts with the outer oxide and corresponds to what was earlier observed during vacuum aging of the electropolished film. The reaction with  $\text{Fe}^{++}$  in solution would follow a nominal equation such as



The rate of this reaction should depend on diffusion of  $\text{FeOH}^+$  in the solution to the oxide surface and would be faster than the solid-state diffusion required in reaction [2].

The effect of pH and  $\text{Fe}^{++}$  concentration on the steady-state potential of the passive film would indicate that the electrochemical reaction determining the potential of the passive film is

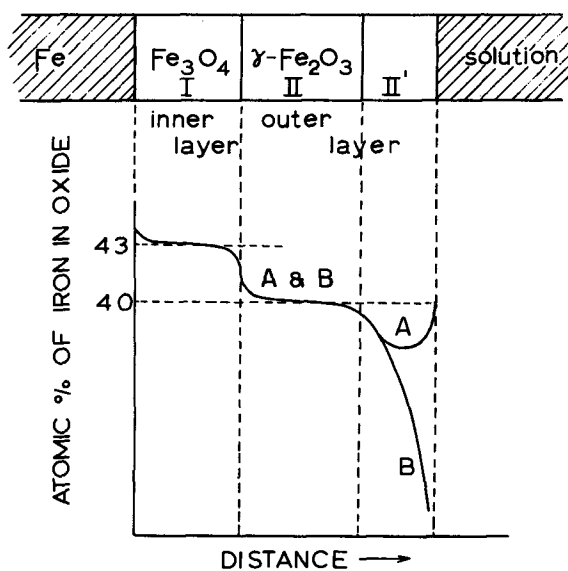


From the potentials measured and the known values of the other reactants one can calculate the free energy of formation of  $\gamma\text{-Fe}_2\text{O}_3$ . This comes out to  $-166.5$  kcal/mole and is quite reasonable in relation

to  $\text{Fe}_3\text{O}_4$  and  $\alpha\text{-Fe}_2\text{O}_3$ .  $\gamma\text{-Fe}_2\text{O}_3$  is intermediate in stability between these two oxides.

On the basis of the above considerations a general picture of the oxide film is shown in Fig. 9. Although phase boundaries are shown these do not exist as real phase boundaries. Rather the oxide is composed of a cubic array of oxygen into which iron atoms fit. Close to the metal surface the oxide has an oxygen-iron ratio close to that of  $\text{Fe}_3\text{O}_4$  while close to the surface it is  $\text{Fe}_{2-x}\text{O}_3$ . In between the ratio is close to that of  $\gamma\text{-Fe}_2\text{O}_3$ . On aging in the solution or in an oxygen-free atmosphere the whole oxide gradually converts to  $\text{Fe}_3\text{O}_4$ . On adding  $\text{Fe}^{++}$  ion the outer layer is quickly converted to  $\gamma\text{-Fe}_2\text{O}_3$ .

*Kinetics of anodic oxidation.*—The good reproducibility obtained during anodic oxidation of iron in the neutral borate-buffer solution indicated that this system could be used for a detailed study of the



POSSIBLE CHANGE OF COMPOSITION OF THE PASSIVE FILM WITH THICKNESS

Fig. 9. Schematic composition of anodic oxide film. A, in the presence of iron; B, in the absence of iron.

kinetics of oxide growth during anodic polarization. This study was reported in two papers on initial and steady-state kinetics (18, 19). Specimens were prepared by anodic oxidation at a low potential for a set time to produce a thin oxide of known thickness. They were then further oxidized potentiostatically by raising the anodic potential and following the change of current with time or galvanostatically by applying a constant current and following the potential change with time. Some results are shown in Fig. 10 and 11. As can be seen in Fig. 10 the total charge is dependent on the applied potential but the slope of the log *i* vs. coulombs curve is constant over the whole potential

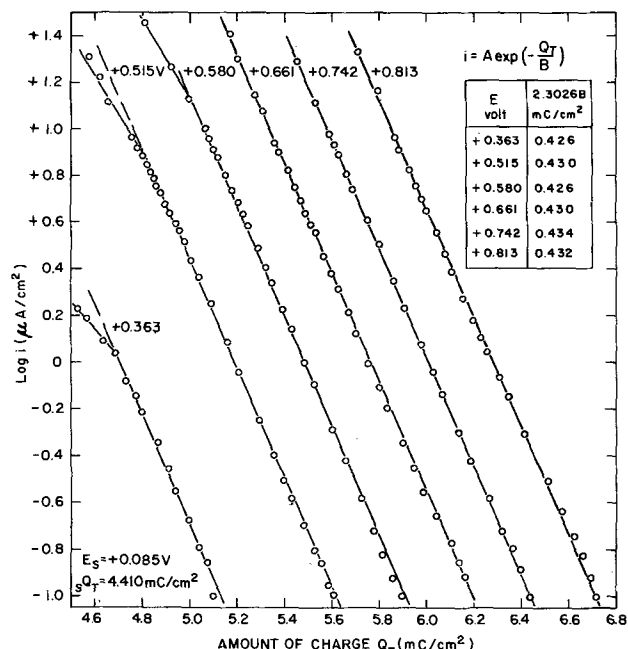


Fig. 10. Potentiostatic oxidation of iron with pre-existing thin oxide film of 4.410 mC/cm<sup>2</sup> formed at +0.085V.

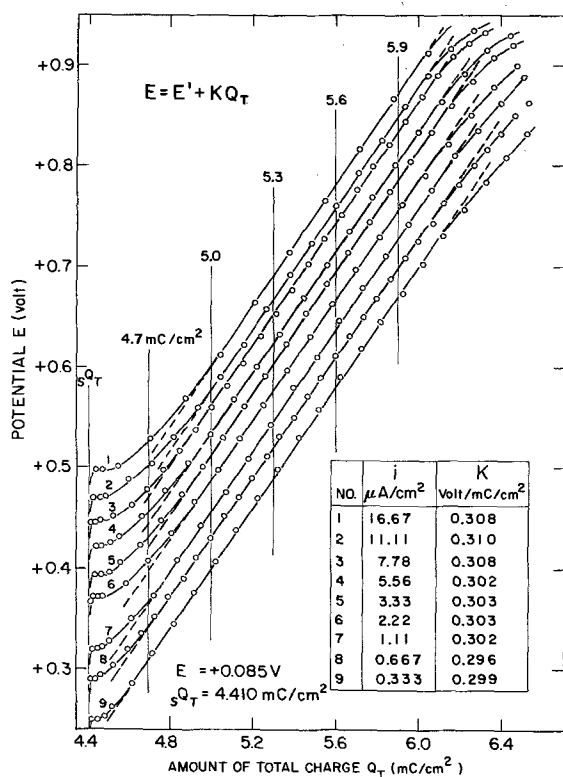


Fig. 11. Galvanostatic oxidation of iron with same pre-existing film as in Fig. 10.

range. All the results could be expressed by the equation

$$i = A \exp\left(\frac{-Q_T}{B}\right) \quad [5]$$

where the value of *A* is dependent on the charging potential and *B* is constant. *Q<sub>T</sub>* is the total charge used in forming the film and hence is a measure of its thickness. One can also obtain an *i/Q<sub>T</sub>* curve from the data of Fig. 11. These agree with the data obtained potentiostatically. Also from Fig. 11 it can be seen that the thickness, (*Q<sub>T</sub>*), is a linear function of the potential with a slope which is independent of the current density. One can also obtain polarization curves (log *i* vs. *E*) at different thicknesses from this data. In the steady growth region the slope is constant and independent of thickness. The slope is also independent of pH.

Some potentiostatic experiments were also run in the temperature range of 0°-35°C. Again curves obeying the equation *i* = *A* exp -*Q<sub>T</sub>*/*B* were obtained. However, the value of *B* changed with temperature.

Although there had been a number of mechanism proposed for explaining the kinetics of anodic growth of thin oxide films, none appeared satisfactory for this set of results. We therefore adapted the place-exchange mechanism which had been proposed for dry oxidation. A more detailed mechanism was worked out (18) which proposed the simultaneous (or cooperative) rotation of rows of atoms. The applied potential supplied part of the driving force. A schematic representation of the process is shown in Fig. 12. The activation energy for growth increases with thickness until it exceeds the activation energy required for diffusion or other growth processes. Because of the applied potential the oxide can become thicker than under conditions of dry oxidation.

**Oxidation in low pressure oxygen.**—We have made a number of attempts to measure the rate of dry oxidation of iron at room temperature. Microbalance measurements, using either a quartz beam type or a sensitive Cahn type, were not sufficiently sensitive. Two techniques were successful. In one of these (20) the reaction was followed by measuring the change of pressure with time at constant volume. With the other the (21, 22) intensity of an electron beam excited *OK<sub>α</sub>* X-ray line was measured to determine the amount of oxygen in the surface.

The pressure-change apparatus was constructed of stainless steel, except for a fused silica specimen chamber. It could be baked and pumped to a base pressure of about 10<sup>-8</sup> Torr. The uptake measurements were made at about 10<sup>-2</sup> Torr. The change of pressure was measured using a calibrated Pirani gauge. The specimens were electropolished and hydrogen reduced before the reaction. Using 10 cm<sup>2</sup> specimens the measurements were sensitive to about 2 × 10<sup>-8</sup> g/cm<sup>2</sup>. With smaller specimens, such as the 2 cm<sup>2</sup> single crystals the sensitivity was less, about 1 × 10<sup>-7</sup> g/cm<sup>2</sup> or the equivalent of just under 1 Å of Fe<sub>3</sub>O<sub>4</sub>.

Results for three different specimens are shown in Fig. 13. The uptake in all cases is approximately logarithmic and the thickness approaches 13-16 Å de-

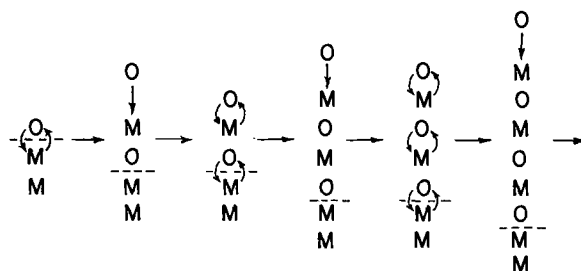


Fig. 12. Illustration of place-exchange mechanism for anodic oxidation of iron. Note simultaneous rotation of rows.

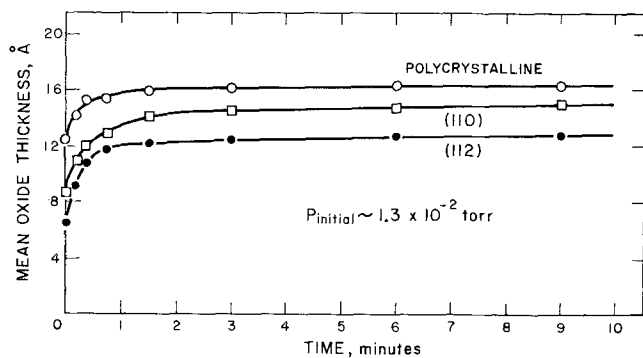


Fig. 13. Kinetics of oxidation of iron at room temperature and low pressure. Note anisotropy of oxidation.

pending on the orientation. The polycrystalline oxide has the highest uptake. The oxide on the single crystal specimens was shown by electron diffraction to be a well-oriented epitaxial microcrystalline oxide of the  $\text{Fe}_3\text{O}_4$ - $\gamma$ - $\text{Fe}_2\text{O}_3$  type, similar to that observed previously for oxide formed by anodic oxidation or air exposure of a cathodically reduced specimen. Surface area measurements were made using krypton adsorption and the surface roughness ( $\approx 1.2$ ) was the same for all the specimens. The small anisotropy of oxidation is probably due to varying grain (or subgrain) size with surface orientation. The observed thickness is about the same as that reported above for iron which was electropolished or etched and exposed to atmospheric air and in the middle range of the thick-

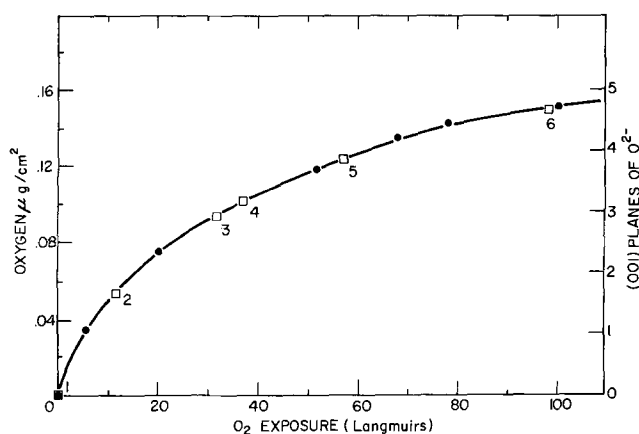


Fig. 14. Oxidation of iron in RHEED-XRE apparatus. The squared numbers were points at which electron diffraction patterns were measured.

nesses formed by anodic oxidation of iron in the borate buffer solution.

A RHEED-XRE apparatus (21) was used to examine the growth of oxide on iron at lower pressures. In this apparatus it was possible both to obtain reflection high energy electron diffraction of the surface and to measure the oxygen uptake by the x-ray emission from the surface oxygen of the  $\text{OK}_\alpha$  line. This x-ray emission could be excited by the high energy electron beam (40-50 kV) or by an auxiliary low energy (500-2000V) beam directed at right angles to the speci-

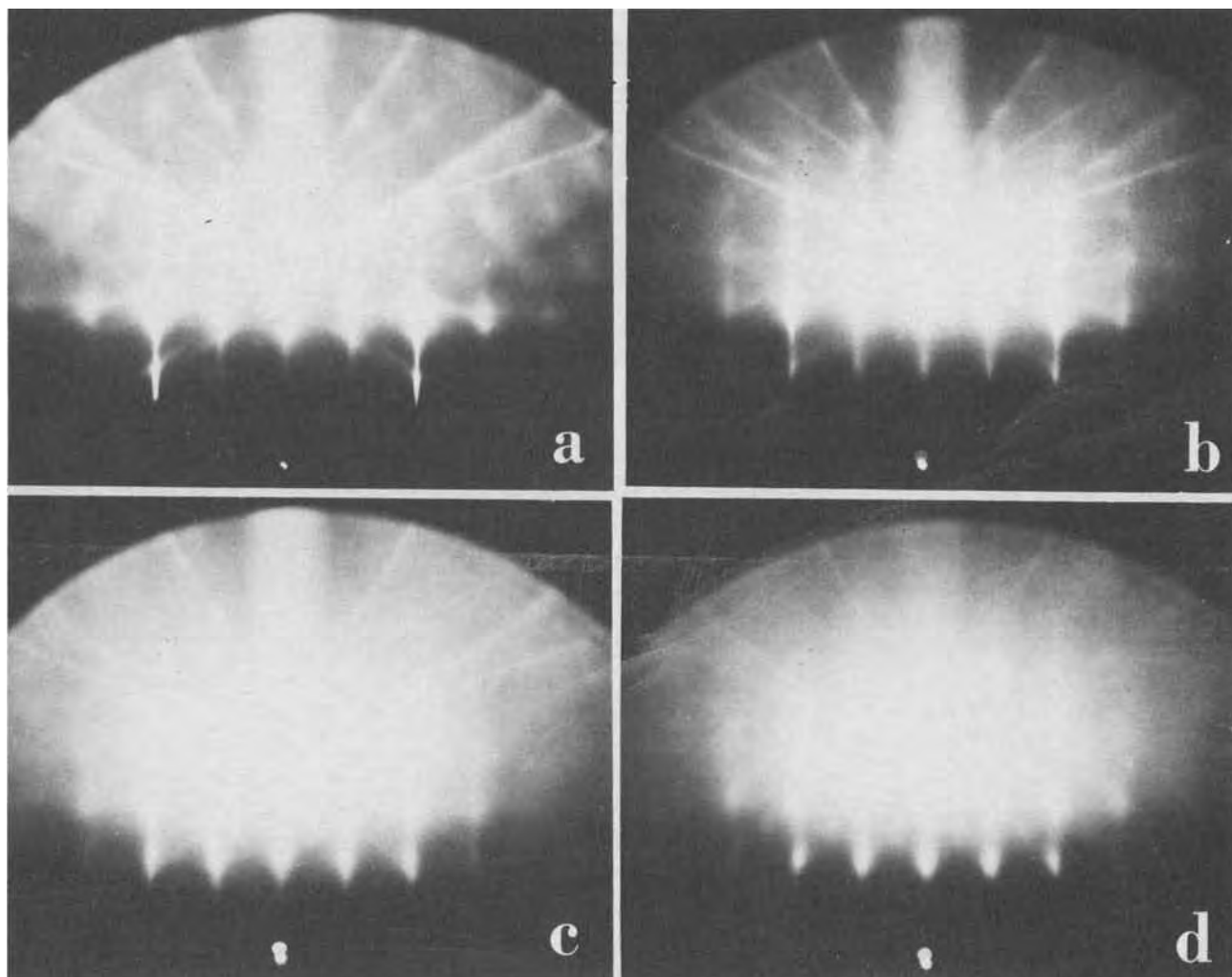


Fig. 15. Electron diffraction patterns of pure (001) iron. (a), Clean. (b), 12L exposure. (c), 37L exposure. Pattern shows both iron and oxide. (d), 57L exposure. Mostly iron oxide pattern.

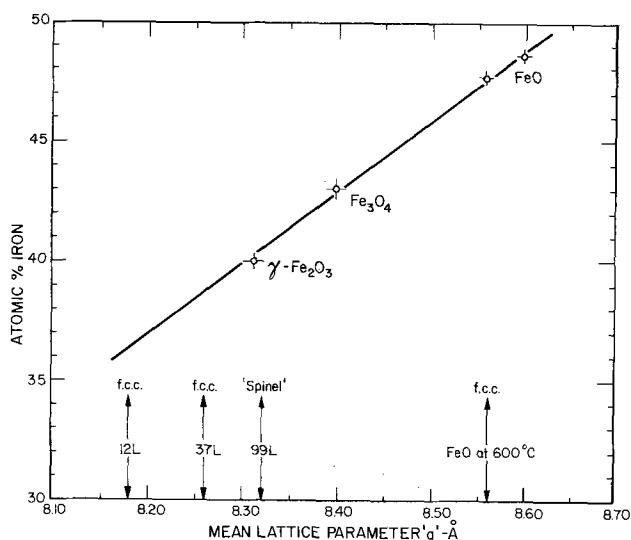


Fig. 16. Variation of oxide lattice parameter with Fe concentration in oxide. The first oxide formed (at 12L) is iron deficient and changes towards the spinel with further exposure.

men. The latter was used in these studies of oxygen take-up (22).

In this study the single crystal high purity iron was further purified in the apparatus to remove carbon, sulfur, and oxygen. It was then exposed to low pressure oxygen, and measurements were made. It was found that over the oxygen pressure range of  $5 \times 10^{-8}$  to  $2 \times 10^{-6}$  Torr and for specimen temperatures from 25° to 150°C, the rate of oxidation at any specific thickness was directly proportional to pressure. In the very early stages of oxidation of a clean surface the sticking coefficient was close to one and dropped to  $10^{-3}$  and lower after some oxide formation. The x-ray emission measurements were calibrated using specimens prepared in the pressure-change apparatus. The sensitivity was, of course, considerably higher than that of the pressure-change equipment.

A typical oxidation curve is shown in Fig. 14. Reflection high energy electron diffraction patterns before and during the oxidation are shown in Fig. 15. Although these measurements were made at 150°C almost identical results are obtained at lower temperatures in this exposure range. The mean lattice parameter parallel to the surface was determined from the diffraction patterns and varied from  $8.18 \pm 0.04$  at low exposures to  $8.34 \pm 0.06$  for long exposure times. The relationship of these observed lattice parameters to those of the oxides of iron is shown in Fig. 16. It can be seen that the oxide starts out with a structure corresponding to an oxide containing even less iron than  $\gamma\text{-Fe}_2\text{O}_3$  and as it thickens (and ages) gradually moves through  $\gamma\text{-Fe}_2\text{O}_3$  to  $\text{Fe}_3\text{O}_4$ . The thickness at 99L ( $L = 10^{-6}$  Torr sec) exposure is about

10Å. With longer times of exposure ( $10^4L$ ) the oxide thickens to about 20Å.

These results are consistent with those obtained with the other techniques of dry oxidation, anodic oxidation, electropolishing, and electropolishing and etching, or cathodic reduction and air exposure. The low lattice parameter (cation vacancies in an essentially  $\gamma\text{-Fe}_2\text{O}_3$  structure) is typical of conditions where oxygen incorporation into the oxide is more rapid than iron diffusion. With time all the oxides tend to "anneal" towards a  $\gamma\text{-Fe}_2\text{O}_3\text{-Fe}_3\text{O}_4$  composition. In all cases the oxide is thin, highly oriented but microcrystalline. The rate of oxidation is essentially logarithmic and hence the oxide is highly protective.

#### Acknowledgment

This work was not done in the author's basement on weekends and evenings. I would therefore like to thank the National Research Council for both facilities and encouragement in doing this work and the many colleagues who have participated in this rather long and difficult but satisfying research into the varied facets of the thin film oxidation of iron.

Manuscript received Feb. 6, 1974.

Any discussion of this paper will appear in a Discussion Section to be published in the December 1974 issue of the JOURNAL. All discussions for the December 1974 Discussion Section should be submitted by Aug. 1, 1974.

#### REFERENCES

1. M. Cohen, *This Journal*, **87**, 255 (1945).
2. M. Cohen, *ibid.*, **89**, 193 (1945).
3. M. Cohen, *ibid.*, **93**, 26 (1948).
4. R. Pyke and M. Cohen, *ibid.*, **93**, 63 (1948).
5. R. Pyke, M. Cohen, and P. Marier, *ibid.*, **96**, 254 (1949).
6. M. J. Pryor and M. Cohen, *ibid.*, **100**, 203 (1953).
7. M. Cohen and A. F. Beck, *Z. Elektrochem.*, **62**, 696 (1958).
8. M. Cohen, *Can. J. Chem.*, **37**, 286 (1959).
9. M. Cohen, *J. Phys. Chem.*, **56**, 451 (1952).
10. M. J. Pryor and M. Cohen, *This Journal*, **98**, 263 (1951).
11. M. J. Pryor, M. Cohen, and F. Brown, *ibid.*, **99**, 542 (1952).
12. P. B. Sewell, C. D. Stockbridge, and M. Cohen, *Can. J. Chem.*, **37**, 1813 (1959).
13. P. B. Sewell, C. D. Stockbridge, and M. Cohen, *This Journal*, **108**, 933 (1961).
14. H. G. Oswin and M. Cohen, *ibid.*, **104**, 9 (1957).
15. M. Nagayama and M. Cohen, *ibid.*, **109**, 781 (1962).
16. M. Nagayama and M. Cohen, *ibid.*, **110**, 670 (1963).
17. D. B. Gibbs and M. Cohen, *ibid.*, **119**, 416 (1972).
18. N. Sato and M. Cohen, *ibid.*, **111**, 512 (1964).
19. N. Sato and M. Cohen, *ibid.*, **111**, 520 (1964).
20. M. J. Graham, S. I. Ali, and M. Cohen, *ibid.*, **117**, 513 (1970).
21. P. B. Sewell, D. F. Mitchell, and M. Cohen, "Developments in Applied Spectroscopy," Vol 7A, p. 61, E. L. Grove and A. J. Perkins, Editors, Plenum Publishing Corp., New York (1969).
22. P. B. Sewell, D. F. Mitchell, and M. Cohen, *Surface Sci.*, **33**, 535 (1972).

# The Current Understanding of Charges in the Thermally Oxidized Silicon Structure

Bruce E. Deal\*

Research and Development Laboratory, Fairchild Camera and Instrument Corporation,  
Palo Alto, California 94304

The publication costs of this article have been assisted by the Fairchild Camera and Instrument Corporation.

## ABSTRACT

Generally accepted facts along with unanswered questions, concerning the four charges,  $Q_{ss}$ ,  $Q_o$ ,  $N_{st}$ , and  $N_{ot}$ , associated with the thermally oxidized silicon system are presented and briefly discussed. The discussions and information presented are based on comprehensive investigations carried out in the semiconductor industry over the past ten years. Although reasonably good empirical information concerning charge dependence on device processing is available, much remains to be learned regarding the physical origin of these charges. A simplified model is presented which indicates that most of the charges can be related to silicon bond defects in the thermally oxidized silicon structure.

In May 1962, the first complete technical session to deal with passivating properties of thermal oxides on silicon was held at the Electrochemical Society Meeting in Los Angeles, California. Prior to that, the only significant work on the subject was from Bell Laboratories, where such scientists as Atalla, Law, Ligenza and Spitzer, Frosch and Derrick, and others (1), had provided the background for oxide passivation of silicon devices.

Ten years ago, in 1963, several companies started programs involving silicon surface studies and MOS development. These programs were later to mushroom into the largest concentrated effort of this type that the industry had seen or perhaps will ever see (2). While these efforts were primarily directed towards MOS devices, the results now also apply to bipolar structures which have become equally sensitive to surface properties due to recently developed technology. Charges present in oxidized silicon structures affect threshold voltages, effective mobilities, and device stability in MOS devices, and also low current beta, junction leakage, noise, and breakdown voltage in discrete transistors and linear and digital integrated circuits. Many of the detrimental effects in bipolar devices are due to channeling or inversion of the silicon surface as a result of charges in the oxide.

It has been adequately demonstrated that the basis for all silicon device passivation is thermal silicon dioxide. While other dielectrics such as vapor deposited silicon oxide or nitride, phosphosilicate glass, or aluminum oxide, are useful, they are generally employed as secondary layers either over the thermal oxide or on top of the metallization. A discussion of charge effects in these double dielectric structures will be presented in a later paper.

This paper will review the current understanding of charges in thermally oxidized silicon. Facts about the four types of charges will be listed and discussed along with comments about unanswered questions. The discussion will be based on the author's experience over the past ten years, as well as on information gained from other investigators.

Since it has been demonstrated that most of the charge effects are directly or indirectly related to the thermal oxidation process, a short discussion of thermal oxidation kinetics will first be presented, followed by a brief description of the four types of

charges. After the primary tabulation and discussion of the facts and unanswered questions about these charges in the  $\text{SiO}_2$ -Si system, the paper will conclude with a hypothesis concerning the possible physical origins and interrelationship of the charges.

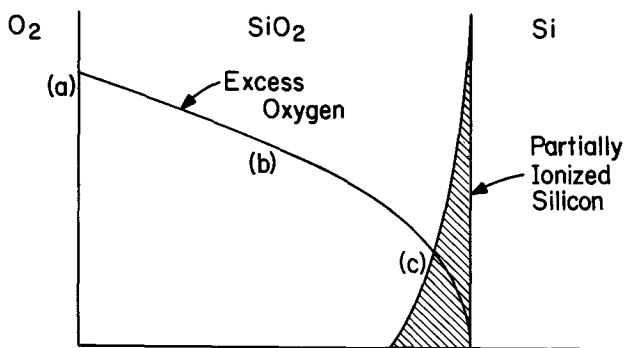
## Thermal Oxidation of Silicon

The thermal oxidation of silicon is commonly carried out in a water vapor or oxygen atmosphere over the temperature range of 800°-1250°C. The oxidation proceeds by three consecutive reactions: (i) the transfer of the oxidizing species into the oxide already formed, (ii) the diffusion of the species through the oxide, and (iii) the reaction of oxygen with silicon at the oxide-silicon interface region to form  $\text{SiO}_2$  (3). These processes are illustrated in Fig. 1. The kinetics of silicon oxidation have been studied in detail (3-7), and a relationship has been established which is based upon all three of the individual reactions mentioned above. This relationship is included in Fig. 1 and agrees with experimental data that have indicated a parabolic, diffusion-controlled oxidation mechanism at high temperatures, a linear, surface-controlled reaction at low temperatures, and a combination of the two at intermediate temperatures. Thus, processing steps, such as boron or phosphorus glass formation, which affect the diffusion process through the oxide, also affect the oxidation rate at high temperatures. On the other hand, anything affecting the nature of the silicon surface, such as crystal orientation, heavy doping, or the like, will affect the oxidation process at low temperatures.

It is interesting to note that the activation energy of 45 kcal/mole determined for the surface reaction controlled, linear rate constant is identical to the Si-Si bond energy reported by Jaccodine (8). Thus, the rate-determining step for the reaction of Si and  $\text{O}_2$  to form  $\text{SiO}_2$  is probably related to the breaking of a Si-Si bond.

As is shown in Fig. 1, a thin region of oxide which contains partially ionized or excess silicon exists near the  $\text{SiO}_2$ -Si interface where diffusing oxygen reacts to form new  $\text{SiO}_2$ . This partially ionized silicon plays an important part in charge formation as will be described in the following sections. The amount or density of the ionized silicon depends upon the final high temperature oxidation or annealing conditions. Unlike the excess silicon, the "excess" oxygen distributed throughout the oxide apparently is not charged in its final form and, thus, does not act as a charge in the thermally oxidized silicon system.

\* Electrochemical Society Active Member.  
Key words: silicon, silicon dioxide, oxide charges, semiconductor passivation.



$$x_0^2 + Ax_0 = B(t + \tau)$$

where:  $A \equiv 2D(1/k + 1/h)$

$$B \equiv 2DC^*/N_1$$

$$\tau \equiv \text{Constant}$$

For "large times,"

$$x_0^2 \approx Bt$$

For "small times,"

$$x_0 \approx \frac{B}{A} (t + \tau)$$

Fig. 1. Schematic illustration of proposed mechanism, plus the general relationship, for the thermal oxidation of silicon (3). The three stages of oxidation are indicated by (a), (b), and (c). In the general relationship, A, B, and  $\tau$  are constants and  $x_0$  is the oxide thickness after time t.

**Charges in Thermal Oxides**

The four types of charges found to be associated with the thermally oxidized silicon structure are shown in Fig. 2. They are as follows:  $Q_{ss}$ , fixed sur-

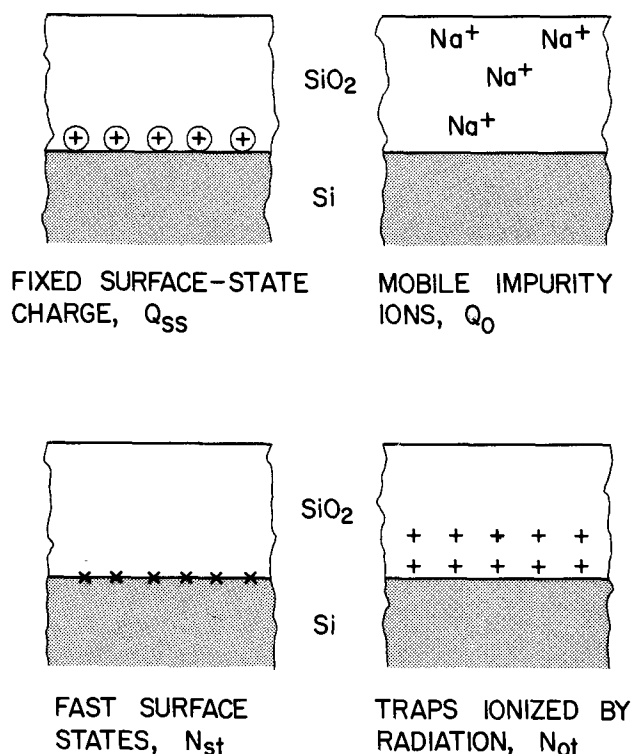


Fig. 2. The four types of charges associated with the thermally oxidized silicon structure.

face state charge;  $Q_o$ , mobile impurity ions;  $N_{st}$ , fast surface states;  $N_{ot}$ , radiation induced charge.

The understanding of the origin and nature of these charges is very important if they are to be reproducibly controlled or minimized during device processing (9-13). The net result of any charge residing in the oxide is to induce a charge of opposite polarity in the underlying silicon. The amount induced will be inversely proportional to the distance of the charge from the silicon surface. Thus, an ion residing in the oxide very near the SiO<sub>2</sub>-Si interface will reflect all of its charge in the silicon, while an ion near the oxide outer surface will cause little or no effect in the semiconductor. The charge is measured in terms of net charge per unit area at the silicon surface.

The author has established that there are at least seventeen basic effects whereby the effective density of one or more of these charges is changed by a particular processing step. These effects have been determined by carefully chosen and controlled experiments, and are locally referred to as the "XVII drifts of silicon oxide technology." It does not have to be emphasized that a proper understanding of these "drifts" is a critical factor in the fabrication of reproducible and reliable devices—either MOS or bipolar. Space does not permit a discussion of all seventeen instabilities, but important examples will be presented in the following sections.

Most oxide charge evaluations can be made using the capacitance voltage (C-V) method of analysis. This method is simple and rapid (14-15) and in most cases provides a quantitative or at least a semiquantitative measure of surface charge.

The value of any given charge such as  $Q_{ss}$ , residing as a sheet near the SiO<sub>2</sub>-Si interface, can be determined using the C-V method of analysis by the following relationship

$$\frac{Q_{ss}}{q} = (-V_{FB} + \phi_{MS}) \frac{C_o}{q} = (-V_{FB} + \phi_{MS}) \frac{k_o \epsilon}{q x_o}$$

where  $V_{FB}$  is flatband voltage;  $\phi_{MS}$ , metal-semiconductor barrier energy difference;  $C_o$ , oxide capacitance; q, electronic charge;  $k_o$ , oxide dielectric constant;  $\epsilon$ , permittivity of free space; and  $x_o$ , oxide thickness.

A typical C-V plot is shown in Fig. 3 where  $Q_{ss}$  can be determined from the above relationship by measuring the flatband voltage  $V_{FB}$ . Additional charges introduced into the oxide will cause a further shift of  $V_{FB}$ , thus displacing the C-V curve along the voltage axis. Other more precise, but also more com-

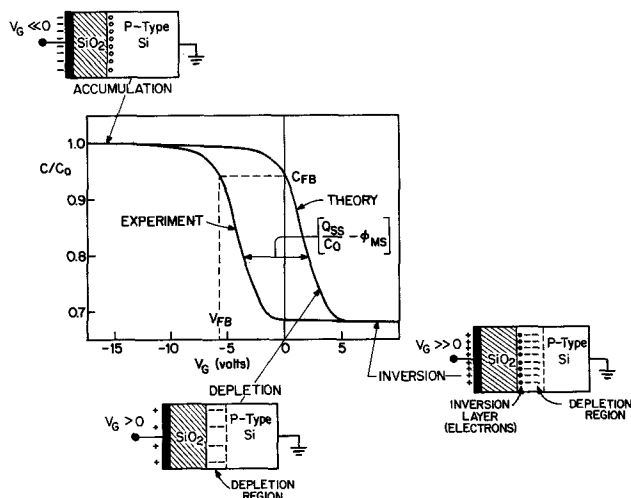


Fig. 3. Determination of fixed surface-state charge  $Q_{ss}$  by comparison of experimental and theoretical capacitance-voltage (C-V) curves. For theoretical curve,  $Q_{ss}$  and  $\phi_{MS} \equiv 0$ .



plicated, methods for charge measurement are reported in the literature, especially for fast state analysis (9, 16-20).

The author has made extensive use of the C-V analysis method over the past ten years and has noted that C-V curves are so sensitive to process variation that it is possible to determine what oxide has been produced in what furnace at what time and even in what mood the operator was that particular day.

### Facts and Unanswered Questions Regarding Oxide Charges

As mentioned in the introductory remarks, a considerable amount of work has been carried out over the past ten years concerning silicon passivation, with emphasis on the four types of charges in thermal oxides. Much is known about each of these charges, and as a result, sophisticated MOS and bipolar devices can be routinely fabricated. On the other hand, many questions remain unanswered. In this section some of the more generally accepted facts will be listed and briefly discussed, along with unanswered questions. It is to be expected, of course, that not everyone will agree on all the facts presented, but it is hoped that this presentation will provide a stimulus for additional thinking and investigation into the subject.

#### Mobile Impurity Ions ( $Q_o$ )

##### Facts.—

1.  $Q_o$  is normally due to positive alkali ions ( $\text{Na}^+$ ,  $\text{K}^+$ ,  $\text{Li}^+$ ) in the oxide. These ions will drift under bias above  $100^\circ\text{C}$  or, in some cases, at lower temperatures, causing device instabilities.
2. Hydrogen ions ( $\text{H}^+$  or  $\text{H}_3\text{O}^+$ ) will drift under bias at room temperature.
3. Under certain conditions negative charges in oxides have been noted. They will not drift, however, in the vicinity of  $300^\circ\text{C}$  or lower over time periods of hundreds of hours.
4. All mobile ions can be gettered at elevated temperatures ( $>900^\circ\text{C}$ ) using a complexing agent such as phosphosilicate glass.

The mobile impurity ions in thermal oxides were the first charge to be extensively investigated since further studies in the  $\text{SiO}_2$  system could not be carried out until the mobile impurity level was minimized. While various mechanisms and origins for the charge were initially proposed, as indicated by Donovan's famous elephant (Fig. 4), experimental evidence proved the alkali ions to be the major cause of this instability (21-22). These ions can be incorporated into the oxide during any or all device processing steps, and any processing material, solvent or ambient can serve as a source (23). Figure 5 shows the rela-

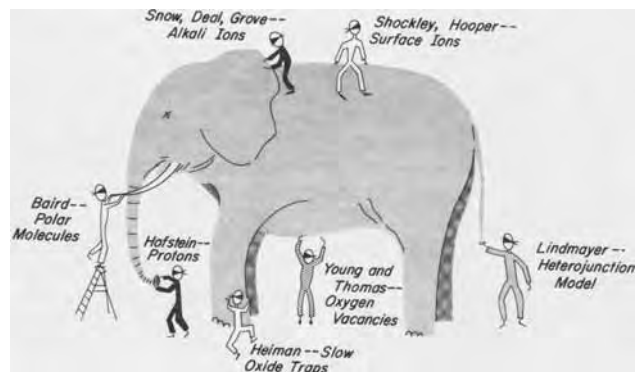


Fig. 4. Indication of early confusion regarding source of MOS instability as represented by Donovan's "blind men and the elephant" drawing. (Courtesy of R. P. Donovan, Research Triangle Institute, RTI Park, North Carolina.)

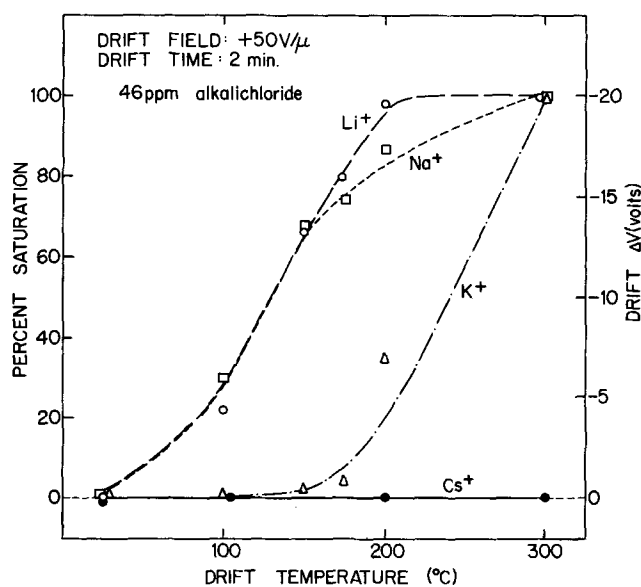


Fig. 5. Comparison of drift rates for various alkali ions through  $0.2\mu$  thermal silicon dioxide over the temperature range  $25^\circ\text{C}$ - $300^\circ\text{C}$ .

tionship among the drifts of  $\text{Li}^+$ ,  $\text{Na}^+$ ,  $\text{K}^+$ , and  $\text{Cs}^+$  at various temperatures. The rate of drift decreases for the heavier elements, which have larger ionic radii and, consequently, lower mobility.

Other species such as mobile protons (24) and immobile negative ions (25-26) have been shown to contribute to ionic charge. Fortunately essentially all such impurities can be removed or complexed by a high temperature gettering step (27), although precaution during device fabrication is considered a safer method for producing more stable and reliable devices (28).

##### Questions.—

1. What is the nature of "inactive" alkali ions?
2. What is the source and mechanism of proton drift?
3. What is the role of chlorine in improving oxide properties, gettering impurities, etc.?

Conflicting data have been presented regarding alkali content, particularly sodium, of thermal oxides. The majority of results to date indicates that more sodium is present than is indicated electrically. Thus, the questions arise as to the nature of the "inactive" sodium, under what circumstances can it be made electrically active, how does it affect other oxide properties and how is it related to other charges in the oxide?

Another question involves proton or hydrogen drift in MOS structures. Initial work by Hofstein (24) indicated that more than one hydrogen species might migrate in oxides along with multiple types of sodium. Unfortunately, measurement of such species is difficult at best and detailed facts about the phenomena are minimal.

The most significant development in thermal oxide technology in recent months has been the incorporation of a chlorine species into the structure (29-30). The reports have indicated that all sorts of good things result. It is reasonably certain that a gettering or complexing of impurity ions occurs, but additional studies are required to establish definite mechanisms and also to verify other reported advantages. In addition, possible detrimental effects, such as corrosion of aluminum interconnections, must be evaluated.

#### Fixed Surface-State Charge ( $Q_{ss}$ )

##### Facts.—

1.  $Q_{ss}$  is a positive, stable charge in the oxide, very close to the  $\text{SiO}_2$ -Si interface. It cannot be

charged or discharged by varying the silicon surface potential.

2. Its value depends upon the final oxidation or annealing conditions (oxygen triangle).
3. Its value is a function of silicon orientation.
4. Its value can be increased by a negative field on the gate of a MOS structure in the temperature range 100°-400°C. The amount of this increase is proportional to the initial  $Q_{ss}$  value and the applied negative field (drift VI).

The presence of a positive, fixed, surface-state charge  $Q_{ss}$  in thermally oxidized silicon is well established (9, 12, 31). It is somehow related to the oxide structure in the interface region between the  $SiO_2$  and the silicon. The value of  $Q_{ss}/q$  can range from the low  $10^{10} \text{ cm}^{-2}$  to  $10^{12} \text{ cm}^{-2}$ . The dependence of the  $Q_{ss}$  density on the annealing ambient, such as  $O_2$ ,  $H_2O$ , nitrogen or argon, and on annealing temperature is also relatively well known (13, 31-32); the oxygen-nitrogen temperature effect is represented by the familiar  $Q_{ss}$  triangle in Fig. 6. Not so well understood is the proposed mechanism which explains the  $Q_{ss}$  dependence upon oxidation and annealing conditions. The latter is indicated in Fig. 6 by the three cross-sections (a), (b), and (c) of the oxidized silicon structure, which will be further discussed in the next section.

A fact not well known is that for extra long annealing times (>60 min) at high temperatures (1200°C) in an inert ambient such as nitrogen, the effective value of  $Q_{ss}$  actually increases. This is contrary to the prediction of Fig. 6, and has caused some investigators difficulties in duplicating the oxygen triangle relationship.

The dependence of  $Q_{ss}$  on silicon orientation is apparently related to the oxidation reaction (6). From the oxidation relationship, values of the surface controlled rate constant  $B/A$  are found to be a function of orientation in the same ratio as is  $Q_{ss}$ . Thus, the origin of  $Q_{ss}$  may well be traced to a Si-Si bond reac-

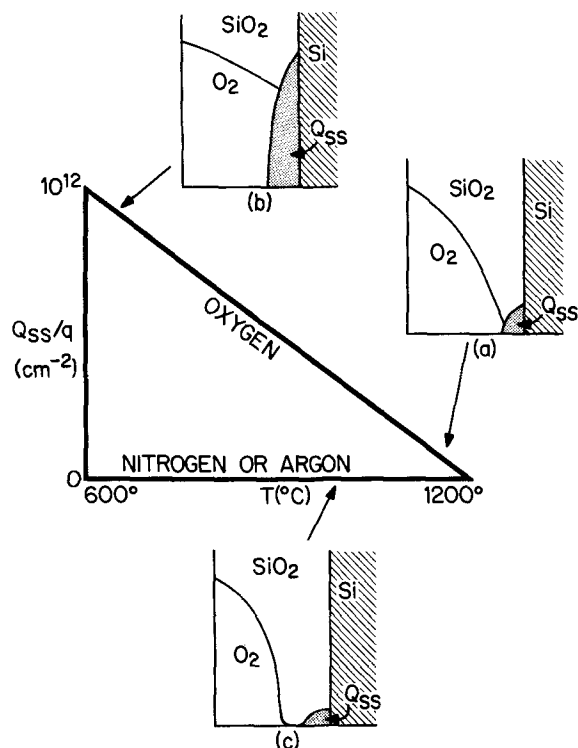


Fig. 6. The dependence of  $Q_{ss}$  on final oxidation temperature and ambient as represented by the  $Q_{ss}$ -oxygen triangle. Data are for (111) oriented silicon. Also shown are sketches of thermal oxide cross section indicating proposed relationship of  $Q_{ss}$  to oxidation conditions.

tion which is also the basis for the surface controlled oxidation reaction.

The effect of a negative field at slightly elevated temperatures on  $Q_{ss}$  is an extremely interesting phenomenon (31, 33-34) and helps to shed considerable light on the origin of  $Q_{ss}$ . The dependence of the amount of  $Q_{ss}$  increase on the initial  $Q_{ss}$  value is shown in Fig. 7, and the significance of this relationship will be discussed in the next section.

Questions.—

1. What is the exact origin of  $Q_{ss}$ ?
2. What is the mechanism of drift VI?
3. What causes the effective  $Q_{ss}$  density to increase with long anneal times in inert ambients at high temperatures?
4. What are the relationships among the origins of the various charges?

The question involving the nature or origin of  $Q_{ss}$  has been the subject of considerable discussion. Most investigators now agree in principle that  $Q_{ss}$  results from a nonstoichiometric silicon-oxygen structure in the Si- $SiO_2$  interface region (see Fig. 1). Whether it is called excess silicon or deficient oxygen is not important; in either case a positive charge results, and the density of this charge is dependent upon the final high temperature annealing or oxidation conditions and the silicon orientation.

Experimental data such as the  $Q_{ss}$  triangle, the dependence upon orientation and oxidation, the negative field effect and the long annealing times in an inert ambient, help to establish more definite conclusions about the origin of  $Q_{ss}$ . For instance, cross section (a) of Fig. 6 shows the proposed origin of  $Q_{ss}$  due to the generation of a thin region of partially ionized silicon in response to the field caused by inward diffusing oxygen as thermal oxidation takes place. At high temperatures, where oxygen diffusion is the rate determining or slower step, most of the excess silicon reacts with oxygen, thus, leaving a minimum amount of  $Q_{ss}$ . In sketch (b) of Fig. 6, the slower process during silicon oxidation at low temperature is the silicon-oxygen reaction. Thus, excess silicon ions are piled up and a high  $Q_{ss}$  density results

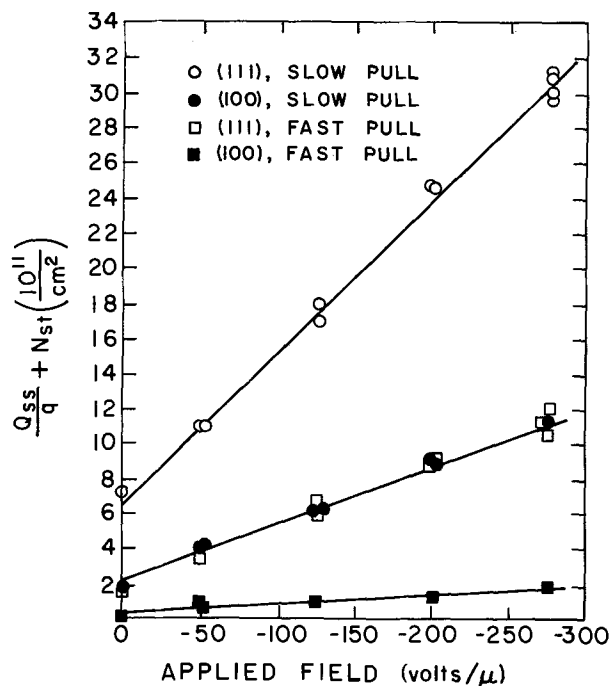


Fig. 7. Steady-state values of  $Q_{ss}/q + N_{st}$  as a function of applied negative field for four different MOS structures with various initial  $Q_{ss}$  values (31). [1200°C dry  $O_2$  oxidation;  $x_0 = 0.20\mu$ ; p-type Si,  $N_A = 1.4 \times 10^{16} \text{ cm}^{-3}$ ].

[Fig. 6(b)]. If, however, the ambient is changed to an inert gas, the situation shown in Fig. 6(c) results, where the excess silicon reacts with oxygen at any temperature, resulting in a low  $Q_{ss}$ . It should be noted that the minimum density of  $Q_{ss}$  under these latter conditions probably represents some equilibrium value, and that under ideal conditions the  $Q_{ss}$  value could go to zero.

Further insight into the origin of  $Q_{ss}$  may be obtained from the drift VI data of Fig. 7. If it is assumed that  $Q_{ss}$  is actually due to partially ionized silicon atoms, such as  $Si^+$ , then it can be proposed that the effect of a negative applied electric field is to break a second (already strained) silicon bond, resulting in a  $Si^{++}$  species. Thus, a dependence on initial  $Q_{ss}$  density is expected.

The increase of effective  $Q_{ss}$  with a long time, high temperature anneal in nitrogen is indicated in Fig. 8. Note that whether the structure initially exhibits a high or low  $Q_{ss}$ , the  $Q_{ss}$  drops to a low value in a short time in  $N_2$ . Subsequent annealing results in a higher effective  $Q_{ss}$  at the higher temperatures. A possible explanation for this effect may also be related to the breaking of Si-Si or Si-O bonds at the interface region—possibly due to thermal energy rather than electrical effects. It might even be possible for oxygen ions to leave the structure or at least the interface region by out-diffusion. In any case, an additional positive charge results. This effect is very similar to that found by Hess and Fowkes (35) when thermal oxides are subjected to a reducing ambient at lower temperatures, e.g., 900°C.

The question of interrelationships among the origins of all the charges, especially  $Q_{ss}$ ,  $N_{st}$ , and  $N_{ot}$ , will be discussed in the final section of this paper. As observations regarding  $N_{st}$  and  $N_{ot}$  are made in the next sections, the possibility of common origins with  $Q_{ss}$  will become more apparent.

#### Fast Surface States ( $N_{st}$ )

##### Facts.—

1.  $N_{st}$  is located at the  $SiO_2$ -Si interface and can be charged or discharged with changing silicon surface potential.
2.  $N_{st}$  includes several types of fast states, appearing both at discrete energy levels and as a con-

tinuous distribution throughout the silicon band-gap.

3. The value of fast state density increases with a high temperature annealing treatment in an inert ambient.
4. Fast state density is initially proportional to  $Q_{ss}$  and exhibits the same silicon orientation dependence.
5. The  $N_{st}$  density can be minimized by a hydrogen anneal above 300°C, including the active metal, "aneal" process.

Fast surface states have been studied over a longer period of time than any of the other charges associated with passivated semiconductors. They were even studied in the early days of germanium; yet they are still the least understood. Fast states derive their name from the fact that the traps responsible are in direct electrical communication with the silicon and, thus, respond rapidly to changes in surface potential. This leads to the familiar charging and discharging as the potential sweeps across the bandgap.

Since the intensive investigations were started approximately ten years ago, considerable empirical data concerning fast states have become available (13, 19, 20, 32, 36). The C-V method of analysis has helped to provide qualitative or even semiquantitative measurements in the  $10^{10}$  or  $10^{11}$   $cm^{-2}$  range. As mentioned in an earlier section, other more sensitive analytical methods are available. Using these techniques, several types of fast states have been identified throughout the silicon bandgap. The general distribution is shown in Fig. 9. Indications of these states can also be noted as distortions in C-V plots [A, B, C, and D of Fig. 10(a)].

The C-V method can also be used to obtain a more accurate measure of fast state density by carrying out the measurement at liquid nitrogen temperature. This method was originally reported by Gray and Brown (18), and an example of the resulting plot is shown in Fig. 10(b).

It has been noted that fast state densities are generally initially proportional to  $Q_{ss}$  and thus also depend on silicon orientation. It is also known that high temperature anneals in inert ambients, such as nitro-

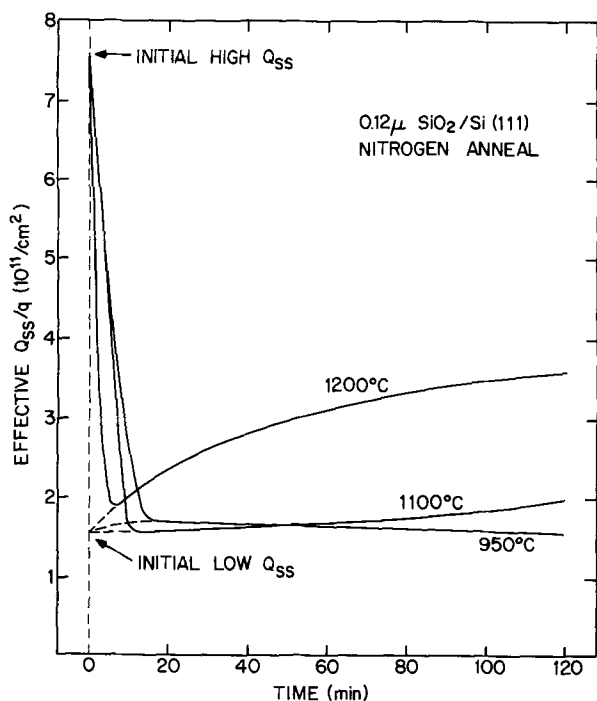


Fig. 8. Dependence of effective  $Q_{ss}/q$  on anneal in nitrogen for times of 0-120 min at various temperatures.

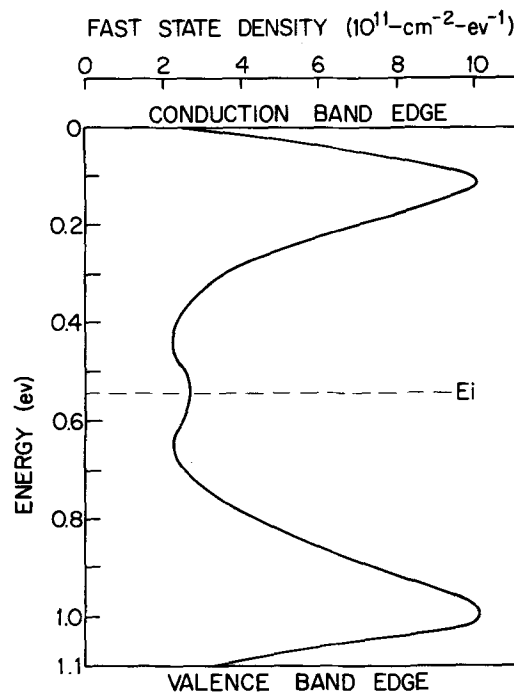


Fig. 9. Approximate distribution of fast states associated with the silicon-silicon dioxide interface produced by thermal oxidation in dry oxygen.

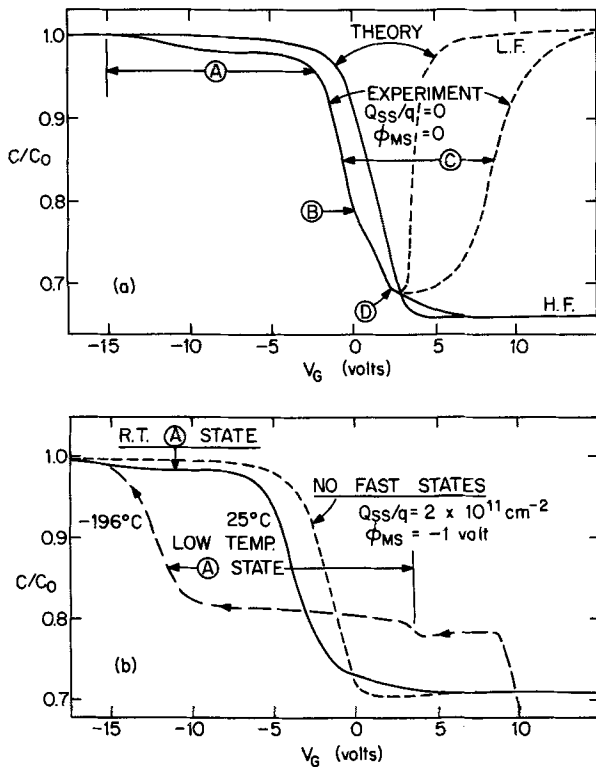


Fig. 10. Examples of fast surface states as indicated in MOS C-V plots; (a) 25°C, (b) 77°K.

gen, will increase fast state density (13, 32). Similarly, treatment in hydrogen or an active hydrogen species produced by the reaction of an active metal with water on the oxide surface (anneal process) will reduce fast state density, supposedly by complexing the defect responsible for  $N_{st}$  (13, 37).

Dependence of many device electrical properties on fast states has been established. These include threshold voltage and transconductance in MOS transistors and junction noise and leakage, low current beta and breakdown characteristics in bipolar devices. Bipolar transistors in linear integrated circuits are especially sensitive to fast states—almost to the same extent as MOS structures.

**Questions.—**

1. What is the physical origin of fast states?
2. What are the differences among the various types of discrete and continuous states?
3. How is  $N_{st}$  related to  $Q_{ss}$  as well as to impurity ions?

The dependence of device properties on fast states as mentioned above makes it imperative that fast states be controlled and minimized during processing. In order to accomplish this, the physical origin of fast states should be known. It is assumed at present that these states result from either defects in the structure of the interface region between the silicon and the oxide, or to impurities in this region, or both. In either case, the net result is trapping of holes or electrons at particular surface potentials or energy levels. The initial relationship of  $N_{st}$  to  $Q_{ss}$  would favor the structural defect mechanism. Also, the fact that additional fast states are formed during the negative field treatment, during ionizing radiation treatment, and during high temperature anneals leads to a similar conclusion. It then follows that a hydrogen species could react with the defect structures to complex the action of the fast state. On the other hand, the presence of impurity ions such as gold, copper and even sodium, can cause effects attributable to fast state action.

The answer to these questions probably indicates that both possibilities are true. Such an assumption

would also explain the various types of states found throughout the bandgap. In any case, it is reasonable to assume that a close relationship exists between the origin of fast states and other charges—particularly  $Q_{ss}$ .

**Radiation Induced Charge ( $N_{ot}$ )**

**Facts.—**

1.  $N_{ot}$  is a positive charge located in the oxide, generally near the  $SiO_2$ -Si interface. It is caused by ionizing radiation such as x-rays, electrons, neutrons, etc.
2. Fast states are also produced at the  $SiO_2$ -Si interface by ionizing radiation.
3. The value of  $N_{ot}$  is a function of the dose and energy of the radiation as well as the field across the oxide during radiation.
4. Both charges,  $N_{ot}$ , and radiation induced fast states, are eliminated by a low temperature anneal in an inert ambient.
5. The annealing of radiation induced charge is hindered by a dense dielectric layer such as silicon nitride over the thermal oxide.

Early in the development of MOS transistors, it was discovered that ionizing radiation would cause a positive space charge in the oxide, leading to a threshold shift of ten's of volts to over one hundred volts. Simultaneously, additional fast states were formed at the Si-SiO<sub>2</sub> interface during the irradiation. Fortunately, both charges could be annealed out at relatively low temperatures (300°C) without the presence of hydrogen. The only disadvantage was that MOS devices could not be used for applications, such as space flights, where radiation would be a factor. Since the time when  $N_{ot}$  was first identified, the phenomenon has been studied continuously (38-41). Most of the efforts have been aimed towards understanding the mechanisms of the radiation induced charge in the oxide and how this charge might be eliminated or minimized.

It has been determined that the number of trapped holes is a function of radiation dose and energy. Also, the amount of resulting charge will depend upon the magnitude and polarity of the electrical field applied across the oxide during radiation (42). The radiation may occur during use of the device in radiation environments or during particular device processing steps, such as electron beam metallization, ion implantation, or sputtering of metals or dielectrics.

Examples of radiation induced space charge formation in various structures are shown in Fig. 11. The effect of gate bias during irradiation as well as the effect of additives or other treatments of the oxide are shown.

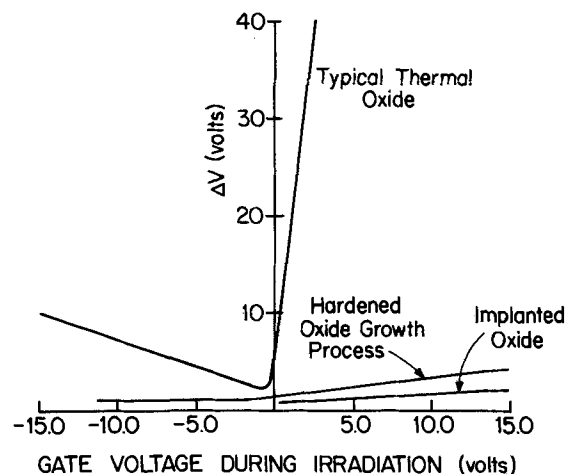


Fig. 11. Dependence of radiation induced charge  $N_{ot}$ , as indicated by MOS threshold voltage shift  $\Delta V$ , on gate voltage during irradiation and on oxide type (41).

It has also been determined, that, while the space charge and fast states produced by radiation can normally be easily annealed out by a 300°C treatment, the presence of a dense dielectric over the thermal oxide retards this annealing. An example of a typical C-V plot before and after radiation, and then after annealing with or without a nitride layer is shown in Fig. 12. Note first that the positive space charge  $N_{ot}$  causes a parallel shift of the C-V curve in the negative direction. Also note that the fast states produced during the irradiation are continuous over the bandgap, unlike the normal oxide fast states which are present at discrete energy levels. Finally, note that without a nitride layer, all fast states are annealed, but that with the nitride layer, the discrete fast states remain as does some of the positive space charge.

#### Questions.—

1. What is the origin and mechanism of the radiation induced space charge  $N_{ot}$ ?
2. How can  $N_{ot}$  be minimized?
3. What is the annealing mechanism for  $N_{ot}$  and associated  $N_{st}$ ?
4. What is the effect of secondary dense layers such as  $Si_3N_4$  on the annealing of  $N_{ot}$ ?

Two schools of thought have developed for postulating a mechanism for the formation of  $N_{ot}$ , the radiation induced positive space charge. One model is based strictly on considerations involving the  $SiO_2$  structure. Electron-hole pairs are produced by the radiation. The holes are trapped by broken silicon-oxygen bonds while the electrons migrate away (41, 43). The traps themselves may or may not be present before radiation. The second model involves the activation of impurity ions such as sodium, which in turn either act as positive charges, or indirectly result in trapped holes (41, 44).

Different solutions to the radiation problem may thus be required depending upon the true mechanism responsible for the charge, or one solution may coincidentally satisfy more than one possibility. Thus far, three solutions are proposed. These are: (i) to modify the  $SiO_2$  structure so that silicon-oxygen bond strain energy is reduced, (ii) to add impurity species such as chromium to compensate trapping centers or to complex impurity ions, or (iii) to produce absolutely pure  $SiO_2$  to eliminate impurity trapping centers. The answer to the question about the annealing mechanism is obviously tied to the formation of  $N_{ot}$  and preventive mechanisms thereof, and an answer to one question will help answer the others.

The effect of dense secondary layers on  $N_{ot}$  formation or annealing is complex due to the possible pres-

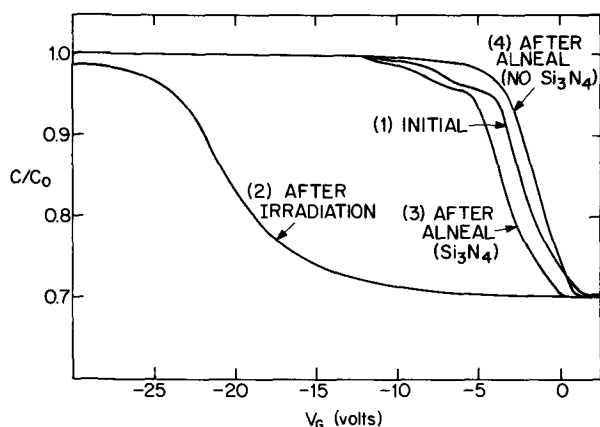


Fig. 12. Effect of irradiation on charges in MOS structures, with and without a silicon nitride layer over thermal oxide, as indicated by C-V plots. Curves (1) and (2) are the plots before and after irradiation, with or without the nitride layer. Curve (3) is the plot after a 450°C hydrogen anneal treatment with the nitride, and curve (4) is the same for no nitride.

ence in the oxide of several types of fast states as well as the space charge. Again, the correct mechanism of radiation induced space charge formation must be understood in order that effects due to added dielectrics can be understood and controlled.

#### Conclusions—Possible Common Origins of Oxide Charges

The current understanding of charges in the thermally oxidized silicon system has been presented. Generally accepted facts about these four types of charges have been listed and briefly discussed along with questions still remaining to be answered. Most of the unanswered questions are related to the origin of the charges or the mechanism of their formation and elimination. On the other hand, a fairly complete set of empirical data is available, providing a reasonable basis for understanding their process dependence. However, for ultimate control of these charges and related device electrical characteristics, a knowledge of their origin and physical nature will be required.

It would seem appropriate at this point to present a possible model of origin for three of the charges— $Q_{ss}$ ,  $N_{st}$ , and  $N_{ot}$ —based on common structural features. The model may well be oversimplified, but on the other hand could provide a basis for more detailed considerations. Figure 13 shows a representation of a thermally oxidized silicon structure. Three regions are indicated: silicon, the transition region between the silicon and the oxide, and the thermal silicon dioxide. Both the silicon and silicon dioxide lattices are represented by a two dimensional network, not necessarily to scale on an absolute or relative basis.

First, the plane separating the bulk silicon from the silicon-oxygen transition region indicates some unsatisfied silicon bonds which are the origin of the traditional fast surface states  $N_{st}'$ . Two of these bonds are shown to be satisfied or complexed by a hydrogen species. A second fast state ( $N_{st}''$ ) results due to a missing oxygen atom. This oxygen deficiency is established during the thermal oxidation process and also resulted in a partially ionized, excess silicon species. The latter, which is located in the oxide-silicon transition region, is believed to be the source of  $Q_{ss}$ .

If a negative field is applied across the oxide, a second silicon-oxygen bond at the partially ionized silicon atom responsible for  $Q_{ss}$  is broken and additional positive charge occurs in the oxide (drift VI). A corresponding additional fast state may also result at some nearby point on the silicon surface. In addition, if the structure is subjected to a long, high temperature anneal in an inert ambient or in a reducing atmosphere, additional silicon-oxygen bonds are broken and/or oxygen ions are removed, producing more positive charge in the oxide (drift XVII).

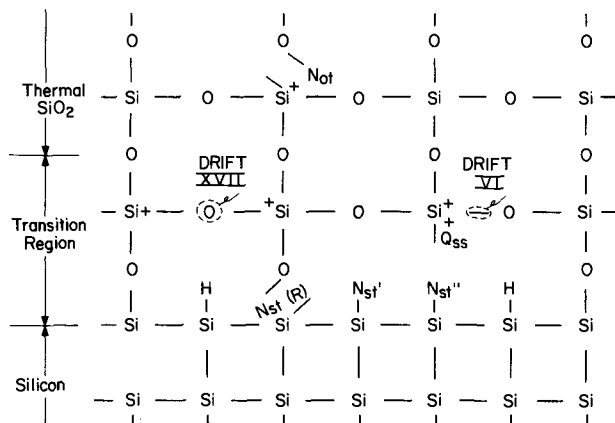


Fig. 13. Two dimension sketch of thermally oxidized silicon structure showing possible origins of charges.

Finally, if the structure is exposed to ionizing radiation, a silicon-oxygen bond in the oxide may be broken (or it already may be broken) and holes formed by electron-hole generation are trapped at the silicon defect. At the same time, a silicon-oxygen bond at the silicon surface is broken, leading to fast state formation.

It is thus obvious that the physical origin of all the charges, except  $Q_{ss}$ , may well be based upon factors related to the silicon bond structure or defects thereof. Whether a particular process causes a silicon bond defect depends on the structural configuration, bond energy, and other considerations. Whether this bond defect in turn will result in either  $Q_{ss}$ ,  $N_{st}$ , or  $N_{ot}$  will depend primarily upon its location in the oxidized silicon structure. Such a proposal does not even rule out the reported effects due to impurity ions such as sodium or aluminum. The presence of these species could physically distort the silicon-oxygen bond structure or result in chemical reactions which would also lead to charge effects.

#### Acknowledgments

The author wishes to thank Maija Sklar for her many contributions during the past ten years in many of the programs referenced in this paper. In addition, valuable assistance has been provided by Phil Fleming, Ed MacKenna, Pat Castro, Pat Kodama, and other persons too numerous to list. Finally, the author values his previous association with Drs. Andy Grove and Ed Snow at the Fairchild Research and Development Laboratory, and acknowledges their outstanding contributions in the various areas of semiconductor device physics and surface passivation technology.

Manuscript submitted Sept 25, 1973; revised manuscript received Dec. 5, 1973.

Any discussion of this paper will appear in a Discussion Section to be published in the December 1974 JOURNAL. All discussions for December 1974 Discussion Section should be submitted by Aug. 1, 1974.

#### REFERENCES

- For a comprehensive review of silicon oxidation studies prior to 1965, see R. P. Donovan, "Integrated Silicon Device Technology, Vol. VII, Oxidation," Technical Report No. ASD-TDR-63-316, Research Triangle Institute (June 1965).
- E. S. Schlegel, *IEEE Trans. Electron Devices*, **ED-14**, 728 (1967); **ED-15**, 951 (1968).
- B. E. Deal and A. S. Grove, *J. Appl. Phys.*, **36**, 3770 (1965).
- J. R. Ligenza and W. G. Spitzer, *Phys. Chem. Solids*, **14**, 131 (1960).
- M. M. Atalla, in "Properties of Elemental and Compound Semiconductors," Vol. 5, H. Gatos, Editor, pp. 163-181, Interscience Publishing Co., New York (1960).
- W. A. Pliskin, *IBM J. Res. Develop.*, **10**, 198 (1966).
- P. J. Burkhardt and L. V. Gregor, *Trans. Met. Soc. AIME*, **236**, 299 (1966).
- R. J. Jaccodine, *This Journal*, **110**, 524 (1963).
- E. H. Nicollian and A. Goetzberger, *Bell System Tech. J.*, **46**, 1055 (1967).
- J. R. Szedon and R. M. Handy, *J. Vacuum Sci. Technol.*, **6**, 1 (1968).
- A. G. Revesz and K. H. Zaininger, *RCA Rev.*, **29**, 22 (1968).
- P. V. Gray, *Proc. IEEE*, **57**, 1543 (1969).
- E. Kooi, "The Surface Properties of Oxidized Silicon," N. V. Philips Gloeilampenfabrieken, Eindhoven, The Netherlands (1967).
- A. S. Grove, B. E. Deal, E. H. Snow, and C. T. Sah, *Solid-State Electron.*, **8**, 145 (1965).
- K. H. Zaininger and F. P. Heiman, *Solid-State Technol.*, **13**, May, p. 49, June, p. 46 (1970).
- L. M. Terman, *Solid-State Electron.*, **5**, 285 (1962).
- C. N. Berglund, *IEEE Trans. Electron Devices*, **ED-13**, 701 (1966).
- P. V. Gray and D. M. Brown, *Appl. Phys. Letters*, **8**, 31 (1966).
- A. Goetzberger and S. M. Sze, "Applied Solid State Science," Vol. 1, p. 154-238, Academic Press, New York (1969).
- H. Deuling, E. Klausmann, and A. Goetzberger, *Solid State Electron.*, **15**, 559 (1972).
- E. H. Snow, A. S. Grove, B. E. Deal, and C. T. Sah, *J. Appl. Phys.*, **36**, 1664 (1965).
- D. S. Kerr, Paper 14 presented at Electrochemical Society Meeting, Cleveland, Ohio, May 1-6, 1966.
- B. Yurash and B. E. Deal, *This Journal*, **115**, 1191 (1968).
- S. R. Hofstein, *IEEE Trans. Electron Devices*, **ED-14**, 749 (1967).
- B. E. Deal, Proc. Silicon Device Processing Symposium, National Bureau of Standards, Gaithersburg, Maryland, June 2-3, 1970.
- E. S. Schlegel and G. L. Schnable, *This Journal*, **119**, 165 (1972).
- D. R. Kerr, J. S. Logan, P. J. Burkhardt, and W. A. Pliskin, *IBM J. Res. Develop.*, **8**, 376 (1964).
- B. E. Deal, U.S. Pat. 3,426,422 (1969).
- R. J. Kriegler, Y. C. Cheng, and D. R. Colton, *This Journal*, **119**, 388 (1972).
- E. MacKenna and P. Kodama, *ibid.*, **119**, 1094 (1972).
- B. E. Deal, M. Sklar, A. S. Grove, and E. H. Snow, *ibid.*, **114**, 266 (1967).
- F. Montillo and P. Balk, *ibid.*, **118**, 1463 (1971).
- Y. Miura and Y. Matukura, *Jap. J. Appl. Phys.*, **5**, 180 (1966).
- F. H. Reynolds, Proc. 11th Annual Reliability Physics Symposium, Las Vegas, Nevada, April 3-5, 1973.
- D. W. Hess and F. M. Fowkes, Paper 303RNP presented at Electrochemical Society Meeting, Chicago, Illinois, May 13-18, 1973; *Appl. Phys. Letters*, **22**, 377 (1973).
- A. Many, Y. Goldstein, and N. B. Grover, "Semiconductor Surfaces," John Wiley and Sons, New York (1965).
- P. Balk, Paper 109 presented at Electrochemical Society Meeting, San Francisco, California, May 9-13, 1965.
- J. P. Mitchell and D. K. Wilson, *Bell System Tech. J.*, **46**, 1 (1967).
- A. G. Stanley, *IEEE Trans. Electron Devices*, **ED-14**, 134 (1967).
- A. G. Holmes-Siedle and K. H. Zaininger, *IEEE Trans. Reliability*, **R-17**, 34 (1968).
- C. W. Gwyn, Sandia Laboratories Development Report No. SLA-73-0013 (January 1973).
- E. H. Snow, A. S. Grove, and D. J. Fitzgerald, *Proc. IEEE*, **55**, 1168 (1967).
- C. W. Gwyn, *J. Appl. Phys.*, **40**, 4886 (1969).
- H. L. Hughes, R. D. Baxter, and B. Phillips, *IEEE Trans. Nuclear Science*, **NS-19**, 256 (1972).



## Electrochemical Aspects of Thrombogenesis— Bioelectrochemistry Old and New

P. N. Sawyer, S. Srinivasan,\* B. Stanczewski, N. Ramasamy,\* and W. Ramsey

*Electrochemical and Biophysical Laboratories of the Vascular Surgical Services,  
Department of Surgery and Surgical Research, State University of New York,  
Downstate Medical Center, Brooklyn, New York 11203*

The fact that living cells such as blood cells carry a surface charge in much the same manner as colloidal particles has been known since the work of Abramson (1, 2). That these surface charges allow the cells and tissues with which they come into contact to exhibit electrochemical properties has only recently been considered. It is the purpose of this review to trace the development of ideas and observations which have led to the use of interfacial electrochemistry to examine biological problems and develop solutions to these problems in the area of thrombosis and related diseases.

Before the details of thrombosis or blood clotting are discussed, it appears appropriate to outline briefly the phenomena involved in intravascular blood coagulation as it appears *in vivo*.

Thrombosis is, by definition, the deposition of polymerized fibrinogen, *i.e.*, fibrin and trapped particulate blood cells including platelets on the blood vessel wall.

Thrombosis occurs at the site of a vascular injury as a multistage process. Blood coagulation during bleeding from blood vessels is the mechanism by which we normally prevent fatal hemorrhage. It is also, in its pathological state, the mechanism by which we experience abnormal vascular occlusion. First the platelets in circulating blood recognize the site of injury and adhere to it. The adhered platelets then aggregate releasing in the process a number of proteins and other agents. This first step is called primary hemostasis. This results in a platelet plug formation which serves as a temporary seal (3, 4).

The blood coagulation cascade is activated leading to a fibrin clot. This process resulting in polymerization of fibrinogen to fibrin is secondary hemostasis (3, 4). The fibrin polymer traps in its strands a number of blood cellular elements including erythrocytes and leukocytes and additional platelets. In a normal system following fibrin polymerization the healing process is initiated by fibroblastic invasion of the thrombus (5).

A study of these interfacial reactions and the ways that thrombosis can be modified, initiated, and/or inhibited by artificial prostheses is the subject of this review.

### Historical

Very early in studies of blood cells and blood vessel walls, there was established a relation between the surface charge carried by the blood cell and the charge on the blood vessel wall.

Between 1925 and 1950, only three or four investigators (3-6) seriously measured the surface charge

characteristics of blood cells and cursorily evaluated blood vessel walls, suggesting both that these charges were related to diapedesis of white cells to points of inflammation and to the interactions of platelets and other cells with blood vessel walls during thrombosis (6). They include Abramson, who did the first meticulous work on electrophoretic characteristics of platelets, red cells, white cells, and proteins (Table I) (1, 2). He found that all of these elements had a consistent cataphoretic mobility in the same range. He also showed that platelets have developmental characteristics which would permit specific adhesion to blood vessel walls through pseudopod formation.

In 1950, members of this group discovered that the vascular wall developed a transmural potential that was negative with respect to an externally applied electrode (Fig. 1) (7, 8). These measurements were made using calomel electrodes; one electrode was connected to the blood stream through a salt bridge while the second electrode was similarly attached to the exterior of the arterial wall. An electrometer was used to make the measurement (Fig. 1). The decrease of surface potential, or its reversal, related to injury, frequently produced surface thrombosis and intraluminal occlusion (6, 7) (Fig. 2).

The concept of injury potential has been expressed possibly by Gerard (9). One may conceive of injury potential as the exposure of the inner content of a cell to the external milieu. An ion flow is supposedly generated yielding an electric (ionic) current. This explanation is obviously simplistic, but the true explanation is unknown. Becker (10) and Pilla (11) have proposed that the phenomena called "injury potentials" are related to interactions between the nervous system,

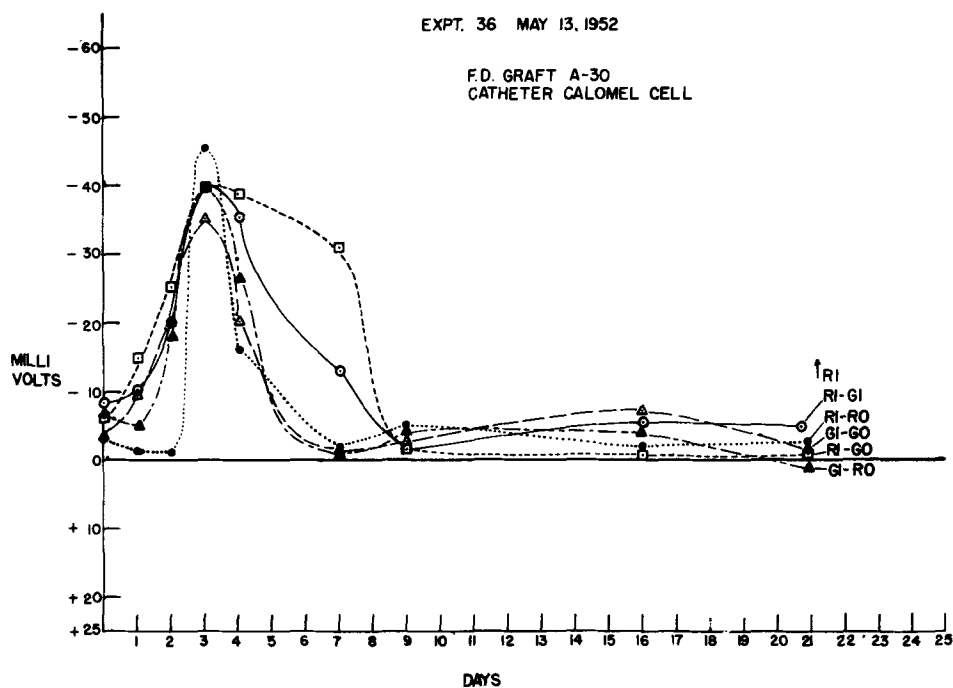
**Table I. The cataphoresis of platelets in plasma. The speed of polymorphonuclear leucocytes is given in the last column. Although red cells and small lymphocytes have different velocities, note that platelets and polymorphonuclear leucocytes have the same velocity (six horses).**

Plasma	Age (hr)	Platelets		Polymorphonuclear leucocytes V (μ/sec/V/cm)
		V <sub>0</sub> (μ/sec/V/cm)	V (μ/sec/V/cm)	
1	30	0.71	0.41	0.46
2	6	0.82	0.59	0.57
	30	0.76	0.55	0.60
3	6	0.65	0.46	0.52
4	6	0.57	0.40	0.43
5	6	0.67	0.51	0.53
6	6	0.68	0.46	0.54
		Mean excluding No. 2	0.45	0.49
		{ potential (mV)	12	13
		(26.5 × μ/sec/V/cm)		

\* Electrochemical Society Active Member.

Key words: thrombogenesis, bioelectrochemistry, blood compatibility, hemostasis, cardiovascular prostheses.

Fig. 1. Transmural potentials in freeze dried grafts and recipient artery. (RI, electrode inside recipient artery; RO, electrode outside recipient artery; GI, electrode inside graft; GO, electrode outside graft.)



body tissues, and tissue regeneration as well as possibly being involved in local cell regeneration.

It was next discovered that the application of an electric field would produce thrombosis on the blood vessel wall beneath a positively charged electrode attached to the external surface of the blood vessel wall, while the area beneath the negative electrode was free of deposits (Fig. 3). This led to the development of a series of experiments in which it was shown that negatively charged electrodes could very effectively delay thrombosis in injured blood vessels (12), the corollary of the positive electrode experiment (7). In the attempt to gain additional information, three sets of experiments were carried out in the subsequent 20 years relating to these original observations.

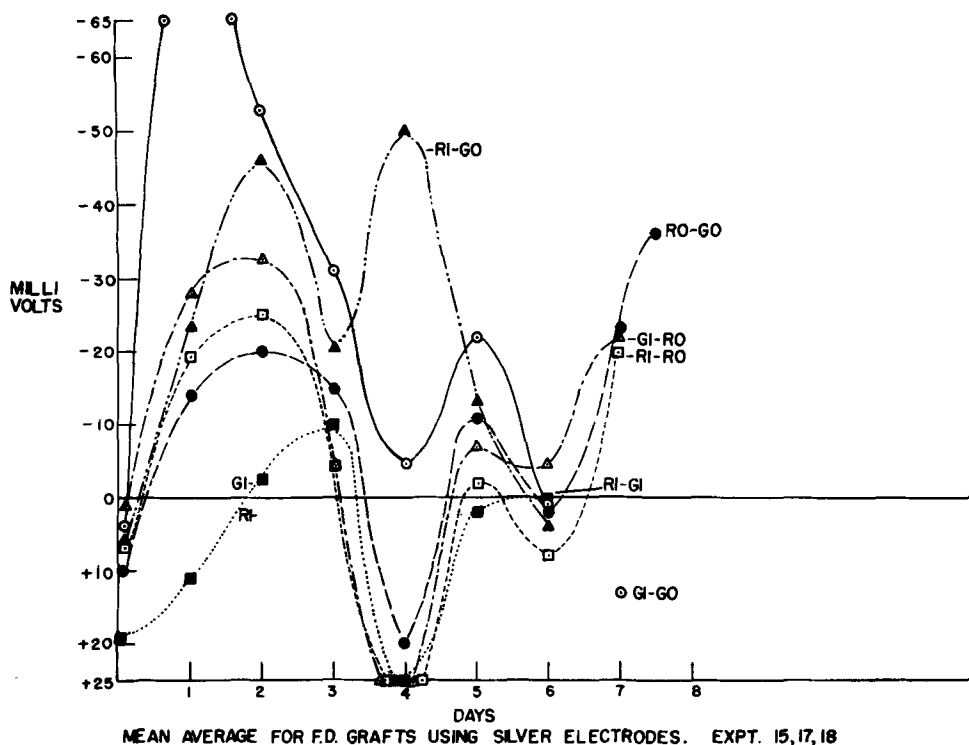
The interfacial phenomena that can occur at solid liquid boundaries in biological systems are represented in Fig. 4. A simplified schematic of a biological membrane and the charge distribution at the membrane

solution interface are shown in Fig. 5. The studies carried out were all related to the phenomena described above (13-20).

The studies on the blood vessel wall included (i) measurement of ion fluxes across the arterial and venous blood vessel walls (13, 14); (ii) the role of metabolic factors in the maintenance of the blood intimal interface of blood vessels (15, 16); (iii) study of the electrokinetic phenomena in the vascular tree and its relationship to thrombogenesis (17, 18); and (iv) the importance of maintaining ion fluxes across the vasculature or graft in determining its patency *in vivo* (19, 20).

The ion transport across the vena cava is one order of magnitude greater than that across the aorta under aerobic conditions. The ion diffusion across the vena cava is opposite from that across the aorta under conditions of no pressure (Fig. 6). The results lend support to the view that the ion diffusion across arteries is

Fig. 2. Transmural potentials across freeze dried grafts and recipient arteries; reversal of sign due to injury or any other local abnormality. (RI, electrode inside recipient artery; RO, electrode outside recipient artery; GI, electrode inside graft; GO, electrode outside graft.)





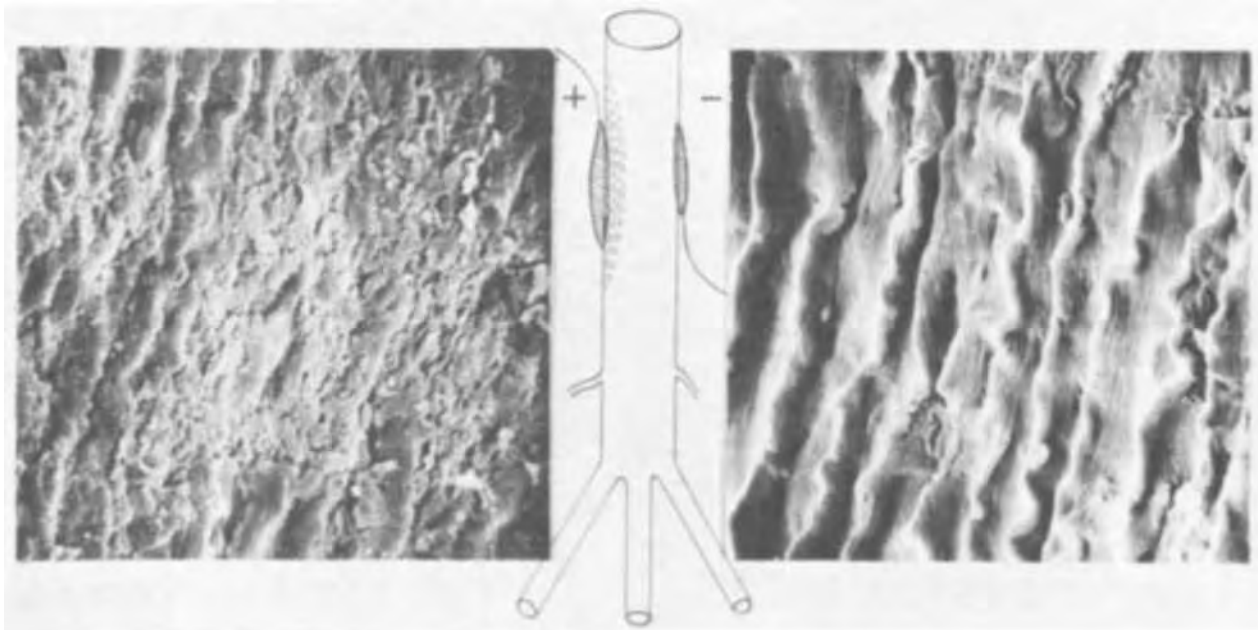


Fig. 3. A positive negative electrode pair applied to aortic wall. SEM photographs of the blood vessel wall (a, left) showing thrombus deposition on the wall beneath the positive electrode and (b, right) showing the area beneath the negative electrode free of deposit.

“controlled diffusion” while venous transport may be “active” in character.

The systematic studies of solid and porous prosthetic surfaces and arterial prostheses during the period of development indicated that porosity was critical to long term function (19, 20) (Fig. 7). Pressure equivalent electro-osmosis or actually “transverse streaming potential” appears important in the maintenance of the charge characteristics of the vascular blood interface.

This is illustrated by the fact that the morphology of a thrombus on arterial and venous surfaces is different (as revealed by histological examination). Thrombosis on arterial surfaces is sculptured by high pressure rapid flow of the arterial stream. On the venous side injury produces a more rapid buildup of transmural thrombosis due to low pressure flow. This occurs probably because the interacting blood elements, platelets, blood cells, and activated blood coagulation proteins involved in thrombosis have a longer contact period with the injured area.

The electrochemical interactions between an electronic conductor and blood cellular elements were studied (21, 22). It was observed that blood cell precipitation on electrodes does occur at potentials more positive than 300-400 mV vs. NHE. The cell precipita-

tion appears to be a potential- and not a current-dependent phenomenon (Fig. 8). This study indicated that intravascular thrombosis on prosthetic metallic materials might also be a potential-dependent process.

Characterized clean metallic surfaces used as arterial and venous blood vessels functioned as thrombus preventing or depositing surfaces depending on their spontaneous corrosion potential in contact with blood (23, 24). With platinum, potentials were set at specific values to either prevent or elicit deposition of thrombi. Copper prostheses were implanted in animals, and the developed junctional thrombi were examined with both light and electron microscopy. These were shown to contain the components of spontaneous intravascular thrombi (25) (Fig. 9 a-c). Most importantly, it was also shown that thrombus formation on electrodes at critical potentials depends on an intact coagulation system

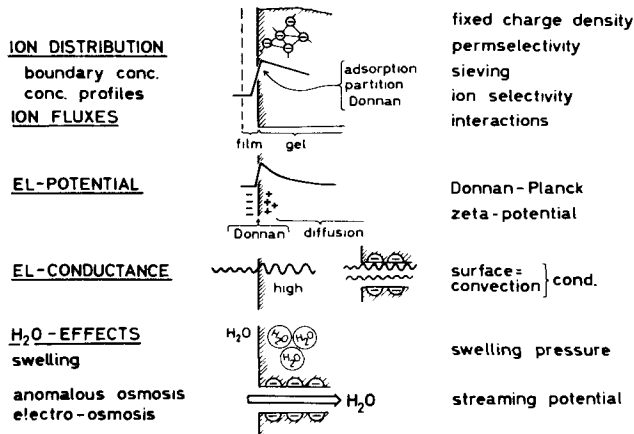


Fig. 4. Scheme of general phenomenology at a fixed charge membrane.

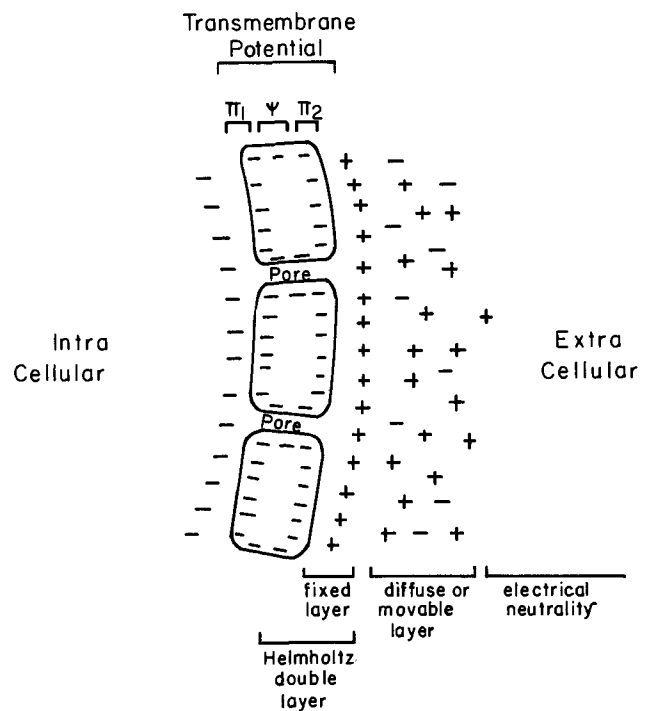


Fig. 5. Molecular scheme of membrane and surface charge

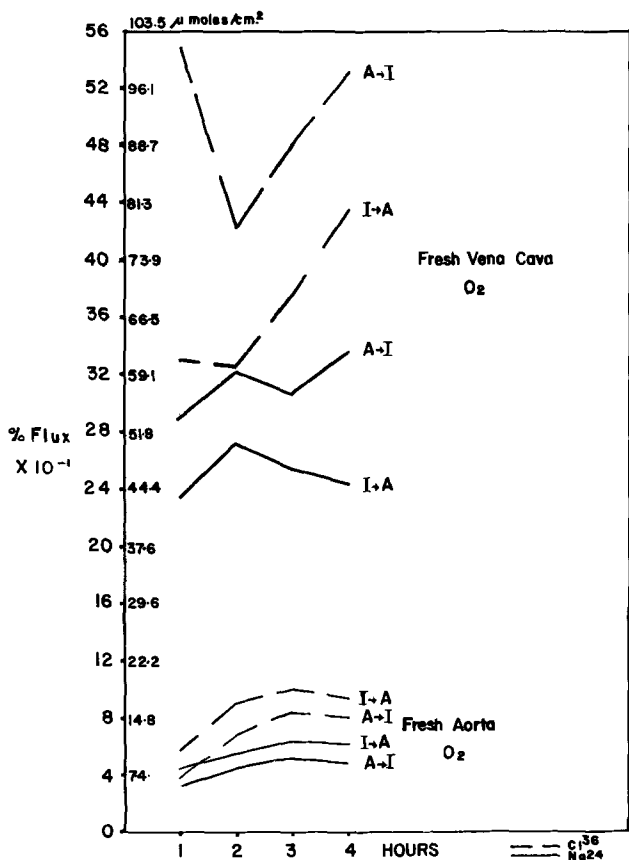


Fig. 6. Selective diffusion, fluxes across blood vessel wall; vena cava at the top, fresh aorta at the bottom under aerobic conditions. I → A, intima to adventitia; A → I, adventitia to intima; - - - - for Cl<sup>-</sup>; — for Na<sup>+</sup>.

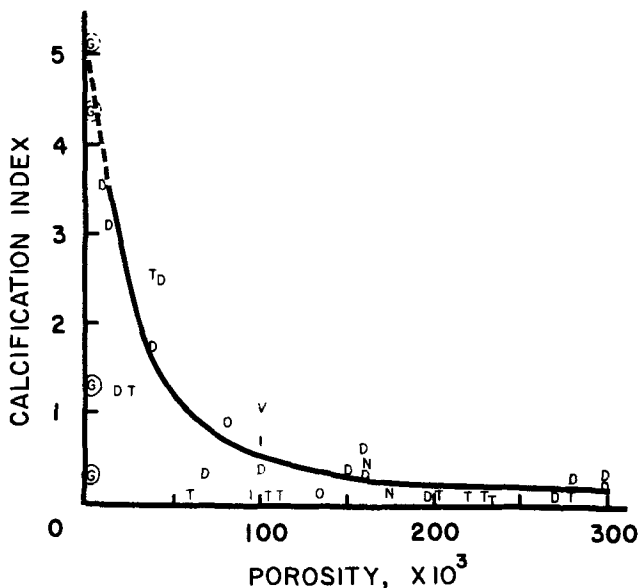
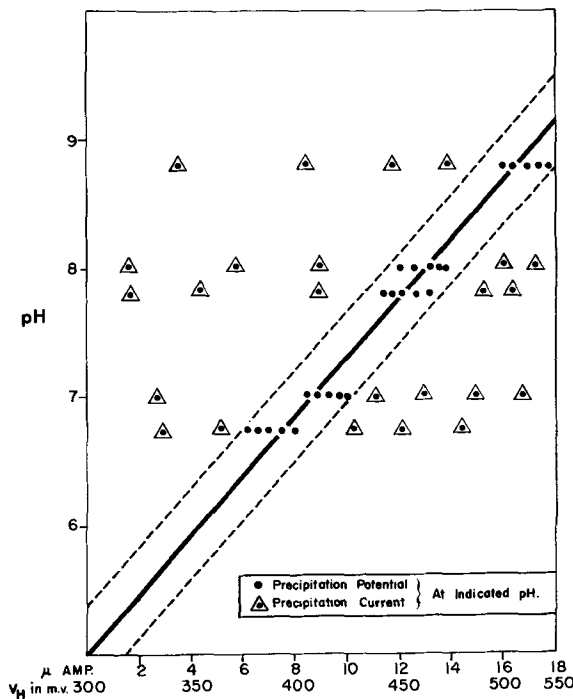


Fig. 7. Calcification porosity index of a blood vessel wall

(26). Thus in hemophiliac dogs (dogs that lack one of the blood coagulation enzymes, Factor VIII) electrical thrombus could not be initiated. This was also the case for dogs which have platelet abnormality, or which, following administration of anticoagulant drugs, do not exhibit potential induced thrombus formation (Table II). Histologic and physiologic evidence was provided in these experiments to show that electrical thrombosis is similar to its biological counterpart, spontaneous thrombosis, and that the triggering of

COMPARATIVE PRECIPITATION POTENTIALS AND CURRENTS AT VARIOUS pH's HUMAN PLATELETS



HUMAN LEUCOCYTE PRECIPITATION AND SEPARATION POTENTIAL (V<sub>H</sub>) VERSUS pH CHANGE

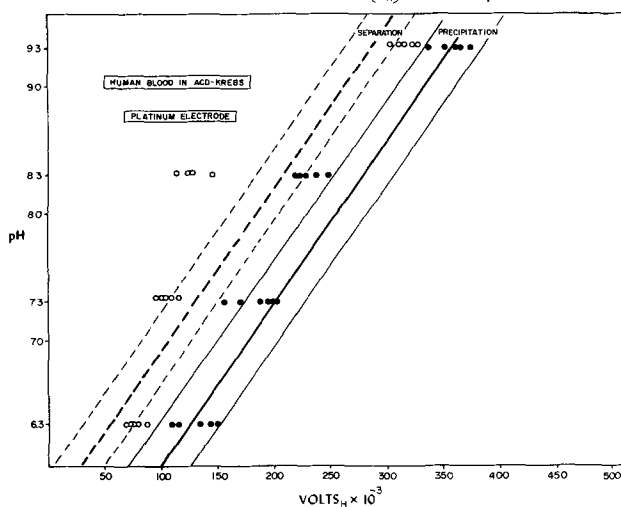


Fig. 8. a(top), Precipitation potentials of human platelets (with respect to normal hydrogen electrode) as a function of pH. The results show that cell deposition is potential not current dependent. b (bottom), Human leukocyte, precipitation potentials on Pt electrodes (with respect to normal hydrogen electrode) as a function of pH.

thrombosis is related to the interfacial potentials of appropriately organized homogeneous surfaces.

The Beginning of Modern Information

*In vivo* streaming potential measurements are a measure of the net surface charge of the blood vessel wall under physiologic conditions. When arteries are removed from the *in vivo* position as high pressure conduits, most of the streaming potential seen *in vivo* can be regained *in vitro* by placing the blood vessel in a streaming potential apparatus in which Ringers or other solutions of known ionic composition are used as the high pressure perfusate (18). Many of the phenomena observed in the vascular tree *in vivo* can be duplicated in a streaming potential apparatus *in vitro*, including the effects of injury, drug effects, changing ion concentration on either side of the blood vessel

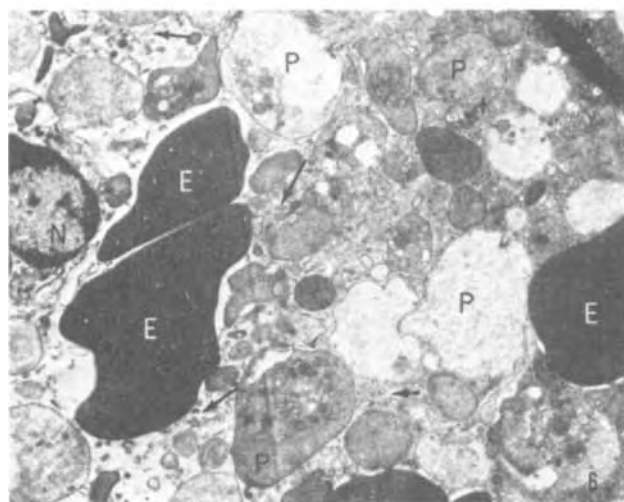
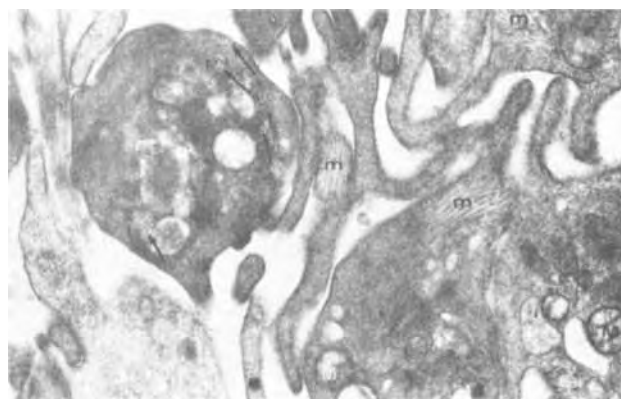
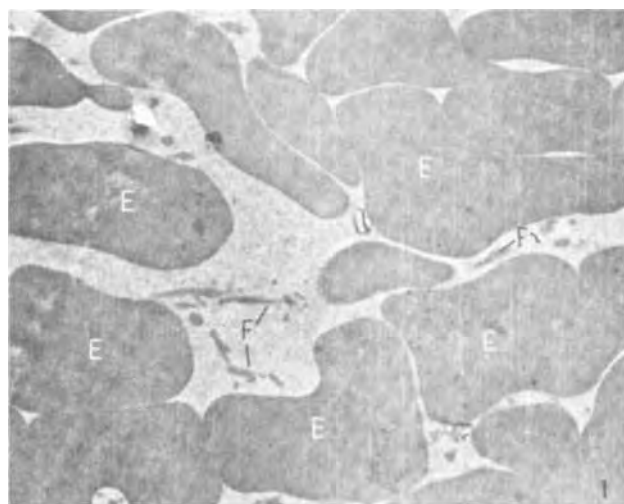


Fig. 9. Electron microscopic photographs of junctional thrombi formed at the junction between a copper tube and its containing vessel. Magnification 7000 $\times$ . a (top left), Multiple masses of erythrocytes (E) agglutinated by a fibrin matrix (F); b (top right), leucocytes, erythrocytes, and platelet masses (m) agglutinated between fibrin sheaths; c (bottom left), degranulated platelets (P) and massed erythrocytes (E) along with granulocytes (N).

wall, etc. (Fig. 10). Some work has also been done evaluating the blood vessel wall as a rectifier (Fig. 11 a and b), and as a diffusion membrane. The vessel wall, because of its porosity and blood pressure, functions as an electro-osmotic membrane. Ion diffusion across the wall appears modulated by enzymatically supported active transport (27). The several enzymatic processes effecting ion transport can be shown to exist by changes produced by hypoxemic conditions, by other types of metabolic inhibition, and by temperature variations.

Recently, a series of more sophisticated studies has been carried out testing the effect of different types of injury on the streaming potential *in vivo* (28).

Four comparative evaluations were carried out: (i) the effect of types of injury on streaming potentials; (ii) the effect of position of the injury on the morphology of proximal and distal artery or vein; (iii) the

type of thrombus deposited following various types of injury; and (iv) the effect of various anticoagulants on the deposited thrombus. The resulting disordered wall with deposited thrombi (Fig. 13) and the modifications brought about by different types of anticoagulant agents during blood interactions with altered surfaces have been examined using both light and scanning electron microscopy (Fig. 14) (29).

### Evolving Concepts

Thus, it has become apparent that intravascular thrombosis has many classic characteristics of a physical chemical phenomenon. Recent studies of several enzymatic reactions which relate to thrombosis seem to illustrate the physical biochemistry of these reactions. Though the results of these studies are frequently semiquantitative, the information seems real and significant.

Table II. Potential dependence of electrical wire thrombosis in dogs (normal, hemophilic, and under the influence of some drugs)

Series	Number of experiments	Electrodes + No. of vessels	Thrombus formation	
			0.2-0.4 NHE Thrombus	Electrodes No. of vessels 0.2-0.4 NHE Thrombus
Normal dogs	25	44	33	47
Hemophilic	2	4	0	—
Heparinized				
2 mg/kg	4	8	0	—
Coumadinized	4	6	0	2
Thrombocytopenic plates				
50,000/mm <sup>3</sup>	4	6	0	2
Control-nitrogen mustard	2	4	4	—

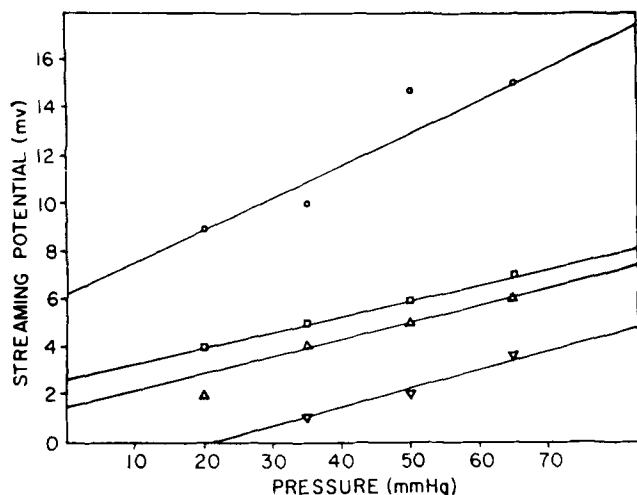


Fig. 10. Effect of change of ionic concentration of the fluid on the streaming potential-pressure behavior of a carotid artery in vitro.  $\circ$ — $\circ$  Krebs/1000;  $\square$ — $\square$  Krebs/100;  $\triangle$ — $\triangle$  Krebs/10;  $\nabla$ — $\nabla$  Krebs/1.

It is now obvious that the blood vascular interface develops an electric field in the range of  $10^6$ – $10^7$  V/cm. Blood cells and blood proteins carry a net negative surface as does the blood vessel wall. The charge on the vessel wall appears to be potentiated by the physico-

chemical phenomena described earlier. Therefore we are in essence statistically unclottable. Special local conditions have to be created to initiate thrombosis.

Weiss (30) has recently suggested mechanisms by which interreactions can occur between cells or platelets and injured blood vessels under these conditions which he calls "tunneling." Recognition occurs between specific configured positive and negative surface charges such as platelets to collagen uncovered by injury. The structure and configuration of recognition induces the active coagulant factor, in this instance platelets, to deposit on the blood vessel wall and become activated with release of ADP (31).

Thus a number of investigators including Nossel (32), Vroman (33), Baier (34), Lyman (35), Salzman (31), and Sawyer (28) and their co-workers appear each to have contributed one segment of our understanding of the *in vivo* reaction. Massini and Luscher (36) and Nossel (32) suggest that it is the recognition of abnormal or disordered surface charges on the wall that stimulates platelet sticking both to collagen, microfibrilae, basement membrane, and ostensibly to any positively charged surface including an injured blood vessel wall, leading ultimately to the development of thrombus.

Wilner, Nossel, and Leroy have shown, using classic techniques, the interaction between platelets and collagen (Fig. 15) in an aggregometer (37). In their *in vitro* studies, they reduced the negative charges of collagen by acetylation of carboxyl groups or pepsin

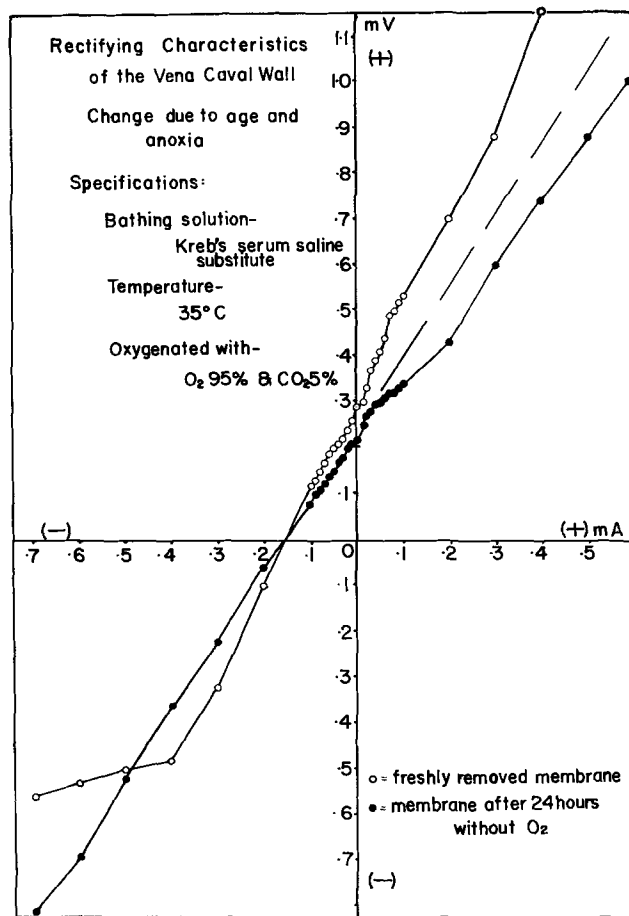
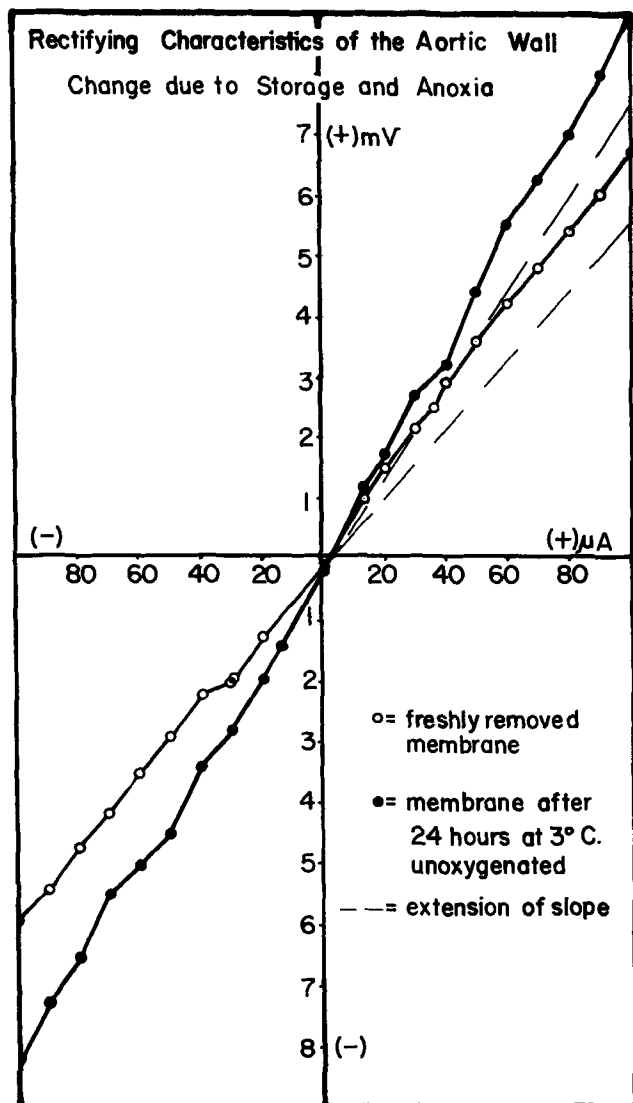
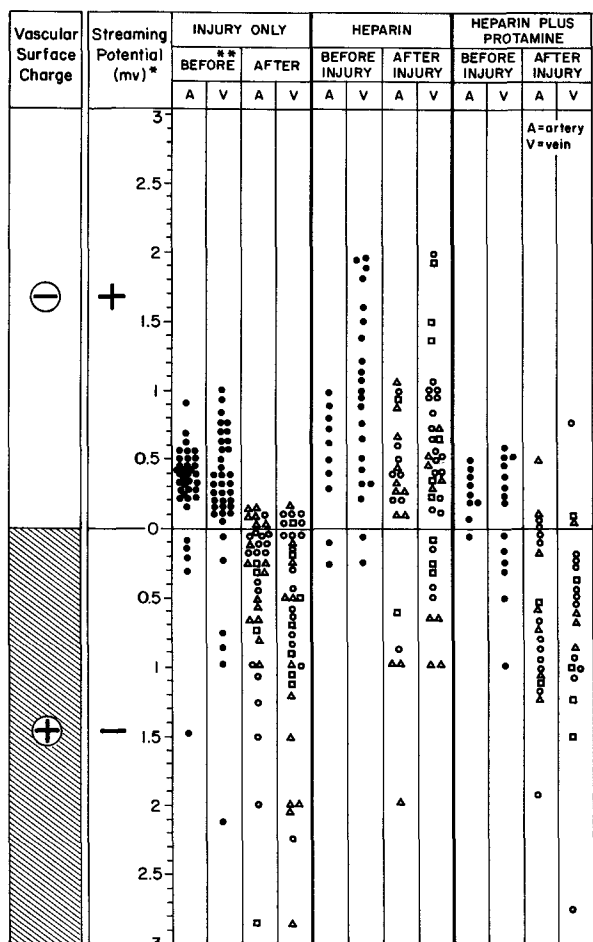


Fig. 11. Rectifying characteristics of (a, left) aortic and (b, right) vena caval walls. Change due to storage and anoxia.



\* A POSITIVE STREAMING POTENTIAL INDICATES A NEGATIVE VASCULAR SURFACE CHARGE AND HENCE A NEGATIVE POTENTIAL ACROSS THE BLOOD VESSEL WALL-BLOOD INTERFACE.  
 \*\* FOLLOWING DISECTION AND EXPOSURE OF THE VESSELS.  
 ● CONTROL  
 ▲ FOGARTY CATHETER INJURY  
 □ HAEMOSTAT CRUSH INJURY  
 ◆ ELECTRICAL INJURY  
 D.C. IMA / 2 HRS

Fig. 12. Effect of injury and of drugs on *in vivo* streaming potentials in canine blood vessels.

treatment of the telo peptides. In a second set of experiments they reduced the positive charges (epsilon amino groups of the lysine) of collagen by deaminating the collagen with nitrous acid or by dinitrofluorobenzene. The investigators were able to show that platelet aggregation was potentiated by highly positively charged collagen but only marginally affected by reduction of the negatively charged groups of collagen.

Baier has used contact angle as a criterion for physicochemical interaction of prosthetic surfaces with blood (38). Dutton and Baier and Petchek have performed additional experiments by measuring coagulation characteristics of blood flowing by a transparent glass slide (39) (Fig. 16a and b). Concomitantly, Vroman has shown that all foreign surfaces adsorb a protein, probably fibrinogen, on exposure to blood (33). The thrombogenic characteristics of a surface appear dependent on subsequent interreactions between the blood proteins and the underlying prosthetic or natural surface. Extreme denaturation of the protein layer initially deposited on surfaces due to high specific activity of the prosthetic surface has been shown to be thrombogenic by Lyman (35).

**Electrochemical Reactions of Blood Coagulation Factors—Their Role in Thrombosis**

Considerable evidence is now developing to show that thrombosis is catalyzed on conducting prosthetic materials when the potential across the interface ex-

ceeds +300 mV/NHE. Thrombus deposition is triggered by a series of reactions involving blood coagulation factors, the last of which is the conversion of fibrinogen to fibrin. Electrochemical studies alone or in combination with optical studies have led to some interesting findings. (i) Using cyclic voltametric techniques, it has recently been shown that a number of the blood coagulation factors, such as fibrinogen (40), prothrombin (41), Factors V and VIII (42), and Factor IX, take part in adsorption and electron transfer reactions across metal-solution interfaces (Fig. 17). (ii) Electrocapillarity (43), ellipsometric (40), and capacitance (44) methods confirm that these blood coagulation factors show potential-dependent adsorption behavior on metal surfaces. (iii) At positive potentials, prothrombin yields a product with thrombinlike activity (41). (iv) A combined electrochemical-electron microscopic investigation has shown that fibrinogen is electropolymerized to a fibrinlike substance at anodic potentials. Electron microscopy reveals that fibrin thus formed is very similar morphologically to enzymatically formed fibrin (45) (Fig. 18). (v) When a platinum electrode is maintained in a fibrinogen containing solution at negative potentials/NHE, the resultant solution shows long term inhibition of fibrinogen coagulation as revealed by thrombin time determinations (46,47). (vi) Heparin inhibits the adsorption of fibrinogen on freshly cleaved mica surfaces (48).

It appears that thrombosis is encouraged on both prosthetic and biological surfaces by the removal of electrons from blood constituents with a normal blood coagulation cascade at potentials more positive than a critical potential, approximately +400 mV vs. NHE, and this occurs with platelet aggregation, whereas thrombosis is normally prevented by the opposite phenomena—electron donation to blood from the blood vessel surface if at a critical potential.

**Biochemical Reactions at the Interface: Molecular Basis for Platelet Aggregation**

Over the past few years, several series of *in vitro* experiments carried out by Jamieson (49), Wolfe and Shulman (50), and others have been reported which illustrate the biochemistry of recognition and, we suggest, facilitated electron exchange during thrombosis formation as described above (49-51). They have shown that enzyme acceptor complexes on platelets, proteins, and other cells interreact with injured blood vessel wall receptor groups (probably underlying collagen that is exposed due to injury) to catalyze platelet adhesion. Salzman and his group, among others, have shown that these reactions are catalyzed and/or inhibited by membrane cyclic AMP (52). Potentiation or increase in intracellular cyclic AMP has been shown to suppress thrombosis and/or platelet aggregation.

Jamieson (49) has related the inhibitory effects of many pharmacologic agents of platelet adhesion to collagen to inhibition of enzyme function of glucosyl transferase present on the surface of platelets (Table III). This enzyme helps in the formation of glucose galactose side chains on collagen by facilitating transfer of glucose from platelet membrane to free galactose side chains of collagen. This may be a possible mechanism of platelet adhesion. The work of Nossel relating the modification of structure of collagen on platelet

Table III. Parallel inhibition of glucosyltransferase and platelet: collagen adhesion

	Conc. (M)	Glucosyl-transferase (% control)	Collagen adhesion (% control)
Control		100	100
+ d-Glucosamine	2 x 10 <sup>-2</sup>	12	16
+ Aspirin	1 x 10 <sup>-3</sup>	25	60
+ Chlorpromazine	4 x 10 <sup>-4</sup>	0	0

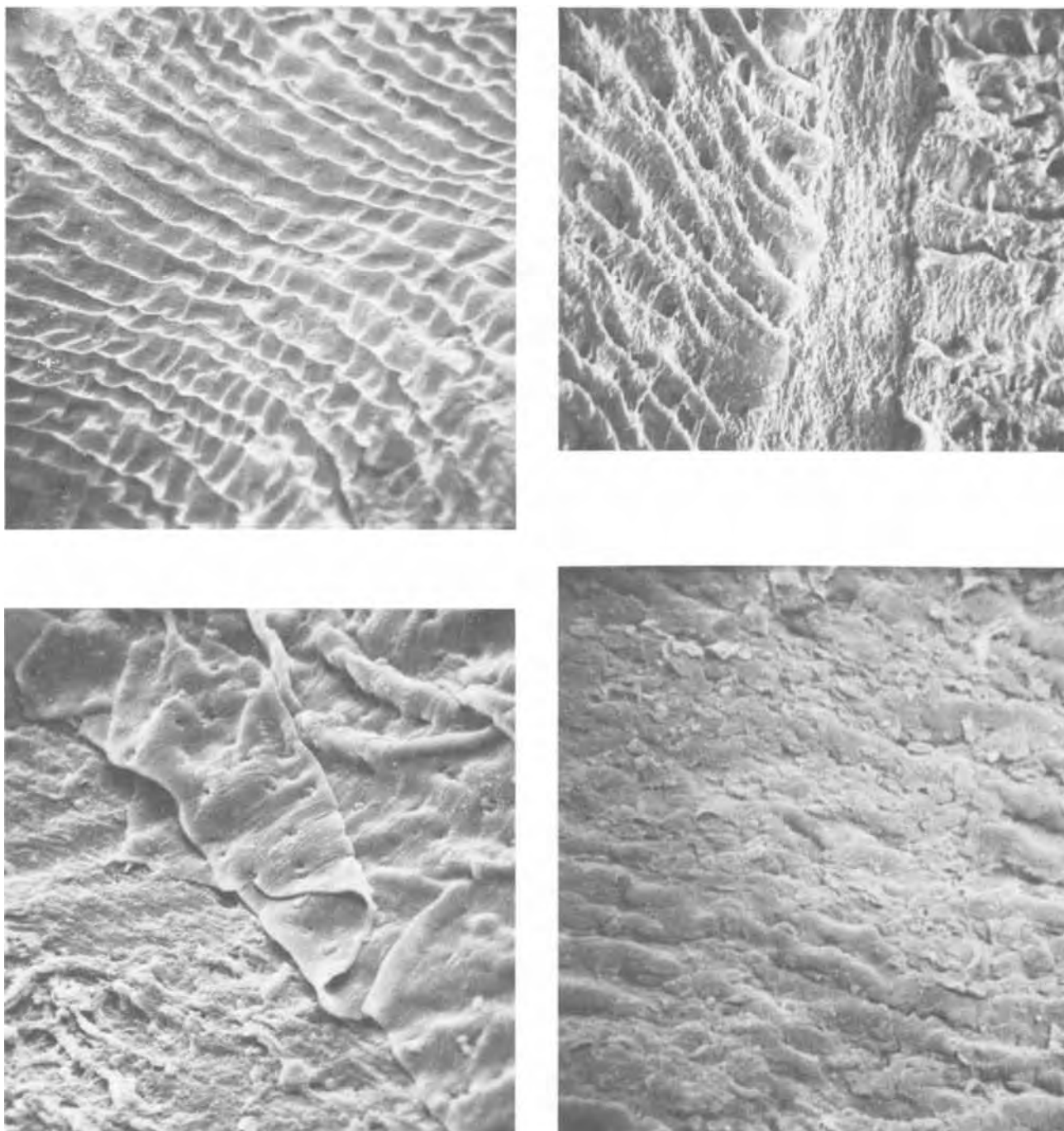


Fig. 13. Scanning electron microscopic photographs (magnification 500 $\times$ ) of a (top left), normal arterial wall; b (top right), hemostatic crush injury produced by Kelly clamp; c (bottom left), rough Fogarty catheterization injury; and d (bottom right), electrical injury to the artery.

adhesion has been discussed earlier. Other pharmacologic agents like prostaglandin ( $\text{PGE}_1$ ) inhibit release of nucleotides and calcium from platelets during aggregation (50) (Fig. 19).

A confirming group of experiments has been completed by Chesney, Harper, and Coleman (51) relating collagen structure to platelet aggregation (Fig. 20) and also relating the critical role of intact galactose side chains of collagen to platelet aggregation. Here the oxidation of a single bond on the galactose side chains was shown to prevent platelet recognition of collagen, blocking subsequent platelet activation and aggregation in an aggregometer. Shulman has categorized other biochemical characteristics which can be assumed operative in the recognition of abnormal exposed surface charges on the blood vessel wall by the platelets and proteins flowing past a point of injury or which are due to abnormal exposure to underlying microfibrillae,

collagen, etc. Epinephrine possibly potentiates an alpha receptor, fibrinogen through thrombin, ADP with a sulfhydryl group on a protein, and antibodies through glycoproteins, and destructured glycoproteins. All of these can be assumed to produce thrombosis through an electron transfer or an equivalent physical chemical mechanism.

Luscher's and Massini's (36) experimental evidence shows that cell recognition occurs because of alteration of charges. This provides an environment for platelet recognition and attachment. These in combination with Weiss's concept (30) of "tunneling" provide a rather satisfactory theoretical picture of the biochemistry of platelet attachment.

#### Anticoagulants—Inhibitory Phenomena in Thrombosis

It is now of interest to show the relevant factors relating to inhibition of these recognition phenomena

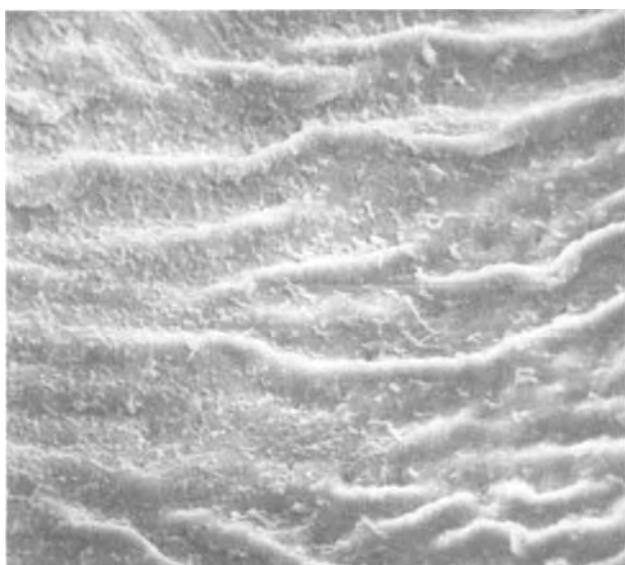
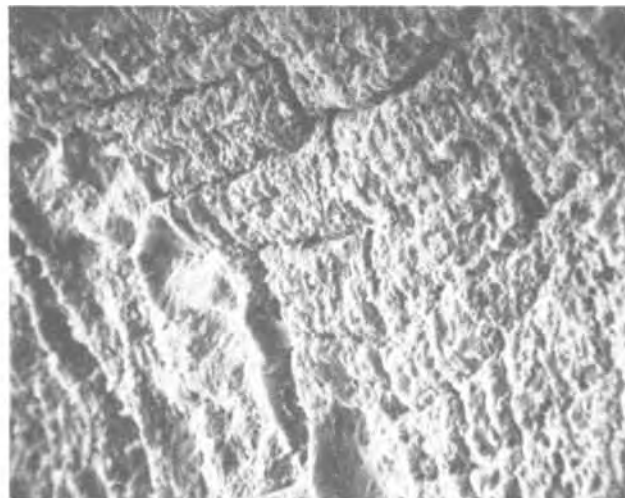


Fig. 14. Effect of heparin perfusion before injury on the nature of thrombus deposit on the artery. Scanning electron microscopic photographs (magnification 1000X) of a (top left), crush injury; b (top right), Fogarty catheter injury; and c (bottom left), electrical injury.

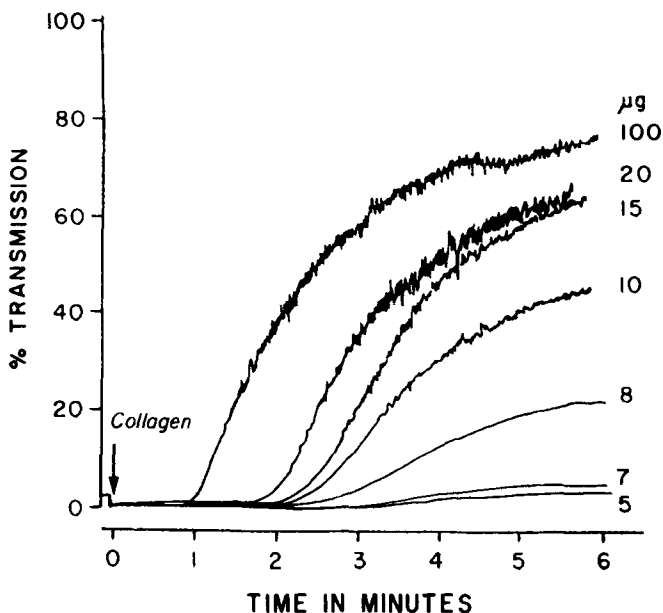


Fig. 15. Effect of collagen concentration on platelet aggregation (as measured by percentage optical transmission) vs. time relations.

which normally result in thrombosis. The direct acting anticoagulant material, heparin, appears to prevent intravascular thrombosis through a physical chemical mechanism potentiating both the normal structure and density of the negative surface charge at the blood vascular interface. The interface potential of both walls and cells is apparently made both more negative and more stable, thus promoting dispersion of all blood cells.

At a recent symposium, Chien (53), Seaman and Brooks (54), Danon (55), Schmidt-Schoenbein (56), and others have shown a possible mechanism of anticoagulant action of dextran. Dextran produces a blanketing phenomenon on red cells increasing the intercellular distance between red cells rouleaux (Fig. 21). Conventional van der Waals effects may thus become non-operational, markedly potentiating the dispersing negative charge and increasing the mutual repellancy of cell-cell and cell-wall interactions. Chien has also shown that dextran alters the viscosity of blood and the extent of aggregation. At relatively low concentrations of dextran (of molecular weight 40,000) it produces antiagglutination. The effects of dextran on blood cells varies with the molecular weight of the polysaccharide (Fig. 22). Work from this laboratory has shown the slight, negative, surface charge enhancing effect of dextran (Fig. 23) (19). Animal experiments with perfusion of dextran before injury to the blood vessel wall indicate significant reduction in thrombus formation on



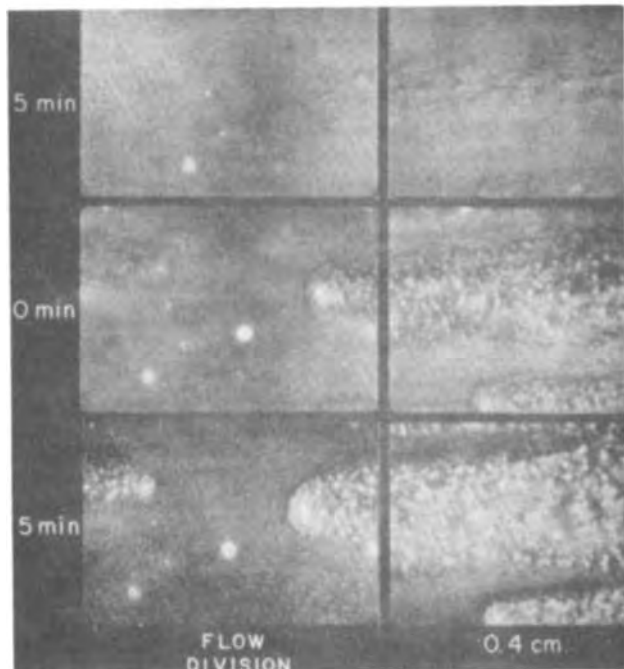
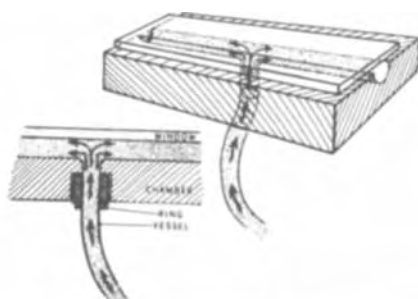


Fig. 16. Baier and Dutton cell (a, top) which allows native blood from a blood vessel to flow through a narrow chamber. The blood flowing beneath the glass cover slip reveals thrombus deposition (b, bottom) at various points on the glass.

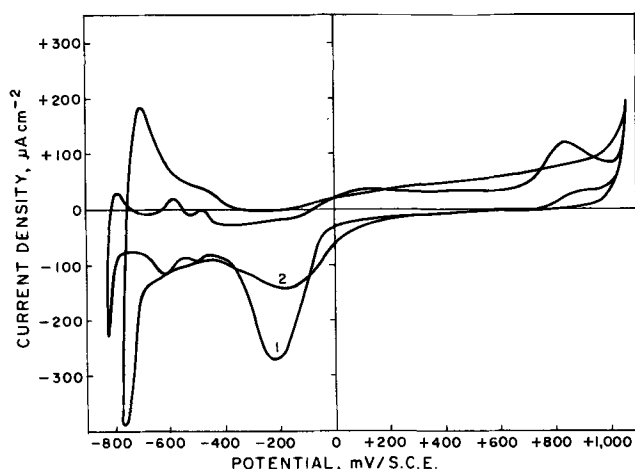


Fig. 17. Cyclic voltammograms of saline (1) and fibrinogen in saline (2) at a concentration of 3 mg/ml with bright platinum electrodes at a scan rate of 50 mV/sec<sup>-1</sup>.

the injured wall (Fig. 24). Snake venoms appear operative by virtue of their blocking the last stage in thrombus formation, the formation of a fibrin clot, by blocking fibrinogen polypeptide A or B separation (57).

### Conclusion

The multiple factors that influence the process of conversion of the colloidal suspension of blood into a gel called thrombus are listed in Table IV. Based on

Table IV

Blood (fluid)	→	Thrombus (gel)
Antithrombogenic		Thrombogenic
Blood vessel porosity		Injury to blood vessel
Ion fluxes		Flow
Transverse streaming potentials		Turbulence
pH		Atherosclerosis
Surface charge		Trauma
Antithrombotic drugs		Evulsion intima (mechanical etc. collagen)
Negatively charged dextran-heparin		Exposure, microfibrillae, basal membrane
Fibrinolytic drugs		Decreased porosity, activated platelets + ADP
Snake venoms		ADP (plasma)
Polymerized fibrin		Chemical activators, coagulation system
Antithrombin factor		Platelets
Cyclic AMP		Cardiac output
		Flow/unit mass tissue (localized)
		Dilution coagulation, enzymes hepatic splenic, filtration
		Cell content (polycythemia)
		Viscosity postoperative hyperplasia

the discussions of the findings of various groups of workers, the surface charge approach to this process of coagulation of blood can be summarized as follows.

The normal vascular tree, with its intact endothelium, and the cellular elements and platelets in blood possess an electric double layer at the solid-solution interface with intense electric field. They all have a net negative surface charge which results in a properly ordered separation of blood cells from one another as well as from the blood vessel wall.

Injury of any sort to the blood vessel wall, including suturing, clamping, destruction of endothelium due to turbulence or chemicals like endo-toxin, and immune response, results in disordering of the negative surface charge density, permitting recognition between platelets and the underlying cell surfaces. This recognition permits attachment of the platelets to underlying collagen, microfibrillae, or injured tissues of any sort which involves disruption of the integrity of the vascular-blood interface change, possibly by a process equivalent to or similar to "tunneling" and "recognition." With attachment of platelets and possibly also leucocytes and erythrocytes, adenine nucleotides, histamine, and other biologically active amines are released from platelets (4). This produces sequential aggregation, with the deposition of thrombus, due to activation of the blood coagulation cascade at multiple levels, producing conversion of prothrombin to thrombin, and fibrinogen to fibrin monomer with polymerization of fibrin monomer to stable fibrin mediated by Factor XIII. The fibrin in its totally polymerized form passivates thrombus formation, so that thrombus deposition may at any time reach sufficient thickness that the disordered charge density may be restructured into normal configuration (58, 59).

Inhibition of thrombosis can be produced by many anticoagulants, such as heparin, which seems to work on the wall and blood cells (by virtue of its negatively charged  $\text{SO}_4^{--}$  groups) at a physical chemical level by enhancing the net negative surface charge by adsorption and possibly at the biochemical level as well. Dextran operates by a different mechanism displacing charges by adsorption on blood cells and resulting in deaggregation or deagglutination. Other pharmacologic blocking agents such as Arvin or Reptilase prevent polymerization of fibrin, thus preventing the formation of an effective fibrin web, the terminal point in thrombus formation.

Thus, the beginning of an understanding of the physical chemistry of ion transport, and of the reactions that occur at the blood vessel wall-blood interface in the initiation or inhibition of thrombosis, is being developed and it encompasses many disciplines.

Manuscript received Aug. 22, 1973.



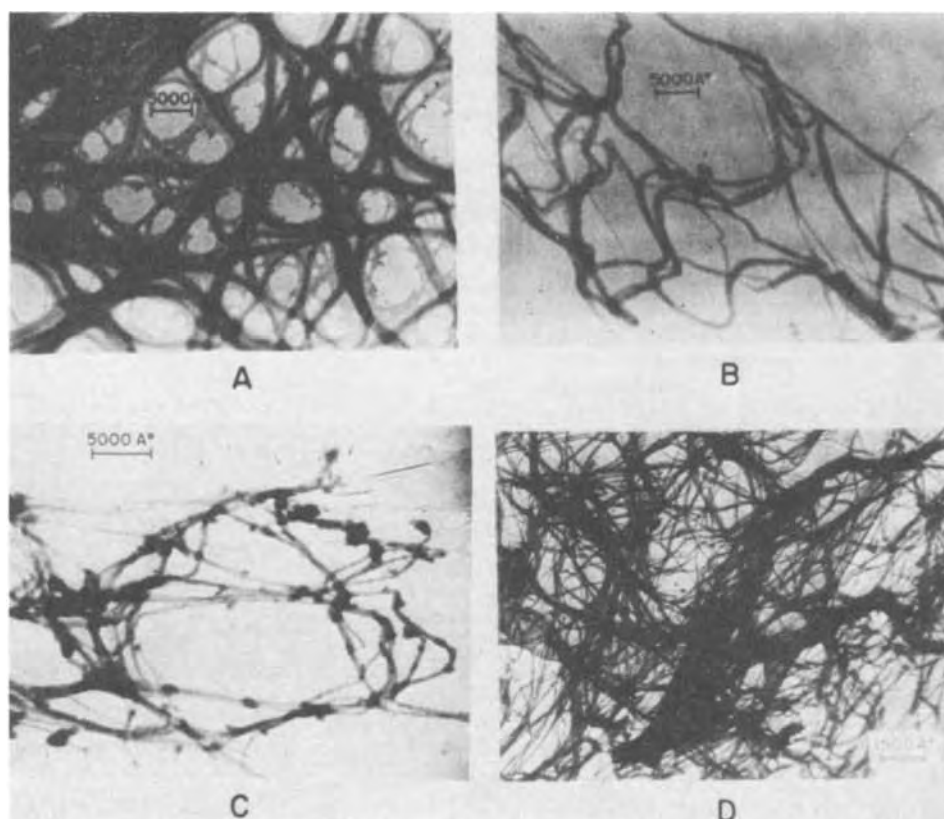


Fig. 18. Electron microscopic photographs of platinum grids maintained at anodic potentials in a phosphate buffer containing fibrinogen with increasing anodic potentials (A-D). The fibrinlike strands are more cross linked.

Any discussion of this paper will appear in a Discussion Section to be published in the June 1975 JOURNAL. All discussions for the June 1975 Discussion Section should be submitted by Feb. 1, 1975.

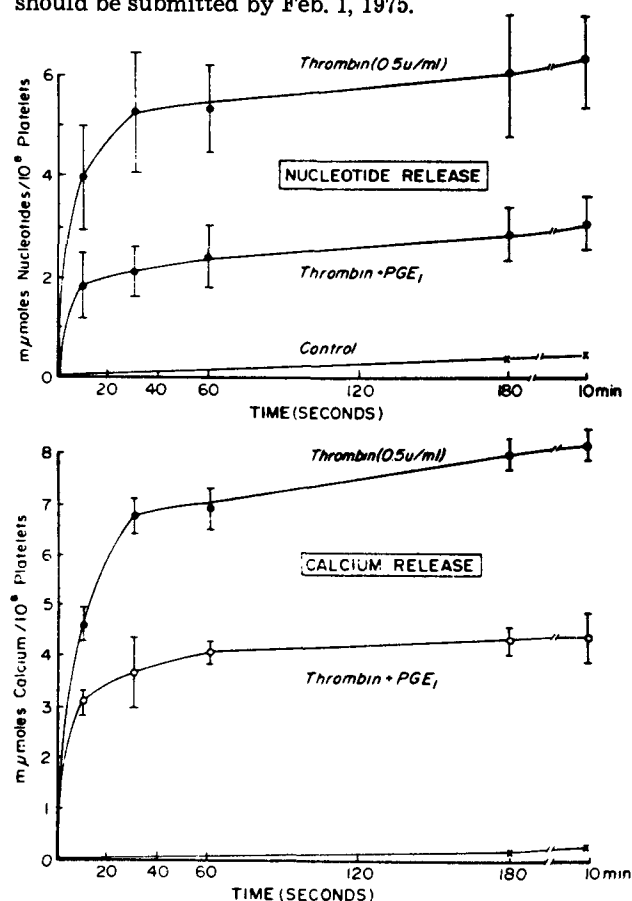


Fig. 19. Effect of prostaglandin E<sub>1</sub> (PGE<sub>1</sub>) on the release of nucleotides and Ca<sup>++</sup> from platelets vessels time relationship.

## GLOSSARY

**Anticoagulant.** A drug which prevents the formation of a coagulum.

**Antithrombotic.** A drug which prevents the formation of a thrombus.

**Charge transfer or electron transfer reactions.** An interfacial reaction where there is transfer of charge across the interface, usually electrons.

**Coagulation.** The formation of a solid from blood (coagulum).

**Interfacial reaction.** A reaction that takes place at the junction of two phases; blood vessel  $\leftrightarrow$  blood interface.

**Coagulation cascade.** Sequential reaction of clotting factors to form a coagulum.

**Coagulum.** The solid formed from blood via the activation of the coagulation cascade. Composed primarily of polymerized fibrin.

**Electrokinetic phenomena.** These arise due to relative movement of ions along the shear plane in the electric double layer across an insulator solution interface. Electrophoresis, streaming potential, and electroosmosis come under this category. Measurement of any of these electrokinetic parameters of blood cells and cellular fragments gives an indication of their surface charge. The measured parameters are related to the zeta-potential.

**Hemostasis.** The cessation of bleeding.

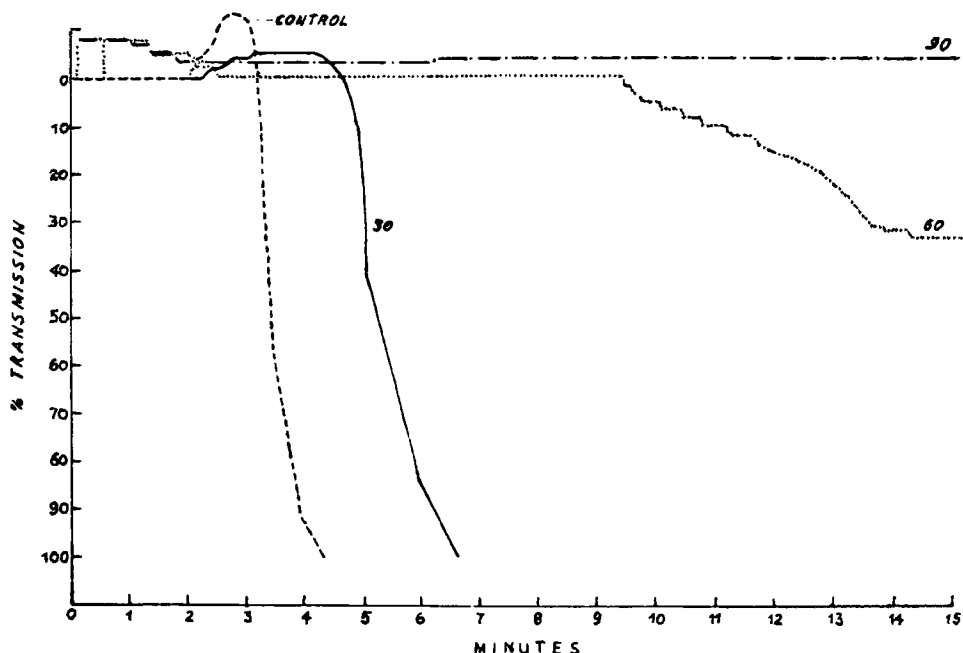
**Platelet aggregation.** The specific binding together of platelets in the formation of a "plug" as an early stage in hemostasis.

**Platelets.** Cell fragments involved in primary hemostasis.

**Primary hemostasis.** The initial cessation of bleeding due to adhesion and aggregation of platelets at the site of injury.

**Prostheses.** Something artificial which replaces a body structure or part.

Fig. 20. Effect of sequential destruction of collagen by collagenase on platelet aggregation as shown by per cent transmission time curves (platelet aggregometer study).



**Red blood cells.** Blood cells that carry hemoglobin and are responsible for  $O_2$  transport. Also called erythrocytes.

**Secondary hemostasis.** The coagulum formed by activation of blood coagulation cascade resulting in polymerization of fibrinogen to fibrin preventing rebleeding.

**Spontaneous potential.** The potential difference developed across a conductor solution interface when it is dipped in an ionic solution. It is measured with reference to the normal hydrogen electrode (NHE) which is the arbitrary zero of the potential scale.

**Thrombogenesis.** The generation of a thrombus or thrombi *in vivo*.

**Thrombus.** A coagulum within a blood vessel.

**White blood cells.** Blood cells involved primarily in host defense (leukocytes).

**Zeta-potentials.** The potential drop across the mobile part of the double layer.

#### REFERENCES

1. H. A. Abramson, *J. Exp. Med.*, **46**, 987 (1927).
2. H. A. Abramson, L. S. Moyer, and M. H. Gorin, "Electrophoresis on Proteins and the Chemistry of Cell Surfaces," Hafner Publishing Co., Inc., New York (1964).
3. H. T. Horowitz and A. R. Spielvogel, in "Thrombosis and Bleeding Disorders—Theory and Methods," N. U. Bang, F. K. Beller, E. Deutsch, and E. F. Mammen, Editors, Chap. IX, Academic Press, New York (1971).
4. R. G. Macfarlane, in "Human Blood Coagulation, Haemostasis and Thrombosis," Rosemary Briggs, Editor, Chap. 20, Blackwell Scientific Publications, Oxford (1972).
5. S. A. Wesolowski, "Evaluation of Tissue and Prosthetic Vascular Grafts," Chap. VIII,

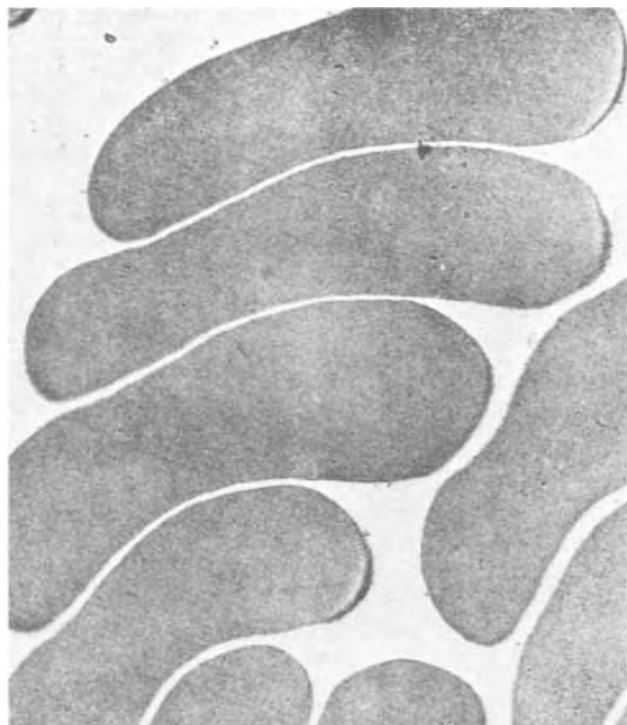


Fig. 21. Effect of dextran on the red cells, electron microscopic study.

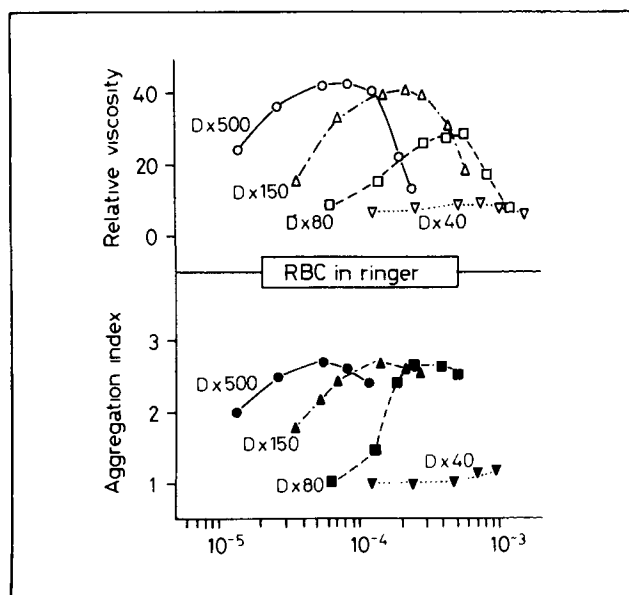


Fig. 22. Effect of dextran on the relative viscosity of blood and aggregation index. (DX 500 dextran of molecular weight 500,000; DX 150, molecular weight 150,000; DX 80, molecular weight 80,000; and DX 40, molecular weight 40,000.)

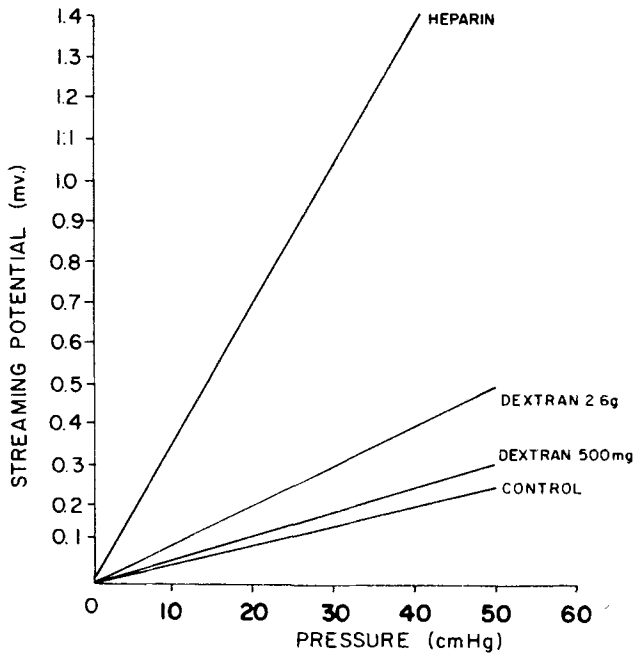


Fig. 23. Effect of heparin and dextran on the streaming potential pressure relations for blood vessel wall *in vitro* in Krebs solution.

Charles C. Thomas, Publisher, Springfield, Ill. (1962).

6. M. McCutcheon, *Physiol. Rev.*, **26**, 319 (1946).
7. P. N. Sawyer and J. W. Pate, *Surgery*, **34**, 491 (1953).
8. P. N. Sawyer and J. W. Pate, *Am. J. Physiol.*, **175**, 113 (1953).
9. G. Ling and R. W. Gerard, *J. Cell Comp. Physiol.*, **34**, 413 (1949).
10. R. O. Becker and D. G. Murray, *Clin. Ortho.*, **73**, 169 (1970).
11. A. Pilla, *Ann. N.Y. Acad. Sci.*, In press.
12. P. N. Sawyer and B. Deutch, *Am. J. Physiol.*, **187**, 473 (1956).
13. P. N. Sawyer, D. W. Harshaw, and S. A. Wesolowski, *Trans. Am. Soc. Artificial Internal Organs*, **8**, 19 (1962).
14. P. N. Sawyer, J. Levine, R. Mazlen, and I. Valmont, *J. Gen. Physiol.*, **45**, 181 (1961).
15. P. N. Sawyer, H. S. Ziskind, and D. H. Harshaw, in "Fundamentals of Vascular Grafting," S. A. Wesolowski and C. Dennis, Editors, McGraw-Hill Book Co., New York (1963).
16. P. N. Sawyer, in "The Etiology of Myocardial Infarction," T. James, Editor, p. 293, Little, Brown & Co., Boston, Mass. (1963).
17. P. N. Sawyer and D. H. Harshaw, *Biophys. J.*, **6**, 653 (1966).
18. S. Srinivasan, C. B. Burrowes, T. R. Lucas, S. B. Bauer, and P. N. Sawyer, *Federation Proc.*, **26**, 550 (1967).
19. S. A. Wesolowski, C. C. Fries, W. J. Liebig, P. N.

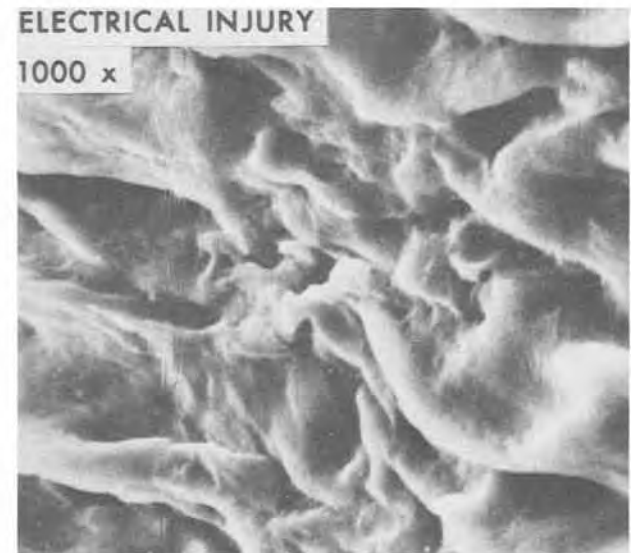
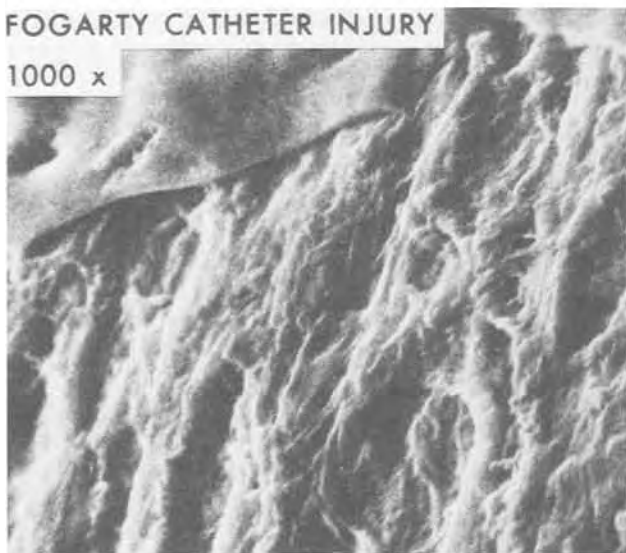


Fig. 24. Effect of dextran perfusion before injury on the nature of thrombus deposit on the artery. Scanning electron microscopy photographs. Magnification 500X.

- Sawyer, and R. A. Deterling, *Arch. Surg.*, **84**, 56 (1962).
20. S. A. Wesolowski, C. C. Fries, K. E. Karslon, M. DeBakey, and P. N. Sawyer, *Surgery*, **50**, 91 (1961).
21. P. N. Sawyer, W. Brattain, and P. Boddy, *Nat. Acad. Sci.*, **51**, 428 (1964).
22. P. N. Sawyer, J. C. Ogoniak, and P. J. Boddy, *Surgery*, **61**, 448 (1967).
23. P. N. Sawyer, K. T. Wu, S. A. Wesolowski, W. H. Brattain, and P. J. Boddy, *Arch. Surg.*, **91**, 735 (1965).
24. P. S. Chopra, S. Srinivasan, T. R. Lucas, and P. N. Sawyer, *Nature*, **215**, 1494 (1967).
25. M. Ranganathan, J. G. Stempak, S. Srinivasan, and P. N. Sawyer, *Thromb. Diath. Haemorrhag.*, **24**, 273 (1970).
26. J. C. Brown, S. M. Lavelle, and P. N. Sawyer, *ibid.*, **21**, 325 (1969).
27. P. N. Sawyer and I. Valmont, *Nature*, **189**, 470 (1961).
28. S. Srinivasan, R. K. Aaron, P. S. Chopra, T. R. Lucas, and P. N. Sawyer, *Surgery*, **64**, 827 (1968).
29. P. N. Sawyer, B. Stanczewski, A. Pomerance, T. R. Lucas, G. Stoner, and S. Srinivasan, *ibid.*, In press.
30. L. Weiss, Presented at Platelets, Drugs and Thrombosis Meeting, McMaster University Medical Center, Hamilton, Ont., Canada, Oct., 1972.
31. E. W. Salzman, *New Engl. J. Med.*, **286**, 358 (1972).
32. H. L. Nossel, Presented at Platelets, Drugs and Thrombosis Meeting, McMasters University Medical Center, Hamilton, Ont., Canada, Oct., 1972.
33. L. Vroman, *J. Biomed. Mat. Res.*, **3**, 43 (1969).
34. R. C. Dutton, A. J. Webber, S. A. Johnson, and R. E. Baier, *ibid.*, **3**, 13 (1969).
35. D. J. Lyman, J. L. Brash, and K. G. Klein, chap. 11, Artificial Heart Program Conference, June 9-13, 1969, United States Government Printing Office, Washington, D. C. (1969).
36. P. Massini and E. F. Lusher, *Thromb. Diath. Haemorrhag.*, **27**, 120 (1972).
37. G. D. Wilner, H. L. Nossel, and E. C. LeRoy, *J. Clin. Invest.*, **47**, 2616 (1968).
38. R. E. Baier, and R. C. Dutton, *J. Biomed. Mat. Res.*, **3**, 191 (1969).
39. R. C. Dutton, R. E. Baier, R. L. Dedrick, and R. L. Dowman, *Trans. Am. Soc. Artificial Internal Organs*, **14**, 57 (1968).
40. N. Ramasamy, M. Ranganathan, L. Duic, S. Srinivasan, and P. N. Sawyer, *This Journal*, **120**, 354 (1973).
41. L. Duic, S. Srinivasan, and P. N. Sawyer, *ibid.*, **120**, 348 (1973).
42. N. Ramasamy, S. Srinivasan, and P. N. Sawyer, *Electrochim. Acta*, **19**, 137 (1974).
43. G. E. Stoner, *J. Biomed. Mat. Res.*, **3**, 655 (1969).
44. G. E. Stoner and S. Srinivasan, *J. Phys. Chem.*, **74**, 1088 (1970).
45. G. E. Stoner and L. Walker, *J. Biomed. Mat. Res.*, **3**, 645 (1969).
46. N. Ramasamy, J. S. Keates, S. Srinivasan, and P. N. Sawyer, Extended Abstracts p. 140, III Congress, The International Society on Thrombosis and Haemostasis, August, 1972, Washington, D. C.
47. N. Ramasamy, J. S. Keates, S. Srinivasan, and P. N. Sawyer, Paper presented at the II International Symposium in Bioelectrochemistry, Pont A Mousson, France, October 1973 (Proceedings published as uncorrected proofs in Bioelectrochemistry and Bioenergetics, **1**, 451 (1973)).
48. G. E. Stoner and S. Srinivasan, *J. Phys. Chem.*, **75**, 2107 (1971).
49. G. A. Jamieson, C. L. Urban, and A. J. Barber, *Nature New Biology*, **234**, 5 (1971).
50. S. M. Wolfe and N. R. Shulman, *Biochem. Biophys. Res. Comm.*, **41:1**, 128 (1970).
51. C. Chesney, E. Harper, and R. Coleman, *J. Clin. Invest.*, **51**, 2693 (1972).
52. E. W. Salzman and L. Levine, *J. Clin. Invest.*, **50**, 131 (1971).
53. Kung-Ming Jan and Shu-Chien, Proceedings of VII Conference on Microcirculation, Aberdeen, Scotland, August 1972, European Society for Microcirculation, J. Ditzel and D. H. Lewis, Editors, p. 54, S. Karger, Basel (1972).
54. G. V. F. Seaman and D. E. Brooks, *ibid.*, Paper 52.
55. D. Danon, Proceedings of VI Conference on Microcirculation, Aalborg, Denmark, June 1972, European Society for Microcirculation, J. Ditzel and D. H. Lewis, Editors, p. 68, S. Karger, Basel (1970).
56. H. Schmidt-Schonbein, E. Volger, G. Gaullusch, and J. N. Mehrishi, Proceedings of VII Conference on Microcirculation, Aberdeen, Scotland, August 1972, European Society for Microcirculation, J. Ditzel and D. H. Lewis, Editors, p. 56, S. Karger, Basel (1972).
57. B. Blomback, Abstracts, p. 46, III Congress International Society on Thrombosis and Haemostasis, Washington, D. C., August 22-26, 1972.
58. Z. Copley, Private communication.
59. S. Niewiarowski, Biomaterials Seminar, Columbia University, New York, February, 1973.

# 1973 F. M. Becket Memorial Award Report

## Heat Capacity of an Ordering Fe-16% Si Alloy Measured with a Spherical Adiabatic Calorimeter

Gary M. Crosbie<sup>1</sup>

*Department of Metallurgy, The University, Sheffield S1 3JD, United Kingdom*

The central matter in the teaching of the subject of alloy steels is the analysis of how various additions affect phase equilibria and transformations of austenite. This face-centered-cubic phase is stable in pure iron only through an intermediate temperature range. At higher and lower temperatures body-centered-cubic phases are stable. Some alloying additions, such as carbon, cause the austenite to be stable over a wider temperature range; others, such as silicon, reduce this temperature range.

Phase diagrams evidence these changes and can be used in the processing of such alloy steels as have been studied. But why is the phase diagram so in each case? And, why is the austenite stable at all? To these questions thermodynamic formalism can provide alternate explanations. The measurements of heat capacity and of heat of transformation are two ways of entering the formalism. For example, it is the lambda-shaped peak in the heat capacity of pure iron, at the Curie point, which raises the Gibbs free energy of the body-centered ferrite above that of the austenite for the intermediate range. Alloy additions which alter the size, shape, and position of this magnetic peak in the heat capacity will, for this reason, alter the range of stability of the austenite.

The group I worked with at the University of Sheffield, Sheffield, United Kingdom, is developing a comprehensive picture of ferrous alloy thermodynamics. Techniques in use include adiabatic calorimetry, isoperibol calorimetry, mass spectrometry, emf methods, and gas equilibrium methods.

Directly, the work of this summer was the final assembly and commissioning of a high temperature adiabatic calorimeter and the use of the apparatus to measure the heat capacity of an Fe-16.1 atomic per cent (a/o) Si alloy. Although the alloy chosen has no stable austenite phase, a knowledge of the magnetic heat capacity will be part of a comparative explanation of why there is no stable austenite. Additionally, since this is an alloy in which atomic ordering occurs, features of the heat capacity curve will relate to the entropy of disordering. This, however, requires a separation of  $C_p$  into components by further experimentation before a link to statistical theories can be made.

### Design and Construction

Following the design of Sale (1970) (1), the adiabatic calorimeter consists of several spherical shells. The centermost shell, which encloses the specimen, has the same temperature as the specimen before, during, and after the injection of heat. In this way, loss of heat to the specimen surroundings is prevented.

The control is achieved by the use of a pair of thermocouple junctions connected in series: one located in the specimen and one on the outer surface of the first shell. The voltage across this differential couple is controlled to zero by adding heat from a small spherical furnace located next out from the center.

Control accuracy is obtained by the use of a three-term solid-state controller.<sup>2</sup> In addition to the proportional term (which alone would make the output signal proportional to the temperature deviation), these are integral and derivative terms to minimize overshoot. Different settings of these terms are determined for each temperature range. Unchanging temperature, before and after the addition of heat is not a sufficient condition for an adiabatic experiment. The error signal must be monitored throughout, to be sure that the adiabatic condition is  $\pm 0.01^\circ\text{C}$  and about a mean of zero. This is obtained when the controller terms are properly set.

While this delicate balance is maintained in the center, the bulk of the energy to keep the calorimeter at temperature is provided by an outer furnace. Though this, too, is controlled by a differential thermocouple with a three-term controller, the shields here are not adiabatic. Clearly, they cannot be so as the electrical energy dissipated by the inner furnace must pass through these outer shells, if the center is not to rise in temperature. Additionally, conduction of heat through supports and furnace leads is a factor in the setting of the nonzero deviation of the outer furnace. A plot of such settings was generated and used to expedite work.

The temperature is measured with thermocouples embedded in the specimen. All couples in the calorimeter are British Standard 1826 Pt/Pt-13%Rh. Deionized ice and water make up the reference junction at  $0^\circ\text{C}$ . A precision decade potentiometer<sup>3</sup> of  $0.1\ \mu\text{V}$  accuracy is used with standard cell, lead-acid batteries, and an amplified galvanometer.

The specimen is cylindrical, with a longitudinal central hole for the specimen heater. This coil of platinum wire, wound on a 1.2 mm alumina shaft, is protected from the specimen by another alumina tube. Power is supplied by a d-c, stabilized, constant-current source. The connections for measuring the voltage drop across the heater are just outside the specimen. Moving coil volt and ammeters, tested to an accuracy of 0.1% were used in this initial setup. Manual timing accuracy was also 0.1%, or 1 sec in 1000.

To permit the calorimeter to be used at temperatures in excess of  $1400^\circ\text{C}$ , special requirements are placed on materials. The spherical shells are either molybdenum or tantalum. Furnace windings and clips are exclusively tantalum. Electrical insulation is high-grade alumina throughout. The only other materials in the calorimeter spheres are the Pt/Pt-13%Rh thermocouples and the ferrous alloy of the specimen.

The whole assembly of shells is protected from the laboratory environment by a vacuum of  $0.5\text{--}1.0 \times 10^{-6}$  Torr. The plinth, on which the spheres rest, is water-cooled, just as is the 316L stainless steel "bell jar." The oil diffusion pump has an automatic timing system for filling its liquid nitrogen cold trap. Multiple reassembly of the vacuum seals, coupled with hydrogen

<sup>1</sup> Present address: Department of Materials Science, The Technological Institute, Northwestern University, Evanston, Illinois 60201.

<sup>2</sup> Manufactured by West Instruments, Brighton, United Kingdom.  
<sup>3</sup> Manufactured by W. G. Fye, Company, Cambridge, United Kingdom.

leak testing, was needed before the desired vacuum was obtained.

### Specimen Manufacture and Analysis

An 800g melt for vacuum induction melting was prepared from deoxidized Japanese electrolytic iron and 99.999% silicon. The major impurities of the iron are oxygen at 0.008 a/o  $\pm 20\%$  and sulfur and carbon at 0.005  $\pm 0.001$  weight per cent (w/o) each. The de-oxidation was done in our laboratory. The melt was preceded by washout melts of the iron with a small quantity of carbon to minimize oxygen contamination from the crucible. The iron-silicon alloy was held just above the solidus temperature for 10 min with 200 Torr argon pressure, then it was teemed into a 25 mm diameter mold. As this alloy was more brittle than the lower silicon alloys in the vacuum melting series, special care was taken in handling.

The analysis showed the alloy to be close to expectations. Wet analysis for silicon indicated 8.80  $\pm 0.02$  w/o Si, or 16.1 a/o Si. Conductimetric analysis of carbon was 0.009  $\pm 0.001$  w/o C. Spectroscopic analysis for eleven metallic impurities found all to be less than 0.02 w/o.

Routine machining was not possible for this alloy. After holding at 1000°C for 2 days and cooling in a vacuum furnace, the specimen diameter was able to be machined with a tungsten carbide tool. However, the holes in the specimen for the heater and thermocouples could not be drilled without pulling out grains. These apertures were obtained by spark erosion, with a cutting speed of 3 mm/hr.

Final heat-treatment in the vacuum furnace consisted of the following: 900°C for 2 days, then cool at an average rate of 7°K/hr, but never more than 15°K/hr, to reach 400°C, then furnace cool. The specimen was then polished and weighed. Total mass was 52.8125g, or 0.989 moles of 16.1 a/o Si alloy.

For calibration of the calorimeter, a second specimen, of zone-refined iron, was machined by ordinary methods. The chief impurities in this specimen were 0.0064 a/o C and 0.0032 a/o Si. This specimen had a mass of 46.524g, or 0.833 moles Fe.

### Commissioning

The first specimen placed in the calorimeter was the zone-refined iron. Heat capacities were measured above and below the Curie point and the ferrite-to-austenite transition. These are shown in Table I. Set points were established and controller terms were found for these temperature ranges. Also, the enthalpy of  $\alpha$ - $\gamma$  transformation was measured on heating and cooling as shown in Table II. These data do not supersede previous work, as they suffer from too rapid heat addition (or subtraction) at the time of completions of the transformation. This causes an ambiguity in the termination point.

After completion of this series, the controllers were exchanged to disassociate the controller with greater touch and vibration sensitivity from the delicate center control. This had been a source of instability at temperatures below 600°C.

Table I. Heat capacity of pure Fe

T°C	T°K	Present $C_p$	Preceding $C_p$	
638.8	912	40.88	43.25	Joules/mole °K
652.6	926	47.06	44.4	
658.0	931	44.74	44.8	
663.8	937	45.21	45.2	
784.0	1057	40.33	46-52	
1059.5	1333	33.63	35.0	

Table II. Enthalpy of ferrite-austenite transformation

Heating	1048 joules/mole
Cooling	789 joules/mole
Accepted value	915 joules/mole $\pm 10$

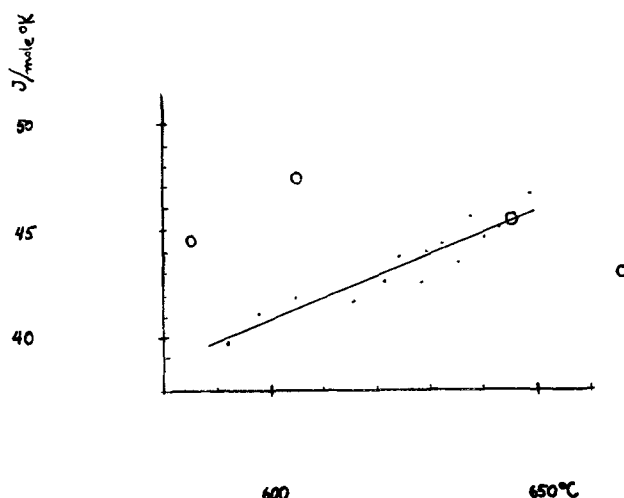


Fig. 1. Heat capacity of Fe-16.1 a/o Si. O, Data of Ettwig and Pepperhoff (7); ●, present data.

### Iron-Silicon Results

The heat capacities are presented in Fig. 1. Only those points for which adiabatic conditions were present before, during, and after the addition of heat are plotted. The temperature of the specimen must not have drifted more than 0.04°K in the 5 min preceding, and the temperature must have leveled in 5 min afterwards. Furthermore, the departure from adiabatic conditions had to be less than 0.02°K throughout, and about a mean of zero.

Other data collected, in the range from 400° to 650°C, are not presented in these results because the above conditions were not met. When a second potentiometer of less accuracy (1.0  $\mu$ V instead of 0.1  $\mu$ V) was used, only temperature changes of about 0.1°K could be discerned. Thus, the drift rate before and after may have exceeded the above-stated requirements. Secondly, those measurements taken when the integral term was removed from the inner furnace control have a steady deviation about a nonzero mean during the time the specimen heater was on. During the heating interval, the specimen was hotter than its surroundings. As there was no way to correct for this, these data were deleted.

Those heat capacity measurements which are left are in the temperature range of 600°-650°C, as shown in Fig. 1. Each heat capacity represents a temperature increment of less than 6°K, and each is plotted at its temperature midpoint. A rise from 40.8 to 45.9 joules/mole°K is found for the interval.

### Discussion

Since the review of Shunk (1969) (2), discussion of the constitution of ordered Fe-Si ferrites has followed two lines. That set forth by Warlimont (1968) (3-4) suggests the existence of two-phase fields and presents transmission electron micrographs to show such microstructures. The other, of Inden and Pitsch (1971-1972) (5-6) and Ettwig and Pepperhoff (1972) (7), suggests that the transformations are continuous and presents x-ray and heat capacity measures as evidence of such. To the first, the second is based on macroscopic properties, and is true only of a metastable state.

The calorimeter constructed and used in the present experimentation has characteristics which enable it to contribute more reliable data. By virtue of using smaller temperature increments than other calorimeters, the departure from equilibrium is less. The calorimeter can be held at temperature for however long is necessary to reach equilibrium. The special care taken in the final anneal of the specimen before inser-

tion into the calorimeter may or may not have been sufficient.

It is not possible to compare features of heat capacity curves when so short a range has been validly studied. Hence, interpretation with respect to ordering and phase constitution is postponed until a broader range has been studied. The data of Ettwig and Pepperhoff (1972) (7) are superimposed on the present results.

The increase of heat capacity with temperature in this range is what would be expected on approaching the Curie temperature reported by Hansen and Anderko (1958) (8).

It is conjectured that the magnetic peak in the heat capacity is reduced from that of pure iron. For the same temperature difference from the Curie temperature, the slope and the value of heat capacity in this alloy is less than that of Fe. If this peak is substantially reduced from that of pure iron and the austenite is little changed, then an explanation for the instability of austenite in this alloy is provided.

#### Summary

A spherical, high temperature (1425°C maximum), adiabatic calorimeter was assembled, commissioned, and used to measure the heat capacity of an Fe-16.1% Si alloy from 600° to 650°C. The design and constructions of the instrument are discussed, as well as the means of manufacturing the specimen of this ordered alloy. This work extends the program of research of thermodynamics of ferrous alloys into ordered iron-silicon alloys.

#### Acknowledgments

I am grateful to Professors B. B. Argent and G. W. Greenwood for their cooperation in the selection of this project and for the provision of laboratory facilities and encouragement for its execution. I wish to thank Dr. A. S. Normanton for the experimental guidance he offered so freely throughout my stay at the University of Sheffield. Of the many other individuals in the Department of Metallurgy who helped, I particularly thank the technicians who spent so many hours assisting in this work.

Finally, I thank the people of The Electrochemical Society and the Union Carbide Corporation for giving me this opportunity to do thermochemical research with the F. M. Becket Award.

#### REFERENCES

1. F. R. Sale, *J. Phys. E: Scientific Instruments*, **3**, 646 (1970).
2. F. A. Shunk, "Constitution of Binary Alloys," 2nd Suppl., pp. 347-349, McGraw-Hill Book Co., New York (1969).
3. H. Warlimont, *Z. Metallk.*, **59**, 595 (1968).
4. H. Warlimont, *J. Met. Soc., Sheffield Univ.*, **7**, 45 (1968).
5. G. Inden and W. Pitsch, *Z. Metallk.*, **62**, 627 (1971).
6. G. Inden and W. Pitsch, *ibid.*, **63**, 253 (1972).
7. H. H. Ettwig and W. Pepperhoff, *ibid.*, **63**, 453 (1972).
8. Hansen and Anderko, "Constitution of Binary Alloys," p. 713, McGraw-Hill Book Co., New York (1958).



## Mechanism and Kinetics of Formaldehyde Oxidation Using a New Fuel Cell Catalyst

W. R. Wolfe\* and K. B. Keating\*

*E. I. du Pont de Nemours and Company, Incorporated, Wilmington, Delaware 19898*

### ABSTRACT

Recently a new class of nonprecious metal anode catalysts has been disclosed. The catalysts are based on the Mo-O-S system and are excellent catalysts for the oxidation of formaldehyde. *IR* free polarization data have been obtained as a function of temperature and formaldehyde concentration and at constant hydrogen ion concentration for formaldehyde in hydrochloric acid electrolyte. The data indicate that the catalyst disassociates the formaldehyde, i.e.,  $\text{H}_2\text{CO} \rightleftharpoons \text{CO} + \text{H}_2$  with subsequent oxidation of the carbon monoxide and hydrogen. The adsorption of the formaldehyde on the catalyst appears to be the rate determining step.

The economic incentive for a methanol fuel cell stems from the relatively low cost of this fuel<sup>1</sup> and the simplicity of electrode construction that accrues to a soluble fuel system. However, the high loadings of precious metal catalysts required to electrochemically oxidize this compound have turned investigators increasingly to consideration of formaldehyde as a fuel (2). Certainly the costs are more favorable than hydrazine, another suggested fuel. The general status of fuel cell electrode and catalyst art for many fuels has been compiled in several excellent reviews (3-6) and will not be covered here.

Recently, a new class of nonprecious metal anode catalysts has been disclosed (7). They consist of at least one oxide of molybdenum and at least one sulfurated compound of molybdenum, with the oxide having the formula  $\text{MoO}_x$  wherein  $x$  has a value of 2-2.88 and the O/S ratio is between 36:1 and 1:36. The catalytic activity in this system increases as the average valence of the Mo approaches 2 and the O/S ratio lies between 10:1 and 1:3.

Because of the excellent activity of these catalysts for formaldehyde oxidation, a study of the kinetics of this oxidation on these catalysts was made for the purpose of optimization of the conditions for fuel cell operation. In these studies the catalyst used was made by heating 18.3g sulfur with 98g of ammonium heptamolybdate  $[(\text{NH}_4)_6\text{Mo}_7\text{O}_{24} \cdot 4\text{H}_2\text{O}]$  in an alumina combustion tube at 450°C in hydrogen for 7 hr. A typical chemical analysis of the resultant acid insoluble compound was as follows

Mo: 64.6 weight per cent (w/o);  
 S: 10.0 w/o; O: 24.0 w/o

### Experimental Procedure

All of the experiments were carried out in the apparatus shown in Fig. 1. In this equipment a batch-

\* Electrochemical Society Active Member.  
 Key words: electrocatalysts, molybdenum, sulfur, HCHO, reaction mechanism, kinetics.

<sup>1</sup> For example, in midyear 1974 the price for methanol was approximately 4 ¢/lb; for formaldehyde it was approximately 10 ¢/lb (1). This means a factor of about 4:1 in favor of methanol in terms of cost of generated power.

type experiment was carried out: the experimental anode was immersed in approximately 250 cm<sup>3</sup> of anolyte and driven against a lead dioxide plate in 250 cm<sup>3</sup> 10% H<sub>2</sub>SO<sub>4</sub>. The anode and cathode compartments were separated by an American Machine and Foundry cation exchange membrane (Series C310). A saturated calomel electrode was used to obtain anode reference potential readings. The current was interrupted every 5 sec using a mercury-wet, relay-type interrupter; this enabled determination of the resistance losses in the electrode so that *IR* free performances could be determined. These data were recorded on a Moseley Model 136-A Autograf X-Y recorder.

Two factors led us to consider that this method of abstracting the polarization due to *IR* losses in the electrodes was legitimate in this case:

(i) Preliminary experiments using an oscilloscope demonstrated that the decay in polarization, interpreted by us as being due to *IR* loss in the electrode, was always less than 1 μsec, eliminating the possibility of this being due to charge transfer.

(ii) For any given electrode configuration, the magnitude of this measured *IR* loss was always directly proportional to the applied current.

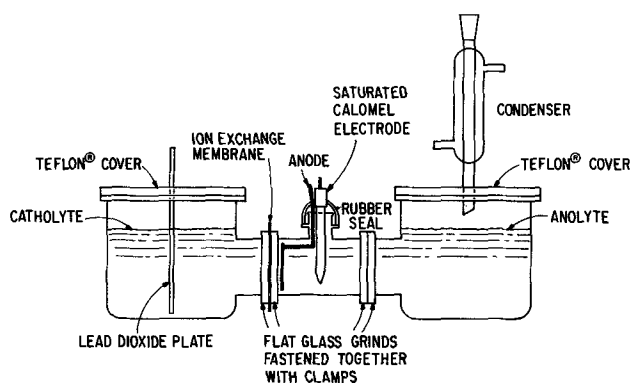


Fig. 1. Apparatus used for fuel cell studies



### Results and Discussion

**Effect of temperature.**—The temperature effect data were taken with an anolyte composition of 9 w/o CH<sub>2</sub>O, 7 w/o HCl, and 84 w/o H<sub>2</sub>O. The data are for the previously described catalyst material which was fabricated into a 1 in. diameter anode containing 2g catalyst, 1g tantalum wool, and 0.2g Teflon® 7 fluorocarbon resin by pressing at approximately 60,000 psi. The thickness of these electrodes was about 50-60 mils. This is the so-called standard anode which was always soaked overnight in the anolyte before determination of the electrochemical parameters.

The data are shown in Fig. 2 which is a plot of current density in milliamperes per square centimeter vs. anode reference potential measured against the saturated calomel electrode (SCE) at the temperature of the experiment.

The temperature effect is quite significant; for example at 15 mA/cm<sup>2</sup> the IR free polarization is about 0.2V vs. SCE at 65°C and about -0.03V vs. SCE at 85°C.

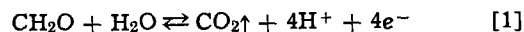
**Effect of electrolyte composition.**—It was found that the polarization characteristics are very sensitive to electrolyte composition. Forty different anolyte compositions were studied. All of these experiments were performed at 85°C. Standard anodes were used in this study also; they were equilibrated overnight with the solution studied. The same apparatus was used as that used for the temperature studies. It was later found that identical performance to this "equilibrated" performance could be achieved by eliminating the Teflon® 7 fluorocarbon resin and pressing the catalyst materials with tantalum wool and making the run almost immediately.

Figure 3 shows the effect of formaldehyde concentration, keeping the hydrogen ion concentration approximately the same. Concentrations of formalde-

hyde lower than 4g in 500 cm<sup>3</sup> solution (0.7% by weight) result in unstable performance; the anode polarizes continuously and the current continues to drop. This effect is not eliminated by stirring. It was also determined that the concentration of formaldehyde remains constant in the bulk solution during the course of the experiment so that depletion of the formaldehyde in the bulk is not the cause of this behavior. Data were also taken in the current density region 0.01-1 mA/cm<sup>2</sup>. These data, taken at 85°C, are shown in Fig. 4 for an anolyte containing 9.3% CH<sub>2</sub>O, 6.2% HCl, 84.4% H<sub>2</sub>O.

Large deviations in the hydrogen ion concentration affect the polarization curves markedly; this effect can be conveniently represented on a ternary diagram as in Fig. 5 which shows contour lines of current density at 0.1V polarization for the concentration at that point. The numbers on the ternary diagram are current densities at 0.1V polarization for the concentration at that point. A sharply defined optimal region in the neighborhood of 24% CH<sub>2</sub>O, 4% HCl, 72% H<sub>2</sub>O is evident.

**Kinetic analysis of data.**—The anode reaction is thought to proceed as follows at the electrode surface



Let us consider the possibility that this reaction occurs in two major steps of the following type



We can now develop the kinetics after Bockris (8) and Christiansen (9) and write the reaction for the net forward velocity

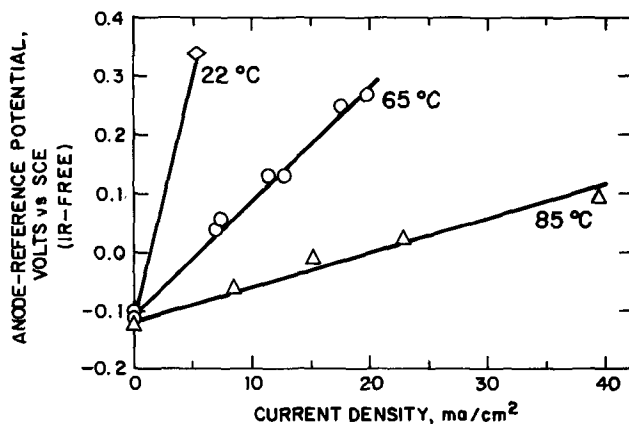


Fig. 2. Effect of temperature on anode performance. Anolyte composition: 9.0% CH<sub>2</sub>O; 7.0% HCl; 84.0% H<sub>2</sub>O.

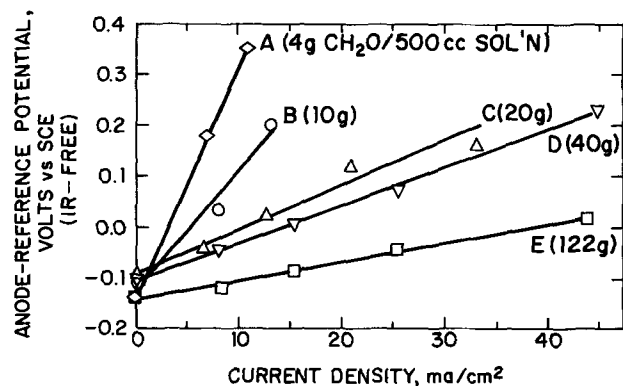


Fig. 3. Effect of concentration on anode performance (temperature, 85°C).

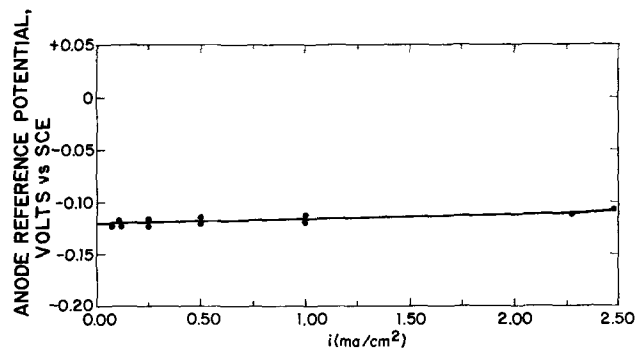


Fig. 4. Plot of  $E$  vs.  $i$  (low current densities). Temperature, 85°C. Standard anode, standard catalyst. Anolyte concentration: 9.0% CH<sub>2</sub>O; 7.0% HCl; 84.0% H<sub>2</sub>O.

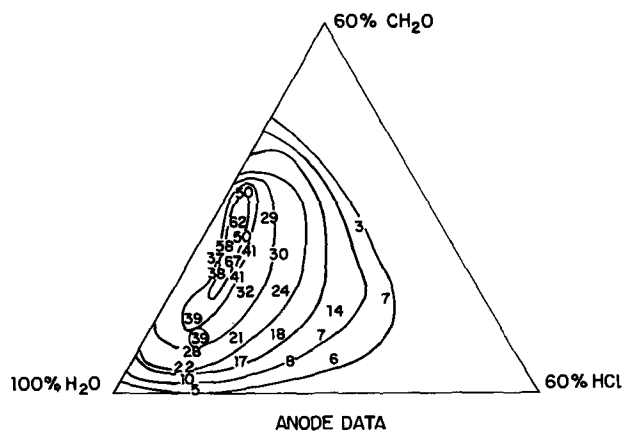
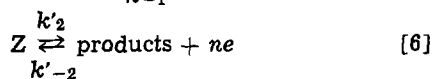


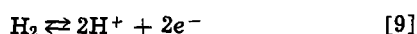
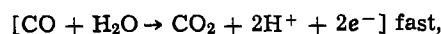
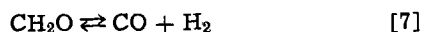
Fig. 5. Ternary diagram of anode. Current density (mA/cm<sup>2</sup>) at 0.1V vs. SCE (IR free) at 85°C.

$$v_f = \frac{k_1 k'_2 A}{k_{-1} + k'_2} \quad [4]$$

Now, if we consider the oxidation of formaldehyde to take place as a first order, nonelectrochemical reaction followed by an electron transfer reaction involving the intermediate, we can write



A set of reactions consistent with this form and with the over-all reaction (Eq. [1]) is



Proceeding as in the simple prototype, we get

$$v_1 = k_1 C_F; v_{-1} = k_{-1} C_Z \quad [10]$$

$$v_2 = k'_2 C_Z e^{\beta f E}; v_{-2} = k'_{-2} C_{\text{prod}} e^{-\alpha f E} \quad [11]$$

where we have made the following substitutions:  $k'_2 = k_2 e^{\beta f E}$  for the oxidation or forward reaction;  $k'_{-2} = k_{-2} e^{-\alpha f E}$  for the reduction or backward reaction.

Here  $f = nF/RT$ ,  $E$  is the anodic polarization,  $\beta$  is the fraction of the potential assisting the forward or oxidation step, and  $\alpha$  is the fraction of the potential assisting the backward or reduction step.

It should be pointed out that in Eq. [10] and [11] the reactions are considered to be first order; also  $k_2$  and  $k_{-2}$  may be functions of temperature.

Now, resubstituting in Eq. [4], we get, for the current density,  $i$

$$i = \frac{nFk_1 k_2 C_F e^{\beta f E}}{k_{-1} + k_2 e^{\beta f E}} \quad [12]$$

This equation will represent the total predicted  $i$ - $E$  behavior, assuming the back reaction is negligible and the temperature is constant.

We now examine the limiting cases. (i) With a small  $E$ , then  $k_{-1} \gg k_2 e^{\beta f E}$ . Therefore

$$i = \frac{nFk_1 k_2 C_F e^{\beta f E}}{k_{-1}} \quad [13]$$

This would predict Tafel-type behavior at low  $E$ , for a given formaldehyde concentration, with reaction [9] controlling.

(ii) With large  $E$ , then  $k_{-1} \ll k_2 e^{\beta f E}$ . Now

$$i = nFk_1 C_F = i_1 \quad [14]$$

or

$$\frac{\partial \log i}{\partial \log C_F} = 1 \quad [15]$$

Thus we get a nondiffusional limiting current ( $i_1$ ) behavior, independent of  $E$ , with reaction [7] rate controlling and a slope of unity for a plot of  $\log i$  vs.  $\log C_F$ .

Returning to Eq. [12] and [14], we get

$$E = \frac{0.059}{\beta n} \left( \frac{T}{298} \right) \log \frac{k_{-1}}{k_2} - \frac{0.059}{\beta n} \left( \frac{T}{298} \right) \log \left( \frac{i_1 - i}{i} \right) \quad [16]$$

We summarize then the three major predictions of this model:

(i) The existence of a limiting current  $i_1$ , proportional to the formaldehyde concentration,  $C_F$  (Eq. [14]).

(ii) A linear plot of  $E$  vs.  $\log \frac{i_1 - i}{i}$ , with a slope of  $\frac{0.059}{n} \frac{T}{298}$ . (See Eq. [16].)

(iii) The current is proportional to the formaldehyde concentration. A plot of  $\log i$  vs.  $\log C_F$  will have a slope unity (Eq. [15]) at large values of  $E$ .

For the purpose of an analysis of the data in terms of this model, let us confine ourselves to data taken on a tieline in the  $\text{CH}_2\text{O}$ - $\text{H}_2\text{O}$ - $\text{HCl}$  ternary diagram at about 4%  $\text{HCl}$  by weight and between 9 and 32% by weight  $\text{CH}_2\text{O}$ .

Figure 6 shows a plot of  $E$ , the anodic polarization, vs.  $\log i$  (on a semilogarithmic plot) for a standard catalyst in anolyte at 85°C containing the formaldehyde concentrations indicated.

Examination of these curves reveals that they do indeed exhibit limiting current behavior as predicted by our model. It is useful at this point to establish that this limiting current behavior is not due to diffusion control. Using the well-known equation for the limiting current in a diffusion controlled process

$$[i_1]_D = \frac{nFD}{\delta} C_F \quad [17]$$

where:  $[i_1]_D$  = diffusion controlled limiting current ( $\text{A}/\text{cm}^2$ );  $n$  = number of electrons involved in reaction;  $D$  = diffusion coefficient of formaldehyde in anolyte ( $\text{cm}^2/\text{sec}$ );  $C_F$  = concentration of formaldehyde in bulk solution (moles/ $\text{cm}^3$ );  $\delta$  = thickness of diffusion film (cm); and  $F$  = Faraday's constant ( $9.65 \times 10^4$  A-sec/mole). We obtain<sup>2</sup> a limiting current of 200-400  $\text{mA}/\text{cm}^2$  at a concentration of  $3.33 \times 10^{-3}$  moles/ $\text{cm}^3$  (50g in 500  $\text{cm}^3$ ) formaldehyde, using conservative values of  $D$  and  $\delta$  ( $10^{-5}$   $\text{cm}^2/\text{sec}$  and 0.03 cm, respectively). This current is far in excess of what any reasonable extrapolation of the data in Fig. 6 would suggest as a limiting current for this concentration. Another experimental indication that diffusion is not controlling the rate of this reaction is that vigorous stirring has no effect on the polarization curves obtained.

Figure 7 shows a plot of  $E$  vs.  $\frac{i_1 - i}{i}$ , where  $i_1$  is estimated from Fig. 6. As can be seen, all of the data can be represented fairly well by a straight line with a slope of  $-0.232$ . This slope provides a value of  $\beta n$  of 0.3, which is reasonable.

Figure 8 shows a plot of  $\log i$  vs.  $\log C_F$  at constant values of  $E$ , the anodic polarization. Statistical anal-

<sup>2</sup> For  $n = 2$ ,  $[i_1]_D = 214$   $\text{mA}/\text{cm}^2$ ; for  $n = 4$ ,  $[i_1]_D = 428$   $\text{mA}/\text{cm}^2$ .

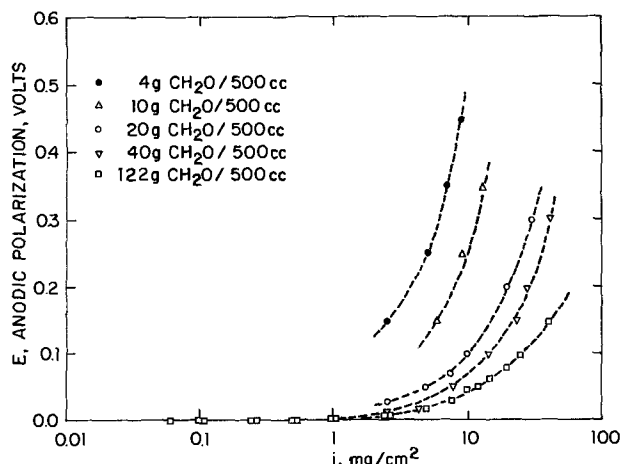
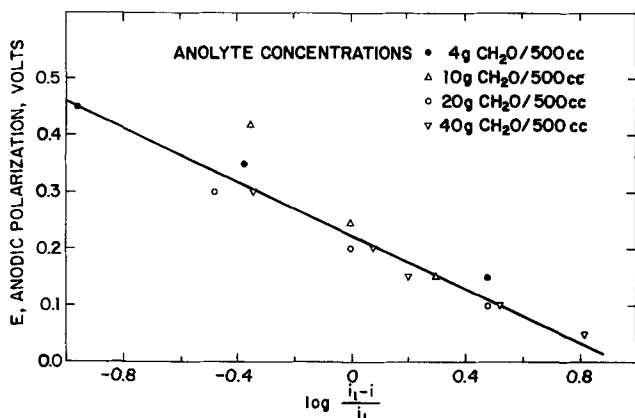
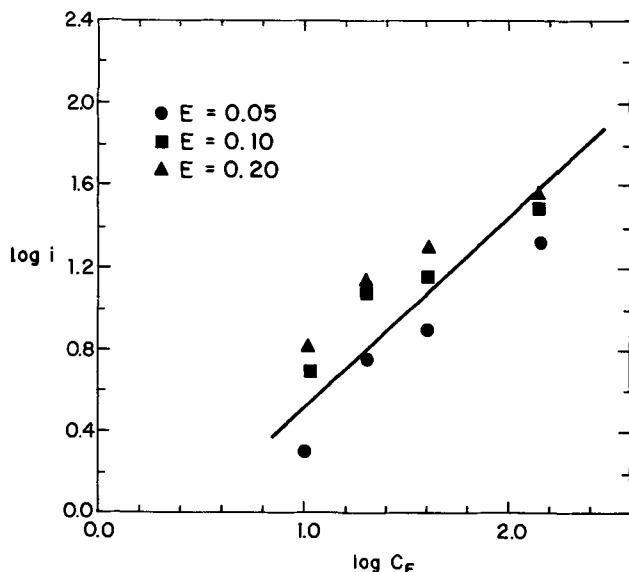


Fig. 6. Plots of  $E$  vs.  $i$  at 85°C. Standard catalyst, standard anode

Fig. 7. Plot of  $E$  vs.  $\log i_1 - i/i_1$  at  $85^\circ\text{C}$ Fig. 8. Plot of  $\log i$  vs.  $\log C_F$  at  $85^\circ\text{C}$ 

ysis of the data shows that a line can be drawn through the data with a slope equal to unity at the 95% level of confidence. Such a line is drawn in Fig. 7. This is in very good agreement with the third major prediction of the model developed for the anode reaction.

At very low current densities, the backward reaction will not be negligible and we will then obtain from Eq. [12] the following expression

$$v = \frac{k_1 k_2 C_F e^{\beta f E} - k_{-1} k_{-2} C_{\text{prod}} e^{-\alpha f E}}{k_{-1} + k_2 e^{\beta f E}} \quad [18]$$

This equation will be important at small  $E$ , therefore  $k_{-1} \gg k_2 e^{\beta f E}$ . Simplifying and introducing the expression for the current, we get

$$\frac{i}{nF} = K_1 k_2 C_F e^{\beta f E} - k_{-2} C_{\text{prod}} e^{-\alpha f E} \quad [19]$$

where

$$K_1 = \frac{k_1}{k_{-1}} \quad [20]$$

For small  $E$ , we can make the following mathematical substitutions

$$e^{\beta f E} \cong 1 + \beta f E \quad [21]$$

$$e^{-\alpha f E} \cong 1 - \alpha f E \quad [22]$$

Then

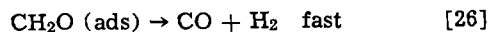
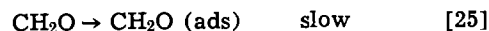
$$\frac{i}{nF} = K_1 k_2 C_F (1 + \beta f E) - k_{-2} C_{\text{prod}} (1 - \alpha f E) \quad [23]$$

and

$$\frac{i}{nF} = E[\beta f K_1 k_2 C_F + \alpha f k_{-2} C_{\text{prod}}] + [K_1 k_2 C_F - k_{-2} C_{\text{prod}}] \quad [24]$$

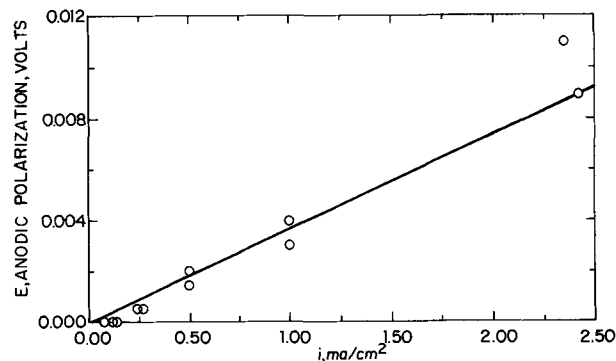
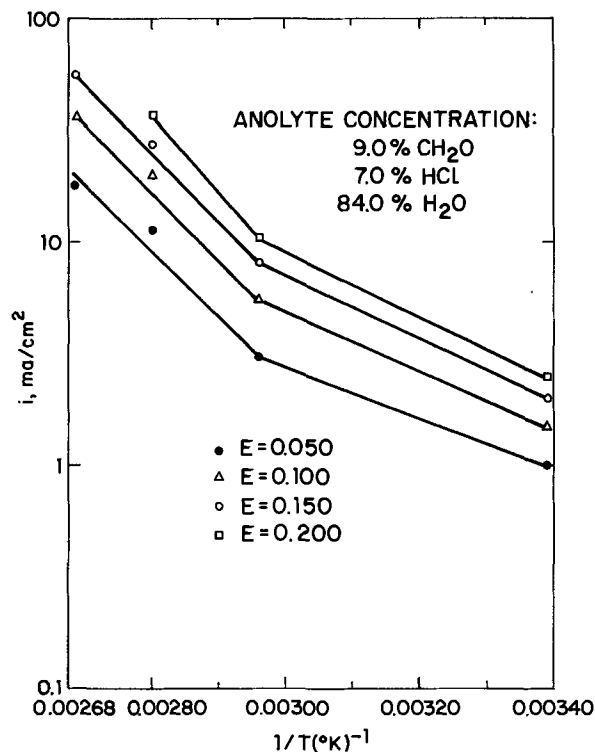
This equation predicts a linear relationship between  $i$  and  $E$  at low values of  $E$ . Figure 9 is such a plot showing this relationship. Above current densities of about  $2.5 \text{ mA/cm}^2$  (corresponding to values of  $E$  of approximately  $10 \text{ mV}$ ) this linear relationship breaks down, presumably because the backward reaction is now negligible.

Our model still holds if what in fact happens is the following



with the rest of the steps following as in Eq. [5] and [6].

An indication that this first slow step may be an adsorption step is the fact that it is necessary to soak the anodes in anolyte overnight before running in order to obtain maximum, reproducible current densities. After 816 hr of soaking a standard electrode in

Fig. 9. Plot of  $E$  vs.  $i$  at  $85^\circ\text{C}$  (low current density region). Anolyte concentration: 9.0%  $\text{CH}_2\text{O}$ ; 7.0%  $\text{HCl}$ ; 84.0%  $\text{H}_2\text{O}$ .Fig. 10. Plot of  $i$  vs.  $1/T$  at constant  $E$ . Anolyte concentration: 9.0%  $\text{CH}_2\text{O}$ ; 7.0%  $\text{HCl}$ ; 84.0%  $\text{H}_2\text{O}$ .

optimized anolyte, it was found that although the formaldehyde concentration had been reduced by about two-thirds, the water concentration (determined by difference, knowing  $\text{Cl}^-$  and  $\text{CH}_2\text{O}$  concentration) actually increased. This suggests that at open circuit  $\text{CH}_2\text{O}$  does not combine with  $\text{H}_2\text{O}$  to form  $\text{CO}_2$ . Thus, Eq. [25] and [26] may indicate the correct course of the reaction.

Figure 10 shows a plot of  $i$  vs. the reciprocal of the absolute temperature ( $1/T$ ) for values of the same polarization. We can immediately discern two separate regimes: the first between 22° and 65°C, in which the heat of adsorption is 4.6 kcal/mole; the second (from 65° to 100°C), in which the heat of adsorption is approximately 13 kcal/mole. These values bracket the value reported for the adsorption of formaldehyde on tungsten carbide, namely 10 kcal/mole (10). In this connection it is interesting to note a report of two adsorbed species for formaldehyde on germania, one very weakly bonded, a second more strongly bonded with a spectrum similar to polyoxymethylene (11). All of these considerations strongly suggest that Eq. [25] is indeed a proper representation of the rate determining step for the oxidation of formadehyde on this catalyst.

#### Acknowledgment

It is a pleasure to acknowledge the contributions of Dr. J. F. Nestor who synthesized the catalysts, Dr.

Allen J. Bard of the University of Texas who aided in the kinetic analysis, and Mr. K. J. P. Karawin who aided in performing many of the experiments.

Manuscript submitted Sept. 21, 1973; revised manuscript received April 26, 1974.

Any discussion of this paper will appear in a Discussion Section to be published in the June 1975 JOURNAL. All discussions for the June 1975 Discussion Section should be submitted by Feb. 1, 1975.

The publication costs of this article have been assisted by E. I. du Pont de Nemours and Company, Incorporated.

#### REFERENCES

1. Chemical Marketing Reporter, February 25, 1974.
2. H. Binder, A. Kohling, W. Kuhn, and G. Sandstede, *Angew. Chem. Intern. Ed. Engl.*, **8**, 757 (1969).
3. S. G. Meibuhr, *Electrochim. Acta*, **11**, 1301 (1966).
4. R. P. Fischer, *ibid.*, **11**, 1309 (1966).
5. S. G. Meibuhr, *ibid.*, **11**, 1325 (1966).
6. S. G. Meibuhr, *ibid.*, **13**, 1973 (1968).
7. W. R. Wolfe, Jr., U.S. Pat. 3,492,164 (1970).
8. J. O'M. Bockris, *J. Chem. Phys.*, **24**, 817 (1956).
9. C. A. Christiansen, *Z. Physik. Chem.*, **B33**, 145 (1936); *ibid.*, **B37**, 374 (1937).
10. G. Schulz-Ekloff, D. Baresel, and J. Heidemeyer, *Collection Czech. Chem. Commun.*, **36**, 928 (1971).
11. J. C. McManus, Kunichi Matsushita, and M. J. D. Low, *Can. J. Chem.*, **47**, 1077 (1969).

## Corrosion and Histopathological Studies on Anode Materials for Implantable Power Sources

Richard B. Beard, Hatim M. Carim, Stephen E. Dubin, and Joseph F. DeRosa

*Biomedical Engineering and Science Program, Drexel University, Philadelphia, Pennsylvania 19104*

and Arthur S. Miller

*Department of Pathology, Temple University School of Dentistry, Philadelphia, Pennsylvania 19122*

#### ABSTRACT

Pacemakers and biotelemeters are being powered by implantable hybrid cells consisting of sacrificial anodes and cathodes where body oxygen is reduced. A high corrosion rate of anode materials for the hybrid cell is a distinct disadvantage because of the cell's proposed goal as a long term power source. *In vitro* and *in vivo* corrosion studies made on anode materials such as aluminum, zinc, and magnesium alloy AZ31B under different loadings have been correlated histopathologically with the tissue reaction at the implant interface. Magnesium and magnesium alloy AZ31B appear to be unacceptable as an anode material due to their high corrosion rates and poor biocompatibility. *In vivo* corrosion measurements on aluminum over 147 days under different loadings demonstrated that a load current density of the order of  $13 \mu\text{A}/\text{cm}^2$  produced a low corrosion rate and good biocompatibility. Although aluminum appears to be more biocompatible than zinc further work needs to be undertaken in order to more completely characterize corrosion mechanisms and the biocompatibility of these materials.

Many thousands of patients have received successfully implanted pacemakers and live useful lives. Recent advances in technology have led to more dependable electrodes and generators so that the average functional life of a pacemaker has increased from six to eighteen months with some as high as thirty-six months (1,2). Ideally an implantable power source should last for ten years, eliminating the necessity of replacing power sources (3). There are a variety of approaches which have been pursued in an attempt to prolong the lifetime of internal power sources (4).

Key words: *in vivo* corrosion, aluminum, zinc, magnesium AZ31B, biocompatibility.

The implantable hybrid cell as a long term power source for cardiac pacemakers has been extensively studied (1, 3-5). The hybrid cell consists of a fuel cell cathode where dissolved oxygen in the body fluids is catalytically reduced and a sacrificial anode is galvanically oxidized.

Previous studies indicated that the primary problem was electrode polarization at the cathode resulting in a loss of power (6). The development of porous palladium black cathodes using powder metallurgy techniques resulted in a substantial increase in the *in vivo* power density obtainable from these cells (7). This paper addresses itself to the corrosion of anode mate-

rials. A high corrosion rate for an anode material for the hybrid cell can be a distinct disadvantage because of its proposed goal as a long term power source, the increase in waste products in the host and the possible weakening of the anode with built up corrosion products (8, 9). Weight loss studies are not sufficiently sensitive to adapt to *in vivo* corrosion studies (9, 10) while for *in vitro* they produce an average corrosion rate with time (11, 12).

A technique that can be used for both *in vitro* and *in vivo* corrosion studies of anodes is the linear polarization method developed by Stern (11-13) and used by Greene *et al.* (9, 10) to study corrosion of surgical implants. The hybrid cell draws 25  $\mu\text{A}/\text{cm}^2$  when driving a commercial pacemaker, thus in order to obtain galvanostatic and potentiostatic anodic and cathodic polarization curves under load conditions anodes were loaded to draw approximately 25  $\mu\text{A}/\text{cm}^2$ . After loading for various periods of time, *i.e.*, for a number of days, polarization, galvanostatic and potentiostatic curves were taken on removal of the load. Besides corrosion rates being determined by linear polarization techniques, rates were estimated similar to Tafel extrapolation by drawing tangents to the polarization curves in the loaded current range. The intersection of these "Tafel" lines with the horizontally drawn line representing  $E_{\text{corrosion}}$  was taken as  $I_{\text{corrosion}}$ .

### Experimental Procedures

**Linear polarization technique for determining corrosion rates (9, 14, 29).**—This method consists of determining the Tafel slopes;  $\beta_a$  and  $\beta_c$  for both anodic and cathodic processes, and the polarization resistance,  $R_{\text{pol}}$ , of the corroding electrode under study. The polarization resistance is the slope of the linear portion of the polarization curve obtained by plotting overpotential *vs.* current density for the first 10-20 mV of overpotential of the electrode.

The values of  $\beta_a$  and  $\beta_c$  and  $R_{\text{pol}}$  are then used to calculate the corrosion rate expressed as a corrosion current  $I_{\text{corr}}$  from the following equation

$$I_{\text{corr}} = \frac{\beta_a \beta_c}{2.3 R_{\text{pol}} (\beta_a + \beta_c)} \quad [1]$$

A Tacussel PIT 20-2X potentiostat and a polarization cell fabricated according to Greene (14) was used for *in vitro* studies. In determining  $R_{\text{pol}}$  and for galvanostatic measurements a constant current source, a Keithley Model 225 was used for accurate low currents. A Lauda Circulator Model K-2 kept samples at a body temperature of  $37^\circ \pm 0.1^\circ\text{C}$ .

In *in vivo* studies the current was passed through a test electrode and a porous palladium black electrode which is implanted with the test electrodes for use as the auxiliary or counterelectrode. The electrical connection to all the electrodes was made by connecting very fine Teflon-coated stainless steel wires to the electrodes and then bringing the other end of the wire out through the skin. The wire connection is insulated by a fluid impermeable neoprene coating covered with Ciba Aradite 6010 epoxy with a final coating of Dow Corning Medical Adhesive Silicon Type A.

The potential of each test electrode was measured with respect to a silver-silver chloride electrode (standard 16 mm Beckman biopotential skin electrode) which was placed on the skin with conductive paste. All samples were 1 or 3  $\text{cm}^2$  in geometric area and were implanted subcutaneously in the lateral abdomen and thorax of dogs.

### Histological Examinations

H & E stains were used for histological staining of the tissue capsules surrounding the implants. Hematoxylin, H, colors basophilic material blue or purple, while eosin, E, colors acidophilic material pink or red. Thus collagen stains pink to red (15). Another staining method used to supplement the H & E is the Gomari

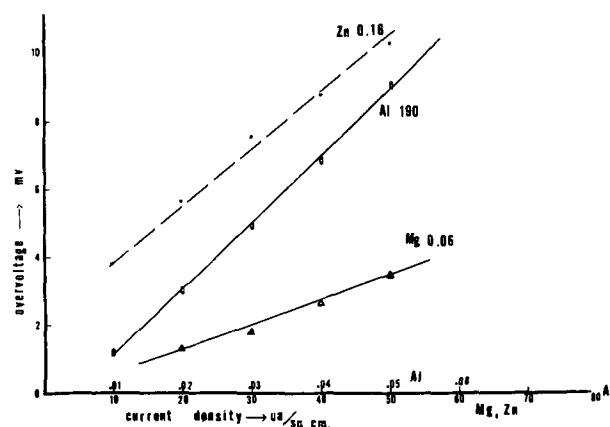


Fig. 1. *In vitro* anodic linear polarization curves under no load used to determine the  $R_{\text{pol}}$  in kilo ohms per square centimeter for Al, Zn, and Mg alloy AZ31B, in 0.9% aqueous NaCl at  $37^\circ\text{C}$  open to atmosphere.

trichrome stain (16) which differentiates between collagen and muscle. Collagen stains a clear green while smooth muscle stains a deep purplish red and fibrin an orange red. In order to differentiate bacteria in tissue a Brown and Brenn method was used.

### Materials

Solid aluminum and zinc were obtained from A. D. Mackay Company with the following purity: aluminum, 99.99%; zinc, 99.9%. The magnesium alloy, AZ31B consisted of magnesium with 3% aluminum and 1% zinc.

### Results and Discussion

***In vitro* measurements.**—Although the anodic and cathodic Tafel slopes varied over a wide range of values the  $I_{\text{corr}}$  can be shown to be approximated by

$$I_{\text{corr}} = \frac{0.026^{(10)}}{R_{\text{pol}}} \quad [2]$$

Figure 1 contains plots of linear polarization curves for determining  $R_{\text{pol}}$  for the various metals under *in vitro* conditions. Table I is a summation of *in vitro* data. It is noted that there is a range of values of  $R_{\text{pol}}$ . The intersection of the Tafel line with  $E_{\text{corr}}$  in Fig. 3 is at 0.2 which checks reasonably well with the values obtained from Eq. [2].

It is noted from Table I that the *in vitro* corrosion rates of zinc and magnesium alloy AZ31B are 2 to 3 orders of magnitude greater than aluminum. The unloaded *in vivo* data of Table II demonstrates that *in vivo* corrosion rates are reduced by an order of magnitude over the *in vitro* corrosion although the relative rates between metals remain approximately the same. Table III illustrates that loading the anode with a current density of 25  $\mu\text{A}/\text{cm}^2$  which has been used for powering present commercially available pacemakers increases the corrosion rate particularly for Al. At this loading the *in vivo* corrosion rates of Al increases with time of implantation as shown in Fig. 2a to arrive at an asymptotic value of  $I_{\text{corr}}$  which is the same order of magnitude as for zinc.

Table I. Comparison of  $I_{\text{corr}}$  of anodic materials under no load conditions 0.9% NaCl,  $T = 37^\circ\text{C}$

Anode	<i>In vitro</i>		
	$R_{\text{pol}}$ (ohms $\times 10^3$ )	$I_{\text{corr}}$ Eq. [2] ( $\mu\text{A}/\text{cm}^2$ )	$i_{\text{corr}}$ Tafel line intersec- tion ( $\mu\text{A}/\text{cm}^2$ )
Solid aluminum	100-330	0.09-0.26	0.1-0.5
Solid zinc	0.14-0.35	52-186	25-45
Solid magnesium alloy AZ31B	0.066-0.242	107-394	35-500

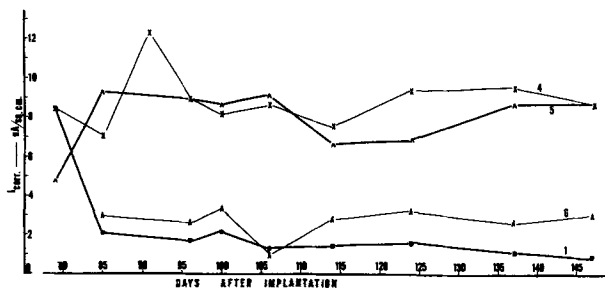


Fig. 2a. Comparison of the time variation of  $I_{corr}$  of aluminum anodes implanted in the lateral thorax of dogs under different loadings. Curve 2 is for a 10 kohm or  $38 \mu A/cm^2$  load while curve 3 is for a 20 kohm or  $19 \mu A/cm^2$  load. Implants sterilized with ethylene oxide.

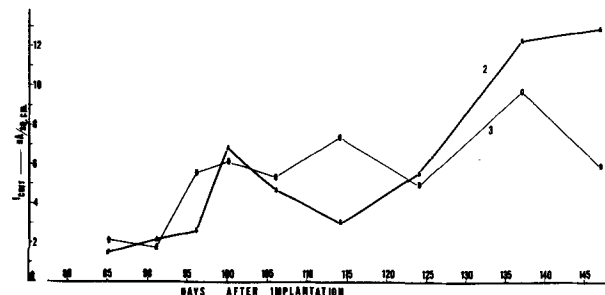


Fig. 2b. Time variation of  $I_{corr}$  for aluminum anodes implanted in dogs under different loadings. Curve 1 represents an electrode heavily loaded at  $75 \mu A/cm^2$  for the first 80 days and then open circuited for a no load. Curve 6 is a loading of  $13 \mu A/cm^2$  for 147 days. Curves 4 and 5 have been loaded for 147 days at approximately  $18.5 \mu A/cm^2$ .

The *in vitro* electrodes unlike the *in vivo* electrodes were not autoclaved so they did not obtain a heavy oxide film. Attempts to make *in vitro* measurements on autoclaved electrodes produced nonreproducible and unstable data. Autoclaved *in vivo* electrodes under no load demonstrated some instability reflected as variations of potential. However, it was possible to obtain reasonably steady values with time which fell in the range of values presented in Tables II and III. Ethylene oxide gas sterilized electrodes under no load *in vivo* behaved similar to the autoclaved as above. Electrodes which were either sterilized in a "Bard" ethylene-oxide gas sterilizer or autoclaved, produced stable potentials under load conditions.

The above results indicate that the oxide film at the aluminum interface may be partially ruptured under load conditions (17-20), increasing the corrosion rate.

Table II. Comparison of  $I_{corr}$  of anodic materials under no load conditions for implantations in dogs  
Electrodes sterilized by autoclaving

Anode	$R_{pol}$ (ohms $\times 10^3$ )	In vivo unloaded	
		$I_{corr}$ Eq. [2] ( $\mu A/cm^2$ )	$I_{corr}$ "Tafel" line extrapolation ( $\mu A/cm^2$ )
Solid aluminum	400-2000	0.013-0.085	0.03-0.23
Solid zinc	6-18	1.4-4.3	0.3-6.66
Solid magnesium alloy AZ31B	3-4	6.5-8.7	14-19

Table III. Comparison of  $I_{corr}$  of anodic materials under an approximate loading of  $25 \mu A/cm^2$   
Electrodes sterilized by autoclaving

Anode	$R_{pol}$ (ohm $\times 10^3$ )	In vivo loaded (for four days)	
		$I_{corr}$ Eq. [2] ( $\mu A/cm^2$ )	$I_{corr}$ "Tafel" line intersection ( $\mu A/cm^2$ )
Solid aluminum	114	0.228	0.5-0.65
Solid zinc	5.8	4.4	5.5-15

Table IV. Showing corrosion data parameters as average values for last 20 days of observation for aluminum implantations of 147 days in dogs

Electrodes sterilized with ethylene-oxide				
Cell No.	Resistor load (K ohms)	Cell potential under load (V)	Load current ( $\mu A/cm^2$ )	Corrosion current range ( $\mu A/cm^2$ )
2*	10	0.3700	38	5.6-13
3*	20	0.3650	18.7	4.9-9.8
4	30	0.5000	18.3	8.6-9.5
5	40	0.8000	19	6.8-8.6
6*	52	0.7000	13.3	2.8-3.1
1	$\infty$	—	0	0.8-1.4

\* Indicates cells loaded 79 days after implantation.

When the hybrid cell is coupled to a pacemaker the whole unit is gas sterilized before implantation. Electrodes were therefore sterilized with ethylene-oxide for *in vivo* measurements under load as given in Table IV.

As expected the disturbance to the corrosion rate of passing a current through the aluminum interface due to its more pronounced oxide coating is greater than that of zinc. *In vivo* corrosion rates for various loadings shown in Table IV illustrates that for  $18 \mu A/cm^2$  the  $I_{corr}$  is approximately 5-12  $\mu A/cm^2$  while at a loading of  $13 \mu A/cm^2$  is on the average 3  $\mu A/cm^2$ . When a sample of solid aluminum was loaded to  $25 \mu A/cm^2$  and then the load removed the  $I_{corr}$  after a number of weeks approached its no load value. *In vivo* data on the magnesium alloy under load conditions was unstable, although these results indicate that under load conditions the corrosion rate is of the same order as under no load conditions.

The following paragraphs discuss the polarization curves used to obtain the data of Tables I-IV.

The intersection of the Tafel line of Fig. 3 with the  $E_{corr}$  line, which in this case is 1V gave the  $I_{corr}$  recorded in Table I.

Figure 4 illustrates the effects of the oxide coating on aluminum with the curve at low current densities being characteristic of the corrosion rate with a substantial oxide coating. The surface appears to be considerably different under loaded current densities of  $25 \mu A/cm^2$ .

Curve 2 of Fig. 4 and 5 demonstrate the upward shift in  $I_{corr}$  with time. The break in the curves of Fig. 4 appears at about 0.5V which checks with the findings of Zahavi *et al.* Figure 4 representing typical curves for a loaded electrode for 4 days and 36 days illustrates that for a given current density the polarization decreased with increasing corrosion rates of electrodes.

A tangent or "Tafel" line was drawn for the curve in the operating range. The  $I_{corr}$  determined from the intersection of the tangent lines with the horizontal  $E_{corr}$  line for the anodic and cathodic galvanostatic curves checks closely.

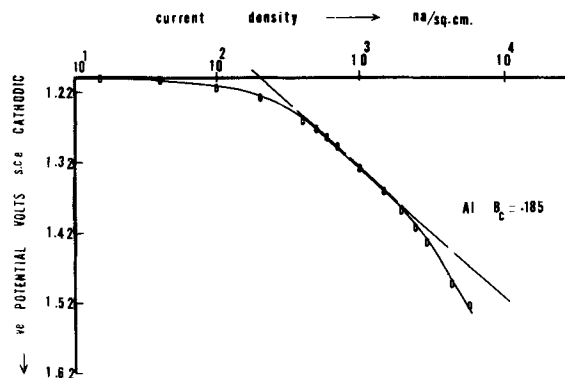


Fig. 3. *In vitro* galvanostatic cathodic polarization curve for solid aluminum in 0.9% aqueous NaCl at 37°C open to atmosphere under no load conditions.

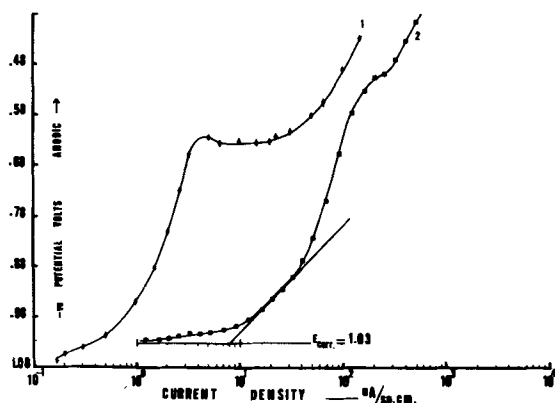


Fig. 4. *In vivo* galvanostatic anodic polarization curves for solid aluminum electrodes implanted in a dog under an approximate loading of  $25 \mu\text{A}/\text{cm}^2$ . The potentials are referenced to a Ag/AgCl skin electrode. Curve 1 was loaded for approximately 4 days and curve 2 for 36 days before measuring the anodic polarization.

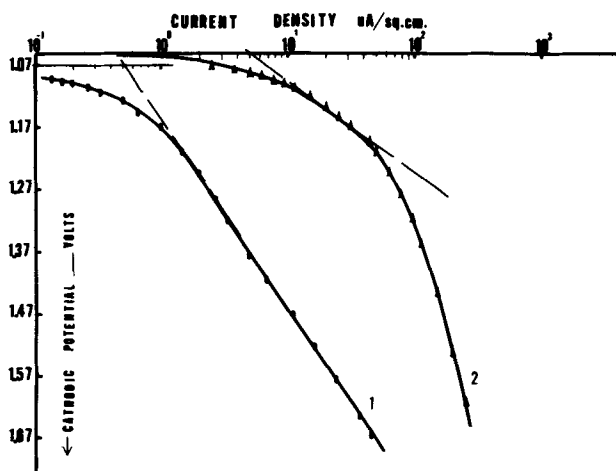


Fig. 5. *In vivo* galvanostatic cathodic polarization curves for solid aluminum electrodes implanted in a dog under an approximate loading of  $25 \mu\text{A}/\text{cm}^2$ . The potentials are referenced to a Ag/AgCl skin electrode. Curve 1 was loaded for approximately 4 days, and curve 2 for 100 days before measuring the cathodic polarization.

Figure 6 is an illustration of linear polarization data under loaded *in vivo* conditions. Although the slopes of the curves vary on a dog, from measurement to measurement and from dog to dog the data points line up well for a given measurement.

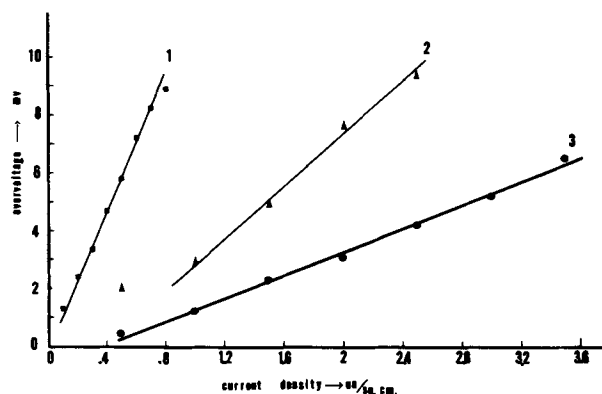


Fig. 6. *In vivo* anodic linear polarization curves of aluminum for determining  $R_{\text{pol}}$  in kilo ohms per square centimeter for electrodes implanted in dogs with a load of approximately  $25 \mu\text{A}/\text{cm}^2$ . The potentials are referenced to a Ag/AgCl skin electrode. Curve 1 represents data taken after 7 days of loading,  $R_{\text{pol}} = 12 \text{ kohms}$ ; curve 2 is from data after 22 days of loading,  $R_{\text{pol}} = 4.26 \text{ kohms}$ ; curve 3 is from data after 67 days of loading,  $R_{\text{pol}} = 2 \text{ kohms}$ .

The present pacemaker system we are using requires  $610 \mu\text{A}$  continuously when operating from a cell voltage of 0.5V. Over a ten year period the faradaic weight loss in an anode of trivalent Al needed to supply the above current is 17.6g. The weight loss based on  $I_{\text{corr}}$  measurements under the above load is 7.4g or about 29% of the faradaic loss. Divalent Zn on the other hand because of a 300 mV higher voltage would need a current of about  $400 \mu\text{A}$  or a faradaic weight loss of 40g over a ten year period. The weight loss based on  $I_{\text{corr}}$  for Zn of an equivalent geometrical area is 11.4-14.7g. Thus for Zn approximately 52g is needed to supply energy over a ten year period, 40g being consumed as useful energy and 12g being lost by way of corrosion, and not converted into usable energy. The efficiency has therefore been defined as the ratio of the faradaic weight loss to the faradaic weight loss plus the weight loss due to corrosion which gives for Zn efficiencies of 73-78% (23). Roy *et al.* (22), in their *in vivo* studies of zinc under various load conditions defined the efficiency as the ratio of the actual life to expected life. They obtained for zinc efficiencies ranging from 73-86%.

Divalent Mg with its 600 mV higher voltage requires a current of approximately  $270 \mu\text{A}$  or a faradaic weight loss of 10.7g. The weight loss based on  $I_{\text{corr}}$  for Mg of an equivalent geometrical area under no load is 8g or 75% of the faradaic weight loss. The corrosion rate under load, although difficult to measure, is estimated to be the order of 1 g/yr which checks with a reported value of 1.2 g/yr (24). After operating *in vivo* under load the Mg galvanostatic and potentiostatic curves were too unstable for corrosion data.

Histopathological examinations of tissue surrounding the aluminum, zinc, and magnesium implants are discussed in the following paragraphs with the help of microscopic photographs.

It is seen in Fig. 7 that a dense capsule composed of fibrous connective tissue has formed around magnesium implanted for 6 months. It is further noted that at the tissue-metal interface, a moderately heavy inflammatory cell reaction is present consisting of granulation tissue with an infiltrate of neutrophils, lymphocytes, and plasma cells.

Figure 8 shows a fibrous connective tissue capsule with a moderately heavy inflammatory cell infiltrate at the tissue-zinc interface after 6 months of implantation. This reaction is characterized by dilated capillaries, infiltrate of neutrophils, lymphocytes, and plasma cells. The adverse tissue response is contrary to the findings of other investigators (4, 28). Further implantations of zinc will be undertaken by us to gain a greater insight into zinc biocompatibility.

Figure 9 shows that under no load conditions histologic examination revealed a well-formed, relatively thick ( $550 \mu$ ) mature fibrous connective tissue capsule which shows only mild aggregates of lymphocytes. No particular matter was observed in the capsule. Under

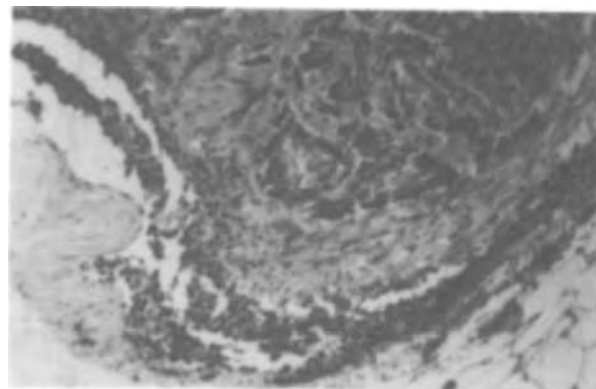


Fig. 7. Tissue surrounding magnesium alloy electrode implanted for 6 months unloaded. Magnification  $100\times$ . E and H stain used.



Fig. 8. Tissue surrounding zinc electrode implanted for 6 months unloaded. Magnification 100 $\times$ . E and H stain used.



Fig. 9. Tissue surrounding aluminum electrode implanted for 6 months unloaded. Magnification 100 $\times$ . E and H stain used.

load conditions removal of aluminum implants after 147 days revealed that they all were encapsulated with a thick wall formed mature fibrous connective tissue capsule. Cells loaded in the range of 18  $\mu\text{A}/\text{cm}^2$  showed little inflammatory reaction. Loads greater than 70  $\mu\text{A}/\text{cm}^2$  produced an open pus drain above the implant. Cells loaded in the 13  $\mu\text{A}/\text{cm}^2$  range were macroscopically free from inflammation.

Magnesium has been reported by Sawyer and Srinivasan (25) as being not only highly corrosive but markedly toxic, destructive of blood cells, and forming magnesium proteinate. On the other hand aluminum was found by them to be nontoxic on tissue surrounding wounds and to have a minimal destruction on red and white blood cells. Determination of aluminum concentrations in blood samples and surrounding tissue of implants by atomic absorption spectrophotometry (26) illustrated that the aluminum concentrations are within the range of values of aluminum of 0.21-0.94 parts per million reported for man (27).

It was further observed by us, that none of the Pd-black cathodes which were coupled and loaded at the same rate as the anodes, showed any visible signs of tissue reaction.

### Conclusions

1. The corrosion rate of aluminum anodes is approximately proportional to the load current density reaching an average steady-state value in 20-30 days after loading.

2. A load current density of 13  $\mu\text{A}/\text{cm}^2$  or less is desirable for lowering of the tissue reaction and corrosion rate.

3. Histopathological data indicate that aluminum is a more biocompatible anode material than magnesium, magnesium alloy AZ31B, or zinc. Further *in vivo* measurements are being conducted on aluminum and zinc implants in order to more completely characterize the biocompatibility of these anode materials.

4. Magnesium and magnesium alloy AZ31B appear to be unacceptable as an anode material due to their high corrosive rates and poor biocompatibility.

### Acknowledgments

This study was made possible by the support of the Biomaterials Program of N.S.F. Grant No. GH33748. The authors acknowledge the contributions of R. Koerner in materials fabrication.

Manuscript submitted March 8, 1974; revised manuscript received May 6, 1974. This will be Paper 76 to be presented at the New York, New York, Meeting of the Society, Oct. 13-17, 1974.

Any discussion of this paper will appear in a Discussion Section to be published in the June 1975 JOURNAL. All discussions for the June 1975 Discussion Section should be submitted by Feb. 1, 1975.

The publication costs of this article have been assisted by Drexel University.

### REFERENCES

1. M. Var, *Schaldach, Wiederbelebung und Organersatz*, 5, 75 (1968).
2. S. Dack and E. Donaso, *Ann. N. Y. Acad. Sci.*, 167, 519 (1969).
3. P. Racine, M.S. Thesis, Drexel University (1966).
4. O. Z. Roy, *Bio-Med. Eng.*, 6, 250 (1971).
5. A. C. C. Tseung, W. J. King, and X. C. Wan, *Med. Biol. Eng.*, 9, 175 (1971).
6. J. F. DeRosa, R. B. Beard, and A. W. Hahn, *IEEE Trans. Bio-Med. Eng.*, BME-17, 324 (1970).
7. R. B. Beard, J. F. DeRosa, R. M. Koerner, S. E. Dubin, and K. J. Lee, *ibid.*, BME-19, 233 (1972).
8. J. H. Payer and R. W. Staehle, in "Corrosion Fatigue," O. E. Devereux, A. J. McEvily, and R. W. Staehle, Editors, p. 211, Nat. Assoc. of Corrosion Eng. (1972).
9. V. J. Colangelo, N. D. Greene, D. B. Kettlekamp, H. Alexander, and C. J. Campbell, *J. Bio-Med. Mater. Res.*, 1, 405 (1967).
10. N. D. Greene and D. A. Jones, *J. Mater.*, 1, 345 (1966).
11. M. Stern and E. D. Weisert, *Proc. Am. Soc. Test Mat.*, 59, 1280 (1959).
12. M. Stern and A. L. Geary, *This Journal*, 104, 56 (1957).
13. M. Stern, *Corrosion*, 14, 60 (1968).
14. N. D. Greene, "Experimental Electrode Kinetics," Rensselaer Polytechnic Institute Publications, Troy, New York (1965).
15. A. W. Ham, "Histology," 5th ed., J. B. Lippincott Co., Philadelphia, Pa. (1965).
16. G. L. Humason, "Animal Tissue Techniques," W. J. Freeman Co., San Francisco, Calif. (1962).
17. R. C. Plumb, "The Aluminum Anode," Alco Research Laboratories, New Kensington, Pa., Report No. 8-58-4.
18. J. E. Lewis and R. C. Plumb, *This Journal*, 105, 496 (1958).
19. R. C. Plumb, *ibid.*, 105, 498 (1958).
20. P. Van Rysselberghe, *ibid.*, 106, 355 (1959).
21. J. Zahavi and M. Metzger, *ibid.*, 119, 1479 (1972).
22. O. Z. Roy, R. W. Wehnert, H. A. Heggveit, and W. G. Waddell, *Ann. N. Y. Acad. Sci.*, 167, 645 (1969).
23. J. F. DeRosa, R. B. Beard, H. M. Carim, and S. E. Dubin, *IEEE Trans. Bio-med. Eng.*, BME-20, 345 (1973).
24. J. Cassel, P. Satinsky, D. Eibling, R. Greenberg, and A. Salkind, *Med. Instr.*, 7, 330 (1973).
25. P. N. Sawyer and S. Srinivasan, "Medical Engineering," C. D. Ray, Editor, Section 1, Chap. 82, Year Book Medical Pub., Inc., Chicago (1974).
26. Sadtler Research Lab., Inc., Philadelphia, Pa., by Atomic Absorption Spectrophotometry outlined in *Analytical Chem.*, 44, 1469 (1972).
27. A. S. Radovsky, M.S. Thesis, Drexel University (1973).
28. J. B. Cooper and A. W. Hahn, *IEEE Trans. Bio-Med. Eng.*, BME-20, 336 (1973).
29. H. M. Carim, R. B. Beard, J. F. DeRosa, and S. E. Dubin, Paper presented at ACS Div. of Organic Coatings and Plastic Chem, Symposium on Biomed. Application of Polymers, Chicago, Aug. 26, 1973.



# High Power Facility for Testing Electrochemical Power Sources

E. J. Dowgiallo, Jr., J. B. O'Sullivan,\* I. R. Snellings, and R. B. Anderson

USAMERDC, Electrochemical Division, Electrotechnology Department, Fort Belvoir, Virginia 22060

## ABSTRACT

A 125 kW programmable power supply has been constructed for testing electrochemical propulsion systems and components. This facility has a number of features which are of value to others for use in broader applications. These features are: voltage programmable for both current and voltage levels, change from charge to discharge in a fraction of a second, fast response, low ripple content, and integral load dissipation. Typical applications are: direct control by field generated profiles, simulation of rapidly changing hybrid charge-discharge regimes, and control techniques such as constant power.

Evaluation and characterization of electrochemical propulsion systems and components for the U.S. Army had reached a stage that required a programmable electrical power system for reproduction, modification, and generation of full-scale test duty cycles. A 125 kW thyristor power system with features that satisfied immediate needs and control techniques that will allow for adaptation to a variety of future requirements is described herein.

The program at the U.S. Army Mobility Equipment Research and Development Center, Fort Belvoir, Virginia, requires evaluation of candidate batteries and fuel cells for propulsion and stationary power applications. Propulsion applications involve construction and materials handling equipment. Evaluation and selection of the most applicable battery for a system requires extensive and realistic testing to particular military regimes.

The thyristor power system described here is the third of four test stations designed to meet these needs. To gain a perspective of its purpose relative to the other stations, all their main functions are briefly presented in the order of progression of a candidate electrochemical power source through them. Station (i), preliminary check of manufacturer's specifications, acceptance tests, and life cycle tests primarily for single cells. Charges and discharges can be controlled to 10V and 3 kW. Station (ii), characterization of systems, load profile tests (25 different preset levels), trial of new test procedures, variable charge/discharge methods, and computer control. Three configurations are available producing maximums of either 8, 16, or 52V, and 14 kW (1). Station (iii), the subject of this paper, has the highest power rating of any of the stations and is more oriented toward full scale or prototype testing. It is programmable by actual averaged wave forms obtained from field testing, or by analog voltages from conventional instrumentation. Station (iv) (now under development), will have a minimum response time of 20  $\mu$ sec enabling further examination of fast pulse charging and more detailed load profile simulations. It is also scheduled to be used for special battery studies of dynamic impedance from very low frequencies to about 50 kHz. This station will have a maximum capability of 50V and 6000W.

## System Description

The thyristor power system of station (iii) was built under contract by Westinghouse Electric Corporation (2). A system was specified that could duplicate the characteristics of conventional chargers and be changed rapidly to extended discharges with an integral dissipation capability. This is, to our knowledge, the first time such a system has been used in this manner. A simplified diagram of the system is shown in Fig. 1. The system may be divided into two main

parts: one is a variable regulator, consisting of operational amplifiers, function modules, and referencing and director logic elements; the other is a thyristor power converter, consisting essentially of a thyristor power modulator, a thyristor power transformer, a basic regulator, and converter sequencing and protective elements. The outer controllers, shown in Fig. 1, are initial input shaping networks; while the inner control loop compensates for basic nonlinearities and time delays.

The variable regulator consists of the outer voltage and current limit controllers. They are driven with two programming input voltages:  $v$  for bus voltage and  $I$  for output current. These controllers are in parallel and the outputs are connected through a diode switching circuit to a common output terminal. Only one controller is in operation at any one time. The outer voltage controller is in operation as long as the programmed current limit is not reached. The current controller is switched off during this time. When the current limit is reached the current controller takes over and the voltage controller is switched off. Switching in and out of the controllers is accomplished smoothly and quickly due to the characteristics of the operational amplifiers used. A current limit controller is used for each polarity of sensed output current. The maximum current in either direction is limited to 1500A. The gate pulse generator output will be suppressed at 1600A.

The basic regulator includes all the components required to close the inner voltage control loop, to sense bus voltage and current, to sense the demand for and execution of current reversals, and to provide gate pulses to the thyristor power modulator. This regulating loop is used to develop the proper signals for current reversals and it helps to overcome the nonlinearities of the power converter when going through a current reversal. This loop makes it possible to consider the converter system for the outer (variable)

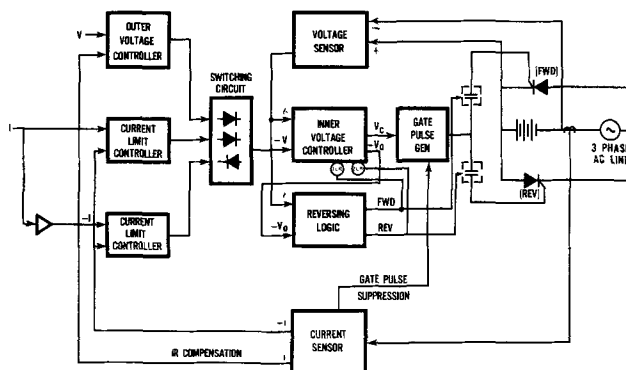


Fig. 1. Regulator system diagram with parallel voltage and current controllers.

\* Electrochemical Society Active Member.  
Key words: controller, simulator, charger.

regulator loops as a "black box" amplifier with nearly ideal characteristics (3). A brief description of the operation of this inner loop follows. The bus voltage,  $v$ , is picked up by the voltage sensor and brought to one input of the inner voltage controller. There it is compared with the reference voltage  $-V$  applied at a second input. Depending on the polarity of the difference of the two voltages, the output voltage  $-V_o$  will swing negative or positive. By comparing this output voltage  $-V_o$  with the bus voltage  $v$ , the polarity of converter conduction can be determined. For example, if the bus voltage  $v$  is smaller than the reference signal  $V$ , forward load current conduction is indicated, and therefore the forward channel of the dual converter should be pulsed. Under this condition,  $-V_o$  is negative, and when compared with  $v$  at the input of the reversing logic module will result in its output picking up relay 1CR and closing the gate pulse distribution switch to the forward converter. If now the reference  $V$  is suddenly reduced to demand reverse current, the opposite sequence of events will take place.

The main power stage, on the right hand of Fig. 1, is a dual type converter which can provide output current in either direction. This consists of an autotransformer in a wye-delta connection, as shown in Fig. 2. The delta transformer drives a thyristor power modulator which converts three-phase, a-c power into voltage adjustable d-c power. The modulator assembly contains 24 thyristors; half for forward (charge) and half for reverse (discharge) operation. The thyristors are connected in a six-phase, double-way circuit. The assembly also has all the necessary voltage protecting networks, current limiting fuses, pulse distribution panel and pulse transformers, and current sensing transformers. The six-phase, double-way converter circuit requires that two legs are conducting simultaneously to complete a current path through the battery. Gating pulses, from the gate pulse generator, occur every  $60^\circ$  and are channeled sequentially to each of the six legs of the converter circuit. This produces six peaks per a-c line cycle for reduced direct voltage ripple and distortion of the alternating current. Figure 2 shows an abbreviated dual converter, antiparallel circuit showing one of the four thyristors in each leg.

The forward (charge) thyristors are labeled with an F and the reverse (discharge) thyristors with an R. Consider the moment when the voltage of  $V-U$  is zero and the voltages of  $U-W$  and  $V-W$  are, respectively,  $\sqrt{3}/2$  and  $-\sqrt{3}/2$  of their maximum values. At this time 1F and 6F are conducting (rectifying) in the

forward direction thereby charging the battery with a voltage determined by the programming reference voltage. In the discharge mode, the forward (F) thyristors are off, and for the same condition as above but with reverse polarities, 1R and 6R would be gated on. This would effectively reverse the battery current. The system now operates in the inverter mode. It is, in effect, a line controlled inverter with the line and system absorbing the battery current. The gate pulse generator gating angle change, determined by the programmed current demand, causes the average output voltage to be enough below the battery voltage to produce the desired current. The difference is determined by the loop drop. This inverter feature eliminates the need for large banks of load dissipation resistors. The system can be operated continuously up to 125V at 1000A d.c., and, in overload to 1500A for a duration of 30 sec.

### System Characteristics

The fluctuation of the d-c voltage about the average value was measured in terms of the root-mean-square (RMS) value. The effect of different autotransformer connections on the ripple was of interest. The results are shown in Table I. The connections were made for 125V d.c. (208V a.c.) and 50V d.c. (83.2V a.c.). A fork lift truck battery was connected at the output and run in the charge mode for the ripple measurements. The per cent change of ripple voltage to the output d-c voltage was improved for the 50V connection to one-tenth of that at the 125V connection. The current ripple was approximately 2A for the 50V connections and 6A for the 125V connections. The inherent ripple in a three-phase, full wave bridge is 4.5% RMS. The system uses an inductive input "L" filter before the output terminals to reduce the ripple. Its unipolar electrolytic capacitors have protective diodes to prevent voltage reversals. A typical battery may have capacitance values in farads at 360 Hz which also reduces the ripple (4).

The output circuit is transformer isolated from the input; either a positive or negative d-c bus can be grounded. Other similar units can be connected in series to 600V. The autotransformer can be wired for 228V a.c., thereby raising the output voltage in the present system to 137V. The system has many protection features. The major ones are a d-c circuit breaker with combined instantaneous magnetic trip and current limiting protection, an overload heater trip, surge suppressors for overvoltage and  $dV/dt$  protection, thyristor fuses, and a protection switch for thyristor over temperature; and finally in case of an a-c power failure, the system will draw less than 50 mA from a 36V fork lift battery.

Total drift in output over an 8 hr interval under constant line, load, and ambient temperature following 30 min warm up was 0.03% for a constant voltage of 40V and 0.03% for a constant current of 500A.

The system has an automatic crossover characteristic that changes the method of regulation from constant voltage to constant current (or vice versa) as dictated by varying load conditions. This is often used in charging batteries where a maximum initial current level is held until battery voltage reaches a preset upper limit after which current drops to a leakage level. To evaluate this capability, system current was set for a maximum of 90A. A load was varied from zero current to short circuit. The difference between an initial falloff of current and the short circuit current expressed as a percentage of the maximum set

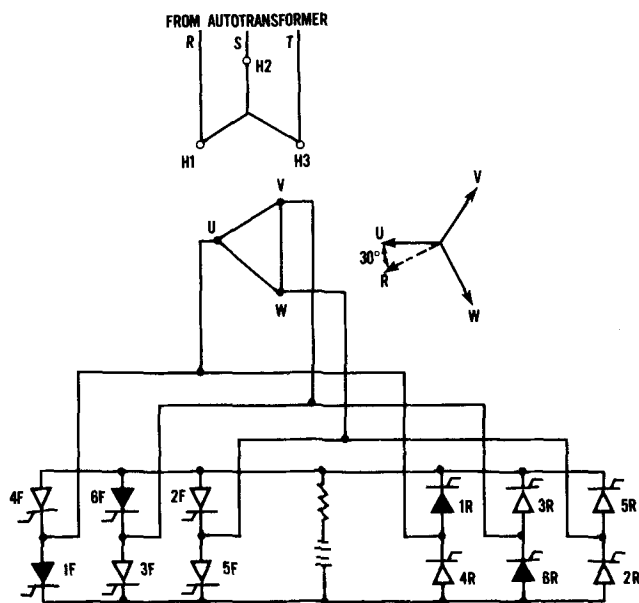


Fig. 2. Dual converter, antiparallel circuit

Table I. Voltage ripple measurements

Maximum voltage connection (V)	Output voltage (V)	Output current (A)	Ripple voltage (True RMS V)	Per cent ripple (%)
125	41.3	291.0	0.418	1.0
50	41.3	291.0	0.045	0.1

Table II. System efficiency

Input a.c. power (kW)	Output d.c.		Efficiency (%)	Dissipated power (kW)
	Voltage (V)	Current (A)		
120.800	118.5	960	94	6.840

current was measured at less than 1% for 30V and 90A.

The efficiency of this system is much higher than any other means of conversion, approaching 93% at rated load and rated volts. Efficiency was calculated based on measurements made with a two-element, polyphase wattmeter with two current transformers on the three-phase a-c input and d-c output power based on the product of measured volts and amperes (5). The system input autotransformer taps were connected for 125V d.c. The a-c meter indicates the average impulse (integral of power over a cycle) and corresponds to the true average power, regardless of the power factor, and is true for nonsinusoidal currents and voltages of any wave form (6). The measurements were made using a load bank. The results are given in Table II.

Input-output correspondence was within 1% for any incremental current programming voltage change from 50 to 1500A and for any incremental voltage programming voltage change from 6 to 50V for the 0-50V range.

Remote programming response is shown in Fig. 3. The upper wave form was applied to the programming voltage input. The two levels of -0.4 and -4V correspond to output voltages of +5 and +50V, respectively. The current programming voltage was fixed at -6.67V producing 1000A output. A fork lift battery was connected at the output, the current level changed from +1000 to -1000A depending on whether the programmed voltage was above or below the battery voltage. The time to change the full current range was about 0.2 sec.

### Applications

To summarize, the system can be viewed as a low frequency, d-c amplifier that can be driven by two 0 to -10V inputs, one for a range of  $\pm 1500$ A and the other to +125V with a response time of less than about 0.1 sec to 1000A. These features can be utilized for simulation of field recorded duty cycles for tests of prototype batteries. Such tests as life cycle and battery system comparisons could be performed at fractions of the field test costs without further costly battery development. An example of the system ability to simulate a field load profile is shown in Fig. 4. The input profile is from a magnetic tape recording of a 4000 lb fork lift truck on a standard military test (7). The current wave form was averaged by a filter prior to recording since the truck current is frequency modulated from about 30 to 150 Hz. The load profile is reproduced with some attenuation of fast spikes due to the previously described response characteristics. In preliminary tests of 6 hr profiles the battery discharged in about the same time as in the field runs. This demonstrated, in a limited way, that smoothing the wave

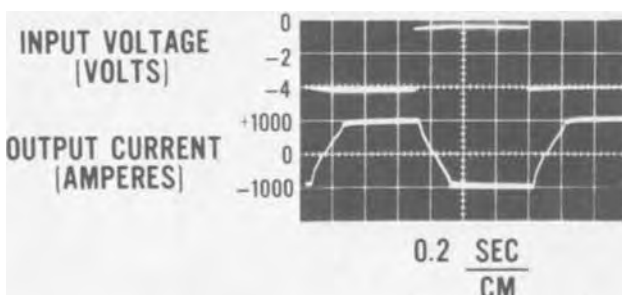


Fig. 3. Remote programming response

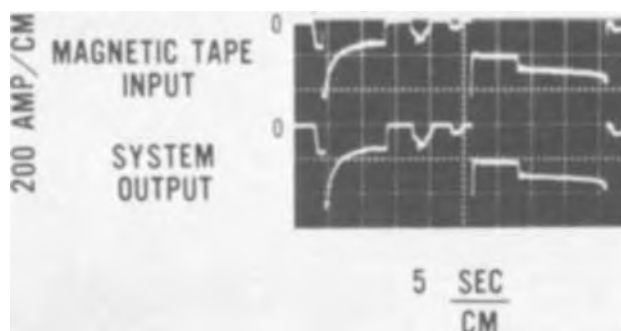


Fig. 4. Fork lift vehicle load profile simulation

form does not significantly effect the simulation of field discharges.

A computer driven digital to analog output channel was also used to produce several precalculated fork lift load profiles which consisted of various voltage levels for durations based on fork lift operations. The profiles were used in both constant current and constant power discharges by driving the system with recordings of the analog outputs. The system can be directly driven by a computer for any desired load profile. An automated control scheme with erasable programmable read only memory chips for making test changes is under development (8).

Testing batteries under constant power discharge conditions is desirable. The energy a battery can produce at constant power accelerations and the number of fixed duration accelerations are conveniently revealed. Horsepower profiles can be easily simulated as input power levels. An external power control circuit that is a modification of one based on voltage-current multiplication incorporated into station (ii) is used to control the thyristor power system (9). In this control scheme an analog division circuit is used. The battery voltage is one input and an analog voltage representing power is the other input. The battery voltage is divided into the reference power level ( $P$ ), and the output voltages ( $v$ ) is fed to the current programming input ( $I$ ) of the thyristor power system with its output connected across the battery. The formula  $I = P/V$  is thereby implemented. Constant power discharges or charges can be performed to 187.5 kW for 30 sec or continuously at any level below 125 kW. The results of a constant power discharge on a fork lift battery are shown in Table III. The voltage decreased 43% and the current increased 56% while power was held to less than a 3% decrease.

### Future Applications

Simulation and other tests requiring rapidly changing wave forms will be performed with four programmable transistorized load banks. The combined dissipation to 50V is 6 kW (10, 11). The step response time is 20  $\mu$ sec for 0-30A and 1.2  $\mu$ sec/A above 30A. This will permit simulation of actual wave forms for battery system comparison tests and depolarization pulses for fast charge studies and for hybrid development where the power battery may only be drained on rapidly changing peaks.

A hybrid fuel cell-battery system development is being planned. The fuel cell energy source will be sized for the average power while the battery power source will be sized to provide short duration power when the load is above the average and to accept

Table III. Constant power discharge variation

Elapsed time (hr)	Voltage (V)	Current (A)	Power (W)
0	36.71	175.2	6432
1	34.78	184.6	6420
2	33.15	192.6	6385
2.77	22.18	281.6	6246
Per cent change based on avg. of 415 readings	-43%	+56%	-3%

power when the load is below average. This requires a test that will effectively reproduce field recorded wave forms. An investigation is planned to determine if the net difference between a smoothed current and its corresponding actual wave form is significant for fork truck discharges. These tests will be performed on scaled-down fork truck batteries that have power ratings compatible with the transistorized load banks. If significant errors are found, a means of modifying the smoothed programming current for correction will be studied. Preliminary field data indicate that less than 30% of the discharge time is spent under solid-state control during which the current is pulsing. The resistive losses resulting from use of an averaged wave form are in appreciable error only during periods in which the "on time" is a small per cent of the total. Since this occurs only at low average power levels during which the over-all losses are low it is felt that a large percentage error during a time of small loss will not significantly effect the cumulative losses.

### Conclusion

The thyristor power system eliminated both the need for switching a contactor to reverse current flow and the large dissipating resistors required for battery discharge with conventional power supplies. The contactors life would be extremely short under fast multiple charge-discharge regimes characteristic of hybrid power sources where current may change direction several times in 1 min. High current and low maintenance requirements exceeded motor generator capabilities. The system has a demonstrated efficiency that is much higher than any other means of conversion. This system makes possible the testing of full size electrical power sources with maximum monitor, accurate control, and fast test change without the necessity for expensive field operation.

The capabilities and applications described here, will, it is hoped, demonstrate what is possible today and serve as a stimulus for the development of new uses by those involved in other areas of electrical power source development.

### Acknowledgment

The authors wish to express their thanks to Gordon Hagensick of Westinghouse Electric Corporation for

his helpful discussions and contributions based on his extensive experience with these systems.

Manuscript submitted Jan. 22, 1974; revised manuscript received May 10, 1974. This was Paper 19 presented at the Boston, Massachusetts, Meeting of the Society, Oct. 7-11, 1973.

Any discussion of this paper will appear in a Discussion Section to be published in the June 1975 JOURNAL. All discussions for the June 1975 Discussion Section should be submitted by Feb. 1, 1975.

The publication costs of this article have been assisted by the Department of the Army.

### REFERENCES

1. E. J. Dowgiallo, U. S. Army Engineering Research and Development Laboratory, Report AD660336, Fort Belvoir, Virginia (1967).
2. Westinghouse Electric Corp., Contract Number DAAK02-71-C-0462, U.S. Army Mobility Equipment Research and Development Center, Fort Belvoir, Virginia.
3. Instruction Leaflet 16-800-126, Westinghouse Electric Corp., Buffalo, N.Y. (1971).
4. E. J. Dowgiallo and R. M. McKechnie, in 23rd Annual Proceedings Power Sources Conference (1969).
5. Department of Defense, U.S.A., "Military Standardization Handbook Generator Sets, Electrical, Measurements and Instrumentations," MIL-HDBK-705A (1961).
6. V. Karapetoff, "Experimental Electrical Engineering," Vol. 1, p. 130, John Wiley and Sons, Inc., New York (1953).
7. Department of Defense, U.S.A., "Military Standard Test and Inspection of Trucks, Lift, Fork," MIL-STD-268C (1963).
8. Reliance Electric Co., Reliance, Automate 32 Users Manual, Cleveland, Ohio (1972).
9. E. J. Dowgiallo, U.S. Pat. 3,487,291 (1969).
10. Acme Electric Corporation, Model PS<sup>2</sup>L-1000 Programmable Solid State Loading Operating Instructions, Cuba, N. Y. (1973).
11. Transistor Devices Inc., Model DLR50-150-3000 Solid State Electrical Loading Operating Instructions, Cedar Knolls, N. J. (1973).

## Passivity and Pitting of Ni-Cu Alloys in NaCl Solutions

T. Koizumi<sup>1</sup> and H. H. Uhlig\*

Department of Metallurgy and Materials Science,  
Massachusetts Institute of Technology, Cambridge, Massachusetts 02139

### ABSTRACT

Passivity of the Ni-Cu alloy series in NaCl solutions is evaluated by means of potentiostatic polarization curves and by measurements of critical pitting potential. Passivity is observed only in alloys of >40% Ni, the actual critical Ni content depending on Cl<sup>-</sup> concentration, sulfate concentration, and pH. Pitting of Ni-Cu alloys is expected and corresponding critical pitting potentials are found only in environments favoring stable passivity.

The passive properties of Ni-Cu alloys in 1N H<sub>2</sub>SO<sub>4</sub> have previously been studied in detail employing potentiostatic anodic polarization curves (1, 2). According to these studies, passivity is clearly a property of Ni and of the high Ni alloys, but not of Cu or low Ni alloys. The critical Ni composition below which a

passive-active transition is no longer observed comes at 30-40% Ni. This critical composition has been related to the approximate filling of the vacant d-band of energy levels in Ni (0.6 vacancy per atom) by electrons supplied by alloyed Cu (1 electron per atom). On this basis, only alloys containing unfilled d-band energy levels have passive properties. In this respect, added solid solution elements contributing more than one electron per atom, e.g., Al, Zn, Ga, shift the critical composition of Ni-Cu alloys to higher Ni values. On

\* Electrochemical Society Active Member.

<sup>1</sup> Present address: The Furukawa Electric Company, Limited, Tokyo, Japan.

Key words: critical pitting potential, electron configuration theory of passivity, potentiostatic polarization curves.

the other hand, those elements adding electron vacancies, e.g., alloyed Fe, Co, Mn, shift the critical Ni composition to lower values (3-7).

But passive properties are not only a function of alloy composition; the environment also plays a role. Pure Ni, for example, loses its passivity in dilute HCl solutions. Also an increasing neutral NaCl concentration tends to break down passivity of otherwise passive Ni-Cu compositions. The question is: How does the factor of electron configuration applying to the passive properties of Cu-Ni alloys in 1N H<sub>2</sub>SO<sub>4</sub> explain the behavior of such alloys in NaCl solutions varying both in concentration and pH?

North and Pryor (8) studied the behavior in NaCl solutions of Cu-Ni alloys containing up to 40% Ni. Here, as their polarization measurements confirmed, the alloys are not passive; that is a passive current density is not a characteristic of their potentiostatic polarization curves. The small deviations in current density which they observed in the Flade potential region at relatively high sweep rates were probably caused by temporary films of soluble or porous corrosion products accumulating on the alloy surface. With slower sweep rates, such discontinuities disappeared and hence the responsible films were not the same as the passive films which typically persist at low sweep rates. Their studies focused mainly on the nature of thick oxide films, protective in some degree as diffusion barriers on Cu and on the low Ni-Cu alloys, but with only limited influence on anodic polarization characteristics typical of truly passive films as discussed above.

Leckie (9) found that protective films are also formed on pure Cu, e.g., in 1M H<sub>2</sub>SO<sub>4</sub> at 0°C or in 10M H<sub>2</sub>SO<sub>4</sub> at 25°C, or in 0.01-1.0M NaOH at 25°C which affect anodic polarization characteristics in potentiodynamic measurements. But these environmental conditions favored insoluble surface reaction products, which combined with characteristics of the reported potential decay characteristics, suggest that relatively thick diffusion barrier films were responsible, rather than the much thinner passive films typical of Ni. The diffusion barrier films have passive properties in accord with definition 2 of the Corrosion Handbook (10) (low reaction rates of metals having a pronounced thermodynamic tendency to react) whereas the thin passive films imparting marked anodic polarization characteristics follow definition 1 and its supplement proposed by Wagner (11). Only the latter type films can give rise to passive-active cells of appreciable potential difference responsible for rapid localized corrosion (pitting).

Since deep pitting corrosion is typical of the higher Ni alloys it is of interest to know how the critical pitting potential varies with Cl<sup>-</sup> concentration and with temperature. Data of this kind are presently reported. They are useful in applying Ni-Cu alloys to sea water environments, desalination equipment and for condenser tube applications in general, where pitting corrosion can be especially damaging.

### Experimental

Alloys were prepared by induction melting in vacuum employing dense pure alumina crucibles. After melting was completed, the furnace was filled with purified argon; ingots were cast by drawing the melt into 7 mm diam Vycor tubes and were water quenched. The ingots were then homogenized in pure argon at 950°C for 20 hr, swaged to 0.42 cm diam, annealed at 750°C for 1 hr, and water quenched. Nickel was carbonyl grade (courtesy of International Nickel Company) and the copper was 99.999% pure. Chemical analyses of the various alloys are given in Table I.

Electrodes were machined to cylinders of about 0.40 cm diam, 1 cm long, then drilled and tapped at one end allowing attachment of a threaded small diameter nickel wire. The nickel wire was enclosed within a glass tube; a water-tight seal was maintained by means

Table I. Composition of Ni-Cu alloys (weight per cent)

Cu	Ni
—	100
4.08	96.0
9.53	90.7
15.4	84.9
17.5	82.6
23.4	76.6
29.0	71.0
34.3	65.8
41.2	58.8
47.2	52.8
50.3	49.7
56.2	43.8
62.0	38.0
64.7	35.3

of a Teflon gasket between electrode and glass tube held firmly in place by a rubber grommet, washer and nut attached to the nickel wire at the other end. Specimens were polished with emery paper and then pickled in dilute nitric acid to remove any cold-worked surface.

The electrolyte for most experiments consisted of various concentrations of NaCl deaerated with purified nitrogen for several hours. Temperature of the air thermostat in which measurements were conducted was 25° ± 0.2°C.

For measuring the critical pitting potential, the procedure was to first polarize the electrodes continuously within the least noble passive region for 30 min in order to achieve steady-state passivity. The potential was then advanced in 40 mV steps, recording the corresponding current after a 5 min wait at each potential. The provisional critical potential was the least noble value at which the current decreased or remained constant in time, whereas just above such a potential the current increased attended by pitting. Additional points were separated at smaller potential intervals in the region of the critical potential. The final value was obtained by polarizing the electrode at a potential just at or below the approximate critical value for a period of several hours and observing the absence of pits employing a low power microscope. No crevice corrosion normally occurred at the Teflon gasket interface; if it occurred, the measurement was repeated.

The critical alloy compositions dividing passive from nonpassive compositions were determined by measuring anodic polarization curves stepwise in deaerated NaCl solutions. The existence of a passive current density smaller in some degree than the critical current density for passivity, and persisting regardless of the time spent at a given potential, defined a passive composition in accord with the definition of passivity proposed by Wagner (11).

### Results

The effect of alloy composition on passivity in neutral 0.5N NaCl is shown by typical potentiostatic anodic polarization curves in Fig. 1. It is obvious that the 65.8% Ni-Cu alloy is not passive in this solution, whereas all the higher Ni composition alloys exhibit a

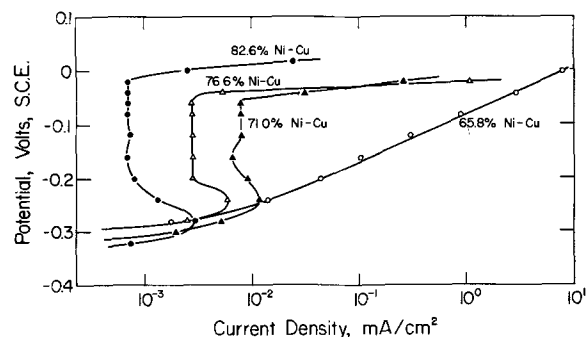


Fig. 1. Potentiostatic anodic polarization curves of Ni-Cu alloys in deaerated 0.5N NaCl, 25°C. Stepwise change of potential.

passive region. The sudden upturn of current at specific potentials for the passive compositions corresponds to the onset of pitting corrosion. Pitting initiates at any potential noble to such critical values, but not below.

Figure 2 shows similar typical anodic polarization data for the 82.6% Ni-Cu alloy in various concentrations of NaCl, other than 0.5N NaCl shown in Fig. 1. The alloy is passive in 1N NaCl and in more dilute solutions, but not in 2.5N or 5.0N NaCl. A summary of data dividing passive from active compositions as a function of nickel content in a variety of neutral NaCl solutions is shown in Fig. 3. These data plus analogous data obtained at pH 3 and 9 are collected in Fig. 4. At pH 3, even spectroscopically pure Ni loses passivity in 1.0N NaCl and above, whereas alloys containing less than about 68% Ni lose passivity at and above 0.01N NaCl. At pH 9, the latter composition alloy retains passivity in 5.0N NaCl, showing that pH as well as NaCl concentration is an important factor establishing conditions for passive behavior. Significantly, all alloys lose passivity regardless of pH or presence of Cl<sup>-</sup> ions below 40% Ni, in agreement with previous results reported by North and Pryor (8). This composition corresponds to the critical composition for passivity established by anodic polarization data in 1N H<sub>2</sub>SO<sub>4</sub> and which is explained by the electron configuration theory. In other words, chlorides can break down passivity of normally passive alloy compositions, but higher Cl<sup>-</sup> concentrations are required the higher the Ni content of the alloy, and less Cl<sup>-</sup> ion is required the lower the pH of the solution. Furthermore, since the minimum alloy composition for passivity at pH 9 re-

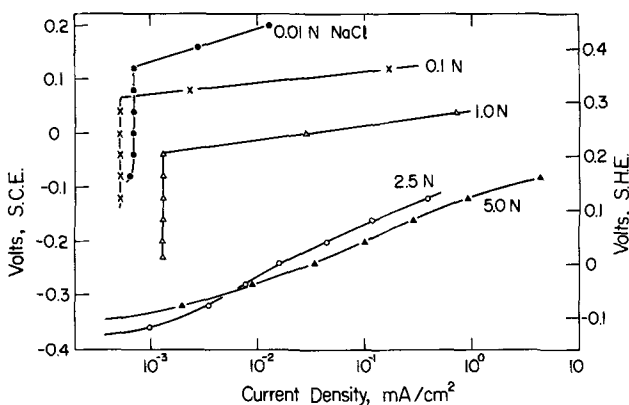


Fig. 2. Potentiostatic anodic polarization curves of 82.6% Ni-Cu alloy in NaCl solutions, 25°C. Stepwise change of potential.

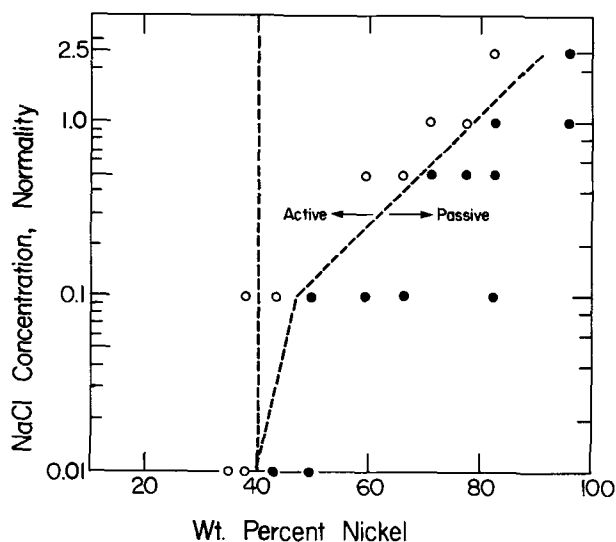


Fig. 3. Effect of NaCl concentration on loss of passivity in Ni-Cu alloys, 25°C.

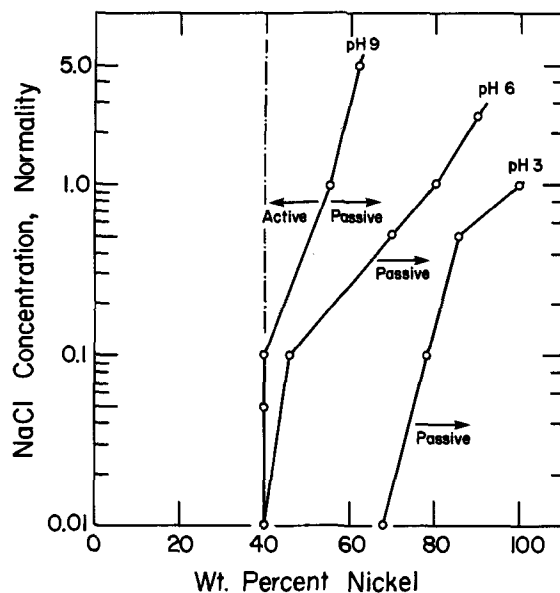


Fig. 4. Effect of NaCl concentration and pH on loss of passivity in Ni-Cu alloys, 25°C.

mains at 40% Ni, hydroxyl ions exert no special passivating effect on alloys containing less than 40% Ni.

Sulfate ions are not as effective as Cl<sup>-</sup> ions in breaking down passivity. If Na<sub>2</sub>SO<sub>4</sub> is added to neutral NaCl solutions, the higher the molal ratio of sulfate to chloride the more nearly does the critical alloy composition for passivity approach the minimum value of 40% Ni for all Cl<sup>-</sup> concentrations. The effect is appreciable for 1.0N NaCl as shown in Fig. 5, but it is small at 0.1N NaCl and it disappears entirely at 0.01N NaCl. At the latter dilute NaCl concentration, chloride ions alone or in presence of sulfates do not destroy passivity of any of the Ni-Cu alloys.

Zamin and Ives (12) showed from anodic polarization curves that Ni does not become passive at a molal ratio SO<sub>4</sub><sup>2-</sup>/Cl<sup>-</sup> = 0.5 in 0.5N H<sub>2</sub>SO<sub>4</sub> indicating, on comparing with data of Fig. 5, that in these solutions as in NaCl solutions (Fig. 4), breakdown of passivity occurs more readily in acid compared to neutral solutions. Similar data of Szklarska-Smialowska (13) also suggest that anodic passivation of Ni is disrupted at a lower concentration of Cl<sup>-</sup> in 0.1N H<sub>2</sub>SO<sub>4</sub> than at 0.1N Na<sub>2</sub>SO<sub>4</sub>.

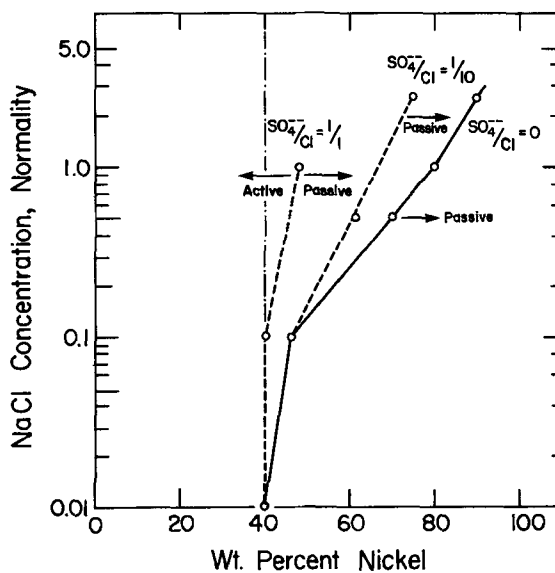


Fig. 5. Effect of sodium sulfate additions to sodium chloride solutions (molal ratios) on loss of passivity in Ni-Cu alloys, 25°C.

### Critical Potential for Pitting

Because pitting potentials refer to values at which the passive film is broken down locally by  $\text{Cl}^-$ , values can be measured only for passive alloy compositions, i.e.,  $> 40\%$  Ni in dilute NaCl solutions (0.01N) and  $> 45\%$  Ni in 0.1N NaCl. Steady-state values in 0.1N NaCl for passive compositions are plotted in Fig. 6. The maximum potential corresponding to maximum resistance to initiation of pitting corrosion is observed at about 85% Ni. The values for Ni, however, depending on source, are shown to fall between 0.21 and 0.26V (SHE). The upper value lies relatively close to the value of 0.28V reported earlier by Horvath and Uhlig (14). Obviously, the critical potential for Ni is surprisingly sensitive to purity of the metal, and this effect very likely enters values reported for the high Ni alloys as well. For example, the critical potential for a commercial 69% Ni-Cu alloy (Monel) lies 0.05V below the interpolated value for the corresponding laboratory melted 69% Ni-Cu alloy (Fig. 6). The difference is far outside the experimental variations of such measurements and indicates the relative order of deleterious effects on pitting resistance induced by impurities common to the commercial alloy. The nature of the responsible impurities has not been investigated; they probably do not include Al or Fe as was shown by preparing alloys of 69-70% Ni-Cu containing 1.1 and 2.1% Fe and 1.1 and 2.4% Al. The critical pitting potentials of these alloys in 0.1N NaCl were all the same within  $\pm 10$  mV compared to the 50 mV displacement in the active direction for Monel.

It is not certain that the value for spectroscopically pure nickel should receive greater weight than the value for commercially pure nickel because of the as yet unknown influence of small amounts of nonmetallic impurities present in the spectroscopically pure material. Heat-treatment of spectroscopically pure Ni was not a factor; the critical potential of the electrode water quenched from 1050°C remained at the same value as before heat-treatment.

The effects of NaCl concentration on critical potentials for Ni and two Ni-Cu alloys are shown in Fig. 7. "Active" designates the approximate NaCl concentration above which uniform passivity breaks down. On the average, the potential becomes more active by about 0.075V for a tenfold increase of NaCl concentration. This can be compared with a corresponding 0.085V change in the active direction for 18-8 stainless steel (15).

The effect of lowering the temperature is to increase the critical potential relative to (noble to) the room temperature value. There is less effect at temperatures above room temperature (Fig. 8). Temperature effects are more pronounced for Ni than for the 84.9% Ni-Cu alloy; they are both less than the temperature effects measured for 18-8 stainless steel (15) but they are correspondingly greater than those measured for aluminum (16).

### Discussion

Anodic polarization data show that the passive film can be destroyed uniformly by increasing the  $\text{Cl}^-$

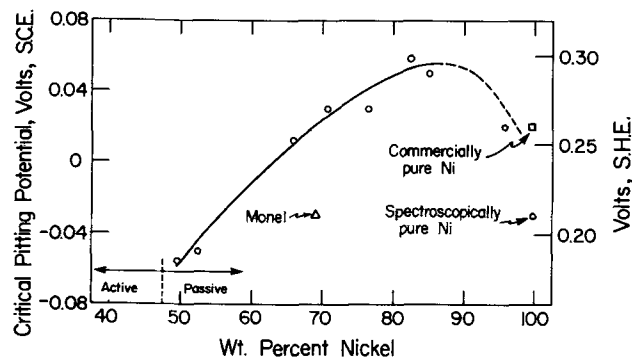


Fig. 6. Critical pitting potentials of Ni-Cu alloys in 0.1N NaCl, 25°C

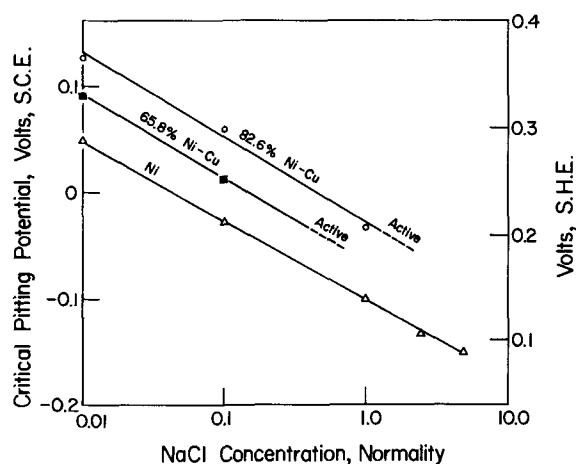


Fig. 7. Effect of NaCl concentration on critical pitting potentials of spectroscopically pure nickel and of Cu-Ni alloys, 25°C.

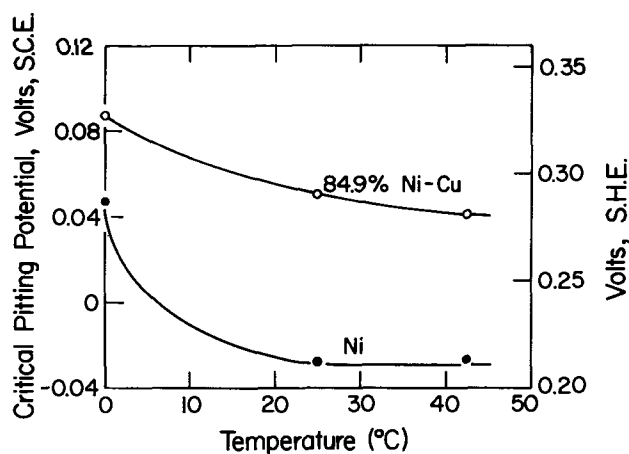


Fig. 8. Effect of temperature on critical pitting potentials of spectroscopically pure Ni and of 84.9% Ni-Cu alloy in 0.1N NaCl.

concentration sufficiently, or it can be broken down locally at lower  $\text{Cl}^-$  concentrations by shifting the applied potential to more noble values. The present data confirm that a passive film as presently defined exists only on alloys containing about 40 or more per cent Ni, whether in sulfuric acid, in acid or alkaline NaCl solutions, or in neutral NaCl plus  $\text{Na}_2\text{SO}_4$  solutions.

Nickel alloys of  $> 40\%$  Ni better resist uniform breakdown of passivity in chloride media the higher the Ni content. This behavior is in line with the more active Flade (decay) potentials observed for Ni-Cu alloys as the Ni content increases (2), corresponding to increased stability of the passive film (17). Extraneous anions like sulfate or hydroxyl, which are less effective than chloride ions in breaking down passivity, when added to NaCl solutions decrease the effectiveness of the chloride ion. In this regard, the extraneous anions compete for sites on the passive surface, hence the passive film is stable at lower Ni composition alloys in a mixture of chloride and sulfate or hydroxyl ions, than in chloride ions alone.

The apparent maximum in critical pitting potential at about 85% Ni has no obvious explanation based on passive properties of these alloys. The conclusion is plausible as mentioned earlier that the maximum is probably not real but represents an impurity effect instead. This conclusion, however, should be verified by additional measurements on carefully purified nickel excluding not only spectroscopically identifiable metallic impurities, but also nonmetallic impurities, e.g., carbon. An effect of degree of purity of Ni on passive properties was also noted by Mansfeld and



Uhlig (2) in their reported potential decay curves in 1N H<sub>2</sub>SO<sub>4</sub>.

The effect of below-room temperature to increase the critical potential to more noble values parallels the situation for 18-8 stainless steel, but with a smaller comparable temperature effect for nickel and for 84.9% Ni-Cu. The effect, as was proposed for 18-8 stainless steel (15), may be one of more pronounced hydration of the passive film at low temperatures. Hydration may serve to stabilize the film against disruption by Cl<sup>-</sup> which proceeds by an exchange mechanism between Cl<sup>-</sup> and the adsorbed oxygen presumably making up the passive film (18). It is less likely that the passive film, conceived as a supposed thick oxide, becomes a better diffusion barrier at low temperatures, e.g., 0° compared to 25° or 40°C. A thick oxide film is probably a source of improved corrosion resistance only in alloys that are not passive as presently defined, i.e., < 40% Ni.

The present results further emphasize that since pitting corrosion occurs only in presence of a passive film as presently studied, only the Ni-Cu alloys containing > 40% Ni are subject to this type of corrosion. Furthermore, > 40% Ni alloys are susceptible only within ranges of NaCl concentration and pH for which the passive film remains intact (Fig. 4). For example, the 70% Ni-Cu alloy would in principle be susceptible to pitting corrosion in aerated 0.01N NaCl, pH 3 in which it remains passive, but it would not be expected to undergo pitting corrosion in 0.1N NaCl or higher concentrations of Cl<sup>-</sup> at this same pH in which it is active. In aerated neutral NaCl solution it would be subject for the same reasons to pitting damage below 0.5N NaCl, but not above.

### Conclusions

1. Passivity in NaCl solutions of any concentration is observed only in copper alloys containing > 40% Ni. Breakdown of passivity occurs at increasingly higher Ni compositions the higher the Cl<sup>-</sup> concentration and the lower the pH.
2. Sulfate and hydroxyl ions added to NaCl solutions shift the alloy composition at which loss of passivity occurs to lower Ni compositions, but not below 40% Ni where the d-band of electronic energy levels is filled.
3. The critical pitting potentials become more noble the higher the Ni content of the alloy. This is in line

with more active Flade potentials and increased stability of the passive film as the Ni content increases. The critical pitting potentials for Ni and high Ni-Cu alloys (e.g., Monel) are appreciably sensitive to unknown impurities in the metal.

4. The critical pitting potentials become more active with increasing Cl<sup>-</sup> concentration, and for Ni and 84.9% Ni-Cu alloy become more noble at 0°C compared to 25° and 40°C.

### Acknowledgment

This research was supported by the Shell Companies Foundation to whom the authors express their appreciation.

Manuscript submitted Jan. 28, 1974; revised manuscript received May 8, 1974.

Any discussion of this paper will appear in a Discussion Section to be published in the June 1975 JOURNAL. All discussions for the June 1975 Discussion Section should be submitted by Feb. 1, 1975.

### REFERENCES

1. J. Osterwald and H. Uhlig, *This Journal*, **108**, 515 (1961).
2. F. Mansfeld and H. Uhlig, *Corrosion Sci.*, **9**, 377 (1969).
3. N. Stolica and H. Uhlig, *This Journal*, **110**, 1215 (1963).
4. F. Mansfeld and H. Uhlig, *ibid.*, **115**, 900 (1968).
5. F. Mansfeld and H. Uhlig, *ibid.*, **117**, 427 (1970).
6. H. Uhlig, *Electrochim. Acta*, **16**, 1939 (1971).
7. H. Uhlig, F. Mansfeld, and M. Kesten, *Z. Physik. Chem., N.F.*, **74**, 216 (1971).
8. N. North and M. Pryor, *Corrosion Sci.*, **10**, 297 (1970).
9. H. Leckie, *This Journal*, **117**, 1478 (1970).
10. "Corrosion Handbook," H. H. Uhlig, Editor, p. 21, John Wiley & Sons, Inc., New York (1948).
11. C. Wagner, *Corrosion Sci.*, **5**, 751 (1965).
12. M. Zamin and M. Ives, *Corrosion*, **29**, 319 (1973).
13. Z. Szklarska-Smialowska, *Corrosion Sci.*, **11**, 209 (1971).
14. J. Horvath and H. Uhlig, *This Journal*, **115**, 791 (1968).
15. H. Leckie and H. Uhlig, *ibid.*, **113**, 1262 (1966).
16. H. Böhni and H. Uhlig, *ibid.*, **116**, 906 (1969).
17. H. H. Uhlig, "Corrosion and Corrosion Control," 2nd ed., pp. 62-65, John Wiley & Sons, Inc., New York (1971).
18. H. Uhlig, *Corrosion Sci.*, **7**, 325 (1967).

## The Anodic Polarization Behavior of Nickel in Acidic Chloride Solution

M. Zamin\* and M. B. Ives

*Institute for Materials Research, McMaster University, Hamilton, Ontario, Canada*

### ABSTRACT

The effect of grain size and cold work on the anodic polarization behavior of polycrystalline nickel in acidic chloride solution has been investigated using potentiostatic techniques and *in situ* microscopic observations. A variation in grain size from 0.025 to 0.330 mm and cold working to 40% does not affect the critical breakdown potential. It is concluded that the critical breakdown potential is not an adequate measure of the electrochemical conditions required for pitting corrosion of nickel.

It has generally been believed (1-3) that metals undergo pitting corrosion only beyond a certain critical potential ( $E_c$ ). This potential has served as one of the fundamental electrochemical criteria charac-

terizing the susceptibility of metals to pitting corrosion. It is believed (4) that at more negative potentials than  $E_c$  the metal exists in a passive state, while above  $E_c$ , active and passive states coexist on the metal surface giving rise to pitting corrosion. Thus, the more positive is  $E_c$ , the more resistant is the metal to pitting corrosion.

\* Electrochemical Society Student Member.

Key words: anodic polarization behavior, critical breakdown potential, *in-situ* microscopic observations, grain size, cold work.



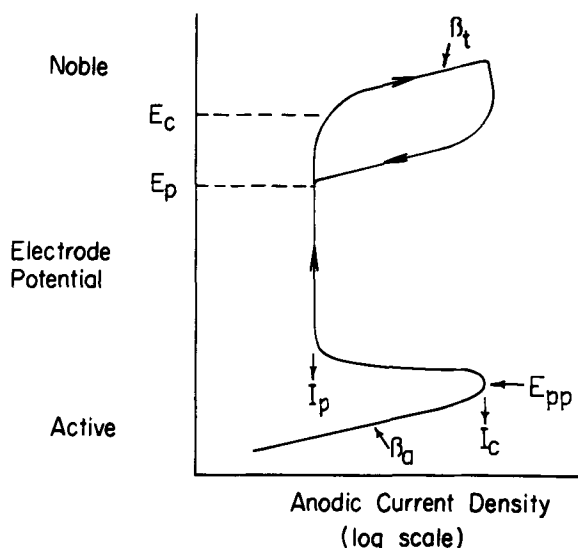


Fig. 1. Schematic representation of the breakdown potential ( $E_c$ ) and the protection potential ( $E_p$ ). Other symbols used in the text are also represented.

Pourbaix *et al.* (5) have distinguished two types of critical potentials: breakdown potential ( $E_c$ ), the potential corresponding to a rapid increase of the current due to pit nucleation, and protection potential ( $E_p$ ), the potential corresponding to the current drop during the reverse potential sweep, caused by the repassivation of the pits (Fig. 1). According to Pourbaix, within the range  $E_p$  to  $E_c$  propagation of already existing pits continues, but nucleation of new pits is restrained, occurring only when  $E \cong E_c$ . However, Wilde (6) has shown that  $E_p$  is not a unique property of a metal and depends on the length of time a pit has been growing.

The effect of cold work on nickel single crystals has been found (7) to increase the passive current density but to decrease the primary passive and critical breakdown potentials. On the other hand, austenitic stainless steels in 3% NaCl solution exhibit no difference in the  $E_c$  values of cold-worked and annealed specimens (8). However, on the cold-worked samples, the pits are smaller and more numerous. The invariance of  $E_c$  with cold work has also been supported by Smialowska and Czachor (9) on 16 Cr-Fe. In this case, no difference was observed in pit density.

Tomashov *et al.* (10) measured the effect of grain size on the  $E_c$  values of Ni-Cr steels. They found that  $E_c$  shifted toward more noble potentials when the grain size increased from 0.005 to 0.07 mm; at greater sizes than 0.07 mm,  $E_c$  was constant. This behavior was interpreted on the basis that small grain size specimens contained more grain boundaries with "heterogeneous inclusions."

It is shown in this paper that the critical breakdown potential ( $E_c$ ) does not adequately describe the electrochemical conditions required for pitting corrosion of nickel.

### Experimental Procedure

The nickel used in this investigation was "low-oxygen nickel" supplied by Falconbridge Nickel Mines Ltd.<sup>1</sup> The material was received as cold-rolled sheets prepared directly from refined cathode material.

Specimen preparation, corrosion cell, potentiostatic circuit, and polarization procedure have been described elsewhere (11, 12). Specimens of 0.36 cm<sup>2</sup> area were metallographically polished to 1 μm diamond. The polarizing solution containing 2 mliters 1N NaCl/100 mliters 1N H<sub>2</sub>SO<sub>4</sub> was flushed with pure dry nitrogen for an hour before commencement of the experiment and the bubbling of nitrogen was continued throughout the experiment. The temperature of the solution was maintained at 24° ± 1°C. Potentials were measured with reference to a saturated calomel electrode (SCE) using an agar-agar salt bridge and the values reported do not incorporate any corrections for junction potentials.

The equilibrium corrosion potential,  $E_{corr}$ , was obtained by allowing the specimen to stand in solution and monitoring the potential until a drift of less than 5 mV in 15 min was obtained.

Two types of metallurgical treatments were adopted: annealing (to modify the grain size) and cold working. Initially, the annealing was done in air. However, for large grain sizes, the results obtained depended on the time period and temperature of anneal. Hence, as a standard procedure, annealing was performed in vacuum. The nickel sheet was cut into strips and sealed in a quartz tube under vacuum (< 10<sup>-5</sup> Torr) before placing in a crucible furnace. The starting material for grain-growth anneal was 1 mm thick, "as-received," nickel sheet.

Cold working was achieved by rolling. The sheet was cut into strips and rolled to various degrees of cold work, defined as the percentage reduction in thickness.

The measurement of the grain size was performed using the ASTM nonferrous grain size standard (13). The microstructure was revealed by etching for about 5 sec in a 1:1 solution of nitric acid (conc) and acetic acid (ice-cooled).

### Results

The anodic polarization curves for eight specimens with grain size ranging from 0.025 to 0.330 mm are shown in Fig. 2. All specimens exhibit an active-passive transition. The anodic dissolution parameters, the anodic Tafel slopes ( $\beta_a$ ), and the slopes in the transpassive region ( $\beta_t$ ) are summarized in Table I.

<sup>1</sup> Analysis in parts per million by weight: O<sub>2</sub> 14; N<sub>2</sub> 2; H<sub>2</sub> 1.5; C 15; P < 2; S 5; Pb 8; Al < 1; Ca 3; Cr < 0.6; Co 60; Cu 8; Fe 40; Mg < 1; Mn 0.7; Si 5; Ti < 1.

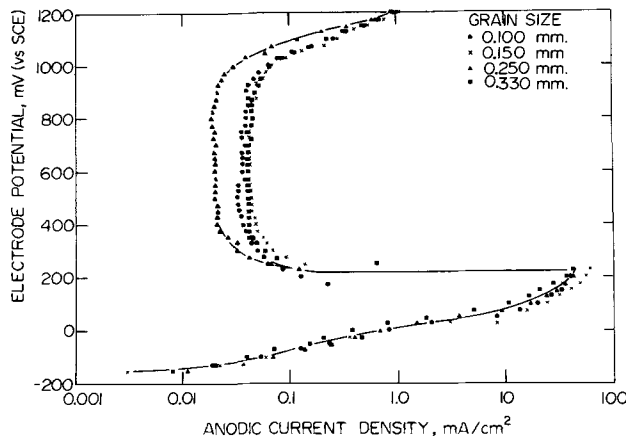
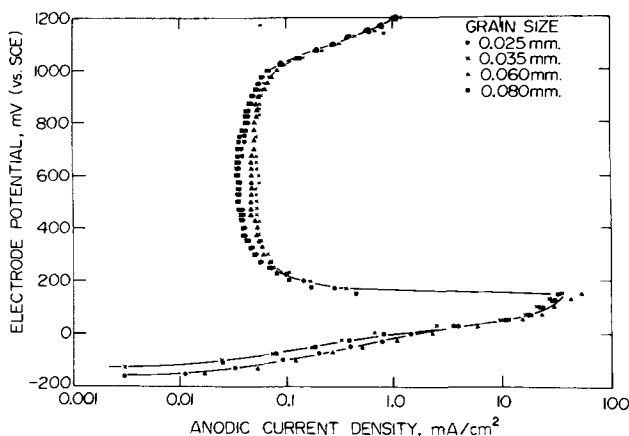


Fig. 2. Anodic polarization curves for polycrystalline nickel of varying grain size in 2 mliters 1N NaCl/100 mliters 1N H<sub>2</sub>SO<sub>4</sub>

Table I. Anodic dissolution parameters, anodic Tafel and transpassive slopes for polycrystalline nickel with varying grain size in 2 mliters 1N NaCl/100 mliters 1N H<sub>2</sub>SO<sub>4</sub>

Grain size, average grain diameter, mm	$E_{corr}$ , mV vs. SCE	$E_{pp}$ , mV vs. SCE	$I_c$ , mA/cm <sup>2</sup>	$I_p$ , mA/cm <sup>2</sup> , lowest recorded value	$E_c$ , mV vs. SCE	$\beta_a$ , mV/decade	$\beta_t$ , mV/decade
0.025	-170	+150	33.3	0.036	+950	80	160
0.035	-130	+150	36.7	0.053	+950	80	165
0.060	-190	+150	52.8	0.047	+950	75	165
0.080	-135	+125	28.3	0.036	+950	70	160
0.100	-165	+150	33.3	0.033	+950	80	158
0.150	-175	+225	61.1	0.042	+950	82	160
0.250	-170	+200	41.9	0.019	+950	95	152
0.330	-220	+225	43.5	0.041	+950	85	172

Table II. Anodic dissolution parameters, anodic Tafel and transpassive slopes for polycrystalline nickel of grain size 0.250 mm with varying amount of cold work in 2 mliters 1N NaCl/100 mliters 1N H<sub>2</sub>SO<sub>4</sub>

Amount of cold work, %	$E_{corr}$ , mV vs. SCE	$E_{pp}$ , mV vs. SCE	$I_c$ , mA/cm <sup>2</sup>	$I_p$ , mA/cm <sup>2</sup> , lowest recorded value	$E_c$ , mV vs. SCE	$\beta_a$ , mV/decade	$\beta_t$ , mV/decade
0	-170	+200	41.9	0.019	+950	95	152
10	-180	+200	46.1	0.022	+950	95	172
20	-245	+225	66.1	0.028	+950	95	142
30	-260	+200	47.2	0.044	+950	92	137
40	-345	+225	69.4	0.032	+950	92	180

It can be seen that the value of the critical breakdown potential ( $E_c$ ) is the same in every case and, within the limits of calculational error, the values of the other parameters do not change significantly over the grain size range.

A definite trend was observed in the nature of the attack in these specimens. At lower grain sizes (0.025-

0.035 mm) pits were formed only along the grain boundaries (Fig. 3a). As the grain size increased to 0.060 mm both grain boundary and grain interior pitting occurred (Fig. 3b). Beyond a grain size of 0.080 mm, pits were formed only within the grains, and their density increased with grain size (Fig. 3c and 3d).

*In-situ* microscopic examination of the specimen surface was performed throughout one polarization run and photomicrographs were taken to record the surface morphology at various stages of polarization. It was found that most of the attack develops in the active region, i.e., before the onset of passivity, and at higher potentials only increases slightly in intensity. This effect will be described in detail elsewhere (14).

The effect of cold work on the critical breakdown potential of nickel was tested for specimens of grain size 0.250 mm. The anodic polarization curves obtained are shown in Fig. 4. The anodic dissolution parameters, along with the anodic Tafel and transpassive slopes, are summarized in Table II. It is evident that cold working has no effect on the value of  $E_{pp}$  and  $E_c$  and within limits of calculational error on  $\beta_a$  and  $\beta_t$  of nickel.

Microscopic examination of the specimens after removal from the polarization cell revealed pits to be nucleated not only along the grain boundaries, but also within the grains. The number of pits within the grains did not change significantly with cold work but pitting along the grain boundaries tended to become continuous.

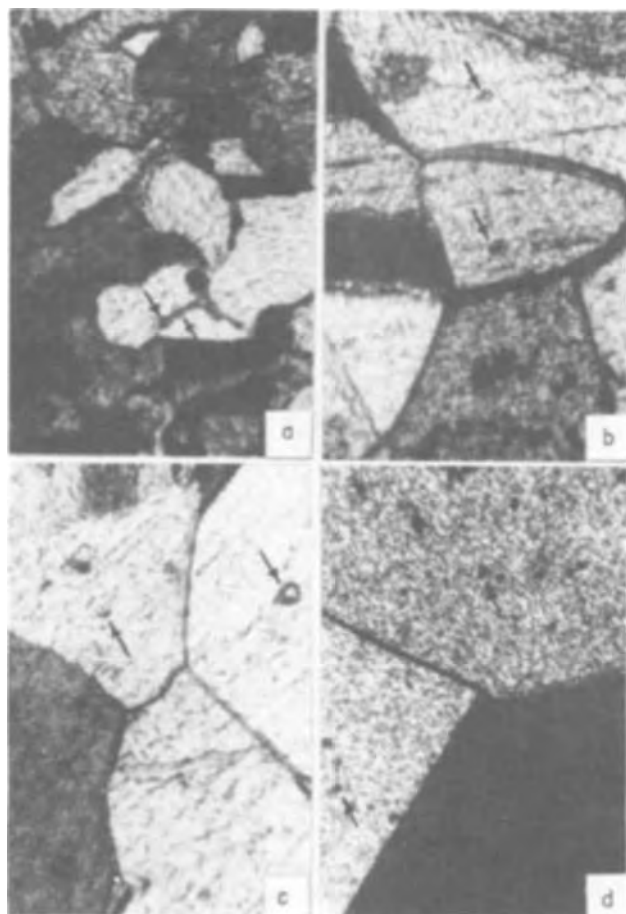


Fig. 3. Nature of attack on polycrystalline nickel with varying grain size in 2 mliters 1N NaCl/100 mliters 1N H<sub>2</sub>SO<sub>4</sub> after polarization to +1200 mV (SCE). (a) Grain size = 0.025 mm, 360 $\times$ . (b) Grain size = 0.060 mm, 360 $\times$ . (c) Grain size = 0.100 mm, 360 $\times$ . (d) Grain size = 0.330 mm, 180 $\times$ . The arrows indicate some regions of localized attack.

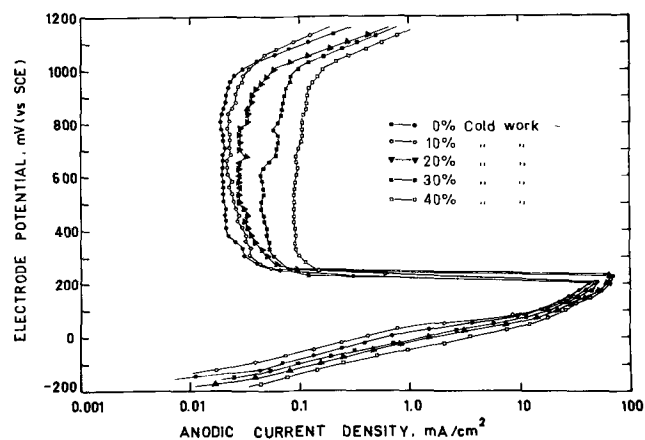


Fig. 4. Anodic polarization curves for polycrystalline nickel of grain size 0.250 mm with varying amount of cold work in 2 mliter 1N NaCl/100 mliters 1N H<sub>2</sub>SO<sub>4</sub>.

The results on air-annealed specimens were similar to those on vacuum-annealed ones. In general, the values of  $E_{pp}$  and  $\beta_a$  were lower,  $E_{corr}$  was more active, and  $\beta_t$  was almost the same. The value of  $E_c$  remained the same in every case.

In order to understand better the significance of the critical potential, specimens of grain sizes 0.025, 0.100, and 0.330 mm were subjected to a passive potential of +400 mV for 28 min (time taken for a normal potentiostatic sweep from -300 to +400 mV) in 1N H<sub>2</sub>SO<sub>4</sub> followed by the addition of 2 mliters 1N NaCl/100 mliters 1N H<sub>2</sub>SO<sub>4</sub> and polarization continued to +1200 mV. The results are presented in Fig. 5. The anodic current density rises linearly with a change in slope between +950 and +1000 mV. The number of pits decreased with grain size even though pit distribution followed the trend shown in Fig. 3. The surface of every specimen remained bright until the addition of Cl<sup>-</sup> ions, after which most of the surface remained in this visual condition (even though pits nucleated) while a small area of the specimen tarnished and by the end of polarization, a faint outline of the grain structure was visible.

Further, a specimen of 0.100 mm grain size was polarized in 1N H<sub>2</sub>SO<sub>4</sub> from -300 to +1200 mV. The solution was removed and a fresh, previously deaerated 1N H<sub>2</sub>SO<sub>4</sub> solution was introduced into the corrosion cell. The specimen was subjected to a potential of -300 mV, held at this potential for 30 min, polarized again up to +400 mV, and then Cl<sup>-</sup> ions added as 2 mliters 1N NaCl/100 mliters 1N H<sub>2</sub>SO<sub>4</sub> and polarization continued up to +1200 mV. Very few pits were formed, all within the grains and they nucleated in the passive region. The critical breakdown potential in the two cases was almost the same, viz., +1000 mV in the former instance and +950 mV in the latter.

### Discussion

In general, the extent of corrosion on a metal surface depends on the active anode/cathode site ratio, being higher if this ratio is large and vice versa. If the sites are fixed with time, localized corrosion is obtained, whereas if they are mobile, general corrosion results. The distribution of the anodic and cathodic sites may be assumed random over the entire specimen surface with both types of sites being present along the grain boundaries as well as within the grains. Which of these sites become activated depends on the conditions existing at the metal/solution interface during polarization. Grain size, cold work, and other aspects of metallurgical condition could all possibly affect the anode/cathode site distribution and, therefore, have a significant effect on the pitting corrosion characteristics of a metal.

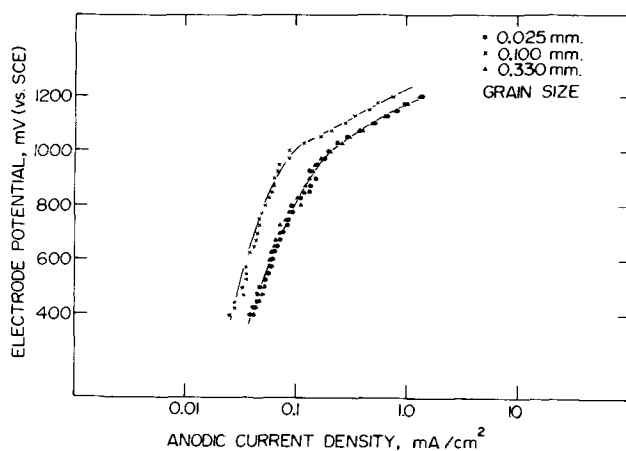


Fig. 5. Potential-current density curves for polycrystalline nickel of varying grain size after being held at +400 mV (SCE) for 28 min followed by addition of Cl<sup>-</sup> ions as 2 mliters 1N NaCl/100 mliters 1N H<sub>2</sub>SO<sub>4</sub>.

The results presented show that it is inappropriate to suppose the critical breakdown potential,  $E_c$ , can be used to predict the pitting corrosion characteristics of nickel in sulfuric acid solutions containing chloride ions. Also, the anodic Tafel slopes show little difference over the entire range of grain size and cold work (Tables I and II). Electrochemically, this fact may be taken to mean that the primary dissolution mechanism, and possibly the characteristics of the passive film, are similar in each case. It is therefore concluded that a variation in grain size from 0.025 to 0.330 mm and cold working up to 40% has no effect on the pitting corrosion characteristics of nickel. The invariance of  $E_c$  with cold work as found in the present case is consistent with instances reported in the literature for austenitic steels (8) and Fe-Cr alloys (9).

The value of the primary passive potential,  $E_{pp}$ , is higher for vacuum-annealed specimens as compared to air-annealed ones. This is in support of the dissolution-precipitation mechanism of passivity (15). Since the vacuum-annealed specimens show lower reactivity, they need to be polarized to higher potentials before the passive state can set in.

The slopes in the transpassive region do not provide any specific information. They cannot be regarded as a measure of the growth rate of the pits because of the multiple events occurring on the surface. Pits that had nucleated grow, new ones might nucleate, and some of the older ones passivate. However, the transpassive slopes,  $\beta_t$ , do provide an idea of the over-all corrosion of the specimen in that potential range. Within limits of computational error ( $\pm 10$  mV/decade), it may be seen that  $\beta_t$  does not significantly change with either grain size or cold work. This is consistent with the observation that neither variation in grain size nor cold working have any effect on the pitting corrosion characteristics of nickel.

Referring to Fig. 5, if one does consider the point of the change of the slope of the curves to have the same significance as the critical breakdown potential, it is around +950 to +975 mV, even though pit formation is observed to occur much earlier. The transpassive slopes for these curves are much higher (ranging between 215-235 mV/decade) which indicates a lower over-all corrosion rate. This is because the pit density in these cases is much lower than in the instance where the specimen is polarized from the beginning of a Cl<sup>-</sup>-containing solution.

The formation of pits in the active region is consistent with the concept of a "balance" between film formation and solution as discussed elsewhere (11), but is in direct conflict with the idea that pitting corrosion cannot occur at potentials more active than some critical potential (1-3). The critical potential thus does not adequately describe the electrochemical conditions required for pitting corrosion of nickel in sulfuric acid solutions containing chloride ions. In view of this conclusion on nickel, it is suggested that considerable caution must be exercised in interpreting data based on critical potentials to assess the pitting susceptibility of metals and alloys.

The critical breakdown potential may be dependent on two factors: (a) internal factors, such as grain size, cold work, inclusions, and compositional inhomogeneity, and (b) external factors, such as the chemistry of either the solution or the passive film. Since  $E_c$  is independent of the internal factors, it is inferred that the critical breakdown potential is chemistry controlled. That the chemistry of the solution affects  $E_c$  has already been demonstrated (11).

The exact mode by which the aggressive ion causes pitting is still unclear. However, since the discharge potential for Cl is very positive (16) (the exact value depending on the concentration of Cl<sup>-</sup> ions) and pitting is observed to occur at negative potentials, as pointed out by Ammar and Darwish (16), the first step leading to the formation of pits is most likely to be associated with Cl<sup>-</sup> ions. It is possible that two mecha-

nisms may be operative simultaneously. One, in which the chloride ion reacts with the nickel in the metal lattice and the other, in which the chloride ion reacts with the passive oxide film; both processes eventually leading to the formation of soluble  $\text{NiCl}_2$ . The incorporation of the chloride ion into the passive oxide film may also be via anion vacancies with the chloride not necessarily of charge,  $-1$ . The details of this mechanism will be the subject of a future communication.

### Conclusions

1. (i) Variation of grain size from 0.025 to 0.330 mm, cold working up to 40%, and annealing atmosphere (air or vacuum) do not affect the critical breakdown potential ( $E_c$ ), and within limits of calculational error, the anodic Tafel slope ( $\beta_a$ ) and the transpassive slope ( $\beta_t$ ) of nickel.

(ii) Cold working up to 40% does not have any significant effect on the primary passive potential ( $E_{pp}$ ) of nickel, although  $E_{pp}$  becomes more positive with increase in grain size from 0.025 to 0.330 mm.

2. At lower grain sizes, pits are formed along the grain boundaries. At larger grain size, the pits are formed within the grains with an increased density.

3. Most of the surface attack and nucleation of pits occurs in the "active" region of the polarization curve, *i.e.*, before the onset of passivity.

4. The critical breakdown potential does not adequately describe the electrochemical conditions required for pitting corrosion of nickel in sulfuric acid solutions containing chloride ions. Considerable caution must be exercised in employing data based on critical potentials to assess the pitting susceptibility of metals and alloys.

### Acknowledgments

We wish to gratefully acknowledge the assistance of Dr. L. A. Morris, Falconbridge Nickel Mines Ltd., for supplying the samples studied in this work. The re-

search was supported primarily by the Defence Research Board of Canada.

Manuscript submitted Dec. 17, 1973, revised manuscript received April 8, 1974.

Any discussion of this paper will appear in a Discussion Section to be published in the June 1975 JOURNAL. All discussions for the June 1975 Discussion Section should be submitted by Feb. 1, 1975.

The publication costs of this article have been assisted by McMaster University.

### REFERENCES

1. Ja. M. Kolotyrykin, *Corrosion*, **19**, 261t (1963).
2. W. Schwenk, *ibid.*, **20**, 129t (1964).
3. Z. Szklarska-Smialowska and M. Janik-Czachor, Proc. of the U. R. Evans International Conference on Localized Corrosion, NACE (1971), In press.
4. Z. Szklarska-Smialowska, *Corrosion*, **27**, 233 (1971).
5. M. Pourbaix, *et al.*, *Corrosion Sci.*, **3**, 239 (1963).
6. B. E. Wilde, Proc. of The U. R. Evans International Conference on Localized Corrosion, NACE (1971), In press.
7. I. Garz and U. Häfke, *Corrosion Sci.*, **11**, 329 (1971).
8. P. Forchhammer and H. J. Engell, *Werkstoffe Korrosion*, **20**, 1 (1969).
9. Z. Szklarska-Smialowska and M. Janik-Czachor, *Brit. Corrosion J.*, **4**, 138 (1969).
10. N. D. Tomashov, O. P. Chernova, and N. Markova, *Zashchita Metal.*, **6**, 21 (1970).
11. M. Zamin and M. B. Ives, *Corrosion*, **29**, 319 (1973).
12. T. Tokuda and M. B. Ives, *Corrosion Sci.*, **11**, 297 (1971).
13. G. L. Kehl, "The Principles of Metallographic Laboratory Practice," p. 293, McGraw-Hill Book Co., Inc., New York (1949).
14. M. Zamin and M. B. Ives, To be published.
15. J. O'M Bockris and A. K. N. Reddy, "Modern Electrochemistry," p. 1321, Plenum Press, New York (1970).
16. I. A. Ammar and S. Darwish, *Electrochim. Acta*, **13**, 781 (1968).

# Ellipsometric Study of the Formation of Films on Iron in Chromate Solutions

Z. Szklarska-Smialowska<sup>1</sup> and R. W. Staehle\*

Department of Metallurgical Engineering, The Ohio State University, Columbus, Ohio 43210

## ABSTRACT

Film growth on iron was studied by ellipsometry in aerated or deaerated chromate solutions of different pH's at open-circuit potentials and at various anodic potentials. It was found that various films can be formed depending on the experimental conditions. At high anodic potentials iron oxide is chiefly produced with an index of refraction of 2.6(1-0.12i). At open-circuit potential the iron and chromium hydroxides with the index of refraction of 1.6-1.7 or a mixture of iron and chromium hydroxides with iron and chromium oxide (with index of refraction of 1.6-1.9 and various absorption coefficients) is formed. The kinetics of the film growth at open-circuit potential is logarithmic, and the kinetics of iron hydroxide formation at constant potentials follow the cubic law.

The aim of this work was to improve the understanding of the mechanism of passivation of iron in chromate solutions. Ellipsometry was used for determining optical parameters and film growth kinetics of the film formed both at open-circuit potential and at anodic potentials. These studies included pH's of 3.9, 7, and 12.

Chromates belong to the most efficient oxidizing type of corrosion inhibitors. They are effective both in aerated and deaerated solutions; they are also effective in neutral and alkaline solutions as well as in acid solutions.

The composition and the growth rate of oxide film on iron formed in chromate solutions has been studied by many authors. During passivation chromates undergo reduction with formation of chromium oxide (1-4). The concentration of chromium in the film can be different, depending on the condition of film formation (oxygen concentration in the solution, solution pH). The amount of reduced chromates during passivation process was determined by Uhlig and King (5), Powers and Hackerman (6), Cohen and Beck (4), Brasher (3), and others. The concentration of oxygen in the solution has an especially large effect on the composition of the film (2, 7, 8). The chromium concentration in the protective layer is decreased as the oxygen in solution is increased or as the surface is exposed to the atmosphere. Films formed in chromate solutions at the open-circuit potential are composed of  $\gamma\text{-Fe}_2\text{O}_3 + \text{Cr}_2\text{O}_3$  and grow according to a logarithmic law (3).

Kruger (9) who was the first to measure the film growth in chromates using ellipsometry found also that the initially air-formed films grew further when immersed in aerated chromate solutions and followed a logarithmic law.

## Experimental

The measurements of polarization curves and ellipsometric measurements of the film growth on iron were performed at 22°C in 0.01N  $\text{Na}_2\text{CrO}_4$  solutions at pH 7 and 12 and in 0.01N  $\text{Na}_2\text{Cr}_2\text{O}_7$  solution at pH 3.9.

Polarization curves were performed potentiokinetically at 20 mV/min in deaerated solutions, starting about 300 mV more negative than corrosion potential. Potentials were measured against the saturated calomel electrode and are expressed in this paper on the calomel scale.

The ellipsometric measurements were made at open-circuit potential and at anodic potentials.

\* Electrochemical Society Active Member.

<sup>1</sup> Present address: Institute of Physical Chemistry, Warsaw, Kasprzaka 44, Poland.

Key words: corrosion inhibitors, ellipsometry, passivity, chromates,

The measurements were performed on specimens of 99.99% purity iron having the form of cylindrical disks with an exposed area of 0.32 cm<sup>2</sup>; the specimens were prepared and the data taken as before (10-12).

The premature formation of films on the iron surfaces was prevented by holding the specimen at 300 mV more negative than the corrosion potential. Other specimens were studied with the initially air-formed film left intact, and these surfaces were neither electropolished nor cathodically reduced prior to the experiment.

Since the solutions in these experiments had an orange or yellow color, it was necessary, before starting the study of films on the metal substrate, to evaluate optical effects due to color. It was found that the values of A (analyzer) and P (polarizer) of the film formed in chromate solutions were the same as in borate solutions (0.15N  $\text{H}_3\text{BO}_3 + 0.15\text{N Na}_2\text{B}_4\text{O}_7$ , pH 8.8). The comparison was performed by first obtaining values of A and P in the chromate solution. The chromate solution was then flushed out by the borate solution, and the values of A and P were again determined and found to be the same as before.

The ellipsometer was Model 436 from Rudolf and Sons, with a mercury arc light source. The vacuum wavelength was 5461Å; the angle of incidence was 70.96°. The optical constants of iron and of the films formed on its surface as well as the film thicknesses were calculated using the Mc Crackin computer program (13) and an IBM 360 computer.

The ellipsometric measurements of the film growth were performed in deaerated chromate of different pH at anodic potentials. The readings of the polarizer and analyzer angles were taken for a period of 1 hr.

Measurements of the film growth in chromate solutions at open-circuit potential were performed under the following conditions:

1. The film was cathodically treated in a deaerated solution, the applied potential was removed, and the open-circuit condition obtained; then the solution was exposed to the atmosphere. Here the solution was aerated slowly.

2. The surface was cathodically treated in an aerated solution, the applied potential was removed, and the open-circuit condition obtained. Here the state of aeration was constant.

3. The air-formed film was left on the surface when exposed to the aerated solution, and there was no cathodic pretreatment.

For the first two circumstances the cathodic potential was 300 mV below the corrosion potential, and at this potential there were no differences observed in the index of refraction. After the readings were taken, the

cathodic current was switched off and the changes of  $A$  and  $P$  and changes of potential with time were noted. The open-circuit potential was monitored at the same time as ellipsometric parameters for films grown in cases 1, 2, and 3.

### Results

**Polarization curves.**—Figure 1 shows anodic polarization curves for the solutions of interest. The polarization curves do not show a transition from the active to the passive state. The current flowing in the passive state does not depend on the pH.

**Optical measurements.**—The complex index of refraction for the substrate was  $2.9(1-1.4i)$ . This value is smaller than the values of refraction indices obtained for the same material in borate, tungstate  $3.21(1-1.26i)$ , and phosphate  $3.14(1-1.14i)$  solutions (10-12).

**Anodic film.**—The results of  $\Delta A$  vs.  $\Delta P$  are plotted in Fig. 2 and 3. Approximately one third of the measurements taken during the 1 hr experiment are plotted as representative values. Figure 2 gives the dependence between  $\Delta A$  and  $\Delta P$  for pH 3.9 and 12. ( $\Delta A$  and  $\Delta P$  are the differences between the clean and the oxide-covered surfaces.) The values in Fig. 2 correspond to the same line independent of the potential and pH.

It is not possible to assign an exact value to the complex refractive index for the data of Fig. 2. The range of possible values of index of refraction is 2.4-2.7. Assuming that we choose a value of 2.6 as a likely value, the complex refractive index is  $2.6(1-0.12i)$  in the range of  $n = 2.6 \pm 0.15$  and  $k = 0.12 \pm 0.015$ . This value corresponds to the indices of refraction which are reported in the literature for anodically formed  $\gamma\text{Fe}_2\text{O}_3$  or  $\text{Fe}_3\text{O}_4$ .

The same kind of measurements were performed in pH 7 and the results are given in Fig. 3. Here two curves are plotted, one for the potential of  $-500$  mV (active region of potential) and the second one for the more positive potentials. All values of  $\Delta A$  vs.  $\Delta P$  obtained at potentials more positive than  $-300$  mV have the same slope as presented in Fig. 2. However, the slope for  $-500$  mV is significantly steeper. At pH

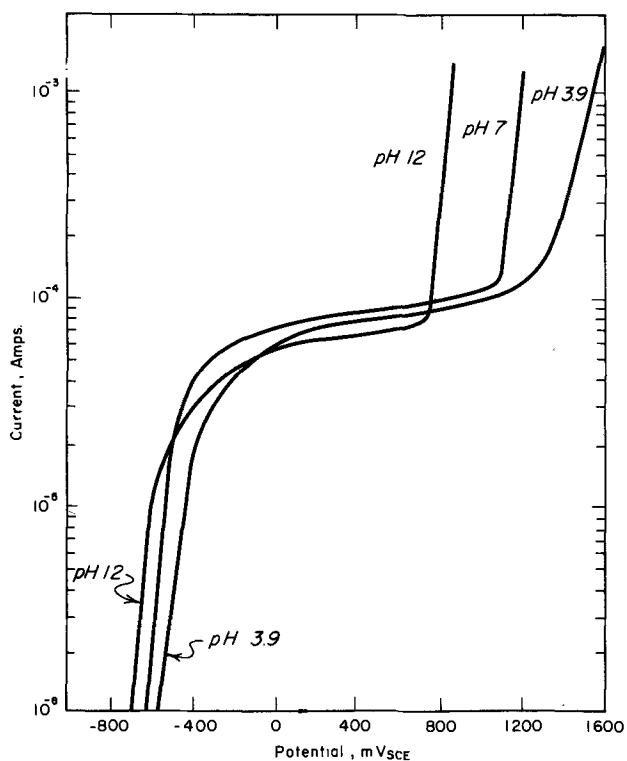


Fig. 1. Current-potential diagrams for iron in chromate solutions of various pH.

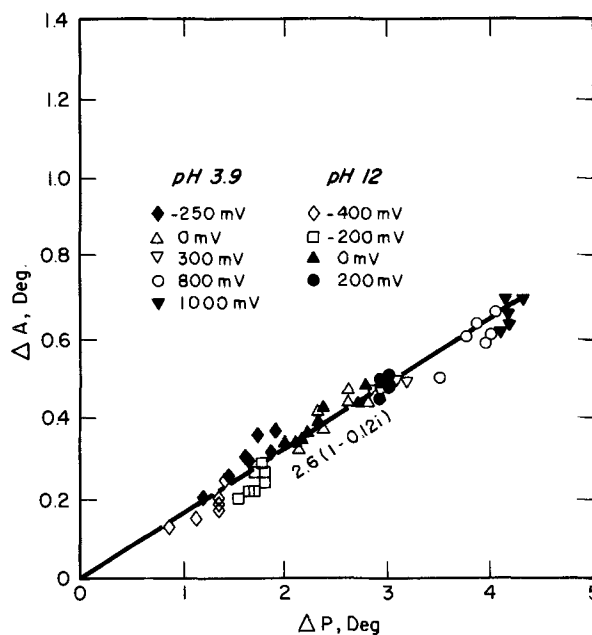


Fig. 2. Relationship between  $\Delta A$  and  $\Delta P$  for a film grown in chromate solutions of pH 3.9 and 12 at different applied potentials.

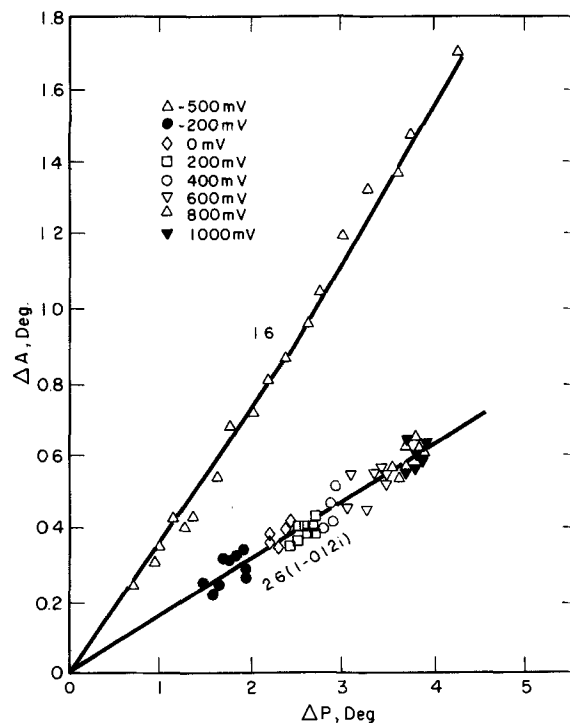


Fig. 3. Relationship between  $\Delta A$  and  $\Delta P$  for films grown in chromate solution of pH 7 at different applied potentials.

7 the slope of  $\Delta A$  vs.  $\Delta P$  is the same for  $-500$  and  $-400$  mV as for the corrosion potential.

**Films obtained at open-circuit potential.**—The formation of films in chromate solutions at open-circuit potential is influenced by the choice of experimental conditions. The results of measurements performed under conditions given above in the experimental section are as follows.

Case 1: The results of the first kind of experiments are presented in Fig. 4 which illustrates the relationship between  $\Delta A$  and  $\Delta P$  for several measurements performed in chromate solutions at pH 3.9, 7, and 12 at open-circuit potential, and also for the measurements made at  $-500$  mV in deaerated  $\text{Na}_2\text{CrO}_4$  solution at pH

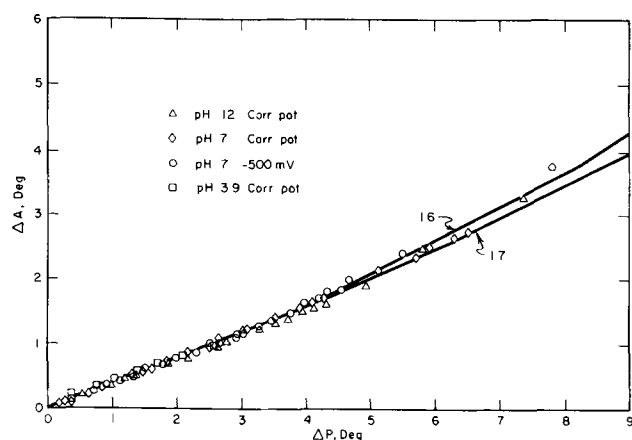


Fig. 4. Relationship between  $\Delta A$  and  $\Delta P$  for a film grown at open-circuit potential at different pH.

7. The curve at open-circuit potential is much steeper than the curve representing the same dependence for iron oxide formation during anodic polarization. This film has an index of refraction of 1.6-1.7.

Case 2: In this case the film growth followed two slightly different patterns, and it seemed that both were equally probable and both of these different from Case 1. The existence of these two different growth processes demonstrates the importance of initial conditions. The first growth pattern is shown in Fig. 5. This curve is composed of two linear segments, the first segment with the small slope and the second one with larger slope than the first. This indicates that two layers, one on top of the other, are formed in such conditions. The first layer is very thin (7Å) and is assumed to be iron oxide since the slope corresponds approximately to Fig. 2. The index of refraction of this layer was assumed to be the same as for the anodic film formed in chromate solutions. The most reasonable values of the refractive indices for the second layer are between 1.6 and 1.9 with their assumed imaginary parts as noted in Fig. 5. Values outside this range give

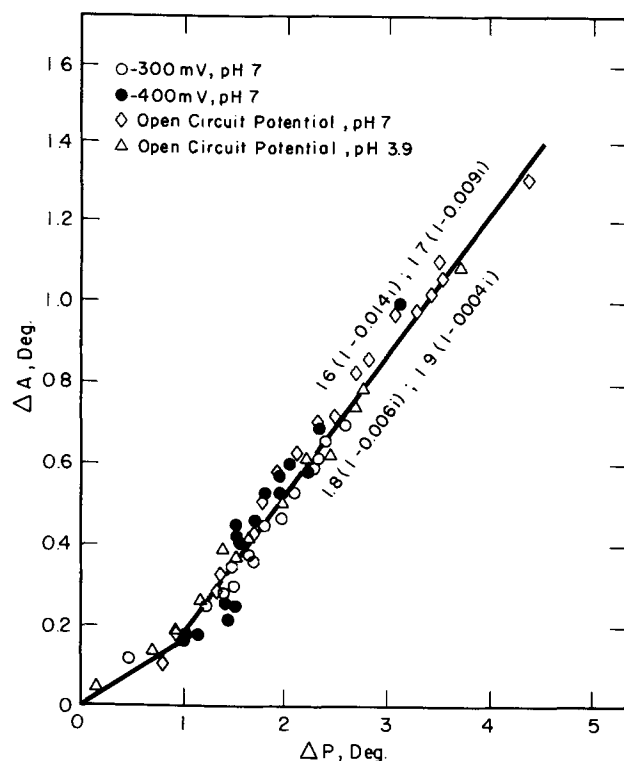


Fig. 5. Relationship between  $\Delta A$  and  $\Delta P$  for a film grown at open-circuit potential when two layers are formed.

improbable values for the imaginary part. This two layer film is obtained when the potential change in the positive direction is more rapid than in Case 1. Still another dependence between  $A$  and  $P$  is observed; namely a linear dependence between  $\Delta A$  and  $\Delta P$  but with smaller slope than in the case when the film with refractive index of 1.6-1.7 is formed. Figure 6 gives an example of such a result obtained in chromate solution of pH 12. Since the changes of both  $P$  and  $A$  are small, it is difficult to determine precisely the index of refraction of the film. As for Case 1, different values are possible from 1.6(1-0.02i) to 1.9(1-0.04i).

Case 3: Here, immersion of the specimen into chromate solutions of pH 7 and 12 causes the formation of the same oxides as for Case 2. However, in the solution of pH 3.9 the film is similar to that in Case 1 with an index of refraction equal to 1.6-1.7.

*Thickness of the films.*—The thickness of the anodic film formed in chromate solutions does not exceed 35Å, even for anodic potentials as high as +1000 mV. However, the thicknesses of the films formed at open-circuit potential with index of refraction equal to 1.6-1.7 are of the order of 100-120Å after 1000 min.

*Kinetics of the film growth.*—Figure 7 shows for Case 1 examples of the thickness vs. time of the films formed at open-circuit potentials for various pH's. The growth rates are logarithmic but the growth of the

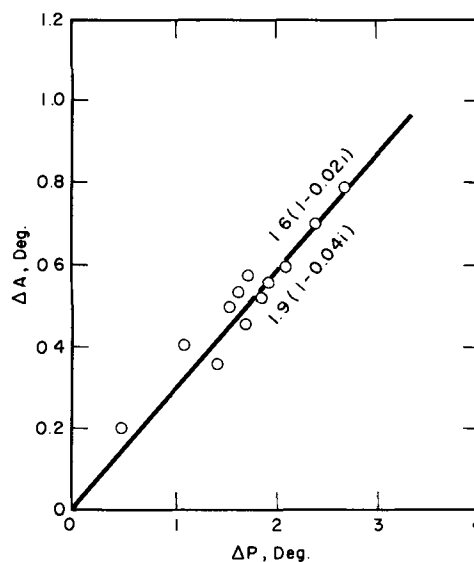


Fig. 6. Relationship between  $\Delta A$  and  $\Delta P$  for a film grown at open-circuit potential when one layer is formed with index of refraction of 1.6-1.9.

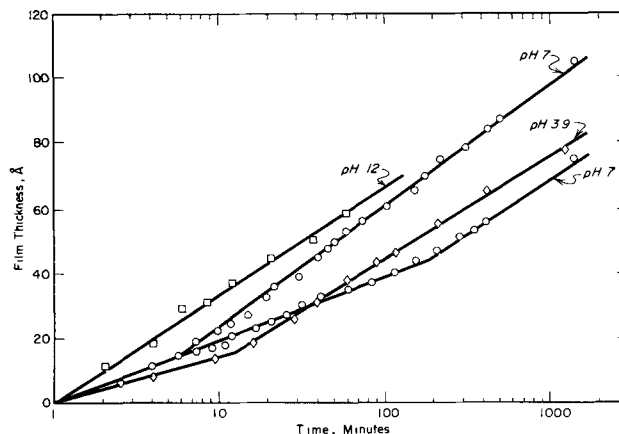


Fig. 7. Film thickness vs. time for the film whose optical constants are given in Fig. 4 (open-circuit potential).

films occurs in two stages. In the initial stage the slope is smaller than in the second stage. The extent and slope of the first stage vary and the reasons for these variations are not presently clear. However, in the second region the slope is the same for all pH's and is about 33 Å/decade.

Figure 8 shows for Case 2, when two layers exist, the thickness vs. time relationship for the two experiments shown in Fig. 5, assuming the complex index of refraction  $1.7(1-0.004i)$ . These films follow the logarithmic law as in Fig. 8. The slope of these curves is 20 Å/decade. There is a somewhat different slope at short times, but the extent of this region is too small to permit assignment of a valid growth law.

The second alternative growth pattern of Case 2 is presented in Fig. 9 showing the relationship between the thickness of the film and time for experiments given in Fig. 6. The two curves in this figure assume indices of refraction of  $1.6(1-0.02i)$  and  $1.9(1-0.04i)$ . The character of the dependence in both cases is the same; the differences are in the film thickness and the slopes. At first the growth of the film is rapid but after 15 min when the film thickness reaches 32 Å (curve 1) and 20 Å (curve 2), the film grows more slowly; and after 1000 min the film increases only 12 Å (curve 1) and 6 Å (curve 2) more. Kinetics of the film growth are logarithmic in both of these regions.

While films formed at the corrosion potential grow according to logarithmic kinetics (see Fig. 7-9), the films formed at applied anodic potentials only slightly greater than the corrosion potential grow according to a cubic law. Such films have indices of refraction in the range of 1.6-1.7. Figure 10 illustrates this kind of film growth kinetics for the specimen in deaerated 0.01N  $\text{Na}_2\text{CrO}_4$  solution at pH 7 polarized at -500 and -400 mV. Figure 11 gives the current accompanying the growth of the film at -500 mV. After reaching 75 Å thickness of the layer, the current decreases remarkably.

*Changes of potential during the film growth at open-circuit potential.*—Figure 12 shows examples of poten-

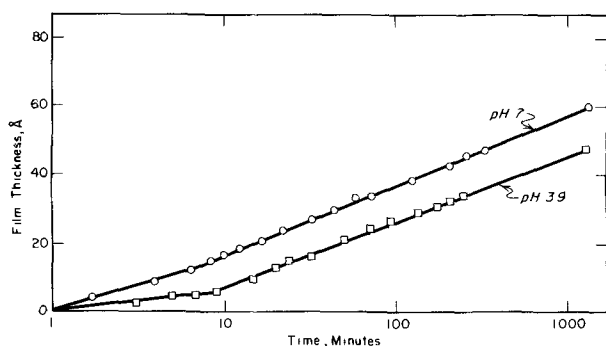


Fig. 8. Film thickness vs. time for the film whose optical parameters are given in Fig. 5 (open-circuit potential).

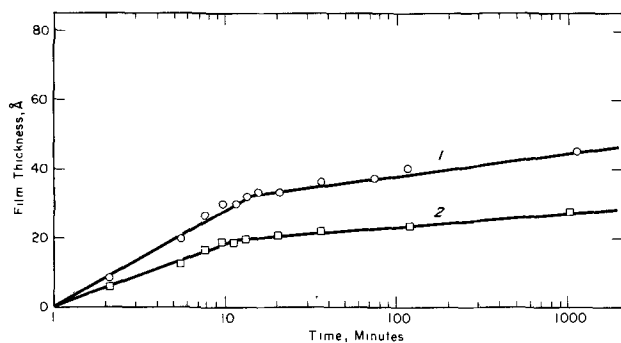


Fig. 9. Film thickness vs. time for the film whose optical parameters are given in Fig. 6 (open-circuit potential): curve 1, complex index of refraction  $1.6(1-0.02i)$ ; curve 2, complex index of refraction  $1.9(1-0.04i)$ .

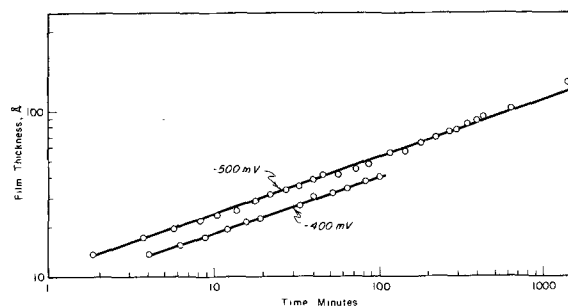


Fig. 10. Film thickness vs. time for films grown in chromate solutions of pH 7 at constant potential.

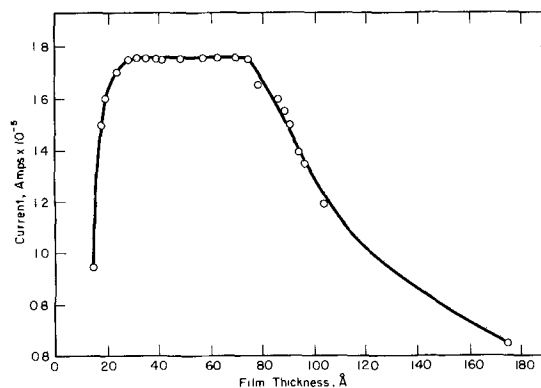


Fig. 11. Changes in current with film thickness for experiments given in Fig. 10,  $E = -500$  mV.

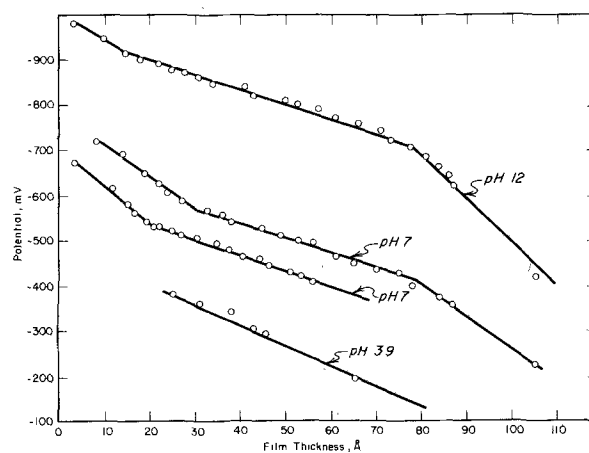


Fig. 12. Potential vs. film thickness for the film whose refractive index is equal to 1.6-1.7.

tial vs. thickness for Case 1 with different pH's. These correspond with circumstances for Case 1 shown in Fig. 4 and 7. As the thickness of the film increases, the potential shifts in the positive direction. Three regions can be distinguished: in the initial period of film growth, the potential changes rapidly; in the second region the rate of potential changes slowly with increase in the film thickness; after a certain value of film thickness the rate of change increases again. This third region can be explained by the formation of a more protective film containing iron oxide on the metal surface. A similar circumstance was observed in the phosphate solution (10). However, the amount of iron oxide seems to be small, because the optical properties of the film do not change. This also parallels the phosphate results.

Figure 13 gives the results of potential vs. time for Case 2, having two layers already shown in Fig. 5 and 8. Figure 13 assumes an index of refraction of  $1.7(1-0.009i)$ . The change of potential vs. thickness is



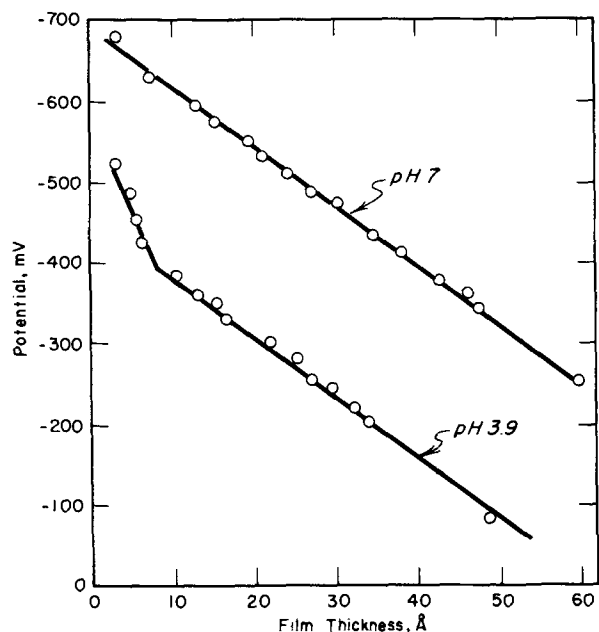


Fig. 13. Potential vs. film thickness for the film whose optical constants are given in Fig. 5. The complex index of refraction of the first layer: 2.6(1-0.12i); and the second layer: 1.7(1-0.009i).

equal to 7.5 mV/Å. The same dependence is shown in Fig. 14 for Case 2 but with only one layer and this corresponds to the experiments presented also in Fig. 6 and 9. For the single layer Case 2, the increase of potential is more rapid than it was for the double layer, and is equal to 17.5 mV/Å (curve 1) and 28 mV/Å (curve 2). Slopes for Fig. 12, 13, and 14 are summarized in Table I.

There is another very important parallel circumstance between the chromate and phosphate experiments. In the phosphate it was observed that above a certain potential the rate of change of potential with film thickness would increase. We hypothesized for the phosphate that this change was preceded by the formation of iron oxide. This hypothesis was checked on

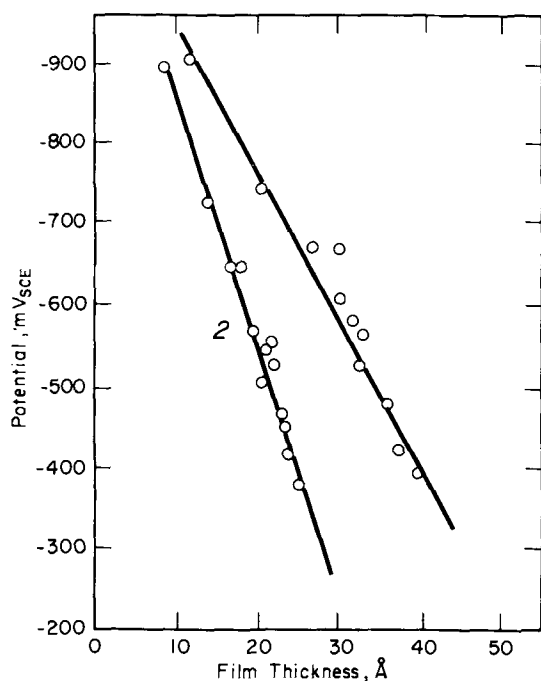


Fig. 14. Potential vs. film thickness for the film whose optical constants are given in Fig. 6: curve 1, complex index of refraction 1.6(1-0.02i); curve 2, complex index of refraction 1.9(1-0.04i).

Table I.

Index of refraction	Change of potential (mV/Å)	Rate of film growth Å/decade of time (in min)	Change of potential in time mV/decade of time (in min)
1.6	I — II 3 III —	— 33 6-8	140
First film 2.6(1-0.12i)			240
Second film 1.7(1-0.009i)	7.5	I 20 II 12	165
1.6(1-0.02i)	17.5		190
1.9(1-0.04i)	28.0	I 20 II 6	

phosphate by allowing the films to grow only at a limited extent followed by applying the higher potential potentiostatically. Since the new iron oxide was a large part of the total, it was then possible to observe a change in optical properties. The same experiment is shown in Fig. 15 for the chromate solution. A film was grown initially at -400 mV; after a short time a potential of +400 mV was applied and at this stage the  $\Delta A$  vs.  $\Delta P$  changed abruptly.

The change of potential vs. time for the Case 1 and 2 films is shown in Fig. 16. These do not provide the same implications as those for potential vs. film thickness. For Case 1 the potential changes slowly until it reaches a parting value and then a rapid change is observed. For Case 2 different patterns are observed for the one and the two layer films.

Discussion

Optical parameters and film composition.—Depending on the experimental condition established on the metal surface, different films of different optical constants are found; these different optical constants imply certainly different chemical compositions. The kind of film does not depend on the pH of the chromate solution; it depends on the potential and initial conditions. The films can be approximately divided into two groups: those with an index of refraction of 2.6 and those with an index of refraction of 1.6-1.9.

It is well known that the anodically produced iron oxide films have the index of refraction about 2.6; however, it is not known what composition corresponds

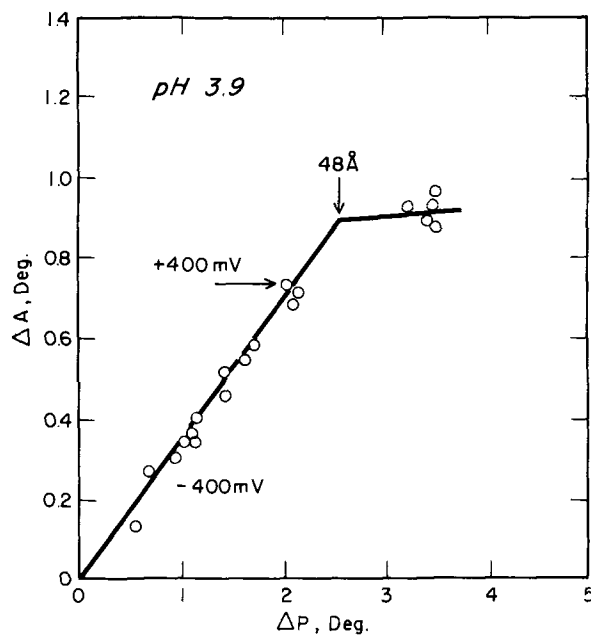


Fig. 15. Effect of anodic polarization on  $\Delta A$  vs.  $\Delta P$  relationship for a film formed in chromate solution of pH 7.

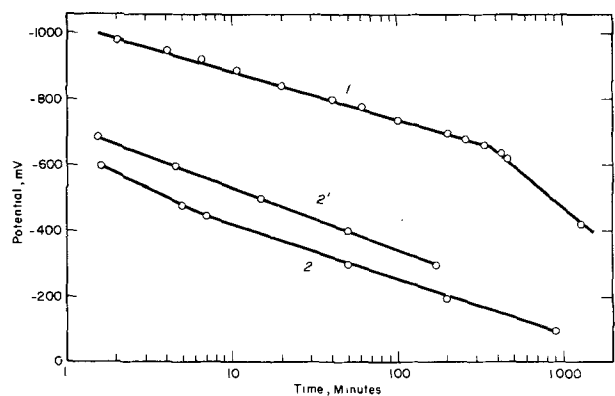


Fig. 16. Potential vs. time for the films of different optical constants produced in chromate solutions: curve 1, 1.6; curve 2, first layer 2.6(1-0.12i), second layer 1.7(1-0.009i); curve 2', 1.6-1.9 with different imaginary parts.

to a film with the index of refraction 1.6-1.7.  $\text{Cr}(\text{OH})_3$  has such a low refractive index (1.62) (17). For  $\text{FeOOH}$  Ord gives the value of 1.7 (16) however, his value differs significantly from those given by other authors (2.2-2.4) (18). Also, the index of refraction of  $\text{Cr}_2\text{O}_3$  is  $2.54 \pm 0.4$  and that of  $\text{CrOOH}$  is  $2.0 \pm 0.1$  (17). These also do not correspond to the range of 1.6-1.7 found in the present study.

If the potential-pH equilibrium diagrams of the system chromium-water and iron-water systems are compared, both chromium hydroxide (oxide) and iron hydroxide (oxide) are stable in the region of potential of the present study. Further,  $\text{Cr}(\text{OH})_3$  is also stable at much more negative potentials than iron oxides. However, to obtain the deposition of  $\text{Cr}(\text{OH})_3$  on the iron surfaces, chromate anions would have to first be reduced. We found that at potentials more negative than the equilibrium potential for  $\text{Fe}/\text{Fe}_2\text{O}_3$  but in the region of  $\text{Cr}(\text{OH})_3$  stability, such cathodic reduction occurred very slowly because we observed very slow formation of a film. However, we noticed that the index of refraction of iron is lower than that obtained in different solutions studied previously (10-12). This indicates that the iron surface is covered by adsorbed chromate molecules or by a thin film of chromium hydroxide. It is well established that trivalent chromium is always present in the film produced in chromate solutions; hence it appears that there is a direct relationship between the reduction of chromate and the oxidation of iron. Details of this coupled reaction are discussed later.

We will not speculate at this time on the exact composition and structure of films with the index of refraction 1.6-1.7, because more studies are necessary. But such a low index of refraction shows that the film cannot be composed of  $\gamma\text{-Fe}_2\text{O}_3$ ,  $\text{Fe}_3\text{O}_4$ , and  $\text{Cr}_2\text{O}_3$ . We presume that this film is some combination of iron hydroxide and chromium hydroxide.

Four different kinds of films can be distinguished according to their optical properties:

1. The films formed at high anodic potentials with a complex index of refraction equal to 2.6 (1-0.12i). The film is composed of  $\gamma\text{-Fe}_2\text{O}_3$  or  $\text{Fe}_3\text{O}_4$  with a negligible concentration of  $\text{Cr}_2\text{O}_3$  (19).

2. The films on the clean surface of iron at open-circuit potentials. During the initial stage of the film growth, high negative potentials occur. The same type of film forms when a constant potential near the open-circuit potential is applied to an initially film-free surface. Such a film is formed also in dichromate solutions on the iron surface having an oxide film formed in the air. The film formed under such conditions has an index of refraction of 1.6-1.7. We suppose that this film is composed of a mixture of iron and chromium hydroxides. After a sufficiently anodic potential is reached,  $\gamma\text{-Fe}_2\text{O}_3$  or  $\text{Fe}_3\text{O}_4$  and  $\text{Cr}_2\text{O}_3$  is also formed.

3. The films formed at open-circuit potentials, when the potential moves more rapidly in positive direction than it was in Case 2. The formed film is composed of two layers. The first layer (thin) on the metal surface appears to be  $\gamma\text{-Fe}_2\text{O}_3$  or  $\text{Fe}_3\text{O}_4$  which is too thin to be protective; on the top of this oxide layer another layer is formed with an index of refraction in the range of  $n = 1.7-1.9$  and  $k = 0.16$  and  $0.04$ , respectively. It seems that such a layer is composed of iron and chromium hydroxides with a small amount of  $\gamma\text{-FeOOH}$ ,  $\gamma\text{-Fe}_2\text{O}_3$  or  $\text{Fe}_3\text{O}_4$  and  $\text{Cr}_2\text{O}_3$ . The same kind of film is formed in chromate solutions of pH 7 and 12 having oxide films formed in the air.

4. The films formed at open-circuit potential with only one layer but with index of refraction in the range 1.6-1.9 with  $k = 0.02$  and  $0.04$ , respectively. This film is also one containing iron and chromium hydroxide but probably contains a higher concentration of  $\gamma\text{-FeOOH}$ ,  $\gamma\text{-Fe}_2\text{O}_3$  or  $\text{Fe}_3\text{O}_4$  and  $\text{Cr}_2\text{O}_3$  than the film formed in Case 3.

*Kinetics of film growth.*—Table I summarizes growth rate of films. Both kinds of film (with the index of refraction 2.6 and 1.6) grow according to the logarithmic law at the open-circuit potential. At constant potentials the film with the index of refraction 1.6-1.9 grows according to the cubic law. Logarithmic and cubic kinetics of oxide film growth show that both films have protective properties. However, the growth rates are different for the various films as given in Table I. The film growth is the most rapid when only iron hydroxide is produced (33Å/decade).

*Changes of potentials during film growth.*—The shift of potential in the noble direction at open-circuit potential during the formation of iron and chromium hydroxide is indicative of the protective properties of iron hydroxide. Table I gives the values of the potential change per Angstrom of film thickness for films studied in the present work. Some differences exist between the various kinds of films. A higher drop of potential is observed on the mixture of iron and chromium oxide than on the mixture of hydroxide and oxide films.

*Mechanism of iron inhibition by chromate.*—There exist two opinions concerning the mechanism of inhibition of iron by chromate. This first view is based on the fact that in neutral solutions of chromate containing oxygen the oxygen reduction is more rapid than the reaction of reduction of chromate. Therefore, the oxygen is in fact the passivator, and chromate adsorbed on the metal surface in a nonreduced form acts only by decreasing the critical current of passivation (14, 15). The second point of view is expressed by Cohen and Beck (4). They assume that the corrosion of iron occurs with formation of the hydroxide of bivalent iron which undergoes oxidation in the presence of oxygen. In the presence of chromates the oxidation occurs directly on the metal surface and causes formation of protective layers of iron oxide with some amount of  $\text{Cr}_2\text{O}_3$ . If a protective layer is already present on the metal surface, then the role of the chromate is limited to healing the weak points on the film and thickening of the film.

Our results suggest that formation of protective films in the presence of chromate anions occurs by successive steps:

1. Iron dissolves forming iron hydroxide,  $\text{Fe}(\text{OH})_2$
2. In the presence of the air or  $\text{CrO}_4^{2-}$  ions,  $\text{Fe}(\text{OH})_2$  is oxidized to  $\text{Fe}(\text{OH})_3$ . Even in the absence of air the chromate anions react with  $\text{Fe}(\text{OH})_2$  producing  $\text{Fe}(\text{OH})_3$  and  $\text{Cr}(\text{OH})_3$ . This reaction occurs at potentials near the initial corrosion potential thereby extending the range of significant corrosion resistance to lower potentials.
3. At higher anodic potentials iron and chromium hydroxides can probably be dehydrated to produce  $\gamma\text{-FeOOH}$  and  $\text{CrOOH}$  and  $\gamma\text{-Fe}_2\text{O}_3$  and  $\text{Cr}_2\text{O}_3$ , corresponding to observations of the higher refractive index.

### Summary

1. Anodic passive films in chromate solutions of pH 3.9, 7, and 12 have the same complex refractive index which is 2.6(1-0.12i). These films are chiefly composed of  $\gamma$ -Fe<sub>2</sub>O<sub>3</sub> or Fe<sub>3</sub>O<sub>4</sub>.

2. At the open-circuit potential on iron surface various films are formed depending on experimental conditions. They are composed of iron and chromium hydroxide (index of refraction 1.6-1.7) or a mixture of iron and chromium hydroxides with iron and chromium oxides (index of refraction 1.6-1.9, with various adsorption coefficients).

3. The films produced on iron surface with an initially formed oxide in aerated chromate solutions of pH 7 and 12 have the index of refraction of 1.6-1.9 with various adsorption coefficients.

4. The kinetics of iron oxide and iron and chromium hydroxide formation at open-circuit potential is logarithmic, and the kinetics of iron hydroxide formation at constant potential is cubic.

5. All films formed in chromate solution have a protective nature.

### Acknowledgment

The authors acknowledge the support of The Ohio State University, the International Nickel Company, and the Office of Naval Research under contract No. N00014-A-0232-0006-NR036-085 in partial support of this research.

Manuscript submitted Dec. 17, 1973; revised manuscript received May 6, 1974.

Any discussion of this paper will appear in a Discussion Section to be published in the June 1975 JOURNAL. All discussions for the June 1975 Discussion Section should be submitted by Feb. 1, 1975.

The publication costs of this article have been assisted by The Ohio State University.

### REFERENCES

1. M. T. Simnad and U. R. Evans, *J. Metals*, **188**, 1220 (1950).
2. D. M. Brasher and E. R. Stove, *Chem. Ind. (London)*, 171 (1952).
3. D. M. Brasher, *Trans. Faraday Soc.*, **61**, 803 (1965).
4. M. Cohen and A. F. Beck, *Z. Elektrochem.*, **62**, 696 (1958).
5. H. H. Uhlig and P. King, *This Journal*, **106**, 1 (1959).
6. R. Powers, N. Hackerman, *ibid.*, **100**, 314 (1953).
7. D. M. Brasher, A. H. Kingsbury, A. D. Mercer, and C. P. De, *Nature*, **180**, 27 (1957).
8. D. M. Brasher and A. H. Kingsbury, *Trans. Faraday Soc.*, **54**, 1214 (1958).
9. J. Kruger, *This Journal*, **110**, 664 (1963).
10. Z. Szklarska-Smialowska and R. W. Staehle, *ibid.*, In press.
11. C. Lukac, Z. Szklarska-Smialowska, J. B. Lumsden, and R. W. Staehle, To be published.
12. C. Lukac, J. B. Lumsden, Z. Szklarska-Smialowska, and R. W. Staehle, In preparation for publication.
13. F. L. McCrackin, "A Fortran Program for Analysis of Ellipsometry Measurements," U.S. Gov. Printing Office, Washington, D. C. (1969).
14. G. H. Cartledge, *J. Phys. Chem.*, **65**, 1009, 1361 (1961).
15. J. G. N. Thomas and T. J. Nurse, *Brit. Corr. J.*, **2**, 13 (1967).
16. F. C. Ho and J. L. Ord, *This Journal*, **119**, 139 (1972).
17. M. A. Genshaw and R. S. Sirohi, *ibid.*, **118**, 1558 (1971).
18. *Handbook of Chemistry and Physics*, 48th edition, The Chemical Rubber Co., (1967-1968).
19. Z. Szklarska-Smialowska, J. B. Lumsden, and R. W. Staehle, To be published.

## Anodic Oxidation of Nickel in Neutral Sulfate Solution

B. MacDougall\* and M. Cohen\*

Division of Chemistry, National Research Council of Canada, Ottawa, Ontario, Canada

### ABSTRACT

The formation and growth of protective oxide films on nickel electrodes was studied in a pH 8.4 Na<sub>2</sub>SO<sub>4</sub> solution. A cathodic treatment of 10 min at -1.35V (vs. Hg<sub>2</sub>SO<sub>4</sub>) was sufficient for removal of the oxide film on electropolished nickel and thereby provided a starting point for the oxidation experiments. Anodization of the nickel electrode into the passive potential region produced a 9-12Å oxide film on the surface, this being ca. 50% thicker than the oxide film on electropolished nickel. Although both types of oxide inhibited nickel dissolution, their cathodic electrochemical behavior was quite different, with the film on anodized nickel not being susceptible to cathodic reduction. Reflection electron diffraction showed that the lattice parameter of the oxide on anodized nickel was closer to stoichiometric NiO than that on electropolished nickel. Formation of the oxide film on anodized nickel is by a direct electrochemical reaction, while that on electropolished nickel is probably due to the subsequent air exposure. The mechanism by which oxide films passivate nickel dissolution is discussed.

The electrochemical behavior of nickel has been the subject of extensive investigation in both acid and alkaline solutions. The typical potentiostatic i-V profile for the anodic polarization of nickel in an aqueous electrolyte shows that nickel dissolution occurs in the "active" potential region but is inhibited at more anodic potentials (e.g., see Fig. 1). The importance of water, and hence probably an oxide film, in the passivation of nickel dissolution has been noted, passivation being absent in anhydrous acetonitrile solutions (1). The

oxide film is believed to inhibit nickel dissolution by forming a physical barrier between the metal and solution, thus preventing bare metal from being in contact with solution (2-5). However, there is some question as to whether the physical presence of the oxide is, by itself, sufficient for passivation since a large potential drop across the oxide film may allow continued dissolution through field-assisted metal cation migration. In the latter case, passivation would occur when the potential gradient across the oxide is too small to allow cation migration and this condition could arise by either a thickening of the oxide or an

\* Electrochemical Society Active Member.

Key words: nickel oxide, passivity, anodic oxidation.

increase in its electronic conductivity. It has also been suggested that the essential step in the passivation of nickel is the conversion of a precursor, nonprotective, oxide film into an electronic conductor through the introduction of nonstoichiometry (6, 7).

The two main mechanisms suggested for oxide formation on nickel are: (i) dissolution-precipitation (6, 8, 9); (ii) direct oxidation of the metal surface (2, 3, 5, 10, 11). In the first case, it is postulated that oxide formation can occur when the solubility of a species such as  $\text{Ni}(\text{OH})_2$  in solution near the electrode is exceeded, thus resulting in a precipitation of the  $\text{Ni}(\text{OH})_2$  onto the electrode. Dependence of the induction time for oxide formation on the rate of solution stirring has been used as support for this mechanism of oxide formation (9); however, the observed dependence might also be due to a concentration overvoltage. The second mechanism of oxide film formation would involve a reaction such as:  $\text{Ni} + \text{H}_2\text{O} \rightarrow \text{NiO} + 2\text{H}^+ + 2\text{e}^-$ , where there is a direct electrochemical reaction between the nickel electrode and water from solution.

The present investigation is a study of the nature of the protective oxide film on nickel and the mechanism for its formation in a neutral  $\text{Na}_2\text{SO}_4$  solution. Electrochemical methods were complemented with electron diffraction, electron microscopy, and x-ray emission spectroscopy, in an attempt to determine more accurately the composition and structure of the film and to decide between the various possibilities given above for oxide formation and passivation.

### Experimental

**Specimen preparation.**—Zone-refined nickel sheet supplied by Materials Research Corporation was used in this work, spark source mass spectrographic analysis showing it to be 99.996% pure. Electrodes of various surface areas (generally 1 cm by 2.5 cm), were degreased with benzene in a soxhlet extractor and chemically polished (12). They were then electropolished for 2 min at 23°C in a 57% sulfuric acid solution at ca.  $0.5\text{A cm}^{-2}$  and annealed at 800°C in a vacuum of  $10^{-8}$  Torr. The specimens were always electropolished again immediately before use in an experiment. Electrical contact was made by spot-welding a nickel wire to the top of the narrow handles of the specimen. The spot-weld was always at least 2 cm above the  $\text{Na}_2\text{SO}_4$  electrolyte during an experiment. A (111) nickel single-crystal disk, the preparation and analysis of which has been described elsewhere (13), was used to obtain detailed information regarding the lattice parameters of the nickel oxides formed under various conditions.

**Reference electrode.**—All potentials quoted in this paper are referred to the  $\text{Hg}_2\text{SO}_4$  electrode (+0.665V with respect to the standard reversible hydrogen electrode).

**Solutions.**—All experiments were conducted at 25°C. A deaerated solution of 0.15N  $\text{Na}_2\text{SO}_4$ , its pH adjusted to 8.4, was used for both the cathodic reduction and the anodic passivation experiments.

**Apparatus.**—A Wenking fast-rise potentiostat was used to obtain controlled potentials and the mode of polarization could be changed to galvanostatic by means of a switch in the circuit (14). A high-speed Brush recorder was used to follow the initial rapid decrease of current after the potential step, with the current and charge measurement being switched over to a slower speed recorder and electronic counter after the rate of current decay had decreased. A Wenking current integrator, Model SS1 70, was used to complement this method of charge determination. Potentials were measured on a Beckman Century pH meter with high input impedance, and/or a Hewlett-Packard strip chart recorder.

The electrochemical cell had the recording and counterelectrodes in the same compartment, the com-

partment usually being filled with 50 ml of solution. The counterelectrode consisted of two large sheets of platinum gauze placed in the cell so that they would be parallel to the nickel sheet electrode. The nickel electrodes were on sliding tru-bore ground glass tubes, thus allowing the electrodes to be immersed into or removed from the electrolyte without admitting air to the system.

**Electrochemical procedure.**—After electropolishing in  $\text{H}_2\text{SO}_4$ , the nickel electrodes were immersed in a deaerated  $\text{Na}_2\text{SO}_4$  solution of pH 8.4 under cathodic polarization at  $-1.35\text{V}$  for 10 min to remove the prior surface oxide. Potentiostatic polarization curves were obtained by changing the potential in 50 mV steps, the current being measured after 60 sec. Galvanostatic charging curves were obtained on both oxide-free and oxide-covered nickel electrodes. The amount of nickel dissolution was measured at various times and potentials.

The potential step method was used for determining oxide coverage on nickel at various anodic potentials,  $V_a$ . The program consisted of a 10 min cathodic reduction of the prior oxide film at  $-1.35\text{V}$  during which time the current changed from ca. 500 to ca.  $35\ \mu\text{A cm}^{-2}$ . This was followed by 10 min at a constant cathodic current density of  $5\ \mu\text{A cm}^{-2}$  to reduce the concentration of molecular hydrogen, produced at  $-1.35\text{V}$ , from the solution. The potential was then stepped to  $V_a$  for the desired period of time, the change of current and anodic charge being followed during this procedure. The nickel electrode was removed from the solution while still potentiostated at  $V_a$ , and the solution was analyzed for nickel. The electrode was immediately rinsed with doubly distilled water and dried in a stream of oil-free compressed air.

The electrochemical behavior of anodized nickel electrodes was studied by two procedures: (i) the electrode was examined in the same solution in which it had been anodized, i.e., the circuit was never broken; (ii) the electrode was removed from the solution on open-circuit, exposed to air, and the solution changed.

When the behavior of nickel electrodes in alkaline solutions was studied, the cathodic reduction of the prior oxide was carried out at pH 8.4 and then the pH of the solution was adjusted to its new value by addition of deaerated NaOH solution. The same type of procedure was employed when the effect of nickel ions was under investigation, i.e., the solution of nickel ions was added after the reduction of the prior oxide in a nickel free  $\text{Na}_2\text{SO}_4$  solution.

**Analysis.**—The solutions were analyzed for nickel by atomic absorption spectroscopy using a carbon rod analyzer. The lower limit of detection by this method was 0.005 ppm. Reflection high energy electron diffraction was used to investigate the orientation, mean particle size, and lattice parameters of the oxide films on nickel. X-ray emission spectroscopy (15, 16) gave the oxygen content in the oxide films along with the amount of foreign atoms, e.g., carbon and sulfur. Replica electron microscopy with a magnification of 30,000 was used to determine the effect of various electrochemical treatments on the smoothness of the nickel surfaces.

### Results and Discussion

**Effect of electrode pretreatment on anodic oxidation of nickel.**—Figure 1 shows the anodic point-by-point polarization curve obtained on a nickel electrode in a pH 8.4  $\text{Na}_2\text{SO}_4$  solution. The electrode had been cathodically pretreated at  $-1.35\text{V}$  to remove the prior oxide film and the potential increment was 50 mV every 60 sec. The rate of active nickel dissolution increases with anodic potential until ca.  $-0.8\text{V}$ , at which point the current begins to decrease with increasing anodic potential. The small current ( $<2\ \mu\text{A cm}^{-2}$ ) which flows between  $-0.5$  and  $+0.3\text{V}$  is independent of

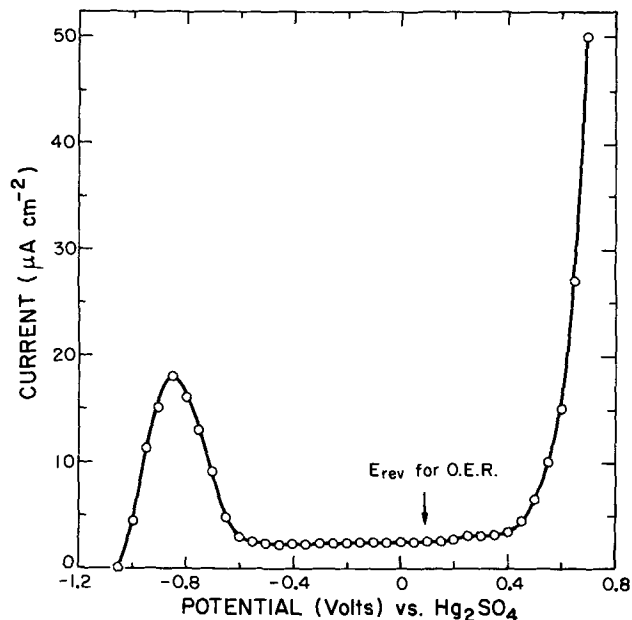


Fig. 1. Anodic potentiostatic current (*i*)-potential (*V*) profile for a previously oxide free nickel electrode in pH 8.4  $\text{Na}_2\text{SO}_4$  solution with potential increments of 0.05V every 60 sec. Measured current is that registered at the end of 60 sec.

potential and continues to decrease slowly with time after 60 sec. At potentials above +0.4V the sharp current increase is due to oxygen evolution on nickel.

It was of critical importance in the present study to determine the electrochemical conditions for obtaining an initial oxide free nickel surface from which to start the oxidation experiments. Figure 2 shows the effect of various cathodic pretreatments on the anodic polarization curves for electropolished nickel. The current maximum for nickel dissolution in the active region increases with increasing cathodic pretreatment until 10 min exposure at -1.35V, after which no significant changes are observed even after polarization for 10 min at -1.6V. Figure 3 shows the change of potential with time of an electropolished nickel electrode in pH 8.4  $\text{Na}_2\text{SO}_4$  upon application of an

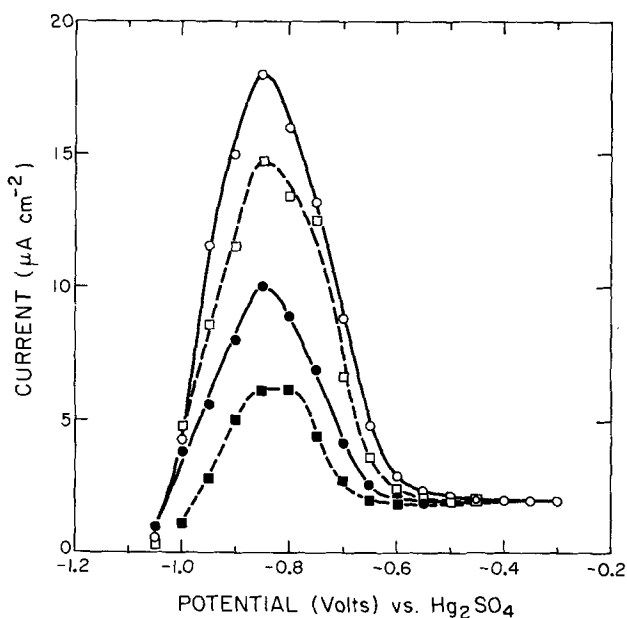


Fig. 2. Anodic potentiostatic *i*-*V* profiles for electropolished nickel electrodes after different cathodic pretreatments in pH 8.4  $\text{Na}_2\text{SO}_4$  solution: (—■—) 1 min at -1.10V; (—●—) 1 min at -1.35V; (—□—) 5 min at -1.35V; (—○—) 10 min at -1.35V.  $\Delta V = 0.05V$  and  $\Delta t = 60$  sec.

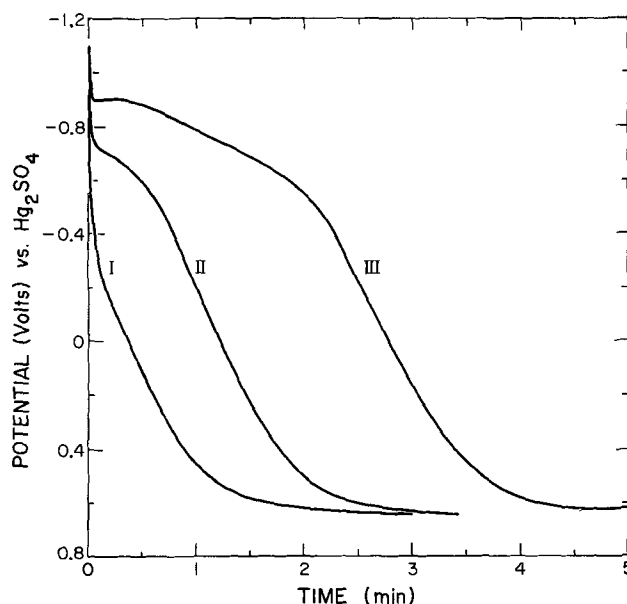


Fig. 3. Anodic galvanostatic charging curves for electropolished nickel in pH 8.4  $\text{Na}_2\text{SO}_4$  solution after prior cathodic treatments at different potentials: (I) 10 min at -1.0V; (II) 10 min at -1.1V; (III) 10 min at -1.35V. Anodic current density =  $50 \mu\text{A cm}^{-2}$ .

anodic current of  $50 \mu\text{A cm}^{-2}$  after various prior cathodic treatments. A cathodic pretreatment of 10 min at -1.35V gives a curve with a significant arrest around -0.8V. In a separate experiment it was found that 90% of the charge associated with this arrest, up to ca. -0.55V, could be accounted for by nickel in the electrolyte. This region of active nickel dissolution is absent with a cathodic pretreatment of 10 min at -1.0V and is quite small for 10 min at -1.1V. Figure 4 shows the dependence of the charge associated with the arrest up to -0.55V, i.e., charge for nickel dissolution, on the cathodic pretreatment. These results indicate that a cathodic pretreatment of 10 min at -1.35V in the  $\text{Na}_2\text{SO}_4$  solution is required to remove the prior oxide on electropolished nickel, further cathodic polarization having no additional effect.

Figure 5 shows the potentiostatic polarization curve for Ni in pH 8.4  $\text{Na}_2\text{SO}_4$  solution in both the anodic and cathodic directions, the direction of potential

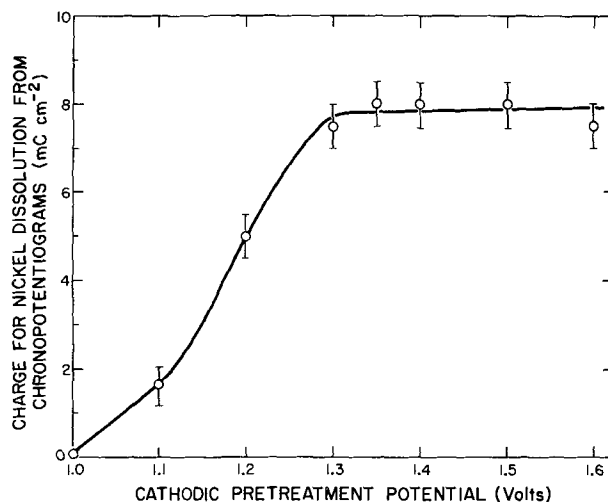


Fig. 4. Dependence of the amount of nickel dissolution as measured by the galvanostatic transient technique of Fig. 3 (and checked by solution analysis) on cathodic pretreatment potential for electropolished nickel in pH 8.4  $\text{Na}_2\text{SO}_4$  solution. 1 mc represents  $0.30 \mu\text{g}$  of nickel which is equivalent to ca. 2 monolayers of nickel on a  $1 \text{ cm}^2$  surface.

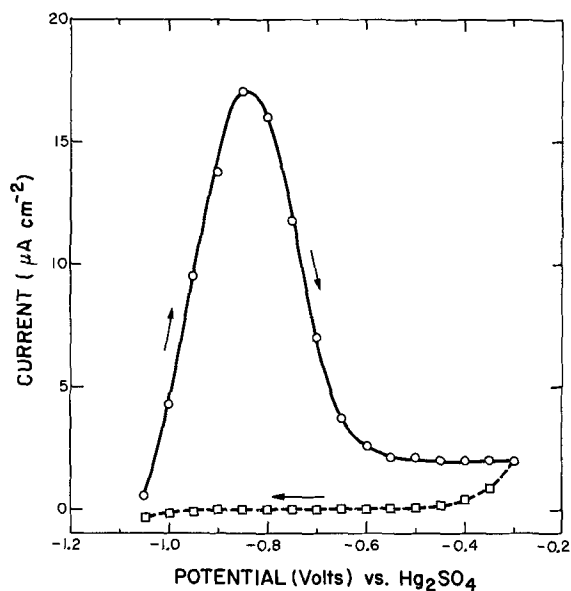


Fig. 5. Potentiostatic  $i$ -V profile for nickel in pH 8.4  $\text{Na}_2\text{SO}_4$  solution in both the anodic and cathodic directions, reversal of potential at  $-0.3\text{V}$ . Oxide film resulting from electropolishing was cathodically reduced at  $-1.35\text{V}$  for 10 min prior to the anodic sweep.  $\Delta V = 0.05\text{V}$  and  $\Delta t = 60\text{ sec}$ .

change being reversed in the passive region at  $-0.3\text{V}$ . No activation of the electrode surface toward nickel dissolution is observed on the cathodic curve. In a separate experiment, an anodic polarization curve was obtained up to  $-0.3\text{V}$  and then the potential was switched back to  $-1.35\text{V}$  for 10 min, after which another anodic polarization curve was taken (Fig. 6). The cathodic treatment which removed the oxide film due to electropolishing in  $\text{H}_2\text{SO}_4$  does not remove, to any significant extent, the oxide film arising from anodic polarization of the nickel electrode to  $-0.3\text{V}$  in pH 8.4  $\text{Na}_2\text{SO}_4$ . The same result was obtained when, after the anodic polarization to  $-0.3\text{V}$ , the nickel electrode was removed from the cell and the solution re-

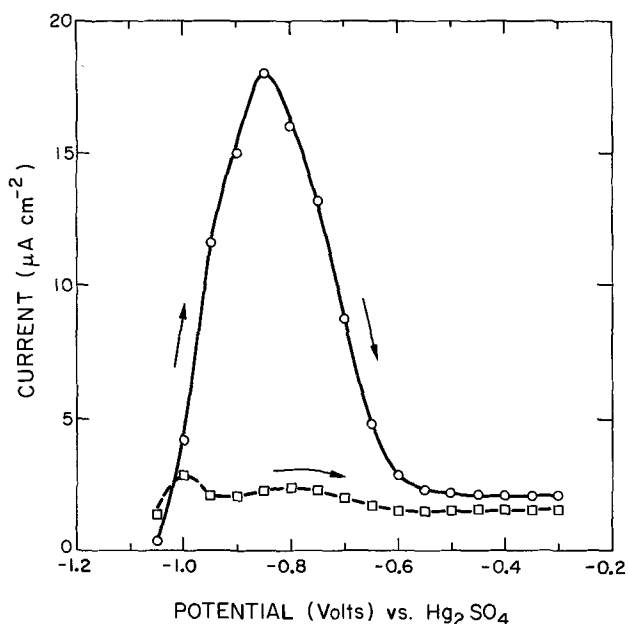


Fig. 6. Anodic potentiostatic  $i$ -V profiles for nickel in pH 8.4  $\text{Na}_2\text{SO}_4$  solution: (—○—) after prior cathodic reduction at  $-1.35\text{V}$  for 10 min of the electropolished nickel electrode; (—□—) after cathodic reduction at  $-1.35\text{V}$  for 10 min of the nickel electrode which had been anodized to  $-0.3\text{V}$  in the first part of Fig. 5.  $\Delta V = 0.05\text{V}$  and  $\Delta t = 60\text{ sec}$ .

placed by a fresh  $\text{Na}_2\text{SO}_4$  solution of pH 8.4 before cathodic polarization.

The galvanostatic charging technique was also used to investigate the possibility of cathodic reduction of the anodized nickel surface<sup>1</sup> in the  $\text{Na}_2\text{SO}_4$  solution. It was found that even with a severe cathodic pretreatment, an arrest corresponding to nickel dissolution was not observed on reanodizing a previously oxidized specimen (see Fig. 7). The same result was also obtained with nickel electrodes anodized without removal of the prior film from electropolishing, i.e., although nickel dissolution is markedly reduced by the presence of oxide from electropolishing, formation of the protective oxide occurs whether or not this oxide is present.

**Potential step technique and oxide coverage.**—In agreement with the electrochemical behavior of anodized nickel surfaces given above, a cathodic galvanostatic transient on an anodized nickel electrode showed no potential arrest corresponding to oxide reduction even at low current densities and hence cathodic coulometry could not be used to determine oxide thickness. The anodic potential step technique was therefore used to determine the amount of oxide on the nickel surface and its dependence on anodization potential. After application of the potential step the initial current was very high (e.g., several hundred mA's at  $V_a = 0\text{V}$ ), but fell very rapidly as an oxide film formed on the surface. The quantity of nickel dissolved during the cathodic pretreatment could not be detected (i.e.,  $<0.005\text{ ppm}$  from a  $5\text{ cm}^2$  nickel electrode). Hence the charge for oxide formation,  $Q_a$ , is simply the total charge,  $Q_T$ , less the calculated charge corresponding to the quantity of nickel in solution,  $Q_{\text{Ni}}$ , i.e.,  $Q_a = Q_T - Q_{\text{Ni}}$ .

If the assumption is made that the oxide stoichiometry is  $\text{NiO}$  and the charge  $Q_a$  converted to oxygen content, the dependence of oxide coverage on anodiza-

<sup>1</sup> In the present work, this term will indicate a nickel electrode whose potential has been taken into the passive region in a pH 8.4  $\text{Na}_2\text{SO}_4$  solution.

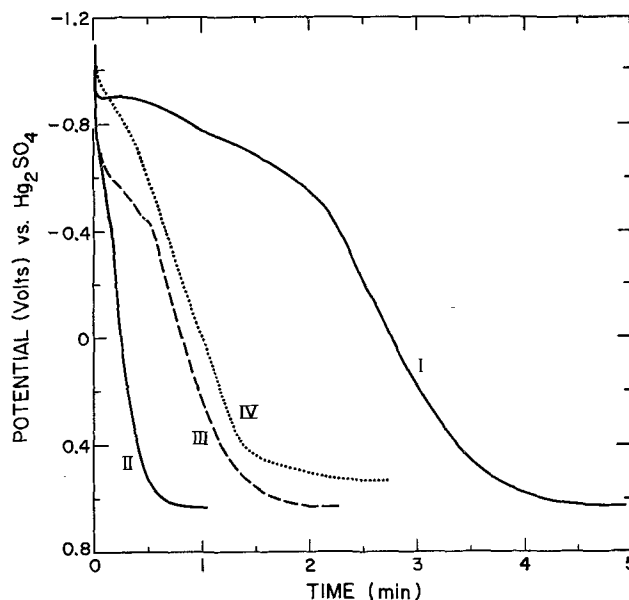


Fig. 7. Anodic galvanostatic charging curves, at  $50\ \mu\text{A cm}^{-2}$ , for nickel in various electrochemical states in pH 8.4  $\text{Na}_2\text{SO}_4$  solution (I to III) and pH 9.6  $\text{Na}_2\text{SO}_4$  solution (IV): (I) electropolished and then cathodically reduced at  $-1.35\text{V}$  for 10 min; (II) anodized to  $0\text{V}$  for 1 hr in pH 8.4  $\text{Na}_2\text{SO}_4$  followed by cathodic reduction at  $-1.35\text{V}$  for 10 min in a fresh pH 8.4  $\text{Na}_2\text{SO}_4$  solution; (III) anodized to  $0\text{V}$  for 1 hr in pH 8.4  $\text{Na}_2\text{SO}_4$  followed by cathodic reduction at  $-1.35\text{V}$  for 10 min in a pH 3.5  $\text{Na}_2\text{SO}_4$  solution; (IV) electropolished and cathodically reduced at  $-1.35\text{V}$  for 10 min in pH 8.4  $\text{Na}_2\text{SO}_4$  solution, then the pH was adjusted to 9.6 and the galvanostatic transient obtained.

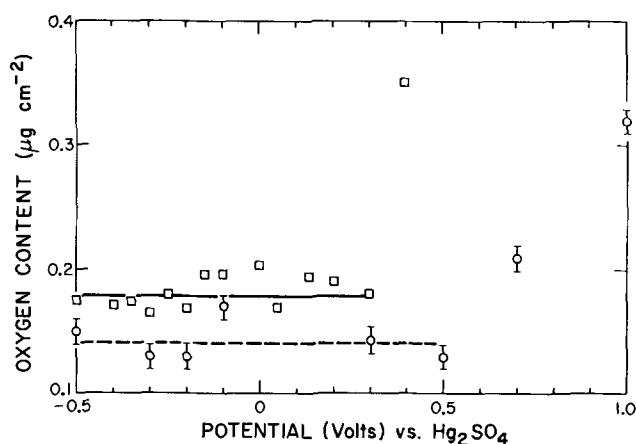


Fig. 8. Dependence of amount of oxygen on nickel on anodization potential,  $V_a$ , using the potential step technique, as determined by coulometry (—□—) and x-ray emission analysis (—○—). Time of anodization was 1 hr.  $0.1 \mu\text{g cm}^{-2}$  of oxygen corresponds to  $6.9\text{\AA}$  of NiO.

tion potential is given in Fig. 8 (see also Table I). The measurements were made 1 hr after initiation of the potential step. Also shown in Fig. 8 are the oxide coverages at different potentials obtained by x-ray emission spectroscopy, also on the basis of an oxide stoichiometry NiO. The oxide thickness agrees to within 20% (Fig. 8 and Table I) with that determined by coulometry, the discrepancy probably being associated with difficulties in preparing accurate nickel standards for the x-ray technique with oxides of less than ca.  $30\text{\AA}$  thickness. The oxide coverage is also seen to be almost independent of  $V_a$  until ca.  $+0.4\text{V}$ . At potentials less than  $+0.4\text{V}$  the residual current after 1 hr of anodic polarization is  $<1 \times 10^{-8}\text{A cm}^{-2}$ , i.e., essentially zero. However, at  $V_a \geq +0.4\text{V}$ , the residual current is finite and measurable and without doubt associated with oxygen evolution (see Fig. 1). The reasonably good agreement between the two sets of data for those potentials below oxygen evolution and the oxide coverage at  $+0.5\text{V}$  determined by the x-ray method indicates that the oxide thicknesses at  $V_a \geq +0.4\text{V}$  calculated from coulometry are incorrect due to oxygen evolution.

The x-ray method gave a thickness of ca.  $6\text{\AA}$ , i.e.,  $0.09 \mu\text{g oxygen cm}^{-2}$ , for the oxide film on nickel after electropolishing in  $\text{H}_2\text{SO}_4$ , the film on anodized nickel being ca. 50% thicker. Cathodic reduction of the electropolished specimen in  $\text{pH } 8.4 \text{ Na}_2\text{SO}_4$  and air-ex-

posure of the resulting oxide free nickel electrode also yielded an oxide film of ca.  $6\text{\AA}$  thickness, this oxide displaying the same electrochemical behavior as that on electropolished nickel. The oxide film on both electropolished and anodized nickel contained<sup>2</sup>  $<0.01 \mu\text{g cm}^{-2}$  of carbon and  $<0.005 \mu\text{g cm}^{-2}$  of sulfur for any potential  $V_a \leq 0.5\text{V}$ , i.e., there was little if any sulfur incorporation into the film even at high anodic potentials.

At  $V_a > \text{ca. } +0.5\text{V}$  the oxide coverage, as measured by oxygen  $K_\alpha$  x-ray emission spectroscopy, increased because of a roughening of the nickel surface. Analysis of the electrolyte after polarization at these potentials shows that large quantities of nickel (ca. 500 monolayers) have dissolved and electron micrographs at  $18,900\times$  (Fig. 9) of the resulting nickel surface show a substantial increase in roughness. In comparison, the nickel surface is very smooth after electropolishing and remains smooth even after the potential step treatments up to  $+0.5\text{V}$ , justifying the use of a roughness factor of 1. The substantial increase in the roughness factor at higher anodic potentials means that the calculated quantity of oxygen  $\text{cm}^{-2}$  of electrode surface, as determined by x-ray emission, will be too high since it is based on a roughness factor of 1.

Bockris *et al.* (6) found that the oxide thickness on nickel in a  $\text{pH } 3.0 \text{ Na}_2\text{SO}_4$  solution was independent of anodic potential, the quoted thickness being from  $60$  to  $100\text{\AA}$  as determined by ellipsometry. This value for oxide thickness is high in comparison with the present  $10$  to  $12\text{\AA}$  film and may be due to the experimental technique of the former. Instead of using a potential step treatment, a point by point anodic polarization technique was employed which probably resulted in heavy etching of the surface because of nickel dissolution. This roughening of the surface would lead to

<sup>2</sup> These represent limits of detection.

Table I. Comparison of total quantity of electricity passed, amount of nickel in solution and oxide film thickness associated with anodization for 1 hr to various potentials,  $V_a$ , using the potential step technique.

Anodization potential $V_a$ (V)	Total charge passed (mC $\text{cm}^{-2}$ )	Charge due to nickel dissolution $\text{cm}^{-2}$ of electrode (mc)	Amount of oxide from charge (μg $\text{cm}^{-2}$ )	% of total charge for oxide formation	Amount of oxide from x-ray measurements (μg $\text{cm}^{-2}$ )
-0.5	5.2	3.13	0.17	40	0.15
-0.3	5.0	3.1	0.16	39	0.13
-0.2	5.5	3.6	0.16	37	0.13
-0.1	6.5	4.1	0.20	37	0.17
+0.15	7.2	4.8	0.20	34	—
+0.3	8.8	6.6	0.18	25	0.14
+0.4	14.2	10.0	0.35*	—	—
+0.5	—	—	—	—	0.13
+0.7	—	—	—	—	0.21**
-0.3***	5.3	—	—	—	0.14

\* Coulometric method is in error because of oxygen evolution.

\*\* X-ray method is in error because of surface roughness.

\*\*\* Potential step technique employed in a solution of  $10 \mu\text{g ml}^{-1} \text{ Ni}^{2+}$ .

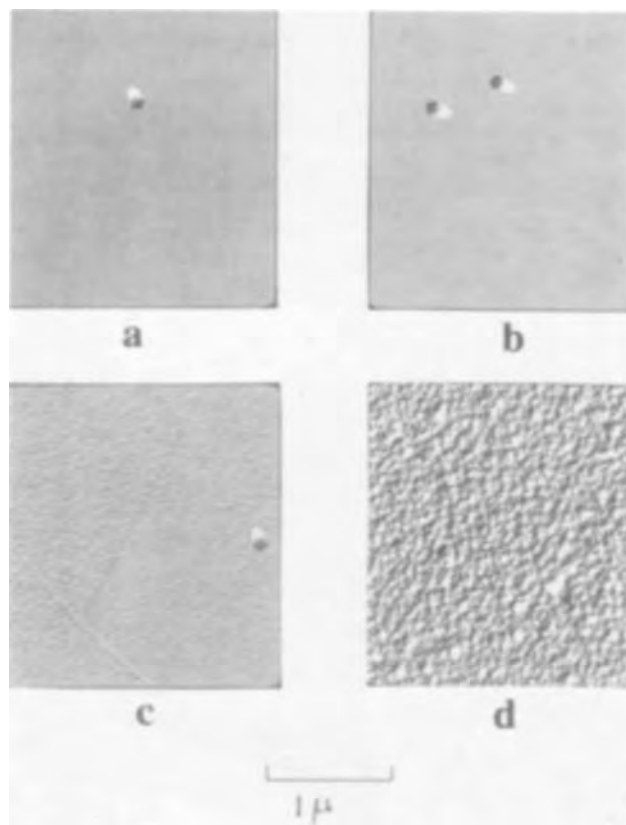


Fig. 9. Electron micrographs at  $18,900\times$  of the nickel surface after different electrochemical treatments: (a) electropolished in  $\text{H}_2\text{SO}_4$ ; (b) anodized to  $0\text{V}$  for 1 hr; (c) as in (b) but with  $V_a = +0.7\text{V}$ ; (d) as in (b) but with  $V_a = +1.0\text{V}$ . Shaded spheres are  $900\text{\AA}$  polystyrene balls.

a large uncertainty in the oxide thickness as measured by the ellipsometric technique (17). The discrepancy in oxide thickness is not associated with the fact that their  $\text{Na}_2\text{SO}_4$  solution was at a  $\text{pH} = 3.0$  since the oxide thickness on nickel obtained in this laboratory at  $\text{pH} = 3.0$  by x-ray spectroscopy, using the potential step technique to  $V_a = 0\text{V}$ , was ca.  $10\text{\AA}$ . Sato *et al.* (18, 19) have recently reported that the oxide thickness on nickel (measured ellipsometrically) in neutral borate buffer solution is dependent on anodic potential in the passive region, the thickness increasing from ca. 5 to  $15\text{\AA}$  with increasing anodic potential. The error limits in the present oxide measurement are  $\pm 1.5\text{\AA}$  (Fig. 8), and this fact taken along with the x-ray measurements would suggest that the discrepancy between our results and those of Sato *et al.* is quite real. Figure 10a shows the change in oxide coverage with time after a potential step to  $-0.3\text{V}$ . The oxide grows very quickly, reaching its maximum thickness after ca. 5 min. Correspondingly, the quantity of nickel in the solution after the potential step to  $-0.3\text{V}$  for various times (Fig. 10b) is found to reach a limit after ca. 5 min, with only a small increase thereafter. As the oxide forms and thickens on the surface, nickel dissolution is inhibited, most of the nickel going into solution when the surface is oxide free.

**Effect of added nickel and solution stirring on oxide formation.**—After a cathodic reduction of the electropolished nickel in  $\text{pH} 8.4 \text{Na}_2\text{SO}_4$  solution at  $-1.35\text{V}$  and with the potential changed to  $-1.1\text{V}$  to remove excess  $\text{H}_2$ , a  $\text{NiSO}_4$  solution was added to the electrolyte. Enough  $\text{NiSO}_4$  was added to give a  $[\text{Ni}^{2+}]$  in solution which was about  $50\times$  higher than would normally be found after the galvanostatic transient (Fig. 3). Reflection electron diffraction on a (111) nickel single crystal (see below) showed that addition of the  $\text{NiSO}_4$  solution during the prior cathodic treatment at  $-1.1\text{V}$  did not alter the electrode surface. This large quantity of added nickel in the solution

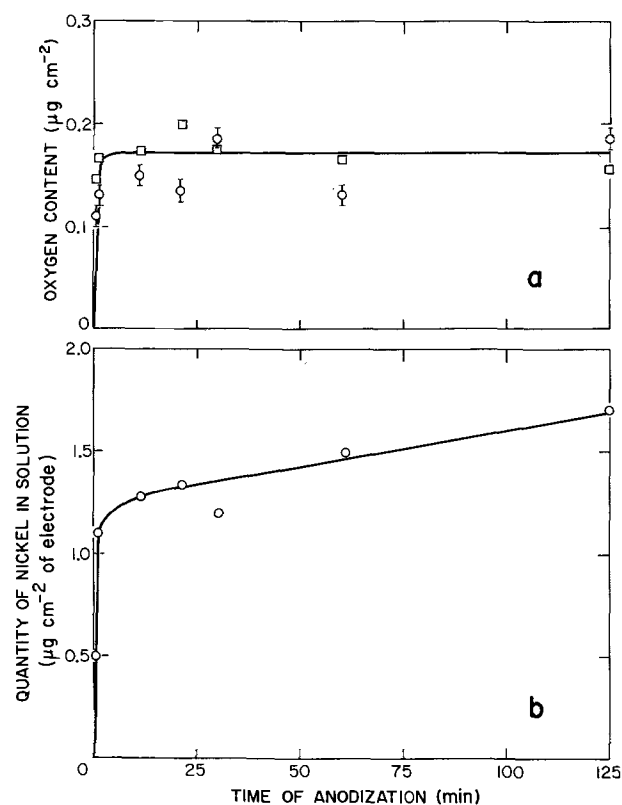


Fig. 10. (a) Variation of oxygen content on nickel with time of anodization after the potential step treatment to  $-0.3\text{V}$ . ( $\square$ ) Coulometric analysis; ( $\bigcirc$ ) x-ray analysis. (b) Variation of the quantity of nickel in solution with time of anodization after the potential step treatment to  $-0.3\text{V}$ .

does not diminish the potential arrest corresponding to nickel dissolution during an anodic charging experiment at  $50 \mu\text{A cm}^{-2}$ . The potential step technique provided an excellent alternative method for determining the mechanism of oxide formation on nickel. When the potential is stepped to  $-0.3\text{V}$  or  $0\text{V}$  in the presence of a large quantity of added nickel ( $10 \mu\text{g ml}^{-1} \text{Ni}^{2+}$ ), the current decays at the same rate as that obtained in an experiment without added nickel.

Identical experiments were carried out, in the absence of added nickel, with and without solution stirring by argon bubbling. The results were independent of solution stirring just as they had been independent of added nickel in the system. These results show that  $\text{Ni}^{2+}$  ions in solution are not an important factor in the oxide formation reaction on nickel under our experimental conditions, i.e., a dissolution-precipitation mechanism does not apply. The results are more consistent with a direct electrochemical reaction between water and metal to form essentially anhydrous  $\text{NiO}$ .

**Electron diffraction study of the oxides on nickel.**—Reflection electron diffraction patterns of an electropolished (111) nickel single crystal are shown in Fig. 11 for both the  $\langle 112 \rangle$  and  $\langle 110 \rangle$  zones. Also shown are the diffraction patterns obtained after anodization, by the potential step method, for 1 hr at  $-0.45$ ,  $+0.4$ , and  $+0.7\text{V}$ . The electropolished surface shows sharp,

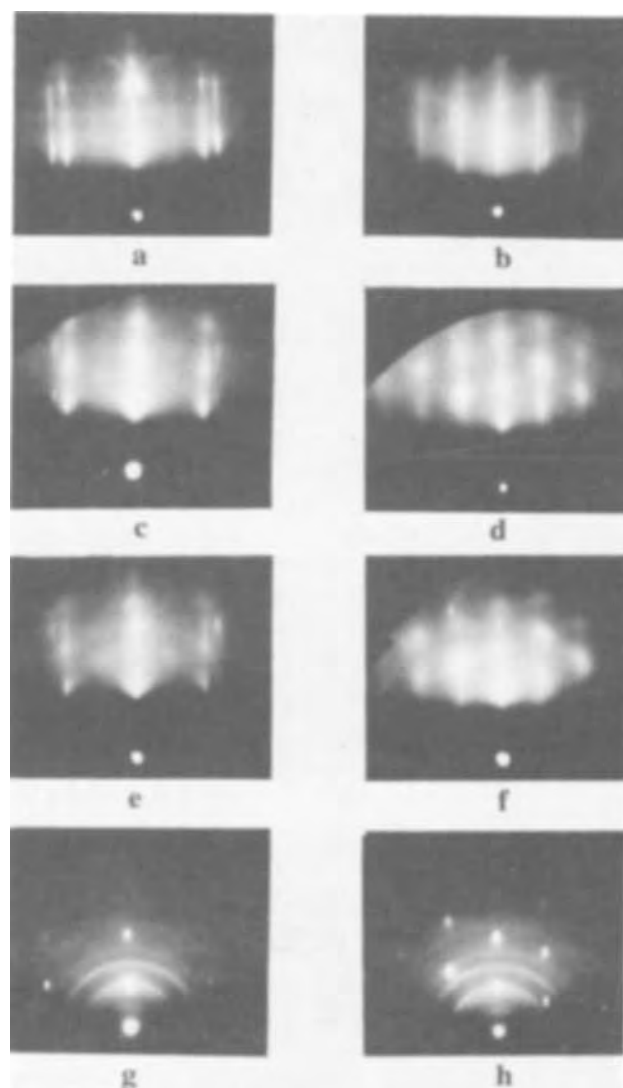


Fig. 11. Reflection electron diffraction patterns from a (111) nickel single crystal, in the  $\langle 112 \rangle$  and  $\langle 110 \rangle$  directions, after various electrochemical treatments: (a-b) electropolished in  $\text{H}_2\text{SO}_4$ ; (c-d) anodized to  $-0.45\text{V}$  for 1 hr; (e-f) as in (c-d) but with  $V_a = +0.4\text{V}$ ; (g-h) as in (c-d) but with  $V_a = +0.7\text{V}$ .



elongated reflections for both metal and oxide, the indication being that the oxide has a highly oriented mosaic structure with a mean particle size of ca. 50Å. The electron diffraction patterns of electropolished specimens which had been cathodically reduced and subsequently air-exposed were similar to those obtained from the electropolished specimens.

Upon anodization in the range  $-0.45$  to  $+0.4V$ , the sharp nickel reflections were less intense, especially in the  $\langle 110 \rangle$  zone, and the oxide reflections became somewhat diffuse. This diffuse characteristic may be due to either a smaller oxide particle size or a roughening of the nickel surface (relative to that existing with electropolished nickel). Since the diffuse oxide spots show a distinct refraction displacement (20), the electrode surface is still smooth and hence the oxide has a finer particle size. Measurement of the half-width of the oxide reflections indicate a 25Å particle size for the highly oriented, parallel oxide. Cathodic polarization at  $-1.35V$  of these anodized nickel electrodes in pH 8.4  $Na_2SO_4$  solution did not alter their electron diffraction patterns, another indication that the oxide film on anodized nickel cannot be cathodically removed in our system.

The nickel reflections are still very distinct in the case of the anodized electrode, providing qualitative support for the earlier observation (Fig. 8) that the oxide film resulting from anodization is only about 50% thicker than that due to electropolishing. Indeed, it is known from the dry oxidation of a smooth, electropolished (111) nickel that an oxide of ca. 15Å thickness completely obscures the reflections from the underlying nickel surface, this upper limit agreeing very well with the 10-12Å value in Fig. 8. The electron diffraction patterns also suggest that the oxide thickness has not changed considerably between the anodization potentials of  $-0.45$  and  $+0.4V$ , further support for the x-ray and coulometric measurements in Fig. 8.

After anodization at  $+0.7V$  for 1 hr, the sharp nickel reflections had become diffuse spots, indicating that the surface was strongly etched (cf. Fig. 9). The oxide now gave a semi-ring pattern corresponding to that expected for polycrystalline NiO. Stepping the potential to  $+0.7V$  for only 90 sec allows the current to fall to a steady value, associated partly with oxygen evolution. However, electron diffraction on such a specimen gave a pattern very much like that obtained with polarization to  $-0.45V$  (Fig. 11), i.e., there was little or no etching of the nickel electrode, and the oxide was highly oriented with a fine grain structure. Etching of the electrode surface and polycrystallinity of the oxide would thus seem to be related.

The diffraction patterns for both the electropolished and anodized nickel electrodes show the presence of the face-centered cubic oxide NiO, reflections from other possible oxides of nickel being absent. The lattice parameter for the nickel oxide formed by electropolishing in a  $H_2SO_4$  solution deviated from that expected for stoichiometric NiO by  $+1.9\%$  and  $+2.2\%$  in the  $\langle 112 \rangle$  zone and  $\langle 110 \rangle$  zone, respectively, i.e., the oxide lattice appears to be somewhat expanded over that of stoichiometric NiO. In the case of nickel electrodes, anodized either galvanostatically or by the potential step technique, the lattice parameter deviated from that of stoichiometric NiO by  $+0.3\%$  in both zones, i.e., the oxide formed by anodization has a lattice parameter which is much closer to that expected for stoichiometric NiO than that obtained by electropolishing. The oxide lattice parameter for an anodized specimen is independent of anodization potential or of the path taken to attain that potential. These changes in the oxide lattice parameter and general appearance of the diffraction patterns upon anodization occur even if the electropolished oxide is not removed prior to the anodization.

The lattice parameters cited above are characteristic of the spacing between planes of atoms which are perpendicular to the surface and says nothing about

the distance between the two planes parallel to the surface (21). Consequently it is impossible to give the exact oxide stoichiometry; however, the electron diffraction results have shown that the oxides in question are NiO as opposed to  $Ni(OH)_2$ ,  $\beta NiOOH$ ,  $\gamma NiOOH$ , or  $NiO_2$ . There is thus correlation with the coulometry and x-ray measurements where an assumption of NiO as the oxide on anodized nickel gave results which were in reasonably good agreement. Indeed, in the present investigation there was no success at preparing a nickel oxide, other than NiO, by the potential step technique in the systems studied. At pH = 11.0 or 13.0, and with a reduction of the prior oxide film, a potential step into the passive region, with  $V_a = 0$  or  $+0.5V$ , gave polycrystalline NiO on the (111) single crystal with a sharp semi-ring diffraction pattern. The random orientation of the oxide in these more alkaline solutions is possibly due to either a faster oxidation rate or a different reaction mechanism (in comparison with the oxidation at pH = 8.4). The quantity of nickel dissolved during a potential step in the alkaline solutions was ca. 25% of that dissolved at pH 8.4, indicating a more rapid oxide formation (cf. Fig. 7), and showing the importance of pH in the oxide formation reaction, i.e.,  $Ni + H_2O \rightarrow NiO + 2H^+ + 2e^-$ .

In an attempt to prepare an NiOOH film on nickel, the potential step technique was employed in pH 8.4  $Na_2SO_4$  solutions containing 5 and 10  $\mu g\ ml^{-1}$  nickel. Reflection electron diffraction on the (111) nickel crystal showed that the above procedure gave the passive, highly oriented NiO film on the (111) crystal (cf. Fig. 11) with no sign of any other oxide reflections. It is, however, possible that long term potential cycling of the nickel electrode would have resulted in the appearance of other oxides of nickel.

The results generally reported in the literature suggest that the "passive" film is nonstoichiometric nickel oxide, e.g.,  $NiO_{1.2}$  or  $NiO_{1.7}$  (6, 22) which is electronically conducting. The present electron diffraction results seem to indicate that the oxide film on anodized (111) nickel is closer to stoichiometric NiO than that on electropolished nickel. The oxide films on both electropolished and anodized nickel are similar in that they inhibit nickel dissolution; however, they differ with regard to their thickness, lattice parameters, and cathodic reducibility. The fact that the oxide on electropolished nickel is converted to the stoichiometric<sup>3</sup> NiO upon anodization would indicate that it is the stoichiometric NiO which is the passive oxide on nickel.

*Cathodic treatment of the oxide on anodized nickel.*  
—It has been noted above that although the surface oxide on electropolished nickel can be removed by cathodic reduction at  $-1.35V$  (Fig. 5), the oxide film formed by anodizing in pH 8.4  $Na_2SO_4$  solution is not removed by such treatment. Upon immersion into the pH 8.4  $Na_2SO_4$  solution at  $-1.35V$ , the electropolished nickel displays initial large cathodic currents (ca. 500  $\mu A\ cm^{-2}$ ) which rapidly fall as the prior oxide is removed. On the other hand, previously anodized nickel electrodes do not give any initial large surge of cathodic current upon immersion at  $-1.35V$  but adjust almost instantaneously to a steady value for this potential. After 10 min of polarization at  $-1.35V$  in pH 8.4  $Na_2SO_4$  solution, the electropolished nickel displays a current of ca. 35  $\mu A\ cm^{-2}$  while the same treatment on the anodized nickel electrode gives a current of ca. 90  $\mu A\ cm^{-2}$ , i.e., 2.5 times larger.<sup>4</sup> Prolonging the cathodic polarization results in only a small decrease in these currents with time; however the 250% difference remains and the prolonged polarization for as much as 2 hr does not affect the subsequent anodic galvanostatic transient. Any attempted cathodic reduction of anodized nickel in the neutral  $Na_2SO_4$  solution is thus

<sup>3</sup> Stoichiometric in the sense that the measured lattice parameters are similar to those obtained with true stoichiometric NiO.

<sup>4</sup> This situation exists over a wide range of potentials; however, because of the neutral, unbuffered nature of the electrolyte, accurate Tafel slope evaluation could not be made.

complicated by the increased rate of hydrogen evolution at  $-1.35\text{V}$ .

It has been postulated that cathodic polarization induced alkalinity plays a significant role in the reduction of the oxides of zirconium (23). In terms of the present nickel experiments, this theory would suggest that since cathodic polarization gives a high rate of hydrogen evolution from passive nickel, the pH may increase enough in the vicinity of the electrode to make the reaction  $\text{NiO} + 2\text{H}^+ + 2\text{e}^- \rightarrow \text{Ni} + \text{H}_2\text{O}$  impossible. A way to test such a theory in the present case is to cathodically polarize the anodized nickel electrodes in an acid solution. It is seen (Fig. 7) that cathodic reduction in a pH 3.5  $\text{Na}_2\text{SO}_4$  solution results in only a slight increase in the activity of the anodized nickel electrodes, and this reflects the difficulty in reducing the passive oxide film even in these acidic solutions where induced alkalinity should not play a role.

The question which naturally arises is whether the difference in cathodic electrochemical behavior between the oxide film on electropolished nickel and that on anodized nickel can be explained in terms of the 50% increase in thickness upon anodization. The oxide film on electropolished nickel is very thin (ca. 6Å), and it will not likely have the properties of bulk stoichiometric NiO. It is possible that the increase in oxide thickness with anodization gives an oxide which more closely resembles bulk NiO as indicated by reflection electron diffraction. This feature could explain the difference in stability of the two oxide films towards cathodic reduction or further thickening by anodization.

*Mechanism of oxide formation on nickel.*—The two principle methods for obtaining nickel oxides were electropolishing and anodization. It has already been concluded that a direct electrochemical reaction is the most probable mechanism of oxide formation on nickel anodized in the neutral solutions. In the case of electropolishing, the question is whether the oxide is formed during the polishing or the subsequent air exposure. It was noted in the results that cathodic reduction at  $-1.35\text{V}$  for 10 min in pH 8.4  $\text{Na}_2\text{SO}_4$  solution removes the prior oxide from electropolished nickel. Subsequent air exposure of the cathodically reduced, bare (and wet) nickel surface gives an oxide whose thickness, lattice parameter, and cathodic and anodic electrochemical behavior are identical to those existing on electropolished nickel. This taken in conjunction with the results of others (10), suggests that the oxide obtained by electropolishing in  $\text{H}_2\text{SO}_4$  solution is a result of the subsequent air exposure of the wet nickel electrode, the electropolishing itself mainly stripping nickel from the surface in a uniform manner and leaving the surface essentially free from oxide.

Both the oxide on electropolished nickel and the wet air-formed oxide are 6-8Å thick nonstoichiometric NiO. The dry air-formed film at room temperature is also 6-8Å in thickness but is basically stoichiometric NiO (13). However, the film formed under anodic conditions is both stoichiometric and somewhat thicker due to the applied potential. The growth rate is approximately logarithmic and could be explained by either a place-exchange mechanism (24, 25) or a Mott-Cabrera type mechanism (26, 27). The electronic conductivity of the film would not suggest a high-field mechanism. A distinction between the various types of mechanism is complicated by the dissolution of nickel during oxide film formation (Fig. 10).

### Summary

1. The anodic dissolution behavior of nickel is highly dependent on the extent of coverage with prior surface oxide.

2. Electropolishing of nickel in  $\text{H}_2\text{SO}_4$  gives a thin (6-8Å) film of NiO which can be removed by cathodic reduction in pH 8.4  $\text{Na}_2\text{SO}_4$  solution at  $-1.35\text{V}$ .

3. Anodization in the pH 8.4  $\text{Na}_2\text{SO}_4$  solution gives a thicker NiO film (9-12Å) which cannot be removed by cathodic reduction.

4. The oxide film on anodized nickel is formed by a direct electrochemical reaction.

5. The lattice spacings of the oxide film on electropolished nickel, as determined by reflection electron diffraction, show a 2% expansion while those on anodized nickel correspond to almost stoichiometric NiO.

6. Although the oxide films on both electropolished and anodized nickel inhibit nickel dissolution, they differ with regard to their thickness, lattice parameters, and cathodic reducibility, the film on anodized nickel being the passive oxide.

### Acknowledgment

The authors thank Dr. D. Mitchell for the x-ray determination of oxygen content, Mr. G. Ducharme for the A.A. analysis for nickel, Mr. I. Sproule for the replica electron micrographs, and Dr. P. B. Sewell for helpful discussions concerning the electron diffraction results.

Manuscript submitted Dec. 10, 1973; revised manuscript received April 1, 1974.

Any discussion of this paper will appear in a Discussion Section to be published in the June 1975 JOURNAL. All discussions for the June 1975 Discussion Section should be submitted by Feb. 1, 1975.

The publication costs of this article have been assisted by the National Research Council of Canada.

### REFERENCES

1. K. Schwabe and W. Schmidt, *Corrosion Sci.*, **10**, 143 (1970).
2. K. Schwabe and U. Ebersbach, "Proc. 4th Inter. Cong. on Met. Corr.," p. 709, Amsterdam, (1969).
3. K. Schwabe, *This Journal*, **110**, 663 (1963); also *Electrochim. Acta*, **3**, 186 (1960).
4. R. L. Cowan and R. W. Staehle, *This Journal*, **118**, 557 (1971).
5. T. S. de Gromoboy and L. L. Shreir, *Electrochim. Acta*, **11**, 895 (1966).
6. J. O'M. Bockris, A. K. N. Reddy, and B. Rao, *This Journal*, **113**, 1133 (1966); also *J. Chem. Phys.*, **42**, 2246 (1965).
7. A. C. Makrides, *This Journal*, **113**, 1159 (1966); also **109**, 977 (1962).
8. W. J. Muller, *Z. Elektrochem.*, **30**, 401 (1922).
9. A. K. N. Reddy and B. Rao, *Can. J. Chem.*, **47**, 2693 (1969).
10. J. Siejka, C. Cherki, and Y. Yahalom, *This Journal*, **119**, 991 (1972); also *Electrochim. Acta*, **17**, 161 (1972).
11. D. Toumi, *This Journal*, **112**, 1 (1965).
12. M. J. Graham and M. Cohen, *ibid.*, **119**, 879 (1972).
13. M. J. Graham, R. J. Hussey, and M. Cohen, *ibid.*, **120**, 1523 (1973).
14. M. Nagayama and M. Cohen, *ibid.*, **109**, 781 (1962).
15. P. B. Sewell, D. F. Mitchell, and M. Cohen, *Develop. Appl. Spectr.*, **7A**, 61 (1969).
16. P. B. Sewell, D. F. Mitchell, and M. Cohen, *Surface Sci.*, **29**, 173 (1972).
17. J. Kruger and J. P. Calvert, *This Journal*, **114**, 43 (1967).
18. K. Kudo and N. Sato, *Corrosion Eng. (Tokyo)*, **21**, 24 (1972).
19. N. Sato, K. Kudo, and M. Miki, *J. Japan Inst. Metals*, **35**, 1007 (1971).
20. P. B. Sewell, C. D. Stockbridge, and M. Cohen, *Can. J. Chem.*, **37**, 1813 (1959).
21. P. B. Sewell, D. F. Mitchell, and M. Cohen, *Surface Sci.*, **33**, 535 (1972).
22. A. M. Sukhotin and P. P. Stanishevsky, "Proc. 3rd Int. Cong. on Met. Corr.," Moscow, Vol. 1, p. 375 (1966).
23. K. Elayaperumal, S. S. Chouthai, and J. Balachandra, *Corrosion*, **29**, 59 (1973).
24. M. A. H. Lanyon and B. M. W. Trapnell, *Proc. Roy. Soc.*, **A227**, 387 (1955).
25. N. Sato and M. Cohen, *This Journal*, **111**, 512 (1964).
26. N. F. Mott, *Trans. Faraday Soc.*, **36**, 472 (1940).
27. N. Cabrera and N. F. Mott, *Rept. Progr. Phys.*, **12**, 163 (1948-1949).

# On the Origin of the Photocatalytic Deposition of Noble Metals on TiO<sub>2</sub>

F. Möllers, H. J. Tolle, and R. Memming

*Philips Forschungslaboratorium Hamburg GmbH, 2 Hamburg 54, Germany*

## ABSTRACT

In connection with studies on the photographic properties of TiO<sub>2</sub> the photocatalytic deposition of palladium and the electrochemical properties of TiO<sub>2</sub> were investigated. In order to study both phenomena simultaneously the experiments were performed with thin, TiO<sub>2</sub> layers deposited on a conducting substrate. It could be shown that the primary step is an anodic photocurrent (O<sub>2</sub> evolution) which catalyzes the cathodic deposition of palladium under open-circuit conditions. Various parameters such as space charge effects, film thickness, and doping were studied and are discussed in detail.

Photocatalytic properties of TiO<sub>2</sub> were reported in 1920 by Renz (1) who observed a darkening of the material by u.v. irradiation. Later on photoreactions with the surrounding medium were also investigated. According to the literature electrons as well as holes produced by light excitation within TiO<sub>2</sub> may be involved in those processes. Obviously the oxidation-reduction behavior of the species in contact with TiO<sub>2</sub> determines whether it will be photoreduced (2) or photo-oxidized (3, 4).

During the last decade the photoreduction of noble metal ions such as, e.g., Ag<sup>+</sup> and Pd<sup>2+</sup> at TiO<sub>2</sub>, found great interest because this reaction can be used as an initial step in a photographic process with TiO<sub>2</sub> (5, 6). In this process the reduced Pd<sup>2+</sup> ions form metal nuclei on the TiO<sub>2</sub> surface, whereas in a second reaction these nuclei may be intensified using chemical metallization (physical developers) in order to give a visible image.

In the primary step the photocatalytic reduction of Pd<sup>2+</sup> must be accompanied by a corresponding oxidation. The Pd<sup>2+</sup> ions need not necessarily be at the surface during the exposure to light but they are also reduced if they are introduced to the solution at the TiO<sub>2</sub> surface immediately afterward. This fact leads to the conclusion that the oxidation must be the initial step and determines the reduction. As proved with TiO<sub>2</sub> powder oxygen is desorbed during illumination. Since the remaining TiO<sub>2</sub> is deficient in oxygen it has become a reducing agent (6, 4).

Information about the primary steps in photocatalytic deposition on TiO<sub>2</sub> can be obtained by studying photographic and electrochemical properties of the same samples. Photographic experiments, however, were only performed with polycrystalline TiO<sub>2</sub> dispersed in organic binders which cannot be used for electrochemical studies. On the other hand, electrochemical experiments were performed with single crystals of TiO<sub>2</sub> which turned out not to be very suitable for photographic experiments. The investigations described in this paper were performed with polycrystalline TiO<sub>2</sub> layers deposited on a substrate. These layers have the advantage of being very transparent and, as far as the photographic properties are concerned, show a higher resolution than the dispersed layers. Electrochemical experiments are easily performed with this type of TiO<sub>2</sub> layers.

## Experimental Technique

The TiO<sub>2</sub> layers are produced by chemical vapor deposition. In this process a solution of titanium-acetylacetonate dissolved in isobutanol was sprayed by a carrier gas on a hot substrate (~ 450°C) on which the titanium salt was oxidized to TiO<sub>2</sub>. As a substrate

either glass plates (Duran/Schott) covered with a conducting SnO<sub>2</sub> layer or titanium sheet metal were used. According to x-ray measurements the TiO<sub>2</sub> film is polycrystalline, the grain size is not larger than 0.1μ. The properties of TiO<sub>2</sub> layers depend strongly on various process parameters such as substrate temperature, deposition rate, and the type of organic titanium compound.

The electrochemical experiments were performed in 0.1N H<sub>2</sub>SO<sub>4</sub> under potentiostatic conditions using a calomel electrode as a reference electrode. The space charge capacities were determined from measurements of impedance and phase angle between a-c current and a-c potential. For this purpose a small a-c voltage of 10 mV and 1 kc was superimposed on the externally applied d-c voltage.

The photocurrent measurements were performed using a mercury, high pressure lamp or a 450W xenon lamp as a light source. In some cases the light was chopped (12.5 Hz) and then the photocurrent measured using lock-in technique.

## Results and Discussion

*Photocurrent measurements.*—The anodic oxygen evolution at n-type TiO<sub>2</sub> electrodes only occurs with a large overpotential (see dotted line in Fig. 1). Under illumination (u.v. light), however, it occurs at much lower potentials, as proved by measuring the photocurrent (solid line in Fig. 1). A saturation current was found which is proportional to the light intensity. This curve is similar to that found by Boddy for a rutile single-crystal electrode (7).

Such behavior of a TiO<sub>2</sub> electrode is typical for n-type semiconductor electrodes if the charge transfer occurs via the valence band. In this case the concentration of holes in the valence band controls the reaction rate. In an n-type semiconductor of large bandgap, as in TiO<sub>2</sub>, the equilibrium concentration of holes is extremely low and the anodic dark current should be determined by diffusion of holes toward the surface or by some generation process. The strong increase of the dark current above 1.5V is due to a tunneling or to an avalanche process which was not further investigated. On the other hand, an illumination by light absorbed by TiO<sub>2</sub> leads to a generation of electron-hole pairs which are separated by the electric field within the space charge region near the TiO<sub>2</sub> surface. Since in the potential range in which a photocurrent was observed the energy bands are bent upward (proved by capacity measurements, see next section), the photogenerated electrons are forced toward the interior and holes toward the surface where they are consumed for the electrochemical process as shown schematically in Fig. 2.

Key words: electrochemistry, semiconductors, photography.

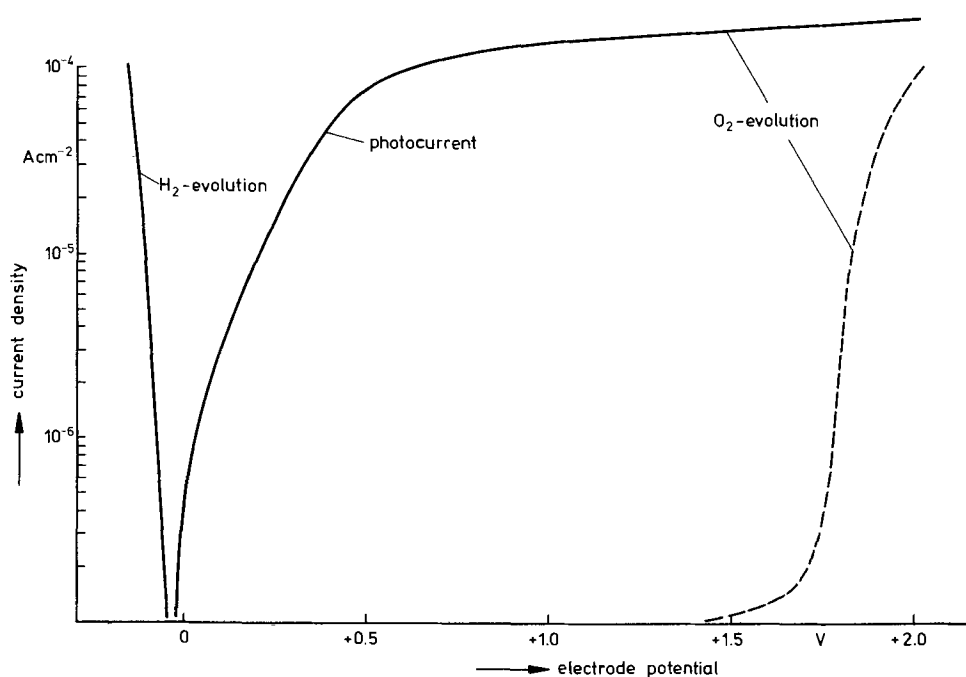
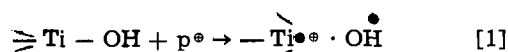


Fig. 1. Dark and photo current vs. electrode potential for TiO<sub>2</sub> layer (deposited on SnO<sub>2</sub>) in 0.1N H<sub>2</sub>SO<sub>4</sub>.

In the charge transfer process at the interface, surface states may also be involved. An influence of surface states in photoelectronic processes at TiO<sub>2</sub> has been assumed, *e.g.*, in the investigations of Vohl (6) and of Addis and Wakim (6). These authors have studied the surface photovoltage and the photoconductivity of TiO<sub>2</sub> in an ambient O<sub>2</sub> atmosphere. They concluded that O<sub>2</sub> may trap conduction band electrons in a chemisorption reaction and form surface O<sup>-</sup> ions. Under illumination these O<sup>-</sup> ions again trap photoholes and O<sub>2</sub> is regenerated.

In aqueous solutions the TiO<sub>2</sub> surface consists of acidic and alkaline Ti-OH groups of equal parts (8). The role of these surface groups in the photoelectrochemical O<sub>2</sub> evolution should be similar to that of O<sup>-</sup> on dry surfaces. The first step may be described by



In consecutive reactions with water the OH radical forms molecular O<sub>2</sub> and the TiO<sub>2</sub> surface is renewed (see Fig. 2). The same surface states of course may act as recombination centers.

Besides the occurrence of photocurrents also a shift of the rest potential during illumination was observed. Whereas in the dark the rest potential is not well de-

fined and varies from sample to sample, it is shifted by ~300 mV toward cathodic potentials by illumination. The rest potential at an illuminated TiO<sub>2</sub> electrode is fixed at such a value where either all photocarriers recombine or the anodic reaction of photoholes is just balanced by a cathodic reaction. Since there is a steep increase of the cathodic current which corresponds to the hydrogen evolution, it may be assumed that the rest potential is indeed determined by the photocatalyzed decomposition of water. The origin of the shift of the rest potential under illumination is also due to the existence of the electric field of the space charge. Measuring the rest potential under open-circuit conditions the potential reached its new value after the light has been turned on. This change of the open-circuit potential is the so-called photopotential. The separation of photocarriers in the electrical field reduces this field and consequently the potential drop across the space charge layer. If the surface photoeffect is exclusively caused by a displacement of charges in the TiO<sub>2</sub>, the open-circuit potential should return to its dark value instantaneously after having switched off the incident light. In all experiments, however, we found a much slower return to its dark value as shown in Fig. 3. The slow decrease of the open-circuit potential after illumination can be explained by the existence of traps within the space charge layer or by surface states.

These traps may also influence the movement of photoexcited charge carriers as indicated by results obtained from nonstationary photocurrent measurements. Corresponding experiments are performed by illuminating an electrode with chopped light causing a pulsed photocurrent. As shown in Fig. 4 there is a pronounced maximum of this photocurrent on varying the electrode potential. It occurs in a potential range where the stationary photocurrent shows its strongest increase with potential. Moreover, the pulsed photocurrent reaches larger values than in the stationary case whereas in the higher potential range the pulsed and stationary photocurrents are almost identical. A similar difference between fast and slow photoeffects were also observed at germanium electrodes by Boddy and Brattain (9). These authors used a galvanostatic arrangement and detected potential changes during illumination with light pulses. They interpreted the fast potential change by a decrease of the band bending due to the formation of electron hole pairs within the space charge layer. In order to get more insight into the mechanism we illuminated the electrode by single light

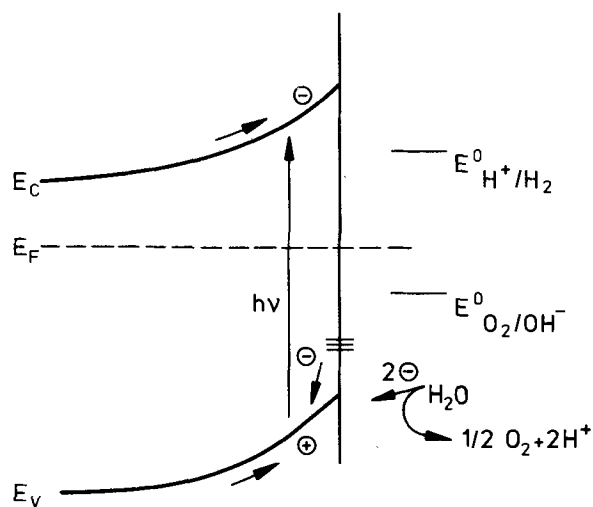
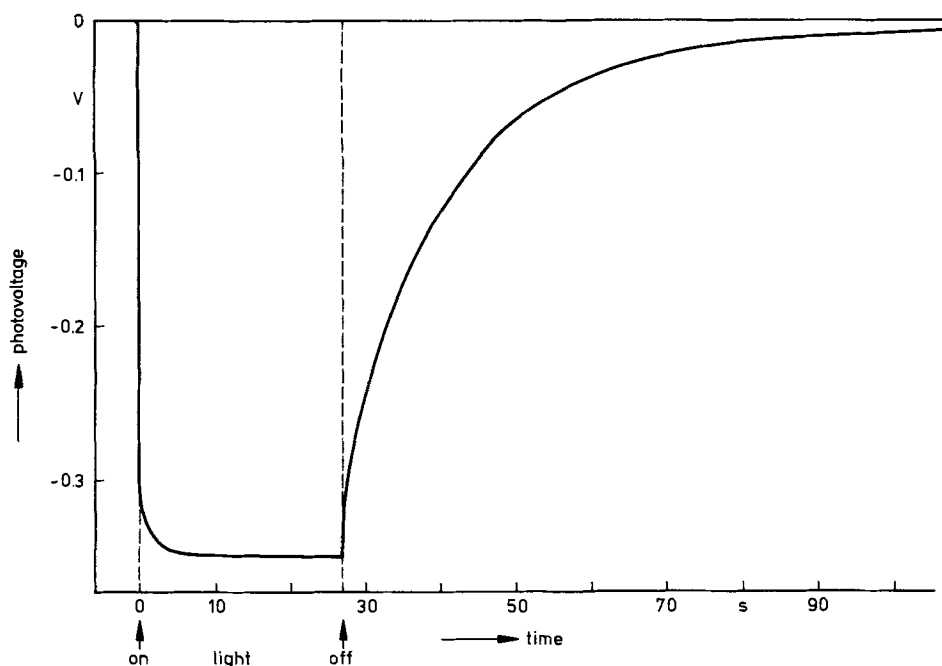


Fig. 2. Schematic diagram of charge transfer process at the TiO<sub>2</sub> electrolyte interface.

Fig. 3. Photovoltage vs. time for  $\text{TiO}_2$  (on  $\text{SnO}_2$  substrate) in  $1\text{N H}_2\text{SO}_4$  (under open-circuit conditions).



flashes. In the lower potential range the photocurrent rises rapidly immediately after the light has been turned on (curve b in Fig. 5), passes a maximum, and decreases down to a stationary value. It is interesting to note that in the following dark period a negative photocurrent also occurs. In the higher potential range those peaks are not observed (curve c), the photocurrent immediately reaches its stationary value. According to this result it has to be assumed that the pulsed photocurrent is due to a displacement of charges, i.e., some of the excited charge carriers are trapped in certain centers. Since the pulsed current passes a maximum the occupation of traps is variable by changing the electrode potential, i.e., by varying the band bending. Consequently, it has to be assumed that the traps have to be located within the space charge layer or even at the surface.

Accordingly the pulsed photocurrent can be described by two terms

$$\Delta i_{\text{ph}} = \Delta i_{\text{st}} + \Delta i_{\text{D}} \quad [2]$$

where  $\Delta i_{\text{st}}$  corresponds to the stationary photocurrent and  $\Delta i_{\text{D}}$  is due to displacement of charges. The latter current is proportional to the variation of the function  $f$  determining the occupation of the traps

$$\Delta i_{\text{D}} \sim \frac{df}{dt} \quad [3]$$

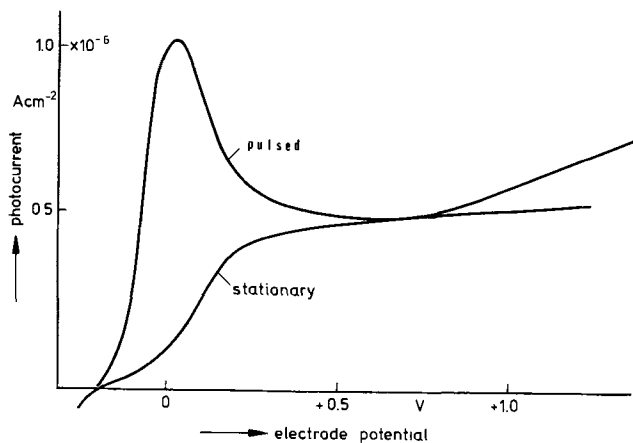


Fig. 4. Potential dependence of photocurrent for  $\text{TiO}_2$  (on  $\text{SnO}_2$  substrate) in  $1\text{N H}_2\text{SO}_4$ .

Since the occupation  $f$  depends strongly on the band bending  $\phi_s$  the pulsed photocurrent is given by

$$\Delta i_{\text{ph}} = \Delta i_{\text{st}} + b \frac{df(\phi_s)}{d\phi_s} \frac{d\phi_s}{dt} \quad [4]$$

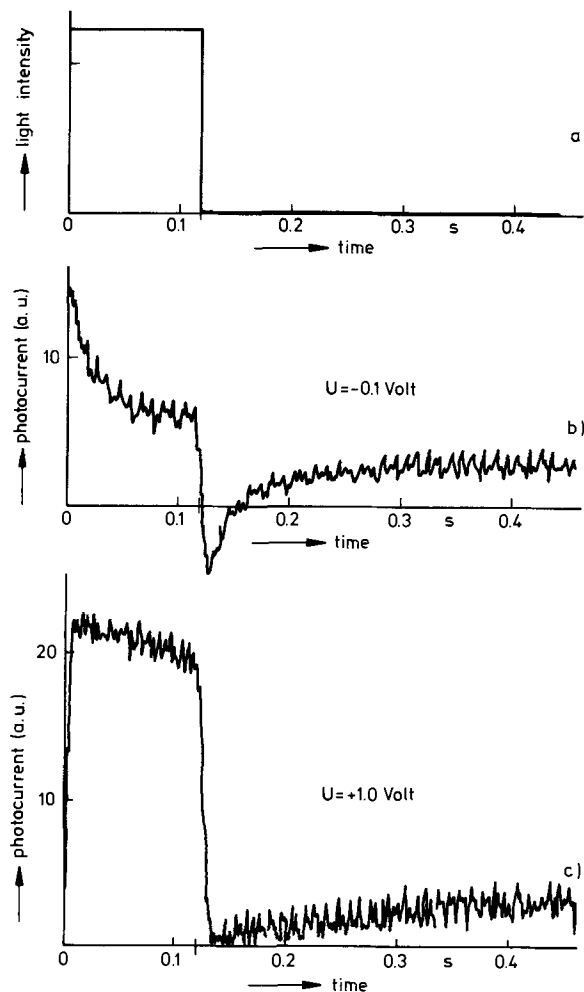


Fig. 5. Photocurrent vs. time for the same electrode as used in Fig. 4.

where  $b$  is a constant containing material and trap parameters.

This interpretation includes the assumption, however, that such a displacement of charges followed by a trapping of excited carriers leads to a small modulation of the band bending ( $d\phi_s/dt$ ) although the potential drop across the whole system is kept constant (potentiostatic measurement). Such a variation of the potential drop across the space charge can only be compensated by a corresponding change of the Helmholtz layer.

This model is supported by measurements of the pulsed current performed with TiO<sub>2</sub> layers of different thickness. Since the additional peak in the lower potential range does not occur for a layer of a very small thickness (Fig. 6) but only for thicker layers, surface effects have to be excluded.

Consequently the traps have to be assumed to be in the space charge layer itself. The trapping effect may decrease or even disappear if the thickness of the whole TiO<sub>2</sub> film becomes smaller than the space charge layer, because then more excited electrons and holes may reach the backside contact and the surface, respectively. Since the maximum of the pulsed current is not visible for a layer thickness of 0.1  $\mu$  the space charge thickness should be larger. This can only be proved by capacity measurements discussed below.

**Potential distribution.**—As discussed above a photoexcitation of electron hole pairs in TiO<sub>2</sub> causes a change of the potential distribution at least under open-circuit conditions, which are relevant to the photographic process. For a more quantitative understanding of the photoeffect it is important to obtain more knowledge about the potential distribution at the TiO<sub>2</sub> electrolyte interface. Such information is easily obtained from capacity measurements.

The space charge of an n-semiconducting electrode is a depletion layer at strong anodic polarization. Its capacity is described by the well-known Schottky-Mott equation

$$C_{sc} = \left( \frac{\epsilon \epsilon_0 N e}{2} \right)^{1/2} \left( \Delta\phi_{sc} - \frac{kT}{e} \right)^{-1/2} \quad [5]$$

$C_{sc}$  is the space charge capacity,  $\Delta\phi_{sc}$  the potential drop across the space charge layer,  $\epsilon$  and  $\epsilon_0$  the dielectric constants of TiO<sub>2</sub> and vacuum, respectively;  $N$  is the concentration of donors and  $e$  and  $kT$  have the usual meaning. Since the space charge capacity becomes smaller with increasing values of  $\Delta\phi_{sc}$  and since it is in series with the larger electrolytic double layer capacity ( $\approx 20 \mu\text{F}/\text{cm}^2$ ), the total capacity of the TiO<sub>2</sub>/electrolyte interface is determined by  $C_{sc}$ . In this case

$$C \approx C_{sc} \quad [6]$$

Provided that a change of the electrode potential  $U$

only leads to a change in  $\Delta\phi_{sc}$  then it may be substituted by

$$\Delta\phi_{sc} = U - U_{fb} \quad [7]$$

$U_{fb}$  is the flatband potential at which  $\Delta\phi_{sc}$  is zero. The validity of these two assumptions (Eq. [6] and [7]) is proved if a linear relation is found between experimental values of  $1/C^2$  and the electrode potential  $U$ . Inserting Eq. [6] and [7] into Eq [5] one obtains

$$1/C^2 = \frac{2}{\epsilon \epsilon_0 N e} \left( U - U_{fb} - \frac{kT}{e} \right) \quad [8]$$

$N$  is readily calculated from the slope of  $1/C^2$  vs.  $U$  lines and the flatband potential by extrapolation of the linear part of the curve to  $1/C^2 = 0$ . Such a linear relation was observed with TiO<sub>2</sub> over a large potential range using single crystals as electrodes (7). We proved these results with rutile electrodes (single crystal), which were reduced by hydrogen in order to get a smaller resistivity. Varying the frequency of the potential modulation between 100 Hz and 10 kHz, however, lines of different slopes were obtained. This may result from slow surface states and was not further investigated. In this case the flatband potential was found around  $-0.3\text{V}$  vs. SCE at  $p\text{H} = 1$ .

Performing capacity measurements with TiO<sub>2</sub> layers the  $1/C^2$  vs.  $U$  curves differ from those obtained with single crystals in so far that not a single straight line but bent curves were found (Fig. 7). This result may be interpreted by assuming that these curves consist of two  $1/C^2$  lines with a steep slope at lower potentials and a much lower slope at higher anodic potentials. On the other hand, a break in a capacity curve may also occur if the space charge thickness is larger than the film thickness. The thickness of the space charge can be defined as follows:

Rewriting the Schottky-Mott equation [8] one obtains

$$C_{sc} = \frac{\epsilon \epsilon_0}{\sqrt{\frac{2\epsilon \epsilon_0}{eN}} \cdot \sqrt{U - U_{fb} - \frac{kT}{e}}} \quad [9]$$

Since the capacity of a normal condenser is given by

$$C = \frac{\epsilon \epsilon_0}{d} \quad [10]$$

the thickness of the space charge can be defined as

$$d_{sc} = \sqrt{\frac{2\epsilon \epsilon_0}{eN}} \sqrt{U - U_{fb} - \frac{kT}{e}} \quad [11]$$

This thickness depends on the electrode potential. If  $d_{sc}$ , however, increases above the film thickness  $d_f$  the capacity is not determined by Eq. [9] but only by

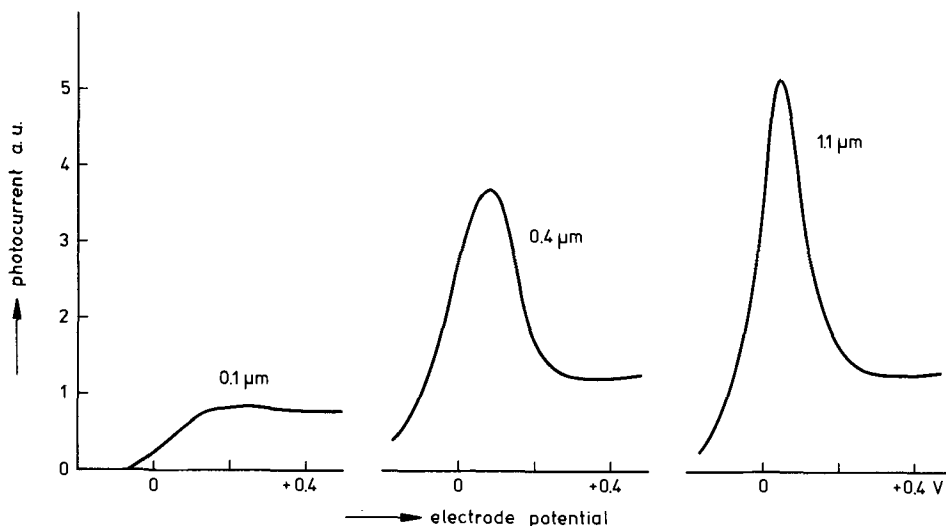


Fig. 6. Alternating photocurrent vs. electrode potential for TiO<sub>2</sub> of different oxide thicknesses in 1N H<sub>2</sub>SO<sub>4</sub>. Light source: Hg-lamp (361 nm). TiO<sub>2</sub> electrode: TiO<sub>2</sub> deposited on Ti-metal.

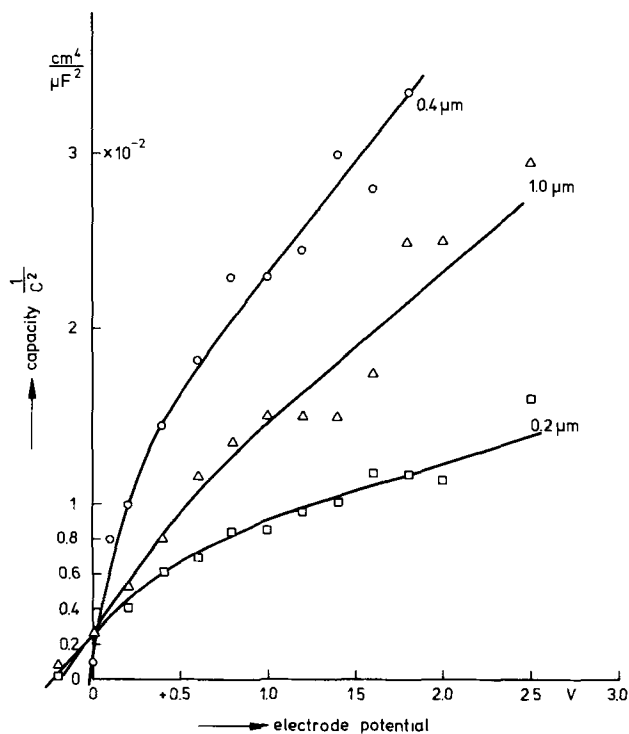


Fig. 7. Schottky-Mott plot of capacity vs. electrode potential for  $\text{TiO}_2$  on  $\text{SnO}_2$  substrate in  $1N \text{H}_2\text{SO}_4$ .

the normal condenser equation, Eq. [10], inserting the film thickness  $d_f$ . Then the capacity curve should show a break where  $d_{sc} = d_f$  and should be independent of potential above a certain potential. Since the thickness of the space charge layer  $d_{sc}$  varies with the square root of the potential, the potential at which the break in the curve occurs should very much depend on the film thickness. The interpretation, however, has to be excluded because the break in the curve appears at about the same potential for all samples of different thickness. It is supported by the fact that the thickness of the space charge layer amounts to  $d_{sc} \approx 0.14\mu$  as obtained from the slopes of the capacity curves in the lower potential range. [For the corresponding calculation we used an average value of  $\bar{\epsilon} = 120$  (10), where we obtained for the donor density  $N$  a value of  $N = 1.2 \cdot 10^{17} \text{cm}^{-3}$ .]

According to Pleskov (11) a break in the capacity curve may also occur if deeper donor levels are present which are not ionized within the bulk. The occupation of these levels may change, however, within the space region increasing the band bending. Assuming only one discrete energy level for such an additional donor of a density  $N'$  a Schottky-Mott equation of two linear slopes can be derived: The first one, measured at small band bendings, is only determined by the ionized shallow donors (density  $N$ ) and the second by the sum of both, the shallow and the deep donor level ( $N = N'$ ).

We assume the latter interpretation to be valid at least for the samples of a film thickness of 0.4 and  $1.0\mu$ , although we could not check whether only one or several types of deep donor levels are involved. Theoretically, all curves obtained with samples of different thickness should be identical. The difference between the  $0.4\mu$ - and  $1\mu$ -samples is due to the layer preparation which has a large influence on the density of donor levels. Many measurements have shown, however, that the slope of the capacity curve of a very thin layer ( $\leq 0.2\mu$ ) was always smaller than that of layers of larger thickness. This may be due to the fact that now the film thickness is of the order of the space charge thickness.

**Influence of film thickness on the stationary photocurrent.**—The photocurrent across the  $\text{TiO}_2$  electrolyte

interface should increase with increasing layer thickness provided that the penetration depth of light is larger than the film thickness itself. The penetration depth of light is determined by the absorption coefficient  $\alpha$ . As shown in Fig. 8, the absorption sets in at about 420 nm which corresponds to an energy gap of 3.2 eV. Since we varied the film thickness up to  $1.4\mu$ , the first condition is fulfilled for wavelengths above 355 nm (see Fig. 8).

Corresponding measurements were performed with various layers using an excitation wavelength of 361 nm or white light. We obtained values which indeed increased with increasing film thickness as long as the film thickness was below about  $0.6\mu$ . For larger thicknesses mostly lower photocurrents were found. Theoretically the photocurrent should be proportional to the absorbed photons, i.e., it should increase with  $(1 - e^{-\alpha d})$ . The large deviation cannot be interpreted by any excitation within the  $\text{SnO}_2$  substrate because even with white light the photocurrent for  $\text{SnO}_2$  is much smaller (12).

More quantitative information about this problem can be obtained from the spectral distribution of the photocurrent as shown in Fig. 9. According to this figure the spectral distribution depends strongly on the film thickness: varying the wavelength of the incident light from higher to shorter wavelengths the photocurrent rises due to the increase of absorption, passes a maximum, and decreases again which is caused by recombination. The  $\text{TiO}_2$  layer of the smallest thickness shows the highest photocurrent and its maximum occurs at shorter wavelengths than for the other layers. It should be mentioned that this experiment was performed with a  $\text{TiO}_2$  layer deposited on Ti metal and the electrodes were illuminated through the electrolyte. The thickness dependence of the spectral distribution, however, is independent of the substrate. This is demonstrated in Fig. 10a which was obtained

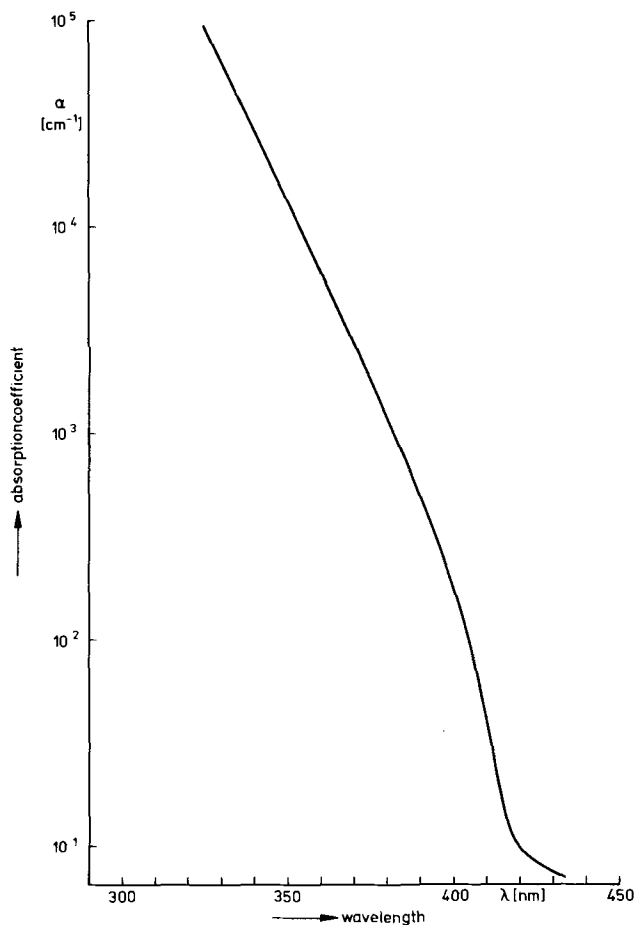


Fig. 8. Absorption coefficient vs. wavelength for  $\text{TiO}_2$  layers

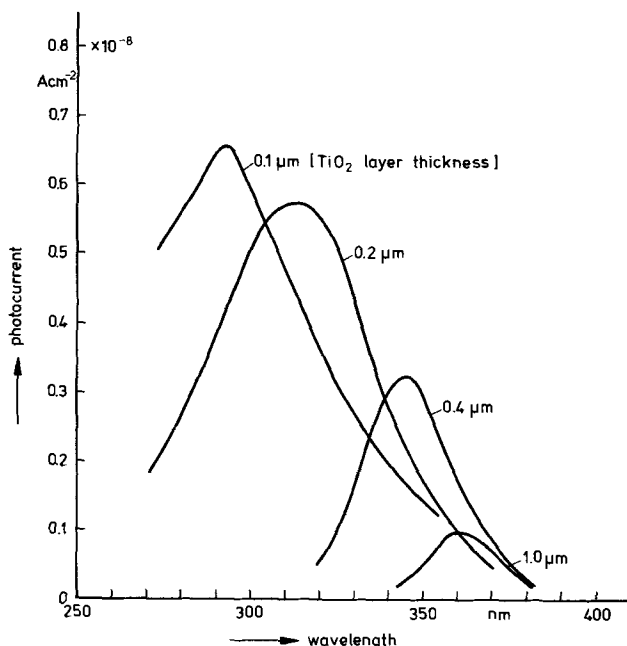


Fig. 9. Spectral distribution of photocurrent for TiO<sub>2</sub> (deposited on titanium, exposure through electrolyte).

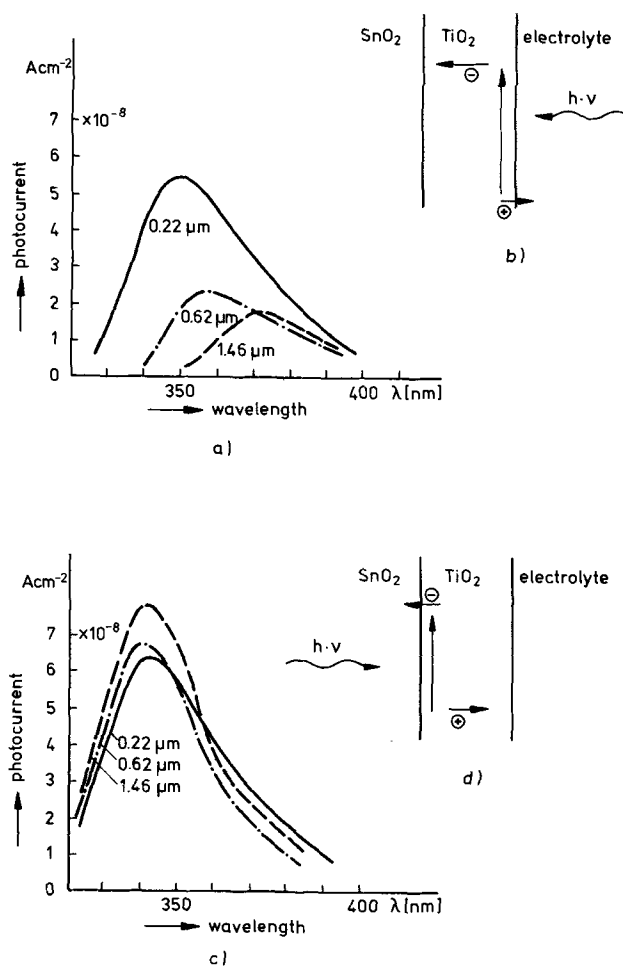


Fig. 10. Spectral distribution of photocurrent for TiO<sub>2</sub> on SnO<sub>2</sub> substrate. (a) Illumination through electrolyte, (c) illumination through SnO<sub>2</sub>, (b) and (d) schematic representation of excitation process.

by using SnO<sub>2</sub> instead Ti as a substrate. Since the bandgap of SnO<sub>2</sub> is considerably larger than for TiO<sub>2</sub> this system could also be illuminated from the re-

verse side, i.e., through the SnO<sub>2</sub> layer (see Fig. 10d). The corresponding spectra were obtained with the same samples as presented in Fig. 10c. In this case the spectral distribution of the photocurrent is independent of the thickness of the TiO<sub>2</sub> layer and its maximum occurs only in the shorter wavelength range.

According to these results it must be concluded that the highest yield for the photocurrent is obtained if the electron-hole pairs are created near the backside contact (Fig. 10d). In this case the electrons produced by light excitations have to move a relatively short distance to the contact, whereas holes have to move all the way through the TiO<sub>2</sub> layer toward the surface where they are consumed in the electrode reaction process. On the other hand, when the electrode is illuminated through the electrolyte, then the electron-hole pairs are created mainly near the TiO<sub>2</sub> electrolyte interface and the electrons have to move across a larger distance, at least in TiO<sub>2</sub> layers of 0.2 μm and of greater thickness. Since in this case the photocurrents are small and since their maxima in the spectral distribution depend on the layer thickness we assume that electrons are more readily trapped than holes and therefore determine the recombination process.

It should be mentioned that the recombination rate is strongly influenced by the structure of the TiO<sub>2</sub> layers and need not be homogeneous over the whole layer. According to our experiments it varied with the decomposition temperature, the substrate, and the Ti compound used in the preparation technique of these layers.

**Photocatalytic deposition of palladium nuclei.**—As already observed with TiO<sub>2</sub> dispersed in polymer binders, palladium is deposited from aqueous solutions on TiO<sub>2</sub> during illumination with ultraviolet light (6). The same effect was observed with TiO<sub>2</sub> layers deposited on SnO<sub>2</sub> by our technique. These experiments were performed with TiO<sub>2</sub> layers on a SnO<sub>2</sub> substrate. It was proved that no palladium was deposited with SnO<sub>2</sub> alone. Following the open-circuit potential of such a TiO<sub>2</sub> electrode in a Pd<sup>2+</sup> solution during illumination a fast shift toward cathodic potentials was observed. After the potential has passed a minimum at around +100 mV it reached a final value of about +200 mV (curve I in Fig. 11a). For comparison we also plotted the open-circuit potential during illumination of a system free from palladium ions as shown by the dashed line in Fig. 11a. The amount of palladium deposited during illumination was determined by subsequent anodic dissolution of palladium under galvanostatic conditions. From the corresponding potential change with time the electrical equivalent of Pd was calculated.

The nature of the photocatalytic deposition of Pd on TiO<sub>2</sub> can easily be interpreted on the basis of the photovoltaic effect of the semiconducting TiO<sub>2</sub>. As discussed in detail above, illumination of TiO<sub>2</sub> electrolyte interface leads to a small rate of the photolysis of water, i.e., holes created by light are consumed for the formation of O<sub>2</sub> and simultaneously an equal amount of electrons for the reduction of H<sup>+</sup> ions. This mechanism can be illustrated by the anodic and cathodic currents involved in this process as shown schematically in Fig. 12. In the dark only a small anodic current (solid line) was observed since almost no holes are available, whereas the cathodic current increases rapidly with increasing cathodic potential (solid line) and hydrogen evolution occurs. Under open-circuit conditions the rest potential  $U_R$  is found at that potential at which anodic and cathodic currents are equal. Illumination causes an anodic photocurrent (dotted curve) leading to oxygen evolution. This anodic partial current sets in at flatband potential  $U_{fb}$  which is more negative than the rest potential  $U_R$  as derived from capacity measurements. Since the cathodic current remains unchanged the new rest potential will occur at  $U_{L(H)}$ . The potential difference



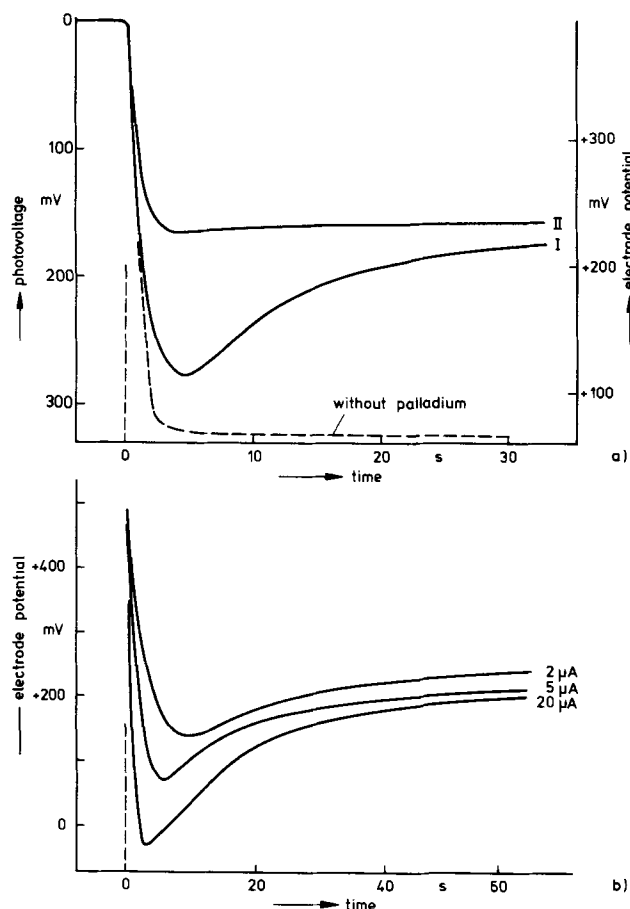


Fig. 11. (a) Photovoltage vs. time for a  $\text{TiO}_2$  electrode (on  $\text{SnO}_2$  substrate) in  $10^{-3}\text{M}$   $\text{PdCl}_2$  in  $0.1\text{N}$   $\text{HCl}$ . Curve I, first run; curve II, second exposure. (b) Electrode potential vs. time without illumination at constant cathodic current as indicated.

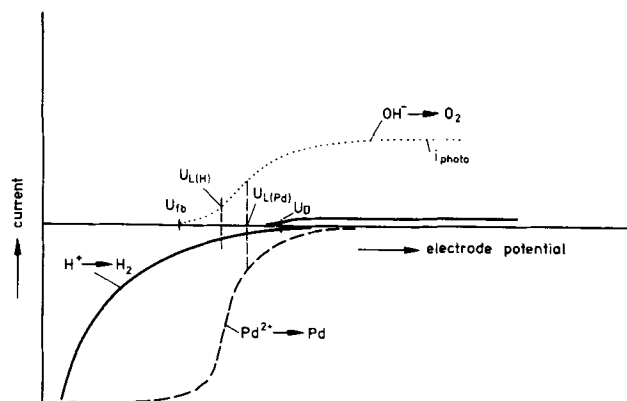


Fig. 12. Schematic current-potential diagram. Symbols are given in text

$U_{L(H)} - U_D$  is the actually observed photovoltage under open-circuit conditions. In the presence of Pd ions an additional cathodic current is possible which appears at less cathodic potentials (dashed curve) than for the hydrogen evolution since the normal potential of  $\text{Pd}/\text{Pd}^{2+}$  is positive. As may be seen from Fig. 12 under illumination the rest potential will now occur at  $U_{L(Pd)}$ , a potential at which the anodic photocurrent and the cathodic deposition current are equal. In this case the corresponding photovoltage is smaller and given by  $U_{L(Pd)} - U_D$ . It should be emphasized that the primary effect is the production of holes by light excitation leading to oxygen evolution represented by an anodic photocurrent. Under open-circuit

conditions a cathodic current of the same magnitude is induced. This current may be either hydrogen evolution or palladium deposition depending on the composition of the electrolyte. This mechanism, which also was principally observed with other semiconductor electrodes, can only work, however, if the flatband potential is more cathodic than the normal hydrogen potential or the normal  $\text{Pd}^{2+}/\text{Pd}$  potential. This condition is, e.g., not fulfilled for  $\text{SnO}_2$ , which explains the fact that no photodeposition of palladium on  $\text{SnO}_2$  was observed.

It is interesting to note that the open-circuit potential in the presence of Pd ions does not immediately reach its final value after light had been turned on but passes a minimum (see Fig. 11a). Repeating this experiment with the same electrode on which palladium was already deposited during the first run, this minimum does not occur again (curve II in Fig. 11a). Obviously an overpotential of more than 100 mV is required for the deposition of the first palladium nuclei. This is a rather large value for the formation of nuclei. We proved this process by depositing palladium by polarizing the electrode with a constant cathodic current. The corresponding potential-time curves also show a pronounced potential minimum due to the formation of palladium nuclei (Fig. 11b). We did not study the nucleation process in detail. It would be interesting to investigate it also at  $\text{TiO}_2$  single crystals since crystal faces and grain boundaries will be of importance.

We only studied the problem of how far the amount of palladium deposited photocatalytically depends on the layer thickness. According to Fig. 13 a considerable increase of the deposited palladium occurs in the range between 0.2 and  $0.5\mu$ , whereas above  $0.5\mu$  it only rises very weakly. As shown in this figure a large amount of scatter is observed in the experimental values. Therefore we could not obtain a reliable spectral distribution of this effect so that a comparison with the thickness dependence of the photocurrent was not possible. Nevertheless, the thickness dependence of the palladium deposition should be determined by two factors: (i) The number of deposited palladium atoms should increase in the thickness range below a value which corresponds to the penetration depth of light (penetration depth  $\delta = 1.5\mu$  at  $\lambda = 361\text{ nm}$ ). (ii) Since the film thickness is of the order of or even smaller than the thickness of the space charge layer for  $d < 0.4\mu$  the effective photovoltage may be smaller leading to a lower deposition rate.

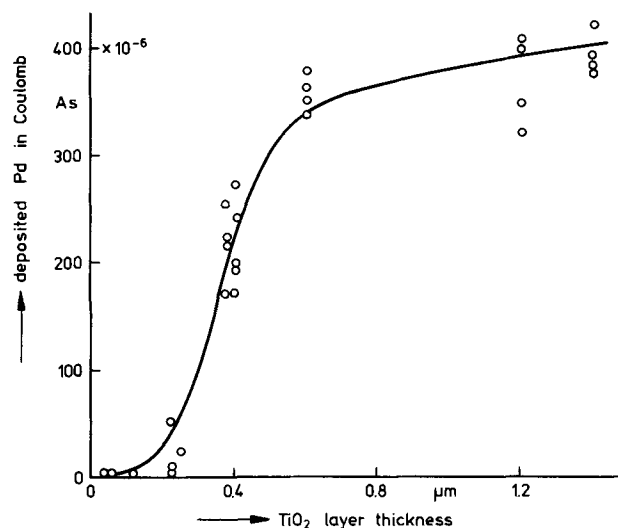


Fig. 13. Amounts of deposited palladium for various film thicknesses after constant exposure for  $\text{TiO}_2$  on  $\text{SnO}_2$  substrate in  $10^{-3}\text{M}$   $\text{PdCl}_2$  in  $0.1\text{N}$   $\text{HCl}$ .

### Acknowledgments

The authors are indebted to Dr. L. K. H. van Beek, Dr. J. J. Kelly, and Dr. C. J. G. F. Janssen of the Philips Research Laboratories in Eindhoven for many stimulating discussions.

Manuscript submitted Jan. 25, 1974; revised manuscript received April 15, 1974.

Any discussion of this paper will appear in a Discussion Section to be published in the June 1975 JOURNAL. All discussions for the June 1975 Discussion Section should be submitted by Feb. 1, 1975.

The publication costs of this article have been assisted by Philips Forschungslaboratorium Hamburg GmbH.

### REFERENCES

1. C. Renz, *Z. Anorg. Chem.*, **110**, 104 (1920); C. Renz, *Helv. Chim. Acta*, **4**, 961 (1921).
2. H. Yonegama, Y. Toyogushi, and H. Tammra, *J. Phys. Chem.*, **76**, 3460 (1972).
3. I. S. McLintock and M. Ritchie, *Trans. Faraday Soc.*, **61**, 1007 (1965).
4. U. Kaluza, Thesis, 1969, Heidelberg.
5. H. Jonker, C. J. G. F. Janssen, C. J. Dippel, Th. P. G. W. Thijssens, and L. Postma, *Phot. Sci. Eng.*, **13**, 45 (1969).
6. G. L. McLeod, *ibid.*, **13**, 93 (1969); E. J. DeLorenzo, L. K. Case, E. M. Stickless, and N. A. Stamoulis, *ibid.*, **13**, 95 (1969); R. R. Addis, Jr. and F. G. Wakim, *ibid.*, **13**, 111 (1963); P. Vohl, *ibid.*, **13**, 120 (1969).
7. P. J. Boddy, *This Journal*, **115**, 199 (1968).
8. H. P. Boehm, *Kolloid-Z. Z. Polymere*, **227**, 17 (1968).
9. P. J. Boddy and W. H. Brattain, *Ann. N. Y. Acad. Sci.*, **101**, 683 (1963).
10. Data from Research Laboratory, Titanium Division, National Lead Company, South Amboy, N. J.
11. V. A. Myamlin and Y. V. Pleskov, "Electrochemistry of Semiconductors," Plenum Press, New York (1967).
12. F. Möllers and R. Memming, *Ber. Bunsengesellschaft Phys. Chem.*, **76**, 469 (1972).

## The Formation of Monolayer Metal Films on Electrodes

W. J. Lorenz,\* H. D. Hermann, N. Wüthrich, and F. Hilbert

*Institute of Physical Chemistry and Electrochemistry, University of Karlsruhe, Karlsruhe, Germany*

### ABSTRACT

The two- and three-dimensional nucleation and the metal ion adsorption process are discussed as initial steps for electrocrystallization on the same or on a foreign substrate. The metal ion adsorption takes place in the underpotential range, which is more positive than the equilibrium potential of the nucleated metal/metal ion electrode. Thermodynamic considerations show that an overlapping of disturbing processes in the underpotential range can be characterized by a factor  $Z_E$ , which is called charge-coverage coefficient or electrosorption valency. It is a function of different independent variables. The metal monolayer model is satisfied only in the simplest case for  $Z_E = z$  (valency of metal ions in solution).

The different experimental methods for determining the thermodynamics, kinetics, and structure of metal ion adsorbates are critically discussed. The most reliable thermodynamic results are obtained by the twin-electrode thin-layer technique. Kinetic data can be obtained by pulse measurements under potentiostatic-galvanostatic conditions. The structure of metal films can be determined by combining different methods including optical investigations.

Results are given for different systems. In the systems Au/Ag<sup>+</sup>, Au/Tl<sup>+</sup>, and Au/Pb<sup>++</sup> the metal monolayer model is practically valid. In the case of Cu<sup>++</sup> ion adsorption on Au the redox reaction forming Cu<sup>+</sup> ions acts as a disturbing process. A cosorption of anions takes place in the system Ag/Pb<sup>++</sup>. The formation of alloys in the underpotential range was observed in the systems Pt/Pb<sup>++</sup> and Bi/Pb<sup>++</sup>.

The structure of metal ion adsorbates must be in correlation with the nucleation phenomena at more negative potentials. In many systems no three-dimensional nucleation overvoltage is observed by using a quasi-steady-state experimental technique. The density of the crystal imperfections and the crystallographic orientation of the surface planes influence the metal ion adsorption process and the structure of films. The results obtained in the systems Ag (poly- and monocrystalline)/Tl<sup>+</sup> can be explained by assuming the formation of superlattices on the electrode surface.

Kinetic investigations in the systems Au/Ag<sup>+</sup>, Au/Tl<sup>+</sup>, and Au/Pb<sup>++</sup> show relatively high exchange current densities for the metal ion adsorption process. In these cases the experimental results can be explained by assuming surface diffusion of adions as the rate determining step in the adsorption process. In the system Au/Cu<sup>++</sup>, a charge transfer step is rate determining, which probably forms precedingly Cu<sup>+</sup> ions.

Crystallization phenomena play an important role in the case of cathodic metal deposition. They include different steps after the metal ion has passed through the electrochemical double layer and is still partially solvated. The final state can be described as the in-

corporation of the discharged metal atom into the bulk of the metal lattice. The following crystallization steps can occur: surface diffusion of metal adatoms or partially charged metal adions, the formation of two- or three-dimensional nuclei, and the growth of formed nuclei and steps. A hindrance of these crystallization steps leads to a crystallization overvoltage, which can be measured experimentally. In most cases this crys-

\* Electrochemical Society Active Member.

Key words: metal ion adsorption, electrocrystallization, thermodynamics, kinetics, structure, experimental methods.

tallization overvoltage is superimposed upon other kinds of overvoltages, especially charge transfer and diffusion overvoltage.

The hindrance of crystallization steps influences the kinetics of the over-all reaction, *i.e.*, the reaction rate and the mechanism. Moreover, the structure of the deposited metal depends on the kinetics. Therefore many mechanical, physical, and electrical properties of the deposited metal are determined by the deposition conditions which are directly connected with the kinetics.

The processes of cathodic metal deposition are practically important in the fields of galvanotechnology and electrometallurgy. On the other hand, the inverse process of metal dissolution is of great interest for metal corrosion and etching.

The important question is, what are the initial steps in electrocrystallization processes? First one has to distinguish between electrodeposition on the same or on a foreign substrate.

In the first case the crystallization steps are a function of the substructure of the substrate. If the density of crystal imperfections is relatively high and a great number of growth sites exist at the surface, then the deposition reaction takes place practically without crystallization overvoltage. Under this condition the charge transfer step takes place directly on these growth sites, *e.g.*, kinks, screw dislocations, and steps. However, if the density of crystal imperfection is relatively low or zero, the formation of two-dimensional nuclei is the rate determining step at low overvoltages and can be considered as the initial step. This was shown impressively by Budevski and co-workers (1, 2) in the case of silver deposition on monocrystalline silver electrodes which were free of dislocations. Similar results were obtained by Fischer and co-workers (3, 4) in the case of  $\text{Cu}^{++}$  deposition on monocrystalline copper substrates and also on polycrystalline copper substrates in the presence of inhibitors in the electrolyte solution.

In the case of metal deposition on a foreign substrate the formation of three-dimensional nuclei had been considered as the initial step for a long time. The theoretical treatment of nucleation phenomena in electrochemistry was already given by Erdey-Gruz and Volmer (5). According to this theory, the three-dimensional nucleation rate is a function of supersaturation and therefore depends on the crystallization overvoltage  $\eta_k$

$$J = A \cdot \exp\left(-\frac{\Delta G_{\text{crit}}}{k \cdot T}\right) = A \cdot \exp\left(-\frac{S}{|\eta_k|^2}\right) \quad [1]$$

with

$$S = \frac{8\pi \cdot \gamma_{N-V} \cdot v^3 \cdot V_M^2}{3kTz^2 \cdot F^2}$$

whereby  $\gamma_{N-V}$  = specific free surface energy of the interphase between nucleus and electrolyte phase, differing for different crystal faces of the nucleus;  $V_M$  = mole volume of nuclei. The other symbols have their usual significance.

This theoretical equation could be confirmed experimentally only in the last decade. Mainly Kaishev and co-workers (6) studied the three-dimensional nucleation phenomena. They investigated the deposition of  $\text{Fe}^{++}$ ,  $\text{Ag}^+$ ,  $\text{Pb}^{++}$ , and  $\text{Hg}^+$  ions on monocrystalline platinum substrates using a potentiostatic pulse technique. They observed high crystallization overvoltages up to more than 100 mV in order to form three-dimensional nuclei. These findings could be confirmed also by Schottky and Mierke (7) in the case of  $\text{Ag}^+$  ion deposition on polycrystalline and monocrystalline platinum substrates, as well as by Fischer and co-workers (8) in the case of  $\text{Cu}^{++}$  ion deposition on a polycrystalline copper substrate in the presence of inhibitors in acidic aqueous solutions.

However, platinum seems to be not the regular case, presumably because of its relatively high adsorption

capacity for hydrogen and oxygen. Adsorption of inhibitors has probably the same effect (8).

During the last decade the specific adsorption of metal ions on foreign substrates was observed in so many systems using different experimental techniques, that this reaction step and the following formation of metal films can now be considered as the regular initial step of electrodeposition on foreign substrates. This conclusion applies for deposition onto bare metallic surfaces in solutions which are free from surface active substances.

The investigations on the metal ion adsorption phenomena are connected with the work of Schmidt and co-workers. They developed new experimental techniques in order to determine exactly the thermodynamics of metal ion adsorption processes and the formation of metal films. On the basis of the earlier findings of Rogers and co-workers (9-17), the adsorption of metal ions on foreign substrates was studied experimentally and theoretically in many systems by Schmidt and co-workers in the last decade (18-40). At present the following groups are mainly dealing with this subject using different experimental techniques: Bruckenstein and co-workers (41-48), Vetter and Schultze (49-53), Bowles (54-59), and Lorenz and co-workers (60-64).

Moreover, metal ion adsorption processes and film formation were also described by some other authors (65-82). Optical investigations of these adsorption phenomena were done by Yeager and co-workers (83) and by Kolb (84, 85). But only very recently have there been some attempts to correlate the adsorption phenomena with electrocrystallization steps (64, 75, 86). Investigations on the metal ion adsorption on semiconductor surfaces are only at the beginning (85). These investigations have great importance for understanding and improving the metallization steps in IC silicon technology and other related semiconductor device applications.

### Metal Ion Adsorption

*Phenomenological considerations.*—The specific adsorption of metal ions on foreign substrates takes place in the so-called "underpotential range," which is more positive than the equilibrium potential of the deposited metal/metal ion electrode

$$\epsilon \cong \epsilon_{0, \text{Me}/\text{Me}z^+} = E_{0, \text{Me}/\text{Me}z^+} + \frac{RT}{zF} \ln \frac{a_{\text{Me}z^+}}{a_{\text{Me}}} \quad [2]$$

This underpotential range extends over several hundred millivolts, however, it depends on the kind of system being investigated.

In order to determine exactly such metal ion adsorption processes cathodically or the reverse desorption processes anodically, it is necessary to measure the corresponding adsorption or desorption currents, respectively, of the corresponding charge amounts.

In the simplest case one can assume that the substrate electrode is ideally polarizable in the underpotential range and no other faradaic or sorption processes occur simultaneously. Here the measured charge amounts correspond exactly to the adsorption or desorption processes of metal ions. In the absence of metal ions in the electrolyte solutions in such systems only capacity current is flowing in order to change the structure of the electrochemical double layer.

However, such ideal conditions are not often realizable. In many systems there is a superposition of disturbing processes, namely faradaic or other sorption processes, *e.g.*, the coverage of the electrode surface with hydrogen or oxygen, the specific adsorption or desorption of other ions, the formation of alloys or intermediate compounds between the substrate and the adsorbed metal ion species, parallel redox reactions, corrosion of the substrate, etc. Under these circumstances the experimental conditions have to be chosen in such a way that these disturbing reactions can be

eliminated or separated either experimentally or by calculations.

**Thermodynamics.**—In the simplest case of an ideally polarizable substrate electrode and no disturbing processes, the metal ion adsorbate can be described by the so-called metal monolayer model. Here the behavior of the adsorbate follows a pseudo-Nernst equation

$$\epsilon = \epsilon_{0, \text{Me}/\text{Me}z^+} + \frac{RT}{zF} \ln \frac{a_{\text{Me}z^+}}{a_{\text{ads}}(\Gamma)} \quad [3]$$

In this equation  $a_{\text{ads}}(\Gamma)$  is the activity of the adsorbed species on the surface at the given surface excess  $\Gamma$ .

Stoichiometric charge measurements show that an equivalent charge amount flows in order to form the adsorbate



The charge amount, integrated over a certain part of the underpotential range, is given by (see Eq. [14])

$$\int_{t_1}^{t_e} i(t) dt = \int_{\epsilon_1, \Gamma_1=0}^{\epsilon_e, \Gamma_e} \left[ \left( \frac{\partial q}{\partial \epsilon} \right)_{\Gamma} d\epsilon + \left( \frac{\partial q}{\partial \Gamma} \right)_{\epsilon} d\Gamma \right] \quad [5]$$

$$= q(\epsilon_e, \Gamma_e) - q(\epsilon_1, \Gamma_1 = 0) \quad [6]$$

$\epsilon_1$  is the equilibrium starting potential at time  $t_1$ , and  $\epsilon_e$  is the equilibrium end potential at time  $t_e$  of single sweep respectively cyclic voltammetry as well as potentiostatic step methods.

The metal ion adsorbate disappears for  $a_{\text{Me}z^+} \rightarrow 0$ , i.e.,  $\mu_{\text{Me}z^+} \rightarrow -\infty$ . In other words, in the electrolyte, which is free of metal ions, there flows only a capacity current. The integral over the same underpotential range is given by

$$\lim_{\mu_{\text{Me}z^+} \rightarrow -\infty} \int_{t_1}^{t_e} i(t) dt = \int_{t_1}^{t_e} i_C(t) dt = q(\epsilon_e, \Gamma_e = 0) - q(\epsilon_1, \Gamma_1 = 0) \quad [7]$$

Subtraction of Eq. [7] from Eq. [6] leads to

$$\begin{aligned} \int_{t_1}^{t_e} [i(t) - i_C(t)] dt &= q(\epsilon_e, \Gamma_e) - q(\epsilon_e, \Gamma_e = 0) \\ &= \Delta q(\epsilon_e, \Gamma_e) \\ &= \int_{\Gamma=0}^{\Gamma} \left( \frac{\partial q}{\partial \Gamma} \right)_{\epsilon_e} d\Gamma \end{aligned} \quad [8]$$

The limiting value of such charge amounts integrated over the total underpotential range up to the equilibrium potential can be written

$$\lim_{\epsilon_e \rightarrow \epsilon_{0, \text{Me}/\text{Me}z^+}} \Delta q(\epsilon, \Gamma) = \Delta q_{\text{max}} \quad [9]$$

The measurable  $\Delta q_{\text{max}}$  values are in the magnitude of a complete metal monolayer, e.g., for  $z = 1$

$$\Delta q_{\text{max}} = 220 \pm 10 \text{ } \mu\text{coulombs} \cdot \text{cm}^{-2}$$

This corresponds to a maximal coverage  $\Gamma_{\text{max}}$

$$\Gamma_{\text{max}} = \frac{\Delta q_{\text{max}}}{z \cdot F} \simeq 2.2 \cdot 10^{-9} \text{ mole} \cdot \text{cm}^{-2}$$

For divalent ions  $z = 2$  and therefore  $\Delta q_{\text{max}}$  is twice, etc.

The saturation coverage  $\Gamma_{\text{max}}$  has been confirmed experimentally in many systems and can be calculated also by taking into consideration an epitaxial adsorption of metal ions on the closest packed lattice plane of the substrate, e.g., the (111) plane in the case of a face-centered cubic lattice. The surface of a polycrystalline substrate is formed by different crystal planes, e.g., (100) and (110) planes in the above-mentioned case. These other planes adsorb a little bit lower

$\Gamma_{\text{max}}$  values as can be seen by calculation. On the other hand, the limiting coverage will be increased somewhat by the roughness factor of the electrode surface. Therefore the experimental data for  $\Gamma_{\text{max}}$  or  $\Delta q_{\text{max}}$  vary somewhat according to the pretreatment of the polycrystalline or monocrystalline electrode surfaces.

If disturbing processes occur simultaneously in the underpotential range, the measurement of  $\Delta q$  values on the working electrode becomes more complex, i.e., the measured  $q_{\mu\epsilon}$  isotherm is different from the  $q\Gamma\epsilon$  isotherm

$$\Delta q \neq zF\Gamma \quad [10]$$

Generally, for the interphase between the substrate electrode and the electrolyte the following thermodynamic considerations must be taken into account:

The surface free energy,  $\sigma$ , is a function of the chemical potentials of all species  $\mu_i$ , which are in the solution, and of the electrode potential  $\epsilon$ . In the presence of an excess of inert electrolyte and with only one common anion the chemical potentials of the supporting electrolyte as well as that of the anion can be assumed as constant. Therefore at  $p, T, \mu_j$  ( $j \neq \text{Me}z^+ = \text{const}$ )

$$\sigma = \sigma(\mu_{\text{Me}z^+}, \epsilon) \quad [11]$$

With the definitions

$$q = \left( \frac{\partial \sigma}{\partial \epsilon} \right)_{p, T, \mu_{\text{Me}z^+}, \mu_j} = q(\mu_{\text{Me}z^+}, \epsilon) \quad [12]$$

and

$$\Gamma = - \left( \frac{\partial \sigma}{\partial \mu_{\text{Me}z^+}} \right)_{p, T, \epsilon, \mu_j} = \Gamma(\mu_{\text{Me}z^+}, \epsilon) \quad [13]$$

it follows

$$q = q(\Gamma, \epsilon) \quad [14]$$

The partial derivative leads to the so-called charge coverage coefficient  $Z_E$

$$\left( \frac{\partial q}{\partial \Gamma} \right)_{\epsilon} = Z_E \cdot F \quad [15]$$

Generally, this coefficient is a function of  $\Gamma$  and  $\epsilon$

$$Z_E = Z_E(\Gamma, \epsilon) \quad [16]$$

There exist three limiting cases:

(i)  $Z_E = z = \text{constant}$ , whereby  $z$  is the charge number of the metal ion  $\text{Me}z^+$ . In this simplest case the metal monolayer model is valid as above mentioned.

(ii)  $Z_E = Z_E(\Gamma)$

(iii)  $Z_E = Z_E(\epsilon)$

In the second and third case it is necessary to measure  $\Gamma_{\mu_{\text{Me}z^+}, \epsilon}$  isotherms in an independent way of that used for  $q_{\mu_{\text{Me}z^+}, \epsilon}$  isotherms in order to determine the metal ion adsorption process exactly. Naturally, the same statement is valid if  $Z_E$  is a mixed function. If such measurements are possible, then the deviations between the two isotherms can be correlated to  $Z_E$  and can be explained by disturbing processes, which take place simultaneously in the underpotential range. Schmidt and co-workers (27-29, 32, 33, 35-37, 39) have given the theoretical treatment as well as the experimental confirmation of the thermodynamic predictions using the newly developed twin-electrode thin-layer technique. Some examples will be demonstrated under Results below.

This twin-electrode thin-layer technique is the only one at present which allows us to determine independently  $\Gamma_{\mu_{\text{Me}z^+}, \epsilon}$  isotherms in a relatively simple manner. Other suitable methods might be radiotracer measurements and in some cases rotating ring disk techniques.

A more detailed interpretation of the deviation of  $Z_E$  from  $z$  is given by Vetter and Schultze (50-52) taking into consideration a geometrical factor for the adsorbed species, a partial charge transfer coefficient,

dipole factors, and a capacitive term. Instead of Z<sub>E</sub> Vetter and Schultze use the symbol  $\gamma$  and call it "electrosorption valency." The disadvantage of this theory is the difficulty of an experimental separation of the different components by electrochemical measurements. Moreover, Vetter and Schultze give a thermodynamic treatment of cosorption processes in order to determine electrosorption valencies for mixed inter-phase reactions (53). It seems that only optical investigations could be applied in order to decide in which charge state exist the adsorbed metal species.

### Experimental Techniques

At present the following electrochemical measurement methods are applied in the field of metal ion adsorption.

**Twin-electrode thin-layer technique.**—This method was developed by Schmidt and co-workers in the last 5 years. In principle the thin-layer cell contains four electrodes; the working or indicator electrode, the generator electrode, and the usual reference and counterelectrodes. The first two are situated parallel at a distance of about  $50\mu$  from each other. The small electrolyte volume between them constitutes the thin layer. This thin layer is separated by small capillaries from the other part of the electrolyte, which contains both the other electrodes. The generator must be a reversible electrode for the ion species being adsorbed on the indicator, e.g., in the case of metal ion adsorption a reversible metal/metal ion electrode. Both, indicator and generator are polarized potentiostatically at different potentials.

The indicator potential is varied cyclic voltammetrically between defined start and end potentials,  $e_1$  and  $e_2$ , using scanning rates of about  $1 \text{ mV} \cdot \text{sec}^{-1}$  and waiting for equilibrium adjusting at these potentials. Integration of current-time transients in the indicator circuit gives changes in  $q$ , as can be seen from Eq. [6].

According to the Nernst equation the fixed generator potential,  $e_G$ ,<sup>1</sup> maintains a certain chemical potential  $\mu_{Me^{z+}}$  of metal ions in the thin layer. Therefore, any concentration changes within the thin layer due to metal ion adsorption or desorption on the indicator are compensated by the generator. The integration of the current-time transients in the generator circuit corresponds directly to  $\Gamma$  changes on the indicator.

The advantages of the two-electrode thin-layer technique are: (i) exact thermodynamic results, especially the possibility to measure  $\Gamma_{\mu e}$  isotherms independently; (ii) simple diffusion conditions in the steady state according to Ficks first law; (iii) the possibility to purify the thin-layer electrolyte to a very great extent by pre-electrolysis. Moreover, this method is not sensitive against electrolyte impurities, because the ratio between electrode surface and electrolyte volume is very high;<sup>2</sup> (iv) the possibility to put in so-called grid electrodes between indicator and generator and to measure potentiostatically the fluxes of different ionic species (39).

The disadvantages are: (i) reversible generator electrodes exist only for a few systems; (ii) pulse measurements are not possible, because the system has too high impedance; (iii) kinetic results cannot be obtained, because the system must be always in quasi equilibrium or in the steady state in order to make possible the mathematical treatment of the findings; (iv) the metal ion concentration in the thin-layer electrolyte is limited by the noise and the stability of the operation amplifiers used in the potentiostatic circuits to about  $10^{-3} \text{ mole} \cdot \text{l}^{-1}$  or less as an upper limit.

A scheme of the arrangement of the two-electrode thin-layer technique is demonstrated in Fig. 1.

**Rotating electrode systems.**—Rotating disk or ring disk electrodes were used in order to simplify the flux

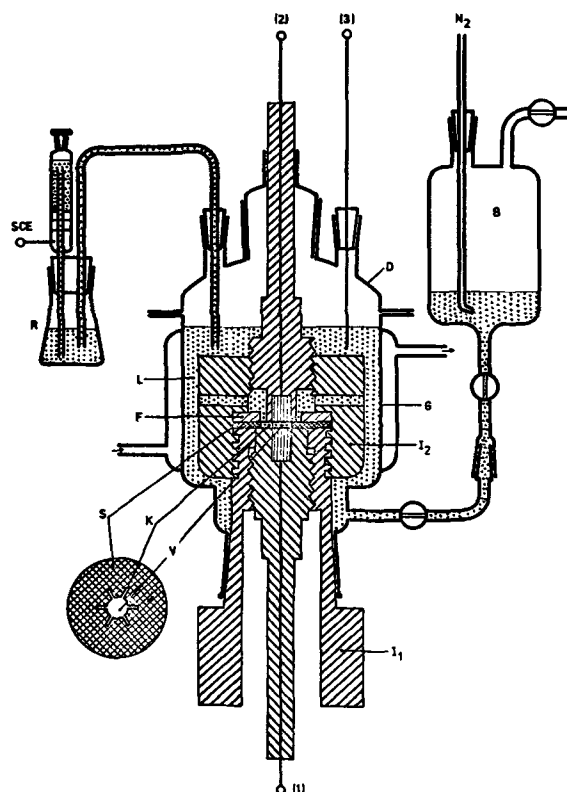


Fig. 1. Twin-electrode thin-layer cell. 1 and 2, Working or indicator electrode and generator electrode, respectively (metal rods, fitted in insulating holders, e.g., Teflon); 3, counterelectrode. I<sub>1</sub>, I<sub>2</sub>, support of insulating material; F, ring of insulating material; K, capillaries cut out of an insulating spacer S; V, thin layer volume cut out of an insulating spacer S; S, spacer of  $50\mu$  thickness; B, electrolyte container; D, glass cover; G, glass cell; L, electrolyte; N<sub>2</sub>, nitrogen; R, container for the reference electrode (SCE).

conditions for the metal ion species and to measure ring currents in the case of anodically stripping experiments. The disadvantage of this and the following methods is the high sensitivity against impurities, because the ratio between electrode surface and electrolyte volume is very small. Moreover, when using this technique it is not so easy to measure independently  $\Gamma_{\mu e}$  isotherms on the ring as in the case of the thin-layer technique. Rotating electrode systems are applied mainly by Bruckenstein and co-workers (41-48).

**Cyclic or linear sweep voltammetry under semi-infinite diffusion conditions.**—These well-known methods give very rapidly useful thermodynamic and kinetic results. The following disadvantages must be taken into account for the interpretation of the results: (i) The obtained thermodynamical data can be correlated only to the simple metal monolayer model, because the  $\Gamma_{\mu e}$  isotherms are not measurable independently. (ii) An exact interpretation of kinetic data in the underpotential range is relatively difficult, because the mathematical treatment of the current-density potential curves is complicated by the additional parameter  $a_{ads}(\Gamma)$  and has not been solved generally up to date.

These methods are used by Harrison and Thirsk (75) and by Lorenz and co-workers (60-64) in the field of metal ion adsorption processes.

**Galvanostatic or potentiostatic rectangular pulse measurements under semi-infinite diffusion conditions.**—Both methods give only limited thermodynamic data as mentioned above. However, the great advantage of nonsteady-state pulse measurements is the possibility to study the kinetics of metal ion adsorption processes. Both methods require pulse techniques with rise times of maximum  $10^{-6} \text{ sec}$ . Usual potentiostats are not able to follow in such time constants under load.

<sup>1</sup>  $e_G = e_0 \cdot \text{Me}/\text{Me}^{z+}$  in Eq. [2] for  $a_{Me} = 1$ .

<sup>2</sup> Assuming that the components of the thin-layer compartment are initially clean. Otherwise this ratio becomes a disadvantage.

Therefore, Lorenz and co-workers (87) are applying multichannel pulse galvanostats, which are very rapid and have a rise time of about  $6.10^{-8}$  sec (88).<sup>3</sup> In addition, this technique also requires an electronic voltage-to-current converter with the same switching time constant in order to change instantaneously from potentiostatically fixed equilibrium conditions to non-steady-state galvanostatic ones (88).

Earlier Schultze (49) had used galvanostatic pulse measurements in order to determine thermodynamics as well as kinetics of the  $\text{Cu}^{++}$  ion adsorption process on polycrystalline platinum substrate. It should be mentioned that the obtained results are problematic due to disturbing processes on platinum electrodes, e.g., adsorption of hydrogen and oxygen. Moreover, no evidence could be given for the adsorption step to be rate determining instead of the reduction of  $\text{Cu}^{++}$  ions to  $\text{Cu}^+$  ions.

**Optical methods.**—In order to determine the formation of metal films on foreign substrates as well as their structures, reflection spectroscopy was applied by Yeager and co-workers (83) and by Kolb (84, 85). The metal ion adsorption changes the reflectivity in a definite way. But the correlation between this change and the structure of the adsorbate seems to be relatively uncertain at present, because of the simplifying assumptions incorporated in the theoretical interpretation of the data.

**Results**

**Au/Ag<sup>+</sup> and Au/Tl<sup>+</sup> systems.**—Figure 2 shows the  $\text{Ag}^+$  ion adsorption on polycrystalline and monocrystalline gold electrodes from sulfuric acid solutions using cyclic voltammetry. The monocrystalline electrode

<sup>3</sup>The apparatus are produced by Mega-Physik Limited, D 7550 Rastatt, Germany.

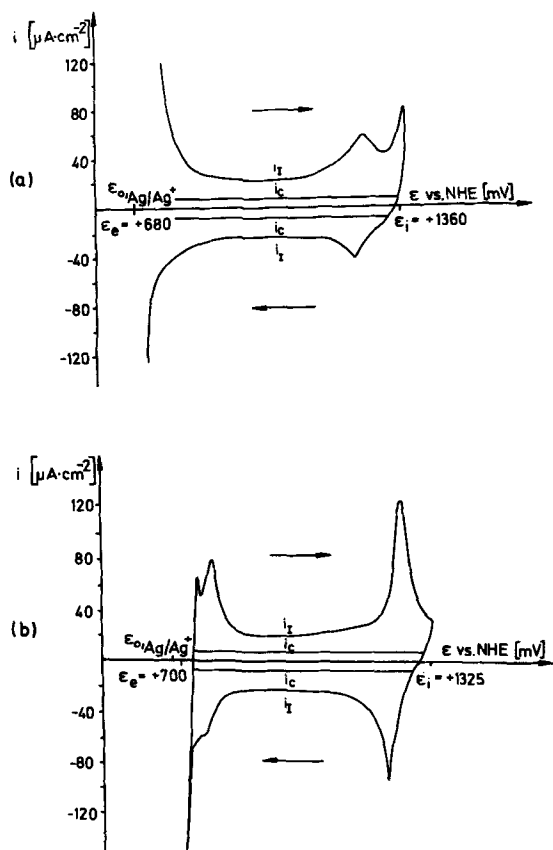


Fig. 2. Au/0.5M H<sub>2</sub>SO<sub>4</sub> + 3.9 × 10<sup>-2</sup>M Ag<sup>+</sup> system.  $\left| \frac{de}{dt} \right| = 50 \text{ mV} \cdot \text{sec}^{-1}$ ;  $T = 298^\circ\text{K}$ ;  $i_i$  = current of the working electrode;  $i_c$  = capacity current at  $c_{\text{Ag}^+} = 0$ . a, Polycrystalline Au; b, monocrystalline Au (111).

surface has a defined crystallographical orientation of (111) plane. Both kinds of electrodes were mechanically and electrolytically polished and preactivated by polarization. In the first approximation this system follows the metal monolayer model. The integrated  $\Delta q_{\text{max}}$  values are about 400  $\mu\text{Coulombs} \cdot \text{cm}^{-2}$  for the polycrystalline and monocrystalline electrode surfaces, respectively. These results are in a good agreement with the theoretical  $\Delta q_{\text{max}}$  value taking into consideration a roughness factor of about 1.5, which could be verified experimentally by measuring the double layer capacity. Moreover, from Fig. 2 it can be seen clearly that the nucleation of metallic silver takes place without any three-dimensional nucleation overvoltage. The  $q_{\mu\epsilon}$  isotherm is represented in Fig. 3.

The system with polycrystalline gold as a substrate and  $\text{Tl}^+$  ions has a quite similar behavior. Figure 4

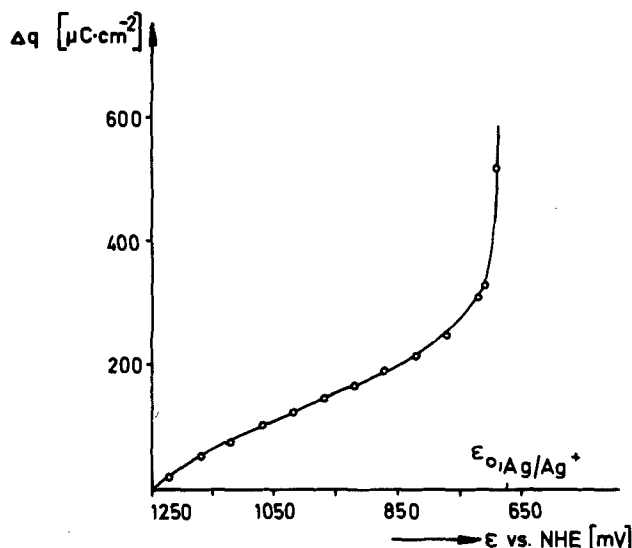


Fig. 3. Au (polycrystalline)/0.5M H<sub>2</sub>SO<sub>4</sub> + 3.9 × 10<sup>-2</sup>M Ag<sup>+</sup> system.  $q_{\mu\epsilon}$  isotherm determined by potentiostatic step measurements under steady-state conditions.  $T = 298^\circ\text{K}$ .

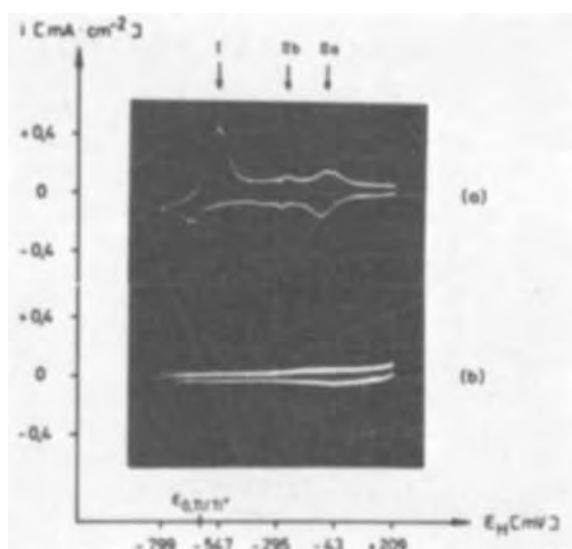
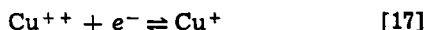


Fig. 4. a, Au (polycrystalline)/0.5M KCl + 4.38 × 10<sup>-4</sup>M Tl<sup>+</sup> system; b, Au (polycrystalline)/0.5M KCl system.  $\left| \frac{de}{dt} \right| = 151 \text{ mV} \cdot \text{sec}^{-1}$ ;  $T = 298^\circ\text{K}$ . I, Anodic dissolution peak of the cathodically deposited Tl metal phase; IIa and IIb, sorption peaks of Tl<sup>+</sup> ions in the underpotential range.

demonstrates cyclic voltammetric measurements in chloride media with and without  $Tl^+$  ions in the electrolyte. The metal ion adsorption occurs mainly at the peak potentials IIa and IIb. In this experiment the end potential was chosen more negative than the equilibrium potential of the  $Tl/Tl^+$  electrode. It can be seen also that the nucleation of metallic thallium happens practically without any crystallization overvoltage.

**Au/Cu<sup>++</sup> system.**—The  $Cu^{++}$  ion adsorption on polycrystalline gold electrodes is shown in Fig. 5 for cyclic voltammetric measurements. In this system the single peak in the underpotential range does not only correspond to the adsorption process cathodically and the desorption process anodically, but it contains also the disturbing faradaic redox process



This follows from the measured  $\Delta q_{max}$  values, which are much higher than the theoretical ones and are dependent on the  $Cu^{++}$  ion concentration in the electrolyte as well as on the scanning rate (61, 62, 89). Investigations in the same system using the twin-electrode thin-layer technique are in a good agreement with the cyclic voltammetric results (34, 62). A mathematical treatment of the experimental results obtained by cyclic voltammetry under semi-infinite diffusion conditions (relatively high  $Cu^{++}$  ion concentrations in the electrolyte and low scanning rates) showed that the diffusion of  $Cu^+$  ions from the electrode surface into the bulk of the solution can be considered as the rate determining step (89).

**Au/Pb<sup>++</sup> system.**—Figure 6 shows the  $Pb^{++}$  ion adsorption on polycrystalline gold electrodes using the twin-electrode thin-layer technique given by Schmidt and Wüthrich (35). It can be seen that the currents of the indicator and generator electrodes are about the same in the opposite direction. In other words, this system follows the metal monolayer model. This was verified by considering the  $q\Gamma\epsilon$  isotherms, which are given in Fig. 7. The measured integrals are situated on the theoretical line for  $Z_E = z = +2$ . In this case the  $\Gamma\mu\epsilon$  isotherms, plotted in the special form  $\theta = \theta(\epsilon_G, \epsilon_G - \epsilon)$ , are all situated on the same curve, which

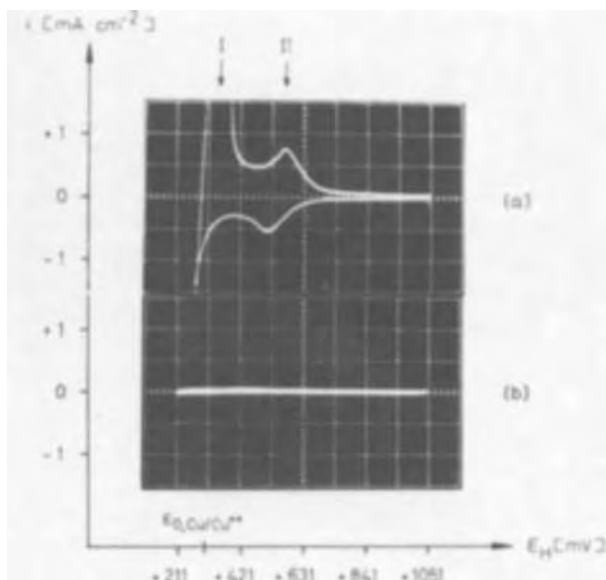


Fig. 5. a, Au (polycrystalline)/0.5M  $H_2SO_4$  + 1M  $Cu^{++}$  system; b, Au (polycrystalline)/0.5M  $H_2SO_4$  system.  $\left| \frac{de}{dt} \right| = 84 \text{ mV} \cdot \text{sec}^{-1}$ ;  $T = 298^\circ\text{K}$ . I, Anodic dissolution peak of the cathodically deposited Cu metal phase; II, sorption peak of  $Cu^{++}$  ions in the underpotential range and disturbing redox reaction  $Cu^+ \rightleftharpoons Cu^{++} + e^-$ .

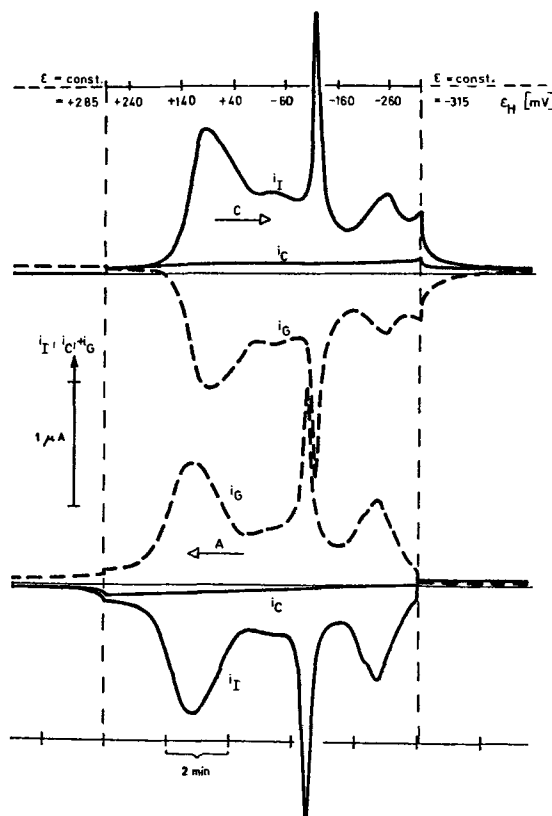


Fig. 6. Au/ $Pb^{2+}$  system. Electrolyte: 0.5M  $NaClO_4$  + acetate-buffer,  $pH = 4.7$  ( $c_{Ac} = 0.5M$ ). Geometric electrode surface:  $0.785 \text{ cm}^2$ .  $\left| \frac{de}{dt} \right| = 1 \text{ mV} \cdot \text{sec}^{-1}$ ;  $T = 298^\circ\text{K}$ ;  $\epsilon_G = -319 \text{ mV}$  vs. NHE  $\Delta \approx 1.8 \times 10^{-4}M \text{ Pb}^{2+}$ ;  $\epsilon_I = 286 \text{ mV}$  vs. NHE;  $\epsilon_e = -314 \text{ mV}$  vs. NHE.  $i_I$ , Indicator current;  $i_G$ , generator current;  $i_C$ , capacity current ( $c_{Pb^{2+}} = 0$ ); C, cathodic sweep; A, anodic sweep.

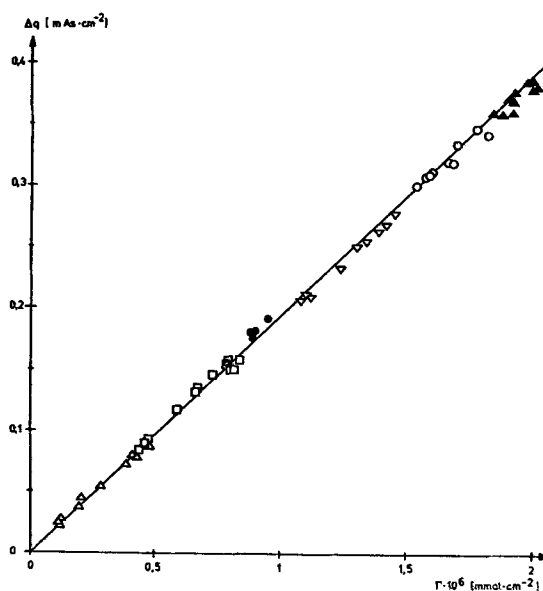


Fig. 7.  $q\Gamma\epsilon$  isotherms in the system Au/ $Pb^{2+}$ . Full line:  $\Delta q = 2 F\Gamma$  (definition of  $\Delta q$  see Eq. [8]).  $\epsilon$  (mV vs. NHE):  $\Delta$ , 121;  $\square$ , 51;  $\bullet$ , -29;  $\nabla$ , -109;  $\circ$ , -359;  $\blacktriangle$ ,  $\epsilon = \epsilon_G + 5 \text{ mV}$ .

is demonstrated in Fig. 8. Hereby  $\epsilon_G$  corresponds to  $\mu_{Pb^{++}}$  and  $\theta$  is given by  $\Gamma/\Gamma_{max}$ .

**Ag/Pb<sup>++</sup> system.**—Schmidt and Wüthrich (33) investigated the  $Pb^{++}$  ion adsorption from chloride media on polycrystalline silver substrates. Figure 9

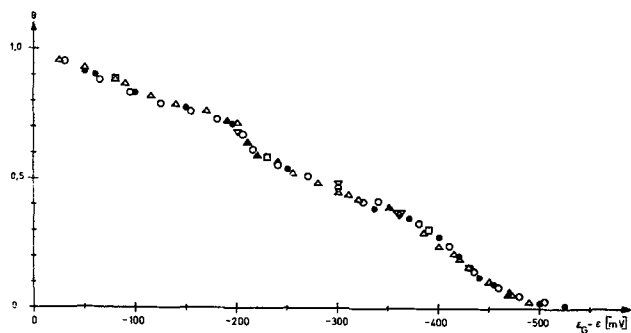


Fig. 8.  $\Gamma\mu\epsilon$  isotherms of the system  $\text{Au}/\text{Pb}^{2+}$  in the special form  $\theta = \Gamma/\Gamma_{\text{max}}$  vs.  $(\epsilon_G - \epsilon)$ .

$\epsilon_G$ (mV vs. NHE)	$c_{\text{Pb}^{2+}}$ (Mole $l^{-1}$ )
○	$1.8 \times 10^{-5}$
▲	$7.6 \times 10^{-4}$
△	$4.0 \times 10^{-4}$
●	$1.8 \times 10^{-4}$
□	$4.0 \times 10^{-5}$
△	$1.8 \times 10^{-5}$

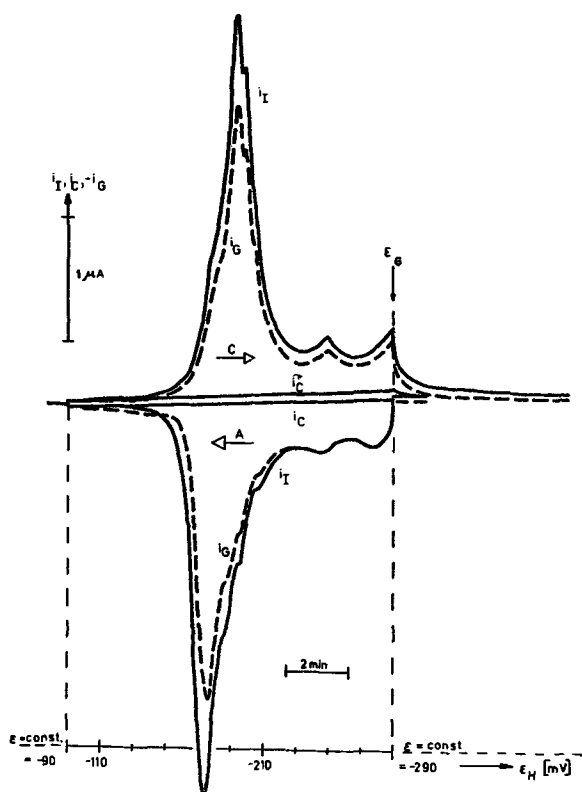


Fig. 9.  $\text{Ag}/\text{Pb}^{2+}$  system. Electrolyte:  $0.5\text{M KCl} + 10^{-3}\text{M HCl}$ . Geometric electrode surface:  $0.785\text{ cm}^2$ .  $\left|\frac{d\epsilon}{dt}\right| = 0.33\text{ mV} \cdot \text{sec}^{-1}$ ;  $T = 298^\circ\text{K}$ ;  $\epsilon_G = -289\text{ mV vs. NHE} \hat{=} 1.8 \times 10^{-4}\text{M Pb}^{2+}$ ;  $\epsilon_I = -89\text{ mV vs. NHE}$ ;  $\epsilon_0 = -289\text{ mV vs. NHE}$ .  $i_I$ , indicator current;  $i_G$ , generator current;  $i_C$ , capacity current ( $c_{\text{Pb}^{2+}} = 0$ ); C, cathodic sweep; A, anodic sweep.

shows the current potential curves for the indicator and generator electrodes. Obviously in this case there are deviations between them. The  $q\Gamma\epsilon$  isotherms, which are represented in Fig. 10, show that in the lower underpotential range  $Z_E = Z_E(\Gamma) > 2$  and in the higher one  $Z_E = Z_E(\Gamma, \epsilon) < 2$ . These deviations were explained by codesorption and coadsorption processes, respectively, of  $\text{Cl}^-$  ions. In this case the special  $\Gamma\mu\epsilon$  isotherms  $\theta = \theta(\epsilon_G, \epsilon_G - \epsilon)$  are different curves for each  $\epsilon_G$ , as it is shown in Fig. 11. The horizontal shift of these curves is correlated to the deviation of  $Z_E$  from  $z = +2$ .

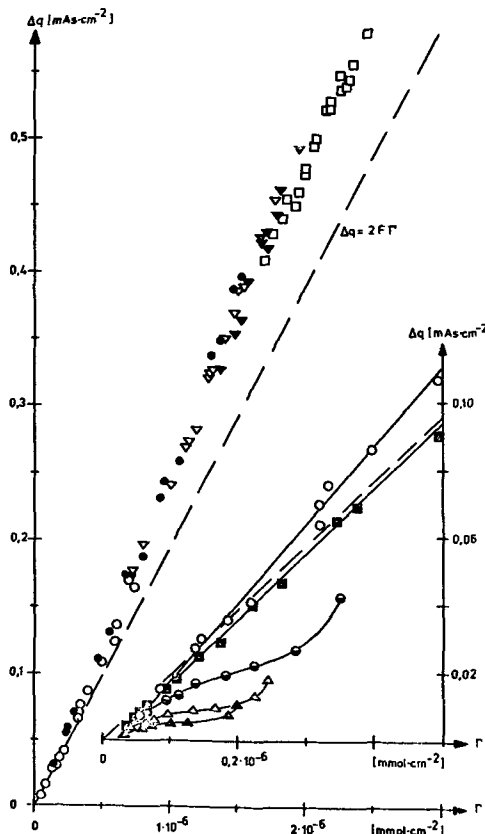


Fig. 10.  $q\Gamma\epsilon$  isotherms in the system  $\text{Ag}/\text{Pb}^{2+}$ . Dashed line:  $\Delta q = 2F\Gamma$  (definition of  $\Delta q$  see Eq. [8]).  $\epsilon$  (mV vs. NHE): ▲, -139; △, -149; ●, -159; ■, -164; ○, -169; ●, -189; ▽, -209; ▽, -229; □, -279.

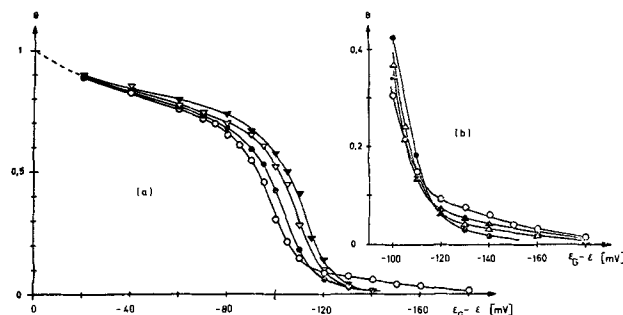


Fig. 11.  $\Gamma\mu\epsilon$  isotherms of the system  $\text{Ag}/\text{Pb}^{2+}$  in the special form  $\theta = \Gamma/\Gamma_{\text{max}}$  vs.  $(\epsilon_G - \epsilon)$ . Diagram (b) is an enlarged part of diagram (a) for low degrees of coverage  $\theta$ .

$\epsilon_G$ (mV vs. NHE)	$c_{\text{Pb}^{2+}}$ (Mole $l^{-1}$ )
○	$8.6 \times 10^{-4}$
▲	$6.1 \times 10^{-4}$
△	$4.0 \times 10^{-4}$
●	$1.8 \times 10^{-4}$
□	$4.0 \times 10^{-5}$
▽	$8.6 \times 10^{-5}$

*Pt/Pb<sup>++</sup> and Bi/Pb<sup>++</sup> systems.*—In these systems Schmidt and Wüthrich (37, 90) found the formation of alloys in the underpotential range. Moreover, the sorption process on the platinum electrode is not reversible. Consequently, thermodynamic treatment could not be applied in these cases.

**Structure of Metal Films**

At present the structure of adsorbed metal ions in the underpotential range is an open question. This problem is not solved because the interpretation of the  $\Delta q_{\text{max}}$  or  $\Gamma_{\text{max}}$  values as the formation of complete metal monolayers on the substrate is only an assumption. The measurable  $\Delta q$  or  $\Gamma$  values are only integrals. They cannot predict anything about the arrange-



ment of the adsorbed species. The formation of multi-atomar metal layers or multiatomar islands in the underpotential range was supposed by Schultze (49), Thirsk (75), Breiter (73, 74), Wüthrich (35, 37, 90), and Kolb (85). The formation of such instable prenuclei would be very interesting in considering the nucleation phenomena of the compact metal at potentials which are more negative than the equilibrium potential  $\epsilon_{0,Me/Mez+}$ . However, a strong argument for the monolayer theory is the fact that in many cases the  $\Delta q_{max}$  respective  $I_{max}$  values correspond just to a monolayer. This constancy could hardly be explained by island formation, which would be much more dependent on pretreatment of electrodes and purity grade of solutions.

In many systems no crystallization overvoltage can be determined using voltammetric techniques under quasi-steady-state conditions, starting from the underpotential range and polarizing to nucleation potentials, which are more negative than the equilibrium potential  $\epsilon_{0,Me/Mez+}$ . In other systems the observed amount of it is only several millivolts and indicates more a two-dimensional rather than a three-dimensional nucleation. In other words, under quasi-steady-state conditions the formation of three-dimensional nuclei as the initial process of electrocrystallization on foreign substrates is improbable in many investigated systems. However, the three-dimensional nucleation could be a kinetic phenomenon. In the case of nonsteady-state pulse experiments the formation of three-dimensional nuclei may occur if the relaxation time is relatively high for the formation of a metal monolayer or instable prenuclei in the underpotential range. On the contrary, under quasi-equilibrium conditions using voltammetry there might be a direct nucleation or growth process starting from the metal adsorbate in the underpotential range.

Another very important problem is the influence of the substructure of the substrate on thermodynamics, kinetics, and structure of metal ion adsorption in the underpotential range. Polycrystalline material as a substrate has a certain density of crystal imperfections, e.g., different kinds of dislocations, lattice deformations, etc. However, the density of crystal imperfections in monocrystalline material is generally lower by several orders of magnitude. Furthermore, the polycrystalline surface consists of different crystal grains belonging to different lattice planes. These grains are separated by large angle boundaries. Each crystal grain consists of subgrains separated by low angle boundaries, which are built up by penetration points of edge dislocations. Monocrystalline material consists also of subgrains. However, the density of subgrain boundaries is much lower than in the case of polycrystalline material.

Consequently two parameters of the substrate have to be taken into account in metal ion adsorption processes: (i) the density of crystal imperfections and (ii) the kind of crystallographic orientation of the surface. Accordingly, Lorenz and co-workers (63, 64) investigated the influence of these two parameters in the case of  $Tl^+$  ion adsorption on silver electrodes. Polycrystalline as well as monocrystalline silver electrodes were used as substrates. The monocrystalline electrode had definite crystallographic surface orientation of (100), (110), and (111) planes and a much lower density of crystal imperfections than the polycrystalline electrodes. Three different electrolyte systems were investigated. The pretreatment of the electrode surfaces was either only mechanical polishing or mechanical polishing followed by electrolytical polishing as carried out by Budevski (91-93). Cyclic voltammograms of mechanical polished electrodes are represented in Fig. 12-14. The obtained results were surprisingly independent of the kind of electrode pretreatment.  $q$  values were determined by integrating only the peak currents, therefore  $q \leq \Delta q_{max}$ . Two important results could be observed:

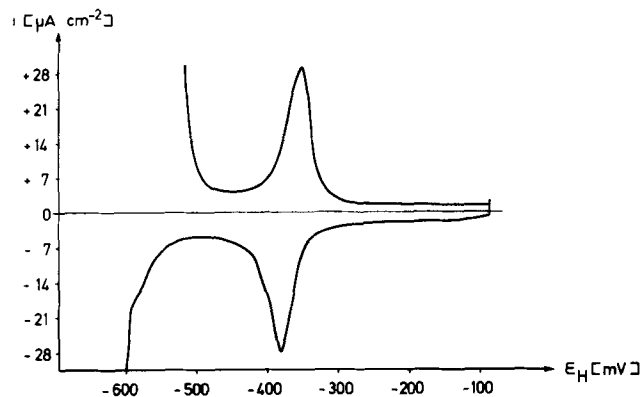


Fig. 12. Ag (polycrystalline)/0.5M KCl +  $3.75 \times 10^{-4}M Tl^+$  system.  $\left| \frac{de}{dt} \right| = 6.1 \text{ mV} \cdot \text{sec}^{-1}$ ;  $T = 298^\circ K$ .

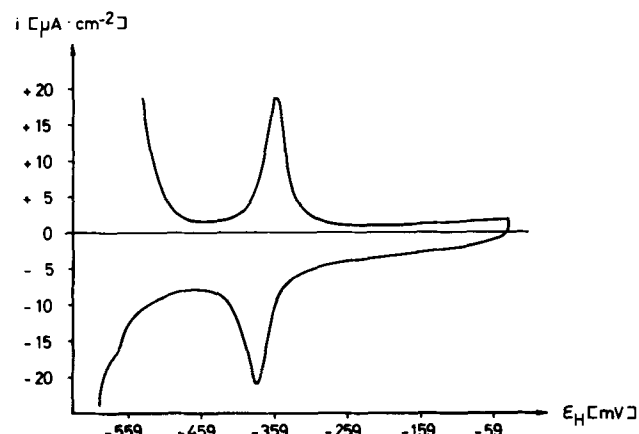


Fig. 13. Ag (110)/0.5M KCl +  $3.75 \times 10^{-4}M Tl^+$  system.  $\left| \frac{de}{dt} \right| = 6.1 \text{ mV} \cdot \text{sec}^{-1}$ ;  $T = 298^\circ K$ .

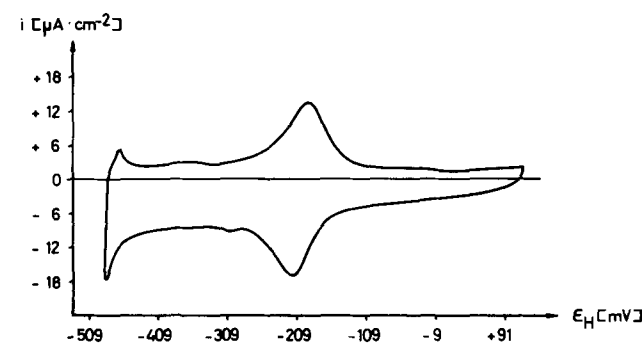


Fig. 14. Ag (100)/0.5M  $NaClO_4$  + 0.01M  $HClO_4$  +  $4 \times 10^{-3}M Tl^+$  system.  $\left| \frac{de}{dt} \right| = 6.1 \text{ mV} \cdot \text{sec}^{-1}$ ;  $T = 298^\circ K$ .

(i) The single current peak, recorded in the underpotential range, corresponds to the  $Tl^+$  ion adsorption and its potential value is not influenced markedly by the kind of substrate. This means that the free energy of adsorption will not mainly depend on the surface orientation. Furthermore, it may be tentatively concluded that this free energy hardly depends on the density of crystal imperfections. This second conclusion depends on how much of the surface deformation caused by mechanical work remains after the last polishing. It is known from the investigations of Samuels and co-workers (94-96) that this remaining surface deformation can be kept quite low. Even without electrochemical polishing it can be kept below the

Table I. Adsorption of  $Tl^+$  ions on polycrystalline and monocrystalline Ag substrates depending on the surface pretreatment, electrolyte system, and scanning rate of cyclic voltammograms ( $T = 298^\circ K$ )

Ag electrode	System	Electrolyte	$ d\epsilon/dt $ (mV)	$q$ ( $\mu\text{coulombs}\cdot\text{cm}^{-2}$ )			
				Polycryst.	(100)	(110)	(111)
Mechanically polished	0.5M KCl + $3.75 \times 10^{-4}M TlNO_3$		6.1	206	145	111	65
With water polished			61	207	128	108	85
Mechanically polished	0.5M NaClO <sub>4</sub> + $3.75 \times 10^{-4}M TlNO_3$		6.1	320	203	201	172
Mechanically + electrochemically polished			6.1	202	224	150	102
	0.5M NaClO <sub>4</sub> + $4 \times 10^{-3}M TlClO_4$		61	189	148	147	104
			5.8	186	256	133	96
	0.01M TlClO <sub>4</sub>		57.4	189	213	148	108
			5.8	186	256	133	96
	Calculated			$96 > q > 68$	96	68	53

detection limit of electron diffraction measurements, if the procedures worked out by this author are carefully followed, as it was done during the present investigations. A further argument for the validity of both conclusions are LEED investigations (97), in which the free energy for CO adsorption on poly- and monocrystalline palladium surfaces was found to be independent of the kind of substrate.

(ii) The measured  $q$  values correspond approximately to the formation of a metal monolayer in the case of polycrystalline substrate. However, in the case of monocrystalline electrodes the  $q$  values depend on the kind of crystallographic orientation. This is illustrated in Table I. Surprisingly the  $q$  values decrease in the following sequence:

$$q(100) > q(110) > q(111)$$

This means that the closest packed lattice plane (111) of the face-centered cubic lattice of silver adsorbs the lowest amount of  $Tl^+$  ions. This can be explained by assuming that the adsorption of  $Tl^+$  ions takes place on interstitial sites between the surface silver atoms and leads to the formation of a superlattice. Such superlattices are well known from LEED investigations dealing with adsorption phenomena from the gas phase. Using this model, the above-mentioned sequence can be calculated. The experimental results are higher than the calculated data. These deviations can be attributed to the influences of crystal imperfections, formation of multilayers or islands, and of the roughness factor. According to the superlattice model, the coverage of the polycrystalline substrate should be placed between the coverages of the (100) and (110) planes, if one does not take into account any influence of the density of crystal imperfections. In two of the three investigated electrolyte systems this statement could be confirmed as Table I indicates. The third system contains  $Cl^-$  ions and here coadsorption or codeposition processes cannot be excluded. A true to scale representation of such superlattices is given in Fig. 15-17 using  $r_{Tl} = 1.70\text{\AA}$  and  $r_{Ag} = 1.44\text{\AA}$ .

#### Kinetics of Metal Ion Adsorption

Up to date only one paper dealt with the subject of the kinetics of metal ion adsorption. Schultze (49) in-

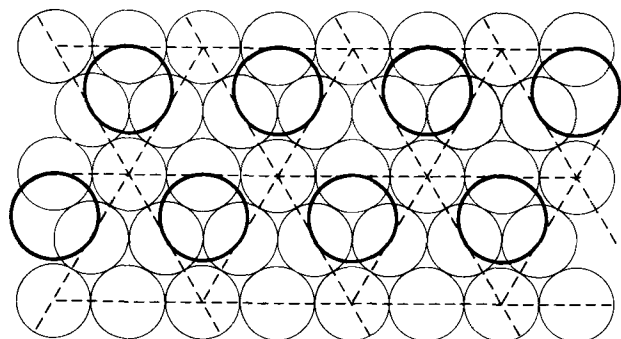


Fig. 15. Hypothetical superlattice in the case of  $Tl^+$  ion adsorption on Ag (111)-(2 × 2) Tl.

vestigated the kinetics of  $Cu^{++}$  ion adsorption on polycrystalline platinum electrodes using galvanostatic pulse measurements after potentiostatically adjusted equilibria. He calculated exchange current densities for the adsorption process in the underpotential range which are higher than those for the corresponding  $Cu/Cu^{++}$  electrode. Naturally, the evaluated values depend on the degree of coverage as well as on the  $Cu^{++}$  ion concentration in the solution. However, the results of Schultze are not without doubt as already mentioned.

Presently a study of adsorption kinetics is being carried out for the systems  $Au/Ag^+$ ,  $Au/Cu^{2+}$ ,  $Au/Pb^{2+}$ , and  $Au/Tl^+$  with (111) orientated monocrystalline and polycrystalline substrates utilizing potentiostatic-galvanostatic pulse techniques (87). The potentiostatically fixed initial states in the underpotential region in this method are equilibrium states, which are characterized by  $\epsilon^*$ ,  $\Gamma^*$ , and  $C_{DL}(\epsilon^*)$ , whereby  $C_{DL}$  represents the double layer capacity. The following galvanostatic pulse width depends on the applied pulse amplitude  $i$  and is chosen in such a way that the change of  $\Delta q$  does not exceed  $1 \mu\text{coulomb}\cdot\text{cm}^{-2}$  and the potential deviations from  $\epsilon^*$  are a few millivolts at most. Under these experimental conditions the  $\Gamma_{\mu\epsilon}$  isotherm can be linearized in the vicinity of the initial state, and therefore potential time transients can be calculated for  $\eta \ll RT/zF$  to fit the experimental curves, assuming simple adsorption kinetics.

Furthermore, the concentrations of metal ions in the electrolyte are chosen high enough to neglect bulk

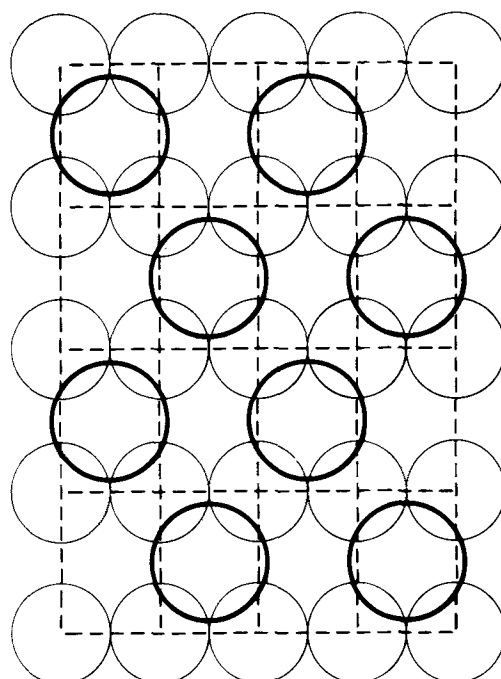


Fig. 16. Hypothetical superlattice in the case of  $Tl^+$  ion adsorption in Ag (110)-c(2 × 2) Tl.

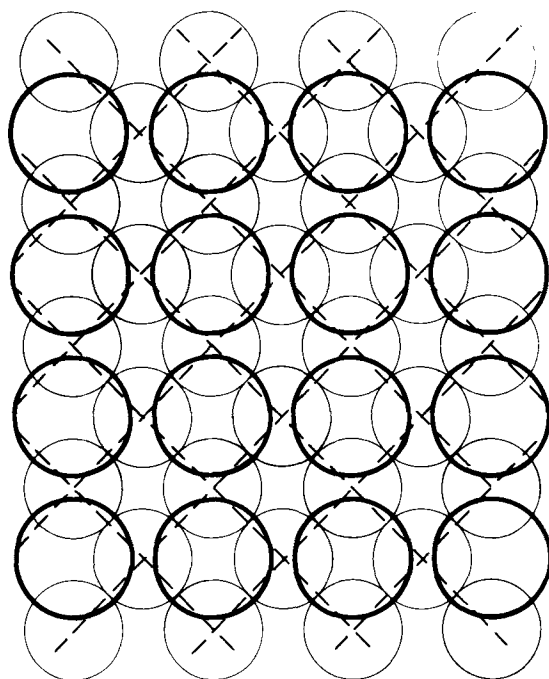


Fig. 17. Hypothetical superlattice in the case of  $Ti^+$  ion adsorption on Ag (100) substrate. Ag (100)- $c(2 \times 2)$  Ti.

diffusion polarization within the experimental time scale. Under this additional condition two extreme cases of adsorption models were tested.

(i) A charge transfer step is rate determining. Assuming kinetic simple steps of metal ion transfer, one is able to show that the working electrode behaves like the equivalent circuit of Fig. 18. Then the potential-time transient is described by the following equation

$$\eta(t) = \epsilon(t) - \epsilon^* = \frac{iR_{ads}C_{ads}^2}{(C_{DL} + C_{ads})^2} \cdot \left[ 1 - \exp\left(-\frac{C_{DL} + C_{ads}}{R_{ads}C_{ads}C_{DL}} t\right) \right] + \frac{i}{C_{DL} + C_{ads}} \cdot t \quad [18]$$

whereby

$$R_{ads} = \frac{RT}{zF} \cdot \frac{1}{i_{0,ads}}$$

with  $i_{0,ads}$  = exchange-current density of adsorption, and

$$C_{ads} = \frac{z^2F^2}{RT} a_{\Gamma^*} \cdot \left( \frac{da_{\Gamma}}{d\Gamma} \right)^{-1}$$

$$C_{DL} = C_{DL}(\epsilon^*)$$

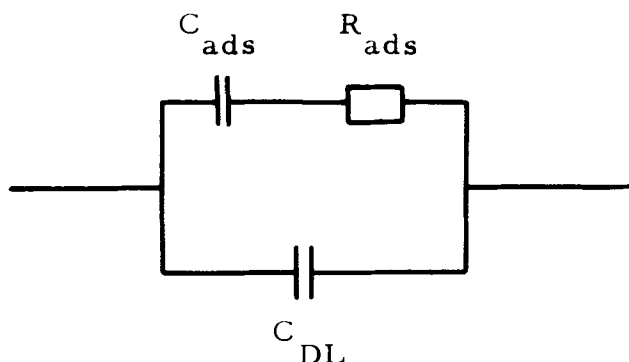


Fig. 18. Equivalent circuit for the kinetics of metal ion adsorption according to the metal monolayer model.  $C_{DL}$  = double layer capacity;  $C_{ads}$  = adsorption capacity;  $R_{ads}$  = adsorption resistance.

(ii) A surface-diffusion step is rate determining. The same well-known linear geometry of an electrode surface as in the adatom model of electrocrystallization was assumed [see Ref. (98) and literature cited there], i.e., the surface was considered to consist of parallel step lines in a distance of  $2l$ . Moreover, the following assumptions were made: In equilibrium the adsorbate is distributed homogeneously; adsorptive charge transfer only occurs at the step lines; within short measuring times ( $<100 \mu\text{sec}$ ), a semi-infinite linear approximation of the diffusion problem is valid. The potential-time transient then may be described by the following equation

$$\eta(t) = \epsilon(t) - \epsilon^* = -\frac{iC_{DL}}{C_{ads}^2} \cdot \frac{l^2}{D} + \frac{2i}{\sqrt{\pi}C_{ads}} \cdot \frac{l}{\sqrt{D}} \cdot \sqrt{t} + \frac{iC_{DL}}{C_{ads}^2} \cdot \frac{l^2}{D} \cdot \exp\left(\frac{C_{ads}^2}{C_{DL}^2} \cdot \frac{D}{l^2} \cdot t\right) \operatorname{erfc}\left(\frac{C_{ads}}{C_{DL}} \cdot \frac{\sqrt{D}}{l} \cdot \sqrt{t}\right) \quad [19]$$

whereby  $D$  is the surface diffusion coefficient (other symbols see above). In both cases,  $C_{ads}$  has to be identical to the thermodynamic adsorption capacity  $-zF(\partial\Gamma^*/\partial\epsilon)_\mu$  which can be evaluated by differentiating  $\Gamma_{\mu\epsilon}$  isotherms, whereas  $C_{DL}$  can be taken from the initial slope of the potential time transient.

In the cases of adsorption of  $Ag^+$ ,  $Pb^{2+}$ , and  $Tl^+$  on gold electrodes, the potential time transients can only be fitted within experimental errors by Eq. [19]. Therefore a surface diffusion step seems to be rate determining. The ratio  $\sqrt{D}/l$ , which is the only experimentally detectable parameter in this case, depends on the surface conditions. As expected this ratio is higher for polycrystalline than for monocrystalline electrode surfaces in the Au/ $Pb^{2+}$  system.

The applicability of Eq. [19] implies a neglectable charge transfer polarization. This means that the exchange current densities of the adsorption processes are relatively high. This could be confirmed by fitting the experimental transients using a program which takes into consideration charge transfer as well as surface diffusion. In the systems Au/0.04M  $Ag^+$ , Au/0.1M  $Pb^{2+}$ , and Au/0.1M  $Tl^+$  one obtains lower limits of  $i_{0,ads}$  of 6.3 and 20  $A \cdot \text{cm}^{-2}$  respectively (87, 99).

Only in the case of  $Cu^{2+}$  adsorption on gold is a charge transfer step rate determining according to Eq. [18]. At a coverage of  $\theta = 0.6$  the exchange current density in the system Au/0.1M  $Cu^{2+}$  is found to be  $10^{-3} A \cdot \text{cm}^{-2}$ . This value is of the same magnitude as the exchange current density of the Cu/ $Cu^{2+}$  electrode which is known to be determined by the preceding redox reaction



Therefore it could be supposed that the rate of  $Cu^{2+}$  adsorption is also determined by this step.

Manuscript submitted Feb. 18, 1974; revised manuscript received May 13, 1974.

Any discussion of this paper will appear in a Discussion Section to be published in the June 1975 JOURNAL. All discussions for the June 1975 Discussion Section should be submitted by Feb. 1, 1975.

#### REFERENCES

1. E. Budevski, W. Bostanov, T. Wittanov, Z. Stoinov, A. Kotzewa, and R. Kaishev, *Electrochim. Acta*, **11**, 1697 (1967).
2. W. Bostanov, R. Roussinova, and E. Budevski, *Chem.-Ing.-Techn.*, **45**, 179 (1973); T. Vitanov, A. Popov, and E. Budevski, *This Journal*, **121**, 207 (1974).
3. D. Postl, G. Eichkorn and H. Fischer, *Z. Physik., Chem. NF.*, **77**, 138 (1972); *ibid.*, **77**, 149 (1972).
4. G. Eichkorn and H. Fischer, *ibid.*, **53**, 1 (1967); G. Eichkorn and H. Fischer, *ibid.*, **61**, 10 (1968);

- N. Dhananjayan, G. Eichkorn, and H. R. Mache, *Electrochim. Acta*, **15**, 617 (1970).
5. T. Erdey-Gruz and M. Vollmer, *Z. Phys. Chem. Abt. A*, **157**, 165, 182 (1931).
  6. R. Kaischev and I. Gutzow, *Electrochim. Acta*, **9**, 1047 (1964).
  7. W. F. Schottky, *Z. Physik., Chem. NF.*, **31**, 40 (1962); G. Mierke and W. F. Schottky, *Ber. Bunsenges. Phys. Chem.*, **72**, 516 (1967); D. B. Knoll and W. F. Schottky, *Z. Physik., Chem. NF.*, **58**, 114 (1968).
  8. G. Eichkorn, F. W. Schlitter, and H. Fischer, *ibid.*, **62**, 1 (1968).
  9. L. B. Rogers, D. P. Krause, J. C. Griess, and D. B. Ehrlinger, *This Journal*, **43**, 21 (1946).
  10. L. B. Rogers, D. P. Krause, J. C. Griess, and D. B. Ehrlinger, *J. (and Trans.) Electrochem. Soc.*, **95**, 33 (1949).
  11. L. B. Rogers, H. H. Miller, R. B. Goodrich, and A. F. Stehney, *Anal. Chem.*, **21**, 777 (1949).
  12. L. B. Rogers and A. F. Stehney, *J. (and Trans.) Electrochem. Soc.*, **95**, 25 (1949).
  13. J. C. Griess, Jr., J. T. Byrne, and L. B. Rogers, *This Journal*, **98**, 447 (1951).
  14. J. T. Byrne, L. B. Rogers, and J. C. Griess, Jr., *ibid.*, **98**, 452 (1951).
  15. J. T. Byrne, L. B. Rogers, and J. C. Griess, Jr., *ibid.*, **98**, 457 (1951).
  16. S. S. Lord, R. C. O'Neill, and L. B. Rogers, *Anal. Chem.*, **26**, 632 (1954).
  17. R. C. de Geiso and L. B. Rogers, *This Journal*, **106**, 433 (1959).
  18. E. Schmidt and H. R. Gygax, *Chimia*, **16**, 165 (1962).
  19. E. Schmidt, P. Moser, and W. Riesen, *Helv. Chim. Acta*, **46**, 2285 (1963).
  20. E. Schmidt and H. R. Gygax, *ibid.*, **48**, 1178 (1965).
  21. E. Schmidt and H. R. Gygax, *ibid.*, **48**, 1584 (1965).
  22. E. Schmidt and H. R. Gygax, *J. Electroanal. Chem.*, **12**, 300 (1966).
  23. E. Schmidt, H. R. Gygax, and P. Boehlen, *Helv. Chim. Acta*, **49**, 733 (1966).
  24. E. Schmidt and H. R. Gygax, *ibid.*, **49**, 1105 (1966).
  25. E. Schmidt and H. R. Gygax, *J. Electroanal. Chem.*, **13**, 378 (1967).
  26. E. Schmidt and H. R. Gygax, *ibid.*, **14**, 126 (1967).
  27. E. Schmidt and N. Wüthrich, *Helv. Chim. Acta.*, **50**, 2058 (1967).
  28. E. Schmidt, *ibid.*, **52**, 1763 (1969).
  29. E. Schmidt and H. Siegenthaler, *ibid.*, **52**, 2245 (1969).
  30. E. Schmidt, H. R. Gygax, and Y. Cramer, *ibid.*, **52**, 649 (1970).
  31. E. Schmidt, *ibid.*, **53**, 1 (1970).
  32. E. Schmidt and H. Siegenthaler, *ibid.*, **53**, 321 (1970).
  33. E. Schmidt and N. Wüthrich, *J. Electroanal. Chem.*, **28**, 349 (1970).
  34. E. Schmidt, P. Beutler, and W. J. Lorenz, *Ber. Bunsenges. Phys. Chem.*, **75**, 71 (1971).
  35. E. Schmidt and N. Wüthrich, *J. Electroanal. Chem.*, **34**, 377 (1972).
  36. E. Schmidt and S. Stucki, *ibid.*, **39**, 63 (1972).
  37. E. Schmidt and N. Wüthrich, *ibid.*, **40**, 399 (1972).
  38. E. Schmidt, H. Christen, and P. Beyeler, *ibid.*, **42**, 275 (1973).
  39. E. Schmidt and S. Stucki, *ibid.*, **43**, 425 (1973).
  40. E. Schmidt, *ibid.*, **47**, 441 (1973).
  41. S. Bruckenstein and D. T. Napp, *J. Am. Chem. Soc.*, **90**, 6303 (1958).
  42. D. T. Napp and S. Bruckenstein, *Anal. Chem.*, **40**, 1036 (1968).
  43. G. W. Tindall and S. Bruckenstein, *ibid.*, **40**, 1051 (1968).
  44. S. H. Cadle and S. Bruckenstein, *ibid.*, **43**, 1858 (1971).
  45. G. W. Tindall and S. Bruckenstein, *Electrochim. Acta*, **16**, 245 (1971).
  46. V. A. Vicente and S. Bruckenstein, *Anal. Chem.*, **44**, 297 (1972).
  47. S. H. Cadle and S. Bruckenstein, *This Journal*, **119**, 1166 (1972).
  48. V. A. Vicente and S. Bruckenstein, *Anal. Chem.*, **45**, 2036 (1973).
  49. J. W. Schultze, *Ber. Bunsenges. Phys. Chem.*, **74**, 705 (1970).
  50. K. J. Vetter and J. W. Schultze, *ibid.*, **76**, 920 (1972).
  51. K. J. Vetter and J. W. Schultze, *ibid.*, **76**, 927 (1972).
  52. J. W. Schultze and K. J. Vetter, *J. Electroanal. Chem.*, **44**, 63 (1973).
  53. J. W. Schultze and K. J. Vetter, *Electrochim. Acta*, Submitted for publication.
  54. B. J. Bowles, *ibid.*, **10**, 717 (1965).
  55. B. J. Bowles, *ibid.*, **10**, 731 (1965).
  56. B. J. Bowles and T. E. Cranshaw, *Phys. Letters*, **17**, 258 (1965).
  57. B. J. Bowles, *Nature*, **212**, 1456 (1966).
  58. B. J. Bowles, *Electrochim. Acta*, **15**, 589 (1970).
  59. B. J. Bowles, *ibid.*, **15**, 737 (1970).
  60. K. Taube and W. J. Lorenz, *J. Electroanal. Chem.*, **25**, 95 (1960).
  61. I. C. Raducanu and W. J. Lorenz, *Electrochim. Acta*, **16**, 1143 (1971).
  62. W. J. Lorenz, I. Moutzias, and E. Schmidt, *J. Electroanal. Chem.*, **33**, 121 (1971).
  63. F. Hilbert, C. Mayer, and W. J. Lorenz, *ibid.*, **47**, 167 (1973).
  64. W. J. Lorenz, *Chem.-Ing.-Techn.*, **45**, 175 (1973).
  65. M. Haissinsky, *J. Chim. Phys.*, **30**, 27 (1933).
  66. M. Haissinsky, *ibid.*, **43**, 21 (1946).
  67. M. Haissinsky, *Experientia*, **8**, 125 (1952).
  68. T. Mills and G. H. Willis, *This Journal*, **100**, 452 (1953).
  69. M. Breiter and C. A. Knorr, *Z. Elektrochem.*, **59**, 681 (1955).
  70. Kh. Z. Brainina, N. F. Zakhavuch, D. P. Synkova, and I. G. Yudelevich, *J. Electroanal. Chem.*, **35**, 165 (1972) and there cited Russian literature.
  71. M. M. Nicholson, *J. Am. Chem. Soc.*, **79**, 7 (1957).
  72. M. M. Nicholson, *Anal. Chem.*, **32**, 1058 (1960).
  73. M. W. Breiter, *This Journal*, **114**, 1125 (1967).
  74. M. W. Breiter, *J. Electroanal. Chem.*, **23**, 173 (1969).
  75. D. J. Astley, J. A. Harrison, and H. R. Thirsk, *ibid.*, **19**, 325 (1968).
  76. A. R. Nisbet and A. J. Bard, *ibid.*, **6**, 332 (1963).
  77. A. R. Nisbet and A. J. Bard, *ibid.*, **18**, 93 (1968).
  78. B. H. Vassos and H. B. Mark, *ibid.*, **13**, 1 (1967).
  79. S. P. Perone, *Anal. Chem.*, **35**, 2091 (1963).
  80. R. C. Propst, *J. Electroanal. Chem.*, **16**, 319 (1968).
  81. J. W. Bixler and W. F. Stafford, *Anal. Chem.*, **40**, 425 (1968).
  82. D. P. Sandoz, R. M. Peekema, H. Freund, and C. F. Harrison, Jr., *J. Electroanal. Chem.*, **24**, 165 (1970).
  83. T. Takamura, K. Takamura, W. Nippe, and E. Yeager, *This Journal*, **117**, 626 (1970); R. Adgc, E. Yeager, and B. D. Cahan, *This Journal*, **121**, 474 (1974).
  84. J. D. E. McIntyre and D. M. Kolb, *Symp. Faraday Soc.*, **4**, 99 (1970).
  85. D. M. Kolb, *Ber. Bunsenges. Phys. Chem.*, **77**, 891 (1973).
  86. V. Klappka, *Collection Czech. Chem. Commun.*, **36**, 1181 (1971).
  87. H. D. Herrmann, Dissertation, Universität Karlsruhe, Germany, 1974.
  88. W. J. Lorenz, H. Meyer, and E. Schmitt, *Z. Instrumentenk.*, **74**, 56 (1966).
  89. H. D. Herrmann, Diplomarbeit Universität Karlsruhe, Germany (1971).
  90. N. Wüthrich, Dissertation, Universität Bern, Switzerland (1973).
  91. E. Budevski, Private note (1972).
  92. Russian Pat. 191,982 (1967).
  93. E. Sewastjanov, T. Witanov, and A. Popov, *Elektrokhimiya*, **8**, 412 (1972).
  94. L. Samuels and J. Sanders, *J. Inst. Metals*, **87**, 129 (1958/1959).
  95. L. Samuels, *Metallurgia*, **66**, 187 (1962).
  96. L. Samuels, *J. Inst. Metals*, **85**, 177 (1956/1957).
  97. H. Conrad, G. Ertl, J. Koch, and E. E. Latta, *Surface Sci.*, **43**, 108 (1974).
  98. J. A. Harrison and H. R. Thirsk, "Electroanalytical Chemistry," Vol. 5, A. J. Bard, Editor, p. 67, Marcel Dekker, Inc., New York (1967).
  99. N. Wüthrich, H. D. Herrmann, and W. J. Lorenz, To be published.

# Analytical Aspects of Energy-Deficient Electrogenerated Chemiluminescence

Terry M. Huret<sup>1</sup> and J. T. Maloy\*

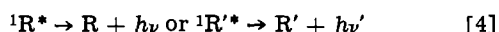
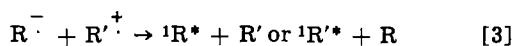
Department of Chemistry, West Virginia University, Morgantown, West Virginia 26506

## ABSTRACT

A potential scan method has been developed for analytical studies of energy-deficient electrogenerated chemiluminescence (ECL) in mixed systems. This method involves the use of an unsymmetrical alternating potential, one portion of which is held at a fixed negative potential, while the other is scanned over a linearly increasing positive potential. This alternating potential program has been used to monitor the intensity of the ECL from 9,10-diphenylanthracene as a measure of the concentration of N,N,N',N'-tetramethyl-*p*-phenylenediamine, N,N-dimethyl-*p*-phenylenediamine, and 10-methylphenothiazine in solution. This ECL intensity was found to be linear with concentration for these compounds for concentrations less than 0.1 mM. Because this method allows the recording of ECL intensity as a function of potential it represents the stationary electrode ECL equivalent of polarography.

Electrogenerated aromatic radical cations and anions can undergo an electron-transfer reaction in an aprotic solvent to produce electrogenerated chemiluminescence (ECL). The radical cation and the radical anion can be formed from the same parent compound, as in the cases of 9,10-diphenylanthracene (DPA) or rubrene, or from different parent compounds, as in the case of the mixed system of N,N,N',N'-tetramethyl-*p*-phenylenediamine (WBP) and DPA. The end result of the electron transfer, or any other subsequent reaction which ensues, is the production of first excited singlet-state molecules of one or both of the compounds. Because ECL arises from first excited singlet-state emission it is usually similar to the fluorescence of the parent compound.

Two main pathways have been proposed for the production of excited singlet-state molecules of the compounds involved in the electron-transfer reaction. The first is an energy-sufficient pathway where the electron-transfer reaction produces enough energy to directly populate the first excited singlet state



where R and R' can be the same compound or different compounds. It has been postulated that the neutral molecule formed in its excited singlet state is that having the lower energy level for its first excited singlet state (1).

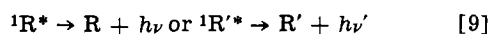
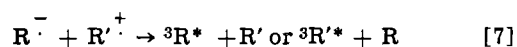
The second pathway by which neutral molecules are produced in the first excited singlet state is an energy-deficient process. Here, the electron-transfer reaction between the electrogenerated reductant and the electrogenerated oxidant does not provide enough energy to produce neutral product molecules in their first excited singlet state, but sufficient energy is available to form the lowest triplet state of the product molecules of one or both of the reactants. Two triplets may then undergo triplet-triplet annihilation to produce a molecule in its first excited singlet state



\* Electrochemical Society Active Member.

<sup>1</sup> Present address: Tennessee Eastman Company, Kingsport, Tennessee 37680.

Key words: nonaqueous solvents, luminescence, voltammetry, chemiluminescence, electroanalysis.



If the electron-transfer reaction energy is sufficient to form either triplet state, it has been postulated that the parent compound with the lower triplet energy will be formed when the electron transfer occurs (2). For the triplet-triplet annihilation reaction to produce molecules to their first excited singlet state, it has also been postulated that the triplet energy of the compound must be at least equal to one-half of its first excited singlet energy (3).

Much experimental work has been done in the characterization of energy-sufficient and energy-deficient reaction schemes (4-6). Some concentration studies have also been performed. Cruser and Bard (7) studied ECL intensity as a function of concentration for single-component, energy-sufficient systems. Fleet, Kirkbright, and Pickford (8) did a quantitative determination of certain fused-ring aromatic hydrocarbons using ECL. Maloy and Bard (9) have used a rotating ring-disk electrode (RRDE) to show that the ECL intensity and efficiency of the energy-deficient WBP-DPA system decreases at high concentrations of the WBP.

In most of the ECL studies performed so far, the cation radicals and the anion radicals have been alternately generated at a single working electrode. Sinusoidal, triangular, and square-wave potential programs have been used. None of these methods involving the alternate formation of the ion radicals at a single working electrode can be used to produce a steady-state ion-annihilation ECL. Therefore, they are difficult to use for the study of the potential dependence of ECL intensity. Nevertheless, Hercules and his co-workers (10) have investigated the potential dependence of ECL by using triangular wave cyclic voltammetry. Zweig *et al.* (11) examined the potential dependence of ECL by manually switching between the required positive or negative potentials and measuring the intensity of the ECL. This method was not only time-consuming, but no steady-state ECL intensity was obtained.

Potential scan ECL experiments have been performed with the RRDE (9,12). In these experiments the ring potential was maintained in the diffusion-limited region for the generation of one of the radical

ions, while the potential of the disk was scanned through regions where the other reactant was generated. Steady-state ECL intensities of one-component, energy-sufficient systems and two-component, energy-deficient systems were produced using this method. This method is difficult to employ generally however, due to the complexity of the RRDE apparatus.

Because no detailed experiments have been done on concentration effects on energy-deficient ECL using two-component systems, and because no simple method of doing easily reproducible potential scan experiments on ECL have been proposed, this present work was undertaken. Its objectives were twofold. The first was to devise a technique that would use a stationary working electrode to approximate the steady-state ECL signal obtained with the RRDE in potential dependence studies on two-component, energy-deficient systems, and thereby avoid some of the experimental difficulties of the RRDE. The second objective was to study, for two-component, energy-deficient systems, the effect of changing the bulk concentration of the parent compound of the electrogenerated oxidant on the intensity of the ECL.

The electrogenerated radical anion of DPA was the reductant used in these studies. It was selected as the reductant because DPA has a high quantum efficiency for fluorescence, a low triplet energy for electron transfer, and is known to produce ECL with a variety of oxidants (2). In an attempt to achieve reproducible conditions regardless of oxidant, the DPA concentration was maintained in at least tenfold excess of the concentration of the parent compound of the electrogenerated oxidant. The three oxidants used in these studies were the radical cations of WBP, WRP (Wurster's Red Parent or *N,N*-dimethyl-*p*-phenyleneamine), and 10 MP (10-methylphenothiazine). These systems were chosen because they had been studied previously (4, 9), and their energy-deficient ECL, produced by the electron-transfer reactions and subsequent triplet-triplet annihilation reactions, was known to be emitted from the first excited singlet state of DPA (2). Also, it had been shown that for one of the mixed systems (WBP-DPA), both the intensity and ECL efficiency decreased with increasing concentration of WBP at a RRDE when the concentration of WBP was greater than 1 mM (9). This study was undertaken to determine if there was a concentration range over which the ECL intensity increased linearly with concentration. Since this concentration range was expected to be below the 1 mM level, the development of a new chemiluminescent method for trace analysis was an indirect objective of this study. The possibilities for a trace analysis method seemed particularly appealing because ion-annihilation ECL results from electron-transfer reactions in the diffusion layer around the electrode; therefore, all ECL of this type must result from faradaic processes, and no correction for nonfaradaic background processes as in conventional voltammetry was anticipated. It was hoped that this would permit the detection of lower concentration levels of the parent compound of the electrogenerated oxidant than conventional electrochemical techniques.

To meet the two objectives of this work, an electrochemical cell and an electronic circuit were designed which allowed concentration and potential scan studies to be carried out concurrently. The specially constructed electrochemical cell employed a stationary working electrode and was equipped with a burette for adding known amounts of the parent compounds of the electrogenerated oxidants used in this study. The electronic circuit was designed to generate an unsymmetrical alternating potential. One portion of this alternating potential was a square wave held at a fixed negative potential. The other portion was a slowly increasing, linear, positive potential ramp. With this circuit, the fixed negative potential of the unsymmetrical square wave was set at the cyclic voltam-

metric peak potential for the formation of the electrogenerated oxidant. Thus, on alternate half-cycles, a slowly varying oxidative potential was applied to the working electrode. The recording of the intensity of the approximate steady-state ECL signal obtained in this manner *vs.* the positive ramp potential provided the ECL equivalent of polarography. Thus, while the magnitude of the maximum ECL signal produced measured the quantity of electrogenerated oxidant present, the ramp potential at which this signal was observed was a characteristic of the parent compound of the oxidant. One of the main results of this study was the investigation and exploitation of the polarographic nature of this analytical technique.

### Experimental

**Electrochemical cell.**—The cell used for these studies is shown in Fig. 1. The cell was a three electrode design with a 5.5 mm 22 gauge platinum wire working electrode, a coiled, platinum counterelectrode, and a coiled, platinum quasi-reference electrode (QRE). The working electrode was made by silver soldering a short piece of platinum wire to a long piece of 20 gauge silver wire which was in turn silver soldered to a short length of nickel-tungsten-nickel alloy sealed into a 10/30 standard taper inner joint. All the wire, except the 5.5 mm of platinum used for the working electrode, was sealed liquid tight in a thin, hollow glass tube which was joined to the 10/30 standard taper inner joint. A small hole in this thin glass tube near the joint allowed the pressure inside and outside

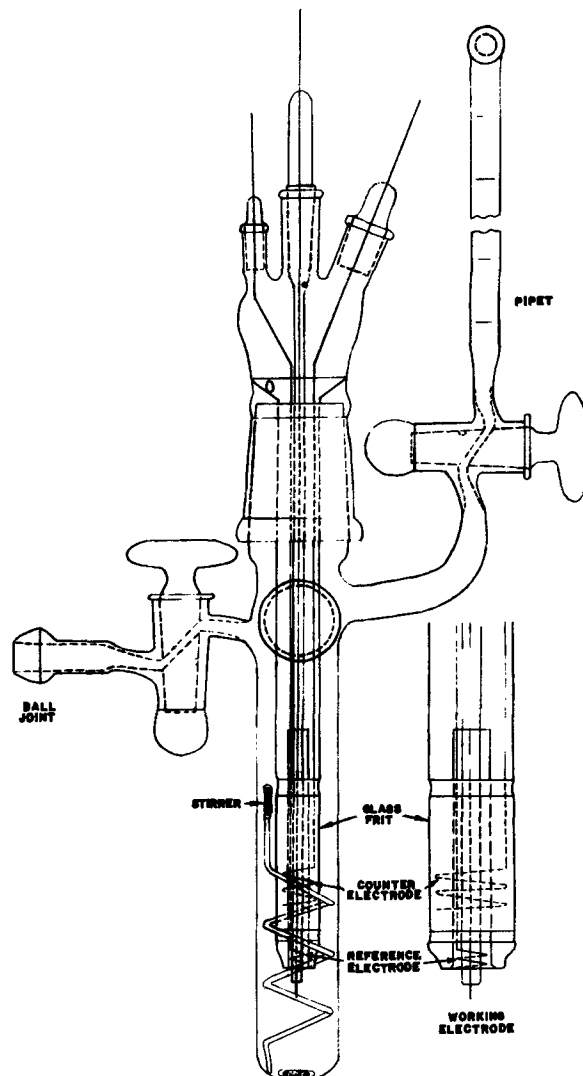


Fig. 1. Electrochemical cell

of this tube to equilibrate. The counterelectrode was a long piece of platinum wire silver soldered to a short length of nickel-tungsten-nickel alloy which was sealed into a 12/18 standard taper inner joint. The quasi-reference electrode was made the same way as the counterelectrode except the coil was smaller, and the alloy connector was sealed into a 7/15 standard taper inner joint. The electrodes were made with joints so that they could easily be removed from the electrochemical cell cap in order to be cleaned between experiments.

The cap of the electrochemical cell was designed to hold all the electrodes in a concentric configuration. In addition, it supported a fritted glass auxiliary compartment. The cap consisted of a 34/45 standard taper outer joint fitted with three outer joints corresponding to the inner joints of the three electrodes. Sealed inside the cap, above the ground surface of the joint, was a flared glass tube with an outer diameter of 15 mm. This tube extended vertically 9 cm below the bottom of the 34/45 standard taper outer joint to a point at which a 6 cm portion of cylindrical, fritted filter tube of identical diameter was attached. Sealed in the Pyrex bottom of the fritted filter tube was a smaller tube of an inner diameter of 5 mm which extended up into the cap assembly 2.4 cm above the end of the fritted glass to a point above the normal solution levels in the cell. The coil of the counterelectrode was large enough to fit over this inner glass tube, and the counterelectrode was long enough so that when it was seated into the cell cap, its coil was positioned between the fritted glass and the inner glass tube. This formed a cylindrical auxiliary electrode compartment to keep any products formed at the counterelectrode during an experiment from mixing with the rest of the solution in the cell. The coiled reference electrode and the wire working electrode, when seated in the cell cap, both extended down through the inner glass tube. The coil of the reference electrode was large enough to slip over the glass tube in which the working electrode was sealed. The tip of the working electrode extended 1 cm below the end of the auxiliary electrode compartment. The reference electrode was ca. 1.5 cm above the working electrode and was just inside the inner glass tube of the cell cap. The electrodes were placed in the cell cap assembly before the cap was placed on the 34/45 standard taper inner joint attached to the main body of the electrochemical cell.

The main body of the electrochemical cell consisted of an electrode chamber, a cold finger, a cap, a calibrated burette connected to the cell through a high-vacuum stopcock, and a ball joint connected to the cell through a high-vacuum stopcock. The electrode chamber was made from glass tubing with an inner diameter of approximately 25 mm and was positioned vertically beneath the electrolysis cell cap. The electrode chamber housed both the glass tube and electrodes which extended downward from the cell cap and the coiled glass stirrer. The electrode chamber extended 2.7 cm below the tip of the working electrode in order to provide an undistorted optical path for the ECL generated at the working electrode. The coiled stirrer was made from thin, hollow glass tubing and contained a small magnet sealed in its top. A horseshoe magnet was used to move this stirrer up and down from outside of the cell to facilitate the mixing of solutions added from the burette. The cold finger, which extended at a right angle to the electrode chamber (coming out of the plane of the paper in Fig. 1) was made of the same inner diameter tubing as the electrode chamber and was about the same length. The cap, which was on the opposite side of the cell as the cold finger, was made from a 24/40 standard taper outer joint. It was attached to the cell by means of a 24/40 standard taper inner joint sealed onto the main body of the cell. This cap allowed entry into the cell when the cell was completely assembled. The burette used for the ECL concentration studies was made from a

10 mliter, calibrated Mohr pipette connected to the cell with a 2 mm high-vacuum stopcock. On top of this burette was a 10 mliter capped bulb (perpendicular to the plane of the paper in Fig. 1). The cap of the burette bulb was made from a 10/30 standard taper outer joint. The whole electrolysis cell could be attached to a vacuum line with the 18/9 ball joint connected to the cell with a 2 mm, high-vacuum stopcock. This electrolysis cell was capable of being evacuated to less than  $10^{-5}$  Torr.

**Instruments.**—Potentials between the working electrode and quasi-reference electrode were controlled by a Wenking Model 68FR0.5 potentiostat modified to have a built-in variable offset of  $\pm 2.0$ V. The potential programs used were supplied by a Wavetek Model 114 Sweep/Trigger Variable Current Generator (VCG). Potentials between the working electrode and quasi-reference electrode were set with and monitored by a Systron Donner Model 7050 digital voltmeter. Cyclic voltammograms, relative ECL intensity vs. ramp potential graphs, and ECL spectra were recorded on a Hewlett-Packard Model 7005B x-y recorder. The ECL was monitored using an 1P21 photomultiplier tube supplied by Hamamatsu, a Model 4-8402 grating monochromator, and a Model 10-267 photomultiplier microphotometer, both of which were supplied by the American Instrument Company.

**Electronic circuit.**—Shown in Fig. 2 is the electronic circuitry used in the ECL studies. The unsymmetrical, alternating potential program which was applied to the working electrode was generated by circuits A and B and the Wavetek VCG and fed through a Model HGS 3074 modified relay (R) to the potentiostat (POT). The square wave of known frequency was generated by the Wavetek VCG, which also, along with the 6V battery (B3), drove the relay which had a switching threshold potential of 8.27V with R5 set at 560 ohms. Circuit A supplied the fixed voltage value of the unsymmetrical square wave. The ten-turn, 100 kohms potentiometer was used to regulate the voltage supplied by the two 1.35V Hg batteries. The linearly ramping portion of the unsymmetrical square wave was produced by circuit B which was a voltage integrator circuit built around a Burr-Brown 3292/14 chopper-stabilized operational amplifier (OA) and a Burr-Brown Model 524 power supply. With the resistors and capacitor shown in Fig. 2, ramp rates of 0.021, 0.0089, 0.0053, and 0.0045 V/sec, were obtained. The unsymmetrical, square wave potential generated by the circuits A and B shown in Fig. 2 was used as the voltage input to the potentiostat. The negative cell potential was alternately fixed at the cyclic voltammetric peak potential for DPA reduction, while the positive cell potential was ramped from 0.00V in a positive direction. The ramp rates were such that the potential of the ramp voltage changed very little

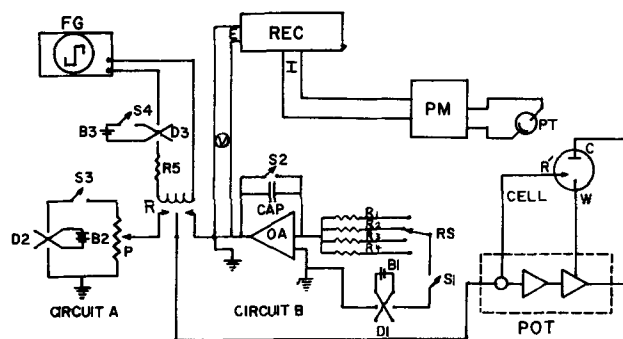


Fig. 2. Electronic circuit. In this figure R1 = 6 Mohms, R2 = 13.6 Mohms, R3 = 22 Mohms, R4 = 25.6 Mohms, R5 = 560 ohms, B1 = 1.35V, B2 = 2.7V, B3 = 6.0V, CAP = 10  $\mu$ f, and P = 100 kohms (ten turn).



during one cycle of the square wave. For instance, at a frequency of 20 Hz and a ramp rate of 0.0089 V/sec, the potential of the ramp changed less than 0.5 mV during one cycle of the square wave.

The voltage output of this circuit is shown in Fig. 3; this potential program is similar to one developed independently by Keszthelyi (13) using somewhat different electronics. Shown also in this figure is a conceptual representation of the ECL signal obtained with this potential program. Two observations are to be inferred from this representation of the ECL output:

1. Because DPA is present in great excess, very little ECL would be expected during the half-cycles when

$\text{DPA}^-$  is being generated; only very small amounts of electrogenerated oxidant would remain in the diffusion layer from the previous oxidation, and when this was depleted, chemiluminescence would cease. On the other hand, during oxidation, the supply of WBP is catalytically regenerated in the diffusion layer by the

reaction of  $\text{WBP}^+$  with excess  $\text{DPA}^-$ ; this regenerated WBP is then available for reoxidation at the electrode

to produce more  $\text{WBP}^+$  which results in more ECL,

so long as the previously generated supply of  $\text{DPA}^-$  is not exhausted. Thus, larger ECL signals would intuitively be expected on the oxidation half-cycles if the concentration of oxidant is small with respect to that of DPA.

2. Because the electronics of the photomultiplier-recorder combination effectively served to average the instantaneous ECL signal, the signal recorded using this potential program should be proportional only to the average ECL output and in no way should it represent a true steady-state signal. Indeed, this was deemed an advantage analytically. This averaged ECL signal is illustrated in Fig. 3, also. Previous authors have used a similar potential program but performed it manually and have found "averaged" plateaus (14).

**Cell holder.**—The cell holder was a block of wood bolted to the face of the monochromator. Drilled into its top was a hole slightly larger than the electrode chamber of the electrochemical cell; another hole, perpendicular to the first, was drilled through the block in line with the entrance slit of the monochromator. When the electrode chamber of the electrochemical cell was placed in this block, the working

electrode of the cell was reproducibly positioned in front of the monochromator entrance slit.

**Reagents.**—Spectroquality N,N-dimethylformamide (DMF) was supplied by Fisher Scientific Company; it was double distilled according to the method of Faulkner and Bard (15) and stored under vacuum in a special flask designed for this purpose. Polarographic grade tetrabutylammonium perchlorate (TBAP) was supplied by Southwestern Analytical Chemicals, Inc. for use as the supporting electrolyte. The compound was dried in a vacuum oven at 90°C for at least 48 hr and stored under vacuum over anhydrous  $\text{P}_2\text{O}_5$ . The 9,10-diphenylanthracene (DPA) used in this study was supplied by City Chemical Corporation and was used as received. N,N,N',N'-Tetramethyl-p-phenylenediamine or Wurster's Blue Parent (WBP) was furnished as the dihydrochloride by Eastman Organic Chemicals. Approximately 2g of the dihydrochloride compound were dissolved in 25 mliters of distilled water and then were neutralized using an excess of a 0.5M solution of sodium carbonate. The WBP was then extracted into benzene. This benzene solution was passed through a column of activated alumina using benzene as the eluting solvent. The fraction of the eluent containing the WBP was collected, and the benzene was evaporated off by passing a stream of dry nitrogen over the WBP solution. The crystals which formed after evaporating away the benzene were purified by vacuum sublimation. N,N-Dimethyl-p-phenylenediamine or Wurster's Red Parent (WRP) was supplied as the dihydrochloride by Eastman Organic Chemicals. It was purified using the same procedure as used for the WBP, with the exception that the eluting solvent used on the activated alumina column was a 1 to 1 mixture of heptane and n-propanol instead of benzene. 10-Methylphenothiazine (10 MP) was obtained from Eastman Organic; it was recrystallized three times from benzene. The prepurified nitrogen and the 99.995% pure helium were supplied by Air Products and Chemicals, Inc. The helium was used as received, but the nitrogen was passed through a column of activated molecular sieves to remove any moisture present.

**Procedure.**—Two methods of preparing the solutions for the studies of the effect of the concentration of the parent compound of the electrogenerated oxidant on the DPA ECL were used, depending on what concentration range of the parent compound was desired. For a solution having a final concentration greater than 0.5 mM of the parent compound the stock solution of the parent compound was prepared directly in the burette of the cell. For a solution having a final concentration of less than 0.5 mM, the stock solution was prepared outside the cell in a glove bag and then transferred into the burette.

In a typical experiment the cell was evacuated and weighed so that solution volumes could be determined gravimetrically. The amount of the parent compound of the electrogenerated oxidant needed to give the final desired concentration in the electrode chamber of the cell was transferred quantitatively into the bulb on top of the burette attached to the cell. The cell was evacuated to a pressure of  $10^{-5}$  Torr with the burette stopcock closed. Then the stopcock of the burette was opened, and the burette and burette bulb were evacuated rapidly to a pressure of about  $10^{-5}$  Torr. The stopcock of the burette was again closed to minimize any chance for sublimation of the parent compound of the electrogenerated oxidant. The cell was removed from the vacuum line, and enough DPA to make approximately a 10 mM solution and enough TBAP to make approximately a 0.2M solution when mixed with ca. 50 mliters of solvent were weighed out and placed in the cold finger of the electrochemical cell through the 24/40 standard taper joint above the cold finger. The cell was reassembled and the main body of the cell was evacuated to approximately  $10^{-5}$  Torr and

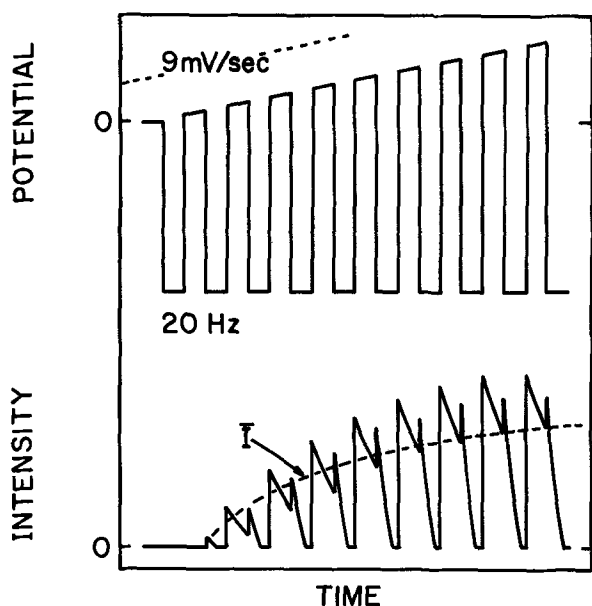


Fig. 3. Potential program and corresponding ECL output. The "averaged" ECL signal obtained using this technique is illustrated by the dashed line.



was outgassed for about an hour to dry the TBAP and DPA completely. After the cell had been sealed, it was removed from the vacuum line and attached to the DMF storage flask. The connecting tubes were evacuated through the storage flask; then DMF was introduced into the cell under helium pressure, and the cell was sealed, removed from the flask, and reconnected to the vacuum line so that the solution could be outgassed by repeated freeze-pump-thaw cycles. After the final freeze-pump-thaw cycle, and the temperature of the cell reached room temperature, the cell was weighed so that the solution volume could be determined. Finally, the stopcock of the burette was opened to allow a measurable volume of the TBAP-DPA solution to enter the burette so that a solution of the parent compound of the electrogenerated oxidant of known concentration could be prepared in the burette.

A second method of preparing the stock solution of the parent compound was used when the amount of the parent compound needed to make up the stock solution was too little to be weighed accurately. The cell was evacuated and filled with solvent, and the solution was outgassed as described above. It was removed from the vacuum line and placed in a glove bag which was flushed with dried, prepurified nitrogen. The cell was opened in the glove bag and sufficient solution was removed to prepare by dilution 10 mliters of solution in which the concentration of the parent of the electrogenerated oxidant was less than 1 mM. This solution was then sealed in the burette and the cell was removed from the glove bag.

After the solutions had been prepared and placed in the cell, the cell was clamped into its holder so that electrochemical experiments could be performed. All electrochemical experiments were conducted with the cell clamped in place so that reproducible ECL signals could be obtained. To avoid any problem of stray radiation, experiments were conducted in a darkroom; this permitted visual and instrumental observation of the ECL produced.

Before any ECL experiments were performed and after every addition of parent compound from the burette into the electrode chamber, both wide and narrow sweep cyclic voltammograms were recorded. Wide sweep voltammetry was conducted over a potential range that included both the one-electron oxidation and reduction of DPA. Narrow sweep voltammograms excluded these redox processes, but included the potential range where the parent compound oxidized; these were recorded at ten or thirty times the current sensitivity as the wide sweep voltammograms. These experiments were performed both to measure the concentration of the parent compound voltammetrically (wherever possible) and to determine the potentials of electrode processes. This was necessary because the potentials of the quasi-reference electrode tended to drift positively a few hundredths of a volt as the experiment progressed. Peak to peak voltages for the reactants stayed the same, however; all potentials cited herein, therefore, were measured against the cyclic voltammetric peak potential for the reduction of DPA.

After the cyclic voltammograms of the solution in the electrode chamber had been obtained, the ECL of the solution was obtained as a function of ramp potential with the circuit shown in Fig. 2. With the Wavetek frequency set at 20 Hz, the constant negative potential portion of the unsymmetrical square wave was set at the peak potential for the formation of the DPA radical anion. The range switch used for the selection of the ramp rate was turned to the desired resistance value; usually a ramp rate of 0.0089 V/sec was used. The monochromator wavelength was set at 433 nm, the wavelength of maximum emission for DPA ECL produced in DMF.

With the lights in the darkroom turned off, the shutter of the photomultiplier tube housing was opened and the function switch of the potentiostat was turned to the current mode. The capacitor discharge switch of

the ramp circuit was opened and the ECL intensity as a function of ramp potential was recorded. The ramp potential was alternately applied to the working electrode until the ECL reached a steady-state value, went through a maximum, or became too great to be recorded at that sensitivity. The solution in the electrode chamber was stirred and at least two more ECL intensity *vs.* ramp potential measurements were taken for a solution of a given concentration of the parent compound of the electrogenerated oxidant. Sometimes more measurements were taken to assure reproducibility. After the ECL measurements were taken, more of the parent compound of the electrogenerated oxidant was added to the electrode chamber from the pipette, and the solution was again stirred. Then the cyclic voltammetry-ECL measurement cycle was repeated.

### Results and Discussion

Typical results are shown in Fig. 4; here, curve A shows the cyclic voltammetry for both radical ions of 9.1 mM DPA in DMF. The cyclic voltammetric peak-to-peak potential for the formation of the DPA radical anion and the DPA radical cation in such a solution was generally found to be 3.32V. Faulkner, Tachikawa, and Bard (4) have reported a peak-to-peak voltage of 3.24V using a saturated calomel reference electrode. Because of the slight instability of the QRE, all potentials have been referenced to the reduction peak potential for DPA.

Curve B shows the background linear sweep voltammetry of the same solution in the potential region where WBP is oxidized; no WBP has been added, however, and the current sensitivity is ten times that which was used to record curve A. Curve D shows the linear sweep voltammetry in the same potential region under identical conditions after a small amount of WBP had been added from the burette to make the bulk concentration of WBP 0.013 mM. Even though the current sensitivity was high, it is clear from this figure that this concentration of WBP lies close to the limit of detectability for linear sweep voltammetry because the current attributable to faradaic processes is not much greater than the background current. In addition, identification of the species undergoing oxidation through its peak potential is virtually impossible; no

peak potential for the formation of  $\text{WBP}^+$  can be discerned easily, if at all.

Curve C shows the ECL *vs.* ramp potential behavior obtained from the solution of DPA (uncontaminated with WBP) using the potential programming circuit shown in Fig. 2. The stepping frequency was 20 Hz while the ramp rate was 0.0089 V/sec. This curve shows that some ECL does occur in solutions containing no known oxidizable species. This low level ECL

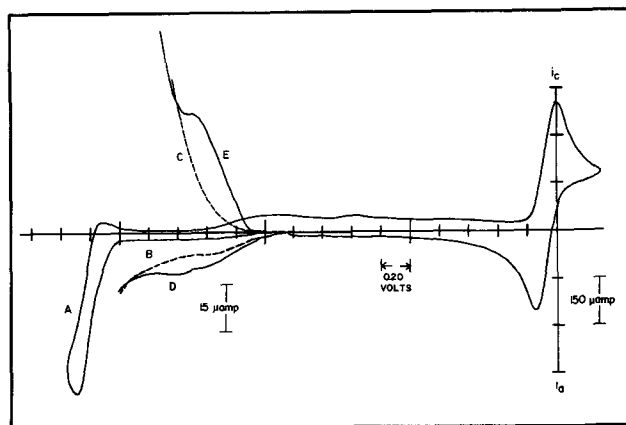


Fig. 4. Typical experimental results. Cyclic voltammetry (A) is for 9.1 mM DPA; high sensitivity linear sweep voltammetry is shown in the absence (B) and presence (D) of 0.013 mM WBP; corresponding ECL behavior is shown in C and E.

is the object of some experiments presented below; at this point it is sufficient to note that a background ECL signal is obtained even in the absence of WBP. Thus, contrary to expectation, all ECL signals obtained from solutions containing WBP had to be corrected for background emission.

That a measurable ECL signal is obtained from solutions containing WBP may be seen in curve E. Here, ECL vs. potential is shown for the solution 0.013 mM in WBP; other experimental conditions are identical to those used to record curve C. Even this small amount of WBP produces an ECL signal significantly larger than background emission. In addition, a potential-dependent maximum in the ECL plot is observed; no such peak may be detected in the corresponding voltammetry.

In an attempt to characterize the potential dependence of the ECL process, a new parameter,  $E_{I_{max}/2}$ , was defined. Like the polarographic half-wave potential, this value is the potential at which half of the maximum ECL intensity due to the presence of the parent compound of the electrogenerated oxidant has been emitted. This potential was determined by finding the potential at which the ECL is one-half its maximum intensity (corrected for background); for curve E in Fig. 4,  $E_{I_{max}/2}$  of the WBP is 2.25V vs.  $E_p$  (DPA/DPA<sup>-</sup>).

The effect of incremental additions of WBP to a 10 mM DPA solution is shown in Fig. 5. Here, curves A through E show the changes in linear sweep voltammetry as the bulk concentration of WBP is increased from  $2.57 \times 10^{-5}$  to  $7.21 \times 10^{-5}$ M. (Curve F shows the cyclic voltammetry for the oxidation of DPA.) Note-worthy is the observation that linear sweep voltammetry would be of little use for analysis in this con-

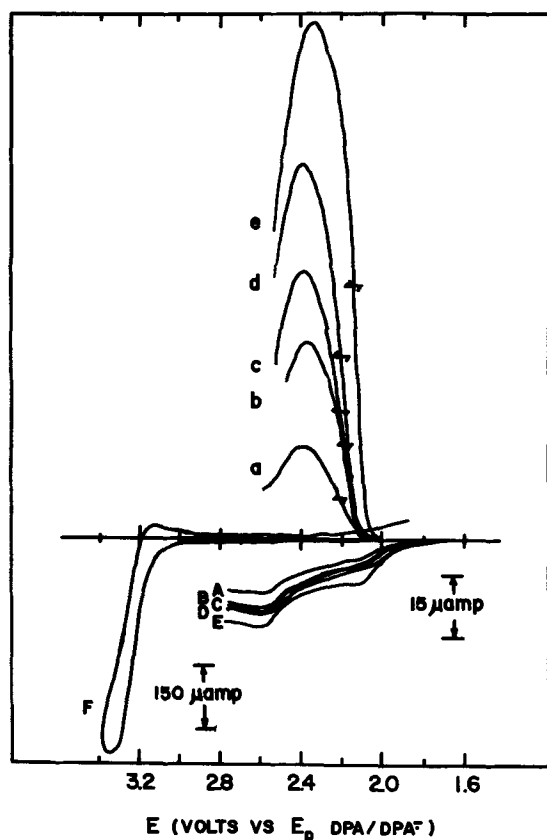


Fig. 5. Concentration effects. Curves A-E show high sensitivity linear sweep voltammetry for solutions containing  $2.57$ ,  $3.82$ ,  $4.93$ ,  $6.00$ , and  $7.21 \times 10^{-5}$ M WBP, respectively; curves a-e show ECL intensity behavior for the same solutions.  $E_{I_{max}/2}$  is indicated on each ECL curve. Curve F shows low sensitivity cyclic voltammetry of DPA.

centration range: it is difficult to detect a change in current with a change in concentration. This may be contrasted with the behavior of ECL intensity for the same solutions when the working electrode is subjected to the potential program described above. Curves a through e demonstrate that analysis by this method is feasible: ECL intensity at all potentials increases regularly with increasing WBP concentration, and in this concentration range this intensity greatly exceeds that attributable to background processes; in addition,  $E_{I_{max}/2}$  is useful in identifying WBP throughout, even at low concentrations. The ECL intensity curves shown in Fig. 5 were independent of ramp rate at rates less than  $0.0098$  V/sec.

While  $E_{I_{max}/2}$  is generally only  $0.10$ V more positive than  $E_p$ ,  $E_{I_{max}}$  itself is usually  $0.25$ V more positive than the corresponding voltammetric oxidation peak. Thus, if  $E_{I_{max}}$  is taken as a measure of the potential at which diffusion-limiting conditions are obtained, considerable uncompensated IR losses must be present in the ECL experiment. This seems reasonable because fairly high current levels are achieved in the alternating potential ECL experiment. That the ECL intensity goes through a maximum rather than reaching a plateau is probably due to two effects. First, any conversion of WBP<sup>+</sup> to electroinactive product (either by

reaction with DPA<sup>-</sup> or by a side reaction) will diminish the amount of WBP available during subsequent cycles; this could result in lower levels of ECL emission as the scan progresses. Second, at potentials where WBP<sup>++</sup> is formed, one would expect a change in ECL output as WBP<sup>++</sup> becomes available to react with DPA<sup>-</sup>. The ECL maximum obtained by this method is fairly broad; the ECL output  $0.15$ V beyond  $E_{I_{max}}$  ( $0.40$ V positive of  $E_p$ ) is still  $90\%$  of  $I_{max}$ . Thus, significant amounts of WBP<sup>++</sup> (peak potential  $0.50$ V positive of  $E_p$ ) are probably being electrogenerated in the potential region where the ECL decreases.

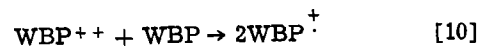
It is of interest to note that the ECL intensity decreases rapidly as the ramp potential approaches that sufficient to form WBP<sup>++</sup>, regardless of concentration and ramp rate. This observation implies that WBP<sup>++</sup>

does not produce ECL when it reacts with DPA<sup>-</sup>; this is in apparent disagreement with a result reported previously for RRDE studies of the same system (9). In these studies, the ECL intensity at the ring (where

DPA<sup>-</sup> was being generated) increased when the disk potential was changed to produce WBP<sup>++</sup> instead of

WBP<sup>+</sup> to be swept into the reaction zone beneath the ring. This apparent discrepancy may be resolved by considering the concentration profiles in each experiment. In the stationary electrode case, WBP<sup>++</sup>

can react with DPA<sup>-</sup> only in a region where small amounts of WBP are present; thus, there is little chance for the reaction



to produce WBP<sup>+</sup> to react secondarily with DPA<sup>-</sup>. On the other hand, in the RRDE experiment, WBP<sup>++</sup> is swept into a region where there is a high relative concentration of WBP, so that in this case, the forma-

tion of WBP<sup>+</sup> is more likely. Thus, the ECL observed upon generating WBP<sup>++</sup> in the RRDE experiment may be attributed only indirectly to the WBP dication.

While extensive studies were conducted with WBP to test the specific applicability of this method to that compound, some experiments were performed with WRP and 10 MP also. Typical experimental results are shown in Table I. These results show that at concentrations less than  $0.1$  mM, both  $I_{max}$  and  $E_{I_{max}/2}$  may be

Table I. Typical experimental results

Parent of oxidant*	Parent concentration ( $\times 10^{-5}M$ )	$i_p/V^{1/2}$ ( $i_{pDPA} V^{1/2} \times 0.01$ )	$E_p$ (V vs. $E_p^{DPA/DPA^{\cdot-}}$ )	$I_{max}$ (relative units)	$E_{I_{max}/2}$ (V vs. $E_p^{DPA/DPA^{\cdot-}}$ )
WBP <sup>(a)</sup>	2.8	—	—	0.55	2.21
	5.5	1.1	2.13	1.24	2.21
	8.5	1.7	2.11	1.90	2.15
	10.8	2.0	2.12	2.21	2.17
	16.0	3.1	2.14	2.19	2.16
WBP <sup>(b)</sup>	21.4	5.0	2.14	1.84	2.17
	1.3	—	—	0.10	2.23
	2.6	—	—	0.30	2.23
	3.8	—	—	0.73	2.23
	4.9	—	—	1.00	2.23
WRP <sup>(c)</sup>	6.0	—	—	1.42	2.23
	7.2	—	—	1.99	2.17
	4.5	0.8	2.14	0.12	2.19
	8.7	1.1	2.12	0.70	2.23
	11.8	2.0	2.13	1.01	2.23
WRP <sup>(d)</sup>	20.2	3.9	2.13	1.30	2.25
	1.9	—	—	0.13	2.20
	3.1	—	—	0.22	2.25
	4.2	—	—	0.45	2.20
	5.4	—	—	0.59	2.19
10 MP <sup>(e)</sup>	2.8	0.6	2.73	1.08	2.76
	6.0	1.8	2.76	2.56	2.75
	9.4	3.0	2.76	3.81	2.75
	13.0	5.7	2.79	4.30	2.75
	15.1	7.0	2.80	4.09	2.73

\* Bulk DPA concentrations were as follows: (a), 10.2 mM; (b), 9.1 mM; (c), 9.5 mM; (d), 8.9 mM; (e), 10.5 mM.

determined more readily than their linear sweep voltammetry counterparts for all three compounds selected. While  $E_{I_{max}/2}$  does not correspond to  $E_p$  for any of the compounds studied, it is generally reproducible within 20 mV at concentrations less than 0.10 mM. In this concentration range there is also a linear relationship between  $I_{max}$  and bulk parent concentration; this may be seen also in the calibration curves presented in Fig. 6. At higher bulk parent concentrations,  $I_{max}$  no longer increases with increasing concentrations and  $E_{I_{max}/2}$  is no longer reproducible. This occurs at a concentration level where linear sweep voltammetry begins to be analytically effective, however. Thus, in this sense, the two methods are complimentary; each is effective at concentration levels where the other is not.

The calibration curves presented in Fig. 6 for multiple runs of each compound give some indication of the reproducibility of the determination from run to run. Different runs (i.e., different DPA solutions) are shown by different symbols. Since most determinations were conducted with WBP, overwhelming evidence of reproducibility is available only for that compound. Indications are good, however, that the behavior of WRP and 10 MP is similarly reproducible. Two of the WBP points show considerable negative deviation from the calibration curve shown. These points were obtained at the end of a run when a considerable amount of electrolysis had taken place at the working electrode. Generally reproducible ECL behavior was obtainable only from relatively fresh solutions.

Because  $I_{max}$  is shown on the same relative intensity scale for all compounds, it is apparent that 10 MP is most efficient at producing ECL upon reacting with

$DPA^{\cdot-}$ , while WRP appears to be least efficient. This concentration efficiency (the slope of the linear portions of the calibration curves) exaggerates the differences in actual current efficiency (photons emitted/electron transferred) for these compounds. Analysis of the linear sweep voltammetry data in Table I reveals that the relative diffusion coefficients of these three compounds increases in the same order as the concentration efficiency; thus, much of the apparent differences in the efficiency of ECL production for these compounds may be attributed to higher average oxidation currents in the order 10 MP > WBP > WRP.

The calibration curves also show that  $I_{max}$  increases linearly with parent concentration only up to 0.10 mM; thereafter, increases in parent concentration bring about no further increases in ECL intensity. This trend,

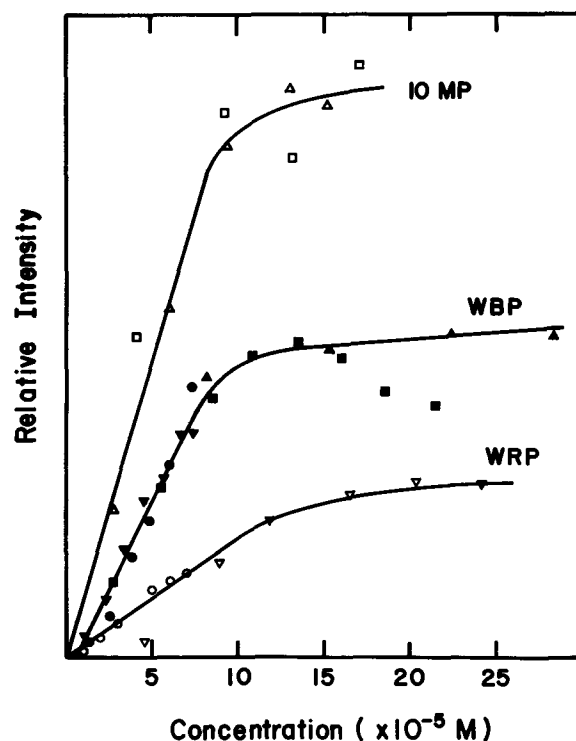


Fig. 6. Calibration curves. Different symbols are used to designate different runs having slightly different concentrations of DPA. For each parent concentration,  $I_{max}$  is shown on the same relative intensity scale.

independent of compound, suggests that the energy deficient ECL from  $DPA^{\cdot-}$  is limited when the concentration of the radical ion oxidant or its precursor is approximately 1% of the DPA concentration. This could be due to a quenching effect attributable to either the radical cation or its parent hydrocarbon.

Because background ECL was not anticipated at the outset of this work, experiments were conducted to determine its probable cause. The actual intensity of this background ECL was quite low. This may be seen in Fig. 7 where background ECL (curve a) was recorded at 100 times the sensitivity of the energy-sufficient ECL (curve b) resulting from the reaction of the

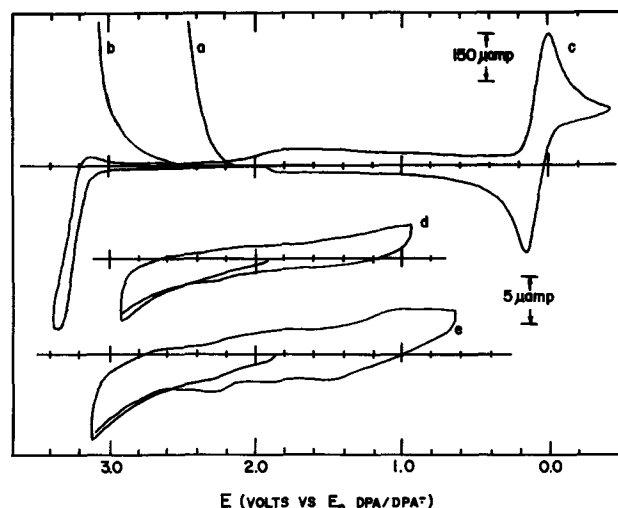


Fig. 7. Background ECL effects. Curve a shows typical high sensitivity background ECL from 10 mM DPA in DMF-TBAI; curve b shows low sensitivity (0.01 times that in curve a) ECL from the same solution. Curve c shows low sensitivity cyclic voltammetry of DPA; curves d and e show high sensitivity cyclic voltammetry of 0.10M TBAP in DMF in the absence of DPA.

radical ions of DPA itself. Since ECL of greater intensity had been detected for solutions containing a known amount of parent compound that was only marginally detectable electroanalytically, it was reasonable to attribute this background ECL to a trace amount of oxidizable species present in the solvent system. High-sensitivity cyclic voltammetry was performed on the DMF-TBAP solvent system (in the absence of DPA) in an attempt to detect this trace amount of oxidizable compound. This is shown by curves d and e in Fig. 7. Admittedly, since no DPA was present in these solutions, the assignment of potentials depends on the agreement of the rest potential of the QRE in the presence and the absence of DPA. If such agreement is assumed for fresh solutions, the high-sensitivity cyclic voltammetry in curves d and e shows that an oxidizable species is generated on the positive potential scan, even though the upper limit of this scan is less than that regarded as sufficient for DPA oxidation. Present at low concentration and detectable only on the second positive potential scan, the oxidizable species found has its peak potential at 2.3V

vs.  $E_p$  DPA/DPA $^{\cdot-}$ ; this corresponds well with the potential onset of background ECL. Since only trace amounts are necessary for ECL production, this species could be present residually from previous positive scans or might be generated in sufficient quantity from any positive scan; it is detectable electroanalytically

following a scan to 2.9V vs.  $E_p$  DPA/DPA $^{\cdot-}$ . This species seems reasonable as the source of background ECL observed.

### Conclusion

The method described herein has been shown to be suitable for the analysis of WBP, WRP, and 10 MP at concentration levels not suitable for ordinary electroanalysis; thus it may find use in trace analysis as the stationary electrode ECL equivalent of polarography. Its use, of course, is limited by the ability of the electrogenerated oxidant to produce ECL upon reaction

with DPA $^{\cdot-}$ . Recent studies (16) indicate that halides electrogenerated from their ions will produce ECL

when reacted with DPA $^{\cdot-}$ . Therefore, there is reason to suspect that the method may be more universal than indicated by this work. Indeed, all that may be necessary is that the electrogenerated oxidant be formed at potentials sufficiently positive to produce

triplet DPA when reacted with DPA $^{\cdot-}$ . Work is presently underway to determine the limitations of the method.

In addition to introducing a simple method to employ ECL analytically, this work provides information about the concentration dependence of the ECL energy-deficient process that was hitherto unavailable. The fact that ECL may be observed from solutions containing a known amount of parent compound that is not detectable electroanalytically supports the contention that only trace amounts of electrogenerated oxidant are necessary to produce ECL upon reaction with DPA $^{\cdot-}$ .

### Acknowledgment

The technical assistance and helpful suggestions of Rein Valdna who constructed all of the glassware used in this work are gratefully acknowledged.

Manuscript submitted Jan. 30, 1974; revised manuscript received April 17, 1974. This was Paper 285 presented at the San Francisco, California, Meeting of the Society, May 12-17, 1974.

Any discussion of this paper will appear in a Discussion Section to be published in the June 1975 JOURNAL. All discussions for the June 1975 Discussion Section should be submitted by Feb. 1, 1975.

### REFERENCES

1. T. M. Siegel and H. B. Mark, Jr., *J. Am. Chem. Soc.*, **94**, 9020 (1972).
2. D. J. Freed and L. R. Faulkner, *ibid.*, **93**, 2097 (1971).
3. A. Weller and K. Zachariasse, *J. Chem. Phys.*, **46**, 4984 (1967).
4. L. R. Faulkner, H. Tachikawa, and A. J. Bard, *J. Am. Chem. Soc.*, **94**, 691 (1972).
5. D. J. Freed and L. R. Faulkner, *ibid.*, **93**, 3565 (1971).
6. R. Bezman and L. R. Faulkner, *ibid.*, **94**, 6317 (1972).
7. S. A. Cruser and A. J. Bard, *ibid.*, **91**, 267 (1969).
8. B. Fleet, G. F. Kirkbright, and C. J. Pickford, *Talanta*, **15**, 566 (1968).
9. J. T. Maloy and A. J. Bard, *J. Am. Chem. Soc.*, **93**, 5968 (1971).
10. D. M. Hercules, R. C. Lansburg, and D. K. Roe, *ibid.*, **88**, 4578 (1966).
11. A. Zweig, A. K. Hoffman, D. L. Maricle, and A. H. Maurer, *ibid.*, **90**, 261 (1968).
12. J. T. Maloy, K. B. Prater, and A. J. Bard, *ibid.*, **93**, 5959 (1971).
13. C. P. Keszthelyi, Ph.D. Thesis, The University of Texas at Austin (1973).
14. K. S. V. Santhanam and A. J. Bard, *J. Am. Chem. Soc.*, **87**, 139 (1965).
15. L. R. Faulkner and A. J. Bard, *ibid.*, **90**, 6284 (1968).
16. T. Kihara, M. Sukigara, and K. Honda, *Electrochim. Acta*, **18**, 639 (1973).

# Effect of the Thickness of Anodic Oxide Films on the Rate of the Oxygen Evolution Reaction at Pt in H<sub>2</sub>SO<sub>4</sub> Solution

## I. Growth at Constant Current

A. Damjanovic, A. T. Ward,\* and M. O'Jea

Xerox Corporation, Rochester Research Center, Webster, New York 14580

### ABSTRACT

Ellipsometry and standard electrochemical techniques are used to determine whether, and if so, how the thickness of an anodic oxide film affects the catalysis of the oxygen evolution reaction at platinum. A prereduced electrode is first polarized in sulfuric acid solution with a constant current density,  $i_p$ , for a given time and then the thickness,  $d$ , of the anodic film and the electrode potential,  $V$ , are determined for various current densities  $i \leq i_p$ . It is found that the thickness of the oxide film affects the catalytic activity in an exponential way, i.e.

$$i = A \exp(-\delta d/2) \exp(FV/2RT)$$

where  $A$  and  $\delta$  are constants. For the same time of polarization both the oxide thickness and the electrode potential increase with the logarithm of the polarization current density,  $i_p$ . The potential dependence is  $dV/d(\log i_p) \approx 170$  mV. This is in contrast with the value of about 115 mV usually reported for the oxygen evolution reaction. The latter value can be obtained only when the electrode is anodically treated at a current density,  $i_p$ , and the  $i$ - $V$  relationship is subsequently determined at current densities  $i < i_p$ . Ellipsometry shows that under these conditions the anodic film thickness remains essentially constant at the value achieved during the initial polarization at a higher current density.

It has been shown that the catalytic activity for the oxygen evolution reaction at platinum in acid solutions is greatly affected by the electrode pretreatment (1). Only after an electrode was kept at a high potential (e.g., 1.7-2.0V), or was subjected to a high anodic current density (e.g.,  $10^{-4}$  to  $10^{-2}$  A/cm<sup>2</sup>) for some time (>10-20 min) was it possible to obtain  $V$ - $\log i$  relationships which were linear over several decades of current density (2-5) and had slopes of 2.3 ( $2RT/F$ ), and then only if the potentials or current densities in the subsequent process of measurement were lower than those used in the electrode pretreatment. No linear  $V$ - $\log i$  relationship could be obtained in a first "run-up" experiment with electrodes that were not so pretreated. In the latter case, the  $dV/d(\log i)$  slopes at any point of current density were higher (1,6) than 2.3 ( $2RT/F$ ). Higher current density or electrode potential and longer time of initial polarization were found to lower the activity. The observed changes in activity were attributed to differences in the thickness of the anodic oxide films that formed during the various electrode pretreatments. The surface oxide film was assumed to act as a barrier to charge transfer, the barrier increasing with increasing thickness of the oxide film. The oxide barrier is in series with the double layer barrier and with it controls the rate of the oxygen evolution reaction.

The experiments of the present study have been designed to verify the assumption that the thickness of the surface oxide film affects the kinetics of the oxygen evolution reaction and to show that an analytical expression can be obtained relating the rate of the reaction to the thickness of the surface film. To achieve this ellipsometry has been combined with a standard electrochemical (galvanostatic) technique and current densities have been determined as a function of the thickness of the oxide film and electrode potential.

\* Electrochemical Society Active Member.  
Key words: anodic films, platinum anodes, catalysis of O<sub>2</sub> evolution.

### Experimental

The procedure involved:

1. Galvanostatic anodic polarization of a highly polished platinum disk electrode in 0.1N H<sub>2</sub>SO<sub>4</sub> for a fixed time. (P.A.R. Model 173 potentiostat in a galvanostatic mode).
2. Measurement of the electrode potential vs. a reversible hydrogen electrode in the same solution (H.E.). (Keithley Model 600 A electrometer).
3. Simultaneous determination of the change in azimuth and ellipticity of monochromatic light reflected from the electrode. (Automated recording ellipsometer, Rudolf Research Incorporated).

The Teflon cell used in the present work was similar to those already described (7). The cell was equipped with a large platinum gauze auxiliary electrode, a Luggin capillary that approached the edge of the disk electrode, and an oxygen gas inlet and outlet. The stream of gas from the inlet served not only to oxygenate the solution prior to polarization but also when necessary, to stir the solution and to displace oxygen bubbles attached to the anode. Except at the highest current densities ( $i > 3.10^{-4}$  A/cm<sup>2</sup>) reliable ellipsometric data could be obtained by displacing these bubbles immediately prior to making a measurement.

The working electrode was a 99.9% pure platinum disk, 1.13 cm<sup>2</sup> in geometrical area, welded to a stainless steel rod. The rod with the disk was enclosed in a shrinkable Teflon sleeve. The face of the disk was polished to a mirror finish, the final polishing being with 0.05 $\mu$  alumina. The electrode was washed with alcohol, alkaline solutions, sulfuric acid, and triply distilled water. Finally, both the electrode and the cell were washed *in situ* with triply distilled water and then acid solution of the same concentration as used in subsequent experiments. Solutions used in this work were prepared from Baker "Analyzed" grade sulfuric acid and triply distilled water. No further purification of the

solution was made. This is because the oxygen evolution reaction at current densities greater than  $10^{-7}$ - $10^{-6}$  A/cm<sup>2</sup> is apparently not affected by trace amounts of impurities. Before measurements, the electrode was subjected to a few high ( $10^{-3}$  A/cm<sup>2</sup>) anodic and cathodic pulses ending with a cathodic pulse. After this pre-treatment the solution was replaced and the electrode was kept at 0.5V for 5 min. The electrode surface at this potential was then used as the reference state.

The changes in azimuth and ellipticity associated with the change in the electrode surface from the initial, freshly reduced film-free state<sup>1</sup> to the final anodically oxidized state were used to calculate the change ( $\Delta_0 - \Delta$ ) in the relative phase retardation,  $\Delta$ , between components of the light polarized perpendicular and parallel to the plane of incidence, respectively. This change was then used to calculate the mean film thickness,  $d$ , using Drude's (8) equation,<sup>2</sup> [ $d = \text{constant} (\Delta_0 - \Delta)$ ], a relationship valid for films thin compared with the wavelength of light.

The optical constants ( $n_1 = 2.80$ ;  $n_2 = 1.94$ ;  $K_2 = 4.36$ ) used here to calculate thickness were taken from the work of Kim, Paik, and Bockris (9) who determined these parameters entirely from ellipsometric data. Here  $n_1$  is the refractive index of the film and  $n_2$  and  $K_2$  are the refractive index and absorption constant, respectively, of the platinum substrate. Other workers have obtained similar values for  $n$  and  $K$  using a combination of optical (ellipsometric, immersion refractive index) and electrical (coulometric) techniques (10, 11). With the experimental angle of incidence corrected for refraction through the cell windows,  $\phi = 75^\circ$ , and wavelength,  $\lambda = 5460\text{\AA}$ , the constant term in Drude's equation is calculated as 3.80  $\text{\AA}/\text{deg}$ . The resulting film thicknesses are then typically less than 10 $\text{\AA}$  so that the use of Drude's equation appears justified.

### Results

In Fig. 1 the phase retardation change,  $\Delta_0 - \Delta$ , observed after a specified time for polarization (125, 750, or 1800 sec) is plotted against the constant current density (C.D.),  $i_p$ , to which a freshly pre-reduced electrode was subjected. The calculated ellipsometric thickness is also shown in the same figure. Likewise, Fig. 2 shows the respective electrode potentials plotted vs.  $i_p$ .

In the examined region of current densities both the thickness and electrode potential change linearly, or very nearly so, with the logarithm of the C.D.,  $i_p$ , with which the electrode was anodically prepolarized. For all times of polarization the  $dV/d(\log i_p)$  slopes are

<sup>1</sup> The film-free condition was assumed to exist under potentiostatic conditions at 0.5V H.E. At 0.98V, the rest potential in the oxygen-saturated system, the phase retardation was somewhat lower reflecting the presence of adsorbed species on the electrode.

<sup>2</sup> The assumption implicit in Drude's equation is that the refractive index of the film is independent of thickness. Since the adsorbed layer and the film ultimately formed may not have the same refractive index the Drude assumption will lead to a small but constant error in the calculated value of thickness.

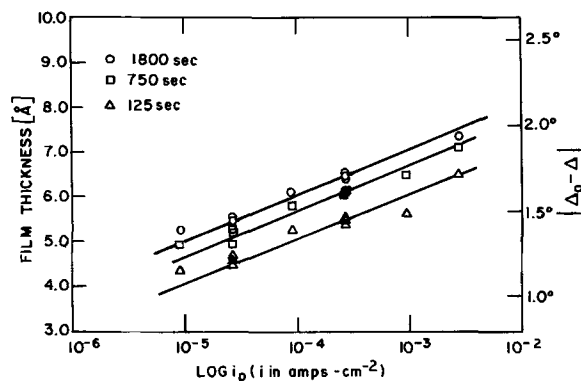


Fig. 1. Plot of anodic film thickness after 125, 750, and 1800 sec vs. log current density of polarization.

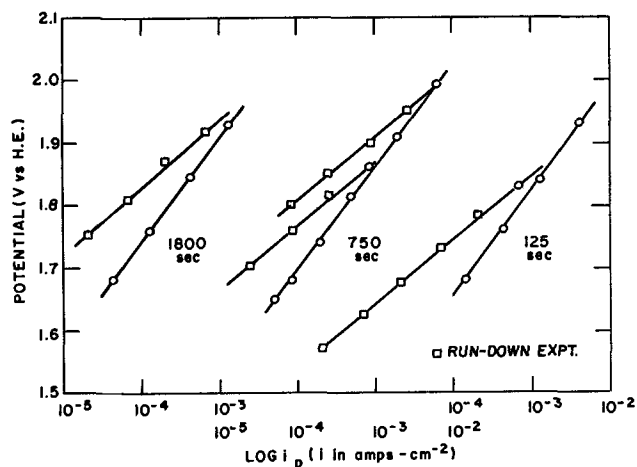


Fig. 2. Plot of electrode potential (H.E.) after 125, 750, and 1800 sec (circles) vs. log current density of polarization. Squares represent subsequent potential-current density relationships for decreasing current densities.

close to 170 mV/decade of C.D., and the  $dd/d(\log i_p)$  slopes are close to 1.0  $\text{\AA}/\text{dec}$ . of C.D.

After an electrode has been polarized for 750 sec with a constant C.D.,  $i_p$ , and the current density,  $i$ , is decreased in steps, no change in thickness,  $d$ , is observed (from A to B in Fig. 3). In contrast to this, the potential,  $V$ , decreases as the C.D.,  $i$ , is decreased (Fig. 2). The  $dV/d(\log i)$  slope is now close to 115 mV/decade of C.D., or to 2.3 ( $2RT/F$ ). The same is observed after the electrode has been prepolarized for 125 or 1800 sec as shown in Fig. 2. (The corresponding thickness data is omitted from Fig. 1 and 3 in order to preserve clarity.)

### Analysis of Data

The important features of the results may be summarized as follows:

- For the same time of polarization at a constant current density,  $i_p$ , both electrode potential and ellipsometric thickness increase with the logarithm of the applied current density. At any applied current density, for a constant time of polarization, the ellipsometric thickness therefore changes, to a good approximation, linearly with electrode potential. This is illustrated in Fig. 4 which is composed from Fig. 1 and 2. Linear  $V$ - $d$  relationships have been observed also in potentiostatic studies both by ellipsometric (10-12) and coulometric (4, 13-15) techniques. Apparently no attempt was made in this earlier work to relate the rate of the oxygen evolution reaction to the thickness of the surface oxide film.

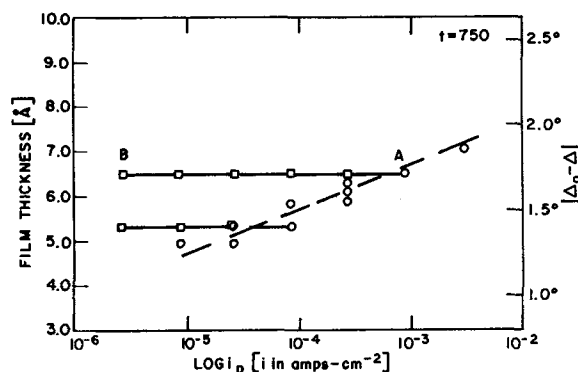


Fig. 3. Plot of anodic film thickness after 750 sec (circles) vs. log current density of polarization. Squares represent subsequent film thickness-current density relationships for decreasing current densities.

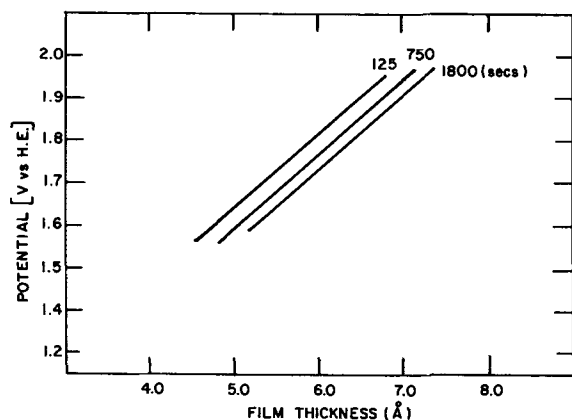


Fig. 4. Plot of electrode potential (H.E.) vs. film thickness after polarization for 125, 750, and 1800 sec at various current densities.

2. An arrest in further growth of the oxide film occurs when, after the initial polarization of a pre-reduced electrode with a constant applied current density, the current density is decreased. Such "hysteresis" has been reported previously in coulometric studies of surface coverages in the potential region lower than that of the present work (13, 14).

3. A  $V$ - $\log i$  relationship which is linear over several orders of magnitude<sup>3</sup> with slope close to  $\partial V/\partial \ln i = 2RT/F$  is obtained under the condition of nearly constant thickness of the surface oxide film. This is self-evident from the comparison of Fig. 2 and 3: in the process of lowering current density, say from point A to B, the thickness represented by point A did not change, i.e.,

$$\left(\frac{\partial V}{\partial \ln i}\right)_d = \frac{2RT}{F} \text{ and } \left(\frac{\partial V}{\partial \ln i}\right)_d \neq f(V, d, i) \quad [1]$$

4. The catalytic activity for the oxygen evolution reaction decreases with increasing thickness of the surface oxide film. This is evident from the change of the electrode potential at the same current density with the thickness of the film as illustrated in Fig. 5. In this figure the potentials from Fig. 1 and 2 are plotted vs. thickness,  $d$ , for two current densities (rather than for a constant time of polarization at different applied current densities as in the case of Fig. 4). As the thickness increases, the potential at the same current density increases linearly, i.e., the catalytic activity decreases. Were the catalytic activity expressed in terms of exchange current densities then it would decrease exponentially with the thickness of the oxide film, i.e.

$$\log i_0 = \text{constant} (-d) \quad [2]$$

as will be shown later in this work.

\* See also Ref. (2) and (3).

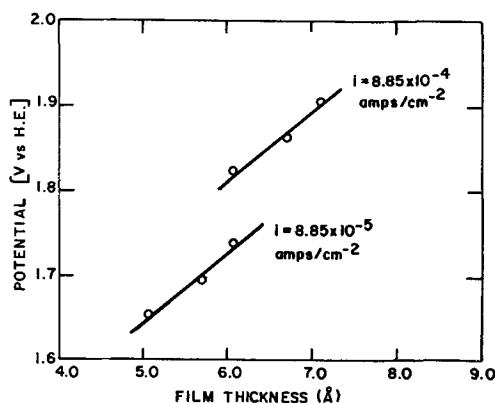


Fig. 5. Plot of electrode potential (H.E.) vs. film thickness after polarization at constant current density for various times.

5. To a fair approximation the slopes of the  $V$  vs.  $d$  lines in Fig. 5 are constant and equal for both current densities, i.e.

$$\left(\frac{\partial V}{\partial d}\right)_i = 0.085 \text{ V/Å} \text{ and } \left(\frac{\partial V}{\partial d}\right)_i \neq f(V, i, d) \quad [3]$$

The difference may be noted at this point between the  $\partial V/\partial d$  slopes of Fig. 4, that refer to a constant time of polarization, and those of Fig. 5, that refer to constant current density. This demonstrates the importance of defining the conditions under which the  $V$  vs.  $d$  relationship is obtained.

6. The mechanism of the oxygen evolution reaction is apparently unaltered with the change in the thickness of the oxide film. This is indicated by the fact that the  $dV/d(\ln i)$  slopes remain the same over the entire, though limited, range of thicknesses of the oxide films examined in the present study. This is in accord with a previous report that the slopes are nearly the same irrespective of the conditions of the anodic pretreatment of the electrodes (1). Also, most of the workers in the field have reported slopes close to  $2RT/F$  although the pretreatments of their electrodes<sup>4</sup> certainly were not identical (2-6, 13, 16-20).

7. Finally, to a good approximation, in the region of current densities and oxide film thicknesses examined here,  $\log i$  is linearly related to both  $V$  and  $d$ , i.e., the function

$$f(V, d, \log i) = \text{constant} \quad [4]$$

represents a plane surface in three dimensions. This follows from the fact that, as illustrated in Fig. 6, the projections of the straight line  $AB^5$  on two perpendicular planes are parallel to the corresponding projections of the straight line  $A'B'$  (or  $A''B''$ ) while intersecting the projection of the third straight line  $AD$ . All these lines lie in the plane  $f(V, \log i, d) = \text{constant}$ .

How well the function  $f(V, \log i, d) = \text{constant}$  approximates a plane surface depends on: (i) how well the  $dV/d(\log i)$  slopes can be taken as independent of the thickness of the surface oxide film [their independence of potential or current density being well established over several decades of current density (2, 3)], and (ii) whether  $(\partial V/\partial \ln i_p)t$  is constant. Now, as already shown, the present experiments as well as the literature give  $dV/d(\log i)$  close to 2.3. ( $2RT/F$ ) irrespective of the conditions of anodic pretreatment of the electrode and, therefore, irrespective of the surface film thickness. Furthermore, it is evident

<sup>4</sup> It is uncertain whether the purity of the platinum metal itself will affect the rate of oxide growth, the thickness of the oxide film or the catalysis mechanism of the oxygen evolution reaction.

<sup>5</sup> The line  $AB$  is not parallel to either of the axes  $V$ ,  $\log i$  or  $d$ .

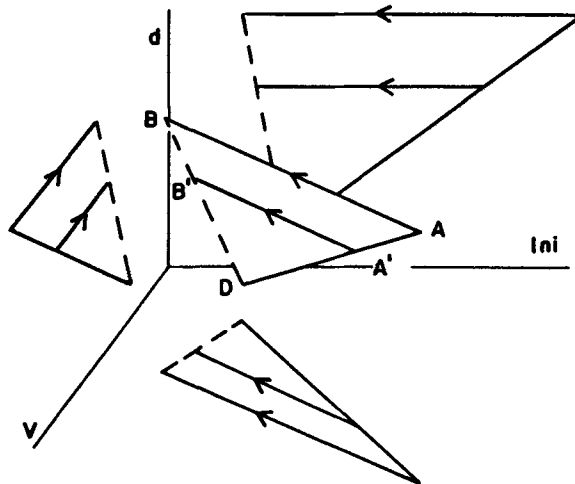


Fig. 6. Representation of the plane  $f(V, \ln i, d) = \text{constant}$  in three dimensions.

from Fig. 2 that  $V$  does indeed depend nearly linearly on  $\log i_p$ .

#### The Rate Equation and the Catalytic Activity for the Reaction

The analytical solution to the expression  $f(V, \log i, d) = \text{constant}$  is given in the Appendix. It is

$$\epsilon V - \left( \frac{2RT\epsilon}{F} \right) \ln i + \left( 1 - \frac{\kappa F}{2RT} \right) d = \text{constant} \quad [5]$$

where

$$\epsilon = \left[ \frac{dd}{d(\ln i_p)} \right]_t \quad [6]$$

is obtained from the data in Fig. 1. It is equal to 1.0 A/decade of C.D. Constant  $\kappa$  is given by

$$\kappa = \left( \frac{dV}{d \ln i_p} \right)_t \quad [7]$$

which, from Fig. 2, is equivalent to 0.170 V/decade.

Now with

$$\frac{2RT - \kappa}{\epsilon RT} = \delta \quad [8]$$

Eq. [5] transforms to

$$i = A \exp \left( \frac{-\delta d}{2} \right) \exp \left( \frac{FV}{2RT} \right) \quad [9]$$

This equation gives the dependence of the rate of the oxygen evolution reaction on both the electrode potential and the thickness of the surface oxide film. For a constant thickness the equation reduces to the well-known rate equation for the oxygen evolution reaction in an acid solution of a given pH

$$i = i_0 \exp \left( \frac{FV}{2RT} \right) \quad [10]$$

It follows from Eq. [9] and [10] that the catalytic activity, expressed as  $i_0$ , decreases exponentially with the thickness of the oxide film

$$i_0 = A \exp \left( -\frac{\delta d}{2} \right) \quad [11]$$

where constant  $A$  contains, among other terms, those which involve the concentration dependence. Differences in the reported catalytic activities can now easily be accounted for in terms of the different thicknesses of the surface oxide films produced in different experiments.

Vetter and Schultze (15) have reported that the coulometric thickness of the surface oxide film at electrodes kept at a constant potential in the region from about 1.0 to 2.0V increases logarithmically with time. From this observation and from Eq. [11] it follows that, at constant potential, current density should decrease with time according to

$$\log (i/i_0) = \beta \log t \quad [12]$$

where constant  $\beta$  has a negative value. Such a dependence has indeed been found by Schultze (21). No relevant data could be traced in the literature that would allow a check of the validity of Eq. [11] under galvanostatic conditions. Bockris and Huq (2) have reported that, at a constant current density, potential increases logarithmically with time of polarization. This would require, according to Eq. [11], that again, under galvanostatic conditions, the thickness of the oxide film increases with time according to a direct logarithmic law. Apparently, no such law for platinum oxide growth has been reported in the literature. Makrides (22), however, reports that at gold anodes, under galvanostatic conditions, oxide films grow according to a direct logarithmic law. The same law of growth<sup>6</sup> has

<sup>6</sup> Vetter and Schultze (15) report for galvanostatic polarization, a linear increase of surface coverage with time. This linear dependence holds only for the initial growth of surface oxides (for, say, less than 10 sec, depending on current density).

been found for other metal electrodes (23, 24). The logarithmic law should be expected for platinum anodes under galvanostatic polarization conditions also. Further study of this question appears desirable and is currently in progress in this laboratory.

#### The Rate Equation for the Current Density Across the Surface Oxide Film

The exponential dependence of the catalytic activity for the oxygen evolution reaction upon film thickness is apparently related to the mechanism of electron transfer from a species in solution or at the electrode surface (e.g., adsorbed water molecules), across the oxide film to the metal itself. As will be discussed in a subsequent paper, the charge transfer occurs by a quantum mechanical tunneling process rather than by electron or hole conduction in the oxide film. This requires the existence of a substantial electric field across the oxide film and also requires that the field change with current density (at a constant surface oxide film thickness). Consequently, the potential difference,  $V_t$ , between the metal itself and the outer Helmholtz plane (in the solution) should be divided into the potential difference across the oxide film,  $V_{of}$ , and the potential difference across the double layer,  $V_{dl}$ . In previous work (1) such a division was introduced in order to account for the observed kinetic parameters for the oxygen evolution reaction in sulfuric acid solutions of different pH. With this division, since the current density across the oxide film,  $i_{of}$ , is equal to the current density for the oxygen evolution reaction across the double layer, it was argued that<sup>7</sup>

$$i = i_{of} = X \exp \left[ \frac{F\Delta V_{of}}{RT} \right] = A \exp \left[ \frac{F\Delta V_{dl}}{RT} \right] \quad [13]$$

In this work,  $X$  contained the dependence of the catalytic activity on the thickness of the oxide film.  $X$  was assumed constant only for a given, strictly controlled pretreatment of the electrodes and only when the  $V$ - $i$  measurements were made at current densities or potentials lower than those at which the electrode was anodically pretreated. It was contended that the observed current density  $i = i_{of} = i_{dl}$  should be given in terms of the total potential difference,  $V_t$ , by the following equation

$$i = (AX)^{1/2} \exp \left[ \frac{F\Delta V_t}{2RT} \right] \quad [14]$$

Now, from this equation and from Eq. [9] of the present work it becomes possible to express  $X$  in terms of the thickness of the oxide film

$$X = X_0 \exp (-\delta d) \quad [15]$$

and thus, the expression for the current density across the oxide film can be written as

$$i_{of} = X_0 \exp (-\delta d) \exp \left[ \frac{F\Delta V_{of}}{RT} \right] \quad [16]$$

This rate expression represents a basis for the study of the mechanism of electron transfer through the surface oxide film. Such study is in progress and will be reported in subsequent publications.

#### Acknowledgment

The authors are grateful to Dr. M. L. Hair for valuable discussions of various topics in this paper. The assistance of E. Gray in making some of the ellipsometric measurements is also gratefully acknowledged.

Manuscript received Dec. 3, 1973. This was Paper 326 presented at the San Francisco, California, Meeting of the Society, May 12-17, 1974.

<sup>7</sup> In this expression  $X$  replaces  $A$  of Ref. (1) and  $A$  replaces  $Bc^{-1}$  of Ref. (1) since pH dependence of the reaction is not considered in the present work.



Any discussion of this paper will appear in a Discussion Section to be published in the June 1975 JOURNAL. All discussions for the June 1975 Discussion Section should be submitted by Feb. 1, 1975.

The publication costs of this article have been assisted by the Xerox Corporation.

## APPENDIX

Equation [5] is obtained by solving the determinant of the coordinates of three points in the plane  $f(V, \ln i, d) = \text{constant}$ . The determinant includes the coordinates  $(V, \ln i, d)$  of point A in Fig. 6 (at the intersection of lines AB, AD) and the coordinates of a point in AB and a point in AD each removed from point A by one  $\ln$  unit of current density, i.e.

$$\begin{vmatrix} V & \ln i & d \\ V - \frac{2RT}{F} & \ln i - 1 & d \\ V - \kappa & \ln i - 1 & d - \epsilon \end{vmatrix} = \text{constant}$$

This transforms to

$$\epsilon V = \frac{2RT\epsilon}{F} \ln i + \left(1 - \frac{\kappa F}{2RT}\right) d = \text{constant}$$

## REFERENCES

1. A. Damjanovic and B. Jovanovic, To be published.
2. J. O'M. Bockris and A. K. M. S. Huq, *Proc. Roy. Soc. Ser. A*, **237**, 227 (1956).
3. A. Damjanovic, A. Dey, and J. O'M. Bockris, *Electrochim. Acta.*, **11**, 791 (1966).
4. W. Visscher and M. A. V. Devanathan, *J. Electroanal. Chem.*, **8**, 127 (1964).
5. G. N. Afon'shin, G. F. Volodin, and Yu. M. Tyurin, *Elektrokhimiya*, **7**, 1338 (1971).
6. J. P. Hoare, *This Journal*, **112**, 602 (1965).
7. Y. C. Chiu and M. A. Genshaw, *J. Phys. Chem.*, **73**, 3571 (1969).
8. P. Drude, *Wied. Ann. Phys.*, **39**, 481 (1890).
9. S. H. Kim, W. K. Paik, and J. O'M. Bockris, *Surface Sci.*, **33**, 617 (1972).
10. W. Visscher, *Optik*, **26**, 407 (1967).
11. A. K. N. Reddy, M. A. Genshaw, and J. O'M. Bockris, *J. Chem. Phys.*, **48**, 671 (1968).
12. R. Parsons and W. Visscher, *J. Electroanal. Chem.*, **36**, 329 (1972).
13. H. A. Laitinen and C. G. Enke, *This Journal*, **107**, 773 (1960).
14. S. Gilman, *Electroanal. Chem.*, **2**, 111 (1967).
15. K. J. Vetter and J. W. Schultze, *ibid.*, **34**, 141 (1972).
16. T. P. Hoar, *Proc. Roy. Soc. Ser. A*, **142**, 628 (1933).
17. T. Erdey-Grúz and O. Golopencza-Bajor, *Acta Chim. Acad. Sci. Hung.*, **34**, 281 (1962).
18. S. Schuldiner, T. B. Warner, and B. J. Piersma, *This Journal*, **114**, 343 (1967).
19. E. I. Krushcheva, O. V. Morovskaya, N. A. Shumilova, and V. S. Bagotskii, *Elektrokhimiya*, **8**, 205 (1972).
20. I. I. Pyshnograeva, A. M. Skundin, Yu. B. Vasilev, and V. S. Bogotskii, *ibid.*, **6**, 142 (1972).
21. J. W. Schultze, *Z. Phys. Chem.*, **73**, 29 (1970).
22. A. C. Makrides, *This Journal*, **113**, 1158 (1966).
23. J. O'M. Bockris, M. A. Genshaw, and V. Brusica, *Symp. Faraday Soc.*, **4**, 177 (1970).
24. N. Sato and M. Cohen, *This Journal*, **111**, 512 (1964).

## Technical Notes



### Morphology of Transgranular Stress Corrosion Crack in Type 304 Stainless Steel Tested in pH 2.5 H<sub>2</sub>SO<sub>4</sub> at 289°C

David A. Vermilyea\*

Corporate Research and Development, General Electric Company, Schenectady, New York 12301

In a previous paper (1) it was reported that annealed as well as cold-worked Type 304 stainless steel was susceptible to transgranular stress corrosion cracking in pH 2.5 H<sub>2</sub>SO<sub>4</sub> at 289°C. The purpose of this note is to present and discuss some unique fractographs which have been obtained from similar tests.

The material used contained 18.3 Cr, 9.3 Ni, 0.045 C, 0.5 Mn, 0.018 P, 0.006 S, 0.43 Si, 0.15 Mo, 0.32 Cu, and 0.088 Co, in weight per cent. Before testing the 0.050 in. wire was electropolished and then notched (30° angle, 0.001 in. root radius, 0.020 in. deep). The test was conducted at a constant crosshead speed of 10<sup>-5</sup> in./min using the apparatus previously described (1), with a potential controlled at zero volts vs. a standard hydrogen electrode. The fracture load was about half the value obtained in a test in air. Test details may be found in the earlier paper (1).

Figures 1-5 show scanning electron micrographs of a typical fracture at several magnifications. In all figures the direction of crack propagation is from

the bottom to the top of the photograph. The fan-shaped areas containing marks roughly parallel to the crack propagation direction are reminiscent of similar features on fractographs produced in boiling MgCl<sub>2</sub> or in H<sub>2</sub>SO<sub>4</sub>-NaCl solutions (2). The unique feature of these fractographs is the pronounced set of striations roughly perpendicular to the crack propagation direction. (The small particles thinly spread over the surface are iron oxide produced by oxidation of ferrous ions in solution.)

In a recent discussion of these photographs Professor Pugh of the University of Illinois pointed out that the marks which run roughly parallel to the crack propagation direction differ from cleavage steps in being very jagged. It can be seen that the irregularities in these marks frequently occur at places where the striations cross them.

It is believed that the striations represent positions at which the crack stopped temporarily during its propagation. Crack propagation is believed to occur by a film rupture mechanism (3, 4), with repeated periods of rapid corrosion and repassivation. Corrosion may leave surfaces which are bounded by certain crystallo-

\* Electrochemical Society Active Member.  
Key words: stress corrosion, fractography, stainless steel, striations.

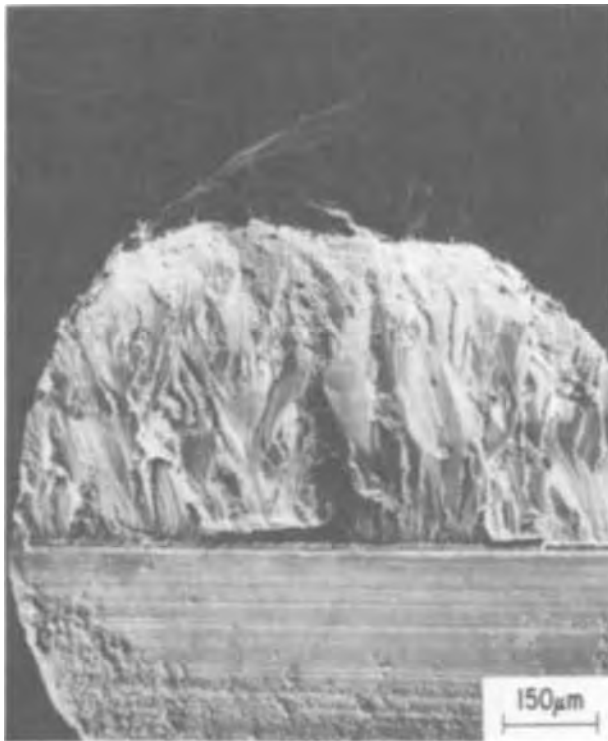


Fig. 1. SEM fractograph of the sample at low magnification; the lower half shows the notch surface.



Fig. 3. Same as Fig. 2



Fig. 2. Area about half-way from notch to outer edge

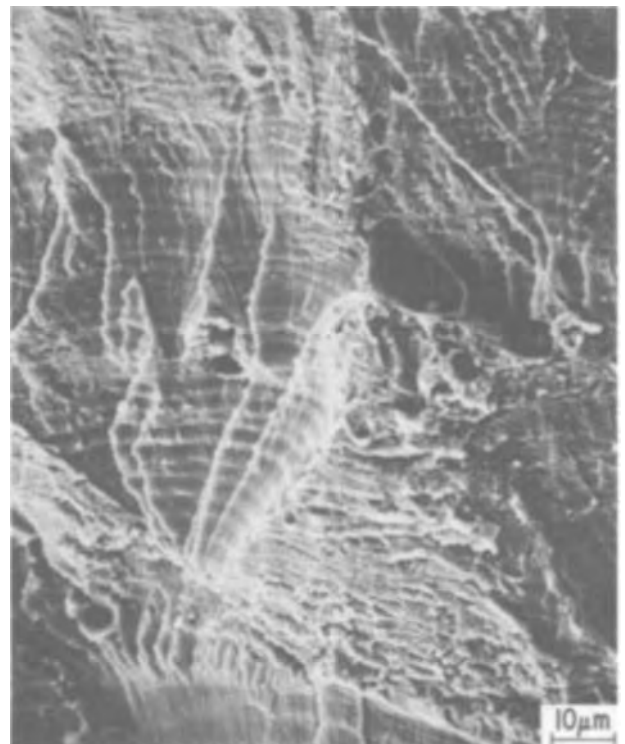


Fig. 4. Area near the outer edge

graphic planes. The marks parallel to the crack propagation direction may then be formed by tearing of material at steps between the crystallographically corroding surfaces, in a manner similar to the way cleavage steps are produced. During crack arrest the striations may be produced by crack blunting due to creep or by continued localized corrosion accompanying the full development of the passive film.

Support for such an interpretation of the fractographs can be obtained from a consideration of the striation spacing. Figure 5 shows that the finest striations are separated by only about  $1-2 \times 10^{-5}$  cm. In a recent paper Vermilyea and Diegle (4) show that the ratio of metal corrosion rate ( $\dot{l}$ ) to the strain rate ( $\dot{\epsilon}$ ) of material being corroded while being continuously strained is roughly equal to the crack advance per film rupture event. This ratio of  $\dot{l}/\dot{\epsilon}$  was measured under the conditions of this test using a smooth specimen and a crosshead speed of 0.05 in./min, and was found to

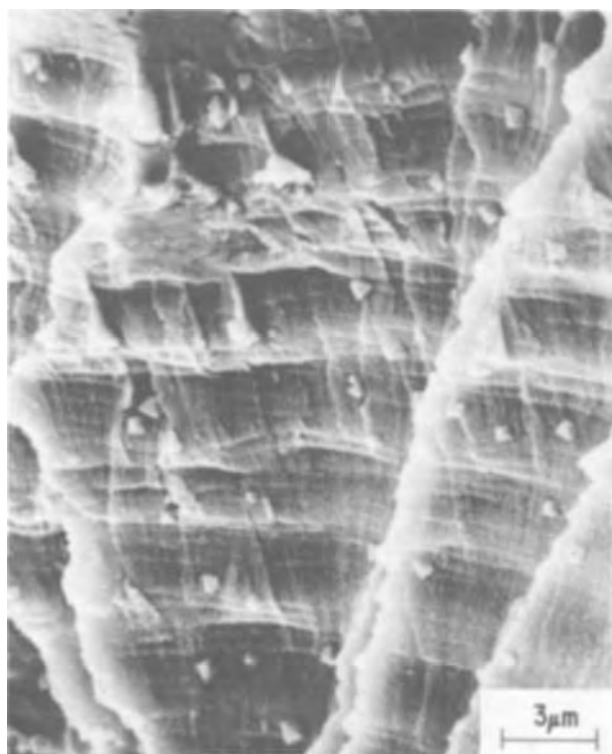


Fig. 5. Same as Fig. 4

be  $2.6 \times 10^{-5}$  cm, in reasonable agreement with the striation spacing.

**Acknowledgments**

The stress-corrosion testing was performed by D. E. Broecker. Fractographs were taken by the Materials Characterization Operation of this laboratory.

Manuscript received April 4, 1974.

Any discussion of this paper will appear in a Discussion Section to be published in the June 1975 JOURNAL. All discussions for the June 1975 Discussion Section should be submitted by Feb. 1, 1975.

The publication costs of this article have been assisted by the General Electric Company.

**REFERENCES**

1. D. A. Vermilyea, *Corrosion*, **29**, 442 (1973).
2. J. C. Scully, "The Theory of Stress Corrosion Cracking in Alloys," p. 127, NATO, Brussels (1971).
3. D. A. Vermilyea, Paper presented at Conference on Stress Corrosion Cracking and Hydrogen Embrittlement of Iron Base Alloys, Firminy, France, 1973, To be published.
4. D. A. Vermilyea and R. B. Diegle, Submitted to *Corrosion*.

## Pitting Resistance of 18% Cr Ferritic Stainless Steels Containing Molybdenum

R. J. Brigham and E. W. Tozer

*Endako Mines Limited, Molybdenum Research, Ottawa, Ontario, Canada*

The pitting resistance of ferritic stainless steel and the effect of Mo content on pitting characteristics at various temperatures have been discussed recently in terms of pitting potentials (1). An alternative approach using temperature as a pitting criterion has been successfully applied to Mo-bearing 18% Cr austenitic stainless steels (2, 3) and appears to be applicable in clarifying the behavior of 18% Cr ferritic stainless steels as well.

It has been shown for austenitic stainless steel that there exists a temperature, which we have called the critical pitting temperature (CPT), below which a steel will not pit when exposed to oxidizing acid chloride solution such as 10% FeCl<sub>3</sub>. An exposure time of 24 hr in this solution has been shown to be sufficient for pit initiation if pitting is to occur at that temperature. For example, an austenitic steel with a CPT of 40°C has been exposed at room temperature varying between 20° and 36°C for more than 600 days and has not initiated pits in that time. The initiation and growth of pits in 10% FeCl<sub>3</sub> solution at a fixed temperature must occur on the flat surface parallel to the rolling plane well removed from the edges of the coupon for the test results to be valid. Crevice, edge, or end-grain attack which may occur at temperatures below CPT are disregarded in judging whether attack by pitting has occurred after exposure at a particular temperature. The test temperature is increased in 2.5°C steps every 24 hr until pitting occurs.

**Key words:** pitting, corrosion, temperature.

In tests below room temperature, care is taken to pre-chill samples before exposure to avoid spurious results.

The series of commercial (AISI 430 and Alloy X) and experimental alloys (Alloys Q, R, S, and T) listed in Table I in order of increasing Mo content have been tested. The experimental alloys were made by a split heat technique, rolled to sheet, annealed for 1 hr at 840°C and furnace cooled. The commercial alloys were tested in the as-received annealed condition. Surface preparation consisted of abrading with 120 grit SiC paper as in the previous studies on austenitic steels (2, 3). The results are plotted in Fig. 1 as CPT vs. per cent Mo using error bars. For each alloy, pitting was not observed at the temperature indicated by the left-hand side of the bar while the right-hand side indicates that temperature (2.5°C higher) at which pitting was observed. The data can be described em-

**Table I. Chemical analyses (weight per cent)**

Alloy	Cr	C	Mn	Si	P	S	Mo	Other
AISI 430	14-18	0.12*	1.0*	1.0*	0.040*	0.030*	nil	
Alloy Q	17.38	0.06	0.80	0.42	0.013	0.018	nil	
Alloy R	17.3†	0.06†	0.80†	0.42†	0.013†	0.018†	0.70	
Alloy S	17.2†	0.06†	0.80†	0.42†	0.013†	0.018†	1.48	
Alloy X	18.95	0.009	0.40	0.37	0.008	0.007	2.00	0.17 Ti
Alloy T	17.1†	0.06†	0.80†	0.42†	0.013†	0.018†	3.11	

\* Denotes maximum value.

† Denotes values estimated from base composition of Alloy Q.

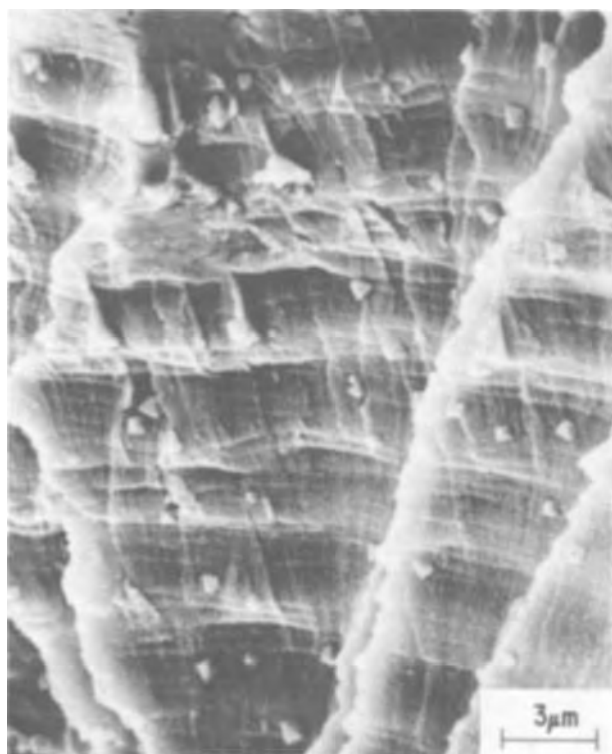


Fig. 5. Same as Fig. 4

be  $2.6 \times 10^{-5}$  cm, in reasonable agreement with the striation spacing.

**Acknowledgments**

The stress-corrosion testing was performed by D. E. Broecker. Fractographs were taken by the Materials Characterization Operation of this laboratory.

Manuscript received April 4, 1974.

Any discussion of this paper will appear in a Discussion Section to be published in the June 1975 JOURNAL. All discussions for the June 1975 Discussion Section should be submitted by Feb. 1, 1975.

The publication costs of this article have been assisted by the General Electric Company.

**REFERENCES**

1. D. A. Vermilyea, *Corrosion*, **29**, 442 (1973).
2. J. C. Scully, "The Theory of Stress Corrosion Cracking in Alloys," p. 127, NATO, Brussels (1971).
3. D. A. Vermilyea, Paper presented at Conference on Stress Corrosion Cracking and Hydrogen Embrittlement of Iron Base Alloys, Firminy, France, 1973, To be published.
4. D. A. Vermilyea and R. B. Diegle, Submitted to *Corrosion*.

## Pitting Resistance of 18% Cr Ferritic Stainless Steels Containing Molybdenum

R. J. Brigham and E. W. Tozer

*Endako Mines Limited, Molybdenum Research, Ottawa, Ontario, Canada*

The pitting resistance of ferritic stainless steel and the effect of Mo content on pitting characteristics at various temperatures have been discussed recently in terms of pitting potentials (1). An alternative approach using temperature as a pitting criterion has been successfully applied to Mo-bearing 18% Cr austenitic stainless steels (2, 3) and appears to be applicable in clarifying the behavior of 18% Cr ferritic stainless steels as well.

It has been shown for austenitic stainless steel that there exists a temperature, which we have called the critical pitting temperature (CPT), below which a steel will not pit when exposed to oxidizing acid chloride solution such as 10% FeCl<sub>3</sub>. An exposure time of 24 hr in this solution has been shown to be sufficient for pit initiation if pitting is to occur at that temperature. For example, an austenitic steel with a CPT of 40°C has been exposed at room temperature varying between 20° and 36°C for more than 600 days and has not initiated pits in that time. The initiation and growth of pits in 10% FeCl<sub>3</sub> solution at a fixed temperature must occur on the flat surface parallel to the rolling plane well removed from the edges of the coupon for the test results to be valid. Crevice, edge, or end-grain attack which may occur at temperatures below CPT are disregarded in judging whether attack by pitting has occurred after exposure at a particular temperature. The test temperature is increased in 2.5°C steps every 24 hr until pitting occurs.

**Key words:** pitting, corrosion, temperature.

In tests below room temperature, care is taken to pre-chill samples before exposure to avoid spurious results.

The series of commercial (AISI 430 and Alloy X) and experimental alloys (Alloys Q, R, S, and T) listed in Table I in order of increasing Mo content have been tested. The experimental alloys were made by a split heat technique, rolled to sheet, annealed for 1 hr at 840°C and furnace cooled. The commercial alloys were tested in the as-received annealed condition. Surface preparation consisted of abrading with 120 grit SiC paper as in the previous studies on austenitic steels (2, 3). The results are plotted in Fig. 1 as CPT vs. per cent Mo using error bars. For each alloy, pitting was not observed at the temperature indicated by the left-hand side of the bar while the right-hand side indicates that temperature (2.5°C higher) at which pitting was observed. The data can be described em-

**Table I. Chemical analyses (weight per cent)**

Alloy	Cr	C	Mn	Si	P	S	Mo	Other
AISI 430	14-18	0.12*	1.0*	1.0*	0.040*	0.030*	nil	
Alloy Q	17.38	0.06	0.80	0.42	0.013	0.018	nil	
Alloy R	17.3†	0.06†	0.80†	0.42†	0.013†	0.018†	0.70	
Alloy S	17.2†	0.06†	0.80†	0.42†	0.013†	0.018†	1.48	
Alloy X	18.95	0.009	0.40	0.37	0.008	0.007	2.00	0.17 Ti
Alloy T	17.1†	0.06†	0.80†	0.42†	0.013†	0.018†	3.11	

\* Denotes maximum value.

† Denotes values estimated from base composition of Alloy Q.

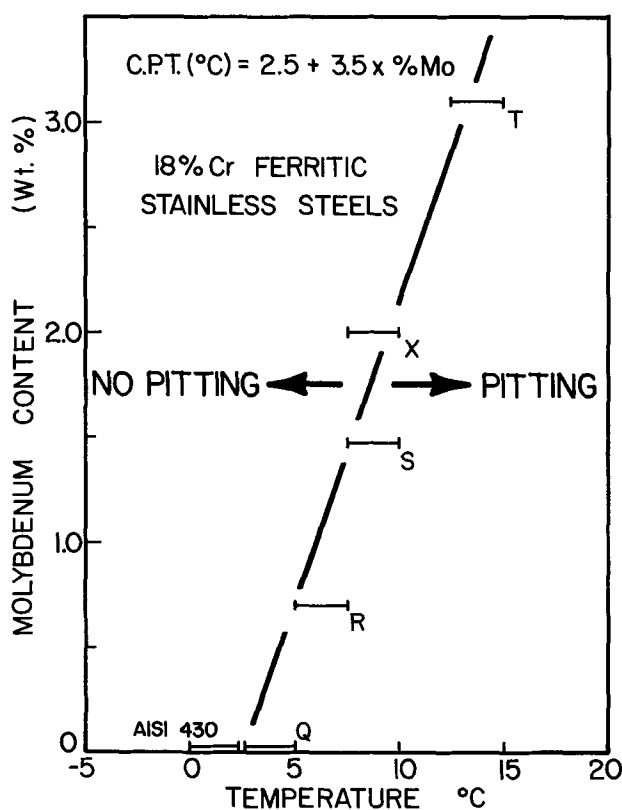


Fig. 1. Critical pitting temperature as a function of Mo content for a series of commercial and experimental 18% Cr ferritic stainless steels.

pirically by

$$CPT (°C) = 2.5 + 3.5 \times \% Mo$$

It can be seen that the pitting resistance increases continuously with increasing Mo content over the range nil to 3% Mo.

The Mo response of these 18% Cr ferritic alloys is only approximately  $\frac{1}{2}$  that for a comparable family of 18% Cr austenitic steels (3) for which

$$CPT (°C) = 5 + 7 \times \% Mo$$

but is entirely consistent with the reduced thermodynamic activity of Mo in ferritic phases. A measure of this lower Mo activity in the ferritic phase is given by the high-temperature partition of Mo between phases to achieve equal thermodynamic activities at equilibrium. A ferritic/austenitic partition ratio of approximately 2 has been observed for molybdenum in duplex stainless steels (4, 5).

#### Acknowledgments

The cooperation of the Physical Metallurgy Division, Department of Energy, Mines and Resources in making their facilities available and helpful discussions with Dr. G. J. Bieffer (Head) and Dr. J. B. Gilmour (Research Scientist) of the Corrosion Section, Physical Metallurgy Division, are gratefully acknowledged. The experimental ferritic alloys were supplied through the good offices of Dr. Bieffer.

Manuscript submitted Feb. 1, 1974; revised manuscript received May 3, 1974.

Any discussion of this paper will appear in a Discussion Section to be published in the June 1975 JOURNAL. All discussions for the June 1975 Discussion Section should be submitted by Feb. 1, 1975.

The publication costs of this article have been assisted by Endako Mines Limited.

#### REFERENCES

1. A. P. Bond, *This Journal*, **120**, 603 (1973).
2. R. J. Brigham and E. W. Tozer, *Corrosion*, **29**, 33 (1973).
3. R. J. Brigham and E. W. Tozer, *Corrosion*, **30**, 161 (1974).
4. R. A. Daemen and F. Dept, *Welding Research Supplement*, 33s-40s (1970).
5. R. J. Brigham and E. W. Tozer, *Can. Met. Quarterly*, **12**, 171 (1973).

## Erratum

In the paper "Activities of Organic Compounds in Aqueous Electrolyte Solutions" by D. M. Mohilner, L. M. Bowman, S. J. Freeland, and H. Nakadomari which appeared on pp. 1658-1662 in the December 1973 JOURNAL, Vol. 120, No. 12, there were three errors in the drawing of the circuit diagram (Fig. 4, p. 1660). One of these errors was major and would render the circuit as drawn inoperable. This major error is that operational amplifier OA7 was shown connected as an

inverting amplifier. OA7 is actually connected as a noninverting amplifier just as is OA6. The other two errors in the drawing are as follows: (i) There should be a 10K resistor connected between the output of OA2 and the terminal labeled integrator out. (ii) The resistor labeled 100 SL on the drawing is actually a 100 ohm resistor. A corrected version of Fig. 4 is shown below.

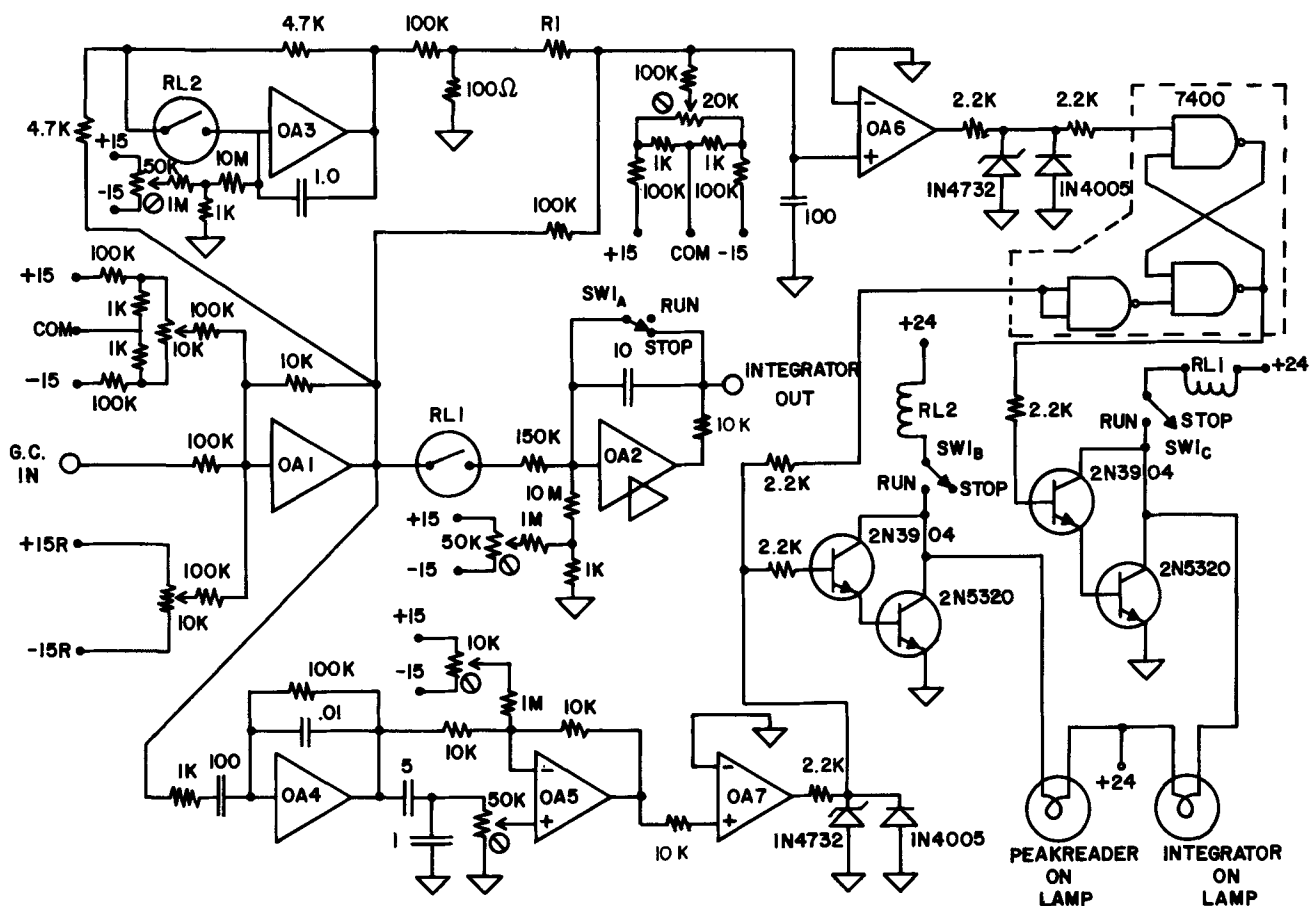


Fig. 4. Circuit diagram of integrator control circuit. The operational amplifiers used are: OA1, Philbrick 1020; OA2, Philbrick 1700, chopper stabilized; OA3, Philbrick 1023; OA4 and OA5, Philbrick S<sub>q</sub>10A and OA7, Model 741.



## Sodium-Induced Barrier-Height Lowering and Dielectric Breakdown on SiO<sub>2</sub> Films on Silicon

C. M. Osburn\* and D. W. Ormond\*

IBM Thomas J. Watson Research Center, Yorktown, Heights, New York 10598

### ABSTRACT

Electrical conduction measurements in SiO<sub>2</sub> films showed that the injecting barrier height was uniformly reduced by a small amount (<1 eV) in proportion to the level of Na contamination. However, at high contamination levels (>10<sup>13</sup> Na<sup>+</sup>/cm<sup>2</sup>) after bias-temperature stressing, a very substantial (≈3 eV), localized barrier lowering was observed. Since this second type of lowering was eliminated after exposure of the film to moisture (in air) and was also seen in uncontaminated samples, it was not attributed to sodium. Accelerated dielectric breakdown measurements at low fields (<2 MV/cm) showed that even a monolayer of Na did not appreciably decrease the wear-out time. Moderately contaminated samples (5 × 10<sup>12</sup> Na<sup>+</sup>/cm<sup>2</sup>) had the same limiting failure times as controls over the temperature range 100°-400°C.

It has been recognized (1) for some time that mobile ions in MOSFET structures lead to threshold voltage shifts. Recently Raider (2) and Osburn and Raider (3) have shown that mobile ions can also lead to a time-dependent dielectric breakdown of a thermally grown SiO<sub>2</sub> film. The electric field due to the charged ions adds to the applied field and causes premature failure. Internal photoemission measurements of DiStefano (4, 5) have revealed another possible breakdown mechanism due to mobile ions: lowering of the height of the injecting barrier resulting in distinctively high conduction levels. But electrical measurements (6) of sodium-free (<10<sup>10</sup>/cm<sup>2</sup>) SiO<sub>2</sub> films prior to breakdown have also shown a large, localized barrier-height lowering. The purpose of this work was to more fully determine the extent of barrier-height lowering due to sodium ions and the effect, with regard to dielectric breakdown, of mobile charge on long term reliability.

Electrical conduction data showing two different types of barrier-height lowering are presented. One component occurred uniformly, was relatively small (≈1 eV), and can be attributed to dipole lowering due to sodium; the second component was large (≈3 eV), localized (≈25Å channels), and is not believed to be due to sodium. This second type of lowering was the same as that seen earlier (6) in uncontaminated samples where it was believed responsible for dielectric breakdown. Measurements of the time interval before breakdown of Na-contaminated examples are also given which do not support the contention that barrier lowering caused by Na ions is responsible for breakdown. Indeed, at typical FET operating fields (2 MV/cm) tests showed that even a monolayer of sodium did not accelerate wear-out.

### Experimental Procedure

Metal-oxide-semiconductor capacitors were fabricated on 2 ohm-cm, n-type, <100>-oriented silicon

\* Electrochemical Society Active Member.

Key words: dielectric breakdown, silicon dioxide, sodium contamination, barrier-height lowering, electrical conduction.

wafers as previously described (3). The silicon dioxide growth was at 1000°C in dry oxygen. Contamination was introduced by evaporating a small amount of NaCl onto the freshly oxidized surface. Aluminum capacitor dots were then evaporated through metal masks. Contamination levels were measured with either the capacitance-voltage flatband shift (1) or the charge-time (Q-t) technique (7). Uncontaminated samples typically had less than 10<sup>10</sup> mobile ions/cm<sup>2</sup> as measured by the triangular voltage sweep (TVS) technique (8).

Both the time to breakdown at constant field and the time dependence of the conduction were determined for contamination levels from less than 10<sup>10</sup> Na<sup>+</sup>/cm<sup>2</sup> to greater than 10<sup>15</sup>/cm<sup>2</sup>. Because large pre-breakdown currents were often seen, the main criterion for the occurrence of dielectric breakdown was an irreversible, step jump in current. A special high-temperature measuring cell, filled with dry nitrogen, was used to insure against stray leakage. The metal was biased positively in all cases in order to drive the sodium to the Si/SiO<sub>2</sub> interface and also to inject electrons from the silicon into the SiO<sub>2</sub>. The electric fields used in this work were low enough so that field enhancement breakdown did not occur (3). Barrier heights were inferred from room-temperature conduction measurements assuming Fowler-Nordheim emission (9). In cases where the calculated barrier height was low, it was recalculated assuming Schottky emission.

### Results and Discussion

**Conduction and barrier-height lowering.**—The conduction current as a function of time for several different temperatures is given in Fig. 1. At room temperature when a bias voltage is applied, the current increased with time until a maximum was obtained, and then decreased (3). This maximum has been explained in terms of the sodium being at an optimal distance (≈30Å) from the Si/SiO<sub>2</sub> interface (10). As the ions moved closer to the silicon, the tunneling distance would increase and hence the current decreased.

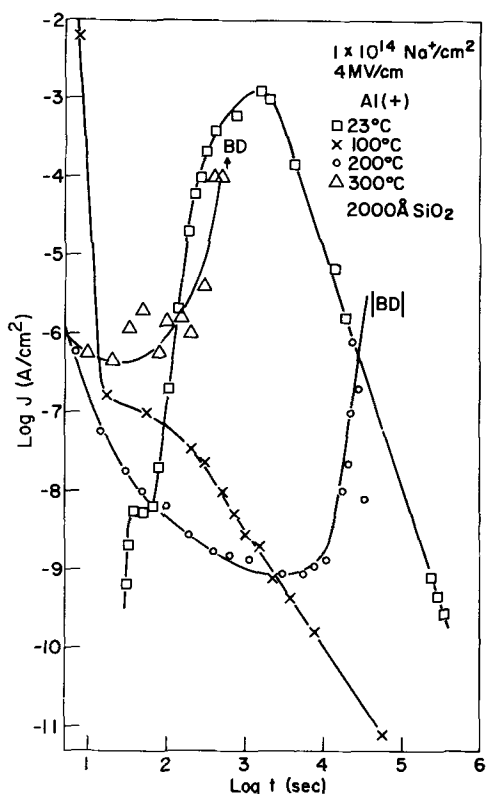


Fig. 1. Current at a fixed electric field as a function of time for several different temperatures.

A minor peak was seen in the current after a very short time and can probably be attributed to the sodium ionic current. At 100°C the ionic decay largely occurred in the first 10 sec (under the conditions of Fig. 1), and the maximum (corresponding to the sodium being about 30Å from the silicon) is seen only as a slope change. At 200° and 300°C a new effect, associated with barrier-height lowering, was seen: after the usual decay, the current increased with time until breakdown occurred. This enhanced current was usually quite erratic, as previously seen with noncontaminated samples (6). The time for the current enhancement to occur increased dramatically with decreasing electric field.

Room-temperature current-voltage characteristics of a capacitor after enhancement are given in Fig. 2. Characteristics of an uncontaminated sample are also shown for reference. Two components of barrier-height lowering are evident: At high fields the barrier was reduced from 3.1 to 2.6 eV and at lower fields the slope of a Fowler-Nordheim plot gave a 0.7 eV barrier. Values of barrier height were calculated from both the slope of the I-V curve and the magnitude of the current. Self-consistent barrier heights as low as 2.5 eV were observed. This compares with a theoretical limit (12) of 1.63 eV and a previously measured (4) value of 1.8 eV (which was not determined to be the absolute minimum obtainable). For barriers less than 2.5 eV, the data suggested that the lowering was localized.

The magnitude of the high-field uniform component of the barrier height after the sodium has been driven to the Si/SiO<sub>2</sub> interface is presented in Fig. 3 as a function of sodium concentration. A 1 MV/cm field was applied for 1 hr at 300°C, at which conditions charge-time measurements confirmed that the sodium drift was very nearly complete. That is, tests showed that the barrier lowering after 20 hr was not substantially greater than that after 1 hr at 300°C at 1 MV/cm. It should be noted, however, that C-V or Q-t measurements could not resolve the position of the sodium ions better than 10-20Å and therefore could not insure that

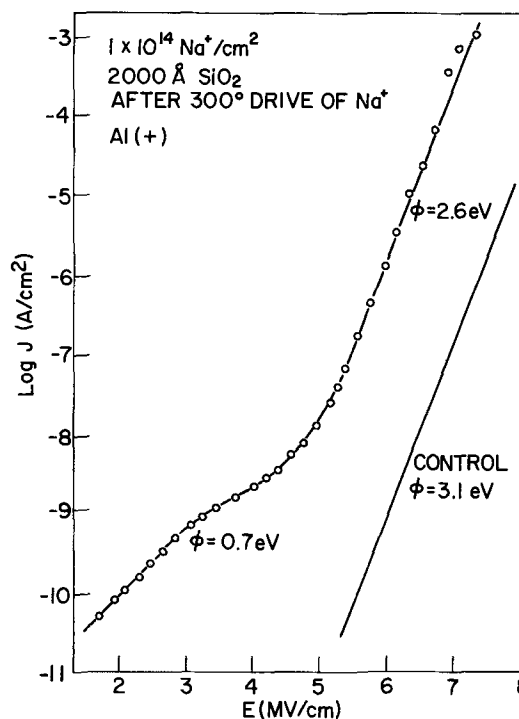


Fig. 2. Room-temperature I-V characteristics after current enhancement.

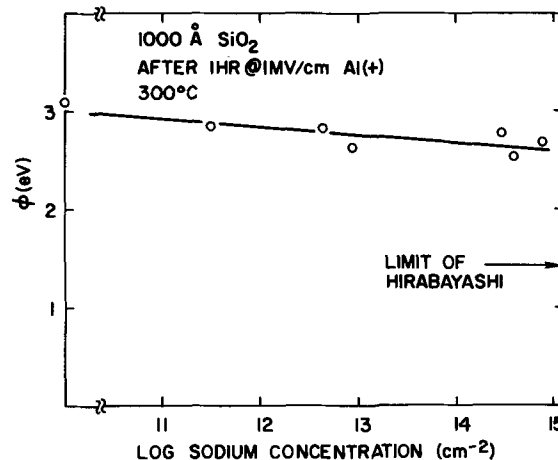


Fig. 3. Barrier height as a function of sodium concentration after bias-temperature stressing.

all the sodium was close enough to the silicon to contribute to barrier lowering.

An alternate analysis of the low-field data in terms of the Schottky conduction model also resulted in a low barrier height. The current density associated with this low barrier (~10 A/cm<sup>2</sup> at 2 MV/cm) is much higher than the average current density that was measured. This discrepancy in current densities could be resolved by (a) inferring that the low-field conduction was localized (25Å diameter channels) or (b) determining that neither the Fowler-Nordheim nor the Schottky mechanism provides a valid description of the conduction. All evidence to date, including data on uncontaminated samples (6), favors the localization model: (a) after enhancement the conduction was dependent on both polarity and electrode material as would be expected of either Fowler-Nordheim or Schottky conductor, (b) the temperature dependence of the conduction was not exponentially activated and was very similar to that seen with Fowler-Nordheim conduction in good SiO<sub>2</sub> films (9), and (c) scanning internal photoemission measurements of DiStefano (4) showed a localized barrier lowering.



The localized component of the barrier lowering is important since the very high current density ( $>1$  A/cm<sup>2</sup>) through this region is of the order of that required for thermal runaway (11) and breakdown. After the conduction enhancement has occurred at elevated temperature, contaminated samples exhibit the same kind of sensitivity to moisture as do uncontaminated samples (6). For example, exposure of the capacitor to room air for a few seconds resulted in a decrease of the current and an increase in the barrier height (often by as much as 2 eV). Locally low barrier heights and sensitivity to atmosphere are not unique to Na-contaminated capacitors but also occur in the purest films available. In uncontaminated samples, the barrier lowering cannot be removed by a reverse bias and hence is not attributed to a mobile species. Likewise, even though a reverse bias moved the sodium away from the Si-SiO<sub>2</sub> interface, measurements showed that the localized lowering remained present and thus was not due to the sodium.

At low measuring fields and higher sodium concentrations, barrier heights were often quite variable from one capacitor to another, and the values did not correlate well with the sodium concentration. It is apparent however that increasing the sodium concentration lowers the barrier and that above  $10^{13}$  Na<sup>+</sup>/cm<sup>2</sup> localization is likely. It also should be noted that barrier heights considerably lower than the 1.63 eV theoretical minimum (12) were observed. Such low barrier heights were also routinely seen (6) in uncontaminated samples and suggest a process more complex than simple barrier lowering due to sodium, e.g., crystallization.

**Dielectric breakdown.**—In order to assess the effect of sodium ions on dielectric integrity of SiO<sub>2</sub> films, breakdown times were obtained as a function of electric field for capacitors having up to  $10^{15}$  Na<sup>+</sup>/cm<sup>2</sup> (see Fig. 4). Breakdown times, of course, are statistical variables since defects in the dielectric cause premature failure (3,6). The maximum time to breakdown ( $t_{max}$ ) of a sampling (10-20 samplings) of MOS

capacitors was chosen for close examination since it was associated with the breakdown time of defect-free SiO<sub>2</sub>. At high electric fields, as Fig. 4 shows, high sodium contamination shortened the life of the capacitors. This is expected because of the field-enhancement from the sodium and is not necessarily related to any barrier-height lowering. At lower fields, like those normally encountered in FET operation, where breakdown might occur induced by barrier lowering, it is seen that even a monolayer of sodium did not shorten the lifetime by more than half an order of magnitude. This effect probably could also be attributed to the increased electric field in the oxide. Flatband voltage measurements (13) as a function of time, made on MOS capacitors having  $10^{12}$  Na<sup>+</sup>/cm<sup>2</sup>, have failed to detect any large scale, lateral, ion motion or neutralization of the sodium and thus eliminate these as mechanisms for improving the life of the contaminated samples.

The temperature dependence of the maximum time to failure (Fig. 5) shows that the wear-out process in SiO<sub>2</sub> films contaminated with  $5 \times 10^{12}$  Na/cm<sup>2</sup> had a  $1.4 \pm 0.2$  eV thermal activation energy from 100° to 400°C. The activation energy is identical to that reported for wear-out (6) and for interface state generation (14) in uncontaminated films. The sodium did not accelerate dielectric wear-out in these films.

Two different breakdown mechanisms have been postulated (6,9) for uncontaminated SiO<sub>2</sub> films depending on the measuring conditions. Normally, the breakdown in SiO<sub>2</sub> films is electronic in nature: electrons gain energy from the high applied field and then ionize centers in the dielectric (9). In this mode, the applied field and the trap ionization energy are important but the current density is secondary. Magnesium and gold injecting electrodes having barrier heights of 1.7 and  $>5$  eV, respectively, and showing at least a 10-decade difference in conduction, give the same MOS dielectric strength (9). After accelerated bias-temperature stressing, breakdown is believed to be thermal in nature (6). The generation of interface states at the injecting electrode lowers the barrier height enough so that an exceedingly high current flow

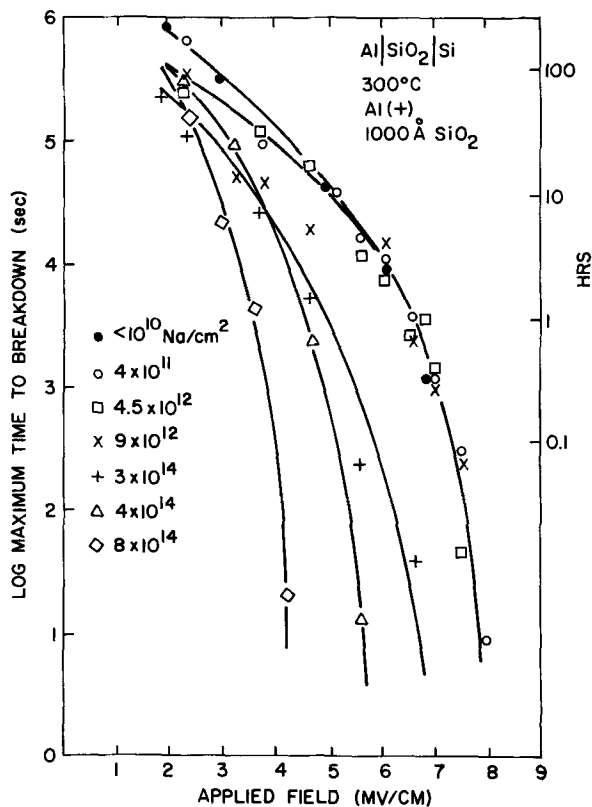


Fig. 4. Breakdown time as a function of electric field for different levels of mobile charge.

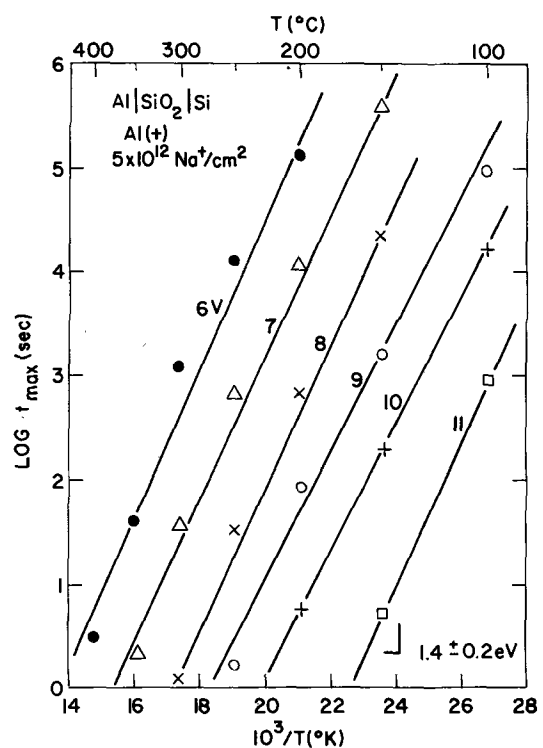


Fig. 5. Temperature dependence of maximum time to breakdown in a 175Å SiO<sub>2</sub> film contaminated with  $5 \times 10^{12}$  Na<sup>+</sup>/cm<sup>2</sup> for various applied voltages.

( $>>1$  A/cm<sup>2</sup>) can initiate thermal runaway. Localized barriers of about 0.5 eV have been frequently observed in uncontaminated films prior to breakdown (6); certainly a barrier height of less than 1 eV would be required to achieve such high current at low fields.

For sodium-related barrier-height lowering to initiate dielectric breakdown at low electric fields ( $<3$  MV/cm), the barrier must be lowered by at least 2 eV. Such a large change has not been observed to occur uniformly even with a monolayer of sodium. Based on this consideration, it is argued that Na-induced barrier-height lowering alone does not enhance uniform wear-out of SiO<sub>2</sub> films.

The localized effects of sodium cannot be ignored since the Na is not uniformly distributed (4, 5, 15) but presumably accumulates at some defect. Although locations of maximum barrier-height lowering and of dielectric breakdown have been correlated (5), the barrier lowering itself may not be the cause of the breakdown. Other mechanisms, notably crystallization (16) or field enhancement (2,3) due to Na trapped at oxide defects could equally well explain the observed correlation.

### Summary

Electrical conduction measurements in SiO<sub>2</sub> films have confirmed scanning internal photoemission findings (4, 5) that the Si-SiO<sub>2</sub> barrier height can be lowered (often locally) by the presence of sodium ions. With the low electric fields typically encountered in FET device operation, a monolayer of Na<sup>+</sup> contamination did not appreciably reduce the maximum time to failure. In addition, moderately contaminated ( $5 \times 10^{12}$  Na<sup>+</sup>/cm<sup>2</sup>) and clean ( $<10^{10}$  Na<sup>+</sup>/cm<sup>2</sup>) oxides had the same maximum failure times over the 100°-400°C range and for oxide thicknesses from 175 to 1000 Å. When the barrier lowering was uniform, its magnitude was less than 1 eV and well within the range observed by DiStefano (4, 5) and predicted by Hirabayashi (12), but yet was still too small to initiate high current and thermal runaway. In view of these findings, the causative relationship between localized barrier lowering and localized breakdown are questioned. Both

field enhancement (2, 3) from Na trapped at oxide defects and Na-induced crystallization (16) provide alternative explanations, but these were not tested in the present experiments.

### Acknowledgments

The authors would like to thank Drs. S. Raider, N. Chou, J. Eldridge, and T. DiStefano for helpful and stimulating discussions during the course of this work.

Manuscript submitted Sept. 17, 1973; revised manuscript received April 4, 1974.

Any discussion of this paper will appear in a Discussion Section to be published in the June 1975 JOURNAL. All discussions for the June 1975 Discussion Section should be submitted by Feb. 1, 1975.

The publication costs of this article have been assisted by the IBM Corporation.

### REFERENCES

1. E. H. Snow, A. S. Grove, B. E. Deal, and C. T. Sah, *J. Appl. Phys.*, **36**, 1664 (1965).
2. S. I. Raider, *Appl. Phys. Letters*, **23**, 24 (1973).
3. C. M. Osburn and S. I. Raider, *This Journal*, **120**, 1369 (1973).
4. T. H. DiStefano, *Appl. Phys. Letters*, **19**, 280 (1971).
5. T. H. DiStefano, *J. Appl. Phys.*, **44**, 257 (1973).
6. C. M. Osburn and N. J. Chou, *This Journal*, **120**, 1377 (1973).
7. W. A. Pliskin, D. A. Kerr, and J. A. Perri, "Physics of Thin Films," Vol. 4, pp. 257-324, Academic Press, Inc., New York (1967).
8. N. J. Chou, *This Journal*, **118**, 601 (1971).
9. C. M. Osburn and E. J. Weitzman, *ibid.*, **119**, 603 (1972).
10. D. R. Kerr, Private communication.
11. C. M. Osburn and D. W. Ormond, *This Journal*, **119**, 591 (1972).
12. K. Hirabayashi, *Phys. Rev.*, **B3**, 4023 (1971).
13. J. S. Logan and D. R. Kerr, Solid State Device Research Conference, Princeton, New Jersey, June 21-23, 1965.
14. A. Goetzberger, A. D. Lopez, and R. J. Strain, *This Journal*, **120**, 90 (1973).
15. D. J. Silversmith, *ibid.*, **119**, 1589 (1972).
16. R. L. Meek and R. H. Braun, *ibid.*, **119**, 1538 (1972).

## The Temperature and Oxygen Pressure Dependence of the Ionic Transference Number of Nonstoichiometric CeO<sub>2-x</sub>

G. J. VanHandel and R. N. Blumenthal

*Metallurgy and Materials Science, College of Engineering, Marquette University, Milwaukee, Wisconsin 53233*

### ABSTRACT

An electrochemical cell technique was used to measure the ionic transference number of sintered specimens of nonstoichiometric CeO<sub>2-x</sub> as a function of temperature (590°-1000°C) and oxygen partial pressure (1-10<sup>-22</sup> atm). The results were described in terms of a high and low oxygen pressure region. The ionic transference number is controlled by impurities in the high oxygen pressure region. In this region the electronic conductivity was p-type at lower temperature and n-type at higher temperatures. In the low oxygen pressure region the ionic transference number is small (e.g., above 700°C,  $t_i < 0.08$ ). The electrical conduction in this region is controlled by the nonstoichiometric defects and is predominantly electronic. Using the value of  $t_i \approx 0.05$ , an estimate of the diffusion coefficient for doubly ionized oxygen vacancies,  $D_{V_{O^{2-}}} \approx 3.5 \times 10^{-5}$  cm<sup>2</sup>/sec at 1000°C was calculated by combining recently obtained thermodynamic and conductivity data with the Nernst-Einstein relation.

Nonstoichiometric cerium dioxide, CeO<sub>2-x</sub>, has been the subject of several x-ray (1-4), thermodynamic (5-8), and electrical conductivity (9-16) investigations.

Key words: ionic conductivity, ionic transference number, diffusion coefficient.

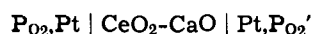
Based on these experimental observations, CeO<sub>2-x</sub> may be classified as a metal-excess, n-type semiconductor. In a recent thermodynamic study (8) the nonstoichiometric defect structure has been characterized in terms of defect model involving doubly ionized

oxygen vacancies,  $V_{O^{\bullet\bullet}}$ , and electrons localized on normal cerium atoms,  $Ce_{Ce^{\bullet}}$ . Although the electrical conduction at lower oxygen pressures has generally been assumed to be predominantly electronic (10, 14-16) there has not been any ionic transference measurements to verify this assumption.

The objective of this study was (i) to measure the ionic transference,  $t_i$ , of  $CeO_{2-x}$  as a function of oxygen partial pressure and temperature and (ii) to combine this data with electrical conductivity and thermodynamic data to obtain information about the oxygen vacancy diffusion coefficient,  $D_{V_{O^{\bullet\bullet}}}$ , in "pure"  $CeO_{2-x}$  and to compare these results with the recently reported values of  $D_{V_{O^{\bullet\bullet}}}$  for CaO-doped cerium dioxide (17).

### Theory

An oxygen concentration cell of the type



was used in this investigation to obtain ionic transference numbers of  $CeO_2$  as a function of  $P_{O_2}$  and temperature. The open-circuit emf of this cell for  $P_{O_2} \neq P_{O_2}'$  is given by the well-known expression

$$E_{meas} = (RT/nF)t_i \ln(P_{O_2}'/P_{O_2}) \quad [1]$$

where  $R$  is the universal gas constant,  $T$  the absolute temperature,  $n$  the number of electrical equivalents,  $F$  Faraday's constant, and  $t_i$  the ionic transference number. The subscript on  $E$  indicates that this is the measured emf. The theoretical or thermodynamic emf of a similar cell with a totally ionic electrolyte ( $t_i = 1$ ) is given by

$$E_{theo} = (RT/nF) \ln(P_{O_2}'/P_{O_2}) \quad [2]$$

If the ionic transference number does vary too much across the electrolyte then  $t_i$  is given by

$$t_i = E_{meas}/E_{theo} \quad [3]$$

The use of Eq. [3] requires that the electrodes act reversibly.

The diffusion coefficient of a nonstoichiometric defect may be determined by combining transport numbers data with the appropriate composition and electrical conductivity data. For example, in nonstoichiometric  $CeO_{2-x}$  the predominate defects are  $V_{O^{\bullet\bullet}}$  and  $Ce_{Ce^{\bullet}}$  (8). Thus the ionic conductivity,  $\sigma_i$ , may be represented by

$$\sigma_i = n_{V_{O^{\bullet\bullet}}} 2e\mu_{V_{O^{\bullet\bullet}}} \quad [4]$$

where  $n_{V_{O^{\bullet\bullet}}}$  is the concentration of oxygen vacancies per cubic centimeter,  $e$  the charge of an electron, and  $\mu_{V_{O^{\bullet\bullet}}}$  the mobility of a doubly ionized oxygen vacancy.

According to the Nernst-Einstein relation

$$D_{V_{O^{\bullet\bullet}}} = \frac{\mu_{V_{O^{\bullet\bullet}}} kT}{2e} \quad [5]$$

Combining Eq. [4] and [5] we obtain

$$\sigma_i = n_{V_{O^{\bullet\bullet}}} 4e^2 \frac{D_{V_{O^{\bullet\bullet}}}}{kT} \quad [6]$$

Since cerium dioxide exhibits a fluorite structure with eight oxygen and four cerium sites per unit cell, the concentration of oxygen vacancies may be related to the deviation from stoichiometry,  $x$ , in  $CeO_{2-x}$  by the expression

$$n_{V_{O^{\bullet\bullet}}} = \frac{4x}{a_0^3} \quad [7]$$

where  $a_0$  is the lattice parameter of  $CeO_{2-x}$

$$\sigma_i = \left( \frac{16e^2}{a_0^3} \right) \frac{x D_{V_{O^{\bullet\bullet}}}}{kT} \quad [8]$$

The conductivity may be calculated from the relation

$$\sigma_i = \sigma_T t_i \quad [9]$$

Combining Eq. [8] and [9] we obtain the following expression for the diffusion coefficient for oxygen vacancies

$$D_{V_{O^{\bullet\bullet}}} = \left( \frac{a_0^3}{16e^2} \right) \frac{kT}{x} \sigma_T t_i \quad [10]$$

Thus, if the transference number data is combined with the appropriate conductivity and composition data,  $D_{V_{O^{\bullet\bullet}}}$  may be calculated from Eq. [10].

### Experimental

Sintered polycrystalline disks were used for the electrolytes in the electrochemical cells. The "pure" cerium dioxide powder was obtained from the Trona Division of American Potash Corporation and was 99.99% pure with respect to other rare earths. The chemical analyses of the  $CeO_2$  powder are given in a previous publication (17). Disks were formed by cold pressing the  $CeO_2$  powder in a  $\frac{3}{4}$  in. diam steel die at approximately 32,000 psi. The green specimens were lightly scraped to remove material deposited on the specimens from the die walls. The disks were fired in flowing argon for 3 hr at 1600°C. Oxygen was introduced at 1300°C during cooling of the sintering furnace. The sintered bulk densities ranged from 80 to 90% of theoretical. The disks were ground to a final size of 13 mm diam by  $\sim 3.2$  mm thick using 180 grit silicon carbide polishing paper.

Pyrex rings were used to seal each electrolyte disk to the end of a  $\frac{1}{2}$  in. OD alumina tube. The rings which were approximately 1.5 mm thick were cut from  $\frac{1}{2}$  in. OD Pyrex tubing. Rubber cement which later burned off was used to hold the electrolyte disk and Pyrex ring in place for insertion into the cell assembly. The electrolyte disk, Pyrex ring, tube assembly was then heated to 1000°C *in situ*. The Pyrex ring softened sufficiently to produce a seal between the tube and disk such that the inside of the tube could be used as one of the electrode chambers.

The cell as used in this investigation is shown schematically in Fig. 1 and 2. The alumina tube with the electrolyte pellet was held in place by the large brass head and rested on a platinum mesh contact. This contact in turn rested on the flat bottom of a quartz support tube. The support tube was cemented to the large brass head. An O-ring compression fitting in the brass head formed a gas seal at the point where the electrolyte tube entered the head.

The electrode-gas atmosphere for the outer electrode was supplied through the brass head which also provided an exhaust exit. Gas atmospheres entering at the

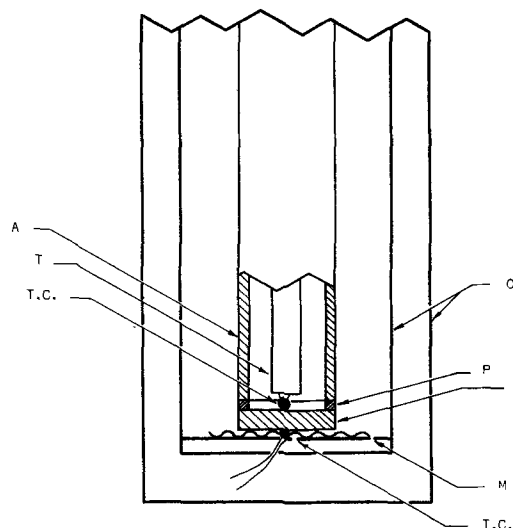


Fig. 1. Schematic detail of cell electrolyte area. A, alumina electrolyte tube; E, electrolyte; M, platinum mesh contact; P, Pyrex seal; Q, quartz tube; T, thermocouple insulator; T.C., Pt/Pt-13% Rh thermocouple.

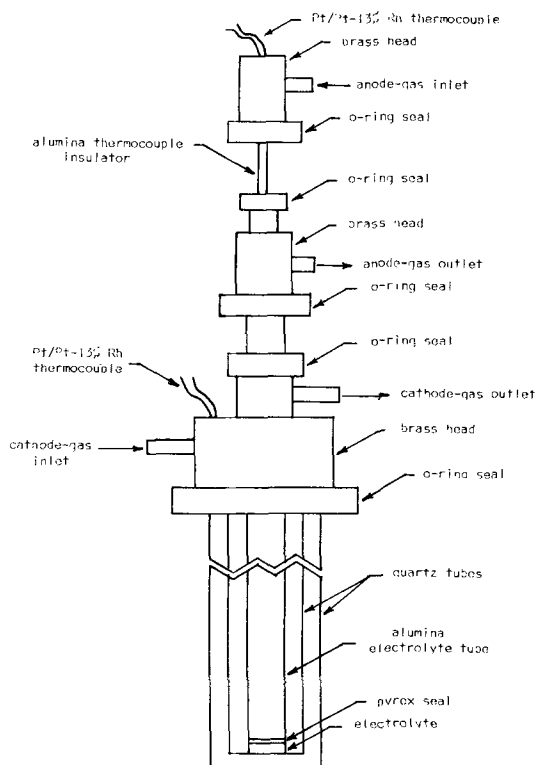


Fig. 2. Schematic of the electrochemical cell assembly

head passed down into the cell and around the outer surface of the electrolyte via a hole in the flat bottom of the quartz support tube.

A Pt/Pt-13% Rh thermocouple was used to measure the temperature at the outer electrode. The leads of this thermocouple passed through a two-hole Kovar seal in the large head. The platinum mesh contact was connected to the platinum lead of this thermocouple which served as the outer potential lead.

A smaller brass head, connected to the  $\frac{1}{2}$  in. alumina tube by means of another O-ring fitting, provided the gas exhaust for the inner electrode chamber and accepted a thermocouple insulator tube.

A third brass fitting on the inner thermocouple insulator was used to supply gas to the inner electrode chamber through the thermocouple insulator. The thermocouple leads exited through a 2-hole Kovar seal in this fitting with platinum lead of this Pt/Pt-13% Rh thermocouple serving as the potential lead for the inner electrode.

Both of the smaller brass fittings were spring-loaded to provide good physical contact between the thermocouple and electrolyte and between the platinum mesh and the electrolyte at all times during heating and cooling of the cell.

Mixtures of  $O_2$ -Ar and CO-CO<sub>2</sub> supplied prepurified, premixed, and analyzed by the Matheson Company were used for the electrode atmospheres. The  $O_2$ -Ar mixtures which ranged from 104 ppm  $O_2$  to pure  $O_2$  were checked with an oxygen gauge using a calcia-stabilized zirconia electrolyte. The oxygen contents as determined from use of the oxygen gauge were used in calculating experimental values of the ionic transference fractions. The CO-CO<sub>2</sub> mixtures ranged from 1000 ppm CO to 97% CO. The Matheson analyses were used in calculations involving these mixtures.

The gas flow rates were controlled by Matheson No. 602 rotometers. Systems of two 3-way glass stopcocks were used to route the gases to the inner and outer chambers as desired. A flow rate of approximately 280 cm<sup>3</sup>/min was used in both chambers.

The cells were heated in a Kanthal resistance furnace to a maximum temperature of 1000°C. The temperature was controlled to  $\pm 1^\circ\text{C}$  with Barber Coleman

Model 477 Capacitrol controllers and Barber Coleman Model 621 power controllers.

The cell emf's were measured with a Keithley Model 630 potentiometric electrometer. The negative lead to the electrometer was maintained at ground potential. All electrical grounds originated at this negative potential lead which was grounded through the electrometer. An electrically grounded Nichrome screen was used to shield the cell from electrical pickup from the furnace windings.

Several experimental observations led to the final cell design. Earlier designs used a gas inlet tube which was separate from the thermocouple insulator in the inner electrode chamber. The cell emf was observed to be a function of the anode-gas flow rate. This effect was more pronounced with the anode gas in the inner chamber. Negligible variations in the emf were observed when the cathode-gas flow rate was varied. This was independent of the chamber used as the cathode.

The emf variations with anode-gas flow rate could not be interpreted as a thermoelectric effect arising from cooling of the electrolyte surface because the change in magnitude of the emf was not consistent with the observed polarity of the thermoelectric power coefficient. Polarization due to insufficient removal rates of oxygen evolved at the anode was suspected as the source of the variations in the emf. To aid in oxygen removal the thermocouple insulator in the inner chamber was used to direct the incoming gas to the point of electrical contact. This procedure appeared to eliminate variations in the emf with gas flow which could not be explained on the basis of surface cooling at the anode. All subsequent measurements were performed with the anode gas in the inner electrode chamber. In addition, gas mixtures differing in oxygen pressure by 1 atm or less were used for any given determination to avoid polarization due to internal currents.

## Results

The ionic transference numbers of sintered specimens of  $CeO_{2-x}$  were measured isothermally at 100°C intervals between 590°-1000°C and from 1 to  $10^{-22}$  atm of oxygen. The results of the transference measurements are shown in Fig. 3: The set of two points at a given value of  $t_i$  corresponds to the two different oxygen pressures of the gas mixtures used to obtain that value of  $t_i$ . A smooth curve was drawn through the center of each set of points.

There are two oxygen pressure regions separated by a gap which widens with decreasing temperature. The data at higher oxygen pressures were obtained with  $O_2$ -Ar mixtures while those at lower oxygen pressures were obtained with CO-CO<sub>2</sub> mixtures. Oxygen pressures in the gap are unobtainable with these gas mixtures at a total pressure of 1 atm. Dashed lines have been drawn in Fig. 3 in an attempt to show how the transition in  $t_i$  from high to low oxygen pressures might look.

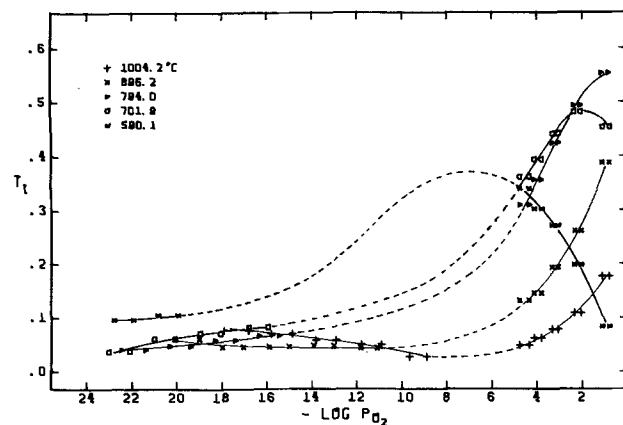
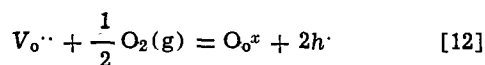


Fig. 3. Isothermal  $t_i$  vs.  $\log P_{O_2}$  for pure  $CeO_2$

For purposes of discussion the  $P_{O_2}$  dependence of  $t_i$  may be described in terms of two oxygen pressure regions.

Region 1: At high oxygen partial pressure (i.e.,  $1-10^{-4}$  atm obtained with  $O_2$ -Ar mixtures) the electrical conductivity has been reported to be influenced by the impurities present in "pure"  $CeO_2$  (14, 15). In this region the deviation from stoichiometry is  $x < 10^{-4}$  which is of the same order of magnitude as the major impurity (e.g., Ca) (8, 15). Thus it appears that in this region  $t_i$  is probably controlled by defects created by Ca ion impurities. The presence of foreign Ca ion has been shown to produce oxygen vacancies in  $CeO_{2-x}$  (17). In similar oxide fluorite structures (e.g.,  $ThO_2$ ) it is believed that near stoichiometry, oxygen vacancies produced by  $y^{+3}$  ions result in the formation of holes according to the following defect reaction (18)



It is interesting to note that in Fig. 3 the shapes of the isotherms at 590°, 702°, and 794°C suggest possible maxima in  $t_i$  which shift to lower oxygen pressures with decreasing temperature. The observed maxima might correspond to a p to n transition where the electronic conductivity is a minimum. The ionic transference number would decrease from its maximum with increasing oxygen pressure because of the increasing importance of hole conductivity with increasing oxygen pressure (e.g., applying Le Chatelier's principle to Eq. [12]).

To determine the effect of temperature on  $t_i$  at higher oxygen pressures a plot of  $t_i$  vs.  $1/T$  at several isobars was made as shown in Fig. 4. This figure shows a maximum in  $t_i$  which shifts to higher temperatures with increasing oxygen pressure. Below ~610°C,  $t_i$  is increasing with decreasing oxygen pressure while the reverse behavior is observed above ~717°C. This behavior is in accord with electronic conductivity which is predominantly p-type at lower temperatures and higher oxygen pressures, and n-type at higher temperatures and lower oxygen pressures where the deviation from stoichiometry is larger (8).

Region 2: In the low oxygen pressure region the ionic transference number is small (e.g., above 700°C,  $t_i < 0.08$ ), thus electrical conduction in this region is predominately electronic. Recent thermodynamic and electrical conductivity studies have shown the predominant defects in this region of  $P_{O_2}$  and temperature are doubly ionized oxygen vacancies and electrons localized on normal cerium sites (8). The electronic conductivity has been shown to be a "hopping" type process where the electrons localized at normal cerium sites move to adjacent cerium sites under the influence of an electric field (19).

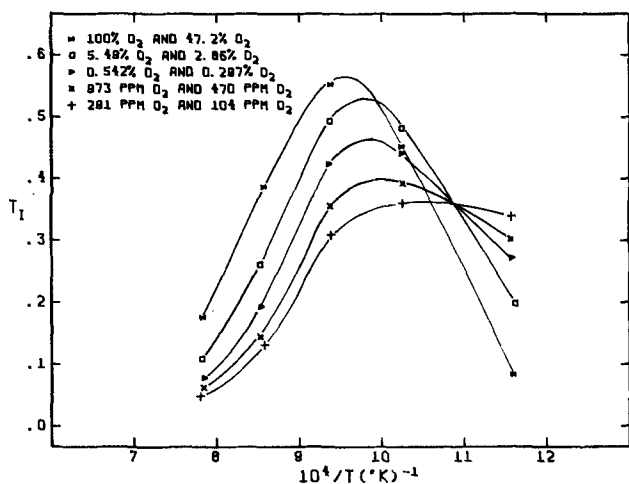


Fig. 4. Isobaric  $t_i$  vs.  $10^4/T$  for pure  $CeO_2$

To determine the effect of the deviation from stoichiometry,  $x$ , on  $t_i$  thermodynamic data (8) [i.e.,  $x = f(T, P_{O_2})$ ] was combined with the  $t_i$  data shown in Fig. 3. The combined data are limited to the temperature region 800°-1000°C and composition region  $x > 10^{-3}$  where the error in  $x$  is less than 4% (8). The results of these calculations are represented by isothermal plots of  $t_i$  vs.  $\log x$  as shown in Fig. 5. In the composition region  $10^{-3} < x < 10^{-2}$ , where the electronic (16) and ionic mobilities should be relatively independent of  $x$ ,  $t_i \approx 0.05$  is relatively constant with the exception of the data points at  $x \sim 10^{-3}$  where  $t_i \sim 0.066$  at 800°C and at 900°C where  $t_i \sim 0.028$ . At larger deviations from stoichiometry ( $x > 5 \times 10^{-2}$ )  $t_i$  appears to increase slightly with  $x$  at 900° and 1000°C. Because of the possibility of relatively large absolute errors in  $t_i$  (i.e., approximately 50% in the low oxygen pressure region) it is difficult to ascribe any particular significance to the apparent variation in  $t_i$  with  $x$  and temperature at this time. It is interesting to note, however, that Floyd and Steele (20) have reported the activation energies for diffusion of oxygen in  $CeO_{2-x}$  is about 4 kcal/mole when  $x \sim 0.2$  whereas in the near stoichiometric state,  $Q \approx 23$  kcal/mole.

Using the value of  $t_i \sim 0.05$  an estimate of the diffusion coefficient for doubly ionized oxygen vacancies,  $D_{V_{O^{\bullet\bullet}}} \approx 3.5 \times 10^{-5}$  cm<sup>2</sup>/sec at 1000°C was calculated by combining recently obtained thermodynamic (8) [ $x = x(T, P_{O_2})$ ] and conductivity data (21) [i.e.,  $\sigma_T = \sigma(T, P_{O_2})$ ] with Eq. [10]. This value of  $D_{V_{O^{\bullet\bullet}}}$  appears to be independent of  $x$  in the region  $10^{-3} < x < 10^{-2}$ . No attempt was made to determine the temperature dependence of  $D_{V_{O^{\bullet\bullet}}}$  because of the uncertainty in  $t_i$  with temperature.

It is interesting to compare the above value of  $D_{V_{O^{\bullet\bullet}}}$  for "pure"  $CeO_{2-x}$  with  $D_{V_{O^{\bullet\bullet}}} \approx 1.1 \times 10^{-5}$  cm<sup>2</sup>/sec calculated at 1000°C from the expression for  $D_{V_{O^{\bullet\bullet}}}$  obtained from a recent electrical conductivity study on CaO-doped  $CeO_2$  (17). Within experimental error the two calculated values of  $D_{V_{O^{\bullet\bullet}}}$  are in relatively good agreement. Since the above expression for  $D_{V_{O^{\bullet\bullet}}}$  was obtained for CaO contents between 1 and 8 mole per cent (m/o), it appears that the presence of CaO at least up to 8 m/o does not have any significant effect on the magnitude of  $D_{V_{O^{\bullet\bullet}}}$ .

#### Acknowledgment

The work reported in this paper was supported by the United States Atomic Energy Commission, Division of Research. This is AEC Report COO-1441-20. This paper is based in part on a dissertation submitted by G. J. VanHandel in partial fulfillment of the requirements for the Ph.D. degree, Marquette University, June 1972.

Manuscript submitted Nov. 9, 1973; revised manuscript received March 18, 1974.

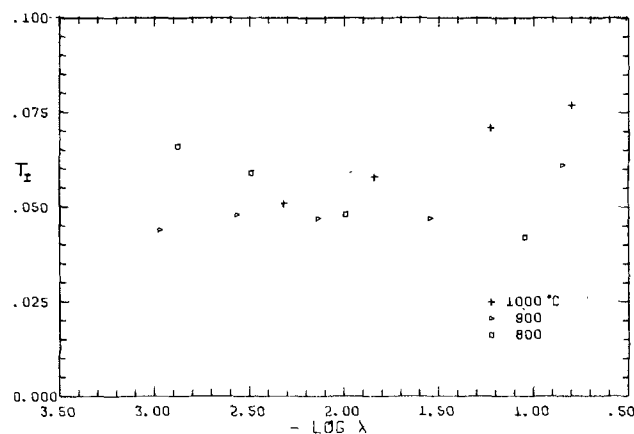


Fig. 5. Isothermal plot of  $t_i$  vs.  $\log x$  for "pure"  $CeO_{2-x}$

Any discussion of this paper will appear in a Discussion Section to be published in the June 1975 JOURNAL. All discussions for the June 1975 Discussion Section should be submitted by Feb. 1, 1975.

The publication costs of this article have been assisted by Marquette University.

## REFERENCES

- G. Brauer and H. Gradinger, *Z. Anorg. Allgem. Chem.*, **277**, 89 (1954).
- D. J. M. Bevan, *J. Inorg. Nucl. Chem.*, **1**, 49 (1955).
- G. Brauer, K. A. Gingerich, and U. Holtzschmidt, *ibid.*, **16**, 77 (1960).
- J. R. Sims, Ph.D. Dissertation, Marquette University, Milwaukee, Wisconsin (1973).
- G. Brauer and K. A. Gingerich, *J. Inorg. Nucl. Chem.*, **16**, 87 (1960).
- F. A. Kuznetsov, V. I. Belyi, and T. N. Rezhukhina, *Dokl. Akad. Nauk SSR, Fiz-Khim*, **139**, 1405 (1961).
- D. J. M. Bevan and J. Kordis, *J. Inorg. Nucl. Chem.*, **26**, 1509 (1964).
- R. J. Panlener, R. N. Blumenthal, and J. E. Garnier, *J. Phys. Chem. Solids*, To be published.
- J. Rudolph, *Z. Naturforsch.*, **14**, 727 (1959).
- E. H. Greener, J. M. Wimmer, and W. M. Hirthe, "Rare Earth Research II," Karl S. Vorres, Editor, p. 539, Gordon and Breach, New York (1964).
- C. J. Kevane, *Phys. Rev.*, **133**, A1431 (1964).
- C. J. Kevane, E. L. Holverson, and James B. Armstrong, Paper presented at the Fifth Rare Earth Research Conference, Ames, Iowa, August 1965.
- I. V. Vinokurov, Z. N. Zonn, and V. A. Ioffe, *Soviet Phys.-Solid State (English Transl.)*, **9**, 2659 (1968).
- R. N. Blumenthal and J. E. Laubach, "Anisotropy in Single-Crystal Refractory Compounds," Vol. 2, p. 137, Plenum Press, New York (1968).
- R. N. Blumenthal, P. W. Lee, and R. J. Panlener, *This Journal*, **118**, 123 (1971).
- R. N. Blumenthal and R. L. Hofmaier, *ibid.*, **121**, 126 (1974).
- F. S. Brugner, R. N. Blumenthal, and J. E. Garnier, *ibid.*, **120**, 1230 (1973).
- J. E. Bauerle, *J. Chem. Phys.*, **45**, 4162 (1966).
- R. N. Blumenthal and R. J. Panlener, *J. Phys. Chem. Solids*, **31**, 1190 (1970).
- B. C. H. Steele and J. M. Floyd, *Proc. Brit. Ceram. Soc.*, **19**, 55 (1971).
- R. N. Blumenthal and R. Sharma, *J. Solid State Chem.*, To be published.

## Microstructural Observations on Gallium Nitride Light-Emitting Diodes

H. P. Maruska,\*<sup>1</sup> L. J. Anderson, and D. A. Stevenson\*

Department of Materials Science, Stanford University, Stanford, California 94305

## ABSTRACT

Microstructural observations, utilizing optical microscopy, scanning electron microscopy, and transmission electron microscopy, were made on gallium nitride (GaN) metal/insulator/n-type semiconductor (m-i-n) light-emitting diodes. The GaN films from which the diodes were fabricated were grown by heteroepitaxial chemical vapor deposition on sapphire substrates, and consisted of an undoped n-layer and a Mg-doped i-layer; a metal contact was subsequently placed on the surface of the i-layer forming an m-i and an n-i junction. Significant observations include the following: optical microscopy and scanning electron microscopy show a faceted surface of the layers and the existence of cell boundaries; the cell boundaries result from the coalescence of the individual crystallites formed on the substrate in the early stages of growth; x-ray Laue patterns consist of spots that are slightly diffuse, indicating that the cells are only slightly misoriented with respect to their adjoining cells; light emission occurs as a pattern of small discrete spots and this pattern of spots correlates with the faceted structure of the film; the light emanates from the cathode regions (the i-n junction with forward bias and the m-i junction with reverse bias); steep electrical potential gradients ( $\sim 10^5$  V/cm), measured using line scan techniques in the scanning electron microscope, occur at the m-i and the n-i junctions. The observations are consistent with an impact ionization model for light emission.

There is considerable interest in the phenomenon of electroluminescence in the III-V compound gallium nitride (GaN) as evidenced by several recent publications (1-6). Light-emitting diodes (LED's) have been fabricated which emit red and yellow (2), green (3), blue (4), and violet light (5, 6). In all of these cases, the basic device is an m-i-n structure, consisting of a layer of n-type GaN, a layer of insulating (i) GaN, and a metal contact to the i-GaN layer. Although numerous emission spectra, current-voltage characteristics, and efficiency characteristics have been published for these diodes, the actual mechanisms responsible for the operation of GaN m-i-n diodes remain unclear. In this paper we present observations made on GaN m-i-n diodes in the optical, scanning

electron, and transmission electron microscopes concerning important structural features of these devices. These observations provide valuable insight concerning the processes that contribute to the operation of the device.

## Experimental Techniques

Films of GaN were grown by heteroepitaxial chemical vapor deposition with the n-i junction structures produced by sequential chemical vapor deposition of first GaN, and then GaN:Mg, on sapphire substrates. Details of the growth process are described elsewhere (5). The devices were made by placing a metal contact over the surface i-layer either by evaporation, painting liquid In-Ga, or by an amalgam technique (6); thus an m-i-n diode structure is formed.

An Advanced Metals Research Model 900 scanning electron microscope (SEM) was used to study the surface characteristics of samples. The SEM is particu-

\* Electrochemical Society Active Member.

<sup>1</sup> Present address: RCA Research Laboratories, Princeton, New Jersey 08540.

Key words: junction structure, light emission pattern, voltage profile, voltage contrast.

larly suited for observations and measurements of junction and space-charge regions in the  $1\mu$  size range. Since an electric field either enhances or retards the emission of secondary electrons, there is a relation between the brightness of the local image and the internal electric field (7). This phenomenon is known as voltage contrast. The voltage contrast may result from an internal electric field in the material due to a concentration gradient of an electrically active species, such as with an n-p junction or an i-n junction, or to an electric field imposed on a device due to an applied bias. A representation of the potential distribution in a sample may be obtained with a line scan. The primary beam is set to sweep one line across the sample and the secondary electron current signal *vs.* distance is displayed on a screen. By taking two of these line scans at the same position across a sample, one with and one without bias, a representation of the potential distribution across the diode can be obtained.

Precipitates and dislocations have been observed in several III-V compounds and have been suggested as potential carrier recombination centers (8). Since the precipitates could be smaller than  $500\text{\AA}$  in diameter, transmission electron microscopy (TEM) provides the only method for definitive examination. Dislocations are also readily observable in single crystalline materials by TEM because the lattice discontinuity they create leads to localized changes in diffraction conditions and consequent contrast in the transmitted image.

A  $10\ \mu\text{m}$  thick, Mg-doped, GaN layer on a  $70\ \mu\text{m}$  thick, n-type layer, that had separated from the sapphire substrate during postgrowth cooling, was ultrasonically cut into 3 mm diameter disks for TEM examination. Low angle ion-milling was used to smooth the faceted surface of the i-layer, and then the n-layer and some of the i-layer were removed in a region near the center of the disk during a 65-hr bombardment on the n-layer side with 10 kV Ar ions in a Commonwealth Scientific Ion Milling Machine. The sample provided an area larger than  $500\ \mu\text{m}^2$  that was thin enough ( $<3000\text{\AA}$ ) for detailed TEM examination.

Optical microscopic studies of the light emission from the diodes were carried out with a Leitz Panphot microscope which allowed focusing at magnifications up to 500X.

### Experimental Results

**Electroluminescence.**—As reported earlier (6), electroluminescence was obtained from Mg-doped GaN m-i-n diodes both with forward (m biased positive with respect to n) and reverse bias. Light emission under forward bias was obtained in the region of 2.86–2.98 eV, with 400 meV half width, and the external quantum efficiency was about 0.005%. Diodes operated in reverse bias exhibited a major emission peak at  $4820\text{\AA}$  (2.57 eV), which is light-blue in color, and another less intense peak at  $6000\text{\AA}$  (2.07 eV) in the yellow-orange; the diodes appear green in reverse bias due to the eye's sensitivity. Photoluminescence in Mg-doped GaN showed an emission spectrum similar to the forward bias electroluminescence spectrum, with a peak at 2.92 eV (independent of temperature) (6). The luminous intensity varies linearly with diode current and superlinearly with applied voltage.

**Growth and surface morphology of GaN.**—The growth and surface morphology of the GaN epitaxial films were studied in order to obtain a better understanding of the processes which control the operation of the LED devices. Gallium nitride crystallizes with the hexagonal wurtzite structure. It was found that a large number of GaN nuclei are formed on the sapphire substrate during the chemical vapor deposition (open-flow vapor phase growth) process. This is reasonable since the deposition temperature used was several hundred degrees below the equilibrium temperature for the chemical reaction. These nuclei grow to form separate hexagonal islands of GaN. An example of these islands is shown in Fig. 1, taken at

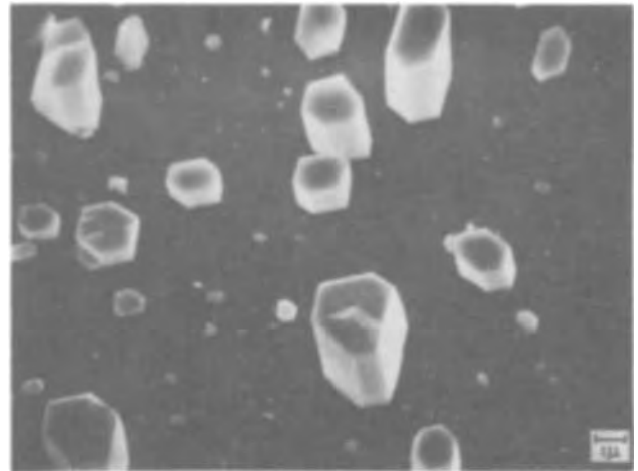


Fig. 1. Hexagonal islands of GaN nucleated on (0001)-sapphire

5000X magnification in the scanning electron microscope. The deposition occurred on an (0001)-oriented sapphire substrate, and the GaN islands have this same orientation. Notice that the individual islands have the form of hexagonal columns, with the respective sides of each column parallel to those of all the other columns. Given sufficient time, all of these islands grow together. This is clearly shown in Fig. 2, where separate islands are still visible on the right side of the micrograph (2000X magnification) while a continuous film has formed on the left side. However, the original island pattern is still visible in the continuous films, which exhibits a faceted surface. This suggests that the various islands may not be exactly aligned. Figure 3 shows the type of GaN surface which occurs for films grown on  $(1\bar{1}02)$ -oriented sapphire substrates. The GaN films have a  $(11\bar{2}0)$  orientation when grown on  $(1\bar{1}02)$  sapphire substrates and the GaN c axis is then parallel to the substrate surface. The size of the facets is directly related to the position of the substrate in the growth tube; the facet size decreases with distance downstream from the ammonia inlet tube, as shown in Fig. 4 for growth on a 5-in. long quartz plate. The thickness of the deposit shows a marked decrease with distance downstream probably due to a small temperature gradient.

A Laue pattern for the faceted  $(11\bar{2}0)$  GaN films, consists only of spots, indicative of a single crystal. There are no rings which would indicate a polycrystalline sample. Therefore, even though many nuclei are involved in the formation of a GaN film, the resulting

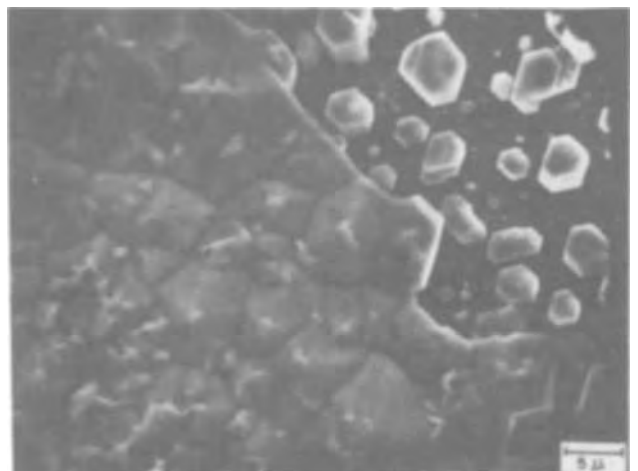


Fig. 2. Hexagonal islands of GaN, which have grown together to form a continuous film on the left side of the picture.



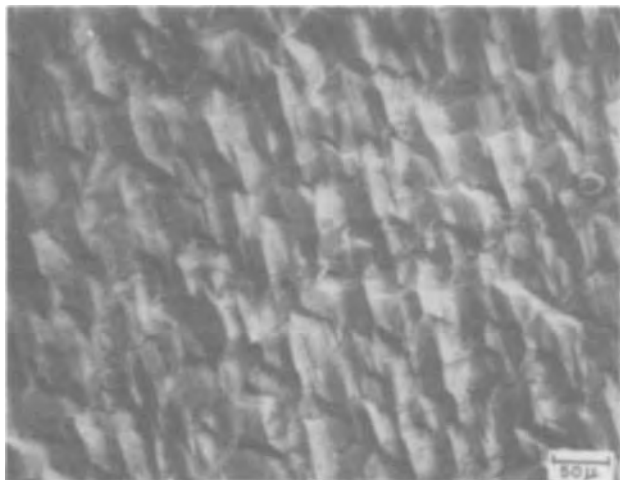


Fig. 3. Typical faceted surface developed in GaN grown on  $(\bar{1}102)$ -sapphire.

film gives x-ray evidence of single crystallinity. However, the Laue pattern spots are not pinpoints but instead show a little smearing, characteristic of slight crystalline misalignment. Thus there are probably subgrain boundaries between the coalescing islands.

*Pattern of light emission.*—It is thus clear that GaN films on sapphire substrates consist of microscopic islands which have coalesced to form a continuous, single-crystalline epitaxial layer with a faceted surface. The microscopic study was extended to actual operating LED's in order to discover how the light emission is correlated with the structure of the crystals.

Chips which separate from the sapphire substrate upon cooling are especially suited for emission pattern observations, since it is possible to directly focus the optical microscope onto the light pattern at magnifications as high as 200X without any dispersion of light due to an intervening sapphire layer. The light emission does not occur uniformly throughout the material but rather takes the form of small discrete spots. The pattern of light spots occurring with forward bias

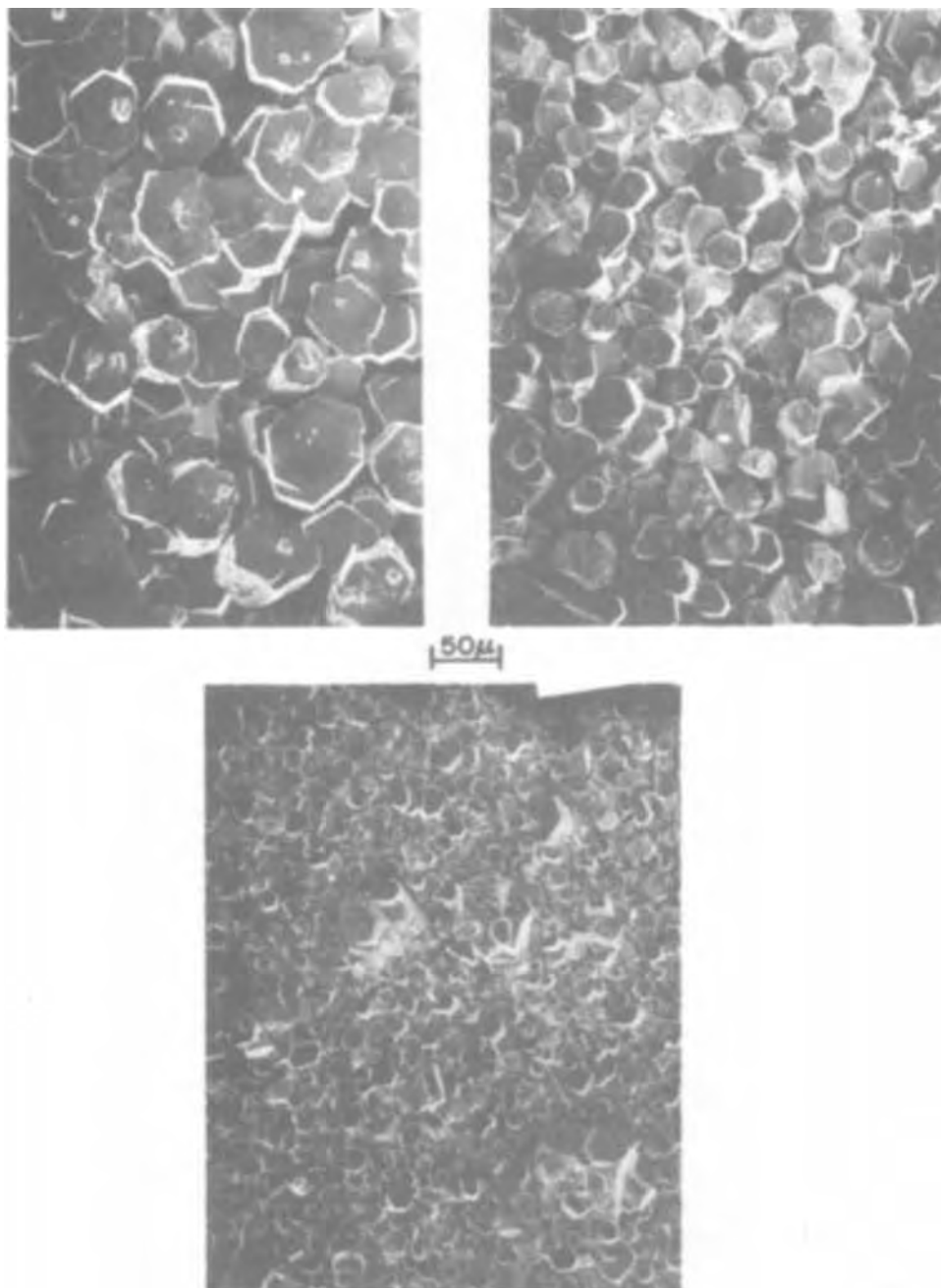


Fig. 4. Polycrystalline gallium nitride films on quartz substrates, showing crystallite size at various distances downstream from the ammonia inlet: (a, top left) 2 in.; (b, top right) 3 in.; (c, bottom) 4 in. Magnification 200X.



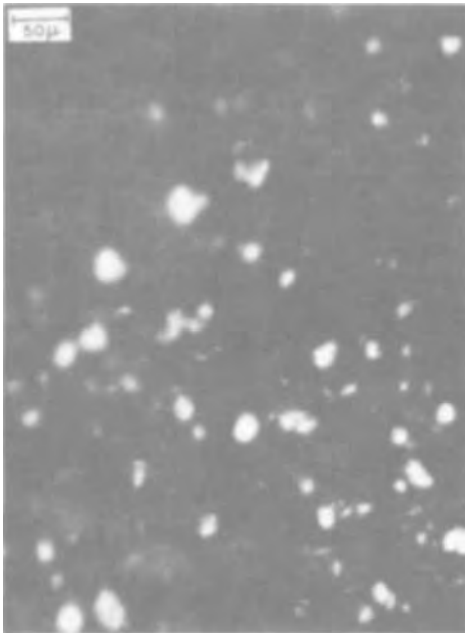


Fig. 5a. Light spot pattern of forward-biased diode at 200 $\times$  magnification.

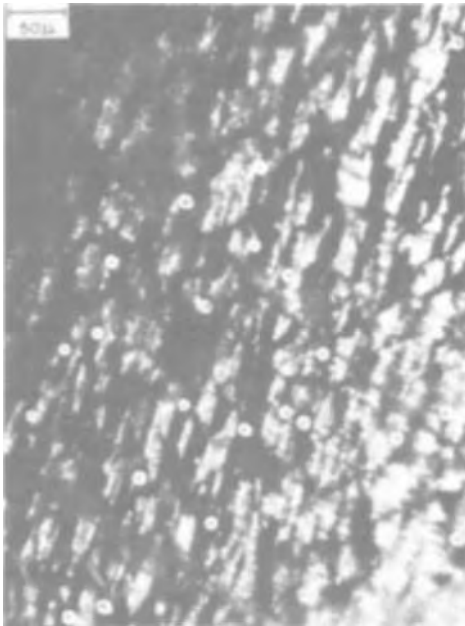


Fig. 5b. Same diode as in Fig. 5a with external illumination and light spot pattern superimposed. Magnification 200 $\times$ .

at 200X magnification is shown in Fig. 5a. The spots appear larger on the film than they actually are due to the exposure time of 6 min. Visual observations of the spots in the microscope indicate that they are less than 10 $\mu$  in diameter.

The same region of the LED of Fig. 5a is shown externally illuminated in Fig. 5b, with the light spot pattern of Fig. 5a superimposed. It can be seen that the light spots can be correlated with the crystal facets; no more than one spot occurs in any facet, and most facets are without spots. For comparison, the facets can be seen more clearly in the scanning electron micrograph shown in Fig. 3. A spotty light emission pattern is also observed with reverse bias, although most of the spot positions are different from the ones seen when a diode is forward biased.

It has been observed that the light spots turn on in a definite, reproducible order as the applied voltage is

increased above a threshold voltage of about 8V. Once all the spots are lighted, they just become brighter as the voltage is further increased. As the voltage is decreased, the spots go out in reverse order. The brighter devices have large numbers of closely spaced light spots, all of which turn on over a short range of voltage increase (about 2-3V). Some diodes only had one or two light spots which increased in brightness with increasing voltage but which burned through before other spots turned on. Any GaN LED will burn through and become a short circuit if the applied voltage is continuously increased sufficiently. In all cases the position of the brightest light spot overheats and burns through leaving a tiny black dot. The device can be salvaged by simply altering the metal contact so that it does not touch this black dot.

It is of interest to determine where the light is actually created inside the device; possible regions are at the m-i junction, the i-n junction, throughout the bulk of the i-layer, or within the n-layer. A sample was mounted perpendicular to a glass slide, so that the various regions (m, i, and n) were visible. Figure 6 is a scanning electron micrograph of the sample and shows, on the right, the sapphire substrate, in the center the GaN n- and i-layers (which are indistinguishable in this picture), and on the left the metal contact to the i-layer. This sample is shown with forward bias applied (and without external illumination) at a magnification of 500X in the optical micrograph of Fig. 7; light spots which were particularly close to the top edge of the chip are clearly seen. They occur about one-eighth of the way from the metal contact on the i-layer to the sapphire substrate. In the next section it is shown that this is the exact position of the i-n junction.

Reverse bias light proved more difficult to study. The size of the reverse bias light spots, when viewed through the n-layer, was the same as the forward bias spots; however, none could be clearly seen and photographed from the edge of the sample. The metal-GaN:Mg interface appeared to glow and there were no signs of light spots anywhere within the i- or the n- regions, thus the reverse-bias light appears to come from the m-i junction.

*Characteristics of the insulating (Mg-doped) region.*—It was appropriate to make a more detailed study of the insulating Mg-doped GaN layer in the diodes. The Mg concentration in the doped material



Fig. 6. Perpendicular view of diodes as seen in the scanning electron microscope. The entire device (including the sapphire substrate) and the two metal contacts (to the n- and i-layers) are visible. Magnification 25 $\times$ .

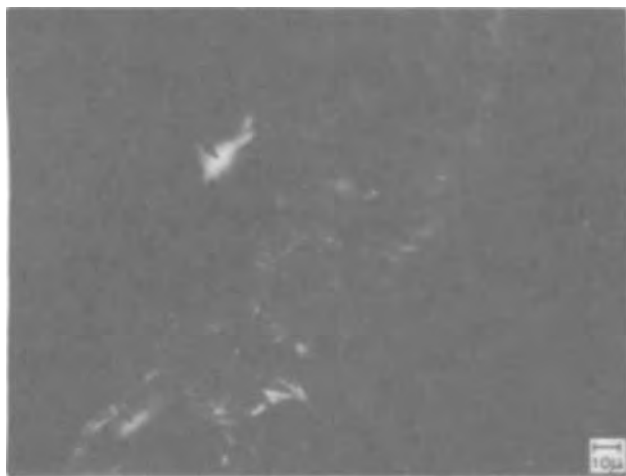


Fig. 7. Light spots observed when diode shown in Fig. 6 was forward biased. The light spots occur within the GaN region. Magnification 500X.

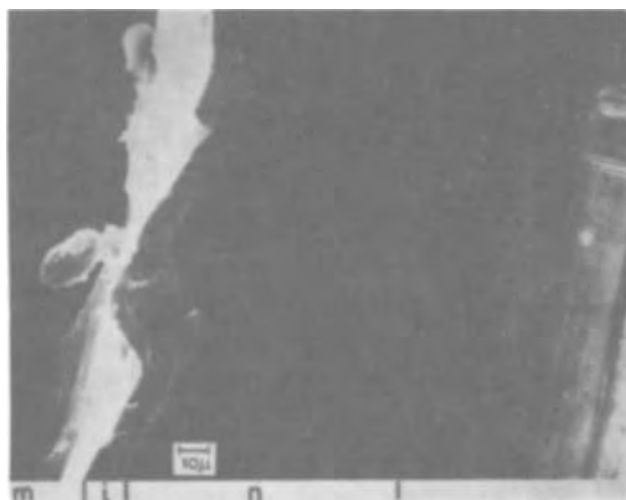


Fig. 8. Scanning electron micrograph of diode at 500X magnification with reverse bias. The insulating (Mg-doped) GaN layer can be clearly distinguished.

was determined by electron microprobe analysis, and dopant concentrations of  $2-6 \times 10^{20}$  atoms/cm<sup>3</sup> were found; however, it is not known what percentage of the dopant is electrically active. The addition of a large quantity of dopant affects the lattice parameters of GaN. Table I presents the lattice parameter measurements of a number of investigations (including the present one) for undoped GaN and for Mg-doped GaN (from the present study). The *a* and *c* values for the doped material were found to increase by 0.14 and 0.21%, respectively, over the average values for undoped material. This is not surprising, since the tetrahedral radius of Mg is larger than that of Ga.

Further studies of the insulating region in the diodes were made with the SEM. Diodes were suitably mounted onto glass slides to expose the two junctions (see Fig. 6). Figure 8 shows a device at 500X magnifi-

cation and with reverse bias. The faceted nature of the GaN surface is apparent, and the extent of the insulating region may be distinguished due to voltage contrast. The *i*-layer is light gray, the *n*-layer is dark gray, and the very white region is the front surface of the *i*-layer which is visible because the metal contact does not come all the way up to the edge and the sample is slightly tilted. Over most of its extent, the *i*-layer is 10 $\mu$  wide, although the width varies up to 25 $\mu$  in sections due to different growth rates of the facet planes. The *m*-*i* junction and the *i*-*n* junction are parallel, and both have a jagged appearance (conforming to the facets), with the *i*-*n* junction one-eighth of the way from the front face to the sapphire substrate. Thus the light spots seen in Fig. 7 were generated at the *i*-*n* junction.

The *n*-Ga<sub>2</sub>N was grown for one-half hour and the *i*-Ga<sub>2</sub>N for one-quarter hour in the diode shown in Fig. 7 and 8; however, the *n*-layer is eight times as thick as the *i*-layer. Therefore the presence of Mg in the vapor during the growth of GaN appears to reduce the growth rate to about one-fourth that of undoped material.

Detailed examination of Mg-doped GaN in the transmission electron microscope revealed no evidence of precipitates or dislocations. Grain boundaries were not observed because of the small size of the thinned area as compared to the known grain size. Selected area diffraction yielded a distinct, single-crystalline GaN pattern. It can be concluded that the *i*-layer is precipitate-free and that the dislocation density is less than  $10^5$  cm<sup>-2</sup> in the interior regions of the crystallites. (It is undoubtedly high in the vicinity of the crystallite boundaries.)

**Electrical potential distribution.**—A representative line scan trace across a diode is displayed in Fig. 9, taken at 1000X magnification at the same position across the sample, with and without forward bias. These traces are superimposed on a standard secondary electron image of the same region. Since for a topographically and compositionally uniform sample, as is the cross section of the sample shown in Fig. 9, the number of secondary electrons emitted from any point on the sample depends on the voltage at that point (7), and since the height of the line scan trace is directly proportional to the number of secondary electrons collected, it is possible to display the voltage profile across the diode for an applied bias (Fig. 10). In a similar manner, voltage profiles were obtained for reverse bias (Fig. 11). In either case, gradients in potential occur only at both the *m*-*i* and the *i*-*n* junctions, and electric field strengths of about  $10^5$  V/cm are encountered. Because of a geometrical spur in the vicinity of the metal contact, there are spurious peaks in the line scan in this region, which are disregarded in Fig. 10 and 11. The diode electrical and electroluminescent properties are not appreciably influenced by changes

Table I. Lattice parameters of undoped and Mg-doped GaN

	<i>a</i> , Å	<i>c</i> , Å	Data source
GaN	3.189	5.185	Maruska and Tietjen, 1969 (9)
GaN	3.190	5.17	Faulkner, <i>et al.</i> , 1970 (10)
GaN	3.189	5.185	Ilegems and Montgomery, 1973 (11)
GaN	3.190	5.184	Present study
GaN:Mg	3.194	5.192	Present study

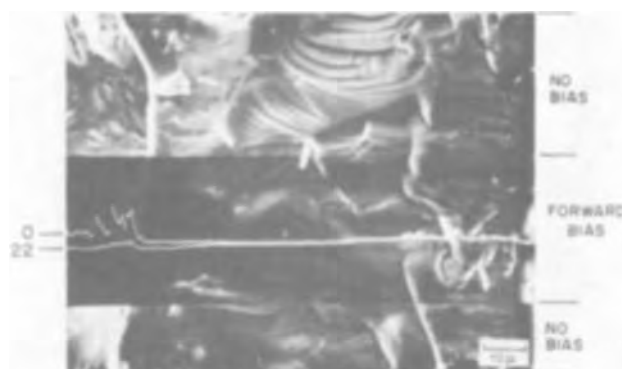


Fig. 9. Superimposed zero bias and forward bias line scan traces and SEM photograph of a gallium nitride light-emitting diode. Magnification 1000X.

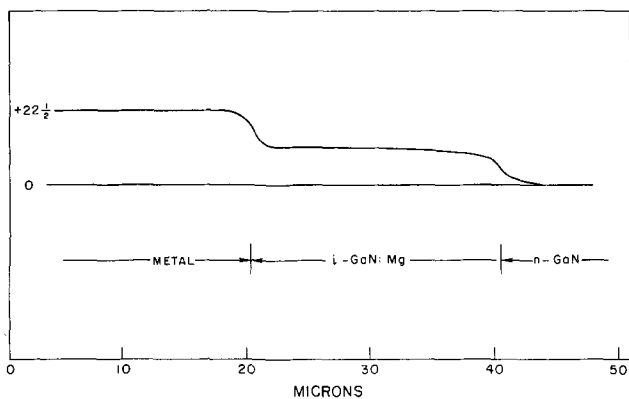


Fig. 10. Electric potential distribution across a gallium nitride light-emitting diode when forward bias is applied.

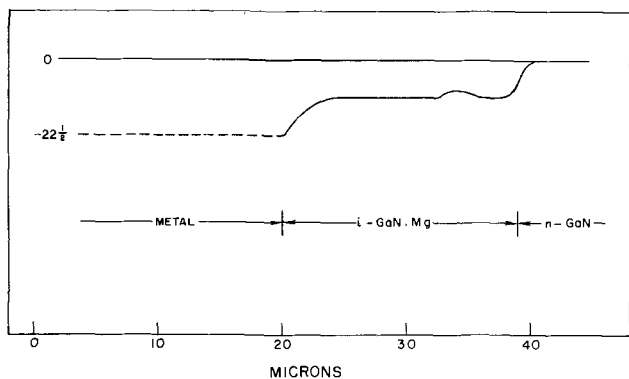


Fig. 11. Electric potential distribution across a gallium nitride light-emitting diode when reverse bias is applied.

in the thickness of the i-layer; diodes grown at the same position in the furnace but with i-layers differing in thickness by an order of magnitude showed virtually no difference in current passed or light emitted at a fixed voltage.

### Summary

The important structural features of GaN m-i-n light-emitting diodes are summarized below.

1. Light-emitting diodes made from GaN:Mg m-i-n structures exhibit violet electroluminescence. Forward bias results in a broad spectrum (400 meV half-width) which peaks at 2.9 eV, with a similar spectrum for photoluminescence.

2. The light emission occurs as a pattern of small, discrete spots, which can be correlated with the GaN crystal facets.

3. The light is emitted at the cathode (i-n junction) with forward bias, and apparently also at the cathode (m-i junction) with reverse bias.

4. Laue patterns indicate that the GaN is single crystalline, but the surface shows a strongly faceted structure. For this reason, the m-i and the i-n junctions are not planar, but follow the faceted nature of the growth.

5. When a bias is applied, steep potential gradients and electric fields of about  $10^5$  V/cm appear at both the m-i and the i-n junctions in the diodes, but not over the bulk of the insulating (i) region.

6. The diode characteristics are not substantially influenced by variations in the i-layer thickness.

The observations of light emission generated at the cathode in the form of small, discrete spots, a high electric field in the depletion region at the negative electrode, a threshold voltage for light emission greater than the bandgap, and brightness proportional to the current are suggestive of an impact ionization mechanism for electroluminescence.

### Acknowledgment

The authors wish to express their thanks to R. Koch and M. de Rojas for technical assistance, and to W. L. Larson and Dr. W. C. Rhines for technical assistance and helpful discussions, and to Dr. E. E. Loebner and Dr. R. A. Burmeister for helpful discussions. This research was supported by the Advanced Research Projects Agency, Grant No. DAHC 15 71-G-6, with facilities provided by the Center for Materials Research at Stanford University.

Manuscript submitted Jan. 28, 1974; revised manuscript received April 23, 1974.

Any discussion of this paper will appear in a Discussion Section to be published in the June 1975 JOURNAL. All discussions for the June 1975 Discussion Section should be submitted by Feb. 1, 1975.

The publication costs of this article have been assisted by Stanford University.

### REFERENCES

1. J. I. Pankove, E. A. Miller, D. Richman, and J. E. Berkeyheiser, *J. Lumin.*, **4**, 63 (1971).
2. J. I. Pankove, E. A. Miller, and J. E. Berkeyheiser, *ibid.*, **6**, 54 (1973).
3. J. I. Pankove, E. A. Miller, and J. E. Berkeyheiser, *RCA Rev.*, **32**, 383 (1971).
4. J. I. Pankove, E. A. Miller, and J. E. Berkeyheiser, *J. Lumin.*, **5**, 84 (1972).
5. H. P. Maruska, W. C. Rhines, and D. A. Stevenson, *Mater. Res. Bull.*, **7**, 777 (1972).
6. H. P. Maruska, D. A. Stevenson, and J. I. Pankove, *Appl. Phys. Letters*, **22**, 303 (1973).
7. N. C. MacDonald and T. E. Everhard, *ibid.*, **7**, 267 (1965).
8. W. C. Rhines and D. A. Stevenson, *J. Electron. Mater.*, **2**, 341 (1973).
9. H. P. Maruska and J. J. Tietjen, *Appl. Phys. Letters*, **15**, 327 (1969).
10. K. R. Faulkner, B. J. Isherwood, B. P. Richards, and I. H. Scoby, *J. Mater. Sci.*, **5**, 308 (1970).
11. M. Ilegems and H. C. Montgomery, *J. Phys. Chem. Solids*, **34**, 885 (1973).

# Liquid Phase Epitaxy of InP

K. Hess,<sup>1</sup> N. Stath, and K. W. Benz

Physikalisches Institut der Universität Stuttgart, 7 Stuttgart 1, West Germany

## ABSTRACT

Liquid phase epitaxy by conventional tipping technique has been employed for the growth of high purity InP epitaxial layers. The layers were grown at 720°–560°C on (100) and (111) oriented InP substrates. Characteristic surface structures for the substrate orientations as a function of the growth temperature were observed. The layers were characterized by Hall data and photoluminescence measurements at low temperatures. The simultaneous observation of the band-acceptor and donor-acceptor pair transition due to the main acceptor in our LPE-layers is reported. The binding energy of this acceptor is determined to  $E_{A1} = 41.0$  meV ( $\pm 1$  meV).

During the last years there has been an increasing interest in high purity epitaxial layers of InP, for instance for Gunn effect applications (1). So far, high purity epitaxial layers were grown by vapor phase epitaxy in particular by the Effer method (2, 3). Net electron concentrations of  $n = 4 \cdot 10^{14}$  cm<sup>-3</sup> and mobilities of  $\mu_{77K} = 87,000$  cm<sup>2</sup> V<sup>-1</sup> sec<sup>-1</sup> were obtained. In the case of GaAs liquid phase epitaxy (LPE) has been very successful in the preparation of high purity epitaxial layers (4-8). One should therefore expect similar good results for the case of InP. In this paper the growth of high purity InP layers is described in connection with Hall data and photoluminescence measurements at low temperatures. Previous works on InP LPE were done by several authors (9-11). The best values for the LPE-layers with  $N_D - N_A = 2 \cdot 10^{15}$  cm<sup>-3</sup> and  $\mu_{77K} = 49,000$  cm<sup>2</sup> V<sup>-1</sup> sec<sup>-1</sup> were reached by Wood *et al.* (11). Recently Astles *et al.* (12) have reported on the growth of InP by LPE from solutions saturated with P from PH<sub>3</sub>. Values of  $N_D - N_A = 3 \cdot 10^{15}$  cm<sup>-3</sup> and  $\mu_{77} = 27,000$  cm<sup>2</sup> V<sup>-1</sup> sec<sup>-1</sup> have been reported.

## LPE—Apparatus and Experimental Procedure

The experience from LPE growth of high purity GaAs has been that the growth results are strongly influenced by the way in which the growth process is performed (13, 14). Important steps are: (i) heating of In-InP solution, (ii) preparation of the single-crystal substrate, (iii) equilibration and homogenization of the solution, and (iv) tipping the solution on the substrate. In the following we describe the corresponding conditions for InP-LPE. For the growth experiments we used a tipping system (14) (schematically shown in Fig. 1). The reaction tube was made of suprasil quartz, the boat for the In-InP solution of high purity graphite. The tube and boat were locked together and could be rotated around the long axis for immersion and withdrawal of the substrate from the solution. To avoid air leaks we used a Pyrex spiral which allowed the rotation of the tube without moving joints. The furnace was transparent (15) in order to observe substrate and solution. The graphite boat was heated at  $T = 1600^\circ\text{C}$  under a vacuum of  $10^{-6}$  Torr for 3 hr. After that, the boat was loaded with 6N In (Johnson Matthey Limited, England) and baked at  $T = 730^\circ\text{C}$  in the reaction tube for 10 hr under a Pd-diffused H<sub>2</sub> gas flow. At the end of this procedure the boat was cooled down to room temperature and the In was removed. We believe that residual impurities on the crucible walls were dissolved in the In. The boat was then loaded again with 10g 6N In and 370 mg 6N InP (MCP, England). Prior to the experiment this In-InP solution was baked at  $T = 730^\circ\text{C}$  for 15 hr and with a H<sub>2</sub> flow rate of 15 liters/hr. During this time the phos-

phorous content of the solution decreases due to phosphorous evaporation.

The amount of P loss during this baking process is very difficult to calculate because it depends on several factors. The concentration of P in the solution is determined by the evaporation of P at the surface and the diffusion in the solution. The diffusion equation involves the diffusion coefficient of P in liquid In, which is not yet known. For this reason the amount of P loss during this baking process and the temperature  $T_S$  at which the solution is saturated cannot be calculated. The tipping temperature  $T_K$  at which the solution was tipped on the substrate was therefore estimated experimentally by observing the temperature at which solid InP appears on the surface of the solution. By this method of determining the starting temperature, the solution was slightly supercooled at  $T_K$ . The temperature was measured near the graphite boat and was controlled within  $\Delta T = \pm 0.5^\circ\text{C}$ . There was no temperature gradient across the tipping zone, the temperature gradient normal to the substrate was negligible.

Under the conditions described above, we have grown single-crystal layers on (111)A, (111)B, and (100) Cr-doped, semi-insulating InP substrates (RRE, England;  $\rho = 1 \cdot 10^3$  ohm-cm). The substrates which were available were cut 2° off orientation and were etched in a solution of 1% bromine in methanol for 10 min. Prior to use, the substrates were rinsed with 18 megohms water. The In-InP-solution was heated up very quickly (within 20 min) to 40°C above  $T_K$  in order to reduce the evaporation of phosphorous. The boat was agitated in order to equilibrate and homogenize the solution. The solution was tipped over the substrate at  $T_K$ . In the different experimental runs,  $T_K$  was varied between 720° and 560°C. The growth time was 2 or 3 hr. The cooling rate was 4°–52°C/hr, however in most cases 6°C/hr. After termination of the experiment, the solution was removed from the substrate by rotation of the crucible.

## Growth Results

Figure 2 shows the growth rate as a function of the tipping temperature  $T_K$  for two different cooling rates. For a cooling rate of 6°/hr a large scatter of data was observed. This is due to differences in the starting

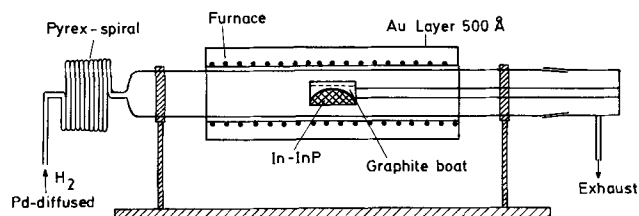


Fig. 1. Schematic drawing of the LPE-apparatus

<sup>1</sup> Present address: Max-Planck-Institut für Festkörperforschung, 7 Stuttgart 1, Heilbronner Strasse 69, West Germany.

Key words: InP, liquid phase epitaxy, photoluminescence.

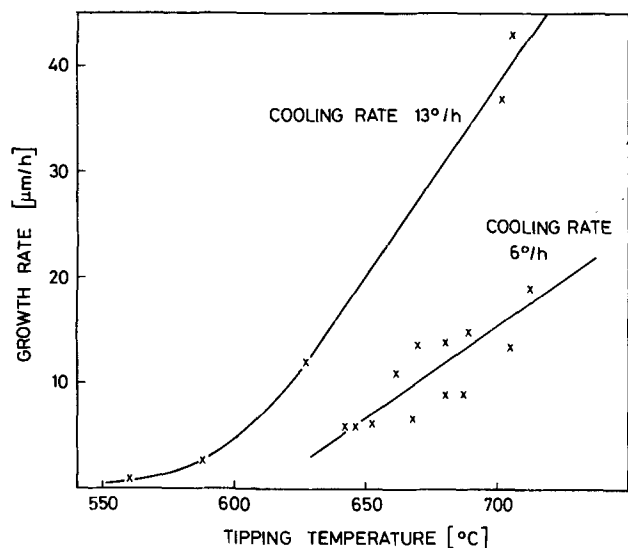


Fig. 2. Growth rate as a function of the tipping temperature for two different cooling rates.

growth conditions. For both cooling rates the growth rate decreases with decreasing tipping temperature.

We have grown epitaxial layers with thicknesses between 5 and 120 μm. Thicknesses were determined either by etching a cleavage plane or by means of a micrometer. The layers grown on (100) and (111) substrates show two types of surface structure: a shed structure of the layers which were grown at tipping temperature  $T > \sim 650^\circ\text{C}$  (Fig. 3a) and a terrace structure of the layers with  $T_K < \sim 650^\circ\text{C}$  (Fig. 3b) was observed in general. No significant differences for the layer structures between (100), (111)A, and (111)B faces were noticed. These structures are due to misorientation of the substrates (16, 17).

The net electron concentrations and the mobilities of our layers were measured by the method of van der Pauw. The best values we have reached were  $N_D - N_A = 5 \cdot 10^{14} \text{ cm}^{-3}$  and  $\mu = 4800 \text{ cm}^2 \text{ V}^{-1} \text{ sec}^{-1}$  ( $T = 300^\circ\text{K}$ ),  $N_D - N_A = 3.4 \cdot 10^{14} \text{ cm}^{-3}$  and  $\mu = 26,000 \text{ cm}^2 \text{ V}^{-1} \text{ sec}^{-1}$  ( $T = 77^\circ\text{K}$ ). Some samples contain deep impurity levels, as seen in luminescence (Fig. 4), which reduce low temperature mobility.

The effect of the baking time of the In-InP-solution is shown in Table I. Layer No. 25 for instance was grown from an In-InP-solution without any baking time, i.e., immediately after its preparation. Layer No. 26 was grown from the same solution after heating it at  $730^\circ\text{C}$  in  $\text{H}_2$  gas flow for 25 hr. One can notice a con-

Table I. Influence of baking of the In-InP solution onto epilayer impurity concentrations and mobilities

Sample	Electron conc (cm <sup>-3</sup> )	300K Mobility (cm <sup>2</sup> V <sup>-1</sup> sec <sup>-1</sup> )	Electron conc (cm <sup>-3</sup> )	77K Mobility (cm <sup>2</sup> V <sup>-1</sup> sec <sup>-1</sup> )
25	$2.7 \cdot 10^{16}$	3200	$2.0 \cdot 10^{15}$	8.800
26	$1.0 \cdot 10^{15}$	3500	$9.0 \cdot 10^{14}$	22.500

Table II. Growth conditions of various samples used for photoluminescence measurements

Sample	Substrate orientation	Growth temperature (°C)	Cooling rate (deg. hr <sup>-1</sup> )	Growth time (hr)	Layer thickness (μm)
31	(100)	688-670	6	3	27
32	(100)	655-635	6	3	19
33	(100)	627-588	13	3	35
34	(100)	587-548	13	3	11
35	(100)	560-521	13	3	4

siderable decrease of the electron concentration and an increase of the mobility for the "baked" sample. Similar effects which are due to evaporation of impurities have been reported for GaAs (13).

Photoluminescence Measurements

The quality of the LPE layers was characterized by low temperature (1.8°K and 77°K) photoluminescence. The crystals were excited by a Kr<sup>+</sup> laser ( $\lambda = 647 \text{ nm}$ ) which was focused to a spot of  $\sim 100 \mu\text{m}$  diameter. The maximal light density was  $I_0 = 400 \text{ mW/cm}^2$ . The intensity of the light could be varied by neutral density filters. A 1m Type 1704 Spex monochromator was used in connection with a RCA 7102 S 1 photomultiplier and conventional lock-in technique.

The growth conditions of the various samples discussed in this section are listed in Table II.

The main features of the observed photoluminescence spectra of high purity InP layers ( $N_D - N_A = 5 \cdot 10^{14} \text{ cm}^{-3}$ ) are shown in Fig. 4. Emission spectra of two epitaxial layers (No. 31 and 34) grown at different temperatures are compared in this figure. The near gap luminescence (energy range 1.42 eV to 1.41 eV) can be attributed predominantly to the radiative decay of free and bound excitons. In the energy range 1.39-1.36 eV InP usually exhibits one or several pair bands and/or band-to-acceptor transitions (18-25) Some spectra show very sharp lines at 1.3866 eV (half width 0.1 meV) (sample 34 at 1.3876 eV) and at 1.3773 eV (half width 0.4 meV). Their intensity decreases rapidly

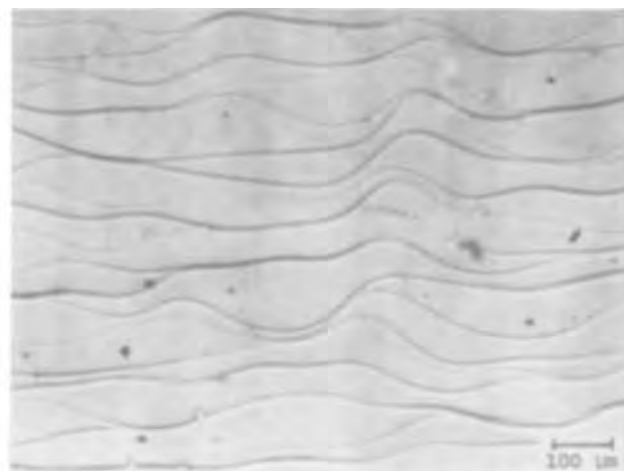
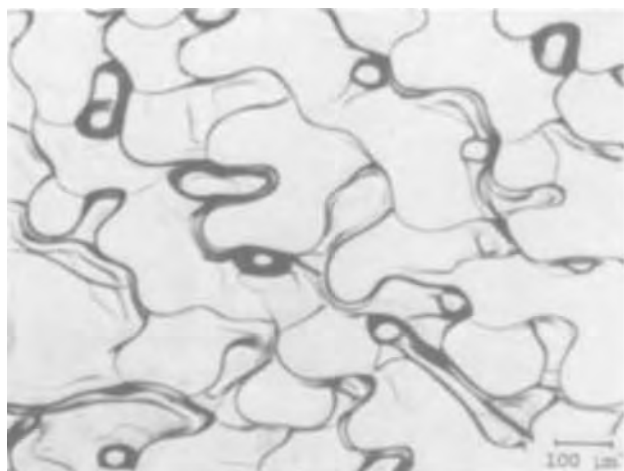


Fig. 3. Characteristic surfaces: (a, left) shed structure for growth temperature  $T > \sim 650^\circ\text{C}$  and (b, right) terrace structure for growth temperatures  $T < \sim 650^\circ\text{C}$ .

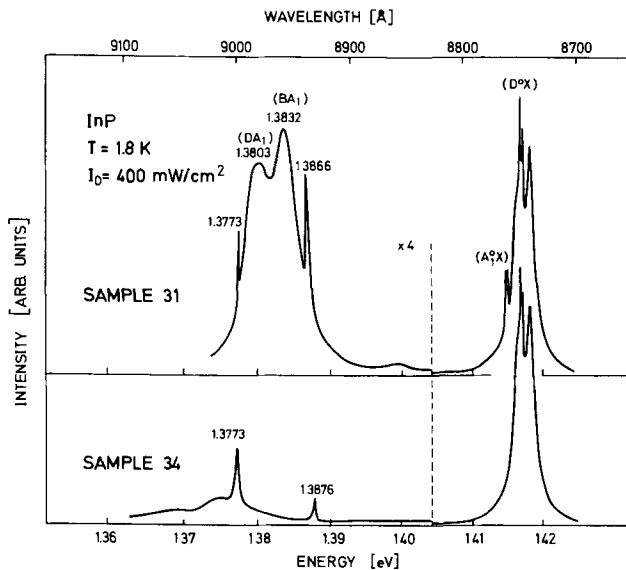


Fig. 4. Photoluminescence spectra of two epitaxial layers grown at different temperatures (No. 31, 688°-670°C; No. 34, 587°-548°C).

with decreasing excitation intensity. They are assumed to contribute to the decay of excitons bound to deep impurities. The concentration of different impurities is monitored by the relative luminescence intensity of the impurity-induced transitions. For quantitative comparison, all spectra are normalized with respect to the peak intensity of a donor-induced near edge emission, labeled (D<sup>0</sup>X) in Fig. 4.

#### Near Gap Emission

Figure 5 shows the near gap luminescence of the two layers for low excitation density at high resolution and in an expanded energy scale. Up to 11 different emission lines (or shoulders) can be observed. The peak at 1.4184 eV has been identified as the free exciton-polariton emission (22, 26). Two weak lines are observed at 1.4181 eV (not previously reported) and at 1.4179 eV, which have not been explained so far. In all our samples the three sharp lines at 1.4174, 1.4172, and 1.4169 eV are the strongest emission. The half widths of these lines are 0.1 meV or less. Such a half width is characteristic for the decay of bound excitons. These transitions appear in the energy range expected for excitons bound to neutral donors (D<sup>0</sup>X) (22, 26).

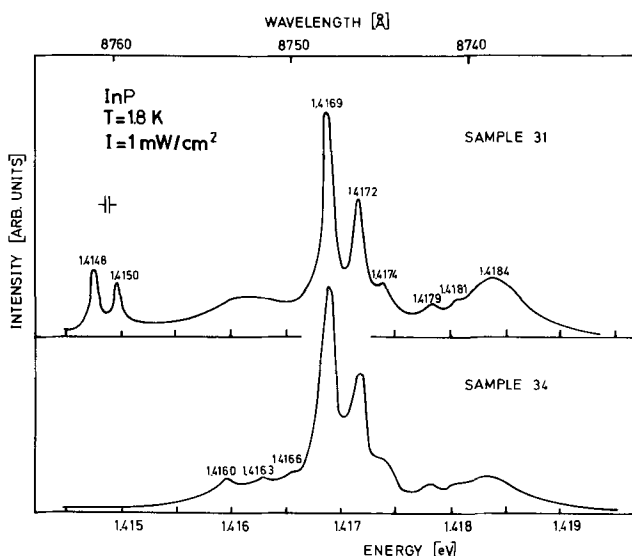


Fig. 5. Near gap luminescence of samples 31 and 34 at low excitation intensities.

The spectra of most layers show a broad emission at 1.416 eV. For layer No. 34 this band can be resolved into three lines at 1.4166, 1.4163, and 1.4160 eV. It is believed that they are associated with the recombination of free holes to neutral donors.<sup>2</sup>

Some layers, e.g., No. 31 (Fig. 5 upper curve), show a doublet centered at 1.4149 eV with spacing ~0.22 meV (the half width is 0.1 meV). This doublet is associated with the recombination of bound excitons at neutral shallow acceptors (22). It always appears together with the emission lines at 1.3832 and 1.3803 eV (Fig. 4). These lines are identified as band-acceptor (BA) and donor acceptor (DA) pair transitions, respectively, which is discussed in detail below. The simultaneous appearance of (A<sub>1</sub><sup>0</sup>X), (BA<sub>1</sub>), and (DA<sub>1</sub>) transitions suggests that one common acceptor element A<sub>1</sub> is involved.

White *et al.* (24) have identified similar doublets and the corresponding (BA) and (DA) lines for the elements Zn and Cd. The energetic positions of the (A<sup>0</sup>X)-doublets vary hardly at all, but the comparison of the (BA) and (DA) emission peak energies shows that A<sub>1</sub> is not identical with Zn or Cd (see Table III). Possible candidates for such a shallow acceptor are C, Si, and Mg. The following considerations may narrow the list of these elements. Astles *et al.* (12) have done LPE doping experiments with Si which yielded to n-type material. There was no evidence for Si-acceptors. Zschauer (28) and Dean *et al.* (29) find that LPE GaAs is dominantly contaminated by C-acceptors, and this element is attributed to the shallowest acceptor in GaAs. Therefore we believe that the shallow acceptor A<sub>1</sub> in our LPE-InP layers is C.

#### Pair Bands and Band-Acceptor Transitions

The band-acceptor transitions and pair bands, we have found in the LPE layers are listed in Table II. The transitions at 1.3775 eV (BA<sub>2</sub>) and 1.3735 eV (DA<sub>2</sub>) are attributed to Zn (24), those at 1.369 eV (BA<sub>3</sub>) and 1.365 eV (DA<sub>3</sub>) to Cd (24). The acceptor ionization energy is  $E_{A_2} = 47.3$  meV for Zn (24) and  $E_{A_3} = 56.3$  meV for Cd (24). Several authors (18-20) have reported an emission band at 1.38 eV. Possibly this emission is caused by the acceptor A<sub>1</sub>, associated with the lines at 1.3832 eV (BA<sub>1</sub>) and at 1.3790 eV (DA<sub>1</sub>)<sup>3</sup> in our samples.

The following arguments lead to the identification of the 1.3790 eV line as a donor-acceptor transition. Figure 6 depicts the intensity dependence of the emission spectra in the energy range around 1.38 eV at constant temperature (1.8°K). At lowest intensities, one line at 1.3790 eV can be observed. This peak shifts to 1.3803 eV as the intensity is increased. The peak energy of this transition depends on the impurity concentration. Samples with high net donor concentration show this line at higher energies. This is typical for a donor-acceptor pair transition.

The emission line at 1.3832 eV is due to a (BA)-transition for the following reasons. At lowest intensities only the line at 1.3790 eV can be observed, as above mentioned. With increasing excitation intensity a new line emerges at 1.3832 eV. This line becomes the strongest emission at highest excitation levels. The peak energy does not change with excitation intensity

<sup>2</sup> Taking  $E_D = 7.65$  meV, reported by Chamberlain *et al.* (27) and  $E_G = 1.4234$  eV (26) the (h,D<sup>0</sup>)-transition is expected at 1.4158 eV.  
<sup>3</sup> DA<sub>1</sub> transition at low excitation density.

Table III. (BA) and (DA) transitions of three shallow acceptors

Photonenergy (eV)	Transition	Acceptor element
1.3832	BA <sub>1</sub>	? (A <sub>1</sub> )
1.3790	DA <sub>1</sub>	? (A <sub>1</sub> )
1.3775	BA <sub>2</sub>	Zn (A <sub>2</sub> )
1.3735	DA <sub>2</sub>	Zn (A <sub>2</sub> )
1.369	BA <sub>3</sub>	Cd (A <sub>3</sub> )
1.365	DA <sub>3</sub>	Cd (A <sub>3</sub> )

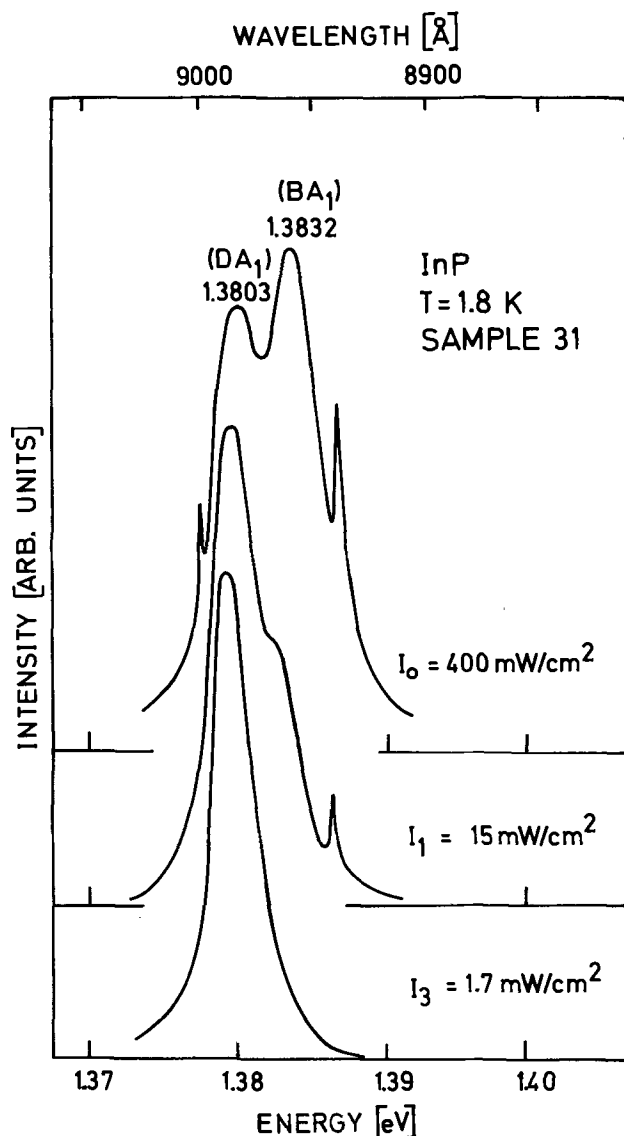


Fig. 6. Intensity dependence of emission spectra in the energy range around 1.38 eV at constant temperature (1.8°K).

as long as the electron temperature remains constant. This is expected for a BA transition. The high energy side of the BA transition has an exponential slope according to the theory of Eagles (30). Using this theory and a bandgap value of  $E_G = 1.4234$  eV the binding energy of the acceptor  $A_1$  becomes  $E_{A_1} = 41.0$  meV ( $\pm 1$  meV).

Finally, the influence of growth temperature on the incorporation of the acceptor  $A_1$  is pointed out. Figure 7 shows the 77°K spectra of the layers No. 31-35 which were grown at different temperatures. It may be noticed that the  $(BA_1)$  transition at 1.378 eV is relatively strong in layers No. 31 and No. 32 (high growth temperatures). The band is relatively weak in samples No. 33-35 (low growth temperatures); therefore, in these layers the  $(BA_2)$  transition dominates. We attribute this effect in the following way to the growth temperature: the acceptor  $A_1$  will be incorporated much stronger at higher temperatures than at lower ones. The change of the incorporation probability rate is especially strong in the temperature range of 600°C.

#### Acknowledgments

The authors would like to thank Professor Dr. M. H. Pilkuhn and Dr. E. Bauser for helpful discussions.

Manuscript submitted Jan. 30, 1974; revised manuscript received April 16, 1974.

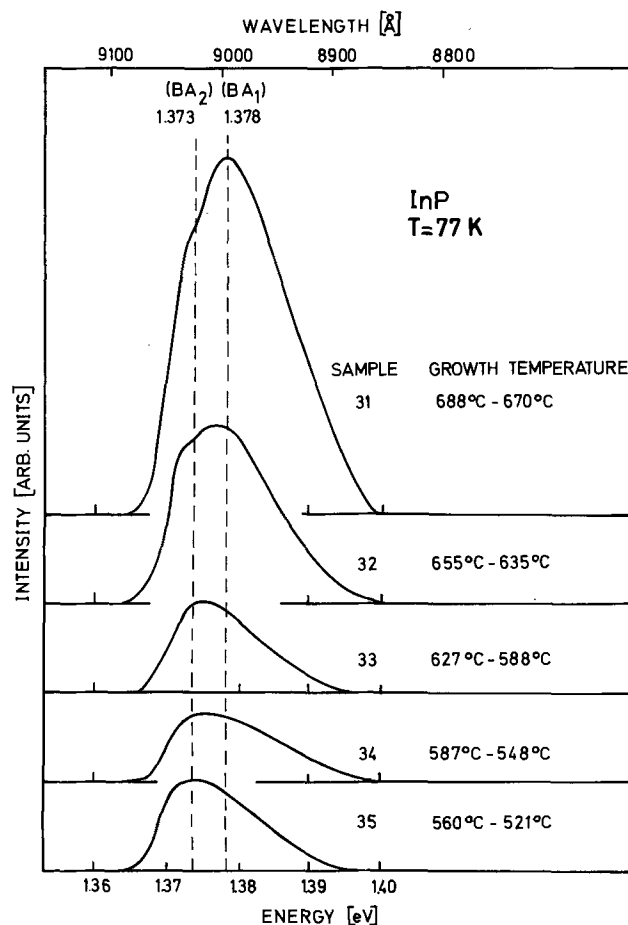


Fig. 7. The 77°K spectra of the layers No. 31-35 and the corresponding growth temperatures. The background of near gap luminescence was eliminated.

Any discussion of this paper will appear in a Discussion Section to be published in the June 1975 JOURNAL. All discussions for the June 1975 Discussion Section should be submitted by Feb. 1, 1975.

The publication costs of this article have been assisted by Physikalisches Institut der Universität Stuttgart.

#### LIST OF SYMBOLS

$E_A$	activation energy for acceptors
$E_D$	activation energy for donors
$E_G$	bandgap energy
$I$	excitation light density
$\lambda$	wavelength
$\mu$	mobility of electrons
$n$	$N_D - N_A =$ net electron concentration
$\rho$	specific resistance
$T$	temperature

#### REFERENCES

1. C. Hilsum and H. D. Rees, *Electron. Letters*, **6**, 277 (1970).
2. R. C. Clarke, B. D. Joyce, and W. H. E. Wilgoss, *Solid State Commun.*, **8**, 1125 (1970).
3. P. W. Braddock and K. W. Gray, *Electron. Letters*, **9**, 2 (1973).
4. C. S. Kang and P. E. Greene, *Appl. Phys. Letters*, **11**, 171 (1967).
5. R. Solomon, "Proc. Int. Symp. GaAs," Dallas Conf. Ser. No. 7, p. 11 (1968).
6. H. G. B. Hicks and D. F. Manley, *Solid State Commun.*, **7**, 1463 (1969).
7. H. Miki and M. Otsubo, *Japan. J. Appl. Phys.*, **10**, 509 (1971).
8. K. Zschauer, "Proc. Int. Symp. GaAs," Boulder Conf. Ser. No. 17, p. 3 (1972).
9. F. E. Rosztochy, G. A. Antypas, and C. J. Casau, "Proc. Int. Symp. GaAs," Aachen Conf. Ser. No. 9, p. 86 (1970).
10. G. M. Blom and J. M. Woodall, *Appl. Phys. Letters*, **17**, 373 (1970).

11. C. E. C. Wood, R. J. Tree, and D. H. Paxman, *Electron. Letters*, **8**, 171 (1972).
12. M. G. Astles, F. G. H. Smith, and E. W. Williams, *This Journal*, **120**, 1750 (1973).
13. J. Vilms and J. P. Garret, *Solid-State Electron.*, **15**, 443 (1972).
14. E. Grobe and H. Salow, *Z. Angew. Phys.*, **32**, 381 (1972).
15. T. B. Reed, Sol. State Res. Rept. Lincoln Labs., p. 21 (1969).
16. R. H. Saul and D. D. Roccasecca, *J. Appl. Phys.*, **44**, 1983 (1973).
17. E. Bauser, M. Frik, K.-S. Löchner, and L. Schmidt, To be published.
18. R. C. C. Leite, *Phys. Rev.*, **157**, 672 (1967).
19. U. Heim, *Solid State Commun.*, **7**, 445 (1969).
20. U. Heim, O. Röder, H. J. Queisser, and M. H. Pilkuhn, *J. Luminescence*, **1**, 2, 542 (1970).
21. O. Röder, U. Heim, and M. H. Pilkuhn, *J. Phys. Chem. Solids*, **31**, 2625 (1970).
22. A. M. White, P. J. Dean, L. L. Taylor, R. C. Clarke, D. J. Ashen, J. B. Mullin, and P. D. Greene, *J. Phys.*, **C5**, 1727 (1972).
23. J. U. Fischbach, G. Benz, N. Stath, and M. H. Pilkuhn, *Solid State Commun.*, **11**, 725 (1972).
24. A. M. White, P. J. Dean, K. M. Fairhurst, W. Bardsley, E. W. Williams, and B. Day, *ibid.*, **11**, 1099 (1972).
25. J. F. Nicolau, K. W. Benz, and J. U. Fischbach, "Proc. Int. Symp. GaAs," Boulder Conf. Ser. No. 17, p. 11 (1972).
26. J. U. Fischbach, G. Benz, N. Stath, M. H. Pilkuhn, and K. W. Benz, *Solid State Commun.*, **11**, 721 (1972).
27. J. M. Chamberlain, H. B. Ergun, K. A. Gehring, and R. A. Stradling, *ibid.*, **9**, 1563 (1971).
28. K. H. Zschau, Private communication.
29. A. M. White, P. J. Dean, D. J. Ashen, J. B. Mullin, M. Webb, and B. Day, *J. Phys.*, **C6**, L 243 (1973).
30. D. M. Eagles, *J. Phys. Chem. Solids*, **16**, 76 (1960).

## Effect of Semiconductor Inhomogeneities on Carrier Mobilities Measured by the van der Pauw Method

R. D. Westbrook

*Solid State Division, Oak Ridge National Laboratory, Oak Ridge, Tennessee 37830*

### ABSTRACT

Carrier mobility is often used to evaluate semiconductor material. A low value of mobility is generally construed to imply the presence of impurities or defects that adversely affect carrier transport. It is shown theoretically that low mobility values will also be obtained by van der Pauw measurements on samples containing certain types of radial inhomogeneities in the distribution of ionized impurities. The theoretical predictions have been confirmed by experiments on germanium slices cut from Czochralski-grown crystals.

The purpose of this work is to show that the apparent charge carrier mobility in a slice of semiconductor material, as measured by the van der Pauw method (1), will be anomalously low if certain types of ionized impurity gradients are present. Crystals grown by the Czochralski method for our high-purity germanium program sometimes contain both p- and n-type regions, as illustrated by the schematic longitudinal section shown in Fig. 1. A slice taken normal to the growth direction at A shows little if any radial gradient in net acceptor concentration. At B, near the point on the axis where the core becomes n-type, the net acceptor concentration is higher at the perimeter of the slice than at the center. At C, there is a radial n-p junction, and the net acceptor concentration increases from the junction to the perimeter. In this case the junction may be considered as a very steep gradient where the net acceptor concentration changes from negative to positive. Similar radial variations in donor and acceptor concentrations in high-purity germanium crystals have been observed at other laboratories, and the effects of these variations on various properties of high-purity germanium photon detectors have been reported (2, 3).

The van der Pauw method (1) is useful in characterizing semiconductor crystals because it permits measurements of the Hall coefficient and resistivity to be made on whole slices taken from a crystal, rather than being limited to measurements on bar-shaped samples taken from each slice. One therefore obtains some average value of the carrier concentration and mobility in the slice according to the relationships

$$n = \frac{1}{eR}$$

$$\mu = R/\rho$$

where  $n$  is the carrier concentration,  $e$  the electronic charge,  $R$  the Hall coefficient,  $\mu$  the mobility, and  $\rho$  the resistivity. In van der Pauw measurements on crystals of the type shown in Fig. 1, it was found that the apparent mobility decreased for slices cut at intervals between A and C. This observation led us to investigate the consequences of positive radial gradients in the carrier concentration on the results of van der Pauw measurements and to determine the degree to which such gradients influence the apparent mobility. (We designate a radial gradient as positive when the carrier concentration increases from the center of a slice to the perimeter.)

### Theory

*Radial n-p junction.*—Wolfe, Stillman, and Rossi (4), (WSR), have developed a general model of apparent mobility in a cylindrically symmetrical semiconductor slice of radius  $a$ , containing an outer region of resistivity  $\rho$  and mobility  $\mu$  and a central region of radius  $b$ , resistivity  $\rho_0$ , and mobility  $\mu_0$  (Fig. 2). They show that van der Pauw measurements will lead to anomalously high values of mobility when  $\rho_0 \ll \rho$  and  $\mu B \ll 1$  (electrostatic units), where  $B$  is the magnetic field ( $\mu B \ll 10^8$  when  $\mu$  is in square centimeters/volt-second and  $B$  is in gauss).

By applying the WSR model to the case where  $\rho_0 \gg \rho$ , which approximates a sample containing a radial n-p junction, it can readily be shown that the apparent Hall coefficient,  $R_{app}$ , is the same as the Hall coefficient,

Key words: impurity distribution, radial gradient, Hall mobility, anomalous mobility.



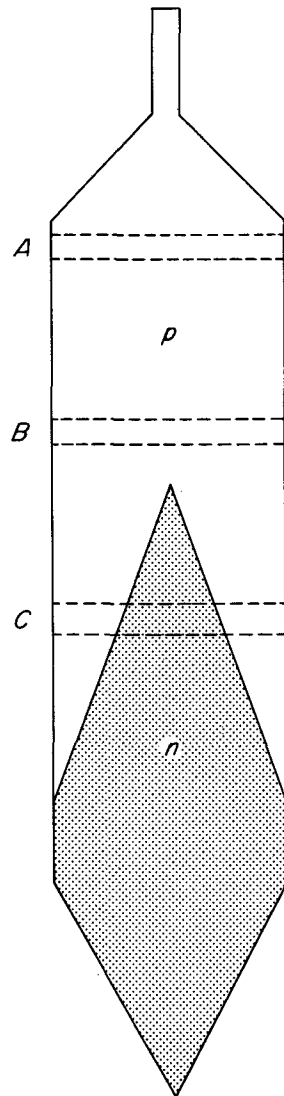


Fig. 1. Location of p- and n-type regions in high-purity germanium crystal grown by the Czochralski method. The positions of three representative slices are indicated by dashed lines.

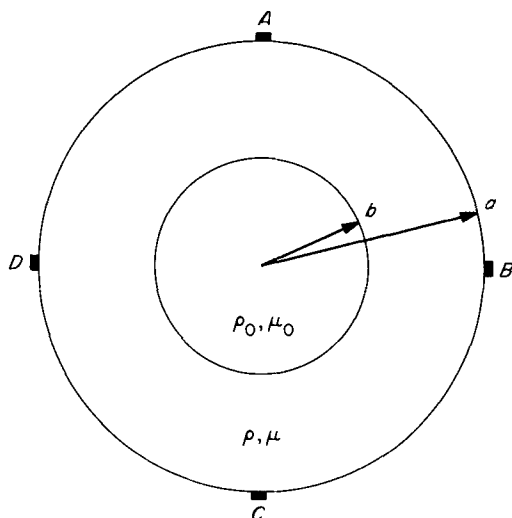


Fig. 2. Sample geometry used in this work. Electrical contacts A, B, C, D at 90° intervals. By the van der Pauw method  $R \equiv R(V_{BD}/I_{AC})$  and  $\rho = \rho(V_{AB}/I_{CD})$ .

$R$ , for a uniform disk with the same carrier concentration as the outer region, while the apparent resistivity,  $\rho_{app}$ , is larger than  $\rho$  by a factor depending upon  $\alpha = b/a$ . Apparent mobilities, therefore, are smaller than the values for the outer region. These results are similar to those of Juretschke, Landauer, and Swanson (5), (JLS), who studied Hall effect and resistivity in porous

material. For samples containing one or more hollow cylinders of arbitrary cross section parallel to the magnetic field and normal to the electric field, they also predict  $R_{app} = R$ , but obtain a somewhat different functional dependence of  $\rho_{app}$  on  $b/a$ .

The relations  $\rho_{app}/\rho$  vs.  $(1 - \alpha)$  for both models are shown as solid lines in Fig. 3. For the WSR model

$$\frac{\rho_{app}}{\rho} = \frac{1}{\ln 2} \sum_{n=1}^{\infty} \frac{(1 + \alpha^{2n})^2 + 2\alpha^{2n}}{(1 - \alpha^{4n})} \cdot \frac{(-1)^{n+1}}{n}$$

for the JLS model

$$\frac{\rho_{app}}{\rho} = \frac{1 + \alpha^2}{1 - \alpha^2}$$

Since  $\mu = R/\rho$  and  $R_{app} = R$ , the ratio of apparent mobility to the mobility in the outer region,  $\mu_{app}/\mu$ , is given by  $(\rho_{app}/\rho)^{-1}$ .

*Ionized impurity gradient.*—If there is a negative radial gradient in the net ionized impurity concentration, WSR show that  $\mu_{app}/\mu$  is expected to be greater than unity. By analogy we expect a positive radial gradient to result in  $\mu_{app}/\mu$  less than unity. This conclusion should apply to the case of a continuous gradient only, as at B in Fig. 1, and also to the case of a step function and a continuous gradient in the outer region as at C in Fig. 1.

### Experimental Procedure

*Radial n-p junction.*—As it was necessary to make van der Pauw measurements under extrinsic condi-

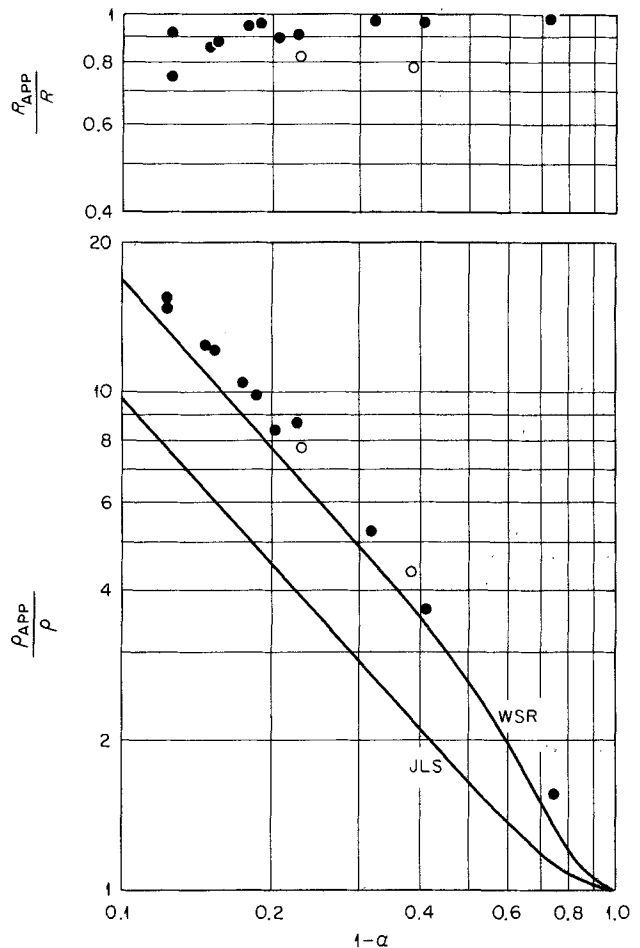


Fig. 3. Relative Hall coefficient and resistivity as a function of  $(1 - \alpha)$  for cored samples, ●, and samples containing radial n-p junctions, ○. Solid lines are theoretical curves from Wolfe, Stillman, and Rossi (WSR), and from Juretschke, Landauer, and Swanson (JLS).

tions, and as our high-purity crystals were intrinsic at room temperature, we worked at 77°K. To be consistent, the doped samples were also measured at that temperature.

Several slices of p-type germanium were cut from a crystal pulled in the  $\langle 100 \rangle$  direction. The material was 20-30 ohm-cm p-type, with a radial variation in resistivity of not more than 5-10% as determined by four-point-probe measurements. Etch pit concentrations were 2000-4000  $\text{cm}^{-2}$ , and there was no evidence of strain, lineage, or slip. A disk of 3.75 cm diameter was cut from each slice to eliminate any possible skin effects and to provide a uniform sample size. After making van der Pauw measurements on a whole disk to determine  $R$  and  $\rho$ , core drills of various diameters were used to cut one or more successively larger concentric holes in the sample to simulate the presence of an n-p junction. The samples were carefully etched before each measurement to minimize surface effects and also as a sensitive test to reveal any cracks that might have occurred during the core-drilling operation. Each cut was followed by a set of electrical measurements to determine  $R_{\text{app}}$  and  $\rho_{\text{app}}$ .

Two similar disks were diffused with lithium to form concentric n-type cores while retaining a uniform outer p-type region.

**Ionized impurity gradient.**—Slices containing radial ionized impurity gradients were cut from high-purity germanium crystals with impurity distributions of the type shown in Fig. 1. Several specimens were taken at intervals above and below the onset of the n-p junction. If a junction was present, it was located by immersing the sample into liquid nitrogen containing a suspension of barium titanate, and applying a high reverse bias voltage. Other methods of locating the junction, such as using thermal, electrical, or optical probes, proved to be less satisfactory.

## Results and Discussion

**Cored and diffused samples.**—Most of the experimental work to determine the effects of radial n-p junctions on the Hall coefficient and resistivity was performed on cored samples. A cored sample was assumed to be the approximate electrical equivalent of a disk containing a radial n-p junction and an outer, uniform p-type portion, under the condition that current flowing in the outer portion of the disk is large compared to the junction saturation current. The validity of this assumption was shown by measurements made on the two p-type samples into which n-type centers had been diffused. At 77°K the saturation current was much less than the sample currents of 10-100  $\mu\text{A}$  used in the van der Pauw measurements. The data points for the apparent resistivities of the diffused samples fell on the experimental curve for the cored samples; however the Hall coefficients of the diffused samples were slightly lower than expected, possibly because of the junction current.

Figure 3 shows the experimental results for  $R_{\text{app}}/R$  and  $\rho_{\text{app}}/\rho$  as functions of  $(1 - \alpha)$ . Representative values of  $R$  and  $\rho$  at 77°K for uniform uncored samples were  $4.5\text{-}6.0 \times 10^4 \text{ cm}^3/\text{coulomb}$  and 1.4-1.0 ohm-cm, respectively. The resistivity data agree rather well with the WSR model; the experimental values are generally a few per cent higher than the theoretical curve. Since  $R_{\text{app}}/R \approx 1$ , the apparent mobility ratio,  $\mu_{\text{app}}/\mu$ , is essentially the same as  $(\rho_{\text{app}}/\rho)^{-1}$  and therefore is not plotted in Fig. 3, but is shown in Fig. 4.

**Continuous concentration gradients.**—For these experiments we chose crystals with the radial characteristics illustrated in Fig. 1. For those slices that contained an n-p junction, as well as a positive radial gradient in net acceptor concentration from the junction to the perimeter, the measured quantities were influenced by both the diameter of the n-type core and the magnitude of the gradient. Values of  $R$  and  $\rho$  could not be assigned to these samples as was possible

in the case of the cored and diffused samples, which initially were of uniform concentration. The apparent mobility measured for each slice was therefore compared to the mobility measured for uniformly doped samples cut from the top of the crystal.

At some point along each crystal,  $\mu_{\text{app}}/\mu$  began to decrease from unity. Beginning at this point the slices were probed for the existence of a radial n-p junction by the barium titanate decoration method. The junctions were not always well defined and occasionally deviated from a circular pattern, so that values of  $\alpha$  often had to be estimated.

The data for  $\mu_{\text{app}}/\mu$  in the high-purity germanium samples are presented in Fig. 4, which includes those for the cored and diffused samples for comparison. In slices taken above the junction, represented in the figure by points along the  $(1 - \alpha) = 1$  axis,  $\mu_{\text{app}}/\mu$  ranges from unity to about 0.4-0.5, showing that the apparent mobility decreases as the radial ionized impurity gradient increases. As the junction appears and its radius increases,  $\mu_{\text{app}}/\mu$  continues to decrease with a slope similar to that for samples containing an n-p junction but no gradient. Therefore, it appears that the contribution of the radial gradient to the decrease in apparent mobility remains essentially constant as a function of length for all the crystals studied.

## Summary

The van der Pauw method of evaluating semiconductor slices will yield erroneously high values of resistivity, and hence erroneously low values of apparent mobility, if the sample contains either a radial n-p junction (and the sample current is large compared to the junction saturation current) or a positive

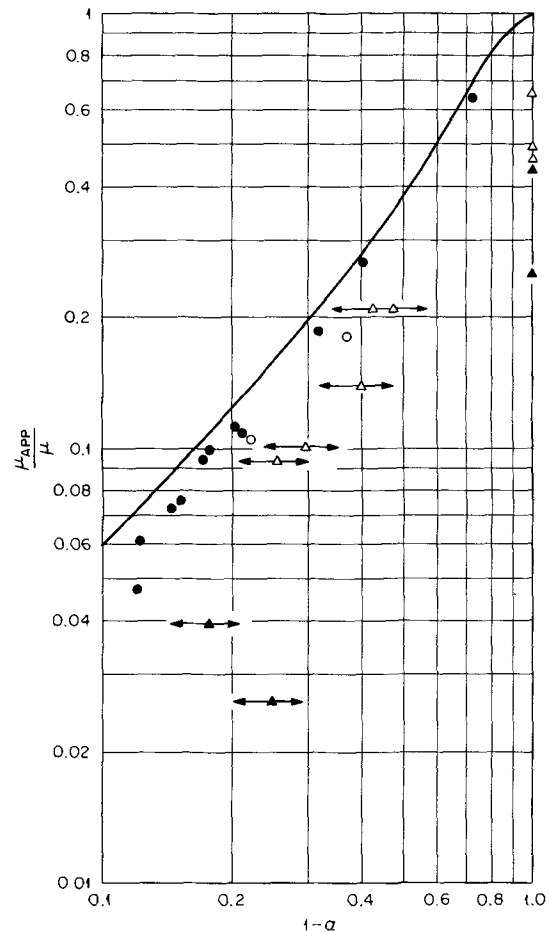


Fig. 4. Apparent mobility as a function of  $(1 - \alpha)$ . Solid curve from the model of WSR.  $\Delta$ , samples from one high-purity crystal containing a radial n-p junction;  $\blacktriangle$ , samples from four similar crystals;  $\bullet$ , cored samples;  $\circ$ , diffused samples. Error bars indicate uncertainty in location of junction.

radial gradient in carrier concentration. If both a junction and a positive gradient in the outer region are present, the effects are additive.

#### Acknowledgment

The author wishes to thank J. W. Cleland, M. Mostoller, and T. Kaplan of this laboratory for many discussions during the course of the work, and also to acknowledge the help obtained through private communication with C. M. Wolfe of M.I.T. Lincoln Laboratory. This research was sponsored by the United States Atomic Energy Commission under contract with Union Carbide Corporation.

Manuscript submitted Feb. 5, 1974; revised manuscript received April 17, 1974.

Any discussion of this paper will appear in a Discussion Section to be published in the June 1975 JOURNAL. All discussions for the June 1975 Discussion Section should be submitted by Feb. 1, 1975.

The publication costs of this article have been assisted by the Oak Ridge National Laboratory.

#### REFERENCES

1. L. J. van der Pauw, *Philips Res. Rept.*, **13**, 1 (1958).
2. E. E. Haller, W. L. Hansen, and F. S. Goulding, *IEEE Trans. Nucl. Sci.*, **NS-20**, 481 (1973).
3. R. D. Baertsch, *ibid.*, **NS-20**, 488 (1973).
4. C. M. Wolfe, G. E. Stillman, and J. A. Rossi, *This Journal*, **119**, 250 (1972).
5. H. J. Juretschke, R. Landauer, and J. A. Swanson, *J. Appl. Phys.*, **27**, 838 (1956).

## A Chemical Etchant for the Selective Removal of GaAs Through SiO<sub>2</sub> Masks

J. J. Gannon and C. J. Nuese

RCA Laboratories, Princeton, New Jersey 08540

#### ABSTRACT

An NH<sub>4</sub>OH:H<sub>2</sub>O<sub>2</sub> etchant has been developed for etching selected regions of GaAs through windows in an SiO<sub>2</sub> mask. This etchant has been found to provide flat etching profiles across the unmasked regions of the GaAs, and has considerably reduced undercutting commonly caused by attack of the SiO<sub>2</sub>. The chemical etching rates have been evaluated and have been found to depend strongly on the concentration of the etching solution and on the crystal orientation of the GaAs. The utility of the NH<sub>4</sub>OH:H<sub>2</sub>O<sub>2</sub> for GaAs device preparation has been demonstrated by its application to the fabrication of interdigitated GaAs bipolar transistors with 5 μm base-emitter separation.

During the years, as the technology of GaAs crystal growth has advanced to the point where it is useful and occasionally unique in device fabrication, many chemical etches have been developed. The most useful of these are Caro's (1), bromine-methanol (2), sodium-hypochlorite, and more recently, a mixture of NH<sub>4</sub>OH:H<sub>2</sub>O<sub>2</sub> (3) used as a chemical-mechanical polishing etch. Each of these etches has its advantages for some applications. Each too has its drawbacks: the acid etches cannot be used in the presence of most metal contacts, while the alkaline etches tend to attack SiO<sub>2</sub> masks commonly used in device technology. A more serious disadvantage common to most of the etches mentioned above is a tendency toward an enhanced etch rate near the edges of an SiO<sub>2</sub> mask (4), presumably due to migration of adsorbed etchant molecules along the mask.

In a previous publication (4), Shaw described a NaOH:H<sub>2</sub>O<sub>2</sub> solution that provided a flat GaAs etching profile over the area of a "window" in an SiO<sub>2</sub> protective surface mask. We found this characteristic attractive when selectively etching through portions of a three-layered GaAs transistor structure to expose a thin inner (base) layer for subsequent contacting (5). For the simple, large-area stripe geometry used in these early prototype transistors, resolution was of little concern.

In subsequent work, we found it necessary to fabricate more sophisticated GaAs bipolar transistors with a closely spaced (~5 μm) interdigitated base-emitter geometry (6). For the fabrication of these devices, the attack of the SiO<sub>2</sub> mask by the NaOH:H<sub>2</sub>O<sub>2</sub> was undesirable, since it provided poor resolution due to undercutting. An alternative chemical etch, described

in this paper, led to a major reduction in the attack of the SiO<sub>2</sub>, resulting in well-defined, closely spaced transistor patterns with highly polished surfaces, free of imperfections. As we will show below, the new etch, a mixture of NH<sub>4</sub>OH and H<sub>2</sub>O<sub>2</sub>, also provides relatively low etching rates for both n- and p-type <100> GaAs, and a flat etching plane over the entirety of the areas defined by the SiO<sub>2</sub> mask. Hence, this etch should be of general value to GaAs device technology.

#### Experimental Procedure

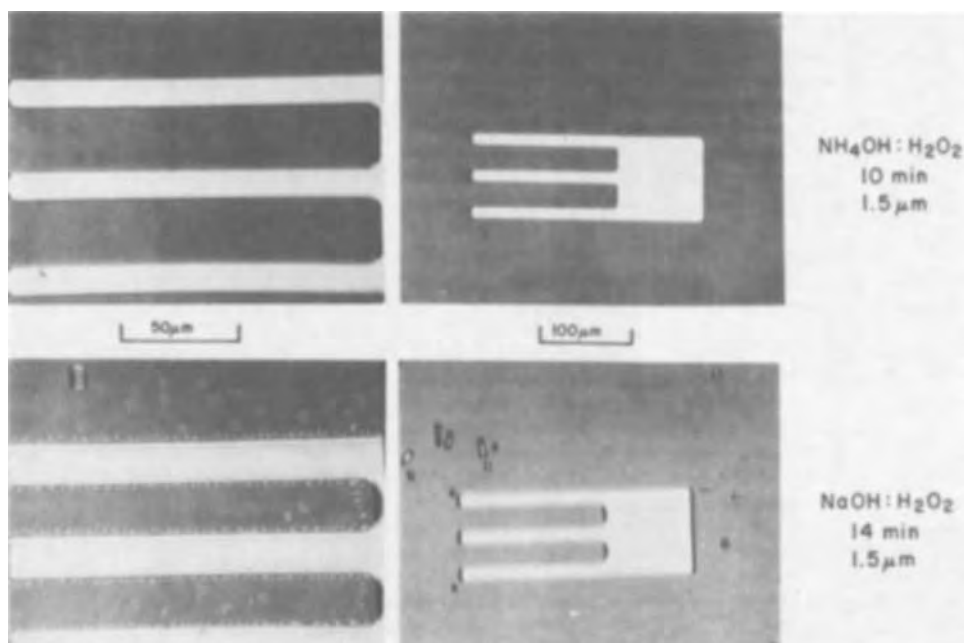
The "standard" NH<sub>4</sub>OH:H<sub>2</sub>O<sub>2</sub> etchant described in this paper was prepared by mixing 20 mliters of NH<sub>4</sub>OH, 7 mliters of 30% H<sub>2</sub>O<sub>2</sub> (stabilized), and 973 mliters of H<sub>2</sub>O to form a 0.3N NH<sub>4</sub>OH:0.1N H<sub>2</sub>O<sub>2</sub> solution. The etchant was always used at room temperature and was freshly mixed prior to each experiment. The SiO<sub>2</sub> masks used in conjunction with this etchant were approximately 3000Å thick and were prepared by reacting silane and oxygen at 350°C (7). The desired geometries (in this case, emitter or base transistor patterns) were defined by standard photoresist techniques using KTFR. Most of the GaAs used in the etching experiments was oriented in the <100> crystallographic direction or 3° off the <100> and was prepared by a vapor-phase growth technique described previously (8). A few experiments were performed on <111>-oriented GaAs to delineate the effects of crystal orientation on etching rates.

#### Results and Discussion

*Undercutting.*—A comparison of the undercutting for the NH<sub>4</sub>OH:H<sub>2</sub>O<sub>2</sub> etch and the previous NaOH:H<sub>2</sub>O<sub>2</sub> etch was made by masking an n-type GaAs epitaxial layer with SiO<sub>2</sub> and defining a "finger"-type transis-

Key words: selective etching, GaAs, bipolar transistors.

Fig. 1. Comparison of undercutting and attack of  $\text{SiO}_2$  mask due to chemical etching with  $\text{NH}_4\text{OH}:\text{H}_2\text{O}_2$  and  $\text{NaOH}:\text{H}_2\text{O}_2$ .



tor pattern with KTFR. Different pieces of this wafer were then exposed to the two etches for a time sufficient to etch about  $1.5 \mu\text{m}$  into the GaAs (10 min for the  $\text{NH}_4\text{OH}:\text{H}_2\text{O}_2$ ; 14 min for the  $\text{NaOH}:\text{H}_2\text{O}_2$ ). The results of this experiment are shown in Fig. 1, where the attack of the  $\text{SiO}_2$  by the  $\text{NaOH}:\text{H}_2\text{O}_2$  is readily apparent in the lower photomicrographs. The crystallographic shape of many of the defects here is probably due to preferential etching of the GaAs beneath pinholes and weak spots in the  $\text{SiO}_2$ , which become enlarged during the etching process by dissolution of the  $\text{SiO}_2$  from both sides of the mask. In contrast, the upper photomicrographs illustrate that the  $\text{NH}_4\text{OH}:\text{H}_2\text{O}_2$  does not give rise to such defects, since it does not attack the  $\text{SiO}_2$  perceptibly.<sup>1</sup> In the lower left-hand photo of Fig. 1, the attack of the  $\text{SiO}_2$  by the  $\text{NaOH}:\text{H}_2\text{O}_2$  is further demonstrated by the significant widening of each of the fingers of the pattern. Here, the finger width was measured to be  $17.4 \mu\text{m}$ , in contrast to a value of  $12.3 \mu\text{m}$  for the pattern etched with  $\text{NH}_4\text{OH}:\text{H}_2\text{O}_2$ . Since the width of the original photoresist mask was  $12.0 \mu\text{m}$ , the finger width after etching represents the amount of lateral etching or undercutting for the two etchants (about  $0.15 \mu\text{m}$  per edge for  $\text{NH}_4\text{OH}:\text{H}_2\text{O}_2$  and about  $2.7 \mu\text{m}$  per edge for  $\text{NaOH}:\text{H}_2\text{O}_2$ ). We should add that the slight widening that occurs for the  $\text{NH}_4\text{OH}:\text{H}_2\text{O}_2$  is thought to arise from enhanced lateral etching rates at the GaAs- $\text{SiO}_2$  interface rather than to dissolution of the  $\text{SiO}_2$  mask. This statement is supported by occasional observations of  $\text{SiO}_2$  layers that extend a small distance ( $<1 \mu\text{m}$ ) over the etched region of the GaAs after a lengthy etching process.

**Etching rates.**—The etching rate for the “standard”  $0.3\text{N NH}_4\text{OH}:\text{H}_2\text{O}_2$  solution was determined for a series of two n-type and two p-type GaAs Czochralski-grown  $\langle 100 \rangle$ -oriented wafers that previously had been polished chemically (in Caro’s etch) to remove any work damage. As shown in Fig. 2, the etching distance was found to have a slightly sublinear dependence on etching time, probably due to a gradual dissociation of the  $\text{H}_2\text{O}_2$  after times on the order of 15–30 min. The maximum etching rate (for 0–10 min) was found to be about  $0.18\text{--}0.2 \mu\text{m}/\text{min}$  for n-type GaAs and  $0.12\text{--}0.14 \mu\text{m}/\text{min}$  for p-type GaAs. Although the dependence of etching rate on doping concentration

has not been evaluated in detail, both the n- and p-type wafers in Fig. 2 yielded somewhat higher etching rates for the more heavily doped sample.

For our applications, where etching distances on the order of  $1\text{--}2 \mu\text{m}$  were usually required, the slow etching rates demonstrated in Fig. 2 were highly desirable. However, for other applications, the rate could be increased significantly by simply increasing the concentration of the aqueous solution, as shown in Fig. 3. Here, for a concentration 10 times larger than the “standard”  $0.3\text{N NH}_4\text{OH}:\text{H}_2\text{O}_2$  solution, an etching rate of about  $1.4 \mu\text{m}/\text{min}$  was obtained for the particular wafer used in Fig. 3. This is about 5.5 times larger than the rate obtained for the more dilute “standard” solution. In addition, the highly polished surface appearance of the GaAs was maintained after etching with each of the  $\text{NH}_4\text{OH}:\text{H}_2\text{O}_2$  mixtures used in Fig. 3. Although it would be interesting to explore the  $\text{NH}_4\text{OH}:\text{H}_2\text{O}_2:\text{H}_2\text{O}$  family of solutions over a much broader range of ratios and concentrations, the etching rates between about  $0.12$  and  $1.4 \mu\text{m}/\text{min}$  illustrated in Fig. 2 and 3 have been sufficient for most GaAs applications encountered to date.

The  $\text{NH}_4\text{OH}:\text{H}_2\text{O}_2$  etchant described in this paper has been mostly used for  $\langle 100 \rangle$ -oriented GaAs sur-

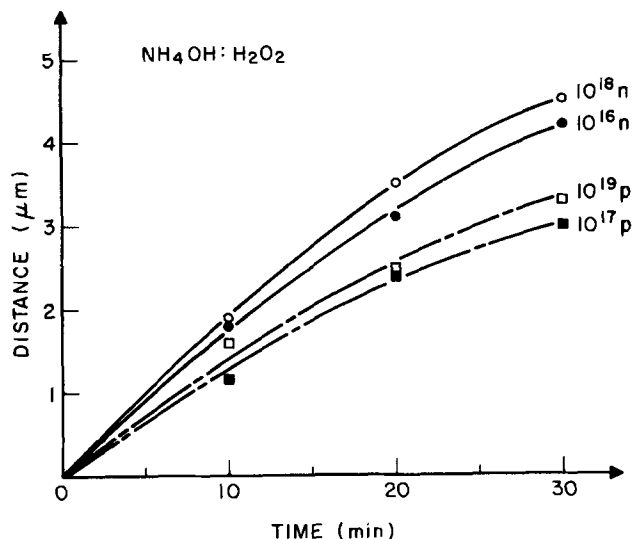


Fig. 2. Etching rates for n- and p-type GaAs in  $0.3\text{N NH}_4\text{OH}:\text{H}_2\text{O}_2$  at room temperature. The crystal orientation is  $\langle 100 \rangle$ .

<sup>1</sup> In an attempt to determine the extent of dissolution of a deposited  $\text{SiO}_2$  layer in  $\text{NH}_4\text{OH}:\text{H}_2\text{O}_2$ , a GaAs wafer covered with  $3000\text{Å}$  of  $\text{SiO}_2$  was placed in  $3\text{N NH}_4\text{OH}:\text{H}_2\text{O}_2$  for 8 hr. (The solution was changed every hour.) At the end of this time, no perceptible change in the  $\text{SiO}_2$  could be observed.

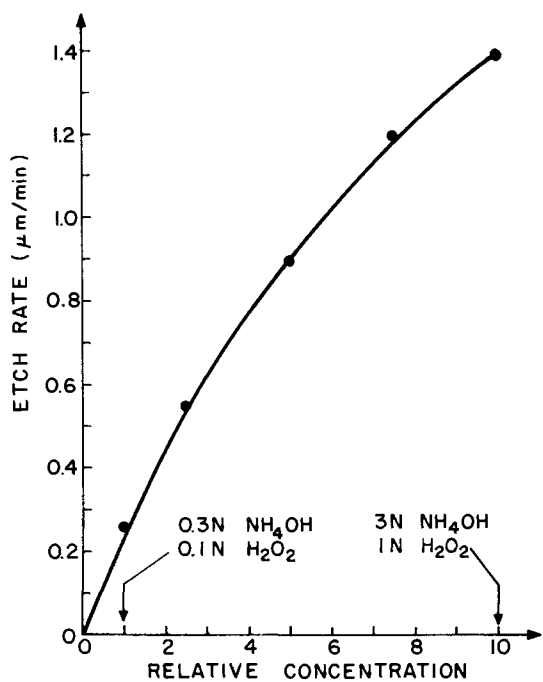


Fig. 3. Dependence of etch rate (in micrometers per minute) on the relative concentration of the  $\text{NH}_4\text{OH}:\text{H}_2\text{O}_2$  etchant for  $\langle 100 \rangle$ -oriented GaAs.

faces. However, it has been evaluated a few times on  $\{111\}$  surfaces. For these experiments, n-type GaAs wafers oriented in the  $\langle 111 \rangle$ A,  $\langle 111 \rangle$ B, and  $\langle 100 \rangle$  crystallographic directions were simultaneously etched in the "standard"  $\text{NH}_4\text{OH}:\text{H}_2\text{O}_2$  solution for 30 min. The etching distances for these orientations are listed in Table I. Immediately evident here is the enhanced etching rate for the  $\{111\}$ B surface and the retarded rate for the  $\{111\}$ A. Similar effects have been previously observed for GaAs etched with  $\text{Br}_2\text{-CH}_3\text{OH}$  (9)

Table I. Effect of crystal orientation on the etch rate of  $\text{NH}_4\text{OH}:\text{H}_2\text{O}_2$

Orientation	Etching distance (μm)	Average etching rate (μm/min)
$\langle 111 \rangle$ B	6.0	0.20
$\langle 100 \rangle$	3.7	0.12
$\langle 111 \rangle$ A	1.1	0.037

and  $\text{H}_2\text{SO}_4:\text{H}_2\text{O}_2$  (10). The enhanced etch rate for the  $\{111\}$ B surface is thought to arise from the unshared electron pairs of each surface atom, while the passive chemical nature of the  $\{111\}$ A surface is due to the absence of unshared bonds (11, 12).

**Preferential etching.**—The preferential etch rates discussed above also were apparent from an observed incline of the edges of the etching pattern, as shown in Fig. 4. Here, a rectangular grid was defined with  $\text{SiO}_2$  on the  $\{100\}$  surface of GaAs, after which the exposed regions of the GaAs were etched with a standard solution of  $\text{NH}_4\text{OH}:\text{H}_2\text{O}_2$ . The etching profile was then examined by cleaving the wafer in orthogonal directions along the  $(011)$  and  $(0\bar{1}1)$  planes. As shown in Fig. 4, the edges of the pattern deviated appreciably from a direction normal to the  $(100)$  surface, in one case sloping downward toward the  $\text{SiO}_2$  [Fig. 4(b)], and in the other, sloping downward away from the  $\text{SiO}_2$  mask [Fig. 4(a)]. This type of etching profile is thought to occur due to the very slow etching rate for the  $\{111\}$ A planes, as we have illustrated previously in Table I. The fact that the direction of incline changes for the two cleavage planes in Fig. 4 merely reflects the change in polarity of the chemical bonds associated with the  $\{111\}$ A planes in zincblende structures upon a  $90^\circ$  crystallographic rotation about the  $\langle 100 \rangle$  axis. Tarui and co-workers (9) have observed similar etching patterns in  $\langle 100 \rangle$ -oriented GaAs etched with bromide-methanol, which also has a very slow etch rate for the  $(111)$ A planes. We should mention that the angle of incline observed in our present

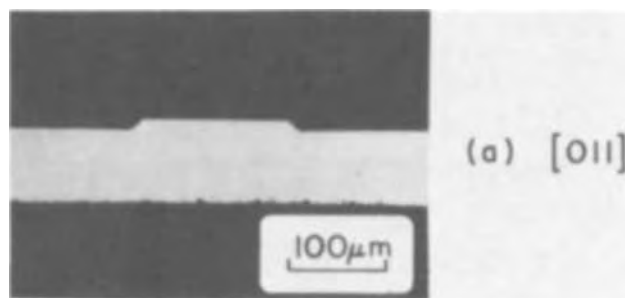
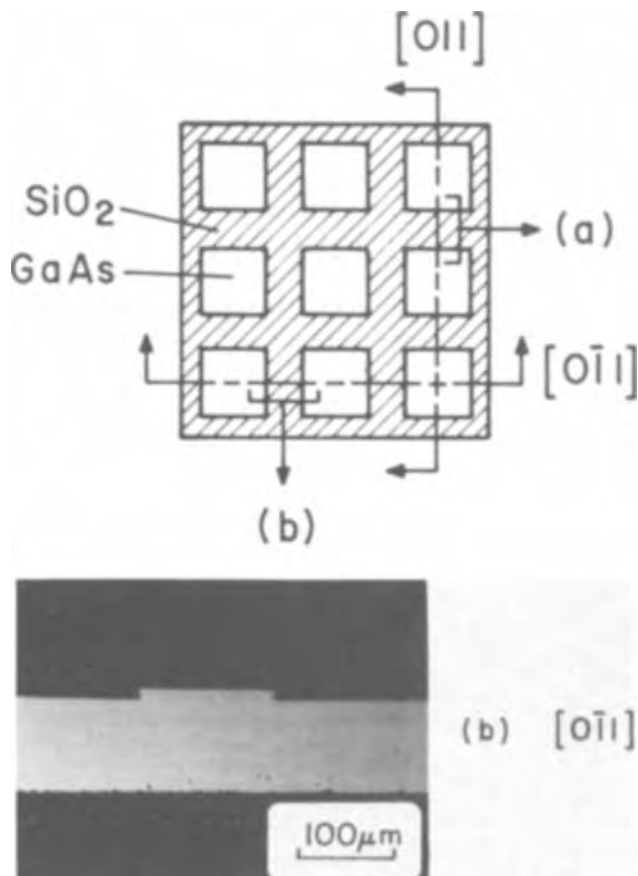


Fig. 4. Etching profile for a square pattern defined by an  $\text{SiO}_2$  mask on GaAs. The etched region was cross sectioned in orthogonal  $\langle 110 \rangle$  directions by cleaving. Note the change in the slope of the edges produced by the  $90^\circ$  crystallographic rotation about the  $\{100\}$  growth axis.

work varied from crystal to crystal in the range of 15°-40° from normal. However, these angles have little physical meaning due to the slight lateral etching near the surface discussed previously.

### Device Application

The  $\text{NH}_4\text{OH}:\text{H}_2\text{O}_2$  etchant whose characteristics were described above has been used extensively for the fabrication of three-layered GaAs bipolar transistors (6). In this final section of our paper, we describe the manner in which the  $\text{NH}_4\text{OH}:\text{H}_2\text{O}_2$  was used for this purpose, since it illustrates the utility of the etchant for general GaAs device fabrication.

For our transistor fabrication, an interdigitated array of emitter and base "fingers" was desired, with a separation of about 5  $\mu\text{m}$ . To obtain this, an emitter contact was first evaporated to the outermost GaAs layer through a  $\text{SiO}_2$  pattern, and sintered to ensure good adhesion [see Fig. 5(a)]. The inner base layer was then exposed for contacting by evaporating  $\text{SiO}_2$  over the emitter, defining a pattern in the  $\text{SiO}_2$  with standard photoresist technology, and etching through the emitter layer (1-2  $\mu\text{m}$  thick) with the  $\text{NH}_4\text{OH}:\text{H}_2\text{O}_2$  etchant [see Fig. 5(b)]. A flat etching profile was essential here to avoid penetrating the base layer, which was only 1  $\mu\text{m}$  thick. The ohmic contact to the base [Fig. 5(c)] was then obtained by using a third  $\text{SiO}_2$  pattern slightly smaller than that used for etching. The utility of the  $\text{NH}_4\text{OH}:\text{H}_2\text{O}_2$  etchant for this fabrication procedure is demonstrated by the sharpness of the edges and by the smoothness of the metallization in Fig. 5(a)-5(c).

A cross-sectional view of a GaAs transistor prepared as described above is illustrated in Fig. 6(a), where a {110} cleavage plane has been used to bisect one of the interdigitated base-emitter patterns. The

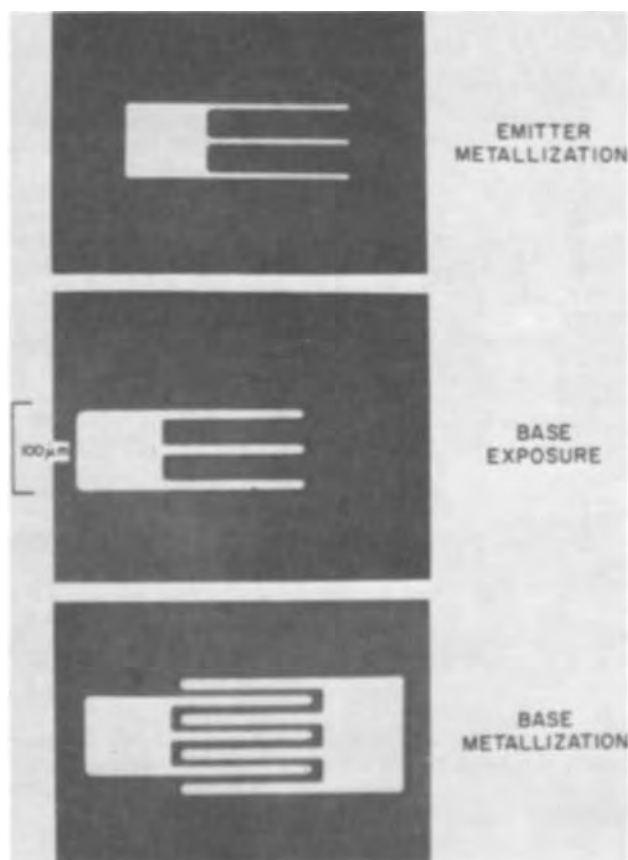


Fig. 5. Photomicrographs of GaAs bipolar transistor fabrication: (top) evaporated emitter metallization, (center) exposure of inner base layer in selected areas by etching with  $\text{NH}_4\text{OH}:\text{H}_2\text{O}_2$ , (bottom) completed base-emitter transistor array following evaporation of base metallization in etched regions.

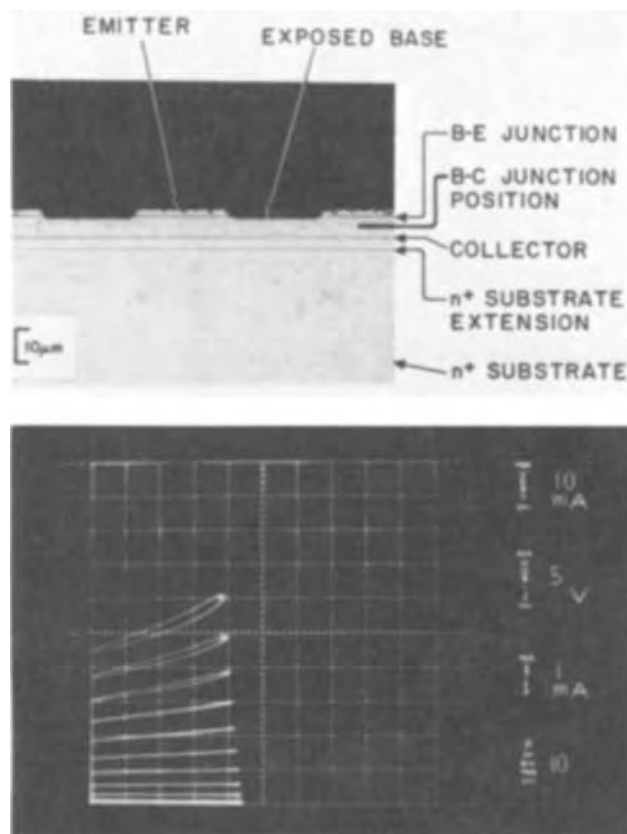


Fig. 6. (Top) {110} cleavage plane of GaAs n-p-n transistor structure after exposing base in selected areas with  $\text{NH}_4\text{OH}:\text{H}_2\text{O}_2$  etch. Note flatness of etching front and its location just below base-emitter junction. Base-collector junction was difficult to stain, but was located approximately where indicated. (Bottom) I-V characteristics of GaAs bipolar transistor after complete fabrication. Current gain is approximately 10.

flatness of the etching front and its position just beneath the emitter-base p-n junction is clearly evident. The p-n junctions for this transistor were delineated by an electrolytic etch after cleaving. The base-collector junction is difficult to accent by this technique because of the light doping in the base and collector layers ( $1 \times 10^{17}$  and  $1 \times 10^{16} \text{ cm}^{-3}$ , respectively), however, the approximate position of the base-collector junction is indicated by the line drawn at the side of the photomicrograph. We should stress that if we had used one of the common GaAs etches that provide enhanced etching rates near the edges of an  $\text{SiO}_2$  mask, the base would have been penetrated in these locations, thereby shorting the emitter to the collector during the subsequent base metallization.

The I-V characteristics of a GaAs transistor fabricated with the  $\text{NH}_4\text{OH}:\text{H}_2\text{O}_2$  etchant is illustrated in Fig. 6(b). Here, a current gain of approximately 10 was obtained, which is about the value expected for GaAs n-p-n transistors with a base width of 1-2  $\mu\text{m}$  (5).

The success of the fabrication procedure described above relies heavily on an etchant that provides a flat etching front and a slow etching rate. In addition, the chemical makeup of the etchant must be such that  $\text{SiO}_2$  masks are not appreciably attacked by the etchant. Clearly, the  $\text{NH}_4\text{OH}:\text{H}_2\text{O}_2$  etchant described in this paper meets these requirements, and should find general usefulness for the fabrication of GaAs devices.

### Summary

An  $\text{NH}_4\text{OH}:\text{H}_2\text{O}_2$  chemical etch for GaAs has been developed that provides a flat etching front when used for selective etching through holes in an  $\text{SiO}_2$  mask. Furthermore, this etchant does not attack  $\text{SiO}_2$  per-

ceptibly, thereby providing improved resolution and definition for fine photoresist patterns.

The etching rate of dilute  $\text{NH}_4\text{OH}:\text{H}_2\text{O}_2$  solutions is on the order of 0.1-0.2  $\mu\text{m}/\text{min}$  (for {100} GaAs) and increases to values greater than 1  $\mu\text{m}/\text{min}$  with increasing solution concentration. The rate depends strongly on crystal orientation, decreasing as the orientation is changed from {111}B to {100} to {111}A. The slow etching rate for the {111}A planes results in inclined etching fronts at the edges of an  $\text{SiO}_2$  mask, similar to those found previously with bromine-methanol solutions (9).

The characteristics mentioned above, as well as the shiny, unblemished surfaces provided by this etchant, make the  $\text{NH}_4\text{OH}:\text{H}_2\text{O}_2$  attractive for a variety of GaAs device applications. As an example, bipolar GaAs transistors with current gains greater than 10 have been routinely fabricated from three-layered n-p-n structures by etching into the inner base layer with  $\text{NH}_4\text{OH}:\text{H}_2\text{O}_2$ .

#### Acknowledgments

The authors wish to thank R. H. Dean and G. H. Olsen for their valuable comments concerning the preferential nature of the etching profile. We also would like to thank J. Alexander for his extensive efforts in the areas of  $\text{SiO}_2$  deposition and photoresist masking, and N. Goldsmith for critical review of this manuscript. This research was supported in part by the National Aeronautics and Space Administration, Huntsville, Alabama, and by RCA Laboratories, Princeton, New Jersey.

Manuscript received Feb. 28, 1974.

Any discussion of this paper will appear in a Discussion Section to be published in the June 1975 JOURNAL. All discussions for the June 1975 Discussion Section should be submitted by Feb. 1, 1975.

The publication costs of this article have been assisted by the RCA Corporation.

#### REFERENCES

1. M. V. Sullivan and L. A. Pompliano, *This Journal*, **108**, 60C (1961). See also J. W. Faust, Jr., in "Preparation of III-V Compounds," Vol. 1, R. K. Willardson and H. L. Goering, Editors, Rheinhold Publishing Corp., New York (1962).
2. C. S. Fuller, *This Journal*, **109**, 880 (1962).
3. J. C. Dymont and G. A. Rozgonyi, *ibid.*, **118**, 1346 (1971).
4. D. W. Shaw, *ibid.*, **113**, 958 (1966).
5. C. J. Nuese, J. J. Gannon, R. H. Dean, H. F. Gosensberger, and R. E. Enstrom, *Solid-State Electron.*, **15**, 81 (1972).
6. C. J. Nuese, Final Report, Contract No. NAS8-27086, National Aeronautics and Space Administration, Huntsville, Alabama 35812, June 1972.
7. N. Goldsmith and W. Kern. *RCA Rev.*, **28**, 153 (1967).
8. J. J. Tietjen and J. A. Amick, *This Journal*, **113**, 724 (1966).
9. Y. Tarui, Y. Komiyama, and Y. Harada, *ibid.*, **118**, 118 (1971).
10. S. Iida and K. Ito, *ibid.*, **118**, 768 (1971).
11. H. C. Gatos and M. C. Lavine, *J. Phys. Chem. Solids*, **14**, 169 (1960).
12. H. C. Gatos and M. C. Lavine, *This Journal*, **107**, 427 (1960).

## A Simplified Method of Measuring Lifetime Using Steady-State Back Illumination of an MOS Capacitor

C. St. L. Rhodes and C. A. T. Salama\*

Department of Electrical Engineering, University of Toronto, Toronto, Ontario, Canada

#### ABSTRACT

The semiconductor minority carrier lifetime in an MOS capacitor can be determined from measurements of back-illumination induced increases in both the steady-state, high frequency, inversion region capacitance and the rate of recovery following deep depletion. The theory of the method is discussed and its application is illustrated by means of experimental results obtained from MOS capacitors fabricated on a silicon substrate. Unlike other MOS deep depletion techniques, this method of minority carrier lifetime determination is not subject to errors due to either peripheral surface-state generation or the assumption of a dominant midgap trap. The over-all simplicity, accuracy, and speed of implementation of this method make it suitable for material specification and process control applications.

Previous authors (1-4) have shown that both surface-state generation effects and the assumption of a midgap trap level in the semiconductor can lead to substantial errors in minority carrier lifetime measurements by standard MOS deep depletion techniques. Rhodes and Salama (4) discussed the response of an MOS capacitor to back illumination under both deep depletion and steady-state conditions, and suggested the possibility of measuring the minority carrier lifetime using this method. This paper describes a simplified procedure for implementing the back-illumination technique, and illustrates a method for rapid reduction of the data, enabling the lifetime to be found readily without graphical analysis using only simple calculations. The method is particularly useful in de-

vice applications where exact specification of the minority carrier diffusion length is important. For example, in the case of charge-coupled imaging devices and photodiode arrays scanned by MOS shift registers, the lifetime affects the integration or storage time of the array and is a very critical parameter in determining the over-all usefulness of these devices as optical sensors in television camera applications.

The method involves application of steady-state back illumination to an MOS capacitor, and measurement of the small signal, high frequency,<sup>1</sup> heavy inversion region capacitance and the recovery of the MOS capacitor from a deeply depleted condition, as illustrated in Fig. 1 and 2. The minority carrier lifetime can be cal-

\* Electrochemical Society Active Member.

Key words: silicon, diffusion length, deep depletion.

<sup>1</sup> Throughout this paper the measurement frequency is assumed to be sufficiently high that light-induced conductance effects in the depletion region are negligible (5).

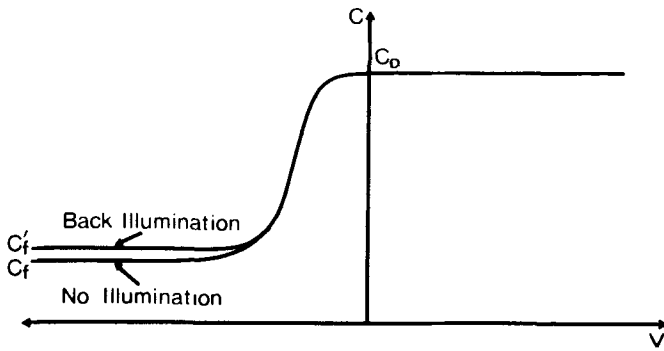


Fig. 1. Effect of back illumination on the steady-state, high frequency, heavy inversion region capacitance of an MOS capacitor on n-type silicon.

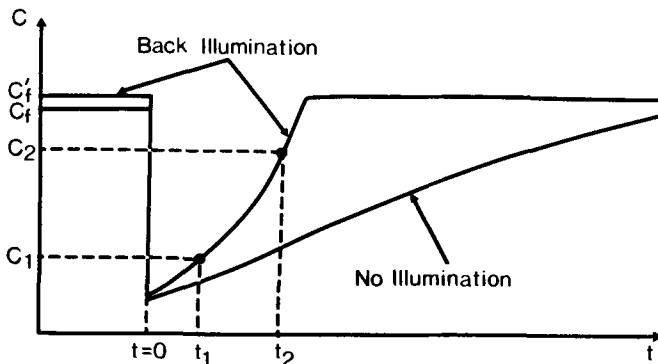


Fig. 2. Effect of back illumination on the transient C-t response following application of a deep depletion voltage step at  $t = 0$ .

culated from the excess minority carrier density obtained from Fig. 1 and the minority carrier diffusion flux obtained from Fig. 2.

### Theory

Zerbst (6) showed that the rate of change of the high frequency capacitance  $C$  of an MOS structure is related to the generation rate per unit area  $g$  by

$$\frac{d}{dt} \left( \frac{C}{C_o} \right) = \frac{K_o}{K_s X_o N} \left( \frac{C}{C_o} \right)^3 g \quad [1]$$

where  $K_o$ ,  $X_o$ , and  $C_o$  are the relative dielectric constant, thickness, and capacitance of the oxide, respectively,  $K_s$  is the relative dielectric constant of the semiconductor, and  $N$  the effective doping density.<sup>2</sup> The generation rate components consist of bulk, surface, and peripheral generation, and a component due to diffusion (1-4, 7).

Under deep depletion conditions with sufficient back illumination,<sup>3</sup> the only non-negligible component of  $g$  is  $g_d'$ , that component due to diffusion from the bulk (3, 4) Since this component is time independent it is easily evaluated by integrating [1] to get

$$g_d' = \frac{K_s X_o N}{2K_o (t_2 - t_1)} \left[ \left( \frac{C_o}{C_1} \right)^2 - \left( \frac{C_o}{C_2} \right)^2 \right] \quad [2]$$

where  $C_1$ ,  $t_1$  and  $C_2$ ,  $t_2$  are coordinates of a pair of arbitrarily chosen points on the C-t recovery curve shown in Fig. 2.

In steady state, with the MOS capacitor biased into the heavy inversion region, band bending causes the recombination rate per unit volume to be much greater in the depletion region than elsewhere. The total recombination rate per unit area, obtained by integrating the recombination rate per unit volume  $R$  over the

space charge region width  $X_d$ , is equal to the available flux of minority carriers. Under sufficient back illumination, this flux is approximately equal to the diffusion flux  $g_d'$  giving

$$g_d' = \int_0^{X_d} R dx \quad [3]$$

Provided the minority carrier diffusion length is greater than  $X_d$ , evaluation of Eq. [3] using Shockley-Read recombination theory and the depletion approximation (4) gives

$$g_d' = \frac{\pi}{2\tau} \left[ \frac{K_s \epsilon_o k T}{q^2 \ln \left( \frac{N}{p_o + \tau} \right)} \right]^{1/2} \quad [4]$$

where  $\epsilon_o$  is the permittivity of free space,  $q$  the electronic charge,  $\tau$  the minority carrier lifetime,  $p_o$  the thermal equilibrium minority carrier (hole) density in the neutral bulk,  $k$  the Boltzmann constant,  $T$  the absolute temperature, and  $\tau$  the excess minority carrier density at the edge of the space charge region under steady-state conditions.

The value of  $\tau$  required to solve Eq. [4] can be obtained from the illumination-induced shift in the high frequency, heavy inversion region capacitance. This shift from  $C_f$  to  $C_f'$  (see Fig. 1) can be related to the parameter  $\eta = (p_o + \tau)/p_o$  by the following equation (4)

$$\ln \eta = \frac{N}{\xi} \left( \frac{C_o}{C_f'} + \frac{C_o}{C_f} - 2 \right) \left( \frac{C_o}{C_f} - \frac{C_o}{C_f'} \right) \quad [5]$$

where  $\xi$  is defined by

$$\xi = \frac{2K_o^2 \epsilon_o k T}{q^2 K_s X_o^2} \quad [6]$$

Substituting  $n_i^2/N$  for  $p_o$ , where  $n_i$  is the intrinsic carrier density, and solving Eq. [4] for  $\tau$  in terms of  $\eta$  gives

$$\tau = \frac{\pi n_i}{2g_d'} \left[ \frac{K_s \epsilon_o (\eta - 1) k T}{q^2 N \ln \left( \frac{N^2}{\eta n_i^2} \right)} \right]^{1/2} \quad [7]$$

Thus the procedure for finding the lifetime  $\tau$  involves the determination<sup>4</sup> of  $N$  from  $C_o$  and  $C_f$ , the calculation of  $\eta$  from  $C_f'$  using Eq. [5] and [6], and finally the determination of  $\tau$  from Eq. [7] using the value of  $g_d'$  given by Eq. [2]. With sufficient illumination the diffusion flux dominates all other components of  $g$ , so the lifetime obtained in the above manner is not subject to errors due to either surface-state or bulk trap thermal generation effects.

### Experimental Procedure

To determine the minority carrier lifetime the apparatus illustrated in Fig. 3 is used for slice probing with back illumination. The associated measurement setup is illustrated in Fig. 4. In practice, the light levels required to make Eq. [2] valid are sufficiently large that the corresponding transient C-t curve is too fast for most mechanical X-Y recorders to follow; requiring the use of a storage oscilloscope or an analog data memory (Biomation Model 610).

The shift in the steady-state inversion region capacitance from  $C_f$  to  $C_f'$  is typically a few per cent of  $C_o$  at these light levels. To facilitate rapid and accurate recording of the steady-state capacitance data, the

<sup>4</sup> The depletion approximation (9) gives the relation

$$N = \frac{2\xi}{\left( \frac{C_o}{C_f} - 1 \right)^2} \ln \left( \frac{N}{n_i} \right)$$

which may be iteratively solved for  $N$  using Putley and Mitchell's (10) relation for  $n_i$

$$n_i = 3.10 \times 10^{10} T^{3/2} \exp \left( \frac{-0.603}{kT} \right) \text{ cm}^{-3}$$

<sup>2</sup> For simplicity, this analysis will be restricted to n-type silicon.  
<sup>3</sup> The back illumination is sufficient if the recovery time under illumination is less than one-tenth of the recovery time without illumination. Typically an incident photon flux of  $2.5 \times 10^{15} \text{ cm}^{-2} \text{ sec}^{-1}$  is sufficient.



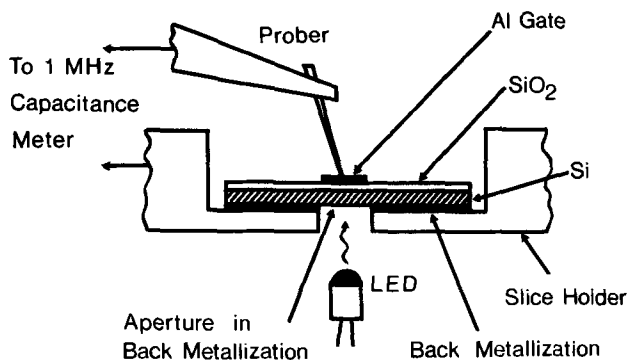


Fig. 3. Apparatus used for slice probing with back illumination

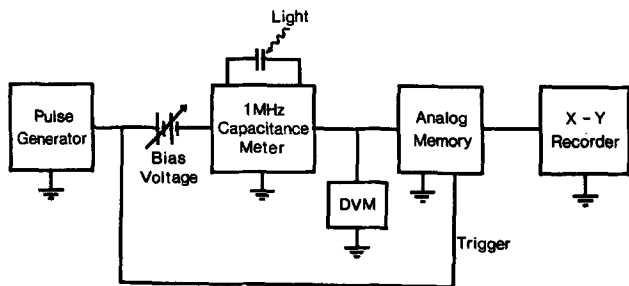


Fig. 4. Minority carrier lifetime measurement setup

capacitance meter output was fed into a digital voltmeter (DVM). Capacitances  $C_f$  and  $C_f'$  were measured at a fixed bias voltage.

The light-emitting diode (LED) used was a Monsanto ME2A, which is a diffused planar gallium arsenide diode with a noncollimating lens. At a current of 1.0A this LED has a minimum total external radiated power of 7.5 mW centered in wavelength at 9000Å, with a spectral half width of 500Å. The measurements described in this paper were conducted at an LED current of 0.75A, resulting in a photon intensity of approximately  $2.5 \times 10^{15} \text{ cm}^{-2} \text{ sec}^{-1}$  incident on the slice.

Since Eq. [7] has an explicit  $n_i$  dependence it is essential that both the steady-state C-V and the transient C-t measurements be made at the same temperature. Errors due to C-t transient end effects and quantization within the analog memory were minimized by choosing the points ( $C_1, t_1$ ) and ( $C_2, t_2$ ) at about  $1/4$  and  $3/4$  of the way along the deep depletion C-t recovery curve with back illumination.

The  $\text{SiO}_2$  thickness was measured using a Talystep, and the value so obtained was cross-checked using a

measurement of the oxide capacitance per unit area. Once the oxide thickness was determined the MOS dots were characterized using only capacitance ratios, thus avoiding precise measurements of their individual areas or absolute capacitances.

To demonstrate the usefulness and practicality of the method, mappings were made of the minority carrier lifetime and doping as a function of position over a portion of a typical n-type (100) orientation silicon slice. This slice was  $250\mu$  thick, 3.2 cm in diameter, and had a nominal resistivity of 10 ohm-cm. A 950Å thick thermal oxide was grown in dry oxygen on the polished surface of the slice and was annealed in  $\text{N}_2$  at  $1100^\circ\text{C}$ .

Using a metal mask, a square array of 0.076 cm diameter aluminum dots with a center to center spacing of 0.125 cm were evaporated onto the oxide. An aluminum back contact with an aperture opposite the portion of the slice to be mapped was also deposited by evaporation.

The numerical work involved in analyzing the data was minimized by using a simple computer program.<sup>5</sup> This program, with data inputs of  $T, C_f/C_o, C_f'/C_o, C_1/C_f', C_2/C_f',$  and  $t_2 - t_1$  for each dot and  $X_o$  for the slice, prints out the values of  $n_i, \xi, N, \eta, g_d',$  and  $\tau$  associated with each set of MOS capacitor measurements.

The area of the slice which was mapped is shown cross-hatched in Fig. 5(a) and the resulting doping and minority carrier lifetime values at room temperature, are shown in Fig. 5(b) and (c). In these figures, X's indicate dots which on probing were found to be defective. Figure 5(b) indicates that the doping is reasonably constant across the slice, exhibiting an average value of  $0.621 \times 10^{15} \text{ cm}^{-3}$  and a root mean square deviation of  $0.0462 \times 10^{15} \text{ cm}^{-3}$ . Figure 5(c) indicates that the minority carrier lifetime varies widely within 0.5 cm (four rows of dots) of the edge of the slice, but is fairly uniform near the center of the slice. For the four rows of dots nearest the edge of the slice the average minority carrier lifetime is  $0.121 \times 10^{-6} \text{ sec}$  and the root mean square deviation is  $0.0617 \times 10^{-6} \text{ sec}$ . For the remaining dots the average minority carrier lifetime is  $0.173 \times 10^{-6} \text{ sec}$  and the root mean square deviation is  $0.0159 \times 10^{-6} \text{ sec}$ . The dots away from the edge of the slice exhibited a much more uniform lifetime distribution than that observed by Schroder and Guldberg (2) using the deep depletion method without back illumination. The high failure rate and wide variations in lifetime exhibited by dots near the edge of the slice seems to indicate that the silicon ingot or the slice preparation is inferior near the slice rim.

<sup>5</sup> Available on request.

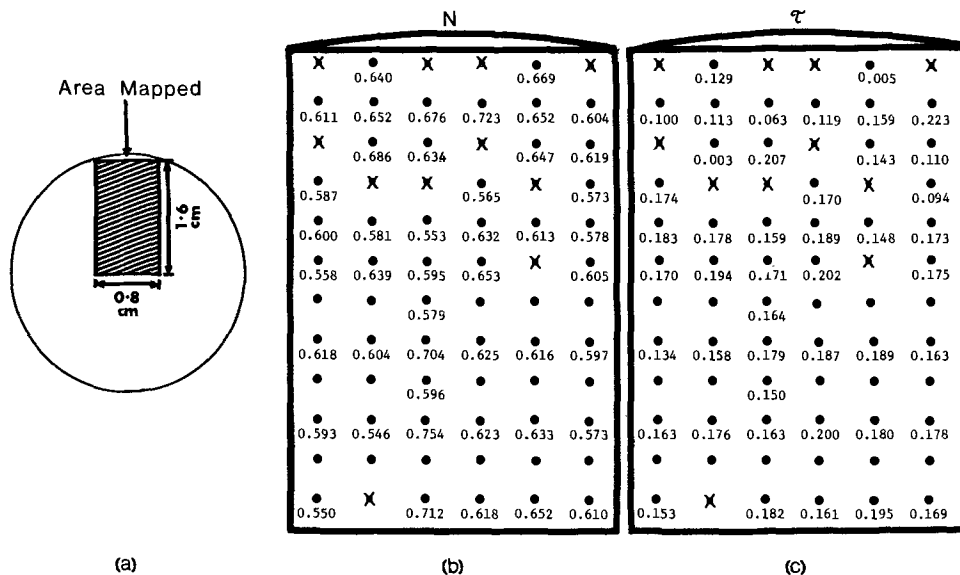


Fig. 5. (a) Plan view of slice showing area mapped. (b) Doping map in units of  $10^{15} \text{ cm}^{-3}$ . (c) Minority carrier lifetime map in microseconds.

For a typical dot near the center of the slice (the one in the lower, left-hand corner of the map) characterized by the data:  $T = 298^\circ\text{K}$ ,  $X_o = 950\text{\AA}$ ,  $C_f/C_o = 0.202$ ,  $C_f'/C_o = 0.223$ ,  $C_1/C_f' = 0.373$ ,  $C_2/C_f' = 0.879$ , and  $t_2 - t_1 = 0.20$  sec, the preceding analysis gave values of:  $N = 5.50 \times 10^{14} \text{ cm}^{-3}$ ,  $\eta = 1.15 \times 10^2$ , and yielded  $\tau = 0.153 \times 10^{-6}$  sec.

### Conclusion

A simple technique using back illumination of an MOS capacitor to measure minority carrier lifetime has been presented. The technique involves measurements which can be analyzed quickly and results in values which are not subject to errors present in other methods of minority carrier lifetime measurements. By using this technique in conjunction with an on-line minicomputer, it is possible to monitor minority carrier lifetime at production rates and to perform slice surveys for doping and minority carrier lifetime.

### Acknowledgments

This work was supported by the Defense Research Board and the National Research Council of Canada. Grateful acknowledgments are also made to the National Research Council for a postgraduate scholarship awarded to one of the authors (C. St. L. Rhodes). The authors would also like to thank V. V. Chettiar for his help with the experimental work.

Manuscript submitted Jan. 22, 1974; revised manuscript received April 18, 1974.

Any discussion of this paper will appear in a Discussion Section to be published in the June 1975 JOURNAL. All discussions for the June 1975 Discussion Section should be submitted by Feb. 1, 1975.

The publication costs of this article have been assisted by the University of Toronto.

### SYMBOLS

$C$	small signal MOS capacitance
$C_f$	thermal equilibrium value of $C$ in the inversion region

$C_f'$	value of $C$ in the inversion region under steady-state illumination
$C_o$	oxide capacitance
$C_1, t_1$	initial measurement point on $C$ - $t$ curve
$C_2, t_2$	final measurement point on $C$ - $t$ curve
$g$	generation rate per unit area
$g_d'$	diffusion flux from bulk with illumination
$k$	Boltzmann's constant
$K_o$	relative dielectric constant of oxide
$K_s$	relative dielectric constant of semiconductor
$n_i$	intrinsic carrier density
$N$	doping density
$p_o$	thermal equilibrium hole density in the neutral bulk
$q$	electronic charge
$r$	excess minority carrier density
$R$	recombination rate per unit volume
$t$	time
$T$	absolute temperature
$X$	distance into semiconductor
$X_d$	space charge region width
$X_o$	oxide thickness
$\epsilon_o$	permittivity of free space
$\tau$	recombination lifetime

### REFERENCES

1. D. K. Schroder and H. C. Nathanson, *Solid-State Electron.*, **13**, 577 (1970).
2. D. K. Schroder and J. Guldborg, *ibid.*, **14**, 1285 (1971).
3. D. K. Schroder, *IEEE Trans. Electron Devices*, **ED-19**, 1018 (1972).
4. C. St. L. Rhodes and C. A. T. Salama, *J. Phys., D. Appl. Phys.*, **6**, 1798 (1973).
5. R. F. Pierret and C. T. Sah, *Solid-State Electron.*, **13**, 269 (1970).
6. M. Zerbst, *Z. Angew. Phys.*, **22**, 30 (1966).
7. H. Preier, *IEEE Trans. Electron Devices*, **ED-15**, 990 (1968).
8. K. H. Zaininger and F. P. Heiman, *Solid State Technol.*, **13**, (5), 49 (1970).
9. A. S. Grove, "Physics and Technology of Semiconductor Devices," John Wiley & Sons, Inc., New York (1967).
10. H. D. Barber, *Solid-State Electron.*, **10**, 1039 (1967).

## Preparation of High-Resistivity Silicon by Vacuum Float Zoning

T. G. Digges, Jr.<sup>1</sup> and C. L. Yaws

Texas Instruments Incorporated, Dallas, Texas 75222

### ABSTRACT

A successful, vacuum float-zone process was developed for the preparation of ultra high-resistivity polysilicon crystals. The high-resistivity polysilicon crystals were then converted to dislocation-free single crystals in an inert atmosphere by the usual Dash float-zone technique. The vacuum float-zone process is based on a semiquantitative purification technique for prediction of silicon bar resistivity after each float-zone pass. Purification is attained by multiple vacuum float zoning on lightly compensated silicon (<0.10 ppb boron). Impurity removal is achieved by a combination of zone refining and evaporation, with evaporation the dominant mode. Equations are derived which permit vacuum float-zone speeds to be determined quantitatively for resistivity targeting. The versatile production process is applicable to a broad product range of single-crystal material: 200-30,000 ohm-cm n-type and 2,000-30,000 ohm-cm p-type silicon.

Dislocation-free silicon crystals up to 1 in. in diameter and 20 in. in length with resistivities greater than

<sup>1</sup>Present address: Spectrolab, Division of Textron Inc., Sylmar, California 91342.

Key words: single-crystal silicon, production process, polydeposition process, polycrystalline silicon.

9000 ohm-cm p-type are being grown in our production float-zone facility as a source of wafers for photon detectors. One apparent way to produce high-resistivity silicon is by vacuum float zoning. This paper describes a successful vacuum float-zone technique

based on semiquantitative purification for prediction of silicon bar resistivity after each pass and presents additional information on purification rates of the impurity species. The versatile production process is applicable to a broad product range of single-crystal material: 200-30,000 ohm-cm n-type and 2,000-30,000 ohm-cm p-type silicon.

**Theory**

The concentration of impurity in a crystal, grown by the float-zone process, when both evaporation and segregation of impurity are occurring, is according to Ziegler (1)

$$\frac{C_f}{C_o} = \left( k - \frac{k}{u} \right) \exp \frac{-ux}{l} + \frac{k}{u} \quad [1]$$

where  $C_f$  is the impurity concentration in the solid,  $C_o$  the initial impurity concentration in the solid,  $k$  the segregation coefficient,  $x$  the distance solidified,  $l$  the zone length, and

$$u = k + \alpha \frac{l}{v} \quad [2]$$

where  $v$  is the growth rate and  $\alpha$  is the evaporation time constant dependent on the impurity species. Assumptions of a cylindrically shaped zone, no diffusion in the solid, uniform concentration in the liquid, and constant  $k$  are made for Eq. [1] and [2].

It is also assumed that the molten zone is instantaneously formed initially. If the evaporation term,  $\alpha(l/v)$ , is zero, Eq. [1] reduces to Pfann's equation (2) for zone melting.

Bradshaw and Mlavsky (3) have derived the vacuum purification equations for normal freezing and give the proportional time constants  $E^{-1}$  for the evaporation of several different impurities. Their  $E^{-1}$  factor is related to  $\alpha$  by

$$al = \frac{2E}{\rho} \quad [3]$$

where  $\rho$  is the specific density of the melt.

From Eq. [1] and [2], it is seen that the maximum purification that can occur for one pass is  $(k/u)$ . For  $n$  passes the ultimate purification is  $(k/u)^n$  at constant zone speed.

The theoretical purification profiles for individual species are given in Fig. 1. It is noticed that the flat

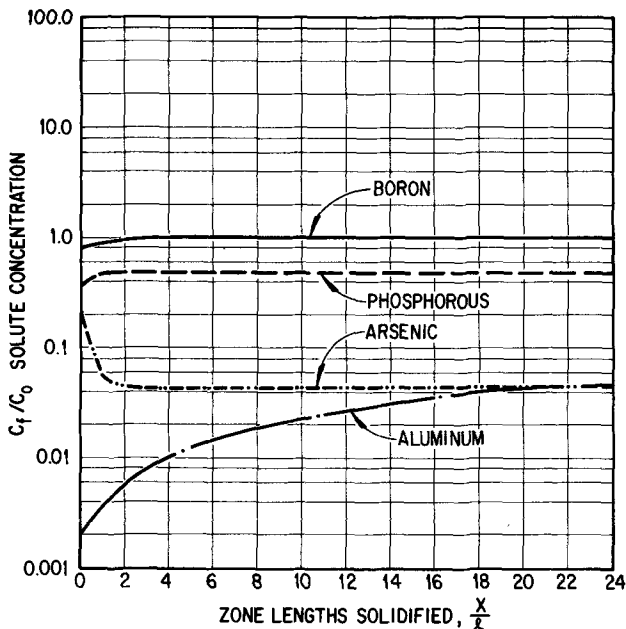


Fig. 1. Vacuum purification profiles for major impurities in silicon (pull rate, 3 in./hr).

portion of the  $(C_f/C_o)$  vs.  $(x/l)$  occurs after three effective zone lengths for all impurities except aluminum. Most aluminum initially present in the polysilicon will be quickly removed by liquid-solid purification (reduced by a minimum factor of 95% per pass). The presence of aluminum can be implied by a failure to reach a flat  $(C_f/C_o)$  vs.  $(x/l)$  curve after one vacuum pass at  $x/l > 10$ . The ultimate purification analysis to be given considers impurities for  $x/l > 3$ , but is valid for any impurity which has a flat portion of  $(C_f/C_o)$  vs.  $(x/l)$  curve.

From the knowledge of  $k$  and  $u$  (a function of  $\alpha$ ), one can in theory predict the purification rate required to attain any resistivity if the impurity species is known. However, in practice there are several factors that make the attainment of high-resistivity silicon ( $>3000$  ohm-cm p-type) difficult. The first is that the starting p-level must be kept below 0.10 ppb to prevent compensation from becoming dominant. The second important factor is to identify and control the n-type impurities that are initially present in the vapor deposited polycrystalline rod.

**Experimental**

*Polycrystalline deposition.*—A material flow diagram for the process is given in Fig. 2. The flow diagram shows the starting point in the process with polycrystalline silicon, the various intermediate processing-testing operations, and the ending point for the high-resistivity silicon crystal which is sliced into wafers for device fabrication.

The polycrystalline silicon was produced from specially purified trichlorosilane, palladium-diffused, purified hydrogen with nondetectable impurities, and high-purity silicon filaments. The equipment was fabricated from materials of construction which were compatible with the hydrogen-chlorine-silicon system. In predeposition, the filaments were selectively etched to remove trace surface contamination. The polydeposition on the filament was next initiated from the pre-

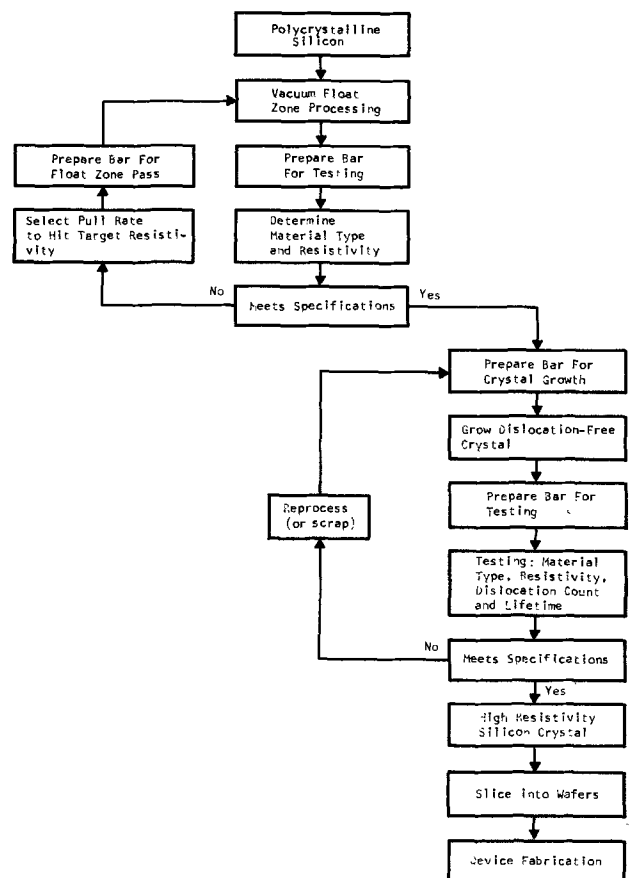


Fig. 2. Process flow diagram for high resistivity silicon

mium quality trichlorosilane and purified hydrogen. Deposition was continued until the rod of desired size (normally 1 to 1¼ in. diam) was attained. During deposition, process parameters such as reactant concentrations, deposition temperature, and various process temperatures were carefully monitored and controlled. By careful control of the process parameters, trace contamination from several sources such as gas phase components in the reactant feed and the process equipment was minimized. Polycrystalline silicon of very high quality with less than 0.1 ppb p-type impurity (boron) was produced.

Polycrystalline silicon was produced from two different reactors in the process. The initial reactor (single hairpin) produced rods in which arsenic was the major n-type impurity as determined by neutron activation analysis as well as data deduced from the rate of evaporation. The next reactor (double hairpin) produced rods in which phosphorus was the major n-type impurity.

**Vacuum float-zone purification.**—The polycrystalline silicon was purified in vacuum float-zone chambers which were specially designed and fabricated by Texas Instruments. The zone was held molten by use of a four-turn robber coil with one reverse turn. The effective molten zone length was determined to be  $0.60 \pm 0.06$  in. The zone length was measured by two separate techniques. The first consisted of using a calibrated telescope to measure the length when purifying. The second method was by metallographic examination after purifying. Metallographic examination revealed that the solid-liquid interface was concave downward at the upper interface and concave upward at the bottom interface. Likewise, the assumed cylindrical portion was concave toward the center, but with an order of magnitude larger radius than the top and bottom portions. Simple calculation revealed that the total volume could be approximated by a cylinder with the diameter (95%) of the largest lateral dimension and the fill coming from the concave portions on the top and bottom. The effective zone length was then determined to be the length of this hypothetical cylinder.

The vacuum was attained with a Model 3103 turbomolecular pump, with a pumping speed of 260 liters/sec, manufactured by the Welch Scientific Company of Skokie, Illinois. This pump was selected primarily because of its unique design which minimizes backstreaming. The vacuum pressure of approximately  $2 \times 10^{-4}$  Torr during zone melting was monitored by Norton gauges (Models 507 and 831). The pull rate of the zoner was controlled by a Leeds and Northrup Electromax II. A Trendrack recorder equipped with a digital output display was utilized to preset or change pull rate during vacuum float zoning.

**Concentration of impurities.**—The initial concentrations of the n- and p-type impurities were essentially the same in each polycrystalline rod produced by vapor deposition in a given reactor.

The concentration of total impurities was experimentally determined in a control rod by the procedure described below. The initial step was to make one float-zone pass in argon to find the net n-type level. Next, the control rod was vacuum purified five or six passes at a slow pull rate (3 in./hr) to insure impurity removal. The resistivity was then plotted vs. zone length for each pass. When there is no further change in resistivity after a subsequent vacuum float-zone pass, the existing resistivity is due to the concentration of the p-type impurity (boron) level in the silicon bar. The concentration of the n-type impurity is then determined from knowledge of the net n-type and the total p-type level.

In silicon, the usual p-type impurities are aluminum and boron. The relative amounts of boron and aluminum can be approximated in several ways. After the control rod has had one or more vacuum passes to produce a flat resistivity profile (at  $x/l > 3$  if boron is

the principal impurity or at  $x/l > 20$  if aluminum is the principal impurity), the rod is melted-in in this flat profile portion under inert atmosphere and a pass made to the end. From the shape of the  $x/l$  curve vs. resistivity an accurate approximation can now be made on the relative amounts of boron and aluminum by knowing the segregation coefficients. In the present work, boron was the predominant p-type impurity.

The n-type impurities can be determined from the change in concentration in the flat portion of the curve from vacuum passes one through six or seven. From the evaporation constants of the different species it is possible to determine the principal n-type impurity. In theory, neutron activation analysis can be employed to identify the n-type contaminants, but the evaporation technique is more amenable for production application. The prominent n-type impurities were determined to be arsenic and phosphorus.

A control rod was processed weekly to ensure that the contaminants did not appreciably change. The consistency in polyquality was accomplished by running the facilities continuously to minimize contamination.

## Results and Discussion

**Theoretical technique.**—Typical results obtained from the purification of over 100 polycrystalline rods, each receiving multiple passes, are illustrated in Fig. 3. The purification chart was constructed by plotting log (total n-type impurity concentration) vs. time that a given section of the silicon rod was molten at each pass. The concentration of impurity plotted after vacuum float zoning was measured in that flat profile portion of the bar where  $x/l > 3$  (see Fig. 1).

There are two curves plotted in Fig. 3. Curve A with the steeper slope is for polycrystalline silicon grown in the initial 2-bar (single hairpin) reactor. Curve B with the less steep slope in Fig. 3 is for polycrystalline silicon deposited in a subsequent 4-bar (double hairpin) reactor.

From data such as found in Fig. 3 estimates have been made of the evaporation constants of phosphorus and arsenic. The evaporation constant  $\alpha_P$  for phosphorus is in general agreement with the value of Bradshaw and Mlavsky. The result is higher than Ziegler's, possibly arising from the float-zone rods here being four times larger than those used by Ziegler. For arsenic, our measured evaporation constant  $\alpha_{As}$  is an order of magnitude less than that reported by Bradshaw and Mlavsky. A comparison of the experimental results is given in Table I.

Peizulaev (4) has derived equations describing evaporation and segregation for purification during

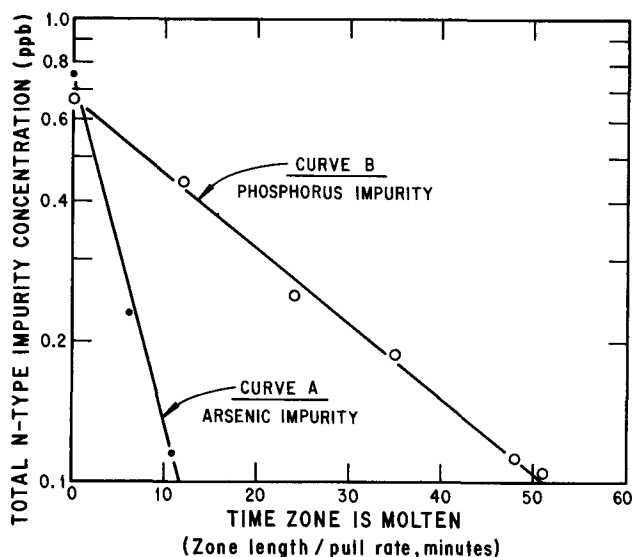


Fig. 3. Typical concentration vs. time plot showing n-type impurity removal.

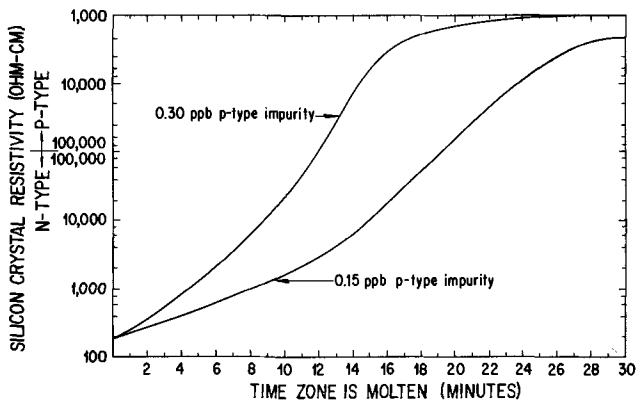


Fig. 4. Effect of p-type impurity on targeting resistivity. Both curves have same n-type contaminant.

multiple zone vacuum passes. His equations pertain to one solute component and may be extended to cover multiple solute components.

For example, to determine,  $n$ , the number of passes and the zone speeds required to attain resistivity  $X$ , analytical techniques can be employed. Assume that the polycrystalline silicon originally contains known amounts of phosphorus and arsenic as impurities. The resistivity is related to the concentration of these impurity components by the relation

$$\frac{1}{X} = (C_{As} + C_P)_n (e\mu_e) \quad [4]$$

where  $C_{As}$  is the concentration of arsenic after  $n$  vac-

Table I. Evaporation constant  $\alpha$  according to different investigations

Impurity species	Evaporation constant $\alpha$		
	This work	Ziegler (1)	Bradshaw & Mivasky (3)
As	$2 \times 10^{-3}$	—	$1 \times 10^{-3}$
P	$6 \times 10^{-4}$	$7 \times 10^{-3}$	$3 \times 10^{-4}$

uum passes are made;  $C_P$ , the concentration of phosphorus after  $n$  vacuum passes are made;  $e$ , the charge of electron;  $\mu_e$ , the mobility of electron; and  $n$ , the number of vacuum passes.

The number of passes,  $n$ , required to obtain  $1/X$  (Eq. [4]) can be analytically determined by the iterative process from the following equation

$$(C_{As} + C_P)_n = \left(\frac{k_{As}}{u_{As}}\right)^{n-1} \left(\frac{k_{As}}{u'_{As}}\right) C_{As}^{\circ} + \left(\frac{k_P}{u_P}\right)^{n-1} \left(\frac{k_P}{u'_P}\right) C_P^{\circ} \quad [5]$$

where  $C_{As}^{\circ}$  is the initial concentration of arsenic and,  $C_P^{\circ}$  the initial concentration of phosphorus,  $u_{As}$  and  $u_P$  are applicable for float-zone passes up to  $n - 1$  (defined by Eq. [2]),  $u'_{As}$  and  $u'_P$  are applicable for the last float-zone pass ( $n$ th pass) (defined by Eq. [2],  $u_{As}$  and  $u_P$  determine the constant pull rate up to the  $n - 1$  pass, whereas  $u'_{As}$  and  $u'_P$  determine the variable pull rate required for the  $n$ th pass.

The technique to iterate Eq. [5] is given in the Appendix.

The experimental concentration vs. time profile for polycrystalline silicon containing both arsenic and

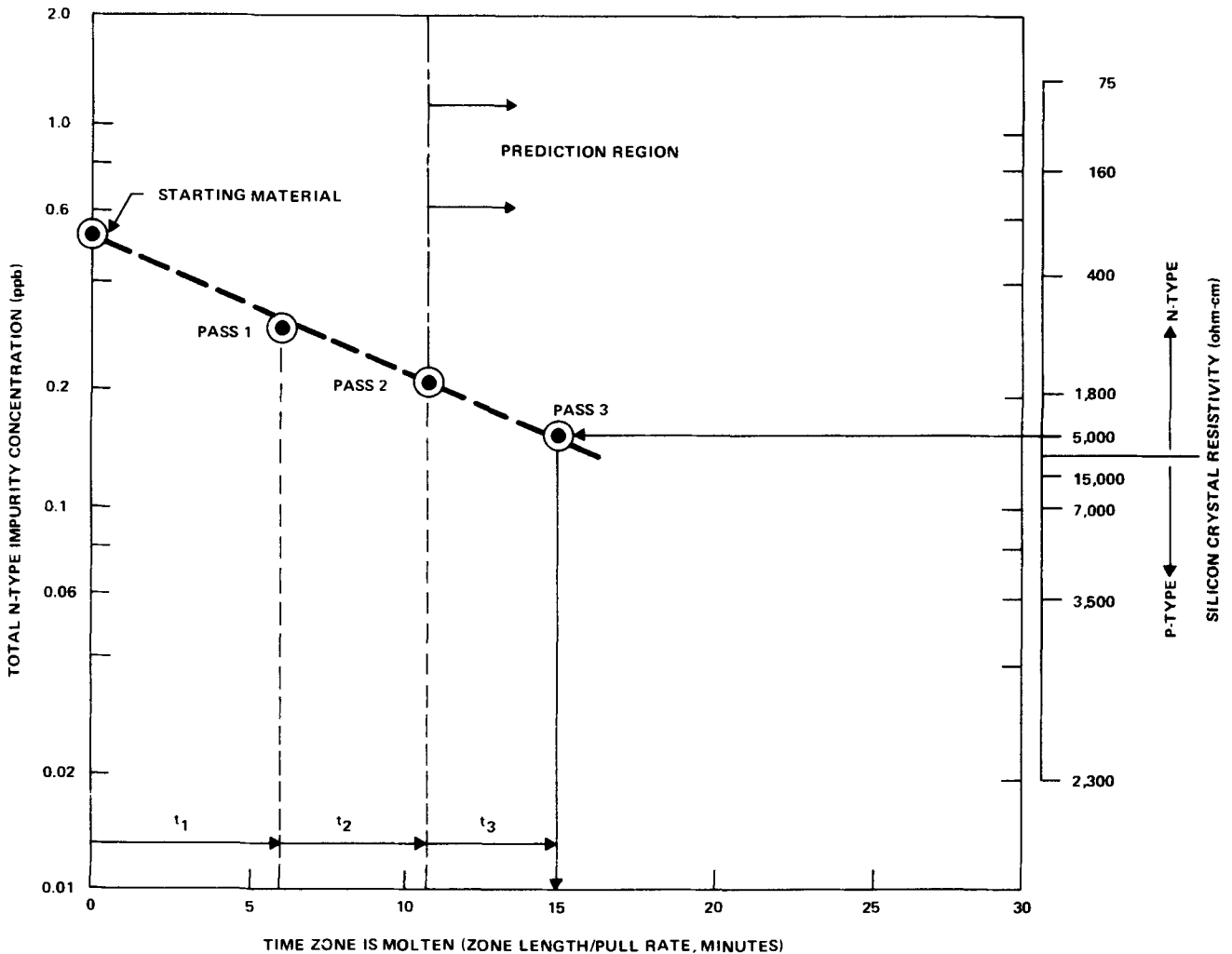


Fig. 5. High resistivity n-type silicon from semiempirical purification technique

phosphorus would lie between curves A and B in Fig. 3 and in general would not be a straight line. This relationship has often been experimentally observed for impurities in silicon. The above theoretical equations can be extended to cover three or more impurity constituents in the polycrystalline silicon.

The above calculations have neglected the effect of compensation. But, if known, then compensation can be directly entered in Eq. [4] by calculating the excess  $C_{As}$  and  $C_P$  required to attain a specific resistivity. The effect of p-type impurity in the starting material on purification is vividly illustrated in Fig. 4. For low-resistivity material, compensation is a minor effect. But as can be seen from the steep slope of the resistivity vs. time curve, for high-resistivity targeting, compensation is a highly damaging effect.

**Semiempirical purification technique.**—The semiempirical purification technique was found to be most valuable for the production of high-resistivity silicon in the process.

The purification technique is based on a knowledge of starting material quality (n- and p-type levels) and construction of a purification chart. The purification chart was constructed by plotting log (total n-type impurity concentration) vs. time the zone was held molten for the applicable section of the bar (flat profile section,  $x/l > 3$ ). The time axis is determined by dividing the zone length by the pull rate. The material quality (n-type level) is plotted at time zero, after the first pass vacuum, and after each of the ensuing vacuum passes. After three or more points are experimentally determined, the general shape of the purification curve can be ascertained. It then becomes possible to semiquantitatively predict the resistivity of the silicon bar after the next vacuum pass. Or conversely, after several passes, it is possible to achieve the targeted resistivity by making the final vacuum pass at a predetermined pull rate based on the semiempirical purification chart.

Use of the technique to produce 5000 ohm-cm n-type silicon is illustrated in Fig. 5. The following data points for the material quality of a particular rod are initially plotted: \*Start 0.52 ppb at  $t = 0$ ; \*Pass 1 0.30 ppb at  $t = t_1 = 6$  min; \*Pass 2 0.215 ppb at  $t = t_1 + t_2 = 6 + 4.5 = 10.5$  min. The purification curve is then constructed through the data points and extended into the prediction region.

The purification curve is extended until it intercepts the target n-type resistivity line (horizontal line at 5000 ohm-cm). The intercept point occurs at that time required to achieve target resistivity material. Determination of the time ( $t_3$ ) for the next pass (Pass 3) is made from the intercept point in the figure as follows

$$\begin{aligned} t_3 &= 15 \text{ (from figure)} - (t_1 + t_2) \\ &= 15 - 10.5 \\ &= 4.5 \text{ min} \end{aligned}$$

Recalling that

$$t_3 = \frac{\text{zone length}}{\text{pull rate for Pass 3}}$$

and solving for pull rate

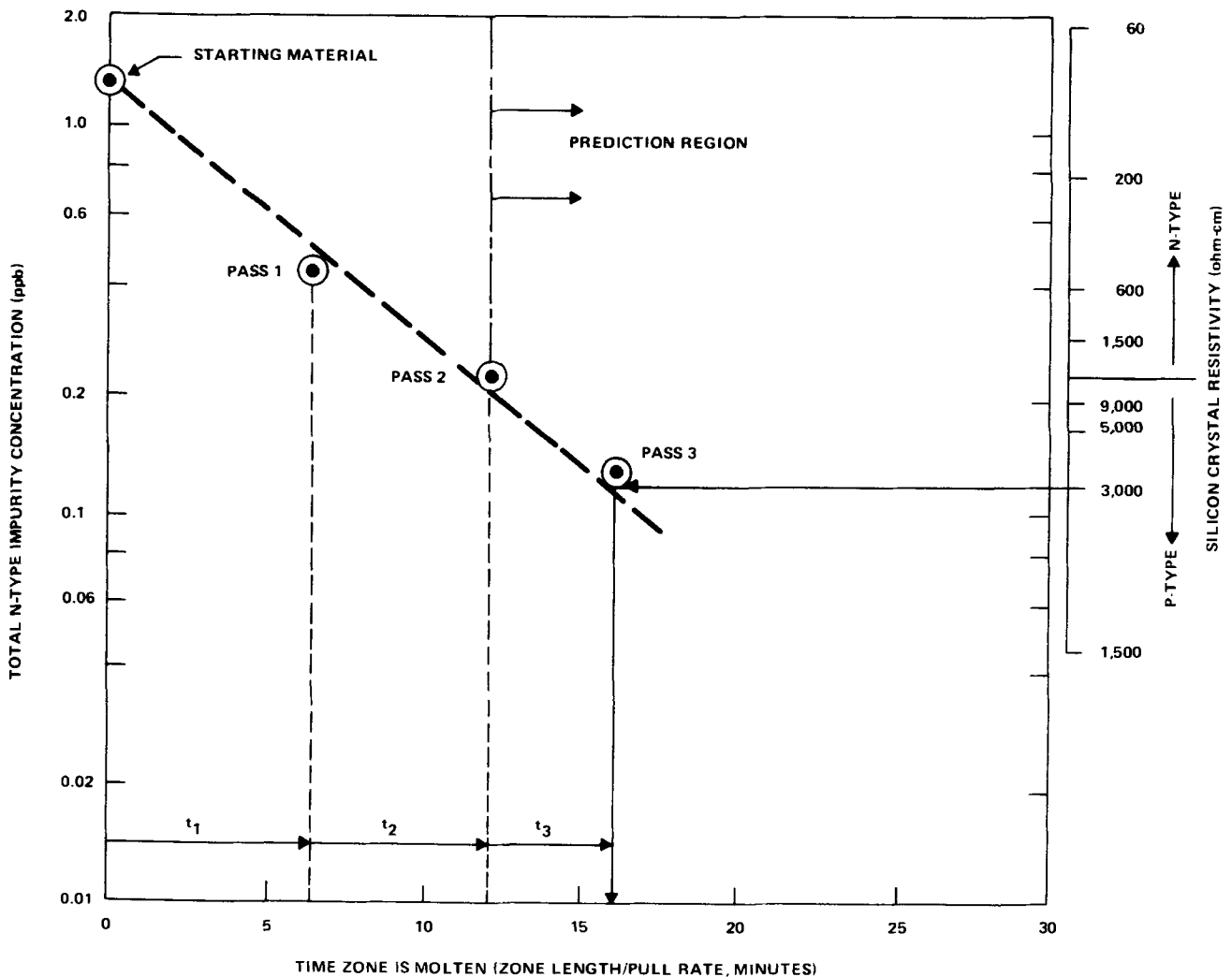


Fig. 6. High resistivity p-type silicon from semiempirical purification technique

Table II. Dislocation-free silicon crystals grown with vacuum float-zone process

Resistivity range (ohm-cm)	Type	Minority carrier lifetime range ( $\mu$ sec)	Quantity of crystals growth
10,000-30,000	p	500-10,000	>10
5,000-10,000	p	750-8,500	>10
2,000-5,000	p	750-7,500	>10
30,000-70,000	n	2,000-4,000	>5
10,000-30,000	n	1,500-6,000	>5
5,000-10,000	n	1,500-6,000	>5
2,000-5,000	n	1,500-6,000	>5
200-2,000	n	1,500-6,000	>5

$$\begin{aligned} \text{Pull rate for Pass 3} &= \frac{\text{zone length}}{t_3} \\ &= \frac{0.6 \text{ in.}}{4.5 \text{ min}} \\ &= 8 \text{ in./hr} \end{aligned}$$

Thus the pull rate for the next vacuum pass (Pass 3) is 8 in./hr to hit the target resistivity of 5000 ohm-cm, n-type material. The next vacuum pass was conducted at this pull rate. Material of 4800-5200 ohm-cm, n-type resistivity (average 5000) was obtained as shown by the data point for Pass 3 in the figure.

Application of the semiempirical purification technique for the production of high-resistivity p-type silicon (3000 ohm-cm) is illustrated in Fig. 6.

Following attainment of the target high-resistivity silicon (n- or p-type) through use of the semiempirical purification technique, dislocation-free single crystals were grown in an inert argon atmosphere. In general, the high resistivity did not change at this step of the process.

Large quantities of n- and p-type, high-resistivity, silicon single crystals were reproducibly prepared in the vacuum float-zone production process with the purification technique. The targeted resistivities varied from 2000-30,000 ohm-cm for p-type material and from 200 to 70,000 ohm-cm for n-type material. Minority carrier lifetime varied from 500-10,000  $\mu$ sec for p-type and 1500-6000  $\mu$ sec for n-type. Crystal orientation was  $\langle 111 \rangle$ .

Resistivities and lifetimes for dislocation-free silicon crystals produced by the process are summarized in Table II.

### Summary and Conclusions

The preparation of ultra high-resistivity silicon single crystals was attained in the vacuum float-zone process. The versatile production process is applicable to a broad product range of single-crystal material: 200-30,000 ohm-cm n-type and 2000-30,000 ohm-cm p-type silicon.

A semiempirical purification technique was successfully used in the process to produce the high-resistivity silicon. With the technique, it is possible to semiquantitatively predict silicon bar resistivity after each float-zone pass. Or conversely, after several passes, it is possible to achieve the target resistivity by making the final vacuum pass at a predetermined pull rate.

Theoretical equations which encompass impurity removal by a combination of zone refining and evaporation are presented for the determination of vacuum float-zone speed to attain target high resistivity. The equations are applicable for silicon with single or multicomponent impurities.

Evaporation coefficients, calculated from the data, for phosphorus and arsenic are reported.

### Acknowledgments

The authors acknowledge the help of Bruce Boggs, Les Connelly, and Marvin Drews. This work was partially supported by the Air Force Materials Laboratory (Contract No. F33615-69-C-1829).

Manuscript submitted Aug. 27, 1973; revised manuscript received March 25, 1974. This was Paper 98 presented in part at the Chicago, Illinois, Meeting of the Society, May 13-18, 1973.

Any discussion of this paper will appear in a Discussion Section to be published in the June 1975 JOURNAL. All discussions for the June 1975 Discussion Section should be submitted by Feb. 1, 1975.

The publication costs of this article have been assisted by Texas Instruments Incorporated.

### APPENDIX

#### Method for Solving Number of Passes and Zone Speed

$$\begin{aligned} (C_{As} + C_P)_n &= \left( \frac{k_{As}}{u_{As}} \right)^{n-1} \left( \frac{k_{As}}{u'_{As}} \right) C_{As}^0 \\ &\quad + \left( \frac{k_P}{u_P} \right)^{n-1} \left( \frac{k_P}{u'_P} \right) C_P^0 \quad [5] \end{aligned}$$

First assume a constant pull rate and calculate  $u_{As}$  and  $u_P$  from Eq. [2]. Next let  $n = 1$ , assume for calculation purposes  $u_{As} = u'_{As}$  and  $u_P = u'_P$  and apply these values to Eq. [5]. If the right-hand side of Eq. [5] is greater than the left-hand side, assume  $n = 2$ ,  $u_{As} = u'_{As}$ , and  $u_P = u'_P$  and recalculate. Whenever the right-hand side becomes less than the left-hand side for positive integral value of  $n$  assuming  $u_{As} = u'_{As}$  and  $u_P = u'_P$  the value of  $n$  is then determined. Once  $n$  has been determined, the final pull rate required to define  $u'_{As}$  and  $u'_P$  can be calculated to satisfy Eq. [5].

### REFERENCES

1. G. Ziegler, *Z. Metallk.*, **49**, 491 (1958).
2. W. G. Pfann, *Trans. AIME*, **194**, 747 (1952).
3. S. E. Bradshaw and A. I. Mlavsky, *J. Electron.*, **2**, 134 (1956).
4. Sh. I. Peizulaev, *Inorganic Mater.*, **3**, 1329 (1967).

## Formation of Silicon Whiskers by Aluminum-Quartz Interaction

P. Rai-Choudhury\* and W. J. Takei

Westinghouse Research Laboratories, Pittsburgh, Pennsylvania 15235

Aluminum diffusion in silicon is normally carried out in a sealed quartz tube under vacuum using elemental aluminum as the dopant source (1). For deep junctions, diffusion temperatures as high as 1200°C are often used. When large diameter wafers (~50-75 mm) are processed at such high temperatures it becomes necessary to back fill the quartz tube with a suitable gas which prevents the tube from collapsing. Back filling with argon consistently results in a nonuniform diffusion with very low surface concentration. If the sealed tube is maintained relatively free from moisture and oxygen, then the source Al remains uncoated with Al<sub>2</sub>O<sub>3</sub>, and an equilibrium Al vapor pressure is maintained throughout the diffusion time. Under these conditions, silicon whiskers grow from the walls of the Al<sub>2</sub>O<sub>3</sub> crucible containing the Al melt. The purpose of this note is to discuss the thermodynamic and kinetic factors which favor the growth of silicon whiskers.

### Experimental Results

Under vacuum conditions ( $p_{Al} \approx 3 \times 10^{-4}$  mm) the evaporated Al molecules leaving the Al<sub>2</sub>O<sub>3</sub> crucible could travel considerable distances without undergoing any collisions. The mean free path of Al is of the order of 180 cm, which, being considerably larger than the diameter of any quartz tube normally used for the diffusion, most collisions occur at the tube wall. An x-ray diffraction analysis of the deposits from the quartz wall indicates that the wall is coated with a mixture of silicon and aluminum oxide. When the entire surface of the quartz is coated with Si and Al<sub>2</sub>O<sub>3</sub>, the interaction between the Al and SiO<sub>2</sub> ceases, and the equilibrium Al vapor pressure present acts only as the diffusion source.

When the quartz tube is filled with argon to provide about one atmosphere pressure at the diffusion temperature, the mean free path of the evaporated Al molecules is reduced to about 1 μm. Thus, the Al molecules suffer numerous collisions in the gas phase and with the Al<sub>2</sub>O<sub>3</sub> crucible walls. Interaction with the quartz walls is only possible by Al transport through molecular diffusion. Assuming a sufficient partial pressure of SiO (see Discussion) in equilibrium with the quartz, silicon could be formed at the inner walls of the Al<sub>2</sub>O<sub>3</sub> crucible by interacting with the Al vapor. Growth of numerous silicon whiskers nucleating at the inner walls of the crucible is observed as shown in Fig. 1.

The majority of the whiskers were 30-40 μm in diameter and approximately 1 cm long with trigonal faceting at the tip as shown in Fig. 2. Analysis by x-ray Weissenberg techniques showed that they had a [111] axis terminated by {111} facets. This is in agreement with the orientation previously reported (2) for Si whiskers grown by other techniques. Other whiskers had approximately the same dimensions but with very

\* Electrochemical Society Active Member.

Key words: x-rays, thermodynamics, reduction, transport, mean free path, silicon, whiskers, quartz, growth.



Fig. 1. Silicon whiskers growing from the inner walls of the alumina crucible at 1050°C in argon atmosphere.

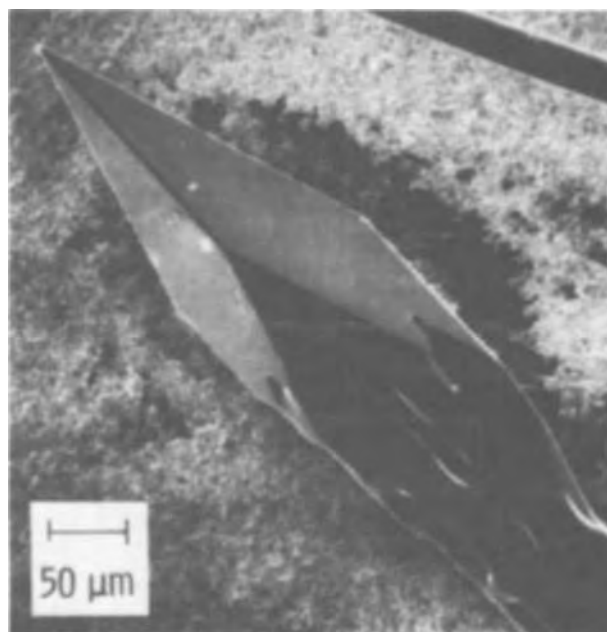


Fig. 2. Silicon whisker showing trigonal faceting at the tip

rough sides, as shown in Fig. 3, and were found to be polycrystalline, giving a spotty ring x-ray pattern. This clearly shows that the development of whisker growth results, not from crystallographic orientation effects, but from the peculiar growth conditions found in this system. A few other whiskers had an appear-



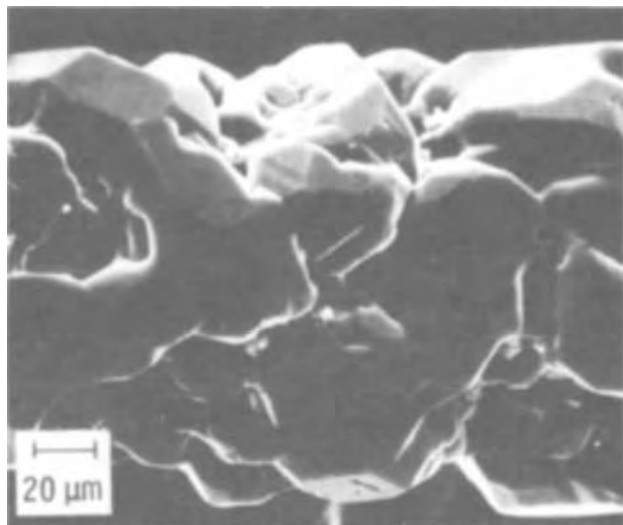
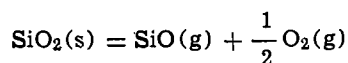


Fig. 3. The stem of a whisker showing rough growth of poly-crystalline silicon.

ance different from those described and examination showed them to possess different growth axes. These were found to be, in decreasing order of occurrence, [112], i.e., the same as Si dendrites and web, [113], and one whisker of [110]. This is not to imply that a more thorough examination may not have revealed other orientations but those that were found and their appearance are summarized in Table I.

#### Discussion

For the growth of silicon whiskers two factors need to be considered, namely, the transport of the reactants to the alumina crucible, and the reaction or reactions by which silicon is produced. Before silicon can be transported  $\text{SiO}_2$  (i.e., quartz) must be reduced to SiO. The thermal reduction of  $\text{SiO}_2$  as represented by



has a reaction free energy of 105.496 kcal at 1400°K, and the equilibrium partial pressure of SiO is negligible. On the other hand, reaction with aluminum vapor

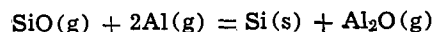


has a standard free energy of -22.869 kcal at 1400°K, and is therefore a likely reaction by which SiO is produced.

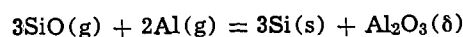
Table I. Description of whiskers found, listed in order of their occurrence

Axis	Appearance	Cross section
[111]	Smooth and rough sides	Approximately equiaxed ~40 $\mu\text{m}$
Poly	Very rough sides	Equiaxed ~40 $\mu\text{m}$
[112]	Smooth	Thin rectangle 20 $\mu\text{m}$ $\times$ 100 $\mu\text{m}$
[113]	Smooth	Very flat rhombohedron 20 $\mu\text{m}$ $\times$ 200 $\mu\text{m}$
[110]	Smooth tapering	Approximately equiaxed 50 $\mu\text{m}$ $\times$ 50 $\mu\text{m}$

An examination of various reactions by which silicon whiskers could grow indicates the likely reaction to be



This reaction has a standard free energy of -75.874 kcal and has no solid reaction by-product. Although the reaction



is thermodynamically favored ( $\Delta F^\circ = -207.227$  kcal) is probably not taking place, because no  $\text{Al}_2\text{O}_3$  could be detected in the whiskers. Also the partial pressures of SiO and Al are probably too low for this reaction to proceed.

#### Summary

The physical conditions under which silicon whiskers can be grown by Al-SiO<sub>2</sub> interaction are described. The most probable reactions are the reduction of SiO<sub>2</sub> to SiO by Al vapor, and a further reduction of SiO to Si in regions of high Al activity. The practical implications of the Al-SiO<sub>2</sub> interaction are that, for successful diffusion of Al in silicon, either the quartz tube should be passivated (e.g., coated with a layer of Al<sub>2</sub>O<sub>3</sub> or silicon), or the oxygen activity reduced in the system.

Manuscript received Dec. 10, 1973.

Any discussion of this paper will appear in a Discussion Section to be published in the June 1975 JOURNAL. All discussions for the June 1975 Discussion Section should be submitted by Feb. 1, 1975.

The publication costs of this article have been assisted by the Westinghouse Electric Corporation.

#### REFERENCES

1. C. S. Fuller and J. A. Ditzenberger, *J. Appl. Phys.*, **24**, 544 (1956); Y. C. Kao, *Electrochem., Technol.*, **5**, 90 (1967).
2. E. R. Johnson and J. A. Amick, *J. Appl. Phys.*, **25**, 1204 (1954).

## The Effect of Silicon Wafer Imperfections on Minority Carrier Generation and Dielectric Breakdown in MOS Structures

C. M. Osburn\* and D. W. Ormond\*

IBM Thomas J. Watson Research Center, Yorktown Heights, New York 10598

A very large amount of work has been done to determine the effect of silicon wafer imperfections on device characteristics or yield (1-26). Although many individual studies (particularly recent ones) have suc-

cessfully correlated device failure with substrate damage, considerable ambiguity remains in this area for several reasons. In the first place, processing induced damage effects (1-9, 13) often exceed those due to defects in the starting materials. Furthermore, device fabrication at high temperatures leads to thermal stresses whose effects are quite dependent on the initial

\* Electrochemical Society Active Member.

Key words: silicon wafer damage, silicon etching, minority carrier generation, dielectric breakdown.

wafer condition [particularly the back side (2)]. Starting with zero dislocation density wafers gives no assurance of obtaining high device yields because float-zone silicon ( $\sim 100/\text{cm}^2$ ) has not generally been proven to be superior to ( $\sim 10^3\text{--}10^4/\text{cm}^2$ ) dislocation density Czochralski material (8). Metallic contaminants (especially those with states near the middle of the Si forbidden band) contribute to the ambiguity by promoting minority carrier generation and diode leakage. Such impurities (3-9, 11, 12, 14, 15, 17, 18, 24, 27) precipitate at locations of Si damage, vacancy clusters, or at oxygen inclusions. Gettering (15-17, 28-31) of metallic impurities reduces the minority carrier generation rate without lowering the defect concentration.

Although many questions are still unresolved, poor device performance has been repeatedly related to silicon imperfection sites. Chynoweth and Pearson (10) found that light was emitted at dislocation sites (as revealed by etching) during p-n junction breakdown. Queisser and Goetzberger (11) observed microplasma breakdown and soft p-n junctions at stacking faults. Soft junctions and diffusion pipes (or shorts) from emitter to collector have been associated with dislocation loops induced by processing (12, 13). Transmission electron micrographs (14) have found that stacking faults at the surface or in an epitaxial layer degrade junctions. Lawrence (5) attributed excessive recombination currents to lattice strain and dislocations as a result of impurity diffusion, and he distinguished between stable, unstable, and impurity-precipitated dislocations (9). High concentrations of stable dislocations had only minor effects on leakage, transistor gain, and storage time; unstable dislocations, *i.e.*, those that move during device fabrication, were somewhat more detrimental. Impurity precipitation caused large p-n junction reverse currents, emitter to collector shorts, and wide variations in transistor gain. Using scanning oscillator topography, Schwuttke has correlated yield with processing induced dislocations (3) and attributed poor MOS storage times to microspits (19).

This study represents another attempt to interrelate silicon wafer damage with device properties. Metal-oxide-semiconductor capacitor structures were chosen as the test vehicle since only one high temperature step is required for fabrication and there are no oxide steps, diffusions, or photoresist operations which might serve to confuse the interpretation of the results. Some samples were gettered with HCl during oxidation in order to assess the influence of metallic impurities. Two different electrical measurements were made: minority carrier generation, which provides a measure of the number of generation centers in the region just below ( $\sim 1\mu$ ) the Si surface, and dielectric breakdown of a thin (400Å) SiO<sub>2</sub> layer, which is very sensitive to oxide and silicon defects. Chemical etching or polishing (32-36) of as-received, chemically and mechanically polished silicon was used to reduce silicon damage to a minimum.

### Experimental

The silicon wafers were 2 ohm-cm, n-type (phosphorus doped),  $\langle 100 \rangle$  single crystal with only the front side polished by a silica gel, chemical-mechanical technique. A series of wafers having a cupric ion polish was also tested for comparison. Initial thicknesses of the  $1\frac{1}{4}$  in. diameter wafers varied from 8 to 10 mils.

Wafers were cleaned both prior to etching and prior to oxidation in solutions of NH<sub>4</sub>OH-H<sub>2</sub>O<sub>2</sub>, HCl-H<sub>2</sub>O<sub>2</sub>, and HF with a final deionized water rinse. Chemical etching was done with a mixture of nitric (70%), acetic, and hydrofluoric (49%) acids (24-28) in the ratio 7:2:1. The etch rate observed here was 11 $\mu$ /min or about one-third that reported by Robbins and Schwartz (32, 33) in freshly sawed (and hence highly damaged) Si; apparently the etch rate is quite sensitive to damage. Etching times of 50 and 500 sec were standardly used to remove 5 and 47 $\mu$  from each side

of the wafer. Another etchant variation used here was a nitric acid to hydrofluoric acid mixture in a ratio of 250:1 ("reactive etch"). This solution dissolved 400-500Å Si/min and was used for total time of 5 min.

The clean, dry  $1\frac{1}{4}$  in. wafers were placed polished side up in  $2\frac{3}{4}$  in. ID Teflon cups. The cup was then filled with 60 ml of etchant and rotated ( $\sim 60$  rpm) while tilted about 40° from the horizontal plane. The rotational speed and the tilt angle were such that the wafer rotated as a wheel inside the cup, producing adequate shearing and mixing of the etchant layer in contact with the wafer (36). A sudden addition of 500 ml of conc. nitric acid (35) followed by 3 liters of deionized water was used to halt the etching process. This procedure was quite critical since uneven quenching resulted in swirl patterns or hazy residues on the surface. The nitric acid addition greatly diminished this problem.

Two ambients were used to grow the 400Å SiO<sub>2</sub> films at 1000°C: high purity oxygen and 97 volume per cent (v/o) O<sub>2</sub>-3 v/o HCl (99.99% purity). To complete the MOS structures, one hundred 32 mil diameter aluminum electrodes were vacuum deposited through a mask onto each wafer using an electron beam heated source. The wafers were then annealed in nitrogen at 500°C for 5 min to remove interface states.

Dislocation densities were measured by counting Sirtl decorated etch pits (37, 38). This etchant is prepared by dissolving 100g chromium trioxide in 200g H<sub>2</sub>O and mixing four parts of this acid with five parts hydrofluoric acid. Thirty milliliters of etchant were added to a clean wafer, placed in a rotating (60 rpm),  $1\frac{1}{8}$  in. Teflon cup tilted  $\sim 40^\circ$  from the horizon. Etching time of 15 sec removed 1.5 $\mu$  (average thickness) of Si to reveal surface damage.

Minority carrier generation was measured (30, 39-41) on fifty MOS capacitors per wafer. Basically, a depleting voltage pulse was applied and the time required to reach a steady-state inversion capacitance was recorded. Dielectric breakdown was measured by applying a ramp voltage to obtain the voltage of the first breakdown event for each capacitor. Care was taken to detect the first breakdown whether or not it was shorting or nonshorting (self-healing) since these events can be interpreted in terms of insulator defects (42). One hundred capacitors were measured on each wafer.

### Results and Discussion

**Wafer damage.**—Chemical etching of silicon wafers was effective in reducing defect levels, as shown by the decrease in Sirtl etch mound density with etching time in Fig. 1. As can also be seen, a longer Sirtl etching time (300 *vs.* 15 sec) reveals a higher etch pit density. The photomicrographs in Fig. 2 show the improvement for both surfaces, when 5 and 47 $\mu$  of Si are removed.

Silicon oxidation greatly increases damage, as can be seen by the photomicrographs in Fig. 3 obtained by growing a 2000Å SiO<sub>2</sub> film at 1000°C on previously etched wafers. Clearly, the amount of damage present after oxidation depends strongly on the degree of perfection of the unoxidized material. Dumin and Henry (2) have noted this earlier: *i.e.*, oxidation induced damage can be markedly reduced by starting with damage-free wafers. Furthermore, Porter *et al.* (26) were able to reduce oxidation induced damage by etching the starting wafers. Both sides of the wafer after oxidation had more nearly equal dislocation densities, suggesting that the back surface dominates the defect growth. It is unfortunate that the quality of the back surface has usually been relegated to secondary importance because the authors have almost invariably found that the backs of wafers, from a half dozen vendors, show visible saw marks and at least 10<sup>5</sup> Sirtl etch pits/cm<sup>2</sup>. This point is demonstrated in Table I. It can also be seen that when the initial back side dislocation density is low, the etch pit density after

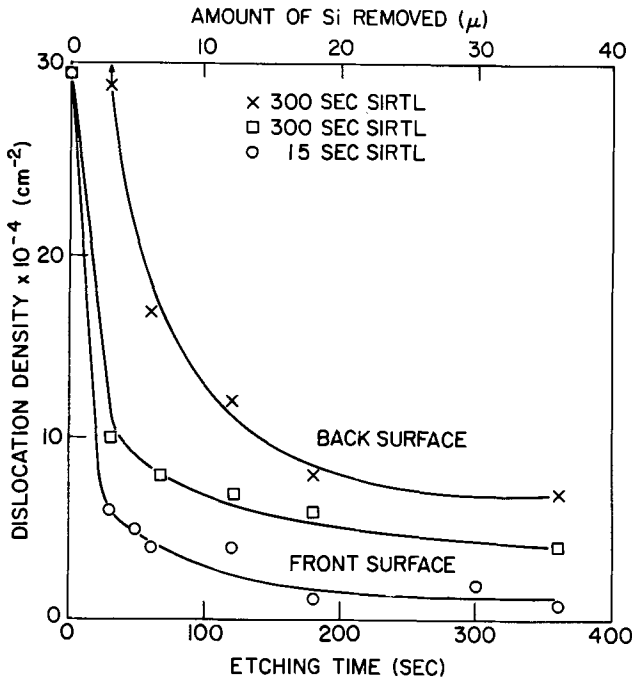


Fig. 1. Dislocation etch mound density for wafer front surface (○, □) and back surface (×) as a function of etching time in HNO<sub>3</sub>-HF-NC<sub>2</sub>H<sub>3</sub>O<sub>2</sub>. Top scale gives amount of silicon removed from each wafer surface. Sirtl etching times of 15 or 300 sec were employed.

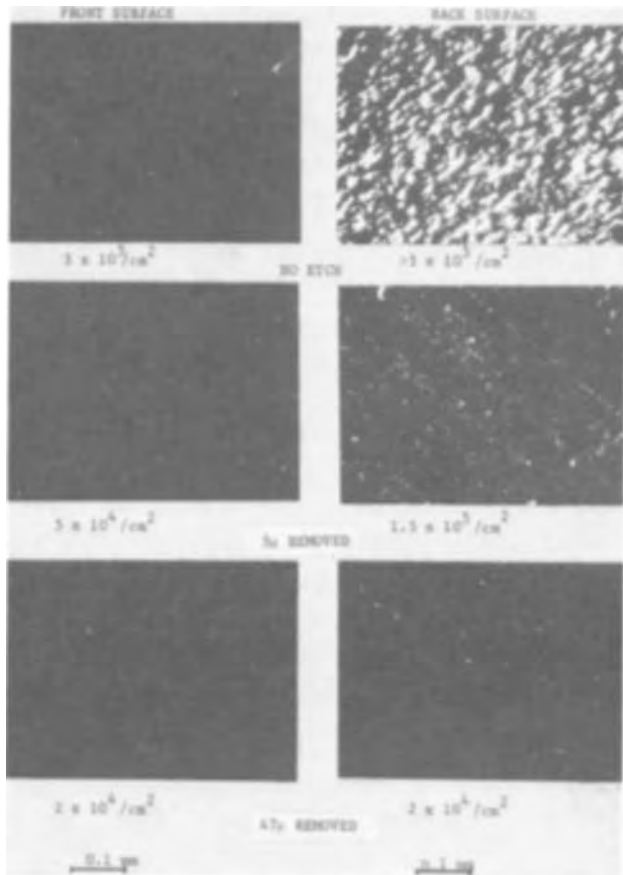


Fig. 2. Effect of silicon removal on wafer damage before oxidation. Wafers were Sirtl etched for 15 sec.

oxidation is also low. Likewise the advantage of using low dislocation density float-zone wafers having heavily damaged back surfaces is eliminated during the oxidation step.

In addition to higher pit counts, the oxidized wafers also show line defects (see Fig. 3, unetched front

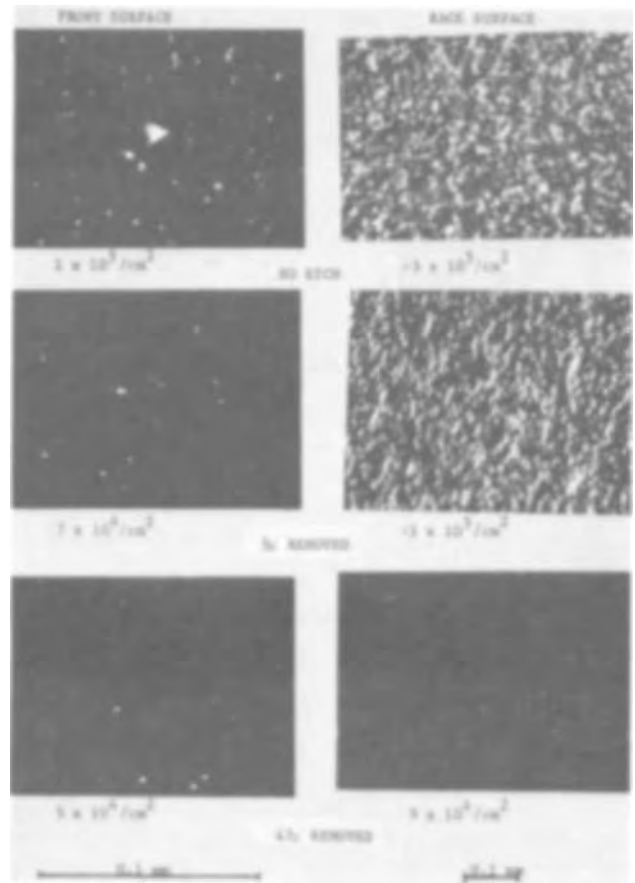


Fig. 3. Effect of silicon removal on wafer damage after oxidation. Wafers were Sirtl etched for 15 sec.

surface). These line defects, in the <110> direction, can be up to 10μ long and generally terminate at dislocations which appear as large bright spots under dark field illumination after Sirtl etching; the dislocation pair is often visible while the line defect cannot be seen. Schwuttke (19) interprets similar line defects in the <110> direction as microsplits with stacking faults at the end. Striation patterns are also revealed by 300 sec Sirtl etching of oxidized wafers. Pre-etching with HNO<sub>3</sub>-HF-HC<sub>2</sub>H<sub>3</sub>O<sub>2</sub> had no effect on the striation pattern. Such patterns were not seen without oxidation and are another (1, 18) example of processing induced changes.

**Electrical properties.**—The results of pulsed capacitance measurements of minority carrier lifetime are summarized in Table II, where the average capacitance relaxation (or inversion) times are given as a function of processing conditions in four different runs. Schroder and Guldberg (41) have found that the relaxation time is directly proportional to minority carrier lifetime in the absence of significant surface generation. Each tabulated value represents the average of 300 capacitors on six wafers in three oxidation runs,

Table I. Sirtl etch pit densities (pits/cm<sup>2</sup>) for wafers supplied by various vendors

Vendor	Before oxidation		After oxidation	
	Front	Back	Front	Back
Czochralski				
1	10 <sup>3</sup>	>10 <sup>5</sup>	1.5 × 10 <sup>4</sup>	>10 <sup>5</sup>
2	10 <sup>4</sup>	5 × 10 <sup>3</sup>	2 × 10 <sup>4</sup>	2 × 10 <sup>4</sup>
3	4 × 10 <sup>2</sup> to 3 × 10 <sup>3</sup>	>10 <sup>5</sup>	10 <sup>4</sup>	>10 <sup>5</sup>
4	1-3 × 10 <sup>4</sup>	>10 <sup>5</sup>	2 × 10 <sup>4</sup> to >10 <sup>5</sup>	>10 <sup>5</sup>
	3 × 10 <sup>3</sup>	10 <sup>4</sup>	8 × 10 <sup>3</sup>	1.5 × 10 <sup>4</sup>
5	7 × 10 <sup>2</sup> to 4 × 10 <sup>4</sup>	>10 <sup>5</sup>	>10 <sup>5</sup>	>10 <sup>5</sup>
Float zone				
1	4 × 10 <sup>3</sup>	>10 <sup>5</sup>	2 × 10 <sup>4</sup>	>10 <sup>5</sup>
2	6 × 10 <sup>2</sup> to 1.2 × 10 <sup>4</sup>	>10 <sup>5</sup>	7 × 10 <sup>3</sup> to 2 × 10 <sup>4</sup>	>10 <sup>5</sup>
6	3 × 10 <sup>3</sup>	>10 <sup>5</sup>	6 × 10 <sup>4</sup>	>10 <sup>5</sup>

Table II. Average capacitance relaxation time as a function of processing (sec)

Control oxidation	Control	0.25 $\mu$ Si removed	5 $\mu$ Si removed	47 $\mu$ Si removed
Silica gel polished Si	33.9 (3.3)*	18.0 (2.6)	50.8 (5.3)	57.4 (2.6)
Cu polished Si	0.01 (0.001)	14.8 (2.6)	—	—
HCl oxidation				
Silica gel polished Si	47.4 (2.7)	73.9 (4.6)	54.0 (2.7)	59.7 (3.3)
Cu polished Si	4.7 (8.8)	15.8 (0.3)	—	—

\* Average standard deviation in parenthesis.

with the exception of the cupric ion polish Si in which 100 capacitors on one wafer were evaluated. Unfortunately, most of the time, the averages of the two identically processed wafers were not statistically identical at the 95% significance level. Chi-squared tests (41) on the statistical distributions of relaxation times further confirmed that more than half of the simultaneously and identically processed wafer pairs were not statistically equal, even at the 99% confidence level. This lack of reproducibility meant that subtle differences due to processing could not be resolved. The variability of the impurity content of the starting wafers presumably accounts for the poor wafer-to-wafer reproducibility. The standard deviation,  $\sigma$  (averaged over the three oxidation runs), is also included in Table II; no substantial variations were discerned.

Despite the serious reproducibility problem, the statistical inversion time distributions revealed several trends. Of the 3000 capacitors tested, those having the longest inversion times were invariably made with etched silicon. Inspection of Table II shows that in five cases out of six, Si etching enhances the relaxation time by 10-70%. It was also observed that the etched samples had a higher than average incidence of very short relaxation time capacitors, possibly as a result of residual surface haze from etching. Wafers having a cupric ion polish (run 4, Table II) showed a dramatic increase in lifetime after even a reactive etch, e.g., more than a thousandfold with standard oxidation. In all cases, the cupric ion polished samples did not have as long a lifetime as did the silica gel polished samples (21, 31). Very likely the improvement seen in these reactively etched samples resulted from removal of a Cu contaminated layer rather than removal of Si imperfections.

Dielectric breakdown characteristics were more reproducible from wafer to wafer than were minority carrier lifetimes (see Table II). In wafers receiving a control oxidation, Si etching rather consistently improved average breakdown strength. It should be emphasized that each entry represents data from 700 capacitors and hence has a very small statistical error. Oxidation in HCl, on the other hand, was seen to degrade reactively etched specimens and to obscure any effect of 50 or 500 sec of etching. The spread of the statistical distribution, as measured by the standard deviation, was not influenced by etching.

The data base generated by these experiments was sufficient to attempt a correlation between minority carrier generation and dielectric breakdown. Both properties were measured on 50 capacitors on a wafer

Table III. Average dielectric breakdown field in the oxide as a function of processing (MV/cm)

	Control	0.25 $\mu$ Si removed	5 $\mu$ Si removed	47 $\mu$ Si removed
Control oxidation	7.3 (0.16)*	7.7 (0.12)	8.1 (0.10)	8.5 (0.11)
HCl oxidation	8.7 (0.12)	6.4 (0.14)	8.5 (0.25)	8.8 (0.09)

\* Average standard deviation in parenthesis.

and the correlation coefficient (43) computed; ten wafers were thus tested. Indeed some wafers did show a high correlation (up to 0.25), but other wafers had a negative coefficient. The average correlation coefficient was about +0.05 while its standard deviation was 0.10. Hence it must be concluded that any relationship between the two properties is very tenuous. Minority carrier generation is a property of the silicon, while dielectric breakdown is a property of the silicon dioxide film.

### Summary

Chemical etching of silicon using the  $\text{HNO}_3$ -HF- $\text{HC}_2\text{H}_3\text{O}_2$  etchant system was found to reduce the density of silicon defects, as revealed by Sirtl etching. Improvements were seen with removal of over 50  $\mu$  per side. Thermal oxidation increased the defect density, making the front and back surfaces more alike. The amount of oxidation induced damage depended on the quality of the starting wafer. The wafer back surface was judged to be particularly important since it contained most of the damage. Sirtl etching of oxidized wafers revealed striation patterns that were not visible before oxidation.

Pulsed capacitance, minority carrier generation measurements showed that removal of 0.25, 5, and 47  $\mu$  of damaged silicon extended the high lifetime end of the statistical distribution and also slightly increased the average lifetime. Wafer-to-wafer reproducibility was exceedingly difficult to attain, presumably because the impurity content of the starting wafers was uncontrolled. On the other hand, Si etching also degraded the lifetime of other samples; this degradation may be attributed to etching residue contaminants. Wafers polished with cupric ions improved dramatically with even a 2500  $\text{\AA}$  Si etch, probably due to removal of residual copper. Etching of the underlying silicon increased the average dielectric breakdown strength of  $\text{SiO}_2$  films by as much as 16% when the oxide was grown in pure  $\text{O}_2$ . Oxide growth in HCl +  $\text{O}_2$  lowered the breakdown strength of oxide over lightly etched Si, and longer etches did not result in any improvement.

### Acknowledgments

The authors are indebted to E. Alley for painstaking measurements of the capacitance relaxation time and also etch pit densities. The careful manuscript review of J. Eldridge is greatly appreciated. They are also grateful for many helpful discussions during the course of this work to Y. J. van der Meulen, C. E. Hallas, Jr., and C. Hauerwas.

Manuscript submitted Jan. 18, 1974; revised manuscript received April 12, 1974.

Any discussion of this paper will appear in a Discussion Section to be published in the June 1975 JOURNAL. All discussions for the June 1975 Discussion Section should be submitted by Feb. 1, 1975.

The publication costs of this article have been assisted by IBM Corporation.

### REFERENCES

1. A. Mayer, *Solid-State Technol.*, 38 (1972).
2. D. J. Dumin and W. N. Henry, *Met. Trans.*, 2, 677 (1971).
3. G. H. Schwuttke, *Microelectron. Rel.*, 9, 397 (1970).
4. M. L. Joshi and J. K. Howard, *Nat. Bur. Std. Spec. Pub.* 337, p. 313 (1970).
5. J. E. Lawrence, *This Journal*, 113, 819 (1966).
6. H. F. John, *Proc. IEEE*, 55, 1249 (1967).
7. H. J. Queisser, in "Semiconductor Silicon," Rolf R. Haberecht and Edward L. Kern, Editors, p. 585, The Electrochemical Society Softbound Symposium Series, New York (1969).
8. J. E. Lawrence, *ibid.*, p. 596.
9. J. E. Lawrence, *This Journal*, 115, 860 (1968).
10. A. G. Chynoweth and G. L. Pearson, *J. Appl. Phys.*, 29, 1103 (1958).
11. H. J. Queisser and A. Goetzberger, *Phil. Mag.*, 8, 1063 (1963).

12. F. Barson, M. S. Hess, and M. M. Roy, *This Journal*, **116**, 304 (1969).
13. E. D. Jungbluth and P. Wang, *J. Appl. Phys.*, **36**, 1967 (1965).
14. K. V. Ravi, C. J. Varker, and C. E. Volk, *This Journal*, **120**, 533 (1973).
15. E. J. Mets, *ibid.*, **112**, 420 (1965).
16. S. W. Ing, Jr., R. E. Morrison, L. L. Alt, and R. W. Aldrich, *ibid.*, **110**, 533 (1963).
17. J. E. Lawrence, *Trans. AIME*, **242**, 484 (1968).
18. A. J. R. de Kock and P. G. T. Boonen, *ibid.*, **119**, 1241 (1972).
19. G. H. Schwuttke, Technical Report 1, Contract DAHC15-72-C-0774 (1963).
20. A. Berman, Private communication.
21. G. Schmidt, Private communication.
22. W. K. Tice, R. C. Lang, and E. B. Shastleen, in "Semiconductor Silicon," Howard R. Huff and Ronald R. Burgess, Editors, p. 639, The Electrochemical Society Softbound Symposium Series, Princeton, N. J. (1973).
23. D. M. Seto, F. Barson, and B. F. Duncan, *ibid.*, p. 651.
24. S. Dash, *ibid.*, p. 626.
25. M. R. Poponiak, W. A. Keenan, and R. O. Schwenker, *ibid.*, p. 701.
26. W. A. Porter, A. Gupta, and J. C. Lewis, *This Journal*, **120**, 92C (1973).
27. G. H. Schwuttke, *ibid.*, **108**, 163 (1961).
28. M. Waldner and L. Sivo, *ibid.*, **107**, 298 (1960).
29. R. S. Ronen and P. H. Robinson, *ibid.*, **119**, 747 (1972).
30. D. R. Young and C. M. Osburn, *ibid.*, **120**, 1578 (1973).
31. A. Berman, D. R. Kerr, and J. Petrak, Private communication.
32. H. Robbins and B. Schwartz, *This Journal*, **107**, 108 (1960).
33. B. Schwartz and H. Robbins, *ibid.*, **108**, 365 (1961).
34. D. R. Turner, *ibid.*, **107**, 810 (1960).
35. R. J. Archer, *J. Phys. Chem. Solids*, **14**, 104 (1960).
36. C. E. Hallas, Jr., *This Journal*, **113**, 318C (1966).
37. ASTM #F47-70.
38. C. E. Hallas, Jr. and E. Mendel, *J. Appl. Phys.*, **42**, 477 (1971).
39. M. Zebst, *Z. Angew. Phys.*, **22**, 30 (1966).
40. P. H. Robinson and F. P. Heiman, *This Journal*, **118**, 141 (1971).
41. D. K. Schroder and J. Guldberg, *Solid State Electron.*, **14**, 1285 (1971).
42. C. M. Osburn and D. W. Ormond, *This Journal*, **119**, 591 (1972).
43. G. P. Wadsworth and J. G. Bryan, "Introduction to Probability and Random Variables," pp. 217, 245, McGraw-Hill Book Co., Inc., New York (1960).

## In Situ Monitoring of Film Deposition Using He-Ne Laser System

### I. Measurements of CVD Insulating Film at 6328Å

Katsuro Sugawara,\* Takeo Yoshimi, Hiroaki Okuyama, and Tatsumi Shirasu

*Semiconductor and Integrated Circuits Division, Hitachi, Limited, Kodaira, Tokyo, Japan*

Chemical vapor deposition (CVD) technology for semiconductor device fabrication has been widely applied to the formation of semiconductor film and insulating films. For these applications, uniformity of both the film thickness and film composition is required to decrease variations of electrical characteristics and to increase the capability of fine photoetching. Consequently, the method of "in-process" monitoring has been strongly in demand. Dumin (1) first devised a technique for "in-process" monitoring of the thickness of heteroepitaxial silicon film grown on sapphire (SOS), utilizing the interference caused by infrared emission radiated from the substrate. This method was subsequently developed into an *in situ* thickness monitor for polycrystalline silicon deposition on SiO<sub>2</sub>-Si substrates by Kamins and Dell'Oca (2) and for alumina deposition by Roberts, Clark, and Dumbri (3). Another method, using an illuminator and a photocell with a filter and a polarizer, was reported by Davidse and Maissel (4) for monitoring the thickness of sputtered SiO<sub>2</sub> films.

To increase control accuracy caused by a coherent single beam and to detect thickness variations even at small, localized spots, a new monitor of CVD film thickness using a laser system was devised. In this paper the experimental method and the results are presented.

Figure 1 shows the layout of the monitoring system using the visible 6328Å He-Ne laser during CVD SiO<sub>2</sub> deposition. A vertical reactor was of the rf heated type with a SiC-coated graphite susceptor. In this reactor, CVD SiO<sub>2</sub> films produced by the SiH<sub>4</sub>-O<sub>2</sub> system were deposited on three different substrates—silicon wafers, thermally grown SiO<sub>2</sub> films formed on silicon

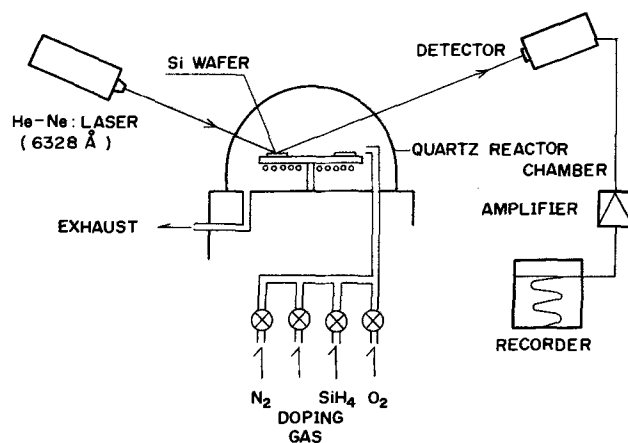


Fig. 1. Layout of monitoring apparatus using a visible He-Ne laser with 6328Å during CVD SiO<sub>2</sub> deposition.

substrates, and aluminum films evaporated on silicon. During deposition, the He-Ne laser beam, (wavelength 6328Å, output power 1 mW, and diameter of beam spot 1 mm) was directed onto the specimens from outside of a quartz reactor chamber of 250 mm inner diameter. As the film was deposited on the substrate, the laser beam was partially reflected at the surface of the deposited SiO<sub>2</sub> film and partially at the interface between the CVD SiO<sub>2</sub> and the silicon substrate, after being transmitted through the CVD SiO<sub>2</sub>. These reflected beams were received by a selenium photocell (maximum sensitivity: 6000Å in wavelength), amplified, and recorded as an interference wave. Since this wave corresponds to the film thickness, the thickness

\* Electrochemical Society Active Member.

Key words: CVD SiO<sub>2</sub> film, Si<sub>3</sub>N<sub>4</sub> film, control of film thickness.

Table I. Standard deposition condition of CVD SiO<sub>2</sub> and PSG films

Condition	CVD SiO <sub>2</sub>	
Flow rate	SiH <sub>4</sub>	56 cm <sup>3</sup> /min
	O <sub>2</sub>	1120 cm <sup>3</sup> /min
	N <sub>2</sub>	20 liters/min
Deposition temperature		450°C

can be determined from the obtained pattern while the film is being subjected to deposit. The standard deposition condition was tabulated as listed in Table I. After deposition, the SiO<sub>2</sub> films were partially removed by etching and the film thickness was measured with a "Talystep."

Figure 2 shows the relation between reaction time and reflective intensity, when the CVD SiO<sub>2</sub> film was deposited on the silicon substrate. The axis of abscissa reveals both reaction time and film thickness measured by the "Talystep;" one cycle of the interference wave is approximately 2900Å. In this figure, the solid line (a) is an observed value and the line of dashes (b) represents the calculated value (5) where the refractive index is taken as 1.44, determined by an ellipsometer. The calculated pattern (b), when 1.44 was used, approximately coincides with the experimental pattern.

When the CVD films were deposited on the silicon substrate, thermally grown SiO<sub>2</sub>, and aluminum film, each interference pattern is drawn on the same chart in Fig. 3. The pattern observed on the silicon substrate is similar to that on the thermally grown SiO<sub>2</sub>, but the pattern on the evaporated aluminum differs from these two. It is considered that this fact was effected by the large extinction coefficient of aluminum, 6.6 at 6500Å in wavelength (6).

The result is reported on applying the visible He-Ne laser to Si<sub>3</sub>N<sub>4</sub> film formation. The Si<sub>3</sub>N<sub>4</sub> film was deposited at 800°C and NH<sub>3</sub>/SiH<sub>4</sub> = 18, in the SiH<sub>4</sub>-NH<sub>3</sub>-N<sub>2</sub> system, the latter parameter was adapted to prevent the formation of excess silicon (7). The interference patterns are shown in Fig. 4, depositing on the oxidized silicon substrate with 1.0 μm thickness. As is evident in Fig. 4, the observed curve (a) practically coincides with the calculated one (b), applied as 2.0 in the refractive index of Si<sub>3</sub>N<sub>4</sub> film (8). The curve (c) shows the obtained one by the infrared radiation system. The laser system is superior in control accuracy; the thickness of one cycle in the interference wave is 1500Å for monitoring by the laser system, while 3200Å for the infrared radiation.

Precise control of CVD film thickness has been required from the standpoints of stable electric properties and accurate photoetching. As one of the countermeasures to meet these demands, a new monitoring method by applying the laser system was devised. This

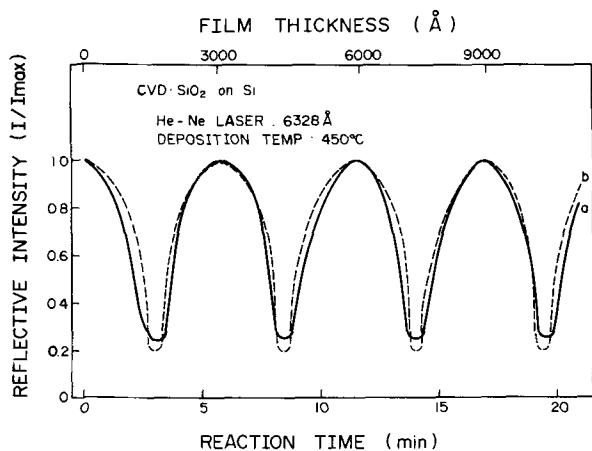


Fig. 2. Observed and calculated interference patterns during CVD SiO<sub>2</sub> film deposition on silicon. a, Observed. b, Calculated as  $n = 1.44$ .

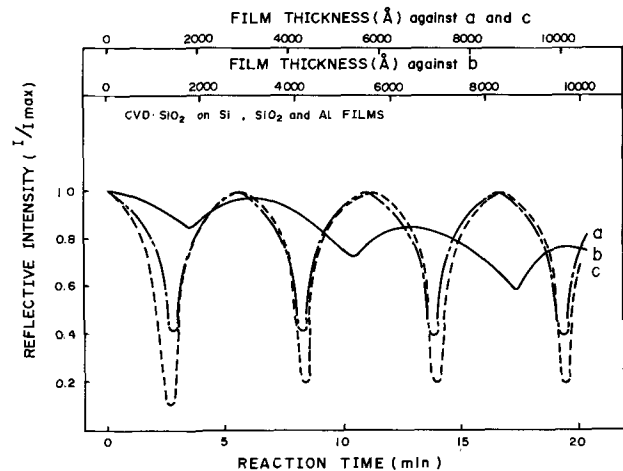


Fig. 3. Observed patterns of interference during CVD SiO<sub>2</sub> deposition on various substrates. a, On silicon substrate. b, On aluminum film evaporated on a silicon substrate. Thickness of aluminum film, 1 μm. c, On thermally grown SiO<sub>2</sub> film formed on silicon substrate. Thickness of thermally grown SiO<sub>2</sub>, 9000Å.

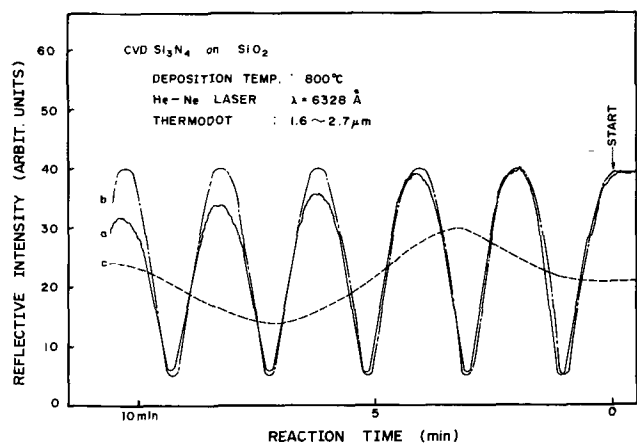


Fig. 4. Observed patterns of interference when CVD Si<sub>3</sub>N<sub>4</sub> film was formed on thermally oxidized silicon wafer. Thickness of SiO<sub>2</sub> film, 1.0 μm. a, Observed pattern by visible He-Ne laser system. b, Calculated pattern as  $n = 2.0$  by laser system. c, Observed pattern by infrared radiation system.

method has several merits: it is precise even at small spots and is widely applicable even to low temperature deposition. The He-Ne visible laser of 6328Å wavelength was adapted for monitoring of insulating films. For CVD SiO<sub>2</sub> film, one cycle of the interference wave was 2900Å; control accuracy was  $\pm 100\text{Å}$  at the minima,  $\pm 250\text{Å}$  at the maxima, and  $\pm 200\text{Å}$  at the remaining parts of the interference patterns. Tendency of the deposition rates of PSG (phosphosilicate glass) films in relation to O<sub>2</sub>/SiH<sub>4</sub> + PH<sub>3</sub> and PH<sub>3</sub>/SiH<sub>4</sub> + PH<sub>3</sub> mole fractions during PSG film formation (9) was confirmed by this monitoring. For Si<sub>3</sub>N<sub>4</sub> film in a higher temperature deposition, it is obvious upon comparing the laser and the infrared radiation system that the control accuracy of film thickness in the former system is improved three times, as a result of shorter wavelength of the laser beam.

#### Acknowledgments

The authors express their deep appreciation to Mr. S. Nishida for his helpful discussions and encouragement during this experiment, to Mr. T. Nohara for ellipsometric measurements, and to Mr. K. Akiba for assistance in fabrication of the experimental equipment.

Manuscript submitted Oct. 24, 1973; revised manuscript received March 26, 1974. This was Paper 213 pre-

sented at the Boston, Massachusetts, Meeting of the Society, Oct. 7-11, 1973.

Any discussion of this paper will appear in a Discussion Section to be published in the June 1975 JOURNAL. All discussions for the June 1975 Discussion Section should be submitted by Feb. 1, 1975.

The publication costs of this article have been assisted by Hitachi, Limited.

#### REFERENCES

1. D. J. Dumin, *Rev. Sci. Instr.*, **38**, 1107 (1967).
2. T. I. Kamins and C. J. Dell'Oca, *This Journal*, **119**, 112 (1972).
3. J. F. Roberts, C. A. Clark, and A. C. Dumbri, *Rev.*

- Sci. Instr.*, **41**, 247 (1970).
4. R. Glang, in "Handbook of Thin Film Technology," L. I. Maissel and R. Glang, Editors, p. 1-114, McGraw-Hill Book Co., New York (1970).
5. M. Born and E. Wolf, "Principle of Optics," p. 323, Pergamon Press, Oxford (1965).
6. O. S. Heavens, "Optical Properties of Thin Solid Films," p. 200, Dover Publications, Inc., New York (1965).
7. V. Y. Doo, D. R. Kerr, and D. R. Nichols, *This Journal*, **115**, 61 (1968).
8. L. V. Gregor, in "Thin Film Dielectrics," p. 447, F. Vratny, Editor, The Electrochemical Society Softbound Symposium Series, New York (1969).
9. M. Shibata, T. Yoshimi, and K. Sugawara, *This Journal*, To be published.

## In Situ Monitoring of Film Deposition Using He-Ne Laser System

### II. Measurements of Polycrystalline Silicon Film in the Infrared

Katsuro Sugawara,\* Takeo Yoshimi, and Hiroaki Okuyama

Semiconductor and Integrated Circuits Division, Hitachi, Limited, Kodaira, Tokyo, Japan

and Yoshio Homma

Central Research Laboratory, Hitachi, Limited, Kokubunji, Tokyo, Japan

In the previous paper (1), the monitoring method was reported applying a visible He-Ne laser for insulating films  $\text{SiO}_2$  and  $\text{Si}_3\text{N}_4$ . Monitoring by the laser system was further developed, and a new method using an infrared He-Ne laser was attempted for polycrystalline silicon film. In this work, the monitoring system was compared with the infrared radiation method (2) and the effect of the deposition condition on monitoring by the laser system was investigated.

A schematic diagram of the monitoring apparatus is shown in Fig. 1. A vertical reactor was of the rf heated type with a SiC-coated graphite susceptor. In this reactor, polycrystalline silicon film was deposited on thermally grown  $\text{SiO}_2$  films formed on silicon substrates by the  $\text{SiH}_4\text{-N}_2$  and  $\text{SiH}_4\text{-B}_2\text{H}_6\text{-N}_2$  systems. Standard thickness of the  $\text{SiO}_2$  films was about 9000Å. The apparatus is similar to that used for CVD  $\text{SiO}_2$  film formation (1) except for the laser and its detector. In this system, an infrared He-Ne laser (wavelength, 1.15

$\mu\text{m}$ ; output power, 3 mW; and diameter of beam spot, 1.4 mm) was adapted. The detector was a silicon solar cell with maximum sensitivity of 7700Å. Besides the laser system, a PbS infrared pyrometer (sensitive to radiation with wavelength between 1.6 and 2.7  $\mu\text{m}$ ) was positioned to detect interference caused by the above-mentioned infrared radiation. Reading the wafer temperature with the infrared pyrometer, emissivity was corrected according to Allen's data (3). The standard deposition conditions are listed in Table I.

The visible He-Ne laser with 6328Å was tested for the deposition of polycrystalline silicon film. As is evident from Fig. 2, when thickness of the deposited film exceeded 4000Å, variation of the reflective intensity was difficult to recognize, because of absorption through the silicon film.

The infrared He-Ne laser beam with 1.5  $\mu\text{m}$  is less absorbed in silicon than the 6328Å beam. The interference pattern obtained by the 1.15  $\mu\text{m}$  beam is shown in Fig. 3. The solid line (a) represents the observed pattern by the laser system, appearing sharp and clear; while the chain line (c) shows interference produced by infrared radiation recorded by the infrared pyrometer. A large difference of film thickness between adjacent maxima, and weak interference can be seen in the interference pattern by the infrared radiation. In this figure, also recorded is the calculated pattern (b) (4), where 3.42, value of the refractive index for the single crystal silicon (5-6) was taken for that of the polycrystalline silicon. Coincidence between the observed (a) and the calculated (b) patterns was good.

\* Electrochemical Society Active Member.  
Key words: polycrystalline silicon film, 1.15  $\mu\text{m}$  He-Ne laser, infrared radiation, control of film thickness.

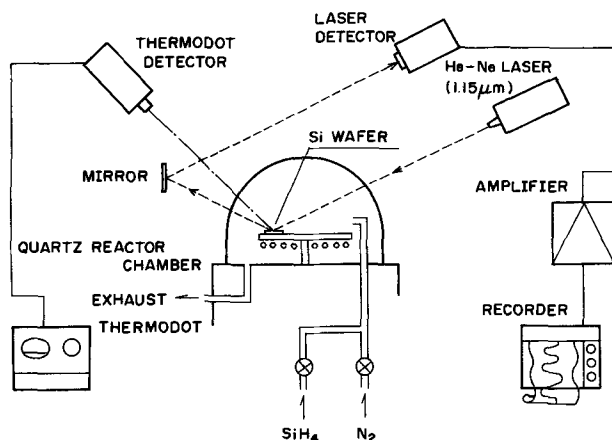


Fig. 1. Layout of monitoring apparatus using the infrared He-Ne laser with 1.15  $\mu\text{m}$  during polycrystalline silicon deposition.

Table I. Standard deposition conditions of polycrystalline silicon films without and with  $\text{B}_2\text{H}_6$  doping

Conditions	Poly. Si without doping	Poly. Si with doping
Flow rate	$\text{SiH}_4$ 56 $\text{cm}^3/\text{min}$ $\text{B}_2\text{H}_6$ — $\text{N}_2$ 20 liters/min	56 $\text{cm}^3/\text{min}$ 0.5 $\text{cm}^3/\text{min}$ 20 liters/min
Deposition temperature	650°C	650°C



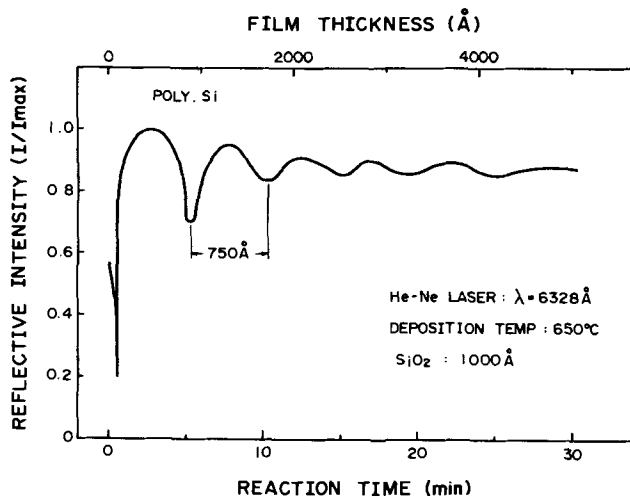


Fig. 2. Observed pattern of interference when the visible He-Ne laser with 6328 Å was used during polycrystalline silicon deposition.

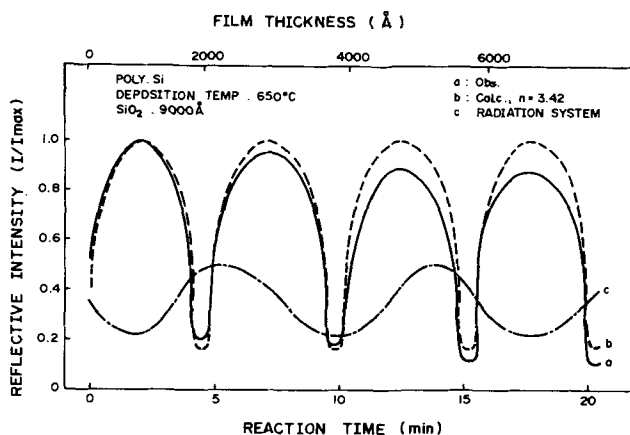


Fig. 3. Comparison between patterns of interference by the infrared laser system and by the infrared radiation system during polycrystalline film deposition. a, Observed pattern by infrared laser system. b, Calculated pattern with infrared laser monitoring as  $n = 3.42$ . c, Observed pattern by infrared radiation system.

Table II. Comparison between laser and infrared radiation systems

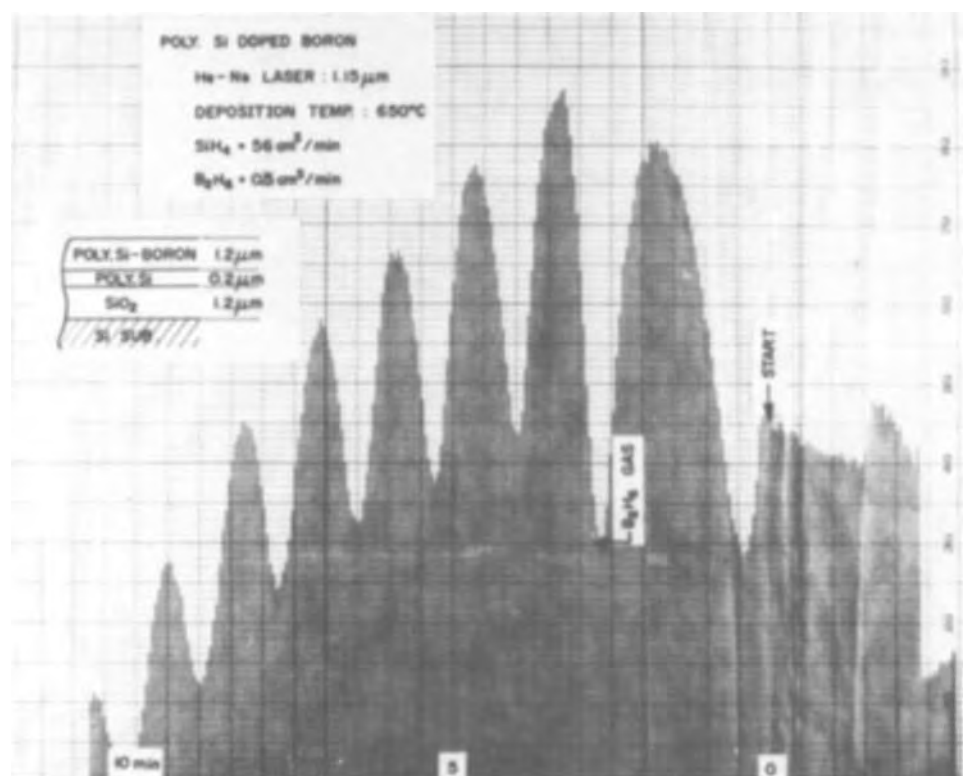
Method	Feature	Problem
Laser system	<ol style="list-style-type: none"> <li>1. More accurate monitoring</li> <li>2. Applicable even to low temp. deposition</li> <li>3. Applicable to thin and thick film</li> </ol>	<ol style="list-style-type: none"> <li>1. Maintenance of alignment</li> <li>2. Sensitivity and area of detector</li> </ol>
Infrared radiation system	<ol style="list-style-type: none"> <li>1. Simple in construction</li> <li>2. Simple to apply</li> </ol>	<ol style="list-style-type: none"> <li>1. Inapplicable to low temp. deposition</li> <li>2. Dispersion</li> <li>3. Large infrared wavelength</li> </ol>

Figure 4 shows the result of a rotating specimen on which the polycrystalline silicon film was deposited, initially without doping and subsequently with  $B_2H_6$  doping of  $0.5 \text{ cm}^3/\text{min}$  at  $650^\circ\text{C}$ . From the moment of doping, the peak-to-peak distance in the interference pattern became shorter, causing an increase of the deposition rate to be noticed.  $B_2H_6$  doping created an increase of the deposition rate while increasing the flow rate, as Eversteyn and his co-worker already pointed out (7). They observed a two-time increase when boron was introduced by more than an atomic fraction  $B/\text{Si} = 0.0025$ , and the result of this experiment shows approximately the same order; the deposition rates without and with  $B_2H_6$  doping were 900 and  $1500 \text{ Å}/\text{min}$ , respectively.

Although the infrared radiation method is simple to apply, it presents problems of precision and minimum specimen temperature, dispersion of radiation beams, and intensity of infrared radiation; while the laser system can be accurately applied to more CVD reactions, based on the single wavelength and injection from outside of the reactor. This method, however, requires more mechanical accuracy for the CVD reactor mechanism—such as that of susceptor rotation—to prevent variations of laser beam reflection. Features and problems of both systems are compared in Table II.

For monitoring the thickness of polycrystalline silicon films, a new method using a He-Ne laser at  $1.15 \mu\text{m}$  wavelength (much less absorbed than the visible He-Ne laser at 6328 Å) was devised. For the infrared radiation system and the laser system, one cycle of the interference wave was 5900 and 3700 Å, and control

Fig. 4. Interference pattern by infrared laser beam during polycrystalline silicon deposition without and with  $B_2H_6$  doping. At the beginning of deposition, the film was formed without doping, and after 3 min with  $B_2H_6$  doping while the specimen was rotated on the susceptor.





accuracy was  $\pm 400$  and  $\pm 200\text{\AA}$ , respectively. Further, the influence of  $\text{B}_2\text{H}_6$  doping was investigated and the deposition rate increment was determined by this monitoring.

### Acknowledgment

The authors express their sincere gratitude to Mr. S. Nishida for his encouragement and to Mr. T. Shirasu for helpful discussions.

Manuscript submitted Oct. 24, 1973; revised manuscript received March 26, 1974. This Paper 213 presented at the Boston, Massachusetts, Meeting of the Society, Oct. 7-11, 1973.

Any discussion of this paper will appear in a Discussion Section to be published in the June 1975 JOURNAL.

All discussions for the June 1975 Discussion Section should be submitted by Feb. 1, 1975.

The publication costs of this article have been assisted by Hitachi, Limited.

### REFERENCES

1. K. Sugawara, T. Yoshimi, H. Okuyama, and T. Shirasu, *This Journal*, **121**, 1233 (1974).
2. T. I. Kamins and C. J. Dell'Oca, *ibid.*, **119**, 112 (1972).
3. F. G. Allen, *J. Appl. Phys.*, **28**, 1510 (1957).
4. P. H. Berning, in "Physics of Thin Films," Vol. 1, p. 69, G. Hass, Editor, Academic Press Inc., New York (1963).
5. H. F. Wolf, "Silicon Semiconductor Data", p. 3, Pergamon Press, Oxford (1969).
6. K. Sato, Y. Ishikawa, and K. Sugawara, *Solid-State Electron.*, **9**, 771 (1966).
7. F. C. Eversteyn and B. H. Put, *This Journal*, **120**, 106 (1973).

## Germanium-Doped GaAs for P-Type Ohmic Contacts

D. R. Ketchow

Bell Laboratories, Murray Hill, New Jersey 07974

Ohmic contacts to epitaxial p-type GaAs, such as those used on double heterostructure lasers, are usually fabricated by deposition of a metal layer on a Zn-diffused ( $p \approx 10^{20} \text{ cm}^{-3}$ ) GaAs layer. Contact to the p-type layer without a Zn diffusion has not been feasible because the hole concentration in the layer was not sufficient for ohmic contact. Previous reports of Ge as a p-type dopant in GaAs used a method not applicable for multilayer growth (1, 2) or did not achieve the level of free carriers necessary for a nonalloyed ohmic contact without a zinc diffusion (3, 4). Carrier concentrations as high as  $8 \times 10^{19} \text{ cm}^{-3}$  were attained in the work reported here. A nonalloyed ohmic contact, with resistance equal to that measured on layers having a Zn diffusion, was achieved without a Zn diffusion.

Single epitaxial GaAs layers were grown on  $\langle 111 \rangle$  B and  $\langle 100 \rangle$  oriented GaAs substrates. Cr-doped substrates were used for carrier concentration experiments. Zn-doped p-type ( $p \approx 10^{18} \text{ cm}^{-3}$ ) substrates were used for contact resistance experiments. The Ge-doped single layers were grown in a graphite slider by the source-seed technique for LPE growth of GaAs-Ga<sub>1-x</sub>Al<sub>x</sub>As double heterostructures as described by Dawson (5).

### Experimental

**Hall measurements.**—Hall measurements were done at room temperature in a magnetic field of 5250 Gauss. The results are shown in Table I. Duplication of sam-

Key words: epitaxy, crystal growth, semiconductor.

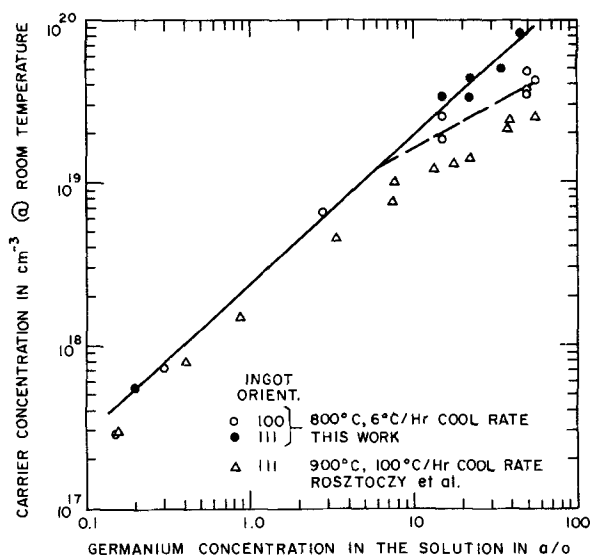


Fig. 1. Room temperature carrier concentration vs. germanium concentration in the solution.

ple numbers indicates that growth occurred simultaneously on two different substrates from the same Ga-Ge-As solution.

Figure 1 shows the effect of Ge concentration in the growth solution on room temperature carrier concen-

Table I. Composition and electrical data of semi-insulating substrate samples

Sample No.	Orient.	Ge concentration in solution (a/o)	Carrier concentration at 25°C (cm <sup>-3</sup> )	Hall mobility at 25°C (cm <sup>2</sup> /Vsec)	Layer thickness (μm)	Carrier
B009	$\langle 100 \rangle$	0.16	$2.9 \times 10^{17}$	239.0	3.96	p
B200	$\langle 111 \rangle$	0.20	$5.5 \times 10^{17}$	207.3	12.34	p
B010	$\langle 100 \rangle$	0.30	$7.3 \times 10^{17}$	195.0	4.96	p
B129	$\langle 100 \rangle$	2.8	$6.5 \times 10^{18}$	66.0	6.15	p
B124a	$\langle 100 \rangle$	15.0	$1.79 \times 10^{19}$	31.4	4.12	p
B124b	$\langle 111 \rangle$	15.0	$3.27 \times 10^{19}$	27.5	1.98	p
Co66	$\langle 100 \rangle$	15.0	$2.49 \times 10^{19}$	31.7	9.7	p
B118a	$\langle 111 \rangle$	22.5	$4.3 \times 10^{19}$	25.0	2.53	p
B119a	$\langle 111 \rangle$	22.5	$3.3 \times 10^{19}$	24.7	2.34	p
B112	$\langle 111 \rangle$	35.0	$5.0 \times 10^{19}$	20.5	3.65	p
B115	$\langle 111 \rangle$	44.5	$8.2 \times 10^{19}$	9.8	1.35	p
C067	$\langle 100 \rangle$	50.0	$3.4 \times 10^{19}$	14.9	4.15	p
C068	$\langle 100 \rangle$	50.0	$4.6 \times 10^{19}$	15.5	7.9	p
C069a	$\langle 100 \rangle$	50.0	$3.77 \times 10^{19}$	15.9	7.6	p
B165	$\langle 100 \rangle$	56.0	$4.2 \times 10^{19}$	12.6	4.0	p

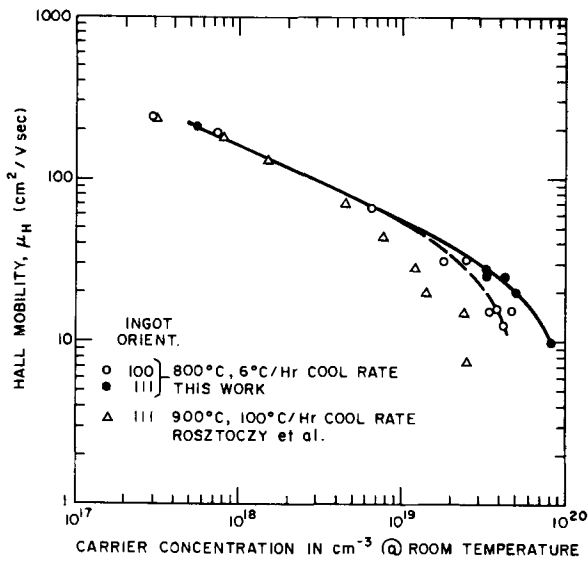


Fig. 2. Hall mobility vs. carrier concentration at room temperature.

tration in the grown layers. On the log-log scale the carrier concentration of layers grown on the <111> oriented substrates increases with a slope of one for growth solutions containing 0.2-44.5 atomic per cent (a/o) Ge. Included also are the data reported by Rosztochy *et al.* (3, 4), on their work using only <111> oriented substrates. All of their data are lower than ours (<111> and <100>), and they have a departure from unit slope at ~4 a/o Ge ( $p \approx 6.5 \times 10^{18} \text{ cm}^{-3}$ ) which we do not observe in our <111> data. The reason for their lower carrier concentration might be their higher average growth temperature (900°-875°C) which could result in lower Ge concentration in the layer and a lower hole concentration for the same Ge concentration. Comparing our data on <111> oriented substrates with that on our <100> substrates we find a departure from unit slope at ~6 a/o Ge ( $p \approx 1 \times 10^{19} \text{ cm}^{-3}$ ) for the latter orientation.

Figure 2 is a plot of the room temperature Hall mobility vs. carrier concentration. The data for our <100> and <111> oriented substrates part agreement again at  $p \approx 1 \times 10^{19} \text{ cm}^{-3}$  with a decrease in the mobility data for the <100> oriented substrates. The higher mobility presented here indicates the layers grown at the lower temperatures are less compensated for the same carrier concentration than those grown by Rosztochy *et al.* at the higher temperature.

**Contact resistance measurements.**—The contact resistance measurements were made across pairs of evaporated metal dots on the grown layers. As may

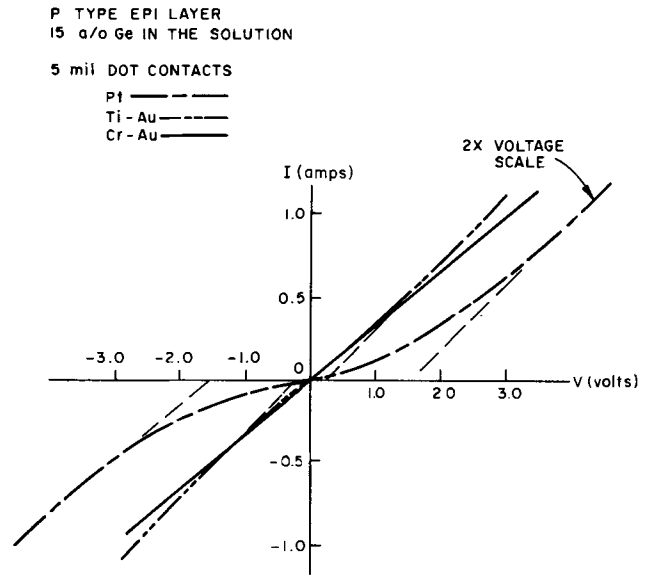


Fig. 3. Typical I/V curves of the contact resistance of three types of metal contacts to epi-layers grown from 15 a/o Ge concentration solutions.

be seen in Table II, the contacts were varied in size from 5 to 10 mils in diameter and were of 3 different metals: (i) 3000Å Pt, (ii) 300Å Cr-5000Å Au, and (iii) 250Å Ti-2400Å Au. They were not alloyed or sintered after evaporation. The a/o Ge concentration in the solutions used to grow the layer ranged from 1.0 a/o ( $p \approx 2.3 \times 10^{18} \text{ cm}^{-3}$ ) to 44.5 a/o ( $p \approx 8.2 \times 10^{19} \text{ cm}^{-3}$ ). Layers with the lower Ge concentrations did not show ohmic behavior. Pt contacts to these layers exhibited blocking voltages three to four times higher than the Cr-Au or the Ti-Au contacts. At 15 a/o Ge concentration in the solution ( $p \approx 2.49 \times 10^{18} \text{ cm}^{-3}$ ) the Pt contacts showed an average of 0.6V blocking voltage while the Ti-Au contacts averaged 0.13V blocking voltage. The Cr-Au contacts showed no blocking voltages on layers grown at this Ge concentration in the solution nor did they show any on layers grown from higher Ge concentration solutions. Figure 3 shows typical I vs. V curves of the three different types of contacts made to layers grown from the 15 a/o Ge solutions. The voltage scale for the Pt contact has been compressed in order for it to fit on the scale of the figure.

The higher Ge concentration samples were used to determine the contact resistance of the grown layers with and without a Zn-diffusion. The three samples were each cleaved into two parts. One part of each was zinc diffused prior to the evaporation of Cr-Au contacts

Table II. Composition and electrical data of p-type substrate samples

Sample No.	Substrate orientation	Ge concn. in solution (a/o)	Carrier* concentration (cm <sup>-3</sup> )	Layer thickness (μm)	Type of contact	Contact dot size (mils)	Avg. contact resistance (ohm) (no diff.)	Avg. contact resistance (ohm) (Zn diff.)	Avg. contact blocking voltage (V)
B168	<111>	1.0	$2.3 \times 10^{18}$	4.8	Ti-Au	5. (10 mil centers)	3.2	—	0.4
	<111>	1.0			Cr-Au	5.	2.9	—	0.33
	<111>	1.0			Pt	5.	8.7	—	1.8
B162	<100>	2.8	$6.5 \times 10^{18}$	4.4	Ti-Au	5.	3.1	—	0.33
	<100>	2.8			Cr-Au	5.	3.0	—	0.44
	<100>	2.8			Pt	5.	10.3	—	1.3
B128	<100>	15.0	$2.5 \times 10^{19}$	3.0	Ti-Au	5.	2.7	—	0.13
	<100>	15.0			Cr-Au	5.	2.6	—	0
	<100>	15.0			Pt	5.	7.2	—	0.6
B118b	<111>	22.5	$4.3 \times 10^{19}$	1.2	Cr-Au	6. (10 mil centers)	0.5 <sup>(E)</sup>	2.5 <sup>(E)</sup>	0
B <sup>#</sup> 119b	<111>	22.5	$3.3 \times 10^{19}$	2.6	Cr-Au	6.	3.4	0.05	0
B111	<111>	35.0	$5.0 \times 10^{19}$	2.2	Ti-Au	10. (20 mil centers)	1.55	—	0
B113	<111>	44.5	$8.2 \times 10^{19}$	2.9	Ti-Au	10.	1.3 <sup>(E)</sup>	—	0
	<111>	44.5			Ti-Au	10.	2.3	—	0
	<111>	44.5			Cr-Au	7. (10 mil centers)	3.1 <sup>(E)</sup>	2.6 <sup>(E)</sup>	0

<sup>R</sup> Ga-Ge solution reused from run preceding.  
<sup>E</sup> Etched mesa contacts.  
 \* Taken from Fig. 2.

on both parts as one unit. There was no significant difference in the contact resistance between the parts to indicate the presence or absence of the zinc diffusion. These results have been confirmed in measurements made on double heterostructure lasers.

### Conclusions

The work presented here shows ohmic contact can be made to p-type Ge-doped layers with carrier concentrations of  $4-8 \times 10^{19} \text{ cm}^{-3}$  without a diffused zinc contact layer. The carrier concentration varies linearly with the amount of Ge in the solution used to grow the layers at 800°-790°C. A comparison of the contact resistance of these layers with and without a zinc diffusion showed little or no difference. The zinc diffusion, therefore, was not the major factor in achieving good ohmic contact. A comparison between types of metal contacts showed the metal species are a factor in achieving good contact. The three types of contacts, Ti-Au, Cr-Au, and Pt used in these comparisons were not alloyed. They were selected because of their availability. No intensive work was done to search for or develop a low contact metal. The Pt contacts showed three times as much resistance and displayed as much as one volt greater blocking voltage than the Ti-Au or Cr-Au contacts. The origin of this discrepancy was not investigated.

### Acknowledgments

Acknowledgment is made to F. Ermanis for some of the Hall effect measurements, G. Barnosky and his co-workers for their patience and skill in evaporating the metal contacts, R. H. Peaker for the use of the pulsed I/V equipment and his cheerful assistance in measuring the contact resistance, and L. R. Dawson and D. L. Rode for their helpful discussions.

Manuscript submitted Nov. 15, 1973; revised manuscript received May 22, 1974.

Any discussion of this paper will appear in a Discussion Section to be published in the June 1975 JOURNAL. All discussions for the June 1975 Discussion Section should be submitted by Feb. 1, 1975.

The publication costs of this article have been assisted by Bell Laboratories.

### REFERENCES

1. R. Solomon, R. Newman, and N. R. Kyle, *This Journal*, **108**, 716 (1961).
2. C. Constantinescu/I. Petrescu-Prahoua, *J. Phys. Chem. Solids*, **28**, 2397 (1967).
3. F. E. Rosztochy *et al.*, *J. Appl. Phys.*, **41**, 1, 264 (1970).
4. F. E. Rosztochy and K. B. Wolfstirn, *ibid.*, **42**, 1, 426 (1971).
5. L. R. Dawson, *J. Cryst. Growth*, In press.

## The Vapor Pressure of Solid Aluminum Bromide

K. G. P. Sulzmann

Department of Applied Mechanics and Engineering Sciences and Institute for Pure and Applied Physical Sciences, University of California, San Diego, La Jolla, California 92037

Vapor pressure measurements for aluminum bromide have been performed in the past by Fischer *et al.* (1) only for the phase equilibrium between the liquid and the vapor at temperatures between about 390° and 523°K. These investigators have shown that the vapor is a dimer of the form  $(\text{AlBr}_3)_2$  for which the degree of dissociation is less than 1% even at the boiling point near 536°K. They also established the heat of fusion at the melting point so that Kelley (2) was able to deduce theoretical data for the phase equilibrium between the solid and the vapor. Over the temperature range between about 320° and 355°K, these data can be fitted by the expression

$$[\log_{10} p(\text{mm Hg})]_{\text{th}} = -4651.16^\circ\text{K}/T + 13.13674 \quad [1]$$

which corresponds to a heat of vaporization for the solid of  $\Delta H = 21,270 \text{ kcal/mole}$ . In the course of absolute infrared band-intensity measurements on AlO produced by shock-heating trace amounts of  $(\text{AlBr}_3)_2$  in argon-oxygen mixtures, we required accurate vapor pressure data between about 315° and 330°K. Therefore, we have made measurements on the purified solid bromide at temperatures between 300° and 335°K, which allowed us to verify the theoretically deduced data.

### Experimental Procedure

The equilibrium vapor pressure of  $(\text{AlBr}_3)_2$  was measured by using a precision capacitance micro-manometer (MKS Baratron gauge, Type 145AHS-10) which has a minimum resolution of  $1 \times 10^{-4} \text{ Torr}$  and a measurement error of less than  $\pm 0.5\%$  of the pressure reading for the pressure range of interest. The gauge was connected to a glass sample reservoir and to a high vacuum pumping station by an all glass system. Backstreaming of diffusion-pump oil was prevented by a glass trap at liquid nitrogen temperature, which

was separated from the system during pressure measurements in order to avoid condensation of the aluminum bromide vapor. The entire measurement apparatus was kept at a temperature above the condensation temperature of the bromide by heating tapes. The system was evacuated routinely to pressures below about  $5 \times 10^{-6} \text{ Torr}$  at a leak rate of less than  $10^{-6} \text{ Torr/min}$  which was achieved by prolonged outgassing procedures and was adequate for our purposes. The gauge was kept at a regulated temperature of about 49°C for measurements at temperatures of up to about 45°C of the sample reservoir, and at a nonregulated temperature of about 71°C for measurements between about 48° and 62°C. The entire system was outgassed after each measurement by heating the gauge to 71°C and by vacuum pumping with the remainder of the measurement portion of the system above about 75°C.

The aluminum bromide used for the vapor pressure measurements was obtained by purifying certified anhydrous samples of an assayed purity of better than 99.98% (Fischer Scientific Corporation). The test sample was pulverized and transferred into the sample reservoir in a dry nitrogen environment in order to prevent oxidation by atmospheric oxygen and water vapor. The measurement apparatus was evacuated, filled and flushed with dry nitrogen before introducing about 20 cm<sup>3</sup> of bromide powder. After filling, the glass reservoir was closed by melting off its filling stud, leaving only one glass stopcock in the system when the diffusion pump with its associated liquid nitrogen trap was separate from the measurement portion of the arrangement. A separate and removable liquid nitrogen glass-trap at the pump-side of the glass valve was used for condensing the aluminum bromide vapors generated while fractionally distilling to waste portions of the sample for further purification. Decomposition of the bromide sample by photon absorption was

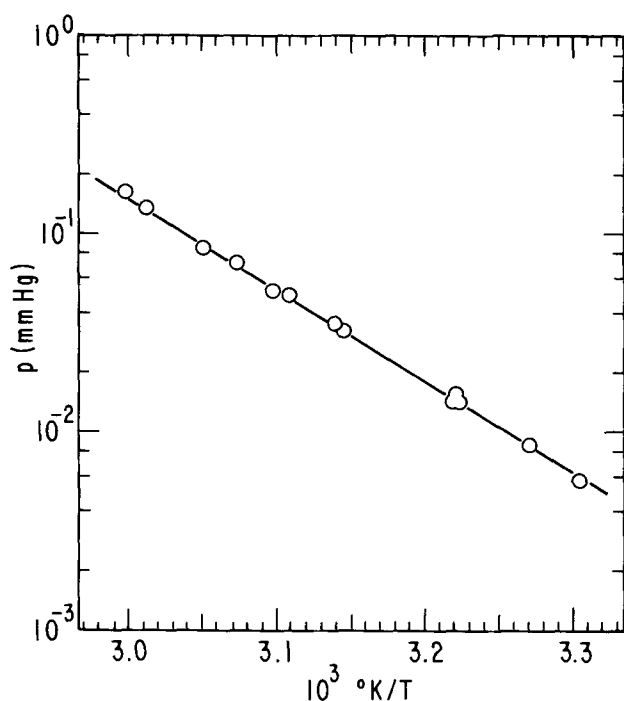


Fig. 1. Measured vapor pressure of  $(\text{AlBr}_3)_2$  for the solid-vapor phase equilibrium ( $\odot$ ). Least squares fit to the experimental data (—).

avoided by shielding the entire apparatus against room light.

After filling and sealing the sample reservoir, the bromide was brought to liquid nitrogen temperature and the whole system was evacuated to pressures of less than  $5 \times 10^{-6}$  Torr. Then the sample was heated to about  $75^\circ\text{C}$  and partly distilled to waste into a separate liquid nitrogen trap by vacuum pumping for at least 2 hr at pressures of less than about  $10^{-5}$  Torr. After purification, the sample was cooled in a water bath to  $0^\circ\text{C}$ , and the system was evacuated to below  $5 \times 10^{-6}$  Torr for half an hour before measurements were conducted at different bath temperatures. Uniform temperature of the water bath was assured by continuous stirring; the bath temperature was measured with an iron-constantan thermocouple gauge within  $0.1^\circ\text{C}$ . Vapor pressure measurements were obtained between about  $29^\circ$  and  $62^\circ\text{C}$ .

### Results

The experimental data obtained are shown in Table I and are plotted in Fig. 1. The results can be represented by an Arrhenius-plot of the form

$$4.573 (\log_{10} p) = -\Delta H/T + B \quad [2]$$

Table I. Vapor pressures of solid aluminum bromide

Temperature ( $^\circ\text{K}$ )	Pressure (mm Hg)	$(\log p)_{\text{obs}} - (\log p)_{\text{exp}}^*$
302.6	0.0058	-0.008
305.9	0.0089	+0.013
310.2	0.0142	+0.007
310.7	0.0142	-0.017
318.1	0.0326	-0.001
310.6	0.0146	0.000
318.5	0.0345	+0.006
321.8	0.0489	+0.009
322.9	0.0517	-0.016
325.5	0.0718	+0.012
327.6	0.0852	-0.004
331.7	0.132	+0.012
334.4	0.161	-0.014

\* Calculated from Eq. [3].

for the equilibrium between the solid and the vapor phase over our limited range of temperatures. A least squares fit to the data is shown in Fig. 1 and results in the experimental relation

$$[\log_{10} p (\text{mm Hg})]_{\text{exp}} = -4610.82^\circ\text{K}/T + 13.0080 \quad [3]$$

From Eq. [2] and [3] we obtain for the heat of vaporization of the solid bromide,  $\Delta H = (21.085 \pm 0.250)$  kcal/mole. These results may be compared with the theoretically derived expression, Eq. [1], which has not been plotted in Fig. 1, since it agrees with our relation [3] within  $+1.2\%$  and  $-1.8\%$  over the range of temperatures used. We consider the experimental and theoretical data in excellent agreement with each other, and we conclude that the theoretically derived results for the phase equilibrium between the solid and the vapor of aluminum bromide have been verified experimentally.

### Acknowledgment

This research was supported by the Advanced Research Projects Agency of the Department of Defense and was monitored by the U.S. Army Research Office-Durham under Contract DAHC04-72-C-0037.

Manuscript received Feb. 19, 1974.

Any discussion of this paper will appear in a Discussion Section to be published in the June 1975 JOURNAL. All discussions for the June 1975 Discussion Section should be submitted by Feb. 1, 1975.

The publication costs of this article have been assisted by the University of California.

### REFERENCES

- W. Fischer, O. Rahlfs, and B. Benze, *Z. Anorg. Allg. Chem.*, **205**, 1 (1932); **200**, 332 (1931).
- K. K. Kelley, "Contributions to Data on Theoretical Metallurgy; Heat and Free Energy of Vaporization Equations," *U.S. Bur. Mines Bull.*, **383** (1935); **601** (1962).

## Surface Preparation of Ceramic Oxide Crystals: Work Damage and Microhardness

Michael F. Ehman\*

Rockwell International, Incorporated, Electronics Research Division, Anaheim, California 92083

The use of single crystalline materials in solid-state devices frequently requires the preparation of surfaces that are strain free and chemically representative of the bulk material. A highly strained surface results whenever materials are cut by abrasive action. This

surface strain is referred to as a damaged layer. The depth of the damaged layer depends on several factors, including hardness of the material, orientation of the surface, abrasive particle size and type, and pressure applied during processing. The primary concern about the depth of damage to date has been in the semiconductor industry where the characteristic elec-

\* Electrochemical Society Active Member.

Key words: sapphire, spinel, beryllia, garnets, polishing.

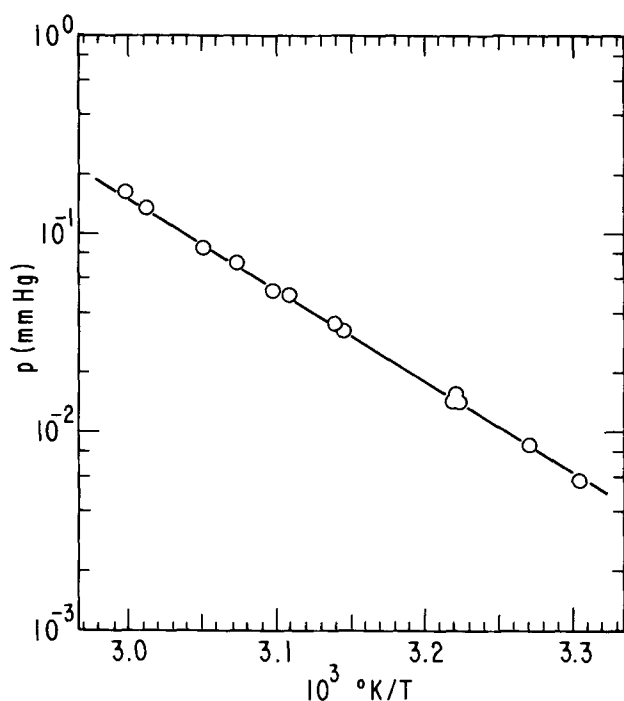


Fig. 1. Measured vapor pressure of  $(\text{AlBr}_3)_2$  for the solid-vapor phase equilibrium ( $\odot$ ). Least squares fit to the experimental data (—).

avoided by shielding the entire apparatus against room light.

After filling and sealing the sample reservoir, the bromide was brought to liquid nitrogen temperature and the whole system was evacuated to pressures of less than  $5 \times 10^{-6}$  Torr. Then the sample was heated to about  $75^\circ\text{C}$  and partly distilled to waste into a separate liquid nitrogen trap by vacuum pumping for at least 2 hr at pressures of less than about  $10^{-5}$  Torr. After purification, the sample was cooled in a water bath to  $0^\circ\text{C}$ , and the system was evacuated to below  $5 \times 10^{-6}$  Torr for half an hour before measurements were conducted at different bath temperatures. Uniform temperature of the water bath was assured by continuous stirring; the bath temperature was measured with an iron-constantan thermocouple gauge within  $0.1^\circ\text{C}$ . Vapor pressure measurements were obtained between about  $29^\circ$  and  $62^\circ\text{C}$ .

### Results

The experimental data obtained are shown in Table I and are plotted in Fig. 1. The results can be represented by an Arrhenius-plot of the form

$$4.573 (\log_{10} p) = -\Delta H/T + B \quad [2]$$

Table I. Vapor pressures of solid aluminum bromide

Temperature ( $^\circ\text{K}$ )	Pressure (mm Hg)	$(\log p)_{\text{obs}} - (\log p)_{\text{exp}}^*$
302.6	0.0058	-0.008
305.9	0.0089	+0.013
310.2	0.0142	+0.007
310.7	0.0142	-0.017
318.1	0.0326	-0.001
310.6	0.0146	0.000
318.5	0.0345	+0.006
321.8	0.0489	+0.009
322.9	0.0517	-0.016
325.5	0.0718	+0.012
327.6	0.0852	-0.004
331.7	0.132	+0.012
334.4	0.161	-0.014

\* Calculated from Eq. [3].

for the equilibrium between the solid and the vapor phase over our limited range of temperatures. A least squares fit to the data is shown in Fig. 1 and results in the experimental relation

$$[\log_{10} p (\text{mm Hg})]_{\text{exp}} = -4610.82^\circ\text{K}/T + 13.0080 \quad [3]$$

From Eq. [2] and [3] we obtain for the heat of vaporization of the solid bromide,  $\Delta H = (21.085 \pm 0.250)$  kcal/mole. These results may be compared with the theoretically derived expression, Eq. [1], which has not been plotted in Fig. 1, since it agrees with our relation [3] within  $+1.2\%$  and  $-1.8\%$  over the range of temperatures used. We consider the experimental and theoretical data in excellent agreement with each other, and we conclude that the theoretically derived results for the phase equilibrium between the solid and the vapor of aluminum bromide have been verified experimentally.

### Acknowledgment

This research was supported by the Advanced Research Projects Agency of the Department of Defense and was monitored by the U.S. Army Research Office-Durham under Contract DAHC04-72-C-0037.

Manuscript received Feb. 19, 1974.

Any discussion of this paper will appear in a Discussion Section to be published in the June 1975 JOURNAL. All discussions for the June 1975 Discussion Section should be submitted by Feb. 1, 1975.

The publication costs of this article have been assisted by the University of California.

### REFERENCES

- W. Fischer, O. Rahlfs, and B. Benze, *Z. Anorg. Allg. Chem.*, **205**, 1 (1932); **200**, 332 (1931).
- K. K. Kelley, "Contributions to Data on Theoretical Metallurgy; Heat and Free Energy of Vaporization Equations," *U.S. Bur. Mines Bull.*, **383** (1935); **601** (1962).

## Surface Preparation of Ceramic Oxide Crystals: Work Damage and Microhardness

Michael F. Ehman\*

Rockwell International, Incorporated, Electronics Research Division, Anaheim, California 92083

The use of single crystalline materials in solid-state devices frequently requires the preparation of surfaces that are strain free and chemically representative of the bulk material. A highly strained surface results whenever materials are cut by abrasive action. This

surface strain is referred to as a damaged layer. The depth of the damaged layer depends on several factors, including hardness of the material, orientation of the surface, abrasive particle size and type, and pressure applied during processing. The primary concern about the depth of damage to date has been in the semiconductor industry where the characteristic elec-

\* Electrochemical Society Active Member.

Key words: sapphire, spinel, beryllia, garnets, polishing.

trical properties of the materials can be realized only after removal of the damage. Depths of damage have been reported for Ge and Si (1) and Si (2), and several III-V intermetallic compounds (3). The more recent use of ceramic oxide crystals as substrates for epitaxially deposited thin films has required the preparation of surfaces of similar quality, i.e., flat, clean, damage free, and chemically representative of the bulk material.

Some of these ceramic crystals include:  $Gd_3Ga_5O_{12}$  (GGG), the primary substrate for magnetic oxide films used in magnetic bubble domain memories, and  $BeO$ ,  $\alpha-Al_2O_3$ , and  $MgAl_2O_4$  which are the most common materials used as substrates for microelectronic devices.

This paper reports the relationship between the penetration of damage and the hardness (bulk and micro-) of different crystal compositions, and the crystallographic orientations within the crystals.

### Experimental

**Crystals.**—The wafers utilized in this study were cut from single crystalline boules grown by the Czochralski technique in the case of GGG,<sup>1</sup>  $\alpha-Al_2O_3$ ,<sup>2</sup> and  $MgAl_2O_4$ .<sup>3</sup> The  $BeO$  crystals were grown from an alkali molybdate flux by a continuous dissolution-precipitation process.<sup>1</sup>

The dislocation densities of the crystals were in the following ranges ( $d/cm^2$ ): GGG,  $<10$ ,  $BeO$ ,  $10^3$ - $10^5$ ;  $MgAl_2O_4$ ,  $10^5$ ;  $\alpha-Al_2O_3$ ,  $10^6$ .

The crystals were oriented to within  $1^\circ$  of the desired orientation by the x-ray Laue back-reflection technique and sliced such that the major surface was at least 20 times larger than the sides to minimize edge contributions to the weight losses (described later).

**Mechanical preparation techniques.**—The crystals were first wafered on an inside-diameter (I.D.) tensioned membrane diamond saw; the blades were 0.015 in. thick with 340 mesh diamond. Typical cutting rates were 0.1 cm/min; with blade speeds of 2000 rpm; the as-sawed wafers were then individually hand-lapped on both sides to produce flat surfaces for subsequent mounting on appropriate individual polishing fixtures.

After the thoroughly cleaned wafers were properly mounted on the polishing fixture with a wax, the wafers are subjected to a machine-lapping step employing a vibratory polisher<sup>4</sup> with a cast-iron lapping plate and a 12  $\mu m$  silicon carbide/ethyleneglycol slurry. The final polishing steps for the crystals were performed on vibratory polishing apparatus with the following abrasives and cloths: GGG, 0.2  $\mu m$  Syton<sup>5</sup> on nylon;  $BeO$ , 0.05  $\mu m$  Cabosil<sup>6</sup> on perforated Pellon<sup>7</sup> cloth;  $MgAl_2O_4$ , 0.05  $\mu m$   $Al_2O_3$ <sup>8</sup> on nylon; and  $\alpha-Al_2O_3$ , 0.25  $\mu m$  top-diamond on perforated Pellon cloth. Thus slicing and lapping steps were identical for all crystals but the polishing step differed in that harder abrasives were used for harder crystals. Both sides of each wafer were given the same surface treatments.

Throughout the lapping steps 350  $g/cm^2$  loads were used on the lapping and polishing fixtures. The loadings were decreased to 300  $g/cm^2$  during polishing steps.

The epitaxial surfaces were free of scratches and polishing pits visible at 100X using Nomarski interference contrast. X-ray topographic analysis of the samples revealed a few scratches only on the  $MgAl_2O_4$  surfaces ( $<0.1\%$  of surface area).

<sup>1</sup> Grown by Crystal Chemistry Group, Rockwell International, Anaheim, California.

<sup>2</sup> Grown by Linde Division, Union Carbide Corporation, San Diego, California.

<sup>3</sup> Grown by Crystal Technology Incorporated, Mountain View, California.

<sup>4</sup> Synton Vibratory Polisher, Synton Company, Homer City, Pennsylvania 15748.

<sup>5</sup> Syton, a product of Monsanto Corporation, St. Louis, Missouri 63166.

<sup>6</sup> Cabosil, a product of Cabot Corporation, Los Angeles, California 90005.

<sup>7</sup> Pellon Fabrication Corporation, Lowell, Massachusetts 01852.

<sup>8</sup> Linde C, a Product of Union Carbide Corporation, San Diego, California 92123.

**Constancy of etch rate technique.**—The constancy of etch rate technique (1) was used to evaluate the depth of damage; the technique is based on the observation that highly strained material etches more rapidly than that with reduced strain. Initially, a chemical etchant attacks a damaged layer vigorously; thus the initial rate is high. As the disturbed layer is removed, the strain decreases and the etch rate decreases accordingly, approaching a constant value which represents that of the bulk material. The point at which the etch rate becomes constant represents that level in the crystal where the damage ends. From the total material loss during removal of the damaged layer, the depth of damage can be determined. Typical etch rate vs. etch time plots are shown in Fig. 1; this example shows the plots for the (111) surface of GGG after sawing, lapping, and polishing.

**Etchants.**—The etchants used in this study are primarily chemical polishes, i.e., they leave a relatively flat, unpitted surface (4). The  $H_3PO_4$  used on the GGG is an effective dislocation etchant at 200°C (5); however, since the total dislocation count was  $<10$  in a 1 in. diameter wafer, it was decided that the effects of pitting would contribute negligible error to weight loss measurements. The  $BeO$  was etched in hot (120°C)  $HCl$  (6). A mixture of  $H_3PO_4/H_2SO_4$  in a 1:1 volume ratio developed by Reisman *et al.* (7) was utilized at 200°C for both the  $\alpha-Al_2O_3$  and  $MgAl_2O_4$ .

Platinum wire mesh baskets were used to hold the samples in the acid. The etchants were magnetically stirred ( $\sim 100$  rpm) in constant temperature baths controlled to  $\pm 0.5^\circ C$ . The surface areas are the apparent surface areas measured by micrometers. The weight losses were measured on a microbalance to  $\pm 2 \mu g$ .

### Results

The depth-of-damage values (in microns) determined for each crystal as a function of surface orientation and type of surface preparation are shown in Table I. The data are average values of the damaged layer measured on four wafers, each with identical surface preparations, of each orientation. The crystals have been arranged in order of increasing bulk (Mohs) hardness. It should be noted that the depth of damage incurred during a given type of surface preparation decreases as the hardness of the material increases. This general relationship also holds when the microhardness (knoop) of a given orientation is compared to the damage incurred by that orientation. The only exception to this general relationship is that the epitaxially polished  $MgAl_2O_4$  has a deeper depth of damage than that measured on epitaxially polished  $BeO$ . This discrepancy can be accounted for though by two factors: one, the  $MgAl_2O_4$  was polished using 0.05  $\mu m$   $Al_2O_3$  which is significantly harder than the 0.05  $\mu m$  Cabosil used on  $BeO$ ; the second factor is that the  $MgAl_2O_4$  surfaces contained numerous scratches and polishing

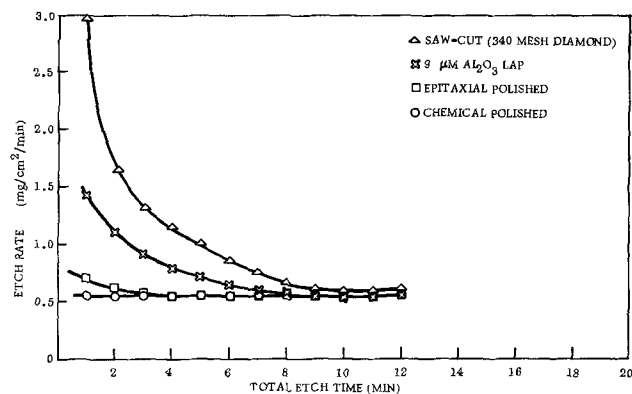


Fig. 1. Depth of damage plot for (111) surfaces of GGG; showing etch rate as a function of total etch time for various surface preparations.

Table I. Depth of damage ( $\mu\text{m}$ ) penetration in ceramic oxide crystals as a function of orientation and microhardness

Crystal	Mohs	Orient.	Knoop	I.D. saw 340 mesh	SiC lap 12 m	Epi- taxial polish
$\text{Gd}_2\text{Ga}_2\text{O}_7$ (GGG)	7½	(111)	1098 (8)	11	3.1	1.0
BeO	8	(1122)	900 (12)	15	1.2	0.16
		(1010)	1000 (10)*	13	1.0	0.15
		(1011)	1075 (12)	12	0.9	0.14
$\text{MgAl}_2\text{O}_4$	8½	(0001)	1250 (9)	9	0.8	0.10
		(100)	1300 (11)	3.8	1.0	0.41
		(111)	1500 (11)	3.4	0.82	0.36
$\text{Al}_2\text{O}_3$	9	(110)	1700 (11)	3.0	0.79	0.22
		(0001)	2050 (8)	1.8	0.22	0.09
		(0112)	2250 (8)	1.6	0.21	0.08
		(1120)	2550 (8)	1.2	0.20	0.08
		(1120) 6° Off	2600	1.2	0.20	0.07
		(1014)	2700 (8)	1.0	0.18	0.07

\* Note that this hardness is dependent on orientation, the average values are reported.

pits during the initial etchings, which would tend to distort the initial weight loss measurements and hence the depth of damage.

Figure 2 shows a plot of the depth of damage penetration into surfaces of various orientation after ID saw wafering vs. the knoop microhardness of the crystal orientation. Similar plots of depth of damage penetration vs. knoop microhardness are shown for surfaces prepared with a 12  $\mu\text{m}$  SiC lap finish and final polish in Fig. 3 and 4. The orientation of each surface has been identified only in Fig. 2 for brevity; the points for a given orientation occur in the same sequences in Fig. 3 and 4. It is interesting to note that within a given crystal, there is a linear relationship between the microhardness and the depth of damage incurred during a given type of preparation, with the exception of the 12  $\mu\text{m}$  SiC lap surface.

If the depth of damage penetration was only a function of the microhardness of the material, then we would expect all of the points, irrespective of crystal type, should fall on a common line. They do not. Not only do they not have such a relation, but the depth values overlap for BeO and spinel.

The tailing off of the curves of 12  $\mu\text{m}$  SiC lap of BeO and spinel are presently unexplained. The curves have been reproduced in three sets of runs, utilizing four wafers per run.

As a check on the accuracy of the values determined above, x-ray rocking curves were made on GGG and

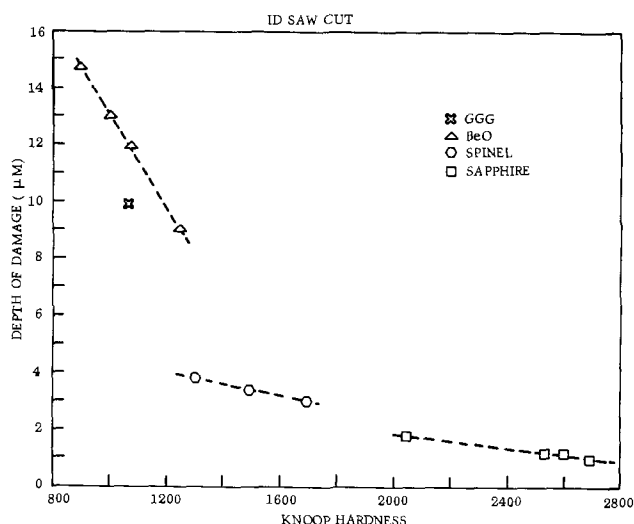


Fig. 2. Plot of depth of damage incurred by surfaces prepared by I.D. saw wafering vs. knoop microhardness of the crystal orientation.

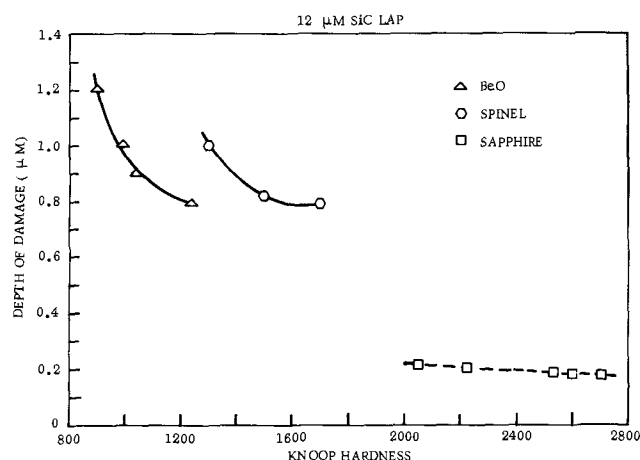


Fig. 3. Plot of depth of damage incurred by surfaces lapped with 12  $\mu\text{m}$  SiC abrasive vs. knoop microhardness of the crystal orientation.

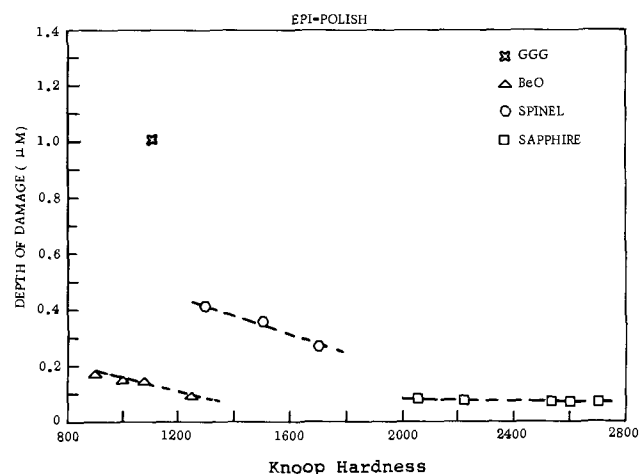


Fig. 4. Plot of depth of damage incurred by epitaxially polished surfaces vs. knoop microhardness of the crystal orientation.

$\text{MgAl}_2\text{O}_4$  samples which had received the same surface treatments. The values for saw-cut and lapped surfaces agreed within 10%. The x-ray analysis was unable to detect any damage on the polished wafers due to the penetration depth of the beam. There was no buildup of dislocations at the epitaxially polished surfaces observable either by dislocation etchants or x-ray techniques.

## Conclusions

The depth of damage incurred by selected ceramic oxide crystals under various types of mechanical surface preparations were measured, showing a linear relationship between the damage penetration and the knoop microhardness of the specific orientation.

It must be concluded that there is a general linear relationship between the damage and hardness within a crystal type, but that other, still unrecognized factors exist between the deformation strain mechanisms of different crystal types.

## Acknowledgments

The author would like to thank Mr. D. Medellin for his assistance in preparing the surfaces and Dr. H. L. Glass for the x-ray analyses. This work was supported in part by the Advanced Research Projects Agency and the Naval Air Systems Command.

Manuscript submitted Sept. 24, 1973; revised manuscript received March 29, 1974. This was Paper 198 presented at the Boston, Massachusetts, Meeting of the Society, Oct. 7-11, 1973.

Any discussion of this paper will appear in a Discussion Section to be published in the June 1975 JOURNAL.

All discussions for the June 1975 Discussion Section should be submitted by Feb. 1, 1975.

The publication costs of this article have been assisted by Rockwell International.

## REFERENCES

1. J. W. Faust, Jr., *Electrochem. Technol.*, **2**, 339 (1964).
2. R. Stickler and G. R. Booker, *Phil. Mag.*, **8**, 859 (1963).
3. E. P. Warekois, M. C. Lavine, and H. C. Gatos, *J. Appl. Phys.*, **31**, 1302 (1960).
4. J. W. Faust, Jr., *Surface Sci.*, **13**, 60 (1969).
5. R. Belt, *J. Appl. Phys.*, **40**, 1644 (1969).
6. M. F. Ehman and S. B. Austerman, *J. Am. Ceram. Soc.*, **56**, 382 (1973).
7. A. Reissman, M. Berkenblit, J. Cuomo, and S. A. Chan, *This Journal*, **118**, 1653 (1971).
8. G. A. Keig, Private communication.
9. C. F. Cline and J. S. Kahn, *This Journal*, **110**, 773 (1963).
10. R. E. Hanneman and J. H. Westbrook, *Phil. Mag.*, **18**, 73 (1968).
11. M. F. Ehman, W. J. Silva, and S. Miscro, To be published.
12. S. B. Austerman, Private communication.





## High Pressure Effects on the EMF of Seawater Battery Electrodes in Chloride Electrolyte

E. M. L. Valeriotte\* and L. D. Gallop

Defence Research Establishment Ottawa, Ottawa, Ontario, Canada K1A 0Z4

### ABSTRACT

Reference electrodes, suitable for use at high pressures in chloride or hydrogen containing solutions, were applied to the study of various buffer equilibria at pressures from 0 to 2.5 kbar. Partial molal volumes of reaction obtained are compared and interpreted in terms of their effects on the solvent structure. Results obtained with anodes of magnesium alloys (AZ 61 and AP 65), aluminum alloys (GB 420 and GB 80S) and pure aluminum, in phosphate and borate buffered and unbuffered chloride solutions, are presented and discussed. Anode potentials were found to be simultaneously controlled by more than one oxidation reaction. In the case of the magnesium anodes, the relative contributions of the three oxidation reactions were clearly determined by both the alloy composition and the ambient pressure. In the case of aluminum this was also true, but the actual reactions taking place were more difficult to identify.

Although a large amount of work has been done on the effect of high pressure on electrolyte systems (1), only little has been directed toward an understanding of electrochemistry or electrode mechanisms at high pressures. These assume particular importance when one considers the operation of seawater batteries at great ocean depths for such purposes as undersea monitoring equipment for military or scientific investigations or for life support systems for bathyscapes or underwater habitats. The present work was intended to explore such pressure effects, particularly as they are related toward the magnesium- or aluminum-silver chloride seawater batteries. The first phase of the work concentrated on the choice of suitable reference electrodes and the second on the effects of pressure on the electrolyte and buffer systems required to simulate seawater conditions. Experiments were then extended to open-circuit measurements for magnesium and aluminum anodes.

The expression for the Gibbs free energy in differential form

$$dG = -SdT + VdP \quad [1]$$

may be expressed suitably for electrochemical systems in terms of the electrochemical potential of species  $i$ ,  $\bar{\mu}_i \equiv (\partial G_i / \partial n_i)$ , and the partial molar quantities  $\bar{S}_i$  and  $\bar{V}_i$

$$d\bar{\mu}_i = -\bar{S}_i dT + \bar{V}_i dP \quad [2]$$

Thus

$$\bar{V}_i = (\partial \bar{\mu}_i / \partial P)_{T, \mu_{j \neq i}} \quad [3]$$

at constant temperature and constant chemical potential of all other species,  $j$ . If this equation is applied separately to each of the products and reactants of a chemical reaction and algebraically summed, one obtains

$$\Delta \bar{V} = \sum_i \bar{V}_i = \sum_i (\partial \bar{\mu}_i / \partial P)_{T, \mu_{j \neq i}} \quad [4]$$

but

$$\sum_i \bar{\mu}_i = \Delta G = -nFE \quad [5]$$

and hence

$$\Delta \bar{V} = -nF(\partial E / \partial P)_{T, \mu} \quad [6]$$

where a partial molar volume change  $\Delta \bar{V}$  accompanies the passage of  $n$  faradays/mole through the cell at the reversible potential difference  $E$ . Thus  $\Delta \bar{V}$  can be obtained from the slope of the emf vs. pressure relationship. Since

$$\bar{\mu}_i = \bar{\mu}_i^0 + RT \ln a_i \quad [7]$$

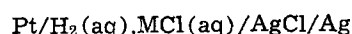
it is also possible to write

$$-nF(\partial E / \partial P)_{T, \mu} = (\partial \Delta \bar{\mu}^0 / \partial P)_{T, \mu} + RT(\partial \ln \pi a_i^{\nu_i} / \partial P)_{T, \mu} \quad [8]$$

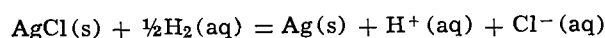
where  $\pi a_i^{\nu_i}$  is the product of the activities of the reaction products raised to their stoichiometric numbers  $\nu_i$  (negative power for reactants) corresponding to a transfer of  $n$  electrons for the over-all cell reaction. Choice of a standard state at unit pressure makes the first term in Eq. [8] zero by definition, and the second term represents the rate of variation of the activities of the potential determining species with pressure. At 25°C Eq. [8] can be integrated to give

$$E_1 - E_p = \frac{59.16}{n} \log \pi a_i^{\nu_i} \text{ mV} \quad [9]$$

For cells of the type



studied in these experiments, the cell reaction is



\* Electrochemical Society Active Member.

Key words: reference electrodes, magnesium, aluminum, reaction volume, buffer.



Equation [9] thus becomes

$$E_1 - E_p = 59.16 \log \frac{[a_{H+(p)} a_{Cl-(p)} a_{H_2(p)}^{-1/2}]}{[a_{H+(1)} a_{Cl-(1)} a_{H_2(1)}^{-1/2}]} \quad [10]$$

and

$$\Delta \bar{V} = V_{Ag} - V_{AgCl} + \bar{V}_{HCl(MCl)} - \frac{1}{2} \bar{V}_{H_2} \quad [11]$$

Some simplification of Eq. [10] is possible.

Since activity coefficients used for electrolytes refer to molal quantities, concentration changes due to compressive effects are reflected in the values of  $\gamma_{\pm}$ , the mean ionic activity coefficients. Therefore concentration changes with pressure need not be considered explicitly. The variation of activity coefficients, due to changes in partial molal volumes with pressure, can be calculated (2) using the equation

$$\begin{aligned} \log \gamma_{\pm} = & (\log \gamma_{\pm})_{p=1} \\ & + 0.888 \times 10^{-5} \left( \frac{3}{2} S_v \right) (P - 1) \sqrt{c} \\ & - 0.444 \times 10^{-5} \left( \frac{3}{2} S_k \right) (P - 1)^2 \sqrt{c} \quad [12] \end{aligned}$$

where  $S_v$  and  $S_k$  are experimental slopes of linear fits of apparent molal volume and compressibility, respectively, to the square root of the molal concentration,  $c$ .

For 0.5M NaCl solutions at 25°C,  $S_v = 2.153$ ,  $S_k = 11.4 \times 10^{-4}$  (7) and  $\gamma_{\pm} = 0.681$  (3) at  $P = 1$ . When the calculations were done using Eq. [12] the potential variation of the Ag/AgCl electrode,  $\Delta E_{\gamma}$ , was found to reach a maximum of 1.13 mV<sup>1</sup> at about 1.9 kbar.

If a calculation was made using an extended Debye-Huckel model for the electrolyte and interpreting the variations in  $\gamma_{\pm}$  as a consequence of variation of dielectric constant (2) with pressure, close agreement at the maximum, and agreement within 0.3 mV over the entire pressure range was obtained. Data for the calculation were taken from measurements of the dependence of the dielectric constant of water on pressure (4, 5) and published  $\bar{a}$  and  $B$  Debye-Huckel parameters (2).

Similar calculations for dilute HCl (<0.05M) in 0.5M NaCl, and for 0.1M KCl solutions, indicated that the pressure variation of  $\gamma_{\pm}$  of the HCl, and those of both HCl and KCl in 0.1M KCl, were negligible.

These calculations have been concerned with estimating changes in activity coefficients for H<sup>+</sup> and Cl<sup>-</sup> ions. They have not, however, dealt with changes in H<sup>+</sup> concentration due to the dissociation of water in unbuffered solutions or the buffering agent in buffered solutions. This will be discussed later, after treatment of the last term in Eq. [10], the variation of the molecular hydrogen activity coefficient with pressure, which is far larger than those of the ionic species already discussed.

The activity of a gas, or its fugacity  $f_p$ , relative to the standard state of unit pressure, can be calculated from compressibility data by considering the deviation of molar volume from ideality, as given by

$$\alpha \equiv RT/P - \bar{V}_p \quad [13]$$

For a gas at constant temperature from Eq. [2]

$$d\mu = RT \ln f_p = \bar{V}_p dp \quad [14]$$

Combining Eq. [13] and [14] gives

$$RT \ln f_p = RT d \ln P - \alpha dP \quad [15]$$

Integrating from  $P = 0$  to  $p$  gives

$$f_p = p \exp \left[ -1/RT \int_0^p \alpha dP \right] \quad [16]$$

Using published compressibility data for hydrogen

(6, 7), values of  $f_p$  and

$$\Delta E_f = 29.58 \log \gamma_{H_2} = 29.58 \log (f_p/f_{1p}) \text{ mV} \quad [17]$$

were calculated. Equation [10] can now be rewritten including the calculated corrections to read

$$(E_1 - E_p) - \Delta E_f - \Delta E_{\gamma} = 59.16 \log [a_{H+(p)}/a_{H+(1)}] \quad [18]$$

For a neutral unbuffered solution the dependence on pressure of the dissociation equilibrium of water must be considered. Thus

$$\frac{a_{H+(p)}}{a_{H+(1)}} = \frac{K_p}{K_1} \cdot \frac{a_{OH-(1)}}{a_{OH-(p)}}$$

but

$$a_{OH-} = a_{H+}$$

hence

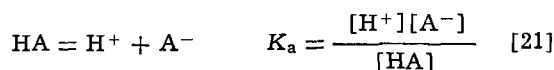
$$\frac{a_{H+(p)}}{a_{H+(1)}} = \left[ \frac{K_{w(p)}}{K_{w(1)}} \right]^{1/2} \quad [19]$$

Therefore Eq. [18] becomes

$$(E_1 - E_p) - \Delta E_f - \Delta E_{\gamma} = 29.58 \log K_{w(p)}/K_{w(1)} \quad [20]$$

A similar equation replacing  $K_w$  by  $K_a$  can be derived for solutions containing weak acids at low concentration.

For acid-buffer solutions the equilibrium



must be considered. In this case

$$\frac{a_{H+(p)}}{a_{H+(1)}} = \frac{K_{a(p)}}{K_{a(1)}} \cdot \frac{a_{HA(p)}}{a_{HA(1)}} \cdot \frac{a_{A-(1)}}{a_{A-(p)}} \quad [22]$$

For most of the buffer concentrations used in these experiments, the concentrations of buffer acid and salt anions do not change appreciably with pressure and the variation of activity coefficients can be shown to be negligible by means of calculations similar to those discussed earlier using Eq. [12]. Hence for buffered solutions Eq. [18] reduces to

$$(E_1 - E_p) - \Delta E_f - \Delta E_{\gamma} = 59.16 \log K_{a(p)}/K_{a(1)} \quad [23]$$

Neglect of the terms discussed is estimated to give rise to errors of no more than 0.2 mV in the left hand side of Eq. [20] and [23] at all the pressures investigated. From Eq. [6], setting

$$E = E_p + \Delta E_f + E_{\gamma}$$

one then obtains

$$\Delta \bar{V} = -nF \partial (E_p - E_1 + \Delta E_f + \Delta E_{\gamma}) / \partial P \quad [24]$$

## Experimental

*Electrochemical cells and pressure vessel.*—Electrochemical cells of two basic designs were used for the measurement of electrode potentials.

A glass cell (Fig. 1a) was used for most of the work described below but some measurements were made using plastic machined cells (Fig. 1b) made of Lexan® (polycarbonate), Teflon®, or nylon. The plastic cells had advantages in ease of fabrication but were difficult to make leak proof at high pressures. Six platinum electrical leads were sealed with epoxy into holes through the screw-type head. However, leakage of hydrogen from the cell, as measured by hysteresis of the hydrogen electrodes in buffered solutions at 1 atm pressure between the beginning and end of a run, was appreciable using the plastic cells, even with the O-ring seal incorporated later in the work. Under similar conditions hydrogen electrodes in the glass cells, with the ground glass joint sealed with a minimum of high vacuum stop-cock grease, remained constant within about 1 mV at 1 atm over the 10-12 hr required for a complete run; in the plastic cells shifts

<sup>1</sup> Values of  $S_v$ , up to 14% smaller than that used here have been reported recently (33, 45). Use of the lower values would give a maximum  $\Delta E_{\gamma}$  of about 1.0 mV.

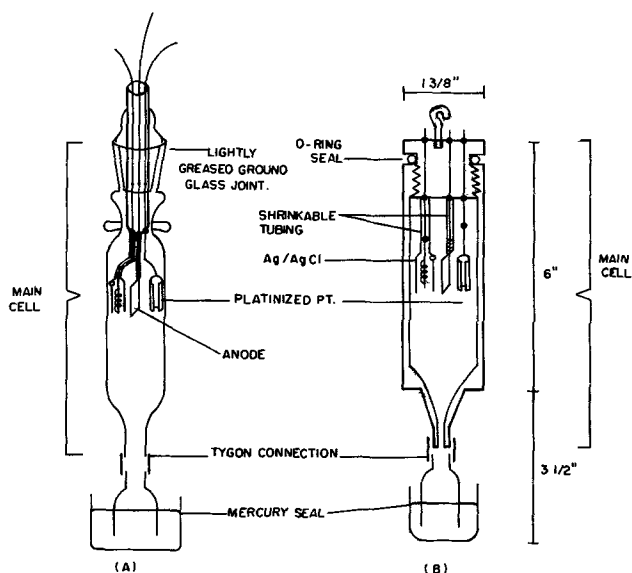


Fig. 1. Electrochemical cells of glass (A) and plastic (B) used to measure the pressure coefficients of cell emf.

of several millivolts toward more positive potentials were observed. Accordingly the plastic cells could only be used when changes of hydrogen concentration due to leakage during the course of a run were unimportant as, for example, when Mg anodes were present in the cell. To prevent leakage from the glass cells, tungsten leads were sealed through the Pyrex head and platinum was welded to the tungsten with a spot welder. Except for the platinized platinum electrodes the electrode leads were insulated from the solution by means of shrinkable polyolefin tubing. Only four or five electrodes could conveniently be incorporated into the glass cells.

The pressure vessel (8) (cavity dimensions  $1\frac{1}{2}$  in. diameter by  $11\frac{1}{2}$  in.) was manufactured by Pressure Products Incorporated, Hatboro, Pennsylvania. Six insulated electrical connections of nichrome wire were sealed into holes in the head using epoxy. After soldering connections to the electrochemical cell, the pressure vessel could be sealed and pressure increased by a hydraulic pump, which compressed the oil in the pressure chamber. Control valves were used for fine adjustments and for decreasing the pressure, which was measured with a 16 in. Bourdon gauge (Heise Bourdon Tube Company, Newport, Connecticut) accurate to  $\pm 2.5$  bars. Pressure was transmitted to the interior of the cell by means of a mercury seal (Fig. 1) which isolated oil from electrolyte. The pressure chamber was immersed in a high thermal conductivity oil bath maintained at  $25.0^\circ\text{C}$  for all experiments.

**Reference electrodes**—Silver-silver chloride reference electrodes were prepared by sealing 0.020 in. platinum wire into sleeves 2-3 cm long made from 7 mm OD glass tubing to protect the electrodes. The sleeves were open at the bottom, and there was a small hole near the top seal to admit solution freely. The platinum was silver-plated in freshly prepared  $\text{KAg}(\text{CN})_2$  solution at  $0.5 \text{ mA/cm}^2$  for 6 hr according to the standard procedures (9) after cleaning in aqua regia and anodizing in concentrated nitric acid. Following soaking in  $\text{NH}_4\text{OH}$  for several hours and thorough rinsing in water (1-3 days), the electrodes were then chloridized in 0.1M HCl for 30-60 min at  $0.8 \text{ mA/cm}^2$ , rinsed and stored in 0.01M KCl.

Platinum foils ( $\sim 1 \text{ cm}^2$ ) for hydrogen reference electrodes were cleaned by immersion in hot aqua regia, hot concentrated nitric acid and thorough rinsing. This was followed by hydrogen flaming to red heat and cathodic cleaning in 1% sulfuric acid so that very small bubbles were evolved uniformly over the

surface. Platinization was then carried out by cathodizing at  $100 \text{ mA/cm}^2$  for 3 min in a solution of 2% chloroplatinic acid containing 0.02% lead acetate.

Both types of reference electrodes were checked against each other and against saturated calomel electrodes and found very stable. Differences between hydrogen electrodes remained constant within a few hundredths of a millivolt and between Ag/AgCl electrodes within a few tenths of a millivolt after equilibration. Differences of 1-3 mV occurred following large changes in pressure or electrolyte concentration before reequilibration.

**Chemicals.**—Chloride solutions were prepared from reagent grade salts without additional recrystallization. Phosphate buffered solutions were made up from Fisher Certified pH 7.0 Buffer, borate buffered solutions from Fisher Certified sodium borax and 2N volumetric hydrochloric acid, and acetate buffered solutions from reagent glacial acetic acid and Fisher Certified volumetric 0.1N sodium hydroxide.

The solvent used was high purity conductivity water (maximum  $0.5 \mu \text{ mho cm}^{-1}$ ) obtained by a pyrodistillation process (10). Mercury was distilled twice under vacuum with an air leak and twice under high vacuum.

Magnesium alloy anodes were cut from 0.030 in. AZ 61 (6% Al, 1% Zn; Dow Corning, Midland, Michigan) or AP 65 (6% Al, 5% Pb; Magnesium Elektron, London, United Kingdom) into  $1 \text{ cm}^2$  foils. Platinum leads were crimped on one edge of the Mg foil and the joint was then sealed with Silastic® (Dow Corning, Midland, Michigan) 731 RTV adhesive sealant. The leads were then protected from solution with shrinkable polyolefin tubing.

Before each run Mg electrodes were briefly immersed several times alternately in 5-10%  $\text{HNO}_3$  and 1-2% HCl solutions and rinsed in water.

Aluminum anodes were similarly constructed from Alcan GB 80S Al alloy (0.45% Sn, 0.05% Ga) and GB 420 ternary (4.5% Zn, 0.15% Sn) alloy (11) (Alcan Research and Development, Kingston, Ontario, Canada). Cleaning of the aluminum was carried out by means of 20-40 sec alternate immersions in 1M NaOH and 33%  $\text{HNO}_3$  solution rinsing with water after each immersion.

**Method and results.**—Initial experimental work was concentrated on the development of reference electrodes suitable for use in seawater related electrolytes. Since seawater is a moderately buffered chloride electrolyte, silver-silver chloride was selected as the chloride reversible electrode and a hydrogen electrode as the pH sensitive electrode. Other possibilities were considered in the event that these were to prove unsuitable. A specially constructed glass electrode has been described (12) for use at pressures up to  $1500 \text{ kg/cm}^2$ .

A three-electrode reference system generating hydrogen *in situ* has been reported by Conway after poor performance had been obtained using a Giner-type system (13). The glass and Giner-type system cannot give thermodynamically meaningful potentials except by calibration using standard systems. Furthermore, the three electrodes and Giner systems would have been undesirable because of the limitation of the cell to 5 or 6 electrical connections. Specially constructed calomel reference electrodes have been used at pressures up to 1000 atm (14).

In order to extend measurements up to 2500 bar and retain the possibility of monitoring hydrogen pressure, as well as pH, in later experiments involving anode materials (and for various other considerations, some of which have been cited) these other possibilities were excluded in selection of the reference electrodes of first choice.

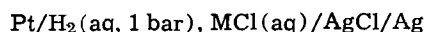
Since the hydrogen electrode is controlled not only by the hydrogen ion activity, but also by the fugacity

<sup>2</sup> 1 standard atmosphere = 1.013 bar =  $1.013 \times 10^5 \text{ nm}^{-2}$  = 1.033  $\text{kg/cm}^2$ .

of the molecular hydrogen in solution, it was essential to maintain the hydrogen pressure as constant as possible during the course of a run. At atmospheric pressures this is usually accomplished by bubbling hydrogen gas over a platinized platinum surface. Except by using *in situ* electrolytic hydrogen generation, this is difficult at high pressures. Accordingly in these experiments solutions, presaturated with hydrogen, were sealed before each run and the hydrogen allowed to exert its own near atmospheric pressure within the cell.

After welding of the electrical leads, sealing all but those for the hydrogen electrodes in shrinkable polyolefin tubing and filling the cell with electrolyte, the main section of the cell was inverted and hydrogen gas was bubbled through the solution using a fine capillary in both the main section and the section including the mercury seal for 30-60 min. The two sections were then joined with a short piece of tygon tubing in such a way as to eliminate any visible gas bubbles or void spaces from the cell, and sealed into the pressure vessel. After each change of pressure, 25-50 min were permitted for thermal and mechanical equilibrium to be reestablished, as indicated by constancy of electrode potentials. Replicate (at least four) measurements of potential were then made at 5 min intervals, and the cycle was repeated for both increasing and decreasing pressure. Pressure increments were usually 500 bars between each set of measurements. Intermediate values of pressure were applied during the decompression period. Atmospheric pressure readings were taken at the beginning and end of every run as a check against hysteresis effects due to H<sub>2</sub> leakage or electrode failure. Thus a complete run up to 2.5 kbars normally included 12 experimental points, half obtained during the compression period.

The first experiments were intended to test the constancy of potential as a function of pressure for cells of the type



where M is a soluble cation.

*Unbuffered systems.*—Measurements of emf were made in unbuffered 0.5M NaCl and in synthetic seawater (0.46M NaCl, 0.02M MgSO<sub>4</sub>, 0.12M MgCl<sub>2</sub> · 6H<sub>2</sub>O) solutions using a DVM accurate to  $\pm 2 \mu\text{V}$ . (In

some of the work on other systems discussed below a DVM accurate to 0.2% was used but the accuracy of either DVM was always better than the precision of the measurements being taken.) These experiments in unbuffered solutions (see Fig. 2a) did not conclusively establish the pressure independence of the electrodes because of time-dependent effects caused either by pH variation or hydrogen loss. Accordingly measurements were then carried out in acidic chloride solutions in order to eliminate any possible pH effects and the glass cells were tightly sealed with high pressure stopcock grease to avoid any loss of hydrogen. The results are displayed in Fig. 2(b-d). The solid lines were calculated from compressibility data for hydrogen, using Eq. [16] and include the correction for variation of activity coefficient of the chloride ion (negligible in the case of the 0.1M HCl solution). The points are experimentally determined and are accurately fitted by a quadratic equation (broken curves) giving a standard error comparable to the mean deviation of the three hydrogen electrodes from their average. Individual hydrogen electrodes were constant to within 0.02 mV during the 20 min of measurements. A linear least squares fit gave a standard error two or three times as large as the quadratic whereas no significant improvement was obtained using a cubic equation (see Table Ib).

At the lower pressures (<800 bars) agreement between experimental and calculated potential differences are excellent. However, at higher pressures the apparent fugacity becomes less than that calculated using compressibility data for dry hydrogen gas. A similar but slightly larger discrepancy was observed for the hydrogen-calomel system (14) and was attributed to the influence of increased hydrogen solubility on the partial molal volume of hydrochloric acid. This interpretation was refuted recently (41) but a residual discrepancy remained of about the same magnitude as in the present work. It is thought that the remaining deviation is due to neglecting the effect of water vapor on the hydrogen fugacity, *i.e.*, compressibility data for hydrogen gas, saturated with water vapor, would have been more appropriate for the present calculations than the data for dry hydrogen which were used. It has also been suggested (42) that some hydrogen loss may occur due to diffusion into the elec-

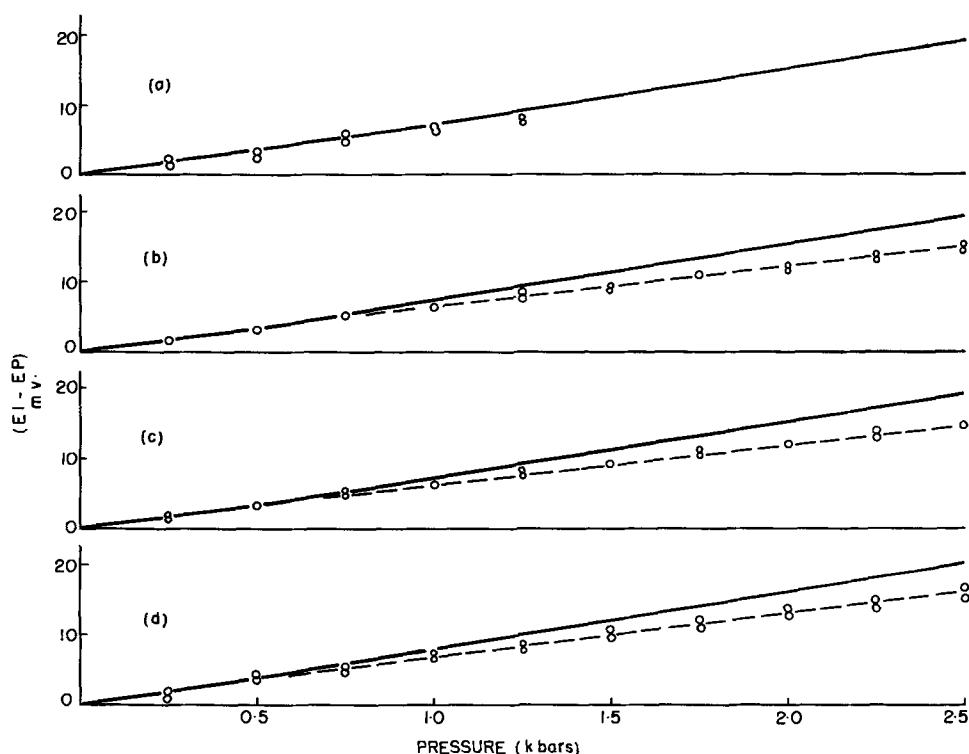


Fig. 2. Increase of hydrogen electrode potential relative to the Ag/AgCl electrode as a function of pressure. Broken curves are fitted to experimental points using a quadratic equation. Solid curves are calculated using compressibility data for hydrogen gas to determine hydrogen fugacity. (a), 0.5M NaCl; (b), 0.5M NaCl + 0.01M HCl; (c), 0.5M NaCl + 0.1M HCl; (d), 0.1M HCl.

trode materials or shrinkable tubing. If this does not occur, then the data of Fig. 2 can be used to determine the fugacity of hydrogen saturated with water vapor. In any case, the cause of the apparent change of fugacity is unimportant to the present work; only its magnitude need be known. Hence in the rest of this paper, the "empirical" fugacity correction, determined from the data (broken lines) of Fig. 2, is applied to the hydrogen electrode potential results in other systems.

Runs were also carried out in 0.5M NaCl solutions saturated with Mg(OH)<sub>2</sub> and Al(OH)<sub>3</sub>. The solutions were prepared by allowing excess Mg or Al to corrode in the salt solutions for a sufficient period of time to assure saturation. Although these electrolytes are buffered by means of the hydroxide equilibria at pH values near 10 and 6, respectively, they have been included in Table I under unbuffered solutions to emphasize the fact that no foreign buffering agent is present.

**Buffered systems.**—Experiments were carried out in the following buffered solutions: (i) 0.1M KCl + 0.2M acetate buffer, pH 4.7; (ii) 0.5M NaCl + 0.01M phosphate buffer, pH 6.6; (iii) 0.5M NaCl + 0.05M phosphate buffer, pH 6.6; (iv) 0.5M NaCl + 0.025M borate buffer, pH 8.1. The results are tabulated in Table I, giving the slope of the linear least squares fit of potential to pressure, the standard error of the linear least squares fit, the standard error of a quadratic least squares fit, and the experimentally attained precision of the emf measurements. As can be seen from the table the data fit a linear equation quite well. However a better fit, giving a standard error in closer agreement with experimental precision, is obtained using a quadratic equation.

**Magnesium and aluminum anodes.**—**Buffered systems.**—Runs were carried out using the following anodes in borate and phosphate buffered solutions of 0.5M NaCl. Potentials were measured relative to a hydrogen and a Ag/AgCl electrode in the same solution.

Mg (AZ 61): 6% Al, 1% Zn

Mg (AP 65): 6% Al, 1% Pb

Al (GB 80S)<sup>3</sup>: 0.5% Sn, 0.05% Ga

Al (GB 420)<sup>3</sup>: 5% Zn, 0.2% Sn

Gas evolution occurs during the course of a run and the hydrogen electrode potentials became sufficiently more negative to indicate that the gas was hydrogen in every case. The magnesium anodes caused an increase of pH and the Al anodes a slight decrease, since the solutions were only partially buffered.

<sup>3</sup> Alcan designation.

Table I.

Buffered solutions (a)	pH	Number of electrodes averaged	Linear E/P fit		Quadratic E/P fit Standard error (mV)	Experimental precision (mV)
			Slope mV/kbar	Standard error (mV)		
(i)	4.7	3	-0.36	0.32	0.15	0.1
(ii)	6.6	1	-13.6	0.37	0.13	<0.1
		1	-13.5	0.45	0.16	<0.1
(iii)	6.6	1	-14.2	0.52	0.23	0.3
		1	-14.2	0.59	0.37	0.4
(iv)	8.1	2	-20.4	0.83	0.38	0.4

Unbuffered solutions (b)	Standard error of fit			Experimental precision (mV)
	Linear	Quadratic	Cubic	
0.1M HCl	0.38	0.29	0.28	<0.1
0.5M NaCl + 0.1M HCl	0.24	0.11	0.11	0.3
0.5M NaCl + 0.01M HCl	0.22	0.12	0.11	0.2
0.5M NaCl: Sat'd Mg(OH) <sub>2</sub>	1.32	1.26	1.24	0.4 (1.1)
0.5M NaCl: Sat'd Al(OH) <sub>3</sub>	4.01	2.64	2.10	0.6 (5)

Standard errors decreased only by about 10% in most cases when the data were fitted to a quadratic equation, in comparison with the linear equation. However rather large standard errors, in comparison to the slopes, were obtained in the corroding systems, particularly in 0.05M phosphate buffers and for Al GB 420 and Mg AP 65 anodes. Reasonably good consistency was observed for AZ 61 in 0.01M phosphate and 0.025M borate buffers and fairly reliable results were obtained for Al GB 80S anodes. In the former cases standard errors were comparable to experimental precision and in the latter the standard error was less than the potential change caused by a 500 bar change in pressure.

Some further observations on the behavior of the anode materials will be useful before discussing the various  $\Delta\bar{V}$  values obtained. The Mg AZ 61 anodes tarnished to a black color and pitted during the course of a run in phosphate solutions, evolving substantial quantities of gas, enough to force more than half of the electrolyte out of the cell upon decompression to atmospheric pressure. In borate solutions less hydrogen was evolved and the anodes remained bright although small tarnish spots appeared particularly near the edges (approximately 15 ml of gas was evolved by 4 cm<sup>2</sup> of magnesium surface over a period of 12 hr). The Mg AP 65 in both buffers blackened and tended to crumble into small black pieces which fell free of the anode as corrosion progressed. A gelatinous grayish-white product also formed in each case, and gas evolution was high (only 15-20 ml of solution remained of the 65 ml cell capacity). The increase in pH, observed for both magnesium alloys, was appreciably greater for AP 65 than for AZ 61 under similar conditions (see Table II).

For the aluminum alloys, the rate of gassing was greater for GB 80S than for GB 420, but both were very low (<5 ml) in comparison to Mg. The GB 80S tarnished only slightly and some white voluminous product formed whereas the GB 420 remained bright with no visible indication of deterioration and only slight amounts of white product formed on it. pH decreased very slightly during a run.

**Unbuffered systems.**—Similar experiments were then carried out in unbuffered (i.e., self-buffered) solutions, made up by adding excess Mg or Al to the 0.5M NaCl to presaturate the electrolyte with the respective hydroxide.

The measured potentials were much more reliably stable and reproducible in these cases and the experimental precision was typically as good or better than that in most of the buffered systems studied. Significant improvement in standard error was obtained when the emf data were fitted to a quadratic equation in comparison to a linear equation. Table II compares experimental errors and standard errors for polynomials of order 2, 3, and 4 for the five anodes investigated. The reproducibility of a single electrode is given in column six and the mean deviation between electrodes is given in column seven (with the number of electrodes in brackets). In the case of the Al GB 420 alloy, two stable ranges of potential were observed

Table II.

Anode	pH	Standard error of fit of emf vs. P for order (mV)			Experimental precision at each pressure (mV)	Mean deviation between electrodes (mV)
		n = 2	n = 3	n = 4		
Mg (AZ 61)	9.9-10.8	1.5	1.1	1.0	0.3	2-5 (2)
Mg (AP 65)	—	4.6	4.5	—	1	3-6 (4)
Al (99.999%)	6.3-6.3	5.7	5.3	—	4	20 (2)
		(21.4)	(21.4)			
Al (GB 420)	5.6-6.3					
Low potentials		5.0	4.1	—	3	5 (4)
High potentials		5.8	5.7	—	1	5
Al (GB 80S)	5.6-7.9	6.8	6.7	—	3	20 (5)
Low potentials		(2.5)	(1.9)	—		

depending on the pressure and history of the sample. At low pressures a high potential region ( $-1.12$  to  $-1.15$  V vs. Ag/AgCl) having a small pressure dependence was obtained. Upon compression the potential dropped to a low potential region ( $-1.03$  to  $-1.10$  V) very suddenly. At lower pressures the electrode potential sometimes recovered to the higher region during the half-hour waiting period between measurements, but at some point it remained low until later decompression, and then returned to the high potential region with some hysteresis observed. The lower potential region was apparently the stable value at high pressures but the exact transition pressure varied from sample to sample. Accordingly in Table II these two cases are given separately. There was some indication that a similar phenomenon occurred for the Al(GB 80S) alloy. However the high potential region was observed only sporadically at atmospheric pressure and only with one sample at pressures greater than 250 bars.

Inspection of the table indicates that only a small further improvement in the fit is obtained for  $n > 2$  except in the cases of Mg (AZ 61) and the low potential region of Al (GB 420).

Gassing of the aluminum anodes was less and that of the magnesium the same or greater than was the case in the buffered solutions. During the course of a run 0.1 ml of gas was evolved from pure Al and Al (GB 420); 2-5 ml from Al (GB 80S) and 12 ml from Mg (AZ 61). The Mg (AP 65) gassed so vigorously that all of the solution was forced out of the cell. So little magnesium metal was left six or seven hours following immersion that potentials were no longer stable and dropped considerably. Accordingly there was no solution remaining with which to measure pH following the run. The run had to be repeated in order to build up enough points to assure their reliability and points obtained after electrode failure were not included in the data analysis.

Much more rapid precipitate formation was observed for AP 65 than for AZ 61.

**Derived results and discussion.—Derived results: buffered systems.**—Typical values of  $(E_p - E_1 + \Delta E_f + \Delta E_\gamma)$ , derived from the experimental data are shown in Fig. 3 for the buffer systems studied. The

solid lines, 1 and 2, were calculated from values of  $K_{a(p)}/K_{a(1)}$ , using Eq. [23] from compressibility data (15) and conductance data (16), respectively.

The error bars shown on line 1 are from the emf data of Distèche (12). Lines 3 and 4 are also experimental emf data (12) but for different concentrations of phosphate buffer and chloride electrolyte than used in the experimental work reported here. The experimental points shown were corrected using the fugacity values, empirically determined in the acidified chloride solutions, except that points corrected using the fugacity determined from dry hydrogen compressibility are also shown for the acetate buffered system for comparison.

Excellent agreement was obtained with conductance data for acetic acid (line 2) but a large difference with density data (line 1) can be seen. It is likely that the density data shown are in error, in spite of agreement with Distèche's emf results. Hamann and Lim (19, 32) have reported density measurements in much closer agreement with the conductance data than those of line 1.

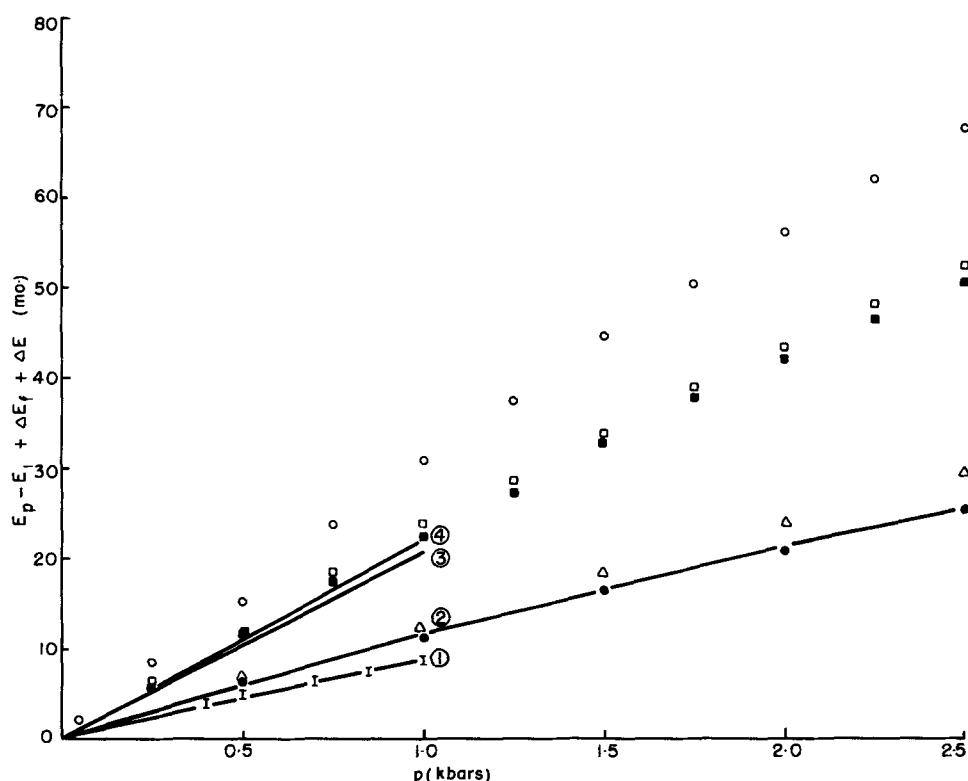
The  $\overline{\Delta V}$  values obtained by other workers and methods can also be used as a basis of comparison and as a measure of the validity of our experimental data.

Figure 4 gives values of  $-\overline{\Delta V}$  obtained by fitting the experimental emf values to a quadratic equation using a least squares method and calculating the analytical slope. (The standard error of the quadratic fit is given in Table Ia.)  $\overline{\Delta V}$  values for formic acid (line 1), phosphoric acid—1st dissociation (lines 2 and 3), bicarbonate buffer (line 4), and carbonic acid (line 5) from other work (17, 31) are included for comparison. Values of  $-\overline{\Delta V}_1^0$  ( $-\overline{\Delta V}$  at 1 atm and infinite dilution), obtained by Distèche (17) using a glass electrode and those obtained by other methods are compared with the present work in Table III.

It may be noted, that except for the low value of  $-\overline{\Delta V}_1^0$  of 9.2 for acetic acid from density measurements, the results of this work are in as good or better agreement with the results of other methods than those obtained using the glass electrode.

**Magnesium and aluminum anodes.**—Figure 5 gives derived  $\overline{\Delta V}$  values obtained from the data for self-buf-

Fig. 3. Decrease with pressure of the hydrogen electrode potential relative to the Ag/AgCl electrode, corrected for the dependences on pressure of the hydrogen fugacity and the chloride ion activity coefficient. 0.1M KCl + 0.2M acetate buffer: ●, experimental points using "empirical fugacity correction" (see text); △, experimental points using fugacity calculated from compressibility data; I, experimental data of Distèche (12) using glass electrode; line ①, calculated from dissociation constants obtained from density measurements (15); line ②, calculated from dissociation constants obtained from conductance data (16). □, 0.5M NaCl + 0.01M phosphate buffer; ■, 0.5M NaCl + 0.05M phosphate buffer; lines ③ and ④, 0.1M KCl + phosphate buffers—glass electrode (12); ○, 0.5M NaCl + 0.025M borate buffer.



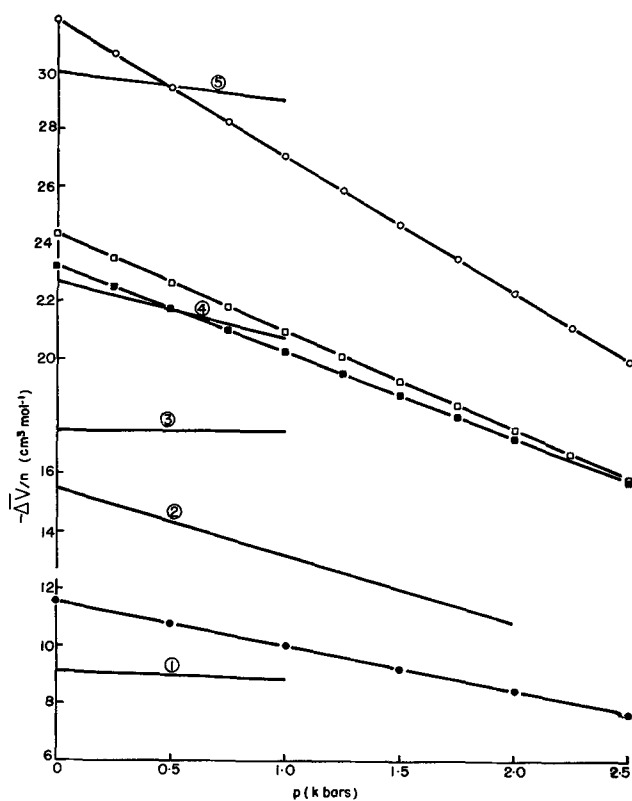


Fig. 4.  $-\overline{\Delta V}/n$  calculated from the slope of a quadratic fit of emf vs. pressure data. Symbols for points refer to the same solutions as in Fig. 3. Numbered lines are from other sources: ①, formic acid (17); ②, phosphoric acid-1st dissociation constant (31); ③, phosphoric acid-1st dissociation constant (17); ④, bicarbonate buffer (17); ⑤, carbonic acid (17).

fered solutions. The solid curves represent the average values of  $\overline{\Delta V}$  from the quadratic and cubic fits. The error bars are conservative in that they give the difference between the two orders of fit or the mean deviation between electrodes, whichever is the larger. Included in Fig. 5 are similar average values calculated from the results in buffered systems. These are the unconnected points and error estimates are not shown but are usually larger than those for the self-buffered systems. In spite of the differences in reproducibility, the results are generally in fairly good semiquantitative agreement.

For the purposes of the discussion in the following section, the  $\overline{\Delta V}$  values for the Mg and Al saturated solutions, derived from the dependence of the hy-

Table III.

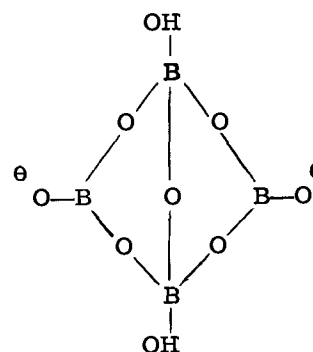
Acid or buffer	Present work emf	Glass electrode (17) emf	Density measurements	Conductivity measurements
(a) Values of $-\overline{\Delta V}_1^0$ (cm <sup>2</sup> /mol) at unit pressure				
Acetic acid or acetate buffer	11.6	11.5	9.2 (15), 11.5 (18)	12.2 (16, 19, 31)
Phosphate buffer	23.2 (0.01M) 24.4 (0.05M)	23.0	24.1 (17) 28.1 (17)	—
Borate buffer	31.8	—	—	—
(b) Values of $-\overline{\Delta V}$ at 1 kbar pressure				
Acetic acid or acetate buffer	10.0	10.8	12.2 (16, 19)	9.8-10.6* (16, 19, 31)
Phosphate buffer	20.2 (0.01M) 21.0 (0.05M)	20.3	23.0	—
Borate buffer	27.1	—	—	—

\* Average  $-\overline{\Delta V}$  for 0-2000 atm.

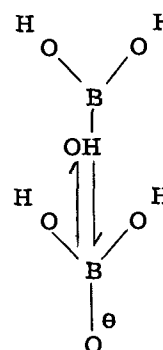
drogen electrode potential on pressure have also been included in Fig. 5. Again the averages of the cubic and quadratic fits are plotted.

*Discussion: buffered systems.*— The significance of the variation of  $\overline{\Delta V}$  with pressure for buffered systems (Fig. 4) can readily be seen in terms of the dissociation equilibrium of the weak acid of the buffer system (Eq. [21]). Thus an increase in applied pressure shifts the equilibrium toward the production of more ions which electrostrict the water structure in their vicinity and thereby reduce the stress in the solution. The negative  $\overline{\Delta V}$  values thus arise principally from the increases in local water density caused by the presence of the orienting fields of the ions produced. In the borate system, the equilibria are complicated by the tendency of polyboric acid formation to occur.

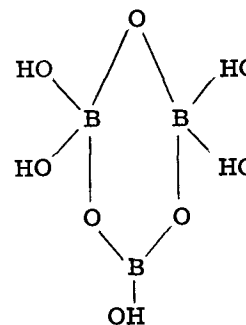
The anion formed  $B_4O_5(OH)_4^-$  consists of a ring structure (18) of two trigonal planar borate  $BO_3$  groups and two tetrahedral  $BO_4$  groups (structure A) which may hydrolyze in solution to form  $B(OH)_3$  monomer (structures B) or other complex borates such as  $B_3O_3(OH)_5^-$  (structure C) or chains of linked tetrahedra and triangles (20).



Structure A



Structure B



Structure C

In crystalline boric acid, layers of  $B(OH)_3$  molecules are held together by hydrogen bonds (20) and it would be expected that in aqueous solution similar hydrogen bonding would occur.

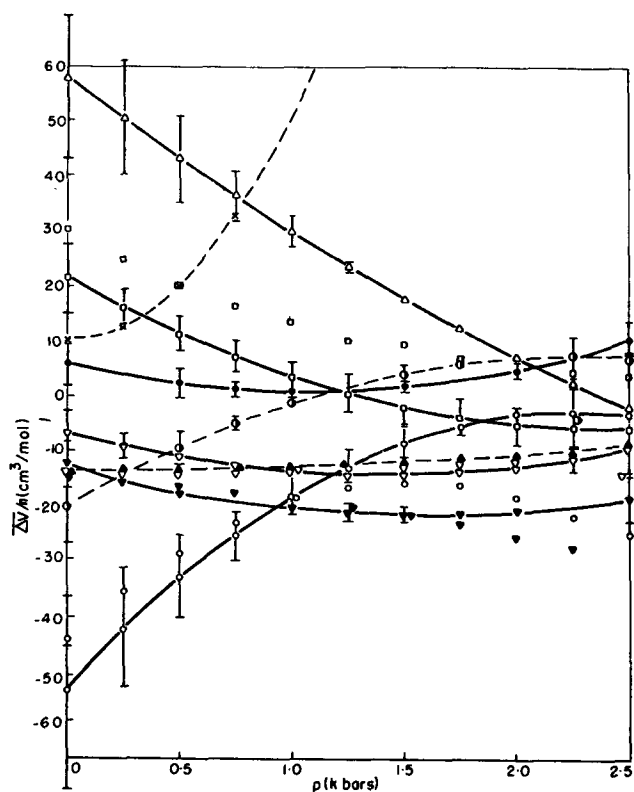


Fig. 5.  $\overline{\Delta V}/n$  for magnesium and aluminum alloys in self-buffered solutions of 0.5M NaCl. Average  $\overline{\Delta V}/n$  of quadratic and cubic fits. Points not falling on the curves are from data of buffered systems. Error bars are conservative (see text).  $\Delta$ , Al (99.999% purity);  $\circ$ , Al (GB 420) low potential region;  $\bullet$ , Al (GB 420) high potential region;  $\square$ , Al (GB 805);  $\times$ , Al (GB 805) possible high potential region;  $\nabla$ , Mg (AZ 61);  $\blacktriangledown$ , Mg (AP 65).  $\overline{\Delta V}/n$  values for the reactions:  $\blacktriangle$ ,  $\text{Mg}(\text{OH})_2 + \text{H}_2(\text{aq}) = \text{Mg}^{++} + 2\text{H}_2\text{O} + 2e^-$ ;  $\circ$ ,  $\text{Al}(\text{OH})_3 + 3/2 \text{H}_2(\text{aq}) = \text{Al}^{+++} + 3\text{H}_2\text{O} + 3e^-$  obtained from the dependence of hydrogen electrode potential on pressure.

As are the borate structures, the acetate ion and phosphate ions are also oxygen acids containing resonance stabilized anions with favorable structures for hydrogen bonding; note for example, hydrogen bonded dimeric acetic acid, with hydrogen bond energies of  $1.8 \text{ kJ mol}^{-1}$  (21). Similar comments apply to the four other systems, formic acid, phosphoric acid—1st dissociation, carbonic acid and bicarbonate buffer, included in Fig. 3 for comparison. A large discrepancy exists in the experimental results for bicarbonate between the emf data of line 3 and those obtained by compressibility data (15); this has been speculatively attributed (12) to unknown effects of pressure on the  $\text{NaHCO}_3$  equilibrium or to complications of hydrolysis reactions. However the author (12) did not explain why such complications would not also be reflected in compressibility or conductivity results; hence the  $\overline{\Delta V}$  values for line 3 may be incorrect. Other values of  $\overline{\Delta V}$  reported for the bicarbonate equilibrium are  $-24.9$  (17) and  $-27.8$  (15).

The magnitudes and pressure dependence of the derived  $\overline{\Delta V}$  values can be rationalized in the following manner: Values of the standard entropy of ionization of the systems of Fig. 3 were calculated from published data (2, 22, 23) and are listed in Table IV.

Comparison of these values of  $\Delta S_i^0$  with the  $\overline{\Delta V}$  values shows an interesting (if imperfect) correlation, in that larger  $-\overline{\Delta V}$  values appear to be associated with larger  $-\Delta S_i^0$  values. This is not surprising when one recalls that volume decreases are caused partially by electrostriction of the water structure, resulting in local ordering of the water dipoles. However, account

Table IV. Values of  $\Delta S_i^0$  and  $\overline{\Delta V}$  (1 atm) for various equilibria

Equilibrium	$\Delta S_i^0$ (cal $\text{K}^{-1} \text{ mol}^{-1}$ )	$\overline{\Delta V}$ ( $\text{cm}^3/\text{mol}$ )
$\text{HCOOH} = \text{HCOO}^- + \text{H}^+$	-17.4	-9.1
$\text{CH}_3\text{COOH} = \text{CH}_3\text{COO}^- + \text{H}^+$	-22.1	-11.5
$\text{H}_2\text{CO}_3 = \text{HCO}_3^- + \text{H}^+$	-23.3	-30.0
$\text{H}_3\text{PO}_4 = \text{H}_2\text{PO}_4^- + \text{H}^+$	-15.7	$-16.5 \pm 1$
$\text{H}_2\text{PO}_4^- = \text{HPO}_4^{2-} + \text{H}^+$	-30.3	$-23.7 \pm 0.6$
$\text{HCO}_3^- = \text{CO}_3^{2-} + \text{H}^+$	-35.3	-22.7
$\text{H}_3\text{BO}_3 = \text{H}_2\text{BO}_3^- + \text{H}^+$	-31.1	-31.9

must also be taken of size effects and structure-breaking entropy (24, 25). For most singly charged anions, there is a considerable increase of disorder and volume. Thus the net entropies in Table IV are due to a difference of ordering and disordering terms. The highly ordered structure around the ion will decrease the volume of the solvent, and the effects of disordering may increase it. However, the differences between molecular and/or ionic sizes also contribute to the  $\overline{\Delta V}$  term whereas their effect on  $\Delta S_i^0$  is less direct. The correlation between the two quantities is therefore not completely straightforward, particularly in a solvent with such an abnormally open structure as water.

In inspecting Table IV there is an anomaly, in the case of phosphoric acid, among the reactions producing singly charged anions by dissociation of the neutral molecular species. On the basis of the  $\overline{\Delta V}$  values one might expect the entropy change for the first dissociation step to be more negative. A possible explanation for this may be that the tetrahedral phosphate group fits better into the water structure than the trigonal carboxyl or bicarbonate groups. Hence the bulk water structure is better preserved with phosphate whereas the other groups cause greater short range ordering effects.

A cage of water molecules forming a clathrate-type structure may act as a transition region between the ion and the bulk water structure.

The equilibria producing doubly charged ions have more negative  $\Delta S_i^0$  and  $\overline{\Delta V}$  values, as expected, due to the greater orienting and compressive effect of the higher ionic fields. However the boric-borate values are far too negative to correspond to the equilibrium as written in the table. They would be far more consistent with the formation of one of the doubly charged borate ions discussed earlier.

The slopes of the  $\overline{\Delta V}/\text{pressure}$  plots calculated from the present data are in the ratio of 3.0:2.0:0.94 for the borate, phosphate, and acetate equilibria, respectively. This may indicate that the borate equilibria involve reversible formation of both singly and doubly charged species simultaneously.

*Magnesium and aluminum electrodes.*—Magnesium and aluminum ions are strong structure makers with large negative  $\Delta S_i$  values. Large negative  $\overline{\Delta V}$  values would be expected if the potential of these anodes were controlled by dissolution of  $\text{Mg}^{++}$  and  $\text{Al}^{+++}$  ions.

The results of Fig. 5 show that this cannot always be the case for aluminum but may be so for magnesium.

Stability constants for complex metal ions (27) indicate that Mg goes into solution in neutral or basic solutions predominantly as hydrated  $\text{Mg}^{++}$  ion and  $\text{MgOH}^+$  ion and that there are no stable complex chloride ions.

For aluminum the picture is much more complicated. Evidence exists (27) for a large number of hydroxyl complex ions such as  $\text{Al}_n(\text{OH})_{3n+1}^-$ ,  $\text{Al}_n(\text{OH})_{2n}^{2-}$ ,  $\text{Al}_n(\text{OH})_{2n}^{n+}$  and  $\text{Al}_{2n}(\text{OH})_{5n}^{n+}$  where  $n = 1, 2, \text{ or } 3$ . The existence of  $\text{Al}(\text{H}_2\text{O})_6\text{Cl}_3$  [as well as  $\text{Mg}(\text{H}_2\text{O})_6\text{Cl}_2$ ] in crystals (28) suggests the likelihood of hexahydrated  $\text{Al}(\text{H}_2\text{O})_6^{+++}$  [and  $\text{Mg}(\text{H}_2\text{O})_6^{++}$ ] in concentrated chloride solutions. Furthermore there is now

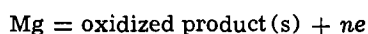


strong, n.m.r. spectroscopic evidence (30) in support of an integral six waters of hydration for  $\text{Al}^{+++}$  and  $\text{Mg}^{++}$  giving stable solvation complexes in aqueous solutions.

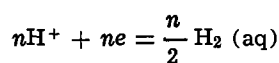
The alloying metals contained in the anodes used are sufficiently noble to be retained in the metallic phase and so have not been considered.

In order to interpret the values of  $\overline{\Delta V}/n$  obtained experimentally, all of the electrochemical reactions controlling the electrode potential must be considered. If these reactions are sufficiently reversible that the present analysis can be applied, the discrepancy between the observed and thermodynamically calculated (29) electrode potentials must be due to mixed potential control.

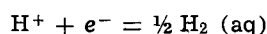
**Magnesium.**—In the case of magnesium, a corrosion potential is measured which must be controlled by the magnesium oxidation reaction(s) and by the hydrogen evolution reaction. Since there is no external current these oxidation and reduction reactions must proceed at equal rates, so that the  $\overline{\Delta V}/n$  value determined will be the sum of the two (or more) processes



and



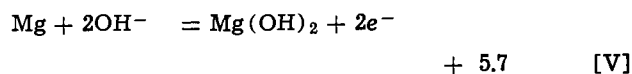
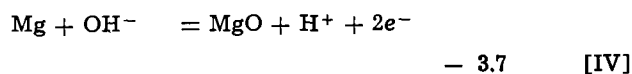
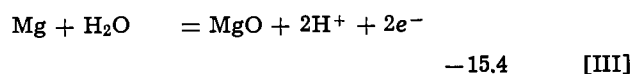
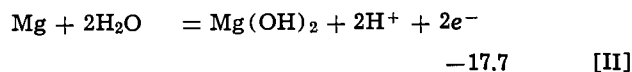
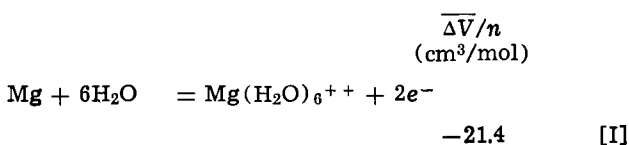
In order to derive a value of  $\overline{\Delta V}$  for the oxidation reaction(s) only, an estimate of  $\overline{\Delta V}/n$  for the hydrogen evolution reaction is required. The most probable value of  $\overline{V}$ , the partial molal volume of a hydrogen ion in aqueous solution at 25°C, is  $-5.0 \text{ cm}^3/\text{mol}$  (33), although there remains some argument in favor of a slightly more positive value (33, 34). The partial volume of solvation of the hydrogen molecule should be small and positive since it probably can be accommodated in the void spaces of the water structure with negligible distortion [cf. Ne, Ar (23)].  $\overline{\Delta V}$  values for the reaction



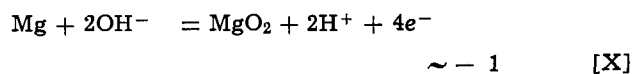
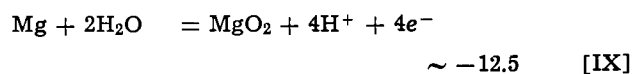
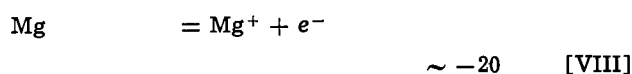
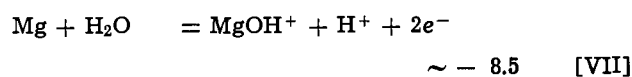
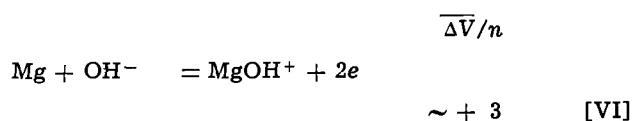
can be obtained from the data of Fig. 2. For the 0.1M HCl and the acidified 0.5M NaCl solutions the value of  $\overline{\Delta V}/n$  obtained at atmospheric pressure is  $+7.5 \pm 0.2 \text{ cm}^3/\text{equivalent}$ . Since it is  $\overline{\Delta V}$  for the over-all reaction which is required, it is not important whether the expansions due to hydrogen ion extraction and molecular hydrogen inclusion are 5.0 and 5.0  $\text{cm}^3/\text{mole}$ , respectively, or 0 and 15  $\text{cm}^3/\text{mole}$ , respectively (or something in between). However the former values appear the more likely.

Accordingly a partial molal volume of  $-5.0 \text{ cm}^3/\text{mole}$  for the hydrogen ion has been assumed for the calculations of  $\overline{\Delta V}$  to follow. From this value and published values of partial molal volumes of electrolytes (33),  $\overline{\Delta V}$  values of +22.8,  $-31.2$ , and  $-57.2 \text{ cm}^3 \text{ mol}^{-1}$  are obtained for  $\text{Cl}^-$ ,  $\text{Mg}^{++}$ , and  $\text{Al}^{+++}$  ions, respectively. From published density data (22) and a  $\overline{\Delta V}$  value of  $-23.4 \text{ cm}^3/\text{mole}$  (2) for the water dissociation reaction, volumes of solid phases could be determined, and a partial molal volume of  $-0.3 \text{ cm}^3/\text{mole}$  for  $\text{OH}^-$  ion was calculated. These values were then used to calculate  $\overline{\Delta V}$  for the electrode reactions considered below. The magnesium results at atmospheric pressure will be discussed first.

The magnesium oxidation reactions considered and their calculated values of  $\overline{\Delta V}/n$  were as follows



In addition the following reactions were considered, in which calculated  $\overline{\Delta V}$  values are approximate since density data were unavailable for  $\text{MgO}_2$  and partial molal volumes for the ions had to be inferred from other ions of similar size and charge



In order to make a comparison with the experimental values of  $\overline{\Delta V}/n$ , correction for the contribution of the hydrogen evolution reaction is required. Table V gives the corrected values with maximum probable experimental error for the various anodes studied. Comparison of the table with the calculated values for magnesium eliminates all of the reactions in which  $\text{OH}^-$  is a reactant species or in which  $\text{MgOH}^+$  is a product. For AZ 61 and AP 65, the formation of  $\text{Mg}^+$  and  $\text{MgO}_2$ , respectively, can also be eliminated except as possible minor parallel reactions. These reactions have been suggested by other workers (29, 35, 36).

The experimental data are consistent with production of  $\text{Mg}^+$  from the AP 65 alloy and  $\text{MgO}_2$  for the magnesium AZ 61. However, at present, scant other evidence exists to support these reactions. Accordingly, having noted these as possibilities, reactions [I]-[III] will be discussed in more detail. The experimental data favor reaction [I] as the oxidation mechanism for AP 65 and reaction [III] for AZ 61. Reaction [II] lies within the experimental error for both alloys however and therefore cannot be ignored. Immersion of these alloys in 0.5M NaCl gives rise to the following phenomena. The AP 65 corrodes rapidly with vigorous gassing and production of grayish-white voluminous precipitate near the surface. In a short time the electrode completely corrodes away and only a white precipitate and

Table V. Corrected experimental  $\overline{\Delta V}/n$  values for the metal oxidation reaction

Anode	$\overline{\Delta V}/n$ ( $\text{cm}^3/\text{equivalent}$ )	Error
Mg AZ 61	-14	$\pm 4$
Mg AP 65	-19.5	$\pm 4$
Al (99.999%)	50	$\pm 15$
Al (GB 80S)	14	$\pm 6$
Al (GB 420)		
High potentials	-1.5	$\pm 3.5$
Low potentials	-60	$\pm 17$

fine black particles remain (presumably from the lead which should not corrode at pH 8-12). The AZ 61 corrodes much less rapidly however and eventually builds up an incomplete black film which retards the rate of corrosion even further.

These observations, in conjunction with the experimental  $\Delta\bar{V}/n$  values, lead to the conclusion that AP 65 corrodes according to reaction [I] by direct dissolution to hexahydrated  $Mg^{++}$  ions (or by reaction [VIII] to  $Mg^+$  ions) followed by solution phase chemical formation of  $Mg(OH)_2$ .

For AZ 61, reaction [III] results in formation of a passivating layer of  $MgO$  on the surface (or  $MgO_2$  by reaction [IX]) which may then be slowly hydrated.

These facts suggest that at higher pressures the mechanism shifts from reaction [III] toward [II] or even [I] for AZ 61 and that reaction [II] is inhibited for AP 65.

Finally at very high pressures  $\Delta\bar{V}$  values begin approaching zero as would be expected when the reaction products can no longer aid in compressing the solvent structure or in reducing the system volume further.

Included in Fig. 5, are values of  $\Delta\bar{V}/n$ , obtained by measuring the hydrogen electrode potentials vs. Ag/AgCl in solutions saturated with  $Mg(OH)_2$  or  $Al(OH)_3$ . The over-all reaction controlling the electrode potential in the case of  $Mg(OH)_2$  is actually the sum of three reactions

		$\Delta\bar{V}$ (cm <sup>3</sup> mol <sup>-1</sup> )
$Mg(OH)_2$	$= Mg^{++} + 2 OH^-$	-56.5
$2H^+ + 2 OH^-$	$= 2H_2O$	+46.8
$H_2(aq)$	$= 2H^+ + 2e^-$	-15.0
$Mg(OH)_2 + H_2(aq) = Mg^{++} + 2H_2O + 2e^-$		-24.7

Direct formation of  $Mg(OH)_2$  by reaction [II] cannot be dismissed completely on the basis of the present evidence. However the mechanisms of the two alloys appear to be so different that it cannot occur, as more than a minor parallel reaction, for both alloys. If it were to occur for AP 65, for example, that would strongly point to reaction [III] for AZ 61. Conversely reaction [I] would be indicated for AP 65 if [II] were accepted for AZ 61. This latter possibility seems unlikely if the errors cited are as conservative as is thought.

Accordingly it is concluded that at atmospheric pressure reaction [I] is the most likely potential controlling oxidation reaction for AP 65 with a possible major parallel contribution by reaction [II]. For AZ 61, the most favored interpretation is that reaction [III] is the principal oxidation process with a possible minor contribution by reaction [II].

In buffered solutions the  $\Delta\bar{V}$  values tended to be somewhat more negative at lower pressures, particularly for AZ 61. Whether this is experimentally significant for AP 65 or not is open to question. However if it is a real effect, it suggests that the buffering agents tend to inhibit oxide formation and possibly dissolution as well. Ion pairing and insoluble salt formation are known to occur between magnesium and phosphate ions in solution and phosphate adsorption on the surface would not be surprising. Furthermore borax is a widely used rust inhibitor. The presence of these agents may very well shift the oxidation reaction path for AZ 61, enhancing the contribution of reaction [II] and reducing that of reaction [III].

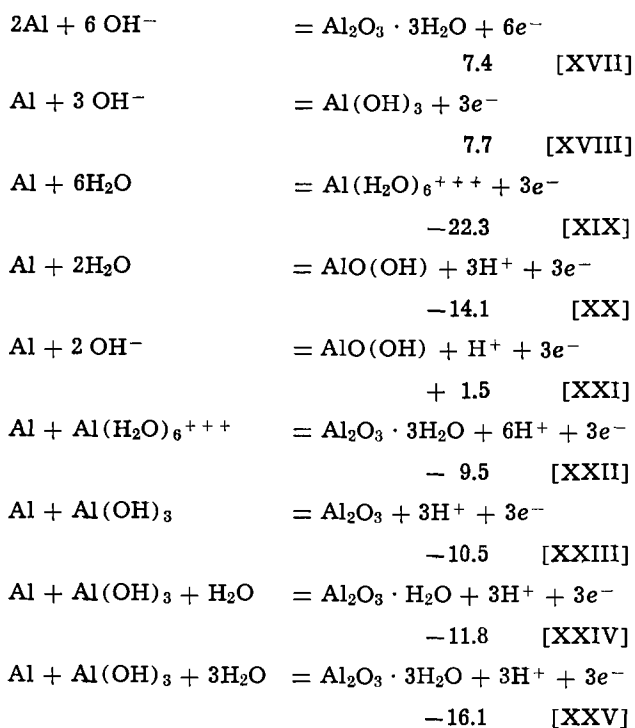
The AP 65 corroded more quickly in the unbuffered than in the buffered solutions even though the pH was higher in the former, also suggesting some shift toward reaction [II] in the presence of phosphate or borate. Differences in corrosion rate were much less for AZ 61, consistent with a shift from reaction [III] to reaction [II] which would have identical pH dependencies.

At higher pressures, both magnesium alloys reacted with more negative  $\Delta\bar{V}$  values than at atmospheric pressure. This would not be expected if a single electrode reaction were occurring at either anode and suggests a shift of mechanism at higher pressures toward the more negative  $\Delta\bar{V}$  reactions. Further evidence that this is occurring for AZ 61 was obtained by the observation that, although AZ 61 did not produce any visible precipitate at atmospheric pressure for several days, a fine white suspension was observed in solution after the alloy had completed an experimental cycle taking it to 2.5 kbars and back to atmospheric pressure again.

The calculated values of  $\Delta\bar{V}$  at 1 atm are shown. The measured value of  $\Delta\bar{V}/n = -13.2 \pm 1.0$  cm<sup>3</sup>/equivalent is in good agreement with the calculated value of -12.4, indicating that the reactions controlling electrode potential in the magnesium system are all reversible. The very small pressure dependence observed suggests that no changes of mechanism occur at higher pressures.

*Aluminum.*—The reason for the rather large experimental scatter of  $\Delta\bar{V}$  values for the aluminum anodes in buffered solutions became more comprehensible when the results for the self-buffered solutions were analyzed. The more evident separation of Al (GB 420) into two distinct potential regions, and the sporadic experimental results, suggesting the same phenomenon was possible (though less favored) for Al (GB 80S), led to the conclusion that at least two potential controlling reactions were important. Furthermore, the hysteresis observed indicated slow attainment of equilibrium between competing species. No high potential region was unambiguously detected in buffered solutions except in the borate buffered system and then at only 1 and 50 bars pressure. Hence the results in buffered systems are in much closer agreement with the low potential self-buffered data than with the high potential results. In the case of aluminum, addition of the buffering agent to the solution raises the pH, the opposite of its effect in the magnesium system. Yet less gassing was observed in the absence of buffering agents, suggesting inhibition either by adsorption of the oxyanion or by a pH effect. In order to interpret the aluminum results, the following reactions were first considered and the  $\Delta\bar{V}/n$  values calculated from published data

		$\Delta\bar{V}/n$
$2Al + 6H_2O$	$= Al_2O_3 \cdot 3H_2O + 6H^+ + 6e^-$	-15.9 [XI]
$2Al + 4H_2O$	$= Al_2O_3 \cdot H_2O + 6H^+ + 6e^-$	-13.7 [XII]
$2Al + 3H_2O$	$= Al_2O_3 + 6H^+ + 6e^-$	-13.1 [XIII]
$Al + 3H_2O$	$= Al(OH)_3 + 3H^+ + 3e^-$	-15.6 [XIV]
$2Al + 3 OH^-$	$= Al_2O_3 + 3H^+ + 6e^-$	- 1.7 [XV]
$2Al + 4 OH^-$	$= Al_2O_3 \cdot H_2O + 2H^+ + 6e^-$	1.9 [XVI]



Other combinations of the above reactions have also been considered.

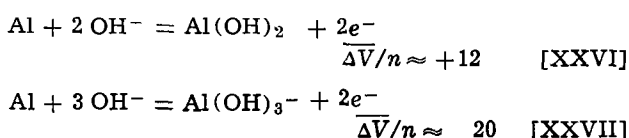
For pure aluminum, for Al (GB 80S), and for the low potential region of Al (GB 420) at atmospheric pressure, none of the above reactions has values of  $\overline{\Delta V}/n$  within the error limits of the experimental values, although reaction [XVIII] lies just outside these limits for Al (GB 80S). For the high potential data of Al (GB 420), only reactions [XV], [XVI], and [XXI] are possible. All of these reactions involve the consumption of hydroxyl ions and production of hydrogen ions and a surface oxide. When the simultaneous hydrogen evolution reaction is added, all would predict no pH dependence.

Estimates of  $\overline{\Delta V}/n$  based on size and charge considerations for reactions producing  $\text{AlO}^+$ ,  $\text{AlOH}^{++}$ ,  $\text{AlO}_2^-$ ,  $\text{Al}(\text{OH})_4^-$ , and  $\text{Al}(\text{H}_2\text{O})_5\text{OH}^{++}$  were also inconsistent with experimental values with some exceptions for the high potential Al (GB 420) results. The partial molal volumes for these species were taken to be approximately +20, -7, +27, +50, and -30  $\text{cm}^3/\text{mol}$ , respectively.

Clearly, either irreversible electrode processes are occurring, or other reactions than those considered above are controlling the electrode potentials.

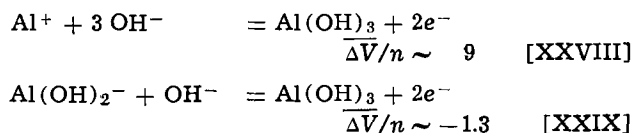
The analysis of the aluminum results has so far carried the tacit assumption that the potential controlling oxidation reaction involves formation of trivalent aluminum from metallic aluminum. Since no reactions have been found to justify this assumption, other oxidation states of aluminum must be considered. This requires estimated  $\overline{\Delta V}/n$  based on approximations, since no density or partial molal volume data exist for such species.

When such estimates were made for reactions in which metallic aluminum is oxidized to the univalent aluminum species  $\text{Al}^+$ ,  $\text{AlOH}$ , or  $\text{Al}(\text{OH})_2^-$  no values of  $\overline{\Delta V}$  calculated were consistent with experimental values. In considering oxidations from metallic aluminum to divalent aluminum by formation of  $\text{Al}(\text{OH})_2$ ,  $\text{Al}_2\text{O}_2 \cdot 3\text{H}_2\text{O}$ ,  $\text{AlO}$ , or  $\text{Al}(\text{OH})_3^-$  only two reactions were found consistent with any of the data. These were



which were only consistent with the Al(GB 80S)  $\overline{\Delta V}/n$  values.

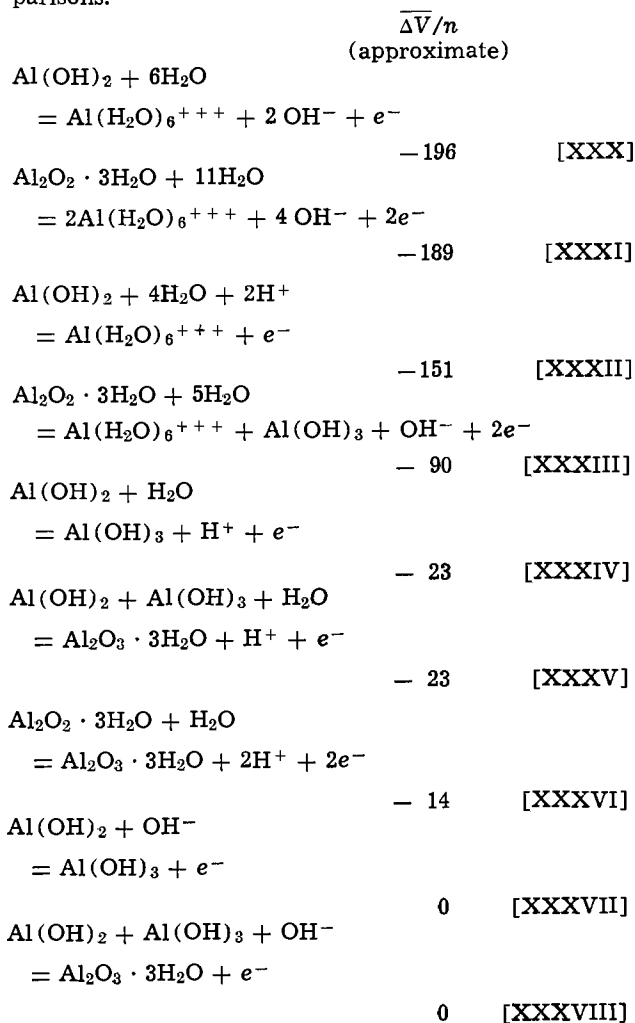
Similarly consideration of oxidations from univalent to trivalent aluminum led to only two possible reactions

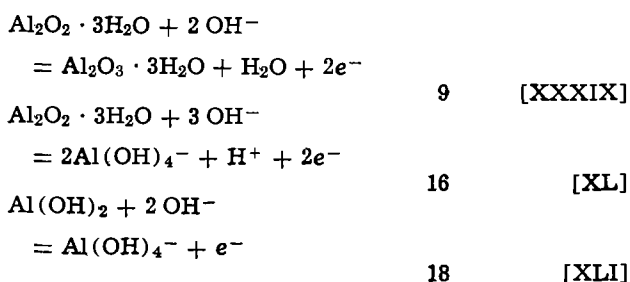


These both would involve the anode, only as a heterogeneous catalyst, and are consistent only with the Al(GB 80S) and Al(GB 420) high potential  $\overline{\Delta V}/n$  values.

Oxidation from divalent to trivalent aluminum is the only remaining case having a stable reactant or product species. The oxygen deficiency of the anodic aluminum barrier layer (adjacent to the solution) has been established (37) and gives rise to an n-type defect structure. The existence of Al(II) has been suggested (38) and infrared absorption studies of barrier layer oxides have been interpreted (39) as indicative of an alumina layer containing divalent aluminum. The structure proposed (39) contained a trivalent cyclic polymeric aluminum oxide trihydrate layer with oxygen deficient terminal groups containing divalent aluminum, at which oxidation and depolymerization could occur to form porous alumina.

The following reactions were considered for oxidation from divalent to trivalent aluminum. It was assumed that divalent solid aluminum phases had the same density as the corresponding trivalent solid phases and estimates of partial molal volumes of ions were made, as before, based on size and charge comparisons.





Reactions [XXX]-[XXXIII] in which divalent aluminum is oxidized to hexahydrated aluminum ion have negative values of  $\overline{\Delta V}/n$  larger than those obtained from the low potential Al (GB 420) data. By themselves they could not explain the experimental results unless another reaction with a more positive  $\overline{\Delta V}/n$  were occurring simultaneously.

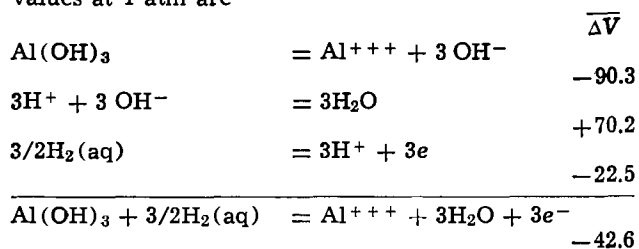
Such a reaction could be any or several of the others already discussed. The most probable are [XI], [XVII], or [XIX] in which metallic aluminum is oxidized to a trivalent solid phase or solution phase species. However the other oxidation reactions cannot be eliminated. It would also be possible to rationalize the other aluminum alloy results in terms of combinations of the reactions cited. However no rationalization of the large positive  $\overline{\Delta V}/n$  values for pure aluminum would be possible from the above reaction schemes.

Aluminum oxide is known to form a negatively charged colloidal sol and it has been suggested (40) that this is of the form  $[\text{Al}_2\text{O}_3 \cdot x \text{H}_2\text{O}] \text{AlO}_2^- \vdots \text{Na}^+$ . No data are available, and it is difficult to estimate the partial molal volume of such a species. If a structure for  $\text{Al}_2\text{O}_3 \cdot 3\text{H}_2\text{O}$  of the form suggested by Dorsey (39) is accepted, a crude estimate of 100-120  $\text{cm}^3/\text{mol}$  can be made. This is based on values for singly charged substituted benzene rings, for which  $\overline{V}^0$  values of about 75-85  $\text{cm}^3/\text{mol}/\text{phenyl group}$  have been obtained (33) and on an estimated value of  $\overline{V}^0$  for  $\text{AlO}_2^-$  of about 30  $\text{cm}^3/\text{mole}$ . Such a value could give an order of magnitude for  $\overline{\Delta V}/n$  consistent with the experimental results for Al (GB 80S) if oxidation from a divalent state took place. However the  $\overline{\Delta V}/n$  values calculated would still be too small to explain the results for pure aluminum.

There remain two other possibilities which will be discussed here. First, if the hydrogen evolved is not adsorbed on the alumina surface in such a way as to dissolve in solution reversibly, and therefore forms gas phase hydrogen, a very large positive  $\overline{\Delta V}$  contribution would appear. Second, if a porous alumina layer is formed by depolymerization according to the model of Dorsey (39), there would be larger positive  $\overline{\Delta V}$  values than those calculated. Unfortunately since the model does not include a detailed geometry for porous layer formation, it is impossible at present to estimate values of  $\overline{\Delta V}$  without entering even more deeply into an area of extreme speculation.

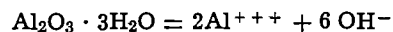
Measurements of the hydrogen electrode potential, in solutions of 0.5M NaCl, in which an excess of Al (GB 80S) was permitted to corrode for several days, were much less reproducible than in  $\text{Mg}(\text{OH})_2$  saturated solutions.

The reactions considered and the calculated  $\overline{\Delta V}$  values at 1 atm are



The calculated value of  $\overline{\Delta V}/n = -14.2$  is in agreement with the experimental value of  $-20 \pm 6 \text{ cm}^3/\text{equivalent}$ . However the strong dependence on pressure and large experimental uncertainty suggest that irreversible processes are occurring and/or there may be other reactions exerting some control on electrode potential.

If the first reaction considered above were



the calculated  $\overline{\Delta V}/n$  for the over-all reaction would be  $+7.0 \text{ cm}^3/\text{equivalent}$ , in close agreement with the observed high pressure values of  $+7.4 \pm 4$ . Hence there could be a change from one mechanism to another as pressure is increased. Other reactions could also be considered, but the comparatively imprecise experimental results for this system do not warrant a high enough degree of confidence to lead to definite conclusions without further evidence.

The aluminum results cannot be definitively explained by the present data. There are many reactions which may be simultaneously occurring to cause this state of affairs, some of which may be irreversible. However the simplest and most likely model which emerges, consistent with the cited facts may be the following.

For Al (GB 420) there are at least two oxidizing reactions occurring: one in which surface alumina containing divalent aluminum is oxidized to hexahydrated aluminum ions (possible reactions [XXX]-[XXXIII]); a second in which metallic aluminum is oxidized to a surface oxide or hydroxide by reaction with hydroxyl ions (possible reactions [XVII], [XVIII], [XIX], [XXVI], [XXVII]); the second reaction might instead involve formation of colloidal or porous alumina.

At atmospheric or low pressures, the second reaction(s) occurs preferentially along cracks or pores in the oxide layer. If the cracks heal or are sealed by the application of pressure, the second reaction is blocked or inhibited and the first becomes favored giving large negative  $\overline{\Delta V}$  values. These mechanisms appear to be consistent with conclusions based on  $\text{O}^{18}$  tracer techniques (43) if the structure proposed by Dorsey (38) and substantiated by electron micrographs (44) is accepted.

For Al (GB 80S), the first reaction does not apparently occur, which suggests that the pores do not seal. A single oxidation reaction might control the electrode potential if divalent aluminum is formed reversibly by reactions [XXVI] or [XXVII]; this seems unlikely. Reactions [XXXIX]-[XLI] are also possible but are not expected to be energetically probable except on a surface without pores. This means that it is also necessary to consider two simultaneous oxidation reactions controlling this alloy's potential. If one reaction is the large positive  $\overline{\Delta V}$  process involving formation of porous or colloidal alumina or gaseous hydrogen, it is impossible to state definitely which of the other 28 reactions, having values of  $\overline{\Delta V}/n$  less than 14, is the second, although some can be eliminated on various grounds.

For pure aluminum, the same unknown reaction(s) as for Al (GB 80S) are possible although a large positive  $\overline{\Delta V}$  process of porous alumina formation or gaseous hydrogen evolution appears to be potential controlling. The latter process would not likely be reversible.

### Conclusion

*Practical significance.*—Pressures much in excess of 1 kbar would not be encountered even at the greatest ocean depths. Hence the present work demonstrates that pressure effects on the electrodes themselves would cause only small changes in most seawater battery voltages.

The elucidation of the electrode mechanisms involved using the present technique should be of some

value in choosing the appropriate alloy for a particular application and in understanding the criteria for such a choice. For example AZ 61 is a superior alloy where sludging in a stagnant electrolyte cannot be tolerated because of the formation of a surface oxide, or in cases where a reduction of corrosion rate during open-circuit periods is essential, as is the case of the personal beacon battery. For a high rate, high voltage, short life application, where circulation of electrolyte is maintained, as in a torpedo battery, AP 65 would be preferred but greater interelectrode spacing would be beneficial.

The reduction of open-circuit emf at high pressures would have to be considered for batteries employing aluminum GB 420 for very deep ocean applications. The increase in open-circuit emf for pure aluminum is of little practical benefit in a battery because of excessive polarization. However an Al (GB 80S) anode coupled with a silver chloride cathode would give a stable voltage independent of depth with only a small increase of OCV with pressure and a low corrosion rate.

### Summary

Reference electrodes, for use at high pressures in chloride or hydrogen containing solutions, were tested in various chloride media, both acidified and buffered. The electrodes were silver chloride, and platinumized platinum in hydrogen saturated electrolyte. The results in unbuffered solutions indicated that the very small ( $\approx 1$  mV over the 2.5 kbar range) pressure dependence of the AgCl electrode could be quantitatively attributed to variation of chloride ion activity with pressure. The larger variation of the hydrogen electrodes were caused by the dependence of hydrogen fugacity on pressure and could be accurately estimated.

The reference electrodes were applied to the study of various buffer equilibria at pressures from 0 to 2.5 kbar. Partial volumes of reaction obtained were linear in pressure to a good approximation. However, there was a slight but definite quadratic dependence which was only detectable due to the high precision of the measurements. The volumes are compared with each other and those obtained by other methods and are interpreted qualitatively in terms of their effect on the solvent structure.

The open-circuit potentials of two magnesium alloy anodes (AZ 61 and AP 65) and three aluminum anodes (99.999% Al, GB 420<sup>4</sup> and GB 80S<sup>4</sup>) were measured relative to AgCl, using hydrogen electrodes to monitor hydrogen evolution. Experiments were done in phosphate and borate buffered sodium chloride solutions, and in 0.5M NaCl, buffered only by the solubility equilibrium of the appropriate metal hydroxide. The partial molal volumes derived for unbuffered (self-buffered) systems were negative for the magnesium alloys ( $-10$  to  $-20$  cm<sup>3</sup>/mol) and were not strongly dependent on pressure. They were positive and strongly dependent on pressure for the pure aluminum (60-0 cm<sup>3</sup>/mol). One of the Al alloys (GB 80S—0.5% Sn, 0.05% Ga) had a positive  $\Delta V$  over most of the pressure range (30 to  $-5$  cm<sup>3</sup>/mol). The other alloy (GB 420—5% Zn, 0.2% Sn) exhibited two stable potentials at certain pressures. The higher (more negative) potential was easier to reproduce at lower pressures, whereas the lower potential often appeared by a rather sudden transition following increase of pressure. It usually remained at the lower values, returning with some hysteresis upon decompression.

The  $\Delta V$  values, associated with the low potentials, were large and negative and more dependent on pressure than the near zero  $\Delta V$  values of the high potential region.

The signs and orders of magnitude of  $\Delta V$  were similar in both the buffered and unbuffered solutions. However, reproducibility was poorer in the former,

possibly as a consequence of adsorption, ion pairing or precipitation caused by phosphate or borate reaction with the metal ion at the electrode surface.

Of the two magnesium anodes investigated, the data indicated that Mg (AZ 61) reacted to produce predominantly a surface oxide, with some hydroxide formation possible, at atmospheric pressure. The Mg (AP 65) produced predominantly hexahydrated magnesium ions and some surface hydroxide. At higher pressures the reactions shifted toward more hydroxide and possibly ion formation for Mg (AZ 61) and less hydroxide and more ion formation for Mg (AP 65).

All aluminum anode potentials also appeared to be controlled by more than one oxidation mechanism. For Al (GB 420), metallic aluminum appeared to be oxidized to a surface oxide by reaction with hydroxyl ions along pores or cracks in the oxide layer at atmospheric pressure. At higher pressures or as the pores healed, the contribution of a reaction involving oxidation of divalent aluminum oxide to hexahydrated aluminum ions, increased in importance.

For Al (GB 80S) and for pure aluminum the interpretation of the data was more equivocal. The formation of porous or colloidal alumina combined with some other oxidation reaction was indicated if the potential controlling processes are reversible. Otherwise the formation of gaseous hydrogen or some other irreversible process controls the potential, rendering the present analysis invalid in such a case.

Manuscript received Dec. 13, 1973. This was Paper 42 presented at the Boston, Massachusetts, Meeting of the Society, Oct. 7-11, 1973.

Any discussion of this paper will appear in a Discussion Section to be published in the June 1975 JOURNAL. All discussions for the June 1975 Discussion Section should be submitted by Feb. 1, 1975.

The publication costs of this article have been assisted by Defence Research Establishment Ottawa.

### REFERENCES

- G. J. Hills and P. J. Ovensen, in "Advances in Electrochemistry and Electrochemical Engineering," Vol. 4, P. Delahay, Editor, Interscience, New York (1966).
- S. Harned and B. B. Owen, "The Physical Chemistry of Electrolytic Solutions," 3rd ed., Reinhold Publishing Corp., New York (1958).
- R. Parsons, "Handbook of Electrochemical Constants," Butterworths, London (1959).
- B. K. P. Scaife, *Proc. Phys. Soc.*, **B68**, 790 (1955).
- S. Kyropoulos, *Z. Physik*, **40**, 507 (1926).
- W. E. Deming and L. E. Shupe, *Phys. Rev.*, **40**, 848 (1932).
- International Critical Tables, **3**: 5.
- I. H. S. Henderson and L. D. Gallop, DREO unpublished work.
- D. J. G. Ives and G. J. Janz, "Reference Electrodes," Academic Press, New York (1961).
- E. E. Criddle, DREO Rept. No. 664, March (1973).
- R. A. Hine and M. W. Wei, *Mater. Protect.*, **3**, 49 (1964).
- A. Distèche, *Rev. Sci. Instr.*, **30**, 474 (1959).
- B. E. Conway and J. Currie, Rept to DRB on Grant No. 5401-11 (Sept. 30, 1972).
- W. R. Hainsworth, H. J. Rowley, and D. A. MacInnes, *J. Am. Chem. Soc.*, **46**, 1437 (1924).
- B. B. Owen and S. R. Brinkley, Jr., *Chem. Rev.*, **29**, 461 (1941).
- S. D. Hamann and W. Strauss, *Trans. Faraday Soc.*, **51**, 1684 (1955).
- A. Distèche, *This Journal*, **109**, 1084 (1962).
- O. Redlick and J. Bigeleisen, *Chem. Rev.*, **30**, 171 (1942). [See also Ref. (27).]
- S. D. Hamann, "Physico-Chemical Effects of Pressure," Butterworths, London (1957).
- L. Pauling, "The Nature of the Chemical Bond," 3rd ed., Cornell University Press, Ithaca, N. Y. (1960).
- M. D. Taylor, *J. Am. Chem. Soc.*, **73**, 315 (1951).
- "Handbook of Chemistry and Physics," 45th ed., Chemical Rubber Co. (1964-1965).

<sup>4</sup> Alcan designation.

23. R. W. Gurney, "Ionic Processes in Solution," Dover Publications, New York (1953).
24. H. S. Frank and M. W. Evans, *J. Chem. Phys.*, **13**, 507 (1945).
25. R. A. Robinson and R. H. Stokes, "Electrolyte Solutions," 2nd ed., Butterworths, London (1968).
26. J. E. Desnoyers and C. Jolicoeur, in "Modern Aspects of Electrochemistry," Vol. 5, P. Delahay and C. Tobias, Editors, pp. 1-89 Interscience, New York (1968).
27. J. Bjerrum, G. Schwarzenback, and L. G. Sillen, "Stability Constants, Part II: Inorganic Ligands," London: The Chemical Society, Special Publication No. 7 (1958).
28. N. V. Sidgwick, "The Chemical Elements and Their Compounds," Vol. 1, Oxford Clarendon Press (1950).
29. M. Pourbaix, "Atlas d'Équilibres Electrochimiques à 25°C," Gauthier-Villars, Paris (1963).
30. J. W. Akitt, *J. Chem. Soc.*, (A), 2347 (1971).
31. A. J. Ellis and D. W. Anderson, *J. Chem. Soc.*, 1765 (1961).
32. S. D. Hamann and S. C. Lim, *Australian J. Chem.*, **7**, 329 (1954).
33. F. J. Millero, in "Water and Aqueous Solutions," R. A. Horne, Editor, Chapter 13, Interscience, New York (1972).
34. M. H. Panckhurst, *Rev. Pure Appl. Chem.*, **9**, 45 (1969).
35. R. L. Petty, A. W. Davidson, and J. Kleinberg, *This Journal*, **76**, 363 (1954).
36. E. J. Casey, R. E. Bergeron, and G. D. Nagy, *Can. J. Chem.*, **40**, 463 (1962).
37. M. A. Heine, D. S. Keir, and M. J. Pryor, *This Journal*, **112**, 24 (1965).
38. M. J. Linevsky, *J. Chem. Phys.*, **41**, 542 (1964).
39. G. A. Dorsey, Jr., *This Journal*, **113**, 284 (1966).
40. S. Glasstone, "Textbook of Physical Chemistry," 2nd ed., p. 1243, Macmillan & Co. Ltd., London (1948).
41. W. R. Howell, Jr., S. H. Woodson, and H. A. Lieb-hafsky, *This Journal*, **119**, 1038 (1972).
42. E. J. Casey, Private communication.
43. C. Cherki and J. Siejka, *This Journal*, **120**, 784 (1973).
44. La Vecchia, G. Piazzesi, and F. Siniscalco, *Electrochim. Metal*, **2**, 71 (1967).
45. W. A. Adams, R. Yank, R. O. Christie, and J. Kruus, *Can. J. Chem.*, In press.

## Additive Ternary Molten Salt Systems—Calculation of Phase Diagrams from Thermodynamic Data of Lower Order Systems

Marie-Louise Saboungi\*<sup>1</sup>

*Laboratoire de Thermodynamique des Sels Fondus, associé au C.N.R.S., Marseille 13013, France*

and Pierre Cerisier

*Département de Thermodynamique et Energétique, Centre St. Jérôme, Université Aix-Marseille I, Marseille 13013, France*

### ABSTRACT

Calculations of the liquidus temperatures of additive ternary molten salt systems are carried out from the conformal ionic solution theory (up to second order terms). The comparison between measured and calculated phase diagrams is made for five systems [(Li,Na,K)F; (Li,Na,Cs)F; (Na,K,Cs)NO<sub>3</sub>; (Li,K,Tl)NO<sub>3</sub>; and Na(F,Cl,I)] chosen according to different types of liquidus and different values of the binary interaction coefficients. For most cases, and in particular when solid solutions are not reported, the agreement between measurements and calculations is found to be very good. In the search for low melting electrolytes for electrochemical applications, these equations should prove useful in predicting the range of compositions where low liquidus temperatures are most likely.

The thermodynamic study of multicomponent molten salt systems has been focused largely on experimental measurements. However, since measurements are generally expensive and time consuming, it is of interest to be able to predict thermodynamic properties of multicomponent systems from known theories by using available data for lower order systems. If this can be achieved with a satisfactory degree of accuracy, general properties of multicomponent systems, unmeasured or inaccessible to conventional measurements, are then *a priori* calculable. As multicomponent molten salt systems appear to be important as low melting stable electrolytes in many electrochemical applications, calculations such as ours should ultimately prove useful in choosing low melting mixtures for particular applications.

Recently, the conformal ionic solution (CIS) theory (1) has been successfully used to calculate the liquidus temperatures (2, 3) and the liquid-liquid miscibility gaps (4) for ternary reciprocal molten salt systems utilizing thermodynamic data for the four pure salts and the four constituent binaries.

In this paper, we shall focus on another class of ternary molten salt systems, the additive ternary systems for which few theoretical investigations (5) have been published. Our main purpose is to apply the conformal ionic solution theory to the additive ternary systems and compare calculated and experimental data.

First, we shall derive by a statistical mechanical treatment a set of equations relating the thermodynamic properties of ternary mixtures to those of the three pure salts and the three constituent binaries; the equations were derived up to second-order terms. Second, the liquidus temperatures are then calculated for

\* Electrochemical Society Active Member.

<sup>1</sup> Present address: Argonne National Laboratory, Argonne, Illinois 60439.

Key words: conformal ionic solution theory, multicomponent systems, liquidus temperatures, thermodynamic properties, fused salts.

the five systems: (Li,Na,K)F; (Li,Na,Cs)F; (Na,K,Cs)NO<sub>3</sub>; (Li,K,Tl)NO<sub>3</sub>; and Na(F,Cl,I) for which published measurements are available. These calculations for the ternary systems were made utilizing only liquidus phase diagram data from the three binary subsystems. Although simplifications in the calculations are used, these simplifications do not greatly influence our results.

Finally, a comparison between the experimental and calculated phase diagrams is carried out with regard to the different types and strengths of interactions of the constituent binaries. For all the cases, the agreement is good. The second-order equations appear to be accurate enough to be used for predicting the general topological behavior of such systems and for determining the compositions of low melting eutectics.

### Conformal Ionic Solution Theory—Extension to Ternary Additive Salt Solutions

Ternary additive molten salt systems are those containing three different anions (or cations) and one common cation (or anion). In this paper, we shall deal with the (A<sup>+</sup>,B<sup>+</sup>,C<sup>+</sup>)X<sup>-</sup> ternary mixture composed of uni-univalent salts AX (component 1), BX (component 2), and CX (component 3). It should be pointed out that the calculations are strictly the same for the A<sup>+</sup>(X<sup>-</sup>,Y<sup>-</sup>,Z<sup>-</sup>) ternary mixture composed of the AX, AY, and AZ salts; the calculations can also be easily extended to other additive systems containing mixtures of salts of multivalent charges (6) and to solutions containing more than three different anions (or cations) but one common cation (or anion). Following the perturbation method of Reiss *et al.* (7), we shall define for each salt *i*, a size parameter *d<sub>i</sub>* (equal to the characteristic sum of the cation and anion radii) and a dimensionless parameter

$$g_i = \frac{d_o}{d_i}$$

where *d<sub>o</sub>* is the size parameter for a "test" salt A<sub>o</sub>X, having, in this case, X<sup>-</sup> as an anion.

In order to calculate the thermodynamic functions for a mixture consisting of *n<sub>A</sub>* moles of A<sup>+</sup>, *n<sub>B</sub>* moles of B<sup>+</sup>, *n<sub>C</sub>* moles of C<sup>+</sup>, and *n* = (*n<sub>A</sub>* + *n<sub>B</sub>* + *n<sub>C</sub>*) moles of X<sup>-</sup>, four separate perturbation calculations must be carried out. At first, in three separate samples, the components are conveniently produced: the size of the cations of the "test" salt varies so that *d<sub>o</sub>* is changed to *d<sub>i</sub>* (*i* = 1, 2, 3). Finally, the ternary mixture is obtained by allowing a fraction, *x<sub>A</sub>*, of the cations of the "test" salt to vary so that *d<sub>o</sub>* is changed to *d<sub>1</sub>*, a fraction *x<sub>B</sub>* to vary so that *d<sub>o</sub>* is changed to *d<sub>2</sub>* and a fraction (*x<sub>C</sub>* = 1 - *x<sub>B</sub>* - *x<sub>A</sub>*) to vary so that *d<sub>o</sub>* is changed to *d<sub>3</sub>*. The fractions *x<sub>i</sub>* are the ionic fractions

$$\begin{aligned} x_A &= \frac{n_A}{n_A + n_B + n_C} = \frac{n_{AX}}{n} \\ x_B &= \frac{n_B}{n_A + n_B + n_C} = \frac{n_{BX}}{n} \\ x_C &= \frac{n_C}{n_A + n_B + n_C} = \frac{n_{CX}}{n} \end{aligned} \quad [1]$$

where *n<sub>AX</sub>*, *n<sub>BX</sub>*, and *n<sub>CX</sub>* are the number of moles of the subscript components.

The perturbations and their effect on the potential energy, *U*, the configurational integral, *Z*, and the Helmholtz free energy, *A*, can be summarized in the following scheme

$$\begin{array}{llll} \text{(i)} & d_o \rightarrow d_1 & U_o \rightarrow U_1 & Z_o \rightarrow Z_1 & A_o \rightarrow A_1 \\ \text{(ii)} & d_o \rightarrow d_2 & U_o \rightarrow U_2 & Z_o \rightarrow Z_2 & A_o \rightarrow A_2 \\ \text{(iii)} & d_o \rightarrow d_3 & U_o \rightarrow U_3 & Z_o \rightarrow Z_3 & A_o \rightarrow A_3 \\ \text{(iv)} & x_A d_o \rightarrow d_1 & & & \\ & x_B d_o \rightarrow d_2 & U_o \rightarrow U_m & Z_o \rightarrow Z_m & A_o \rightarrow A_m \\ & x_C d_o \rightarrow d_3 & & & \end{array} \quad [2]$$

According to the definition of the conformal ionic solution (7), the potential energy *U<sub>i</sub>* for a salt *i* in a particular configuration is expressed by

$$U_i = \sum_c^n \sum_a^n g_{ifca}(g_i r) + \sum_c^n \sum_a^n h_{ca}(r) + \sum_{a < a'}^n \sum_{c < c'}^n u_{aa'} + \sum_{c < c'}^n \sum_{c < c'}^n u_{cc'} \quad [3]$$

where *c* and *a* refer to a cation and an anion, respectively. The configurational integral, *Z<sub>i</sub>*, is expressed by

$$Z_i = \frac{1}{(n!)^2} \int \dots \int \exp(-U_i/kT) (d\tau)^{2n} \quad [4]$$

and the Helmholtz free energy *A<sub>i</sub>* by

$$A_i = -kT \ln Z_i \quad [5]$$

Similarly, for the mixture (A<sup>+</sup>, B<sup>+</sup>, C<sup>+</sup>)X<sup>-</sup>

$$U_m = \sum_c^{n_A} \sum_a^n g_{1fca}(g_1 r) + \sum_c^{n_B} \sum_a^n g_{2fca}(g_2 r) + \sum_c^{n_C} \sum_a^n g_{3fca}(g_3 r) + \sum_c^n \sum_a^n h_{ca}(r) + \sum_{a < a'}^n \sum_{c < c'}^n u_{aa'} + \sum_{c < c'}^n \sum_{c < c'}^n u_{cc'} \quad [6]$$

$$Z_m = \frac{1}{n_A! n_B! n_C! n!} \int \dots \int \exp(-U_m/kT) (d\tau)^{2n} \quad [7]$$

and

$$A_m = -kT \ln Z_m \quad [8]$$

One mole of the ternary solution can be considered as consisting of *x<sub>A</sub>* mole of AX, *x<sub>B</sub>* mole of BX, and *x<sub>C</sub>* mole of CX; then the excess Helmholtz free energy of mixing is expressed by

$$\Delta A_m^{xs} = A_m - x_A A_1 - x_B A_2 - x_C A_3 - RT(x_A \ln x_A + x_B \ln x_B + x_C \ln x_C) \quad [9]$$

In order to calculate  $\Delta A_m^{xs}$ , the functions *A<sub>i</sub>* and *A<sub>m</sub>* are expanded about the values of the "test" salt up to the second order as follows

$$\begin{aligned} -\frac{A_1}{kT} &= \ln Z_1 = \ln Z_o + (g_1 - 1) \left( \frac{\partial \ln Z_1}{\partial g_1} \right)_{(g=1)} \\ &+ \frac{1}{2} (g_1 - 1)^2 \left( \frac{\partial^2 \ln Z_1}{\partial g_1^2} \right)_{(g=1)} + \dots \quad [10] \\ -\frac{A_m}{kT} &= \ln Z_m = \ln Z_o + \sum_{i=1}^3 (g_i - 1) \left( \frac{\partial \ln Z_m}{\partial g_i} \right)_{(g=1)} \\ &+ \frac{1}{2} \sum_{i=1}^3 \sum_{j=1}^3 (g_i - 1)(g_j - 1) \left( \frac{\partial^2 \ln Z_m}{\partial g_i \partial g_j} \right)_{(g=1)} + \dots \quad [11] \end{aligned}$$

where *Z<sub>o</sub>* refers to the configurational integral of the "test" salt and the symbol *g* = 1 designates the limit as *g<sub>1</sub>*, *g<sub>2</sub>*, and *g<sub>3</sub>* approach unity. The calculations are identical to those given by Blander (8) for the binary systems; by keeping the same notation, the results for the excess Helmholtz free energy of mixing lead to the following second-order equation

$$\Delta A_m^{xs} = \Delta A_{12}^{xs} + \Delta A_{13}^{xs} + \Delta A_{23}^{xs} \quad [12]$$

where

$$\Delta A_{12}^{xs} = \Gamma(T, V) (g_1 - g_2)^2 x_A x_B$$

$$\Delta A_{13}^{xs} = \Gamma(T, V) (g_1 - g_3)^2 x_A x_C$$

$$\Delta A_{23}^{xs} = \Gamma(T, V) (g_2 - g_3)^2 x_B x_C \quad [13]$$

$\Gamma(T, V)$  is a combination of integrals depending only on the properties of the "test" salt and is a constant quantity for binary ionic conformal mixtures having  $X^-$  as a common anion. It should be noted that the terms of the first-order development cancel exactly as for binary mixtures.

The difference between the Helmholtz free energy  $A$  and the Gibbs free energy  $G$  can be considered as negligible in the second-order theory; then, the expression for the total excess free energy of mixing,  $\Delta G_m^{xs}$ , of the ternary mixture is deduced from Eq. [12]

$$\Delta G_m^{xs} = \Delta G_{12}^{xs} + \Delta G_{13}^{xs} + \Delta G_{23}^{xs} \quad [14]$$

In order to be self-consistent we shall include only second-order terms so that

$$\begin{aligned} \Delta G_{12}^{xs} &= \lambda_{12}x_Ax_B \\ \Delta G_{13}^{xs} &= \lambda_{13}x_Ax_C \text{ etc.} \end{aligned} \quad [15]$$

$\lambda_{ij}$  being an energy coefficient which can be determined experimentally in the case of common ion systems. For one mole of ternary solution, the excess free energy of mixing is then expressed by

$$\Delta G_m^{xs} = x_Ax_B\lambda_{12} + x_Ax_C\lambda_{13} + x_Bx_C\lambda_{23} \quad [16]$$

Assuming that the ternary mixture is regular and the heat of mixing of each of the constituent binaries is a symmetrical parabolic function of composition, Lumsden (9) has previously suggested that the heat of mixing of the ternary solution may be represented by the equation

$$\Delta H_m = x_Ax_B\lambda_{12} + x_Ax_C\lambda_{13} + x_Bx_C\lambda_{23} \quad [16a]$$

The right hand side of this equation is identical to Eq. [16]. Lumsden applied Eq. [16a] to calculate the excess free energy for silver chloride in the LiCl-KCl eutectic melt; the agreement between his calculation and the experimental results is within the limits of the error in estimating the coefficients,  $\lambda_{ij}$ .

Finally, it should be pointed out that the higher order terms in Eq. [10]-[11] do not cancel. Blander and Hagemark (10) using the quasi-chemical theory gave a higher order equation for the excess free energy of mixing for ternary mixtures, taking into account terms which correspond to some of the third-order terms of the CIS. Because of limitations in the quasi-chemical theory, all the third-order terms cannot be obtained. In any case, these terms appear to be small in the systems we studied; using the equation of Blander and Hagemark (10), we have numerically estimated the third-order terms for our systems and in the most extreme cases, the correction was negligibly small.

### Calculations of Ternary Phase Diagrams—Discussion

*Method of calculation.*—The activity coefficient,  $\gamma_{ij}$ , of any component can be calculated from Eq. [16] with the aid of the following relation

$$RT \ln \gamma_{ij} = \frac{\partial(n\Delta G_m^{xs})}{\partial n_{ij}} = \frac{\partial(n\Delta H_m)}{\partial n_i} \quad [17]$$

the number of moles  $n_{ij}$  of any component being, in this case, equal to the number of moles of the cations,  $n_i$ . For example, for the AX component, one obtains

$$RT \ln \gamma_{AX} = x_B(1 - x_A)\lambda_{12} + x_C(1 - x_A)\lambda_{13} - x_Bx_C\lambda_{23} \quad [18]$$

Similar equations can be derived for the other components by changes in the subscripts in Eq. [18] as follows

$$\begin{aligned} \text{for BX change } A \rightarrow B \quad B \rightarrow A \quad 1 \rightarrow 2 \text{ and } 2 \rightarrow 1 \\ \text{for CX change } A \rightarrow C \quad C \rightarrow A \quad 1 \rightarrow 3 \text{ and } 3 \rightarrow 1 \end{aligned}$$

The ternary liquidus temperatures may be calculated from expressions as

$$R \ln a_1 = R \ln \gamma_1x_A = -\Delta H_f \left( \frac{1}{T} - \frac{1}{T_f} \right) \quad [19]$$

where the enthalpy of fusion  $\Delta H_f$  has been assumed to be temperature independent; this assumption does not have any significant effect on our conclusions.

Indeed, if one takes into consideration the variation of the heat of fusion  $\Delta H_f$  with the temperature,  $\Delta H_f$  is then expressed by

$$\Delta H_f(T) = \Delta H_f(T_f) - \int_T^{T_f} \Delta C_p dT$$

where  $\Delta H_f(T)$  and  $\Delta H_f(T_f)$  are the enthalpies of fusion at  $T$  and  $T_f$ , respectively, and  $\Delta C_p = C_p(\text{liq}) - C_p(\text{s})$ . If  $\Delta C_p$  is expressed by

$$\Delta C_p = \Delta a + T\Delta b + T^{-2}\Delta c$$

one obtains

$$\begin{aligned} R \ln a_1 = & -\Delta H_f(T_f) \left( \frac{1}{T} - \frac{1}{T_f} \right) \\ & + \Delta a \left( \frac{T_f}{T} - \ln \frac{T_f}{T} \right) + \frac{\Delta b}{2} \left( \frac{T_f^2}{T} - 2T_f + T \right) \\ & + \frac{\Delta c}{2} \left( \frac{1}{T} - \frac{1}{T_f} \right)^2 \end{aligned} \quad [19a]$$

The terms containing the correction for the variation of  $\Delta H_f$  with the temperature have a very small contribution, in the range of temperatures considered in this paper. For example, for  $\Delta T = T_f - T = 540^\circ$  which corresponds to the case of NaF, the error in  $a_1$  would be about 4.6%. However, Eq. [19] will also be used to obtain the coefficients  $\lambda_{ij}$  from binary phase diagrams. This self-consistent procedure considerably reduces the uncertainties inherent in the use of Eq. [19] (rather than Eq. [19a]) for the calculation of the ternary liquidus temperatures.

Table I lists the values of  $\Delta H_f$  and  $T_f$  used; the values of the melting points of the pure salts  $T_f$  are those given in the published phase diagrams, our main purpose being the comparison of calculated and measured ternary liquidus temperatures.

Values of the  $\lambda_{ij}$  coefficients are calculated from known binary phase diagrams in a manner described previously (1,2). Combining Eq. [19] with the following simplified relations

$$RT \ln \gamma_i = \lambda_{ij}x_j^2 \text{ and } RT \ln \gamma_j = \lambda_{ij}(1 - x_j)^2 \quad [20]$$

one obtains

$$\begin{aligned} T(\text{eutectic}) = & [\lambda_{ij}(1 - x_j)^2 + \Delta H_{f,i}] / \\ & [(\Delta H_{f,i}/T_{f,i}) - R \ln x_j] \\ = & [\lambda_{ij}x_j^2 + \Delta H_{f,j}] / \\ & [(\Delta H_{f,j}/T_{f,j}) - R \ln(1 - x_j)] \end{aligned} \quad [21]$$

Table I. Values of enthalpies of fusion and melting points used in calculations

Salt	$\Delta H_f^{(a,b)}$ (kcal mole <sup>-1</sup> )	$T_f^{(c)}$ (°K)
LiF	6.47	1119, 1117
LiNO <sub>3</sub>	6.12	528, 530
NaF	8.03	1263
NaCl	6.69	1073
NaI	5.64	943
NaNO <sub>3</sub>	3.49	581
KF	6.75	1129
KNO <sub>3</sub>	2.80	610
RbF	6.15	1053
CsF	5.19	958
CsNO <sub>3</sub>	3.37	680
TlNO <sub>3</sub>	2.29	479

<sup>a</sup> A. S. Dworkin and M. A. Bredig, *J. Phys. Chem.*, **64**, 269 (1960); *ibid.*, **67**, 697 (1963).

<sup>b</sup> M. Blander, in "Molten Salt Chemistry," p. 127, Interscience Publishers, New York, (1964).

<sup>c</sup> The melting points are taken from the phase diagrams for which calculations are made. They are usually consistent with works cited in footnotes (a) and (b). In the case of the lithium fluoride melting point, we used the two slightly different values measured.



Table II. Calculated and experimental values of the interaction coefficients  $\lambda_{ij}$  and the eutectic compositions ( $x_{AX}$ ) for binary systems

AX-BX or AX-AY	Calculated		Experimental		$4 \Delta H_{m,0.5}$ (cal mole <sup>-1</sup> )	T(eut)*
	$\lambda_{ij}$ (cal mole <sup>-1</sup> )	$x_{AX}$	$\lambda_{ij}$ (cal mole <sup>-1</sup> )	$x_{AX}$		
LiF-NaF	-1293	0.603	-1300 <sup>a</sup>	0.610	-1930 <sup>b</sup>	923
	-1207	0.605				925
LiF-KF	-4213	0.509	-3600 <sup>a</sup>	0.500	-4647 <sup>b</sup>	765
LiF-CsF	-3051	0.480	-3000 <sup>a</sup>	0.525	-3860 <sup>b</sup>	(720)
LiNO <sub>3</sub> -NaNO <sub>3</sub>	-129	0.497	-540 <sup>a</sup>	0.540	-470 <sup>c</sup>	469
LiNO <sub>3</sub> -CsNO <sub>3</sub>	-2650	0.506	—	0.570	-3000 <sup>c</sup>	(423)
LiNO <sub>3</sub> -TlNO <sub>3</sub>	-693	0.269	-1150 <sup>a</sup>	0.295	-885 <sup>c</sup>	405
LiNO <sub>3</sub> -KNO <sub>3</sub>	-2884	0.436	-2300 <sup>a</sup>	0.5780	-1800 <sup>b</sup>	393
NaF-NaCl	54	0.341	0 <sup>a</sup>	0.340	—	948
NaF-NaI	370	0.213	700 <sup>a</sup>	0.190	—	876
NaF-KF	337	0.376	250 <sup>a</sup>	0.400	-90 <sup>b</sup>	983
NaF-CsF	766	0.199	0 <sup>a</sup>	0.220	—	891
NaCl-NaI	853	0.660	700 <sup>a</sup>	0.624	465 <sup>d</sup>	843
NaNO <sub>3</sub> -KNO <sub>3</sub>	104	0.495	—	0.500	-442	(475)
NaNO <sub>3</sub> -CsNO <sub>3</sub>	-1306	0.557	—	0.530	-1258 <sup>c</sup>	451
KNO <sub>3</sub> -CsNO <sub>3</sub>	-140	0.592	—	0.590	-133 <sup>c</sup>	493
KNO <sub>3</sub> -TlNO <sub>3</sub>	806	0.226	—	0.270	439 <sup>c</sup>	(435)

<sup>a</sup> J. Lumsden, "Thermodynamics of Molten Salt Mixtures," Academic Press, New York (1936); G. J. Janz, "Molten Salts Handbook," Academic Press, New York (1967).

<sup>b</sup> J. L. Holm and O. J. Kleppa, *J. Chem. Phys.*, 49, 2425 (1968).

<sup>c</sup> M. Blander, in "Molten Salt Chemistry," Interscience Publishers, New York (1964).

<sup>d</sup> M. E. Melnichak and O. J. Kleppa, *J. Chem. Phys.*, 57, 5231 (1972).

\* The eutectic temperatures are taken from phase diagrams for which the calculations are made. Parentheses indicate extrapolated values for the binaries where solid solutions or some intermediate compounds are reported.

From the eutectic temperature and from Eq. (21), unique values for the energy coefficient  $\lambda_{ij}$  and the eutectic composition  $x_j$  may then be numerically calculated.

This procedure applies for simple binary systems where neither solid solutions nor binary compounds are reported. The calculated values obtained for  $\lambda_{ij}$  and  $x_j$  are given in Table II and are in reasonable agreement with the experimental values within experimental uncertainties. Our procedure constrains our calculations so as to include the binary eutectic point in the calculated phase diagram.

When solid solutions or binary compounds are known to exist, Eq. [20] and [21] if applied, would lead to higher values of  $\lambda_{ij}$ . In this case, we estimate a eutectic which would occur in the absence of solid solutions or binary compounds such that the calculated values of  $\lambda_{ij}$  are then consistent with available calorimetric or emf data (Table II). This procedure leads to a better representation of the thermodynamic properties at most compositions not close to the binary in question.

### Comparison of Measured and Calculated Ternary Liquidus Temperatures

Experimental data for some ternary additive molten salt systems are available (10). The phase diagram is plotted in an equilateral triangle; each composition of the solution fixed by a point is defined by the corresponding triangular coordinates.

In order to adopt a uniform method to represent the calculated phase diagrams, the isotherms are drawn in

each phase field for intervals of 50°C. For consistency, the binary data (*i.e.*, the eutectic temperatures) we use in the present calculations are those given by the same workers who made the ternary measurements, rather than values given in more recent work; for some binary systems included in more than one ternary phase diagram and measured by different authors, there are some discrepancies in the eutectic temperatures; in these cases, we use the value of  $T(\text{eutectic})$  given in the corresponding ternary.

For the present purpose of comparing measured values with those calculated from lower order systems using the above equations, five systems have been examined; four of these are systems composed of salts containing a common anion and are characterized by relatively large negative binary interaction coefficients; the last is a system composed of salts containing a common cation and is characterized by small positive binary interaction coefficients ( $\leq 1$  kcal mole<sup>-1</sup>).

Figures 1-5 give both measured and calculated phase diagrams for several types of ternary additive systems. The range of applicability of the theory and the approximations used can then be discussed.

For the simplest ternary systems (*i.e.*, those in which the binary subsidiary solutions have eutectics and a ternary eutectic is reported) such as the (Li,Na,K)F and Na(F,Cl,I) systems (11), the differences between the measured and calculated phase diagrams are small and reflect, in part, uncertainties in the measured phase diagram (Fig. 1 and 5). For example, differences in the location and shape of some iso-

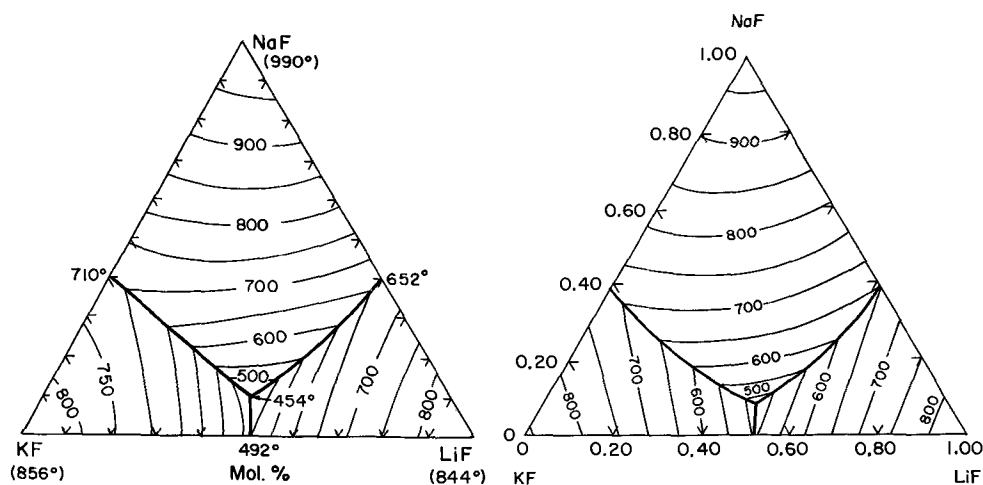


Fig. 1. Phase diagrams of the (Li,Na,K)F system. a (left), Measured [Ref. (11)]; b (right), calculated.

Fig. 2. Phase diagrams of the (Li,Na,Cs)F system. a (left), Measured [Ref. (12)]; b (right), calculated.

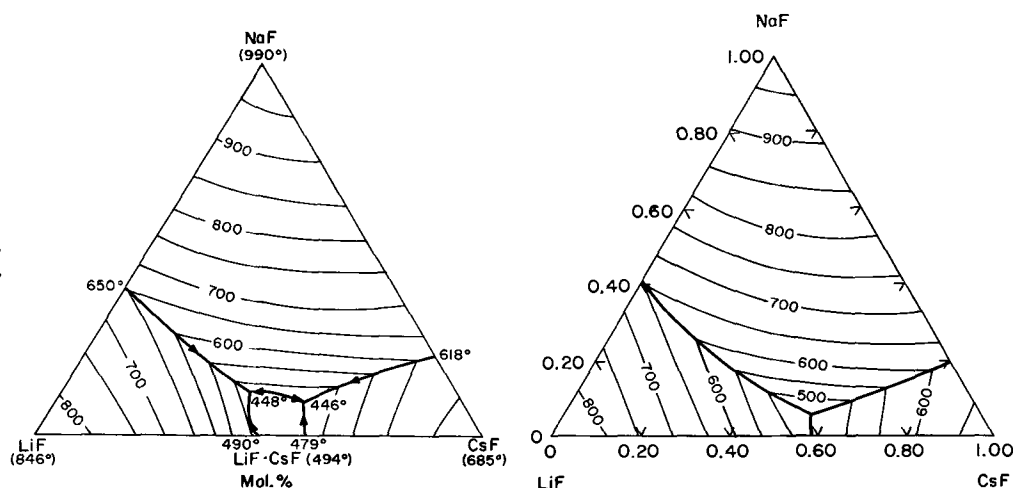


Fig. 3. Phase diagrams of the (Na,K,Cs)NO<sub>3</sub> system. a (left), Measured [Ref. (13)]; b (right), calculated.

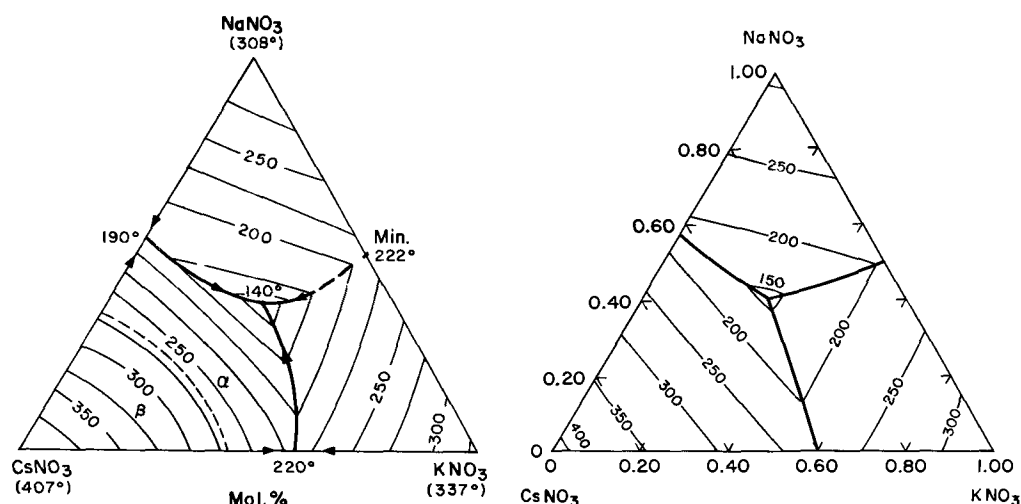
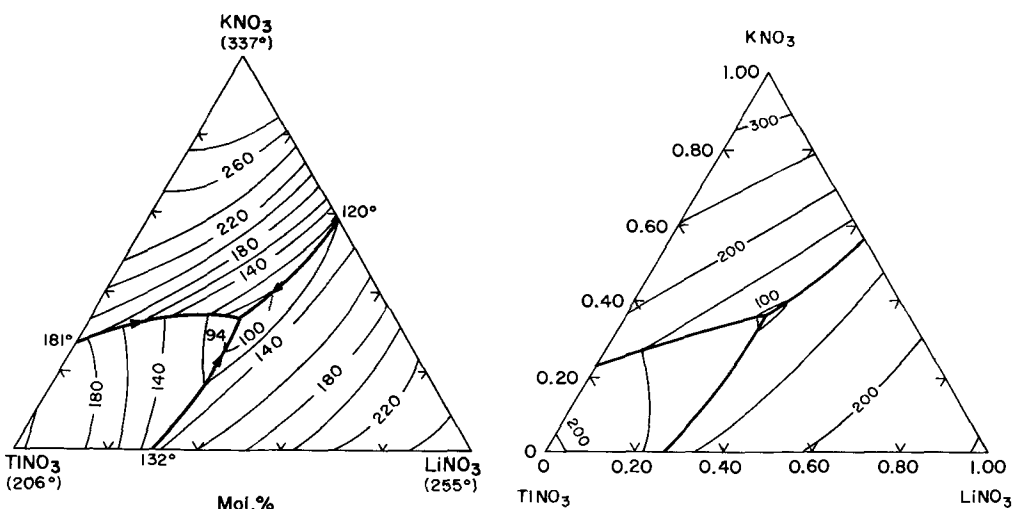


Fig. 4. Phase diagrams of the (Li,K,Tl)NO<sub>3</sub> system. a (left), Measured [Ref. (14)]; b (right), calculated.



therms (i.e., in Fig. 1, the 900 and 800 isotherms in the phase field of NaF and 750 isotherm in the phase field of KF, and in Fig. 5 the isotherms in the phase field of NaF) are within the experimental uncertainties and the limits of error in calculating the interaction coefficients.

Two ternary invariants are reported in the (Li,Na,Cs)F system (12) (Fig. 2a). For the binary LiF-CsF where the compound LiF · CsF exists, we have estimated a single hypothetical eutectic temperature by extrapolation from the phase fields of the pure components LiF and CsF. From the hypothetical eutectic temperature (lower by 32° than the experimental eutectic temperature) and from Eq. [20] and [21], the calculated value of  $\lambda_{ij}$  is in agreement with both the measured calorimetric data and the value

calculated using the dilute branches of the binary liquidus (Table II). The calculated phase diagram (Fig. 2b) accurately reproduces the measured phase diagram except in the small area subtended by the phase field of the compound LiF · CsF.

For ternary systems where solid solutions are known to exist as in the systems (Na,K,Cs)NO<sub>3</sub> (13), (Li,K,Tl)NO<sub>3</sub> (14), the calculated phase diagrams (Fig. 3b and 4b) are in good agreement with measurements (Fig. 3a and 4a). The same approximative procedure is used to calculate the interaction coefficients  $\lambda_{ij}$  and the eutectic compositions  $x_{ij}$  for the binaries NaNO<sub>3</sub>-KNO<sub>3</sub>, KNO<sub>3</sub>-TlNO<sub>3</sub>. The hypothetical eutectic temperatures are found to be about 20° lower than the lowest measured temperatures; this procedure allows us to obtain a better fit between calculated and mea-

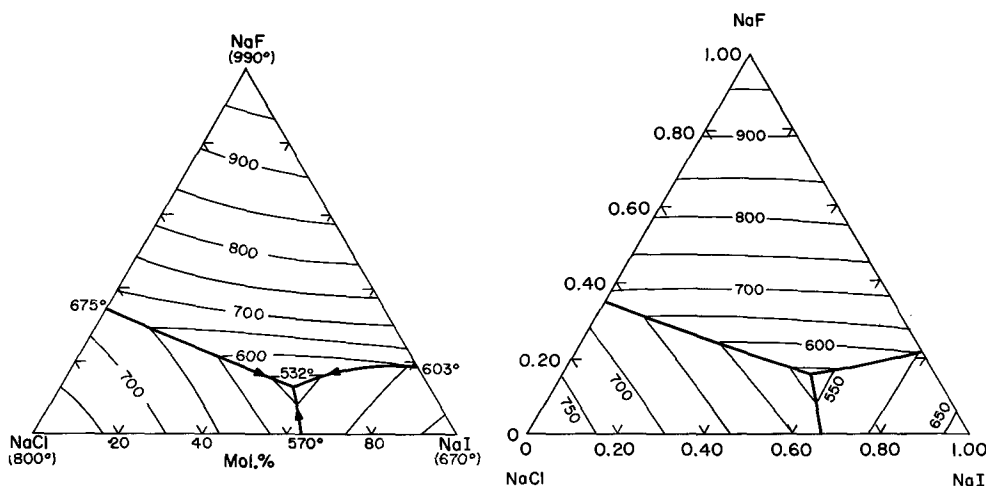


Fig. 5. Phase diagrams of the Na(F,Cl,I) system. a (left), Measured [Ref. (11)]; b (right), calculated.

sured interaction coefficients (Table II). Although the general topology is not affected by these approximations, some discrepancies result.

For example, because the hypothetical eutectic temperatures used for the binaries  $\text{NaNO}_3\text{-KNO}_3$  and  $\text{KNO}_3\text{-TiNO}_3$  is lower than the reported minimum temperatures, the phase fields of  $\text{NaNO}_3$  and  $\text{TiNO}_3$  occupy a slightly smaller area in Fig. 3b and 4b than in Fig. 3a and 4a, respectively. In addition, the calculated eutectic valley separating the phase fields of the pure components has a curvature different from the measurements; for example in Fig. 3 and 4 compare the curvature of the eutectic valley separating the phase fields of  $\text{CsNO}_3$  and  $\text{KNO}_3$  and of  $\text{KNO}_3$  and  $\text{TiNO}_3$ , respectively. Again, this difference results from the fact that solid solutions do form and are not taken into account in our calculations.

However, the correspondence between measurements and calculations is good in the region of the phase diagrams where solid solutions do not form and where Eq. [20]-[22] are rigorously applicable.

It should be pointed out that the magnitude of the binary interaction coefficients does not have a large effect on the applicability of the calculations. The calculated phase diagrams are consistent with measurements in ternary systems which have different values of the three binary interaction coefficients. The  $\lambda_{ij}$ 's are strongly negative for systems as  $(\text{Li,Na,K})\text{F}$ ,  $(\text{Li,Na,Cs})\text{F}$  and positive for the system  $\text{Na}(\text{F,Cl,I})$ .

Finally, the phase diagrams of three other systems (15, 16, 11),  $(\text{Li,Na,Cs})\text{NO}_3$ ,  $(\text{Li,Na,Rb})\text{F}$ , and  $\text{K}(\text{F,Cl,I})$ , were also calculated. We do not report them here since they do not have any special significance.

### Conclusion

The prediction of the liquidus temperatures of ternary systems from the phase diagrams of the subsidiary binaries using the equations given in this paper is good. An empirical approximation may be successfully used for slightly more complex cases where solid solutions or intermediate compounds exist; the correspondence between the calculations and the experiments can be improved if solid solutions or intermediate compounds are taken into account. It must finally be emphasized that the results of this present study are promising since the prediction *a priori* of ternary liquidus temperatures is possible without ternary experimental data; modifications, such as including higher order terms, have to be considered in order to study a broader range of systems.

### Acknowledgments

We are indebted to Dr. M. Blander of Argonne National Laboratory for stimulating comments. One of the

authors (M.-L.S.) expresses her appreciation to the C.N.R.S. of Lebanon for their support.

Manuscript submitted Jan. 2, 1974; revised manuscript received April 8, 1974.

Any discussion of this paper will appear in a Discussion Section to be published in the June 1975 JOURNAL. All discussions for the June 1975 Discussion Section should be submitted by Feb. 1, 1975.

The publication costs of this article have been assisted by the University of Provence, Marseille, France.

### REFERENCES

1. M. Blander and S. J. Yosim, *J. Chem. Phys.*, **39**, 2610 (1963).
2. M. Blander, and L. E. Topol, *Inorg. Chem., U.S.A.*, **10**, 1641 (1966); M. L. Saboungi and M. Blander, *High Temp. Sci.*, **6**, 37 (1974).
3. C. E. Johnson and M. S. Foster, *This Journal*, **116**, 1612 (1969); C. E. Johnson, R. Sridhar, and E. Cairns, In preparation.
4. M. L. Saboungi, H. Schnyders, M. Foster, and M. Blander, *J. Phys. Chem.*, **78**, 11 (1974).
5. K. Hagemark, *ibid.*, **72**, 527 (1968); P. J. Spencer, F. H. Hayes, and O. Kubaschewski, *Rev. Chim. Min.*, **9**, 13 (1972).
6. M. L. Saboungi, C. Vallet, and Y. Doucet, *J. Phys. Chem.*, **77**, 1699 (1973).
7. H. Reiss, J. Katz, and O. J. Kleppa, *ibid.*, **36**, 144 (1962).
8. M. Blander, "Advances in Chemical Physics," Vol. XI, p. 83, Interscience Publishers, New York (1967).
9. J. Lumsden, "Thermodynamics of Molten Salt Mixtures," p. 96, Academic Press, New York (1966).
10. M. Blander and K. Hagemark, *Nucl. Metall.*, **15**, 579 (1969); Conf. 690801 Clearinghouse for Federal Scientific and Technical Information, N.B.S. U. S. Dept. of Commerce, Springfield, Virginia 22151.
11. N. K. Voskresenskaya, "Handbook of Solid-Liquid Equilibria in Systems of Anhydrous Inorganic Salts," Vol. I and II, *Isdatel'stvo Akademicheskikh Nauk SSSR, Moskva-Leningrad* (1961); E. M. Levin, C. R. Robbins, and H. F. McMurdie, "Phase Diagrams for Ceramists," American Ceramic Society, Inc., Columbus, Ohio (1969).
12. G. A. Bukhalova and D. V. Sementsova, *Zh. Neorgan. Khim.*, **10**, 1880 (1965). English translation: *Russ. J. Inorg. Chem.*, 1025 (1965).
13. G. G. Diogenov and I. F. Sarapulova, *Zh. Neorgan. Khim.*, **10**, 1937 (1965). English translation: *Russ. J. Inorg. Chem.*, 1055 (1965).
14. P. I. Pratsenko and K. K. Shelotov, *Zh. Obshch. Khim.*, **23**, 9 (1953).
15. G. G. Diogenov and I. F. Sarapulova, *Zh. Neorgan. Khim.*, **10**, 1932 (1965). English translation: *Russ. J. Inorg. Chem.*, 1052 (1965).
16. E. P. Dergunov, *D.A.N. SSSR*, **58**, 1369 (1947); C. J. Barton, L. M. Bratcher, J. P. Blakely, and W. R. Grimes, in "Phase Diagrams of Nuclear Reactor Materials," R. E. Thoma, Editor, ORNL-2548 (1959).

# Surface-Catalyzed Anodes for Hydrazine Fuel Cells

## I. Preparation of the Substrate

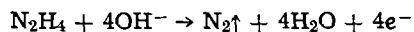
S. G. Meibuhr\*

Electrochemistry Department, Research Laboratories, General Motors Corporation, Warren, Michigan 48090

### ABSTRACT

Surface-catalyzed anodes for the electrochemical oxidation of  $N_2H_4$  were prepared by first codepositing a porous layer of Mond Ni powder with Ni on an electroformed Ni sheet substrate and then catalyzing by chemically precipitating nickel boride into the porous Ni layer. The parameters associated with the codeposition step were studied for their effect on (i) the structure and texture of the resultant deposit, and (ii) the electrochemical performance of the subsequently catalyzed electrode. Scanning electron micrographs were made after the Mond Ni was codeposited. The catalyzed electrodes were operated at  $2 \text{ kA/m}^2$  ( $200 \text{ mA/cm}^2$ ) and the anode vs. reference potential was monitored. The most influential parameters was the total number of coulombs used during the codeposition process. When 1200 coulombs on  $48 \text{ cm}^2$  were exceeded, the rough texture of the Mond Ni was destroyed and the  $Ni_2B$  catalyst was quickly shed during the electrochemical test.

Numerous catalysts have been examined for their activity toward the electrochemical oxidation of hydrazine (1-3). The over-all anodic reaction is described by



The most widely used catalysts have included Ru metal (3), Pd metal (3-7), and the borides of Ni and Co (8-10). Open-circuit potentials of about  $-1.10V$  (referred to the Hg/HgO reference electrode) were achieved with the best catalysts. The best catalysts also gave anodes that polarized less than 80 mV at the highest density of  $1 \text{ kA/m}^2$  ( $100 \text{ mA/cm}^2$ ). However, there have been few published data on the performance of hydrazine anode catalysts operating at current densities greater than  $1 \text{ kA/m}^2$ , nor have there been many data on the performance of surface catalyzed, nonporous substrates when used as hydrazine anodes (11).

Early work at the laboratories showed that hydrazine anodes yielding  $1.5 \text{ kA/m}^2$  at an  $iR$ -free potential of  $-0.95V$  could be prepared by using surface-catalyzed, nonporous substrates. These anodes were prepared by chemically depositing nickel boride ( $Ni_2B$ ) onto a nonporous substrate. However, because of the  $N_2$  gas evolution during the anodic oxidation of hydrazine, the  $Ni_2B$  catalyst quickly shed from the substrate in all instances except one (12). This latter substrate was prepared by codepositing<sup>1</sup> Mond 255 Ni powder<sup>2</sup> (13) with electroplated Ni onto an electroformed, scrobiculated Ni sheet. This paper describes the optimized preparation of this substrate.

### Experimental

The steps involved in the preparation of surface catalyzed, nonporous electrodes for hydrazine fuel cells were: (i) electroform the Ni sheet; (ii) codeposit the Mond Ni powder with Ni; (iii) catalyze with  $Ni_2B$ .

**Electroformation of the sheets.**—Scrobiculated Ni sheets ( $0.05 \text{ mm}$  thick) were electroformed on a Cr-plated stainless steel mandrel from an 18 liter Ni sulfamate/chloride bath. The geometric area of the scrobiculated portion was  $48 \text{ cm}^2$ . The nominal bath composition and the operating conditions for the electroforming process are listed in Table I, column A. Two types of scrobiculated sheets were made. Initially, a dimpled design was utilized; however, in the latter

stages of this work, a corrugated design was used to better meet the engineering requirements of the project. No differences resulted from this design change.

**Codeposition of the Mond powder.**—The codeposition of Mond Ni powder with Ni was performed in the three-piece plastic half-box cell shown in Fig. 1. The top section fitted inside the middle section which was bolted to the base to hold in position the electroformed Ni sheet. The steps in the codeposition process were:

1. Separate the electroformed scrobiculated Ni sheet from the mandrel.
2. Position the Ni sheet on the base and bolt the middle piece to the base forming the half-box cell.
3. Add the 500 ml of sulfamate/chloride Ni plating solution maintained at  $50^\circ C$ .
4. Position the top section of the cell so that the counterelectrode (Ni anode) is located 62 mm from the Ni sheet (cathode). This distance is fixed by the cell design.
5. Position the stirrer above the anode.
6. Add 0.5g of Mond powder, turn on the stirrer, and apply current to the cell for the appropriate time to codeposit the Mond Ni powder with the electrodeposited Ni on the scrobiculated portion of the Ni sheet (see Fig. 2). Turn off the stirrer after an appropriate time.

The exact procedure in step 6 was varied so that the following codeposition parameters could be studied: speed of the impeller (1,000-10,000 rpm measured under no-load), duration of stirring (0.5-10 min), solution pH, plating time, cell voltage and current, bath composition, and particle size of Mond powder. A high-stress Ni-plating bath was also used in one ex-

Table I. Nickel plating bath composition and plating conditions

	A	B
	Concentration ( $\text{kg/m}^3$ )	Concentration ( $\text{kg/m}^3$ )
Nickel sulfamate	300	—
Nickel chloride	6	300
Boric acid	30	38
pH	3.5-4.2	3.4
Temperature	$45^\circ \pm 5^\circ C$	$45^\circ \pm 5^\circ C$
Anti pitting agent*	**	
Current density	$500 \text{ A/m}^2$	$500 \text{ A/m}^2$
Plating time	$\sim 1 \text{ hr}$	$\sim 1 \text{ hr}$

\* Electrochemical Society Active Member.

Key words: nickel-boride, hydrazine, catalyst, Mond Ni.

<sup>1</sup> The term "codeposition" refers to a process in which inert or conductive powders are included into an electrodeposition metal.

<sup>2</sup> International Nickel Company.

\* SNAP, Sulfamate Nickel Anti Pitting Agent, proprietary compound from Barrett Chemical Products Division of Allied Research Products Incorporated.

\*\* Sufficient to maintain a film in a  $0.076 \text{ m}$  diameter ring.

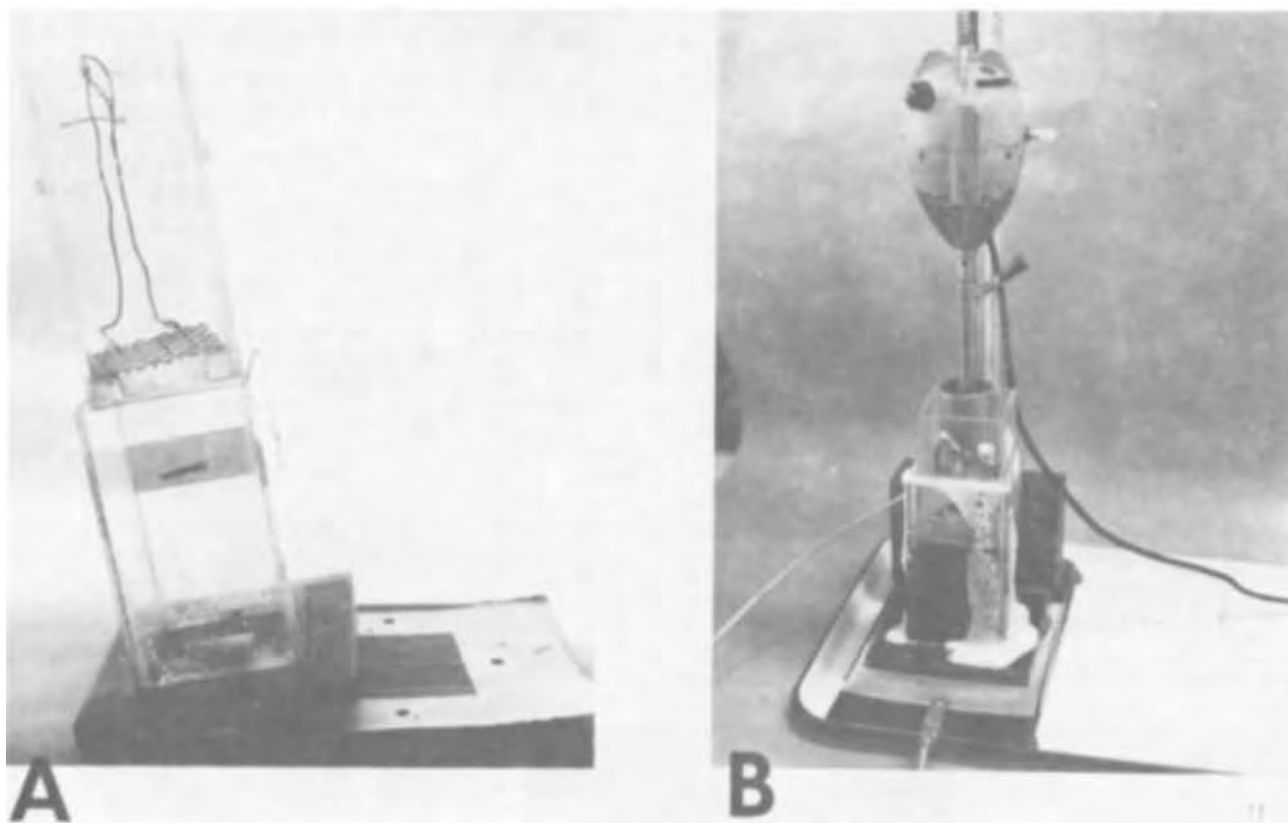


Fig. 1A. The half-box cell showing various components. B. The half-box cell during the codeposition process

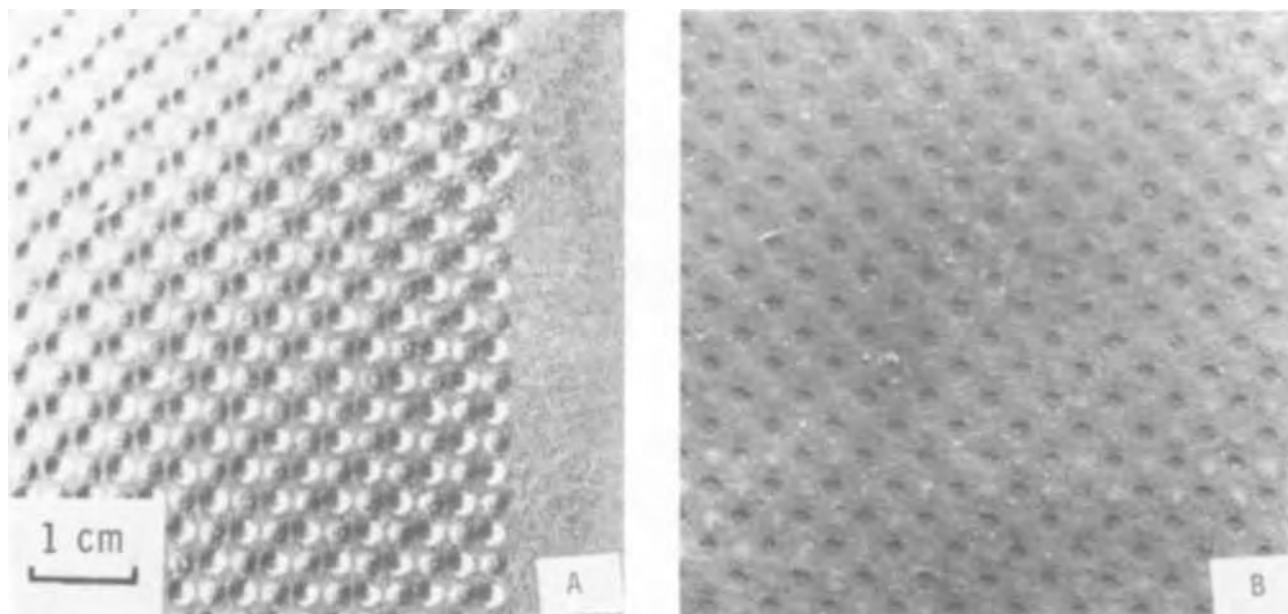


Fig. 2. Dimpled surfaces of the electroformed sheet. A, Before the codeposition of Mond Ni powder; B, the Mond surfaces. Both are at 1.4X magnification.

periment to codeposit the Mond powder. The composition of this bath is also given in Table I, column B (14).

Duplicate substrates were made at each experimental condition. One substrate was chemically catalyzed with  $\text{Ni}_2\text{B}$  and was tested as an anode in a hydrazine half-cell. The other substrate was cut to yield samples for use in the scanning electron microscope (SEM); cross section and top view samples were taken for each substrate, both before and after chemical catalyzation. Consequently, both microscopic and elec-

trochemical data were taken on substrates for every experimental condition of the codeposition process.

*Chemical catalyzation.*—Approximately  $3 \text{ mg/cm}^2$  of  $\text{Ni}_2\text{B}$  catalyst was chemically deposited onto the substrate surface by thrice alternately dipping the substrate into a 5% nickel acetate solution and a 10%  $\text{NaBH}_4$  solution, just long enough for the initial, violent reaction to subside. Excess solution was drained from the electrode before it was inserted into the other solution. The substrates were positioned hori-

zontally in these solutions. The electrodes were tested immediately after a final rinse.

**Electrochemical test procedure.**—The catalyzed anodes (48 cm<sup>2</sup> active area) were operated in 5.7M (33%) KOH containing 1M (3.2%) N<sub>2</sub>H<sub>4</sub> at a constant current density of 2 kA/m<sup>2</sup> for about 2 hr before the initial resistance-free polarization data were taken. The electrolyte temperature was 31°±1°C; the electrolyte flow rate was about 16 times stoichiometric for a current density of 2 kA/m<sup>2</sup>. Subsequent polarization data were taken regularly and the anode was operated at 2 kA/m<sup>2</sup> between polarization runs.

### Results

**Scanning electron micrographs.**—As a frame of reference, the SEM micrographs are displayed in Fig. 3 for the two Mond Ni powders used in this study: Mond 255 and Mond 128. These photos confirm the particle sizes to be approximately 3 and 8 μm (13) for the 255 and 128 powders, respectively.

The effect of varying the stirring impeller speed from 1,000 to 10,000 rpm on the codeposition of Mond 255 powder from the sulfamate/chloride Ni bath is seen in Fig. 4. The top row of micrographs is at 10,000X magnification and the bottom row is at 5,000X. Figure 4 (A-D) correspond to 1,000, 4,000, 7,100, and 10,000 rpm, respectively. As these micrographs show, there is little effect of stirring impeller speed on the

surface structure and texture of these substrates. Hence, substrates were subsequently prepared at 7100 rpm.

The effect of stirring time (0.5-10 min) during codeposition demonstrated that whereas there was no obvious difference in the surface texture as seen by the SEM, there was a difference in the structure as seen by the unaided eye. The stirring time that gave reproducibly the most uniform substrate was 1 min. Consequently, the preparation of substrates was standardized using an impeller speed of 7100 rpm to stir the bath for only the first minute of the total 10 min during which current flowed.

Although the SEM micrographs presented in Fig. 4 represent substrates prepared by codeposition from a bath at pH=4, they also could represent substrates codeposited from a bath of pH=2. No differences were evident in the surface texture, nor in the subsequent electrochemical performance of catalyzed substrates. Consequently, the pH value of the codeposition bath was maintained in the range of 2.8-4.

Variation in the length of the plating time (at 2A) produced striking changes in the appearance of the substrate. These micrographs are displayed in Fig. 5 where (A-E) represent plating times of 30, 20, 10, 5, and 2 min, respectively (3600, 2400, 1200, 600, and 240 coulombs). It is evident that at plating times of only 5 min, there is some loss in surface area (compare

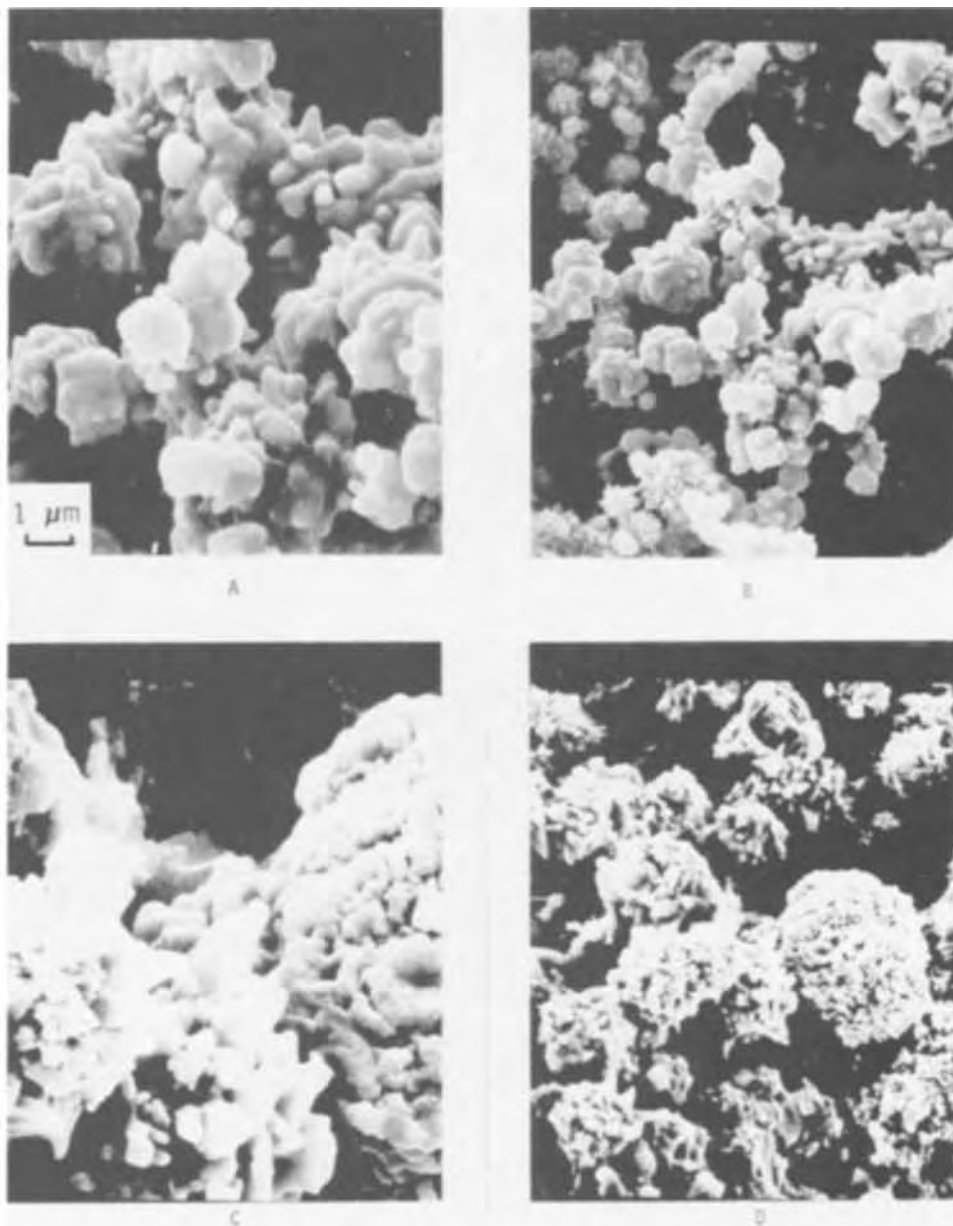


Fig. 3. Mond Ni powder. A, M255 at 10,000X magnification; B, M255 at 5000X magnification; C, M128 at 10,000X magnification; D, M128 at 3000X magnification.

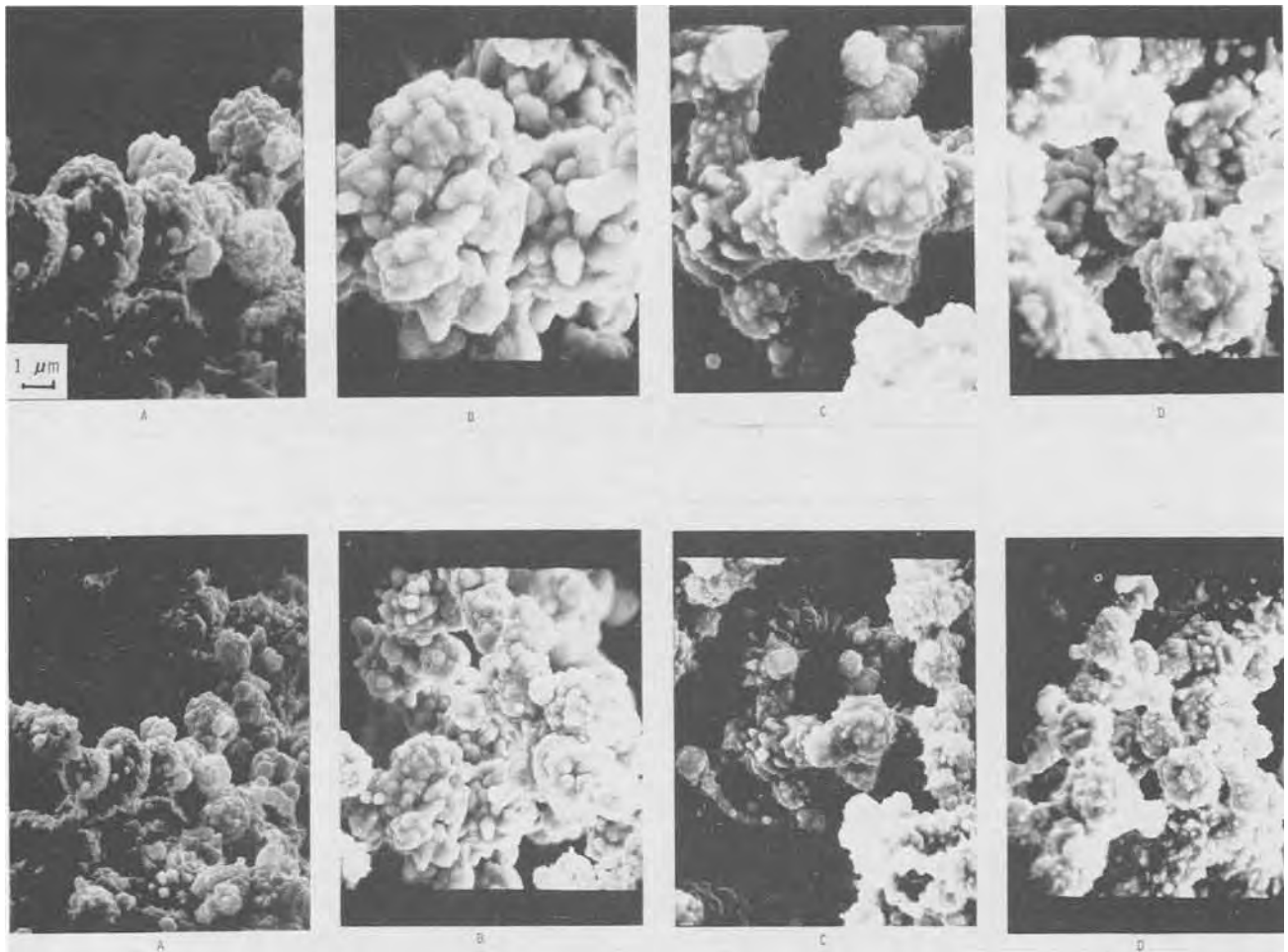


Fig. 4. The effect of stirring speed during the codeposition of Mond 255 powder. A, 1000 rpm; B, 4000 rpm; C, 7100 rpm; D, 10,000 rpm. Magnification: top row, 10,000X; bottom row, 5000X.

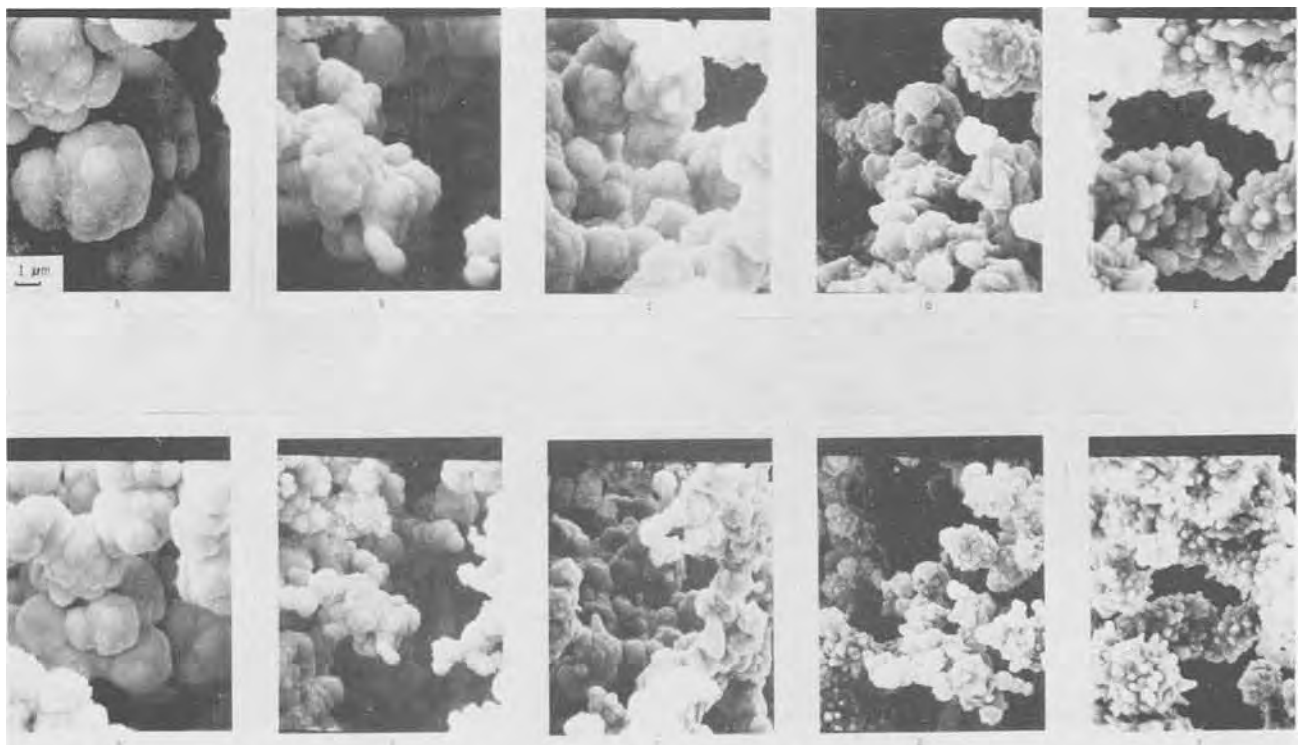


Fig. 5. The effect of plating during the codeposition of Mond 255 powder. A, 30 min; B, 20 min; C, 10 min; D, 5 min; E, 2 min. Magnification: top row, 10,000X; bottom row, 5000X.



with Fig. 3). However, the electrochemical performance of the subsequently catalyzed substrates did not show the earlier problem of shedding until the plating time exceeded 10 min. The micrographs (A) and (B) of Fig. 5 clearly demonstrate the significant loss in surface area; fuel cell anodes prepared from these two substrates showed the original problem of catalyst shedding after only 1-2 hr under current load. In contrast, the shedding problem was absent with anodes prepared using plating times of 10 min or less at 2A.

Parts D and E of Fig. 5 show a surface texture that is very desirable as a substrate for the anode catalyst. The texture is rough, and the true surface area appears to approach that of the powder. However, in Fig. 5E, the plating time of only 2 min was used, and there was only 3 min allowed for the preparation: 1 min stirring and 2 min plating. Under these conditions, there is insufficient time to permit the Mond powder to settle. These latter two substrates have poor coverage and distribution of the Mond powder. Because these times, as represented by Fig. 5D and E, are too short to permit adequate disposition of the powder, some modification to these two preparation methods may yield better coverage and distribution, and still produce a substrate with a surface texture as represented by Fig. 5D and E. Two possibilities are immediately evident.

1. Adjust the current to a lower value so that the total number of coulombs does not exceed that represented by Fig. 5C (1200 coulombs). Continue the plating throughout the total preparation time. Under these conditions (1A for 20 min = 1200 coulombs), a substrate was produced that had uniform coverage of the Mond powder. The SEM micrographs for this substrate are shown in Fig. 6A and B at 5,000X and 10,000X magnification, respectively. The resultant surface texture approximates that represented by Fig. 5D (2A for 5 min). These SEM micrographs indicate that the substrate of Fig. 6 should yield an anode that would not shed its catalyst, although no electrochemical test was performed. No further work with this codeposition condition (1A for 20 min) was performed because it

was desirable to minimize the time involved in the codeposition process and no significant improvement resulted over that achieved by using the standard procedure.

2. Maintain the present standard current value (2A) but adjust the plating sequence to include a settling time, for example, 1 min stirring, 8 min settling (no stirring and no plating), 2 min plating (total coulombs = 240) or 10 min plating (total coulombs = 1200). Using the condition of only 2 min plating time, the resultant substrate was neither uniformly nor densely covered with the Mond powder. A large portion of the powder remained suspended in solution. The micrograph of this sample showed a rough surface texture similar to that shown in Fig. 5E. This substrate was unsuitable for testing because of the sparse, nonuniform coverage by the Mond powder. Using the condition of 10 min plating time, however, the resultant substrate was uniformly and densely covered with the Mond powder. The SEM micrograph taken from this sample showed a surface texture similar to that shown in Fig. 5C. Although the surface texture was considered to be good, no further testing of this modification was employed, because no improvement was achieved over that obtained by using the standard procedure of 1 min stirring, and no current followed by 10 min plating at 2A with no stirring.

All of the previously described substrates were prepared from the low-stress sulfamate/chloride Ni plating bath. The Mond 255 powder was also codeposited at standard conditions from a high-stress, Ni plating bath whose composition is given in Table I. The resultant surface texture was similar to that shown in Fig. 5C and D. Hence, no further work was performed using this bath.

In two separate codeposition experiments with Mond 255, the interelectrode distance was increased from 62 to 140 mm. In one experiment, the cell voltage was maintained at the usual value of 6V; the resulting current was only 0.8A. In the other experiment, the current was maintained at the usual value of 2A; the

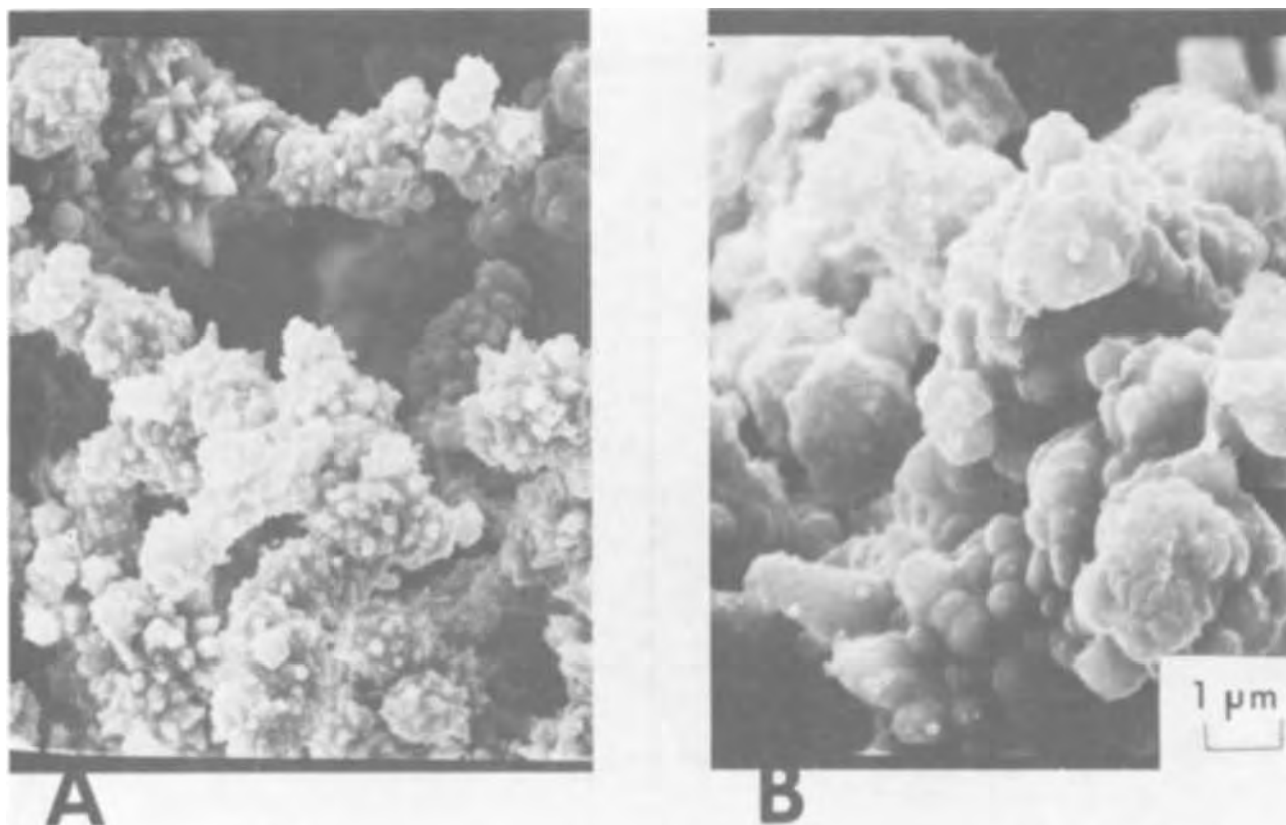


Fig. 6. The effect of a lower current (1A, 20 min) during codeposition of Mond 255 powder



resulting voltage was about 10V. In neither case was the rough surface texture altered significantly from the standard shown in Fig. 5. However, in the former of these two experiments, the resultant substrate was poorly covered with the Mond powder. No further work was performed using either of these procedures.

**Heating the codeposited Mond substrate.**—The prime function of the codeposited Ni is to act as "glue" to bond the Mond Ni to the substrate without destroying the rough surface texture required for the adhesion of a catalyst. This electrochemical preparation method is superior to a thermal diffusion bonding method. For example, when the codeposited Ni powder was heated at 800°C (a temperature commonly used to anneal Ni) for 2 hr in a reducing atmosphere, the original rough surface texture was destroyed. The micrograph of Fig. 7 shows this loss in texture. When this substrate was catalyzed and tested as an hydrazine anode, the Ni<sub>2</sub>B catalyst quickly shed.

In a separate experiment, a sample of the codeposited Mond Ni substrate was mounted in the hot-stage of a SEM and the temperature was increased. Figure 8A shows the Mond surface unchanged at temperatures to 400°C; Fig. 8B shows the surface at temperatures above 600°C up to about 1000°C. An important area to note is area 1, consisting of a chain of 6 or 7 spheres. In Fig. 8B, the spheres have fused and are no longer distinct. Note also the area marked 2. The rough surface texture evident in Fig. 8A has been destroyed by heating. It is clearly evident that the Mond 255 Ni substrate begins to lose its desirable characteristic surface features at some temperature between 400° and 600°C.

**Polarization data.**—Electrodes prepared from substrates for which more than 1200 coulombs (at 2A) were used during the codeposition process resulted in the catalyst being shed from the substrate even before the initial polarization data could be taken. The black catalyst particles were observed floating in the KOH electrolyte. However, with electrodes prepared from substrates for which less than 1200 coulombs (at 2A)

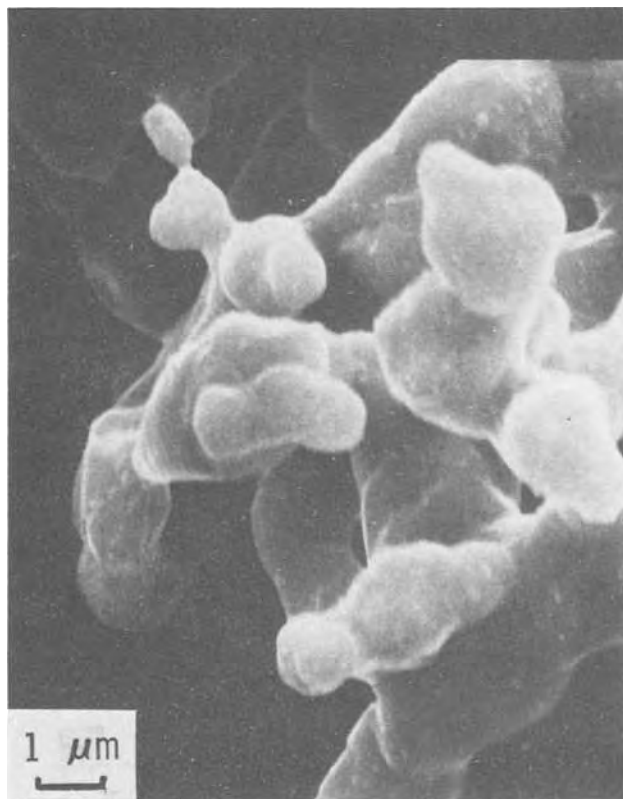


Fig. 7. A codeposited Mond 255 substrate heat-treated at 800°C for 2 hr. (10,000X).

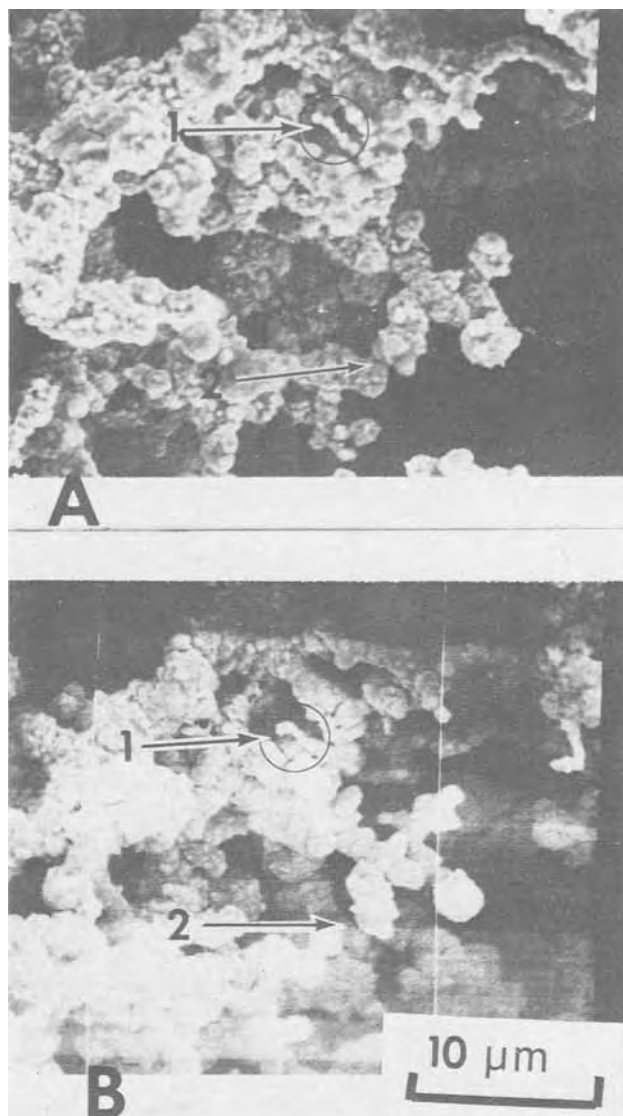


Fig. 8. Effect of heating on the surface texture of a codeposited Mond Ni surface. Magnification, 3000X. A, Temperature up to 400°C; B, temperature from 600°-1000°C.

were used to codeposit the Mond 255 powder, no shedding of the catalyst was evident. Typical initial polarization data for these latter electrodes are given in Fig. 9. Duplicate runs, while not giving exactly the same potential values, did fall within the shaded area. The use of Mond 128 Ni powder yielded substrates which when catalyzed gave anodes that had polarization data represented by the same curve. There was no detectable difference in polarization.

### Discussion

Although inclusion plating (the incorporation of metallic or nonmetallic particles into an electrodeposit) is well documented (15-18), this is the first known application of this approach to the formation of fuel cell electrodes. The usual applications of electrodeposited composite coatings (ECC) obtained by inclusion plating involve improving some characteristic of the electroplate itself, such as wear resistance, frictional behavior, or electrical contacts. In each instance, the value of the desirable property of the ECC begins to decrease when the included portion of the coating increases to about 40 weight per cent (w/o). For the fuel cell application, the desirable property of surface roughness begins to decrease when the included portion of the coating (the Mond Ni powder) drops below about 60 w/o. This value corresponds to the 10 min plating time at 2A (Fig. 5C). The amount

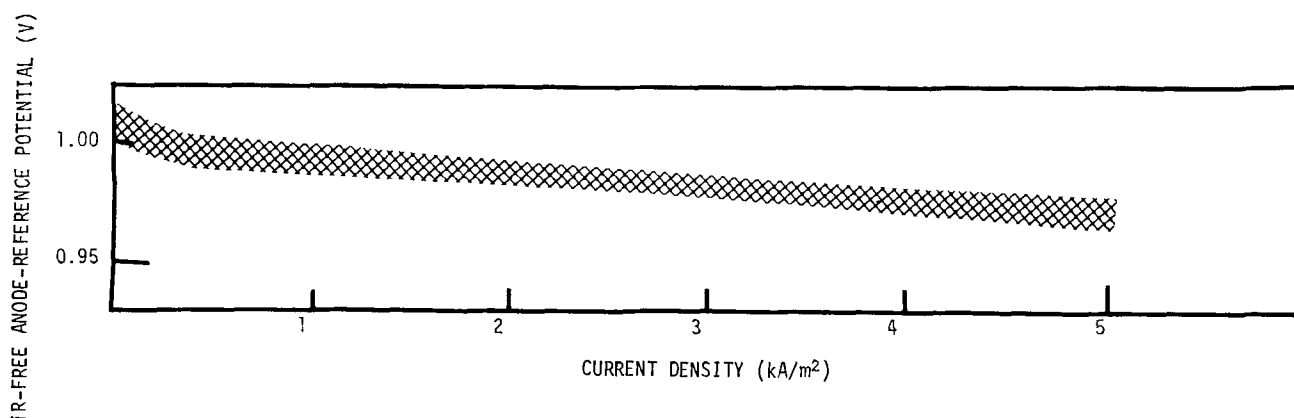


Fig. 9. Current density-*i*R free potential data at operating time ( $\Delta t$ ), 2 hr

of Mond Ni can approach 87 w/o (Fig. 5E) and still yield a suitable substrate, although this latter substrate is sparsely coated with the Mond powder and as such is less desirable than a substrate that is more densely coated.

In general, the results of this study showed that there were two parameters that affected the quality of codeposited Mond Ni powder and the subsequent electrochemical performance of the catalyzed-codeposited surface: (i) the duration of stirring, and (ii) the number of coulombs used in the codeposition process, although this parameter is not unequivocal because of limited data at different plating currents.

If stirring continued beyond about 10% of the time for codeposition, the resultant substrate was nonuniformly and sparsely coated with the Mond powder. The extended stirring was sufficient to maintain the powder in suspension. When a substrate had both nonuniform and sparse distribution of Mond, there was insufficient amount of the powder to retain the Ni<sub>2</sub>B catalyst. If the number of coulombs exceeded 1200/48 cm<sup>2</sup>, corresponding to 10 min plating time at 2A, the resultant Mond surface texture was too smooth to provide enough adhesion sites for the catalyst. However, catalyst shedding during the oxidation of hydrazine would probably not be a problem if there were no phase change involved in the electrochemical reaction.

#### Acknowledgments

The author is grateful to Mr. E. J. Zeitner, Jr. and Mr. M. E. Wheatley of this department who jointly designed the half-box cell used to codeposit the Ni powder; to Mr. R. L. Adams of this department for making the SEM micrographs; to Mr. R. F. Paluch of this department for performing the electrochemical portions of this work; and to Mr. T. Schreiber of the Analytical Chemical Department for operating the SEM during the hot-stage experiments.

Manuscript submitted Nov. 30, 1973; revised manuscript received June 3, 1974.

Any discussion of this paper will appear in a Discussion Section to be published in the June 1975 JOURNAL.

All discussions for the June 1975 Discussion Section should be submitted by Feb. 1, 1975.

The publication costs of this article have been assisted by the General Motors Corporation.

#### REFERENCES

1. S. Akhtar, C. T. Grein, and D. Beinstock, *U.S. Bur. Mines, Bull.* 652 (1970).
2. M. B. Clark and K. V. Kordesch, Final Report AD 693846, Union Carbide Co., Parma, Ohio (Sept. 1969).
3. L. G. Austin, "Fuel Cells—A Review," pp. 261-274, NASA (1967).
4. M. I. Gillibrand and E. R. Lomax, in "Proceedings 3rd International Symposium on Batteries, Bournemouth 1962," D. H. Collins, Editor, p. 221, Pergamon Press, Oxford (1963).
5. S. S. Tomter and A. P. Antony, *Chem. Engineering Handbook, "Fuel Cells,"* p. 22, American Institute of Chemical Engineers, New York (1963).
6. P. Terry, J. Gallegher, R. Salathe, and J. O. Smith, in "Proc. 20th Ann. Power Sources Conf.," p. 39, Atlantic City, N. J. (1966).
7. J. Perry, in "Proc. 22nd Ann. Power Sources Conf.," p. 10, Atlantic City, N. J. (1968).
8. R. Jasinski, *Electrochem. Technol.*, **3**, 129 (1965).
9. K. V. N. Rao, Papers 258 and 258A presented at Electrochemical Society Meeting, New York, New York, May 4-9, 1969.
10. J. Perry, in "Proc. 21st Ann. Power Sources Conf.," p. 16, Atlantic City, N. J. (1967).
11. B. Warszawski, Alstom Report (Oct. 1968).
12. E. J. Zeitner, M. E. Wheatley, R. R. Witherspoon, and S. G. Meibuhr, U.S. Pat. 3,772,086 (Nov. 13, 1973).
13. V. A. Tracey and N. J. Williams, *Electrochem. Technol.*, **3**, 3 (1965).
14. "Modern Electroplating," F. A. Lowenheim, Editor, pp. 282-283, John Wiley and Sons, Inc., New York (1963).
15. R. V. Williams, *Electroplating Metal Finishing*, **19**, 92 (March 1966).
16. E. C. Kedward, *ibid.*, **25**, 20 (Sept. 1972).
17. M. Viswanathan and K. S. G. Doss, *Metal Finishing*, **70**, 83 (Feb. 1972).
18. R. Bazzard and P. J. Boden, *Trans. Inst. Metal Finishing*, **50**, 63 (1972).

# Anodic Behavior of Aluminum Straining and a Mechanism for Pitting

S. B. de Wexler and J. R. Galvele

Comision Nacional de Energia Atomica, Departamento de Metalurgia, Buenos Aires, Argentina

## ABSTRACT

The anodic behavior of pure aluminum during straining at a constant potential in various electrolytes was studied. In sodium sulfate solutions, up to 1.84V, and both in sodium chloride solutions and in sodium nitrate solutions below the pitting potential, the exposure of bare metal to the solution leads to repassivation. At potentials higher than the pitting potential, pitting localization depends on the rate of pitting nucleation. Under conditions of fast pitting nucleation generalized pitting was observed, while under conditions of slow pitting, pits nucleated preferentially on the slip lines and might eventually have led to transgranular stress corrosion cracking. Pitting is the result of localized acidification on the metal-solution interphase due to metal dissolution and hydrolysis of the metal ions. To maintain such acidification, compensation for the loss of protons by hydrogen evolution and by diffusion to the bulk of the solution is necessary. Such compensation will occur if the electrode potential of the metal is higher than its corrosion potential in the locally acidified solution. No pitting will propagate at or below that corrosion potential, which is, for aluminum in chloride solutions,  $-0.64V$ .

The study of anodic behavior of straining metals has been widely applied to the investigation of the mechanism for stress corrosion cracking (SCC) (1-4). In the present work, the same technique has been used to study the mechanism for the pitting of aluminum. It was found that the exposure of bare metal to a solution, at a potential lower than the pitting potential, leads to the repassivation of the metal. It is only at potentials higher than the pitting potential that the reaction changes from repassivation to anodic dissolution. The change in behavior is correlated to the type of anodic and cathodic reactions occurring on the bare metal.

The above results have also been used to propose a mechanism for transgranular SCC initiation. In many cases the SCC of a metal starts at the pitting potential (5). The reason for this correlation is clear for high strength steels (5, 6) and for aluminum alloys (5), but it is not so in cases where transgranular SCC is observed as is the case with stainless steels in hot chloride solutions.

## Experimental

The straining experiments were made with aluminum wires. "Analar" 99.9% aluminum wires, 0.6 mm diameter, and "Leico" 99.999% aluminum wires, 1 mm, diameter, were used. The specimens were about 10 cm long. The wires were previously annealed for 20 min at 400°C in an argon atmosphere, and water quenched. Before the straining experiments the wires were electropolished in a solution of Butilcellosolve, 10% HClO<sub>4</sub>, at 0°C and 25V. The cell used for the straining experiments was described in a previous publication (5).

Static experiments were performed on 99.99% aluminum coupons of 10 × 30 mm. The heat-treatment of these specimens was the same as for the wires. The edges and the surface of the specimens were covered with a cured-epoxy resin, leaving an uncovered area of about 1 cm<sup>2</sup>. These specimens were electropolished in the same way as the wires.

The solutions were prepared with analytical grade reagents and were deaerated with purified N<sub>2</sub> (7). A saturated calomel reference electrode was used for the experiments in NaCl solutions, and a mercurous sulfate reference electrode in NaNO<sub>3</sub> and in Na<sub>2</sub>SO<sub>4</sub> solutions. All the potentials are reported on the normal

hydrogen electrode (NHE) scale. The straining experiments were done at room temperature (20° ± 2°C) and at constant potentials, the current changes were recorded during the experiments.

Polarization of aluminum specimens was controlled by a Tacussel PRT 20-2X potentiostat, and the potential was measured with a Tacussel Aries 10000 electronic millivoltmeter. The current was recorded on a Tacussel EPL2 multirange recorder.

The straining of the wires was done with a motor-driven Hounsfield Tensometer at constant rate of cross head displacement, using initial strain rates of 1.6, 5, 21, and 90%/min. Before straining the wires, they were prestressed below the yield stress and kept at a desired passive potential until a constant current was attained. For the experiments at higher than the pitting potential the specimens were kept for 10 min at a constant potential below the pitting potential, and switched to the working potential simultaneously with the straining machine.

## Results

*Straining aluminum in neutral 1.0 NaCl solution.*—The anodic current was observed to increase significantly when 99.9% aluminum was strained in 1.0M NaCl solution at a constant potential. As soon as the plastic deformation of the wire started, the current began to increase but attained a steady-state value after about 5% elongation. Over a wide range of potentials the steady-state current density observed during deformation was independent of the potential but varied with the strain rate. Figure 1 shows typical results obtained with wires yielding at a constant strain rate of 90%/min with potentials ranging from  $-0.80$  to  $-0.56V$ . The mean value of the steady-state current density observed at this strain rate was  $2.5 (\pm 0.5) \times 10^{-5}$  A/cm<sup>2</sup>. Wide scattering of the steady-state current density was found in experiments at  $-0.53V$  (Fig. 2). The current density measured at this potential was  $5 (\pm 2) \times 10^{-5}$  A/cm<sup>2</sup>. At potentials higher than  $-0.53V$  the steady-state current density became potential dependent, and a potential increase of 20 mV produced a 100 times increase in the current density. The potential at which steady-state current density became potential dependent was the same for all the strain rates tested, and was equal (8) to the pitting potential of aluminum in the test solution (Fig. 3).

Below the pitting potential, the steady-state current density during straining depended on the strain rate

**Key words:** aluminum, straining metal, pitting, transgranular SCC, chloride solutions, nitrate solutions, pitting potential.

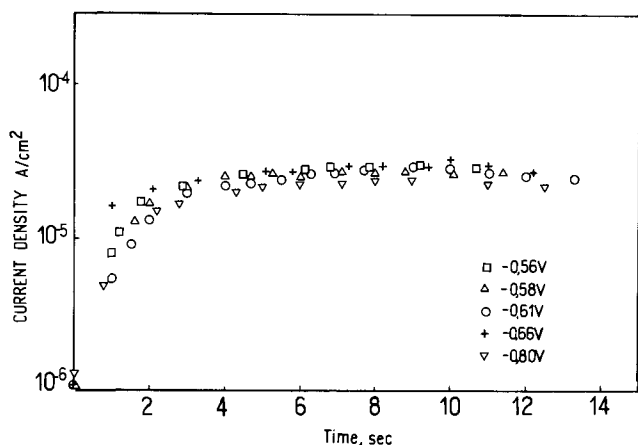


Fig. 1. Potentiostatic current density/time curves at various potentials for aluminum straining at 90%/min in 1M NaCl solution.

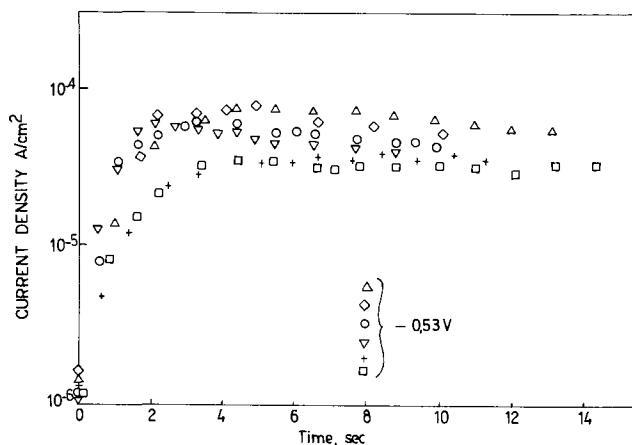


Fig. 2. Potentiostatic current density/time curves near the pitting potential for aluminum straining at 90%/min in 1M NaCl solution.

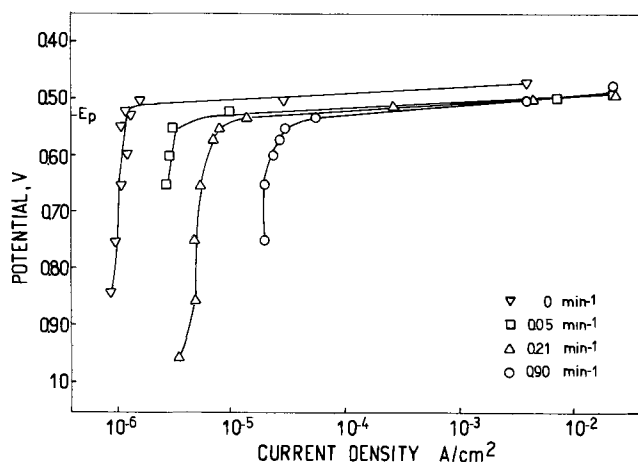


Fig. 3. Steady-state current densities for aluminum during straining in 1M NaCl solution at different potentials and at different strain rates.

(Fig. 4). Above the pitting potential this current was practically independent of the strain rate (Fig. 3).

At potentials lower than the pitting potential, interruption of straining caused a drop in the current density which after a couple of seconds reached the value observed before straining. At the pitting potential and above, interruption of straining also caused a drop in the current, but the drop was less severe than in the previous case. At potentials 100 mV higher than the

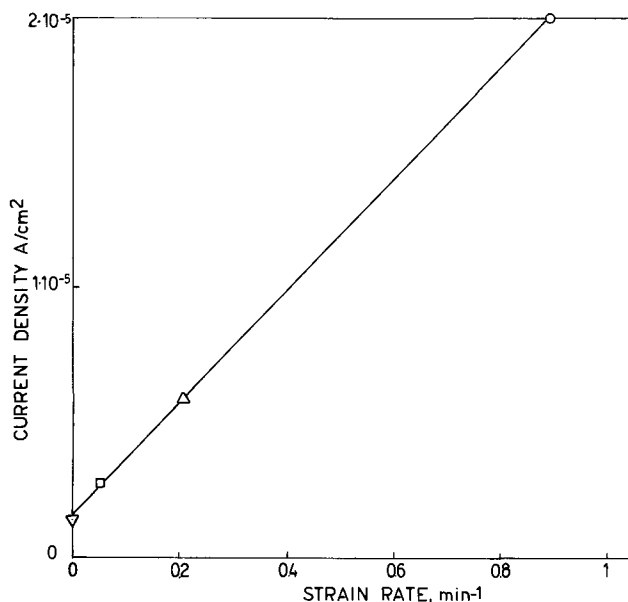


Fig. 4. Relation between steady-state current density and strain rate for aluminum straining in 1M NaCl solution.

pitting potential no current drop was observed after interruption of straining.

After the tests all the wires were examined under both an optical and a scanning electron microscope. No evidence of corrosion was observed on wires strained below the pitting potential. On the other hand, extensive pitting was found on wires which were potentiostated above the pitting potential. The density of the pitting observed was much higher than usually observed on nonstrained or static specimens, but the pits were smaller. Pitting on aluminum in NaCl solutions is known to nucleate very easily without showing any induction time (8). The straining of the metal does not introduce any change in the type of attack except that it offers more sites for pit nucleation, leading to higher density of pits.

*Straining aluminum in neutral 0.5M Na<sub>2</sub>SO<sub>4</sub> solution.*—Figure 5 shows the typical results of the anodic behavior of straining 99.9% aluminum in 0.5M Na<sub>2</sub>SO<sub>4</sub> solution. Up to a potential of above 0.9V the steady-state current density was independent of the potential and of the same order of magnitude as that found during straining in 1M NaCl solution below the pitting potential (Fig. 1). At higher potentials a slight potential dependence was observed probably due to

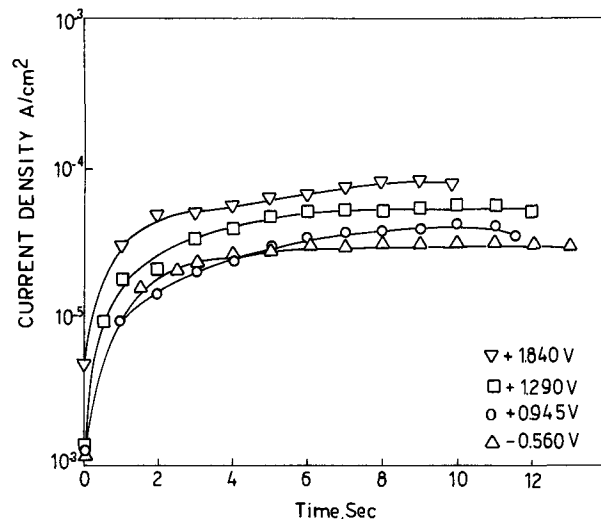


Fig. 5. Potentiostatic current density/time curves at various potentials for aluminum straining at 90%/min in 0.5M Na<sub>2</sub>SO<sub>4</sub> solution.

oxygen evolution on the bare metal. The strained wires did not show any sign of corrosion, and no passivity breakdown was detected at potentials up to 1.84V.

**Straining aluminum in 0.9M Na<sub>2</sub>SO<sub>4</sub> plus 0.1M NaCl solution.**—The anodic behavior of 99.9% aluminum during straining at constant potentials was studied in a mixture containing 0.9M Na<sub>2</sub>SO<sub>4</sub> plus 0.1M NaCl. The results were similar to those found in 1M NaCl solution, with a potential independent region and a potential dependent region. The transition potential, -0.35V, coincided with the pitting potential reported for aluminum in the same solution (9).

**Straining aluminum in 1.0M NaNO<sub>3</sub> solution.**—The anodic behavior during straining at a constant potential in deaerated 1.0M NaNO<sub>3</sub> solution was studied with 99.9% aluminum and 99.999% aluminum wires. Similar results were obtained with both grades of purity.

Below the pitting potential of aluminum in nitrates,  $E_p = 1.70V$ , the current density after about 5% elongation reached a steady-state value, as found in the previous solutions (Fig. 6). The values of current density, however, are slightly higher than those found in chloride or in sulfate solutions. The steady-state current density was also observed to be slightly dependent on the applied potential. No traces of corrosion were to be found on the strained wires below the pitting potential. Interruption of straining at those potentials caused a rapid drop in the current, which in a couple of seconds reached the same value observed before straining.

When aluminum was strained in nitrate solutions, at potentials higher than 1.70V, the current did not reach a steady value, but kept increasing all through the experiment. The rate of current increase was a function of the potential, and it became higher as the potential increased. No pitting was observed on the strained metal up to potentials 100 mV higher than the pitting potential, provided that the exposure time was not too long. However white corrosion products covering the slip lines could be observed under a microscope.

As described in a recent paper (5), the rate of current increase for aluminum straining in nitrate solu-

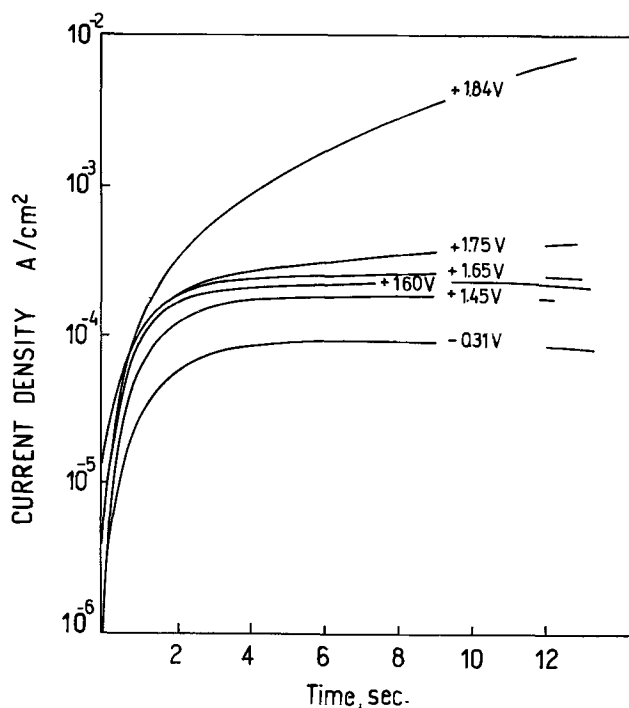


Fig. 6. Potentiostatic current density/time curves at various potentials for aluminum straining at 90%/min in 1M NaNO<sub>3</sub> solution.

tions at potentials higher than the pitting potential followed a square root law (Fig. 7). It was then explained that such a law was the result of pitting nucleation on the slip lines. Recent electron microscopy done in our laboratory confirmed that semicylindrical channels are formed on the slip lines under conditions of the square root law behavior (10).

The rates of current increase for static aluminum and for straining aluminum in nitrate solutions at constant potential are shown in Fig. 8 and 9. It was ob-

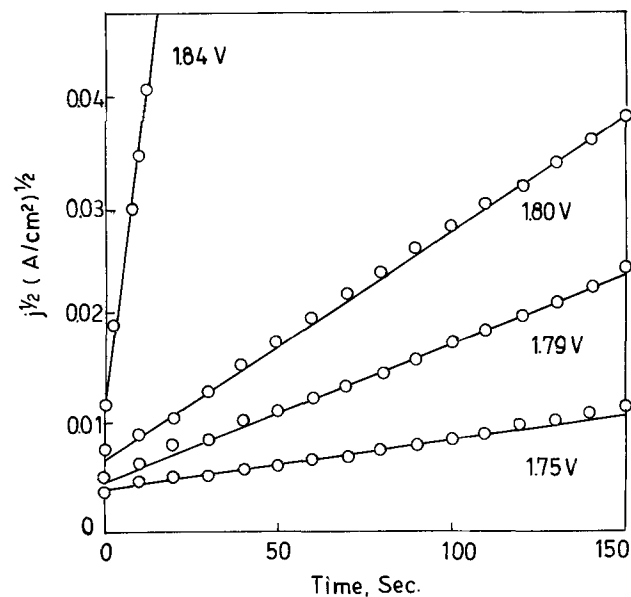


Fig. 7. Potentiostatic current density/time curves for aluminum straining at 1.6%/min in 1M NaNO<sub>3</sub> solution at potentials higher than the pitting potential.

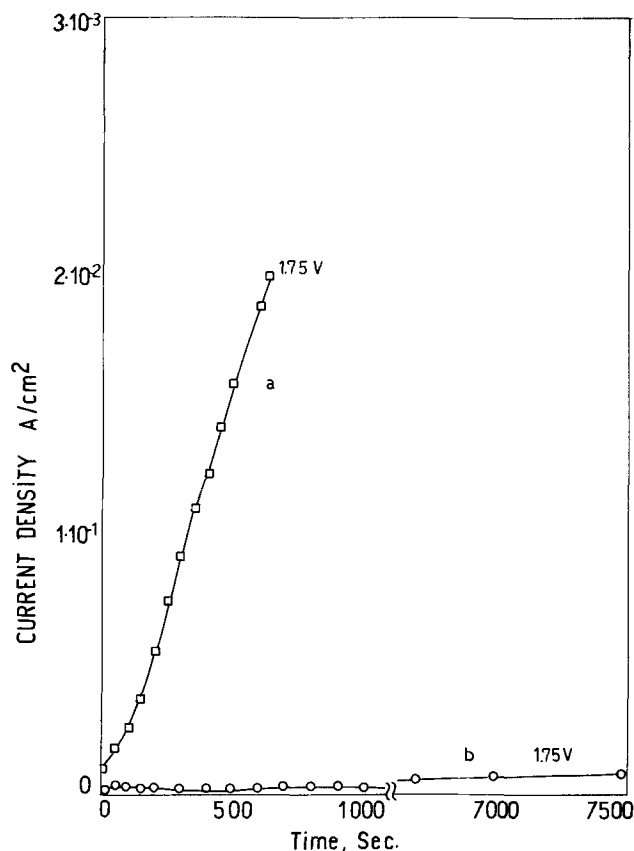


Fig. 8. Potentiostatic current density/time curves for aluminum in 1M NaNO<sub>3</sub> solution at a potential 50 mV higher than the pitting potential. a, Specimen straining at 1.6%/min; b, static specimen.

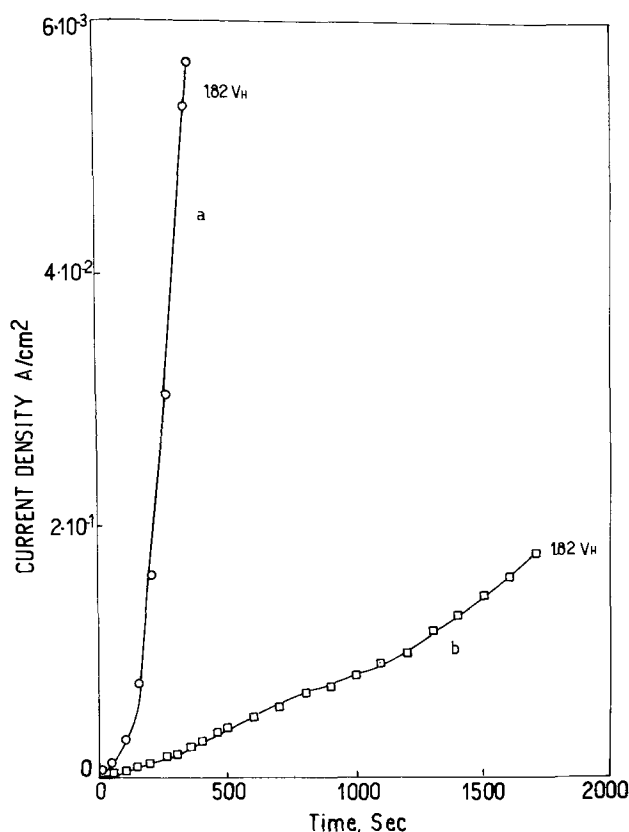


Fig. 9. Potentiostatic current density/time curves for aluminum in 1M  $\text{NaNO}_3$  solution at a potential 120 mV higher than the pitting potential. a, Specimen straining at 1.6%/min; b, static specimen.

served that there was a great difference between the anodic behavior of the static metal and that of the straining metal. A slow strain rate of 1.6%/min was used to minimize the contribution of the repassivation process, as described above (Fig. 4). The straining metal showed a much faster current increase than the static metal. The difference in behavior was more pronounced at potentials slightly higher than the pitting potential. At 1.75V the current density for the static metal, after an exposure of several hours, is only a small fraction of that obtained after a few minutes of straining. The rate of current rise for the static metal increased with the potential, and at 1.82V the current density for the static metal became significant. If the current density for the static metal corresponds to hemispherical pitting, and that for the straining metal to the corrosion on slip lines, assuming that both processes do not interfere with each other, Fig. 8 shows that compared to corrosion at slip steps, very little pitting should be expected on the metal at fracture time. On the other hand, at 1.82V, the strained metal should have corrosion on slip lines and also hemispherical pits on the surface at fracture time (Fig. 9).

### Discussion

**Mechanism of the pitting of aluminum.**—After a comparison of the several mechanisms proposed for the pitting initiation on aluminum, the most conflicting point appears to be the role assigned to the oxide film. In one line of thought, supported mainly by Pryor *et al.* (11-16), it is considered that a very important step for pit initiation is the contamination of the oxide film by chloride ions. This contamination increases the conductivity of the oxide film leading to enhanced localized dissolution (pitting). While these authors do not elaborate on the effect of the potential, Hoar *et al.* (17, 18) suggest that the migration of the chloride ions should start at the pitting potential. On the other hand, Wood and Richardson (19, 20), taking into consideration observations with the scan-

ning electron microscope, suggest that the oxide film acts mainly as an inert barrier, with no effect on the mechanism of pitting. According to them the pits will start in flaws always present in the oxide film. The existence of such flaws has been questioned by Pryor (15, 16).

The straining method, as used in the present work, avoids discussion of the existence of flaws in the oxide film, since these flaws are continually produced during straining. Before straining, the aluminum wire carries an air-formed oxide film of the order of 30Å (15). The plastic deformation of the aluminum produces slip displacements of the order of 600Å (21). As the aluminum oxide film is very fragile (22) in deformation the film breaks easily, and the bare metal is exposed to the solution.

In the potentiostatic straining experiments it was observed that there is a range of potentials at which the anodic behavior of aluminum is independent of the electrolyte used. The current density observed during straining in  $\text{Na}_2\text{SO}_4$  solution (Fig. 5) was similar to that found below the pitting potential in NaCl solution (Fig. 1) and in a mixture of aqueous NaCl plus  $\text{Na}_2\text{SO}_4$  solution. Similar values were obtained by Bubar and Vermilyea (22) for straining aluminum at -0.06V in ammonium borate solutions. The similarity of anodic behavior in the different electrolytes, as well as the absence of any sign of corrosion on the slip steps, suggest that the exposure of bare metal to a NaCl solution, below the pitting potential, leads to the reformation of an oxide film as the only reaction. The linear relation between the steady-state current density and the strain rate, in Fig. 4, as expected from the straining of passive metals (4), confirms this supposition. These results suggest that if there are flaws in the oxide film below the pitting potential, they will not last long, since the bare metal will quickly repassivate.

The straining experiments show that the behavior of aluminum in NaCl solution is similar to that in a  $\text{NaNO}_3$  solution. In both cases repassivation occurs below the pitting potential, and the attack of the metal starts only at the pitting potential. In the case of nitrates, because of its large size, it is doubtful whether the nitrate ion could migrate through the aluminum oxide film. The migration of chloride ions in the aluminum oxide film, as found by Pryor, could produce weak points in the film which would account for the ease at which the pitting in NaCl solutions starts.

As for the changes in behavior observed at the pitting potential, they are visualized as follows. When an oxide-free metal is exposed to the solution a rapid dissolution of the metal will occur



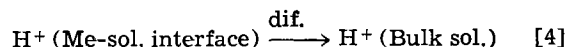
In solutions of weak acid salts, like ammonium borate, the solubility point of the aluminum hydroxide will be quickly exceeded, and it will precipitate on the bare metal inhibiting further dissolution.

In the presence of a strong acid salt, like NaCl, a localized acidification will occur as the result of hydrolysis of the metal salt, which allows further dissolution



The existence of local acidity will be favored if the rate of metal dissolution is increased.

Two other important processes occurring in the acidified zone will be hydrogen evolution and proton diffusion to the bulk of the solution

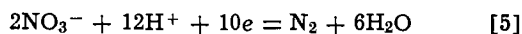


These two processes will oppose the existence of the localized acidity. The rate of metal dissolution, and hence acidity production, has to be high enough to

compensate the loss of protons by diffusion and by reaction.

Reactions [1] plus [3] will give aluminum a certain corrosion potential, or mixed potential. If the potentiostatically controlled potential of the specimen is higher than the corrosion potential of the metal in the acidified solution, the anodic dissolution of the metal will lead to localized corrosion, reactions [1] plus [2]. On the other hand, if the potential of the specimen is maintained below the corrosion potential the reaction of hydrogen evolution, reaction [3], will predominate. In addition there will be no localized acidity, and the oxide film will precipitate on the bare metal. According to this, the pitting potential of aluminum in sodium chloride solutions should be higher than the corrosion potential of aluminum in  $\text{AlCl}_3$  solutions, so that reactions [1] and [2] might maintain the localized acidity in spite of [3] and [4]. The corrosion potential of aluminum in saturated  $\text{AlCl}_3$  solutions was found to be  $-0.640\text{V}$  (23), and the pitting potential in 1M NaCl solution was reported as  $-0.530\text{V}$  (8). The same relation between corrosion potentials and pitting potentials was found for several aluminum binary alloys (24).

The high pitting potential of aluminum in nitrate solutions is attributed to the interference by a cathodic reaction with the localized acidification process, i.e., reduction of the nitrate ions. Gas evolution was observed during the pitting of aluminum in sodium nitrate solutions. Analysis by explosion showed that this gas was neither hydrogen nor oxygen. Preliminary results of gas chromatography suggested that the main component of this gas was nitrogen. Such a cathodic reaction will produce a high consumption of protons, thus preventing the formation of localized acidity



In this case the anodic reaction will predominate only at potentials at which the nitrate reduction becomes negligible. According to Pourbaix diagrams (25), in an acidic solution the nitrate ion will become stable at potentials higher than 1.0-1.2V. It is only at such high potentials that the current density during straining in nitrate solutions becomes potential dependent (Fig. 6) indicating an increasing contribution of the anodic reaction.

Basically the pitting mechanism described above is similar to the "autocatalytic" process for localized corrosion proposed by Edeleanu and Evans in 1950 (26). The main difference is that these authors did not make any reference to the electrode potential. In the present work an explanation for the existence of a pitting potential is given.

*Anodic behavior of straining metals.*—The above-described results show that the anodic behavior of a straining metal varies substantially with the composition of the media and with the electrode potential. The differences in behavior can be classified into three different categories: (i) repassivation of the metal, (ii) fast pitting nucleation, and (iii) slow pitting nucleation. When repassivation of the metal is the dominant reaction, straining will have little effect on the anodic behavior of the metal. An increase in the anodic current density will be observed as a result of the rupture and reformation of the oxide film, but no localized corrosion will be detected. This is the case for aluminum in sodium sulfate solutions from  $-0.56$  to  $+1.8\text{V}$ , in ammonium borate solutions at  $-0.06\text{V}$  (22), or at potentials lower than the pitting potential in solutions containing NaCl or  $\text{NaNO}_3$ . This type of behavior was also observed by Muratta and Staehle for nickel in sulfuric acid solutions (4).

The second type of behavior corresponds to those cases where pitting nucleation occurs very easily. In such cases the straining of the metal will have little effect on the anodic attack, and pitting will be observed over the whole surface on the metal. An example of this behavior is that of aluminum in NaCl solutions above

pitting potential as observed in the present work. Another example of this behavior is the one reported by Muratta and Staehle for stainless steel in KCl plus  $\text{H}_2\text{SO}_4$  solutions at potentials much higher than the pitting potential. This type of behavior is also observed when straining aluminum in nitrate solutions at potentials much higher than the pitting potential.

The third type of behavior corresponds to the conditions of difficult pitting nucleation. In the present work it was found that aluminum in nitrates, at potentials slightly higher than the pitting potential, is one of those cases. Another very well-known instance of difficult pitting nucleation is stainless steel in chloride solutions. This case is well documented in the literature and leads to different pitting potentials under different conditions of measurement (27-29). In these cases straining produces a high increase in the current density. The oxide film acts as an inert barrier, but anodic dissolution on the bare metal exposed at slip steps leads to pitting. When the metal is strained at the pitting potential, pitting will start at the slip steps thus creating conditions that will eventually lead to transgranular SCC initiation.

### Acknowledgments

We thank the Programa Multinacional de Metalurgia (Programa Regional de Desarrollo Científico y Técnico-O.A.S.) and the Consejo Nacional de Investigaciones Científicas y Técnicas of Argentina for partial financial support.

Manuscript submitted Nov. 27, 1973; revised manuscript received May 20, 1974.

Any discussion of this paper will appear in a Discussion Section to be published in the June 1975 JOURNAL. All discussions for the June 1975 Discussion Section should be submitted by Feb. 1, 1975.

### REFERENCES

1. T. P. Hoar and J. C. Scully, *This Journal*, **111**, 348 (1964).
2. T. P. Hoar and J. R. Galvele, *Corrosion Sci.*, **10**, 211 (1970).
3. J. J. Podesta, G. P. Rothwell, and T. P. Hoar, *ibid.*, **11**, 241 (1971).
4. T. Murata, Ph.D. Dissertation, The Ohio State University (1971).
5. J. R. Galvele, S. M. de De Micheli, I. L. Muller, S. B. de Wexler, and I. L. Alanis, "U. R. Evans International Conference on Localized Corrosion," Williamsburg, Virginia, (Dec. 1971).
6. J. R. Galvele and C. J. Semino, *Anais do II Simposio Sul-Americano de Corrosao Metalica*, IBP, ABRACO, Rio de Janeiro 1971, p. 275.
7. D. Gilroy and J. Mayne, *J. Appl. Chem.*, **12**, 382 (1962).
8. J. R. Galvele and S. M. de De Micheli, *Corrosion Sci.*, **10**, 795 (1970).
9. S. M. de De Micheli and J. R. Galvele, *Metallurgia*, **27**, 589 (1971).
10. I. Maier and J. R. Galvele, In press.
11. J. J. McMuller and M. J. Pryor, "Proc. 1st Int. Congr. Metall. Corrosion," p. 52, Butterworths, London (1961).
12. M. A. Heine and M. J. Pryor, *This Journal*, **110**, 1205 (1963).
13. M. A. Heine, D. S. Keir, and M. J. Pryor, *ibid.*, **112**, 24 (1965).
14. M. A. Heine and M. J. Pryor, *ibid.*, **114**, 1001 (1967).
15. M. J. Pryor, *Corrosion Sci.*, **11**, 463 (1971).
16. M. J. Pryor, "U. R. Evans International Conference on Localized Corrosion," Williamsburg, Virginia, (Dec. 1971).
17. T. P. Hoar, D. C. Mears, and G. P. Rothwell, *Corrosion Sci.*, **5**, 279 (1965).
18. T. P. Hoar and R. Jacob, *Nature*, **216**, 1299 (1967).
19. J. A. Richardson and G. C. Wood, *Corrosion Sci.*, **10**, 313 (1970).
20. G. C. Wood and J. A. Richardson, "U. R. Evans International Conference on Localized Corrosion," Williamsburg, Virginia, (Dec. 1971).
21. G. Thomas and J. Nutting, *J. Inst. Metals*, **85**, 1 (1956-1957).
22. S. I. Bubar and D. A. Vermilyea, *This Journal*, **114**, 882 (1967).

23. S. M. de De Micheli and J. R. Galvele, In preparation.
24. I. L. Muller and J. R. Galvele, In preparation.
25. M. Pourbaix, "Atlas of Electrochemical Equilibria," p. 499, Pergamon Press, (1966).
26. C. Edeleanu and U. R. Evans, *Trans. Faraday Soc.*, **47**, 1121 (1951).
27. G. Hersleb and W. Schwenk, *Corrosion Sci.*, **9**, 615 (1969).
28. H. P. Leckie and H. H. Uhlig, *This Journal*, **113**, 1262 (1966).
29. N. Pessal and C. Liu, *Electrochim. Acta*, **16**, 1937 (1971).

## Electrodissolution Kinetics of Iron in Chloride Solutions

### V. Neutral Solutions Containing Benzotriazole

S. Asakura, C. C. Lu, and Ken Nobe\*

School of Engineering and Applied Science, University of California, Los Angeles, California 90024

#### ABSTRACT

The anodic transient and steady-state behavior of iron in neutral chloride solutions containing benzotriazole (BTA) was examined by a potential pulse technique. The results suggest the formation of a resistive film on iron at open circuit. The electrical resistance of the film ( $R_{sf}$ ) was dependent on the BTA concentration, and decreased with the duration of anodic polarization and the magnitude of the current. Where  $i_a$  is the anodic current at steady state,  $\log(R_{sf}i_a)$  varied linearly with the anodic potential with a slope of 80 mV/decade, and the plot was independent of the concentration of BTA. A porous film model is proposed to interpret the electrochemical behavior. The Bockris reaction mechanism is shown to be valid for both the anodic and cathodic reactions.

In a previous investigation (1), the mechanism of iron dissolution in neutral chloride solutions has been described. The present paper extends that work to determine the effect of benzotriazole (BTA) on the kinetics and mechanism of iron dissolution in neutral chloride solutions. Recent work (2, 3) has shown that BTA inhibits the rate of hydrogen evolution on iron in acidic solutions but does not change the mechanism. On the other hand, the effect of BTA on the mechanism of iron dissolution has not been examined, although it has been shown that BTA reduces the rate of anodic dissolution of iron in acidic solutions (3, 4).

#### Experimental

The solutions were prepared by adding the benzotriazole to 1N KCl. Two concentrations of BTA, 2.3 mM and 15.5 mM were used. Deaeration of the solution by prepurified nitrogen was performed for at least 4 hr before a run. The preparation of the iron electrodes has been described previously (1). Potentiostatic pulses were generated by combining a potentiostatic (1  $\mu$ sec rise time) with a pulse generator. The interval between pulses was always greater than 200 times the pulse duration. The temperature was maintained at  $25^\circ \pm 1^\circ$  C.

#### Results

**Anodic potential pulse polarization.**—The open-circuit potential,  $E_o$ , of inhibited iron was  $-660$  and  $-640$  mV vs. SCE for 2.3 and 15.5 millimolar (mM) BTA, respectively. For uninhibited iron,  $E_o = -780$  mV. The anodic potential pulse,  $\Delta E_a$ , was imposed at open circuit as shown schematically in Fig. 1. The pulse is imposed at  $t = 0$  and terminated at  $t = \tau$ . The current immediately after  $t = 0$  is expressed by  $i_{ap}$ , and the currents immediately before  $t = \tau$  and immediately after  $t = \tau$  are designated as  $i_{as}$  and  $i_{cp}$ , respectively. Figure 2 is a plot of  $i_{ap}$  vs.  $\Delta E_a$ . A linear relationship was obtained and the slope of the line changed with the concentration of BTA.

The current drop at the termination of the pulse,  $i_{as} + |i_{cp}|$ , is plotted against the pulse potential,  $\Delta E_a$ ,

in Fig. 3 and compared with the  $i_{ap}$  vs.  $\Delta E_a$  plot. When the magnitude of the potential pulse was small enough, the  $i_{ap}$  and  $(i_{as} + |i_{cp}|)$  plots were superimposed. However, as  $\Delta E_a$  increased, the plot of  $(i_{as} + |i_{cp}|)$  deviated from that of  $i_{ap}$ .

The current transients are analyzed utilizing the equivalent circuit shown in Fig. 4.  $C_{dl}$ ,  $R_r$ ,  $R_{sf}$ , and  $R_s$  represent the double layer capacitance, charge transfer resistance, the resistance due to the surface film, and the solution resistance, respectively.  $R_s$  is a constant and independent of the polarization current and polarization time. However,  $R_{sf}$  may change with polarization since the nature of the surface film may change during the electrode reaction. The parameters

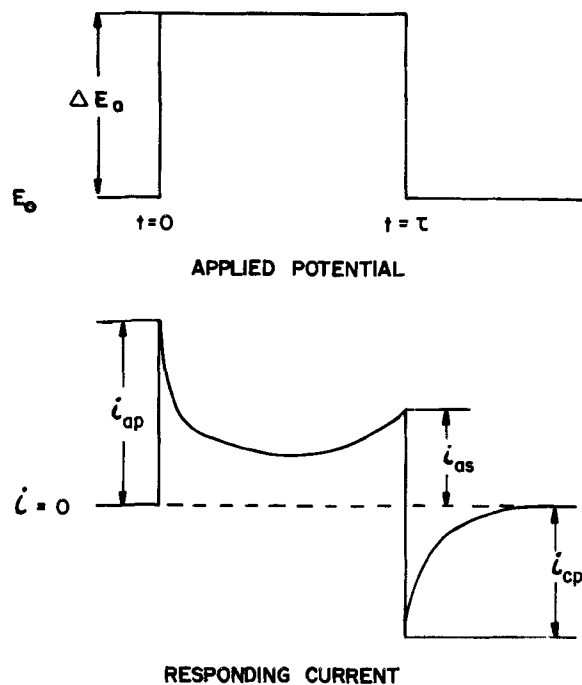


Fig. 1. Anodic potential pulse and the current transients

\* Electrochemical Society Active Member.

Key words: anodic dissolution, corrosion inhibition.



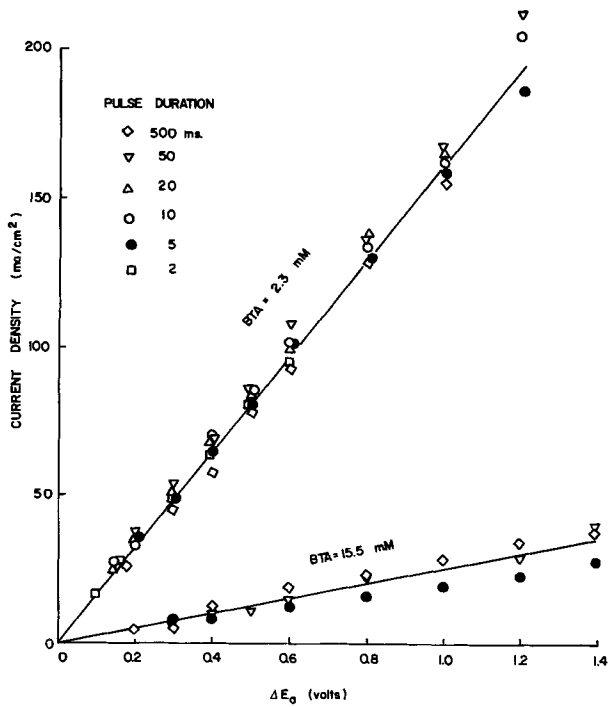


Fig. 2. Plot of  $i_{ap}$  vs.  $\Delta E_a$

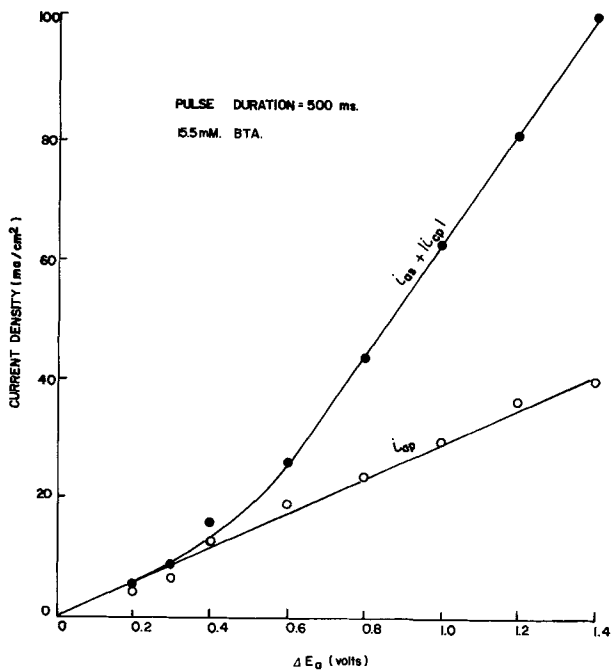


Fig. 3. Comparison of  $i_{ap}$  and  $i_{as} + |i_{cp}|$  plots vs.  $\Delta E_a$

shown in Fig. 4 can be obtained by the experimental procedures described (1).

During the potential pulse,  $\Delta E_a$  is equal to the sum of the potential difference,  $e_1$ , and ohmic potential drop,  $e_2$ , i.e.

$$\Delta E_a = e_1 + e_2, \quad 0 < t < \tau \quad [1]$$

Immediately after the potential pulse is initiated,  $e_1$  is zero due to the double layer capacitance. Thus

$$(e_2)_{t=0+} = \Delta E_a \quad [2]$$

Consequently

$$R_s + R_{sf,0} = \Delta E_a / i_{ap} \quad [3]$$

where  $R_{sf,0}$  is the surface film resistance at open circuit. The slopes of the lines in Fig. 2 are equal to  $1/[R_s + R_{sf,0}]$  according to Eq. [3]. This means that the film resistance at open circuit was dependent on

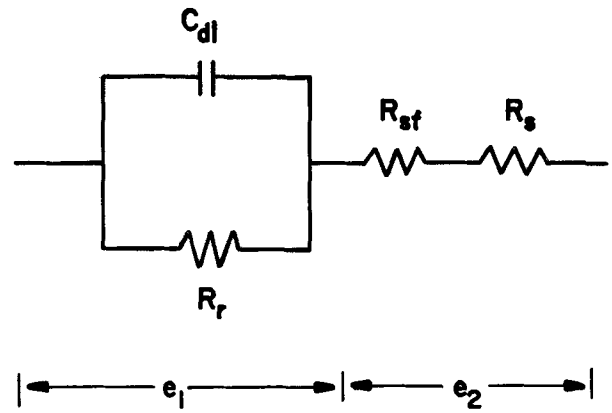


Fig. 4. Equivalent electrical circuit for the electrode system

the concentration of BTA. The solution resistance,  $R_s$ , was determined by applying the same procedure to the system without BTA. If it is assumed that the addition of BTA did not change the solution conductivity,  $R_{sf,0}$  can be calculated by subtracting  $R_s$  from  $[R_s + R_{sf,0}]$ . The surface resistance at open circuit,  $R_{sf,0}$ , was about 40 and 1.0 ohm-cm<sup>2</sup> for 15.5 and 2.3 mM BTA, respectively, and was independent of the anodic pulse duration as shown in Fig. 5. These results indicate that the surface returned to the initial open-circuit condition before the next pulse was imposed. Since significant differences in  $R_{sf,0}$  with concentration of BTA were observed, it seems reasonable that the resistive surface film was formed at the open circuit by the reaction of iron with BTA.

Immediately before the pulse is terminated, the potential drop across the double layer is  $(e_1)_{t=\tau-}$ . Thus

$$(e_1)_{t=\tau-} = \phi_a - E_0 \quad [4]$$

where  $\phi_a$  is the electrode potential during the potential pulse. Also

$$(e_2)_{t=\tau-} = i_{as}[R_s + R_{sf,\tau}] \quad [5]$$

Immediately after the current is terminated

$$(e_1)_{t=\tau+} + (e_2)_{t=\tau+} = 0 \quad [6]$$

and

$$(e_2)_{t=\tau+} = [R_s + R_{sf,\tau}] i_{cp} \quad [7]$$

At this instant, the potential difference across the double layer is given by Eq. [4] since

$$(e_1)_{t=\tau+} = (e_1)_{t=\tau-} \quad [8]$$

By combining Eq. [1], [5], [6], [7], and [8]

$$R_s + R_{sf,\tau} = \Delta E_a / (i_{as} + |i_{cp}|) \quad [9]$$

The film resistance at  $t = \tau$ ,  $R_{sf,\tau}$ , can be determined from Eq. [9] and  $R_s$  which was obtained experimentally as described above. A comparison of Eq. [3]

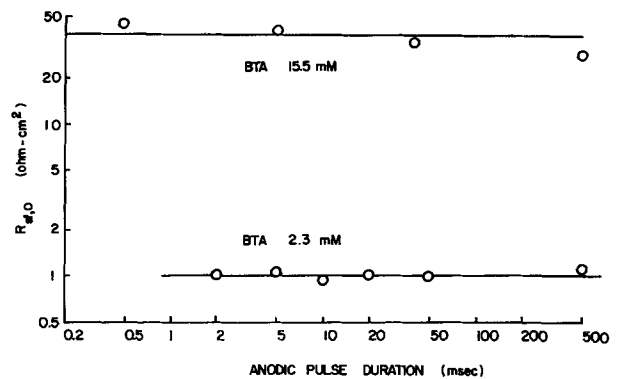


Fig. 5. Surface film resistance,  $R_{sf,0}$ , vs. the anodic pulse duration.

and [9] indicates that the deviation between the lines in Fig. 3 is due to the difference in the film resistance. These results show that the surface state of iron in neutral chloride solutions containing benzotriazole changed with pulse anodic polarization for the larger  $\Delta E_a$  values. Furthermore, Fig. 6 shows that  $R_{sf,\tau}$  increased and approached  $R_{sf,0}$  as  $i_{as}$  and the pulse duration decreased.

**Cathodic potential pulses during steady-state anodic polarization.**—Five milliseconds cathodic potential pulses were imposed on iron during steady-state anodic polarization. The interval between pulses was about 1 sec. The cathodic potential pulses were selected to be short enough so as not to perturb appreciably the anodic process. The cathodic current ( $i_c$ ) transient during the cathodic potential pulse is shown in Fig. 7. An instant after the cathodic pulse is initiated a maximum negative current,  $i_{ci}$ , is observed. Then the initial sharp decay which corresponds to charging of the double layer is followed by a slower decay

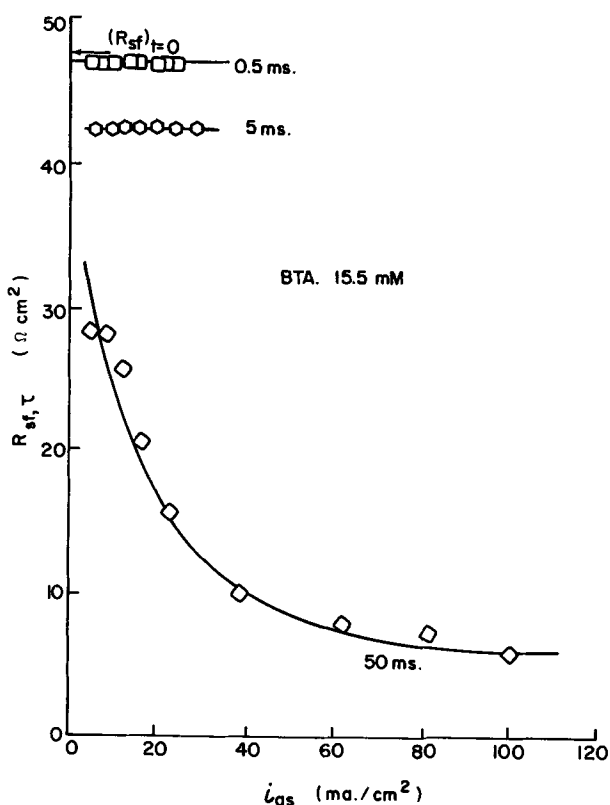


Fig. 6. Surface film resistance,  $R_{sf,\tau}$ , vs.  $i_{as}$

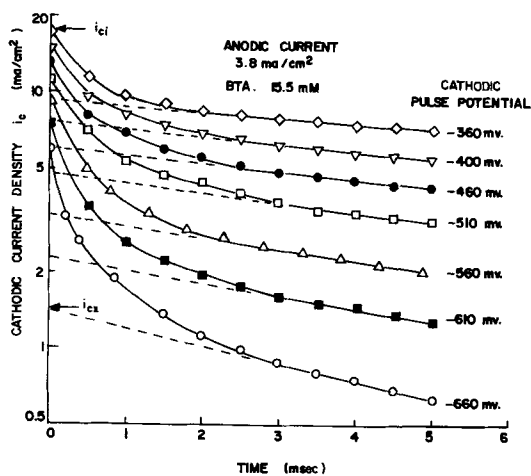


Fig. 7. Cathodic current transient during cathodic potential pulse

region. Subsequently,  $\log |i_c|$  decreased linearly with time. This slow current decrease is ascribed to a change in surface state. The extrapolation of this linear portion of the curve to  $t = 0$  gives the cathodic current,  $i_{cx}$ , corresponding to the surface state during steady-state anodic polarization. The effect of double layer charging on  $i_{cx}$  can be neglected.

The maximum negative current,  $i_{ci}$ , is plotted vs. the cathodic pulse potential for 15.5 mM BTA in Fig. 8. By applying the previous analysis (1) to the equivalent circuit in Fig. 4,  $i_{ci}$  is related to the cathodic pulse potential,  $E_c$ , and the anodic electrode potential,  $\phi_a$ , which is corrected for the ohmic potential drop, as given in Eq. [10]

$$i_{ci} = (E_c - \phi_a) / (R_s + R_{sf}) \quad [10]$$

Equation [10] and Fig. 8 show that for iron in solutions containing BTA, the resistive component,  $R_s + R_{sf}$ , varied with the steady-state anodic current,  $i_a$ , and was much larger than the solution resistance. Therefore, it seems reasonable to assume the existence of a resistive surface film on iron in accord with the above results.  $R_s$  was determined by applying the cathodic pulse to iron in BTA-free solutions. The surface film conductance,  $k_{sf} (= 1/R_{sf})$ , obtained is plotted against the steady-state anodic current in Fig. 9.

According to Eq. [10], the anodic electrode potential,  $\phi_a$ , can be deduced by extrapolating the plot in Fig. 8 to  $i_{ci} = 0$ . The potential,  $\phi_a$ , and  $\log i_a$  is plotted in Fig. 10. In the presence of 15.5 mM BTA, an inversion in the current-potential plot at high current densities is observed.

A plot of  $\log |i_{cx}|$  vs. the cathodic electrode potential,  $\phi_c$ , is shown in Fig. 11, where  $\phi_c$  has been corrected for the ohmic potential drop. For both concentrations of BTA, 15.5 and 2.3 mM, these plots give straight lines with slopes of  $-120$  mV/decade, i.e.

$$\left( \frac{\partial \phi_c}{\partial \log |i_{cx}|} \right)_{i_a} = -120 \text{ mV/decade} \quad [11]$$

The dependence of the cathodic current,  $i_{cx}$ , on the steady-state anodic current for  $\phi_c = -670$  mV vs. SCE is shown in Fig. 12.  $\log |i_{cx}|$  is linearly related to  $\log i_a$  with a slope of  $1/2$

$$\left( \frac{\partial \log |i_{cx}|}{\partial \log i_a} \right)_{\phi_c} = 1/2 \quad [12]$$

It is shown that this plot is independent of the con-

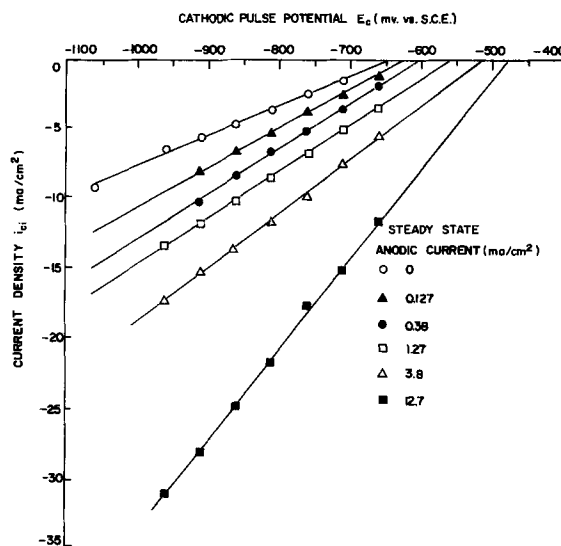


Fig. 8. Cathodic pulse potential,  $E_c$ , vs. cathodic current,  $i_{ci}$ , at the instant the reducing pulse is imposed during steady-state anodic polarization. 15.5 mM BTA.

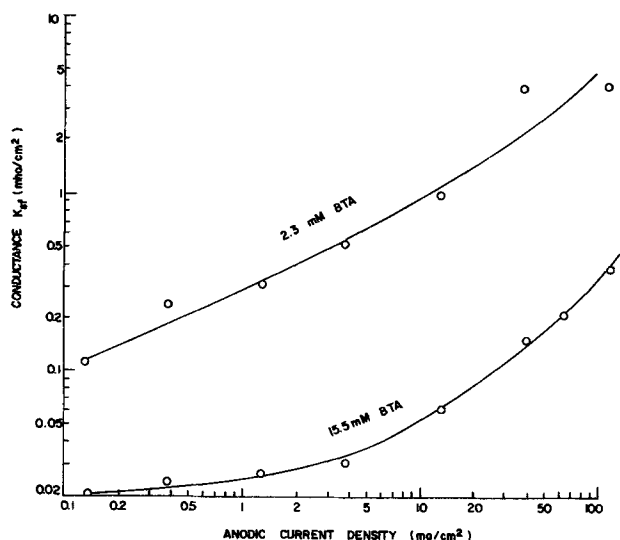


Fig. 9. Dependence of surface film conductance on the steady-state anodic current.

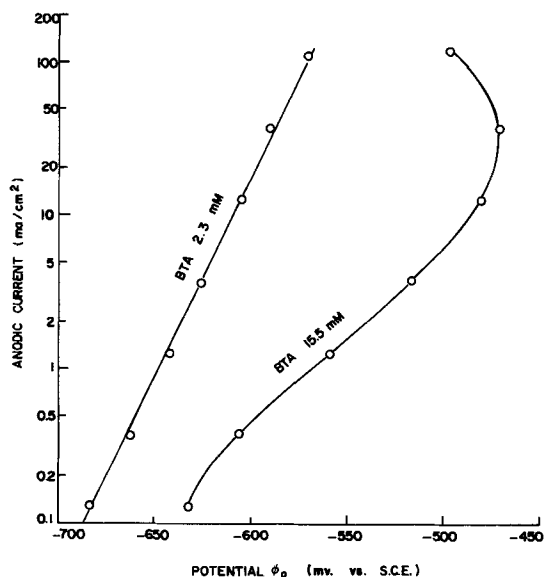


Fig. 10. Steady-state anodic current vs. anodic potential (corrected for ohmic potential drop),  $\phi_a$ .

centration of BTA. Thus,  $i_{cx}$  can be expressed as a function of  $i_a$  and  $\phi_c$

$$i_{cx} = -k_1 \sqrt{i_a} \exp\left(-\frac{F}{2RT} \phi_c\right) \quad [13]$$

where  $k_1$  is independent of the concentration of BTA.

**Discussion**

As shown in Fig. 9, the surface film conductance during steady-state anodic polarization,  $k_{sf}$ , increases with anodic current and decreases with concentration of BTA. These results are consistent with the pulse anodic polarization experiments. The inversion in the current-potential plot for 15.5 mM BTA in Fig. 10 is similar to the results obtained by Sathianandhan *et al.* (3). They attributed this phenomenon to a change in the dissolution mechanism.

Correlation between  $k_{sf}$  and the potential-current behavior can be obtained by a plot of  $\log(i_a/k_{sf})$  vs.  $\phi_a$  as in Fig. 13. A linear relation was obtained with a slope of 80 mV/decade, *i.e.*

$$\frac{\partial \phi_a}{\partial \log(i_a/k_{sf})} = 80 \text{ mV/decade} \quad [14]$$

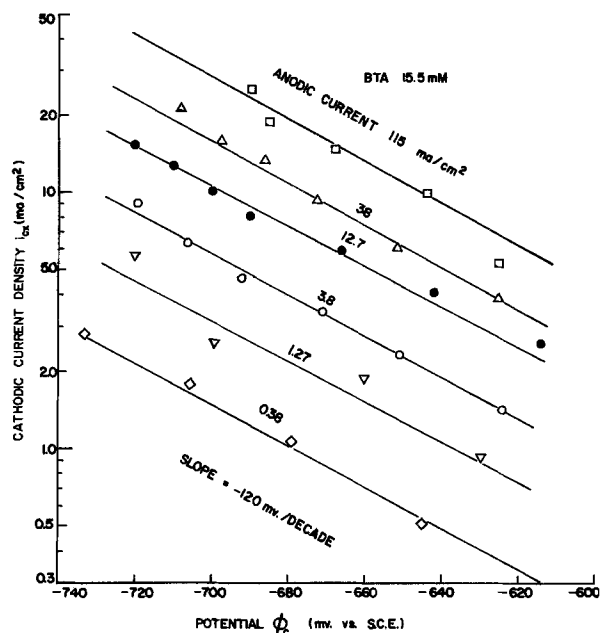


Fig. 11. Cathodic Tafel plots of  $i_{cx}$  vs.  $\phi_c$  at various steady-state anodic currents.

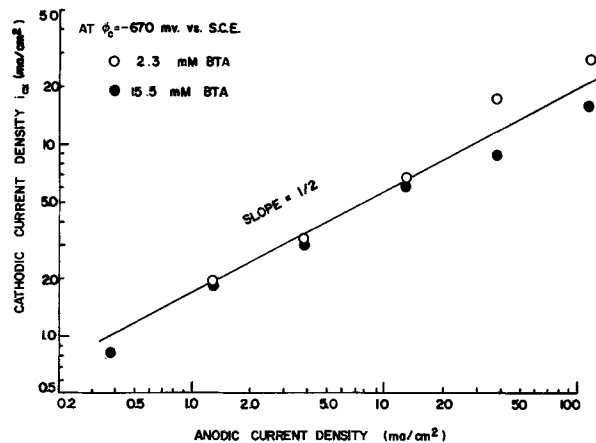


Fig. 12. Cathodic current,  $i_{cx}$ , vs. steady-state anodic current

This plot is shown to be independent of the concentration of BTA. The empirical relationship

$$i_a = k_2 k_{sf} \exp\left(\frac{3F}{4RT} \phi_a\right) \quad [15]$$

is obtained from Fig. 13 where  $k_2$  is a constant and independent of the BTA concentration.

Based on the experimental results the following model of the iron surface is proposed. As seen in Fig. 14, the surface is covered with an electrical resistive film C and an adsorbed layer B. The surface film C is surmised to be an organo-iron complex consisting of  $\text{OH}^-$ ,  $\text{Cl}^-$ , and  $\text{Fe(II)}$  and BTA. Pores exist in the surface film C through which diffusion of dissolved substances can occur. Thus, the electrolyte can penetrate film C and make electrical contact with the electrode surface. Layer B represents a thin adsorbed complex which has a negligible ohmic resistivity.

For the simple pore structure shown in Fig. 14, electrical conductivity of layer C can be given as

$$k_{sf} = \frac{k}{l} \gamma \quad [16]$$

where  $k$ ,  $l$ , and  $\gamma$  are the conductivity of the electro-

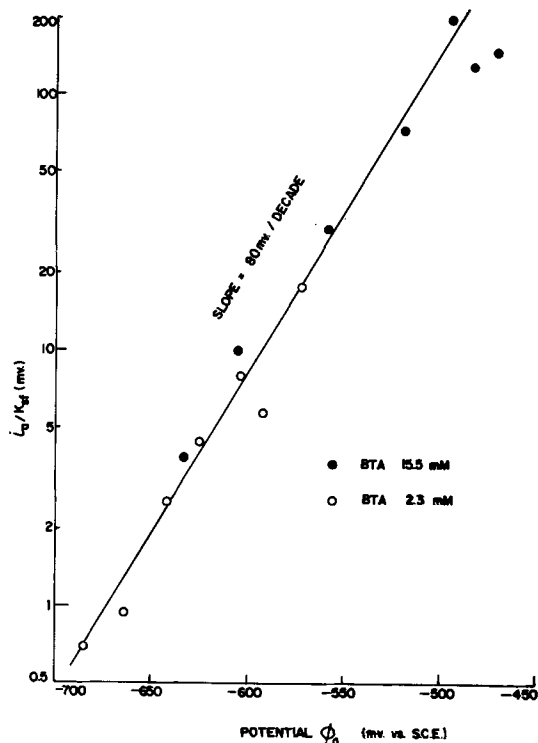
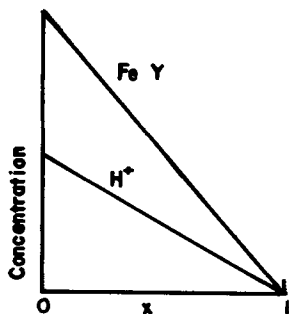
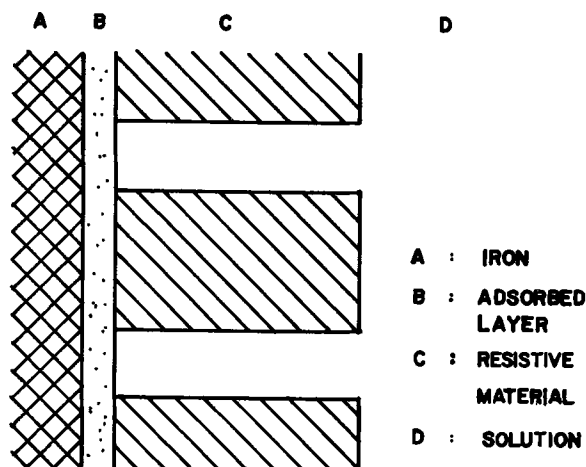
Fig. 13. Plot of  $\log (i_a/k_{st})$  vs. anodic potential,  $\phi_a$ 

Fig. 14. Porous film model

lyte, thickness of layer C, and the ratio of the pore area to the apparent total area, respectively. The effective current density,  $i_{eff}$ , can then be expressed as

$$i_{eff} = i_a/\gamma \quad [17]$$

Thus

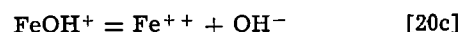
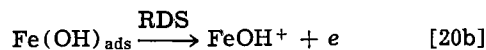
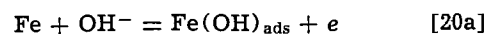
$$i_a = \left(\frac{l}{k}\right) k_{st} i_{eff} \quad [18]$$

If  $i_{eff}$  follows the expression

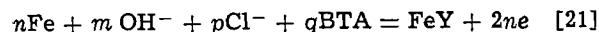
$$i_{eff} = k_3 \exp\left(\frac{3F}{4RT} \phi_a\right) \quad [19]$$

and is independent of the concentration of BTA, Eq. [15] can be obtained by substituting  $k_3 = (k/l)k_2$  and Eq. [16] and [17] into Eq. [19]. Thus, the Tafel slope for the plot of  $i_{eff}$  vs.  $\phi_a$  is 80 mV/decade in accord with that obtained for uninhibited iron in neutral chloride solutions (1) and indicates that, although the rate is decreased, the mechanism of anodic dissolution is not affected by the presence of BTA.

The anodic Tafel slope of 80 mV/decade can be obtained by assuming the Bockris mechanism for electro-dissolution of iron (5) and a pH change at the electrode-solution interface due to formation of a hydroxochloro-iron complex (1). The reaction steps in the electro-dissolution of iron (5) can be given as



where Eq. [20b] is the rate-determining step. The over-all reaction for the formation of the organo-iron complex can be expressed by



where  $m \neq 0$  and FeY is given the general formula  $[\text{Fe}_n(\text{OH}^-)_m(\text{Cl}^-)_p(\text{BTA})_q]$ . The independence of  $k_3$  in Eq. [19] with respect to the concentration of BTA indicates that the adsorbed layer B is not a function of BTA concentration when it is 2.3 mM or greater and suggests that the electrode surface during anodic dissolution is already saturated with BTA at this concentration.

The cathodic Tafel slope of Eq. [11] obtained from the cathodic pulse potential experiments during steady-state anodic polarization indicates that Eq. [20b] is also the rate-determining step in the cathodic deposition reaction. The details of the analysis have been given previously (1).

#### Acknowledgment

This work was supported by a grant from the Office of Saline Water, U.S. Department of the Interior.

Manuscript submitted March 1, 1974; revised manuscript received June 7, 1974.

Any discussion of this paper will appear in a Discussion Section to be published in the June 1975 JOURNAL. All discussions for the June 1975 Discussion Section should be submitted by Feb. 1, 1975.

The publication costs of this article have been assisted by the University of California.

#### LIST OF SYMBOLS

$C_{dl}$	capacitance of electrical double layer, $\mu\text{f}/\text{cm}^2$
$E_c$	applied cathodic potential pulse, mV vs. SCE
$E_o$	open-circuit potential, mV vs. SCE
$e_1$	potential difference as shown in Fig. 4, V
$(e_1)_{t=\tau+}$	right-hand limit of $e_1$ at $t = \tau$ , V
$(e_1)_{t=\tau-}$	left-hand limit of $e_1$ at $t = \tau$ , V
$e_2$	potential difference as shown in Fig. 4, V
$(e_2)_{t=0+}$	right-hand limit of $e_2$ at $t = 0$ , V
$(e_2)_{t=\tau+}$	right-hand limit of $e_2$ at $t = \tau$ , V
$(e_2)_{t=\tau-}$	left-hand limit of $e_2$ at $t = \tau$ , V
$F$	Faraday's constant, coulombs/equiv.
$i_a$	steady-state anodic current density, $\text{mA}/\text{cm}^2$
$i_{ap}$	current density as shown in Fig. 1, $\text{mA}/\text{cm}^2$
$i_{as}$	current density as shown in Fig. 1, $\text{mA}/\text{cm}^2$
$i_c$	cathodic current density, $\text{mA}/\text{cm}^2$
$i_{eff}$	effective anodic current density as defined in Eq. [17], $\text{mA}/\text{cm}^2$
$i_{cl}$	maximum cathodic current density as shown in Fig. 7, $\text{mA}/\text{cm}^2$
$i_{cx}$	extrapolated cathodic current density as shown in Fig. 7, $\text{mA}/\text{cm}^2$

$k$	electrical conductivity of the electrolyte, mho-cm <sup>-1</sup>	$t$	time after imposition of potential pulse, msec
$k_1$	constant in Eq. [13]	$\Delta E_a$	applied anodic potential pulse, V
$k_2$	constant in Eq. [15]	$\phi_a$	anodic electrode potential (corrected for IR drop), mV vs. SCE
$k_3$	constant in Eq. [19]	$\phi_c$	cathodic electrode potential (corrected for IR drop), mV vs. SCE
$k_{sf}$	surface film conductance during steady-state anodic polarization, mho/cm <sup>2</sup>	$\gamma$	ratio of pore area to apparent total area
$l$	thickness of surface film, cm	$\tau$	time period as shown in Fig. 1, msec
$R$	gas constant		
$R_r$	charge transfer resistance, ohm-cm <sup>2</sup>		
$R_s$	solution resistance, ohm-cm <sup>2</sup>		
$R_{sf}$	surface film resistance at steady-state anodic polarization, ohm-cm <sup>2</sup>		
$R_{sf,0}$	surface film resistance at open circuit, ohm-cm <sup>2</sup>		
$R_{sf,\tau}$	surface film resistance at termination of anodic potential pulse of time duration, $\tau$ , ohm-cm <sup>2</sup>		
$T$	absolute temperature, °K		

## REFERENCES

1. S. Asakura and Ken Nobe, *This Journal*, **118**, 13 (1971).
2. R. J. Chin and Ken Nobe, *ibid.*, **118**, 545 (1971).
3. B. Sathianandhan, K. Balakrishnan, and N. Subramanyan, *Brit. Corr. J.*, **5**, 270 (1970).
4. Robert Jackson Chin, Ph.D. dissertation, UCLA, September 1971.
5. J. Bockris, D. Drazic, and A. R. Despic, *Electrochim. Acta*, **4**, 325 (1961).

## Mobility of Metallic Foreign Atoms during the Anodic Oxidation of Aluminum

W. D. Mackintosh, F. Brown,\* and H. H. Plattner

Chalk River Nuclear Laboratories, Atomic Energy of Canada Limited, Chalk River, Ontario, Canada

## ABSTRACT

Metallic foreign atoms introduced into the surface layers of aluminum specimens are shown to be mobile during anodic oxidation. The direction of motion depends on whether the initial distribution of the foreign atoms is located in aluminum metal under the natural air-formed oxide or entirely contained within a thin preformed surface film of anodic oxide. For a number of the fifteen elements studied, the rate of motion relative to aluminum ions was determined. The results of these experiments are of intrinsic interest in the eventual understanding of the processes involved and have immediate practical consequences for sectioning techniques which involve anodizing and stripping.

In a previous paper (1) it was shown that the energy spectra of He ions backscattered from aluminum, recorded before and after anodic oxidation, could be interpreted to give the thickness of the oxide films and the final position of foreign atoms introduced into the surface layers of the metal before oxidation. Noble gas, halogen, or alkali metal atoms were introduced into the surface layer by implantation with an isotope separator capable of accelerating a chosen ion to energies of a few tens of kilovolts (2). As they are immobile (3), the positions of noble gas atoms were used to deduce the transport number of metal and oxygen. The alkali metals and the halogens were found to be mobile during anodization, the former moving toward the oxide/electrolyte interface, the latter toward the metal/oxide interface. The alkali metals, K, Rb, and Cs, were less mobile than Al; the halogens, Cl, Br, and I, were less mobile than oxygen. In both series the mobility decreased with increasing atom size. Further, there was no significant difference in the behavior between atoms introduced initially into metal and those introduced initially into a preformed anodic oxide film  $\sim 11 \mu\text{g}/\text{cm}^2$  thick.

Using the same techniques of ion implantation and analysis by Rutherford scattering we have extended these studies. The previous work had encompassed only species likely to be singly charged. In order to compare their mobility with species likely to be doubly charged we selected the series Ca, Ba, and Sr. We also chose to investigate Ga, In, and Tl because they are in the same group of the periodic table as Al.

During the course of these latter experiments we discovered that, unlike the alkali metals and alkaline earths, the behavior of Ga, In, and Tl depended on the location of the implanted material (*i.e.*, whether in metal or preformed oxide film). To explore the extent of this phenomenon, we eventually included metals representing as many groups of the periodic table as we could within the capabilities of our mass separator. The elements investigated were: Cu, Ag; Hg; V; Cr; Mn; Fe, Co, and Ni.

## Experimental

The aluminum specimens were 0.9 cm diameter disks 0.5 mm thick. Surfaces were first prepared by mechanical and vibratory polishing (4). This was followed by four cycles in which the specimen was anodized and then stripped of oxide with a solution of phosphoric and chromic acids at 95°. This particular stripping contaminates the specimen with chromium and phosphorus. Therefore, when studying the elements Co, Fe, and Mn whose masses are close to chromium we used a final cleaning with phosphoric acid only. This solution is corrosive to aluminum metal, hence the exposure was kept to a minimum. Some samples were then exposed to the air at room temperature for a few hours, some were anodized to an oxide thickness of 30V or 11  $\mu\text{g}/\text{cm}^2$ .

The foreign atoms were implanted into these specimens at energies of 20-40 keV. Within this energy range the greater part of the implanted atoms were located in the metal of those specimens covered only with the air-formed oxide and entirely located within the oxide layer of those specimens covered with the preformed oxide. This can be inferred from a knowl-

\* Electrochemical Society Active Member.

Key words: anodic oxidation, ion implantation, Rutherford, backscattering, aluminum, metallic foreign atoms.

edge of the ion ranges (2, 5) and the thickness of the oxides. The thickness of the preformed anodic oxides is known from a previous calibration (1) of thickness *vs.* voltage. We measured the thickness of air-formed oxide by using Rutherford scattering and working with single-crystal aluminum, following the principles described by Meyer *et al.* (6). The values obtained in two experiments were 0.5 and 0.7  $\mu\text{g}/\text{cm}^2$ . A few experiments were made using higher energy implants; these are designated in the appropriate sections below and any experiment not specially designated refers to implants at energies of 20-40 keV. The number of ions implanted was commensurate with the sensitivity of the Rutherford scattering method for each species; they were in the range  $10^{14}$ - $10^{15}$  ions/ $\text{cm}^2$ .

All anodization was done in a saturated solution (~5%) of ammonium pentaborate in water at a temperature of 23°C. The current was kept constant at 2 mA/ $\text{cm}^2$ . The desired oxide thickness was achieved by terminating the oxidation at a voltage corresponding to the desired thickness obtained from a previously prepared calibration curve and was checked by the subsequent Rutherford backscattering analysis.

The experimental arrangement for obtaining the spectra of backscattered He ion was identical with that described in Ref. (1). Briefly it consists of a Van de Graaff accelerator delivering a beam of 2 MeV He ions, a target chamber, and a surface barrier detector (resolution 17 keV FWHM), placed to observe ions scattered through 150°, together with the usual electronics and pulse height analyzer.

The basis of the Rutherford scattering technique for surface analysis, for film thickness measurements, and for locating the position of foreign atoms has been described extensively [(7) and references therein]. The application of the technique to the particular problem of anodic oxide films on Al and the behavior of implanted foreign atoms is described in detail in Ref. (1). The essence of the method is that, if a He ion of known energy (in this case 2 MeV) is scattered from a surface atom, the resultant energy loss can be calculated from the kinematics of the system. Any additional energy loss observed is due to the fact that the struck atom is not on the surface and therefore the He ion suffers energy loss in both its ingoing and outgoing trajectories. This loss can be interpreted to give the depth of the atom.

The area of the peak obtained by backscattering from implanted ions is dependent on the number of implanted atoms present. It is possible to obtain the absolute amounts (7) but for these experiments it was sufficient to compare areas after normalization to the same integrated beam current (*i.e.*, same number of incident particles) to observe any changes in the relative amount of implant occurring during anodization.

The details of how the spectra are interpreted are, again, given in Ref. (1). We present a very brief illustration by means of Fig. 1 and 2. The former was obtained from a specimen of Al in which the implanted Ag is located in the metal underlying an air-formed oxide film, the latter was obtained from the same specimen after the oxide had been thickened anodically to 100  $\mu\text{g}/\text{cm}^2$ . In both spectra the peak to the right is derived from scattering from the Ag. The continuum to the left of the spectrum of Fig. 1 is derived from scattering by the Al atoms of the substrate.

The continuum in Fig. 2 has a marked step. The portion at the right-hand side, in which the height is reduced, comes from scattering of He by Al atoms in the oxide. The higher level portion at the left comes from scattering by Al atoms in the underlying metal. The width of the step is a measure of the oxide and this can be calculated as described in Ref. (1).

The position of the Ag peak on the energy scale of Fig. 1 corresponds to Ag atoms at a depth of 6  $\mu\text{g}/\text{cm}^2$  (the implant depth). The Ag peak position in Fig. 2 is shown displaced to one of lower energy. This indicates the Ag atoms were buried beneath the surface during oxidation. The change in depth of the Ag is cal-

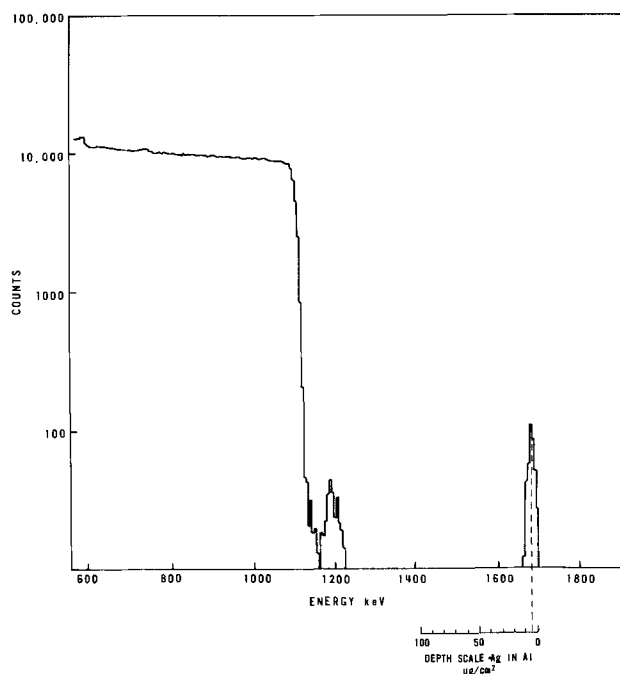


Fig. 1. Spectrum from  $2 \times 10^{14}$  Ag atoms implanted in Al. The incident energy of the  $\text{He}^+$  was 1965 keV.

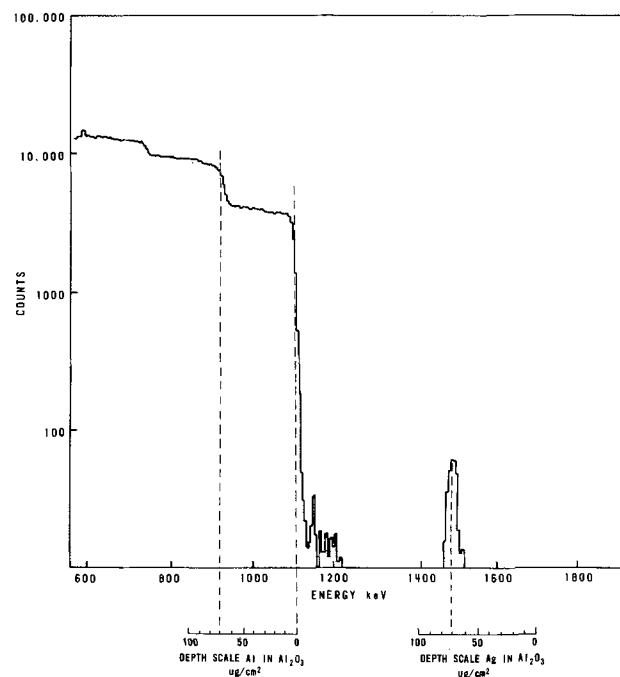


Fig. 2. Spectrum from  $2 \times 10^{14}$  Ag atoms buried beneath an oxide layer (70  $\mu\text{g}/\text{cm}^2$  thick) on the surface of Al. The incident energy of the  $\text{He}^+$  was 1965 keV.

culated from this energy shift. The area of the Ag peak in Fig. 2 is 90% of the area in Fig. 1 so that 10% of the Ag is no longer within the boundaries of the principle distribution.

The depth resolution of the technique is  $\sim 2 \mu\text{g}/\text{cm}^2$  and is essentially constant over the range of depths involved in the work. It is set mainly by the detector resolution. The resolution sets a limit to precision when one is attempting to measure the depth at which atoms are located. The precision obviously depends on the magnitude of the distance one is measuring in each particular case. It is not possible to tell the difference between atoms on top of the substrate surface or within the first 2-3  $\mu\text{g}/\text{cm}^2$  of the substrate. In Ref. (1) we found the relative standard deviation at a

depth of  $35 \mu\text{g}/\text{cm}^2$  to be 6.0%. Likewise, the measurements of oxide thickness have limited precision. In Ref. (1) we found a relative standard deviation of 2.0% for four thickness measurements made on the same oxide, which had a thickness of  $93 \mu\text{g}/\text{cm}^2$ . Thus, the position of foreign atoms relative to the metal/oxide interface is somewhat imprecise, subject to both the error in depth measurement and the error in oxide thickness measurement. It is not possible to assert from the Rutherford scattering data alone whether foreign atoms close to the interface lie within the metal or within the oxide.

On occasion and as a matter of convenience, the Rutherford scattering experiments were supplemented by experiments in which radioactive  $^{204}\text{Tl}$  tracer and conventional radio-assay methods were employed. These are indicated in the relevant section under Results.

**Results**

*Implants in preformed oxides.*—In this section we describe the behavior of ions, implanted into preformed oxide, when the oxide film is subsequently thickened by a number of anodic oxidation steps. The preformed oxide thickness is  $t = 11 \mu\text{g}/\text{cm}^2$  and the thickness at each successive stage is designated  $T$ . In Fig. 3 we illustrate qualitatively, the various phenomena observed. For convenience we consider the results in three groups, as follows:

(a) When  $T \approx 25 \mu\text{g}/\text{cm}^2$  all the implanted Ba ions were found in the oxide, close to but not at the outer (oxide-electrolyte) interface. Since 4/10 of the new oxide is formed outside the original surface by outward movement of Al [Ref. (1)] the Ba must also move outward, but not quite as fast as the Al. The same behavior was observed on further thickening the oxide ( $T_2 = 60$ ), Fig. 3B, and ( $T_{3-4} = 75$  and  $95 \mu\text{g}/\text{cm}^2$ ). The Ba ion mobility can be described in terms of a migration number which we defined in Ref. (1) as the ratio of the distance moved by the implanted atoms to the total thickness of the oxide grown after implantation. The value for Ba averaged 0.39.

(b) The group, Ag, Co, Cr, Hg, Ni, and V, on the other hand, disappeared from the solid when  $T \approx 25$

$\mu\text{g}/\text{cm}^2$ , leaving, at most, a just detectable trace on the surface of the oxide. They also must move outward, but at a faster rate than Al atoms. No migration number can be assigned, except that it must exceed the Al value (0.4).

(c) The remaining group, as shown in Fig. 3A, Cu, Ca, Fe, Ga, In, Mn, Sr, and Tl implants, also move outward; but display a behavior intermediate between groups (a) and (b). That is, a portion is lost to the electrolyte while the remainder is found close to the outer surface. The fraction remaining at the surface layer varies from species to species, and is not reproducible from specimen to specimen of the same species. For Ca, Cu, Ga, and Sr the amount retained at  $T = 25 \mu\text{g}/\text{cm}^2$  was  $< 50\%$  and at  $T = 50 \mu\text{g}/\text{cm}^2$  they had entirely disappeared (Fig. 3B). Essentially then, these ions move faster than Al. In the case of Fe, In, Mn, and Tl the amount remaining at  $T = 25 \mu\text{g}/\text{cm}^2$  was  $> 75\%$  and when  $T = 100 \mu\text{g}/\text{cm}^2$  (the maximum available), appreciable quantities remained, always located close to the outer surface. These then, move more rapidly than Al and only slowly dissolve in the electrolyte, or, they move at much the same rate as Al and are reduced by dissolution of the alumina matrix or by some other process. Loss of any species to the electrolyte not only involves movement through the oxide but dissolution into the electrolyte and possibly dissolution of the alumina surface layers [2% of the Al converted to  $\text{Al}_2\text{O}_3$  is known to dissolve (8)]. Thus once an implanted ion reaches the surface layers its rate of egress will depend on factors other than the rate of movement through the oxide. These factors were not investigated in the present work. Some such studies have been carried out with  $\text{Ta}_2\text{O}_5$  (9).

In order to distinguish between movement within the oxide and these rather complex surface effects, we carried out another experiment. We preformed oxide films  $43 \mu\text{g}/\text{cm}^2$  thick and sent the specimens to the University of Aarhus, Denmark, where they were implanted with indium to a depth of  $34 \mu\text{g}/\text{cm}^2$  and with thallium to a depth of  $20 \mu\text{g}/\text{cm}^2$  (Fig. 4A) using the 600 keV heavy ion accelerator. In this way we substantially increased the path length over which the ions would have to move before they could reach the

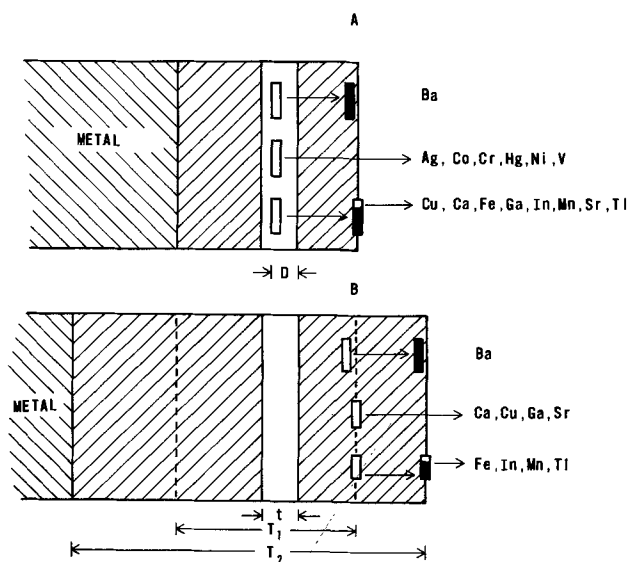


Fig. 3. The position of ions implanted into preformed oxide films after thickening by anodic oxidation in two stages. A, first oxidation; B, second oxidation.  $T_1$  and  $T_2$  are the thicknesses of the 1st and 2nd oxides, respectively,  $t$  the thickness of the preformed oxide film, and  $D$  the depth of the implant before thickening. □ is the position before thickening; ■ after thickening. □ indicates part of implant retained and part moving farther. The height of the latter two rectangles corresponds approximately to the fraction of implanted material in the position indicated.

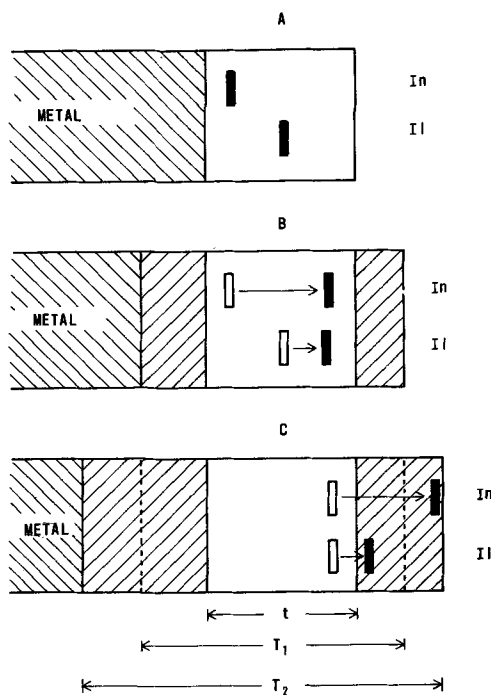


Fig. 4. The position of In and Tl ions implanted into thick preformed oxide films before (A) and after thickening (B).  $t$  is the thickness of the preformed oxide,  $T_1$ ,  $T_2$ , and  $T_3$  are the thicknesses of anodically grown films. ■ is the position of the implants, □ the positions held before thickening.

surface. After thickening the oxide ( $T_1 = 74 \mu\text{g}/\text{cm}^2$ , Fig. 4B) we found all the implanted material within the oxide film and could therefore obtain migration numbers. They were 0.83 and 0.34 for the In and Tl, respectively. On further thickening ( $T_3 = 102 \mu\text{g}/\text{cm}^2$ , Fig. 3C) the In was located close to the surface, while the Tl was still well within the oxide. For both species the values of the respective migration numbers were the same as before. Thus In moves faster than Al and its presence at the surface in the earlier experiments where it reached the surface quickly must have been due to preference for remaining in the surface rather than dissolving in the electrolyte. The Tl moves at much the same rate as Al. The gradual decrease in amount in the earlier experiments must have been due to alumina dissolution or possibly to the fact that if Tl moves at about the same rate as Al and also suffers any broadening of its distribution, then a small fraction will in fact move faster than the Al; a small degree of broadening is difficult to observe due to the detector resolution.

Such experiments involving deeper implants have not been carried out with Fe and Mn. It is therefore not known whether these move faster than Al and remain on the surface because they are subject to some surface effect or whether they move at the same rate as Al.

**Implants into aluminum metal.**—The positions of species, implanted into metal under an air-formed oxide film, after the specimens had been anodized are shown in Fig. 5A.

Barium behaved exactly as it did when implanted into preformed oxides, i.e., all of it moved outward to

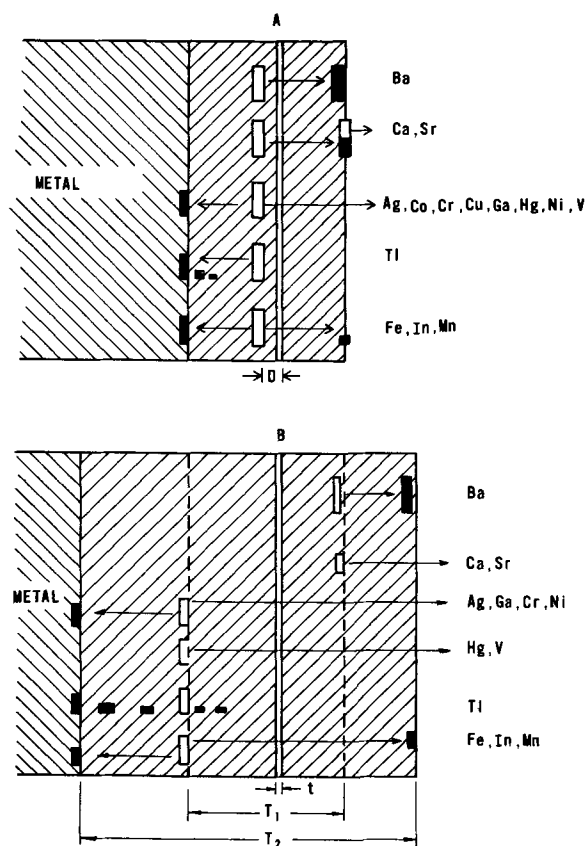


Fig. 5. The position of ions implanted into metal under the air-formed oxide after thickening by anodic oxidation. A, first oxidation; B, second oxidation.  $T_1$  and  $T_2$  are the thicknesses of the 1st and 2nd oxides, respectively,  $t$  the thickness of the air-formed oxide, and  $D$  the depth of the implant (in metal) before thickening.  $\square$  is the position before thickening,  $\blacksquare$  after thickening.  $\blacksquare$  indicates part of implant retained, part moving farther. The height of the latter two rectangles corresponds approximately to the fraction of the implanted material in the position indicated.

a location just below the surface. When  $T_1 = 28 \mu\text{g}/\text{cm}^2$ , the migration number obtained was 0.38 which agrees with the previously obtained value. Further thickening of  $T$  to successively 44, 64, 83, and  $104 \mu\text{g}/\text{cm}^2$  gave values which averaged 0.39.

Also, as before, a part of both Ca and Sr was located at the surface when the first film was grown ( $T_1 = 50 \mu\text{g}/\text{cm}^2$ , Fig. 5A) and disappeared during further growth ( $T_2 = 100 \mu\text{g}/\text{cm}^2$ , Fig. 5B).

By contrast the behavior of all other elements (Fig. 5A) was strikingly different from that observed for implants into preformed oxide. After anodizing, a large fraction of the implanted material was found in a sharp peak corresponding to a depth, within the experimental resolution, that is equal to the oxide thickness, i.e., at the metal/oxide interface. By stripping off the oxide and analyzing again it was found that the implant was, in fact, in the metal and is, within the limit of resolution, at the metal surface. Since it has been shown that the anodic oxidation of Al proceeds, in part, by inward movement of oxygen, the implanted ions retained in the metal must have retreated before the advancing oxide front, moving in a direction opposite to that observed in the preformed oxide experiments.

The amount of implant found at the interface does not fully account for the original amount; Table I shows that fractions were retained at the interface at the end of the first oxidation step. The fractions of Ag, Co, Cr, Cu, Hg, Ga, Ni, and V not retained at the interface were not observed elsewhere in the spectra. They either passed into the electrolyte or the small amounts of material involved were dispersed throughout the oxide too sparsely to be detected. The first alternative seems likely in the case of Hg because a relatively larger amount is missing from the interface region (Table I) and Hg, being heavy, is easily detected in very small amounts. Such behavior would be consistent with that of Hg ions implanted into preformed oxide films where Hg disappeared quickly from the solid system. The Tl not retained at the interface was dispersed in oxide in a concentration gradient decreasing from the oxide/metal interface outward as indicated on Fig. 5B. This too is consistent with previous experiments where Tl was found to move in the oxide at much the same rate as Al. Some Fe, In, and Mn were observed at the outer surface. This too, is the same as the behavior of these species implanted in preformed oxide.

As the oxides were thickened the fraction remaining of Ag, Ga, Cr, and Ni at the metal/oxide interface decreased; Co and Cu did not. For Hg and V the loss was 100% after forming  $100 \mu\text{g}/\text{cm}^2$  of oxide, the other species lost amounts varying in the range 10-50%. Again, except for Fe, In, Mn, and Tl, the material not at the interface could not be located. Thallium was found in the oxide, decreasing in concentration from the metal/oxide interface outward. In the case of Fe, In, and Mn, the fraction leaving the interface was at the outer surface.

Table I. Fractions located at oxide/metal interface

Implanted species	Oxide thickness ( $\mu\text{g}/\text{cm}^2$ )	Fraction at interface* (% of implanted amount)
Ag	27	56
Co	27	92
Cr	50	84
Cu	28	100
Fe	52	75
Ga	48	100
Hg	35	62
In	28	89
Mn	53	72
Ni	27	92
Tl	31	90
V	26	100

\* This fraction varied as much as 15% from one experiment to the next.



The rate at which Tl leaves the metal as the oxide film is thickened was determined by experiments using radioactive  $^{204}\text{Tl}$ . Specimens of aluminum metal were implanted with  $^{204}\text{Tl}$  and also with stable Tl to bring the dose up to  $2 \times 10^{14}$  ions/cm<sup>2</sup>. The activity was measured by  $\beta$ -counting. The specimens were then anodized, the oxide stripped off, and the residual activity measured. This procedure was then repeated many times so that the gradual disappearance of Tl could be followed. The amount lost on the first step was variable, but thereafter the rate of loss showed first-order dependence on the amount of Tl remaining, Fig. 6. The amount lost in a given step is also proportional to the thickness of oxide grown, i.e., to the time of anodizing at constant current. Thus the amount removed by forming a thick oxide will be the same as that removed in successive small steps of total thickness equaling the large one.

### Conclusion

These experiments have shown that the behavior of implanted ions depends on the location of the implant. All metal ions implanted in a preformed oxide move outward. However most metal species implanted into Al metal under the natural air-formed oxide exhibit the opposite effect, remaining in the metal and moving inward with the advancing oxide front.

The migration numbers for In and Tl, measured by using deep implants, show that In moves faster than Al whereas Tl moves at about the same speed. A large number of other species clearly move more quickly than Al because they are lost to the electrolyte during anodizing. These are Ag, Co, Cr, Cu, Ga, Hg, Ni, and V. Migration numbers for these species can only be determined by deep implants in thicker oxides as were done for In and Tl. At present, we cannot do this without help from an outside laboratory but equipment now being assembled will shortly remedy this situation.

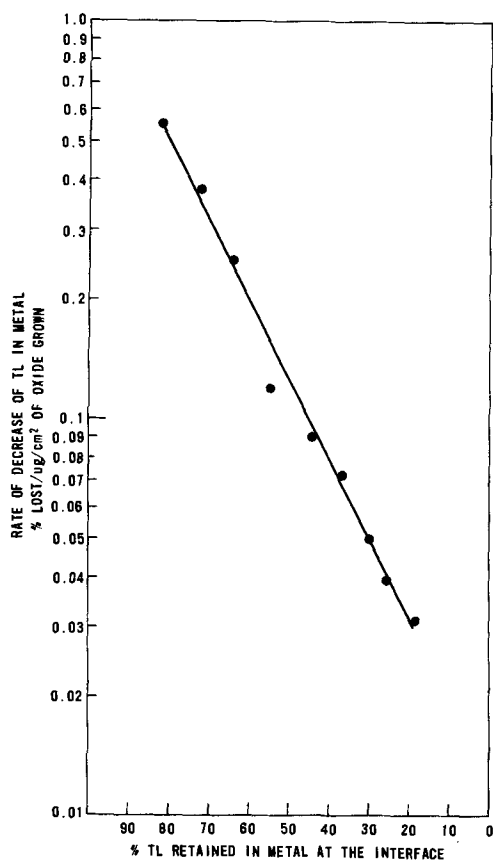


Fig. 6. The rate of decrease of Tl in the metal substrate at the interface as a function of the concentration of the Tl in the metal. The concentration shown is the average for each oxidation-dissolution step.

Only one of the species, Ba, moved more slowly than Al. The other two alkali earths Ca and Sr are more mobile than K, Rb, and Cs (1). If it is assumed that these species move as ions, one can attribute the greater mobility of Ca, Sr, and Ba to the double charge on their ions. It was found in Ref. (1) that mobility decreased in the sequence K, Rb, Cs. Although Ca and Sr move faster than Ba, suggesting the same pattern obtains, the relative mobility of Ca and Sr can only be unambiguously determined with deep implants. However, Sr was retained in greater amounts at the surface than was Ca. In both cases, whether oxide or metal, they should be soluble in the aqueous electrolyte and thus it is not implausible that the greater amount of Sr is due to slower migration, i.e., mobility decreases in the sequence Ca, Sr, Ba. In both sequences this appears to be an effect of size rather than electropositivity (which increases rather than decreases in the two sequences).

The results of the deep implant experiments with In and Tl also exhibit the apparent dependence on size as the mobility of indium is considerably greater than that of thallium.

One further fact emerges from these experiments; all ions which clearly move more slowly than Al, viz., K, Rb, Cs, and Ba, are appreciably greater in size than those which clearly move faster, Ag, Co, Cr, Cu, Ga, Hg, In, Ni, and V.

The most striking feature of the present work is that many metallic species, when implanted into aluminum metal, are retained to a large extent in the aluminum when the specimen is anodized. The over-all pattern fits with normal electrochemical behavior. Species with lower oxidation potentials than aluminum (K, Rb, Cs, Ca, Sr, and Ba) are oxidized and incorporated into the  $\text{Al}_2\text{O}_3$ . Species with higher oxidation potentials than aluminum (all the remaining metallic species studied) are not oxidized and remain in the metal, although the fraction so retained does vary considerably between different species. The anodic oxidation of aluminum proceeds, in part, by inward movement of oxygen. Hence if an implanted atom is retained in the metal it must, in effect retreat before the advancing oxide front. This implies that the implanted atoms must have a high degree of mobility in the aluminum metal close to the metal-oxide interface due to a high concentration of vacancies in this region.

The phenomenon appears to be similar to that observed in thermal oxidation of alloys where oxides containing only one of the components can be found. In these cases the component with the lower heat of formation remains in the metal [see for example Ref. (10)].

When the oxide front moves through the implant region it does not sweep every atom of the implanted species before it. The amounts vary from species to species. Further as the front moves inward, i.e., beyond the implant region into a hitherto undisturbed region, it continuously loses a fraction of the atoms that had been moved inward from the original position. In the more detailed studies with Tl it was shown that the amounts transferred across the interface into the oxide is dependent on the concentration of the Tl atoms at the interface. Atoms not swept along by the oxide front as it passes through the implant region and thus transferring into the oxide evidently behave in the same fashion as the particular species involved does when implanted into preformed oxides.

In addition to the intrinsic interest in formulating a plausible mechanism for the process, this phenomenon has some significant practical consequences. Anodic oxidation and stripping has been used as means of "sectioning" aluminum to determine range profiles and to study diffusion. These procedures are subject to error, or could be totally useless, if the foreign atoms in question do not pass into the oxide (11). Anodizing-stripping cycles and also electrochemical polishing are useful techniques for preparing good surfaces. However, we have found that if they are applied to alu-

minum alloys they will perturb the concentration of additive in the surface region (11). Furthermore, with due consideration of the oxidation potentials involved, similar effects could well be observed with matrix metals other than aluminum.

#### Acknowledgments

We are indebted to Professor E. Bögh, Aarhus University, for implants of In and Tl in thick oxide. The assistance of O. Westcott, C. Sitter, G. Sims, and J. Lori in operation of the mass separator and Van de Graaff is gratefully acknowledged.

Manuscript received Feb. 13, 1974.

Any discussion of this paper will appear in a Discussion Section to be published in the June 1975 JOURNAL. All discussions for the June 1975 Discussion Section should be submitted by Feb. 1, 1975.

The publication costs of this article have been assisted by Atomic Energy of Canada Limited.

#### REFERENCES

1. F. Brown and W. D. Mackintosh, *This Journal*, **120**, 1096 (1973).
2. J. A. Davies, F. Brown, and M. McCargo, *Can. J. Phys.*, **41**, 829 (1963).
3. J. P. S. Pringle, *This Journal*, **119**, 482 (1972).
4. J. L. Whitton, *J. Appl. Phys.*, **36**, 3917 (1965).
5. B. Domeij, F. Brown, J. A. Davies; and M. McCargo, *Can. J. Phys.*, **42**, 1624 (1964).
6. O. Meyer, J. Gyulai, and J. W. Mayer, *Surface Sci.*, **22**, 263 (1970).
7. W. D. Mackintosh and J. A. Davies, *Anal. Chem.*, **41**, 26A (1969).
8. J. A. Davies, Chalk River Nuclear Laboratories, Chalk River, Private communication, 1972.
9. D. Phillips and J. P. S. Pringle, *This Journal*, **120**, 1067 (1973).
10. K. Hauffe, "Oxidation of Metals," Plenum Press, New York (1965).
11. W. D. Mackintosh, Proc. Int. Conf. Application of Ion Beams to Metals, Albuquerque, New Mexico, October 1973, To be published.

## The Effect of Brine Level on the Voltage of Mercury-Type Chlor-Alkali Cells

Peter A. Dana<sup>\*1</sup>

Olin Corporation, Stamford, Connecticut 06904

#### ABSTRACT

One of the neglected variables affecting the operating voltage of mercury-type chlor-alkali cells is the level of the cell brine relative to the tops of the graphite anodes within the cell. Laboratory data have been analyzed and scaled up to predict the magnitude of this effect in a typical commercial mercury cell.

It is well known that varying the slot and hole configuration of graphite anodes can reduce the cell voltage of a mercury-type chlor-alkali cell (1, 2). The voltage decrease is the result of improved brine circulation rates which in turn result in more rapid chlorine bubble detachment from the graphite as well as minimization of localized depletion of the brine. Brine circulation rates depend on hydrodynamic forces commonly known as the "gas lift pump" principle. In the present application, one critical variable affecting the rate of circulation via the gas lift pump principle is the difference in hydrostatic head which results between the brine-bubble mixture within an operating anode and the relatively bubble-free mixture of the bulk electrolyte in the cell. The relationship of this variable to cell brine level can be understood as follows.

Figure 1 shows a cross section of a portion of a typical graphite anode. Bubbles of chlorine are formed in the anode-cathode gap by the oxidation of chloride ions in the brine solution. These bubbles then rise up through the slotted lower section of the anode ( $h_2$ ) and enter the upper drilled section of the anode ( $h_1$ ). As these bubbles rise and fill the slot and hole volume a bubble-brine mixture of density  $\rho_M$  is created. The brine around the outside of the anode is relatively bubble free due to gas disengagement when the bubble-brine mixture emerges from the top of the anode. Thus the brine outside the anode is of density  $\rho_B$ . Due to void fraction of the mixture within the anode  $\rho_B$  is greater than  $\rho_M$ . In this way circulation of brine and removal of the bubbles from the reaction zone result from the driving force caused by the difference in hydro-

drostatic head between the outside bubble-free brine and the bubble-brine mixture within the anode.

As shown in Fig. 2, brine circulation around a typical anode in commercial use takes place not only down through the interelectrode gap (path A), but also through the ends of the anode slots (path B). Since the primary benefit to voltage reduction is obtained when chlorine bubbles are rapidly swept out of the anode-cathode gap, path A circulation is by far the

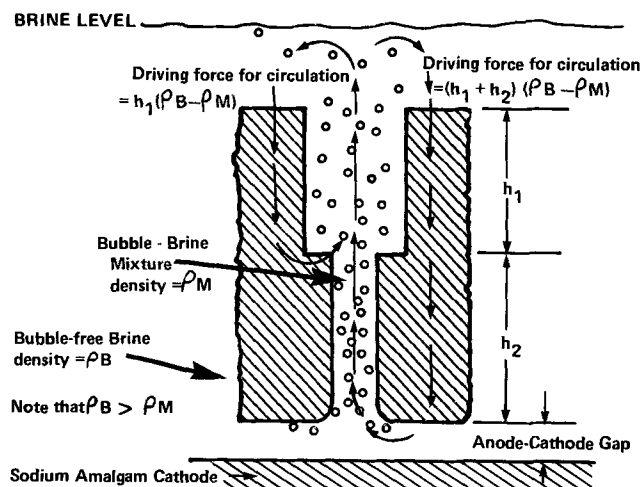


Fig. 1. Anode hydrodynamics

\* Electrochemical Society Active Member.

<sup>1</sup> Present address: The Marstolin Group, Hamilton 5, Bermuda.

Key words: hydrodynamics, anodes, scale-up, gas lift pump.

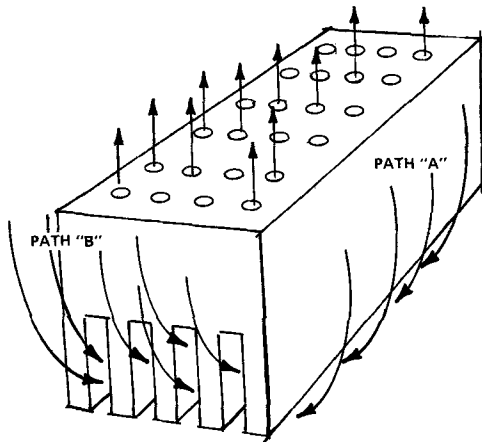


Fig. 2. Typical brine circulation paths

most important to achieving low operating voltages. A patent has been issued to Olin Corporation wherein all brine circulation is forced to also be gap circulation by using several novel anode designs (3).

**Experimental**

In the present series of studies the experimental anode was 610 mm long  $\times$  229 mm wide  $\times$  152 mm high. This is one-half the length of a commercial Olin E-510 cell anode. The test apparatus consisted of a brine feed system, mercury pumping system, and a steel bottomed Lucite cell large enough to accommodate the anode and provide clearances around the anode equivalent to those commercially used. Flow rates for brine and amalgam as well as cell temperature were consistent with industrial operating conditions.

**Results and Conclusions**

For the purpose of isolating the brine level effect in this analysis we will assume that all other cell variables which are a function of anode position in the cell do not interact with brine level effects and remain constant. Actual experimental data showed that only minor errors are introduced by this assumption.

Neglecting dynamic head effects, the brine level relative to the bottom of the graphite anode plane is a straight line function of the slope. If the cell brine inlet level is at 45 mm above the bottom plane of the anodes, and using the dimensions shown in Fig. 3, we can derive the equation

$$(BL)_N = 45 \text{ mm} + \left[ 6 \frac{\text{mm}}{\text{m}} \times \frac{0.612\text{m}}{\text{anode}} \times (N - 1) \right] \quad [1]$$

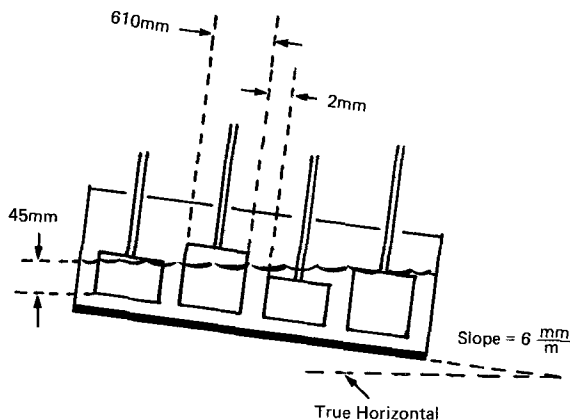


Fig. 3. Brine level vs. anode position

where  $(BL)_N$  is the brine level at the leading edge of an anode in position  $N$ ; and  $1 \leq N \leq 20$ . Note that for this example  $N$  and bus bar number are identical since we are assuming only one post per anode and a bus bar for each post.

Figure 4 graphically depicts the method of numbering and assumed cell arrangement used in this example. For simplicity of electrical circuit analysis we assume our commercial cell room consists of 250 cells, each 1 anode wide and 20 anodes long. As is usual in mercury cell plants, anodes in any cell are electrically in parallel while anodes in the same position from cell to cell are electrically in series.

The anode age distribution for any given bus number is linear. For example, suppose one measures all anodes in position 5 from cell No. 1 through No. 250 inclusive. If the oldest (thinnest) anode is then called No. 1 and the newest (thickest) called No. 250 a straight line age distribution will result from new to "throw away" (or stub loss) thickness. The anodes in this example are 152 mm thick when new. If 100 mm of the anode is used and 52 mm is stub loss, the anodes along any bus in the cell room are linearly distributed in thickness from 52 to 152 mm. The solid black line of Fig. 5 depicts this relationship. From Eq. [1], the brine level at any row position can also be calculated. Typical values are shown as horizontal dotted lines in Fig. 5. The fraction of anodes  $F_s$  submerged at row  $N$  can then be calculated. For any given row, the number of anodes submerged is given by the intersection of the brine level in that row with the age distribution line of Fig. 5. The fraction of anodes submerged ( $F_s$ ) is simply the anode number of the intersection point divided by the total number of anodes (250 in this case).

The average circuit voltage drop along any bus is given by the weighted average voltage drop at that bus position for each cell. This results in the general equation

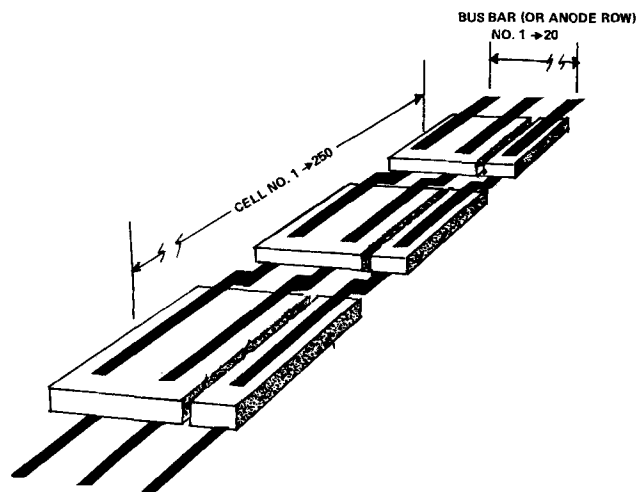


Fig. 4. Schematic of cell and anode positions

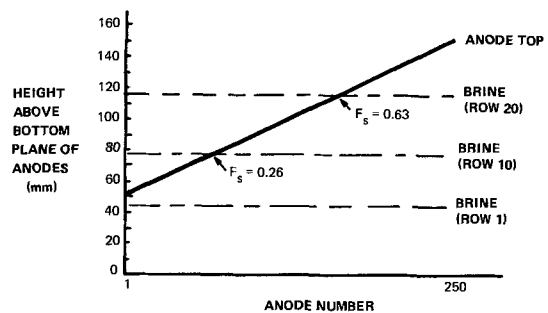


Fig. 5. Relation between brine level and anode age

$$V_N = F_S V_S + (1 - F_S) V_U \quad [2]$$

where  $V_N$  = circuit voltage along a given bus bar  
 $F_S$  = fraction of anodes submerged along bus bar N  
 $V_S$  = experimentally determined voltage of submerged anode at given current density  
 $V_U$  = experimentally determined average voltage of unsubmerged anodes over the range of nonsubmergence

For any given anode design,  $V_U$  as well as  $V_S$  must be determined experimentally. Figure 6 gives the shape of typical experimental data obtained in this study. Note that increasing the brine level above the top of the anode does not result in additional voltage improvement. However, decreasing brine level below the top of the anode at any current density results in considerable worsening of the voltage. This effect is more noticeable as the current density increases. This is probably due to the critical need for increased circulation rates at higher current densities and indicates that anodes should be designed according to the current density at which they are to operate.

With the experimental data represented by Fig. 6, the average voltage ( $V_U$ ) for those anodes which are unsubmerged in any particular row as well as the voltage for submerged anodes can then be substituted into Eq. [2]. Thus, the cell room voltage at a given current density along any particular bus can be predicted.

Figure 7 gives experimentally determined data obtained for one particular graphite anode design investigated in this study.

Note that the typically shaped qualitative curve described in Fig. 6 again reappears quantitatively in Fig. 7. Upon examination of Fig. 7, the importance of the gas lift pump principle to low voltage operation can be further appreciated.

At brine levels between 0 mm and about -50 mm an increase in current density produced an increase in voltage as shown. However, at brine levels which were lower than about -70 mm relative to the top of the anode a much greater increase in voltage was experienced for a given current density increase. The point of inflection occurring between about -50 and -70 mm represents a change of hydrodynamic mechanism.

The anode used for the data of Fig. 7 was the typical slot and hole design shown in Fig. 2. The top of the slot started 51 mm below the top of the anode. Thus, one can explain the more severe voltage increases at low brine levels by realizing that once the brine level dropped below the top of the slot, gas lift pump or percolation-type circulation was no longer possible and circulation reverted to the mechanism of free convective lift due to bubble buoyancy. The smaller vertical separation of current density lines to the left of the -50 mm level of Fig. 7 is direct evidence of the voltage advantage due to the rapid brine cir-

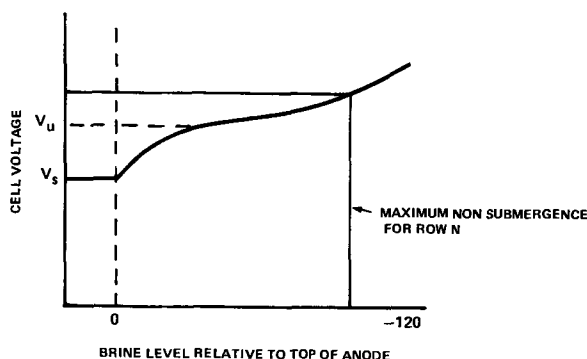


Fig. 6. Typical functional relation between anode voltage and brine level.

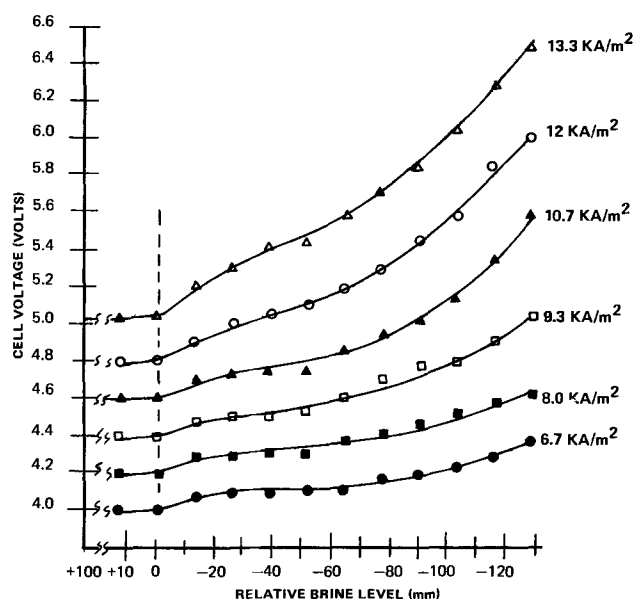


Fig. 7. Cell voltage as a function of brine level relative to the top of a graphite anode.

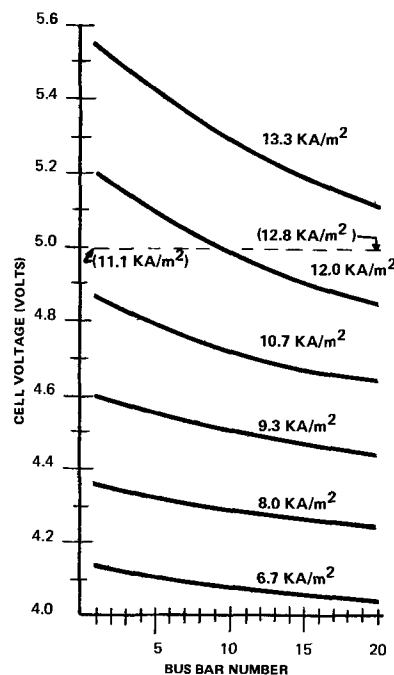


Fig. 8. Cell voltage profile at various current densities as a function of bus bar number.

ulation and bubble detachment provided by the gas lift pump principle.

Using the data of Fig. 7 and Eq. [2] one can plot the cell voltage at any bus bar position with current density as a parameter. The result is given in Fig. 8.

Two points of significant importance should be noted from Fig. 8. Firstly, let us suppose that the cell room is operated under a condition of uniform current density; i.e., the current in each bus bar is equal. Under this condition, due to the brine level effect alone, the average circuit voltage from bus to bus along the length of a given cell will decrease and the control panel rectifier voltage will indicate some value of an average cell voltage.

Secondly, if the cell room anodes are adjusted to a given voltage (say 5V as indicated in Fig. 8) then the current density at the inlet bus position is significantly different from the current at the outlet bus. In this example the brine level effect results in a more

than 10% increase in current density from the inlet to the outlet end of the cell.

### Summary

It has been shown that brine level is an important variable affecting the operating voltage of graphite anodes in mercury-type chlor-alkali cells. In addition, a method of analyzing laboratory data has been presented which enables one to predict the effect of this variable on the operating voltage and current distribution in a commercial cell room.

Manuscript received Nov. 19, 1973. This was Paper 147 presented at the Houston, Texas, Meeting of the Society, May 7-11, 1972.

Any discussion of this paper will appear in a Discussion Section to be published in the June 1975 JOURNAL. All discussions for the June 1975 Discussion Section should be submitted by Feb. 1, 1975.

The publication costs of this article have been assisted by The Marstolin Group.

### REFERENCES

1. W. C. Gardiner, *Electrochem. Technol.*, **1**, 71 (1963).
2. K. Takata and H. Morishita, *Denki Kagaku*, **32**, 586 (1964).
3. P. A. Danna, U.S. Pat. 3,558, 464 (1971).

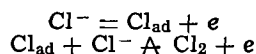
## Studies on the Mechanism of the Chlorine Electrode Process

Fumio Hine\* and Masaki Yasuda

Nagoya Institute of Technology, Nagoya 466, Japan

### ABSTRACT

The chlorine electrode process on the graphite anode under real conditions of chlor-alkali cells has been studied. In relatively low potential range up to 1.25V vs. SCE, two consecutive charge-transfer reactions occur, and the second is rate determining



The potential deviates from the Tafel line at high current densities, where the carbon oxide (C-O<sub>H</sub>) forms on the electrode surface, and the active sites for the chlorine electrode process diminish.

Substantial development of both science and engineering has taken place in the chlor-alkali industry during the past 20 years. Reduction of the cell voltage at high current densities is a most important goal in practical cell operation. The chlorine overvoltage and the IR drop near the graphite anode are major factors in the voltage balance of the amalgam-type cell (1). Even in the diaphragm cell, the situation is essentially the same.

The chlorine electrode in molten salts has been studied by some authors (2-8), but relatively few studies have been made in aqueous solutions (8-11). Electrode behavior in aqueous solutions is complicated by the formation of an oxide layer on the surface of graphite anode during electrolysis of chloride solution because of discharge of H<sub>2</sub>O and/or OH<sup>-</sup> with chlorine. Thus the effect of the carbon oxide layer on the chlorine evolution reaction should be considered (12, 13). Formation of the higher oxide [designated as (C-O<sub>H</sub>) hereafter] becomes a major factor in the electrochemical consumption of graphite anodes; furthermore, the oxide causes an increase in chlorine overvoltage due to occupation of the active sites on the working electrode (13).

The mechanism of the chlorine electrode process will be discussed with respect to results obtained using rotating-disk and rotating-cylinder graphite electrodes in acidified NaCl solutions. A large Tafel slope rather than the theoretical value ( $2.3 \times 2RT/F$ ) at high current densities will also be discussed with assumption of formation of (C-O<sub>H</sub>) on the electrode.

### Experimental Procedure

Rotating-disk and rotating-cylinder graphite electrodes were used. Properties of the specimen were as follows: specific gravity, 1.71; specific resistance,  $55 \times 10^{-5}$  ohm·cm; vanadium content, 3 ppm; ash, less

than 0.1%. A graphite rotating disk of 11 mm diam (ca. 0.95 cm<sup>2</sup> working area) and 25 mm long was screwed at the end of the Ti-shaft with a Teflon sleeve. A graphite cylinder, 12 mm diam and 10 mm long, was mounted to the Ti-shaft, and graphite surface was covered with chlorine-resistant plastic resin except for a small part (ca. 0.2 cm<sup>2</sup>) as working surface. These electrodes were treated in 6N HCl at 40-50 A/dm<sup>2</sup> for at least one month. The electrode was placed at the center of the measurement cell of ca. 1 liter in capacity having a Pt counterelectrode which was separated by a sintered glass diaphragm. Preelectrolysis of the electrode was carried out at 5 A/dm<sup>2</sup> for an hour prior to measurement.

A calomel electrode in contact with 3.3N KCl was used as reference, and a very small liquid junction potential was found. The current interruption method was employed to eliminate a large IR drop near the working electrode due to bubbles.

Although preelectrolysis of the solution was not necessary according to Yokoyama and Enyo (14), pretreatment with graphite anode and Pt cathode was sometimes made. Results obtained were not affected. Moisture and temperature of chlorine or mixture of Cl<sub>2</sub> and N<sub>2</sub> were brought to equilibrium before sending to the cell. Temperature was 50°C.

### Results and Discussion

Preelectrolysis of the working electrode shown above is most important for reproducibility of the polarization measurement. The surface roughness of graphite was not determined, but the specimen was not degraded during experiment. The graphite anode in practical chlor-caustic cell becomes rough (9), but graphite is resistive toward roughening in HCl (12). The chlorine overvoltage decreased gradually, then stabilized after eight weeks. Penetration of solution would be one reason (15), but it could also be due to slow conversion of the carbon oxide on the working surface into adatoms of chlorine (13). After the sur-

\* Electrochemical Society Active Member.

Key words: chlorine electrode, graphite anode, carbon oxide layer, coverage on graphite anode.

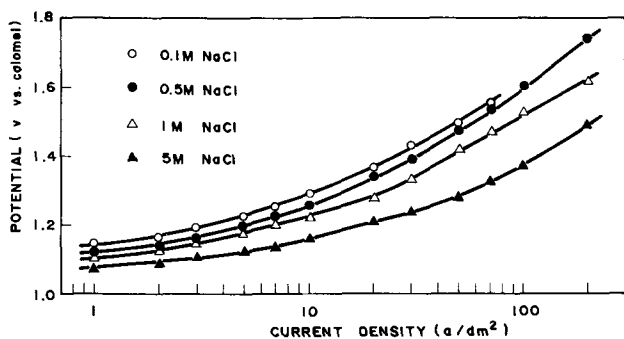


Fig. 1. Polarization curves of graphite anode in acidic NaCl solution (0.1M HCl) at 50°C.

face is stabilized, the chlorine electrode process takes place mostly at the surface, while micropores would also be working. But it was confirmed that the polarization curve was no longer affected by the micropores.

The anodic polarization is a function of the NaCl concentration as shown in Fig. 1. It is independent of the rotating speed, and hence no slow mass transfer step is involved. The Tafel slope at  $E < 1.25V$  is 120-130 mV/decade, but the potential rises quickly with current density thereafter. Full logarithm plot of the current density vs.  $Cl^-$  activity has a slope of 0.6 as shown in Fig. 2. The activity coefficient of  $Cl^-$  was estimated to be 0.8 in 5.1M NaCl at 50°C (16). The electrochemical reaction order for  $Cl^-$  is represented as follows (17)

$$z_{Cl^-} = \left( \frac{\partial \log i}{\partial \log a_{Cl^-}} \right)_{E, a_{Cl_2}} \cong 0.6 \quad [1]$$

The reaction order  $z_{Cl^-}$  in the previous paper (13) was unity because the process consisted of the chlorine electrode reaction only. On the other hand, the process under discussion here took the effects of the carbon oxide on the anode, and hence a small value of  $z_{Cl^-}$  was obtained.

The anodic polarization curves in chlorine saturated and chlorine-free solutions are shown in Fig. 3. Ionization of  $Cl_2$  occurs at  $E < 1.15V$  in chlorine saturated solution. In chlorine-free solution, the reversible potential is very low, and no backward reaction takes place even at less than 1.1V with the slope of 40 mV/decade.

The cathodic polarization in Fig. 4 is affected by the  $Cl_2$  concentration at a given rotating speed. It also depends on the rotating speed. The cathodic reaction is, therefore, controlled by diffusion of  $Cl_2$ .

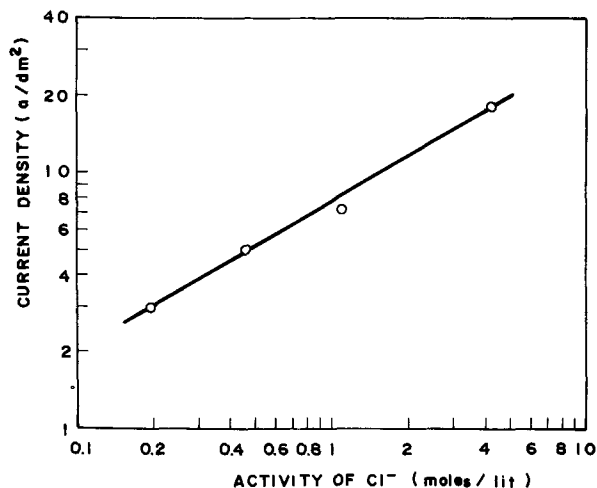


Fig. 2. Current density vs.  $Cl^-$  activity curve (logarithmic scale) at constant potential (1.2V vs. calomel).

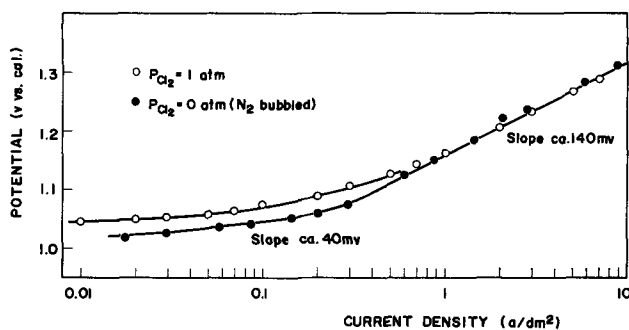


Fig. 3. Polarization curves of graphite anode in saturated NaCl (pH ca. 1.0) at 50°C.  $E_{eq} = 1.044V$  vs. calomel.

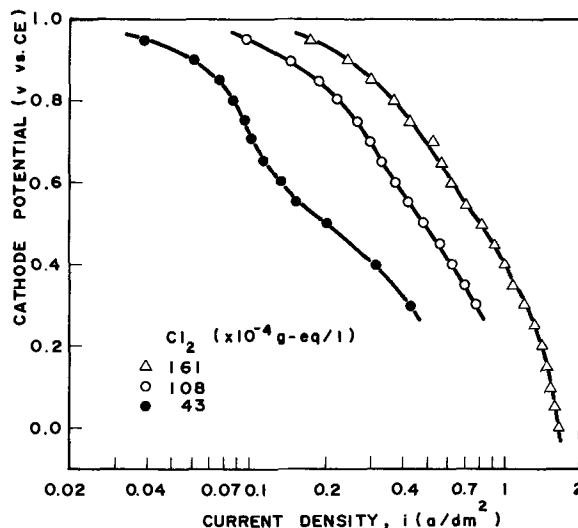


Fig. 4. Polarization curves of graphite cathode in saturated NaCl containing chlorine at 50°C. Rotating speed, 2130 rpm; pH, ca. 0.5.

The current density,  $i$ , controlled by diffusion of  $Cl_2$  at a rotating speed,  $m$ , is as follows (18)

$$i = A ([Cl_2] - [Cl_2]_s) \sqrt{m} \quad [2]$$

where  $A$  is a constant, and  $[Cl_2]$  and  $[Cl_2]_s$  are the  $Cl_2$  concentration in the bulk of solution and at the electrode surface, respectively. Also, the diffusion limiting current density,  $i_d$ , is represented by

$$i_d = A [Cl_2] \sqrt{m} \quad [3]$$

At the overvoltage more than 70 mV, the backward reaction is negligible, and hence

$$i = k [Cl_2]_s^{z_{Cl_2}} \quad [4]$$

where  $k$  is the electrochemical rate constant, and  $z_{Cl_2}$  is the reaction order for  $Cl_2$ . From Eq. [2]-[4]

$$\log i = \log k + z_{Cl_2} \log \left( 1 - \frac{i}{i_d} \right) [Cl_2] \quad [5]$$

The reaction order,  $z_{Cl_2}$ , is unity as shown in Fig. 5, and hence, Eq. 5 becomes simply

$$i = k [Cl_2] \left( 1 - \frac{i}{i_d} \right) \quad [6]$$

or

$$\frac{1}{i} = \frac{1}{i_r} + \frac{1}{A [Cl_2] \sqrt{m}} \quad [7]$$

where  $i_r = k [Cl_2]$ , and can be evaluated by projection of the  $1/i$  vs.  $1/\sqrt{m}$ . The intercept obtained from this extrapolation is very limited in accuracy since the rotation dependence has only been plotted over a small range. Coefficient  $A$  can be calculated by the equation

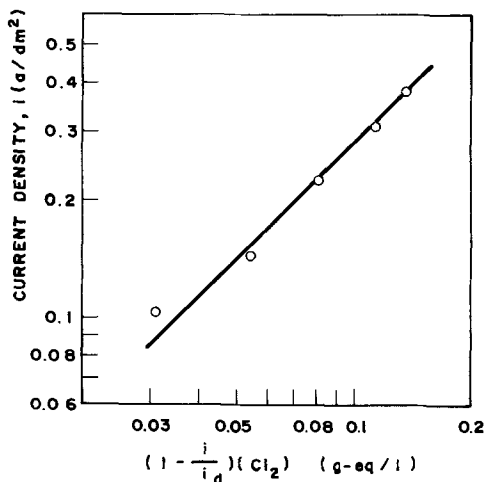


Fig. 5. Current density vs. Cl<sub>2</sub> concentration curve in saturated NaCl (pH ca. 0.1) at 50°C. Rotating speed, 2150 rpm.  $i$  and  $i_a$  were measured at 900 mV vs. calomel and 0V, respectively.

$$A = 0.62 nFD^{2/3} \left( \frac{\mu}{\rho} \right)^{-1/6} [Cl_2] (2\pi m)^{1/2}$$

But reliable data for the diffusion coefficient,  $D$ , of Cl<sub>2</sub> were not available. Experiments were repeated and the potential was set in several stages. From these data,  $A$  was computed by the method of least squares.

The potential vs. logarithm of  $i_r$  with the slope of 120 mV/decade is independent of the Cl<sup>-</sup> concentration as shown in Fig. 6, therefore, the reaction order with respect to Cl<sup>-</sup> is zero.

The exchange current density of the chlorine electrode process on a graphite electrode in a saturated NaCl (pH 0.5) is ca. 0.12 A/dm<sup>2</sup> (Fig. 7).

The overvoltage vs. current density curve in the range of very low overvoltage ( $|\eta| < 20$  mV) is exactly straight (Fig. 8), and hence the two directions of the chlorine electrode process are symmetrical. The polarization resistance is 0.15 ohm · dm<sup>2</sup>.

The stoichiometric number,  $\nu$ , is represented as follows

$$\nu = \frac{nF}{RT} (i_0) \left( \frac{\partial \eta}{\partial i} \right)_{\eta=0} = 1.2 \quad [8]$$

where  $n$  is the number of charge transfer for the overall reaction. Those experiments have been carried out in the range of low overvoltage as described above, and it has been confirmed that the cathode process has not been controlled by diffusion.

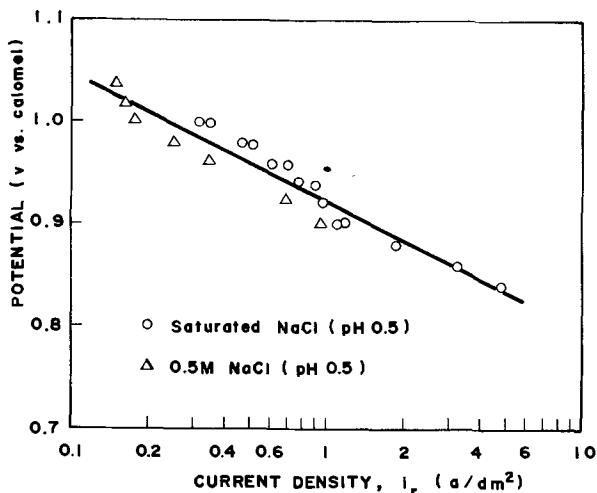


Fig. 6. Polarization curve of graphite cathode in NaCl at 50°C.  $p_{Cl_2} = 1$  atm.

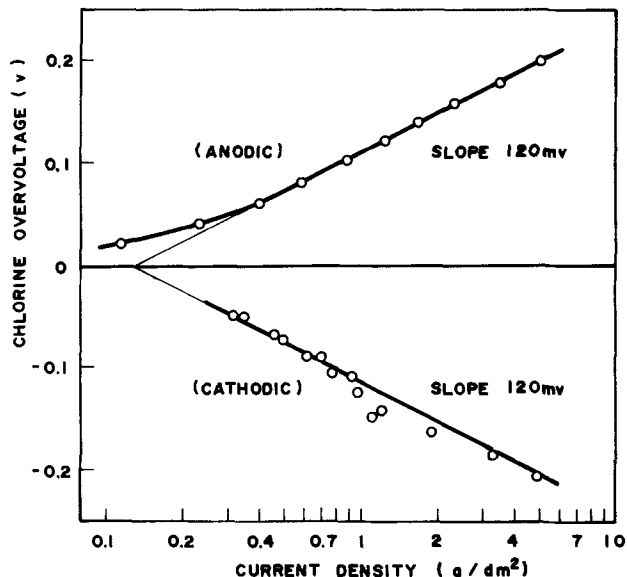


Fig. 7. Anodic and cathodic polarization curves of graphite in saturated NaCl solution (pH ca. 0.5) at 50°C.  $p_{Cl_2} = ca. 1$  atm.

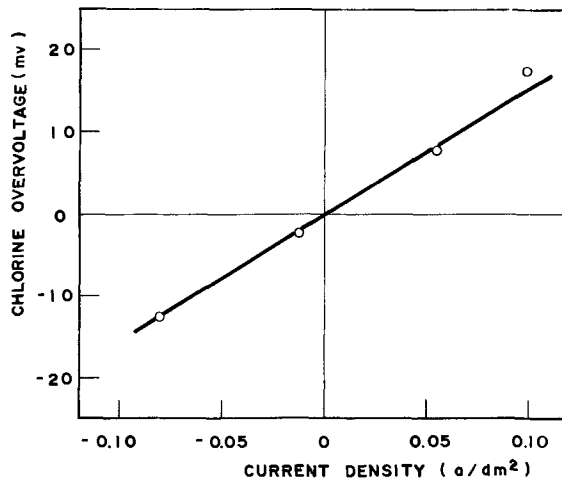


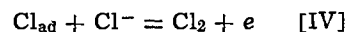
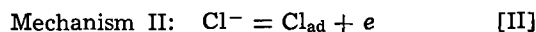
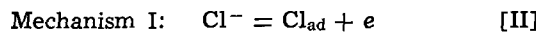
Fig. 8. Overvoltage vs. current density curve at low current densities. Saturated NaCl (pH ca. 0.8) at 50°C.  $p_{Cl_2} = ca. 1$  atm.

Various parameters evaluated from the experimental results are shown in Table I.  $z_{Cl^-}$  for anodic process in this table is 1 instead of 0.6 in Fig. 2. The results obtained by the galvanostatic anodic transient method is unity (13). Deviation of  $z_{Cl^-}$  might be due to disturbance of (C-OH) on the working electrode.

The over-all reaction of the chlorine/chloride system is



But the elementary reactions involved are as follows (7)



The parameters on the electrode kinetics corresponding to these mechanisms are listed in Table II, where the Langmuir-type isotherm is proposed for adsorption of Cl with the coverage  $\theta_{Cl}$ .

In the potential range up to 1.25V, the Tafel slope under  $p_{Cl_2} = 1$  atm is about 120 mV/decade. On the other hand, the slope is about 40 mV/decade at low current densities with  $p_{Cl_2} = 0$  (N<sub>2</sub> bubbled solution)

Table I. Parameters for the chlorine electrode process (experimental)

	Stoichiometric number, $\nu$	Tafel slope (mV/decade)	Reaction order		Exchange current density, $i_0$ (A/dm <sup>2</sup> )
			ZnCl <sup>-</sup>	ZnCl <sub>2</sub>	
Anodic	1 (ca. 1.2)	ca. 40 at low C.D.* 120 ~ 130 at high C.D.**	—	—	$(i_0)_{an.} = (i_0)_{ca.} = 0.12$ In sat'd NaCl (pH 0.5), $p_{Cl_2} = 1$ atm at 50°C.
Cathodic	1 (ca. 1.2)	ca. -120	1 (ca. 0.6) 0	0 1	

\* The backward reaction is negligible because  $p_{Cl_2} = 0$ .

\*\*  $E < ca. 1.25V$  vs. calomel. The Tafel slope increased very much at  $E > ca. 1.25V$ .

Table II. Parameters for the chlorine electrode process (theoretical)\*

Mechanism	Rate-determining step	$\nu$	Tafel slope**		ZnCl <sup>-</sup>		ZnCl <sub>2</sub>		
			$\theta_{Cl} \rightarrow 0$	$\theta_{Cl} \rightarrow 1$	$\theta_{Cl} \rightarrow 0$	$\theta_{Cl} \rightarrow 1$	$\theta_{Cl} \rightarrow 0$	$\theta_{Cl} \rightarrow 1$	
Anodic	I	Cl <sup>-</sup> = Cl <sub>ad</sub> + e	2	2RT/F	2RT/F	1	1	0	0
	II	2Cl <sub>ad</sub> = Cl <sub>2</sub>	1	RT/F	$\infty$	2	0	0	0
Cathodic	I	Cl <sup>-</sup> = Cl <sub>ad</sub> + e	1	2RT/F	2RT/F	1	1	0	0
		Cl <sub>ad</sub> + Cl <sup>-</sup> = Cl <sub>2</sub> + e	1	2RT/3F	2RT/F	2	1	0	0
	II	Cl <sub>2</sub> = 2Cl <sub>ad</sub>	1	—	—	—	—	1	0
		Cl <sub>ad</sub> + e = Cl <sup>-</sup>	2	—	—	0	0	1/2	0
		Cl <sub>2</sub> + e = Cl <sub>ad</sub> + Cl <sup>-</sup>	1	-2RT/F	-2RT/F	0	0	1	0
		Cl <sub>ad</sub> + e = Cl <sup>-</sup>	1	-2RT/3F	-2RT/F	-1	0	1	0

\* Langmuir-type isotherm was adopted for adsorption of Cl<sub>ad</sub>.

\*\* When  $\alpha = 0.5$ .

as shown in Fig. 3. The rate of the cathodic process [I] is negligible in this case. The Tafel slope for the anodic process of Mechanism II should be  $2.3 \times 2RT/F$  (=120 mV) at  $\theta_{Cl} = 1$  and  $2.3 \times 2RT/3F$  (=40 mV) at  $\theta_{Cl} = 0$ , and is in agreement with the experimental results. Thus, it is concluded that Mechanism II is appreciable, and reaction [IV] is rate determining.

Results of a previous paper (13) show that formation of the carbon oxide on PG- and GC-anodes in 1M HClO<sub>4</sub> increases with the anode potential, i.e., all of the surface oxide tend to the "higher oxide (C-O<sub>H</sub>)" at the potential range over ca. 1.3V. (C-O<sub>H</sub>) may form even in chloride solution, of course, the amount of formation decreases with increase in the Cl<sup>-</sup> concentration. The exchange between oxide (or adatom of oxygen) and chlorine depends on the potential and is significantly irreversible.

It is evident that the graphite anode is consumed by a considerable amount if it is preelectrolyzed at very high current densities such as 250 A/dm<sup>2</sup>. The rough surface after corrosion resembles the surface of the anode polarized in HClO<sub>4</sub> at high current densities where the oxygen electrode reaction may take place.

The polarization curves of the graphite anode preelectrolyzed in a saturated NaCl (pH ca. 2) at 250 A/dm<sup>2</sup> for about 6 hr is shown in Fig. 9. The chlorine current efficiency (volume ratio of chlorine to total gas) is also shown. At high current densities over 10 A/dm<sup>2</sup>, the potential deviates from the Tafel line, and

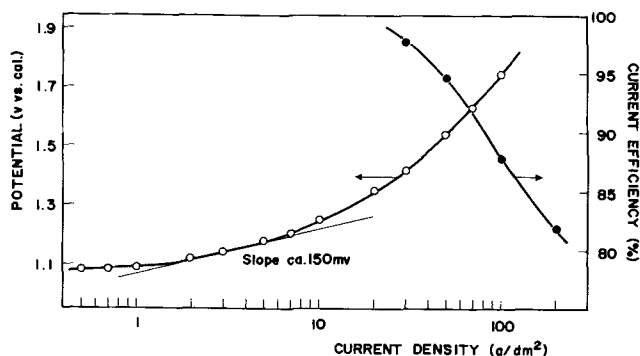


Fig. 9. Polarization curve and current efficiency for chlorine evolution reaction with graphite anode having rough, or corroded, surface in saturated NaCl (pH 2.3) at 50°C.

the chlorine current efficiency decreases with increase in current density. It is considered that the effect of the oxide layer on the anode is a major reason for deviation from the Tafel line at high current densities, and also the oxygen electrode process is not negligible even in a saturated NaCl solution at low pH such as 2 in the potential range over 1.7V.

In conclusion, Mechanism II is acceptable for the chlorine electrode process at relatively low current densities or at the potential range up to 1.25V, and reaction [IV] is rate determining.

Since the backward reaction is negligible at high potential ranges, Eq. [9] is obtained

$$i = k_D [Cl^-] \theta_{Cl} \exp(\alpha FE/RT) \quad [9]$$

where  $k_D$  is the reaction rate for the anodic direction of reaction [IV], and  $\alpha$  is the transfer coefficient (= ca. 0.5).  $\theta_{Cl}$  is the coverage of adatom of chlorine, and is assumed to be about unity.  $\theta_{Cl}$  decreases with formation of (C-O<sub>H</sub>), at high potential over 1.3V. In a small range of potential (ca. 1.25-1.5V), it can be assumed that the amount of the oxide is proportional to the potential, therefore,  $\theta_{Cl}$  decreases with potential

$$\theta_{Cl} = 1 - \theta_0 \quad (E > ca. 1.25V) \quad [10]$$

where  $\theta_0$  is the coverage of carbon oxide. Thus, we have

$$i' = k_D [Cl^-] (1 - \theta_0) \exp(\alpha FE/RT) \exp[-(1 - \alpha)f\theta_0] \quad [11]$$

where  $fRT$  is Temkin's parameter, and hence, the last term will show the factor of increase in the apparent activation energy for the chlorine electrode reaction due to existence of the oxide layer on the surface of the working electrode (19). From Eq. [9] and [11]

$$\frac{i'}{i} = (1 - \theta_0) \exp(-f\theta_0/2) \quad [12]$$

The straight line with the slope of  $2.3 \times 2RT/F$  in Fig. 10 is represented by Eq. [9], whereas the curve labeled  $i'$  follows Eq. [11]. Figure 11 represents the relationship between  $E$  vs.  $(i'/i)$  obtained from the polarization data such as Fig. 1. The chlorine current efficiency obtained by gas analysis was quite high at high current densities such as 250 A/dm<sup>2</sup> (Fig. 12). Therefore, the oxygen evolution reaction is negligible during experiment shown in Fig. 1.  $\theta_0$  is approximately proportional to the potential in a small range of potential (13).



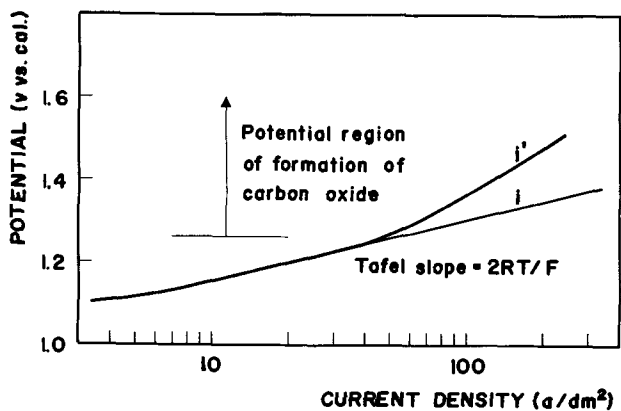


Fig. 10. Polarization curve of graphite in NaCl solution.  $i$ , Polarization curve represented by Eq. [9];  $i'$ , polarization curve represented by Eq. [11].

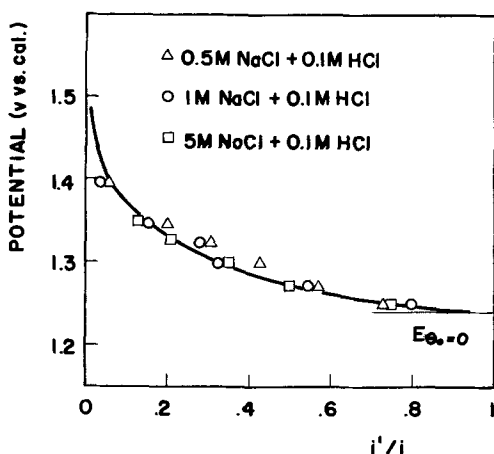


Fig. 11. Potential vs.  $(i'/i)$  curve

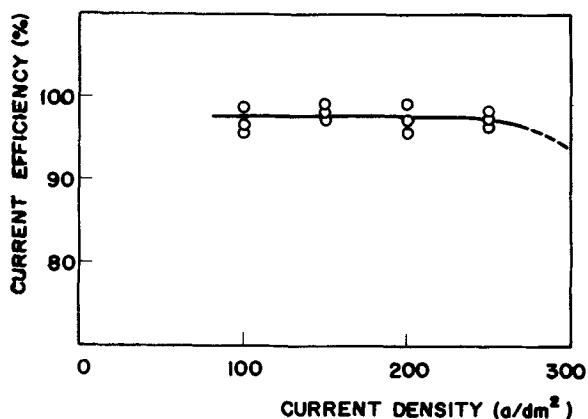


Fig. 12. Chlorine current efficiency vs. current density curve. The graphite anode was preelectrolyzed enough. Solution, saturated NaCl (pH 0.6-1.5) at 50°C.

Since the surface of graphite anode is rough, the oxygen electrode process might not be detected unless the current density is extremely high. It is therefore difficult to explain the exact relationship between  $\theta_0$  and  $E$ , but the relationship between  $\theta_0$  and  $(1 - \theta_0) \exp(-f\theta_0/2)$  in Fig. 13, which was obtained with PG and GC electrodes (13), resembles Fig. 11. The potential  $E_{\theta_0=0}$  can be estimated to be ca. 1.25V, while  $E_{\theta_0=1}$  is not obtained from Fig. 11. The active sites for the chlorine electrode process decrease with disturbance of adatom of oxygen and/or oxide layer, and the activation energy for the chlorine electrode may increase with increase in  $\theta_0$ .

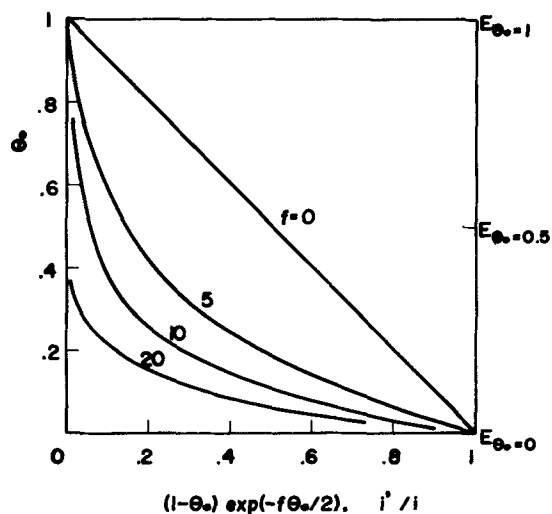
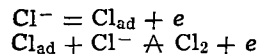


Fig. 13.  $\theta_0$  vs.  $(1 - \theta_0) \exp(-f\theta_0/2)$  curves under the assumption of  $\theta_0 \sim E_{\theta_0}$ .

It has been considered that the surface oxide affects the chlorine current efficiency, graphite consumption, and the overvoltage as well. The chlorine evolution reaction may not take place on the carbon-oxide layer. The "over-all oxygen electrode reaction," which involves formation of  $O_2$ ,  $CO$ , and  $CO_2$ , may take place on the graphite anode at high current densities even in concentrated chloride solutions, and the graphite anode might be corroded in this potential range.

**Conclusion**

The mechanism of the chlorine electrode process on the graphite anode under real conditions of chlor-alkali cells has been discussed. The electrochemical reaction takes place mostly at the surface of graphite anode, while very small current would pass through micropores of several millimeters deep of graphite. In the potential range less than 1.25V, the consecutive charge transfer reactions occur



and the second step is rate determining.

At higher potential ranges, the anode surface is covered by the carbon oxide, and the potential becomes high due to decrease of the active sites for the chlorine electrode process.

**Acknowledgment**

This work has been conducted as a part of the Ph.D. thesis of M. Yasuda, Kyoto University. The author wishes to express many thanks for the support of Olin Research Center, New Haven, Connecticut, and also for the kind suggestions of Dr. W. C. Gardiner.

A part of this research work was carried out with the financial support of the Ministry of Education, Japan, 743016.

Manuscript submitted Aug. 30, 1973; revised manuscript received ca. April 15, 1974.

Any discussion of this paper will appear in a Discussion Section to be published in the June 1975 JOURNAL. All discussions for the June 1975 Discussion Section should be submitted by Feb. 1, 1975.

The publication costs of this article have been assisted by F. Hine.

**REFERENCES**

1. F. Hine, *Electrochem. Technol.*, **6**, 69 (1968).
2. P. Drossbach, *This Journal*, **103**, 700 (1956).
3. A. M. Shams El Din, *Electrochim. Acta*, **4**, 242 (1961).
4. Iu. K. Delimanski and G. V. Shilna, *ibid.*, **10**, 973 (1965).
5. D. A. J. Swinkels, *This Journal*, **113**, 6 (1966).
6. P. Drossbach, *Electrochim. Acta*, **11**, 667 (1966).
7. W. E. Triaca, C. Solomons, and J. O'M. Bockris, *ibid.*, **13**, 1949 (1968).

8. P. Drossbach and H. Hoff, *ibid.*, **14**, 89 (1969).
9. L. J. J. Janssen and J. G. Hoogland, *ibid.*, **14**, 1097 (1969).
10. L. J. J. Janssen and J. G. Hoogland, *ibid.*, **15**, 339, 941 (1970).
11. L. J. J. Janssen and J. G. Hoogland, *ibid.*, **15**, 1667 (1970).
12. F. Hine and M. Yasuda, *Denki Kagaku (J. Electrochem. Soc. Japan)*, **39**, 530 (1971).
13. F. Hine, M. Yasuda, and M. Iwata, *This Journal*, **121**, 749 (1974).
14. T. Yokoyama and M. Enyo, *Electrochim. Acta*, **15**, 1921 (1970).
15. O. S. Ksenzhek and V. V. Stender, *Soviet Electrochem.*, **3**, 197 (1961).
16. "Denki Kagaku Binran" (Handbook of Electrochemistry, Japan), p. 121, Maruzen Publ., Tokyo (1964).
17. K. J. Vetter, "Transactions of the Symposium on Electrode Processes," E. Yeager, Editor, p. 47, John Wiley and Sons Inc., New York (1961).
18. V. G. Levich, "Physico-Chemical Hydrodynamics," p. 69, Prentice-Hall, Englewood Cliffs, N. J. (1962).
19. B. E. Conway, "Theory and Principles of Electrode Processes," p. 118, Ronald Press, New York (1965).

## Electroinitiated Polymerization of Tetrahydrofuran

A. N. Dey\* and E. J. Rudd

P. R. Mallory & Company, Incorporated, Laboratory for Physical Science, Burlington, Massachusetts 01803

### ABSTRACT

Electroinitiated polymerization of tetrahydrofuran (THF) was accomplished in 1M LiClO<sub>4</sub>-THF organic electrolyte solutions by anodic electrolysis on platinum electrodes in a three-compartment cell. THF was found to polymerize to form a viscose gel at 25°C. The rate of polymerization was followed by measuring the electrical resistance of the organic electrolyte solution as a function of time after the electroinitiation. The rate of polymerization was found to increase with the increase in the anodic charge passed. The average molecular weight of the polymer was determined to be  $2 \times 10^5$  by viscometry. The polymer was found to be "living" in nature. Electrochemical evidence was presented to show that the initiation occurred as a result of the electro-oxidation of THF rather than the ClO<sub>4</sub><sup>-</sup> anion.

The chemical polymerization of THF has been studied extensively (1). It has been established that the polymerization occurs strictly by a cationic mechanism and the catalysts are of the strong acid or Lewis acid type or of salts derived from them. Electroinitiated polymerization of THF has also been reported (2-4). The mechanism proposed (3) for the electroinitiation involved the oxidation of the anion, e.g. ClO<sub>4</sub><sup>-</sup> rather than the THF itself. In this paper we wish to present evidence which indicates that electroinitiation occurs as a result of the electro-oxidation of THF itself. The results reported here have also a direct bearing on the high energy density organic electrolyte lithium batteries (5-8) with THF as a solvent.

### Experimental

**Materials.**—Tetrahydrofuran (Eastman Kodak practical grade) was purified by pretreating with lithium aluminum hydride and subsequent distillation under argon atmosphere. Anhydrous lithium perchlorate (G. Frederick Smith Chemical Company) was dried under vacuum at 120°-140°C for 48 hr. Lithium foil (Foote Mineral Company) was used as received.

LiClO<sub>4</sub> solutions in THF were prepared in an argon-filled dry box. The water content of the solutions was determined by gas chromatography (Perkin Elmer Model No. 801, hot wire detector) using a 15 × 0.25 in. column of Porapak Q at 125°C with a helium gas flow of 20 cm<sup>3</sup>/min. The moisture contents of the solutions were typically 0.01% or less.

**Electrodes.**—The working electrode was made of a smooth platinum wire sealed through a glass tube. The geometric surface area of the exposed portion of the platinum wire was approximately 0.3 cm<sup>2</sup>. The reference and the counterelectrodes were made by

pressing lithium foil on expanded stainless steel current collector.

**Cells.**—A three-compartment glass cell was used for both the electroinitiated polymerization and the voltammetric measurements. The central compartment contained the working electrode, the counterelectrode compartment was connected to the central compartment via a fritted glass disk of medium porosity, and the reference electrode compartment was connected by a Luggin capillary which was placed close to the working electrode. For the electroinitiated polymerization experiments, the working electrode compartment was modified to allow the insertion of two platinized platinum electrodes used for the measurement of electrical resistance of the solution. This was measured at 1 kc employing an impedance bridge (General Radio Company, Type No. 1650-A).

**Polymerization.**—Electroinitiated polymerization experiments were carried out by anodically electrolyzing the solution in the working electrode (Pt) compartment at constant currents of 0.2 and 1 mA corresponding to current densities of 0.67 and 3.3 mA/cm<sup>2</sup>, respectively. After a certain time the electrolysis was stopped and two platinized platinum electrodes (from a conductivity cell) were inserted in the cell in order to measure the electrical resistance of the solution. The solution became progressively viscose with time as a result of the polymerization of THF and the electrical resistance of the solution increased accordingly. The rate of polymerization of THF was followed by measuring the resistance (instead of the viscosity) of the solution as a function of time at 25°C. There was no polymerization of THF in either the reference or the counterelectrode compartments. Presence of either the Li metal or the moisture (0.5% or more) in the working electrode compartment inhibited the polymerization. Electroinitiation occurred on both Pt and graphite electrodes.

\* Electrochemical Society Active Member.

Key words: polytetrahydrofuran, electroinitiation, organic electrolytes, polymerization, living polymer, lithium perchlorate, tetrahydrofuran, lithium batteries, high energy density batteries, organic electrolyte batteries.

The THF polymers were isolated by terminating the reaction with addition of excess distilled water to the solution of the working electrode compartment, and filtering the precipitated polymer. The polymer was purified by successive (three times) dissolution in pure THF and reprecipitation in distilled water. The material was finally dried under vacuum to remove excess monomeric THF and was weighed to determine the conversion. Equilibrium conversions of 30-40% were realized at 25°C.

**Molecular weight.**—The average molecular weights of the polymers were determined by viscometry in benzene at 30°C in a Cannon Fenske viscometer. Molecular weights were computed from the relation (9)

$$[\eta] = 1.31 \times 10^{-3} \bar{M}_v^{0.60}$$

where  $\bar{M}_v$  is the average molecular weight. The intrinsic viscosity  $[\eta]$  was determined by extrapolating the linear plots of  $\eta_{sp}/C$  vs.  $C$  where the concentration ( $C$ ) of polymer was expressed in grams/100 mliters. Specific viscosity ( $\eta_{sp}$ ) was calculated from the measured relative viscosity ( $\eta_r$ ) according to the relations (9)

$$\eta_{sp} = \eta_r - 1$$

$$\eta_r = t_{\text{solution}}/t_{\text{solvent}}$$

where  $t_{\text{solution}}$  is the flow time of the polymer solutions and  $t_{\text{solvent}}$  is the flow time of the pure solvent (benzene).

**Electrochemical measurements.**—Cyclic voltammetric and the steady-state measurements were carried out on Pt wire electrodes in 1M LiClO<sub>4</sub>-THF solutions in the regions of potential anodic to Li/Li<sup>+</sup> potential using a Wenking potentiostat (6354-TR), a Wavetek function generator, and a x-y recorder.

### Results and Discussion

**Rate of polymerization.**—The electroinitiation of the polymerization of THF was carried out at constant currents of 1 and 0.2 mA. The durations of electrolysis were 1 and 4 hr at 1 mA, and 20 hr at 0.2 mA, corresponding to total charges of 3.6 coulombs, and 14.4 coulombs, respectively. The rates of polymerization as reflected from the plots of the electrical resistance of the solution after electroinitiation at 1 mA for 1 hr increased with time for approximately 130 hr and, thereafter, it leveled off indicating that the polymerization reaction reached an equilibrium. The viscosity of the solution increased progressively and the final material had the appearance of a clear viscous gel. There was no evidence of salting out of LiClO<sub>4</sub> electrolyte salt. The rate of polymerization, as determined from the slopes of the plots shown in Fig. 1, was found to increase drastically with the increase in the total anodic charge ( $Q$ ) passed during electroinitiation. Assuming that the electroinitiation of the THF polymer occurs as a result of electrochemical generation of the initiating species, the increase in the polymerization rate with the anodic charge is expected (10), assuming that the current efficiency of electroinitiation remains unchanged.

**Molecular weight.**—The average molecular weights of the polymer as determined from viscometry are shown in Table I. Although the data are insufficient to draw any conclusions in regard to the dependence

Table I. Average molecular weight of the electroinitiated THF polymer as determined from viscometry (9) in benzene at 30°C

Electroinitiating conditions			
Current (mA)	Time of anodic electrolysis (hr)	Intrinsic viscosity	Average molecular weight, $\bar{M}_v$
0.2	20	2.04	$2.1 \times 10^5$
1.0	4	2.40	$2.7 \times 10^5$
1.0	1	1.73	$1.6 \times 10^5$

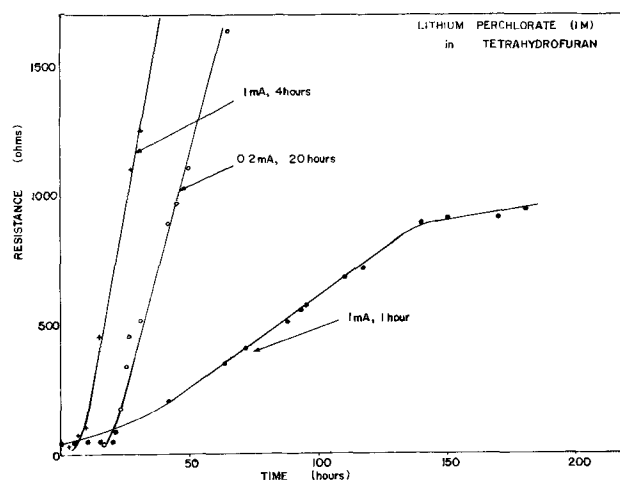


Fig. 1. Change in electrical resistance of the 1M LiClO<sub>4</sub>-THF solution with time after electroinitiation at 1 mA for 1 hr, 0.2 mA for 20 hr, and 1 mA for 4 hr.

of the molecular weight on the initiating condition, it is clear that a true polymer with molecular weights<sup>1</sup> in the range of  $2 \times 10^5$  is formed by anodic electrolysis of 1M LiClO<sub>4</sub>-THF organic electrolyte. The dried polymer had the appearance of a stiff white solid very much like polyethylene or polypropylene.

**“Living” polymer.**—The “living” nature of the electroinitiated THF polymer was established by studying the change in the electrical resistance of 1M LiClO<sub>4</sub>-THF solutions (which was initiated at 4 mA for 1.2 hr) with time of equilibration at different temperatures and is shown in Fig. 2. In a “living” polymer system the polymer molecules establish an equilibrium with the monomer units at any given temperature by either depolymerizing (with increasing temperature) or polymerizing (with decreasing temperature). This is reflected in Fig. 2. It is seen that at 25°C the resistance increases steadily with time, indicating the process of polymerization. On increasing the temperature to 54°C, the resistance drops; first sharply (indicating the effect of temperature on the resistance), and then steadily for 25 hr indicating the process of depolymerization. On decreasing the temperature to 40°C, the resistance increases again and on further decrease to 14°C, there is again a sharp rise followed by a steady rise in resistance for 50 hr and

<sup>1</sup> One reviewer suggests that discrepancy in the dependence of the molecular weights on the total charge may be explained in terms of current efficiency of initiation.

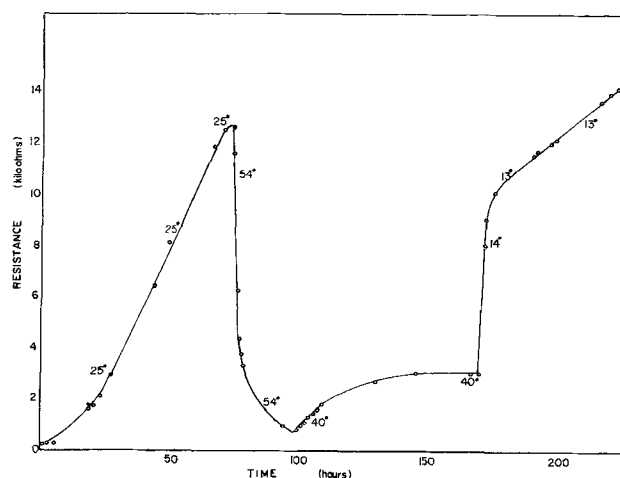


Fig. 2. Change in electrical resistance of 1M LiClO<sub>4</sub>-THF solution with time at different temperatures of equilibration after electroinitiation at 4 mA for 1.2 hr.

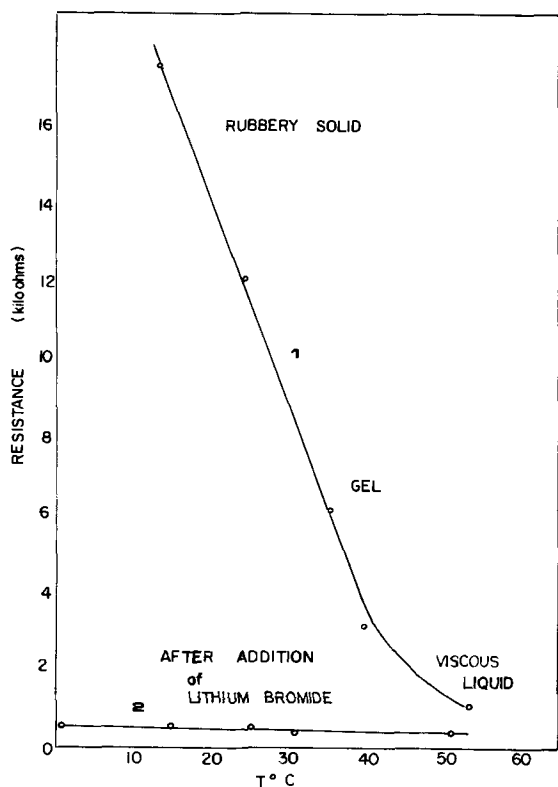


Fig. 3. Equilibrium electrical resistance of 1M  $\text{LiClO}_4$ -THF polymer solutions as a function of temperature, curve 1 before and curve 2 after addition of excess LiBr (termination).

more. The initial sharp rise in resistance is due to the temperature effect and the sustained rise in resistance over 50 hr is due to the process of repolymerization at low temperature.

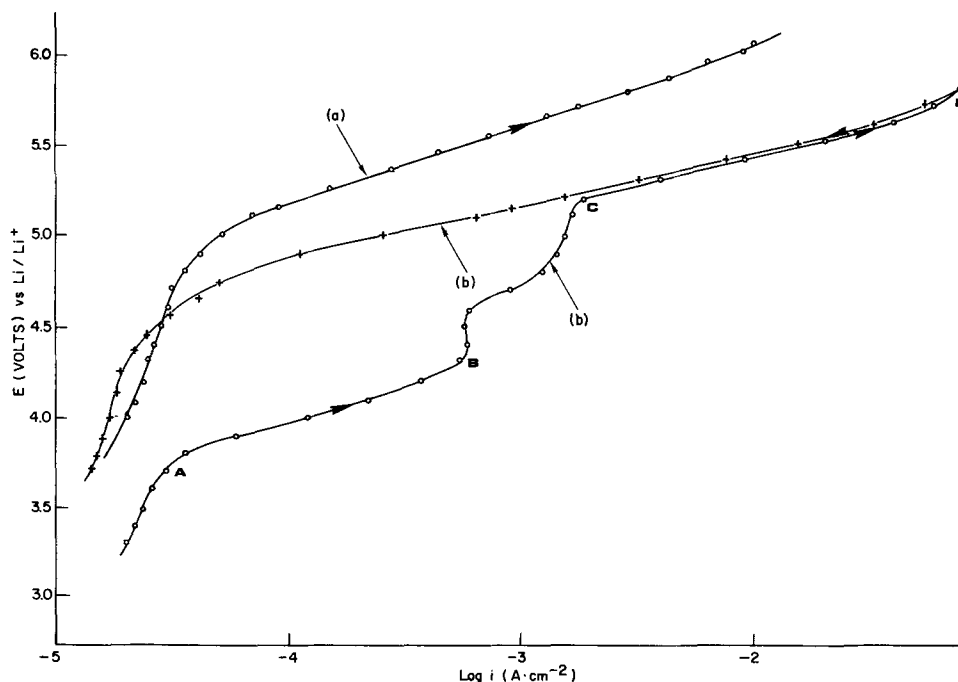
The "living" nature of the polymer was further demonstrated by comparing the equilibrium resistance of the solution as a function of temperature, before and after the termination of the "living" polymer, and is shown in Fig. 3. Curve 1 represents the behavior of the "living" polymer before the termination. The consistency of the solution at the various regions of temperature is shown on the curve itself.

At 54°C the solution assumes the consistency of a viscous liquid. To this liquid, a saturated solution of anhydrous LiBr in THF was added to terminate (11) the THF polymer so that they lose their "living" nature. The behavior of the "terminated" polymer solution is shown in curve 2. The resistance as well as the consistency of the terminated solution remain relatively unchanged with change in temperature compared to the "living" system.

**Electrochemical studies.**—Voltammetric studies were carried out in an attempt to understand the electrochemical reactions involved in the process of electroinitiation of the THF polymers. The steady-state current potential curves obtained on a smooth platinum electrode in 1M  $\text{LiClO}_4$ -THF solution are shown in Fig. 4, curve b. Significantly large anodic currents are evident at potentials of 4.0V vs.  $\text{Li/Li}^+$  from the ascending portion of the curve b. The process appears to be partially inhibited (region BC of curve b) and in this region the formation of a black film on the electrode surface was observed. This film remained on the surface during the descending portion of the curve and the inhibiting effect is reflected in the hysteresis. This film is most likely due to the rapid initiation of the polymerization of THF in the vicinity of the electrode where the initiating species are formed. The hysteresis may be due to the impedance of the polymer film. Prolonged electrolysis at 4.0V vs.  $\text{Li/Li}^+$  led to an extensive polymerization of THF. The steady-state current potential curve was also obtained in a nonpolymerizing medium, viz., 1M  $\text{LiClO}_4$  in propylene carbonate (PC) and is shown in Fig. 4, curve a. It is seen that no significant oxidation occurs below the potential of 5.0V vs.  $\text{Li/Li}^+$  reference and there was no formation of a passive film on the Pt surface. Since the only difference between the two mediums is the solvent, it is reasonable to conclude that the large anodic current at 4.0V vs.  $\text{Li/Li}^+$  reference obtained in 1M  $\text{LiClO}_4$ -THF medium is due to the oxidation of the solvent THF.

The current-potential curves were also obtained by triangular sweep voltammetry in 1M  $\text{LiClO}_4$ -THF and 1M  $\text{LiClO}_4$ -PC and are shown in Fig. 5 (i) and (ii), respectively. Again, the oxidation occurs at markedly less anodic potential in 1M  $\text{LiClO}_4$ -THF than in 1M  $\text{LiClO}_4$ -PC. The cathodic profile of the curves may correspond to the reduction of the oxidized species. Voltammograms were also obtained in 1M  $\text{LiPF}_6$ -THF and in 1M  $\text{LiBF}_4$ -THF and were identical to

Fig. 4. Steady-state current-potential behavior in (curve a) 1M  $\text{LiClO}_4$ -PC and (curves b) 1M  $\text{LiClO}_4$ -THF solutions on smooth Pt electrodes.



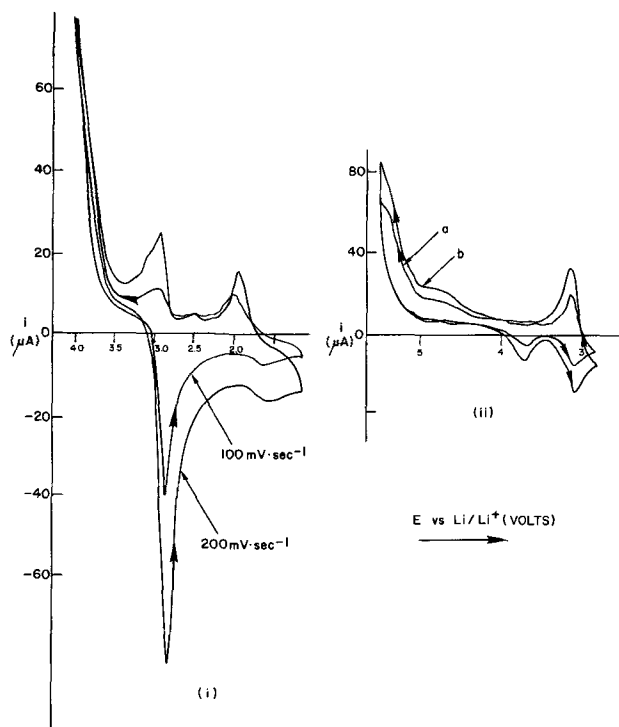
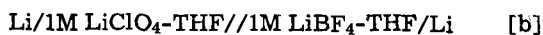


Fig. 5. Cyclic voltammograms of (i) 1M LiClO<sub>4</sub>-THF and (ii) 1M LiClO<sub>4</sub>-PC solutions at Pt electrode; (a) Scan rate 100 mV sec<sup>-1</sup>, (b) scan rate 200 mV sec<sup>-1</sup>.

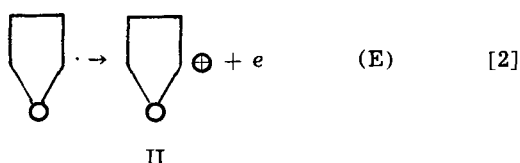
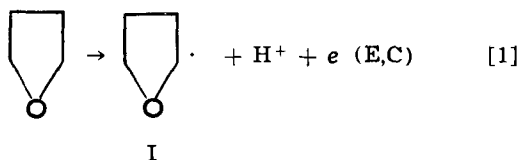
those in 1M LiClO<sub>4</sub>-THF, indicating the oxidation of the solvent rather than the anion. Electroinitiated polymerization occurred with LiPF<sub>6</sub> and LiBF<sub>4</sub> salts as well.

It may be argued that the comparison of cyclic voltammograms of the two solvent systems, viz., THF and PC, and the salts, viz., LiClO<sub>4</sub>, LiBF<sub>4</sub>, and LiPF<sub>6</sub>, is not valid because of the possible change in the potential of the Li/Li<sup>+</sup> reference electrode. This was checked by measuring the potential of the following cells with liquid junctions

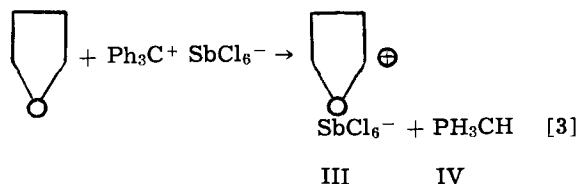


The potential differences of cells [a] and [b] were 0.085 and 0.022V, respectively. The above potential differences include the liquid junction potential. Therefore, the change in the Li/Li<sup>+</sup> reference potential from THF to PC is insignificant compared to the difference in oxidation potentials of approximately 1.5V observed between the two systems in the potentiostatic and cyclic voltammetric measurements shown in Fig. 4 and 5, respectively.

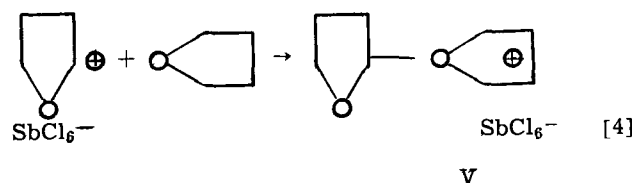
**Mechanism.**—On a first approximation the electro-oxidation of THF may be represented by an ECE mechanism, *i.e.*, electron transfer step-chemical step-electron transfer step, as has been used to describe the electro-oxidation of related compounds (12-15)



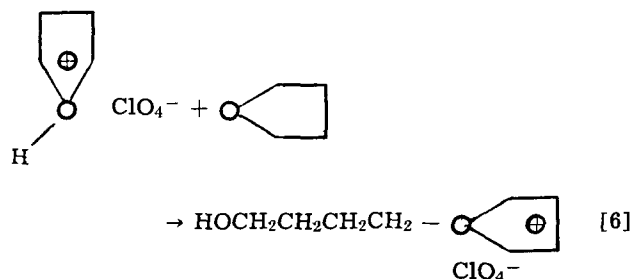
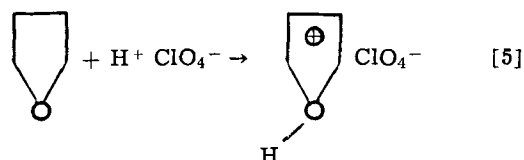
It has been established (1) that the initiation requires the formation in some manner of a THF Oxonium ion  $\left( \text{R} - \text{O}^{\oplus} \right)$  in order for the propagation reaction to take place. It was shown (16) that the chemical polymerization of THF with catalysts such as Ph<sub>3</sub>C<sup>+</sup>SbCl<sub>6</sub><sup>-</sup> was initiated by the transfer of a hydride ion from THF to the carbonium ion salt catalyst



The formation of Ph<sub>3</sub>CH (IV) was demonstrated by NMR spectroscopy. The THF cation (III) formed as a result of the hydride ion abstraction from the α-carbon atom of THF, reacts (17) with another molecule of THF to form the Oxonium ion (V) which starts the propagation (1)



The end group is an acetal. The electrochemically formed THF cation (II) is expected to initiate polymerization reaction in a similar manner. The counterion for the THF cation in this case will be ClO<sub>4</sub><sup>-</sup> instead of SbCl<sub>6</sub><sup>-</sup>. The proton formed in the electrochemical reaction [1] may also initiate polymerization (18) by forming the THF Oxonium salt



The end group in this case is a hydroxyl. No end group analysis was carried out to distinguish the polymerization reactions. However, Nakahama *et al.* (3) carried out the end group analysis of THF polymers made by electroinitiation at 0°C employing Bu<sub>4</sub>NClO<sub>4</sub> salt, and determined that end groups were primarily hydroxyl. Nakahama *et al.* (3) suggested that the electroinitiation occurred as a result of the oxidation of ClO<sub>4</sub><sup>-</sup> anion rather than the oxidation of THF itself. We have shown by cyclic voltammetry as well as by steady-state current potential measurements that in solutions of LiClO<sub>4</sub>, LiBF<sub>4</sub>, or LiPF<sub>6</sub> in THF the major oxidation peak occurs at a potential of 3.5V anodic to the Li/Li<sup>+</sup> reference electrode irrespective of the anion, whereas in solution of LiClO<sub>4</sub> in propylene carbonate the major oxidation peak occurs at approximately 5.0V anodic to the Li/Li<sup>+</sup> reference elec-

trode. This is a strong evidence in favor of our hypothesis that the electroinitiation step involves the oxidation of THF itself rather than the anion as suggested by Nakahama *et al.*

Manuscript submitted Jan. 7, 1974; revised manuscript received May 11, 1974. This was Paper 187 presented at the Chicago, Illinois, Meeting of the Society, May 13-18, 1973.

Any discussion of this paper will appear in a Discussion Section to be published in the June 1975 JOURNAL. All discussions for the June 1975 Discussion Section should be submitted by Feb. 1, 1975.

The publication costs of this article have been assisted by P. R. Mallory & Company, Incorporated.

#### REFERENCES

1. P. Dreyfuss and M. P. Dreyfuss, *Advan. Polymer Sci.*, **4**, 528 (1967).
2. C. F. Heins, *Polymer Letters*, **7**, 625 (1969).
3. S. Nakahama, S. Hino, and N. Yamazaki, *Polymer J.*, **2**, 56 (1971).
4. M. R. Rifi, U. S. Pat. 3,645,986 (1972).
5. A. N. Dey, U. S. Pat. 3,658,592 (1972).
6. A. N. Dey and B. P. Sullivan, U. S. Pat. 3,655,585 (1972).
7. A. N. Dey and M. L. B. Rao, Paper 53, presented at Electrochemical Society Meeting, Boston, Massachusetts, October 7-11, 1973.
8. A. N. Dey, Paper 54, presented at Electrochemical Society Meeting, Boston, Massachusetts, October 7-11, 1973.
9. J. Brandrup and E. H. Immergert, "Polymer Handbook," Vol. IV, p. 34, Interscience Publishers, Inc., New York (1966).
10. D. Vofsi and A. V. Tobolsky, *J. Polymer Sci.*, **A3**, 3261 (1965).
11. S. Smith and A. J. Hubin, *Am. Chem. Soc., Polymer Preprints*, **13**, (1) 66 (1972).
12. E. J. Rudd, M. Finkelstein, and S. D. Ross, *J. Org. Chem.*, **37**, 1753 (1972).
13. S. D. Ross, J. F. Barry, M. Finkelstein, and E. J. Rudd, *J. Am. Chem. Soc.*, **95**, 2193 (1973).
14. L. L. Miller, J. F. Wolf, and E. A. Mayeda, *ibid.*, **93**, 3306 (1971).
15. G. Sundholm, *J. Electroanal. Chem.*, **31**, 265 (1971).
16. I. Kuntz, *J. Polymer Sci.*, **B4**, 427 (1966).
17. I. Kuntz, *Am. Chem. Soc., Polymer Preprints*, **7**(1), 187 (1966).
18. M. P. Dreyfuss, J. C. Westfahl, and P. Dreyfuss, *ibid.*, **7**, (2) 413 (1966).

## Electrical Conductivities and Molar Volumes in the Binary Systems $\text{MnCl}_2\text{-LiCl}$ , $\text{MnCl}_2\text{-NaCl}$ , $\text{MnCl}_2\text{-KCl}$ , $\text{MnCl}_2\text{-RbCl}$ , $\text{MnCl}_2\text{-CsCl}$

A. S. Kucharski and S. N. Flengas\*

Department of Metallurgy and Materials Science, University of Toronto, Toronto, Ontario, Canada

#### ABSTRACT

The densities and the electrical conductivities of the five binary  $\text{MnCl}_2\text{-ACl}$  systems, where A = Li, Na, K, Rb, and Cs, have been measured. The molar volumes exhibit increasing positive deviations from additivity, as the size of the alkali metal cation in ACl is increased from  $\text{Li}^+$  to  $\text{Cs}^+$ , and have a maximum positive deviation at approximately  $X_{\text{MnCl}_2} = 1/3$ . The molar conductances exhibit an increasing negative deviation from ideality, with a minimum occurring approximately at  $X_{\text{MnCl}_2} = 1/3$ . The concentration dependence of the molar volumes and of the electrical conductivities in these systems is interpreted in terms of a complex ion model (1) proposed previously for the purpose of interpreting their thermodynamic properties. According to this model the solutions of  $\text{MnCl}_2$  with alkali chlorides are characterized by the presence of the  $\text{MnCl}_4^{2-}$  complex anions. The difference between a "free" chloride anion and a chloride anion bonded within a complex configuration, lies in differences in the strength of the anion-to-cation bonds in these two configurations. In this respect, the continuity of the quasilattice structure of a molten salt is not disrupted by the presence of complex species and the latter are not expected to occupy single "lattice" sites within the liquid, as local electrical neutrality is always maintained. Good agreement is obtained between the experimental and the theoretical values for the electrical conductivities and the molar volumes in the systems  $\text{MnCl}_2\text{-KCl}$ ,  $\text{MnCl}_2\text{-RbCl}$ , and  $\text{MnCl}_2\text{-CsCl}$ . The deviations from ideal behavior are small in the systems  $\text{MnCl}_2\text{-LiCl}$  and  $\text{MnCl}_2\text{-NaCl}$ . The coefficients for thermal expansion and the activation energies for specific and molar conductances were also calculated from the experimental results and their concentration dependences are also indicative of complex formation.

There have been few density and electrical conductivity measurements on transition metal chlorides and their mixtures with alkali chlorides. However, extensive investigations on other fused salt systems have been made, and these have been compiled by Janz (2), Klemm (3), and Sundheim (4).

\* Electrochemical Society Active Member.  
Key words: manganous chloride, densities, conductances, alkali chlorides, melt.

In examining the literature, the molar volumes and electrical conductivities of these divalent metal chloride-alkali metal chloride systems indicate certain general trends. In the presence of small alkali metal cations which create strong polarizing fields, such as  $\text{Li}^+$  or  $\text{Na}^+$ , the molar volumes exhibit an additive concentration dependence or indicate slight positive deviations from additive behavior. However, as the polarizing power of the larger alkali metal cation

such as,  $K^+$ ,  $Rb^+$ , or  $Cs^+$  becomes weaker, larger positive deviations from additivity occur. For example, the systems  $PbCl_2$ - $ACl$  (5) ( $A = Na, Rb, Cs$ );  $CdCl_2$ - $ACl$  (5) ( $A = Rb, Cs$ );  $BaCl_2$ - $ACl$  (6) ( $A = Li, Na, K, Cs$ );  $CaCl_2$ - $NaCl$  (7),  $CaCl_2$ - $KCl$  (8); and  $MgCl_2$ - $KCl$  (9),  $MgCl_2$ - $LiCl$  (10) support this general trend.

The molar electrical conductivities of the solutions show slight negative deviations with cations like  $Li^+$  and  $Na^+$  and progressively larger deviations as the size of the alkali metal cation becomes larger. The  $CdCl_2$ - $ACl$  (11),  $PbCl_2$ - $ACl$  (11, 12),  $MgCl_2$ - $ACl$  (10, 13, 14) systems illustrate this behavior.

These deviations have been ascribed to the formation of "complex" species (15) but specific complexes have not been established conclusively. In the present study the densities and electrical conductivities of the  $MnCl_2$ - $ACl$  solutions where  $A = Li, Na, K, Rb, Cs$  have been determined. Only the conductivities and densities of the  $MnCl_2$ - $KCl$  system (16) are reported to date in the literature. The present study along with the previously reported emf measurements (17) was conducted to ascertain the relationship between the structure of the molten salts and the corresponding thermodynamic and electrical properties.

### Experimental

The densities were measured using the Archimedean method as shown by Fig. 1. The apparatus is similar to that used previously in this laboratory (18, 19) and had the advantage of creating a totally closed system. The technique involved the measurement of the weight change of a quartz sinker filled with platinum, using a quartz-spring type balance. The quartz spring could take a maximum static load of 5g and

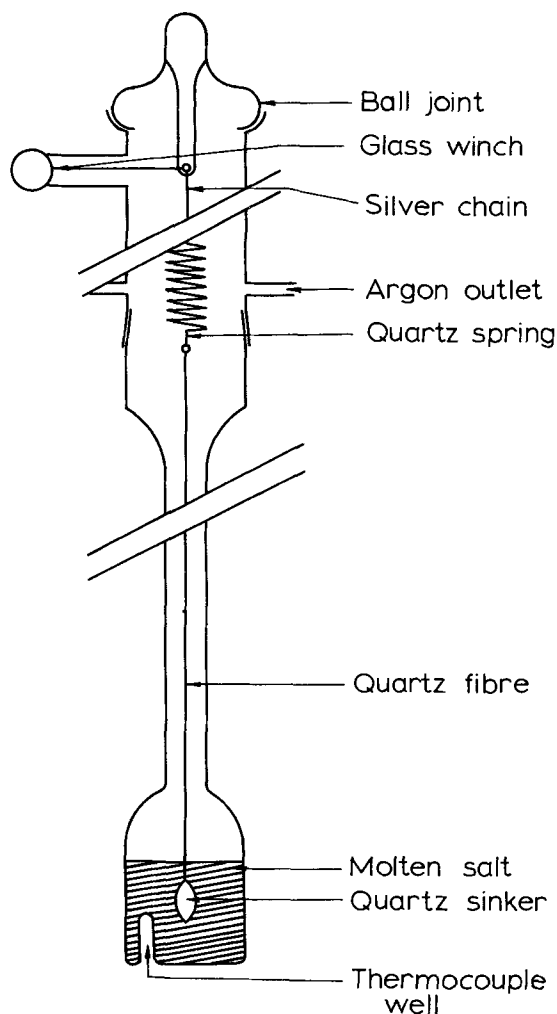


Fig. 1. Apparatus for measuring densities

the spring extension could be measured with an accuracy of  $\pm 0.005$  cm on the cathetometer's vernier scale. With a spring constant of  $0.0742$  g  $cm^{-1}$ , the absolute accuracy of the weight measurement was  $\pm 0.0036$ g. The lower half of the density cell was made narrower than the melt-containing cavity to minimize the volatilization of salt and subsequent condensation on the connecting suspension fiber. The effectiveness of this design was verified by conducting a separate experiment in which only the connecting fiber was suspended over pure molten  $MnCl_2$ . For convenience and accuracy all measurements and calibrations were made with respect to a reference quartz fiber which was suspended parallel to the spring.

The electrical conductivity measurements were determined using a U-tube conductivity cell of the type described previously (18, 19) from this laboratory. The cell constant was obtained by calibrating the cell with 1.0 demal  $KCl$  solution (20). For this calibration, the cell was at a constant temperature using an oil bath kept at  $25^\circ \pm 0.01^\circ C$ . The capillary U-tube section of the cell was about 10 cm in length and represented cell constants ranging from 500 to 700  $cm^{-1}$ .

The electrodes were constructed from 10 mm diameter platinum disks spot welded to platinum wires. All measured resistivities were corrected for lead resistance. No correction was applied for the change of the cell constant with temperature, as quartz expands very little on heating (21).

To establish a constant temperature zone of at least 10 cm long and also for electrical shielding, the conductivity cells were contained in graphite cylinders, 20 cm long by 5 cm in diameter packed with alumina fibre refrax insulation. A quartz tube 8 mm in diameter containing the thermocouple was placed along with the cell into the hole drilled in the graphite.

Initially, conductivities were measured with an a-c resistance bridge at frequencies of 2500, 3500, and 4500 Hz, and there was less than 0.1% difference between the measurements. Subsequently, all resistance readings were taken at a frequency of 3500 Hz. The quartz cell was not attacked by the melts except with the  $MnCl_2$ - $LiCl$  solutions at high temperatures. Conductivity cells were individually calibrated for each composition.

The molar volumes of a binary system can be calculated from the density data using the equation

$$V_M = \bar{M}/\rho \quad [1]$$

where,  $\rho$  is the density of the solution and  $\bar{M}$  the average molecular weight of the binary system given by

$$\bar{M} = X_1 M_1 + X_2 M_2 \quad [2]$$

where,  $M$ 's are molecular weights and  $X$ 's are the mole fractions of the components. The molar conductance in units  $ohm^{-1} cm^2 mole^{-1}$  can be calculated from

$$\Lambda = V_M \kappa \quad [3]$$

where  $\kappa$  is the specific conductance, and  $V_M$  is the molar volume.

### Density Results

The density results for the five binary systems can be represented by linear equations of the type

$$\rho = a + bt \quad [4]$$

The experimental data were fitted to this equation by the least squares method and the resulting constants are shown in Table I, along with the standard and maximum deviations.

Errors in density measurements have been discussed by Bloom *et al.* (5) and Mellors and Senderoff (22). For a suspension fiber 0.043 cm in diameter Bloom ascribed a surface tension error of 0.1-0.2%. The use of a fine quartz suspending fiber (0.012 cm in diameter)

Table I. Density measurements of manganese chloride-alkali chloride melts linear least square fits for  $\rho$  vs. temperature at various compositions in the  $\text{MnCl}_2$ -ACl systems

		(A = alkali)			
$X_{\text{MnCl}_2}$	Temperature range ( $^{\circ}\text{C}$ )	$\rho = a + bt$ ( $^{\circ}\text{C}$ ) ( $\text{g cm}^{-3}$ )		Deviation	
		$a$	$-b \times 10^3$	Standard	Maximum
<b>MnCl<sub>2</sub>-LiCl</b>					
1.000	696-815	2.6984	0.5211	0.001	0.001
0.700	595-742	2.6213	0.6236	0.002	0.002
0.400	578-740	2.3740	0.6075	0.001	0.001
0.305	591-755	2.2492	0.5659	0.001	0.001
0.0	627-744	1.7662	0.4360	0.001	0.001
<b>MnCl<sub>2</sub>-NaCl</b>					
1.000	696-815	2.6984	0.5211	0.001	0.001
0.800	640-817	2.6538	0.5963	0.003	0.003
0.600	547-838	2.5873	0.7039	0.003	0.005
0.500	484-838	2.4898	0.6576	0.003	0.006
0.400	537-842	2.4052	0.6445	0.003	0.003
0.300	688-839	2.2715	0.5633	0.003	0.004
0.200	743-845	2.1787	0.5617	0.002	0.002
0.0	816-947	1.9802	0.5327	0.001	0.001
<b>MnCl<sub>2</sub>-KCl</b>					
1.000	696-815	2.6984	0.5211	0.001	0.001
0.900	657-816	2.6710	0.5973	0.001	0.002
0.800	630-742	2.6876	0.7159	0.001	0.001
0.700	599-820	2.5864	0.6896	0.001	0.002
0.600	583-794	2.4895	0.6707	0.002	0.004
0.550	627-790	2.4387	0.6628	0.002	0.003
0.500	563-774	2.3873	0.6553	0.004	0.005
0.450	576-825	2.3276	0.6436	0.002	0.004
0.400	498-819	2.2755	0.6305	0.003	0.004
0.333	527-812	2.1917	0.5981	0.002	0.004
0.300	534-694	2.1861	0.5870	0.002	0.003
0.200	637-774	2.1082	0.5928	0.001	0.001
0.100	736-885	1.9777	0.5115	0.003	0.002
0.0	788-913	1.9734	0.5778	0.001	0.001
<b>MnCl<sub>2</sub>-RbCl</b>					
1.000	696-815	2.6984	0.5211	0.001	0.001
0.900	640-809	2.7617	0.6184	0.001	0.002
0.800	618-798	2.8153	0.7180	0.001	0.002
0.700	541-794	2.8378	0.7921	0.003	0.004
0.600	589-782	2.7973	0.7847	0.001	0.002
0.550	592-782	2.7769	0.7827	0.002	0.002
0.500	583-788	2.7658	0.7801	0.001	0.001
0.450	576-796	2.7299	0.7561	0.002	0.002
0.400	561-791	2.6971	0.7282	0.001	0.002
0.300	480-807	2.7147	0.7506	0.002	0.003
0.200	632-808	2.7559	0.7815	0.002	0.003
0.100	685-816	2.8426	0.8576	0.006	0.010
0.0	766-829	2.8916	0.8951	0.001	0.002
<b>MnCl<sub>2</sub>-CsCl</b>					
1.000	696-815	2.6984	0.5211	0.001	0.001
0.900	650-802	2.8329	0.6477	0.001	0.002
0.800	581-800	2.9388	0.7644	0.002	0.002
0.700	569-807	2.9925	0.8220	0.001	0.001
0.600	678-801	2.9856	0.8184	0.002	0.002
0.550	633-814	3.0066	0.8325	0.001	0.001
0.500	630-810	2.9989	0.8191	0.001	0.002
0.400	588-804	3.0125	0.8069	0.001	0.002
0.300	557-816	3.0784	0.8378	0.001	0.001
0.200	564-803	3.2148	0.9240	0.001	0.002
0.100	630-788	3.3558	1.0025	0.001	0.001
0.0	678-806	3.4894	1.0704	0.001	0.001

in this study diminishes the surface tension errors and accordingly corrections may be neglected. Considering this error and others such as parallax and weighing errors, the total error of 0.3% would be a fair assessment of the present results. The reproducibility of the results would also lie in the same uncertainty range.

#### Densities of Pure $\text{MnCl}_2$ and ACl

The densities of pure alkali halides have been compiled and critically appraised by Janz *et al.* (2). The density results of this investigation are shown in Table II, along with the values taken from Janz (2).

The compilation by Janz *et al.* (2) for the density of the alkali chlorides are taken mainly from the precise work by Yaffe and Van Artsdalen (23, 24). The uncertainties in these results for LiCl, NaCl, KCl, RbCl, and CsCl are given by Janz as 0.2, 0.2, 0.5, 0.4, and 0.1%, respectively. The maximum departure of the present work from the Janz compilation is: 0.2% for LiCl, 0.2% for NaCl, 0.1% for KCl, 0.2% for RbCl, and 0.3% for CsCl.

Due to the poor description of the available density experiments on  $\text{MnCl}_2$ , Janz did not attempt to evalu-

Table II. Comparison of densities of pure alkali chlorides and manganese chloride

Salt	700 $^{\circ}\text{C}$	800 $^{\circ}\text{C}$	900 $^{\circ}\text{C}$
LiCl	1.4630 1.4610 (1.6109)	1.4197 1.4174 1.5566	1.3765* 1.3738** 1.5023*
NaCl	(1.6074) (1.5685)	1.5540 1.5101	1.5008** 1.4519*
KCl	(1.5694)	1.5112	1.4534**
RbCl	2.2615 2.2650	2.1732 2.1755	2.0849* 2.0850**
CsCl	2.7328 2.7401	2.6263 2.6334	2.5198* 2.5263**
$\text{MnCl}_2$	2.3311 2.3336	2.2873 2.2815	2.3436* 2.2294**

\* Janz (2).  
\*\* This study.

ate the accuracy. The maximum differences between the present results for  $\text{MnCl}_2$  and those reported by Murgulescu and Zuca (16) is 0.6%.

#### Electrical Conductivity Results

*Pure salts.*—The conductivities of the five pure alkali chlorides and of pure  $\text{MnCl}_2$  were measured. The data were fitted by the method of least squares to equations of the form

$$\kappa = a + bT + cT^2 \quad (\text{ohm}^{-1} \text{cm}^{-1}) \quad [5]$$

The coefficients  $a$ ,  $b$ , and  $c$  are tabulated in Table III. The specific conductance results for pure LiCl agree within 2% of the values reported by Yaffe and Van Artsdalen (23, 24). The agreement is much better at lower temperatures (better than 1%) where the corrosive effect of LiCl is not as pronounced. Yaffe and Van Artsdalen also reported that considerable corrosion occurred at high temperatures. Similar corrosion of the cells was experienced in the present work in spite of the care used to remove the last traces of water from LiCl. The specific conductance of pure LiCl obtained in this work also agrees to within 1% of the conductance reported by Smirnov *et al.* (25).

The specific conductances of NaCl and KCl agree to within 2 and 1%, respectively, with the above reference. The uncertainty in the specific conductance of pure NaCl and KCl ascribed by Janz *et al.* (2) to the results reported by Yaffe and Van Artsdalen is 0.8 and 2.6% for NaCl and KCl, respectively. The results obtained in this work for NaCl and KCl are slightly outside this uncertainty limit, with the uncertainty for NaCl being the greatest. However, at lower temperatures the specific conductances for NaCl are within the uncertainty of the data reported by Yaffe and Van Artsdalen (23, 24).

The specific conductances obtained in this investigation for RbCl are within the uncertainty limits given to the data of Yaffe and Van Artsdalen (23). The uncertainty limit for RbCl given by Janz (2) is 3.5% and the present results are within this limit. The specific conductances of CsCl obtained in this study are slightly outside the 5.0% uncertainty limit imposed by Janz and co-workers. However, the specific conductances for CsCl measured by Smirnov *et al.* (25) are in good agreement (less than 1%) with the present results. The conductances found by Klemm (26) for RbCl and CsCl are also in good agreement with the present measurements.

There have been two previous determinations of the specific conductances of  $\text{MnCl}_2$  to date. Murgulescu and Zuca (16) have determined the conductance of pure  $\text{MnCl}_2$  from 923 $^{\circ}$  to 1123 $^{\circ}\text{K}$ . However, the conductance as determined by Winterhager and Werner (27) has maximum departure of 27% from the former data. The present determination supports the data of Murgulescu and Zuca (16) to within 1%.

*$\text{MnCl}_2$ -ACl binary solutions.*—The conductivity of five binary solutions have been determined, namely:



Table III. Least square fit for electrical conductivity  $\kappa$  vs. temperature at various compositions in the  $\text{MnCl}_2$ - $\text{ACl}$  systems

Mole fraction		$\kappa = a + bT + cT^2$ ohm <sup>-1</sup> cm <sup>-1</sup>			Deviation	
$X_{\text{MnCl}_2}$	Temperature range (°C)	-a	b × 10 <sup>-3</sup>	-c × 10 <sup>-6</sup>	Standard	Maximum
<b>MnCl<sub>2</sub>-LiCl</b>						
1.0000	658-833	0.9810	3.2128	0.6205	0.004	0.010
0.8210	626-778	1.6049	5.0367	1.3074	0.009	0.012
0.4752	598-743	4.9340	12.9548	4.9288	0.009	0.014
0.2929	605-743	6.1300	16.2036	6.2287	0.025	0.040
0.1000	661-750	10.0849	28.4502	12.4449	0.032	0.066
0.0	656-785	-3.3285	2.9091		0.030	0.040
<b>MnCl<sub>2</sub>-NaCl</b>						
1.0000	658-833	0.9810	3.2128	0.6205	0.004	0.010
0.9056	643-846	2.3707	5.9566	1.8701	0.002	0.003
0.7444	605-851	3.4280	8.2267	2.9287	0.003	0.004
0.7089	575-849	3.7800	8.9804	3.2587	0.002	0.004
0.5912	493-839	3.8383	9.4771	3.5323	0.006	0.010
0.4978	502-835	4.0876	10.0894	3.8714	0.004	0.010
0.3971	460-827	4.0085	10.0107	3.7799	0.008	0.004
0.2985	611-801	7.5943	17.5013	7.5219	0.020	0.034
0.1998	704-855	6.7308	15.6262	6.3088	0.006	0.010
0.0994	780-870	1.2112	5.2029	1.1199	0.007	0.007
0.0	826-901	1.1689	24.6597	9.7619	0.005	0.010
<b>MnCl<sub>2</sub>-KCl</b>						
1.0000	658-833	0.9810	3.2128	0.6205	0.004	0.010
0.9003	638-830	2.2687	5.4992	1.6712	0.002	0.003
0.8032	733-869	4.0861	9.0482	3.4855	0.007	0.010
0.7050	598-850	3.0229	6.8765	2.3726	0.003	0.005
0.6025	532-817	3.0383	7.0615	2.6158	0.003	0.007
0.5068	535-843	2.9172	6.6887	2.3970	0.005	0.012
0.4500	536-849	2.1883	5.2233	1.6854	0.003	0.008
0.3999	491-857	2.1259	5.0081	1.5293	0.002	0.003
0.2995	500-851	2.3592	5.4105	1.6559	0.001	0.001
0.1988	649-860	5.1623	10.8741	4.1560	0.015	0.030
0.0961	753-867	7.4924	15.0838	5.8683	0.005	0.010
0.0	808-904	5.1141	10.9182	3.8095	0.001	0.002
<b>MnCl<sub>2</sub>-RbCl</b>						
1.0000	658-833	0.9810	3.2128	0.6205	0.004	0.010
0.9000	683-830	2.1706	5.2596	1.6344	0.006	0.012
0.7900	575-833	3.2523	7.2067	2.6114	0.002	0.005
0.7000	505-831	3.1456	7.0208	2.6141	0.006	0.004
0.6000	543-824	2.9132	6.9038	2.8456	0.007	0.016
0.5000	595-832	1.1241	2.8741	0.7062	0.004	0.009
0.4000	624-817	1.8122	4.0335	1.2240	0.002	0.004
0.3000	512-814	1.9015	4.1632	1.2316	0.001	0.002
0.2036	609-832	2.3477	5.1002	1.6155	0.002	0.003
0.0967	730-831	4.0662	8.4769	3.0819	0.002	0.002
0.0	726-834	1.7294	4.1531	0.9054	0.004	0.005
<b>MnCl<sub>2</sub>-CsCl</b>						
1.0000	658-853	0.9810	3.2128	0.6205	0.004	0.010
0.9000	630-809	2.2537	4.1358	1.5304	0.004	0.007
0.8000	585-829	2.4727	0.4909	1.8236	0.005	0.007
0.7000	578-816	2.1605	4.9192	1.6829	0.002	0.004
0.6000	627-837	1.7402	4.0857	1.4118	0.002	0.002
0.5000	640-822	1.1556	2.7501	0.7682	0.002	0.002
0.4000	579-823	1.2889	2.7847	0.7186	0.001	0.001
0.2500	561-778	1.7891	3.8090	1.1301	0.002	0.003
0.2000	580-827	1.8164	3.8579	1.0879	0.002	0.003
0.1000	661-823	1.6598	3.7122	0.9295	0.002	0.003
0.0	680-830	3.0306	6.4693	2.1303	0.002	0.003

$\text{MnCl}_2$ - $\text{LiCl}$ ,  $\text{MnCl}_2$ - $\text{NaCl}$ ,  $\text{MnCl}_2$ - $\text{KCl}$ ,  $\text{MnCl}_2$ - $\text{RbCl}$ , and  $\text{MnCl}_2$ - $\text{CsCl}$ . To define the concentration dependence in the simple  $\text{MnCl}_2$ - $\text{LiCl}$  binary system only six compositions were studied. In each of the other four systems at least eleven compositions were studied to ascertain the concentration dependence of the conductivities.

The data were fitted to Eq. [5] to determine the three coefficients in the conductivity-temperature equation. The results of this least squares analysis are shown in Table III, along with the data for the pure salts.

Table III shows that there are somewhat greater deviations in the  $\text{LiCl}$  system, the greater scatter in the data being due to the corrosive nature of  $\text{LiCl}$ . However, this scatter is partially compensated by the fact that the specific conductances in this system are much higher than in the other alkali halide systems and hence become less important.

The remaining systems are well represented by the equations given, since 90% of the compositions studied have standard deviations of less than  $0.006 \text{ ohm}^{-1}\text{cm}^{-1}$ . Assessment of errors in the conductivity measurements is difficult, but a total error of 2% would be a fair estimate. The reproducibility of the results lies in the same error range.

## Discussion of Results

In previous publications from this laboratory (1, 17) it has been shown that the formation of a tetrahedrally coordinated complex species of the type  $\text{A}_2\text{MnCl}_4$  accounts for the unusual concentration behavior of the enthalpy and entropy of mixing in the  $\text{MnCl}_2$ - $\text{ACl}$  systems. Similarly, the present results indicate that the concentration dependence of the molar volumes, of the molar conductances of the coefficients of thermal expansion, and of the activation energies for conduction in the  $\text{MnCl}_2$ - $\text{ACl}$  type solutions, are directly related to the presence of the complex species in the fused salt solutions.

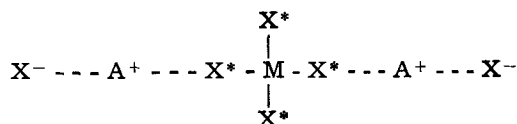
The concept of complexes in fused salts was based upon the following postulates (1):

1. The fused salt is a continuous and highly electrified medium, and as a result interlocking anionic and cationic quasilattices exist to preserve local electrical neutrality.

2. A nonionic solvent, such as water which is capable of separating ionic species is not present.

3. The differences between a complexed and a non-complexed state, involving a cation  $\text{M}^{+2}$  and an anion  $\text{X}^-$ , is simply defined by a characteristic "shorter" bond distance  $\text{M-X}^*$  for the complexed state as compared to the  $\text{M-X}$  bond distance for the noncomplexed state.

4. Complexed ionic species must still belong to their respective quasilattices and not disrupt the continuity of the molten structure. Hence the ligands  $\text{X}^*$  in a complex  $\text{MX}_n^*$  interact with the surrounding  $\text{A}^+$  cations in the sequence



whereby an anion  $\text{X}$  is always a cation "bridging" specie.

5. Under such restrictions, the complex represents a coordinated configuration of the type  $\text{MX}_n^*$  which may be treated as a statistical entity.

6. The formation of a complex is initiated by the presence of foreign cations which "compete" with the central cations  $\text{M}^{+2}$  for the same ligands  $\text{X}^-$ . Accordingly, the size of the foreign cation is related to its capability of promoting or preventing the formation of complexes.

7. The coordination number of a given monovalent cation is taken to be one-half of that of a divalent cation, with respect to a monovalent anion ligand. The coordination number of a solution containing both mono- and divalent cations is taken to be the ion-fraction average of that of the two cations.

Regarding the preferred coordination of complex ions in fused salts, the accumulated experimental evidence indicates that such coordinations are relatively simple. Thus, mixtures of monovalent cations appear to prefer the 2-ligand configuration representing a linear array or angular structure as in  $\text{Ag}(\text{CN})_2^-$  (28). Mixtures of mono- with divalent cations appear to follow the tetrahedral coordination as in  $\text{MgCl}_4^{2-}$  (1) and  $\text{MnCl}_4^{2-}$  (17). Finally, mixtures of mono- and tetravalent cations as in  $\text{ZrCl}_4$ ,  $\text{TiCl}_4$ , and  $\text{HfCl}_4$  with alkali chlorides, prefer to form octahedrally coordinated complexes of the type  $\text{ZrCl}_6^{2-}$ ,  $\text{TiCl}_6^{2-}$ , and  $\text{HfCl}_6^{2-}$  (29). From the previous discussion it follows that complex species in fused salts are not expected to dissociate in the same manner as their counterparts in aqueous solutions. The formation of the new type  $\text{M-X}^*$  bond is initiated by the presence of the  $\text{A}^+$  cations in solution, and each added  $\text{A}^+$  cation as  $\text{AX}$  is expected to disturb the  $\text{M-X}$  bonds in  $\text{MX}$  and the "complex" should form stoichiometrically.

Table IV. Molar conductances, molar volumes, coefficients for thermal expansion, and activation energies in the  $MnCl_2$ -ACl molten solutions at 700°C

( $\text{cal}_{th} = 4.184\text{J}$ )

$X_{MnCl_2}$	$\Lambda_M$ ( $\text{ohm}^{-1}\text{cm}^2$ $\text{mol}^{-1}$ )	$V_M$ ( $\text{cm}^3$ )	$\alpha_p^{(a)}$ $\times 10^4$ ( $\text{K}^{-1}$ )	$\Delta E^*_{\text{s}}$ ( $\text{cal}$ $\text{mol}^{-1}$ ) ( $\pm 100$ $\text{cal}$ )	$\Delta E^*_{\text{v}}$ ( $\text{cal}$ $\text{mol}^{-1}$ ) ( $\pm 50$ $\text{cal}$ )	$\Delta E^*_{\text{M}}$ ( $\text{cal}$ $\text{mol}^{-1}$ ) ( $\pm 150$ $\text{cal}$ )
<b>MnCl<sub>2</sub>-LiCl</b>						
1.00	84.00	53.93	2.291	2440	430	2870
0.821	100.84	49.00	2.600	2290	490	2780
0.475	122.9	40.90	3.000	2120	570	2690
0.293	136.9	36.60	3.080	2070	580	2650
0.100	161.5	31.70	2.800	1570	530	2100
0.0	178.75	29.02	2.047	880	390	1270
<b>MnCl<sub>2</sub>-NaCl</b>						
1.00	84.00	53.93	2.291	2440	430	2870
0.906	86.33	52.16	2.560	2650	480	3130
0.74	89.15	49.41	2.708	2650	510	3160
0.71	90.17	48.81	3.000	2670	570	3240
0.59	93.63	47.31	3.418	2490	650	3140
0.50	93.74	45.40	3.293	2340	620	2960
0.40	93.95	43.60	3.362	2330	640	2970
0.30	96.95	41.90	3.053	2340	580	2920
0.20 <sup>(b)</sup>	—	—	3.193	2540	600	3140
0.10 <sup>(b)</sup>	106.97	38.32	3.300	2050	620	2670
0.0 <sup>(b)</sup>	111.42	36.36	3.296	790	620	1410
<b>MnCl<sub>2</sub>-KCl</b>						
1.0	84.00	53.93	2.291	2440	430	2870
0.9	80.00	53.26	2.683	2840	510	3350
0.8	74.97	52.86	3.327	3030	630	3660
0.7	74.66	52.51	3.35	3010	630	3640
0.6	70.47	52.14	3.373	2750	640	3390
0.507	68.85	51.95	3.457	2900	650	3550
0.45	67.55	52.01	3.475	2830	660	3490
0.40	67.36	51.84	3.496	2960	660	3620
0.30	68.57	51.26	3.404	3100	640	3740
0.20	74.33	50.09	3.557	3560	670	4230
0.096 <sup>(b)</sup>	80.14	49.20	3.212	4260	610	4870
0.0 <sup>(b)</sup>	90.45	47.52	3.744	3490	710	4200
<b>MnCl<sub>2</sub>-RbCl</b>						
1.00	84.00	53.93	2.291	2440	430	2870
0.90	75.33	53.82	2.694	2810	510	3320
0.80	69.50	53.98	3.155	3130	600	3730
0.70	65.94	54.46	3.604	3020	680	3700
0.60	61.16	55.09	3.554	2330	670	3000
0.55	—	55.38	—	—	—	—
0.50	55.95	55.74	3.477	2630	660	3290
0.45	—	55.93	—	—	—	—
0.40	53.55	56.16	3.385	3280	640	3920
0.30	54.95	55.88	3.485	3400	660	4060
0.20	59.87	55.16	3.603	3410	680	4090
0.10 <sup>(b)</sup>	68.41	54.12	3.787	3710	720	4430
0.0 <sup>(b)</sup>	77.60	53.35	4.034	3110	760	3870
<b>MnCl<sub>2</sub>-CsCl</b>						
1.00	84.00	53.93	2.291	2440	430	2870
0.90	70.77	54.67	2.764	3160	520	3680
0.800	63.91	55.89	3.239	3220	620	3840
0.700	59.34	57.34	3.462	3010	650	3660
0.600	53.20	59.21	3.477	2820	660	3480
0.550	—	59.81	—	—	—	—
0.500	48.09	60.85	3.435	3000	650	3650
0.400	45.78	61.84	3.355	3550	640	4190
0.300	—	62.44	—	—	—	—
0.25	52.86	62.43	3.419	3600	650	4250
0.200	56.48	62.25	—	—	—	—
0.100	66.30	61.83	3.849	3360	730	4090
0.0	76.63	61.44	4.071	3530	770	4300

(a) Constant over the temperature range indicated by the density measurements in Table I.

(b) Extrapolated from measurements taken at higher temperatures to below the melting points.

### Molar Volumes and Thermal Expansivities

The molar volumes can be calculated from Eq. [1] and the data given in Table I. The results of these calculations for the temperature of 700°C are shown in Table IV and are plotted in Fig. 2a to 2e. For the  $MnCl_2$ -ACl system (where A = Li, Na, K, Rb, and Cs), the molar volumes follow the trends indicated in the literature survey for all the solutions containing divalent metal chlorides and alkali metal chloride. They illustrate the general behavior in that in the LiCl and NaCl binary systems the molar volumes of the solutions are additive and that increasing positive deviations from additivity are observed beginning with the KCl binary system through to CsCl. The most pronounced positive deviations appear to occur at approximately  $X_{MnCl_2} = 1/3$ . In the  $MnCl_2$ -NaCl system there is some indication for a positive departure from

ideality. This observation is in disagreement with the data of Murgulescu and Zuca (16) for  $MnCl_2$ -rich concentrations in the  $MnCl_2$ -KCl system. It should be mentioned that these authors used a density apparatus open to the atmosphere and only few unspecified measurements were taken under a stream of HCl gas. In the present work it was found necessary to handle  $MnCl_2$  with extreme caution in order to avoid the formation of oxides or oxychlorides by reaction with atmospheric moisture and oxygen.

The concentration dependence of the molar volumes in the systems  $MnCl_2$ -KCl,  $MnCl_2$ -RbCl, and  $MnCl_2$ -CsCl may be understood in terms of the formation of the  $MnCl_4^{2-}$  complex configuration.

For the calculation of finite partial molar volume  $\bar{V}_C$  shall be assigned to the  $MnCl_4^{2-}$  complex ion. Similarly, the simple "free" ions  $Mn^{2+}$ ,  $A^+$ , and  $Cl^-$  shall be assigned finite partial molar volumes,  $\bar{V}_{Mn^{2+}}$ ,  $\bar{V}_A$ , and  $\bar{V}_{Cl^-}$ , respectively. The molar volume of a  $MnCl_2$ -ACl solution can be estimated from a simple model if it is assumed that each ion contributes a volume element proportional to its concentration and the volume of the solution is the sum of the volume contribution from all ions present. The partial molar volumes of the constituent species in solution shall be assumed to be independent of concentration and have the same values as for the pure components.

Considering the complex forming reaction



a solution containing the mole fractions  $X_{MnCl_2}$  and  $X_{ACl}$ , may be represented by the ionic concentrations given in Table V. The corresponding ionic contributions to the total volume are also included in this table. In the concentration range  $1.0 > X_{MnCl_2} > 0.333$ , the total volume of the solution is

$$V_{\text{total}} = (0.5X_{ACl})\bar{V}_C + (X_{MnCl_2} - 0.5X_{ACl})\bar{V}_{Mn^{2+}} + (2X_{MnCl_2} - X_{ACl})\bar{V}_{Cl^-} + (X_{ACl})\bar{V}_A \quad [6]$$

and in the concentration range  $0.333 > X_{MnCl_2} > 0$

$$V_{\text{total}} = (X_{MnCl_2})\bar{V}_C + (1 - 3X_{MnCl_2})\bar{V}_{Cl^-} + (X_{ACl})\bar{V}_A \quad [7]$$

The ideal or additive molar volume based on the non-complexed components  $MnCl_2$  and ACl may be written as

$$V_{\text{ideal}} = X_{MnCl_2}(\bar{V}_{Mn^{2+}} + 2\bar{V}_{Cl^-}) + X_{ACl}(\bar{V}_A + \bar{V}_{Cl^-}) \quad [8]$$

The excess volume can be obtained

$$\Delta V^{xs} = V_{\text{total}} - V_{\text{ideal}} \quad [9]$$

For  $1.0 > X_{MnCl_2} > 0.333$

$$\Delta V^{xs} = 0.5X_{ACl}(\bar{V}_C - \bar{V}_{Mn^{2+}} - 4\bar{V}_{Cl^-}) = 0.5X_{ACl}\delta \quad [10]$$

where  $\delta = \bar{V}_C - \bar{V}_{Mn^{2+}} - 4\bar{V}_{Cl^-}$ , given in  $\text{cm}^3 \text{mole}^{-1}$  and for  $0.333 > X_{MnCl_2} > 0$

$$\Delta V^{xs} = X_{MnCl_2}(\bar{V}_C - \bar{V}_{Mn^{2+}} - 4\bar{V}_{Cl^-}) = X_{MnCl_2}\delta \quad [11]$$

Experimentally the excess molar volume is obtained by subtracting the additive volume of the pure components from the measured molar volume of a solution. The results of the calculations are shown in Fig. 3. The solid lines represent excess molar volumes determined experimentally and the dashed lines represent the values calculated from the model. The value for  $\delta$  was obtained for each system by substituting for  $\Delta V^{xs}$  in a solution rich in alkali chloride where the model is expected to hold best. The values for  $\delta$  found in this manner are positive and increase beginning with the  $MnCl_2$ -NaCl through the  $MnCl_2$ -CsCl systems. The positive deviations from additivity are indicative

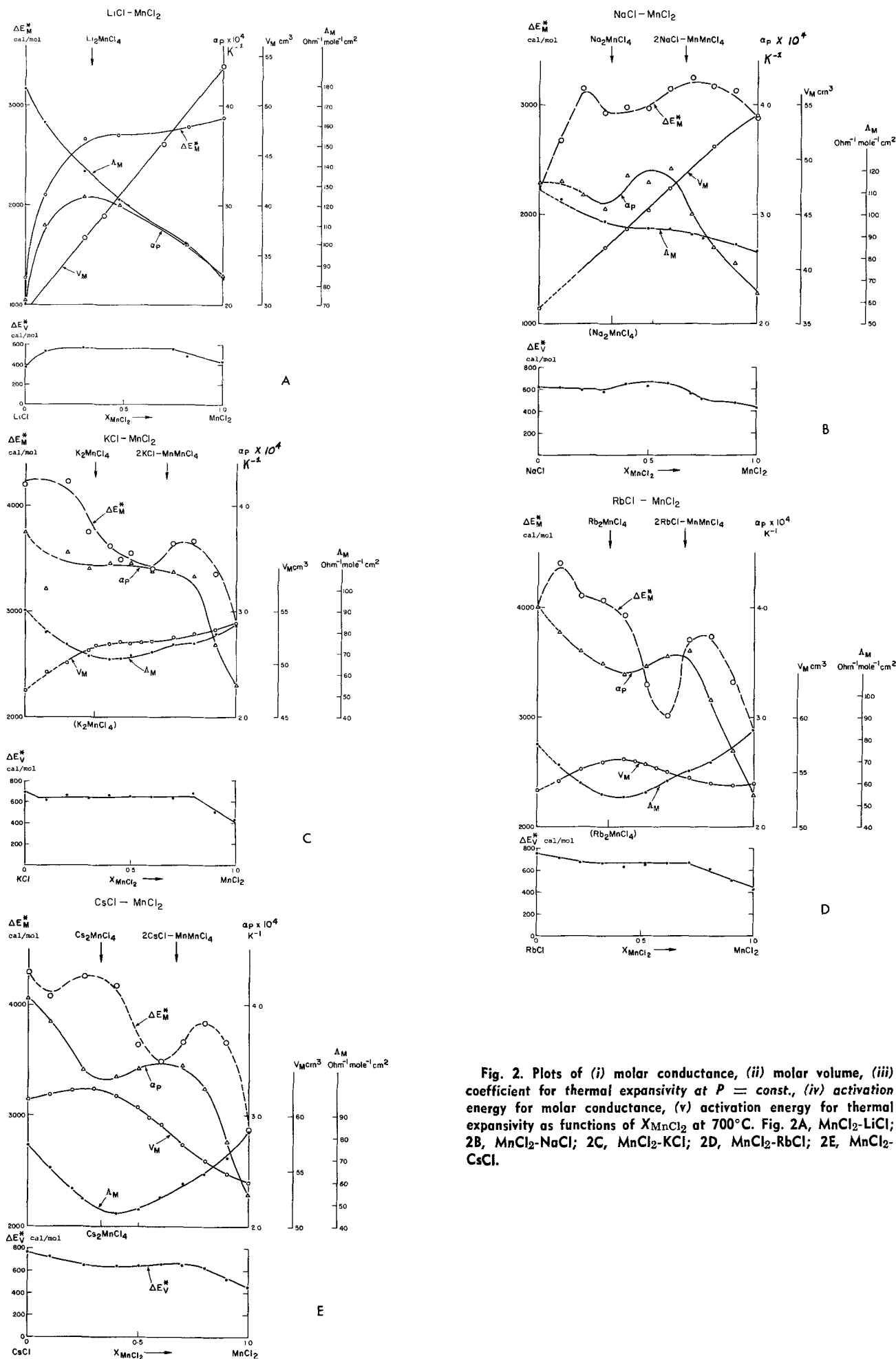


Fig. 2. Plots of (i) molar conductance, (ii) molar volume, (iii) coefficient for thermal expansivity at  $P = const.$ , (iv) activation energy for molar conductance, (v) activation energy for thermal expansivity as functions of  $X_{MnCl_2}$  at 700°C. Fig. 2A, MnCl<sub>2</sub>-LiCl; 2B, MnCl<sub>2</sub>-NaCl; 2C, MnCl<sub>2</sub>-KCl; 2D, MnCl<sub>2</sub>-RbCl; 2E, MnCl<sub>2</sub>-CsCl.

Table V. Mass balance for the  $\text{MnCl}_2$ -ACl system

A <sup>+</sup>	$\text{MnCl}_4^{2-}$	$\text{Mn}^{+2}$
Cl <sup>-</sup>	A <sup>+</sup>	Cl <sup>-</sup>
$\text{MnCl}_4^{2-}$	$\text{Mn}^{+2}, \text{Cl}^-, \text{A}^+$	
Cl <sup>-}, \text{A}^+</sup>	$\text{MnCl}_4^{2-}$	
0	0.333	1.0
ACl	$\text{A}_2\text{MnCl}_4$	$\text{MnCl}_2$
$X_{\text{MnCl}_2} \rightarrow$		
For, $1.0 > X_{\text{MnCl}_2} > 0.333$		
Subsystem $\text{MnCl}_2$ - $\text{A}_2\text{MnCl}_4$		
$n_{\text{MnCl}_2}$	$= X_{\text{MnCl}_2} - 0.5X_{\text{ACl}}$	
$n_{\text{A}_2\text{MnCl}_4}$	$= 0.5X_{\text{ACl}}$	
$n_{\text{ACl}}$	$= 0$	
Ionic composition		
Ionic volume contribution		
$n_{\text{Mn}^{+2}}$	$= X_{\text{MnCl}_2} - 0.5X_{\text{ACl}}$	$(X_{\text{MnCl}_2} - 0.5X_{\text{ACl}})\bar{V}_{\text{Mn}^{+2}}$
$n_{\text{A}^+}$	$= X_{\text{ACl}}$	$(X_{\text{ACl}})\bar{V}_{\text{A}^+}$
$n_{\text{Cl}^-}$	$= 2X_{\text{MnCl}_2} - X_{\text{ACl}}$	$(2X_{\text{MnCl}_2} - X_{\text{ACl}})\bar{V}_{\text{Cl}^-}$
$n_{\text{MnCl}_4^{2-}}$	$= 0.5X_{\text{ACl}}$	$(0.5X_{\text{ACl}})\bar{V}_{\text{C}}$
$0.333 > X_{\text{MnCl}_2} > 0$		
Subsystem ACl- $\text{A}_2\text{MnCl}_4$		
$n_{\text{MnCl}_2}$	$= 0$	
$n_{\text{A}_2\text{MnCl}_4}$	$= X_{\text{MnCl}_2}$	
$n_{\text{ACl}}$	$= X_{\text{ACl}} - 2X_{\text{MnCl}_2}$	
Ionic composition		
Ionic volume contribution		
$n_{\text{Mn}^{+2}}$	$= 0$	0
$n_{\text{A}^+}$	$= X_{\text{ACl}}$	$(X_{\text{ACl}})\bar{V}_{\text{A}^+}$
$n_{\text{Cl}^-}$	$= X_{\text{ACl}} - 2X_{\text{MnCl}_2}$	$(1 - 3X_{\text{MnCl}_2})\bar{V}_{\text{Cl}^-}$
$n_{\text{MnCl}_4^{2-}}$	$= X_{\text{MnCl}_2}$	$(X_{\text{MnCl}_2})\bar{V}_{\text{C}}$

X indicates the original mole fractions in the solution which is prepared by mixing the components ACl and  $\text{MnCl}_2$ .  
 $n_i$  indicates the moles of a component  $i$  after the reaction has taken place.

of inefficient ionic packing within the liquid structure which is usually attributed to complex formation.

This simple model should hold the best in the ACl-rich concentrations and especially for large alkali metal cations in the presence of which the complex species have been shown to be most stable.

In solutions rich in alkali chloride the excess molar volumes in the systems  $\text{MnCl}_2$ -KCl,  $\text{MnCl}_2$ -RbCl, and  $\text{MnCl}_2$ -CsCl are approximately the same and indicate a linear dependence on concentration. This behavior is consistent with Eq. [11], which is applicable to the alkali chloride rich concentration.

It is also probable that the specific accommodation requirements of the various alkali metal cations in the liquid structure depend upon ionic size and bonding and are not strictly an additive property. For example, pure LiCl has a molar volume which is about one half of that for  $\text{MnCl}_2$ , indicating that the volume of the solution is determined mainly by the anions. With large cations like  $\text{Cs}^+$ , which occupy by themselves about twenty times the volume of a  $\text{Li}^+$  ion, the alkali metal cation size should also become a factor determining the total volume of the solution.

The approximate partial molar volumes of  $\text{MnCl}_2$  in this region were calculated graphically from the molar volume isotherm at  $800^\circ\text{C}$ . The results are shown in Fig. 4, and support this interpretation. The partial molar volumes of  $\text{MnCl}_2$  are almost constant in the rich  $\text{MnCl}_2$  compositions, and deviate at higher ACl compositions. Poor packing of  $\text{MnCl}_2$  in the  $\text{MnCl}_4^{2-}$  species in excess KCl, RbCl, and CsCl is shown by the high partial molar volumes of 60-70  $\text{cm}^3$ , respectively.

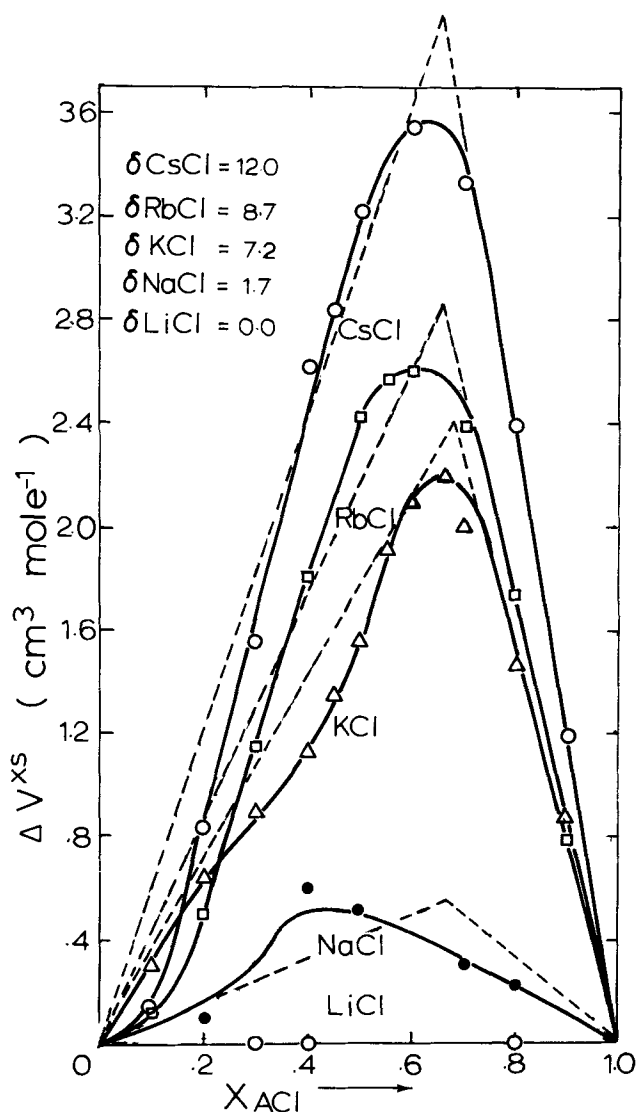


Fig. 3. Excess molar volumes in the  $\text{MnCl}_2$ -ACl systems, where, A = Li, Na, K, Rb, and Cs, plotted vs.  $X_{\text{ACl}}$  for the temperature of  $800^\circ\text{C}$ . — Experimental and - - - - - model.

It can be seen from Fig. 3 that the model presented here holds reasonably well in the ACl-rich concentrations but in the  $\text{MnCl}_2$ -rich concentrations some deviations occur.

The coefficients for thermal expansion at constant pressure  $\alpha_p$  may be calculated from the temperature dependence of the molar volumes using the expression

$$\alpha_p = (1/V) (\partial V / \partial T)_P = (\partial \ln V / \partial T)_P \quad [12]$$

The plots of  $\ln V$  vs.  $T$  for all systems are strictly linear, indicating that the coefficients  $\alpha_p$  are temperature independent over the temperature ranges indicated in Table I.

The coefficients for thermal expansion calculated from Eq. [12] are also given in Table IV and their concentration dependence is shown in Fig. 2.

If the thermal expansion of a solution is considered to represent an activated process, then

$$(\partial \ln V / \partial T)_P = \Delta E^*_{\text{v}} / RT^2 \quad [13]$$

where,  $\Delta E^*_{\text{v}}$ , is the activation energy for thermal expansion. Combining Eq. [12] and [13] it follows that

$$\Delta E^*_{\text{v}} = \alpha_p RT^2 \quad [14]$$

Activation energies for thermal expansion calculated at  $700^\circ\text{C}$  are also included in Table IV.

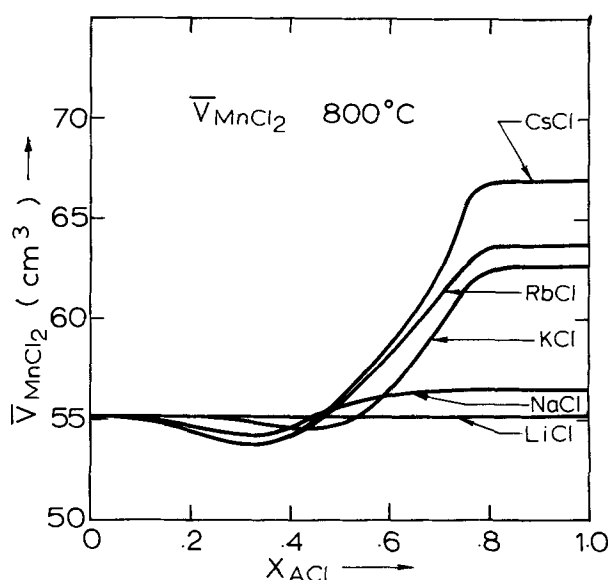


Fig. 4. Partial molar volumes of the  $MnCl_2$  solutions plotted vs.  $X_{ACl}$  at a temperature of  $800^\circ C$ .

The concentration dependence of the coefficients for thermal expansion in the five  $MnCl_2$ - $ACl$  systems indicate the following trends.

For the highly complexed systems,  $MnCl_2$ - $RbCl$  and  $MnCl_2$ - $CsCl$ , the coefficients for thermal expansion for the alkali chlorides decrease upon addition of  $MnCl_2$  and reach a minimum at about 33 mole per cent (m/o)  $MnCl_2$ , at a point corresponding to the maximum in the curves representing the dependence of molar volumes upon concentration. This composition represents approximately the stoichiometric ratio for  $ACl/MnCl_2$  required for the formation of the complex  $MnCl_4^{2-}$  species. At higher  $MnCl_2$  concentrations the molar volumes of the solutions decrease continuously while the thermal expansivity coefficients increase up to about a  $MnCl_2$  content of 70-80 m/o, after which they decrease continuously to the value representing the thermal expansion coefficient for pure molten  $MnCl_2$ .

The minimum in the thermal expansivity curves should be associated with the availability of "free" volume indicated by the maximum in the molar volume curves. This "free" volume is attributed to poor packing arrangements of the complex  $MnCl_4^{2-}$  configurations within the liquid structure. Upon heating this "free" volume is apparently capable of accommodating the thermally expanding liquid structure so that the over-all thermal expansion coefficient for a solution reaches a minimum. At concentrations higher than 33 m/o, the excess  $MnCl_2$  added appears to enter the solution by filling the "free" volume present in the  $A_2MnCl_4$  structure. Accordingly, the molar volume of the solution decreases from its maximum value and the thermal expansivity increases in the more densely populated structure to a maximum representing a concentration of 70-80 m/o  $MnCl_2$ .

It is of interest to note that in this composition range which is at the midpoint between "pure"  $A_2MnCl_4$  and pure  $MnCl_2$ , the filling of "free" volume may be assigned to the following exchange reaction



If the electrostatic interactions between the large monovalent cations, like  $K^+$ ,  $Rb^+$ , or  $Cs^+$ , and bonded  $Cl^*$  specie in a  $MnCl_4^{2-}$  type complex, are compared with those of the much smaller  $Mn^{2+}$  "free" cations, it is evident that the interatomic distance between  $Mn$  and bonded chlorine in the  $A_2MnCl_4$  configuration should also be smaller than that in the  $Mn(MnCl_4)$  configuration. Therefore the addition of excess  $MnCl_2$  in the  $ACl$ - $MnCl_2$  melts of composition beyond 33 m/o  $MnCl_2$  is expected to result in a relaxation of the

$Mn-Cl^*$  type of bonds in the  $MnCl_4^{2-}$  complex configurations existing in  $A_2MnCl_4$ , followed by more efficiently packed ionic arrangements.

The "activation energies" for thermal expansion are also given in Fig. 2 and in Table IV. These activation energies are rather small and do not indicate any unusual trends.

### Molar Conductances

Molar conductances were calculated from the specific conductance results and the density results, using Eq. [3]. In some instances it was found necessary to interpolate the molar volume isotherm to obtain the molar volume for the compositions corresponding to the conductivity data.

The isotherms of the molar conductances as a function of melt composition at  $700^\circ C$  are given in Fig. 2. It is seen that molar conductances exhibit increasing negative departures from additivity to the extent of -8% in  $LiCl$ , -6% in  $NaCl$ , -23% in  $KCl$ , -32% in  $RbCl$ , and -39% in  $CsCl$ , at  $X_{ACl} = 2/3$ .

For the  $MnCl_2$ - $KCl$  system molar conductance data reported by Murgulescu and Zuca (16) agree reasonably well with the present results, except for the  $MnCl_2$ -rich solutions probably due to the uncertainties in the molar volumes determined by these workers.

The concentration dependence of the molar conductances in the  $KCl$ - $MnCl_2$ ,  $RbCl$ - $MnCl_2$ , and  $CsCl$ - $MnCl_2$  systems, may also be explained by the complex anion model.

If the concentration range,  $1.0 > X_{MnCl_2} > 0.333$ , the solution consists of unreacted  $MnCl_2$  and the complex  $A_2MnCl_4$ . The conducting species in this range are the ions  $Mn^{2+}$ ,  $A^+$ ,  $Cl^-$  (free), and the  $MnCl_4^{2-}$  coordinated complex. The molar conductances may be obtained from the general expression

$$\Lambda_M = F \sum_i e_i z_i b_{ij} \quad [16]$$

where,  $F$  is the Faraday constant,  $e_i$  is the number of carriers of type  $i$  present in one mole of solution,  $Z_i$  is the valence and  $b_{ij}$  is the relative mobility of the  $i$  carrier with respect to another ion  $j$  as the frame of reference (3).

For solutions having the ionic compositions given in Table V, the molar conductance is obtained from Eq. [16] by referring all mobilities to the "free" chloride ions  $Cl^-$  as the frame of reference.

These equations are shown below. For the concentration range  $1.0 > X_{MnCl_2} > 0.333$

$$\Lambda_{total} = F[(2X_{MnCl_2} - X_{ACl})b_{14} + X_{ACl}b_{34} + X_{ACl}b_{24} + (2X_{MnCl_2} - X_{ACl})b_{44}] \quad [17]$$

and for  $0.333 > X_{MnCl_2} > 0$

$$\Lambda_{total} = F[X_{ACl}b_{24} + 2X_{MnCl_2}b_{34} + (X_{ACl} - 2X_{MnCl_2})b_{44}] \quad [18]$$

The quantities  $b_{14}$ ,  $b_{24}$ ,  $b_{34}$ , and  $b_{44}$  are the relative mobilities of the ions  $Mn^{2+}$ ,  $A^+$ ,  $MnCl_4^{2-}$ , and  $Cl^-$ , respectively, where  $b_{44} = 0$ .

It should be noted that according to the proposed complex ion model, the  $MnCl_4^{2-}$  specie should not be considered as an independent carrier. It seems likely that both the  $Mn^{2+}$  and  $Cl^-$  species, which are present in  $MnCl_4^{2-}$  are independent carriers each having mobilities which are different from those of "free"  $Mn^{2+}$  and "free"  $Cl^-$  ions. It is also to be expected that the shielding of the  $Mn^{2+}$  specie in the  $[MnCl_4^{2-}]$  configuration by the chloride ligands should make the mobility of the "bonded"  $Mn^{2+}$  lower than that of the "free"  $Mn^{2+}$  in solution. Irrespective of the individual behavior of each of the manganese and chloride species bonded within the complex  $MnCl_4^{2-}$ , the relative mobility  $b_{34}$  should be taken as representing a combination of these two contributions. Assuming that the mobilities are concentration independent and have the

same values in pure component as in the solutions, Eq. [17] and [18] reduce to

$$\Lambda_{\text{total}} = (X_{\text{MnCl}_2} - 0.5X_{\text{ACl}})\Lambda^{\circ}_{\text{MnCl}_2} + 0.5X_{\text{ACl}}\Lambda^{\circ}_{\text{A}_2\text{MnCl}_4} \quad [17a]$$

and

$$\Lambda_{\text{total}} = X_{\text{ACl}}\Lambda^{\circ}_{\text{ACl}} + 2X_{\text{MnCl}_2}(b_{34} - b_{44})F \quad [18a]$$

where

$$\Lambda^{\circ}_{\text{ACl}} = F(b_{24} + b_{44}) \quad [19]$$

$$\Lambda^{\circ}_{\text{MnCl}_2} = 2F(b_{14} + b_{44}) \quad [20]$$

and

$$\Lambda^{\circ}_{\text{A}_2\text{MnCl}_4} = 2F(b_{24} + b_{34}) \quad [21]$$

are the molar conductances of the pure molten compounds ACl, MnCl<sub>2</sub>, and A<sub>2</sub>MnCl<sub>4</sub>, respectively.

At the stoichiometric composition for the formation of the complex compound A<sub>2</sub>MnCl<sub>4</sub>,  $X_{\text{MnCl}_2} = 0.333$ , and Eq. [17a] yields

$$\begin{aligned} \Lambda_{\text{total}} &= X_{\text{ACl}}(b_{24} + b_{34})F \\ &= 0.5X_{\text{ACl}}\Lambda^{\circ}_{\text{A}_2\text{MnCl}_4} \end{aligned} \quad [22]$$

Equation [18a] predicts that at  $X_{\text{MnCl}_2} = 0.333$ , the total conductance should reduce to  $2/3 \Lambda^{\circ}_{\text{ACl}}$ , if the mobilities of the MnCl<sub>4</sub><sup>2-</sup> and Cl<sup>-</sup> species are not significant. As seen in Fig. 2d and 2e, in the highly complexed systems like MnCl<sub>2</sub>-RbCl and MnCl<sub>2</sub>-CsCl the total molar conductance at  $X_{\text{MnCl}_2} = 0.333$  is approximately equal to two-thirds of the total conductance of the pure alkali chloride.

In the binary systems, MnCl<sub>2</sub>-KCl, MnCl<sub>2</sub>-NaCl, and MnCl<sub>2</sub>-LiCl, the Mn<sup>2+</sup> ions are not able to form a strong complex anion and the total conductance at  $X_{\text{MnCl}_2} = 0.333$  is higher than  $2/3 \Lambda^{\circ}_{\text{ACl}}$ . For the "ideal" solution the molar conductance is given as

$$\Lambda_{\text{ideal}} = X_{\text{ACl}}\Lambda^{\circ}_{\text{ACl}} + X_{\text{MnCl}_2}\Lambda^{\circ}_{\text{MnCl}_2} \quad [23]$$

where  $\Lambda^{\circ}_{\text{ACl}}$  and  $\Lambda^{\circ}_{\text{MnCl}_2}$  are the conductances of the pure ACl and MnCl<sub>2</sub>, respectively. In terms of mobilities this equation takes the form

$$\Lambda_{\text{ideal}} = F[(b_{24} + b_{44})X_{\text{ACl}} + 2X_{\text{MnCl}_2}(b_{14} + b_{44})] \quad [24]$$

Excess conductances are obtained by subtracting Eq. [24] from Eq. [17] and [18], respectively. Hence at  $1.0 > X_{\text{MnCl}_2} > 0.333$

$$\begin{aligned} \Delta\Lambda^{\text{xs}} &= 0.5X_{\text{ACl}}(2b_{34} - 2b_{14} - 4b_{44})F \\ &= 0.5X_{\text{ACl}} \cdot \Delta m \end{aligned} \quad [25]$$

where

$$\Delta m = (2b_{34} - 2b_{14} - 4b_{44})F \quad [25a]$$

and at  $0.333 > X_{\text{MnCl}_2} > 0$

$$\Delta\Lambda^{\text{xs}} = X_{\text{MnCl}_2} \cdot \Delta m \quad [26]$$

The quantity  $\Delta m$  is expected to be negative for low  $b_{34}$  values. Accordingly, excess conductances are expected to be negative and be proportional to  $X_{\text{MnCl}_2}$  or  $X_{\text{ACl}}$ . The model should be applicable to systems having the least polarizing alkali cations like Cs<sup>+</sup> and Rb<sup>+</sup> which also form strong complex anions (1, 17).

The excess conductances for the five binary systems calculated from the specific conductance data at the temperature of 800°C are presented in Fig. 5. The values for  $\Delta m$  are obtained by substituting an experimental value of the molar conductance into Eq. [25] or [26], respectively. From the  $\Delta m$  values, the expected excess molar conductances are calculated over the entire concentration range and compared with the experimental results. In Fig. 5 the solid curves are experimental and the dashed curves are calculated from the model. The model is best applicable to the ACl-rich compositions. In the MnCl<sub>2</sub>-rich side the model deviates by about 12% from the experimental data. In the MnCl<sub>2</sub>-NaCl, MnCl<sub>2</sub>-LiCl systems the model does not appear to be applicable as the conductivity behavior of the solution is almost ideal.

Activation energies for the specific conductances  $\Delta E^*_s$  were also calculated from the data presented in Table III.

From the temperature dependence of the specific conductance  $\kappa$  given as

$$\kappa = a + bT + cT^2$$

the activation energies at any given temperature may be calculated through the transformation

$$d \ln \kappa / dT = (1/\kappa)(d\kappa/dT) = \Delta E^*_s / RT^2 \quad [27]$$

or

$$\Delta E^*_s = RT^2(b + 2cT)/(a + bT + cT^2) \quad [28]$$

Similarly, the activation energy for molar conductance  $\Delta E^*_M$  is calculated at any temperature from Eq. [3], [13], [27], and [28], as

$$\Delta E^*_M = \Delta E^*_s + \alpha_p RT^2 \quad [29]$$

where  $\alpha_p$ , represents the coefficient for thermal expansion.

The quantities  $\Delta E^*_s$  and  $\Delta E^*_M$  were calculated at the common temperature of 700°C and the results are presented in Table IV. The molar activation energies for conductance are also plotted in Fig. 2.

The molar activation energies for KCl, RbCl, and CsCl have much higher values than that for MnCl<sub>2</sub>, probably due to a smaller temperature effect on the mobilities of the large alkali metal cations.

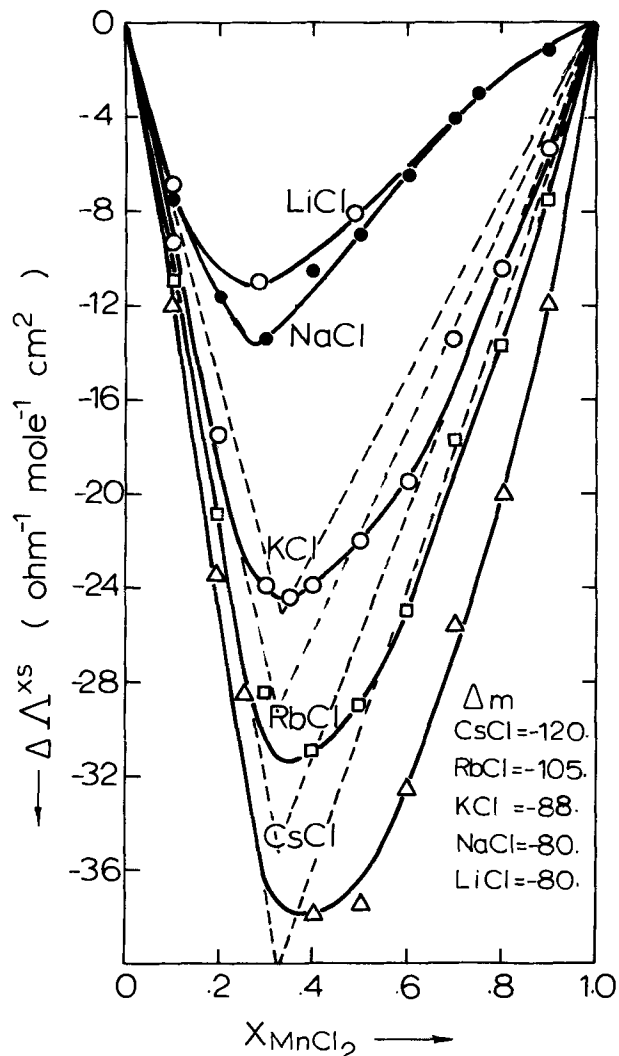
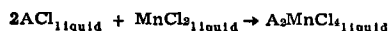


Fig. 5. Excess molar conductances in the MnCl<sub>2</sub>-ACl systems, where, A = Li, Na, K, Rb, and Cs, plotted vs.  $X_{\text{MnCl}_2}$  at a temperature of 800°C. — Experimental and - - - - - model.

Table VI. Comparison between thermodynamic and structural properties in the  $MnCl_2$ -ACl solutions

Sys-tem	$b_R$ (17) (cal/mol) (a)	$\Delta V^{xs}$ at $X_{MnCl_2}$ $= 0.333$ ( $cm^3 mol^{-1}$ )	$\delta$ ( $cm^3 mol^{-1}$ )	$\Delta m$ ( $ohm^{-1} cm^2 mol^{-1}$ )	$r_{A^+}$ ( $^\circ$ )
LiCl	-1,100	0	0	(-80)	0.60
NaCl	-4,950	0.5	1.7	-80	0.95
KCl	-10,680	2.2	7.2	-88	1.33
RbCl	-13,500	2.6	8.7	-105	1.48
CsCl	-15,720	3.5	12.0	-120	1.69

(a)  $b_R$  represents the enthalpy of formation of the complex compounds  $A_2MnCl_4$  according to the reaction



Upon the addition of  $MnCl_2$  to either NaCl, KCl, RbCl, or CsCl, the activation energies for molar conductance of the solutions indicate significant maximum values in the concentration ranges in which the  $A_2MnCl_4$  and  $Mn-MnCl_4$  complex configurations appear to predominate. In general, however, the concentration dependence of the activation energy curves is not as simple as that of the molar conductances.

From Fig. 2d and 2e, it is of interest to note that the molar conductance and the thermal expansivity curves in the systems  $MnCl_2$ -RbCl and  $MnCl_2$ -CsCl indicate a minimum at approximately the same composition for which the molar volume curves indicate their maximum. This characteristic concentration corresponds to the stoichiometric composition required by the formation of a  $MnCl_4^{2-}$  complex specie.

If the activation energy for the conductivity process is thought to be related to the energy of dissociating the complex species present in solution, then at  $X_{MnCl_2} = 1/3$  the activation energies should be directly related to the enthalpy of formation of the various  $A_2MnCl_4$  compounds.

In Fig. 6, the reaction parameters  $b_R$ , which represent the heats of mixing (17) in the various  $MnCl_2$ -ACl system at a mole ratio of  $ACl/MnCl_2 = 2$ , are plotted vs. the corresponding activation energies  $\Delta E^*_M$ . The exact linearity of this plot demonstrates clearly the relationship. Table VI represents a summary of the various structural and thermodynamic parameters determined in the course of our investigations. It should also be noted that the effects of the exchange reactions [15] on the thermodynamic behavior of the systems, were also taken into account in our previous treatment on enthalpies of mixing (17).

Accordingly, it may be concluded that the simple quasichemical complex ion model presents a reasonable

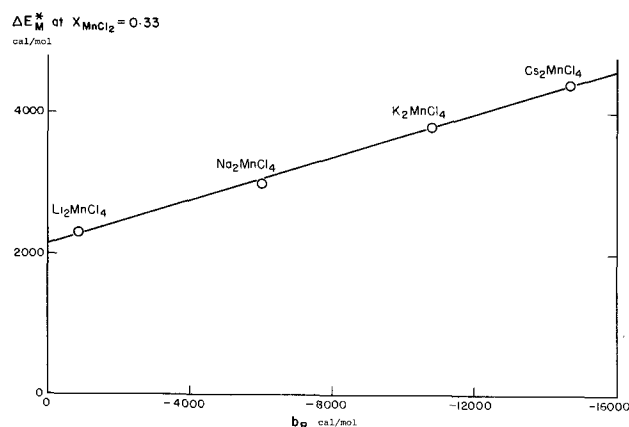


Fig. 6. Plot of activation energy for molar conductances at  $X_{MnCl_2} = 1/3$  vs.  $b_R$ , where  $b_R$  represents the enthalpy of formation of the compounds  $A_2MnCl_4$  according to the reaction  $(MnCl_2)_{liq} + 2(ACl)_{liq} \rightarrow (A_2MnCl_4)_{liq}$

interpretation for both thermodynamic and structural properties.

### Acknowledgments

We wish to acknowledge our thanks to the National Research Council of Canada for its financial assistance to one of us (ASK).

Manuscript submitted March 19, 1973; revised manuscript received Oct. 10, 1973.

Any discussion of this paper will appear in a Discussion Section to be published in the June 1975 JOURNAL. All discussions for the June 1975 Discussion Section should be submitted by Feb. 1, 1975.

The publication costs of this article have been assisted by the University of Toronto.

### LIST OF SYMBOLS

$\rho$	density, $g cm^{-3}$
$t$	temperature, $^\circ C$
$T$	temperature, K
$V_M$	molar volume, $cm^3$
$\Delta V^{xs}$	excess molar volume, $cm^3$
$\kappa$	specific conductance, $ohm^{-1} cm^{-1}$
$\Delta_M$	molar conductance, $ohm^{-1} cm^2$
$\Delta \Delta^{xs}$	excess molar conductance, $ohm^{-1} cm^2$
$b_{ij}$	internal mobility of i ion with respect to j ion $cm^2 sec^{-1} V^{-1}$
$X_i$	mole fraction of component i
$n$	number of moles
$F$	Faraday's constant
$A$	alkali atom
$\alpha_p$	coefficient of thermal expansion, $K^{-1}$
$\Delta E^*_s$	activation energy for specific conductance, $cal mol^{-1}$ , (Eq. [27])
$\Delta E^*_v$	activation energy for thermal expansion, $cal mol^{-1}$ , (Eq. [13])
$\Delta E^*_M$	activation energy for molar conductance, $cal mol^{-1}$ , (Eq. [29])
$\bar{V}_i$	partial molar volume of i ion, $cm^3$
$e_i$	number of carriers of type i in one mole of solution.
$\Delta m$	defined by Eq. [25a]

### REFERENCES

- S. N. Flengas and A. S. Kucharski, *Can. J. Chem.*, **49**, 24 (1971).
- S. J. Janz, F. W. Dampier, G. R. Lakshminarayanan, P. K. Lorenz, and R. P. T. Tomkins, "Electrical Conductance, Density and Viscosity," NSRDS-NB595, National Standard Reference Series, National Bureau of Standards, **1** (1968).
- M. Blander, Editor, "Molten Salt Chemistry," Interscience Publishers, Inc., New York (1964).
- B. Sundheim, Editor, "Fused Salts," p. 165, McGraw-Hill Book Co., Inc., New York (1964).
- H. Bloom, P. W. D. Boyd, J. L. Laver, and J. Wong, *Australian J. Chem.*, **19**, 1591 (1966).
- G. A. Yogubyan and G. A. Bukhalova, *Russ. J. Inorg. Chem.*, **13**, 1162 (1968).
- C. Sandonnini, *Gazz. Chim. Ital.*, **51**, 289 (1910).
- S. Fuseya and K. Ouchi, *J. Electrochem. Soc. Japan*, **17**, 254 (1949).
- J. A. Reding, *J. Chem. Eng. Data*, **10**, 1 (1965).
- T. Matsushima and T. Ito, *Japan Inst. Metals Trans.*, **10**, 161 (1969).
- H. Bloom and E. Heymann, *Proc. Roy. Soc. (London)*, **A188**, 825 (1947).
- H. Bloom, *Pure Appl. Chem.*, **7**, 385 (1963).
- R. W. Huber, E. V. Potter, and H. W. St. Clair, U.S. Bur. Mines Rept. Invest., 4858 (1952).
- K. P. Batashov, *Metallurg*, **10**, 100 (1935).
- H. Bloom, "The Chemistry of Molten Salts," Benjamin, New York (1967).
- L. S. Murgulescu and S. Zuca, *Acad. Rep. Populare Romine Studii Cercetari Chim.*, **7**, 325 (1959).
- A. S. Kucharski and S. N. Flengas, *This Journal*, **119**, 1170 (1972).
- M. C. Bell and S. N. Flengas, *ibid.*, **111**, 569 (1964).
- A. K. Garbee, Ph.D. Thesis, University of Toronto (1969).
- S. Jones and B. C. Bradshaw, *J. Am. Chem. Soc.*, **55**, 1780 (1933).

21. J. O'M. Bockris, J. L. White, and J. D. Mackenzie, Editors, "Physico-Chemical Measurements at High Temperatures," p. 248, Butterworth Scientific Publications, London (1959).
22. G. W. Mellors and S. Senderoff, *J. Phys. Chem.*, **64**, 294 (1960).
23. E. R. Van Artsdalen and I. S. Yaffe, *ibid.*, **60**, 118 (1955).
24. E. R. Van Artsdalen and I. S. Yaffe, *ibid.*, **60**, 1127 (1956).
25. M. V. Smirnov, V. A. Khokhov, and Puzanova, *Electrochem. Molten Solid Electrolytes*, **6**, 15 (1968).
26. W. Klemm and W. Biltz, *Z. Physik Chem.*, **110**, 318 (1924).
27. H. Winterhager and L. Werner, Forschungsber. Wirtsch Verkehrsministeriums Nordrhein-Westfalen, 341 (1956).
28. S. N. Flengas and Sir Eric Rideal, *Proc. Roy. Soc.*, **A233**, 443 (1956).
29. S. N. Flengas and P. Pint, *Can. Met. Quart.*, **8**, 151 (1969).

## Electrochemical Behavior of the Fluorographite Electrode in Nonaqueous Media

William Tiedemann\*

*Corporate Applied Research Group, Globe-Union Incorporated, Milwaukee, Wisconsin 53201*

### ABSTRACT

The open-circuit voltage of the fluorographite,  $(CF)_n$ , electrode can be interpreted as a mixed potential resulting from the anodic reaction of the solvent in question coupled with the cathodic reaction of fluorographite,  $(CF)_n$ . The Tafel slope was found to be relatively constant as a function of solution composition and discharge state of the  $(CF)_n$ . An exchange current of  $10^{-21}$  A/cm<sup>2</sup> was estimated based on a thermodynamically predicted open-circuit voltage of the  $(CF)_n$  electrode. An average charge transfer coefficient of 0.4 was calculated for the  $(CF)_n$  reaction.

Organic electrolyte systems have been studied for a relatively long time because of their potential capabilities of providing a high specific energy, high specific power, wide temperature range battery. Recently (1-5) there has been an interest in the use of lamellar-type compounds of graphite as cathode materials. The technical feasibility of an organic electrolyte battery comprising a lithium anode and a fluorographite cathode,  $(CF)_n$ , (a lamellar type compound) has been demonstrated (1, 3-5).

Little information exists on the fundamental electrochemical behavior of the  $(CF)_n$  electrode and little is known concerning its limiting performance characteristics. Electrochemical investigations of  $(CF)_n$  are complicated by the following facts: (i)  $(CF)_n$  is a non-conductor and must be supported on an electrically conductive phase which is in intimate contact with the electrolyte solution; (ii) the reaction products (C and LiF) are insoluble and tend to cover the available surface; and (iii) a very small electrochemical reaction rate of  $(CF)_n$  necessitates the use of large effective surface areas in order that currents obtained may be measured accurately. These conditions necessitate the use of a test electrode which has a relatively large active surface area, is electronically conducting, and is porous. Porous electrodes tend to complicate the analysis of the polarization results; however, it will be shown below that certain test conditions exist which greatly reduce the complexity of the analysis.

### Experimental

**Chemicals.**—Propylene carbonate (PC), dimethyl sulfite (DMSI), and dimethoxyethane (DME) were obtained in reagent grade form, dried over 4A molecular sieves, and vacuum distilled twice, the middle fraction being retained in each instance. Each solvent was stored in vacuum sealed glass vials until used.

Ultrapure  $LiClO_4$  was obtained from Anderson Physics Laboratory and used without further treatment.

\* Electrochemical Society Active Member.  
Key words: porous electrodes, mixed potential, double layer charging.

One molar solutions of  $LiClO_4$  were prepared from combinations of PC/DMSI in a ratio of 30% PC to 70% DMSI by volume, and PC/DME in a ratio of 30% PC to 70% DME by volume. These solutions were stored in vacuum sealed glass vials until used.

$(CF)_n$  was obtained from three sources ((i) Ozark-Mahoning Company, Tulsa, Oklahoma,  $x = 0.96 \pm 0.05$ ; (ii), Air Products and Chemicals, Allentown, Pennsylvania,  $x = 1.04 \pm 0.05$ ; (iii), MarChem, Incorporated Houston, Texas,  $x = 1.06 \pm 0.04$ ) and used without further treatment. Conductex SC (Columbian Carbon Company) powder was selected as the conductive diluent and Teflon molding powder as the binder. These three materials were vacuum dried at 250°F for 50 hr.

**Electrode preparation.**—The porous  $(CF)_n$  electrode was prepared from a mixture of  $(CF)_n$ , Conductex SC carbon, and Teflon molding powder (1:0.2:0.2 ratio by weight) by pressing the resulting powder onto an expanded nickel grid at 200°C and 4000 psi. Prismatic electrodes measuring  $5.38 \times 5.38 \times 0.132$  cm had theoretical capacities of 1.8 A-hr, an effective matrix conductivity of 0.2 mho/cm, a porosity of 0.56, and a specific interfacial surface area of  $10^6$  cm<sup>2</sup>/cm<sup>3</sup>.

The lithium electrodes were prepared by Foote Mineral Company (Exton, Pennsylvania) by pressing lithium metal onto expanded nickel foil. They were used as received without further treatment.

**Cell design.**—Experiments were performed on a cell comprising one  $(CF)_n$  electrode sandwiched between two lithium electrodes with a solid lithium reference electrode positioned adjacent to the  $(CF)_n$  electrode. A 0.0025 cm thick microporous polypropylene separator was inserted between the Li and  $(CF)_n$  electrodes. The resulting electrode stack was sealed into an aluminum laminated polypropylene bag and placed in a testing fixture which prevented expansion of the electrode stack. Electrical connections were taken out through seals in the laminate.

**Experimental procedure.**—The test cell was filled with solution, placed in a vacuum to remove trapped gas, sealed, and placed in a vise-type testing fixture.

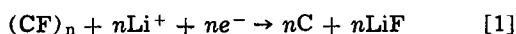


Approximately 4 ml of solution were used in each cell. This operation was performed in a vacuum dry box with an argon atmosphere and equipped with  $N_2$ ,  $O_2$ , and  $H_2O$  recirculating dry trains. The temperature of the dry box was maintained at  $28^\circ \pm 1^\circ C$ . Polarization studies were performed both inside and outside the dry box; however, all assembly, filling, and sealing operations occurred in the dry box.

A Wenking potentiostat was employed for the constant potential polarization studies. Prior to each polarization study the fresh  $(CF)_n$  was placed on a  $0.035 \text{ mA/cm}^2$  constant current discharge for 9 hr. Approximately 0.05% of the electrode coulombic capacity was removed in this period. The electrode was then allowed to stand at open circuit for a minimum of 24 hr before testing was continued. Current, as a function of time, was recorded on an Esterline Angus chart recorder. Polarization of the electrode was terminated when the current density reached approximately  $3 \text{ mA/cm}^2$ . All potentials mentioned below are measured with respect to a lithium reference electrode. The maximum  $IR$  included in these measurements was less than 1 mV.

### Treatment of Polarization Data

The reaction which is postulated to occur at the  $(CF)_n$  electrode is (1)



The reversibility of this reaction will be discussed below. Analysis of the system is somewhat complicated by the fact that the  $(CF)_n$  electrode is porous which suggests the possibility of nonuniform current distribution within the electrode. An equation applicable to this situation is

$$\frac{di(x)}{dx} = A_a i_{o,a} \exp \left[ \frac{\alpha_a F}{RT} \eta_s(x) \right] - A_c i_{o,c} \exp \left[ - \frac{\alpha_c F}{RT} \eta_s(x) \right] \quad [2]$$

where uniform concentrations have been assumed. Uniformity of current distribution in a porous electrode over the so-called Tafel region can be estimated in terms of the parameter

$$\delta = L|i|(1 - \alpha_c)(nF/RT)(1/\kappa + 1/\sigma) \quad [3]$$

For  $\delta \approx 0.1$ , the current distribution in a porous electrode is nearly uniform (6). The system presently being examined yields  $\delta \approx 0.1$ . Analysis of the  $(CF)_n$  electrode is therefore simplified and Eq. [2] reduces to

$$i = A_a Li_{o,a} \exp \left( \frac{\alpha_a F}{RT} \eta_s \right) - A_c Li_{o,c} \exp \left( - \frac{\alpha_c F}{RT} \eta_s \right) \quad [4]$$

In effect Eq. [4] states that a uniform current distribution exists throughout the depth of the electrode and the subsequent behavior can be equated to that of a flat electrode with a surface area ( $LA$ ) times greater.

### Results and Discussion

Potentiostatic measurements on the  $(CF)_n$  electrode are made difficult by the relatively large surface area of a porous electrode. While the steady-state current related to the  $(CF)_n$  reaction might be  $10^{-4} A$  for a 2 mV overpotential, the initial current associated with charging the double layer of the porous electrode was of the order of  $10^{-2} A$ . Subsequent variations in the controlled potential of less than  $10 \mu V$  produced current oscillations of  $\sim 10^{-4} A$ . Approaching a steady-state current reading is further complicated by a large time constant of double layer charging of the porous electrode. Due to these complications, linear polarization data of the  $(CF)_n$  electrode could not be obtained. As the electrode became more discharged, the amount

of carbon increased, and therefore the double layer charging area increased. Double layer charging will be discussed below as it relates to the observed behavior of the  $(CF)_n$  electrode.

Figure 1 contains a typical polarization curve of a porous  $(CF)_n$  electrode. The large uncertainty limits at low overpotentials are associated with current oscillations resulting from charging of the double layer. A reasonable Tafel region (linear dependence of  $\eta_s$  vs.  $\log i$ ) is observed for both solutions examined, and similar Tafel behavior is shown in Fig. 2 for  $(CF)_n$  at different states of charge. The Tafel slopes of these four curves were found to be nearly equal. An average value of  $\alpha_c$  was calculated to be 0.4. As the current approaches  $3 \cdot 10^{-2} A$ , the assumptions of constant concentration and uniform current distribution are no longer valid. Nonuniform current distribution is a subject beyond the scope of the present investigation.

Initial open-circuit voltages (O.C.V.) of the  $(CF)_n$  electrode in 1M  $LiClO_4$ -PC/DMSI and -PC/DME solution were 3.20 and 3.35V (vs. a lithium reference electrode), respectively. The reversible O.C.V. of  $(CF)_n$  has been calculated (7) to be approximately 4.5V (vs. lithium) based on free energy of formation data. Figure 3 shows that the O.C.V. of the  $(CF)_n$  electrode decreases as the discharge state of the electrode increases. The most rapid decrease in the O.C.V. is observed in the first 10-15% of the discharge followed by a moderate decline of the electrode potential until

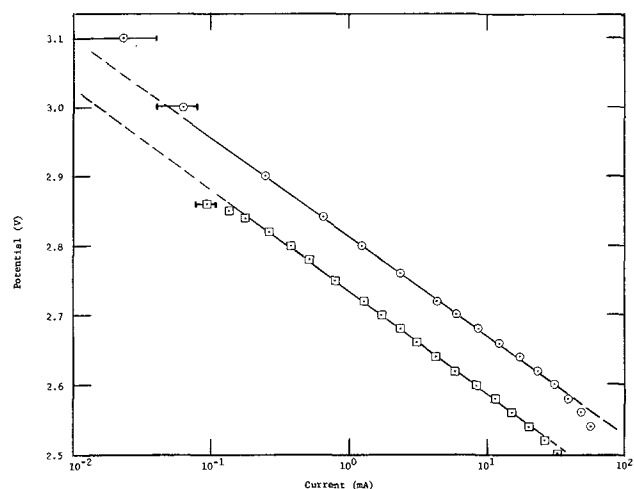


Fig. 1. Potentiostatic polarization of a porous  $(CF)_n$  electrode.  $\odot$ , 1M  $LiClO_4$  PC/DME;  $\square$ , 1M  $LiClO_4$  PC/DMSI. Temperature =  $25^\circ C$ ; area =  $29 \text{ cm}^2$ ; thickness =  $0.132 \text{ cm}$ .

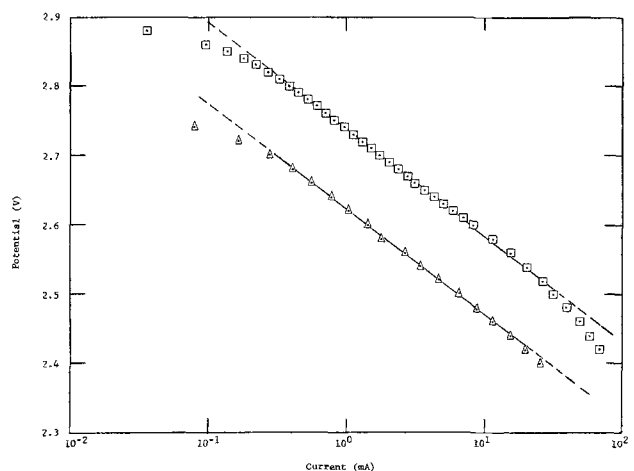


Fig. 2. Potentiostatic polarization of a porous  $(CF)_n$  electrode as a function of discharge state. 1M  $LiClO_4$  PC/DMSI.  $\square$ , 0.05% discharged;  $\Delta$ , 10% discharged. Temperature =  $25^\circ C$ ; area =  $29 \text{ cm}^2$ ; thickness =  $0.132 \text{ cm}$ .

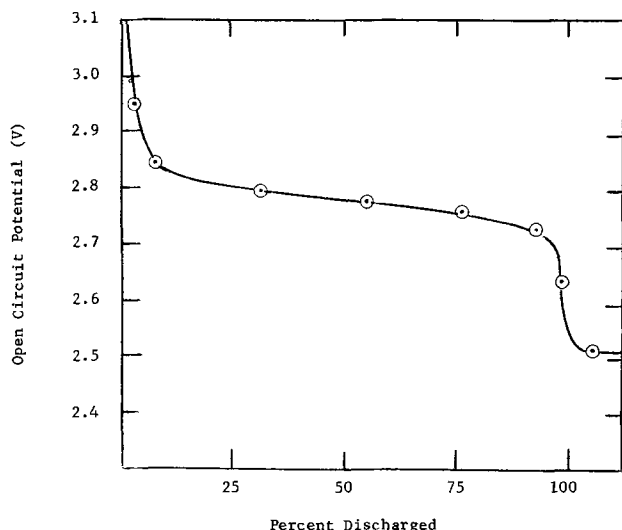


Fig. 3. Open-circuit voltage of a porous  $(CF)_n$  electrode as a function of its state of charge. 1M  $LiClO_4$  PC/DMSI.

about 90-95% of the discharge is reached. The O.C.V. of a completely discharged  $(CF)_n$  electrode is approximately 2.5V (vs. a lithium reference electrode).

The observed behavior of the O.C.V. of  $(CF)_n$  can possibly be attributed to a mixed potential resulting from the anodic decomposition of the solvent(s) coupled with the cathodic reaction of  $(CF)_n$ . Most solvents, including the ones studied here, undergo some degree of oxidation at potentials greater than 3V. The degree of oxidation is subject to the nature of the catalytic surface (in this case, carbon) and to the total accessible surface area. As  $(CF)_n$  is discharged according to Eq. [1], electronically conductive carbon is generated, and one can expect the oxidation of the solvent(s) to increase due to the increase in reactive carbon area. At the same time the cathodic reaction of  $(CF)_n$  must increase resulting in a decrease of the O.C.V. This implies that the intercept of the Tafel slope with the O.C.V. gives an estimate of the corrosion (or self-discharge) current and can be used to predict the activated shelf life of the  $(CF)_n$  electrode as a function solvent(s). One would expect self-discharge to increase with increasing discharge of  $(CF)_n$ .

Using 4.57V as the true O.C.V. of the  $(CF)_n$  electrode and extrapolating the Tafel slope in Fig. 1 to this value, a value of the exchange current density of  $\sim 10^{-21}$  A/cm<sup>2</sup> is calculated. This implies that recharging the  $(CF)_n$  electrode in a reasonable length of time would require over 6V (vs. a lithium reference electrode). There are virtually no solvents which are stable at this voltage. All attempts to recharge the  $(CF)_n$  electrode have been unsuccessful; only decomposition of the solvents was observed.

The discharge behavior of the  $(CF)_n$  electrode suggests that the reaction mechanism does not involve a soluble  $(CF)_n$  intermediate since the electronically conductive carbon surface area increases by more than an order of magnitude during the time when the rate capability of the  $(CF)_n$  electrode is decreasing (Fig. 2). The decrease in rate capability corresponds directly to the decrease in the active area of the  $(CF)_n$ .

As the electrode becomes more discharged, the time required for the electrode potential to reach its open-circuit value, after polarization has been terminated, increases markedly (Fig. 4). The slow recovery time appears to be linked to the small value of  $i_0$ , the decrease in the electrochemically active surface area, and the increasing value of the electronically conducting carbon surface area. These effects are coupled through charging or discharging the double layer capacity of the electrode. An estimation of the relaxation time can be given by

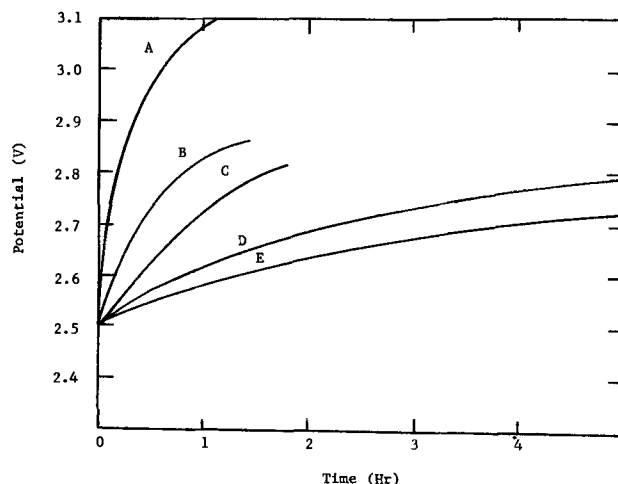


Fig. 4. Voltage recovery of a porous  $(CF)_n$  electrode as a function of its discharge state. A = 0%; B = 5%; C = 10%; D = 30%; E = 50%.

$$\tau = \frac{RTCA_a}{F i_0 A_c} \quad [5]$$

For a 6% discharged electrode we obtain  $\tau \cong 10^4$  sec. Therefore, as the end of the discharge is approached, the recovery of the electrode potential (after the cell is open circuited) can take as long as 50 hr. Conversely, in the initial stages of discharge, the electrode potential can recover in a matter of seconds. Time required to charge the double layer can also affect the polarization readings at small currents.

### Conclusions

The open-circuit voltage of the  $(CF)_n$  electrode is a mixed potential resulting from the anodic reaction of the solvent(s) with the cathodic reaction of  $(CF)_n$ . The intercept of the Tafel slope with the O.C.V. can be interpreted as a corrosion or self-discharge current and represents an estimate of the activated shelf life of the  $(CF)_n$  electrode.

It should be noted that larger O.C.V.'s do not imply higher energy densities for the  $(CF)_n$  electrode, since useful currents are obtained only when the  $(CF)_n$  electrode has been cathodically polarized to 2.7V (vs. a lithium reference electrode).

Double layer charging of the carbon surface of the porous  $(CF)_n$  coupled with the small exchange current density of the  $(CF)_n$  reaction results in slow attainment of steady-state polarization readings.

### Acknowledgments

The author wishes to thank Professor John Newman for many valuable discussions concerning the contents of this paper. The author also wishes to thank Globe-Union Incorporated for permission to publish this paper and for their cooperation and support that have made this research possible.

Manuscript submitted April 26, 1974; revised manuscript received June 4, 1974.

Any discussion of this paper will appear in a Discussion Section to be published in the June 1975 JOURNAL. All discussions for the June 1975 Discussion Section should be submitted by Feb. 1, 1975.

The publication costs of this article have been assisted by Globe-Union Incorporated.

### LIST OF SYMBOLS

- $A_a$  specific interfacial area for the anodic reaction, cm<sup>2</sup>/cm<sup>3</sup>  
 $A_c$  specific interfacial area for the cathodic reaction, cm<sup>2</sup>/cm<sup>3</sup>  
 $C$  double layer capacity, f/cm<sup>2</sup>

<b>F</b>	Faraday's constant, coulombs/equiv
<b>i</b>	normal current density at the electrode surface, A/cm <sup>2</sup>
<b>i<sub>o,a</sub></b>	exchange current density of the anodic reaction, A/cm <sup>2</sup>
<b>i<sub>o,c</sub></b>	exchange current density of the cathodic reaction, A/cm <sup>2</sup>
<b>L</b>	electrode half-thickness, cm
<b>n</b>	number of electrons, equal to one
<b>R</b>	universal gas constant, joule/mole-deg
<b>T</b>	absolute temperature, °K
<b>α<sub>a</sub>, α<sub>c</sub></b>	parameters in kinetic expression (see Eq. [2])
<b>δ</b>	current distribution parameter (see Eq. [3])
<b>σ</b>	matrix conductivity, mho-cm <sup>-1</sup>
<b>η<sub>s</sub></b>	surface overpotential, V
<b>κ</b>	solution conductivity, mho-cm <sup>-1</sup>
<b>τ</b>	double layer charging time constant, sec

## REFERENCES

1. M. Fukuda and T. Iijima, Abstract 41, p. 100, Electrochemical Society Extended Abstracts, Fall Meeting, Cleveland, Ohio, Oct. 3-7, 1971.
2. J. S. Dunning, W. H. Tiedemann, L. Hsueh, and D. N. Bennion, *This Journal*, **118**, 1886 (1971).
3. Herbert F. Hunger and George J. Heymach, *ibid.*, **120**, 1162 (1973).
4. J. J. Auborn, K. W. French, S. I. Lieberman, V. K. Shah, and A. Heller, *ibid.*, **120**, 1613 (1973).
5. W. K. Behl, J. A. Christopoulos, M. Romirez, and S. Gelman, *ibid.*, **120**, 1619 (1973).
6. J. Newman and C. Tobias, *ibid.*, **109**, 1183 (1962).
7. J. Wood, R. Bodachharpe, R. Lagow, and J. Margrave, *J. Phys. Chem.*, **73**, 3139 (1969).

# Technical Note



## The Influence of Electrolyte Impurities on Mercury Losses in the Electrolysis of Aqueous NaCl Solutions

I. T. Rodeanu

*Str. Dr. Ratiu 24, bloc 8, ap. 18, Turda, Romania*

Experimental work undertaken in laboratories and in industrial installations has shown that impurities in the electrolyte, such as calcium, magnesium, aluminum, iron, and silica compounds, can influence the electrolysis of aqueous sodium chloride in mercury cells. Several papers (1-5) have investigated how metal salts (vanadium, chromium, nickel, barium, magnesium, iron, copper, and arsenic) may intensify amalgam decomposition within the electrolyzer, resulting in unwanted hydrogen evolution.

The object of this paper is to examine and to determine the dependency of mercury losses on electrolyte purification procedures and on the soluble and insoluble constituents which contaminate the electrolyte.

### Experimental Procedures and Results

Experiments were undertaken in an industrial electrolysis installation of aqueous sodium chloride solution in a mercury cell. The impurities contained in eight samples of raw electrolyte material are given in Table I. The samples were taken at twenty-day intervals from the salt introduced in the saturator.

In addition, daily measurements were made of the impurities in the electrolytic solution. Table II gives

mean values for each working day over a four-week period.

Experiments were carried out with use of electrolyte which had been pretreated by one of three different methods: (a) "Imposed" working conditions: remove chlorites and hypochlorites with hydrochloric acid, remove calcium ions with sodium carbonate, remove sulfate ions with barium chloride, remove magnesium and ferric ions with sodium hydroxide. (b) "Normal working conditions: incomplete purification of electrolyte consisting only of treatment with sodium hydroxide and hydrochloric acid. (c) "Uncontrolled" working conditions; no prepurification. In this condition, the electrolyte contained a suspension of NaCl crystals and insoluble impurities which were carried from the settler and were not retained by the filters.

With use of electrolyte prepared by these three methods, measurements were made of the hydrogen content in the chlorine gas leaving the electrolysis cell. Table III gives typical comparative data for how the hydrogen content varies with impurity constituents in the electrolyte. Under imposed working conditions, less than 1.05% hydrogen was found; under normal conditions, between 1.05 and 1.44% hydrogen was found; over 1.44% was found for uncontrolled conditions.

Key words: mercury losses, mercury cell, impurity effects, industrial processing, sodium chloride electrolysis.

Table I. Impurity content of the NaCl

Impurities determined	Content, %							
	1	2	3	4	5	6	7	8
NaCl	98.42	98.26	98.2	98.5	98.33	97.93	98.8	97.47
CaCl <sub>2</sub>	0.083	0.076	0.028	0.018	—	—	0.028	0.107
MgCl <sub>2</sub>	0.01	0.008	—	—	—	—	—	0.047
Na <sub>2</sub> SO <sub>4</sub>	0.16	0.29	—	—	—	—	—	—
CaSO <sub>4</sub>	0.41	0.39	0.27	0.29	0.31	0.26	0.26	0.563
Fe <sub>2</sub> O <sub>3</sub> <sup>+</sup>	—	—	—	—	—	—	—	—
Al <sub>2</sub> O <sub>3</sub>	0.042	0.058	0.026	0.020	0.05	0.082	0.011	0.014
Insoluble	0.74	0.84	0.61	0.6	0.44	0.63	0.73	0.70

Table II. Impurity content of the electrolyte

Name of impurity	No. of mean sample	Content in g/liter					
		I	II	III	IV	V	VI
ClO <sub>2</sub> <sup>-</sup>	1	0.29	0.54	0.29	0.26	0.27	0.48
	2	0.43	0.54	0.25	0.21	0.30	0.39
	3	0.51	0.50	0.27	0.29	0.29	0.34
	4	—	0.44	0.23	0.23	0.55	0.46
SO <sub>4</sub> <sup>2-</sup>	1	3.09	3.38	3.02	3.14	3.18	3.90
	2	3.34	3.14	2.68	3.09	3.09	2.90
	3	3.49	3.04	2.99	3.14	3.14	3.14
	4	—	3.08	3.14	3.14	2.90	3.20
Fe <sup>2+</sup>	1	0.0002	Traces	Traces	Nil	Traces	Traces
	2	Traces	Traces	Traces	Traces	Traces	Nil
	3	Nil	Nil	Nil	Traces	Nil	Traces
	4	—	Traces	Traces	Traces	Traces	Traces
Ca <sup>2+</sup>	1	0.80	0.78	0.80	0.84	0.88	0.74
	2	0.77	0.74	0.70	0.75	0.88	0.65
	3	0.78	0.80	0.88	0.86	0.82	0.78
	4	—	0.84	0.84	0.78	0.72	0.62
Mg <sup>2+</sup>	1	Nil	Traces	Traces	Traces	Nil	Nil
	2	Nil	Nil	Nil	Traces	Traces	Traces
	3	Nil	Nil	0.0048	Traces	Nil	Traces
	4	—	Traces	Traces	Traces	Traces	Nil

Table III. Comparative data regarding the hydrogen content in chlorine and impurities in the electrolyte

Content of impurities in the electrolyte in g/liter	H <sub>2</sub> content in Cl <sub>2</sub> in volume per cent	H <sub>2</sub> content in Cl <sub>2</sub> in volume per cent		
		0.6-0.8	1.05-1.44	4.0-6.2
ClO <sub>2</sub> <sup>-</sup>	0.05	0.362	0.362 + susp	
SO <sub>4</sub> <sup>2-</sup>	1.06	3.212	3.212 + susp	
Fe <sup>2+</sup>	0.00025	0.0002	0.0002 + susp	
Ca <sup>2+</sup>	0.08	0.85	0.85 + susp	
Mg <sup>2+</sup>	0.0045	0.0048	0.0048 + susp	

Mercury losses under normal and uncontrolled conditions were determined simultaneously by sampling the electrolyte at four locations in the electrolyte flow circuit. Samples were taken at the electrolyzer outlet, at the inlet to the precipitation tank, at the outlet of the settling tank, and at the electrolyzer inlet. Mercury in the electrolyte was determined by the dithizone (6) method, which is suitable over the range of 1-

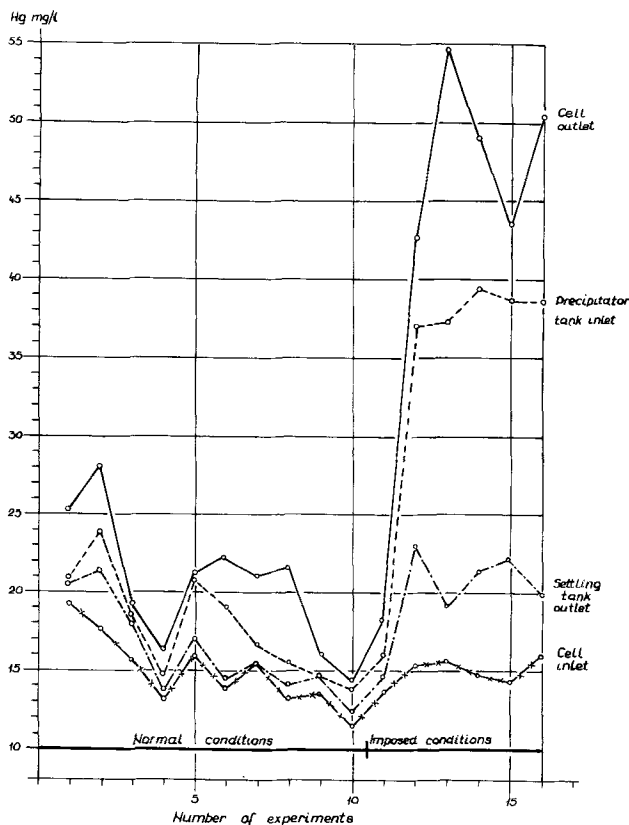


Fig. 1. Results obtained at the determination of the mercury losses in normal and uncontrolled working conditions.

55 mg Hg/liter. The presence of Fe, Co, Ni, Bi, Pb, and Mn does not interfere with the determination provided that their concentrations are less than 10<sup>-2</sup> mol/liter. Results are shown in Fig. 1 for a number of successive experiments.

During uncontrolled conditions, i.e., in the absence of electrolyte prepurification, a suspension of sodium chloride crystals and impurity precipitation products was carried from the settling tank and was not retained in the filtering system. Several samples of electrolyte containing such suspensions were withdrawn and examined under a microscope. Typical observations are shown in Fig. 2, 3, and 4. The suspensions, of unknown structure, surround and become attached to the sodium chloride crystals. Microscopic observations during fouling of fresh NaCl crystals were also

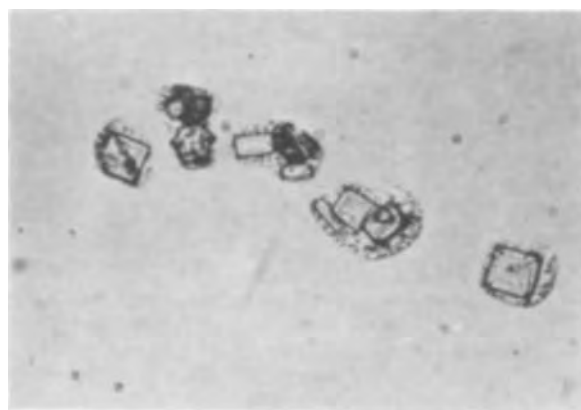


Fig. 2. Sample taken in uncontrolled working conditions from the level flask.



Fig. 3. Sample taken in uncontrolled working conditions from the level flask.



Fig. 4. Sample taken in uncontrolled working conditions from the level flask.

carried out. Figure 5 illustrates several fresh crystals which, after fouling, eventually take the forms shown in Fig. 6. Figure 7 shows the region in the vicinity of a fouled NaCl crystal after it has been perturbed by stirring during microscopic observation.

#### Interpretation of Results

The data in Table III indicate a quantitative relation between the content of soluble impurities in the electrolyte and the hydrogen content in the chlorine gas. The  $\text{Ca}^{+2}$  and  $\text{Mg}^{+2}$  do not bring about the decomposition of the amalgam, especially in acid media. Their presence, in addition to other impurities, contributes to increasing the hydrogen content in the chlorine gas from only 0.6-0.8 to 1.05-1.44%. These results confirm the studies undertaken by Hauck (4) and Balej (5). These results are clearly important in



Fig. 5. Experiment carried out by microscopic observation.



Fig. 6. Experiment carried out by microscopic observation and fouled on purpose with impurities coming from the decantor.

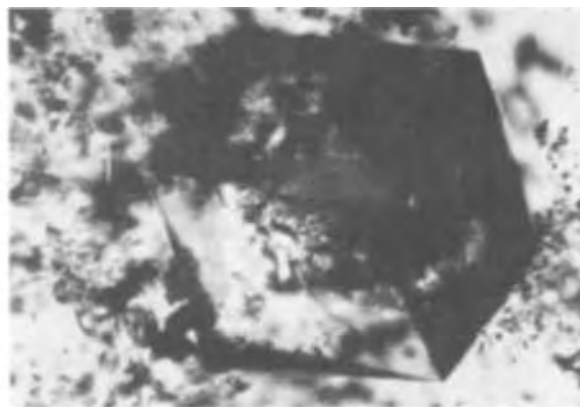


Fig. 7. Sample fouled and disturbed on purpose

selecting an optimum purification procedure. Under uncontrolled conditions, the presence of suspensions in the electrolytic solution brings about an abrupt additional increase of hydrogen in the chlorine gas, to values in the range 4.9-6.2%.

Mercury losses vary usually between 7.3 mg Hg/liter under normal purification conditions to 33.55 mg Hg/liter for uncontrolled conditions. In Fig. 1 it is seen that the mercury content varies with position in the plant. Under normal conditions, the mean values at the four locations are: at cell outlet, 22.15 mg Hg/liter; in the saturator, 19.2; at the outlet of the settling tank, 16.4; and at the cell inlet, 14. Under controlled conditions, the mercury losses at the same locations were: at the cell outlet, 42.6-54.7 mg Hg/liter; in the saturator, 37.0-39.4; at the outlet of the settling tank, 19.1-23.0; and at the cell inlet, 14.3-15.9.

The lost mercury was found in the mud in the saturator, in the precipitates deposited in the filters which were periodically purged to the waste-dump, and in the sludge of the settling tank. These results establish that part of the mercury contained by the electrolyte remains bound and deposits with precipitates and settled sludge. These events take place both in the acid medium in which saturation is achieved and in the alkaline medium in which precipitation, decantation, and filtration of impurities take place.

Although the mercury losses are greater under uncontrolled working conditions, the mean mercury content of electrolyte by the time it is recycled to the cell is not much different from that observed under normal conditions of purification. This observation seems to indicate the existence of a minimum solubility threshold of mercury in the electrolyte. It also appears that mercury losses depend on the presence of soluble and insoluble impurities and on the processes which occur within the electrolyzer under their influence.

From Fig. 2, 3, 4, one ascertains a close physical association between the insoluble impurities and the newly formed NaCl crystals which leave the electrolyzer and are carried by the sludge. Attachment of impurities to NaCl crystals is achieved at the junction points, on the edges, and at the less order overlapping of the edges with adjacent planes.

This mechanism of attachment is confirmed by the observations of Fig. 5, 6, and 7. The mechanism does not, as was initially expected, permit a chaotic or homogeneous distribution of impurities in the bulk of the electrolyte. Rather, it is seen that electrolyte purification processes should be designed in such a manner as to create voluminous associations between NaCl and impurities which then could be decanted in a shorter time. By comparing the data in Table III and Fig. 1 with the observations of Fig. 2-7, it is seen that both the increase of hydrogen content in the chlorine gas and the increase of mercury losses under uncontrolled conditions are due to the presence of insoluble impurities in the electrolyte phase. These im-

purities exist as calcium sulfates, magnesium and iron hydrates, aluminum oxide, silica, etc., which are attached to NaCl crystals. It appears that the insoluble materials form active decomposition centers on the surface of the amalgam, and that the cathodic hydrogen overvoltage on the remainder of the mercury surface is not decreased. In this manner, the excessive increase of hydrogen content simultaneously with the increase of mercury losses in the electrolyte may be explained.

### Conclusions

During the electrolysis of aqueous NaCl solutions in mercury cells, the mercury losses into the electrolyte phase, which are subsequently deposited at various positions throughout the flowsheet, were found to increase with an increase in the soluble and insoluble impurity constituents in the electrolyte. Excessive amounts of hydrogen in the chlorine gas are correlated with large mercury losses when the electrolyte is not prepurified. These occurrences result from the presence in the electrolyte of insoluble impurities which have the structure of impurities attached to the NaCl crystals which form. Thus one has proof of the existence of impurity agglomeration centers which, during

normal conditions of electrolyte purification, might bring about a more rapid formation of bulky precipitation products which would have a higher settling speed.

### Acknowledgment

This paper was rewritten in JOURNAL style by R. Alkire, Department of Chemical Engineering, University of Illinois, Urbana, Illinois 61801.

Manuscript submitted Feb. 21, 1974.

Any discussion of this paper will appear in a Discussion Section to be published in the June 1975 JOURNAL. All discussions for the June 1975 Discussion Section should be submitted by Feb. 1, 1975.

### REFERENCES

1. G. Angel and R. Brännland, *This Journal*, **99**, 442 (1952); **100**, 39 (1953).
2. H. Sanders, W. C. Gardiner, and I. Wood, *Ind. Eng. Chem.*, **45**, 1824 (1953).
3. Canadian Pat. No. 491,854.
4. G. Hauck and W. Dürr, *Chem. Ing.-Tech.*, **39**, 12 (1967).
5. J. Balej and I. Praseka, *ibid.*, **39**, 12 (1967).
6. *Z. Anal. Chem.*, **2**, 182 (1961).

# Brief Communications



## Measurement of Beta-Alumina Impedance with Constant Current Pulses

G. C. Farrington\*

General Electric Company, Research and Development Center, Schenectady, New York 12301

The ionic impedance of a polycrystalline solid electrolyte arises in two regions: within its constituent individual grains and at the boundaries between those grains. Since the intergrain impedance is dominant in a typical polycrystalline beta-alumina ceramic, its separation and characterization from its intragrain counterpart is essential for guiding the optimization of ceramic properties. While such separation can be effected with multifrequency a-c measurements (1), a d-c constant current pulse technique described here yields the same data over an effective frequency range of d.c. to ca. 60 MHz with relative simplicity. Results are presented for a tube of polycrystalline beta-alumina.

The gross electrical response of polycrystalline beta-alumina resembles that of the circuit shown in Fig. 1 in which  $R_1$  and  $R_2C_2$  represent intragranular and intergranular impedances, respectively. This simplified model neglects intragrain capacitance and lumps all intergrain impedances into one RC combination. The voltage rise as a function of time occurring across this circuit during passage of a pulse of constant current of magnitude  $I$  is related to  $R_1$ ,  $R_2$ , and  $C_2$  by the following expression in which  $t$  is the elapsed time since pulse initiation (time into pulse) (2)

$$V = I[R_1 + R_2(1 - e^{-t/R_2C_2})]$$

Since  $C_2$  shunts  $R_2$ , for a short time after pulse ini-

tiation  $Z$  is essentially  $R_1$ . If the pulse is of sufficient duration,  $C_2$  gradually charges and  $Z$  rises exponentially to the sum of  $R_1 + R_2$ .  $C_2$  can be determined from the characteristics of the transition region between these two extremes. Clearly, as the product  $RC$  decreases, definition of the circuit parameters requires pulses of shorter and shorter risetimes.

To illustrate this behavior, the model circuit shown in Fig. 1 was assembled with  $R_1 = 200$  ohms,  $R_2 = 2000$  ohms, and  $C_2 = 0.0092 \mu\text{F}$ . A small constant current pulser was constructed using a 2N3564 transistor as the current switch. The pulser was triggered either with a PAR Model 175 Universal Programmer or a Tektronix 114 Pulse Generator. A typical output pulse rose in  $7 \times 10^{-9}$  sec (10-90%) overshooting its ultimate value, which was attained after ca.  $10^{-7}$  sec, by 30%. The behavior of the model circuit was consistent enough, as was that of a beta-alumina tube, that repetitive identical pulses, separated by pauses

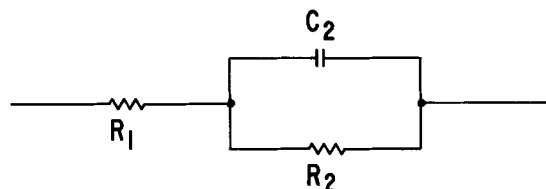


Fig. 1. Circuit modelling the impedance of a polycrystalline solid electrolyte.

\* Electrochemical Society Active Member.

Key words: beta-alumina, impedance, pulse, conductance, solid electrolyte.

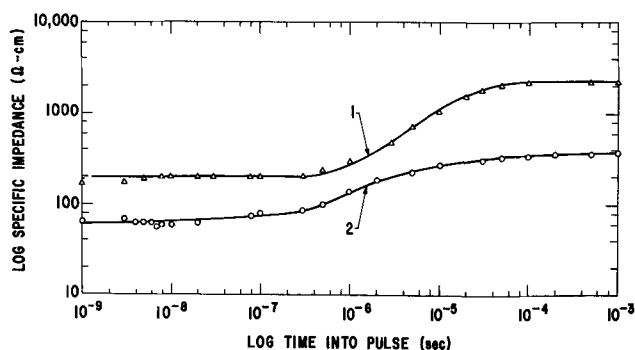


Fig. 2. Log specific impedance vs. log time into pulse plot for model circuit (curve 1) and polycrystalline beta-alumina tube (curve 2).

equal to the pulse width, could be used for measurement, obviating any need for capturing single-shot events.

A repetitive train of constant current pulses of known magnitude ( $50\text{--}1000\ \mu\text{A}$ ) and  $10^{-7}\text{--}10^{-3}$  sec in duration was applied to the model circuit while the potential buildup across the circuit was monitored as a function of time with a Tektronix 7A11 Probe/Amplifier and 7704A Mainframe (170 MHz bandwidth). Useful potential data could be obtained at times as short as  $1 \times 10^{-9}$  sec after pulse initiation, defined as that time the pulse had risen 10%, by computerized interpolation of points along the rising edge.

Figure 2, curve 1 details the log impedance vs. log time into pulse behavior of the model circuit. From these data,  $R_1$ ,  $R_2$ , and  $C_2$  were determined to be  $199 \pm 4$  ohm-cm,  $2027 \pm 40$  ohm-cm, and  $0.0088 \pm 0.002\ \mu\text{F}$ , respectively. These results compare favorably with the individual component values cited previously which were measured singly at 1 kHz with a General Radio 1650A Impedance Bridge.

Similar measurements were made on a polycrystalline beta-alumina tube of 6 cm length, 1.1 cm OD, and 0.8 cm ID. Four contacts were made along the tube with loops of Pt wire. A saturated solution of  $\text{NaClO}_4$  in propylene carbonate was used to wet the contact interfaces. Repetitive, identical constant current pulses were applied to the outer two contacts while the voltage rise as a function of time at the inner electrodes was recorded during each pulse. From these data the net impedance rise between the two inner electrodes was calculated as a function of time and corrected for any current inconstancy observed across a 500 ohm resistor in series with the sample.

Figure 2, curve 2 details the results. At short times, an intragranular impedance of  $63 \pm 5$  ohm-cm is observed, consistent with the single crystal impedance of 71 ohm-cm reported by Whittingham and Huggins (3).

$Z$  increases to  $365 \pm 5$  ohm-cm after  $10^{-4}$  sec. At the midpoint of the impedance rise  $C_2 = 0.012\ \mu\text{F-cm}$ . The more indistinct slope of the beta-alumina transition region compared to that of the model circuit verifies, as expected, that the intergranular impedance of a real ceramic cannot be modelled by a single RC circuit but, rather, is the sum of many such RC combinations.

Manuscript received April 16, 1974.

Any discussion of this paper will appear in a Discussion Section to be published in the June 1974 JOURNAL. All discussions for the June 1975 Discussion Section should be submitted by Feb. 1, 1975.

The publication costs of this article have been assisted by the General Electric Company.

#### REFERENCES

1. R. W. Powers and S. P. Mitoff, In press.
2. M. F. Gardner and J. L. Barnes, "Transients in Linear Systems," Vol. 1, p. 338, John Wiley and Sons Inc., New York (1942).
3. M. S. Whittingham and R. A. Huggins, *J. Chem. Phys.*, **54**, 414 (1971).

## The Electro-Oxidation of Carbon Monoxide on Platinum

K. F. Blurton\* and J. M. Sedlak\*

*Energetics Science, Incorporated, Elmsford, New York 10523*

Recently an instrument for the measurement of carbon monoxide in ambient air based on electrochemical principles was developed and described (1-3). During the development of this instrument a study was made of the relationship between the CO oxidation current and the potential of a Pt electrode, and the results of these experiments are reported here.

Previous studies of CO electro-oxidation on smooth Pt electrodes by cyclic voltammetry (4-6) showed that in the anodic sweep (0.4-1.6V) there was no oxidation current from 0.4 to 0.9V, the current sharply increased at 0.91V and thereafter decreased linearly with increasing potential. In the cathodic sweep (i.e., 1.6-0.4V) the current was less than on the anodic sweep in the range 1.6-0.9V, it was slightly greater in the range 0.9-0.7V and zero from 0.7 to 0.4V.

In the present work steady-state currents for CO oxidation were determined at a potentiostatically controlled Pt electrode. By making these measurements the electrode is closer to steady-state condition, and hence the influence of the surface Pt oxide on CO oxidation current can be determined. These results, coupled with recent studies (7-10) of oxide formation

on Pt electrodes, demonstrate that PtOH is the most active electrocatalytic species for CO electro-oxidation.

#### Experimental

The electrochemical cell was similar to that used in the CO monitor and it was described previously (2). Essentially it consisted of a three electrode electrochemical cell with 3.4M  $\text{H}_2\text{SO}_4$  solution as electrolyte. The anode (sensing) and counterelectrodes were Pt-catalyzed, Teflon-bonded diffusion electrodes (11), and the reference electrode was a mercury/mercury sulfate electrode. The geometric area of the sensing electrode was  $5\text{ cm}^2$  and the effective area measured electrochemically (12) was  $1.2\text{ m}^2$ . All potentials refer to the standard hydrogen electrode potential.

The potentiostat was designed and constructed in-house (3). The current due to the electro-oxidation of CO was measured by determining the potential drop across a standard resistor with a recorder (Hewlett-Packard Company, Model 680). In order to conform to the experimental conditions of air pollution analysis, the CO oxidation currents were determined in a CO/air mixture. CO/air mixtures (48.5 ppm CO and 84.0 ppm) and UHP grade air were obtained from Matheson Gas Products Company.

\* Electrochemical Society Active Member.

Key words: carbon monoxide, platinum electrode, gas sensor, diffusion electrode.

### Results and Discussion

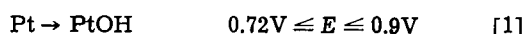
Figure 1 shows the CO oxidation current *vs.* the potential of the Pt electrode. These results were obtained by initially potentiostating the cell at 0.8V for 24 hr. Then the oxidation currents were determined when UHP air and the CO/air mixtures were introduced into the cell. The sensing electrode potential was increased stepwise to 1.5V and the corresponding oxidation currents were determined after potentiostating for 24 hr at each potential (Fig. 1, curve a). Subsequently, the electrode potential was decreased stepwise from 1.5 to 0.8V (Fig. 1, curve b), and finally it was increased to 1.1V (Fig. 1, curve c). These results show that the shape of the current/potential curve would probably differ if the electrode was potentiostated at another potential prior to taking the measurements at 0.8V.

At each potential there was a small current (approximately 10  $\mu$ A) when no gas and when UHP air was passed into the sensor, and this was subtracted from the value determined when CO was introduced into the cell. The potential range was restricted to 0.8-1.5V since the currents due to oxygen reduction and to oxygen evolution were negligible. The values of the current/ppm of CO agreed within 3% for the two CO concentrations, and this is within the precision of the CO analysis.

The mechanism of CO electro-oxidation involves the reaction of adsorbed CO with platinum oxide (4-6). The observed variation of CO oxidation current with potential (Fig. 1) occurs as a result of changes in the oxidation state of the Pt electrode surface. This variation may be explained from recent studies of the surface state of the Pt electrodes in this potential region (7-9).

A mechanism for the oxidation of Pt electrodes has recently been proposed (7-9) and it can be summarized as follows.

Stage I: Reversible electrosorption of OH species on Pt



- Potential increased from 0.8V to 1.5V
- Potential decreased from 1.5V to 0.8V
- △ Potential increased from 0.8V to 1.1V

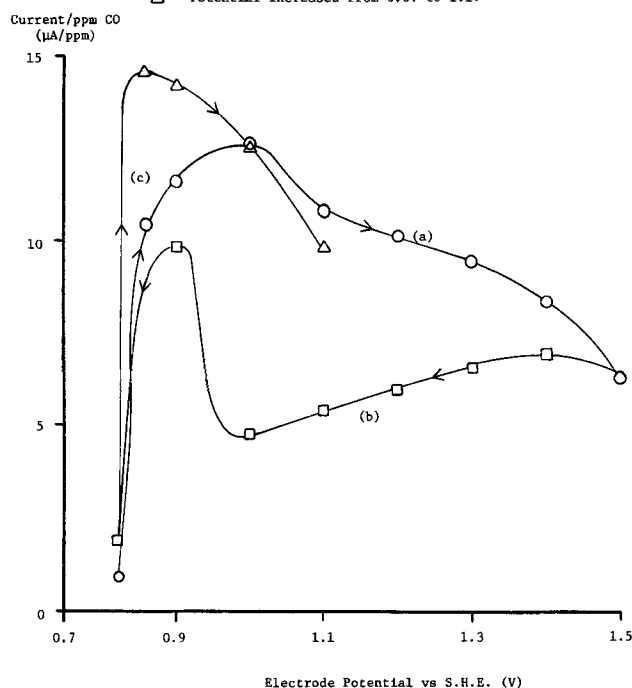
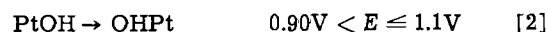
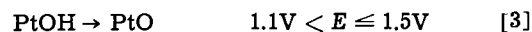


Fig. 1. CO oxidation current as a function of Pt electrode potential. ○, Potential increased from 0.8 to 1.5V; □, potential decreased from 1.5 to 0.8V; △, potential increased from 0.8 to 1.1V.

Stage II: Rearrangement of surface PtOH species



Stage III: Conversion of PtOH species to PtO



As the surface is oxidized at successively higher potentials or is held for longer times at a given potential, the irreversibility of the reaction for the reduction of rearranged OHPt and the PtO species is increased.

The increase in CO oxidation current in the range 0.8-1.0V (Fig. 1, curve a) parallels the increase in reversibly bound OH species on the Pt surface (Eq. [1]). Between 1.0 and 1.1V there is a sharp decrease in current (Fig. 1, curve a) corresponding to the rearrangement in the surface layer (Eq. [2]). At more anodic potentials the continuing decrease in current with increasing potential is in accordance with the diminished availability of surface PtOH groups (Eq. [3]).

On decreasing the potential from 1.4 to 1.0V (Fig. 1, curve b) the current decreased linearly with potential, due to the retention of PtO which was formed at 1.5V together with the decreasing overvoltage for the reaction. At 0.9V the current increased sharply, and this corresponds to the reforming of electrosorbed PtOH (Eq. [1]). On the further decrease of the potential to 0.8V the CO oxidation current decreased to a small value in accordance with the decrease of surface PtOH concentration.

On the subsequent increase of potential (Fig. 1, curve c) very high currents were observed at 0.85 and 0.90V which are attributed to extensive surface coverage with PtOH. On increasing the potential beyond the reversible PtOH formation region (Eq. [1]) the CO oxidation current decreased markedly due to the rearrangement of electrosorbed OH (Eq. [2]). The CO oxidation current at 1.1V at the end of these experiments (Fig. 1, curve c) was only about 10% lower than the current observed at that potential on the first anodic sequence (Fig. 1, curve a). The final electrochemical area of the Pt electrode was the same as the initial area (*i.e.*, 1.2 m<sup>2</sup>).

An estimate of the time involved before the attainment of steady state at the Pt surface was obtained by measuring the CO oxidation current at 1.2V as a function of time. This was done with 20 electrodes and with each the current decreased to a steady value of about 15% lower than the initial value after 35 ± 10 days. This was confirmed to be associated with the change in state of the Pt electrode surface since the current did not decay when the sensor remained on open circuit and only potentiostated for the short period required to measure the CO oxidation current.

The measurement of the CO oxidation rate has been shown to be a useful tool for the study of Pt surfaces. The results demonstrate that: (i) oxidized Pt electrodes are more electroactive for CO electro-oxidation than unoxidized Pt, (ii) PtOH is the preferred catalytic sites and PtO is catalytically active to a lesser extent, (iii) the oxidation of the Pt surface in the potential range 0.8-1.0V is reversible while that in the range 1.0-1.5V is irreversible, and (iv) the Pt electrode does not attain a steady state at 1.2V until it has been under potentiostatic control for 35 days.

Manuscript received April 15, 1974.

Any discussion of this paper will appear in a Discussion Section to be published in the June 1975 JOURNAL. All discussions for the June 1975 Discussion Section should be submitted by Feb. 1, 1975.

The publication costs of this article have been assisted by Energetics Science, Incorporated.

### REFERENCES

1. H. W. Bay, K. F. Blurton, H. C. Lieb, and H. G. Oswin, *Am. Laboratory*, 4, 57 (1972).



2. H. W. Bay, K. F. Blurton, J. M. Sedlak, and A. M. Valentine, *Anal. Chem.*, In press.
3. K. F. Blurton and H. W. Bay, Presented to Air Pollution Control Association Meeting, Denver, Colorado, June 1974.
4. S. Gilman, *J. Phys. Chem.*, **66**, 2657 (1962).
5. S. Gilman, *ibid.*, **68**, 70 (1964).
6. E. Gileadi, in "Modern Aspects of Electrochemistry", Vol. IV, pp. 100-102, J. O'M. Bockris, Editor, Butterworths, London, (1966).
7. H. Angerstein-Kozłowska, B. E. Conway, and W. B. A. Sharp, *J. Electroanal. Chem.*, **43**, 9 (1973).
8. B. E. Conway and S. Gottesfeld, *J. Chem. Soc., Faraday Trans.*, **1**, 1091 (1973).
9. B. V. Tilak, B. E. Conway, and H. Angerstein-Kozłowska, *J. Electroanal. Chem.*, **48**, 1 (1973).
10. S. Shibata, *Electrochim. Acta*, **17**, 395 (1972).
11. K. F. Blurton, *This Journal*, **119**, 1605 (1972).
12. K. F. Blurton, P. Greenburg, H. G. Oswin, and D. Rutt, *ibid.*, **119**, 559 (1972).



## A Study of Low Temperature Diffusion of Copper in Single Crystalline Gold Using a CuCl Solid Electrolyte

J. Goldman<sup>1</sup> and J. B. Wagner, Jr.

Department of Materials Science, Northwestern University, Evanston, Illinois 60201

### ABSTRACT

A galvanic cell of Cu|CuCl|Au was used to measure the diffusion coefficient of copper in single crystalline gold in the temperature range of 355°-400°C. Results are in good agreement with tracer data extrapolated to the lower temperatures. Using polarization measurements, electronic conductivity of single crystalline CuCl and the double layer capacitance at the CuCl|Au interface were determined.

The principle of measuring diffusivities by electrochemical methods is well established. Recently, Ramanarayanan *et al.* (1) studied oxygen diffusion in liquid tin and solid silver using a stabilized zirconia electrolyte. Chu *et al.* (2) also used stabilized zirconia to study oxygen diffusion in wustite. They also measured silver diffusion in silver sulfide using AgI as the electrolyte. Oxygen diffusion in silver was measured by Rickert and Steiner (3) using stabilized zirconia. Takahashi *et al.* (4) obtained values for the diffusion of silver in Ag<sub>2</sub>Se and Ag<sub>2</sub>Te using a RbAg<sub>4</sub>I<sub>5</sub> electrolyte. Raleigh and Crowe (5) used a polarization cell of the type Ag|AgBr|Au(Ag) to study silver diffusion in gold alloys. They applied a negative potential to the left-hand electrode, thus fixing the silver activity at the AgBr|Au interface. They reported the presence of a low level electronic leakage current which, until very long times, was small relative to the current due to the silver flux. The electronic carriers in AgBr are n-type, and, therefore, application of higher potentials will cause the electronic leakage current to reach a saturation value (6).

Joshi (7) and Wagner (8) have discussed the problems in using a p-type electrolyte for diffusion and other transient measurements. The electronic leakage current in a p-type electrolyte does not saturate on application of higher potentials (6), but continues to increase exponentially. The purpose of the present study was to test the use of a p-type electrolyte, in this case CuCl, as a medium for solid-state titration into an electronic conductor, in this example single crystalline gold. In addition, this investigation was conducted to evaluate effects of electronic leakage through single crystalline CuCl and double layer capacitance at the CuCl-gold interface.

Cu-Au, which is a well-documented system, was chosen for study because of the uncertainty in assessing the effect of a large electronic leakage current through CuCl on the ability to see the diffusion process. Diffusion data for copper in pure gold has been reported (9), as have two different electrochemical investigations of the thermodynamics of the copper-gold system (10, 11).

A polarization cell of the type, Cu|CuCl|Au was used. As pointed out by Hebb (12) and Wagner (13), a given copper activity,  $a$ , may be fixed at the CuCl|Au surface by applying a potential to the cell with the copper electrode negative. The value of the activity is

$$a = e^{-EF/RT} \quad [1]$$

where  $E$  is the applied potential,  $F$  the Faraday constant,  $R$  is the gas constant, and  $T$  the absolute temperature. If the potential is suddenly changed to a new value, a time dependent current will flow through the external circuit. At least three different phenomena make contributions to this current. First, diffusion of copper into the gold electrode requires the electrochemical transport of copper through the CuCl to maintain the copper activity at the gold interface, and there will be a corresponding current through the external circuit. The second contribution comes from the re-equilibration of electron holes within the electrolyte. The third contribution results from an inherent double layer capacitance which is present at the CuCl|Au interface (7). When the potential is changed, the capacitor charges or discharges, giving rise to an external current. There are also faradaic processes at the electrodes, which in this experiment are assumed not to be rate determining. Mathematical expressions for the first three contributions will be given below.

Consider first the diffusion of copper into the gold. Treating the gold as a semi-infinite solid, and given the boundary conditions

$$\begin{aligned} C(t=0) &= C_0 & 0 \leq x < \infty \\ C(0,t) &= C_1 \end{aligned}$$

the flux of copper,  $J$ , at the CuCl|Au interface is (12)

$$J = \frac{-(C_1 - C_0)}{63.5} \sqrt{\frac{D}{\pi t}} \quad [2]$$

where  $D$  is the diffusion coefficient for copper in gold and  $t$  is time. The concentrations are expressed in grams/cubic centimeter and the flux is in equivalents/square centimeter-second. The atomic weight of copper, 63.5, is inserted in Eq. [2] to convert the flux from grams/square centimeter-second to equivalents/square centimeter-second. These boundary conditions per-

<sup>1</sup> Present address: Motorola, Inc., Phoenix, Arizona 85008.  
 Key words: CuCl solid electrolyte, Cu-Au diffusion, electronic leakage, double layer capacitance.

tain to an experiment in which a potential corresponding to a copper concentration of  $C_0$  at the CuCl|Au interface is applied to the cell, and held until the concentration is effectively uniform through the Au. This is  $t = 0$ . During the next instant the potential is changed to a new value corresponding to a concentration,  $C_1$ , at the CuCl|Au interface. Faraday's law relates the electrochemical transport in the cell to the diffusion contribution to the external current,  $I_D$ , as

$$I_D = JAF$$

where  $A$  is the area in square centimeters. Substituting Eq. [2] into Eq. [3] gives

$$I_D = \frac{-(C_1 - C_0)AF}{63.5} \sqrt{\frac{D}{\pi t}} \quad [4]$$

At infinite time, the diffusion ceases and  $I_D$  ceases. This equation does require a correction for phase boundary motion (14), which is negligible for small concentration steps.

The concentrations are determined experimentally by measuring the potential difference across a cell using a set of standard copper-gold alloys. Such experiments have been carried out by Chiche (10) and by Weibke *et al.* (11). The diffusion coefficient may be determined by obtaining an experimental slope of Eq. [4],

$dI_D/d(1/\sqrt{t}) = S$ , and rearranging to solve for  $D$

$$D = \left( \frac{S 63.5 \sqrt{\pi}}{(C_1 - C_0) AF} \right)^2 \quad [5]$$

Next, the current due to rearrangement of electron holes in the CuCl on applying a potential step will be considered. As discussed above, CuCl exhibits p-type behavior. The hole concentration at the CuCl|Au interface is given by

$$c_{\oplus} = c_{\oplus}^0 \exp \{EF/RT\} \quad [6]$$

where  $c_{\oplus}^0$  is the electron hole concentration in coulombs/cubic centimeter at the reversible electrode, the Cu|ClCl interface. When a potential step is applied to the cell the concentration of electron holes changes within the CuCl. The boundary conditions for the hole concentrations in CuCl are

$$c(x, 0) = c_{\oplus}^0 + (c_{\oplus}^1 - c_{\oplus}^0) \frac{x}{L} \quad [7]$$

and

$$c(x, \infty) = c_{\oplus}^0 + (c_{\oplus}^2 - c_{\oplus}^0) \frac{x}{L} \quad [8]$$

$c_{\oplus}^1$  and  $c_{\oplus}^2$  are the initial and final hole concentrations at the gold electrode given by the initial and final potentials  $E_1$  and  $E_2$ , respectively, and can be calculated using Eq. [6].  $L$  is the length of the CuCl pellet. The flux of electron holes measured at  $L$  is (15)

$$J_{\oplus} = - \frac{D_{\oplus} (c_{\oplus}^2 - c_{\oplus}^0)}{L} + \frac{2D_{\oplus}}{L} (c_{\oplus}^1 - c_{\oplus}^2) \sum_{n=0}^{\infty} \exp(-n^2 \pi^2 D_{\oplus} t/L^2) \quad [9]$$

The flux,  $J_{\oplus}$ , in amperes/square centimeter can be converted to a current simply by multiplying by  $A$ . Doing this, expressing the concentrations in terms of Eq. [6], and recalling that  $\sigma_{\oplus}^0$ , the CuCl hole conductivity, is  $c_{\oplus}^0 D_{\oplus} F/RT$  yields

$$I_{\oplus} = \frac{-RTA}{LF} \sigma_{\oplus}^0 (e^{E_2 F/RT} - 1) + \frac{2RTA}{LF} \sigma_{\oplus}^0 (e^{E_1 F/RT} - e^{E_2 F/RT}) \sum_{n=0}^{\infty} \exp \left[ - \frac{n^2 \pi^2 D_{\oplus} t}{L^2} \right] \quad [10]$$

The current in Eq. [10] approaches a steady-state value as the summation term goes to zero at long times. The resulting well-known expression for the steady-state electron hole leakage current,  $I_{\oplus ss}$ , through the cell is (13)

$$I_{\oplus ss} = \frac{RTA}{LF} \sigma_{\oplus}^0 (e^{E_2 F/RT} - 1) \quad [11]$$

The current due to charging a double layer capacitance is the third contribution on applying a potential step. The equation for the current through a series RC circuit is

$$I_c = \frac{\Delta E}{R} \exp(-t/RC)$$

where  $C$  is the capacitance,  $\Delta E/R$  is the applied potential divided by the AC resistance of the electrolyte, and is equal to the initial value of the current,  $I_0$ .

### Experimental

In the present work, a single-crystal CuCl pellet was used, which was obtained from Dr. F. Okabe of Shizuoka University. He has described his method of preparation (16). The pellet length was 0.12 cm, and the diameter, 0.85 cm. The gold single crystal was grown from five-nines purity material by the Bridgman method, and electron channeling patterns obtained on a Cambridge S4 scanning electron microscope showed the gold to be single crystalline. A 0.78 cm diameter by 0.3 cm disk was cut from a single crystal, mechanically polished by conventional metallographic techniques, then electropolished in a cyanide solution (17). Electron channeling patterns made after the surface preparation revealed no surface damage. The cell was springloaded into a glass tube, through which dry argon was passed. The entire apparatus was placed in a resistance furnace and heated using a d-c power supply. Potential steps were applied using a Keithley No. 260 nanovolt source and a specially designed circuit which stores two potential values, and produces a low-noise, rapid potential step. Measurements of current *vs.* time to determine the capacitive effects were carried out at 228°C. Contributions from diffusion, and hole conduction should be small at this temperature. The current was measured using a Tektronix oscilloscope to measure the voltage across 100 ohms, which is about two orders of magnitude less than the electron hole resistance of the sample at the highest temperatures of this study. Therefore,  $IR$  drop across the measuring resistor is not significant. Plots of the  $\log I$  *vs.* time for various voltage steps are shown in Fig. 1.

Figure 2 shows a plot of  $I_0$ , the initial value of the current *vs.*  $\Delta E$ . The slope yields a value for the AC resistance of the CuCl pellet of  $2.23 \times 10^3$  ohm-cm. The AC resistivity, determined from the resistance and the sample dimensions is  $10.6 \times 10^3$  ohm-cm, which is in reasonably good agreement with the published value  $7.7 \times 10^3$  ohm-cm (18, 19).

The capacitance, determined from the slopes of the curves in Fig. 1 has a value of  $3.7 \times 10^{-4}$  farads. These calculations assume that the only contribution to the current comes from interface charging.

One other point that should be mentioned is that some electronic leakage current was apparently present, as can be seen by noting that the  $\log I$  *vs.* time curves in Fig. 1 are not quite linear. All curves ap-

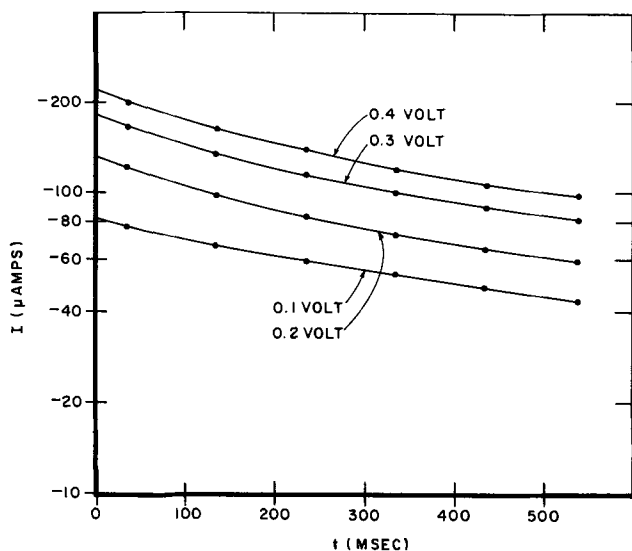


Fig. 1. Plot of  $\log I_c$  against time at 228°C. Slope indicates time constant,  $RC$ , and intercept is  $\Delta E/R$ .

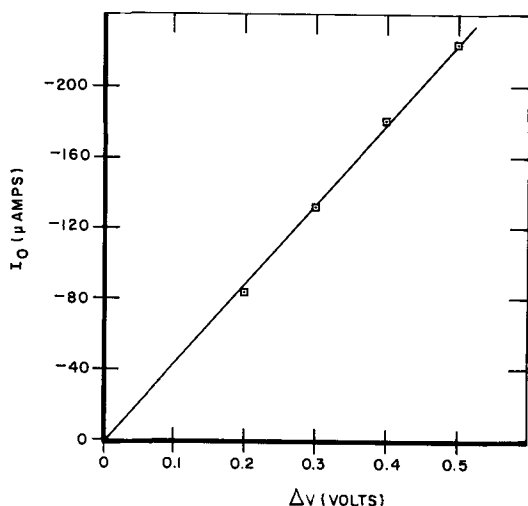


Fig. 2. Initial current,  $I_0$  as a function of  $\Delta E$ . Slope is linear, and is equal to  $1/R$ .

proach a constant slope, equal to  $1/2.3RC$ , very quickly, indicating that the electron hole current dies out very fast.

Diffusion experiments were conducted at 355°, 370°, 385°, and 400°C. The procedure was to apply a potential, of about 0.2V, wait 3 hr, instantaneously lower the potential by 3 mV, and monitor the current for one-half hour, apply another potential, wait three more hours, and so on. It was found experimentally that a 3-hr wait between potential steps was sufficient to allow the current from previous steps to decay to a point where it would not make a contribution to the current from a new potential step. Longer waits produced identical current-time characteristics. While 3 hr is obviously not long enough to completely equilibrate the gold sample at a particular activity, it is long enough to permit the current to decay to a level below the resolution of the measuring technique. The current was measured on a Doric digital voltmeter across 100 ohms. The results of the experiments carried out at 370°C are shown in Fig. 3. The experimental currents are linear with  $1/\sqrt{t}$ . The mean copper mole fractions for each of the curves are from top to bottom: 0.05, 0.175, 0.225, 0.275, and 0.325, corresponding to potentials of 0.25, 0.22, 0.20, 0.18, and 0.105, respectively. Results for other temperatures are similar. The diffusion coefficients were calculated from the ex-

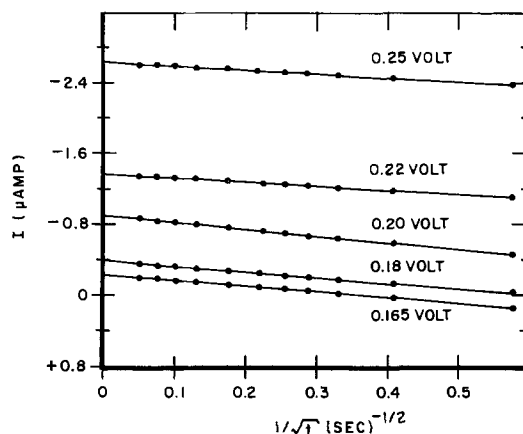


Fig. 3. Experimental current vs.  $1/\sqrt{t}$  at 370°C. Slope is linear indicating that the observed time variation is due to chemical diffusion of copper into gold. Residual current at infinite time is due to electronic leakage.

perimental slopes, such as those in Fig. 3, and Eq. [5]. The values of  $D$ , corresponding to a potential step of 0.220-0.217V for the four temperatures are shown in Fig. 4. All applied potentials were below the decomposition voltage of CuCl (7).

Values for the hole conductivity in CuCl have also been obtained. The steady-state current obtained when  $1/\sqrt{t} = 0$  was plotted against  $\exp \{EF/RT\}$ . According to Eq. [11], this plot should be linear with a slope proportional to the conductivity, as long as the exponential term is much greater than unity. Figure 5 shows that the relation is indeed linear, and that the slope increases with increasing temperature. Figure 6 shows the hole conductivity as a function of reciprocal temperature plotted along with the data obtained by Joshi (7). Joshi's ionic conductivity data are also shown.

Discussion

It has been demonstrated that solid electrolytes in which the minority charge carriers are electron holes are useful in studying low temperature diffusion in solids. Copper diffusion in gold, using a cuprous

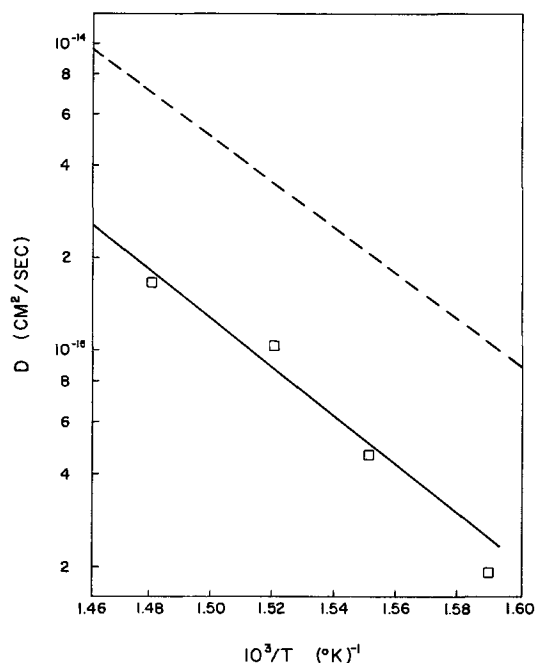


Fig. 4. Calculated diffusion coefficients for copper in gold at 355°, 370°, 385°, and 400°C. Dotted curve is extrapolated data of Vignes et al. (9).

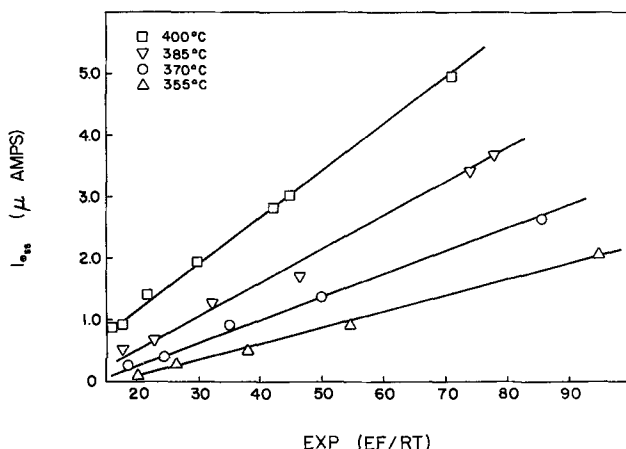


Fig. 5. Steady-state electron hole leakage,  $I_{\text{ess}}$ , as a function of  $\exp\{EF/RT\}$ . Slope is proportional to the hole conductivity,  $\sigma_{\oplus}$ , for CuCl.

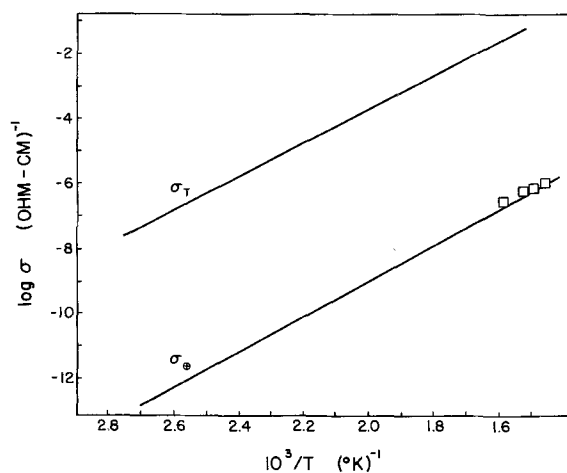


Fig. 6. Hole conductivities for CuCl determined in this investigation plotted along with the data of Joshi (7). Upper curve is total conductivity.

chloride solid electrolyte was the particular system studied. The cell arrangement was Cu|CuCl|Au, where the gold electrode was held at a positive potential. As described earlier in this paper, a potential step was applied which produced a step in the copper activity at the CuCl|Au interface. The external current was measured and, through Eq. [3], related to the flux of copper atoms into the gold. It was necessary to take account of all possible contributions to the external current to be certain that the measured current was only due to copper diffusion.

On application of a 3 mV potential step, in addition to the diffusion current, there is a transient, Eq. [10], due to electron hole rearrangement in the CuCl. There is also a transient, given by Eq. [12], from the discharging of the double layer capacitance at the CuCl|Au interface. After these transients have relaxed, there remains a steady-state leakage of electron holes, Eq. [11]. It will be shown that these transients relax very quickly, provided the CuCl pellet is sufficiently thin, and that the external current is only the sum of the diffusion current and the steady-state electron-hole leakage.

Using Eq. [10] and Joshi's (7) conductivity values we see that at 400°C, the transient current due to the rearrangement of electron holes decays in 3 sec to less than 1% of the steady-state leakage current. Because the first data point was taken 3 sec after applying a potential step, neglecting the transient hole current is justified at this temperature. An identical conclusion may be reached by making the calculation at other temperatures.

If the electrolyte sample were, say, 1 cm long instead of 0.12 cm, this conclusion would not be justified. For example, if a measurement of the current were made 10 sec after applying a potential step the transient electron hole current would still be almost 20% away from the steady-state value, and would be making a substantial contribution to the experimental current transient. It is probably possible to separate the diffusional current from that due to the electron hole transient by computational methods, but the entire problem may be eliminated by using a sufficiently thin electrolyte, as has been done in this investigation.

In evaluating the double layer capacitance transient, account must be taken of the time constant,  $RC$ , in Eq. [12].  $RC$  is the time for the double layer current to decay to  $1/e$  of its initial value. Beyond a time equivalent to ten times the value of the time constant, it is assumed that the contribution due to double layer charging or discharging is negligible. At 400°C, 10 times  $RC$  is about 13 msec, and at 355°C, it is about 45 msec, both well under the 3 sec which elapse before the initial data point is taken.

Another consideration is the effect of current transients on the sharpness of the concentration step. The activity change at the Au electrode as predicted by Eq. [1] is valid only if there is no appreciable  $IR$  drop in the circuit. This is unavoidable immediately after applying the potential step, because of the large initial value of the current. When  $IR$  drop effects are appreciable, the potential, which fixes the copper activity at the Au electrode will be time dependent. Since it has been shown that the  $I_c$  and  $I_{\oplus}$  transients decay quickly, relative to the time at which the taking of diffusion data is begun, it is felt that the concentration step is sufficiently sharp.

The fact that the current transient at 228°C was represented fairly well by a series  $RC$  circuit model supports the assumption that faradaic effects are probably small. The good agreement between the literature and measured values for the  $AC$  resistivity further supports this assumption.

The only unsteady current left is due to diffusion. Figure 3 shows that the experimental current is indeed linear with  $1/\sqrt{t}$  as predicted by Eq. [10], the expression for the diffusion current. Equation [10] also predicts that the diffusion current goes to zero at infinite time ( $1/\sqrt{t}=0$ ). In Fig. 3 it is apparent that there is still a current flowing at infinite time, and that the magnitude of the current increases with increasing applied potential. Since it has been shown that all the transients decay well before the first data point is taken, this offset can only be due to the steady-state electron hole leakage through the cell. The steady-state current was therefore plotted against  $\exp\{EF/RT\}$  in Fig. 5, and, as predicted by Eq. [11], the slope is constant. The hole conductivities were obtained from the slopes in Fig. 5 and compared with the values obtained by Joshi (7), Fig. 6. The agreement is excellent, confirming that the steady-state current is due to the leakage of electron holes. Joshi's total conductivity data,  $\sigma_T$ , are also shown.

Unlike the n-type electrolytes, in which the application of higher potentials produces a saturation electronic leakage, in p-type electrolytes higher potentials result in larger leakage currents. As long as the sample is thin, however, for a given applied potential, the diffusional current is displaced along the current axis a constant amount by the steady-state electronic leakage.

It is seen in Fig. 3 that the slopes of the current  $-1/\sqrt{t}$  lines decrease with increasing applied potential. This is because a larger concentration step for a given potential step is being applied at lower voltages. This is expected for solutions which are ideal, or show negative departures from ideality,<sup>2</sup> and is consistent

<sup>2</sup> For an ideal solution,  $E = -(RT/F) \ln X$  so that  $\Delta E/\Delta X = RT/FX$ . For a given  $\Delta E$ ,  $\Delta X$  is larger as  $X$  is larger ( $E$  is smaller). A similar argument applies for solutions showing negative departures from ideality.

with Chiche's data. Weibke's  $E$  vs.  $X$  data are essentially linear and thus do not predict the behavior seen in Fig. 3. Therefore, it is felt that new emf-concentration measurements would be needed to correctly interpret the concentration dependence from the data in Fig. 3. At a constant mole fraction of Cu of 0.175 the use of Weibke's data in conjunction with the present results yields values of  $D$  shown in Fig. 4. The dotted curve is the extrapolated data of Vignes *et al.* (9) for copper diffusion in pure gold. The agreement is excellent considering that Vignes' data was extrapolated over several hundred degrees. While not a great deal of significance should be attached to the fact that actual low temperature data fall slightly below the extrapolated curve, it may be a real effect. It is expected that copper diffusion in an alloy would be slower than in pure gold (20).

It has been demonstrated that the determination of Cu diffusion coefficients down to almost  $10^{-16}$  cm<sup>2</sup>/sec may be accomplished by this method. While gold was chosen for this study, any material which is not reactive with CuCl may be substituted, provided thermodynamic data are available for the analysis of the data. The presence of a large steady-state leakage current does not hamper the technique in any way.

Manuscript submitted May 9, 1973; revised manuscript received May 1, 1974.

Any discussion of this paper will appear in a Discussion Section to be published in the June 1975 JOURNAL. All discussions for the June 1975 Discussion Section should be submitted by Feb. 1, 1975.

The publication costs of this article have been assisted by Northwestern University.

## REFERENCES

1. T. A. Ramanarayanan and R. A. Rapp, *Met. Trans.*, **3**, 3239 (1972).
2. W. F. Chu, H. Rickert, and W. Weppner, "Fast Ion Conductors," W. Van Gool, Editor, American Elsevier Publishing Co., Inc., New York (1973).
3. H. Rickert and R. Steiner, *Z. Physik. Chem.*, **49**, 127 (1966).
4. T. Takahashi and O. Yamamoto, *This Journal*, **118**, 1051 (1971).
5. D. O. Raleigh and H. R. Crowe, *ibid.*, **116**, 40 (1969).
6. D. O. Raleigh, in *Prog. Solid State Chem.*, **3**, 83 (1967).
7. A. V. Joshi, Ph.D. Thesis, Northwestern University (1972).
8. J. B. Wagner, Fast Ion Transport in Solids, Solid State Batteries and Devices; A Nato Sponsored Advanced Study Institute, Belgirate, Italy, 1972.
9. Vignes and J. Haeussler, *Compt. Rend.*, **263**, Series C, 1504 (1966).
10. P. Chiche, *Compt. Rend.*, **234**, 830 (1952).
11. F. Weibke and U. von Quadt, *Z. Electrochem.*, **45**, 715 (1939).
12. M. H. Hebb, *J. Chem. Phys.*, **20**, 185 (1952).
13. C. Wagner, *Z. Electrochem.*, **60**, 4 (1956).
14. K. B. Oldham and D. O. Raleigh, *This Journal*, **118**, 252 (1971).
15. J. Crank, "Mathematics of Diffusion," Oxford University Press (1956).
16. M. Soga, R. Imaizumi, Y. Kondo, and F. Okabe, *This Journal*, **115**, 388 (1967).
17. P. B. Hirsch, A. Howie, R. B. Nicholson, D. W. Pashla, and M. J. Whelan, "Electron Microscopy of Thin Crystals," Plenum Press, New York (1965).
18. J. B. Wagner and C. Wagner, *J. Chem. Phys.*, **26**, 1597 (1957).
19. V. W. Hsueh and R. W. Christy, *ibid.*, **39**, 3519 (1963).
20. A. G. Guy, "Introduction to Materials Science," McGraw-Hill Book Co., New York (1971).

## The Growth of Hydrus Oxide Films on Aluminum

Robert S. Alwitt\*<sup>1</sup>

Sprague Electric Company, North Adams, Massachusetts 02147

### ABSTRACT

The weight gains of Al specimens immersed for short times in water at 50°-70°C were measured. An analysis of these data and published results at other temperatures indicated that the kinetics of pseudoboehmite film growth in the temperature range 50°-100°C is determined initially by the nucleation and growth of hydrolysis sites on the amorphous oxide surface, and subsequently by solid-state diffusion through the pseudoboehmite layer. At 40°C, pseudoboehmite and bayerite were observed to grow simultaneously at first, with bayerite crystallization eventually becoming the dominant process. The two oxide phases occupied completely separate layers.

Aluminum reacts readily with water to form a hydrous oxide film. The initial product is pseudoboehmite, a poorly crystallized oxyhydroxide that is similar to boehmite (AlOOH) but contains excess water (1, 2). Pseudoboehmite has a lamellar structure (2) and in the film the lamellae are oriented approximately perpendicular to the substrate surface (3); this layer has a substantial void fraction and high specific area (4). Electron micrographs have shown that while the outer surface is highly porous there is an absence of porosity at the metal interface, and it seems likely that a thin amorphous barrier oxide layer exists between the

metal and the hydrous oxide (1). Pseudoboehmite may be the sole reaction product at higher temperatures, but moderate temperatures or longer reaction times promote the growth of bayerite crystal (Al(OH)<sub>3</sub>) on the pseudoboehmite surface (3).

The essential steps of the aluminum + water reaction appear to be (i) formation of amorphous oxide, (ii) dissolution of this oxide, and (iii) precipitation of the dissolved species as hydrous oxide (1).

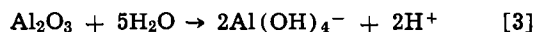
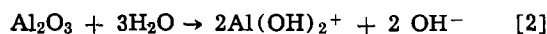
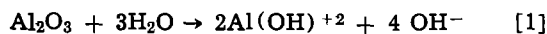
In step (i), the amorphous oxide is continuously replenished by an electrochemical process in which barrier film growth is the anodic half-cell reaction, coupled with the cathodic reduction of water. In step (ii), the exact nature of the oxide dissolution process is not known, but it must involve a surface hydrolysis reaction. The particular hydrolyzed aluminum species

\* Electrochemical Society Active Member.

<sup>1</sup>Present address: United Chemi-Con Inc., R&D Laboratory, 380 Union St., West Springfield, Massachusetts 01089.

Key words: bayerite, pseudoboehmite, surface hydrolysis, surface nucleation.

found in solution depends on temperature, pH, and aluminum concentration. In dilute solutions at 25°C, the major aluminum monomer species varies with pH in this fashion:  $\text{Al}^{+3}$  for  $\text{pH} < 3$ ,  $\text{Al}(\text{OH})^{+2}$  for  $\text{pH} 4-5$ ,  $\text{Al}(\text{OH})_2^+$  for  $\text{pH} 5-6$ , and  $\text{Al}(\text{OH})_4^-$  for  $\text{pH} > 6.5$  (5-7). The hydrolyzed species could be produced by these surface reactions



The formation of aluminate anion at lower pH is favored by increasing temperature. For example, at 25°C gibbsite is in equilibrium with  $10^{-4}\text{M}$   $\text{Al}(\text{OH})_4^-$  at about pH 10, but at 100°C this same equilibrium is achieved at about pH 7 (6). Thus, with increasing temperature and pH the most likely surface hydrolysis shifts from reaction [1] to [2] to [3].

At higher aluminum concentrations and elevated temperatures, hydrolyzed aluminum readily forms polynuclear complexes. These appear to be transitory species that eventually coalesce to form a solid phase (7). Complex cations as large as  $[\text{Al}_{14}(\text{OH})_{34}]^{+8}$  have been identified (8) and it has been suggested that this species is the precursor of boehmite precipitation under hydrothermal conditions (9). It has not been demonstrated that such complexes are involved in step (iii), precipitation leading to film growth, but this is certainly a possibility.

Vedder and Vermilyea (1) have proposed that the rate-controlling step for film growth is the transport of dissolved aluminum species to deposition sites on the hydrous oxide. According to their model, transport is by diffusion in the liquid phase within the interstices of the film. However, recent radiotracer experiments in our laboratory (10) have shown, at least for films grown in boiling water, that there is an inner region of the pseudoboehmite layer that is impermeable to phosphate anions, and presumably other solvated species. Film growth has been found to continue even after this region is established, so ionic diffusion across this layer must eventually be the rate-limiting process, rather than transport in solution.

A characteristic of the aluminum + water reaction is the occurrence of an initial induction period during which there is no weight change, or other sign that a reaction has occurred (11, 12). The length of this period decreases with increasing temperature and depends, among other things, on surface preparation (11). In the Vedder and Vermilyea model the induction period is due to the development of a saturated surface layer that stifles further dissolution until film deposition occurs (1), presumably through localized critical supersaturation. However, one of the experiments reported here demonstrates that the induction period is controlled by events on the surface and not in the solution phase.

Thus, in several respects the existing model for film growth and structure seemed deficient, but it was not possible to synthesize a new explanation without more information about the kinetics at short reaction times. Such results are presented here, and a new model for film growth is discussed.

During the course of this work, some experiments were performed at conditions where pseudoboehmite growth was accompanied by bayerite crystallization. Some preliminary observations of this sequence have already been reported (13), and further details are presented here.

### Procedure

Coupons of 99.99% aluminum foil were electropolished in a perchloric acid-acetic anhydride bath and stored in dry air prior to use. In an earlier study (4) it had been found that the weight gain in boiling water of samples prepared in this way was the same as for evaporated aluminum films, suggesting the absence of in-

terfering surface films from electropolishing. Specimens were hung vertically in distilled water in an unstirred jacketed Pyrex beaker for the required reaction time. The reaction temperatures were in the range 40°-80°C and each temperature was maintained to  $\pm 0.1^\circ\text{C}$ . After immersion, the specimen was rinsed in acetone and air dried. Sample weight, before and after immersion, was measured with an accuracy of about  $\pm 0.5 \mu\text{g}/\text{cm}^2$ .

Specimens were prepared for scanning electron microscopy by evaporation of a thin aluminum film over the sample surface. Bayerite crystal surface density and size distribution were measured by examining SEM photographs of low temperature films in a Quantimet Image Analyzer (14). To do this, use was made of the ability of the image analyzer to determine the maximum chord length, in the horizontal direction, of each particle in the field of view. Moreover, it is possible to preselect a chord length so that the number of particles with a maximum chord length greater than the preselected value are counted. For the particular photographs being examined, chord lengths less than about  $0.23 \mu\text{m}$  could not be readily distinguished from background noise. The number of bayerite crystals was taken to be the number of particles with maximum chord length greater than  $0.23 \mu\text{m}$ . This number was not significantly different from that obtained by using the image analyzer in the full-feature mode (14). Successive countings with preselections of increasing longest chord gave the particle size distribution function. Subtracting these values from each other yielded the distribution density.

### Results

*Induction period.*—The induction times found in these experiments, as well as those reported by other investigators, are shown in Fig. 1 for temperatures ranging from 40° to 100°C. There was excellent agreement between the present results and the times reported for evaporated aluminum films (1), which is further evidence for the absence of a significant polishing film from the perchloric acid-acetic anhydride bath.

An activation energy of 18.7 kcal/mole was calculated from the slope of the line in Fig. 1. There appeared to be a sharp increase in activation energy at

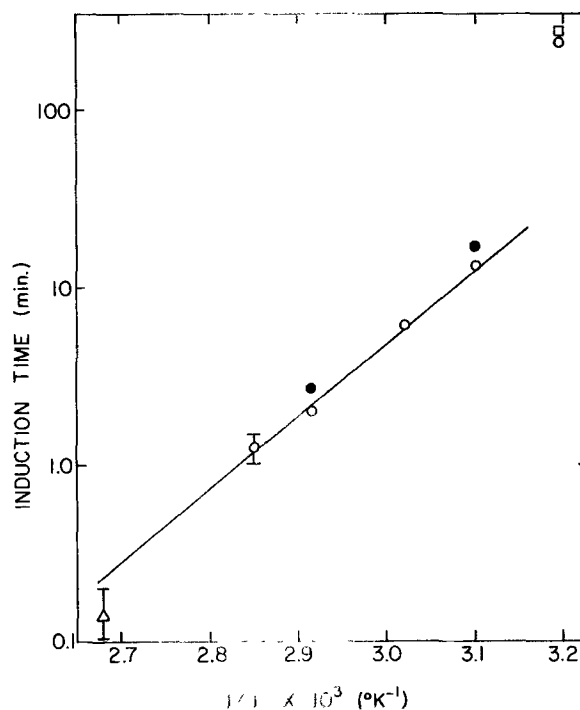


Fig. 1. Temperature dependence of the induction period for film growth on electropolished foil in distilled water. The data are from Ref. (1),  $\bullet$ ; Ref. (3)  $\square$ ; Ref. (10),  $\Delta$ ; and this work,  $\circ$ .

40°C; Hart (3) also found a 4-hr induction period at 40°C, in agreement with the long time observed here.

The pH dependence of the induction time ( $t_0$ ) was examined at 78°C in 0.01N sodium nitrate, adjusted with NaOH or HNO<sub>3</sub> to the desired pH. The value of  $t_0$  was found to remain between 1 and 1½ min while the pH was varied between 4 and 10. This is consistent with an observation that the early rate of film growth at 100°C was independent of pH over this same range (1).

In order to establish whether  $t_0$  is due to events on the solid surface or in solution, an experiment was performed in which specimens were given a series of successive immersions, each one for a time less than  $t_0$ , but with a total reaction time greater than  $t_0$ . Between immersions, the specimens were rinsed in water at room temperature. If  $t_0$  depended on reaching a certain condition in the solution adjacent to the surface, then no weight change would be expected for these specimens. The particular conditions were a reaction temperature of 70°C, and a series of seven immersions each for 1 min. At 70°C, the induction time is 2 min. It was found that there were weight gains of 20 and 22 µg/cm<sup>2</sup> for two specimens, which can be compared with an expected weight gain of 19 µg/cm<sup>2</sup> for an uninterrupted immersion of 7 min. This difference is within the observed reproducibility and is not significant. The induction period must be a property of a process occurring on the solid surface.

**Reaction rate.**—The weight gains found in these experiments at 50°, 60°, and 70°C are shown in Fig. 2 as a function of  $(t-t_0)$ ; data reported by other investigators at 70° and 100°C are also included. At the lowest temperatures, 40° and 50°C, very irreproducible results were obtained at the shortest reaction times, up to times of about  $2t_0$ ; these data are not presented here. This problem was particularly acute when chemically polished foil was used in some preliminary work suggesting that it may have been due to some surface contamination. The data collected at longer times at 50°C and at higher temperatures seemed sufficient for our purposes so this phenomenon was not pursued. At 40°C bayerite crystals, as well as pseudoboehmite, deposited on the surface so the weight gain of these samples could not be used to examine pseudoboehmite growth kinetics. The results obtained at this temperature are treated in a separate section.

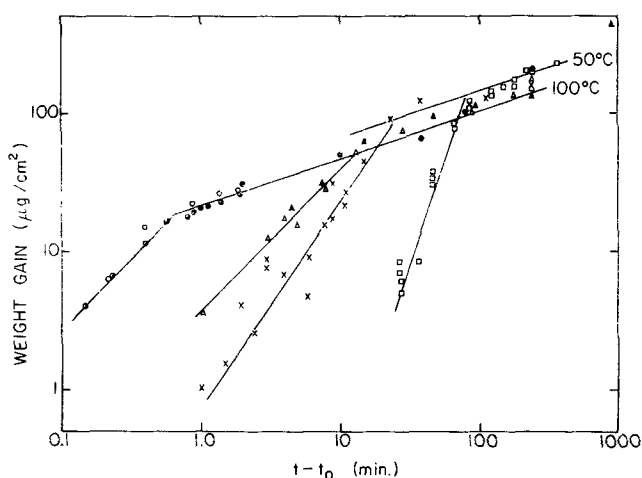


Fig. 2. Film growth on electropolished aluminum in distilled water.

Symbol	Temp (°C)	Ref.
○	100	21
●	100	1
◐	100	10
△	70	This work
▲	70	1
X	60	This work
□	50	This work

As noted by others (1, 12), at each temperature there appeared to be two reaction periods: an initial period during which the rate was constant or increasing with time, and then a period in which the rate steadily decreased. The lines drawn in Fig. 1 through the data of the initial period have slopes of 1 for 70° and 100°C, 3/2 for 60°C, and 3 for 50°C. At the higher temperatures the lines provide a very good fit for the data; at 50° and 60°C there is more scatter, but it is apparent that a power law is a good approximation and that the exponent increases with decreasing temperature. From the rates at 70° and 100°C an activation energy of 16.3 kcal/mole was found, which is only slightly less than that for the induction period.

At each temperature there was a relatively sharp transition to the next stage, a period of slow growth. This period was best defined at 100°C where, over more than two decades of time, the weight gain was proportional to  $(t-t_0)^{1/3}$ . This relationship appeared to be followed at lower temperatures, too, although the 50°C results might be as well described by an exponent of ½. A remarkable feature, noted by previous investigators (1), is that the weight gain not only showed very little dependence on reaction temperature, but sometimes more film was found at lower temperatures. This is illustrated in Fig. 2, where the two lines labeled 50°C and 100°C delineate the narrow band of observed weight gains for a 50° range of reaction temperatures.

**Films grown at 40°C.**—After about 4 hr, a duplex surface film developed consisting of a uniform, finely textured layer covered with relatively large crystals (13). Although Hart (3) reported that the uniform layer gave the electron diffraction pattern of boehmite (presumably pseudoboehmite), our attempts to obtain a diffraction pattern were not successful, indicating a noncrystalline film. On the other hand, the film had the platelet structure expected of pseudoboehmite (13), and replicas of the surface had the appearance of the pseudoboehmite film produced in boiling water, albeit with coarser detail (Fig. 3). Perhaps the uniform layer can be described as retaining the pseudoboehmite structure, but much more poorly crystallized than films grown at higher temperatures.

Small areas of the film sometimes spalled during preparation for microscopy, revealing the film cross section and the metal substrate, as shown in Fig. 4a. Pits in the metal substrate were sometimes associated with these regions, suggesting that stress due to localized corrosion was a cause for film separation. Except for these occasional pits, the metal surface appeared structureless up to about 12,000X magnification. Film thicknesses were estimated from these cross sections, as well as from an occasional "head-on" view of a lifted film, as in Fig. 4b. After 8 and 16 hr immersions, the pseudoboehmite film was 1.2 and 1.8 µm thick, based on single measurements. Between 24 and 98 hr, film thicknesses were  $2.5 \pm 0.4$  µm, with no trend to greater thicknesses evident.

The crystals resting on the pseudoboehmite layer gave a diffraction pattern for bayerite, as found also by previous investigators (3, 15). The number of crystals increased with immersion time as  $(t-t_0)^2$ , as shown in Fig. 5. For times up to 24 hr, there was sufficient separation between crystals to get a size distribution in terms of the chord length measured on the image analyzer. The distributions for two typical fields are shown in Fig. 6. The chord length interval was about 0.45 µm and the points in Fig. 6 are placed at the midpoint of each interval. The limit of resolution of 0.23 µm determined the lower cut-off point of the distribution. With the crude assumption that each crystal was a cube with sides equal to chord length, the volume and hence the weight gain due to bayerite growth was calculated. Although the smallest particles were most numerous, they contributed relatively little to the calculated weight. These calculated points are shown in Fig. 7, along with the



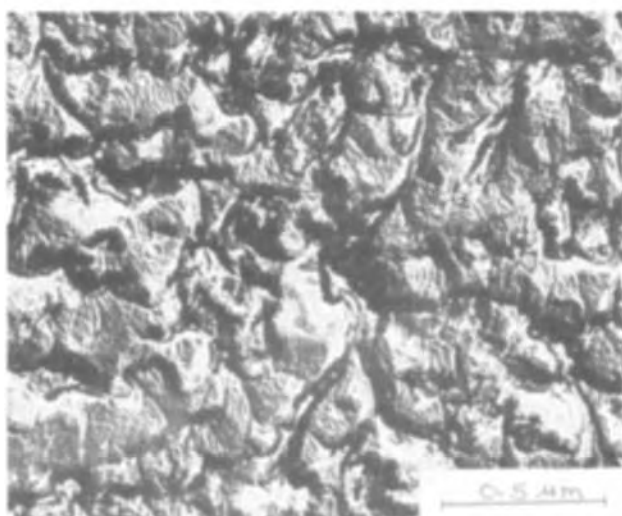
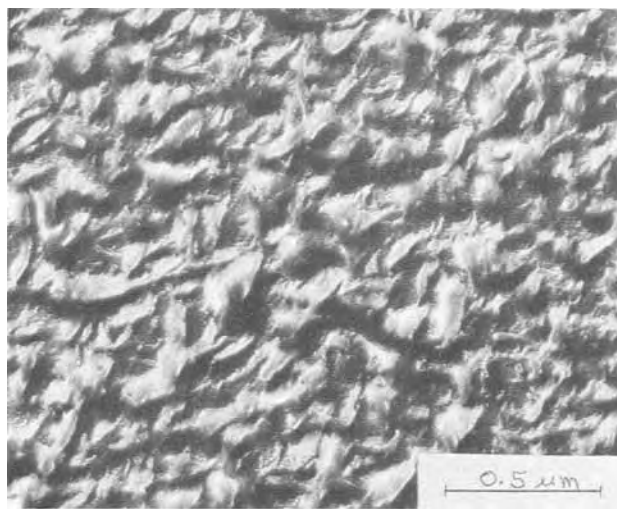
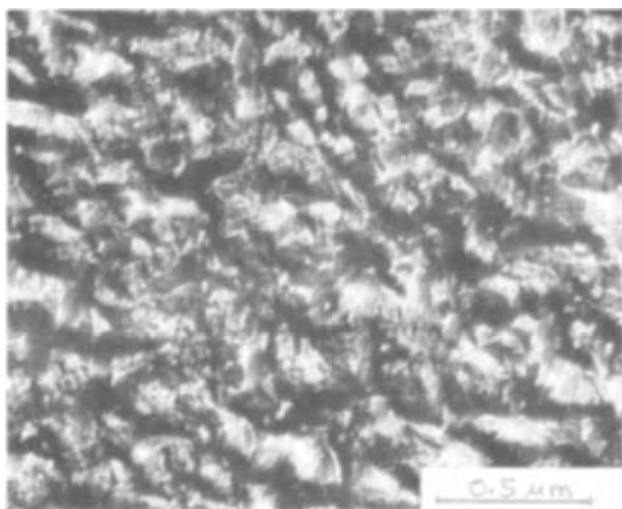


Fig. 3. Transmission electron micrographs of negative replicas of film surface shadowed with Au-Pd at 45°. Reaction conditions were: a (above left), 4 hr at 40°C; b (below left), 8 hr at 40°C; and c (above right), 5 min at 100°C.

observed total weight gain. The weight of pseudo-boehmite, taken as the difference, was found to be unchanged between 16 and 24 hr. The constant film thickness at longer times suggests that no further pseudo-boehmite growth occurred beyond 24 hr, and that all the weight gain at these times was due to bayerite growth. The dotted lines in Fig. 7 have been drawn according to this interpretation. From the thickness and weight it is estimated that the pseudo-boehmite film had a porosity of about 50%.

A puzzling feature of this duplex film is that the two layers always remained quite separate, even when both were undergoing growth. For example, between 8 and 16 hr the number of bayerite crystals increased fourfold (see Fig. 5) while the pseudo-boehmite layer increased in thickness by about 0.6  $\mu\text{m}$ . Yet at 16 hr, or at any other time, no bayerite crystals were found embedded in the bottom layer or surrounded by pseudo-boehmite. The crystals always appeared to be simply sitting on the surface.

### Discussion

An induction period is frequently observed during the formation of a new phase, as in precipitation or crystallization (15, 16). The induction period arises from the need to achieve a minimum size before a particle of the new phase can sustain its identity. Particles smaller than this "critical nucleus" tend to revert back to starting material, whereas the free energy of the system is reduced by the growth of critical nuclei into still larger particles (15). These events occur at the submicroscopic level; for example, a critical nucleus typical of precipitation of a crystalline solid from aqueous solution might have a diam-

eter on the order of 100Å (15). The induction period is just the time required to produce a sufficient number of critical nuclei to cause an observable change in the system.

The induction period found in the system under investigation suggests that initially the hydrolysis reaction takes place at surface sites that must achieve a critical size in order to sustain the reaction. The mechanism of the reaction is not known, but it very likely involves diffusion of water, perhaps as protons and hydroxyl groups, into the amorphous oxide surface. It may be that sufficient water must enter an oxide region so that thermal fluctuations of the distorted lattice will produce a localized configuration suitable for release of a hydrolyzed monomer. Such regions would constitute the critical nuclei.

The observation that  $t_0$  was independent of pH is consistent with the idea that diffusion of water into the oxide lattice is the rate-determining step. The activation energy for the induction period was found to be 18.7 kcal/mole. The activation energy for a nucleation process should exceed that for the corresponding diffusion process by an amount equal to the maximum free energy for nucleus formation (17). Values of the activation energy for  $\text{H}_2\text{O}$  diffusion in amorphous  $\text{Al}_2\text{O}_3$  have not been reported; the closest available figures are for  $\text{D}_2\text{O}$  diffusion in boehmite, given as 12.8 (18) and 15.7 (19) kcal/mole. The free energy for nucleus formation would be expected to be relatively small, perhaps on the order of the hydrogen bond energy between water and the oxide which would be several kcal/mole. Thus, the observed activation energy is reasonable for the process that has been postulated.

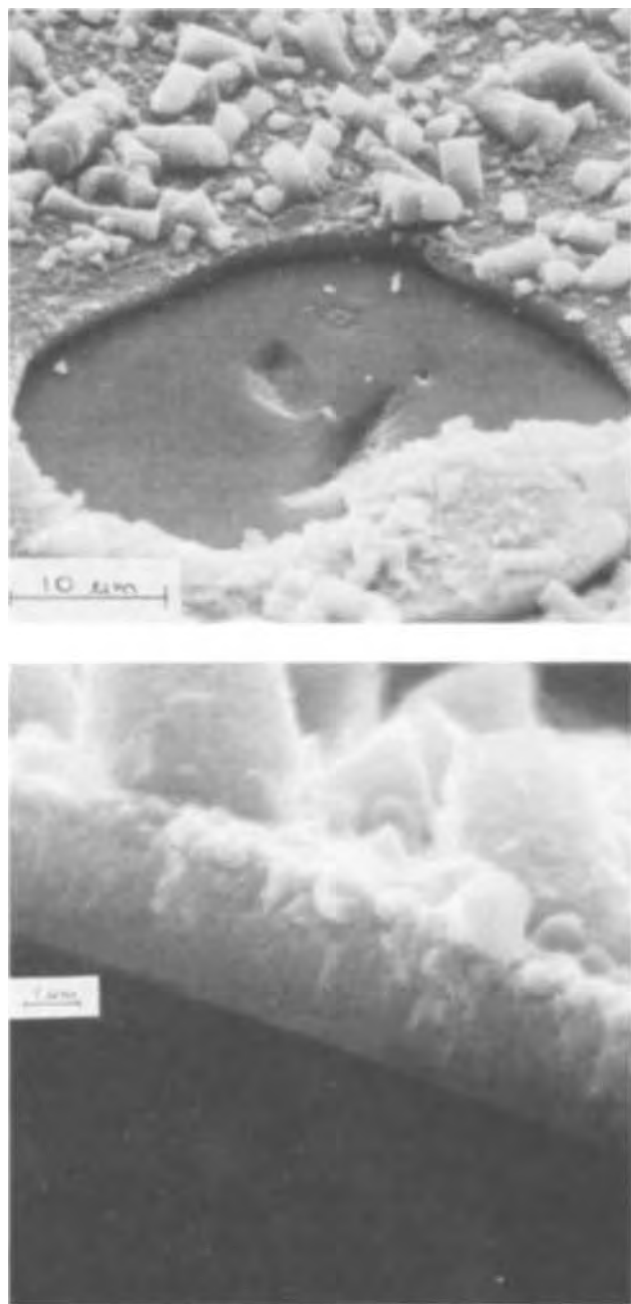


Fig. 4. Scanning electron micrographs of film grown at 40°C for 2 days. a, Top; b, bottom.

The initial growth rate at 100°C has also been found to be independent of pH (1) and is reported here to have about the same activation energy as for  $t_0$ . This suggests that nucleation and growth of hydrolysis sites in the amorphous oxide continues to be rate controlling after the induction period has ended. Of course, as the amorphous oxide is dissolved, new amorphous barrier oxide would be produced by an electrochemical reaction governed by the emf between anodic and cathodic surface sites.

The aluminum oxides are so sparingly soluble (20) that once surface hydrolysis is proceeding at a significant rate, *i.e.*, at the end of  $t_0$ , the critical supersaturation would be quickly reached adjacent to the surface and hydrous oxide would be precipitated on low energy surface sites. The pseudoboehmite platelets are exceedingly thin and are attached to the substrate only along an edge (1). For some time then, the deposited material would occupy only a small fraction of the surface and probably would not interfere with the dissolution reaction.

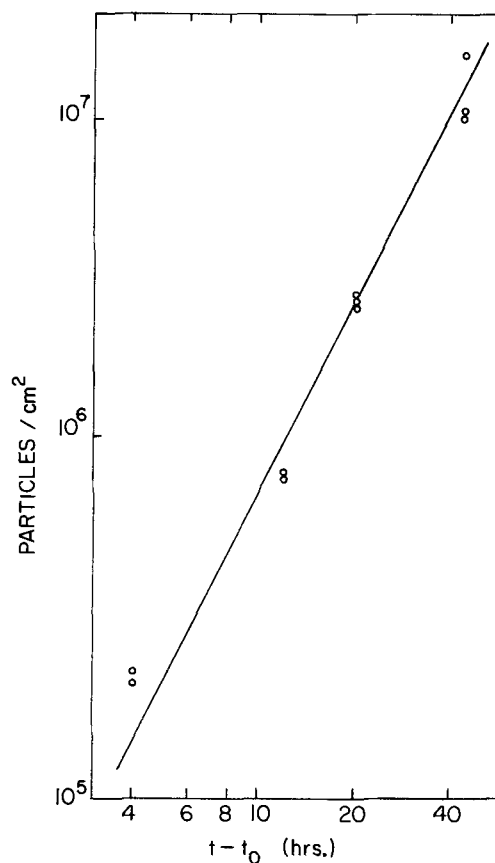


Fig. 5. Density of bayerite crystals at 40°C

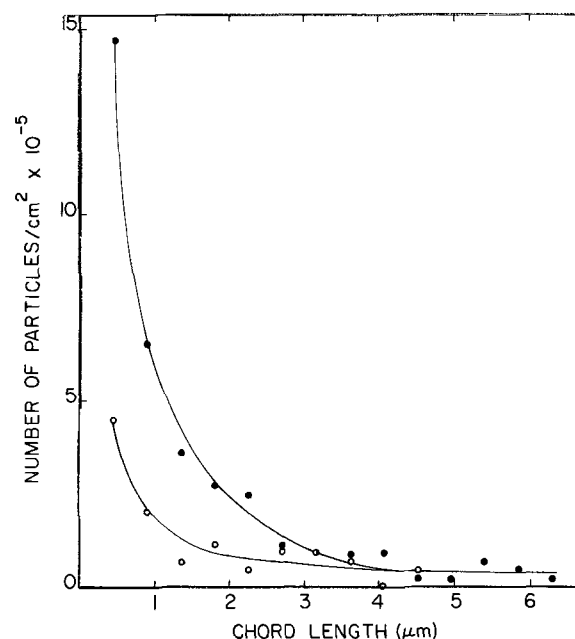


Fig. 6. Size distribution of bayerite crystals after 16 hr (○) and 24 hr (●) at 40°C.

According to the rate equations developed by Jacobs and Tompkins (21), the kinetics during the initial growth period best fit a process consisting of nucleation followed by two-dimensional growth. On a crystalline surface two-dimensional growth might arise from dissolution occurring at steps spreading over the surface, but it is not clear what surface structure supports this growth on an amorphous surface. Slow random nucleation followed by normal two-dimensional growth can give rise to  $\Delta W \propto (t - t_0)^3$ , as ob-

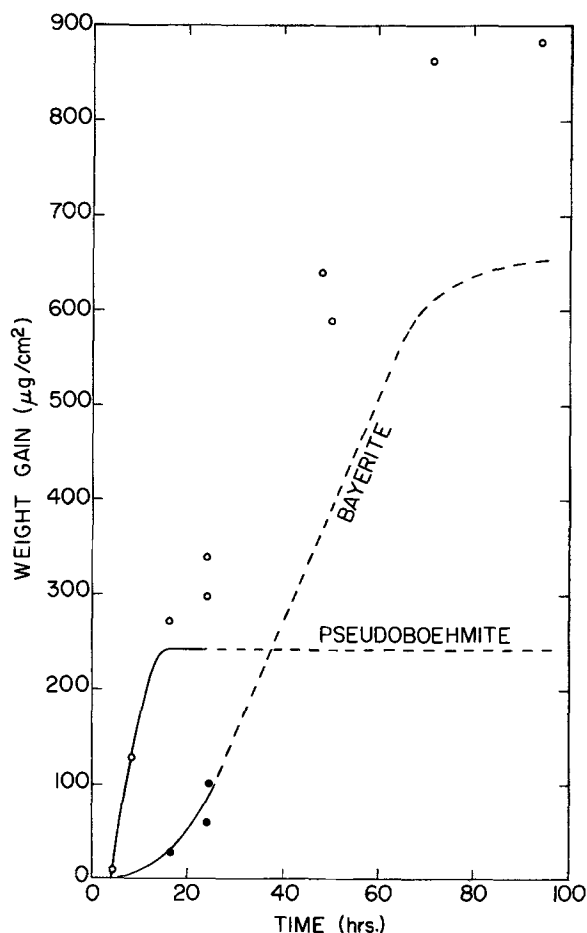


Fig. 7. Weight gain of Al specimens at 40°C. From the total weight gain (○) has been subtracted the calculated weight of bayerite (●) to give the pseudoboehmite component.

served at 50°C. More rapid nucleation reduces the value of the exponent of  $(t - t_0)$ , until extremely rapid nucleation followed by rapid growth can give rise to a linear dependency for a short initial period, as seen at 70° and 100°C.

The platelets would increase in number and thickness as the reaction proceeded until they impinged upon each other. Finally, the platelet layer would become sufficiently dense so as to block the movement of solvated species, as observed for the case of film produced in a 5-min reaction at 100°C (10), and further growth must occur by solid-state diffusion through the film. The most likely diffusing species is water, diffusing inward perhaps as  $H^+$  and  $OH^-$  (18). One would expect growth to now obey a  $t^{1/2}$  relationship and this may be the case at 50°C, but at 100°C the weight gain is clearly proportional to  $t^{1/3}$ .

There is a complete parallel between the kinetics observed during this reaction stage and those observed for the oxidation of  $Cu_2O$  to  $CuO$  in the 800°-1000°C range (22). In this latter case, the weight increased as  $t^{1/3}$  and was not very dependent on reaction temperature. The results were explained as being due to an aging effect that decreased the permeability of the oxide with increasing time and temperature and thus opposed the normal temperature dependence. A similar argument could certainly be applied to pseudoboehmite films since they have been found to exhibit other aging effects, such as a decrease in specific surface area and changes in dielectric properties (4).

The growth process at 40°C differed substantially from that at higher temperatures, the most obvious change being the presence of a second oxide phase. Hart (3) reported that bayerite did not appear until the (pseudo)boehmite film was well established, but

we found that the induction time was about the same for both oxide phases. It is likely that his method of detection was not sensitive enough to identify bayerite when only a relatively few crystals were on the surface. The total weight gains shown in Fig. 7 are in excellent agreement with those reported by Hart, whose representation of the data suggests the two-stage growth process we have found [see Fig. 2 in Ref. (3)]. The observed  $t^2$  dependency for bayerite nucleation implies that either two successive events are required to form a stable nucleus, or that nucleation involves a reaction between a surface site and an active intermediary formed in solution at a constant rate (21). One of the polynuclear complexes could be such an intermediary.

Bayerite has a much lower solubility than pseudoboehmite (23) so after an appreciable amount of bayerite had crystallized the concentration of soluble aluminum species at the outer surface would drop below that required for pseudoboehmite deposition. Figure 7 was drawn to indicate complete cessation of pseudoboehmite growth after 16 hr, but it is possible that the film density continued to increase even though the thickness remained unchanged. This could arise from the fact that a concentration gradient of hydrolyzed species would exist within the interstices of the pseudoboehmite layer so that in the inner regions of the film deposition could still be expected.

The pseudoboehmite layer grown at 40°C was much thicker than films grown at high temperatures, say 100°C (4), and also had a considerable porosity, estimated from weight and thickness to be about 50%. This structure, when considered along with the observation that bayerite continued to deposit even after pseudoboehmite growth had ceased, strongly suggests that the low temperature pseudoboehmite layer does not have an impermeable region but rather is open for outward diffusion of hydrolyzed aluminum, as in the Vedder and Vermilyea model. This may be associated with the poorer crystallinity of these films.

Because of the difference in solubilities, the pseudoboehmite should all dissolve eventually and recrystallize as bayerite, as observed for colloidal suspensions (24). There was no indication that this was occurring, which could mean either that the hydrolyzed species precipitated directly as bayerite, or that there was a steady state between pseudoboehmite deposition and dissolution (13). The eventual decrease in bayerite growth was probably due to blockage of the surface with bayerite crystals, which prevented outward diffusion of soluble species and inward diffusion of water.

The absence of any mutual penetration of the two oxide phases cannot be explained. One would infer from this observation that pseudoboehmite layer growth occurs primarily by internal deposition. This might produce stresses that cause a shearing action between platelets, resulting in an expansion of the layer. However, this scheme is difficult to reconcile with the high porosity of the layer.

## Conclusions

At temperatures between 50° and 100°C the pseudoboehmite film produced by the reaction of aluminum with water grows initially at a rate determined by the nucleation and growth of hydrolysis sites on the amorphous oxide. The rate-limiting step is probably diffusion of water into the oxide surface. As the oxide thickens, rate control shifts to solid-state diffusion, probably of water, through the pseudoboehmite structure.

At 40°C, a thick porous hydrous oxide layer, probably pseudoboehmite, grows to a limiting thickness. Bayerite crystallization occurs simultaneously with this film growth, and becomes the dominant process at longer times.

### Acknowledgment

Part of this work was carried out in the Department of Metallurgy and Materials Science, University of Nottingham, England, during the tenure of a Senior Fellowship from the Science Research Council (U.K.). Assistance from Dr. L. C. Archibald, Mrs. G. Hutchins, and Mrs. E. Vigna during different phases of this study was most helpful.

Manuscript submitted Jan. 14, 1974; revised manuscript received March 26, 1974.

Any discussion of this paper will appear in a Discussion Section to be published in the June 1975 JOURNAL. All discussions for the June 1975 Discussion Section should be submitted by Feb. 1, 1975.

The publication costs of this article have been assisted by the Sprague Electric Company.

### REFERENCES

1. W. Vedder and D. A. Vermilyea, *Trans. Faraday Soc.*, **65**, 561 (1969).
2. B. C. Lippens and J. J. Steggerda, in "Physical and Chemical Aspects of Adsorbents and Catalysts," B. G. Linsen, Editor, p. 171, Academic Press, New York (1970).
3. R. K. Hart, *Trans. Faraday Soc.*, **53**, 1020 (1957).
4. R. S. Alwitt, *This Journal*, **118**, 1730 (1971).
5. C. R. Frink and M. Peech, *Inorg. Chem.*, **2**, 473 (1963).
6. D. D. MacDonald and P. Butler, *Corrosion Sci.*, **13**, 259 (1973).
7. R. W. Smith, *Adv. Chem.*, **106**, 250 (1971).
8. R. E. Mesmer and C. F. Baes, Jr., *Inorg. Chem.*, **10**, 2290 (1971).
9. D. D. MacDonald, P. Butler, and D. Owen, *J. Phys. Chem.*, **77**, 2474 (1973).
10. R. S. Alwitt and W. J. Bernard, *This Journal*, **121**, 1019 (1974).
11. W. J. Bernard and J. J. Randall, Jr., *ibid.*, **107**, 483 (1960).
12. W. J. Bernard and J. J. Randall, Jr., *ibid.*, **108**, 822 (1961).
13. R. S. Alwitt and L. C. Archibald, *Corrosion Sci.*, **13**, 687 (1973).
14. H. Schmeisser and M. Harsdorff, *Thin Solid Films*, **14**, 321 (1972).
15. K. H. Lieser, *Angew. Chem. (Internat. ed.)*, **8**, 188 (1969).
16. W. J. Dunning, in "Nucleation," A. C. Zettlemoyer, Editor, Chap. 1, Marcel Dekker, New York (1969).
17. D. Turnbull and J. C. Fisher, *J. Chem. Phys.*, **17**, 7 (1949).
18. Y. Wei and R. B. Bernstein, *J. Phys. Chem.*, **63**, 738 (1959).
19. A. Mata Arjona and J. J. Fripiat, *Trans. Faraday Soc.*, **63**, 2936 (1967).
20. E. Deltombe and M. Pourbaix, *Corrosion*, **14**, 496T (1956).
21. P. W. M. Jacobs and F. C. Tompkins, in "Chemistry of the Solid State," W. E. Garner, Editor, Chap. 7, Academic Press, New York (1955).
22. J. L. Meijering and M. L. Verheijke, *Acta Met.*, **7**, 331 (1959).
23. R. S. Alwitt, in "The Anodic Behavior of Metals and Semiconductors," J. S. Diggle and A. K. Vijh, Editors, Vol. 3, Marcel Dekker, New York. To be published in 1974.
24. G. C. Bye and J. G. Robinson, *Kolloid Z.*, **198**, 53 (1964).

## Interface Stability in the Electrolytic Decomposition of Silicon Dioxide Films at Elevated Temperatures

J. W. Hinze,<sup>\*1</sup> J. A. Baker,<sup>2</sup> and J. W. Patterson\*

Department of Metallurgy and Engineering Research Institute, Iowa State University, Ames, Iowa 50010

### ABSTRACT

The stability of planar Si<sub>3</sub>SiO<sub>2</sub> interfaces was investigated in the electrolytic decomposition of SiO<sub>2</sub> films at 850°C. It was found that voltages greater than the reversible emf of the cell Si|SiO<sub>2</sub>|O<sub>2</sub> (P<sub>O<sub>2</sub></sub> = 1 atm) applied cathodic to silicon rendered the planar geometry unstable so that localized, electrolysis-induced breakdown occurred. This finding is in disharmony with previous observations by Jorgensen. A mechanism for electrolysis-induced dielectric breakdown was proposed to explain the observed breakdown morphologies and voltages. The magnitudes of the observed voltages indicate that ionic as opposed to neutral oxygen transport predominates in SiO<sub>2</sub> films at elevated temperatures.

The intrinsic nature of mass and charge transport in SiO<sub>2</sub> films at elevated temperatures has received increased attention in recent years owing to the technological importance of Si<sub>3</sub>SiO<sub>2</sub> devices in the electronics industry. Karube *et al.* (1) and Jorgensen (2) have demonstrated that silicon is immobile in SiO<sub>2</sub> compared to oxygen; however, there is controversy concerning the nature and effective charge of the mobile oxygen species (3-6). In an effort to resolve this issue, Jorgensen (2) studied the effect of applied electric fields on silicon oxidation and concluded that oxygen in the form of monatomic divalent ions is mobile in SiO<sub>2</sub>. However that study sparked another con-

troversy concerning the reliability of information to be gained from such studies (5, 7, 8).

In a more recent work, Jorgensen (9) studied the decomposition of SiO<sub>2</sub> films at elevated temperatures to further substantiate the migration of divalent oxygen ions. A cell arrangement similar to that shown in Fig. 1 was used for the decomposition experiments. Constant applied currents, with silicon as the cathode, were reported to cause planar thinning of the Si<sub>3</sub>SiO<sub>2</sub> interface. The cell voltage, monitored with time, was reported to decrease in a fashion qualitatively consistent with a uniform thinning of the resistive SiO<sub>2</sub> film. After a time, the voltage reached a steady-state value indicating that a balance had been achieved between the rate of decomposition and the rate of formation of SiO<sub>2</sub>. The observed steady-state voltage was approximately 1.75V at 850°C which corresponds closely to the reversible cell emf one would calculate

\* Electrochemical Society Active Member.

<sup>1</sup> Present address: Systems Research Laboratories, Incorporated, Dayton, Ohio 45400.

<sup>2</sup> Present Address: Dow Corning Corporation, Hemlock, Michigan 49626.

Key words: silicon dioxide, mass transport, electrolysis, dielectric breakdown, silicon dioxide interface.

from free energy data for the formation of amorphous SiO<sub>2</sub> (10), assuming four equivalents are transferred in the cell reaction.

In a more general vane, however, planar thinning of the SiO<sub>2</sub> films under such conditions would seem rather unlikely; especially in view of past observations of instability of planar electrode interfaces in other electrochemical systems. For example, Rapp (11) and Wagner (12) have observed nonplanar interface growth in the double decomposition of oxides and halides. Conditions were outlined for which the transition from planar to nonplanar morphologies would take place. Tubandt (13) observed the formation of dendritic filaments of silver in his attempts to measure the ionic transference number of AgBr in symmetric cells with silver as the cathode and anode materials. Dendrites originating at the silver cathode grew to the anode thus causing a short circuit to occur. Similarly, metallic sodium dendrites have been observed to form in  $\beta$ -alumina during the charging of sodium sulfur cells (14-15). Finally, unless special precautions are taken, metallic dendrite formation at the cathode is commonly observed during the electrolytic deposition of metals from fused salt and aqueous electrolytes and during the charging of fused salt electrolytic cells.

Dendritic growth in the above instances is not without theoretical justification. In fact, it is to be expected on the basis of simple laws of diffusion. For example, if a small protuberance should form at the cathode, its growth will be favored. This is because the diffusion path length from the anode is shorter to the tip of the protuberance than it is to the trailing planar interface whereas the voltage difference is the same in both cases. Thus the average voltage gradient (the driving force for ion migration) will be greater between the tip and the anode than anywhere else. Therefore, the highest ionic current densities occur immediately between the tip and the anode so that the growth of the protuberance is not only preferential but also self-accelerating.

In view of the foregoing arguments, it seemed surprising to us that some form of localized decomposition was not observed by Jorgensen (9) in his experiments and this prompted the present investigation.

#### Experimental Procedures and Apparatus

Ultra high purity, high resistivity (1000 ohm-cm) silicon single-crystal specimens were used in this study. The specimens were obtained from Dow Corning Corporation as  $\frac{1}{4}$  in. thick disks with a  $\frac{1}{2}$  in. diameter. Thin planar faces, which were parallel to the (111) crystallographic plane, had been electrochemically polished to a mirror finish.

The following procedure was used in the construction of the decomposition cells. The silicon specimens were cleaned by ultrasonic agitation in the following reagents sequentially: trichloroethylene, methanol, distilled water, buffered hydrofluoric acid, distilled water, nitric acid, and distilled water followed by a 5 min rinse in a jet of distilled water. Excess water was stripped off of the specimens with paper tissues, and the specimens were finally dried in an air stream.

After a brief exposure to vacuum at 850°C, purified oxygen at 1 atm pressure was introduced to oxidize the specimens to a thickness the order of 5000Å. Platinum anodes were then applied to each planar interface by electron beam evaporation to a thickness of 1000Å. Into the cylindrical side surface of each of the silicon specimens was drilled a small hole into which a platinum wire with a beaded tip was press fitted. This cell was then placed between two platinum foils on a cell support and electrical leads were attached. During all of the above operations, extreme care was taken to avoid sodium contamination. The specimens were not contacted with the fingers or contaminated laboratory surfaces and tools.

#### Results and Discussion

Preliminary experiments were conducted to determine the open-circuit emf ( $E_w$ ) across the cells shown

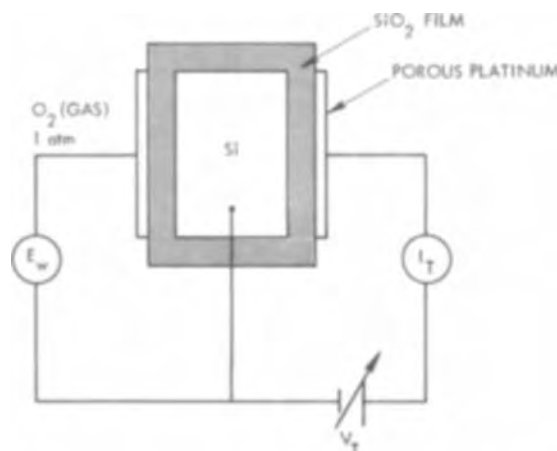


Fig. 1. Schematic diagram of the cell arrangement and external electrical circuitry used to study the kinetics of SiO<sub>2</sub> electrolyte decomposition at elevated temperatures.

in Fig. 1. These emf's were found to be approximately 420 mV which are around 200 mV lower than those reported by Jorgensen (2). Further preliminary measurements of the silicon oxidation rate under open-circuit conditions were conducted without the platinum electrodes intact. Linear plots of the square of the thickness *vs.* time were observed which yielded a scaling rate constant of  $1.25 \times 10^{-11}$  cm<sup>2</sup>/hr at 850°C in good agreement with Jorgensen's results (2). The partial surface control observed by Deal and Grove (16) in determinations of the oxidation rate of doped silicon was not observed here.

Decomposition experiments were conducted at 850°C on the cells shown in Fig. 1. Due to the symmetric nature of the cells only half of the cell was used for the study while the open-circuit emf and conductance were measured across the other half as shown in Fig. 1. Formation of a platinum-silicon eutectic at 830°C (17) generally limited cell life because of local deterioration at the center electrode. However with proper care in cell construction useful cell life was on the order of 2-3 weeks. Both constant voltage and constant current decomposition experiments were carried out as part of the present study.

Constant voltages in the range  $1.80 < V_T < 5.00$ V (silicon as cathode) were applied with the use of an appropriate operational amplifier circuit. A uniform planar decomposition of the Si<sub>3</sub>SiO<sub>2</sub> interface should result in a timewise current increase as the resistive SiO<sub>2</sub> layer becomes thinner. Instead, localized breakdown of the SiO<sub>2</sub> films occurred as evidenced by intermittent and highly sporadic bursts of current. Moreover, this phenomenon was observed in all the potentiostatic experiments where voltages greater than 1.8V were applied. Thus these constant voltage observations in themselves seem to be inconsistent with the observations of Jorgensen because even though he used constant currents, his constant current voltage always exceeded the thermodynamic emf (1.75V). Indeed his voltages decayed through precisely the same range of values ( $1.8 < V < 5.0$ V) and yet his films reportedly did not fail locally. Further confirmation of this inconsistency was provided later with constant current experiments as pointed out below.

Figure 2 shows the planar surface of a typical specimen after exposure to a potentiostatic decomposition experiment at 850°C. In Fig. 2a the specimen had been prepared by first etching the platinum electrode away in aqua regia and then removing most of the SiO<sub>2</sub> with HF. This leaves the silicon substrate surface only partially exposed while the remainder is still covered with adherent flakes of SiO<sub>2</sub> scale. It is evident from Fig. 2a that localized pits have been excavated in the silicon substrate, some have penetrated through the SiO<sub>2</sub> flakes, and finally some appear to be forming beneath undamaged regions of these flakes. Figure 2b

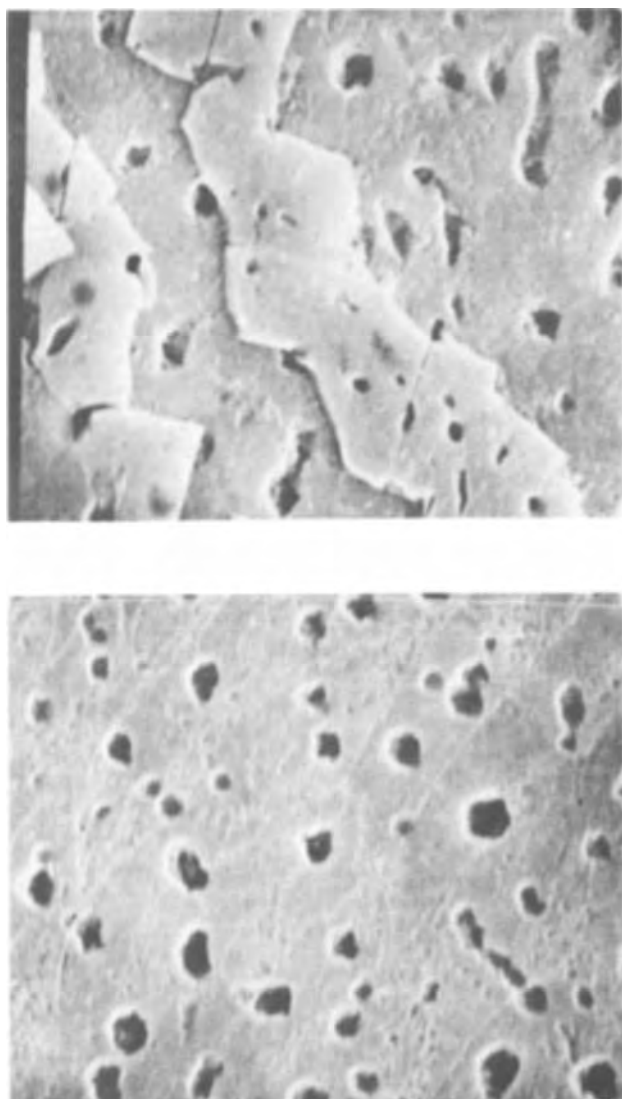


Fig. 2. SEM micrographs of damage to the Si/SiO<sub>2</sub> interface in a decomposition experiment. (a, top) Partially etched specimens showing breakdown damage pits in the silicon substrate surface and in the retained flakes of SiO<sub>2</sub> (magnification  $\times 3000$ ). (b, bottom) Pits in the silicon substrate of a fully etched specimen (magnification  $\times 3000$ ).

merely shows the same specimen (different region) after complete removal of the SiO<sub>2</sub> with the HF etchant. Features of these types were observed for all decomposition voltages greater than 1.8V and the following explanation in terms of localized electrolytic decomposition followed by catastrophic dielectric breakdown is offered.

According to Klein (18) catastrophic dielectric breakdown as opposed to electrolytic breakdown occurs in three stages. In the initial stage a localized avalanche of carriers is initiated when the local voltage gradient exceeds some critical value typically in the range of  $10^5$ - $10^7$  V/cm for insulators. Snow and Deal (19) found this critical value to be  $8 \times 10^6$  V/cm for SiO<sub>2</sub> films at room temperature. Localized  $I^2R$ -type heating results which causes the current to run away during the second phase of breakdown because the conductivity of insulator materials increases exponentially with temperature. In the final stage, current arcing vaporizes the electrode materials as well as the interposed dielectric insulator in the immediate vicinity of the arc. The damaged region then becomes a nonconductive void, and the breakdown is said to be self-healing (18).

In addition to dielectric breakdown, electrolytic breakdown can also occur if mobile ions prevail in the

compound. A most important difference between these two modes of breakdown is that electrolytic breakdown is induced by a critical voltage difference (namely, the thermodynamic emf if no neutral transport exists) but is otherwise independent of the voltage gradient in the specimen. Dielectric breakdown, on the other hand, commences only after a critical voltage gradient is surpassed but is otherwise independent of total applied voltage. In view of these concepts the observed breakdown effects can be rationalized with the aid of the sequence shown in Fig. 3.

In the initial stage, shown in Fig. 3a, electrolysis of SiO<sub>2</sub> commences at the Si/SiO<sub>2</sub> interface. Suppose that small protuberances form as highly conductive, partially reduced pockets of SiO<sub>2</sub> (Fig. 3b). Then once formed, the tip of the most protruding SiO<sub>2</sub> pocket propagates ahead of the others and ahead of the planar interface. That is, the oxygen removal rate from the tip of this protuberance is greater than that from all the other points. This is because the average field gradient from that tip to the anode is greater than that between all the other cathode locations and the anode. Thus the pocket of partially reduced SiO<sub>2</sub> evolves into a dendritic spike in a runaway mode of propagation. Of course, the same analysis holds if the dendrite is silicon which has been produced by the total reduction of SiO<sub>2</sub>.

As the tip of the reduced SiO<sub>2</sub> dendrite gets closer to the anode, the local voltage gradient in front of it continues to increase even though the applied voltage remains constant. Eventually the critical gradient (about  $8 \times 10^6$  V/cm) required for the catastrophic dielectric breakdown of SiO<sub>2</sub> is exceeded. At this point arcing vaporizes the remaining path length as shown schematically in Fig. 3c. Vaporization due to arcing causes the circuit to be broken (*i.e.*, the breakdown is said to be "self-healing"), and the whole process starts over again at the next largest conductive protuberance on the cathode.

The electrolytic breakdown phenomenon observed here provides strong evidence for the domination of charged over uncharged oxygen migration in SiO<sub>2</sub>. Significant migration of neutral oxygen would act to annihilate the protuberances as they approached the anode. Furthermore, the electrolytic breakdown phenomenon occurred whenever a voltage greater than the thermodynamic emf was applied cathodic to silicon. Were the flux of neutral oxygen nonzero, an applied voltage perceptibly greater than  $E_{TH}$  would have been necessary to cause electrolytic breakdown. These findings lead us to agree with Jorgensen that doubly charged oxygen ions have high mobility in SiO<sub>2</sub> films, at least when electric fields are applied.

In our view, the same basic arguments should apply to galvanostatic decomposition experiments. This view holds that the SiO<sub>2</sub> scale is unstable with respect to

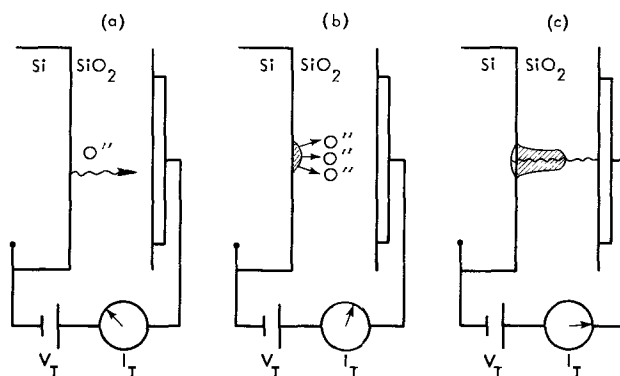


Fig. 3. Proposed sequence for electrolysis-induced dielectric breakdown for SiO<sub>2</sub> layers at elevated temperatures. (a) Initial decomposition of Si/SiO<sub>2</sub> interface. (b) Formation of region of highly reduced SiO<sub>2</sub>. (c) Growth of reduced region with subsequent arcing due to dielectric breakdown.



electrolytically induced localized breakdown as long as the applied voltage is of the proper polarity and magnitude to reverse the flow of mobile ions. In other words, the voltage need only be cathodic to silicon and greater than the thermodynamic emf for localized, electrolytically induced breakdown to proceed. Thus when these conditions hold, electrolytic decomposition proceeds preferentially from localized instabilities (protuberances) irrespective of how the applied current (or voltage) may vary with time. Finally, because both the foregoing requirements must necessarily be fulfilled during galvanostatic decomposition, it would seem that localized breakdown, as opposed to the uniform thinning reported by Jorgensen should result in the case of constant current decomposition.

For these reasons two galvanostatic decomposition experiments were carried out at 850°C. In both cases the applied current was fixed at 4  $\mu$ A and in both cases the voltage over the SiO<sub>2</sub> layer continuously increased and within minutes surpassed the thermodynamic emf. Shortly thereafter the measured voltage suffered intermittent instantaneous decreases (sometimes to zero) with the behavior eventually becoming so erratic as to preclude accurate recording. This behavior is interpreted as catastrophic breakdown preceded by electrolytic decomposition issuing as before from localized sites on the silicon cathode. While this was born out by subsequent visual inspection, no detailed scanning electron microscope examinations were carried out.

To further substantiate the proposed mechanism of electrolysis-induced breakdown, potentiometric studies were conducted with applied voltages of opposite polarity, (i.e., silicon as the anode). Such voltages would not be expected to give rise to pockets of electrolytically reduced SiO<sub>2</sub> because the pockets would now have to form by virtue of oxygen depletion at the platinum electrode. However the abundance of oxygen gas at this electrode would be expected to immediately reoxidize the pockets. Such oxidation would thus reconvert the pockets to insulators thus arresting the electrolysis current required for the breakaway propagation mode and planar geometries would remain stable. If all this is true, catastrophic breakdown with reverse bias should require much larger applied voltages because now the critical gradient on the order of  $8 \times 10^6$  V/cm (19) must be set up over the entire thickness of the SiO<sub>2</sub> film. For an initial thickness of 5000Å the required voltage would be about 400V at room temperature. The experiments revealed no breakdown up to about 120V with catastrophic breakdown taking place above this value. The observed voltage is sufficiently close to the predicted value of 400V (and sufficiently far from 1.8V) to serve as a confirmation.

Actually the critical breakdown voltage gradient at elevated temperatures has not been previously measured; however, it does not seem unreasonable that the observed voltage should be somewhat less than that predicted from the critical gradient of ( $8 \times 10^6$  V/cm) given by Snow and Deal (19) for room temperature. In other words, the present study merely suggests that the high temperature value of the critical gradient is about one fourth the room temperature value.

The cell used for this study was observed under the scanning electron microscope with the platinum electrode still intact. SEM micrographs of the breakdown pits are shown in Fig. 4. In the lower SEM micrograph, breakdown seems to have caused a crack in the silicon substrate. The pits which formed with reverse polarity are much larger than those shown in Fig. 2. This reflects the fact that much more energy is released in pure catastrophic breakdown than in electrolysis-induced breakdown.

### Conclusion

Two important conclusions result from the above experimental observations. It has been shown that applying voltages greater than the thermodynamic emf

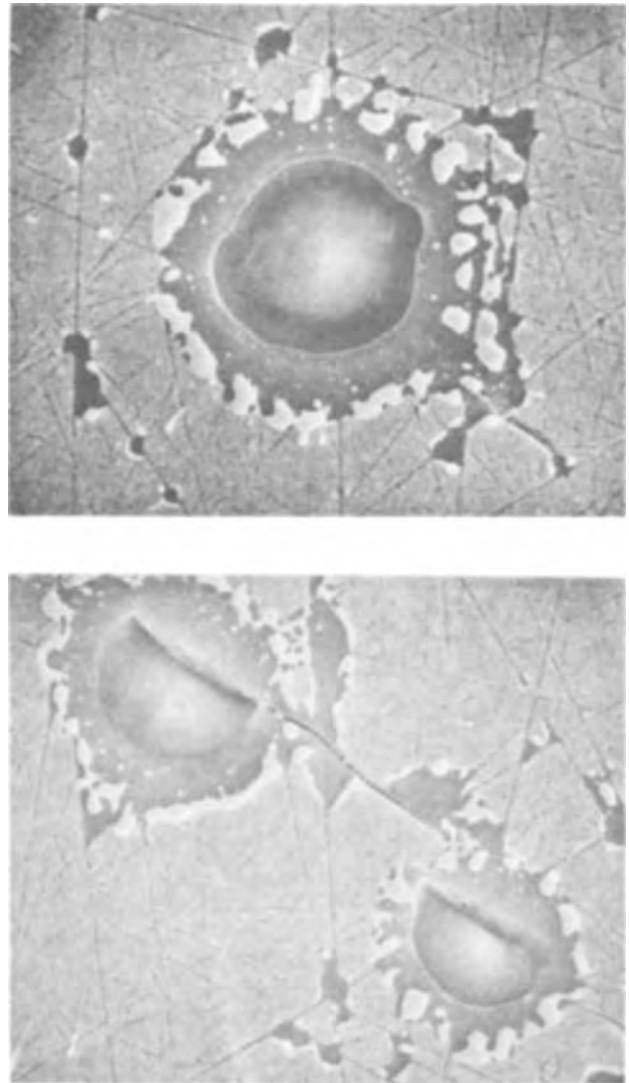


Fig. 4. SEM micrographs of self-healing electrical breakdown of a SiO<sub>2</sub> film induced by a large accelerating field. (a, top) Breakdown in a defect-free region of the SiO<sub>2</sub> film (magnification  $\times 1500$ ). (b, bottom) Breakdown along an imperfection (magnification  $\times 1500$ ).

across SiO<sub>2</sub> films (the silicon substrate being the cathode) rendered the initially planar scale geometry unstable. In all the decomposition experiments, highly localized damage resulted due to electrolysis-induced dielectric breakdown. In view of the arguments presented above, this phenomenon would be expected to occur in the electrolytic decomposition of all scaling layers as long as cathodic protuberances are more conductive than the surrounding phase, that is, whenever the electric field gradient ahead of the protuberance is greater than it is from the anode to the planar interface of the cathode.

Secondly, on the basis of the breakdown voltages and morphologies for the SiO<sub>2</sub> films, it is concluded that divalent oxygen ions are capable of carrying significant currents in SiO<sub>2</sub> and that neutral oxygen fluxes are negligible by comparison.

### Acknowledgments

This research was conducted under the auspices of the Engineering Research Institute at Iowa State University through funds provided by the Aerospace Research Laboratories, Office of Aerospace Research, United States Air Force, Contract F 33615-68-C-1034.

The authors wish to thank Dr. Jon Schieltz and Mr. Frederick Schmidt for providing our specimens with the electron beam evaporated electrodes used in this study.

Manuscript submitted Dec. 26, 1972; revised manuscript received March 15, 1974.

Any discussion of this paper will appear in a Discussion Section to be published in the June 1975 JOURNAL. All discussions for the June 1975 Discussion Section should be submitted by Feb. 1, 1975.

## REFERENCES

1. K. N. Karube, K. Yamamoto, and M. Kamiyama, *Japan J. Appl. Phys.*, **2**, 11 (1963).
2. P. J. Jorgensen, *J. Chem. Phys.*, **37**, 874 (1962).
3. R. Brückner, *J. Non-Crystalline Solids*, **5**, 177 (1971).
4. G. H. Frischat, *Glastech. Ber.*, **45**, 309 (1972).
5. D. O. Raleigh, *This Journal*, **113**, 782 (1966).
6. R. H. Doremus, To be published in Proc. of the Am. Soc. Met. Materials Science Seminar on Diffusion, Cleveland, Ohio, October 1972.
7. P. J. Jorgensen, *This Journal*, **114**, 820 (1967).
8. D. O. Raleigh, *ibid.*, **115**, 111 (1968).
9. P. J. Jorgensen, *J. Chem. Phys.*, **49**, 1594 (1968).
10. JANAF Thermochemical Data, Dow Corning Co., Midland, Mich., Dec. 31, 1960.
11. R. A. Rapp, Paper 119 presented at the Electrochemical Society Meeting, Atlantic City, New Jersey, Oct. 4-8, 1970.
12. C. Wagner, *Z. Anorg. Allgem. Chem.*, **236**, 320 (1938).
13. C. Tubandt, *ibid.*, **115**, 105 (1920).
14. L. Hsueh and D. N. Bennion, Report 69-68, December 1969, UCLA Contract, No. DA 44-009-AMC-1661 (T).
15. J. T. Kummer, Paper presented at a workshop on Materials Problems and Opportunities in Energy Storage, Philadelphia, Pa., March 1971.
16. B. E. Deal and A. S. Grove, *J. Appl. Phys.*, **36**, 3770 (1965).
17. M. Hansen, "Constitution of Binary Alloys," 2nd ed., McGraw-Hill Book Co., New York (1958).
18. N. Klein, *Advan. Electron. Electron Physics*, **26**, 309 (1969).
19. E. H. Snow and B. E. Deal, *This Journal*, **113**, 263 (1966).

## The Effect of Heat-Treatment on Photoluminescence Efficiency and Minority Carrier Lifetime in LEC-GaP(Zn,O)

R. Caruso and A. R. Von Neida

Bell Laboratories, Incorporated, Murray Hill, New Jersey 07974

## ABSTRACT

High temperature heat-treatment in the interval between 1300° and 1200°C followed by slow cooling (2°-50°C/hr) to 500°C has been found to increase the photoluminescence efficiency ( $\eta_{\text{red}}$ ) of LEC-GaP(Zn,O) (typically 0.00015% in the seed end to 0.06% in the tail end) to within a factor of 4 of solution grown crystals ( $\eta_{\text{red}} \approx 0.7\text{-}4\%$ ) with comparable hole concentrations. The effect of high temperature annealing is to increase substantially the minority carrier lifetime by reducing the density of nonradiative electron trapping (killer) centers. Subsequent cooling from 1200°-500°C produces an increase in Zn-O pairs over that obtained in as-grown LEC material. The activation energy for the high temperature process involving the removal of killer centers is  $6.2 \pm 0.5$  eV with a relaxation time of 2.1 hr at 1300°C. Arguments are presented to identify further the killer center with a Ga vacancy and the activation energy with that for Ga vacancy diffusion in GaP. Thus, there appears to be an inherent thermodynamic limitation, rather than any impurity-related limitation, to the radiative efficiency of as-grown LEC-GaP(Zn,O). Since annealing appears to be capable of yielding p-type GaP(Zn,O) with  $\eta_{\text{red}}$  ranging from at least 0.5 to 1.0% over an entire crystal, this material may be useful in a single epitaxial growth process for device application.

In this paper we characterize the change in photoluminescence properties of LEC-GaP(Zn O) with heat-treatment at elevated temperature. We present data which show that a significant increase in internal red photoluminescence quantum efficiency ( $\eta_{\text{red}}$ ) can be realized by suitable annealing.

As-grown LEC-GaP(Zn,O) crystals show markedly reduced  $\eta_{\text{red}}$  (<0.06%) from that obtained in liquid phase epitaxial (LPE) layers or in solution grown (SG) platelets (>1%) (1). Efficient diodes have been prepared with single LPE growth on SG-GaP(Zn,O) substrates (2), but faced with the low  $\eta_{\text{red}}$  of the LEC material, single LPE on LEC-GaP(Zn,O) substrates has not been successful. Obviously, an increase in  $\eta_{\text{red}}$  of the pulled crystals to the 1% region would make the LEC p-type material an attractive substrate for device fabrication using single LPE techniques.

The high-temperature annealing experiments are suggested by the results of measurements on LEC-GaP(Zn,O) grown from nonstoichiometric, Ga-rich, melts (3, 4) in which it was found that lower growth

temperatures (down to 1200°C) produced material having substantially longer minority carrier lifetimes and higher red photoluminescence efficiency than stoichiometrically grown material.

The minority carrier lifetime of LEC-GaP(Zn,O) crystals is typically two orders of magnitude shorter than equivalently doped SG platelets (1). The major nonradiative shunt path, or killer center, responsible for this short minority carrier lifetime does not appear to be related to impurity effects, notably Si, B, C, N, As, or to changes in the LEC growth parameters. Rather, the killer center appears to be a native defect related to Ga vacancies or Ga vacancy complexes (4). The role of Ga vacancies in determining luminescence efficiency has also been reported in GaAs (5).

Insofar as there are competing centers for electron recombination the photoluminescence efficiency of GaP(Zn,O) is also determined by the number of Zn-O pairs. The seed-to-tail variation in the Zn-O pair concentration in LEC crystals is typically of the order of 1:30 (1). This gradient cannot be completely accounted for by Zn partitioning since the Zn seed-

Key words: GaP(Zn,O), photoluminescence, minority carrier lifetime, light-emitting diode.



to-tail concentration varies typically by 1:6 (1). However, at the same time, there does not appear to be a lower oxygen concentration at the seed end (with either  $\text{Zn}(\text{PO}_3)_2$  or  $\text{Ga}_2\text{O}_4$  dopants), since measurements of the total oxygen concentration using He (3) activation analysis show an approximately uniform oxygen content (within a factor of 2) in the LEC crystals (6). Apparently then, much of the oxygen in the seed end is not available for pairing with Zn, being interstitial, precipitated, or paired with other species. As will be shown, the results of the high temperature heat-treatment indicate that the seed-end oxygen is most probably complexed with Ga vacancies.

### Experimental

The samples for heat-treatment were obtained from 10 p-type LEC-GaP crystals (50-100g). For each annealing experiment a number of pie-shaped samples were cut from a 1/4 in. thick slice and a control sample was saved for representation of the as-grown condition at that point in the crystal. The slices were cut from near the seed and tail ends of these crystals, which had been doped with Zn in the  $10^{17}$ - $10^{18}$   $\text{cm}^{-3}$  range and with 100-300 mg  $\text{Ga}_2\text{O}_3$  added to the melt. All heat-treatments were made in a tube furnace at temperatures of 1152°, 1200°, and 1300°C.

In a number of preliminary experiments pie-shaped sections ( $\approx 1$ g) were sealed under vacuum in 1.5 in. long silica tubes containing Ga and sufficient powdered GaP to form a saturated solution at the annealing temperature. These samples showed only a 10% increase in minority carrier lifetime ( $\tau_m$ ) after annealing 30 days at 1200°C. However, when similar samples were treated as above but without the addition of any Ga or powdered GaP,  $\tau_m$  improved by a factor of 10 after 8 days at temperature. Although the tube furnace gradient was uniform to within 1°C over a 3 in. length we were often not able to keep these samples from transporting within the vials, particularly at the highest temperature (1300°C). Accordingly, a system was devised by which the samples could be heat-treated under encapsulation by  $\text{B}_2\text{O}_3$  (termed liquid encapsulation annealing, LEA). In this way the transport of the samples caused by the temperature gradients was eliminated. Hot-pressed high-purity BN boats, each with a series of 3/4 in. diameter isolated holes, to allow simultaneous heat-treatment of a number of samples, were used to contain the specimens. BN is quite inert to both GaP and  $\text{B}_2\text{O}_3$  (to 1300°C) but must be kept from reacting with air, so a  $\text{N}_2$  ambient was used in the tube furnace. Each sample was covered with about a 5 mm thick layer of  $\text{B}_2\text{O}_3$ . Gaseous phosphorus could be observed emanating from the samples shortly after they were introduced into the furnace. After heating, the samples were removed from the furnace and dropped into boiling water to remove the  $\text{B}_2\text{O}_3$ . Usually the surface of the samples was spalled to a depth of around 20 mils by adhering  $\text{B}_2\text{O}_3$ .

Samples were subsequently thinned and polished to 15 mils thickness for above gap (4880Å) and below gap (5682Å) photoluminescence measurements (at room temperature), from which the minority carrier lifetimes and internal red photoluminescence quantum efficiencies were obtained. This measurement technique has been described explicitly elsewhere (7).

### Results

Figure 1a shows the time dependence of heat-treatment at 1200°C on the reciprocal minority carrier lifetime for a seed-end slice and a tail-end slice of LEC grown GaP(Zn,O). In Fig. 1b and c we show the same effect for temperatures of 1300° and 1152°C, respectively, on tail-end slices. It is seen that heat-treatment significantly increases minority carrier lifetime.

In order to determine whether this lifetime change occurs uniformly throughout the crystal two cubes,

1/4 and 1/8 in. on a side, were cut from an LEC slice with the cube centers equidistant from the center of the slice. These cubes were heat-treated together at 1200°C for 2 days. This time period was chosen since it is short compared to the time required for a 1/4 in. thick sample to approach a limiting minority carrier lifetime ( $\approx 16$  days, Fig. 1a). The minority carrier lifetime at the center of both cubes increased by a factor of 2.4. If we assume that this lifetime change occurs by diffusion of trapping centers to the crystal surface, then the three-dimensional solution (8) for diffusion out of a 1/8 in. cube with the surface boundary conditions set by the limiting minority carrier lifetime gives a value of  $3 \times 10^{-8}$   $\text{cm}^2\text{-sec}^{-1}$  for the diffusion coefficient. Using this value to calculate the lifetime change to be expected at the center of the larger cube we find that there should be a negligible change for the same period of time. Since, in fact, the change is the same we assume that the minority carrier lifetime increase with annealing occurs mainly by diffusion of electron trapping centers to internal sinks rather than by diffusion to the surface.

A simple model for diffusion of centers to internal sinks would provide the following equation for the time dependence of minority carrier lifetime ( $\tau_m$ ) on heat-treatment (9)

$$(1/\tau_m - 1/\tau_{m,0}) / (1/\tau_{m,i} - 1/\tau_{m,0}) \approx e^{-t/\tau_a} \quad [1]$$

where  $\tau_{m,i}$  and  $\tau_{m,0}$  are the initial and temperature-limiting values of the minority carrier lifetime,  $\tau_a$  is the relaxation time which depends on the diffusion coefficient of the center and the geometry and density of sinks. The electron capture rate ( $1/\tau_m$ ) is actually a summation of rates for electron capture by zinc-oxygen (Zn,O), isolated oxygen on phosphorus sites ( $\text{O}_P$ ), and nonradiative trapping centers. However, the low photoluminescence quantum efficiencies of these samples, even after heat-treatment ( $< 0.10\%$ ), indicates that the capture rate by the radiative centers ( $\text{O}_P$  and Zn-O) is small compared to that by nonradiative centers. Thus we can take the measured electron capture rate as a quantity proportional to the concentration of nonradiative trapping centers.

In Fig. 2a, we show the results for heat-treatment at 1152° and 1200°C, and in Fig. 2b for heat-treatments at 1300°C when plotted in accordance with Eq. [1]. The agreement seems sufficient to assume a mechanism of the kind described above. The scatter probably reflects differences in initial trapping center concentration and sink density for each of the sections cut from an as-grown slice used in a heat-treatment run. The values for  $1/\tau_{m,i}$ ,  $1/\tau_{m,0}$ , and  $1/\tau_a$  for isothermal heat-treatment at the three temperatures are summarized in Table I. With this data, in Fig. 3, a plot of  $1/\tau_a$  vs.  $1/T$  is used to obtain an activation energy of  $6.2 \pm 0.5$  eV for the annealing process.

Below gap (5682Å excited) photoluminescence spectra taken before and after heat-treatment can be used for determining relative changes in concentration of zinc-paired and unpaired oxygen (7). In this study the spectra can be directly compared, since it was found that heat-treatment does not significantly: (i) change the absorption characteristics of the samples within the wavelength region of excitation and emission (5,682-10,000Å), (ii) change the hole (p) concentration (as evidenced by no significant change in absorption at 10,000Å), and (iii) decrease the nonradiative center concentration to a level where radiative centers can compete in the retrapping of thermalized electrons. In Fig. 4a below gap (5682Å excited) photoluminescence spectra are shown for seed-end samples before and after annealing at 1200°C for 15 days. Similar spectra for the tail-end samples are shown in Fig. 4b. Taking the ratio of peak heights before and after heat-treatment for both the Zn-O exciton band (at 7000Å) and the  $\text{O}_P$  free-to-bound band (at 9200Å) as measures of the change in Zn-O and  $\text{O}_P$  concentrations we find that the result of heat-treatment is to produce

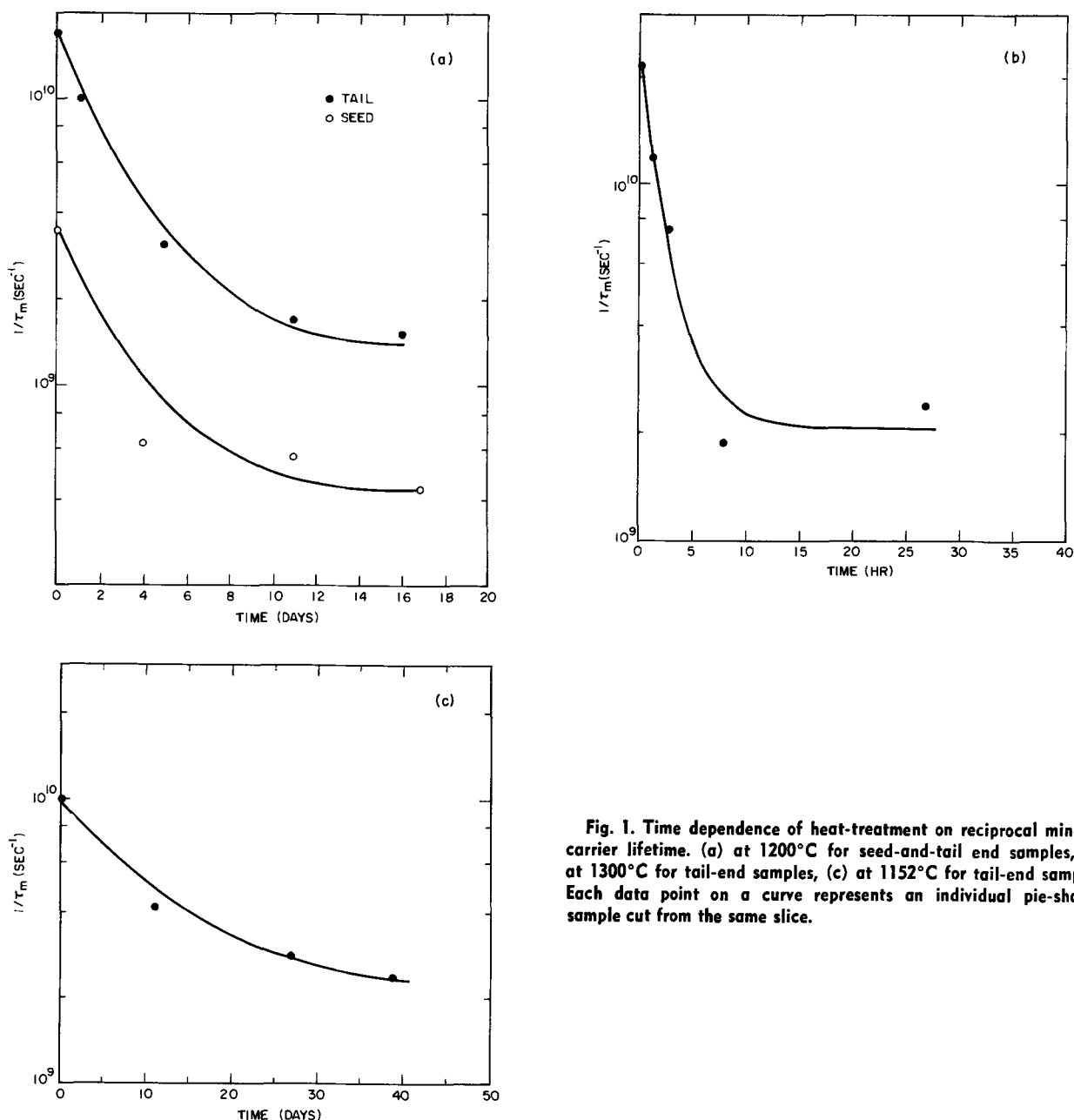


Fig. 1. Time dependence of heat-treatment on reciprocal minority carrier lifetime. (a) at 1200°C for seed-and-tail end samples, (b) at 1300°C for tail-end samples, (c) at 1152°C for tail-end samples. Each data point on a curve represents an individual pie-shaped sample cut from the same slice.

a significant increase in concentration of isolated substitutional oxygen ( $O_P$ ) in the seed-end samples (Fig. 4a), and no change in the tail-end samples (Fig. 4b). The slight decrease in Fig. 4b is within the  $\pm 20\%$  variation we normally found in samples cut from a single slice of GaP. Further, by taking into account the hole ( $p$ ) dependence of the radiative efficiencies of the Zn-O exciton band and the  $O_P$  free-to-bound band, one may also compare the concentrations of  $O_P$  and Zn-O pairs in the seed-end and tail-end samples (7, 10). These results are shown in Table II. We can conclude that the 1200°C heat-treatment brings the seed-end  $O_P$  concentration up to the same level as in the tail-end samples. The lower Zn-O pair concentration in the seed-end slice, when compared to the tail-end

slice after heat-treatment, reflects the lower Zn (hole) concentration in the seed end.

In addition to high temperature annealing experiments which were concerned with the reduction of nonradiative centers in LEC(GaP), a lower temperature heat-treatment range was studied with respect to reformation of Zn-O pairs dissociated at the high temperatures, and possible association of nonradiative trapping centers with another specie. Accordingly, two seed-end samples were treated using a schedule of one day at 1300°C followed by five days at 1200°C (from the kinetic data this anneal has been calculated to be equivalent to 16 days at 1200°C, see Fig. 1a). One sample was then removed and plunged into boiling water. The remaining sample was furnace cooled to

Table I. Effect of heat-treatment on reciprocal minority carrier lifetime

Sample	Heat-treat. temp (°C)	$1/\tau_{m,1}$ (sec <sup>-1</sup> )	$1/\tau_{m,\infty}$ (sec <sup>-1</sup> )	$\tau_a$ (hr)
Tail-end slice	1152	$1.0 \times 10^{10}$	$2.2 \times 10^9$	238
Tail-end slice	1200	$1.7 \times 10^{10}$	$1.4 \times 10^9$	60.5
Seed-end slice		$3.5 \times 10^9$	$4.2 \times 10^8$	
Tail-end slice	1300	$2.1 \times 10^{10}$	$2.1 \times 10^9$	2.1

Table II. Effect of 1200°C heat-treatment on luminescence center concentrations in LEC-GaP (Zn,O)

Sample	Hole conc. (cm <sup>-3</sup> )	$N_{Zn,O}$ relative	$N_{O_P}$ relative
Seed, as-grown	$4 \times 10^{17}$	4.6	8.2
Seed, heat-treated	$4 \times 10^{17}$	10.4	85
Tail, as-grown	$2 \times 10^{18}$	106	132
Tail, heat-treated	$2 \times 10^{18}$	46	87

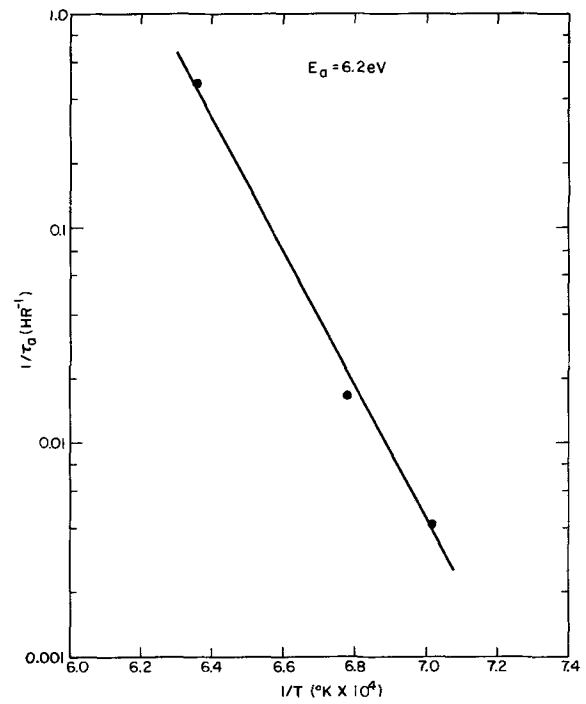
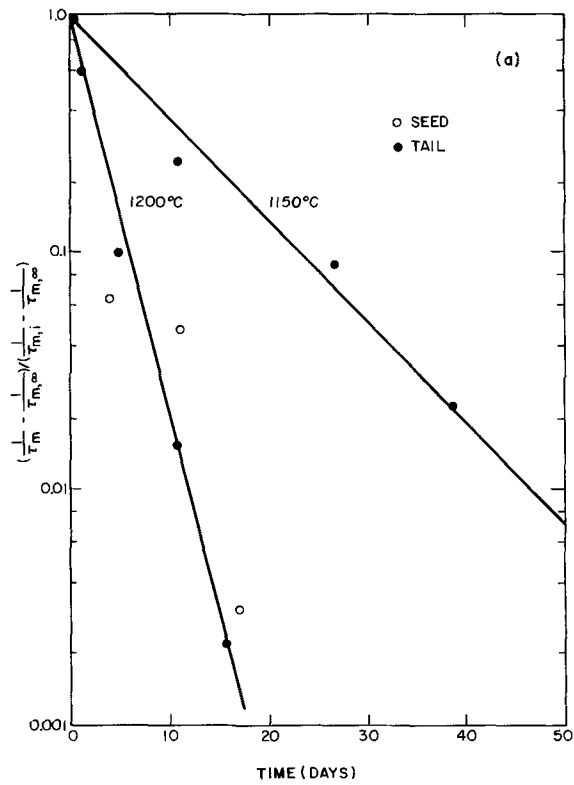


Fig. 3. An Arrhenius plot of the reciprocal relaxation time at the heat-treatment temperatures 1152°, 1200°, and 1300°C.

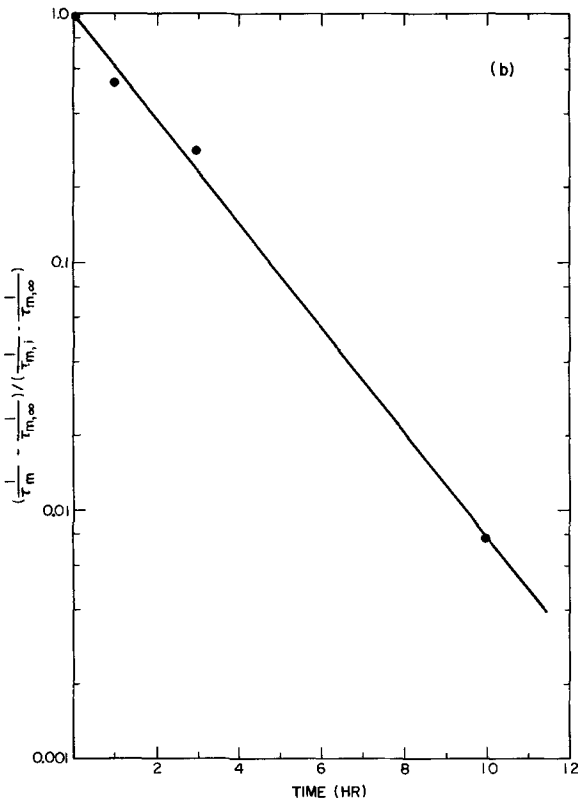


Fig. 2. The equilibrium annealing data at (a) 1152° and 1200°C and at (b) 1300°C plotted in accordance with Eq. [1].

500°C at a rate of 15°C/hr, then removed, and immersed in boiling water. The effect of these differing heat-treatments on minority carrier lifetime and internal above gap red photoluminescence quantum efficiency,  $\eta_{red}$ , is presented in Table III, which shows that slow cooling from the equilibrated 1200°C condition produces a factor of 2 increase in  $1/\tau_m$  and a factor of 15 increase in  $\eta_{red}$  (Table III-C) over the quenched sample (Table III-B). Moreover, the effect of heat-treatment B on the increase in minority carrier life-

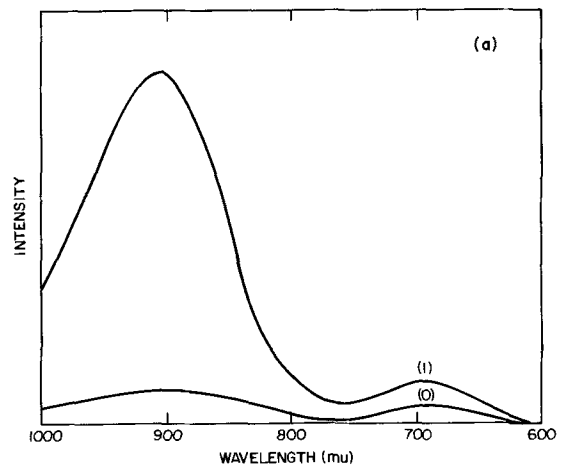


Fig. 4(a). Below gap (5628Å excited) photoluminescence spectra for a seed-end sample (curve 0) as-grown, and (curve 1) heat-treated at 1200°C for 17 days. (Uncorrected for detector response.)

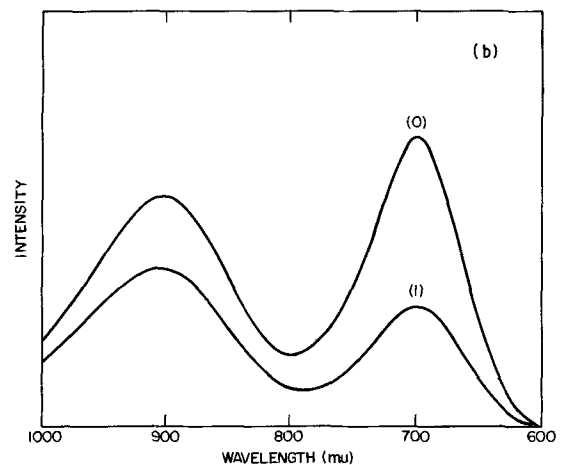


Fig. 4(b). Below gap (5682Å excited) photoluminescence spectra for a tail-end sample (curve 0) as-grown, and (curve 1) heat-treated 1200°C, 16 days. (Uncorrected for detector response.)

Table III. Effect of 15°C/hr cool down to 500°C on red photoluminescence efficiency and reciprocal minority carrier lifetime of heat-treated LEC-GaP(Zn,O)

Heat-treatment conditions	$1/\tau_m$ (sec <sup>-1</sup> )	$\eta_{red}(\%)$
A. As-grown	$3.5 \times 10^9$	0.0015
B. 1 day at 1300°C, 5 days at 1200°C, immersed in H <sub>2</sub> O	$3.0 \times 10^8$	0.030
C. 1 day at 1300°C, 5 days at 1200°C, 1200°C → 500°C at 15°C/hr, immersed in H <sub>2</sub> O	$1.6 \times 10^8$	0.45

Table IV. Effect of variation in rate of cooling down from 1200° to 500°C on red photoluminescence efficiency and reciprocal minority carrier lifetime of high temperature heat-treated LEC-GaP(Zn,O)

Crystal slice	p (cm <sup>-3</sup> )	Cool down rate (°C/hr)	$\eta_{red}(\%)$	$1/\tau_m \approx 1/\tau_n$ (sec <sup>-1</sup> )
A	$1.6 \times 10^{17}$	15	1.0	$1.0 \times 10^8$
B <sub>1</sub>	$4.0 \times 10^{17}$	2.5	0.33	$2.7 \times 10^8$
B <sub>2</sub>	$4.0 \times 10^{17}$	15	0.45	$1.6 \times 10^8$
C <sub>1</sub>	$7.5 \times 10^{17}$	2.5	0.13	$2.7 \times 10^8$
C <sub>2</sub>	$7.5 \times 10^{17}$	50	0.18	$3.0 \times 10^8$
D <sub>1</sub>	$8.0 \times 10^{17}$	2.5	0.56	$2.9 \times 10^8$
D <sub>2</sub>	$8.0 \times 10^{17}$	50	0.13	$3.6 \times 10^8$
E <sub>1</sub>	$8.0 \times 10^{17}$	2.5	0.60	$2.1 \times 10^8$
E <sub>2</sub>	$8.0 \times 10^{17}$	50	0.65	$4.0 \times 10^8$

time is comparable to annealing 16 days at 1200°C (See Fig. 1a).

We can further elaborate on these changes with the use of below gap photoluminescence spectra which are shown in Fig. 5. Note that the spectra a (as grown) and b (heat-treatment B), which are similar to those in Fig. 4a, show an increase in the O<sub>P</sub> band (9200Å) with high temperature annealing. However, as the sample is now cooled to 500°C (spectra c) the O<sub>P</sub> band decreases and the Zn-O band (7000Å) increases due to the pairing up of oxygen with available zinc to produce additional Zn-O pairs. With the data from Table III and the spectra from Fig. 5, we can explain the ~20× increase in  $\eta_{red}$  with heat-treatment B as being due to ~10× decrease in  $1/\tau_m$  and a ~2× increase in Zn-O pairs. Then, cooling from 1200° to 500°C (condition C) yields an additional ~15× increase in  $\eta_{red}$  of which ~7× can be ascribed to the increased Zn-O pairing and 2× to a decrease in  $1/\tau_m$ , which may be due to a pairing of the trapping center with another specie.

Table IV shows the effect of varying the cooling rate upon both  $\eta_{red}$  and  $1/\tau_m$ . Slices taken from the different crystals were equilibrated at 1200°C and then cooled to 500°C at rates of 2.5°, 15°, 50°C/hr. The slower

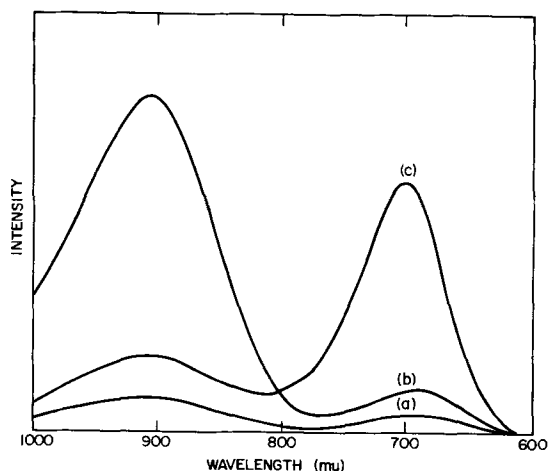


Fig. 5. Below gap (5682Å excited) photoluminescence spectra for a seed-end sample of LEC GaP(Zn,O) (curve a) as-grown, (curve b) after heat-treatment B, (curve c) after heat-treatment C. (Uncorrected for detector response.)

cooling rate is only slightly more effective (at most a factor of 2) in decreasing  $1/\tau_m$ , which suggests that this additional mechanism for increasing the minority carrier lifetime is a relatively fast process having a low activation energy. Similarly, there is no significant trend in  $\eta_{red}$  with variation of the 1200°-500°C cooling rate. The scatter in the  $\eta_{red}$  data may reflect the different initial oxygen concentrations among the various crystals from which these samples were taken. The Ga<sub>2</sub>O<sub>3</sub> additions to the melt varied by as much as a factor of three among these crystals.

### Discussion of Results

It has been suggested that the major nonradiative electron trapping center in GaP(Zn, O) is a gallium vacancy or a gallium vacancy associated complex (4). This conclusion resulted from the observation that in crystals grown from 1465° to 1200°C the computed Ga vacancy concentration (which changes by two orders of magnitude) is linear with the measured nonradiative center concentration. The computed P vacancy concentration change over this temperature interval is no more than a factor of two. More recently the solidus boundary of GaP has been constructed by a coulometric titration technique for determining the gallium content of crystals grown at various temperatures (11). The gallium content of an LEC crystal heat-treated at 1200°C until the minority carrier lifetime approached its limiting value increased from 50.0104 to 50.0163%. These values are in close agreement with the solidus composition at 1465° and 1200°C indicating (i) that the depletion of trapping centers is coincident with the depletion of Ga-vacancies and (ii) that when the Ga-vacancy concentration has decreased to its equilibrium value, the trapping center concentration no longer decreases. This result provides additional evidence for our identification of the nonradiative trapping centers with Ga vacancies.

The fact that the decrease in Ga vacancy concentration occurs more rapidly by LEA heat-treatment than by heat-treatment in saturated Ga-GaP solutions, and further that the decrease is uniform, suggests that vacancy equilibration occurs by different mechanisms. In the LEA case, the crystal rapidly loses phosphorus which could leave in the bulk a network of internal gallium sources or equivalently gallium vacancy sinks. Equilibration could then occur mainly by the diffusion of Ga vacancies to these sinks. In the case of crystals annealed in contact with a GaP-Ga saturated solution a phosphorus pressure is quickly established in the gas phase through dissolution of the powdered GaP in Ga. The bulk composition of the crystal is left relatively unaltered and equilibration would occur mainly by diffusion of Ga vacancies to the surface.

The activation energy obtained from the heat-treatment results,  $6.2 \pm 0.5$  eV, can be equated with the activation energy for Ga vacancy diffusion in GaP. This quantity has not been reported in the literature. With the addition of 1.4 eV (11) for the enthalpy of Ga vacancy formation in GaP we obtain a Ga self-diffusion activation energy of 7.6 eV, which can be compared with values of 5.6 (12) and 3.15 (13) eV for GaAs and GaSb, respectively. This trend, which follows the decrease in melting points (1740°, 1511°, and 979°K) and bandgaps (2.2, 1.4, and 0.72 eV), appears reasonable since the Ga self-diffusion activation energy must be related to bonding strengths of the constituent atoms.

Evidence has been reported for the existence in GaP of a complex center consisting of a Ga vacancy associated with an oxygen atom on a phosphorus site (14, 15). Furthermore, this complex, V<sub>Ga</sub>-O<sub>P</sub>, is almost completely dissociated above ~1100°C. This information can be used to explain the additional decrease in  $1/\tau_m$  obtained by slow cooling from 1200° to 500°C (Table III). The low temperature heat-treatment permits some of the Ga vacancies, already decreased by the high temperature treatment, to pair

up with substitutional oxygen, thus decreasing the killer center density.

The existence of  $V_{Ga}-O_P$  pairing can also be used to explain the seed-to-tail variation in isolated substitutional oxygen concentration in as-grown LEC-GaP(Zn, O), and its subsequent elimination on high temperature heat-treatment. The already pulled portion of an LEC crystal undergoes some annealing during the pulling operation and can see temperatures below  $\sim 1100^\circ\text{C}$ , whereas the tail end is essentially quenched at a temperature much closer to the growth temperature. Therefore we could expect a seed-to-tail decrease in  $V_{Ga}-O_P$  pairs and as a result a seed-to-tail increase in isolated substitutional oxygen. High temperature heat-treatment would then eliminate this gradient by breaking up the  $V_{Ga}-O_P$  pairs preferentially formed in the seed end.

One can compare the rate of electron capture by nonradiative centers ( $1/\tau_n$ ) in SG GaP(Zn, O) with that in the heat-treated LEC crystals ( $1/\tau_m \approx 1/\tau_n$ ) GaP(Zn, O). It has been found that in SG material  $1/\tau_n$  is linearly dependent on hole concentration. For crystals grown over a temperature interval of  $1140^\circ\text{--}900^\circ\text{C}$  with hole concentrations ranging from  $1.6$  to  $8 \times 10^{17} \text{ cm}^{-3}$ ,  $1/\tau_n$  ranges from  $\sim 0.7$  to  $4 \times 10^8 \text{ (sec}^{-1}\text{)}$  (16). We find that the measured values for the heat-treated crystals (see Table IV) also fall in this range. The agreement cannot be expected to be exact insofar as the thermal histories of the SG material and the LEC heat-treated crystals are not the same.

A comparison of the above gap red photoluminescence efficiencies of the LEA-LEC crystals with the same SG crystals shows that the efficiencies of the SG crystals are higher by approximately a factor of four over the same zinc-doping range. Since the rates of electron capture by nonradiative centers in the two sets of crystals are approximately the same, the lower efficiency in the LEC heat-treated crystals results from a lower zinc-oxygen pair concentration. In general, the total oxygen concentration in LEC crystals ( $\approx 2 \times 10^{18} \text{ cm}^{-3}$ ) (6) as well as the  $O_P$  concentration ( $\approx 5 \times 10^{16} \text{ cm}^{-3}$ ) (2) is found to be lower than the respective values ( $\approx 2 \times 10^{19} \text{ cm}^{-3}$ ) (6) and ( $\approx 1 \times 10^{17} \text{ cm}^{-3}$ ) (16) in SG material. This could in part account for the lower Zn-O pair concentration in the LEC heat-treated samples.

### Conclusion

The high activation energy, 6.2 eV for Ga vacancy diffusion in GaP implies that the vacancies are essentially frozen in at the growth temperature equilibrium concentration. Therefore the smaller  $\eta_{\text{red}}$  of LEC GaP(Zn, O) when compared to material grown at a lower temperature is due to a higher concentration of Ga vacancies which act as very effective nonradiative electron trapping centers. The marked tail-to-seed de-

crease in Zn-O concentration results from additional pairing of oxygen with Ga vacancies in the seed end which undergoes partial annealing during growth. High temperature ( $1300^\circ\text{--}1200^\circ\text{C}$ ) LEA heat-treatment (for removal of Ga vacancies) and low temperature heat-treatment (for pairing of Zn with O) can be used to increase the  $\eta_{\text{red}}$  of an entire LEC grown crystal to about 1%. At this level this material may be suitable for a single n on p epitaxial growth technique for LED fabrication.

### Acknowledgment

The authors wish to thank L. J. Oster for his excellent technical assistance with the annealing treatments, S. Knight and J. W. Nielsen for their encouragement throughout the course of the work and for review of the manuscript, and A. S. Jordan for many helpful discussions.

Manuscript submitted Feb. 28, 1973; revised manuscript received Feb. 18, 1974. This was Paper 48 presented at the Chicago, Illinois, Meeting of the Society, May 13-18, 1973.

Any discussion of this paper will appear in a Discussion Section to be published in the June 1975 JOURNAL. All discussions for the June 1975 Discussion Section should be submitted by Feb. 1, 1975.

The publication costs of this article have been assisted by Bell Laboratories.

### REFERENCES

1. R. Caruso, M. DiDomenico, Jr., H. W. Verleur, and A. R. Von Neida, *J. Phys. Chem. Solids*, **33**, 689 (1972).
2. R. H. Saul, J. Armstrong, and W. H. Hackett, Jr., *Appl. Phys. Letters*, **15**, 229 (1969).
3. A. R. Von Neida, L. J. Oster, and J. W. Nielsen, *J. Crystal Growth*, **13/14**, 647 (1972).
4. A. S. Jordan, A. R. Von Neida, R. Caruso, and M. DiDomenico, Jr., *Appl. Phys. Letters*, **19**, 394 (1971).
5. A. Y. Cho and I. Hayashi, *Solid State Electron.*, **14**, 125 (1971).
6. C. K. Kim, *J. Appl. Phys.*, **45**, 243 (1974).
7. R. Caruso, *ibid.*, **42**, 5055 (1971).
8. H. S. Carslaw and J. C. Jaeger, "Conduction of Heat in Solids," Clarendon Press, Oxford (1959).
9. J. Bauerle and J. Koehler, *Phys. Rev.*, **107**, 1493 (1957).
10. J. M. Dishman, M. DiDomenico, Jr., and R. Caruso, *ibid.*, **B2**, 1988 (1970).
11. A. S. Jordan, A. R. Von Neida, R. Caruso, and C. K. Kim, *This Journal*, **121**, 153 (1974).
12. B. Goldstein, *Phys. Rev.*, **121**, 1305 (1961).
13. F. H. Eisen and C. E. Birchenall, *Acta. Met.*, **5**, 265 (1957).
14. P. J. Dean, *Phys. Rev.*, **B4**, 2596 (1971).
15. P. J. Dean, *Solid State Comm.*, **9**, 2211 (1971).
16. A. S. Jordan, L. Derick, R. Caruso, and M. Kowalchik, *This Journal*, **119**, 1585 (1972).

# Energy Transfer Between $\text{Pb}^{2+}$ and $\text{Eu}^{3+}$ in Germanate Glass

R. Reisfeld and N. Lieblich

Department of Inorganic and Analytical Chemistry, The Hebrew University of Jerusalem, Jerusalem, Israel

## ABSTRACT

Energy transfer from  $\text{Pb}^{2+}$  to  $\text{Eu}^{3+}$  in germanate glass was detected from the increase of  $\text{Eu}^{3+}$  fluorescence on excitation via  $\text{Pb}^{2+}$ . It was found that the transfer is mostly nonradiative, with a small radiative contribution. Probabilities of transfer were calculated from experimental fluorescence data.

Sensitization of fluorescence by energy transfer is potentially of great importance in increasing laser efficiency. In several recent papers (1-3) the advantage of germanate glass as a laser host material was emphasized.

It is the purpose of this work to investigate energy transfer in a germanate glass system in which  $\text{Pb}^{2+}$  serves as a donor and  $\text{Eu}^{3+}$  as an acceptor.

Transfer of energy can occur by nonradiative or radiative means. The first theories for nonradiative transfer were given by Förster (4). Dexter (5) extended the theory of Förster for multipolar interactions. The transfer probabilities of electric dipole or quadrupole are proportional to  $R^{-6}$  and  $R^{-8}$ , respectively, when  $R$  is the separation of the two ions. Another nonradiative mechanism is that of spin exchange, which is supposed to be effective only between the nearest neighbors. The radiative transfer occurs when light emitted by the donor is absorbed by the acceptor and reemitted as its fluorescence. A review on energy transfer between rare-earth ions in glasses can be found in Ref. (6). The conditions necessary for an efficient energy transfer to occur are high cross section of light absorption of the donor, and a good overlap between donor emission and the acceptor absorption. A narrow emission band is required for laser materials. These demands are fulfilled in the  $\text{Pb}^{2+}$ - $\text{Eu}^{3+}$  system.

## Experimental

The materials from which germanate glasses of final composition  $17\text{K}_2\text{O}\cdot 17\text{BaO}\cdot 66\text{GeO}_2$  mole per cent (m/o) (7) were prepared, were:  $\text{GeO}_2$  Fluka Buchs 99.999%;  $\text{K}_2\text{O}_3$  Mallinckrodt;  $\text{BaCO}_3$  Baker Analyzed. The  $\text{Eu}^{3+}$  added to the glass was  $\text{Eu}_2\text{O}_3$  Molycorp 99.9% and the  $\text{Pb}^{2+}$  was  $\text{PbO}$  of B.D.H.

Five series of glasses of the following compositions were prepared:

1.  $\text{Eu}^{3+}$  1,2,3,5,7 weight per cent (w/o)
2.  $\text{Pb}^{2+}$  0.5,1,1.5 w/o
3.  $\text{Pb}^{2+}$  0.5% and  $\text{Eu}^{3+}$  1,2,3,5,7 w/o
4.  $\text{Pb}^{2+}$  1% and  $\text{Eu}^{3+}$  1,2,3,5,7 w/o
5.  $\text{Pb}^{2+}$  1.5% and  $\text{Eu}^{3+}$  1,2,3,5,7 w/o

The glasses were prepared by mixing the materials in an electric vibrator for 10 min and then melting them at  $1250^\circ\text{C}$  for 12 hr in Pt crucibles. Glass disks 1 mm thick and 12 mm in diameter were prepared by molding the melt on a tile.

Emission and excitation spectra were obtained by using a xenon light source and a spectrofluorimeter built in our laboratory (8).

Decay time of  $\text{Pb}^{2+}$  fluorescence was measured<sup>1</sup> by a pulse of 10 nsec duration from a  $\text{N}_2$  laser of  $\lambda$  3371Å. All measurements were taken at room temperature.

## Results

The absorption and emission spectra of  $\text{Eu}^{3+}$  in germanate glass were described in Ref. (2) and those of  $\text{Pb}^{2+}$  in Ref. (9).

**Key words:** fluorescence europium, fluorescence lead, lead germanate glasses, europium germanate glasses.

<sup>1</sup> We acknowledge the help of Mr. Gilyora Doytsch for these measurements.

The evidence for the energy transfer between  $\text{Pb}^{2+}$  and  $\text{Eu}^{3+}$  can be seen; (a) in the excitation and emission spectra of  $\text{Eu}^{3+}$ , (b) in the emission spectrum of  $\text{Pb}^{2+}$ , and (c) in the fluorescent lifetime of  $\text{Pb}^{2+}$ .

Figure 1 compares an excitation spectrum of  $\text{Eu}^{3+}$  only and  $\text{Eu}^{3+}$  in the presence of  $\text{Pb}^{2+}$ . The excitation is monitored at  $^5\text{D}_0 \rightarrow ^7\text{F}_2$  transition of  $\text{Eu}^{3+}$  at 612 nm. In the glasses doped both by  $\text{Pb}^{2+}$  and  $\text{Eu}^{3+}$ , an additional band peaking at 317 nm appears. This band is characteristic of the excitation of  $\text{Pb}^{2+}$  in germanate glass (9).

Figure 2 represents the emission spectrum of  $^5\text{D}_0 \rightarrow ^7\text{F}_2$  of  $\text{Eu}^{3+}$  excited at 317 nm in two glasses; one containing  $\text{Eu}^{3+}$  only and the other  $\text{Eu}^{3+}$  and  $\text{Pb}^{2+}$ . A fivefold increase in the emission intensity of  $\text{Eu}^{3+}$  is observed as a result of coexistence with  $\text{Pb}^{2+}$ . The results of the increase of  $\text{Eu}^{3+}$  fluorescence in singly

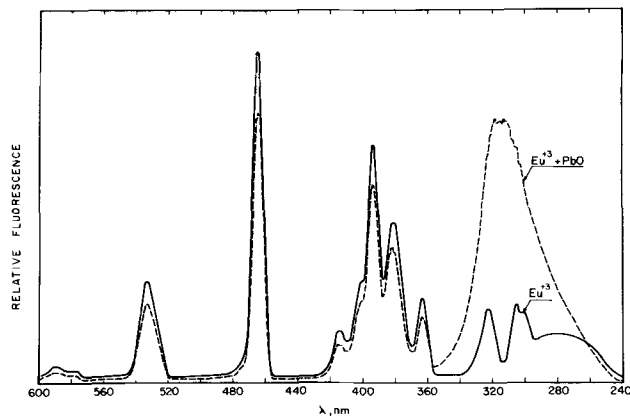


Fig. 1. Excitation spectrum of  $\text{Eu}^{3+}$  in germanate glass monitored at  $^5\text{D}_0 \rightarrow ^7\text{F}_2$  (612 nm).

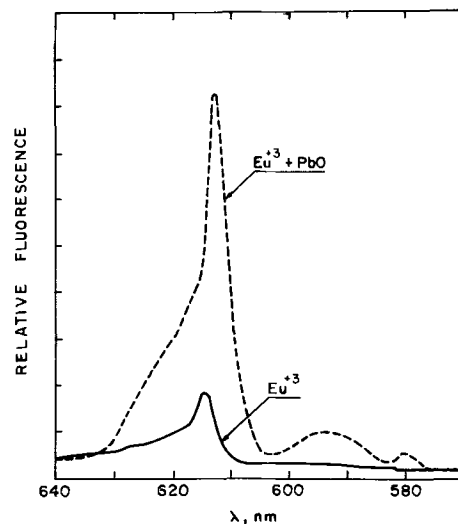


Fig. 2. Increase in the emission spectrum of  $\text{Eu}^{3+}$  in the presence of  $\text{Pb}^{2+}$ . Excitation at 317 nm.

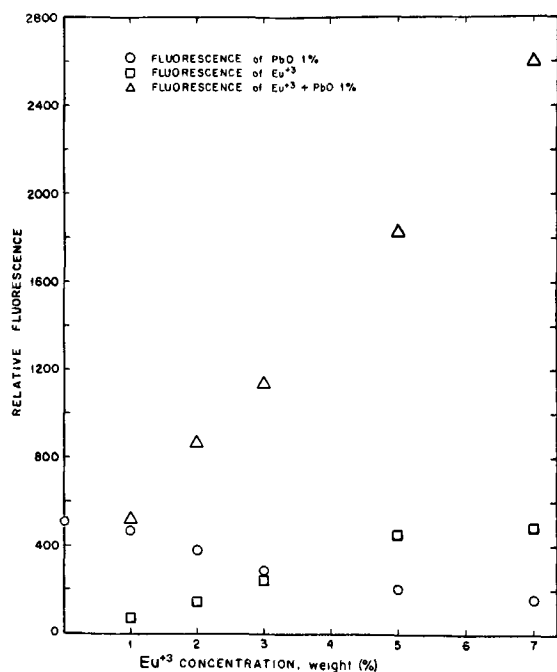


Fig. 3. Concentration dependence of fluorescence. □ 612 nm fluorescence of Eu<sup>3+</sup> in glasses doped by Eu<sup>3+</sup> only. △ 612 nm fluorescence of Eu<sup>3+</sup> in glasses doped by Eu<sup>3+</sup> and 1% w.p. Pb<sup>2+</sup>. ○ 430 nm fluorescence of 1 w/o Pb<sup>2+</sup>, as a function of Eu<sup>3+</sup> concentration.

and doubly doped glasses as a function of Eu<sup>3+</sup> concentration, are presented in Fig. 3. A decrease in Pb<sup>2+</sup> fluorescence in the presence of Eu<sup>3+</sup> is also demonstrated in this figure. As the Eu<sup>3+</sup> concentration increases, the Pb<sup>2+</sup> fluorescence decreases. Intensity data for three series each containing a constant concentration of Pb<sup>2+</sup>, and a varied concentration of Eu<sup>3+</sup>, are summarized in Table I.

In the fluorescence decay curves of Pb<sup>2+</sup> two components are observed: a short lifetime of 10<sup>-8</sup> sec and a long lifetime of 10<sup>-7</sup> sec. The explanation for the existence of two components in the lifetime of mercury-like ions can be found in Ref. (10). In the presence of Eu<sup>3+</sup> both components are shortened; their values are given in Table II.

Calculations were made for energy transfer probabilities and efficiency by using the following formulas (11).

The efficiency of energy transfer can be expressed by

Table I. Increase of Eu<sup>3+</sup> fluorescence in presence of Pb<sup>2+</sup> and decrease of Pb<sup>2+</sup> fluorescence in presence of Eu<sup>3+</sup>. R.F. is the relative fluorescence

Eu <sup>3+</sup> (w/o)	Relative fluorescence, R.F., of Eu <sup>3+</sup>	0.5% Pb <sup>2+</sup> R.F. 333		1% Pb <sup>2+</sup> R.F. 515		1.5% Pb <sup>2+</sup> R.F. 648	
		ΔR.F. Eu <sup>3+</sup>	Pb <sup>2+</sup>	ΔR.F. Eu <sup>3+</sup>	Pb <sup>2+</sup>	ΔR.F. Eu <sup>3+</sup>	Pb <sup>2+</sup>
1	125	+220	-8	+405	-45	+308	-268
2	160	+362	-77	+764	-128	+779	-298
3	300	+620	-98	+870	-210	+1038	-364
5	430	+705	-177	+1380	-315	+1700	-443
7	443	+808	-235	+2432	-340	+2357	-492

Table II. Fluorescent lifetime of Pb<sup>2+</sup> in germanate glasses containing Pb<sup>2+</sup> only and Pb<sup>2+</sup> in presence of Eu<sup>3+</sup>

	τ, nsec	τ, nsec
1% Pb <sup>2+</sup>	29	260
1% Pb <sup>2+</sup> + 3% Eu <sup>3+</sup>	24	178
1% Pb <sup>2+</sup> + 7% Eu <sup>3+</sup>	20	104

$$\eta_t = 1 - (\eta/\eta_0) \quad [1]$$

where η<sub>0</sub> and η are the fluorescence yields of the donor alone, and the donor in the presence of an acceptor, respectively.

The probability for energy transfer can be expressed as

$$P = \frac{1}{\tau d} \left( \frac{\eta_0}{\eta} - 1 \right) \quad [2]$$

where τd is the radiative lifetime of the pure donor level from which energy transfer takes place. In this work the long lifetime of Pb<sup>2+</sup> was taken.

The mean distance between the ions was calculated by

$$R = \sqrt[3]{1/C_t} \quad [3]$$

where C<sub>t</sub> is the sum of Pb<sup>2+</sup> and Eu<sup>3+</sup> ions in 1 cm<sup>3</sup> glass.

These results are given in Table III.

Discussion

As seen from the experimental results, the fluorescence intensity of germanate glass doped by Eu<sup>3+</sup> can be increased by energy transfer from Pb<sup>2+</sup>. Possibility of excitation of Eu<sup>3+</sup> by energy transfer at 317 nm is especially important in germanate glasses, since the charge transfer band of Eu<sup>3+</sup> lies in a region where the host glass absorbs, and therefore it cannot be used for excitation of Eu<sup>3+</sup>.

The mechanism of the transfer in the system studied occurs both by radiative and nonradiative modes. The nonradiative transfer can be seen from the decrease of the donor's lifetime and the total decrease of Pb<sup>2+</sup> emission. The radiative transfer can be seen from the dips in the envelope of the emission curve of Pb<sup>2+</sup> in the presence of Eu<sup>3+</sup>, in wavelengths at which Eu<sup>3+</sup> has the highest absorption: 394 nm and 464 nm, Fig. 4. The relative amount of the two modes can roughly be obtained by comparing the difference between the emission spectrum of Pb<sup>2+</sup> alone and Pb<sup>2+</sup> with Eu<sup>3+</sup>, to the area of the "dips" in the emission curve caused by the direct absorption of Eu<sup>3+</sup>.

The mechanism of multipolar nonradiative transfer between two rare-earth ions was obtained by us (11-14) from the dependence of the transfer probability P on the power of the dopants' concentration. A straight line was obtained when P was plotted against C<sub>t</sub><sup>6/3</sup> in cases of transfer between Gd<sup>3+</sup>-Tb<sup>3+</sup>, Gd<sup>3+</sup>-Sm<sup>3+</sup>, and Tm<sup>3+</sup>-Er<sup>3+</sup>, indicating a dipole-dipole mechanism, and against C<sub>t</sub><sup>8/3</sup> in Sm<sup>3+</sup>-Eu<sup>3+</sup> in dipole-quadrupole mechanism. In this work a straight line is obtained when values of P are plotted against the first power of C<sub>t</sub>. Such dependence does not fit the classical theory of multipolar interactions. Recently, Fong and Diestler (15) proposed a mechanism for a nonradiative energy transferred between ions in crystals by a many body process in which a prediction is made for a linear dependence of energy transfer rate on concentration. Our experimental results are in accordance with this theory. The difference between the concentration dependence found in this work and in our previous work may be attributed to: (i) the higher concentration of the dopants which could be due to the higher dissolving property of the germanate glass (the upper limit

Table III. Energy transfer probabilities P and transfer efficiencies η<sub>t</sub> as a function of the concentration of donor and acceptor. C<sub>t</sub> expressed in number of ions per cubic centimeter. R is the mean distance in angstroms between the ions

1% Pb <sup>2+</sup> + Eu <sup>3+</sup> (w/o)	C <sub>t</sub> × 10 <sup>20</sup>	R(Å)	η <sub>t</sub>	P × 10 <sup>8</sup>
1	2.6	15.7	0.09	3.3
2	4.1	13.5	0.25	11.4
3	5.6	12.1	0.41	23.7
5	8.6	10.5	0.59	50.0
7	11.6	9.5	0.68	73.2

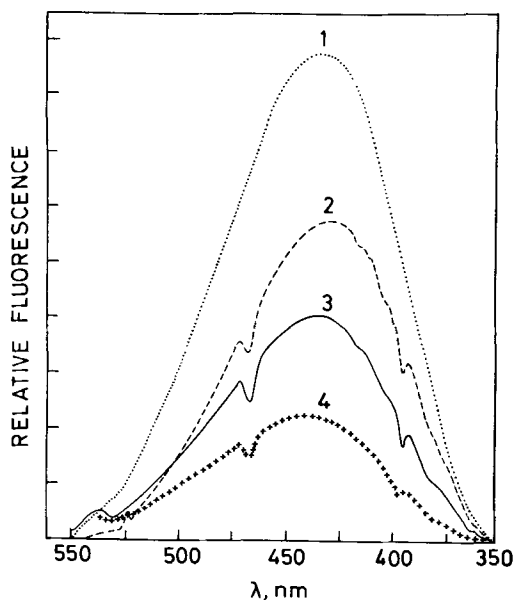


Fig. 4. Changes in the emission spectrum of  $Pb^{2+}$  as a result of energy transfer to  $Eu^{3+}$ . Curve 1, 1%  $Pb^{2+}$ ; curve 2, 1%  $Pb^{2+}$  + 3%  $Eu^{3+}$ ; curve 3, 1%  $Pb^{2+}$  + 5%  $Eu^{3+}$ ; curve 4, 1%  $Pb^{2+}$  + 7%  $Eu^{3+}$ .

of the activator concentration was 3.5 w/o in borate and phosphate glasses (11-14), while in germanate glasses a concentration of 7 w/o could be easily obtained), and (ii) the fact that the emission of the donor  $Pb^{2+}$  results from allowed transition and has a broad band which overlaps with several absorption bands of  $Eu^{3+}$ .

In conclusion, we have shown the existence of energy transfer between  $Pb^{2+}$  and  $Eu^{3+}$  in germanate glass and this can be utilized for sensitization of  $Eu^{3+}$  fluorescence. The exact mechanism via which the energy transfer takes place is still an open question.

#### Acknowledgment

The work reported in this paper was partially supported by the European Office of the United States Army Contract DAJA 37-73-C-1581.

Manuscript submitted Jan. 2, 1974; revised manuscript received April 22, 1974.

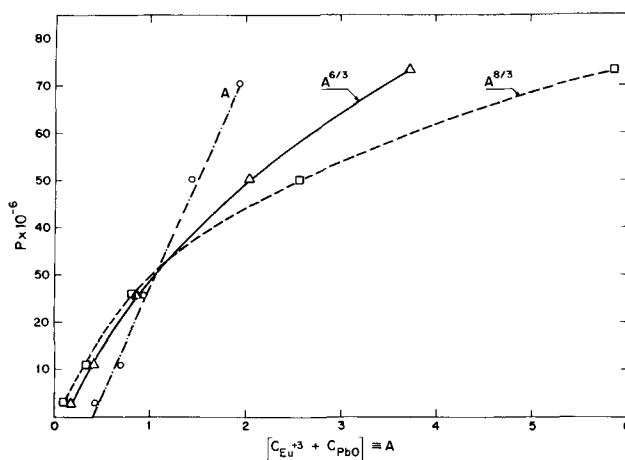


Fig. 5. Dependence of the transfer probability  $P$  on various powers of total concentration of donor and acceptor ions.

Any discussion of this paper will appear in a Discussion Section to be published in the June 1975 JOURNAL. All discussions for the June 1975 Discussion Section should be submitted by Feb. 1, 1975.

#### REFERENCES

1. C. Hirayama, F. E. Camp, N. T. Melamed, and K. B. Steinbruegge, *J. Non-crystalline Solids*, **6**, 342 (1971).
2. R. Reisfeld and N. Lieblich, *J. Phys. Chem. Solids*, **34**, 1467 (1973).
3. R. Reisfeld and Y. Eckstein, *J. Non-crystalline Solids*, **12**, 357 (1973).
4. Th. Forster, *Ann. Physik*, **2**, 55 (1948).
5. D. L. Dexter, *J. Chem. Phys.*, **21**, 836 (1953).
6. R. Reisfeld, *Structure and Bonding*, **13**, 53 (1972).
7. C. Hirayama and F. E. Camp, *This Journal*, **115**, 1275 (1968).
8. R. Reisfeld, A. Honigbaum, G. Michaeli, L. Harel, and M. Ish-Shalom, *Israel J. Chem.*, **7**, 613 (1969).
9. R. Reisfeld and N. Lieblich, *J. Non-crystalline Solids*, **12**, 207 (1973).
10. R. Reisfeld, *J. Res. Nat. Bur. Std.*, **76A**, 443 (1972).
11. R. Reisfeld, E. Greenberg, R. Velapoldi, and B. Barnett, *J. Chem. Phys.*, **56**, 1698 (1971).
12. R. Reisfeld, E. Greenberg, and E. Biron, *J. Solid State Chem.*, **9**, 224 (1974).
13. R. Reisfeld and Y. Eckstein, *J. Non-crystalline Solids*, **11**, 261 (1973).
14. R. Reisfeld and L. Boehm, *J. Solid State Chem.*, **4**, 417 (1972).
15. F. K. Fong and D. J. Diestler, *J. Chem. Phys.*, **56**, 2875 (1972).



# Enhanced Conversion of X-Rays into Visible Light in Thin Composite Layers (Composite Anthracene-PbCl<sub>2</sub> Screens)

W. Albers and L. A. H. van Hoof

Philips Research Laboratories, Eindhoven, Netherlands

## ABSTRACT

The absorption of x-rays by a solid organic phosphor can be enhanced to a great extent by the inclusion of a disperse second solid phase that consists of heavy atoms. In consequence the x-ray to visible light conversion can be enhanced by one or two orders of magnitude when using composite screens. Experiments on composite anthracene-PbCl<sub>2</sub> screens reveal an amplification factor of about 30. The experimental results are discussed and are compared with existing theories.

Since 1947 luminescent organic substances, such as anthracene, have been used as scintillators to detect high-energy particles and quanta, such as x-rays, and to measure their energy (1). An anthracene crystal converts x-rays into visible light near u.v. The luminescent radiation output depends on (i) the absorption of the x-rays, during which secondary electrons are released, that lose their energy by means of many processes, one of them being a transition of anthracene molecules from the ground state to excited states that can return to the ground state while emitting visible light of wavelengths between 400 and 470 nm, a process which consumes only a few per cent of the total energy of the secondary electrons (2), (ii) the absorption and scattering of the luminescent light, the scattering occurring both at the outer surfaces of the crystal and at internal interfaces, due to inhomogeneities such as grain boundaries, inclusions, and cracks.

The absorption coefficient of organic phosphors for x-rays is undesirably low due to the low density and to the low atomic number of the constituent atoms. By separating the functions of x-ray to secondary electron conversion and the secondary electron to visible light conversion [*i.e.*, using the concept of composite product properties (3)] the absorbed fraction of the incident x-rays can be enhanced to a great extent by the inclusion of a disperse second solid phase that (partially) consists of heavy atoms and consequently exhibits a high absorption coefficient for x-rays. The included phase does not need to be a phosphor, but it has to be transparent to the luminescent light of the matrix phase. At a given thickness of the composite layer and at a definite ratio of the volume fractions of the two phases, the x-rays (*e.g.*, of 100 keV energy) will be absorbed predominantly in the second phase releasing secondary electrons. These secondary electrons have a mean free path of the order of 10  $\mu\text{m}$  in the second phase and spend most of their range in the phosphor matrix if the heavy phase particles are substantially smaller than 10  $\mu\text{m}$ . They excite the phosphor matrix resulting in luminescent emission. In this way the x-ray to visible light conversion can be enhanced by more than an order of magnitude in an anthracene screen by the addition of finely dispersed PbCl<sub>2</sub> particles.

## Experimental

**Preparation.**—The expectations expressed above have been experimentally verified on the anthracene-PbCl<sub>2</sub> composite. PbCl<sub>2</sub> exhibits only a poor luminescence, has an energy bandgap of 3.85 eV (4), and is trans-

**Key words:** composite materials, product properties, luminescence.

parent among others to light of 400–470 nm wavelengths.

At 250°C solid PbCl<sub>2</sub> grains (diameter 1–10  $\mu\text{m}$ ) and liquid anthracene (mp anthracene, 216°C; mp PbCl<sub>2</sub>, 501°C) were stirred together in a sealed evacuated quartz tube with a pointed base. After homogenization the PbCl<sub>2</sub> particles were allowed to precipitate partially and then the mixture was cooled down and solidified. Thus the upper part of the tube consisted of crystalline anthracene, saturated with traces of dissolved PbCl<sub>2</sub> [the matrix material, denoted as anthracene(m); the PbCl<sub>2</sub> concentration being < 500 ppm according to chemical analyses]. The lower part consisted of anthracene-PbCl<sub>2</sub> composite material. Matrix samples of varying thicknesses were cut from the upper part, and from the lower part composite samples containing 30 volume per cent (v/o) PbCl<sub>2</sub> grains. The samples were coarsely ground in order to reduce specular reflection at the surface. The surface of the samples was normalized. The thicknesses of the samples varied between 0.01 and 0.4 cm.

**Optical measurements.**—These samples, situated on a dim black substrate, were subjected to both x-ray and u.v. irradiations perpendicular to the surfaces of the samples in order to determine the conversion efficiency and to characterize the luminescent center in the anthracene-PbCl<sub>2</sub> composites.

**X-ray to visible light conversion.**—The x-rays were delivered by an x-ray tube of the Müller MG 150 Type. The electrode voltage was varied between 50 and 150 kV<sub>p</sub>. No filters were used, *i.e.*, the x-ray beams were not monochromatic. The intensity of the backwards emitted luminescent light, (*i.e.*, the direction opposed to that of the incident x-rays) was measured as a function of the sample thickness by means of a photomultiplier (Philips 150 UVP), directed under 45 angular degrees with respect to both the sample surface and the x-ray beam (Fig. 1). The sensitivity of the photomultiplier was the same to within 10% for wavelengths between 400 and 470 nm. Typical results (for 150 kV<sub>p</sub>, *i.e.*, a mean value of the x-ray energy of about 100 keV) are shown in Fig. 2. The circles, triangles, and squares correspond to the composite, the anthracene matrix, and the PbCl<sub>2</sub> samples, respectively.

**Emission spectra.**—The emission spectra of composite samples and of anthracene(m) samples of a thickness of 0.055 cm have been measured both under x-ray irradiation of 60 keV (Fig. 3a and 3b) and under u.v. irradiation of 254 nm wavelength (Fig. 4a and 4b).

## Discussion

From Fig. 2 it is evident that the conversion factor of composite material is considerably enhanced and

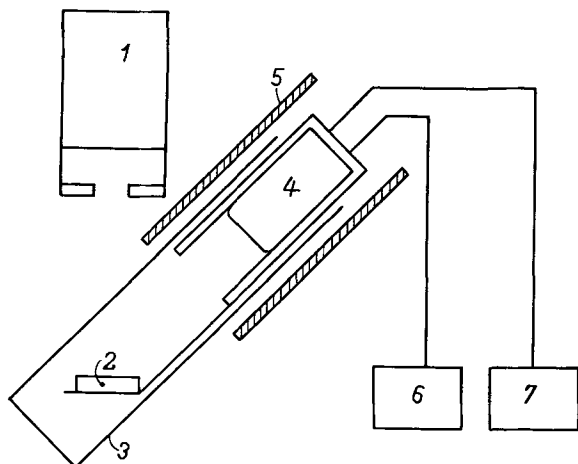


Fig. 1. Equipment for the measurement of the backwards luminescent light. 1, X-ray tube; 2, sample; 3, cardboard tube; 4, photomultiplier; 5, lead shields; 6, power supply for the photomultiplier; 7, detector.

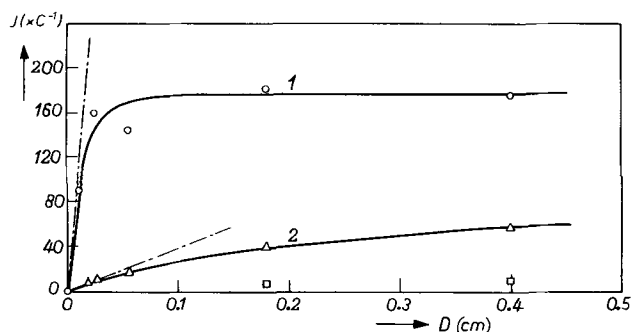


Fig. 2. Intensity of the backwards emitted luminescent light  $J$  in arbitrary units as a function of the thickness,  $D$ , of the sample. Curve 1, experimental points and theoretical curve for the anthracene- $\text{PbCl}_2$  composite; curve 2, experimental points and theoretical curve for the anthracene matrix. The squares correspond to single-phase  $\text{PbCl}_2$ .

exceeds that of single-phase anthracene(m) by a factor of about 30 for thin films. The luminescence contribution of single phase  $\text{PbCl}_2$  (squares) is negligible.

The emission spectra shown in Fig. 3 and 4 are essentially the same and are in accordance with pub-

lished data on the emission spectrum of pure crystalline anthracene (5, 6, 12) exhibiting peaks at about 400, 420, 450, and 470 nm. The x-ray emission spectrum (Fig. 3b) of the anthracene(m) shows the peaks at 470 and 450 nm, but the two peaks at 420 and 400 nm are absent. The x-ray emission spectrum of the anthracene- $\text{PbCl}_2$  composite has the peaks at 470, 450, and 420 nm, while the peak at 400 nm is missing (Fig. 3a). In Fig. 4 (u.v. excitation) all peaks are present. The differences can be explained in terms of self-absorption of the luminescent light, due to the fact that the emission and absorption spectra of anthracene mutually overlap (7). The penetration depth of u.v. in both the anthracene(m) and the composite is very small (a few micrometers), such that the self-absorption of the backwards emitted luminescent light is small. For x-rays, however, the penetration depth in the anthracene(m) is considerably larger than in the composite (as argued above), but both are much larger than for u.v. As a consequence the absence of one peak in Fig. 3a and two peaks in Fig. 3b can be attributed to an increase of the self-absorption of the luminescent light.<sup>1</sup> Therefore the diagrams of Fig. 3 and 4 are basically the same and it can be concluded that the presence of dissolved  $\text{PbCl}_2$  and solid  $\text{PbCl}_2$  grains does not affect the molecular luminescence mechanism typical for pure anthracene. Consequently the intensities given in Fig. 2 for anthracene(m) and for the anthracene- $\text{PbCl}_2$  composite can be compared directly.

The experimental points of Fig. 2 for the composite (circles) can be described by a simple curve (solid line 1) of the form

$$J_{(\text{comp})} = 180C(1 - e^{-60D}) \quad [1]$$

where  $J_{(\text{comp})}$  is the response of the photomultiplier to the luminescent light emitted backwards by the composite sample,  $D$  is the thickness of the sample, and  $C$  a constant. Similarly the experimental results of the anthracene(m) (triangles) correspond to

$$J_{(\text{anth.m})} = 66.2C(1 - e^{-5.9D}) \quad [2]$$

(see solid curve 2), the slopes,  $R$ , at  $D = 0$  (dashed lines) being

$$R_{(\text{comp})} = 10800C \text{ and } R_{(\text{anth.m})} = 390C \quad [3]$$

These experimental results of Fig. 2 can be related to physical parameters by considering the luminescence

<sup>1</sup> This is true in spite of the fact that the absorptivity for the luminescent light is larger in the composite than in the anthracene(m), because the absorption coefficient for x-rays has increased much more (see below).

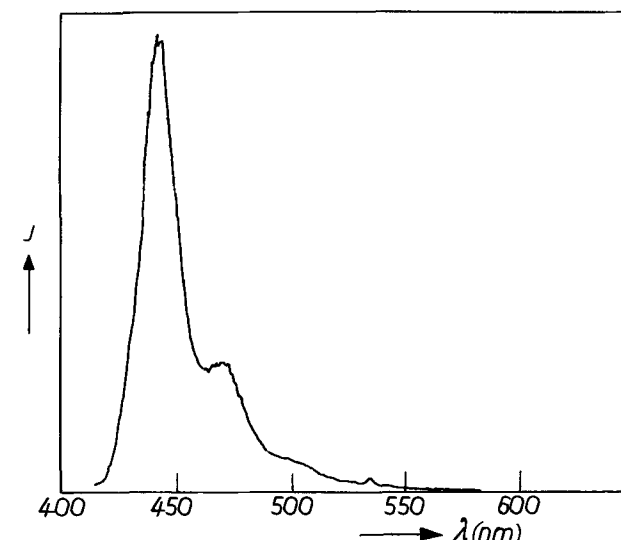
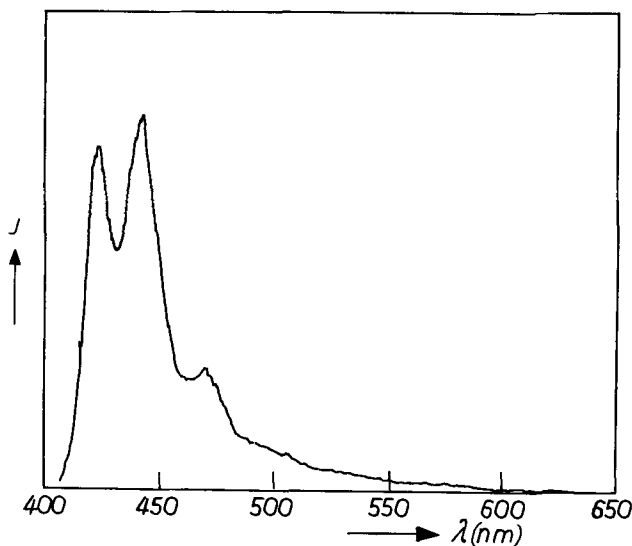


Fig. 3. X-ray emission spectrum.  $J$  denotes the spectral power in arbitrary units. a (left), For the anthracene- $\text{PbCl}_2$  composite; b (right), for the anthracene matrix.

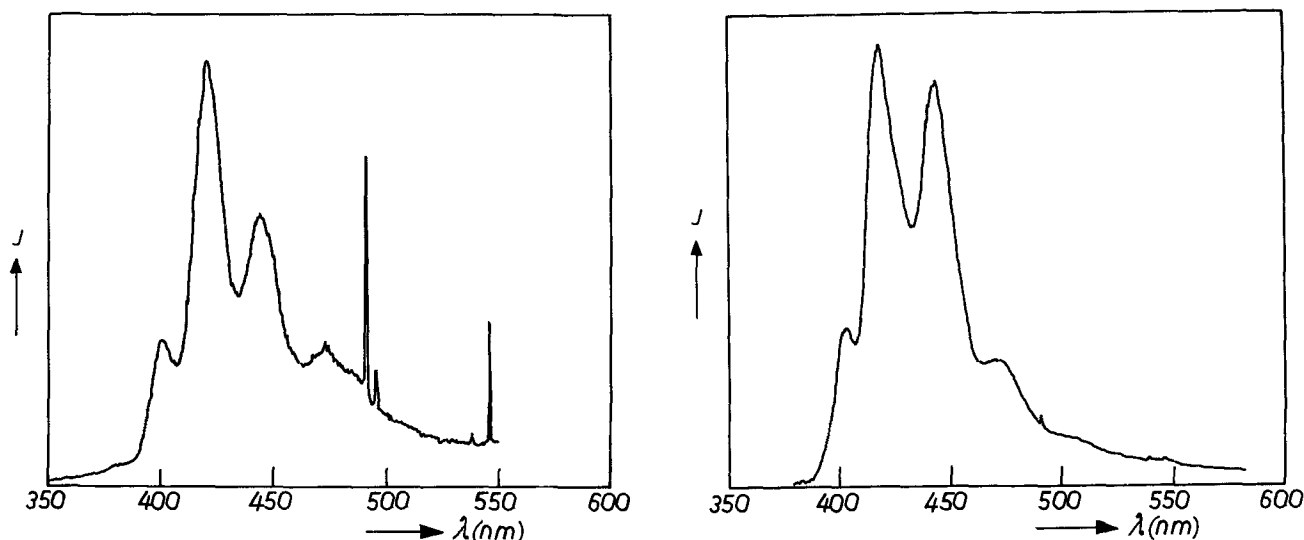


Fig. 4. U.V. emission spectrum.  $J$  has the same meaning as in Fig. 3. a (left), For the anthracene-PbCl<sub>2</sub> composite (the sharp peaks at 492 and 546 nm originate from the u.v. mercury excitation source); b (right), for the anthracene matrix.

and the absorption processes in more detail (8-10). The luminescent light generated by the incident x-rays travels through the sample and is subject to absorption and to scattering before it leaves the sample through the surface and can be detected by the photomultiplier. The one-dimensional case is considered in Fig. 5. The total luminescent radiant flux passing an infinitesimal thin layer  $dx$  is split up into two parts, *viz.*,  $J_F$  in the x-axis (*i.e.*, the direction of the incident x-ray beam) and  $J_B$  in the opposite direction.<sup>2</sup> A fraction  $\tau J_F dx$  of  $J_F$  will be absorbed and a fraction  $s J_F dx$  will be lost by scattering in a backward direction, but a fraction  $s J_B dx$  will be added by scattering from flux  $J_B$ , as well as a quantity  $\frac{1}{2} f \mu I_0 e^{-\mu x} dx$ , being the half of the radiation excited by the x-rays in  $dx$  (the other half contributes to  $J_B$ ), such that

$$\frac{dJ_F}{dx} = -(\tau + s)J_F + s J_B + \frac{1}{2} f \mu I_0 e^{-\mu x} \quad [4a]$$

and similarly

$$\frac{dJ_B}{dx} = (\tau + s)J_B - s J_F - \frac{1}{2} f \mu I_0 e^{-\mu x} \quad [4b]$$

where  $\tau$  and  $s$  are the absorption coefficient and the coefficient of internal scattering of the luminescent radiation,  $I_0$  and  $\mu$  the intensity and the absorption coefficient of the incident x-rays, and  $f$  the luminescence efficiency factor. By common principles the general solution of Eq. [4] has been found to be (8)

$$J_F = A(1 - \beta)e^{\sigma x} + B(1 + \beta)e^{-\sigma x} - \frac{1}{2} f \mu I_0 \frac{\mu + \sigma/\beta}{\mu^2 - \sigma^2} e^{-\mu x} \quad [5a]$$

and

$$J_B = A(1 + \beta)e^{\sigma x} + B(1 - \beta)e^{-\sigma x} + \frac{1}{2} f \mu I_0 \frac{\mu - \sigma/\beta}{\mu^2 - \sigma^2} e^{-\mu x} \quad [5b]^3$$

where  $\sigma$  is the absorptivity, comprising both absorption and internal scattering of the luminescent light according to  $\sigma = \sqrt{\tau(\tau + 2s)}$  and  $\beta = \tau/\sigma$ . The constants

<sup>2</sup> Sideways directions are not considered because in layers with a large surface compared with the thickness the loss in sideways directions is compensated by an equal contribution from the neighboring parts of the layer.

<sup>3</sup> In Eq. [29] of Ref. (8) printing errors occur in the terms

$$\frac{1}{2} f \mu I_0 \frac{\mu + \sigma/\beta}{\mu^2 - \sigma^2} e^{-\mu x} \text{ and } \frac{1}{2} f \mu I_0 \frac{\mu - \sigma/\beta}{\mu^2 - \sigma^2} e^{-\mu x}$$

a factor  $\beta$  has been lost. For the same reason Eq. [154] of Ref. (10) should be rewritten.

$A$  and  $B$  can be determined by the boundary conditions  $J_F = r_1 J_B$  at  $x = 0$  and  $J_B = r_2 J_F$  at  $x = D$ , respectively, in which  $r_1$  and  $r_2$  are the reflection coefficients of the front surface (facing the incident x-rays) and the opposing surface, respectively.

Neglecting specular reflection of the luminescent light at the front surface of the sample (*i.e.*, putting  $r_1 = 0$ ) and for the case where the dim black substrate (see above) has the same reflectivity as a luminescent layer of infinite thickness [which will be true for the composite samples due to the high absorptivity  $\sigma$ , and also for the anthracene(m) samples if it is assumed that in anthracene(m) internal scattering is absent and that the black substrate has a zero reflectivity] then from Eq. [4] and [5] it follows (8, 9)

$$J_B = \frac{f \mu I_0}{(1 + \beta)(\mu + \sigma)} \{1 - e^{-(\mu + \sigma)D}\} \quad [6]$$

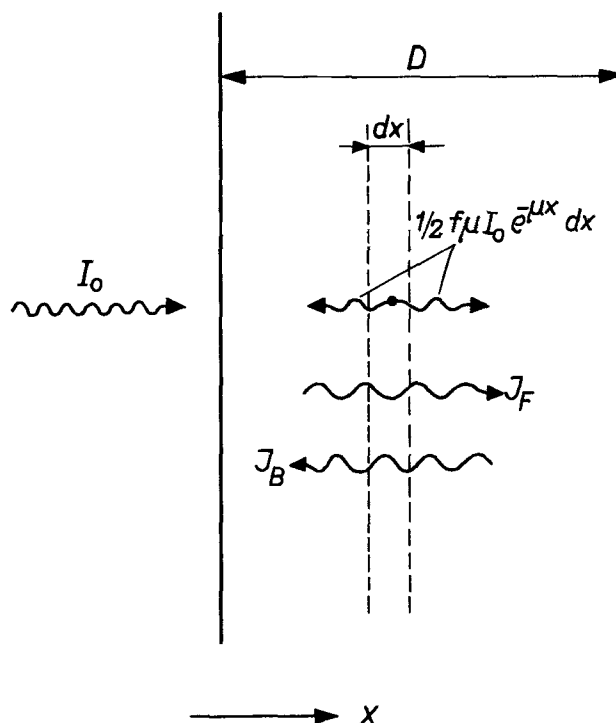


Fig. 5. X-ray luminescence.  $I_0$  = incident x-ray beam;  $J_F$  = forward flux of the luminescent light;  $J_B$  = backward flux;  $D$  = thickness of the sample;  $\frac{1}{2} f \mu I_0 e^{-\mu x} dx$  see text.

Equation [6] and Eq. [1] and [2], which also apply to backwards radiation, are of the same form. Therefore from these equations it follows

$$\mu_c + \sigma_c = 60 \text{ cm}^{-1} \quad [7]$$

and

$$\mu_m + \sigma_m = 5.9 \text{ cm}^{-1} \quad [8]$$

where the suffixes c and m refer to the anthracene-PbCl<sub>2</sub> composite and to the anthracene(m), respectively. With  $\mu_m = 0.20 \text{ cm}^{-1}$  at 100 keV (11) and assuming  $s_m = 0$  (see above), or  $\sigma_m = \tau_m$ , it follows from Eq. [8]

$$\tau_m = 5.7 \text{ cm}^{-1} \quad [9]$$

Because the major part of the composite consists of anthracene(m), and because, according to preliminary absorption measurements  $\sigma_{\text{PbCl}_2}$  equals about  $1 \text{ cm}^{-1}$  to a good approximation the following holds

$$\tau_c = \tau_m \quad [10]$$

The parameter  $\mu_c$  can be obtained from

$$\mu_c = V\mu_{\text{PbCl}_2} + (1 - V)\mu_m \quad [11]$$

where  $V$  is the volume fraction of PbCl<sub>2</sub>. Equation [11] has been derived by substituting a model for the disperse composite consisting of two layers with equal surfaces, and of thicknesses proportional to  $V$  and  $(1 - V)$ , the first layer being PbCl<sub>2</sub> and the other anthracene(m). With  $\mu_{\text{PbCl}_2}$  (100 keV) =  $20 \text{ cm}^{-1}$ , calculated according to Ref. (11) and  $V = 0.3$ , from Eq. [11] it follows that

$$\mu_c = 6 \text{ cm}^{-1} \quad [12]$$

and from Eq. [7] that

$$\sigma_c = 54 \text{ cm}^{-1} \quad [13]$$

The fact that  $\sigma_c \gg \tau_m$  can be attributed both to the pronounced internal reflection of the composite (due to the difference in the refractive indices of the PbCl<sub>2</sub> grains and the anthracene matrix) and to the fact that the degree of reabsorption is higher in the anthracene samples (larger penetration depth of the incident x-rays) than in the composite samples. The reabsorption tends to decrease the intensity of the short-wave luminescence and to increase the intensity of the long-wave luminescence via the photon cascade process (7, 12-14). In consequence the mean absorption coefficient of the anthracene samples will approach to the absorption coefficient of the luminescent light of 450 nm wavelength ( $\tau_{450} \approx 5 \text{ cm}^{-1}$ ) (14, 15) while that of the composite samples will tend more to the absorption coefficient of the luminescent light of 420 nm wavelength, being of the order of  $100 \text{ cm}^{-1}$  (14). From Eq. [6] it follows for the slopes  $R$  at  $D \rightarrow 0$

$$R_c = \frac{f_c \mu_c I_0}{1 + \beta_c} \quad \text{and} \quad R_m = \frac{f_m \mu_m I_0}{1 + \beta_m} \quad [14]$$

With the above-derived values for the  $\mu$ 's, while putting  $\beta_m = 1$  (no contribution by the internal scattering) and  $\beta_c = 0.3$  (internal scattering), for the amplification factor  $U_{\text{th}} = R_c/R_m$  it follows from Eq. [14] that

$$U_{\text{th}} = 46 \frac{f_c}{f_m} \quad [15]$$

The luminescence efficiency factor,  $f_c$ , contains a factor  $Q$  that is a function of the volume fraction  $V$ .  $Q$  varies between 1 (for  $V = 0$ ) and 0 (for  $V = 1$ ). In the latter extreme case the composite does not contain any luminescent material and consequently  $f_c$  falls to zero (if the PbCl<sub>2</sub> luminescence is neglected). The factors  $f_c$  and  $f_m$  are independent of the degree of self-absorption and photon cascade because the efficiency of (cascade) photoluminescence of crystalline anthracene at room temperature is almost unity (7).

The experimental amplification factor,  $U_{\text{exp}}$ , at  $D \rightarrow 0$  according to Eq. [3] is

$$U_{\text{exp}} = 28 \quad [16]$$

From Eq. [15] and [16] it follows that the agreement between theory and experiment is good, if  $f_c = 0.6 f_m$ .

The above-calculated values have to be considered as mean values, due to the nonmonochromatic character of the incident x-rays and the luminescent light, the range of the secondary electrons in the anthracene can amount up to 10-100  $\mu\text{m}$ , the photon cascade process, the inhomogeneities in the samples, etc.

Finally it has to be remarked that in principle the x-ray to visible light conversion can also be enhanced by covering the anthracene sample with a PbCl<sub>2</sub> layer. However the result will be poor compared to the composite. Only a small fraction of the x-rays will be absorbed if the PbCl<sub>2</sub> layer is 1-10  $\mu\text{m}$  thick, and if the PbCl<sub>2</sub> layer is thicker than 10  $\mu\text{m}$  most secondary electrons, released in the PbCl<sub>2</sub> layer, will be trapped in the PbCl<sub>2</sub> layer before reaching the underlying anthracene. In the composite structure, however, the incident x-rays successively hit many PbCl<sub>2</sub> particles of small dimensions, and as a consequence the conversion is maximum.

### Conclusion

For phosphors of a low density and consisting of atoms of a low atomic number the x-ray to visible light conversion can be enhanced by one or two orders of magnitude by the addition of finely dispersed particles (globules, rods, lamellae, etc.) of a heavy phase.

### Acknowledgment

Thanks are due to Messrs. J. A. de Poorter, G. de Vries, and R. E. Breemer for the measurements of the emission spectra and to Dr. A. Brill for the stimulating discussions.

Manuscript received Nov. 12, 1973.

Any discussion of this paper will appear in a Discussion Section to be published in the June 1975 JOURNAL. All discussions for the June 1975 Discussion Section should be submitted by Feb. 1, 1975.

The publication costs of this article have been assisted by Philips Research Laboratories.

### LIST OF SYMBOLS

$\beta$	$\tau/\sigma$
$C$	a constant including the photomultiplier properties
$D$	thickness of the sample, cm
$f$	luminescence efficiency factor
$I_0$	intensity of the incident x-rays
$J$	luminescent radiation output
$\mu$	absorption coefficient of the incident x-rays, $\text{cm}^{-1}$
$R$	slope of $J$ vs. $D$ at $D = 0$
$\tau$	absorption coefficient of the luminescent radiation, $\text{cm}^{-1}$
$s$	coefficient of internal scattering of the luminescent radiation, $\text{cm}^{-1}$
$\sigma$	absorptivity of the luminescent radiation, $\text{cm}^{-1}$
$U$	luminescence amplification factor
$V$	volume fraction of the PbCl <sub>2</sub> particles
$X$	distance from the surface, cm

### REFERENCES

1. N. Riehl, "Einführung in die Lumineszenz," Karl Thieme, München (1971).
2. F. B. Harrison, *Nucleonics*, **10**, No. 6, 40 (1952).
3. J. van Suchtelen, *Philips Res. Repts.*, **27**, 28 (1972).
4. Y. Sost and L. Langouët, *Compt. Rend. Acad. Sci. Paris*, **264B**, 1603 (1967).
5. P. Pringsheim, *Trans. Faraday Soc.*, **35**, 28 (1939).
6. L. Roth, *Phys. Rev.*, **75**, 983 (1949).
7. G. T. Wright, *Proc. Phys. Soc. London*, **B68**, 241 (1955).
8. H. C. Hamaker, *Philips Res. Repts.*, **2**, 55 (1947).
9. H. A. Klasens, *ibid.*, **2**, 68 (1947).
10. G. Kortüm, "Reflexionsspektroskopie," Springer-Verlag, Berlin, Heidelberg, New York (1969).

11. K. Siegbahn, "Alpha-, Beta- and Gamma-Ray Spectroscopy," Vol. I, pp. 286, 840 ff., North Holland Publ. Co., Amsterdam (1968).
12. J. B. Birks and W. A. Little, *Proc. Phys. Soc.*, **A66**, 921 (1953).
13. L. A. Kravtsov, *Bull. Acad. Sci. USSR Phys. Ser.*, **27**, 724 (1964).
14. B. J. Mulder, Thesis, Eindhoven (1967).
15. N. Shiomi, *Bull. Inst. Chem. Res. Kyoto Univ.*, **46**, 23 (1968).

## A Comparison of the Semiconducting Properties of Thin Films of Silicon on Sapphire and Spinel

G. W. Cullen\* and J. F. Corboy

*RCA Corporation, David Sarnoff Research Center, Princeton, New Jersey 08540*

### ABSTRACT

The Hall mobilities in 0.5 and 1.0  $\mu\text{m}$  thick heteroepitaxial silicon on  $(\bar{1}102)$  sapphire and (100) and (111) spinel substrates are compared. The substrates employed were Czochralski sapphire, alumina rich flame fusion spinel, stoichiometric Czochralski spinel, and a "modified" alumina-rich Czochralski spinel. The semiconducting properties of the silicon on the spinels are similar if the Czochralski grown substrate surfaces are air annealed prior to deposition. The reproducibility achieved in electrical properties in silicon on spinel is related to the method of preparation of the substrate. In comparing the semiconducting properties in silicon on sapphire with silicon on spinel, one finds that the MOS transistor mobilities are more similar than the Hall mobilities.

It is of interest to identify the factors which limit the semiconducting properties of thin (1  $\mu\text{m}$  and less) heteroepitaxial silicon on insulating substrate materials. To this end, it is informative to compare the properties of films deposited on substrates with distinctly different crystallographic and chemical properties. In order to optimize the characteristics of complementary pair MOS transistor (CMOST) circuitry fabricated in silicon on insulators, the effort is directed toward achieving carrier mobilities as similar as possible to bulk values in heteroepitaxial films as thin as 0.5  $\mu\text{m}$ . Therefore, the nature of the substrate material is under continual reexamination.

During the development of the silicon-on-insulator technology, sapphire has been the most commonly employed substrate material (1-3). Excellent progress has been made, and semiconducting properties useful for application in commercial devices have been realized (4-6). Spinel has been considered as a possible alternate substrate because of the relatively good crystallographic match to, and relatively low chemical reactivity with, silicon (7-10). Higher mobilities have been achieved for some, but not all carrier types, orientations, and thicknesses of silicon on spinel (11, 12). As the demand for larger substrate diameters (2 in. and greater) arose to meet the needs of advancing IC technologies, there was a general shift from flame fusion to Czochralski grown material, although at least one organization has adopted the approach of developing methods for the growth of large diameter flame fusion spinel (13). In the case of sapphire, the flame fusion and Czochralski material are chemically identical; therefore, the same conditions can be used for the deposition of silicon on both types of substrates. In the case of spinel, however, the properties of concern for use as a substrate material are a strong function of the method used for the growth of the crystal, and therefore the substrate surface preparation and/or the conditions employed for silicon deposition must be adjusted accordingly (11, 12).

The semiconducting properties in thin silicon films on sapphire have improved as the growth temperature has been decreased and the growth rate increased.

These deposition conditions have been used to suppress the chemical interactions between the deposition constituents and the substrate (3). The mismatch between the crystal lattice of the rhombohedral sapphire and the cubic silicon appears not to have been as limiting a factor (12) as was originally anticipated (2). The chemical reactivity of the spinel has proven to be a strong function of the chemical composition, which in turn is influenced by the method of growth (11). Very different semiconducting properties have been observed in silicon deposited on spinels with such subtle differences in the chemical composition that the lattice constants are very nearly the same (11). Here again, it is clear that the chemical reactivity between silicon (and  $\text{H}_2$ , the carrier gas) and the substrate predominates over lattice matching considerations. On the other hand, on the relatively unreactive flame fusion spinel, mobilities equivalent to bulk silicon mobilities have been measured in p-type 1.5  $\mu\text{m}$  thick (111) silicon (10). This suggests that, under very specific conditions, the influence of lattice matching is seen. It is difficult to explain why the near bulk mobilities have not been achieved in other crystalline orientations or in n-type films; it may be a stress effect (8).

We have previously reported the properties of silicon deposited in a hydrogen atmosphere on Czochralski sapphire (3) and flame fusion spinel (3, 10), and of silicon deposited in a helium atmosphere on stoichiometric Czochralski spinel (12). In this paper the properties are summarized of silicon deposited in hydrogen on alumina-rich flame fusion spinel, stoichiometric Czochralski spinel, and a modified alumina-rich Czochralski spinel. These properties are compared with the characteristics of silicon deposited on sapphire, also in a hydrogen atmosphere.

### Substrate Materials

The substrates employed in this study are:

(i) Czochralski sapphire (Union Carbide Corporation, Crystal Products Division, San Diego, California).

(ii) Czochralski spinel, nominally stoichiometric (*i.e.*,  $\text{MgO} \cdot \text{Al}_2\text{O}_3$ ). The crystals are grown in an inert atmosphere with small additions of oxygen to suppress the formation of iridium (the crucible material) inclu-

\* Electrochemical Society Active Member.

Key words: heteroepitaxial growth, silicon on insulators, single-crystal sapphire and spinel, thin film semiconductor.

sions. In this report this spinel is referred to as stoic.-Czo. spinel. The crystals used in this study were both prepared in-house and at Union Carbide.

(iii) Czochralski spinel, alumina rich ( $\text{MgO} \cdot x\text{Al}_2\text{O}_3$ ;  $1 < x < 1.7$ ). These crystals are grown in-house in a high humidity ambient in an effort to simulate the chemical composition of flame fusion spinel (14). This material is referred to as the "modified" Czochralski spinel.

(iv) Flame fusion (f.f.) spinel, alumina rich ( $x \sim 1.7$ ) grown in-house using procedures previously described (15).

### Substrate Surface Preparation and Silicon Growth

Prior to deposition of the silicon, the polished sapphire (polished by Union Carbide or Insaco, Quakertown, Pennsylvania) is exposed to a hydrogen ambient for 30 min at  $1300^\circ\text{C}$ . During this treatment  $\sim 1 \mu\text{m}$  of material is removed from the surface (16, 17). The temperature is sufficiently high that annealing of the subsurface work damage also takes place (18). The polished flame fusion spinel (polished by RCA or Insaco) is exposed to hydrogen for 30 min at  $1150^\circ\text{C}$ . Both the modified and unmodified polished Czochralski spinel substrate wafers are air-annealed for 5 hr at  $1500^\circ\text{--}1600^\circ\text{C}$ . This procedure is similar to that reported by Reisman *et al.* (19) for the stoic.-Czo. spinel.

The silicon is deposited in a pure hydrogen ambient using silane as the source gas. A growth temperature of  $1000^\circ\text{C}$  is used for the deposition of silicon on sapphire, and  $1100^\circ\text{C}$  for the deposition of silicon on spinel. The latter deposition temperature, which was considered to be optimum for the deposition of silicon on (111) spinel (10), was not changed for the deposition on the (100) spinel. In both cases, a deposition rate of  $2 \mu\text{m}/\text{min}$  is employed. The substrates are placed on inductively heated pyrolytic carbon coated carbon susceptors in a quartz water-cooled growth ampul. Diborane is used as the p-type dopant source, and arsine is used as the n-type dopant source. Other details of the deposition method have been previously reported (3, 10).

It proved to be possible to reproducibly obtain highly reflective, clear silicon deposits. The high-temperature air anneal appeared to have alleviated the problems that had previously been experienced in obtaining clear samples on the stoichiometric Czochralski spinel. A hazy silicon surface always indicates a degradation in semiconducting properties, and is usually associated with either a leak in the deposition system or the incomplete removal of substrate subsurface work damage. No problems were experienced in surface crazing or substrate cracking with the alumina rich spinels or the sapphire substrates.

### Hall Mobilities

The carrier mobilities are measured by the Hall method. The patterns are chemically etched in the silicon. Although this is a destructive method, considerably less scatter has been observed using the Hall method than the van der Pauw method (20). Just prior to making the Hall measurements, the silicon dioxide is stripped from the sample in an aqueous HF solution. This is done in order to provide a reproducible surface-state density. The Hall values reported here were gathered over a period of more than a year, and thus the scatter observed provides a measure of the long-term reproducibility. Except in the case of the stoichiometric Czochralski spinel, less scatter is observed if the films are deposited within a brief time period on a group of substrates prepared at the same time.

Under the conditions described, the mobilities observed on the three types of spinel are similar, and therefore the values have been grouped on one set of curves.

Typical hole mobilities, as a function of the hole concentration, are shown for 0.5 and 1.0  $\mu\text{m}$  thick (100) silicon on (1102) sapphire (Fig. 1), (100) silicon on (100) spinel (Fig. 2), and (111) silicon on (111) spinel (Fig. 3). In order to facilitate comparison of these data, the curves presented in Fig. 1 are reproduced (without data points) in Fig. 2, and the curves of Fig. 2 are reproduced on Fig. 3. Due to the scatter observed in the Hall values the curves were not drawn by mathematical methods and are included only to facilitate a general comparison of mobilities of the two film thicknesses on the two substrate substances.

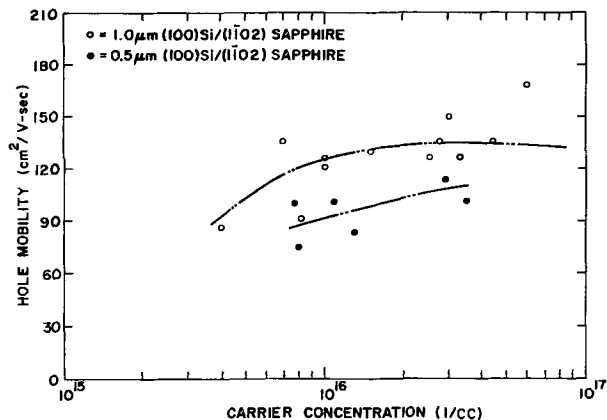


Fig. 1. Hall mobility as a function of hole concentration in 0.5 and 1.0  $\mu\text{m}$  thick (100)Si/(1102)sapphire.

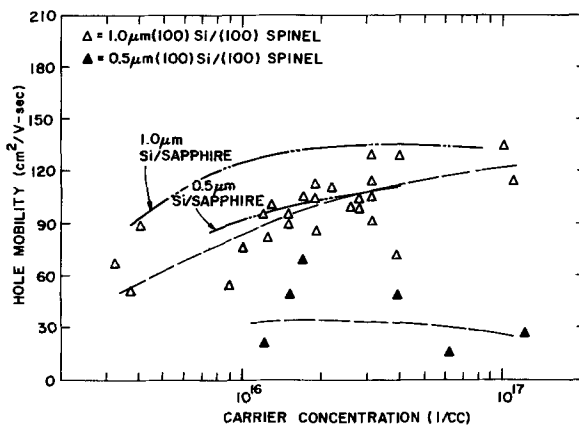


Fig. 2. Hall mobility as a function of hole concentration in 0.5 and 1.0  $\mu\text{m}$  thick (100)Si/(100)spinel. Curves for (100)Si/(1102) sapphire are included (without data points) for reference.

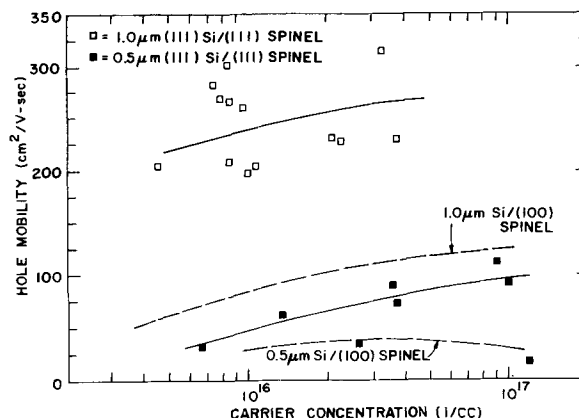


Fig. 3. Hall mobility as a function of hole concentration in 0.5 and 1.0  $\mu\text{m}$  thick (111)Si/(111)spinel. Curves for (100)Si/(100) spinel are included (without data points) for reference.

Typical electron mobilities, as a function of the electron concentration, are shown for 0.5 and 1.0  $\mu\text{m}$  thick (100) silicon on (1102) sapphire (Fig. 4), (100) silicon on (100) spinel (Fig. 5), and (111) silicon on (111) spinel (Fig. 6). As with the p-type data, the curves of Fig. 4 are superimposed on Fig. 5, and the curves of Fig. 5 are included in Fig. 6.

A summary of typical carrier mobilities at a carrier concentration of  $\sim 1 \times 10^{16}/\text{cm}^3$  is presented in Table I.

It is informative to compare the electron mobilities in silicon deposited on the three types of spinel if they are all hydrogen annealed prior to silicon deposition. The electron mobilities in Si/f.f. spinel fall on the

Table I. Typical as-deposited carrier mobility values for 1.0 and 0.5  $\mu\text{m}$  silicon on sapphire and silicon on spinel for a carrier concentration of  $1 \times 10^{16}/\text{cm}^3$

Film thickness ( $\mu\text{m}$ )	Substrate composition and orientation	Mobility ( $\text{cm}^2/\text{V-sec}$ )	% of bulk
	p-type		
	Bulk silicon	350	
1.0	(100)Si/(1102)sapphire	120	34
0.5	(100)Si/(1102)sapphire	90	26
1.0	(111)Si/(111)spinel	240	69
0.5	(111)Si/(111)spinel	50	14
1.0	(100)Si/(100)spinel	80	23
0.5	(100)Si/(100)spinel	30	9
	n-type		
	Bulk silicon	1100	
1.0	(100)Si/(1102)sapphire	500	45
0.5	(100)Si/(1102)sapphire	430	39
1.0	(111)Si/(111)spinel	480	44
0.5	(111)Si/(111)spinel	200	18
1.0	(100)Si/(100)spinel	300	27
0.5	(100)Si/(100)spinel	140	13

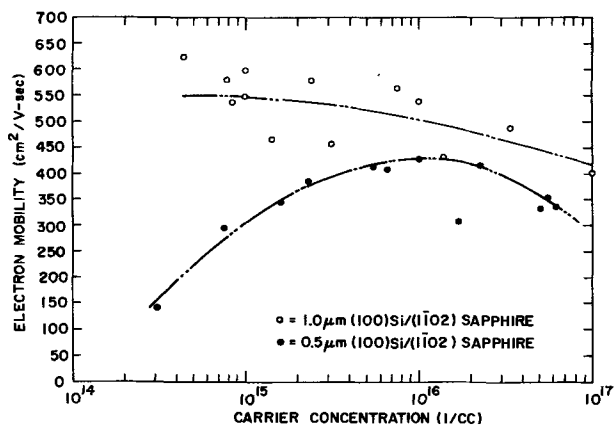


Fig. 4. Hall mobility as a function of electron concentration in 0.5 and 1.0  $\mu\text{m}$  thick (100)Si/(1102)sapphire.

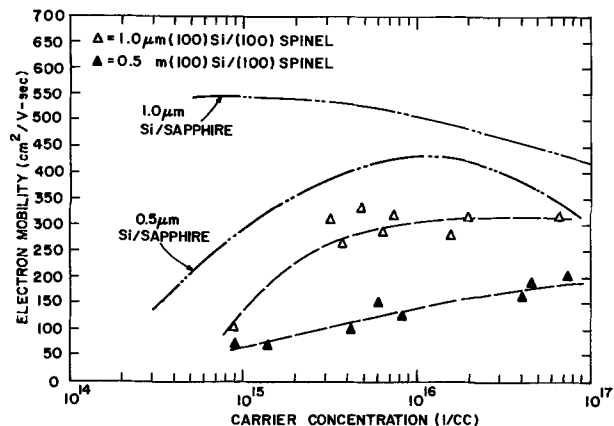


Fig. 5. Hall mobility as a function of electron concentration in (100)Si/(100)spinel. Curves for (100)Si/(100)sapphire are included (without data points) for reference.

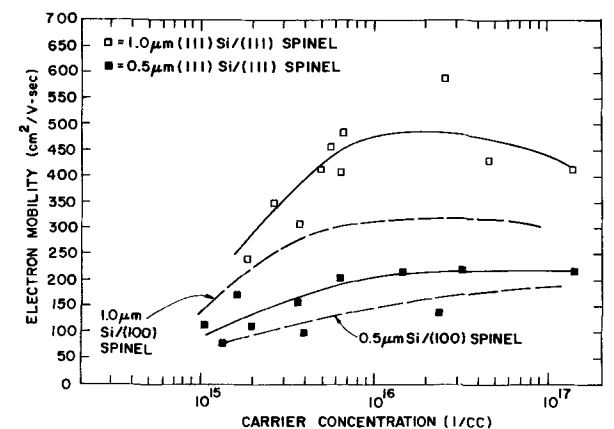


Fig. 6. Hall mobility as a function of electron concentration in (111)Si/(111)spinel. Curves for (100)Si/(100)spinel are included (without data points) for reference.

curves shown above. Some electron mobilities in Si/modified Czo. spinel fall on the curves, but the values are scattered. It is difficult to obtain n-type Si/stoic.-Czo. spinel if the substrate is hydrogen fired. Air annealing of the Czo. spinel substrates has provided reproducibility in electron mobilities in the Si/modified spinel and has made it possible to achieve as-deposited n-type Si/stoic.-Czo. spinel.

Mobility values for (111)Si/(0001)sapphire are not shown here because the values are too low to be of interest in 1  $\mu\text{m}$  thick films. Other investigators have achieved usable mobilities in (111)Si/(1120)sapphire (21). The electron mobilities in the 1  $\mu\text{m}$  thick (annealed) (111)Si/(1120)sapphire appear to be similar to the values reported here for as-deposited 1  $\mu\text{m}$  (111)Si/(111)spinel. Since (111)Si/(1120)sapphire hole mobilities are reported for thicker films ( $>2 \mu\text{m}$ ), it is not possible to make meaningful comparisons with the hole mobility values reported here.

Recently considerable effort has been directed toward minimizing the changes in the semiconducting properties in the heteroepitaxial silicon during thermal oxidation (3, 22, 23). Exposure to dry  $\text{O}_2$  for 1 hr at 1100°C has been taken as approximately equivalent to the thermal treatment employed during processing of the MOS transistor structures. In 1.0  $\mu\text{m}$  silicon on both sapphire and spinel, for carrier concentrations greater than  $\sim 2 \times 10^{16}/\text{cm}^3$ , the carrier mobility typically changes by less than 10%, and the carrier concentration typically changes by less than a factor of 1.5 on thermal oxidation. In films less than 1  $\mu\text{m}$  in thickness, and for carrier concentrations less than  $2 \times 10^{16}/\text{cm}^3$ , the magnitude of the changes on thermal oxidation are scattered and difficult to use as a "material quality" factor. Clear conclusions in this respect must be derived from device data.

Effective (MOST) Mobilities

Typical mobilities measured in MOS transistors fabricated in 1.0 and 0.5  $\mu\text{m}$  thick (100) silicon on sapphire and spinel are shown in Table II. Leakage

Table II. MOS transistor characteristics in (100) silicon on sapphire and spinel

Substrate orientation and type	Silicon thickness ( $\mu\text{m}$ )	n-channel		p-channel	
		$\mu_{\text{eff}}$ ( $\text{cm}^2/\text{V-sec}$ )	$I_L$ (A/mil $\times 10^{12}$ )	$\mu_{\text{eff}}$ ( $\text{cm}^2/\text{V-sec}$ )	$I_L$ (A/mil $\times 10^{12}$ )
(1102) sapphire	1.0	420	150	210	170
	0.75	410			
	0.50	340	135		
(100) spinel	1.0	350	150	210	95
	0.5	250	100		

$\mu_{\text{eff}}$  measured at  $V_{\text{gate}} - V_{\text{threshold}} = 5\text{V}$  (+ or -, depending on the conductivity type).

currents (at 5V source drain) are also included in this table. The Hall characteristics of the (111) silicon on the (0001) sapphire have been too low to warrant fabrication of devices in these films, and insufficient data have been developed in devices fabricated in (111) silicon on (111) spinel to include here.

### Discussion

**Reproducibility—substrate type and surface treatment.**—The sensitivity of the semiconducting properties to preparative variables is a strong function of the reactivity of the substrate to the deposition constituents ( $H_2$ ,  $SiH_4$ , Si, and dopants) and the annealing ambient. It has been previously demonstrated that the stoic.-Czo. spinel reacts with hydrogen, and therefore, higher carrier mobilities are achieved on this substrate using helium as the carrier gas (12). A somewhat surprising result of the previous study was that good mobility values are obtainable in silicon deposited on unannealed stoic.-Czo. spinel. It was proposed that work damage was removed by reaction with the silicon (12). Good mobilities have been occasionally observed in silicon deposited in hydrogen on the unannealed stoic.-Czo. spinel. But when the substrate is not heat-treated prior to silicon deposition, the semiconducting properties, and the reproducibility of the properties, are critically dependent on the quality of the final surface finishing (11). An alternative procedure for the use of the stoic.-Czo. spinel is to anneal the surface in air and deposit the silicon in hydrogen. To date, however, using this procedure, the reproducibility in the semiconducting properties of deposited silicon has not been good, particularly for n-type films.

In respect to chemical reactivity, the modified Czo. spinel is more similar to flame fusion spinel than to the stoic.-Czo. spinel (14). Here the problem is more to achieve reproducibility in the chemical composition of the substrate material. While good semiconducting properties are achievable in silicon deposited in hydrogen on hydrogen annealed modified spinel, better reproducibility is realized on air annealed substrates. The flame fusion spinel has proven to be the least reactive of the spinels in a hydrogen ambient.

**Hall mobilities,  $n < 1 \times 10^{16}/cm^3$ .**—The decrease in the Hall mobilities with decreasing carrier concentration below  $1 \times 10^{16}/cm^3$  in both p- and n-type silicon on sapphire and spinel has previously been attributed to scattering by space charge regions around crystalline heterogeneities (8, 24). It was proposed that as the carrier concentration decreases, the effective space charge region increases, resulting in degradation of the carrier mobility. More recently, Ham (25) has suggested that the effect is associated with depletion of the carriers in the thin lightly doped films by surface charges. If the films are partially depleted by surface charge, one cannot make the assumption that the current is evenly distributed throughout the thickness of the sample. For any fixed value of surface charge, as the carrier concentration decreases, the thickness of the layer depleted from the silicon/silicon dioxide interface increases and effectively the thickness of the layer in which the Hall measurement is made decreases. While the average mobility measurement is independent of thickness, in the silicon on the insulating substrates the mobility is degraded near the silicon/substrate interface (26) by the relatively high impurity content and poor crystallinity, and thus the net result is that the Hall mobility decreases with decreasing carrier concentration. The analysis of the measured carrier concentration in the lightly doped films is complicated not only by the possibility that the carrier concentration is a function of the film thickness (27), but also by the limitation of the current (by the space charge) to only a portion of the film while the entire film thickness is used in the calculation of the carrier concentration. Ham (25) has demonstrated the influence of the surface charge by

measuring the Hall voltage in a gated structure in which the film can be biased to flatband. This provides "bulk" values (*i.e.*, values unaffected by surface charges) wherein it is assumed that the current flow is evenly distributed throughout the thickness of the sample. The mobility value of most interest is the effective MOS transistor mobility, in which carriers only within  $\sim 500\text{\AA}$  of the silicon/silicon dioxide interface are active. Thus, significantly different values for the transport properties in the thin films may be derived using different measurement techniques. In the conventional (ungated) Hall measurement, the properties near the silicon/substrate interface are weighed in thin ( $< 1 \mu m$ ) lightly doped ( $< 1 \times 10^{16}/cm^3$ ) films. In the gated-Hall-bar measurement (when the film is biased to flatband) the characteristics derived represent an integrated value of properties throughout the thickness of the film. In the effective MOS transistor measurement, the properties near the silicon/silicon oxide interface are weighted. Gated-Hall-bar and MOS transistor measurements require the deposition of a clean oxide and considerable processing. Using these techniques, it is difficult to acquire feedback within the time frame practical in the development of deposition conditions. The unbiased Hall measurements can be made within minutes of a deposition run.

For the reasons outlined above, the Hall mobility *vs.* carrier concentration (unbiased) relationships cannot be used on an absolute scale to compare thin lightly doped film and bulk properties. On the other hand, if the surface charge is fixed immediately prior to the measurement by stripping the oxide in an aqueous HF solution (25), the Hall values are reproducible and characteristic of the specific deposition conditions, film thickness, and type of substrate. Thus, on a relative scale, the unbiased Hall values are useful in the development of deposition conditions and the choice of various film thicknesses and substrate orientations and types.

The optimization of the low carrier concentration thin heteroepitaxial silicon properties is of interest for application in deep-depletion MOS transistor geometries (3). It has been demonstrated that, particularly when spinel is used as the substrate material, the semiconducting properties of the low carrier concentration films are considerably more dependent on the deposition conditions than are the properties of the high carrier concentration films (10).

**Hall and MOST mobilities,  $n \sim 1 \times 10^{16}/cm^3$ .**—In order to avoid the ambiguities discussed above, in this section a comparison of Hall and MOST mobilities is made for films with a carrier concentration of  $\sim 1 \times 10^{16}/cm^3$ . Heteroepitaxial silicon with  $n \geq 1 \times 10^{16}/cm^3$  is of interest for application in enhancement type CMOS transistor structures fabricated in silicon on sapphire by the "two-stage" method; *i.e.*, discrete n- and p-type silicon areas are deposited on the same substrate (3, 28).

Hall mobilities of  $120 \text{ cm}^2/\text{V-sec}$  are typically observed in  $1 \mu m$  thick p-type (100)Si/(1102)sapphire. On the other hand, the effective mobilities of MOS transistors fabricated in films of the same thickness are typically  $210 \text{ cm}^2/\text{V-sec}$ . While significantly lower Hall mobilities of  $80 \text{ cm}^2/\text{V-sec}$  are observed in  $1 \mu m$  thick (100)Si/(100)spinel, the effective mobilities of MOS transistors fabricated in  $1 \mu m$  thick silicon on the two substrates are similar. The mobilities in (100) silicon on spinel degrade more rapidly with decreasing film thickness than the (100) silicon on sapphire. In  $0.5 \mu m$  thick films, hole mobilities are typically  $90 \text{ cm}^2/\text{V-sec}$  in (100)Si/(1102)sapphire and  $30 \text{ cm}^2/\text{V-sec}$  in (100)Si/(100)spinel. Insufficient data have been collected in p-channel MOS transistors fabricated in the  $0.5 \mu m$  thick (n-type) films to make meaningful comparisons between the effective device and Hall mobilities in these films.



Relatively high (Hall) hole mobilities of 240 cm<sup>2</sup>/V-sec are typically observed in (111)Si/(111)spinel, but as in the case of the (100)Si/(100)spinel, the electrical properties are a strong function of the film thickness, and the mobilities drop to 50 cm<sup>2</sup>/V-sec in 0.5 μm thick (111)Si/(111)spinel. The mobilities observed in (111)Si/(0001)sapphire are too low to be of interest, and other more favorable sapphire orientations for the growth of (111) silicon have not been pursued in this study.

As in the case of the hole mobilities, the effective electron mobilities in the 1 μm thick films of 420 cm<sup>2</sup>/V-sec in (100)Si/(1102)sapphire and 350 cm<sup>2</sup>/V-sec in (100)Si/(100)spinel are more similar than the Hall electron mobilities of 500 cm<sup>2</sup>/V-sec and 300 cm<sup>2</sup>/V-sec, respectively. The effective n-channel mobilities are lower than the Hall electron mobilities in (100)Si/(1102)sapphire, but slightly higher in (100)Si/(100)spinel. This same trend in electron mobilities is observed in the 0.5 μm thick silicon, except that with the degradation of the Hall electron mobilities in the thinner (0.5 μm) (100)Si/(100)spinel, the effective p-channel value of 250 cm<sup>2</sup>/V-sec is 1.8× the Hall electron mobility of 140 cm<sup>2</sup>/V-sec. The corresponding values in the 0.5 μm thick (100)Si/(1102)sapphire are: p-channel mobility, 340 cm<sup>2</sup>/V-sec; and Hall electron mobility, 430 cm<sup>2</sup>/V-sec.

While the Hall hole mobilities in 1.0 μm thick (111)Si/(111)spinel were double the values observed in (100)Si/(1102)sapphire, this relationship does not hold up in the n-type films. The Hall electron mobility in 1.0 μm thick (111)Si/(111)spinel of 480 cm<sup>2</sup>/V-sec is very similar to the values typically observed in (100)Si/(1102)sapphire of 500 cm<sup>2</sup>/V-sec. As was previously observed, the Hall mobilities in the silicon on spinel are a strong function of the thickness, and the Hall electron mobility of 200 cm<sup>2</sup>/V-sec in 0.5 μm (111)Si/(111)spinel is less than half of that observed in the 1.0 μm thick film.

Since the unbiased Hall mobility measurement is weighted by the properties of the material near the silicon/substrate interface, and the (enhancement mode) device measurement is characteristic of the carrier mobilities only within ~500Å of the silicon surface most remote from the silicon-substrate interface, it is not unexpected that the device mobilities are significantly higher than the Hall mobilities for holes in silicon on both sapphire and spinel, and for electrons in silicon on spinel. It is difficult to explain, however, why the n-channel device mobilities in the silicon on sapphire are lower than the Hall electron mobilities measured in equivalent films. It cannot be attributed to the effect of oxidation during device processing, since in general the Hall electron mobilities increase as the compensating aluminum autodoping is deactivated during thermal oxidation (17, 23). In general, however, processing results in the degradation in the carrier mobility even in bulk silicon devices. If the effective (electron) mobility is expressed in terms of the per cent of the mobility commonly observed in MOS transistors fabricated in bulk silicon (~500 cm<sup>2</sup>/V-sec) (4), it is found that the per cent of bulk device mobilities in the transistors fabricated in 1.0 μm silicon on sapphire is in excess of 80%, and in 1 μm thick silicon on spinel ~70%. The effective hole mobilities in the 1 μm thick films are similar to the mobility commonly observed in fabricated devices (~200 cm<sup>2</sup>/V-sec) (4). Thus, on this basis, the per cent of bulk device mobility values are considerably in excess of the per cent of bulk Hall mobilities.

It is interesting to note that the Hall mobilities in 0.5 and 1.0 μm thick films are more similar in silicon on sapphire than in silicon on spinel. This can be explained on the basis of the differences in the nature of film growth prior to complete coverage of the substrate surface. We have demonstrated previously that the primary reaction which leads to the contamina-

tion of the silicon is the chemical reduction of the substrate by silicon (12). Since the reaction products are gaseous, the contamination of the growing film takes place primarily during the period prior to complete coverage of the substrate, and is stopped as the substrate is completely covered and the evolution of gaseous reaction products is blocked off (3). Therefore, the thickness of the heavily contaminated silicon layer adjacent to the substrate can be related to the thickness at which complete coverage of the surface is realized. Under the deposition conditions employed in this study, the surface of the sapphire is completely covered at film thicknesses of ~300Å, while the surface of the spinel is typically covered at a silicon thickness of ~1000Å. It is reasonable to assume that the semiconducting properties improve as the level of contamination by substrate reaction products decreases, and thus the semiconducting properties of the 0.5 μm thick silicon are more similar to the properties of the 1.0 μm thick films on sapphire than on spinel. The reason for the striking differences in the nature of the early growth on the two substrate materials is the subject of current investigation.

### Application

Within this organization sapphire is the favored substrate material because of the advantages realized in processing devices in the very thin (<1 μm) (100) heteroepitaxial films. The commercial availability of single-crystal sapphire from a number of sources is also a factor in the choice of sapphire as a substrate material. Interest continues in the silicon-spinel system for special applications of heteroepitaxial semiconductor structures, particularly where other cubic materials (such as the III-V compounds) are included in the device structure and latitude in the choice of cubic orientations is desirable (29). In these applications carrier mobility within the silicon is not specifically the desired property, but good crystallinity is essential, and mobility has been used as a sensitive measure of the crystalline perfection.

### Summary

The Hall and effective device mobilities of 0.5 and 1.0 μm thick heteroepitaxial silicon on sapphire and spinel are compared. Larger differences are observed in the Hall mobilities than in the device mobilities. The surface reactivity of the Czochralski spinel can be suppressed by growth of the crystal in a high humidity atmosphere. The differences in the chemical nature of the spinel prepared by the various growth techniques to a large extent can be "leveled" by pre-deposition surface treatments. The Hall mobilities in 1 μm thick p-type (111)Si/(111)spinel are ~2× the mobilities observed in (100)Si/(1102)sapphire, but in n-type films the corresponding mobilities are similar. The Hall mobilities in the (100)Si/(1102)sapphire are higher than in (100)Si/(100)spinel for 0.5 and 1.0 μm, n- and p-type films. The Hall mobilities in 0.5 and 1.0 μm thick films are more similar in silicon on sapphire than in silicon on spinel. This can be related to the observation that, under the deposition conditions employed, the surface of the sapphire is completely covered at a thickness of ~300Å, while the surface of the spinel is covered at a thickness of ~1000Å.

### Acknowledgments

The MOS transistors were fabricated and characterized by W. W. Clauhs. Spinel substrate crystals were prepared by Messrs. S. Bolin, J. Creamer, H. Temple, and A. Wasielewski.

Manuscript submitted Nov. 16, 1973; revised manuscript received May 29, 1974.

Any discussion of this paper will appear in a Discussion Section to be published in the June 1975 JOURNAL. All discussions for the June 1975 Discussion Section should be submitted by Feb. 1, 1975.

The publication costs of this article have been assisted by the RCA Corporation.

## REFERENCES

- H. M. Manasevit and W. I. Simpson, *J. Appl. Phys.*, **35**, 1349 (1964).
- J. D. Filby and S. Nielson, *Brit. J. Appl. Phys.*, **18**, 1357 (1967).
- G. W. Cullen, *J. Crystal Growth*, **9**, 107 (1971).
- E. Boleky, J. R. Burns, J. E. Meyer, and J. H. Scott, *Electronics*, p. 82 (July 1970).
- J. E. Meyer, J. R. Burns, and J. H. Scott in, "IEEE ISSCC Digest of Technical Papers," p. 200 (1970).
- E. Boleky, *RCA Rev.*, **31**, 372 (1970).
- H. M. Manasevit and D. H. Forbes, *J. Appl. Phys.*, **37**, 734 (1966).
- H. Schlötterer, *Solid-State Electron.*, **11**, 947 (1968).
- P. H. Robinson and D. J. Dumin, *This Journal*, **115**, 75 (1968).
- G. W. Cullen, G. E. Gottlieb, C. C. Wang, and K. H. Zaininger, *ibid.*, **116**, 1444 (1969).
- G. W. Cullen and C. C. Wang, *ibid.*, **118**, 640 (1971).
- G. W. Cullen and F. C. Dougherty, *J. Crystal Growth*, **17**, 230 (1972).
- H. Schlötterer, Personal communication.
- G. W. Cullen, S. Bolin, J. Creamer, J. F. Corboy, and A. Wasielewski, To be published.
- C. C. Wang, *J. Appl. Phys.*, **40**, 3433 (1969).
- T. A. Zeveke, L. N. Kornev, and V. A. Tolomasov, *Sov. Phys. Cryst.*, **13**, 493 (1968).
- G. E. Gottlieb, Ph.D. Thesis, Rutgers University (1971).
- C. C. Chang, *J. Vacuum Sci. Technol.*, **8**, 500 (1971).
- A. Reisman, M. Berkenblit, J. Cuomo, and S. A. Chan, *This Journal*, **10**, 1653 (1971).
- L. J. van der Pauw, *Philips Res. Rept.*, **13**, 1 (1958).
- R. P. Ruth, A. J. Hughes, J. L. Kenty, H. M. Manasevit, D. Medellin, A. C. Thorsen, Y. T. Chan, C. R. Viswanathan, and M. A. Ring, Final Report, Contract No. DAAH01-70-C-1311, Advanced Research Projects Agency, August 1973.
- G. E. Gottlieb, J. F. Corboy, G. W. Cullen, and J. H. Scott, *Met. Trans.*, **2**, 653 (1971).
- G. E. Gottlieb and J. F. Corboy, *J. Crystal Growth*, **17**, 261 (1972).
- L. R. Weisberg, *J. Appl. Phys.*, **33**, 1817 (1962).
- W. E. Ham, *Appl. Phys. Letters*, **21**, 440 (1972).
- A. C. Ipri, *ibid.*, **20**, 1 (1972).
- D. J. Dumin and P. H. Robinson, *J. Crystal Growth*, **3**, 4, 214 (1968).
- J. H. Scott and J. R. Burns, Paper 138 presented at Electrochemical Society Meeting, Los Angeles, California, May 10-15, 1970.
- G. W. Cullen, M. T. Duffy, and C. C. Wang, in "Chemical Vapor Deposition," G. F. Wakefield and J. M. Blocher, Jr., Editors, p. 247, The Electrochemical Society Softbound Symposium Series, Princeton, N. J. (1973).

## The Solid Solubility of Gold in Doped Silicon by Oxide Encapsulation

T. A. O'Shaughnessy\* and H. D. Barber\*

*Linear Technology, Inc., Hamilton, Ontario, Canada*

D. A. Thompson

*Department of Engineering Physics, McMaster University, Hamilton, Ontario, Canada*

and E. L. Heasell

*University of Waterloo, Waterloo, Ontario, Canada*

### ABSTRACT

The solubility of gold has been measured in phosphorus-doped silicon by the method of oxide encapsulation. At high phosphorus concentrations an enhanced solubility was observed. This enhanced solubility is extremely temperature dependent, increasing from a factor of 1.4 at 1200°C to  $\approx 15$  at 800°C in silicon doped with  $4 \times 10^{19}$  phosphorus/cm<sup>3</sup>. A reasonable agreement has been obtained between the measured enhancement and that calculated using the Shockley-Moll theory.

The effect of gold on the electrical properties of silicon is of technological importance in the semiconductor device field. Gold introduces two known energy levels in silicon; a donor at  $E_v + 0.35$  eV and an acceptor at  $E_c - 0.54$  eV (1). These levels act as effective recombination centers (2) with the charge state determining the recombination process. Hence, when gold can be controllably introduced into silicon it is possible to effectively control the minority carrier lifetime. This has application in high speed switching transistors. However, when gold is present as an unwanted and uncontrolled contaminant, device parameters can be seriously degraded. Surface contamination of silicon with gold has been observed on wafers that have been subjected to normal processing procedures (3, 4). In a previous paper (5), the authors have shown that gold plates out of a standard HF solution to the

extent that one monolayer of gold will form in minutes over the surface of a silicon wafer immersed in 10 ml of HF solution contaminated with gold to 1 ppm by weight.

Most metals exhibit a retrograde solubility in silicon. This has also been observed for gold in silicon by Collins *et al.* (1). Therefore in device processing, where each diffusion step is at a lower temperature than the preceding one, gold present to the limit of solid solubility during an earlier step would be expected to form precipitates in the bulk or to be rejected to the surface due to the high diffusion coefficient. Hence, accurate knowledge of the solubility of gold in doped silicon would be very desirable. Much work has already been carried out in this area (1, 6-8) but there is substantial disagreement between published data. The fact that gold can reside both interstitially and substitutionally in the silicon lattice is partially responsible for such disagreement. The work

\* Electrochemical Society Active Member.

Key words: silicon, gold, solubility, enhancement, encapsulation.

of Struthers (7) and Collins *et al.* (1) give values of the solubility which Wilcox and LaChappelle (9) determined to be the substitutional solubility. The earlier work of Struthers (6) and data given by Boltaks *et al.* (8) appear to be incorrect due to incomplete equilibration.

Additional complications arise since gold solubility is dependent on the initial impurity type and concentration in silicon. An enhanced gold solubility has been observed by Wilcox *et al.* (10) in silicon containing a high phosphorus concentration. Joshi and Dash (11) and Cagnina (12) found a similar effect. In two cases (10, 11) good agreement was found between this enhancement and the Reiss (13) and Shockley-Moll (14) theories in which the solubility is dependent on the position of the Fermi level. The even greater enhanced solubility found by Cagnina (12) was interpreted as due to the formation of an Au-P compound in addition to the electronic effect resulting from the position of the Fermi level.

Dorward and Kirkaldy (15) argued that if enhanced solubility occurred in heavily doped n-type silicon, then a reduced solubility should be observed in silicon doped heavily p-type. Their experimental observations showed a 40% reduction in the solubility of gold in silicon doped with  $10^{19}$  boron atoms/cm<sup>3</sup> over that doped with  $\sim 10^{13}$  boron atoms/cm<sup>3</sup>. In contrast, Gubenko and Shmelev (16) observed enhanced solubility of gold in silicon doped with Ga at concentrations of  $10^{17} - 4 \times 10^{19}$ /cm<sup>3</sup>. This enhancement is probably due to high mechanical stress within the samples.

It was felt that there was considerable scope for further work in this area especially if some of the problems from which previous work suffered could be eliminated. The data presented in this paper was obtained using an oxide encapsulation technique in which the equilibrated sample is encapsulated in a thermally grown oxide. The oxide prevents gold loss on cooling and reduces errors resulting from high concentrations of residual surface gold.

### Oxide Encapsulation

Shown below are the diffusion coefficients for gold in silicon (assuming a vacancy-controlled mechanism) and for silicon dioxide

Silicon (9)

$$D = 4 \cdot 10^{-9} \text{ cm}^2/\text{sec at } 1000^\circ\text{C}$$

$$D = 2.5 \cdot 10^{-7} \text{ cm}^2/\text{sec at } 1200^\circ\text{C}$$

Silicon dioxide (17)

$$D = 3 \cdot 10^{-18} \text{ cm}^2/\text{sec at } 1000^\circ\text{C}$$

$$D = 10^{-15} \text{ cm}^2/\text{sec at } 1200^\circ\text{C}$$

Also, the solid solubilities at 1100°C of gold in silicon and silicon dioxide are  $3 \times 10^{16}$ /cm<sup>3</sup> (1) and  $3 \times 10^{14}$ /cm<sup>3</sup> (18), respectively. Hence, if following the equilibration step, an oxide is grown on the silicon surface, problems related to gold migration toward the surface during cooling should be minimized without having to resort to quenching procedures.

In the present experiments, prior to removal from the furnace, the equilibrated sample was oxidized in dry oxygen to form about 1000Å of SiO<sub>2</sub>. During the formation of the oxide, most of the excess gold remaining on the silicon surface is rejected to the oxide surface from which it can easily be removed in aqua regia. Measurements of the gold distribution throughout the Si-SiO<sub>2</sub> (5) system show an accumulation of gold in the interface region. This accumulated gold lies in the oxide layer and is distributed over a region  $\sim 200\text{Å}$  from the silicon surface.

Measurements of the gold in the silicon indicate no depletion of gold near the interface when excess gold is present before oxidation. The interfacial gold is therefore part of the excess gold and is removed with the oxide before measurements are made. Because no gold is removed from the silicon following equilibration, the measurements remain accurate regardless of

the final distribution of the gold within the silicon itself.

### Experimental

In order to avoid some of the errors made in earlier measurements, the time required to saturate the silicon with gold was experimentally determined. Slices of silicon had their surfaces coated with gold containing some radioactive Au<sup>198</sup>. The gold was then diffused for times ranging from 1 hr to 1 week depending on the diffusion temperature. In Fig. 1, the equilibration data is given for a 0.008 in. thick silicon wafer diffused with gold at 1050°C. The experimentally determined, time-dependent gold concentration in the silicon was accurately described by the vacancy controlled diffusion coefficients of Wilcox and LaChappelle (9). It was found that 95% of the solid solubility at 1050°C was reached after 24 hr. The times required to reach 95% saturation were determined for all temperatures of interest. In the case of diffusion at 800°C, the silicon sample was thinned to 0.002 in. prior to diffusion. Also, samples containing a high concentration of phosphorus were thinned down to 0.004 in. and the diffusion times increased to compensate for the expected increase in the gold solubility limit. The diffusions were carried out in a nitrogen atmosphere. Following the diffusion step each sample was oxidized as indicated in the oxide encapsulation technique.

Surface damage can effect the solubility of gold in silicon. Figure 2 shows the profiles of gold in the sur-

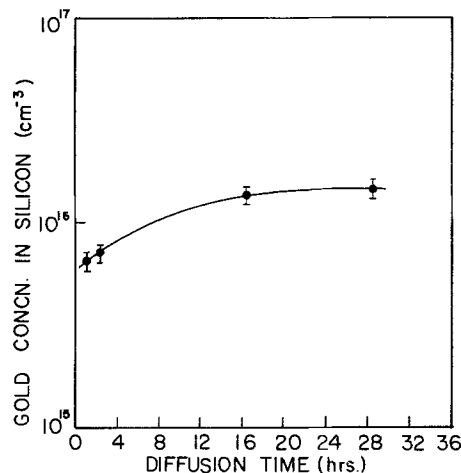


Fig. 1. Equilibration of gold in silicon at 1050°C

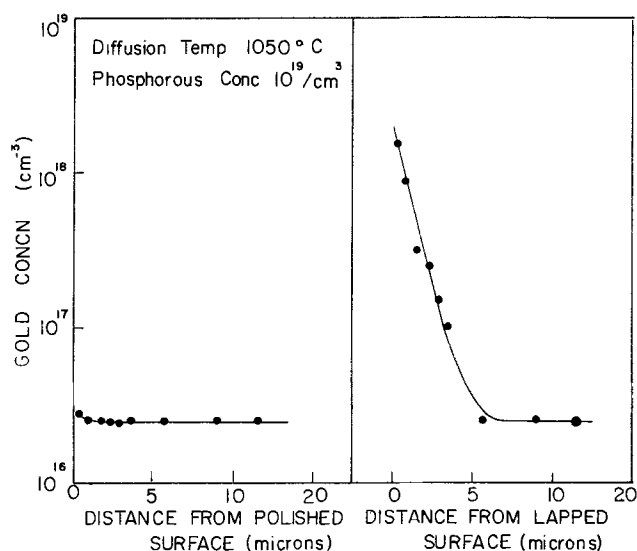


Fig. 2. Distribution of gold at a polished and a lapped silicon surface.

face region for a lapped and a polished surface. In order to avoid errors arising from damage enhanced solubility in the surface layer all samples were prepared with polished surfaces only. Each wafer was counted front and back and again after removal of  $12\mu$  of silicon to check that indeed no damage enhancement of the solubility was present.

The gold concentration in the sample was determined by  $\beta$ -particle counting. With  $\beta$ -particle counting it is necessary to correct for attenuation of the radiation due to the distributed nature of the source. The sample was counted with the front and back surfaces alternately facing the detector. If the counts measured were  $C_F$  and  $C_B$ , then the total count,  $N$ , corresponding to all the gold atoms in the sample is given by

$$N = F(C_F + C_B)/2$$

where  $F$  is the correction factor for the distributed source. For a uniformly distributed source

$$F = t\lambda/[1 - \exp(-\lambda t)]$$

where  $t$  is the sample thickness (cm) and  $\lambda$  is the  $\beta$ -particle absorption coefficient which was measured to be  $= 50.41 \text{ cm}^{-1}$ . The  $F$  factor was evaluated for the extremes of nonuniformity in source distribution and was found to vary by less than 4% from the uniform case.

### Results and Discussion

The solid solubility of gold in silicon, in the temperature range  $1000^\circ\text{--}1200^\circ\text{C}$  is shown in Fig. 3 for silicon initially doped with phosphorus to the levels  $5.5 \times 10^{14}$  and  $4 \times 10^{19}/\text{cm}^3$ . The enhanced gold solubility in the heavily doped sample is clearly evident. In the temperature range considered, the solubility was investigated for initial phosphorus doping levels of  $5.5 \times 10^{14}$ ,  $4.5 \times 10^{15}$ ,  $1.2 \times 10^{17}$ ,  $10^{19}$ , and  $4 \times 10^{19}/\text{cm}^3$ . For temperatures above  $1000^\circ\text{C}$ , solubility enhancement was observed only in the  $4 \times 10^{19}/\text{cm}^3$  phosphorus doped sample.

A solubility enhancement factor  $R_S$  is defined as

$$R_S = \frac{\text{gold solubility in heavily doped sample}}{\text{gold solubility in a reference sample}}$$

For the current experiments, the solubility in  $5 \times 10^{14}/\text{cm}^3$  doped silicon was used as the reference level.

In Fig. 4, the solubility enhancement factor is given over the temperature range  $1000^\circ\text{--}1200^\circ\text{C}$  in silicon doped with  $4 \times 10^{19}$  phosphorus atoms/ $\text{cm}^3$ .

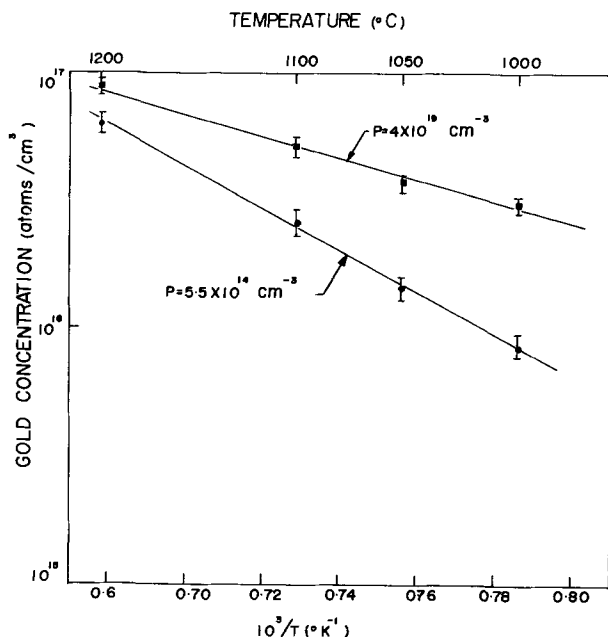


Fig. 3. Measured solubility of gold in phosphorus-doped silicon

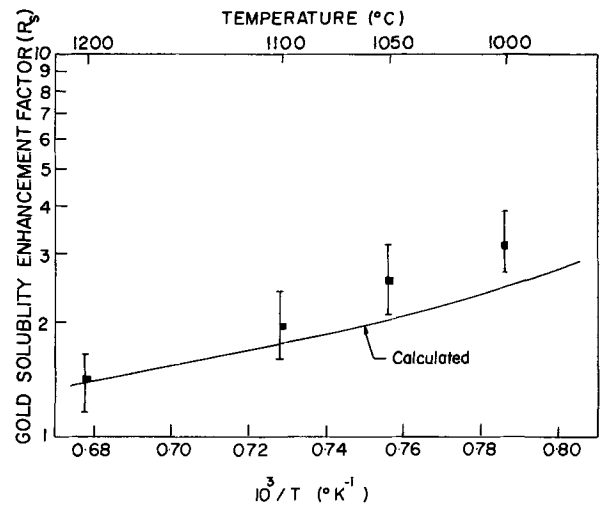


Fig. 4. Temperature dependence of the solubility enhancement of gold in silicon doped with  $4 \times 10^{19}$  phosphorus atoms/ $\text{cm}^3$ .

Reiss *et al.* (13) have shown that the solubility of impurities in semiconductors may depend on the charge state of the impurity. This idea was further developed by Shockley and Moll (14) such that the total concentration of gold can be written as

$$N_{\text{Au}} = \sum_{j=0}^2 N_{\text{Au}}(j) \quad [1]$$

where

$$\frac{N_{\text{Au}}(j)}{N_{\text{Au}}} = \frac{g(j) \exp\{(jE_F - E(j))/kT\}}{\sum_{j=0}^2 g(j) \exp\{(jE_F - E(j))/kT\}} \quad [2]$$

where  $N_{\text{Au}}(j)$  is the concentration of gold centers occupied by  $j$ -electrons and  $g(j)$  and  $E(j)$  are the degeneracies and total energies of such centers, respectively (20).

Since the theory postulates that  $N_{\text{Au}}(1)$ , the neutral center concentration is independent of the Fermi level position, Eq. [2] may be used to express the  $N_{\text{Au}}(j)$  in terms of  $N_{\text{Au}}(1)$

$$\frac{N_{\text{Au}}(j)}{N_{\text{Au}}(1)} = \{g(j)/g(1)\} \exp\{((j-1)E_F - (E(j) - E(1)))/kT\} \quad [3]$$

If  $N_{\text{Au}}^R$  and  $N_{\text{Au}}^F$  are the solubilities in the reference and test samples respectively, Eq. [1] and [3] yield the solubility ratio  $R_S$

$$R_S = N_{\text{Au}}^F/N_{\text{Au}}^R$$

$R_S$  was calculated using the parameters

$$g(0) = 1, g(1) = 4, g(2) = 6$$

The energy levels were assumed referenced to a linearly extrapolated energy gap of 1.205 eV at  $0^\circ\text{K}$

$$E(0) = (0.35 + E_V) \text{ eV at } 0^\circ\text{K}$$

$$E(2) = (0.97 + E_V) \text{ eV at } 0^\circ\text{K}$$

and were assumed to maintain the same relative location in the gap at other temperatures (21, 22).

The degeneracy factors are those corresponding to a simple valence bond model of the gold center, forming 0, 1, and 2 bonds in the donor, neutral, and acceptor states. These values correspond to  $g = 3/2$ ,  $g = 1/4$ ,  $E_A = 0.54 \text{ eV}$ , and  $E_D = 0.35 \text{ eV}$  in the Shockley and Last notation (23).

The Fermi level was computed using the modified band model described by Barber (24) and extended by Heasell (25). Shallow level excited states were in-

cluded and an empirical adjustment made for the doping dependence of activation energies (26).

The results of one such calculation are shown in Fig. 4. It can be seen that the experimental results show a slightly greater rate of solubility enhancement than predicted on the Shockley-Moll theory.

Samples were also diffused at 800°C. A comparison of calculated and measured enhancement factor as a function of phosphorus doping is shown in Fig. 5. It can be seen that enhancement now occurs at the  $10^{18}$  phosphorus atoms/cm<sup>3</sup> level.

In some samples a phosphorus diffusion was also carried out at 1050°C at the same time as the gold diffusion. The surface concentration of phosphorus in the diffused layer was  $10^{21}$ /cm<sup>3</sup>. According to the present model an enhanced solubility factor of  $\approx 70$  might be expected taking a mean phosphorus concentration throughout the diffused layer of  $5 \times 10^{20}$ /cm<sup>3</sup>. Etching of the first 2 $\mu$  of surface (i.e., the phosphorus diffused layer), a gold concentration of  $1.25 \times 10^{18}$  atoms/cm<sup>3</sup> was observed in the diffused layer. This represents an enhancement factor of 80.

In almost all the measurements the enhanced solubility was slightly greater than that predicted by the model used.

The effects of the gold concentration on the electrical resistivity were also measured. For the samples with initial phosphorus concentrations of  $1.2 \times 10^{17}$ /cm<sup>3</sup> and greater, gold concentrations of  $8 \times 10^{16}$ /cm<sup>3</sup> had no measurable effect. At lower values of phosphorus concentration, the resistivity varied drastically. The results are shown in Fig. 6 compared with the recent theoretical results of Bullis (19). With an initial phosphorus concentration of  $5 \times 10^{14}$ /cm<sup>3</sup> the silicon converts to p-type when the gold concentration reaches  $\sim 6 \times 10^{15}$ /cm<sup>3</sup>. At  $4.5 \times 10^{15}$  phosphorus atoms/cm<sup>3</sup>, conversion to p-type occurs with a gold concentration of  $\sim 1.5 \times 10^{16}$ /cm<sup>3</sup>.

### Summary and Conclusions

Solid solubility measurements were carried out by encapsulating gold in silicon by growing a 1000Å thick layer of SiO<sub>2</sub> over the sample following the diffusion step. This method allowed the total gold taken up by

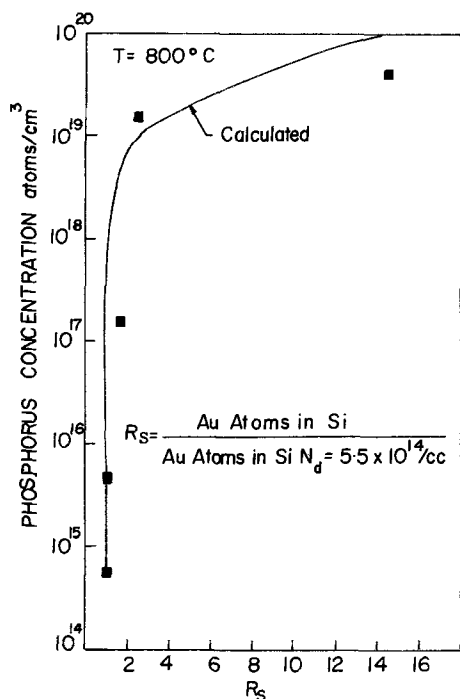


Fig. 5. Solubility enhancement factor at 800°C for gold as a function of phosphorus concentration. The calculated dependence is shown for comparison.

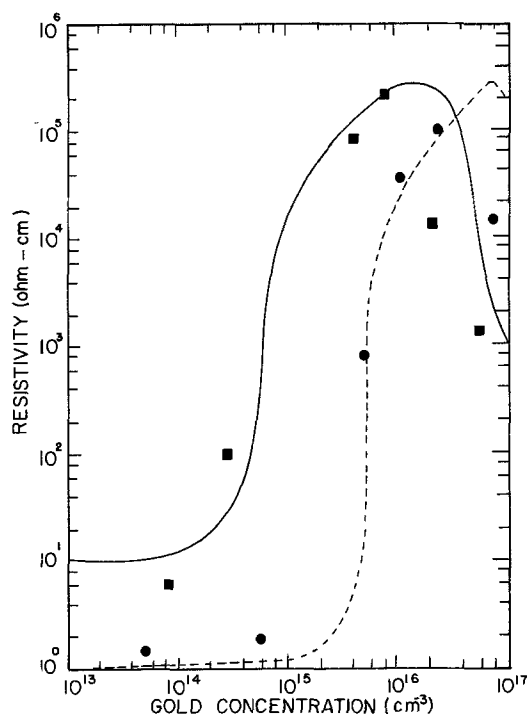


Fig. 6. Effect of gold concentration on the electrical resistivity for silicon with phosphorus concentrations of  $5.5 \times 10^{14}$  cm<sup>-3</sup> (■) and  $4.5 \times 10^{15}$  cm<sup>-3</sup> (●). The lines give the extrapolated theoretical dependence given by Bullis (19).

the silicon at the diffusion temperature to be determined and eliminated the need to quench the samples.

The time required to equilibrate the silicon wafers indicated that the vacancy controlled process was the diffusion mechanism.

Phosphorus doping of the silicon resulted in enhanced solid solubility for the gold. A reasonable agreement between the experimental results and the Shockley-Moll theory was obtained. It is not certain whether this mechanism alone accounts for the total enhancement. Uncertainties arise in the calculated values of enhancement since the degeneracy factors and temperature dependence of the energy levels of the gold states are not accurately known. It is possible that ion-pairing or compound formation may be occurring (e.g., Au<sup>-</sup>-P<sup>+</sup>). However, if this were a substantial effect, the gold acceptor level would be neutralized and agreement between the gold radio-tracer measurements and the electrical compensation would not have been obtained.

Manuscript submitted Nov. 26, 1973; revised manuscript received April 23, 1974.

Any discussion of this paper will appear in a Discussion Section to be published in the June 1975 JOURNAL. All discussions for the June 1975 Discussion Section should be submitted by Feb. 1, 1975.

The publication costs of this article have been assisted by McMaster University.

### REFERENCES

1. C. B. Collins, R. O. Carlson, and C. J. Gallagher, *Phys. Rev.*, **105**, 1168 (1957).
2. G. Bemski, *ibid.*, **111**, 1515 (1958).
3. H. F. John, J. W. Faust, and R. Stickler, *IEEE Trans.*, **PMP-2**, 51 (1966).
4. R. O. Carlson, *J. Appl. Phys.*, **29**, 1001 (1958).
5. T. A. O'Shaughnessy, H. D. Barber, D. A. Thompson, and E. L. Heasell, in "Semiconductor Silicon 1973," Howard R. Huff and Ronald R. Burgess, Editors, The Electrochemical Society Soft-bound Symposium Series, Princeton, N. J. (1973).
6. J. D. Struthers, *J. Appl. Phys.*, **27**, 1560 (1956).
7. J. D. Struthers, *ibid.*, **28**, 516 (1957).

8. B. I. Boltaks, G. S. Kulikov, and R. Sh. Malkovich, *Sov. Phys.-Solid State*, **2**, 2134 (1960).
9. W. R. Wilcox and T. J. La Chappelle, *J. Appl. Phys.*, **35**, 240 (1964).
10. W. R. Wilcox, T. J. La Chappelle, and D. H. Forbes, *This Journal*, **111**, 1377 (1964).
11. M. L. Joshi and S. Dash, *J. Appl. Phys.*, **37**, 2453 (1966).
12. S. F. Cagnina, *This Journal*, **116**, 498 (1969).
13. H. Reiss, C. S. Fuller, and F. J. Morin, *Bell System Tech. J.*, **35**, 535 (1956).
14. W. Shockley and J. L. Moll, *Phys. Rev.*, **119**, 1480 (1960).
15. R. C. Dorward and J. S. Kirkaldy, *This Journal*, **116**, 1284 (1969).
16. A. Ya. Gubenko and Yu. I. Shmelev, *Akad. Nauk SSSR, Neorganicheski Materialy*, **7**, 731 (1971).
17. D. R. Collins, D. K. Schroder, and C. T. Sah, *Appl. Phys. Letters*, **8**, 323 (1966).
18. T. A. O'Shaughnessy, Ph.D. Thesis, University of Waterloo (1971).
19. W. M. Bullis, *Nat. Bur. Std. Tech. Note* 743, 15 (1973).
20. P. T. Landsberg, "Semiconductors and Phosphors," Braunschweig, Vieweg & Son (1958).
21. H. D. Barber, Ph.D. Thesis (London) (1965).
22. L. C. Parrillo and W. C. Johnson, *Appl. Phys. Letters*, **20**, 104 (1972).
23. W. Shockley and J. Last, *Phys. Rev.*, **107**, 392 (1957).
24. H. D. Barber, *Solid State Electron.*, **10**, 1039 (1967).
25. E. L. Heasell, *ibid.*, **16**, 651 (1973).
26. G. L. Pearson and J. Bardeen, *Phys. Rev.*, **75**, 865 (1949).

## The Incorporation of Phosphorus in Silicon Epitaxial Layer Growth

J. Bloem,\* L. J. Giling, and M. W. M. Graef

*University of Nijmegen, Laboratory of Physics, Department of Solid State Chemistry,  
Toernooiveld, Nijmegen, Holland*

### ABSTRACT

A study has been made of the mechanism governing the incorporation of phosphorus during epitaxial growth of silicon. Several possibilities are mentioned and it is shown that the position of the Fermi level in the solid and the equilibria in the gas phase determine the outcome of the experiment. When  $\text{PH}_3$  in  $\text{H}_2$  is used as a dopant at the temperatures of interest,  $\text{P}$ ,  $\text{P}_2$ ,  $\text{P}_4$ ,  $\text{PH}$ , and  $\text{PH}_2$  are present also. It is shown that there is a close correlation between the partial pressure of monoatomic P in the gas and the phosphorus concentration in the solid as long as intrinsic conditions apply. Only at high dopant concentration ( $P > 3 \cdot 10^{19} \text{ cm}^{-3}$ ) and low temperature ( $T < 1500^\circ\text{K}$ ) does the influence of the position of the Fermi level become important.

The incorporation of phosphorus in epitaxial silicon layers grown from the vapor phase has been studied in considerable detail by many workers (1-5). For low partial pressures of the dopant (mostly in the form of phosphine,  $\text{PH}_3$ ), the concentration of phosphorus atoms in silicon is proportional to the partial pressure of the phosphine gas present in the gas mixture, and the slope of a log-log plot of the  $\text{P}^+$  concentration in the solid ( $[\text{P}^+]$ ) vs. the initial (input) phosphine partial pressure ( $p^{\circ}\text{PH}_3$ ) is 1.0. At higher  $\text{PH}_3$  pressures a deviation is found and the slope changes from 1.0 to 0.5. A number of explanations have been given for this behavior, of which the most important are: (i) variation of growth rate which may influence the dope concentration; (ii) clustering of phosphorus in the silicon matrix during cooling, which causes a decrease of the concentration of charge carriers and thus flattening of the curve; (iii) transition from intrinsic to extrinsic conditions at high donor concentrations; and (iv) the degree of aggregation of phosphorus in the gas mixture.

As yet no clear picture exists as to which effect is dominating. In order to elucidate which mechanism is responsible for the incorporation, a series of precise measurements was started.

### Experimental

Silicon doped with phosphorus was epitaxially grown in a horizontal water-cooled reactor having an effective cross section of  $12 \text{ cm}^2$ . Substrates were one-side polished p-type Czochralski-grown silicon wafers

with a resistivity between 2 and 5 ohm-cm. The orientation of the surface was  $3^\circ$  from the (111)-plane in the nearest  $\langle 110 \rangle$ -direction. The slices were placed on a SiC-coated graphite susceptor and heated by means of a rf coil. Epitaxial growth was performed by silane,  $\text{SiH}_4$ , using  $\text{H}_2$  as a carrier gas at a velocity of 42 cm/sec. The  $\text{SiH}_4$  partial pressure was kept at a constant value of  $2.2 \times 10^{-3} \text{ atm}$  giving a growth rate of  $0.45 \mu\text{/min}$ .  $\text{PH}_3$  was used as a dopant gas at pressures varying between  $10^{-10}$  and  $10^{-3} \text{ atm}$ . The purity of the hydrogen gas was continuously controlled ( $\text{O}_2 < 1 \text{ ppm}$  and  $\text{H}_2\text{O} < 2-3 \text{ ppm}$ ).

Before any growth experiment the Si surface was etched *in situ* for 1 min by 1% HCl at  $1400^\circ\text{K}$ . The composition of the gas mixture was monitored and controlled by calibrated flow meters. Temperature measurements were made during the reaction, using a calibrated Leeds and Northrup optical pyrometer, and corrected for the emissivity of silicon and for the reflection and absorption of the epitaxial system.

The epitaxial layer thickness was measured using a bevel and stain technique; the layer thicknesses were kept between 4.5 and  $8.5 \mu\text{m}$ . The resistivity of the layers was determined at room temperature by the four-point probe technique; carrier concentrations were calculated using Irving's (6) mobility data. The phosphorus concentration in the crystal is then assumed to be equal to the number of free electrons measured at room temperature (5).

### Results and Discussion

The experimental data from experiments at  $1400^\circ$ ,  $1500^\circ$ , and  $1600^\circ\text{K}$  are collected in Fig. 1, where the

\* Electrochemical Society Active Member.

Key words: silicon, phosphorus dope, incorporation mechanism, vapor phase epitaxy, gas phase equilibria.

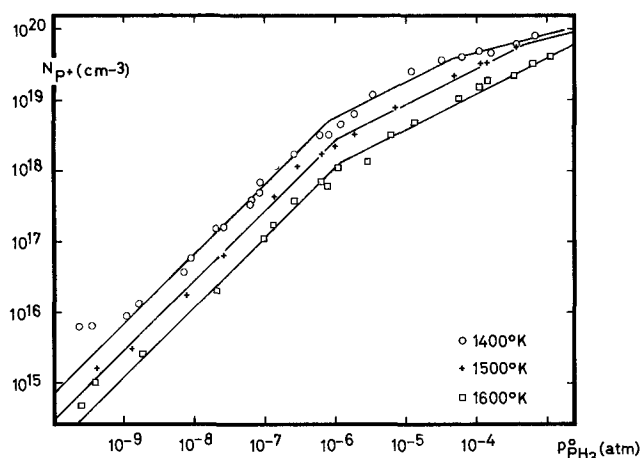


Fig. 1. The experimentally determined concentration of phosphorus donor centers in silicon ( $\text{cm}^{-3}$ ) as a function of the partial pressure of phosphine in the incoming gas. The carrier gas is hydrogen, the silicon growth rate is  $0.45 \mu/\text{min}$ .

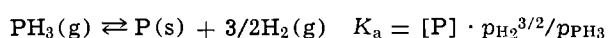
logarithm of the concentration of incorporated phosphorus is plotted against the logarithm of the initial phosphine partial pressure. The experimental points were obtained over a period of several months and the reproducibility of the data is considered to be within  $\pm 10\%$ . Essentially one can consider the curves to be constructed from straight lines with one or two breaks. The principal interest concerns the slope of the lines and the origin of the change of this slope at the breaks. At low  $\text{PH}_3$  pressures the slope is unity, at higher pressures the slope changes to 0.5. This change in slope occurs at lower values of  $[\text{P}^+]$  for higher temperatures. Further it can be noticed that at  $1400^\circ\text{K}$  for partial pressures of  $\text{PH}_3$  exceeding  $10^{-5}$  atm a second change in slope from 0.5 to 0.25 occurs.

Concerning the mechanism of incorporation of phosphorus in silicon the following possibilities are present.

*Effects in the solid.*—(i) Regarding the correlation between the incorporation of phosphorus and the growth rate of silicon, Rai-Choudhury and Salkovitz (2) found that the Si deposition rate does not influence the doping level. Bloem (7), however, showed that growth rates higher than  $1 \mu/\text{min}$  caused an appreciable increase in phosphorus concentration in the solid, using a constant  $\text{PH}_3$  pressure in the gas phase. In order to prevent this type of kinetic effects and to be able to study the equilibrium segregation of P in Si, a growth rate of  $0.45 \mu/\text{min}$  was chosen by using a constant  $\text{SiH}_4$  partial pressure of  $2.2 \times 10^{-3}$  atm. (At the highest  $\text{PH}_3$  concentrations the growth rate appeared to be 10% less.)

(ii) A second reason for the flattening of the curve at high  $\text{PH}_3$  pressures is the clustering of phosphorus in the silicon upon cooling, which would cause a decrease in the number of electrically active P atoms. Nakanuma (5) showed by radiotracer analysis a one to one correlation between the total concentration of P and the conductivity of the layers, thus making clear that clustering of P can be neglected for concentrations as high as  $3 \times 10^{19}$  atoms/ $\text{cm}^3$  at least. The experimental data of Nakanuma are in good agreement with the present results.

(iii) The change from intrinsic to extrinsic conditions in the solid will cause a change in the slope of  $\log [\text{P}^+]$  vs.  $\log p_{\text{PH}_3}$  with a factor two which follows from the ionization equilibrium of phosphorus in the silicon matrix together with the appropriate equilibrium constant



giving

$$[\text{P}^+] = K_b[\text{P}] / n = K_a K_b p_{\text{PH}_3} / (n \cdot p_{\text{H}_2}^{3/2})$$

for  $p_{\text{H}_2} \approx 1$  atm this becomes

$$[\text{P}^+] = K_a K_b p_{\text{PH}_3} / n$$

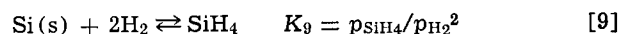
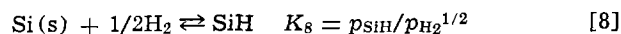
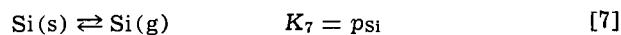
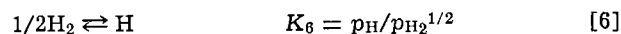
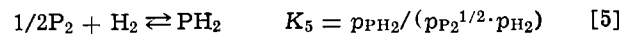
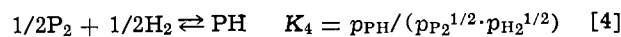
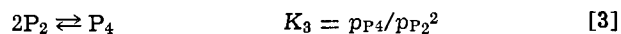
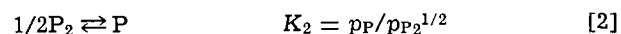
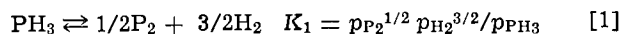
For intrinsic conditions  $n = k_i^{1/2}$ ,  $k_i$  being the intrinsic constant and  $[\text{P}^+] \sim p_{\text{PH}_3}$ , whereas for extrinsic conditions with  $[\text{P}^+] = n$ ,  $[\text{P}^+] \sim p_{\text{PH}_3}^{1/2}$  (8). In the results presented in Fig. 1 it is seen that the change in slope from 1.0 to 0.5 is found at a lower value of  $[\text{P}^+]$  for higher temperatures which is in disagreement with a behavior, based on an intrinsic-extrinsic conversion. Moreover, according to Morin and Maita (9) the intrinsic concentrations at the temperatures used are:  $3 \times 10^{19} \text{ cm}^{-3}$  at  $1400^\circ\text{K}$ ,  $6 \times 10^{19} \text{ cm}^{-3}$  at  $1500^\circ\text{K}$ , and  $1.2 \times 10^{20}$  at  $1600^\circ\text{K}$ , much higher than the value of  $10^{18}$  encountered here. Later in this section it will be shown that the break in the curve from 0.5 to 0.25 for  $1400^\circ\text{K}$  at high concentrations could be due to this intrinsic-extrinsic transition.

*Effects in the gas phase: thermodynamic discussion.*—In the foregoing it has been shown that reactions in the solid cannot explain the main features of the experimental data, therefore the gas phase has to be given closer attention. Rai-Choudhury (2, 3) and Hurlle *et al.* (4) performed calculations of the gas phase composition of various phosphorus compounds in hydrogen; however, they did not take into account the presence of  $\text{PH}_3$  and monoatomic P,  $\text{P}_4$ ,  $\text{PH}$ , and  $\text{PH}_2$ , respectively.

These compounds are stable at the temperatures of interest and are present in concentrations high enough to be of considerable importance. The possible occurrence of other phosphorus-containing compounds, such as  $\text{PSi}$ ,  $\text{PSi}_2$ ,  $\text{PH}_2\text{SiH}_3$ ,  $\text{PSiH}_3$ ,  $\text{P}^+$ ,  $\text{P}_2^+$ , etc., is likely to be of minor importance. At least this seems to follow from the present state of knowledge about the relevant thermodynamic data.

Using the most recent JANAF data (10) the equilibrium concentration in hydrogen of P,  $\text{P}_2$ ,  $\text{P}_4$ ,  $\text{PH}$ ,  $\text{PH}_2$ , and  $\text{PH}_3$  were computed as a function of the input concentration of  $\text{PH}_3$  at the temperatures of interest. It is assumed, because of the low growth rate which is being used, that equilibrium in the gas phase is attained near the silicon surface, and that transport effects are of minor importance. In that case a thermodynamical approach is allowed.

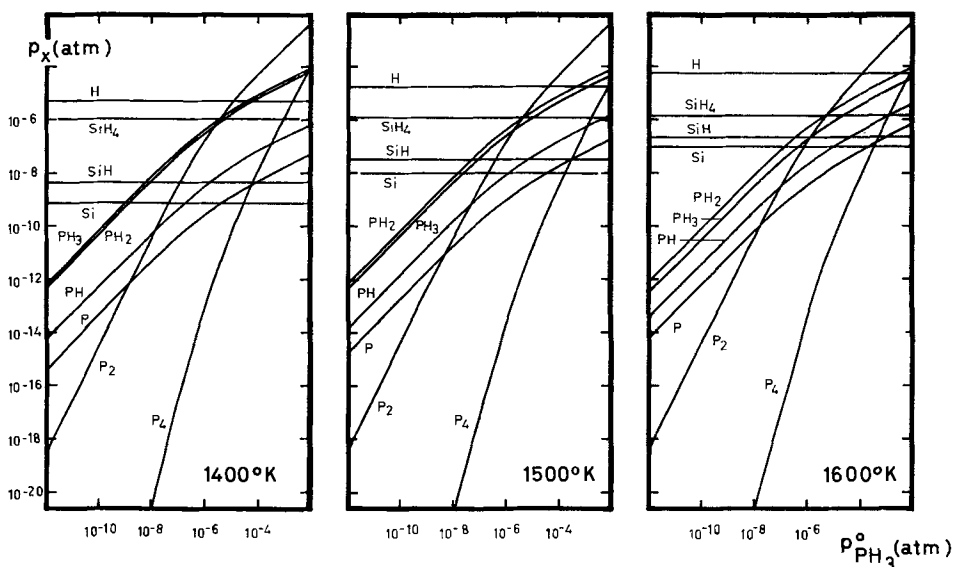
The equilibria in which the above-mentioned phosphorus components are present may be described by the following reactions and equilibrium constants



The composition of the system is now solved by means of an iterative computer procedure subject to the conditions that (a) the sum of all the partial pressures remains 1 atm, (b) the silicon partial pressure is determined by its solid-vapor equilibrium, and (c) the phosphorus-hydrogen ratio is determined by the input quantities of  $\text{PH}_3$ ,  $\text{SiH}_4$ , and  $\text{H}_2$ . The various equilibrium constants which are used are collected in Table I.

Calculations were made for the partial pressures of P,  $\text{P}_2$ ,  $\text{P}_4$ ,  $\text{PH}$ ,  $\text{PH}_2$ ,  $\text{PH}_3$ ,  $\text{H}_2$ ,  $\text{H}$ ,  $\text{SiH}_4$ ,  $\text{SiH}$ , and  $\text{Si}$ . The results are presented in Fig. 2. Over the range of initial

Fig. 2. Computed curves giving the equilibrium partial pressures of the components of the gas mixture vs. the initial partial pressure of  $\text{PH}_3$  ( $p_{\text{PH}_3}^0$ ) for three temperatures.



phosphine partial pressures that were considered in these experiments, the main gas components at low pressures appear to be  $\text{PH}_3$  and  $\text{PH}_2$ ; at higher initial pressures  $\text{P}_2$  has the highest partial pressure. The most significant feature however is that the calculated profiles of  $\text{P}$ ,  $\text{PH}$ ,  $\text{PH}_2$ , and  $\text{PH}_3$  are completely analogous to what empirically has been found for the incorporation of  $\text{P}$  in the silicon matrix. Since the concentrations of all phosphorus-containing compounds are related by equilibrium equations one is permitted to consider the segregation as originating from one of these compounds. In addition as there is no evidence for the presence of  $\text{P}_2$ ,  $\text{P}_4$ ,  $\text{PH}$ ,  $\text{PH}_2$ , and  $\text{PH}_3$  in the solid state, the segregation of phosphorus in the silicon matrix is best correlated with the vapor pressure of monoatomic  $\text{P}$  in the gas phase according to



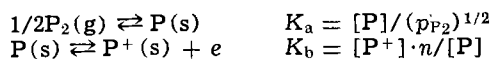
The calculated results for monoatomic phosphorus are collected in Fig. 3. These curves are in good agreement with the shape of the experimental curves found at the three temperatures (Fig. 1). Attention must be given to the fact that the relative order of the curves is different: the monoatomic phosphorus pressure increases with increasing temperature (Fig. 3), whereas the amount of phosphorus incorporated in silicon decreases with increasing temperature (Fig. 1), demonstrating the temperature dependence of the incorporation process.

Discussing the data in Fig. 1, it can be stated that the slope 1.0 is due to the linear relation between monoatomic  $\text{P}$  and  $\text{PH}_3$  at  $1400^\circ\text{K}$  or between  $\text{P}$  and  $\text{PH}_2$  at  $1500^\circ\text{K}$ , respectively,  $\text{PH}_3$  and  $\text{PH}_2$  being the main gas components at these temperatures. The slope 0.5 expresses the quadratic relation of  $\text{P}$  to  $\text{P}_2$  in the gas phase.

Table I. The logarithms (to base 10) of the equilibrium constants of the heterogeneous system  $\text{Si-P-H}$  at  $1400^\circ\text{K}$ ,  $1500^\circ\text{K}$ , and  $1600^\circ\text{K}$  (from Ref. 10). The equilibrium constants correspond to Eq. [1]-[9] given in the text

	$\log_{10}K$	$1400^\circ\text{K}$	$1500^\circ\text{K}$	$1600^\circ\text{K}$
$\text{P}_2$	(Ref. state)	0.000	0.000	0.000
$\text{H}_2$	(Ref. state)	0.000	0.000	0.000
$\text{Si}(\text{s})$	(Ref. state)	0.000	0.000	0.000
$\text{PH}_3$	$\log K_1$	+2.975	+3.154	+3.308
$\text{P}$	$\log K_2$	-6.164	-5.548	-5.008
$\text{P}_4$	$\log K_3$	0.620	0.073	-0.404
$\text{PH}$	$\log K_4$	-5.051	-4.645	-4.289
$\text{PH}_2$	$\log K_5$	-3.060	-2.979	-2.907
$\text{H}$	$\log K_6$	-5.315	-4.756	-4.266
$\text{Si}$	$\log K_7$	-9.107	-7.998	-7.029
$\text{SiH}$	$\log K_8$	-8.378	-7.463	-6.664
$\text{SiH}_4$	$\log K_9$	-5.979	-5.924	-5.875

At  $1400^\circ\text{K}$  a second transition of the slope from 0.5 to 0.25 is found. This can be recognized by the intrinsic-extrinsic transition mentioned in the first section, and which occurs at  $3 \times 10^{19}$  atoms/cm<sup>3</sup> at  $1400^\circ\text{K}$  (9). In this case one has the following equilibria



giving

$$[\text{P}^+] = \frac{K_b \cdot [\text{P}]}{n} = K_a K_b (p_{\text{P}_2})^{1/2} / n$$

For intrinsic conditions  $n = k_i^{1/2}$  and

$$[\text{P}^+] \sim p_{\text{P}_2}^{1/2}$$

For extrinsic conditions  $[\text{P}^+] = n$ , thus

$$[\text{P}^+] \sim p_{\text{P}_2}^{1/4}$$

At higher temperatures the intrinsic carrier concentration of silicon shifts to a higher level and is outside the present range of measurements. For this reason no clear second break is found in the curves at  $1500^\circ$  and  $1600^\circ\text{K}$ , although an indication is given at  $1500^\circ\text{K}$  in the figure.

The exact position of the change in slope from 1 to 0.5 in the experimental curves deviates slightly from the same position in the calculated curves. This may

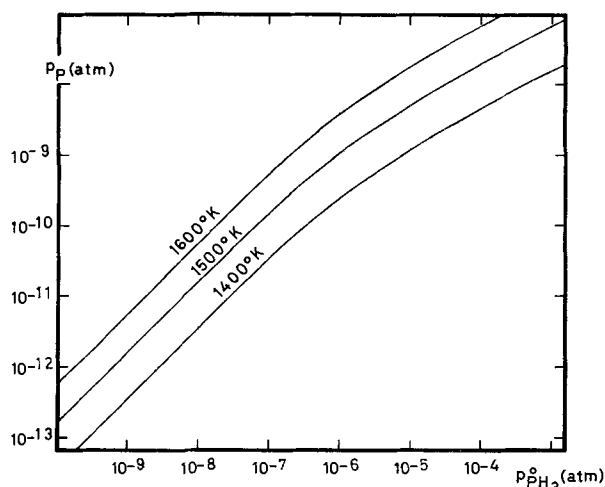


Fig. 3. Computed partial pressures of monoatomic phosphorus ( $p_{\text{P}}$ ) vs.  $p_{\text{PH}_3}^0$  as collected from Fig. 2 for the three temperatures quoted.



be due to the influence on the equilibria of additional compounds mentioned before which were not taken into account in the calculations. However the correspondence is such as to have confidence in the given interpretation. The agreement between the experimental data and the calculated curves also indicates that Henry's law defined as  $k = p_P/[P]_{Si}$  is obeyed over the whole range of phosphorus concentrations, which were far below the maximum solubility of P in Si ( $\sim 1.5 \times 10^{21}/\text{cm}^3$ ) (11).

### Conclusion

The mechanism for the incorporation of phosphorus in epitaxial silicon is governed by the position of the Fermi level in the solid and the chemical equilibria in the gas phase. With increasing phosphine partial pressures a slope bending from 1.0 to 0.5 is found due to transitions in the gas phase, at low temperatures a second break to 0.25 occurs when the donor concentration becomes equal to the intrinsic electron concentration of the silicon matrix.

These results also indicate that the gas phase reactions at or near the silicon surface proceed sufficiently rapidly that equilibrium concentrations of the components may be assumed to be present.

### Acknowledgment

The authors gratefully acknowledge the stimulating discussions about the calculation of the above given gaseous equilibria by means of iterative procedures with Ir. A. W. C. van Kemenade of Philips Research Laboratories in Eindhoven, Holland, and Dr. P. Z. A. M. van der Putte of this laboratory. In this respect we also want to mention the assistance of Dr. H. Lydtin from Philips Forschungslaboratorium Aachen, Ger-

many. In addition we are grateful to Mr. P. A. M. de Groot who performed the first experiments on this subject and whose practical advice was of considerable value.

Manuscript submitted Feb. 27, 1974; revised manuscript received May 6, 1974.

Any discussion of this paper will appear in a Discussion Section to be published in the June 1975 JOURNAL. All discussions for the June 1975 Discussion Section should be submitted by Feb. 1, 1975.

The publication costs of this article have been assisted by the University of Nijmegen.

### REFERENCES

1. W. H. Shepherd, *This Journal*, **115**, 541 (1968).
2. P. Rai-Choudhury and E. I. Salkovitz, *J. Crystal Growth*, **7**, 353 (1970).
3. P. Rai-Choudhury and E. I. Salkovitz, *ibid.*, **7**, 361 (1970).
4. D. T. J. Hurle, R. M. Logan, and R. F. C. Farrow, *ibid.*, **12**, 73 (1972).
5. S. Nakanuma, *This Journal*, **111**, 1199 (1964).
6. S. M. Sze and J. C. Irving, *Solid State Electron.*, **11**, 599 (1968).
7. J. Bloem, in "Semiconductor Silicon 1973," Howard R. Huff and Ronald R. Burgess, Editors, p. 213, The Electrochemical Society Softbound Symposium Series, Princeton, N. J. (1973).
8. F. A. Kröger, "The Chemistry of Imperfect Crystals," p. 347, North-Holland Publishing Company, Amsterdam (1964).
9. F. J. Morin and J. P. Maita, *Phys. Rev.*, **96**, 28 (1954).
10. JANAF Thermochemical Tables, 2nd edition (1971), NSRDS-NBS 37.
11. F. A. Trumbore, *Bell System Tech. J.*, **39**, 205 (1960).

## Vapor Phase Epitaxy and Thermodynamic Calculations of $\text{GaAs}_{1-x}\text{P}_x$ ( $0.3 < x < 0.5$ )

T. Y. Wu<sup>\*1</sup>

Research Laboratories, General Motors Corporation, Warren, Michigan 48090

### ABSTRACT

Various relationships between gas concentrations and solid composition have been established for the vapor phase epitaxy of  $\text{GaAs}_{1-x}\text{P}_x$  ( $0.3 < x < 0.5$ ). A  $\text{GaCl-AsH}_3\text{-PH}_3\text{-H}_2$  process was used to grow such materials at a satisfactory temperature of  $790^\circ\text{C}$ . The crystal composition was measured as a function of the input flow rates. Based on these reproducible data, thermochemical calculations were performed with thermodynamic constants evaluated from the literature or determined by fitting the measured data to the calculated equations. The results agree nicely with all the experimental data when the input flow rate ratio  $f^{\circ\text{HCl}}/f^{\circ\text{H}_2}$  is higher than 0.01. For  $f^{\circ\text{HCl}}/f^{\circ\text{H}_2} < 0.01$ , disagreements occur and the gas-solid relationships are hence established by experimental extrapolations. The crystal composition is strongly affected by  $f^{\circ\text{HCl}}/f^{\circ\text{H}_2}$  and  $f^{\circ\text{AsH}_3}/f^{\circ\text{H}_2}$ , in addition to  $f^{\circ\text{PH}_3}/f^{\circ\text{AsH}_3}$ . Such phenomena are briefly discussed.

The  $\text{GaAs}_{1-x}\text{P}_x$  materials have been of practical importance for electronic applications. At the present time, commercial light-emitting diodes (LED's) are mainly fabricated with these materials. Red-emitting  $\text{GaAs}_{1-x}\text{P}_x$  ( $x \approx 0.4$ ) diode indicators and displays were successfully developed a few years ago. More recently, following the observations (1-3) of efficient nitrogen trap processes in indirect  $\text{GaAs}_{1-x}\text{P}_x$ , yellow and orange LED's with reasonable efficiency have also been made in such materials with  $0.9 > x > 0.6$ . Be-

sides electroluminescent applications, high speed current limiting (4) and microwave switching (5) have been achieved in  $\text{GaAs}_{0.7}\text{P}_{0.3}$  due to its velocity-field saturation characteristics. Furthermore, Blakeslee (6) has made superlattice structures in  $\text{GaAs}_{1-x}\text{P}_x$  with a period as small as  $110\text{\AA}$  by vapor growth. Such structures may very well exhibit novel transport and optical properties like a negative conductance (7).

Although  $\text{GaAs}_{1-x}\text{P}_x$  materials are highly desirable and the  $\text{AsH}_3\text{-PH}_3\text{-GaCl-H}_2$  vapor phase epitaxy (VPE) technique has been used extensively, detailed and practical relationships between the input gas concentrations and the resulting crystal composition for such a process have not been available in the literature.

\* Electrochemical Society Active Member.

<sup>1</sup> Present address: IBM Laboratories, San Jose, California 95193.  
Key words:  $\text{GaAs}_{1-x}\text{P}_x$ , vapor phase growth, epitaxial deposition, thermodynamics, computer calculations.

These relationships are necessary to guide experiments in order to achieve a particular composition as desired. It is the objective of the present study to establish such relationships for a crystal composition range of  $0.3 < x < 0.5$  at a growth temperature of  $790^\circ\text{C}$ . Such a composition range is of particular interest for red LED's.

Ideally, if the growth atmosphere is close to thermodynamic equilibrium with the grown crystal, one can describe the gas-solid interface entirely by theoretical calculations. However, in practice, the growth interface can be far off thermochemical equilibria. Thus theoretical treatments alone cannot produce accurate results. On the other hand it is too time-consuming to establish the entire relationships by experiments. A semi-empirical approach was therefore necessary in order to obtain accurate gas-solid relationships. Such an approach was used in the present study.

### Experimental

**Procedures.**—The reactor system employed in this study is shown in Fig. 1. It is similar to the one used by Tietjen and Amick (8). But, in the present system, the HCl flow can bypass the Ga source for vapor etching of the substrate and is guided to the Ga boat during the growth period to ensure nearly complete conversion of HCl into GaCl. The reactor tube is 5 cm in diameter and 91 cm in heated length. The introduced  $\text{AsH}_3$  and HCl are 10% mixtures in  $\text{H}_2$ , and  $\text{PH}_3$  is a 5% mixture in  $\text{H}_2$ . All the gases are of electronic grade. Ga of 99.99999 purity, loaded in a pyrolytic graphite boat, was used throughout this study. The surface area of the Ga source was around  $18\text{ cm}^2$ . Preliminary experiments established that such a source can convert HCl into GaCl almost completely under the present experimental conditions. Chemically polished GaAs of  $\{100\}$  orientation was employed.

As is shown in Fig. 1, the temperatures selected for growth were  $900^\circ$ ,  $940^\circ$ , and  $790^\circ\text{C}$  for the source, the center zone, and the substrate. Such a profile was found to yield good preliminary growth. At the beginning of a run, this profile was reached with  $\text{H}_2$  flowing inside the reactor and the substrate in the cold zone.  $\text{AsH}_3$  flow was then established to prevent thermal etching of the GaAs surface and the substrate moved into the deposition zone. Afterward, vapor etch was carried out with a small HCl stream introduced through the upper tubing (see Fig. 1). Three minutes later, HCl was switched into the lower tubing and set at the desired flow rate to initiate the deposition of GaAs. After GaAs was epitaxially grown for 1 hr, the  $\text{PH}_3$  flow was started and gradually increased so as to deposit a taper region with  $x$  changing from 0 to a certain desired value  $x_0$ . And finally a layer of  $\text{GaAs}_{1-x_0}\text{P}_{x_0}$  was grown with the required thickness.

The following ranges of flow rates were used for growth:  $\text{H}_2$  (750-1000 ml/min),  $\text{AsH}_3$  (5-20 ml/min), HCl (5-25 ml/min), and  $\text{PH}_3$  (0.3-4.0 ml/min). Precautions were taken to eliminate deposition on the reactor upstream of the substrate so as to ascertain that all the

introduced gases contribute to the growth atmosphere in the substrate region. Such precautions, together with the fact that the input HCl is almost completely converted into GaCl in the present design, allows correlation of the growth atmosphere with the input gas concentration.

**Results.**—Growth morphologies were examined and compared at different flow rate conditions. When the growth atmosphere is nonstoichiometric, pyramids or pits are developed on the as-grown surfaces depending on whether the deposition region is rich in group III element or group V elements. On the other hand, in the stoichiometric case, as-grown surfaces are generally smooth and specularly reflective. Details of such observations were reported previously (9).

Typical layers consisted of 30-50  $\mu\text{m}$  of GaAs, 40-100  $\mu\text{m}$  of graded  $\text{GaAs}_{1-x}\text{P}_x$  and 50-200  $\mu\text{m}$  of  $\text{GaAs}_{1-x_0}\text{P}_{x_0}$ . Electron microprobe analysis was carried out across the cross section of every layer to determine the crystal compositions. Very uniform  $x_0$  through the final layer has been observed in all cases. The values of  $x_0$  and their corresponding sets of flow rates at a growth temperature of  $790^\circ\text{C}$  are listed in Table I. Such data were checked and found to be reproducible. It was estimated that all the values of  $x_0$  should be accurate within  $\pm 0.01$  and the various flow rate ratios to be within  $\pm 5\%$ . Extreme care was taken to check the reproducibilities and to keep the results within the above accuracies. It should also be pointed out that such correspondence can be used to describe the gas-solid relationships at the growth interface, since, as mentioned above, the input flow rate conditions in the present setup can be related accurately to the growth atmosphere. Part of the data in Table I was therefore adopted in the following calculation to adjust theoretical parameters.

### Thermodynamic Calculations

**Theoretical model.**—The theoretical approach used in this study is formulated with the following assumptions: (i) Dynamic thermochemical equilibria are established in a deposition region of uniform temperature and pressure. Such equilibria at the gas-solid interface control the growth of  $\text{GaAs}_{1-x}\text{P}_x$ . (ii) All the gas species obey the ideal gas law and the GaAs-GaP solid can be described by regular solution behavior. (iii)

Table I. Relationships between the input flow rates and the grown crystal composition obtained in the present experiments

$f^{\circ}\text{HCl}/f^{\circ}\text{H}_2$ ( $\times 10^{-3}$ )	$f^{\circ}\text{AsH}_3/f^{\circ}\text{H}_2$ ( $\times 10^{-3}$ )	$f^{\circ}\text{PH}_3/f^{\circ}\text{H}_2$ ( $\times 10^{-3}$ )	$f^{\circ}\text{PH}_3/f^{\circ}\text{AsH}_3$ ( $\times 10^{-2}$ )	$x$ ( $\times 10^{-2}$ )
5.0	15.0	1.5	10	34
11.0	15.0	1.5	10	36
10.0	20.0	2.0	10	44
15.0	20.0	2.0	10	36
17.5	30.0	3.0	10	40
27.5	40.0	4.0	10	33
9.0	8.0	1.6	20	44
12.5	10.0	2.0	20	42
16.5	12.0	2.4	20	40
20.0	15.0	3.0	20	39
19.0	20.0	4.0	20	50
25.0	20.0	4.0	20	43
33.0	20.0	4.0	20	33
33.0	30.0	6.0	20	46
15.0	5.0	1.5	30	37
17.0	10.0	3.0	30	49
20.0	10.0	3.0	30	43
30.0	10.0	3.0	30	34
30.0	20.0	6.0	30	49
11.0	2.5	1.0	40	38
2.5	5.0	2.0	40	50
7.5	5.0	2.0	40	57
11.0	2.5	1.0	40	40
20.0	4.5	1.8	40	40
30.0	5.0	2.0	40	33
8.0	7.0	2.8	40	62
25.0	7.0	2.8	40	40
30.0	10.0	4.0	40	42
30.0	15.0	6.0	40	51
5.0	15.0	3.75	25	46
6.3	11.0	2.75	25	44
11.0	12.5	3.1	25	59
11.0	11.0	1.65	15	40
13.0	13.0	1.95	15	41
18.0	17.0	2.6	15	36
23.0	22.0	3.3	15	34

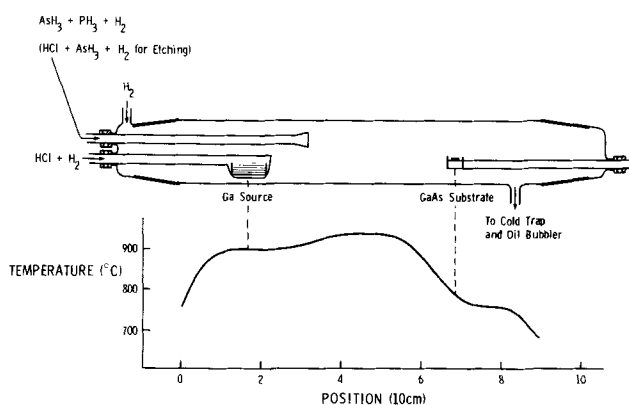
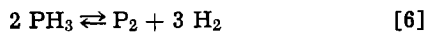
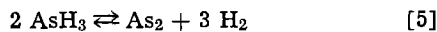
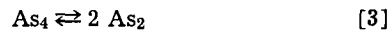
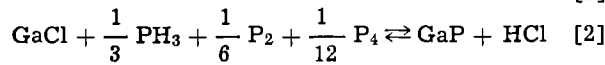
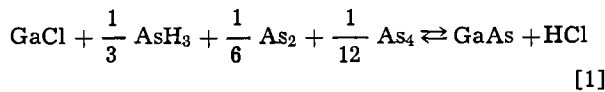


Fig. 1. Schematic diagram of the epitaxial reactor with the temperature profile used in this study.

HCl is completely converted into GaCl by reaction with Ga in the source region. (iv) No deposition occurs upstream of the substrate. (v)  $M_2$ ,  $M_4$ , and  $MH_3$  ( $M = \text{As}$  or  $\text{P}$ ) contribute equally to the deposition of  $\text{GaAs}_{1-x}\text{P}_x$ , while various mixed species of the type  $\text{As}_y\text{P}_z$  can be neglected.

Assumptions (iii) and (iv) were found to be reasonably true in the present case. A mass-spectrometric study by Ban (10) has determined the relative abundances and deposition reactivities of various M-containing species at 680°, 780°, and 880°C. Such results indicate that assumption (v) should also be a good approximation. However, on the other hand, assumptions (i) and (ii) deviate to a good degree from the actual cases. These deviations make it impossible to obtain accurate relationships between the gas concentrations and the solid composition based on a theoretical approach alone. Incorporation of experimental data is therefore necessary. Indeed, it was found here that the equations derived with the above theoretical assumptions could be used to describe the vapor growth of  $\text{GaAs}_{1-x}\text{P}_x$ , only if the thermodynamic constants were properly adjusted to fit experimental data. A similar technique has been applied successfully by Wu and Pearson (11) to the liquid phase epitaxy of  $\text{In}_x\text{Ga}_{1-x}\text{As}$ .

Based on the assumptions (i-v), one can write the following reactions to illustrate the equilibria existing around the gas-solid interface



The equilibrium constant  $K_j$  of reaction (j) can be expressed as follows

$$K_1 = \frac{(1-x) \gamma_{\text{GaAs}} p_{\text{HCl}}}{p_{\text{GaCl}} (p_{\text{AsH}_3})^{1/3} (p_{\text{As}_2})^{1/6} (p_{\text{As}_4})^{1/12}} \quad [7]$$

$$K_2 = \frac{x \gamma_{\text{GaP}} p_{\text{HCl}}}{p_{\text{GaCl}} (p_{\text{PH}_3})^{1/3} (p_{\text{P}_2})^{1/6} (p_{\text{P}_4})^{1/12}} \quad [8]$$

$$K_3 = \frac{(p_{\text{As}_2})^2}{p_{\text{As}_4}} \quad [9]$$

$$K_4 = \frac{(p_{\text{P}_2})^2}{p_{\text{P}_4}} \quad [10]$$

$$K_5 = \frac{p_{\text{As}_2} (p_{\text{H}_2})^3}{(p_{\text{AsH}_3})^2} \quad [11]$$

$$K_6 = \frac{p_{\text{P}_2} (p_{\text{H}_2})^3}{(p_{\text{PH}_3})^2} \quad [12]$$

where  $p$  and  $\gamma$  designate the partial pressure and the activity coefficient, respectively. Since we are dealing with an open-flow system with  $\text{H}_2$  as the major gas specie and the GaAs-GaP solid is assumed to be regular, we have

$$p_{\text{H}_2} \approx 1 \text{ atm} \quad [13]$$

and

$$\gamma_{\text{GaAs}} = \exp \left[ \frac{\alpha x^2}{RT} \right] \quad [14]$$

$$\gamma_{\text{GaP}} = \exp \left[ \frac{\alpha (1-x)^2}{RT} \right] \quad [15]$$

where  $\alpha$  is the interaction parameter between GaAs and GaP.

Thus we have established relationships between the solid composition and the partial pressures of various gas species in the deposition region. These partial pressures can be further related to the input flow rates through consideration of mass conservation due to the validity of assumptions (iii) and (iv). The conservation of chlorine, arsenic, and phosphorus can be described, respectively, as

$$p_{\text{HCl}} + p_{\text{GaCl}} = p^{\circ}_{\text{HCl}} \approx \frac{p^{\circ}_{\text{HCl}}}{p^{\circ}_{\text{H}_2}} = \frac{f^{\circ}_{\text{HCl}}}{f^{\circ}_{\text{H}_2}} \quad [16]$$

$$p_{\text{AsH}_3} + 2p_{\text{As}_2} + 4p_{\text{As}_4} + (1-x) p_{\text{HCl}} = p^{\circ}_{\text{AsH}_3} \approx \frac{f^{\circ}_{\text{AsH}_3}}{f^{\circ}_{\text{H}_2}} \quad [17]$$

and

$$p_{\text{PH}_3} + 2p_{\text{P}_2} + 4p_{\text{P}_4} + x p_{\text{HCl}} = p^{\circ}_{\text{PH}_3} \approx \frac{f^{\circ}_{\text{PH}_3}}{f^{\circ}_{\text{H}_2}} \quad [18]$$

where  $f^{\circ}$  is the flow rate of the incoming gas and  $p^{\circ}$  represents the partial pressure of this input gas in the growth region prior to deposition.

With Eq. [7]-[18], one can solve for the crystal composition and the partial pressures at any given incoming gas concentrations, once all the equilibrium constants and the interaction parameter are determined.

*Determination of constants.*—The above approach can be used for any growth temperature. But the present calculation was performed with 790°C, which was found to be satisfactory for  $0.3 < x < 0.5$ .

The equilibrium constants, i.e.,  $K_1$ ,  $K_2$ ,  $K_3$ ,  $K_4$ ,  $K_5$ , and  $K_6$  were evaluated from Kirwan's results (12) to be  $10^4$ ,  $80$ ,  $10^{-5}$ ,  $9 \times 10^{-5}$ ,  $3 \times 10^{17}$ , and  $3 \times 10^2$  atm units, respectively, at 790°C. Panish and Ilegems (13) have reported a value of 0.4 kcal/mole for  $\alpha$ . Based on these parameters, preliminary calculations resulted in significant deviations from the experimental data obtained in this study. This can be expected due to the fact that complete thermochemical equilibria do not exist and kinetic effects such as adsorption, surface reaction, and desorption cannot be neglected in actual cases, as were reported by Shaw (14, 15). In order to obtain accurate results with the above-described equations, one thus has to adjust appropriate parameters to fit experimental data. Such adjustments will invalidate some of the above assumptions and thus result in inconsistency in the theoretical model. However, the main purpose of this paper is to establish correct gas-solid relationships for practical use. The adoption of simple, unrealistic assumptions was merely to set up calculation equations to start with.

Since we are mainly interested in calculation of the crystal composition at given gas concentrations, such adjustments should be made with parameters which have major influences on the depositions of GaAs and GaP. Adjustable parameters should therefore be selected among  $K_1$ ,  $K_2$ , and  $\alpha$ , which can affect the deposition reactions directly.

By following the same techniques used in Ref. (11), it was found that, with  $K_2 = 3 \times 10^2$  atm units,  $\alpha = (4.2-3.8x)$  kcal/mole, and other equilibrium constants given above, the calculation resulted in good agreement with the experimental data.

*Calculation results.*—Such a calculation was carried out to determine the crystal composition  $x$  at any given  $f^{\circ}_{\text{HCl}}/f^{\circ}_{\text{H}_2}$ ,  $f^{\circ}_{\text{AsH}_3}/f^{\circ}_{\text{H}_2}$ , and  $f^{\circ}_{\text{PH}_3}/f^{\circ}_{\text{AsH}_3}$ . The results are shown in Fig. 2 and 3 together with the experimental data obtained in the study. The solid lines are calculated results and the dashed lines are experimental extrapolations. Good agreement was obtained for  $f^{\circ}_{\text{HCl}}/f^{\circ}_{\text{H}_2} > 0.01$ . However, when  $f^{\circ}_{\text{HCl}}/f^{\circ}_{\text{H}_2}$  is smaller than 0.01, the calculation fails and the relationships were established entirely by experiments. The failure of the calculation in this region indicates that such a semi-empirical approach can only be applied in limited regions since the actual deposition process can be far more complicated.

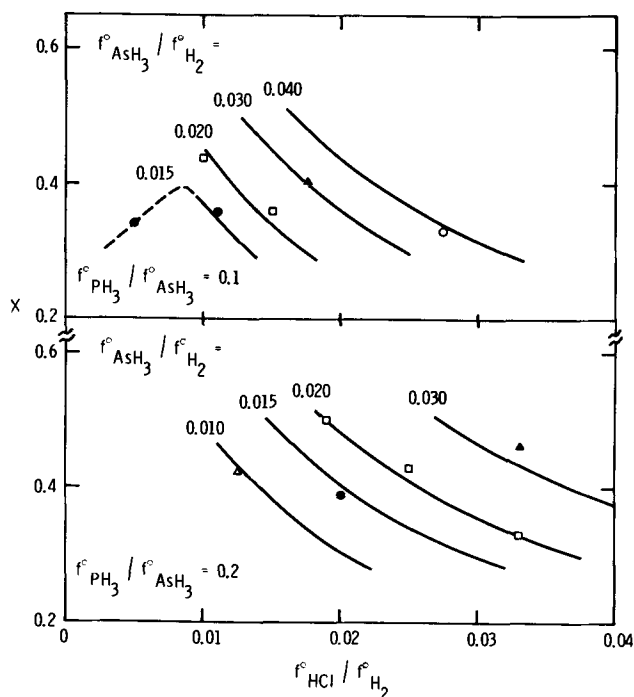


Fig. 2. Crystal composition  $x$  as a function of input flow rate ratios  $f_{\text{HCl}}^0/f_{\text{H}_2}^0$ ,  $f_{\text{AsH}_3}^0/f_{\text{H}_2}^0$ , and  $f_{\text{PH}_3}^0/f_{\text{AsH}_3}^0$  ( $= 0.1$  and  $0.2$ ) at a growth temperature of  $790^\circ\text{C}$ . Solid lines are calculated results. The dashed line is experimental extrapolation. The values of  $f_{\text{AsH}_3}^0/f_{\text{H}_2}^0$  for various measured data are:  $0.010$  ( $\Delta$ ),  $0.015$  ( $\bullet$ ),  $0.020$  ( $\square$ ),  $0.030$  ( $\blacktriangle$ ), and  $0.040$  ( $\circ$ ).

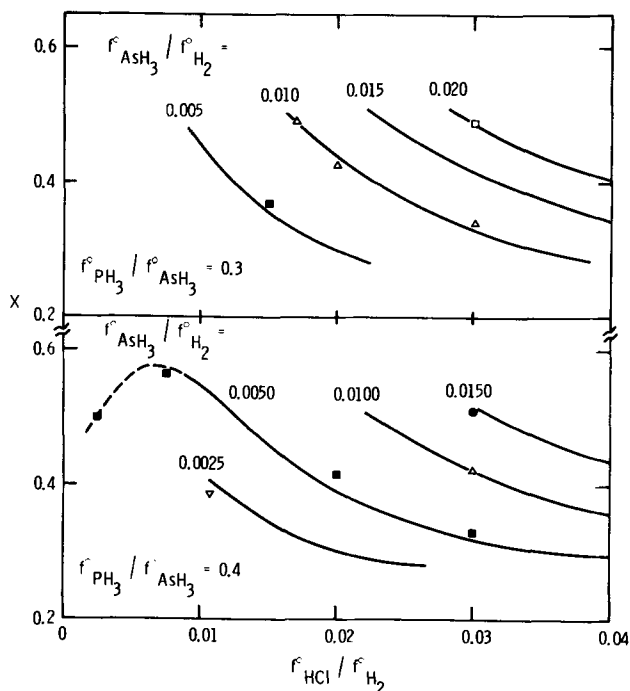


Fig. 3. Crystal composition  $x$  as a function of input flow rate ratios  $f_{\text{HCl}}^0/f_{\text{H}_2}^0$ ,  $f_{\text{AsH}_3}^0/f_{\text{H}_2}^0$ , and  $f_{\text{PH}_3}^0/f_{\text{AsH}_3}^0$  ( $= 0.3$  and  $0.4$ ) at a growth temperature of  $790^\circ\text{C}$ . Solid lines are calculated results. Dashed line is experimental extrapolation. The values of  $f_{\text{AsH}_3}^0/f_{\text{H}_2}^0$  for various measured data are:  $0.0025$  ( $\nabla$ ),  $0.0050$  ( $\blacksquare$ ),  $0.0100$  ( $\Delta$ ),  $0.0150$  ( $\bullet$ ), and  $0.020$  ( $\square$ ).

Figure 4 gives the relationships among the incoming flow rates required to grow  $\text{GaAs}_{0.6}\text{P}_{0.4}$  under the present experimental conditions. All the lines are drawn from Fig. 2 and 3, together with the corresponding experimental data in Table I. Similar plots can be obtained for other  $x$  and serve as guides to achieve specific compositions.

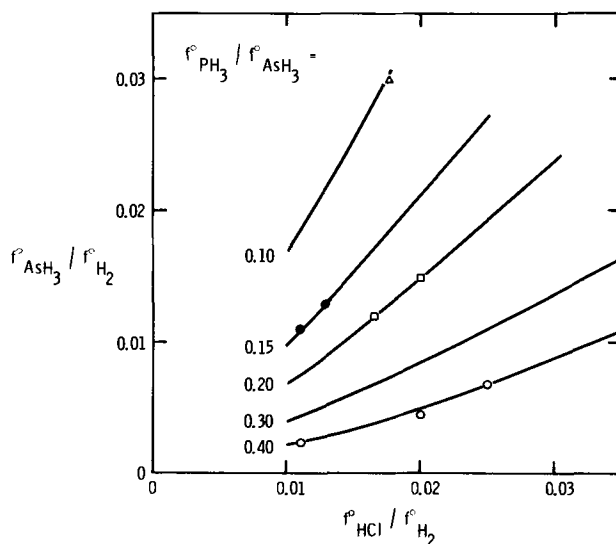


Fig. 4. Input flow rate ratio  $f_{\text{AsH}_3}^0/f_{\text{H}_2}^0$  required to achieve  $x = 0.4 \pm 0.02$  with various fixed  $f_{\text{HCl}}^0/f_{\text{H}_2}^0$  and  $f_{\text{PH}_3}^0/f_{\text{AsH}_3}^0$  at  $790^\circ\text{C}$ . All the lines are calculated results. The values of  $f_{\text{PH}_3}^0/f_{\text{AsH}_3}^0$  for various measured data are:  $0.10$  ( $\Delta$ ),  $0.15$  ( $\bullet$ ),  $0.20$  ( $\square$ ), and  $0.40$  ( $\circ$ ).

## Discussion

From the above results, the crystal composition is not only determined by  $f_{\text{PH}_3}^0/f_{\text{AsH}_3}^0$ , but is also affected to a great extent by  $f_{\text{HCl}}^0/f_{\text{H}_2}^0$  and  $f_{\text{AsH}_3}^0/f_{\text{H}_2}^0$ . In particular, at constant  $f_{\text{AsH}_3}^0/f_{\text{H}_2}^0$  and  $f_{\text{PH}_3}^0/f_{\text{AsH}_3}^0$ ,  $x$  increases along with  $f_{\text{HCl}}^0/f_{\text{H}_2}^0$  when  $f_{\text{HCl}}^0/f_{\text{H}_2}^0 < 0.01$  but decreases as  $f_{\text{HCl}}^0/f_{\text{H}_2}^0$  is increased further. It is difficult to explain such behavior in much detail since precise thermochemistry at a real growth interface is not known. Nevertheless the following interpretations can be made here.

The crystal composition is influenced by two factors: (i) the reactant partial pressures and (ii) the reactivities of various M-containing species with GaCl. When  $f_{\text{HCl}}^0$  is much greater than  $f_{\text{AsH}_3}^0 + f_{\text{PH}_3}^0$ , there is more than sufficient GaCl in the deposition region. In that case, the reactivity influence is overruled by the pressure influence and the crystal composition  $x$  is mainly determined by  $f_{\text{PH}_3}^0/(f_{\text{PH}_3}^0 + f_{\text{AsH}_3}^0)$ . As  $f_{\text{HCl}}^0/f_{\text{H}_2}^0$  is reduced while keeping  $f_{\text{PH}_3}^0/f_{\text{AsH}_3}^0$  and  $f_{\text{AsH}_3}^0/f_{\text{H}_2}^0$  constant, the relative reactivities of M-containing species will then become increasingly important. The fact that  $x$  increases with decreasing  $f_{\text{HCl}}^0/f_{\text{H}_2}^0$  ( $> 0.01$ ) can hence be explained by the over-all higher reactivity of P-containing reactants in this range. The same explanation also holds for the increasing  $x$  when  $f_{\text{AsH}_3}^0/f_{\text{H}_2}^0$  is increased with constant  $f_{\text{PH}_3}^0/f_{\text{AsH}_3}^0$  and  $f_{\text{HCl}}^0/f_{\text{H}_2}^0$ .

Sedgwick (16) proposed a "quasi-equilibrium" model to describe the  $\text{H}_2$  reduction of  $\text{SiCl}_4$ . In this model, only a fraction  $\beta$  of the incoming gases equilibrates with the condensed phase. Shaw (14) has found such a model can be successfully applied to calculate GaAs deposition rates for certain limited growth conditions if a constant, empirical  $\beta$  is assumed. The present results agree with such previous observations. The adjustment of  $K_2$ , in the present case, is equivalent to the quasi-equilibrium treatment. It was also found here that such a treatment can be successfully used to calculate  $x$  for certain growth conditions, namely,  $f_{\text{HCl}}^0/f_{\text{H}_2}^0 > 0.01$  in the present case.

Although the use of a composition-dependent  $\alpha$  is inconsistent with the assumption of regular solution behavior between GaAs and GaP, it yields some accurate and practical results in the present calculations. After all, the GaAs-GaP solid solution is by no means strictly regular. Rao and Tiller (17) have found composition-dependent  $\alpha$ 's can be used to describe similar systems.

It should also be pointed out here that the empirical adjustments of  $K_2$  and  $\alpha$  were performed based on part of the reproducible data in Table I only. But the remaining data were also found to agree with the calculated results nicely. This suggests such a semiempirical approach is a good technique for interpolation and reasonable extrapolation with a limited amount of data.

In a previous paper (9), an optimum growth condition was reported for the process used in this study, namely,  $f_{\text{HCl}}^0/f_{\text{H}_2}^0 = (f_{\text{AsH}_3}^0 + f_{\text{PH}_3}^0)/f_{\text{H}_2}^0 = 0.02$ . Such a condition together with the relationships given in Fig. 4 indicate that  $\text{GaAs}_{0.6}\text{P}_{0.4}$  can be best grown with  $f_{\text{HCl}}^0/f_{\text{H}_2}^0 = 0.02$ ,  $f_{\text{AsH}_3}^0/f_{\text{H}_2}^0 = 0.0165$ , and  $f_{\text{PH}_3}^0/f_{\text{AsH}_3}^0 = 0.19$  at a temperature of 790°C.

Although the present relationships are established for the  $\text{AsH}_3$  and  $\text{PH}_3$  process, they can be applied equally well to the  $\text{AsCl}_3$  and  $\text{PCl}_3$  process since the thermochemistry at the gas-solid interface is the same for both processes. As a matter of fact, the trichloride process can be considered as a special case of the hydride process, which satisfies  $p_{\text{HCl}}^0 = 3(p_{\text{AsH}_3}^0 + p_{\text{PH}_3}^0)$  with  $p_{\text{AsH}_3}^0$  and  $p_{\text{PH}_3}^0$  equal to  $p_{\text{AsCl}_3}^0$  and  $p_{\text{PCl}_3}^0$ , respectively. Thus, the present relationships can be reduced for use in the trichloride case by introducing a restriction that  $f_{\text{HCl}}^0/f_{\text{H}_2}^0$  is equal to  $3(f_{\text{AsH}_3}^0 + f_{\text{PH}_3}^0)/f_{\text{H}_2}^0$ . It was indeed found that the results so obtained agree well with the calculated relationships by Bleicher (18) for the trichloride process.

### Conclusions

A thermochemical investigation on the VPE of  $\text{GaAs}_{1-x}\text{P}_x$  ( $0.3 < x < 0.5$ ) has been carried out and the following conclusions can be made:

1. The crystal composition  $x$  ( $0.3 < x < 0.5$ ) as a function of the input flow rate ratios  $f_{\text{PH}_3}^0/f_{\text{AsH}_3}^0$ ,  $f_{\text{AsH}_3}^0/f_{\text{H}_2}^0$ , and  $f_{\text{HCl}}^0/f_{\text{H}_2}^0$  at 790°C has been obtained for the hydride process. A semiempirical approach was used to establish such relationships. Such an approach demolishes the theoretical consistency, but is certainly a simple way to establish accurate, practical relationships. Similar techniques can be used for other ranges of  $x$  or other materials.

2. The flow rate dependences of  $x$  for  $f_{\text{HCl}}^0/f_{\text{H}_2}^0 > 0.01$  can be explained by the relative abundances and reactivities of various vapor sources.

3. It is concluded that  $\text{GaAs}_{0.6}\text{P}_{0.4}$  vapor epitaxial layers can be best grown with  $f_{\text{HCl}}^0/f_{\text{H}_2}^0 = 0.02$ ,  $f_{\text{AsH}_3}^0/f_{\text{H}_2}^0 = 0.0165$ , and  $f_{\text{PH}_3}^0/f_{\text{AsH}_3}^0 = 0.19$  at 790°C. Such information is particularly important for red-emitting diode application.

4. The above relationships can be reduced and used for the trichloride process which is actually a special case of the hydride process.

5. The results established here are applicable to any such reactors where the input flow rates can be correlated with the incoming gas concentrations in the substrate region.

### Acknowledgments

The author would like to acknowledge the competent and enthusiastic technical assistance of L. Green. Thanks are also due to A. Dolenga for construction of the quartz reactor, to T. P. Schreiber and A. C. Ottolini for electron microprobe measurements, and to J. C. Price for computer programming.

Manuscript submitted Oct. 1, 1973; revised manuscript received April 15, 1974. This was Paper 174 presented at the Boston, Massachusetts, Meeting of the Society, Oct. 7-11, 1973.

Any discussion of this paper will appear in a Discussion Section to be published in the June 1975 JOURNAL. All discussions for the June 1975 Discussion Section should be submitted by Feb. 1, 1975.

The publication costs of this article have been assisted by the General Motors Corporation.

### REFERENCES

1. W. O. Groves, A. H. Herzog, and M. G. Craford, *Appl. Phys. Letters*, **19**, 184 (1971).
2. N. Holonyak, Jr., D. R. Scifres, M. G. Craford, W. O. Groves, and D. L. Keune, *ibid.*, **19**, 256 (1971).
3. N. Holonyak, Jr., D. R. Scifres, H. M. Macksey, R. D. Dupuis, Y. S. Moroz, C. B. Duke, G. G. Kleiman, and F. V. Williams, *Phys. Rev. Letters*, **28**, 230 (1972).
4. A. Majerfeld and G. L. Pearson, *IEEE Trans. Electron Devices*, **ED-14**, 632 (1967).
5. G. A. Foggiato and G. L. Pearson, *Proc. IEEE*, **60**, 456 (1972).
6. A. E. Blakeslee, *This Journal*, **118**, 1459 (1971).
7. L. Esaki and R. Tsu, *IBM J. Res. Develop.*, **14**, 61 (1970).
8. J. J. Tietjen and J. A. Amick, *This Journal*, **113**, 724 (1966).
9. T. Y. Wu, *J. Crystal Growth*, **21**, 85 (1974).
10. V. S. Ban, *ibid.*, **17**, 19 (1972).
11. T. Y. Wu and G. L. Pearson, *J. Phys. Chem. Solids*, **33**, 409 (1972).
12. D. J. Kirwan, *This Journal*, **117**, 1572 (1970).
13. M. B. Panish and M. Ilegems in "Progress in Solid State Chemistry," H. Reiss and J. O. McCaldin, Editors, Vol. 7, pp. 39-83, Pergamon Press, Oxford (1972).
14. D. W. Shaw, *This Journal*, **117**, 683 (1970).
15. D. W. Shaw, *J. Crystal Growth*, **8**, 117 (1971).
16. T. O. Sedgwick, *This Journal*, **111**, 1381 (1964).
17. M. V. Rao and W. A. Tiller, *J. Phys. Chem. Solids*, **31**, 191 (1970).
18. M. Bleicher, *This Journal*, **119**, 613 (1972).

# The Growth of High Quality Epitaxial Silicon over Ion Implanted Buried Arsenic Layers

R. A. Moline and R. Lieberman\*

Bell Laboratories, Murray Hill, New Jersey 07974

J. Simpson

Bell Laboratories, Whippany, New Jersey 07981

and A. U. Mac Rae

Bell Laboratories, Murray Hill, New Jersey 07974

## ABSTRACT

High structural quality epitaxial Si layers have been grown over implanted As patterns. For As doses  $\geq 5 \times 10^{14}/\text{cm}^2$ , it has been necessary either to implant into a heated substrate or to remove the damaged region prior to epitaxial growth. This can be conveniently done by diffusing in an oxygen ambient; consuming part of the damage by oxidation while diffusing the donor impurities away from the damaged silicon. Sheet resistivities of less than 10 ohms/ $\square$  have been attained as have minority carrier lifetimes over 20  $\mu\text{sec}$  in the epitaxial layer, with no lifetime difference observed on control areas or regions grown over the buried layers.  $\text{SiO}_2$ , photoresist and silicon contact masks have been successfully employed. For implantation doses of  $3 \times 10^{15}/\text{cm}^2$ , driven to a junction depth of 3  $\mu\text{m}$ , sheet resistivities of 20 ohms/ $\square$  were obtained. The existence of HF staining of the damaged region prior to annealing has been observed.

The need for techniques to reproducibly grow high quality epitaxial silicon layers over low sheet resistivity buried collector diffusions of n-type impurity atoms has been a continuing problem in the fabrication of bipolar integrated circuits. The ability to grow high lifetime, low strained epitaxial films over arsenic buried layers requires a reproducible diffusion source free of variables such as attack of the  $\text{SiO}_2$  masked areas, variable etching characteristics, arsenic rich precipitates, etc. Chemical diffusion sources generally suffer from some of the above problems, resulting in the subsequent formation of epitaxial defects especially over impurity rich diffusion "rosettes." As part of an over-all examination of arsenic buried layer sources, ion implanted arsenic techniques were investigated. This paper describes the experimental details which form the basis of the results reported earlier (1).

It was recognized that crystallographic disorder introduced in the silicon lattice by implantation of buried layers could be a potential problem in the epitaxial growth process which is sensitive to minor lattice disorder. The investigation studied the use of room temperature and high temperature implantations followed by epitaxial deposition, and also the use of room temperature implantations followed by a high temperature diffusion drive-in prior to epitaxial deposition. It was found in all cases that although the epitaxial process was extremely sensitive to residual crystallographic damage in the implanted substrates it was equally sensitive to the cleaning sequence used to process the substrates after implantation.

This work has shown that good results are obtained using ion predeposition followed by a diffusion drive-in at 1200°C. Epitaxial silicon layers have been grown consistently free of structural defects and comparable to layers grown on nondiffused, melt doped substrates. In particular "rosettes" have not been observed since the oxide mask used never contains sufficient arsenic to form the necessary arsenic rich oxide phase. High

quality base-collector junctions have been fabricated over buried layers formed in the above fashion.

## Experimental Procedures

**Implantation.**—The early work was done with beam energies of 300 keV giving a profile peaked at approximately 0.2  $\mu\text{m}$  (2). This was later reduced to 150 keV. The majority of the substrates were implanted at room temperature, but some experiments were performed with the substrates held on a heated support at temperatures between 500°-600°C to reduce the radiation damage in the Si (3) caused by the implantation.

**Diffusion drive-in.**—These were performed at 1200°C in pure oxygen for most of this work. Some runs used 10%  $\text{O}_2$ -90%  $\text{N}_2$ , 50%  $\text{O}_2$ -50%  $\text{N}_2$ , or a short  $\text{O}_2$  drive-in followed by a  $\text{N}_2$  drive-in. These variations had minor effects on the sheet resistivity of the buried diffusions but no effect on the subsequent epitaxial growth process.

**Epitaxial growth.**—Epitaxial films in the 2.0-4.0  $\mu\text{m}$  thickness range were grown in a single slice vertical reactor system described previously (4). Growth rates of 0.5  $\mu\text{m}/\text{min}$  were used at 1000°C utilizing the silane pyrolysis process. Ten ohm-cm p-type, "Syton" polished substrates misoriented by 3° to the  $\langle 111 \rangle$  axis were used. The early experiments used substrates which were HCl vapor etched in the epitaxial reactor prior to ion implantation to eliminate minor variations in substrate surface perfection but later work showed that "Syton" polished surfaces were adequate for our purposes. Where no drive-in had been performed the standard preepitaxial, *in situ* HCl vapor etch at 1000°C was eliminated to prevent etching away the implanted As zone.

**Epitaxy and substrate characterization.**—The structural perfection of the ion implanted substrates with and without epitaxial layers was examined by x-ray topography, interference contrast microscopy, and ellipsometry. Berg-Barrett reflection topography was used with a lateral resolution of two microns, utilizing the  $\text{CrK}\alpha$  (220) reflection with an approximate penetra-

\* Electrochemical Society Active Member.  
Key words: bipolar, silicon, technology.

tion of  $1.5 \mu\text{m}$ , or the  $\text{Fe}_{k\alpha}$  (311) with an approximate penetration of  $6.5 \mu\text{m}$ . The use of geometric patterns such as device patterns or simple grids enabled a comparison to be made between the implanted areas and the surrounding silicon matrix. In addition interference microscopy at  $\times 698$  was used to compare the surface relief of the epitaxy over implanted areas with the matrix structure and to examine stacking faults, etc. The ellipsometric measurements served to monitor the cleanness of the substrates prior to and subsequent to ion implantation. It also was useful in monitoring the annealing of implanted silicon surfaces as the disordered surface had an apparently low refractive index which reverted to the characteristic silicon value after annealing. The sheet resistivities were measured using a four-point probe and the minority carrier lifetime using a pulsed MOS (C-V) technique (5).

## Results

### Ion-Implanted Substrates

The first experiments studied doses which yielded sheet resistivities between 10 and 4000 ohms/ $\square$  after an anneal but without a diffusion drive-in. Four strips were implanted into a slice held at room temperature with doses of  $5 \times 10^{14}$ ,  $10^{14}$ ,  $2 \times 10^{13}$ , and  $4 \times 10^{12}$  300 keV arsenic ions/cm<sup>2</sup>, the substrates having been HCl vapor etched immediately prior to implantation. Of these implantations only the heaviest dose rendered the lattice amorphous as seen by x-ray topography and also reflection microscopy. A twenty minute anneal at 1000°C in the epitaxial reactor in hydrogen returned the refractive index of the  $5 \times 10^{14}$ /cm<sup>2</sup> implanted area to its bulk value, but x-ray topographs indicated that the crystallographic structure was not that of the surrounding matrix. The growth of  $2.5 \mu\text{m}$  epitaxial layers over these stripes showed that excellent quality silicon was obtained over all areas except the heaviest dose region. In Fig. 1a, the x-ray topograph shows the epitaxy in the heaviest dose region to be highly dislocated, perhaps oriented polycrystalline material, and observation under phase contrast microscopy (Fig. 1b) confirms that the layer is highly disordered Si.

To ascertain whether the defective epitaxial layer was caused by residual damage due to a dose above that required to render Si amorphous, implantations were done into samples held at temperatures high enough that the amorphous transition is not expected (6). Doses of  $5 \times 10^{14}$ ,  $5 \times 10^{15}$ , and  $10^{16}$  300 keV As/cm<sup>2</sup>, all above the amorphous transition damage range for As in Si at room temperature, were implanted with the substrate held between 500°-600°C. By x-ray and reflectance examination this material was indistinguishable from the nonimplanted zone immediately after implantation. At an implantation dose of  $10^{16}$ /cm<sup>2</sup> the epitaxial texture was only slightly different from the nonimplanted material. Lang transmission x-ray topographs (7) indicated single-crystal material with dislocation densities of several thousand/square centi-

Table I. Etching conditions for epitaxial growth over ion implanted buried layers

Drive-in conditions	Amount HCl etched	HCl etch temperature	Epitaxial visual quality
O <sub>2</sub> , 15 min; N <sub>2</sub> , 4 hr	None	—	Very poor
O <sub>2</sub> , 4 hr	None	—	Poor
(0.35 $\mu\text{m}$ SiO <sub>2</sub> )	0.1 $\mu\text{m}$	1000°C	Good
(0.35 $\mu\text{m}$ SiO <sub>2</sub> )	0.2 $\mu\text{m}$	1000°C	Excellent
(0.35 $\mu\text{m}$ SiO <sub>2</sub> )	0.3 $\mu\text{m}$	1000°C	Excellent
(0.35 $\mu\text{m}$ SiO <sub>2</sub> )	0.5 $\mu\text{m}$	1000°C	Excellent
(0.35 $\mu\text{m}$ SiO <sub>2</sub> )	1.5 $\mu\text{m}$	1200°C	Excellent

meter but this value was also obtained for the non-implanted area. It would appear that the dislocations were not due to the implantation per se but perhaps related to the method of holding the sample on the heater block during implantation.

Although implanting into a hot substrate gave sheet resistivities  $\sim 10$  ohms/ $\square$ , the technique was found to be too sensitive to residual surface impurities without HCl vapor etch prior to epitaxial growth. Also, heating the sample during the implantation is generally cumbersome.

### Ion Predeposition and Drive-In

*HCl vapor etching.*—It was decided to use a standard  $10^{16}$ /cm<sup>2</sup> implantation dose at 150 keV for the diffusion experiments, with a drive-in of 4 hr at 1200°C in O<sub>2</sub>. During the implantation the substrates were held near room temperature. These conditions gave a junction depth of  $3.0 \mu\text{m}$  and a sheet resistivity of 7-8 ohms/ $\square$ . To determine the minimum amount of Si necessary to be removed so that any residual damage in the implanted zone would not affect the epitaxial process, a series of drive-ins and *in situ* (prior to epi growth) vapor etchings were performed as listed in Table I. Since during the 4 hr period at 1200°C approximately  $0.35 \mu\text{m}$  of SiO<sub>2</sub> are formed and subsequently removed by an HF etch prior to epitaxial deposition,  $0.15 \mu\text{m}$  of the original surface will be consumed without any HCl etch. Thus, in two runs, no HCl etching was performed to test whether this in itself was sufficient to give high quality epitaxy. It appears that although cosmetically acceptable epitaxy can be grown this way, x-ray topography indicated clearly that a  $0.2 \mu\text{m}$  HCl etch was necessary to obtain reproducible results.

*KMER masks.*—The above results were obtained with large area implantations. During processing, some form of mask definition will be required. The simplest approach in terms of number of processing steps would be to use a photoresist mask thick enough to stop the As ions. KMER-II was used and proved to be adequate for the purpose. Substrates were coated with  $1 \mu$  of KMER-II and buried layer patterns developed. After the ion predeposition was performed, the KMER-II was stripped and then the substrate cleaned and put in the drive-in furnace.

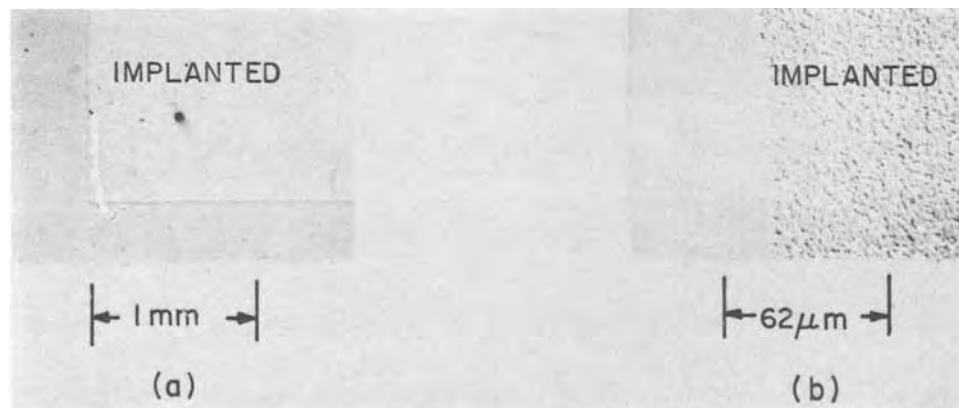


Fig. 1. (a) X-ray topograph and (b) photomicrograph of epitaxial layer grown over  $5 \times 10^{14}$  As/cm<sup>2</sup> implanted region (25°C).



It was found that excellent epitaxy could usually be grown as characterized under interference contrast. However, variation occurred in the quality of the epitaxy, and faceted pads, which by x-ray showed considerable surface damage, were sometimes observed. This was correlated with the ability to remove the polymerized KMER resist after ion implantation and before drive-in. Due to the additional cross linking induced in resist by ion implantation, J-100<sup>1</sup> chemical stripper is insufficient for the total removal of the organic contaminants.

The lack of a readily observable pattern in a mask alignment microscope makes the use of a resist mask somewhat impractical.

**Oxide masks.**—SiO<sub>2</sub> masks were examined. It was found that the oxide stopped the As implanted into the SiO<sub>2</sub> from diffusing through the oxide during drive-in. During the drive-in in O<sub>2</sub>, a 0.1-0.3 μm step was formed in the substrate. This simplifies alignment to these buried features.

**Contact (shadow) masks.**—At this point the variables noted in the cleaning stimulated an examination of the possible use of "shadow" masking. The potential for minimizing chemical contamination of the Si surface during implantation appeared attractive. Initial results with a Mo mask indicated that sputtering of contaminant Mo onto the Si surface with subsequent drive into the surface at 1200°C could occur (Fig. 2a). Replacement of Mo by a Si mask on the presumption that sputtered Si would not be a contaminant proved correct. Figure 2b and the related topograph Fig. 2c show that high quality epitaxy, with barely a trace of the slightly strained implanted area, can indeed be obtained by this method. The heavily doped, buried layers oxidized faster than the surrounding silicon, and thus steps of ≈ 300Å were formed around the edge of the buried layers during the drive-in in O<sub>2</sub>.

**Effect of HF staining.**—Many of the initial results showed staining effects which subsequently gave rough epitaxial surfaces. This has been traced to the original use of an oxide mask which was removed by HF etching prior to the 1200°C drive-in in an attempt to minimize the subsequent step in the substrate. Heavily implanted As surfaces appear to react preferentially with HF forming a stained compound which forms considerable defects during the epitaxial growth stage. Even when the original oxide mask is left on, if the

<sup>1</sup> Proprietary solvent: Indust-Ri-Chem Laboratory, Richardson, Texas.

holes are cleaned using 100:1 H<sub>2</sub>O:HF prior to drive-in, the problem occurs (in a less dramatic form).

Figure 3 illustrates the texture of epitaxial layers grown over buried layers cleaned in various concentrations of HF before drive-in. Figure 3a (no HF) shows excellent epitaxial Si with no sign of the implanted regions in an x-ray topograph. Figure 3b is from a region with a 50:1 HF etch and Fig. 3c from a region with a 48% HF etch treatment. Both HF cleaned regions show faceted, striated epitaxy. X-ray topographs also show harmful effects of the HF cleans.

**Electrical measurements.**—Four-point probe measurements have shown that sheet resistivities of 7-8 ohms/□ are obtained for a dose of 10<sup>16</sup>/cm<sup>2</sup> after drive-in and are only slightly increased by a 0.2 μm vapor etch. For 5 × 10<sup>15</sup>/cm<sup>2</sup>, ρ<sub>s</sub> was 15 ohms/□ and for 10<sup>15</sup>/cm<sup>2</sup>, ρ<sub>s</sub> was 80 ohms/□. Minority carrier lifetimes measured on undoped epitaxy over both the buried layers and the surrounding matrix gave values greater than 20 μsec, the upper reliable limit of the method.

### Discussion

The growth of epitaxial silicon over implanted buried layers has shown interesting effects related to the decoration of residual implantation damage by the epitaxial growth process. The region shown in Fig. 2 is amorphous after implantation and although after the 1000°C anneal, by resistivity measurements the impurity atoms are incorporated into a Si lattice and the reflectance is identical with bulk Si, the area still shows that residual damage exists by both x-ray topography and by the disordered epitaxial film that forms. The observations of Bicknell and Allen (8) of residual damage existing in P implanted Si after annealing at 1027°C could account for this. The epitaxial growth of Si on such a lattice would be greatly hindered and the meaning of an x-ray topograph of such highly dislocated material would be problematical (9). An alternative concept would be the existence of a high density of point defects in such a disordered lattice resulting in epitaxial disorder. One might expect such a grouping of vacancies to segregate at high temperatures, however, and to precipitate out as stacking faults. No such aggregation of stacking faults has been seen.

The hot implantation (600°C) proved that no residual implantation damage which would affect epitaxial growth existed after a 1000°C anneal even at doses 20-100 times greater than room temperature implantation which yielded poor epitaxial layers. It

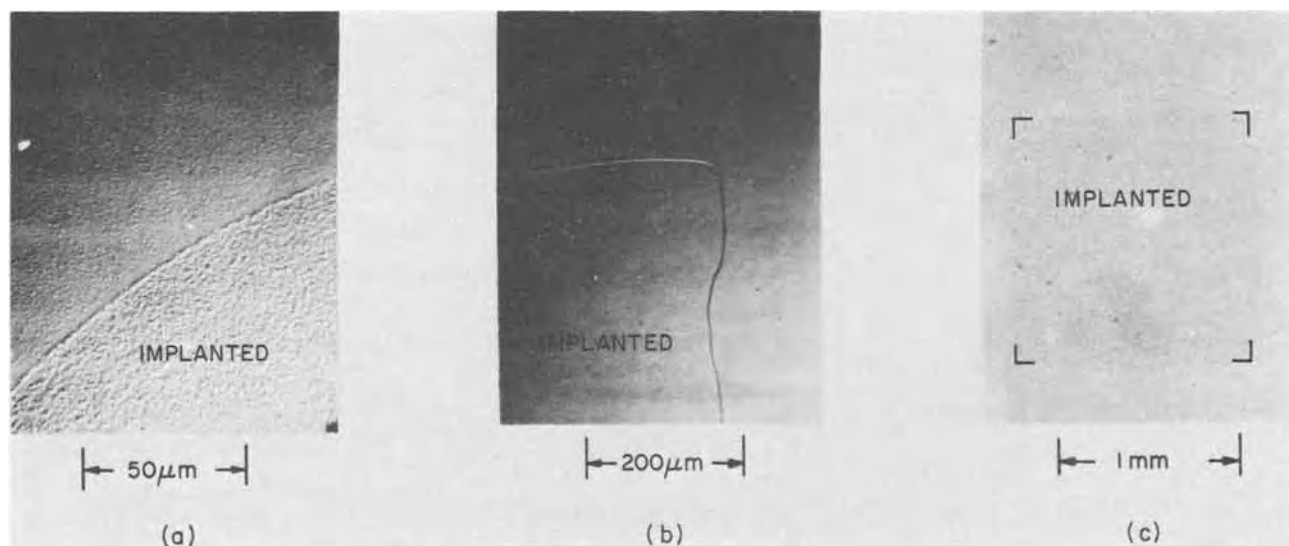


Fig. 2. Epitaxial layers grown over shadow masked implantations. (a) Mo mask photomicrograph, (b) Si mask photomicrograph, and (c) Si mask x-ray topograph.



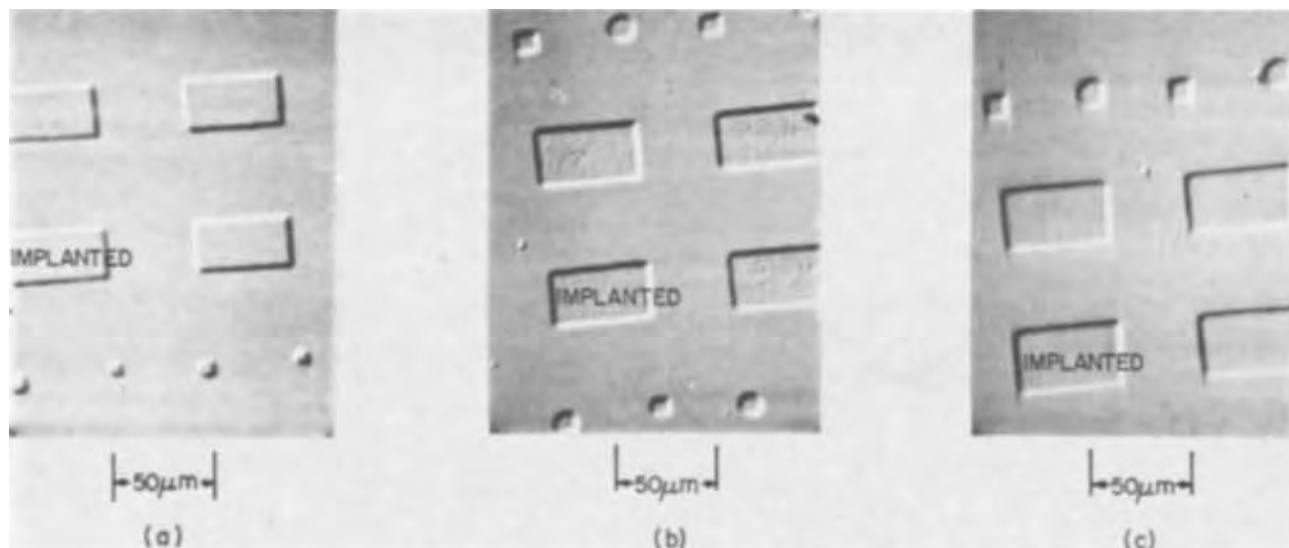


Fig. 3. Photomicrographs of epitaxial layers grown over (a) non-HF treated substrate, (b) 50:1 HF etched substrate, and (c) 48% HF etched substrate.

would appear that high quality epitaxy could be grown under such implantation conditions.

In terms of the vapor etch experiments it would appear that a  $0.2 \mu\text{m}$  HCl *in situ* etch prior to epitaxial deposition is essential. The incorporation of between  $0.15$  and  $0.2 \mu\text{m}$  of the implanted substrate surface by oxide formation during the  $1200^\circ\text{C}$   $\text{O}_2$  drive-in may not remove all the residual damage, or, in fact, some of the damage may propagate into the substrate during oxidation as dislocations or vacancy migration. The x-ray topography indicates that the additional  $0.2 \mu\text{m}$  vapor etch removes the vestigial damage and also any surface contamination likely to produce traditional structural defects. It is interesting to note that no significant damage propagates more than  $0.2 \mu\text{m}$  from this highly disordered region.

The effect of HF etching on the implanted As areas prior to drive-in seems to relate to a complex chemical reaction at the surface resulting in an inert stain. This reaction appeared strongest for the highest implantation dosage, and the strongest HF etchant solution. The additional reactive energy available in the large number of disordered lattice bonds might create a highly activated surface.

The use of shadow masking and photoresist masking is interesting because of the high structural quality of the resulting epitaxy grown over such buried layers and the processing simplicity. The oxide mask method is compatible with current device processing technology and has been shown to yield excellent epitaxy which is readily processed.

The results shown in Fig. 2a underscore the importance of using masking materials which do not serve as a source of contaminants. Significant quantities of materials get backsputtered off the mask and redeposit on the silicon. The sputtering yield is generally  $>1$  for heavy projectiles and thus tens of monolayers of the mask are removed, some of which will redeposit in the windows. Also, if there is a thin surface layer over the windows of the Si, significant quantities of this material can recoil into the Si. Recent measurements have shown (10) that heavy projectiles passing through a thin oxide layer can recoil several ( $>2$ ) oxygen atoms/projectile into the substrate.

The ability to tailor buried layer concentrations accurately, reproducibly, and without structural defects is a positive step toward controlled processing. The low As concentration in the oxide mask prevents the formation of As rich precipitates which can cause oxide breakdown. Ellipsometric measurements of the As im-

planted  $\text{SiO}_2$  mask have shown it is easily removed by HF to a residual  $\text{SiO}_2$  film equivalence of  $5\text{\AA}$ .

The  $20 \mu\text{sec}$  lifetimes measured in the epitaxy are encouraging.

### Conclusions

1. Structurally perfect epitaxy can be grown over room temperature As implanted Si substrates up to a dose of  $1 \times 10^{14}/\text{cm}^2$  after annealing.
2. Similarly, epitaxial layers have been grown over As implanted at  $600^\circ\text{C}$  up to a dose of  $10^{16}/\text{cm}^2$ .
3. A process has been developed utilizing a room temperature ion predeposition, up to a dose of  $10^{16}/\text{cm}^2$  followed by a diffusion drive-in at  $1200^\circ\text{C}$  in pure  $\text{O}_2$ , or in  $\text{O}_2\text{-N}_2$  mixtures.
4. Sheet resistivities as low as  $7 \text{ ohms}/\square$  have been attained by this method with a  $3 \mu\text{m}$  junction depth; lower sheet resistivities can be obtained by driving the junction in deeper (11).
5. Either  $\text{SiO}_2$ , photoresist or contact masks may be used with the process.
6. The existence of HF staining of implanted As areas (before anneal) has been noted as a processing variable.

### Acknowledgments

Thanks are due P. Miller for encouragement in utilizing the implant approach for buried layers; also, R. H. Kaiser for helpful ellipsometric advice, and R. W. Treible for performing the implantations.

Manuscript submitted Jan. 30, 1974; revised manuscript received April 26, 1974.

Any discussion of this paper will appear in a Discussion Section to be published in the June 1975 JOURNAL. All discussions for the June 1975 Discussion Section should be submitted by Feb. 1, 1975.

The publication costs of this article have been assisted by Bell Laboratories.

### REFERENCES

1. A. U. Mac Rae, "Proceedings of the II International Conference on Ion Implantation in Semiconductors," I. Ruge and J. Graul, Editors, p. 329, Springer-Verlag, New York (1971).
2. D. Eirug Davies, *Solid-State Electron.*, **13**, 229 (1970).
3. J. A. Davies, J. Denhartog, L. Eriksson, and J. W. Mayer, *Can. J. Phys.*, **45**, 4053 (1967).
4. J. Simpson, A. C. Adams, and M. H. Hanes, NBS Special Publication 337, Proceedings of Symposium on Silicon Device Processing, Gaithersburg, Maryland, p. 87 (June 1970).

5. M. Zerbst, *Z. Angew. Phys.*, **22**:1, 30 (1966).
6. F. F. Morehead, Jr., and B. I. Crowder, *Radiation Effects*, **6**, 27 (1970).
7. K. E. Benson, Private communication.
8. R. W. Bicknell and R. M. Allen, "Ion Implantation," Fred H. Eisen and Lewis T. Chadderton, Editors, p. 63, Gordon and Breach, Science Pub. Ltd., (1971).
9. E. S. Meieran, *Siemens Review*, **37**, 39 (1970).
10. R. A. Moline, G. W. Reutlinger, and J. C. North, Paper VIII 6 in, "Proceedings of 5th International Conference on Atomic Collisions in Solids (Sept. 1973), Plenum Press, New York, To be published.
11. C. M. Drum and P. Miller, Paper 17.7, Abstracts of International Electron Device Meeting, Washington (Oct. 1971).

## An Analysis of the Temperature Distribution During Crystal Growth by THM

R. O. Bell

*Tyco Laboratories, Inc., Waltham, Massachusetts 02154*

### ABSTRACT

The temperature distribution during crystal growth by the traveling heater method (THM) has been calculated by numerical integration of the Laplace equation for a cylindrical geometry. The boundary between the liquid and solid, which have different physical properties, was assumed to be an isotherm. The radial and longitudinal temperatures, the isotherms, and the interface shape have been calculated for different heater temperatures, interface temperatures and geometries. Also briefly described are a one-dimensional model that neglects radial gradients and an analytical solution for an idealized geometry and boundary conditions. When numerical values are determined, parameters appropriate to the growth of CdTe by Te are used. Some of the practical implications with regard to crystal growth behavior are discussed.

Recently, the traveling heater method of crystal growth (THM) has been applied to a number of compounds including CdTe (1, 2), GaAs (3), GaP (4, 5), CuCl (6), and ZnO (7), and also to several solid solutions such as (Ga, Al) As (3), (Ga, In)P (3), (Hg, Zn)Te (5), and (Pb, Sr)TiO<sub>3</sub> (8). This is a relatively new technique, and the basic process has been analyzed using idealized geometries and temperature distributions, primarily in papers by Wolff and co-workers (3, 9-11).

The usual cylindrical geometry (Fig. 1) has a heater, typically a hot metal ring, which heats the solvent by radiation. The solvent zone is made to migrate along the ampul containing the material of interest by the relative motion of the heater. Heat is transported by thermal conduction along the feed material and growing crystal and then is lost by convection and reradiation. The general heat flow is thus balanced between the heat input from the central heater and loss from the ends of the ampul. As discussed by Chalmers (12, 13), it is important that the growing interface, which will be an isotherm, have minimal curvature. A concave<sup>1</sup> surface is undesirable if nucleation of new crystals from the walls is to be avoided and a highly convex<sup>1</sup> surface should also be avoided to prevent the solvent near the perimeter of the ampul from becoming starved of the material in solution. Thus, one very important parameter is the temperature distribution during THM, which will to a large degree determine the liquid-solid interface shape.

Some experimental measurements of temperature profiles have been made (13), but precise results are difficult to obtain; therefore, we have found it very useful to calculate the temperature distribution. Both the temperature of the solid-liquid interface and the concentration in solution, will be determined by the thermal conditions and by the phase diagram. Changes in physical parameters, such as the amount of solvent

or the heater temperature, will change the length of the solvent zone and thus the interface temperature, so the entire process is fairly complicated. This paper is not meant to be an analysis of the entire situation but to provide some guidance with regard to the practical understanding of THM.

THM crystal growth is quite slow (not more than 1 to 2 cm/day and usually something more like 5 mm/day); thus it is not necessary to consider the latent heat associated with the phase transformation or other dynamical properties. To a high degree of approximation, the temperature will be given by the equilibrium situation. In some work on GaP and CdTe, direct rf coupling to the solvent to produce heat throughout the

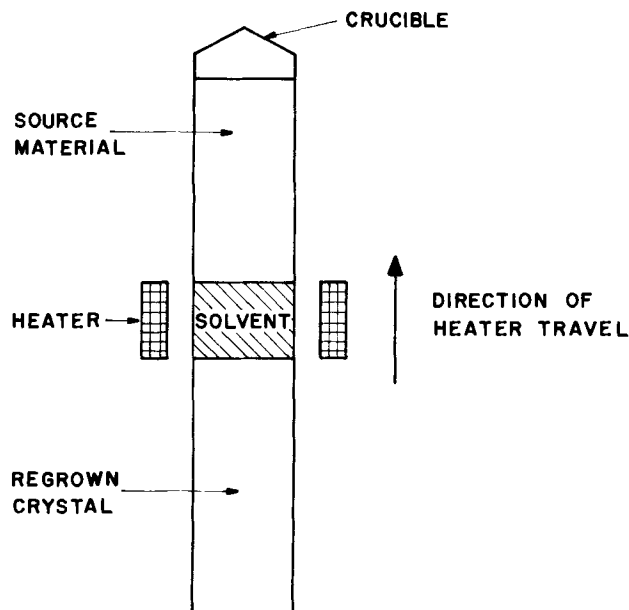


Fig. 1. Schematic of THM crystal growth procedure

Key words: crystal growth, temperature distribution, traveling heater method, numerical integration, interface shape, cadmium telluride.

<sup>1</sup> In this communication, concave and convex will refer to the shape of the growing crystal, i.e., the solid.

volume has been used (4, 13), but we will only consider the more usual case where thermal radiation from an external source is used.

### Theory

A number of different approaches to the calculation of thermal distribution are possible, of which we have investigated three. The first is a one-dimensional model which neglects radial gradients and gives only the average temperature along the ampul (see the Appendix). This particular model is easily formulated to obtain numerical results with the major drawback, of course, that no isotherms are obtained. The second approach is to analytically solve the Laplace equation in three dimensions (see the Appendix), but in order to obtain a simple series solution of the appropriate equations, it is necessary to assume that the regrowth, solvent, and feed all have homogeneous thermal properties. Even more importantly, thermal radiation which involves a  $T^4$  term cannot be handled directly, but, rather, an effective linear heat transfer coefficient must be used. The third, and most realistic, case and the one on which we will concentrate is the direct numerical integration of the Laplace equation and the boundary conditions to obtain the liquid-solid interface shapes. The principal approximations made in this case relate to the practical impossibility of producing an abrupt temperature step because of longitudinal spreading of the incident radiation between the heater and rod and neglect of the effect of things such as the conductivity of the walls of the ampul, although, in principle, they could be included.

In this paper we will discuss this last case and show some of the results and insights we have obtained. A brief outline of the first two models is given in the Appendix. The numerical methods are also outlined and, although we have not included the FORTRAN computer programs, enough information is given so that the programming should be straightforward.

The approach used here is to integrate the Laplace equation and the boundary conditions numerically using the geometry shown in Fig. 2. The rod is assumed to be symmetrically located in the heater. The set of equations governing the temperature,  $T$ , in a cylindrical coordinate system are

$$\frac{1}{r} \frac{\partial}{\partial r} \left( r \frac{\partial T}{\partial r} \right) + \frac{\partial^2 T}{\partial z^2} = 0 \quad [1]$$

$$-k_l \left( \frac{\partial T}{\partial r} \right)_{r=a} = q_{i,j} \quad [2]$$

$$-k_l \left( \frac{\partial T}{\partial z} \right)_{z=d} = q_{i,j} \quad [3]$$

$$-k_l \left( \frac{\partial T}{\partial r} \right)_{r=0} = 0 \quad [4]$$

$$-k_l \left( \frac{\partial T}{\partial z} \right)_{z=0} = 0 \quad [5]$$

$$-k_l \frac{\partial T}{\partial n} = -k_s \frac{\partial T}{\partial n} \text{ at the interface where } T = T_m \quad [6]$$

and

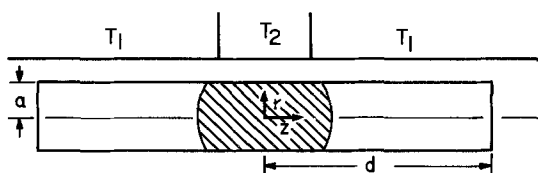


Fig. 2. Geometry assumed for numerical solution of temperature distribution. The interface is assumed to be at a fixed temperature,  $T_m$ .

$$q_{i,j} = \sigma \epsilon_l (T^4 - T_j^4) + h_s (T - T_a)^{1.25} \quad [7]$$

where  $k_l$  is the thermal conductivity of the liquid,  $k_s$ , or solid, depending on whether the temperature is above or below that of the interface; similarly, this applies to the emissivities  $\epsilon_l$  and  $\epsilon_s$ .  $T_j$  is either the temperature of the heater,  $T_2$ , or of the outside environment,  $T_1$ .  $T_m$  is the temperature of the interface, and  $T_a$  the temperature of the air.  $\sigma$  is the Stefan-Boltzmann constant and  $h_s$  is the effective heat transfer coefficient for convection.

In Eq. [7] which gives the heat flux across the surface, the first term on the right-hand side is the contribution by thermal radiation and the second represents the convective heat transfer. It should be pointed out, though, that the form of this last term is only for free laminar convection across an isothermal surface (14, 15) and thus is only an approximation.

An area where convection has been neglected is in the liquid zone where the heat transport is assumed to be solely by conduction. In principle it should be possible to include convection by using the Navier-Stokes equation coupled to the Laplace equation which has been modified to include the effects of fluid flow (16) but the additional complications were not deemed worth the effort for this initial analysis.

It has also been assumed that the system is opaque making radiative transfer unimportant. For partially transmitting media coupled radiation and convection must be considered (17, 18).

Another approximation that has been made is to assume perfectly abrupt transitions from the hot to the cool zone. In practice, there will be a more or less continuous change which will smooth out the transition. The principal effect will be to decrease the gradient, primarily in the transition region. For the case where the interface is within the heater, this will not be as important as when near or outside in the cool zone.

The equations are converted to difference equations and used to solve for the temperature as a function of the  $r$  and  $z$  coordinates.

For the numerical solution write Eq. [1] as a difference equation with a spacing of  $h$

$$(2m-2)(T_{n-1,m} + T_{n+1,m}) + (2m-1)T_{n,m+1} + (2m-3)T_{n,m-1} - 8(m-1)T_{n,m} = 0 \quad [8]$$

Here, the  $m$  index is for the  $r$  coordinate and runs from 1 at  $r=0$  to  $M$  at  $r=a$ . Similarly, the  $n$  index is for the  $z$  coordinate and runs from 1 at  $z=0$  to  $N$  at  $z=d$ . Equation [2] becomes

$$-k_l(T_{n,M} - T_{n,M-1}) + hq_{i,j}(T_{n,M}) = 0 \quad [9]$$

Equation [4] gives

$$T_{n,1} - T_{n,2} = 0 \quad [10]$$

Similar expressions for Eq. [3] and [5] are

$$-k_l(T_{1,m} - T_{2,m}) + hq_{i,j}(T_{1,m}) = 0 \quad [11]$$

$$T_{N,m} - T_{N-1,m} = 0 \quad [12]$$

This gives enough equations so one could, in principle, solve for each  $T_{n,m}$ , but because Eq. [9] and [11] are nonlinear in  $T$ , a closed form solution is probably impossible. We have thus chosen to first assume values for  $T_{n,m}$  and use these in an iterative process (Gauss-Seidel method) to calculate new values. Because of the rather slow convergence, it is necessary to use over-relaxation to speed the process (19).

Figure 3 shows a plot of the temperature as a function of length for the center and outer surface of the ampul where we assumed that the 6 cm long and 1 cm diameter ampul is symmetrically located within a 2 cm hot zone at 1000°C. Physical parameters appropriate to the growth of CdTe with a Te solvent were used (Table I). Figures 4 and 5 are plots of isotherms for two different values of the liquid-solid interface (600° and 750°C). Note that only near the junction of the high and the low temperature regions does a nearly flat zone

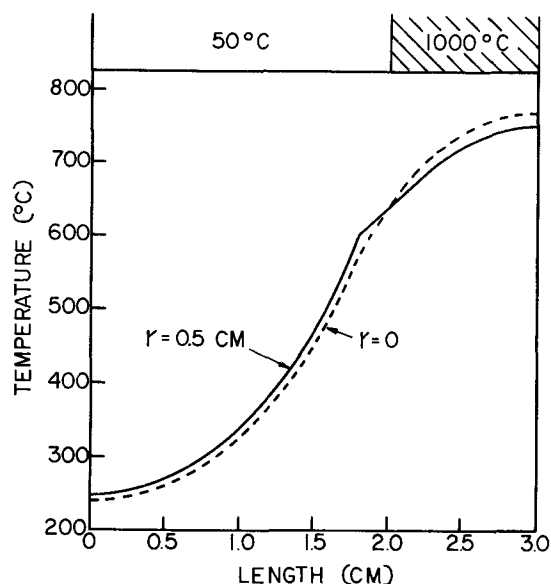


Fig. 3. Temperature distribution along the ampul at the center,  $r = 0$ , and on the outer surface,  $r = 0.5$  cm. An interface temperature of  $600^\circ\text{C}$  was assumed. The rod is 6 cm long and is symmetrically located in the 2 cm heater. A heater temperature of  $1000^\circ\text{C}$  and air temperature of  $50^\circ\text{C}$  was assumed. Parameters given in Table I were used for the calculation.

occur and even here the isotherm is never perfectly flat. The curvature changes from concave (the shape of the growing crystal) when the interface is out of the heater (Fig. 4) to convex when the interface is within the hot zone (Fig. 5). The latter condition is more desirable for preventing new crystallites that nucleate on the walls from growing into the crystal. Naturally a perfectly flat growth interface is ideal, but if that is not possible, then a slightly convex shape is probably better than concave.

Rather than making a complete temperature map for each set of conditions, it is more effective just to look at the shape and position of the interface while holding all parameters fixed except for one which is allowed to vary. Figure 6 shows the changes as the interface temperature changes. The further the interface is from the heater junction, the greater the curvature. Figure 7 shows the result of changing the heater temperature with the interface temperature held constant at  $650^\circ\text{C}$ . The highest heater temperatures expand the zone and produce a strongly concave shape. In actual physical situations the effect will not be as drastic because as the temperature is increased the solution will become more concentrated and the liquid-solid transition temperature generally will increase, by an amount given by the phase diagram.

### Conclusions

During THM, many different parameters can interact to affect the geometry and temperature of the inter-

Table I. Physical characteristics used for calculation of temperature distribution during THM growth of CdTe with a Te solvent

Parameter	Value
$k_1$ , thermal conductivity of CdTe	$0.035\text{W cm}^{-1}\text{K}^{-1}$ *
$k_2$ , thermal conductivity of Te	$0.10\text{W cm}^{-1}\text{K}^{-1}$ **
$\epsilon_{1,2}$ , emissivity	1
$h_s$ , heat transfer coefficient	$0.0006\text{W cm}^{-2}\text{K}^{-1}$ †
$T_a$ , air temperature	$50^\circ\text{C}$

\* Obtained from extrapolation of data to  $500^\circ\text{C}$ , from G. A. Slack and S. Galginaitis, *Phys. Rev.*, 133, A253 (1964).

\*\* Value at  $700^\circ\text{C}$  after being increased by 50% to partially account for heat transport by convection in the Te solvent. C. Y. Ho, R. W. Powell, and P. E. Liley, *J. Phys. Chem., Ref. Data*, 1, 279 (1972).

† Air value from W. H. McAdams, "Heat Transmission," p. 165, McGraw-Hill Book Co., New York (1954).

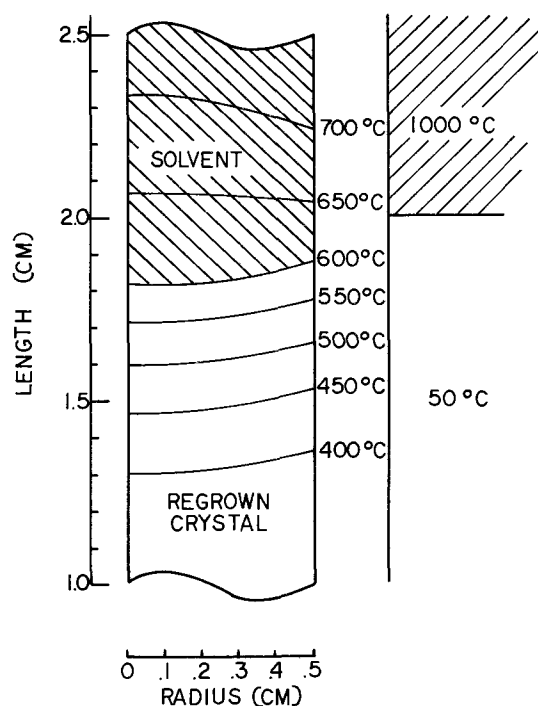


Fig. 4. Plot of temperature isotherms for an interface temperature of  $600^\circ\text{C}$ . Other dimensions and parameters the same as in Fig. 3.

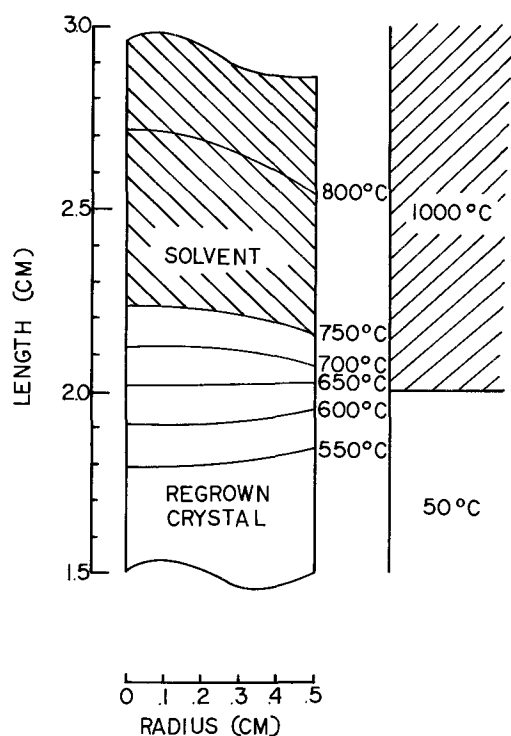


Fig. 5. Plot of temperature isotherms for an interface temperature of  $750^\circ\text{C}$ . All other parameters the same as in Fig. 3 and 4.

face. The amount of material in solution will be determined by the interface temperature which, in turn, is determined by the relative position of the heater and interface. To complicate matters still further, the length of the solvent zone will depend, to some extent, on the amount of feed material in solution.

Naturally, the final adjustment of the growth parameters must be done experimentally, but calculations such as these for a particular solvent-solute will make the problem much easier.

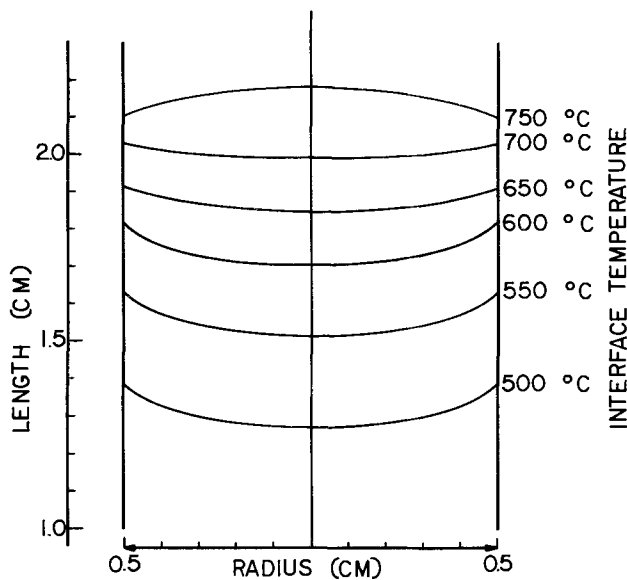


Fig. 6. Shape and position of the liquid-solid interface for various interface temperatures. All other parameters were the same as for Fig. 3.

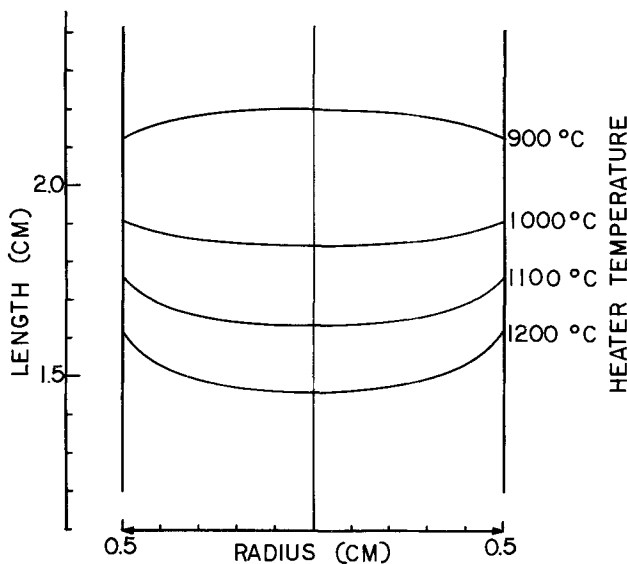


Fig. 7. Shape and position of the liquid-solid interface for various heater temperatures. An interface temperature of 650°C was used, otherwise all other parameters were the same as for Fig. 6.

Some practical implications that have become apparent from these calculations and those in the Appendix are:

1. Only near the junction of the high and low temperature regions does a reasonably flat isotherm occur, and here it is apparently never absolutely flat. For shorter solvent zones, the interface becomes convex and for longer zones, concave. From the point of view of the best crystallinity, a short solvent zone with a long heater is desirable, but in order to obtain fast growth rates and to prevent constitutional supercooling, a large gradient, which implies a short heater, is necessary. Thus, the optimum configuration must be determined for each different crystal-solvent system.

2. If the thermal history of the crystal is important, for example, to control the defect structure, it is necessary to be aware of the thermal distribution and how it changes as the position of the crystal relative to the heater changes. Longer ingots will be annealed at lower temperatures.

3. Keeping other parameters constant, increasing the radius will decrease the thermal gradients along the rod. This is because the heat gain or loss is through the surface whose area is proportional to the radius, but heat transport is along the rod whose cross-sectional area is proportional to the square of the radius.

4. At the beginning and end of THM growth, where only one end of the ampul sticks out of the furnace, a substantial increase in the temperature of the solvent zone can occur. This is because the heat loss can only occur in one direction rather than in two, as at an intermediate position. One way to overcome this is by the use of dummy ends. Naturally, use of an extra long ingot and discarding the ends would work, but the slow growth speeds do not make this very attractive.

5. The temperature is a very strong function of the length of the heater and of the thermal conductivity of the material. Because of this, attempts to determine the absolute thermal profile with a bare thermocouple without the ampul present may be misleading, although relative values make some sense. Since the length of the ampul will have a pronounced effect on the temperature, reproducible experiments can only be made with careful control of the geometry. The principal effect of going to a longer ingot is to decrease the temperature because more radiating surface is available and the heat input can only increase slightly.

### Acknowledgments

I would like to acknowledge the support of the United States Atomic Energy Commission (Contract No. AT(11-1)-3545), and the Advanced Research Project Agency (Order No. 1846) for this work. I would especially like to thank Mr. Fritz Wald of Tyco Laboratories, Inc. for many interesting discussions which greatly stimulated this contribution.

Manuscript submitted July 13, 1973; revised manuscript received March 11, 1974.

Any discussion of this paper will appear in a Discussion Section to be published in the June 1975 JOURNAL. All discussions for the June 1975 Discussion Section should be submitted by Feb. 1, 1975.

### APPENDIX

In addition to the direct numerical integration of the Laplace equation, two other models have been used and proved useful for determining the effect of various parameters on the temperature distribution during THM. They are briefly discussed in this Appendix.

*One-dimensional temperature distribution.*—This model is a one-dimensional approximation that neglects radial gradients. Assume that the rod of radius,  $a$ , and length,  $d$ , can conduct heat along its length and is in thermal equilibrium with its surroundings when radiation and convection are considered. The solvent is located between  $b$  and  $c$  (Fig. 8a).

The hot zone is at a temperature  $T_2$ , the outside at  $T_1$ , and the air temperature is  $T_a$ . By looking at the heat flow along a small section of the rod and neglecting radial gradients, the equation governing the temperature,  $T$ , as a function of position,  $x$ , can easily be shown to be

$$\pi a^2 k_i \frac{d^2 T}{dx^2} = 2\pi a \epsilon_i \sigma (T^4 - T_1^4) + 2\pi a h_s (T - T_a)^{1.25} \quad [\text{A-1}]$$

where  $k_i$  is the thermal conductivity of material in region  $i$ ,  $\sigma$  is the Stefan-Boltzmann constant,  $\epsilon_i$  is the emissivity of material in region  $i$ , and  $h_s$  is the heat transfer coefficient for convection.

The boundary conditions for insulated ends are

$$\left. \frac{dT}{dx} \right|_{x=0,d} = 0 \quad [\text{A-2}]$$

i.e., heat flux from the ends is neglected. For freely conducting ends the heat flux should naturally be equated to the loss via radiation and convection. Also, at the interface between two materials of different con-

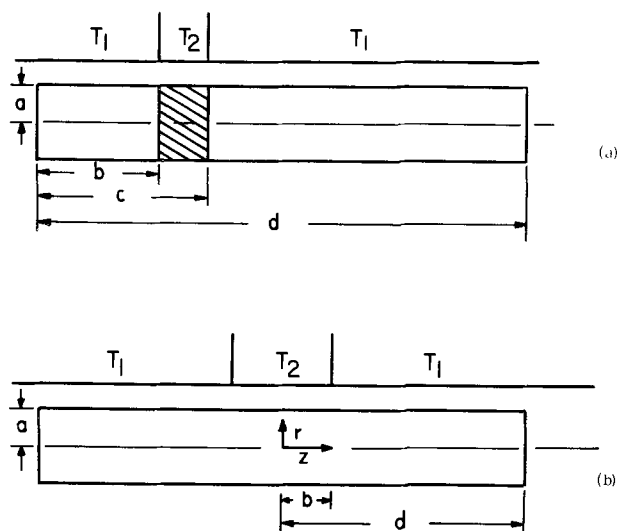


Fig. 8. (a) Geometry used to analyze one-dimensional temperature distribution. The air temperature is  $T_a$ . The thermal conductivity and emissivities are different in different regions. (b) Geometry assumed to calculate temperature distribution in a homogeneous rod. The distribution will be symmetrical about  $z = 0$ .

ductivities, the flux and temperature must be continuous.

To obtain numerical values after dividing through by  $\pi a^2 k_i$ , Eq. [A-1] and [A-2] are written as difference equations with a spacing of  $h$ : and solved for  $T_{n+1}$  and  $T_1$

$$T_{n+1} = 2T_n - T_{n-1} + h^2 f(T_n) \quad [\text{A-3}]$$

$$T_1 = T_0 + h^2 f(T_0)/2 \quad [\text{A-4}]$$

where

$$f(T) = \frac{2\epsilon_1\sigma}{k_1 a} (T^4 - T_1^4) + \frac{2h_s}{k_1 a} (T - T_a)^{1.25} \quad [\text{A-5}]$$

A value of the temperature on the left-hand side, i.e.,  $T_0$ , was assumed and by successive application of the difference equation and requiring the continuity of the flux at the interface of the two different materials, the temperature, and, therefore, the thermal gradient on the right-hand side was determined. A different value of the initial temperature was assumed and a new gradient at  $x = d$  was calculated. An extrapolation was made to provide a starting temperature that satisfies

the boundary conditions at  $x = d$ , Eq. [A-2]. This new starting temperature was used to iterate the whole procedure until the appropriate distribution was determined (20).

Some results are shown in Fig. 9, where the effect of making the total ampul longer and longer is examined. Note that the gradient in the Te zone is smaller than in the CdTe because of the larger thermal conductivity of the Te. The hot zone is assumed to be as long as the Te solvent, although this is not necessary but is only done for convenience. The principal effect of going to a longer ingot is to decrease the temperature, obviously, because more radiating surface is available and the heat input can only increase slightly.

Another interesting result is to compare the temperature distribution when the ampul is symmetrically located and when it is displaced (Fig. 10). A substantial increase in the solvent temperature occurs in the asymmetric case with an increase of temperature at zone center.

*Analytical solution for temperature distribution.*—If we want a reasonably simple analytical solution, we must restrict our generality. Boundary conditions where thermal radiation is involved require  $T^4$  terms and do not often produce neat or closed form results. We will thus use an effective heat transfer coefficient so that the flux across the surface will be proportional to the temperature difference. We also assume that the thermal properties of the rod are homogeneous and isotropic. For a steady temperature, the equation governing the heat distribution is the Laplace equation.

Using the geometry shown in Fig. (8b), the radius of the rod is  $a$ , the total length is  $2d$ , and the length of the heater, which is centered, is  $2b$ . The heater temperature is  $T_2$  and the temperature around the rest of the ampul is  $T_1$ . It is easy to show that the temperature as a function of radius  $r$ , and length,  $z$ , is given by the series

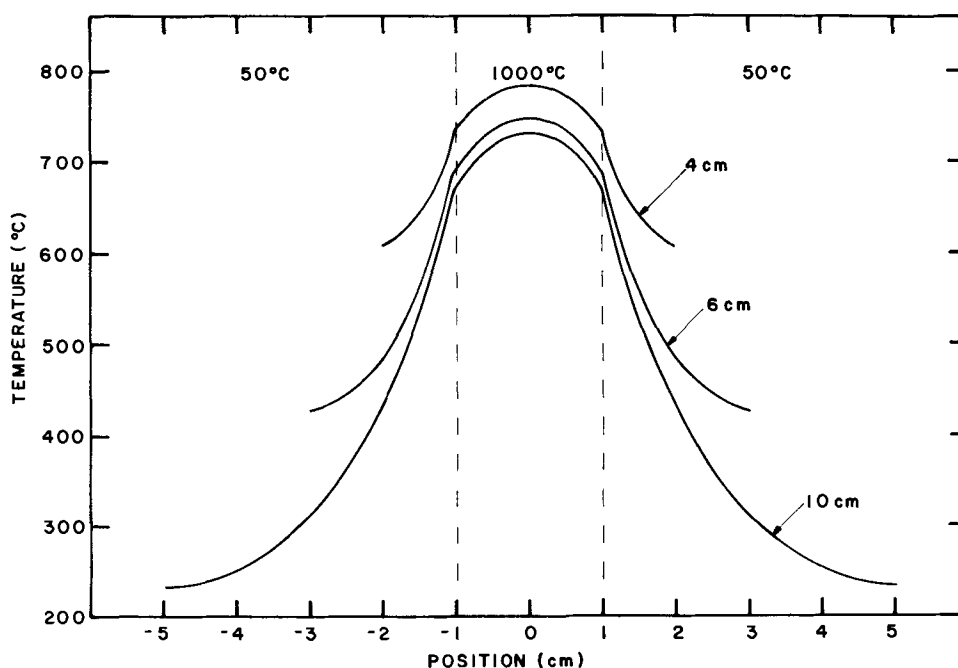
$$T = T_2 + \sum_{n=1}^{\infty} C_n \cosh(\alpha_n z) J_0(\alpha_n r) \quad 0 < z < b \quad [\text{A-6}]$$

$$T = T_1 + \sum_{n=1}^{\infty} [A_n \sinh(\alpha_n z) + B_n \cosh(\alpha_n z)] J_0(\alpha_n r) \quad b < z < d \quad [\text{A-7}]$$

The solution will be symmetrical about  $z = 0$ ; thus for  $z < 0$ , it is necessary to replace  $A_n$  by  $-A_n$ .  $\alpha_n$  is the  $n$ th root of the characteristic equation

$$\alpha_n J_0'(\alpha_n a) + h J_0(\alpha_n a) = 0 \quad [\text{A-8}]$$

Fig. 9. Temperature along a 1.2 cm diameter ampul for lengths of 4, 6, and 10 cm. For a one-dimensional model, parameters given in Table I were used for the calculation.



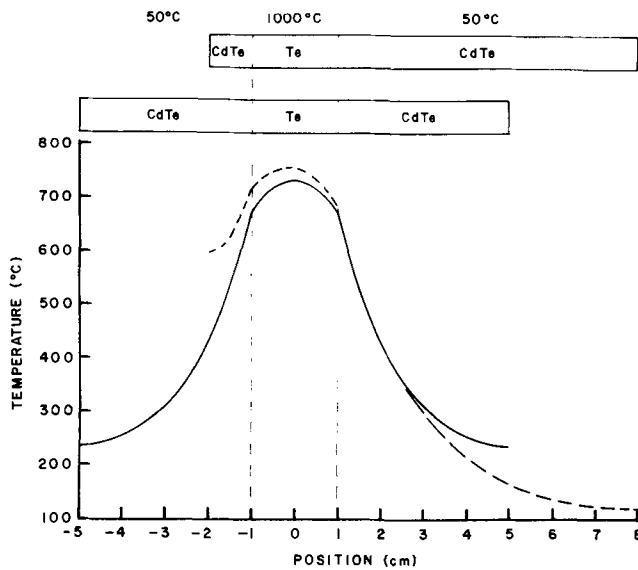


Fig. 10. Temperature distribution for the case of a symmetrically located ampul (solid line) and an ampul displaced 3 cm to the right (dashed line) for a one-dimensional model. Parameters given in Table I were used for the calculation.

$J_0(x)$  is the zeroth order Bessel function. The prime indicates differentiation with respect to the argument.

$h = H/K$  where  $K$  is the thermal conductivity and  $H$  is the linear heat transfer coefficient related to the heat flux through the surface,  $F$ , by the boundary condition

$$F = -K\nabla T = H(T - T_1) \quad [\text{A-9}]$$

The boundary conditions for uninsulated ends are

$$\frac{\partial T}{\partial z} + h(T - T_1) = 0 \quad \text{for } z = d \quad [\text{A-10}]$$

$$\frac{\partial T}{\partial r} + h(T - T_2) = 0 \quad \text{for } r = a \text{ in Eq. [A-6]} \quad [\text{A-11}]$$

$$\frac{\partial T}{\partial r} + h(T - T_1) = 0 \quad \text{for } r = a \text{ in Eq. [A-7]} \quad [\text{A-12}]$$

$$T^+ = T^- \quad \text{for } z = b \quad [\text{A-13}]$$

$$\frac{\partial T}{\partial z} = \frac{\partial T}{\partial z} \quad \text{for } z = b \quad [\text{A-14}]$$

Equations [A-11] and [A-12] are already satisfied by the form of the solutions chosen and the characteristic equation. The general procedure to follow is to use Eq. [A-7] to substitute for  $T$  in Eq. [A-10].

Multiply by  $rJ_0(\alpha_m r)$ , integrate from  $r = 0$  to  $r = a$  and using the properties of integrals involving Bessel functions such as given by Carslaw and Jaeger (21) find

$$B_n = -A_n \frac{\alpha_n + h \tanh(\alpha_n d)}{\alpha_n \tanh(\alpha_n d) + h} \quad [\text{A-15}]$$

Similar procedures can be used on boundary conditions Eq. [A-13] and [A-14] to obtain

$$A_n = -\Delta T \sinh(\alpha_n b) \frac{2h_a}{[(\alpha_n a)^2 + (ha)^2]} \frac{1}{J_0(\alpha_n a)} \quad [\text{A-16}]$$

and

$$C_n = B_n + A_n \operatorname{ctnh}(\alpha_n b) \quad [\text{A-17}]$$

where  $\Delta T = T_2 - T_1$ . This along with the solution to the characteristic equation, Eq. [A-8], are enough to allow us to calculate  $T$  as a function of  $r$  and  $z$ . This result is similar to that obtained by Cook *et al.* (22) who used modified Bessel functions. It is only slightly more difficult to treat the case where three different lengths of the rod are exposed to three different temperatures, but because the expressions for the coefficients are more cumbersome than Eq. [A-15], [A-16], and [A-17], it would add little to the discussion to write them down.

Solutions have been calculated but are not reported here since the numerical integration presented in the foregoing is a better approximation to physical reality.

#### REFERENCES

1. R. O. Bell, F. Wald, and N. Hemmat, *Phys. Status Solidi*, (a) **1**, 375 (1970).
2. R. O. Bell and F. Wald, *IEEE Trans. Nucl. Sci.*, **NS-17** (3), 241 (1970).
3. N. Hemmat, C. B. Lamport, A. A. Menna, and G. A. Wolff, *Proc. ACCG Conf. on Crystal Growth*, p. 79 (1969).
4. T. S. Plaskett, S. E. Blum, and L. M. Foster, *This Journal*, **114**, 1304 (1967).
5. G. A. Wolff, H. E. LaBelle, Jr., and B. N. Das, *Trans. Met. Soc., AIME*, **242**, 436 (1968).
6. B. Perner, *J. Crystal Growth*, **6**, 86 (1969).
7. G. A. Wolff and H. E. LaBelle, Jr., *J. Am. Ceram. Soc.*, **48**, 441 (1965).
8. B. diBenedetto and C. J. Cronan, *ibid.*, **51**, 364 (1968).
9. G. A. Wolff and A. I. Mlavsky, *Proc. Intern. Conf. on Absorption and Crystal Growth, Nancy, France*, **152**, 711 (1965).
10. J. D. Broder and G. A. Wolff, *This Journal*, **110**, 1151 (1963).
11. N. Hemmat, C. B. Lamport, A. A. Menna, and G. A. Wolff, *Proc. Mat. Engr. and Sci. Div., Biennial Conf., Am. Inst. Chem. Eng., Atlanta, Georgia* (1970).
12. B. Chalmers, Private communication.
13. F. Wald, R. O. Bell, and A. A. Menna, Interim Technical Report, NYO-4202-1 for U. S. Atomic Energy Commission, Division of Isotopes Development, by Tyco Laboratories, Inc., July 1971.
14. H. S. Carslaw and J. C. Jaeger, "Conduction of Heat in Solids," 2nd Edition, p. 21, Clarendon Press, Oxford (1959).
15. W. H. McAdams, "Heat Transmission," p. 165, McGraw-Hill Book Co., New York (1954).
16. N. Kobayashi and T. Arizumi, *Japan. J. Appl. Phys.*, **9**, 361 (1970).
17. R. Gardon, *J. Am. Ceram. Soc.*, **39**, 278 (1956).
18. G. K. Chui and R. Gardon, *ibid.*, **52**, 548 (1969).
19. Francis Scheid, "Sahum's Outline of Theory and Problems of Numerical Analysis," p. 341, McGraw-Hill Book Co., New York (1968).
20. *Ibid.*, pp. 386-387.
21. H. S. Carslaw and J. C. Jaeger, "Conduction of Heat in Solids," 2nd edition, pp. 196-198, Clarendon Press, Oxford (1959).
22. J. S. Cook, D. R. Mason, and P. H. Smith, *Electrochem. Technol.*, **1**, 300 (1963).

# Diffusion as the Rate Controlling Step in the Reaction of Tungsten Hexafluoride with Tungsten and the Role of Tungsten Pentafluoride

Lewis V. McCarty,\* William E. Reith,<sup>1</sup> and Mariellen T. Simon<sup>2</sup>

Lighting Research and Technical Services Operation, General Electric Company, Nela Park, Cleveland, Ohio 44112

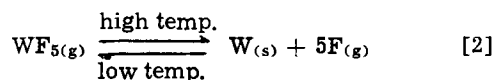
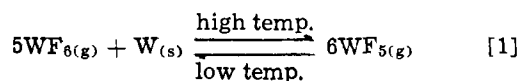
## ABSTRACT

Estimated thermodynamic properties of the molecule tungsten pentafluoride indicate that it may be the reactive intermediate formed at high temperatures when tungsten hexafluoride etches tungsten. The calculated concentration of tungsten pentafluoride that can form at equilibrium is adequate to explain the etching reaction between 1500°-2680°K, and it becomes sufficiently unstable above 2300°K to explain the transition from etching to deposition at higher temperatures. The differences in reaction rates in the three carrier gases argon, nitrogen, and helium, point to a diffusion controlled reaction. The reaction rates from diffusion calculations of tungsten hexafluoride into, and tungsten pentafluoride out of the Langmuir sheath are in good agreement with experiment for helium, and are reasonable for argon and nitrogen. Convective distortion of the Langmuir sheath is suspected as the cause of the higher than expected etching rates in the latter two gases as well as the higher than expected rates as the temperature increases.

Tungsten hexafluoride reacts with tungsten in a series of complex reactions. From about 900° to 2300°K the important reaction etches the metal and transports tungsten to cooler parts of the system. Tungsten powder deposits on cold surfaces as the result of a disproportionation reaction that reforms tungsten hexafluoride.

At higher temperatures whatever intermediate compound forms decomposes to tungsten metal and fluorine atoms. Presumably the decomposition reaction has a large enthalpy of reaction, at least larger than that of the etching reaction, and above 2500°K, depending upon the partial pressure of fluorine compounds, it overwhelms the etching reaction and tungsten deposits from the gas. This qualitative reaction scheme is implicit in work reported by Schroeder (1).

More recently Schroeder and Grewe (2) have reported on the preparation of tungsten pentafluoride, and Schroeder and Sieben (3) on its enthalpy of formation. When their data is extrapolated to high temperatures, it suggests that the reactive intermediate may be tungsten pentafluoride. The important reactions would then be



One purpose of this report is to discuss how well this reaction scheme fits the experimental data.

The experimental part of this work used 25W-1100 hr tungsten coils. Early work indicated that the relatively long cool zone at each end of an electrically heated straight filament caused serious errors during the determination of rates of reaction. This error can be minimized, but not eliminated, by using small wire sizes in coil form.

The use of coils introduces another complication in these measurements. The light from between the turns

of the incandescent coil is brighter than the light from the outside of the coils because of internal reflections (4, 5). An empirical correction curve was established for the 25W coils, and all of the optical pyrometer measurements of temperature have been so corrected.

When a filament or coil is heated to incandescence in an inert gas, a Langmuir sheath surrounds the coil (16) with properties that vary depending upon the kinetic parameters of the gas. Variations in reaction rate for tungsten hexafluoride with tungsten in the gases nitrogen, argon, and helium have been observed and are compared with calculated rates of diffusion.

## Experimental

Gas flows were measured into a 1/8 in. copper manifold to mix and conduct the gases to the reaction chamber. Nitrogen, argon, or helium were controlled with one Pyrex flowmeter, and a small Pyrex flowmeter with a sapphire ball and Nichrome wire ball retainers measured the tungsten hexafluoride flow. When not in use, both flowmeters, the manifold, and the reaction chamber were flushed with dry, lamp-grade nitrogen. Teflon and Kel-F plastic parts were avoided because they degenerated during repeated use and seemed to absorb tungsten hexafluoride which was released slowly when not wanted.

The reaction chamber was made from 2 in. OD Pyrex tubing with an inlet near the bottom, a 65/40 Pyrex ball joint with an O-ring seal, 1/4 in. nickel electrodes, and an exit to a long surge chamber to prevent air sucking into the reaction chamber when the coils were turned off.

Electrically heated, 25W-1100 hr tungsten coils, 49.1-50.7 mm in length, weighing  $8.03 \pm 0.10$  mg were used for the solid reactant. The wire diameter was 1.21 mils, and they were wound on 4.2 mil mandrels with a 118% pitch. A razor blade flattened 3-5 turns on each end of the coils to form an attachment to small bronze clips spaced 17 mm apart on the ends of the nickel leads. When heated the coils sagged under their own weight to a pitch near 140%.

Voltage to the Variacs for a.c., and to the Variacs and rectifier system for d.c., for heating the coils was regulated by a Sola transformer to  $\pm 0.1V$ . Electrical power to the filament was turned on and off by a mercury relay inserted just ahead of the coil to eliminate any time lag required to energize the electrical equip-

\* Electrochemical Society Active Member.

<sup>1</sup> Present address: Lincoln Electric Company, 22801 St. Clair Avenue, Euclid, Ohio 44117.

<sup>2</sup> Present address: 1271 Bunts Road, Lakewood, Ohio 44107.

Key words: diffusion, Langmuir sheath, estimated equilibria, reaction rates, etching.



ment. The mercury relay was controlled by a 40 sec timer with an adjustable "on" time cycle. The timer also controlled an electric stopwatch and recorded "on" times to a tenth of a second but was estimated to the nearest hundredth second. In early work 60 cycle a.c. was used to heat the coils for the tests in nitrogen between 2546° and 2716°K. The ripple in light emission from a-c heated coils amounts to several per cent which corresponds to several tens of degrees variation in temperature. To eliminate any possible effect in the reaction zone, d.c. was used for the nitrogen work between 1451° and 1894°K, all of the argon work, and for most of the helium work; a.c. was used for the two helium rate determinations at 2552° and 2636°K. So far as could be determined there was no observable effect caused by changing from a.c. to d.c.

The reaction chamber was flushed for at least 4 min with inert gas for the usual case of a flow of 1517 ml/min measured at 741.7 Torr and 24.0°C, and correspondingly longer times for lower flow rates. The coils were heated to the intended reaction temperature for at least 1 min to remove dirt and oxides from the surface before measuring the current and voltage needed to give a predetermined temperature. They were weighed after cooling and remounted in the reaction chamber. Each was again flushed for at least 4 min with the inert gas, 4-5 min with a mixture of inert gas and tungsten hexafluoride (20.0 ml/min measured at 741.7 Torr and 24.0°C in the usual case), flashed at the predetermined voltage for measured times, flushed once again with pure inert gas, flashed to remove traces of fluoride from the surface, and reweighed.

Temperature measurements of the coils with an optical pyrometer is less than satisfactory because it is difficult to match colors with the calibrated filament. A better technique (6) places a wide ribbon filament back of the coil to be measured, and it is easier to match the coil to this broad area than to the relatively smaller pyrometer filament. In our case an 18A, 75-80 mil ribbon filament, spectrographic lamp was matched to the desired temperature with the optical pyrometer which was focused on the test coil, and not on the ribbon filament. Although the ribbon is out of focus and the edges are apparently "low" in temperature, the central portion is wide enough to appear uniform. After establishing the current to maintain the ribbon at the desired temperature, the coil is matched to the ribbon using the pyrometer telescope and filter. Too much magnification is not an advantage because it becomes difficult to match colors if the individual turns are clearly resolved. Refraction effects in the Langmuir sheath also interfere with the images making complete disappearance into the background impossible.

In spite of the obvious difficulties with the optical determination of coil temperature, a calibration of the technique was accomplished by measuring apparent temperatures of coils and comparing with the true temperature obtained by focusing a micropyrometer on the outside of an individual turn at 125X magnification for the same current. The correction factors,  $\Delta$ , are fitted by the equation

$$\Delta = [({}^\circ\text{K}^{3.237}) / (7.218 \times 10^8)] \pm 7^\circ$$

The emissivity data for tungsten published by DeVos (7) was used to calculate temperature.

### Results

The data in Fig. 1 are typical of the individual weight changes found in this work. The slopes of straight lines such as these have been plotted in Fig. 2, 3, 4, and 5. Figure 2 shows that the etching reaction is more rapid in helium than in nitrogen, and comparable data for argon in Fig. 3 are somewhat slower.

The rate of reaction is proportional to the tungsten hexafluoride concentration in the etching region below

2200°K according to the data of Fig. 3 and 4. There is also a marked lowering of the transition temperature between the etching and deposition regions as the concentration decreases.

Figure 5 shows that the reaction rate is independent of flow rate below one liter per minute, 59 cm/min in this equipment, and increases modestly at higher flow rates.

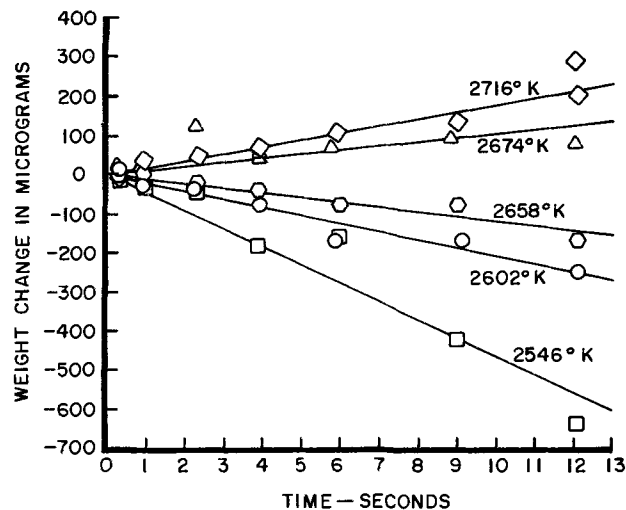


Fig. 1. Weight changes of 25W-1100 hr coils in 0.0127 atm of  $\text{WF}_6$  in nitrogen.

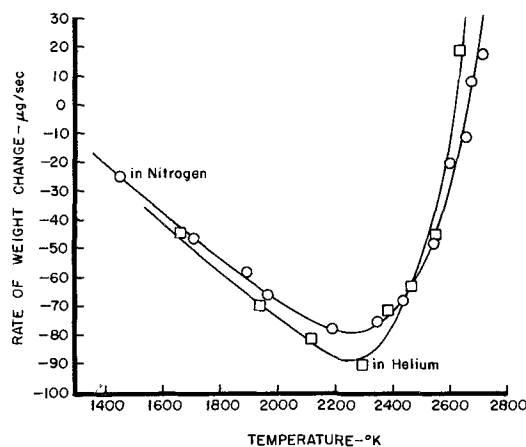


Fig. 2. Rate of weight change vs. temperature for 25W-1100 hr tungsten coils in 0.0127 atm of  $\text{WF}_6$  in nitrogen and helium.

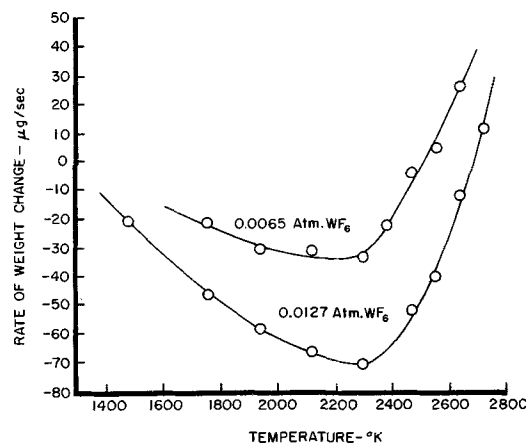


Fig. 3. Rate of weight change vs. temperature for 25W-1100 hr tungsten coils in 0.0065 and 0.0127 atm of  $\text{WF}_6$  in argon.

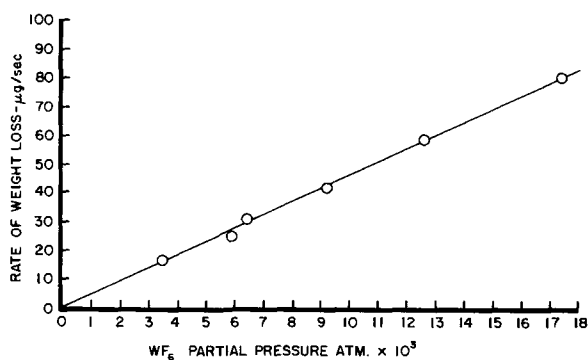


Fig. 4. Rate of weight loss vs. WF<sub>6</sub> partial pressure for 25W-1100 hr coils at 1939°K in argon.

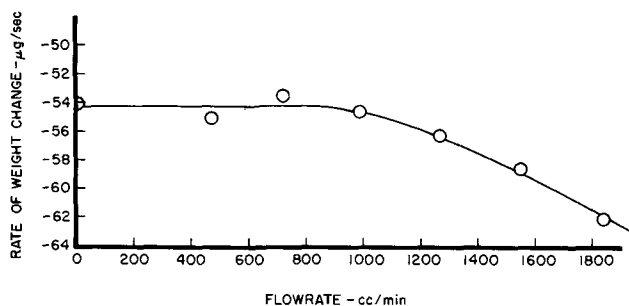


Fig. 5. Rate of weight change vs. total flow rate for 25W-1100 hr coils in 0.0127 atm of WF<sub>6</sub> in argon at 1939°K.

### Discussion

The results in Fig. 2 and 3 illustrate that the inert gas has an influence on the rate of the reaction and the transition from an etching reaction to a deposition reaction. The etching reaction is most rapid in helium and the transition temperature is lowest. Both effects are likely related to diffusion controlled processes, and part of this discussion will be concerned with the role of diffusion through the Langmuir sheath surrounding the hot filament.

Another feature of interest is the shape of the curves. This can be related to the kind of intermediate or lower valence tungsten fluorides that are formed. An attempt has been made to estimate thermodynamic functions for tungsten pentafluoride gas, and its role will be discussed first.

**Estimated thermodynamic functions for the molecule WF<sub>5(g)</sub>.**—Tungsten forms hexahalides with the three halogens bromine, chlorine, and fluorine. The hexabromide is the least stable and will decompose upon gentle warming to the pentabromide. The hexachloride is more stable and can be heated to its boiling point 346.7°C. The vapor density above the boiling hexachloride shows evidence of dissociation (8), however, and thermodynamic data (9) can be used to show that one of the products is probably tungsten pentachloride. Schroeder and Grewe (2) have shown that 10 Torr of tungsten hexafluoride in contact with tungsten at 500°–700°C will generate tungsten pentafluoride which condenses on a surface cooled to –50° to –60°C. Experimentally, the pentahalides can be formed from the hexahalides, and the temperature at which this occurs is related to the stability of the latter.

The only reliable thermodynamic data for tungsten pentafluoride is as the solid. Schroeder and Sieben (3) used fluorine bomb calorimetry to measure the enthalpy of the fluorination of WF<sub>5(s)</sub> to WF<sub>6(g)</sub>. This value was combined with the enthalpy of formation of WF<sub>6(g)</sub> to give the enthalpy of formation of WF<sub>5(s)</sub> quoted in Table I. Unfortunately, no other experi-

Table I. Thermodynamic properties of WF<sub>5(c)</sub>, WF<sub>5(l)</sub>, and WF<sub>5(g)</sub>

#### Known values:

$$\Delta H^{\circ}_f = -346.1 \begin{matrix} +2.6 \\ -1.0 \end{matrix} \text{ kcal/mole (3) at } 298^{\circ}\text{K for WF}_{5(c)}$$

#### Estimated values:

Melting point of WF <sub>5(c)</sub>	~ 399°K
Heat of fusion of WF <sub>5(c)</sub>	~ 4 kcal/mole
Boiling point of WF <sub>5(l)</sub>	~ 521°K
Heat of vaporization of WF <sub>5(l)</sub>	~ 12 kcal/mole
Heat capacity of WF <sub>5(c)</sub>	~ 31.7 gibbs/mole
Heat capacity of WF <sub>5(l)</sub>	~ 34.7 gibbs/mole
Heat capacity of WF <sub>5(g)</sub>	~ 26.4 gibbs/mole (298°–521°)

$$\Delta H^{\circ}_f = -328.6 \text{ kcal/mole at } 298^{\circ}\text{K for WF}_{5(g)}$$

$$S^{\circ} = 79 \text{ gibbs/mole at } 298^{\circ}\text{K for WF}_{5(g)}$$

mental data for tungsten pentafluoride solid or gas is available. All of the information needed for the thermodynamic cycles to give the enthalpy of WF<sub>5(g)</sub> in Table I has been estimated. Fortunately, the absolute value of the estimated enthalpy for the sublimation of the pentafluoride at 298°K is only +17.5 kcal/mole. Because it is so much less than the enthalpy of either species, errors in the estimates are somewhat less important than they might ordinarily be.

Heat capacity data are needed to calculate free energy and equilibrium values at high temperatures. The heat capacity for WF<sub>5(g)</sub> should be somewhat less than that given for WCl<sub>5(g)</sub> in the JANAF tables (9). What seemed like a reasonable correction for the difference between five tungsten-fluorine and five tungsten-chlorine bonds was obtained by taking 5/6 of the difference between the heat capacities for WCl<sub>6(g)</sub> and WF<sub>6(g)</sub>. Values were calculated for each 100° interval; some are listed in Table II.

The function  $H_T - H_{298}$  in Table II was calculated by averaging the heat capacity values for a 100° interval, multiplying by 100°, and adding to the accumulated function. The entropy as a function of temperature was determined by a similar technique; the entropy increment for each 100° was approximated by dividing the average heat capacity by the average temperature, and successively adding to the original estimate at 298°K, 79 gibbs/mole. The free energy function  $-(G^{\circ}_T - H^{\circ}_{298})$  was calculated from

$$\frac{T}{(H^{\circ}_T - H^{\circ}_{298})} \text{ Free energy function}$$

the function  $S^{\circ}_T - \frac{T}{(H^{\circ}_T - H^{\circ}_{298})}$ . Free energy function values for F<sub>2(g)</sub> and W<sub>(s)</sub> from the JANAF (9) tables were combined with the estimated values for WF<sub>5(g)</sub> to give the estimated free energy values,  $\Delta G^{\circ}$ , in Table II.

Neumann and Knatz (17) have independently estimated free energies for WF<sub>5(g)</sub> which are within 2 kcal/mole of the values in Table II up to 3000°K.

**Estimated partial pressures of WF<sub>6(g)</sub>, WF<sub>5(g)</sub>, and F<sub>(g)</sub> at the surface of hot tungsten.**—The estimated free energy values for WF<sub>5(g)</sub> have been combined with the values available for WF<sub>6(g)</sub> and F<sub>(g)</sub> from the JANAF tables (9) to provide free energies of reaction for reactions [1] and [2] between 1400° and 2800°K. The equilibrium constants derived from the free energies of reaction were combined with a mass balance constraint to calculate equilibrium partial pressures of the three gaseous species for the two initial partial pressures of interest in Fig. 6.

A comparison of Fig. 6 with Fig. 3 shows that several of the main features of the reaction can be re-

Table II. Estimated thermodynamic functions for WF<sub>5(g)</sub>

Temp (°K)	C <sub>p</sub> (gibbs/mol)	H <sub>T</sub> - H <sub>298</sub> (cal/mol)	S <sub>T</sub> (gibbs/mol)	$\frac{(G^{\circ}_T - H^{\circ}_{298})}{T}$ (gibbs/mol)	$\Delta G^{\circ}$ (cal/mol)
298	23.774	0	79.000	79.000	-313.723
1000	30.768	20,208	112.960	92.752	-279.094
2000	31.859	51,604	134.672	108.869	-231,316
3000	32.504	83,809	147.720	119.784	-184,074

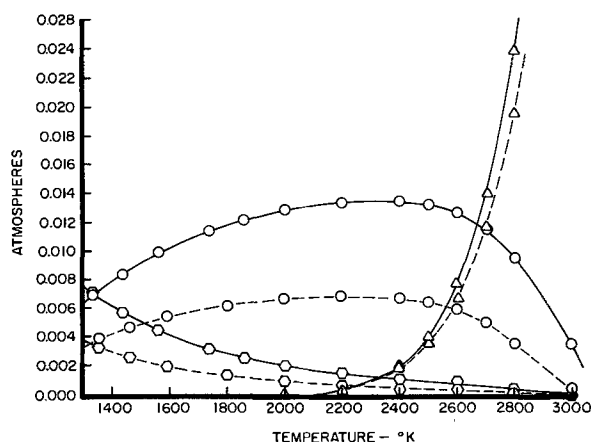


Fig. 6. Estimated  $WF_6$  (O),  $WF_5$  (O), and F atom ( $\Delta$ ) concentrations; ——— 0.0127 atm of  $WF_6$  initially, - - - - - 0.0065 atm of  $WF_6$  initially.

lated to the amount of tungsten pentafluoride formed. According to reaction [1] it is the agent responsible for transporting tungsten from the hot coil surface to the cooler gas where disproportionation reforms  $WF_{6(g)}$  and solid tungsten as a powder. According to Fig. 6 there should be substantial reaction at 1400°K which increases in amount up to some maximum in the 2200°-2400°K range which agrees with the experimental data of Fig. 3 fairly well. But this simple mechanism would still transport tungsten from the coil to the cooler gas even above 2800°K which is not true.

Reaction [2] becomes important above 2200°K, and when the fluorine atom concentration equals the  $WF_{5(g)}$  concentration, etching effectively stops because of the reaction



in the cooler gas. At higher temperatures greater amounts of fluorine atoms are evaporating from the coil surface, and deposition of tungsten metal occurs. Because of the rapid increase in fluorine atom concentration at higher temperatures, deposition occurs even though  $WF_{5(g)}$  is still an important species in this system.

A good test of whether reactions [1] and [2] account for this system is how well the calculated transition temperature for the etching to deposition ranges agrees with experiment. For 0.0127 atm of  $WF_{6(g)}$  initially in Fig. 6, the partial pressures of  $F_{(g)}$  and  $WF_{5(g)}$  are equal at 2670°K and the experimental value is 2680°K in Fig. 3. For 0.0065 atm of  $WF_{6(g)}$  initially the calculated value in Fig. 6 at 2580°K compares with 2510°K determined experimentally.

In spite of the good qualitative agreement of the calculated data based on simple equilibria with experiment, there are quantitative discrepancies in the rates of reaction at lower temperatures. Between 1500° and 2300°K the rate of tungsten removal in Fig. 3 increases by a factor of at least three while the calculated increase in  $WF_{5(g)}$  concentration is less than one and one-half. The rate of reaction is not directly proportional to the amount of  $WF_{5(g)}$  expected to form.

*The role of  $WF_{2(g)}$ .*—Neumann and Knatz have estimated a free energy of formation for  $WF_{2(g)}$  (17). Calculations by Neumann and Gottschalk (18) indicate that this molecule is so stable that only etching reactions should have been observed in the temperature range of the present experimental work. This is clearly not the case which suggests that  $WF_{2(g)}$  may not be as stable as originally thought. For similar reasons Dittmer *et al.* (19) also estimate a lower stability for  $WF_{2(g)}$ .

*The diffusion of  $WF_{6(g)}$  through the Langmuir sheath.*—In the etching region, the reaction rates are slowest in argon and greatest in helium, but the rates do not differ as much as expected for a reaction controlled entirely by diffusion. Nevertheless, it was felt worth while to try to estimate the rates on the basis of a diffusion model.

A calculated diffusion value in terms of moles of  $WF_6$  transported to the coil per centimeter per second requires a diffusion coefficient and a thickness of the Langmuir sheath. The diffusion coefficient is a function of temperature, but the temperature profile as a function of distance from the filament is not known accurately. It was assumed that the temperature dependence was a simple linear function of the radius.

The diffusion coefficient,  $D_{12}$ , for gas 1 diffusing into gas 2 is given by Kennard (10) as

$$D_{12} = \frac{3}{8\sqrt{2\pi} N_0} \frac{(RT)^{3/2}}{P} \frac{\sqrt{\frac{1}{M_1} + \frac{1}{M_2}}}{d_{12}^2}$$

where  $N_0 = 6.023 \times 10^{23}$  molecules/mole, the Avogadro number;  $R = 8.3144 \times 10^7$  g cm<sup>2</sup> sec<sup>-2</sup> deg<sup>-1</sup> mole<sup>-1</sup>;  $P =$  dynes cm<sup>-2</sup>; and  $d_{12} =$  intermolecular distance in cm. The quantity  $d_{12}$  is half the sum of the molecular diameters of tungsten hexafluoride and the inert gas. Molecular diameters in Table III for the inert gases were obtained (11) from gas viscosity measurements. The  $WF_6$  molecular diameter is assumed to be equal to twice the tungsten fluorine bond distance (12), plus twice the fluoride ion radius (13). Substitution of the appropriate intermolecular distances in the diffusion coefficient equation gives the calculated diffusion coefficients of Table IV.

Langmuir sheath thicknesses have been calculated for an 0.0099 cm filament by Covington for a variety of gases (14) from the equation

$$b \ln(b/a) = K_3 \left(\frac{\eta}{\rho}\right)^{2/3} (\theta\beta)^{-1/3}$$

where  $b =$  Langmuir sheath diameter, cm;  $a =$  filament diameter, cm;  $K_3 =$  constant, 2.41 for horizontal filaments and 2.82 for vertical filaments;  $\eta =$  gas viscosity at average temperature, g sec<sup>-1</sup> cm<sup>-1</sup>;  $\rho =$  gas density at average temperature, g cm<sup>-3</sup>;  $\theta =$  difference between filament and bulb temperature, °K; and  $\beta =$  coefficient of thermal expansion, °K<sup>-1</sup>. The Langmuir sheath sizes in Table V were recalculated for the 25W-1100 hr coils as if they were simple cylinders with an outside diameter of 0.0168 cm. The coils were used

Table III.

Gas	Molecular weight	Molecular diameter
Argon	39.948	$2.86 \times 10^{-8}$ cm
N <sub>2</sub>	28.0134	$3.16 \times 10^{-8}$ cm
He	4.0026	$2.00 \times 10^{-8}$ cm
WF <sub>6</sub>	297.84	$6.44 \times 10^{-8}$ cm

Table IV. Diffusion coefficients for  $WF_6$  in various gases

Gas mixture	300°K	2300°K
WF <sub>6</sub> -A	0.0772 cm <sup>2</sup> sec <sup>-1</sup>	1.64 cm <sup>2</sup> sec <sup>-1</sup>
WF <sub>6</sub> -N <sub>2</sub>	0.0849 cm <sup>2</sup> sec <sup>-1</sup>	1.80 cm <sup>2</sup> sec <sup>-1</sup>
WF <sub>6</sub> -He	0.280 cm <sup>2</sup> sec <sup>-1</sup>	5.94 cm <sup>2</sup> sec <sup>-1</sup>

Table V. Langmuir sheath diameters for 0.0168 cm horizontal coils

Gas	1475°K	1663°K	2300°K
He		1.44 cm	1.68 cm
N <sub>2</sub>	0.46 cm		0.55 cm
A	0.44 cm		0.54 cm

in a "V" shape with the legs somewhat more than 16° from the vertical. Covington (14) has shown that a filament tilted 20° from the vertical behaves like a horizontal filament, and sheath sizes for horizontal filaments were used in the present work.

Diffusion in this system is taking place through a distorted cylinder around a relatively straight length of coil. An equation for cylindrical diffusion through a stagnant film of inert gas was developed that is similar to the spherical case discussed by Bird, Stewart, and Lightfoot (20). For the case of a linear temperature profile represented by the equation

$$T = a - br$$

where  $r$  is the radius, the equation becomes

$$Q = \frac{2\pi PD_{12,T_2} \sqrt{a} \ln [X_{B_2}/X_{B_1}]}{RT_2^{3/2} \ln \left[ \frac{T_1^{1/2} - \sqrt{a}}{T_1^{1/2} + \sqrt{a}} \cdot \frac{T_2^{1/2} + \sqrt{a}}{T_2^{1/2} - \sqrt{a}} \right]}$$

In this equation  $Q$  = moles of  $WF_6$  transported,  $cm^{-1} sec^{-1}$ ;  $D_{12,T_2}$  = diffusion coefficient,  $cm^2 sec^{-1}$ , at  $T_2$ ;  $R = 82.0567 cm^3 atm deg^{-1} mole^{-1}$ ;  $T_2$  = temperature of coil surface;  $T_1$  = room temperature, 300°K;  $X_{B_2}$  = mole fraction of inert gas at coil surface; and  $X_{B_1}$  = mole fraction of inert gas outside of Langmuir sheath surface. Rates of  $WF_6$  transport were calculated for the etching region by using the estimated equilibrium concentration at the coil surface to determine the mole fraction of inert gas at the inside boundary of the Langmuir sheath, and the mole fraction of inert gas for 0.0127 atm of  $WF_6$  at the outer boundary. For this purpose, species like  $WF_5$  and fluorine atoms were treated as inert. Since five molecules of  $WF_6$  are required to remove one atom of tungsten according to Eq. [1], the transport rates for  $WF_6$  were divided by five to obtain the calculated rates of tungsten metal removal in Table VI.

The experimental rates in argon at 1475°K, and helium at 1663°K, were determined from the experimental data by dividing by 4.98 cm, the coil length, and 183.84, the atomic weight of tungsten. Data for the other experimental rates in Table VI were read from their respective plots in Fig. 2 and 3.

In Table VI, the calculated rates in helium are 22% too high at 1663°K and 12% too low at 2300°K. In the heavier gases, nitrogen and argon, the calculated values are 34 and 26% too low at 1475°K, and both calculated values are 62% low at 2300°K. All calculated values are within a factor of three of the experimental rates.

Thus, over-all agreement, and the really very good agreement for the helium case, indicates that diffusion is the rate controlling process. It is clear, however, that some process related to higher molecular weight of the inert gas causes a relative increase in reaction rates in argon and nitrogen, and all experimental rates increase more rapidly than predicted by the diffusion model as the temperature increases.

In its originally suggested form, the Langmuir sheath was a relatively viscous, immobile layer of gas around a hot filament in which diffusion controlled the important rate determining properties, and convection was assumed to be unimportant. Brödy and

Körösy (15) suggested that this is an oversimplification, and that convection accounted for as much as 10% of the heat transfer observed. Convective flow in nitrogen and argon should be more rapid than in helium because of the greater density difference for a given temperature gradient, and its effects should be more pronounced at higher temperatures as observed in all three gases. Convective flow compresses the lower side of the Langmuir sheath of a nonvertical filament and distorts it so that it is no longer circular. While some allowance for this distortion was made for these diffusion calculations, the results indicate that convective distortion for chemical transport may be more serious than indicated by heat transfer calculations. Convective distortion of the Langmuir sheath provides one reasonably satisfying way of accounting for the discrepancies from a simple diffusion limited rate model.

Figure 5 shows a modest increase in etching rate as the flow rate increases which is believed to be a distortion of the sheath by bulk transport akin to that caused by convection.

*The diffusion of  $WF_{5(g)}$  through the Langmuir sheath.*—If one assumes that the  $WF_5$  molecule is a hexagonal bipyramid in structure, then its radius of interaction with other molecules as a hard sphere should be the same as a  $WF_6$  molecule. On this basis, the somewhat smaller molecular weight of  $WF_5$  increases its calculated diffusion coefficient 0.4% over the corresponding value for  $WF_6$  in argon where the change is greatest. When these coefficients are used in the diffusion equation with the calculated amounts of  $WF_5$  at the coil surface, and assuming zero concentration at the outer edge of the Langmuir sheath, the calculated transport of  $WF_5$  from the coil surface to the outer boundary of the sheath is almost exactly the same as the rate at which it forms from the transport of  $WF_6$  into the tungsten. The values are 0.3% low for  $WF_5$  at 1475°C and about 2% at 2300°K, but at the latter temperature, the equilibrium calculations show the formation of fluorine atoms as well as  $WF_5$ .

*The effect of  $WF_6$  partial pressure on the rate of tungsten weight loss.*—Figure 4 shows that the rate of weight loss is proportional to the partial pressure of tungsten. The diffusion model developed here requires a dependence on  $P_{WF_6}^{0.98}$  which would be difficult to distinguish from the linear equation.

#### Acknowledgments

We are indebted to E. J. Covington for help in understanding Langmuir sheath phenomena. Drs. E. G. Zubler and S. K. Gupta, and Prof. Leo Brewer discussed the thermodynamic problems with us. Drs. S. C. Kim and R. J. Petti made useful suggestions for the diffusion calculations.

Manuscript submitted Aug. 6, 1973; revised manuscript received May 5, 1974. This was Paper 237 presented at the Boston, Massachusetts, Meeting of the Society, Oct. 7-11, 1973.

Any discussion of this paper will appear in a Discussion Section to be published in the June 1975 JOURNAL. All discussions for the June 1975 Discussion Section should be submitted by Feb. 1, 1975.

*The publication costs of this article have been assisted by the General Electric Company.*

#### REFERENCES

1. J. Schroeder, Paper 34, Division of Fluorine Chemistry, American Chemical Society 148th Meeting, Chicago, Illinois, Aug.-Sept. 1964; Abstract K34. *Chem. Eng. News*, p. 77, Sept. 14, 1964.
2. J. Schroeder and F. J. Grewe, *Angew. Chemie*, **7**, 132 (1968).
3. J. Schroeder and F. J. Sieben, *Chem. Ber.*, **1970**, 103 (1), 76-81.
4. I. M. Langmuir, *Phys. Rev.*, **6**, 138 (1915).
5. J. E. Gibbs and G. W. Gordon-Smith, *Brit. J. Appl. Phys.*, **12**, 257 (1961).

Table VI. Comparison of experimental rate of tungsten removal with rates calculated from kinetic theory for 0.0127 atm of  $WF_6$

Temp (°K)	Gas mixture	Exp. rate of W removal (moles $cm^{-1} sec^{-1}$ )	Calcd. rate of W removal (moles $cm^{-1} sec^{-1}$ )
1475	WF <sub>6</sub> -A	$2.3 \times 10^{-8}$	$1.7 \times 10^{-8}$
1475	WF <sub>6</sub> -N <sub>2</sub>	$2.9 \times 10^{-8}$	$1.9 \times 10^{-8}$
1663	WF <sub>6</sub> -He	$4.9 \times 10^{-8}$	$6.0 \times 10^{-8}$
2300	WF <sub>6</sub> -A	$7.8 \times 10^{-8}$	$3.0 \times 10^{-8}$
2300	WF <sub>6</sub> -N <sub>2</sub>	$8.6 \times 10^{-8}$	$3.3 \times 10^{-8}$
2300	WF <sub>6</sub> -He	$9.7 \times 10^{-8}$	$8.5 \times 10^{-8}$

6. We are indebted to Mr. A. G. Stainsby, The City University, London, England, for suggesting this technique.
7. J. C. de Vos, *Physica*, **20**, 690-714 (1954).
8. M. V. Sidgwick, "Chemical Elements and Their Compounds," p. 1034, Clarendon Press, Oxford University, England (1950).
9. Joint Army-Navy-Air Force Thermochemical Tables, U.S. Dept. of Commerce, PB168,370 (1965), PB168-370-1 (1966), PB168-370-2 (1967) and PB168-370-3 (1968).
10. E. H. Kennard, "Kinetic Theory of Gases," p. 194, McGraw-Hill Publishing Co., New York (1938).
11. W. J. Moore, "Physical Chemistry," 3rd ed., p. 229, Table 7.5, Prentice Hall, Englewood Cliffs, N. J. (1962).
12. G. D. Rieck, "Tungsten and Its Compounds," p. 113, Pergamon Press (1967).
13. F. A. Cotton and G. Wilkinson, "Advanced Inorganic Chemistry," p. 43, Interscience Publishers, New York (1962).
14. E. J. Covington, *Illum. Eng.*, **63**, 134 (1968).
15. I. Brödy and F. Körösy, *J. Appl. Phys.*, **10**, 584 (1939).
16. I. M. Langmuir, *Phys. Rev.*, **34**, 401 (1912).
17. G. M. Neumann and W. Knatz, *Z. Naturforsch.*, **26a**, 863 (1971).
18. G. M. Neumann and G. Gottschalk, *ibid.*, **26a**, 870 (1971).
19. G. Dittmer, A. Klopfer, D. S. Ross, and J. Schroeder, *J. Chem. Soc., Chem. Communications*, No. 22, 846 (1973).
20. R. B. Bird, W. E. Stewart, and E. N. Lightfoot, "Transport Phenomena," p. 528, John Wiley and Sons, Inc., New York (1960).

## Boron Diffusion Coefficient Increased by Phosphorus Diffusion

H. Nakamura, S. Ohyama, and C. Tadachi

*Musashino Electrical Communication Laboratory, Nippon Telegraph and Telephone Public Corporation,  
Midori-cho, Musashino-shi, Tokyo, Japan*

### ABSTRACT

The emitter dip effect has been studied quantitatively at 900°C in boron-base phosphorus-emitter doubly diffused structure. An approximate expression for the emitter dip effect is derived. Experimental results are consistent with this expression. Using this expression and the experimental results, the effective boron diffusion coefficient, which is increased by phosphorus diffusion, is calculated and shown to be increased linearly with phosphorus surface concentration. It is suggested that the emitter dip effect occurs during emitter diffusion, not during cooling, and is not necessarily accompanied with diffusion induced dislocation.

Phosphorus diffusion into silicon has been very important in the semiconductor device industry. However, many anomalous effects have been reported on phosphorus diffusion, e.g., emitter dip effect (1-9), anomalous phosphorus concentration profile (10-13), and diffusion coefficient dependent on concentration (14, 15). The emitter dip effect has been attributed to enhanced base impurity diffusion due to increase of vacancy concentration during emitter diffusion. To explain the mechanism in which the vacancy concentration is increased by emitter diffusion, several models have been reported, e.g., the Fermi level effect (1, 16), dislocation climb (5, 8), or precipitation (4). Although those models seem plausible for the emitter dip effect caused by phosphorus-emitter diffusion, at least two experimental clarifications are required to determine the probable mechanism. One is to clarify the time when the emitter dip effect occurs. The other is whether this effect occurs necessarily accompanied with the diffusion-induced dislocation or not.

The present work was undertaken to clarify the problems described above, and to obtain the diffusivity of boron increased by phosphorus diffusion. First, an approximate analytic expression of the relationships between the amount of dip and various diffusion process parameters, which is analogous to that by Hu and Yeh (8), is derived. Then the experiments are performed carefully to verify the expression and its assumptions. Using this expression and the experimental results, the enhanced diffusion coefficient of boron during phosphorus diffusion is calculated. The significance of the phosphorus surface concentration in the increase of boron diffusion coefficient is determined.

**Key words:** emitter dip effect, enhanced diffusion, approximate expression.

### Derivation of Approximate Expression

An approximate expression of the amount of dip is derived analytically under the condition that the base diffusion is performed by single heat-treatment with constant surface concentration followed by the emitter diffusion.

Assumptions used in the course of derivation of the expression are discussed with relation to the applicable experimental conditions. The base profile after the base diffusion cannot be expressed by complementary error function, because of concentration dependence of boron diffusion coefficient (17). During the emitter diffusion, the surface concentration of the base layer cannot be constant, because the base impurity source is removed. Furthermore, the diffusivity of the base impurity may be positionally affected by a built-in electric field produced by emitter diffusion (6, 7, 18), or some other interaction between impurities and carriers (22). At present, however, it is assumed that the base impurity profile is approximated by complementary error function, both during base and emitter diffusion. This assumption is assumed to be valid in determining the effective diffusion coefficient, if the change of base surface concentration and the interaction between base and emitter impurities are negligible. The former corresponds to the penetration of the base during emitter diffusion being small compared to the initial base depth. The latter corresponds to the base width being large.

Next, it is assumed that the enhancement of base diffusion occurs during emitter diffusion, but not during the cooling process. This assumption is confirmed in a later section of this paper.

It is now possible to analytically derive an expression of the amount of dip. The diffusion process and

the notations used are shown in Fig. 1. The base layer depth after base diffusion  $x_{j1}$ , is given by

$$x_{j1} = 2 \sqrt{D_{B1} t_1} \operatorname{erfc}^{-1} (C_b/C_{SB}) \quad [1]$$

where  $D_{B1}$  and  $t_1$  are the diffusion coefficient and the time of the base diffusion,  $C_b$  is the bulk concentration, and  $C_{SB}$  is the surface concentration of the base. After the emitter diffusion, the junction depth at the singly diffused region is given by

$$x_{j2} = 2 \sqrt{D_{B1} t_1 + D_{B2} t_2} \operatorname{erfc}^{-1} (C_b/C_{SB}) \quad [2]$$

At the doubly diffused region, it is given by

$$x^*_{j2} = 2 \sqrt{D_{B1} t_1 + D^*_{B2} t_2} \operatorname{erfc}^{-1} (C_b/C_{SB}) \quad [3]$$

where  $D_{B2}$  and  $D^*_{B2}$  are the base impurity diffusion coefficient of the singly diffused and the doubly diffused region, respectively, and  $t_2$  is the emitter diffusion time. Then the amount of dip  $\Delta x_j$  is defined by the difference between Eq. [3] and [2]

$$\Delta x_j = 2 (\sqrt{D_{B1} t_1 + D^*_{B2} t_2} - \sqrt{D_{B1} t_1 + D_{B2} t_2}) \operatorname{erfc}^{-1} (C_b/C_{SB}) \quad [4]$$

As described previously, the present derivation prefers a condition where the penetration of base-collector junction during the emitter diffusion is small, compared to  $x_{j1}$ . This means that  $D^*_{B2} t_2$  and  $D_{B2} t_2$  are much smaller than  $D_{B1} t_1$ . Then Eq. [4] is expanded to

$$\Delta x_j = 2\sqrt{D_{B1} t_1} \left\{ \frac{1}{2} (D^*_{B2} - D_{B2}) t_2 / D_{B1} t_1 - \frac{1}{4} (D^{*2}_{B2} - D^2_{B2}) t_2^2 / (D_{B1} t_1)^2 + \dots \right\} \operatorname{erfc}^{-1} (C_b/C_{SB}) \quad [5]$$

When  $D_{B2}$  is much smaller than  $D^*_{B2}$ , Eq. [5] is reduced. Then, combining with Eq. [1], we obtain

$$\Delta x_j = 2 \{ \operatorname{erfc}^{-1} (C_b/C_{SB}) \}^2 x_{j1}^{-1} D^*_{B2} t_2 \quad \text{for } D_{B1} t_1 \gg D^*_{B2} t_2 \gg D_{B2} t_2 \quad [6]$$

From Eq. [6], it is seen that  $\Delta x_j$  increases linearly with  $t_2$  and  $D^*_{B2}$ , and is inversely proportional to  $x_{j1}$ . The effect of the base surface concentration is involved in complementary error function term.

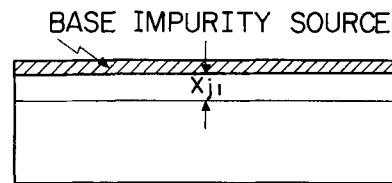
### Experimental Procedure

The silicon wafers used in this work were mirror polished, 1 ohm-cm, phosphorus-doped Czochralski crystal cut to the (111) surface. The etch pit density was less than  $3000 \text{ cm}^{-2}$ .

The boron-doped oxide films, which were used as a diffusion source, were deposited on the wafers in an atmosphere of silane, diborane, oxygen, and nitrogen at  $400^\circ\text{C}$ . The boron surface concentration was varied by changing the boron content in the oxide layer. The boron base was diffused at  $1050^\circ$  or  $1150^\circ\text{C}$  in a nitrogen atmosphere. The boron surface concentration was calculated from the sheet resistance and the junction depth, using data published by Irvin (21).

After the base diffusion, the oxide layer was partly removed by etching in aqueous HF solution, then phosphorus emitter was diffused at  $900^\circ\text{C}$ . Here, the diffusion sources used were the phosphorus-doped oxide in an ambient of nitrogen and 1000 ppm  $\text{POCl}_3$  in an ambient of nitrogen with 1.4% oxygen. The phosphorus-doped oxide films were deposited in an atmosphere of silane, phosphine, oxygen, and nitrogen at  $400^\circ\text{C}$ . The phosphorus surface concentration was obtained by the differential conductance method, repeating the anodic oxidation in N-methylacetamide- $\text{KNO}_3$  solution. In Fig. 2, the phosphorus surface concentration is plotted against the molar ratio of phosphine to silane, where the surface concentration corresponding

## I BASE DIFFUSION STEP



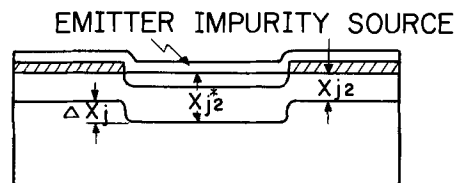
Temp. :  $1050^\circ\text{C}$  or  $1150^\circ\text{C}$

Time :  $t_1$

Surface Conc. :  $C_{SB}$

Diffusion Coeff. :  $D_{B1}$

## II EMITTER DIFFUSION STEP



Temp :  $900^\circ\text{C}$

Time :  $t_2$

Diffusion Coeff. at Single layer :  $D_{B2}$

Diffusion Coeff. at Double layer :  $D^*_{B2}$

Fig. 1. Diffusion process and notations used

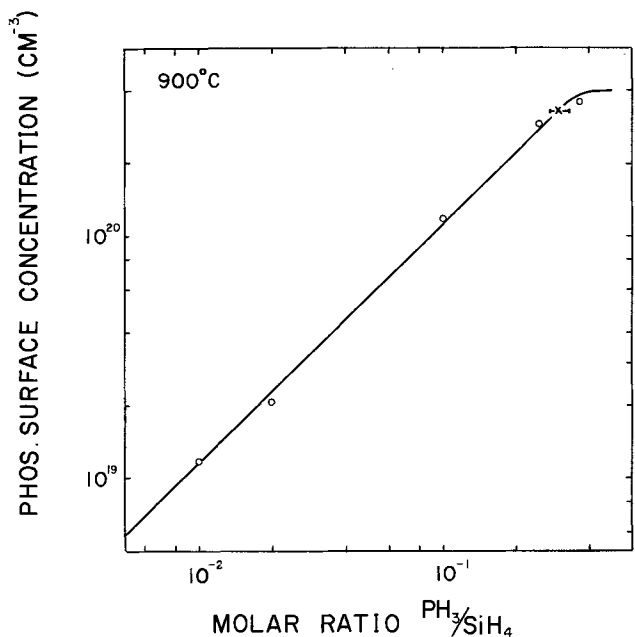


Fig. 2. Phosphorus surface concentration as a function of  $\text{PH}_3/\text{SiH}_4$ . Surface concentration corresponding to 1000 ppm  $\text{POCl}_3$  source is presented by the crossing point.

to the  $\text{POCl}_3$  source is indicated by the crossing point. Junction depth was measured by beveling the specimens and etching in HF- $\text{HNO}_3$  solution. The diffusion induced dislocation was examined by Sirtl etching technique.

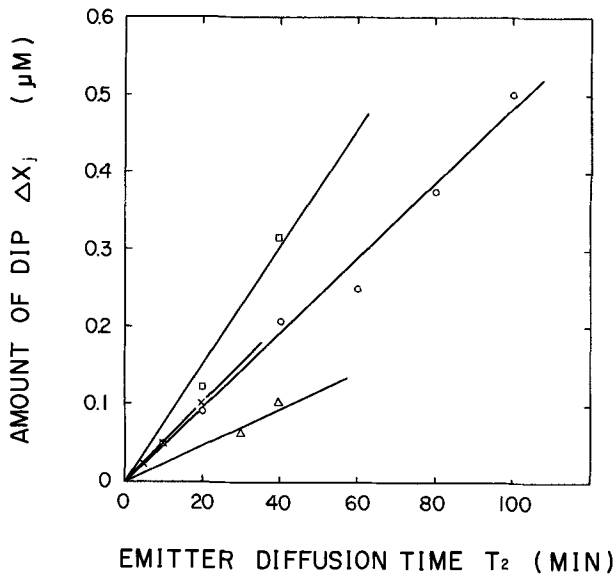


Fig. 3. Amount of dip as a function of emitter diffusion time.   
 ○,  $C_{sB} = 2.4 \times 10^{20} \text{ cm}^{-3}$ ,  $x_{j1} = 0.85 \text{ μm}$ ,  $\text{PH}_3/\text{SiH}_4 = 0.36$ ;   
 □,  $C_{sB} = 3.9 \times 10^{19} \text{ cm}^{-3}$ ,  $x_{j1} = 0.48 \text{ μm}$ ,  $\text{PH}_3/\text{SiH}_4 = 0.36$ ;   
 ×,  $C_{sB} = 1.2 \times 10^{19} \text{ cm}^{-3}$ ,  $x_{j1} = 0.48 \text{ μm}$ ,  $\text{PH}_3/\text{SiH}_4 = 0.36$ ;   
 △,  $C_{sB} = 1.2 \times 10^{19} \text{ cm}^{-3}$ ,  $x_{j1} = 0.48 \text{ μm}$ ,  $\text{PH}_3/\text{SiH}_4 = 0.18$ .

Results and Discussion

Experimental verification of Eq. [6].—In this section, the validity of Eq. [6] and assumptions used to derive it are experimentally verified.

Figure 3 shows the dependence of the amount of dip on the emitter diffusion time. Here, after boron bases with various surface concentrations and junction depths were diffused, phosphorus was diffused for 5-100 min at 900°C, using the phosphorus-doped oxide as a source. It was observed that no increment of base-collector junction depth at the singly diffused region was caused during emitter diffusion. This suggests that the condition  $D_{B1} t_1 \gg D_{B2} t_2$  in Eq. [6] is satisfied in the present work. In Fig. 3 it is clearly seen that the amount of dip increases linearly with the emitter diffusion time  $t_2$ , regardless of various base and emitter diffusion conditions, which is expected from Eq. [6]. The linear relationship between  $\Delta x_j$  and  $t_2$  strongly supports the concept of emitter dip effect occurring during emitter diffusion, which is one of the present assumptions. Additional experiments were carried out to investigate the effect of cooling rate on the amount of dip. The boron-base with 0.35 and 0.49  $\mu\text{m}$   $x_{j1}$  were diffused, followed by phosphorus diffusion for 20 min using 1000 ppm  $\text{POCl}_3$ . The time to remove the wafers was varied from 1 sec to 3 min. Furthermore, the 900°C heat treatment for 5 sec was repeated 3 times after the emitter diffusion for two of the wafers. The results are shown in Table I, where it is found that the amount

Table I. Effect of cooling processes on amount of dip

$x_{j1}$ ( $\mu\text{m}$ )	Cooling process	$\Delta x_j$ ( $\mu\text{m}$ )
0.49	Time to remove slices (sec)	
	1	0.05
	10	0.06
	60	0.07
	180	0.06
	900°C, 5 sec heat-treatment for 3 times	0.06
0.35	Time to remove slices (sec)	
	1	0.08
	10	0.07
	60	0.08
	180	0.06
	900°C, 5 sec heat-treatment for 3 times	0.08

Phosphorus emitter was diffused at 900°C for 20 min, using 1000 ppm  $\text{POCl}_3$  as a source.

of dip ranges from 0.05 to 0.07  $\mu\text{m}$  for 0.49  $\mu\text{m}$   $x_{j1}$  and from 0.06 to 0.08  $\mu\text{m}$  for 0.35  $\mu\text{m}$   $x_{j1}$ , independently of cooling rate and heat-treatment. Therefore, it is concluded that the emitter dip effect occurs during emitter diffusion, not during cooling.

This conclusion is inconsistent with that of Gereth *et al.* (3), who suggested that the amount of dip was not dependent on the emitter diffusion time and was increased by slow cooling, and concluded that this effect occurs during cooling. In their cooling effect experiment, the cooling rate was very low (3°C/min) compared to that of the present experiment. It is expected that the very slow cooling would result in the increase of the effective emitter diffusion time and then in increase of the amount of dip. Further, in Fig. 5 of their work, the amount of dip seems to increase with emitter diffusion time. The diffusion temperature of phosphorus in their work was 1000°C, where the penetration of base layer during emitter diffusion in the singly diffused region cannot be neglected. In such a case, it is expected from Eq. [4], that the amount of dip is weakly dependent on the emitter diffusion time.

Next, the effect of the base-collector junction depth upon the amount of dip is studied. The boron-base was diffused, varying the junction depth from 0.25 to 1  $\mu\text{m}$  with constant surface concentrations of 1 and  $4 \times 10^{19} \text{ cm}^{-3}$ . Phosphorus was diffused using a 1000 ppm  $\text{POCl}_3$  source for 10 and 20 min at 900°C. The result is shown in Fig. 4, where it is found that the amount of dip increases linearly with the inverse of the base-collector junction depth. This result is also consistent with Eq. [6]. From the linear relationships of the amount of dip with  $t_2$  and with  $1/x_{j1}$ , it is suggested that the penetration of base-collector junction is not retarded by built-in electric field (6, 7, 18) or by interaction between impurity atoms (22). If the penetration of base layer was affected by those two effects, the slopes in Fig. 3 and 4 would not be constant, but show a tapering off of the increase in a longer emitter diffusion time in Fig. 3, and in a smaller base-collector junction depth in Fig. 4. Therefore, it is concluded that the base width is large enough in the present experimental conditions to allow neglecting these effects.

The experimental results described above support the concept that Eq. [6] and its assumption are valid. Now, it is possible to calculate the effective diffusion

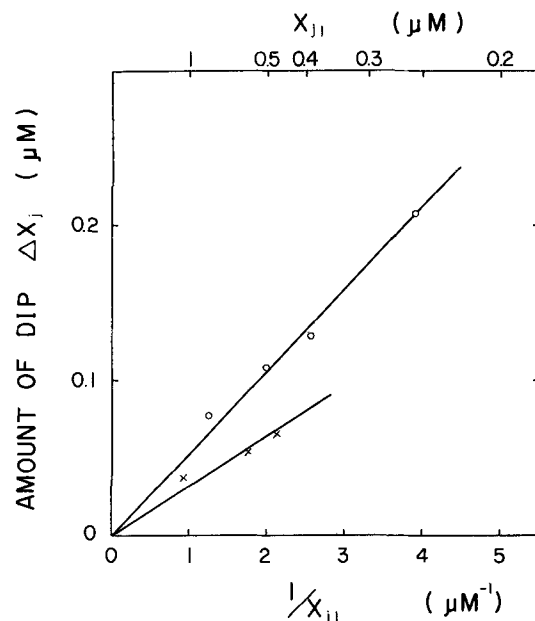


Fig. 4. Amount of dip as function of the reciprocal of the initial base collector junction depth. Phosphorus was diffused using 1000 ppm  $\text{POCl}_3$  as a source,   
 ○,  $C_{sB} = 4 \times 10^{19} \text{ cm}^{-3}$ ,  $t_2 = 20$  min;   
 ×,  $C_{sB} = 1 \times 10^{19} \text{ cm}^{-3}$ ,  $t_2 = 10$  min.

coefficient of boron increased by phosphorus diffusion using Eq. [6].

**Effect of boron concentration.**—The effect of boron surface concentration upon the amount of dip appears explicitly in the term,  $\operatorname{erfc}^{-1}(C_b/C_{sB})$ , in Eq. [6]. Simultaneously, it is expected that  $D_{B2}$  and  $D^*_{B2}$  also include the dependence of boron concentration. In Fig. 5,  $D_{B2}$  and  $D^*_{B2}$  are plotted against boron surface concentration  $C_{sB}$ . Here, to obtain  $D^*_{B2}$ , boron was diffused while varying the surface concentration from  $8 \times 10^{18}$  to  $2 \times 10^{20} \text{ cm}^{-3}$  with a junction depth of about 0.4–0.5  $\mu\text{m}$  followed by phosphorus diffusion at 900°C, using the 1000 ppm  $\text{POCl}_3$  as a source. To obtain  $D_{B2}$ , boron was diffused with various surface concentrations at 900°C. Using the junction depth and the surface concentration,  $D_{B2}$  was calculated assuming complementary error function. In Fig. 5, it is seen that both  $D_{B2}$  and  $D^*_{B2}$  increase with the boron surface concentration.

The net effect of phosphorus diffusion upon the enhancement of boron diffusion is defined by  $D^*_{B2}/D_{B2}$ , and is plotted in Fig. 5. The ratio  $D^*_{B2}/D_{B2}$  is almost constant in the lower boron surface concentration region below about  $4 \times 10^{19} \text{ cm}^{-3}$ . The slight decrease of the ratio above it in Fig. 5 cannot be explained at present.

**Effect of phosphorus surface concentration.**—In Fig. 6,  $D^*_{B2}/D_{B2}$  is plotted as a function of the phosphorus surface concentration. Here, after boron was diffused with surface concentration of  $4 \times 10^{19} \text{ cm}^{-3}$  and to junction depth of 0.47  $\mu\text{m}$ , phosphorus was diffused using the phosphorus-doped oxide as a source, with the surface concentration ranging from 1 to  $4 \times 10^{20} \text{ cm}^{-3}$ . From this figure, it is seen that the ratio  $D^*_{B2}/D_{B2}$  increases approximately linearly with the surface concentration of phosphorus and is about 40 at  $4 \times 10^{20} \text{ cm}^{-3}$ .

This result is interesting when it is compared with the observation by Yoshida, Arai, Nakamura, and Terunuma (15), who extensively studied the concentration dependence of phosphorus diffusion coefficient at 900°C. They obtained the phosphorus diffusion coefficient experimentally using Boltzmann-Matano's method and found that the phosphorus diffusion coefficient

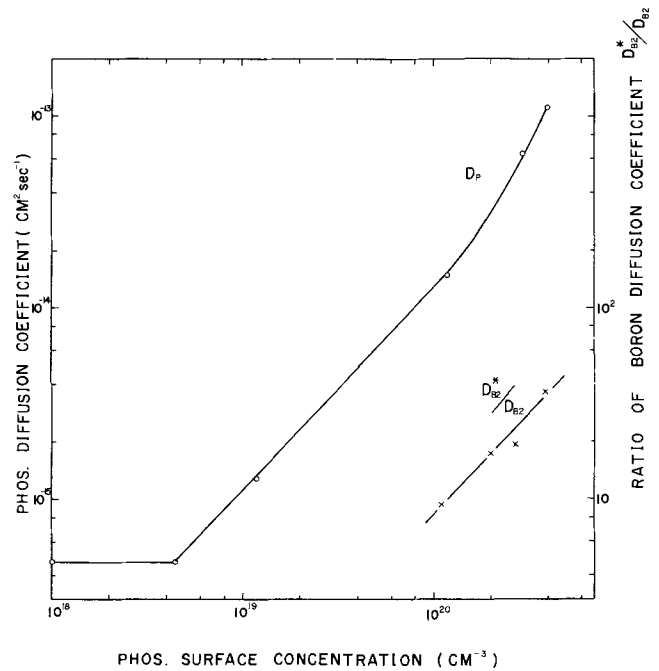


Fig. 6.  $D^*_{B2}/D_{B2}$  and phosphorus diffusion coefficient as a function of phosphorus surface concentration.

depends not only on the concentration at each point of the diffusion profile, which has been previously reported by Tannenbaum (14), but also on the surface concentration of phosphorus. Their result is reproduced in Fig. 6, indicating the linear relationship between the surface concentration and diffusion coefficient of phosphorus at concentration of  $1 \times 10^{18} \text{ cm}^{-3}$ . It is seen that the phosphorus diffusion coefficient at  $4 \times 10^{20} \text{ cm}^{-3}$  of surface concentration is about 300 times larger than the value at the surface concentration below  $5 \times 10^{18} \text{ cm}^{-3}$ . Assuming boron and phosphorus diffusion by a vacancy mechanism, an increase in diffusivity corresponds to an increase of vacancy concentration. There is a difference of an order of magnitude between the effect of phosphorus surface concentration on the boron diffusion coefficient ( $40 \times$ ) and on the phosphorus diffusion coefficient ( $300 \times$ ). Although this cannot be explained at present, it is assumed that the vacancy concentration in silicon is increased linearly by phosphorus diffusion with the surface concentration of phosphorus.

**Diffusion-induced dislocation.**—From the fact that the emitter dip effect occurs during emitter diffusion, it is suggested that the Fermi level effect (1, 16) and the precipitation (4) cannot be the cause of this phenomenon, because those two models require that the emitter dip effect occurs in a nonequilibrium state, such as during cooling. On the other hand, the present experimental observations are qualitatively in good agreement with the analytically derived approximate expression by Hu and Yeh (8). Using Prussin's model (19), they calculated the increase of base diffusion coefficient, assuming that the excess vacancy is generated by dislocation climb during emitter diffusion.

To examine the diffusion-induced dislocation, phosphorus was diffused into Si wafers at 900°C, for 30 min to 10 days, using phosphorus-doped oxide films of 0.36 and 0.25  $\text{PH}_3/\text{SiH}_4$  ratios. The results are shown in Table II, where it is seen that the diffusion-induced dislocation was not observed within 23 hr of phosphorus diffusion time. In the present work, the longest time  $t_2$  is 100 min which is short enough not to produce the diffusion-induced dislocation. Also in the doubly diffused wafers, the dislocation-induced dislocation was not observed. Therefore, it is concluded that the dislocation climb is not the cause of the emitter dip effect observed in the present experimental conditions.

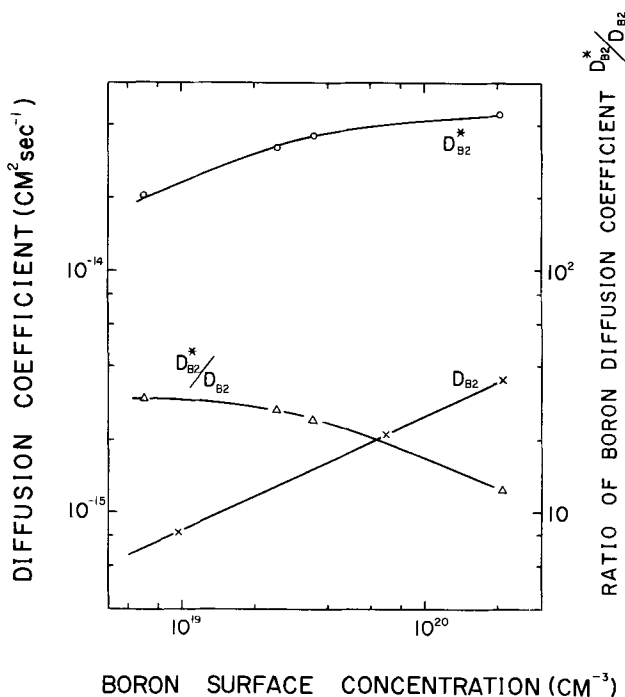


Fig. 5. Boron diffusion coefficients in the doubly diffused and singly diffused region and the ratio of those two as a function of boron surface concentration. Phosphorus was diffused using a 1000 ppm  $\text{POCl}_3$  source.



Table II. Dislocation induced by phosphorus diffusion at 900°C

PH <sub>3</sub> /SiH <sub>4</sub>	Diffusion time	Diffusion-induced dislocation
0.36	30 min	None
	1 hr	None
	4 hr	None
	7 hr	None
	23 hr	None
	3 days	Some few
	7 days	Great many
0.25	30 min	None
	2 hr	None
	23 hr	None
	3 days	Few
	10 days	Great many

Examined by Sirtl etching technique.

In Ref. (15), cited before, Yoshida *et al.* proposed a new model to explain the effect of surface concentration upon phosphorus diffusion coefficient. The new model consists of vacancies in a state of supersaturation generated in the range of at least 20  $\mu\text{m}$  from a surface when phosphorus atoms enter from the surface into the bulk. Some of the present observations, *e.g.*, the linear relationship of  $D^*_{B2}/D_{B2}$  with phosphorus surface concentration and the fact that the emitter dip effect occurs without diffusion-induced dislocation, can be qualitatively explained in terms of this model, although the time dependence of the enhancement due to this model, etc. are not clear at present. The surface effect is suggested to decrease with increasing diffusion temperature (20). Based on this model, it is expected that the emitter dip effect decreases in a higher diffusion temperature.

### Conclusion

Quantitative relationships between the emitter dip effect caused by phosphorus diffusion at 900°C and the various diffusion process parameters were obtained experimentally through Eq. [6]. The main results of the present work are summarized as follows:

1. The emitter dip effect occurs during emitter diffusion.
2. The diffusion coefficient of boron at the doubly diffused region is increased linearly with surface concentration of phosphorus.
3. Net effect of the phosphorus diffusion upon the enhancement of boron diffusion, *i.e.*,  $D^*_{B2}/D_{B2}$  is approximately independent of the boron surface concentration in the boron surface concentration region below  $4 \times 10^{19} \text{ cm}^{-3}$ .
4. The emitter dip effect is not necessarily accompanied by the diffusion-induced dislocation.

In order to explain the results described above, it is probably attributable to the excess vacancy generation due to the surface effect of phosphorus diffusion (15).

### Acknowledgment

The authors are indebted to Dr. M. Yoshida and Mr. E. Arai for numerous discussions and important suggestions in the course of this work, and to Mr. Y. Terunuma for supplying information about his work on boron diffusion.

Manuscript submitted Aug. 23, 1973; revised manuscript received May 20, 1974.

Any discussion of this paper will appear in a Discussion Section to be published in the June 1975 JOURNAL. All discussion for the June 1975 Discussion Section should be submitted by Feb. 1, 1975.

The publication costs of this article have been assisted by the Nippon Telegraph and Telephone Public Corporation.

### REFERENCES

1. P. Baruch, C. Constantin, J. C. Pfister, and R. Saintesprit, *Discuss. Faraday Soc.*, **31**, 76 (1961).
2. Y. Sato and H. Arata, *Japan. J. Appl. Phys.*, **3**, 511 (1964).
3. R. Gereth, P. G. G. van Loon, and V. Williams, *This Journal*, **112**, 323 (1965).
4. R. Gereth and G. H. Schwuttke, *Appl. Phys. Letters*, **8**, 55 (1966).
5. J. E. Lawrence, *J. Appl. Phys.*, **37**, 4106 (1966).
6. M. Okamura, *Japan. J. Appl. Phys.*, **7**, 1067 (1968).
7. M. Okamura, *ibid.*, **7**, 1231 (1968).
8. S. M. Hu and T. H. Yeh, *J. Appl. Phys.*, **40**, 4615 (1969).
9. D. B. Lee and A. F. W. Willoughby, *ibid.*, **43**, 245 (1972).
10. M. C. Duffy, F. Barson, J. M. Fairfield, and G. H. Schwuttke, *This Journal*, **115**, 84 (1968).
11. J. Makris, A. Ferris-Prabhu, and M. L. Joshi, *IBM J. Res. Develop.*, **15**, 132 (1971).
12. F. N. Schwettmann and D. L. Kendall, *Appl. Phys. Letters*, **21**, 2 (1972).
13. S. Maekawa, *J. Phys. Soc. Japan*, **17**, 1952 (1962).
14. E. Tannenbaum, *Solid-State Electron.*, **2**, 123 (1961).
15. M. Yoshida, E. Arai, H. Nakamura, and Y. Terunuma, *J. Appl. Phys.*, **45**, 1498 (1974).
16. M. F. Millea, *J. Phys. Chem. Solids*, **27**, 315 (1966).
17. G. L. Vick, and K. M. Whittle, *This Journal*, **116**, 1142 (1969).
18. S. M. Hu and S. Schmidt, *J. Appl. Phys.*, **39**, 4272 (1968).
19. S. Prussin, *ibid.*, **32**, 1876 (1961).
20. S. Matsumoto, M. Yoshida, and T. Niimi, *Japan. J. Appl. Phys.*, To be published.
21. J. C. Irvin, *Bell System Tech. J.*, **41**, 387 (1962).
22. J. F. Ziegler, G. W. Cole, J. E. E. Baglin, *Appl. Phys. Letters*, **21**, 177 (1972).



## A Nonaqueous Electrolyte for Anodizing GaAs and GaAs<sub>0.6</sub>P<sub>0.4</sub>

Edward B. Stoneham

Stanford Electronics Laboratories, Stanford University, Stanford, California 94305

A solution of potassium permanganate in acetone has proved to be effective as an electrolyte for anodizing GaAs and GaAs<sub>0.6</sub>P<sub>0.4</sub>. This electrolyte may possess advantages over previously reported aqueous electrolytes (1-7) in which difficulties are encountered with pH control, inclusion of H<sub>2</sub>O in anodic oxide films, or partial dissolution of the oxide during growth.

Samples of low resistivity n-type GaAs and samples of  $3 \times 10^{17}$  cm<sup>-3</sup> n-type GaAs<sub>0.6</sub>P<sub>0.4</sub> epi grown on low resistivity n-type <100>-oriented GaAs substrates were anodized at various voltages between 0 and 250V. In each case the sample was suspended face down from the end of a 1/16 in. OD aluminum tube attached to a suction pump, the tube making electrical contact to the back of the sample. Only the face of the sample was immersed in the electrolyte which filled an aluminum container of 3 cm<sup>3</sup> volume that acted as the cathode. Fresh electrolyte and a clean container were used for each anodization. The electrolyte was prepared by mixing one volume of a saturated acetone solution of reagent grade KMnO<sub>4</sub> at room temperature with 25 volumes of electronic grade acetone. Since the electrolyte was observed to decompose slowly, with visible changes becoming noticeable after about 24 hr of standing at room temperature, the electrolyte was always used within 6 hr of mixing.

Power was furnished by a voltage-regulated supply with a variable current limiter. The current limiter was required for anodizations at 100V or more to prevent bubbling at the sample surface. It was found, for example, that with a current limit of 20 mA, bubbling commenced at the surface of an 8.9 × 6.9 mm sample of GaAs<sub>0.6</sub>P<sub>0.4</sub> when the anodizing cell voltage reached 200V. Boiling of the acetone due to the high power dissipation at the sample surface may be responsible.

Each anodization was performed by first bringing the sample into contact with the electrolyte and then connecting the power supply with its voltage  $V_0$  and current limit  $I_0$  preset. Once the anodizing cell voltage reached a plateau the current  $I$  would begin to drop monotonically, continuing this way until it reached a value  $I_{min}$  at which it would begin to jump upward occasionally. Allowing  $I$  to drop below  $I_{min}$  resulted in nonuniformity of the anodic oxide and pitting of the sample surface. Therefore, anodization was generally terminated by disconnection of the power supply at a predetermined current  $I_f$  somewhere between  $I_{min}$  and  $4I_{min}$ . In this way, anodic oxide layers with no visible nonuniformities were obtained at voltages  $V_0$  up to 150V on a 10.0 × 6.8 mm sample of GaAs and up to 200V on an 8.9 × 6.9 mm sample of GaAs<sub>0.6</sub>P<sub>0.4</sub>. At higher voltages the coatings became nonuniform.

The value of  $I_{min}$  depended on the composition and size of the sample and was roughly proportional to  $V_0$ . With  $V_0$  at 100V and  $I_0$  at 20 mA, the current  $I$

Key words: gallium arsenide, gallium arsenide phosphide, anodization, oxidation, native oxide.

dropped to the value  $I_{min} = 2.5$  mA in 43 sec when a 10.0 × 6.8 mm sample of GaAs was anodized. Under the same conditions, an 8.9 × 6.9 mm sample of GaAs<sub>0.6</sub>P<sub>0.4</sub> gave  $I_{min} = 2.0$  mA in 27 sec.

The anodic oxide thickness on a GaAs sample of 0.5 cm<sup>2</sup> surface area anodized at  $V_0 = 100$ V and  $I_0 = 20$  mA with final current  $I_f = 10$  mA was approximately 1800Å, and approximately 1100Å of GaAs was consumed. The corresponding amounts for a GaAs<sub>0.6</sub>P<sub>0.4</sub> sample with the same surface area anodized at  $V_0 = 200$ V and  $I_0 = 20$  mA with  $I_f = 10$  mA were approximately 1800 and 1200Å, respectively. Examination of these anodized samples with a scanning electron microscope revealed smooth, featureless oxides. Areas in which oxides had been stripped off in concentrated hydrochloric acid appeared clean and smooth.

One sample of GaAs<sub>0.6</sub>P<sub>0.4</sub> was anodized and stripped 50 times in succession with  $V_0 = 50$ V and still maintained a smooth optically polished appearance. More than 1μ of material had been removed.

Another sample of GaAs<sub>0.6</sub>P<sub>0.4</sub> was anodized at 100V and then submerged in the electrolyte and allowed to stand for 35 hr. No change in the oxide's light blue interference color was noticeable, indicating at least a fair degree of stability of the oxide in the electrolyte.

The permanganate-in-acetone electrolyte has been used successfully to rapidly profile 6 × 6 mm zinc-diffused samples of GaAs<sub>0.6</sub>P<sub>0.4</sub> by anodizing and stripping between measurements, each anodization taking less than 10 sec.

It should be noted also that the electrolyte was effective in anodizing samples of InSb at up to 100V.

### Acknowledgment

This work was supported by the National Science Foundation and performed under the auspices of Prof. James F. Gibbons of the Electrical Engineering Department at Stanford University.

Manuscript submitted July 19, 1973; revised manuscript received April 1, 1974.

Any discussion of this paper will appear in a Discussion Section to be published in the June 1975 JOURNAL. All discussions for the June 1975 Discussion Section should be submitted by Feb. 1, 1975.

The publication costs of this article have been assisted by Stanford University.

### REFERENCES

1. R. A. Logan, B. Schwartz, and W. J. Sundburg, *This Journal*, **120**, 1385 (1973).
2. J. M. Poate, P. J. Silverman, and J. Yahalom, *ibid.*, **120**, 844 (1973).
3. T. J. Magee, *Rev. Sci. Instr.*, **43**, 1218 (1972).
4. C. J. Dell'Oca, G. Yan, and L. Young, *This Journal*, **118**, 89 (1971).
5. W. W. Harvey and J. Kruger, *Electrochim. Acta*, **16**, 2017 (1971).
6. A. K. Revesz and K. H. Zaininger, *J. Am. Ceram. Soc.*, **46**, 606 (1963).
7. J. F. Dewald, *This Journal*, **104**, 244 (1957).

# Few Characteristics of Epitaxial GaN—Etching and Thermal Decomposition

Yasuo Morimoto

Research Laboratory, OKI Electric Industry Company, Limited, 550-5, Higashiasakawa, Hachioji, Tokyo 193, Japan

GaN is a III-V compound semiconductor noticed as a material for blue or violet LED's, but its etching behavior has not been extensively studied with only two reports by Chu (1) and Pankove (2). The former was effective for GaN grown by vapor phase epitaxy using GaBr<sub>3</sub> and NH<sub>3</sub> (1) but not effective (2) for GaN grown by vapor phase epitaxy using Ga, HCl, and NH<sub>3</sub> (3). The latter etched GaN electrolytically in 0.1N NaOH by anodizing the crystal. We have tried to etch GaN crystals by hot phosphoric acid (85%) referring the fact that the nitrides are generally etched with hot phosphoric acid and obtained positive results. The behavior of thermal decomposition of GaN was also investigated in several different ambients at elevated temperature. The GaN crystals used here were grown epitaxially from Ga, HCl, NH<sub>3</sub>, and Ar (3) at 1050°C on sapphire substrates. Typical values of the flow rate were 4, 300, and 1000 cm<sup>3</sup>/min for HCl, NH<sub>3</sub>, and Ar, respectively. Ga metal was placed at 1000°C.

## Etching by Hot Phosphoric Acid

The etching depth of GaN is plotted against etching time in Fig. 1(a). The parameter is the temperature of phosphoric acid. ○, ×, and △ indicate the data on good GaN crystals with smooth surface, while ● the data on wrong samples with rough surface (somewhat porous). As is clear from Fig. 1(a) such crystals with a rough

Key words: semiconductor, etching, annealing.

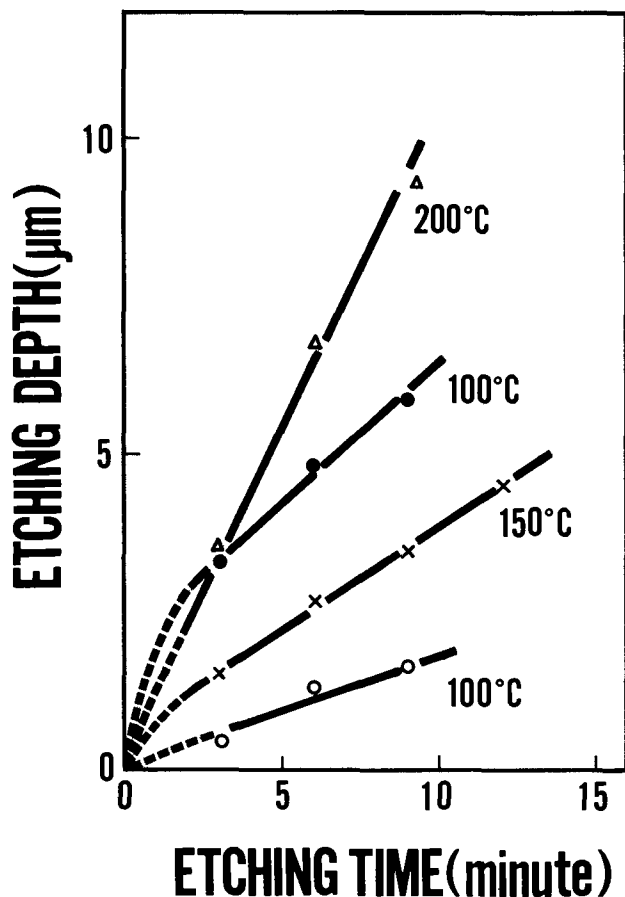


Fig. 1 (a). Etching depth plotted against etching time. The reason why the line joining each point does not cross the origin is mentioned in the text.

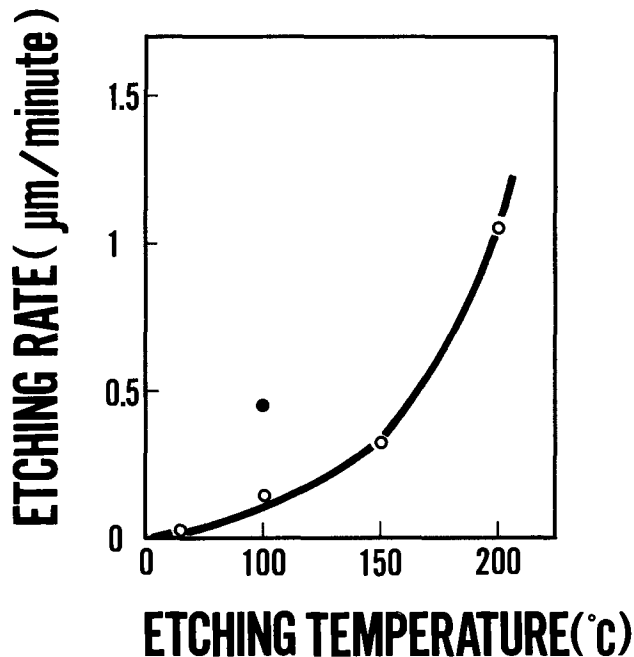


Fig. 1 (b). Temperature dependence of the etching rate. The etchant is phosphoric acid.

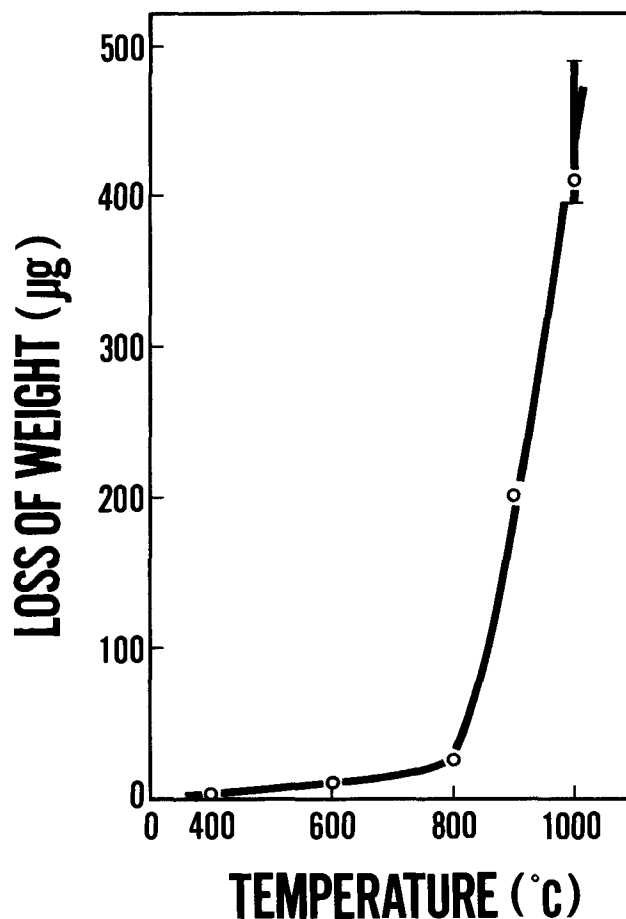


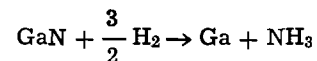
Fig. 2. Weight loss of GaN in H<sub>2</sub> atmosphere at elevated temperature. The annealing time is 20 min.

surface were etched more quickly than those with a smooth surface. Crystals with a smooth surface were colorless and transparent, on the other hand crystals with a rough surface were brownish and not transparent. The crystal growth was not perfectly uniform over all the surface. The rough surface was formed in part of the substrate where the etching rate was faster than on the other smooth part. This effect is observed in Fig. 1(a), that is, the line joining each point does not cross the origin. The etching rate is plotted against the temperature of phosphoric acid in Fig. 1(b). Below 100°C it was negligible. Above 180°C the etching rate was fast, but the smooth surface became rough. The mirror-like surface was not lost by the etching below 170°C for about 1 hr. Thus it was found that the hot phosphoric acid (100° ~ 170°C) was a useful etchant for GaN crystals.

### Thermal Decomposition

The weight loss of GaN crystals was measured in N<sub>2</sub>, air, and H<sub>2</sub> atmosphere by annealing at elevated temperature to investigate the behavior of thermal decomposition. The annealing time was 20 min. In N<sub>2</sub> and air, no weight loss could be detected, and no change of the crystal surface was observed up to 1000°C. In H<sub>2</sub> at-

mosphere weight loss could be observed above 400°C as shown in Fig. 2. The surface did not change up to 600°C, but it became a little rough by the annealing at 800°C. Simultaneously the weight loss also became noticeable as shown in Fig. 2. Annealing above 900°C produced small liquid Ga balls (20 ~ 30 μm in diameter) on the surface which became completely gray. Considering the fact that Ga is left on the surface it is evident that the decomposition of GaN proceeds as follows



Manuscript submitted May 3, 1974; revised manuscript received June 7, 1974.

Any discussion of this paper will appear in a Discussion Section to be published in the June 1975 JOURNAL. All discussions for the June 1975 Discussion Section should be submitted by Feb. 1, 1975.

The publication costs of this article have been assisted by the OKI Electric Industry Company, Limited.

### REFERENCES

1. T. L. Chu, *This Journal*, **118**, 1200 (1971).
2. J. I. Pankove, *ibid.*, **119**, 1118 (1972).
3. M. Ilegems, *J. Cryst. Growth*, **13/14**, 360 (1972).



## Corrosion of Pure and Amalgamated Zinc in Concentrated Alkali Hydroxide Solutions

L. Ž. Vorkapić, D. M. Dražić, and A. R. Despić

*Electrochemistry Department, Institute of Chemistry, Technology and Metallurgy, Beograd, Yugoslavia*

### ABSTRACT

Corrosion of pure and amalgamated zinc in pure concentrated KOH solutions was investigated using two methods: (a) galvanostatic measurements of the kinetics of hydrogen evolution with electrodic assessment of corrosion properties of the system, and (b) volumetric measurement of the hydrogen evolution reflecting directly the rate of corrosion. The latter was followed as a function of time during 150 hr. It was found that the corrosion rate varies considerably with time and was suggested that different factors control the initial and the steady-state corrosion. The initial corrosion rate increases with increasing KOH concentration which is indicative of the chemical mechanism of hydrogen evolution. The change of the corrosion rate with time and the steady-state corrosion rate can be explained in terms of formation of an impermeable ZnO film at the surface. In such a case the concentration dependence of the corrosion rate is inverse with time, which explains some results reported in literature. The amalgamated zinc surface gives complex galvanostatic transients which indicate a new phase formation in the process of initiation of hydrogen evolution, which could pertain to some solid potassium-zinc-mercury alloy.

The problem of corrosion of zinc in alkaline solutions has become a topic of considerable interest with the increasing use of zinc as the anode in a variety of alkaline batteries (primary alkaline zinc battery, secondary silver-zinc, and both primary and secondary zinc-air batteries), some of which contain great promise for propulsion of electric vehicles. This corrosion process is the basic cause for self-discharge and a relatively short shelf life of all the zinc-containing batteries, and one of its products, the gaseous hydrogen, creates problems when sealed batteries are to be produced. However, relatively little work has been done which could help toward a more fundamental understanding of the mechanism and kinetics of reactions constituting the corrosion process and this with some controversial results.

Thus, Snyder and Lander (1) studied corrosion of a system similar to that used in primary batteries by measuring the rate of hydrogen evolution and found that the amount of hydrogen evolved in a given time decreased with increasing KOH concentration. This finding is confirmed by comparable measurements of Dirkse and Timmer (2) both on pure (99.999%) and amalgamated zinc in pure KOH solutions, while in those saturated by zinc oxide much lower corrosion rates were found and no unambiguous concentration dependence.

Contrary to that, Ruetschi (3) found hydrogen evolution on amalgamated zinc to increase with increasing KOH concentration, which is in line with the kinetic work on hydrogen overpotential on zinc in al-

kaline solutions done earlier by Jofa, Komlev, and Bagotskii (4) and also by Lee (5).

The effect of saturation of the electrolyte by zincate also remained obscure. Ruetschi (3) assumed the large effect to be due to a more rapid formation of a protective film of zinc oxide on the electrode surface in the saturated electrolyte than in pure KOH. The existence of such a film seems indeed to be proved by the microscopic investigations of Powers (6). It is interesting that Powers claims even a catalytic activity of such a film for hydrogen evolution. However, Mansfield and Gilman (7) deny the necessity of that film formation for the explanation of the corrosion behavior and maintain that addition of zinc oxide acts by reducing the activity of water as the reactant for hydrogen evolution.

It is in this situation that the present work has been undertaken with the ambition to clarify the reasons for the discrepancy between results of different authors and to throw some more light onto the problem.

### Experimental

Two kinds of experiments have been carried out.

*Galvanostatic transient measurements.*—Those were carried out on a pure (99.99% made by Zorka-Šabac) zinc in pure KOH solution of different concentrations (1, 3, 6, and 10M) and on amalgamated zinc in 10M KOH. Zinc electrodes were made from zinc wire imbedded in Teflon and were placed in a closed, thermostated cell as normally used in electrodic investigations. The transients were obtained by perturbing the system with a conventional homemade galvanostat and were recorded on the CRO Tektronix 543B.

**Key words:** hydrogen evolution on zinc, galvanostatic investigation of the corrosion of zinc, zinc oxide film on corroding zinc, amalgamated zinc surface.

Amalgamation of the zinc surface was done by immersing the electrode into  $\text{HgCl}_2$  solution of a known mercury content and leaving it in until all the mercury had precipitated on the sample (checked by the KJ and by the copper test). Amounts of mercury were taken so as to render zinc with 0.5, 1, and 2% mercury calculated on the bulk amount of zinc. Since diffusion of mercury into the metal is slow the concentration of mercury in the surface layer must have been higher than the figures cited, but in some proportion with them.

**Volumetric measurements of the rate of hydrogen evolution.**—This has been done by enclosing pure (99.99%) and amalgamated zinc 5 cm long and 0.5 cm in diameter, machined out of zinc blocks, into a glass tube with a graded side-arm pipette, similar to that used by Dirkse and Timmer (2), where the amount of hydrogen evolved is found from the volume of solution expanded into the pipette. The glass tubes were thermostated to  $25^\circ \pm 0.05^\circ\text{C}$ . No stirring of the electrolyte was employed. Amalgamation of the zinc surface has been done in the same way as for zinc electrodes.

### Results

**Electrode investigations.**—For pure zinc good and reproducible galvanostatic cathodic transients were obtained with well-defined plateaus of the activation polarization for hydrogen evolution.

When the electrodes were left for a certain period in the electrolyte to stay at the established mixed potential, as well as when they were submitted to short anodic pulses, a lower potential plateau would appear with well-defined transition time. This could be ascribed to the reduction of zinc dissolved by corrosion or during the anodic pulse.

Figure 1 represents the Tafel lines obtained from the upper potential plateaus, pertaining to hydrogen evolution.<sup>1</sup>

Characteristic are: (a) well-defined straight lines over more than two powers of current density with slopes of  $120 \text{ mV dec}^{-1}$ , and (b) decrease of the polarization at a given current density with increasing concentration of KOH. This produced the dependence of the current density on concentration at a constant potential shown in Fig. 2 with the slope of the log-log plot (the reaction order) equal to one.

The corrosion current was also obtained by extrapolating the Tafel lines to the spontaneously established corrosion potentials and the dependence of the obtained result on KOH concentration is also shown in Fig. 2.

The dependence of the corrosion potential on KOH concentration is given in Fig. 3.

<sup>1</sup> All potentials in this and subsequent diagrams are referred to the hydrogen electrode in the same solution.

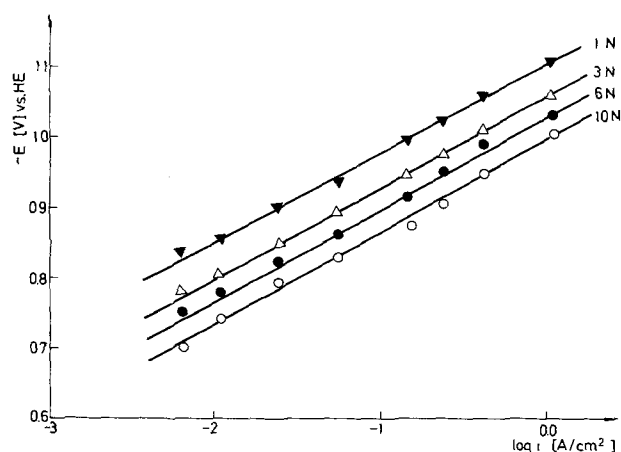


Fig. 1. Cathodic Tafel plots for zinc in KOH solutions of different concentrations.

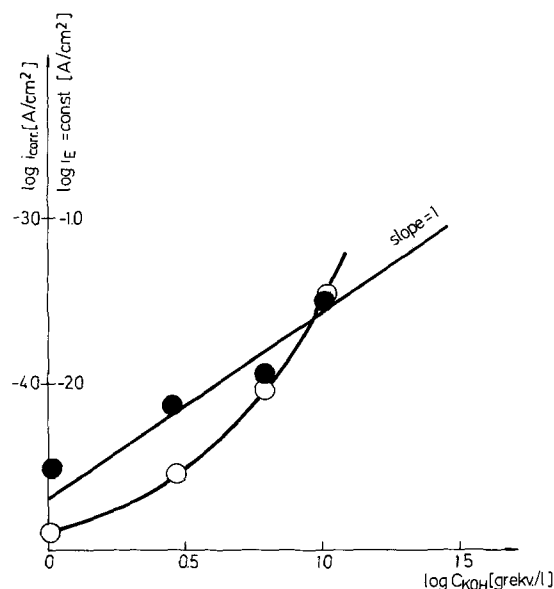


Fig. 2. Concentration dependence of the initial corrosion current density ( $\circ$ ) and of the current density at a constant potential of  $0.79\text{V vs. HE}$  ( $\bullet$ ) in same solution for zinc in KOH solutions.

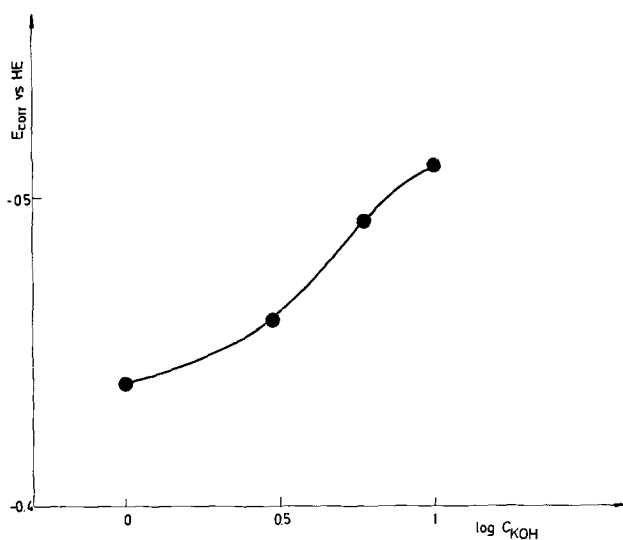


Fig. 3. Open-circuit potential of zinc as a function of the activity of the KOH solutions.

Galvanostatic transients of the freshly amalgamated zinc were of more complex structure than those on pure zinc as shown in Fig. 4a for charging and Fig. 4b for decay.

Characteristic of the rise is (a) a sharp increase (after a short transition time which disappears at higher current densities) to a first potential level which is then changing more slowly in an almost linear fashion within a time interval  $\tau_u$  and (b) a potential dip lasting over a period  $\tau_m$ , upon which (c) the potential is getting onto the plateau which could be ascribed to a steady-state hydrogen evolution.

The duration of the potential dip,  $\tau_m$ , decreases with increasing current density, while the extent to which the potential falls seems to be independent of it. The potential dip does not appear if the amalgamated zinc is left to stay in the cell for 24 hr before measurements.

Figure 5 shows the dependence of the duration of the linear potential rise  $\tau_u$  on current density for the freshly amalgamated zinc and for that after 24 hr. Obviously in both cases the product  $i \cdot \tau_u$  appears to be constant and in the first case it is  $1 \text{ mC/cm}^2$  while in the second it is  $3 \text{ mC/cm}^2$ .

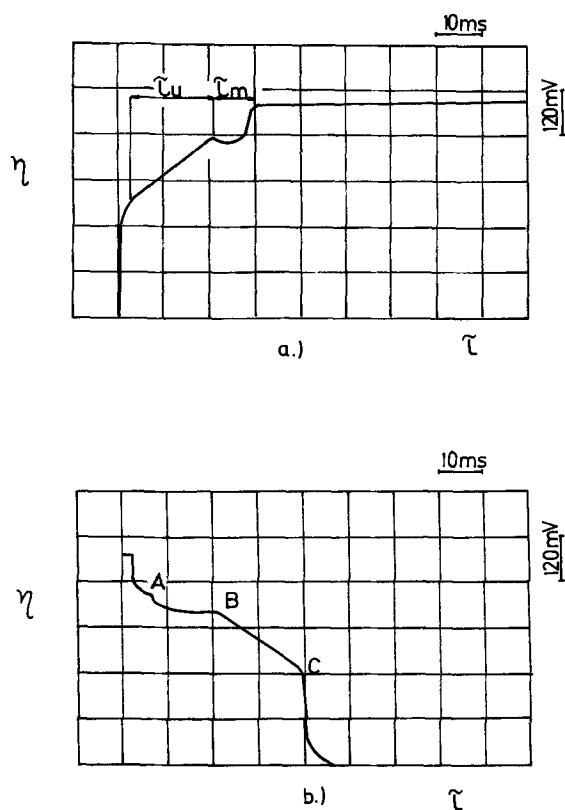


Fig. 4. (a) Galvanostatic cathodic charging curve for amalgamated zinc in 10N KOH solution for 25 mA/cm<sup>2</sup>.  $\tau_u$  is time interval till the appearance of the potential dip.  $\tau_m$  is duration of the potential dip. (b) Potential decay after the galvanostatic pulses.

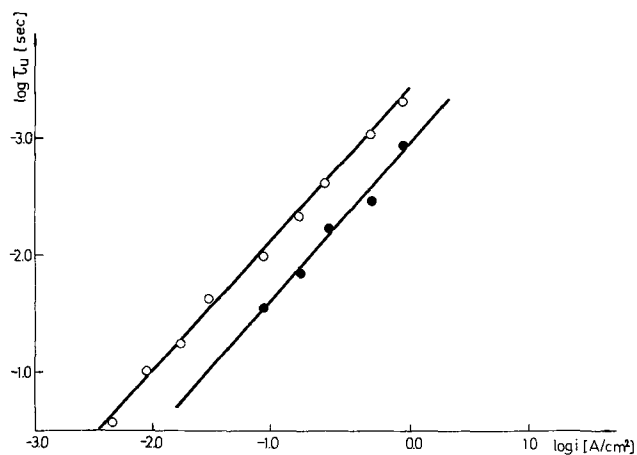


Fig. 5. The dependence of  $\tau_u$  on current density.  $\circ$ , Freshly amalgamated surface;  $\bullet$ , amalgamated surface after 24 hr of rest.

The decay curve (Fig. 4b) exhibits two potential arrests A and B, a linear decay to C, and a fast decay portion back to the original mixed potential.

The Tafel lines for hydrogen evolution indicate significant inhibition compared to pure zinc as shown in Fig. 6. The corrosion current obtained by extrapolation is about 50 times smaller at the former than on the latter.

It seems to be practically independent of the amount of mercury absorbed (above 0.5%) indicating that the surface layer is saturated with mercury.

Tafel lines are also different for the freshly amalgamated surface and the one after 24 hr as shown in Fig. 7. Both the hydrogen overvoltage at a given current density and the Tafel slope change, the first being considerably larger and the second somewhat lower

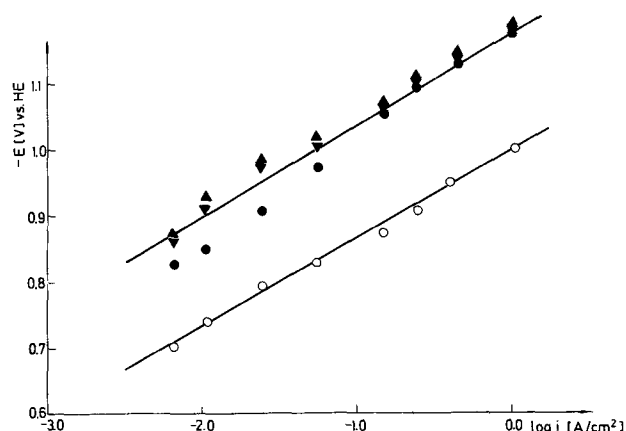


Fig. 6. Cathodic Tafel plots for pure zinc ( $\circ$ ) and zinc containing 0.5% ( $\bullet$ ), 1% ( $\blacktriangledown$ ), and 2.5% ( $\blacktriangle$ ), Hg, in 10N KOH.

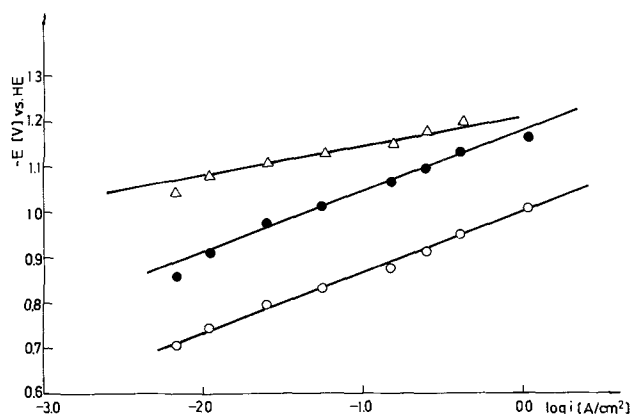


Fig. 7. Cathodic Tafel plots for pure zinc ( $\circ$ ), freshly amalgamated zinc ( $\blacktriangle$ ), and amalgamated zinc after 24 hr ( $\bullet$ ) in 10N KOH.

(60 vs. 120 mV dec<sup>-1</sup>) in the case of the freshly amalgamated zinc than in the case of the aged surface.

*Rate of hydrogen evolution at the corrosion potential.*—Typical results of the volumetric measurements are shown in Fig. 8 as the volume of hydrogen evolved as a function of time from a pure zinc sample in different concentrations of KOH. This was followed for more than 150 hr. The rates of hydrogen evolution at any moment are obtained as corresponding slopes of the curves. These are presented in Fig. 9. Three characteristic features should be noted: (i) in all the investigated cases the rate of hydrogen evolution (i.e., the corrosion rate) is strongly time dependent and within the time of observation it is reduced by more than one order of magnitude; (ii) the rates are dependent on KOH concentration; (iii) the concentration dependence may be different for the initial corrosion rates than for those after more than 100 hr. Thus, a straightforward increase in the initial corrosion rate with KOH concentration is observed, while after more than 100 hr the rate of corrosion in 10M KOH becomes smaller than in 6M solution. This crossover has been confirmed several times and hence can be considered to be beyond doubt, i.e., outside the possible experimental error.

### Discussion

The most important result of the present investigation is that corrosion of zinc in pure concentrated alkaline solution is strongly time-dependent and that a period of the order of 100 hr is needed before a steady state (or a negligibly slow change of the rate) is reached. Hence, the initial and the steady-state corrosion rates represent separate problems. In as much as

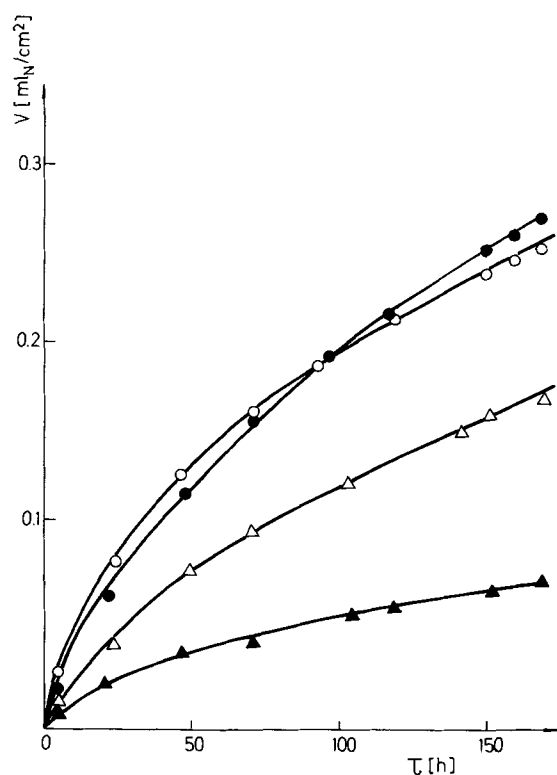


Fig. 8. Volume of evolved hydrogen on zinc in 1N (▲), 3N (△), 6N (●), and 10N (○) KOH solution as a function of time.

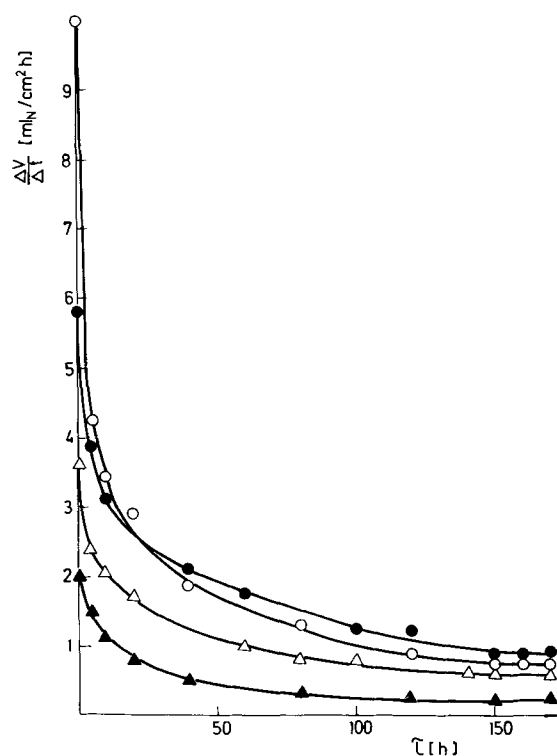


Fig. 9. Rate of hydrogen evolution on zinc in 1N (▲), 3N (△), 6N (●) and 10N (○) KOH solution as a function of time.

the mechanism of corrosion may stay the same it is quite likely that the rate-controlling factors are changing from one to the other.

#### Initial Corrosion Phenomenon

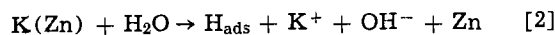
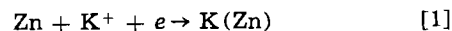
**Hydrogen evolution kinetics on pure zinc.**—Galvanostatic investigation of the cathodic reaction on pure

zinc rendered Tafel lines pertaining to hydrogen evolution well in line with the results of Jofa *et al.* (4) and Lee (5). No doubt is left that at a given potential the rate of hydrogen evolution increases with the increase in KOH concentration and a somewhat surprising result is that this was found to be a straightforward, first-order dependence. The increase in KOH concentration is known to produce also an increase in the activity of KOH, while the activity of water decreases along that change (16).

Jofa *et al.* (4) went into a complex analysis of the possible changes in the double layer structure to show that it is feasible that water discharge is a rate-determining step and still to have the increase in rate at the same time when the activity of that species is decreasing. This however, is hardly necessary when one takes into account the possible effectiveness of some other mechanisms. The first one was popular in the last century and was revived recently by a number of authors [Frumkin, Korshunov, and Bagozkaya (8) on mercury and partly on indium amalgam, Matsuda and Notoya (9) on platinum, and Matsuda and Ohmori (10) on nickel] namely the mechanism according to which the alkali metal cation is discharged electrochemically and the alkali metal formed reacts chemically with water.

This mechanism is made more likely by the findings of Kabanov (11) of the incorporation of alkali metals into lattices of solid electrodes including zinc [Aleksandrova, Kiseleva, and Kabanov (12)] during hydrogen evolution.

The mechanism should consist of the following steps



The transfer coefficients and reaction orders with respect to the alkali metal ions, water, and  $\text{OH}^-$  ions can be obtained from the following rate equations:

In the case of the rate-determining discharge

$$i = \bar{k}_1 \frac{\gamma_{\text{K}^+}}{\gamma_{\neq}} C_{\text{K}^+} \exp \left[ -\frac{\beta F}{RT} E \right] \quad [4]$$

where  $\gamma_{\text{K}^+}/\gamma_{\neq}$  is the ratio of activity coefficients of  $\text{K}^+$  ion and the activated complex, and  $E$  is the electrode potential measured with respect to a reference electrode (*e.g.*, vs. NHE) while  $\bar{k}_1$  is the electrochemical rate constant at the reference electrode potential.

In the case of rate-determining chemical reaction [2] with the first step in electrochemical equilibrium

$$i = \frac{\bar{k}_2}{\gamma_{\neq}} a_{\text{K}} a_{\text{H}_2\text{O}} \quad [5]$$

and

$$a_{\text{K}} = a_{\text{K}^+} \exp \left[ -\frac{F(E - E_{0,\text{K}})}{RT} \right] \quad [6]$$

$E_{0,\text{K}}$  being the standard electrode potential for  $\text{K}^+$  discharge. Hence

$$i = \frac{\bar{k}_2'}{\gamma_{\neq}} a_{\text{K}^+} a_{\text{H}_2\text{O}} \exp \left[ -\frac{FE}{RT} \right] \quad [7]$$

In the case of rate-determining recombination

$$i = \frac{\bar{k}_3}{\gamma_{\neq}} a_{\text{H}_{\text{ads}}}^2$$

$$\begin{aligned} a_{\text{H}_{\text{ads}}} &= k_2 \frac{a_{\text{K}} a_{\text{H}_2\text{O}}}{a_{\text{K}^+} + a_{\text{OH}^-}} \\ &= k_2 \frac{a_{\text{H}_2\text{O}}}{a_{\text{OH}^-}} \exp \left[ -\frac{F(E - E_{0,\text{K}})}{RT} \right] \quad [8] \end{aligned}$$



and, hence

$$i = \bar{k}_3 (k_2')^2 \frac{a_{\text{H}_2\text{O}}^2}{a_{\text{OH}^-}^2} \exp \left[ - \frac{2FE}{RT} \right] \quad [9]$$

The diagnostic criteria arising from the above equations for the cases of the three possible rate-determining steps are summarized in Table I.

It is seen that the obtained value of the Tafel slope is compatible only with the case of the first step being rate determining. However, such a slope would be obtained also in the case of a straight-forward discharge of water. Still, it is the reaction order of one with respect to the potassium ions (as shown in Fig. 2) which is indicative of the mechanism suggested here.

Indeed, it is surprising that a value so much in accordance with theory is obtained, when in such concentrated solutions the activity of water was not kept constant with changing KOH concentration and thus changed the solvation of the species. The result actually means that the ratio of the two activity coefficients (that of potassium ion to that of the activated state) is equal to one, indicating structural similarity between the two states.

Another possibility exists for a mechanistic interpretation of the positive reaction order with respect to the alkali metal which so far was not considered in the literature and was suggested by one of the present authors (D.D.) on the basis of the results of Šepa, Vojnović, and Bugarin [cf. (20)]. It is quite likely that hydrogen of the water molecules in the first hydration sheet of alkali metal ions is more loosely bound than this in free water molecules because of the additional polarization of the molecule which occurs in the strong electrostatic field of the ion. In such a case there could be a preference for hydrogen discharge from these water molecules, and this could also be expected to be first order with respect to alkali metal ions. This is supported by the findings of Šepa, Vojnović, and Bugarin that the decrease in hydrogen overvoltage at one and the same concentration of alkali hydroxide follows the order K, Na, Li; whereas in the case of alkali metal ion discharge (e.g., on mercury) Li is deposited at the most negative potentials, followed by Na and K.

One could easily show that if this new mechanism was operative and if discharge was rate determining, the same rate equation [4] would be applicable as for the alkali metal ion discharge; hence, also the same diagnostic criteria as given in Table I.

**Zinc dissolution kinetics.**—This has been fairly thoroughly studied in a number of recently published papers [cf., Bockris, Nagy, and Damjanović (13)]. It appears that dissolution follows a complex reaction path with two one-electron transfer unit steps and chemical reaction of the species formed, with OH<sup>-</sup> ions to render a very short lived dihydroxy monovalent zinc

Table I. Diagnostic criteria arising from the chemical mechanism of hydrogen evolution from alkaline solutions

	Rate-determining step			Found
	Zn + K <sup>+</sup> + e → K(Zn)	K(Zn) + H <sub>2</sub> O → H <sub>ads</sub> + K <sup>+</sup> + OH <sup>-</sup> + Zn	2H <sub>ads</sub> → H <sub>2</sub>	
Cathodic transfer coefficient	0.5	1	2	0.5
$\left( \frac{\log i}{\log C_{\text{K}^+}} \right)_{a_{\text{H}_2\text{O}}, a_{\text{OH}^-}, E}$	1	1	0	1
$\left( \frac{\log i}{\log C_{\text{H}_2\text{O}}} \right)_{a_{\text{K}^+}, a_{\text{OH}^-}, E}$	0	1	2	—
$\left( \frac{\log i}{\log C_{\text{OH}^-}} \right)_{a_{\text{K}^+}, a_{\text{H}_2\text{O}}, E}$	0	0	-1	0*

\* The value of Jofa et al. (4).

complex intermediate, as well as tetrahydroxy divalent zinc complex as the reaction product. Since, the second electron exchange is rate determining and this is preceded by the reaction of the zinc species with 3 OH<sup>-</sup> ions, the kinetics should be third order with respect to OH<sup>-</sup> ions. Since equilibria are established in all steps prior to the formation of the activated state, it is the activity of OH<sup>-</sup> ions which should affect the kinetics.

To assess the latter in the case when zinc is dissolving into solutions free of zincate ions one should use the approach of Kimball (17), i.e., the concept of the "floating" electrode extended to cover the case of divalent metal dissolution (18).

If it is accepted that the univalent intermediate is so unstable that it practically reacts all at the electrode (diffusion away neglected) one could write for the current density

$$i = k_{\text{Zn}}^{\circ} a_{\text{Zn}} a_{\text{OH}^-}^3 \exp \left[ \frac{\alpha_a F}{RT} E \right] - k_{\text{Zn(II)}}^{\circ} a_{\text{Zn(II)}} a_{\text{OH}^-} \exp \left[ - \frac{\alpha_c F}{RT} E \right] \quad [10]$$

where  $k_{\text{Zn}}^{\circ}$  and  $k_{\text{Zn(II)}}^{\circ}$  are the specific rates at unit activities and at the potential equal to the reference electrode potential, while  $\alpha_a$  and  $\alpha_c$  have values of 1.5 and 0.5, respectively, as found by Bockris, Nagy, and Damjanović.

The material balance equation taking into account diffusion of the reaction product away from the electrode can be written as

$$\frac{da_{\text{Zn(II)}}}{dt} = \frac{i}{2F} - \frac{D_{\text{Zn(II)}} a_{\text{Zn(II)}}}{\delta} = 0 \quad [11]$$

where  $D_{\text{Zn(II)}}$  and  $\delta$  are the diffusion coefficient of the Zn(II) species and the diffusion layer thickness, respectively.

Hence, replacing [10] into [11] and rearranging, one obtains

$$a_{\text{Zn(II)}} = \frac{k_{\text{Zn}}^{\circ} a_{\text{Zn}} a_{\text{OH}^-}^3 \exp \left[ \frac{\alpha_a F}{RT} E \right]}{k_{\text{Zn(II)}}^{\circ} a_{\text{OH}^-} \exp \left[ - \frac{\alpha_c F}{RT} E \right] + 2FD_{\text{Zn(II)}}/\delta} \quad [12]$$

and the current density comes to be

$$i = \frac{k_{\text{Zn}}^{\circ} a_{\text{Zn}} a_{\text{OH}^-}^3 \exp \left[ \frac{\alpha_a F}{RT} E \right]}{k_{\text{Zn(II)}}^{\circ} a_{\text{OH}^-} \exp \left[ - \frac{\alpha_c F}{RT} E \right] + 2FD_{\text{Zn(II)}}/\delta} \quad [13]^2$$

In the case when the cathodic reaction is much faster than diffusion away from the Zn(II) species formed by anodic dissolution, as could well be the case considering the relatively high  $i_0$  values found in the literature [up to 0.37 A/cm<sup>2</sup> (13)], Eq. [13] reduces to

$$i = 2F \frac{k_{\text{Zn}}^{\circ} a_{\text{Zn}}}{k_{\text{Zn(II)}}^{\circ}} \frac{D_{\text{Zn(II)}}}{\delta} a_{\text{OH}^-}^2 \exp \left[ \frac{2F}{RT} E \right] \quad [14]$$

i.e., the reaction becomes second order with respect to OH<sup>-</sup> and the Tafel slope obtains a value of 30 mV dec<sup>-1</sup>. Hence, the Tafel line shifts by 60 mV to the negative side for each power of ten of increase in activity of KOH.

<sup>2</sup> Kaesche (19) has obtained a similar equation, which was subsequently used by Mansfeld and Gilman (7) for calculating Tafel lines for dissolving zinc. That equation, however, suffers from the application of a relatively poorly defined quantity  $i_{\text{t,Zn}}$  relying on the assumption of the concentration of the reaction product in solution.

In the adverse case

$$i = (k^{\circ}_{Zn} a_{Zn}) a^3_{OH^-} \exp \left[ \frac{\alpha_a F}{RT} E \right] \quad [15]$$

i.e., third-order dependence is expected with respect to OH<sup>-</sup> and a Tafel slope of 40 mV dec<sup>-1</sup>. Hence, the Tafel line should shift by 120 mV to the negative side for a tenfold increase in activity of KOH.

The corrosion process on pure zinc.—Since the cathodic and the anodic processes are known, schematic Wagner-Traud type diagrams can be established as shown in Fig. 10, for the two extreme cases of anodic dissolution kinetics [case (a) and case (b)] exemplified by Eq. [14] and [15], respectively.

Considering that the equation for the hydrogen evolution kinetics is also known (Eq. [4]), one can derive quantitative expressions for the rate of corrosion and the corrosion potential.

Thus, from Eq. [4] and [14] and taking C<sub>K<sup>+</sup></sub> = C<sub>KOH</sub> and a<sub>OH<sup>-</sup></sub> = a<sub>KOH</sub>, one obtains

$$i_{corr} = K C_{KOH}^{\left(\frac{1}{1+\beta/2}\right)} a_{KOH}^{\left(\frac{\beta}{1+\beta/2}\right)} = K C_{KOH}^{0.8} a_{KOH}^{0.4} \quad [16]$$

where

$$K = \left\{ \left[ \frac{k^{\circ}_{Zn} a_{Zn}}{2F} \frac{D_{Zn(II)}}{\delta} \right]^{\beta/2} \frac{\gamma K^+}{\bar{k}_1 \gamma^{\neq}} \right\} \left( \frac{1}{1+\beta/2} \right) \quad [17]$$

Also

$$E_{corr} = E^{\circ}_{corr} + \frac{RT}{(2+\beta)F} \ln C_{KOH} a_{KOH}^{-2} \quad [18]$$

where E<sup>o</sup><sub>corr</sub> is the corrosion potential at C<sub>KOH</sub> a<sub>KOH</sub><sup>-2</sup> = 1.

Using Eq. [4] and [15] one obtains

$$i_{corr} = K' C_{KOH}^{\left(\frac{1}{1+\beta/\alpha_a}\right)} a_{KOH}^{\left(\frac{3\beta/\alpha_a}{1+\beta/\alpha_a}\right)} = K' C_{KOH}^{0.75} a_{KOH}^{0.75} \quad [19]$$

where

$$K' = \left[ \frac{\gamma K^+}{\bar{k}_1 \gamma^{\neq}} (k^{\circ}_{Zn} a_{Zn})^{\beta/\alpha_a} \right] \left( \frac{1}{1+\beta/\alpha_a} \right) \quad [20]$$

Also

$$E_{corr} = E^{\circ}_{corr} + \frac{RT}{(\alpha_a + \beta)F} \ln C_{KOH} a_{KOH}^{-3} \quad [21]$$

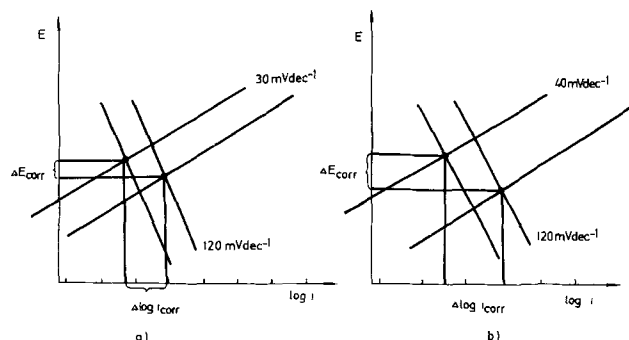


Fig. 10. Change of corrosion potential ( $\Delta E_{corr}$ ) and corrosion current ( $\Delta \log i_{corr}$ ) for a tenfold increase in KOH concentration represented by the schematic Wagner-Traud diagram for the corrosion of zinc in alkaline solutions. (a) In the case of dominant hydrogen evolution control and (b) in the case of mixed hydrogen evolution and zinc dissolution control.

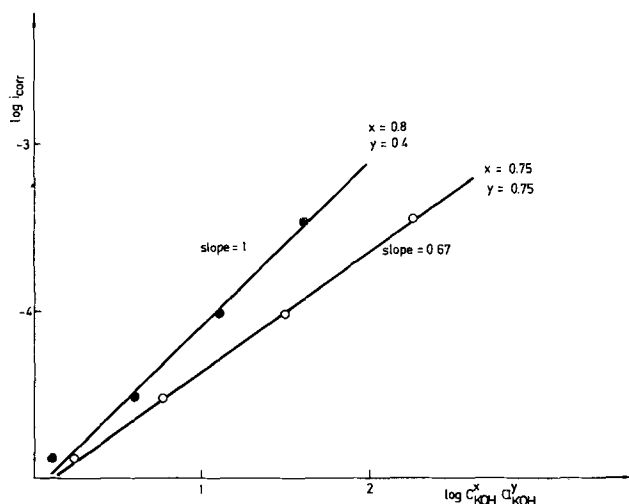


Fig. 11. The dependence of the log corrosion current density of zinc in KOH solutions on the complex variable  $\log C_{KOH}^x a_{OH^-}^y$  (see Eq. [14] and [15]).

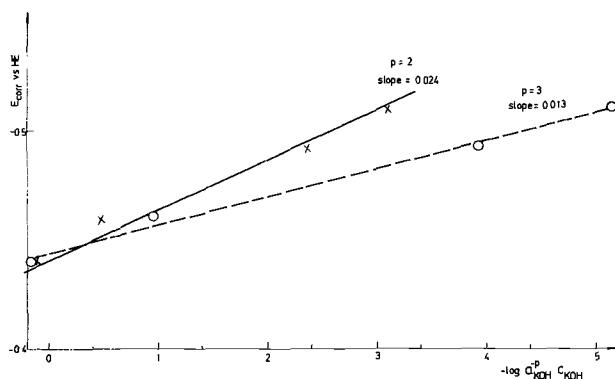


Fig. 12. Plot of  $E_{corr}$  as a function of the complex variable  $\log C_{KOH} a_{KOH}^{-p}$  corresponding to Eq. [18] and [21] with  $p = 2$  and  $3$ , respectively.

It is seen that the two cases (a) and (b) (Fig. 10) should differ by the dependence of both corrosion current and corrosion potential on the activity of KOH. The numerical values of the exponents in Eq. [16] and [19] were obtained taking  $\beta = 0.5$  and  $\alpha_a = 1.5$  [as shown in Ref. (13)].

To test the model, plots of  $i_{corr}$  and  $E_{corr}$  vs.  $\log C_{KOH} a_{KOH}^y$  and  $\log a_{KOH}^{-p} C_{KOH}$ , respectively, with  $x, y$ , and  $p$  arising from Eq. [16], [18], [19], and [21] are shown in Fig. 11 and 12.<sup>3</sup> The slope of 24 mV dec<sup>-1</sup> in Fig. 12 corresponding to Eq. [18], both figures clearly show that the first model is the adequate one.

Kinetic behavior of amalgamated zinc.—Galvanostatic transients reveal complex relationships in the polarization of freshly amalgamated zinc electrodes. The shape of the curve can be interpreted in one of two ways: (i) The first kink in the charging curve can be due to the activation overpotential of hydrogen evolution on pure zinc amalgam. As the current flows, there occurs a codeposition of potassium metal into the amalgam and this inhibits hydrogen evolution, i.e., raises the polarization to a new steady-state level. (ii) The first kink corresponds to the deposition of potassium. As the concentration of potassium increases, so does the polarization, until after about 1 mC/cm<sup>2</sup> of deposited alkali metal a new phase is formed, mercury is depleted temporarily of potassium and thus accepts potassium more readily (lower polarization). This undergoes, however, further concentration polarization, until a steady state is established in which hy-

<sup>3</sup> The activity of KOH was calculated at each concentration using the activity coefficient data of Bender and Ackerloff (16).

drogen is evolved by chemical reaction of potassium with water at the same rate at which potassium is deposited.

The second explanation seems more likely, for in the first case it is difficult to explain the appearance of the potential dip. A creation of a new phase, however, would instantaneously decrease the concentration of potassium in the amalgam and hence, would reduce polarization, until a new accumulation takes place which leads to a new rise up to the steady state.

The assumption of the accumulation of potassium in the amalgam can be justified only if on a freshly amalgamated surface the chemical reaction between potassium and water (second step) is the rds rather than  $K^+$  discharge.

In support of this stands not only the fact that the hydrogen evolution is known to be much more inhibited on Hg than on Zn, but also the experimental finding (Fig. 7) that the Tafel line on a freshly amalgamated surface has a slope of  $60 \text{ mV dec}^{-1}$ , i.e., suggests a transfer coefficient of one.

The potential decay curve supports the above consideration. The two arrests, however, indicate a transient existence of two different phases. Insufficient information is available for speculation about the structures of those phases. They seem to need a certain amount of mercury, for they do not appear when mercury dissolves deeper into zinc with time (after 24 hr), i.e., reduces in the surface concentration.

Even then and if the rds becomes the  $K^+$ -discharge as in the case of pure zinc, a build up of potassium concentration may be needed before the steady-state decomposition rate with the evolution of hydrogen is achieved. This is in accordance with the fact that according to quantitative results more charge is spent for potassium pileup ( $3 \text{ mC/cm}^2$ ) when less mercury is present at the surface (after 24 hr).

#### Steady-State Corrosion of Zinc

The change in the corrosion rate with time can be interpreted as due to increasing coverage of the surface by an impermeable film of zinc oxide. In such a case a  $(1 - \theta_{\text{ZnO}})$  factor should be introduced into Eq. [15]. In order to assess how  $\theta_{\text{ZnO}}$  changes with time one has to consider a complex kinetics at the surface. The  $\text{Zn(OH)}_2$  was seen to be formed by the corrosion of the electrode and reaction between  $\text{Zn}^{2+}$  ions and  $\text{OH}^-$  ions. It partly diffuses away, and partly undergoes dehydration forming the insoluble and compact  $\text{ZnO}$ . If one assumes the first-order kinetics for the latter one could write the rate equation as

$$\frac{dn_{\text{ZnO}}}{dt} = \frac{k_{\text{ZnO}}}{\gamma^{\neq \text{ZnO}}} a_{\text{Zn(OH)}_2} \quad [22]$$

and a steady-state material balance equation for  $\text{Zn(OH)}_2$

$$\frac{k_{\text{Zn(OH)}_2}}{\gamma^{\neq \text{Zn(OH)}_2}} a_{\text{Zn}^{2+} + \text{a}^2\text{OH}^-} - \frac{k_{\text{ZnO}}}{\gamma^{\neq \text{ZnO}}} a_{\text{Zn(OH)}_2} - \frac{DC_{\text{Zn(OH)}_2}}{\delta} = 0 \quad [23]$$

Taking into account that

$$\frac{d\theta_{\text{ZnO}}}{dt} = \frac{1}{(n_{\text{ZnO}})_{\text{max}}} \frac{dn_{\text{ZnO}}}{dt} \quad [24]$$

and

$$\frac{dn_{\text{Zn}^{2+}}}{dt} = \frac{i_{\text{corr},0}(1 - \theta_{\text{ZnO}})}{2F} - \rho \frac{k_{\text{Zn(OH)}_2}}{\gamma^{\neq \text{Zn(OH)}_2}} a_{\text{Zn}^{2+} + \text{a}^2\text{OH}^-} = 0 \quad [25]$$

where  $\rho$  is the thickness of the reaction layer, combining then [22] with [23] and [25] and replacing into [24] one obtains for the rate of increase of surface

coverage by  $\text{ZnO}$

$$\frac{d\theta_{\text{ZnO}}}{dt} = \frac{1/\rho}{(n_{\text{ZnO}})_{\text{max}}} \frac{k_{\text{ZnO}}/\gamma^{\neq \text{ZnO}}}{[k_{\text{ZnO}}/\gamma^{\neq \text{ZnO}} + D/\delta] \cdot i_{\text{corr},0}(1 - \theta_{\text{ZnO}})} \quad [26]$$

which suggests the first-order kinetics for the film formation. One can solve this for the surface coverage as

$$\theta_{\text{ZnO}} = (1 - e^{-A i_{\text{corr},0} t}) \quad [27]$$

where

$$A = \frac{1/\rho}{(n_{\text{ZnO}})_{\text{max}}} \frac{k_{\text{ZnO}}/\gamma^{\neq \text{ZnO}}}{k_{\text{ZnO}}/\gamma^{\neq \text{ZnO}} + D/\delta} \quad [28]$$

Now, for the effective corrosion rate at any time,  $t$ , one can write

$$i_{\text{corr},t} = i_{\text{corr},0}(1 - \theta_{\text{ZnO}}) \quad [29]$$

and introducing [27] into [29] one obtains

$$i_{\text{corr},t} = i_{\text{corr},0} e^{-A i_{\text{corr},0} t} \quad [30]$$

The correctness of the above derivation can be checked by the experimental time dependence of the rate of hydrogen evolution for this is directly related to the rate of corrosion. Hence

$$\log r_{\text{H}_2} = (\log r_{\text{H}_2})_0 - A i_{\text{corr},0} t \quad [31]$$

and the appropriate plot is shown in Fig. 13.

It is seen that, except for 1N KOH solution, the plots exhibit fair linearity after a certain induction period. The slopes increase with increasing KOH concentration as should be expected, for they contain the  $i_{\text{corr},0}$ . The values of the corrosion rate extrapolated to zero time follow the same pattern. The induction period is to be expected since the theoretical relationship has been derived under the assumption that all of the  $\text{ZnO}$  formed precipitates immediately into an impermeable film. This could be true of a solution saturated with  $\text{ZnO}$ .

Indeed, in the earlier work cited (2), the corrosion rate was shown to be much lower in  $\text{ZnO}$ -saturated

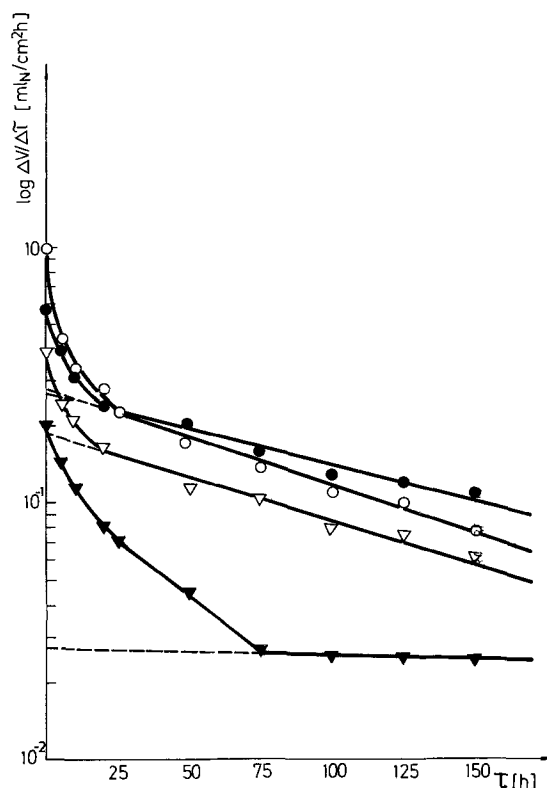


Fig. 13. Plot of log of the rate of hydrogen evolution vs. time for zinc in 1N ( $\blacktriangledown$ ), 3N ( $\nabla$ ), 6N ( $\bullet$ ), and 10N ( $\circ$ ) KOH solution.

solution than in fresh KOH. The solutions used in the present work contained no ZnO to start with and some period of accumulation of ZnO to reach saturation is normally expected.

On the whole one can say that the model contains quite a number of simplifying assumptions so that the agreement with the experiment cannot be but crude. However, it reveals one important feature which helps understand some of the experimental puzzles and in particular the reasons for controversial results on the effect of KOH concentration.

It is seen that the initial corrosion rate,  $i_{\text{corr},0}$ , acts not only as a proportionality constant, but is contained also in the exponent of Eq. [30]. Hence, as this quantity has been shown to be larger at higher KOH concentrations this also means that the decay of the corrosion rate is getting faster as the latter is increased. This explains the crossover of the curves of Fig. 8 and 13 for the 6 and 10M KOH after a certain period of time. But one can foresee also that under some other conditions of experiment under which the  $i_{\text{corr},0}$  has a faster increase with the increase in KOH concentration, this crossover can take place much earlier and the concentration dependence of the rate of corrosion is inverse if measured after that has happened. The fact is that, e.g., the data on the rate of corrosion reported by Dirkse and Timmer (2) were taken 1 hr after the immersion of zinc into the electrolyte and, hence, are not the initial corrosion rate values but rather those given by Eq. [24].

Also, Snyder and Lander (1) observed the corrosion in terms of the gassing rate over a long period of time and reported the first values after 2 days.

Addition of zinc oxide to the electrolyte to saturation complicates the interpretation of the results for Eq. [14] is no longer valid and the concept of supersaturation must be introduced if the phenomena are to be explained in the same semiquantitative terms as the ones above. However, one can speculate qualitatively that, if anything, the rate of diffusion of the corrosion products away from the electrode must be slower and, hence, for the same period of time the surface coverage by ZnO in a saturated electrolyte must be much larger than in the pure one. Hence, the corrosion must be correspondingly depressed.

### Acknowledgment

The authors acknowledge gratefully the sponsorships of The National Science Foundation, Washington, D.C., (Project GF-31570) and Research Fund of the SR Serbia.

Manuscript submitted Jan 7, 1974; revised manuscript received June 18, 1974.

Any discussion of this paper will appear in a Discussion Section to be published in the June 1975 JOURNAL. All discussions for the June 1975 Discussion Section should be submitted by Feb. 1, 1975.

### REFERENCES

1. R. N. Snyder and J. J. Lander, *Electrochem. Technol.*, **3**, 161 (1965).
2. T. P. Dirkse and R. Timmer, *This Journal*, **116**, 162 (1969).
3. P. Rüetschi, *ibid.*, **114**, 301 (1967).
4. Z. A. Jofa, L. V. Komlev, and V. S. Bagočkii, *Zh. Fiz. Khim.*, **35**, 1571 (1961).
5. T. S. Lee, *This Journal*, **118**, 1278 (1971).
6. R. W. Powers, *ibid.*, **118**, 5 (1971).
7. F. Mansfeld and S. Gilman, *ibid.*, **117**, 1328 (1970).
8. A. N. Frumkin, V. N. Korshunov, and J. A. Bagotzskaya, *Electrochim. Acta*, **15**, 289 (1970).
9. A. Matsuda and R. Notoya, *J. Res. Inst. Catalysis, Hokkaido Univ.*, **14**, 165 (1966).
10. A. Matsuda and T. Ohmori, *ibid.*, **10**, 215 (1962).
11. B. N. Kabanov, *Usp. Khim.*, **35**, 1873 (1965).
12. A. P. Aleksandrova, J. G. Kiseleva, and B. M. Kabanov, *Zh. Fiz. Khim.*, **38**, 1493 (1964).
13. J. O'M. Bockris, Z. Nagy, and A. Damjanović, *This Journal*, **119**, 285 (1972).
14. J. O'M. Bockris and A. R. Despić, in "Physical Chemistry An Advanced Treatise," H. Eyring, Editor, pp. 611-723, Academic Press, New York (1970).
15. A. R. Despić, and Dj. S. Jovanović, *Bull. Soc. Chim. Belgrade*, **38**, 255 (1973).
16. G. C. Akerlof and P. Bender, *J. Am. Chem. Soc.*, **70**, 2366 (1948).
17. G. E. Kimball, *J. Chem. Phys.*, **8**, 199 (1940).
18. J. O'M. Bockris and A. R. Despić, in "Physical Chemistry," H. Eyring, D. Henderson, and W. Jost, Editors, Vol. 9B, Chap. 7, Academic Press, New York (1970).
19. H. Kaesche, "Die Korrosion der Metalle," Springer-Verlag, Berlin (1966).
20. Lj. Bugarin, Diploma Thesis, Faculty of Technology and Metallurgy, Beograd, 1974.

# Ellipsometric Study of the Formation of Films on Iron in Orthophosphate Solutions

Z. Szklarska-Smialowska<sup>1</sup> and R. W. Staehle\*

Department of Metallurgical Engineering, The Ohio State University, Columbus, Ohio 43210

## ABSTRACT

Ellipsometry was used to study optical properties and kinetics of film growth on iron in 0.1N sodium orthophosphate solutions differing in pH. Properties and thicknesses of films grown at room temperature (22°C) were found to vary within wide limits depending upon pH, potential, and presence or absence of oxygen. In aerated Na<sub>3</sub>PO<sub>4</sub> solution,  $\gamma$ -Fe<sub>2</sub>O<sub>3</sub> or Fe<sub>3</sub>O<sub>4</sub> film is formed with a refractive index  $n = 2.6$  and absorption coefficient  $k = 0.20$ . At anodic polarization potentials and at pH 7 or higher, iron oxide films are also formed. On the other hand, at open-circuit potentials in aerated solutions of pH 7.0 and pH 9.1, a multiple phosphate film is produced. It is composed of several layers with  $n$  values oscillating between 1.4 and 1.5, and  $k$  values from 0 to 0.14. Such a film decreases the corrosion rate of iron shifting its open-circuit potential to more noble values. As a potential is reached at which iron oxide forms, a film composed of both iron oxide and iron phosphate is produced. The growth rate of iron oxide films, and that of phosphate films at higher pH values than 7.2, follow a logarithmic law. Below pH 7.2, both in aerated and deaerated solutions, an unprotective phosphate film is formed. It is composed of several layers with  $n$  values oscillating between 1.34 and 1.36, and  $k$  values from 0.013 to 0.45. Its thickness is a linear function of time.

The aim of the present work was to elucidate the kinetics of the film growth on iron in phosphate solutions at various values of pH in the presence and absence of air and to determine the optical parameters of these surface layers. Such data are pertinent to understanding the nature of the inhibition provided by phosphate additions.

Phosphates belong to the most popular corrosion inhibitors used for steel in aqueous nearly neutral solutions. It is commonly assumed that they are active in the presence of oxygen only.

Mayne and Menter (1) used electron diffraction to determine the composition of protective films on iron in aerated dibasic and tribasic phosphate solutions. In both solutions the protective film was composed mainly of a cubic oxide having the structure of Fe<sub>3</sub>O<sub>4</sub>,  $\gamma$ -Fe<sub>2</sub>O<sub>3</sub>, or an intermediate compound. However, in disodium hydrogen phosphate, particles of FePO<sub>4</sub> · 2H<sub>2</sub>O were found imbedded in a matrix of the cubic oxide. On the basis of corrosion measurements and film composition studies, the authors concluded that in 0.1N trisodium phosphate in the presence of air, the weak areas in the air-formed film are repaired by the formation of  $\gamma$ -Fe<sub>2</sub>O<sub>3</sub>, Fe<sub>3</sub>O<sub>4</sub>, or an intermediate compound with traces of ferric phosphate. In 0.1N disodium hydrogen phosphate, FePO<sub>4</sub> · 2H<sub>2</sub>O was found in the protective film what, as the authors assume, is essential for the inhibition when the air-formed film is weak.

Kolotyркиn *et al.* (2) assume that in neutral phosphate solutions a passivating monolayer of FeHPO<sub>4</sub> and a porous film of Fe<sub>3</sub>(PO<sub>4</sub>)<sub>2</sub> is formed.

According to Pryor and Cohen (3), the inhibition of the corrosion of iron by sodium phosphate solutions in the presence of air is caused by oxygen. They assume that oxygen dissolved in the phosphate solution is mainly responsible for the capacity of phosphate solutions to inhibit the corrosion of iron. Namely, oxygen adsorbed on the metal surface takes part in the reaction with surface iron atoms to form  $\gamma$ -Fe<sub>2</sub>O<sub>3</sub>. They also suggest that the formation of a protective film of  $\gamma$ -Fe<sub>2</sub>O<sub>3</sub> is not instantaneous, and the initial stages of film formation are accompanied by a very slow

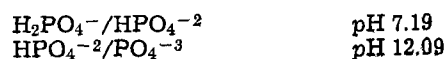
electrochemical attack, which leads to the formation of hydrated ferric phosphates. Neither the thickness of the protective films nor the kinetics of their formation in phosphate solutions were studied in their work.

## Experimental

All experiments were performed on specimens of 99.99% purity iron in the form of cylindrical disks with exposed area of 0.32 cm<sup>2</sup>. The specimen was mounted in a Teflon holder.

The specimen was first rough ground to a 600 grit finish through a series of metallographic papers and then mechanically polished with diamond abrasives to a final finish of 1 $\mu$ . After mechanical polishing, the specimen was cleaned, degreased, and electropolished. The electropolishing solution was composed of 20 parts of glacial acetic acid with 1 part of 70% perchloric acid. The specimens were exposed for 2 sec at room temperature and a current density of 4 A/cm<sup>2</sup>; the specimen was then washed with methanol, dried and placed in the ellipsometric cell.

The ellipsometric measurements were performed in different solutions, either deaerated or maintained in free contact with air. As the pH changes, the composition of the anion changes; regions for the existence of the phosphate ions are (4)



Since we wished to investigate domains of existence of each anion, the following solutions were used: 0.1N Na<sub>3</sub>PO<sub>4</sub> (pH 12.3), 0.1N Na<sub>2</sub>HPO<sub>4</sub> (pH 9.1), 0.1N NaH<sub>2</sub>PO<sub>4</sub> (pH 4.5), and 0.1N Na<sub>2</sub>HPO<sub>4</sub> with NaH<sub>2</sub>PO<sub>4</sub> (pH 7). The solutions were deaerated by bubbling for 24 hr prepurified helium through the solution. All experiments were conducted at 22°C. The electrode potential was measured with reference to a saturated calomel electrode and all data are reported in the calomel scale. Experiments were conducted at open-circuit potential, at different anodic potentials, and sometimes at slightly cathodic potentials.

The ellipsometer was Model 436 from Rudolf and Sons with mercury arc light source. The vacuum wave length of light was 5461Å, and the angle of incidence was 70.96°.

Before measuring the optical parameters of the pure substrate, the specimen was treated with a constant

\* Electrochemical Society Active Member.

<sup>1</sup> Present address: Institute of Physical Chemistry, Warsaw, Kasprzaka 44, Poland.

Key words: corrosion inhibitors, ellipsometry, passivity, phosphates, thin films, refractive index.

cathodic current of 40  $\mu\text{A}/\text{cm}^2$  in the solution to be studied to remove any air-formed film and to maintain a clean surface. The measurements of the optical constants of iron were made as rapidly as possible.

The optical constants of iron and of the films formed on its surface, and the film thicknesses were calculated using the McCrackin computer program (5) and an 360 computer. In the case of multiple films, their refractive indices were calculated under the assumption that there was a stack of several homogeneous layers with different optical parameters.

**Results**

**Polarization curves.**—Anodic polarization curves were determined to characterize the general electrochemical response of the iron to the various phosphate solutions. The measurements of the polarization curves were performed in deaerated solutions at a scanning rate of 20 mV/min; the potential sweep started from potentials more negative than the corrosion potential.

Figure 1 gives the polarization curves for all the solutions studied. The critical potential of passivation manifests itself distinctly only in the solution of pH 7. In the 0.1N  $\text{NaH}_2\text{PO}_4$  solution iron does not passivate.

**Index of refraction of film-free substrate.**—The index of refraction of the film-free substrate for each experiment was determined; the value of the refractive index was 3.14-3.26 and the absorption coefficient was 3.6-4.0. This applied for aerated and deaerated solutions at all values of pH studied.

**Iron oxide films at pH 12.3 and 9.1.**—Figure 2 shows changes in analyzer angles ( $\Delta A$ ) vs. changes in polarizer angles ( $\Delta P$ ) for iron in the three environmental conditions: The first two cases involve 0.1N  $\text{Na}_3\text{PO}_4$  (pH 12.3) and 0.1N  $\text{Na}_2\text{HPO}_4$  (pH 9.1), each taken at a series of applied potentials. The former was taken from -700 to +600 mV<sub>SCE</sub>. Every value of potential was maintained constant for 60 min and during this time the changes in A and P were noted. Approximately one-third of the measurements taken during 1 hr are plotted. Thus, at -700 mV<sub>SCE</sub> the (x) symbol refers to values of  $\Delta A$  and  $\Delta P$  taken at the same potential over a period of 1 hr. The surface was freshly prepared for each experiment. The third case in Fig. 2 shows the changes with time of  $\Delta A$  and  $\Delta P$  for speci-

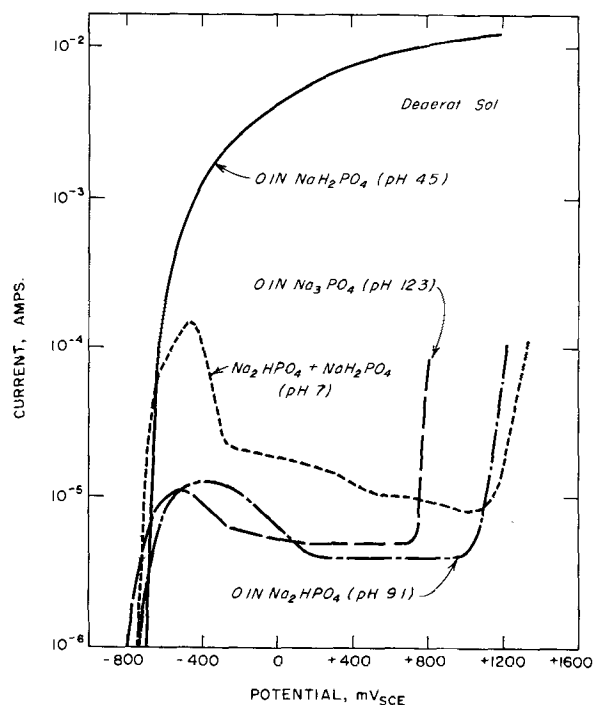


Fig. 1. Current-potential diagrams for iron in phosphate solutions of various pH.

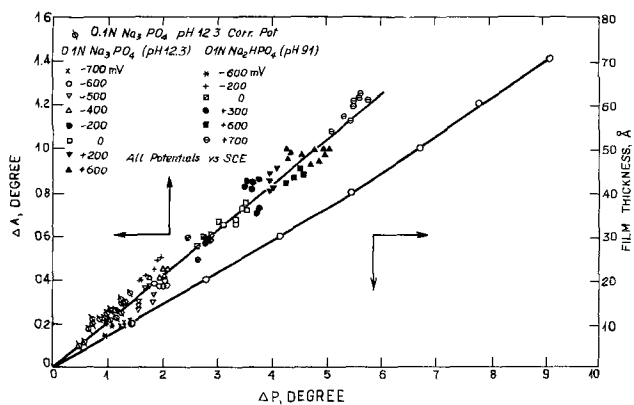


Fig. 2. Relationship of  $\Delta A$  vs.  $\Delta P$  for a film grown in 0.1N  $\text{Na}_3\text{PO}_4$  and 0.1N  $\text{Na}_2\text{HPO}_4$  solutions at different applied potentials, and relationship between  $\Delta P$  and thickness of the film whose complex index was equal to 2.6 (1-0.08i).

mens immersed in 0.1N  $\text{Na}_3\text{PO}_4$  at the open circuit potential. These points lie along the same line which was found for the films formed at constant anodic potentials.

From Fig. 2 it is possible to calculate an average complex refractive index which applies to all three cases including the whole set of applied potentials at two pH's and the open-circuit potentials at pH 12.3. The data in Fig. 2 give an average refractive index of 2.6 (1-0.08i)<sup>2</sup> with  $n = 2.6 \pm 0.1$  and  $k = 0.21 \pm 0.05$ . These values correspond either to  $\gamma\text{-Fe}_2\text{O}_3$  or  $\text{Fe}_3\text{O}_4$ . However, the imaginary part of the refractive index is smaller than the range of 0.12-0.20 usually given in the literature for the same type of film (6-8).

Figure 2 also shows the relationship between the thickness of the film and  $\Delta P$ .

Figure 3 shows that the time dependence of the film thickness under open circuit conditions at pH 12.3 is logarithmic. The growth rate of approximately 5Å per decade is higher than that for the iron base alloys studied by Goswami and Staehle (9) in borate buffer solutions of pH 8.4 where values of 0.9 to 1.5 Å/decade were obtained at constant applied potentials. The growth of the film was accompanied by a substantial increase in potential, shown in Fig. 4. This change corresponds to 35 mV/Å.

**Films at pH 9.1 at open-circuit potentials.**—Figure 2 showed a series of measurements for the pH 9.1 solution at constant anodic potentials. Here the optical properties of the protective film were identical to those for open-circuit and applied anodic potentials at pH 12.3. However, at open-circuit potential at pH 9.1 quite

<sup>2</sup> The complex index,  $N$ , of a substance is defined by the equation:  $N = n - i \cdot k$ , or  $N = n(1 - i \cdot K)$  where  $nK = k$ ,  $n =$  refractive index,  $k =$  absorption coefficient,  $K =$  extinction coefficient.

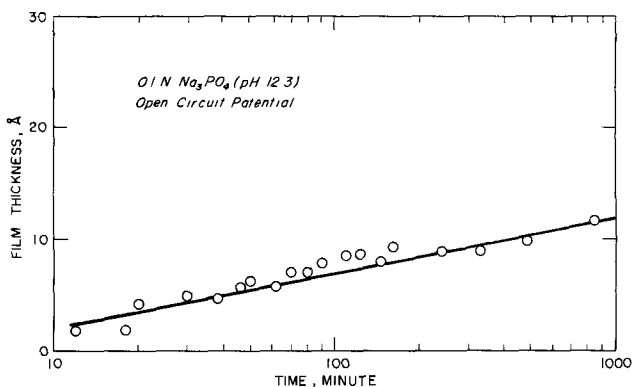


Fig. 3. Film thickness vs. time for iron at open-circuit potential in 0.1N  $\text{Na}_3\text{PO}_4$  solution.

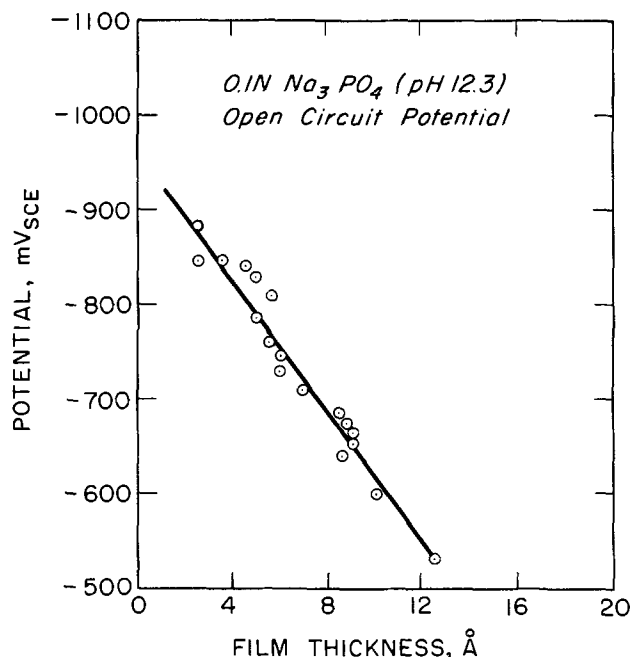


Fig. 4. Dependence of the open circuit potential on thickness of the oxide film formed in 0.1N Na<sub>3</sub>PO<sub>4</sub> solution.

different results from those at applied anodic potentials were obtained. Figures 5-8 show as an example the results of an experiment where optical and electrochemical parameters were determined for films grown under open circuit conditions at pH 9.1. In this experiment the initial solution was deaerated and the specimen had been cleaned by cathodic reduction. After the experiment started, the solution was brought into contact with air.

Figure 5 shows analyzer vs. polarizer readings. These are correlated with regions of film thicknesses and different refractive indices. These measurements were continued until the readings of A and P could be made with sufficient accuracy, because reliable interpretation of ellipsometric data depends upon a reasonable amount of light transmission in the film. When the experiment was terminated, five different refractive indices had been found. Their values and the extent of the applicable thickness ranges is not consistent in detail, although the over-all behavior is generally similar.

If these experiments had been continued, additional layers of similar refractive indices would probably be formed.

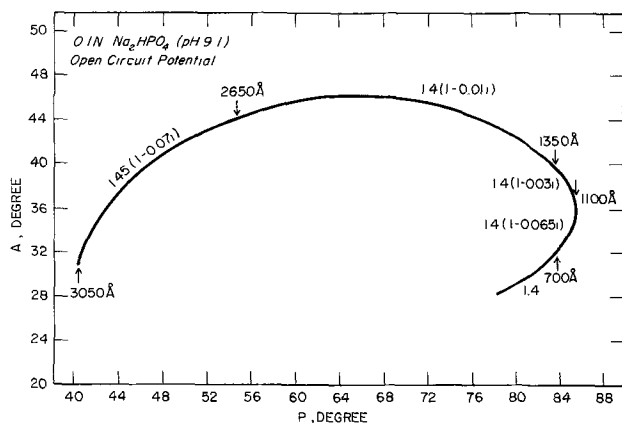


Fig. 5. Values of P and A for a film formed at corrosion potential in 0.1N Na<sub>2</sub>HPO<sub>4</sub> solution. Thickness corresponds to limits where specific optical constants were observed.

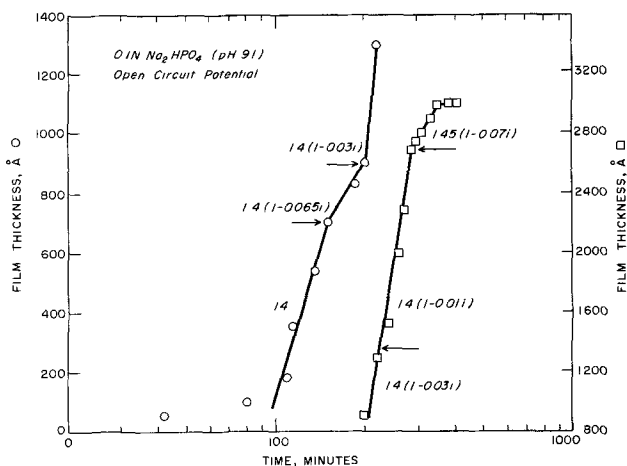


Fig. 6. Film thickness vs. time for the film whose optical parameters are given in Fig. 5.

Figure 6 shows film thickness vs. time. As can be seen, the maximum film thicknesses are very large compared to those in Fig. 2 for films found at pH 12.3. The changes in the slopes of film thickness vs. log time correspond generally to changes in the refractive index, and there is no progressive trend in the rates, i.e., they do not progressively increase or decrease in any clear order. The reasons for this behavior are not clear. However, some lack of reproducibility for the first film formed would be expected in view of the uncertainties in surface preparation and because the surface was maintained initially at cathodic potentials. Also hydrogen effusion for the cathodic potential could disturb the initially formed film. The early stage of film growth is slow, since the surface is at a relatively low potential and the rate of production of iron ions is low. When the potential begins to rise, the rate of formation of iron ions increases, and it is then possible to produce sufficient material to form the rapidly growing film. It is difficult to assign a specific growth law to this early stage of film growth.

Growth rates for the films of Fig. 6 are tabulated in Table I along with other data from the other experiments. These rates are three orders of magnitude greater than the rates in pH 12.3 or at anodic polarization at pH 9.1.

The open-circuit potential increases in the noble direction with time at pH 9.1 as shown in Fig. 7. The figure exhibits an intermediate range where the potential changes very little; this corresponds to the highest imaginary value of K. The highest values of absorption coefficients are connected with high semiconductive properties of the films (10); thus, a relatively negligible change in potential in this region seems to correlate well with a relatively higher electronic conductivity.

The relationship between film thickness and potential is shown in Fig. 8. The initial rate of change of potential is 0.031 mV/Å. This increases at -670 mV to a rate of 0.23 mV/Å. This potential of -670 mV<sub>SCE</sub> (-430 mV<sub>H</sub>) is substantially noble to the potentials for the formation of Fe<sub>2</sub>O<sub>3</sub>.<sup>3</sup> Despite the fact that the iron oxide forms, no change was observed in the refractive index. Since the film of Fig. 8 was so thick before the iron oxide formed it was difficult to see any influence of the new iron oxide on the refractive index. Therefore it was decided to grow a thinner initial film prior to forming the iron oxide. This was accomplished by growing films at controlled potentials. A potential -720 mV<sub>SCE</sub> was selected as the initial polarizing potential. This was in a range where the optical constant was clearly not that of an iron oxide, and was clearly low enough so that the iron oxide

<sup>3</sup> Equilibrium potentials for Fe/Fe<sub>2</sub>O<sub>3</sub> are -785, -590, and -472 mV<sub>H</sub> for pH's of 12.3, 9.1, and 7, respectively (4).

Table I. Number and thickness of phosphate layers within films formed during experiments shown in Fig. 6, 10, 18, 20, and 24

Number*	Range of thickness, Å	Growth rate, Å/decade	Complex index N	Refractive index n	Absorption coefficient k
Film formed at open circuit potential in 0.1N Na <sub>2</sub> HPO <sub>4</sub> of pH 9.1 with free access of air (Fig. 5)					
1	0-100†			1.4	
2	100-700	3400	1.4	1.4	
3	700-1100	1250	1.4(1-0.065i)	1.4	0.09
4	1100-1350	7800	1.4(1-0.03i)	1.4	0.049
5	1350-2850	7800	1.4(1-0.01i)	1.4	0.014
6	2850-3050	3150	1.45(1-0.07i)	1.45	0.10
Film formed at -680 mV in deaerated 0.1N Na <sub>2</sub> HPO <sub>4</sub> + NaH <sub>2</sub> PO <sub>4</sub> solution of pH 7 (Fig. 20)					
1	0-100†		1.35(1-0.001i)	1.35	0.013
2	100-400	740	1.35(1-0.001i)	1.35	0.013
3	400-600	740		1.5	
4	600-850	1800	1.4(1-0.05i)	1.4	0.07
5	850-1000	1800	1.4(1-0.1i)	1.4	0.14
6	1000-1340	4800	1.4(0.004i)	1.4	0.005
7	1340-1965	(8 A/min)	1.4(1-0.01i)	1.4	0.014
8	1965-2740		1.48(1-0.001i)	1.48	0.0015
9	2740-2915		1.52(1-0.02i)	1.52	0.03
10	2915-4115	4800		1.38	
	4115-4740		1.39(1-0.02i)	1.39	0.028
Film formed at -750 mV in deaerated 0.1N Na <sub>2</sub> HPO <sub>4</sub> + NaH <sub>2</sub> PO <sub>4</sub> solution of pH 7 (Fig. 18)					
1	0-250	(12.5 A/min)	1.36(1-0.01i)	1.36	0.013
2	250-280	(1.15 A/min)	1.34(1-0.34i)	1.34	0.45
3	280-580	(1.15 A/min)	1.34(1-0.2i)	1.34	0.27
Film formed at open circuit potential in 0.1N NaH <sub>2</sub> PO <sub>4</sub> of pH 4.5 with free access of air (Fig. 24)					
1	0-250	25 A/min	1.36(1-0.012i)	1.36	0.016
2	250-670	1.5 A/min	1.34(1-0.24i)	1.34	0.32

\* The layers within the given film are numbered starting from the metal surface.  
 † We have omitted from this table growth rate of the earliest films since the kinetics law was uncertain.

would not form. Figures 9 and 11 show that this low optical constant of  $N = 1.4$  was maintained so long as the potential of  $-720$  mV was maintained. The growth rate of these early stages is very high similar to that in Fig. 6. These experiments showed that the expected result occurred, i.e., the refractive index changed when the iron oxide was formed. The earliest growth pattern did not follow a distinct law; this is the same as the earlier results from Fig. 6. The first very steep growth curves of Fig. 10 and 12 showed rates of 2950 and 1650 Å/decade, respectively. While these are lower than that of Fig. 6, they are obtained potentiostatically. They are, nonetheless, very high. After applying the high anodic potentials, these rates were reduced to 100 and 45 Å/decade, respectively. Also, for these thinner films it was possible to see the change in the refractive index when iron oxide formed which had not been possible for the thicker films.

Films at pH 7.0.—In deaerated solution of pH 7 at corrosion potential, no conclusive results as to the

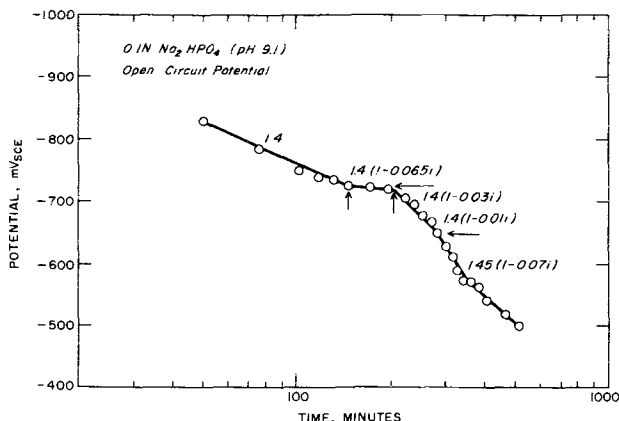


Fig. 7. Potential vs. time during growth of the same film as in Fig. 5 and 6.

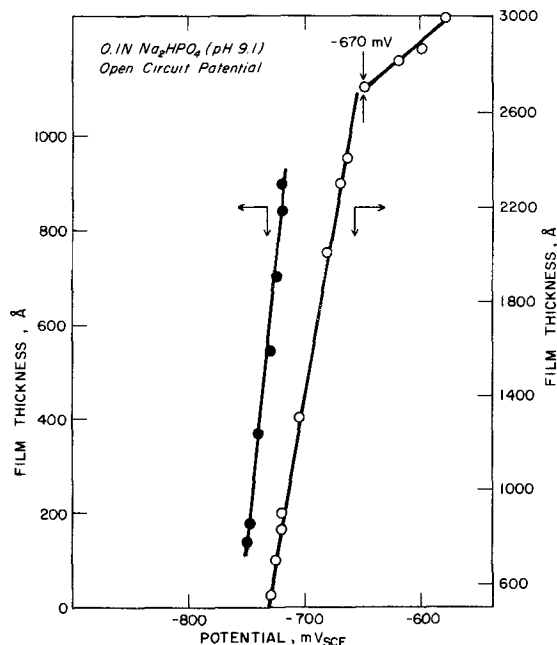


Fig. 8. Dependence of the open-circuit potential on thickness of the film produced in 0.1N Na<sub>2</sub>HPO<sub>4</sub> solution.

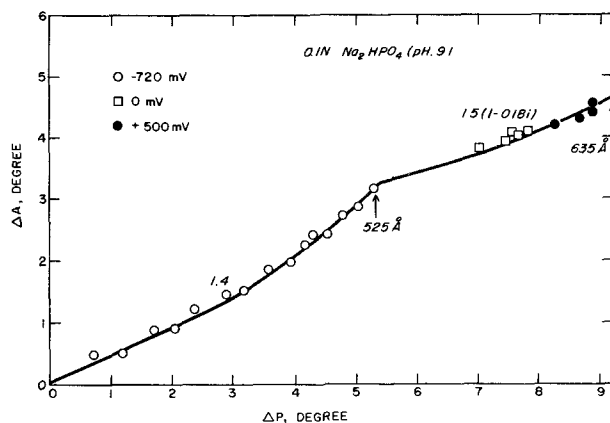


Fig. 9. Effect of anodic polarization on  $\Delta A$  vs.  $\Delta P$  relationship for a film formed in 0.1N Na<sub>2</sub>HPO<sub>4</sub> solution.

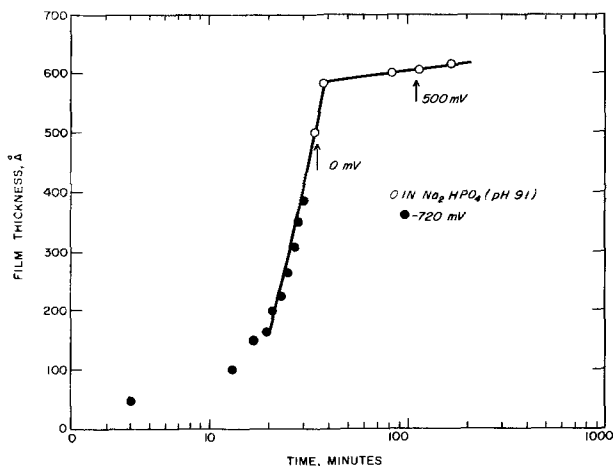


Fig. 10. Film thickness vs. time for the film whose optical parameters are given in Fig. 9.

optical parameters of the produced film have been observed. On the contrary, at potentials more positive and more negative than the corrosion potential, the re-



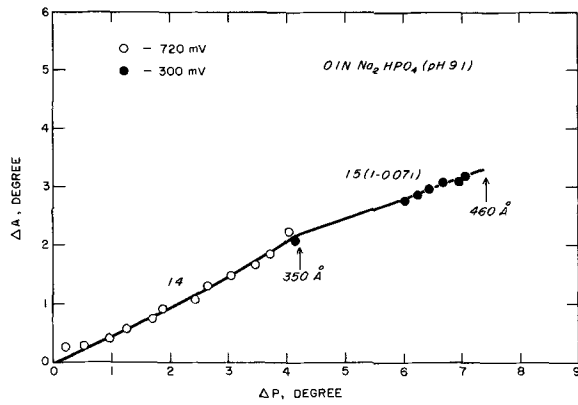


Fig. 11. Effect of anodic polarization on  $\Delta A$  vs.  $\Delta P$  relationship for a film produced in 0.1N  $\text{Na}_2\text{HPO}_4$  solution.

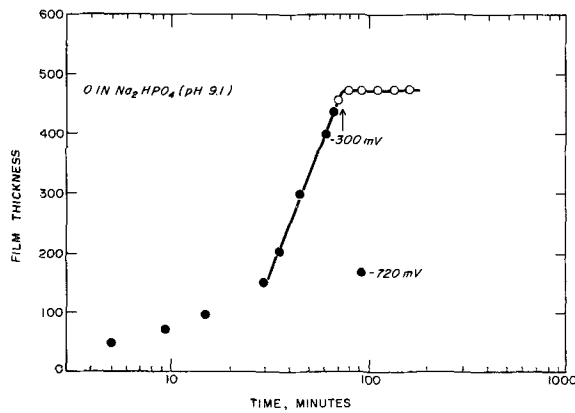


Fig. 12. Effect of time on thickness of the film whose optical parameters are given in Fig. 11.

sults are more reproducible and have shown that quite different films are produced in both cases. At pH 7 the properties of the films below ( $-750$  mV) and above ( $-680$  mV) the corrosion potential were studied. Optical parameters, film growth, kinetics, and current-time behavior were determined. Below the corrosion potential a film was formed, and it grew to a thickness of  $600\text{\AA}$  in 300 min, as shown in Fig. 13 and 14. Figure 13 shows  $\Delta A$  vs.  $\Delta P$  for the 0.1N ( $\text{NaH}_2\text{PO}_4 + \text{Na}_2\text{HPO}_4$ ) solution at  $-750$  mV; Fig. 14 shows film thickness and current vs. time for the same conditions. Two clearly different but linear growth laws were obtained. Below  $250\text{\AA}$ , the film growth rate was  $12.5$  A/min and above, it was  $1.15$  A/min. The initial film

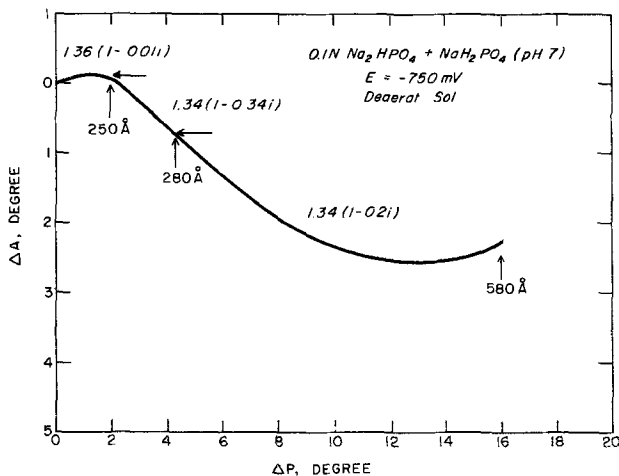


Fig. 13. Relationship of  $\Delta A$  vs.  $\Delta P$  of a film produced at  $-750$  mV in deaerated solution of pH 7.

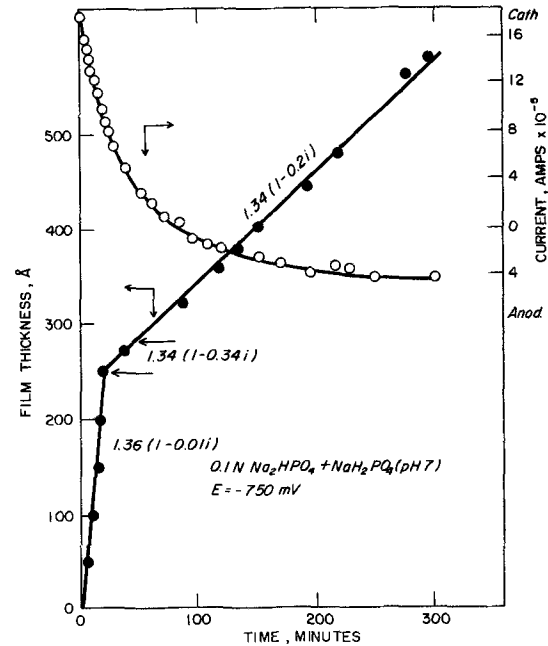


Fig. 14. Thickness and current vs. time during the growth of the film whose optical parameters are given in Fig. 13.

corresponded to a refractive index of  $1.36(1-0.01i)$ ; a transition film seems to exist from  $250$  to  $280\text{\AA}$  with a substantial increase in  $K$  and is  $1.34(1-0.34i)$ . The remainder of the film grew to  $580\text{\AA}$  with a similar refractive index.

Figures 15-18 show data taken above the corrosion potential at  $-680$  mV. These films are very complex and exhibit ten layers after 230 min. Further, the film grows to slightly more than ten times the thickness in the same exposure time, as does the film at  $-750$  mV. Figures 15 and 16 show patterns exceedingly more complex than their counterparts obtained under open-circuit conditions at pH 9.1 (Fig. 5). The changes in slopes of film growth rates in Fig. 16 are generally similar to those of Fig. 6. These growth rates are compared with those of previous experiment in Table I. A particular linear dependence between film thickness and time from  $2000$  to  $2800\text{\AA}$  was present, and it is shown in detail in Fig. 17.

The relationship between film thickness and current at  $-680$  mV is shown in Fig. 18. The behavior is complex but after reaching  $800\text{\AA}$  the current decreases and the film becomes protective. The current becomes slightly cathodic and stays very close to zero.

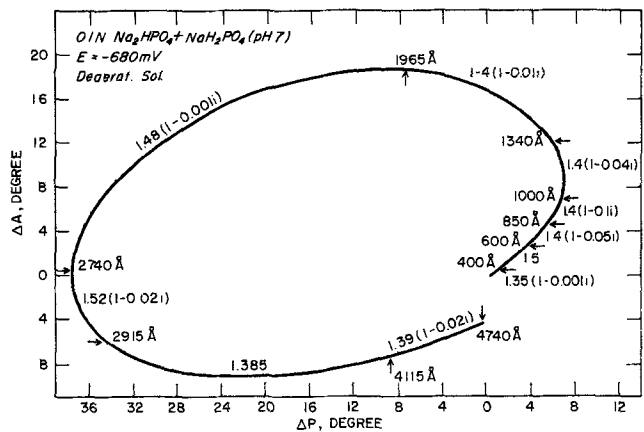


Fig. 15. Relationship of  $\Delta A$  vs.  $\Delta P$  of a film grown at  $-600$  mV in deaerated solution at pH 7.

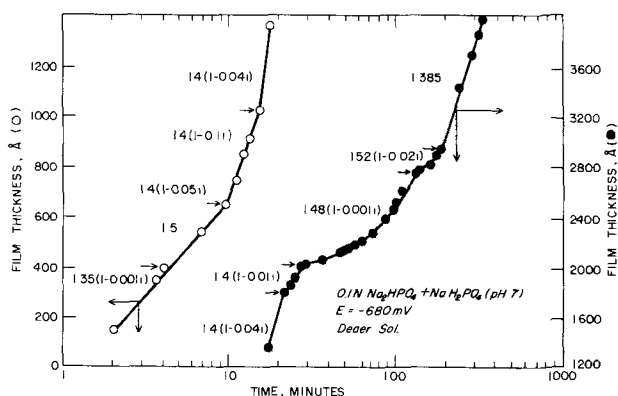


Fig. 16. Film thickness vs. time of the film whose optical parameters are given in Fig. 15.

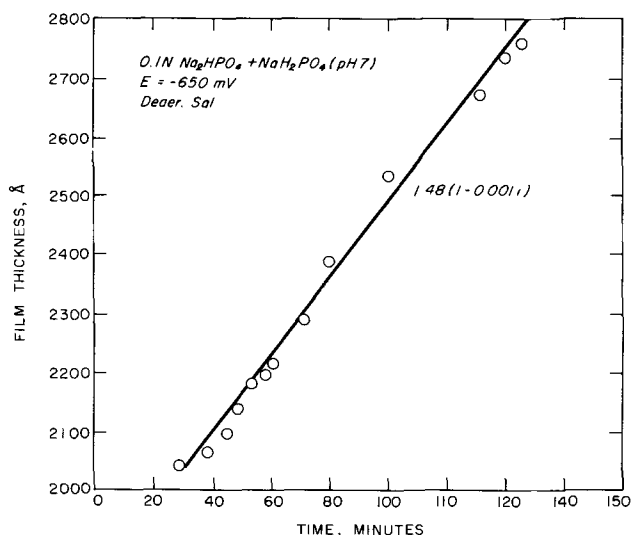


Fig. 17. Effect of time on thickness of a phosphate layer whose complex index  $1.48(1-0.001i)$  is indicated in Fig. 15 for the de-aerated solution of pH 7.

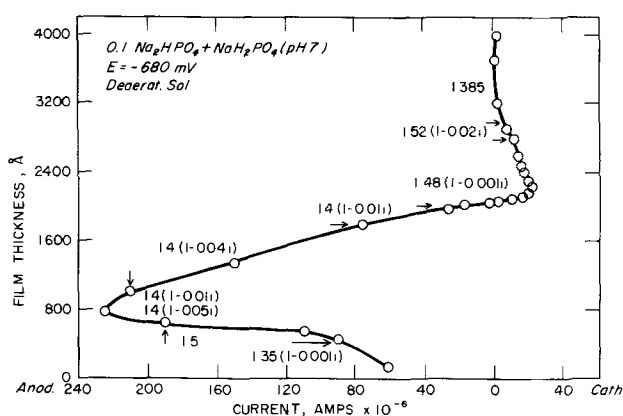


Fig. 18. Changes in current with film thickness for experiment given in Fig. 15.

**Films at pH 4.5.**—Since Fig. 1 shows that there is no passive state, the film growth was investigated only at the corrosion potential at pH 4.5 in the  $0.1N$   $NaH_2PO_4$  solution. The plots of  $\Delta A$  vs.  $\Delta P$  and film thickness vs. time in Fig. 19 and 20 at pH 4.5 are similar to Fig. 13 and 14 for the region below the corrosion potential ( $-750$  mV) at pH 7. There is a transition in the growth rates at the same value of  $250\text{Å}$ . The early film grows at a rate of  $25\text{Å}/\text{min}$  while the

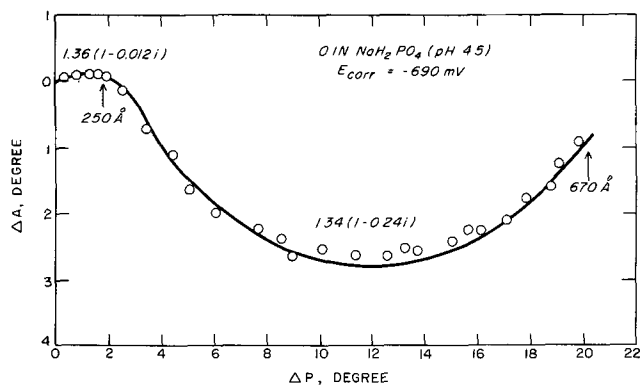


Fig. 19. Relationship of  $\Delta A$  vs.  $\Delta P$  of a film produced in de-aerated  $0.1N$   $NaH_2PO_4$  solution at open-circuit potential.

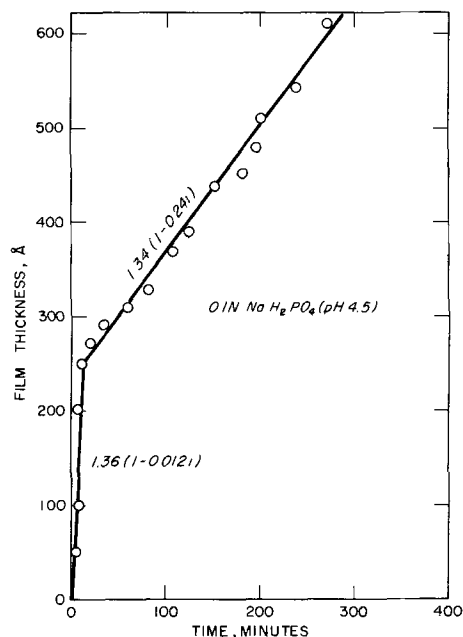


Fig. 20. Film thickness vs. time of the film whose optical parameters are given in Fig. 19.

slow rate at greater thickness is  $1.5\text{Å}/\text{min}$ . These rates are comparable to ones in Fig. 14.

**Effect of initial oxide.**—To study the effect of the surface being initially covered by an oxide film on the formation of successive deposits in aerated solutions of phosphates, measurements similar to the above were performed without initially reducing the air-formed oxide film on the iron surface. It was found that at pH 9.1 at open-circuit potential the oxide film continued to grow. At pH 7, a film was produced with refraction index equal to 1.4–1.5. At pH 4.5, a layer with  $n = 1.34$ – $1.36$  was formed.

## Discussion

**Polarization curves.**—The anodic polarization curves of Fig. 1 exhibit three important patterns. First, the polarization curve for pH 4.5 exhibits no tendency towards passivation. Secondly, the peak potentials of Fig. 1 are substantially noble to the values for the equilibrium formation of the iron oxides. This result has been observed by many authors (11). A third important feature of the polarization curves involves the comparison with film thickness as determined ellipsometrically at potentials active to the peak potential. In all cases a film of optical significance was found in a region active to the peak potential. For the experiments at pH 9.1 and 12.3 there were iron oxide films

and for pH 7 these probably were phosphate films. At potentials noble to the peak potential the protective capacity of these films increases. This pattern has also been observed by Sato and Kudo (8) for iron oxide films formed in borate buffer solutions.

In general there are four classes of films formed on iron in phosphate solutions. The existence of these regions depends upon pH and oxygen present (or potential).

While a considerably greater amount of information is required relative to effects of concentration of the phosphate ions, a broader range of pH and potential, we have identified the following important general classes of films.

**Class I films.**—Class I is the compact iron oxide film produced at pH 12.3 in both open circuit in aerated solutions and in applied anodic potential conditions at pH 9.1. These films have the same optical properties over a wide range of potentials and are so similar to iron oxide as to leave only the conclusion that the films are in fact the  $\gamma$ -Fe<sub>2</sub>O<sub>3</sub> or Fe<sub>3</sub>O<sub>4</sub>. These films are characterized by a relatively low logarithmic growth rate (5 Å/decade) and a high value of the field strength equal to 35 mV/Å.

**Class II films.**—Class II are the relatively complex multilayered films produced at pH 9.1 under open-circuit conditions in deaerated solutions below the potential of iron oxide formation and at pH 7 at -680 mV. These films grow very much thicker than those of Class I with 3000-4000 Å being obtained in less than 1000 min. The existence of the multiple layers in the Class II films are easily recognized by changes in optical properties, corresponding generally to changes in slope of the thickness-time and potential-time data. The optical constants correspond directly to the separable kinetic regions. These films have a very low field strength of 0.031 mV/Å compared to the very high value of Class I films. As shown in Table I, the refractive index varies between 1.4 and 1.52, and the absorption coefficients range from 0 to 0.14. The changes in the complex indices are not quite systematic, but a certain general tendency can be noted. Namely, the refractive indices of the first layer numbered starting from the iron surface are comparatively low; they increase with thickness, and finally, they decrease again. The absorption coefficients show a similar tendency; that for the first layer is 0 or close to it, the next layer has a considerable  $k$  value, and the coefficients of further layers are low again. The Class II films appear to produce an ultimately protective condition despite the much greater thickness than the Class I films.

**Class III films.**—These films are similar to those of Class II but differ in one important respect: the protective properties are improved due to the simultaneous formation of an iron oxide.<sup>4</sup> However, no changes in the refractive index are observed under these conditions, as shown in Fig. 5. Evidently, a small content of Fe<sub>2</sub>O<sub>3</sub> in the thick film does not affect its optical properties. On the other hand, when the film with the refractive index equal to 1.4-1.5 is not too thick, as shown in Fig. 9 and 11, the formation of a mixture of oxides and of the compound with the refractive index 1.4-1.5 involves an increase of both the  $n$  and  $k$  values.

**Class IV films.**—The Class IV films are epitomized by those found below the corrosion potential at pH 7 and at the open-circuit potential at pH 4.5. These films at these conditions are nonprotective; they have similar optical and kinetic properties. These Class IV films are characterized also by the following: (i) the growth laws are linear for the first two layers; (ii) the real parts of the refractive indices are relatively lower than for Class II films; (iii) the transitions between growth laws for the two pH's occur at approximately the same thickness; (iv) the imaginary parts of the

films are substantially lower for the first layer than the second; (v) the imaginary part of the second layer of the Class IV films is much larger than any of those in Class II and Class III. The Class IV film is sufficiently porous and nonprotective that the corrosion potential remains relatively constant.

**Optical constants.**—The consideration of optical constants is inextricably involved with the previous discussion of multiple layers and the relative protective behavior of the films. However, several specific points should be made here.

The question arises as to how far from reality are the complex indices and the number of layers calculated on the basis of ellipsometric measurements. All the  $A$  vs.  $P$  relationships were obtained experimentally, but the refractive indices were computed for different segments of the curves in such a way to fit them best to the results of measurements. In some cases, for the same segment of the curve, different optical parameters could be obtained, but the differences were small and did not essentially influence the calculated film thicknesses.

Figure 21 gives, as an example, the theoretical shape of  $A$  vs.  $P$  relationships for iron whose complex index is 3.2(1-1.24i), and on whose surface homogeneous films with different refraction indices are present. The dashed curve represents our experimental curve also shown in Fig. 5. As it may be seen, the latter does not correspond to any of the theoretical curves describing the optical parameters of films composed of only one homogeneous layer. This suggests that the real film must be composed of several layers differing in optical parameters.

The correctness of the calculated optical constants seems verified by the good agreement of any particular optical constant with specific region on the thickness-time or potential-time plots. Further, when the optical constants change, the thickness-time and potential-time slopes change also. In some cases a change in optical constants does not produce a change in thickness or potential vs. time slopes when there is a relatively small difference in successive optical constants in the same experiment. An example of no change in the thickness-time behavior with a small change in optical constants is shown in Fig. 6. A similar result for potential-time is shown in Fig. 7. Here the slope changes very little for slight changes in the optical constants.

The changes in refractive indices may be due to variations in the density and in the molecular weight of the compounds being formed (12), e.g., the water content can vary within considerable limits. The changes in absorption coefficients are presumably related to the unstoichiometric composition of the film.

It is necessary to remark here that in the case of the actively dissolving iron, the roughness of the surface should be taken into consideration since it affects the  $P$  and  $A$  values. Unfortunately, any accurate theoretical treatment of this influence is lacking. In our case

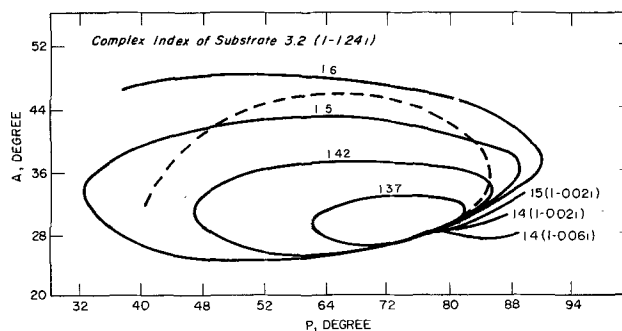


Fig. 21. Theoretical  $A$  vs.  $P$  relationships (full lines) for homogeneous films with different complex indices, and experimental curve (dashed) as in Fig. 5.

<sup>4</sup> When such a layer is formed, the shift of potential is higher than in the case of Class II films, namely 0.1-0.23 mV/Å.

an intensive corrosion occurred in  $\text{NaH}_2\text{PO}_4$  solution at pH 4.5, but no visible roughening or pitting was observed during these experiments. Nevertheless, we fully realize that some of the calculated values of the refractive indices can be inaccurate.

**Composition of films formed on iron in phosphate solutions.**—Depending upon the domain of existence of different phosphate anions and upon the presence or absence of oxygen, the films being formed on iron show various optical parameters and protective capacities. The composition and the structure of these films *in situ* is not known. All previous investigations were made after putting the specimens out from the solution, and this could change the composition of the film.

In deaerated monosodium phosphate at pH 4.5 Pryor and Cohen (3) have found by chemical analysis a product of the formula  $\text{Fe}_3(\text{PO}_4)_2 \cdot 9\text{H}_2\text{O}$ . By x-ray analysis they have identified this compound as vivianite  $\text{Fe}_3(\text{PO}_4)_2 \cdot 8\text{H}_2\text{O}$ . In the presence of air,  $\text{FePO}_4 \cdot x\text{H}_2\text{O}$  has been found, with  $x$  equal to about 30. The refractive index of vivianite is 1.58 to 1.65 (13), which is different from our value found for the film formed at corrosion potential at pH 4.5.

In aerated disodium hydrogen phosphate Mayne and Menter (1) have observed the presence of  $\text{FePO}_4 \cdot 2\text{H}_2\text{O}$  in addition to iron oxides.

In tribasic phosphate solution mainly  $\text{Fe}_3\text{O}_4$  or  $\gamma\text{-Fe}_2\text{O}_3$  is formed (1). The formation of iron oxides in this solution is confirmed by our ellipsometric studies, because the refractive index of the film formed in this solution is in the range of values found by different authors for anodic films and for  $\text{Fe}_3\text{O}_4$  or  $\gamma\text{-Fe}_2\text{O}_3$  obtained by gaseous oxidation of iron.

Under our experimental conditions, when the measurements are performed *in situ*, other compounds are probably formed in mono- and disodium phosphates. The occurrence of a sharp difference between the optical and the protective properties of films produced within the domain of relative predominance of  $\text{H}_2\text{PO}_4^-/\text{HPO}_4^{2-}$  (pH 7.2) suggests that the films produced under these conditions have different structures and chemical compositions. It is possible that below pH 7.2 the compound  $\text{Fe}(\text{H}_2\text{PO}_4)_2 \cdot x\text{H}_2\text{O}$  is formed, while above 7.2 until pH 12  $\text{FeHPO}_4 \cdot x\text{H}_2\text{O}$  is produced. Such compounds have been found to occur in the  $\text{Fe}_2\text{O}_3\text{-P}_2\text{O}_5\text{-H}_2\text{O}$  system (14). In the presence of oxygen these ferrous salts can be oxidized to ferric phosphates.

**Inhibition of iron by phosphates.**—In agreement with Pryor and Cohen's viewpoint (3), the passivation of iron in  $\text{NaH}_2\text{PO}_4$  solution (pH 4.5) does not occur. The film with refractive index from 1.34 to 1.36, composed probably of  $\text{Fe}(\text{H}_2\text{PO}_4)_2$ , is unprotective. The corrosion potential does not change during corrosion, and with time a linear growth of the film is observed. The low

refractive index of this film seems to indicate that it is not composed of a solid deposit, but rather of a super-saturated solution of iron phosphate.

The films produced in  $\text{Na}_2\text{HPO}_4$  and  $\text{Na}_3\text{PO}_4$  are protective. In deaerated  $\text{Na}_2\text{HPO}_4$  solutions at first iron undergoes corrosion connected with the formation of some kind of phosphate film with refractive index from 1.4 to 1.52. This film is probably composed of  $\text{FeHPO}_4$ . By blocking the metal surface, it shifts the potential to more positive values. The phosphate films are thick and grow according to logarithmic laws. At higher anodic potentials the iron oxide is formed together with iron phosphates improving the protective capacity of the film. Similarly, in  $\text{Na}_3\text{PO}_4$ , on a clean surface, at first a protective phosphate film (refractive index 1.4-1.5) is produced, and hereafter the iron oxide is also formed. In the last case, i.e., in the presence of iron oxide, the film grows much more slowly.

The protective capacity of phosphates is less than that of iron oxide. A direct evidence of this fact is the magnitude of the potential drop on 1Å film thickness: it is higher in the case of oxide (35 mV/Å) than in the case of phosphate (0.031 mV/Å). When a mixture of phosphate and oxide is formed, this value is equal to 0.23 mV/Å.

When an air-formed film is left on the metal surface before starting the experiment, different trends are observed, but the patterns are understandable in terms of different classes described before. Thus, when the air-formed film is present on the iron surface at pH 9.1, an iron oxide film grows at open-circuit potential, instead of the phosphate film produced on a clean surface. This is due to the fact that the potential of the primarily oxidized specimen quickly attains a value at which the iron oxide forms. However, at pH 7, iron phosphates are formed with refractive indices from 1.4 to 1.52. This means that the air-formed film is not protective at that pH value, and the relatively high corrosion rate produces a thicker film which eventually reaches a protective capacity.

Table II surveys the types of films grown in phosphate solutions at open-circuit potentials. The importance of the initial surface condition: clean or pre-oxidized, and the correlations with the refractive indices are quite obvious. Not knowing surely the chemical composition of phosphate films formed in solutions at different pH's, we can distinguish them only after their refractive indices.

Table I shows that among the classes of films the real part of the refractive index correlates well with the protective capacity of the films. A value of 2.4 corresponds to Class I, which is the most protective; values from 1.4 to 1.5 correspond to Classes II and III, which are less protective; and values from 1.34 to 1.36 correspond to Class IV, which is unprotective.

Table II. Types of films grown in phosphate solutions at open-circuit potential

Phosphate conc. 0.1N	pH	Iron surface	Solution	Suggested film composition	Protective ability	Optical parameters $n$	$k$
$\text{Na}_2\text{PO}_4$	12.3	clean	deaerated	iron phosphates*	weak	1.4 ÷ 1.52	0 ÷ 0.14
$\text{Na}_2\text{PO}_4$	12.3	clean	free access of air	iron oxide	yes	2.6	0.20
$\text{Na}_2\text{PO}_4$	12.3	with air-formed oxide film	free access of air	iron oxide	yes	2.6	0.20
$\text{Na}_2\text{HPO}_4$	9.1	clean	deaerated	iron phosphates*	weak	1.4 ÷ 1.52	0 ÷ 0.14
$\text{Na}_2\text{HPO}_4$	9.1	clean	free access of air	mixture of iron oxide and iron phosphate on a phosphate layer	yes	1.4 ÷ 1.52	0 ÷ 0.14
$\text{Na}_2\text{HPO}_4$	9.1	with air-formed oxide film	free access of air	iron oxide	yes	2.6	0.20
$\text{Na}_2\text{HPO}_4$	7.0	clean	deaerated	iron phosphates	no	1.34 ÷ 1.36	0.013 ÷ 0.4
$\text{NaH}_2\text{PO}_4$	7.0	clean	free access of air	iron phosphates	no	results inconclusive	
mixture	7.0	with air-formed film	free access of air	iron phosphates (probably with some iron oxide)	weak	1.4 ÷ 1.52	0 ÷ 0.14
$\text{NaH}_2\text{PO}_4$	4.5	clean	deaerated	iron phosphates	no	1.34 ÷ 1.36	0.013 ÷ 0.45
$\text{NaH}_2\text{PO}_4$	4.5	clean	free access of air	iron phosphates	no	1.34 ÷ 1.36	0.013 ÷ 0.45
$\text{NaH}_2\text{PO}_4$	4.5	with air-formed film	free access of air	iron phosphates	no	1.34 ÷ 1.36	0.013 ÷ 0.45

\* After reaching the potential of iron oxide formation, a protective mixture of iron oxide and iron phosphate is formed on the phosphate layer.

### Summary

1. The type of films produced on iron in 0.1N sodium orthophosphate solutions at open-circuit potentials depends upon the pH, potential, and presence of oxygen and may be considered as four separate classes.

Class I: At pH 12, i.e., in the presence of  $\text{PO}_4^{3-}$  ions, the iron oxide film is formed with a refractive index  $n = 2.6$ , and an absorption coefficient  $k = 0.20$ .

Class II: At pH values higher than 7.2, and at potentials below the potential of iron oxide formation in the presence of  $\text{HPO}_4^{2-}$  ions, phosphate films manifesting higher refractive indices, from 1.4 to 1.52, and absorption coefficients from 0 to 0.14, are produced. They exhibit some protective capacity; in the presence of these films the open-circuit potential shifts to more positive values which are greater with increasing thickness. Below the potential of iron oxide formation the shift of potential is small, namely 0.031 mV per 1Å.

Class III: These are similar to Class II films but contain iron oxide which forms simultaneously with the iron phosphates. The shift of potential at potentials higher than that of the iron oxide formation is 0.1-0.23 mV per 1Å. This indicates that the protective properties of the film composed of iron oxide and iron phosphate are much better than those of the film formed at lower potentials.

Class IV: At pH values lower than 7, i.e., in the presence of  $\text{H}_2\text{PO}_4^-$  ions in the solution, a phosphate film with a low refractive index of 1.34-1.36 and an absorption coefficient of 0.013-0.45 is formed. This film does not protect the iron against corrosion. The open-circuit potential of iron does not change during the film growth. The properties of films grown in deaerated and aerated solutions are alike.

2. The kinetics of the film growth on iron in 0.1N sodium orthophosphate solutions depend upon the type of the film being formed. In  $\text{H}_2\text{PO}_4^-$  solutions, the thickness of the film is a linear function of time, while in  $\text{HPO}_4^{2-}$  solutions it follows a logarithmic law. The thickness of iron oxide films growing in  $\text{PO}_4^{3-}$  solution also follows a logarithmic law but at a very much lower rate than in the  $\text{HPO}_4^{2-}$  solution.

3. There appears to be a correlation between the real part of the refractive index and the protective

capacity of the film. Lower values correspond to a less protective film.

### Acknowledgments

The authors acknowledge the support of The Ohio State University, the International Nickel Company, and the Office of Naval Research under contract No. N00014-A-0232-0006-NR036-085 in partial support of this research.

Manuscript submitted Nov. 21, 1973; revised manuscript received Feb. 25, 1974.

Any discussion of this paper will appear in a Discussion Section to be published in the June 1975 JOURNAL. All discussions for the June 1975 Discussion Section should be submitted by Feb. 1, 1975.

The publication costs of this article have been assisted by The Ohio State University.

### REFERENCES

1. J. E. O. Mayne and J. W. Menter, *J. Chem. Soc.*, **1954**, 103.
2. Ja. M. Kolotyrkin, Ju. A. Popov, and A. A. Vasilev, *Electrokhimia*, **9**, 1855 (1973).
3. M. J. Pryor and M. Cohen, *This Journal*, **98**, 263 (1951).
4. M. Pourbaix, "Atlas of Electrochemical Equilibria in Aqueous Solutions," Pergamon Press, New York (1966).
5. F. L. McCrackin, "A Fortran Program for Analysis of Ellipsometry Measurements," U.S. Govt. Printing Office, Washington, D.C. (1969).
6. J. Kruger and J. Calvert, *This Journal*, **114**, 43 (1967).
7. L. Ord and D. J. De Smet, *ibid.*, **113**, 1258 (1966).
8. N. Sato and K. Kudo, *Electrochim. Acta*, **16**, 447 (1971).
9. K. N. Goshwami and R. W. Staehle, *ibid.*, **16**, 1895 (1971).
10. T. Moss, "Optical Properties of Semiconductors," Academic Press, New York (1959).
11. K. J. Vetter, "Electrochemical Kinetics. Theoretical and Experimental Aspects," Academic Press, New York (1967).
12. F. Seitz, "The Modern Theory of Solids," McGraw-Hill Book Co., New York (1940).
13. "Handbook of Chemistry and Physics," 48th Edition, The Chemical Rubber Co. (1967-68).
14. S. R. Carter and N. H. Hartshorne, *J. Chem. Soc.*, **1926**, 363.

# The Anodization of Several Rare Earth Metals in Sodium Silicate Solutions

Leonard Gruss\* and Thomas Mackus

Pitman-Dunn Laboratory, Frankford Arsenal, Philadelphia, Pennsylvania 19137

## ABSTRACT

The rare earth metals, *e.g.*, Sm, Gd, Dy, Ho, Er, and Yb including Y, were anodized in a 0.1N solution of reagent grade sodium metasilicate. A current density of 0.16 A/cm<sup>2</sup> was employed in all reactions. The reaction cell was thermostated at 14.5° ± 0.5°C. Dielectric breakdown (sparking) was observed with all of the metal-electrolyte combinations investigated. The anodic spark reaction process produced coatings the components of which were derived from the anion constituent of the electrolyte. Orthosilicate coatings were produced on samarium and gadolinium metals and mixtures of orthosilicate and a distorted sesquioxide coating were produced on yttrium, dysprosium, holmium, erbium, and ytterbium metals. Powder x-ray diffraction techniques were utilized to identify the anodic spark reaction products. Diffuse reflectance spectra between 200 and 700 mμ were also obtained for the anodic spark products. The reflectance spectra confirmed the results of the x-ray diffraction study that single compounds exist in the anodic products for samarium and gadolinium metals and mixtures exist in the anodic products of yttrium, dysprosium, holmium, erbium, and ytterbium metals when these metals were anodized in sodium silicate solutions.

Numerous authors (1-10), beginning with Giuscá in 1934, synthesized various rare earth silicate compounds. The orthosilicate (1:1) and the pyrosilicate (1:2) compounds are the most common variety for rare earth silicates. The usual procedure for the preparation of polycrystalline rare earth silicates involves firing a rare earth sesquioxide with silica at temperatures in excess of 1000°C.

This investigation was undertaken to study the preparation, structure, and composition of a variety of rare earth silicates by the anodic spark reaction of rare earth metals in sodium silicate solution. It was shown previously (11, 12) that the rare earth metals are typical of those metals which form oxide barrier films at their interfaces. Greene and Lee (11) studied the electrochemical characteristics of the rare earth metals in dilute phosphoric acid solution using potentials up to 4V in the noble direction. Gruss and Mackus (12) prepared rare earth aluminates by anodic oxidation of rare earth metals in sodium aluminate solution. The anodic spark reaction process produced aluminates with perovskite structures when the base metal was samarium, europium, or gadolinium. Mixtures of perovskite and garnet structured coatings were produced with dysprosium, holmium, erbium, yttrium, and even yttrium.

## Experimental

The rare earth metals in rod form were mounted in tight-fitting Teflon sleeves. These sleeves served to mask the anode at the air-electrolyte interface and to fix the area for anodization. Prior to anodization the metals were polished with a series of silicon carbide abrasive papers down to a 3/0 emery and finally with microcut polishing paper (GRIT=600 soft) and washed with absolute ethanol. Samarium, gadolinium, yttrium, dysprosium, holmium, erbium, and ytterbium metal rods (99.9% pure) were anodized in a 0.1N solution of reagent grade sodium metasilicate. A current density of 0.16 A/cm<sup>2</sup> was employed in all reactions. The reaction cell was thermostated at 14.5° ± 0.5°C. The cell was equipped with a magnetic stirrer and a platinum cathode whose area was at least equal to the anode surface area in all experiments.

The voltages were monitored by an Electronic Measurements constant current power supply and a Hew-

lett-Packard 410c voltmeter and recorded on a Speedo-max strip chart recorder.

The analyses of the anodic spark reaction products were performed on the insoluble material which was ejected from the anode surface during the spark reaction. X-ray diffraction patterns were obtained on all samples using a Debye-Scherrer 114.59 mm camera (Norelco) and a Norelco basic x-ray diffraction unit employing nickel filtered copper K<sub>α</sub> radiation. The results of powder x-ray diffraction analysis on the anodic products are shown in Table I.

Diffuse reflectance spectra between 220 and 700 mμ were obtained for the anodic spark products using a Cary Model 14 Spectrophotometer equipped with a Model 1411 diffuse reflectance (ring collector) accessory.

## Results

The composite voltage-time curves for the anodic reactions of six rare earth metals and yttrium in sodium silicate solution are shown in Fig. 1. The curves of Sm, Gd, Y, Dy, Ho, and Er are typical of metals which form thin oxide-barrier films at their interfaces, *i.e.*, Ta and Zr. Extremely large slopes occurring within the first 15-20 sec of anodization are evident and correspond to the growth of thin transparent insulating films.

Yb, which tends to be anomalous compared to the other rare earths (*e.g.*, anomalous atomic volume, melting point, and density), also exhibited significantly different voltage-time curves. The curve for Yb is somewhat typical of valve metals except that a much longer period of time was required to achieve dielec-

Table I. The anodic spark reaction products of the rare earth metals when anodized in sodium silicate solutions

Metal	Products
Samarium	Sm <sub>2</sub> SiO <sub>5</sub>
Gadolinium	Gd <sub>2</sub> SiO <sub>5</sub>
Yttrium	Y <sub>2</sub> SiO <sub>5</sub>
	Distorted Y <sub>2</sub> O <sub>3</sub>
Dysprosium	Distorted Dy <sub>2</sub> SiO <sub>5</sub>
	Dy <sub>2</sub> O <sub>3</sub>
Holmium	Distorted Ho <sub>2</sub> SiO <sub>5</sub>
	Ho <sub>2</sub> O <sub>3</sub>
Erbium	Distorted Er <sub>2</sub> SiO <sub>5</sub>
	Er <sub>2</sub> O <sub>3</sub>
Ytterbium	Distorted Yb <sub>2</sub> SiO <sub>5</sub>
	Yb <sub>2</sub> O <sub>3</sub>

\* Electrochemical Society Active Member.

Key words: rare earth metals, rare earth silicates, anodic spark reaction, diffuse reflectance spectra.

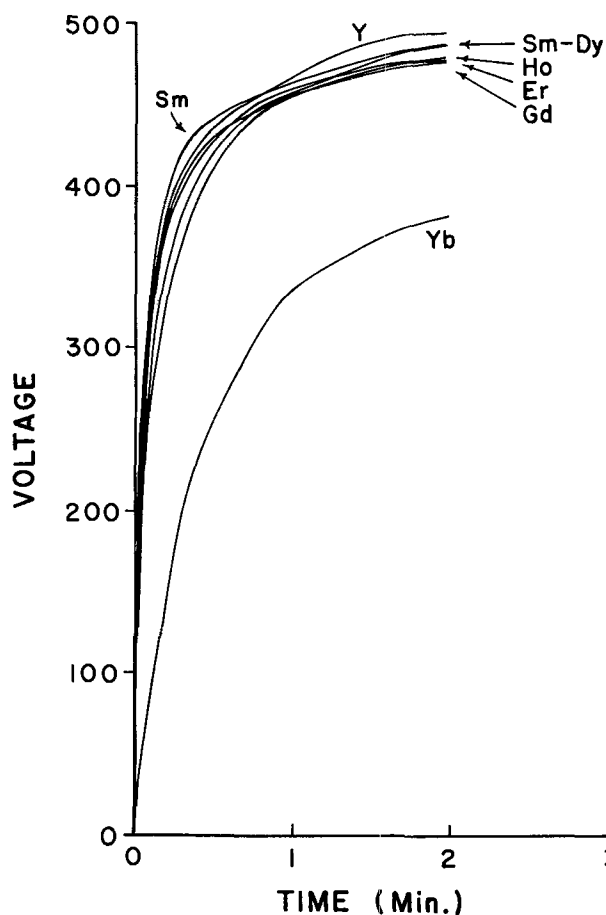


Fig. 1. The voltage-time curves for a variety of rare earth metals and yttrium anodized in  $0.1N Na_2SiO_3 \cdot 9H_2O$ .

tric breakdown. Electroluminescence was observed with all of the metal-electrolyte combinations investigated. The electroluminescence appeared over the entire anodic film at voltages below the spark potential and was present with spark discharges at 400V. The color of the electroluminescence varied from one rare earth metal to another but no color variations were noted with increases in voltage.

The appearance of sparking was noted with all of the rare earth metals including yttrium. The sparks were as described by Guntherschulze (13), *i.e.*, increasing in size and becoming less mobile as the voltage increased toward the maximum. The potentials at both initial and highly energetic sparking conditions and the final potentials are given in Table II. The final potentials were obtained from the constant current density experiments after 30 min of anodization. The voltage-time curve was found, in all cases, to be strongly correlated with both the initial and highly energetic sparking condition. Initial sparking and the first significant change in the slope occurred simultaneously. Highly energetic sparking was concurrent

Table II. Spark initiation, high energetic, and maximum anodization potentials for anodic films on rare earth metals when anodized in  $Na_2SiO_3 \cdot 9H_2O$

Metal	Initial spark potential, V	Highly energetic spark potential, V	Maximum potential, V
Samarium	299	373	535
Gadolinium	291	373	530
Yttrium	268	363	545
Dysprosium	254	348	530
Holmium	241	348	530
Erbium	241	338	540
Ytterbium	220	310	535

Table III. Color description of the anodic coatings deposited on the rare earth metals by the anodic spark process

Metal	Color
Samarium	Light brown
Gadolinium	Light tan (off-white)
Yttrium	Pale blue-green
Dysprosium	Pale yellow
Holmium	Peach
Erbium	Dark pink (magenta)
Ytterbium	Tan

with the onset of the second major change in slope.

The very strong adherent anode coatings display striking colors characteristic of the individual rare earth cations. The colors are described in Table III. These coatings were very hard and had the appearance of fired ceramics.

The anodic spark reaction process produced coatings (Table I) the components of which are derived from the anion constituent of the electrolyte. Orthosilicate coatings were produced on samarium and gadolinium metals, and mixtures of orthosilicate and a distorted sesquioxide coating were produced on yttrium, dysprosium, holmium, erbium, and ytterbium metals. It is possible that noncrystalline or silicate glass compounds may also be present, but if so they are undetected in the x-ray diffraction analysis.

Diffuse reflectance spectra in the near u.v. to visible range were obtained for the spark reaction products. The reflectance spectra for samarium, holmium, and ytterbium products are shown in Fig. 2. In these re-

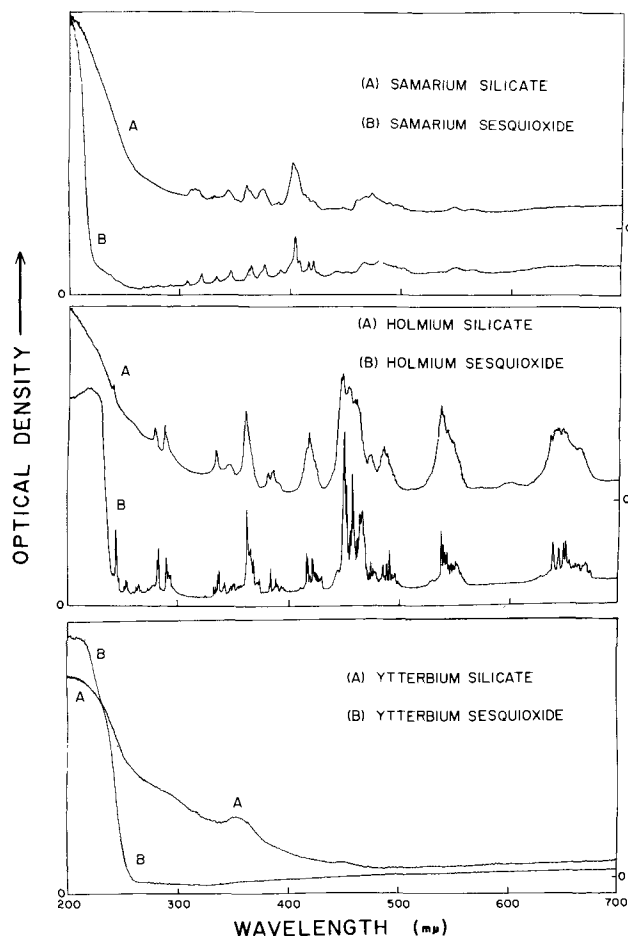
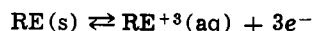


Fig. 2. Comparison of the diffuse reflectance spectra of the spark reaction products of samarium, holmium, and ytterbium metals with the reflectance spectra of the sesquioxides of these metals, respectively.

gions of the spectrum the sharp absorption peaks characteristic of the rare earth ion were observed. These peaks are intra f-f transitions of predominantly electric dipole character (14) resulting from spin-orbit interactions, and to a lesser extent, due to the extent of the crystalline field. For the samarium and gadolinium products the spectra contained slightly displaced peaks from the corresponding peaks of similar sesquioxides. In addition, in the region of strong optical absorption only a single absorption edge was observed for the orthosilicate product, indicative of a single compound. The spectra for dysprosium, holmium, and erbium products also contained slightly shifted peaks when compared to the corresponding sesquioxides. The observed spectra in the region of strong optical absorption for the orthosilicate-distorted sesquioxide products are suggestive of the existence of two absorption peaks as is found in a mechanical mixture. This datum apparently confirms the results of the x-ray diffraction study that single compounds exist in the anodic products for samarium, and that gadolinium metals and mixtures exist in the anodic products of yttrium, dysprosium, holmium, erbium, and ytterbium metals when these metals are anodized in sodium silicate solutions. In addition, many of the peak intensities of the orthosilicate and orthosilicate-distorted sesquioxide products increase and/or decrease from similar peaks found in the sesquioxides.

### Discussion

It is noted in Table II that both the initial spark potential and highly energetic spark potentials decrease with a decrease in size of the rare earth metal atom. This decrease in the spark potentials from Sm to Yb is similar to the decreasing values for the standard oxidation potentials of the rare earths described by the equation (15)



The high values of the standard oxidation potentials which are in accord with their electropositive character places yttrium metal between gadolinium and dysprosium metals. The values of both the initial and highly energetic spark potentials also place yttrium metal between gadolinium and dysprosium. This was also found when the rare earth metals were anodized in a sodium aluminate solution (12). The chemistries of the rare earths (16) in the +3 oxidation state are nearly identical although slight quantitative differences exist varying systematically from lanthanum through lutetium with yttrium being placed approximately between dysprosium and holmium.

X-ray diffraction analyses showed that the anode metal was chemically combined in the crystalline spark reaction products forming stable orthosilicate or orthosilicate-distorted sesquioxide rare earth compounds (Table I). This was true with all rare earth metals studied. The diffraction lines of the metal sesquioxide are shifted toward small d spacings or small lattice parameters. This is in agreement with Si (0.42Å, atom radius) incorporated into the rare earth oxide lattice. Emission spectroscopy studies confirmed the fact that a large amount of Si is present in the anodic products.

The crystalline orthosilicate spark products obtained from the anodic reactions of Sm, Gd, Y, Dy, Ho, Er, and Yb metals in 0.1N sodium silicate solutions are similarly produced when Sm<sub>2</sub>O<sub>3</sub>, Gd<sub>2</sub>O<sub>3</sub>, Y<sub>2</sub>O<sub>3</sub>, Dy<sub>2</sub>O<sub>3</sub>, Er<sub>2</sub>O<sub>3</sub>, and Yb<sub>2</sub>O<sub>3</sub>, respectively, and silica are carefully mixed, pressed into pellets or cylinders, and fired in an atmosphere using a program controlled furnace in excess of 1000°C (2-4, 7).

The growth mechanism which apparently accounts for the compositions of the anodic coating formed in sodium silicate solutions is similar to that reported by McNeill and Gruss (17) and by Gruss and Mackus (12) who studied anodic film growth by anion deposition in sodium aluminate solution. Gruss and

Mackus showed that the rare earth metals and yttrium form a film of oxide of the anode metal prior to the deposition of the anion constituent. The metal oxide film is apparently the anodic barrier film common to anodes such as Ta and Zr which exhibit strong tendencies to form these barrier films in most electrolytes. With silicate solutions this is followed by precipitation of the anion constituent on the anode surface possibly as H<sub>2</sub>SiO<sub>3</sub> (or SiO<sub>2</sub>) which apparently dehydrates to SiO<sub>2</sub> at elevated temperatures. It seems likely that sparking induces the reaction between the metal oxide and the anion constituent. In addition to the reactions described, there are undoubtedly other anodic phenomena occurring simultaneously at the anode, i.e., at high pH (pH of sodium silicate is 12.3) SiO<sub>4</sub><sup>-4</sup> anions exist which can combine with the rare earth cations formed at the anode surface.

If a rare earth ion such as Yb<sup>+3</sup> is added to a rare earth sesquioxide lattice, i.e., Er<sub>2</sub>O<sub>3</sub>, no interactions take place between the erbium and ytterbium cations in the solid solutions (18). The electrostatic field generated by the Yb<sup>+3</sup> ion in the erbium oxide lattice has no effect on the erbium ion. In other words, the erbium ion when in the ground state is completely independent of the ytterbium ion. However, when Si<sup>+4</sup> is added to a rare earth sesquioxide lattice the tightly bound f electron levels are no longer shielded from the changes in the electrostatic field produced by the addition of Si<sup>+4</sup> to the rare earth oxide lattice. This was observed in the diffuse reflectance spectra of the rare earth silicates where the f-f transition absorption peaks were shifted. In addition, there are variations in the transition probability as indicated by the increases and/or decreases in some of the peak intensities. Where mixtures occurred as with orthosilicate-distorted sesquioxide products, the extra peaks, already mentioned, are merely the absorption peaks of the two compounds some of which are superimposed upon each other, and others are shifted when compared to the rare earth oxide absorption peaks.

Manuscript received July 8, 1974.

Any discussion of this paper will appear in a Discussion Section to be published in the June 1975 JOURNAL. All discussions for the June 1975 Discussion Section should be submitted by Feb. 1, 1975.

The publication costs of this article have been assisted by the Department of the Army.

### REFERENCES

1. D. Giusca, *Bull. Lab. Mineral. Univ. Bucuresti*, **1**, 27 (1934).
2. N. A. Toropov, F. Ya. Galakhov, and S. F. Konvalova, *Izv. Akad. Nauk SSSR, Otd. Khim. Nauk*, 539 (1961).
3. N. A. Toropov and I. A. Bondar, *ibid.*, 544 (1961).
4. N. A. Toropov, F. Ya. Galakhov, and S. F. Konvalova, *ibid.*, 1365 (1961).
5. N. A. Toropov and I. A. Bondar, *ibid.*, 1372 (1961).
6. I. Warshaw and R. Roy, "Progress in the Science and Technology of the Rare Earths," p. 203, The Macmillan Co., New York (1964).
7. I. A. Bondar, N. A. Toropov, and L. N. Koroleva, *Inorg. Mater.*, **1**, 512 (1965).
8. L. A. Harris and C. B. Finch, *Am. Mineralogist*, **50**, 1493 (1965).
9. J. Ito and H. Johnson, *ibid.*, **53**, 1940 (1968).
10. N. A. Toropov, R. G. Grebenshchikov, and A. N. Sokolov, *Inorg. Mater.*, **5**, 266 (1968).
11. N. Greene and L. Lee, U.S. Atomic Energy Commission Report TID-18697 (1963).
12. L. Gruss and T. Mackus, *This Journal*, **120**, 337 (1973).
13. A. Guntherschulze and H. Betz, *Z. Physik.*, **7**, 196 (1932).
14. B. G. Wybourne, "Spectroscopic Properties of Rare Earths," p. 205, Interscience Publishers, Inc., New York (1965).
15. W. M. Latimer, "The Oxidation States of the Ele-



- ments and Their Potentials in Aqueous Solutions," 2nd ed., Chap. 20, Prentice-Hall, Inc., Englewood Cliffs, N. J. (1962).
16. F. A. Cotton and G. Wilkinson, "Advanced Inorganic Chemistry," p. 882, Interscience Publishers, Inc., New York (1962).
17. W. McNeill and L. Gruss, *This Journal*, **110**, 853 (1963).
18. L. Gruss and R. E. Salomon, *J. Phys. Chem.*, **74**, 3969 (1970).

## The Rate of Electroless Copper Deposition by Formaldehyde Reduction

James Dumesic, James A. Koutsky, and Thomas W. Chapman\*

Department of Chemical Engineering, University of Wisconsin, Madison, Wisconsin 53706

### ABSTRACT

*In situ* measurement of electroless plating rates of copper onto glass substrates has been achieved. The technique employs optical absorption measurements of the depositing copper film on rotating cylindrical glass substrates which are immersed in the plating solution. The substrates have been sensitized and activated by tin and silver solutions, respectively. Effects of stirring and composition of the plating solutions on the copper deposition rates are reported. It appears that the copper deposits at an anomalous initial rate which usually decreases with time to a steady final rate. The initial and final rates behave differently with respect to composition of the plating solution. Dissolved oxygen has a significant effect in retarding the initial rate of deposition. Structural characteristics of the film produced from such solutions are also reported.

The qualitative aspects of electroless deposition are well known (1). The patent literature is filled with reports on bath stabilization, control, and regeneration, plate improvement, prevention of stardusting, and metal ductility improvement (2-23). Fundamental studies, however, are relatively few, and mechanistic conclusions often seem to contradict one another. Of primary concern is understanding the deposition processes of the sensitizer (usually a  $\text{SnCl}_2$  solution), the activator species (usually a noble metal), and the growth of the electroless metal film. Sard's work on carbon substrates indicated a time-dependent deposition of small sensitizer particles (24). Fillar concluded for glass substrates that sensitization was highly dependent on the rate of particle formation which was directly related to pH and hydrodynamic conditions of the rinsing step after removal from the sensitizing bath (25). Cohen *et al.* (26) have investigated the sensitization mechanism using Mössbauer spectroscopy. Their results indicate that stannic hydroxide is found in a colloidal state. The surface of the colloid appears to contain bound stannous ions. Feldstein and co-workers found that aged solutions of stannic chloride led to a polymeric form of  $\beta$ -stannic acid and that this material improves sensitizer performance (27-30). The efficiency of the sensitization step is improved giving a greater density of sites for electroless deposition.

Activation is believed to be the reduction by the tin of a heavy metal which aids the subsequent electroless deposition. The reduction appears to be at the  $\text{SnCl}_2$  precipitate surface (24). Growth of the electrolessly deposited metal film appears also to be initiated at the particle surfaces.

The adhesion strength and uniformity of the electrolessly deposited film appears to be a complex function of surface roughness and the condition of both sensitization and activation steps. It has been reported that the bond between the substrate and the metal plate is mainly mechanical (31). This view is reflected in the rationale for such pretreatment as tumbling and blasting of the substrate or various chemical roughening techniques (3, 5, 7, 9, 23, 32-34).

This paper reports the results of a study of the rates of copper deposition on activated glass substrates. The system chosen for study was the formaldehyde reduction of copper with  $\text{SnCl}_2$  sensitization and  $\text{AgNO}_3$  activation.

### The Rate of Copper Deposition During Electroless Plating

In order to understand more clearly the nature of the deposition process, as well as to establish optimum plating conditions, one would like to have quantitative information regarding the rate of metal reduction. Specifically, it would be desirable to elucidate the mechanisms of the chemical reactions in electroless plating so that the relation of plating conditions to metal film properties might be correlated on a sound theoretical basis.

There have been several studies of the rate of electroless plating, but most of these have yielded an integral or average reaction rate (1). That is, rates are reported as the total amount of metal deposited in a finite reaction time. Furthermore, in most of these experiments no special care was taken to control the mass transfer conditions so that the surface concentrations of reactants were not known. Under these circumstances it is difficult to analyze the data in terms of molecular mechanisms or even to relate a rate to the proper solution composition.

Donahue has measured differential deposition rates by monitoring the changing resistance of a metal foil or wire as the cross section was increased by electroless deposition (35). A possible problem with this approach is that it gives the rates of deposition only on solid metal surfaces but not on a developing electroless deposit. The latter situation is of more basic interest than the former because the initial reaction on the activated substrate must be critical in determining adhesion and other film properties.

We have sought to develop an experimental method for measuring the kinetics of electroless deposition that avoids the difficulties mentioned above. In particular, we wanted a method for measuring differential electroless deposition rates on activated substrates under known mass transfer conditions.

\* Electrochemical Society Active Member.

Key words: copper, formaldehyde, electroless plating.

Morphological studies of the deposited films were also made in order to understand more fully the basic mechanisms with regard to copper deposition. Specifically, it was desired to see if the morphology of the film was related to the rate data. Also, it was desired to compare the morphology obtained qualitatively with results of other authors (2, 27-30, 36, 37).

### Experimental Method and Procedure

A simple geometry for which mass transfer rates are uniform and have been quantitatively characterized is the rotating cylinder. This system is a suitable one for studying heterogeneous processes. The rotation of the inner cylinder of a concentric pair provides efficient stirring for species transport to the cylindrical surfaces. Even for processes that are partially mass-transfer limited, the correlations developed by Eisenberg *et al.* (38) make it possible to compute the surface concentrations from the bulk concentrations if fluxes are known.

A rotating cylinder apparatus, consisting of a glass Beckman colorimeter tube (OD = 24.23 mm) inserted into an 80 mliter beaker, was assembled. The colorimeter tube was mounted on the shaft of a variable speed stirring motor (0-1600 rpm) and aligned coaxially with the beaker. A sketch of the apparatus appears in Fig. 1.

The outer surface of the colorimeter tube was sensitized and activated in the usual way. The active surface was prepared by washing the tube in concentrated nitric acid, rinsing in distilled water, rotating at 200 rpm for 10 sec in the sensitizer, rotating at 200 rpm for 60 sec in tap water, rotating at 200 rpm for 30 sec in activator, and rotating at 200 rpm for 10 sec in distilled water. The rate of withdrawal from the sensitizer was 1 in./sec. Tap water was used in the second rinse because it appears to give more uniform sensitization over the surface than is the case with distilled water or an alkaline rinse (25).

The tube was placed in the beaker containing the copper-formaldehyde plating solution so that copper deposition occurred on the activated surface. In subsequent tests it was established that an immersion in a formaldehyde solution prior to the plating solution gave some interesting results. It was found that the amount of copper deposited from the plating solution could be monitored continuously *in situ* by visible spectroscopy. Light of wavelength 630 m $\mu$  from a helium-neon gas laser was passed through the active surfaces of the inner tube to a 2 mm diameter phototransistor. The transmittance of the copper film, measured as the voltage output of the photocell, was correlated with copper deposition, in micrograms Cu/square centimeter, by dissolving the copper from various samples with nitric acid and determining the mass of copper by atomic absorption spectroscopy. The precision of the calibration was about 5% over the thickness range of interest.

Filling the inner tube with distilled water rather than air reduced the refraction of the light beam and decreased the noise to signal ratio. The illumination of the photocell could be adjusted to a suitable (linear response) range by the use of polarizing filters in the beam.

According to the established correlation between optical transmittance and copper coverage, it was possible to convert the measured photocell signals directly to plots of copper coverage *vs.* time. In this way it was possible to monitor the progress of the reaction from zero time up to a coverage of 150  $\mu\text{g Cu/cm}^2$  or about 1600 $\text{\AA}$  in thickness, at which point the film becomes too opaque to permit further measurements.

A number of experiments were done at various values of rotation speed (0-1100 rpm), copper concentration (0.003-0.03M), formaldehyde concentration (0.06-0.38M), and pH (0.0055-0.0175M OH<sup>-</sup>). The EDTA/Cu<sup>+2</sup> ratio was held constant at 1.05, and the temperature was 21°C. Oxygen was excluded from the plating bath by continuously sweeping nitrogen across the plating bath surface.

Ordinary sodium silicate glass was used in this investigation. Qualitative microscopic studies were made on glass slides whereas the rate studies used cylindrical glass tubes. Substrate surfaces were first washed in "Alconox" solution and subsequently immersed in concentrated nitric acid for 10 sec. They were then thoroughly rinsed with distilled water.

Table I indicates the solution recipes used for most of the investigation. Solutions were made with distilled water. The solutions were always freshly prepared and kept in brown glass containers. The long term instability of the AgNO<sub>3</sub> solution is well known and care must be taken in its use.

For the microscopic studies cleaned glass slide substrates were dipped into the sensitizing solution and kept immersed for various times. They were then removed manually at an approximate rate of 1 in./sec. The surfaces were rinsed by immersion in tap water and withdrawn again at nearly 1 in./sec and placed into the activation bath for various times. They were removed at the same rate, rinsed in distilled water, and immersed into the electroless copper bath for various times.

Bright field reflectance and transmission optical microscopy were used to characterize the deposits and the glass substrate surfaces. The deposits were also characterized by electron diffraction and bright field electron microscopy. In order to do this, we removed the deposits from the substrate by first evaporating a thin supporting carbon film onto the specimens at 10<sup>-4</sup> Torr. Polyacrylic acid solution was placed on the carbon film and after drying, the hardened polyacrylic acid was mechanically removed from the substrate. The copper deposits were removed by this procedure because they more readily adhered to the carbon than to the glass substrate. In the case of thicker deposits the supporting carbon film was not necessary. The

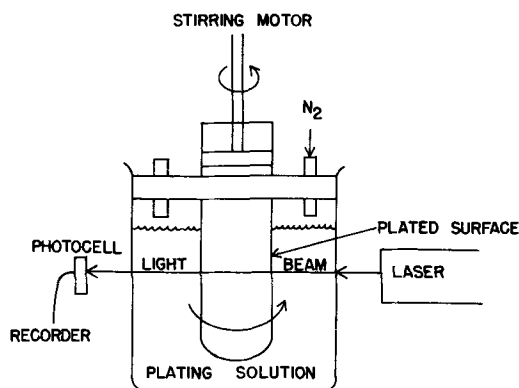


Fig. 1. Schematic diagram of apparatus

Table I. Recipes for electroless coating solutions

Sensitization solution		
SnCl <sub>2</sub> ·2H <sub>2</sub> O		10 g/liter
HCl (conc)		40 cm <sup>3</sup> /liter
Activation solution		
AgNO <sub>3</sub>		5 g/liter
NH <sub>4</sub> OH (conc)		15 cm <sup>3</sup> /liter
Standard copper plating solution		
CuSO <sub>4</sub>	0.02 moles/liter	HCHO 0.31 moles/liter
EDTA*	0.021 moles/liter	NaOH 0.005 moles/liter
Ranges of composition variation of standard plating solution used to study influence on rate of plating		
CuSO <sub>4</sub> : 0.003-0.03 moles/liter		HCHO: 0.06-0.38 moles/liter
EDTA: constant $\frac{\text{EDTA}}{\text{Cu}^{+2}}$ ratio = 1.05		
OH <sup>-</sup> : 0.0055-0.0175 moles/liter		

\* EDTA acid form.

polyacrylic acid was readily dissolved by water, and by flotation the specimen film was picked up on electron microscope grids.

**Experimental Results**

Some typical experimental results of the rate studies are presented in Fig. 2, 3, and 4. Precision of data is well within 10% in measurement of copper coverage. Figure 2 shows the growth of the copper film with time in a standard plating bath at various stirring speeds. Figure 3 gives the growth curves with good stirring at two different copper levels. Figure 4 shows the effect of formaldehyde concentration on film growth. Note that  $10 \mu\text{g Cu/cm}^2$  corresponds to an average copper film

thickness of  $112\text{\AA}$ , based on a solid film with the bulk density of metallic copper.

Perhaps the most striking feature of the film growth curves is the apparent existence of two distinct growth regions. At surface coverages above  $30 \mu\text{g Cu/cm}^2$  one finds a constant rate of film growth, which we refer to as the final rate. At short times, or at coverages less than  $25 \mu\text{g Cu/cm}^2$ , the rate of copper deposition is generally different from the steady final rate. In most cases it appears that the deposition rate is approximately constant at coverages from zero to about  $25 \mu\text{g Cu/cm}^2$  and that this initial rate is usually larger than the subsequent final rate. At coverages around  $25 \mu\text{g Cu/cm}^2$  there is a distinct break in the film growth curves where the deposition rate changes abruptly from the initial rate to the final rate. In cases where the initial rate is considerably higher than the final rate, there is actually an arrest in the growth curve at the transition point (point A in Fig. 3).

In order to represent the results in a relatively concise form, we have calculated the slopes of the two portions of the growth curves to report initial and final rates in micrograms Cu/square centimeter-minute for each experimental condition. The initial rates are presented in Fig. 5, 6, and 7 as functions of copper, formaldehyde, and hydroxide concentrations, respectively. Final rates are given as functions of the same variables in Fig. 8, 9, and 10.

*Effect of stirring.*—The primary reason for choosing the rotating cylinder geometry for these experiments was to make possible the estimation of mass transfer rates and surface concentrations. This arrangement not

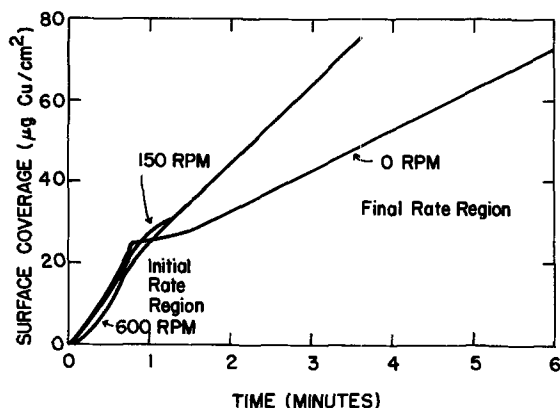


Fig. 2. Surface coverage as a function of time at three different stirring speeds. Bath composition was  $0.186\text{M HCHO}$ ,  $0.02\text{M CuSO}_4$ ,  $(\text{NaOH}) = 0.005\text{M}$ .

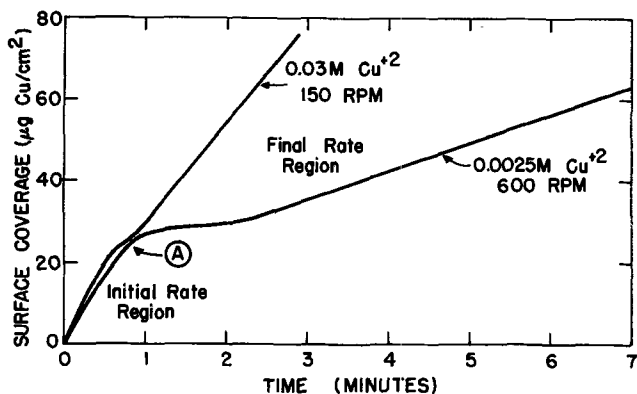


Fig. 3. Surface coverage as a function of time at two different copper levels.  $(\text{HCHO}) = 0.186\text{M}$ ;  $(\text{NaOH}) = 0.005\text{M}$ .

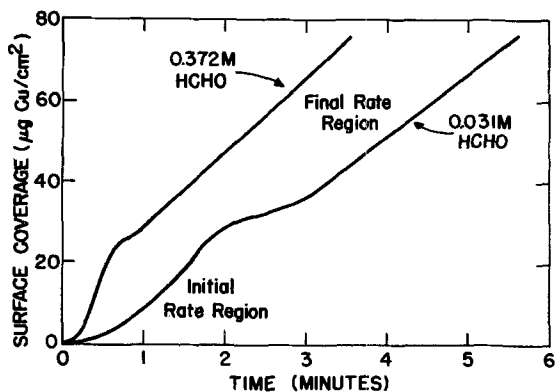


Fig. 4. Surface coverage as a function of time at two different formaldehyde levels at 600 rpm.  $(\text{CuSO}_4) = 0.02\text{M}$ ;  $(\text{NaOH}) = 0.005\text{M}$ .

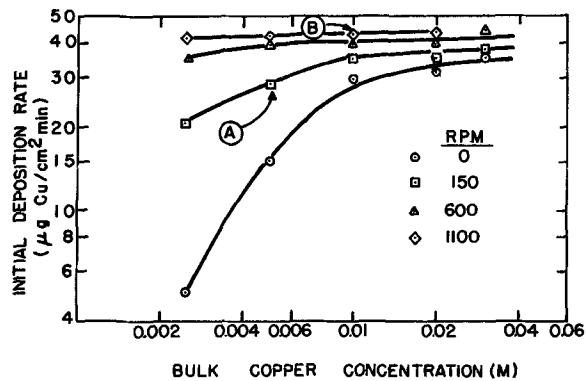


Fig. 5. Initial deposition rate as a function of copper concentration at various stirring speeds.  $(\text{HCHO}) = 0.186\text{M}$ ;  $(\text{NaOH}) = 0.005\text{M}$ .

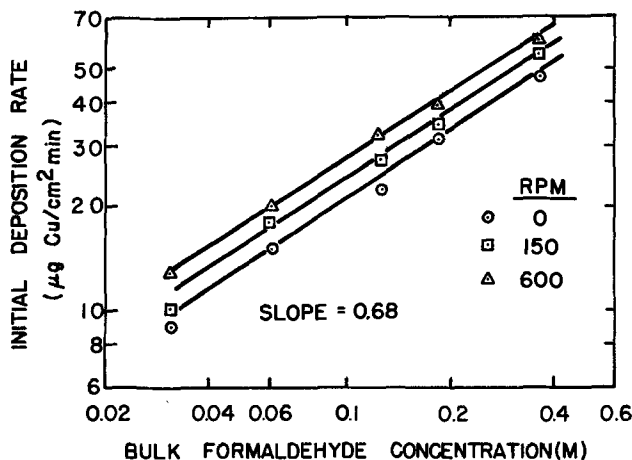


Fig. 6. Initial deposition rate as a function of formaldehyde concentration at various stirring speeds.  $(\text{CuSO}_4) = 0.02\text{M}$ ;  $(\text{NaOH}) = 0.005\text{M}$ .

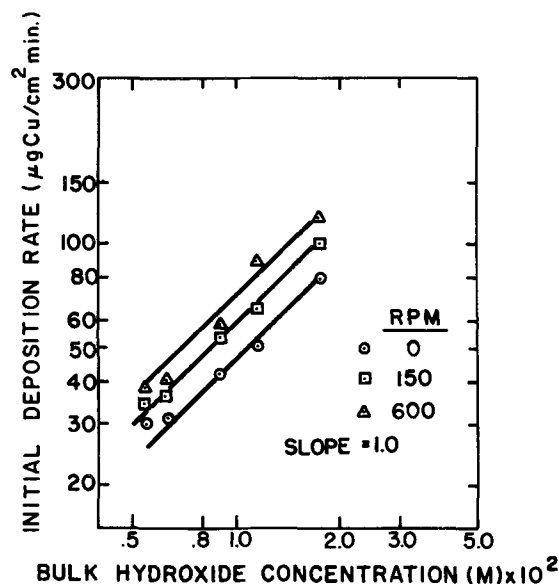


Fig. 7. Initial deposition rate as a function of hydroxide concentration at various stirring speeds. ( $\text{CuSO}_4$ ) = 0.02M; (HCHO) = 0.186M.

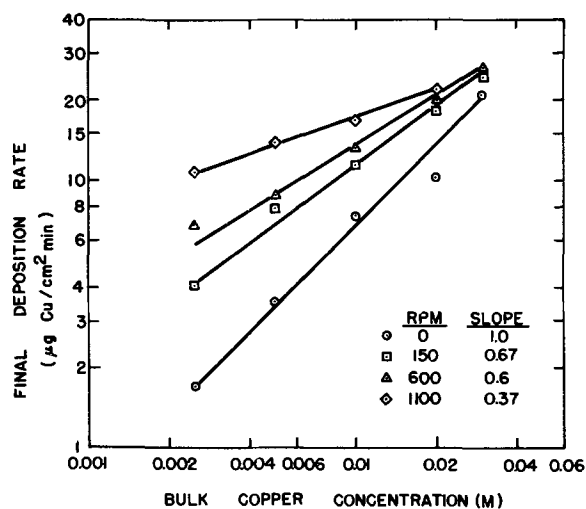


Fig. 8. Final deposition rate as a function of copper concentration at various stirring speeds. (HCHO) = 0.186M; (NaOH) = 0.005M.

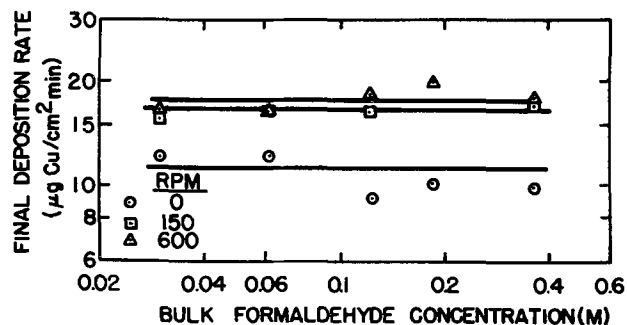


Fig. 9. Final deposition rate as a function of formaldehyde concentration at various stirring speeds. ( $\text{CuSO}_4$ ) = 0.02M; (NaOH) = 0.005M.

only provides uniform stirring but also lends itself to quantitative investigation according to the correlation of Eisenberg *et al.* (38). The mass transfer correlation may be expressed as

$$\text{Nu} = 0.0791 \text{Re}^{0.7} \text{Sc}^{0.356} \quad [1]$$

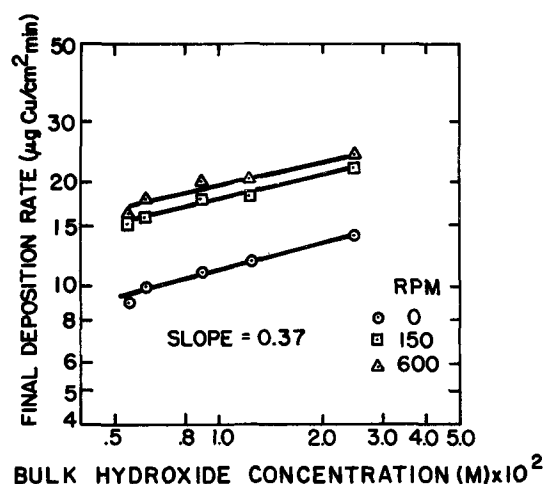


Fig. 10. Final deposition rate as a function of hydroxide concentration at various stirring speeds. ( $\text{CuSO}_4$ ) = 0.02M; (HCHO) = 0.186M.

where

$$\text{Nu} \equiv \frac{k_c d}{D}$$

$$\text{Re} \equiv \frac{d^2 \Omega}{\nu}$$

$$\text{Sc} \equiv \nu / D$$

An estimate of the mass transfer coefficient  $k_c$  from Eq. [1] allows computation of the surface concentrations of reactants according to

$$\Delta c_i = N_i / k_c \quad [2]$$

where  $\Delta c_i$  is the difference between the bulk and surface concentrations and  $N_i$  is the flux of species  $i$  at the surface. Assuming  $(\text{Sc})_{\text{Cu}^{+2}} = 3000$ ,  $D_{\text{Cu}^{+2}} = 3 \times 10^{-6} \text{ cm}^2/\text{sec}$ , and  $\nu = 10^{-2} \text{ cm}^2/\text{sec}$ , we can estimate the copper concentration difference as a function of deposition rate and stirring speed.<sup>1</sup> The results are given in Table II where  $\Delta c_i$  for copper,  $\Delta c_{\text{Cu}^{+2}}$ , is given for various deposition rates and stirring speeds. These calculations indicate that mass transfer limitations should be significant only at high deposition rates, low stirring speeds, and low copper concentrations. According to Fig. 5 and 8, this effect was important at copper concentrations below 0.03M  $\text{Cu}^{+2}$  if the stirring rate was less than 1100 rpm for the high initial rates and below 0.02M  $\text{Cu}^{+2}$  at less than 600 rpm for the final rate.

For example, for the experimental point A in Fig. 5 where the observed deposition rate was  $28 \mu\text{g Cu}/\text{cm}^2\text{-min}$ , Table II indicates that the surface concentration of  $\text{Cu}^{+2}$  was about  $3 \times 10^{-3}$  moles/liter rather than the bulk value of  $5 \times 10^{-3}$  moles/liter. On the other hand, at point B, where the observed rate was  $42 \mu\text{g Cu}/\text{cm}^2\text{-min}$ , Table II indicates that the surface concen-

<sup>1</sup> The Reynolds numbers attained in this study ( $10^3$  at 150 rpm) were somewhat higher than those covered in Eisenberg's experiments. Equation [1] probably gives a conservative estimate of  $k_c$  at these higher Reynolds numbers.

Table II. Effect of stirring speed on copper concentration differences between bulk and surface values

Deposition rate ( $\mu\text{g Cu}/\text{cm}^2\text{-min}$ )	$\Delta c_{\text{Cu}^{+2}}$ (moles/liter)		
	$\Omega = 150 \text{ rpm}$ ( $k_c = 4 \times 10^{-3} \text{ cm/sec}$ )	$\Omega = 600 \text{ rpm}$ ( $k_c = 1 \times 10^{-2} \text{ cm/sec}$ )	$\Omega = 1100 \text{ rpm}$ ( $k_c = 1.6 \cdot 10^{-2} \text{ cm/sec}$ )
5	$0.3 \times 10^{-3}$	$0.1 \times 10^{-3}$	$0.08 \times 10^{-3}$
10	$0.6 \times 10^{-3}$	$0.3 \times 10^{-3}$	$0.2 \times 10^{-3}$
20	$1.3 \times 10^{-3}$	$0.5 \times 10^{-3}$	$0.3 \times 10^{-3}$
30	$2.0 \times 10^{-3}$	$0.8 \times 10^{-3}$	$0.5 \times 10^{-3}$
40	$2.6 \times 10^{-3}$	$1.0 \times 10^{-3}$	$0.7 \times 10^{-3}$
100	$6.6 \times 10^{-3}$	$2.6 \times 10^{-3}$	$1.6 \times 10^{-3}$

tration of  $\text{Cu}^{+2}$  was about  $9 \times 10^{-3}$  moles/liter, which was relatively much closer to the bulk value of  $10^{-2}$  moles/liter. Therefore, under conditions of point A, the observed rate was probably controlled at least partly by mass transfer rather than entirely by reaction kinetics; at point B the transport effects are less important.

Similar calculations could be made for formaldehyde and hydroxide. These species, however, should not be mass-transfer limited in the range of concentrations studied because of the large excess of formaldehyde and the high mobility of hydroxide.

**Effect of copper concentration.**—Aside from the mass transfer limitations observed at low copper concentrations and slow stirring, the initial rate of deposition (Fig. 5) appears to be independent of copper concentration. On the other hand, the final rate (Fig. 8) is dependent on copper level. There is no clear asymptotic behavior with respect to stirring in Fig. 8, but at 1100 rpm the order with respect to copper appears to be 0.37.

**Effect of formaldehyde concentration.**—In all experiments a large excess of formaldehyde was present. It is interesting to observe from Fig. 6 that the initial rate is first order in formaldehyde with very high rates being attainable. On the other hand the final rates shown in Fig. 9 are nearly independent of formaldehyde level.

**Effect of hydroxide concentration.**—As with the formaldehyde the hydroxide has a strong effect on the initial rate, the order of the reaction appearing to be unity (see Fig. 7). According to Fig. 10, the pH has less of an effect on the final rate since the order with respect to  $(\text{OH}^-)$  is 0.37.

#### Qualitative Observations Related to Deposition Rates

In addition to the quantitative rate measurements described above there were a number of interesting qualitative observations made in the course of this study that may be of some help in elucidating the mechanism of this complex process.

**Effect of dissolved oxygen.**—In early experiments no effort was made to exclude oxygen from the plating bath. It was found under these conditions that an initial induction period of negligible deposition rate was encountered after which plating proceeded at a constant rate. The length of the induction period was a function of stirring speed, ranging from 2 min with no stirring to 16 min at 600 rpm. The plating bath appeared to become more effective with repeated use, the induction period getting shorter, but bubbling of oxygen between platings led to constant induction times which depended only on stirring speed.

Subsequent tests indicated that the effect of dissolved oxygen was to form an oxide layer on the catalytic surface. Only after formaldehyde reduces the oxide layer can plating occur. For example, if plating is interrupted during the final rate period and the specimen is exposed temporarily to a water bath containing dissolved oxygen, plating can be resumed only after a finite induction period of several minutes in the plating bath. A similar treatment in the absence of oxygen yields no delay in the resumption of plating.

Further evidence for surface oxidation is obtained from optical measurements. When a freshly formed copper surface is exposed to oxygen, the optical absorbance (at  $630 \text{ m}\mu$ ) decreases slowly. Quantitative measurements by dissolution and atomic absorption analysis show that no copper is being lost from the surface. Instead, a changing surface causes decreased reflectivity. Exposure to the formaldehyde in the plating bath increases the absorbance to its original value very rapidly.

**Effect of formaldehyde pretreatment of the activated surface.**—To avoid complications from oxygen in the kinetic measurements, we excluded oxygen from the plating bath, and the activated (Ag) substrate was ex-

posed to a formaldehyde solution for 1-2 min. This latter procedure prevented a delay in the copper plating reaction, possibly reducing any silver.<sup>2</sup> This procedure led to the deposition kinetics described above. If an activated substrate which has been left in the formaldehyde solution for 5 min or more is placed in the plating solution, neither an initial rate period nor an induction time is observed. That is, the final steady deposition rate is attained over the entire range of measurement.

This phenomenon can be related to the physical appearance of the substrate. The freshly activated substrate has a brown color and when it is placed in the formaldehyde bath, it turns yellow immediately. After about 5 min in the pretreatment solution, the substrate slowly turns to a brown color again. It is only when the substrate is in the yellow state that a high initial plating rate without an induction time upon placement in the electroless copper solution is observed. When the substrate is brown in color a constant final rate is observed with or without an induction time.

**Effect of activation conditions on plating rates.**—In the rate measurements described above, standardized conditions (solution concentrations indicated in Table I) were used in the sensitization and activation steps. Variation of the tin concentration in the sensitizing bath or of the rinsing conditions can alter the amount of tin and hence silver on the activated surface. Tests were made with a plating bath that yielded an initial rate of 30 and a final rate of  $13 \mu\text{g Cu/cm}^2\text{-min}$  under standard conditions. When less tin and silver were placed on the substrate, an initial rate of  $17 \mu\text{g Cu/cm}^2\text{-min}$  was observed. With heavier activation an initial rate of  $54 \mu\text{g Cu/cm}^2\text{-min}$  occurred. In all cases the final rate was approximately the same.

**Observations at the point of rate change.**—Near the point at which the deposition rate undergoes a discontinuous change it was observed that gas evolution begins. At about the same time the copper film first becomes shiny in appearance.

The question of whether the onset of gas evolution is a determining factor in the rate change was investigated by measuring the copper film growth with the plating bath under a positive pressure of 13 psig. Pressurization prevented bubble formation, but the deposition rates were unchanged, and the rate transition was not affected. It should be mentioned, however, that fine cracks developed in the copper deposit when the bath was depressurized. This could be due to gas, probably hydrogen, being nucleated rapidly within the film as the pressure is released (39). The large stresses produced by the formation of the expanding gas could rupture the film.

**Microscopic observations.**—Electron microscopy gave interesting qualitative results reminiscent of previous investigators (24,27-30,36). The sensitization and activation steps left small particulate deposits which were distributed over the surface in varying degrees of surface density as shown in Fig. 11.

It appears that the colloidal tin particles which were initially on the substrates became enveloped with silver deposits. It appeared that prolonged immersion in the sensitizing solution had little effect on the resulting density of particles after activation. Also varying times of immersion in the activation solution from 10 sec to 5 min did not affect the density and size of particles. It is interesting to note that a large fraction of even the smallest particles are bridged in some manner (see arrows in Fig. 11), which is similar behavior to that observed in vacuum deposited metals during the initial nucleation and growth steps (40,41).

Subsequent electroless deposition of copper to a coverage of about  $80 \mu\text{g/cm}^2$  produced a rather open network structure (Fig. 12). A diffraction study (Fig. 13) of the copper deposit reveals random orientation which was also reported by Sard (24). Note the bridged

<sup>2</sup> There was not sufficient HCHO carried over to cause any significant copper reduction.

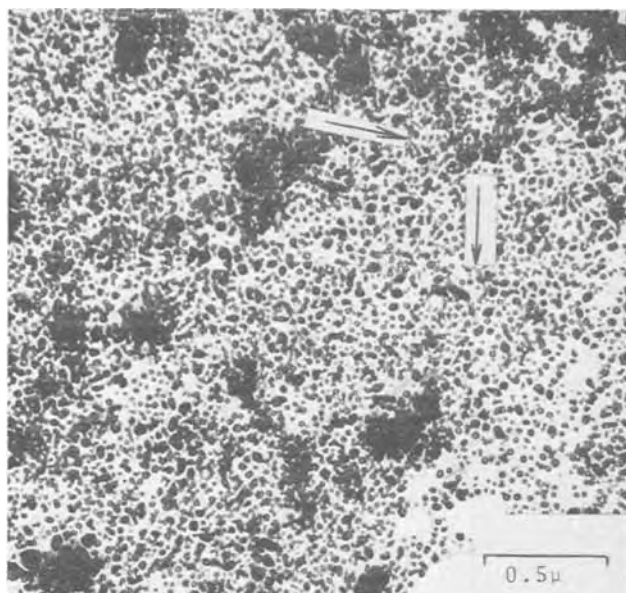


Fig. 11. Electron micrograph of a detachment replica of a silver-tin activated surface. Silver-tin particles are characteristically bridged (see arrows). Particle density corresponds to about  $10^{11}/\text{cm}^2$ . Magnification bar is  $0.5\mu$ .

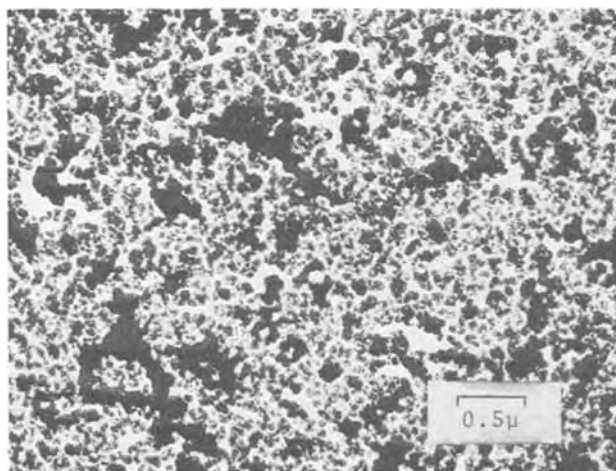


Fig. 12. A copper film coverage corresponding to  $80\ \mu\text{g}\ \text{Cu}/\text{cm}^2$ . Note film is highly porous at this stage. The copper forms an interconnecting network of crystals. Magnification bar is  $0.5\mu$ .

structures which exist in the thicker copper film with no indication of specific crystallographic branching. The growth of the film appears to be a three-dimensional type with impingement of crystals forming bridges.

The copper film appears to grow in a random fashion with no epitaxial or texture orientation indicating that the growth is not as specific as for metal deposition from the vapor onto solid substrates or for certain metals, notably nickel and cobalt, which are deposited electrolessly from solution in a textured fashion (36, 37, 42). It appears that the initial and final growth rates of copper cannot be explained in terms of a textured growth which predominates in the final rate step. Note the high degree of porosity which indicates that calculation of thickness from mass based on a solid film would give values considerably lower than actual values.

#### Discussion

From this work it appears that a constant deposition rate occurs only after a contiguous film of copper has been formed. Initially a different mechanism may operate which manifests itself as differences in both rate

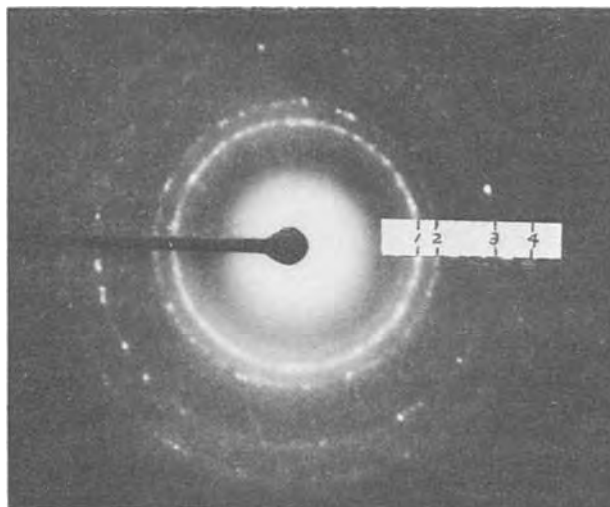


Fig. 13. A diffraction pattern of the copper film shown in Fig. 12. Pattern is of polycrystalline copper with the strong (111) and (200) reflections (lines 1 and 2, respectively) and the moderately strong (220) and (311) reflections (lines 3 and 4, respectively). Note that there is no preferential orientation.

and rate dependence on solution composition. Specifically, the final rate appears to be independent of formaldehyde concentration whereas the initial rate is independent of copper concentration but depends strongly on formaldehyde concentration.

One might question whether the shape of the film growth curves is just an artifact of the optical measurements. Our direct measurements of the absorbance *vs.* coverage calibration which included points from 3 to  $70\ \mu\text{g}/\text{cm}^2$  establish a clear, unambiguous observation. It is possible that minor errors in coverage measurements could arise from structural differences related to bath compositions. Therefore an experimental calibration should be determined for any particular plating system.

Microscopic investigation led us to suspect that the observed change from the initial to the final rate could be related to coverage of the catalytic silver-tin particles by the growing copper film. From Fig. 11 it is possible to estimate the silver-tin particle surface area within an order of magnitude. There are about  $10^{11}$  particles/ $\text{cm}^2$  and the average size of a particle is about  $200\text{\AA}$ . Therefore, a total particle area of about  $1\ \text{cm}^2/\text{cm}^2$  of nominal area of substrate is estimated from the micrographs. On the basis of monolayer coverage of copper atoms on the silver-tin particles this area corresponds to about  $10^{15}$  Cu atoms/ $\text{cm}^2$  of substrate at total coverage. The value of surface coverage of  $25\ \mu\text{g}/\text{cm}^2$  corresponds to about  $10^{17}$  Cu atoms/ $\text{cm}^2$  of substrate. This calculation indicates that the change in the deposition mechanism which was observed in the rate studies occurs when a copper film of about  $10^2$  atoms in thickness has been established. This is probably the point at which the silver particles are in fact completely covered with copper and at which the surface film becomes a true copper surface. The specific chemical mechanisms which occur in the two regions are not yet clear and require further study. Paunovic's work (43) shows that the electroless reduction of copper by formaldehyde on a copper surface is a mixed potential process, which should occur at a constant rate as long as the solution composition is constant. In his study he used a plating bath containing  $0.1\text{M}\ \text{CuSO}_4$ ,  $0.05\text{M}\ \text{HCHO}$ ,  $0.175\text{M}\ \text{EDTA}$ , and  $\text{NaOH}$  to make the pH 12.5. The rate he measured, both electrochemically and directly, was  $1.8 \times 10^{-3}\ \text{A}/\text{cm}^2$  or  $33\ \mu\text{g}\ \text{Cu}/\text{min}\text{-}\text{cm}^2$ . This rate agrees well with the final rates we have observed (cf. Fig. 8). Unfortunately, Paunovic did not vary his solution composition so that more extensive comparison is not possible. It is interesting to observe from his individual electrode polarization studies that

the reduction of copper is more reversible than the oxidation of formaldehyde. The shapes of the polarization curves [Fig. 8 in Ref. (43)] may explain why the final rate is apparently independent of formaldehyde concentration. It would be interesting to see how these polarization curves do in fact depend on reagent concentrations.

Whether the initial rate of deposition results from a mixed-potential process is not clear at this time. If it does, our observations indicate that the electrocatalysis of the two half-reactions must be quite different on the silver-tin particles than on a fresh copper surface. On the other hand, a completely different chemical mechanism may be operating in this region.

The most crucial step of the electroless deposition process with respect to adhesion and probably with respect to film structure and strength as well, must be the initial growth of the metallic film when metal-substrate bonds are being formed. The unusual rate phenomena observed in this work should be studied more thoroughly to understand the basic mechanisms of reduction, deposition, and film growth. In particular, it would be desirable to make rate measurements of the type described here for other activating systems such as palladium chloride and for various substrates and reducing agents of practical interest.

For plating baths of the type we have studied, the kinetics of deposition are relatively fast. In any commercial plating process which uses these solutions and does not make special provisions for efficient stirring, however, the average deposition rate and metal coverage will probably be controlled by diffusion and mass transfer.

### Conclusions

An experimental technique has been developed for the direct measurement of electroless plating rates. The advantages of this method are that it can reveal the initial growth of the metallic film on an activated substrate and it provides uniform and well-characterized stirring.

The deposition of copper from a formaldehyde-EDTA plating solution onto a tin-silver-activated glass substrate exhibits a dramatic change in mechanism when the copper film reaches an average coverage of about  $25 \mu\text{g}/\text{cm}^2$ .

The initial rate period is independent of copper concentration but varies with formaldehyde concentration. The converse is true during the final rate. All rates depend on pH. Oxygen in the system can have a severe inhibiting effect on the deposition rate. The chemistry of this process is very complex and not yet understood very well. It seems likely, however, that the observed phenomena are caused by changes in the nature of the catalytic surface.

Microscopic observations have shown that the metallic films start from very small (200A), highly dispersed, and partially bridged silver-tin particles and grow into a fairly rough and porous, polycrystalline copper film. No texturization or oriented overgrowth of the electroless copper film was observed.

### Acknowledgments

We wish to thank the Research Committee of the Graduate School, the University of Wisconsin and the du Pont Corporation for providing summer salary support for James Dumesic in this work.

Manuscript submitted June 25, 1973; revised manuscript received Feb. 18, 1974.

Any discussion of this paper will appear in a Discussion Section to be published in the June 1975 JOURNAL. All discussions for the June 1975 Discussion Section should be submitted by Feb. 1, 1975.

### LIST OF SYMBOLS

$c_i$  concentration of species  $i$  (moles/liter)  
 $d$  outer diameter of rotating cylinder (cm)

$D$  diffusion coefficient of species in solution ( $\text{cm}^2/\text{sec}$ )  
 $k_c$  mass transfer coefficient for transport to rotating cylinder surface (cm/sec)  
 $M$  concentration (moles/liter)  
 $N_i$  molar flux of species  $i$  at the rotating surface (moles/ $\text{cm}^2\text{-sec}$ )  
 $\Omega$  angular speed of rotating cylinder ( $\text{sec}^{-1}$  or rpm)  
 $\nu$  kinematic viscosity of solution ( $\text{cm}^2/\text{sec}$ )  
 $Nu$  Nusselt number  
 $Re$  Reynolds number  
 $Sc$  Schmidt number

### REFERENCES

- W. Goldie, "Metal Coating of Plastics," Electrochemical Publications Ltd., Great Britain (1968).
- J. Berenato, Neth. Pat. Appl. 6,614,993 (April 24, 1967); U.S. Appl. (Oct. 23, 1965).
- T. Bisset and W. Goldie, Brit. Pat. 1,043,233 (Sept. 21, 1966).
- G. C. Blytas, E. S. Slott, and E. R. Bell, U.S. Pat. 3,524,754 (Aug. 18, 1970).
- K. C. Davis and G. V. Elmore, Ger. Pat. Offen. 1,911,041 (Sept. 25, 1969); U.S. Appl. (Mar. 6, 1968).
- O. B. Dutkewych, U.S. Pat. 3,745,186 (Oct. 28, 1969).
- W. M. Emons, Jr. and S. Charms, U.S. Pat. 3,425,946 (Feb. 4, 1969).
- N. Feldstein, Ger. Pat. Offen. 1,505,385 (May 14, 1969).
- P. S. Francis and L. D. McGraw, U.S. Pat. 3,466,232 (Sept. 9, 1969).
- H. Gerlach and K. Loeschner, Ger. (East) Pat. 63,251 (Aug. 5, 1968).
- T. Hirai, Japan Pat. 6,921,673 (Sept. 16, 1969).
- D. S. Kneppel, Ger. Pat. Offen. 1,916,727 (Nov. 6, 1969); U.S. Appl. (April 1, 1968).
- R. Lacal, Fr. Pat. 1,564,064 (April 18, 1969).
- C. A. Levine, U.S. Pat. 3,367,792 (Feb. 6, 1968).
- F. A. Lowenheim, "Metal Coating of Plastics," Noyes Data Corp. (1970).
- B. M. Luce, M. M. Selker, and M. P. Makowski, Ger. Pat. 1,258,699 (Jan. 11, 1968).
- Pernix Enthone, Fr. Pat. 1,560,236 (Mar. 21, 1969).
- B. W. Wilson, U.S. Pat. 3,421,922 (Jan. 14, 1969).
- B. S. Schaaper, Neth. Pat. Appl. 68 01088 (July 28, 1969).
- A. G. Schering, Fr. Pat. 1,553,375 (Jan. 10, 1969); Ger. Appl. (Feb. 3, 1967).
- F. W. Schneble, Ger. Pat. Offen. 2,005,032 (Aug. 20, 1970); U.S. Appl. (Feb. 4, 1969).
- A. Sergienko, U.S. Pat. 3,418,143 (Dec. 24, 1968).
- R. E. Sutherland, U.S. Pat. Off. 869,021 (Dec. 30, 1969).
- R. Sard, *This Journal*, **117**, 864 (1970).
- E. Fillar, "The Sensitization of Nonmetallics with Stannous Solutions," Master's Thesis, Univ. of Wisconsin (1966).
- R. L. Cohen, J. F. D'Amico, and K. W. West, *This Journal*, **118**, 2042 (1971).
- N. Feldstein, J. A. Weiner, and G. L. Schnable, *ibid.*, **119**, 1486 (1972).
- N. Feldstein and J. A. Weiner, *ibid.*, **120**, 475 (1973).
- N. Feldstein and J. A. Weiner, *Plating*, **59**, 140 (1973).
- N. Feldstein, S. L. Chow, and M. Schlesinger, *This Journal*, **120**, 875 (1973).
- K. C. Davis and G. V. Elmore, *ibid.*, **116**, 1455 (1969).
- E. B. Atkinson, P. R. Brooks, T. D. Lewis, R. R. Smith, and K. A. White, *Plastics Inst. Trans. J.*, **35** (117), 549 (1967).
- H. Ebnet and W. Klimaschewski, *Metal Finishing J.*, (London), **15** (177), 317 (1969).
- E. B. Saubestre, Technical Paper, Soc. Plastics Engrs., Connecticut Section.
- F. M. Donahue and C. V. Yu, *Electrochim. Acta*, **15**, 237 (1970).
- A. Frieze, R. Sard, and R. Weil, *This Journal*, **115**, 586 (1968).
- A. Frieze, R. Sard, and R. Weil, *ibid.*, **116**, 821 (1969).
- M. Eisenberg, C. W. Tobias, and C. R. Wilke, *ibid.*, **101**, 306 (1954).
- H. M. Ghorashi, "Copper Deposition on ABS Plastic," Master's Thesis, Department of Chemical Engineering, University of Wisconsin (1973).



40. R. F. Adamsky and R. E. LeBlanc, *Trans. Tenth Nat. Vacuum Symposium, Am. Vacuum Soc.*, 453 (1963).  
 41. G. A. Bassett and D. W. Pashley, *J. Inst. Metals*, 87,

449 (1958-1959).  
 42. P. Cavallotti and G. Salvago, *This Journal*, 116, 818 (1969).  
 43. M. Paunovic, *Plating*, 2-8 (Nov. 1968).

## Voltammetry of (E)-1-Phenyl-2-Nitro-1-Propene in N,N-Dimethylformamide Solutions

R. Allensworth and J. W. Rogers

*Department of Chemistry, Midwestern University, Wichita Falls, Texas 76308*

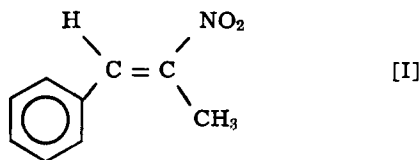
and George Ridge and Allen J. Bard\*

*Department of Chemistry, University of Texas at Austin, Austin, Texas 78704*

### ABSTRACT

The electrode reduction mechanism of (E)-phenyl-2-nitro-1-propene (PNP) in N,N-dimethylformamide (DMF) has been studied by polarographic, cyclic voltammetric, and rotating disk techniques. The compound is reduced in two polarographic steps in DMF and DMF-water solutions. Data taken at potentials of the first polarographic plateau suggest that the compound is reduced to a product via a mechanism involving coupling of the ion radicals of the precursor. The rate of the coupling reaction has been studied as a function of concentration of the PNP and water content of the solvent. Oscilloscopic recording of rapid cyclic voltammetry experiments demonstrate that the second polarographic step represents a two-electron reduction of the parent compound, PNP.

A wealth of electrochemical and electron spin resonance data demonstrate the great stability of the anion  $\pi$ -radicals of a large variety of aromatic nitro compounds in aprotic solvents such as acetonitrile, dimethylsulfoxide, and N,N-dimethylformamide (DMF) (1, 2). Nitro group elimination (3) and aromatic ring-halide elimination (4, 5) represent some decay pathways of certain species of this general type. Hoffman *et al.* (6) found that the anion radicals of various electrochemically generated tert-alkyl nitro compounds are intrinsically unstable, cleaving to nitrite ion and corresponding alkyl free radicals in glyme solvent. The small amount of data presented relative to nitroalkene  $\pi$ -radicals, intermediate to the above examples in extent of resonance stabilization, is inconclusive as to the general behavior of such species in aprotic media (7-9). As part of a systematic study into this matter, the compound 1-phenyl-2-nitro-1-propene (PNP) [I] was synthesized and its electrochemical behavior in DMF and DMF-water solutions observed. Techniques employed in the study include conventional d-c polarography, rotating disk, and cyclic voltammetry.



### Results

**Polarography.**—The compound PNP features two polarographic waves in DMF containing 0.1M tetra-N-propylammonium perchlorate (TPAP) (Fig. 1). The waves exhibit half-wave potentials ( $E_{1/2}$ ) of  $-0.99$  and  $-1.68$ V vs. saturated calomel electrode (SCE) and are diffusion controlled. Complete polarographic data are presented in Table I. The diffusion current constant ( $I_d$ ) of the more negative potential plateau in dry DMF<sup>1</sup> is much less than that for a one-electron

\* Electrochemical Society Active Member.

Key words: (E)-1-phenyl-2-nitro-1-propene, electrochemistry, dimerization.

<sup>1</sup> DMF containing less than 0.03% water.

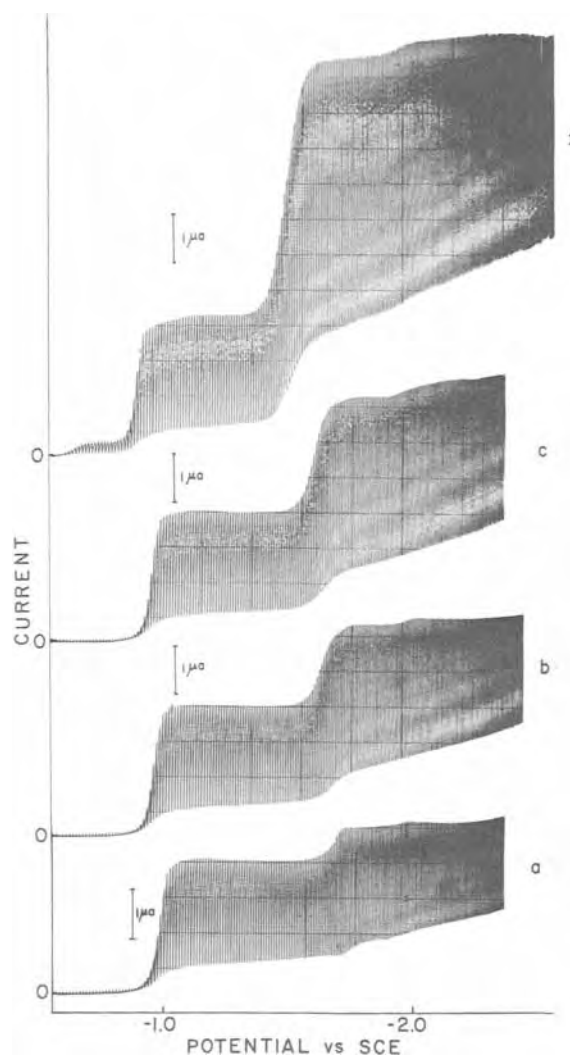


Fig. 1. Polarograms of PNP 1 mM in DMF containing (a) no water, (b) 220 mM H<sub>2</sub>O, (c) 660 mM H<sub>2</sub>O, (d) 6600 mM H<sub>2</sub>O.



Table I. Polarographic data for (E)-1-phenyl-2-nitro-1-propene in DMF, DMF-H<sub>2</sub>O, and DMF-HQ mixtures<sup>a</sup>

H <sub>2</sub> O <sup>b</sup> (mM)	First wave		Second wave	
	-E <sub>1/2</sub> (V)	I <sub>d</sub> (μAmM <sup>-1</sup> sec <sup>-1/2</sup> ) <sup>c</sup>	-E <sub>1/2</sub> (V)	I <sub>d</sub> (μAmM <sup>-1</sup> sec <sup>-1/2</sup> ) <sup>c</sup>
0	0.99	1.82	1.68	0.59
220	0.95	1.82	1.65	1.52
440	0.95	1.82	1.61	1.95
660	0.94	1.82	1.61	2.15
1,100	0.93	1.82	1.56	3.08
2,200	0.89	1.82	1.50	4.71
6,600	0.87	1.82	1.47	5.51
11,000	0.86	1.82	1.37	5.37
HQ (mM)				
0.0	0.99	1.82	1.68	0.59
1.82	0.99	1.82	1.43	2.52
9.10	0.98	1.83	1.35	4.22
18.20	0.97	1.81	1.29	4.81
36.40	0.97	1.81	1.25	4.81
145.60	0.92	1.81	1.24	4.81

<sup>a</sup> All solutions were 1 mM in PNP and 0.1M in TPAP supporting electrolyte.

<sup>b</sup> Concentration computed based on water added to solvent.

<sup>c</sup> All diffusion currents measured at a mercury head height of 60 cm. The electrode characteristics measured at 60 cm mercury head and at open circuit were  $m = 2.41$  mg/sec and  $t = 3.1$  sec.

transfer process involving materials of comparable diffusion coefficients. Addition of the proton donors water and hydroquinone (HQ) to the test solution had no effect on the diffusion current or shape of the first plateau (Fig. 1). The  $E_{1/2}$  of the wave is, however, shifted towards less negative potentials by large ratios of proton donor to electroactive compound. The characteristics of the second polarographic wave proved to be sensitive to added proton donors (Table I, Fig. 1). The diffusion current is increased to a limiting value, a factor of ten greater than that of the wave in pure solvent, upon addition of large quantities of water or HQ. This change is accompanied by a significant positive shift in the  $E_{1/2}$  of the wave (Table I). Consistent with previously published data, HQ proved to be much more effective than water as a donor in DMF (10). Similar polarographic behavior is reported by Baizer and co-workers for several 1,2-diacetylated olefins (11, 12).

**Cyclic voltammetry.**—Typical cyclic voltammograms of PNP recorded at a planar platinum disk electrode (ppde) at varying concentrations in DMF are shown in Fig. 2. Data for voltammetric studies at concentrations of 0.1 and 1 mM PNP are presented in Table II.

Voltage excursion and reversal 120 mV cathodic of the first plateau revealed cyclic voltammetric waves with very little anodic current in solutions containing 1 and 10 mM PNP in dry DMF (Fig. 2). The potential sweep rate ( $v$ ) ranged to a maximum of 12.48 V/min in experiments conducted on 1 mM solutions (Fig. 2). In a series of experiments conducted at 1 mM PNP the cathodic peak potential [( $E_p$ )<sub>c</sub>] shows negative shifts of 30 mV per tenfold increase in  $v$ . This cathodic shift is accompanied by a 9% decrease in the current function, ( $ip$ )<sub>c</sub>/ $v^{1/2}$  (Table II).

Similar voltammetric experiments in solutions containing 0.1 mM PNP in dry DMF produced cyclic waves possessing significant anodic currents (Fig. 2). The ( $E_p$ )<sub>c</sub> and current function of the recorded voltammograms were essentially constant with respect to a varying potential sweep rate (Table II). The cathodic to anodic peak separation [( $E_p$ )<sub>c</sub>-( $E_p$ )<sub>a</sub>] is 60 mV at all values of  $v$ .

Chronoamperometric experiments were conducted in conjunction with the cyclic voltammetric experiments at the same ppde and under identical conditions of concentration of PNP and supporting electrolyte at potentials corresponding to the first polarographic plateau. Diffusion current plots,  $it^{1/2}/C$  vs.  $t$ , of data taken from current-time decay curves (0.3-1.4 sec) of the reduction of PNP at 0.1 and 1.0 mM in dry DMF correspond closely to similar plots for the known one-

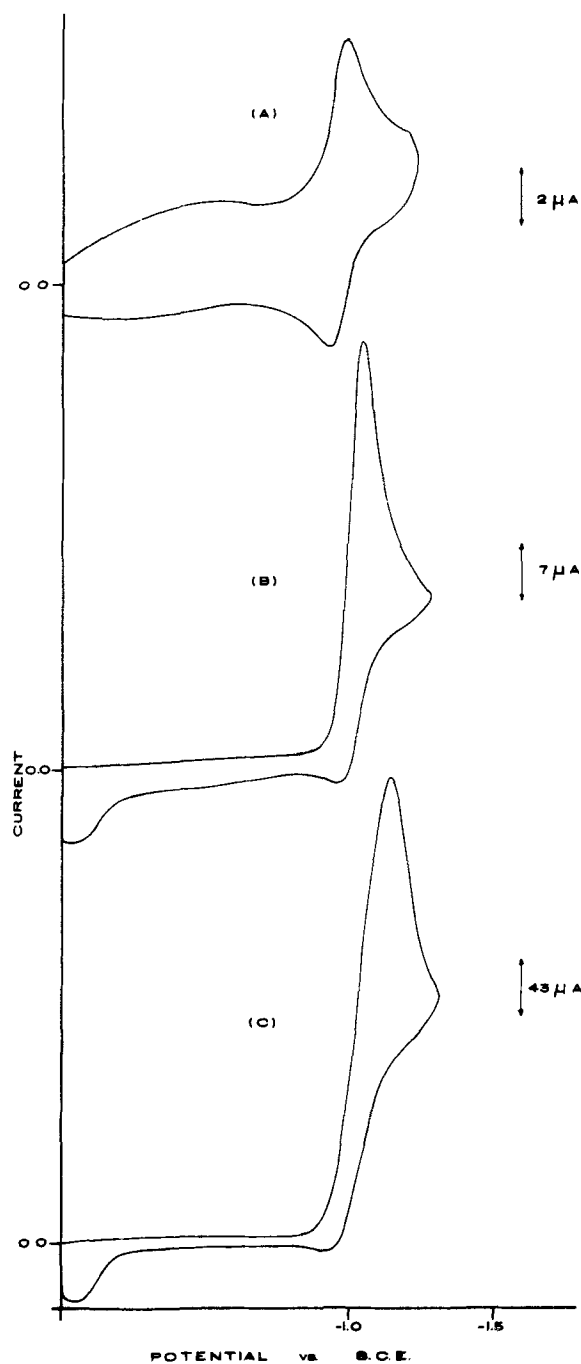


Fig. 2. Single sweep cyclic voltammograms taken at a ppde at potentials of first polarographic wave in DMF containing 0.1M TPAP and (a) 0.1 mM PNP recorded at 12.48 V/min. (b) 1 mM PNP recorded at 12.48 V/min. (c) 10 mM PNP recorded at 9.65 V/min.  $E_{\lambda}$  is 120 mV.

electron reduction of nitrobenzene under the same experimental conditions.

The influence of water on the process occurring at potentials of the first polarographic wave was studied with cyclic voltammetry at a ppde (Table II). Controlled quantities of water were added to solutions 0.1 and 1.0 mM in PNP and cyclic voltammograms were recorded. Addition of water to solutions 0.1 mM in PNP had a slight but discernible influence on the ( $E_p$ )<sub>c</sub>, current function, and anodic to cathodic current ratio [( $ip$ )<sub>a</sub>/ $(ip)$ ]<sub>c</sub> of the cyclic curves (Table II). At a proton donor to PNP ratio of  $2.4 \times 10^4$  moles to one, a 10% decrease in the current function and a 20 mV negative shift in the cathodic wave is noted to accompany a tenfold increase in  $v$ . Only an immeasurably small anodic current is observed on the reverse sweep

Table II. Cyclic voltammetric data for (E)-1-phenyl-2-nitro-1-propene in DMF and DMF-H<sub>2</sub>O at a ppde<sup>a</sup>

H <sub>2</sub> O <sup>b</sup> (mM)	$v$ (V/min)	$-(E_p)c$ (V)	$(E_p)c$ $-(E_p)a$ (mV)	$(i_p)a/$ $(i_p)c^c$	$(i_p)c/v^{1/2}$ $\mu A \text{ volt}^{-1/2} \text{ min}^{1/2}$
(E)-1-phenyl-2-nitro-1-propene (0.1 mM)					
0	12.48	1.00	60	1.0	2.59
	9.38	1.00	60	1.0	2.48
	6.24	1.00	60	1.0	2.38
	3.12	0.99	60	1.0	2.46
	1.25	0.99	60	1.0	2.66
600	12.48	0.97	62	0.66	2.62
	9.38	0.97	60	0.64	2.50
	6.24	0.96	60	0.62	2.41
	3.12	0.96	— <sup>d</sup>	— <sup>d</sup>	2.40
	1.25	0.95	— <sup>d</sup>	— <sup>d</sup>	2.65
1200	12.48	0.95	70	0.66	2.47
	9.38	0.95	70	0.64	2.42
	6.24	0.95	70	0.61	2.38
	3.12	0.94	— <sup>d</sup>	— <sup>d</sup>	2.46
	1.25	0.94	— <sup>d</sup>	— <sup>d</sup>	2.65
2400	12.48	0.93	70	0.63	2.39
	9.38	0.93	70	0.62	2.40
	6.24	0.92	— <sup>d</sup>	— <sup>d</sup>	2.40
	3.12	0.92	— <sup>d</sup>	— <sup>d</sup>	2.43
	1.25	0.91	— <sup>d</sup>	— <sup>d</sup>	2.65
(E)-1-phenyl-2-nitro-1-propene (1 mM)					
0	4.68	1.05	— <sup>d</sup>	— <sup>d</sup>	23.25
	3.12	1.04	— <sup>d</sup>	— <sup>d</sup>	23.45
	1.56	1.03	— <sup>d</sup>	— <sup>d</sup>	25.00
	0.47	1.02	— <sup>d</sup>	— <sup>d</sup>	25.34
	0.47	1.02	— <sup>d</sup>	— <sup>d</sup>	22.90
600	4.68	1.02	— <sup>d</sup>	— <sup>d</sup>	22.90
	3.12	1.02	— <sup>d</sup>	— <sup>d</sup>	23.90
	1.56	1.01	— <sup>d</sup>	— <sup>d</sup>	25.78
	0.47	0.99	— <sup>d</sup>	— <sup>d</sup>	25.63
	0.47	0.99	— <sup>d</sup>	— <sup>d</sup>	22.15
1200	4.68	1.00	— <sup>d</sup>	— <sup>d</sup>	22.15
	3.12	0.99	— <sup>d</sup>	— <sup>d</sup>	23.68
	1.56	0.97	— <sup>d</sup>	— <sup>d</sup>	25.47
	0.47	0.97	— <sup>d</sup>	— <sup>d</sup>	25.05
	0.47	0.97	— <sup>d</sup>	— <sup>d</sup>	21.63
2400	4.68	0.97	— <sup>d</sup>	— <sup>d</sup>	21.63
	3.12	0.96	— <sup>d</sup>	— <sup>d</sup>	22.34
	1.56	0.95	— <sup>d</sup>	— <sup>d</sup>	24.20
	0.47	0.94	— <sup>d</sup>	— <sup>d</sup>	23.71

<sup>a</sup> All solutions were 0.1M in TPAP.

<sup>b</sup> Concentration computed based on water added to solvent.

<sup>c</sup>  $E_\lambda$  (switching potential) = 120 mV and ratio computed after method of Nicholson *et al.* (15).

<sup>d</sup> Anodic current not reliably measurable.

segment of cyclic experiments conducted at a  $v$  of less than 6.24 V/min (Table II, Fig. 3). Only a positive shift in  $(E_p)c$  relative to the same values in dry solvent is noted in water addition experiments conducted at 1 mM PNP (Table II).

The dependence of cyclic peak characteristics on the concentration of PNP in dry DMF is significant to the interpretation of the electrochemical process responsible for the first diffusion plateau. In general, the cyclic voltammetric data taken at 0.1 mM PNP suggests the reversible, one-electron formation of an intermediate followed by a chemical reaction slow relative to the voltage excursion rate (13, 14). At higher concentrations of PNP (1.0 and 10.0 mM) the behavior suggests a rapid chemical reaction coupled to an initial electron-transfer process. The influence of the precursor concentration on the rate of the coupled homogeneous chemical reaction and the chronoamperometric data is consistent with second order kinetics involving dimerization of intermediate radicals of the precursor (hydrodimerization). Nicholson *et al.* (15) and Saveant *et al.* (16) have presented the theory of cyclic voltammetry for an electrochemically initiated homogeneous dimerization reaction with diagnostic criteria analogous to those developed for other electrochemical reaction mechanisms (13, 14). The cyclic voltammetric data in Table II for PNP are in general good agreement with the dimerization criteria.

Oscilloscopic recording of current response to rapid voltage excursion and reversal past the diffusion plateau of the diminished second wave, revealed data definitive of the electrochemical process responsible for the wave. Cyclic voltammograms recorded at a ppde in 1 mM PNP at 24 and 240 V/min (Fig. 4) show that the cathodic current of the second wave grows in intensity with increased sweep rate to a limiting value equal to that of the first wave, a one-electron process.

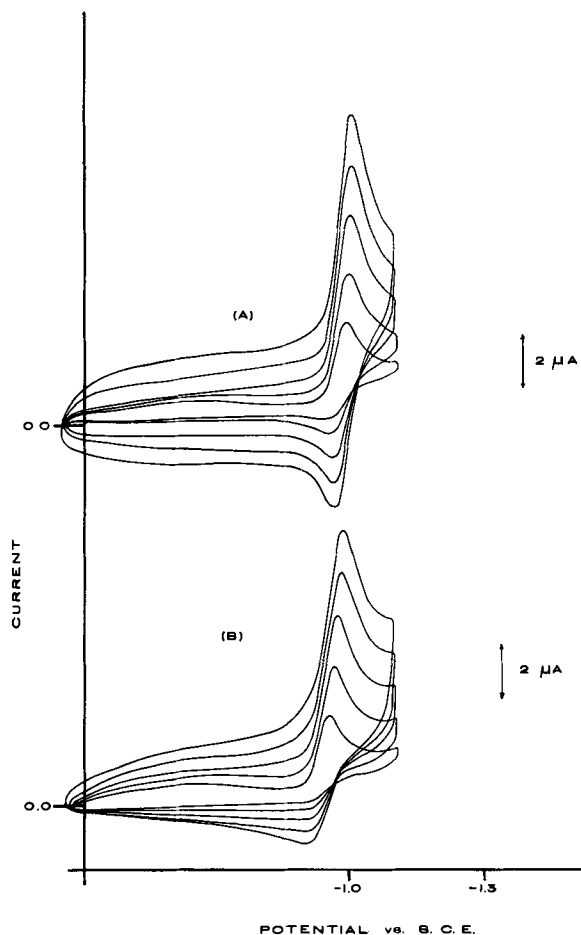


Fig. 3. Single sweep cyclic voltammograms of PNP at 0.1 mM in DMF recorded at a ppde at potentials of first polarographic wave. (a) Solution contained no added water and voltammograms recorded at 12.48, 9.38, 6.24, 3.12, and 1.25 V/min. (b) Solution contained 2.4M H<sub>2</sub>O and voltammograms recorded at 12.48, 9.38, 6.24, 3.12, and 1.25 V/min.  $E_\lambda$  is 120 mV.

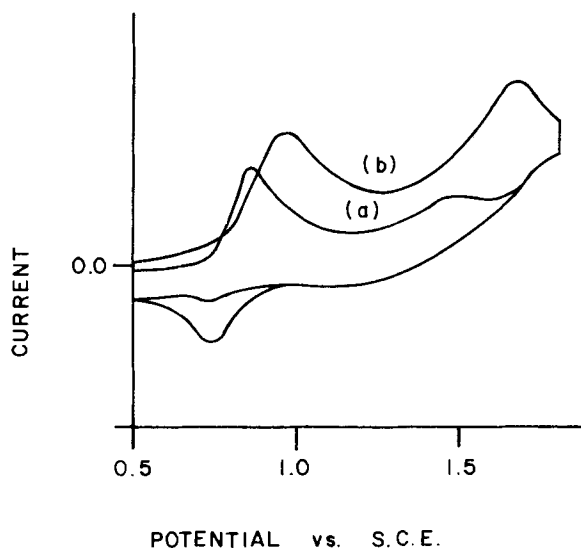


Fig. 4. Trace from film of oscilloscopic recording of single sweep cyclic voltammograms at a ppde of a 1 mM solution of PNP at (a) 24 V/min and (b) 240 V/min.  $E_\lambda$  is approximately 120 mV.

These data and the enhanced anodic current of the first wave recorded under the same conditions are consistent with an electrochemical reduction process involving an initial one-electron transfer to the parent

Table III. Rotating disk electrode data for the first reduction wave of (E)-1-phenyl-2-nitro-1-propene (PNP)<sup>a</sup>

Limiting disk current $i_{d,1}$ ( $\mu\text{A}$ )	Rotation rate $\omega$ ( $\text{sec}^{-1}$ )	$\frac{i_{d,1}}{\omega^{1/2}C}$
Concentration of PNP = 2.78 mM		
110	48	5.73
155	99	5.61
190	150	5.58
220	201	5.58
244	253	5.52
274	305	5.64
294	358	5.59
314	409	5.59
330	461	5.53
350	512	5.56
368	564	5.58
384	616	5.57
Concentration of PNP = 3.20 mM		
259	201	5.72
Concentration of PNP = 4.79 mM		
212	48	6.41
297	99	6.25
305	105	6.21
420	201	6.18
473	253	6.20
516	305	6.16
573	358	6.17
594	409	6.13
631	461	6.13
668	512	6.13
703	564	6.18
773	616	6.17

<sup>a</sup> Solutions were 0.1M TBAI in DMF.

compound at the first wave and a subsequent one-electron addition to the ion radical at the second wave. Chemical reactions following the first transfer are not apparent at very rapid potential excursion rates. The sensitivity of the second wave to small quantities of proton donors (Fig. 1) is consistent with a rapid protonation of an initially produced dianion of PNP. In summary the cyclic voltammetric data are consistent with a general reduction scheme of the type

## First Wave

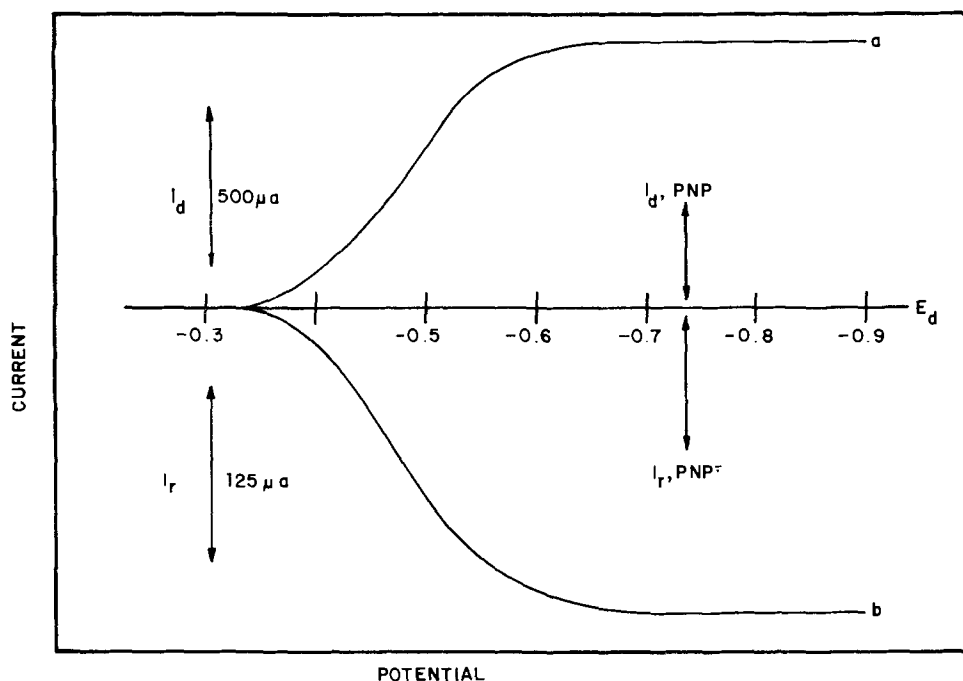
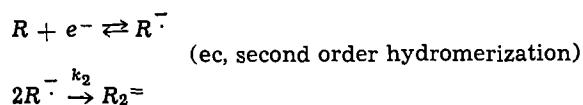
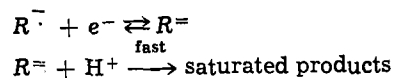


Fig. 5. RRDE voltammograms of PNP at 2.89 mM in DMF determined at a scan rate of 30 mV/sec and a rotation rate of 201 rad/sec. (a)  $i_d$  vs.  $E_d$  (b)  $i_r$  vs.  $E_d$ ,  $E_r = -0.10\text{V}$  vs. Ag R.E.

## Second Wave



*Rotating ring-disk electrode studies.*—Confirmation of hydrodimerization as the major reduction pathway of PNP in DMF at its first polarographic step and a determination of the rate constant for the coupling reaction (RRDE) techniques. Rotating disk electrode voltammograms taken at scan rates of 20-25 mV/sec of 1 mM solutions of PNP in DMF show a reduction wave with  $E_{1/2} = -0.49\text{V}$  vs. Ag reference electrode. Values of the Levich constant,  $i_{d,1}/C_R\omega^{1/2}$  (where  $i_{d,1}$  is the disk current on the mass transfer limiting plateau) given in Table III, show no dependence on rotation rate ( $\omega$ ). The diffusion coefficient for PNP,  $D$ , evaluated from the Levich equation

$$i_{d,1} = 0.62nFAD^{2/3}\nu^{-1/6}C_R\omega^{1/2}$$

(where  $n = 1$ , and  $\nu$ , the kinematic viscosity, is  $0.00849\text{ cm}^2/\text{sec}$  for DMF) was found to be  $2.4 \times 10^{-5}\text{ cm}^2/\text{sec}$ . Coulometry carried out at  $-1.10\text{V}$  vs. Ag-R.E. shows  $n_{\text{app}}$  values of 0.97 and 0.98 for 2.78 and 4.79 mM solutions, respectively. The independence of the Levich constant with rotation rate and the above coulometry data suggest the absence of polymerization which often accompanies hydrodimerization reactions in aprotic solvents (e.g., for diethyl fumarate and fumaronitrile) (14, 20).

Rotating ring-disk electrode experiments were performed to gather additional data relative to the mechanistic characteristics of the reduction process. A typical RRDE voltammogram of this system is shown in Fig. 5. Collection efficiency ( $N_K$ ) (where  $N_K = i_r/i_d$ ) measurements as a function of disk current (CONI) (where  $\text{CONI} = i_d/i_{d,1}$ ) were made at various rotation rates ( $\omega$ ) and concentrations. Representative data of these experiments are presented in Table IV. The trend of increasing  $N_K$  with decreasing CONI has been shown to be indicative of a hydrodimerization reaction proceeding by a coupling of radical anions rather than attack of the parent compound by radical anions (17, 20). The experimental points were fit by simulating such a mechanism for different values of the simulation rate constant parameter

Table IV. Experimental collection efficiency ( $N_K$ ) data for (E)-1-phenyl-2-nitro-1-propene<sup>a,b</sup>

$i_r$ ( $\mu A$ )	$i_a$ ( $\mu A$ )	$N_K$	CONI
Concentration PNP = 2.78 mM			
23.4	54.6	0.429	0.199
44.7	113.9	0.392	0.414
61.7	175.5	0.352	0.638
71.3	220.4	0.324	0.801
76.6	247.7	0.309	0.900
78.8	260.5	0.303	0.947
80.0	267.2	0.300	0.972
80.5	272.3	0.296	0.990
81.0	273.8	0.296	0.996
81.0	275.0	0.295	1.000
Concentration PNP = 4.79 mM			
16.5	20.0	0.525	0.047
18.0	37.0	0.486	0.086
28.0	64.0	0.438	0.149
36.0	90.2	0.400	0.209
37.8	106.8	0.353	0.249
42.5	135.1	0.315	0.314
47.5	149.9	0.317	0.349
55.0	208.0	0.264	0.484
60.0	234.7	0.255	0.547
62.0	250.0	0.248	0.581
65.0	280.3	0.232	0.651
70.0	315.0	0.222	0.732
70.0	319.7	0.219	0.744
71.0	359.8	0.197	0.837
75.0	400.0	0.189	0.930
76.0	419.9	0.181	0.977
78.0	430.0	0.181	1.000

<sup>a</sup> Solutions were 0.1M TBAI in DMF.

<sup>b</sup> Rotation rate = 201.1 radians/sec.

$XKTC = (0.51)^{-2/3} \nu^{1/3} D^{-1/3} D \omega^{-1} k_2$ . The lines in Fig. 6 correspond to  $XKTC$  values of 2.2 for line b and 0.9 for line a. These lines correspond to the following experimental conditions: line a, concentration of PNP equal to 2.78M at a rotation rate of 305 radians/sec; line b, concentration of PNP equal to 4.79 mM at a rotation rate of 201 radians/sec. Values of  $k_2$ , determined

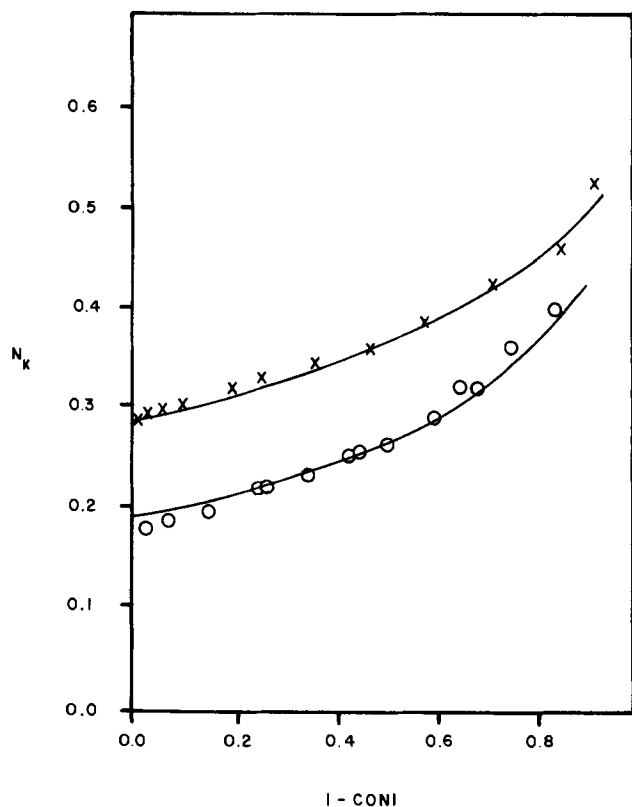


Fig. 6. Collection efficiency ( $N_K$ ) vs. 1-CONI for a 2.78 mM PNP solution (X), and a 4.79 mM PNP solution (O). The rotation rates were 305 rad/sec and 201 rad/sec respectively. Solid lines are theoretical curves corresponding to dimerization mechanism and for (X)  $XKTC = 2.2$  and (O)  $SCTC = 0.9$ .

Table V. Calculated rate constants for reactions of radical anion of PNP obtained from RRDE results<sup>a</sup>

$\omega$ (sec <sup>-1</sup> )	Concentration (mM)	$XKTC^b$	$k_2$ (1/mole-sec)
99	2.78	2.1	$1.5 \times 10^4$
	4.79	3.1	1.3
201	2.78	1.0	1.5
	3.20	1.3	1.6
305	4.79	2.2	1.8
	2.78	0.9	1.3
			Avg = $1.7 \times 10^4$

<sup>a</sup> The solutions were all 0.1M TBAI in DMF.

<sup>b</sup>  $XKTC = (0.51)^{-2/3} \nu^{1/3} D^{-1/3} D \omega^{-1} k_2$ ,  $\nu = 0.00849$  cm<sup>2</sup>/sec.

from these  $XKTC$  values and the diffusion coefficient are given in Table V; an average of  $1.7 \times 10^4 M^{-1} sec^{-1}$  is obtained.

### Discussion of Results

Cyclic voltammetric, chronoamperometric, and rotating-ring disk data suggest that a dimeric coupling reaction (hydrodimerization) represents a major mode of decay of the anion radical of the compound PNP, produced by an initial one-electron transfer in DMF solvent. The compound is reduced also at more negative potentials via an *ec* process involving protonation of the dianion of the parent.

The radical anion coupling rate found here for PNP,  $1.7 \times 10^4 M^{-1} sec^{-1}$ , is intermediate to those found for other substituted olefins (17-20); the dialkyl fumarate radical anions couple with a  $k_2 \approx 10^2 M^{-1} sec^{-1}$ , while that for fumaronitrile radical anions is  $6 \times 10^5 M^{-1} sec^{-1}$ . The 1-phenyl, 2-cyano substituted olefin, cinnamionitrile, yielded a  $k_2$  value of  $9 \times 10^2 M^{-1} sec^{-1}$ .

Baizer and co-workers (11) found that the radical anion of benzalacetophenone in DMF decayed most rapidly of the five, 2-substituted 1-phenyl olefins he studied ( $-CO\phi > -CN > -COOC_2H_5 > -CON(CH_3)_2 > -C_6H_5$ ) with a lifetime approximately 1/40th of that of diethyl fumarate. Comparison of the  $k_2$  computed for PNP with these data illustrated the relatively great reactivity of radical ions of nitrosubstituted olefins.

The cyclic voltammetric data from the study of the influence of water on the electrochemical reaction occurring at potentials of the first polarographic plateau suggests that proton donors influence the rate of chemical reactions coupled to the electron transfer but do not alter the mechanism of the processes controlling the shape and behavior of the cyclic curves (15). Similar conclusions were reached by Baizer and co-workers (11) and Bard and co-workers (18) from a variety of data. The magnitude of the influence of water is slight but data taken at precursor concentrations of 0.1, 1.0, and 10.0 mM are consistent with an increase in the rate of reactions coupled to the initial electron transfer (Table II, Fig. 3).

Studies of *cis-trans*-pairs of some activated olefins (19) have demonstrated that the anion of the *cis*-isomer may undergo a rapid isomerization to form the *trans*-radical anion as well as react more rapidly in self or cross-coupling reactions. No evidence of such behavior by the E-isomer of PNP is found in the short-term electrochemical data presented herein. The fact that only the E-isomer is produced in the synthesis of PNP, by the condensation of benzaldehyde, with nitroethane is probably pertinent to this point.

### Experimental

**Apparatus.**—The ppde employed in the cyclic voltammetric experiments was a Beckman platinum buton electrode with an area of 80 mm<sup>2</sup>. The reference electrode employed in the polarographic and cyclic voltammetry experiments, an aqueous saturated calomel electrode, made contact with the solution through an agar plug behind a Pyrex frit. Water leakage

through this tip was found to be negligible. The cyclic voltammetric data were recorded on a Bolt-Barnak-Newman X-Y Plotter using a Wenking potentiostat and exact wave form source for potential variation and control. The polarograms were recorded with a Beckman Electroscan 30 electroanalytical system.

A Tascussel Electronique Bipotentiostat, Model Bipad 2, was used for all RRDE experiments. A Digitec digital voltmeter, Model 204, and a Fairchild digital multimeter, Model 7050, were used to measure the steady-state ring and disk currents simultaneously. A Wavetek function generator provided a d-c potential ramp for voltammetric experiments recorded on a Mosley Model 2D-2 X-Y recorder. The platinum-Teflon rotating ring-disk electrode, having a disk radius ( $r_1$ ) of 0.187 cm and inner ( $r_2$ ) and outer ( $r_3$ ) ring radii of 0.200 and 0.332 cm, respectively, was constructed by Pine Instrument Company, Grove City Pennsylvania. The maximum collection efficiency,  $N$ , for the RRDE used in these experiments was 0.555 (20). The reference electrode was a silver wire spiral.

**Chemicals.**—Spectroquality DMF containing approximately 0.03% water was obtained from Eastman Organic Chemicals. The solvent was vacuum distilled from anhydrous  $\text{CuSO}_4$  before use. Hydroquinone was obtained from J. T. Baker Chemical Company and was recrystallized from a 50% water-ethylether solution. All nitroalkenes were synthesized by the method of Hass, Susie, and Heider (21). The compound PNP exhibited a melting point of 64°C after several recrystallizations from absolute ethanol.

#### Acknowledgment

The authors gratefully acknowledge the financial support of the Robert A. Welch Foundation; J. W. Rogers—(Grant No. AO-337), A. J. Bard—(Grant No. F-079), and National Science Foundation (GP-31414X).

Manuscript submitted May 13, 1974; revised manuscript received June 24, 1974.

Any discussion of this paper will appear in a Discussion Section to be published in the June 1975 JOURNAL.

All discussions for the June 1975 Discussion Section should be submitted by Feb. 1, 1975.

The publication costs of this article have been assisted by the Robert A. Welch Foundation and the National Science Foundation.

#### REFERENCES

1. D. H. Geske and A. H. Maki, *J. Am. Chem. Soc.*, **82**, 2671 (1960).
2. J. Gendell, J. H. Freed, and G. K. Frankel, *J. Chem. Phys.*, **37**, 2832 (1962).
3. J. Q. Chambers and R. N. Adams, *J. Electroanal. Chem.*, **9**, 400 (1965).
4. J. G. Lawless and M. D. Hawley, *ibid.*, **21**, 365 (1969).
5. J. G. Lawless and M. D. Hawley, *ibid.*, **23**, 1 (1969).
6. A. K. Hoffmann, W. G. Hodgson, D. L. Maricle, and W. H. Jura, *J. Am. Chem. Soc.*, **86**, 631 (1964).
7. J. Armand and O. Convert, *Coll. Czech. Chem. Comm.*, **36**, 351 (1971).
8. A. I. Prokofev, V. M. Chibrikov, O. A. Yuzhakova, and R. G. Kostyanovskii, *Izv. Akad. Nauk.*, **6**, 1105 (1966).
9. H. B. Hass and E. F. Riley, *Chem. Rev.*, **28**, 373 (1941).
10. J. R. Jesorek and H. B. Mark, Jr., *J. Phys. Chem.*, **74**, 1627 (1970).
11. J. P. Petrovich, M. M. Baizer, and M. R. Ort, *This Journal*, **116**, 743 (1969).
12. J. P. Petrovich, M. M. Baizer, and M. R. Ort, *ibid.*, **116**, 749 (1969).
13. R. S. Nicholson and I. Shain, *Anal. Chem.*, **37**, 178 (1965).
14. R. S. Nicholson and I. Shain, *ibid.*, **36**, 706 (1964).
15. M. L. Olmstead, R. G. Hamilton, and R. S. Nicholson, *ibid.*, **41**, 260 (1960).
16. L. Nadjo and J. M. Saveant, *J. Electroanal. Chem.*, **33**, 419 (1971).
17. V. I. Puglisi and A. J. Bard, *This Journal*, **120**, 241 (1973).
18. W. V. Childs, J. T. Maloy, C. P. Keszthelyi, and A. J. Bard, *ibid.*, **118**, 874 (1971).
19. A. J. Bard, Vincent J. Puglisi, J. V. Kenkel, and Ann Lomax, *Trans. Faraday Society*, In press.
20. V. J. Puglisi and A. J. Bard, *This Journal*, **119**, 829 (1972).
21. H. B. Hass, A. G. Susie, and R. L. Heider, *J. Org. Chem.*, **15**, 8 (1950).

## The Electrocapillary Phenomena at the Lead Electrode

Ikram Morcos\*

Hydro-Quebec Institute of Research, Varennes, Quebec, Canada

#### ABSTRACT

The electrocapillary phenomena was studied on the lead electrode by the method of meniscus rise in  $\text{Na}_2\text{SO}_4$  solutions. The potential and concentration dependence of meniscus rise at potentials approximately cathodic to the pzc suggest that the electrode is polarizable. A sharp increase in the interfacial tension at  $-1.1\text{V}$  is attributed to anion adsorption. Charge density and differential capacity values are calculated from the meniscus rise data for 0.01M  $\text{Na}_2\text{SO}_4$  solution, and are compared to the results of electrocapillary and capacity measurements on both mercury and lead electrodes, respectively. A reduction in the increase of meniscus rise with potential starting at about  $-1.55\text{V}$  with 1M  $\text{Na}_2\text{SO}_4$  suggests the occurrence of cation specific adsorption.

An adequate understanding of the electrochemical activity of solid electrodes requires a better knowledge than is presently available of the electrode/electrolyte interface. The meniscus rise technique has been shown (1-10) to be valuable in previous studies of the inter-

facial tension at solid electrodes. An extensive application of this technique to various systems is therefore desirable.

The development of the meniscus rise technique, and hence that of the interfacial phenomena at solid electrodes, requires, besides the examination of different systems, some comprehensive measurements on a given

\* Electrochemical Society Active Member.

Key words: electrocapillary phenomena, lead electrode, meniscus rise, interfacial tension, double layer.

system. During the past few years both approaches were examined and on the basis of the experimental data (both published and unpublished), it was concluded that a proper interpretation of the results of one comprehensive study, involving such variables as the electrolyte's nature and concentration, cannot be realized before the outline of the general features of interfacial phenomena at solid electrodes is well understood. Unfortunately the nature of the problem is such that progress can be only very slowly made and that there is not one single system that can be applied to reveal all the complexities of the problem. The following explain more precisely the nature of such complexities.

1. The chemical and electrochemical nature of the solid surface strongly influences the potential dependence of the interfacial tension. In the absence of a theory to explain the role played by the electrode surface it is necessary to obtain experimental data on various surfaces of different nature. A consideration of the data obtained on mercury-plated gold (1-6), platinum (3-5), gold (3-5), silver (7), cleavage graphite (3, 8, 9), and silicon (10) electrodes illustrate this point.

2. In addition to electrode's polarizability, variables such as surface roughness and heterogeneity influence the experimental values of meniscus height. While it is possible to obtain an electrode surface which satisfies just a certain degree of the theoretical requirements, it is almost impossible to find a solid surface which is polarizable and free of both surface roughness and heterogeneity. Even variation in surface roughness and heterogeneity can be sometimes more easily realized by using different types of metals than by treating the surface of one metal.

3. Some of the electrochemically inert electrodes, which would have been ideal for a comprehensive study of the effect of ionic nature and concentration, have certain properties which severely limit their use for such studies. Examples are the cleavage surface of single-crystal graphite and silicon electrode in acid medium. The former surface has a lower surface tension (8) than that of water which almost prevents the adsorption of solvated ions. The result is that the potential dependence of meniscus rise is very slightly influenced by either the nature (9) or the concentration of ionic species. In the case of silicon (10) where a polarizable oxide layer forms in acid medium, the interpretation of concentration dependence of meniscus rise is complicated by the presence of potential drops across the space charge and oxide layers and the limiting effect of surface states on surface charge density.

4. The effect of nature and concentration of ions on the potential dependence of meniscus rise on solid metals indicates a completely different type of adsorption between the anion and the metal surface as compared to that observed on mercury. The understanding of the nature of this adsorption requires among other things a comparison between the data observed on different metals.

The aim of the present paper has been to examine the interfacial phenomena at the lead electrode. Recent work on the voltammetry (11) of that electrode suggests the presence of a relatively wide polarizable region. Although the softness of lead and its rapid oxidation on air make it difficult to prepare an ideal surface for the meniscus rise measurement, the indicated polarizable behavior is a sufficient justification for the study.

### Experimental Procedure

Most experimental aspects concerning the apparatus and procedure of measuring the meniscus rise were discussed in previous papers. The test electrodes used in the study were polycrystalline lead plates 2 cm wide, 4 cm long, and about 0.05 cm thick. The preparation of a smooth, bright lead plate constituted a par-

ticularly difficult problem. Several methods of preparing the surface were tried and the best surface finishing was obtained by chemically polishing the lead plates after mechanical polishing with sandpapers No. 240, 320, 400, and 600 followed by 0.3 alumina on a felt wheel. Chemical polishing was done in a mixture prepared by adding 80 mliters of glacial acetic acid to 20 mliters of 30% H<sub>2</sub>O<sub>2</sub>. The electrodes were then thoroughly washed in triply distilled water. Several plates were usually treated in the described manner before one could be found eligible for use. Only those plates that continued to exhibit their brightness were used. In meniscus rise experiments, the final test for the eligibility of a certain surface is based on observing a horizontally straight solid/liquid contact line (meniscus edge).

Test solutions were prepared from A.R. quality sodium sulfate, ultra pure sulfuric acid, and triply distilled water twice from a permanganate solution. Solutions of 1.0, 0.1, and 0.01M Na<sub>2</sub>SO<sub>4</sub> and 0.01M H<sub>2</sub>SO<sub>4</sub> were used. The pH of the test solution was measured from samples taken from the cell after each experiment and was found to be 5.2, 4.95, 5.88, and 2.1, respectively. A mercury-mercurous sulfate electrode, which has been prepared several weeks prior to the measurements, was used as a reference electrode. The stability of this reference electrode was tested as a function of both time and pH. This was carried out in 1M Na<sub>2</sub>SO<sub>4</sub> solution against a two-phase lead amalgam lead sulfate electrode. The emf between the two electrodes was found to be remarkably stable during a period of 1 hr and between pH 2.75 and 12.59. The emf read at both pH extremes was -0.981 and -0.980, respectively.

A large Teflon cell of 12.3 cm diameter was applied. The counterelectrode consisted of a spectroscopic grade rod of graphite.

The advancing equilibrium meniscus rise was measured at prefixed potentiostatically controlled potential values and the measurement was carried out from the most cathodic to the most anodic potential value. The measurement was carried out under helium atmosphere and in helium-saturated solutions. The current density was calculated for the immersed area of the electrode and was found not to exceed 10  $\mu$ A/cm<sup>2</sup>.

### Results and Discussion

Figure 1 shows plots of potential dependence of the advancing meniscus rise on partially immersed polycrystalline lead plates in 0.01, 0.1, and 1.0M Na<sub>2</sub>SO<sub>4</sub> solutions. The three plots show well-defined minima located in the potential region between -1.35 and -1.25V (*vs.* Hg/Hg<sub>2</sub>SO<sub>4</sub>). The plots also show that at -1.1V the meniscus rise drops sharply and, therefore, results in the occurrence of well-defined maxima. Differential capacity measurements carried out by several investigators (12-16) in sulfate solutions show that the pzc of lead is located at potentials between -0.62 and -0.67V (*vs.* NHE). These values agree with the minima of Fig. 1 and, therefore, the latter minima should correspond to the pzc of lead in the same solutions.

A detailed discussion of the electrocapillary curves of Fig. 1 can be more conveniently carried out if one considers the corresponding variation in interfacial tension with potential. Irrespective of the polarizability of the electrode and subject only to the thermodynamic validity of the contact angle at the three phase region, the interfacial tension  $\gamma_{SL}$ , at the solid/liquid interface is related to the advancing meniscus rise by an equation previously (6) derived

$$\gamma_{SL} = \gamma_{SV} - \gamma_L (2kh^2 - k^2h^4)^{1/2} \quad [1]$$

where

$$k = \frac{\rho g}{2\gamma_L} \text{ and } \gamma_{SV} = \gamma_S - \pi$$

and the different terms are as follows:  $\gamma_S$  and  $\gamma_L$  the

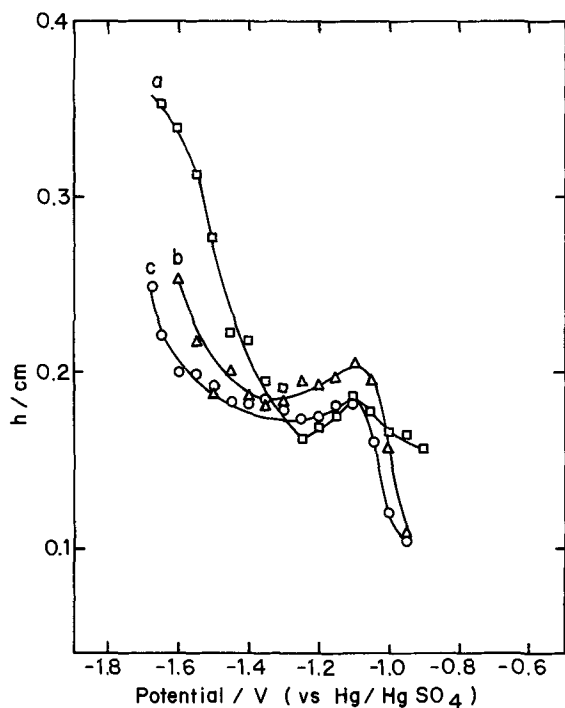


Fig. 1. Meniscus rise vs. potential relationships on chemically polished polycrystalline lead electrode in helium atmosphere. Curve a, 1.0M  $\text{Na}_2\text{SO}_4$ ; curve b, 0.1M  $\text{Na}_2\text{SO}_4$ ; curve c, 0.01M  $\text{Na}_2\text{SO}_4$ .

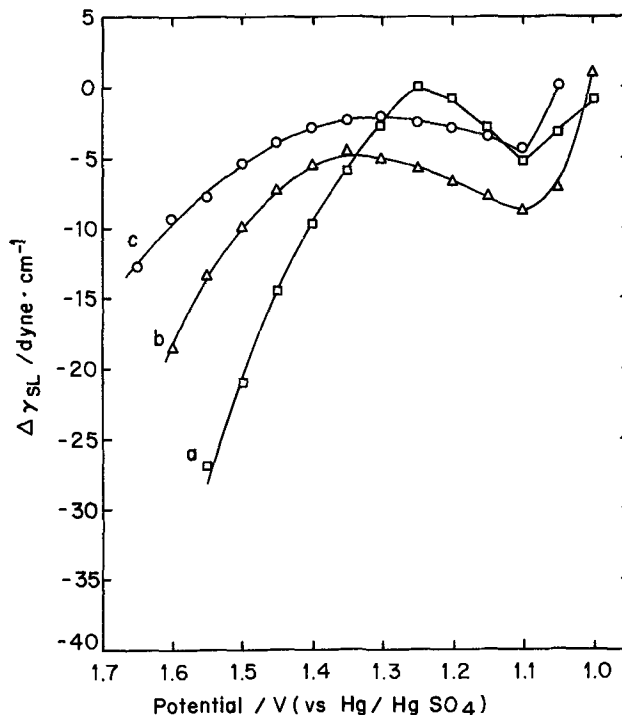


Fig. 2. Interfacial tension vs. potential relationships on chemically polished polycrystalline lead electrode in helium atmosphere. Data calculated by Eq. [1] using plots of Fig. 1. Curve a, 1.0M  $\text{Na}_2\text{SO}_4$ ; curve b, 0.1M  $\text{Na}_2\text{SO}_4$ ; curve c, 0.01M  $\text{Na}_2\text{SO}_4$ .

solid's and liquid's surface tensions, respectively,  $\pi$  the spreading pressure of water,  $\rho$  the liquid's density, and  $g$  the gravitational constant. In the absence of gas evolution, which is the case with the lead electrode as shown by voltammetry (11), the thermodynamic validity of the contact angle (and hence that of the meniscus rise) is justifiable (10). A knowledge of the absolute value of  $\gamma_{\text{SL}}$  requires a knowledge of  $\gamma_{\text{S}}$ . But since the latter quantity cannot be obtained, only variations in  $\gamma_{\text{SL}}$  as a function of the potential can be evaluated assuming that the values of both  $\gamma_{\text{SV}}$  and  $\gamma_{\text{L}}$  are independent of the potential.

Figure 2 shows those plots of  $\Delta\gamma_{\text{SL}}$  as a function of the applied potential which have been obtained by means of Eq. [1] from the data of Fig. 1. In calculating  $\Delta\gamma_{\text{SL}}$  the value of  $\gamma_{\text{S}} - \gamma_{\text{SL}}$  which corresponds to the minimum meniscus height in 1M  $(\text{Na})_2\text{SO}_4$  solution has been taken as a reference point. At any given potential and concentration  $\Delta\gamma_{\text{SL}}$  is given by

$$\Delta\gamma_{\text{SL}} = (\gamma_{\text{S}} - \gamma_{\text{SL}}) - (\gamma_{\text{S}} - \gamma_{\text{SL}})_{\text{at minimum } h \text{ in } 1.0\text{M } \text{Na}_2\text{SO}_4}$$

With regard to the polarizability of the lead electrode, Fig. 2 indicates that as the potential is increased in the anodic direction, the metal surface exhibits three relatively well-defined states.

At potentials more negative than about  $-1.3$  (which corresponds to the pzc) both the potential and concentration dependence of  $\gamma_{\text{SL}}$  strongly suggest a polarizable surface. In this region, with both 0.01 and 0.1M solutions  $\Delta\gamma_{\text{SL}}/\Delta E$  shows a satisfactory agreement with  $\Delta\gamma/\Delta E$  observed on mercury. With 1M solution the variation in  $\Delta\gamma_{\text{SL}}$  is higher than the corresponding variation in mercury but is still within the same order of magnitude. The higher value probably results from the effect of solid surface roughness which becomes more influential with the increase in concentration.

At potentials more positive than  $-1.1\text{V}$ ,  $\gamma_{\text{SL}}$  shows a sudden increase with all concentrations. This potential coincides almost exactly with the cathodic side of the bottom of the current peak which is observed in fast, anodic, linear potential sweeps on the lead electrode in sulfate mediums (11). The peak occurs at  $-0.342$  (vs. NHE) and is attributed to the formation

of  $\text{PbSO}_4$ . That leaves little doubt that the increase in interfacial tension observed at  $-1.1$  (vs.  $\text{Hg}/\text{HgSO}_4$ ) is connected with the chemisorption of  $\text{SO}_4^{=}$  on the lead electrode. In that respect it seems that the variation in the interfacial tension is more sensitive than linear sweep voltammetry with regard to anion chemisorption. The mere adsorption of anions causes a sharp increase in the interfacial tension while the peak in voltammetry sweep does not appear before the potential of  $\text{PbSO}_4$  formation is reached. It could be argued that the increase in interfacial tension (drop in meniscus rise) at  $-1.1$  is due to the adsorption of  $\text{OH}^-$  rather than  $\text{SO}_4^{=}$  ion. Figure 3, however, shows that the same drop in meniscus rise takes place with 0.01  $\text{H}_2\text{SO}_4$  at exactly the same potential, which confirms that the observed effect is due to  $\text{SO}_4^{=}$  ion.

The increase in  $\gamma_{\text{SL}}$  due to anion adsorption is contrary to what usually takes place on mercury where anion adsorption reduces  $\gamma$ . The most probable interpretation for the increase in  $\gamma_{\text{SL}}$  is that anion adsorption must have resulted in reducing the charge density at the surface by interacting with the available free charge. It is interesting to note that from measurement of surface conductance on a gold electrode, Anderson and Hansen (17) have concluded that adsorption of  $\text{SO}_4^{=}$  ion reduces the amount of free charge at the gold surface.

In the potential region between  $-1.1$  and  $-1.3\text{V}$  (vs.  $\text{Hg}/\text{HgSO}_4$ ) the potential dependence of meniscus rise suggests the occurrence of slight  $\text{SO}_4^{=}$  adsorption. This suggestion is based on the fact that  $\Delta\gamma_{\text{SL}}/\Delta E$  is less than that observed on mercury. Carr *et al.* (12) reached the same conclusion from measurement of differential capacity. According to the latter authors (12), differential capacity vs. potential plots in dilute sulfuric acid solutions give rise to curves with well-defined minima only when the electrode was exposed before each fixed potential to a fixed negative potential of about  $-1.77$  (vs.  $\text{Hg}/\text{HgSO}_4$ ). In meniscus rise measurement, caution must, however, be taken in interpreting the concentration dependence of  $\gamma_{\text{SL}}$  near the potential of zero charge because surface roughness and

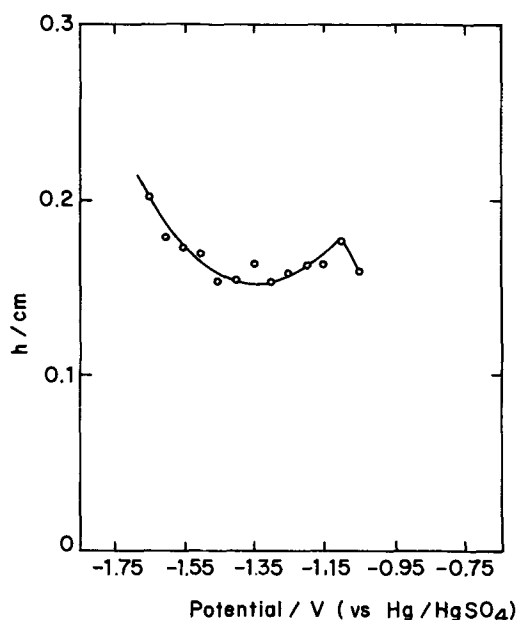


Fig. 3. Meniscus rise vs. potential relationship on chemically polished polycrystalline lead electrode with 0.01M  $H_2SO_4$  and helium atmosphere.

heterogeneity exerts their maximum effects in this potential region.

A quantitative comparison between the data of meniscus rise and differential capacity,  $C_d$ , on both the lead and mercury electrodes is desirable. This can only be realized by differentiating twice the meniscus rise vs. potential plots, and calculating  $C_d$  according to (9)

$$q = (2k)^{1/2} \gamma_L \frac{1 - kh^2}{(1 - \frac{1}{2}kh^2)^{1/2}} \left( \frac{\partial h}{\partial E} \right)_\mu \quad [3]$$

$$C_d = \frac{\partial q}{\partial E} \quad [4]$$

Figure 4 shows the charge density vs. rational potential plot calculated by means of Eq. [3] using the data of Fig. 3 for 0.01M  $Na_2SO_4$ . Figure 5 shows the differential capacity vs. potential calculated by means of

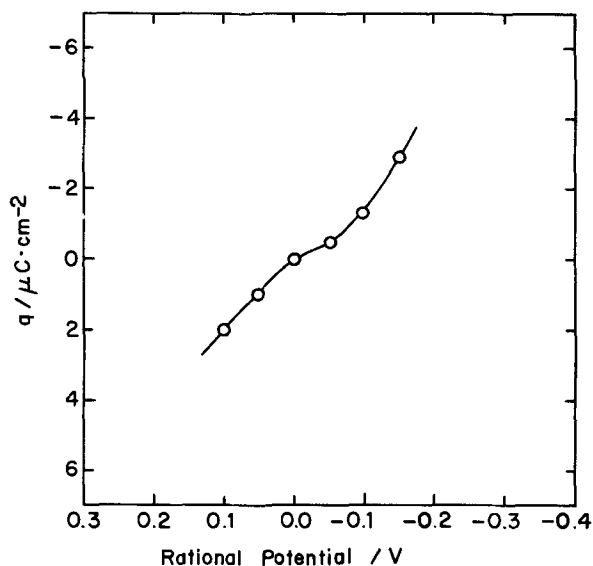


Fig. 4. Charge density vs. rational potential relationship on a polycrystalline chemically polished lead electrode with 0.01M  $Na_2SO_4$  and helium atmosphere. Data are calculated by Eq. [3] from curve c of Fig. 1.

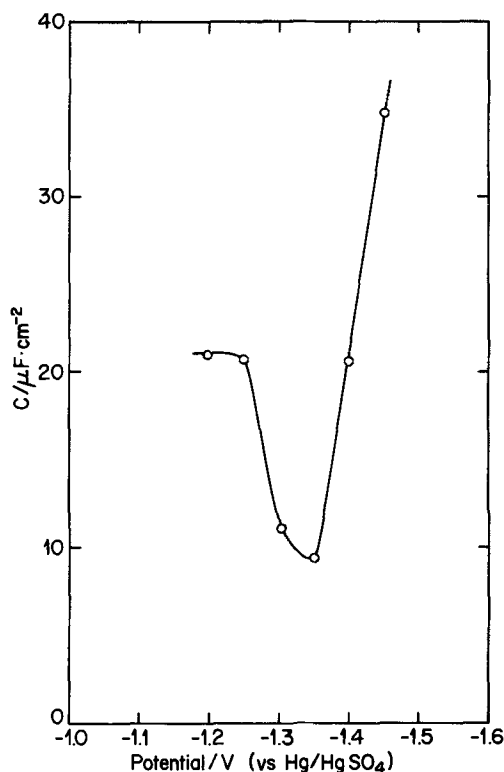


Fig. 5. Differential capacity vs. potential relationship on a polycrystalline polished lead electrode with 0.01M  $Na_2SO_4$  and helium atmosphere. Data calculated by Eq. [4] from Fig. 4.

Eq. [4] using the data of Fig. 4. At potentials more negative than  $-1.35$  (vs.  $Hg/HgSO_4$ ) the plot shows a satisfactory agreement with the same data directly measured on either lead or mercury. At potentials more positive than the above-mentioned value the effect of anion adsorption limits the increase in capacity.

Much of the deviation from polarizability discussed above results from anion adsorption. It is noticed however that with 1.0M  $Na_2SO_4$  solution, the rate of meniscus rise increase with potential decreases at potentials more cathodic than about  $-1.55V$  (vs.  $Hg/HgSO_4$ ). Since hydrogen is known to adsorb only poorly on the lead electrode and since this cathodic decrease in  $\Delta h/\Delta E$  is not observed with dilute solutions of 0.01 and 0.1M, its occurrence with 1.0M solutions probably results from some specific adsorption of the sodium ion on the lead surface.

#### Acknowledgment

The author wishes to thank Mr. A. Gendron for his assistance in the physical realization of the work.

Manuscript submitted Feb. 25, 1974; revised manuscript received ca. May 21, 1974.

Any discussion of this paper will appear in a Discussion Section to be published in the June 1975 JOURNAL. All discussions for the June 1975 Discussion Section should be submitted by Feb. 1, 1975.

The publication costs of this article have been assisted by the Hydro-Quebec Institute of Research.

#### REFERENCES

1. I. Morcos and H. Fischer, *J. Electroanal. Chem.*, **17**, 7 (1968).
2. I. Morcos, *Collection Czech. Chem. Commun.*, **36**, 689 (1971).
3. I. Morcos, *J. Colloid Interface Sci.*, **37**, 410 (1971).
4. I. Morcos, Paper presented at CITCE, Prague, September 1970.
5. I. Morcos, Paper 291 presented at the Electrochemical Society Meeting, Los Angeles, Calif., May 10-15, 1970.



6. I. Morcos, *J. Chem. Phys.*, **56**, 3996 (1972).
7. I. Morcos, *J. Electroanal. Chem.*, **20**, 479 (1969).
8. I. Morcos, *J. Chem. Phys.*, **57**, 1801 (1972).
9. I. Morcos, *J. Phys. Chem.*, **76**, 2750 (1972).
10. I. Morcos, in "Proceedings of the Symposium on Oxide-Electrolyte Interfaces," R. S. Alwitt, Editor, pp. 143-154, Electrochemical Society Soft-bound Symposium Series, Princeton, N. J. (1973).
11. J. P. Carr, N. A. Hampson, and R. Taylor, *J. Electroanal. Chem. and Interfac. Electrochem.*, **33**, 109 (1971).
12. J. P. Carr, N. A. Hampson, S. N. Holley, and R. Taylor, *ibid.*, **32**, 345 (1971).
13. T. Borisova, B. Ershler, and A. N. Frumkin, *Zh. Khim.*, **22**, 925 (1948).
14. G. M. Deriaz, Ph. D. Thesis, University of Birmingham, 1951.
15. N. V. Nikolaeva, N. S. Shapino, and A. N. Frumkin, *Dokl. Akad. Nauk SSSR*, **86**, 581 (1952).
16. A. N. Frumkin, *J. Res. Inst. Catalysis, Hokkaido Univ.*, **15**, 61 (1967).
17. W. J. Anderson and W. N. Hansen, *J. Electroanal. Chem.*, **43**, 329 (1973).

## Cyclic Voltammetry and Chronocoulometry with $trans\text{-Rh}(\text{en})_2\text{Cl}_2^+$ at Mercury Electrodes

Janis Gulens,<sup>1</sup> Dusan Konrad,<sup>2</sup> and Fred C. Anson

Arthur Amos Noyes Laboratory of Chemical Physics,  
California Institute of Technology, Pasadena, California 91109

### ABSTRACT

Cyclic voltammetric, coulometric, and chronocoulometric data associated with the reduction of  $\text{Rh}(\text{en})_2\text{Cl}_2^+$  at mercury electrodes are reported that confirm previous results indicating the occurrence of a two-electron reduction to produce the hydrido complex,  $\text{Rh}(\text{en})_2\text{H}(\text{OH}_2)^{2+}$ , which engages in a pH dependent equilibrium involving  $\text{Rh}(\text{en})_2^+$ :  $\text{Rh}(\text{en})_2\text{H}(\text{OH}_2)^{2+} + \text{OH}^- \rightleftharpoons \text{Rh}(\text{en})_2^+ + 2\text{H}_2\text{O}$ . The resulting presence of  $\text{Rh}(\text{en})_2^+$  at the electrode surface has a number of interesting consequences which are described. Among these are the electrochemical production of metal-metal bonded rhodium-mercury adducts, apparent strong adsorption of  $\text{Rh}(\text{en})_2^+$  on the electrode surface, and anomalous cyclic voltammograms with inverted peaks.

As part of a study of the possible role of adsorbed transition metal complexes in the catalysis of electrode processes, we have been investigating the electrochemistry of some complexes of rhodium(III) because of their prominence as catalysts in homogeneous reactions (1, 2). Previous polarographic and controlled potential electrolytic studies of various hexacoordinate chloroaminorhodium(III) complexes (3-6) have established a common pattern of a single, two-electron reduction in which halide is liberated and tetra-coordinate rhodium(I) complexes are produced. In the case of the  $trans\text{-Rh}(\text{py})_4\text{Cl}_2^+$  complexes the polarographic behavior observed was taken to indicate that the rhodium(I) product was adsorbed on the mercury electrode (4).

We chose to investigate the electrochemical behavior of  $trans\text{-Rh}(\text{en})_2\text{Cl}_2^+$  in the hope of generating  $\text{Rh}(\text{en})_2^+$  as an intermediate which might be reacted with added, electrochemically inactive substrates. We were further intrigued by the reports (7) that controlled potential, electrolytic reduction of this complex under certain conditions yielded a rhodium(II) product which is a rare oxidation state for rhodium (1). In a recent paper (8) it was shown that the electrolysis product thought to contain rhodium(II) (7) was actually a rhodium(I) adduct of mercury(II) formed by a combination of electrochemical and chemical reactions at the surface of the mercury pool electrode. During the course of that study there came to light a number of features of the electrochemistry of  $trans\text{-Rh}(\text{en})_2\text{Cl}_2^+$  at mercury electrodes which have not been previously described. They form the basis for this report.

### Experimental

The preparations of the complexes  $trans\text{-Rh}(\text{en})_2\text{Cl}_2^+$ ,  $(\text{en})_2\text{RhHgRh}(\text{en})_2^{4+}$ , and  $(\text{en})_2\text{RhHg}(\text{OH}_2)^+$  were described previously (8). The experiments reported here were performed in supporting electrolytes consisting of sodium methane sulfonate plus added buffering agents, but the behavior in nitrate or perchlorate supporting electrolytes is essentially identical [ $trans\text{-Rh}(\text{en})_2\text{Cl}_2^+$  and  $[(\text{en})_2\text{Rh}]_2\text{Hg}^{4+}$  complexes are only sparingly soluble in  $\text{NaClO}_4$ ]. All solutions were prepared from triply distilled water and were deaerated with prepurified nitrogen.

Cyclic voltammograms were obtained with a conventional, operational amplifier based electrochemical apparatus and were recorded by photographing the traces stored on a Tektronix Model 564 oscilloscope. The cells and hanging mercury drop electrode (area = 0.029 cm<sup>2</sup>) were conventional. Potentials were measured and are quoted with respect to a sodium chloride saturated calomel reference electrode which had a potential 5 mV more negative than a SCE.

Chronocoulometry (9) was performed using the previously described digital data acquisition and analysis system (10). Usually 100 data points were taken at 200  $\mu\text{sec}$  intervals. The chronocoulometric values for surface concentrations of adsorbed electroactive species were obtained by subtracting the charge changes measured in rhodium-free solutions from the intercepts of charge-(time)<sup>1/2</sup> plots or, in some cases, from the charge value of the first data point (acquired 200  $\mu\text{sec}$  after the potential step was applied). The accuracy of the resulting values of the quantity of adsorbed species is discussed in the text.

Controlled potential electrolyses at stirred mercury pool electrodes were carried out by means of a Wenking potentiostat (Model TR). The electrolyses currents and their time integrals were displayed on a pen and

<sup>1</sup> Present address: Atomic Energy Canada Limited, Chemistry and Materials Division, Chalk River, Ontario, Canada K0J 1J0.

<sup>2</sup> Present address: ESB Research, Incorporated, Yardley, Pennsylvania 19067.

Key words: rhodium complexes, adsorption, rhodium-mercury bonds.

ink recorder. Changes in solution pH resulting from electrolysis were determined with a conventional pH meter and a Fisher Scientific Company "Blue Glass" pH electrode which was calibrated so that its readings could be converted directly to the analytical concentrations of H<sup>+</sup> and OH<sup>-</sup> in the range from 10<sup>-3</sup> to 10<sup>-1</sup>M.

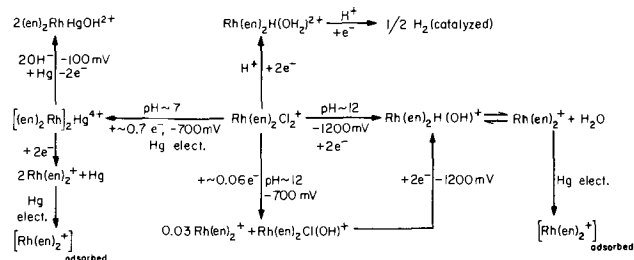
Steady-state background currents continued to flow at the end of the controlled potential electrolysis of solutions of *trans*-Rh(en)<sub>2</sub>Cl<sub>2</sub><sup>+</sup> or *trans*-Rh(en)<sub>2</sub>-Cl(OH)<sup>+</sup> at -1100 or -1200 mV. The magnitude of these currents increased as the applied potential became more negative but they were typically of the order of 20-30 μA/cm<sup>2</sup> after a 40-50 min electrolysis. Under these conditions the background correction (Q<sub>background</sub> = i<sub>steady state</sub> × t<sub>electrolysis</sub>) amounted to ca. 10-15% of the total charge consumed.

Spectra of the electrolysis solutions were obtained at various stages during an electrolysis by transferring aliquots under nitrogen to previously purged spectrophotometer cells and recording the spectra with a Cary Model 11 or Beckman spectrophotometer.

### Results and Discussion

The electrochemical behavior of *trans*-Rh(en)<sub>2</sub>-Cl<sub>2</sub><sup>+</sup> is complicated by a tendency toward severe "maxima" related stirring of the solution at both hanging and dropping mercury electrodes. Further complications are introduced by the pH dependent chemical reactions engaged in by the initial product of the electrode reaction to yield electroinactive final products. A combination of pulse techniques and controlled potential electrolyses with continual spectral monitoring of the solution was employed to try to deal with the many experimental obstacles inherent in the electrochemistry of this complex and its reduction products. Because the behavior observed is quite dependent on pH it seems profitable to divide the description of the results on the basis of the solution pH.

The most prominent of the electrochemical and coupled chemical processes exhibited by the Rh(en)<sub>2</sub>Cl<sub>2</sub><sup>+</sup> system are summarized in Scheme I which may be useful as a reference guide during the discussion to follow.



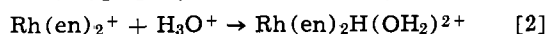
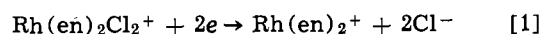
Scheme I - Electrode Reactions of Rh(en)<sub>2</sub>Cl<sub>2</sub><sup>+</sup> on Mercury

**Reduction of *trans*-Rh(en)<sub>2</sub>Cl<sub>2</sub><sup>+</sup> in the presence of protons.**—In acidic solutions the *trans*-Rh(en)<sub>2</sub>Cl<sub>2</sub><sup>+</sup> complex displays its least complicated behavior. Cyclic voltammetry in solutions in which the hydrogen ion concentration is greater than the concentration of the complex gives two well-separated waves during potential scans in the direction of more negative potentials and no corresponding oxidation waves when the scan direction is reversed. The peak potential of the first reduction wave varies with the scan rate (−E<sub>p</sub> = 580, 630, and 700 mV for scan rates of 0.46, 4.6, and 46 V/sec, respectively) while the peak current varies linearly with the concentration of the complex and with the square root of the scan rate. The potential of the second reduction wave also shifts with scan rate (−E<sub>p</sub> = 1140, 1190, and 1280 mV for the same three scan rates) and the peak current is proportional to the square root of the scan rate and to the sum of the

concentrations of the rhodium(III) complex and hydrogen ion.

The number of electrons consumed in the charge-transfer process associated with the first reduction peak under pulsed conditions was determined chronocoulometrically (9) from the slope of charge-(time)<sup>1/2</sup> plots for a potential step from -200 to -700 mV. Such plots were linear with slopes (ca. 600 μcoulombs cm<sup>-2</sup> sec<sup>-1/2</sup> mM<sup>-1</sup>) consistent with diffusion controlled reduction of the complex with the consumption of two electrons. The intercept of these plots on the charge axis matched that obtained in rhodium-free solutions indicating that the complex is not adsorbed on the electrode in detectable quantities.

Controlled potential reduction of *trans*-Rh(en)<sub>2</sub>Cl<sub>2</sub><sup>+</sup> at a Hg pool cathode at -700 mV proceeds normally in acidic solutions without any spectral evidence for the formation of an intermediate product. The starting complex is converted quantitatively to *trans*-Rh(en)<sub>2</sub>-H(OH<sub>2</sub>)<sup>2+</sup> which was identified from its known ultraviolet spectrum (7). The electrolyses consumed 2 Faradays of electricity and 1 mole of protons per mole of *trans*-Rh(en)<sub>2</sub>Cl<sub>2</sub><sup>+</sup>. The electrode process under both pulsed and controlled potential electrolytic conditions thus appears to proceed as follows



Cyclic voltammetry conducted in acidic solutions containing only *trans*-Rh(en)<sub>2</sub>H(OH<sub>2</sub>)<sup>2+</sup> gives rise to a single reduction wave with a peak potential near -1200 mV which matches the second wave obtained with solutions of Rh(en)<sub>2</sub>Cl<sub>2</sub><sup>+</sup>. There is no oxidation wave during the positive going potential scan. The peak current is proportional to the concentration of hydrogen ion and controlled potential electrolyses (at -1300 mV) of acidic solutions of *trans*-Rh(en)<sub>2</sub>-H(OH<sub>2</sub>)<sup>2+</sup> result only in the consumption of hydrogen ion with 100% faradaic efficiency. The large initial electrolyses currents decay smoothly to large steady-state currents and result in an increase in solution pH. Coulometric measurements showed that 1 Faraday of charge is consumed per mole of hydrogen ion reduced. Further reduction at -1300 mV at the steady-state current level results in a continuous increase in pH with the production of 1 mole of hydroxide ion for each Faraday of charge consumed. The cathodic peak present in acidic solutions at -1200 mV was absent from the electrolysis solutions at this point. The u.v. spectrum of the *trans*-Rh(en)<sub>2</sub>H(OH<sub>2</sub>)<sup>2+</sup> complex remained unchanged throughout the electrolyses as the pH increased from 3 to 11. The *trans*-Rh(en)<sub>2</sub>H(OH<sub>2</sub>)<sup>2+</sup> complex thus appears to be effective in decreasing the hydrogen overvoltage at mercury, but the mechanism for this catalytic action is uncertain.

**Reduction of *trans*-Rh(en)<sub>2</sub>Cl<sub>2</sub><sup>+</sup> at intermediate and high pH values.**—The cyclic voltammetric behavior of *trans*-Rh(en)<sub>2</sub>Cl<sub>2</sub><sup>+</sup> in neutral and alkaline solutions becomes increasingly more complicated as the concentration of the complex is increased and/or the potential scan rate is decreased. However, relatively straightforward behavior can be obtained by working with dilute solutions (0.1 mM) at sweep rates from 0.5 to 50 V/sec and the results of experiments conducted under these conditions will be analyzed first. Figure 1 shows a typical set of voltammograms obtained at pH 12 in which two reduction waves, at ca. -650 and -1100 mV, and an oxidation wave near -200 mV are present. The ratio of the peak current to the square root of the scan rate becomes larger as the scan rate is increased for both the first reduction wave and the oxidation wave. At a fixed scan rate the peak current for the oxidation wave does not increase linearly with the concentration of the complex but at a somewhat lower rate.

Controlled potential electrolyses of alkaline solutions of *trans*-Rh(en)<sub>2</sub>Cl<sub>2</sub><sup>+</sup> at -700 mV consume only

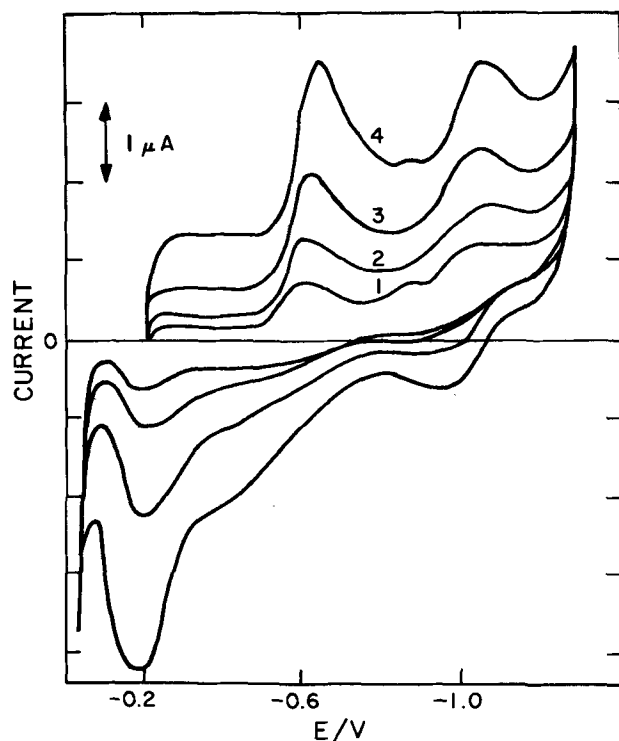


Fig. 1. Cyclic voltammograms for  $\text{trans-Rh(en)}_2\text{Cl}_2^+$  at pH 12. Conc. of complex: 0.1 mM. Supporting electrolyte: 1M  $\text{CH}_3\text{SO}_3\text{Na}$  (sodium methane sulfonate), 0.01M NaOH. Scan rates (V/sec): curve 1, 0.46; curve 2, 0.92; curve 3, 1.84; curve 4, 3.68.

ca. 0.05 Faradays of electricity per mole of the complex before the electrolysis current decreases to a very small value. Spectral analysis of the resulting solutions shows that the initial complex has been converted quantitatively into  $\text{trans-Rh(en)}_2\text{Cl(OH)}^+$ , the spectrum of which has been reported (11). A cyclic voltammogram of this solution, Fig. 2, contains a single reduction wave with a scan rate dependent peak potential near  $-1000$  mV. This conversion of the dichloro

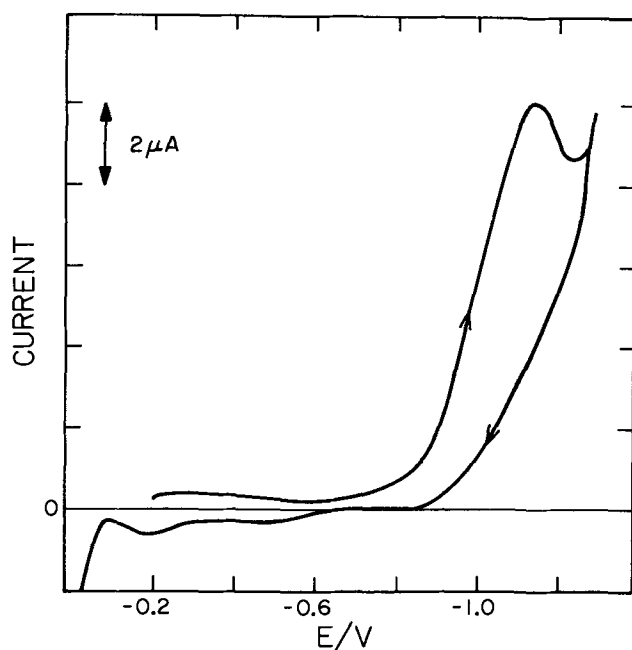
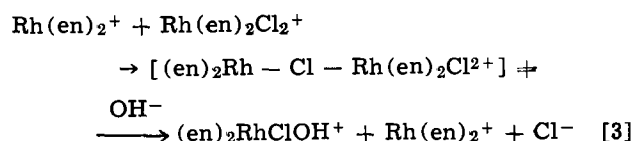


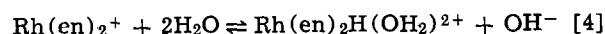
Fig. 2. Cyclic voltammogram for  $\text{trans-Rh(en)}_2\text{Cl(OH)}^+$  at pH 12. Conc. of complex: 0.9 mM. Supporting electrolyte as in Fig. 1. Scan rate: 0.46 V/sec.

to the monochloro complex most likely proceeds by means of a Rh(I)-catalyzed inner sphere redox reaction in which the  $\text{Rh(en)}_2^+$  generated electrochemically, reaction [1], catalyzes the loss of one and only one chloride from the dichloro complex by reducing it via a chloride bridged transition state, reaction [3] (12-14)



Since the  $\text{trans-Rh(en)}_2\text{Cl(OH)}^+$  product is reduced at considerably more negative potentials than the initial  $\text{trans-Rh(en)}_2\text{Cl}_2^+$  complex, only a small amount of electricity is consumed during the controlled potential electrolysis at  $-700$  mV before the solution is converted to an electroinactive form. This same catalytic decomposition of  $\text{Rh(en)}_2\text{Cl}_2^+$  by a product of its reduction is responsible for the peak current for reduction of  $\text{trans-Rh(en)}_2\text{Cl}_2^+$  near  $-650$  mV (Fig. 1) being disproportionately large at high sweep rates when less time is available for the decomposition to occur. However, even at the highest sweep rates employed in Fig. 1, the appearance of the second reduction wave near  $-1100$  mV gives evidence of some  $\text{trans-Rh(en)}_2\text{Cl(OH)}^+$  having been formed within the diffusion layer via reaction [3].

Controlled potential electrolysis of neutral and alkaline solutions of either  $\text{trans-Rh(en)}_2\text{Cl}_2^+$  or  $\text{trans-Rh(en)}_2\text{Cl(OH)}^+$  at  $-1200$  mV proceeds smoothly without any evidence for the formation of an intermediate, and 2 Faradays/mole of rhodium are consumed (after correcting for the background currents; see the Experimental section). The spectrum of the resulting solution is consistent with that reported for  $\text{trans-Rh(en)}_2\text{H(OH}_2\text{)}^{2+}$  (7), which is in equilibrium with  $\text{Rh(en)}_2^+$  according to reaction [4] (7)



Chronocoulometry was employed to demonstrate that the number of electrons involved during pulsed electrolysis of  $\text{trans-Rh(en)}_2\text{Cl}_2^+$  is the same as that consumed during controlled potential electrolysis, namely two electrons per molecule of complex. Charge vs.  $(\text{time})^{1/2}$  plots were analyzed as a function of the concentration of  $\text{trans-Rh(en)}_2\text{Cl}_2^+$  and the electrode potential (Fig. 3 and 4). Linear plots result when the potential is stepped from  $-200$  to  $-800$  mV with the most dilute solutions but the slopes of the plots are about 25% smaller than would correspond to a diffusion controlled two-electron reduction. At higher concentrations of the complex the deviations from linearity of the plots in Fig. 3 doubtless reflect the increased importance of reaction [3] in the presence of the larger concentrations of the  $\text{Rh(en)}_2^+$  catalyst being generated in the diffusion layer. When the potential is stepped to more negative potentials such as  $-1100$  mV (Fig. 4), both  $\text{trans-Rh(en)}_2\text{Cl}_2^+$  and  $\text{trans-Rh(en)}_2\text{Cl(OH)}^+$  are reduced at diffusion controlled rates and the chronocoulometric plots are linear for all initial concentrations of the complex. The ratio of the slopes of the plots to the concentrations of rhodium(III) present are also correct for a two-electron, diffusion controlled reduction.

The electrolysis product obtained at  $-1100$  or  $-1200$  mV was identified spectrally (7) as  $\text{Rh(en)}_2\text{H(OH}_2\text{)}^{2+}$ . This complex gives no reduction wave in alkaline solutions before the evolution of hydrogen which is, however, catalyzed by the presence of the complex.

Cyclic voltammograms for  $\text{trans-Rh(en)}_2\text{Cl}_2^+$  recorded in neutral, unbuffered supporting electrolyte (1M sodium methane sulfonate) are shown in Fig. 5. These voltammograms resemble those obtained at pH 12 (Fig. 2). The only significant differences are the shifts in the peak potentials to more positive values for

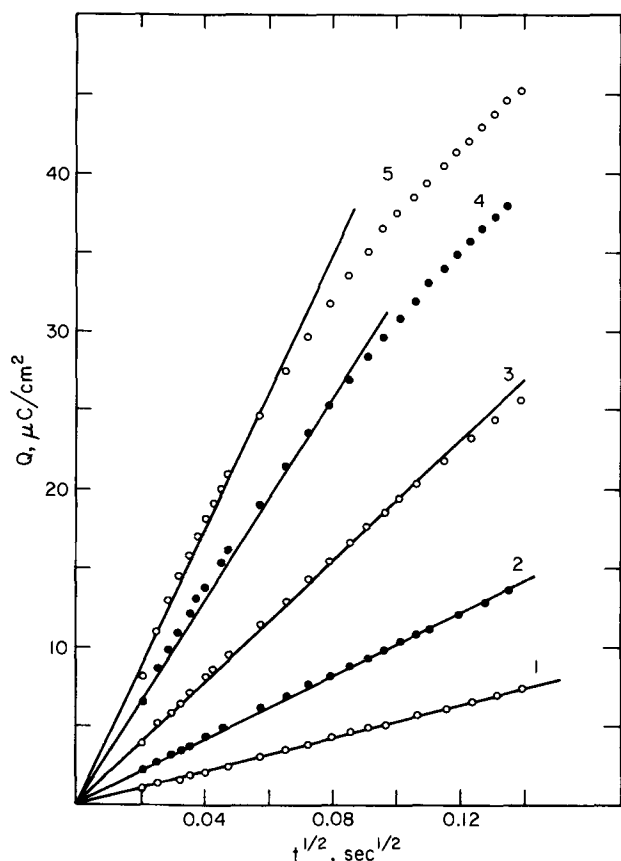


Fig. 3. Chronocoulometric plots for the reduction of  $\text{trans-Rh(en)}_2\text{Cl}_2^+$  at  $-800$  mV. Supporting electrolyte as in Fig. 1. Initial potential:  $-200$  mV. The double-layer charging blank,  $Q_{d.l.}$ , was subtracted from each point. Conc. of the complex (mM): curve 1, 0.1; curve 2, 0.2; curve 3, 0.4; curve 4, 0.65; curve 5, 0.9.

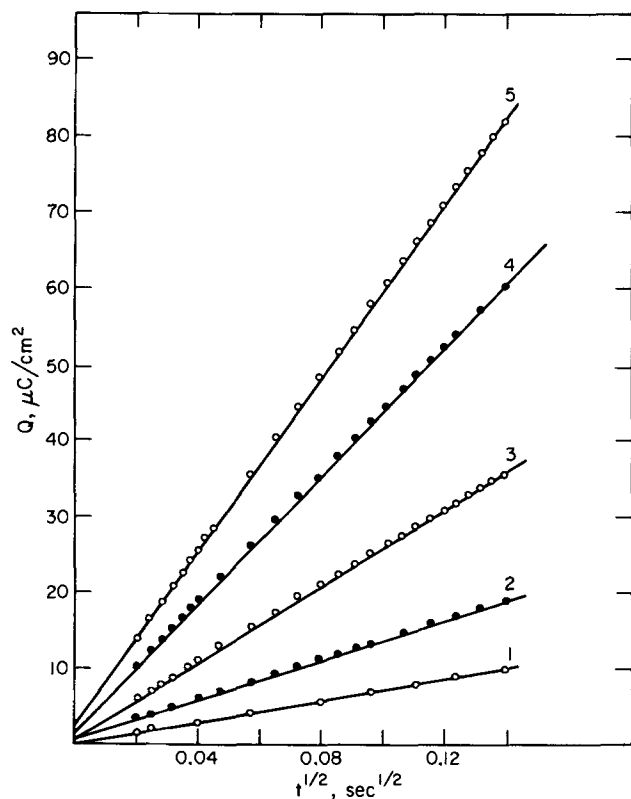


Fig. 4. Chronocoulometric plots for the reduction of  $\text{trans-Rh(en)}_2\text{Cl}_2^+$  at  $-1100$  mV. All other conditions as in Fig. 3.

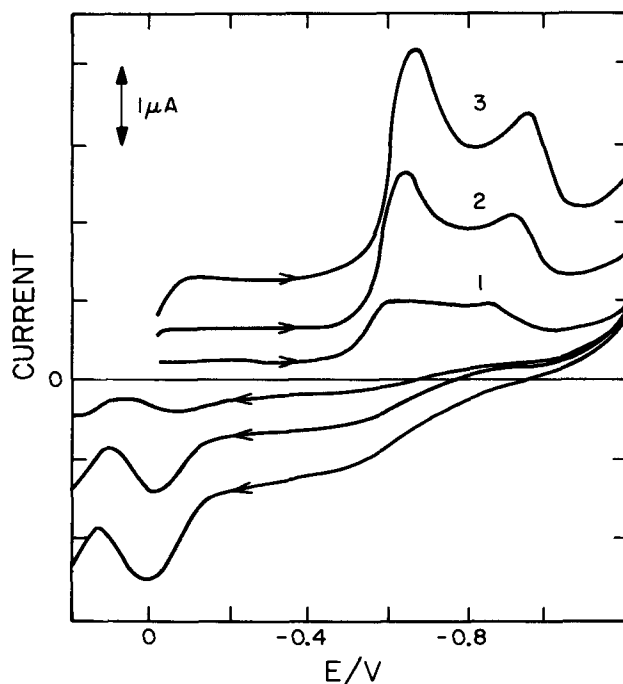


Fig. 5. Cyclic voltammograms for  $\text{trans-Rh(en)}_2\text{Cl}_2^+$  at pH 7. Conc. of complex: 0.1 mM. Supporting electrolyte: 1M  $\text{CH}_3\text{SO}_3\text{Na}$ . Scan rates (V/sec): curve 1, 0.46; curve 2, 1.84; curve 3, 3.7.

the second reduction wave ( $-900$  vs.  $-1100$  mV at pH 12) and the single oxidation wave (0 vs.  $-200$  mV at pH 12) as well as a decrease in the magnitude of the peak current for the oxidation wave.

The chronocoulometric charge-(time) $^{1/2}$  plots measured at  $-700$  mV in neutral supporting electrolytes show deviations from linearity that become quite pronounced as the initial concentration of  $\text{Rh(en)}_2\text{Cl}_2^+$  is increased (Fig. 6A). At the higher concentrations the rate of accumulation of charge, i.e., the current, is considerably below the rate that would correspond to a diffusion controlled, two-electron reduction. However, when the potential to which the electrode is stepped in the chronocoulometric experiment is made more negative, e.g.,  $-1100$  mV, linear, two-electron, diffusion controlled, charge-(time) $^{1/2}$  plots are obtained (Fig. 6B).

Controlled potential electrolysis of initially neutral, unbuffered solutions of  $\text{trans-Rh(en)}_2\text{Cl}_2^+$  at  $-1200$  mV consumes 2 Faradays/mole of complex and yields solutions of higher pH (pH 10-11 depending on the initial concentration of complex) with a spectrum matching that of  $\text{Rh(en)}_2\text{H(OH)}_2^+$ . However, when the electrolysis is conducted at potentials between  $-700$  and  $-1000$  mV, where deviant chronocoulometric plots are obtained, a new, highly colored electrolysis product appears and attains a maximum concentration after 0.7 to 1.2 Faradays of charge per mole of complex have been passed. The spectra of this new species is quite similar to that reported by Gillard and co-workers (7) who have previously described controlled potential electrolyses of neutral solutions of  $\text{trans-Rh(en)}_2\text{Cl}_2^+$ . They believed they had generated a dimeric complex of Rh(II) to which they ascribed the spectrum of the colored product, but recent experiments (8) have identified the species as a mercurated adduct of Rh(I),  $(\text{en})_2\text{RhHgRh(en)}_2^{4+}$  which is formed by the simultaneous occurrence of a reduction and an oxidation reaction at the mercury electrode at potentials between  $-700$  and  $-1000$  mV. The reactions by which this intermediate is thought to be generated are as follows (8)



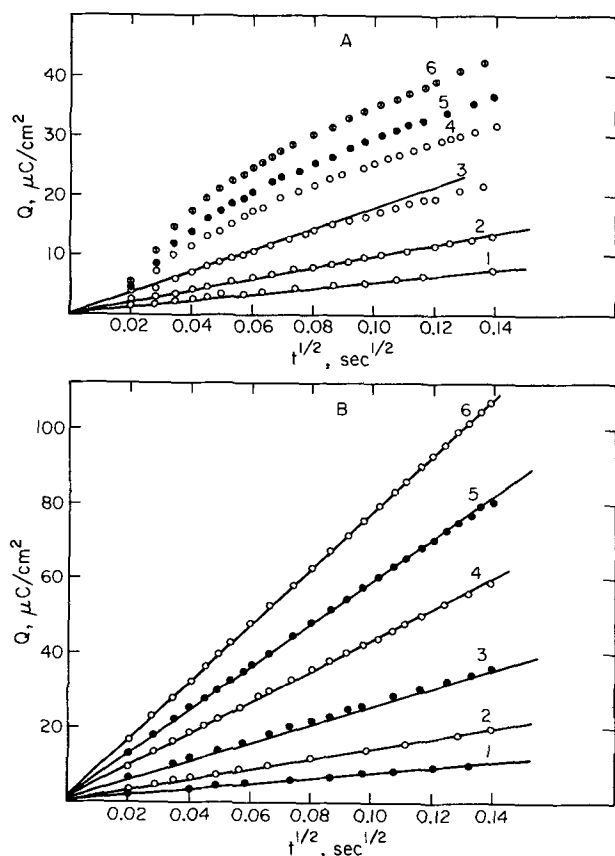


Fig. 6. Chronocoulometric plots for the reduction of  $\text{trans-Rh(en)}_2\text{Cl}_2^+$  at pH 7. Supporting electrolyte: 1M  $\text{CH}_3\text{SO}_3\text{Na}$ . Conc. of complex (mM): curve 1, 0.1; curve 2, 0.2; curve 3, 0.4; curve 4, 0.7; curve 5, 0.95; curve 6, 1.3. Initial potential:  $-200$  mV. Final potential: A,  $-700$  mV; B,  $-1100$  mV. The double-layer charging blank,  $Q_{dl}$ , was subtracted from each point.

The fact that electrons are liberated in reaction [5] is the main reason that chronocoulometric plots having slopes well below the level corresponding to a two-electron reduction of  $\text{trans-Rh(en)}_2\text{Cl}_2^+$  are obtained at  $-700$  mV (Fig. 6A) despite the fact that all of the Rh(III) is reduced to Rh(I). And the increasing deviations of these slopes from the two-electron value at larger initial concentrations of  $\text{trans-Rh(en)}_2\text{Cl}_2^+$  reflects the increasing importance of reaction [5] as the concentration of  $\text{Rh(en)}_2^+$  generated at the electrode surface in reaction [1] increases. The reason that the mercurated product is not observed at low pH is that the concentration of  $\text{Rh(en)}_2^+$  generated in acid solutions is much lower because the equilibrium involved in reaction [2] lies far to the right. At high pH, the  $\text{trans-Rh(en)}_2\text{Cl}_2^+$  initially present is converted to  $\text{trans-Rh(en)}_2\text{Cl(OH)}^+$  very early in the electrolysis (*vide supra*) and the latter complex can be reduced only at more negative potentials where reaction [5] proceeds at an insignificant rate (8).

**Oxidation of  $\text{trans-Rh(en)}_2\text{H(OH}_2\text{)}^{2+}$ .**—No oxidation waves for  $\text{trans-Rh(en)}_2\text{H(OH}_2\text{)}^{2+}$  appear in acidic solutions, but in neutral and especially in alkaline solutions this complex does exhibit oxidation waves. Figure 7 shows a cyclic voltammogram for this complex in 1M NaOH in which the potential was first scanned to more positive values and then reversed. The two reduction waves observed during the last half of the cycle only appear when the positive scan is allowed to traverse the potential region around  $-300$  mV where the single oxidation wave appears. The oxidation wave moves steadily to more positive potentials as the scan rate is increased until it merges with the background current corresponding to oxida-

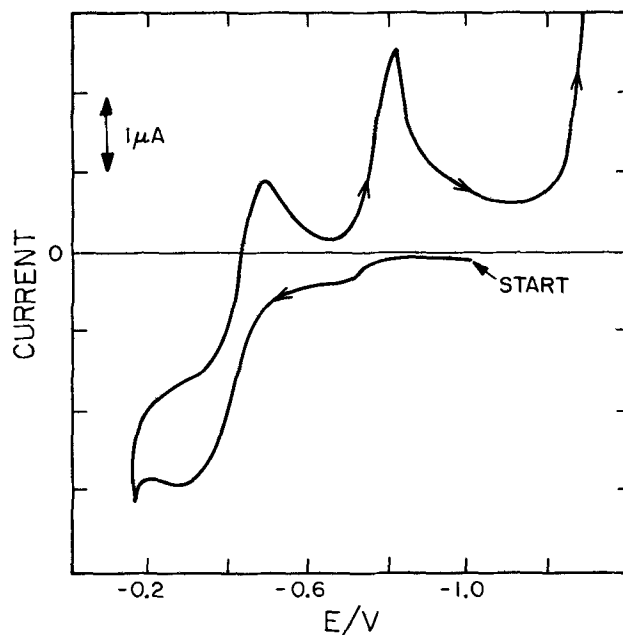
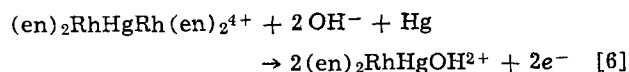


Fig. 7. Cyclic voltammogram for  $\text{trans-Rh(en)}_2\text{H(OH}_2\text{)}^{2+}$  in 1M NaOH. Conc. of complex: 1 mM. Scan rate: 0.18 V/sec.

tion of the mercury electrode in the highly alkaline electrolyte.

Controlled potential electrolysis of the same solution at  $-100$  mV leads to the stepwise formation of two mercurated complexes according to reactions [5] and [6] which each liberate 1 Faraday/mole of rhodium (8)



Thus these two rhodium-mercury complexes are the logical candidates for assignment to the two reduction waves observed during the last half of the cyclic voltammogram in Fig. 7. This assignment was confirmed by recording the voltammogram for alkaline solutions of  $(\text{en})_2\text{RhHgOH}^{2+}$  and  $[(\text{en})_2\text{Rh}]_2\text{Hg}^{4+}$  (prepared electrolytically). These voltammograms, Fig. 8 and 9, show that  $(\text{en})_2\text{RhHgOH}^{2+}$  gives rise to a reduction wave having a peak potential between  $-500$  and  $-600$  mV while  $[(\text{en})_2\text{Rh}]_2\text{Hg}^{4+}$  is reduced between  $-800$  and  $-900$  mV. Thus the reduction wave

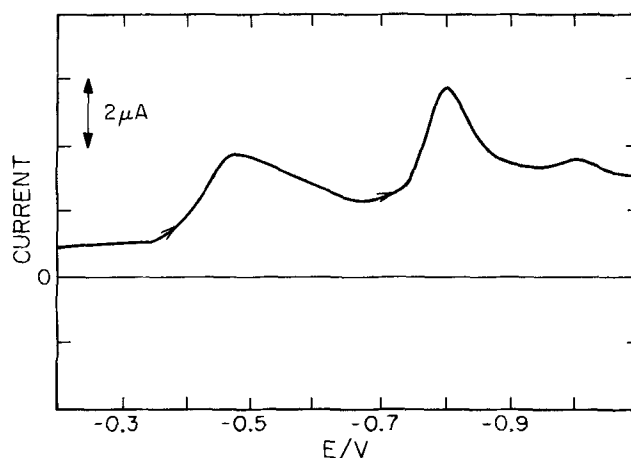


Fig. 8. Voltammogram for  $(\text{en})_2\text{RhHgOH}^{2+}$ . Conc. of complex, 1 mM. Supporting electrolyte: 0.1M  $\text{CH}_3\text{SO}_3\text{Na}$ , 0.1M NaOH. Scan rate: 0.46 V/sec.

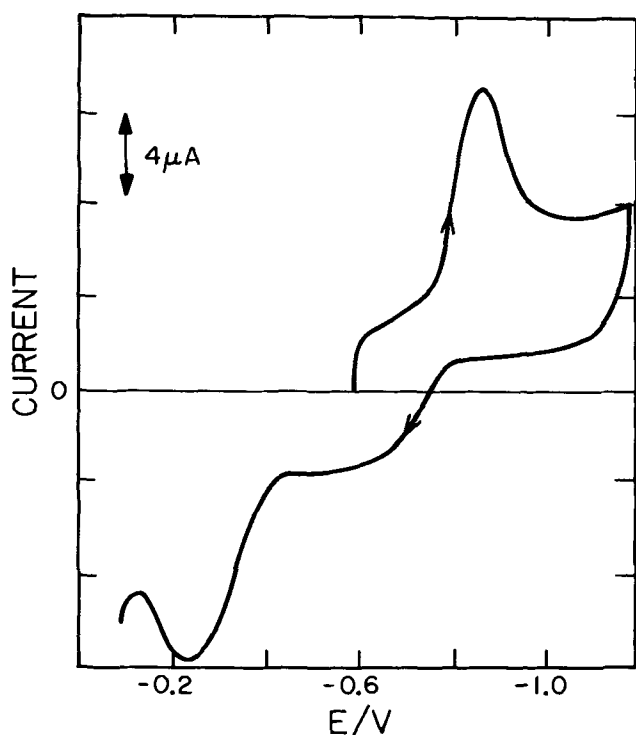
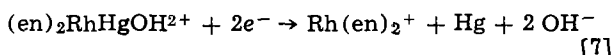
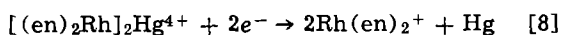


Fig. 9. Cyclic voltammogram for  $(en)_2RhHgRh(en)_2^{4+}$ . Conc. of complex: 0.5 mM. Supporting electrolyte: 0.1M  $CH_3SO_3Na$ , 0.1M  $NaOH$ . Scan rate: 4.6 V/sec.

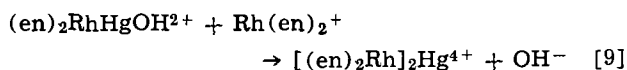
near  $-500$  mV in Fig. 7 can be attributed to reaction [7]



and the wave near  $-800$  mV to reaction [8]



Although  $[(en)_2Rh]_2Hg^{4+}$  is not present in the solution used to record Fig. 8, a reduction wave for this complex appears because it is formed in the diffusion layer next to the electrode by reaction between  $(en)_2RhHgOH^{2+}$  and the  $Rh(en)_2^+$  that is generated at the electrode during the first reduction wave



Controlled potential electrolysis of alkaline solutions of  $(en)_2RhHg(OH)^{2+}$  at  $-1000$  mV produced results that are consistent with this interpretation. The concentration of  $(en)_2RhHg(OH)^{2+}$ , determined spectrophotometrically (8) during the course of the electrolysis, decreases linearly with the quantity of electricity consumed while the concentration of  $[(en)_2Rh]_2Hg^{4+}$  increases. The maximum concentration of the latter is reached after approximately 1 Faraday of charge/mole of complex has been consumed, at which point the concentration of  $(en)_2RhHgOH^{2+}$  has become essentially zero. Continued electrolysis at  $-1000$  mV requires an additional Faraday per mole of rhodium and converts all of the  $[(en)_2Rh]_2Hg^{4+}$  into  $Rh(en)_2H(OH_2)^{2+}$ .

The foregoing results allow the oxidation wave appearing near  $-300$  mV in Fig. 7 during an initially positive potential scan with alkaline solutions of  $Rh(en)_2H(OH_2)^{2+}$  to be ascribed to reactions [5] and [6] occurring at potentials too close together to yield separate waves. The same reactions are also presumed to account for the oxidation waves observed during the second, oxidative portion of the cyclic voltammograms of *trans*- $Rh(en)_2Cl_2^+$  (Fig. 1) and *trans*- $Rh(en)_2ClOH^+$  (Fig. 2) because  $Rh(en)_2H(OH_2)^{2+}$

and (therefore)  $Rh(en)_2^+$  are generated at the electrode during the initial reductive potential scan. The oxidation wave exhibits a peak potential that is more negative (ca.  $-300$  mV) at pH 14 (Fig. 7) than in less alkaline solutions (ca.  $-50$  mV in Fig. 1). This pH dependence could result from the pH dependence of equilibrium (2) that produces the  $Rh(en)_2^+$  intermediate as well as from the direct involvement of hydroxide in the second stage of the oxidative electrode reaction (Reaction [6]).

**Possible adsorption of  $Rh(en)_2^+$ .**—The strong tendency for  $Rh(en)_2^+$  to behave as a Lewis base to form rhodium-mercury bonds (8) made it seem likely that this complex would be adsorbed on the surface of mercury electrodes. To examine this possibility, chronocoulometric experiments were conducted with solutions of  $Rh(en)_2H(OH_2)^{2+}$  at pH values from 5.3 to 14 in the expectation that equilibrium (2) would provide a source of  $Rh(en)_2^+$  in these solutions. Single potential steps were applied to the electrode from various initial values (between  $-1200$  and  $-400$  mV) to the most positive value possible at each pH without producing direct oxidation of the electrode to give  $Hg(OH)_2$ . The charge-time data resulting from each potential step were recorded every 200  $\mu$ sec. (Table I shows a typical set of data points obtained, in this case, at pH 14.) Examination of the data on a point-by-point basis reveals that the initial rate of charge consumption is quite large, exceeding in some cases the rate at which the bulk complex could be directly oxidized under diffusion limited conditions (Table I). However, the high initial rates diminish within a few hundred microseconds to values far below the diffusion limited values. This pattern of charge-time behavior is consistent with the presence of an adsorbed complex, e.g.,  $Rh(en)_2^+$ , whose rate of oxidation is limited by charge-transfer kinetics at the most positive accessible potentials. The rapid decline in the rate of accumulation of charge indicates that when the adsorbed complex is oxidatively removed its rate of replenishment from the reservoir of unreacted  $Rh(en)_2H(OH_2)^{2+}$  complex is quite low.

Inasmuch as we were unable to find conditions where diffusion controlled oxidation rates could be sustained, the chronocoulometric data could not be analyzed in the usual way by plotting the charge *vs.*  $(time)^{1/2}$  and extrapolating to zero time to determine the quantity of adsorbed reactant (9). Instead, the first data point, recorded 200  $\mu$ sec following the positive potential step, was taken as an approximate measure of the quantity of adsorbed complex. The double-layer charging blank, measured by stepping the potential between the same two values in rhodium-free electrolyte, was subtracted from the first data point to obtain approximate values for the adsorption. This procedure will underestimate the amount of adsorption if the rate of oxidation of the adsorbed complex is too low for the reaction to be complete in 200  $\mu$ sec, but the fact that the rate of charge accumulation is considerably smaller by the time 400  $\mu$ sec has elapsed (Table I)

Table I. Charge-time data during the oxidation of a 1.06 mM solution of  $Rh(en)_2H(OH_2)^{2+}$  at  $-200$  mV in 1M  $NaOH$

Time, msec after potential step	Charge, $\mu$ coulombs/cm <sup>2</sup> for initial potentials (mV) of					Calculated charge for a two-electron diffusion controlled case
	-1200	-1000	-800	-600	-400	
0.2	8.1	16.2	19.3	13.9	8.6	9.0
0.4	10.3	19.6	22.7	17.1	10.9	12.7
0.6	10.8	20.1	23.2	17.7	11.3	15.6
0.8	11.3	20.6	23.6	18.2	11.7	18.0
1.0	11.4	20.7	23.6	18.3	11.8	20.1
2.0	12.0	21.4	24.3	19.1	12.5	28.4
20.0	15.8	24.8	27.7	24.0	16.4	90.0

\* The double-layer charging blanks,  $Q_{dl}$ , were subtracted from the charge values at each potential.

makes this an unlikely source for serious error. An overestimate of the adsorption will result if the true double-layer charging blank is diminished by the adsorption or if significant unadsorbed reactant diffuses to the electrode during the first 200  $\mu\text{sec}$ . Neither of these sources of possible error appeared to be significant enough to affect the qualitative features observed.

The fact that the oxidative current falls rapidly to very low values could reflect a sluggishness in the rate of reaction [2]. Mild evidence against this interpretation was obtained by extending the measurements to much longer times and observing no significant increase in the slopes of the charge-(time)<sup>1/2</sup> plots. An alternative possible origin of the brevity of the oxidation currents is that the product of the oxidation of the adsorbed complex is itself adsorbed. This could result in a sizable diminution in the rate of an oxidation reaction which required the formation of mercury-rhodium bonds by depriving the rhodium complex of access to the mercury surface.

Figure 10 summarizes the estimated adsorption as a function of initial potential and solution pH. In converting the measured charges into moles of adsorbed complex it was assumed that the electrode reaction releases two electrons per molecule of  $\text{Rh}(\text{en})_2^+$ , i.e., that the net reaction product is  $(\text{en})_2\text{RhHgOH}^{2+}$ . The uniform increase in adsorption with pH is the strongest evidence for the suggestion that the adsorbing

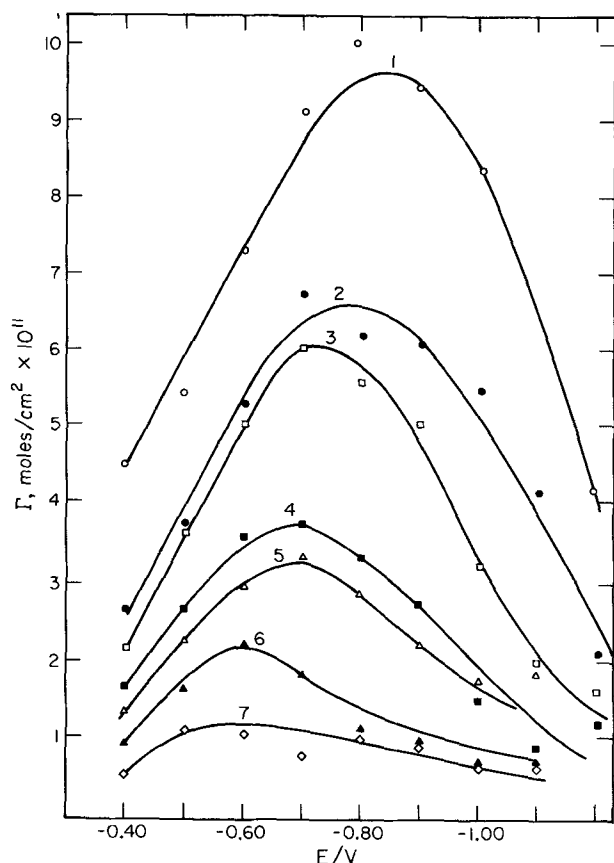


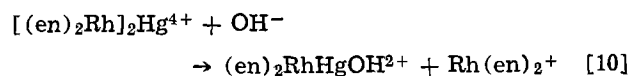
Fig. 10. Approximate adsorption of what is thought to be  $\text{Rh}(\text{en})_2^+$  (see text) as a function of pH and electrode potential. The solution contained 1.06 mM  $\text{Rh}(\text{en})_2\text{H}(\text{OH}_2)^{2+}$ , 1M  $\text{CH}_3\text{SO}_3\text{Na}$ , and NaOH to adjust the pH. The plotted values of  $\Gamma$  are based on the total charge passed 200  $\mu\text{sec}$  after an anodic potential step was applied less the double-layer charging blank. The initial potentials are plotted as abscissa. The final potentials and pH values were: curve 1, -200 mV, pH 14; curve 2, -150 mV, pH 13; curve 3, -150 mV, pH 11.9; curve 4, -50 mV, pH 10.8; curve 5, -50 mV, pH 10.1; curve 6, +100 mV, pH 9; curve 7, +100 mV, pH 5.3.

species is  $\text{Rh}(\text{en})_2^+$  formed via the equilibrium expressed in reaction [4].

The dependence of the adsorption on the initial electrode potential lacks a ready rationalization. The decrease in the adsorption at the most positive potentials no doubt results from the partial oxidation of the adsorbed complex at the initial potential because small anodic currents were obtained at initial potentials of -500 or -400 mV in these solutions. The decrease in adsorption at the most negative potentials may be a reflection of the Lewis acid base nature of the adsorption reaction. The Lewis acidity of the mercury surface will be a function of its charge density, increasing at positive charges and declining at negative charges (15). At the most negative charge densities the formation of the rhodium-mercury adsorption bond may be hindered because the mercury based orbitals into which the rhodium(I) complex donates electrons becomes increasingly occupied.

Whatever the origin of the potential dependence of the adsorption, it is worth noting that it may afford a simple and direct means for generating high local concentrations of (unadsorbed)  $\text{Rh}(\text{en})_2^+$ . Exposing a mercury electrode to a solution of  $\text{Rh}(\text{en})_2\text{H}(\text{OH}_2)^{2+}$  at potentials between -600 and -800 mV appears to result in the adsorption of  $\text{Rh}(\text{en})_2^+$ . If the potential is now stepped in the negative direction to, say, -1200 mV, a portion of the adsorbed complex should be desorbed but no faradaic reduction current will flow. If suitable substrates are added to the solution, it may be possible to observe an enhancement in their rates of (e.g., oxidative addition) reaction with the  $\text{Rh}(\text{en})_2^+$  because of its transiently increased concentration. Experiments to test this possibility are planned.

**Chronocoulometry of  $[(\text{en})_2\text{Rh}]_2\text{Hg}^{4+}$ .**—In alkaline solutions  $[(\text{en})_2\text{Rh}]_2\text{Hg}^{4+}$  can be oxidized (reaction [6]) as well as reduced (reaction [8]). Figure 11 shows charge-(time)<sup>1/2</sup> plots for the reduction reaction at several potentials. The slopes correspond to a two-electron, diffusion controlled reduction and the small intercepts indicate little or no adsorption of the complex. By contrast, when the potential is stepped to values where the complex is oxidized, the chronocoulometric plot (Fig. 12) displays a large intercept indicative of substantial adsorption of an oxidizable species. The slope of the plot corresponds to a two-electron, diffusion controlled oxidation reaction. A possible explanation for this superficially discrepant behavior takes advantage of the fact that adsorbed  $\text{Rh}(\text{en})_2^+$  will contribute to the intercepts of anodic but not to cathodic chronocoulometric plots because it is not reduced. Adsorbed  $\text{Rh}(\text{en})_2^+$  may be produced at intermediate potentials in alkaline solutions of  $[(\text{en})_2\text{Rh}]_2\text{Hg}^{4+}$  as follows



Reaction [10] resembles reaction [2] and the resulting  $\text{Rh}(\text{en})_2^+$  would adsorb on the electrode and contribute to anodic but not cathodic chronocoulometric intercepts. The fact that the apparent adsorption of  $\text{Rh}(\text{en})_2^+$  is larger in solutions of  $[(\text{en})_2\text{Rh}]_2\text{Hg}^{4+}$  than in solutions of  $\text{Rh}(\text{en})_2\text{H}(\text{OH}_2)^{2+}$  may reflect the difference in the equilibrium quotients for reactions [2] and [10].

Note that reduction of solutions of  $[(\text{en})_2\text{Rh}]_2\text{Hg}^{4+}$  at -1200 mV will produce high local concentrations of  $\text{Rh}(\text{en})_2^+$  from the combination of the desorption of the initially adsorbed  $\text{Rh}(\text{en})_2^+$  and the faradaic reduction of  $[(\text{en})_2\text{Rh}]_2\text{Hg}^{4+}$  according to reaction [8]. Thus, solutions of this cation offer another route to  $\text{Rh}(\text{en})_2^+$  which has the advantage [over the previously described desorptive route via  $\text{Rh}(\text{en})_2\text{H}(\text{OH}_2)^{2+}$ ] that the  $\text{Rh}(\text{en})_2^+$  can be generated

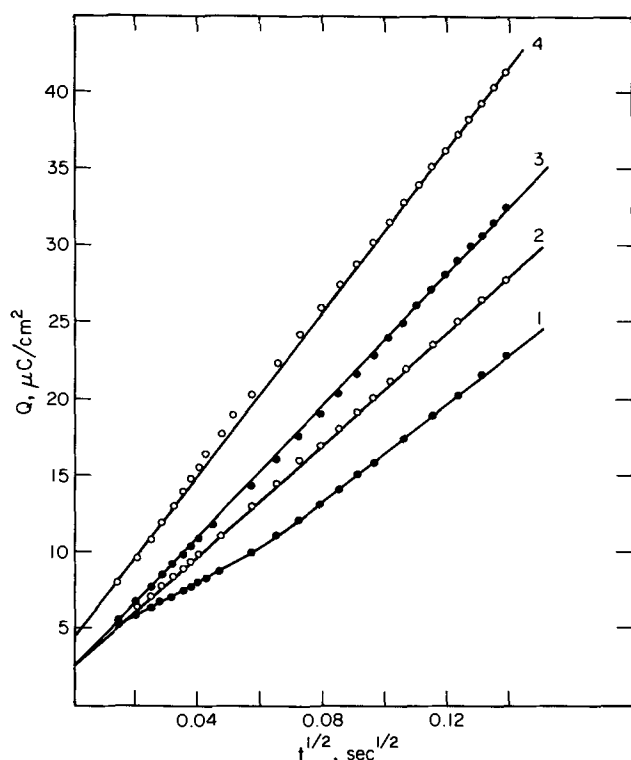


Fig. 11. Chronocoulometric plots for the reduction of  $(en)_2RhHgRh(en)_2^{4+}$ . Conc. of complex: 0.57 mM. Supporting electrolyte: 1M  $CH_3SO_3Na$ , 0.1M  $NaOH$ . The double-layer charging blank,  $Q_{dl}$ , was subtracted from each point. Initial potential: -600 mV. Final potential (mV): curve 1, -900; curve 2, -1000; curve 3, -1100; curve 4, -1200.

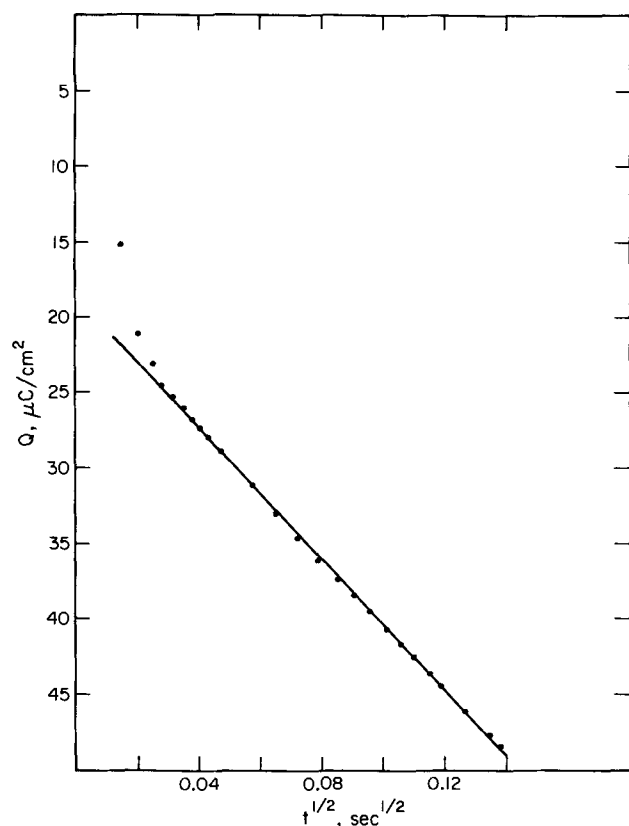


Fig. 12. Chronocoulometric plot for the oxidation of  $(en)_2RhHgRh(en)_2^{4+}$  at -150 mV. All other conditions as in Fig. 11.

steadily at a rate limited only by the diffusion of the mercurated complex to the electrode surface.

When  $[(en)_2Rh]_2Hg^{4+}$  is reduced at intermediate potentials (-700 or -800 mV) the currents are smaller than the diffusion limited current and their time dependence gives evidence of an apparent inhibition of the electrode process by a product of the reaction. The adsorption of  $Rh(en)_2^+$  which is maximal at these potentials (Fig. 10) would produce an electrode surface bearing a net positive charge (the quantity of adsorbed cations exceeds the negative electronic charge) that could easily result in a sharp decrease in the rate of reduction of a tetrapositive reactant,  $[(en)_2Rh]_2Hg^{4+}$ , because of its repulsion from the diffuse double layer. Such an effect would also help to account for the previous observation (8) that  $[(en)_2Rh]_2Hg^{4+}$  is slowly reduced at -700 mV although this is also the potential where the same complex can be generated during the reduction of *trans*- $Rh(en)_2Cl_2^+$  via reactions [1] and [5]. During the initial stages of such an electrolysis when the concentration of  $Rh(en)_2^+$  is largest, its adsorption on the electrode could be responsible for the temporary inhibition of reaction [5] while reaction [1] proceeds. Later, when the *trans*- $Rh(en)_2Cl_2^+$  has been largely consumed, the concentration of  $Rh(en)_2^+$  at the electrode surface will be smaller and its adsorption will decrease which could lead to an increase in the rate of reduction of  $[(en)_2Rh]_2Hg^{4+}$  as its repulsion from the diffuse layer diminishes. Additional measurements are needed to verify this line of speculative reasoning but the evidence clearly indicates the presence of some kind of inhibitive coupling between the electrode reaction and its product.

*Anomalous cyclic voltammograms.*—As mentioned earlier, most of the complexes studied exhibited unusual cyclic voltammetric behavior at higher concentrations and with scan rates that require several seconds for the recording of the voltammogram. Figure 13 is an example of the kind of voltammetric behavior typically observed under these conditions. The major anomalous feature in the voltammogram is the appearance of a reductive current peak during the oxidative half of the potential cycle. Often this feature is

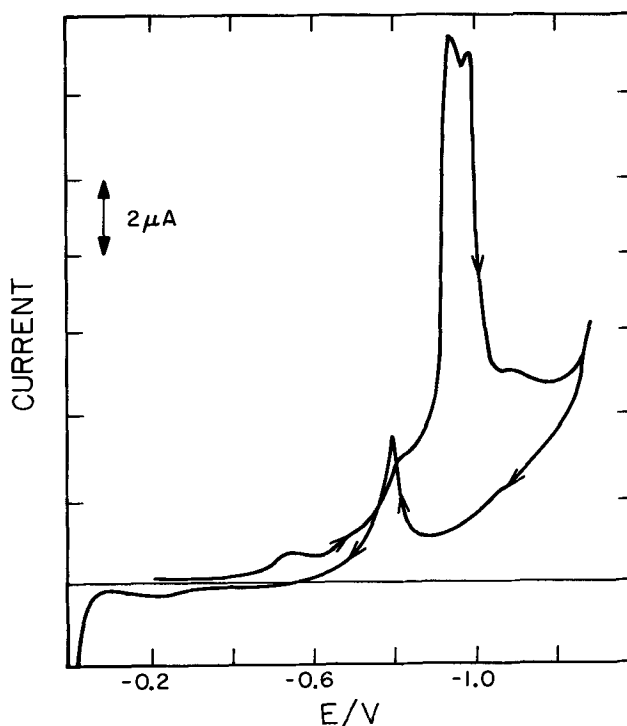


Fig. 13. Cyclic voltammogram for 0.9 mM *trans*- $Rh(en)_2Cl_2^+$  at a low scan rate: 0.18 V/sec. All other conditions as in Fig. 1.



preceded by the appearance of several, less prominent current peaks during the reductive half of the potential cycle. Such "wrong-way" current peaks in cyclic voltammograms have been previously reported in a variety of systems (16-19), especially those involving the generation of free radicals capable of spontaneous reactions with mercury electrode surfaces to yield organomercurial products (16-18). Although we were usually able to find conditions (high scan rates, low concentrations) where these anomalies were absent, it seems worthwhile to report their prominence under other conditions and to express our concurrence with the suggestion (16) that their origin is related to that of polarographic maxima, namely convective stirring of the electrode-electrolyte interface (20). The sudden changes in interfacial tension usually associated with such stirring of the interfacial region are accentuated by rapid changes in the concentrations of adsorbing species,  $\text{Rh(en)}_2^+$  in the present case. The fact that the "wrong-way" current peaks appear at just the potentials where the chronocoulometric data show the greatest adsorption of  $\text{Rh(en)}_2^+$  adds support to this interpretation, as does the similarity between the chemistry of organic radicals and  $\text{Rh(en)}_2^+$ , both of which attack mercury electrodes to produce mercurated products (8, 16, 18).

#### Acknowledgments

We thank the National Science Foundation (U.S.A.), the U.S. Army Research Office (Durham), the National Research Council (Canada), and the Petroleum Research Fund, administered by the American Chemical Society, for support of various portions of this work. Helpful discussions with Drs. John Bercaw, Steven Frank, and Robert Rodgers are a pleasure to acknowledge.

Manuscript submitted April 18, 1974; revised manuscript received July 1, 1974.

Any discussion of this paper will appear in a Discussion Section to be published in the June 1975 JOURNAL. All discussions for the June 1975 Discussion Section should be submitted by Feb. 1, 1975.

The publication costs of this article have been assisted by the California Institute of Technology.

#### REFERENCES

1. W. P. Griffith, "The Chemistry of the Rarer Platinum Metals," Interscience Publishers, New York (1967).
2. "Transition Metals in Homogeneous Catalysis," G. N. Schrauzer, Editor, Marcel Dekker, Inc., New York (1971).
3. R. D. Gillard, J. A. Osborn, and G. Wilkinson, *J. Chem. Soc.*, 4107 (1965).
4. L. E. Johnston and J. A. Page, *Can. J. Chem.*, **47**, 2123 (1969).
5. L. E. Johnston and J. A. Page, *ibid.*, **47**, 4241 (1969).
6. D. R. Crow, *Inorg. Nucl. Letters*, **5**, 291 (1969).
7. R. D. Gillard, B. T. Heaton, and D. H. Vaughan, *J. Chem. Soc. (A)*, 3126 (1970); 734 (1971).
8. J. Gulens and F. C. Anson, *Inorg. Chem.*, **12**, 2568 (1973).
9. F. C. Anson, *Anal. Chem.*, **38**, 54 (1966).
10. G. Lauer, R. Abel, and F. C. Anson, *ibid.*, **39**, 765 (1967).
11. H. L. Bott and A. J. Poe, *J. Chem. Soc. (A)*, 205 (1967).
12. J. V. Rund, F. Basolo, and R. G. Pearson, *Inorg. Chem.*, **3**, 658 (1964).
13. J. V. Rund, *ibid.*, **1**, 24 (1968).
14. R. D. Gillard, B. T. Heaton, and D. H. Vaughan, *J. Chem. Soc. (A)*, 1840 (1971).
15. D. J. Barclay, *J. Electroanal. Chem.*, **19**, 318 (1968).
16. B. Fleet and R. D. Jee, *ibid.*, **25**, 397 (1970).
17. D. A. Tysee, *ibid.*, **30**, App. 14 (1971).
18. J. H. Wagenknecht, *This Journal*, **119**, 1494 (1972).
19. K. E. Johnson and D. T. Sawyer, *J. Electroanal. Chem.*, **49**, 95 (1974).
20. H. H. Bauer, *Electrochim. Acta*, **18**, 427 (1973).

## Electromigrational Depletion (ED) Chronopotentiometry Temperature Dependence of Diffusion in Molten $\text{BeF}_2\text{-LiF}$

C. E. Vallet,<sup>1</sup> H. R. Bronstein, and J. Braunstein

Chemistry Division, Oak Ridge National Laboratory, Oak Ridge, Tennessee 37830

#### ABSTRACT

New chronopotentiometric measurements with a Be anode in highly viscous molten 95 mole per cent  $\text{BeF}_2$ -5 mole per cent LiF mixture are described in the range of temperature 564°-704°C. The transition is a result of electromigrational depletion (ED) of mobile nonelectroactive lithium ions. The equation of the chronopotentiogram is derived with the linear phenomenological equations of the thermodynamics of irreversible processes. Interdiffusion coefficients are derived from analysis of emf-time data along the chronopotentiograms rather than from a transition time alone. The low values,  $3 \times 10^{-9}$ - $3 \times 10^{-7}$  cm<sup>2</sup>/sec and high Arrhenius energy, 50.5 kcal/mol, are compared with the results of molecular dynamics computer experiments and the values of other transport coefficients in this and related systems.

Transport and thermodynamic properties of beryllium fluoride-alkali fluoride mixtures are of interest in connection with theories of ionic liquids and structural relationships to silicates and other glass-forming systems. Although studies of thermodynamic properties (1), transference numbers (2), and electrical conductance (3) have been reported for  $\text{BeF}_2$ -rich fluoride systems, little diffusional behavior has been reported,

<sup>1</sup> On leave from the Laboratoire de Thermodynamique, Associe au C.N.R.S., Universite de Provence, France.

Key words: beryllium electrode,  $\text{BeF}_2$  distillation apparatus, glasses, irreversible thermodynamics, transference number.

except for recent molecular dynamics (MD) computer experiments (4).

Recently we have shown that on the basis of unicationic conduction (2) in MF- $\text{BeF}_2$  mixtures (by  $\text{M}^+$  relative to  $\text{F}^-$ ) a chronopotentiometric transition is expected, and was demonstrated, at a Be anode in molten  $\text{BeF}_2$ -rich mixtures containing NaF (5). The transition is a result of electromigrational depletion of mobile nonelectroactive alkali ions rather than, as in ordinary chronopotentiometry (6), faradaic depletion of electrically immobile electroactive constituents (5).

This phenomenon, which we shall term ED, has been observed also with an aluminum anode in alkali chloride-aluminum chloride melts (7). Mutual diffusion coefficients were estimated from measured transition times with the Sand equation (6), which had been derived approximately for ED chronopotentiometry (5). The calculations also required estimation of the activity coefficients and the electrode areas (5, 7).

In this paper we derive the equation of the chronopotentiogram more rigorously with the linear phenomenological equations of the thermodynamics of irreversible processes (8), considering the possible coupling between migrational and diffusional flows and focusing attention on the assumptions in the derivation. We also present new chronopotentiometric data at five temperatures in the system 95 mole per cent (m/o) BeF<sub>2</sub>-5 m/o LiF for which activity coefficient data are available (1). Beryllium anodes of known area and geometry were employed. We present the computation of the diffusion coefficient from emf-time data along the chronopotentiogram, rather than from the transition time alone. Finally, we discuss the resulting diffusion coefficients and their temperature dependence in the light of the MD computer experiments and the values of other transport coefficients in this system.

### ED Anodic Chronopotentiometry of Be in BeF<sub>2</sub>-Rich Mixtures with Alkali Fluorides

**Conditions for ED chronopotentiometry.**—The distinction between ED and ordinary chronopotentiometry may be indicated with reference to Fig. 1, which illustrates schematically the various flows in a voltammetric experiment with a binary electrolyte mixture, here LiF-BeF<sub>2</sub>. In chronopotentiometry a constant current is caused to flow between a working electrode or indicator electrode and a counterelectrode. The potential is measured between the indicator electrode, which becomes concentration polarized, and a reference electrode (or reference half cell) through which no current flows. The indicator electrode current may be made anodic or cathodic, depending on the properties of the system and the aim of the investigation.

In ordinary chronopotentiometry (6) the electroactive constituent is present at very low concentration in a supporting electrolyte. The function of this supporting electrolyte is to suppress migration of the dilute electroactive solute whose electrical mobility may be as high as or higher than that of one of the supporting electrolyte's ionic constituents. Under these circumstances the transference number of the constituent

$$t_i = \frac{e_i Z_i c_i' u_i}{\sum_j e_j Z_j c_j' u_j} \quad [1]$$

where the  $e$  are the signs of the ionic charges ( $\pm 1$ ),

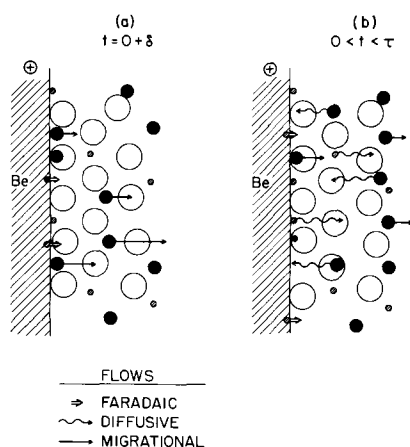


Fig. 1. Schematic representation of faradaic, diffusive, and migrational flows in anodic chronopotentiometry of Be in BeF<sub>2</sub>-LiF mixtures. Ion constituents: ●, Be<sup>2+</sup>; ●, Li<sup>+</sup>; ○, F<sup>-</sup>.

the  $Z$  are ionic charge magnitudes,  $u$  the mobilities, and  $c'$  the molar concentrations, is constrained to be essentially zero. If the faradaic process at the electrode consumes the dilute electroactive constituent and convection is absent, only diffusion can resupply it to the electrode, since its electrical migration has been suppressed. As the diffusion layer extends further from the electrode surface, the region near the electrode becomes depleted of electroactive constituent and a sharp change of emf, or chronopotentiometric transition, occurs as a new faradaic process must take place to sustain the constant current. The current is carried by the supporting electrolyte which is present at high concentration. If the solute is sufficiently dilute, the supporting electrolyte also provides a uniform environment so that the activity coefficients do not change during the electrolysis.

ED chronopotentiometry is possible in a system where the electroactive constituent has very low electrical mobility relative to the reference constituent. For example, in molten LiF-BeF<sub>2</sub> mixtures, the transference number of Be<sup>2+</sup> is zero and that of Li<sup>+</sup> is one, relative to fluoride, over a wide range of compositions (2). [In silicates (9) and in cryolite mixtures (10), the current is carried by alkali ions, and the situation is probably similar in alkali halide-aluminum halide mixtures (7).] When a constant anodic current is initiated at a Be electrode, the faradaic process is the formation of BeF<sub>2</sub> at the electrode surface. If the current relative to fluoride ion constituent is carried only by Li<sup>+</sup> ion constituent, the fluoride ions in the vicinity of the electrode would be depleted of Li<sup>+</sup> virtually instantaneously. However, back diffusion of Li<sup>+</sup> (actually interdiffusion of Be<sup>2+</sup> and Li<sup>+</sup>), driven by the concentration gradient, supplies Li<sup>+</sup> to the electrode to sustain the current, as illustrated in Fig. 1. The emf of the Be electrode relative to a reference electrode changes as electrolysis continues to form BeF<sub>2</sub>. The emf undergoes an abrupt change when nearly all the Li<sup>+</sup> in the region near the electrode has been replaced by Be<sup>2+</sup>. Electromigrational depletion of the nonelectroactive solute Li<sup>+</sup> is thus the characteristic feature of ED chronopotentiometry that is the analog of the faradaic depletion of electroactive constituent in ordinary chronopotentiometry. ED analogs of polarography, linear sweep voltammetry, and other electrochemical scanning methods should also be observable.

**Phenomenological equations for binary systems.**—Since the melt has only two components, a single diffusional flow is possible, mutual diffusion of LiF and BeF<sub>2</sub>. In addition there is an electrical flow. Thus one might write the linear phenomenological equations in terms of these flows (5), the forces consisting of a gradient of chemical potential ( $\nabla\mu$ ) and a gradient of electrical potential ( $\nabla\psi$ ); but this formulation is non-symmetric and does not in general satisfy the Onsager reciprocal relations.

The proper flows for symmetric formulation of the phenomenological equations may be derived from the dissipation function,  $\Phi$ , written initially in terms of the flows of the ionic constituents lithium, beryllium, and fluoride. The forces are the gradients of electrochemical

potential [ $\tilde{\nabla}\mu_i = \nabla(\mu_i + F e_i Z_i \psi)$ ] of these constituents. Thus

$$\Phi = J_L \tilde{\nabla}\mu_L + J_B \tilde{\nabla}\mu_B + J_F \tilde{\nabla}\mu_F \quad [2]$$

In order to simplify the equations, the flows ( $J_i$ ), concentrations ( $c_i$ ), chemical potentials ( $\mu_{ij}$ ), and electrochemical potentials ( $\tilde{\mu}_i$ ) will be taken to refer to equivalents rather than moles.<sup>2</sup>

<sup>2</sup> The equations are thus applicable to charge unsymmetric binary mixtures as well as to mixtures of univalent salts without the need for carrying the ionic charge magnitudes through the derivation. Note, however, that the chemical potential per equivalent will be simply the molar chemical potential divided by the number of equivalents, e.g.,  $\mu_{BF} = \frac{1}{2} \mu_{BeF_2(m)}$  so that the activity coefficients need not be redefined to correspond to an equivalent fraction concentration scale.

The flows of  $\text{Li}^+$ ,  $\text{Be}^{2+}$ , and  $\text{F}^-$  are related to the current density

$$J_L + J_B - J_F = I/F \quad [3]$$

and the ionic electrochemical potentials may be combined to give the chemical potentials of the components

$$\mu_{LF} = \tilde{\mu}_L + \tilde{\mu}_F; \quad \mu_{BF} = \tilde{\mu}_B + \tilde{\mu}_F \quad [4]$$

The two chemical potential gradients are related through the Gibbs-Duhem equation

$$c_L \nabla \mu_{LF} + c_B \nabla \mu_{BF} = 0 \quad [5]$$

The dissipation function, with flows all written relative to any common reference frame, becomes

$$\Phi = [J_B - (c_B/c_L)J_L - I/F] \nabla \mu_{BF} + I/F \nabla \tilde{\mu}_B \quad [6]$$

The appropriate phenomenological equations, incorporating the Onsager reciprocal relation, may be written<sup>3</sup>

$$- [J_B^F - (c_B/c_L)J_L^F - I/F] = \mathcal{D} \nabla \mu_{BF} + L \nabla \tilde{\mu}_B \quad [7]$$

$$- I/F = L \nabla \mu_{BF} + K \nabla \tilde{\mu}_B \quad [8]$$

where the flows are taken relative to fluoride ion constituent. The left-hand side of Eq. [7] may be simplified using Eq. [3], and the gradient of electrochemical potential can be eliminated by combining Eq. [7] and [8] to give

$$(1 + c_B/c_L)J_L^F = (\mathcal{D} - L^2/K) \nabla \mu_{BF} - (L/K)I/F \quad [9]$$

*Identification of the phenomenological coefficients.*—The conventional transport coefficients may be related to the phenomenological coefficients in the usual way. Thus Eq. [8] reduces, with  $\nabla \mu_{BF} = 0$ , to Ohm's law, whence

$$K = \kappa/F \quad [10]$$

where  $\kappa$  is the specific conductance. Division of Eq. [7] or [9] by  $I/F$  and allowing the chemical potential gradient to vanish shows that

$$L/K = - (1 + c_B/c_L)t_L^F \quad [11]$$

where  $t_L^F = [J_L^F/(I/F)]|_{\nabla \mu_{LF}=0}$  is the Hittorf transference number of lithium relative to fluoride. Similarly, the term  $\mathcal{D} - L^2/K$  may be related to the Fick's law mutual diffusion coefficient,  $D$ , in the volume fixed frame of reference if the partial equivalent volumes are constant.

$$D = - \frac{J_B^V}{\nabla c_B} = - \frac{J_L^V}{\nabla c_L} \quad [12]$$

From Eq. [7] and [8], noting that the left-hand side of Eq. [7] is independent of reference frame and  $\mu_{BF} = \mu_{BF}^0 + RT \ln c_B f_{BF}$

$$(\mathcal{D} - L^2/K) = - \frac{J_B^V - (c_B/c_L)J_L^V - \left(\frac{L}{K} + 1\right) \frac{I}{F}}{(RT/c_B) \nabla c_B} \quad [13]$$

where

$$\Gamma = \left(1 + \frac{d \ln f_{BF}}{d \ln c_B}\right) \quad [14]$$

The equivalent concentrations and partial equivalent volumes are related as

$$c_B \bar{V}_B + c_L \bar{V}_L = 1; \quad \bar{V}_B \nabla c_B + \bar{V}_L \nabla c_L = 0; \quad \bar{V}_F = \frac{c_L \bar{V}_L + c_B \bar{V}_B}{c_L + c_B} \quad [15]$$

<sup>3</sup> Although the friction coefficient formalism is now frequently employed, we found the derivation in terms of the flow coefficients simpler in this case and more closely related to the measured transport parameters. In any case, these are insufficient data to calculate the entire set of ionic friction or flow coefficients for the  $\text{LiF}-\text{BeF}_2$  system. The development, however, somewhat parallels Laity's general treatment in the friction coefficient formalism (8b, c).

Combining Eq. [13], [12], and [15], and allowing  $I$  to vanish

$$(\mathcal{D} - L^2/K) = D(1 + c_B \bar{V}_B/c_L \bar{V}_L) c_B/RT \quad [16]$$

*Mutual diffusion coefficient.*—Substitution of Eq. [11] and [16] into Eq. [9] leads finally to the relations between the current density, concentration gradient, and mutual diffusion coefficient<sup>4</sup>

$$J_L^F = -D \frac{\bar{V}_F}{\bar{V}_B} \frac{\partial c_L}{\partial x} + t_L^F I/F = -D \frac{\partial c_L}{\partial \xi} + t_L^F I/F \quad [17a]$$

$$I \left[ J_L^F = 0 \right]_{(x=0)} = \mathbf{F} J_B^F \Big|_{(x=0)} = \mathbf{F} (D/t_L^F) \left[ \frac{\bar{V}_F}{\bar{V}_B} \right] \frac{\partial c_L}{\partial x} = \mathbf{F} (D/t_L^F) \frac{\partial c_L}{\partial \xi} \quad [17b]$$

In the above equations,  $\xi$  is a distance variable such that equal increments  $d\xi$  contain equal numbers of fluoride,  $d\xi = (\bar{V}_B/\bar{V}_F)dx$ . Equation [17b] provides one of the boundary conditions for the system, since  $J_L^F$  must vanish at the electrode surface ( $x = 0$ ), as no lithium ion constituent crosses the electrode surface.  $\bar{V}_F$  is the equivalent volume of the mixture. Differentiation of Eq. [17a] with respect to the distance variable leads to the analog of Fick's second law (11). In the first approximation, constancy of  $D$ ,  $t_L^F$ , and  $\bar{V}_F$  are assumed.

$$\frac{\partial c_L}{\partial t} = \frac{\partial}{\partial \xi} D \frac{\partial c_L}{\partial \xi} - I/F \frac{\partial t_L^F}{\partial \xi} \cong D \left[ \frac{\bar{V}_F}{\bar{V}_B} \right] \frac{\partial^2 c_L}{\partial x^2} \quad [18]$$

The other boundary condition is that of semi-infinite linear plane diffusion

$$c_i(x \rightarrow \infty) = c_i^0, \quad 0 < t < \infty \quad [19]$$

where the superscript zero refers to the initially uniform concentration. The initial condition is also the usual one of initially uniform composition

$$c_i(t = 0) = c_i^0, \quad 0 < x < \infty \quad [20]$$

In the system  $\text{LiF}-\text{BeF}_2$ , as in many binary molten salt mixtures, the partial equivalent volumes (12) are constant so that the single volume fixed Fick's law diffusion coefficient applies. In the  $\text{LiF}-\text{BeF}_2$  system, furthermore, the partial equivalent volumes are very nearly equal, so that the bracketed term in the boundary condition Eq. [17b] is very close to unity. If also  $t_L^F = 1$ , the diffusion equation together with the initial and boundary conditions reduce to those for ordinary chronopotentiometry (6); however,  $D$  cannot be considered constant since the medium composition and viscosity change drastically during the chronopotentiogram. As a first approximation, nevertheless, we calculate, with the Sand equation an average value of  $D$  or (more correctly) of

$$\bar{D}/t_L^{F^2} \quad \bar{D}/t_L^{F^2} \left[ \frac{\bar{V}_F}{\bar{V}_B} \right]$$

which we shall designate  $\bar{D}$ .

In a subsequent paper we shall analyze the concentration dependence of the diffusion coefficients as determined from the mean values obtained with differing initial melt compositions. Here we shall be concerned principally with the above mean value calculated from the chronopotentiogram.

#### Computation of the Mean Diffusion Coefficient

*Equation of the chronopotentiogram.*—Although  $\bar{D}$  may be calculated from a measured transition time

<sup>4</sup> The same result (Eq. [17b]) would be obtained with flows written in the volume fixed frame of reference as in Eq. [13] since, at the electrode surface ( $x = 0$ ),  $J_B^V = I/F$  and  $J_L^V = 0$ .

with the Sand equation, there are several reasons why it seems worthwhile to analyze the experimental chronopotentiograms avoiding the graphical concept of transition time (13) and, rather, to focus on the early portion of the chronopotentiogram rather than only the later portion. As Bos and Van Dalen (14) have pointed out for ordinary chronopotentiometry, the final part of a chronopotentiogram is very sensitive to various errors involving, e.g., the geometry of the cell, convection in the melt, and capacity current. In ED chronopotentiometry, especially in systems such as LiF-BeF<sub>2</sub>, there is the additional complication that large changes of *D* and of *t<sub>L</sub>* may occur in the composition region near that corresponding to the transition time, here pure BeF<sub>2</sub>.

The emf along the chronopotentiogram (corrected for the IR drop) may be obtained by integration of Eq. [8] and has been shown to be given (2, 5, 15) by

$$\frac{2FE}{RT} = \left[ \ln \frac{y}{(1-y)^2} - \ln \frac{y_0}{(1-y_0)^2} \right] \bar{t}_{L^F} + \frac{2FE^E}{RT} \quad [21]$$

where *y* is the mole fraction of BeF<sub>2</sub> (the zero subscript referring to the initial composition) and the second term of the right-hand side is the "excess term" calculated from activity coefficient data. If the transference number varies with composition, *t<sub>L</sub><sup>F</sup>* represents its mean value. Here we proceed with the assumption *t<sub>L</sub><sup>F</sup>* = 1 - *t<sub>B</sub><sup>F</sup>* = 1. Equation [21] may be solved numerically by successive approximations to give the concentration as a function of time

$$y(t) = F(E, t, E^E(y(t)))$$

The diffusion coefficient can then be calculated at each time (or each concentration) from the chronopotentiometric expression for the concentration at the electrode surface for a constant diffusion coefficient (5, 6).

$$c_{LiF} = c_{LiF}^0 - \alpha t^{1/2} \quad [22]$$

where  $\alpha = (2/\pi^{1/2})I/(F\bar{D}^{1/2})$  and the equivalent concentrations are related to the mole fraction as indicated previously (5).<sup>5</sup>

**Excess term.**—In the absence of the excess term in Eq. [21] it is possible to solve Eq. [21] explicitly for the concentration as a function of time along the chronopotentiogram. Although the contribution from nonideality is small for high BeF<sub>2</sub> content melts, the computation presented here takes it into account, so that this procedure can be applied without change at lower BeF<sub>2</sub> contents. From the data given by Hitch and Baes (1) between 500° and 700°C, the activity coefficient of LiF,  $\gamma_{LiF}$ , on the mole fraction scale, for solutions dilute in LiF, i.e., between 85 and 100% BeF<sub>2</sub>, is well described by

$$\ln \gamma_{LiF} = \text{constant} + 5.34y \quad [23]$$

The Gibbs-Duhem relation leads to the relation for the activity coefficient of BeF<sub>2</sub> in this composition range

$$d \ln \gamma_{BeF_2} = -5.34 \left( \frac{1-y}{y} \right) dy \quad [24]$$

and the "excess term" becomes (5)

$$\frac{2FE^E}{RT} = -5.34(\ln(y/y_0) + (y - y_0)) \quad [25]$$

**Diffusion coefficient.**—In practice, some 10-25 (E, time)<sub>i</sub> pairs were read from a recorded chronopotentiogram. The combination of Eq. [21] and [25] was solved by computer successive approximations to give a set of (time, *y*)<sub>i</sub> pairs. The final value of *y<sub>i</sub>* is ap-

<sup>5</sup> It should be noted that  $\bar{V}_B$  refers to the partial equivalent volume of BeF<sub>2</sub> in this paper and  $V_{BeF_2}$  referred to the partial molar volume of BeF<sub>2</sub> ( $\bar{V}_{BeF_2} = 2V_B$ ) in Ref. (5).

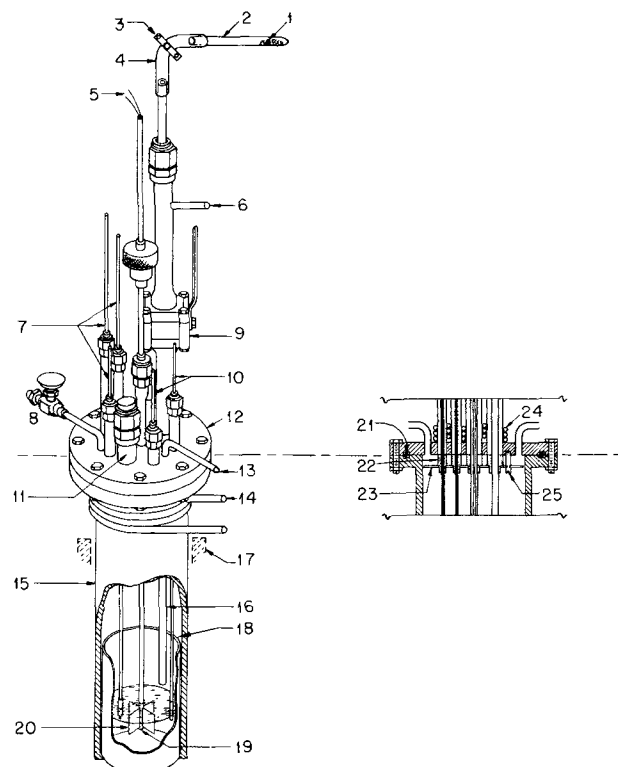
proached to better than  $5 \times 10^{-11}$ , and this precision was found necessary for the description of the chronopotentiograms at long times.

The corresponding (time, *c<sub>LiF</sub>*)<sub>i</sub> pairs also were calculated and, by applying Eq. [22], a diffusion coefficient  $\bar{D}_i$  corresponding to each (E, time)<sub>i</sub> pair was obtained. The results of these computations will be presented later as plots of  $\bar{D}$  vs. *c<sub>LiF</sub>* and  $\bar{D}$  vs. time.

**Experimental**

**Apparatus.—Instrumentation.**—Measurements were made with a modified Q2943-cyclic voltammeter (16), designed and built at the Oak Ridge National Laboratory and operated in the chronopotentiometric mode with a three-electrode system, the counterelectrode being grounded. Readout of the voltage-time curve was on a Minneapolis-Honeywell X-Y recorder with 11 × 18 in. chart paper.

**Cell.**—The cell, shown in Fig. 2, was of all-metal construction except for Teflon insulators in the cool region, boron nitride spacers which were not in contact with melt, and beryllium oxide insulators for the beryllium working electrodes. The cell containing the molten fluoride mixture was a crucible of nickel into which dipped the electrodes and thermocouple well. The cell envelope, of stainless steel, was in two sections, fitted with a Teflon O-ring and bolted together to provide a vacuum-tight seal. The upper part of the container was water cooled and the cover was provided with risers for entry of the electrodes, thermocouple well, manual stirrer, gas entry and exit, and a port for sample additions. The latter port was provided with a ball-valve to which a sample container could



**Fig. 2.** All metal cell and container assembly for chronopotentiometry in LiF-BeF<sub>2</sub>. 1, LiF crystals; 2, glass tubing; 3, pinch clamp; 4, Teflon tubing; 5, thermocouple leads; 6, helium or vacuum inlet; 7, working electrodes; 8, valve; 9, ball valve; 10, reference electrodes; 11, reserve port; 12, stainless steel flange; 13, helium or vacuum inlet; 14, cooling water; 15, stainless steel container; 16, sample tube; 17, Marshall furnace (3½ in. core); 18, nickel crucible; 19, thermocouple junction; 20, manual stirrer; 21, Teflon O-ring; 22, boron nitride spacer; 23, stainless steel support for boron nitride spacers; 24, cooling coils (not shown on perspective drawing); 25, support (typical of three).

be connected, evacuated, and sparged with cover gas before opening the valve and adding the sample. The electrode leads could be moved vertically through Teflon sleeves in the Swage-Lok<sup>®</sup> fittings. The sample-addition port also permitted insertion of a new electrode if necessary. The cell was heated in a Marshall furnace, with automatic temperature control provided by a Leeds and Northrup DAT controller and Chromel-Alumel thermocouple. Temperature measurements of the melt were made with a Chromel-Alumel thermocouple using a precision Rubicon potentiometer and a Brown Electronik recorder having a full scale chart span of 1 mV.

**Electrodes.**—The counterelectrode was the crucible itself, in electrical contact with the grounded cell container. The reference electrode was a beryllium rod (about 2 mm in diameter and 2 cm in length, threaded to a nickel rod). Working electrodes, as illustrated in Fig. 3, were employed after several previous attempts to provide a well-defined area. The machined solid cylindrical beryllium slug, the top of which was machined to a conical taper, was attached to a threaded tantalum rod through a cylindrical copper spacer so that thermal expansion would not loosen the tight fit of the beryllium slug against the beryllium oxide insulator. An uninsulated beryllium rod was apparently wetted by the salt, resulting in a gradually changing area. Although an inert metal lead such as tantalum should in principle not interfere with the anodic chronopotentiograms, erratic results and spurious emf readings resulted from electrodes without the BeO insulators. With only Be and BeO exposed to the melt, reproducible chronopotentiograms were obtained over long periods of time. The geometric area of exposed beryllium was calculated from micrometric measurements and measurements with an optical microscope of the dimensions. A typical area was about 0.28 cm<sup>2</sup>.

**Materials.**—Chemicals employed were single-crystal chips of optical grade LiF from Harshaw and twice-

<sup>®</sup> Crawford Fitting Company, Solon, Ohio.

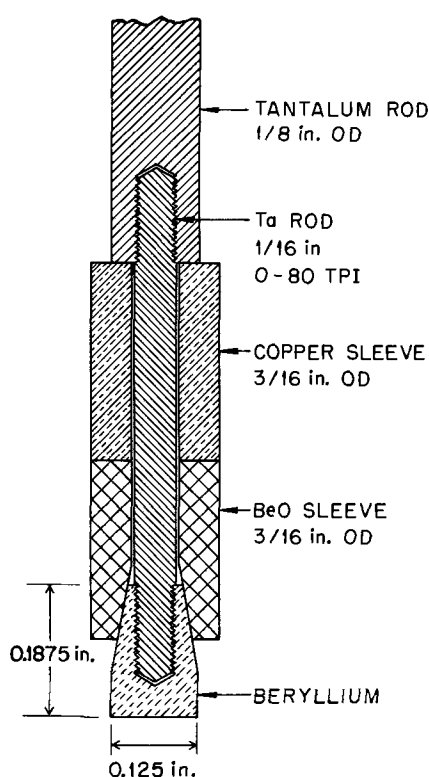


Fig. 3. Beryllium working electrode for chronopotentiometry of BeF<sub>2</sub>-alkali fluoride mixtures.

distilled BeF<sub>2</sub>. The distillation apparatus of all nickel construction employed to purify the beryllium fluoride is illustrated in Fig. 4. The BeF<sub>2</sub> was loaded into the upper cup which had a center tube for insertion of the thermocouple well of the outer jacket when the apparatus was assembled. The unit as shown was raised into a rigidly mounted Marshall furnace by means of laboratory jacks. A Chromel-Alumel thermocouple in the upper well permitted control of the distillation temperature. The still was evacuated to a pressure of several microns of mercury and the distillation of the BeF<sub>2</sub> was accomplished by maintaining the temperature of the upper cup at 850° while the lower funnel and receiving cup were maintained at about 300°. The condensate of BeF<sub>2</sub> on these cooler surfaces was in the form of a fine powder. At the end of the distillation period, usually 2-3 days, the powder was treated with an HF-H<sub>2</sub> mixture and then sparged with He. The apparatus was then raised farther into the furnace and the temperature in the region of the funnel and receiving cup was adjusted so that the BeF<sub>2</sub> would melt and collect in the receiving cup. The unloading of the apparatus was done in a large dry box. A typical analysis of the optically clear material showed the following elements detected (concentration in ppm): K, 7; Li, 15; Na, 70; Ca, 20; Mg, 3; Mn, 16; Cr, 10; Ti, 5.

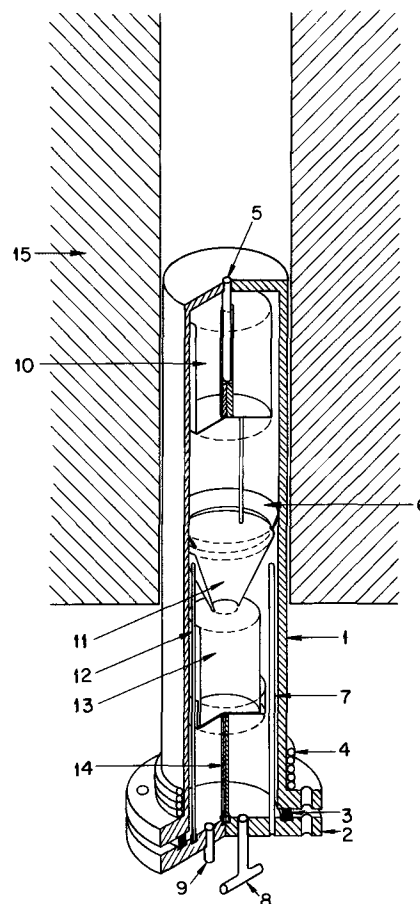


Fig. 4. Nickel apparatus for purification of BeF<sub>2</sub> by hydrofluorination, sublimation, and melting under vacuum. 1, Nickel container vessel (ca. 3/4 in. × 14 in.); 2, bottom flange; 3, Teflon O-ring; 4, cooling coils for water circulation; 5, thermocouple well which fits into the upper cup, 10, sleeve; 6, permanent guide welded to container wall to prevent material from dropping elsewhere than into the funnel, 11, and thence into the lower cup, 13; 7, thermocouple well for measuring temperature near funnel; 8, gas or vacuum exit; 9, exit for gases; 10, upper (loading) cup; 11, funnel; 12, support members for funnel and upper cup; 13, lower (receiving) cup; 14, support and holder for lower cup, 13; 15, furnace (3 1/2 in. core).

**Procedure.**—The chronopotentiograms were run anodically in a conventional manner, but since the instrument operates from a fixed initial potential of the working electrode, this potential was first adjusted precisely to the open-circuit voltage of the cell consisting of the working and reference electrode. This was generally within a few millivolts of zero since both electrodes are of beryllium, but it was found essential to avoid current flow through the electrode prior to the chronopotentiogram for reproducible results. Cathodic half-cycles showed no migrational depletion transition (5), nor would one be expected from the theory of ED with  $t_{B^F} = 1$ . The initial  $IR$  drop in cathodic half-cycles was very close to that in the anodic half-cycles. Following a chronopotentiogram, the emf was monitored, with occasional manual stirring, during the decay of the cell emf to a steady near-zero value before the next chronopotentiogram.

### Results

**Chronopotentiograms.**—The above experimental and computational procedure were used for the temperature dependence study of interdiffusion coefficients in molten  $LiF-BeF_2$  mixtures of high  $BeF_2$  content. The composition was 95 m/o  $BeF_2$ , and the temperature range was 564° to 704°C. As reported by Cantor *et al.* (12), viscosity of the melts increases drastically with increasing  $BeF_2$  content. According to their data, the melt studied here has a viscosity at 600°C of about  $5.7 \times 10^3$  P; this high viscosity probably accounts for the reproducibility of fairly long time chronopotentiograms without interference by convection.

Typical chronopotentiograms are shown in Fig. 5. First of all, they demonstrate the reproducibility of recordings obtained under identical conditions at different times. During the week separating the recording of the two chronopotentiograms, measurements were performed at higher and lower temperatures with the same melt and electrodes.

The chronopotentiograms are characterized by an initial  $IR$  drop corresponding to the low specific conductance expected for  $BeF_2$ -rich  $LiF-BeF_2$  melt from data (3) for 34 to 70 m/o  $BeF_2$  and for pure  $BeF_2$  (17). The initial rise is correspondingly smaller for chronopotentiograms at lower  $BeF_2$  contents. Although the initial  $IR$  drop is appreciable, we believe that the variation during the course of the chronopotentiogram is not. Successive chronopotentiograms at short time in-

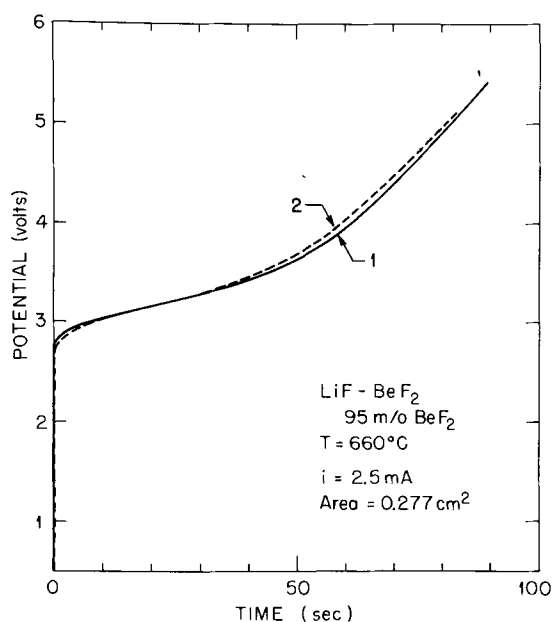


Fig. 5. Typical recorded chronopotentiograms taken eight days apart: temperature, 660°C; current, 2.5 mA; current density, 0.009 A/cm<sup>2</sup>.

tervals show virtually the same  $IR$  drop even when the successive transition times decrease markedly because the higher  $BeF_2$  concentration at the electrode surface has not had time to decay to the bulk concentration. When the concentration has become uniform, as indicated by a constant low emf value between working and reference electrode, both  $IR$  drop and over-all chronopotentiogram show reproducibility comparable to Fig. 5.

The initial rise is very rapid and showed no evidence of significant charging current for time scales down to 2-3 sec even with an oscilloscope. However, at long times the chronopotentiograms do not rise sharply. This lack of sharpness may have a contribution from a charging current and from convection, but must also be due to the fact as the melt composition in the vicinity of the electrode approaches pure  $BeF_2$  the transference number of  $Be(II)$  must approach unity unless other constituents (e.g., trace impurities or electrons) become significant for current transport relative to fluoride. In any case the assumption  $t_{B^F} = 0$  probably becomes invalid for pure  $BeF_2$ . Because of the voltage output characteristics of the cyclic voltammeter, the high resistance of the melt prevented the use of higher current densities which would provide shorter transition times, and even with low current densities, as shown in Fig. 5, the recording of the potential at higher times was limited. In melts of lower  $BeF_2$  content this problem is reduced, and transition times of the order of 10 sec or less are feasible. Clearly, graphical determination of a transition time would be uncertain and might lead to erroneous values of the diffusion coefficient.

**Diffusion coefficients.**—The chronopotentiograms for 95 m/o  $BeF_2$  were analyzed by first calculating  $\bar{D}$  and  $c_{LiF}$  (the concentration at the electrode surface) from the recorded emf-time data with Eq. [21], [22], and [25], and plotting  $\bar{D}$  vs.  $t$  or  $\bar{D}$  vs.  $c_{LiF}$ . The sensitivity of the calculated values to experimental errors varied. Thus, an error in temperature of as much as 5°, or in the zero of time of as much as 1 sec, would have virtually no effect. Variations in reading the initial  $IR$  drop had appreciable effects at very short times, decreasing rapidly with time. An error in the electrode area or initial composition had relatively little effect at short times, and an increasing effect at longer times. A plot of  $\bar{D}$  vs.  $c_{LiF}$  calculated from the chronopotentiograms in Fig. 5 is shown in Fig. 6 along with points calculated with variations of 10% in the electrode area, 0.5 m/o in the initial composition, 50 mV in the initial  $IR$  drop, 5° in temperature and 1 sec in the time. Although the effect of an error in area or initial composition is large at low  $c_{LiF}$  (long times), extrapolation to the bulk concentration nevertheless leads to values of  $\bar{D}$  in agreement with the other calculations. Too large an estimated  $IR$  drop leads to exceptionally high values of  $\bar{D}$  at very short times, and too low an estimate gives low values of  $\bar{D}$  at very short times.

This behavior was useful for checking the consistency of the estimated  $IR$  drop. In addition, plots of  $IR$  drop vs. current, when data for different currents were available, showed the expected proportionality, and the slope increased strongly with decreasing temperature, as seen in Fig. 7.

Figure 8 shows, as functions of time and of calculated  $LiF$  concentration, calculated diffusion coefficients obtained at 660°C with four different current densities. At each current density, as seen in Fig. 8a, the calculated  $\bar{D}$  is found to increase, the rate of increase with time becoming faster with increasing current density. However, we do not believe that these variations with current density derive from convection or joule heat; for the results may all be superimposed and show no systematic variation with current density if compared in terms of the calculated values of  $c_{LiF}$  as seen in Fig. 8b. In the absence of further information

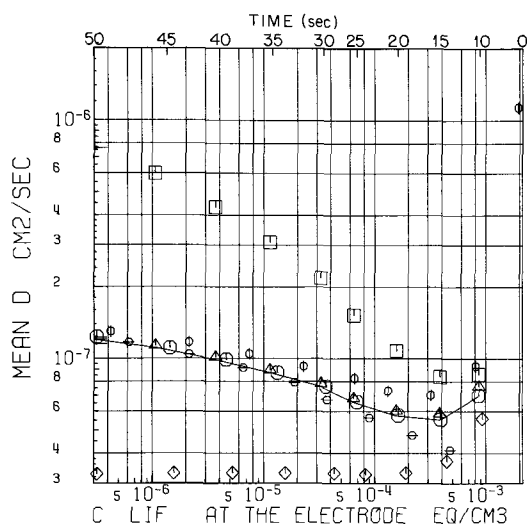


Fig. 6. Effect of various errors on calculated mean interdiffusion coefficient  $\bar{D}$  calculated at different LiF concentrations at the electrode (same data as in Fig. 5). —, Standard values;  $\square$ ,  $\delta \text{ area/area} = -0.1$ ;  $\diamond$ ,  $\delta \gamma_0 = -0.005$ ;  $\triangle$ ,  $\delta T = +5^\circ\text{K}$ ;  $\circ$ ,  $\delta t = +1 \text{ sec}$ ;  $\diamond$ ,  $\delta(IR \text{ drop}) = +50 \text{ mV}$ ;  $\circ$ ,  $\delta(IR \text{ drop}) = -50 \text{ mV}$ .

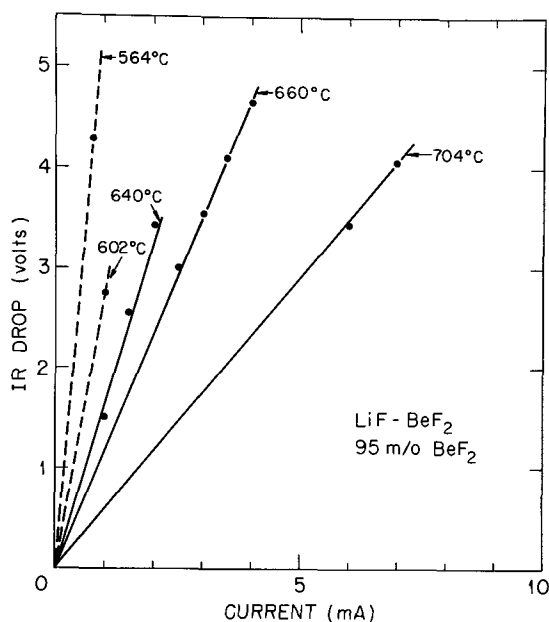


Fig. 7. IR drop vs. current at the five temperatures investigated

on the form of the variation of the diffusion coefficient (and transference number) with concentration, we initially focused on the nearly constant values of  $\bar{D}$  obtained from the early part of the chronopotentiograms, but beyond the initial uncertainty of emf, in order to obtain values corresponding to melt composition as near 95 m/o  $\text{BeF}_2$  as possible. (The region of near constancy in Fig. 6 and 8b,  $\bar{D} = 6 \times 10^{-8} \text{ cm}^2/\text{sec}$ , is  $10^{-3} > c_{\text{LiF}} > 10^{-4}$  and corresponds to  $\text{BeF}_2$  concentrations  $0.97 < y < 0.997$ .) Because of uncertainties in the composition dependence and weighting, this seemed more appropriate than a least squares fit or extrapolation. It may be noted that the values of  $\bar{D}$  are determined largely by the region of the chronopotentiogram near, but generally before, the inflection. A further refinement and check of the reasonableness of the values was made by comparison of the early portion of experimental chronopotentiograms with curves calculated for different constant diffusion coefficients.

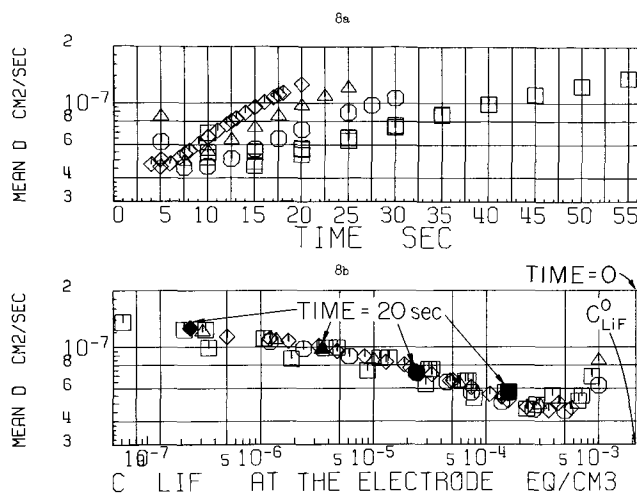


Fig. 8. Computer plots of interdiffusion coefficient  $\bar{D}$  calculated from chronopotentiograms at  $660^\circ\text{C}$  with area =  $0.277 \text{ cm}^2$  and current densities,  $\text{A}/\text{cm}^2$ .  $\diamond$ , 0.0144;  $\triangle$ , 0.0126;  $\square$ , 0.0108;  $\circ$ , 0.0090. The abscissas are: (a, upper) time; (b, lower) LiF concentration at the electrode.

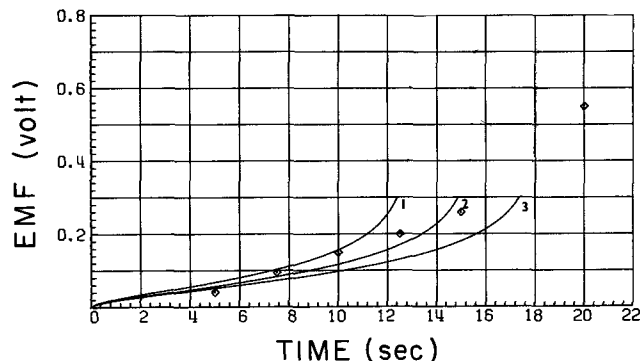


Fig. 9. Comparison of calculated and experimental chronopotentiograms with three values of constant  $\bar{D}$ . The experimental points ( $\diamond$ ) are for 0.95  $\text{BeF}_2$ -0.05 LiF at  $704^\circ\text{C}$ .  $i = 7 \text{ mA}$ , area =  $0.277 \text{ cm}^2$ ; —, calculated chronopotentiograms:  $\bar{D}/\text{cm}^2/\text{sec}$  = curve 1,  $2.5 \times 10^{-7}$ ; curve 2,  $3 \times 10^{-7}$ ; curve 3,  $3.5 \times 10^{-7}$ .

Figure 9 shows a comparison of points from an experimental curve, recorded at  $704^\circ\text{C}$  with a current of 7 mA, and chronopotentiograms calculated with  $\bar{D}$  values of  $2.5 \times 10^{-7}$ ,  $3.0 \times 10^{-7}$ , and  $3.5 \times 10^{-7} \text{ cm}^2/\text{sec}$ , showing that the value of  $\bar{D}$  is between  $2.5$  and  $3.0 \times 10^{-7}$  (but closer to the former value). From similar calculations at this temperature with chronopotentiograms at the same and other current densities, the value of  $\bar{D}$  is found to be  $2.5 \pm 0.2 \times 10^{-7}$ . Constancy of  $\bar{D}$  with changing current density, shown by  $\bar{D}$  vs.  $c_{\text{LiF}}$  plots for the  $660^\circ\text{C}$  data in Fig. 8b, is indicated for the  $640^\circ\text{C}$  data by means of chronopotentiograms calculated with fixed  $\bar{D}$  and compared with the experimental chronopotentiograms at different current densities in Fig. 10. These checks are analogous to the check of  $i\tau^{1/2}$  product constancy in ordinary chronopotentiometry. The results at different temperatures are summarized in Fig. 11 and Table I. The value at the lowest temperature was obtained only from  $\bar{D}$  vs.  $c_{\text{LiF}}$  plots, since the high resistivity at this temperature led to a very limited emf-time trace in the chronopotentiograms. Absolute errors of  $\bar{D}$  may, indeed, be larger than the reproducibilities listed in Table I. As shown in Fig. 6, uncertainties in the initial IR drop, electrode area, and initial composition may have a significant effect in calculated  $\bar{D}$  values in the region of near con-

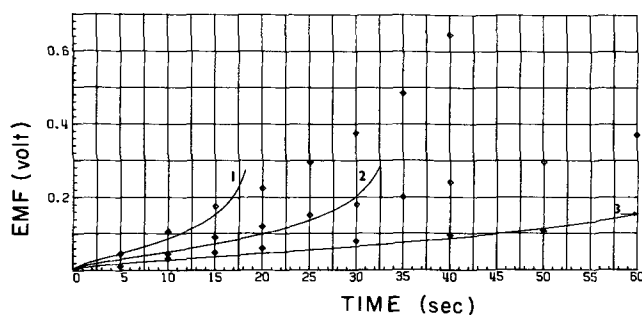


Fig. 10. Constancy of  $\bar{D}$  with different current densities in 0.95  $\text{BeF}_2$ -0.05  $\text{LiF}$  at  $640^\circ\text{C}$ . The lines are calculated with a fixed value of  $\bar{D}$ ,  $3.0 \times 10^{-8} \text{ cm}^2/\text{sec}$ . Curve 1,  $i/\text{mA} = 2$ ; curve 2,  $i/\text{mA} = 1.5$ ; curve 3,  $i/\text{mA} = 1$ . The points are the experimental emf-time data.

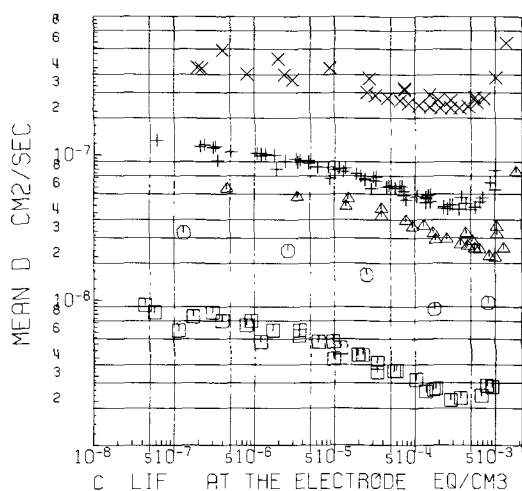


Fig. 11. Summary of chronopotentiometric results at different temperatures.  $\bar{D}$  vs.  $c_{\text{LiF}}$ .  $\times$ ,  $704^\circ\text{C}$ ;  $+$ ,  $660^\circ\text{C}$ ;  $\Delta$ ,  $640^\circ\text{C}$ ;  $\odot$ ,  $602^\circ\text{C}$ ;  $\square$ ,  $564^\circ\text{C}$ .

stancy of  $\bar{D}$  in the  $\bar{D}$  vs.  $c_{\text{LiF}}$  plots. The probable error in estimating the initial  $IR$  drop is  $\pm 5 \text{ mV}$  which would lead to an additional uncertainty of about 2.5% in  $\bar{D}$ . An estimate of limits of error in the electrode area obtained by repeating the micrometric measurements was found to be of the order of 1%, corresponding to a 2% additional uncertainty in  $\bar{D}$ . The error in the bulk concentration was estimated from the weighing errors to be 0.03%, leading also to a possible error of about 2.5%.

In conclusion, we estimate the over-all uncertainties in mean diffusion coefficients to be between 5 and 10%. Since most of the above errors probably have small temperature dependence, they will introduce less error into the Arrhenius coefficient than into the absolute value of  $\bar{D}$ . In Fig. 12, values of interdiffusion coefficients are plotted logarithmically as a function of the reciprocal temperature. The results indicate a mean activation energy for diffusion of 50.5 ( $\pm \sim 0.5$ ) kcal/mole. Within the estimated error limits, it is not possible to determine unambiguously whether the plot is linear or curved, but it may be noted also that logarithmic viscosity-reciprocal temperature or conduc-

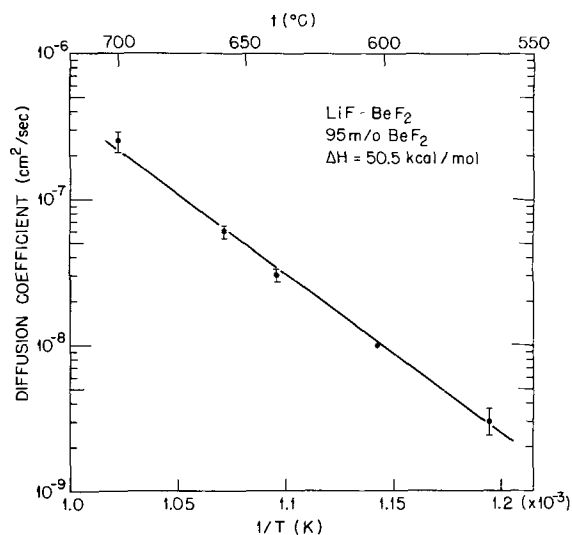


Fig. 12. Temperature dependence of interdiffusion coefficients in 95 m/o  $\text{BeF}_2$ ,  $\text{LiF-BeF}_2$ , melt.

tivity-reciprocal temperature plots show no or very little curvature (12, 17).

### Discussion

The strong composition and temperature dependence of transport properties in  $\text{BeF}_2$ - $\text{LiF}$  mixtures clearly indicate the need for measurements at more closely spaced initial compositions and temperatures in order to obtain reliable values. We believe that the reasonableness of the values reported here demonstrates the potential of ED voltammetry for such studies.

The high mean Arrhenius activation energy for diffusion, in 0.95  $\text{BeF}_2$ -0.05  $\text{LiF}$ , 50.5 kcal/mole in the temperature range  $564^\circ\text{C}$ - $704^\circ\text{C}$ , reflects the high values of the temperature coefficients of other transport parameters in this system. Thus Cantor *et al.* (12) report activation energies for viscous flow of 40 kcal/mole for 95 m/o  $\text{BeF}_2$ , 52 kcal/mole for 99 m/o  $\text{BeF}_2$ , and 59.6 kcal/mole for pure  $\text{BeF}_2$ . The activation energy for electrical conductance (17) in pure  $\text{BeF}_2$  is 44 kcal/mole. The values of  $\bar{D}$  reported in this paper, obtained for mixtures of initial composition 95 m/o  $\text{BeF}_2$ , are calculated from the region of near constancy of  $\bar{D}$  in the chronopotentiograms. This region, as noted above, corresponds to  $\text{BeF}_2$  mole fraction at the electrode surface  $0.97 < y < 0.997$ .

The temperature coefficient of  $\bar{D}$  is less sensitive than its absolute value to errors in electrode area and shape, but also to uncertainty in the transference number or the form of the concentration dependence of  $\bar{D}$ . Thus the same value of the activation energy is found if calculated from  $\bar{D}$  at any fixed value of the calculated  $c_{\text{LiF}}$  at the electrode surface.

Regarding the shape of the electrode, the equations employed have been based on linear diffusion to a plane electrode, while the actual electrode was a short cylinder. The correction for cylindrical diffusion has been treated by Evans *et al.* (18) in terms of the index  $\theta = D^{1/2} \tau^{1/2}/r_0$  (where  $r_0$  is the electrode radius). The value of  $\theta$  is  $\sim 0.005$  for a diffusion coefficient of  $3 \times 10^{-8} \text{ cm}^2/\text{sec}$  in our system, indicating a correction less than 0.5%. Although the equations of Evans *et al.* cannot be expected to apply accurately to ED

Table I. Calculated values of  $\bar{D}$  and reproducibility

$t/^\circ\text{C}$	564	602	640	660	704
$\bar{D}/\text{cm}^2/\text{sec}$	$3.0 (\pm 0.5) \times 10^{-9}$	$1.0 \times 10^{-8}$	$3.0 (\pm 0.2) \times 10^{-8}$	$6.0 (\pm 0.5) \times 10^{-8}$	$2.5 (\pm 0.2) \times 10^{-7}$
Number of current densities	1	1	3	4	2
Number of chronopotentiograms	3	1	3	7	3



chronopotentiometry of LiF-BeF<sub>2</sub> systems, the very low diffusion coefficients, although not constant, lead to very thin diffusion layers, even during times up to 20 and 30 sec. Figure 13 is a plot of calculated LiF concentration as a function of distance from the electrode at times between 0.05 and 24 sec (assuming  $\bar{D} = 6 \times 10^{-8}$  cm<sup>2</sup>/sec) at 660°C and a current density of 0.0090 A/cm<sup>2</sup>. The concentration rises from that at the electrode surface to the bulk concentration in shorter distances than in "ordinary" chronopotentiometry of dilute aqueous solutions with transition times below 2 sec (6a, b). These curves, together with the high viscosity, indicate why convection is not a serious problem even with fairly long times.

The diffusivity is expected to fall with increasing BeF<sub>2</sub> content in qualitatively the same manner as the electrical conductance and the fluidity. Hence the relatively small variation of  $\bar{D}$  along the chronopotentiogram, with an increase indicated in, e.g., Fig. 6, 8, and 11, was not at first expected. It may reflect a value of  $t_{L^+}^F$  decreasing faster than the decrease of  $D$  in the ratio  $\bar{D}/t_{L^+}^F$ , and indicates the need for extension of transference number measurements to higher BeF<sub>2</sub> contents. Such measurements would be of interest also in connection with a distinction between mass transport mechanisms in silicate glasses and in fluoride glasses and crystals. In molten LiF-BeF<sub>2</sub> at compositions between 30 and 70 m/o BeF<sub>2</sub>, as in molten silicates, the Hittorf transference number of the alkali ions is unity. In the silicate glasses, the alkali ion transference number (relative to the lattice) remains unity up to virtually pure silica, while for fluoride glasses and for fluoride crystals, fluoride ions rather than alkali ions are the current carriers (19).

The interdiffusion coefficients  $D_{Li-Be}$  reported in Table I are smaller than diffusion coefficients measured in ordinary molten salt solutions (7, 20-22), but this is to be expected in view of the high viscosity and low electrical conductivity of these melts. (If the transference number of Be<sup>2+</sup> becomes nonzero ( $t_{L^+}^F < 1$ ), the calculated values of  $D$  would be still smaller.) Although to our knowledge, no direct measurements of diffusivities have been reported for binary LiF-BeF<sub>2</sub>

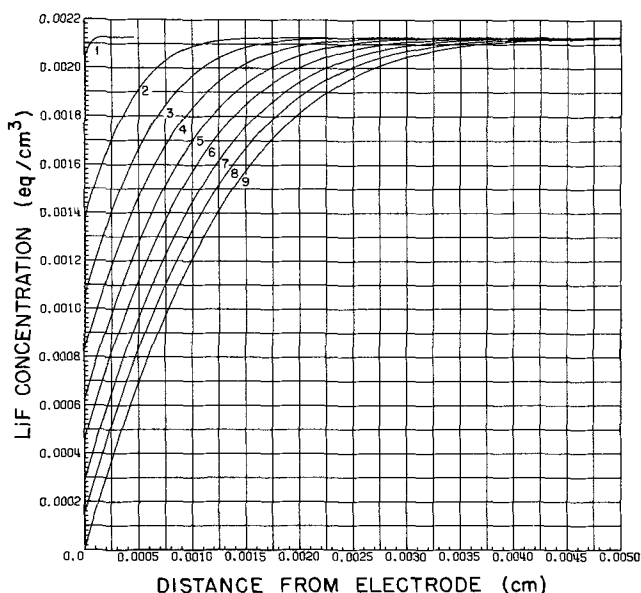


Fig. 13. LiF concentration vs. distance from electrode at different times during a chronopotentiogram at 660°C,  $D$  is assumed to be constant,  $6 \times 10^{-8}$  cm<sup>2</sup>/sec and the current is 2.5 mA. Curve 1, time = 0.05 sec; curve 2, time = 3.05 sec; curve 3, time = 6.05 sec; curve 4, time = 9.05 sec; curve 5, time = 12.05 sec; curve 6, time = 15.05 sec; curve 7, time = 18.05 sec; curve 8, time = 21.05 sec; curve 9, time = 24.05 sec.

melts, it is interesting to compare our results with conductance data and with self-diffusion coefficients calculated from molecular dynamics computer experiments for BeF<sub>2</sub>-containing melts (4). It should be noted, however, that the authors of these MD computations have pointed out that at this stage the results for transport properties must be considered of a more qualitative nature than the structural data derived from their MD pair correlation functions (4).

As has been shown (8, 23), the interdiffusion coefficient approaches the self-diffusion coefficient of a constituent (here lithium ion) as its concentration approaches zero. Our chronopotentiometric diffusion coefficient, measured in 95 m/o BeF<sub>2</sub>, is a mean value over the concentration range 95-100 m/o BeF<sub>2</sub>, and should be close to the self-diffusion coefficient of Li<sup>+</sup>. Because of the high activation energy it would be preferable to compare results at the same temperature. The MD computations for 74 BeF<sub>2</sub>-1 LiF (98.7% BeF<sub>2</sub>) (4) were carried out for only a single temperature, 837°K, the lowest for which we have experimental results. Here, our results were least precise because of the high resistivity, but are in accord with our higher temperature results.

Although the Nernst-Einstein relation is not expected to be accurate, it will probably not be off by an order of magnitude, and provides a means to compare the magnitudes of the diffusional mobilities estimated from available conductance data (3). Furthermore, it has been noted (24) for a number of molten salt systems that, as the temperature (and, consequently, the fluidity) decreases toward the glass transition temperature, and the density of mobile particles decreases correspondingly, the validity of the Nernst-Einstein equation approaches that for crystals. At higher temperatures the diffusional mobility becomes higher than the electrical mobility. The specific conductance may be expressed, in terms of external mobilities,  $u_i$ , as

$$\kappa = F [(u_B/u_L)c_B - (u_F/u_L)c_F + c_L]u_L \quad [26]$$

where  $c_i$ 's are in equivalents per cubic centimeter. If the reference frame is taken the same as that for the self-diffusion coefficient of an ion,  $D_i$ , the latter may be expressed (25) in terms of the Nernst-Einstein equation as

$$D_i = (RT/F)|u_i| \quad [27]$$

By combining Eq. [26] and [27], the specific conductance may be written in terms of self-diffusion coefficient as

$$\kappa = (F^2/RT) [(D_B/D_L)c_B + (D_F/D_L)c_F + c_L]D_L \quad [28]$$

The specific conductance of pure BeF<sub>2</sub> (17) is  $2.3 \times 10^{-7}$  ohm<sup>-1</sup>cm<sup>-1</sup> at 837°K, and the specific conductance of 95 m/o BeF<sub>2</sub> is assumed to be of the order of  $10^{-5}$  ohm<sup>-1</sup>cm<sup>-1</sup>. The MD calculations suggest a diffusion coefficient ratio of 1/10 for  $D_B/D_L$  and nearly equal self-diffusion coefficients for Be<sup>2+</sup> and F<sup>-</sup>, whence  $D_F/D_L \approx 0.1$ .

For pure beryllium fluoride at 1153°K, Eq. [28] becomes

$$\kappa = (F^2/RT) [c_B + (D_F/D_B)c_F]D_B \quad [29]$$

and the result  $D_F/D_B \approx 1$  of the MD calculations (4) was employed. The conductance value at 1153°K was estimated by extrapolation with the equation reported to fit the data in the range 800°-960°K.

For 50 m/o BeF<sub>2</sub>, although here the Nernst-Einstein equation indubitably does not apply, conductance data (3) were extrapolated to the temperature of the MD computation, 1035°K.

Table II summarizes estimates of self-diffusion coefficients for several compositions in the BeF<sub>2</sub>-LiF system.

In the 50% mixtures the estimated self-diffusion coefficient of Li<sup>+</sup> from the conductance results is of the same order of magnitude as the MD result, and of the magnitude expected in normal molten salts; these val-

Table II. Estimated self-diffusion coefficients in BeF<sub>2</sub>-LiF

m/o BeF <sub>2</sub>	Temperature/°K	Type of experiment	Self-diffusion coefficient/cm <sup>2</sup> /sec or N.E. self-diffusion coefficient
50	1035	Conductance <sup>(a)</sup>	$D_L = 5 \times 10^{-5}$
50	1035	MD <sup>(b)</sup>	$D_L = 2 \times 10^{-5}$
95	837	ED chronopotentiometry	$D_L = 3.0 \times 10^{-9}$
95	837	Conductance <sup>(c)</sup>	$D_L = 4 \times 10^{-10}$
98.7	837	MD <sup>(b)</sup>	$D_L = 1.5 \times 10^{-9}$ $(D_B = 1.1 \times 10^{-7})$ $(D_F = 1.6 \times 10^{-7})$
100	1153	Conductance <sup>(d), (e)</sup>	$D_B = D_F = 7 \times 10^{-9}$
100	1153	MD <sup>(b)</sup>	$D_B \cong D_F < 5 \times 10^{-9}$

<sup>(a)</sup> From Ref. (3) extrapolated with fitting equation in the range 673°-803°K;  $D_B$  and  $D_F$  are estimated as  $0.1 \times D_L$ .

<sup>(b)</sup> From Ref. (4).

<sup>(c)</sup> From Ref. (3); conductance is estimated from pure BeF<sub>2</sub> data.

<sup>(d)</sup> From Ref. (3) extrapolated with fitting equation in the range 803°-963°K.

<sup>(e)</sup> Assuming MD result  $D_B \cong D_F$ .

ues are quite close also to the voltammetric diffusion coefficient of U(IV) in a LiF-BeF<sub>2</sub>-ZrF<sub>4</sub> solvent mixture containing 34% BeF<sub>2</sub> at 480°-600°C (22) where extrapolation to 1035°K would lead to a value of  $1 \times 10^{-5}$  cm<sup>2</sup>/sec. At high BeF<sub>2</sub> contents, and in pure BeF<sub>2</sub>, the MD computations do not show as much of a decrease in magnitude as both the chronopotentiometric and conductance results. Although the comparison is only qualitative, it indicates the need for further theoretical and experimental work to resolve the discrepancy, particularly since MD is one of the most promising new tools for investigating models of molten salt structure and transport (26).

Finally we would like to point out other areas where the concepts of ED voltammetry may be useful. These may include studies of polarization and transport in membranes (27), in crystals such as sodium beta alumina (28) and in ionic glasses (29); however, in rigid glasses space charge phenomena, that are probably not significant in liquid systems, must be considered (29).

Migrational contribution to the chronopotentiometric transition in ordinary (faradaic depletion) chronopotentiometry has been considered previously (30) in terms of corrections to the Sand equation and enhancement of the transition. Chronopotentiometry in the absence of supporting electrolyte has been proposed as a means to determine transference numbers (31). In these cases, however, the basis of the chronopotentiometric transition has been the faradaic process. In contrast, as we have tried to indicate, the basis of ED chronopotentiometry is migrational depletion of a mobile nonelectroactive constituent.

### Acknowledgment

The authors wish to thank: Dr. T. R. Mueller (Analytical Chemistry Division, ORNL) for his interest, help, and suggestions, especially with the instrumentation; Mr. D. Brown (ORAU Research Trainee from Kenyon College, Gambier, Ohio) for his active participation during the initial stage of the computer programming. In addition, one of us (C. E. V.) gratefully acknowledges support from the Ministère des Affaires Étrangères Français during the academic year 1972-1973 and from the Centre National de la Recherche Scientifique. This research was sponsored by the United States Atomic Energy Commission under contract with the Union Carbide Corporation.

Manuscript submitted March 19, 1974; revised manuscript received June 24, 1974.

Any discussion of this paper will appear in a Discussion Section to be published in the June 1975 JOURNAL. All discussions for the June 1975 Discussion Section should be submitted by Feb. 1, 1975.

The publication costs of this article have been assisted by the Union Carbide Corporation.

### LIST OF SYMBOLS

B	(subscript) beryllium ion (equivalents)
BF	(subscript) BeF <sub>2</sub> component (equivalents)
c <sub>i</sub>	concentration of i (equivalents per cm <sup>3</sup> )
c <sub>i</sub> <sup>0</sup>	concentration of i in bulk solution (equivalents per cm <sup>3</sup> )
c <sub>i</sub> '	concentration of i (moles per cm <sup>3</sup> )
D	self-diffusion coefficient, Fick's law diffusion coefficient
$\bar{D}$	corrected average value of D
$\mathcal{D}$	phenomenological coefficient
E	emf
e <sub>i</sub>	(= ±1) sign of ionic charge
F	(subscript) fluoride ion equivalent
F	the Faraday (96,487 coulombs)
f <sub>i</sub>	activity coefficient of component i on equivalents/cm <sup>3</sup> concentration scale
I	current density, A/cm <sup>2</sup>
i	current, mA
J <sub>i</sub>	flow of i, equivalents/cm <sup>2</sup> · sec
J <sub>i</sub> <sup>j</sup>	flow of constituent i relative to constituent j, equivalents/cm <sup>2</sup> · sec
J <sub>i</sub> <sup>v</sup>	flow of constituent i in volume fixed reference frame, equivalents/cm <sup>2</sup> · sec
K	phenomenological coefficient
L	phenomenological coefficient
L	(subscript) lithium ion equivalent
LF	(subscript) LiF component (equivalent)
R	gas constant (8.3143 M.K.S.)
r <sub>0</sub>	radius of cylindrical electrode
T	temperature in Kelvins
t	time in sec
t <sub>i</sub> <sup>j</sup>	transference number of i relative to j
u <sub>i</sub>	mobility of constituent i
V <sub>i</sub>	partial equivalent volume of constituent i
x	distance from electrode surface
y	mole fraction of BeF <sub>2</sub> at electrode
y <sub>0</sub>	mole fraction of BeF <sub>2</sub> in bulk melt
Z <sub>i</sub>	magnitude of ionic charge of ion i
α	rate of decrease of concentration with $\sqrt{t}$
Γ	activity coefficient correction to diffusion coefficient
γ <sub>i</sub>	activity coefficient of component i on mole fraction concentration scale
θ	chronopotentiometric correction parameter for cylindrical electrodes
κ	specific electrical conductance
μ <sub>ij</sub>	chemical potential of constituent ij (per equivalent)
μ <sub>i</sub> <sup>0</sup>	standard chemical potential of ion i
μ <sub>ij</sub> <sup>(m)</sup>	molar chemical potential of constituent ij
~	
μ <sub>i</sub>	electrochemical potential of ion i
ξ	distance variable
τ	transition time
Φ	dissipation function (rate of dissipation of free energy)
ψ	electrical potential

### REFERENCES

- (a) B. F. Hitch and C. F. Baes, *Inorg. Chem.*, **8**, 201 (1969). (b) K. A. Romberger, R. E. Thoma, and J. Braunstein, *J. Phys. Chem.*, **76**, 1154 (1972). (c) J. Braunstein, K. A. Romberger, and R. Ezell, *J. Phys. Chem.*, **74**, 4383 (1970).
- K. A. Romberger and J. Braunstein, *Inorg. Chem.*, **9**, 1273 (1970).
- G. D. Robbins and J. Braunstein, in "Molten Salts. Characterization and Analysis," G. Mamantov, Editor, p. 443, Marcel Dekker, New York (1969); G. D. Robbins and J. Braunstein, Oak Ridge National Laboratory, ORNL-4548, p. 156, February 1970.
- A. Rahman, R. H. Fowler, and A. H. Narten, *J. Chem. Phys.*, **57**, 3010 (1972); H. A. Levy, A. H. Narten, and A. Rahman, Oak Ridge National Laboratory, ORNL-4891, September 1973, p. 120. A. Rahman, Abstract 263, p. 643, Electrochemical Society, Extended Abstracts, Spring Meeting, Chicago, Illinois, May 13-18, 1973.
- J. Braunstein, H. R. Bronstein, and J. Truitt, *J. Electroanal. Chem.*, **44**, 463 (1973).
- (a) P. Delahay, "New Instrumental Methods in Electrochemistry," p. 179, Interscience Publishers, Inc., New York (1954). (b) "Physical Methods of Chemistry," Vol. I, Part IIA, Chapt. V, VI,

- VII, VIII, pp. 297-644, A. Weissberger and B. W. Rossiter, Editors, Wiley-Interscience, New York (1971).
7. B. Gilbert, D. L. Brotherton, and G. Mamantov, *This Journal*, **121**, 773 (1974).
  8. (a) R. Haase, "Thermodynamics of Irreversible Processes," pp. 61, 261, 289, 296, Addison-Wesley Press, Reading, Mass. (1969). (b) R. W. Laity and J. D. E. McIntyre, *J. Am. Chem. Soc.*, **87**, 3806 (1965). (c) R. W. Laity, *J. Chem. Phys.*, **30**, 682 (1959), *J. Phys. Chem.*, **67**, 671 (1963). (d) D. G. Miller, *Chem. Revs.*, **60**, 15 (1960). (e) C. Wagner, in "Advances in Electrochemistry and Electrochemical Engineering," P. Delahay, Editor, Vol. 4, p. 1, Interscience Publishers, Inc., New York (1966).
  9. J. O'M. Bockris, J. A. Kitchener, and A. E. Davis, *Trans. Faraday Soc.*, **48**, 536 (1952).
  10. W. B. Frank and L. M. Foster, *J. Phys. Chem.*, **61**, 1531 (1957).
  11. J. Crank, "The Mathematics of Diffusion," p. 219, Clarendon Press, Oxford (1956).
  12. S. Cantor, W. T. Ward, and C. T. Moynihan, *J. Chem. Phys.*, **50**, 2874 (1969); C. T. Moynihan and S. Cantor, *ibid.*, **48**, 115 (1968).
  13. M. L. Olmstead and R. S. Nicholson, *J. Phys. Chem.*, **72**, 1650 (1968).
  14. P. Bos and E. Van Dalen, *J. Electroanal. Chem.*, **45**, 165 (1973).
  15. J. Braunstein and H. Braunstein, in "Experimental Thermodynamics," Vol. 2, B. Vodar and B. LeNeindre, Editors, I.U.P.A.C., In press.
  16. T. R. Mueller and H. C. Jones, *Chem. Instr.*, **2**, 65 (1969).
  17. G. D. Robbins and J. Braunstein, Oak Ridge National Laboratory, ORNL-4396, February 1969, p. 184.
  18. D. H. Evans and J. E. Price, *J. Electroanal. Chem.*, **5**, 77 (1963); D. I. Dornfeld and D. H. Evans, *ibid.*, **20**, 341 (1969).
  19. K. Hughes and J. O. Isard, in "Physics of Solid Electrolytes," Vol. 2, Chap. 10, J. Hladik, Editor, Academic Press, New York (1972).
  20. J. Richter, *J. Chem. Eng. Data*, **18**, 401 (1973).
  21. D. Inman, Dj. Jovanović, and S. H. White, *J. Electroanal. Chem.*, **43**, 37 (1973).
  22. G. Mamantov and D. L. Manning, *Anal. Chem.*, **38**, 1494 (1966).
  23. L. S. Darken, *Trans. AIME*, **175**, 184 (1948).
  24. C. A. Angell, *J. Phys. Chem.*, **69**, 399 (1965); F. S. Howell, R. A. Bose, P. B. Macedo, and C. T. Moynihan, *J. Phys. Chem.*, Submitted.
  25. A. Klemm, in "Molten Salt Chemistry," M. Blander, Editor, p. 537, Interscience Publishers, Inc., New York (1964).
  26. L. V. Woodcock, in "Advances in Molten Salt Chemistry," Vol. III, J. Braunstein, G. P. Smith, and G. Mamantov, Editors, Plenum Publishing Co., New York (1974), in press.
  27. M. Block and J. Kitchener, *This Journal*, **113**, 947 (1966).
  28. M. S. Whittingham and R. A. Huggins, *J. Chem. Phys.*, **54**, 414 (1971).
  29. P. M. Sutton, *J. Am. Ceram. Soc.*, **47**, 188 (1964); P. B. Macedo, C. T. Moynihan, and R. A. Bose, *Phys. and Chem. Glasses*, **13**, 171 (1972).
  30. M. D. Morris and J. J. Lingane, *J. Electroanal. Chem.*, **6**, 300 (1963); M. D. Morris, *ibid.*, **8**, 1 (1964); H. L. Kies, *ibid.*, **4**, 156 (1962); G. Mamantov and P. Delahay, *J. Am. Chem. Soc.*, **76**, 5324 (1954); H. J. S. Sand, *Phil. Mag.*, **1**, 45 (1901).
  31. J. Broadhead and G. J. Hills, *J. Electroanal. Chem.*, **13**, 354 (1967).

## Equivalent Circuit for the Uncompensated Resistances Occurring at Ring-Disk Electrodes

Mani Shabrang\* and Stanley Bruckenstein\*\*

*Chemistry Department, State University of New York at Buffalo, Buffalo, New York 14214*

### ABSTRACT

An equivalent circuit for the ring-disk electrode is proposed and tested. The model assumes that the resistance between the auxiliary electrode and the disk (or ring) electrode is the series combination of two resistances. One resistance is shared by both the disk and the ring electrodes, whereas the other is characteristic of the disk (or the ring) electrode. Changing the position of the Luggin capillary tip produces different uncompensated ohmic potential drops. The IR drops can be interpreted by assuming that the tip of the Luggin capillary is being located somewhere on these resistances.

A detailed interpretation of results obtained at the rotating ring-disk electrode requires a thorough understanding of current and potential distributions in the electrochemical cell. This point is well appreciated at a rotating disk electrode and extensive theoretical and experimental work on this problem has been carried out (1-7). However, only Gabrielli *et al.* (8) and Miller and Bellavance (4) have investigated ohmic potential effects at ring-disk electrodes. In their studies they found that current passing through the disk electrode affected the ring electrode potential, and vice versa. Their results were represented by a set of linear equations involving the ring and the disk current and the electrode potentials. However, to our knowledge, no work has been done proposing and verifying a simple equivalent circuit for a ring-disk

electrode that could serve as an experimental framework for further studies of ohmic potential effects.

This work is concerned with testing a proposed equivalent circuit for a ring-disk electrode where the ohmic and nonohmic components are represented as shown in Fig. 1. A conventional, four-electrode, ring-disk potentiostat (9-14) is assumed to be used. Point T represents the tip of the Luggin capillary which can be anywhere on resistances in the three branches of the equivalent circuit, and  $R_{\text{aux}}$  represents the resistance between the capillary and the auxiliary electrode.

An uncompensated resistance exists between the tip of the Luggin capillary and the disk electrode,  $R_C + R_D$ . Similarly an uncompensated resistance exists between the tip of the Luggin capillary and the ring electrode,  $R_C + R_R$ .  $R_C$  is assumed to be common to both the disk and the ring electrodes. The values of  $R_C$ ,  $R_R$ , and  $R_D$  depend on the physical dimensions of

\* Electrochemical Society Student Member.

\*\* Electrochemical Society Active Member.

Key words: pseudocollection, resistance measurement, ohmic coupling.

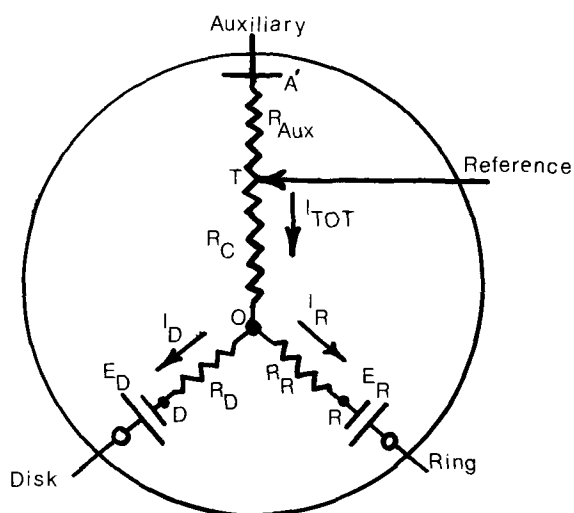


Fig. 1. Equivalent circuit of ring-disk electrode

the electrode and the location of the Luggin capillary.  $E_D$  represents the half-cell potential of the disk electrode and  $I_D$  is the disk current in question.  $E_R$  and  $I_R$  are the corresponding values for the ring electrode.  $E_D$  and  $E_R$  are assumed to contain all the impedances associated with double layer and faradaic processes. Thus,  $R_C$ ,  $R_D$ , and  $R_R$  in the equivalent circuit are associated with the current distribution characteristic of the resistance measurement techniques. In our experiments, the current distribution was a primary one.

As is shown below, experiments can be devised to determine  $R_C$  and various combinations of  $R_C$  and the other resistances in Fig. 1. The number of independent experiments exceeds the number of unknown resistances in our model, hence the system is overdetermined and the validity of the equivalent circuit can be verified.

The utility of this equivalent circuit lies in the fact that it provides a framework for correcting ohmic potential effects of the ring on the disk electrode, and vice versa. This utility is only slightly diminished by the fact that changes in current distribution with potential will have a small effect in the measured value of the resistances.

It is, of course, necessary to keep in mind that the resistances referred to are calculated quantities, and that the fundamental analysis of the ring-disk system will eventually have to be done in terms of current distribution and ohmic potential drop.

### Experimental

**Reagents.**—Solutions of 0.01M sulfuric acid were prepared from triply distilled water and a Baker reagent grade sulfuric acid.

**Cell.**—The glass cell and the auxiliary equipment are described elsewhere (15-16).

**Electrodes.**—The two electrodes used in the experiments were: (i) A platinum-ring, platinum-disk with a disk diameter,  $d_1$ , of 7.6 mm and ring-inner diameter,  $d_2$ , of 8.0 and ring-outer diameter,  $d_3$ , of 8.4 mm. Teflon was the insulating material. (ii) A platinum disk electrode with a diameter of 2.20 mm. Teflon was the insulator.

These electrodes were electrochemically pretreated before each experiment as discussed in Ref. (17), and were all polished to a final mirror finish using  $0.05\mu$  alumina on Buehler microcloth.

**Instrumentation.**—A lock-in amplifier, Model RJB made by Electronics and Missiles and Communication Inc., Mount Vernon, New York, was used for a-c studies.

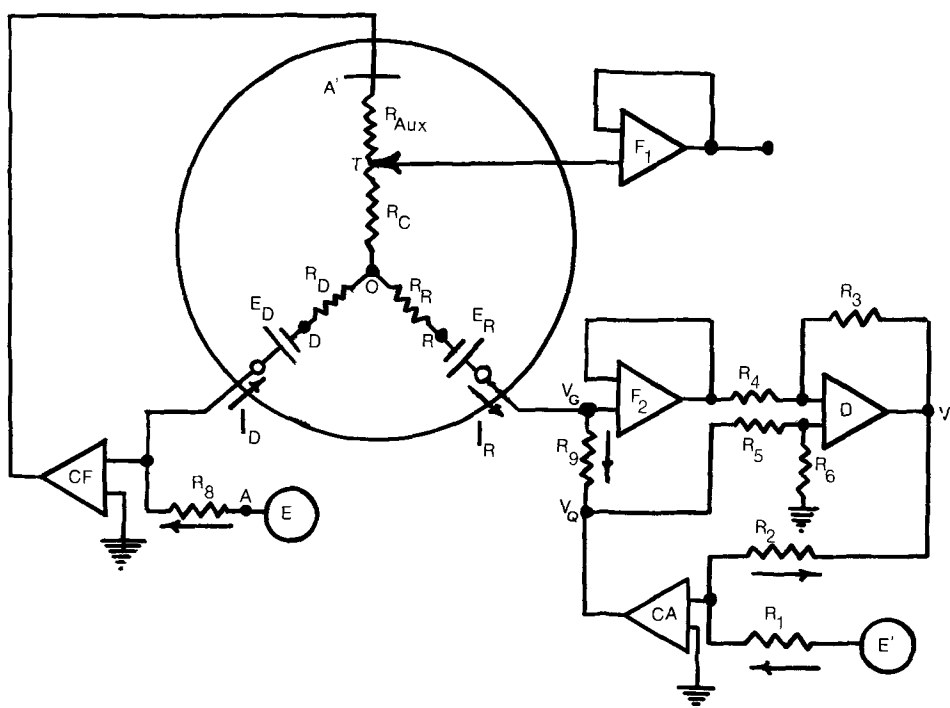
Hewlett-Packard Model 3300A and Heathkit Model IG-18 function generators were used to supply the modulation signal and the reference signal of the lock-in amplifier.

All potentials were measured and reported vs. the saturated calomel electrode. Experiments were run at  $25^\circ \pm 2^\circ\text{C}$ .

**Resistance measurements.**—Small changes in the conventional four-electrode potentiostat, allowing independent control of the ring and the disk electrode potentials (9), convert it to an instrument that provides independent galvanostatic control of both the ring and the disk electrodes, Fig. 2. This circuit was used to determine  $R_C$ .

Measurements of the total resistive component of the impedance between the Luggin capillary and the ring or disk electrodes were carried out by means of a modulation technique using the lock-in amplifier at 1000 Hz. The arrangement for this measurement is

Fig. 2. Circuit for independent galvanostatic control of the ring and the disk electrode. The direction of the current inside and outside of the cell is shown.



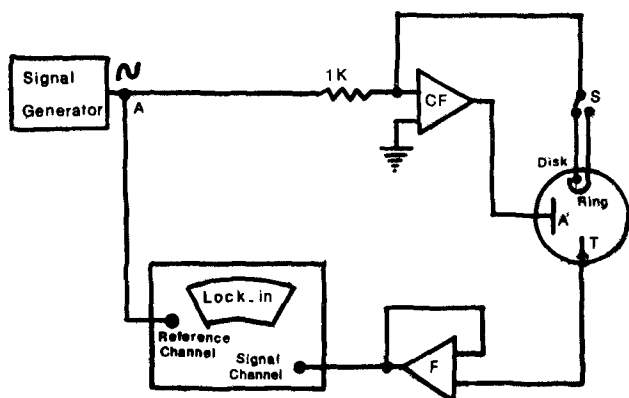


Fig. 3. Schematic of the a-c modulation technique used to measure the uncompensated resistance for the disk and ring electrodes.

shown in Fig. 3. A 0.5-2V a-c signal was applied at the point A resulting in an a-c current of 0.5-2 mA through the auxiliary electrode and the ring and the disk electrode. The uncompensated a-c ohmic potential drop appears at the output of amplifier F.

The resistance between the ring and the disk electrodes was measured using the arrangement shown in Fig. 4. Its value is the ratio of the in-phase component of  $V_O$  and  $i$ . The operational amplifier follower F is used to measure the potential of point O in the equivalent circuit of Fig. 1.

The Luggin capillary was positioned, by eye, to lie on the axis of rotation, unless otherwise stated.

### Theoretical

**Determination of  $R_C$ .**—The potentials at the points O, T, and D in Fig. 1 are represented by  $V_O$ ,  $V_T$ , and  $V_D$ . If the ring current,  $I_R$ , is zero we can write

$$V_{T''} - V_D = I_D R_C + I_D R_D \quad [1]$$

where  $I_D$  is the disk current and  $V_{T''}$  is the potential at the point T when there is no ring current. Now if some current passes through the ring electrode and  $I_D$  is held constant, using Kirchoff's current law at the point O, we can write

$$V_T - V_D = I_D R_C + I_R R_C + I_D R_D \quad [2]$$

Note that  $V_D$ , the potential of the disk electrode, does not change since  $I_D$  is constant even though the potential at point T has changed from  $V_{T''}$  to  $V_T$ .

Subtracting Eq. [1] from Eq. [2] yields

$$V_T - V_{T''} = I_R R_C \quad [3]$$

The change in potential at point T is the same as change in the output of the operational amplifier

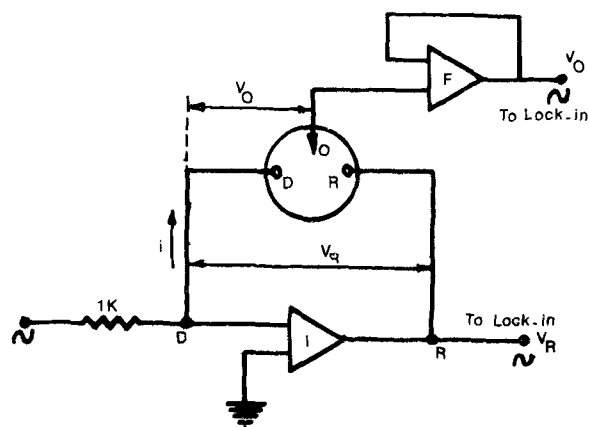


Fig. 4. Schematic of the setup for voltage divider test

follower  $F_1$  in Fig. 2. Hence  $R_C$  can be determined from Eq. [3].

$R_C$  can also be determined in a similar manner, if we hold  $I_R$  constant and control the disk current at two values, zero and  $I_D$ . In this case we measure  $V_{T''}$ , where  $V_{T''}$  is the potential at T when  $I_D = 0$ , and we obtain

$$V_{T''} - V_R = I_R R_C + I_R R_R \quad [4]$$

When current  $I_D$  is passed through the disk we write

$$V_T - V_R = I_R R_C + I_D R_C + I_R R_R \quad [5]$$

where  $V_R$  is the potential at point R. Note that since  $I_R$  does not change,  $V_R$  in Eq. [5] and [4] has the same value. Subtracting Eq. [4] from Eq. [5] yields

$$V_T - V_{T''} = R_C I_D \quad [6]$$

Hence, we have two independent ways to determine  $R_C$ .

Note that if the Luggin capillary tip is positioned at a point in space equivalent to point O in Fig. 1,  $R_C$  is zero and  $V_T - V_{T''}$  ( $V_{T''}$  in Eq. [3] (and [6]) is zero. If the Luggin capillary tip is positioned at a point in space that effectively lies on  $R_D$  (or  $R_R$ ),  $V_T - V_{T''}$  (or  $V_{T''}$ ) becomes a negative quantity and  $R_C$  appears to take on negative values. Such negative values have no physical significance and arise only due to formulation of the problem. In practice, the Luggin capillary tip must be placed very close to the plane of the rotating ring-disk electrode to observe these "negative resistances," and the quantitative aspects of this work will deal only with positive values of  $R_C$ .

Determination of  $R_D$  and  $R_R$ , the equivalent circuit associated with the a-c impedance measurements illustrated in Fig. 3, is shown in Fig. 5 (18). Point T corresponds to point T in Fig. 1 and 2, and point W in Fig. 5 corresponds to point D of Fig. 1 and 2 if the disk electrode is involved, or point R if the ring electrode is involved.  $R_{ohm}$  in Fig. 5 corresponds to the appropriate combination of uncompensated primary resistances, either  $R_C + R_D$  or  $R_C + R_R$ . At high frequencies, only  $R_{ohm}$  determines the voltage difference between the reference and the working electrode and the total ohmic resistance between W and T is then given by

$$R_{ohm} = \frac{V_T}{I} \quad [7]$$

where  $V_T$  is the in phase voltage response measured by the lock-in amplifier and  $I$  is the modulation current. Thus  $R_D$  and  $R_R$  can be calculated by subtracting  $R_C$  from the corresponding  $R_{ohm}$  value.

If the disk and the ring electrodes are shorted together, according to the equivalent circuit in Fig. 1, the measured value of  $R_{ohm,tot.}$  will correspond to  $R_C$  in series with the parallel combination of  $R_D$  and  $R_R$ , i.e.

$$R_{ohm,tot.} = R_C + \frac{R_D R_R}{R_D + R_R} \quad [8]$$

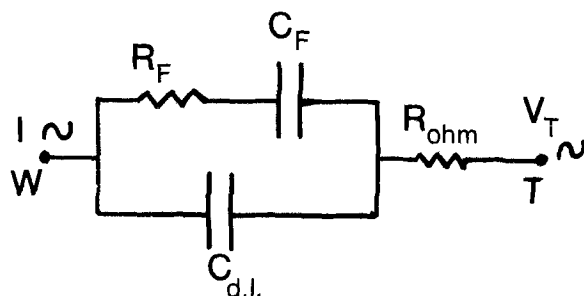


Fig. 5. Equivalent circuit for a-c measurements (18).  $C_F$ ,  $R_F$  = faradaic capacitance and resistance, respectively;  $C_{d.l.}$  = double layer capacitance;  $R_{ohm}$  = ohmic resistance; W = working electrode; T = reference electrode;  $I$  = modulation current;  $V_T$  = voltage response.

Another experiment to further confirm the validity of our model, involves passing current only through the disk and ring electrode with no current passing through the auxiliary.  $R_D$  and  $R_R$  then form a voltage divider between points D and R in Fig. 1 and the reference electrode can be used to determine the potential at point O. Equation [9] gives the relation between the uncompensated resistances  $R_D$ ,  $R_R$ , and the measured potentials

$$\frac{R_D}{R_D + R_R} = \frac{V_O}{V_R} \quad [9]$$

$V_O$  is amplitude of the a-c potential of point O, measured by operational amplifier follower F;  $V_R$  is the amplitude of the a-c output of the operational amplifier I, in phase with  $V_O$ . It is the a-c potential of the ring electrode vs. the disk electrode, which is at ground potential.

## Results and Discussion

### Resistance Common to Ring and Disk Electrodes

$R_C$  was measured by the method described in the preceding section for a particular fixed distance between the ring-disk electrode and the Luggin capillary corresponding to a position in space lying between O and A' in Fig. 1. The values of  $R_C$  were calculated using, as it was appropriate, either Eq. [3] or [6]. Table I gives the results found with electrode No. 1 in 0.01M sulfuric acid, and it is seen that the precision of the measurements approaches 2% with increasing current level. The direction of the current does not affect the calculated value of the common resistance, and thus confirms the ohmic behavior of  $R_C$ .

In their experiments, Gabrielli *et al.* (8) measured two resistances,  $R_R^D$  and  $R_D^R$ , which they called the coupling resistance of the ring on the disk and the disk on the ring, respectively. The values of these two resistances were reported to be within 5% of each other, and for a primary current distribution presumably correspond to the value of the common resistance,  $R_C$ , in our equivalent circuit. Also, their resistances  $R_R^R$  and  $R_D^D$  should correspond to  $R_R$  and  $R_D$ , respectively.

Table I.  $R_C$  values

$I_D$ ( $\mu$ A)	$I_R$ ( $\mu$ A)	$V_T^{**}$ (mV)	$V_T$ (mV)	$R_C$ (ohm)
Using Eq. [3]				
100	-100	328	323	$5 \times 10^1$
100	100	328	333	$5 \times 10^1$
-100	-100	-1400	-1405	$5 \times 10^1$
-100	100	-1400	-1496	$4 \times 10^1$
500	-500	380	353	54
500	500	380	406	52
-500	-500	-1570	-1597	54
-500	500	-1570	-1545	50
1000	-1000	427	374	53
1000	1000	427	479	52
-1000	-1000	-1706	-1756	50
-1000	1000	-1706	-1657	49
1400	-1400	500	431	49
1400	1400	500	570	50
-1400	-1400	-1800	-1870	50
-1400	1400	-1800	-1730	50
Using Eq. [6]				
100	-100	343	337	$6 \times 10^1$
100	100	343	349	$6 \times 10^1$
-100	-100	-1500	-1505	$5 \times 10^1$
-100	100	-1500	-1496	$4 \times 10^1$
500	-500	401	376	50
500	500	401	427	52
-500	-500	-1650	-1680	60
-500	500	-1650	-1622	56
1000	-1000	459	411	48
1000	1000	459	508	49
-1000	-1000	-1770	-1818	48
-1000	1000	-1770	-1717	53
1400	-1400	460	388	51
1400	1400	460	533	52
-1400	-1400	-1710	-1778	49
-1400	1400	-1710	-1640	50

The values of  $R_C$  decreased the closer the tip of the Luggin capillary was placed to the surface of the ring-disk electrode. We found that up to a distance of nearly 5 mm,  $R_C$  values calculated using either of the methods based on Eq. [3] or Eq. [6], were equal to each other.

### Total Uncompensated Ohmic Resistance

**Disk electrode.**—The modulation technique for determining the uncompensated ohmic resistance that is represented in Fig. 3 was tested by using disk electrode No. 2 in 0.01M sulfuric acid (specific conductivity  $\kappa = 0.00616 \text{ ohm}^{-1}\text{-cm}^{-1}$ ) in the current range of 0.5-2.0 mA. The Luggin capillary was placed at different distances, all far from the disk electrode, and the in-phase uncompensated ohmic potential drop between the tip of the Luggin capillary and the disk electrode was measured using a-c currents of 0.5-2.0 mA about a zero current level. At 1000 Hz, the calculated mean resistance,  $R_x$ , was  $377 \pm 4$  ohms in agreement with Newman's formula (1) which predicted 369 ohms. The results of all a-c measurements were reproducible in the range of frequencies between 100 Hz and 10 kHz.

**Ring-disk electrode.**—The above results validated the a-c technique of Fig. 3 as a reliable method for determining uncompensated ohmic potential drops, *i.e.*, the primary resistance. Next,  $R_x$  was determined for the disk of ring-disk electrode No. 1, yielding a value of  $R_x = 96 \pm 2$  ohms. If the ring of this electrode is insulated from the solution using varnish,  $R_x = 110 \pm 2$  ohms, which compares favorably with the theoretical value for a 7.6 mm diameter disk electrode, 107 ohms (1). The decrease of  $R_x$  produced by a ring electrode is in the expected direction, when one qualitatively considers the changes in the potential field produced by a conductor in the insulating plane surrounding the disk electrode. The effect of the ring electrode on the disk electrode primary resistance prevents us from using Newman's formula (1) in the interpretation of results presented below.

Next, the modulation technique was applied using electrode No. 1 to determine  $R_C + R_D$ ,  $R_C + R_R$ , and  $R_C + R_D R_R / (R_D + R_R)$  for six locations of the Luggin capillary by placing switch S in Fig. 3 in the appropriate position, or by shorting the ring to disk electrode with the switch in either position.  $R_C$  was determined simultaneously as described in the preceding section. The results are given in Table II, where  $R_{\text{ohm,tot.}} = R_C + R_D R_R / (R_D + R_R)$ .

Values of  $R_D$  and  $R_R$  were calculated from the initial values of  $R_C$  and  $R_{\text{ohm}}$ . These values of  $R_C$ ,  $R_R$ , and  $R_D$  were then used to calculate  $R_{\text{ohm,tot.}}$ , and agree well (1-2%) with the value measured when the ring and disk are shorted.

Table III shows the results of the experiment carried out to verify Eq. [9] for runs 2, 4, and 5 of Table II. In the last entry of Table III the ring and disk were interchanged such that the output of the operational amplifier I,  $V_D$ , was the potential of the disk vs. the virtually grounded ring electrode. The results are in good agreement with the predicted values.

### Effect of $R_C$ , $R_D$ , and $R_R$ on $I$ - $E$ Curves at Ring-Disk Electrode

An uncompensated voltage drop equal to  $(I_D + I_R)R_C$  will be shared between the disk and the ring. This common uncompensated  $IR$  drop will have a significant effect on the  $I$ - $E$  curves obtained simultaneously for the disk and the ring electrodes. For example, if  $\Delta I_D$  and  $\Delta I_R$  represent changes in the disk and the ring current, respectively, the potential of the ring electrode will vary by an amount  $R_C(\Delta I_D + \Delta I_R) + R_R \Delta I_R$ . Thus a changing disk current will produce a change in the ring potential sufficient to change the ring current by  $\Delta I_R$ . If the ring electrode is potentiostated on the rising portion of an  $I$ - $E$  curve,  $\Delta I_R$  will change markedly as opposed to the change when the

Table II. Resistance data for ring-disk electrode No. 1

All resistances are in ohms. Runs 1-6 represent separate experiments in which the Luggin capillary was positioned approximately on the electrode axis, about 1-2.5 cm away from the disk.

	$R_0$	$R_{ohm}$		$R_D$	$R_R$	$R_{ohm,tot.}$	
		Disk	Ring			Experimental	Theoretical
1	51	77	92	26	41	67	67
2	57	84	104	27	47	75	74
3	57	96	132	39	75	82	83
4	60	88	116	28	56	79	79
5	63	89	122	26	59	81	81
6	63	89	111	26	48	79	80

Table III. Results of experiment to verify Eq. [9]

All resistances are in ohms.

$R_D$	$R_R$	$V_0/V_D$	$V_0/V_R$	$R_D/(R_D + R_R)$	$R_R/(R_D + R_R)$
27	47	0.37	—	0.36	0.64
28	56	0.35	—	0.34	0.66
26	59	0.34	0.61	0.31	0.69

ring potential is on a limiting current region. An example of this phenomenon is shown in Fig. 6 where the ring electrode, being potentiostated on the rising portion of the hydrogen evolution curve, behaves as if it is collecting a soluble species being generated at the disk electrode.

Similar effects, presumably due to such an interaction, were studied by Gabrielli *et al.* (8) using ring-disk electrodes of different dimensions in the case of the anodization of iron in 2N sulfuric acid. Miller and Bellavance (4) also considered such interactions, using a potentiometric ring-disk experiment.

Rapid changes in current at the disk electrode will produce a rapid change in potential at the ring electrode as a result of the change in potential of the ring electrode double layer capacitance, so that even in the absence of a faradaic ring electrode process a current will flow in the ring electrode circuit. This phenomenon has been observed by Alberly (19) in his studies of ring electrode current when an a-c current is passed through the disk electrode.

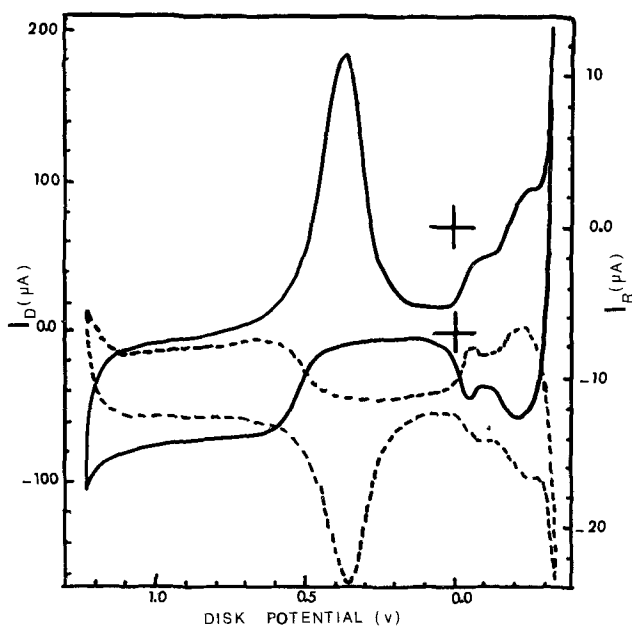


Fig. 6. Cyclic voltammogram in 0.01M  $H_2SO_4$  using electrode No. 1. Solid curve and dashed curve represent disk and ring voltammogram, respectively. Ring is potentiostated at  $-0.450V$ . Scan rate = 100 mV/sec. Rotation speed = 2500 rpm. These  $I-E$  curves were recorded on an EAI, X-Y-Y' 1131 Variplotter.

We propose that the term "pseudocollection" be used to denote changing ring electrode currents arising because of uncompensated ohmic potential effects at ring-disk electrodes. We also propose the term "inverse pseudocollection" to represent the analogous effect of changing disk electrode currents arising because of uncompensated ohmic potential effects at ring-disk electrodes.

We have observed, as has Miller (20), that it is possible to reverse the direction of the pseudocollection effect by positioning the tip of the Luggin capillary very close to the plane of the rotating ring-disk electrode. In the case of electrode No. 1, on the axis of rotation, the reversal appears when the Luggin capillary is closer than 2 mm. This reversal of the sign of the pseudocollection effect corresponds to a negative value of  $R_C$ , i.e., position of the Luggin capillary along the resistor  $R_D$ , as interpreted in the theoretical section.

The formulation of Gabrielli *et al.* (8) would formally predict this change in signs of the pseudocollection effect if negative resistance values would have been considered by them. However, in the absence of an equivalent circuit such as Fig. 1, there is no justification for introducing the concept of a negative resistance, nor would there be the obvious idea of moving the Luggin capillary tip toward the electrode to find a "negative resistance" region.

We have also been able to find positions in space which produce a change in the sign of the inverse pseudocollection effect. Generally, regions close to the ring electrode produce this change in the sign of the inverse pseudocollection effect.

Finally, there is a locus of points for which both the pseudo- and inverse pseudocollection effects disappear simultaneously. This result, along with the negative resistance effects are decisive tests of the equivalent circuit given in Fig. 1.

Pseudocollection effects will be most significant when large disk currents flow, when the disk current changes rapidly, or when the supporting electrolyte resistance is large, as for example, in dilute aqueous solution or in many nonaqueous solvents. In principle, they may also be observed if the ohmic potential drop changes become large enough to shift the ring electrode potential from the limiting current plateau to the rising portion of a current potential curve.

It is, of course, necessary to recognize that the test of the equivalent circuit we have proposed is based on a primary current distribution. Thus, somewhat different values of  $R_C$ ,  $R_D$ , and  $R_R$  will be found for the same position of the Luggin capillary for different current distributions resulting from kinetics and mass transfer effects. However, our model suggests strategies that will be successful in minimizing the pseudocollection effect for any current distribution.

### Conclusion

The proposed equivalent circuit, involving a common uncompensated resistance with the uncompensated resistances of the ring and the disk electrodes, agrees well with experiment. Using this model there should be little difficulty in designing circuits to feed back the necessary  $IR$  correction for the ring and disk potentiostat, and thus eliminate much of the undesirable interactions that can occur because of the coupling these uncompensated resistances produce between ring and disk electrodes.

### Acknowledgment

This research was supported in part by The Electrochemical Society Summer Fellowship and Henry Woodburn Fellowship from S.U.N.Y.A.B. (M.S.) and by AFSOR Grant No. 505034A.

Manuscript submitted Feb. 18, 1974; revised manuscript received June 21, 1974.

Any discussion of this paper will appear in a Discussion Section to be published in the June 1975 JOURNAL.

All discussions for the June 1975 Discussion Section should be submitted by Feb. 1, 1975.

The publication costs of this article have been assisted by the State University of New York at Buffalo.

## REFERENCES

1. J. Newman, *This Journal*, **113**, 501 (1965).
2. J. Newman, *ibid.*, **113**, 1235 (1966).
3. S. Bruckenstein and B. Miller, *ibid.*, **117**, 1044 (1970).
4. B. Miller and M. I. Bellavance, *ibid.*, **120**, 42 (1973).
5. V. Marathe and J. Newman, *ibid.*, **116**, 1704 (1969).
6. W. J. Albery and M. L. Hitchman, *Trans. Faraday Soc.*, **67**, 2408 (1971).
7. W. H. Smyrl and J. Newman, *This Journal*, **119**, 208 (1972).
8. C. Gabrielli, M. Keddani, and H. Takenouti, *J. Chim. Phys.*, **4**, 737 (1972).
9. D. T. Napp, D. C. Johnson, and S. Bruckenstein, *Anal. Chem.*, **39**, 481 (1967).
10. S. H. Cadle, Ph.D. Thesis, S.U.N.Y.A.B. (1972).
11. D. C. Johnson, Ph.D. Thesis, University of Minnesota (1967).
12. D. F. Untereker, Ph.D. Thesis, S.U.N.Y.A.B. (1972).
13. V. Vicente, Ph.D. Thesis, S.U.N.Y.A.B. (1972).
14. M. Z. Hassan, Ph.D. Thesis, University of Minnesota (1972).
15. D. C. Johnson and S. Bruckenstein, *This Journal*, **117**, 460 (1970).
16. D. T. Napp, Ph.D. Thesis, University of Minnesota (1967).
17. D. F. Untereker and S. Bruckenstein, *Anal. Chem.*, **44**, 1009 (1972).
18. K. J. Vetter, "Electrochemical Kinetics," Chap. 2, Academic Press, New York (1967).
19. W. J. Albery, Private communications.
20. B. Miller, Private communications.

## Triangular Sweep Voltammetry Studies on Porous Silver in KOH: Effect of Temperature and Sweep Rate on Double-Layer Capacitance

E. G. Gagnon\*

*Electrochemistry Department, Research Laboratories, General Motors Corporation, Warren, Michigan 48090*

## ABSTRACT

Triangular sweep voltammetry data for commercially available porous silver in 31 weight per cent KOH between 21° and -47°C are presented. Experimental problems with distributed capacitance and impurity effects are discussed. When experimental conditions are optimized, however, the double-layer capacitance of the porous electrode, based upon the BET area of the electrode, compares well with literature values for solid silver.

One method of characterizing flooded porous electrodes is to determine the double-layer capacitance (DLC) of the electrode in the environment in which it is to be used. The wetted surface area obtained from DLC measurements does not, however, always agree with the dry areas obtained from BET data. In part, DLC measurements using classical methods such as a-c bridge or interrupter methods meet with difficulties introduced by ohmic effects within the pore structure of the electrode. Recently, the effect of electrolyte resistivity within the pores of the electrode was treated mathematically (1) for the triangular voltage sweep method. The theory was later verified experimentally for porous electrodes constructed of silver (2) and nickel (3). This paper gives additional information regarding the effect of temperature and sweep rate on the DLC of porous silver.

## Experimental

**Materials.**—Silver electrodes (99.8% pure) were punched from a sheet of sintered, porous silver, battery plaque available commercially. The test electrodes had a diameter of 3.5 cm, a thickness of 0.127 cm, a porosity of 62%, and a BET area of 0.175 m<sup>2</sup>/g (or 8660 cm<sup>2</sup> of internal area). Copper was identified to be the major impurity by spectrographic analysis ( $\approx 0.20\%$ ). The electrolyte was a 31 weight per cent (w/o) KOH solution and was prepared by diluting reagent grade 45 w/o KOH with distilled water (specific resistance of  $3 \times 10^5$  ohm-cm) obtained from a Barnstead still; the major impurity in the electrolyte was  $2 \times 10^{-4}\%$  Cu.<sup>1</sup>

**Cell.**—The electrochemical cell and the Teflon test electrode holder were described before (2). A Hildebrand-type Hg/HgO (31 w/o KOH) reference electrode with a Luggin capillary was used. The complete cell and the reference electrode were assembled in a Tenney constant-temperature cabinet (Model TR-5) and tests were conducted between 21° and -47°C. Prior to all testing, the electrolyte was equilibrated at the test temperature for periods of at least 18 hr (overnight).

**Measurements.**—Triangular voltage sweeps (TVS) were performed using a Wenking (Model 66TS10) potentiostat in conjunction with an Exact (Model 5000 series) signal generator. A Moseley (Model 7004 AM) X-Y recorder recorded voltammetry data from which capacitances were calculated. Results using sweep rates of 6 and 59 mV/sec are discussed; higher sweep rates could not be used because of severe distributed capacitance effects (2). Voltage excursions of 140 mV were used to (i) minimize transient faradaic currents (2) and (ii) determine capacity solely as a function of potential; sweep results over a wide range of potentials often give smeared-out voltammetry curves in which the behavior of the electrode at one potential reflects changes that occurred at another potential.

## Results and Discussion

Figure 1 shows a composite of eleven single-sweep voltammetry curves obtained for a porous silver electrode in 31 w/o KOH at 21°C. The first sweep is emphasized by the darker line and begins at -0.10V vs. Hg/HgO. The potential is then varied cathodically to -0.24V at a sweep rate of 59 mV/sec and then anodically back to -0.10V at the same sweep rate. Each successive cathodic sweep begins in intervals of 50 mV

\* Electrochemical Society Active Member.

Key words: voltammetry studies, porous silver, potassium hydroxide, double-layer capacity.

<sup>1</sup> Spectrographic analysis.



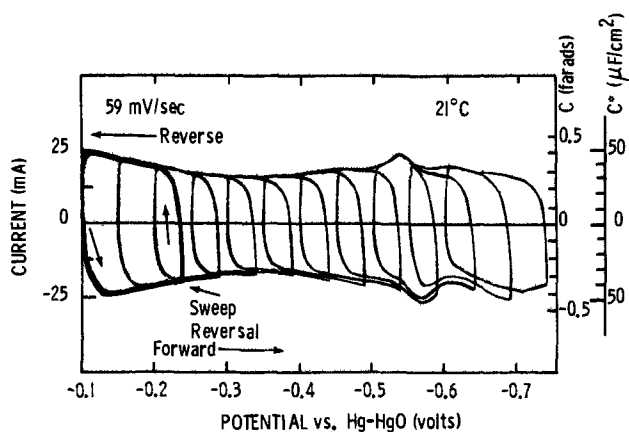


Fig. 1. TVS data at 21°C;  $k = 59$  mV/sec

and at zero current. Over most of the potential region scanned, the results superimpose to form an envelope of potential vs. current. The apparent capacity,  $C$ , is readily calculated from the voltammetry data simply from

$$C = i/k \quad [1]$$

where  $i$  is the measured current (mA);  $k$  is sweep rate (mV/sec); and  $C$  is capacity (farads). The apparent capacity,  $C$ , and the capacity per BET area of the electrode,  $C^*$  ( $\mu\text{f}/\text{cm}^2$ ) are plotted at the right ordinate in Fig. 1. Capacitance varies with potential and minimums are seen at  $-0.350\text{V}$  (forward direction) and  $-0.325\text{V}$  (reverse direction); pseudocapacity peaks are also observed in the vicinity of  $-0.55\text{V}$ . Similar results at  $-18^\circ$ ,  $-33^\circ$ , and  $-47^\circ\text{C}$  are shown in Fig. 2, 3, and 4, respectively; the results were obtained with the same electrode over a period of several days and are typical of data obtained with this particular porous silver sample.

**Impurities.**—Anodic and cathodic pseudocapacity peaks of about  $50 \mu\text{f}/\text{cm}^2$  occur at about  $-0.55\text{V}$  (Fig. 1). Also in the vicinity of  $-0.175\text{V}$ , anodic and cathodic peaks are seen most clearly at  $-33^\circ$  and  $-47^\circ\text{C}$ ; perhaps the peaks are not as noticeable at the higher temperatures because they are masked by small

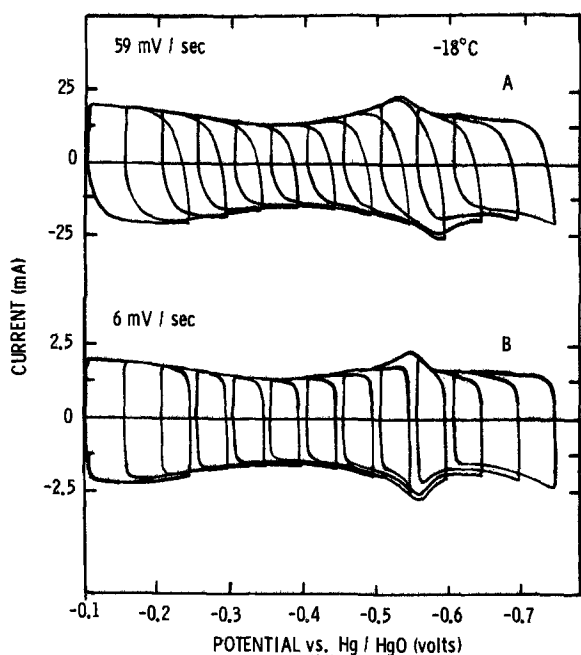


Fig. 2. TVS data at  $-18^\circ\text{C}$ : A,  $k = 59$  mV/sec; B,  $k = 6$  mV/sec.

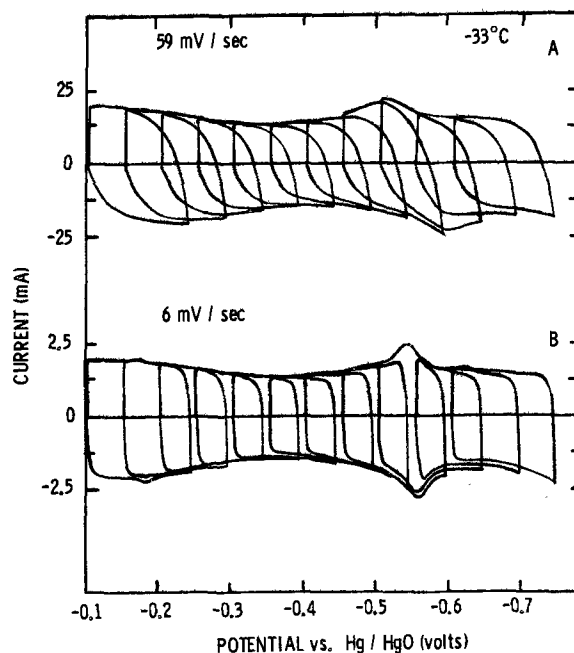


Fig. 3. TVS data at  $-33^\circ\text{C}$ : A,  $k = 59$  mV/sec; B,  $k = 6$  mV/sec.

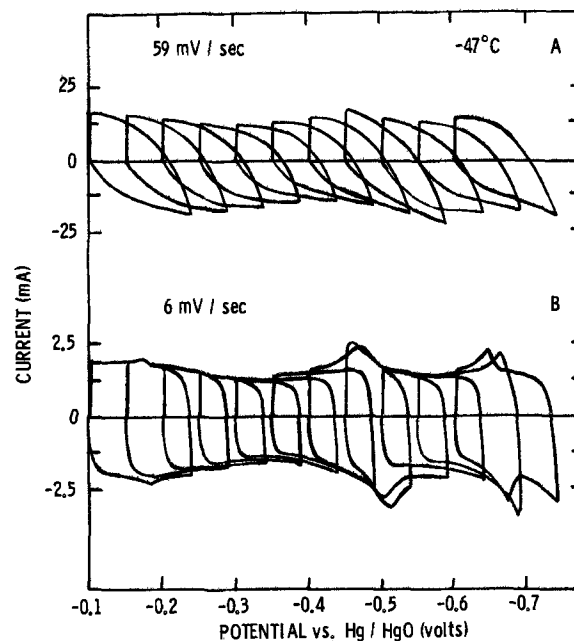
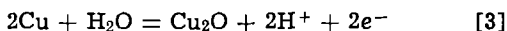
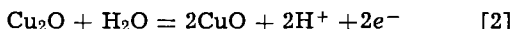


Fig. 4. TVS data at  $-47^\circ\text{C}$ : A,  $k = 59$  mV/sec; B,  $k = 6$  mV/sec.

amounts of faradaic current. Similar peaks were reported by others (4, 5) using porous silver electrodes. In all probability, the peaks are due to impurities present in the electrode which are desorbing and readsorbing within the pore structure. This is because the peak separation decreases with decreasing sweep rate, which often is a good indication of adsorption-desorption processes (6). The charge associated with the various peaks, however, corresponds to a very small fraction of a monolayer and therefore to a small amount of impurities. For example, the charge associated with the largest cathodic peak at  $-0.57\text{V}$  (Fig. 1) is about  $0.6 \mu\text{coulomb}/\text{cm}^2$ . This is approximately 0.3% of the  $210 \mu\text{coulomb}/\text{cm}^2$  value for monolayer coverage (7); it also corresponds very nearly to the level of copper impurity in the metal. Bird *et al.* (4), using a potential step method, concluded that the various peaks observed in

1M KOH were due to copper impurities in their electrodes, according to the following reactions



where the respective  $E^\circ$  values are pH-dependent according to

$$E^\circ = 0.747 - 0.059 \text{ pH} \quad [2a]$$

$$E^\circ = 0.471 - 0.059 \text{ pH} \quad [3a]$$

In this study, additions of copper ions to the electrolyte enhanced the peaks in question. Thus, it is postulated that the peaks are associated with the Cu(II)/Cu(I) couple at  $-0.18\text{V}$  and the Cu(I)/Cu(0) couple at  $-0.55\text{V}$ .

**Distributed capacity effects.**—Figure 5 illustrates the behavior expected with a porous electrode as a function of temperature for the case where capacity is constant and faradaic current is negligible (1). The figure shows the time to reach a steady current after the sweep begins ( $t'$ ) and after the sweep reverses ( $t''$ ) increases as temperature decreases. The current density during the initial portion of the sweep is predicted (1) from

$$i(L) = \beta_1 k C' \quad [4]$$

where  $i(L)$  is the current density;  $k$  is the sweep rate ( $dV/dt$ ), and  $C'$  is the apparent capacity per geometric area of the electrode. The parameter  $\beta_1$  has a numerical value between 0 and 1 and is dependent on two dimensionless parameters  $L\lambda/d$  and  $t/\rho_e C' L$ , where  $L$  is the thickness of the electrode,  $\lambda$  is the labyrinth factor,  $d$  is the distance between the tip of the Luggin capillary and the surface of the electrode, and  $\rho_e$  is the effective specific resistance of the electrolyte in the pores of the electrode. When  $\beta = 1$  (dashed line, Fig. 5), distributed capacity effects are negligible. Conditions which increase  $L\lambda/d$  (e.g., thicker electrodes) and/or decrease  $t/\rho_e C' L$  (e.g., lower temperatures and higher resistivities) enhance distributed capacity effects (solid lines, Fig. 5). Similarly, the current density after sweep reversal is predicted (1) from

$$i(L) = \gamma k C' \quad [5]$$

where  $\gamma$  is a function of basically the same dimension-

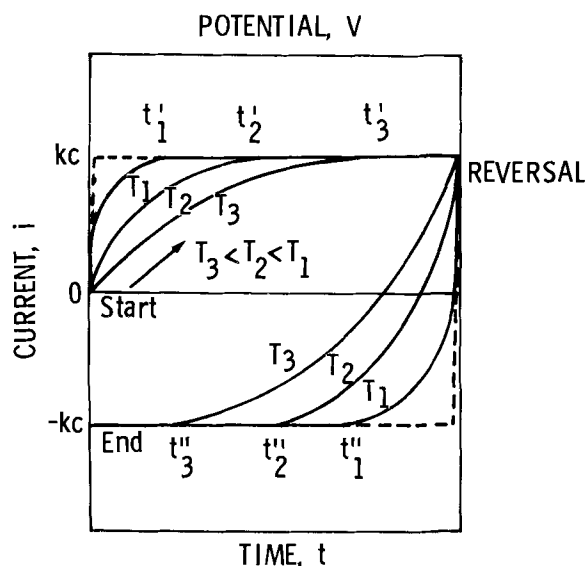


Fig. 5. Current vs. time or potential during a TVS for cases where capacity is constant and faradaic current is negligible. Solid lines illustrate distributed capacity effects as a function of temperature. Dashed line illustrates case where distributed effects are negligible.

less parameters as  $\beta_1$ , except its value ranges between +1 and -1 as the value of  $t/\rho_e C' L$  increases.

The experimental results (Fig. 1-4) given here clearly follow the general pattern expected, even though there are potential regions where capacity is obviously not constant (e.g., in the vicinity of  $-0.55\text{V}$ ). It can be shown (8) that when all other parameters are kept constant (e.g.,  $k, L, C$ , etc.),  $t'$  (Fig. 5) is proportional to  $\rho_e$ . Values of  $t'$  estimated from sweeps beginning at  $-0.30\text{V}$ , such as shown in Fig. 1-4, are plotted as a function of temperature in Fig. 6; also included are values of  $\rho_e$  (solid line) which are calculated using

$$\rho_e = \rho \lambda \quad [6]$$

and experimentally determined values of the bulk resistivity,  $\rho$ , of 31 w/o KOH (9) and the labyrinth factor,  $\lambda$ , of 2 determined previously (2).

**Capacitance data.**—A capacitance minimum occurs in both the forward ( $-0.35\text{V}$ ) and reverse ( $-0.325\text{V}$ ) directions. At  $21^\circ\text{C}$ ,  $C_{\text{min}}$  is about  $32 \mu\text{f}/\text{cm}^2$  and is independent of sweep rate. As temperature decreases, there occurs an apparent shift in the potential of the cathodic minimum,  $E_{\text{min}}^c$  (Fig. 7) and in the capacitance  $C_{\text{min}}$  (Fig. 8). Between  $21^\circ$  and  $-47^\circ\text{C}$ ,  $E_{\text{min}}^c$  shifts 80 mV cathodically at 59 mV/sec, whereas at 6 mV/sec, the shift is 20 mV. Similarly, over the same temperature range,  $C_{\text{min}}$  decreases about  $10 \mu\text{f}/\text{cm}^2$  at 59 mV/sec and about  $2 \mu\text{f}/\text{cm}^2$  at 6 mV/sec. The higher sweep rate results show significant shifts in  $C_{\text{min}}$  and  $E_{\text{min}}^c$  with decreasing temperature, but with the slower sweep rate the shifts over the same temperature range

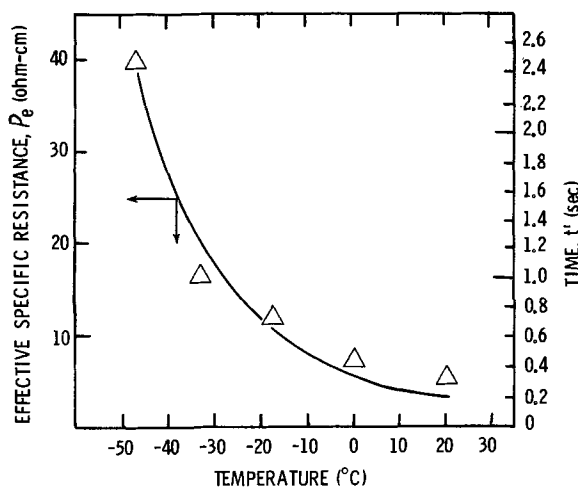


Fig. 6. Effective specific resistance of the electrolyte in the pores of the electrode (solid line) and times to reach a constant current,  $t'$  (points), vs. temperature.

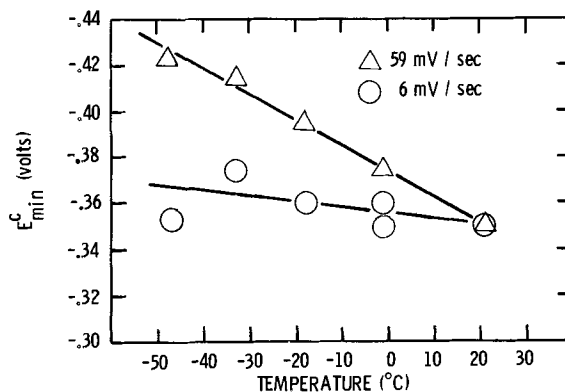


Fig. 7. The potential of the capacitance minimum,  $E_{\text{min}}^c$  (forward direction) vs. temperature as a function of sweep rate.

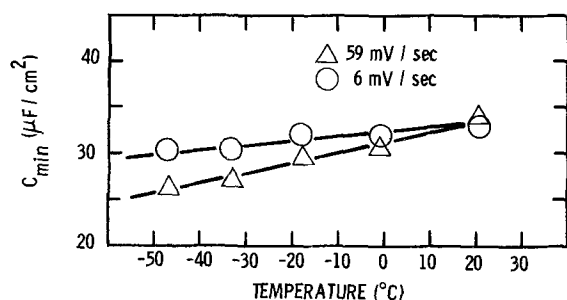


Fig. 8. The capacitance minimum,  $C_{\min}$ , vs. temperature as a function of sweep rate.

are markedly reduced. Thus it would appear that the high sweep rate results are mostly artifacts of the system and the result of a distributed capacitance effect. The magnitude of the results is specific to this particular electrode/electrolyte system and does not necessarily apply to other porous silver electrodes. This is especially true if the physical properties (e.g.,  $\rho$ ,  $\lambda$ ,  $L$ , etc.) of the electrodes differ.

The pzc is usually taken as the potential at which a well-defined minimum occurs in the potential-capacity data (10) with dilute solutions (0.01M or less). With concentrated solutions, however, the pzc is not well defined even with mercury surfaces. For solid silver, reported pzc values show a wide variation including 0.046V vs. NHE in  $\text{KNO}_3$  (11); -0.70V vs. NHE in  $\text{Na}_2\text{SO}_4$  (12), and  $\text{NaClO}_4$  (13). It is even more difficult to determine the pzc with porous electrodes. For example, consider the case where an adsorption pseudo-capacitance due to a faradaic process occurs in the same potential region as the pzc. Normally, with mercury surfaces, measurements at high frequencies often eliminate the contribution of an adsorption pseudo-capacitance (10). With porous electrodes, however, high frequency techniques are not always applicable because of distributed capacity effects. Also, the use of dilute solutions to determine the diffuse layer capacitance near the pzc is not possible, again because of massive distributed capacity effects. Although the pzc is an important parameter of the metal, it depends markedly on the properties of the solution in contact with the particular metal. Therefore, it is not clear at this point whether the  $C_{\min}$ , observed in this work actually corresponds to the pzc, even though both often occur in the same vicinity.

The capacity values obtained over the entire potential range (32 to 50  $\mu\text{F}/\text{cm}^2$ ) are in good accord with literature values for solid silver in 1M  $\text{Na}_2\text{SO}_4$  (14), 1M  $\text{K}_2\text{SO}_4$  (15), 1M  $\text{KNO}_3$  (15), and 30 w/o KOH (16). When one wishes to compare the electrochemically active surface area of porous silver electrodes, it is best done at the  $E_{\min}$ , preferably under similar test conditions. Thus, a proper sweep rate must be selected; it can be estimated using the equations discussed in the paper or determined experimentally. Obviously the same principles apply to other porous electrode systems. Using these concepts, it is possible to understand why Evans (17) was unable to use fast sweep rates in determining the capacitance of carbon powders in NaCl solutions while the use of slow sweep rates gave consistent and meaningful results.

### Conclusions

The TVS technique is a fast and effective method of electrochemically studying the surface characteristics

of porous silver in alkaline solutions. The technique is very sensitive to trace amounts of electrochemically active species present at the surface (i.e., coverages of less than a monolayer can be detected). DLC, free from pseudocapacity effects can be determined, however, only in certain potential regions where a capacitance minimum occurs in the vicinity of -0.35V vs. Hg/HgO. Values of capacitances based on the BET area of the electrode agree with literature values for solid silver. Methods of avoiding some experimental difficulties arising from the porous nature of the electrode are discussed in terms of a distributed capacitance model.

### Acknowledgments

The author thanks Professor E. B. Yeager for helpful and stimulating discussions during the course of this work.

Manuscript submitted Dec. 17, 1973; revised manuscript received June 4, 1974. This was Paper 354 presented at the San Francisco, California, Meeting of the Society, May 12-17, 1974.

Any discussion of this paper will appear in a Discussion Section to be published in the June 1975 JOURNAL. All discussions for the June 1975 Discussion Section should be submitted by Feb. 1, 1975.

The publication costs of this article have been assisted by the General Motors Corporation.

### REFERENCES

- L. G. Austin and E. G. Gagnon, *This Journal*, **120**, 251 (1973).
- E. G. Gagnon, *ibid.*, **120**, 1052 (1973); Abstract 242, p. 548, Electrochemical Society Extended Abstracts, Spring Meeting, Chicago, Illinois, May 13-18, 1973.
- E. G. Gagnon, *This Journal*, **121**, 512 (1974); Abstract 44, p. 108, Electrochemical Society Extended Abstracts, Fall Meeting, Boston, Massachusetts, Oct. 7-11, 1973.
- J. Bird, H. Feng, J. Giner, and M. Turchan, Tyco Laboratories, Inc., Waltham, Mass., Contract No. DA 49-186-AMC-39(D), April 1968.
- R. A. Myers, W. F. Cowherd, and W. H. Steuernagel, HDL-TR-1578, Harry Diamond Laboratories, Washington, D. C., December 1971.
- R. H. Wopschall and I. Shain, *Anal. Chem.*, **39**, (13), 1535 (1967).
- S. Gilman, *J. Phys. Chem.*, **67**, 78 (1963).
- E. G. Gagnon and L. G. Austin, HDL-065-4 Contract No. DAAG-39-67-C-0065, Department of Material Sciences, Pennsylvania State University, University Park, Pa., p. 60, September 1971.
- E. G. Gagnon and L. G. Austin, *This Journal*, **118**, 497 (1971).
- S. D. Argade and E. Gileadi, "Electrosorption," E. Gileadi, Editor, pp. 87-115, Plenum Press, New York (1967).
- V. I. Veselovsky, *Acta Physicochim., U.R.S.S.*, **11** (6), 815 (1939).
- D. I. Leikis, *Dokl. Akad. Nauk SSSR*, **135**, 1429 (1960).
- N. A. Hampson, D. Larkin, and J. R. Morley, *This Journal*, **114**, 817 (1967).
- J. J. McMullen and H. Hackerman, *ibid.*, **106**, 341 (1959).
- M. A. Devanathan and K. Ramakrishnaiah, *Electrochim. Acta*, **18**, 259 (1973).
- J. McCallum, R. W. Hardy, and R. F. Redmond, Contract No. AF 33(615)-2225, Report No. AFAPL-TR-66-31, Battelle Memorial Institute, Columbus, Ohio, May 1966.
- S. Evans, *This Journal*, **113**, 165 (1966).

# Current Distribution on a Plane below a Rotating Disk

Robert V. Homsy and John Newman\*

*Inorganic Materials Research Division, Lawrence Berkeley Laboratory, and Department of Chemical Engineering, University of California, Berkeley, California 94720*

## ABSTRACT

The current distribution on a stationary disk electrode below a rotating disk at high Schmidt numbers is calculated at various fractions of the limiting current. Numerical results for the case of Tafel polarization show that the current density on the plane becomes more nonuniform as the limiting current is approached.

The rotating disk system has been used extensively in electrochemical investigations primarily because the disk is a surface of uniform accessibility and it is easy to use. A slightly more complicated system consisting of a fluid driven by a rotating disk above a stationary plane has been studied recently (1-3). The electrode surface is a coaxial disk imbedded in the stationary plane. Figure 1 shows the system. A diffusion-layer solution to the equation of convective diffusion was found for high Schmidt numbers at conditions of limiting current (1). The current distribution was found to be nonuniform, increasing from zero at the center of the electrode to infinity at the leading edge. We shall apply here the same procedure which has been used previously (4-10) for various geometries to study the behavior of this system at current densities below the limiting current.

In the treatment of the problem the following assumptions are made:

1. The working electrode is a coaxial disk imbedded in an infinite, insulating plane.
2. The rotating disk acts as a counterelectrode at infinity. (For the case in which the separation distance between the rotating disk and the plane is finite, Laplace's equation should be solved in a different way for the potential in the solution outside the diffusion layer, in order to account for the fact that the rotating disk is an insulator, or another electrode, as the case might be.)
3. The flow is fully developed and laminar.
4. Dilute solution theory applies with constant diffusion coefficients, mobilities, and activity coefficients.
5. Radial diffusion is negligible (valid at high Péclet numbers).
6. The treatment presented here applies to either metal deposition from a single salt solution or electrode reactions with an excess of supporting electrolyte.

## Mathematical Formulation

At high Schmidt numbers the concentration varies from its bulk value only in a thin diffusion layer near the electrode surface, well within the hydrodynamic boundary layer. It is then valid to approximate the radial velocity by the first term in an expansion in distance from the electrode

$$v_r = -y\beta(r) \quad [1]$$

where  $\beta = -\partial v_r / \partial y$  at  $y = 0$ . A full discussion of the hydrodynamics of this system may be found elsewhere (1). For this system  $\beta = -r\Omega\sqrt{\Omega/\nu} F'(O)$ , where  $F'(O)$  is a constant determined by the dimensionless separation distance,  $\beta = L\sqrt{\Omega/\nu}$ .

The axisymmetric diffusion-layer solution may be superposed (8) to yield the concentration derivative evaluated at the electrode surface in terms of the derivative of the surface concentration

$$\left. \frac{\partial c}{\partial y} \right|_{y=0} = -\frac{\sqrt{r\beta}}{\Gamma(4/3)} \times \int_0^x \frac{dc_0}{dx} \bigg|_{x=x_0} \frac{dx_0}{\left[ 9D \int_{x_0}^x r\sqrt{r\beta} dx \right]^{1/3}} \quad [2]$$

where  $x = r_0 - r$  is the distance from the edge of the electrode. Substitution for  $x$  and  $\beta$  yields

$$\left. \frac{\partial c}{\partial y} \right|_{y=0} = -\frac{(1-\xi)^{1/3}}{r_0\Gamma(4/3)} \left( \frac{2Pe}{3} \right)^{1/3} \times \int_0^\xi \frac{dc_0}{d\xi} \bigg|_{\xi=\xi_0} \frac{d\xi_0}{(\xi-\xi_0)^{1/3}} \quad [3]$$

where  $Pe = \beta r_0^3 / 2rD = -\frac{1}{2}F'(O) Sc Re^{3/2}$  is a Péclet number,  $Re = r_0^2 \Omega / \nu$  is the Reynolds number based on the radius of the electrode,  $\xi = 1 - \xi^3$ , and  $\xi = r/r_0$  is the dimensionless radius.

The current density normal to the surface of the electrode is related to the concentration derivative by the relation

$$i = \frac{nFD}{1-t} \left. \frac{\partial c}{\partial y} \right|_{y=0} \quad [4]$$

where  $n$  is the number of electrons produced when one reactant ion or molecule reacts and  $t$  is the transference number.

The potential in the solution outside the diffusion layer is the same as that for the rotating disk. At the surface of the electrode the potential is given by (4)

$$\phi_0 = \frac{RT}{ZF} \sum_{m=0}^{\infty} B_m P_{2m}(\eta) \quad [5]$$

where  $Z = -z_+z_-/(z_+ - z_-)$  for a single salt and

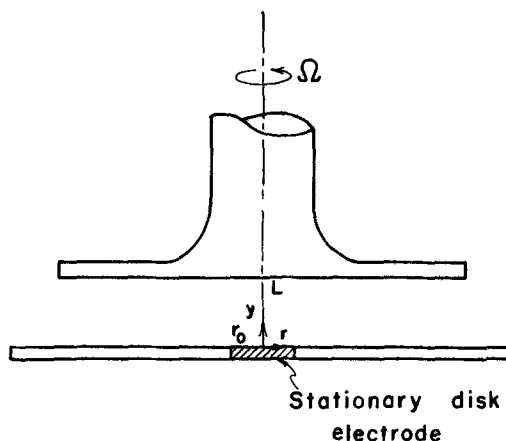


Fig. 1. Disk electrode imbedded in a stationary plane below a rotating disk.

\* Electrochemical Society Active Member.

Key words: current distribution, mass transfer, electrode kinetics.

— $n$  with supporting electrolyte,  $P_{2m}(\eta)$  is the Legendre polynomial of order  $2m$  and  $\eta = \sqrt{1 - \xi^2}$  is the rotational elliptic coordinate at  $y = 0$ . The expansion coefficients  $B_m$  are given by

$$B_m = -\frac{ZF r_0}{\kappa RT} \pi \frac{(4m+1)[(2m)!]^2}{2(2^m m!)^4} \int_0^1 i \eta P_{2m}(\eta) d\eta \quad [6]$$

where  $\kappa$  is the conductivity of the bulk solution.

The electrode potential is the sum of the potential drop in the solution  $\Phi_0$ , the concentration overpotential  $\eta_c$ , and the surface overpotential  $\eta_s$

$$V = \Phi_0 + \eta_c + \eta_s \quad [7]$$

The concentration overpotential is taken to be (11)

$$\eta_c = \frac{RT}{ZF} \left[ \ln \left( \frac{c_0}{c_s} \right) + t \left( 1 - \frac{c_0}{c_s} \right) \right] \quad [8]$$

while the surface overpotential may be related to the current density by the Butler-Volmer expression

$$i = i_0 \left( \frac{c_0}{c_s} \right)^\gamma \left[ \exp \left( \frac{\alpha ZF}{RT} \eta_s \right) - \exp \left( -\frac{\beta ZF}{RT} \eta_s \right) \right] \quad [9]$$

where  $i_0$  is the exchange current density at the bulk concentration, and  $\alpha$ ,  $\beta$ , and  $\gamma$  are kinetic parameters. It is convenient to refer the current density to the average limiting current density (1)

$$\langle i_{lim} \rangle = -\frac{i_0}{\Gamma(4/3)} \frac{N}{J} \quad [10]$$

where

$$N = -\frac{nZF^2 D c_0}{RT\kappa(1-t)} \left( \frac{2Pe}{3} \right)^{1/3} \quad [11]$$

and

$$J = \frac{i_0 r_0 ZF}{RT\kappa} \quad [12]$$

are dimensionless parameters.

Equations [3]–[9] constitute a set of seven equations containing the seven unknowns,  $c_0$ ,  $\partial c/\partial y$  at  $y = 0$ ,  $i$ ,  $\Phi_0$ ,  $B_m$ ,  $\eta_c$ , and  $\eta_s$ . The numerical method of calculation is the same as has been used previously (7). There are six parameters which must be specified in the dimensionless problem:  $N$ ,  $J$ ,  $t$ ,  $\alpha$ ,  $\beta$ , and  $\gamma$ , along with the fraction of limiting current we wish to study. The latter may be set by specifying the current density at the leading edge of the electrode,  $i(1)$ . Such a choice eliminates an iteration loop in the numerical procedure.

### Results and Discussion

Because mass-transfer effects are important at higher current densities, we have used Tafel polarization throughout in calculating the current distributions. Thus, we have taken the exchange current density  $i_0$  to be much less than the average current density, so that the surface overpotential  $\eta_s$  is large and one of the terms on the right in Eq. [9] can be neglected. When operation is at an appreciable fraction of limiting current, this means that  $J \ll N$  according to Eq. [10]. In the figures,  $J = 0$  designates the use of the Tafel approximation.

Figures 2 and 3 show, respectively, the dimensionless current density and concentration distributions on the surface of the electrode for  $N = 10$  at various fractions of the limiting current. All other parameters were arbitrarily set at 0.5. The limiting current curve was obtained from previous work (1). Figures 4 and 5 show the effect of increasing  $N$  on the current density and surface concentration for a fixed current density at the leading edge ( $i/\langle i_{lim} \rangle = 1.429$ ).

Figure 2 shows that the current density rises monotonically from zero at the center of the electrode to a finite value at the leading edge for current densities

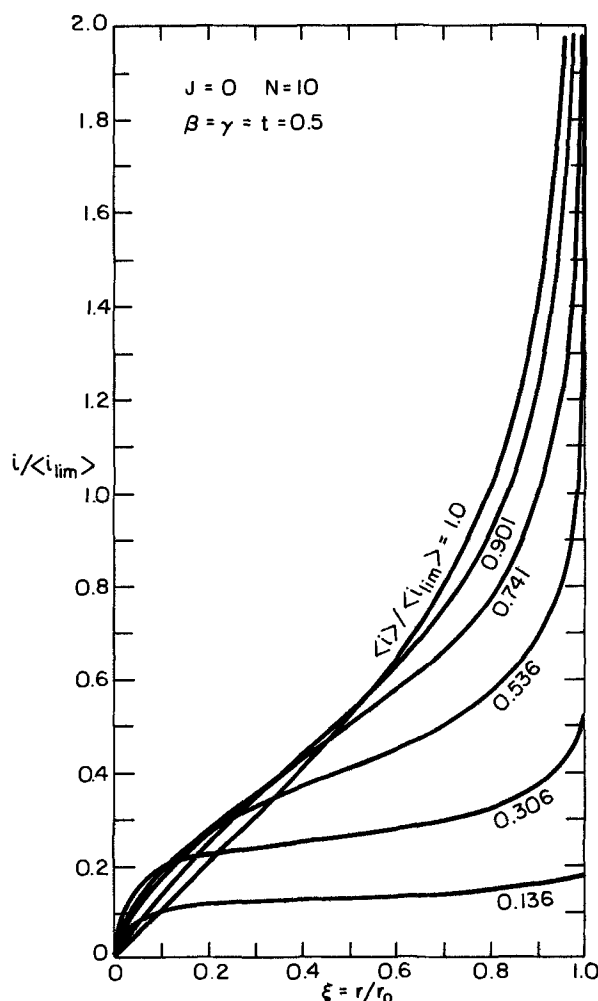


Fig. 2. Current distribution for Tafel polarization

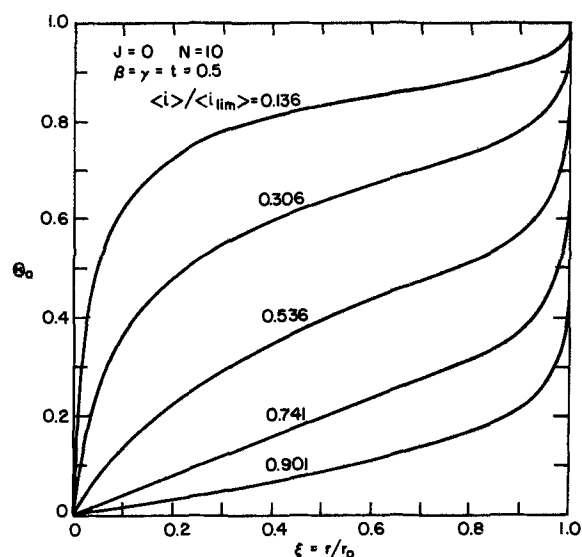


Fig. 3. Surface concentration distribution for Tafel polarization

below limiting. This behavior would be expected since both the limiting (1) and primary (4) current distributions are infinite at the leading edge of the electrode. The current density becomes more nonuniform as the limiting current is approached and is seen to exceed the limiting current locally near the center of the electrode. This latter behavior has been ob-

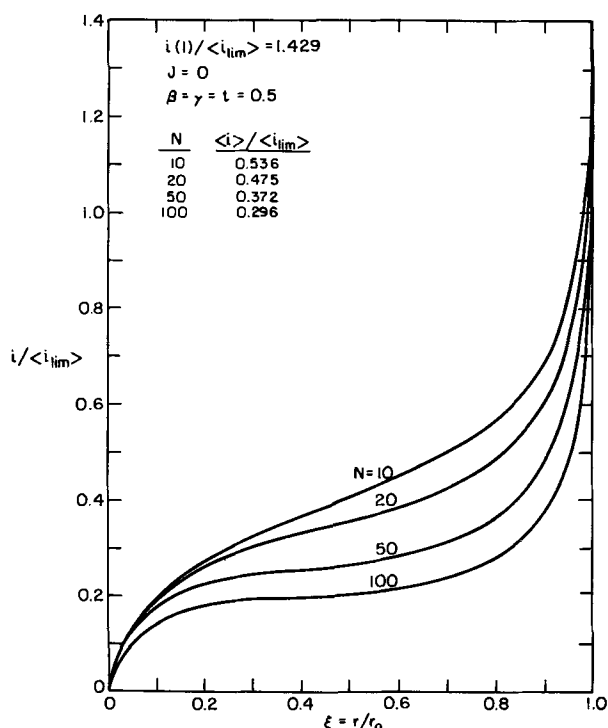


Fig. 4. Effect of variation of  $N$  on the current distribution for Tafel polarization.

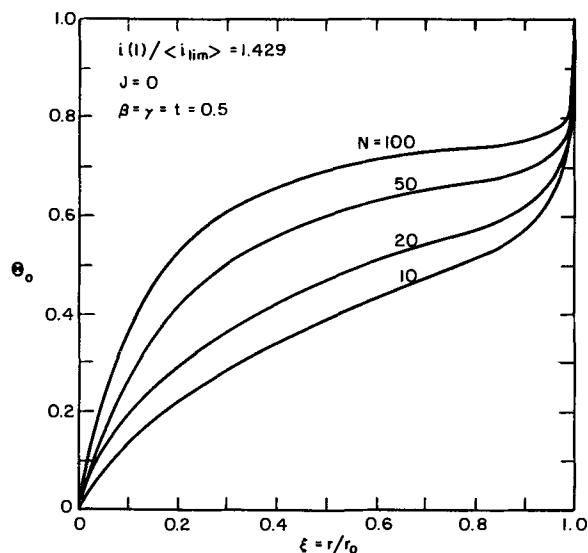


Fig. 5. Effect of variation of  $N$  on the surface concentration distribution for Tafel polarization.

served for other geometries (4, 6, 7, 10). The surface concentration increases monotonically from zero at the center of the electrode to its bulk value at the leading edge (see Fig. 3). As the current density approaches its limiting value, the surface concentration tends toward zero. Figures 4 and 5 show that as  $N$  is increased, both the current density and concentration distributions tend to be more uniform, as might be expected since the rate of stirring (Péclet number) is increased.

### Summary

The current density and concentration distributions on the surface of an electrode imbedded in a stationary plane below a rotating disk have been calculated at various fractions of the limiting current. At high

Schmidt numbers the concentration varies from its bulk value only in a thin diffusion layer near the electrode surface. The potential distribution in the diffusion layer is determined from a superposition of the diffusion-layer solution to the equation of convective diffusion and electrode kinetic expressions, while the potential in the bulk of the solution is obtained from Laplace's equation. The calculation method used here is the same as was applied previously to the rotating disk and sphere and plane electrodes. Results for the case of Tafel polarization show that the current density becomes more nonuniform as the limiting current is approached.

### Acknowledgment

This work was supported by the United States Atomic Energy Commission.

Manuscript submitted Sept. 10, 1973; revised manuscript received June 24, 1974.

Any discussion of this paper will appear in a Discussion Section to be published in the June 1975 JOURNAL. All discussions for the June 1975 Discussion Section should be submitted by Feb. 1, 1975.

The publication costs of this article have been assisted by the University of California.

### LIST OF SYMBOLS

$B_m$	expansion coefficients in the series for the potential
$c$	concentration of the reactant, mole/cm <sup>3</sup>
$c_0$	concentration of the reactant at the electrode surface, mole/cm <sup>3</sup>
$c_\infty$	concentration of the reactant in the bulk, mole/cm <sup>3</sup>
$D$	diffusion coefficient of the reactant, cm <sup>2</sup> /sec
$F$	Faraday's constant, 96,487 coulombs/equiv.
$F'(0)$	dimensionless radial velocity derivative evaluated at the plane
$i$	normal current density at the electrode surface, A/cm <sup>2</sup>
$i_0$	exchange current density, A/cm <sup>2</sup>
$\langle i \rangle$	average current density, A/cm <sup>2</sup>
$\langle i_{lim} \rangle$	average limiting current density, A/cm <sup>2</sup>
$J$	dimensionless exchange current density
$L$	separation distance between stationary plane and rotating disk, cm
$m$	index of summation in the series for the potential
$n$	number of electrons produced when one reactant ion or molecule reacts
$N$	dimensionless parameter related to the significance of mass transfer (see Eq. [11])
$P_{2m}$	Legendre polynomial of order $2m$
$Pe$	Péclet number, $-F'(0) Sc Re^{3/2}/2$
$r$	radial coordinate, cm
$r_0$	radius of electrode, cm
$R$	universal gas constant, 8.3143 joule/mole-deg
$Re$	Reynolds number, $r_0^2 \Omega / \nu$
$Sc$	Schmidt number, $\nu/D$
$t$	transference number of reactant
$T$	absolute temperature, °K
$v_r$	radial velocity component, cm/sec
$V$	potential of the electrode, V
$x$	distance from the edge of the electrode, cm
$x_0$	integration variable in Eq. [2]
$y$	normal distance from the electrode surface, cm
$z_i$	charge number of species $i$
$Z$	$-z_+ z_- / (z_+ - z_-)$ for a single salt $-n$ for reactions with excess supporting electrolyte
$\mathcal{L}$	dimensionless separation distance between stationary plane and rotating disk, $L\sqrt{\Omega/\nu}$
$\alpha, \beta, \gamma$	parameters in the kinetic expression (see Eq. [9])
$\beta(r)$	radial velocity derivative at the plane, $-\partial v_r / \partial y$ at $y = 0$ , sec <sup>-1</sup>
$\Gamma(4/3)$	the gamma function of $4/3$ , 0.89298
$\xi$	$1 - \xi^3$
$\xi_0$	integration variable in Eq. [3]
$\eta$	rotational elliptic coordinate at $y = 0$ , $\sqrt{1 - \xi^2}$
$\eta_c$	concentration overpotential, V
$\eta_s$	surface overpotential, V

$\theta_0$	dimensionless concentration of the reactant at the electrode surface, $c_0/c_e$
$\kappa$	conductivity of the bulk solution, $\text{ohm}^{-1}\text{-cm}^{-1}$
$\nu$	kinematic viscosity, $\text{cm}^2/\text{sec}$
$\xi$	dimensionless radial coordinate, $r/r_0$
$\pi$	3.14159
$\Phi_0$	potential in the bulk extrapolated to the electrode surface, V
$\Omega$	angular velocity of rotating disk, $\text{rad}/\text{sec}$

## REFERENCES

1. R. V. Homsy and John Newman, *Am. Inst. Chem. Engrs. J.*, **19**, 929 (1973).
2. K. A. Smith and C. K. Colton, *ibid.*, **18**, 949 (1972).
3. C. K. Colton and K. A. Smith, *ibid.*, **18**, 958 (1972).
4. John Newman, *This Journal*, **113**, 1235 (1966).
5. John Newman, *ibid.*, **114**, 239 (1967).
6. W. R. Parrish and John Newman, *ibid.*, **116**, 169 (1969).
7. W. R. Parrish and John Newman, *ibid.*, **117**, 43 (1970).
8. W. H. Smyrl and John Newman, *ibid.*, **119**, 212 (1972).
9. Richard Alkire and A. A. Mirarefi, *ibid.*, **120**, 1507 (1973).
10. Kemal Nisancioğlu and John Newman, *ibid.*, **121**, 241 (1974).
11. John Newman, *Intern. J. Heat Mass Transfer*, **10**, 983 (1967).

## Electrochemical Oxidation of Nitrite Ions at Platinum, Gold, and Glassy Carbon Anodes in Acetonitrile

H. W. Salzberg\*

Department of Chemistry, The City College of the City University of New York, New York, New York 10031

## ABSTRACT

Electrochemical oxidation of nitrite ions has been studied in nominally anhydrous acetonitrile at platinum, gold, and glassy carbon electrodes. Tafel slopes, a-c polarography, and potential values indicate the electron transfer is reversible. It is believed that the  $\text{NO}_2$  radical-molecule leaves the carbon and platinum surfaces by a unimolecular step, most probably desorption, and that the  $\text{NO}_2$  leaves the gold surface by dimerization as well as by unimolecular desorption.

Until recently, the electrochemical oxidation of nitrite ion in organic media was terra incognita. The first on the subject was by Cauquis and Serve (1) who worked in nitromethane, nitrobenzene, and acetonitrile, running polarographic and cyclic voltammetric measurements on a smooth platinum rotating electrode. Their conclusion was that the discharge is reversible and bimolecular, forming  $\text{N}_2\text{O}_4$  in one step, followed by various chemical processes in a complicated over-all pattern. The half-wave potential, relative to  $\text{Ag}/\text{AgCl}_{(s)}$ , was about +0.77V.

Wargon and Avia (2) studied the oxidation of  $\text{NaNO}_2$  at platinum electrodes, with dimethyl sulfide as solvent, and concluded that the rate-determining step (rds) was the discharge of the nitrate ion, which was therefore irreversible. Castellano, Wargon, and Arvia (3) reported on the electrochemical oxidation of  $\text{AgNO}_2$  in acetonitrile on platinum. By analysis of product mixtures they concluded that the initial oxidation is followed by a large number of simultaneous competing processes, between initial products and water or nitrite ion. However, they do not commit themselves as to whether or not the first electrochemical oxidation is reversible.

Unpublished work in this laboratory had indicated that on platinum in acetonitrile, the discharge was reversible but that the subsequent rds was unimolecular. This study was therefore undertaken.

### Experimental

The principal measurement techniques were steady-state voltammetry and a-c polarography.

Voltammetric measurements were made using the familiar interrupter method to eliminate ohmic drop. Interruption was by a positive 5-10  $\mu\text{sec}$  pulse every millisecond, from a General Radio 1340 pulse generator, through a pnp transistor in series with the elec-

trolysis cell. During the interruption period, the potential, vs. a reference, was observed with a 5103N dual trace Tektronix memory oscilloscope. The second trace on the scope was used to observe the potential drop across a 1000 ohm resistor in series with the cell, to make sure that the current was completely interrupted. Cell current was obtained potentiometrically rather than with a microammeter. The measurement gave only the average current during the on-off cycle but since the interruption period was only about 0.5-1% of the cycle, the error is negligible.

The a-c polarographic measurements were made with a Heathkit EUA19-2 polarography module, the a.c. being supplied from a Wavetek 134 function generator and the output being fed into the oscilloscope.

The cell was a lipless beaker with a Teflon cap through which the electrodes were inserted. The platinum and the gold electrodes were Beckman button type, with the metal recessed in glass, so that no edges were exposed. Two platinum anodes were used, one 0.24  $\text{cm}^2$  and the other 0.18  $\text{cm}^2$  in area. The gold anode was 0.0079  $\text{cm}^2$  and the carbon anode 0.031  $\text{cm}^2$ . The carbon was a Chemtrix A-111 glassy carbon electrode, modified by using a carbon rod to make contact with the glassy carbon surface. No roughness factors were measured. The cathode was a 0.24  $\text{cm}^2$  platinum electrode. Two alternative references were used. One was a silver wire, the other a platinum electrode which had been silver plated. The potential difference between them was less than the minimum value to which potentials were measured.

Before use, the electrodes were washed with nitric acid and distilled water. Sometimes they were then air dried, sometimes washed with acetone, and sometimes wiped with filter paper. No differences in performance could be ascribed to different pretreatments, except that failure to clean with nitric acid often resulted in discrepant and irreproducible behavior.

The solvent was acetonitrile, reagent grade, not distilled but dried over Linde Molecular Sieves, 3Å. The

\* Electrochemical Society Active Member.

Key words: nitrite electro-oxidation, gold, carbon, platinum, anodes.

electrolytes were reagent grade  $\text{LiNO}_3$ , vacuum dried at  $150^\circ\text{--}200^\circ\text{C}$ , anhydrous  $\text{LiClO}_4$ , used as obtained from the supplier, Alpha Inorganics, reagent grade  $\text{AgNO}_3$ , used without pretreatment, and  $\text{AgNO}_2$ , prepared by precipitation from aqueous  $\text{AgNO}_3$  and  $\text{NaNO}_2$  followed by filtration, washing, drying, and prolonged vacuum desiccation. No differences in performance could be ascribed to different batches of solvent and electrolyte.

During measurements, the cell was isolated from the atmosphere by being kept in a resin assembly vessel surrounded by desiccant. Electrical contact was with copper wires thrust through cork stoppers held in the necks of the lid. During runs, dry nitrogen was passed through the cell to remove any oxygen. The scrubber nitrogen gave no polarographic oxygen peak and so was used without additional treatment. The combination of nitrogen scrubbing and surrounding desiccant kept water and oxygen at a minimum, although not eliminating these two potential trouble makers.

The electrolytes were weighed out in the laboratory atmosphere before being put into the cell. A test sample of  $\text{AgNO}_2$  showed no weight gain after several hours in the laboratory. However, weighing the  $\text{LiNO}_3$  and the  $\text{LiClO}_4$  in the laboratory air must have introduced some traces of water.

After the addition of the silver nitrite, the solvent was added to the cell through a tube leading into the desiccator, without opening the system. During this addition, about  $20\text{--}30\text{ cm}^2$  of liquid surface were exposed to the laboratory air for about half a minute or more. Some oxygen and water must have been absorbed.

When  $\text{LiClO}_4$  or  $\text{LiNO}_3$  or  $\text{AgNO}_3$  was to be added, a set of data was first obtained using  $\text{AgNO}_2$  only, to act as a base line. The reaction chamber was then opened and the additional electrolyte added.

Usually,  $50\text{--}60$  mliters of acetonitrile were added to  $1.5\text{ g}$  of  $\text{AgNO}_2$ , not all of which dissolved. The solutions may, therefore, be considered saturated with respect to  $\text{AgNO}_2$  and about  $0.15\text{--}0.1\text{ M}$ . The concentration of  $\text{Ag}^+$  must have decreased slightly during the runs, since some silver did plate out on the cathode, but the concentration change was so slight that the reference potentials may be considered to have remained constant during the run.

All runs were made with all the electrodes in the solution at the same time, so that differences between potentials could not be ascribed to measuring at different times with different solutions. Sometimes the complete curves for each electrode were obtained

sequentially. At other times, measurements were obtained by switching back and forth between electrodes after each point. The results were the same. Each set of measurements was made on freshly prepared solution.

To measure decay times, the current was run for several minutes at a selected value, usually in the  $10^{-5}$   $\text{A/cm}^2$  range, until the potential had reached a steady state. The circuit was then opened manually, triggering the scope for a single sweep in the memory mode. The procedure was repeated until fairly reproducible decay times were observed, the decay time being defined here as the time for the potential to drop to a point which then did not change for at least  $20\text{--}30$  sec.

To measure equilibrium potentials,  $\text{NO}_2$  gas was produced by adding concentrated  $\text{H}_3\text{PO}_4$  to solid  $\text{NaNO}_2$ . The evolved gas was then passed through the cell and solution. When brown fumes were observed in the gases exiting from the reaction chamber, the gas stream was diverted and the electrode potentials were measured. Measurements were made with the oscilloscope, using a  $1$  megohm probe, with the reference electrode grounded. The measurements used about  $70$  nA with current densities in the microampere/square centimeter range.

## Discussion

**Tafel lines.**—Figure 1 shows typical results of potential-current density measurements. The potentials reported are relative to an  $\text{Ag/AgNO}_2$  reference. Table I summarizes data taken on different days, some with different batches of solvent and electrolyte. The day-to-day variations for each anode are less than the spread between results with different metals. Table II lists the range of potential values (taken from the experimental Tafel curves) for the electrodes at  $10^{-5}$  and  $10^{-3}$   $\text{A/cm}^2$ . Except for carbon and gold at  $10^{-3}$ , the curves, although quite close to each other, do not overlap. The large ( $0.24\text{ cm}^2$ ) platinum electrode consistently registered higher potentials, at corresponding current densities, than the smaller ( $0.018\text{ cm}^2$ ) platinum electrode. The difference was usually about  $25\text{--}30$  mV and could possibly be due to differences in roughness.

The addition of sufficient  $\text{AgNO}_3$  or  $\text{LiNO}_3$  to make the concentration of added salt about  $0.1\text{--}0.2\text{ M}$  had no discernible effect. On addition of enough  $\text{LiClO}_4$  to make the solution  $0.1\text{--}0.2\text{ M}$ , the Tafel slopes remained the same but the curves were shifted slightly toward more positive potentials, about  $10\text{--}15$  mV on gold and platinum and even less on carbon. This effect probably was due to adsorption.

Fig. 1. Tafel lines. ●, Platinum anode; the slope is 0.071. ○, Gold anode; the slope is 0.045. X, Carbon anode; the slope is 0.059.

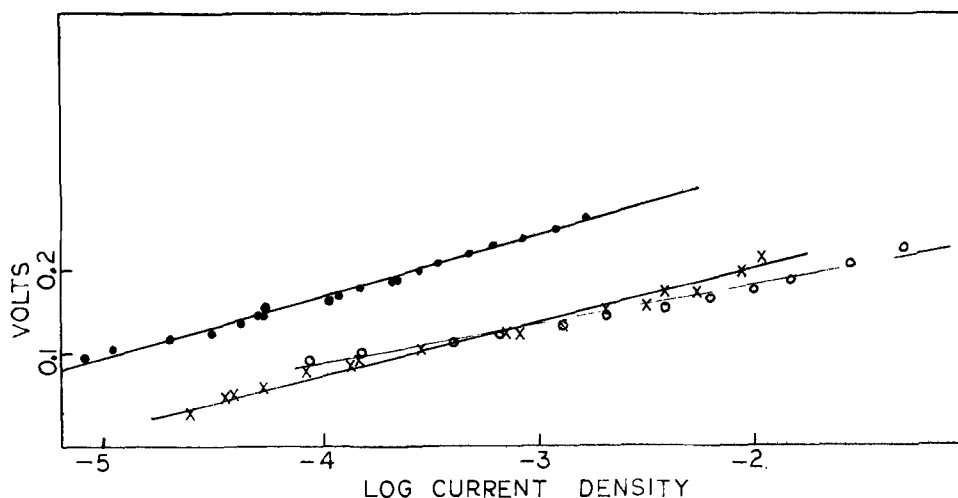




Table I. Least squares slopes of Tafel plots

Electrode	Slope
Platinum, large	0.069
	0.067
	0.078
	0.071 ± 0.004
Platinum, small	0.068
	0.071
	0.077
	0.072 ± 0.003
Gold	0.048
	0.045
	0.043
	0.044*
	0.045 ± 0.002
Carbon	0.059
	0.053
	0.051
	0.061*
	0.056 ± 0.004

\* NO<sub>2</sub><sup>-</sup> added.

Table II. Potential ranges

Electrode	10 <sup>-5</sup> A/cm <sup>2</sup> , V	10 <sup>-3</sup> A/cm <sup>2</sup> , V
Platinum, large	0.100-0.125	0.250-0.270
Platinum, small	0.078-0.098	0.220-0.240
Gold	0.050-0.070	0.140-0.160
Carbon	0.025-0.045	0.130-0.150

Table III. Decay times

Electrode	Time, sec
Pt	0.050
C	0.1
Au	1

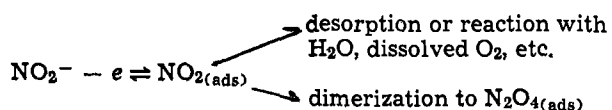
*Decay times.*—Table III shows the time taken for potentials to drop to open-circuit values when the current was interrupted.

*Equilibrium potentials.*—Table IV shows the potentials at open circuit in saturated AgNO<sub>2</sub> with the mixture of NO<sub>2</sub> and N<sub>2</sub>O<sub>4</sub> at one atmosphere.

*A-C polarography and cyclic voltammetry.*—These results were not graphed. The cyclic voltammograms showed no reverse (cathodic) wave at sweeps as high as 10 V/min. The a-c polarograms were produced by superimposing 5 mV of 400 Hz a.c. on d.c., using LiNO<sub>3</sub> or LiClO<sub>4</sub> as indifferent electrolyte. Small but definite a-c peaks of about 2-3 μA were observed in the region 0.4-IV, positive to the reference. The actual potentials were unimportant since they included an unknown ohmic drop. However, the fact that the a-c peaks were observed only within a potential range indicates that they were not the results of capacitance but indicated a reversible electron transfer.

### Discussion

Most of the foregoing results are consistent with the following picture



On all three electrodes, the electron transfer is reversible and the rate-determining step is the removal of the adsorbed NO<sub>2</sub>.

The reversible currents in a-c polarography are direct evidence for the reversibility of the electron transfer step.

Indirect evidence for Nernstian reversibility consists of the slopes of the Tafel lines in Fig. 1 and the close approximation of working potentials as shown in Table

II. The spread between the potentials at the gold, carbon, and the smaller platinum electrode was less than 100 mV and even taking into account the higher potentials on the larger platinum electrode, the greatest spread was only 120 mV. For electron transfer processes known to be irreversible, differences in electrode potentials are much higher. For example, hydrogen overvoltages at different metals show differences of as much as a volt. Large potential differences would indicate Nernstian reversibility and the small differences shown here are a necessary, but not sufficient, condition for reversibility.

The small potential differences observed here could be at least partly due to differences in surface roughness but are more likely due to differences in surface spacings. Entities as large as nitrite ions and NO<sub>2</sub> molecules should be adsorbed on several surface atoms at the same time. Since the surface spacings of these three electrode materials are not the same, even if the total area were the same, the fraction available for nitrite ion adsorption would be different and the true current densities could differ considerably from apparent current densities. Also, since the surfaces are polycrystalline and heterogeneous, the activities of the adsorbed NO<sub>2</sub> molecules should be different for each electrode at a given current density and should increase somewhat with increasing coverage.

The results shown in Table IV are also necessary but not sufficient for reversibility of the rate-determining step. For the electron transfer at the working electrodes to be reversible, it would have to be reversible under open-circuit conditions in the presence of NO<sub>2</sub> gas. Under such conditions the potentials observed should be equilibrium potentials, dependent only on the free energies of the nitrite ions in solution and the dissolved NO<sub>2</sub> molecules and independent of electrode material. As shown in Table IV, these potentials are just about the same at all three electrodes, allowing for the crudity of the measurement.

The slopes of the Tafel lines shown in Fig. 1 and Table I offer further evidence for reversibility of electron transfer. A reversible one-electron transfer would yield a Tafel slope of 0.06 if the following rate-determining step (rds) is first order with respect to the product of the electron transfer. If the rds is bimolecular, the slope would be 0.03. If the slow process following the electron transfer is a combination of simultaneous first- and second-order steps proceeding at comparable velocities, the Tafel slope should be intermediate between 0.03 and 0.06.

If the reversible step involved the transfer of two electrons, the slopes should be 0.03 for a first-order rds and 0.015 for a second-order rds.

The slopes of carbon and gold are both intermediate between 0.03 and 0.06, arguing for a simultaneous dimerization of the adsorbed NO<sub>2</sub> and removal by desorption or reaction with dissolved oxygen, or water, or NO<sub>3</sub><sup>-</sup>, or similar substances that might be present. The slope on carbon, being so close to 0.06, would indicate that very little dimerization occurred. Support for this argument comes from the data of Table III, which shows that the decay time for gold is ten times that for carbon and twenty times that for platinum. This means either that there is a very high surface concentration of NO<sub>2</sub> on gold, which in turn would mean a high potential, or that adsorbed N<sub>2</sub>O<sub>4</sub> is present and disassociates into NO<sub>2</sub>. Since the potentials on gold are lower than on platinum, rather than higher, the latter explanation would hold rather than the former.

Table IV. Equilibrium potentials

Electrode	Potential vs. Ag/AgNO <sub>2</sub> (s)
Pt	+0.078
C	+0.060
Au	+0.068

In the case of the platinum electrodes, the slopes are about 0.07, slightly higher than that expected for a normal first-order removal of the product of a reversible one-electron transfer. If the surface were to be covered with a tightly held monolayer of adsorbed  $\text{NO}_2$  further nitrite oxidation would then take place on this monolayer producing  $\text{N}_2\text{O}_4$  in a bimolecular two-electron process, with a Tafel slope of 0.09. A Tafel slope of 0.07 could then be considered to be a combination of such a process with a simultaneous reversible one-electron unimolecular removal. However, the data of Table III show that the removal of  $\text{NO}_{2(\text{ads})}$  from platinum is faster than from carbon, which suggests that the  $\text{NO}_2$  is not strongly adsorbed and that such a monolayer would not form. Also, if there were a monolayer of strongly adsorbed  $\text{NO}_2$ , one would expect to see a cathodic wave in running cyclic voltammetry. No such wave was observed.

An alternative explanation for the increase in Tafel slope would be based on surface heterogeneity. For a reversible electron transfer process, the Nernst equation holds and the potential is a function of the activity and therefore activity coefficient of the  $\text{NO}_{2(\text{ads})}$ . If over each decade change in current, the surface free energy of the adsorbed  $\text{NO}_2$  increased by about 250 cal/mole, the increase in activity coefficient would produce an increase in potential of 12 mV, which is the difference between the observed 0.072 slope and the 0.06 slope expected. This, of course, assumes a tenfold increase in concentration of adsorbed  $\text{NO}_2$ , which is contradictory, since any increase in surface free energy would increase the rate constant for the desorption process. However, since  $\text{NO}_2$  molecules do attract each other and dimerize, intermolecular attractions should at least partly counterbalance increased

desorption rates, and increased activity coefficients could account for the Tafel slope being 0.072 rather than 0.060.

I am troubled by the discrepancy between my observed potentials and the value of 0.77V vs.  $\text{Ag}/\text{AgCl}_{(\text{s})}$  reported by Cauquis and Serve (1), who are very careful, scrupulous, and competent workers. I can only cite the differences in solvent, concentration, supporting electrolyte, reference electrode, and method of measurement.

### Conclusions

To summarize, on gold, glassy carbon, and bright platinum, in acetonitrile, the oxidation of nitrite ion is a reversible one-electron process. The subsequent removal of  $\text{NO}_{2(\text{ads})}$  on gold and carbon is by simultaneous dimerization and either desorption or reaction with water, oxygen, or  $\text{NO}_3^-$ , or some combination thereof. On platinum, the rate-determining step is the first-order removal of adsorbed  $\text{NO}_2$ .

Manuscript submitted April 10, 1974; revised manuscript received June 17, 1974.

Any discussion of this paper will appear in a Discussion Section to be published in the June 1975 JOURNAL. All discussions for the June 1975 Discussion Section should be submitted by Feb. 1, 1975.

### REFERENCES

1. G. Cauquis and D. Serve, *Compt. Rend., Ser. G*, **270**, 1773 (1970).
2. J. A. Wargon and A. J. Arvia, *Electrochim. Acta*, **17**, 640 (1972).
3. C. E. Castellano, J. A. Wargon, and A. J. Arvia, *J. Electroanal. Chem. and Interfacial Electrochem.*, **47**, 372 (1973).

## Technical Notes



### Solution-Precipitation Mechanism in Lead-Acid Cell Electrode Reactions

J. L. Weininger\*

General Electric Company, Corporate Research and Development, Schenectady, New York 12301

One of the most interesting aspects of the reaction mechanism at electrodes of galvanic couples is the path by which the reaction proceeds, whether through the solid state or by the way of the electrolyte. Solution transport of the electroactive material (in the solution-precipitation mechanism) is known to occur at lead, cadmium, zinc, and other electrodes.

Archdale and Harrison (1) have used rotating-disk and ring-disk electrodes to demonstrate the solution-precipitation mechanism for Pb dissolving in  $\text{H}_2\text{SO}_4$  at low anodic potential with the formation of  $\text{Pb}^{2+}$  and subsequent precipitation of  $\text{PbSO}_4$ . They also found that at more anodic potential the reaction may proceed in the solid state by nucleation and growth.

Hughel and Hammar (2) first applied scanning electron microscopy (SEM) to the electrode materials of the lead-acid battery. They showed the morphology

of the various battery materials before cycling. Others have also used SEM to investigate the behavior of lead alloys in acid solutions (3) and the function of lignin in the negative electrode (4). In the present work this method has been extended to cycled negative electrodes. In addition to the expected isotropic structure of the porous electrode, at sufficiently large magnification there were observed extremely intricate, open, symmetrical crystal structures which derived from a solution-precipitation mechanism. This report also attempts to relate the observed dimensions of the microcrystals to a recently developed criterion of Vetter (5) which involves an evaluation of the concentration gradients in the electrolyte relative to the minimum solubility necessary for solution transport of the electroactive material.

### Experimental

The structure of the negative electrode was monitored during cycle life. It differed from conventional

\* Electrochemical Society Active Member.

Key words: scanning electron microscopy, lead negative electrode, lead and lead sulfate crystal structure.

lead-acid battery electrodes by having a lead-plated copper screen substrate and by the addition of a polymeric binder (neoprene) to the paste. The purpose of the polymer addition was to produce a flexible, more durable negative electrode. Addition of carbon black compensated for the conductivity lost by the presence of polymer.

The same active material,<sup>1</sup> containing a leady oxide (approximately 25% Pb and 75% PbO) and an organic expander was used for the test electrode and for the control electrode.

The polymer-bonded electrode had an area of  $5 \times 5$  cm, 0.3 cm thickness, and a theoretical capacity of 3.0 A-hr. It was charged and discharged at the C/4 rate (6 mA/cm<sup>2</sup>) against two conventional positive electrodes with a combined higher capacity than the negative. Periodically, small samples of the negative were taken from a location near the edge of the electrode, washed in distilled water, and mounted for examination in SEM. Micrographs in this report are of samples taken during cycles 29 and 73. To illustrate the SEM method a few micrographs of conventional electrodes after their formation and at the end of cycle life are also shown.

### Scanning Electron Microscopy

The initial appearance of the active electrode materials, after formation but before cycling, is shown for conventional negative (Fig. 1) and positive (Fig. 2) pasted electrodes. The original outline of the litharge

<sup>1</sup> Grenox 111-G, a product of NL Industries.

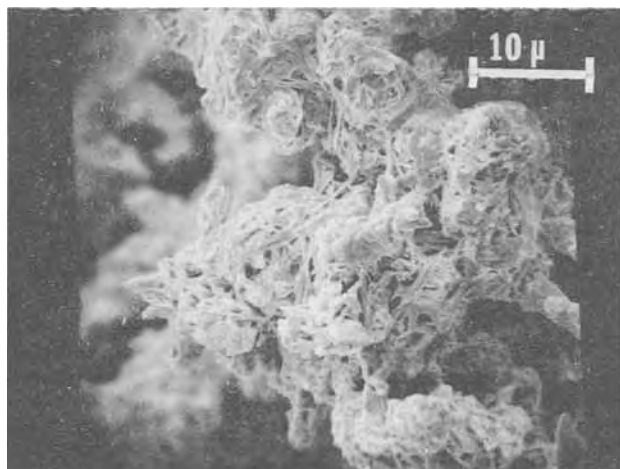


Fig. 1. Negative plate after formation, 2000X

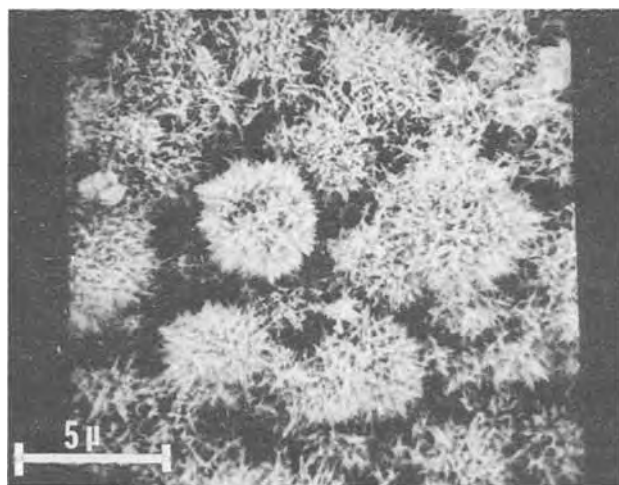


Fig. 2. Positive plate after formation, 5000X

particles from which the materials were formed can be noted in both cases. At the negative plate, formation produced acicular lead crystals as long as  $15\mu$  and approximately  $0.75\mu$  thick; at the positive plate PbO<sub>2</sub> dendrites, 500-1500Å wide, with dendrite separation of about 500Å, were produced.

Figures 3, 4, and 5 are micrographs of the polymer-bonded electrode at the end of discharge in cycle 29. Figure 3 shows a field of star-like PbSO<sub>4</sub> crystals, one of these structures is enlarged in Fig. 4. The individual crystals are  $1.4\mu$  wide and up to  $50\mu$  long. In the central cluster the separation of crystals varies from 0 to about  $1.6\mu$ . Small dots or balls are also visible in these micrographs. At the much larger magnification of 40,000× these clumps have a coral structure (Fig. 5). The individual coral strands are 500-750Å wide and have a similar distance of separation between individual strands.

Figures 6, 7, and 8 are micrographs obtained at the end of charge during cycle 73. Figure 6 shows very

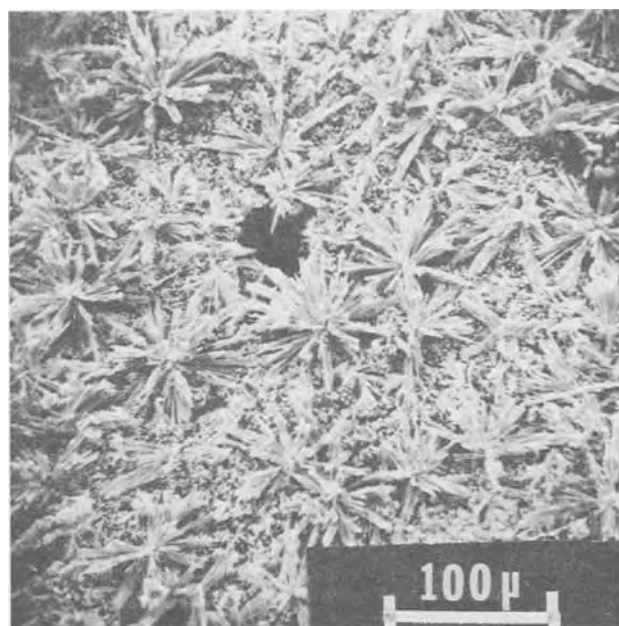


Fig. 3. Negative electrode at the end of cycle 29, 2000X

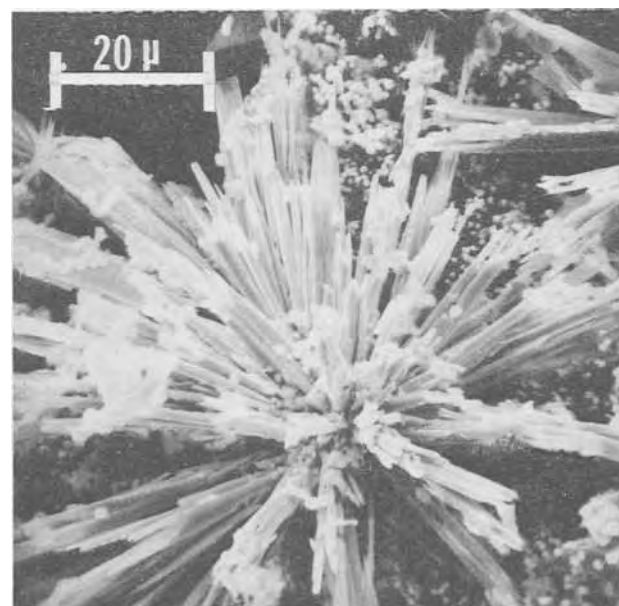


Fig. 4. Portion of Fig. 3 enlarged, 10000X

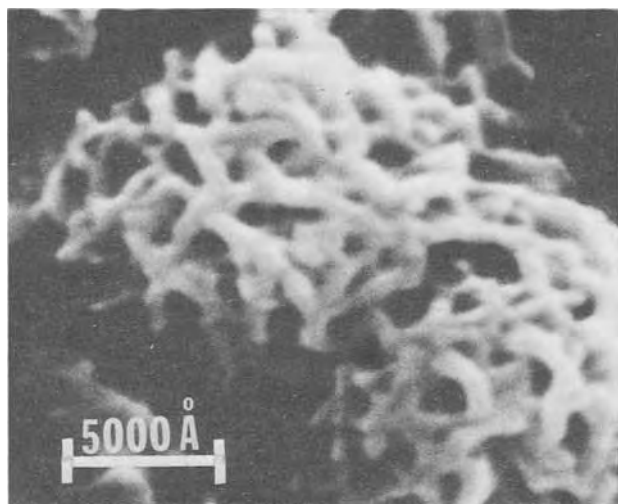


Fig. 5. Portion of Fig. 4 enlarged, 40,000X



Fig. 6. Negative electrode at end of charge 73,500X

large,  $0.65\mu$  thin blades of crystals. In Fig. 7 similar crystals are covered with round structures which on further magnification (Fig. 8) have a remarkable flower-like structure. The central part has petals, about  $0.5\mu$  thick, separated from each other at a distance of  $0.1-0.2\mu$ .

Finally, returning to conventional pasted electrodes, Fig. 9 depicts a negative electrode at the end of cycle life, after 163 cycles when the cell could no longer accept a reasonably large charge. The bulky crystals are  $0.5-5\mu$  large with an average distance of separation of about  $2\mu$ . They resemble a sponge lead structure, shown by Hughel and Hammar (2) for a formed negative plate without expander.

#### Solution-Precipitation Mechanism

The above micrographs indicate that the microcrystals were grown by a solution transport mechanism. For a more quantitative description of this process, Vetter established the criterion

$$\Delta c \ll c$$

where  $\Delta c$  is the concentration gradient of  $PbSO_4$  or that of  $Pb(II)$  ions and  $c$  is the solubility of  $PbSO_4$ . The value of  $c_{PbSO_4}$  in 1.12 sp. gr. and 1.26 sp. gr.  $H_2SO_4$  at  $25^\circ C$  is, respectively,  $21.8 \times 10^{-6}$  and  $6.6 \times 10^{-6}$  mole/

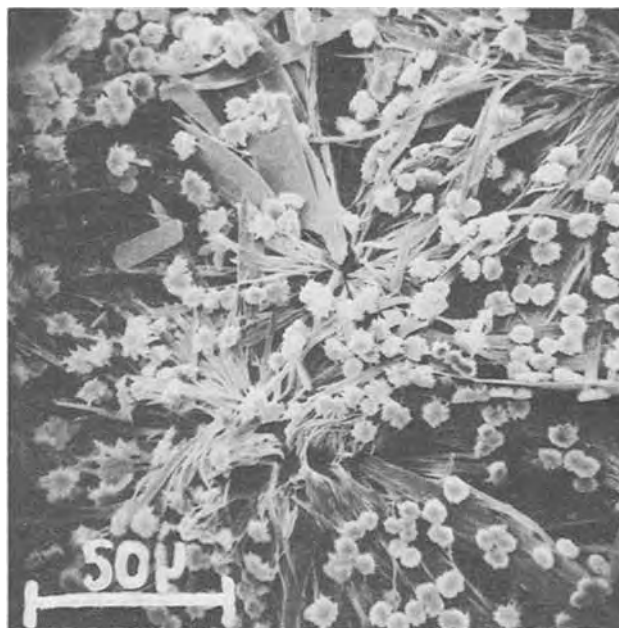


Fig. 7. Negative electrode at end of charge 73,500X

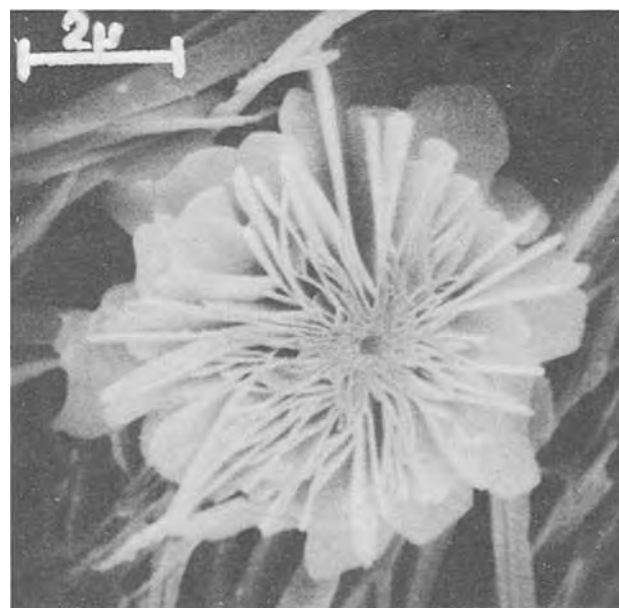


Fig. 8. Portion of Fig. 7 enlarged, 10,000X

liter (6).  $\Delta c$  can be estimated from the electrode, diffusion, and electrical parameters by the expression

$$\Delta c = \frac{I \cdot 2P}{A^2 \cdot \rho^2 \cdot (1 - P)^2 \cdot d \cdot nF \cdot D}$$

where  $I$  (in  $A/cm^2$ ) is the current density applied to the electrode, having a porosity  $P$  (pore volume/total volume), internal surface area  $A$  ( $cm^2/g$ ), density  $\rho$  ( $g/cm^3$ ), electrode thickness  $d$  (cm), and a diffusion coefficient  $D$  ( $cm^2/sec$ ) of the soluble species. Burbank, Simon, and Willihnganz (7) quote internal surface area of  $7-24.5 m^2/g$  for positive electrodes. A smaller internal surface area is expected for negative electrodes (compare, for example, Fig. 1 and 2), for which a reasonable assumption of internal surface area would be  $0.1$  to  $1 m^2/g$ . Taking the lower value of  $0.1 m^2/g$  and evaluating  $\Delta c$  from the experimental conditions used in cycling the electrodes shown in the micrographs, one obtains  $\Delta c = 6.6 \times 10^{-7}$  mole/l from these parameters:  $I = 0.006 A/cm^2$ ,  $P = 0.5$ ,

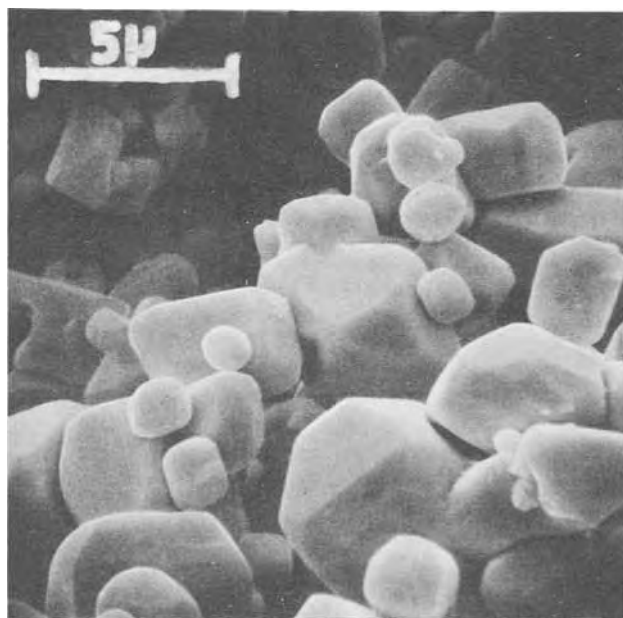


Fig. 9. Negative plate at end of cycle life-cycle, 5000X

$A = 10^3 \text{ cm}^2/\text{g}$ ,  $\rho = 11 \text{ g/cm}^3$ ,  $d = 0.3 \text{ cm}$ ,  $n = 2$ ,  $F = 10^5 \text{ A} \cdot \text{sec}/\text{equiv.}$ , and  $D = 5 \times 10^{-6} \text{ cm}^2/\text{sec}$ . Compared to  $c = 6.6 \times 10^{-6} \text{ mole/liter}$ , this fulfills Vetter's criterion for the condition of the solution-precipitation mechanism.

In this order of magnitude calculation Vetter's criterion,  $\Delta c \ll c$ , applies equally to the charge and discharge mechanisms of the electrode reaction, for at steady-state dendrite growth is controlled by the diffusion of Pb(II) ions from or to the solution, depending on whether Pb or PbSO<sub>4</sub> is formed.

For the charging process, corresponding to Fig. 6-8, the specific gravity of 1.26, the density of Pb, and the solubility of PbSO<sub>4</sub> in that solution are used. Even with the small internal surface of 0.1 m<sup>2</sup>/g the criterion  $\Delta c \ll c$  is fulfilled by a factor of 10; the factor would increase to 1000 for 1 m<sup>2</sup>/g. For the discharged

electrode, corresponding to the conditions in Fig. 3-5, the density of PbSO<sub>4</sub> and its solubility in the less concentrated 1.10 sp. gr. acid would be used.

The structures shown in the micrographs vary widely in terms of internal surface area and porosity. However, they can be placed in context with Vetter's criterion. It can be postulated that the structures shown in series of Fig. 3-5 and Fig. 6-8 cease to grow by solution-precipitation in the open areas because of large porosity in those locations which depletes the concentration of active soluble material ( $\Delta c$  is large). On the other hand, in the dense tight central structures with large internal surface areas the mechanism proceeds and allows unique crystal structures to grow.

#### Acknowledgment

This paper was presented at a symposium sponsored by the Ministry of Electrical Engineering Industries of the U.S.S.R. and the General Electric Company in Leningrad, U.S.S.R., February 21, 1974.

Manuscript submitted March 25, 1974; revised manuscript received June 28, 1974.

Any discussion of this paper will appear in a Discussion Section to be published in the June 1975 JOURNAL. All discussions for the June 1975 Discussion Section should be submitted by Feb. 1, 1975.

The publication costs of this article have been assisted by the General Electric Company.

#### REFERENCES

1. G. Archdale and J. A. Harrison, *J. Electroanal. Chem.*, **34**, 21, 357 (1972).
2. T. J. Hughel and R. H. Hammar, "Power Sources 1970, Proc. 7th Internatl. Symp., Brighton," D. H. Collins, Editor, p. 35, Pergamon Press.
3. T. E. Parker, *This Journal*, **119**, 13C (1972).
4. P. Gurlusky, J. R. Pierson, A. C. Simon, and S. M. Caulder, Paper 31, p. 82, Electrochemical Society Extended Abstracts, Fall Meeting, Boston, Mass., October 7-11, 1973.
5. K. J. Vetter, *Chem.-Ing. Tech.*, **45**, 213 (1973).
6. D. N. Craig and G. W. Vinal, *J. Res. Natl. Bur. Std.*, **22**, 55 (1939).
7. J. Burbank, A. C. Simon, and E. Willihnganz, *Advan. Electrochem. Electrochem. Eng.*, **8**, 180 (1971).

## Some Observations on Rechargeable Lithium Electrodes in a Propylene Carbonate Electrolyte

R. Selim and P. Bro\*

P. R. Mallory and Company, Incorporated, Laboratory for Physical Science,  
Northwest Industrial Park, Burlington, Massachusetts 01803

Organic electrolyte lithium systems have been reported which give promising results when operated as rechargeable batteries (1-8). It is characteristic of most of this work that either the discharges were initiated shortly after the completion of the charges, the stoichiometric lithium capacities were in a considerable excess of the charge per cycle, or the capacities of deposition were far less than those likely to be useful in practical cells (of the order of 5 mA-hr/cm<sup>2</sup>). These circumstances tend to obscure the intrinsic cycling characteristics of the lithium electrode and may lead to tenuous conclusions about the suitability of a system as a rechargeable organic electrolyte lithium battery.

\* Electrochemical Society Active Member.

Key words: batteries, electrodeposition, organic electrolytes.

In our work (1) with such solvents as propylene carbonate, butyrolactone, dimethylformamide, and dimethylsulfoxide, as well as in subsequent unpublished work with other solvents, we have found the behavior of lithium on electrodeposition, as well as anodic discharge of the electrodeposit, to be similar for different solvents. We have recently performed some further experiments designed to give a clearer picture of the cyclability of the lithium electrode in a propylene carbonate solution of lithium perchlorate. The results will be found, we believe, to be similar in nature to those found under equivalent conditions in other solvent systems. We believe the methodology described herein reflects more accurately the intrinsic properties of lithium under practical conditions than do other methods

reported so far. A brief description of the experiments and some results will be given in this report.

**Experimental**

The cell arrangement was extremely simple and was designed to insure a uniform current distribution across the face of the working electrode. The cell was a 3¼ in. length of a ¼ in. diameter glass tubing supported vertically in a heavy brass base to minimize vibration. The working electrode, in the bottom of the tube, was a brass cylinder with an O-ring which was machined to fit tightly in the glass tube. The top of the cell was closed by a rubber stopper through which projected a stainless steel lead connected within the cell to an expanded stainless steel circle on which was pressed a circle of lithium foil. This served as the counterelectrode and was positioned parallel to and about 1½ in. above the face of the brass working electrode.

Solutions were prepared from distilled propylene carbonate and vacuum oven-dried LiClO<sub>4</sub> and contained about 40 ppm of water. Before each run the working electrode surface of the brass cylinder was metallographically polished. Solutions were prepared and the cells assembled, filled, and closed in a dry box in an inert argon atmosphere.

Cathodic deposition and anodic stripping were done at constant current and the cell voltage was monitored. The end of anodic stripping was signalled by an abrupt voltage excursion. The stripping efficiency was calculated by dividing the number of coulombs passed before this rapid polarization by the total number of coulombs passed during the previous deposition. The amount of metallic lithium remaining on the electrode was calculated from the volume of gas evolved when the rubber stopper was removed and the cell placed in a closed system containing water.

**Results and Discussion**

The efficiency of the charging process was close to 100% as determined by the chemical analysis of the lithium deposit within a few hours of the charging cycle (Fig. 1). When the lithium deposit was permitted to age the amount of metallic lithium present on the electrode decreased, most likely because of its reaction with the solvent. About 15% of the lithium was lost from the electrode in 40 hr at 25°C. The appearance of the deposit suggested a mossy structure and

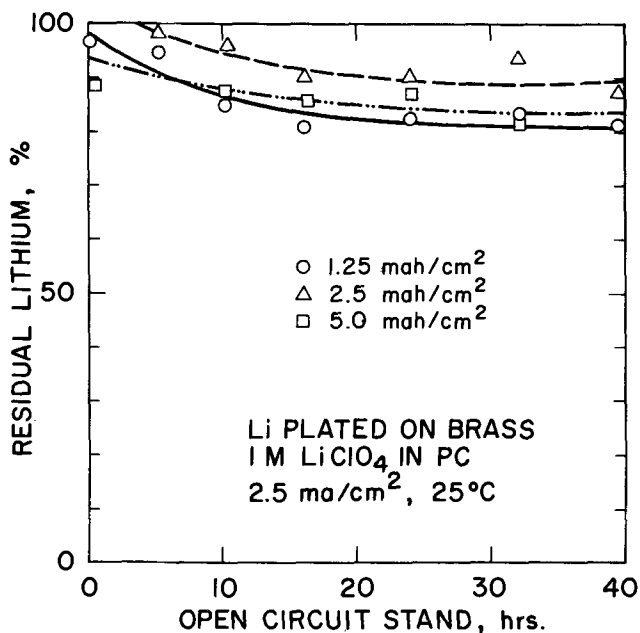


Fig. 1. Chemical analysis of lithium deposition efficiency

some of the loss may have been physical rather than chemical.

In a parallel series of experiments it was found that the discharge efficiency of the fresh lithium deposit was about 60% (Fig. 2). However, the discharge efficiency decreased much more rapidly with an increasing age of the deposit than did the lithium content of the deposit. After 40 hr at 25°C it approached zero even though the deposit still contained 80% of the original metallic lithium. None of the residual lithium was available for discharge. Our tentative conclusion is that the chemical reaction(s) between the lithium and the electrolyte had gradually changed the physical structure of the lithium deposit to render most of the lithium inaccessible to the current collector.

An illustration that lithium/electrolyte reactions may have such an effect is given in Fig. 3 where it may be seen that the deliberate addition of water to

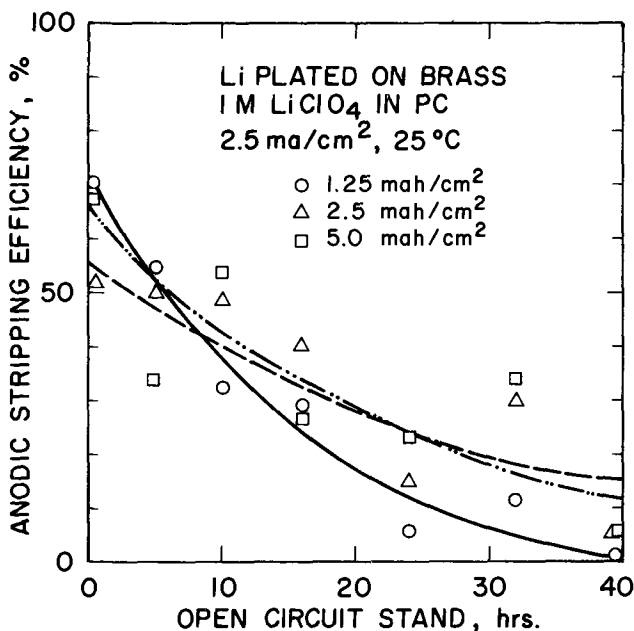


Fig. 2. The discharge efficiency of electrodeposited lithium

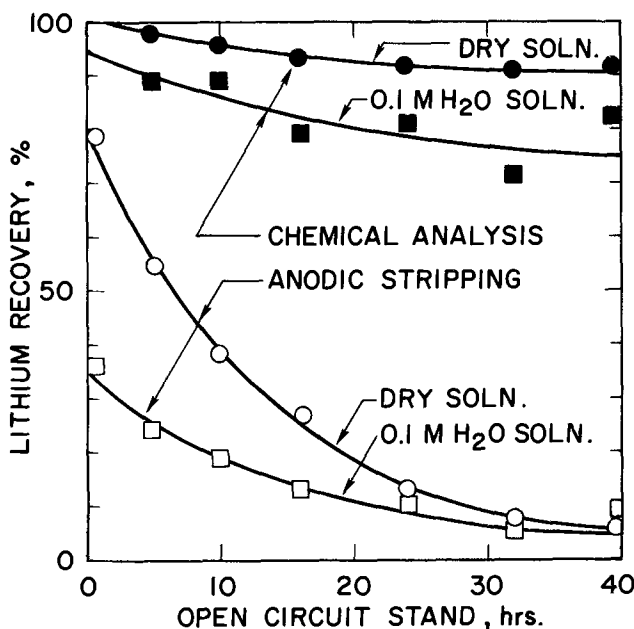


Fig. 3. Chemical and electrochemical availability of electrodeposited lithium in wet and dry electrolytes. 1M LiClO<sub>4</sub> in PC at 25°C, 2 mA/cm<sup>2</sup>, 2.5 mA-hr/cm<sup>2</sup>.



the electrolyte decreased the discharge efficiency markedly relative to that observed in the dry electrolyte. The discharge efficiency of the fresh lithium was 80% in the dry electrolyte and 35% in the 0.1M H<sub>2</sub>O electrolyte. After 40 hr, the efficiencies had decreased to almost zero despite the presence of about 90 and 75% of the original metallic lithium in the electrodes for the dry and the wet electrolytes, respectively. It was interesting to note that the lithium deposit was quite compact in the 0.1M water solutions and almost completely nondendritic in nature.

If the lithium/electrolyte reactions were that significant in affecting the discharge efficiency, they should also affect the charging efficiency at some current density. The data in Fig. 4 show that this was so. In the dry electrolytes the charging efficiency decreased noticeably below 0.1 mA/cm<sup>2</sup>; in the 0.3M H<sub>2</sub>O electrolyte it decreased below 2 mA/cm<sup>2</sup>. At a current density of 0.01 mA/cm<sup>2</sup>, the charging efficiencies were comparable for the two solutions.

The contributions of dendritic or loose lithium to the discharge inefficiencies of fresh lithium deposits may be judged from the data in Fig. 5. The electrolyte was swirled about the lithium electrodes by strong hand-shaking to dislodge dendrites and loose fragments

from the lithium deposits, and the electrodes were then either discharged or analyzed for residual metallic lithium. At a current density of 5 mA/cm<sup>2</sup> for the charging cycle it was found that the fraction of dendrites and loose fragments amounted to 5% at 1 mA-hr/cm<sup>2</sup> and 30% at 10 mA-hr/cm<sup>2</sup>, as determined by chemical analyses. The discharge efficiencies of the undisturbed deposits decreased from about 50 to 30% over the same specific capacity range, and only slightly lower values were obtained when the dendrites and loose fragments were removed from the lithium electrode prior to the discharge. The difference between the lithium contents as determined by chemical analyses after dendrite removal and the lithium contents as determined by electrochemical discharge showed that the discharge inefficiencies must be attributed to the physical state or morphology of the deposit proper and are not attributable to gross dendrites or loose lithium fragments. An arbitrary distinction is made here between the microscopic dendrites that form a mossy structure and the large dendrites that may be seen protruding well above the surface of the mossy deposit.

The experimental results raise some questions in regard to the suitability of lithium electrodes for rechargeable organic electrolyte batteries. It would seem that a low intrinsic lithium/electrolyte reactivity may be a prerequisite for the satisfactory cycling of such a battery. It is our concern, however, that any polar solvent is intrinsically reactive toward lithium because of the existence of an electron deficient region about a highly electronegative atom, which forms the positive end of the dipole. This intrinsic reactivity may go undetected by static experiments but may be crucial in deposition and reanodization experiments of the type described herein.

We would encourage investigators of rechargeable organic electrolyte lithium batteries to include in their reports data on cells with stoichiometric anode capacities comparable to the coulombic charge per cycle and data on cells that are permitted to remain on open circuit for various extended periods of time after charging and prior to discharge. The satisfactory performance of an organic electrolyte lithium battery in such experiments is a necessary, but not sufficient, condition for satisfactory cyclability.

Manuscript submitted April 4, 1974; revised manuscript received July 10, 1974.

Any discussion of this paper will appear in a Discussion Section to be published in the June 1975 JOURNAL. All discussions for the June 1975 Discussion Section should be submitted by Feb. 1, 1975.

The publication costs of this article have been assisted by P. R. Mallory and Company, Incorporated.

#### REFERENCES

1. R. G. Selim, K. R. Hill, and M. L. B. Rao, Tech. Rept. NASA-CR-54969, N66-35218, Oct. 1965.
2. M. Shaw, in Proc 20th Power Sources Symposium, p. 70, Atlantic City, N. J. (1966).
3. H. F. Bauman, J. E. Chilton, and A. E. Hultquist, Tech. Rept. AFAPL-TR-67-104, July 1967.
4. A. Lyall, H. Seiger, and J. Orshick, Tech. Rept. AFAPL-TR-68-71, July 1968.
5. M. Shaw, O. A. Paez, and F. Ludwig, Tech. Rept. NASA WRD-392, N69-14677, Jan. 1969.
6. J. P. Gabano, G. Lehmann, G. Gerbier, and J. F. Laurent, in Proc. 7th International Power Sources Symposium, p. 297, Brighton, England (1970).
7. D. E. Semones and J. McCallum, in Proc. 24th Power Sources Symposium, p. 16 Atlantic City, N. J. (1970).
8. J. S. Dunning, W. H. Tiedemann, L. Hsueh, and D. N. Bennion, *This Journal*, **118**, 1886 (1971).

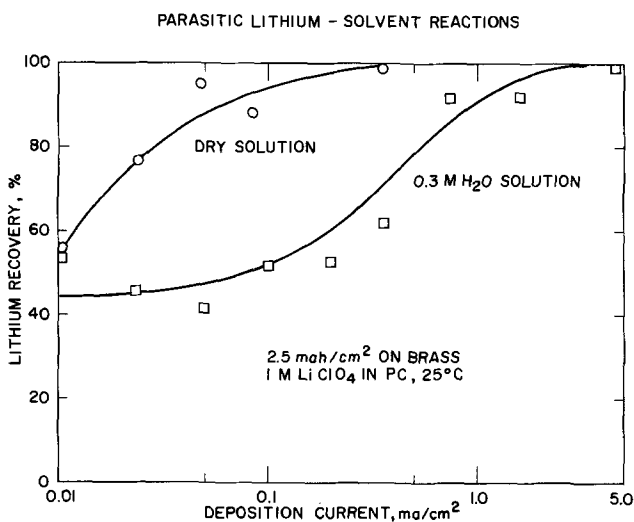


Fig. 4. The effect of parasitic reactions on the charging efficiency.

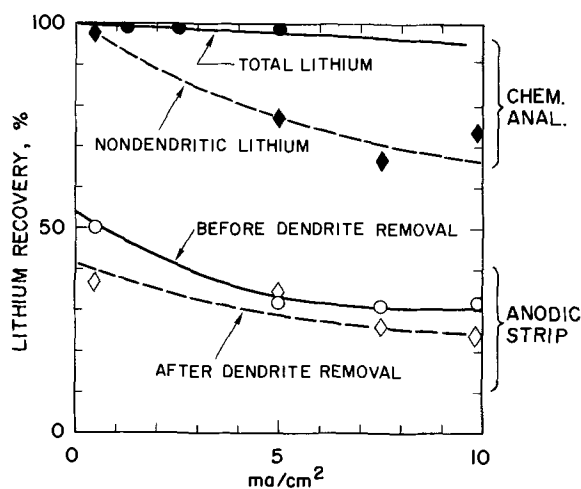


Fig. 5. The effect of the lithium morphology on the charge recovery. 1M LiClO<sub>4</sub> in PC at 25°C, 5 mA/cm<sup>2</sup>.



## Discharge Behavior of Li/MoO<sub>3</sub> Cells

Nehemiah Margalit\*

ESB Incorporated, Technology Center, Yardley, Pennsylvania 19067

The system Li/MoO<sub>3</sub> was proposed, as early as 1965 by Knapp (1), for use in nonaqueous cells using organic solvents. Since then several investigators have used the system (2-8) but the cathode reaction remained unknown. The assumption was made that the cathode reaction involved a two-electron transfer per molecule of MoO<sub>3</sub> and that reported coulombic efficiencies did not exceed 75% to a 1.8V cutoff. Campanella and Pistoia (2) using Li/0.9M LiAlCl<sub>4</sub>  $\gamma$ -butyrolactone/MoO<sub>3</sub> cells recognized that the operating voltages of their cells exceeded the open circuit voltage predicted from thermodynamic data, assuming the products to be Li<sub>2</sub>O and MoO<sub>2</sub> or Mo<sub>2</sub>O<sub>5</sub>. Further investigation by the latter led them to the conclusion that the electrochemical reaction involves a two-electron transfer (6).

Li/MoO<sub>3</sub> cells discharged in our laboratory (4, 8) exhibited two useful discharge plateaus at the end of which a maximum of 1.5 Faradays per mole of MoO<sub>3</sub> was obtained. Therefore, an attempt was made to verify both the two-electron hypothesis and the true nature of the discharge curve using a slow, continuous discharge of a complete cell.

### Experimental

Standard button cell hardware was used as casing for making cells 0.41 cm high and 1.1 cm in diameter. The anode was punched from a high purity lithium ribbon (Foote Mineral Company, 99% pure) and rinsed twice with hexane (MC/B, Manufacturing Chemists, spectroquality grade). The cathode was made from MoO<sub>3</sub> powder (Mallinckrodt, analytical reagent), porous carbon powder, and Teflon in several ratios with the active material weighing between 85 and 95% of the finished cathode. The solvent,  $\gamma$ -butyrolactone (Eastman), was distilled on a spinning band column (Nester/Faust, NF 276) at 5 mm Hg. The middle fraction, boiling between 68.0 and 68.8°C (uncorrected) was collected. The salt LiAsF<sub>6</sub> (U.S. Steel), was used as received. One point five molar solutions prepared in a dry room and sealed in a glass vessel were stored for periods exceeding 5 months without apparent deterioration. Cells were assembled in the dry room, allowed to reach a constant open circuit voltage, and finally discharged at room temperature across  $15 \times 10^3$  ( $\pm 1\%$ ) ohm resistors. Readings were obtained daily, manually, using a high internal impedance digital voltmeter.

### Results and Discussion

Initial open circuit voltages exceeded 3V in agreement with Knapp and Dey (1, 7). However, these voltages were reduced to 2.85V after standing for several days at room temperature. Discharge data indicated utilization of about 50% based on 2 Faraday per mole of MoO<sub>3</sub>. The discharge curves consistently exhibited what appeared to be an end of a first plateau at

about one-third of the obtained discharge capacity. Of particular interest was the discharge behavior at 35°C as shown in Fig. 1. Such cells delivered better than 70% of their theoretical capacity and the end of what appears as a first plateau was at about one-third of the obtained capacity. Such cells delivered 0.5 Faraday/mole, at the end of the first plateau, and a total of 1.5 Faraday/mole for the total discharge.

A re-examination of other authors' published discharge data (2-4, 7, 8) indicates that similar points of inflection are characteristic of Li/MoO<sub>3</sub> systems. Indeed what seems to be a slowly growing concentration polarization is consistently ending at about 25% utilization on the basis of two electrons/molecule for highly efficient systems (3, 4, 7, 8), i.e., 0.5 Faraday/mole. Indeed such a distinct two plateaus discharge has been shown by Dey (7) for a battery. Such discharge characteristics of MoO<sub>3</sub> have been recently reported for both nonaqueous and aqueous systems. Popov and Laitinen (9) obtained, in a molten salt environment, a product whose empirical formula is Li<sub>5</sub>Mo<sub>2</sub>O<sub>8</sub>. In such a product, the formal oxidation state of molybdenum is +5.5. At the same time Gabano *et al.* (10) reported that upon reducing MoO<sub>3</sub> in 7N H<sub>2</sub>SO<sub>4</sub>, one observes a major reduction plateau starting at a calculated product composition of about MoO<sub>2.8</sub> and ending at a calculated product composition of about MoO<sub>2.2</sub>. A comparison of the latter data with those presented here reveals that in both cases, formal charges of +5.5 and +4.5 can be calculated for the boundary of what seems to be the major plateau. The formation of a new cathode material in our Li/MoO<sub>3</sub> cells after the apparent  $n = 0.5$  reduction is further confirmed by a 2.4-2.5V open circuit voltage observed for partially discharged cells.

The above is not in disagreement with the reduction mechanisms proposed by Popov and Laitinen (9), Gabano (10), or Campanella and Pistoia (6) as the initial electrochemical reaction could involve a two-electron step. However, as Popov and Laitinen propose, the primary reaction product probably reacts further with MoO<sub>3</sub> to form polymolybdates, hence the net observed changes of 0.5 electrons per MoO<sub>3</sub> molecule with initial open circuit voltages of 2.85V.

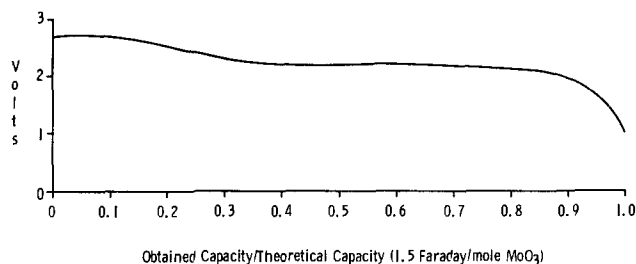


Fig. 1. Discharge behavior of Li/1.5M LiAsF<sub>6</sub>- $\gamma$ -butyrolactone/MoO<sub>3</sub> cells. 35°C,  $15.0 \times 10^3$  ohm load, 577 hr of discharge.

\* Electrochemical Society Active Member.

Key words: lithium cells, molybdenum trioxide, nonaqueous electrolytic solutions.



Further work aimed at identification and characterization of the reduction products is presently being pursued in our laboratory.

Manuscript submitted Feb. 4, 1974; revised manuscript received June 6, 1974.

Any discussion of this paper will appear in a Discussion Section to be published in the June 1975 JOURNAL. All discussions for the June 1975 Discussion Section should be submitted by Feb. 1, 1975.

The publication costs of this article have been assisted by ESB Incorporated.

#### REFERENCES

1. H. R. Knapp, Tech. Rept. ECOM-2632, October 1965.
2. L. Campanella and G. Pistoia, *This Journal*, **118**, 1905 (1971).

3. A. N. Dey U.S. Pat. 3,681,143 (1972) (citing application U.S. Ser. No. 55,170, filed July 15, 1970).
4. F. W. Dampier, Paper 4 presented at Electrochemical Society Meeting, Miami Beach, Florida, October 8-13, 1972.
5. L. F. Athearn and C. C. Liang, U.S. Pat. 3,726,716 (1973).
6. L. Campanella and G. Pistoia, *This Journal*, **120**, 383 (1973).
7. A. N. Dey, Paper 54 presented at Electrochemical Society Meeting, Boston, Massachusetts, October 7-11, 1973.
8. F. W. Dampier, *This Journal*, **121**, 656 (1974).
9. B. N. Popov and H. A. Laitinen, *ibid.*, **120**, 1346 (1973).
10. J. P. Gabano, Y. Jumel, and J. P. Gomis, Paper 55 presented at Electrochemical Society Meeting, Boston, Massachusetts, October 7-11, 1973.

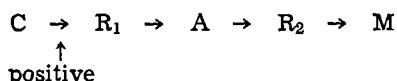
## On the Ultraviolet Inhibition of Electroless Plating on Plastics

M. Schlesinger and B. K. W. Baylis

Department of Physics, University of Windsor, Windsor, Ontario, Canada

In a recent communication (1) we reported on the inhibition of electroless metal plating on glass using ultraviolet light. We employed in that study the so-called conventional sensitizing activating surface pretreatment path. The observation was made that u.v. inhibition had not proved possible if the catalyzing (PdCl<sub>2</sub>/SnCl<sub>2</sub>/HCl) accelerating (HCl or NaOH and similar) path was followed.

It is the aim of the present note to give some results concerning the successful u.v. inhibition and growth patterning of electroless deposition on plastics using the catalyzing path. Specifically, our results to date show that the effect of u.v. light can be presented as follows



where C stands for the combined PdCl<sub>2</sub>/SnCl<sub>2</sub>/HCl catalytic bath [Shipley 9F (2)], R for a DI water rinse, A for the accelerator, and M for the metallizing bath [a room temperature Ni-P bath, the composition of which is reported in Ref. (3)].

If u.v. light is applied after catalyzing, deposition of the positive occurs essentially only on the areas protected by the mask, resulting in sharply defined metal strips separated by bare plastic. Exposure of the substrate to ultraviolet radiation at other stages in the above sequence results in either "positives" or even "negatives" (1) depending on the specific stage at which the irradiation takes place. The resulting images show markedly less contrast because there is considerable background remaining.

As noted in Ref. (5) the substrate and its condition seem to play an important role in determining the activity of the catalyst. It seems to play an important role also in determining the effectiveness of the u.v.

Key words: electroless, u.v. inhibition, catalytic systems, plating.

inhibition or promotion of growth (i.e., the creation of a positive or negative image of the photomask).

Most of the above observations were made on platable grade ABS<sup>1</sup> which had been properly pre-cleaned. Other plastics on which it has been possible to obtain patterns are epoxy, Plexiglas, Formvar, Polyamide, and cellulose acetate. It would appear at this stage that deglazing or some roughening of the surface prior to the sequence of premetallizing baths is of prime importance.

Further study of the above effects is being undertaken in our laboratory.

#### Acknowledgment

The skillful technical assistance of Mr. A. Busuttill is gratefully acknowledged.

Manuscript received June 21, 1974.

Any discussion of this paper will appear in a Discussion Section to be published in the June 1975 JOURNAL. All discussions for the June 1975 Discussion Section should be submitted by Feb. 1, 1975.

The publication costs of this article have been assisted by the University of Windsor.

<sup>1</sup> Kindly supplied by International Tools Limited, Windsor, Ontario, Canada. The approved sources for this plastic are (i) Borg-Warner Corporation, MARBON EPA 3530, (ii) Monsanto Chemical Company, PG 299, and (iii) B. F. Goodrich Company, ABSON 89151.

#### REFERENCES

1. M. Schlesinger, *This Journal*, **121**, 667 (1974).
2. C. R. Shipley, U.S. Pat. 3,011,920 (1961).
3. J. P. Marton and M. Schlesinger, *This Journal*, **115**, 16 (1968).
4. S. L. Chow, N. E. Hedgecock, M. Schlesinger, and J. Rezek, *Ibid.*, **119**, 1013 (1972).
5. N. Feldstein, M. Schlesinger, N. E. Hedgecock, and S. L. Chow, *ibid.*, **121**, 738 (1974).

# Direct Electrochemical Determination of Hammett Substituent Constants

Thomas L. Riechel,<sup>1</sup> Janice J. Kim,<sup>2</sup> and Peter A. Rock\*

Department of Chemistry, University of California at Davis, Davis, California 95616

Probably the best known, and the most successful, semi-empirical, linear-free-energy relationship is that proposed by Hammett (1, 2). The Hammett rho-sigma equation

$$\log \frac{k}{k'} = \rho\sigma \quad [1]$$

has been found to correlate the rate and equilibrium constants of a great variety of side-chain reactions of *meta*- and *para*-substituted benzoic acid derivatives. In this equation  $k$  is a rate or equilibrium constant of a substituted benzoic acid derivative,  $k'$  is the corresponding constant for the unsubstituted derivative,  $\rho$  is the reaction series constant, and  $\sigma$  is the substituent constant. The reaction series constant is independent of the nature of the substituent, but depends on the solvent, the temperature, and the particular reaction series. The Hammett substituent constant  $\sigma$  is defined (1) by the equation

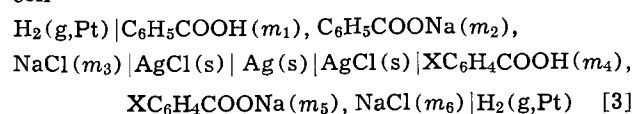
$$\sigma \equiv \log \frac{K}{K'} \quad [2]$$

wherein  $K$  is the thermodynamic acid dissociation constant for a *meta*- or *para*-substituted benzoic acid in water, and  $K'$  is the acid dissociation constant for benzoic acid in water, both at 25°C.

The calculation of  $\sigma$  values using Eq. [2] together with separately determined experimental values of  $K$  and  $K'$ , yields  $\sigma$  values as small differences between two (relatively) large numbers, that is,  $\sigma = \log K - \log K'$ . The determination of accurate ( $\pm 0.004$  or better)  $\sigma$  values requires even more accurate ( $\pm 0.002$  or better)  $pK$  values in aqueous solution for benzoic acid and its *meta*- and *para*-derivatives.

The potentially most accurate method for the determination of  $pK$  values for benzoic acids in water is from electrochemical cell data. The most extensive electrochemical study of the ionization constants of benzoic acids in water is that reported by Briegleb and Bieber (3). However, the accuracy of the  $pK$  values reported by Briegleb and Bieber has been criticized in two review articles on the ionization constants of acids (4, 5). Furthermore, there are disagreements between the electrochemically determined  $pK$  values of Briegleb and Bieber and the spectrophotometrically determined  $pK$  values of Wilson *et al.* (6). The possible uncertainties ( $\sim \pm 0.02$   $pK$  units) in the measured  $pK$  values of benzoic acids may give rise to considerable uncertainties ( $> \pm 0.04$   $pK$  units) in the values of the Hammett substituent constants calculated from these  $pK$  values.

The inherent difficulties associated with the determination of  $\sigma$  values as small differences between two large numbers can be eliminated by a direct measurement of  $\sigma$ . We have used the electrochemical double cell



(where X represents a *meta*- or *para*-substituent, and

\* Electrochemical Society Active Member.

<sup>1</sup> Present address: Department of Chemistry, University of California, Riverside, California 92501.

<sup>2</sup> Present address: Department of Chemistry, University of California, Berkeley, California 94700.

Key words: hydrogen, Hammett, substituent, electrode, sigma.

the  $m_i$  values are molalities) for the direct electrochemical determination of Hammett  $\sigma$  values; this communication outlines the basic method and reports our results for the  $\sigma$  value of *meta*-methylbenzoic acid.

## Experimental

The cell electrolytes were prepared in a glove box under a nitrogen atmosphere. The distilled water used to prepare the cell solutions was boiled and stored under a nitrogen atmosphere. The benzoic acid and the *m*-methylbenzoic acid (Eastman reagent grade) were dissolved in  $\text{CO}_2$ -free  $\text{NaOH}(\text{aq})$  and recrystallized by addition of  $\text{HCl}(\text{aq})$ . Primary standard  $\text{NaCl}$ , constant-boiling  $\text{HCl}(\text{aq})$ , and carbon dioxide-free  $\text{NaOH}(\text{aq})$  were used to prepare the cell solutions.

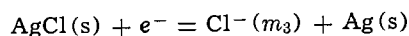
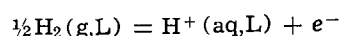
The hydrogen electrodes (7) were closed-loop, platinum coils, 5 mm in diameter and 20 mm in length, consisting of seven turns of 0.020 in. diameter Pt wire. The coils were soaked in reagent-grade acetone, and cathodically cleaned at 50 mA in 3M  $\text{H}_2\text{SO}_4(\text{aq})$  overnight. After the acid cleaning, the electrodes were rinsed in distilled water and a light coating of Pt black was electroplated onto the coils [5 mA for 5 min and then 10 mA for 6 min in 10%  $\text{H}_2\text{PtCl}_6 \cdot 6\text{H}_2\text{O}$  in 2M  $\text{HCl}(\text{aq})$  plating solution]. Bias potentials between hydrogen electrodes were found to be less than 20  $\mu\text{V}$ . New electrode coils were prepared for each cell. The platinum electrode lead was brought into the cell from above through a Pt-to-soft-glass seal. The silver-silver chloride electrodes were prepared on closed-loop platinum coils using the thermal electrolytic method (7). Bias potentials of aged electrodes were less than 20  $\mu\text{V}$ .  $\text{Ag}/\text{AgCl}$  electrode leads were brought into the cell from above via a Pt-to-soft-glass seal.

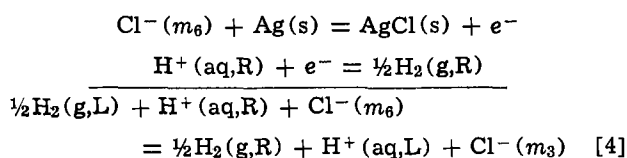
The design of each half of the double cell was of the basic H-type with a large-bore, ground-glass stopcock between the chambers. A  $\text{H}_2$  gas presaturation chamber was attached to each of the hydrogen electrode compartments. The  $\text{H}_2$  gas was run through a DEOXO hydrogen purifier (Englehard Industries), then through the presaturator (filled with cell electrolyte), and then into the cell.

The electrodes were presoaked in cell electrolyte overnight, then the cell was filled with electrolyte and the electrodes were mounted in the cell by means of ground-glass joints. The respective halves of the double cell were connected externally and the entire assembly was immersed in an oil bath (recirculation sump type). The temperature of the oil bath thermostat ( $\pm 0.002^\circ\text{K}$ ) was maintained by a proportional heater and monitored with a certified Leeds and Northrup Company platinum resistance thermometer and a G-2 Mueller bridge. Hydrogen gas was bubbled through the cell for approximately 1 hr before the emf measurements were begun. The cells were then closed and the double cell emf was measured on a certified Leeds and Northrup Company universal potentiometer. The cells attained a stable ( $< \pm 0.1$  mV) voltage within 1-2 hr.

## Results

The over-all reaction of cell [3] can be obtained as follows (L = left, R = right hand side cell electrolyte)





Application of the Nernst equation to this reaction under conditions where  $a_{\text{H}_2(\text{R})} = a_{\text{H}_2(\text{L})}$  (equal hydrogen pressures) yields ( $\mathcal{E}^\circ = 0$ )

$$\mathcal{E} = -\frac{RT}{F} \ln \left\{ \frac{a_{\text{H}^+(\text{L})} a_{\text{Cl}^-(m_3)}}{a_{\text{H}^+(\text{R})} a_{\text{Cl}^-(m_6)}} \right\} \quad [5]$$

We now define

$$K' = \frac{a_{\text{H}^+(\text{L})} a_{\text{C}_6\text{H}_5\text{COO}^-}}{a_{\text{C}_6\text{H}_5\text{COOH}}} \quad [6]$$

and

$$K = \frac{a_{\text{H}^+(\text{R})} a_{\text{XC}_6\text{H}_4\text{COO}^-}}{a_{\text{XC}_6\text{H}_4\text{COOH}}} \quad [7]$$

Combination of Eq. [6], [7], and [2] with Eq. [5] yields

$$\begin{aligned} \mathcal{E} &= +2.3026 \left( \frac{RT}{F} \right) \sigma \\ &- \frac{RT}{F} \ln \left\{ \frac{m_3[m_1 - m_{\text{H}^+(\text{L})}][m_5 + m_{\text{H}^+(\text{R})}]}{m_6[m_4 - m_{\text{H}^+(\text{R})}][m_2 + m_{\text{H}^+(\text{L})}]} \right\} \\ &- \frac{RT}{F} \ln \left\{ \frac{\gamma_{\text{C}_6\text{H}_5\text{COOH}} \cdot \gamma_{\text{Cl}^-(m_3)}}{\gamma_{\text{XC}_6\text{H}_4\text{COOH}} \cdot \gamma_{\text{Cl}^-(m_6)}} \right. \\ &\quad \left. \cdot \frac{\gamma_{\text{XC}_6\text{H}_4\text{COO}^-(m_5)}}{\gamma_{\text{C}_6\text{H}_5\text{COO}^-(m_6)}} \right\} \quad [8] \end{aligned}$$

Under conditions where the ionic strengths of the L and R solutions are approximately equal, Eq. [8] reduces to

$$\begin{aligned} \mathcal{E} &= + \left( \frac{2.3026 RT}{F} \right) \sigma \\ &- \frac{RT}{F} \ln \left\{ \frac{m_3[m_1 - m_{\text{H}^+(\text{L})}][m_5 + m_{\text{H}^+(\text{R})}]}{m_6[m_4 - m_{\text{H}^+(\text{R})}][m_2 + m_{\text{H}^+(\text{L})}]} \right\} \quad [9] \end{aligned}$$

This equation shows that the use of the double cell [3] yields a direct relationship between the measured cell voltage and the Hammett substituent constant. A determination of  $\mathcal{E}$  to  $\pm 0.1$  mV, which is not difficult to achieve in cells of the type of cell [3], yields a  $\sigma$  value to within  $\pm 0.003$  units.

An example of the type of results that can be obtained from emf measurements on cells of the type of cell [3] is provided by the following data for the case where X is *meta*-methyl. For a cell with the concentrations:  $m_1 = 1.824 \times 10^{-4}$  mole  $\cdot$  kg $^{-1}$ ;  $m_2 = 1.734 \times 10^{-4}$  mole  $\cdot$  kg $^{-1}$ ;  $m_3 = 0.1013$  mole  $\cdot$  kg $^{-1}$ ;  $m_4 = 1.614 \times 10^{-4}$  mole  $\cdot$  kg $^{-1}$ ;  $m_5 = 1.933 \times 10^{-4}$  mole  $\cdot$  kg $^{-1}$ ; and  $m_6 = 0.1020$  mole  $\cdot$  kg $^{-1}$ , the following voltages were obtained:  $-4.82$  mV (25.228°C);  $-3.94$  mV (30.000°C);  $-3.14$  mV (35.326°C);  $-2.41$  mV (40.221°C);  $-2.13$  mV (45.323°C);  $-1.87$  mV (50.314°C). The ionic strengths of the two cell electrolyte solutions were 0.1015 (L) and 0.1022 (R).

The procedure used to calculate a  $\sigma$  value was as follows:  $K_a$  values for benzoic acid and *meta*-methylbenzoic acid were calculated from the data summarized by Larson and Hepler (5), (benzoic acid "best values" were used); these  $K_a$  values were used to estimate  $m_{\text{H}^+(\text{L})}$  and  $m_{\text{H}^+(\text{R})}$  from solution of the quadratic equation; the values of  $m_{\text{H}^+(\text{L})}$  and  $m_{\text{H}^+(\text{R})}$  were then used to calculate the second term (call it the molality term) on the right-hand side of Eq. [9]; a value of  $\sigma$  was then calculated from Eq. [9] using the measured emf value and the estimated value of the molality term. A revised value of  $K_a$  for *meta*-methylbenzoic acid was then calculated from the  $\sigma$  value using Eq. [2] and

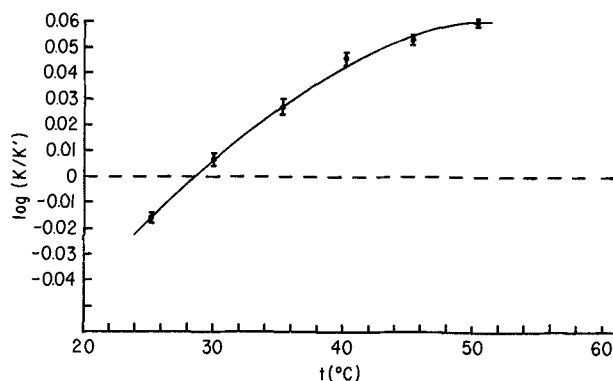


Fig. 1. Plot of  $\log(K/K')$  vs. temperature ( $^{\circ}\text{C}$ ) for *meta*-methylbenzoic acid in water.

Larson's and Hepler's "best" value for the  $K_a$  of benzoic acid. The revised value of  $K_a$  for *meta*-methylbenzoic acid was then compared with the original value. If the difference was greater than or equal to  $1 \times 10^{-7}$ , then  $\sigma$  was recalculated using the revised  $K_a$  value. Iterations were continued until the difference between  $K_a$  estimates was less than  $1 \times 10^{-7}$ . Computer runs starting with both high and low initial estimates for the  $K_a$  value of *meta*-methylbenzoic acid were made to insure that the function was converging on the true value of  $\sigma$ . These initial variations of the value of  $K_a$ , as well as variations over the range of reported  $K_a$  values for benzoic acid itself, did not significantly affect the final value of  $\sigma$ . In each case five or six iterations were necessary to reach the chosen maximum error limit. The  $\log(K/K')$  values obtained at the various temperatures are:  $\log(K/K') = -0.016 \pm 0.002$  (25.2°C);  $+0.007 \pm 0.002$  (30°C);  $+0.027 \pm 0.003$  (35.3°C);  $+0.046 \pm 0.002$  (40.2°C);  $+0.053 \pm 0.002$  (45.3°C); and  $+0.060 \pm 0.001$  (50.3°C).

A plot of  $\log(K/K')$  vs. temperature for *meta*-methylbenzoic acid is given in Fig. 1. It can be seen in this figure that, in terms of the usual interpretation of Hammett  $\sigma$  values, the *meta*-methyl group might be regarded as either electron donating or electron withdrawing relative to hydrogen, depending on whether the temperature chosen to define  $\sigma$  is below or above about 29°C, respectively.

The value of  $\sigma$  obtained at 25°C ( $-0.016$ ) is in fair agreement with that calculated from the data given in Ref. (3), namely,  $\sigma = -0.03$ ; a value of  $\sigma = -0.07$  is calculated from data given in Ref. (6). Extrapolations of the data given in Ref. (3) and (6) also lead to the conclusion that  $\log(K/K')$  changes sign; however, the sign change occurs at temperatures of 48° and 44°C, respectively.

#### Acknowledgment

The computer time used to carry out the calculations was paid out of NSF Computer Grant GJ-462 funds. This research was supported by UCD Committee on Research funds.

Manuscript received May 9, 1974.

Any discussion of this paper will appear in a Discussion Section to be published in the June 1975 JOURNAL. All discussions for the June 1975 Discussion Section should be submitted by Feb. 1, 1975.

The publication costs of this article have been assisted by the University of California.

#### REFERENCES

1. L. P. Hammett, "Physical Organic Chemistry," 2nd Ed., pp. 355, 404, McGraw-Hill Book Co., New York (1970).
2. P. R. Wells, "Linear Free Energy Relationships," pp. 1-56, Academic Press, New York (1968).
3. G. Briegleb and A. Bieber, *Z. Electrochem.*, **55**, 250 (1951).
4. G. Kortüm, W. Vogel, and K. Andrussow, *J. Pure Appl. Chem.*, **1**, 352 (1960).

5. J. W. Larson and Loren G. Hepler, in "Solute-Solvent Interactions," J. F. Coetzee and C. D. Ritchie, Editors, Chap. 1, Marcel Dekker, Inc., New York (1969).
6. J. M. Wilson, N. E. Gore, J. E. Sawbridge, and F. Cardenas-Cruz, *J. Chem. Soc.(B)*, 852 (1967).
7. D. J. G. Ives and G. J. Janz, Editors, "Reference Electrodes," Academic Press, New York (1961).



## The Growth of Anodic Aluminum Oxide Layers after a Heat-Treatment

C. Crevecoeur and H. J. de Wit

*Philips Research Laboratories, Eindhoven, The Netherlands*

### ABSTRACT

Aluminum was anodized in a solution of ammonium pentaborate in ethylene glycol with a current density of  $0.25 \text{ mA/cm}^2$  to voltages between 9.8 and 183V. After annealing to  $400^\circ\text{C}$  in oxygen the specimens were reanodized in the same solution, either with a constant rate of voltage increase or at constant voltage. In both cases the current displays a peak as a function of time. With increasing voltage the peak occurs slightly above the original forming voltage, at constant voltage an induction period occurs before the current starts to increase. After passage of the peak annealed and unannealed specimens behave in the same way. The efficiency of the reanodization after annealing has remained unity: the layer grows. Transmission electron micrographs of layers stripped after interruption of the reanodization show that in the peak growth occurs inhomogeneously: black spots occur which are thickenings of the layer, the surface of which increases as the reanodization is interrupted in a later stage. The effect can formally be described as a two dimensional phase transformation. A model in which the theory of the kinetics of phase transformations is combined with the experimental exponential relation between ionic current and field during anodization leads to an equation which in most cases accurately describes the reanodization curves.

Heating of anodic oxide layers is customary during the production of electrolytic capacitors. In dry capacitors, for instance, in which the counterelectrode consists of a layer of so-called "manganese dioxide," the latter is applied by dipping the anodized metal in a solution of manganese nitrate in water and oxidizing the wet sample at  $300^\circ\text{--}500^\circ\text{C}$  in air. This procedure does not improve the quality of a capacitor and the question arises whether the heating of the anodic oxide is on its own, at least partly, responsible for this effect.

With this in mind we investigated the influence of annealing on the properties of anodic oxide layers. We have concentrated our attention on aluminum. This is a suitable metal with which to investigate annealing effects, because the anodic oxide remains noncrystalline and protects the metal from oxidation during heating. Heating of anodic tantalum oxide on the other hand causes a reaction between the oxide and the metal (1) as well as sharpening of the x-ray diffraction diagram (2) as reported by Vermilyea. A disadvantage of aluminum is its low melting point.

In general, when during anodization the current or voltage is suddenly changed or interrupted and reapplied, transient effects can be observed. Evidently adaption of the conductivity of the layer to the newly applied field requires some time. The transient becomes very pronounced if the oxide layer is heated ( $250^\circ\text{--}450^\circ\text{C}$ ) before being submitted to further anodization. Reanodization curves of annealed films, obtained by regularly increasing the voltage across the cell, exhibit a very characteristic current peak, as

reported first by Dignam (3). He showed that the ionic conductivity of the aluminum oxide after annealing was very small but that it could be restored by the application of a high electric field. Earlier Vermilyea (1) had reported that the ionic conductivity of anodic tantalum oxide decreased after annealing. After applying a constant voltage, new oxide would grow preferentially at metal grain boundaries and singularities within the grains, until finally the growth became uniform. Recently Kudo, Watase, and Kato (4) reanodized heated anodic tantalum oxide by the application of a constant voltage. They concluded that the relatively small number of charge carriers present after heating was increased not only by the applied electric field but also by the current.

We have made a detailed investigation of the reanodization of anodic aluminum oxide and found that, after annealing, further growth started inhomogeneously. This is shown in Fig. 10. The process can formally be described as a two dimensional phase transformation in which the annealed oxide with a low ionic conductivity is transformed into oxide with a normal ionic conductivity. A model will be presented in which the theory of the kinetics of phase transformations developed by Johnson and Mehl (5) and Avrami (6) is combined with the experimental exponential relation between ionic current and applied electric field for anodization as found by Güntherschulze and Betz (7) and Bernard and Cook (8). This leads to an equation which in most cases gives an accurate description of the reanodization curves.

### Experimental

In a reanodization experiment an aluminum sample is successively cleaned, anodized, annealed, and re-

**Key words:** annealing of anodic films, reanodization, heterogeneous growth, phase transformation, surface gain after electroetch.

anodized. In this section the details of these different stages are described.

#### Pretreatment

Samples were punched from aluminum foil 0.3 mm thick, supplied by Merck, purity 99.95%, the main impurity being Si. The samples were spoons with a circular area of 14 mm diameter and a handle 4 mm wide and 2 cm long. The anodized surface used was about 3.7 cm<sup>2</sup>.

The samples were roughly cleaned by immersion in an aqueous solution of caustic soda, 4g NaOH per liter, at 50°C for 15 sec, and more thoroughly by electropolishing in a bath consisting of 140 mliters C<sub>2</sub>H<sub>5</sub>OH, 40 mliters HClO<sub>4</sub> (70%), and 20 mliters 2-butoxy-ethanol (9). To avoid recrystallization of the aluminum during the experiments the samples were heated at 600°C for 15 min. To remove the thermal oxide layer and to polish, the samples were electropolished in the above-mentioned bath again for 2 min at 0.2 A/cm<sup>2</sup>.<sup>1</sup> Then the samples were stored. Deionized water was used for rinsing.

Before anodization, the surface layer of the samples was removed by immersion in a bath containing 1.5 mliters HF (50%), 10 mliters H<sub>2</sub>SO<sub>4</sub> (96%), and 90 mliters water at room temperature for 15-30 sec, followed by rinsing in methanol.

#### Anodization

Immediately hereafter the sample was anodized in a solution of 17g ammonium pentaborate in 100 mliters glycol (10). This electrolyte was chosen because it was known that anodic oxide layers were formed with a current efficiency of unity and because layers formed in this electrolyte showed a good thermal stability. The electrolyte was prepared at 90°C in the absence of air.

The anodization process was performed at 24° ± 1°C at constant current density, viz., 0.25 mA/cm<sup>2</sup>. The voltage was measured relative to a platinum cathode. The voltage drop across the electrolyte was small (about 0.2V). When the voltage across the cell had reached a previously determined value, V<sub>f</sub>, the current was interrupted. This voltage is called the forming voltage in this investigation and is therefore defined only for this particular current density. Rinsing in methanol completed the anodizing process.

#### Annealing

Finally the samples were heated for 15 min in oxygen at 400°C and immediately afterward used in one of the following experiments.

#### Reanodization

Reanodization was carried out in two ways, either with a regularly increasing voltage or with a constant voltage applied across the cell. The former method gives a good qualitative indication of the effects, whereas only the latter method is suitable to obtain quantitative results.

*Reanodization with a constant rate of voltage increase.*—Anodic oxide films were, after annealing, reanodized by applying a voltage increasing at a constant rate. Once the voltage reached the original forming voltage, V<sub>f</sub>, the current started to increase and displayed a peak at the voltage V<sub>max</sub>. After passage of the peak the current eventually reached the anodizing value, which depended on the choice of dV/dt. The characteristic maximum in the current is caused by annealing: a nonheated sample shows below V<sub>f</sub> a gradual increase in the reanodization current, until the final anodization value has been reached.

These phenomena were investigated by Dignam (3) with thin films. He remarked that the charge required to reach, at reanodization, a voltage > V<sub>f</sub> was the same for heated and nonheated films. He concluded

<sup>1</sup> Electropolishing is improved if the thermally grown oxide layer is first removed by etching.

that a heat-treatment hindered the growth of the anodic oxide film. Our results obtained on thick films are in complete agreement with those of Dignam. In Fig. 1 reanodization curves of a heated and a nonheated layer have been plotted. During the passage of the peak the film becomes thicker, as follows from capacitance and ellipsometric measurements. At voltages beyond V<sub>max</sub> the current-time relations of the two layers coincide.

Some difference remains, however. When anodization of the heated sample is continued, say, beyond 150V, small breakdowns take place, attended by evolution of gas and a current efficiency less than unity. A nonannealed sample can be anodized with hardly any evolution of gas at up to 210V in this particular electrolyte.

When etched foil, as used in capacitors, is anodized, the current density and therefore also the thickness of the anodic oxide layer are unknown. This is also the case if for some reason the oxide layer has been thinned chemically. The occurrence of the peaks can be used to determine the forming voltage, V<sub>f</sub>, which in this investigation is used as a measure of the layer thickness. To that purpose peaks have been measured with a constant rate of voltage increase on annealed samples. Figure 2 shows the relation between V<sub>f</sub> and

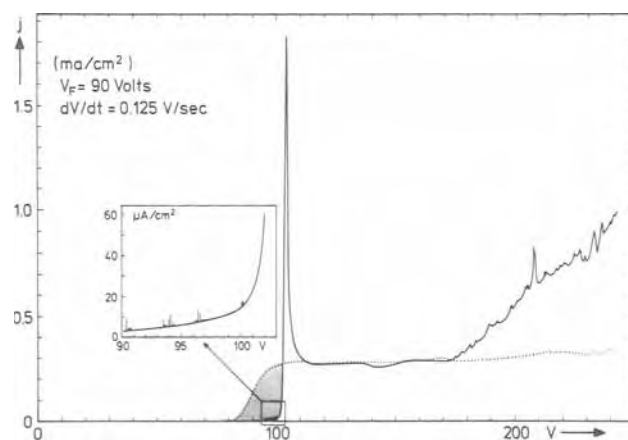


Fig. 1. Current density as function of voltage increasing at a constant rate. The dotted line shows the reanodization of a non-annealed sample, the solid line represents the reanodization of an annealed sample. The shaded areas are equal.

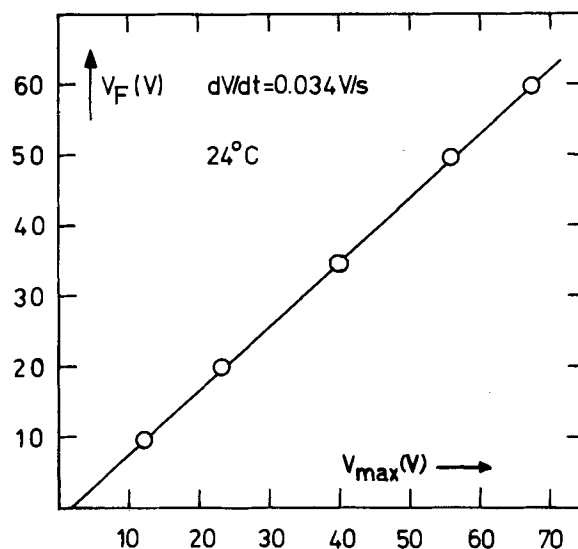


Fig. 2. The forming voltage V<sub>f</sub> as function of V<sub>max</sub>, the voltage of which the current is maximum, when a heated sample is reanodized with dV/dt = 0.034 V/sec. From this plot the layer thickness can be obtained.

$V_{\max}$ . Similar relations can be found in Dignam's work (3).

**Reanodization at constant voltage.—Nonheated films.**—Let us first consider the reanodization of a nonannealed sample. The dotted line in Fig. 3 represents the reanodization of such a sample, measured by the application of a constant voltage across the aluminum and the electrolyte. The current varies in inverse proportion with time, as it should do (10). This  $1/t$  law is obtained by means of the fact that the thickness of the anodic layer,  $L$ , is proportional to the charge passed per square centimeter,  $q$ :  $L = \alpha \lambda q$ , in combination with the exponential dependence of the ionic current density  $j$  on  $F$ , the applied field:  $j = j_0 \exp(BF)$ ; here  $\alpha$  is the current efficiency,  $\lambda$  the ratio of the equivalent weight of aluminum oxide to the product of the Faraday number times the density of the oxide. At a constant voltage across the cell, this leads to the differential equation

$$dt = \frac{1}{\alpha \lambda j_0} \exp\left(-\frac{BF}{L}\right) dL$$

Integration gives

$$j = \frac{q_f}{BF} \left( \frac{1}{t + t_0} \right) \quad [1]$$

where use has been made of the fact  $BF \gg 1$  (11, 12).  $q_f$  is the charge per centimeter square consumed during the anodization up to  $V_f$ , during which a layer with a thickness of, say,  $L_0$  was built up;  $t_0$  may then be considered as the time it would take to anodize a layer to the same thickness  $L_0$  at constant voltage starting from the bare metal (if this were possible).

$t_0$  is given by

$$t_0 = \frac{q_f}{j_0 BF} \exp(-BF)$$

The charge consumed during the reanodization at time  $t$  is

$$q \equiv \int_0^t j dt = \frac{q_f}{BF} \ln\left(\frac{t + t_0}{t_0}\right) \quad [2]$$

$t_0$ , a quantity which we shall use later on, can be obtained from plots of  $1/j$  vs.  $t$  or from plots of  $q$  vs.  $\log t$ . Extrapolation, in the latter plot, of the straight line for large values of  $t$  toward  $q = 0$  gives  $t_0$  directly. The broken lines in Fig. 4a and b represent examples of the growth of nonannealed samples at constant voltages.

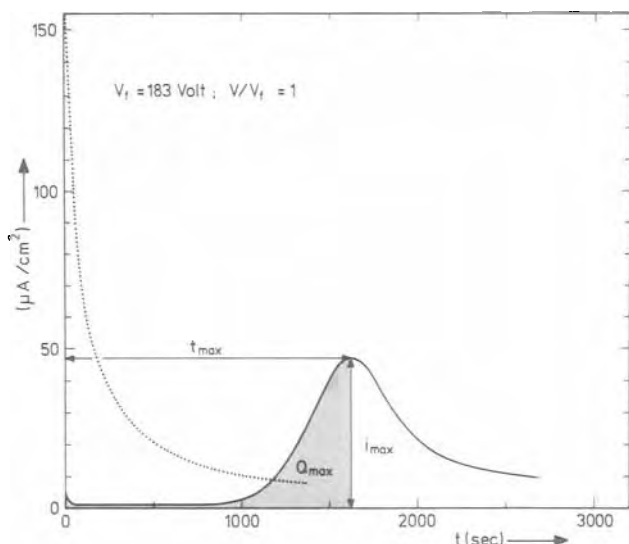


Fig. 3. Reanodization at a constant voltage  $V$  of a nonheated sample (dotted line) and a heated sample (solid line). The meaning of the symbols is explained in the text.

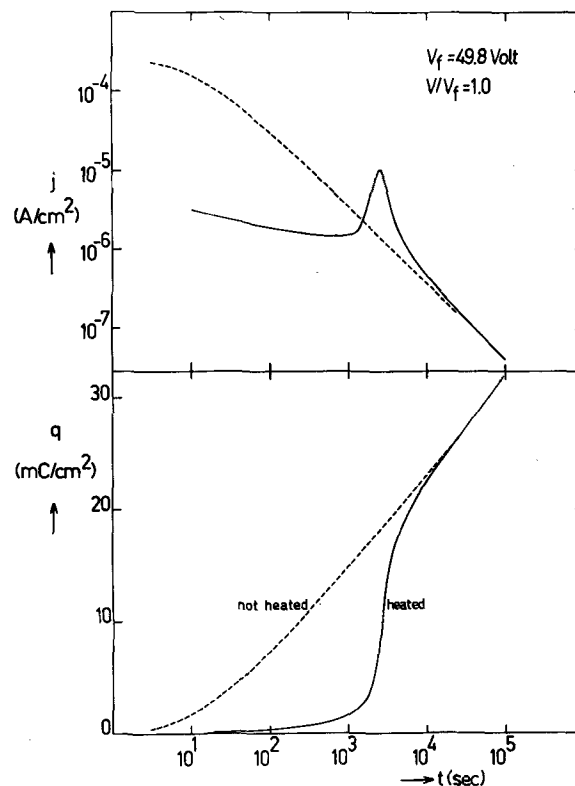


Fig. 4. Reanodization, at a constant voltage of 50V, of heated and nonheated samples. (a, upper) The current as a function of time; (b, bottom) the charge consumed during reanodization as a function of time.

**Annealed films.**—When a constant voltage is applied to an annealed film, the current will first charge the capacitor and then drop to low values. After some time, however, the current starts to rise and displays a peak. An example of such a peak is represented by the solid line in Fig. 3. During passage of the peak the capacitance of the sample diminishes and again we associate the peak current with film growth. Compared with the nonannealed film the annealed layer starts growing only after an induction period, which is clearly demonstrated in Fig. 4a. At longer times the current decays and the annealed and nonannealed samples become the same.

In Fig. 4b the charges are plotted as a function of  $\log t$ . In the annealed sample the charge begins to flow at a later stage as compared with the nonannealed sample, but again in the case of long periods of time the curves merge, indicating that the efficiency of the reanodization after annealing has remained unity.

**Properties of the peak.**—The occurrence of a current peak after a heat-treatment is a general phenomenon. Peaks have been observed when different electrolytes (e.g., ammonium hydrocitrate in water or an oxygen discharge) as well as different heating temperatures (250°–450°C) were used.

The time after which the current peak appears in Fig. 3 as well as its form, are very sensitive to experimental conditions. It is important to remove, before anodization, any layer already present on the bare metal (and to replace it by another one!). Also the manner of rinsing after the first anodization may influence the peak. To obtain reproducible results, the complicated ritual of pretreatments described in the preceding section had to be developed. More experimental results are given in Ref. (13).

The characteristics of the peak have been examined as functions of the applied field, of the thickness of the film, of the temperature at which reanodization takes place, of the chemical treatments of the film, and of

the electrolyte composition. In this paper only the dependence on the first two parameters is discussed.

The time needed to reach the maximum current ( $t_{\max}$ ) has been measured with samples of three different thicknesses as a function of the applied field and is plotted in Fig. 5.  $V/V_f$  is proportional to the applied field. According to Bernard and Cook (8) the field is  $8.6 \times 10^6$  V/cm for  $V/V_f = 1$  at the current density of  $0.25$  mA/cm<sup>2</sup> used by us.  $t_{\max}$  depends exponentially on the applied field and does not depend very much on the thickness of the film. About the same field dependence has been found for the current at the maximum ( $j_{\max}$ ). It appears that  $j_{\max}$  increases as the thickness of the film increases, which results in high maximum currents (of the order of several milliamperes) when thick layers are measured at high fields. In such cases the spacing between cathode and sample was reduced to  $\approx 1$  mm, resulting in a cell

resistance of about 25 ohms. The disadvantage of this is that the temperature may rise and the supply of electrolyte may be inadequate.

Another quantity of interest is the charge per centimeter square necessary to reach the maximum current density,  $q_{\max} \equiv \int_0^{t_{\max}} j dt$ . This quantity is plotted in Fig. 6. It does not, as one might think at first, depend on the applied field. In order to compare the form of the peaks, measured on layers with different thicknesses, we plotted the current and time in reduced units:  $j/j_{\max}$  and  $t/t_{\max}$ . An example of such a plot is given in Fig. 7. At low fields the peaks are more or less of the same form, although the layer with  $V_f = 50$  V shows a high current in the beginning. As we shall show afterward this current, which we shall call the induction current, also represents growth of the layer.

Fig. 5. The field dependence of  $1/t_{\max}$ . The value  $V/V_f = 1$  corresponds to a field of  $8.6 \times 10^6$  V/cm.

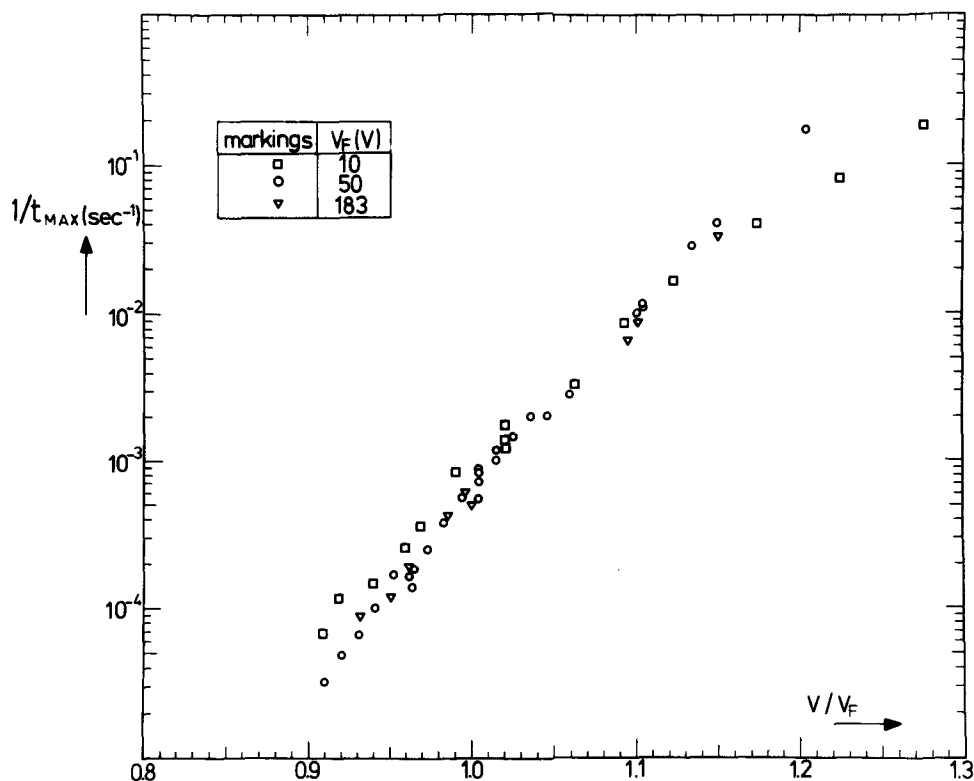
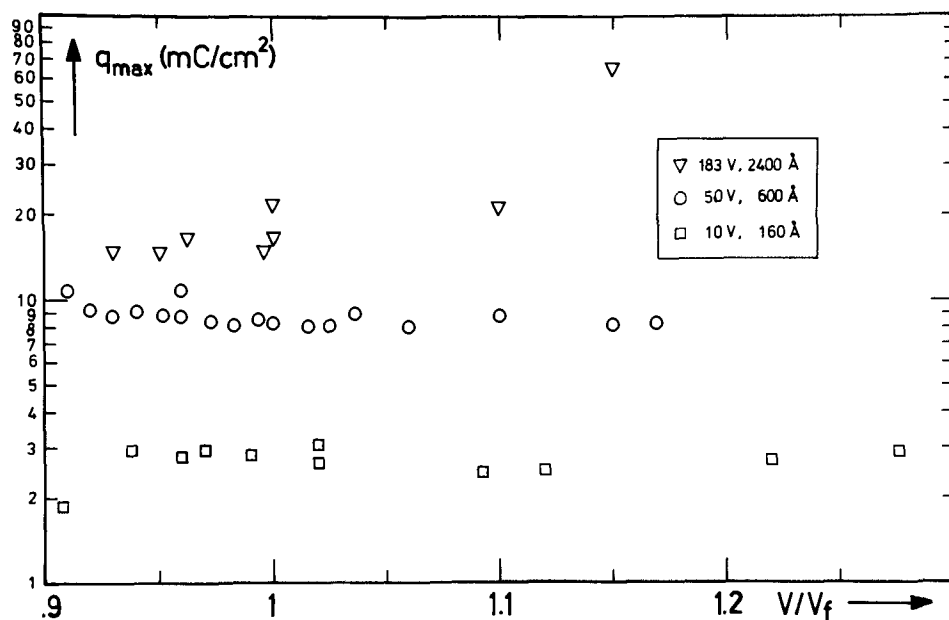


Fig. 6. The field dependence of the charge necessary to reach the maximum.





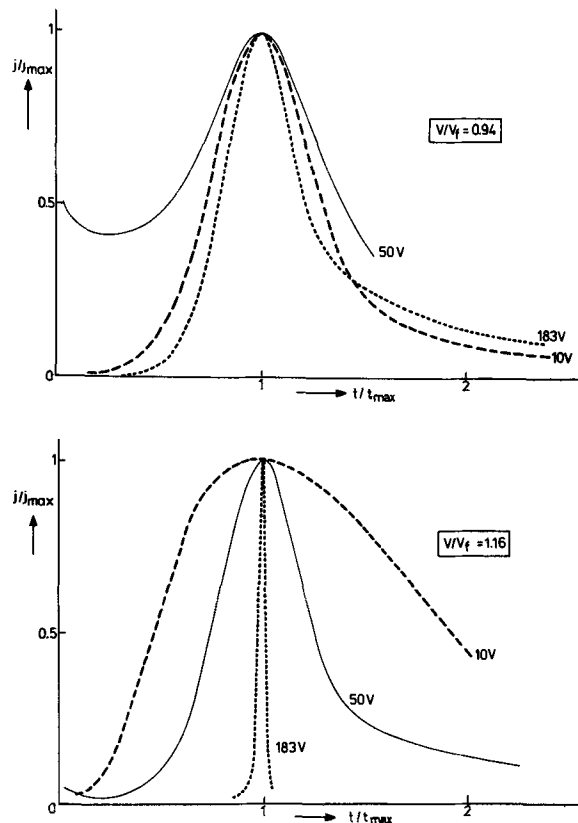


Fig. 7. The field dependence of the shape of peaks, measured at constant voltage and plotted in reduced units  $j/j_{max}$  and  $t/t_{max}$ .

At high fields the form of the current peaks of the three layers is very different. The thin layer shows a very broad peak, the thick layer a very narrow one. In Fig. 8 we have plotted the width  $b$ , taken from the reduced plots at  $j/j_{max} = 0.5$ , as a function of the reduced field. The contrasting behavior of layers having  $V_f = 10V$  and  $V_f = 180V$  is evident. In particular the 180V

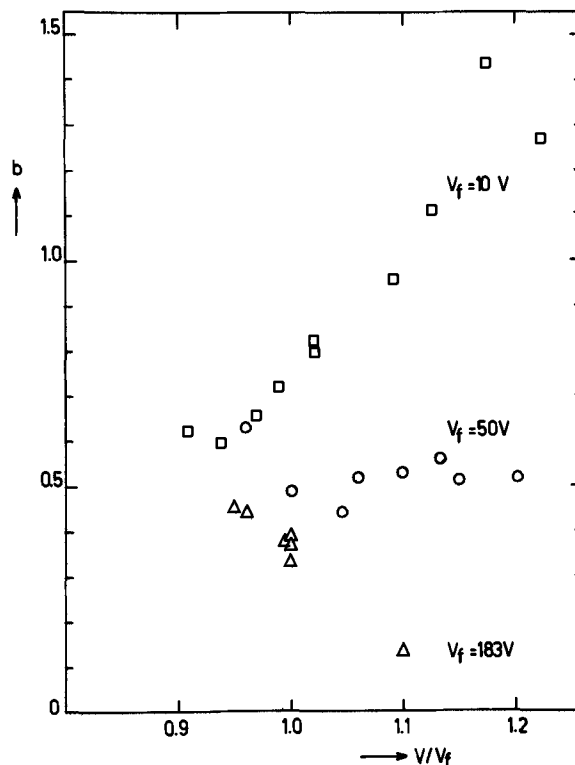


Fig. 8. The width  $b$ , taken from plots in reduced units as presented in Fig. 7, as a function of the field. The values of  $b$  are taken at  $j/j_{max} = 0.5$ .

peak at a high field shows the presence of an induction time, prior to which hardly any growth of the layer occurs.

*Optical and electron microscopic observations.*—In Fig. 9 we have once more plotted a reanodization curve measured with a constant  $dV/dt$ . The plot is surrounded by dark field photographs of the surface of

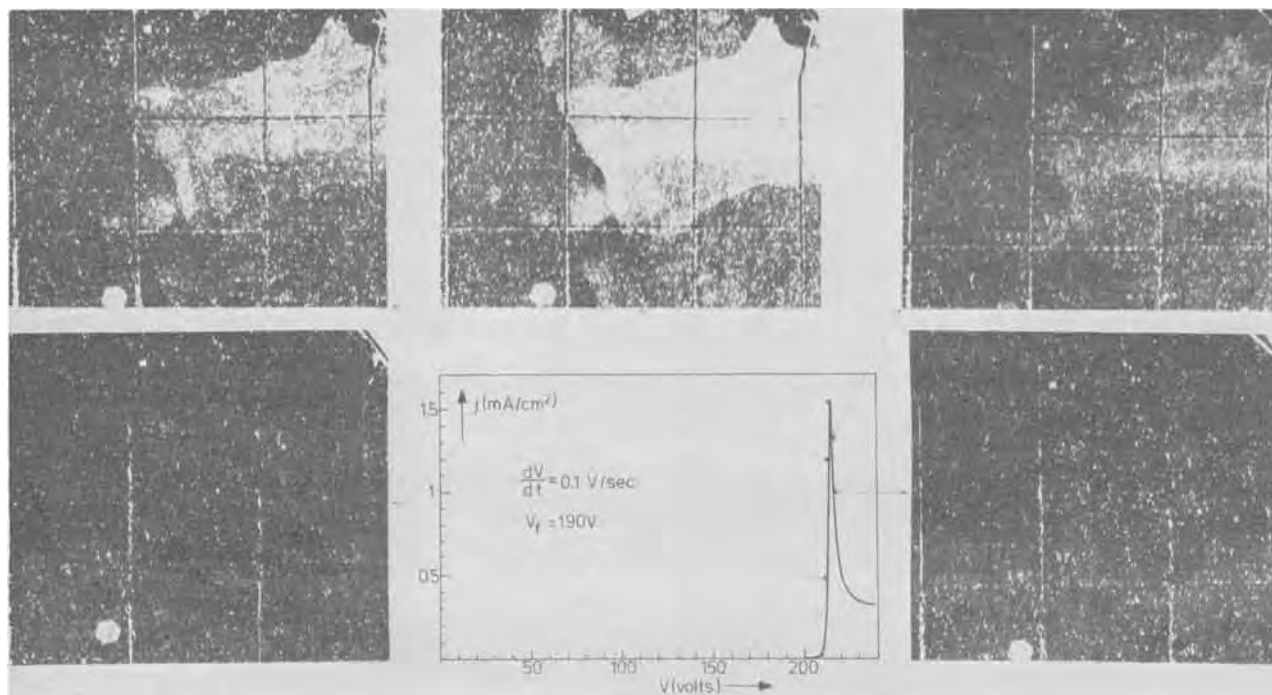


Fig. 9. The change of the reflectivity of a heated sample during reanodization. The arrows indicate the moment the pictures were taken. At a lower value of  $dV/dt$  the reflectivity change is more uniform. The peak is rounded off as compared with the one in Fig. 1, because of a higher cell resistance (about 2000 ohms).

the specimen taken during the reanodization. The surface of the specimen changes as the current reaches its peak. Beyond it the sample regains its original appearance. The pattern of white spots visible on the sample consists of small crater like holes, already present on the bare metal. It does not change during the treatments.

The reflectivity changes are visible only with thick layers. We have examined this phenomenon in more detail with an electron microscope. For greater simplicity we shall restrict ourselves to reanodization at constant voltage.

At different stages of the reanodization process the current was interrupted and the sample was immersed in a solution of bromine in methanol. After dissolution of the aluminum, the anodic oxide layers could be isolated and examined in transmission. We were able to investigate, with the microscope working at 80 kV, layers up to 1500 Å thick.

Nonannealed and reanodized samples do not show heterogeneities on reanodization. Heated and reanodized layers, however, showed a number of dark spots on the screen of the microscope. Since these spots do not show any crystallinity, we must conclude that the spots are thicker places in the layer. Hardly any contrast is found over a spot and it has about the same thickness everywhere.

An example of such an experiment on 600 Å thick layers, reanodized at  $V/V_f = 1$  is shown in Fig. 10. The number and size of the spots increase as the reanodization proceeds. At the maximum of the peak about 50% of the surface of the sample is covered and a number of spots are in contact with each other. Finally the whole surface is dark, a situation roughly coinciding with the end of the peak. (The photographs were printed with a maximum of contrast.)

Such observations are characteristic of reanodization experiments of heated films. The heterogeneous growth is also observed if reanodization is performed

with a constant  $dV/dt$  or with a constant current. The electrolyte has an influence on the form of the dark spots but not on the fact that heterogeneous growth takes place.

### Discussion

First of all we want to summarize the main results. The ionic conductivity of an anodic oxide layer becomes very small in heated as compared with nonheated specimens. If a heated layer is reanodized by the applying of a constant voltage, heterogeneous growth will start after an induction period. As seen in the electron microscope, this phenomenon is very reminiscent of a phase transformation: poorly conducting  $Al_2O_3$ , white in the micrographs, is transformed into  $Al_2O_3$  with a normal ionic conductivity, which becomes thicker and shows up as black material. In view of this we will describe the process formally with terms borrowed from the theory of phase transformations like phase and nucleus, without implying that these "phases" are defined in the chemical sense. Therefore we say that as the current increases, nuclei arise which grow out in a direction parallel to the surface of the sample, transforming the nonconducting into conducting oxide. Since the  $Al_2O_3$  layer is very thin, the phase transformation is essentially two dimensional. When the whole surface has been covered, the layer behaves again like a nonheated sample.

In the following we shall construct a model to describe the reanodization behavior after annealing. Since we do not know even qualitatively what causes nucleation and why an incubation time ( $t_{inc}$ ) is necessary, we shall only consider processes occurring after the incubation period. Only the stage in which nuclei are growing, where the peak in the current appears, is treated. Two assumptions, namely, (a) why the nuclei grow at all, and (b) how the oxide grows after ionic conductivity has been restored, underlie this model.

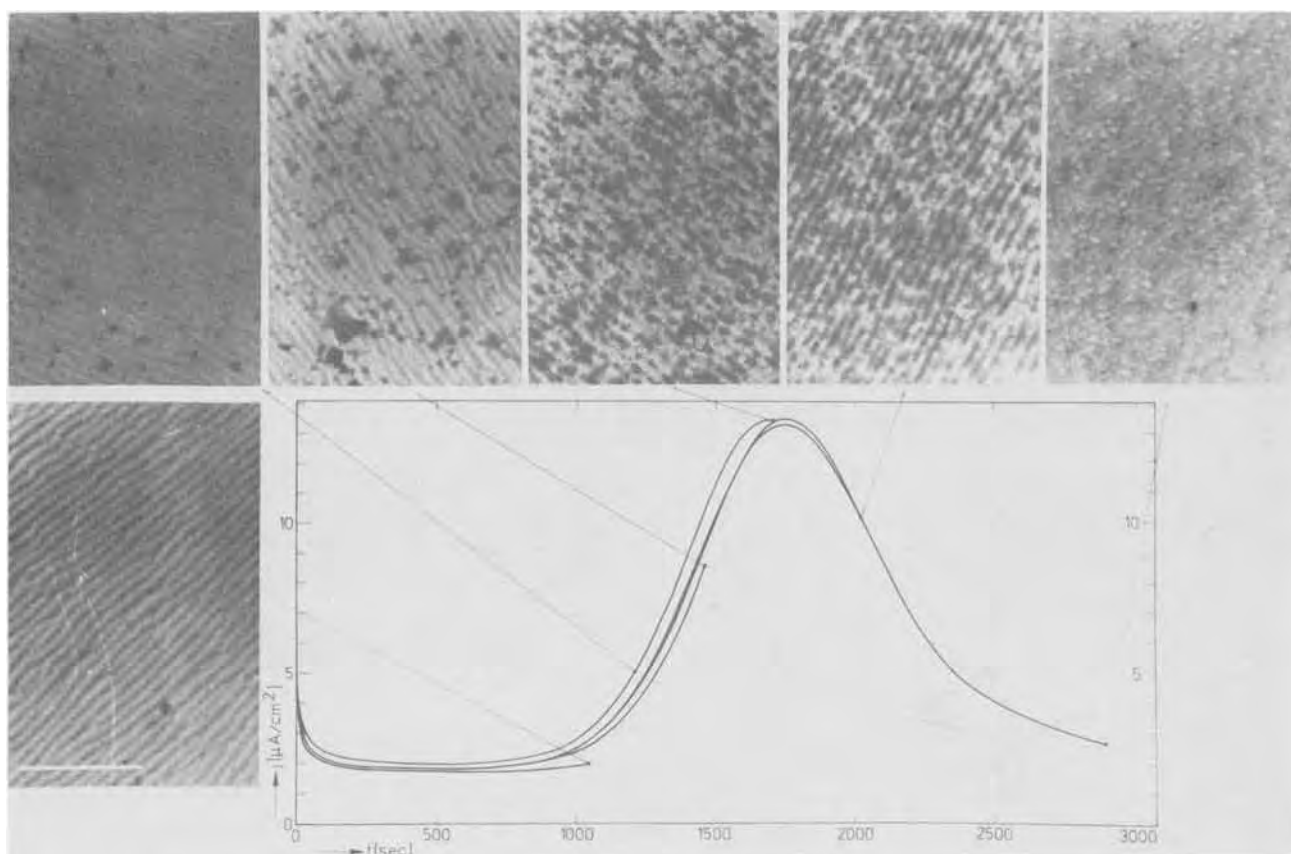


Fig. 10. Transmission electron micrographs showing heterogeneous growth at reanodization of six heated layers. The arrows indicate the moments at which the current through a sample was interrupted.  $V_f = 50V$ ;  $V/V_f = 1$ . The bar represents 1  $\mu$ .

(a) As soon as the ionic conductivity has been restored locally, the layer will become thicker at that particular spot and a step is formed on the oxide film, as is shown very schematically in Fig. 11. Close to such a step the lines of constant potential and the field lines in the anodic oxide layer are shown. It is evident that the highest electric field is to be found in the old nonconducting oxide near the edge of the step. We suppose that this high field causes the annealed oxide to become conducting. The anodic oxide will start to grow rapidly in the vertical direction which means that the step moves along the surface until it collides with another growing spot. Because the field distribution near the step does not change, this model leads to a constant lateral growth velocity.

(b) We have shown that, to a first approximation, the growth beyond the peak is the same as with a nonannealed sample. Such evidence is contained in Fig. 4, where annealed and nonannealed films are compared at long reanodization times. In Fig. 3, remembering that annealing causes postponed growth, we can make the current decay of the nonannealed sample coincide with that of the annealed sample by a mere shift of the former by 1500 sec. Finally the appearance of the sample before and after the peak is the same (Fig. 9). Therefore we suppose that, as soon as the ionic conductivity of the layer has been restored, the thickening of the oxide will follow the relations valid for the growth of an anodic oxide at constant voltage.

Let us suppose that at time  $t'$  a surface  $O(t')$  has been transformed into a conducting oxide.  $O(t')$  is the surface of all the dark spots in the electron micrographs. At time  $t' + dt'$  this surface will have increased by an amount  $dO$ , because the size of the spots has increased and in addition new spots have been formed. The situation at  $t'$  and  $t' + dt'$  has been sketched in Fig. 12.

The current at time  $t$  due to the region  $dO$  transformed between  $t'$  and  $t' + dt'$  will be given by

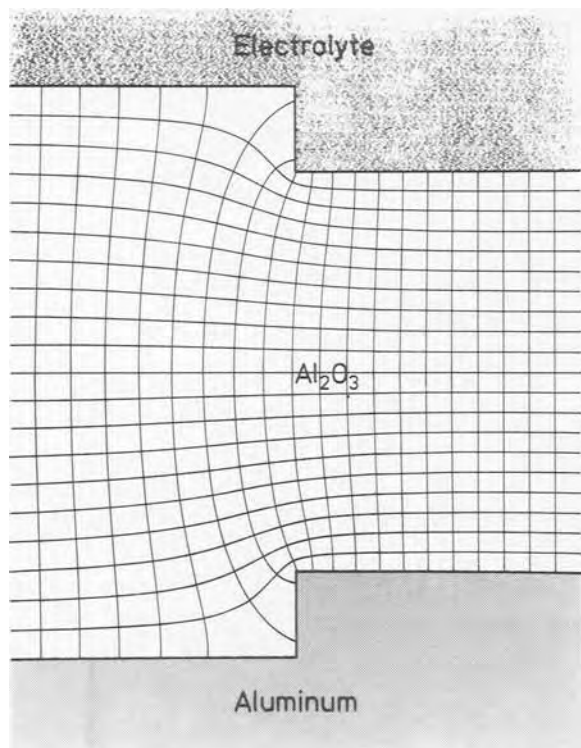


Fig. 11. The field distribution and lines of constant potential near a step in the oxide. The high field inside the old, "nonconducting" oxide near the edge of the step, explains the lateral growth of the step.

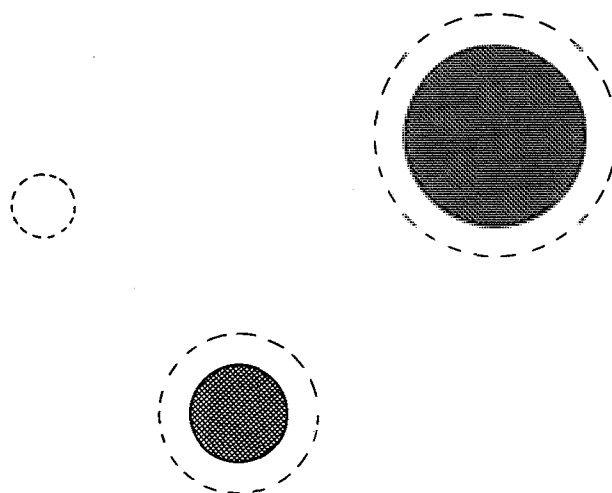


Fig. 12. Schematic presentation of the heterogeneous growth at reanodization. The solid line shows the situation at time  $t$ , the "black spots" are growing at a constant speed. The broken line represents the situation at time  $t + \Delta t$ . Lateral growth has taken place and a new spot is present.

$$di(t) = \frac{qf}{BF} \frac{dO}{t_0 + t - t'} \quad [3]$$

To find an expression for the total current we have to integrate over  $t'$ , and therefore we replace  $dO$  by  $(dO/dt') dt'$ .

Since the nuclei start to grow only after an incubation time we have

$$i(t) = \frac{qf}{BF} \int_{t_{inc}}^t \frac{dO/dt'}{t_0 + t - t'} dt' \quad [4]$$

$(dO/dt')$  can be obtained from the theory of the kinetics of phase transformations developed by Johnson and Mehl (5) and Avrami (6). In our case we have to apply this theory to the case of two dimensions and to assume furthermore that the growth velocity of a nucleus is constant, that the number of nuclei increases linearly with time, and that nucleation is random. Then the theory leads to the following equation for the fraction of the surface  $\alpha$  which at time  $t'$  has been transformed from phase 1 into phase 2 (translated into our language, this means: from nonconducting oxide into conducting oxide):  $\alpha = 1 - \exp(-kt'^3)$  in which  $k$  is the rate constant of this transformation. For small values of  $t'$ , when the nuclei do not yet touch each other,  $\alpha \sim (t')^3$ , as follows directly from our assumptions that the number of nuclei is proportional with time and that the area of a single nucleus is proportional to the square of the time. At longer times,  $\alpha$  will tend to unity because the transformation will then be near completion.

Instead of the rate constant  $k$  of the reaction phase  $1 \rightarrow$  phase 2, we shall use the quantity  $w = k^{-1/3}$ . Since the transformation of nonconducting oxide into conducting oxide only starts at  $t = t_{inc}$  we must use  $t' - t_{inc}$  rather than  $t'$ . Thus at the time  $t'$  the fraction of the surface which is covered with conducting oxide is

$$1 - \exp - \left( \frac{t' - t_{inc}}{w} \right)^3 = \frac{O(t')}{S}$$

where  $S$  is the surface area of the sample.  $w$  is found to represent with fair accuracy the width of the peak at half the height of the current maximum.<sup>2</sup> Differen-

<sup>2</sup>  $w$  has to be distinguished from the quantity  $b$  introduced earlier which is the width of the peak at half the height of the current maximum expressed in the reduced time  $t'/t_{max}$ .

tiating this expression and using Eq. [4], we obtain for the current density

$$j(t) = \frac{3q_t}{wBF} \int_{t_{inc}}^t \frac{\left(\frac{t' - t_{inc}}{w}\right)^2 \exp\left(-\frac{t' - t_{inc}}{w}\right)^3}{t_0 + t - t'} dt' \quad [5]$$

which can be written, with  $y \equiv \frac{t' - t_{inc}}{w}$  and  $z = \frac{t - t_{inc}}{w}$

$$j = \frac{3q_t}{wBF} \int_0^z \frac{y^2 \exp(-y^3)}{t_0/w + z - y} dy \quad [6]$$

Figure 13 shows that beyond the incubation period this equation accurately describes the reanodization current.

The parameters  $w$  and  $t_{inc}$  have to be fitted, the other quantities ( $q_t/BF$ , and  $t_0$ ) in Eq. [5] can be obtained from measurements of nonannealed films. We also fitted these, however, and used the values obtained in this way as a check of the correctness of the equation. In Fig. 14, values of  $t_0$  of annealed samples, obtained by means of relation [6], and of nonannealed samples, obtained with the help of the relations [1] or [2], are compared. From the reasonable agreement shown in Fig. 14 and also from the fits of calculated and observed peaks, an example of which is given in Fig. 13, we conclude that the growth of an annealed anodic oxide layer follows the laws (Eq. [1] and [2]) holding for the nonannealed films. A further result of this description is that formula [6] immediately leads to a value of  $q_{max}$  which is independent of  $V/V_f$ . In Fig. 16 we have once more plotted the charge  $q$ , consumed during reanodization, but now as a function of time at three different values of the applied field. It is obvious that the values of  $q_{max}$ , which are given here by the points of inflection of the curves, remain the same when the field is changed. To calculate the charges we have to integrate Eq. [6]

$$q(t'') = \int_0^{t''} j(t) dt = w \int_0^{z''} j(z) dz$$

$$= q_t/BF \int_0^{z''} dz \int_0^z \frac{3y^2 \exp(-y^3)}{t_0/w + z - y} dy$$

This shows that the charge is a function of only the quantity  $(t_0/w)$ . Indeed it can be shown that to a good approximation  $q_{max}$  is given by

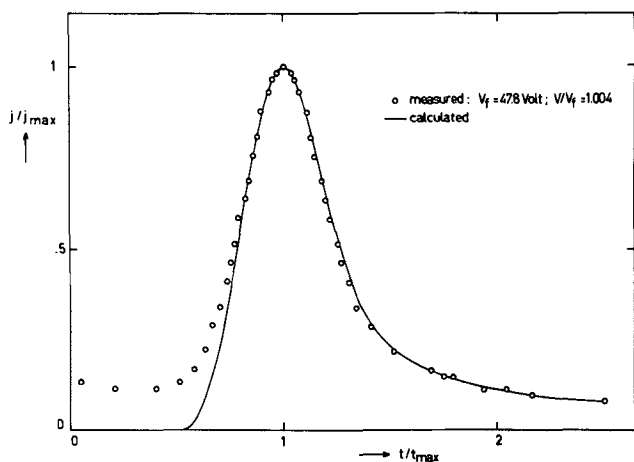


Fig. 13. Comparison between a measured and a calculated peak, plotted in reduced units.

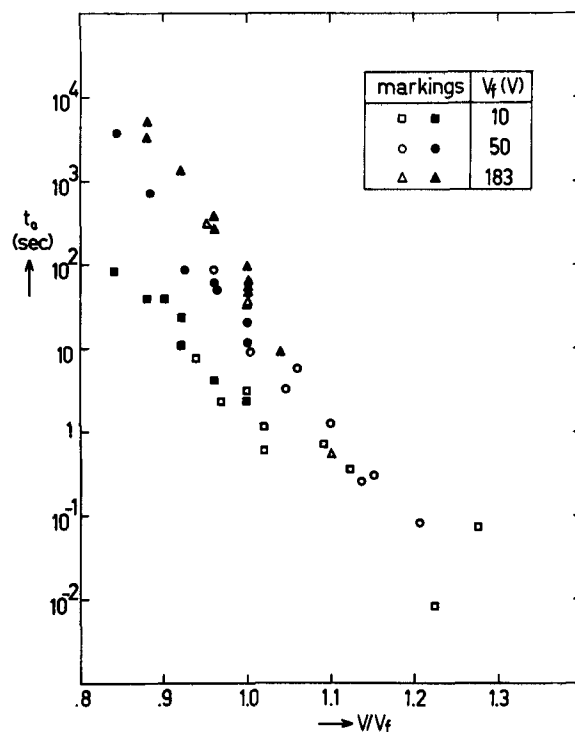


Fig. 14. The field dependence of  $t_0$ . The black markings represent values obtained in reanodization measurements of nonheated samples. The open markings were obtained by the fitting of formula [6] to the reanodization curves of heated samples.

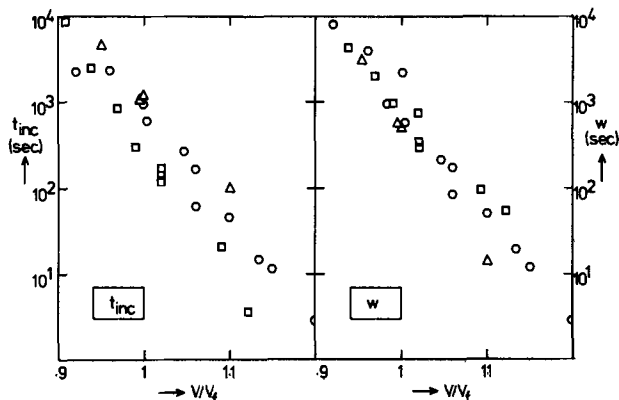


Fig. 15. The field dependence of  $t_{inc}$  and the width  $w$  of the peaks. The meaning of the markings corresponds to those of Fig. 14.

$$q_{max} = q_t/BF \ln(w/t_0) \{1 - \exp(-z_{max}^3)\} \quad [7]$$

in which the factor between brackets is the fraction of the surface covered with new oxide.

In Fig. 15,  $w$  and  $t_{inc}$  are plotted as a function of  $V/V_f$ . Comparison with Fig. 14 shows that the field dependence of  $w$  and  $t_0$  is essentially the same, so that the quantity  $\ln(w/t_0)$  is hardly dependent on the field. In other words: the shape of the  $q - \ln(t)$  curves in Fig. 16 which is determined by the relation between  $t_0$ ,  $w$ , and  $t_{inc}$ , is independent of the field; the curve is only shifted as a whole, but this keeps the height of  $q_{max}$  unaltered. It is also evident from Fig. 14 and 15 that  $t_0$  is very small as compared with  $w$ . Since, for anodizing at constant voltage,  $q \sim \ln(t/t_0)$ , the growth of the oxide that has become conducting occurs mainly within a few times  $t_0$ . Consequently the height of the step is the same almost everywhere and the schematic drawing of Fig. 11 represents the actual situation reasonably well. This explains why the optical density of the electron micrographs is so uniform

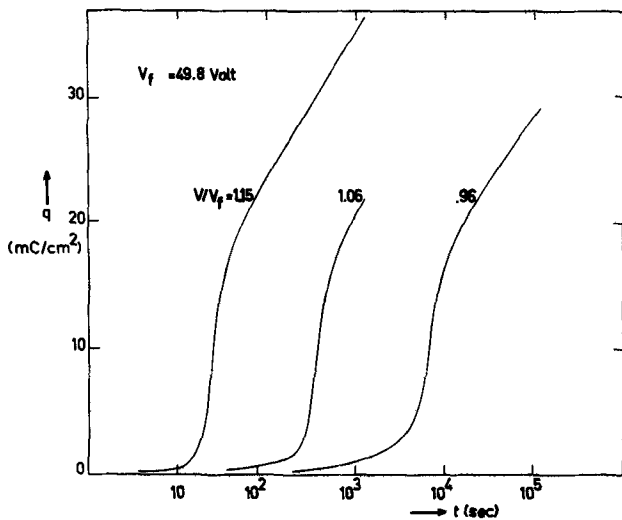


Fig. 16.  $q$  as function of time at different field strengths. The main effect of a different field is a translation of the curve along the abscissa.

over the dark spots. The thickness change after passage of the front of the nucleus can be calculated as well

as measured. The measurement was performed by dipping an anodized and annealed sample halfway into the solution and then reanodizing this part of the sample until the current maximum occurred. Afterward the reanodized part of the sample was compared with the rest of the sample. With an ellipsometer and on the assumption that, on reanodization, 50% of the oxide had been transformed, an increase in thickness  $\Delta L$  was found of 65Å for a 50V layer.

A thickness change due to the annealing itself could not be demonstrated either by ellipsometry or by measurement of the capacitance. According to formula [7] the increase in thickness,  $\Delta L$ , should be  $\Delta L = (L/2BF) \ln(w/t_0)$ . For a 600Å thick layer ( $V_f = 50\text{V}$ )  $\Delta L = 75\text{Å}$ , which is of the right order of magnitude.

Finally we used our experiments to determine the surface area of etched aluminum foil. Such foil is used in the production of electrolytic capacitors to obtain a large surface in a small volume. The etching was performed on a specimen similar to those used in the anodization experiments, by passing 50 coulombs/ $\text{cm}^2$  through the sample in a solution of 200g NaCl in 1 liter water at 90°C. The sample was rinsed in deionized water, ultrasonically cleaned, dipped into a chromic acid-phosphoric acid-water solution at 95°C, and rinsed in methanol.

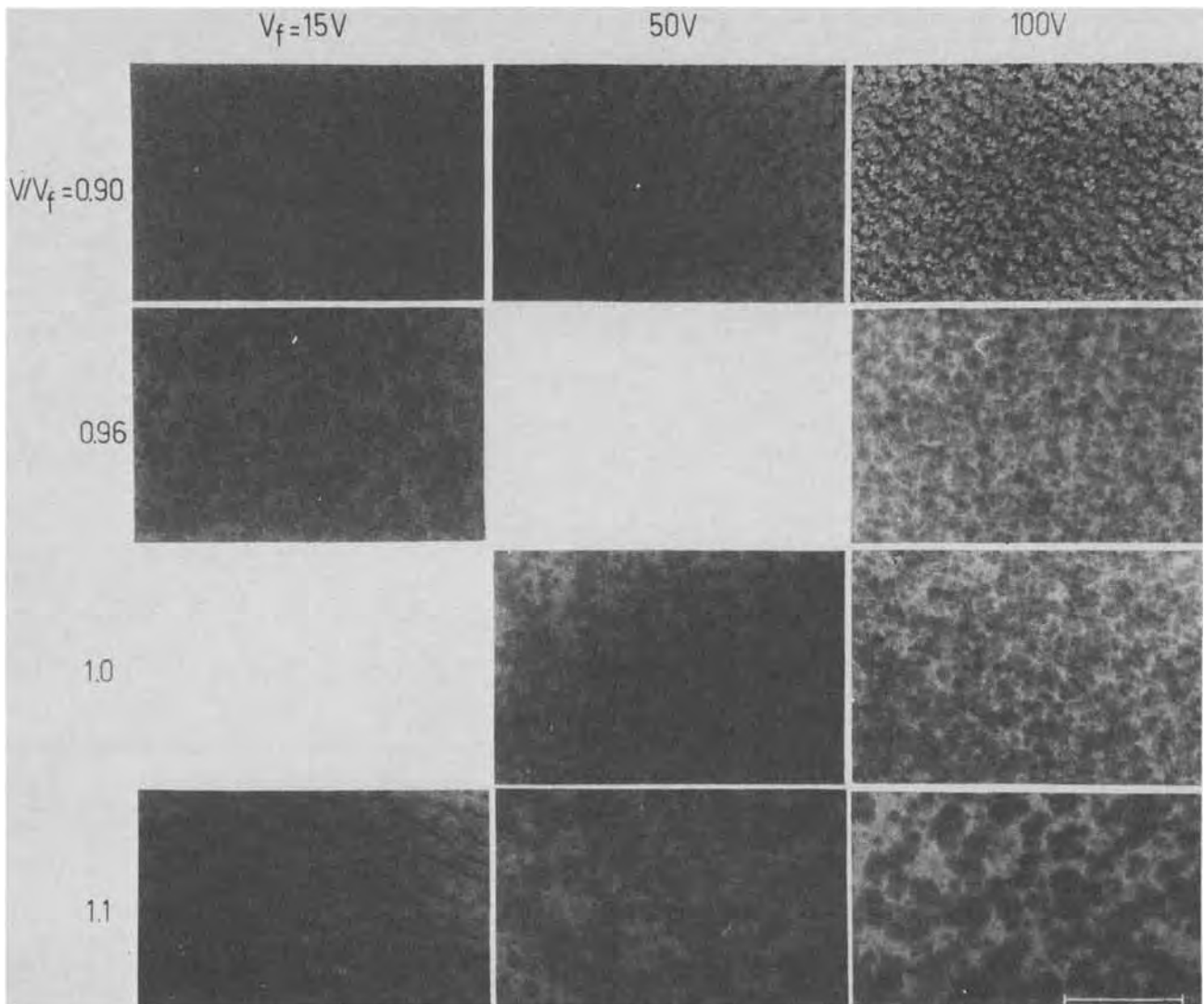


Fig. 17. Electron transmission photographs of layers reanodized with a constant voltage after heating. The current was interrupted at the maximum of the peak. The bar in the lower right corner represents  $1\mu$ . Layers reanodized with  $V/V_f = 0.9$  and the layer with  $V_f = 15\text{V}$  and reanodized with  $V/V_f = 1.1$  show a second growth mechanism which seems to be related to the surface area of the dissolved aluminum.

(a) The sample was anodized at up to 50V with a constant  $dV/dt$  of 0.043 V/sec.<sup>3</sup> As compared with a nonetched sample, the etched sample needed a 9.4 times greater current.

(b) From capacitance measurements of this anodized sample at frequencies for which  $\tan \delta$  is minimum on the etched and a nonetched sample it followed that the capacity had increased by a factor of 9.7.

(c) The etched sample was heated at 400°C during 15 min and reanodized at constant voltage to measure  $t_{max}$ . By means of Fig. 5,  $V_f$  could be obtained and, together with the charge used for anodization, the surface covered by anodic oxide was obtained, which increased by a factor of 9.2 again as compared with a nonetched sample.

(d) The use of Fig. 6 and  $q_{max}$  of the same sample revealed the etch factor to be 9.4 immediately.

**Thickness dependence of the growth mechanism.**—In this section we shall summarize gaps in our knowledge of the growth mechanism of annealed oxide layers, and illustrate these with a few more experiments.

The quantities  $w$  and  $t_{inc}$  are at present only numbers that follow from curve-fitting, but their behavior is still largely unknown. A detailed knowledge of the nucleation process and of the factors determining the growth velocity of a nucleus is still lacking. Therefore the remarkable field dependence of the width of the peak as given, in Fig. 7b, in reduced units as a function of specimen thickness, which is governed by the ratio of  $w/t_{inc}$ , remains unexplained and is the more puzzling since  $t_{max}$ , the time until the maximum of the peak appears, is hardly dependent on thickness.

In Fig. 17 a number of transmission electron micrographs of layers with different thickness have been collected. The layers were reanodized at different values of  $V/V_f$  and the reanodization was stopped in the maximum of the peak. Figure 17 clearly shows that the local growth, as described above, is not always evident. Especially with low fields, the growth may be characterized by the appearance of many nuclei not growing out in all directions. The nuclei form a pattern that may be related to the aluminum substrate removed. At any rate it will be evident that in these cases formula [5] cannot represent the whole curve.

Another interesting point is the relatively high "incubation" current of the layer having  $V_f = 50V$  in Fig. 7a. This measurement is only a weak reflection of another growth mechanism which we are studying at present and which, at room temperature, shows its maximum effect with layers obtained with  $V_f = 35V$ . Figure 18 shows plots of peaks measured at the same applied field. The vanishing of the peak, as well as a shift in  $t_{max}$ , can be observed. The sharp decay of the current after the small peak, which in our model represents the impinging of growing nuclei on each other, indicates nevertheless that there still exists something like a peak. Since also in this case we measured a current efficiency of unity we conclude that another, still unknown mechanism is operating. It may be that the growth of such layers is governed by a surface layer as is suggested by the following experiment. We also prepared layers having  $V_f = 35V$  in another way. We anodized the aluminum samples up to  $V_f = 50V$ , annealed them, and dissolved part of the layer in the above-mentioned HF solution. Then part of the sample was scanned at constant  $dV/dt$  and, with Fig. 2 we obtained a value for  $V_f$ . An example of such a peak is shown likewise in Fig. 18.

The greatest challenge, however, is to know what happens during annealing of the anodic oxide film. Diffraction of x-rays or electrons did not reveal the slightest change after annealing. From the experiments in which part of the layer is dissolved after annealing

<sup>3</sup> The influence on the peaks of the current density used to anodize the samples will be discussed in a later paper.

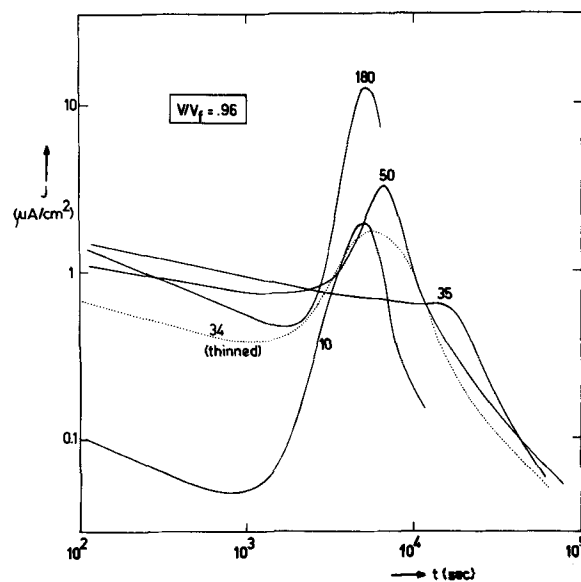


Fig. 18. Peaks obtained on layers having different thicknesses. The forming voltage  $V_f$  is indicated in the figure. A layer with  $V_f = 35V$  does not show a well resolved peak on being reanodized. The peak is present, however, when a layer with  $V_f = 50V$  is partly dissolved, as indicated by the dotted line.

it will be clear that the peaks are not due to some barrier near the interface electrolyte-anodic oxide. We will deal with these problems in a later paper.

#### Acknowledgment

We would like to thank Miss G. Stienstra and Mr. H. B. Haanstra for the electron microscopic investigation of our samples, Mr. L. P. van Kemenade and Mr. C. Wyenberg for the performance of the many experiments, and Mr. C. J. Loyen and Dr. F. Meyer for the ellipsometric measurements.

Manuscript received Feb. 11, 1974. This was Paper 18 presented at the Chicago, Illinois, Meeting of the Society, May 13-18, 1973.

Any discussion of this paper will appear in a Discussion Section to be published in the JUNE 1975 JOURNAL. All discussions for the JUNE 1975 Discussion Section should be submitted by Feb. 1, 1975.

The publication costs of this article have been assisted by Philips Research Laboratories.

#### REFERENCES

1. D. A. Vermilyea, *Acta Met.*, **5**, 113 (1957).
2. D. A. Vermilyea, *This Journal*, **104**, 485 (1957).
3. M. J. Dignam, *ibid.*, **109**, 184 (1962).
4. T. Kudo, M. Watase, and M. Kato, 24th Meeting of ISE, Eindhoven, 1973.
5. W. A. Johnson and R. F. Mehl, *Trans. Am. Inst. Min. Met. Engrs.*, **135**, 416 (1939).
6. M. Avrami, *J. Chem. Phys.*, **7**, 1103 (1939); **8**, 212 (1940).
7. A. Güntherschulze and H. Betz, *Z. Physik*, **92**, 367 (1934).
8. W. J. Bernard and J. W. Cook, *This Journal*, **106**, 643 (1959).
9. P. A. Jacquet, *Bull. Soc. Chim. France*, **3**, 705 (1936).
10. R. W. Santway and R. S. Alwitt, *This Journal*, **117**, 1282 (1970).
11. A. Charlesby, *Proc. Phys. Soc.*, **66**, 317 (1953).
12. R. Dreiner, *This Journal*, **111**, 1350 (1964).
13. C. Crevecoeur and H. J. de Wit, Abstract 18, p. 43, Electrochemical Society Extended Abstracts, Spring Meeting, Chicago, Illinois, May 13-18, 1973.

# Fine Structure in the Optical Spectra of Divalent Europium in the Alkaline Earth Sulfates

F. M. Ryan,\* W. Lehmann,\* D. W. Feldman, and J. Murphy

Westinghouse Research Laboratories, Pittsburgh, Pennsylvania 15235

## ABSTRACT

Fine structure has been observed in the fluorescence and excitation spectra of  $\text{Eu}^{+2}$  in  $\text{CaSO}_4$  and in the fluorescence spectrum of  $\text{Eu}^{+2}$  in  $\text{BaMg}(\text{SO}_4)_2$ . The fine structure in the fluorescence of  $\text{Eu}^{+2}$  in  $\text{CaSO}_4$  is identified as a zero phonon line with many sharp phonon replicas. The fine structure in its excitation spectrum is due to the closely spaced energy levels in the excited state produced by a strong exchange interaction splitting of the  $4f^65d$  states. The fine structure in the fluorescence of  $\text{Eu}^{+2}$  in  $\text{BaMg}(\text{SO}_4)_2$  is due to the normal splitting of the  $4f^7$  excited state and the dominance of  $4f^7 \rightarrow 4f^7$  transitions.

The alkaline earth sulfate compounds activated with  $\text{Eu}^{2+}$  generally exhibit broad, featureless fluorescence and excitation spectra. Their decay times are relatively short ( $\sim 0.1 \mu\text{sec}$ ) and the resulting fluorescence is located in the near ultraviolet. These are familiar characteristics that are common to a great many other  $\text{Eu}^{+2}$  activated phosphors. The fast decay has been attributed to the fluorescence being an "allowed"  $f^6d \rightarrow f^7$  transition. The broad featureless fluorescence envelopes are accounted for by a large Stokes' shift due to the different coupling to the lattice modes of the excited  $f^6d$  states relative to the  $f^7$  ground state.

In recent years, it has become apparent that in certain hosts  $\text{Eu}^{+2}$  can exhibit much more interesting optical spectra characterized by sharp fluorescence and/or absorption lines. The presence of such sharp line spectra has caused some detailed experimental measurements and theoretical analyses to be made on these systems. There are four types of such spectra which have been reported to date: (type 1) sharp structure in the  $f^6d \rightarrow f^7$  transitions in both absorption and fluorescence due to local vibrational modes, (type 2) sharp structure in the  $f^6d \rightarrow f^7$  fluorescence and absorption transitions due to selective coupling to certain lattice modes and/or to structure in the phonon density of states of the lattice modes, (type 3) sharp structure in absorption due to a splitting of the  $f^6$  levels by interaction with the single  $5d$  electron and the crystal field, and (type 4) sharp structure in fluorescence due to  $f^7 \rightarrow f^7$  transitions in the special case where the lowest lying excited state is an  $f^7$  state rather than an  $f^6d$ .

Type 1 spectra are exhibited by  $\text{Eu}^{+2}$  in the alkali halides (1) where the  $\text{Eu}^{+2}$  is substituting for a monovalent ion and an adjacent compensating vacancy forms. The high energy and low damping of the local vibrational modes about the vacancy give sharp structure to both the optical fluorescence and absorption spectra. Types 2 and 3 spectra have been reported for  $\text{Eu}^{+2}$  in calcium fluoride (2, 3) where a zero phonon line accompanied by sharp vibrational sidebands have been observed in fluorescence while some sharp lines can be seen in absorption. Type 4 spectra have been reported for  $\text{Eu}^{+2}$  only in the alkaline earth aluminum fluorides (4, 5) and in potassium and sodium magnesium fluoride (6).

We have examined  $\text{Eu}^{2+}$  in the alkaline earth sulfates. We have observed sharp line spectra in only two compounds,  $\text{CaSO}_4:\text{Eu}^{+2}$  and  $\text{BaMg}(\text{SO}_4)_2:\text{Eu}^{+2}$ . Our interpretation of the data is that  $\text{CaSO}_4:\text{Eu}^{+2}$  exhibits types 2 and 3 spectra for  $\text{Eu}^{+2}$  and  $\text{BaMg}(\text{SO}_4)_2:\text{Eu}^{+2}$  exhibits the type 4 spectrum. The purpose of this paper is to present the optical spectra of  $\text{Eu}^{+2}$  in these two compounds and to compare the spectra with theory. Possible explanations will be given for the unique-

ness of such spectra to  $\text{CaSO}_4$  and  $\text{BaMg}(\text{SO}_4)_2$  among all of the alkaline earth sulfates.

## Sample Preparation and Structure

The simple sulfates of Ca, Sr, and Ba used in our investigations were precipitated from purified nitrate solutions with  $\text{H}_2\text{SO}_4$ .  $\text{MgSO}_4$  was formed by reacting  $\text{MgO}$  with  $\text{H}_2\text{SO}_4$ . The phosphors were made by firing these sulfates with a mixture of europium oxide and  $(\text{NH}_4)_2\text{SO}_4$ . The firing was done in capped quartz tubes at  $900^\circ\text{C}$  in a nitrogen atmosphere. The resulting phosphor cakes were washed in water or methanol to remove unreacted  $(\text{NH}_4)_2\text{SO}_4$ , and then air dried. Compounds were also prepared containing two cations, such as  $\text{BaMg}(\text{SO}_4)_2$ . They were formed by firing the individual sulfates together at  $900^\circ\text{C}$ . In addition to  $\text{BaMg}(\text{SO}_4)_2$ , only two other compounds containing two divalent cations were found to exist,  $\text{Mg}_2\text{Ca}(\text{SO}_4)_3$  and  $\text{MgSr}(\text{SO}_4)_3$ . The structures of these compounds are unknown but their existence is established by powder x-ray analysis. No attempt was made to form sulfate compounds containing more than two divalent cations. The structures of the compounds that have been determined are summarized in Table I along with the cation site symmetry and the number of oxygen neighbors of the cation site (7, 8).

$\text{CaSO}_4$  has several crystalline modifications. When prepared according to the conditions we employed it has an orthorhombic crystal structure ("anhydrite") with the space group  $D_{17h}^{2h}$  (Cmcm). In this structure the calcium ions are surrounded by eight nearest neighbor oxygen atoms belonging to the various sulfate groups about it. The calcium sites are all crystallographically equivalent with point group symmetry  $C_{2v}$  ( $\text{mm}2$ ) which lacks inversion symmetry. The divalent europium ions would be expected to substitute for calcium ions without compensation of any kind and therefore to have  $C_{2v}$  ( $\text{mm}2$ ) site symmetry.

$\text{MgSO}_4$  has two crystalline modifications, the  $\alpha$  form exists above  $800^\circ\text{C}$  and the  $\beta$  form below  $800^\circ\text{C}$ . They differ only slightly and both forms have an orthorhombic crystal structure.

Table I. The determined crystal structures, cation site symmetries, and numbers of oxygen nearest neighbors of the alkaline earth sulfate compounds

Compound	Crystal structure	Cation site symmetry	Oxygen neighbors
$\alpha$ - $\text{MgSO}_4$	Orthorhombic	( $C_1 = T$ )	6
$\beta$ - $\text{CaSO}_4$	Anhydrite (orthorhombic)	( $C_{2v} = \text{mm}2$ )	8
$\text{BaSO}_4$	Barite (orthorhombic)	( $C_{1h} = m$ )	12
$\text{SrSO}_4$	Barite (orthorhombic)	( $C_{1h} = m$ )	12

\* Electrochemical Society Active Member.

Key words: luminescence, divalent, europium, sulfates, spectra.



The crystal structure of  $\text{BaMg}(\text{SO}_4)_2$  has not been determined but powder x-ray diffraction photographs show it to possess a structure that differs from both  $\text{BaSO}_4$  (orthorhombic "barite") and  $\text{MgSO}_4$  ( $\alpha$  or  $\beta$  orthorhombic). Ionic size considerations suggest that the europium ions would replace only barium ions in this structure. This is confirmed by x-ray diffraction data. Samples prepared by balancing the europium doping level with a corresponding reduction in the barium concentration, typically  $\text{Ba}_{0.95}\text{Eu}_{0.05}\text{Mg}(\text{SO}_4)_2$ , show an identical x-ray pattern to undoped  $\text{BaMg}(\text{SO}_4)_2$ . On the other hand, samples prepared by attempting to balance the europium doping with a corresponding reduction in the magnesium concentration show additional lines in their x-ray patterns due to a second phase of  $\text{BaSO}_4$ . The europium atoms must therefore be substituting for barium atoms in  $\text{BaMg}(\text{SO}_4)_2$ .

### Experimental

Low temperature optical measurements were performed with the samples immersed directly in either liquid nitrogen ( $77^\circ\text{K}$ ) or liquid helium below the  $\lambda$  point ( $1.8^\circ\text{K}$ ). The powder samples were formed into solid disks by saturating them with a potassium silicate cement. This prevented them from being eroded by the liquid refrigerants used.

Fluorescence spectra were taken with either a 0.25m Jarrel-Ash spectrometer (low resolution) or a 0.5m Jarrel-Ash spectrometer operating in 2nd order (high resolution). The detector used was an EMI 9558QA photomultiplier tube with an S-20 photosurface. All fluorescence data were corrected for the variation in response of the detector and the spectrometers at the various wavelengths studied.

For obtaining excitation spectra, the 0.25m spectrometer and the photomultiplier monitored the fluorescence of the samples at the desired wavelength while excitation energy was obtained from a 500W xenon short-arc lamp followed by a double 0.25m Jarrel-Ash spectrometer. The dependence of the output energy of this system on wavelength was determined and used in correcting the excitation spectra.

To measure the fluorescence decay times the samples were mounted on a cold finger inside of a vacuum chamber. Short rectangular pulses of 10 keV electrons were used for exciting their fluorescence. The current densities of excitation were kept well below  $10^{-6}$  A/cm<sup>2</sup> to avoid producing saturation effects such as non-exponential decays. The fluorescence was passed through a 0.25m spectrometer adjusted to the wavelength of interest and the radiation was detected with a 9558QA photomultiplier tube. A multichannel storage analyzer was used to measure the time constants of the weak and very fast signals by using a sampling oscilloscope as a "fast" to "slow" time transducer. The output of the oscilloscope was stored on a "slow" 100 channel analyzer (PAR Model TDH-9). Decay times as short as 10 nsec could be measured with this arrangement so that the decay times measured were always much longer than the limits of the system.

Raman measurements were performed to gather further data on lattice vibrations. The excitation source used in obtaining the Raman spectra was an argon ion laser with a power level of about one watt in the 5145Å line. The monochromator was a Spex 1400 double monochromator in tandem with a 0.25m Jarrel-Ash monochromator used as a band pass filter to further block scattered 5145Å light. The detector was an EMI 95025 photomultiplier with an S-11 photosurface and was used in the d-c current mode. The samples were powders which were pressed into a recess in a metal block with the laser beam focused onto the surface.

### Theoretical Discussion of the Excited States of $\text{Eu}^{+2}$

The energy level diagram and some of the features one might expect to see in the spectra of  $\text{Eu}^{+2}$  in various hosts are shown in Fig. 1.

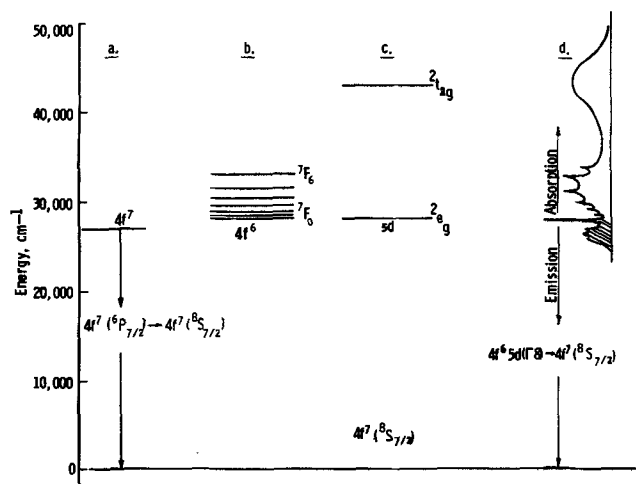


Fig. 1. The energy level diagram for  $\text{Eu}^{+2}$

In the ground state of the  $\text{Eu}^{+2}$  ion there are seven 4f electrons which arrange themselves into a  $4f^7$  ( $8S_{7/2}$ ) configuration. The lowest lying excited states may be formed from states within the  $4f^7$  configuration or from states within the  $4f^65d$  configuration. Excited states within the  $4f^7$  configuration are isoelectronic with  $\text{Gd}^{+3}$ . The lowest lying of them is  $6P_{7/2}$ , then  $6P_{5/2}$ , and so on. The decay time of transitions from these states would be in the millisecond range and transitions from the ground state to them would be very weak. Transitions between the ground state and excited states of the type  $4f^7 \rightarrow 4f^65d$  are allowed transitions and would completely dominate any  $4f^7 \rightarrow 4f^7$  type transitions except in fluorescence if the lowest lying excited states are  $4f^7$  states. Fluorescence transitions from these  $4f^7$  states would then be observed unless thermal depopulation to the fast-decaying nearby  $4f^65d$  states occurs. In almost all  $\text{Eu}^{+2}$  hosts the  $4f^65d$  states are lower in energy than the  $4f^7$  levels and  $4f^7 \rightarrow 4f^7$  transitions are not observed.

Some general features of the  $4f^65d$  states are shown in the center of Fig. 1. In this configuration there are six 4f electrons which, in the absence of any interaction with the 5d electron, would arrange themselves into seven levels,  $7F_0$  through  $7F_6$ , shown at Fig. 1b, analogous to the ground states of  $\text{Eu}^{+3}$ . There are a total of 49 states contained within these seven spin-orbit energy levels which will be further split by the crystal field. There is also a single 5d electron. Under the influence of a cubic crystal field, but ignoring any interaction with the  $4f^6$  electrons, the states of the 5d electron would be split into two bands, a  $2t_{2g}$  and an  $2e_g$  shown at Fig. 1c. The  $2e_g$  level is expected to be much lower and is 4-fold degenerate. When combined with the 49 states of the  $4f^6$  configuration this  $2e_g$  state yields a total of 196 nearly degenerate states. If the interaction between the  $4f^6$  electrons and the 5d electron is sufficiently strong, the states are strongly mixed and much of this degeneracy can be lifted. The  $4f^65d$  system therefore can potentially exhibit a large number of distinct optical transitions in its absorption or excitation spectra. In many cases, however, the interaction is weak and the composite  $4f^65d$  system retains much of the character of the uncoupled  $4f^6$  and 5d levels. On the right side of Fig. 1, the unshaded part of 1d, is shown this type of absorption spectrum. It has been observed for  $\text{Eu}^{+2}$  in  $\text{CaF}_2$ ,  $\text{EuO}$ ,  $\text{EuSe}$ , and  $\text{EuF}_2$  (9). Two broad bands are seen in absorption corresponding to transitions to the  $2e_g$  and  $2t_{2g}$  bands of the 5d electron. Superimposed on the lower  $2e_g$  bands are seven narrow bands, referred to as a "staircase spectrum," which retain the character of the seven  $4f^6$  levels. No structure is seen in the  $2t_{2g}$  band probably because the spin orbit splitting which occurs only in  $2t_{2g}$  washes out any structure.



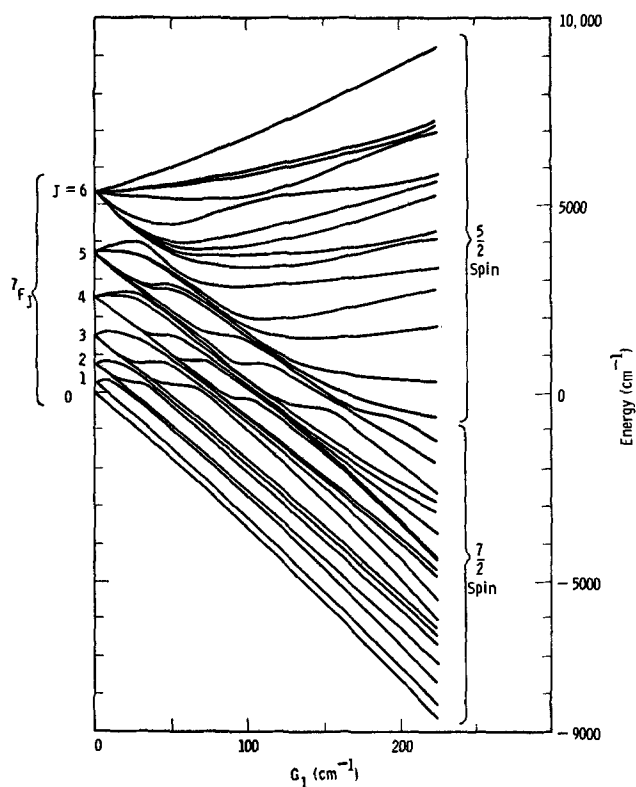


Fig. 2. The quartet energy levels of the  $4f^6 5d$  system as a function of the exchange parameter,  $G_1$ .

In the case of strong interaction between the  $4f^6$  electrons and the  $5d$ , one would expect that very little of the characteristic  $4f^6$  structure would remain and that the absorption spectrum would reflect only the nature of the composite  $4f^6 5d$  system. Weakliem (10) has recently made the first calculation of the energy levels of the  $4f^6 5d$  system taking into account the exchange interaction between the  $4f^6$  electrons and the  $5d$ . The results of his calculation are shown in Fig. 2 which shows the set of  $4f^6 ({}^7F_J) 5d ({}^2e_g)$  energy levels of the system as a function of the exchange parameter,  $G_1$ .<sup>1</sup> In the limit of weak exchange the levels resemble the  $4f^6$  levels. As the exchange interaction is increased all resemblance to the  $4f^6$  levels ceases and the levels separate into two groups, a group of levels with spin =  $5/2$  and a group with spin =  $7/2$ . The six  $4f$  electrons have a total spin of 3 and the  $d$  electron a spin of  $1/2$ . The  $5/2$  spin levels arise from the case where the  $5d$  electron spin is antiparallel to the spin of the  $4f^6$  electrons, leading to a small exchange energy, and the  $7/2$  spin levels when the spins are parallel, leading to a large exchange energy. Therefore, in the region of large exchange parameter  $G_1$ , the  $7/2$  levels have a large slope while the  $5/2$  levels tend to become independent of  $G_1$ . A conclusion which can be drawn from Fig. 2 is that at large values of  $G_1$ , the  $7/2$  spin levels are well defined and distinct from the  $5/2$  spin levels. Thus spin selection rules should be obeyed. Only the quartet levels are shown on Fig. 2. Interspersed with these are also the doublet levels of the system which behave similarly. They have been omitted from Fig. 2 to keep it from being too cluttered.

We will now calculate the number of discrete levels that one might expect to observe in the absorption spectrum of  $\text{Eu}^{2+}$  in a host with site symmetry  $C_{2v}$  (typical of  $\text{CaSO}_4$ ) in the region of strong exchange interaction ( $G_1 \sim 200 \text{ cm}^{-1}$ ). Consider the two electronic systems composed of the six  $4f$  electrons forming the  ${}^7F_J$  levels and the single  $d$  electron forming the  ${}^2e_g$  level coupled together by an exchange interaction. The crystal field splitting of the  $5d$  energy levels can be

represented by the dominant term, the cubic field component ( $O_h$ ). The single  $d$  electron state,  ${}^2e_g$ , transforms as  $D_{3/2}$  of the  $O_h$  double group. The product of the  $D_{3/2}$  representation with the representations of the cubic field-split sublevels of the  ${}^7F_J$  states are shown in Table II. There are 33  $D_{3/2}$  quartet levels of the total system, and 16  $D_{1/2}$  and 16  $S$  doublet levels. Reducing the symmetry to  $C_{2v}$  will split the 33  $D_{3/2}$  quartets into 66 doublets so that the number of levels in  $C_{2v}$  symmetry will be  $66 + 32 = 98$ . Since we are concerned only with the spin  $7/2$  states, the degeneracy ratio of the  $7/2$  to the  $5/2$  states yields  $4/7 \times 98 = 56$  levels that might be observable in optical absorption or fluorescence excitation in  $C_{2v}$  symmetry and strong exchange. This number will be referred to later in the paper.

A final feature shown on the right in Fig. 1 (the shaded area of Fig. 1d) is the type of fluorescence that might be observable in a transition from the lowest lying  $4f^6 5d$  level to the ground state. Ordinarily this will be a narrow band. If in a particular host the Stokes' shift is small enough (particularly at low temperatures), a zero phonon line and some sharp phonon sidebands might also be observable. This fluorescence should exhibit a decay time in the order of tenths of a microsecond.

#### Discussion of the Observed Fluorescence Spectrum of $\text{Eu}^{2+}$ in $\text{CaSO}_4$

The  $1.8^\circ\text{K}$  fluorescence spectrum of  $\text{Eu}^{2+}$  in  $\text{CaSO}_4$  is shown in Fig. 3 and 4. Fine structure can also be seen at higher temperatures but some thermal broadening occurs and the structure is seen best at low temperatures. The line marked  $E_0$  in fluorescence is located at exactly the same energy in absorption as in fluorescence. We therefore conclude that  $E_0$  is a zero phonon line (a purely electronic transition involving no phonons). In absorption (here actually fluorescence excitation)  $E_0$  is labeled  $A_0$ .  $E_0$  has a fluorescence decay time of  $0.40 \pm 0.04 \mu\text{sec}$ .

We assign the lines  $E_1$  through  $E_{16}$  as phonon replicas of  $E_0$ . In order to make this assignment it is first necessary to show that it is very unlikely that any of these lines are due to purely electronic transitions. These lines are separated from one another and from  $E_0$  by some hundreds of  $\text{cm}^{-1}$ . In order for them to be due to purely electronic transitions these separations must be accounted for by having transitions from different excited states to the same ground state, as any splitting of the  ${}^8S_{7/2}$  ground state should be much smaller than  $100 \text{ cm}^{-1}$ . If they are due to transitions from different excited states separated by some hundreds of  $\text{cm}^{-1}$ , one would only observe such a multitude of transitions at low temperature if the transition rate to the ground state from each excited state was much faster than the nonradiative single phonon emission relaxation rates

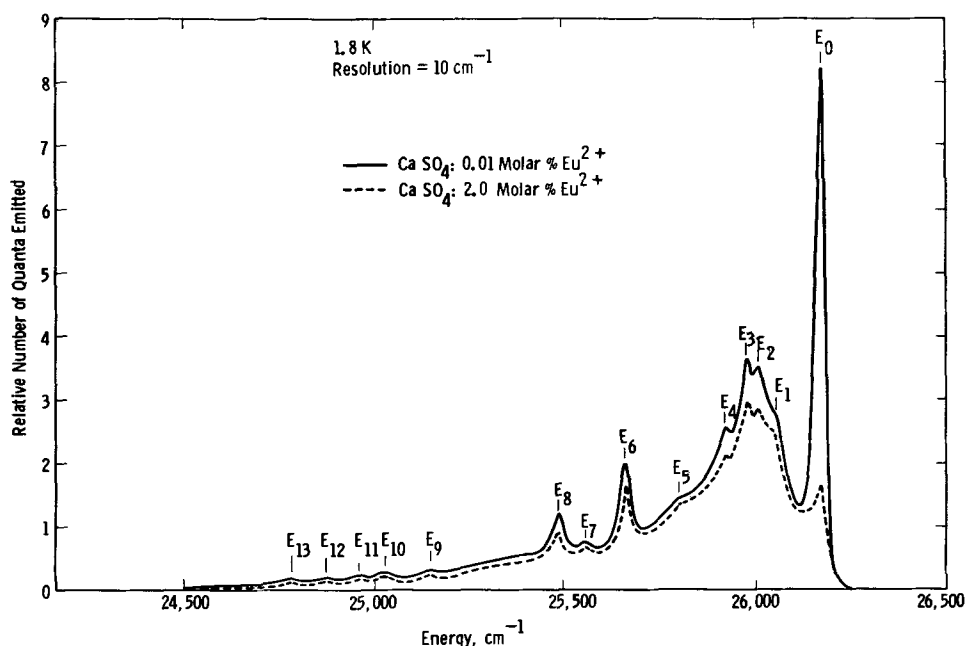
Table II. The product of the  $D_{3/2}$  representation with the representations of the cubic field split sublevels of the  ${}^7F_J$  state [from Ref. (12)]

State	Products	Terms	Number of levels
${}^7F_0$	$A_1 \times D_{3/2}$	$D_{3/2}$	1
${}^7F_1$	$T_1 \times D_{3/2}$	$2D_{3/2} + D_{1/2} + 2S$	4
${}^7F_2$	$T_1 \times D_{3/2}$	$3D_{3/2} + 2D_{1/2} + 2S$	7
${}^7F_3$	$E \times D_{3/2}$ $A_2 \times D_{3/2}$ $T_1 \times D_{3/2}$ $T_2 \times D_{3/2}$	$5D_{3/2} + 2D_{1/2} + 2S$	9
${}^7F_4$	$A_1 \times D_{3/2}$ $E \times D_{3/2}$ $T_1 \times D_{3/2}$ $T_2 \times D_{3/2}$	$6D_{3/2} + 3D_{1/2} + 3S$	12
${}^7F_5$	$E \times D_{3/2}$ $2T_1 \times D_{3/2}$ $T_2 \times D_{3/2}$	$7D_{3/2} + 4D_{1/2} + 4S$	15
${}^7F_6$	$A_1 \times D_{3/2}$ $A_2 \times D_{3/2}$ $E \times D_{3/2}$ $T_1 \times D_{3/2}$ $2T_2 \times D_{3/2}$	$9D_{3/2} + 4D_{1/2} + 4S$	17

Total 65

<sup>1</sup>The authors would like to thank Dr. Weakliem for granting permission to reproduce this figure from Ref. (10).

Fig. 3. The 1.8°K fluorescence envelopes of  $\text{Eu}^{2+}$  in  $\text{CaSO}_4$  at high and low  $\text{Eu}^{2+}$  concentrations.



between the excited states. The experimentally measured fluorescence decay rates of  $E_1$  through  $E_{16}$  are all identical and equal to that of  $E_0$  ( $0.40 \pm 0.04 \mu\text{sec}$ ). The nonradiative interexcited state relaxation rate could hardly be slower than this and should be  $\sim 10^{-10}$  sec or faster (11). We therefore rule out the possibility of any of the lines  $E_1$  through  $E_{16}$  being other than phonon replicas of  $E_0$ .

The assignment of  $E_1$  through  $E_{16}$  as phonon replicas of  $E_0$  is consistent with some experimental observations of their properties. One expects the fluorescence of phonon replicas to decay at the same rate as the zero phonon line. As previously mentioned, the experimentally determined fluorescence decay times of all of the lines from  $E_0$  to  $E_{16}$  are identical at  $0.40 \pm 0.04 \mu\text{sec}$ . Another observation is that  $E_0$  is the only fluorescence line that shows self-absorption. If the concentration of luminescence centers is increased one expects only the zero phonon line to show self-absorption, the absorbed energy being redistributed among the phonon lines. One sees in Fig. 3 that as the europium concentration is increased from 0.01-2 molar per cent (m/o),  $E_0$  drops considerably in intensity relative to the other lines. The spectrum of the 2 m/o sample in Fig. 3 has been scaled down to better display this change.

The conclusion we reach from these observations and arguments is that our assignment of  $E_1$  through  $E_{16}$  as phonon replicas of  $E_0$ , while not absolutely certain, is undoubtedly correct. Figure 4 shows all of the lines

observed in detail. The separations of the lines from  $E_0$  are listed in Table III.

Hobdon (3) has observed similar sharp phonon structure for  $\text{Eu}^{2+}$  in  $\text{CaF}_2$ . The europium site in  $\text{CaF}_2$  has inversion symmetry, so that only even phonons will be observed in a fully allowed electric dipole transition. Hobdon explained the sharpness of the phonon sidebands as being due to a combination of this selective coupling and peaks in the phonon density of states distribution in  $\text{CaF}_2$ . The ( $C_{2v}$ ) europium site in  $\text{CaSO}_4$  lacks inversion symmetry so that all phonons may be involved. The sharpness of the phonon sidebands therefore may reflect structure in the phonon density of states curve in  $\text{CaSO}_4$ . An alternate explanation is that at least some of the lines could be due to resonant modes introduced by the addition of europium to the  $\text{CaSO}_4$ . In hopes of testing these models we took Raman spectra of both pure  $\text{CaSO}_4$  samples and samples containing various amounts of europium, up to a 10% molar replacement of calcium. The phonon energies observed are listed in Table III. The second column of Table III shows the separations in energy of the phonon peaks from the zero phonon line, obtained from the fluorescence data. The energies of these peaks range from about  $100 \text{ cm}^{-1}$  to more than  $1000 \text{ cm}^{-1}$ . If one assumes that these are due to normal lattice vibrational modes the lower energy peaks would be due to vibra-

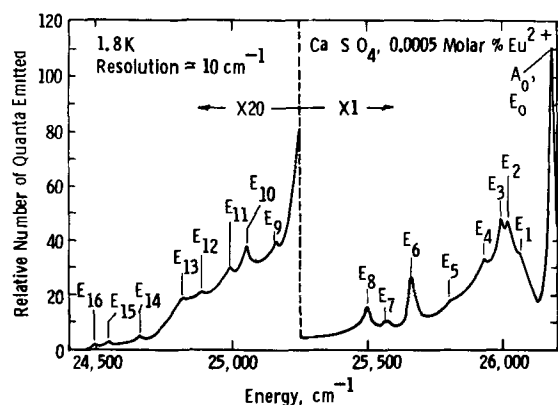


Fig. 4. The 1.8°K fluorescence envelope of  $\text{Eu}^{2+}$  in  $\text{CaSO}_4$  showing all of the sharp phonon structure.

Table III. The energies of the 1.8°K phonon lines in the fluorescence of  $\text{Eu}^{2+}$  in  $\text{CaSO}_4$ , the Raman lines in pure  $\text{CaSO}_4$ , and the new Raman lines due to  $\text{Eu}^{2+}$  doping in  $\text{CaSO}_4$

No. of line	Phonon lines in fluorescence, $\text{cm}^{-1}$	Raman lines in pure $\text{CaSO}_4$ , $\text{cm}^{-1}$	New Raman lines due to $\text{Eu}^{2+}$ doping, $\text{cm}^{-1}$
$E_1$	116	128	132
$E_2$	163-S	135	156
$E_3$	181-S	154	189
$E_4$	251-S	172	203
$E_5$	372	235	221
$E_6$	513-VS	420-S	334-S
$E_7$	617	445-S	448-S
$E_8$	682-S	502-VS	469
$E_9$	1018	612-S	606
$E_{10}$	1128	632-S	651
$E_{11}$	1185	680-VS	
$E_{12}$	1297	1005-S	
$E_{13}$	1358	1114-S	
$E_{14}$	1518	1128-S	
$E_{15}$	1633	1163-S	
$E_{16}$	1685		

S—Strong; VS—Very Strong.

tions between the cations and the  $\text{SO}_4$  groups. The high energy peaks would be due to internal modes of the  $\text{SO}_4$  groups. The peaks probably represent peaks in the density of states of the various lattice modes as the selection rules allow all phonons to be coupled to. The third column of Table III shows the phonon energies obtained by Raman spectroscopy for pure  $\text{CaSO}_4$ . The phonons observed by Raman spectroscopy are located

at  $k = 0$  rather than at the point of maximum density. Consequently, good agreement between the energies listed in the center column and the fluorescence phonon energies should not occur. Typically, the energy at the zone boundary is 10-20% greater than the energy at  $k = 0$  for optical modes, and therefore the disagreement may be expected to be of this order. The Raman data does show, however, that normal lattice vibrations do occur over the energy range in which the fluorescence phonon sidebands are observed. The assignment of these peaks to structure in the density of states of the normal lattice modes of  $\text{CaSO}_4$  is therefore a reasonable one.

One cannot rule out the possibility that at least some of the phonon peaks are due to resonant vibrational modes caused by the disruption of the lattice by the addition of europium ions. To investigate this possibility we took Raman spectra on  $\text{CaSO}_4$  samples containing various  $\text{Eu}^{+2}$  concentrations ranging up to 10%. In addition to the Raman lines seen in pure  $\text{CaSO}_4$ , new lines appeared in the samples doped with  $\text{Eu}^{+2}$ . The strengths of these new lines are linearly proportional to the  $\text{Eu}^{+2}$  concentration. Since x-ray photographs verify that the  $\text{Eu}^{+2}$  forms a perfect mechanical mixture with the  $\text{Ca}^{+2}$  ions in  $\text{CaSO}_4$  (up to at least 10%  $\text{Eu}^{+2}$ ) with no formation of second phases, it must be concluded that the new lines are indeed resonant modes due to substitutional  $\text{Eu}^{+2}$ . The energies of these lines are listed in the right-hand column of Table III. None of the phonon peaks seen in fluorescence have energies identical with the resonance lines seen by Raman spectroscopy, which one might expect if they were both due to resonant modes. We therefore conclude that lines  $E_1$  through  $E_{16}$  are due to density of states peaks in the normal lattice modes of  $\text{CaSO}_4$  and are not due to resonant modes. Why we have failed to observe the resonant modes in the fluorescence sidebands is not clear. We can speculate that perhaps they are broader in the fluorescence spectrum than they are in the Raman spectrum, and that the resonant sideband peaks are hidden under the broad sideband fluorescence envelope. It is also possible that the relative strength of the resonant modes is greater in a Raman process than in fluorescence, as the coupling mechanisms are different in the two cases.

**Excitation.**—The excitation spectrum of  $\text{Eu}^{+2}$  in  $\text{CaSO}_4$  is shown in Fig. 5. This spectrum was taken on a sample containing only 0.0005 m/o  $\text{Eu}^{+2}$  and at 1.8°K

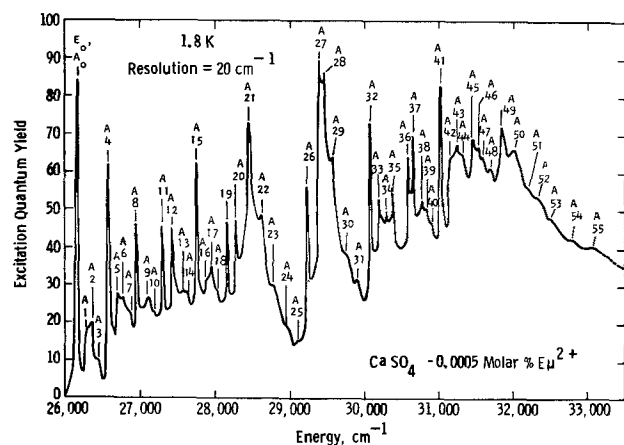


Fig. 5. The 1.8°K excitation spectrum of  $\text{Eu}^{+2}$  in  $\text{CaSO}_4$

in order to display all of the fine structure present. The zero phonon line which was labeled as  $E_0$  in fluorescence, is here also labeled  $A_0$ . A total of 56 lines have been counted in this spectrum spread over an 8000  $\text{cm}^{-1}$  width. The excitation spectrum beyond 33,000  $\text{cm}^{-1}$  is not shown on Fig. 5 but it consists of a broad envelope peaking at 41,200  $\text{cm}^{-1}$  which has no fine structure contained in it. Several sharp lines in the absorption spectrum of  $\text{Eu}^{+2}$  in  $\text{CaF}_2$  have been seen by Kaplyanskii and Feofilov (2) but nowhere in the literature has such a profusion of lines been reported. One possible reason for the failure of others to see such a spectrum is that they measured absorption spectra and not fluorescence excitation spectra. In order to observe impurity ion absorption in solids by direct absorption it is necessary to keep the doping level fairly high. High ion concentrations however broaden the sharp line spectra reported here so that they cannot be directly observed. The experimental sensitivity in measuring excitation spectra is much higher so the spectra of impurity ions at low doping levels can be measured easily.

We attribute the multitude of sharp lines observed in the excitation spectrum of  $\text{Eu}^{+2}$  in  $\text{CaSO}_4$  to purely electronic transitions to the various levels of the  $4f^6(7F_1)5d(e_g)$  system, split by a strong exchange interaction between the 4f electrons and the 5d. The theory presented in a previous section predicts 56 levels and we have counted 56 lines. Such an extremely good agreement is, perhaps, fortuitous. Some of the lines seen in the excitation spectrum may, in fact, be phonon replicas and conversely, some of the exchange split lines may be unresolvable due to proximity to nearby lines. We do however believe that the spectrum is principally due to exchange interaction, and the existence of the large number of levels observed is our main evidence for this identification. No assignment of these lines to particular energy levels is given but their energies and relative excitation strengths are listed in Table IV.

#### Discussion of the Optical Spectra of $\text{Eu}^{+2}$ in $\text{BaMg}(\text{SO}_4)_2$

**Fluorescence.**—Fluorescence spectra of  $\text{Eu}^{+2}$  in  $\text{BaMg}(\text{SO}_4)_2$  at 300° and 77°K are shown on Fig. 6 and the 1.8°K spectrum of some of the higher energy lines in Fig. 7. Their energies are listed in Table V. At 300°K the spectrum consists of a broad band with some sharp lines superimposed. Upon cooling to 77°K the band emission has disappeared and only the sharp lines remain at this and lower temperatures. The sharp lines labeled D and E have disappeared at 77°K and line C is reduced considerably in strength relative to line  $B_0$ . The decay time of the broad band as well as the sharp lines at 300°K is equal to 0.05  $\mu\text{sec}$ . The decay times of all of the sharp lines at 77°K and below are equal and have a value of 3.5 msec. This is in contrast to the value of 0.40  $\mu\text{sec}$  found in  $\text{CaSO}_4$ .

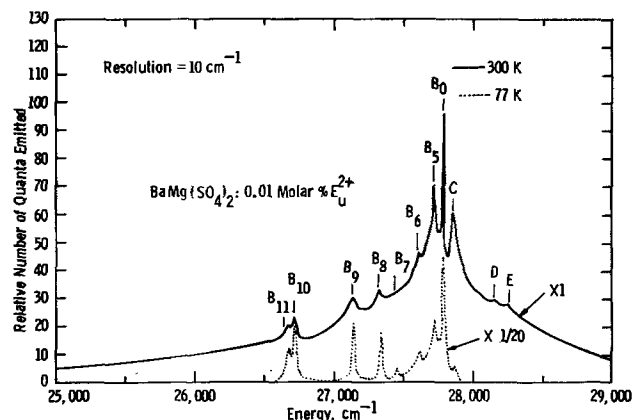


Fig. 6. The 300° and 77°K fluorescence envelopes of  $\text{Eu}^{+2}$  in  $\text{BaMg}(\text{SO}_4)_2$ .

Table IV. The energies of the 1.8°K excitation lines of  $\text{Eu}^{+2}$  in  $\text{CaSO}_4$ 

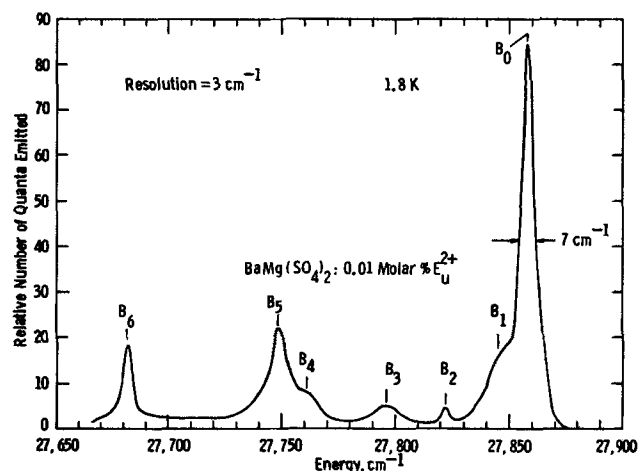
Line No.	Energy, $\text{cm}^{-1}$	Relative height
A <sub>0</sub>	26,178	63
A <sub>1</sub>	26,301	2
A <sub>2</sub>	26,353	16
A <sub>3</sub>	26,434	2
A <sub>4</sub>	26,582	49
A <sub>5</sub>	26,696	5
A <sub>6</sub>	26,770	3
A <sub>7</sub>	26,852	2
A <sub>8</sub>	26,961	28
A <sub>9</sub>	27,114	11
A <sub>10</sub>	27,210	1
A <sub>11</sub>	27,314	32
A <sub>12</sub>	27,434	25
A <sub>13</sub>	27,570	2
A <sub>14</sub>	27,616	3
A <sub>15</sub>	27,770	41
A <sub>16</sub>	27,878	4
A <sub>17</sub>	27,960	13
A <sub>18</sub>	28,034	1
A <sub>19</sub>	28,169	29
A <sub>20</sub>	28,284	20
A <sub>21</sub>	28,449	33
A <sub>22</sub>	28,612	6
A <sub>23</sub>	28,778	3
A <sub>24</sub>	28,947	5
A <sub>25</sub>	29,118	2
A <sub>26</sub>	29,239	48
A <sub>27</sub>	29,398	55
A <sub>28</sub>	29,455	20
A <sub>29</sub>	29,563	12
A <sub>30</sub>	29,748	4
A <sub>31</sub>	29,881	6
A <sub>32</sub>	30,079	47
A <sub>33</sub>	30,202	24
A <sub>34</sub>	30,280	8
A <sub>35</sub>	30,385	24
A <sub>36</sub>	30,585	21
A <sub>37</sub>	30,656	38
A <sub>38</sub>	30,778	6
A <sub>39</sub>	30,835	3
A <sub>40</sub>	30,911	1.5
A <sub>41</sub>	31,028	58
A <sub>42</sub>	31,162	2
A <sub>43</sub>	31,230	24
A <sub>44</sub>	31,289	6
A <sub>45</sub>	31,468	12
A <sub>46</sub>	31,535	4
A <sub>47</sub>	31,590	4
A <sub>48</sub>	31,685	4
A <sub>49</sub>	31,847	22
A <sub>50</sub>	32,000	5
A <sub>51</sub>	32,206	1
A <sub>52</sub>	32,362	1
A <sub>53</sub>	32,488	3
A <sub>54</sub>	32,786	1
A <sub>55</sub>	33,079	6

Table V. The energies and assignments of the 1.8°K fluorescence lines of  $\text{Eu}^{+2}$  in  $\text{BaMg}(\text{SO}_4)_2$ 

Line	Energy, $\text{cm}^{-1}$	Transition
E	28,274	${}^6\text{P}_{5/2} \rightarrow {}^8\text{S}_{7/2}$
D	28,194	${}^6\text{P}_{5/2} \rightarrow {}^8\text{S}_{7/2}$
C	27,914	${}^6\text{P}_{7/2} \rightarrow {}^8\text{S}_{7/2}$
B <sub>0</sub>	27,858	${}^6\text{P}_{7/2} \rightarrow {}^8\text{S}_{7/2}$
B <sub>1</sub>	27,845	+
B <sub>2</sub>	27,822	+
B <sub>3</sub>	27,796	+
B <sub>4</sub>	27,761	+
B <sub>5</sub>	27,745	+
B <sub>6</sub>	27,682	+
B <sub>7</sub>	27,490	+
B <sub>8</sub>	27,369	+
B <sub>9</sub>	27,198	+
B <sub>10</sub>	26,689	+
B <sub>11</sub>	26,618	+

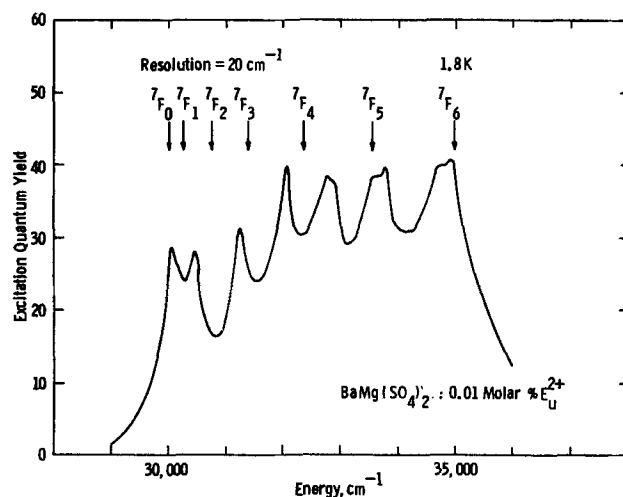
+ Phonon replicas of B<sub>0</sub>.

Similar slowly decaying sharp line spectra have been reported by Hoffman *et al.* (4, 5) for  $\text{Eu}^{+2}$  in the alkaline earth aluminum fluorides. They concluded that the sharp lines are due to transitions within the 4f configuration which occurs when the lowest lying excited state is a  $f^7$  state rather than a  $f^6d$ . Our assignment of the sharp lines in the spectrum is the following: Line B<sub>0</sub> is a zero phonon line due to the transition  ${}^6\text{P}_{7/2} \rightarrow {}^8\text{S}_{7/2}$  and the lines at lower energy than line B<sub>0</sub> are phonon replicas of line B<sub>0</sub>. Line C is at 56  $\text{cm}^{-1}$  higher energy than B<sub>0</sub> and is due to a transition from another state which is thermally populated following a Boltzmann distribution. It is probably a level of the  ${}^6\text{P}_{7/2}$  excited state that is split by the noncubic crystal field

Fig. 7. The 1.8°K fluorescence of  $\text{Eu}^{+2}$  in  $\text{BaMg}(\text{SO}_4)_2$ . Phonon replicas of B<sub>0</sub> with energies less than 27,650  $\text{cm}^{-1}$  are not shown.

at the  $\text{Eu}^{+2}$  site. Lines D and E, which lie about 300  $\text{cm}^{-1}$  above line B<sub>0</sub> and also show marked temperature dependence are probably associated with  ${}^6\text{P}_{5/2} \rightarrow {}^8\text{S}_{7/2}$  transitions. At 300°K the  $f^6d$  state is strongly populated and the fast decay characteristics of an  $f^6d \rightarrow f^7$  transition is observed. Since the  ${}^6\text{P}_{7/2}$  levels are in thermal equilibrium with the  $f^6d$  levels they also exhibit the fast decay time at this temperature. Our assignments of the transitions responsible for the observed lines are also listed in Table V.

**Excitation.**—The excitation spectrum of  $\text{Eu}^{+2}$  in  $\text{BaMg}(\text{SO}_4)_2$  is shown in Fig. 8. Seven well-defined narrow bands can be seen, located between 30,000 and 35,000  $\text{cm}^{-1}$ . Another excitation band exists at higher energy but it has no structure to it and is not included on Fig. 8. The structure in the lower band is due to transitions to the seven  ${}^7\text{F}_J$  levels of the  $\text{Eu}^{+3}$  core superimposed on top of the  ${}^2e_g$  state of the additional 5d electron (9). Also shown in Fig. 8 is a best fit of the seven bands to the free ion spacing of the 4f<sup>6</sup> levels assuming a spread of 5040  $\text{cm}^{-1}$ . This fit is reasonable even though the spacings between the levels do not coincide perfectly with the free ion spacings. The effect of the crystal field on the free ion levels will be different in the various states contained within each  ${}^7\text{F}_J$  level. Certain states will be shifted in energy more than others and the transition probabilities may be altered. Exchange coupling, which has so far been ignored, will also have some effect. As a result, some distortion of the envelope shapes or positions is to be expected. Because the distortion is small the excited state 4f<sup>6</sup>5d configuration of  $\text{Eu}^{+2}$  in  $\text{BaMg}(\text{SO}_4)_2$  rep-

Fig. 8. The 1.8°K excitation spectrum of  $\text{Eu}^{+2}$  in  $\text{BaMg}(\text{SO}_4)_2$

resents an example of weak exchange interaction of the  $4f^6$  and  $5d$  electrons.

### The Optical Properties of $\text{Eu}^{+2}$ in the Other Alkaline Earth Sulfates

The optical spectra of  $\text{Eu}^{+2}$  in the remaining alkaline earth sulfates will not be presented in this paper. The fluorescences of these compounds are all fast in decay and are located at various wavelengths in the near-ultraviolet. In all of these compounds the crystal field has depressed the  $2e_g$  band well below the lowest lying  $4f^7$  configuration so that no  $4f^7 \rightarrow 4f^7$  transitions may be observed. They all have much broader fluorescence envelopes than in  $\text{CaSO}_4$  due probably to larger Stokes' shifts. As a result, none of them exhibit a zero phonon line and therefore none of the interesting phonon structure seen in  $\text{CaSO}_4$ . While some structure can be seen in the excitation spectra of these compounds it is not nearly as detailed as that of  $\text{CaSO}_4$  so that its presentation would be of little value.

### Conclusion and Discussion

We have observed types 2 and 3 optical spectra for  $\text{Eu}^{+2}$  in  $\text{CaSO}_4$  and type 4 in  $\text{BaMg}(\text{SO}_4)_2$ . At low temperatures a strong zero phonon line is observed in fluorescence for  $\text{Eu}^{+2}$  in  $\text{CaSO}_4$  accompanied by many sharp phonon sidebands, reflecting the phonon density of states distribution in  $\text{CaSO}_4$ . The fast fluorescence transition is  $4f^65d \rightarrow 4f^7$  as the lowest lying excited state is a  $4f^65d$  level. The many sharp lines seen in the excitation spectrum can be accounted for by a strong exchange splitting of the  $4f^65d$  states.

The lowest lying excited state of  $\text{Eu}^{+2}$  in  $\text{BaMg}(\text{SO}_4)_2$  is a  $4f^7$  state so that slow  $4f^7 \rightarrow 4f^7$  fluorescence transitions with vibronic sidebands are observed. The excitation spectrum shows that in  $\text{BaMg}(\text{SO}_4)_2$  there is a weak exchange interaction between the  $4f^6$  electrons and the  $5d$ .

It is interesting to question why such spectra are not observed in the other alkaline earth sulfates, or for that matter in many other hosts. The conclusions we reach are listed below for types 2, 3, and 4 spectra. [The conditions necessary for observing type 1 is discussed in Ref. (1).] These conclusions should be applicable to  $\text{Eu}^{+2}$  in any host, although we specifically address ourselves to the question of why certain types of spectra appear in certain alkaline earth sulfates and not in others.

**Type 2.**—In order to observe a type 2 spectrum in fluorescence it is necessary that the coupling to the phonons in the excited state of the  $\text{Eu}^{+2}$  ion differ from the coupling in the ground state by a small enough degree so that a zero phonon line can be observed. That is, a small Stokes' shift must occur. This condition is met in  $\text{CaSO}_4$  whose fluorescence envelope is much narrower than that for the other hosts studied where  $4f^65d \rightarrow 4f^7$  transitions dominated. If the phonon spectrum of the host has sharp structure in it or if resonant modes are present, the phonon replicas of the zero phonon line will exhibit this sharp structure, as in the case of  $\text{CaSO}_4$ .

**Type 3.**—In order to see many sharp lines in the excitation or absorption spectrum of  $\text{Eu}^{+2}$  there must be a strong exchange interaction between the  $5d$  electron and the  $4f^6$  electrons. In the alkaline earth sulfates only  $\text{CaSO}_4$  shows this strong exchange term. This suggests

that  $\text{CaSO}_4$  is the least covalent compound of the alkaline earth sulfates.

**Type 4.**—In order to observe a type 4 spectrum the lowest lying  $4f^65d$  level must be located above the lowest lying  $4f^7$  level. There are two conditions that must be met in order for this to be the case. The first is that the crystal field strength cannot be too large. A strong crystal field splitting of the  $d$  states will depress the  $2e_g$  state so that it in combination with  $4f^6$  lies below the lowest  $4f^7$  level. Apparently the strengths of the crystal field at the  $\text{Eu}^{+2}$  site in  $\text{BaMg}(\text{SO}_4)_2$  is less than in the other hosts studied so that this condition is satisfied. This would occur, for example, if the nearest neighbor spacing of the oxygen atoms to the  $\text{Eu}^{+2}$  ions were greater in the  $\text{BaMg}(\text{SO}_4)_2$  lattice than in the other hosts. In the absence of structural data this suggestion must remain speculative, as must arguments based on the different oxygen coordinations in the structures. The second condition that must be is that the exchange interaction cannot be too strong. A strong exchange interaction will depress the  $4f^65d$  levels as shown on Fig. 2. As we have shown, the exchange interaction of the  $5d$  electron with the  $4f^6$  electrons is very weak ( $50 \text{ cm}^{-1}$ ) in  $\text{BaMg}(\text{SO}_4)_2$ . The exchange interaction would depend on the degree of localization of the  $5d$  electron near the  $\text{Eu}^{+2}$  core. This localization would be dependent on the degree of covalency present in the interaction of the  $5d$  electron with the surrounding ions. We therefore suggest that in  $\text{BaMg}(\text{SO}_4)_2$  a greater degree of covalency exists and that this is responsible for the weak exchange term.

### Acknowledgments

The authors would like to thank Dr. R. W. Warren for many constructive discussions.

Manuscript received April 8, 1974. This was Paper 30 presented at the Chicago, Illinois, Meeting of the Society, May 13-18, 1973.

Any discussion of this paper will appear in a Discussion Section to be published in the June 1975 JOURNAL. All discussions for the June 1975 Discussion Section should be submitted by Feb. 1, 1975.

The publication costs of this article have been assisted by Westinghouse Research Laboratories.

### REFERENCES

1. W. E. Bron and M. Wagner, *Phys. Rev.*, **139A**, 233 (1965).
2. A. A. Kaplyanskii and P. P. Feofilov, *Opt. Spectry. (USSR)*, **13**, 129 (1962).
3. M. V. Hobden, *Phys. Letters*, **15**, 10 (1965).
4. R. A. Hewes and M. V. Hoffman, *J. Luminescence*, **3**, 26 (1971).
5. M. V. Hoffman, *This Journal*, **119**, 905 (1972).
6. S. N. Bodrug, E. G. Valyashko, V. N. Mednikova, D. T. Sviridov, and R. K. Sviridov, *Opt. Spectry.*, **34**, 176 (1973).
7. R. W. G. Wyckoff, "Crystal Structures," Vol. 3, pp. 19, 38, 41, 56, Interscience Publishers, New York (1965).
8. *Structure Reports*, **16**, 285 (1952); **22**, 448 (1958); **27**, 606 (1962).
9. M. J. Freiser, S. Methfessel, and F. Holtzberg, *J. Appl. Phys.*, **39**, 900 (1968).
10. H. A. Weakliem, *Phys. Rev.*, **6B**, 2743 (1972).
11. W. M. Yen, W. C. Scott, and A. L. Schawlow, *Phys. Rev.*, **136**, A 271 (1969).
12. J. Prather, *Nat. Bur. Stds. Monograph* 19, (Feb. 24, 1961).

# Infrared Reflectivity and Free Carrier Absorption of Si-Doped, N-Type GaAs

J. K. Kung and W. G. Spitzer

Departments of Physics and Materials Science, University of Southern California, Los Angeles, California 90007

## ABSTRACT

The infrared plasma reflectivity and free carrier absorption of heavily Si-doped n-type GaAs are examined and the results show that shallow reflectivity minima ( $R_m \approx 14\%$ ) and increased free carrier absorption cross sections are a consequence of high levels of compensation in the samples. The frequency dependence of the extinction coefficient  $k$  in compensated as well as uncompensated samples is found to be different from that described by the Drude-Zener theory in the frequency region near or higher than the plasma-edge frequency. Based on the experimentally observed frequency dependence of  $k$ , correction factors are evaluated in determining carrier concentration from the frequency of the infrared plasma reflectivity minimum when the reflectivity minimum is shallow. The correction factors are applied to the measured results of a series of samples and the resulting carrier concentrations are compared with those obtained from Hall effect measurements.

Infrared plasma reflectivity and free carrier absorption measurements of n-type GaAs have been reported by a number of investigators. The reflectivity of samples with a carrier concentration  $n_e > 10^{17} \text{ cm}^{-3}$  shows the effect of a plasma frequency  $\omega_p$  which is higher than that for the fundamental lattice reflectivity band (1) (restrahl). A reflectivity minimum is observed (1) at a frequency above the plasma-edge frequency. The minimum is deep with  $R_m \leq 2\%$  and the frequency  $\omega(R_m) \equiv \omega_m$  has been used as a measurement (2, 3) of  $n_e$ . In some cases  $n_e$  is determined from another measurement and the reflectivity data have been used with  $n_e$  to obtain carrier effective mass values in a number of semiconductor materials (1, 4).

In some recently reported measurements (3) of Si-doped GaAs it was found that the  $R_m$  value could vary from  $<4\%$  to as large as  $14\%$ . The Si doping level and the thermal history of the sample both influence the  $R_m$  value. The present study relates the presence of the shallow reflectivity minimum (large  $R_m$ ) to an increase in the free carrier absorption cross section. The validity of using  $\omega_m$  as a measure of  $n_e$  for a sample with a shallow minimum is also examined.

## Background

The classical Drude-Zener theory for the free carrier contribution to the complex dielectric constant gives the well-known expression (6)

$$\epsilon = \epsilon_1 + i\epsilon_2 = \epsilon_\infty - \frac{4\pi n_e e^2}{m^*} \left\langle \frac{\tau^2}{1 + \omega^2 \tau^2} \right\rangle + i \frac{4\pi n_e e^2}{m^* \omega} \left\langle \frac{\tau}{1 + \omega^2 \tau^2} \right\rangle \quad [1]$$

where  $m^*$  is the carrier effective mass,  $\tau$  is the carrier scattering relaxation time, and  $\epsilon_\infty$  is the limiting value for the high frequency dielectric constant. If  $(\omega\tau)^2 \gg 1$  then one has

$$\epsilon_1 = n^2 - k^2 = \epsilon_\infty \left( 1 - \frac{\omega_p^2}{\omega^2} \right) \quad [2]$$

and

$$\epsilon_2 = 2nk = \frac{\epsilon_\infty \omega_p^2}{\omega^3} \left\langle \frac{1}{\tau} \right\rangle \quad [3]$$

where  $\omega_p^2 = \frac{4\pi n_e e^2}{\epsilon_\infty m^*}$ ,  $\omega_p$  is the plasma frequency, and  $n$  and  $k$  are the optical constants, refractive index and extinction coefficient, respectively.

Key words: carrier concentration, compound semiconductor, reflectivity minimum frequency, free electron absorption cross section.

Reflectivity curves with  $R_m$  near zero, like those labeled (a) and (b) in Fig. 1, have been widely interpreted (1, 4, 5) by using the Drude-Zener (D-Z) theory. The normal incidence reflectivity is given by the usual expression

$$R = \frac{(n-1)^2 + k^2}{(n+1)^2 + k^2} \quad [4]$$

As will be discussed  $k$  is proportional to an inverse power of the frequency and an  $R_m$  value near zero means  $k$  is small ( $k^2 \ll 1$ ) at  $\omega \cong \omega_m$ . Setting  $k = 0$  gives  $R_m = 0$  when  $n = 1$  and hence Eq. [2] becomes

$$\left( \frac{\omega_p}{\omega_m} \right)^2 = \frac{\epsilon_\infty - 1}{\epsilon_\infty} \quad [5]$$

or

$$\omega_m^2 = \frac{4\pi n_e e^2}{(\epsilon_\infty - 1)m^*} \quad [6]$$

Because of the small  $k$  value  $\epsilon_2$  has little influence on  $R$  for  $\omega \cong \omega_m$  and also has little influence on the value of  $\omega_m$ . If  $m^*$  and  $\epsilon_\infty$  are known then Eq. [6] shows that  $n_e$  is determined from a measurement of  $\omega_m^2$  and this method of obtaining  $n_e$  has been used (3, 7, 8) because it is nondestructive and needs no physical contacts to the samples. The  $n_e$  values obtained in this way are in good agreement with those measured by the Hall effect.

Moss *et al.* (9) and Köhl (10) have considered the situation when  $k_m$ , the value of  $k$  at  $\omega_m$ , is not small and thus  $R_m$  is not near zero. A relationship between  $n_m$ ,  $k_m$ , and  $\epsilon_\infty$  is obtained from Eq. [2], [3], and [4] and if  $(\omega\tau)^2 \gg 1$  this relationship is

$$k_m^2 = \frac{(\epsilon_\infty - n_m^2)(n_m^2 - 1)}{5n_m^2 + 3\epsilon_\infty - 2} \quad [7]$$

Also if one assumes  $\tau$  is energy independent so that the energy averages  $\langle \rangle$  can be omitted, then Eq. [1] can be used to obtain a modified form of Eq. [5]

$$\frac{\omega_p^2}{\omega_m^2} = \frac{\epsilon_\infty - n_m^2 + k_m^2}{\epsilon_\infty} + \frac{4n_m^2 k_m^2}{\epsilon_\infty (\epsilon_\infty - n_m^2 + k_m^2)} \quad [8]$$

If  $(\omega\tau)^2 \gg 1$ , the second term on the right becomes negligible. The procedure used is to assume  $n_m$  values for a given  $\epsilon_\infty$ , calculate the  $k_m$  and use these to obtain  $R_m$  and  $(\omega_p/\omega_m)^2$ . Thus the dependence of  $(\omega_p/\omega_m)^2$  on  $R_m$  is established and the measurement of both  $\omega_m$  and  $R_m$  should give  $n_e$ .

There are some difficulties with the above procedure when applied to n-type GaAs. Equation [7] is obtained

from Eq. [2] and [3] and depends upon their validity. Equation [2] has not been established for shallow minimum cases although it is known to be correct for deep minimum samples (1). From free-carrier absorption measurements Eq. [3] is known to be valid for n-type GaAs only under very restrictive conditions (11, 12). For the samples used in the present study Eq. [3] does not apply. Moreover, the second term on the right side of Eq. [8] is dependent upon the validity of Eq. [3].

The inability of the D-Z theory to correctly predict  $\epsilon_2$  and hence the free carrier absorption for samples with  $n_e \cong 1 \times 10^{17} \text{ cm}^{-3}$  and  $\omega \cong \omega_p$  is seen from the following considerations. When  $(\omega_p/\omega)^2 \ll 1$  then  $\epsilon_1 \cong \pi^2 \cong \epsilon_\infty$  while the  $\epsilon_2$  equation becomes

$$k \cong \frac{\epsilon_\infty^{1/2} \omega_p^2}{2} \left\langle \frac{1}{\tau} \right\rangle \omega^{-3}$$

Thus the classical theory predicts  $k \propto \omega^{-3}$  when  $(\omega\tau)^2 \gg 1$  and  $\omega^2 \gg \omega_p^2$ . It has been established that under these conditions (1, 13, 14) the measurements of samples with  $n_e \cong 1 \times 10^{17} \text{ cm}^{-3}$  show an absorption coefficient  $\alpha = 2\omega k/c$  which is  $\omega^{-3}$  and hence  $k \propto \omega^{-4}$ . For  $n_e \cong 1 \times 10^{17} \text{ cm}^{-3}$ , the  $\omega^2 \gg \omega_p^2$  means that the frequency range considered will be  $\cong 300 \text{ cm}^{-1}$  which is the region measured in the studies referred to in Ref. (1, 13, 14). The behavior of  $k$  near  $\omega_p$  is not known from measurements of n-type GaAs. It has been shown (12) in samples with  $n_e < 10^{16} \text{ cm}^{-3}$  and

for frequency  $\leq 200 \text{ cm}^{-1}$  the classical  $k \propto \omega^{-3}$  dependence is observed. This latter result agrees with the theoretical expectation (15, 16) that for  $kT \gg \hbar\omega \gg \hbar/\tau$  the quantum and classical theories produce the same results.

In the present discussion we will be confined to  $\omega > 300 \text{ cm}^{-1}$ ,  $n_e \cong 10^{17} \text{ cm}^{-3}$ , and room temperature where the  $k \propto \omega^{-4}$  dependence is observed. In this region the absorption has been explained (16) in quantum mechanical calculations as a linear combination of optical and acoustical mode lattice scattering absorption and impurity scattering absorption. Thus, the total free carrier absorption coefficient,  $\alpha_{fc}$ , can be written at any frequency as

$$\alpha_{fc}(\omega) = A_L(\omega)n_e + B_I(\omega)n_eN_I \quad [9]$$

where  $A_L$  and  $B_I$  are the frequency dependent terms from the lattice scattering and impurity scattering calculations, and  $N_I$  is the total ionized impurity concentration. If  $n_e = N_D - N_A$  and  $N_I = N_D + N_A$  then  $N_I = n_e + 2N_A$  and

$$\alpha_{fc} = A_L n_e + B_I n_e^2 + 2B_I n_e N_A \quad [10]$$

Thus when an n-type sample is heavily compensated the absorption cross section,  $\alpha_{fc}/n_e$  is increased by  $2B_I N_A$  over that of a singly doped sample. An increase in  $\alpha_{fc}/n_e$  of double-doped samples has been observed in both n-type Ge (17) and Si (18).

In a recent study (3) of annealing effects in n-type, heavily Si-doped GaAs it was observed that samples

which have Si concentrations  $[\text{Si}] > 10^{19} \text{ cm}^{-3}$ , the  $n_e$  can be changed substantially by annealing and the changes are reversible. The  $n_e$  was varied from  $8 \times 10^{18} \text{ cm}^{-3}$  to  $1.5 \times 10^{18} \text{ cm}^{-3}$  for material with  $[\text{Si}] = 4 \times 10^{19} \text{ cm}^{-3}$ . All of the samples, but particularly those with smaller  $n_e$ , had  $R_m$  values which were larger than those previously observed for Te- and Se-doped material. A comparison is given in Fig. 1 which uses some previously published data (1) along with measurements made in this study.

In the present work the following properties will be studied for samples with shallow reflectivity minima:

1. To experimentally establish the magnitude and frequency dependence of  $k$  and  $\epsilon_2$  for  $\omega \cong \omega_p$  and  $(\omega\tau)^2 \gg 1$ .

2. To use the measurements of reflectivity and absorption to determine if the D-Z expression for  $\epsilon_1$  is satisfied.

3. To determine the relationship between  $\omega_m$  and  $R_m$  by using  $\epsilon_1$  and  $\epsilon_2$  functions which are consistent with experiment. This relationship has not been determined properly for samples with deep as well as shallow minima.

### Experimental Results and Discussion

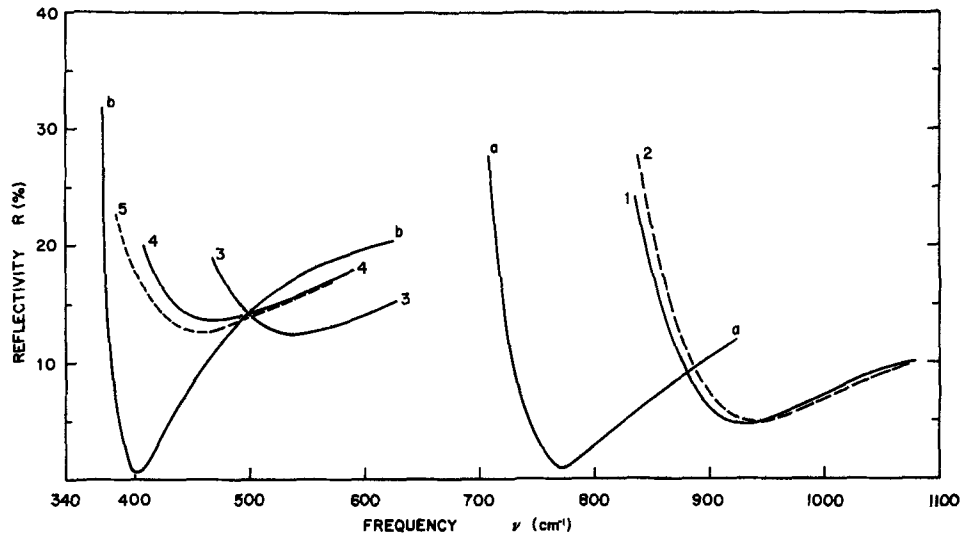
*Absorption in samples with large  $R_m$ .*—Figure 1 shows the reflectivity of five Si-doped samples taken from the same section of an ingot but with the samples in various anneal stages. Samples 3, 4, and 5 all have  $R_m$  near 13% and are referred to as shallow minimum samples. Relevant information on these samples is listed in Table I. The measured extinction coefficient for these same five samples is shown in Fig. 2 for  $\omega > \omega_m$ . Since  $\omega_p/\omega_m < 1$  we also have  $\omega > \omega_p$ . As Fig. 2 indicates, the  $k \propto \omega^{-4}$  dependence is also observed in the shallow minimum cases. Figure 3 shows the measured  $\alpha = 2k\omega/c$  at a frequency of  $1250 \text{ cm}^{-1}$  ( $\lambda = 8.0 \mu\text{m}$ ) plotted against  $n_e$  for the five samples of Fig. 1 and 2 as well as the values for a series of samples with deep minima taken from a previous study (1) and one Te-doped sample measured here and called 6. All of the deep minimum samples lie on a smooth curve and the fact that the curve is not a straight line of slope 1 is an indication of the presence of the  $B_I n_e^2$  term in Eq. [10]. Samples 1 and 2 lie close to the extrapolation of the curve, however samples 3, 4, and 5 are all well above the curve indicating a large contribution from the  $2B_I N_A n_e$  term. This result is consistent with the interpretation that the decrease in  $n_e$  between samples 1 and 2 and samples 3, 4, and 5 is at least partially because of increased compensation as a result of annealing rather than solely the loss of ionized impurity through, for example, precipitation. Since the predicted frequency dependence (16) of  $B_I$  is  $\omega^{-3.3}$  it is also consistent that samples 3, 4, and 5 which have larger contributions from impurity scattering than singly doped samples of the same  $n_e$  will also continue to have  $\alpha \propto \omega^{-3}$  (or  $k \propto \omega^{-4}$ ) as indicated in Fig. 2. Therefore the samples with shallow minima are indeed samples of larger than usual absorption cross section.

Table I. List of samples studied in this work  
Samples a and b are taken from Ref. (1)

Sample No.	Dopant	$N_I$	Anneal condition	$n_e$ (Hall effect) ( $\pm 10\%$ )	$R_m$	$\omega_m$ ( $\text{cm}^{-1}$ )
1	Si	$4 \times 10^{19} \text{ cm}^{-3}$	1100°C/15 min	$8.0 \times 10^{19}$	4.7%	935
2	Si	$4 \times 10^{19} \text{ cm}^{-3}$	600°C/290.5 hr + 1100°C/15 min	$8.0 \times 10^{18}$	4.9%	940
3	Si	$4 \times 10^{19} \text{ cm}^{-3}$	750°C/320 hr	$1.9 \times 10^{18}$	12.5%	542
4	Si	$4 \times 10^{19} \text{ cm}^{-3}$	600°C/290.5 hr	$1.5 \times 10^{18}$	13.7%	465
5	Si	$4 \times 10^{19} \text{ cm}^{-3}$	400°C/1178 hr	$1.5 \times 10^{18}$	12.6%	456
6	Te	—	as grown	$2.8 \times 10^{18}$	3.7%	594
a	Se	—	•	$5.4 \times 10^{18}$	1.0%	770
b	Te	•	•	$1.1 \times 10^{18}$	0.6%	440

\* Samples a and b are from Ref. (1). The  $N_I$  and anneal condition are unknown.

Fig. 1. Reflectivity in per cent as a function of frequency  $\nu$  ( $\text{cm}^{-1}$ ) of seven samples. Curves a and b are reproduced from Ref. (1), Fig. 5. All seven samples are listed in Table I.



Verification of the Drude-Zener  $\epsilon_1$  expression for large  $R_m$  cases.—The infrared transmission measurements of samples 5 and 6 of Table I were made over an extended frequency range  $\omega \cong \omega_m$ . The measurements near  $\omega_m$  will permit us to obtain experimental  $n$  and  $k$  values near  $n_m$  and  $k_m$  and thus test the validity of Eq. [1] near  $\omega_m$ . Sample 5 is a shallow minimum sample with  $R_m = 12.6\%$ , while sample 6 is a fairly deep minimum sample having  $R_m = 3.7\%$ . Since  $R$  is changing with  $\omega$  in the range of the transmission measurements we use the customary practice of determining  $\alpha$  from both  $T$  and  $R$  measurements at each  $\omega$  by using

$$T = \frac{(1 - R)^2 e^{-\alpha x}}{1 - R^2 e^{-2\alpha x}}$$

where  $x$  is the sample thickness. Having  $\alpha$  and hence  $k$  one obtains  $n$  from Eq. [4]. Thus the experimental frequency dependence of  $k$ ,  $nk$ , and  $n^2 - k^2$  can be

given for each sample. Figure 4 gives  $k$  and Fig. 5 gives  $nk$  for both samples. Figure 6 gives  $\epsilon_\infty - n^2 + k^2$  which should be equal to  $\epsilon_\infty \omega_p^2 / \omega^2$  if D-Z theory is obeyed and  $(\omega\tau)^2 \gg 1$  as in Eq. [2]. For both samples the  $k$  curves of Fig. 4 are close to  $\omega^{-4}$  dependencies throughout the  $\omega > \omega_m$  region. However, the Te-doped, deep minimum sample No. 6 shows a substantial steepening of the slope as  $\omega$  approaches  $\omega_m$  while the shallow minimum sample No. 5 maintains the near  $k \propto \omega^{-4}$  dependence through its  $\omega_m$  position. However, Fig. 5 shows a reversal of this behavior for the  $nk$  curves in that sample No. 5 deviates from the  $\omega^{-4}$  dependence. From these figures it is not clear whether  $k \propto \omega^{-4}$  or  $nk \propto \omega^{-4}$  is the better approximation near  $\omega_m$ . In Fig. 6, the value of  $\epsilon_\infty$  used is 11.0 and the points

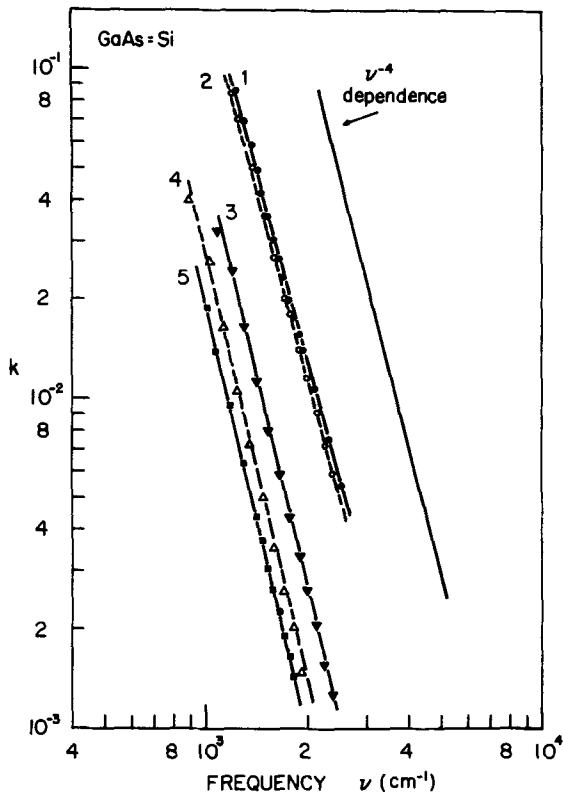


Fig. 2. The measured extinction coefficient  $k$  vs. the frequency  $\nu$  ( $\text{cm}^{-1}$ ) of samples 1-5 of Fig. 1.

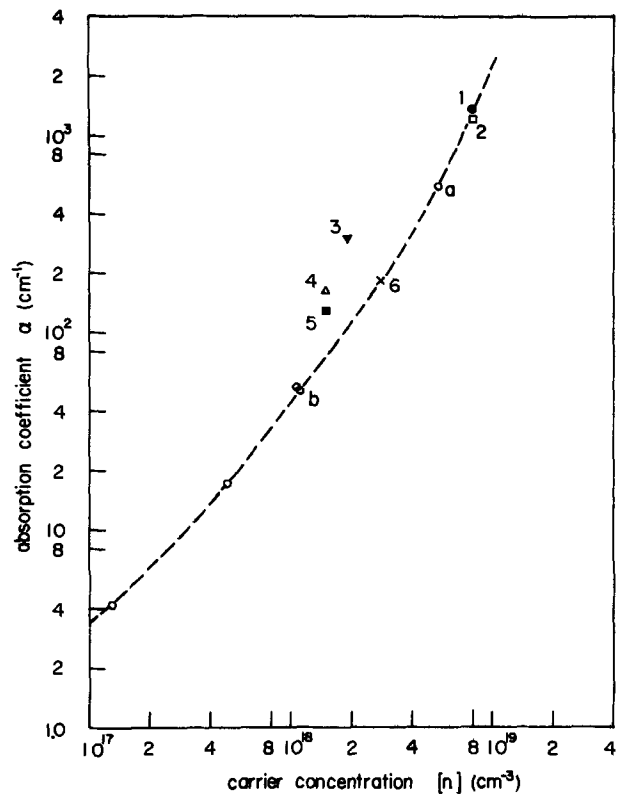


Fig. 3. Absorption coefficient,  $\alpha$ , as a function of carrier concentration at frequency  $\nu = 1250 \text{ cm}^{-1}$  ( $\lambda = 8 \mu\text{m}$ ). Data points labeled 1-6 and a, b are from samples listed in Table I. The data points drawn as open circles are obtained from Fig. 3 of Ref. (1).



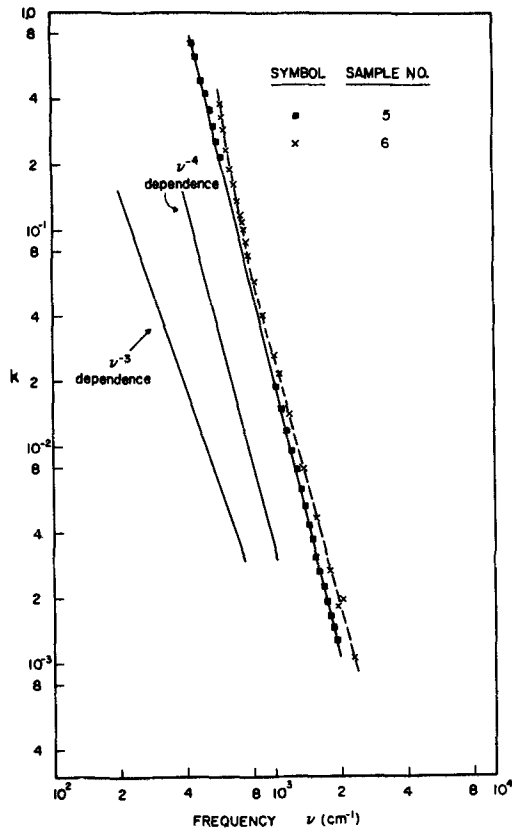


Fig. 4. Measured extinction coefficient,  $k$ , of samples 5 and 6 vs. frequency  $\nu$  ( $\text{cm}^{-1}$ ). The frequency range includes the frequency of the reflectivity minimum for each sample.

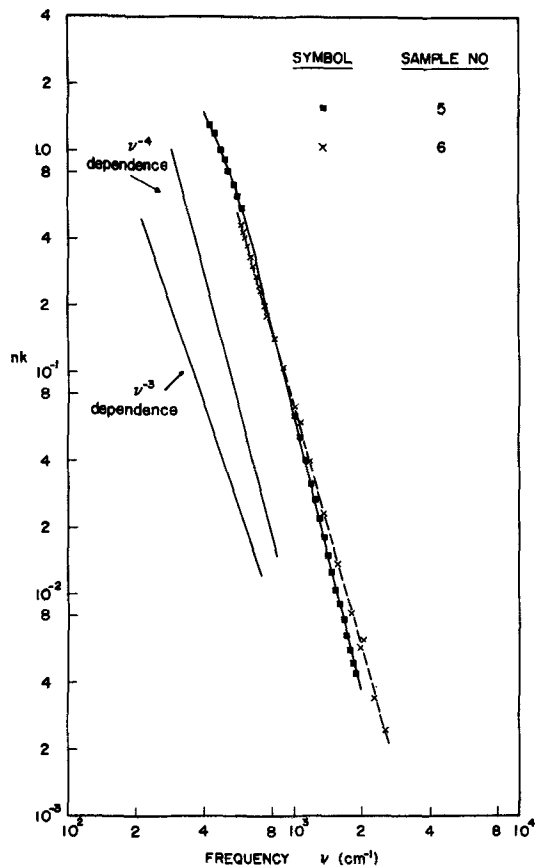


Fig. 5. The  $nk$  product of samples 5 and 6 vs. frequency  $\nu$  ( $\text{cm}^{-1}$ )

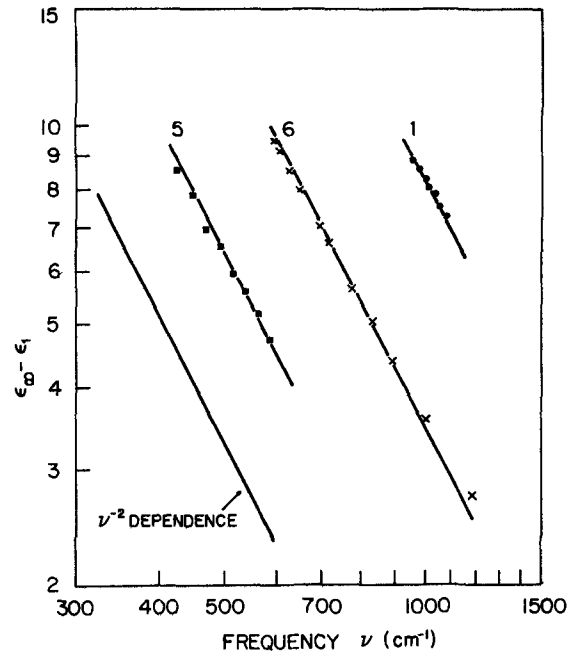


Fig. 6.  $\epsilon_{\infty} - \epsilon_1$  vs. frequency of samples 1, 5, and 6. The lines are drawn with a slope of  $-2$ .

for both samples lie close to lines of slope negative 2 indicating that  $(\epsilon_{\infty} - n^2 + k^2) \propto \omega^{-2}$  and the  $m^*$  values obtained are  $0.085 m_0$  for sample No. 5 and  $0.074 m_0$  for sample No. 6. For completeness, sample No. 1 of Table I which has an  $n_e = 8.0 \times 10^{18} \text{ cm}^{-3}$  was also measured and  $m^* = 0.088 m_0$  was obtained. These values compare favorably with literature values (19) of  $0.076 m_0$ ,  $0.078 m_0$ , and  $0.091 m_0$  for samples No. 5, 6, and 1, respectively, although sample No. 5 value is about 12% high. It appears that  $(\omega_m \tau)^2 \gg 1$  is a reasonable assumption for the shallow minimum case as well as the deep one and Eq. [2] is correct for  $\omega = \omega_m$  as well as  $\omega > \omega_m$ .

**Relationship between  $R_m$  and  $\omega_p/\omega_m$ .**—It is clear from the sections above that the D-Z equation for  $\epsilon_1$  is valid for both deep and shallow minimum samples and that  $(\omega_m \tau)^2 \gg 1$ . It is also clear now that the calculations made by previous authors in which  $R_m$  as a function of  $\omega_p/\omega_m$  was determined by using Eq. [3] for  $\epsilon_2$ ,

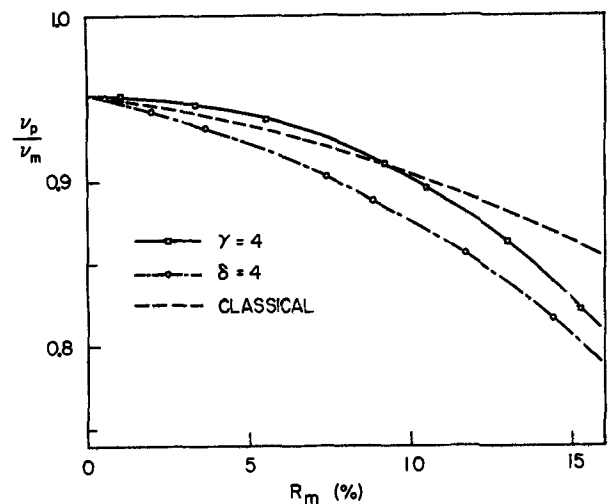


Fig. 7. Plasma frequency divided by the frequency of reflectivity minimum as a function of the value of the minimum reflectivity. The curve labeled "classical" is taken from Ref. (9) for comparison.

Table II. Comparison of carrier concentration determined from plasma edge reflectivity measurement (corrected and uncorrected) with that from Hall effect  
Samples 1-6 and a, b are the same as listed in Table I

Sample No.	$R_m$	$\omega_m$ (cm <sup>-1</sup> )	$n_e$ (in units of 10 <sup>18</sup> cm <sup>-3</sup> )				% Deviation compared with Hall effect	
			From measured $\omega_m$	Corrected by $\gamma = 4$	Corrected by $\delta = 4$	Hall effect ( $\pm 10\%$ )	With measured $\omega_m$	Corrected by $\gamma = 4$
1	4.7%	935	8.1	8.0	7.8	8.0	+1.3%	0.0%
2	4.9%	940	8.1	8.0	7.8	8.0	+1.3%	0.0%
3	12.5%	542	2.3	1.8	1.8	1.9	+21%	-5.3%
4	13.7%	465	1.7	1.3	1.2	1.5	+13%	-13%
5	12.6%	456	1.6	1.3	1.2	1.5	+6.7%	-13%
6	3.7%	584	3.0	2.8	2.7	2.8	+7.1%	0.0%
7	5.7%	677	3.9	3.8	3.7	4.4	-11%	-14%
8	13.1%	470	1.7	1.4	1.3	1.5	+13%	-6.7%
9	4.8%	949	8.7	8.1	8.0	8.4	+3.6%	-3.6%
10	4.7%	926	8.0	7.9	7.7	8.5	-5.9%	-7.1%
11	12.4%	460	1.7	1.4	1.3	1.9	-10.5%	-26.3%
12	11.4%	530	2.2	1.9	1.8	2.3	-4.3%	-17.4%
a	1.0%	770	5.4	5.4	5.4	5.4	0.0%	0.0%
b	0.6%	440	1.2	1.2	1.2	1.1	+9.1%	+9.1%

are not correct for n-type GaAs. We will replace  $\epsilon_2$  with two different forms and obtain relationships for each case. In both cases we use  $\epsilon_s - n^2 + k^2 = C/\omega^2 + \tau^{-2}$ , where  $C = \omega_p^2 \epsilon_s$ .

1. Let  $k = D\omega^{-\gamma}$  where  $D = \text{constant}$  and  $\gamma$  is a power. If  $(\omega\tau)^2 \gg 1$  and by using the condition that

$$\frac{d}{d\omega} \left( \frac{1+R}{1-R} \right)_{\omega=\omega_m} = 0$$

then one can get

$$k_m^2 = \frac{(n_m^2 - 1)(\epsilon_s - n_m^2)}{(3\gamma - 2)n_m^2 + (1 - \gamma) + \epsilon_s} \quad [11]$$

Since the experiments show that  $k_m^2 \ll 1$  a term involving  $k_m^4$  was dropped in obtaining Eq. [11].

2. Let  $nk = G\omega^{-\delta}$  and in similar manner to 1 we obtain

$$k_m^2 = \frac{(n_m^2 - 1)(\epsilon_s - n_m^2)}{(3\delta - 4)n_m^2 + (1 - \delta) + 3\epsilon_s} \quad [12]$$

If  $\delta = 3$  we then have the D-Z model and Eq. [12] reduces to Eq. [7].

Since Eq. [2] is still correct, then again with  $(\omega_m\tau)^2 \gg 1$  we obtain

$$\left( \frac{\omega_p}{\omega_m} \right)^2 = \frac{\epsilon_s - n_m^2 - k_m^2}{\epsilon_s} \quad [13]$$

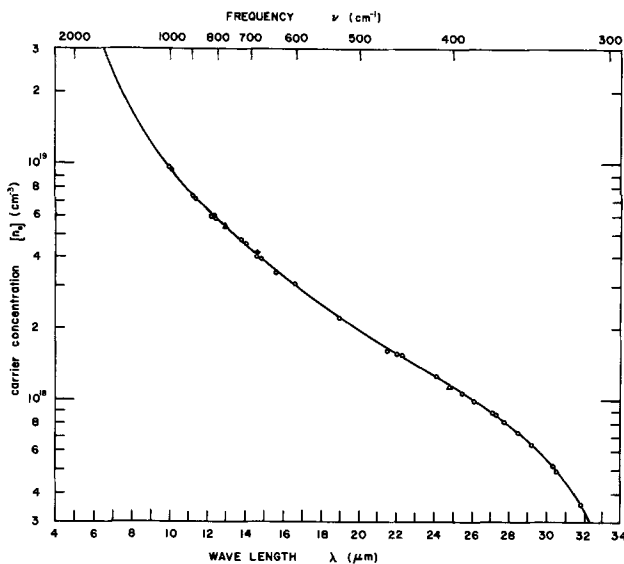


Fig. 8. Carrier concentration as a function of frequency and wavelength for the plasma edge reflectivity minimum. This curve is taken from Ref. (7).

In both cases we can get  $k_m$  for  $\epsilon_s = 11.0$  and  $\gamma = \delta = 4$  by letting  $n_m$  assume a range of values. For each set of  $n_m$  and  $k_m$  values we obtain  $(\omega_p/\omega_m)^2$  from Eq. [13] and an  $R_m$  from Eq. [4]. The results are given in Fig. 7 where the classical curve is calculated (9) with the D-Z model and not assuming  $(\omega\tau)^2 \gg 1$ . All three cases agree within 8% for  $\omega_p/\omega_m$  if  $R_m \leq 15\%$ . The results of these calculations were tested as follows: a series of samples were measured to determine  $R_m$  and  $\omega_m$ . From the curves in Fig. 7 the  $\omega_m$  was corrected to its value when  $R_m = 0$  and this corrected  $\omega_m$  was used with the curve of Okada and Oku (7) (see Fig. 8 for this curve) to give  $n_e$ . The results are given in Table II in which the  $n_e$  obtained as described are compared with Hall data for the same samples. The reproducibility of the Hall data is estimated to be  $\pm 10\%$ . Except for sample No. 3 all  $n_e$  values from the Hall effect and  $\omega_m$  without any correction agree within 15% and in most cases within 10%. When  $\omega_m$  is corrected with the  $\gamma = 4$  curve and used to obtain  $n_e$  the comparison with the Hall values is not substantially improved. The values for only two of the 14 samples disagree by more than 15% while the majority are again within 10% agreement. It appears that the measured  $\omega_m$  is a reliable method of determining  $n_e$  within the stated errors for both deep and shallow minimum ( $R_m < 15\%$ ) samples and that application of the calculated corrections does not necessarily improve the reliability.

#### Acknowledgment

This work was supported in part by the National Science Foundation under Grant GK 25144 and by the Joint Services Electronics Program through the Air Force Office of Scientific Research/AFSC under Contract F44620-71-C-0067.

Manuscript submitted Aug. 10, 1973; revised manuscript received ca. July 1, 1974.

Any discussion of this paper will appear in a Discussion Section to be published in the June 1975 JOURNAL. All discussions for the June 1975 Discussion Section should be submitted by Feb. 1, 1975.

The publication costs of this article have been assisted by the University of Southern California.

#### REFERENCES

- W. G. Spitzer and J. M. Whelan, *Phys. Rev.*, **114**, 59 (1959).
- I. V. Mitchell, J. W. Mayer, J. K. Kung, and W. G. Spitzer, *J. Appl. Phys.*, **42**, 3982 (1971).
- J. K. Kung and W. G. Spitzer, *ibid.*, **44**, 912 (1973).
- W. G. Spitzer and H. Y. Fan, *Phys. Rev.*, **106**, 882 (1957).
- A. Kahan, Air Force Cambridge Research Laboratories, Physical Sciences Research Papers, No. 537, AFCLR-TR-73-0122 (1973).
- H. A. Lyden, *Phys. Rev.*, **134A**, 1106 (1964).

7. K. Okada and T. Oku, *Japan J. Appl. Phys.*, **6**, 276 (1967).
8. N. Goldsmith and W. Oshinsky, *RCA Rev.*, **24**, 546 (1963).
9. T. S. Moss, T. D. F. Hawkins, and G. J. Burrell, *J. Phys. C.*, **1**, 1435 (1968).
10. F. Köhl, *Optics Commun.*, **2**, 157 (1970).
11. S. Perkowitz, *J. Appl. Phys.*, **40**, 3751 (1969).
12. S. Perkowitz, *J. Phys. Chem. Solids*, **32**, 2267 (1971).
13. M. G. Mil'vidskii, V. B. Osvenskii, E. P. Rashevskaya, and T. G. Yugova, *Soviet Phys.-Solid State*, **7**, 2784 (1966).
14. E. P. Rashevskaya and V. I. Fistul', *Soviet Phys.-Solid State*, **9**, 1443 (1967).
15. W. P. Dumke, *Phys. Rev.*, **124**, 1813 (1961).
16. E. Haga and H. Kimura, *J. Phys. Soc. Japan*, **19**, 658 (1964).
17. H. Y. Fan, W. G. Spitzer, and R. J. Collins, *Phys. Rev.*, **101**, 566 (1956).
18. W. G. Spitzer and H. Y. Fan, *ibid.*, **108**, 268 (1957).
19. H. Piller, "Proc. International Conference on the Physics of Semiconductors," Kyoto, p. 206 (1966).

## Diffusion of Gallium Through Silicon Dioxide Films into Silicon

Sigurd Wagner

*Bell Telephone Laboratories, Incorporated, Holmdel, New Jersey 07733*

and Edward I. Pivilonis

*Bell Telephone Laboratories, Incorporated, Murray Hill, New Jersey 07974*

### ABSTRACT

Metal-oxide-silicon capacitors with shallow ( $\sim 0.1 \mu\text{m}$ ) diffusions of gallium through silicon dioxide films into silicon were studied with capacitance-voltage techniques. The first part of the paper is a discussion of the ionization of the gallium acceptor in the silicon space charge region, and of the unusual capacitance-voltage characteristics of very shallow diffused layers. It is concluded that in a space charge region even a comparatively deep level like that of gallium is largely ionized so that nearly all of the dissolved gallium contributes to the C-V signal. Furthermore, very shallow diffusions give C-V curves identical to those of the bulk substrate material. However, the entire curve is shifted on the voltage axis in linear proportion to the amount of indiffused impurity. This voltage shift is used to determine the amount of gallium in silicon. In the second part the following experimental results are reported: After comparatively short diffusion times the concentration of gallium in silicon is linearly proportional to  $(p_{\text{H}_2}/p_{\text{H}_2\text{O}})$  in an ambient gas containing hydrogen and water over  $\beta\text{-Ga}_2\text{O}_3$  at  $850^\circ\text{-}1050^\circ\text{C}$ . This implies that initially the gallium concentration is a function of  $p_{\text{Ga}_2\text{O}}$  rather than  $p_{\text{Ga}}$ . The diffusion coefficient of gallium in the oxide film, derived from the amount of gallium which diffused through the film into the silicon at  $800^\circ\text{-}900^\circ\text{C}$  is  $D_{\text{Ga}(\text{SiO}_2)} = 0.73 \times \exp(-2.46 \text{ eV}/kT)$ . The density of mobile charge in the  $\text{SiO}_2$  film was found to be higher than  $1 \times 10^{12} \text{ cm}^{-2}$  under all diffusion conditions except when  $\text{Ga}_2\text{O}$  vapor is suppressed.

The rate of diffusion of gallium through silicon dioxide films is several orders of magnitude higher than that of the other Group III and Group V elements used as dopants for silicon (1-3). Thus silicon dioxide does not "mask" against gallium. By the same token silicon can be doped with gallium even when covered with oxide.

We have studied the formation of shallow Ga diffusion layers in Si covered by  $\text{SiO}_2$ . The purpose of this work was to find a reliable technique for the prevention of conductivity-type inversion at p-Si/ $\text{SiO}_2$  interfaces. When thick native oxide layers are grown on boron-doped silicon, boron is depleted from Si because of a distribution coefficient which favors dissolution in  $\text{SiO}_2$ . The concurrent reduction of the acceptor density in Si facilitates the formation of an n-type inversion layer under the influence of an electric field originating at positively charged conductors on top of the  $\text{SiO}_2$ , or at positive charges within the  $\text{SiO}_2$ . This inversion can be prevented by diffusing Ga through the  $\text{SiO}_2$  film to form a shallow but highly doped p-type layer in the Si.

In the work presented here the diffusion length of gallium in silicon was of the order of  $0.1 \mu\text{m}$ . When

such profiles are established in n-type substrates, their resistivity and doping level cannot be conveniently measured by profiling and four-point probing. Under the load needed to make good contact the points punch through the junction. In addition, angle lapping and staining reveal p-n junctions which must be estimated if they are less than  $0.1\text{-}0.2 \mu\text{m}$  deep. Therefore we diffused gallium into p-type substrates and determined concentrations, or amounts, of gallium from capacitance-voltage measurements. These measurements are carried out after diffusion with the metal-silicon dioxide-silicon capacitor formed by the deposition of aluminum field plates on the oxide film.

Two aspects of C-V measurements on shallow diffusions of gallium deserve some attention. One is the comparatively deep acceptor level of gallium in silicon and the consequent deionization in the silicon space charge region. The other aspect arises from the unusual C-V characteristics of very shallow profiles. Their evaluation is different from that used for bulk doped material. The next section of this paper is devoted to this discussion. The reader who is primarily interested in the experimental results is asked to proceed immediately to the section on Diffusion of Gallium.

**Key words:** diffusion, silicon dioxide films, silicon, gallium.

## Capacitance-Voltage Characteristics of Shallow Gallium Diffusions

### Deionization of Gallium Acceptors

In equilibrium, not all of the gallium dissolved in the silicon is ionized when its concentration exceeds  $\sim 10^{18}$   $\text{cm}^{-3}$  (4). This deionization occurs because the Fermi function becomes a significant fraction of unity at the energy level of the gallium impurity. At low gallium concentrations this level is comparatively deep. Its ionization energy is 65 meV.

During the measurement of the resistivity or of the Hall coefficient the holes acquire little kinetic energy. They are virtually in equilibrium with the lattice. Therefore the measured quantity is converted first to the concentration of ionized acceptors by using the appropriate low-field mobility. Second, the total concentration of donors, ionized and un-ionized, is calculated using the equilibrium relation between ionized and total dopant concentration

$$N_{\text{Ga}} = N_{\text{Ga}^-} \times \left[ 1 + g \times \exp\left(\frac{E_{\text{Ga}} - E_{\text{F}}}{kT}\right) \right] \quad [1]$$

This equation is derived from one given by Wolfstirn (4). The degeneracy,  $g$ , is 4 (5).<sup>1</sup>  $E_{\text{F}}$  is the Fermi energy and  $E_{\text{Ga}}$  is the acceptor energy. Wolfstirn has shown that the ionization energy of the gallium acceptor,  $\epsilon_{\text{Ga}} = \Delta E_{\text{gap}} - E_{\text{Ga}}$ , depends on the concentration of gallium. The simplest model for such a dependence assumes  $\epsilon_{\text{Ga}}$  to be a linear function of the average separation between gallium atoms (6, 7). In Fig. 1 this linear least squares fit of the first set of Wolfstirn's data is shown.  $\epsilon_{\text{Ga}}$  was taken to be constant at its low concentration value of 65 meV up to  $N_{\text{Ga}} = 4.3 \times 10^{17}$   $\text{cm}^{-3}$ . Above this concentration the ionization energy is  $\epsilon_{\text{Ga}} = 23.2 + 31.5 \times 10^6 / (N_{\text{Ga}})^{1/3}$  or, after substitution with  $r_{\text{Ga}} = (3/4\pi N_{\text{Ga}})^{1/3}$ ,  $\epsilon_{\text{Ga}} = 23.2 + 50.5 \times 10^6 r_{\text{Ga}}$  (meV). If no band edge tailing or broadening of the impurity level occurs the Fermi level coincides with the valence band edge at  $N_{\text{Ga}} > 5 \times 10^{19}$   $\text{cm}^{-3}$ . The maximum solubility of Ga in Si is  $4 \times 10^{19}$   $\text{cm}^{-3}$  (8). Thus, by extrapolating beyond  $N_{\text{Ga}} = 1.62 \times 10^{18}$   $\text{cm}^{-3}$ , we set up the curve drawn in Fig. 2 for conversion of  $N_{\text{Ga}^-}$  to  $N_{\text{Ga}}$  using Eq. [1].

With MOS capacitances the evaluation of total dopant concentrations from measured data is conceptually less straightforward. MOS capacitors under

<sup>1</sup>  $g = 4$  is taken from Ref. (4). This value is accurate within about 10% (5).

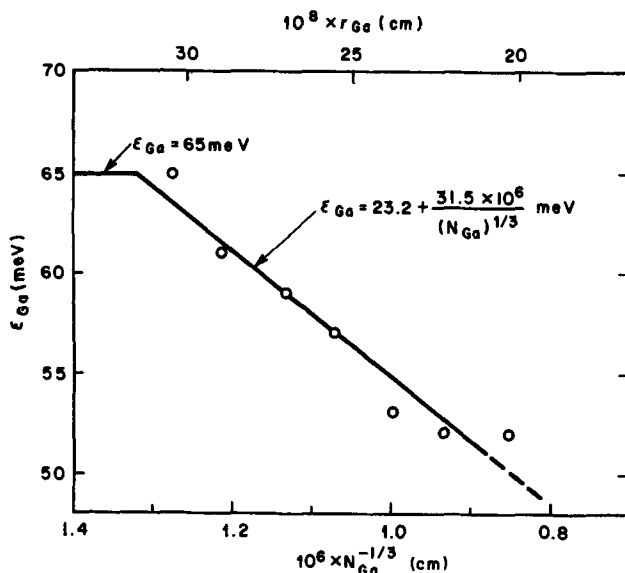


Fig. 1. Dependence of the energy level of the gallium acceptor,  $\epsilon_{\text{Ga}}$ , on the mean distance between gallium atoms. The data are taken from Wolfstirn (4).

bias are in quasi equilibrium. The Fermi level is constant throughout the semiconductor. However, the potential of the band edges and the impurity levels varies between the edge of the space charge region and the oxide-silicon interface. Over a large portion of the depletion layer the Fermi level lies much higher than the acceptor level,  $E_{\text{F}} \gg E_{\text{Ga}}$ . Then, regardless of the gallium concentration,  $N_{\text{Ga}} \cong N_{\text{Ga}^-}$ .

In a uniformly doped semiconductor in depletion the band bending is parabolic. The electrostatic potential  $\psi(x)$  at a distance  $x$  from the interface is a quadratic function of  $(x - x_2)$  where  $x_2$  denotes the edge of the depletion region

$$\psi(x) = \frac{q}{2\epsilon_s} (N_{\text{Ga}^-}) (x - x_2)^2$$

where  $q$  is the electronic charge and  $\epsilon_s$  is the permittivity of the semiconductor. At  $x > x_2$  the exponent of Eq. [1] is determined by the energy difference between the gallium impurity level and the Fermi level in the bulk of the silicon. At  $0 < x < x_2$  the exponent is modified to

$$E_{\text{Ga}} - E_{\text{F}}(x < x_2) = E_{\text{Ga}} - E_{\text{F}}(x \geq x_2) - \psi(x)$$

Ten per cent or more deionization may be considered significant. This occurs when  $E_{\text{Ga}} - E_{\text{F}}(x < x_2)$  is more positive than  $-5 kT/q$ , i.e., with  $N_{\text{Ga}} \gtrsim 2 \times 10^{18}$   $\text{cm}^{-3}$  (Fig. 2).

As described in the next section, we derive  $N_{\text{Ga}}$  from the voltage and the capacitance at inversion where the band bending is at a maximum. It is possible to estimate the portion of the depletion region where ionization is incomplete ( $E_{\text{Ga}} - E_{\text{F}}(x_i) \cong -5 kT/q$ ) and to estimate the accuracy of  $N_{\text{Ga}}$  extracted from these measurements. We assume a highly doped substrate with  $E_{\text{Ga}} = E_{\text{F}}$ . For this case  $N_{\text{Ga}} = 5 N_{\text{Ga}^-}$  (Eq. [1]).  $N_{\text{Ga}}$  can be determined by numerically solving the equation  $E_{\text{Ga}} - E_{\text{F}} = 0$ , or by locating the intercept of the line  $N_{\text{Ga}} = 5 N_{\text{Ga}^-}$  with the curve of Fig. 2. The resulting values are  $N_{\text{Ga}^-} = 2.5 \times 10^{18}$   $\text{cm}^{-3}$  and  $N_{\text{Ga}} = 1.25 \times 10^{19}$   $\text{cm}^{-3}$ . The corresponding bulk Fermi level is about  $20 kT/q$  below midgap and the surface potential in inversion is  $\psi_s = 40 kT/q$ . Then

$$\frac{(x_1 - x_2)^2}{x_2^2} = \frac{\psi(x_1)}{\psi(x=0)} = \frac{5}{40}$$

and

$$\frac{x_1 - x_2}{x_2} \cong 0.35$$

It follows that for this worst case assumption of a very high and uniform gallium concentration the acceptors are completely ionized over two-thirds of the space charge layer. Extensive deionization ( $E_{\text{Ga}} - E_{\text{F}} \cong -$

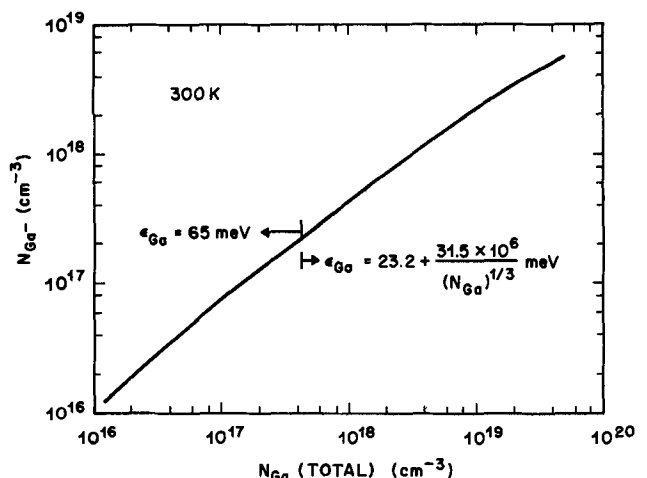


Fig. 2. Density of ionized gallium acceptors,  $N_{\text{Ga}^-}$ , as a function of the total gallium concentration,  $N_{\text{Ga}}$ .

$2kT/q$ ) occurs within  $0.8 x_2 \leq x < x_2$ . At inversion 80% or more of the gallium dissolved in the depletion layer is ionized and contributes to the capacitance signal. When the doping level is uniformly lower than in this example, or when a diffusion profile with high  $N_{Ga}$  at  $x = 0$  and low  $N_{Ga}$  at  $x_2$  is measured, nearly all of the gallium will be ionized at inversion. A similar argument shows the edge of the depletion layer,  $x_2$ , to be slightly but not significantly deeper than  $x_2$  for the completely ionized case.

We conclude that the inversion voltage and the minimum capacitance give closely the total amount of gallium atoms in the depletion layer.

**Shallow Diffused Layers**

Two basic types of high frequency C-V curves are obtained with shallow diffusion profiles of gallium in p-type silicon. Their occurrence depends on the Ga concentration in the profile and on the depth of the diffusion. The depth is defined by the point where the concentration of the indiffused Ga is equal to the net acceptor concentration of the substrate, which was about  $2 \times 10^{15} \text{ cm}^{-3}$  in this study.

In the first type of C-V curve, the depletion width in inversion is smaller than the depth of the Ga profile. A C-V curve similar to one for uniformly doped silicon is obtained. The minimum capacitance corresponds to a weighted average density of ionized acceptors in the depletion region. In this case, the average gallium concentration was obtained by a graphical method (9).

The second type of C-V curve is obtained when the depletion width in inversion is larger than the diffusion depth. The C-V curve is then typical for the substrate material, but the entire curve is shifted to more positive voltages. This voltage shift is proportional to the amount of indiffused Ga. A shift of the inversion voltage, or the threshold voltage, of a metal-oxide-semiconductor transistor has been discussed recently, in the light of diffusion (10, 11) and of ion implantation (12-16) of dopants, or as a general feature of nonuniformly doped surfaces (17, 18).

C-V curves which are intermediates between these two types are obtained when the depletion width at inversion is comparable to the depth of the Ga diffusion.

The properties of MOS capacitors with shallow diffusions are calculated for a capacitor with a "box" diffusion profile. The capacitor is schematically shown in Fig. 3. Numerical results of the calculations are demonstrated on a capacitor with a bulk doping level  $N_B = 2 \times 10^{15} \text{ cm}^{-3}$ , and an oxide thickness  $t_{ox} = 0.1 \mu\text{m}$ , as a function of  $N_A$ , the concentration of indiffused acceptors, and  $x_1$ , the depth of this diffusion (Fig. 4).

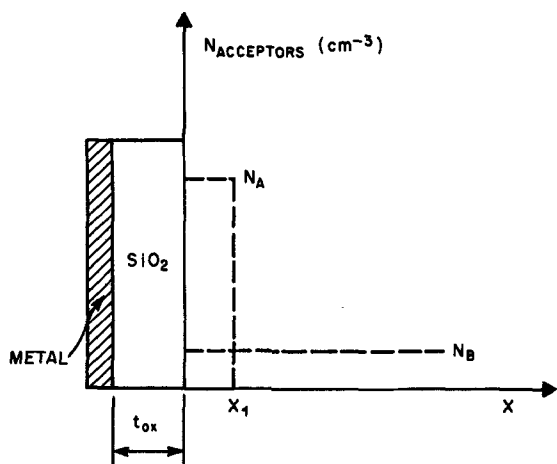


Fig. 3. Metal-oxide-silicon capacitor with a "box" diffusion profile with concentration  $N_A$  and depth  $x_1$  in silicon with bulk doping  $N_B$ .

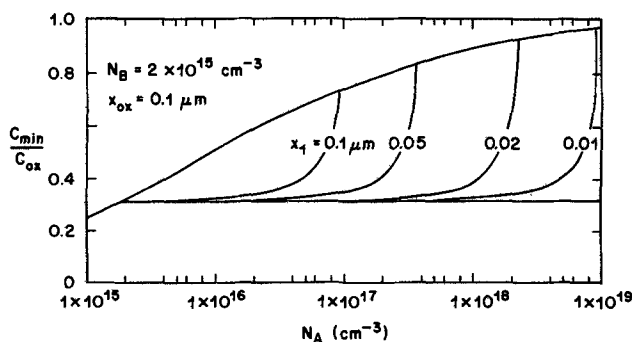


Fig. 4. Normalized minimum capacitance,  $C_{min}/C_{ox}$ , of a MOS capacitor with a "box" diffusion profile of concentration  $N_A$  and depth  $x_1$ .

In the following derivation  $N_A$  and  $N_B$  are taken to be independent of depth and the density of fixed charge and the density of interface states are assumed to be zero. Also, the depletion approximation is used, i.e., the space charge in the silicon is assumed to be made up only of ionized acceptors.

First, the work function difference between the silicon and the metal,  $\psi_{MS}$ , is defined. Then the Poisson equation for the capacitor of Fig. 3 is solved to give a relation between surface potential,  $\psi_s$ , and depletion width,  $x_2$ . Using this equation, the normalized high frequency capacitance in inversion,  $C_{min}/C_{ox}$ , and the inversion voltage,  $V_i$ , are calculated.

**Work function difference.**—For the doping profile given in Fig. 3, the Fermi potential in the bulk is  $\phi_{F,2} = (kT/q) \ln (N_B/n_i)$ . That for surface region is  $\phi_{F,1} = (kT/q) \ln (N_A + N_B)/n_i$ , where  $k$  is the Boltzmann constant,  $T$  the absolute temperature,  $q$  has the magnitude of the electronic charge, and  $n_i$  is the carrier concentration of intrinsic silicon. The work function difference between the Si and the metal is determined by the work function of the Si in the surface region,  $\psi_{Si,1} = \psi_{Si,i} + (kT/q) \ln (N_A + N_B)/n_i$ , with  $\psi_{Si,i}$  denoting the work function of intrinsic silicon, which is the reference state for potentials.

The flatband condition in the absence of fixed or mobile charge and of interface states obtains at a voltage

$$V_{FB} = \psi_M - \psi_{Si} = \psi_M - \psi_{Si,i} - \frac{kT}{q} \ln \frac{N_A + N_B}{n_i}$$

The equations derived in this section, however, will be applied to capacitors in inversion, i.e., when the space charge extends beyond  $x_1$  to  $x_2$ . It is then more convenient to retain the flatband condition for the original material (doping  $N_B$  throughout), and to redefine flatband for the diffused silicon as the condition where there is no electrostatic potential difference between the surface ( $x = 0$ ) and the bulk ( $x_2$ ). This condition is realized when the actual surface potential is  $\psi_s = (kT/q) \ln (N_A + N_B)/N_B$ . This surface potential is taken into account by redefining the work function of the Si to be that of the bulk material with  $N_B$  acceptors

$$\begin{aligned} \psi_{Si} &= \psi_{Si,i} + \frac{kT}{q} \ln \frac{N_A + N_B}{n_i} - \frac{kT}{q} \ln \frac{N_A + N_B}{N_B} \\ &= \psi_{Si,i} + \frac{kT}{q} \ln \frac{N_B}{n_i} \end{aligned}$$

This definition is made to facilitate a comparison of the equations for diffused with those for undiffused capacitors. In addition, the inversion potential of the capacitor becomes formally independent of the acceptor concentration in the surface region.

**Surface potential and depletion width.**—The one-dimensional Poisson equation at points between the edge of the depletion region,  $x_2$ , and  $x_1$  is

$$\frac{d^2\psi}{dx^2} = \frac{q}{\epsilon_S} N_B \quad (x_1 < x < x_2)$$

where  $\epsilon_S$  is the permittivity of the silicon. For  $0 < x < x_1$  it is

$$\frac{d^2\psi}{dx^2} = \frac{q}{\epsilon_S} (N_A + N_B) \quad (0 < x < x_1)$$

The signs on the right are positive because of the negatively charged acceptors. By integration with the boundary condition  $E(x > x_2) = 0$  one obtains the field strength  $E(x)$ . A second integration with the boundary condition  $\psi(x_2) = 0$  leads to the surface potential,

$\psi_S = [\psi(x = 0) - \psi(x_1)] + \psi(x_1) = \frac{q}{2\epsilon_S} (N_A x_1^2 + N_B x_2^2)$ . The depletion width  $x_2$ , as a function of the surface potential  $\psi_S$  is

$$x_2 = \left( \frac{2\epsilon_S}{qN_B} \psi_S - \frac{N_A}{N_B} x_1^2 \right)^{1/2} \quad [2]$$

**High frequency capacitance in inversion.**—At the point of inversion a small amount of electrons,  $\delta q$ , removed from the field plate induces  $1/2 \delta q$  of electrons at the SiO<sub>2</sub>/Si interface and  $1/2 \delta q$  ionized acceptors at the edge of the depletion region. Therefore, the surface potential of inversion is determined by the doping level at the edge of the depletion region. It is equal to twice the bulk Fermi potential. A term of  $3(kT/q)$  is added to bring the capacitor into deep inversion for more realistic calculated  $C_{\min}/C_{\text{ox}}$  values

$$\psi_{S,i} = \frac{kT}{q} \left( 2 \ln \frac{N_B}{n_i} + 3 \right)$$

The depletion width in inversion, from Eq. [2], is

$$x_{2,i} = \left( \frac{2\epsilon_S}{qN_B} \psi_{S,i} - \frac{N_A}{N_B} x_1^2 \right)^{1/2}$$

The capacitance per unit area of the space charge layer in the silicon is given by

$$C_{S,i} = \frac{\epsilon_S}{x_{2,i}}$$

Adding the reciprocal capacitances of this depletion layer and of the oxide layer one obtains an expression for the high frequency inversion, or minimum, capacitance normalized to the capacitance of the oxide layer

$$\begin{aligned} \frac{C_{\min}}{C_{\text{ox}}} &= \frac{1}{1 + \frac{C_{\text{ox}}}{C_{S,i}}} \\ &= \left[ 1 + \frac{\epsilon_{\text{ox}}}{\epsilon_S} \frac{1}{t_{\text{ox}}} \left( \frac{2\epsilon_S}{qN_B} \psi_{S,i} - \frac{N_A}{N_B} x_1^2 \right)^{1/2} \right]^{-1} \end{aligned}$$

In Fig. 4,  $C_{\min}/C_{\text{ox}}$  of a capacitor with a 0.1  $\mu\text{m}$  SiO<sub>2</sub> layer and  $N_B = 2 \times 10^{15} \text{ cm}^{-3}$  is plotted vs.  $N_A$  for several values of  $x_1$ . These curves demonstrate that the doping level in the diffused layer can become quite high before the minimum capacitance rises above the value for the substrate. The bottom horizontal line is for  $x_1 = 0$  which represents a concentration profile of gallium in the form of a delta function at the SiO<sub>2</sub>/Si interface. It has the same effect as a fixed negative charge. The top curve corresponds to  $C_{\min}/C_{\text{ox}}$  of substrates uniformly doped with  $N_A$ . The sharp intercepts with this curve are artifacts resulting from the simplifying assumption of an abrupt transition of the hole concentration from  $(N_A + N_B)$  to  $N_B$  at  $x_1$ .

**Inversion voltage.**—The inversion voltage,  $V_i$ , is the sum of the surface potential in inversion and the voltage drop across the insulator

$$\begin{aligned} V_i &= \psi_{S,i} + \frac{Q_s}{C_{\text{ox}}} \\ &= \psi_{S,i} \\ &\quad + \frac{1}{C_{\text{ox}}} \left[ N_A x_1 + N_B \left( \frac{2\epsilon_S}{qN_B} \psi_{S,i} - \frac{N_A}{N_B} x_1^2 \right)^{1/2} \right] \end{aligned}$$

$V_i$  is a virtually linear function of  $N_A x_1$  for  $x_1$  up to  $x_1 = x_2$ . An example is shown in Fig. 5.  $N_A x_1$  is the amount of indiffused gallium which acts like a negative fixed charge at the SiO<sub>2</sub>/Si interface.

Conversely, the amount of gallium in the silicon can be determined from the inversion voltages before and after the diffusion

$$N_A x_1 \cong C_{\text{ox}} \Delta V_i = C_{\text{ox}} (V_i, \text{ after Ga} - V_i, \text{ before Ga})$$

If the diffusion profile follows a complementary error function, the concentration of dopant at the interface ( $x = 0$ ) is

$$N(x = 0) \cong \frac{\sqrt{\pi}}{2\sqrt{D_2 t}} C_{\text{ox}} \Delta V_i$$

where  $D_2$  is the diffusion coefficient of the dopant in silicon, and  $t$  is the diffusion time.

### Diffusion of Gallium

Following a survey of the literature on the diffusion of gallium in silicon and in silicon dioxide, the experimental procedures and the equipment are described. Next, results are presented concerning the dependence of the Ga concentration in Si on the ratio of the partial pressures of H<sub>2</sub> and H<sub>2</sub>O over the Ga<sub>2</sub>O<sub>3</sub> source. The Ga concentration in Si is found to depend on the Ga<sub>2</sub>O pressure in the gas phase. Another paragraph deals with the determination of the effective coefficient of diffusion of Ga in SiO<sub>2</sub>. The section concludes with a discussion of the mobile ionic charge introduced to the SiO<sub>2</sub> by the Ga diffusion.

### Previous Studies

The first investigation of the coefficient of diffusion of gallium in silicon was carried out by Fuller and Ditzenberger (19). Using bare crystals and a small quantity of Ga<sub>2</sub>O<sub>3</sub> as a source in quartz ampuls initially filled with 10<sup>-3</sup> mm air, these authors determined  $D_{\text{Ga}}(\text{Si}) = 3.6 \times \exp(-3.51 \text{ eV}/kT) \text{ cm}^2 \text{ sec}^{-1}$  for temperatures between 1105° and 1360°C. Frosch and Derick

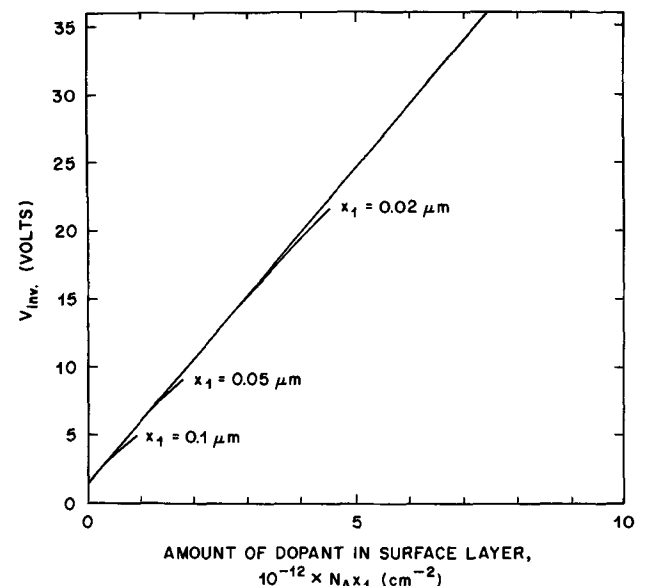


Fig. 5. Inversion voltage  $V_{\text{inv}}$ , of a MOS capacitor with a "box" diffusion profile, as a function of the indiffused amount of dopant,  $N_A x_1$ .

(2) developed a two temperature zone open tube technique to diffuse Ga into Si at 1200° and 1300°C using a Ga<sub>2</sub>O<sub>3</sub> source and a wet hydrogen carrier gas; in a later study (20), they determined the weight loss of Ga and of Ga<sub>2</sub>O<sub>3</sub> in H<sub>2</sub>-H<sub>2</sub>O mixtures at 950°C, and the surface concentration of Ga in Si wafers as a function of the composition of the carrier gas (H<sub>2</sub>-H<sub>2</sub>O and CO-H<sub>2</sub>O mixtures) flowing over a Ga<sub>2</sub>O<sub>3</sub> source. Kurtz and Gravel (21) employed the technique of Frosch and Derick, with a Ga source and a dry argon carrier, to determine the diffusion coefficient in bare Si at 1130°-1358°C,  $D_{\text{Ga}}(\text{Si}) = 164 \times \exp(-4.07/kT)$ . Boltaks and Dzharov (22) annealed "in gallium vapor" at 1180°-1340°C silicon wafers into which high concentrations of antimony had been diffused and found accelerated diffusion of Ga in comparison to control samples where  $D_{\text{Ga}} = 2.1 \exp(-3.51/kT)$ . In the first radiotracer study Kren, Masters, and Wajda (23) used an elemental radioactive gallium source for diffusion into oxide-covered silicon at 1200°C in evacuated ampuls. The concentration profile of Ga followed a complementary error function with  $D_{\text{Ga}} = 2.9 \times 10^{-12} \text{ cm}^2 \text{ sec}^{-1}$ , while the density of holes as determined by incremental sheet resistance measurements was found to be lower than  $N_{\text{total}}$  at  $N_{\text{total}} \geq 1 \times 10^{18} \text{ cm}^{-3}$ . (In tracer measurements on bulk Ga-doped Si, Wolfstirn (4) had found considerable deionization.) The results of Kren and co-workers are supported by the data of Okamura (24) who neutron activated Ga diffused at 1250°C ( $D_{\text{Ga}} = 1.3 \times 10^{-11} \text{ cm}^2 \text{ sec}^{-1}$ ) from a Ga droplet on a Si wafer in an ampul filled with dry argon, and also found deionization at  $N_{\text{total}} \geq 1 \times 10^{18} \text{ cm}^{-3}$ . Makris and Masters (25) diffused Ga in evacuated ampuls at 900°-1050°C from Ga-doped Si powder into Si wafers. The Ga diffusion profiles were measured after neutron activation, and the resulting diffusion coefficients were combined with data from Ref. (19, 21-23) to give  $D_{\text{Ga}}$  (intrinsic Si) =  $60 \times \exp(-3.89 \text{ eV}/kT)$ . The diffusion coefficient of Ga in highly boron-doped Si was found to increase linearly with the boron concentration at  $N_{\text{B}} \geq 1 \times 10^{19} \text{ cm}^{-3}$ . In a study of the diffusion of Ga into Si from Ga doped ( $1-4 \times 10^{18} \text{ cm}^{-3}$ ) epitaxial silicon layers covered with Si<sub>3</sub>N<sub>4</sub>, Ghoshtagore (26) determined the coefficient "free from surface effects"  $D_{\text{Ga}} = 0.374 \times \exp(-3.39 \text{ eV}/kT)$  between 1143°-1393°C. In three studies Okamura (24, 27, 28) observed retardation of gallium diffusion both during codiffusion with donors and during diffusion into heavily doped n-type silicon as well as enhanced solubility in the latter. Retardation of the Ga diffusion during codiffusion with arsenic and phosphorous is also described in a communication by Nakajima and Ohkawa (29). An increase of the hole lifetime by the preparation of a Si-Ga alloy from Ga films spread over Si wafers has been reported (30).

Frosch and Derick (2) demonstrated the high diffusivity of Ga through SiO<sub>2</sub> films. Using their two temperature zone technique with Ga<sub>2</sub>O<sub>3</sub> as a source in wet nitrogen-hydrogen gas, Grove, Leistiko, and Sah (3) determined the diffusion coefficient of Ga in SiO<sub>2</sub> through 1 to 4 μm SiO<sub>2</sub> films at 1100° and 1250°C. From the measurement of the junction depths, they arrived at a value for  $D_{\text{Ga}}(\text{SiO}_2) = 1.04 \times 10^5 \times \exp(-4.17 \text{ eV}/kT)$ , as well as at a value for the distribution coefficient between Si and SiO<sub>2</sub>,  $m \approx 20$ . In a recent communication, Nakajima and Ohkawa (31) reported more rapid diffusion of Ga at 1000°C in Si under SiO<sub>2</sub> than in bare Si. They used evacuated quartz ampuls and enough elemental Ga to establish a saturated vapor atmosphere.

#### Experimental

Si wafers 9-11 mil thick, 1 1/4 in. diameter, with (111) surfaces from one p-type (boron-doped) ingot with  $\rho = 4-9 \text{ ohm-cm}$  ( $1.5-4 \times 10^{15} \text{ cm}^{-3}$ ) and 9-11 mil thick, 1 1/4 in. diameter (111) wafers from one phosphorus-doped ingot with  $\rho = 6-7 \text{ ohm-cm}$  ( $7-8 \times 10^{14} \text{ cm}^{-3}$ ) were used. The silicon oxide films were

grown in steam at 1050°C (for  $t_{\text{ox}} \leq 1 \text{ μm}$ ) and at 1200°C (for  $t_{\text{ox}} = 2 \text{ μm}$ ). After the oxidation the wafers were annealed for 1/2 hr at 1050°C in pure nitrogen to reduce the fixed charge density at the SiO<sub>2</sub>/Si interface.

The gallium diffusions were carried out in a quartz container with a quartz furnace tube. The atmosphere of the furnace consisted of forming gas (15% H<sub>2</sub>, 85% N<sub>2</sub>) with varying amounts of water introduced as shown schematically in Fig. 6. The quartz container is shown in Fig. 7; it incorporates a rack for holding the wafers as well as two crucibles filled with the gallium source. Other than in a few preliminary experiments with elemental Ga, β-Ga<sub>2</sub>O<sub>3</sub> was used as a source material.

After the gallium diffusions the oxide layers were etched back by 100Å in dilute HF and aluminum was then evaporated through shadow masks for field plates. The metallization was followed by a 1/2 hr anneal at 400°C in hydrogen for reduction of the interface state density. The capacitance measurements were carried out with equipment and procedures similar to those described by Lopez (32).

The mobile ionic charge in the oxide films was derived from the ion drift current measured by the ramp method (33, 34). At a temperature of 300°C the voltage ramp was started at  $-1 \times 10^6 \text{ V-cm}^{-1}$  with a rate of voltage change of  $0.048 \text{ V-sec}^{-1}$ . Some samples were measured with the bias-temperature stress technique at 300°C and  $1 \times 10^6 \text{ V-cm}^{-1}$  with a stressing time of 10 min.

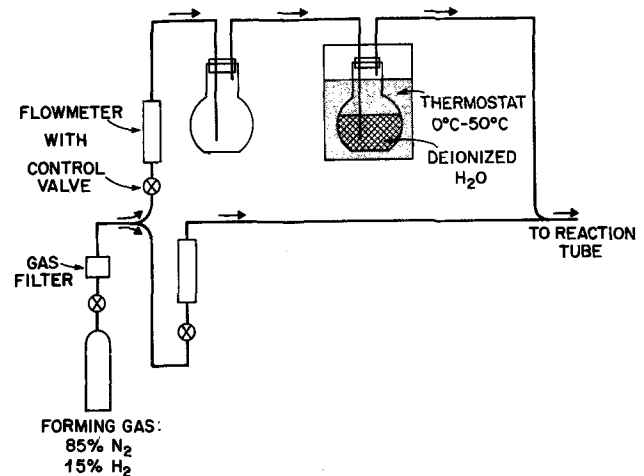


Fig. 6. The gas train of the diffusion furnace

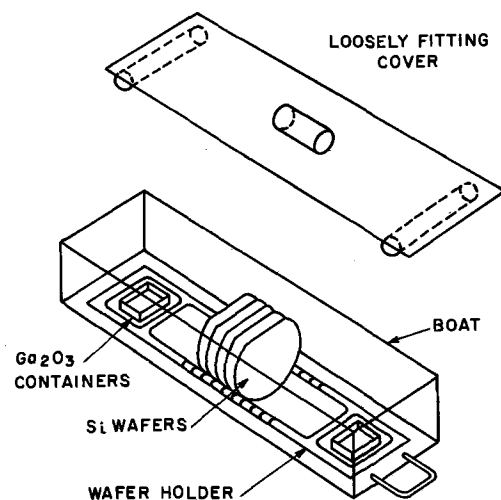
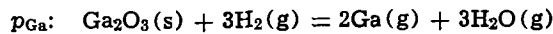


Fig. 7. Boat, cover, wafer holder, and Ga<sub>2</sub>O<sub>3</sub> containers in the diffusion furnace. All material is clear fused quartz.

### Mass Transport Species

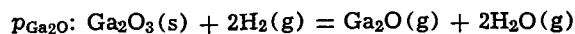
Three gallium-containing species are known to exist over  $\text{Ga}_2\text{O}_3$ : Ga,  $\text{Ga}_2\text{O}$ , and GaO (35, 36). GaO is a typical high temperature species with a positive heat of formation at room temperature [ $\Delta H_{f,298}\text{GaO}(\text{g}) = 66.8 \text{ kcal}$  (37)]. Its maximum partial pressure at  $1000^\circ\text{C}$  is of the order of  $10^{-18} \text{ atm}$ . Therefore it is not considered in the following discussion about the mass transport species. The molecule which performs the mass transport to the silicon can be determined from the dependence of the concentration of gallium in the silicon at  $x = 0$  on the ratio  $(p_{\text{H}_2}/p_{\text{H}_2\text{O}})$  in the gas phase. Ga was diffused into wafers covered by  $0.1 \mu\text{m}$   $\text{SiO}_2$  at  $850^\circ$ ,  $950^\circ$ , and  $1050^\circ\text{C}$  with  $(p_{\text{H}_2}/p_{\text{H}_2\text{O}})$  ranging from 1.23 to 2020. To be useful in device processing the diffusion times were the shortest still leading to reproducible high concentrations of Ga in Si at the  $\text{SiO}_2/\text{Si}$  interface,  $N_{\text{Ga}}(x = 0)$ . The resulting gallium concentrations as a function of temperature,  $T$ , and of  $(p_{\text{H}_2}/p_{\text{H}_2\text{O}})$  are listed in Table I, and are plotted in Fig. 8. In an intermediate range,  $N_{\text{Ga}}(x = 0)$  depends linearly on  $(p_{\text{H}_2}/p_{\text{H}_2\text{O}})$ . A linear dependence points to  $\text{Ga}_2\text{O}$  as the species dominating the transport of gallium to the silicon. This follows from the equations relating  $p_{\text{Ga}}$  and  $p_{\text{Ga}_2\text{O}}$  to  $(p_{\text{H}_2}/p_{\text{H}_2\text{O}})$ , which are derived below.

The vapor pressures of Ga and  $\text{Ga}_2\text{O}$  over  $\text{Ga}_2\text{O}_3(\text{s})$  are determined by the ratio  $(p_{\text{H}_2}/p_{\text{H}_2\text{O}})$  as follows:



$$K_{p,1} = p_{\text{Ga}}^2 \left( \frac{p_{\text{H}_2\text{O}}}{p_{\text{H}_2}} \right)^3$$

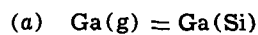
$$p_{\text{Ga}} = (K_{p,1})^{1/2} \left( \frac{p_{\text{H}_2}}{p_{\text{H}_2\text{O}}} \right)^{3/2}$$



$$K_{p,2} = p_{\text{Ga}_2\text{O}} \left( \frac{p_{\text{H}_2\text{O}}}{p_{\text{H}_2}} \right)^2$$

$$p_{\text{Ga}_2\text{O}} = K_{p,2} \left( \frac{p_{\text{H}_2}}{p_{\text{H}_2\text{O}}} \right)^2$$

The oxide is virtually saturated with respect to the diffusing Ga species. Therefore the activity of the species dissolved in the oxide at the  $\text{SiO}_2/\text{Si}$  interface equals that at the gas/ $\text{SiO}_2$  surface and the silicon surface is in equilibrium with the gas phase. The net reactions for the dissolution of the Ga carriers in Si are:



$$a_{\text{Ga}(\text{Si})} = x_{\text{Ga}(\text{Si})} \times \gamma_{\text{Ga}(\text{Si})} = p_{\text{Ga}}/p_{\text{Ga}}^0$$

For dilute solutions of Ga in Si,  $\gamma_{\text{Ga}(\text{Si})}$  is assumed to be constant. It is, after reformulation of the atomic fraction  $x_{\text{Ga}(\text{Si})}$  as the number of Ga atoms in one cubic centimeter of Si,  $N_{\text{Ga}(\text{Si})}$ , inversely proportional to Henry's constant,  $H_{\text{Ga}}$

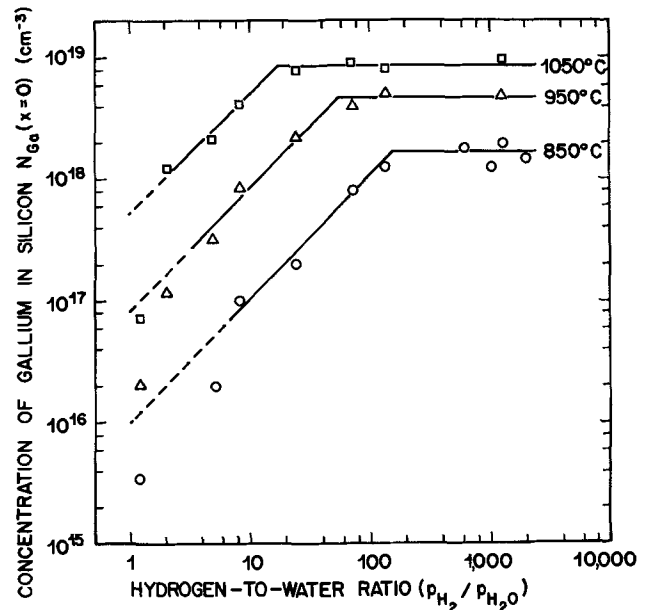
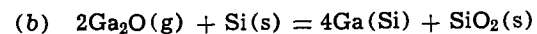


Fig. 8. The concentration of gallium in silicon at the  $\text{SiO}_2/\text{Si}$  interface,  $N_{\text{Ga}}(x = 0)$ , as a function of  $(p_{\text{H}_2}/p_{\text{H}_2\text{O}})$ , and of temperature.

$$N_{\text{Ga}(\text{Si})} = H_{\text{Ga}} \times p_{\text{Ga}} = H_{\text{Ga}} \times K_{p,1}^{1/2} \left( \frac{p_{\text{H}_2}}{p_{\text{H}_2\text{O}}} \right)^{3/2} \\ = \text{const}(T) \times \left( \frac{p_{\text{H}_2}}{p_{\text{H}_2\text{O}}} \right)^{3/2}$$



$$K_3 = \frac{a_{\text{Ga}(\text{Si})}^4}{p_{\text{Ga}_2\text{O}}^2}$$

$$a_{\text{Ga}(\text{Si})} = K_3^{1/4} \times p_{\text{Ga}_2\text{O}}^{1/2}$$

Introducing a formal Henry constant

$$N_{\text{Ga}(\text{Si})} = H_{\text{Ga}} \times K_3^{1/4} \times p_{\text{Ga}_2\text{O}}^{1/2}$$

$$= H_{\text{Ga}} \times K_3^{1/4} \times K_{p,2}^{1/2} \left( \frac{p_{\text{H}_2}}{p_{\text{H}_2\text{O}}} \right) \\ = \text{const}(T) \times \left( \frac{p_{\text{H}_2}}{p_{\text{H}_2\text{O}}} \right)$$

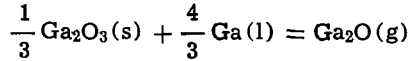
Thus, if the species responsible for the doping of the silicon is Ga vapor, the concentration of Ga in Si,  $N_{\text{Ga}}(x = 0)$ , has to be proportional to  $(p_{\text{H}_2}/p_{\text{H}_2\text{O}})^{3/2}$ . However, it is found experimentally (Fig. 8) that  $N_{\text{Ga}}(x = 0)$  is linearly proportional to  $(p_{\text{H}_2}/p_{\text{H}_2\text{O}})$  in accordance with the preceding equation. The  $\text{Ga}_2\text{O}$  vapor is therefore the source of the gallium dissolved in the silicon.

Table I. Concentration of gallium in silicon at the  $\text{SiO}_2/\text{Si}$  interface,  $N_{\text{Ga}}(x = 0)$ , and density of mobile charge,  $Q_{\text{mob}}$ , as a function of  $(p_{\text{H}_2}/p_{\text{H}_2\text{O}})$  and of temperature

$(p_{\text{H}_2}/p_{\text{H}_2\text{O}})$	$N_{\text{Ga}}(x = 0) \text{ (cm}^{-3}\text{)}$			$Q_{\text{mob}} \text{ (e}^{-}\text{/cm}^2\text{)}$		
	850°C (4 hr)	950°C (1 hr)	1050°C (½ hr)	850°C (4 hr)	950°C (1 hr)	1050°C (½ hr)
1.23	$3.5 \times 10^{15}$	$2.1 \times 10^{16}$	$7.2 \times 10^{17}$	$6.8 \times 10^{12}$	$6.1 \times 10^{12}$	$1.5 \times 10^{13}$
2.06	—	$1.2 \times 10^{17}$	$1.2 \times 10^{18}$	—	$4.3 \times 10^{12}$	$3.9 \times 10^{12}$
5.10	$1.9 \times 10^{16}$	$3.3 \times 10^{17}$	$2.1 \times 10^{18}$	$6.8 \times 10^{12}$	$2.4 \times 10^{12}$	$2.3 \times 10^{13}$
8.20	$9.7 \times 10^{15}$	$8.5 \times 10^{17}$	$4.2 \times 10^{18}$	$2.2 \times 10^{12}$	$3.0 \times 10^{12}$	$4.2 \times 10^{13}$
24.9	$2.0 \times 10^{17}$	$2.2 \times 10^{18}$	$7.8 \times 10^{18}$	$1.4 \times 10^{12}$	$4.7 \times 10^{12}$	—
72.1	$7.9 \times 10^{17}$	$3.9 \times 10^{18}$	$9.1 \times 10^{18}$	$1.4 \times 10^{12}$	$4.7 \times 10^{12}$	—
138	$1.3 \times 10^{18}$	$5.0 \times 10^{18}$	$8.0 \times 10^{18}$	$2.5 \times 10^{12}$	$1.4 \times 10^{13}$	—
715	$1.7 \times 10^{19}$	—	—	—	—	—
1050	$1.2 \times 10^{19}$	—	—	—	—	—
1420	$1.9 \times 10^{19}$	$4.8 \times 10^{19}$	$9.4 \times 10^{19}$	$4.8 \times 10^{13}$	$6.9 \times 10^{13}$	—
2020	$1.4 \times 10^{19}$	—	—	—	—	—



Above a certain ratio ( $p_{\text{H}_2}/p_{\text{H}_2\text{O}}$ ),  $N_{\text{Ga}}(x=0)$  is found to remain constant. This limit of ( $p_{\text{H}_2}/p_{\text{H}_2\text{O}}$ ), which depends on the temperature, is reached when the vapor pressure of gallium,  $p_{\text{Ga}}$ , reaches the equilibrium pressure over the liquid gallium. The ensuing formation of a condensed gallium phase reduces the number of degrees of freedom by one. According to the phase rule,  $p_{\text{Ga}_2\text{O}}$  is then constant for a given temperature. It is determined by the equilibrium



$$K_{p,3} = p_{\text{Ga}_2\text{O}}$$

The pressures of the gaseous species participating in this equilibrium,  $p_{\text{Ga}}$  and  $p_{\text{Ga}_2\text{O}}$ , are plotted as a function of  $1/T$  in Fig. 9. Also shown in Fig. 9 is the equilibrium constant for the formation of  $\text{Ga}_2\text{O}(\text{g})$  from  $\text{Ga}_2\text{O}_3(\text{s})$  in a  $\text{H}_2$ - $\text{H}_2\text{O}$  atmosphere,  $K_{p,2}$ . When  $p_{\text{H}_2} = p_{\text{H}_2\text{O}}$ ,  $p_{\text{Ga}_2\text{O}}$  is equal to this constant. The curve ( $p_{\text{H}_2}/p_{\text{H}_2\text{O}}$ )<sub>max</sub> denotes the hydrogen-to-water ratio needed to raise  $p_{\text{Ga}_2\text{O}}$  to its maximum value, viz., in equilibrium with  $\text{Ga}_2\text{O}_3$  and Ga.

The sources of the thermodynamic data used in this graph are: ( $\text{fef}_T$  is the free energy function)  $\Delta H^\circ_{f,298}$  of  $\beta$ - $\text{Ga}_2\text{O}_3$ , Wagman *et al.* (37);  $\Delta H^\circ_{f,298}$  of  $\text{Ga}_2\text{O}(\text{g})$ , Thurmond and Frosch (38);  $\text{fef}_T$  of  $\text{Ga}_2\text{O}_3(\text{s})$  and of  $\text{Ga}_2\text{O}(\text{g})$ , Cochran and Foster (39);  $\text{fef}_T$  of Ga(g), Munir and Searcy (40);  $\text{fef}_T$  of  $\text{H}_2(\text{g})$ ,  $\text{fef}_T$  of  $\text{H}_2\text{O}(\text{g})$ , and  $\Delta H^\circ_{f,298}$  of  $\text{H}_2\text{O}(\text{g})$ , JANAF Tables (41).

The sharp drop of  $N_{\text{Ga}}(x=0)$  as ( $\text{H}_2/\text{H}_2\text{O}$ ) is going to unity is due to the insensitivity of the inversion voltage shift method to very small ( $< 2 \times 10^{11} \text{ cm}^{-2}$ ) amounts of indiffused Ga. This tends to give values for  $N_{\text{Ga}}(x=0)$  which are too low (Fig. 8).

Our results imply that  $\text{SiO}_2$  constitutes a diffusion barrier for Ga, but not for  $\text{Ga}_2\text{O}$ . The four points obtained by Frosch and Derick (20) on pre-oxidized silicon agree with our data. On the other hand  $N_{\text{Ga}}(x=0)$  reaches the solubility limit (8),  $\sim 4 \times 10^{19} \text{ cm}^{-3}$ , after long diffusion times (42).  $N_{\text{Ga}}(x=0)$  is then deter-

mined by the chemical potential of gallium. The unpublished study by Moore who is reported (43) to have found  $N_{\text{Ga}} \propto (p_{\text{H}_2}/p_{\text{H}_2\text{O}})^{3/2}$  was presumably carried out on bare silicon or with long diffusion times on oxidized wafers.

#### Coefficient of Diffusion of Ga in $\text{SiO}_2$

The diffusion coefficient of Ga in  $\text{SiO}_2$  films was determined from the amount of Ga diffused into the Si. At a given temperature and for a given diffusion time, this amount depends on the thickness of the oxide film. Sah and co-workers (44) have solved the equations for this sequential diffusion. The dopant concentration in the semiconductor as a function of position and time is

$$N_2(x, t) = m(1 - \alpha) N_0 \sum_{n=0}^{\infty} \alpha^n \text{erfc} \frac{(2n + 1)t_{\text{ox}} + rx}{2\sqrt{D_1 t}}$$

$t$  is the time,  $N_0$  is the solubility of the diffusant in the oxide,  $t_{\text{ox}}$  is the thickness of the oxide layer,  $x$  is the depth in the silicon measured from the  $\text{SiO}_2/\text{Si}$  interface,  $D_1$  is the diffusion coefficient in the  $\text{SiO}_2$ , and  $D_2$  that in the Si.  $m = N_2/N_1$  is the distribution coefficient between Si and  $\text{SiO}_2$ ,  $\alpha = (m - r)/(m + r)$ , with  $r = \sqrt{(D_1/D_2)}$ .

The total amount of gallium diffused into the silicon up to time  $t$  is

$$Q(t) = \sum_{x=0}^{\infty} N_2(x, t) dx = 4m N_0 (1 - \alpha) D_1 t \sum_{n=0}^{\infty} \alpha^n \text{ierfc } y(0) \quad [3]$$

with

$$y(0) = \frac{(2n + 1)t_{\text{ox}}}{2\sqrt{D_1 t}}$$

From the work of Grove *et al.* (3)  $\alpha$  is known to be smaller than unity. In an argument similar to the one presented by these authors we reason that the value of  $\text{ierfc } y(0)$  drops rapidly with increasing  $y(0)$ . As a consequence the series in Eq. [3] converges strongly and is well approximated by its first term to give

$$Q(t) \cong 4m N_0 \alpha (1 - \alpha) D_1 t \text{ierfc} \frac{t_{\text{ox}}}{2\sqrt{D_1 t}}$$

$Q(t)$  was determined at  $800^\circ\text{C}$  ( $t = 4 \frac{1}{2}$  hr),  $850^\circ\text{C}$  ( $t = 1$  hr), and  $900^\circ\text{C}$  ( $t = 10$  min) for  $0.1 \leq t_{\text{ox}} \leq 2.0 \mu\text{m}$ . The diffusion length of gallium in bare silicon,  $2\sqrt{D_2 t}$ , was taken from the paper by Makris and Masters (25). It ranges from 0.015 to  $0.020 \mu\text{m}$  under these conditions (Table II). The depletion width in inversion,  $x_2$ , is then larger than the depth of the profile regardless of the surface concentration. We have discussed earlier in this paper that  $Q(t)$  can be determined from the shift of the inversion voltage  $\Delta V_i$  which results from the indiffusion of gallium

$$Q(t) \cong C_{\text{ox}} \cdot \Delta V_i$$

$\Delta V_i$  for the wafers diffused at  $800^\circ$ - $900^\circ\text{C}$  is listed in Table III.

The logarithm of the first integral of the complementary error function is very closely a linear function of  $t_{\text{ox}}/2\sqrt{D_1 t}$  with the slope depending on the

Table II. Diffusion coefficient of gallium in silicon,  $D_2$ , taken from Makris and Masters (25), diffusion time  $t$ , and diffusion coefficient of gallium in  $\text{SiO}_2$ ,  $D_1$  (this study)

T ( $^\circ\text{C}$ )	$D_2$ ( $\text{cm}^2 \text{sec}^{-1}$ )	t (sec)	$D_1$ ( $\text{cm}^2 \text{sec}^{-1}$ )
800	$5.9 \times 10^{-17}$	16,200	$2.0 \times 10^{-12}$
850	$2.1 \times 10^{-16}$	3,600	$8.3 \times 10^{-12}$
900	$1.1 \times 10^{-15}$	600	$1.9 \times 10^{-11}$

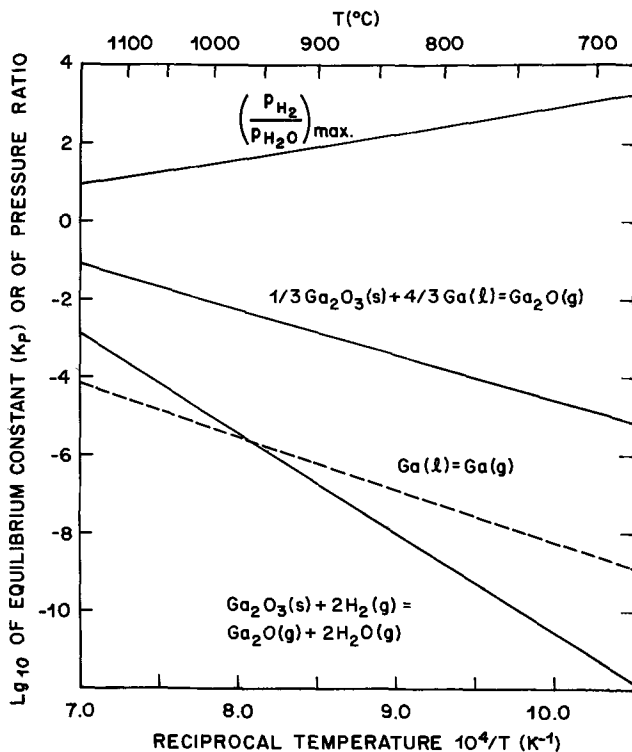


Fig. 9. Equilibrium constants for the formation of  $\text{Ga}_2\text{O}$  vapor and of Ga vapor (see text for references.) ( $p_{\text{H}_2}/p_{\text{H}_2\text{O}}$ )<sub>max</sub> is the ratio needed to bring  $p_{\text{Ga}_2\text{O}}$  in the reaction listed at the bottom up to the maximum  $p_{\text{Ga}_2\text{O}}$  given by the equilibrium between  $\text{Ga}_2\text{O}_3(\text{s})$  and Ga(l).

Table III. Shift of the inversion voltage,  $\Delta V_L$ , and amount of gallium diffused through  $\text{SiO}_2$  of thickness  $t_{\text{ox}}$ , as a function of temperature.  $(p_{\text{H}_2}/p_{\text{H}_2\text{O}}) = 1200$

$t_{\text{ox}}$ ( $\mu\text{m}$ )	$\Delta V_L$ (V)			$Q_t$ ( $\text{cm}^{-2}$ )		
	800°C	850°C	900°C	800°C	850°C	900°C
0.1	4	7	17	$8.6 \times 10^{11}$	$1.5 \times 10^{12}$	$3.7 \times 10^{12}$
0.2	6.5	11.5	27	$7.0 \times 10^{11}$	$1.2 \times 10^{12}$	$3.0 \times 10^{12}$
0.3	10	13.5	36	$7.2 \times 10^{11}$	$9.7 \times 10^{11}$	$2.6 \times 10^{12}$
0.4	11	20	48	$5.9 \times 10^{11}$	$1.1 \times 10^{12}$	$2.6 \times 10^{12}$
0.5	17	24	50	$7.3 \times 10^{11}$	$1.0 \times 10^{12}$	$2.2 \times 10^{12}$
1.0	21	30	60	$4.5 \times 10^{11}$	$6.5 \times 10^{11}$	$1.3 \times 10^{12}$
2.0	—	28	32	—	$3.0 \times 10^{11}$	$3.5 \times 10^{11}$

$$Q(t) = \frac{1}{q} C_{\text{ox}} \Delta V_L = 2.16 \times 10^6 \times \frac{\Delta V_L \text{ (V)}}{t_{\text{ox}} \text{ (cm)}} \text{ (cm}^{-2}\text{)}$$

range of this approximation. For  $0 < t_{\text{ox}}/2\sqrt{D_1 t} \lesssim 1$ , the slope is  $B = -1.05$  with base 10 logarithms

$$\log_{10} \text{ierfc}(t_{\text{ox}}/2\sqrt{D_1 t}) \cong \log_{10}(1/\sqrt{\pi}) + B(t_{\text{ox}}/2\sqrt{D_1 t})$$

Thus

$$\begin{aligned} \log_{10} C_{\text{ox}} \Delta V_L &\cong \log_{10} \left[ \frac{4}{\sqrt{\pi}} m N_0 \alpha (1 - \alpha) D_1 t \right] \\ &\quad + B(t_{\text{ox}}/2\sqrt{D_1 t}) \\ &= \lim_{t_{\text{ox}} \rightarrow 0} (\log_{10} C_{\text{ox}} \Delta V_L) - 1.05(t_{\text{ox}}/2\sqrt{D_1 t}) \end{aligned}$$

In Fig. 10,  $Q(t)$  is plotted logarithmically vs.  $t_{\text{ox}}$ . The slopes in Fig. 10 were evaluated for  $D_1$  which is listed in Table II. A least squares treatment gives for the temperature range from 800° to 900°C,  $D_{\text{Ga}}(\text{SiO}_2) = 0.73 \times \exp(-2.46 \text{ eV}/kT)$ . Combined with the data points of Grove *et al.* (3) for 1100° and 1250°C,  $D_{\text{Ga}}(\text{SiO}_2) = 1.0 \times 10^5 \times \exp(-4.17 \text{ eV}/kT)$ , an equation covering the range from 800° to 1250°C is obtained

$$D_{\text{Ga}}(\text{SiO}_2) = 5.2 \times 10^{-4} \times \exp(-1.77 \text{ eV}/kT)$$

This is the line plotted in Fig. 11. The lack of agreement between the results of Grove and co-workers and of the present study is certainly not satisfactory. It is understandable in view of the numerous approxima-

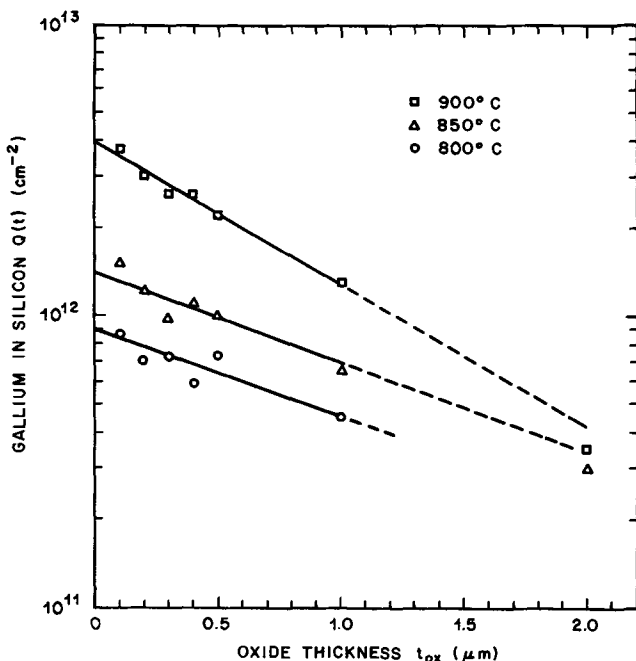


Fig. 10. Semilogarithmic plot of the amount of gallium diffused through  $\text{SiO}_2$ ,  $Q(t)$ , as a function of oxide thickness,  $t_{\text{ox}}$ , and of temperature.  $(p_{\text{H}_2}/p_{\text{H}_2\text{O}}) = 1200$ .

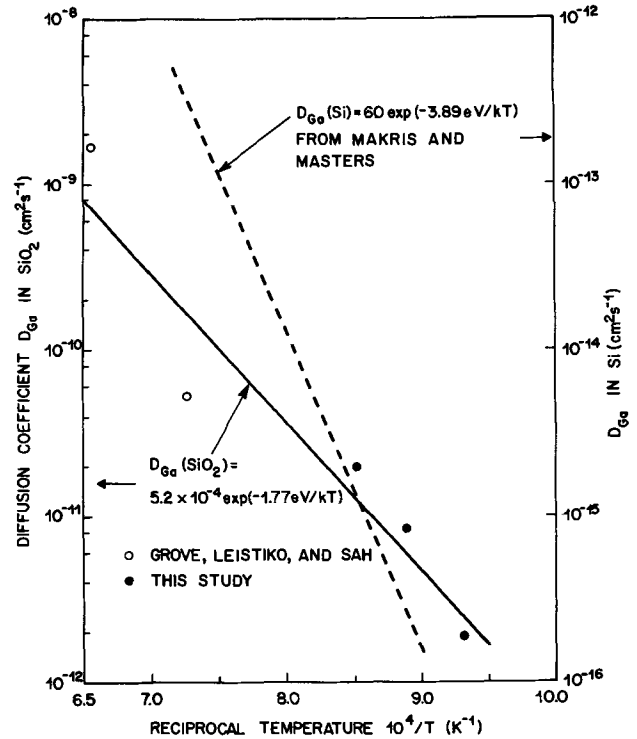


Fig. 11. Left ordinate: Diffusion coefficient of gallium through  $\text{SiO}_2$  films. The straight line is from a least squares regression on the data of Grove *et al.* (3) and of this study. Right ordinate: Diffusion coefficient of gallium in silicon, selected by Makris and Masters (25).

tions which had to be made in both investigations. In view of the results on the mobile charge in  $\text{SiO}_2$ , presented in the next section, one may speculate that our study gives a coefficient for the diffusion of " $\text{Ga}_2\text{O}$ " through  $\text{SiO}_2$ , while Grove *et al.* measured the coefficient for the diffusion of " $\text{Ga}$ ." Then, of course, it would not be permissible to combine these data to the line shown in Fig. 11. This plot, however, was found to be useful and realistic for device development work.

With the intention of reproducing the results of Nakajima and Ohkawa (31) who found Ga diffusions which were deeper in  $\text{SiO}_2$  covered Si than in bare Si, we diffused Ga into bare and oxidized (0.1, 0.5, and 1.0  $\mu\text{m}$   $\text{SiO}_2$ ) n-type wafers. At 950°C (5 hr) and  $(p_{\text{H}_2}/p_{\text{H}_2\text{O}}) = 66.0$ , and at 1050°C (20 min) and  $(p_{\text{H}_2}/p_{\text{H}_2\text{O}}) = 7.67$  we found junctions to be deeper in bare Si by about 0.1  $\mu\text{m}$ . It was quite difficult to delineate the junctions in the oxide-covered portions by angle lapping and staining. They were found to be very diffuse and prone to either under or overstaining.

#### Mobile Charge in $\text{SiO}_2$ after Ga Diffusion

In samples where the gallium dissolved at the surface of the silicon,  $N_{\text{Ga}}(x=0)$ , has reached its equilibrium value, the equilibrium concentration is also attained by the gallium species in the oxide film. A correlation between these two concentration values may be expected.

During C-V measurements on highly gallium-doped substrates we noticed effects typical of mobile positive charge in  $\text{SiO}_2$ . High frequency C-V curves shifted parallel to the voltage axis after bias at room temperature. The inversion capacitance increased with increasing positive voltage, a characteristic of lateral a-c current flow brought about by positive charge in the oxide (45). It was reasonable to expect this positive charge, which had been introduced during the gallium diffusion, to be related to the gallium dissolved in the oxide. Then the positive charge in the equilibrated oxides should be correlated with  $N_{\text{Ga}}(x=0)$ . In the simplest case of constant chemical activity coefficients, and of all positive charge being mobile at 300°C, a linear

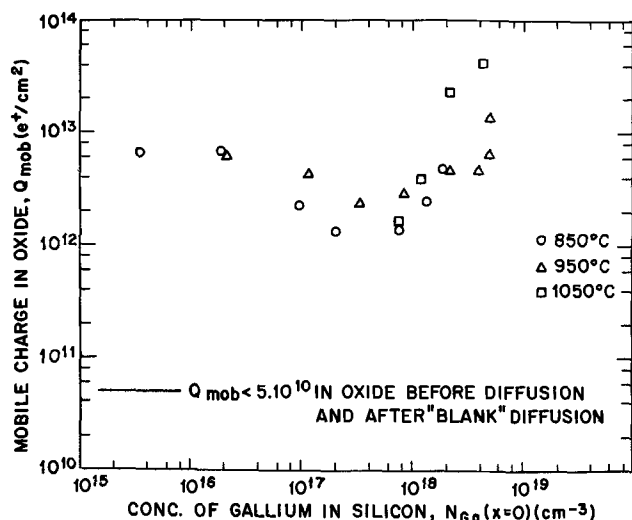


Fig. 12. Mobile charge in  $\text{SiO}_2$ ,  $Q_{\text{mob}}$ , plotted vs. the concentration of gallium in silicon at the  $\text{SiO}_2/\text{Si}$  interface,  $N_{\text{Ga}}(x=0)$ . The samples are those used for Fig. 8.

dependence of this mobile charge,  $Q_{\text{mob}}$ , upon  $N_{\text{Ga}}(x=0)$  is expected.

The mobile charge measured with the ramp technique is listed in Table I and plotted in Fig. 12 vs.  $N_{\text{Ga}}(x=0)$ . Voltage shifts after bias-temperature stressing gave similar results. The stressing of most oxide films, however, resulted in dielectric breakdown. Some samples could not be measured even with the ramp technique because of breakdown.

The mobile charge in the oxide films before the gallium diffusion was equal to or less than  $5 \times 10^{10} e^+/\text{cm}^2$ . The quartz boat and the  $\text{Ga}_2\text{O}_3$  were also free of mobile charge as demonstrated by the following experiment. An oxide covered wafer was annealed for 3 hr at  $850^\circ\text{C}$  in the boat on the wafer rack and in the presence of the  $\text{Ga}_2\text{O}_3$  source. In the oxidizing gas (2%  $\text{O}_2$  in  $\text{N}_2$ ) no gallium was transported from the source to the wafer, and indeed the  $Q_{\text{mob}}$  was less than  $5 \times 10^{10} e^+/\text{cm}^2$ .

It is surprising to see  $Q_{\text{mob}}$  to be large and approximately constant independent of the value of  $N_{\text{Ga}}(x=0)$ . (At  $N_{\text{Ga}}(x=0) > 2 \times 10^{18} \text{cm}^{-3}$  the oxide films were visibly damaged; we ascribe the rise of  $Q_{\text{mob}}$  in this range to a change in the properties of the oxide.) Two qualitative explanations come to mind: first, the amount of gallium dissolved in the oxide is equal to a constant and uniform concentration of native defects in the oxide; second, that most of the gallium dissolved resides near the interfaces, and that the amount of gallium is determined by the characteristics of these interfaces.

All data in Fig. 12 are for  $0.1 \mu\text{m}$  thick oxide films.  $Q_{\text{mob}}$  in  $0.5$  and  $1.0 \mu\text{m}$  oxides was comparable to that shown in Fig. 12. Therefore  $Q_{\text{mob}}$  is not proportional to the volume of the oxide and the first explanation cannot be correct. The alternate interpretation of a strong accumulation of gallium near the interfaces is more likely. This interpretation is supported by the analogy of  $\text{Ga}_2\text{O}$  to  $\text{Na}_2\text{O}$ .  $\text{Ga}_2\text{O}$  vapor may dissolve in  $\text{SiO}_2$  in the same manner as  $\text{Na}_2\text{O}$  leading to the U-shaped concentration profiles which have been measured for sodium (46). It is possible to calculate distribution profiles for these ionic impurities using the image force model put forward by Williams and Woods (47). A maximum concentration of the order of  $10^{18}$  ions per  $\text{cm}^2$  of interface can be estimated in qualitative agreement with our data. However, both the theoretical basis and the existing experimental data are insufficient for a rigid treatment and the agreement mentioned above may be fortuitous.

Qualitative experiments on the removal of the mobile charge were carried out. It was found that a variety of controlled annealing procedures as well as the

formation of a phosphate glass layer can reduce the density of mobile ions.

### Summary

It was shown in this study that:

1. The amount of dopant in shallow diffused layers in Si covered with  $\text{SiO}_2$  films can be obtained from the shift of the MOS inversion voltage which arises from the diffusion.
2. For comparatively short diffusion times the concentration of Ga in Si covered with  $\text{SiO}_2$  films is linearly proportional to  $(p_{\text{H}_2}/p_{\text{H}_2\text{O}})$  over a  $\beta\text{-Ga}_2\text{O}_3$  source. Therefore, the molecule  $\text{Ga}_2\text{O}$  performs the transport of gallium to the silicon.
3. The diffusion coefficient of Ga in  $\text{SiO}_2$  films in the temperature range from  $800^\circ$  to  $900^\circ\text{C}$  has not been measured previously. It is  $D_{\text{Ga}(\text{SiO}_2)} = 0.73 \times \exp(-2.46 \text{ eV}/kT)$ .
4. Mobile charge with a density of at least  $1 \times 10^{12} \text{cm}^{-2}$  is introduced to the  $\text{SiO}_2$  films under all diffusion conditions except when the molecule  $\text{Ga}_2\text{O}$  is not present.

### Acknowledgments

The authors are indebted to E. N. Fuls and P. J. Boddy for their support. They would like to thank C. F. Gibbon, J. R. Brews, H. C. Casey, Jr., B. Tell, A. S. Jordan, and M. E. Weiner for helpful discussions, and C. D. Thurmond for several clarifying comments.

Manuscript submitted March 18, 1974; revised manuscript received June 24, 1974.

Any discussion of this paper will appear in a Discussion Section to be published in the June 1975 JOURNAL. All discussions for the June 1975 Discussion Section should be submitted by Feb. 1, 1975.

The publication costs of this article have been assisted by Bell Laboratories.

### REFERENCES

1. M. Ghezzeo and D. M. Brown, *This Journal*, **120**, 146 (1973).
2. C. J. Frosch and L. Derick, *ibid.*, **104**, 547 (1957).
3. A. S. Grove, O. Leistiko, and C. T. Sah, *J. Phys. Chem. Solids*, **25**, 985 (1964).
4. K. B. Wolfstirn, *ibid.*, **16**, 279 (1960).
5. S. Sze, Private communication.
6. G. L. Pearson and J. Bardeen, *Phys. Rev.*, **75**, 865 (1949).
7. G. F. Neumark, *Phys. Rev.*, **B5**, 408 (1972).
8. F. A. Trumbore, *Bell System Tech. J.*, **39**, 205 (1960).
9. S. Wagner and C. N. Berglund, *Rev. Sci. Instr.*, **43**, 1775 (1972).
10. T. Tanaka, *Japan. J. Appl. Phys.*, **10**, 84 (1971).
11. G. Schottky, *Solid-State Electron.*, **14**, 467 (1971).
12. H. Hara, *Electron. Commun., Japan*, **55-C**, 99 (1972).
13. T. Warabisako, I. Yoshida, and T. Tokuyama, *J. Japan. Soc. Appl. Phys., Supplement*, **42**, 181 (1973).
14. K. G. Aubuchon, "International Conference on Properties and Use of M.I.S. Structures, Grenoble, June 17-20, 1969," J. Borel, Editor; pp. 575-590. Centre d'Etudes Nucléaires de Grenoble, (1969).
15. R. M. Swanson and J. M. Meindl, *IEEE Solid-State Circuits*, **SC-7**, 146 (1972).
16. T. W. Sigmon and R. Swanson, *Solid-State Electron.*, **16**, 1217 (1973).
17. S. D. Brotherton and P. Burton, *ibid.*, **13**, 1591 (1970).
18. G. Doucet and F. van de Wiele, *ibid.*, **16**, 417 (1973).
19. C. S. Fuller and J. A. Ditzenberger, *J. Appl. Phys.*, **27**, 544 (1956).
20. C. J. Frosch and L. Derick, *This Journal*, **105**, 695 (1958).
21. A. D. Kurtz and C. L. Gravel, *J. Appl. Phys.*, **29**, 1456 (1958).
22. B. I. Boltaks and T. D. Dzharov, *Soviet Phys. Solid State*, **5**, 2649 (1964).
23. J. G. Kren, B. J. Masters, and E. S. Wajda, *Appl. Phys. Letters*, **5**, 49 (1964).

24. M. Okamura, *Japan. J. Appl. Phys.*, **10**, 434 (1971).
25. J. S. Makris and B. J. Masters, *J. Appl. Phys.*, **42**, 3750 (1971).
26. R. N. Ghoshtagore, *Phys. Rev.*, **B3**, 2507 (1971).
27. M. Okamura, *Japan. J. Appl. Phys.*, **7**, 1067 (1968).
28. M. Okamura, *ibid.*, **7**, 1231 (1968).
29. Y. Nakajima and S. Ohkawa, *ibid.*, **10**, 1745 (1971).
30. J. L. Lambert and G. Köhl, *Solid-State Electron.*, **14**, 430 (1971).
31. Y. Nakajima and S. Ohkawa, *Japan. J. Appl. Phys.*, **11**, 1742 (1972).
32. A. D. Lopez, *Rev. Sci. Instr.*, **44**, 200 (1973).
33. N. J. Chou, *This Journal*, **118**, 601 (1971).
34. M. Kuhn and D. J. Silversmith, *ibid.*, **118**, 966 (1971).
35. S. A. Shchukarev, G. A. Semenov, and I. A. Ratkovskii, *Zh. Prikl. Khim.*, **35**, 1454 (1962).
36. R. P. Burns, *J. Chem. Phys.*, **44**, 3307 (1966).
37. D. D. Wagman, W. H. Evans, V. B. Parker, I. Halow, S. M. Bailey, and R. H. Schumm, *Nat. Bur. Std. Tech. Note 270-3*, U.S. Government Printing Office, Washington, D. C. (1968).
38. C. D. Thurmond and C. J. Frosch, *This Journal*, **111**, 184 (1964).
39. C. N. Cochran and L. M. Foster, *ibid.*, **109**, 144 (1962).
40. Z. A. Munir and A. W. Searcy, *ibid.*, **111**, 1170 (1964).
41. JANAF Interim Thermochemical Tables, Thermal Laboratory, Dow Chemical Company, Midland, Michigan (1960).
42. S. M. Spitzer, Private communication.
43. A. S. Grove, "Physics and Technology of Semiconductor Devices," p. 44, John Wiley & Sons, Inc., New York (1967).
44. C. T. Sah, H. Sello, and D. A. Tremere, *J. Phys. Chem. Solids*, **11**, 288 (1959).
45. E. H. Nicollian and A. Goetzberger, *IEEE Trans. Electron Dev.*, **ED-12**, 108 (1966).
46. E. Yon, W. H. Ko, and A. B. Kuper, *IEEE Trans. Electron Dev.*, **ED-13**, 276 (1966).
47. R. Williams and M. H. Woods, *Appl. Phys. Letters*, **22**, 458 (1973).

## Optical Investigation of Different Silicon Films

Ch. Köhl, H. Schlötterer,\* and F. Schwidofsky

Siemens AG, Forschungslaboratorien, München, Germany

### ABSTRACT

In the case of weak absorption, the spectral reflectance of a thin film on a nonabsorbing substrate can be used to determine the spectral dependence of the absorption constant. For this purpose, a relatively simple method is described evaluating the envelopes of the interference extrema. This method as well as a Kramers-Kronig analysis were applied to epitaxial, polycrystalline, and amorphous silicon films in the energy range 0.5-5.5 eV. With decreasing crystal quality, changes in the spectral dependence of the optical constants of these films are observed. This can be understood in terms of a decreasing long range order.

Optical investigations are very promising for evaluating film properties because of the nondestructive measuring technique. In order to examine the quality of semiconducting thin films on insulating substrates, electrical and optical measurements can be performed. Evaluating electrical measurements with very thin films can sometimes be problematical because of the increasing surface contribution with decreasing film thickness. Results of optical investigations in the region of weak absorption can easily be assigned to the volume of the thin film.

The determination of the optical constants of an absorbing material seems to be somewhat difficult. Many optical measurement techniques applied to thin films already exist and are summarized, e.g., by Heavens (1). Schopper (2) measures amplitude and phase of the reflected and the transmitted beams on both sides of the film and calculates the refractive index  $n$ , the absorption index  $k$ , and the thickness  $d$  of the film. Malé's (3) evaluation requires the reflectance at each side of the film and the transmittance of the film. Then a set of curves must be drawn giving reflectance and transmittance vs. thickness for a set of values of  $n$  and  $k$ . Brattain and Briggs (4) measure the transmittance of the films of several thicknesses and fit the values of  $n$  and  $k$  by a trial-and-error method. Howson (5) determines the optical constants of the film from transmission measurements, evaluating the transmittance halfway on the  $h\nu$ -axis between two neighboring interference extrema. Also common for determining the optical constants of relatively thin films is the analysis of elliptically polarized light.

In the present paper, a method of determining the spectral dependence of the optical constants is described in which only the reflectance of one single film is required. Since in the case of multiple interference both the reflection and the transmission coefficients contribute to the amplitude of the reflected beams, reflection measurements also provide information similar to transmission measurements. One advantage of evaluating reflection measurements rather than transmission measurements for thin films is based on the fact that, contrary to the transmittance, the average oscillatory reflectance does not slope down to zero with increasing film absorption. Therefore, the reflectance extrema can be better located and analyzed. Furthermore, the reflection measurements are independent both of the quality of the rear surface and of the plane parallelism of the substrate; films on higher absorbing substrates can easily be measured, too.

### Experimental

Reflection measurements were performed with a Zeiss two beam spectrophotometer Model DMR 21 having a wave number range of  $\nu^* = 1/\lambda = \nu/c = 4-50 \times 10^3 \text{ cm}^{-1}$  (corresponding to  $\lambda = 2.5-0.2 \mu\text{m}$  or  $E = 0.5-6.2 \text{ eV}$ ). For this purpose, a reflection attachment had to be constructed which is not commercially available, since the Zeiss spectrophotometer is designed for transmission measurements only. The angle of incidence is  $\theta = 30^\circ$ . In order to obtain absolute values for the reflectance of the samples, the absolute reflectance of the aluminum mirror used in the reference beam had to be known. The reflectance of that mirror was obtained using a Beckman two beam spectrophotometer Model DK 2A with a special "VW" re-

\* Electrochemical Society Active Member.

Key words: thin film, absorption, refractive index, Kramers-Kronig-analysis, optical interferences.

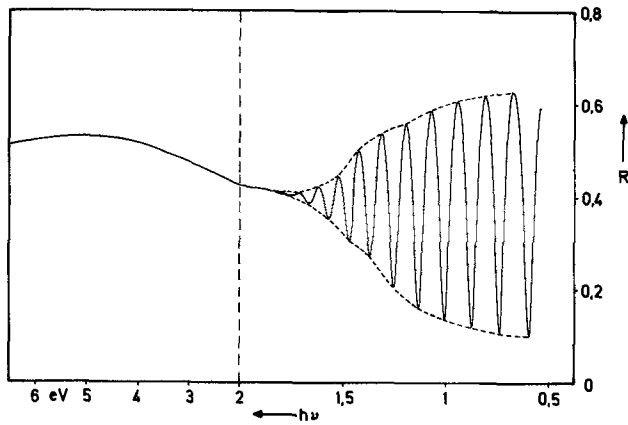


Fig. 1. Spectral reflectance curve of a polycrystalline silicon film. The dashed lines represent the envelopes of the reflectance extrema.

flection attachment (6). Thus, a reflectance calibration of our attachment for the Zeiss spectrophotometer was performed. Measurements were made with a series of epitaxial, polycrystalline, and amorphous silicon films on several substrates. Figure 1 shows a typical reflectance interference curve of a polycrystalline silicon film on spinel (sample 2 of Table I). The envelopes connect the extrema of the interference fringes and are used to determine the absorption constant. Silicon films with different substrate temperatures were investigated and for the present paper the results of the silicon films listed in Table I are shown, each one representative for the respective substrate temperature. Samples 1 and 2 were obtained by chemical vapor deposition with thermal decomposition of silane, whereas sample 3 was obtained by vacuum evaporation in a diffusion pumped system using an electron beam gun. The size of the coherently scattering regions near the surface was obtained by means of reflection electron diffraction (7). The geometrical film thickness was measured with a Perthen stylus tracer Model ECW-L.

**Method of Analysis**

*Theory.*—Let us consider a homogeneous, isotropic, plane parallel, thin film with the thickness  $d_1$  and the complex refractive index  $\bar{n}_1 = n_1 - ik_1$  ( $n_1$  denotes the real refractive index, and  $k_1$  the absorption index) at normal incidence of the light (Fig. 2). The adjoining media air ( $n_0$ ) and substrate ( $n_2$ ) are assumed to be nonabsorbing ( $k_0 = k_2 = 0$ ) and infinite.

In an absorbing medium, the intensity of light decreases exponentially with  $e^{-\alpha x}$ , where  $x$  denotes the light path in the film and  $\alpha$  the absorption constant which is related to  $k$  by  $\alpha = 4\pi k\nu^*$ . Taking into account multiple interference, the complex amplitude reflectivity can be obtained by summing up all interfering beams leaving the film surface. The amplitude reflection  $\bar{r}$  and transmission coefficients  $\bar{t}$  at an interface are given by the Fresnel coefficients listed in Table II. For simplicity, in the following we shall omit for the film the index and only write  $n, k, \alpha, d$ .

Using the complex Fresnel coefficients the complex amplitude reflectance of the film is given (1) by

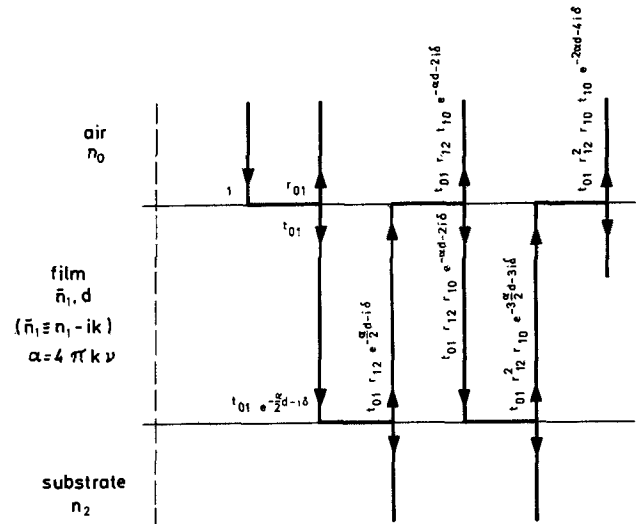


Fig. 2. Amplitudes of light for an absorbing thin film in the case of multiple interference at normal incidence. For simplicity and clearness: no oblique incidence contrary to the experiment, and lateral displacement of the light rays.

$$\bar{r} = \bar{r}_{01} + \frac{\bar{t}_{01}\bar{r}_{12}\bar{t}_{10}e^{-\alpha d - 2i\delta}}{1 - \bar{r}_{12}\bar{r}_{10}e^{-\alpha d - 2i\delta}} \quad [1]$$

where  $\delta = 2\pi n_1 d \nu^*$  denotes the phase difference caused by traversing the film once from one interface to the other. With the simplifying assumption  $k^2 \ll n^2$ , which is fulfilled for silicon films in the infrared and part of the visible region we obtain for the intensity reflectance

$$R = |\bar{r}|^2 = \frac{r_{01}^2 e^{\alpha d} + r_{12}^2 e^{-\alpha d} + 2r_{01}r_{12} \cos 2\delta}{e^{\alpha d} + r_{01}^2 r_{12}^2 e^{-\alpha d} + 2r_{01}r_{12} \cos 2\delta} \quad [2]$$

where  $r_{ij}$  denotes the real part of the complex Fresnel coefficient  $\bar{r}_{ij}$  (Table II).

The extrema of the reflectance  $R(h\nu)$  are determined by the extrema of the  $\cos 2\delta$  terms ( $\cos 2\delta = \pm 1$ ). With increasing  $\alpha d$ ,  $\Delta R$  decreases, where  $\Delta R = R_{\max} - R_{\min}$  and  $R_{\max}, R_{\min}$  denote the values of the corresponding envelopes at a certain energy.

*Application.*—Figure 1 shows that there are two regions of the reflectance curve that can be evaluated. The region where interference fringes are registered is treated first. Here the wave number position as well as the absolute height of the extrema of the interference fringes can be analyzed. The refractive index of the film is obtained from the wave number position of the extrema (8) provided the film thickness is known. The condition  $\cos 2\delta = \pm 1$  is fulfilled for both kinds of extrema when  $\delta = z\pi$  with  $z = 0, 1/2, 1, 3/2, \dots$  yielding  $n = z/2d\nu^*$ .

The absorption constant can be obtained by analyzing the height of the reflectance curve. Here either the zero passages or the extrema of the  $\cos 2\delta$  term in Eq. [2] can be regarded. The condition of  $\cos 2\delta = 0$  is satisfied halfway on the  $h\nu$ -axis between two neighboring extrema. In that way, Howson (5) determines the absorption constant but applied to transmission-measurements. His method of analysis seems to be

Table I. Silicon films used in this investigation

Sample	Crystal quality	Substrate	Substrate temperature, °C	Deposition rate, μm/min	Film thickness, μm
1	Single crystalline	Sapphire	1050	1	0.65
2	Polycrystalline	Spinel	680	0.05	0.83
3	Amorphous	Spinel	20	1	0.44

Table II. Fresnel coefficients for the interfaces air-film, film-air, and film-substrate

$\bar{r}_{01} = \frac{n_0 - \bar{n}_1}{n_0 + \bar{n}_1}$	$\bar{r}_{10} = \frac{\bar{n}_1 - n_0}{\bar{n}_1 + n_0}$	$\bar{r}_{12} = \frac{\bar{n}_1 - n_2}{\bar{n}_1 + n_2}$
$\bar{t}_{01} = \frac{2n_0}{n_0 + \bar{n}_1}$	$\bar{t}_{10} = \frac{2\bar{n}_1}{\bar{n}_1 + n_1}$	$\bar{t}_{12} = \frac{2\bar{n}_1}{\bar{n}_1 + n_2}$

rather inaccurate because of the relatively steep slope of the interference fringes. From the maximum and minimum reflectance values which satisfy the condition  $\cos 2\delta = \pm 1$  the envelopes mentioned before can be constructed. At a definite energy either the difference or the quotient of these envelopes can be regarded. However, the quotient method is advantageous as it is nearly independent of a possible error in the reflectance calibration of the spectrometer, which is not the case with the difference method.

Calculating the quotient  $Q = R_{\max}/R_{\min}$  from Eq. [2] yields the following equation for  $e^{4\alpha d}$

$$e^{4\alpha d} - (r_{01}^2 - 1) \frac{2r_{12}}{r_{01}} \left( \frac{Q+1}{Q-1} \right) e^{3\alpha d} + \left\{ \frac{r_{12}^2}{r_{01}^2} (r_{01}^2 - 1)^2 - 2r_{12}^2 \right\} e^{2\alpha d} + (r_{01}^2 - 1) \frac{2r_{12}^3}{r_{01}} \left( \frac{Q+1}{Q-1} \right) e^{\alpha d} + r_{12}^4 = 0 \quad [3]$$

Only one of the four solutions of this equation is physically suitable, namely

$$e^{\alpha d} = \frac{r_{01}r_{12} - r_{12}/r_{01}}{Q-1} \left( \frac{Q+1}{2} + \sqrt{Q} \right) + \sqrt{\left( \frac{r_{01}r_{12} - r_{12}/r_{01}}{Q-1} \right)^2 \cdot \left( \frac{Q+1}{2} + \sqrt{Q} \right)^2 + r_{12}^2} \quad [4]$$

Using Eq. [4], it is possible to determine absolutely the spectral dependence of  $\alpha$  or  $k$  by means of the quotient of the envelopes of the reflectance interference curve of the film. For this purpose, the spectral dependence of the refractive index of the film, the refractive index of the substrate, and the film thickness have to be known. It must be kept in mind, that  $\alpha$  represents a mean value of the exponential loss of light intensity throughout the film volume including volume scattering. However, surface scattering, due to interface irregularities of the film is considered where necessary by taking into account the intensity loss at both interfaces. The wavelength dependence of the specular reflectance of a rough surface is treated according to the method of Bennett *et al.* (9). The roughness correction was tested by comparing the absorption constant thus obtained with the absorption constant of the same film, but subsequently polished (no correction necessary). There was a good agreement between both results within  $\pm 4\%$ .

Equation [4] has been derived for the case of normal incidence of the light. Since we measure at oblique incidence ( $\theta = 30^\circ$ ), we have to correct the refractive index of the film regarding the angle of incidence by substituting  $n$  by

$$n' = \sqrt{n^2 - \sin^2\theta} \approx n - \frac{\sin^2\theta}{2n} \quad [5]$$

Other effects due to the oblique incidence of light such as polarization effects are neglected, as we measure with natural light.

The validity of the approximations of Eq. [4] and [5] has been tested by comparison with numerical calculations based on the Fresnel formulas for oblique incidence without any approximations. This comparison shows that the error in  $\alpha$  calculated according to Eq. [4] for silicon films with a film thickness  $\sim 1 \mu\text{m}$  is smaller than  $\pm 2\%$ , thus justifying our approximations globally.

Taking into account all possible sources of errors, namely, the determination of  $Q$ , the film thickness with a possible gradient, the refractive index of both film and substrate, the mathematical simplifications, and the roughness correction, the error  $\Delta\alpha$  of the determination of the absorption constant with the quotient method is estimated to be  $\Delta\alpha \leq \pm (10\% + 100 \text{ cm}^{-1})$  for silicon films in the thickness range  $d = 0.2-$

$2 \mu\text{m}$ . Using the same substrate for the films, the uncertainty of  $\pm 100 \text{ cm}^{-1}$  caused by the possible error in the refractive index of the substrate can be neglected when different films are to be compared.

The region where no interference fringes are recorded can be evaluated with a Kramers-Kronig analysis with respect to  $n$  and  $k$  (10). Since the energy range was rather limited with our measurements, a method of Roessler was applied (11) allowing for the unknown reflectance values by taking into account the absorption index measured at a definite energy.

### Results with Silicon Films

Both, refractive index  $n$  and absorption index  $k$  of the samples 1, 2, and 3 listed in Table I have been determined in the whole measured spectral region. The slight dispersion of the refractive index of the spinel (sapphire) substrate (12, 13) from  $n_2 = 1.74$  ( $n_2 = 1.78$ ) at  $\lambda = 0.435 \mu\text{m}$  to  $n_2 = 1.695$  ( $n_2 = 1.738$ ) at  $\lambda = 2 \mu\text{m}$  has been taken into account. The rear surface of the spinel is unpolished and therefore its contribution to the finally reflected intensity can be neglected because of the small aperture of the spectrometer.

Figure 3 shows that in the region where interference fringes can be recorded both the polycrystalline and the amorphous silicon film have a higher refractive index than the epitaxial film, whereas the latter does not differ essentially from bulk silicon, regarding the refractive index.

In the adjoining region, where no interference fringes are recorded, and the Kramers-Kronig analysis can be applied, the refractive index of the epitaxial silicon film shows three maxima which are located at nearly the same energies as the corresponding maxima of bulk silicon. The polycrystalline and amorphous silicon films show only one broad maximum. With decreasing crystal quality (size of the coherently scattering regions: for the polycrystalline film 4 nm, for the amorphous film 0.7 nm) that maximum is shifted toward smaller energies.

Figure 4 shows the spectral dependence of the absorption index also evaluated both from the interference fringes and by means of a Kramers-Kronig analysis. It can be seen clearly that, in the region where interference fringes are recorded, the absorption index strongly increases with increasing lattice disorder, thus offering a quick and reliable criterion for the crystal quality of the films. Again, the polycrystalline and amorphous silicon films, unlike the epitaxial film, show only one broad maximum.

### Discussion

The spectral dependence of the refractive index shows a discontinuity at the energy where detectable interference fringes end and the pure surface reflectance without interference fringes begins. The occur-

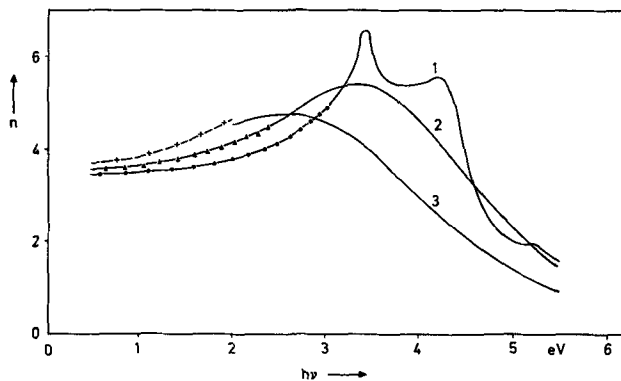


Fig. 3. Spectral dependence of the refractive index for different silicon films. Curve 1, epitaxial; curve 2, polycrystalline, and curve 3, amorphous. ●▲+, Film volume (by interference method); —, film surface (by Kramers-Kronig analysis).

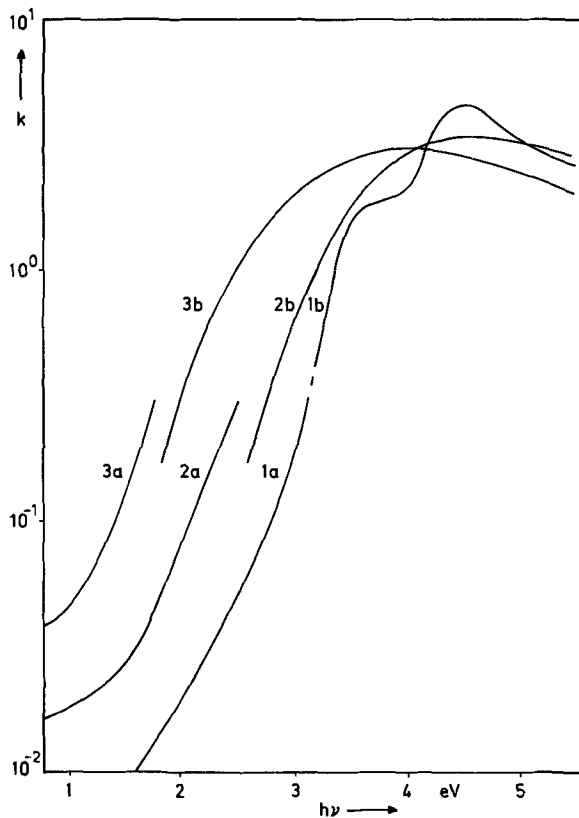


Fig. 4. Spectral dependence of the absorption index for different silicon films. Number 1, epitaxial; 2, polycrystalline; and 3, amorphous. a, Film volume (by interference method); and b, film surface (by Kramers-Kronig analysis).

rence of the discontinuity can be understood if one considers the different light paths the two methods comprise. As the light traverses through the whole film in the case of an interference measurement, one obtains the mean value of the local optical constants. On the other hand, the results of the Kramers-Kronig analysis evaluating the surface reflectance of the film yield the optical constants of a very thin region near the surface, showing a lower value of the refractive index compared to the value obtained by the interference method. It has been reported in an earlier paper that the infrared refractive index of similar films decreases with increasing grain size (14). It has been shown, too, that for polycrystalline silicon films the surface grain size increases with increasing thickness (15). Thus, the discontinuity of the spectral dependence of the refractive index obtained by the two methods of analysis can be understood assuming a gradient of the refractive index, the smaller value being at the surface. Some interference measurements with films of different thicknesses have confirmed these assumptions. The discontinuity of the spectral dependence of the absorption constant can analogously be explained by a gradient of  $k$ .

In order to have a continuous reflectance curve for the Kramers-Kronig analysis in the interference region the reflectance values were calculated according to the effective refractive index, and then fitted by a constant of proportionality to the surface reflectance curve.

To be able to analyze the different spectral behavior of sample 1, 2, and 3 a plot of  $\epsilon'' = 2nk$  is shown in Fig. 5. Since  $\epsilon''$  is mainly determined by energy band structure properties, the optical transitions with the epitaxial silicon film can easily be assigned to the respective maxima of the  $\epsilon''$ -spectrum. Thus the first peak at 3.6 eV corresponds to transitions  $\Gamma'_{25} - \Gamma_{15}$  for  $\mathbf{k} = (000)$ , the second peak at 4.3 eV, to  $X_4 - X_1$  for

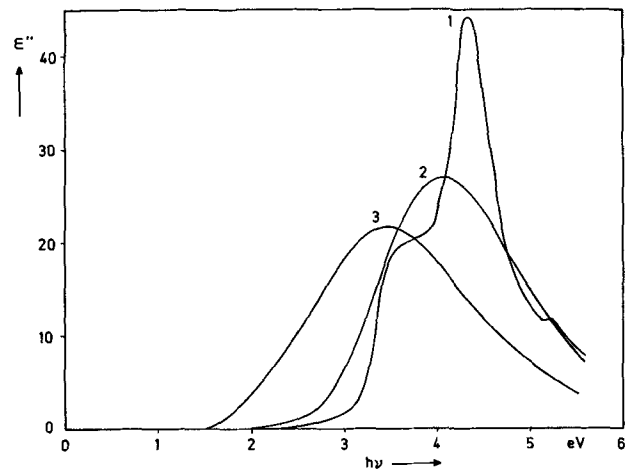


Fig. 5. Spectral dependence of the imaginary part  $\epsilon''$  of the dielectric constant for different silicon films. Curve 1, epitaxial; curve 2, polycrystalline; and curve 3, amorphous.

$\mathbf{k} = 2\pi/a (100)$ , and the third peak at 5.3 eV, to  $L'_3 - L_3$  for  $\mathbf{k} = 2\pi/a (1/2 \ 1/2 \ 1/2)$  (16). According to Kramer (17), the band edges near the axis  $L - \Gamma$  are less influenced by disorder than at other  $\mathbf{k}$ -points in the first Brillouin zone. A comparison of the epitaxial silicon film with the amorphous one shows clearly that the second maximum corresponding to  $X_4 - X_1$  transitions is affected the most by the disorder of the film and disappears. This is in good agreement with Kramer's statement.

The only maximum of the amorphous film lies at nearly the same energy as the first maximum of the epitaxial silicon film, but it is considerably broader than the latter. The broadening of the maximum can be understood considering the smearing of the band edges with crystals of high disorder contrary to the sharp band edges observed with single crystals. This can also be expressed as a lifetime broadening (17) consisting in the increase of the energy uncertainty with decreasing lifetime of the crystal electrons, i.e., decreasing coherence length of the lattice.

Figure 3 shows a shift of the extrema of the  $n$ -spectrum toward lower energies with increasing crystal disorder, which is also observed with the corresponding  $\epsilon'$ -curves ( $\epsilon' = n^2 - k^2$ ). A similar shift in the  $\epsilon'$ -curves will be obtained by increasing the damping factor in the classical dispersion relation often used for the description of the spectral dependence of the refractive index.

In the infrared, the refractive index of polycrystalline and amorphous silicon films is increased compared with epitaxial silicon films. This fact can be understood with a model described in a previous paper (18), giving a connection to the internal surface. The increase of the refractive index has been confirmed by applying the optical sum rules (19) as has been done by Philipp (20) for silicon and  $\text{SiO}_y$  films. The first sum rule is given by

$$\epsilon_{0,\text{eff}} = 1 + \frac{2}{\pi} \int_0^{E_0} E^{-1} \epsilon''(E) dE$$

where  $\epsilon_{0,\text{eff}}$  is the optical dielectric constant for  $h\nu = 0$ , associated with optical transitions in the energy range  $E \leq E_0$ . For our silicon films, a plot of  $\epsilon_0$  vs.  $E_0$  shows that the saturation value of  $\epsilon_0$  is close to the increased  $n^2(0)$  as has been expected. [ $n(0)$ : refractive index as extrapolated to  $E = 0$  from the Kramers-Kronig calculations.] The  $\epsilon_{0,\text{eff}}$  vs.  $E_0$  curve of our amorphous silicon film differs from that reported by Philipp. As it is known [see e.g., (14)] that the preparation conditions have a distinct influence on the optical properties of films, those differences can be due to different preparation parameters.

Further information is obtained applying the second sum rule (19), which is given by

$$n_{\text{eff}} = \frac{8\pi\epsilon_0 m}{h^2 N e^2} \int_0^{E_0} E \epsilon''(E) dE \quad (\text{in SI-units})$$

where  $m$  is the free electron mass,  $N$  the atom density, and  $n_{\text{eff}}$  the effective number of electrons per atom in the energy range  $E \leq E_0$ . For our silicon films with increasing  $E_0$ ,  $n_{\text{eff}}$  approaches asymptotically a value of approximately 4, independent of the crystal disorder. Comparing this result with the results of Philipp (20) for  $\text{SiO}_2$  films, a noticeable oxygen content can be excluded for our silicon films.

Altogether it has been shown that the difference in the spectral dependence of the optical constants of epitaxial, polycrystalline, and amorphous silicon films both in the region where interference fringes can be recorded and in the adjoining region where Kramers-Kronig analysis can be applied, can be understood by considering the degree of crystal disorder of the films.

#### Acknowledgments

The authors wish to express their appreciation to Mr. R. Gessner, Mr. U. Klein, and Mrs. S. Rheinboldt for providing the samples used in this investigation and to Dr. E. Preuss for valuable discussions.

Manuscript submitted Oct. 15, 1973; revised manuscript received June 5, 1974.

Any discussion of this paper will appear in a Discussion Section to be published in the June 1975 JOURNAL. All discussions for the June 1975 Discussion Section should be submitted by Feb. 1, 1975.

The publication costs of this article have been assisted by Siemens AG.

#### REFERENCES

- O. S. Heavens, "Optical Properties of Thin Solid Films," Dover Publications, New York (1965).
- H. Schopper, *Z. Phys.*, **131**, 215 (1952).
- D. Malé, *Compt. Rend. Acad. Sci., Paris*, **230**, 1349 (1950).
- W. H. Brattain and H. B. Briggs, *Phys. Rev.*, **75**, 1705 (1949).
- R. P. Howson, *Brit. J. Appl. Phys., J. Phys. D.*, **1**, 15 (1968).
- H. Lappe, *Beckman Rept.*, **2**, 26 (1970).
- G. Schimmel, "Elektronenmikroskopische Methodik," p. 45, Springer Berlin, Heidelberg, New York (1969).
- W. G. Spitzer and W. Tanenbaum, *J. Appl. Phys.*, **32**, 744 (1961).
- H. E. Bennett and J. O. Porteus, *J. Opt. Soc. Am.*, **51**, 123 (1961).
- T. S. Robinson, *Proc. Phys. Soc. (London)*, **B65**, 910 (1952).
- D. M. Roessler, *Brit. J. Appl. Phys.*, **16**, 1119 (1965).
- F. Rinne, *N. Jb. Mineral.(A), Beil.-Bd.*, **58**, 43 (1928).
- I. H. Malitson, *J. Opt. Soc. Am.*, **52**, 1377 (1962).
- R. Hezel and F. Schwidetsky, *Siemens Forsch. Entw.-Ber.*, **1**, 297 (1972).
- R. Hezel, *Verhandl. DPG(VI)*, **8**, 260 (1973).
- M. Cardona and F. H. Pollack, *Phys. Rev.*, **142**, 530 (1966).
- B. Kramer, *Phys. Status Solidi (b)*, **47**, 501 (1971).
- F. Schwidetsky, *Thin Solid Films*, **18**, 45 (1973).
- D. L. Greenaway, "Optical Properties and Band Structure of Semiconductors," p. 13, Pergamon Press, Oxford (1968).
- H. R. Philipp, *J. Phys. Chem. Solids.*, **32**, 1935 (1971).

## Polymeric Resists for X-Ray Lithography

L. F. Thompson, E. D. Feit, M. J. Bowden, P. V. Lenzo, and E. G. Spencer

Bell Laboratories, Murray Hill, New Jersey 07974

#### ABSTRACT

It has been demonstrated that high resolution patterns can be delineated in poly(methyl methacrylate) using x-ray radiation modulated by an absorbing mask. For this technique to be effective, families of both positive and negative x-ray resists must be available which have properties that allow exploitation of x-ray lithography. This paper describes the evaluation of several polymeric electron resists for x-ray resists and demonstrates a good correlation between x-ray energy absorbed and electron energy absorbed for equivalent degrees of chemical reaction. The incorporation of heavy atoms in the resist to enhance the x-ray energy absorption and hence increase the material sensitivity has been demonstrated. The effects of a resist's contrast on ultimate pattern resolution and fidelity is discussed in relationship to the x-ray mask contrast.

It has been demonstrated that high resolution patterns can be delineated in poly(methyl methacrylate) (PMMA) using x-ray radiation modulated by an absorbing mask (1-3). PMMA is at present the most widely used resist material for x-ray (1) and electron lithography, and has been used with both techniques to delineate high resolution patterns. PMMA dissolves more rapidly after irradiation (4) and is classified as a positive resist. A negative resist crosslinks and becomes insoluble on exposure to actinic radiation.

Recently, several new positive and negative polymeric resists sensitive to electron beam irradiation have been developed. The evaluation of these seven

materials as resists for x-ray lithography is reported here.

When a moderate energy electron (5-20 kV) or an x-ray photon enters a polymer film multiple chemical events are initiated. It is commonly accepted that organic polymers (those containing carbon, hydrogen, oxygen and/or nitrogen) will exhibit similar sensitivities (G-values) to both x-ray or electron irradiation. Two reactions of interest which may occur are chain scission and/or crosslinking. Energy absorption in the resist film is an important consideration when comparing x-ray and electron sensitivities. Electron energy absorption using a phenomenological approach has been described elsewhere (5) and is used in calculating electron doses in this paper. X-ray energy absorption is more straight forward to calculate, utilizing the following general expression (6)



Table I. Dose values of several polymer resists to both x-ray radiation and electrons

Material	Electron, coulombs/cm <sup>2</sup>	Electron, joules/cm <sup>2</sup>	X-ray, joules/cm <sup>2</sup>	Ratio of electron to x-ray dose
PMMA (POS)	1 × 10 <sup>-5</sup>	400	500	0.8
PBS (POS)	2 × 10 <sup>-6</sup>	80	14	5.71
PVFc	1 × 10 <sup>-4</sup>	4400	150	29.0
PDOP	1 × 10 <sup>-6</sup>	32.5	14	2.3
CER	8 × 10 <sup>-7</sup>	26	25	1.0
P (GMA-co-EA)	3 × 10 <sup>-7</sup>	9	5	1.8
EPB	1 × 10 <sup>-7</sup>	3	1	3.0
PB	2 × 10 <sup>-6</sup>	65	20	3.2

(a) Electron doses for negative resists are those required to yield ~50% gel remaining with a 0.5 $\mu$  initial film and a 10 kV electron beam. The positive resist doses are those to result in a relief image in a 0.5 $\mu$  initial film without affecting unirradiated film.

$$I = I_0 e^{-(\mu/\rho)t} \quad [1]$$

where  $I_0$  is the intensity of incident x-rays;  $I$  the intensity of x-rays after penetration through a thickness,  $t$ , of a homogeneous material having a linear absorption coefficient  $\mu$  for x-rays; and  $\rho$  the bulk density of the material.

The absorption coefficient ( $\mu$ ) is an additive function of the various atomic species present in the material (6). For a 0.5-1.0  $\mu$ m film of an organic polymer, it has been found that ~5-10% of the incident intensity of an 8 $\text{\AA}$  x-ray is absorbed. The effective sensitivity of a resist to x-ray radiation can be increased by chemically incorporating atoms of higher atomic number into the resist to increase the x-ray absorption, and poly(vinylferrocene) has been used as a model compound to illustrate this point, cf. Table I.

### Experimental

The preparation of poly(vinyl ferrocene) (PVFc) (7), crosslinking electron resist (CER) (8), poly(butene-1-sulfone) (PBS) (9, 10), epoxidized poly(butadiene) (EPB) (11, 12), poly(glycidyl methacrylate-co-ethylacrylate) [P(GMA-co-EA)] (13), and poly(diallyl-ortho-phthalate) (PDOP) (14) has been described elsewhere.

The resists were spin coated on the substrate and processed as shown in Table II. X-rays were produced by bombardment of an Al target with 6.25 keV electrons and the 8.34 $\text{\AA}$  K $\alpha$  line (1.486 keV) was the primary radiation used. X-ray exposure doses were determined as described by Lenzo and Spencer (3). An x-ray dose of 500 j/cm<sup>2</sup> (2.5 × 10<sup>-2</sup> j/cm<sup>2</sup> for a 500 nm film) was used as a standard reference exposure for PMMA (1, 2).

Some consideration should be given to doses used in the paper (both electron and x-ray) for positive and negative resists. The dose for negative resists was that necessary to result in 250 nm of an initial 500 nm film

after development. The electron sensitivities were determined (or normalized) with a 10 kV electron beam. The bulk doses listed in Table I (joules/cm<sup>2</sup>) have been corrected for the energy absorbed in the developed volume of film. Sensitivity of a positive resist is the dose which results in complete dissolution of the irradiated polymer while not dissolving unirradiated material. Bulk doses are for a 500 nm initial film. The ratio of x-ray to electron dose is given for convenience of comparing relative sensitivities of these materials used for both applications.

X-ray exposure requires a mask which consists of a substrate somewhat transparent to x-rays and a patterned absorber. This is described in detail by Smith, Spears, and Bernacki (2). The mask used in this paper consisted of a silicon substrate with gold absorbers. The Si/Au masks were fabricated with electron lithography using either EPB or P(GMA-co-EA) as electron resists. The resist was exposed using a flying spot scanner (15) interfaced to a Cambridge Mark II SEM and processed as previously described (12). The 400 nm Au absorption layer was subsequently ion etched and the Si transmission windows thinned to 3-10 $\mu$  using electrochemical etching (16).

### Results and Discussion

The resists evaluated in this study are listed below and summarized in Tables I and II.

1. Poly(butene-1-sulfone) (PBS) (9, 10) is a positive resist exhibiting an electron sensitivity of ~2 × 10<sup>-6</sup> coulombs cm<sup>-2</sup> when a 500 nm film is exposed with a 10 kV electron beam. The material is resistant to most chemical etching solutions, but does not withstand ion beam etching.

2. Epoxidized polybutadiene (EPB) (11, 12) is a low contrast, negative electron resist with a sensitivity of ~8 × 10<sup>-8</sup>-2 × 10<sup>-7</sup> coulombs cm<sup>-2</sup>. The polymer is highly reactive and must be handled carefully.

3. A terpolymer of methyl methacrylate, ethyl acrylate, and glycidyl methacrylate partially esterified with methyl acrylic acid (CER) (8, 17) is a medium contrast negative resist which exhibits a sensitivity of ~8 × 10<sup>-7</sup> coulombs cm<sup>-2</sup>. It is resistant to acidic and basic etching solutions and to ion etching.

4. Poly(diallyl ortho-phthalate) (PDOP) (14) is a negative resist that has a sensitivity of ~2 × 10<sup>-6</sup> coulombs cm<sup>-2</sup> and withstands high temperature processing (>150°C).

5. Poly(glycidyl methacrylate) (PGMA) and especially copolymers with ethyl acrylate [P(GMA-co-EA)] (13) are high contrast negative resists with a range of sensitivities between 8 × 10<sup>-9</sup> and 1 × 10<sup>-6</sup> coulombs cm<sup>-2</sup>. The copolymers exhibit high contrast and have excellent resistance to both chemical and ion etching.

6. Polybutadiene (PB) is a low sensitivity (1-2 × 10<sup>-6</sup> coulombs cm<sup>-2</sup>) medium contrast negative resist.

Table II. General processing conditions for several electron resists used as x-ray resists

Material	Spinning solvent	Prebake, °C	Electron dose, coulombs/cm <sup>2</sup>	Developer <sup>(d)</sup>	Postbake	Etching
PMMA	Ethylcellosolve	150°C, 1 hr	5 × 10 <sup>-5</sup>	MIBK-(g)2-propanol	170°C, 10-40 min	(a), (b), (e)
EPB	Dioxane	No	3 × 10 <sup>-7</sup>	Dioxane-MEK <sup>(f)</sup>	140°C, 5 min	(a), (b), (e)
P (GMA-co-EA)	Chlorobenzene	65°C, 5 min	3 × 10 <sup>-7</sup>	5:2 MEF <sup>(f)</sup> ethanol	70°C, 30 min	(a), (b), (e)
PDOP	(e)	25°C, 30 min	2 × 10 <sup>-6</sup>	(h)	240°C, 15 min	(a), (b), (e)
PVFc	Chlorobenzene	120°C, 10 min	1 × 10 <sup>-4</sup>	Chlorobenzene	200°C, 15 min	(a), (b), (e)
CER	Toluene	80°C, 10 min	8 × 10 <sup>-7</sup>	Toluene	120°C, 15 min	(a), (b), (e)
PBS	Cyclohexanone/ MEK <sup>(f)</sup>	110°C, 15 min	1 × 10 <sup>-6</sup>	MEK <sup>(f)</sup> 2-propanol	110°C, 15 min	(a), (b)
PB	Toluene	70°C, 10 min	3 × 10 <sup>-6</sup>	Toluene	110°C, 30 min	(a), (b), (e)

(a) Withstands acid etching solutions.

(b) Withstands basic etching solutions.

(c) Withstands ion etching techniques.

(d) The developers are given as examples. Other solvent combination may be used.

(e) As supplied from Dynachem.

(f) MEK, methyl ethyl ketone.

(g) MIBK, methyl isobutyl ketone.

(h) Proprietary.

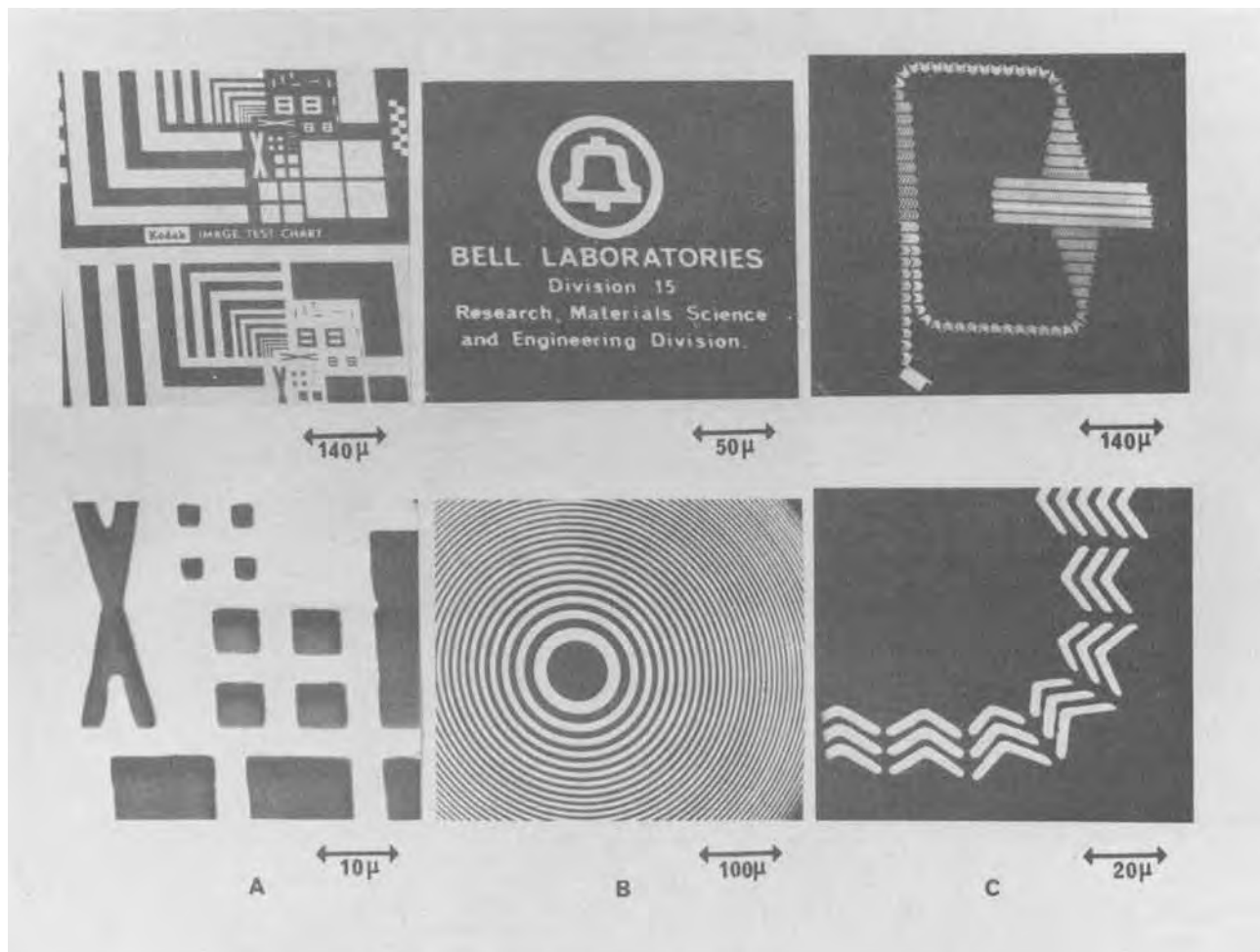


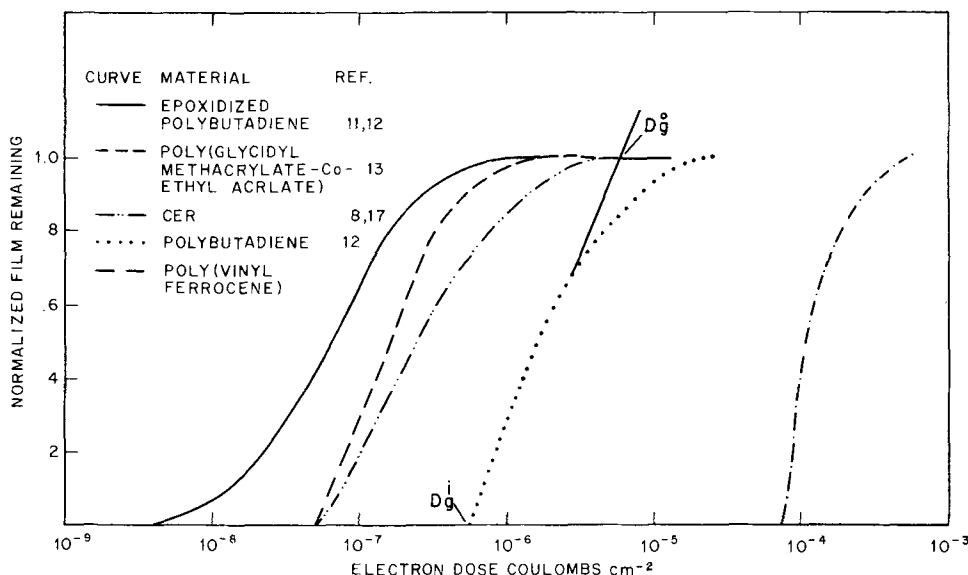
Fig. 1. Scanning electron micrographs of gold absorber pattern on a thin silicon substrate used as an x-ray mask.

7. Poly(vinylferrocene) (PVFc) is an extremely high contrast, low sensitivity negative resist, containing 24% iron, and used as an archetype compound to illustrate a method of enhancing x-ray sensitivity.

The x-ray doses for organic resists containing only first and second row elements are in good agreement with electron doses as expected, Table I. For these polymers the ratio of x-ray to electron doses was found to be 1-3. Poly(butene-1-sulfone) contains a heavier atom, sulfur, and the ratio was 5.2. Incorporation of

~24% iron into the polymer resulted in a ratio of 29, a gain of ~10 in sensitivity toward x-ray radiation. A gain of 3-4 was expected on the basis of absorption considerations. Clearly, this method of increasing the amount of energy absorbed by the resist by incorporating materials with high linear absorption coefficients for the exposing wavelength, is a powerful technique that, in principle at least, permits a resist to be specifically designed for the wavelength of irradiation employed.

Fig. 2. Electron dose-thickness curve for several electron resists.



**Masks.**—Some typical mask patterns that were fabricated for x-ray lithography by electron lithography are shown in Fig. 1. There were 25 similar patterns ion beam etched in 400 nm of Au on Si on each substrate. Patterns with less than  $2\mu$  resolution were readily produced. The Si was subsequently thinned electrochemically to  $\sim 3\text{--}7\ \mu\text{m}$ . Beryllium may also be an acceptable substrate material since it has a low absorption coefficient and may be obtained sufficiently thin to eliminate the need for the electrochemical thinning step.

Unlike electron exposure, x-ray exposure results in the entire resist surface receiving some dose, because the mask absorber will transmit an x-ray beam diminished according to Eq. [1]. Due largely to this effect the contrast,  $\gamma$ , of a resist becomes an important parameter. Contrast for a negative resist is defined as the slope of the extrapolated linear portion of a plot of normalized film remaining as a function of log dose and may be expressed as

$$\gamma = \left[ \log \frac{D_g^0}{D_g^i} \right]^{-1} \quad [2]$$

where  $D_g^i$  is the dose at 0 film thickness and  $D_g^0$  is the dose at 100% film remaining (5, 17), using the extrapolated linear portion of the dose-thickness curve, Fig. 2. The contrast has been found similar for both electron and x-ray exposure. Figure 2 represents electron exposure characteristics for several negative resists and is included to clarify the above definitions.

The ratio of x-ray transmission through the absorber to substrate will determine the contrast and exposure levels required for the resist. Table III gives electron contrasts for several negative resists and may be used as a guide in selecting an x-ray resist.

### Conclusions

This paper shows (i) that there is a good correlation between x-ray energy absorbed and electron energy absorbed for 1st and 2nd row elements; (ii) that absorption can be increased for x-rays more than for electrons with a resist containing a 3rd row element, and (iii) the transmission ratio of the transparent and opaque region of an x-ray mask will determine the resist contrast required.

Manuscript submitted Dec. 3, 1973; revised manuscript received May 15, 1974.

Any discussion of this paper will appear in a Discussion Section to be published in the June 1975 JOURNAL.

Table III. Values of the contrast,  $\gamma$ , for various negative electron resists

Material	Contrast
PVFc	1.5
P (GMA-co-EA) <sup>(a)</sup>	1.07
CER	0.78
PDOP	0.78
EPB	0.56

<sup>(a)</sup> High contrast form.

All discussions for the June 1975 Discussion Section should be submitted by Feb. 1, 1975.

The publication costs of this article have been assisted by Bell Laboratories.

### REFERENCES

- D. L. Spears and H. I. Smith, *Solid State Technol.*, **15**, 21 (1972).
- D. L. Spears and H. I. Smith, *Electron. Letters*, **8**, 102 (1972); H. I. Smith, D. L. Spears, and S. E. Bernacki, *J. Vacuum Sci. Technol.*, **10**, 913 (Nov. 1973).
- P. V. Lenzo and E. G. Spencer, *Appl. Phys. Letters*, **24**, 289 (1974).
- M. Hatzakis, *This Journal*, **116**, 1033 (1969).
- R. D. Heidenreich, L. F. Thompson, C. M. Melliar-Smith, and E. D. Feit, *J. Appl. Phys.*, **44**, 4039 (1973).
- E. F. Kaelble, "Handbook of X-rays," pp. 1-20, McGraw-Hill Book Co., New York (1967).
- L. F. Thompson, *This Journal*, in press.
- E. D. Feit and J. L. Bartelt, *ibid.*, Submitted.
- M. J. Bowden and L. F. Thompson, *J. Appl. Poly. Sci.*, **17**, 3211 (1973).
- L. F. Thompson and M. J. Bowden, *This Journal*, **120**, 1722 (1973).
- T. Hirai, Y. Hatanu, and S. Nonogaki, *ibid.*, **118**, 669 (1971).
- E. D. Feit, R. D. Heidenreich, and L. F. Thompson, Organic Coatings and Plastic Preprints of the April 1973 ACS Meeting, Dallas, Texas.
- L. F. Thompson, E. D. Feit, and R. D. Heidenreich, Society of Plastics Engineers, Ellenville Conf., October 1973; L. F. Thompson and E. D. Feit, Unpublished results.
- J. L. Bartelt, Organic Coating and Plastic Preprints of the April 1973 ACS Meeting, Dallas, Texas.
- C. M. Melliar-Smith and A. R. Storm, *Rev. Sci. Instr.*, **44**, 1282 (Sept. 1973).
- R. L. Meek, *This Journal*, **118**, 1240 (1971).

## Photolithographic Contact Printing of 4000Å Linewidth Patterns

Henry I. Smith, N. Efremow, and P. L. Kelley

Massachusetts Institute of Technology, Lincoln Laboratory, Lexington, Massachusetts 02173

### ABSTRACT

Surface acoustic wave transducers with 4000Å linewidth interdigital electrodes have been fabricated by photolithographic contact printing using conformable photomasks and AZ 1350H photoresist. The exposure time could be varied over a factor of three, indicating that line broadening due to diffraction is suppressed either by the optical nonlinearity or by the exposure development characteristics of the photoresist, or both.

Photolithographic contact printing, or "shadow printing," is widely used in the fabrication of semiconductor, surface acoustic wave, thin-film optical, and bubble domain devices. It is generally believed that the

**Key words:** photolithography, photoresist, submicron lines, conformable masks, acoustic surface waves.

technique cannot be used to expose submicrometer linewidth patterns, and that optical projection (1, 2), electron lithography (3, 4), or x-ray lithography (5-8) must be used in this domain. In this paper we will show that interdigital electrode structures of 4000Å linewidth can be readily produced on smooth, flat sub-

strates, through the use of conformable photomasks and AZ 1350 type photoresists.<sup>1</sup>

In order to contact print submicrometer linewidth patterns in photoresist films, the detrimental effects of optical diffraction outside the photoresist have to be avoided by eliminating any gap between the photomask and the top surface of the photoresist. Diffraction still occurs in the photoresist. In principle, the gap can effectively be made zero by employing photomasks and substrates which are much flatter than an optical wavelength, by making the thickness of photoresist films uniform to the same tolerance, by excluding all dust and surface asperities, and by bringing the photomask into optical contact with the photoresist. Such an approach is impractical because photomasks and most substrates are not so flat. Moreover, for substrates of large area, it is generally impossible to completely exclude all dust. An alternative approach to intimate contact is to use conformable photomasks (9-11). A conformable photomask consists of a pattern in thin-film chromium (500-1000Å) or Fe<sub>2</sub>O<sub>3</sub> (1300Å) on Corning Type 0211 glass,<sup>2</sup> 0.2 mm thick. Such photomasks readily conform to the contours of a substrate, and wherever an occasional dust particle occurs, they deform so as to minimize the area of noncontact (usually <1 mm

<sup>1</sup> Shipley Company, Incorporated, Newton, Massachusetts 02182.

<sup>2</sup> Corning Type 0211 glass for use as conformable photomasks is obtained from Corning Glass Works, Electronic Materials Department, Corning, New York 14830. Chromium and Fe<sub>2</sub>O<sub>3</sub> coated 0211 glass can be obtained from Electronic Materials Corporation, Sierra Madre Villa, Pasadena, California 91107.

diameter) as well as the local stress. A simple vacuum frame can be used to obtain uniform intimate contact over large areas (11). The standard type of photomask used in the semiconductor industry is on 1.5 mm thick glass, and it is not well suited to obtaining uniform intimate contact. Commercially available mask alignment systems are likewise unsuitable for submicrometer linewidth photolithography.

Figure 1 shows a cross-sectional profile of a portion of an 8000Å periodicity grating exposed in AZ 1350 H photoresist, 9800Å thick on a glass substrate, using a mercury arc lamp and a conformable photomask in intimate contact. The photomask was made by scanning electron beam lithography. With intimate contact, the photoresist thickness and the exposure time are found experimentally not to be critical parameters. The same 4000Å linewidth patterns have also been exposed in 15,000Å thick AZ 1350 H on glass substrates. Using photoresist relief structures such as shown in Fig. 1, together with the metal lift-off process (10), surface acoustic wave transducers with five interdigital electrodes of 4000Å linewidth have been routinely fabricated in 2000Å thick aluminum on LiNbO<sub>3</sub> substrates. When the exposure time was varied by a factor of three, the linewidth increased by only about 20%. It has been established that the metal lift-off technique will work only if the photoresist sidewalls are vertical or slightly undercut (10). Transducers with 8000Å linewidths have been used in high performance L-band

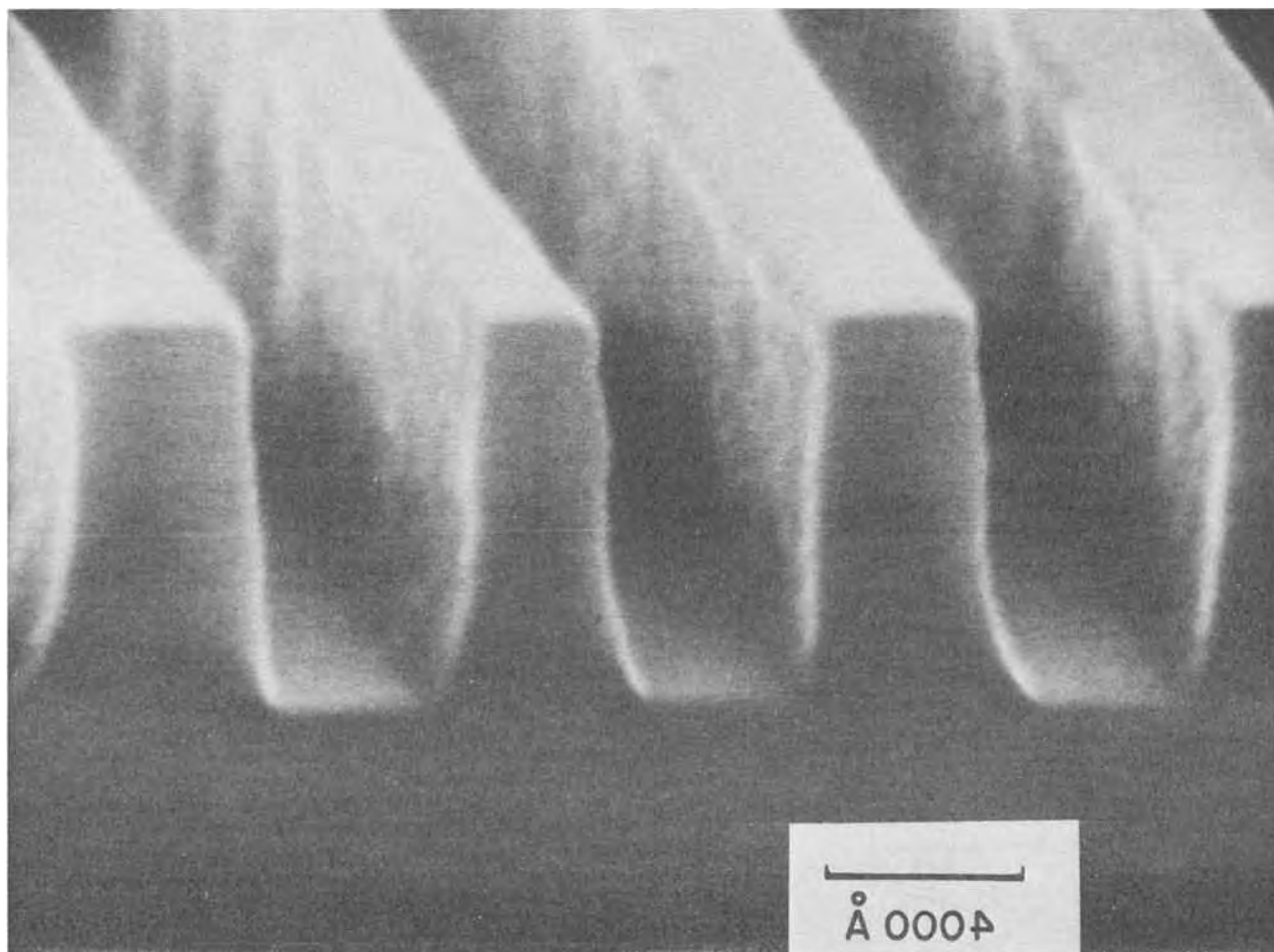


Fig. 1. Scanning electron micrograph of the cross section of a grating pattern exposed in AZ1350H photoresist on a glass substrate using a high pressure mercury arc lamp and the conformable photomask intimate contact technique. The photoresist is 9800Å thick. Because of the angles used in microscopy, vertical dimensions are foreshortened relative to lateral dimensions. The scale refers to lateral dimensions only. The photomask consisted of five slits in an 800Å thick chromium film. It was made by scanning electron beam lithography and chemical etching of the chromium, which caused irregularities along the edges of the slits. These small irregular features are replicated in the photoresist. The smaller space between two of the slits was in the original mask and was caused by an error in the scanning electron beam pattern generator.

reflective-array pulse compression filters (12). In exposing these patterns, the latitude in exposure time was a factor of eight for  $\text{LiNbO}_3$  substrates and 10,000Å thick AZ 1350 H. Gratings of 7000Å period, with several thousand lines, have been exposed in 3500Å thick AZ 1350 photoresist on silicon and other reflecting substrates. Following development, gratings in thin-film chromium were produced by metal lift-off. The exposure time was not critical to within almost a factor of two. Although no effort has been made to explore the ultimate limitations of the conformable mask photolithography, our observations lead us to speculate that narrower linewidths than reported here are probably possible, but may require the exercise of finer control over photoresist thickness and exposure parameters.

When a photoresist film is exposed by contact printing using a photomask in intimate contact, the relief structure obtained is determined by the near-field diffraction pattern of the photomask, and the exposure development characteristics of the photoresist. The near-field diffraction pattern of the photomask used to expose the structure in Fig. 1 is difficult to calculate exactly. Existing rigorous diffraction theory (13) deals only with perfectly conducting masks. Moreover, AZ 1350 H photoresist is not a simple linear medium. As discussed below, the light intensity (and perhaps also the phase delay) at any position in the photoresist changes with time during the course of an exposure, and this greatly complicates any diffraction calculations. For linear media, B. J. Lin has developed an approximation method for calculating the very near-field diffraction from narrow apertures in perfectly conducting opaque masks (14). Some of his results are presented in Fig. 2 for the case of a plane wave incident normally on a mask having three slits of width  $2\lambda$ , with E polarized parallel to the slits (15). For the case of unpolarized polychromatic radiation, somewhat more diffraction broadening occurs (15).

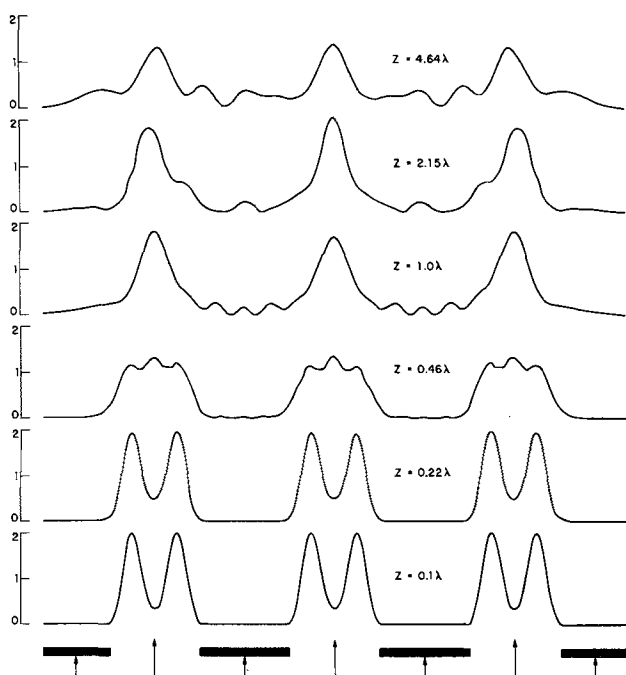


Fig. 2. Plots of light intensity in the near field of a grating consisting of three slits of width  $2\lambda$ . The strips between the slits are also  $2\lambda$  wide, as indicated by the solid bars at the bottom of the figure.  $Z$  is the perpendicular distance away from the grating into the near field. The plots were made from calculations provided through the courtesy of B. J. Lin, and they are for the case of a normally incident plane wave whose E field is polarized parallel to the slits. Note that at a distance  $Z = 2.15\lambda$  there is significant intensity in between the slits.

It is interesting to compare the intensity distribution of Fig. 2 with the results of Fig. 1. If we assume that the index of refraction of the AZ 1350 H photoresist ( $n = 1.612$ ) is merely a scaling factor, then the wavelengths of the prominent lines of the mercury arc lamp used (4358, 4047, and 3663Å) become 2700, 2510, and 2270Å, respectively, inside the photoresist, and the slit widths in the photomask correspond to less than  $2\lambda$ . The photoresist thickness in Fig. 1 is approximately  $z = 4\lambda$ . For a given exposure time, one can construct from Fig. 2 surfaces of equal energy deposition per unit volume for a linear medium. These surfaces would have shapes similar to the structure shown in Fig. 1, but the "linewidth" would rapidly widen as a function of exposure time. The fact that the photoresist relief structures obtained by intimate contact printing do not change rapidly as a function of exposure time indicates that they cannot be identified as surfaces of equal energy deposition per unit volume. Indeed, because of the exposure development characteristics of AZ 1350 H photoresist one would not expect this to be the case.

The AZ 1350 type photoresists are composed of a base resin plus diazide compounds. The latter are strong absorbers at blue and ultraviolet wavelengths, and undergo photochemical decomposition leading to reduced optical absorption or "bleaching." The ultraviolet transmission of AZ 1350 is thus a function of an absorber concentration which decreases with exposure time. Herrick (16) has given solutions to the nonlinear partial differential equations which describe the bleaching of photoresist films. The development of AZ 1350 photoresist is based on the fact that as the diazide compound is decomposed, the solubility of the photoresist in an aqueous alkaline solution increases very rapidly in an almost thresholdlike manner (17-19). Dill and Neureuther have shown that by using Herrick's solutions to the bleaching equations, together with a mathematical model of the development process, one can calculate numerically the relief structure obtained in an AZ 1350 film given the light intensity distribution, the exposure time, and the development time for the case of negligible diffraction in the photoresist (17-19). Incorporating the effects of diffraction in the photoresist is a more difficult problem, and has not yet been treated rigorously. Nevertheless, we believe that the present results, in particular the insensitivity of linewidth to exposure time, indicate that line broadening due to diffraction is suppressed to some degree either by the optical nonlinearity or the exposure development characteristics of the photoresist, or both. In a future publication (20) we will discuss this tentative conclusion more thoroughly and describe in detail various equipment and techniques which have been developed for conformable mask photolithography, including means for registering a conformable photomask relative to patterns already existing on a substrate surface.

#### Acknowledgments

The authors are especially grateful to B. J. Lin for making his calculations of near-field diffraction patterns available to us. A. R. Neureuther and F. H. Dill kindly provided some of their unpublished work. We thank R. J. Hawryluk and R. C. Williamson for helpful discussions and R. Eager for the scanning electron microscopy.

This work is sponsored by the Department of the Army and the Department of the Air Force.

Manuscript submitted March 6, 1974; revised manuscript received June 3, 1974.

Any discussion of this paper will appear in a Discussion Section to be published in the June 1975 JOURNAL. All discussions for the June 1975 Discussion Section should be submitted by Feb. 1, 1975.

The publication costs of this article have been assisted by the Lincoln Laboratory, Massachusetts Institute of Technology.

## REFERENCES

1. H. J. Schuetz and K. E. Hennings, *SCP Solid State Technol.*, **9**, 31 (1966).
2. S. Middelhoek, *IBM J. Res. Develop.*, **14**, 117 (1970).
3. G. R. Brewer, *IEEE Spectrum*, **8**, 23 (1971).
4. A. N. Broers and M. Hatzakis, *Sci. Am.*, **227**, 34 (1972).
5. D. L. Spears and H. I. Smith, *Electron. Letters*, **8**, 102 (1972).
6. D. L. Spears, H. I. Smith, and E. Stern, in "Electron and Ion Beam Science and Technology," Fifth International Conference, R. Bakish, Editor, pp. 80-91, The Electrochemical Society Softbound Symposium Series, Princeton, N.J. (1972).
7. D. L. Spears and H. I. Smith, *Solid State Technol.*, **15**, 21 (1972).
8. H. I. Smith, D. L. Spears, and S. E. Bernacki, *J. Vacuum Sci. Technol.*, **10**, 913 (1973).
9. H. I. Smith, *Rev. Sci. Instr.*, **40**, 729 (1969).
10. H. I. Smith, F. J. Bachner, and N. Efrechow, *This Journal* **118**, 821 (1971).
11. R. C. Williamson and H. I. Smith, *IEEE Trans. Microwave Theory Techniques*, **MTT-21**, 195 (1973); H. I. Smith, *Proc. IEEE*, To be published.
12. R. C. Williamson, V. S. Dolat, and H. I. Smith, in *Proc. 1973 Ultrasonics Symposium*, J. DeKlerk, Editor, pp. 490-493, Institute of Electrical and Electronics Engineers, New York (1973).
13. J. C. Bouwkamp, *Rept. Progr. Phys.*, **17**, 35 (1954).
14. B. J. Lin, *J. Opt. Soc. Am.*, **62**, 976 (1972).
15. B. J. Lin, Personal communication.
16. C. E. Herrick, *IBM J. Res. Develop.*, **10**, 2 (1966).
17. F. H. Dill and A. R. Neureuther, Paper 15, Device Research Conference, University of Colorado, Boulder, Colorado, June 26-28, 1973.
18. A. R. Neureuther and F. H. Dill, in *Proc. Microwave Research Institute Symposium XXIII*, New York, April 16-18, 1974.
19. F. H. Dill, Paper 30-2, International Magnetism Conference, Toronto, Canada, May 14-17, 1974.
20. H. I. Smith, N. Efrechow, R. C. Williamson, J. Melngailis, and P. L. Kelley, To be published.

## Epitaxial Growth of $\text{In}_x\text{Ga}_{1-x}\text{As}$ Waveguide Detectors for Integrated Optics

C. M. Wolfe,\* G. E. Stillman, and I. Melngailis

Lincoln Laboratory, Massachusetts Institute of Technology, Lexington, Massachusetts 02173

### ABSTRACT

An  $\text{In}_x\text{Ga}_{1-x}\text{As}$ -GaAs growth process, which reduces the effects of lattice mismatch, is used to integrate regions of  $\text{In}_{0.2}\text{Ga}_{0.8}\text{As}$  into GaAs waveguide structures by selective epitaxial deposition. With this technique an optimal waveguide detector configuration for  $1.06\ \mu\text{m}$  radiation is obtained.

The compound semiconductor system  $\text{In}_x\text{Ga}_{1-x}\text{As}$ -GaAs has several advantages for use in integrated optics: (i) It can be used to generate and detect radiation at wavelengths compatible with low-loss optical fibers. (ii) It exhibits a variety of physical phenomena which can be used to process optical signals at these wavelengths. (iii) It has a well-developed technology, i.e., large area, single crystal GaAs is readily available for device fabrication and epitaxial substrates, and most of the devices to perform the above functions are well understood and can be fabricated with reasonable yield in their discrete form. (iv) It is possible to integrate a number of these devices into a monolithic structure by epitaxial techniques.

The principal disadvantage of the  $\text{In}_x\text{Ga}_{1-x}\text{As}$ -GaAs system is the lattice mismatch between GaAs and the alloy, which can be as high as 7.2% for  $x = 1.0$  and tends to degrade the crystalline quality of the material. Thus, it is desirable to utilize a graded compositional region between the GaAs substrate and the desired alloy composition to reduce the effects of lattice mismatch. In this paper we discuss the epitaxial growth system used to provide compositional grading and describe the incorporation of regions of  $\text{In}_x\text{Ga}_{1-x}\text{As}$  into GaAs waveguide structures (1) by selective epitaxial deposition.

### Epitaxial Growth System

The method we have used to grow  $\text{In}_x\text{Ga}_{1-x}\text{As}$  on GaAs substrates is different from methods previously described (2-7) and is shown schematically in Fig. 1. The epitaxial growth system consists of two separate chambers for indium and gallium melts with  $\text{AsCl}_3$  as the source for arsenic and chlorine to transport the indium and gallium. An electronic feedback system is used to control flow rates and hence the alloy composi-

tion. Mass flow transducers produce output voltages which are directly proportional to flow rates. These voltages are fed into error detection networks where they are compared to reference voltages. The difference signals are then used to drive motorized needle valves. Palladium-purified hydrogen is bubbled through two  $\text{AsCl}_3$  reservoirs which are temperature controlled at  $12.0^\circ\text{C}$  by a circulating bath. The hydrogen is saturated with  $\text{AsCl}_3$  at this temperature, and the resulting gas mixtures are then passed over pre-saturated indium and gallium melts (8) which are maintained at  $850^\circ\text{C}$ . A mixing chamber at  $900^\circ\text{C}$  is located between the source and growth regions to homogenize the vapors and to smooth out small fluctuations in gaseous composition. Epitaxial growth is obtained on GaAs substrates at a temperature of  $700^\circ\text{C}$  in a gradient of about  $8^\circ\text{C}/\text{min}$ . Growth is initiated with zero flow over the indium melt<sup>1</sup> and this flow is gradually increased<sup>2</sup> until the desired alloy composition is attained.

Under the conditions described above the alloy composition of the epitaxial layer is largely determined by the flow rates of  $\text{AsCl}_3\text{-H}_2$  over the indium and gallium melts.<sup>3</sup> In Fig. 2 we have plotted the mole per cent (m/o) InAs in the constant composition region of the growth<sup>4</sup> vs. the ratio of the flow rate over the indium

<sup>1</sup> The flow rate over the gallium melt was held constant at a value that gave a total flow of 250 ml/min after the grading process. This rate depends on the desired alloy composition and can be obtained from Fig. 2.

<sup>2</sup> The desired rate of change of this flow varies with growth rate, which in turn varies with substrate orientation and the desired final alloy composition. Thus, it must be changed empirically to achieve the approximate required compositional gradient.

<sup>3</sup> The boats for the indium and gallium melts were 10 cm long with linear flow rates over the melts from 10 to 40 cm/min. Thus, the melts and gas mixtures were close to equilibrium.

<sup>4</sup> Alloy compositions were determined by electron microprobe analyses and were typically uniform over the layers to within 3% of the mole fraction.

\* Electrochemical Society Active Member.

Key words: epitaxy, InGaAs, detector, waveguide.

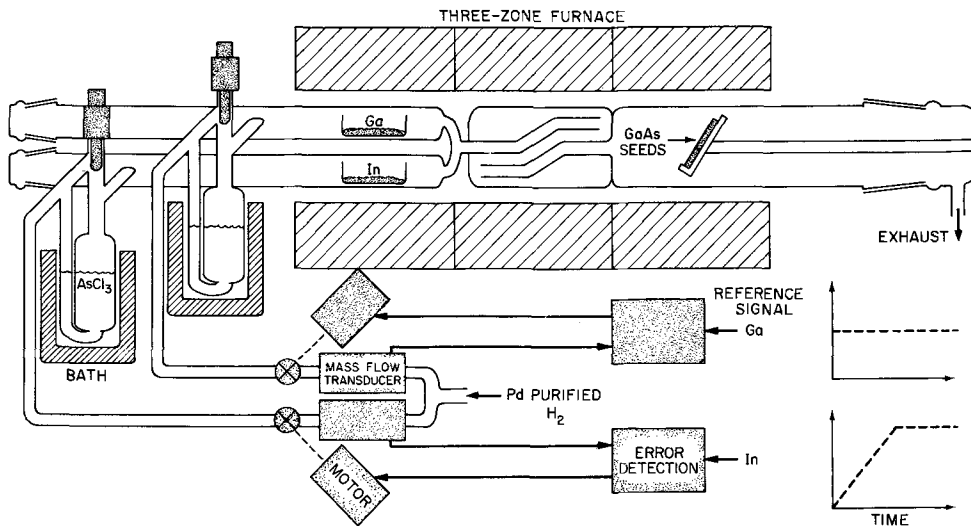


Fig. 1. Epitaxial  $\text{In}_x\text{Ga}_{1-x}\text{As}$  growth system showing the electronic feedback circuit used to control flow rates.

melt to the flow rate over the gallium melt. The dashed lines indicate the approximate run-to-run scatter in the data (open circles) which is largely due to different melt depletion rates. These results show that alloy composition is a linear function of the ratio of flow rates. Thus, for relatively constant growth rate (which is indicated by experiment) and constant flow rate over the indium melt produces an approximately linear increase in alloy composition.

Continuous epitaxial layers of  $\text{In}_{0.2}\text{Ga}_{0.8}\text{As}$  for 1.06  $\mu\text{m}$  avalanche photodiodes (9) have been grown on GaAs {100}, {111}Ga, and {111}As substrates using this grading process with compositional gradients of 0.01 mole fraction  $\text{InAs}/\mu\text{m}$ . These layers are free from gross defects, and preliminary study of the defect structure, using etchants developed for GaAs (10), indicates dislocation densities of the order of  $10^6 \text{ cm}^{-2}$  and stacking fault densities of the order of  $10^4 \text{ cm}^{-2}$ . These values show that about 99.999% of the lattice mismatch is maintained elastic (11) with the grading and growth process employed. Under equivalent conditions the small area growth discussed in the next section exhibits substantially less defect structure, and comparable quality material can be obtained with compositional gradients of about 0.05 mole fraction  $\text{InAs}/\mu\text{m}$ .

**Selective Epitaxial Deposition Process**

Using this growth process, we have integrated small regions of  $\text{In}_{0.2}\text{Ga}_{0.8}\text{As}$  into GaAs waveguide structures

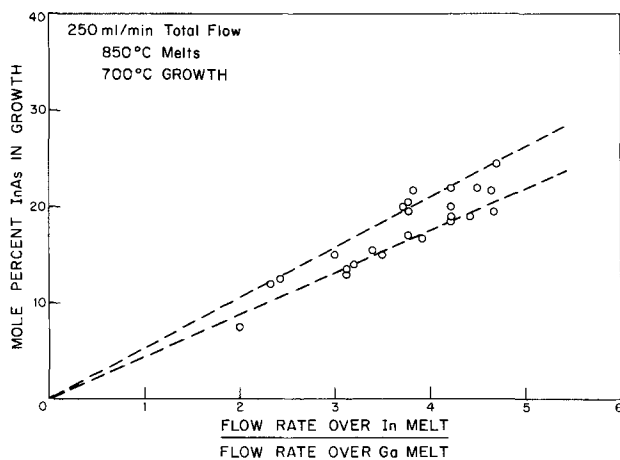


Fig. 2. Mole per cent  $\text{InAs}$  in the constant composition region of the epitaxial growth as a function of the ratio of flow rates. The dashed lines bracket the approximate scatter in the data (open circles).

by the selective epitaxial deposition (12) process shown in Fig. 3. The waveguide structures shown in Fig. 3(a) are formed by growing a 5-20  $\mu\text{m}$  layer of high purity ( $N_D + N_A \sim 10^{14} \text{ cm}^{-3}$ ) GaAs on a heavily doped ( $n \sim 10^{18} \text{ cm}^{-3}$ ) GaAs substrate using techniques previously described (13). Optical guiding can be obtained in the high purity n-layer since plasma effects reduce the refractive index in the heavily doped  $n^+$  substrate. A pyrolytic  $\text{SiO}_2$  is then deposited over this waveguide structure and circular regions are opened in the  $\text{SiO}_2$  using standard photolithographic techniques. This patterned  $\text{SiO}_2$  is then used as an etch mask and holes are etched through the high purity layer to the heavily doped substrate to obtain the structure shown in Fig. 3(b). Depending on the crystallographic orientation and etchant, a variety of hole geometries can be pro-

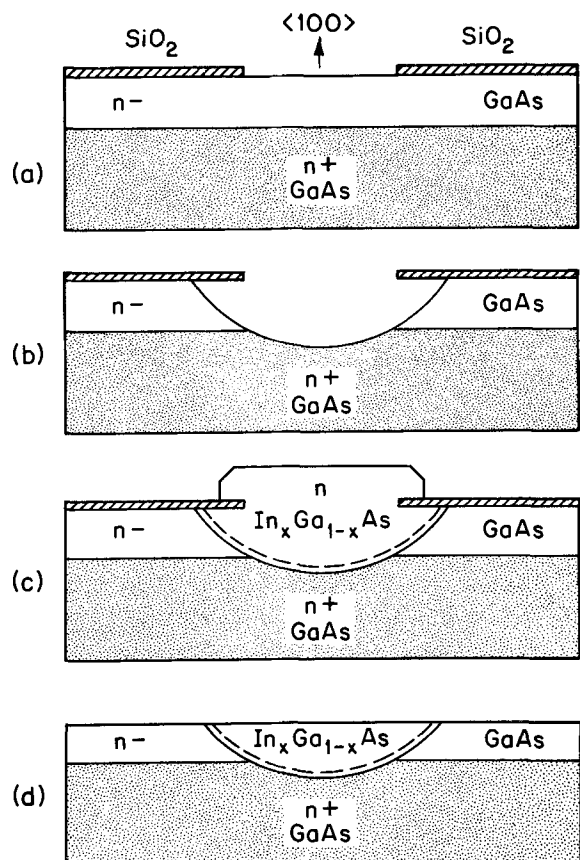


Fig. 3. Selective epitaxial process for forming waveguide detector structures.



duced (14). However, as will be discussed later, the most suitable geometry for a waveguide detector is a hemisphere. To obtain a hemispherical hole we use a nonpreferential etch of 5 H<sub>2</sub>SO<sub>4</sub>:1 H<sub>2</sub>O<sub>2</sub>:1 H<sub>2</sub>O on a {100} surface. This etchant is allowed to cool for about 10 min to approximately room temperature before use to obtain a slower etch rate.

The resulting structure shown in Fig. 3(b) is then placed in the epitaxial reactor, where the SiO<sub>2</sub> now serves as a mask against growth. Thus, epitaxial growth of In<sub>x</sub>Ga<sub>1-x</sub>As is obtained only in the holes etched in the GaAs waveguide structure. The composition of the alloy is graded out to some region, indicated by the dashed line in Fig. 3(c), where the alloy composition is maintained constant at the desired value. For reasons discussed below, the In<sub>x</sub>Ga<sub>1-x</sub>As should be doped to a value at least a factor of five higher than the GaAs waveguide (15). Although it would be desirable to terminate growth at the edge of the SiO<sub>2</sub>, in practice this is somewhat difficult. Generally, the growth proceeds out of the hole and over the SiO<sub>2</sub>, giving a faceted structure as indicated in Fig. 3(c). To obtain the waveguide structure indicated in Fig. 3(d), the SiO<sub>2</sub> is removed and the faceted In<sub>x</sub>Ga<sub>1-x</sub>As and the GaAs waveguide are mechanically chemically polished to the desired thickness with 20 CH<sub>3</sub>OH:1 Br on a rotating pad.

### Waveguide Detector Structures

Figure 4 shows a scanning electron micrograph, a diagram of the upper surface, and a cleaved cross section of a region of In<sub>0.2</sub>Ga<sub>0.8</sub>As grown in a GaAs waveguide structure. The faceting indicated in Fig. 3(c) is evident and is typical of that obtained for <100>-orientated growth in GaAs (14) as well as in In<sub>x</sub>Ga<sub>1-x</sub>As. The diameter of the grown-in region is about 125 μm. The interfaces between the grown-in 10<sup>16</sup> cm<sup>-3</sup> In<sub>0.2</sub>Ga<sub>0.8</sub>As, the 10<sup>14</sup> cm<sup>-3</sup> GaAs waveguide, and the 10<sup>18</sup> cm<sup>-3</sup> GaAs substrate are delineated by a 1 HF:3 HNO<sub>3</sub>:4 H<sub>2</sub>O etch. The change in curvature at the interface between the waveguide and the grown-in region, which is undesirable for reasons discussed below, is caused by a slight *in situ* furnace etch. The desired structure can be obtained by polishing below this change in curvature.

Figure 5 shows an optical micrograph and a diagram of the cleaved cross section through a similar grown-in region in a 5 μm thick waveguide. A Schottky barrier placed over this hemispherical region of In<sub>0.2</sub>Ga<sub>0.8</sub>As and over part of the waveguide surrounding this region produces an essentially ideal detector structure for 1.06 μm radiation propagating through the GaAs waveguide. This structure has the following advantages: (i) The heavily doped 10<sup>18</sup> cm<sup>-3</sup> GaAs substrate, in addition to giving the change in refractive index to provide guiding in the 10<sup>14</sup> cm<sup>-3</sup> GaAs layer, also acts as a closely spaced back contact for a low resistance, high band-

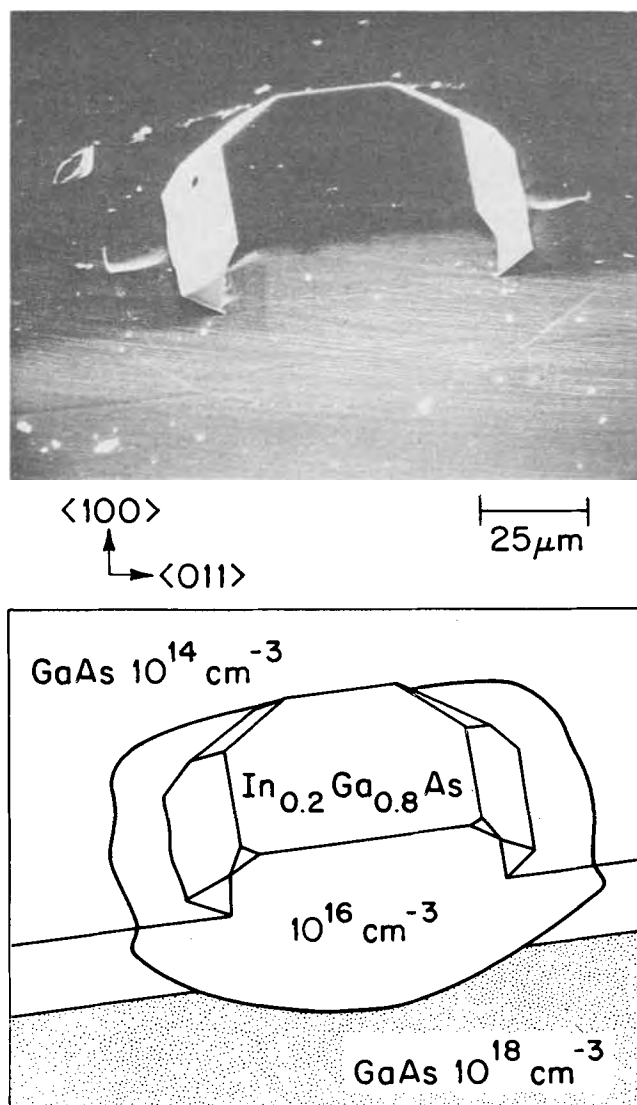


Fig. 4. Scanning electron micrograph and diagram showing the upper surface and cleaved cross section of an In<sub>0.2</sub>Ga<sub>0.8</sub>As region grown in a GaAs high purity waveguide.

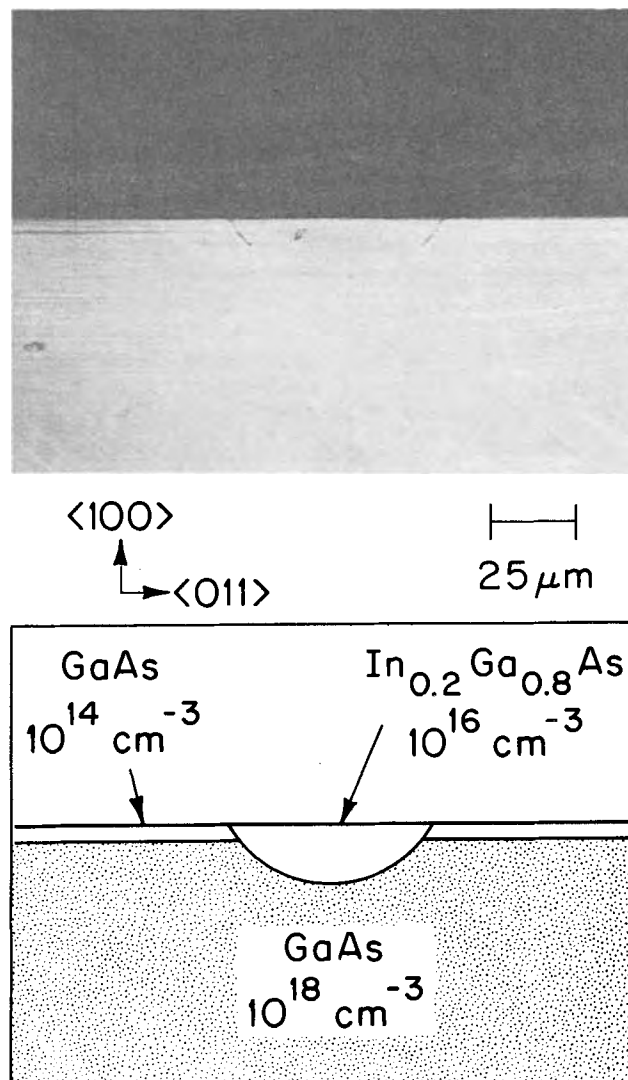


Fig. 5. Optical micrograph and diagram showing the cleaved cross section through a waveguide detector structure.



width device. (ii) The  $10^{14}$  cm<sup>-3</sup> GaAs waveguide also serves as a guard ring (15) for the  $10^{16}$  cm<sup>-3</sup> In<sub>0.2</sub>Ga<sub>0.8</sub>As device material, since the reverse bias breakdown voltage is higher in the lighter doped waveguide material than in the heavier doped detector material. (iii) The hemispherical geometry produces an inverted mesa structure, which reduces the component of electric field along the critical interface region and thereby tends to suppress edge breakdown. (iv) The increased refractive index in the inverted mesa alloy region tends to deflect radiation from the waveguide into the high field region of the diode.

With this guarded, inverted mesa geometry, one should be able to reverse bias these detector structures to sufficiently high voltages to observe multiplication or avalanche gain. Present device results show that bulk breakdown voltages can be achieved in these structures with dark currents comparable to those observed in discrete GaAs Schottky barrier devices (about  $10^{-7}$  A at breakdown). These structures have also been used to detect 1.06  $\mu$ m Nd-doped YAG radiation propagating along the GaAs waveguide with a quantum efficiency of 60% and with multiplication gain (16).

### Conclusion

From the results described above, we conclude that this selective epitaxial deposition process provides a useful means of fabricating optimal waveguide detector structures for integrated optics at wavelengths compatible with low loss optical fibers. The small area growth is of better crystalline quality than continuous layers grown under equivalent conditions. Thus, we anticipate that with additional development, the performance of such integrated avalanche photodiodes should be equal or superior to the performance of similar discrete devices (9).

### Acknowledgments

We would like to thank M. C. Finn for the electron microprobe analyses, and L. Krohn, Jr. and J. M. Lawless for expert technical assistance.

This work was sponsored by the Defense Advanced Research Projects Agency.

Manuscript submitted Feb. 25, 1974; revised manuscript received June 7, 1974.

Any discussion of this paper will appear in a Discussion Section to be published in the June 1975 JOURNAL. All discussions for the June 1975 Discussion Section should be submitted by Feb. 1, 1975.

The publication costs of this article have been assisted by the Lincoln Laboratory, Massachusetts Institute of Technology.

### REFERENCES

1. C. M. Wolfe, G. E. Stillman, and I. Melngailis, Paper presented at OSA-IEEE Topical Meeting on Integrated Optics, New Orleans, Jan. 21-24, 1974.
2. H. T. Minden, *This Journal*, **112**, 300 (1965).
3. E. W. Mehal and G. R. Cronin, *Electrochem. Technol.*, **4**, 540 (1966).
4. R. W. Conrad, P. L. Hoyt, and D. D. Martin, *This Journal*, **114**, 164 (1967).
5. H. Olsen, H. Robbins, and R. K. Willardson, *ibid.*, **114**, 64C (1967).
6. R. E. Enstrom, D. Richman, M. S. Abrahams, J. R. Appert, D. G. Fisher, A. H. Sommer, and B. F. Williams, in Proc. 3rd Int. Symp. GaAs, p. 30, Institute of Physics, London (1971).
7. H. M. Manasevit and W. I. Simpson, *This Journal*, **118**, 291C (1971).
8. R. N. Hall, *ibid.*, **110** 385 (1963).
9. G. E. Stillman, C. M. Wolfe, A. G. Foyt, and W. T. Lindley, *Appl. Phys. Letters*, **24**, 8 (1974).
10. J. L. Richards and A. J. Crocker, *J. Appl. Phys.*, **31**, 611 (1960).
11. J. H. van der Merwe, *Phil. Mag.*, **7**, 1433 (1962).
12. B. D. Joyce and J. A. Baldrey, *Nature*, **195**, 485 (1962).
13. C. M. Wolfe and G. E. Stillman, in Proc. 3rd Int. Symp. GaAs, p. 3, Institute of Physics, London (1971).
14. D. W. Shaw, *This Journal*, **113** 904 (1966).
15. C. M. Wolfe and W. T. Lindley, *ibid.*, **116**, 276 (1969).
16. G. E. Stillman, C. M. Wolfe, and I. Melngailis, Paper presented at OSA-IEEE Topical Meeting on Integrated Optics, New Orleans, Jan. 21-24, 1974; *Appl. Phys. Letters*, **25**, 36 (1974).

## Compatibility of Oxide Passivation and Planar Junctions with Al, Ga, and P Diffusions

P. Rai-Choudhury,\* Y. C. Kao,\* and G. G. Sweeney

Westinghouse Research Laboratories, Pittsburgh, Pennsylvania 15235

### ABSTRACT

With the emergence of sophisticated high voltage devices it is becoming necessary to integrate deep junctions with the planar technology. Because of the many disadvantages of the conventional p-type dopant, namely boron, use of aluminum and gallium is common practice in the fabrication of deep junctions. Sealed tube Al or Ga diffusion results in a damaged surface layer ( $\sim 1 \mu$ m) on silicon wafers. During subsequent heat-treatment in oxidizing ambient these dopants outdiffuse, causing depletion in the silicon and forming their respective oxides at the Si-SiO<sub>2</sub> interface. The pile up of the dopants near the silicon surface and their interaction with the SiO<sub>2</sub> seriously degrade the masking properties of the oxide during phosphorus diffusion. Phosphorus induced crystallization of the amorphous oxide compounds the problem of mask failure. Possible solutions to minimize the degradation of the thermal oxide during device processing are discussed.

In the fabrication of planar devices, phosphorus and boron diffusions have been commonly used. Due to their small ionic radii (1.07Å for P<sup>+</sup> and 0.98Å for B<sup>-</sup>)

these dopants frequently cause massive dislocation generation in silicon (1). Presence of any surface oxides and/or precipitates in the bulk silicon could prevent boron diffusion locally and thus cause nonuniform diffusion. Boron diffusion is also sensitive to ambient gases (2). Boron is known to form stable

\* Electrochemical Society Active Member.

Key words: oxidation, segregation, masking, passivation, crystallization.

compounds with silicon, such as  $\text{SiB}_4$  and  $\text{SiB}_6$  (3). Thus, boron is unattractive as a dopant and is used because it is the only p-type dopant that can be effectively masked by silicon dioxide. Phosphorus diffusion, on the other hand, is not commonly used to form a high voltage blocking junction. Its use as an emitter dopant has some merits in providing high surface concentration and gettering of undesirable metallic ions. For deep emitters (typically 10–20  $\mu\text{m}$ ) diffusion induced (shallow) dislocations are not considered harmful.

The use of aluminum or gallium as diffusants to form blocking junctions has some attractive features. The ionic radii of these two dopants (1.29Å for  $\text{Al}^-$  and 1.27Å for  $\text{Ga}^-$ ) compare favorably to the tetrahedral covalent radius of silicon (1.17Å) and the elastic limit of silicon is not reached, even at the solid solubility limit (4). Therefore, dislocations cannot be generated in silicon by the diffusion induced stress alone. Compared to boron, both aluminum and gallium (at higher temperature) diffuse more rapidly, which is a desirable feature for deep junctions. Neither Al nor Ga form any intermetallic compounds with silicon. The use of Al and Ga diffusions has some additional advantages from the point of view of device performance. The diffused junctions yield better blocking voltages than that formed by boron diffusion.

Both Al and Ga diffusions, however, suffer from a few disadvantages of their own. When the diffusion is carried out in a sealed system under vacuum or an inert ambient, a thin layer of damaged silicon is produced at the surface. Also, due to the high diffusivity of Al and Ga species in silicon dioxide, they cannot be diffused selectively in the usual way to fabricate planar junctions. In addition, during any subsequent oxidations and heat-treatments both Al and Ga atoms outdiffuse and produce an inhomogeneous oxide film which is not an effective mask against phosphorus diffusion. Furthermore, the oxide may be degraded during the phosphorus diffusion due to catalyzed crystallization (5). This degraded oxide also does not etch uniformly during the delineation of the metalization mask. As a consequence of the dopant outdiffusion and crystallization of the oxide, direct shorting of the emitter junction at the surface is frequently observed.

This investigation is undertaken to explore the compatibility of the oxide passivation and the planar junction with Al, Ga, and P diffusion. Here we examine the surface of the Si wafers following Al and/or Ga diffusion, the quality of the oxide grown on these surfaces, the outdiffusion of the dopants during oxidation, and the effects of P diffusion. The purpose of the study is to compare the various diffusion processes, which is helpful in selecting a compatible process for a given device.

### Experimental Procedure

Silicon wafers used were n-type, 1.25 in. in diameter, 28–44 ohm-cm, float zoned, having a (111) oriented surface. The wafers were chemically polished prior to diffusion (nonselective) with Al or Ga in a temperature range of 1050°–1175°C for 16 hr. The wafers were then thermally oxidized at 1200°C or 1235°C for 2–3 hr. Following photolithography and etching steps to open emitter windows, wafers were phosphorus-diffused at 1150°–1200°C for 1–2 hr and redistributed at 1200°C for 4–16 hr in an oxidizing ambient. After each high temperature treatment, five wafers were withdrawn from the batch for evaluations.

The impurity concentration profiles following diffusion and various heat-treatment operations were measured by the spreading resistance technique (6). Secondary ion mass spectrometry (SIMS) and electron beam microanalysis were used to detect any Al and Ga pile up at or near the oxide-silicon interface. X-ray topography was used to examine the silicon surface layers, the quality of the oxide, and in the identifica-

tion of any second phase particles. Reflection electron diffraction was used to detect very shallow damaged layers on the silicon surface following various processing steps. Finally, the reverse current voltage characteristics of the emitter junctions were checked to establish their quality.

### Results

The results are presented in four sections, namely, outdiffusion of Al and Ga, defects at the silicon-silicon dioxide interface, phosphorus induced defects in the silicon and the oxide, and the quality of the emitter junction.

*Outdiffusion of Al and Ga.*—Both Al and Ga diffusions were carried out in an inert or vacuum ambient which results in a diffusion from a constant surface concentration with a complementary error function type of profile. Surface concentrations begin to deplete only during subsequent heat-treatment operations. Fig. 1 (a and b) shows the effect of the outdiffusion of Al and Ga during oxidation and phosphorus diffusion. Here the impurity concentration is plotted as a function of the normalized junction depth. In Fig. 1(a) the impurity profiles following the sealed tube Al diffusion, the oxidation, and after phosphorus redistribution are shown. Similarly, in Fig. 1(b) the impurity profiles after the sealed tube Ga diffusion, after oxidation and redistribution of Ga at 1235°C for 16 hr, after a second oxidation and phosphorus redistribution are shown. Results shown in Fig. 1 indicate significant outdiffusion of both Al and Ga. In the case of Al, the concentrations at the surface is found to decrease from  $2.5 \times 10^{18}$  atoms/cm<sup>3</sup> after Al diffusion to  $1.5 \times 10^{16}$  atoms/cm<sup>3</sup> after phosphorus diffusion. The outdiffusion permits larger penetration of the emitter junction in the lateral direction at the surface than that in the vertical direction, as is observed by beveling and staining technique. The decreased surface concentration leads to a higher emitter junction breakdown voltage.

The Al diffused wafers were examined by secondary ion mass spectrometry to further explore the nature of outdiffusion and any clustering of electrically inactive dopants. The technique used has been described elsewhere (7) and is shown to be reproducible. Figure 2 shows the Al concentration profile (relative intensity) near the surface in a silicon wafer that has been processed through Al diffusion to phosphorus emitter redistribution. The processed wafer was cleaned to remove any oxide and surface films before analysis using  $\text{O}_2^+$  as the primary ion beam. The figure shows the Al pile up near the silicon surface which is electrically inactive. This is followed by a depletion region and a maximum Al concentration, which is probably bonded to oxygen. The intense peak at the surface is usually attributed to a chemical enhancement, i.e., the ionization efficiency of Al is much higher when it is bound to oxygen.

It is suspected that any Al pile up at the  $\text{SiO}_2$ -Si interface and electrically inactive Al in silicon may be bound to oxygen. To investigate this point, SIMS measurements were carried out through the oxide layer using argon as the primary ion beam. Figure 3(a) shows the Al profile (relative intensity) through  $\text{SiO}_2$  and into the silicon. The  $\text{SiO}_2$  layer extends to about 5000Å and contains relatively little Al. At depths below 5000Å a large number of Al clusters are observed in the  $\text{SiO}_2$ -Si interface regions and in the surface layers of silicon. Figure 3(b) was obtained by monitoring the  $\text{AlO}^+$  ionic species and indicates a rise in the intensity just before the  $\text{SiO}_2$  interface is reached, suggesting some reaction between Al and the  $\text{SiO}_2$  layer. The initial rise is followed by a depletion region (above about 5000Å) which corresponds to the maximum of Al clustering in Fig. 3(a). The fact that  $\text{AlO}^+$  clustering is observed indicates that aluminum is present in oxidized form. Thus, it appears that Al is rejected by the silicon during various

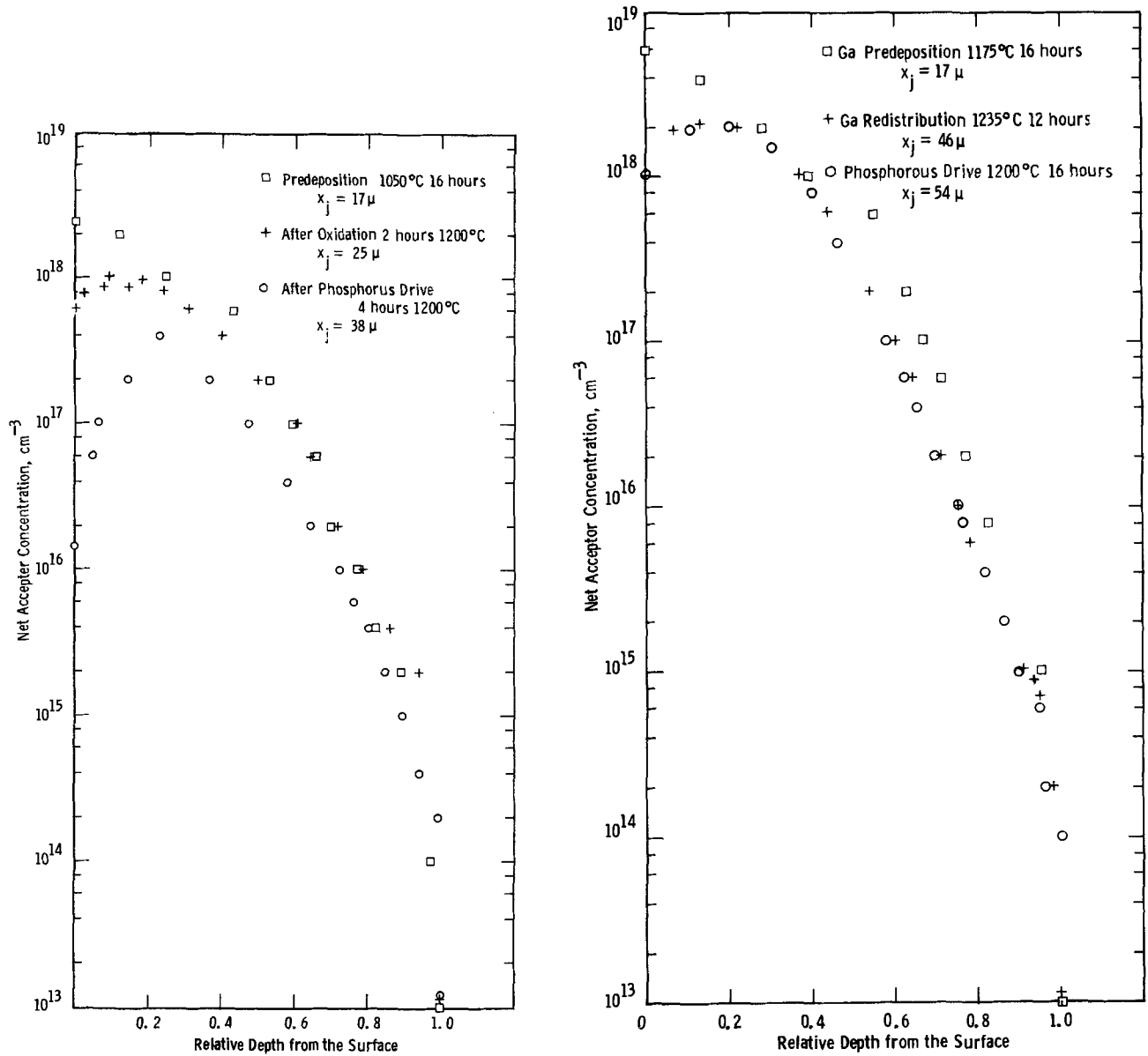


Fig. 1. Effects of oxidation and phosphorus diffusion on the depletion of Al and Ga concentrations. a (left), Al diffusion conditions: 1050°C for 16 hr; oxidation conditions: 1200°C for 2 hr; phosphorus diffusion conditions: 1200°C for 4 hr. b (right), Ga diffusion conditions: 1175°C for 16 hr; oxidation conditions: 1235°C for 12 hr; phosphorus diffusion conditions: 1200°C for 16 hr.

oxidation heat-treatment operations and is piled up as Al and Al-O clusters at and near the silicon surface.

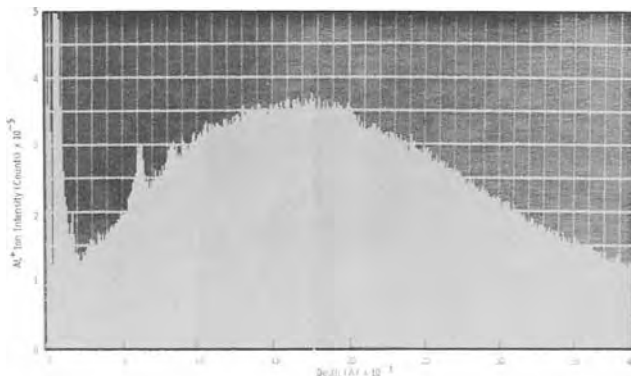


Fig. 2. Al concentration (relative intensity) profile showing depletion and clustering of Al near the surface. The silicon wafer has been processed through Al diffusion to P emitter redistribution and is analyzed by SIMS using  $O_2^+$  ion beam. Vertical:  $5 \times 10^3$  counts full scale; horizontal:  $4 \mu m$  full scale.

A similar analysis of Ga diffused samples by SIMS indicates that Ga is piled up in the oxide and, unlike Al, no accumulation in the silicon is noticeable.

*Defects at the silicon-silicon dioxide interface.*—The surface of the silicon wafer appears to be damaged following the sealed tube diffusion in the case of both Al and Ga. The presence of these damaged surfaces is revealed by the reflection electron diffraction patterns shown in Fig. 4 and 5, both of which indicate the presence of a polycrystalline component. These damaged regions are very shallow and disappear when  $1 \mu$  or so of the surface is chemically etched. The damage from Ga diffusion seemed to be more pronounced or extensive than that from Al diffusion. Both Al and Ga diffused wafers are free from any diffusion induced dislocations as revealed by the x-ray topography.

The outdiffusion of Al becomes increasingly noticeable with increasing heat-treatment time and temperature in an oxidizing ambient. Figure 6 shows a reflection electron diffraction pattern of a silicon surface which received an oxidation of 2 hr at 1200°C followed by phosphorus diffusion (4 hr at 1200°C). The wafer is dipped in HF to remove the phosphorus glass and the thermal oxide, and the diffraction pat-

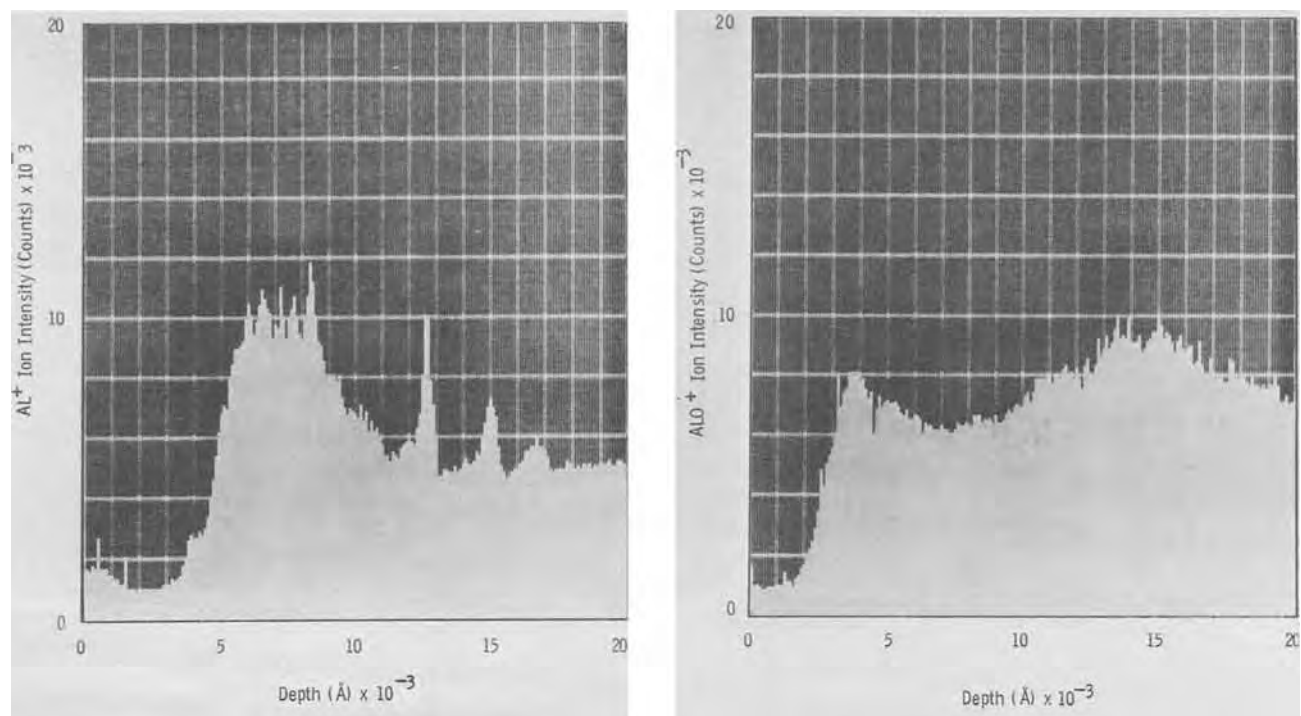


Fig. 3. a (left) Al concentration profile (relative intensity) through  $\text{SiO}_2$  indicating presence of some clusters measured by SIMS using Ar beam. Vertical:  $2 \times 10^4$  counts full scale; horizontal:  $2 \mu\text{m}$  full scale. b (right), AlO profile, scales same as in (a).

tern is obtained from the areas that were masked during the phosphorus drive. The extra reflections in the figure resemble  $\eta\text{-Al}_2\text{O}_3$  and could not be removed by boiling in HCl,  $\text{H}_2\text{SO}_4$ , or  $\text{H}_3\text{PO}_4$ .

The outdiffusion of Ga is similar to that of Al in many respects. Figure 7 shows a diffraction pattern from a silicon surface following Ga diffusion at  $1175^\circ\text{C}$  for 16 hr and an oxidation cycle for Ga redistribution. The wafer was dipped in HF prior to examination in the electron microscope. The diffraction patterns indicate the presence of polycrystalline silicon and  $\beta\text{-Ga}_2\text{O}_3$ . The reflections due to gallium oxide disappear when the sample is boiled in hot acids (e.g., HCl,  $\text{H}_2\text{SO}_4$ , aqua regia), but the polycrystalline silicon component is still present. Gallium oxide is found to reappear if the cleaned sample is oxidized again. When the oxide near the silicon-silicon dioxide interface is examined by transmission electron microscopy (TEM), a dispersed second phase could be detected as shown in Fig. 8. This second phase does not give any diffraction pattern and is believed to be induced by the outdiffusion of gallium. A freshly grown oxide on the same wafer after the original oxide was removed and the



Fig. 4. Reflection electron diffraction from the surface of a silicon wafer following sealed tube Al diffusion indicating the presence of a faint ring pattern.

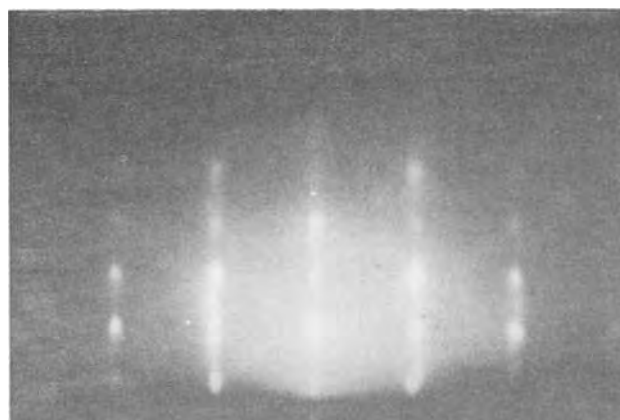


Fig. 5. Reflection electron diffraction from silicon surface after sealed tube Ga diffusion showing the presence of polycrystalline silicon.



Fig. 6. Reflection electron diffraction pattern from a silicon surface which received Al diffusion, oxidation, and P diffusion heat-treatment. The surface is characterized by the presence of polycrystalline silicon and extra reflections resembling  $\eta\text{-Al}_2\text{O}_3$ .

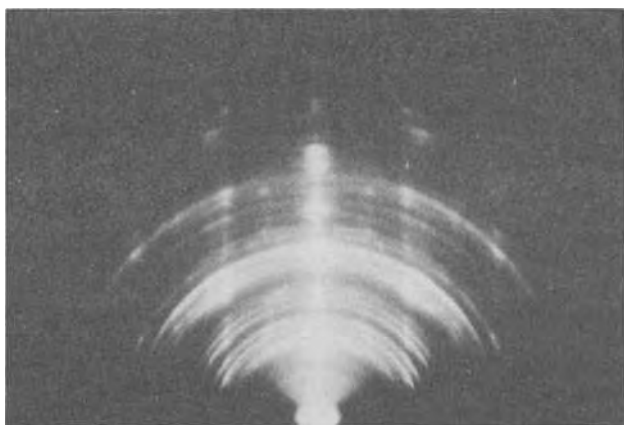


Fig. 7. Reflection electron diffraction from a silicon surface following Ga diffusion and a Ga redistribution oxidation cycle, indicating presence of polycrystalline silicon and  $\beta$ -Ga<sub>2</sub>O<sub>3</sub>.

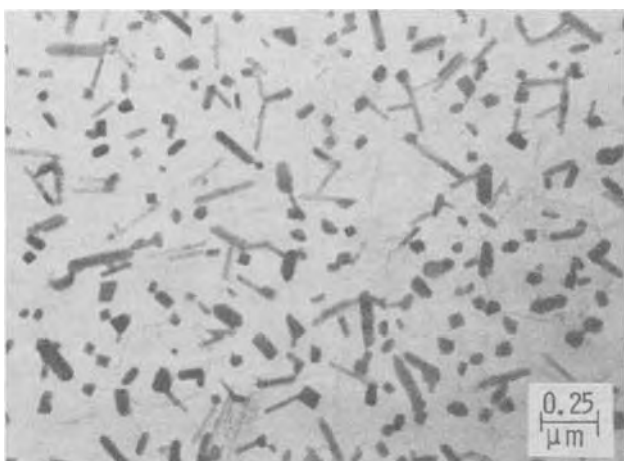


Fig. 8. Transmission electron micrograph of the Ga redistribution cycle oxide showing the presence of a dispersed second phase; note the growth of hexagonal shapes in the background.

wafer cleaned in boiling acids, is found to be free of this second phase particles. However, the silicon surface under the oxide is still damaged, and a polycrystalline component could be observed from the diffraction pattern.

The surface of the diffused silicon wafer, following Ga redistribution heat-treatment, was examined by an electron probe microanalyzer. Spectral line analysis indicated the presence of both Ga and O on the surface. This is a good indication of the fact that Ga is clustering with oxygen at the silicon-silicon dioxide interface. A similar test with the Al diffused samples failed to detect any Al on the silicon surface.

**Phosphorus induced defects.**—The diffusivity of P in the phosphosilicate glass region has been found to vary over several orders of magnitude, depending on the concentration of P<sub>2</sub>O<sub>5</sub> in SiO<sub>2</sub> (8). The catalytic influence of P leading to crystallization of amorphous oxide has been observed by several investigators (5). Schmidt *et al.* (9) have identified one of the main crystalline phases to be SiO<sub>2</sub> · P<sub>2</sub>O<sub>5</sub>. In this study we have observed highly crystallized regions of the oxide along with the frequent presence of polycrystalline silicon within the oxide. Figure 9 shows a TEM and a diffraction pattern of crystallized regions in the oxide following a 16 hr phosphorus redistribution heat-treatment at 1200°C. The fact that the crystallization was P induced was confirmed by the absence of any polycrystalline regions in the original amorphous SiO<sub>2</sub> following prolonged heat-treatments (up to 64 hr at 1200°C). It is interesting to note the presence of very

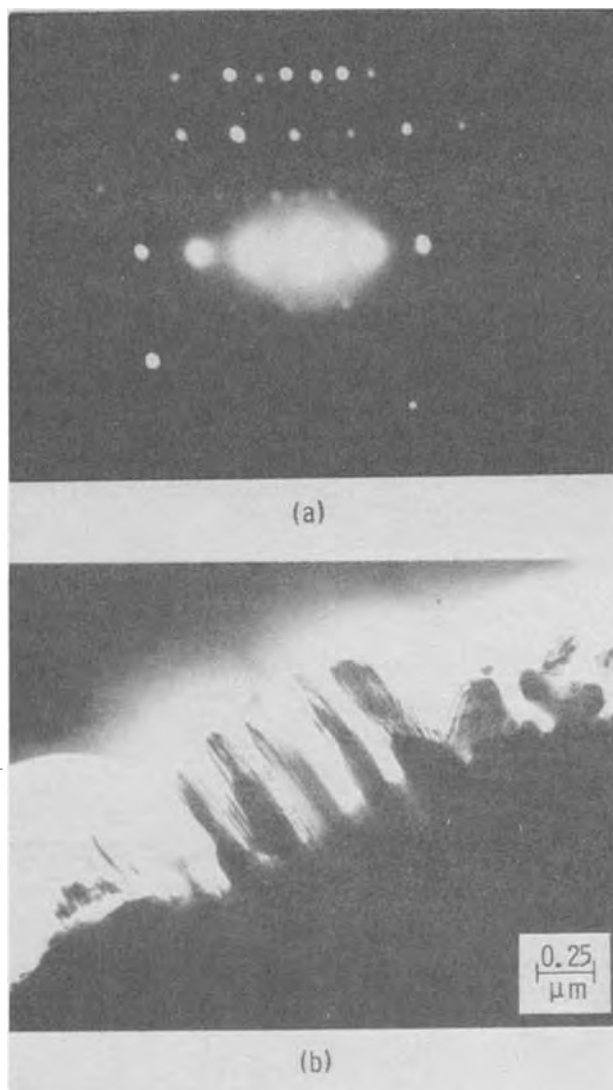


Fig. 9. Diffraction pattern (a) and transmission of electron micrograph (b) of crystallized regions in the oxide following 16 hr P redistribution heat-treatment at 1200°C.

fine grain (1000Å) silicon at various stages of growth inside the oxide film. Figure 10 shows a fairly large aggregate of polycrystalline silicon growth in oxide following P redistribution heat-treatment. The presence of such crystallized oxides and elemental silicon could increase the conductivity of the passivation oxide and might severely affect the junction leakage current.

Different types of interdigitated emitter patterns were used for phosphorus diffusion. X-ray topographs of wafers indicate the phosphorus diffused regions to be heavily dislocated. The delineation of the emitter fingers and the oxide along the emitter base junction appear to be very nonuniform, as shown by the XRT in Fig. 11. Frequently, initial masking oxides grown at high temperature and degraded by dopant outdiffusion gave poor results. Such oxides either became crystallized and failed to passivate the emitter junction or gave rise to numerous n<sup>+</sup> pipes in the p-base region during phosphorus diffusion. These crystallized oxides also have poor etching properties. Figure 12 shows a scanning electron micrograph of the emitter base junction prior to metallization. Note the complete absence of the passivation oxide near the center of the photograph, thus exposing the bare junction. The presence of bare silicon in the supposedly passivated region was confirmed by using the x-ray attachment of the scanning electron microscope. This type of inhomogeneous

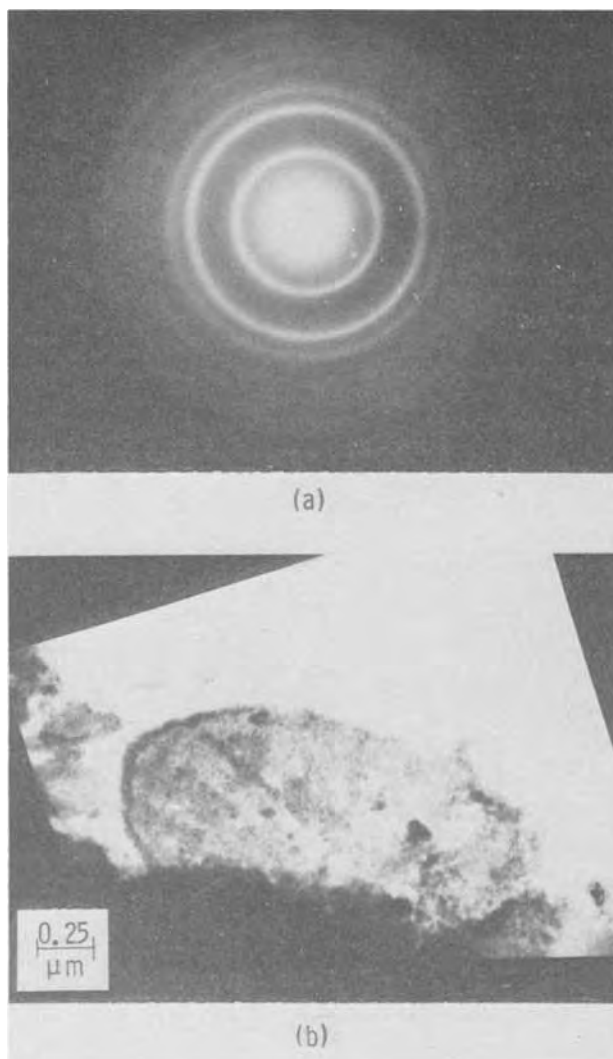


Fig. 10. Diffraction pattern (a) and transmission electron micrograph (b) showing the presence of very fine grain silicon within the oxide.

geneous etching of the oxide is avoided by minimizing P induced crystallization of the oxide.

**Emitter junction.**—At the end of the diffusions the emitter junction I-V characteristics of the devices were measured. On devices with an Al diffused base layer the emitter junction was found to be shorted after metallization. This shorting could be removed by etching the silicon surface between the emitter and the p-base contacts. After etching the measured breakdown voltage was around 20-25V, and the leakage current of the mesa junction ranged between microamperes to milliamperes. On the best units the leakage current density was around  $10^{-6}$  A/cm<sup>2</sup>.

On devices with a Ga diffused base layer, planar emitter junctions with acceptable I-V characteristics have been obtained when the silicon surface was cleaned and boiled in acids prior to oxidation and when the oxidation temperature was lowered from 1235° to 1200°C. After metallization, the measured breakdown voltage ranged from 15 to 20V with a leakage current less than 1 mA. However, the measured I-V curve indicated that the leakage current was dominated by a channel current with a pinch off voltage between 1-3V. The leakage current density at 5V was around  $10^{-4}$  A/cm<sup>2</sup>. Comparing with boron diffused devices on which the measured breakdown voltage was around 10V and the leakage current density at 5V around  $10^{-7}$  A/cm<sup>2</sup>, Al or Ga diffused devices showed a higher breakdown voltage but a much

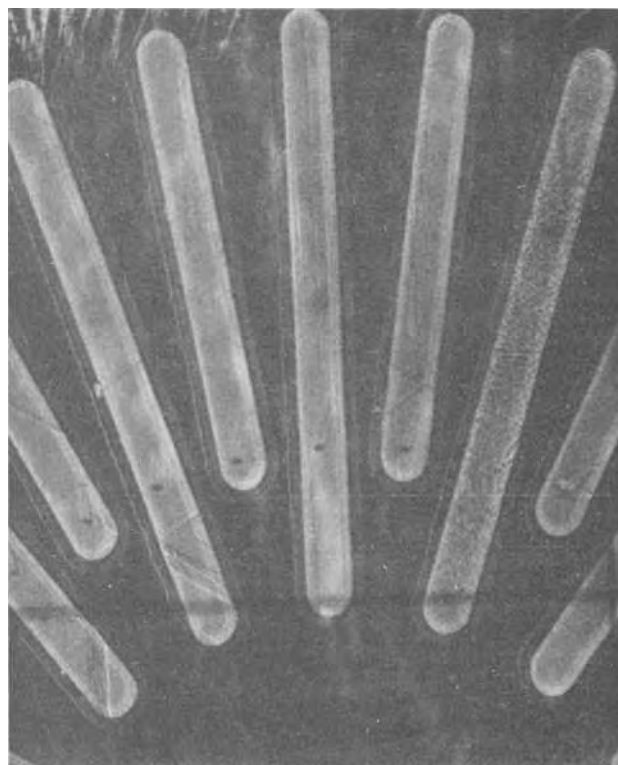


Fig. 11. X-ray topograph of a diffused wafer showing heavily dislocated emitter fingers, inhomogeneous etching of the passivation oxide along the emitter-base junction, and the poor quality oxide giving additional contrasts in the topograph.

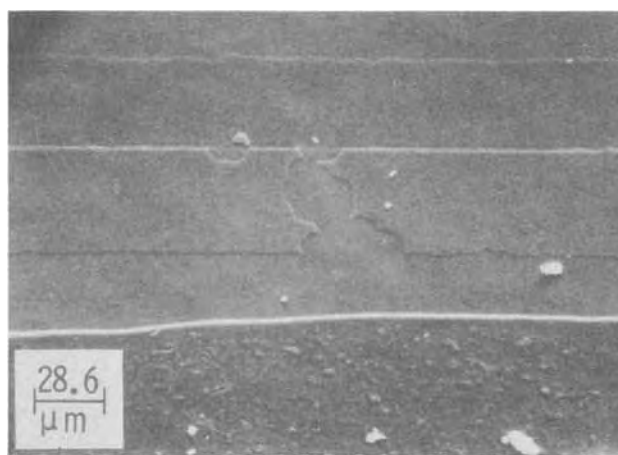


Fig. 12. Scanning electron micrograph of the emitter base interface region showing the absence of the passivation oxide near the center.

higher leakage current. The presence of the surface channel current on devices with a Ga diffused base layer and the need to etch the silicon surface on devices with an Al diffused base layer strongly suggested that high leakage currents were originated at the surface. With an Al diffused base, the continuous interaction between the aluminum and the oxide during the oxidation period rendered the oxide ineffective against phosphorus diffusion. This problem, together with localized phosphorus penetrations through crystallized oxides, have led to the shorting of the emitter junction at the surface. With Ga diffusion, cleaning the silicon surface in boiling acids seemed to improve the oxide quality in masking against the phosphorus diffusion



and resulted in devices with acceptable emitter junction I-V characteristics.

### Discussion

The damaged silicon surface that results from the sealed tube Al and Ga diffusions appears to be related to the formation of the respective alloys. Examining the case of Al first, we note that the eutectic composition is 12.3% silicon. The vapor pressure of Al at 1050°C is about  $3 \times 10^{-4}$  mm Hg, and it reacts with the quartz walls until a protective coating of silicon and  $\text{Al}_2\text{O}_3$  is built up. Al is also a fast diffusant in silicon when compared with Ga. Thus, the formation of Al-Si eutectic at the wafer surfaces is limited by the availability of Al. Consequently, the lattice disorder introduced at the silicon surface is confined to a very shallow depth. In the case of Ga, however, the damage to the silicon lattice could be more extensive. At a diffusion temperature of 1175°C the vapor pressure of Ga is about  $10^{-1}$  mm Hg, and its interaction with the quartz tube is negligible. Thus, a relatively large quantity of Ga is available for diffusion and formation of surface alloys. Further, Ga-Si eutectic requires very little silicon (10) and could easily form during cooling of the wafers following diffusion. As may be expected, the damage to the silicon lattice due to Ga is more extensive than that from Al (see Fig. 4 and 5). In order to remove these damaged layers about 1-2  $\mu\text{m}$  of silicon should be etched from the wafers following the sealed tube diffusion. Otherwise, the silicon-silicon dioxide interface over the planar junction would contain a damaged silicon layer which will introduce excess junction leakage current (generation current under reverse bias and recombination current under forward bias).

Even if the damaged silicon is removed following the sealed tube diffusion, subsequent oxidation causes both Al and Ga to outdiffuse and form disordered mixed phases at the interface. The important parameters governing the redistribution of impurities during thermal oxidation are the segregation coefficient ( $m = C_{\text{Si}}/C_{\text{Ox}}$ ) of the impurity at the oxide-silicon interface, the ratio of the diffusion coefficient of the impurity in the oxide to its diffusion coefficient in Si, and the ratio of the parabolic rate constant of the oxidation to the square root of the impurity diffusion coefficient in silicon ( $A/\sqrt{D_{\text{Si}}}$ ). The case of Ga outdiffusion has been treated by Grove *et al.* (11). At about 1200°C the segregation coefficient for Ga is approximately 20, indicating that Ga should be rejected by the oxide and should pile up in the silicon. The reason for depletion of Ga during oxidation is its high diffusivity in the oxide ( $D_{\text{Ga}}^{\text{ox}}/D_{\text{Si}}^{\text{ox}} \approx 322$ ). Reasonably high vapor pressure of Ga at 1200°C allows it to escape to the gas phase. At a given temperature, the value of  $A/\sqrt{D_{\text{Si}}}$  is higher for wet oxidation (steam) than for dry oxidation ( $\text{O}_2$ ), and the impurity depletion is reduced by lowering this ratio. Thus, dry oxidation would result in minimum redistribution and depletion of impurities.

The case of Al outdiffusion during thermal oxidation is somewhat more complex because of its interaction with  $\text{SiO}_2$ . In this case a segregation coefficient ( $m < 10^{-3}$ ) is difficult to define because Al, instead of dissolving in  $\text{SiO}_2$ , reduces it to Si or  $\text{SiO}$ . In contrast with Ga, the oxide here accepts Al until all the  $\text{SiO}_2$  is reduced. This point has been substantiated by diffusing Al through an oxidized silicon and noting the disappearance of the oxide. Significant interaction between  $\text{Al}_2\text{O}_3$  and  $\text{SiO}_2$  may not be expected at the typical diffusion temperature (12) (the eutectic is at 1595°C). The value of the diffusivity ratio is much greater than 1, similar to Ga. Unlike Ga, however, Al is not likely to be transported to the gas phase due to its considerably lower vapor pressure and strong affinity for oxygen. About the only form in which Al could leave the surface is by forming suboxides such as  $\text{Al}_2\text{O}$  and  $\text{AlO}$ . The outdiffused Al should, therefore,

be found as  $\text{Al}_2\text{O}_3$  in the silicon-silicon dioxide interface. This is consistent with our experimental results. As long as we have an Al diffused junction, oxidation will always result in a disturbed silicon-silicon dioxide interface. Thus, at a high Al surface concentration this process is incompatible with a silicon dioxide masked planar junction.

The presence of elemental silicon in the oxide was occasionally observed in steam or dry oxygen grown oxide on high resistivity, undiffused wafers. This tends to indicate that the presence of impurities, such as Al and Ga, is not essential in the formation of the silicon phase. Nucleation of the silicon clusters does not seem to be associated with any observable crystallographic defects. One possibility is through the formation of  $\text{SiO}$  in the presence of excess silicon, and the subsequent disproportionation to Si and  $\text{SiO}_2$  on cooling. The activity of  $\text{SiO}$  is expected to be significant at the diffusion temperatures of interest (e.g.,  $p_{\text{SiO}}^e \sim 6 \times 10^{-4}$  atm at 1500°K).

### Summary

The compatibility of Al, Ga, and P diffusion with oxide passivation and planar junction is briefly examined. Al and Ga diffusion introduce a surface layer of damaged silicon through formation of respective alloys and eutectics during cooling. These damaged silicon layers may be removed by chemical etching. During heat-treatments under oxidizing ambients both Al and Ga outdiffuse and could adversely affect the silicon-silicon dioxide interface, the bulk of the oxide, and the shape of the impurity profile. Consequently, compatibility with oxide passivation is difficult to achieve, unless high surface concentration of the dopants is avoided. By maintaining a reasonably low surface concentration, rejecting the redistribution oxide, and growing a fresh oxide along with suitable acid treatments of the wafers, a significant improvement is made in the quality of the junction passivation. Phosphorus emitter diffusions frequently catalyze the formation of crystalline oxide which has poor masking and etching properties. Mask failure in the base regions results in  $n^+$  pipes, and inhomogeneous etching exposes the emitter base junctions resulting in increased leakage current. With gallium diffusion, cleaning the silicon surface in boiling acids improves the oxide quality in masking against the phosphorus diffusion and resulted in devices having acceptable emitter junctions.

### Acknowledgments

The authors wish to thank Drs. A. J. Noreika and W. J. Takei for their assistance with the TEM and x-ray topography measurements and Drs. R. N. Ghoshtagore and D. J. Page for helpful discussions. They are also grateful to J. H. Rieger, L. S. Saxon, and R. J. Pfeil for carrying out the experimental work.

Manuscript submitted Feb. 28, 1974; revised manuscript received June 27, 1974.

Any discussion of this paper will appear in a Discussion Section to be published in the June 1975 JOURNAL. All discussions for the June 1975 Discussion Section should be submitted by Feb. 1, 1975.

The publication costs of this article have been assisted by Westinghouse Research Laboratories.

### REFERENCES

1. E. Levine, J. Washburn, and G. Thomas, *J. Appl. Phys.*, **38**, 81 (1967); **38**, 87 (1967).
2. M. Ghezzi and D. M. Brown, *This Journal*, **120**, 146 (1973).
3. R. P. Elliot, "Constitution of Binary Alloys, First Supplement," p. 134, McGraw-Hill Book Co., New York (1965).
4. J. E. Lawrence, *J. Appl. Phys.*, **37**, 4106 (1966).
5. D. R. Campbell, E. I. Alessandrini, K. N. Tu, and J. E. Lewis, Paper 252 presented at Electrochemical Society Meeting, Miami Beach, Florida, October 8-13, 1972.

6. R. G. Mazur and D. H. Dickey, *This Journal*, **113**, 255 (1966).
7. H. B. Kim, D. L. Barrett, and G. G. Sweeney, 1972 Proc. 4th Int. Symp. GaAs, p. 88, Institute of Physics, Conf. Ser. No. 17; J. M. Morabito and R. K. Lewis, *Anal. Chem.*, **45**, 869 (1973).
8. C. T. Sah, H. Seilo, and D. A. Tremere, *J. Phys. Chem. Solids*, **11**, 288 (1959); M. O. Thurston, J. C. C. Tsai, and K. D. Kang, ASTIA Report AD 261 201 (1961).
9. P. F. Schmidt, W. van Gelder, and J. Drobek, *This Journal*, **115**, 79 (1968).
10. R. P. Elliot, "Constitution of Binary Alloys, First Supplement," p. 457, McGraw-Hill Book Co., New York (1965).
11. A. S. Grove, O. Leistiko, Jr., and C. T. Sah, *J. Appl. Phys.*, **35**, 2695 (1964).
12. E. M. Levin, C. R. Robbins, and H. F. McMurdie, "Phase Diagram for Ceramists," The American Ceramic Society (1964).

## Influence of Gas-Phase Stoichiometry on the Defect Morphology, Impurity Doping, and Electroluminescence Efficiency of Vapor-Grown GaAs P-N Junctions

R. E. Enstrom,\* C. J. Nuese, J. R. Appert, and J. J. Gannon\*

RCA Laboratories, Princeton, New Jersey 08540

### ABSTRACT

The vapor-hydride method of GaAs epitaxial growth permits separate control of the flow rates of both the AsH<sub>3</sub> and HCl reactant species. In the present work, these variables have been independently adjusted to provide gas-phase compositions ranging from Ga-rich to As-rich. The surface defect morphology has been found to be a strong function of the HCl flow rate, changing from pits at low flow rates to hillocks at higher flow rates. In contrast, the AsH<sub>3</sub> flow rate for constant HCl flows principally affects the size of the defects. The growth rate increases slightly with increasing AsH<sub>3</sub> flow rate, but decreases with increasing HCl flow rate over the range normally used. The Se-donor and Zn-acceptor concentrations both decrease with increasing HCl flow rate, suggesting that crystal stoichiometry is not strongly influenced by the HCl flow rate.

Electroluminescent diode efficiencies range between 0.1 and 0.5% at room temperature and between 1 and 2.6% at 80°K. Peak efficiency values have been attained with slightly As-rich gas-phase conditions.

Vapor-grown p-n junctions of GaAs are useful for a variety of electroluminescence (1-3) and microwave (4-6) applications. Several of the first-order, vapor-growth parameters relevant to such structures have been examined previously (1), such as the carrier concentrations, layer thicknesses, growth temperatures, etc.; however, the role of gas-phase stoichiometry (and perhaps crystal stoichiometry) is more subtle and has only recently begun to be determined.

For example, several workers (7-9) have examined the influence of Ga/As flow ratios on the background (reactor) concentrations of unintentionally doped GaAs with  $n \sim 10^{14}$ - $10^{15}$  cm<sup>-3</sup>. In these studies, the gas-phase stoichiometry was found to influence the incorporation of the donor and/or acceptor impurities; however, the effects of gas-phase stoichiometry on the electrical properties of epitaxial layers with significantly higher impurity concentrations have not been previously explored. Furthermore, the relative (and perhaps absolute) flow rates used to transport the Group III and Group V atoms have recently been found to directly influence the defect morphology (pits and hillocks) on the surface of vapor-grown GaAs (10-12) and GaAs<sub>1-x</sub>P<sub>x</sub> (13) epitaxial layers. For the case of GaAs, the absolute amount of Ga in the vapor is found to determine the defect morphology (10-12), whereas for GaAs<sub>1-x</sub>P<sub>x</sub>, the ratio of Group III to Group V vapor species seems to be the dominant factor (13). Gas-phase stoichiometry is also known to influence the growth rate of GaAs under certain vapor-growth conditions (14).

As a result of the effects described above, it becomes essential to examine the influence of gas-phase stoichi-

ometry on a practical device structure, whose ultimate performance depends critically on the interdependence of several factors. In the present study, we specifically consider the effects of vapor stoichiometry on the surface defect morphology, growth rate, impurity incorporation, and electroluminescence efficiency of heavily doped ( $10^{17}$ - $10^{19}$  cm<sup>-3</sup>) p-n junction structures of GaAs. For this study, we have employed the vapor-hydride growth technique (15), where the amounts of Ga and As species in the gas phase can be independently varied over a relatively wide range. In contrast, the other commonly used vapor-growth technique (16, 17) for preparing GaAs utilizes AsCl<sub>3</sub>, where the ratio of Ga to As vapor species is fixed at 3/1. As we will show in the sections below, both the surface defect morphology and the incorporation of donors and acceptors are relatively strong functions of the HCl flow rate, but are not nearly as strongly affected by the amount of As species in the vapor phase.

### Experimental Procedure

The apparatus and procedures used for the vapor growth of the p-n junction layers have been described in detail previously (15, 18). In brief, AsH<sub>3</sub>, HCl, and Ga are the reactant species, and Pd diffused H<sub>2</sub> is used as a carrier gas. The gases in all cases are of high purity so that background impurity concentrations of less than  $1 \times 10^{15}$  donors/cm<sup>3</sup> are generally achieved (7). The metal (Alusuisse, 99.9999% pure) is transported as GaCl (19) by passing HCl over a 75g metallic Ga source with a surface area of approximately 15 cm<sup>2</sup>. In these experiments, the HCl flow rate was varied from 2 to 20 cm<sup>3</sup>/min, and the flow rate of AsH<sub>3</sub> (Precision Gas Products), employed as a 10% AsH<sub>3</sub> in H<sub>2</sub> mixture, was varied from 25 to 350 cm<sup>3</sup>/min. The effec-

\* Electrochemical Society Active Member.

Key words: III-V compounds, crystal growth, vapor-phase epitaxy, chemical vapor deposition.



tive flow rate of the  $\text{AsH}_3$  alone therefore ranged between 2.5 and 35  $\text{cm}^3/\text{min}$ . All other vapor-growth conditions were held approximately constant. The total  $\text{H}_2$  flow was about 2500  $\text{cm}^3/\text{min}$ , which is much higher than that used for  $\text{AsCl}_3$  vapor-growth experiments. The growth temperature was approximately 725°C.

The p-n junction structures used in the present study consisted of n<sup>+</sup>-n-p<sup>+</sup> epitaxial layers prepared sequentially in a single vapor-growth operation. The substrates were Czochralski-grown GaAs oriented 3° off <100> toward <110>, and were chemically polished prior to growth. The thicknesses of the epitaxial layers were determined by cleaving and measuring {110} transverse cross sections and were typically 7-15  $\mu\text{m}$  for the n<sup>+</sup>-layer, 10-35  $\mu\text{m}$  for the n-layer, and 3-10  $\mu\text{m}$  for the p<sup>+</sup>-layer. The n-type epitaxial layers were doped with a 100 ppm  $\text{H}_2\text{Se}$  in  $\text{H}_2$  mixture using a flow rate of 50  $\text{cm}^3/\text{min}$  of the mixture for the initial n<sup>+</sup>-layer and 20  $\text{cm}^3/\text{min}$  for the n-layer. These flow rates yield GaAs donor concentrations on the order of  $1 \times 10^{18}$  and  $5 \times 10^{17} \text{ cm}^{-3}$ , respectively, for our typical vapor-growth conditions. The flow rates of the HCl and  $\text{H}_2\text{Se}$  were measured to within about 0.1  $\text{cm}^3/\text{min}$  with mass flow meters.<sup>1</sup> The p-type layers were prepared by doping with zinc acceptor impurities to a concentration of  $5 \times 10^{18} \text{ cm}^{-3}$  from a heated metallic zinc source. No intentional acceptor impurities were introduced on the n-side of the junction, and no intentional donor impurities were introduced on the p-side.

The impurity concentrations incorporated into the p- and n-type epitaxial layers of these structures were determined from photoluminescence measurements on the as-grown wafers and from capacitance-voltage measurements on the p-n junctions after diode fabrication. For the photoluminescence measurements, a pulsed argon laser emitting at 5145Å was focused to a spot size of 0.25 mm on the surface of the p-type GaAs layers. Since the optical absorption coefficient for the high energy radiation is about  $2 \times 10^4 \text{ cm}^{-1}$ , the penetration of the light was restricted to within 1  $\mu\text{m}$  of the surface. The p-n junction diodes were prepared using procedures described previously (1). Briefly, the junction wafers were lapped to about 100  $\mu\text{m}$  thickness, after which ohmic contacts were applied using gold and silver base alloys (20). The diode electroluminescence efficiencies at 300° and 77°K under direct-current forward bias were measured with a Hoffman 2A silicon solar cell.

### Results and Discussion

**Defect morphology.**—A striking feature of the vapor-grown layers was the occurrence of surfaces having either pits or hillocks. Initial examination showed that the pits occurred for low HCl flow rates, whereas the hillocks were associated with higher HCl flow rates. Accordingly, the conditions leading to each type of defect were investigated further.

For the growth of GaAs, about 17.5  $\text{cm}^3/\text{min}$  of  $\text{AsH}_3$  and 5  $\text{cm}^3/\text{min}$  of HCl are routinely used. The effect on the morphology of varying the HCl flow rate between 2 and 20  $\text{cm}^3/\text{min}$  for a constant  $\text{AsH}_3$  flow rate of 17.5  $\text{cm}^3/\text{min}$  is illustrated in Fig. 1. The 2  $\text{cm}^3/\text{min}$  flow of HCl [Fig. 1(a)] results in a matte surface, consisting of an array of fine pits, while the 20  $\text{cm}^3/\text{min}$  flow of HCl [Fig. 1(d)] results in a smoother surface, containing only a few hillocks. A transition from pits to hillocks is seen to occur at an HCl flow rate between 5 and 10  $\text{cm}^3/\text{min}$  [Fig. 1(b) and 1(c)]. It should be noted that the surfaces prepared at about 10  $\text{cm}^3/\text{min}$  of HCl are of good crystalline quality and have a low average defect density.

The effect of the  $\text{AsH}_3$  flow rate on the defect morphology was examined for HCl flow rates producing either pits or hillocks. The effect on the pit morphology of varying the  $\text{AsH}_3$  flow rate, while keeping the HCl flow rate fixed at 5  $\text{cm}^3/\text{min}$ , is shown in Fig. 2. Here, variations in the  $\text{AsH}_3$  flow rate are shown to affect only the size and density of the defect, in this case a

pit, but do not change the type of defect. It appears that for an HCl setting of 5.0  $\text{cm}^3/\text{min}$ , an  $\text{AsH}_3$  flow rate between 8 and 17.5  $\text{cm}^3/\text{min}$  is best to minimize the density and size of the pits.

The effect of the  $\text{AsH}_3$  flow rate on the hillock morphology for an HCl flow rate of 20.0  $\text{cm}^3/\text{min}$  is shown in Fig. 3. Here we see that increasing the  $\text{AsH}_3$  flow rate from 3 to 17.5  $\text{cm}^3/\text{min}$  increases the size and the definition of the hillock, but does not result in pits. Hence, in both of the experiments illustrated in Fig. 2 and 3, the type of defect was not altered over a wide range of  $\text{AsH}_3$  flow rates. From further examination of Fig. 2 and 3 we also conclude that the pit-to-hillock transition is related to the HCl flow rate rather than to the HCl/ $\text{AsH}_3$  ratio, since Fig. 2(a) (HCl/ $\text{AsH}_3$  ratio = 1.43) shows pits and Fig. 3(c) (HCl/ $\text{AsH}_3$  ratio = 1.14) has very pronounced hillocks for similar gas flow ratios. These conclusions are consistent with those of Kennedy and Potter (12) for vapor-grown GaAs, and those of Blakeslee (10) for vapor-grown  $\text{GaAs}_{1-x}\text{P}_x$ , but differ from those of Wu (13), who found the absence of pits or hillocks related to the gas-phase stoichiometry (Ga/As+P ratio).

The present results on the transition from pits to hillocks on {100} GaAs surfaces shed light on the defect morphology in alloy systems prepared by the hydride method. Epitaxial layers of GaAs and  $\text{GaAs}_{1-x}\text{P}_x$  prepared with  $\text{AsH}_3$  and  $\text{PH}_3$  tend to form pits (18), while  $\text{In}_x\text{Ga}_{1-x}\text{As}$  and  $\text{In}_{1-x}\text{Ga}_x\text{P}$  form hillocks (21). The present work suggests that this difference is observed because the GaAs and  $\text{GaAs}_{1-x}\text{P}_x$  alloys are generally prepared with low HCl flow rates (15) (less than 10  $\text{cm}^3/\text{min}$ ), whereas  $\text{In}_x\text{Ga}_{1-x}\text{As}$  (HCl = 20  $\text{cm}^3/\text{min}$ ) (22) and  $\text{In}_x\text{Ga}_{1-x}\text{P}$  (HCl  $\approx$  40  $\text{cm}^3/\text{min}$ ) (21) alloys have much higher HCl flows because of two-metal transport.

Our results also help to explain the morphology (23-25) of <100>-oriented GaAs prepared by the  $\text{AsCl}_3$  method. Increasing the flow rate of  $\text{AsCl}_3$  from low to high values causes a transition from pits to hillocks (23). This transition may be explained by the increasing GaCl partial pressure rather than by a changing Ga/As ratio in the vapor phase, as suggested earlier (26).

The normally observed defect type for GaAs prepared by the  $\text{AsCl}_3$  technique is the hillock (27), while that for the hydride method is the pit (18, 28). This difference probably arises from a difference in the GaCl species concentration in the two types of systems, as shown below.

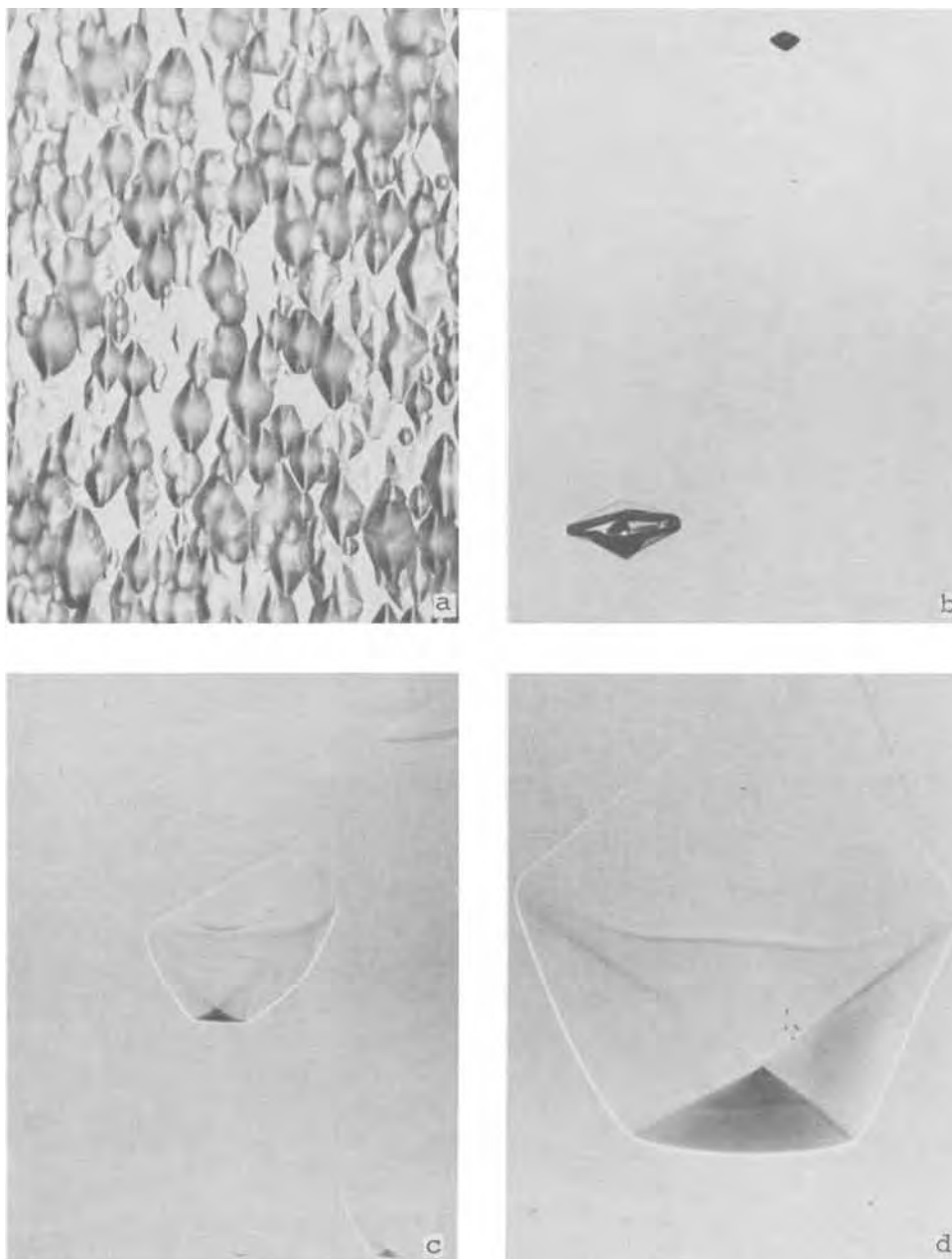
For GaAs grown in the  $\text{AsH}_3$  system at 725°C, pits are observed at a gas-phase concentration of about  $1 \times 10^{-3}$  (HCl/ $\text{H}_2$  = 2.5/2500) and hillocks are predominant at  $8 \times 10^{-3}$ , with relatively smooth surfaces observed at  $2-4 \times 10^{-3}$ . For the  $\text{AsCl}_3$  system (25) at 710°C, a concentration of  $4-6 \times 10^{-3}$  of  $\text{AsCl}_3$  in  $\text{H}_2$  produces smooth surfaces, while a value of  $10-18 \times 10^{-3}$  of  $\text{AsCl}_3$  produces many hillocks. Thus, the regimes for hillock formation are about the same for <100>-oriented GaAs prepared by both the hydride and the  $\text{AsCl}_3$  growth systems (about  $10 \times 10^{-3}$ ). For smooth growth, a concentration of about  $4 \times 10^{-3}$  is used in both systems, but values range on the low side of  $4 \times 10^{-3}$  for hydride growth and on the high side for  $\text{AsCl}_3$  growth, thereby leading to pits and hillocks, respectively.

Finally, the cross-sectional structures of the two types of defects are compared in Fig. 4. For the hillock, the thickness of both the n- and p-type layers is increased considerably at the defect site, whereas for the pit, the thickness of the n-layer is locally reduced. The n<sup>+</sup>-substrate interface is flat for both types of defect, and the defects start in the n-layer rather than at the substrate.

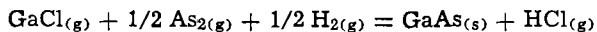
**Growth rate.**—Examination of the cleaved {110} edge of multilayer wafers prepared under the various growth conditions shows that the growth rate also is a function of the gas-phase composition, consistent with

<sup>1</sup> Hastings-Raydist and Tylan Corporation.

Fig. 1. Optical photomicrographs of GaAs vapor-grown layers prepared with  $17.5 \text{ cm}^3/\text{min}$  of  $\text{AsH}_3$  and  $\text{HCl}$  flow rates varying from 2 to  $20 \text{ cm}^3/\text{min}$ . a, Run 1121,  $2 \text{ cm}^3/\text{min}$  of  $\text{HCl}$ ;  $\text{Ga}/\text{As} = 0.114$ ;  $500\times$  magnification; defects are pits. b, Run 1124,  $5 \text{ cm}^3/\text{min}$  of  $\text{HCl}$ ;  $\text{Ga}/\text{As} = 0.286$ ;  $200\times$  magnification; defects are pits. c, Run 911,  $10 \text{ cm}^3/\text{min}$  of  $\text{HCl}$ ;  $\text{Ga}/\text{As} = 0.572$ ;  $200\times$  magnification, defects are hillocks. d, Run 1127,  $20 \text{ cm}^3/\text{min}$  of  $\text{HCl}$ ;  $\text{Ga}/\text{As} = 1.14$ ;  $200\times$  magnification; defect is hillock.



the previous observations of Shaw (14). In Fig. 5(b), for a constant  $\text{HCl}$  flow rate, it is seen that the n-layer thickness increases with increasing  $\text{AsH}_3$  flow rate, as might be expected from mass-action considerations for the reaction (19)



That is, as more reactant (e.g.,  $\text{As}_2$  or  $\text{As}_4$ ) is added, the amount of product ( $\text{GaAs}$ ) increases. The curve saturates at high  $\text{AsH}_3$  flow rates because of the limited amount of  $\text{GaCl}$  available to react with the  $\text{As}$ -vapor species. The increase in growth rate with increasing values of  $\text{AsH}_3$  or  $\text{As}_4$  partial pressure has also been observed by several other investigators (9, 14). It should be noted that a growth rate of  $30\text{--}35 \mu\text{m}/\text{hr}$  is about the maximum value normally observed for growth of  $\text{GaAs}$  on the  $\{100\}$  surface.

In contrast, for a given  $\text{AsH}_3$  setting, the growth rate first increases, then decreases [Fig. 5(a)] with increasing  $\text{HCl}$  flow rate. The decrease does not result from incomplete reaction of  $\text{HCl}$  with the  $\text{Ga}$  metal source. In separate experiments, comparison of the moles of  $\text{Ga}$  and  $\text{HCl}$  gas consumed, as determined by weight loss and wet chemical analysis, respectively, showed that 98% of a  $20 \text{ cm}^3/\text{min}$   $\text{HCl}$  flow rate reacts with the

$\text{Ga}$  metal source to form  $\text{GaCl}$  in the vapor-growth tube used for the present experiments. Thus, virtually all of the  $\text{HCl}$  in the range  $2\text{--}20 \text{ cm}^3/\text{min}$  injected into the vapor-growth apparatus is converted to  $\text{GaCl}$ .

The reduced growth rate for increasing  $\text{HCl}$  flow rates shows that the growth rate is not directly related to the reactant partial pressures, as is the case for  $\text{AsH}_3$ . Instead, the limitation of the growth rate at  $725^\circ\text{C}$  is probably related to adsorption of  $\text{GaCl}$  (14, 29) and subsequent reaction with  $\text{As}_x$  on the  $\text{GaAs}$  crystal surface to form the epitaxial  $\text{GaAs}$  layer. The nature of this reaction has been examined previously by Shaw (14), whose data are also shown in Fig. 5. Surprisingly good agreement is found for the dependence of the growth rate on the  $\text{HCl}$  and  $\text{AsH}_3$  flow rates in the present study and on  $\text{GaCl}$  and  $\text{As}_4$  partial pressures determined previously by Shaw (14), who used significantly different growth conditions (i.e., growth on the reactor walls prevented by injecting auxiliary unreacted  $\text{HCl}$ , an 80% lower total  $\text{H}_2$  flow rate, and a solid  $\text{As}$  source).

Several authors (8, 26) have previously related the growth rate to the  $\text{Ga}/\text{As}$  ratio in the vapor phase, and have shown a peak value of the growth rate in the range of  $1\text{--}4 \text{ Ga}/\text{As}$ . However, the present study, as

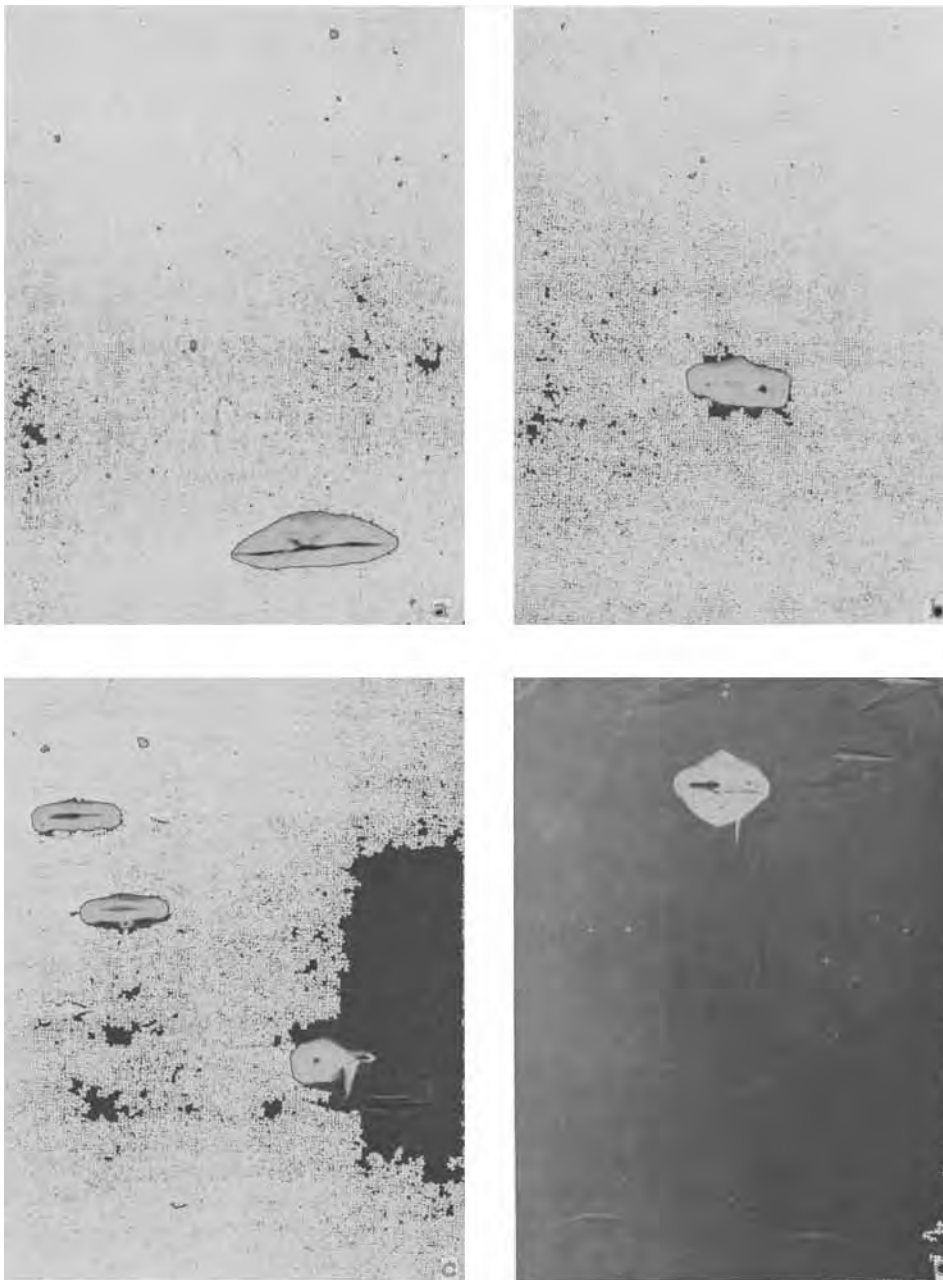


Fig. 2. Optical photomicrographs of GaAs vapor-grown layers prepared with 5 cm<sup>3</sup>/min of HCl and AsH<sub>3</sub> flow rates varying from 3.5 to 35 cm<sup>3</sup>/min. 200× magnification. All defects are pits. a, Run 881, 3.5 cm<sup>3</sup>/min of AsH<sub>3</sub>; Ga/As = 1.43. b, Run 905, 8 cm<sup>3</sup>/min of AsH<sub>3</sub>; Ga/As = 0.65. c, Run 910, 17.5 cm<sup>3</sup>/min of AsH<sub>3</sub>; Ga/As = 0.28. d, Run 880, 35 cm<sup>3</sup>/min of AsH<sub>3</sub>; Ga/As = 0.14.

well as other recent works (9, 12, 14), suggests that the growth rate is related to the partial pressure of the individual reactants, GaCl and AsH<sub>3</sub> or As<sub>4</sub>, rather than to the Ga/As gas ratio. Since increasing AsH<sub>3</sub> flow rates increase the growth rate, in accord with thermodynamic expectations, and increasing HCl flow rates decrease the growth rate, contrary to equilibrium thermodynamics (17), it appears that GaCl is the chemical species limiting the growth rate. This could arise at high HCl flow rates by nearly complete filling of adsorption sites with GaCl on the crystal surface, to the exclusion of the As-species. Adsorbed As-species atoms on the crystal surface are necessary for reaction with the GaCl to form GaAs, and if insufficient As is available, a lower growth rate should result. Since our experiments with Zn- and Se-doped vapor-grown layers (to be described in the next section) show that both the donor and acceptor concentrations are strong functions of the HCl flow rate, it is not unreasonable to suspect that the incorporation of dopant atoms is also affected by the preferential adsorption of GaCl on the growing surface.

The growth rate was also found to decrease with increasing elapsed growth time. This probably occurs because growth of GaAs on the quartz tube walls in-

creases with time, and these polycrystalline deposits increasingly compete with growth on the single-crystalline substrate. It was also observed that the GaAs deposits on the walls of the quartz tube increased in thickness as the HCl flow rate increased. For low HCl flow rates (2 cm<sup>3</sup>/min) only a thin GaAs layer formed on the quartz, whereas for higher HCl flow rates (20 cm<sup>3</sup>/min) a dense GaAs wall deposit was observed.

*Impurity doping.*—Since the epitaxial layers used in this investigation were prepared in the form of p-n junction structures, the carrier concentrations could not be determined by Hall measurements. However, as described in detail below, straightforward photoluminescence and capacitance measurements could be used to characterize both the outermost Zn-doped layer and the adjacent Se-doped layer, respectively.

*Zn doping.*—The hole concentration in the p-type layer was evaluated from room temperature photoluminescence measurements. The spectral halfwidth was used as a measure of the free hole concentration, since it depends directly on doping for concentrations greater than about  $2 \times 10^{18}$  cm<sup>-3</sup> (30). This correlation allowed us to correctly label the right-hand ordinate in the plots of spectral halfwidth vs. gas flow rate shown

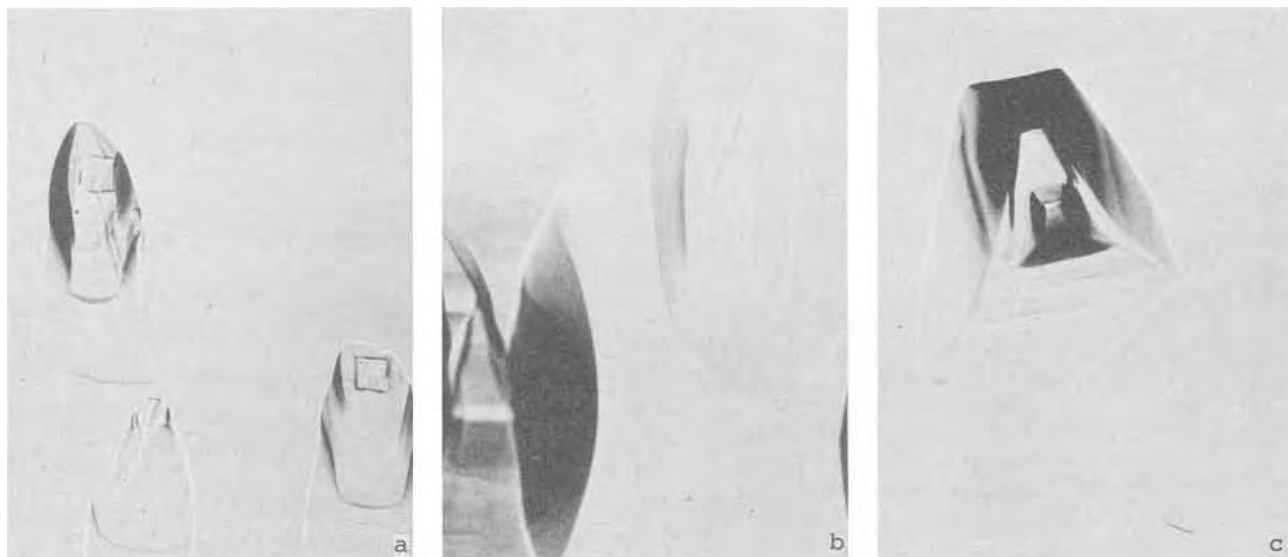


Fig. 3. Optical photomicrographs of GaAs vapor-grown layers prepared with 20 cm<sup>3</sup>/min of HCl and AsH<sub>3</sub> flow rates varying from 3.0 to 17.5 cm<sup>3</sup>/min. 200× magnification. All defects are hillocks. a, Run 907, 3.0 cm<sup>3</sup>/min of AsH<sub>3</sub>; Ga/As = 6.66. b, Run 904, 10 cm<sup>3</sup>/min of AsH<sub>3</sub>; Ga/As = 2.0. c, Run 882, 17.5 cm<sup>3</sup>/min of AsH<sub>3</sub>; Ga/As = 1.14.

in Fig. 6. Here, for HCl flow rates increasing from 2 to 20 cm<sup>3</sup>/min, the Zn carrier concentration decreases from approximately  $2 \times 10^{19}$  to  $5 \times 10^{18}$  cm<sup>-3</sup> for a Zn source at 450°C, and from  $5 \times 10^{18}$  to  $1.5 \times 10^{18}$  cm<sup>-3</sup> for a source at 410°C. The hole concentration depends less strongly on the AsH<sub>3</sub> flow rate, increasing from  $5 \times 10^{18}$  to  $1 \times 10^{19}$  cm<sup>-3</sup> over the range evaluated (3.5-35 cm<sup>3</sup>/min).

The relative photoluminescence intensity of each of the Zn-doped GaAs layers is plotted in Fig. 7 as a function of the Zn concentration (determined from the halfwidths in Fig. 6). The increase in intensity with increasing carrier concentration is consistent with Cusano's (30) cathodoluminescence data for p-type GaAs. Since the carrier concentrations for our experiments are less than about  $2 \times 10^{19}$  cm<sup>-3</sup>, an intensity degradation usually associated with Zn precipitation (30) at high concentrations is not observed. The self-

consistency of the photoluminescence data of Fig. 6 and 7 clearly indicates that large HCl flow rates give rise to a reduction in the amount of Zn incorporated into the GaAs lattice.

*Se doping.*—Since the n-type layer of our vapor-grown structures is sandwiched between the GaAs substrate and the p-type layer, it is not exposed for photoluminescence measurements. Accordingly, the donor concentration in the n-type layers was estimated from standard capacitance-voltage and reverse-bias breakdown measurements performed after complete diode fabrication. The donor concentrations determined by both methods were in excellent agreement.

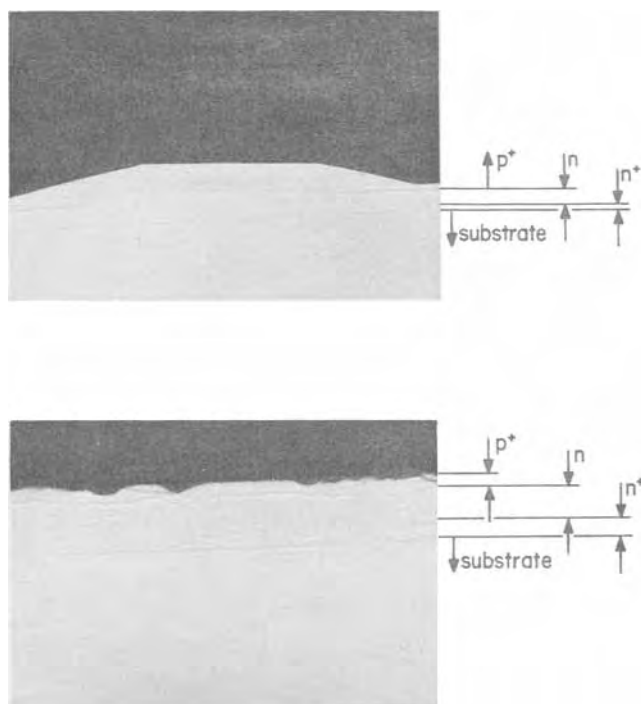


Fig. 4. Optical photomicrographs of {110} cleavage planes intersecting hillock (top) and pit (bottom).

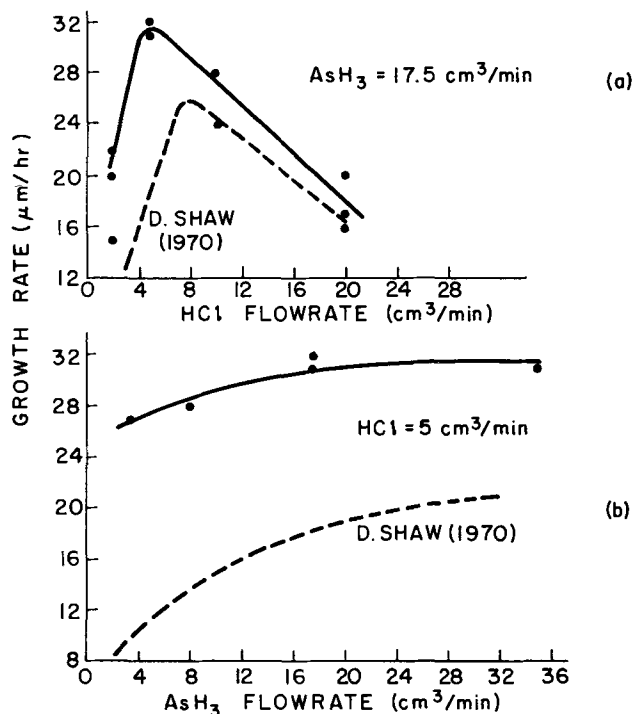


Fig. 5. (a) Growth rate vs. HCl flow rate for GaAs epitaxial layers prepared with AsH<sub>3</sub> flow rate of 17.5 cm<sup>3</sup>/min. (b) Growth rate vs. AsH<sub>3</sub> flow rate for GaAs epitaxial layers prepared with HCl flow rate of 5 cm<sup>3</sup>/min. Substrate orientation is  $\langle 100 \rangle$ . Dashed lines are from Shaw's previous study (14).

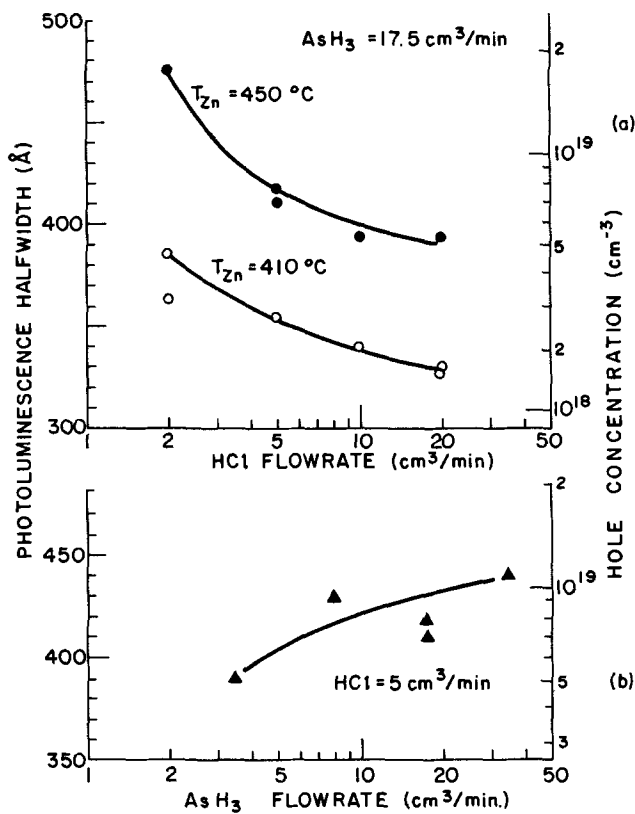


Fig. 6. Room temperature photoluminescence halfwidth (in angstroms) vs. (a) HCl flow rate, and (b) AsH<sub>3</sub> flow rate. Two different Zn source temperatures (410° and 450°C) were used for the layers whose halfwidths were evaluated in the top figure. The right-hand vertical axis (hole concentration) was calibrated from the known relationship [Ref. (30)] between spectral halfwidth and hole concentration in GaAs.

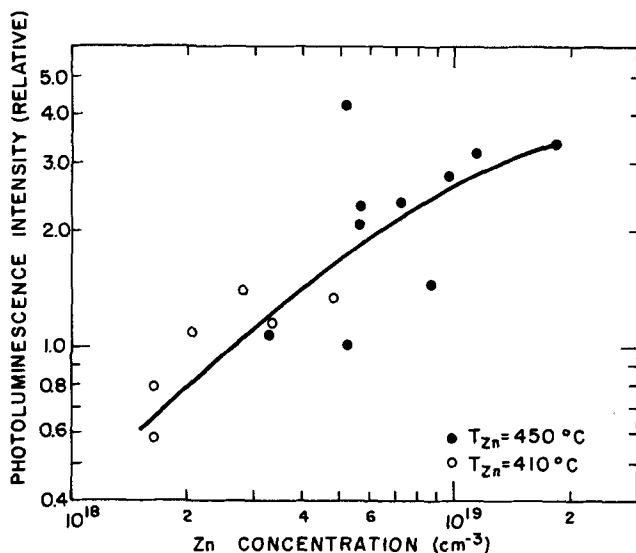


Fig. 7. Photoluminescence intensity vs. Zn acceptor concentration for the GaAs layers whose halfwidths are shown in Fig. 6 (a and b).

The free electron concentration, as determined from the above measurements, is plotted as a function of the HCl and AsH<sub>3</sub> flow rates in Fig. 8. In Fig. 8(a) the electron concentration decreases from  $6 \times 10^{17}$  to  $1 \times 10^{17}$  cm<sup>-3</sup> for HCl flow rates increasing from 2 to 20 cm<sup>3</sup>/min. For these samples, the AsH<sub>3</sub> flow rate was held at 17.5 cm<sup>3</sup>/min. In Fig. 8(b), the effect of AsH<sub>3</sub> flow rate on the electron concentration is shown for growths where the HCl is held constant at 5 cm<sup>3</sup>/min.

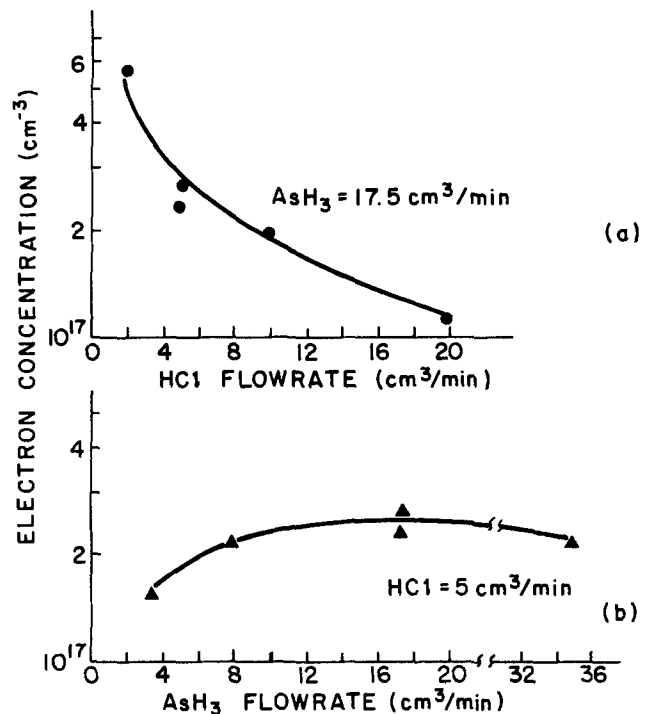


Fig. 8. Electron concentration on the n-side of the junction vs. (a) HCl flow rate, and (b) AsH<sub>3</sub> flow rate. The electron concentration was determined from C-V and voltage-breakdown measurements.

The electron concentration is only weakly dependent on the AsH<sub>3</sub> flow rate, increasing by about 40% over the range of flow rates used here.

Several different mechanisms are possible to explain the flow rate dependence of the doping concentration, including changes in crystal stoichiometry and differences in the rate of adsorption of impurity atoms. Concerning crystal stoichiometry, a change in the Ga or As vacancy concentration with changing gas flow conditions should enhance the incorporation of one type of impurity (either donors or acceptors), while retarding the incorporation of the other. In fact, previous work has shown that the background donor concentration of vapor-grown GaAs layers can be influenced by gas-phase (Ga/As) ratios for donor concentrations in the range of  $10^{14}$ - $10^{15}$  cm<sup>-3</sup> (7, 9). But the impurity concentrations here, particularly for the case of Zn where  $p \sim 10^{19}$  cm<sup>-3</sup>, are probably too large to be directly affected by deviations in crystal stoichiometry. Accordingly, since both the Zn-acceptor and the Se-donor concentrations were found to decrease with increasing HCl flow rate, it appears that varying the gas-phase stoichiometry alters the rate of incorporation (i.e., the sticking coefficient) of both types of impurity atoms from the gas phase into the growing solid layer rather than changing the crystal stoichiometry or unintentional reactor impurity concentrations.

In addition, changes in the crystal stoichiometry might be expected to alter the characteristics of the low-energy luminescence spectra of the GaAs samples (31, 32). In our work, both the photoluminescence spectra of the p-type layers and the electroluminescence spectra of the p-n junctions were examined at 300° and 77°K; although weak, low energy emission at 1.2-1.3 eV was observed for all samples at 77°K, the magnitude of this emission (relative to the near band-gap emission at  $\sim 1.5$  eV) did not change significantly over the range of gas-flow conditions studied here. Therefore, consistent with our electrical data described above, the luminescence spectra at 77°K give no indication of significant changes in crystal stoichiometry.

*External electroluminescent diode efficiency.*—The diode electroluminescence efficiency at 300°K is given

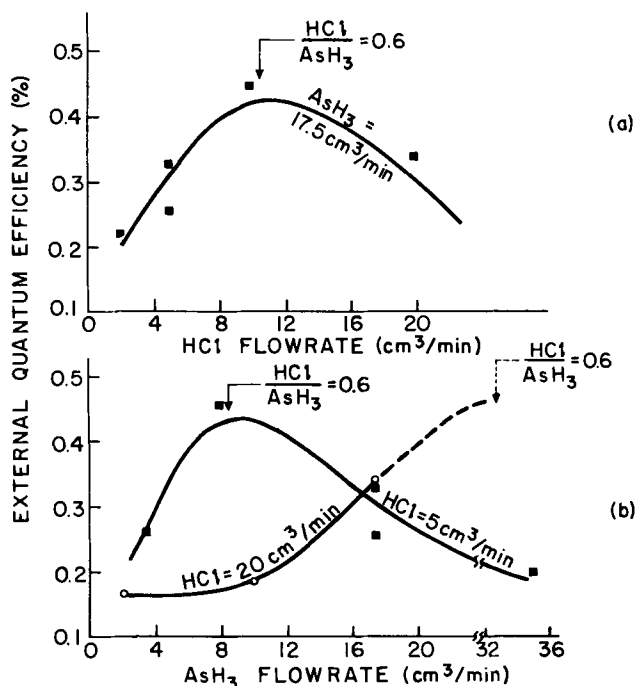


Fig. 9. The room temperature external quantum efficiency vs. (a) HCl flow rate, and (b) AsH<sub>3</sub> flow rate for GaAs electro luminescent diodes fabricated from the vapor-grown layers.

in Fig. 9 as a function of the HCl and AsH<sub>3</sub> flow rates. Here, two rather unexpected results are observed. First, the external quantum efficiency in Fig. 9(b) is seen to depend strongly on the AsH<sub>3</sub> flow rate, in contrast to the weak dependence on AsH<sub>3</sub> found for the defect morphology (Fig. 2 and 3), growth rate (Fig. 5), and doping concentrations (Fig. 6 and 8). Second, for both the solid curves in Fig. 9(a and b), a maximum efficiency of approximately 0.45% is attained at an HCl/AsH<sub>3</sub> ratio of 0.6, in contrast to each of the early dependences (Fig. 1, 5, 6, and 8) on HCl only. Thus, empirically it appears that a slightly As-rich, gas-phase composition is desirable for our vapor-grown electro luminescent diodes. For comparison, vapor-grown GaAs produced by the AsCl<sub>3</sub> method has an HCl/As ratio of 3, which, according to the present results, might limit electro luminescent diode efficiencies.

The maximum values of 0.45% at 300°K are about the same as previously attained with optimized Se and Zn concentrations (1). At 80°K, efficiencies approaching 3% were attained, close to the theoretical maximum for a single-surface, rectangular emitter with no absorption losses (33).

The shape of the curves in Fig. 9 probably reflects the variation of several factors, including defects, carrier concentrations, and layer thicknesses. These affect the bulk radiative recombination efficiency in the p-layer, the injection efficiency of electrons into the p-layer, the effectiveness of shunting nonradiative centers at the junction, and optical absorption of the light passing through the p-layer. Because of the complex manner in which these many parameters interact, it is difficult *a priori* to predict the effect of HCl or AsH<sub>3</sub> flow rates on the electro luminescent diode efficiencies. However, in view of the earlier results of this study, it is not surprising that extreme flow rates of either AsH<sub>3</sub> or HCl are detrimental. For example, at the low HCl flow rates in Fig. 9(a), the high density of pits would be expected to reduce the junction perfection. Similarly, large HCl and small AsH<sub>3</sub> flow rates would reduce the acceptor concentration in the p-layer, thereby reducing the radiative recombination efficiency there, as shown in Fig. 7.

## Summary and Conclusions

The defect morphology of vapor-grown, <100>-oriented GaAs epitaxial layers is not related to the HCl/AsH<sub>3</sub> (or Ga/As) gas-phase ratio. Rather, the occurrence of pits is associated with low HCl flow rates (2-5 cm<sup>3</sup>/min), and hillocks are associated with high HCl flow rates (10-20 cm<sup>3</sup>/min). These results are consistent with observations for GaAs prepared by the AsCl<sub>3</sub> growth method, where low flow rates of AsCl<sub>3</sub> (i.e., GaCl or HCl) produce pits and higher AsCl<sub>3</sub> flow rates produce hillocks. The AsH<sub>3</sub> flow rate appears to influence the size and density rather than the type of defect present.

The crystal growth rate increases monotonically with AsH<sub>3</sub> flow rate but shows a maximum at intermediate values of increasing HCl flow rate. The growth rates obtained in a Ga/HCl/AsH<sub>3</sub>/H<sub>2</sub> growth system using high H<sub>2</sub> flow rates (2500 cm<sup>3</sup>/min) are in nearly quantitative agreement with Shaw's earlier results (14) for significantly different vapor-growth conditions. Since both the Zn-acceptor and Se-donor concentrations decrease with increasing HCl flow rate, it appears that varying the gas-phase stoichiometry alters the rate of incorporation of both types of impurity atoms from the gas-phase into the growing solid layer rather than changing the crystal stoichiometry (Ga and As vacancy concentrations) or unintentional reactor impurity concentrations. The electro luminescent diode efficiency depends strongly on both the AsH<sub>3</sub> and HCl flow rates, in contrast to the weak dependence on AsH<sub>3</sub> found for the defect morphology, growth rate, and doping concentrations. A maximum efficiency of 0.45% at 300°K is attained for a slightly As-rich, gas-phase mixture. At 80°K, efficiencies approaching 3% are attained, close to the theoretical maximum for this geometry.

## Acknowledgments

The authors wish to acknowledge the technical assistance of R. W. Snedeker. Discussions with D. Richman, V. S. Ban, R. T. Smith, and M. Ettenberg have been helpful and are appreciated.

Manuscript submitted Dec. 3, 1973; revised manuscript received May 24, 1974.

Any discussion of this paper will appear in a Discussion Section to be published in the June 1975 JOURNAL. All discussions for the June 1975 Discussion Section should be submitted by Feb. 1, 1975.

The publication costs of this article have been assisted by RCA Laboratories.

## REFERENCES

- C. J. Nuese, J. J. Tietjen, J. J. Gannon, and H. F. Gossenberger, *Trans. Met. Soc. AIME*, **242**, 401 (1968).
- J. I. Pankove, H. Nelson, J. J. Tietjen, I. J. Hegyi, and H. P. Maruska, *RCA Rev.*, **28**, 560 (1967).
- J. J. Tietjen and S. Ochs, *Proc. IEEE*, **53**, 180 (1965).
- J. J. Tietjen, G. Kupsky, and H. F. Gossenberger, *Solid-State Electron.*, **9**, 1049 (1966).
- P. A. Levine, A. B. Dreeben, and A. R. Triano, *Proc. IEEE*, **59**, 1128 (1971).
- K. P. Weller, C. P. Wen, A. F. Young, and A. B. Dreeben, *Proc. Cornell Conf. High Frequency Generation Amplification*, **3**, 191 (1971).
- B. E. Berson, R. E. Enstrom, and J. F. Reynolds, *RCA Rev.*, **31**, 20 (1970).
- D. W. Shaw, R. W. Conrad, E. W. Mehal, and O. W. Wilson, *Gallium Arsenide*, Conf. Series No. 3, p. 10, Institute of Physics and the Physical Society, London (1967).
- P. Merenda, *J. Crystal Growth*, **13/14**, 331 (1972).
- A. E. Blakeslee, *Proc. Third Intern. Symp. Gallium Arsenide and Related Compounds*, p. 283, Institute of Physics, London (1971).
- R. E. Enstrom, C. J. Nuese, J. R. Appert, and J. J. Gannon, *Second National Conf. Crystal Growth*, Princeton, N. J., Aug. 2, 1972.
- J. K. Kennedy and W. D. Potter, *ibid.*, Late News Paper, See also *J. Crystal Growth*, **19**, 85 (1973).
- T. Y. Wu, *ibid.*, **21**, 85 (1974).

14. D. Shaw, *This Journal*, **117**, 683 (1970).
15. J. J. Tietjen and J. A. Amick, *ibid.*, **113**, 724 (1966).
16. D. Effer, *ibid.*, **112**, 1020 (1965).
17. J. R. Knight, D. Effer, and P. R. Evans, *Solid-State Electron.*, **8**, 178 (1965).
18. R. E. Enstrom and J. R. Appert, *Gallium Arsenide*, Conf. Series No. 7, p. 213, Institute of Physics and the Physical Society, London (1969).
19. V. S. Ban, *J. Crystal Growth*, **17**, 19 (1972).
20. C. J. Nuese and J. J. Gannon, *This Journal*, **115**, 327 (1968).
21. R. E. Enstrom, C. J. Nuese, V. S. Ban, and J. R. Appert, *Gallium Arsenide and Related Compounds*, Conf. Series No. 17, p. 37, The Institute of Physics, London (1973).
22. R. E. Enstrom, D. Richman, M. S. Abrahams, J. R. Appert, D. G. Fisher, A. H. Sommer, and B. F. Williams, *ibid.*, Conf. Series No. 9, p. 30, The Institute of Physics, London (1971).
23. H. T. Minden, *J. Crystal Growth*, **8**, 37 (1972).
24. A. E. Blakeslee, *Trans. Met. Soc. AIME*, **245**, 577 (1969).
25. J. V. DiLorenzo, *J. Crystal Growth*, **17**, 189 (1972).
26. R. E. Ewing and P. E. Green, *This Journal*, **111**, 1266 (1964).
27. B. D. Joyce and J. B. Mullin, *Solid State Commun.*, **4**, 463 (1966).
28. J. J. Tietjen, M. S. Abrahams, A. B. Dreeben, and H. F. Gossenberger, *Gallium Arsenide*, Conf. Series No. 7, p. 55, Institute of Physics and the Physical Society, London (1969).
29. Chr. Belouet, *J. Crystal Growth*, **13/14**, 342 (1972).
30. D. A. Cusano, *Solid State Commun.*, **2**, 353 (1964); see also M. Ettenberg and C. J. Nuese, To be published.
31. A. Y. Cho and I. Hayashi, *Solid-State Electron.*, **14**, 125 (1971).
32. L. L. Chang, L. Esaki, and R. Tsu, *Appl. Phys. Letters*, **19**, 143 (1971).
33. W. N. Carr, *Infrared Phys.*, **6**, 1 (1966).

## Antimony Diffusion into P-Type $Pb_{1-x}Sn_xTe$

R. L. Guldi and G. A. Antcliffe

*Texas Instruments Incorporated, Dallas, Texas 75222*

### ABSTRACT

The characteristics of Sb diffusion into p-type  $Pb_{1-x}Sn_xTe$  with  $0.08 < x < 0.21$  were investigated by measuring radioactive Sb profiles and n-p junction depths. Values for the Sb diffusion coefficient in  $Pb_{0.79}Sn_{0.21}Te$  range from  $2 \times 10^{-14}$  cm<sup>2</sup>/sec at 500°C to  $4 \times 10^{-10}$  cm<sup>2</sup>/sec at 750°C. The Sb diffusion coefficient and solubility are essentially independent of Sn content and substrate hole concentration. In contrast the rate of n-p junction diffusion increases with decreasing substrate hole concentration. The Sb concentration at the n-p junction, determined by using the radioactive Sb profiles, is considerably higher than the hole concentration before diffusion. Mechanisms that might account for this behavior include the formation of Sb precipitates, compensation of Sb by native defect acceptors, or amphoteric doping behavior of Sb.

$Pb_{1-x}Sn_xTe$  is a pseudobinary semiconductor compound with a bandgap that depends upon alloy composition. The phase fields for undoped  $Pb_{1-x}Sn_xTe$  of various Sn compositions have been well established (1). Samples containing a stoichiometric excess of metal (*i.e.*, Pb and Sn) show n-type conductivity while those containing excess Te are p-type, because the native defects responsible for these deviations from stoichiometry act as donors and acceptors, respectively. The alloys discussed in this paper fall in the composition range  $0.08 < x < 0.21$ . Crystals of such alloys grown within 100°C of the melting point always contain excess Te and are therefore strongly p-type. A common method for obtaining n-p junctions in  $Pb_{1-x}Sn_xTe$  is to diffuse a metal-rich layer into the p-type substrate (1). An alternative method which has proven quite successful involves diffusing a donor impurity such as Sb into the p-type substrate (2, 3). This paper will discuss some of the characteristics of Sb diffusion into p-type  $Pb_{1-x}Sn_xTe$  determined from radioactive Sb profiles and junction depths found by thermoelectric probe measurements. The ranges of temperatures, alloy compositions, and substrate hole concentrations which were studied are those of importance in the fabrication of junction lasers and photovoltaic detectors for the 8-12 μm spectral region.

### Experimental Procedure

The crystals used were either 9 or 25 mm diameter single crystals grown at temperatures from 820° to 850°C by vapor transport from metal-rich source material (4). The dislocation density was typically in the mid  $10^4$  cm<sup>-2</sup> range. The hole concentration in the as-grown crystals, as determined by van der Pauw measurements at 77°K, was equal to  $2 \times 10^{18}$ ,  $5 \times 10^{18}$ , and  $2 \times 10^{19}$  cm<sup>-3</sup> for the 8, 12.4, and 21 mole per cent (m/o) SnTe compositions, respectively. The as-grown

ingots were cut with a string saw into either (100)- or (111)-oriented wafers. Saw damage was removed by polishing and etching, using HBr + 2% Br<sub>2</sub> as a final etch. The diffusion slices were typically 0.5-1.0 mm thick. In some cases, prior to Sb diffusion, the slices were preannealed in metal-rich vapor to adjust the stoichiometry, giving material with lower hole concentrations (1) (see Table I).

The diffusion samples were sealed in quartz ampuls which were evacuated to a pressure of approximately  $10^{-6}$  Torr and backfilled with H<sub>2</sub> to a pressure of about 2 atm in order to prevent thermal etching of the samples. Radioactive Sb-124 (half-life = 60.2 day) was obtained by neutron activation of Sb (6-9's) at the Union Carbide reactor facilities at Tuxedo, New York. In the majority of the diffusions, a 1-2 mg charge of metallic Sb was used as a diffusion source. Some diffusions however used an Sb-doped ( $Pb_{0.79}Sn_{0.21}$ )<sub>0.505</sub>Te<sub>0.495</sub> source. [The Sb content was approximately 5 atomic per cent (a/o).] In either case the Sb charge was in contact with the crystal

Table I. Solubilities and diffusion coefficients of antimony in  $Pb_{1-x}Sn_xTe$

Composition	Substrate hole concentration (cm <sup>-3</sup> )	Temperature (°C)	Solubility of antimony (cm <sup>-3</sup> )	Diffusion coefficient of antimony (cm <sup>2</sup> /sec)
$Pb_{0.92}Sn_{0.08}Te$	$2 \times 10^{18}$	700	$6 \times 10^{19}$	$6 \times 10^{-11}$
	$2 \times 10^{18}$	640	$6 \times 10^{19}$	$1 \times 10^{-11}$
$Pb_{0.79}Sn_{0.21}Te$	$2 \times 10^{19}$	750	$7 \times 10^{19}$	$4 \times 10^{-10}$
	$2 \times 10^{19}$	700	$7 \times 10^{19}$	$6 \times 10^{-11}$
	$5 \times 10^{18} \dagger$	700	$1 \times 10^{20} \ast$	$6 \times 10^{-11}$
	$2 \times 10^{19}$	640	$7 \times 10^{19}$	$1 \times 10^{-11}$
	$6 \times 10^{17} \dagger$	600	$6 \times 10^{19}$	$3 \times 10^{-12}$
	$2 \times 10^{19}$	561	$6 \times 10^{19}$	$1 \times 10^{-12}$
	$6 \times 10^{17} \dagger$	561	$6 \times 10^{19}$	$1 \times 10^{-12}$
	$2 \times 10^{19}$	502	$5 \times 10^{19}$	$2 \times 10^{-14}$

† Substrate preannealed.

\* Sb-doped ( $Pb_{0.79}Sn_{0.21}$ )<sub>0.505</sub>Te<sub>0.495</sub> diffusion source used.

Key words: lead tin telluride, infrared devices, p-n junctions, chalcogenides, ternaries.



14. D. Shaw, *This Journal*, **117**, 683 (1970).
15. J. J. Tietjen and J. A. Amick, *ibid.*, **113**, 724 (1966).
16. D. Effer, *ibid.*, **112**, 1020 (1965).
17. J. R. Knight, D. Effer, and P. R. Evans, *Solid-State Electron.*, **8**, 178 (1965).
18. R. E. Enstrom and J. R. Appert, *Gallium Arsenide*, Conf. Series No. 7, p. 213, Institute of Physics and the Physical Society, London (1969).
19. V. S. Ban, *J. Crystal Growth*, **17**, 19 (1972).
20. C. J. Nuese and J. J. Gannon, *This Journal*, **115**, 327 (1968).
21. R. E. Enstrom, C. J. Nuese, V. S. Ban, and J. R. Appert, *Gallium Arsenide and Related Compounds*, Conf. Series No. 17, p. 37, The Institute of Physics, London (1973).
22. R. E. Enstrom, D. Richman, M. S. Abrahams, J. R. Appert, D. G. Fisher, A. H. Sommer, and B. F. Williams, *ibid.*, Conf. Series No. 9, p. 30, The Institute of Physics, London (1971).
23. H. T. Minden, *J. Crystal Growth*, **8**, 37 (1972).
24. A. E. Blakeslee, *Trans. Met. Soc. AIME*, **245**, 577 (1969).
25. J. V. DiLorenzo, *J. Crystal Growth*, **17**, 189 (1972).
26. R. E. Ewing and P. E. Green, *This Journal*, **111**, 1266 (1964).
27. B. D. Joyce and J. B. Mullin, *Solid State Commun.*, **4**, 463 (1966).
28. J. J. Tietjen, M. S. Abrahams, A. B. Dreeben, and H. F. Gossenberger, *Gallium Arsenide*, Conf. Series No. 7, p. 55, Institute of Physics and the Physical Society, London (1969).
29. Chr. Belouet, *J. Crystal Growth*, **13/14**, 342 (1972).
30. D. A. Cusano, *Solid State Commun.*, **2**, 353 (1964); see also M. Ettenberg and C. J. Nuese, To be published.
31. A. Y. Cho and I. Hayashi, *Solid-State Electron.*, **14**, 125 (1971).
32. L. L. Chang, L. Esaki, and R. Tsu, *Appl. Phys. Letters*, **19**, 143 (1971).
33. W. N. Carr, *Infrared Phys.*, **6**, 1 (1966).

## Antimony Diffusion into P-Type $Pb_{1-x}Sn_xTe$

R. L. Guldi and G. A. Antcliffe

*Texas Instruments Incorporated, Dallas, Texas 75222*

### ABSTRACT

The characteristics of Sb diffusion into p-type  $Pb_{1-x}Sn_xTe$  with  $0.08 < x < 0.21$  were investigated by measuring radioactive Sb profiles and n-p junction depths. Values for the Sb diffusion coefficient in  $Pb_{0.79}Sn_{0.21}Te$  range from  $2 \times 10^{-14}$  cm<sup>2</sup>/sec at 500°C to  $4 \times 10^{-10}$  cm<sup>2</sup>/sec at 750°C. The Sb diffusion coefficient and solubility are essentially independent of Sn content and substrate hole concentration. In contrast the rate of n-p junction diffusion increases with decreasing substrate hole concentration. The Sb concentration at the n-p junction, determined by using the radioactive Sb profiles, is considerably higher than the hole concentration before diffusion. Mechanisms that might account for this behavior include the formation of Sb precipitates, compensation of Sb by native defect acceptors, or amphoteric doping behavior of Sb.

$Pb_{1-x}Sn_xTe$  is a pseudobinary semiconductor compound with a bandgap that depends upon alloy composition. The phase fields for undoped  $Pb_{1-x}Sn_xTe$  of various Sn compositions have been well established (1). Samples containing a stoichiometric excess of metal (*i.e.*, Pb and Sn) show n-type conductivity while those containing excess Te are p-type, because the native defects responsible for these deviations from stoichiometry act as donors and acceptors, respectively. The alloys discussed in this paper fall in the composition range  $0.08 < x < 0.21$ . Crystals of such alloys grown within 100°C of the melting point always contain excess Te and are therefore strongly p-type. A common method for obtaining n-p junctions in  $Pb_{1-x}Sn_xTe$  is to diffuse a metal-rich layer into the p-type substrate (1). An alternative method which has proven quite successful involves diffusing a donor impurity such as Sb into the p-type substrate (2, 3). This paper will discuss some of the characteristics of Sb diffusion into p-type  $Pb_{1-x}Sn_xTe$  determined from radioactive Sb profiles and junction depths found by thermoelectric probe measurements. The ranges of temperatures, alloy compositions, and substrate hole concentrations which were studied are those of importance in the fabrication of junction lasers and photovoltaic detectors for the 8-12 μm spectral region.

### Experimental Procedure

The crystals used were either 9 or 25 mm diameter single crystals grown at temperatures from 820° to 850°C by vapor transport from metal-rich source material (4). The dislocation density was typically in the mid  $10^4$  cm<sup>-2</sup> range. The hole concentration in the as-grown crystals, as determined by van der Pauw measurements at 77°K, was equal to  $2 \times 10^{18}$ ,  $5 \times 10^{18}$ , and  $2 \times 10^{19}$  cm<sup>-3</sup> for the 8, 12.4, and 21 mole per cent (m/o) SnTe compositions, respectively. The as-grown

ingots were cut with a string saw into either (100)- or (111)-oriented wafers. Saw damage was removed by polishing and etching, using HBr + 2% Br<sub>2</sub> as a final etch. The diffusion slices were typically 0.5-1.0 mm thick. In some cases, prior to Sb diffusion, the slices were preannealed in metal-rich vapor to adjust the stoichiometry, giving material with lower hole concentrations (1) (see Table I).

The diffusion samples were sealed in quartz ampuls which were evacuated to a pressure of approximately  $10^{-6}$  Torr and backfilled with H<sub>2</sub> to a pressure of about 2 atm in order to prevent thermal etching of the samples. Radioactive Sb-124 (half-life = 60.2 day) was obtained by neutron activation of Sb (6-9's) at the Union Carbide reactor facilities at Tuxedo, New York. In the majority of the diffusions, a 1-2 mg charge of metallic Sb was used as a diffusion source. Some diffusions however used an Sb-doped ( $Pb_{0.79}Sn_{0.21}$ )<sub>0.505</sub>Te<sub>0.495</sub> source. [The Sb content was approximately 5 atomic per cent (a/o).] In either case the Sb charge was in contact with the crystal

Table I. Solubilities and diffusion coefficients of antimony in  $Pb_{1-x}Sn_xTe$

Composition	Substrate hole concentration (cm <sup>-3</sup> )	Temperature (°C)	Solubility of antimony (cm <sup>-3</sup> )	Diffusion coefficient of antimony (cm <sup>2</sup> /sec)
$Pb_{0.92}Sn_{0.08}Te$	$2 \times 10^{18}$	700	$6 \times 10^{19}$	$6 \times 10^{-11}$
	$2 \times 10^{18}$	640	$6 \times 10^{19}$	$1 \times 10^{-11}$
$Pb_{0.76}Sn_{0.24}Te$	$2 \times 10^{19}$	750	$7 \times 10^{19}$	$4 \times 10^{-10}$
	$2 \times 10^{19}$	700	$7 \times 10^{19}$	$6 \times 10^{-11}$
	$5 \times 10^{18} \dagger$	700	$1 \times 10^{20} \dagger$	$6 \times 10^{-11}$
	$2 \times 10^{19}$	640	$7 \times 10^{19}$	$1 \times 10^{-11}$
	$6 \times 10^{17} \dagger$	600	$6 \times 10^{19}$	$3 \times 10^{-12}$
	$2 \times 10^{19}$	561	$6 \times 10^{19}$	$1 \times 10^{-12}$
	$6 \times 10^{17} \dagger$	561	$6 \times 10^{19}$	$1 \times 10^{-12}$
	$2 \times 10^{19}$	502	$5 \times 10^{19}$	$2 \times 10^{-14}$

† Substrate preannealed.

\* Sb-doped ( $Pb_{0.76}Sn_{0.24}$ )<sub>0.505</sub>Te<sub>0.495</sub> diffusion source used.

Key words: lead tin telluride, infrared devices, p-n junctions, chalcogenides, ternaries.



only through the vapor phase. The diffusions were conducted in furnaces which were controlled to  $\pm 0.5^\circ\text{C}$  and had isothermal heat pipes to provide a constant temperature zone. At the termination of a diffusion run the ampuls were removed from the furnace and allowed to cool in air. Each diffused sample was characterized by measuring either the Sb-124 diffusion profile or the n-p junction depth.

The radioactive Sb diffusion profiles were measured by conventional lapping and counting techniques. The samples were sectioned by successively lapping away thin (typically 1-2  $\mu\text{m}$ ) layers on 4/0 Emery paper and counting the activity in the material which collected on the paper. A  $7.5 \times 7.5$  cm NaI(Tl) well detector in conjunction with a single-channel analyzer and timer scaler was used to count in the integral mode with the discriminator at 470 keV. The thickness of the removed layers was determined from the sample area, the density of  $\text{Pb}_{1-x}\text{Sn}_x\text{Te}$  (5), and the difference in sample weight before and after lapping. Autoradiograms taken at various stages of lapping indicated that the Sb concentration was uniform in the plane normal to the diffusion direction.

Measurements of n-p junction depths were made by the standard technique of angle lapping ( $1^\circ$  angle) and thermoelectric probing. Junction depths were measured at  $300^\circ$  and  $77^\circ\text{K}$  and found to be the same at both temperatures. The position of the junction can be measured to within  $\pm 2 \mu\text{m}$ , and the measured depths were quite reproducible within that range.

### Results and Discussion

**Radioactive Sb diffusion profiles.**—We have measured Sb-124 profiles for diffusions into as-grown  $\text{Pb}_{0.92}\text{Sn}_{0.08}\text{Te}$  and  $\text{Pb}_{0.79}\text{Sn}_{0.21}\text{Te}$  with hole concentrations of  $2 \times 10^{18}$  and  $2 \times 10^{19} \text{ cm}^{-3}$ , respectively, and for diffusions into annealed  $\text{Pb}_{0.79}\text{Sn}_{0.21}\text{Te}$  with lower hole concentrations. In all cases the Sb concentration is well described by a complementary error function. In a few cases, there is a small deviation from this function within the region 0-5  $\mu\text{m}$  from the surface, where the Sb profile is less steeply graded. The fact that the profiles can be described by error functions, except possibly near the surface, suggests that the diffusion coefficient is constant throughout most of the sample. We have verified the constancy of the diffusion coefficient and the dependence of the profiles on the square root of time by diffusing  $\text{Pb}_{0.79}\text{Sn}_{0.21}\text{Te}$  samples at  $600^\circ\text{C}$  for 72, 168, and 576 hr.

Table I summarizes the values for the solubility of Sb and for the Sb diffusion coefficients which have been obtained by fitting complementary error functions to our data. Each of these values was obtained by fitting each of several profile measurements to obtain a surface concentration ( $C_0$ ) and a diffusion coefficient ( $D$ ) and averaging the  $C_0$  and  $D$  values for the different profiles. The accuracy of the average values thus obtained is estimated to be  $\pm 15\%$ . The surface concentrations have been taken to be the Sb solubility values. The Sb solubilities are essentially independent of Sn content and temperature over the range  $500^\circ$ - $750^\circ\text{C}$ . A lower surface Sb concentration was observed, however, in annealed  $\text{Pb}_{0.79}\text{Sn}_{0.21}\text{Te}$  which was diffused from a Sb-doped ( $\text{Pb}_{0.79}\text{Sn}_{0.21}$ ) $_{0.505}\text{Te}_{0.495}$  source instead of from a metallic Sb source. The diffusion coefficient at a given temperature is also essentially independent of the Sn content, even though the hole concentrations which reflect native defect concentrations differ by an order of magnitude for the two Sn compositions. Similarly  $D$  is independent of substrate hole concentration for the diffusions into  $\text{Pb}_{0.79}\text{Sn}_{0.21}\text{Te}$  at  $700^\circ$  and  $561^\circ\text{C}$ .

Since the donor behavior of Sb has been attributed to the substitution of Sb on Pb sites (6), it is interesting that the  $D$  values are independent of native defect concentrations. The temperature dependence of the Sb diffusion coefficient in  $\text{Pb}_{0.79}\text{Sn}_{0.21}\text{Te}$  is shown in Fig. 1. The data can be represented by an Ar-

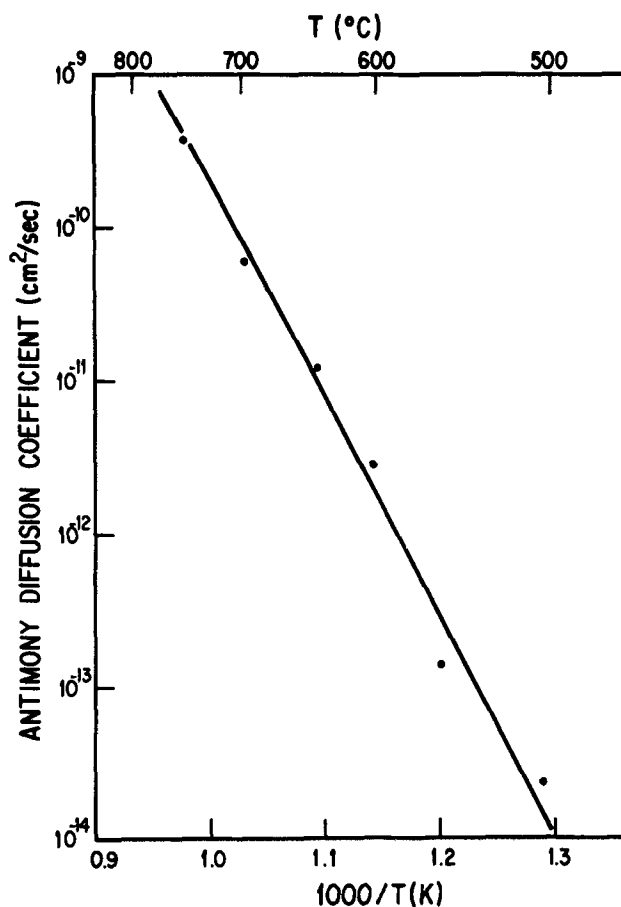


Fig. 1. Antimony diffusion coefficient in  $\text{Pb}_{0.79}\text{Sn}_{0.21}\text{Te}$  as a function of temperature.

henius-type expression in which  $D$  ( $\text{cm}^2/\text{sec}$ ) =  $1.08 \times 10^{-4} \exp(-2.74 \text{ eV}/kT)$ . The Sb diffusion coefficients are at least two orders of magnitude smaller than the interdiffusion coefficients responsible for controlling the stoichiometry of PbTe (7, 8). The measured  $D$  values are also independent of substrate orientation. This is consistent with the cubic symmetry of the rocksalt lattice structure of  $\text{Pb}_{1-x}\text{Sn}_x\text{Te}$  (9).

It should be pointed out that our experiments were not carried out under true "tracer diffusion" conditions (in which there are no gradients other than the tracer) (8, 10), but rather under conditions appropriate for the fabrication of devices. Under these conditions, it is not rigorously correct to interpret the data in terms of diffusion mechanisms, jump frequencies, and activation energies because the defect conditions may vary during the diffusion if the Sb doping is amphoteric or if native defects compensate the Sb (see following section).

**Junction depths.**—Figure 2 shows the depth of the n-p junction produced by Sb diffusion at  $700^\circ\text{C}$  as a function of the square root of time for as-grown  $\text{Pb}_{0.92}\text{Sn}_{0.08}\text{Te}$ ,  $\text{Pb}_{0.879}\text{Sn}_{0.124}\text{Te}$ , and  $\text{Pb}_{0.79}\text{Sn}_{0.21}\text{Te}$ . The junction depth increases linearly as the square root of time for junctions less than 25  $\mu\text{m}$  deep. For longer diffusion times, however, there is a more rapid increase in depth. The rate of junction penetration is about three times faster for  $\text{Pb}_{0.92}\text{Sn}_{0.08}\text{Te}$  than for  $\text{Pb}_{0.79}\text{Sn}_{0.21}\text{Te}$ . The more rapid junction movement in the lower Sn content alloys is expected because these materials have lower as-grown hole concentrations than the higher Sn content alloys. Indeed, we have found that  $\text{Pb}_{0.79}\text{Sn}_{0.21}\text{Te}$  annealed to  $2 \times 10^{18}$  holes/ $\text{cm}^3$  shows the same junction depth as as-grown  $\text{Pb}_{0.92}\text{Sn}_{0.08}\text{Te}$  with the same hole concentration. Thus an interesting comparison can be made between the junction diffusion data and the Sb diffusion coeffi-

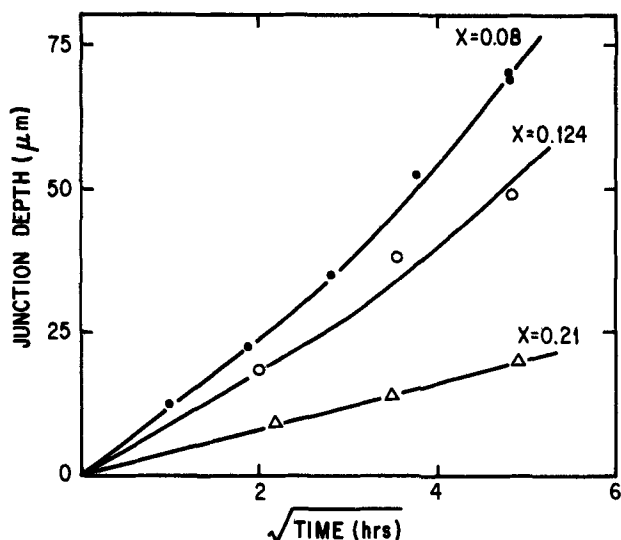


Fig. 2. Junction depths produced by Sb diffusion at 700°C into as-grown  $Pb_{1-x}Sn_xTe$ .

ents in that the junction depths correlate with substrate hole concentration, while the Sb diffusion coefficients are essentially independent of substrate hole concentration.

Values for the Sb concentration at the position of the electrical junction were determined by locating the position of the junction on the Sb-124 profile measured for the same diffusion conditions. Table II compares values for the Sb concentration at the junction with values for the substrate hole concentration before diffusion. The Sb concentration at the junction is always higher than the initial hole concentration, with a larger discrepancy observed for diffusions into substrates with low hole concentrations. This behavior suggests that the doping of Sb in  $Pb_{1-x}Sn_xTe$  is amphoteric, as has been suggested by Strauss for PbTe (6), or that the introduction of Sb into  $Pb_{1-x}Sn_xTe$  may be accompanied by the formation of compensating native defect acceptors. However, other effects such as the formation of Sb precipitates cannot be ruled out at this point.

Figure 3 shows the temperature dependence of the junction depth for an 8 hr diffusion of Sb into as-grown  $Pb_{0.92}Sn_{0.08}Te$ . It is not possible to obtain junction diffusion coefficients from these data because of uncertainties in the boundary conditions. The difference between the donor and acceptor defect concentration at the surface of the material is not known because the extent of compensation of the Sb by native defects and the extent of amphoteric Sb doping have not been determined. Nevertheless, a qualitative comparison can be made between the temperature dependence of the junction depth and that of the Sb diffusion coefficient by comparing the ratio of the squares of the junction depth at 700° and 640°C to the ratio of the diffusion coefficients at these temperatures. The former ratio is equal to 26, while the latter

Table II. Comparison of antimony concentration at the n-p junction with substrate hole concentration

Composition	Temperature (°C)	Diffusion time (hr)	Substrate hole concentration ( $cm^{-3}$ )	Sb concentration at n-p junction ( $cm^{-3}$ )
$Pb_{0.92}Sn_{0.08}Te$	700	4	$2 \times 10^{18}$	$5 \times 10^{18}$
	640	24	$2 \times 10^{18}$	$2 \times 10^{19}$
$Pb_{0.79}Sn_{0.21}Te$	700	24	$2 \times 10^{19}$	$5 \times 10^{19}$
	640	72	$2 \times 10^{19}$	$5 \times 10^{19}$
	600	173	$7 \times 10^{17}\dagger$	$2 \times 10^{19}$

† Substrate preannealed.

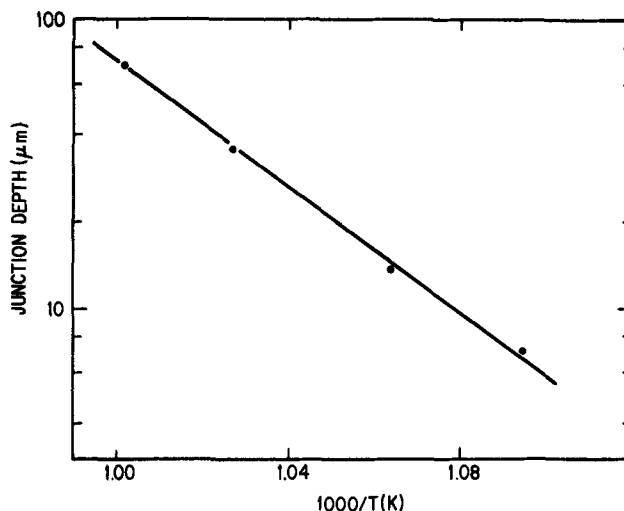


Fig. 3. Temperature dependence of junction produced by Sb diffusion into as-grown  $Pb_{0.92}Sn_{0.08}Te$  (normalized to 8-hr diffusion).

is 7. Hence, the junction depth exhibits a stronger temperature dependence than the diffusion coefficients.

Summary

Antimony diffusion profiles and n-p junction depths in  $Pb_{0.92}Sn_{0.08}Te$  and  $Pb_{0.79}Sn_{0.21}Te$  have been measured under experimental conditions of interest for device fabrication processes. The solubility of Sb is essentially independent of temperature between 500° and 750°C. Both the solubility and diffusion coefficients are independent of Sn content even though the substrate hole concentration varies by a factor of ten between the two different alloys. In contrast, the n-p junction depth shows a strong dependence on Sn content with the junction depth about three times deeper for  $Pb_{0.92}Sn_{0.08}Te$  than for  $Pb_{0.79}Sn_{0.21}Te$ . The junction depths can be correlated with substrate hole concentration.

This study has clarified many aspects of Sb diffusion in  $Pb_{1-x}Sn_xTe$ . However, there are other aspects that could be studied. These include the identification of the mechanism for Sb diffusion, the extent of compensation of Sb by native defects, the extent of precipitation of Sb, and possible amphoteric doping behavior.

Acknowledgments

The authors would like to thank R. G. Carroll and P. K. Bunch for preparing the samples and G. Garza for performing the counting experiments. The crystals used were grown by Dr. S. G. Parker. The authors also acknowledge the helpful discussions of Drs. R. E. Johnson, D. W. Bellavance, and J. A. Keenan.

Manuscript submitted Jan. 22, 1974; revised manuscript received June 10, 1974. This was Paper 166 presented at the Boston, Massachusetts, Meeting of the Society, Oct. 7-11, 1973.

Any discussion of this paper will appear in a Discussion Section to be published in the June 1975 JOURNAL. All discussions for the June 1975 Discussion Section should be submitted by Feb. 1, 1975.

The publication costs of this article have been assisted by Texas Instruments Incorporated.

REFERENCES

1. A. R. Calawa, T. C. Harman, M. Finn, and P. Youtz, *Trans. Met. Soc. AIME*, **242**, 374 (1968).
2. G. A. Antcliffe and J. S. Wrobel, *Appl. Phys. Letters*, **17**, 290 (1970).
3. G. A. Antcliffe and S. G. Parker, *J. Appl. Phys.*, **44**, 4145 (1973).

4. S. G. Parker, R. E. Johnson, and J. E. Pinnell, *J. Electron. Mater.*, To be published.
5. N. R. Short, *Brit. J. Appl. Phys. (J. Phys. D)*, **1**, 129 (1968).
6. A. J. Strauss, *J. Electron. Mater.*, **2**, 553 (1973).
7. L. Goldstein, *C. R. Acad. Sci. Paris*, **268B**, 686 (1969).
8. J. N. Walpole and R. L. Guldi, *J. Nonmetals*, **1**, 227 (1973).
9. A. J. Strauss, *Trans. Met. Soc. AIME*, **242**, 354 (1968).
10. J. R. Manning, "Diffusion Kinetics for Atoms in Crystals," p. 18, D. Van Nostrand Co., New York (1968).

## Effects of Calcium, Tin, and Bismuth on the Early Strength of Calcium-Lead Alloys

M. Myers, H. R. Van Handle, and C. R. DiMartini

American Smelting and Refining Company, Central Research Laboratories, South Plainfield, New Jersey 07080

### ABSTRACT

The effects of calcium content as well as additions of tin and bismuth on the mechanical properties of calcium-lead alloys have been investigated. The alloys were wrought and heat-treated in order to avoid the problems raised by the presence of casting variables. The previously reported increase in the rate of hardening with increasing calcium content was confirmed. Binary alloys containing less than 0.04% calcium showed no strengthening 1 hr after quench from the solution treatment temperature, while 0.1% calcium nearly doubled in tensile strength in only 5 min. Tin, in additions of 0.5 and 1%, completely restrained hardening in the first hour after quench in both 0.06 and 0.1% calcium alloy. Bismuth additions were made up to 1000 ppm. No effect was noted on the early strength of the 0.1% calcium alloys, but the rate of hardening of the 0.06% calcium alloys was significantly enhanced by the presence of bismuth. This effect, as well as the increase in hardening rate due to increased calcium are shown by means of transformation kinetics calculation to be the result of grain refinement in the alloys caused by calcium and bismuth. These findings show that early strength of calcium-lead alloys may be improved by: (i) limiting tin content; (ii) increasing calcium content; or (iii) adding bismuth to lower calcium alloys.

Over the last several years, interest in calcium-lead alloys for use as grids in SLI batteries has greatly increased due to the expected requirement for maintenance-free (low gassing) batteries in the automotive industry.

The effect of calcium level in these alloys has been well studied (1, 2, 7). The literature also contains many articles on calcium-lead, covering such subjects as aging behavior (1-4, 6, 7), casting properties (2, 3, 6, 7), battery grid growth (3, 5), and corrosion resistance (3, 5).

An area of interest which has not heretofore been reported upon in detail is the effects of tin and bismuth on the early strength of the calcium-lead system. The "early strength" is the strength during the first minutes of age hardening. This strength is important to the successful handling of cast grids up to and during the pasting operation and could conceivably be affected by impurity content or alloy composition.

Bismuth is of interest in this regard as it is usually present in primary and secondary lead as an impurity and has been reported to be deleterious to the early strength of grid alloys (3). Tin is of interest as it is frequently added in amounts of 0.5-1.0% in calcium-lead alloys. Caldwell and Sokolov (6) have studied the superficial hardness during aging of cast calcium-lead of various bismuth contents up to 180 ppm. They found essentially no effect on the hardness or on the electrochemical properties of the alloys. They also reported that the presence of tin slowed the onset of hardening.

An understanding of the age hardening characteristics of cast calcium-lead grids is the practical interest of this investigation. However, because of the many difficult to control variables introduced by any casting operation, the authors decided to use wrought,

heat-treated specimens to insure uniform distribution of calcium in the individual tensile bars. This allows for the study of the metallurgical behavior of the alloy system under highly reproducible conditions.

### Experimental Procedures

Four categories of alloys were prepared; they were: (i) calcium-lead binaries with varying calcium levels and minimum impurities; (ii) 0.06 and 0.1% (0.09% Ca actual) calcium-leads with 3-1000 ppm bismuth and no tin; (iii) 0.06 and 0.1% calcium-leads with 0-2% tin and 5 ppm bismuth; and (iv) 0.06% calcium with combined additions of tin and bismuth.

The materials used for all of these alloys were low bismuth 1% calcium-lead hardener and 99.99+ % pure lead (see spectrographic analysis, Table I). Tin and bismuth were added as pure metal.

Individual 2000g melts containing the desired levels of calcium, bismuth, and tin were prepared under a dynamic inert gas atmosphere to protect the calcium from oxidation. They were cast at 400°-450°C into a graphite book mold. The resultant ingots were 4 × 5 × 1 in. These ingots were sampled, top and bottom. Segregation was found to be minimal.

The ingots were rolled at room temperature to sheet approximately 0.1 in. thick. This sheet was then

Table I. Spectrographic and chemical analyses of lead used

Element	
Ca	<0.0001
Bi	0.0003
Sn	<0.0001
Sb	0.0003
Cu	0.0003
Ag	0.0003
As	0.0001

Key words: grids, batteries, calcium, tin, bismuth.

sheared to strips which were, in turn, milled to standard tensile bar shape. Gauge lengths were 1 in. long and 0.25 in. wide. All specimens were numbered individually.

With the exception of aging time at room temperature, all specimens were treated alike. The as-rolled test bars were solution heat-treated at  $300^{\circ} \pm 5^{\circ}\text{C}$  for 5 hr and then rapidly water quenched to room temperature. Time of quench was accurately recorded for each specimen. At predetermined intervals (1, 5, 10, 20, and 60 min after quench), the specimens were tested in tension on an Instron Machine at a strain rate of  $0.5 \text{ min}^{-1}$ . Elongation was measured using inscribed 1 in. marks on the specimen gauge length.

Variations in strength and the rate of hardening were noted with varying compositions. The surface appearance of the specimens after fracture, which was related to grain size, also seemed to vary with composition. A study of grain size vs. strength and composition was, therefore, made using x-ray techniques.

**Results and Discussion**

The data presented herein show calcium, bismuth, and tin concentrations to have very marked effects on the early strength of calcium-lead alloys.

In the lead-calcium binary system, no significant hardening is noted 1 min after quench for calcium levels below 0.06% (Fig. 1). After 1 hr at room temperature, no hardening is noted for alloys with up to 0.04% calcium. A rapid increase in strength at 1 min is obtained between 0.06 and 0.08%, the UTS improving from 1900 to 3500 psi over that range. Above 0.08% calcium, the rate of improvement in strength with increasing calcium content is much less rapid.

The effect of bismuth on binary 0.06% calcium-leads is shown to be beneficial for aging up to 1 hr (Fig. 2). For longer aging periods, upwards of 24 hr, all 0.06% calcium-lead alloys had the same tensile strengths irrespective of bismuth content. Variations in bismuth content, up to 500 ppm, have no effect on higher calcium level alloys (0.09%, Fig. 3). This may be due to a grain refining of the 0.06% calcium alloy by bismuth which is masked by the grain refining effect of calcium at higher calcium levels.

This is more clearly illustrated by Fig. 4 in which effects of bismuth on the strength of 0.06 and 0.09% calcium-leads at 1 min after quench are shown.

The effects of tin content on 0.06 and 0.1% calcium-lead alloys (low bismuth) are shown in Fig. 5 and 6.

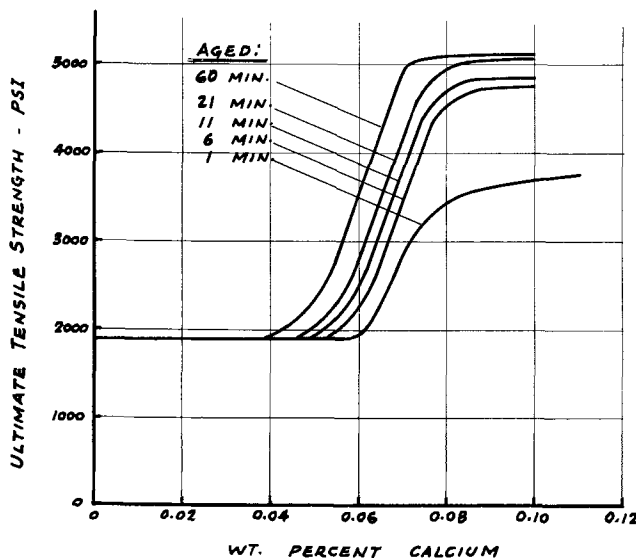


Fig. 1. Tensile strength vs. Ca content showing effect of aging time. All specimens solution treated for 5 hr at  $300^{\circ}\text{C}$  and water quenched.

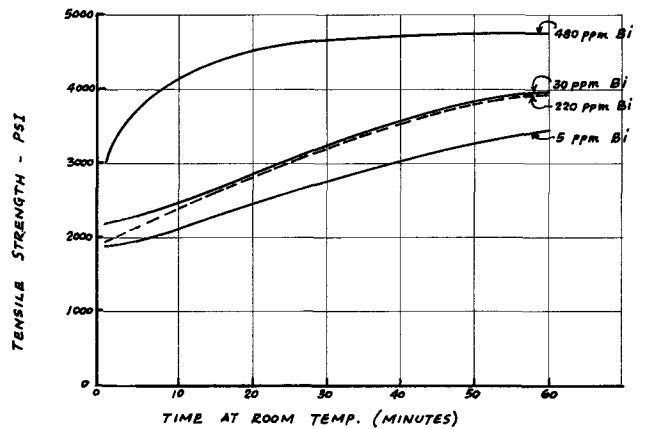


Fig. 2. Tensile strength vs. aging time for 0.06 Ca at varying Bi levels.

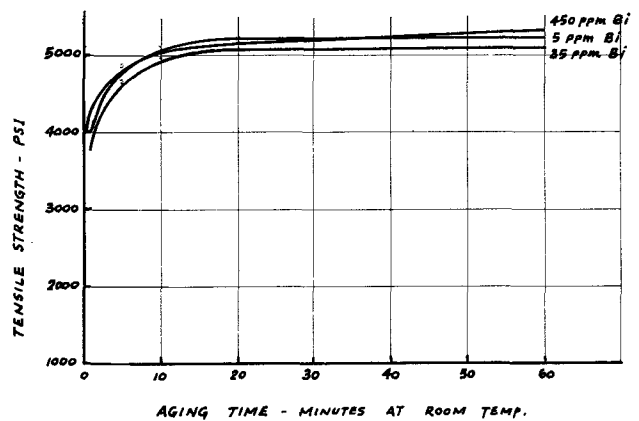


Fig. 3. Tensile strength vs. aging time for 0.09 Ca at varying Bi levels.

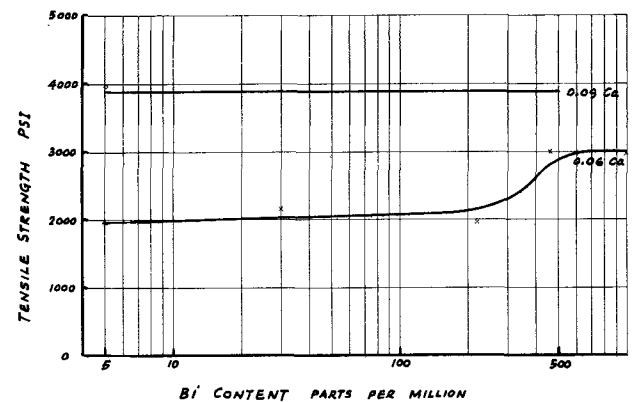


Fig. 4. Tensile strength vs. Bi content for 0.06 and 0.09 Ca aged at room temperature for 1 min.

Clearly the addition of tin inhibits all hardening during the first hour after quench in these alloys. As the addition of tin to 0.06% calcium-lead caused behavior opposite in nature to that caused by additions of bismuth to that alloy, it was interesting to observe the behavior of alloys containing both tin (0-1%) and bismuth (500 ppm). The results obtained from these alloys are plotted in Fig. 7. It may be seen that some increase in strength is obtained at 0.5% tin, but that at 1% tin no hardening occurs even in the presence of 500 ppm bismuth.

An attempt was made to predict from theory the increase in the rate of hardening with increasing bismuth and calcium. The work of Scharfenberger and

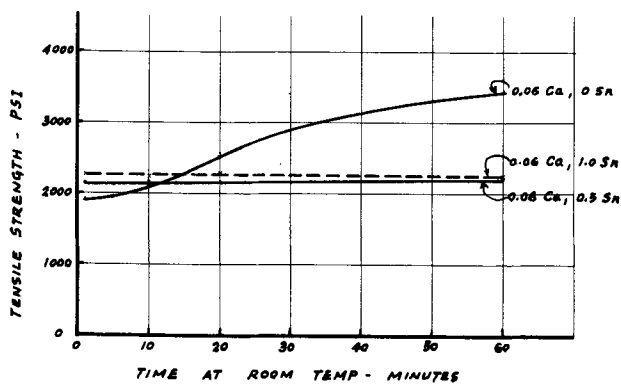


Fig. 5. Tensile strength vs. aging time for 0.06 Ca at varying Sn levels.

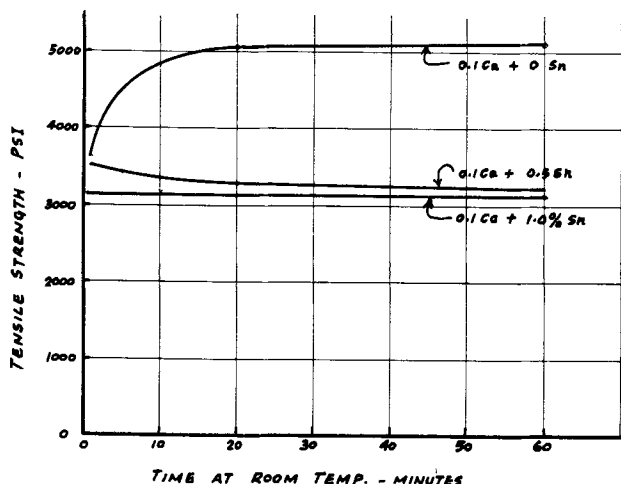


Fig. 6. Tensile strength vs. aging time for 0.1 Ca at varying Sn levels.

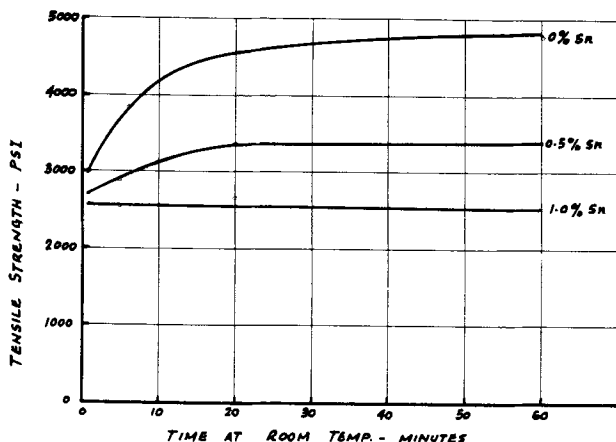


Fig. 7. Tensile strength vs. aging time for 0.06 Ca with 500 ppm Bi and varying Sn levels.

Henkel (7) is a detailed study of the mechanism and kinetics of precipitation in the calcium-lead system. It has long been known that hardening in this system occurs by the precipitation of extremely fine  $\text{CaPb}_3$  particles at low temperature from the high temperature solid solution structure. Scharfenberger and Henkel reported the interesting finding that age hardening of calcium-lead occurs by two discontinuous nucleation and growth transformations, each analogous to the growth of pearlite in steel. This differs from most aging alloys which harden as a result of a continuous precipitation, as in, for example, aluminum-copper alloys. This finding is of significance in ex-

plaining the results of this report, as grain size, which has been shown herein to vary with alloy composition, is an important variable in determining the rate of discontinuous transformation.

This mode of transformation is modeled mathematically by Cahn and Hagel (8) by the equation

$$X = 1 - e^{-2BGt} \quad [1]$$

where  $X$  = volume fraction transformed,  $B$  = grain surface area, ( $\text{mm}^2/\text{mm}^3$ ) [Fig. 8, Ref. (9)],  $G$  = cell growth velocity ( $\text{mm}/\text{min}$ ) [Fig. 9, Ref. (7)], and  $t$  = time after quench (min).

Equation [1] models the over-all transformation rate for the case in which nucleation of the new, hard structure occurs rapidly all along the grain boundary surfaces. The only variables which affect the rate of transformation in this mechanism are growth rate,  $G$ , and grain size, upon which the grain boundary area per unit volume depends. For a specific composition, the only variable is grain size. (Variations in grain boundary area per unit volume with alloy chemistry are shown in Fig. 8. Grain boundary area varies inversely with the grain size.)

Thus, Eq. [1] can be used to predict the rate at which transformation from the solid solution to the hardened state occurs. This, in turn, can be used to compare the predicted rate with our experimental results and thus determine if the means by which alloy composition changes hardening rate is, in fact, grain refinement.

The growth rates used in our calculations are taken from Ref. (7). Growth rates were reported which varied with calcium content and with the amount of transformation completed. For ease of calculation, we assume that the rate reported at 50% transformed is constant for each calcium level. A plot of growth rate  $G$  vs. calcium level derived from the data of Ref. (7) is presented in Fig. 9.

Using this growth rate chart, and the grain size data of Fig. 8, time transformation curves were calculated. The calculated curves of volume fraction transformed vs. time for three conditions of interest (combinations of growth rate and grain size) are shown in Fig. 10. A growth rate of 0.008 mm/min corresponds to a calcium content of about 0.08%, while 0.0055 mm/min corresponds to about 0.06% calcium.

These curves are clearly similar in shape to the curves of tensile strength vs. time shown in Fig. 2 and 3. By employing two assumptions, it was possible to transpose the curves of Fig. 10 to the form of the curves of Fig. 2 and 3. These assumptions are: (i) that immediately after quench, all specimens had the same tensile strength,  $S_0 = 1900$  psi (this is implied by the data of Fig. 1); and (ii) that the fraction change in strength on age hardening is directly related to the volume fraction transformed.

These assumptions are combined in the equation

$$S_t = S_0 + X_t(S_f - S_0) \quad [2]$$

where:  $S_t$  = tensile strength (psi) at aging time,  $t$ ;  $S_0$  = tensile strength at time = 0, 1900 psi;  $X_t$  = volume fraction transformed at time  $t$ ; and  $S_f$  = tensile strength at the end of hardening (strength at which the aging experimental curve levels off).

Values for  $S_f$  are approximate and were taken from the data of Fig. 1 and 2. The curves obtained by applying Eq. [2] to the data of Fig. 10 are shown in Fig. 11 as calculated tensile strength vs. time, compared to experimental data. The calculated curves agree reasonably well with the experimental curves for the rapid hardening alloys. The disagreement is somewhat larger for the slow transforming alloy. This may be due to the inherent error introduced in determining the grain size of large-grained specimens. In any case, the agreement is good enough to support grain refinement as a mechanism by which bismuth and calcium increase the rate of hardening in calcium-lead alloys.

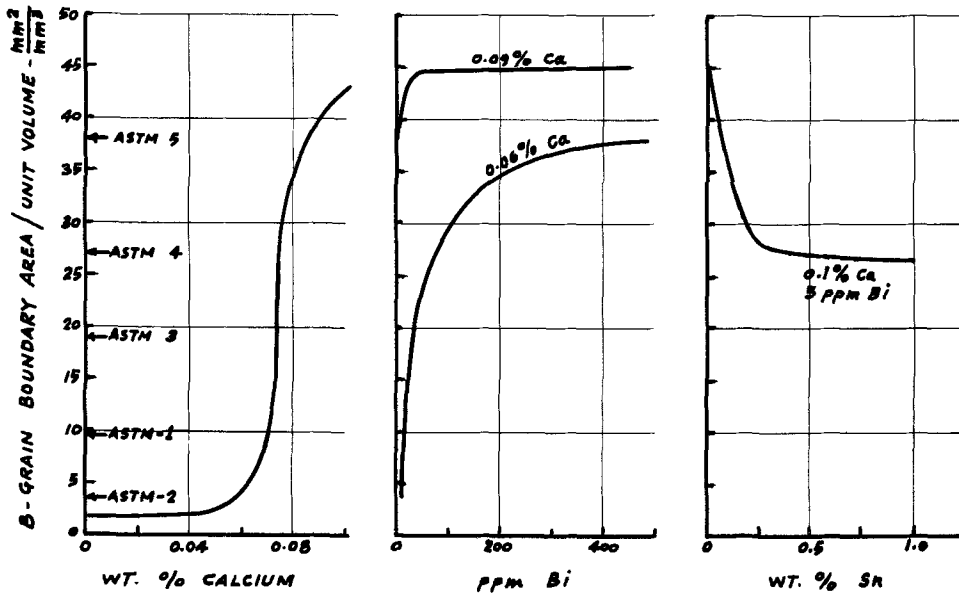


Fig. 8. Effects of calcium, bismuth, and tin on grain boundary surface area [Ref. (9)]. a (left), Grain boundary area vs. calcium content. b (center), Grain boundary area vs. bismuth content. c (right), Grain boundary area vs. tin content.

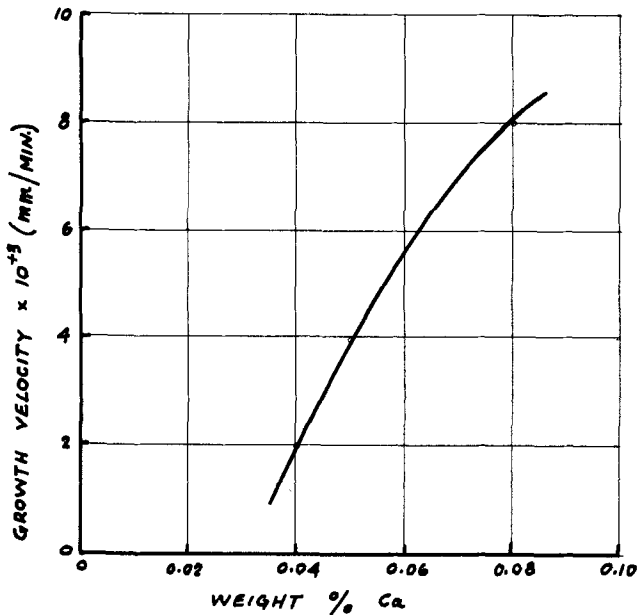


Fig. 9. Approximate growth velocity at 50% completion of the first reaction. Derived from the data of Scharfenberger and Henkel (7).

This effect was noted in Ref. (7) for calcium, although it was felt that grain refinement did not account for all of the change.

Additions of tin to calcium-lead have the effect of increasing the grain size (Fig. 8) and inhibiting completely the early hardening reaction (Fig. 5 and 6). It seems likely that the presence of tin has the effect of changing the mechanism of hardening in the calcium-lead system, perhaps to a continuous precipitation mechanism with an extended incubation period.

Alloys containing combinations of bismuth and tin show some hardening at the 0.5% tin level but none in alloys containing higher levels of tin (see Fig. 7).

**Conclusions**

Calcium and bismuth are shown to increase the rate at which calcium-lead alloys age harden. Increasing calcium also increases the ultimate aged strength, while bismuth additions (up to 1000 ppm) only increase the rate of hardening.

The mechanism by which calcium and bismuth achieve the rate increase is shown to be grain refinement. The finer grains have a larger surface area and smaller diameter thus allowing the growth of the hardened structure to proceed to completion more rapidly. No deleterious effects on strength associated with bismuth have been observed.

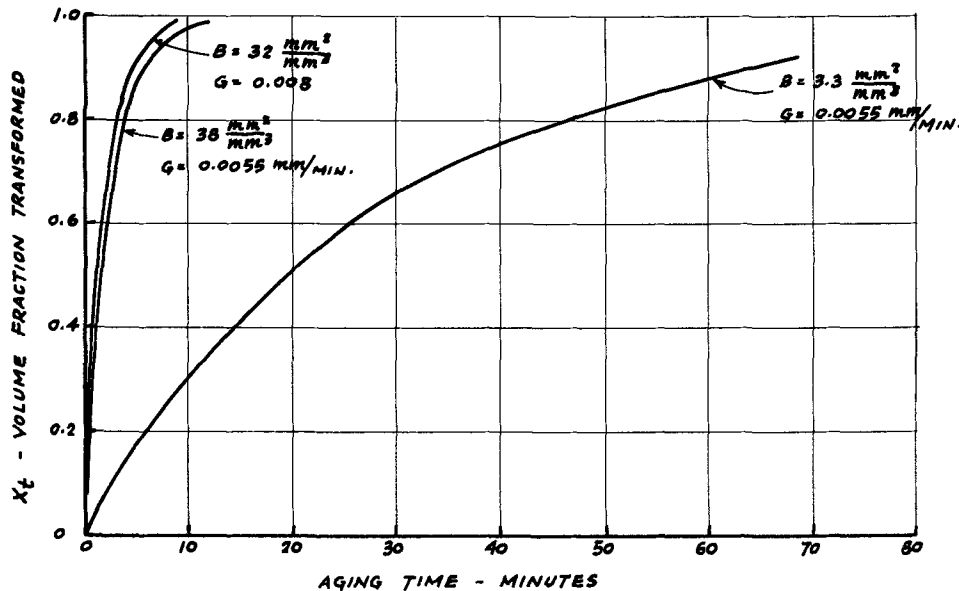


Fig. 10. Calculated curves of volume fractions transformed vs. aging time.

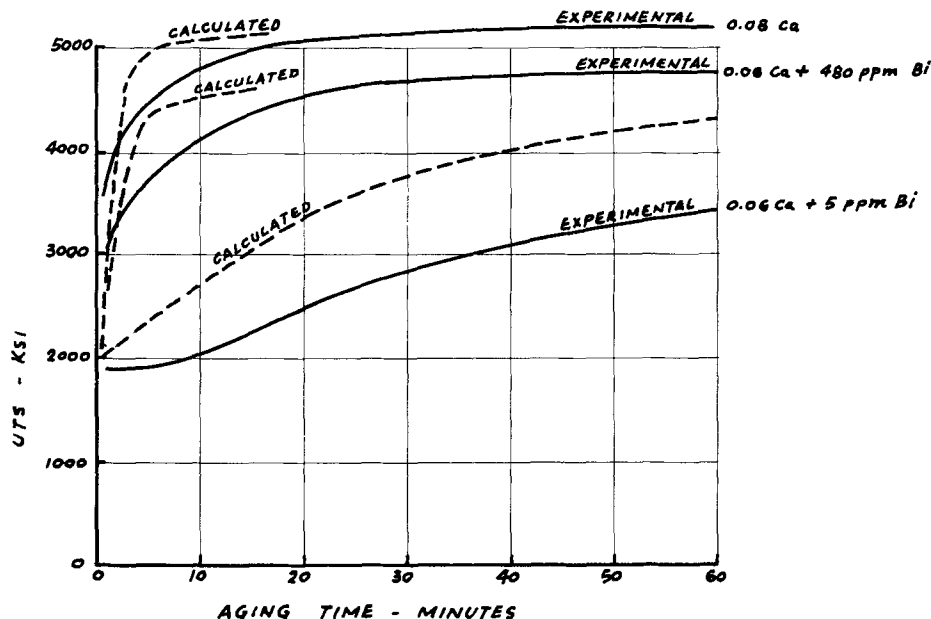


Fig. 11. Calculated and experimental aging curves for three alloys.

Additions of tin have been found to increase grain size and to strongly inhibit the early hardening process. It is likely that tin changes, basically, the mechanism of hardening in this system.

Although these conclusions are based upon studies of wrought alloys, such grain size effects should be similarly manifested in cast alloys. Work is currently underway to validate this and will be reported upon at a later date.

Manuscript submitted March 6, 1974; revised manuscript received May 13, 1974.

Any discussion of this paper will appear in a Discussion Section to be published in the June 1975 JOURNAL. All discussions for the June 1975 Discussion Section should be submitted by Feb. 1, 1975.

The publication costs of this article have been assisted by American Smelting and Refining Company.

#### REFERENCES

1. E. E. Schumacher and G. M. Bouton, *Metals and Alloys*, 1, 405 (1930).
2. A. B. Townsend, Union Carbide Nuclear Company, Report No. Y-1307, Dec. 1960.
3. E. J. Ritchie, Final Report ILZRO Projects LE-82 and LE-84, Dec. 1971.
4. W. W. Canary, Union Carbide Oak Ridge Y-12 Plant, Report No. Y-1855, Sept. 1972.
5. G. W. Mao, J. G. Larson, and P. Rao, *This Journal*, 120, 11 (1973).
6. T. W. Caldwell and U. S. Sokolov, *ibid.*, To be published.
7. W. Scharfenberger and S. Henkel, *Z. Metallk.*, 64, 478 (1973).
8. J. W. Cahn and W. C. Hagel, "Decomposition of Austenite By Diffusional Processes," p. 141, Interscience Publishers, Inc., New York (1962).
9. "Metals Handbook," T. Lyman, Editor, p. 405, American Society for Metals, Novelty, Ohio (1948).

## A Thermodynamic Investigation of Cubic Sodium Tungsten Bronze, $\text{Na}_x\text{WO}_3$

T. A. Ramanarayanan and W. L. Worrell\*

Department of Metallurgy and Materials Science, University of Pennsylvania, Philadelphia, Pennsylvania 19174

#### ABSTRACT

The partial molar free energy of solution of sodium in cubic sodium tungsten bronze,  $\text{Na}_x\text{WO}_3$ , has been measured in the composition range from  $x = 0.45$  to  $x = 0.8$  and at temperatures between  $500^\circ$  and  $800^\circ\text{C}$ . An electrochemical cell using Pyrex as a sodium ion conducting solid electrolyte has been employed. The standard state for sodium is chosen such that the activity of sodium is unity for the composition  $\text{NaWO}_3$ . Using this standard state, the partial molar free energy of solution of sodium is  $-16.6$  kcal/g atom of sodium in  $\text{Na}_{0.45}\text{WO}_3$  and  $-6.1$  kcal/g atom of sodium in  $\text{Na}_{0.8}\text{WO}_3$  at  $700^\circ\text{C}$ . The thermodynamic factor  $\partial \ln a_{\text{Na}} / \partial \ln x$  has been calculated from the variation of the cell emf with composition. The thermodynamic factor is combined with values for the chemical diffusivity of sodium to evaluate the partial sodium ion conductivity in cubic  $\text{Na}_{0.78}\text{WO}_3$ .

Sodium tungsten bronzes are nonstoichiometric compounds having the general formula,  $\text{Na}_x\text{WO}_3$ , where  $x$  is less than 1. At values of  $x$  between 0.15 and

0.28, two tetragonal phases coexist; the tetragonal phase of higher sodium content has a homogeneity range from  $x = 0.28$  to 0.38 (1). A cubic phase occurs at values of  $x > 0.43$  (1). The crystal structures of the various sodium tungsten bronzes have been estab-

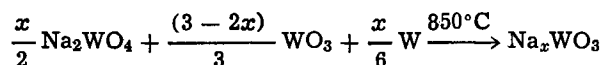
\* Electrochemical Society Active Member.  
Key words: sodium thermodynamics, cubic sodium tungsten bronze, partial sodium ion conductivity.

lished by Hägg and Magneli using x-ray techniques (2). The crystal structure of  $\text{NaWO}_3$  is that of perovskite, in which a tungsten atom is at the center of a cube, surrounded octahedrally by six oxygen atoms at the face centers. The corners of the cube are occupied by sodium atoms. In cubic sodium tungsten bronzes with the general formula  $\text{Na}_x\text{WO}_3$ , a fraction  $(1-x)$  of sodium atoms is missing from the corners (3). The bronzes can be regarded as a solution of sodium in  $\text{WO}_3$ . The conductivity of the cubic bronzes is metallic (4, 5).

The present study is a measurement of sodium activities in the cubic bronzes using Pyrex as a solid electrolyte. Sodium ions are the predominant conducting species in Pyrex. Several investigators (6-8) have used a sodium ion conducting glass as a solid electrolyte to determine the thermodynamic properties of alloys containing sodium.

### Experimental Procedure

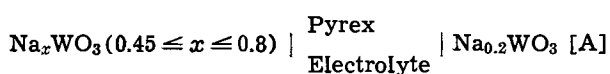
Tungsten (99.99%),  $\text{WO}_3$  (99.95%), and  $\text{Na}_2\text{WO}_4$  (99.95%) powders were used to prepare the sodium tungsten bronzes. The preparation was based on the reaction (3)



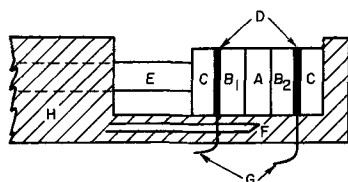
The reactants were weighed accurately in the appropriate proportions, mixed thoroughly, and heated for approximately 10 hr at  $850^\circ\text{C}$  in an alumina boat under purified argon. The weight change after reaction was within 0.1% of the original weight, and an x-ray diffraction pattern of the reaction product indicated that only the bronze phase was present. The bronzes were crushed to a powder, pressed in a 1 cm diam die without binder at 20 tsi, and sintered at  $850^\circ\text{C}$  under purified argon to yield pellets of approximately 1 cm diam by 0.5 cm thickness.

Pyrex disks of 0.5 cm thickness were cut from a rod of 1 cm diam. The faces of the Pyrex disk were polished to a smooth finish using  $6\mu$  diamond polishing compound, and thoroughly cleaned with acetone.

The composition of the reference electrode was  $\text{Na}_{0.2}\text{WO}_3$ , which was a mixture of two tetragonal phases. The other electrode was a cubic bronze,  $\text{Na}_x\text{WO}_3$ , with  $x$  between 0.45 and 0.8. The electrochemical cell



was assembled in an alumina tube as shown in Fig. 1. Platinum wires were used as leads, and a Pt-Pt (10%



- A PYREX ELECTROLYTE
- B<sub>1</sub> Na<sub>0.2</sub>WO<sub>3</sub> REFERENCE ELECTRODE
- B<sub>2</sub> Na<sub>x</sub>WO<sub>3</sub> ELECTRODE
- C ALUMINA DISCS
- D Pt DISC CONTACTS
- E ALUMINA PUSH ROD
- F Pt-Pt (10% Rh) THERMOCOUPLE
- G Pt-LEAD WIRES
- H ALUMINA CELL HOLDER

Fig. 1. Electrochemical cell arrangement

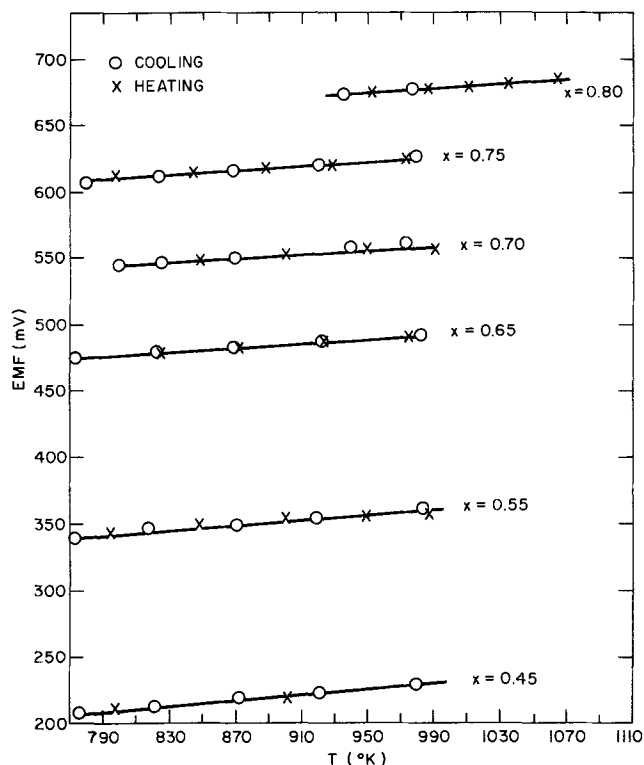


Fig. 2. Emf of cell [A] as a function of temperature

Rh) thermocouple, placed within 0.5 cm of the cell, was used to measure the temperature. The cell was heated to  $700^\circ\text{C}$  under an argon atmosphere (purified by passing through anhydrous  $\text{CaSO}_4$ , anhydrous magnesium perchlorate, and Ti-Zr chips held at  $800^\circ\text{C}$ ) in the constant temperature ( $\pm 1/2^\circ\text{C}$ ) zone of a Hoskin's alloy resistance furnace. Light pressure was exerted on the cell by means of an alumina push-rod to ensure good electrode-electrolyte contact. The open-circuit voltages were measured to within  $\pm 0.02$  mV using a Keithley 630 high impedance ( $> 10^{13}$  ohms) potentiometric electrometer. Equilibrium was taken to be established when the open-circuit cell voltage remained constant ( $\pm 0.5$  mV) over a 5 hr period. Cell voltages were measured on heating and on cooling over a temperature range from  $500^\circ$  to  $800^\circ\text{C}$ .

### Results and Discussion

The measured open-circuit cell voltages for cell [A] are shown as a function of temperature in Fig. 2. The reproducibility of the data is  $\pm 2$  mV. Table I shows the temperature-dependent equations for the cell emf. At a given temperature, the cell emf is related to the sodium activities at the electrodes through the relation

$$E = \frac{RT}{F} \ln \frac{a_{\text{Na}}}{a_{\text{Na}}^*} \quad [1]$$

where  $a_{\text{Na}}$  is the sodium activity in the cubic bronze and  $a_{\text{Na}}^*$  is the activity in the reference bronze  $\text{Na}_{0.2}\text{WO}_3$ . To describe the thermodynamics of the various Na- $\text{WO}_3$  solutions, a standard state is selected such that the sodium activity is unity for the composi-

Table I. Emf values as a function of temperature for cell [A]

$x$	Expression for cell emf (mV)
0.45	$E = 126.58 + 0.104 T$
0.55	$E = 270.01 + 0.091 T$
0.65	$E = 418.31 + 0.074 T$
0.70	$E = 477.61 + 0.083 T$
0.75	$E = 540.38 + 0.086 T$
0.80	$E = 592.75 + 0.086 T$



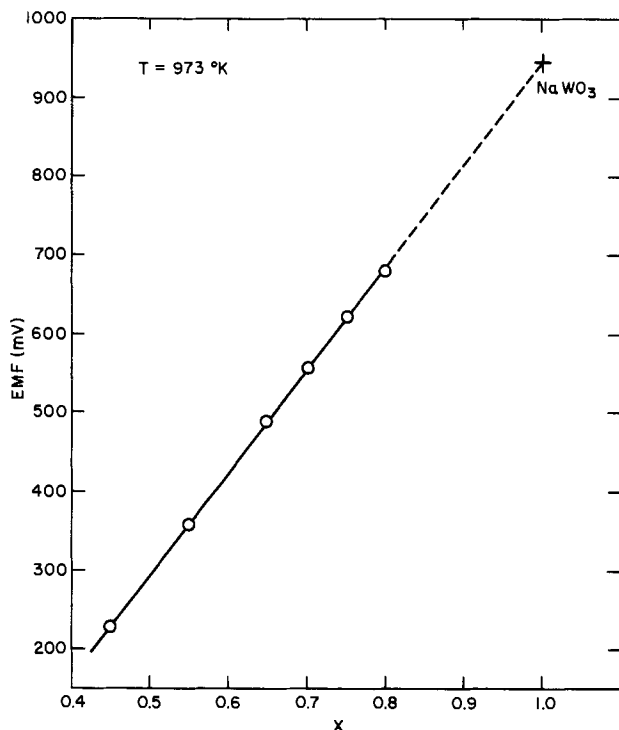


Fig. 3. Emf of cell [A] as a function of  $x$  at 973°K

tion  $\text{NaWO}_3$ . In  $\text{NaWO}_3$ , all the available sodium positions are occupied, and it is reasonable to assign unit sodium activity to the bronze of this composition.

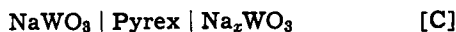
The emf of cell [A] at 973°K has been plotted vs.  $x$  in Fig. 3. An extrapolation of the straight line in Fig. 3 to  $x = 1$  gives 944 mV for the emf of the cell



at 973°K. The temperature dependence of the emf of cell [B] follows the equation

$$E = 875.75 + 0.07T \quad [2]$$

On subtracting the emf's of cell [A] shown in Table I from Eq. [2], one obtains the emf's for the cell



Expressions for the temperature dependence of the emf of cell [C] are presented in Table II. For the selected standard state, the emf of cell [C] is given by

$$E = \frac{RT}{F} \ln a_{\text{Na}} \quad [3]$$

where  $a_{\text{Na}}$  is the sodium activity in the cubic bronze relative to that in  $\text{NaWO}_3$ . The partial molar free energy of solution of sodium ( $\overline{\Delta G}_{\text{Na}}$ ) per g atom of sodium is related to the emf of cell [C] through the equation

$$\overline{\Delta G}_{\text{Na}} = \overline{\Delta H}_{\text{Na}} - T\overline{\Delta S}_{\text{Na}} = -FE \quad [4]$$

where  $\overline{\Delta H}_{\text{Na}}$  and  $\overline{\Delta S}_{\text{Na}}$  refer to the partial molar heat and entropy of solution, respectively, of sodium in the cubic bronze. Table III lists the values of  $\overline{\Delta G}_{\text{Na}}$  at 973°K vs.  $y$ , the atom fraction of sodium in the  $\text{NaWO}_3$  binary;  $y$  and  $x$  are related by

Table II. Emf values as a function of temperature for cell [C]

$x$	Expression for cell emf (mV)
0.45	$E = 749.17 - 0.034 T$
0.55	$E = 605.74 - 0.021 T$
0.65	$E = 457.44 - 0.004 T$
0.70	$E = 398.14 - 0.013 T$
0.75	$E = 335.37 - 0.016 T$
0.80	$E = 283.00 - 0.016 T$

Table III. Partial molar free energies of solution of sodium in cubic bronzes,  $\text{Na}_x\text{WO}_3$ , as a function of the sodium atom fraction,  $y$ , at 973°K

$y = x/(1+x)$	$\overline{\Delta G}_{\text{Na}}$ (kcal/g atom)
0.310	-16.6
0.355	-13.5
0.394	-10.5
0.412	-8.9
0.429	-7.4
0.444	-6.1

$$y = x/(1+x) \quad [5]$$

In Fig. 4, the partial molar free energies of solution at 973°K are plotted as a function of the atom fraction of sodium. Using Eq. [4] and the emf equations tabulated in Table II, one obtains very small  $\overline{\Delta S}_{\text{Na}}$  values ( $< 0.8$  eu). Thus the partial molar heat of solution is approximately equal to the partial molar free energy of solution. It should be noted that  $\overline{\Delta G}_{\text{Na}}$  and  $\overline{\Delta H}_{\text{Na}}$  are not the usual solution quantities, but represent the energy changes which occur on removing sodium atoms from the  $\text{NaWO}_3$  lattice. In view of the small entropy changes, the large free energy changes shown in Table III most likely indicate a decreasing Fermi level with decreasing sodium content in  $\text{Na}_x\text{WO}_3$ .

The thermodynamic factor of sodium in cubic bronze,  $\partial \ln a_{\text{Na}} / \partial \ln C_{\text{Na}}$  (where  $C_{\text{Na}}$  is the sodium concentration in moles/cm<sup>3</sup>), may be evaluated from the present experiments. The sodium concentration,  $C_{\text{Na}}$ , is related to  $x$  in the formula  $\text{Na}_x\text{WO}_3$  by

$$C_{\text{Na}} = x/V_m \quad [6]$$

where  $V_m$  (cm<sup>3</sup>/mole of  $\text{Na}_x\text{WO}_3$ ) is the molar volume of the cubic bronze. From Eq. [6]

$$d \ln C_{\text{Na}} = d \ln x - d \ln V_m \cong d \ln x \quad [7]$$

if changes in molar volume with composition are ignored. The variation of the lattice parameter of the cubic bronze with composition (9) indicates that the molar volume changes only by 2% when  $x$  is changed from 0.45 to 0.8. Thus, using Eq. [7], one obtains

$$\frac{\partial \ln a_{\text{Na}}}{\partial \ln C_{\text{Na}}} = \frac{\partial \ln a_{\text{Na}}}{\partial \ln x} \quad [8]$$

Differentiation of Eq. [1] with respect to  $\ln x$  for a given temperature yields

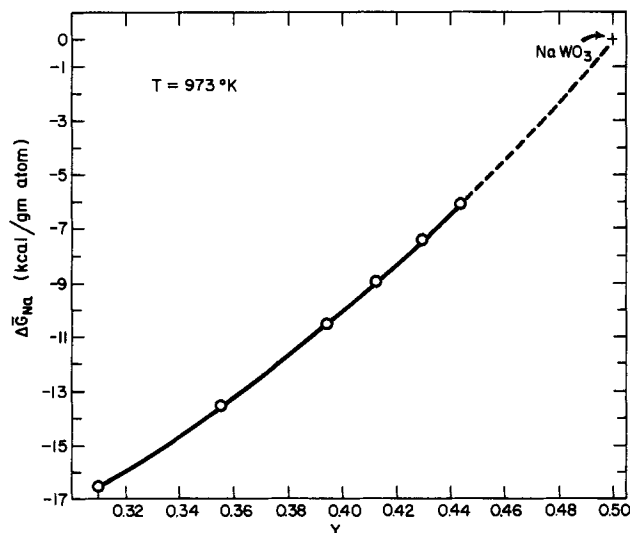
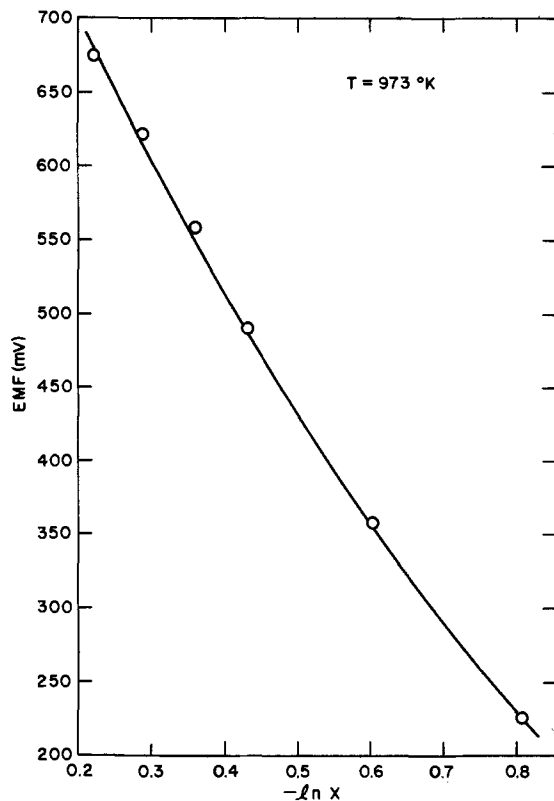


Fig. 4. The partial molar free energy of solution of sodium in cubic  $\text{Na}_x\text{WO}_3$  as a function of  $y$  at 973°K.

Fig. 5. Emf of cell [A] as a function of  $\ln x$  at 973°K

$$\frac{\partial E}{\partial \ln x} = \frac{RT}{F} \left( \frac{\partial \ln a_{\text{Na}}}{\partial \ln x} \right) \quad [9]$$

A plot of  $E$  vs.  $\ln x$  at  $T = 973^\circ\text{K}$  is shown in Fig. 5. From the slope of the line in Fig. 5, the thermodynamic factor may be calculated for any composition using Eq. [9].

The thermodynamic factor may be combined with data for the chemical diffusivity of sodium in the cubic bronze to obtain the partial sodium ion conductivity. In the presence of a concentration gradient and in the absence of an electrical potential gradient, the flux of sodium in the  $z$  direction may be written (10) as

$$J_{\text{Na}} = -\frac{C_{\text{Na}}B_{\text{Na}}}{N} \left( \frac{\partial \mu_{\text{Na}}}{\partial z} \right) \quad [10]$$

where  $J_{\text{Na}}$  is the sodium flux (moles/cm<sup>2</sup>-sec),  $B_{\text{Na}}$  is the absolute mobility of the sodium ion (particle-cm<sup>2</sup>/cal-sec),  $N$  is the Avogadro number (particles/mole), and  $\mu_{\text{Na}}$  is the chemical potential of sodium (cal/mole). In view of Eq. [8], Eq. [10] may be written as

$$J_{\text{Na}} = -\frac{B_{\text{Na}}RT}{N} \left( \frac{\partial \ln a_{\text{Na}}}{\partial \ln x} \right) \frac{\partial C_{\text{Na}}}{\partial z} \quad [11]$$

From Fick's first law, the sodium flux,  $J_{\text{Na}}$ , is given by

$$J_{\text{Na}} = -D_{\text{Na}} \left( \frac{\partial C_{\text{Na}}}{\partial z} \right) \quad [12]$$

Upon combining Eq. [11] and [12]

$$D_{\text{Na}} = \frac{B_{\text{Na}}RT}{N} \left( \frac{\partial \ln a_{\text{Na}}}{\partial \ln x} \right) \quad [13]$$

The partial sodium ion conductivity of the bronze is related to the concentration of sodium and its mobility (10) through

$$\sigma_{\text{Na}} = z_{\text{Na}}^2 e^2 F B_{\text{Na}} C_{\text{Na}} = \frac{z_{\text{Na}}^2 e^2 F B_{\text{Na}} x}{V_m} \quad [14]$$

Here  $\sigma_{\text{Na}}$  is the sodium ion conductivity in (ohm cm)<sup>-1</sup>

Table IV. Partial sodium ion conductivity in Na<sub>0.78</sub>WO<sub>3</sub> as a function of temperature

Temp (°K)	$D_{\text{Na}}^\dagger$ (cm <sup>2</sup> /sec)	$\frac{\partial \ln a_{\text{Na}}}{\partial \ln x}$	$\sigma_{\text{Na}} T$ (ohm cm <sup>-1</sup> )
873	$9.35 \times 10^{-14}$	14.75	$1.6 \times 10^{-7}$
923	$4.70 \times 10^{-13}$	14.15	$8.7 \times 10^{-7}$
973	$2.01 \times 10^{-12}$	12.17	$4.1 \times 10^{-6}$
1023	$7.45 \times 10^{-12}$	12.00	$1.5 \times 10^{-5}$

† From Ref. (11).

$z_{\text{Na}}$  is the valence of the sodium ion, and  $e$  is the electronic charge. Combining Eq. [13] and [14] and noting that  $eN = F$  and  $z_{\text{Na}} = 1$ , one obtains

$$\sigma_{\text{Na}} T = \frac{D_{\text{Na}} F^2 x}{V_m R} \left/ \left( \frac{\partial \ln a_{\text{Na}}}{\partial \ln x} \right) \right. \quad [15]$$

Values of the thermodynamic factor,  $\partial \ln a_{\text{Na}} / \partial \ln x$ , for  $x = 0.78$  are shown in Table IV for four different temperatures. Smith and Danielson (11) have measured the chemical diffusivity of sodium in Na<sub>0.78</sub>WO<sub>3</sub> under a concentration gradient. On combining values of  $\partial \ln a_{\text{Na}} / \partial \ln x$  from Table IV with the  $D_{\text{Na}}$  values according to Smith and Danielson, one can calculate values of  $\sigma_{\text{Na}} T$  for Na<sub>0.78</sub>WO<sub>3</sub> using Eq. [15]. The values so obtained are shown in Table IV. Figure 6 is a plot of  $\log \sigma_{\text{Na}} T$  vs.  $\frac{1}{T}$ ; the straight line fits the least squares expression

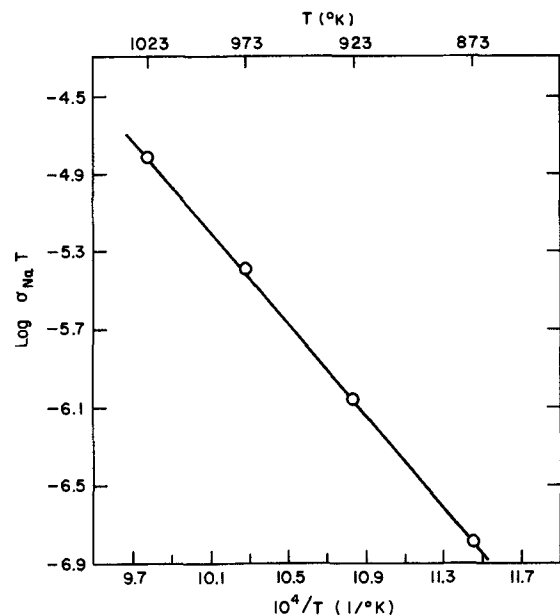
$$\sigma_{\text{Na}} T =$$

$$5.9 \times 10^6 \exp(-54,200/RT) \text{ohm}^{-1} \text{cm}^{-1} \text{°K} \quad [16]$$

According to measurements of Brown and Banks (4), Na<sub>0.77</sub>WO<sub>3</sub> has a total conductivity,  $\sigma_t$ , of approximately  $10^4$  (ohm cm)<sup>-1</sup> at 973°K. From Eq. [16],  $\sigma_{\text{Na}}$  for Na<sub>0.78</sub>WO<sub>3</sub> at 973°K is  $3.7 \times 10^{-9}$  (ohm cm)<sup>-1</sup>. Thus the ionic transference number ( $t_{\text{Na}} = \sigma_{\text{Na}} / \sigma_t$ ) is  $3.7 \times 10^{-13}$  for a bronze of approximate composition Na<sub>0.78</sub>WO<sub>3</sub>.

#### Acknowledgments

The authors gratefully acknowledge the financial support provided by the National Science Foundation, which funded this research through the National

Fig. 6. The partial sodium ion conductivity-temperature product of Na in Na<sub>0.78</sub>WO<sub>3</sub> as a function of reciprocal temperature.

Center for Energy Management and Power and through the Laboratory for Research on the Structure of Matter at the University of Pennsylvania.

Manuscript submitted Aug. 13, 1973; revised manuscript received June 12, 1974.

Any discussion of this paper will appear in a Discussion Section to be published in the June 1975 JOURNAL. All discussions for the June 1975 Discussion Section should be submitted by Feb. 1, 1975.

The publication costs of this article have been assisted by the University of Pennsylvania.

#### REFERENCES

1. A. S. Ribnick, B. Post, and E. Banks, *Advan. Chem. Ser.*, **39**, 247 (1963).
2. G. Hägg and A. Magneli, *Rev. Pure Appl. Chem.*

- (Australia), **4**, 235 (1954).
3. P. G. Dickens and M. S. Whittingham, *Quart. Rev. Chem. Soc.*, **22**, 30 (1968).
4. B. W. Brown and E. Banks, *Phys. Rev.*, **84**, 609 (1951).
5. W. R. Gardner and G. C. Danielson, *ibid.*, **93**, 46 (1954).
6. K. Hauffe, *Z. Elektrochem.*, **46**, 348 (1940).
7. K. Hauffe and A. L. Vierk, *ibid.*, **3**, 151 (1949).
8. D. Yuan and F. A. Kröger, *J. Phys. Chem.*, **73**, 2390 (1969).
9. B. W. Brown and E. Banks, *J. Am. Chem. Soc.*, **76**, 963 (1954).
10. C. Wagner, "Proc. CITCE, 7th meeting, Lindau (1955)," Butterworth Scientific Publ., London (1957).
11. J. F. Smith and G. C. Danielson, *J. Chem. Phys.*, **22**, 266 (1954).

## The Oxidation of Thin Single Crystals of Iron

P. L. Fan and L. O. Brockway

Department of Chemistry, University of Michigan, Ann Arbor, Michigan 48104

#### ABSTRACT

Single crystal (001) films of iron treated with mixtures of oxygen and nitrogen at  $10^{-7}$  Torr and  $700^{\circ}\text{C}$  form individual oxide grains observable in transmission electron microscopy. The three reaction products ( $\text{FeO}$ ,  $\text{Fe}_2\text{O}_4$ , and " $\text{Fe}_4\text{N}$ ") all have a fixed epitaxy with (001) parallel to the iron film. The grain size and distribution of the product phases are reported as well as a curious growth behavior of  $\text{FeO}$ .

The reaction of iron with oxidizing atmospheres has been the subject of very many investigations. Most of the reported work has dealt with the formation of continuous oxide layers on polycrystalline iron surfaces. Some oxidation work on single crystals of iron has been done by Sewell and co-workers (1-3) and by Graham and Cohen (4). Gulbransen (5) worked with the formation of iron oxide whiskers. Epitaxial formation of iron oxide on iron was reported and the identities of the oxide phases have been studied, but very little work has been done under conditions affording observations on the formation and growth of individual oxide grains. Such observations seem necessary for the understanding of the earlier stages of the reaction between oxygen and metal surface.

The use of thin metal films and transmission electron microscopy for the study of the formation of individual oxide grains has been employed by Brockway, Marcus, Rowe, and Adler (6-10) on copper. A similar technique has now been applied to the study of the formation, epitaxy, nucleation sites, and growth rate of individual iron oxide grains on iron.

#### Experimental

Single crystal (001) iron films of about 1000Å thickness were obtained by deposition of iron vapor from an electron beam evaporator onto polished (001) surfaces of sodium chloride at  $350^{\circ}\text{C}$  with a deposition rate of 8-10 Å/sec and a residual pressure of  $5 \times 10^{-6}$  Torr. The films were floated off of the substrate onto water and mounted on stainless steel support grids. They were annealed and oxidized in a bakeable vacuum line constructed of 1-1/2 in. diam stainless steel tubing and fittings with a 1 in. diam quartz tube in a tubular furnace as a reaction zone. The ultimate vacuum attained after baking for 8 hr at  $250^{\circ}\text{C}$  (the temperature limit imposed by the materials of the valves) was about  $4 \times 10^{-8}$  Torr. A typical compo-

sition read on a residual gas analyzer was 45% nitrogen, 25% water, and 25% hydrogen.

The iron films mounted on grids were annealed in hydrogen at 1 atm and  $700^{\circ}\text{C}$  for 1 hr. Because of the strong preferential adsorption of water on the stainless steel walls, it was imperative to reduce the water content of the hydrogen as far as possible. Electrolytic hydrogen filtered through palladium contained a troublesome amount of water (on the order of  $10^{-7}$ ), which was significantly lowered by passage through a trap filled with glass beads at liquid nitrogen temperature.

The oxidation experiments were carried out immediately following the anneal treatment and a subsequent baking at  $250^{\circ}\text{C}$  under vacuum for 8 hr. The oxidation pressures used ranged from  $1 \times 10^{-7}$  to  $2 \times 10^{-6}$  Torr; the reaction times were from 15 to 240 min, and the temperature was  $550^{\circ}$  or  $700^{\circ}\text{C}$ . Only the reactions at  $700^{\circ}\text{C}$  and pressures in the range from  $1$  to  $8 \times 10^{-7}$  Torr gave distinguishable individual oxide grains. Since this pressure range of interest was not far above the residual background pressure ( $4 \times 10^{-8}$  Torr), it was not feasible to achieve high purity of oxygen in the unit as constructed. A typical composition observed at a total pressure of  $2 \times 10^{-7}$  Torr was 38% oxygen, 40% nitrogen, 9% water, and 7% hydrogen. It may be noted that carbon monoxide has the same mass number as nitrogen (i.e., 28), but any appreciable fraction of CO present would have been indicated by a much higher peak for C (12) than was observed in any of the mass spectra recorded by the residual gas analyzer.

The annealed and oxidized films were examined by electron micrographs and diffraction patterns taken on JEOLCO 6A and JEOLCO 7 microscopes.

#### Results

The annealed films gave good single crystal (001) diffraction patterns with no deviation greater than

about  $1^\circ$ . Micrographs (Fig. 1) showed smooth films with areas of about  $0.1 \mu^2$  enclosed by low angle boundaries running along the  $\langle 110 \rangle$  directions. Dislocations appeared with an average density of  $5 \times 10^9 \text{ cm}^{-2}$  usually piled up along the boundaries; no stacking faults were observed.

The identification and epitaxial orientation of the oxidation products was determined with the aid of a series of diffraction patterns taken at room temperature; one example is shown in Fig. 2 for an iron film treated at  $700^\circ\text{C}$  for 240 min at  $2 \times 10^{-7}$  Torr total pressure. Table I lists the primary reflections observed for Fe, FeO, and  $\text{Fe}_3\text{O}_4$ ; all reflections are of the form (hk0). All of the reflections possible for these three phases within the range of scattering angle recorded are observed, when it is recognized that the (001) planes of the oxides are parallel to the (001) plane of the iron and the [110] directions of the oxide grains are parallel to the [100] of iron. For all these reflections the observed  $d$  values agree with the calculated ones (using the cubic cell edges listed in Table I) within the experimental error of the measurements, amounting to about 3% for the smallest angles and to less than 1% at the larger



Fig. 1. Electron micrograph of grid-annealed film. Low angle grain boundaries are marked by piled-up dislocations.



Fig. 2. Diffraction pattern of oxidized film ( $700^\circ\text{C}$ ,  $2 \times 10^{-7}$  Torr, 240 min). Four phases show: Fe, FeO,  $\text{Fe}_3\text{O}_4$ ,  $\text{Fe}_4\text{N}$ .

Table I. Phases and primary reflections (hk0) observed in diffraction patterns from iron films treated for 240 min at  $700^\circ\text{C}$  and  $2 \times 10^{-7}$  Torr

Fe $a = 2.86\text{\AA}$	FeO $a = 4.30\text{\AA}$	$\text{Fe}_3\text{O}_4$ $a = 8.40\text{\AA}$	" $\gamma'$ - $\text{Fe}_4\text{N}$ " $a = 3.80\text{\AA}$
110	200	220	110
200	220	400	200
220	400	440	220
310	420	620	
400	600	800	
330	620	660	
420		840	
		10.2.0	

angles; moreover, the individual reflections in each of the (hk0) forms are correctly positioned. The phases Fe and FeO contribute most strongly in Fig. 2.

The diffraction patterns illustrated in Fig. 2 show many more spots than can be accounted for by the individual planes of the forms listed in Table I. There are evidently many double diffraction spots formed when the electron beam incident on the specimen is reflected strongly by one phase and the reflected beam passes through a layer of a second phase and is partially scattered again. A few of the extra spots arise from combinations of Fe and FeO reflections. The presence of a fourth cubic phase with cube edge of approximately  $3.80\text{\AA}$  and oriented with its axes parallel to those of the iron film does account for all of the many extra spots. Three primary reflections observed from this phase are listed under " $\gamma'$ - $\text{Fe}_4\text{N}$ " in Table I. The double reflections are of the following kinds: (200), (400), and (420) of FeO each reflected by (110), (200), and (220) of the extra phase; (110), (220), and (310) of Fe reflected again by the three planes of the extra phase. No second scattering of  $\text{Fe}_3\text{O}_4$  reflections was found.

A search of the current A.S.T.M. Powder Diffraction File discloses only one compound containing iron and having three strong diffraction lines with  $d$  values of 2.67, 1.89, and  $1.33\text{\AA}$ ; for this reason the fourth phase is designated  $\gamma'$ - $\text{Fe}_4\text{N}$ , whose strongest (hk0) reflections do correspond to the observed spacings.

The oxidation experiments at  $550^\circ\text{C}$  yielded  $\text{Fe}_3\text{O}_4$  as the only oxidized phase, while all oxidations at  $700^\circ\text{C}$  produced both FeO and  $\text{Fe}_3\text{O}_4$  in treatment times ranging from 15 to 240 min. The  $\text{Fe}_4\text{N}$  also appeared with treatment times of 120 to 240 min at  $2 \times 10^{-7}$  Torr. The amounts of  $\text{Fe}_4\text{N}$  indicated by the relative intensities of the diffraction spots were less in the treatment having a  $\text{N}_2/\text{O}_2$  ratio of 3.4 than in the others where the  $\text{N}_2/\text{O}_2$  ratio was 1.0 or less.

The appearance and distribution of oxide grains is illustrated in the micrographs of Fig. 3 (15 min) and Fig. 4 (240 min). After the short treatment well-defined grains of uniform size (about  $0.03\mu$ ) are distributed randomly over the film without any observable relation to the dislocation sites or grain boundaries of the iron. After the long treatment the sizes are far from uniform; some of the grains have scarcely grown at all while others have reached sizes in the  $0.3\text{--}0.5\mu$  range. Grains of intermediate sizes are rare. The average diameters of the thirty largest grains at different treatment times are shown in Fig. 5. The standard deviations for such measurements are indicated by the magnitude of the bars. The lineal growth rate appears to be uniform at  $0.088\mu \text{ hour}^{-1}$  at  $700^\circ\text{C}$  and  $2 \times 10^{-7}$  Torr.

Further examination of the treated films by electron microscopy and diffraction gave information on the distribution of the phases. By the use of dark field microscopy the large grains produced at longer times are shown to be mainly FeO with some  $\text{Fe}_4\text{N}$  included.  $\text{Fe}_3\text{O}_4$  is spread across the whole film. This is supported by selected area diffraction experiments showing that FeO and  $\text{Fe}_3\text{O}_4$  are distributed across the film while  $\text{Fe}_4\text{N}$  is scarcely detected away from



Fig. 3. Electron micrograph of oxidized film (700°C,  $2 \times 10^{-7}$  Torr, 15 min). FeO grains are randomly distributed.

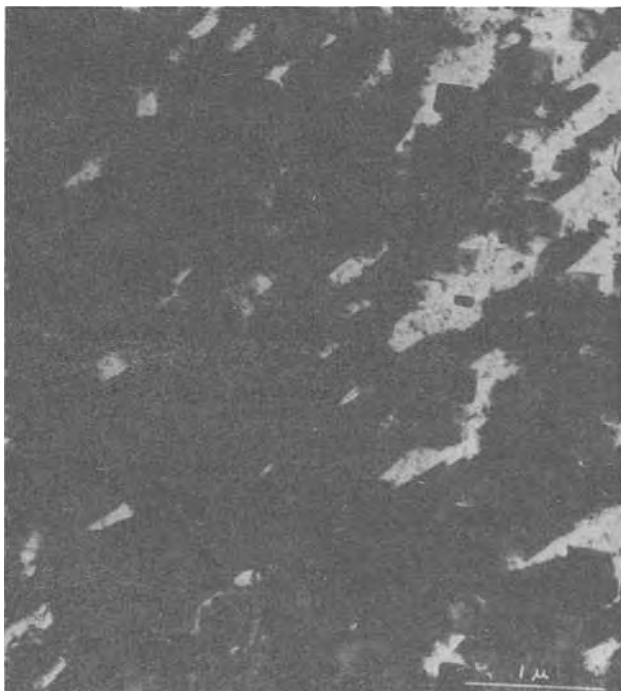


Fig. 4. Electron micrograph of oxidized film, (700°C,  $2 \times 10^{-7}$  Torr, 240 min). Large FeO grains appear.

the large FeO grains. Further corroboration comes from the Moire fringe patterns observed in the high resolution micrograph of Fig. 6; the fringe spacings inside the large grain can be accounted for only by an overlay of  $\text{Fe}_4\text{N}$  on FeO while the spacings away from the large grain arise, respectively, from FeO on Fe and  $\text{Fe}_3\text{O}_4$  on Fe.

#### Discussion

The observed epitaxy of FeO and  $\text{Fe}_3\text{O}_4$  agrees with the results of Bardolle and Benard (11) for oxidation at  $10^{-1}$  Torr and with the calculations of Collins and Heavens (12). The presence of imperfec-

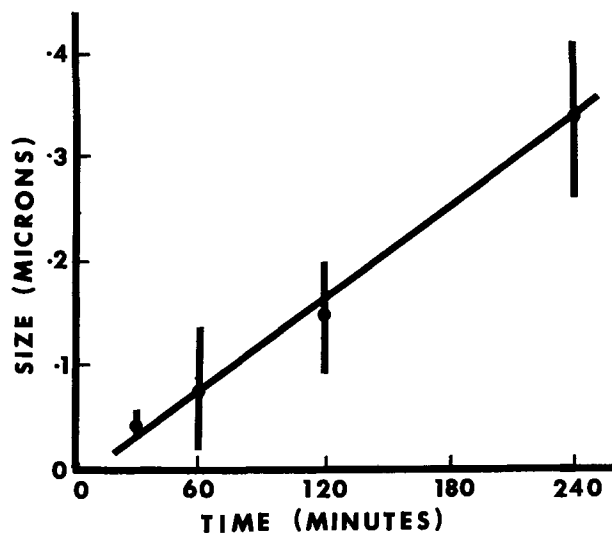


Fig. 5. Relation between average diameter of large FeO grains (700°C,  $2 \times 10^{-7}$  Torr) and oxidation time.



Fig. 6. Electron micrograph of oxidized film (700°C,  $2 \times 10^{-7}$  Torr, 240 min). At high resolution three distinct sets of moire fringes appear.

tions (dislocations and low angle boundaries) in the iron failed to influence the sites of oxide nucleation in agreement with the observations of Pease and Ploc (13), who reported a dependence of nucleation sites on dislocations only when the iron contained impurities much in excess of the 0.001% concentration in the present experiments.

A possible effect of imperfections in the iron may lie in the greatly disparate oxide growth rates observed in the treatments at 700°C and  $2 \times 10^{-7}$  Torr. About 0.8% of the oxide grains observed after 15 min grow to ten times their original diameters in 4 hr while a very large fraction of the grains have not shown any apparent growth. Some variation in the texture of the iron film causes abnormal growth at certain grain sites; accelerated diffusion of iron atoms at dislocations could plausibly account for the unusual growth. It should be noted that a new phase,

Fe<sub>4</sub>N, is being formed on the larger grains at the later times, and the growth rate observations can not be interpreted in terms of the increase of a single phase.

The apparent formation of Fe<sub>4</sub>N was surprising. It is found only after FeO and Fe<sub>3</sub>O<sub>4</sub> have been well established. Because it is associated almost exclusively with the large FeO grains, it might be supposed that the surface of the large FeO grains enables the formation of the nitride in a way which does not occur with the small-grained FeO, with Fe<sub>3</sub>O<sub>4</sub>, or with iron. The thermodynamic possibilities for the reaction of formation cannot be confidently assessed since the standard free energies are not adequately known for the conditions here, *i.e.*, mixtures of fine particles (0.3 $\mu$  and much smaller) in specific crystallographic orientations. The dilemma could be resolved by reactions with the nitrogen pressure varied from very low to very high with respect to oxygen; this would require a new ultrahigh vacuum line capable of reaching a background pressure far below the total pressure required ( $\sim 10^{-7}$  Torr) to yield isolated grains of oxide.

Finally it is possible to suggest a series of stages in the formation of oxide layers under the conditions of the present experiments. The first step of adsorption of oxygen and other gases is not observed by electron microscopy or transmission diffraction. Next (in less than 15 min) is the formation of grains of two phases, FeO and Fe<sub>3</sub>O<sub>4</sub>, too small to show contrast effects in micrographs but detected by their diffraction patterns. Later, individual grains of FeO are detected with diameters of 0.03 $\mu$ . Many of these remain practically the same size after 4 hr while a few grow to more than ten times the original diameters. During the last half of this period Fe<sub>4</sub>N is formed on the FeO large grains, but the growth of the grains is mainly due to added FeO. The space between the large grains continues to show the small FeO grains but never does develop detectable individual grains of Fe<sub>3</sub>O<sub>4</sub>. A continuous thick layer of oxide is finally formed by the lateral growth and coalescence of the larger FeO grains.

#### Summary

Single crystal (001) films of iron were exposed to oxidizing atmospheres under conditions which permitted the formation of individual oxide grains observable in transmission electron microscopy. These conditions were a temperature of 700°C and a pressure range of  $1-8 \times 10^{-7}$  Torr for a gas composition of about 40% each of oxygen and nitrogen with the balance mainly water and hydrogen. Grains of FeO and Fe<sub>3</sub>O<sub>4</sub> were observed for treatment times from 15 to 240 min; for the longer treatment times Fe<sub>4</sub>N was also formed. All three phases were oriented with (001)

planes parallel to the iron film. By contrast at 550°C the only oxidized phase observed was Fe<sub>3</sub>O<sub>4</sub> in continuous films with no grains resolved.

The FeO grains originally observed at 15 min showed a uniform size of about 0.03 $\mu$  diameter. While most of these appeared to be unchanged after 4 hr, about 1% had grown to ten times greater diameters at a rate of 0.088 $\mu$  hour<sup>-1</sup>.

#### Acknowledgments

We are grateful to Professor W. C. Bigelow, Mrs. A. P. Rowe, and Mr. L. F. Allard of The University of Michigan for technical assistance and valuable discussions. We also wish to thank Mr. T. A. Nolan of the Oak Ridge Gaseous Diffusion Plant operated by the Union Carbide Corporation, Nuclear Division, for the Atomic Energy Commission, for preparing high resolution micrographs and diffraction patterns.

Manuscript submitted May 15, 1973; revised manuscript received May 31, 1974.

Any discussion of this article will appear in a Discussion Section to be published in the June 1975 JOURNAL. All discussions for the June 1975 Discussion Section should be submitted by Feb. 1, 1975.

The publication costs of this article have been assisted by The University of Michigan.

#### REFERENCES

1. C. D. Stockbridge, P. B. Sewell, and M. Cohen, *This Journal*, **108**, 928 (1961).
2. P. B. Sewell and M. Cohen, *ibid.*, **111**, 501, 308 (1964).
3. N. Ramasubramanian, P. B. Sewell, and M. Cohen, *ibid.*, **115**, 12 (1968).
4. M. J. Graham and M. Cohen, *ibid.*, **116**, 1430 (1969).
5. E. A. Gulbransen and R. L. Tallman, Clearinghouse for Federal Scientific and Technical Information, AD 653723 (1967).
6. L. O. Brockway and R. B. Marcus, *J. Appl. Phys.*, **34**, 921 (1963).
7. L. O. Brockway, R. B. Marcus, and A. P. Rowe, in "Single Crystal Films," M. H. Francombe and H. Sato, Editors, p. 231, Macmillan, New York (1964).
8. A. P. Rowe and L. O. Brockway, *J. Appl. Phys.*, **37**, 2703 (1966).
9. L. O. Brockway and A. P. Rowe, "Proc. Symp. Fundamentals of Gas-Surface Interactions," p. 147, Academic Press, New York (1967).
10. L. O. Brockway and I. M. Adler, *This Journal*, **119**, 899 (1972).
11. J. Bardolle and J. Benard, *Rev. Met.*, **49**, 613 (1952).
12. L. E. Collins and O. S. Heavens, *Proc. Phys. Soc.*, **70**, 265 (1957).
13. R. F. W. Pease and R. A. Ploc, *Trans. Met. Soc. AIME*, **233**, 1949 (1965).



## An Investigation of the Structure of Pd<sub>2</sub>Si Formed on Si

S. S. Lau and D. Sigurd<sup>1</sup>

California Institute of Technology, Pasadena, California 91109

Recent investigations of the electrical and metallurgical properties of palladium silicide (Pd<sub>2</sub>Si) have shown that this metal silicide is a useful contact material in integrated circuit applications (1-4). It has been reported that of the possible intermetallic compounds in the Pd/Si system Pd<sub>2</sub>Si is predominantly formed when a Si wafer with an evaporated layer of Pd (<10,000Å) is heat-treated at temperatures up to 750°C (2, 3, 5-7). In a few cases small amounts of Pd<sub>3</sub>Si and PdSi have been observed (5).

Experimental observations indicated (6, 7) a strong tendency for Pd<sub>2</sub>Si to grow with the hexagonal basal plane parallel to the substrate surface ([001] fiber texture) regardless of the substrate orientation, and in particular, Pd<sub>2</sub>Si grown on (111)-oriented Si substrate is epitaxially oriented.

The transformation kinetics of the Pd<sub>2</sub>Si phase has been investigated in our laboratory by MeV <sup>4</sup>He<sup>+</sup> ion backscattering in a previous investigation (7). The formation rate of the Pd<sub>2</sub>Si layer on Si wafers in the temperature range of 200°-275°C was found to be diffusion limited, and independent of the substrate orientation, i.e., the same transformation kinetics were observed on (111), (100), and (110) oriented Si single crystal substrates as well as on amorphous (evaporated Si on single crystal substrate) Si substrates. The growth kinetics can be described by an Arrhenius type of equation and the activation energy for growth was found to be 1.5 ± 0.1 eV. A lower activation energy of 1.27 eV was reported by Hutchins and Shepela (6) for the growth of Pd<sub>2</sub>Si on (111) Si substrates using an optical technique. This discrepancy might be due to the sensitivity of different analytical techniques. They also observed a *t*<sup>1/2</sup> time dependence for the Pd<sub>2</sub>Si growth rate. They further suggested that the growth kinetics should be the same for Pd<sub>2</sub>Si formed on (100), (110), and (111) oriented Si substrates since Pd<sub>2</sub>Si grows with a [001] fiber textures on these substrates.

It is our objective in the present work to investigate the structure, such as grain size and preferred orientation, of the as-deposited Pd films and the silicide films formed on Si substrates of various orientations, and their possible relationship with the transformation kinetics of the Pd<sub>2</sub>Si phase.

### Experimental

Samples were prepared by e-gun evaporation of 500-3000Å Pd films onto (100) and (111) Si wafers and on Si wafers with approximately 3000Å thick evaporated Si (amorphous) films. The evaporation rate was about 10 Å/sec, and the pressure during evaporation was ~5 × 10<sup>-7</sup> Torr. The temperature of the substrates at the end of the evaporation was estimated to be about 100°C. Pd films were evaporated on all three types of

substrates at the same time. Prior to evaporation, the Si substrates were treated in HF followed by rinsing in H<sub>2</sub>O.

Heat-treatments of the samples at 260° and 550°C for 30-60 min were performed in a vacuum furnace operated at pressures between 1 to 5 × 10<sup>-5</sup> Torr. After the vacuum annealing, the compositions of the reacted samples were examined by backscattering and the phase structure was identified using the x-ray thin film camera technique.

Transmission electron microscopy was used to examine the structure of the Pd and the Pd<sub>2</sub>Si films. The Pd films were stripped off from the Si substrate in a HF solution and the Pd<sub>2</sub>Si samples were prepared by chemically etching away the Si substrate in a water-amine solution (8).

### Results

**Amorphous Si substrate.**—The as-deposited Pd film (~500Å) on amorphous Si substrate had grains ranging from 50 to 150Å in size (Fig. 1). There were apparently some very fine precipitates of Pd<sub>2</sub>Si distributed throughout the film. It has been suggested (6) that Pd<sub>2</sub>Si was formed by a rapid nondiffusion controlled process during the deposition of the Pd films, therefore, the actual thickness of the Pd films may have been thinner than the expected 500Å. The diffraction pattern for the as-deposited Pd films shows a random orientation (Fig. 2). When the Pd/Si (amorphous) composite structure was heat-treated for 30 min at 260°C, a Pd<sub>2</sub>Si phase with grains of 50 to 150Å in size was formed (Fig. 3). Selective area diffraction (SAD, aperture size ~25 μm) experiments indicated

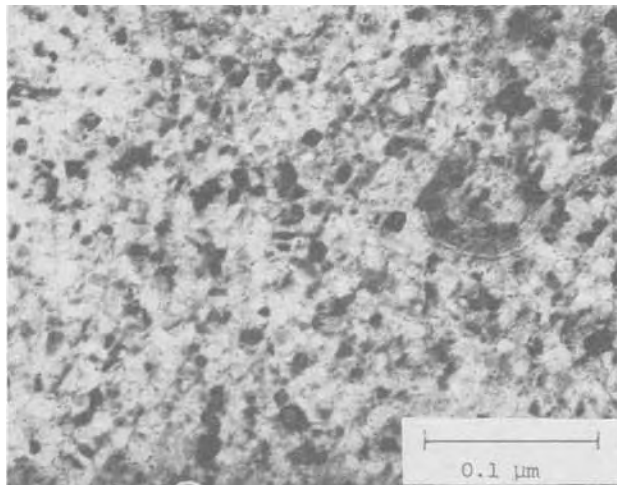


Fig. 1. Transmission electron micrograph of as-deposited Pd film on amorphous Si substrate.

<sup>1</sup>Permanent address: Research Institute for Physics, Stockholm, Sweden.

Key words: silicide formation, electron microscopy, diffusion.



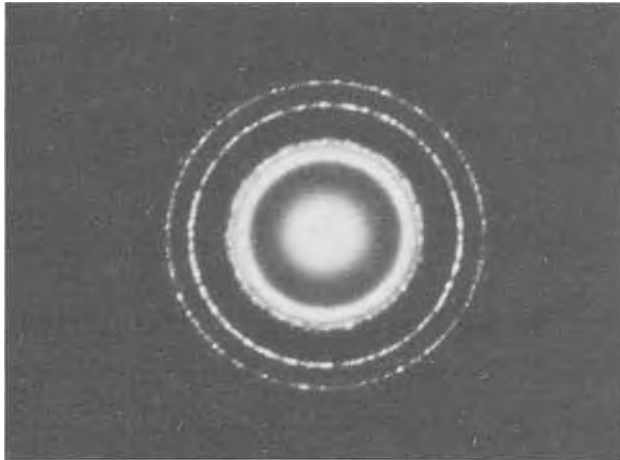


Fig. 2. Diffraction pattern of the as-deposited Pd film on amorphous substrate.

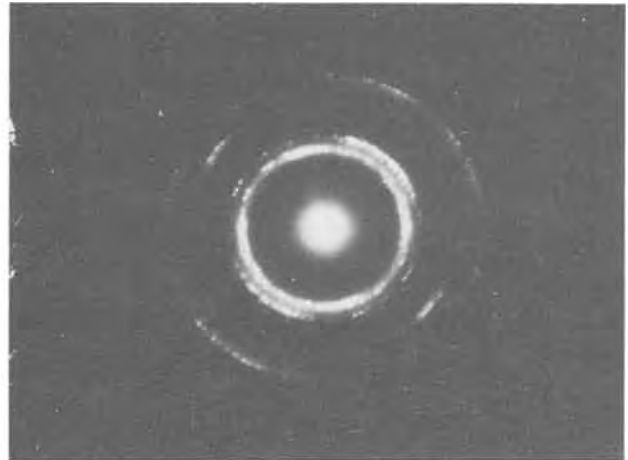


Fig. 4. Diffraction pattern of as-deposited Pd film on (100) Si substrate.

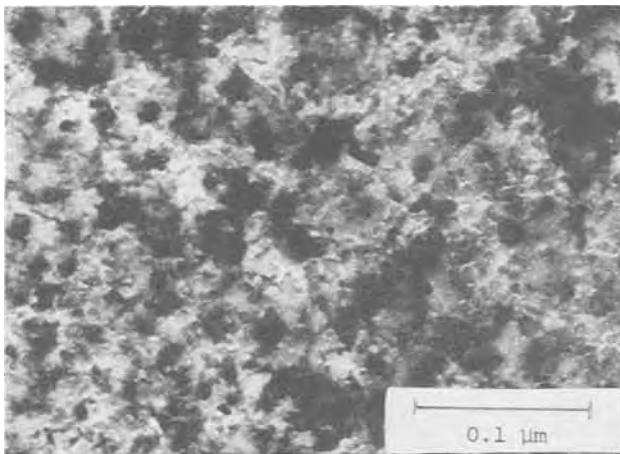


Fig. 3. Transmission electron micrograph of Pd<sub>2</sub>Si formed on amorphous Si substrate at 260°C.

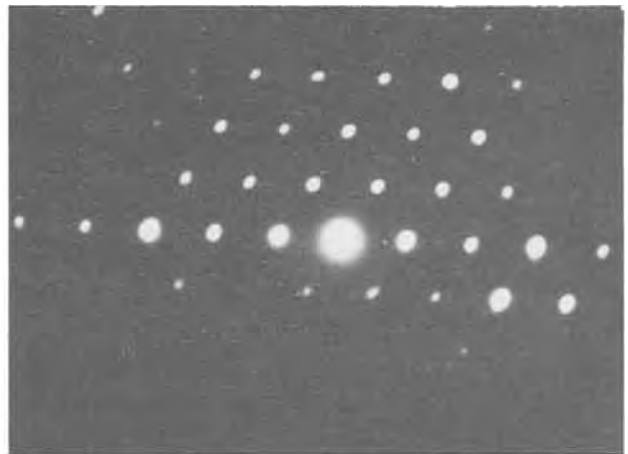


Fig. 5. Diffraction pattern of Pd<sub>2</sub>Si formed on (100) Si substrate at 550°C.

that the basal planes of these grains were preferentially oriented parallel to the substrate surface, in agreement with reported observations (6, 7). No specimens were heat-treated at 550°C to avoid possible crystallization of the amorphous Si film.

**(100) Si substrate.**—The as-deposited Pd films on (100) Si substrates had grains ranging from 100 to 400Å in size. It is interesting to note that the SAD pattern (Fig. 4) indicated a fiber texture (weak 220 reflection) for the as-deposited Pd films, while a random SAD pattern for Pd films deposited on amorphous Si substrates was observed (see Fig. 2 and 4). When the samples were heat-treated at 260°C, polycrystalline Pd<sub>2</sub>Si with grains ranging between 200 and 500Å was formed. Heat-treating the samples at 550°C resulted in the formation of the Pd<sub>2</sub>Si phase with grains ranging from 100 to 300Å. The reasons for this reduction in grain size when the heat-treatment temperatures were increased from 260° to 550°C are not clear at present. In localized areas of the Pd<sub>2</sub>Si layer formed at 550°C single crystal diffraction patterns with the basal plane parallel to the substrate surface were observed (Fig. 5). This can be possibly related to the crystallographic structure of the oriented as-deposited Pd films deposited on (100) Si substrates. Voids were observed in the Pd<sub>2</sub>Si films formed both at 260° and 550°C.

**(111) Si substrates.**—The as-deposited Pd films had grains ranging between 50 and 200Å. The SAD pattern showed random orientation of the Pd films. The Pd<sub>2</sub>Si

phase formed at 260°C was generally epitaxial and the grains had mosaic block structure (9) with block size ranging between 200 and 500Å (Fig. 6). No voids were observable at 80,000×. The Pd<sub>2</sub>Si phase formed at 550°C was also generally epitaxial with 200-500Å mosaic blocks, however, small voids in the films were observed.

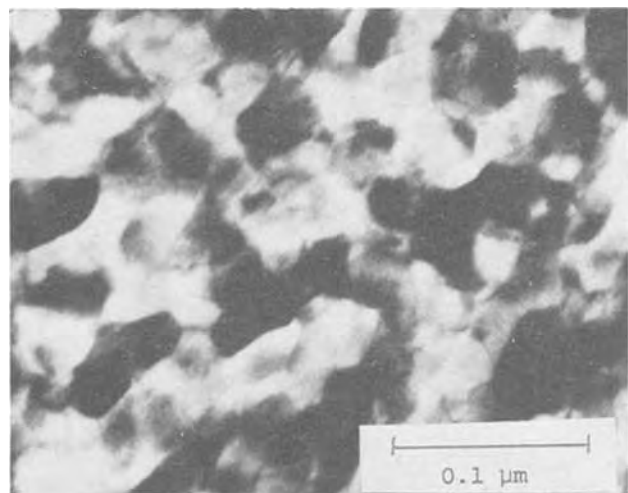


Fig. 6. Transmission electron micrograph of Pd<sub>2</sub>Si formed on (111) Si substrate at 260°C.



### Discussion and Summary

Judging from the experimental observations in the present study and those obtained from the previous backscattering investigation (7), we propose that the lattice diffusion of materials through the Pd<sub>2</sub>Si layer is the rate-controlling step for Pd<sub>2</sub>Si formation. The reasons are as follows: It was observed that the grain sizes of the as-deposited Pd films were different for various substrates. The grain size of Pd<sub>2</sub>Si formed on amorphous Si at 260°C (50-150Å) was smaller than the grain size or the mosaic block size (200-500Å) of Pd<sub>2</sub>Si formed on (100) and (111) substrates, respectively. This observation in conjunction with the previously reported MeV <sup>4</sup>He<sup>+</sup> backscattering results that the transformation kinetics of the Pd<sub>2</sub>Si phase was independent of the substrate orientations (7) seem to suggest that the grain size of the Pd films and the grain size or the grain structure (large angle grain boundaries vs. small angle mosaic block boundaries) of Pd<sub>2</sub>Si do not play a role in the growth kinetics of the Pd<sub>2</sub>Si phase. At 550°C, the transformation kinetics are expected to follow the same Arrhenius equation that governs the growth rate of Pd<sub>2</sub>Si at lower temperatures for all substrates investigated. The grain size of Pd<sub>2</sub>Si formed at 550°C was found to be different on different substrates in the present work, again the results suggest the independence of growth rate of Pd<sub>2</sub>Si on grain size or grain structure.

If the transformation process is governed by the diffusion of Si along the grain boundaries of Pd<sub>2</sub>Si and/or Pd and subsequent diffusion and transformation in the Pd grains, then the transition front between the Pd<sub>2</sub>Si and Pd layers will not be uniform and would cause a gradual slope in the backscattering spectra. The fact that sharp edges were observed in the spectra [see Fig. 2 in Ref. (7)] indicating a sharp and uniform front for the Pd<sub>2</sub>Si layer seems to rule out the grain boundary diffusion process. Buckley and Moss (3) suggested that at least in the case of growth

of Pd<sub>2</sub>Si on (111) Si substrates, the controlling step is the diffusion of Si atoms through the Pd<sub>2</sub>Si lattice. Our observations on grain size and the backscattering data reported earlier (7) are in agreement with the hypothesis that lattice diffusion of materials through the Pd<sub>2</sub>Si layer is apparently the rate-controlling step. Experiments to determine the moving species are now in progress.

### Acknowledgment

The authors would like to express their gratitude to Dr. J. W. Mayer for his encouragement during the course of this work, to Mr. Henri Arnal for his assistance in electron microscopy, and to the Air Force Cambridge Research Laboratory for their financial sponsorship.

Manuscript submitted May 10, 1974; revised manuscript received July 12, 1974.

Any discussion of this paper will appear in a Discussion Section to be published in the June 1975 JOURNAL. All discussions for the June 1975 Discussion Section should be submitted by Feb. 1, 1975.

The publication costs of this article have been assisted by the California Institute of Technology.

### REFERENCES

1. W. V. T. Rush and C. A. Burrus, *Solid-State Electron.*, **11**, 517 (1968).
2. C. J. Kircher, *ibid.*, **14**, 507 (1971).
3. W. D. Buckley and S. C. Moss, *ibid.*, **15**, 1331 (1972).
4. A. Shepela, *ibid.*, **16**, 477 (1973).
5. J. Drobek, R. C. Sun, and T. C. Tisone, *Phys. Status Solidi (a)*, **8**, 243 (1971).
6. G. A. Hutchins and A. Shepela, *Thin Solid Films*, **18**, 343 (1973).
7. R. W. Bower, D. Sigurd, and R. E. Scott, *Solid-State Electron.*, **16**, 1461 (1973).
8. R. M. Finne and D. L. Klein, *This Journal*, **114**, 965 (1967).
9. D. Sigurd, R. W. Bower, W. F. van der Weg, and J. W. Mayer, *Thin Solid Films*, **19**, 319 (1973).



## Polymer-Bonded Negative Electrodes for Lead-Acid Batteries

J. L. Weininger and F. W. Secor

General Electric Company, Corporate Research and Development, Schenectady, New York 12301

### ABSTRACT

Negative lead electrodes were pasted and bonded to lead alloy substrates with activated carbon and a polymer. Scanning electron microscopy was used to follow structural changes of the polymer-bonded electrodes during cycle life. With lead-calcium alloy substrates the electrode performance of the polymer-bonded electrode was superior to conventionally pasted electrodes with respect to cycle life, charge acceptance, and lack of gassing. Different substrates of the same Pb-0.06%Ca-1%Sn alloy gave similar results.

It is common practice to blend polymers with active materials of an electrode in order to improve physical and electrochemical properties of the electrode. In the patent literature there are many descriptions of electrode structures incorporating a variety of polymers. This is exemplified by the work of Duddy (1) who was one of the first to introduce polyethylene, polyvinyl chloride, and their copolymers as porous carriers of electrode materials. Other examples of processes which are based on the principle of polymer bonding are (a) bonding fuel cell electrodes with polytetrafluoroethylene to render them hydrophobic and to bind the catalyst (2); (b) compounding metal oxides with polymers to produce conductive coatings (3); and (c) forming rechargeable electrodes with a polymeric binder (4).

This report describes polymer bonding the active material of the negative lead electrode. The method improves the cycle life, charge acceptance, and lack of gassing of the lead-acid cell over that of commercially available ones. Scanning electron microscopy (SEM) was used to follow structural changes of the polymer-bonded electrodes during cycle life. This also supplied corroborating evidence for the dissolution-precipitation mechanism of the electrode reaction (5).

### Method of Polymer Bonding

For use in the lead-acid cell, a solution of neoprene in toluene was mixed with carbon black and Grenox battery grade PbO, a product of NL Industries. The mixture was suitable for pasting battery grids and after evaporation of the solvent no further curing of the electrode was needed.

Several paste formulations were developed for the negative electrode. The two preferred compositions are given in Table I.

Composition 1 was used for the series of experiments described below. Sodium benzoate was added to composition 2 for making a more porous electrode structure by removing the benzoate in a further leaching step in water. This more porous structure was believed to give greater flexibility and larger high-rate discharge capability. Preliminary tests showed even a longer life for a composition 2 electrode. Nevertheless, composition 1 was chosen for the present experiments,

because the primary objective of this work was to prove out the efficacy of polymer bonding without the introduction of another component.

### Experimental

The negative electrodes had an area of  $5 \times 5$  cm, 0.3 cm thickness, and a theoretical capacity of 3.0 A-hr. They were placed in bags of Daramic (W. R. Grace Company) porous polyethylene separators and were sandwiched between two conventional, pasted, positive electrodes (Type B-80, Atlantic Battery Company). The positive electrodes had a combined higher capacity (9.8 A-hr) than the negative electrode.

Table II lists the structure and function of the six negative electrodes which were life-tested.

The two control electrodes were pasted and cured in the conventional manner; the polymer-bonded electrodes were prepared as described above. Formation of the plates was performed at charge rates of C/20 for 24 hr in 1.05 sp gr acid, followed by C/24 for 20 hr in 1.28 sp gr acid, except that positive and negative electrodes had to be formed separately against corresponding counterelectrodes because of the above-indicated imbalance of their capacities.

The cells were cycled at constant current to cut-off voltages of 2.70V on charge and 1.75V on discharge. Cycling was performed manually for the first two cycles at about a 6-hr rate (see Table III); thereafter cycling was automatic at the 4-hr rate.

Table III indicates that the normal controls had a slightly higher initial utilization and capacity compared to the polymer-bonded electrodes. These first two cycles also established the normal capacity for determining cycle life.

Table I. Composition of polymer-bonded negative electrodes

	Composition 1		Composition 2	
	Weight %	Volume %	Weight %	Volume %
PbO*	87.4	53.6	81.3	40.1
Carbon (Shawin-igan Black)	7.5	22.5	7.0	16.7
Neoprene**	5.1	24.0	7.0	26.5
Sodium benzoate	—	—	4.7	16.8

\* Grenox 111-G or any other suitable battery-grade PbO.

\*\* du Pont Type AD-10.

Key words: lead-acid battery, lead electrode structure, lead-calcium alloy, polymer bonding, scanning electron microscopy.

Table II. List of negative electrodes

Experiment Number	Structure	Substrate	Function
PN-C1	Pasted grid	Cast grid* Pb/Sb alloy	Control
PN-C2	Pasted grid	Expanded grid**	Control
PN-12	Polymer-bonded	Pb-plated Cu screen	Experimental
PN-13	Polymer-bonded	Expanded grid** 500/1 pattern	Experimental
PN-14	Polymer-bonded	Expanded grid** 3/0 pattern	Experimental
PN-15	Polymer-bonded	Expanded grid** Dystex pattern***	Experimental

\* Type A-70, Atlantic Battery Company.

\*\* RDP-16, St. Joe Minerals Company (composition: Pb-0.06% Ca-1.0% Sn).

\*\*\* Exmet Corporation.

Table III. Performance of negative electrodes during cycles 1 and 2

	PN-C1	PN-C2	PN-12	PN-13	PN-14	PN-15
Cycle 1						
Time (hr)	5.94	6.75	5.75	5.58	5.08	5.07
Capacity (A-hr)	1.48	1.69	1.44	1.40	1.27	1.27
Utilization (%)	49	56	48	46	42	42
Cycle 2						
Time (hr)	5.63	6.42	5.47	5.30	5.04	4.97
Capacity (A-hr)	1.41	1.61	1.37	1.33	1.26	1.24
Utilization (%)	47	54	46	44	42	41
Decrease in capacity (%)	5	5	5	5	1	2

Starting with cycle 3, at the higher C/4 rate, the negative electrodes had a steady 1.16-1.20 A-hr discharge capacity for many cycles. Their behavior over the total cycle life is shown in Fig. 1. The curves in this figure are drawn through experimental points, ignoring only a few excursions, which were clearly due to instrumental error, e.g., a premature cut-off of discharge due to electronic noise or cycles in which the positive electrodes became limiting.

In spite of the initial mismatch of capacities the positive electrodes had a much shorter cycle life so that they had to be replaced twice, or even three times in cells lasting over 200 cycles. In all cases, Fig. 1 shows the cell performance in which the negative electrode limited the discharge capacity.

The behavior of individual cells is described below.

Cell PN-C1 had a discharge capacity of 1.16 A-hr to cycle 50 and a decrease to 0.6 A-hr at cycle 155.

Cell PN-C2 maintained a discharge capacity of 1.18 A-hr only for the first 20 cycles, then dropped rapidly to 0.6 A-hr at cycle 90. For both these control cells the efficiency, i.e., the percentage of discharge capacity

with respect to charge, was in the 95-98% range when the cells had a steady discharge. It was 80% or less during the decline of cell performance.

Cell PN-12 held steady at 1.18 A-hr until cycle 150, then declined to 0.6 A-hr at cycle 183. Efficiency was in the range 90-100% even during the period of decline.

Cell PN-13 had a discharge capacity of 1.19 A-hr to cycle 185 with only a small decline to 1.11 A-hr at cycle 257 (end of test). Efficiency was 90-100% throughout cycle life; it was 100% during the cycle period 230-257.

Cell PN-14 was comparable in cycle life to PN-12, having a discharge capacity of 1.16 A-hr to cycle 110, followed by a slow decrease to 0.6 A-hr at cycle 191. Efficiency of this cell was nearly 100% to cycle 170 and between 85 and 95% for the last 20 cycles.

The discharge capacity of cell PN-15 was unchanged at 1.16 A-hr for the duration of the test to cycle 233. Efficiency was 95-100%.

### Scanning Electron Microscopy

Electrode PN-12 was chosen for monitoring the structure of the polymer-bonded electrode during cycle life. Small samples were taken from a location near the edge of the electrode, washed in distilled water, and mounted for examination in the scanning electron microscope (SEM). Micrographs were obtained during cycles 5, 29, 73, and at the end of the life test after cycle 204.

Some of these micrographs have been published in a report (5) that related the morphology of the electrode to the solution-precipitation mechanism of the electrode reactions of the lead acid cell. Other micrographs are included in the present report. For example, Fig. 2 and 3 are the previously shown views of the electrode at the end of the 73rd charge (5). Figure 4 represents the same general location of the electrode after the discharge of cycle 73. The flowerlike crystal structures as well as the underlying bandlike crystals have been converted into finely divided small crystalline particles, interspersed between large rhombohedral crystals. This appearance was typical for both the edge of the electrode and its interior. It signifies that the crystalline structures of Fig. 2 and 3 represent active lead in the charged condition. The rhombohedral crystals after discharge are  $\text{PbSO}_4$  crystals which were at least partially passivated.

The remaining SEM's, Fig. 5-11, were taken of different electrodes at the end of the cycle life of the cells. This was defined as the time when the cell failed to accept a minimum charge. Consequently, the electrodes were removed at the end of a charge cycle but this does not imply that the particular areas examined by SEM were of charged active material. At least

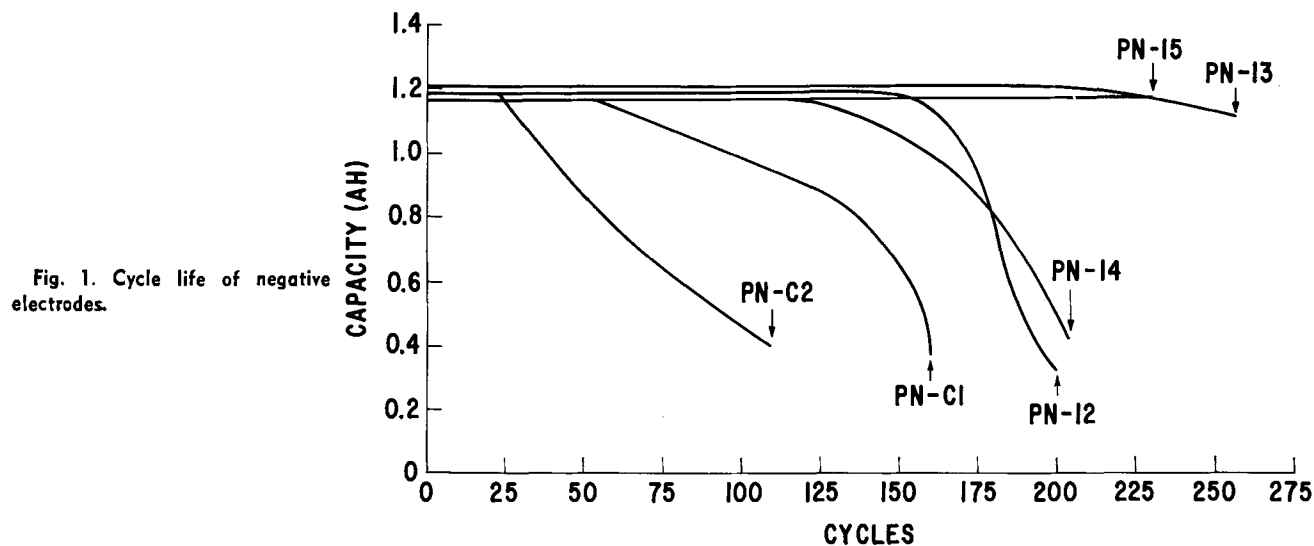


Fig. 1. Cycle life of negative electrodes.

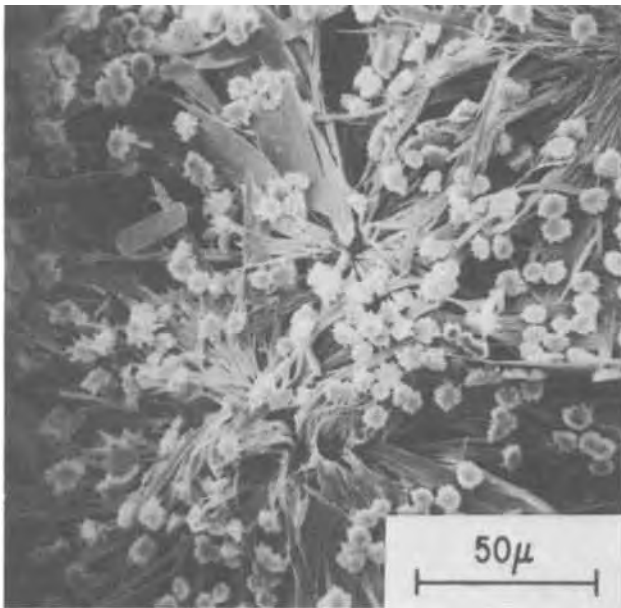


Fig. 2. Negative electrode PN-12 at end of charge 73. Magnification 5000X.

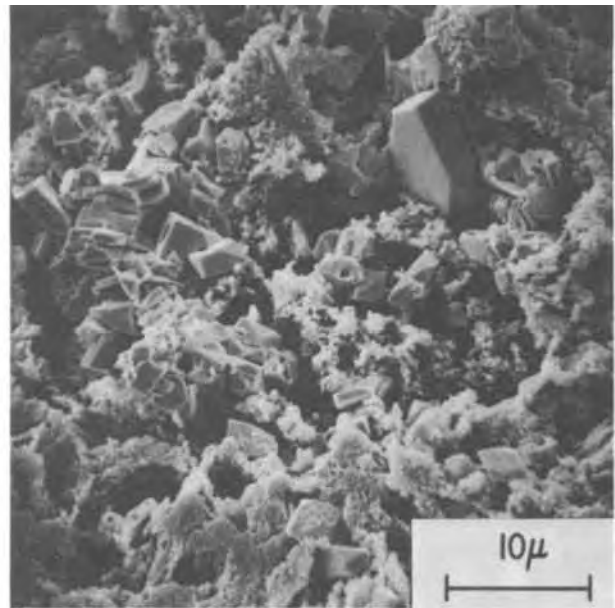


Fig. 4. Negative electrode PN-12 at end of discharge 73. Magnification 2000X.

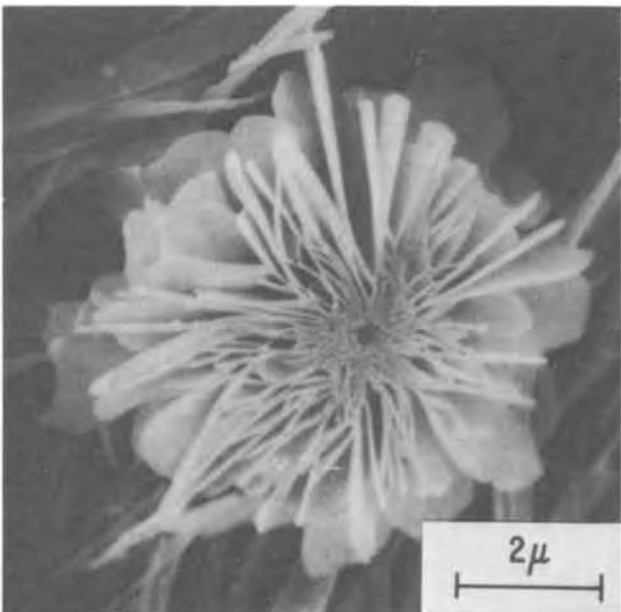


Fig. 3. Negative electrode PN-12 at end of charge 73. Magnification 5000X.

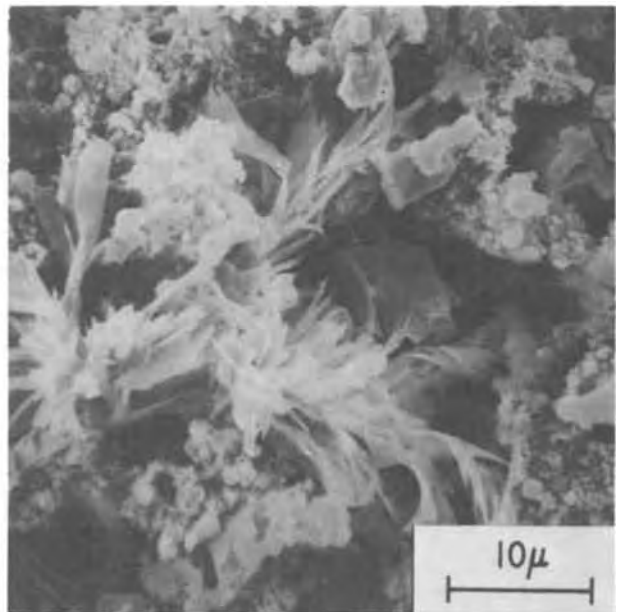


Fig. 5. Surface of negative electrode PN-12 at end of cycle 204. Magnification 2000X.

some of the crystals appear to be large passivating  $\text{PbSO}_4$  crystals.

Figures 5, 6, and 7 represent the electrode at the end of cycle life (cycle 204) when the discharge capacity had dropped below 0.6 A-hr. Figures 5 and 6 are views of the surface of electrode PN-12. In one case (Fig. 5) there are still needlelike crystals, resembling the active material in Fig. 2 and 3, but in Fig. 6 there are large passivated crystals. They result from the growing together of smaller ones. Such crystals, some of them larger than  $15\mu$ , were only observed at the electrode surface. Figure 7 is typical of the structure and crystal size in the interior of the electrode after cycle 204.

By comparison, the interior of the negative electrode at the end of cycle life of the control cell PN-C1 is shown in Fig. 8. It has an entire crystal field of rhombohedral crystals, characteristic of spongy electrodes without any active material [see also Fig. 9 of Ref. (5) for a SEM of the surface of this electrode].

Although the presence and effect of the polymer in the electrode structure is implicit in the above discussion, the polymer phase cannot be seen in the micrographs. One can see the polymer phase in a different polymer-bonded electrode for which SEM's are shown in Fig. 9, 10, and 11. Samples for these micrographs were taken from a negative electrode with the same polymer-bonding formulation as above, but the electrode had larger external dimensions and was one of two negative electrodes used in a 10 A-hr cell. Figures 9-11 represent this electrode at the end of the cell's cycle life (68 cycles) which was limited by the positive and not by these negative electrodes. Figure 9 is a top view of the polymer-bonded electrode. Crystalline shapes appear to be coated and held together by a porous polymer. Figure 10 is taken from the same general area as Fig. 9. On further enlargement of Fig. 10, the crystalline structure near the center of the SEM appears in Fig. 11 as a hollow, three-dimensional, leaf-

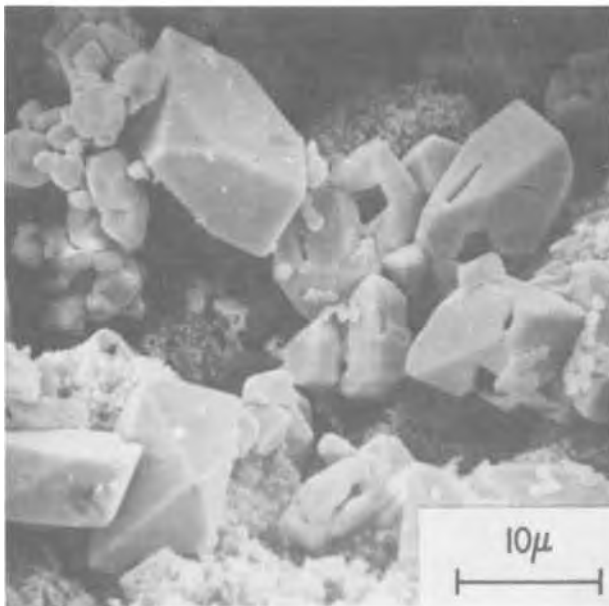


Fig. 6. Surface of negative electrode PN-12 at end of cycle 204. Magnification 2000X.

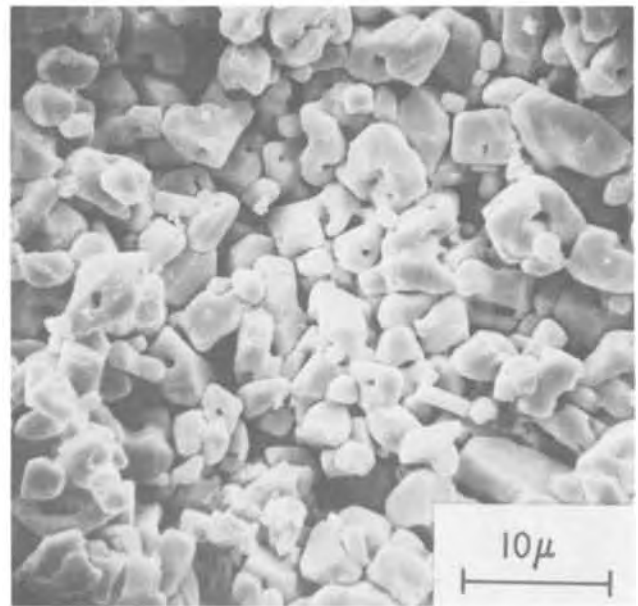


Fig. 8. Interior of electrode PN-C1 at end of cycle 163. Magnification 2000X.

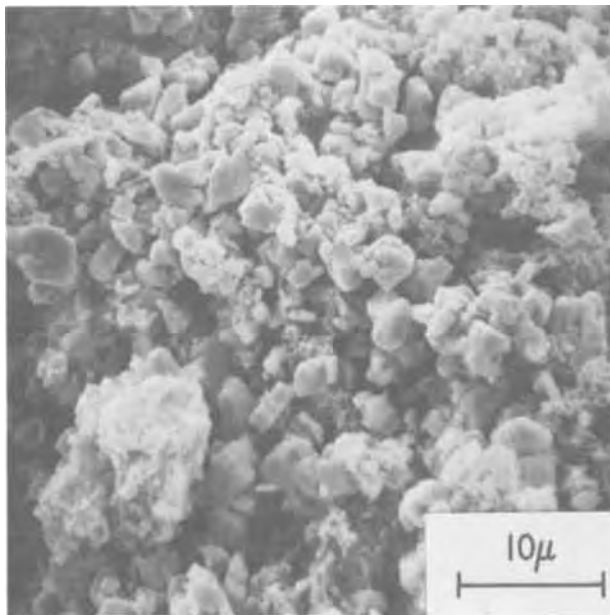


Fig. 7. Interior of negative electrode PN-12 at end of cycle 204. Magnification 2000X.

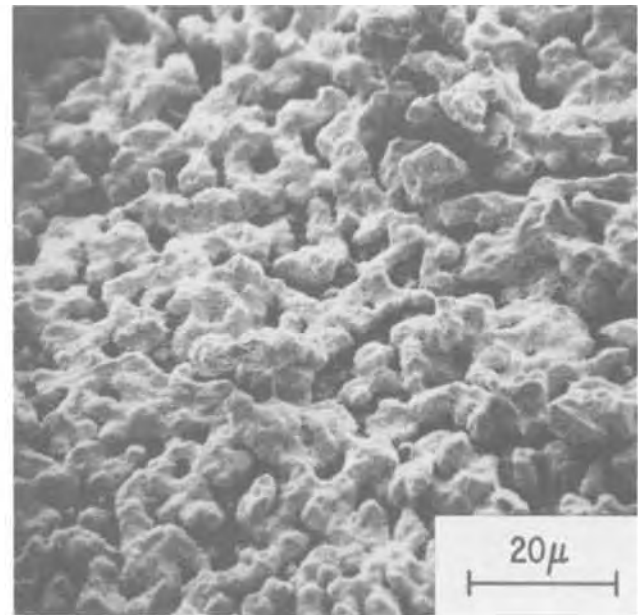


Fig. 9. Polymer-bonded electrode. Magnification 1000X

like structure. From this series of SEM's the large porosity, crystalline nature of the active material and the presence of polymer are apparent.

#### Discussion

Tests have shown that polymer-bonded electrodes have a life of 200 or more cycles in a 4-hr rate, 100% depth of discharge cycling regime. Under the same conditions, control cells having pasted electrodes had a shorter cycle life. Taking 1.2 A-hr as the nominal capacity of the electrodes (equivalent to 40% utilization) and considering a 50% drop in capacity as the end of cycle life, Table IV gives the life-times of the tested electrodes.

Comparison of polymer-bonded electrodes with each other is less certain. Although PN-12 and PN-14 had a shorter life than PN-13 and PN-15, it may have been caused by instrumental difficulties or by the deleteri-

ous influence of the positive electrodes. The SEM sampling procedure for PN-12 may also have shortened the life of that electrode.

The close to 100% efficiency of all the polymer-bonded electrodes indicated that charge acceptance limited the discharge capacity. Inspection of the electrodes at the end of cycle life showed that all of the polymer-bonded electrodes were in good condition and had not changed in appearance from the start of the life test. Nor was any of the active material sloughed-

Table IV. Cycle life of negative electrodes

Electrode	PN-C1	PN-C2	PN-12	PN-13	PN-14	PN-15
Cycles	155	90	183	>257*	191	>233*

\* End of cycle life test; electrodes still functioning satisfactorily.

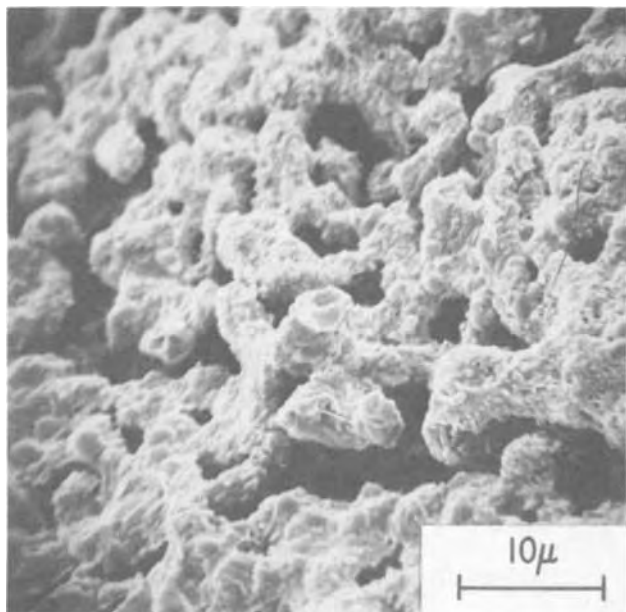


Fig. 10. Polymer-bonded electrode. Magnification 2000X

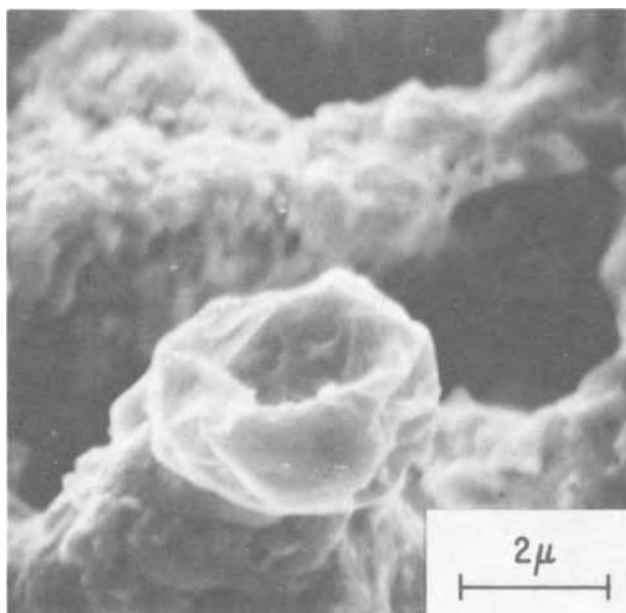


Fig. 11. Enlargement of Fig. 10. Magnification 10,000X

off into the separator bag. By contrast, the control electrodes had badly corroded grids, were spongy and very porous, had swelled to 3 or 4 times their original thickness, and a considerable amount of sloughed-off material was found in their separator bags.

The change of efficiency as the electrodes deteriorated also showed a different mechanism of failure of the control cells vs. those containing polymer-bonded electrodes. In the control cells the efficiency changed from 90-100% to less than 80% as the electrodes de-

teriorated. This indicated that the accepted charge could no longer be maintained or that it was partly lost to the corrosion of the grid, to gas evolution, or to passivation of previously active material. This was not the case with polymer-bonded electrodes. Where discharge capacity dropped off (cells PN-12 and PN-14) the efficiency of the cells still remained higher than 90%. This supports the above suggestion that in these cases charge acceptance may have been limited by other causes than by the negative electrodes and confirms the post-mortem observation of the serviceable appearance of electrodes PN-12 and PN-14.

The consistently high value of efficiency for the polymer-bonded electrodes also showed that there was little loss of charge due to gassing at the negative electrode. This is important because the addition of carbon black to the electrode mix required a high hydrogen overvoltage at carbon as well as at the Pb/Ca/Sn alloy. This is now confirmed.

In summary, it is concluded that polymer-bonded electrodes were superior to conventional (control) electrodes with respect to cycle life, charge acceptance, and lack of gassing. This has also been consistently the case in other tests in which pasted and polymer-bonded electrodes were studied under comparable conditions. Comparison of the effect of different substrates based on the St. Joe RDP-16 alloy is uncertain. The Dystex pattern in the expanded grid of PN-15 appeared to give best results but the difference to other patterns was too marginal to draw any conclusions concerning the most favorable substrate structure. In fact, a nonantimonial molded grid, possibly of the same alloy, would be equally effective in combination with polymer bonding the active materials by the present method.

#### Acknowledgments

The authors greatly appreciate discussions of polymer bonding with J. H. Lupinski and the scanning electron microscopy performed by M. D. McConnell and W. T. Hatfield. Thanks are due also to J. Young of St. Joe Minerals Company for making available the expanded grids of the Pb/Ca/Sn alloy.

Manuscript submitted May 6, 1974; revised manuscript received June 28, 1974. This was Paper 44 presented at the New York, New York, Meeting of the Society, Oct. 13-17, 1974.

Any discussion of this paper will appear in a Discussion Section to be published in the June 1975 JOURNAL. All discussions for the June 1975 Discussion Section should be submitted by Feb. 1, 1975.

The publication costs of this article have been assisted by the General Electric Company.

#### REFERENCES

1. J. C. Duddy and A. J. Salkind, *This Journal*, **108**, 717 (1961); J. C. Duddy, U.S. Pat. 2,968,686 (to ESB Company), January 1961.
2. L. W. Niedrach and H. R. Alford, *This Journal*, **112**, 117 (1965); U.S. Pat. 3,432,355 (to General Electric Company), March 1969.
3. J. H. Lupinski, *J. Appl. Polymer Sci.*, **17**, 1889 (1973); U.S. Pat. 3,619,382 (to General Electric Company), November 1971.
4. G. Rampel, U.S. Pat. 3,630,781 (to General Electric Company), December 1971.
5. J. L. Weininger, *This Journal*, **121**, 1474 (1974).

# Thermal Decomposition Mechanism of Formed and Cycled Lead Dioxide Electrodes and Its Relationship to Capacity Loss and Battery Failure

S. M. Caulder\*

*International Lead Zinc Research Organization Research Associate at the Naval Research Laboratory, Washington, D.C. 20375*

and A. C. Simon\*

*Electrochemistry Branch, Naval Research Laboratory, Washington, D. C. 20375*

## ABSTRACT

The structural changes accompanying capacity loss in the  $\text{PbO}_2/\text{PbSO}_4$  electrode were followed using differential thermal analysis. The thermal decomposition mechanism of formed plates was found to differ, depending on the method of manufacture. All cycled plates, however, gave the same decomposition mechanism after a few cycles. The major changes in the DTA curves, as the positive electrode was cycled to failure, was the gradual disappearance of the exothermic peak at  $200^\circ\text{C}$  and the endothermic peak at  $358^\circ\text{C}$ . It is believed that these peaks are associated with an electrochemically active amorphous form of  $\text{PbO}_2$ . As the electrochemically active  $\text{PbO}_2$  is cycled to failure it is converted to an electrochemically inactive form of  $\text{PbO}_2$ . This latter form of  $\text{PbO}_2$  gives DTA results similar to those obtained on reagent  $\text{PbO}_2$ . The continual conversion of electrochemically active  $\text{PbO}_2$  to the electrochemically inactive  $\text{PbO}_2$  is one of the major factors that accounts for the loss in battery capacity and ultimate failure.

The structure of the lead dioxide electrode after formation and cycling has been studied by optical (1) and electron microscopy (2, 3), neutron and x-ray diffraction (4), nuclear magnetic resonance (5), and by thermal analysis (6). The thermal analysis study was limited to one type of formed electrode and to an electrode with only a few cycles. Previous investigations (1-3, 7) have shown that parameters such as grid alloy, oxide blend, and curing process affect the microstructure of formed lead dioxide electrodes and subsequently, the initial part of the life cycle.

The thermal decomposition of active material obtained from the  $\text{PbO}_2/\text{PbSO}_4$  electrode involves the nucleation of  $\text{PbO}_x$  compounds on the  $\text{PbO}_2$  active material particles. These nucleation sites may be the same as the nucleation sites involved during the electrochemical oxidation and reduction of the  $\text{PbO}_2/\text{PbSO}_4$  electrode. No information is available regarding the  $\text{PbO}_2$  thermal decomposition mechanism of formed electrodes with respect to their method of preparation or microstructure. Information is also lacking as to whether the mechanism is altered along with the structural changes the  $\text{PbO}_2/\text{PbSO}_4$  electrode undergoes during subsequent reduction and reoxidation.

The purpose of this investigation was to determine whether the method of electrode preparation and subsequent cycling would influence the thermal characteristics of the  $\text{PbO}_2$  active material and, if so, how the structural changes of the active material are related to battery life and failure mechanism. The thermal results of this paper were correlated with results obtained from optical microscopy, mass spectrometry, x-ray diffraction, and nuclear magnetic resonance.

## Experimental Method

The four series of commercial electrodes used in this investigation were selected on the basis of their similarity in cycling routines, similarity in points at which oxidized and reduced samples were removed from

cycling, and the dissimilarity in appearance of the as-formed active material, as observed by optical microscopy. The last criterion was used since it was anticipated that these electrodes would give different microstructures upon cycling. The plates that were used were obtained from four different manufacturers, two in the United States and two overseas. Two of the series were prepared in the laboratory of the concerned companies, while the others were taken from production and routinely plant cycled. The active material of all plates were pasted on Pb-Sb alloy grids.

The DTA, TGA, NMR, x-ray diffraction, and mass spectroscopy samples were obtained by punching out sections of positive active material and then grinding with a mortar and pestle. Additional sample sections were cut from the electrodes, impregnated with a catalyzed polyester resin, and examined microscopically (1).

Reference samples of  $\alpha\text{-PbO}_2$  were prepared chemically and electrochemically using the methods of Angstadt (8) and Bode (9). Samples of reagent  $\beta\text{-PbO}_2$  were obtained from various chemical manufacturers.

The thermal decomposition equipment utilized in this investigation was a du Pont Model 900 differential thermal analyzer and a Model 950 thermogravimetric analyzer. The DTA samples (25 mg) were placed in 4 mm quartz sample holders. No diluent was added to the samples. A thermally inert reference sample,  $\text{Al}_2\text{O}_3$ , was placed in two adjacent quartz holders. Chromel-Alumel thermocouples were placed in the center of the sample and reference materials. Two of the thermocouples measured the temperature difference ( $\Delta t$ ) between sample and reference, while the third measured the temperature of the heating block. The heating block assembly was then covered by a thermal shield. The entire sample cell assembly was enclosed in a bell jar. Careful control of parameters such as sample weight, particle size, sample assembly geometry, and heating rate was maintained.

Prior to running the  $\text{PbO}_2$  samples the DTA apparatus was calibrated by measuring the melting and freezing points of pure samples of  $\text{AgCl}$ ,  $\text{Ag}_2\text{SO}_4$ , and

\* Electrochemical Society Active Member.  
Key words: differential thermal analysis, lead dioxide electrode, lead dioxide, electrochemically inactive  $\text{PbO}_2$ , capacity loss, battery failure.



Pb. A heating rate of  $15^{\circ}\text{C min}^{-1}$  in stationary air, using 4 mm tubes, was used on all subsequent runs. Isothermal decomposition products were obtained by heating  $\text{PbO}_2$  samples in aluminum blocks at  $225^{\circ}$ ,  $315^{\circ}$ , and  $355^{\circ}\text{C}$  for varying periods of time.

X-ray diffraction patterns were obtained using a Norelco diffractometer equipped with a scintillation counter. Nickel-filtered copper radiation was used. The decomposition products were identified by their diffraction patterns.

In the thermogravimetric experiments a sample of 5-25 mg was placed in a platinum weighing boat. The boat was attached to the balance arm incorporated within the instrument. The sample was heated at  $15^{\circ}\text{C min}^{-1}$  in a nitrogen atmosphere. A Chromel-Alumel thermocouple approximately 4 mm above the sample measured the temperature of the environment.

### Thermal Analysis Results

**Basis of the problem.**—Lead dioxide contains sufficient adsorbed water, as well as lattice water and/or hydroxyl ions, to provide for a Pb:O ratio of 1:2. Upon heating,  $\text{PbO}_2$  loses  $\text{O}_2$  and  $\text{H}_2\text{O}$  down to a Pb:O ratio of about 1.80 before experiencing a phase change. Between  $\text{PbO}_{1.90}$  and  $\text{Pb}_3\text{O}_4$  a nearly continuous series of nonstoichiometric lead oxides with decreasing oxygen content have been reported (10-14).

Recent investigations (15-17) on the thermal properties of the lead-oxygen system have shown that only two distinct oxide phases exist between  $\text{PbO}_{1.90}$  and  $\text{Pb}_3\text{O}_4$ . These intermediate oxides, designated  $\alpha\text{-PbO}_x$  and  $\beta\text{-PbO}_x$  by Byström (10), have very similar crystal structures. The crystallographic system to which these oxides belong is still subject to controversy. The Pb:O ratio over which  $\alpha\text{-PbO}_x$  exists is generally accepted as 1.60-1.51 and that for  $\beta\text{-PbO}_x$  as 1.50-1.44. These oxides are based on an oxygen deficient metal fluoride type structure containing both divalent and tetravalent lead ions. It is the reordering between the divalent and tetravalent lead ions and the oxygen lattice vacancies that account for these intermediate oxides. This ordering of the lattice with the evolution of  $\text{O}_2$  and  $\text{H}_2\text{O}$  is accompanied by an enthalpy change, as shown on the DTA curves. Additional evidence for this reordering is obtained from x-ray diffraction patterns which show a shifting of major lines, accompanied by intensity changes. Thermal gravimetric analysis also shows weight plateaus for these intermediate oxides.

Certain experimental parameters must be carefully controlled to obtain reproducible thermal results, since maximum peak temperatures are not solely dependent on the decomposition reaction. Careful control of parameters such as sample weight, particle size, sample assembly geometry, and heating rate are all important. The effect of heating rate and sample size, for example, have been summarized in Table I. The DTA results were obtained with chemically prepared  $\text{PbO}_2$ .

**Thermal analysis of reference samples of  $\alpha$ - and  $\beta$ - $\text{PbO}_2$ .**—The positive electrodes used in these experiments contained both  $\alpha$ - and  $\beta$ - $\text{PbO}_2$  so that it was necessary to subject reference samples of these two allomorphs to thermal analysis in order to obtain reference DTA curves. The DTA curves, x-ray analysis, and mass spectroscopy results, obtained from the reference samples, were used to interpret the DTA results obtained from the positive plate active material.

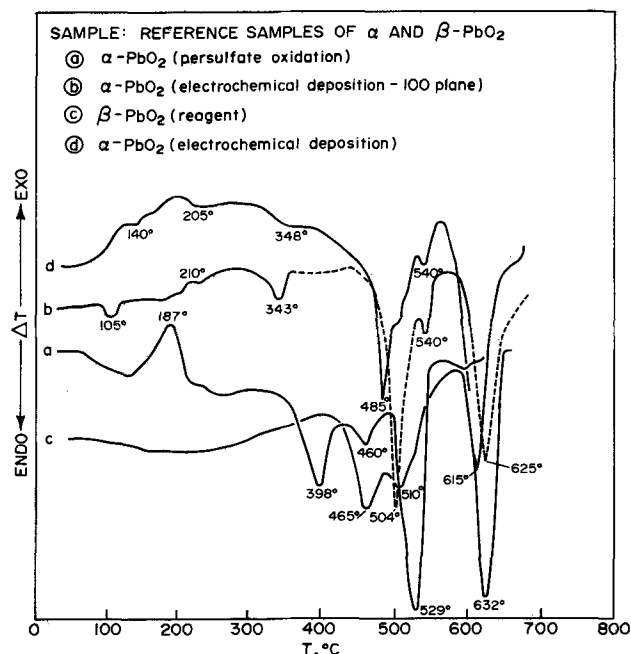
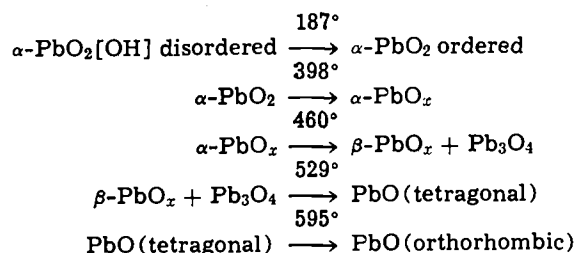


Fig. 1. DTA curves of reference samples of  $\alpha$ - and  $\beta$ - $\text{PbO}_2$ . Curve a,  $\alpha\text{-PbO}_2$  prepared by ammonium persulfate oxidation of lead acetate; curve b,  $\alpha\text{-PbO}_2$  prepared by electrochemical deposition (preferred orientation); curve c, General Chemical Corporation reagent  $\beta\text{-PbO}_2$ ; curve d,  $\alpha\text{-PbO}_2$  prepared by electrochemical deposition.

The DTA curves of the  $\alpha\text{-PbO}_2$  prepared by ammonium persulfate oxidation of ammoniacal lead acetate (8) and by electrochemical oxidation of an alkaline solution of  $\text{Pb}(\text{NO}_3)_2$  (9) are given in Fig. 1. Also shown is the curve for General Chemicals reagent  $\beta\text{-PbO}_2$ . The x-ray analysis of the decomposition reaction intermediates,  $\alpha\text{-PbO}_x$  and  $\beta\text{-PbO}_x$ , are summarized below in Table II and III. These results are compared with those of Byström (10), Weiss (12), and Angstadt (8).

The chemically prepared  $\alpha\text{-PbO}_2$  gave a broad exothermic peak at  $187^{\circ}\text{C}$  and a series of endothermic peaks at  $398^{\circ}$ ,  $460^{\circ}$ ,  $529^{\circ}$ , and  $595^{\circ}\text{C}$ . These peaks were associated with the following decomposition reactions



Angstadt *et al.* (8) in their thermal studies on  $\alpha\text{-PbO}_2$  prepared by persulfate oxidation did not observe a second intermediate compound ( $\beta\text{-PbO}_x$ ). However, they employed a different experimental technique. Gillibrand and Halliwell, using DTA, obtained curves similar in shape to the one shown in Fig. 1, except

Table I. Effect of heating rate and sample size on the decomposition of lead dioxide (chemical preparation)

Heating rate: Sample size:	$5^{\circ}\text{C/min}$ 63.7 mg	$10^{\circ}\text{C/min}$ 71.0 mg	$15^{\circ}\text{C/min}$ 62.3 mg	$20^{\circ}\text{C/min}$ 69.0 mg	$20^{\circ}\text{C/min}$ 215.8 mg
T max, 1st peak, $^{\circ}\text{C}$	427	446	452	458	452
T max, 2nd peak, $^{\circ}\text{C}$	465	485	490	497	490
T max, 3rd peak, $^{\circ}\text{C}$	490	510	514	528	520
T max, 4th peak, $^{\circ}\text{C}$	508	528	533	541	542
T max, 5th peak, $^{\circ}\text{C}$	597	612	618	634	627



Table II. X-ray analysis of  $\alpha$ - and  $\beta$ -PbO<sub>2</sub> decomposition product at 1st endothermic peak ( $\alpha$ -PbO<sub>x</sub>)

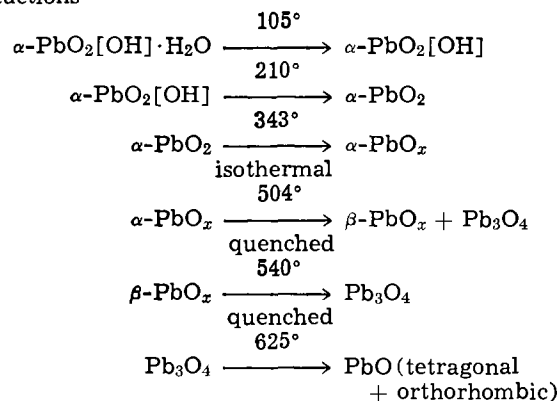
Obtained from:	Chemical $\alpha$ -PbO <sub>2</sub>	Electro-chemical $\alpha$ -PbO <sub>2</sub>	Chemical $\beta$ -PbO <sub>2</sub>	Bystrom chemical $\beta$ -PbO <sub>2</sub>	Weiss chemical $\beta$ -PbO <sub>2</sub>	Angstadt chemical $\alpha$ -PbO <sub>2</sub>	Angstadt chemical $\beta$ -PbO <sub>2</sub>
	3.148	3.142	3.149	3.149	3.147	3.137	3.148
	2.742	—	2.746	2.758	2.747	2.728	2.738
	2.721	—	2.713	2.716	2.712	2.708	2.708
	—	—	—	—	—	—	2.244
d(A)	1.920	1.927	1.933	1.953	1.928	1.926	1.928
	—	1.917	1.917	1.927	1.910	1.918	1.913
	—	—	1.653	1.909	—	—	—
	—	—	1.646	1.654	1.653	—	—
	—	—	1.632	1.646	1.645	1.647	1.647
	—	—	—	1.632	1.636	1.636	1.635

Table III. X-ray analysis of  $\alpha$ - and  $\beta$ -PbO<sub>2</sub> decomposition product at 2nd endothermic peak ( $\beta$ -PbO<sub>x</sub>)

Obtained from:	Chemical $\alpha$ -PbO <sub>2</sub>	Electro-chemical $\alpha$ -PbO <sub>2</sub>	Chemical $\beta$ -PbO <sub>2</sub>	Bystrom chemical $\beta$ -PbO <sub>2</sub>	Weiss chemical $\beta$ -PbO <sub>2</sub>	Angstadt
	3.175	3.170	3.170	3.179	3.186	
	3.155	3.142	3.142	3.149	3.147	No $\beta$ -PbO <sub>x</sub> observed
	2.742	—	—	2.750	2.752	
d(A)	2.721	2.725	2.737	2.736	2.737	
	—	—	—	—	—	
	1.937	1.928	1.936	1.938	1.943	
	—	—	1.912	1.916	1.917	
	—	1.748	—	1.655	1.656	
	1.654	1.649	1.648	1.641	1.642	
	—	1.643	—	—	—	
	—	1.634	—	—	—	

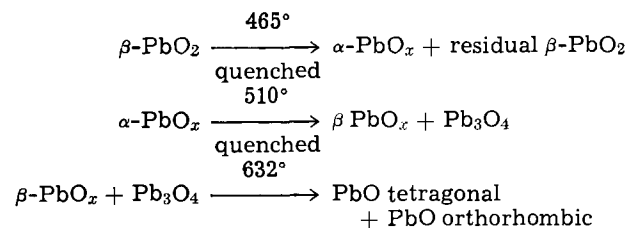
they did not observe an exothermic peak at 187°C. Kordes (4), using x-ray and neutron diffraction, found this  $\alpha$ -PbO<sub>2</sub> compound to be between 40-60% crystalline when compared to a reference PbO<sub>2</sub> standard. His DTA results on this material are in excellent agreement with ours. It was concluded from our DTA-TGA and x-ray diffraction results that due to the noncrystallinity of the  $\alpha$ -PbO<sub>2</sub> it decomposed along two simultaneous reaction paths. It is believed that the noncrystalline material decomposes to Pb<sub>3</sub>O<sub>4</sub> without going through the  $\alpha$ - $\beta$ -PbO<sub>x</sub> intermediates. Low temperature (225°-250°) isothermal studies on this compound as well as other  $\alpha$ - and  $\beta$ -PbO<sub>2</sub> compounds have shown that a small amount of Pb<sub>3</sub>O<sub>4</sub> appears after extended heating periods, along with the original ordered PbO<sub>2</sub> compound.

Electrochemical oxidation of an alkaline solution of Pb(NO<sub>3</sub>)<sub>2</sub> produced two products. The initial compound deposited was a hard black form of  $\alpha$ -PbO<sub>2</sub> with preferred orientation of the (100) planes parallel to the surface. The DTA curve for this product is shown in Fig. 1. The second product, which could be scraped from the surface of the electrode, was a softer, less crystalline, brownish form of  $\alpha$ -PbO<sub>2</sub> with no preferred orientation. Its DTA curve is also given in Fig. 1. The DTA curve (Fig. 1) of a predominantly black sample gave endothermic peaks at 105°, 343°, 504°, 540°, and 625° and a small exothermic peak at 210°C. These peaks were associated with the following reactions



The reagent  $\beta$ -PbO<sub>2</sub> gave no exothermic peak in the vicinity of 200°C, thus indicating no structural reorder-

ing. X-ray analysis of samples that had been preheated gave identical patterns to those not heated. The following mechanism was found for the  $\beta$ -PbO<sub>2</sub>



Other preparations of  $\beta$ -PbO<sub>2</sub> gave results similar to those obtained by Gillibrand and Halliwell (6). In all cases it was found that  $\alpha$ -PbO<sub>2</sub> decomposed before  $\beta$ -PbO<sub>2</sub>.

*Thermal analysis of formed electrodes.*—The DTA curves obtained from the four formed electrodes are shown in Fig. 2. The x-ray diffraction analysis and maximum peak temperatures of the quenched products are given in Table IV.

The formed plate from each series gave its own characteristic DTA curve with respect to the number

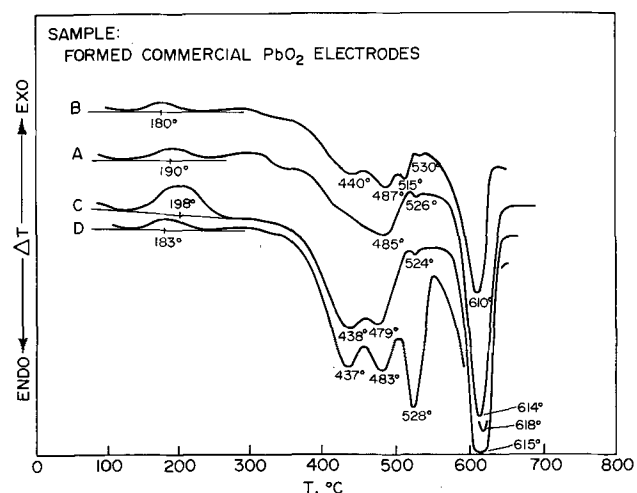
Fig. 2. DTA curves of four commercially formed PbO<sub>2</sub> electrodes

Table IV. Decomposition temperature maxima and x-ray analysis for formed PbO<sub>2</sub> electrodes

Series	1st peak exothermic	Analysis	2nd peak endothermic	Analysis	3rd peak endothermic	Analysis	4th peak endothermic	Analysis	5th peak endothermic	Analysis
A	190	$\alpha + \beta\text{-PbO}_2$ Some Pb <sub>3</sub> O <sub>4</sub>	—	—	485	$\beta\text{-PbO}_x$ Pb <sub>3</sub> O <sub>4</sub>	526	$\beta\text{-PbO}_x$ Pb <sub>3</sub> O <sub>4</sub> , PbO <sub>R</sub>	614	PbO Tetragonal
B	180	$\alpha, \beta\text{-PbO}_2$	440	$\alpha\text{-PbO}_x$	487	$\beta\text{-PbO}_x$ Pb <sub>3</sub> O <sub>4</sub>	515 530	$\beta\text{-PbO}_x$ Pb <sub>3</sub> O <sub>4</sub>	610	PbO Tetragonal
C	198	$\alpha, \beta\text{-PbO}_2$	439	$\alpha\text{-PbO}_x$	479	$\beta\text{-PbO}_x$ Pb <sub>3</sub> O <sub>4</sub>	524	Pb <sub>3</sub> O <sub>4</sub>	615	PbO Tetragonal
D	183	$\alpha, \beta\text{-PbO}_2$	437	$\alpha\text{-PbO}_x$	483	$\beta\text{-PbO}_x$ Pb <sub>3</sub> O <sub>4</sub>	528	Pb <sub>3</sub> O <sub>4</sub>	618	PbO Tetragonal

of peaks, maximum peak temperature, and relative area under each peak. However, the over-all decomposition mechanism for three of the four electrodes (B, C, D) were the same. Series A deviates from the general decomposition mechanism in that no peak was observed for an  $\alpha\text{-PbO}_x$  intermediate.

The exothermic peak exhibited by the formed active material between 180°-198°C was associated with the reordering of the  $\alpha$ - and  $\beta$ -PbO<sub>2</sub> and the evolution of O<sub>2</sub>, adsorbed and bound water. A portion of this water was incorporated in the anion lattice network as was evidenced by the results obtained by heating samples in conjunction with a mass spectrometer. The mass spectra taken under isothermal conditions at various temperatures and at 10<sup>-6</sup> mm pressure showed that as the temperature increased from 27° to 180°C three water peak maxima occurred. The reordering of the PbO<sub>2</sub> lattice was evidenced by comparing the x-ray diffraction patterns of the original samples with those obtained before and after the exothermic peak. The original sample did not show the high 2 $\theta$  angle K $\alpha$  doublets for  $\beta$ -PbO<sub>2</sub>. After heating to 180°-190°C these doublets were resolved, in addition to a shifting of the low 2 $\theta$  angle values. A few additional lines also appeared for both  $\alpha$ - and  $\beta$ -PbO<sub>2</sub>. The mass spectra of the active material effluent also showed peaks for CO<sub>2</sub>, occluded air (O<sub>2</sub> and N<sub>2</sub>), and organic compounds. These organics were due to leaching out of organic materials from the separators and the migration of these expander products from the negative to the positive electrode.

X-ray studies on the active material held isothermally at 225° for periods of time ranging from 2 hr to several weeks gave x-ray patterns for ordered  $\alpha$ - and  $\beta$ -PbO<sub>2</sub>. Thermogravimetric experiments over the temperature range 100°-225°C showed a very small weight loss which could be attributed to adsorbed water since mass spectrometry showed that every sample contained some. After prolonged heating, duration of up to several months, some of the samples gave lines for Pb<sub>3</sub>O<sub>4</sub>. However, three of the four electrodes had contained residual Pb<sub>3</sub>O<sub>4</sub> in the formed electrode. Series D, which contained no Pb<sub>3</sub>O<sub>4</sub> in the original oxide blend, also showed several Pb<sub>3</sub>O<sub>4</sub> diffraction lines.

Continued heating of the electrode active material showed that each sample began to decompose endothermically at 290°C with the active material from series B, C, and D giving peak maxima at 440°, 434°, and 437°C, respectively. No temperature maxima in this range was observed for series A. X-ray analysis of quenched and isothermally held samples of series B, C, and D gave patterns for  $\alpha\text{-PbO}_x$ . X-ray analysis of quenched and isothermally held samples of series A taken between 375°-440°C gave x-ray patterns for  $\beta\text{-PbO}_x$ . Isothermal runs on a number of A series samples held at 325° for varying periods of time gave a few samples whose x-ray patterns were close to  $\alpha\text{-PbO}_x$ .

The third endothermic peak maximum was observed between 480°-487°C for all electrode samples. X-ray analysis showed the major product to be  $\beta\text{-PbO}_x$ .

The fourth endothermic peak maxima were between 515°-530°C and were associated with the decomposition of  $\beta\text{-PbO}_x$  to Pb<sub>3</sub>O<sub>4</sub>. The area under this peak varied considerably. Series B and D gave peaks which were more characteristic of pure samples of

chemically prepared  $\alpha$ - and  $\beta$ -PbO<sub>2</sub> while series A and C gave much smaller peaks thus indicating that simultaneous decomposition reactions were occurring. This was confirmed by x-ray diffraction analysis of samples quenched from the 480° endothermic peak.

The final endothermic peak between 610°-618°C was due to the decomposition of Pb<sub>3</sub>O<sub>4</sub> to PbO tetragonal.

*Thermal analysis of cycled lead dioxide electrodes.*—Thermal analysis of the four samples of active material gave identical DTA curves. A representative DTA curve is shown in Fig. 3. The DTA curves obtained from these cycled electrodes were unlike any of the curves obtained from the active material of the formed electrodes. The main differences between the formed and cycled electrodes were that there was a general decrease in area under the first exothermic peak at 200°C; the occurrence of an endothermic peak at 358°C; and the appearance of one large endothermic peak at 465°C which replaced the two endothermic peaks observed with three of the formed electrodes (B, C, and D) between 434°-480°C.

The DTA curves of the oxidized material from cycled electrodes consisted of five peaks. An exothermic peak at approximately 200°C and four endothermic peaks at 358°, 465°, 536°, and 617°C. These peaks were associated with the following thermal decomposition reactions. This decomposition mechanism applies only to nonequilibrium runs with samples removed at each peak maximum. All of the cycled samples contained adsorbed water.

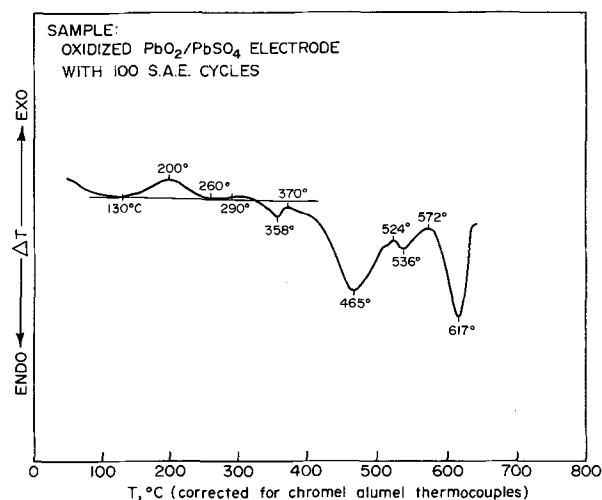
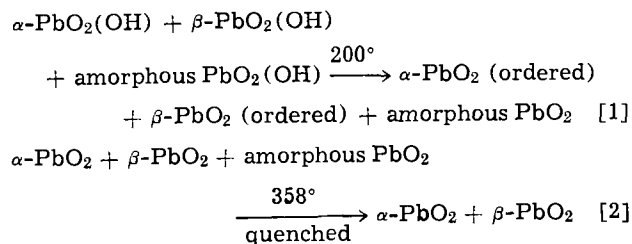
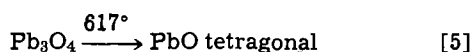
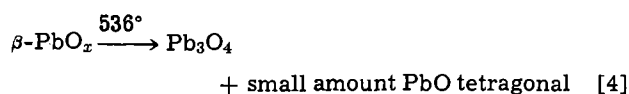
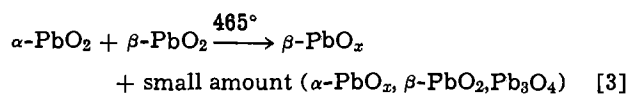


Fig. 3. A representative DTA curve of a PbO<sub>2</sub> electrode cycled 100 SAE cycles.



The exothermic peak at 200° was the result of reordering of the PbO<sub>2</sub> lattice with the evolution of H<sub>2</sub>O and O<sub>2</sub>. This reaction was also observed in each of the formed electrodes. Continued heating of the active material produced an endothermic peak at 358°C. X-ray diffraction patterns of quenched samples showed lines for ordered  $\alpha\text{-PbO}_2$  and  $\beta\text{-PbO}_2$ . TGA showed a slight weight loss over the 290°-360°C temperature range. A rerun of a sample which had previously been run to 358° gave no endothermic peak. X-ray analysis of this sample showed lines for  $\beta\text{-PbO}_2$  and  $\alpha\text{-PbO}_x$ . The material in this sample responsible for the endothermic peak at 358° must therefore be associated with  $\alpha\text{-PbO}_2$  or a possible amorphous form of PbO<sub>2</sub>. Evidence strongly favors the existence of such an amorphous form since samples containing no  $\alpha\text{-PbO}_2$  still gave an endothermic peak at 358°C. Microscopic studies of the original active material show two distinct forms of PbO<sub>2</sub> (1). The predominant form, approximately 85-95% of the total, occurs at brown, brownish-orange, or bright orange, individual crystals of small size and translucent appearance. The other form occurs in dense black or slate gray masses, of glassy appearance and with no definite form, and does not appear to be translucent. Both forms appear unreactive to ammonium acetate and appear in electrodes which show only  $\beta\text{-PbO}_2$  lines, as well as those showing both  $\alpha\text{-}$  and  $\beta\text{-PbO}_2$  thus indicating that the material is not  $\alpha\text{-PbO}_2$ . Microscopic examination of samples that were heated to the 358° peak, and then quenched, showed that most of the black material had been replaced by a red material. Samples of this red material gave the major lines for Pb<sub>3</sub>O<sub>4</sub>.

The black form of  $\alpha\text{-PbO}_2$ , which was prepared electrochemically (Fig. 1) gave an endothermic peak of similar magnitude at 345°, whereas all of the  $\beta\text{-PbO}_2$  preparations studied gave much larger enthalpy changes at around 400° or higher. DTA curves run on discharged electrodes gave a 358° endothermic peak of approximately the same magnitude as that observed in the charged plate. These samples had not experienced large capacity losses at this time. The other peaks associated with PbO<sub>2</sub> decomposition had diminished in area. Microscopical studies showed that the black material was still present in a discharged electrode. This material evidently does not undergo oxidation or reduction to an appreciable extent after the first few cycles. The most logical explanation of the above facts appears to be that the black PbO<sub>2</sub> is an amorphous form or contains an amorphous form of PbO<sub>2</sub> that is relatively inactive.

While as yet no evidence has been obtained that would directly link the two cases of unreactive material, recent pulsed nuclear magnetic resonance studies (5) have revealed the presence of a hydrogen species in the electrochemically prepared PbO<sub>2</sub> structure which appears to be related to the loss of capacity of the lead acid battery. This hydrogen species has not been found in chemically prepared  $\beta\text{-PbO}_2$ , and the latter is known to be unsatisfactory as a battery electrode. Upon heating the electrochemically prepared PbO<sub>2</sub> to 150°C this hydrogen species disappears. This temperature roughly corresponds to the exothermic peak observed at 180° on the differential thermal analyzer. This peak was not observed when the chemically prepared  $\beta\text{-PbO}_2$  was heated.

The endothermic peak at 463°C was due to the decomposition of  $\alpha\text{-PbO}_x$  and residual PbO<sub>2</sub> to  $\beta\text{-PbO}_x$ . Also occurring simultaneously was the decomposition of  $\alpha\text{-PbO}_x$  and  $\beta\text{-PbO}_x$  to Pb<sub>3</sub>O<sub>4</sub>.

The endothermic peak at 535°C was due to the decomposition of  $\beta\text{-PbO}_x$  (from  $\beta\text{-PbO}_2$ ) to Pb<sub>3</sub>O<sub>4</sub> and the decomposition of Pb<sub>3</sub>O<sub>4</sub> to PbO tetragonal (from  $\alpha\text{-PbO}_2$ ). As the amount of  $\alpha\text{-PbO}_2$  increased in the original sample the peak at 535°C decreased. This would be expected if this peak was due to the decomposition of  $\beta\text{-PbO}_2$  to Pb<sub>3</sub>O<sub>4</sub>.

The endothermic peak at 618°C was due to the decomposition of Pb<sub>3</sub>O<sub>4</sub> to tetragonal PbO.

The above analysis was based on cycled samples taken from electrodes which had showed only a slight loss in its initial capacity. As the electrodes were cycled to failure the major changes in the DTA curves were the gradual disappearance of the exothermic peak at 200°C and the endothermic peak at 358°C. The other endothermic peaks were only reduced slightly indicating that the plate still possessed a high PbO<sub>2</sub> content. This PbO<sub>2</sub> was electrochemically inactive. X-ray analysis also showed that the electrode had a high PbO<sub>2</sub> content and a low PbSO<sub>4</sub> content at failure. The DTA curve obtained from this electrochemically inactive PbO<sub>2</sub> resembled the DTA curves obtained from reagent PbO<sub>2</sub>.

### Conclusions

1. From the evidence that has been obtained it is concluded that an amorphous form of PbO<sub>2</sub> exists in positive plate active material, in addition to  $\alpha\text{-}$  and  $\beta\text{-PbO}_2$ . This material appears to possess thermal properties similar to  $\alpha\text{-PbO}_2$ .

2. It was concluded from thermal, mass spectroscopy, NMR, and microscopy results that as the PbO<sub>2</sub>/PbSO<sub>4</sub> electrode was cycled the electrochemically active PbO<sub>2</sub>, which may be an amorphous compound, underwent a structural reordering with the loss of a hydrogen species. This structural reordering led to an electrochemically inactive PbO<sub>2</sub> compound which gave NMR, DTA, and mass spectroscopy results similar to those obtained on reagent PbO<sub>2</sub>. The continual conversion of electrochemically active PbO<sub>2</sub> to the electrochemically inactive form is one of the major factors that causes battery capacity loss and ultimate failure.

3. The thermal decomposition mechanism of formed plates has been found to differ, depending on the method of manufacture. However, after a number of cycles all plates gave the same thermal decomposition mechanism.

4. It was also concluded that similar DTA, NMR, and mass spectroscopy results are obtained when electrochemically active PbO<sub>2</sub> is cycled to failure or when it is heated isothermally at 225°C.

### Acknowledgment

We wish to thank the Naval Research Laboratory for the support of this joint investigation and for permission to publish this work. Appreciation is also expressed to the International Lead-Zinc Research Organization, Incorporated, which has assisted in this and other investigations by maintaining the position of Research Associate at the Naval Research Laboratory. Appreciation is also expressed to Mr. Michael McDowell for running the mass spectroscopy samples.

Manuscript submitted April 22, 1974; revised manuscript received July 3, 1974.

Any discussion of this paper will appear in a Discussion Section to be published in the June 1975 JOURNAL. All discussions for the June 1975 Discussion Section should be submitted by Feb. 1, 1975.

The publication costs of this article have been assisted by the International Lead Zinc Research Organization, Incorporated.

### REFERENCES

1. A. C. Simon and S. M. Caulder, *This Journal*, **118**, 659 (1971).

2. J. Burbank and E. J. Ritchie, *ibid.*, **116**, 125 (1969).
3. E. J. Ritchie and J. Burbank, *ibid.*, **117**, 299 (1970).
4. D. Kordes, *Chem. Ing. Tech.*, **38**, 638 (1966).
5. S. M. Caulder, J. S. Murday, and A. C. Simon, *This Journal*, **120**, 1515 (1973).
6. M. I. Gillibrand and B. Halliwell, "Power Sources," D. H. Collins, Editor, p. 179, Pergamon Press, New York (1966).
7. A. C. Simon, S. M. Caulder, and E. J. Ritchie, *This Journal*, **117**, 1264 (1970).
8. R. T. Angstadt, C. J. Venuto, and P. Rüetschi, *ibid.*, **109**, 177 (1962).
9. H. Bode and E. Voss, *Z. Electrochem.*, **60**, 1053 (1956).
10. A. Byström, *Arkiv. Kemi, Mineralog. Geol.*, **20A**, No. 11 (1945).
11. T. Katz and R. Faivre, *Ann. Chim.*, **5**, 5 (1950).
12. R. Weiss, Thesis, Nancy, France (1959).
13. G. Butler and J. L. Copp, *J. Chem. Soc.*, **1956**, 725.
14. J. S. Anderson and M. Sterns, *J. Inorg. Nucl. Chem.*, **11**, 272 (1959).
15. W. B. White and R. Roy, *J. Am. Ceram. Soc.*, **47**, 242 (1964).
16. D. Fogue, P. Fouilloux, P. Bussiere, D. Weigel, and M. Prettre, *J. Chim. Phys.*, **62**, 1088 (1965).
17. E. M. Otto, *This Journal*, **113**, 525 (1966).

## Effect of Gaseous Pretreatment on Oxidation of Iron

A. W. Swanson\*<sup>1</sup> and H. H. Uhlig\*

*Department of Metallurgy and Materials Science, Massachusetts Institute of Technology,  
Cambridge, Massachusetts 02139*

### ABSTRACT

Gaseous pretreatment of pure iron surfaces may either increase the subsequent thin film oxidation rate or decrease it, depending on the gas. The effect is less than for copper. Traces of impurities including carbon may explain diminished faceting of iron, and also lower oxidation rates in low-pressure O<sub>2</sub>.

In previous papers (1, 2) it was shown that gaseous pretreatment of single-crystal and polycrystalline Cu has a large effect on subsequent thin film oxidation rates in oxygen. Surface facets are formed, the orientation and oxidation rate of which vary with the gas used for pretreatment. It was found that the pretreatment of single-crystal Cu, whatever the crystal face, in hydrogen at 350°-450°C favors formation of the slowly oxidizing (111) face; on the other hand pretreatment in nitrogen favors formation of the much more rapidly oxidizing (100) face. Both pretreated and untreated copper surfaces follow two-stage logarithmic oxidation kinetics when oxidized at 175°-225°C in 1 atm O<sub>2</sub>.

Tammann and Köster (3) first observed that oxidation of Fe at low temperatures (thin oxide films) follows the direct logarithmic equation. Similar behavior for Fe in air at 300°C was reported by Lustman and Mehl (4), in air up to 200°C by Vernon *et al.* (5), in air up to 300°C by Davies *et al.* (6), and in  $1.3 \times 10^{-2}$  Torr O<sub>2</sub> up to 200°C by Graham *et al.* (7). Runk and Kim (8) observed two-stage logarithmic behavior for 0.2, 0.4, and 0.8% C steels in 100 Torr O<sub>2</sub> at 200°-350°C; similar behavior was reported by Needham *et al.* (9) for zone-refined Fe in  $4 \times 10^{-6}$  Torr O<sub>2</sub> up to 350°C. In some of these investigations, a wide variety of oxide thicknesses were reported under otherwise comparable conditions but various metal surface treatments were used prior to oxidation. It was the purpose of the present investigation to determine to what extent Fe similar to Cu oxidizes in the thin film region at rates dependent on the type of gaseous pretreatment.

### Experimental

Two kinds of iron were used. The first was Armco iron sheet 0.0037 in. (0.0094 cm) thick decarburized in wet H<sub>2</sub> to 0.0013% C (by chemical analysis). The second was Battelle zone-refined iron containing <0.0005% C, with other impurities consistently low,

cold rolled to 0.015 in. (0.038 cm), and subsequently annealed in argon at 800°C for 1 hr.

Oxidation and pretreatment tests were run in a 3 cm ID fused silica tube inserted into a horizontal tube furnace maintained automatically at  $\pm 1.5^\circ\text{C}$ . A 0.5 cm wall stainless steel tube surrounding the silica tube insured a more uniform furnace temperature. The furnace could be slid along runners bringing it into or out of the specimen zone. Gases were led through an inner small diameter silica tube to the rear of the larger silica tube, thereby preheating the gas before it impinged on the specimen.

Dried nitrogen, hydrogen, and argon were purified by passing over Cu chips at 400°C; the argon was additionally purified over Ti chips at 800°C. All the foregoing gases were then dried through a trap immersed in solid CO<sub>2</sub> and acetone. Oxygen was dried using CaCl<sub>2</sub>. Specific mixtures of CO-CO<sub>2</sub> were obtained by monitoring the flow of the individual gases through flow meters. Specific H<sub>2</sub>O-H<sub>2</sub> mixtures were obtained by bubbling H<sub>2</sub> through distilled H<sub>2</sub>O maintained at a prescribed temperature.

The  $3 \times 10$  cm iron sheet specimens bent into a semicircle were pickled for 2 min at room temperature in 10 volume per cent (v/o) conc HNO<sub>3</sub>, rinsed four times in distilled water, and then dried by immersing in acetone, followed by benzene in a nitrogen atmosphere. It was suspected that carbon tended to migrate to the metal surface during heating of the specimens (as detected by reduced oxidation rates of the iron), requiring a further oxidation-reduction treatment of the surface in order to remove it. Holm (10) earlier observed that carbon migrating to the surface of iron reduced the thickness of a previously formed oxide film; Uhlig *et al.* (11) noted the same effect with nickel. Sewell (12) found similarly that the oxidation rate of nickel is affected by only a few parts per million of carbon migrating to the surface. Blickwede (13) showed through surface analysis of commercial steels that marked surface enrichment in carbon occurs after annealing in N<sub>2</sub>-H<sub>2</sub> mixtures.

To avoid such effects with the present specimens, both Armco and zone-refined iron were subjected to

\* Electrochemical Society Active Member.

<sup>1</sup> Present address: Raytheon Company, Research Division, Waltham, Massachusetts 02154.

Key words: iron oxidation, effect of surface pretreatment, surface carbon films, thin film oxidation, initial oxidation.

the following procedure: the specimen was heated in O<sub>2</sub> at 1 atm to 250°C for 1 min, followed by heating at 720°C in N<sub>2</sub> at 1 atm. Any carbon diffusing to the metal surface in the N<sub>2</sub> atmosphere reduced the thin oxide. If the oxide was visibly changed, the oxidation treatment was repeated until the oxide remained unaffected by the 720°C treatment. The residual oxide film was then reduced with H<sub>2</sub> at 250°C.

Surface pretreatment runs were made by bringing the specimen to temperature in N<sub>2</sub>, then flowing the pretreatment gas over the specimen at 1000 ml/min for the required time. The specimen was then allowed to cool to 250°C in the same gaseous atmosphere. After flushing with N<sub>2</sub>, the introduction of O<sub>2</sub> marked the beginning of oxidation time. Cooling of the specimen after oxidation was carried out in N<sub>2</sub>.

### Oxide Thickness Measurements

Iron oxide thickness, in contrast to cuprous oxide thickness, could not be determined by the convenience of coulometric reduction. An attempt was made to use coulometry employing various fused salt electrolytes, but without success. Cohen and co-workers (14, 15) tried to electrochemically reduce Fe<sub>3</sub>O<sub>4</sub> films on iron in aqueous electrolytes but never achieved a well-defined current efficiency even closely approaching 100%. The method we finally adopted employed an oxide film stripping technique using a 10% solution of iodine dissolved in anhydrous methyl alcohol previously distilled over metallic Ca. The method was similar to that described by Vernon *et al.* (16) and made use of a glass setup equipped with ball and socket joints and Teflon stopcocks (Fig. 1). Purified N<sub>2</sub> filled the apparatus and was also used to circulate the methanolic solution or methanol itself. A sample of oxidized iron specimen cut to 1.3 × 8.1 cm was placed in the stripping cell C and covered with the I<sub>2</sub>-CH<sub>3</sub>OH solution. The stripped oxide was rinsed five times with small portions of CH<sub>3</sub>OH from flask A, thereby insuring removal of stripping solution and ferrous iodide (as checked by chemical tests of aqueous wash solutions). The washed oxide was then dissolved in 6N HCl and both the ferrous iron and total iron determined using the *o*-phenanthroline method in conjunction with a spectrophotometer operating at a wavelength of 508 mμ. The oxide by such analysis was found to have a ratio of total iron to Fe<sup>2+</sup> of 2.95 ± 0.05 corresponding to Fe<sub>3</sub>O<sub>4</sub>. This composition for the oxide formed on iron in the 250°C range is in agreement with that determined by others (17-19), employing mostly x-ray. The thickness of the oxide film was calculated from the iron analyses assuming a density for Fe<sub>3</sub>O<sub>4</sub> of 5.18 and a surface roughness factor of unity.

### Results

Oxidation data for polycrystalline Armco and zone-refined iron were found to follow the direct logarithmic equation and in particular two-stage logarithmic behavior as shown in Fig. 2-3. The data for first-stage oxidation follow the relation  $y = k_1 \log(t/\tau + 1)$  where  $y$  is oxide thickness,  $t$  is the time, and  $k_1$  and  $\tau$  are constants. Values of  $\tau$  were obtained by extrapolating  $y$  vs.  $\log t$  to  $y = 0$ , emphasizing points for which  $t \gg \tau$ . Values of  $\tau'$  for second-stage oxidation were obtained on the basis of the following equation

$$y - L = k_1' \log(t/\tau' + 1)$$

where  $L$  is the thickness of oxide at the transition from 1st to 2nd stage oxidation. The value of  $\tau'$  is then the time at which  $y$  equals  $L$ . Values of  $k_1$ ,  $k_1'$ ,  $\tau$ , and  $\tau'$  are listed in Table I

The oxidation data for preoxidized Armco iron, the air-formed film of which was reduced at 250°C, are shown in Fig. 2 ("No Pretreatment"). Within experimental variations, these data coincide with those for iron specimens pretreated in dry H<sub>2</sub>, in dry N<sub>2</sub>, or in dry Ar at 800° and 1000°C. Zone-refined iron pretreated in dry H<sub>2</sub> or in dry N<sub>2</sub> behaves essentially the same as does Armco iron. Impurities normal to Armco iron, therefore, are not important. However, for both

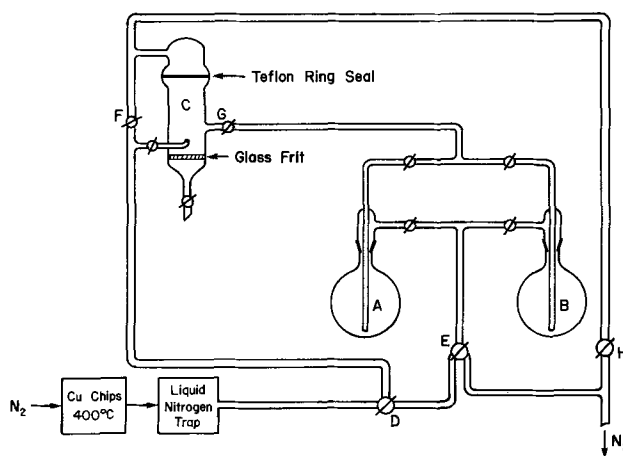


Fig. 1. Apparatus for oxide film removal

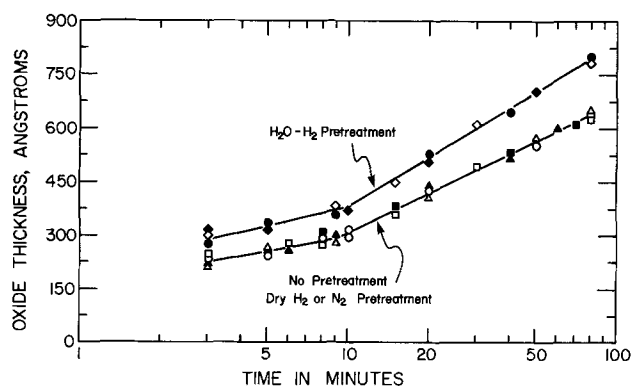


Fig. 2. Oxidation of decarburized Armco and zone-refined iron in 1 atm O<sub>2</sub>, 250°C. Pretreatment times: 150 min.

Armco iron	Zone-refined iron	
○	—	No pretreatment
□	■	Pretreated dry N <sub>2</sub> , 800°C
△	▲	Pretreated dry H <sub>2</sub> , 800°C
●	◇	Pretreated p <sub>H<sub>2</sub>O</sub> /p <sub>H<sub>2</sub></sub> = 10 <sup>-1</sup> , 800°C
—	◆	Pretreated p <sub>H<sub>2</sub>O</sub> /p <sub>H<sub>2</sub></sub> = 10 <sup>-1</sup> , 1000°C

Table I. Rate parameters for iron oxidizing in 1 atm O<sub>2</sub> at 250°C

Pretreatment conditions		k <sub>1</sub> (Å)	τ (min)	k <sub>1</sub> ' (Å)	τ' (min)	L (Å)
Armco	Zone refined					
None						
N <sub>2</sub> , H <sub>2</sub> , or Ar, 800° or 1000°C	N <sub>2</sub> or H <sub>2</sub> , 800°C	129	0.06	363	9.3	297
p <sub>H<sub>2</sub>O</sub> /p <sub>H<sub>2</sub></sub> = 10 <sup>-1</sup> , 800°C	p <sub>H<sub>2</sub>O</sub> /p <sub>H<sub>2</sub></sub> = 10 <sup>-1</sup> , 800° or 1000°C	175	0.07	460	10.0	380
p <sub>H<sub>2</sub>O</sub> /p <sub>H<sub>2</sub></sub> = 10 <sup>-0.5</sup> , 800°C		140	0.02	470	9.0	360
p <sub>H<sub>2</sub>O</sub> /p <sub>H<sub>2</sub></sub> = 10 <sup>-1.5</sup> , 1000°C		140	0.02	470	9.0	360
p <sub>CO</sub> /p <sub>CO<sub>2</sub></sub> = 2.33, 800°C		103	0.03	352	10.4	265
p <sub>CO</sub> /p <sub>CO<sub>2</sub></sub> = 3.0, 1000°C		103	0.03	352	10.4	265

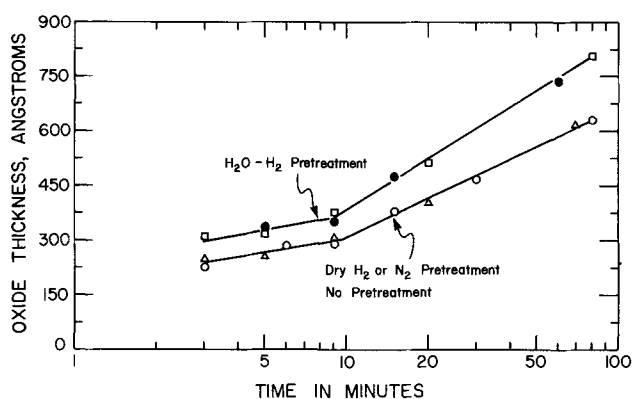


Fig. 3. Oxidation of decarburized Armco iron in 1 atm  $O_2$ , 250°C. Pretreatment times: 150 min.  $\Delta$ , Pretreated dry  $N_2$ , 1000°C;  $\circ$ , pretreated dry  $H_2$ , 1000°C;  $\square$ , pretreated  $p_{H_2O}/p_{H_2} = 10^{-0.5}$ , 800°C;  $\bullet$ , pretreated  $p_{H_2O}/p_{H_2} = 10^{-1.5}$ , 1000°C.

irons, pretreatment with reducing  $H_2O-H_2$  mixtures with  $p_{H_2O}/p_{H_2} = 10^{-0.5}$ ,  $10^{-1.0}$ , and  $10^{-1.5}$  for 150 min increased the subsequent oxidation rates by an amount equal to about 25-35%. A longer time of pretreatment in  $H_2O-H_2$  for up to 300 min did not alter subsequent rates (Table II). Pretreatment in noncarburizing  $CO-CO_2$  mixtures ( $p_{CO}/p_{CO_2} = 2.33$  and 3.00) caused a slight decrease (10-20%) in the first-stage oxidation rate. These data are shown in Fig. 4. The pretreatment gas ratios were chosen at values which avoided either carburization on the one hand, or oxidation on the other, in accord with data provided by Austin (20).

### Discussion

The observed changes of oxidation rate produced by various gaseous pretreatments are much smaller than parallel effects observed for Cu. The changes in iron can be ascribed either to changes in surface roughness or to the development of surface facets having an orientation corresponding to the lowest metal surface energy. In view of the pronounced and reversible effects of pretreatment on faceting of Cu, as confirmed by electron micrographs, a similar explanation for the oxidation behavior of Fe based on faceting is plausible. A change of roughness factor is not an equally valid explanation for the results on Cu, and probably not for the results on Fe. Electron micrographs of  $H_2O-H_2$  and  $CO_2-CO$  pretreated Fe showed a definite surface rearrangement but the facets were less pronounced than those appearing on Cu and the resolution was not of sufficient quality to justify reproduction. The electron micrographs were similar to those pictured by Sewell *et al.* (21) for Fe after vacuum or  $H_2$  treatment at 800°C for 120 min. Although the latter authors indicate that all low index planes of Fe develop similar facets, one would assume that, as in the case of Cu and in accord with discussions by Gjostein (22), the orientation of facets which develop on any single-crystal face is a function of the kind and partial pressure of the gas in contact.

Since thin film oxidation of iron, as for Cu, increases in the order (111) < (100) (23), the lesser

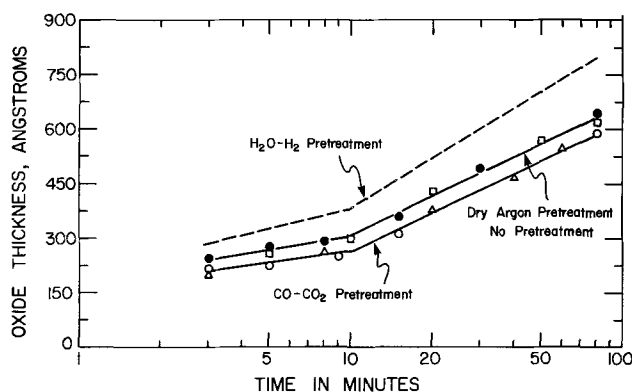


Fig. 4. Oxidation of decarburized Armco iron in 1 atm  $O_2$ , 250°C. Pretreatment times: 150 min.  $\square$ , Pretreated dry argon, 800°C;  $\bullet$ , pretreated dry argon, 1000°C;  $\circ$ , pretreated  $p_{CO}/p_{CO_2} = 2.33$ , 800°C;  $\Delta$ , pretreated  $p_{CO}/p_{CO_2} = 3.0$ , 1000°C.

effects of gaseous pretreatment on oxidation of Fe may result from a lesser tendency of Fe to facet in the pretreatment gases presently chosen. The latter tendency in turn may be inherent to Fe or it may be caused by surface contamination by carbon or other impurities, which, despite all precautions, reached the metal surface in monolayer or lesser amounts during gaseous pretreatment or  $O_2$  exposures. Such a partial monolayer is expected to exert a major effect on surface energies and, in turn, on facet formation.

A comparison between presently reported oxide thicknesses on Fe and values previously reported by other investigators also suggests an effect of surface contamination rather than of differences in faceting. The results divide themselves into two categories. All investigations carried out in relatively high  $O_2$  pressures are reasonably consistent. For example, at the end of 10 min, presently measured thickness of the  $Fe_3O_4$  film on iron at 250°C, 1 atm  $O_2$ , is 297Å; Wagner *et al.* (23) (1 atm  $O_2$ ) obtained about 450Å at 250°C; Boggs *et al.* (17) (0.01-100 Torr  $O_2$ ) reported about 350Å at 270°C; and Runk and Kim (8) (100 Torr  $O_2$ ) for 0.2% C steel reported 420Å at 300°C. On the other hand, at consistently lower pressures, the reported oxide thickness is about an order of magnitude less. At the end of 10 min, Graham *et al.* (7) ( $1.3 \times 10^{-2}$  Torr  $O_2$ ) reported 60Å at 200°C although their  $O_2$  pressure overlapped the lowest pressure employed by Boggs *et al.*; and Needham *et al.* (9) ( $4 \times 10^{-6}$  Torr  $O_2$ ) reported 36Å at 285°C.

The zone-refined iron used by Needham *et al.*, Boggs *et al.*, and by us was supplied by Battelle Memorial Institute and hence observed differences in oxidation rates are not likely to be caused by differences in impurities. Our present similar results on Armco and zone-refined Fe also make it clear that impurities are not a major factor. Furthermore the oxidation rate in low pressure in contrast to higher pressure  $O_2$  is not controlled by diffusion of  $O_2$  to the surface in view of observed logarithmic behavior, and also because the time separating first- from second-stage oxidation is about 10 min in our measurements and also in those of Needham *et al.* and in those of Runk and Kim, the latter investigators working with 0.2-0.8% C steels. There is the possibility that the semiconducting properties of the  $Fe_3O_4$  film are affected by oxygen pressure in such a direction as to decrease the rate as the pressure is lowered. Such a trend, however, is opposite to the effect of oxygen pressure within the range 0.01-100 Torr reported by Boggs *et al.* Graham and Cohen (24) reported an increasing rate with  $O_2$  pressure at 350° and 400°C but their results apply to the parabolic region of oxidation and not necessarily to the logarithmic range presently considered. Boggs *et al.* found little if any pressure dependence in the definitely parabolic region at 450°C. It seems reasonable to suggest,

Table II. Effect of time of  $H_2O-H_2$  pretreatment\* at 800°C on oxide thickness formed subsequently at 1 atm  $O_2$ , 250°C, 20 min

Specimen	Oxide thickness	
	2.5 hr pre-treatment, Å†	5 hr pre-treatment, Å†
Armco iron	520 ± 40	510 ± 35
Zone-refined iron	512 ± 42	525 ± 32

\*  $p_{H_2O}/p_{H_2} = 10^{-1}$ .

† Averaged for 3 or 4 specimens. Deviations are maximum values.

therefore, that contamination of an iron surface by monolayer or lesser amounts of carbon (which is difficult to avoid) has a much larger effect on oxidation rates carried out in low pressure  $O_2$  than in higher pressure  $O_2$  approaching 1 atm, the carbon contamination in low pressure measurements markedly reducing the oxidation rate. This suggestion is in accord with the results of Needham *et al.* showing that surface carbon contamination in their low pressure measurements exerted a retarding effect on oxidation. In addition, the low oxidation rates they reported at  $4 \times 10^{-6}$  Torr  $O_2$  are also explained by a diminished electric field within the  $Fe_3O_4$  film caused by decreased adsorption of oxygen on the outer oxide surface. Such a reduced electric field slows down the oxidation-rate controlling escape of electrons from metal to adsorbed oxygen in accord with the theory of thin film oxidation described by one of us (25).

In accord with the theory of thin film oxidation referred to (25), it is possible from observed values of  $k_1$  to calculate the density of sites  $n$  at which electrons become trapped in oxide adjacent to the metal surface. The increasing thickness of negative space charge thus created retards the escape of electrons from metal to oxygen adsorbed on the oxide surface. On the basis of the values of  $k_1$  observed for Fe reduced in  $H_2$  at  $250^\circ C$ ,  $n = 6.4 \times 10^{15}$ . This is intermediate between values for Cu at  $250^\circ C$  ( $0.6 \times 10^{14}$ ) (25) and for Zn at  $206^\circ C$  ( $2.4 \times 10^{17}$ ) (26). Accordingly, one of the reasons Cu oxidizes more rapidly and Zn less rapidly than Fe in the thin film region is the differing oxide space charge densities.

### Conclusions

1. Gaseous pretreatment of iron with reducing  $H_2O-H_2$  mixtures at  $800^\circ-1000^\circ C$  increases the subsequent oxidation rate in 1 atm  $O_2$  at  $250^\circ C$  by 25-35%.

2. Similar pretreatment with noncarburizing  $CO-CO_2$  mixtures decreases oxidation by 10-20%.

3. Both decarburized Armco iron and zone-refined iron oxidize in 1 atm  $O_2$  at  $250^\circ C$  at the same rate; both follow similar two-stage logarithmic kinetics. A much lower oxidation rate reported by other investigators in low pressure  $O_2$  is probably caused by the retarding effect of contaminating surface carbon; such carbon contamination does not similarly retard oxidation in 1 atm  $O_2$ . In addition, diminished adsorption of oxygen on oxide may also explain lower oxidation rates in low pressure gas.

4. Iron in the thin-film region oxidizes at a rate intermediate between Cu and Zn. This is interpreted in terms of an intermediate space charge density in  $Fe_3O_4$  compared to that in  $Cu_2O$  and  $ZnO$  adjacent to the metal surface.

### Acknowledgment

This research was supported by the National Steel Corporation to whom the authors express their appreciation.

Manuscript submitted Jan. 28, 1974; revised manuscript received July 11, 1974. This was Paper 104 presented at the Boston, Massachusetts, Meeting of the Society, Oct. 7-11, 1973.

Any discussion of this paper will appear in a Discussion Section to be published in the June 1975 JOURNAL. All discussions for the June 1975 Discussion Section should be submitted by Feb. 1, 1975.

The publication costs of this article have been assisted by the National Steel Corporation.

### REFERENCES

1. W. Bradley and H. Uhlig, *This Journal*, **114**, 669 (1967).
2. A. Swanson and H. Uhlig, *ibid.*, **118**, 1325 (1971).
3. G. Tammann and W. Köster, *Z. Anorg. Allgem. Chem.*, **123**, 196 (1922).
4. B. Lustman and R. Mehl, *Trans. Am. Inst. Min. Met. Engrs.*, **143**, 246 (1941).
5. W. Vernon, E. Calnan, C. Clews, and T. Nurse, *Proc. Roy. Soc.*, **A216**, 375 (1953).
6. D. Davies, U. Evans, and J. Agar, *ibid.*, **A225**, 443 (1954).
7. M. Graham, S. Ali, and M. Cohen, *This Journal*, **117**, 513 (1970).
8. R. Runk and H. Kim, *Oxid. Metals*, **2**, 285 (1970).
9. P. Needham, H. Leavenworth, and T. Driscoll, *This Journal*, **120**, 778 (1973).
10. V. Holm, *J. Res. Nat. Bur. Std.*, **28**, 569 (1942).
11. H. Uhlig, J. Pickett, and J. MacNairn, *Acta Met.*, **7**, 111 (1959).
12. P. Sewell, Private communication.
13. D. Blickwede, *Metal Progr.*, **96**, 77 (1969).
14. K. Buob, A. Beck, and M. Cohen, *This Journal*, **105**, 74 (1958).
15. G. Oswin and M. Cohen, *ibid.*, **104**, 9 (1957).
16. W. Vernon, F. Wormwell, and T. Nurse, *J. Chem. Soc., (London)*, 621 (1939).
17. W. Boggs, R. Kachik, and G. Pellissier, *This Journal*, **112**, 539 (1965).
18. R. Grauer and W. Feitknecht, *Corrosion Sci.*, **6**, 301 (1966).
19. M. Cahoreau and M. Gillet, *Mem. Sci. Rev. Met.*, **63**, 976 (1966).
20. J. Austin, in "Corrosion Handbook," pp. 1123-1127, H. Uhlig, Editor, John Wiley & Sons, Inc., New York (1948).
21. P. Sewell, E. Brewer, and M. Cohen, *J. Phys. Chem.*, **67**, 2008 (1963).
22. N. Gjostein, *Acta Met.*, **11**, 957, 969 (1963).
23. J. Wagner, K. Lawless, and A. Gwathmay, *Trans. Met. Soc. AIME*, **221**, 257 (1961).
24. M. Graham and M. Cohen, *This Journal*, **116**, 1430 (1969).
25. H. Uhlig, *Acta Met.*, **4**, 541 (1956).
26. V. Nwoko and H. Uhlig, *This Journal*, **112**, 1181 (1965).

# Electrochemically Generated Colored Films of Insoluble Viologen Radical Compounds

H. T. van Dam and J. J. Ponjé

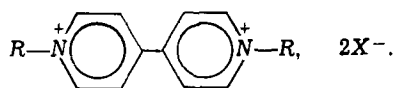
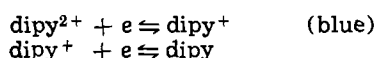
Philips Research Laboratories, Eindhoven, The Netherlands

## ABSTRACT

Electrochemical reactions that produce a change of light absorption in the visible region can be used in display devices. The reduction of the 4,4'-dipyridinium compounds or viologens to stable blue radicals is very promising in this respect. It was found that in aqueous solution the solubility of the radical is remarkably lower than that of the oxidized form. It turned out that the solubility depends on the kind of anion and the magnitude of the viologen radical ion.

An increasing demand for all sorts of display devices with which electrical information can be made visible, has stimulated the search for electrochemical processes to provide the electro-optical effect in such a device. The most obvious processes are electrochemical reactions in which the light-absorbing characteristics of one of the reacting substances change dramatically. The reduction of metal ions to a metal film on a transparent electrode and the color change of pH or redox indicators are examples of such reactions (1).

In our laboratory the feasibility of a display based on an electrochemical color change was investigated using the group of redox indicators known as the viologens. This name was given by Michaelis and Hill (2) to the 4,4'-dipyridinium compounds (I) because they become deeply blue-purple on reduction. Designating I as dipy  $X_2$  we have the following reactions



I

From several investigations (3) it is known that the first step is a simple, reversible, one-electron reduction giving the stable blue, radical ion. There is no reaction with a proton involved, a rare occurrence in organic redox reactions. The electron transfer reaction is so fast that the reduction is diffusion controlled only, even at large current densities. This property is of importance in display applications where a response as fast as possible is required. Response times of 10 msec have been obtained.

The stability and the intensive color of the radical ion result from the extensive delocalization of the electron that is added on reduction to the  $\pi$ -electron system of the dipyridium skeleton. As long as the substituent R does not influence this  $\pi$ -electron system one expects no influence of R on the energy needed to add an electron, i.e., the viologens should all have more or less the same redox potential. This argument is supported by the fact that the EPR spectra of some of the viologens with different substituents are practically identical (4). The respective redox potentials measured in water at inert electrodes however, show large differences, e.g., ethyl viologen  $-0.680\text{V}$  vs. SCE and benzyl viologen  $-0.597\text{V}$  vs. SCE. In addition, the value of the redox potential of a particular viologen in an organic solvent such as acetonitrile differs from that in aqueous solution. One wonders whether this last fact is connected with the differences in color in

the above solvents: blue ( $\lambda_{\text{max}} = 605\text{ nm}$ ) in acetonitrile as well as in dilute aqueous solutions, purple (increase of shoulder at  $\lambda = 545\text{ nm}$ ) in more concentrated aqueous solutions. This behavior has been explained (3, 5) in terms of a dimer formation in aqueous solutions. The absence of the dimer in organic solvents is attributed to ion-pair formation which somehow prevents dimerization. However Dimroth and Frister (6) noted the deepening of the purple color and even the possibility of salting-out the radical compound of 4,4'-dipyridyl by adding iodide ions, which suggests that the kind and the concentration of the anion are important. Some of the viologens we synthesized gave insoluble purple products on reduction even in dilute solutions. In order to find an explanation for the differences in redox potentials we have determined the half-wave potentials of a number of substituted viologens at various concentrations and in one case with different supporting electrolytes. The existence of insoluble reduction products is of practical importance in display applications. On electrodes of any desired shape these products can be deposited in the form of thin films. This property provides a memory effect without any power consumption and ensures that the oxidation of the colored product to the colorless state is fast (7). Erasure times of 10 msec have been obtained.

## Experimental

The dipyridinium salts were prepared with the use of the Menshutkin reaction in which an amine is quarternized with an alkyl halide (8). The halides obtained in this way were transformed into compounds with different anions by double displacement reactions. Simply by adding concentrated solutions of their sodium salts the tetrafluoroborates as well as the perchlorates could be precipitated.

A Metrohm Polarograph E 261 R was used for the polarographic measurements, in some cases together with the iR-compensator E 446. Large Ag/AgCl electrodes were used as reference and counterelectrodes. In the measurements of solutions in acetonitrile these electrodes were connected through a bridge filled with acetonitrile saturated with supporting electrolyte. The viologen concentration was  $10^{-3}\text{ mol liter}^{-1}$ . A series of measurements was performed at  $25 \pm 0.1^\circ\text{C}$  but since the influence of the temperature on  $E_{1/2}$  is slight this practice was discontinued and most experiments were done at room temperature.

The preparation of viologen radical films for measurement of the static emf of the cell

Pt/viologen radical film/viologen soln/AgCl/Ag

was done with the help of a Wenking potentiostat in that cell at about  $-0.70\text{ vs. Ag/AgCl}$ . This potential was maintained until the current became negligibly small. In this way the poor reproducibility of these

Key words: viologen, electrochromics, display.



Table I. Half-wave potentials for viologen tetrafluoroborates in acetonitrile

R	$-E_{1/2}$ 1st reduction step vs. Ag/AgCl (V)	$-E_{1/2}$ 2nd reduction step vs. Ag/AgCl (V)
Ethyl	0.48	0.89
n-Propyl	0.47	0.90
Allyl	0.44	0.85
n-Butyl	0.45	0.98
n-Amyl	0.45	0.89
iso-Amyl	0.46	0.90
Hexyl	0.49	0.93
Heptyl	0.41	0.88

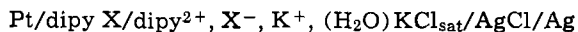
measurements, due to changes inside the layers, especially in the case of heptyl viologen bromide, could be improved upon. Pt electrodes of different shapes were used. They were cleaned in 2N nitric acid, rinsed with water, and kept in a dilute  $\text{FeSO}_4$  solution.

The solutions were stirred continuously and oxygen-free nitrogen was bubbled through. A heptyl viologen bromide film was prepared electrolytically on a transparent conducting  $\text{SnO}_2$  substrate part of a cell filled with a heptyl viologen dibromide solution. Its spectrum was measured with a Cary 15 spectrophotometer. A matched cell filled with the same solution was placed in the reference beam.

### Results

The half-wave potentials for the first and second reduction steps for a number of viologen tetrafluoroborates in acetonitrile are given in Table I. It is noted that, irrespective of the substituent, all values are close together compared with the differences observed between, e.g., ethyl and benzyl viologen in water, as pointed out earlier in this paper. In acetonitrile only the tetrafluoroborates and the perchlorates are sufficiently soluble to allow variation of the anion concentration over two decades. No change in the half-wave potentials was found over this range. A similar result holds for acetonitrile water mixtures 1:1.

Heptyl viologen is one of the compounds that gives an insoluble product on reduction in water and we selected this compound for polarographic measurements with different supporting electrolytes. The results for KCl and  $\text{NH}_4\text{BF}_4$  are given in Fig. 1. For anions other than these a comparison at a fixed concentration of  $10^{-1}$  mol liter $^{-1}$  was made and a sequence could be set up for monovalent anions in which the absolute value of the measured half-wave potential of the first reduction step decreases  $\text{F}^- > \text{Cl}^- > \text{Br}^- > \text{BF}_4^- > \text{ClO}_4^-$ . It is noted that the radius of the anions increase in this sequence. Since a precipitate is formed the approximate equivalence of the half-wave potential and the redox potential is no longer true, but now stationary measurements are possible after the formation of a layer of the insoluble product on an inert electrode. Measurements of the emf of the following cell are given in Fig. 2



A number of different viologens have been prepared primarily to test their possible usefulness for display applications. We observed therefore whether it was possible to prepare a permanent film by electrochemical reduction in the aqueous solutions of the dibromides. In Table II we give the results, where + indicates the fact that the solubility of the bromide is sufficiently small to make a permanent film. We have arranged the substituents in the order of increasing length of the alkyl groups and we have compared other substituents with these in terms of the number of  $\text{CH}_2$  units. With less than 4-5 of these units in R the films dissolve slowly or do not exist at all.

In Fig. 3 the spectrum of the heptyl viologen bromide layer formed electrochemically on a  $\text{SnO}_2$  electrode is given as well as that of the solution in acetonitrile and that of ethyl viologen chloride in water for

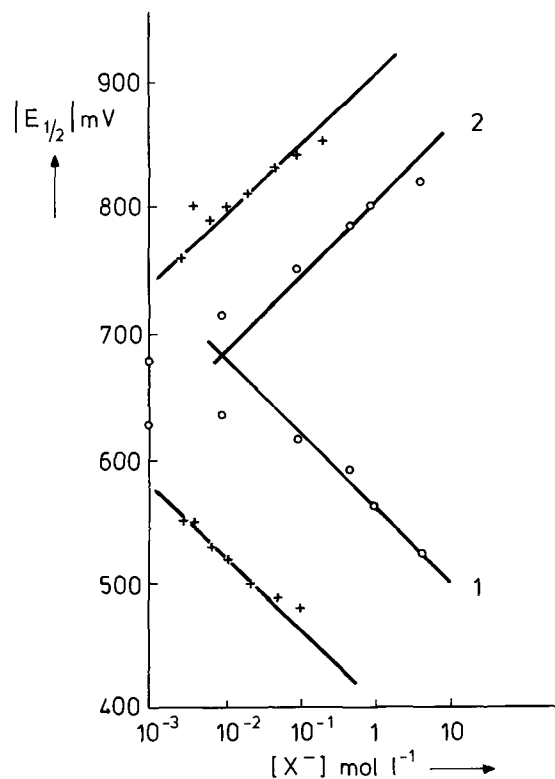


Fig. 1. Half-wave potentials as function of the anion concentration  $\text{X}^-$ . +,  $\text{BF}_4^-$ ; O,  $\text{Cl}^-$ . Heptyl viologen concentration  $10^{-3}$  mol liter $^{-1}$ . 1, First reduction step; 2, second reduction step.

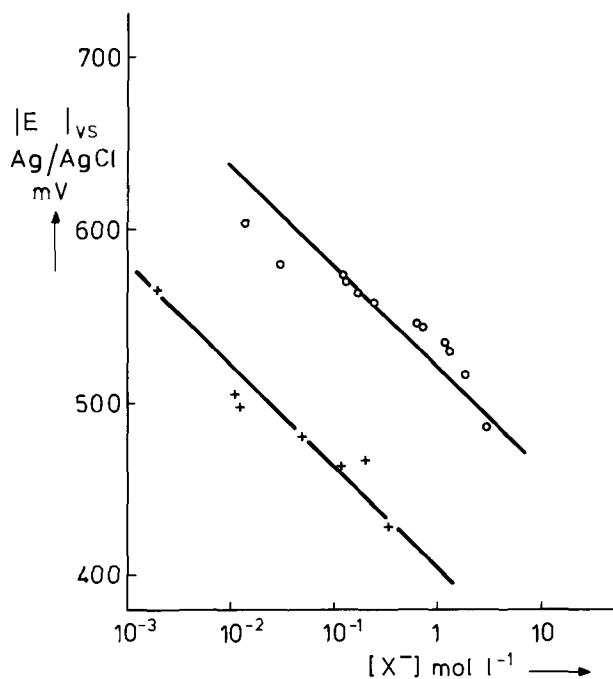


Fig. 2. EMF of the cell Pt/viologen radical film/viologen solution/AgCl/Ag as function of the anion concentration  $\text{X}^-$ . O,  $\text{Cl}^-$ ; +,  $\text{Br}^-$ . Heptyl viologen concentration  $10^{-3}$  mol liter $^{-1}$ .

comparison. The absorption band with a maximum at 605 nm is no longer present in the solid layer and the shoulder at 545 nm, present in both solutions, is now the major absorption band. One can say that the anomalous spectral behavior of aqueous solutions of viologens becomes extreme in the case of heptyl viologen.

Table II. Electrochemical reduction of viologens in aqueous solutions of dibromides for preparation of permanent film

R	Effective length of R in units CH <sub>2</sub>	Permanent film
CH <sub>3</sub>	1	-
C <sub>2</sub> H <sub>5</sub>	2	-
C <sub>3</sub> H <sub>7</sub>	3	-
C <sub>4</sub> H <sub>9</sub>	4	-
C <sub>5</sub> H <sub>11</sub>	5	+
C <sub>6</sub> H <sub>13</sub>	6	+
C <sub>7</sub> H <sub>15</sub>	7	+
C <sub>8</sub> H <sub>17</sub>	8	+
iso-C <sub>8</sub> H <sub>17</sub>	4	+
C <sub>6</sub> H <sub>5</sub> -CH <sub>3</sub>	4-5	+
Cl-CH <sub>2</sub> -O-CH <sub>3</sub>	4	-
CH <sub>2</sub>		
CH <sub>2</sub> -CH=CH-CH <sub>3</sub>	4	-
CH <sub>2</sub> =CH-C <sub>6</sub> H <sub>5</sub>	4-5	-
NC-C <sub>6</sub> H <sub>7</sub>	4-5	-

### Discussion

The dependence of the half-wave potential on the anion concentration found for several substituents R suggests that a solubility product  $L = [\text{dipy}^+][\text{X}^-]$  for the insoluble radical compounds can be defined, for with the help of such a product we have the following Nernst-type equations for the two reduction steps

$$E^{(1)} = E_o^{(1)} + 0.06 \log \frac{[\text{dipy}^{2+}][\text{X}^-]}{L} \quad \text{1st step} \quad [1]$$

$$E^{(2)} = E_o^{(2)} + 0.06 \log \frac{L}{[\text{X}^-][\text{dipy}]} \quad \text{2nd step} \quad [2]$$

These are the equations of the lines in Fig. 1 for adjusted  $E_o$  values. These  $E_o$  values cannot be identified with the redox potentials for the following reason. Such an identification is based on the fact that at the half-wave potential just half of the amount of the reacting substance present at the electrode is reduced. This makes the concentration ratio in the Nernst equation equal to 1 and the whole concentration term vanishes. When however the reaction product precipitates on the electrode surface this is no longer true. It also follows that we do not know the value of  $[\text{dipy}^{2+}]$  in the first step. We do know this value when no current flows and the first step can therefore be used in conjunction with the measurements in Fig. 2 to calculate  $L$ . Now  $E_o$  can be identified with the redox potential and all we need to know is its value for the couple  $\text{dipy}^{2+}/\text{dipy}^+$ . If we take the half-wave potential of ethyl viologen in water, which does not depend on the anion concentration in the range studied, to be equal to

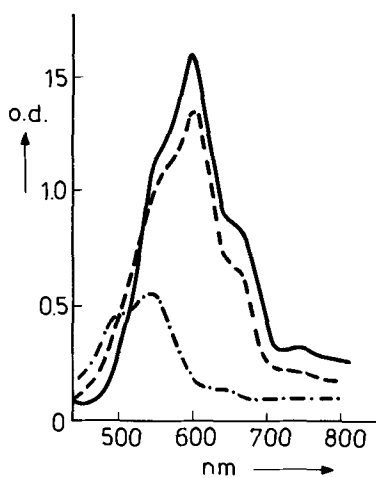
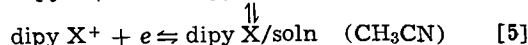
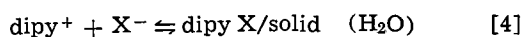
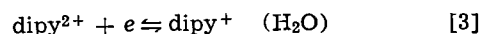
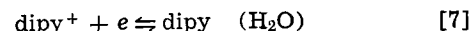
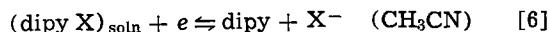


Fig. 3. Spectra of viologens: (---) ethyl viologen chloride  $10^{-4}$  mol liter<sup>-1</sup> in water; (—) heptyl viologen tetrafluoroborate  $10^{-4}$  mol liter<sup>-1</sup> in acetonitrile; (-.-.-) heptyl viologen bromide film on SnO<sub>2</sub> substrate.

$E_o^{(1)} = -0.66\text{V}$  vs. Ag/AgCl, we find for heptyl viologen chloride  $L = 8.5 \times 10^{-6}$ , for the corresponding bromide  $L = 3.9 \times 10^{-7}$ . Noting further that the absolute values of the redox potentials of the first and second reduction step are lower and higher, respectively, in acetonitrile than in water we are led to the following reaction scheme. For the first step



and for the second step



The difference in the redox potentials in acetonitrile and in water can now be interpreted as a consequence of equilibrium [4] on the one hand and the strong association of the second X<sup>-</sup> ion with the viologen cation in CH<sub>3</sub>CN on the other. The assumption of this association, which holds for all the viologens, seems reasonable in view of measurements by Brody and Fuoss (9) of the conductivity of bis-quaternary salts in methanol such as diethyl sulfide bis-trimethyl ammonium diiodide, which resemble the viologens somewhat in their charge distribution; they find that all such salts show association of one anion to the doubly charged cation. From our own measurements of the conductivity of heptyl viologen dibromide in water, to be published later, we know that ionization is complete which justifies Eq. [3], but that already a strong association exists which increases when the dielectric constant becomes lower and therefore supports the assumption underlying [5].

The influence of the substituent R and the anion X<sup>-</sup> on the redox potential can now be found in reaction [4] and not in the reduction reaction [3] itself, as expected. We see that a correlation exists between the size of R as well as X<sup>-</sup> and the solubility of the radical compound. This correlation can be understood if a sandwich-type structure is formed in which the anion knits the dipyrindinium ions together and the R groups protect the anion from the solvent molecules. The larger the radius of X<sup>-</sup> the smaller the electrostatic repulsion between the dipyrindinium ions and the greater the stability of such a structure. Normally the double positive charge prevents the formation of large clusters in this way, but on reduction such clusters are electrically neutral and precipitation results. When R and X<sup>-</sup> are not large enough to cause a precipitate to be formed the spectral changes in concentrated solutions point to similar smaller clusters. Because of the essential role of the anion and the fact that the solid precipitate is strongly paramagnetic (4) we feel that a description of spectral anomalies in terms of dimers, where spin-pairing would be expected, is confusing.

Manuscript submitted March 11, 1974; revised manuscript received July 9, 1974.

Any discussion of this paper will appear in a Discussion Section to be published in the June 1975 JOURNAL. All discussions for the June 1975 Discussion Section should be submitted by Feb. 1, 1975.

The publication costs of this article have been assisted by Philips Research Laboratories.

### REFERENCES

- British Pat. 328,017 (1929); U.S. Pat. 3,451,741 (1969); S. Zaromb, *This Journal*, **109**, 903 (1962).
- L. Michaelis and E. S. Hill, *J. Gen. Physiol.*, **16**, 859 (1933).
- W. M. Schwarz, Thesis University of Wisconsin (1961); R. M. Eloffson and R. L. Edsberg, *Can. J. Chem.*, **35**, 646 (1957); J. Volke and V. Volková, *Collection Czech. Chem. Comm.*, **34**, 2037 (1969).

4. C. S. Johnson and H. S. Gutowsky, *J. Chem. Phys.*, **39**, 58 (1963); own observations for heptyl viologen bromide.
5. E. M. Kosower and J. L. Cotter, *J. Am. Chem. Soc.*, **86**, 5524 (1964); S. Hünig, J. Gross, and W. Schenk, *Liebigs Ann. Chem.*, **1973**, 324; S. Hünig and H. Chr. Steinmetzer, *Tetrahedron Letters*, No. 8, 643 (1972); S. Hünig and J. Gross, *ibid.*, No. 21, 2599 (1968).
6. O. Dimroth and F. Frister, *Ber.* **55**, 3693 (1922).
7. C. J. Schoot, J. J. Ponjeé, H. T. van Dam, R. A. van Doorn, and P. T. Bolwijn, *Appl. Phys. Letters*, **23**, (2), 64 (1973); (with S. van Houten), *SID Int. Symp.* 1973, p. 146.
8. N. Menshutkin, *Z. Phys. Chem.*, **5**, 589 (1890), *ibid.*, **6**, 41 (1890).
9. O. V. Brody and R. M. Fuoss, *J. Phys. Chem.*, **60**, 156 (1956).

## Theoretical and Experimental Study of Hydrodynamically Modulated Current-Potential Curves at Rotating Disk Electrodes under Conditions of Mixed Electron and Mass Transfer Control

Barry Miller\* and Stanley Bruckenstein\*<sup>1</sup>

Bell Laboratories, Murray Hill, New Jersey 07974

### ABSTRACT

When a rotating disk electrode is subjected to an appropriate superimposed sinusoidal modulation of its rotation speed, the modulated component of the disk current may be governed by both mass transport and kinetic processes. In this study, mixed electron transfer and convective diffusion control conditions are considered, and the relationships among modulated current response, average current, potential, relevant species concentrations, and kinetic and transport parameters are derived. The theoretical predictions are experimentally verified for the two limiting cases of totally reversible and irreversible reactions, and for the general case of mixed control.

Sinusoidal modulation of a disk electrode's rotation speed about a center value produces a disk current having a component at the modulation frequency. This modulated current is governed by mass transport and kinetic processes, provided the amplitude and frequency of modulation are chosen to maintain an effective hydrodynamic steady state (1, 2). In this paper we consider, under these conditions, the case of mixed electron transfer and convective diffusion control in order to obtain the relationships that exist among modulated current response, average current, potential, relevant species concentrations, and kinetic and transport parameters. The theoretical results permit comparing conventional rotating disk electrode (RDE) data with hydrodynamically modulated rotating disk electrode (HMRDE) data.

These developments make it feasible to consider determining electron transfer kinetics at electrodes that are undergoing simultaneous electrochemical surface processes, only one of which is controlled by convective diffusion. For example, one might determine the variation of the rate of an electron transfer step proceeding with concurrent formation of a surface oxide on the electrode and then correlate the electron transfer rate constant and surface oxide coverage. As another example, one might separate modulated current kinetic data from the currents occurring at the limits of supporting electrolyte stability.

The theoretical predictions obtained below have been verified for the case of the totally irreversible limit using the Pd/Pd(II) couple, for the case of mixed kinetic and convective diffusion control using the Fe(III)/Fe(II) couple at gold in 1M HCl, and for the case of fast electron transfer (convective diffusion control) using the Fe(CN)<sub>6</sub><sup>3-</sup>/Fe(CN)<sub>6</sub><sup>4-</sup> couple at gold in 1M KCl.

\* Electrochemical Society Active Member.

<sup>1</sup> Permanent address: Department of Chemistry, State University of New York, Buffalo, New York 14214.

Key words: electrode kinetics, convective diffusion, sinusoidal modulation.

### Theoretical

The process we consider is  $Ox + ne = Red$ , with standard rate constant  $k_0$  and standard potential  $E^\circ$ , at some applied current,  $i$ . The general rate equation is

$$i = nFAk_0\{C_{red}^s Red(E) - C_{ox}^s Ox(E)\} \quad [1]$$

where

$$Ox(E) = \exp\{-\alpha_c F(E - E^\circ)/RT\} \quad [2]$$

$$Red(E) = \exp\{\alpha_a F(E - E^\circ)/RT\} \quad [3]$$

anodic currents and overpotentials are taken as positive, and electrons transferred are not separated out of the exponential factor in this paper.

According to the Levich equation

$$C_{ox}^s = C_{ox}^0 + i/L_{ox}\omega^{1/2} \quad [4]$$

and

$$C_{red}^s = C_{red}^0 - i/L_{red}\omega^{1/2} \quad [5]$$

where  $C^s$  represents the surface concentration and  $C^0$  the bulk concentration of the subscripted species,  $\omega$  the angular velocity, and  $L$  the remaining constant factors of the Levich equation ( $0.62nFAD^{2/3}\nu^{-1/6}$ ).

Substituting Eq. [2]-[5] into Eq. [1] and solving for  $i$  yields

$$i = \frac{nFAk_0\{C_{red}^0 Red(E) - C_{ox}^0 Ox(E)\}}{1 + \frac{nFAk_0}{\omega^{1/2}} \left[ \frac{Ox(E)}{L_{ox}} + \frac{Red(E)}{L_{red}} \right]} \quad [6]$$

If we differentiate  $i$  in Eq. [6] with respect to  $\omega^{1/2}$  at constant potential and define

$$k_E = nFAk_0\{Ox(E)/L_{ox} + Red(E)/L_{red}\} \quad [7]$$

it can be shown that

$$di/i = (d\omega^{1/2}/\omega^{1/2}) \{k_E/(k_E + \omega^{1/2})\} \quad [8]$$

In our experiments we have used an angular velocity program of the form

$$\omega^{1/2} = \omega_0^{1/2} \{1 + \Delta\omega^{1/2}(\sin 2\pi ft)/2\omega_0^{1/2}\} \quad [9]$$

where  $f$  is the frequency of modulation,  $\omega_0$  is the center angular velocity, and  $\Delta\omega^{1/2}$  is the peak-to-peak amplitude of the sinusoidal modulation of the square root of the angular velocity. If  $\Delta\omega^{1/2} \ll \omega_0^{1/2}$ , then

$$d\omega^{1/2}/\omega_0^{1/2} \approx \Delta\omega^{1/2}/\omega_0^{1/2} \quad [10]$$

Also

$$di/i \approx \Delta i/\bar{i} \quad [11]$$

where  $\Delta i$  is the peak-to-peak amplitude of the sinusoidal current response at frequency  $f$  and  $\bar{i}$  is the current at  $\omega_0$ . Hence

$$\Delta i/\bar{i} = (\Delta\omega^{1/2}/\omega_0^{1/2})k_E/(k_E + \omega_0^{1/2}) \quad [12]$$

If Eq. [12] is rearranged in the form

$$\frac{\Delta\omega^{1/2}/\omega_0^{1/2}}{\Delta i/\bar{i}} = 1 + \omega_0^{1/2}/k_E \quad [13]$$

the result suggests a convenient plot to be used for determining  $k_E$ . Since  $k_E$  can be determined as a function of  $E$ , for  $E = E^\circ$  it follows from Eq. [7] that

$$k_{E^\circ} = nFAk_0(1/L_{\text{Ox}} + 1/L_{\text{Red}}) \quad [14]$$

Equation [14] is suitable for calculating  $k_0$  from  $k_{E^\circ}$  after the transport factors,  $L$ , are measured.

For any couple with reasonably symmetrical parameters ( $L_{\text{Ox}} \cong L_{\text{Red}}$ ,  $\alpha_a \cong \alpha_c$ ),  $k_E$  will be a minimum at or very close to  $E = E^\circ$  and  $k_E$  will be a relatively slowly changing function near  $E^\circ$ . For example, with  $\alpha_a = \alpha_c = 1/2$  and  $L_{\text{Red}} = L_{\text{Ox}}$ ,  $k_E$  increases by only 50% for a 50 mV excursion either side of  $E^\circ$ , and by only 12% for one of 25 mV. Very little error would be made in estimating the value of  $k_{E^\circ}$  by assuming that the minimum of a  $k_E$  vs.  $E$  plot occurs at  $E^\circ$  and Eq. [14] applies.

We next consider three limiting cases of the general result, Eq. [12].

Case 1.—At either a cathodic or anodic limiting current, the quantity containing  $k_E$  in Eq. [12] goes to unity. The resulting expression, where the subscript  $L$  refers to the disk electrode limiting convective diffusion condition

$$\Delta i_L/\bar{i}_L = \Delta\omega^{1/2}/\omega_0^{1/2} \quad [15]$$

is the one predicted by the Levich equation, and it has been amply confirmed for pure convective diffusion controlled situations (1, 2).

Case 2.—If the standard rate constant is very large (as with a reversible reaction), then at all potentials  $k_E \gg \omega^{1/2}$  and Eq. [15] without the subscript  $L$  applies. Thus, the normalized plots of  $\bar{i}/i_L$  vs.  $E$  and  $\Delta i/\Delta i_L$  vs.  $E$  should superimpose, as should the corresponding logarithmic forms of these data.

Case 3.—For a totally irreversible reaction,  $k_E$  approaches one of two limits. On the cathodic side

$$k_E = nFAk_0\{\text{Ox}(E)/L_{\text{Ox}}\} \quad [16]$$

and on the anodic side

$$k_E = nFAk_0\{\text{Red}(E)/L_{\text{Red}}\} \quad [17]$$

If Eq. [16] or [17] is substituted into the correspondingly limited form of [1] and  $L_{\text{Ox}}$  or  $L_{\text{Red}}$  is eliminated using [4] or [5], we obtain

$$k_E/(k_E + \omega_0^{1/2}) = (C^\circ - C^s)/C^\circ = \bar{i}/i_L \quad [18]$$

for both situations. Substituting Eq. [18] into [12] and using Eq. [15] yields the simple interrelationship between modulated and conventional disk electrode currents

$$\bar{i}_L/\bar{i} = \sqrt{\Delta i_L/\Delta i} \quad [19]$$

For this totally irreversible case, Eq. [19] permits facile comparison of RDE and HMRDE data. The equation for the irreversible wave of the Ox/Red couple is given by

$$E = E_{1/2} \pm RT/\alpha F \ln[(\bar{i}_L/\bar{i}) - 1] \quad [20]$$

where  $E_{1/2}$  is the observed half-wave potential, which is related to the kinetic parameters of the electron transfer process, not to  $E^\circ$ . The positive sign applies on the cathodic side, and the negative on the anodic. Substituting Eq. [19] into Eq. [20] yields the potential observed under HMRDE conditions,  $E^{\text{mod}}$ , in terms of the conventional  $E_{1/2}$  found from the  $\bar{i}$ - $E$  curve and the modulation currents.

$$E^{\text{mod}} = E_{1/2} \pm RT/\alpha F \ln[\sqrt{\Delta i_L/\Delta i} - 1] \quad [21]$$

Defining  $E^{\text{mod}}_{1/2}$  as the potential at which  $\Delta i = 0.5\Delta i_L$ , it follows from Eq. [21] that at 25°C

$$E_{1/2} - E^{\text{mod}}_{1/2} = \pm 0.02265/\alpha \text{ volt} \quad [22]$$

i.e., the HMRDE half-wave potential is shifted about 45 mV when  $\alpha = 1/2$ . The direction of the shift is cathodic for reductions and anodic for oxidations. Also, we see from Eq. [20] and [21] that  $E_{1/2} = E^{\text{mod}}_{1/4}$  and that  $E_{0.707} = E^{\text{mod}}_{1/2}$ .

The various relationships that exist between the RDE and HMRDE curves for the completely reversible and irreversible extremes are summarized in Fig. 1. The ordinate represents a normalized current variable, either  $\bar{i}/i_L$  or  $\Delta i/\Delta i_L$ . For the reversible electrode reaction, the normalized RDE and HMRDE plots superimpose, while this is not the case for the completely irreversible process. In the latter situation, the difference between the RDE and HMRDE plots decreases as the normalized current variable approaches unity. This property is advantageous in applications involving limiting current measurements, since, for practical purposes, the same potential can be used to determine both  $\bar{i}_L$  and  $\Delta i_L$ .

The totally irreversible reduction of a metal ion,  $M^{+n} + ne = M$ , follows the cathodic forms of Eq. [18] through [22] found for the Ox/Red couple.

## Experimental

The speed control methodology and electronic elements are identical to those recently described (2), parts of which derive from an earlier version (1). Experiments were run in two different hydrodynamic modes with the usual one involving fixed sinusoidal modulation superimposed on a constant speed. The second mode was only employed in the testing of Eq. [13] and utilized fixed amplitude sinusoidal modulation superimposed on a linear increase of  $\omega_0^{1/2}$  with time. All measurements were made under potentiostatic or potential scan conditions at ambient temperature, ~24°C.

A gold disk electrode of 0.178 cm<sup>2</sup> area, polished to a 0.3 $\mu$  Linde A finish, was employed for all experiments. Solutions were prepared from triply distilled water and reagent grade chemicals without further

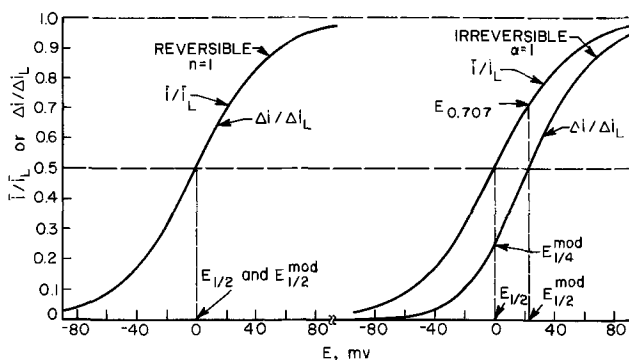


Fig. 1. Normalized current plots of  $\bar{i}/i_L$  and  $\Delta i/\Delta i_L$  vs. potential for the cases of a reversible one-electron reaction and an irreversible reaction with an  $\alpha$  of one.

purification. Pd(II) and  $\text{Fe}(\text{CN})_6^{4-}$  solutions were prepared determinatively from  $\text{K}_2\text{PdCl}_4$  and  $\text{K}_4\text{Fe}(\text{CN})_6$ , respectively. The Fe(III) stock solution was standardized by  $\text{SnCl}_2$  reduction and ceric titration. All experiments were run under deaeration by house nitrogen.

### Results and Discussion

**Oxidation of  $\text{Fe}(\text{CN})_6^{4-}$ .**—Plots of RDE and HMRDE curves for the oxidation of 1.57 mM  $\text{Fe}(\text{CN})_6^{4-}$  in 1M KCl at gold are given in Fig. 2 along with the conventional RDE logarithmic analysis. A potential scan rate of 0.5 mV/sec was employed, and the time constant was 2 sec in the electronics that converted the modulated current response to a d-c voltage. Under these conditions, the experimental HMRDE curve is shifted no more than a few millivolts from the curve found at constant potential, i.e., a couple of time constants. The measured separation at  $E_{1/2}$  in Fig. 2 is between 3 and 4 mV. A point by point determination of RDE and HMRDE  $i$ - $E$  curves was not practical since trace impurities present in solution are adsorbed and poison the electrode surface in such experiments. Poisoning also occurs when very slow scan rates are used. However, averaging the traces for an anodic-cathodic cycle obtained at a finite scan rate eliminates any time constant induced hysteresis when the electrode surface is stable.

The conventional wave analysis of the single scan RDE data in Fig. 2 confirms that the oxidation of  $\text{Fe}(\text{CN})_6^{4-}$  proceeds reversibly under the experimental conditions used (59 mV/decade slope). Thus, according to the result obtained in the theoretical section under limiting case 2 and shown in Fig. 1, the RDE and HMRDE curves should superimpose if the RDE and HMRDE current data are properly weighted. This weighting was accomplished during the experiment by adjusting the  $\bar{i}$  and  $\Delta i$  current scales so that the chart recorder pen deflection for  $\bar{i}_L$  equaled that for

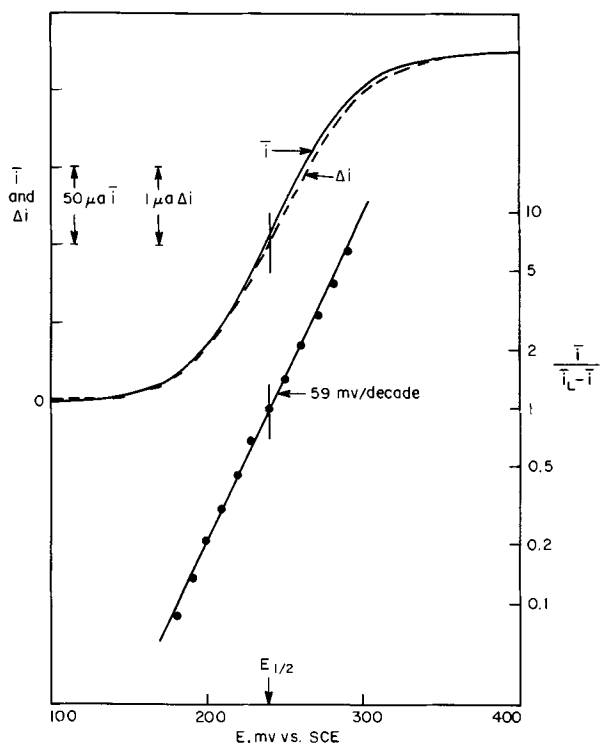


Fig. 2. RDE and HMRDE current-potential curves (left ordinate) for the oxidation of 1.57 mM  $\text{Fe}(\text{CN})_6^{4-}$  in 1M KCl at a 0.178  $\text{cm}^2$  gold disk. Logarithmic analysis of RDE curve also given (right ordinate). Potential scan rate = 0.5 mV/sec, averaging time constant = 2 sec, rotation speed = 3600 rpm,  $\Delta\omega^{1/2} = 1.3 \text{ rpm}^{1/2}$ , modulation frequency = 3 Hz. Current sensitivities,  $E_{1/2}$ , and log slope as marked.

$\Delta i_L$ . As is seen in Fig. 2, the RDE and curves do essentially superimpose as required for a reversible system.

**Reduction of Pd(II).**—The RDE and HMRDE curves for the reduction of 1.01 mM  $\text{K}_2\text{PdCl}_4$  in 2M KCl are given in Fig. 3. These curves are appreciably different in shape and clearly do not superimpose as they would for a reversible system. Figure 4 gives normalized plots of these data for comparison with the theoretical predictions, i.e., the RDE curve is plotted as  $\bar{i}/i_L$  vs.  $E$ , while the HMRDE data are plotted in two forms, that for the reversible case,  $\Delta i/\Delta i_L$  vs.  $E$ , and that for the irreversible one,  $\sqrt{\Delta i/\Delta i_L}$  vs.  $E$ . The irreversible HMRDE plot virtually superimposes on the RDE data for  $\bar{i}/i_L > 0.35$ , while there is no agreement of the reversible HMRDE plot with the RDE data at any potential outside of the limiting current region. A gold disk electrode was used in this experiment, and the deviation at the lower part of the reduction wave probably arises because the palladium activity on the surface varies until the gold is entirely covered.

The data for the fully covered, palladium electrode ought then to conform to the expectations of a totally irreversible cathodic reaction, case 3 in the theoretical section, for metal ion reduction. Thus,

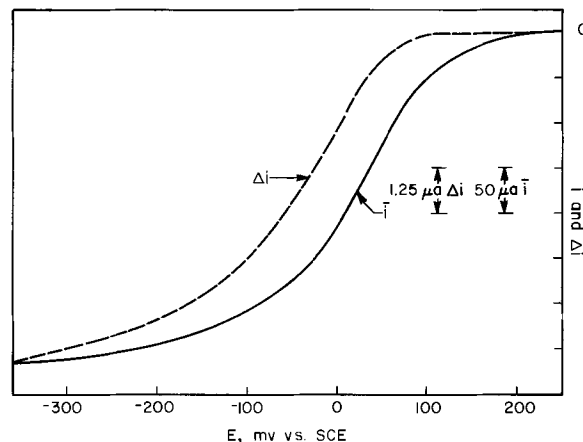


Fig. 3. RDE and HMRDE curves for the reduction of 1.01 mM  $\text{K}_2\text{PdCl}_4$  in 2M KCl. Potential scan rate = 1 mV/sec, averaging time constant = 1 sec, rotation speed = 3600 rpm,  $\Delta\omega^{1/2} = 1.6 \text{ rpm}^{1/2}$ , modulation frequency = 3 Hz.

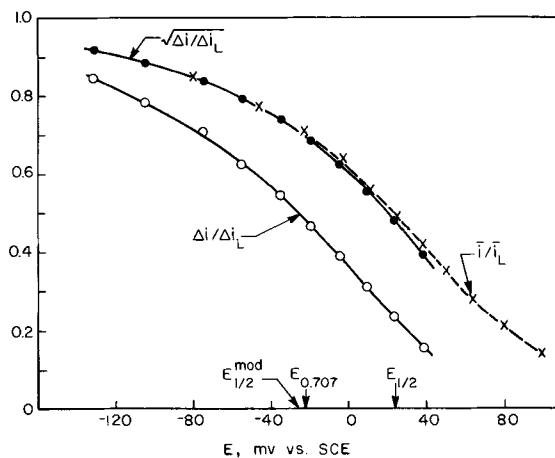


Fig. 4. Normalized Fig. 3 current plots,  $\bar{i}/i_L$  and  $\Delta i/\Delta i_L$ , vs. potential. Calculated plot of  $\sqrt{\Delta i/\Delta i_L}$  also shown. Ordinate common to the three current functions. Values of  $E_{1/2}^{\text{mod}}$ ,  $E_{0.707}$ , and  $E_{1/2}$  indicated on abscissa.

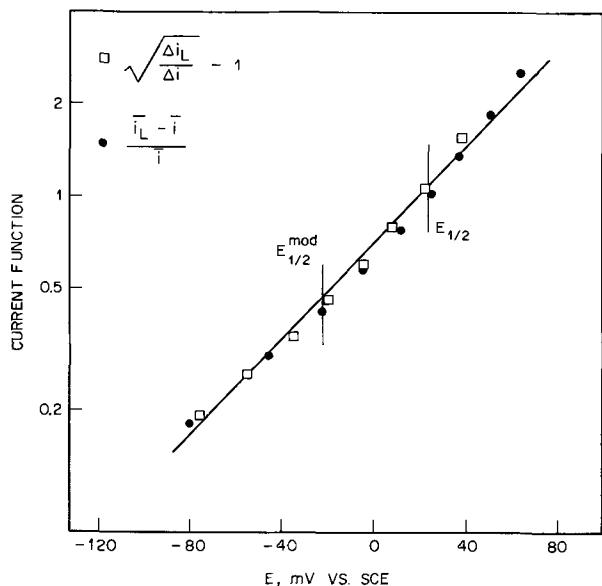


Fig. 5. Plots of  $(\bar{i}_L - \bar{i})/\bar{i}$  and  $\sqrt{\Delta i_L / \Delta i} - 1$  vs. potential for Fig. 3 data.  $E_{1/2}$  and  $E_{1/2}^{\text{mod}}$  as indicated on plot.

these  $i$ - $E$  data are plotted logarithmically against potential according to Eq. [20] and [21] in Fig. 5. The RDE and HMRDE data are coincident, within the experimental scatter and the anticipated small shift due to the response lag of a 1 mV/sec scan rate and a 1 sec averaging time constant in the modulation current electronics. The average line thus drawn has a slope of 130 mV/decade. This corresponds to  $\alpha_c = 0.45$ .  $\alpha_c$  can also be obtained using Eq. [22]. From Fig. 4,  $E_{1/2} - E_{1/2}^{\text{mod}} = +50$  mV, hence  $\alpha_c = 0.45$ , in agreement with the estimate from the RDE data. This agreement is significant because it shows that the value of  $\alpha$  obtained by varying  $E$  at constant  $\omega$  is the same as the value obtained by varying  $\omega$  at constant  $E$ .

**Reduction of Fe(III).**—The general case of mixed electron and mass transfer control was tested with Fe(III) reduction in 0.1M HCl-1M NaCl at a gold disk. This system had been previously examined under identical solution and electrode conditions by means of the technique of isosurface concentration voltammetry (3).

A potential scan showing the normalized  $\Delta i - E$  and  $\bar{i} - E$  curves at 1.94 mM Fe(III) is given in Fig. 6. A clear separation between the  $\Delta i$  and  $\bar{i}$  curves is shown, particularly near the limiting current region. The data were actually scaled by rotation speed adjustment to superimpose the limiting currents,  $\Delta i_L$  and  $\bar{i}_L$ , in the recorded traces. Included in Fig. 6 is a calculated curve of  $(\bar{i}/\bar{i}_L)^2$ , clearly well separated from the measured  $\Delta i/\Delta i_L$  result with which it would have superimposed in the irreversible case. Similarly, considering Eq. [19],  $\sqrt{\Delta i/\Delta i_L}$  is well separated from the unmodulated result. This implies that the general relationship of Eq. [12] may be needed to interpret the data and the  $k_E$  and  $\omega_0^{1/2}$  are comparable quantities, rather than one or the other being dominant as in the limiting cases already discussed. The departure from reversibility, case 2, is much more apparent from the difference between the  $\Delta i/\Delta i_L$  and  $\bar{i}/\bar{i}_L$  curves in Fig. 6 than it is from the slope of a conventional  $E$  vs.  $\log[(\bar{i}_L - \bar{i})/\bar{i}]$  plot, which gives 67 mV/decade, not far from the reversible 59 mV/decade. Thus, the comparison of modulated and conventional currents, when scaled as described, is a useful diagnostic test for the presence of a departure

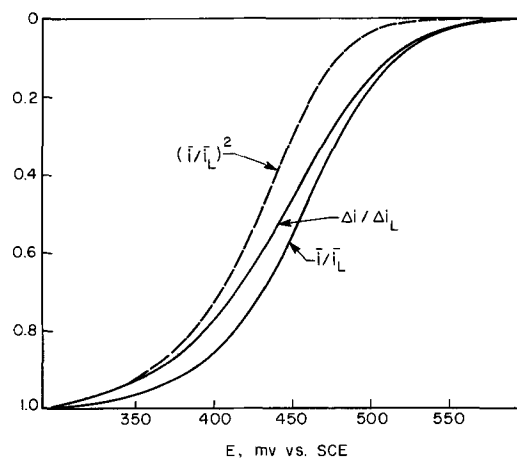


Fig. 6. Normalized current plots,  $\bar{i}/\bar{i}_L$  and  $\Delta i/\Delta i_L$ , vs. potential for RDE and HMRDE reduction of 1.94 mM Fe(III) in 0.1M HCl-1M NaCl at 0.178 cm<sup>2</sup> gold disk. Calculated plot (dashed line) of  $(\bar{i}/\bar{i}_L)^2$  also shown. Cathodic potential scan rate = 1 mV/sec, averaging time constant = 1 sec, rotation speed = 3600 rpm,  $\Delta\omega^{1/2} = 1.3$  rpm<sup>1/2</sup>, modulation frequency = 3 Hz. Actual current values  $\bar{i}_L = 250$   $\mu$ A,  $\Delta i_L = 5.00$   $\mu$ A, on original recording.

from mass transfer control, i.e., some kinetic factor in the  $\bar{i}$ - $E$  behavior.

In order to test Eq. [13], the following experiment was carried out at a set of 10 fixed potentials on the rising part of the wave and at one potential in the limiting current region. A fixed, small  $\Delta\omega^{1/2}$  (about 1 rpm<sup>1/2</sup>) was chosen and  $\omega_0^{1/2}$  slowly scanned linearly with time so as to retain effective hydrodynamic equilibrium (1) over a considerable range of  $\omega_0^{1/2}$ . Concurrently  $\Delta i$  and  $i$  were measured and recorded vs.  $\omega_0^{1/2}$ . The gold disk was held at +800 mV vs. SCE between  $\omega_0^{1/2}$  scans to activate the surface by slight anodic etching and cleaning.

Several plots of Eq. [13] for this experiment are shown in Fig. 7 for the range of  $\omega_0^{1/2}$  from 40 to 90 rpm<sup>1/2</sup>. The scan data for the run at the limiting current ( $E = 0.00$ V vs. SCE), included in Fig. 7, were used to confirm the lower  $\omega_0^{1/2}$  limit ( $\sim 40$  rpm<sup>1/2</sup>),

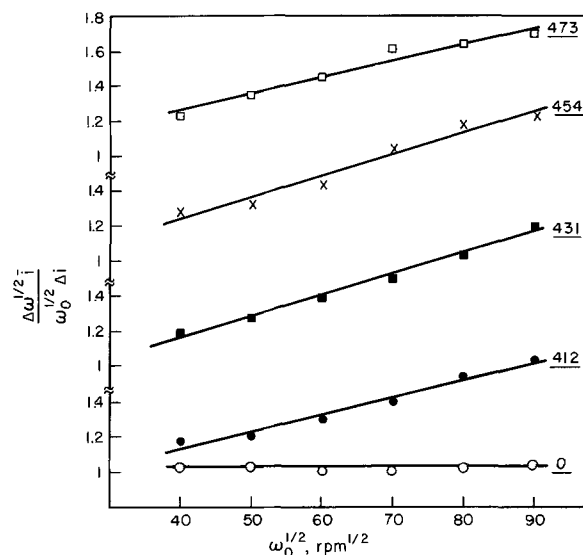


Fig. 7. Plots of  $\Delta\omega^{1/2} \bar{i} / \omega_0^{1/2} \Delta i$  vs.  $\omega_0^{1/2}$  for Fe(III) system of Fig. 6. Constant potential in millivolts vs. SCE for each  $\omega_0^{1/2}$  scan shown at right of corresponding line. Fixed  $\Delta\omega^{1/2}$  of 1.09 rpm<sup>1/2</sup> for each scan. Rotation speed scan rate = 0.25 rpm<sup>1/2</sup>/sec, averaging time constant = 4 sec, modulation frequency = 1 Hz.

above which Levich conditions were met for the experiment. It further served to check the predicted unit value of the ordinate and the zero slope of the plot of Eq. [13] in the limiting condition of  $k_E \gg \omega_0^{1/2}$ . In that case, trace O in Fig. 7, a least squares fit gave  $1.019 + 0.00014 \omega_0^{1/2}$ . The value of 1.019 is in excellent agreement with the expected value of one, especially considering the data were not corrected for a typical loss of 2% in  $\Delta i$  due to the filtering network, which would account for the total difference. The slope is nearly zero (i.e.,  $k_E \sim 7000$ ), as expected. The plots for the other representative potentials shown are acceptably linear in the measured region of  $\omega_0^{1/2}$ , although the extrapolations all fall below unity at  $\omega_0^{1/2} = 0$ , for reasons that are presently unresolved.

Figure 8 shows a plot of the values of  $k_E$  determined from slopes of the least squares fits according to Eq. [13] vs. potential, for all 10 potentials employed. The range of potentials in Fig. 8 is 82 mV and includes the Fe(III)/Fe(II) standard potential in this medium, which was estimated from the 1M HCl formal potential to be  $\sim 0.45V$  vs. SCE.

Previous limiting current measurements in this system (3) gave  $L_{red}/L_{ox} = 1.06$ , from  $D_{Fe(II)} = 5.58 \times 10^{-6}$  cm<sup>2</sup>/sec and  $D_{Fe(III)} = 5.12 \times 10^{-6}$  cm<sup>2</sup>/sec. These are sufficiently close in magnitude to allow approximating an average Levich constant by their arithmetic mean,  $L_{avg}$ , of 2.3 A-cm<sup>3</sup>/mole-rpm<sup>1/2</sup>. The kinetic parameters for this system were determined previously using the independent rotating disk method of isosurface concentration voltammetry, and gave  $k_0 = 5.6 \times 10^{-3}$  cm/sec and  $\alpha = 0.48$  (3). This value of  $k_0$  and the above  $L_{avg}$  yield a calculated  $k_E$  of 83 rpm<sup>1/2</sup> assuming  $E^\circ = 445$  mV vs. SCE,  $L_{red} = L_{ox} = L_{avg}$ , and  $\alpha = 1/2$ .  $k_E$  may readily be calculated from Eq. [7] as a function of potential and such a plot is shown as the dashed line in Fig. 8. Also shown in Fig. 8 are the experimental points obtained in this study. Within experimental error, the agreement of the present theory and experiment with the previous values of  $k_0 = 5.6 \times 10^{-3}$  cm/sec and  $\alpha = 0.48$  is satisfactory.

The repeated electrode activation steps required in this experiment produced a gradual trend toward higher  $k_E$  values with time because the etching pretreatment at +800 mV vs. SCE roughened the electrode surface. Probably, it is the major source leading to scatter in the  $k_E$  vs.  $E$  plot. For example, three of the four points above the dashed line in Fig. 8 result from the last three experiments. Similar activation sensitivity was noticed in the previous study (3), where it was found that, without the anodic pretreatment, the

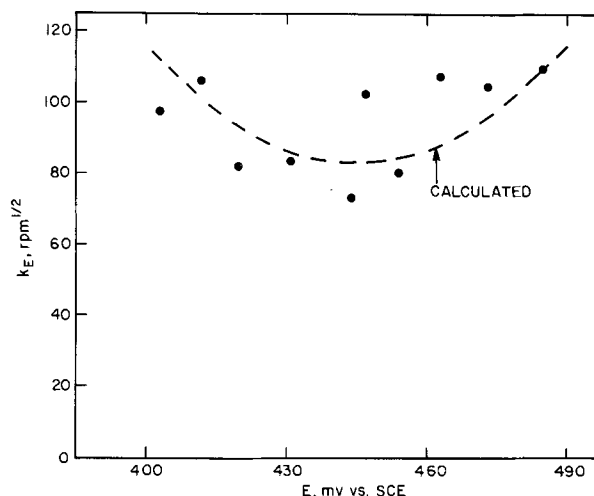


Fig. 8. Values of  $k_E$  from least squares slope of Fig. 7 type plots vs. potential. Dashed line calculated (see text) with  $k_E$  taken as 83 at 445 mV vs. SCE.

electrode surface is both less active and less reproducible during constant potential experiments.

At the  $E^\circ$  of the Fe(III)/Fe(II) couple,  $k_E = 83$  rpm<sup>1/2</sup> and the factor  $k_E/(k_E + \omega_0^{1/2})$  in Eq. [12] would be  $1/2$  at a rotation speed of  $(83)^2$  or about 6900 rpm. Considering this and the fact that both constant speed and hydrodynamic modulation data begin to deviate from convective-diffusion theory below about  $(20)^2$  rpm, it is clear that mixed mass and electron transfer control will be seen for this couple at all feasible rotation speeds.

The average literature value (4) for  $k_0$  in the Fe(CN)<sub>6</sub><sup>3-</sup>/Fe(CN)<sub>6</sub><sup>4-</sup> system is at least ten times higher than that of the Fe(III)/Fe(II) system in Cl<sup>-</sup> media at gold. This higher value of  $k_0$  accounts for the essentially reversible appearance of the Fe(CN)<sub>6</sub><sup>4-</sup> wave in the modulation experiment depicted in Fig. 2. A rotation speed of the order of 40,000 rpm would be required before significant effects due to kinetics would be observable.

### Summary and Conclusions

A theoretical analysis of superimposed sinusoidal modulation of the rotation speed of a disk electrode for the situation of mixed mass and electron transfer control of the electrode current has been carried out and has been shown to yield relatively simple forms for the modulated current response as a function of potential, rate and transport parameters, and concentration of electroactive species. These results have been confirmed experimentally for the limiting cases dominated by either electron or mass transfer kinetics and for the general case of mixed control.

The significance of the hydrodynamic modulation technique for obtaining kinetic parameters with the RDE becomes particularly evident when its unique application to situations obscured in conventional RDE approaches by interfering contributions to the total current is considered. As has been shown in an application to trace electroanalysis (2), convective-diffusion limited currents may be isolated by HMRDE methods from, among others, currents due to purely surface processes, double layer charging processes, and irreversible supporting electrolyte reactions. By the use of the transformations of  $\Delta i$  and  $\bar{i}$  discussed in this paper, considerable information may be obtained about the current-potential relation of many reactions that are inaccessible to ordinary solid electrode voltammetric techniques. Further applications will be considered elsewhere (5). It may also be noted that, even for simple conditions in which conflicting sources of current are absent, the ratio of modulated current to average current has a marked diagnostic sensitivity and produces an attractive direct readout convenience for the detection of kinetic complications, when compared to other means of analyzing voltammetric curves.

### Acknowledgment

The authors are indebted to P. C. Milner for a critical review of the manuscript.

Manuscript submitted March 20, 1974; revised manuscript received July 8, 1974.

Any discussion of this paper will appear in a Discussion Section to be published in the June 1975 JOURNAL. All discussions for the June 1975 Discussion Section should be submitted by Feb. 1, 1975.

The publication costs of this article have been assisted by Bell Laboratories.

### REFERENCES

1. B. Miller, M. I. Bellavance, and S. Bruckenstein, *Anal. Chem.*, **44**, 1983 (1972).
2. B. Miller and S. Bruckenstein, *Anal. Chem.*, **46**, 2026 (1974).
3. B. Miller, M. I. Bellavance, and S. Bruckenstein, *This Journal*, **118**, 1082 (1971).
4. M. Spiro, *Electrochim. Acta*, **9**, 1531 (1964).
5. B. Miller and S. Bruckenstein, To be published.

# Precipitation and Dissolution Potentials of Electrolytes in D<sub>2</sub>O, Acetone, and Formamide

R. P. Rastogi, R. D. Shukla,<sup>1</sup> and S. Bhagat<sup>2</sup>

Department of Chemistry, University of Gorakhpur, Gorakhpur, Uttar Pradesh, India

## ABSTRACT

Precipitation, dissolution, diffusion, and phase potentials of KCl, KBr, and NaCl have been measured in D<sub>2</sub>O, acetone, and formamide in nitrogen atmosphere. The techniques adopted were similar to those used previously by Rastogi and Shukla for KCl, NaCl, BaCl<sub>2</sub>, and NH<sub>4</sub>Cl in H<sub>2</sub>O. The true dissolution and precipitation potentials were found to be negative for KCl and NaCl in H<sub>2</sub>O and D<sub>2</sub>O (smaller numerically in the latter) and for KBr in D<sub>2</sub>O. However, the dissolution potential of KCl and KBr in acetone and formamide and of NaCl in acetone is positive and of higher magnitude. The temperature, concentration, and time dependence of the dissolution potentials have been investigated. The decay of the precipitation potential and of the apparent diffusion potential with time has been studied. The experimental results show that the precipitation potential increases with undercooling. The transport number of K<sup>+</sup> and Br<sup>-</sup> in formamide has also been measured. The results support the hypothesis that the precipitation and dissolution potentials arise on account of the unequal mobilities of the ions moving to and away from the crystal face.

A comprehensive study of the precipitation and the dissolution potentials of several chlorides in H<sub>2</sub>O has been reported in a recent communication (1). These potentials were discovered by Rastogi, Dass, and Batra (2) in 1961. It has been pointed out that these potentials arise because of the unequal mobilities of the ions being incorporated into or detached from the crystal lattice (1). These mobilities would depend on the crystal binding energy and the medium. Obviously, for the same electrolytes, the sign as well as the magnitude of the potentials would be determined by the nature of the medium. Accordingly, the present investigation was undertaken. D<sub>2</sub>O, acetone, and formamide were chosen as the solvents. D<sub>2</sub>O was chosen since it is known that the ionic mobility of K<sup>+</sup> is considerably reduced (3) in D<sub>2</sub>O, while the latter two were chosen since the cationic mobility for several electrolytes is known to be less than the anionic mobility in acetone and formamide. For the detailed study experiments were made with KCl, KBr, and NaCl. In order to assess the ionic mobilities of KBr in formamide, transport number measurements were made in this system.

When the crystallization or dissolution of an electrolyte occurs on a bright platinum electrode surface, concentration and temperature gradients tend to be developed in the region near the electrode on which these processes are occurring. These tend to give rise to diffusion and thermodiffusion potentials. The observed P.D. measured relative to a bare bright platinum electrode dipping in the same medium and corrected for any asymmetry potentials between two electrodes would include Nernst and phase potentials at the solution/crystal interface. Thus, the observed P.D. would be made up of the true precipitation or dissolution potential, the apparent diffusion potential, the thermodiffusion potential, the phase potential, and the Nernst potential as defined in the Appendix. In order to estimate the true precipitation or dissolution potential, these potentials have to be measured experimentally or estimated from theory. For this purpose, the apparent diffusion potential and the phase potentials have been measured. The thermodiffusion potential and the Nernst potential are found to have low

magnitude and therefore these can be neglected. In order to throw light on the mechanism, the temperature and concentration dependence of the dissolution potential in the temperature range 10°–95°C and in the concentration range 0.0001–2.0M have been investigated.

## Experimental

**Materials.**—B.D.H. (A.R.) KCl, KBr, and NaCl were purified by recrystallization in conductivity water. Acetone was purified by the method described by Weissberger and Proskauer (4). Heavy water of isotopic purity >99.4% supplied by Bhabha Atomic Research Centre (India) was used without any further purification. The density of acetone at 30°C was 0.7794 g/cm<sup>3</sup> [literature (5) 0.7793]. Formamide (E. Merck) was purified by distillation under reduced pressure three to four times. It was further purified by fractional crystallization. The specific conductivity and density of a purified sample were  $1.0-1.5 \times 10^{-5}$  ohm<sup>-1</sup> cm<sup>-1</sup> and 1.1296 g/cm<sup>3</sup>, respectively. The corresponding values reported in the literature (6) are  $0.9-1.5 \times 10^{-5}$  ohm<sup>-1</sup> cm<sup>-1</sup> and 1.1296 g/cm<sup>3</sup>. It was stored in a dry nitrogen atmosphere.

**Platinum electrodes.**—Platinum electrodes as described earlier (1) were used in this investigation. The asymmetry potential was estimated for each run.

**Measurement of potentials.**—Because of the high resistance of the system (about 10<sup>7</sup>–10<sup>10</sup> ohms) under investigation a Lindemann electrometer was used for the measurement of the potentials. In order to annul the effects of stray external fields, coaxial cables were used. The experimental cells for the measurement of the dissolution potential, the precipitation potential, the apparent diffusion potential, and the phase potentials were similar to those described earlier (1). All the measurements were made in a nitrogen atmosphere. The decay of the dissolution, precipitation, and diffusion potentials with time was studied. The effect of temperature and solute concentration on the magnitude of the potentials in the three solvents was also investigated. The consistency of the phase potential was checked from the decay experiments as described earlier (1).

**Measurement of transport number of K<sup>+</sup> in formamide.**—A conventional Hittorf's apparatus as modified by Steel and Stokes (7) was utilized. Platinum electrodes in the form of a helix were used. These

<sup>1</sup> Present address: Chemistry Department, Regional College of Education, Bhubaneswar, Orissa, India.

<sup>2</sup> On study leave from T.N.B. College, Bhagalpur University, Bhagalpur, Bihar, India.

Key words: electrochemistry, crystal growth, precipitation and dissolution potentials, interface phenomena, transient potentials.



Table I. Transport number of K<sup>+</sup> in solution of KBr in formamideTemperature = 30°C; C<sub>1</sub> (eq dm<sup>-3</sup>) = 0.07788

Run	C <sub>2</sub> (eq dm <sup>-3</sup> )	q (coulombs)	V (cm <sup>3</sup> )	t <sub>K+</sub>
1	0.083566	39.6410	31.642	0.4380
2	0.082626	32.8676	31.502	0.4389
3	0.081316	23.8442	31.642	0.4400
4	0.082356	31.3140	31.682	0.4370
			Mean	0.4385 ± 0.0010

were coated with silver and one of the electrodes to be used as cathode was subsequently reduced to silver bromide electrolytically.

Stable current for electrolysis (4-5 mA for 3-4 hr) was obtained using a storage cell and an electronic current stabilizer. The current was measured by a Leeds and Northrup potentiometer employing a sensitive galvanometer across a standard 100 ohms resistance placed in series with the experimental cell. The total current could be estimated correct to ±0.01%.

The change in concentration was estimated by conductivity measurements. When the current was switched off the specific conductance of the solution was determined. In order to estimate the change in concentration, a measured quantity of the original solution was taken in a conductance cell. A known amount of concentrated solution was added dropwise from a weight pipette until the specific conductance of the solution became exactly equal to that of the cathode solution. Since the concentration of the solution added was known, the change in concentration could easily be estimated. This procedure is simple and straightforward but it is not very accurate since the specific conductance is very small and is not very sensitive to changes in concentration. However, it is adequate for the present investigation.

The transport number of the cation t<sub>K+</sub> was estimated from the equation

$$t_{K^+} = F(C_2 - C_1)V/1000q \quad [1]$$

where **F** is the Faraday, C<sub>1</sub> and C<sub>2</sub> are initial and final concentrations in eq dm<sup>-3</sup>, q is the quantity of electricity in coulombs, and V is the volume of the cathode compartment expressed in cubic centimeters. The results of the transport number measurements are summarized in Table I.

**Results.**—The observed dissolution and precipitation potential, the phase potential, and the apparent diffusion potentials of electrolytes are recorded in Table II. The results on the transport number of K<sup>+</sup> in a solution of KBr in formamide are recorded in Table I.

### Discussion

Following the operational definition of the different types of potentials described in the Appendix, the true

precipitation and the true dissolution potentials would be given by the following

$$\begin{aligned} \text{True dissolution potential} &= \text{Observed dissolution potential} \\ &\quad - (\text{Phase potential} + \text{Apparent} \\ &\quad \text{diffusion potential} + \text{Nernst} \\ &\quad \text{potential} - \text{Thermodiffusion} \\ &\quad \text{potential}) \end{aligned} \quad [2]$$

$$\begin{aligned} \text{True precipitation potential} &= \text{Observed precipitation potential} \\ &\quad - (\text{Phase potential} - \text{Theoretical} \\ &\quad \text{diffusion potential} - \text{Nernst} \\ &\quad \text{potential} + \text{Thermodiffusion} \\ &\quad \text{potential}) \end{aligned} \quad [3]$$

For a typical case of KCl in D<sub>2</sub>O the thermodiffusion potential for ΔT = 12.5 kelvins was experimentally found to be 1.57 mV. The Nernst potential at 30°C for C<sub>1</sub> = 5.01 mol/liter and C<sub>2</sub> = 4.38 mol/liter was calculated to be 3.51 mV. Since these are much smaller than the experimental uncertainty we can write

$$\begin{aligned} \text{True dissolution potential} &= \text{Observed dissolution potential} \\ &\quad - (\text{Phase potential} + \text{Apparent} \\ &\quad \text{diffusion potential}) \end{aligned} \quad [4]$$

Thermodiffusion and Nernst potentials would also have a much smaller magnitude for the case of the precipitation potential. Further the calculated diffusion potential is found to be +0.0385 mV when C<sub>1</sub> = 5.01 mol/liter and C<sub>2</sub> = 4.38 mol/liter in the case of KCl in D<sub>2</sub>O. Since this can also be neglected, we have

$$\begin{aligned} \text{True precipitation potential} &= \text{Observed precipitation potential} \\ &\quad - \text{Phase potential} \end{aligned} \quad [5]$$

Using Eq. [4] and [5], the true precipitation and dissolution potentials can be estimated from the experimental data. These are recorded in Table II in columns 8 and 9.

The results recorded in Table II lead to the following conclusions:

1. The true dissolution potential of KCl and NaCl (Table II) is negative in H<sub>2</sub>O and D<sub>2</sub>O but has a lower magnitude in D<sub>2</sub>O. However, in acetone<sup>3</sup> and formamide, the potentials are positive and considerably larger in magnitude.

2. The true precipitation potentials of KCl, KBr, and NaCl (Table II) have the same sign (negative) and magnitude both in D<sub>2</sub>O and H<sub>2</sub>O within experimental error.

3. The phase potential has similar sign (negative) in D<sub>2</sub>O, H<sub>2</sub>O, and acetone but in acetone the magnitude is quite high. However, in formamide the phase potential is positive.

The magnitude of the dissolution potential decreases with the increase in temperature in D<sub>2</sub>O. The data are plotted in Fig. 1. The behavior is similar to that ob-

<sup>3</sup> Preliminary measurements were made by Prashant Rastogi.

Table II. Dissolution, precipitation, phase, and apparent diffusion potentials of electrolytes

Electrolyte	Solvent	Observed dissolution potential (mV)	Observed <sup>(a)</sup> precipitation potential (mV)	Phase potential (mV)		Apparent diffusion potential (mV)	True dissolution potential (mV)	True <sup>(a)</sup> precipitation potential (mV)
				30°C	30°C			
Temperature =		30°C	38°C	30°C	30°C	30°C	30°C	38°C
KCl <sup>(b)</sup>	D <sub>2</sub> O	-105 ± 8	-66	-17	-14	-33 ± 4	-55 ± 12	-49 ± 10 <sup>(c)</sup>
KCl <sup>(d)</sup>	H <sub>2</sub> O	-182 ± 6	-76	-21	-20	-63 ± 4	-98	-55
KBr <sup>(b)</sup>	D <sub>2</sub> O	-131 ± 3	-70	-21	-19	-42 ± 4	-68 ± 7	-49 ± 4
NaCl <sup>(b)</sup>	D <sub>2</sub> O	-97 ± 6	-73	-24	-18	-31 ± 5	-42 ± 11	-49 ± 12
NaCl <sup>(d)</sup>	H <sub>2</sub> O	-170 ± 4	-78	-24	-17	-73 ± 5	-73	-54
KCl <sup>(b)</sup>	Acetone	268 ± 18	—	-73	—	+83 ± 3	258 ± 21	—
KBr <sup>(b)</sup>	Acetone	279 ± 6	—	-84	—	+75 ± 2	288 ± 8	—
NaCl <sup>(b)</sup>	Acetone	211 ± 12	—	-52	—	+69 ± 4	194 ± 16	—
KCl <sup>(b)</sup>	Formamide	289 ± 9	—	+19	—	+83 ± 7	187 ± 16	—
KBr <sup>(b)</sup>	Formamide	307 ± 8	—	+24	—	+77 ± 4	206 ± 12	—

<sup>(a)</sup> Saturation temperature = 50°C, undercooling of the experiment = 12 kelvins.

<sup>(b)</sup> This work.

<sup>(c)</sup> When the Nernst potential (3.355 mV) and the thermodiffusion potential (1.57 mV) for KCl in D<sub>2</sub>O are taken into account the true dissolution and precipitation potentials would be equal to -56.79 mV and -47.177 mV, respectively. The difference between these and the values in the last column in this table is well within the experimental error.

<sup>(d)</sup> Rastogi and Shukla (1).

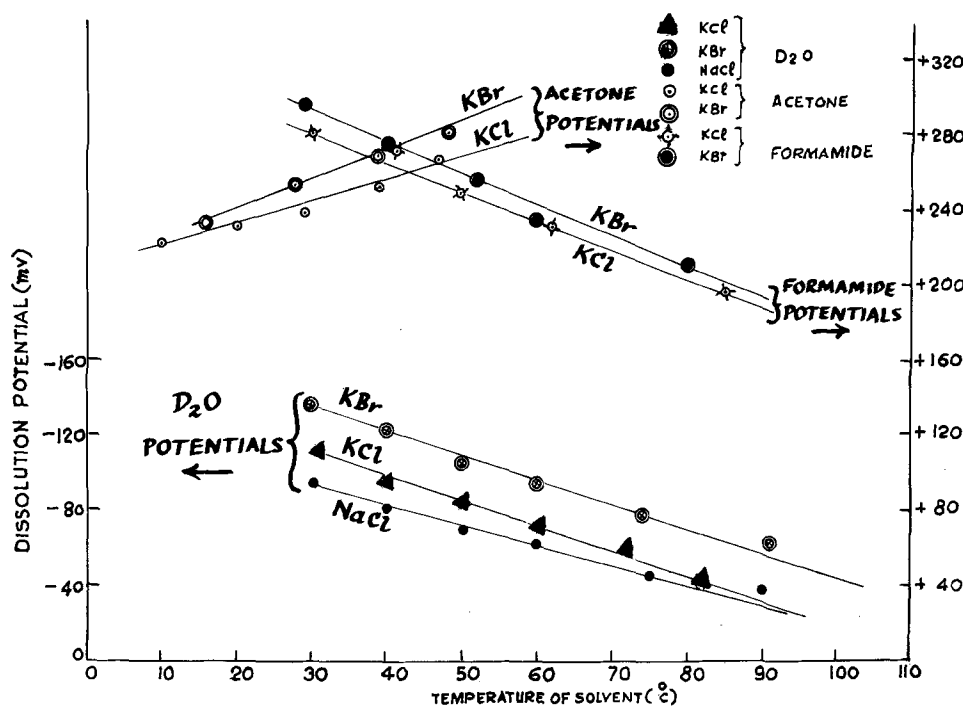


Fig. 1. Dependence of dissolution potential on temperature. (Minus scale on left refers to D<sub>2</sub>O and plus scale on right to acetone and formamide.)

served in H<sub>2</sub>O earlier (1). As expected (1), the dissolution potential also decreases with the increase in molarity of the solution (Fig. 2). The dissolution potential decays exponentially with time (Fig. 3) in conformity to the behavior observed in water. Similar is the decay behavior in acetone (Fig. 4). The precipitation potentials of KCl, KBr, and NaCl in D<sub>2</sub>O (Fig. 5) increase (in the negative direction) with the increase in the degree of undercooling below the saturation temperature of 50°C. The precipitation potentials of KCl, KBr, and NaCl decay exponentially, the plot of  $\log |\Delta\phi|$  against time is a straight line (Fig. 6) where  $\Delta\phi =$  observed precipitation potential - phase potential. The decay of the apparent diffusion potential with time is plotted in Fig. 7, which shows a similar pattern. The plot of the logarithm of the apparent diffusion potential against time gives a straight line (Fig. 8) as is found in the case of H<sub>2</sub>O (1). This behavior is similar to the decay of a condenser through a resistance.

The apparent dissolution potential of KCl, KBr, and NaCl decays exponentially with time in D<sub>2</sub>O and acetone (Fig. 3 and 4). The trend is similar in formamide (Fig. 9). The decay curve is similar to that observed for the diffusion potential (Fig. 8) showing that the functional dependence of both the diffusion and the dissolution potential on an electrolyte concentration which is varying with time, is perhaps similar. This is further confirmed by the study of the dependence of the dissolution potential on the concentration of the medium in which the dissolution takes place. Figure 10 shows that the plot of the dissolution potential vs. the logarithm of concentration is a straight line. The slopes for KCl, KBr, and NaCl are 21.8, 26.0, and 9.26 mV, respectively, whereas the Nernst slope ( $2.303 RT/F$ ) is equal to 60.16 mV at 30°C.

The above results can easily be explained in the light of the mechanism postulated by Rastogi and Shukla (1) which is as follows. In a growing crystal, anions and cations separately migrate to the solution/crystal interface and get attached to the lattice. Both ions do not get attached to the growing crystal simultaneously because of the unequal mobilities of the ions. Hence, a certain P.D. is developed. In the case of dissolution, there would be a competition between the two ions to get detached from the lattice which would ultimately be responsible for the development of P.D.

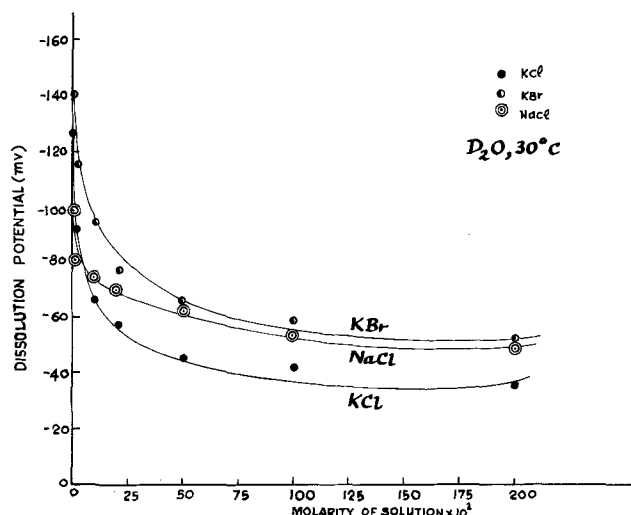


Fig. 2. Dependence of dissolution potential on the concentration of solution.

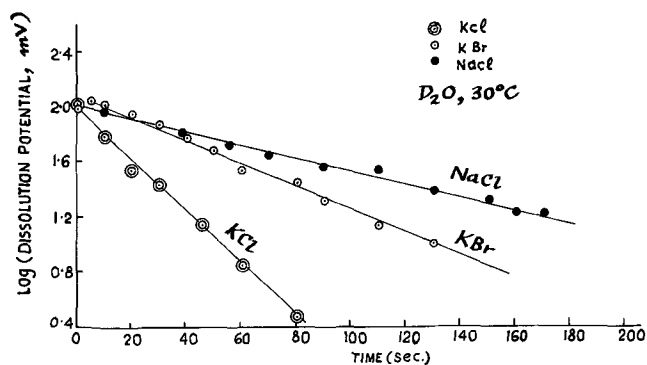


Fig. 3. Dependence of dissolution potential on time in D<sub>2</sub>O

The values of ionic mobilities are recorded in Table III. From Table III, it is obvious that (i) the precipitation potential and the dissolution potential of the alkali

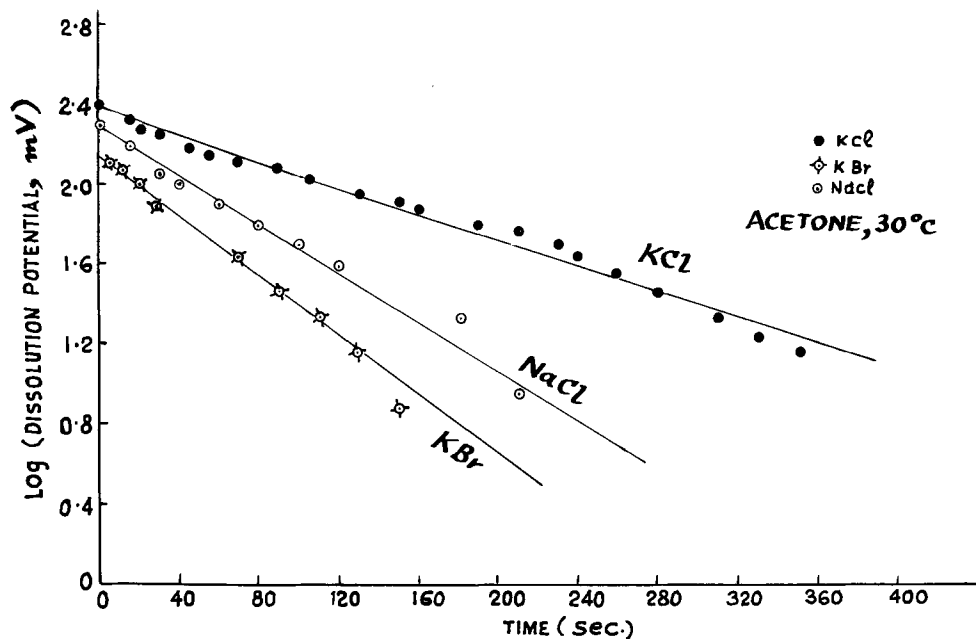


Fig. 4. Dependence of dissolution potential on time in acetone.

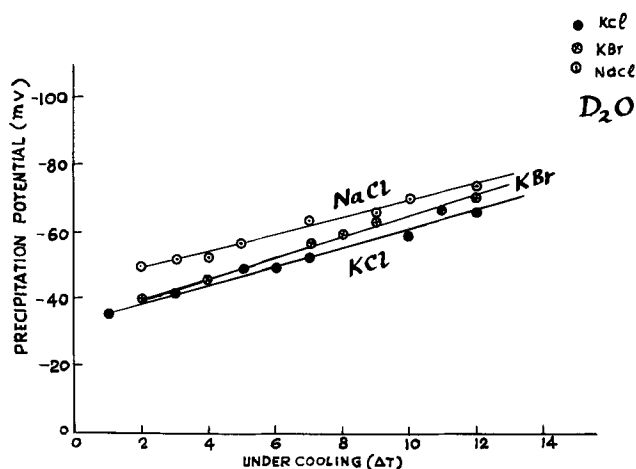


Fig. 5. Dependence of precipitation potential on undercooling. Saturation temperature 50°C.

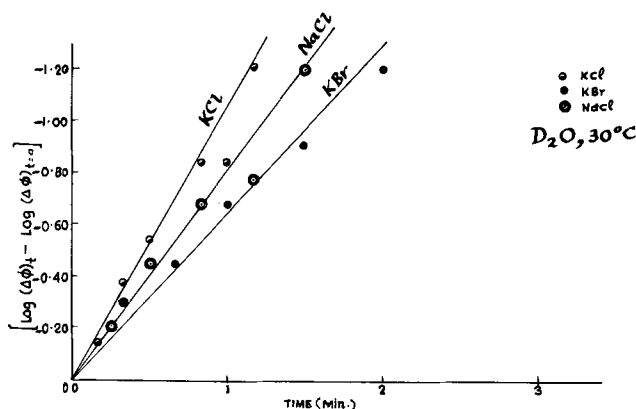


Fig. 6. Plot of  $\log |\Delta\phi|_t - \log |\Delta\phi|_{t=0}$  vs. time where  $|\Delta\phi|$  is the absolute value of  $\Delta\phi =$  observed precipitation potential - phase potential.

halides in  $D_2O$  are negative and (ii) the magnitude is about half the corresponding value for water. As pointed out above these potentials arise because of the unequal mobilities of the ions moving to and away from the lattice. The mobility of the halide ion is greater than the metal ions and the former also has

less tendency for hydration. Hence, the electrode on which crystallization is taking place would be negative. However, during dissolution, cations would leave the lattice faster on account of hydration and hence the dissolution occurs on the negative electrode. Since the magnitude of  $(U_{K^+} - U_{X^-})$  is less in  $D_2O$  as compared to that in  $H_2O$ , the magnitude of the precipitation and dissolution potentials is less in  $D_2O$  as compared to water.  $X^-$  represents the halide ion.

The results obtained in the case of acetone as the medium can also be explained on the basis of the hypothesis suggested earlier (1). The values of the ionic mobilities of  $K^+$  and  $Cl^-$  in acetone, recorded in Table III, show that in acetone the chloride ion moves faster than the cation. This trend is also observed for other electrolytes in acetone. On account of this fact as well as the fact that the ions have less tendency to be solvated in acetone as compared to water, the dissolution potential would be expected to be positive as is found to be the case. Further, since the difference between the ionic mobilities of the cation and the anion is much greater as compared to the other case, the magnitude of the dissolution potential is higher. This is also the situation in formamide (cf. Table I).

It is therefore clear that the dissolution potential and the precipitation potentials depend on (i) temperature, (ii) time, (iii) concentration of the medium, and (iv) nature of the electrolyte. It would be worthwhile to guess the functional dependence. Results for the dissolution potential in  $D_2O$ , acetone, and formamide show (i) linear dependence on temperature, (ii) exponential dependence on time, (iii) linear dependence on the logarithm of the concentration of the medium, and (iv) dependence on the nature of the electrolyte which probably governs the relative speed of detachment or attachment of the ions on the crystal lattice. Evidently the precipitation and dissolution po-

Table III. Ionic mobilities at infinite dilution  
Temperature = 25°C

Solvents	Mobilities $\times 10^5$ $U_{K^+}$	Mobilities ( $cm^2/sec V$ )	
		$U_{Cl^-}$	$U_{Br^-}$
$H_2O$ (8)	76.217	79.057	81.057
$D_2O$ (13)	63.810	65.240	67.015 (8)
Acetone (9)*	84.974	115.020	117.098
Formamide (10)	12.901	17.875	18.259

\* The values agree with that estimated from ionic conductance at infinite dilution (11) and transport number (12).

tentials depend on temperature, concentration, and time in the same manner as in the case of the diffusion potential. Exponential dependence of potentials on time would somehow be related to the capacitive-resistive properties of the system. Linear dependence on log concentration would appear to tie in with the Nernst equation but the slope is not identical with the Nernst slope.

Since the speeds of attachment and detachment of the ions on the crystal lattice are not known, we may assume in the first instance that these are related to ionic mobilities. Accordingly, the true precipitation and dissolution potential would be related either to  $U - V$  or  $(U - V)/(U + V)$  where  $U$  is the mobility of cation and  $V$  that of anion at infinite dilution. The latter factor is known to be important in diffusion potentials. In Table IV values of  $U - V$  and  $(U - V)/(U + V)$  for KCl in various solvents have been recorded. Keeping in view the fact that the dissolution potential decreases with an increase in temperature in  $D_2O$  and formamide, it is obvious from Table IV that the dissolution potential would be related to  $(U - V)/(U + V)$  and not to  $U - V$  since the former decreases with a rise in temperature. In acetone, the dissolution

Table IV. Variation of  $U - V$  and  $(U - V)/(U + V)$  with temperature in different solvents for KCl

Solvent	T °C	$(U - V) \times 10^5$	$(U - V)/(U + V)$
$D_2O$ (13)	18	-1.471	0.0134
	21.5	-1.440	0.0120
	25	-1.430	0.0110
Acetone (9)	18	-27.875	0.1485
	25	-30.050	0.1502
	37	-32.120	0.1490
Formamide (10)	15	-3.927	0.2602
	25	-4.974	0.1616
	35	-5.212	0.1407

potential increases with an increase in temperature. Here again Table IV clearly indicates that the dissolution potential would be related to  $(U - V)/(U + V)$  and not to  $U - V$ . Further studies are needed to corroborate the above conclusions.

**Acknowledgments**

The authors are grateful to C.S.I.R. (India) for supporting the investigation. We wish to thank Dr. Kehar Singh for useful discussions.

Manuscript submitted June 15, 1972; revised manuscript received June 6, 1974.

Any discussion of this paper will appear in a Discussion section to be published in the June 1975 JOURNAL. All discussions for the June 1975 Discussion Section should be submitted by Feb. 1, 1975.

**APPENDIX**

**Dissolution potential.—Operational definition—**The dissolution potential is the potential of a platinum electrode coated with a uniform thick layer of an electrolyte deposited by controlled crystallization from a solution of the electrolyte saturated at 75°C and dipped mechanically in a cell filled with conductivity water, measured by reference to the potential of another similar bare platinum electrode dipping in the same conductivity water. The observed dissolution potential is corrected for any asymmetry (bias) potential existing between the two platinum electrodes as determined before and after the dissolution run. The potential difference is measured electrostatically by means of a Lindemann electrometer.

**Conceptual definition.—**The dissolution potential is the potential difference arising from an electrical double

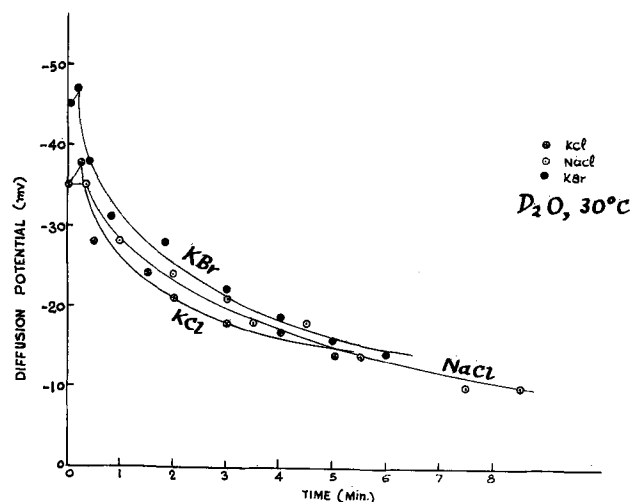


Fig. 7. Decay of diffusion potential in  $D_2O$

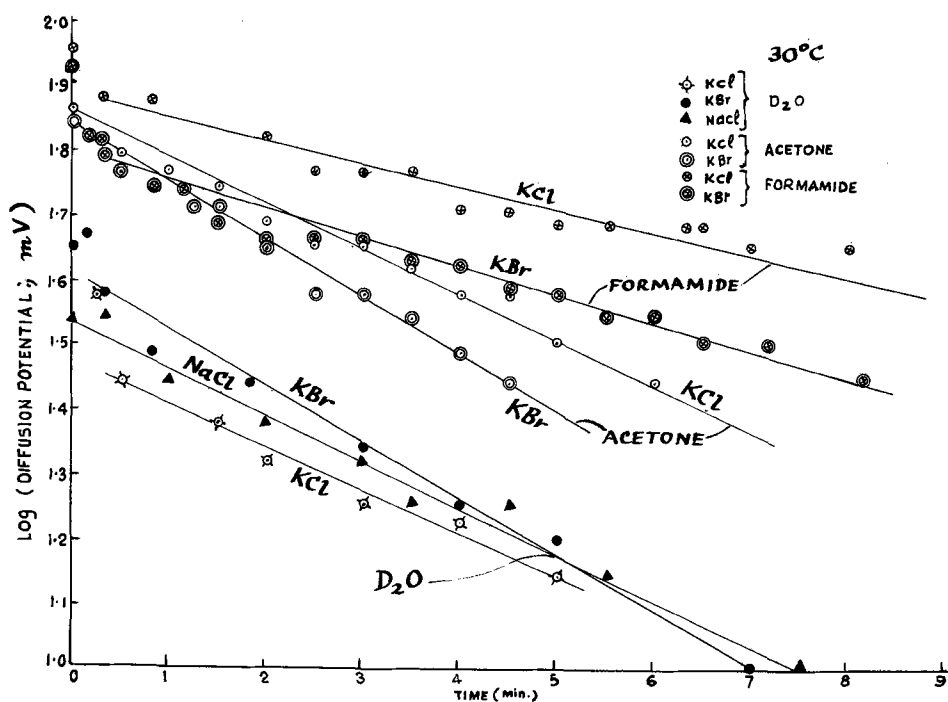


Fig. 8. Dependence of diffusion potential on time.

layer developed at a liquid/crystal interface by the process of crystal dissolution (ion migration) into the liquid phase. The algebraic sign of the dissolution potential is the same as the electrostatic polarity, (+) or (-), of the end of the dipolar double layer on the crystal side of the interface.

**Precipitation potential.—Operational definition.**—The precipitation potential is the potential of a platinum electrode coated with a layer of an electrolyte deposited by crystallization from a supersaturated solution at a temperature  $T$  less than the saturation temperature  $T_s$ .  $T_s - T$  is called the degree of undercooling. The reference potential is a similar bare platinum electrode which is dipped in the above supersaturated solution once the crystallization has started. The observed precipitation potential is corrected for any asymmetry potential existing between the two platinum electrodes before the precipitation run. The potential difference is measured electrostatically by means of a Lindemann electrometer.

**Conceptual definition.**—The precipitation potential is the potential difference arising from an electrical double layer developed at a liquid/crystal interface by the ion migration from the liquid phase. The algebraic sign of the precipitation potential is the same as the electrostatic polarity, (+) or (-), of the end of the dipolar double layer on the crystal side of the interface.

**Phase potential.—Operational definition.**—The phase potential is the potential of a platinum electrode coated with a uniform thick layer of an electrolyte deposited by controlled crystallization from a solution of the electrolyte saturated at  $75^\circ\text{C}$ , and dipped mechanically in a cell filled with saturated solution of the electrolyte

at the saturation temperature  $T_s$ . The phase potential is measured by reference to the potential of another similar bare platinum electrode dipping in the saturated solution. The observed phase potential is corrected for any asymmetry potential existing between the two platinum electrodes as determined before the run. The potential difference is measured electrostatically by means of a Lindemann electrometer.

**Conceptual definition.**—The phase potential is the potential difference arising from an electrical double layer developed at a liquid/crystal interface as a result of the dynamic equilibrium of ion migration from the liquid phase to the crystal phase and vice versa. The algebraic sign of the phase potential is the same as the electrostatic polarity, (+) or (-), of the end of the dipolar double layer on the crystal side of the interface.

**Phase potential from decay.—Experiment.—Operational definition.**—The phase potential from the decay experiment is the potential of a platinum electrode coated with a thick layer of an electrolyte dipped mechanically in a supersaturated solution when the concentration of the solution approaches the concentration corresponding to the saturation concentration at the temperature of observation. This situation is obtained when the observed potential attains a steady value on decay. The potential is measured by reference to the potential of another similar bare platinum electrode dipping in the saturated solution. The potential difference is measured electrostatically by means of a Lindemann electrometer.

**Conceptual definition.**—The conceptual definition of the phase potential from the decay experiment is the same as that of the phase potential.

**Apparent diffusion potential.—Operational definition.**—The apparent diffusion potential is the potential of a platinum electrode dipped mechanically in a cell filled with a saturated solution at a particular temperature,  $T_s$ . The potential is measured by reference to the potential of another similar bare platinum electrode dipping in pure solvent, the solvent being connected to the saturated solution by a narrow opening in the cell. The observed apparent diffusion potential is corrected for any asymmetry potential existing between the two platinum electrodes after the diffusion run. The potential difference is measured electrostatically by means of a Lindemann electrometer.

**Conceptual definition.**—The apparent diffusion potential is the potential difference arising at the interface of the solutions of two concentrations  $C_1$  and  $C_2$  by the process of ion migration from one solution to the other. The algebraic sign of the diffusion potential depends on the difference in the ionic mobilities of the ions leaving the dilute solution/concentrated solution inter-

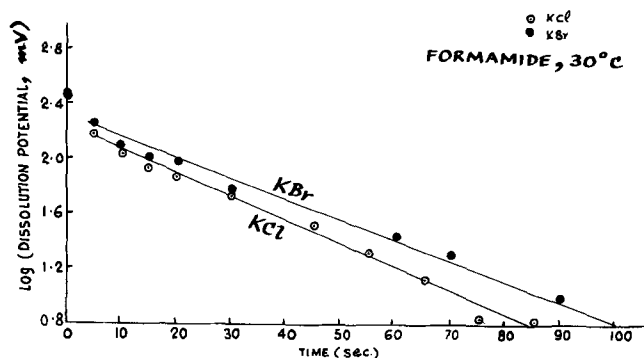


Fig. 9. Dependence of dissolution potential on time in formamide.

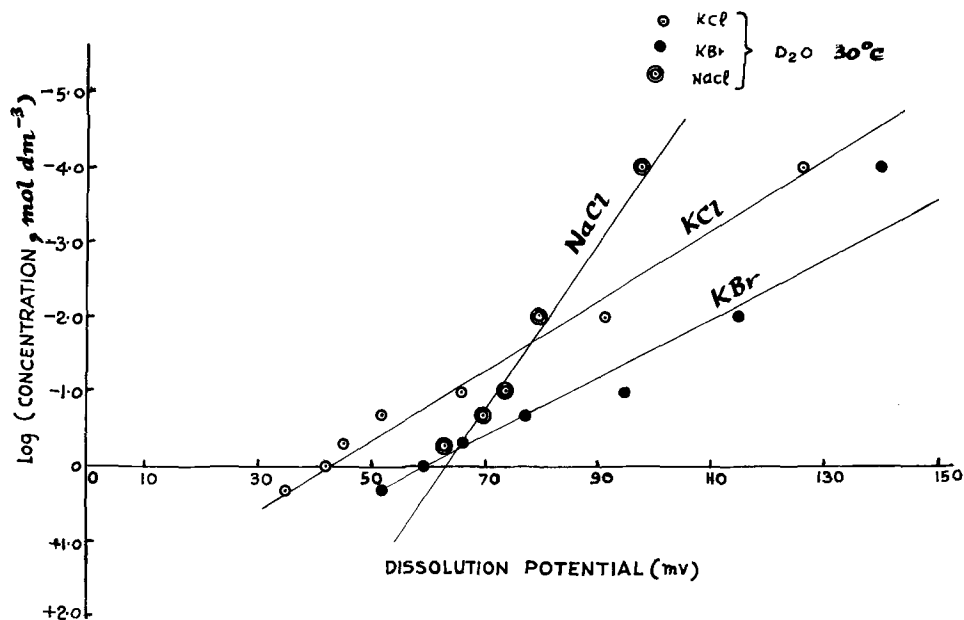


Fig. 10. Dependence of dissolution potential on the concentration in  $\text{D}_2\text{O}$ .

face. If cations move faster, the concentrated solution will be negatively charged.

*Thermodiffusion potential.—Operational definition.—*

The thermodiffusion potential is the potential of a silver/silver chloride electrode kept in a solution of an electrolyte saturated at the ice-point ( $T_s = 0^\circ\text{C}$ ) and maintained at a temperature higher than that of the reference electrode (which is maintained at a temperature higher than  $0^\circ\text{C}$ ). The thermodiffusion potential is related to the temperature difference  $\Delta T$ . The observed thermodiffusion potential was corrected for any asymmetry potential by making the measurement for  $\Delta T = 0$ . The potential difference was measured by means of a Pye precision potentiometer.

*Conceptual definition.—*The thermodiffusion potential is the potential difference arising from the migration of ions at the interface of two solutions on account of temperature difference. The algebraic sign of the thermodiffusion potential depends on the difference in ionic mobility when a temperature difference is imposed in the system.

*True dissolution potential.—Operational definition.—*The true dissolution potential is given by the following equation

$$\begin{aligned} \text{True dissolution potential} &= \text{Observed dissolution potential} \\ &- (\text{Phase potential} + \text{Apparent diffusion potential} + \text{Nernst potential} \\ &- \text{Thermodiffusion potential}) \end{aligned}$$

In the above equation the Nernst potential is given by  $(RT/F) \ln C_1/C_2$ , where  $C_1$  and  $C_2$  are the concentrations in the two regions ( $C_1 > C_2$ ). The Nernst potential is the difference between the potential of the electrode in the concentrated solution and the potential of the electrode in the dilute solution. In most of the cases the calculated Nernst potential and the experimentally measured thermodiffusion potential are well within the experimental uncertainty in the observed dissolution potential and hence can be neglected.

*Conceptual definition.—*The conceptual definition of the true dissolution potential is the same as that given earlier for the dissolution potential.

*True precipitation potential.—Operational definition.—*The true precipitation potential is given by the following equation

$$\begin{aligned} \text{True precipitation potential} &= \text{Observed precipitation potential} \\ &- (\text{Phase potential} - \text{Theoretical diffusion potential} - \text{Nernst potential} \\ &+ \text{Thermodiffusion potential}) \end{aligned}$$

where the theoretical diffusion potential is given by  $-[(U - V)/(U + V)] (RT/F) \ln C_1/C_2$ . The theoretical diffusion potential is the potential at the dilute

solution/concentrated solution interface so that the sign is determined with respect to concentrated solution.  $C_1$  is the concentration of the supersaturated solution and  $C_2$  is the concentration prevailing at the crystal interface, i.e., the saturation concentration at the temperature of the experiment. The theoretical diffusion potential is usually found to be less than 1 mV and hence the sum of the theoretical diffusion potential, the Nernst potential, and the thermodiffusion potential can be neglected.

*Conceptual definition.—*The conceptual definition of the true precipitation potential is the same as that given earlier for the precipitation potential.

#### SYMBOLS

$t_{K^+}$	transport number of cation
$F$	Faraday, coulomb $\text{eq}^{-1}$
$C_1$	initial concentration, $\text{eq dm}^{-3}$
$C_2$	final concentration, $\text{eq dm}^{-3}$
$V$	volume, $\text{cm}^3$
$q$	quantity of electricity, coulomb
$\Delta T$	difference between the saturation temperature and the temperature of the experiment, kelvins
$\Delta\phi$	observed precipitation potential - phase potential, mV
$U$	mobility of cation, $\text{cm}^2/\text{sec V}$
$V$	mobility of anion, $\text{cm}^2/\text{sec V}$

#### REFERENCES

1. R. P. Rastogi and R. D. Shukla, *J. Appl. Phys.*, **41**, 2787 (1970); *J. Sci. Industrial Res.*, (India), **29**, 317 (1970).
2. R. P. Rastogi, R. K. Dass, and B. P. Batra, *Nature*, **191**, 764 (1961).
3. L. G. Longworth and D. A. MacInnes, *J. Am. Chem. Soc.*, **59**, 1666 (1937).
4. A. Weissberger and E. S. Proskauer, in "Technique of Organic Chemistry," Vol. VII, p. 381, Revised Second Edition, J. A. Riddick and E. E. Toops, Editors, Interscience Publishers Ltd., London (1955).
5. J. Timmermans, "Physico-Chemical Constants of Pure Organic Compounds," p. 355, Elsevier Publishing Co., Inc., New York (1950).
6. L. R. Dawson, E. D. Wilhoit, and P. G. Seers, *J. Am. Chem. Soc.*, **79**, 5906 (1957).
7. B. J. Steel and R. H. Stokes, *J. Phys. Chem.*, **62**, 450 (1958).
8. R. L. Kay and D. F. Evans, *ibid.*, **70**, 2325 (1966).
9. A. Lannung, *Z. Physik. Chem.*, **161** (4/5), 255 (1932).
10. R. Gopal and O. N. Bhatnager, *J. Phys. Chem.*, **68**, 3892 (1964); **69**, 2382 (1965); **70**, 3007, 4070 (1966).
11. T. C. Waddington, "Non-aqueous Solvents System," p. 237, Academic Press, London (1966).
12. B. E. Conway, "Electrochemical Data", p. 169, Elsevier Publishing Co., Amsterdam (1952).
13. E. Ron Hess, D.K.N.V.S. *Forhandlinger Bd XII*, Nr 38 (1940).

# Electrode Surface Conductance Measurements in an Electrochemical Cell

W. J. Anderson\*

Aerospace Research Laboratories, Wright-Patterson Air Force Base, Ohio 45433

and W. N. Hansen\*\*

Physics Department, Utah State University, Logan, Utah 84322

## ABSTRACT

A quantitative theory of the electrode surface conductance decrease caused by adsorbed ions is discussed that shows good agreement with the measured results. Conductance measurements are shown to provide a reliable measure of adsorbed ion surface concentration. The sensitivity of conduction measurements to adsorbing ions and surface free electron density changes is discussed. Changes in the adsorbed state are detected as a function of electrode potential. The conductance measurements are used to measure the ionic diffusion rate of  $I^-$  through an aqueous electrolyte.

Thin film electrode conductance measurements have proved to be a sensitive method of observing the electrode surface, *in situ*, in an electrochemical cell. This technique was first developed by Shimizu (1-3) to investigate the hydrogen evolution and dissolution mechanism at the platinum electrode. Bockris *et al.* (4) later used conductivity measurements to detect ionic adsorption from concentrated solutions on thin platinum films. Recently Niki and Shirato (5) have discussed the applicability of the electrode resistance measurements to detect the adsorption of organic compounds on thin gold electrodes. The resistance measurements have been shown to be sensitive to electrode charging (6, 7) and adsorption on the electrode surface (4, 8). As the electrode potential is varied, the relative change in conductance is equal to the relative change in the total number of conduction electrons in a metallic film. In addition to this effect, when point charges are adsorbed on the electrode surface, they increase the conduction-electron surface scattering thus causing a decrease in electrode conductance (9). The change in electrode conductance caused by the change in free electrons per unit of electrode area and the surface scattering can easily be detected in a thin film electrode, thus providing a sensitive method of observing fundamental electrode processes. All of our results have been obtained on thin (approximately 10 nm) gold and copper electrodes (8).

The purpose of this paper is to quantitatively develop the conductance theory for adsorbed ions, compare the results to measurements, and to demonstrate the versatility of conductance measurements in understanding ionic adsorption. The relative conductance change of a thin film electrode is shown to decrease linearly with the specifically adsorbed ion surface concentration, for small surface coverages. The magnitude of this conductance change is calculated from a previously developed theory of surface scattering and shown to be in good agreement with the measured values. The sensitivity of conduction measurements to electrode charging and ionic adsorption is derived as a function of the film thickness, free electron concentration, and conduction electron mean free path length.

The diffusion coefficient of  $I^-$  is calculated from the change in conductance as a function of time. Conductance measurements on thin film electrodes are shown to be useful as a fundamental electrochemical technique of monitoring the electrochemical interphase.

\* Electrochemical Society Student Member.

\*\* Electrochemical Society Active Member.

Key words: conductance, electrode surface, adsorption, thin film electrode.

## Theory

The conductance of a thin film is a function of its free electron concentration, expressed in electrons per unit area, as can be seen from simple solid-state theory. Bonfiglioli *et al.* (10) have shown experimentally that the conductance of a thin gold film varies linearly with the film's charge. The conductance,  $G$ , of a thin gold film electrode has been shown to vary with the total number of conduction electrons per unit area,  $N$ , as

$$\Delta G/G = \Delta N/N \quad [1]$$

where  $\Delta G$  and  $\Delta N$  are small changes in  $G$  and  $N$ , respectively (7).

The sensitivity of the conductance measurements,  $S_N$ , to a change in  $N$  can be defined as

$$S_N \equiv 1/(\Delta N)_{\min.} = 1/(N \Delta G/G)_{\min.} \quad [2]$$

where  $(\Delta N)_{\min.}$  is defined as the minimum observable  $(\Delta N)$ .

$$S_N = (1/N) (G/\Delta G)_{\max} \quad [3]$$

The minimum relative change in conductance that can be detected with our experimental setup is  $10^{-4}$ . Then  $(G/\Delta G)_{\max}$  is at least  $10^4$ . For a 10 nm film with electron density of bulk gold ( $6 \times 10^{22} \text{ cm}^{-3}$ ) then  $N = 9.6 \times 10^{-3} \text{ coulomb/cm}^2$  and  $S_N \approx 96$ .  $S_N$  is increased by either decreasing  $N$  or by decreasing the fractional change in conductance that we can observe. For example, the maximum thickness of a gold film (bulk electron density of  $5.9 \times 10^{22} \text{ cm}^{-3}$ ) that can be used to detect a change in  $N$  is approximately  $0.1 \mu\text{m}$  while for a semiconducting film such as tin oxide (electron density  $\approx 10^{20} \text{ cm}^{-3}$ ) a  $10 \mu\text{m}$  film can be used. The film thickness is limited even further if the temperature of the film does not remain constant as the current is changed although no problems have been observed in our measurements.

Conductance measurements provide a reliable method of quantitatively measuring the adsorbed ion concentration on an electrode surface. Several investigators (11-13) measuring adsorption from the gas phase have shown that the relative change in conductivity of thin metal films (10-40 nm thick) decreases in direct proportion to the fractional coverage of the adsorbed species. They attributed the decrease in conductivity to a localizing of the conduction electrons caused by the formation of chemical bonds.

Another effect that better explains conductance change is the surface scattering of free electrons caused by the adsorbed particles. The conductance of a thin

film is strongly dependent on the surface scattering of the free electrons when the film thickness is approximately equal to or less than the free electron mean free path length in the bulk material. Fuchs (14) has derived an expression for the conductance of a thin film as a function of the probability of specular reflection from the film surface by the conduction electrons,  $P$ , and their angle of incidence,  $\theta$ . The conductivity,  $\sigma$  is

$$\sigma = \sigma_0 \left\{ 1 - (3/4) \int_0^\pi \sin^3\theta [1 - P] K' d\theta + (3/4) \int_0^\pi \sin^3\theta [1 - P]^2 K' \exp(-K') \times [1 - P \exp(-K')]^{-1} d\theta \right\} \quad [4]$$

where

$$K' = (\lambda_0/h) |\cos \theta|$$

$\sigma_0$  is the bulk conductivity,  $\lambda_0$  is the electron mean free path length, and  $h$  is the film thickness. The derivation of Eq. [4] assumes elastic collisions with the surface.

The film surface roughness causes some inherent scattering that decreases the film conductivity. Adsorbed ions on the film surface cause bumps in the equipotential surfaces as shown in Fig. 1. These deformations increase the surface scattering thus decreasing the conductance. The adsorbed ions only have an effect approximately 0.1 nm into the metal because of the free electron screening. The electron wavelength for a metal such as gold is about 0.5 nm [see Ref. (15), p. 248, Table 1, where  $\lambda_f = 2\pi/k_f$ ]. This model treats the adsorbed ion as a point charge at the surface with no electron sharing between the ion and the electrode. Greene (16) has derived an expression for  $P(\theta)$  as a function of the charge density of point charges adsorbed on the film surface. A screened coulomb potential,  $V$ , is used to approximate the scattering potential so that

$$V = (e^2/r) \exp(-q_0 r) \quad [5]$$

where

$$q_0 = (4me^2/\hbar^2) (3n_0/\pi)^{1/3}$$

$r$  is the distance from the film surface,  $e$ ,  $m$ , and  $n_0$  are the free electron charge, mass and volume density, respectively, and  $\hbar$  is Planck's constant/ $2\pi$  [see Ref. (15), p. 227]. Equation [5] is for spherical symmetry and only approximates adsorbed charges on a plane surface. The expression for  $P(\theta)$  is derived by considering the perturbation of the free electron wave functions caused by Eq. [5] using the Born approximation such that

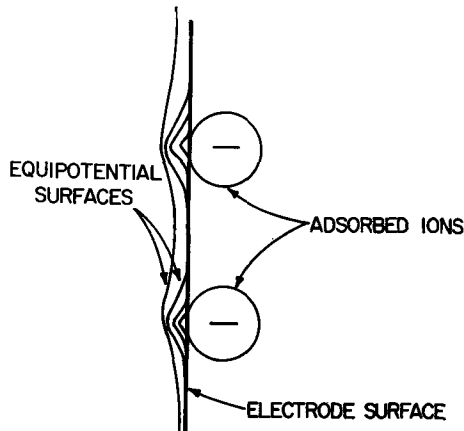


Fig. 1. The metal electrode surface with adsorbed ions

$$P = 1 - (2\pi\Gamma/\mu) (me^2/h^2 k^2) [-2(\epsilon^2 + 2)^{-1} - \mu^2(1 - \mu^2)^{-1} \ln((2 + \epsilon^2)/\epsilon^2) + (\epsilon^2 + \mu^2)(1 - \mu^2)^{-1} (s\mu)^{-1} \ln((s + \mu)/(s - \mu))] \quad [6]$$

where

$$\epsilon^2 = q_0^2/2k^2, s = [(1 + \epsilon^2)^2 + \mu^2 - 1]^{1/2}, \mu = \cos \theta$$

$k$  is the free electron wave vector, and  $\Gamma$  is the area concentration of adsorbed surface charges. Reference (16) contains a more thorough discussion of the derivation of Eq. [6].

The change in  $P$ , calculated from Eq. [6], caused by an adsorbed charge density of  $5 \mu\text{coulombs/cm}^2$  is zero at grazing angles of incidence increasing to 0.0023 at normal incidence for a gold film electrode. (Although impossible to obtain because of electrostatic repulsion effects, a complete monolayer coverage would be approximately  $200 \mu\text{coulombs/cm}^2$ .) As an approximation for the purpose of estimating the conductance change,  $P$  was assumed to be 0.002, independent of angle of incidence. Equation [4] assumes  $P$  is the same for both sides of the film. Since the ions adsorb only one side of the film,  $P$  only changes on one side. Juretschke (17) has shown that for a film whose surfaces scatter differently, the  $P$  in Eq. [4] is approximately the average of both surfaces. Therefore, the  $P$  in Eq. [4] changes by approximately 0.001 for an adsorbed charge density of  $5 \mu\text{coulombs/cm}^2$ . The relative change in  $G$  caused by a change in  $P$  is dependent on the initial value of  $P$ . The surface scattering of a thin film cannot be calculated from film resistance measurements because thin films probably have other scattering mechanisms, e.g., film thickness variations can cause an additional decrease in conductance (18). The predominant scattering mechanism in thin films is more likely to be due to structural imperfections than surface effects. An initial value for  $P$  of 0.20 is a reasonable specular reflection probability for a gold film. With these assumptions and using Eq. [4] the relative change in conductance,  $\Delta G/G$ , is 0.0011 for a  $5 \mu\text{coulombs/cm}^2$  adsorbed charge density.

The surface scattering term varies linearly with  $\Gamma$ . The conductivity  $\sigma$ , varies almost linearly with  $P$  for small change in  $P$ ; therefore

$$\Delta G/G \approx K\Gamma \quad [7]$$

where  $K$  is a constant. By the above calculations  $K$  is equal to  $3.5 \times 10^{-7} \text{ cm}^2$ .

This is only a rough approximation and could vary by as much as a factor of two depending on the assumptions made in the calculation. The calculation only considers the surface scattering caused by the perturbed equipotential lines at the electrode surface and does not include other possible effects, i.e., electron tunneling between adsorbed particles and the conduction band, creation of chemical bonds at the surface, or new surface states created by the adsorbed particle, all of which will affect the conductance.

The sensitivity of the conductance to a change in  $P$  can be defined as

$$S_p \equiv |\Delta G/G|/\Delta P \quad [8]$$

Sondheimer (19) has derived approximations for Eq. [3] good when  $h \gg \lambda_0$

$$\sigma = 8h\sigma_0/\lambda_0 (8(h/\lambda_0) + 3P) \quad [9]$$

and when  $h \ll \lambda_0$  and  $P \approx 0$

$$\sigma = 3\sigma_0 (h/\lambda_0) \ln(\lambda_0/h)/4P \quad [10]$$

This gives for  $h \gg \lambda_0$  and  $P \approx 0$

$$S_p \approx 3\lambda_0/8h \quad [11]$$

and for  $h \ll \lambda_0$  and  $P \approx 0$

$$S_p \approx 1/P \quad [12]$$



From Eq. [11] and [12] it can be seen that a thin film made of a substance whose conduction electrons have a long mean free path length compared to the film thickness will be most sensitive to the surface scattering. A 6 nm thick gold film with  $\lambda_0 \cong 3.5$  nm should be very sensitive to adsorbed ions while a 1  $\mu\text{m}$  thick tin oxide film with  $\lambda_0 \cong 5$  nm should not permit detection of adsorbed charges.

### Experimental Method

Standard techniques are used with the electrochemical cell. The cell and electrode used for most of the measurements along with the conductance monitoring technique have previously been described in Ref. (7). All potentials are referred to a saturated calomel electrode (SCE). The electrode used in Ref. (7) performed well for slow potential sweep rate measurements (0.1 V/sec) but as the sweep rate was increased a slight electrode resistance difference between each contact of the conductance bridge and the potentiostat contact caused a fickle voltage to appear on the conductance bridge. The electrode design of Fig. 2 was devised to eliminate this problem. Resistances  $R_2$  and  $R_4$  are 10 ohm potentiometers used to balance the electrode current. The potential difference between contacts 1 and 3 caused by the potentiostat current can be made zero by adjusting either  $R_2$  or  $R_4$  (one is always left at zero to eliminate any serious error in the true potential measurement of the system). This electrode design was used when the potential sweep rate exceeded approximately 5 V/sec.

A standard bridge circuit is used to monitor the conductance change of the thin-film electrode as a function of potential [see Ref. (7) and (8)]. Relative changes in conductance of 0.0001 could be measured without difficulty. The conductance was plotted as a function of potential with an x-y recorder for the slow sweep rates and with a storage oscilloscope for the fast sweep rates.

The preparation and properties of the gold film electrodes are described in Ref. (7). The film thicknesses were measured optically using the method described in Ref. (20). The tin oxide film was approximately 1  $\mu\text{m}$  thick and had a resistance of 38 ohms- $\square^{-1}$ . The electron density was unknown.

### Experimental Results and Discussion

The relative conductance change is equal to the relative change in free electron density when no change in ionic adsorption occurs. Figure 3 contains the voltammetric electrochemical curve and conductance change for a 1  $\mu\text{m}$  tin oxide electrode. The total free electron change per unit area of the tin oxide film is calculated from the charging current to be 22.5  $\mu\text{Coulombs/cm}^2$ . The free electron density of the tin oxide

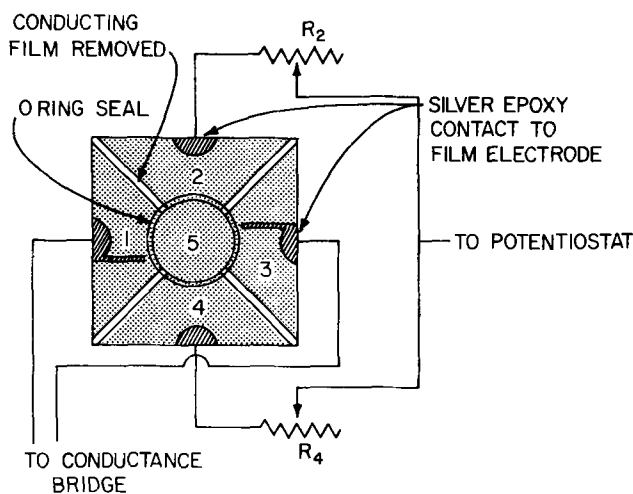


Fig. 2. The electrode design for fast potential sweep rates

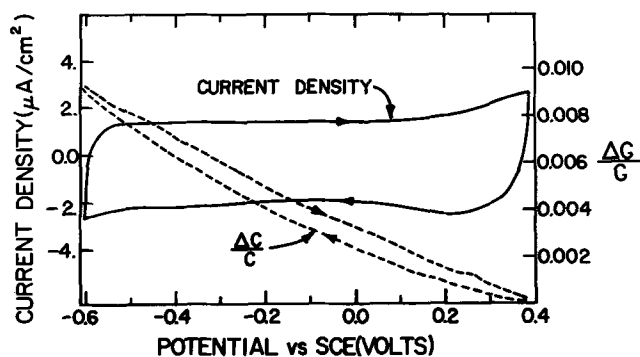


Fig. 3. Voltammetric electrochemical curve (—) and conductance change (---) for a 1.04  $\mu\text{m}$  tin oxide electrode in a 0.01M  $\text{Na}_2\text{SO}_4$  solution with a pH of 6. The curves are traversed every 19 sec.

film is then calculated from the conductance change using Eq. [1] and the measured tin oxide thickness. The effective free electron density of the tin oxide film is calculated to be  $1.4 \times 10^{20}$  electrons/ $\text{cm}^3$ . No ionic adsorption (conductance dip) could be detected on the tin oxide film by the conductance measurement. The film thickness for the tin oxide film is much larger than the free electron mean free path, therefore the surface scattering should not affect the conductance by a detectable amount. There is a slight hysteresis in the charging curve in Fig. 3 that is probably the result of a small oxidation-reduction reaction at the electrode surface.

Ionic adsorption at the electrode surface causes the conductance to decrease linearly with the adsorbed charge density as in Eq. [6]. The conductance-change proportionality constant,  $K$ , is different for each film and depends on a variety of fickle film characteristics, e.g., film surface roughness, surface impurities, thickness, free electron properties, and lattice defects. Figure 4 contains the cyclic voltammetry curves for a 6 nm gold film with and without  $\text{I}^-$  adsorption. The shaded area represents the increased charge density caused by  $\text{I}^-$  specifically adsorbing on the electrode surface. The model we have used in both the anion and cation adsorption involves no Faradaic current. The adsorption current is caused only by the increase in the double layer capacitance as the charged ion adsorbs on the surface of the electrode (21, 22). The adsorbing  $\text{I}^-$  charges add an additional component to the electrode current as they adsorb. The adsorbed  $\text{I}^-$  charge density is 4.8  $\mu\text{Coulombs/cm}^2$  and represents approximately a 2.0% surface coverage. We will assume this small surface coverage of adsorbed charges

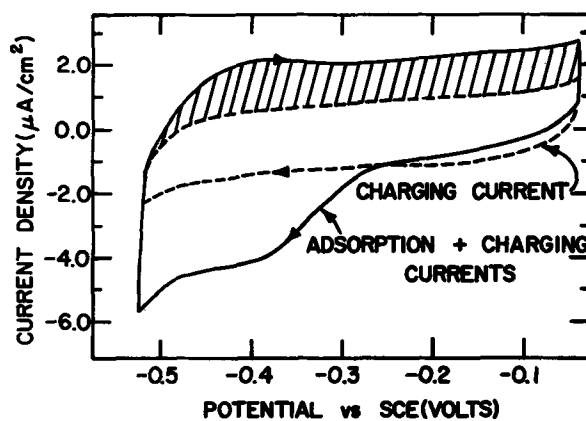


Fig. 4. Voltammetric electrochemical curves for a 6.0 nm thick gold film electrode. The electrolytes are 0.1M  $\text{Na}_2\text{SO}_4$  (---) and 0.1M  $\text{Na}_2\text{SO}_4$  plus 5.9 mM  $\text{NaI}$  (—) with a pH of 3.0. The curves are traversed every 13 sec.

probably affects the electrode charging current only slightly. Therefore, the change in the conductance caused by the  $I^-$  adsorption is the difference between the conductance change with and without  $I^-$  adsorption. The conductance change with and without  $I^-$  adsorption was 0.0038 and 0.0011, respectively, for the cyclic voltammetric curves of Fig. 4. This gives a  $K$  of  $9.0 \times 10^{-17} \text{ cm}^2$  for this gold film. This is more than a factor of two larger than the value predicted previously of  $3.5 \times 10^{-17} \text{ cm}^2$ . Figure 5 contains the results of several similar gold films of the same thickness (curves a-c) compared to the theoretical value (curve d). The variation in the sensitivity to adsorbed ions of the different gold films is probably caused by the slightly different surface characteristics of each film. These results do show that the electron scattering by point-surface charges is probably a major contributor to the conductance decrease although there probably are other effects occurring as previously mentioned. A partial sharing of electrons or formation of surface states will increase the surface scattering. For a more detailed theory of adsorption see Ref. (23).

As the adsorbed ion surface coverage increases above a few per cent the adsorbed ion charge density is no longer equal to the difference between the cyclic voltammetric curves as in Fig. 4. The adsorbed ionic layer acts more like a charged plane than a few randomly spaced point charges and thus the electron charging contribution to the conductance change is affected also. Figure 6 contains the conductance change as a function of apparent charge density (calculated as mentioned above) for  $Cs^+$  and  $I^-$  adsorption for a potential sweep from 0.0 to  $-1.0V$  vs. SCE. The  $Cs^+$  ion probably causes a greater change in the conductance because the electrode is charged negatively for  $Cs^+$  adsorption, increasing the electron density near the adsorbed charges at the surface while for  $I^-$  adsorption the electrode is charged positively. The value of  $K$  for these curves appears to be about three times larger than measured with smaller surface coverages. The approximate adsorbed ion surface concentrations can be calculated by using Eq. [6], the measured conductance change, and a  $K$  of  $9.0 \times 10^{-17} \text{ cm}^2$ . Figure 6 also shows the similarity in surface scattering by ions of opposite charge as predicted by Eq. [6].

Measuring the conductance can be a very sensitive way of detecting ionic adsorption. Figure 7 is the conductance change for  $Cd^{++}$  adsorption as the ionic concentration is increased. An ionic concentration on the order of  $100 \text{ nM}$  can easily be detected using a thin gold electrode. As is discussed in the remainder of this section, the ionic adsorption is diffusion limited for small concentrations, therefore, the sensitivity can be improved by decreasing the voltage sweep rate. The

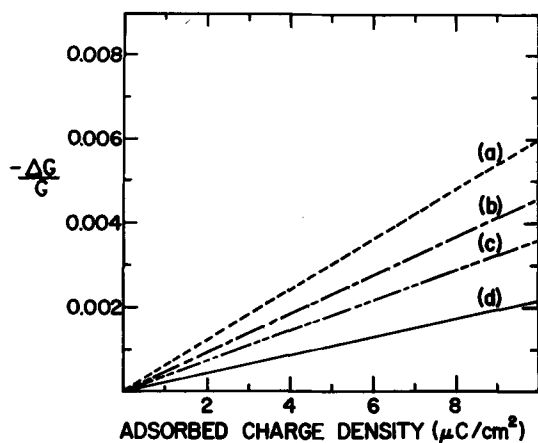


Fig. 5. The measured (curves a-c) and calculated (curve d) electrode conductance change for several different 6.0 nm thick gold electrodes as a function of adsorbed charge density.

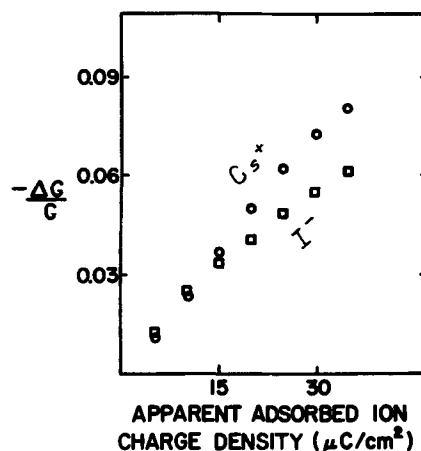


Fig. 6. The conductance change for  $Cs^+$  ( $\circ$ ) and  $I^-$  ( $\square$ ) adsorption as a function of the apparent adsorbed ion charge density. The potential sweep was from 0.0 to  $-1.0V$  at a rate of 0.06 V/sec. The electrolyte was 0.1M  $Na_2SO_4$  and 0.01M  $NaI$  or 0.01M  $Cs_2SO_4$  with a pH of 4.0.

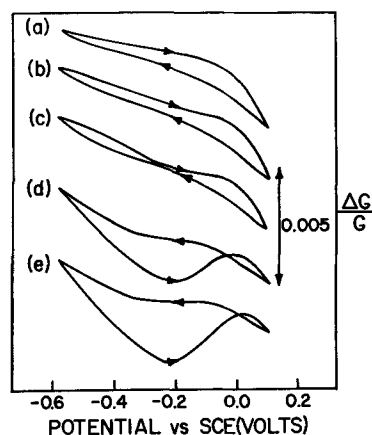


Fig. 7. Conductance curves for a gold electrode with a 0.01M  $Na_2SO_4$  electrolyte with a pH of 3.9 and (a) no  $CdSO_4$ , (b) 0.2 mM  $CdSO_4$ , (c) 0.53 mM  $CdSO_4$ , (d) 6.9 mM  $CdSO_4$ , (e) 13.5 mM  $CdSO_4$ . The curves are traversed every 18 sec.

impurity ion adsorption then becomes the limiting factor in detecting small adsorbed ion concentrations.

The conductance curves in Fig. 7 appear to have more occurring than simple charging and surface scattering. There seems to be two different adsorbed states for the  $Cd^{++}$  ion as observed from the decrease in conductance caused by adsorption, than the increase in conductance possibly caused by the reduction of  $Cd^{++}$ . A better explanation of this effect will require a more detailed study. Figure 7 illustrates the usefulness of conductance measurements in detecting differences in the adsorption process.

The ionic adsorption rate becomes diffusion limited with an increase in the electrode potential sweep rate. Figure 8 is the conductance change for a 10 mM  $NaI$  electrolyte with a pH of 6 for several different sweep rates. The conductance decrease at 0.0V is not as great for the faster sweep rates because the  $I^-$  adsorption is diffusion limited. The conductance at  $-1.0V$  does not change as the sweep rate is increased indicating that the desorption is complete at  $-1.0V$ .

Conductance measurements provide a reliable method of measuring the ionic diffusion coefficient,  $D$ . The conductance decrease caused by the ionic adsorption is a direct measure of  $\Gamma$ , as already demonstrated. Stepping the electrode potential from a position of no adsorption to a value where adsorption occurs and observing  $\Delta G/G$  as a function of time is a di-

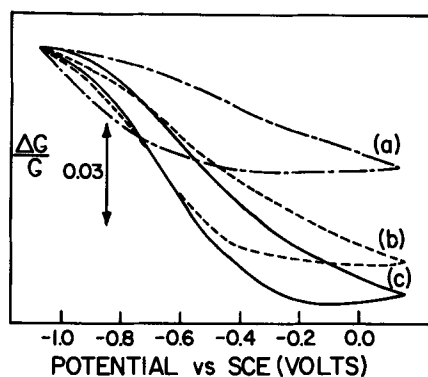


Fig. 8. The conductance of a gold film electrode with a 10 mM NaI electrolyte. The potential sweep rate is (a) 20 V/sec, (b) 2 V/sec, (c) 0.2 V/sec.

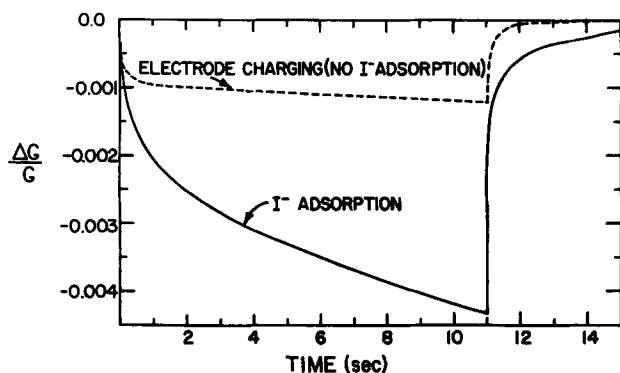


Fig. 9. The conductance as a function of time for a potential step from  $-0.05$  to  $-0.55$  V at  $t = 0$  sec and back again at  $t = 11$  sec. The electrolyte is the same as in Fig. 4.

rect measure of the ionic adsorption. The solid line in Fig. 9 is the electrode conductance, as a function of time, for the gold electrode and electrolyte used in Fig. 4 as the electrode potential is stepped from  $-0.05$  to  $-0.55$  V. The dotted line is the electrode conductance as the electrode potential is stepped without any NaI in the electrolyte. The difference between the dotted and solid lines should be directly proportional to  $\Gamma$ . Since the electrode charge is effectively screened within the first 1 nm of the electrolyte, the diffusion constant is the dominant factor controlling the rate of change of  $\Gamma$  as a function of time. Parsons (24) has shown that  $\Gamma$  depends upon the time,  $t$ , as

$$\Gamma/\Gamma_{eq} = 1 - \exp(-Dt/K_0^2) \operatorname{erfc}[(Dt)^{1/2}/K_0] \quad [10]$$

where  $\Gamma_{eq}$  is the equilibrium value of  $\Gamma$  for the potential step used and  $K_0$  is the isotherm constant. The equilibrium surface coverage,  $\Gamma_{eq}$ , is measured by holding the potential at  $-0.05$  V for 300 sec and measuring the change in the conductance,  $(\Delta G/G)_{eq}$ . The equilibrium value of  $\Delta G/G$  was 0.0088. The isotherm constant is approximated by using the relationship

$$K_0 = \Gamma_{eq}/C_0 \quad [11]$$

where  $C_0$  is the bulk adsorbing ion concentration. From Eq. [7] it is obvious that

$$(\Delta G/G)/(\Delta G/G)_{eq} = \Gamma/\Gamma_{eq} \quad [12]$$

The squares in Fig. 10 are the fractional surface coverage as a function of time measured from Fig. 9. The solid line is the fractional surface coverage calculated from Eq. [10] and using a  $D = 1.21 \times 10^{-5}$  cm<sup>2</sup>/sec. The similarity in shape of the measured and calculated curves is a good indication of the reliability of the data. The conductance measurements

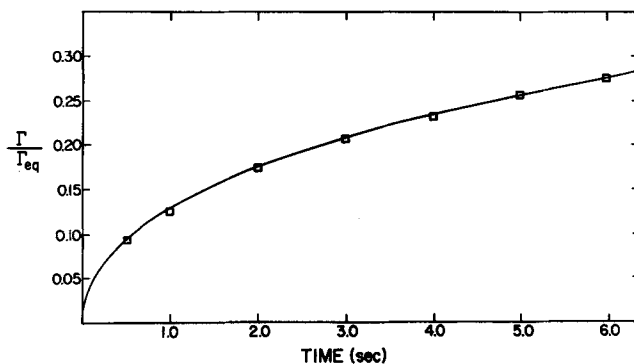


Fig. 10. The calculated (—) and observed (□) fractional change in the  $I^-$  surface coverage of a gold film electrode as a function of time. The observed values are taken from Fig. 9.

have provided a reliable method of measuring ionic diffusion coefficients.

### Conclusions

The conductance decrease caused by adsorbed ions is probably a result of the free electron scattering by the surface point charges. Other effects probably contribute to the conductance change, e.g., electron tunneling, creation of chemical bonds at the surface, or surface states created by the adsorbed particle. The conductance measurements provide a reliable method of quantitatively measuring the adsorbed ion density at the electrode surface. The sensitivity of the conduction measurements to changes in surface free electron concentration is inversely proportional to the free electron charge density per unit area of the film. The sensitivity to changes in adsorbed ion concentration is directly proportional to the ratio of electron mean free path length to film thickness. Conductance measurements can be sensitive to different types of adsorption as demonstrated with the adsorption of  $Cd^{++}$  on gold. Thin film conductance measurements provide a versatile method of studying many basic electrode processes.

### Acknowledgment

This work was partially supported by the National Science Foundation Grant No. GP 13767.

Manuscript submitted May 21, 1973; revised manuscript received July 10, 1974. This was Paper 276 presented at the Chicago, Illinois, Meeting of the Society, May 13-18, 1973.

Any discussion of this paper will appear in a Discussion Section to be published in the June 1975 JOURNAL. All discussions for the June 1975 Discussion Section should be submitted by Feb. 1, 1975.

The publication costs of this article have been assisted by the U.S. Government.

### SYMBOLS

$C_0$	adsorbing ion concentration in ions/cm <sup>3</sup>
$D$	diffusion coefficient
$e$	electron charge
$h$	film thickness (nm)
$\hbar$	Planck's constant/ $2\pi$
$G$	electrical conductance
$\Delta G$	the change in $G$
$k$	free electron wave vector
$K$	conductance change proportionality constant
$K_0$	isotherm constant
$m$	electron mass
$n$	free electron volume density
$N$	total number of conduction electrons per unit area of a film
$\Delta N$	the change in $N$
$P$	the probability of specular reflection from the film surface of the conduction electrons
$r$	distance from electrode surface

$S_N$	sensitivity of conductance to free electron density changes
$S_D$	sensitivity of conductance to free electron surface scattering
$t$	time
$V$	screened coulomb potential
$\Gamma$	number of adsorbed charges per unit area
$\Gamma_{eq}$	the equilibrium value of $\Gamma$
$\theta$	angle of incidence of the conduction electrons with the film surface
$\lambda_0$	free electron mean free path length
$\sigma$	thin film conductivity
$\sigma_0$	bulk conductivity

## REFERENCES

- H. Shimizu, *Electrochim. Acta*, **13**, 27 (1968).
- H. Shimizu, *ibid.*, **13**, 45 (1968).
- H. Shimizu, *ibid.*, **14**, 55 (1969).
- J. O'M. Bockris, B. D. Cahan, and G. E. Stoner, *Chem. Instrum.*, **1**, 273 (1969).
- Katumi Niki and Takehide Shirato, *J. Electroanal. Chem.*, **42**, App 7 (1973).
- W. N. Hansen, *Surface Sci.*, **16**, 205 (1969).
- W. J. Anderson and W. N. Hansen, *J. Electroanal. Chem.*, **43**, 329 (1973).
- W. J. Anderson and W. N. Hansen, *ibid.*, **47**, 229 (1973).
- R. F. Greene, in "Solid State Surface Science," Vol. I, p. 87, Mino Green, Editor, Marcel Dekker, New York (1969).
- G. Bonfiglioli, E. Coen, and R. Malvano, *Phys. Rev.*, **101**, 1281 (1956).
- P. Zwietering, H. L. T. Koks, and C. Van Heerden, *Phys. Chem. Solids*, **11**, 18 (1959).
- G. Ehrlich, *J. Chem. Phys.*, **35**, 2165 (1961).
- J. Kirkland and J. Joe, *J. Anal. Chem.*, **26**, 1340 (1954).
- K. Fuchs, *Proc. Cambridge Phil. Soc.*, **34**, 100 (1938).
- Charles Kittell, "Introduction to Solid State Physics," 3rd edition, John Wiley & Sons, Inc., New York (1966).
- R. F. Greene and R. W. O'Donnell, *Phys. Rev.*, **147**, 599 (1966).
- H. J. Juretschke, *Surface Sci.*, **2**, 40 (1964).
- Y. Namba, *J. Appl. Phys.*, **39**, 6117 (1968).
- E. H. Sondheimer, *Advan. Phys.*, **1**, 1 (1952).
- W. N. Hansen, *J. Opt. Soc. Am.*, **63**, 793 (1973).
- R. Parsons and A. Stockton, *J. Electroanal. Chem.*, **25**, App 10 (1970).
- Richard Payne, *ibid.*, **41**, 277 (1973).
- Robert Gomer and Lynn W. Swanson, *J. Chem. Phys.*, **38**, 1613 (1963).
- Roger Parsons, in "Advances in Electrochemistry and Electrochemical Engineering," Vol I, p. 27, Paul Delahay, Editor, Interscience Publishers, New York (1961).

## Studies of a Nitrogen Dioxide Sensitive, Chalcogenide Glass Electrode

Raymond Jasinski,\* Gabriel Barna, and Isaac Trachtenberg\*

Texas Instruments Incorporated, Dallas, Texas 75222

## ABSTRACT

Properly activated  $Fe_nSe_{60}Ge_{28}Sb_{12}$  electrodes, when exposed to nitrogen dioxide in air, develop shifts in their steady-state potentials and, at constant potential, develop cathodic currents which are functions of the  $NO_2$  concentration in the gas phase. This reversible response, and the selectivity in the presence of  $O_2$ ,  $CO$ ,  $SO_2$ ,  $CH_4$ ,  $NO$ ,  $NO_3^-$ , and  $NO_2^-$ , cannot be reconciled with conventional redox, pH, or solubility product mechanisms, but must involve a specific chemisorption of the  $NO_2$  by the electrode surface.

The potentiometric measurement of species in solution may be accomplished through a number of physicochemical processes, e.g., selective diffusion of ions within membranes (the glass pH electrode) and the mass action control of electrode solubility coupled with selective diffusion of ions within the electrode structure (the silver sulfide and lanthanum fluoride electrodes). The catalysis of electron transfer processes by otherwise inert electrodes such as platinum has been used to measure, potentiometrically and amperometrically, the concentration of oxidizing and reducing agents.

Described in this paper are some of the properties of a chalcogenide glass electrode ( $Fe_nSe_{60}Ge_{28}Sb_{12}$ ), in an aqueous electrolyte, for sensing directly nitrogen dioxide in air and other gases. As will be shown, the performance of this electrode cannot be readily reconciled with such "classical" sensing mechanisms but appears to involve specific adsorption of  $NO_2$  onto the electrode surface.

## Experimental

Two test cell configurations were used to provide the sample, electrolyte, electrode interface necessary for sensing electroactive gases. The first, the "gas dif-

fusion electrode configuration," consisted of porous sensor, reference and counterelectrodes separated by an inert matrix containing the electrolyte. This system was particularly well suited: (a) for the measurement of current generated, at constant potential, by sensors exposed to  $NO_2$ , (b) for minimizing reaction of nitrogen dioxide with the bulk of the aqueous electrolyte, as well as (c) for providing short term, steady-state potential data. The sensor electrodes used with this configuration were formed by heating to  $290^\circ C$  for 3 min, a paste of Teflon emulsion and approximately 0.12g of powdered glass ( $\approx 200$  mesh) that had been spread onto a  $5\text{ cm}^2$  tantalum screen disk. The electrolyte was contained in two 30 mil thicknesses of fiber glass filter paper. The cell end plates were machined from Teflon block. Gas was delivered into the cell via stainless steel fittings screwed into the end plates; electrical contact was accomplished by screwing these fittings onto tantalum screens in contact with the test, counter, and reference electrodes. Anodized silver chloride and silver sulfate on silver screen were used as the reference electrodes in the appropriate electrolytes.

The second test assembly, more suited for long term, quantitative potentiometric studies was the "ion specific electrode configuration" (subsequently designated as "ISE configuration") and made use of the sensor material in the form of a nonporous disk, 7 mm in diameter. The assembly, discussed in more detail elsewhere (1),

\* Electrochemical Society Active Member.

Key words: nitrogen dioxide, gas sensors, chalcogenide glass electrodes, ion selective electrodes, specific chemisorption.

involved a wick taped over the sensing surface of the electrode. In this way the sensing element, which protruded above the surface of the electrolyte, was directly exposed to the gas being monitored, while only that minimal amount of electrolyte necessary to complete the solution circuit reached the electrode surface by capillary action from an electrolyte reservoir.

A perforated commercial Teflon membrane was used to separate the ISE sensor electrode from the gas phase, serving primarily to minimize drying of the electrolyte on the wick, while still permitting access of the gas to the sensor surface. The same selectivities and sensitivities were obtained in the ISE configuration with the membrane in place and in the gas diffusion electrode configuration in which a membrane was not used. The PermaProbe (Beckman Instruments Inc.) was used as the reference electrode in these experiments.

Preanalyzed gas mixtures of  $\text{NO}_2$  in air and in  $\text{N}_2$  were purchased from Matheson Company in concentrations of 1.2, 25, 100, 350, and 392 ppm. Mixtures of  $\text{CH}_4$ ,  $\text{CO}$ , and  $\text{NO}$  in nitrogen were obtained from the same supplier.

The glass sensing materials were prepared as described in Ref. (2) and (3). The term "Fe 1173" is used to designate the material  $\text{Fe}_n\text{Se}_{60}\text{Ge}_{28}\text{Sb}_{12}$ , where  $n$  falls between 1.3 and 2. A correlation of composition with performance was not made for the sensing process described in this paper. Since there was a variation in activity from batch to batch of glass melt, a dependence of activity on composition must exist. A similar situation was found in the use of this glass for sensing ferric ion in solution (3).

The pretreatment steps necessary to convert this glass material into a  $\text{NO}_2$  selective sensor are discussed below.

Potential measurements were made with a Hewlett-Packard 3440A digital voltmeter; a Keithley Model 610C electrometer provided the necessary impedance matching. A Wenking Model 61-TR potentiostat was used for the constant potential measurements.

### Results and Discussion

Shown in Table I are the potentials of a properly activated, (see below) porous, Teflon-bonded, Fe 1173 electrode exposed to a series of gases; the electrolyte was 7N  $\text{H}_2\text{SO}_4$ . The electrochemical activity of these gases on platinum is also shown in the table. Results similar to these were obtained with an electrolyte of 1M KCl, pH 6 and with  $(\text{NH}_4)_2\text{HPO}_4$ , pH 8 in the ISE configuration.

Essentially then, the Fe 1173 electrode responded only to  $\text{NO}_2$ , and gave no response to reducing agents and to oxygen. Stronger oxidizing agents such as  $\text{H}_2\text{O}_2$  also gave significant responses, similar to results reported previously (2).

Included in the table are the responses of the undoped 1173 glass. Since the parent glass itself responds to reducing agents, in much the same manner as does a poor platinum black, and the iron-doped glass does not, it can be concluded that the two phase, iron-doped material does not consist of a particular iron-rich phase in a matrix of substantially unreacted, excess 1173 glass.

The potentiometric response of the Fe 1173 glass to  $\text{NO}_2$  in air and in nitrogen, over the concentration range of 1-392 ppm, yielded a potential-log concentra-

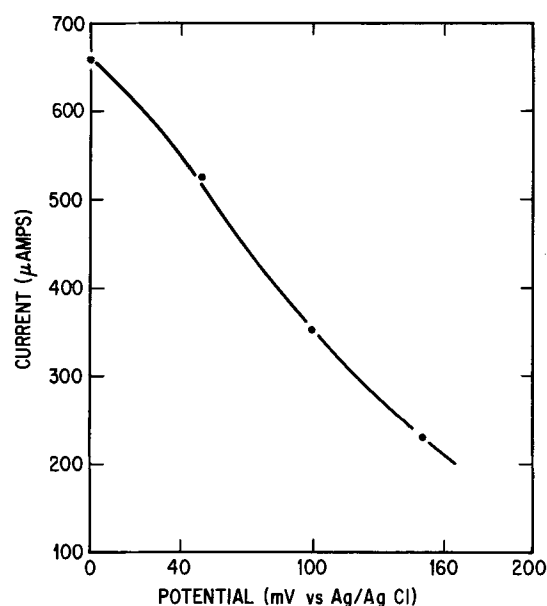


Fig. 1. Shown is the cathodic current-potential relationship for a Teflon-bonded, porous Fe 1173 electrode exposed to 350 ppm  $\text{NO}_2$  in  $\text{N}_2$ ; 1M KCl, pH 2 was the electrolyte.

tion dependence of a nominal slope of 70 mV/decade (1).

As previously described (3), Fe 1173 is an electronic conductor, which property is apparently maintained after heating in air (during the preparation of the Teflon-bonded structure). This therefore provided the possibility of sensing  $\text{NO}_2$  in air amperometrically as well as potentiometrically. Shown in Fig. 1 is the potential dependence of the steady-state current for one Teflon-bonded electrode exposed to a constant 350 ppm  $\text{NO}_2$  in nitrogen; 1M KCl, pH 2 was the electrolyte. At potentials more positive than +100 mV (vs. Ag/AgCl) no signal was observed from air,  $\text{SO}_2$ , or 100 ppm  $\text{NO}$  in the gas cavity. These results then are consistent with the potentiometric selectivity data shown in Table I. At more negative potentials, cathodic oxygen reduction was observed; at zero millivolts, a current of 40  $\mu\text{A}$  was generated by 100%  $\text{SO}_2$ . The fact that this sensing current is potential dependent does not, of course, obviate a concentration dependence; the exchange current for a general redox process involves concentration terms (5). For this particular experimental system, the cathodic current resulting from the passage of variable concentrations of nitrogen dioxide over the electrode surface held at a potential of +150 mV, was directly proportional to the concentration of nitrogen dioxide in the gas phase. Similar potential-concentration dependence situations have been reported for the amperometric determination of  $\text{CO}$  and ethanol on platinum (6, 7).

The upper operating limit of  $\text{NO}_2$  concentration has not been explored in any detail. A concentration of 10%  $\text{NO}_2$  was detrimental, concentrations of 390 ppm had not brought about any immediate adverse effects. However daily exposure ( $\approx 4$  weeks) of the sensor to 390 ppm nitrogen dioxide resulted in a slow deactivation of the electrode surface. This was signaled by a gradual increase in the response time and a slow decrease in the net signal observed, which, of course, may have also involved the slow approach to steady state. The initial potential remained relatively constant; altering the position of the wick on the ISE configuration did not restore activity. Teflon-bonded electrodes, not continuously exposed to  $\text{NO}_2$ , maintained their activity for at least 6 months.

These then are the general performance characteristics of this material for sensing nitrogen dioxide directly. The remainder of this paper is concerned with

Table I. Sensor potentials vs. gas composition (vs. Ag/Ag $_2\text{SO}_4$ )

Gas	Platinum black, mV	Fe 1173, mV	1173, mV
$\text{N}_2$	+620	+41	+152
Air	+720	+45	+161
$\text{NO}_2$ (350 ppm in $\text{N}_2$ )	+791	+365	+415
$\text{NO}$ (100 ppm in $\text{N}_2$ )	—	+44	—
$\text{CO}$ (1% in $\text{N}_2$ )	+100	+47	+106
$\text{SO}_2$ (100%)	-52	+48	-30
$\text{CH}_4$ (1% in $\text{N}_2$ )	—	+44	—

establishing, at least in general terms, some of the characteristics of the sensing mechanism.

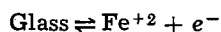
First of all, the experiments carried out to develop the potentiometric response indicated that the sensing process was reversible, *i.e.*, removal of NO<sub>2</sub> from the gas phase restored the electrode to its initial potential and hence its initial condition.

Second, the chemical composition and oxidation state of the electrode surface were particularly critical features of the sensing process. An "activation" step was required before the sensitivity and selectivity properties could be reproducibly observed. Mechanical removal of the surface of a deactivated electrode, followed by a repetition of the activation step restored performance. Of the variety of techniques considered for "activation," only heating in air at 290°C for 3 min was effective in generating reproducibly, a highly active surface with fast response time and a high degree of selectivity. A number of sensors showed activity and selectivity for sensing NO<sub>2</sub> without pretreatment. The majority yielded slow responses, if at all, to nitrogen dioxide and varying degrees of selectivity relative to oxygen. Such electrodes could not be activated by chemical oxidation, such as equilibration with 30% H<sub>2</sub>O<sub>2</sub>, or by potentiostating at +400 mV *vs.* Ag/AgCl. Equilibration of these electrodes with 10<sup>-1</sup> molar ferric nitrate did not produce sensitivity to NO<sub>2</sub>, although such a procedure was effective, in almost all cases, in generating activity for ferric ion (3).

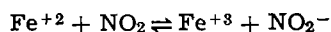
Although the ferric ion sensitive electrodes were not particularly sensitive to NO<sub>2</sub>, the NO<sub>2</sub> active electrode was indeed sensitive to ferric ion, after, not before, subsequent equilibration in 10<sup>-1</sup>M Fe<sup>+3</sup> solution, the normal activation procedure (3) for ferric ion sensing. The potential-log ferric ion concentration dependence was identical to that reported for the ferric ion activated electrode, except that the actual potentials were shifted more cathodic by about 300 mV after activation for nitrogen dioxide by heating in air. Since air normally affords a potential shift of the order of 30-40 mV (*vs.* N<sub>2</sub>) on a low selectivity, nonactivated electrode, this 300 mV shift cannot solely represent a deactivation of the electrode toward oxygen sensing.

It would appear from these experiments that: (i) there is a similarity, if not an identity in the electrode sites involved in sensing NO<sub>2</sub> and Fe<sup>+3</sup> (before adsorption of Fe<sup>+3</sup>), (ii) additional sites are involved, at least in part, in determining the base line potential (*i.e.* in the absence of nitrogen dioxide and ferric ion), and (iii) these sites are distinctly different in the two sensing systems. This point is discussed again below.

The sensitivity of the NO<sub>2</sub> electrode to ferric ion could imply a sensing mechanism "of the second kind," *i.e.*, whereby the electrode surface is in equilibrium with iron species dissolved off the electrode surface, which concentration is altered by NO<sub>2</sub>. Using ferrous ion as an example, the following processes could, in principle, take place



followed by

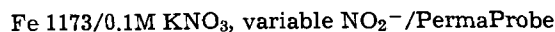


The ferric ion would then be sensed by the electrode. There are a number of problems with this mechanism. For example, (i) oxygen in the air has the same potential as 350 ppm NO<sub>2</sub> to bring about the oxidation of ferrous ion or other reduced species, and yet there is no response to oxygen, Table I, and (ii) there is no obvious process by which the electrode would be reversible, after nitrogen dioxide is removed from the gas phase, *i.e.*, by which the ferric ion or other oxidized species would be removed from the electrode surface in order to restore the electrode to its initial potential.

Consider next a number of possible redox mechanisms to account for the sensitivity and selectivity of the electrode material. The lack of interaction of the glass with NO (Table I) and the high potential-log concentration slope (1) precludes catalysis of the NO<sub>2</sub>/NO

couple. If the surface were interacting with the NO<sub>2</sub>/NO<sub>2</sub><sup>-</sup> couple, as might be implied by this slope, it would be expected that the electrode would be responsive to nitrite ion, *i.e.*, equilibrium must be approachable from both ends of the redox couple.

Shown in Table II are the potentials for the sensor (ISE configuration) in the following cell



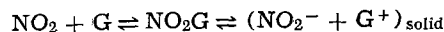
Thus over at least three orders of magnitude the electrode is insensitive to nitrite ion. The small increase in potential between 10<sup>-4</sup> and 10<sup>-3</sup>M could be ascribed to air oxidation of nitrite, which was likely. Furthermore it would be expected that exposure of the electrode to the reduced half of the couple would lower potential rather than increase potential. Identical responses of the electrode to NO<sub>2</sub> were obtained with and without 10<sup>-2</sup>M nitrite in a 1M KNO<sub>3</sub>, pH 9.2 electrolyte. The generation of a cathodic current in the amperometric sensing of nitrogen dioxide removes the possibility of involvement of the NO<sub>2</sub>/NO<sub>3</sub><sup>-</sup> couple.

A possible, indirect sensing mechanism would be that the electrode is actually detecting a pH change via a solution reaction of NO<sub>2</sub>, *e.g.*, 2NO<sub>2</sub> + H<sub>2</sub>O → HNO<sub>2</sub> + H<sup>+</sup> + NO<sub>3</sub><sup>-</sup>.

However the potential of the NO<sub>2</sub> active electrode was independent of pH in the range of 2.5-8.5. This observation is also consistent with an electrode mechanism not involving the dissolution of iron species off the electrode, as described above, since the solubilities of ferric and ferrous hydroxides vary considerably over this pH range while the electrode potential does not.

Thus to explain sensor performance we are left with specifying some form of interaction of NO<sub>2</sub> with the electrode rather than a conventional catalysis of solution redox couples. The argument has been put forth, for Fe<sup>+3</sup> sensing (1), that the electrode itself was the reduced form of the couple. This may well be true, and would account for the sensitivity of the electrode to strong oxidizing agents such as peroxide and persulfate (3). However it is still necessary to explain, or rationalize, why the electrode is not further reducible by an atmosphere of 100% SO<sub>2</sub>. It is also necessary to explain why this "reduced" electrode is not responsive to oxygen in air, even though weaker oxidizing agents such as 1 ppm NO<sub>2</sub> and 10<sup>-5</sup>M Fe<sup>+3</sup> evoke electrode responses.

It is therefore proposed that this specific interaction of nitrogen dioxide and the sensor surface is one of reversible chemisorption, *i.e.*



where G represents the properly activated surface. This mechanism then can be viewed as a redox process but preceded by adsorption reaction which provides the specificity observed. The absence of a pH response implies that this adsorption process does not involve displacement of hydroxide ion from the surface.

If charge is delivered to the surface, as in the amperometric sensing mode, the above reaction could continue, presumably through the irreversible generation of nitrite ion in solution: (NO<sub>2</sub><sup>-</sup> + G<sup>+</sup>) + e<sup>-</sup> → NO<sub>2</sub><sup>-</sup> + G, restoring the original activated glass.

A somewhat heuristic rationalization for the behavior of the electrode relative to the activation step and electrode activity can be made as follows. There are two classes of electrochemically active sites (designated

Table II. Sensor response in variable nitrite solution

Concentration NO <sub>2</sub> <sup>-</sup> added, M	Potential, mV
0	+122
10 <sup>-6</sup>	+119
10 <sup>-4</sup>	+119
10 <sup>-3</sup>	+126

nated as G and G') initially present in the original Fe 1173 glass, but differing in concentration from sensor slice to sensor slice. It is postulated that sites G' can catalyze the  $O_2/H_2O$  couple, resulting a dependence of potential for untreated sensors on the oxygen content of the atmosphere above the sensor. Since this would be a mixed potential, the degree of oxygen sensitivity would depend on the concentration of G' sites in the particular glass. It is also postulated that these G' sites strongly adsorb  $O_2$  which is only slowly displaced via purging the gas cavity with nitrogen, accounting for the small change in potential (30 mV) obtained on substituting  $N_2$  for air in the gas phase. This is consistent with the behavior of platinum black electrodes under identical experimental conditions (Table I). It is also likely that the G' sites also set the initial potential via a corrosion-dissolution process. In any event, air oxidation at 290°C destroys these sites, while leaving sites G appreciably unaffected and it is these sites that are active to adsorption of nitrogen dioxide. This destruction of potential-determining G' sites would account for the 300 mV cathodic shift in potential for  $Fe^{+3}$  sensing obtained by heating the electrode in an oxidizing atmosphere (air). Since these G' sites are removed, the  $NO_2$  active sites now dominate the potential-determining properties of the glass and high sensitivity of  $NO_2$  results.

Since activity to ferric ion remains after activation for nitrogen dioxide but at more cathodic potentials, it is inferred that these G sites are the same described previously (3) as "oxidized Fe 1173." These are the sites which interact strongly with ferric ion to generate a new set of sites which are active in ferric ion sensing. Since the ferric ion activated electrodes are poorly sensitive to nitrogen dioxide, if at all, it is to be inferred that these "new" sites do not adsorb nitrogen dioxide, being blocked by the presence of strongly adsorbed ferric ion. Following from this argument then is a possible mechanism for electrode deactivation. Slow solubility product dissolution (or corrosion) of the electrode injects ferric ion into the electrolyte, which then adsorbs onto the nitrogen dioxide active sites. Further data are required to evaluate this deactivation mechanism.

Now is such an adsorption-sensing mechanism plausible? The energy of the adsorption process was estimated as follows. Little potential change was observed below 0.3 ppm  $NO_2$ . Extrapolating the potential change from 1 ppm  $NO_2$  (mole fraction  $10^{-6}$ ) to mole fraction unity, at 70 mV/decade, and converting to units of kilocalories/equivalent yields a value of 8-9 kcal, which is of a reasonable order of magnitude for weak and reversible chemisorption.

As precedence, are cited the adsorption of chloride ion onto platinum which has been shown (8) to provide linear potential-log concentration plots over the range of  $10^{-1}$ - $10^{-4}$ M chloride. Such processes are apparently characterized by potential log concentration slopes in excess of the values expected from the Nernst equation based on charge transfer.

The adsorption of chloride onto platinum gave a slope of approximately 90 mV/decade.

### Summary

A properly activated Fe 1173 electrode is inherently sensitive to nitrogen dioxide in air. With the use of a porous, Teflon-bonded gas diffusion electrode, measurements of  $NO_2$  can also be made amperometrically,

i.e., current proportional to concentration at fixed potential.

The electrode response is reversible, i.e., removing  $NO_2$  from the gas phase restores the initial potential, and hence the initial state of the electrode surface. This precludes any mechanism involving permanent change of the electrode surface and/or the electrolyte by  $NO_2$ .

The absence of an electrode response of  $NO$ ,  $NO_2^-$ ,  $NO_3^-$ , and  $H^+$ , in both the amperometric and potentiometric modes, precludes sensing mechanisms based on redox couples involving these species. The absence of an electrode response to high concentrations of oxygen, CO, and  $SO_2$ , normally electroactive gases, further precludes a general redox mechanism and implies a specific reaction between the glass and nitrogen dioxide. The necessity for appropriately pretreating the electrode surface to generate selectivity and sensitivity, taken together with the variable initial performance of freshly prepared (unactivated) sensor, leads to a dual site theory for the determination of electrode potential. The response of electrodes, as activated for nitrogen dioxide, to ferric ion reinforces this dual site concept and identifies similarities in surface composition for the two sensing systems.

It is further postulated that these nitrogen dioxide active sites function via a specific chemisorption mechanism, which involves the glass itself as the "reduced half of the couple." The energy calculated from the observed potential shifts on contacting the electrode with nitrogen dioxide is consistent with such a mechanism. Precedence is also available for adsorption effects resulting in linear potential-log concentration dependencies and with slopes greater than expected from charge transfer processes.

Manuscript submitted Jan. 1, 1974; revised manuscript received July 18, 1974. This was Paper 358 presented at the San Francisco, California, Meeting of the Society, May 12-17, 1974.

Any discussion of this paper will appear in a Discussion Section to be published in the June 1975 JOURNAL. All discussions for the June 1975 Discussion Section should be submitted by Feb. 1, 1975.

The publication costs of this article have been assisted by Texas Instruments Incorporated.

### REFERENCES

1. G. Barna and R. Jasinski, *Anal. Chem.*, **42**, 1834 (1974).
2. C. Baker and I. Trachtenberg, *This Journal*, **118**, 571 (1971).
3. R. Jasinski and I. Trachtenberg, *ibid.*, **120**, 1169 (1973).
4. P. Delahay, "Double Layer and Electrode Kinetics," p. 164, John Wiley & Sons, Inc., New York (1965).
5. H. Bay, K. Blurton, H. Lieb, and H. Oswin, *Am. Lab.*, p. 57 (July 1972).
6. G. Holleck, J. Bradspies, and S. Brummer, Paper 285 presented at Boston, Massachusetts, Meeting of the Society, Oct. 7-11, 1973.
7. R. Jasinski, M. Salomon, and H. Furumoto, in "Electrochemical Contributions to Environmental Protection," Theodore R. Beck, Christie G. Enke, Olin B. Cecil, John McCallum, and Stanley T. Wlodek, Editors, pp. 108-120, The Electrochemical Society Softbound Symposium Series, Princeton, N. J. (1972).
8. A. Frumkin, in "Transactions of the Symposium on Electrode Processes," E. Yeager, Editor, p. 2, John Wiley & Sons, Inc., New York (1961).



# A Palladium Hydride pH Electrode for Use in Buffered Fluoride Etch Solutions

Raymond Jasinski\*

Texas Instruments Incorporated, Dallas, Texas 75222

## ABSTRACT

pH measurements can be made in aerated, concentrated, aqueous  $\text{NH}_4\text{F-HF}$  etch solutions with palladium electrodes cathodically charged to palladium hydride. Electrode life and stability in ammonium fluoride, as well as in  $\text{NH}_2\text{SO}_4$ , pH 3.6 sodium citrate and in pH 8 ammonium phosphate are enhanced by maximizing the palladium hydride concentration, electrode volume as well as volume to surface ratio. Electrode lifetimes have been measured in the range of 7-14 days for all solutions, times which are significantly longer than have been reported previously in the literature for palladium hydride electrodes.

Ammonium fluoride-hydrogen fluoride solutions are widely used in the electronics industry as etchants (1, 2). The etch rates of these solutions are a function of pH, a parameter which must therefore be monitored and controlled. Because of the reactivity of these solutions, the glass pH electrode, obviously, is not applicable to this measurement. Use of the platinum  $\text{H}_2/\text{H}^+$  electrode for pH measurements on a routine basis is complicated: (i) by the need for a constant partial pressure of hydrogen in the test solution; and, to a lesser extent, (ii) by the possibility of evaporating HF during the hydrogen equilibration period and thus altering the pH. The use of the quinhydrone electrode to measure pH in HF solutions has been described (3-5). Besides the inconvenience of adding a chemical (quinhydrone) to the test solution, this electrode is subject to interference by the large amounts of ammonium ion present in these "buffered etch" solutions (6); indeed pronounced discoloration and potential drift were found. Interference from ammonium ion is also to be expected with ion exchange membrane pH electrodes recently proposed for use with acid HF solutions (7).

This paper describes the application of the palladium hydride/ $\text{H}^+$  couple to the direct measurement of pH in concentrated, undiluted  $\text{NH}_4\text{F-HF}$  solutions.

The literature on palladium/palladium hydride electrodes up to 1961 is reviewed in Ref. (6); subsequent developments are summarized in Ref. (8); other and more recent examples of application are given in Ref. (9-12). No literature is available, however, on application of this electrode system to the buffered fluoride etch solutions. Furthermore, the published lifetimes of the palladium hydride electrode in solutions containing dissolved air have been of the order of a few hours to a day, times which are too short for the purposes of routine, quality control pH monitoring.

According to the literature (13-16), dissolved oxidants (including oxygen) also result in inaccurate pH and reference electrode potentials due to depolarization of the palladium hydride electrode. It is shown below that electrode lifetimes of the order of 1-2 weeks can be obtained by proper selection of the electrode volume and surface to volume ratio, even in the presence of dissolved oxygen.

## Experimental

The palladium metal used in these experiments (99.99% pure) was obtained from Engelhard Industries, Incorporated. Electrodes were formed from: (i) foil, 1  $\text{cm}^2$  10 mil thick (after plating with palladium black), sealed into acrylic plastic; (ii) rod, 0.25 in.

diameter, 1 cm long, imbedded in acrylic plastic and imbedded in Teflon; (iii) rod, 0.25 in. diameter, with a 2 cm length exposed to the test solution, and with 0.5 cm imbedded in the acrylic rod; (iv) rod, 0.25 in. diameter, 2 mm exposed to solution, and 8.0 mm imbedded in Teflon. The second test electrode configuration will be referred to in the text as the "disk configuration." Ohmic contacts were made within the electrode bodies so that palladium was the only metal in contact with the solution (17). Some testing was made with palladium wire (2 cm  $\times$  50 mil diameter) containing 1000 ppm nickel, as well as some copper (200 ppm) and gold (100 ppm). The trends observed with this electrode were comparable to those obtained with the purer material, except that the potentials were about 20 mV more negative.

Before use, all electrodes were cleaned with aqua regia and immediately plated with palladium black in the standard manner (6). It was also possible to form palladium black by first charging the smooth cleaned surface to palladium hydride and then immersing the electrode in standard palladium plating solution. Electrodes which were previously plated and used in the studies to be described, were replated in this manner without removal of the previous plate. This reactivation procedure was carried out before and after each recharging cycle. Unless this was done, abnormal, pronounced stirring dependencies were observed.

Palladium hydride was always formed by cathodizing the electrode in 1N  $\text{H}_2\text{SO}_4$  under nitrogen at constant current or at constant potential (provided by a Wenking Model 70 HC 3 potentiostat). The details of the charging procedure are discussed below. Platinum screen was used as the counterelectrode; Orion double junction electrodes (designated "dj") and the Beckman PermaProbe were used as references. The maximum theoretical input charge is based on the mass of palladium present and the composition  $\text{PdH}_{0.6}$ .

It has been pointed out in Ref. (8), that a constant current charge is 60-90% efficient in forming palladium hydride, the remainder of the charge going into the formation of  $\text{H}_2$ . It is assumed, in this work, that the charging process approaches 100% in efficiency. As will be shown, this assumption is consistent with the observed forms of the charging curves at constant current and at constant potential. The general conclusions to be drawn from this work remain valid as long as a constant fraction of the total input charge is converted to palladium hydride. Since the most likely mechanism for loss of PdH during charges is recombination to  $\text{H}_2$  (see below), the assumption of "constant fraction" is likely to be valid.

The platinum  $\text{H}_2/\text{H}^+$  electrode was established by purging with tank hydrogen for 30 min the appropriate

\* Electrochemical Society Active Member.  
Key words: palladium hydride, pH electrode, fluoride etch solutions.



electrolyte containing a platinized platinum wire sealed with heat-shrinkable Teflon tubing.

Electrolytes were prepared from reagent grade chemicals. No attempt was made to remove the trace heavy metal content which might plate on the palladium hydride electrode. The primary test solutions used to evaluate electrode design and consistency of performance with published data (6-12) were: 1N  $H_2SO_4$ , 0.1M sodium citrate (pH 3.6), and 0.5M  $(NH_4)_2HPO_4$  (pH 8). pH calibration was accomplished with commercial buffers. The compositions of the various ammonium fluoride-hydrogen fluoride solutions used are given in the text.

Stirring was accomplished with a paddle stirrer rotated at approximately 250 rpm in a constant solution volume of 175 ml. The stirring dependencies discussed below refer to the potential shifts obtained 1 min after this stirrer was turned off. There was no distinguishable effect of purging the test solutions with air vs. stirring in an open beaker after first saturating the solution with air. Since the pH 8 solution absorbed carbon dioxide from the air resulting in a decrease in pH, the data reported were taken after readjusting the pH to 8 with sodium hydroxide.

The measurements in the aerated pH 3.6 citrate solution were complicated by the formation, after about 5 days, of a gelatinous precipitate on the electrodes. This was accompanied by a slow drift of the cell potentials to more negative values and a decrease in the stirring dependence. Daily replacement of the test solutions avoided repetition of this phenomenon; data was taken immediately after the electrodes were exposed to fresh aerated solution.

The electrode life studies in semiconductor grade Texas Instruments Incorporated "common oxide etch" were made on stirred, aerated solutions. Because of the evaporation of water, fresh solution was put into the electrode twice daily, before recording data.

Potentials were measured to 0.1 mV with a Corning Model 101 Digital Electrometer.

### Results

Shown in Fig. 1 is a typical cathodic charging curve for palladium foil electrodes subjected to a constant 6 mA charge in the sulfuric acid electrolyte. Curves of similar form were also obtained with constant potential charge (current vs. time).  $PdH_{0.6}$  corresponds, in

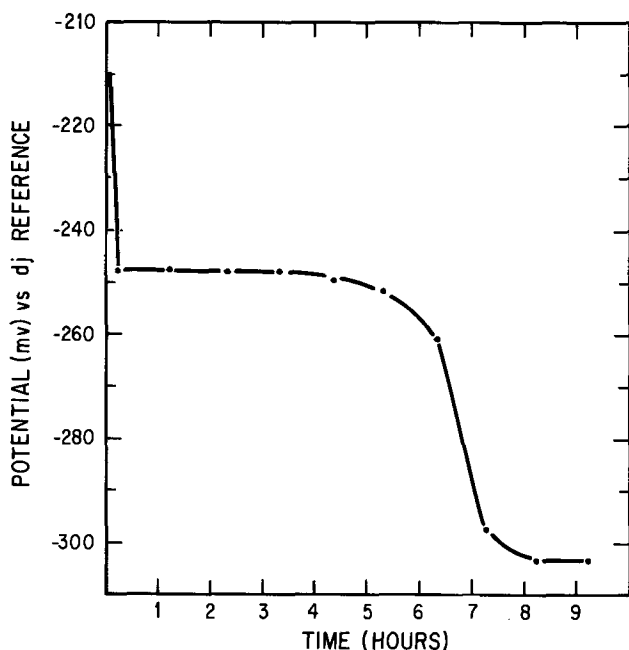


Fig. 1. Charging curve for the palladium foil electrode at 6 mA in 1N  $H_2SO_4$  under  $N_2$ .

Fig. 1, to a charging time of 6.9 hr. The correspondence in the break in the charging curve with that expected from the literature (8,17,18) implies that substantially all the charge put into the electrode resulted in the formation of palladium hydride, and thus formed the basis of assuming essentially 100% charging efficiency, as discussed above.

Shown in Fig. 2 is the subsequent potential-time curve for the same electrode subsequently immersed in aerated sulfuric acid. Both curves obviously resemble the potential-time behavior and the potential-Pd/H ratio curves in Ref. (8), (17), and (18). These same general forms were obtained with all the palladium electrodes studied. The duration of the constant potential plateau did vary with the geometry of the electrode, which is the primary subject of this paper. In subsequent discussion, electrode life is arbitrarily taken as the time at which the electrode potential reached a value 20 mV more positive than the plateau voltage (16 hr in Fig. 2). This is a reasonable criterion for the 1N  $H_2SO_4$  solutions, but is much less rigorous for the higher pH solutions (see Fig. 4 and 5).

That the potential of the palladium electrode in the plateau region is pH dependent has been well demonstrated in the literature. The palladium foil electrode discussed above yielded a slope of  $-59$  mV/pH, over the range of pH 4-7, a response identical to that obtained with a glass pH electrode in the same solutions.

The lifetime of the electrode described by Fig. 2 is similar to published data (6-12). However such times are too short for the purposes required, i.e., an electrode suitable for routine quality control measurements. As mentioned above, a prime reason given for this low lifetime is the reaction of the palladium hydride at the electrode surface with oxygen dissolved in the electrolyte. It is to be expected, therefore, that, if this is indeed the case, decreasing the area for a fixed electrode volume would proportionately increase electrode life. Accordingly the foil electrode was coated with paraffin wax over half its surface after charging to capacity as shown in Fig. 1. Indeed the expected doubling in electrode life was obtained.

It is also to be expected that electrodes containing more charge (palladium hydride) would also have a proportionately longer electrode life. The quantity of charge which can be delivered to the electrode is, of course, proportional to electrode volume. Listed in

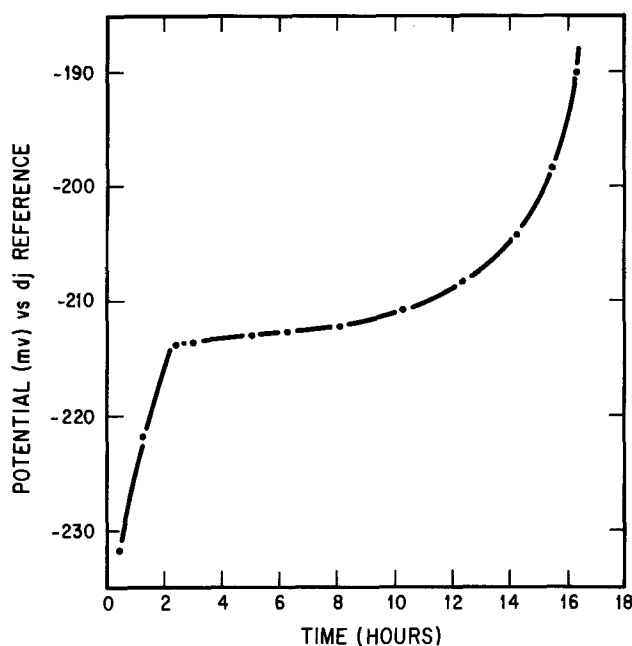


Fig. 2. Potential-time (in hours) curve for the charged palladium foil in aerated 1N  $H_2SO_4$ .

Table I. Comparison of electrode performance with configuration (1N H<sub>2</sub>SO<sub>4</sub>)

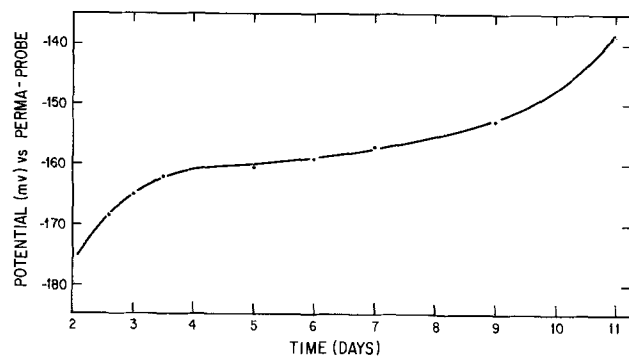
Electrode	Volume (cm <sup>3</sup> )	V/S ratio (cm)	Charge (A-min)	Life (days)	Loss rate (mA)
Wire	0.024	0.016	2.8	1.0	1.9
Foil	0.025	0.012	2.4	0.7	2.5
Disk	0.317	1	3.9	7.0	0.39
Rod (2 mm)	0.317	0.44	11.9	8.0	1.0
Rod (2 cm)	0.793	0.18	58.2	10.0	4.0

Table I are typical lifetimes (in aerated 1N H<sub>2</sub>SO<sub>4</sub>), the dimensional parameters, and the input charge for the five palladium hydride electrode configurations investigated. Since each electrode had been charged and discharged prior to taking the data listed, they contained a residual ampere-hour capacity over and above that shown in Table I. This point is discussed more fully below. Also given in Table I are the rates of loss (in milliamperes) of palladium hydride to the solution. These numbers are the input charge (in milliampere-minutes) divided by the electrode life (also in minutes). Shown in Fig. 3 is the potential-time stability curve of the palladium rod electrode.

The following general trends are apparent: (i) increasing electrode volume increased electrode life; (ii) electrode lifetimes in excess of 1 week were achieved; (iii) for a constant electrode volume, decreasing the electrode surface area exposed to the solution decreased the rate of loss of palladium hydride to the solution. A more quantitative correlation of electrode life with total charge in the electrode and the dimensional parameters is developed below.

Taking advantage of the lower self-discharge rate of the disk electrode configuration in order to obtain a long-lived electrode is influenced, in practice, by the time available for electrode charging. Shown in Table II are the times required to reach PdH<sub>0.6</sub> at a constant current density of 2.3 mA/cm<sup>2</sup>, the maximum value used with the 2 cm palladium rod which avoided hydrogen evolution throughout the charge period. Thus from the point of view of rapid charging with a reasonable electrode lifetime, the palladium rod with the greater exposed surface is the more desirable electrode.

Illustrated in Table III is the effect of electrolyte pH on the lifetime of this palladium rod electrode (2 cm exposed length). Shown in Fig. 4 is the potential-time curve for the rod electrode in the pH 8 ammonium phosphate solution. Note the compressed time scale relative to Fig. 3. As implied above, deciding on the electrode "life" is much less rigorous than for the sulfuric acid solutions; here electrode life is taken as 15 days. Similar curves were developed with the citrate and ammonium fluoride solutions (see Fig. 5). The slopes of the various portions of the potential-time curve are also listed in Table III.

Fig. 3. Potential (vs. PermaProbe)-time (in days) relationship for charged palladium rod in aerated 1N H<sub>2</sub>SO<sub>4</sub>.Table II. Charging times as a function of configuration (in N<sub>2</sub> saturated 1N H<sub>2</sub>SO<sub>4</sub>)

Configuration	Current (mA)	Time (days)
Rod (2 cm length)	10	5.7
Rod (2 mm length)	1.4	16.2
Disk	0.5	45.4

Table III. Lifetime vs. pH

Electrolyte	Life (days)	Loss rate (mA)	Initial slope (pH/hr)	Midcurve slope (pH/hr)	Final slope (pH/hr)
1N H <sub>2</sub> SO <sub>4</sub>	11	3.7	0.01	0.002	0.01
pH 3.6 citrate	15.5	2.8	0.01	0.0007	0.003
pH 8 phosphate	15.0	2.8	0.014	0.0007	0.002

Table IV. Stirring dependencies of electrode potential

1N H <sub>2</sub> SO <sub>4</sub>		pH 3.6 citrate		pH 8 phosphate	
Pd/H ratio	Δ potential, mV	Pd/H ratio	Δ potential, mV	Pd/H ratio	Δ potential, mV
0.44	-1.1	0.49	-2.0	0.52	-2.1
0.31	-2.1	0.39	-2.8	0.49	-0.8
0.26	-2.2	0.23	-2.9	0.35	-1.8
0.10	-3.4	0.15	-8.0	0.29	-3.3
0.06	-4.2				
0.03	-5.3	0.03	-10.4		

Obviously the electrode life increased with increasing pH, and obviously periodic recalibration will be required, particularly with a freshly charged electrode.

As mentioned above, palladium hydride electrodes have been reported to have stirring dependence in aerated solutions. Shown in Table IV are the shifts in potential for the palladium rod electrode (2 cm exposed length), as a function of Pd/H ratio, after the stirring was terminated in aerated 1N H<sub>2</sub>SO<sub>4</sub>, pH 3.6 citrate and pH 8 phosphate.

Obviously, the stirring dependence is dependent upon the PdH content of the electrode. It would also seem that the higher pH solutions have a higher stirring dependence, particularly as the Pd/H ratio increases. Essentially identical results were obtained with the disk configuration, except that the potential shifts below PdH<sub>0.05</sub> were of the order of 7-10 mV. The practical significance of these stirring dependencies is determined, of course, by the accuracy of the results desired; a 2 mV shift corresponds to a pH shift of 0.03 pH units. These data do point out the

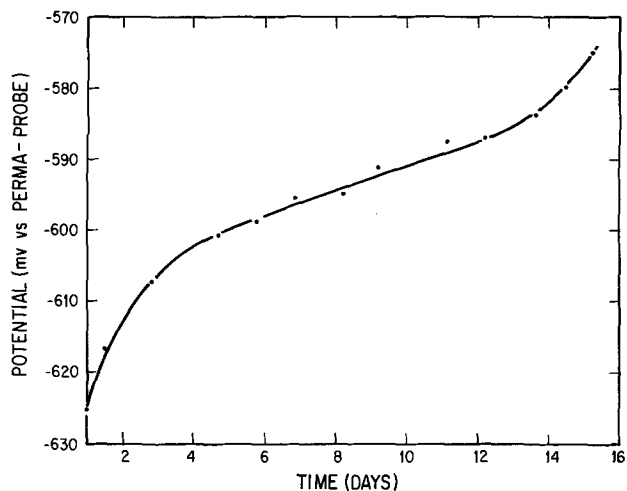
Fig. 4. Potential (vs. PermaProbe)-time (days) relationship for a cathodically charged palladium rod in pH 8 (NH<sub>4</sub>)<sub>2</sub>HPO<sub>4</sub>.

Table V. pH of fluoride etch solutions

Composition	PdH electrode	Pt H <sub>2</sub> /H <sup>+</sup> electrode
13.4M NH <sub>4</sub> F + 4.54M HF	4.50	4.52
15.9M NH <sub>4</sub> F + 5.40M HF	4.74	4.80
18.9M NH <sub>4</sub> F + 6.4M HF	5.03	5.08

desirability of working with a fully charged electrode to minimize this problem. The specific sources of these stirring dependencies are discussed below.

Having thus demonstrated that long electrode lifetimes (11-15 days), with minimal perturbation from dissolved oxygen, can be achieved by large volume, high charge capacity, palladium hydride electrodes, performance in the ammonium fluoride-HF etch solutions was studied. Shown in Table V are the pH values obtained with the palladium rod (2 mm exposed length) Teflon holder electrode, charged to PdH<sub>0.22</sub>. Also shown are the pH values obtained with the platinum H<sub>2</sub>/H<sup>+</sup> electrode. Corrections for the different ionic strengths of the standard buffers and the concentrated fluoride solutions have not been made. Application and interpretation of these data will be discussed in a subsequent paper.

The glass pH electrode gave pH values of the order of 6.4, reflecting the influence of the etching reaction of these solutions. On return of the PdH electrode to the 1N H<sub>2</sub>SO<sub>4</sub> test solution, in which the electrode life was being monitored, potential readings were obtained which were identical to those measured before the fluoride solution experiments, implying no degradation of the electrode surface. These pH measurements in the etch solutions were repeated 5 times over a 7 day period with the same pH electrode. Values identical to those shown in Table V were obtained, as long as the electrode was recalibrated in the standard buffer solutions before each test.

Shown in Fig. 5 is a potential-time curve for a palladium disk, Teflon electrode, charged at constant potential to PdH<sub>0.14</sub> and operated as described in Texas Instruments Incorporated semiconductor grade common oxide etch (nominal 16M NH<sub>4</sub>F + 5.4M HF). For this electrode, life was taken as 11.5 days, giving a loss rate of 0.30 mA. As with the rod electrode in pH 3.6 sodium citrate, this loss rate was less than observed in 1N H<sub>2</sub>SO<sub>4</sub> (Table I). The slope of the curve between 2 and 11.5 days corresponds to  $2 \times 10^{-4}$  pH/hr. Data on the stirring dependence in these etch solutions, as a function of PdH content, is given in Table VI.

It is not possible to compare these data directly with those given in Table V because of the differences in electrode configuration. The same general trend,

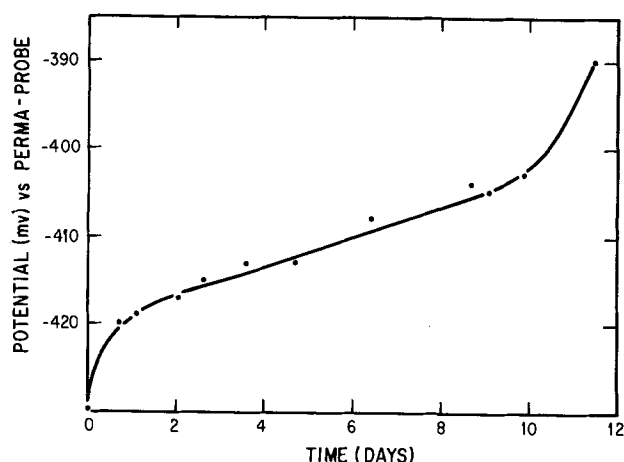


Fig. 5. Potential (vs. PermaProbe)-time (days) relationship for a cathodically charged palladium disk electrode in NH<sub>4</sub>F+HF etch.

Table VI. Stirring dependencies vs. PdH content

PdH content	Δ potential (mV)
0.22*	<0.1
0.14	1
0.09	4
0.07	6
0.04	9

\* Previous test.

however, is observed as with the other electrodes in other solutions, i.e., lower PdH contents result in higher stirring dependencies, and a highly charged electrode,  $\approx$  PdH<sub>0.22</sub>, has a negligible stirring dependence.

This electrode was then used to monitor a titration with 1N NaOH of 1/100 diluted etch. The curve so obtained is compared in Fig. 6 with that measured by a commercial glass electrode. Identical results, within experimental error for these experiments, were obtained with the electrodes in separate and in the same solutions. For the purposes of direct comparison, the potentials of both electrodes were normalized to the millivolt readings at 1 ml NaOH added. Readings were taken in static solution, 2 min after the increment of titrant was added and the electrolyte volume was stirred. The magnitude of the potential drifts throughout the titration was essentially identical for both electrodes, although generally in the opposite direction. Although the titration curves were somewhat different in form, the end points were obviously identical. This subject of the shape of the titration curve as a function of the H<sup>+</sup> chemistry in these solutions will be treated in another paper.

The operational life of a glass pH electrode used on a routine basis in the titrations was of the order of 5 days. A PdH electrode has been used continuously for over 1 month, at the present writing, with overnight recharge every 2 days. An electrode charged to PdH<sub>0.22</sub> lasted 11 days without recharge. However, as indicated, the stirring dependence became unacceptable after about 5 days.

### Discussion

In order to obtain a more rigorous correlation of electrode performance in terms of dimensional parameters, consideration must be given to the electrode mechanism in terms of the depolarization processes involved. The shape of the potential-time curve (Fig.

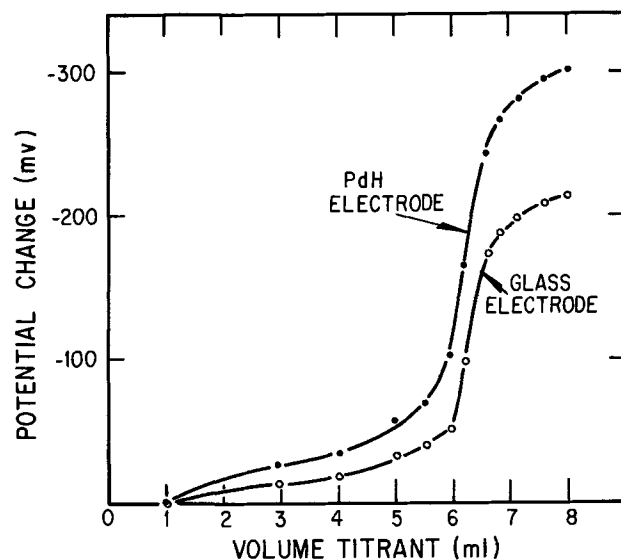


Fig. 6. Potentiometric titration of 1/100 diluted common oxide etch with 1N NaOH. (●, Glass electrode; ○, PdH electrode.)

2 and 3) of a charged palladium hydride electrode in the test solutions is rationalized as follows. The initial portion of the curve (up to 3 days in Fig. 3) represents the loss of PdH from the electrode surface to the test solution and to the bulk of the electrode, eventually establishing a surface hydrogen-palladium ratio of less than 0.6 [0.36 according to Ref. (7)]. Immediately after charge, it is reasonable that the surface concentration is in excess of this value, particularly in view of the low diffusion coefficient of hydrogen in palladium. This same bulk diffusion mechanism has been proposed in Ref. (8). Throughout the midtime region, palladium hydride, in the  $\alpha + \beta$  phase, slowly reacts with the solution. At the latter portion of the curve (>11 days, Fig. 3), sufficient hydride has been removed from the surface to reduce the H/Pd ratio to below 0.03. There is at this point insufficient palladium hydride remaining in the bulk of the electrode to deliver hydrogen to the surface at a rate equal to or faster than the surface reaction rate. As a consequence, potential of the palladium electrode becomes more positive (17, 18).

One of the major solution processes accounting for this continual loss of palladium hydride from the surface is reported to be the reaction with dissolved oxygen (13, 14). The extent of this process, as a function of electrolyte pH, is indicated by the stirring dependencies shown in Table IV. The rates of oxygen depolarization are higher at and above pH 3.6 than in 1N H<sub>2</sub>SO<sub>4</sub>. However, as shown in Table IV, the life of the electrode is significantly less in 1N H<sub>2</sub>SO<sub>4</sub> than in the pH 3.6 and 8 solutions. This implies an additional electrode degradation process in the acid solution that does not proceed at as rapid a rate in the more basic solutions. It is postulated that this process is the acid catalyzed recombination of PdH to yield H<sub>2</sub>. It is presumably this process which accounts for the observation (17) that "when the circuit is opened, hydrogen is spontaneously evolved until a potential of 0.050V and a H/Pd ratio of 0.36 is reached."

Not all the hydride formed by cathodic charging of the palladium electrode is "available" for maintaining a constant potential. According to the proposed mechanism for the electrode discussed above, sufficient hydride to establish solely the  $\alpha$ -PdH phase, i.e., PdH<sub>0.03</sub>, must remain in the electrode bulk at the end of electrode life as defined above. However, it was also observed that when solution stirring was stopped for such a "depleted" electrode, the potential fell to that of the  $\alpha + \beta$  phase, indicating a greater PdH content in the bulk of the electrode structure. It was also observed that charge inputs to a previously uncharged electrode (1 cm  $\times$  0.256 in. diameter) equal to or less than 2.3 A-min yielded short lived electrodes ( $\leq 3$  hr). Thus the residual hydride can be separated into two parts, that for the  $\alpha$ -phase (PdH<sub>0.03</sub>) and an additional concentration to establish the minimal diffusion concentration gradient, yielding a total of PdH<sub>0.042</sub> (equivalent to the 2.3 A-min referred to above). These considerations then result in the following empirical formula relating electrode life to the charge input and electrode dimensions

$$t(\text{days}) = k(ch - 5.17V - 2.08V)/A$$

with A the exposed surface area in cm<sup>2</sup>, V the electrode volume in cm<sup>3</sup>, and ch the total charge in the electrode in A-min. The two numerical coefficients (in units of charge per cm<sup>2</sup>) were derived from the residual charge considerations described above. This equation then is the quantitative representation of the general concept expressed above, that electrode life is proportional of the volume to surface ratio.

As indicated, electrode life, for a given electrode configuration, is also a function of pH and a function of the dissolved oxygen content as well as its mass transport rate. For the experimental setup described above, in 1N H<sub>2</sub>SO<sub>4</sub>, the proportionality constant k has a value of 0.569. Shown in Table VII is a comparison

Table VII. Application of correlation formula

Electrode	Charge input (A-min)	Measured life (days)	Calculated life (days)
Disk, Teflon	6.0*	7.0	6.8
Disk, Teflon	5.3*	5.2	4.9
Disk, Acrylic	3.9	7.0	6.3
Rod, 2 mm exposed	11.9	8.0	8.0
Rod, 2 cm exposed	58.2	10.0	8.0
Rod, 2 cm exposed	83.6*	8.8	10.0
Rod, 2 mm exposed	9.8	6.8	6.2
Wire, 2 cm exposed	2.8	1.0	1.2
Foil	2.88*	0.69	0.76

\* Containing no residual PdH.

of the measured lifetimes with those calculated from the electrode dimensions and the input charge.

Thus the correlation formula does account within  $\pm 25\%$  for the geometric and residual charge factors involved in establishing the electrode life. This is not an unreasonable agreement considering the method of determining electrode life. Interpretation of the constant k in terms of solution processes has not been possible with the cells studied due to poor definition of the mass transport conditions for this particular experimental setup, and due to the lack of information on the PdH recombination processes involved in the acid solution.

The data for the performance of these electrodes in concentrated NH<sub>4</sub>F-HF solutions indicates similar electrode mechanisms to those operating in the other test solutions. Electrode life is superior to that in 1N H<sub>2</sub>SO<sub>4</sub>, and the stirring dependencies are less, due probably to a lower solubility of air in the concentrated fluoride salt solutions and a lower PdH recombination rate. Constant k has a value of approximately 0.70 in the empirical formula given above for concentrated NH<sub>4</sub>F-HF etch solutions.

Manuscript submitted Feb. 1, 1974; revised manuscript received July 18, 1974.

Any discussion of this paper will appear in a Discussion Section to be published in the June 1975 JOURNAL. All discussions for the June 1975 Discussion Section should be submitted by Feb. 1, 1975.

The publication costs of this article have been assisted by Texas Instruments Incorporated.

## REFERENCES

- J. Judge, *This Journal*, **118**, 1772 (1971).
- I. Lawrence, in "Oxide-Electrolyte Interfaces," R. Alwitt, Editor, p. 171, The Electrochemical Society, Softbound Symposium Series, Princeton, N. J. (1973).
- J. Entwistle, C. Weedon, and T. Hayes, *Chem. Ind. (London)*, **9**, 433 (1973).
- L. Warren, *Anal. Chem. Acta*, **53**, 199 (1971).
- H. Farrer and F. Rossotti, *J. Inorg. Nucl. Chem.*, **26**, 1959 (1964).
- D. Ives and G. Janz, "Reference Electrodes," p. 111, Academic Press, Inc., New York (1961).
- T. Eriksson and G. Johansson, *Anal. Chim. Acta*, **63**, 445 (1973).
- M. Vasile and C. Enke, *This Journal*, **112**, 865 (1965).
- W. Grubb, U.S. Pat. 3,671,414 (1972).
- J. Dobson, *J. Electroanal. Chem.*, **35**, 129 (1972).
- K. Slevogt, E. Seelos, J. Heilboch, and W. Rautenstrauch, *Vom Wasser*, **37**, 123 (1970).
- M. Fleischmann and M. Thirsk, *Trans. Faraday Soc.*, **51**, 71 (1955).
- J. P. Schwing and L. B. Rogers, *Anal. Chim. Acta*, **15**, 379 (1956).
- J. Stock, W. Purdy, and Th. Rogers, *ibid.*, **20**, 73 (1959).
- T. Franklin and J. McDaniel, *This Journal*, **116**,

1524 (1969).

16. R. LaDietra and G. Castellan, *ibid.*, **111**, 1276 (1964).17. S. Schuldiner, G. Castellan, and J. Hoare, *J. Chem.**Phys.*, **28**, 16 (1959); *ibid.*, **28**, 20 (1959); *ibid.*, **28**, 22 (1959).18. P. Aben and W. Burgers, *Trans. Faraday Soc.*, **58**, 1989 (1962).

## The Complex Solubilities of Silver Halides in Acetone-Water Mixtures

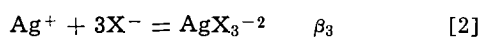
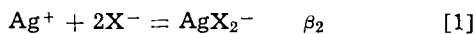
Mark Salomon\*

Power Sources Technical Area, U.S. Army Electronics Technology and Devices Laboratory,  
Fort Monmouth, New Jersey 07703

### ABSTRACT

The over-all formation constants and solubility products for the silver chlorides, bromides, and iodides have been determined at 25°C in acetone-water mixtures of the following weight per cent acetone: 80.03, 91.23, and 98.53. In the concentration ranges studied, values of  $\beta_2$  and  $\beta_3$  corresponding, respectively, to the formation of  $\text{AgX}_2^-$  and  $\text{AgX}_3^{-2}$  ( $\text{X} = \text{Cl}, \text{Br}, \text{I}$ ) could be determined.  $\text{AgX}_2^-$  is the predominant species and the formation of  $\text{AgX}_3^{-2}$  decreases rapidly as the water content is increased.  $\log K_{s0}$  and  $\log \beta_2$  values for pure acetone were evaluated by an extrapolation procedure and the results are compared to previous work.

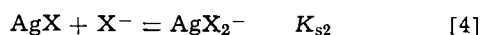
The work reported in this paper is a continuation of our studies on the effect of solvent composition on the complex solubilities of the silver halides (1). In particular, the following equilibria have been studied



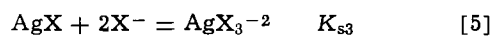
and



In Eq. [1]-[3],  $\text{X} = \text{Cl}, \text{Br}, \text{and I}$ ; the  $\beta$ 's are the over-all formation constants (or stability constants) and  $K_{s0}$  is the solubility product. Once determined, the above equilibrium constants can be used to evaluate the solubility of  $\text{AgX}$  according to



and



The effect of solvent composition on these equilibria are of interest in theoretical treatments of ionic solvation and in treatments concerning ion-solvent interactions. In the present paper, the above equilibria have been studied in several mixtures of water and acetone.

### Experimental

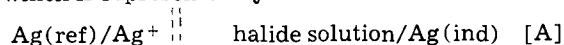
**Materials.**—All salts were treated as reported earlier (1). Tetrapropylammonium halide (TPAX) and perchlorate (TPAP) solutions were prepared such that the total ionic strength was maintained at a constant 0.1000M (molar). These solutions were titrated with 0.1000M  $\text{AgClO}_4$  using a Gilmont 2.0 ml microburette.

Histological grade acetone (Fisher) was refluxed with  $\text{KMnO}_4$  for at least 5 hr and then distilled onto vacuum dried type 4A molecular sieves. This solvent was further distilled in a Nester-Faust spinning band still and a constant boiling fraction (56°-57°C) was collected at atmospheric pressure. Distilled water was used to prepare three solvents of the following weight per cent acetone: 80.03, 91.23, and 98.53. All solutions were prepared in the laboratory atmosphere at 25.0° ± 0.1°C. The halide solutions were prepared the day prior to their use; each  $\text{AgClO}_4$  solution was prepared prior

to each solvent run and stored in the dark for a period of 1-2 weeks.

**Emf measurements.**—A Doric model DS-100 microvoltmeter was used for the emf measurements. Reproducibility of this instrument is ± 0.1 mV. The emf measurements were generally stable to within ± 0.2 mV in unsaturated solutions and ranged from ± 0.2 to ± 1 mV in the saturated solutions: Cl and Br solutions were consistently stable while I solutions were the least stable (particularly near the saturation point).

The electrochemical cell was a 125 ml three-neck flask which is represented by



Here "ref" and "ind" refer, respectively, to the reference and indicator electrodes. The dashed lines indicate the liquid junction and since all solutions were of a constant ionic strength of 0.1M, it is assumed that the liquid junction potential is virtually constant. A silver wire plated with silver from a cyanide bath served as the indicator electrode and a silver wire in ~0.02M  $\text{AgClO}_4$  in TPAP served as the reference electrode. The reference electrode was separated from the study solution by a sealed ST 7/25 joint. Twenty milliliters of TPAX + TPAP solution were placed in the cell which was fitted with a Gilmont 2.0 ml burette containing 0.1M  $\text{AgClO}_4$  in the given solvent mixture. The sealed cell was thermostated at 25.0° ± 0.1°C and vigorous magnetic stirring was maintained during each potentiometric titration.

### Results and Calculations

The measured emf of the above cell,  $E$ , is given by

$$E = E' + (2.3RT/F) \log[\text{Ag}^+] \quad [6]$$

where  $E'$  is a formal potential; i.e., it contains contributions from the liquid junction and nonideality of the electrolyte solutions.  $E'$  was determined by titrating 0.1M  $\text{AgClO}_4$  into 25.0 ml of 0.1M TPAP solution. The Nernst slope of 59.2 mV was obeyed to within 0.2 mV in all solutions except the 98.53% acetone solution for which a slope of 60.0 mV was obtained. This is probably due to ion-pairing effects (see below). Activity coefficient effects will be discussed further on in conjunction with the Davies equation (Eq. [14]).

\* Electrochemical Society Active Member.

Key words: silver halides, water-acetone mixtures, over-all formation constants, solubility products, medium effects.

The over-all formation constants are calculated from the titration data in unsaturated solutions by a non-linear least squares method in which the relative error,  $U$ , is minimized. For  $i$  data points,  $U$  is defined (1-3) by

$$U = \sum_1^i (1 - x_i/fx_i)^2 \quad [7]$$

where

$$x_i = (C_{X,i} - [X^-]_i)/[Ag^+]_i \quad [8]$$

and

$$fx_i = \beta_1[X^-]_i + 2\beta_2[X^-]_i^2 + \dots + n\beta_n[X^-]_i^n \quad [9]$$

In these equations  $[X^-]$  is the halide ion concentration,  $[Ag^+]$  is the silver ion concentration which is obtained from the measured emf via Eq. [6], and  $C_X$  is the total halide concentration present in solution (below  $C_{Ag}$  is used for the total silver concentration in solution). All concentrations are based on the molar scale. To obtain  $[X^-]_i$  values, an iterative procedure was used which is based on the average ligand number,  $\bar{n}$ , defined by

$$\bar{n} = (C_{X,i} - [X^-]_i)/C_{Ag,i} \quad [10a]$$

and

$$\bar{n} = \frac{\sum_1^n n\beta_n[X^-]^n}{\sum_0^n \beta_n[X^-]^n} \quad [10b]$$

Equation [10a] is used to start the calculations by assuming a value for  $\bar{n}$  (usually around 1.5-2.5) and obtaining initial  $[X^-]_i$  values. The  $\beta$ 's are obtained from the least squares using Eq. [7] to minimize the relative errors. The iteration is begun by using these  $\beta$ 's to calculate new  $\bar{n}$  values via Eq. [10b] and the process is continued until the  $\beta$ 's converge to within 0.001%. The standard deviations of the  $\beta$ 's were calculated by Sillén's method (4). The solubility product,  $K_{s0}$ , was calculated from each point in the saturated region of the titration curve using the relation

$$\{C_x - C_{Ag} + [Ag^+]\}/[Ag^+] = \frac{K_{s0}}{[Ag^+]^2} + \sum_2^n (n-1)\beta_n \left\{ \frac{K_{s0}}{[Ag^+]} \right\}^n \quad [11]$$

The Newton-Raphson iterative method is used to solve Eq. [11] and the average  $K_{s0}$  value is reported along with the standard deviation. The solubility constants  $K_{s2}$  and  $K_{s3}$  are obtained from

$$K_{s2} = K_{s0}\beta_2 \quad [12]$$

$$K_{s3} = K_{s0}\beta_3 \quad [13]$$

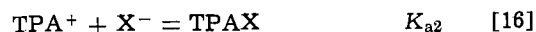
The experimental data are given in the Appendices. It should be noted that those data points marked with an asterisk were omitted from the calculations because they gave rise to abnormally large errors. The majority of these rejected points lie very close to the saturation

point; this is attributable to supersaturation and the failure to reach equilibrium. Each point was recorded usually within 10-30 min and if equilibrium was not reached within 1 hr, additional titrant was added and the experiment continued. For the concentration ranges studied, statistically meaningful solutions to Eq. [7] were obtained only for  $\beta_2$  and  $\beta_3$ . In the 80.03 and 91.23% acetone solutions,  $\beta_3$  values for the iodides could not be refined. The results of the calculations are given in Table I. Activity coefficient corrections were made by use of the Davies (5) equation

$$\log \gamma_{\pm} = -\frac{AM}{1 + M^{1/2}} + 0.3AM \quad [14]$$

where  $A$  is the Debye-Hückel "A" factor and  $M$  is the molarity. Dielectric constants and densities of the acetone-water mixtures were interpolated from the data of Albright (6). The Debye-Hückel "A" factors for the present acetone-water mixtures are given in Table I. The Davies equation was chosen for activity coefficient corrections rather than a simpler Debye-Hückel equation because of its successful application to a variety of other nonaqueous solvents (9, 20).

Above it was pointed out that the high Nernst slope in the 98.53% acetone solution was probably due to ion pairing. It is well known (7-9) that ion-association constants in pure acetone are quite large ( $\sim 10^2$ ) even for the tetraalkyl halides, perchlorates, and picrates. In correcting for ion-pair formation in the 98.53% acetone solution, the following equilibria were assumed to be of importance



The possible formation of the triple-ion  $\text{TPA}_2\text{AgX}_3$  was not considered. Because specific data on the  $K_a$ 's in Eq. [15]-[18] are not available, it was assumed that  $K_{a1} = K_{a2} = K_{a3} = K_{a4} = K_a$ . An approximate value of 50 was found for  $K_a$  by a method discussed below. The results of these calculations are given in Table II. The standard deviations are not included in this table: they are expected to be about 5-10% higher than the corresponding values given in Table I due to the uncertainties in the use of Eq. [14]-[18]. It is noted that  $K_{s2}$  is independent of the effects described by Eq. [14]-[18].

The ion association constant in 98.53% acetone and values for the equilibrium constants in pure acetone were evaluated as follows. First the  $\log K^{\circ}_{s0}$  data for the 80.03, 91.23, and 98.53% acetone solutions were fit to the equation

$$\log K = a + bP + cP^2 \quad [19]$$

where  $P$  = per cent acetone.  $K_a$  for the 98.53% acetone solution was varied until the predicted value of  $\log K^{\circ}_{s0}$  in pure acetone agreed with the published values (9) for AgBr and AgCl. Once  $K_a$  was evaluated, Eq.

Table I. Equilibrium constants at 25°C

Weight per cent acetone*	Salt	$-\log K_{s0}$	$\log \beta_2$	$\log \beta_3$	$\log K_{s2}$	$\log K_{s3}$
80.03 (2.005)	AgCl	13.17 ± 0.06	11.598 ± 0.003	11.60 ± 0.02	-1.58 ± 0.06	-1.57 ± 0.06
	AgBr	14.79 ± 0.05	12.98 ± 0.04	14.855 ± 0.004	-1.81 ± 0.06	0.07 ± 0.05
	AgI	17.64 ± 0.04	17.09 ± 0.02		-0.55 ± 0.05	
91.23 (2.767)	AgCl	14.96 ± 0.004	14.321 ± 0.002	14.40 ± 0.04	-0.641 ± 0.005	-0.56 ± 0.04
	AgBr	16.38 ± 0.04	16.202 ± 0.002	15.44 ± 0.11	-0.18 ± 0.04	-0.94 ± 0.12
	AgI	18.70 ± 0.05	18.956 ± 0.019		0.25 ± 0.07	
98.53 (3.581)	AgCl	17.95 ± 0.02	19.097 ± 0.004	20.37 ± 0.06	1.15 ± 0.02	2.42 ± 0.06
	AgBr	18.67 ± 0.07	19.915 ± 0.004	21.34 ± 0.07	1.24 ± 0.07	2.67 ± 0.10
	AgI	20.21 ± 0.06	21.339 ± 0.003	22.79 ± 0.03	1.13 ± 0.06	2.58 ± 0.07

\* The numbers in parentheses are the Debye-Hückel "A" factors (see Eq. [14]) in units of mole<sup>-1/2</sup> liter<sup>1/2</sup>.

Table II. Equilibrium constants at 25°C corrected to zero ionic strength

Weight per cent acetone	Salt	$-\log K^{\circ}_{s0}$	$\log \beta^{\circ}_2$	$\log \beta^{\circ}_3$	$\log K^{\circ}_{s2}$	$\log K^{\circ}_{s3}$
80.03	AgCl	13.36	11.78	11.88	-1.58	-1.48
	AgBr	14.98	13.17	15.13	-1.81	0.15
	AgI	17.82	17.28		-0.55	
91.23	AgCl	15.22	14.56	14.78	-0.64	-0.44
	AgBr	16.63	16.46	15.82	-0.18	-0.81
	AgI	18.96	19.21		0.25	
98.53	AgCl	19.46	20.60	22.63	1.15	3.17
	AgBr	20.18	21.42	23.60	1.24	3.42
	AgI	21.72	22.85	25.05	1.13	3.33
98.53*	AgCl	19.90	21.05	23.52	1.15	3.61
	AgBr	20.62	21.86	24.49	1.24	3.86
	AgI	22.16	23.29	25.93	1.13	3.77

\* Also corrected for ion pairing,  $K_a = 50$ .

Table III. Equilibrium constants in pure acetone at 25°C

Salt	$-\log K^{\circ}_{s0}$			$\log \beta^{\circ}_2$		
	a	b	c	d	a	c
AgCl	16.4		21.2	21.2	16.7	22.8
AgBr	18.7		21.7	21.6	19.7	23.3
AgI	20.9	22.0	23.0		22.2	24.4

a is from Ref. (10).  
 b is from Ref. (11).  
 c are the present results.  
 d is from Ref. (9).

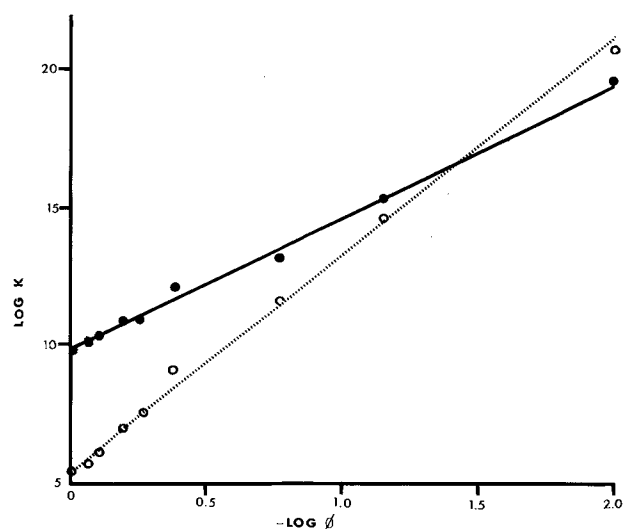
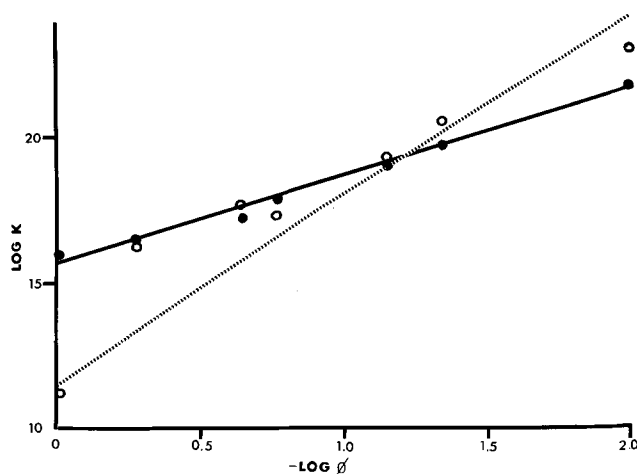
[19] was used to calculate  $\log K^{\circ}_{s0}$  for AgI and the  $\beta^{\circ}_2$  values in pure acetone. Table III lists the calculated values along with those values obtained by other workers. The values obtained by Luehrs *et al.* (10) are certainly in error as they are generally much too large. There is some discrepancy between the present results for the AgI data and Mackor's data (11). In the Discussion section below, evidence is presented which indicates that some of Mackor's data may be in error.

### Discussion

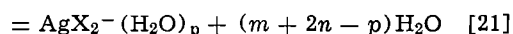
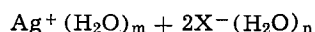
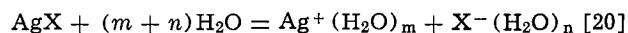
Table IV lists the available data for the silver halide equilibrium constants in various water-acetone mixtures. The data in pure water were obtained from Ref. (12), (13), and (14) for AgCl, AgBr, and AgI, respectively. Data for the AgCl and AgI systems, other than those reported here, were obtained from Ref. (15) and (11), respectively. Using the data in Table IV, some function was sought to give linear relationships between the equilibrium constants and water or acetone composition. The only functions that could be found were those of  $\log \phi_w$  or  $\log a_w$  ( $\phi_w$  is the volume fraction of water and  $a_w$  is the activity of water); other functions, including the volume fraction of acetone, were not linear. Figures 1 and 2 are examples of plots of  $\log K$  vs.  $\log \phi_w$  for the AgCl and AgI systems. The plot for the AgBr system is not shown but is very similar to the AgCl system (Fig. 1). Mackor's data for  $\beta^{\circ}_2$  (AgI) do not fall on a single line which is contrary to the analogous results for AgCl and AgBr. For

Table IV. Equilibrium constants in acetone-water mixtures at 25°C

Weight per cent acetone	$-\log K^{\circ}_{s0}$			$\log \beta^{\circ}_2$			$\log K^{\circ}_{s2}$		
	Cl	Br	I	Cl	Br	I	Cl	Br	I
0	9.8	12.3	16.0	5.4	7.6	11.2	-4.4	-4.7	-4.8
9.6	10.1			5.7			-4.4		
19.8	10.3			6.1			-4.2		
34.4				7.0			-3.9		
42.1	11.0			7.6			-3.5		
43.9		16.4				16.3			-0.1
54.2	12.1			9.1			-3.0		
73.7		17.2				17.6			0.5
80.0	13.4	15.0	17.8	11.8	13.2	17.3	-1.6	-1.8	-0.6
91.2	15.2	16.6	19.0	14.6	16.5	19.2	-0.6	-0.2	0.3
94.5			19.7			20.6			0.9
98.5	19.9	20.6	22.2	21.1	21.9	23.3	1.2	1.2	1.1
100.0	21.2	21.6	23.0	22.8	23.3	24.4	1.6	1.7	1.4

Fig. 1. Plots of  $\log K^{\circ}_{s0}$  and  $\log \beta^{\circ}_2$  for the AgCl systems against  $\log \phi$  ( $\phi$  is the volume fraction of water).  $\circ$ ,  $\log \beta^{\circ}_2$  values;  $\bullet$ ,  $-\log K^{\circ}_{s0}$  values.Fig. 2. Plots of  $\log K^{\circ}_{s0}$  and  $\log \beta^{\circ}_2$  for the AgI systems against  $\log \phi$  ( $\phi$  is the volume fraction of water).  $\circ$ ,  $\log \beta^{\circ}_2$  values;  $\bullet$ ,  $-\log K^{\circ}_{s0}$  values.

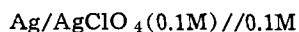
this reason it is suggested that the accuracy of these  $\beta^{\circ}_2$  values is questionable. The dashed line in Fig. 2 (for  $\beta^{\circ}_2$ ) was drawn neglecting Mackor's values. Figures 1 and 2 were suggested by Feakins and French (16) and by Marshall (17) to have the following significance. Equations [1] and [3] can be written to include the solvent,  $H_2O$ , involved in hydrating the various ionic species: *i.e.*,



Plots of  $\log K^{\circ}_{s0}$  and  $\log \beta^{\circ}_2$  should be linear with slopes, respectively, of  $m+n$  and  $m+2n-p$ . For AgCl the plot in Fig. 1 gives  $m+n=5$ ; assuming  $m=2$  and  $n=3$ , it is found that  $p=16$  which seems unreasonably large. The failure of this treatment over a large range of solvent compositions is not surprising as the original treatments (16,17) were intended to apply to those systems where the cosolvent (acetone in the present case) is inert. Over the range where the cosolvent composition is small, the relations in Eq. [20] and [21] apparently hold (15,16). Over the solvent composition range studied here, no particular

theoretical significance can be attached to the plots shown in Fig. 1 and 2.

Inspection of Table IV shows monotonical behavior: for each salt  $K^{\circ}_{s0}$  becomes smaller and  $\beta^{\circ}_2$  becomes larger as the acetone content is increased. In solutions of high acetone content, the  $AgX_2^-$  and  $AgX_3^{-2}$  species becomes more stable than  $X^-$  which is typical of these salts in aprotic solvents (1, 3, 9-11, 14). That the  $AgX_2^-$  species is indeed more stable can be demonstrated by considering individual ionic medium effects. Table V gives values of the individual ionic free energies of transfer,  $\Delta G^{\circ}_t(\text{ion})$ , from water to pure acetone. The data are based on the extrathermodynamic assumptions of: Bax *et al.* (18) who used an extrapolation procedure, and Parker *et al.* (9) who assumed that there is negligible liquid junction potentials for the reference half cells

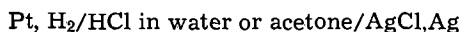


tetraethylammonium picrate//

and the present values which are based on the approximate relation (1)

$$\Delta G^{\circ}_t(Ag^+, AgCl_2^-) + \Delta G^{\circ}_t(Ag^+, AgBr_2^-) \approx 2\Delta G^{\circ}_t(Ag^+) \quad [22]$$

In Table V, those values given in parenthesis were obtained by the additivity rule using the present values for  $\Delta G^{\circ}_t(Ag^+, X^-)$  and  $\Delta G^{\circ}_t(Ag^+, AgX_2^-)$ . Using Parker's (9) and the present values for  $\Delta G^{\circ}_t(Cl^-)$  a value for  $\Delta G^{\circ}_t(H^+)$  was obtained from the calculated value of  $\Delta G^{\circ}_t(HCl)$ . This latter quantity was calculated from the emf's of the cells



using the relation

$$\Delta G^{\circ}_t(HCl) = F(E^{\circ}_w - E^{\circ}_{ac}) \quad [23]$$

For acetone  $E^{\circ}_{ac} = -0.542V$  (19) and in water,  $E^{\circ}_w = 0.222V$ . Inspection of Table V shows that even though the  $\Delta G^{\circ}_t(\text{ion})$  values are not very consistent for the three works, the relation  $\Delta G^{\circ}_t(AgX_2^-) < \Delta G^{\circ}_t(X^-)$  holds for each method of evaluation. While it is desirable to produce a common list of  $\Delta G^{\circ}_t(\text{ion})$  values, it is not necessary if our primary object is to qualitatively understand the nature of ion solvation in the various solvents. One inherent difficulty involved in producing common  $\Delta G^{\circ}_t(\text{ion})$  values is that values of  $\Delta G^{\circ}_t(\text{salt})$  often differ considerably. For example the value of  $\Delta G^{\circ}_t(HCl)$  calculated from Eq. [23] is 12.6 kcal mole<sup>-1</sup>. Bax *et al.* use a value of 12.6 kcal mole<sup>-1</sup>, and Parker and the present author arrive at a value 7.4 kcal mole<sup>-1</sup> for  $\Delta G^{\circ}_t(HCl)$ . Additional but less severe discrepancies can be found for the values of  $\Delta G^{\circ}_t(Ag^+, Br^-)$  and  $\Delta G^{\circ}_t(Ag^+, I^-)$  obtained by Parker *et al.* and by the present author.

Manuscript submitted Sept. 10, 1973; revised manuscript received July 15, 1974.

Table V. Free energies of transfer for single ions from water to acetone at 25°C

Ion	$\Delta G^{\circ}_t(\text{ion}), \text{kcal mole}^{-1}$		
	a	b	c
H <sup>+</sup>	-4.9	-4.9	-2.5
Ag <sup>+</sup>	(-1.8)	3.3	5.7
Cl <sup>-</sup>	17.5	12.3	9.9
Br <sup>-</sup>	15.4	8.7	7.0
I <sup>-</sup>	(11.4)	4.9	3.9
AgCl <sub>2</sub> <sup>-</sup>	(9.2)	(4.1)	1.7
AgBr <sub>2</sub> <sup>-</sup>	(5.8)	(0.7)	-1.7
AgI <sub>2</sub> <sup>-</sup>	(2.9)	(-2.1)	-4.6

a is from Ref. (18) and is based on molal units.  
b is from Ref. (9) and is based on molal units.  
c are the present results.

Any discussion of this paper will appear in a Discussion Section to be published in the June 1975 JOURNAL. All discussions for the June 1975 Discussion Section should be submitted by Feb. 1, 1975.

The publication costs of this article have been assisted by the U.S. Army Electronics Technology and Devices Laboratory.

#### LIST OF SYMBOLS

$\beta_n$	over-all stability constant for the formation of species $Ag_n^{1-n}$ uncorrected for activity effects.
$\beta^{\circ}_n$	over-all stability constant corrected for activity effects
$U$	relative error defined by Eq. [7]
$C_X$	total concentration of species X in moles per liter or millimoles per liter as denoted in text
$\bar{n}$	average ligand number
$\Delta G^{\circ}_t(X)$	free energy of transfer of species X from water to the mixed or pure acetone solvent
$[Ag^+]$	concentration of silver ion in moles per liter or millimoles per liter

#### APPENDICES

The experimental data are given below. All concentrations are reported in units of mM (millimoles per liter) and potentials are given in volts. Those points marked with an asterisk were not used in the least squares refinement of the equilibrium constants. The symbols used below have the following significance:  $E'$  = formal potential;  $E$  = potential measured during the titration;  $[Ag^+]_{ref}$  = silver ion concentration in the reference electrode solution;  $C_{Ag}$  = total silver concentration in the experimental solution;  $C_X$  = total halide concentration in the experimental solution.

Data for the 98.53% Acetone Solutions  
( $E' = 0.0776V$ ;  $[Ag^+]_{ref} = 30.48 \text{ mM}$ )

Chloride Solutions			
$C_{Ag}$	$C_{Cl}$	$-E$	
0.3508	3.776	0.9598	
0.4856	3.771	0.9473	
0.6122	3.766	0.9359	
0.7503	3.761	0.9246	
0.8959	3.755	0.9134	
1.065	3.749	0.8978	
1.201	3.744	0.8845	
1.342	3.738	0.8686	
1.513	3.732	0.8418*	unsaturated solutions ↑
1.656	3.726	0.8092*	unsaturated solutions ↓
1.776	3.722	0.7543	saturated solutions ↓
1.857	3.719	0.7545	
1.994	3.714	0.7527	
2.164	3.707	0.7502	
2.374	3.699	0.7462	
2.557	3.692	0.7423	
2.735	3.685	0.7376	
2.954	3.677	0.7303	
3.165	3.669	0.7204	
3.376	3.661	0.7042	
3.499	3.656	0.6861	
3.592	3.653	0.6596	
Bromide Solutions			
$C_{Ag}$	$C_{Br}$	$-E$	
0.3587	3.938	1.0100	
0.4579	3.934	1.0015	
0.5411	3.931	0.9933	
0.6359	3.927	0.9860	
0.7267	3.923	0.9789	
0.8645	3.918	0.9682	
1.002	3.913	0.9574	
1.135	3.907	0.9455	
1.268	3.902	0.9325	
1.404	3.897	0.9176	
1.536	3.891	0.8990	unsaturated solutions ↑
1.757	3.883	0.8419*	unsaturated solutions ↓
1.853	3.879	0.7971	saturated solutions ↓
1.938	3.876	0.7958	
2.068	3.870	0.7937	
2.214	3.865	0.7920	
2.439	3.856	0.7887	
2.671	3.847	0.7828	
2.875	3.839	0.7769	
3.243	3.824	0.7619	
3.434	3.816	0.7495	
3.546	3.812	0.7347	
3.678	3.807	0.6986	



## Iodide Solutions

$C_{Ag}$	$C_I$	$-E$	
0.3547	3.626	1.0905	
0.4341	3.623	1.0821	
0.5173	3.620	1.0738	
0.6083	3.617	1.0662	
0.6912	3.614	1.0590	
0.8251	3.609	1.0479	
0.9430	3.605	1.0365	
1.072	3.600	1.0240	
1.209	3.595	1.0100	
1.334	3.591	0.9920*	
1.462	3.586	0.9695*	unsaturated solutions ↑
1.590	3.581	0.9374*	
1.672	3.578	0.9145*	saturated solutions ↓
1.795	3.574	0.8918	
1.919	3.569	0.8901	
2.034	3.565	0.8853	
2.206	3.559	0.8769	
2.378	3.553	0.8658	
2.597	3.545	0.8428*	
2.758	3.406	0.8002*	

Data for the 91.23% Acetone Solutions  
( $E' = 0.1163V$ ;  $[Ag^+]_{ref} = 11.76 \text{ mM}$ )

## Chloride Solutions

$C_{Ag}$	$C_{Cl}$	$-E$	
0.8920	38.23	0.7413	
1.129	38.14	0.7349	
1.408	38.03	0.7287	
1.695	37.92	0.7232	
1.979	37.81	0.7183	
2.218	37.72	0.7145	
2.443	37.63	0.7110	
2.720	37.52	0.7072	
2.949	37.43	0.7041	
3.221	37.33	0.7008	
3.494	37.22	0.6975	
3.713	37.14	0.6948	
3.942	37.05	0.6922	
4.215	36.94	0.6893	
4.482	36.84	0.6863	
4.791	36.72	0.6832	
5.105	36.60	0.6801	unsaturated solutions ↑
5.414	36.48	0.6771	
5.796	36.34	0.6741	saturated solutions ↓
6.091	36.22	0.6730	
6.448	36.08	0.6729	
6.859	35.93	0.6725	
7.407	35.71	0.6720	

## Bromide Solutions

$C_{Ag}$	$C_{Br}$	$-E$	
0.2354	24.44	0.8638	
0.3786	24.41	0.8522	
0.5134	24.37	0.8438	
0.6537	24.34	0.8371	
0.8133	24.30	0.8315	
0.9430	24.27	0.8265	
1.084	24.23	0.8221	
1.229	24.20	0.8182	
1.414	24.15	0.8133	
1.608	24.11	0.8090	
1.783	24.06	0.8052	
1.976	24.02	0.8015	
2.164	23.97	0.7985	
2.332	23.93	0.7954	
2.511	23.89	0.7923	
2.786	23.82	0.7881	
3.003	23.76	0.7845	
3.285	23.70	0.7804	
3.557	23.63	0.7765	
3.772	23.58	0.7734	
4.001	23.52	0.7701	
4.182	23.48	0.7676	
4.411	23.42	0.7644	
4.635	23.36	0.7614	
4.838	23.32	0.7584	
5.109	23.25	0.7547	
5.377	23.18	0.7511	unsaturated solutions ↑
5.627	23.12	0.7474	
5.881	23.06	0.7436	saturated solutions ↓
6.153	22.99	0.7399	
6.416	22.93	0.7362	
6.706	22.86	0.7318	
7.032	22.78	0.7307	
7.473	22.67	0.7298	
7.966	22.55	0.7290	
8.789	22.35	0.7273	
9.259	22.23	0.7263	
10.10	22.03	0.7243	
11.03	21.80	0.7220	
11.68	21.64	0.7202	
12.46	21.45	0.7177	
13.44	21.21	0.7144	

## Iodide Solutions

$C_{Ag}$	$C_I$	$+E$	
2.412	18.70	0.9390	
2.606	18.66	0.9355	
2.845	18.61	0.9315	
3.071	18.57	0.9277	
3.292	18.53	0.9238	
3.531	18.48	0.9201	
3.744	18.44	0.9164	
3.977	18.40	0.9126	
4.218	18.35	0.9088	
4.420	18.31	0.9051	
4.662	18.27	0.9014	
4.876	18.23	0.8981	
5.105	18.18	0.8942	
5.371	18.13	0.8900	
5.589	18.12	0.8862*	
6.072	18.00	0.8782*	unsaturated solutions ↑
6.539	17.94	0.8708*	
7.346	17.79	0.8589*	saturated solutions ↓
7.810	17.66	0.8518	
8.092	17.61	0.8485	
8.428	17.54	0.8471	
8.846	17.46	0.8445	
9.276	17.38	0.8420	
9.757	17.29	0.8385	
10.14	17.22	0.8358	
10.63	17.12	0.8311	
11.16	17.02	0.8254	
12.12	16.84	0.8160	

Data for the 80.03% Acetone Solutions  
( $E' = 0.0976V$ ;  $[Ag^+]_{ref} = 26.49 \text{ mM}$ )

## Chloride Solutions

$C_{Ag}$	$C_{Cl}$	$-E$	
0.6122	99.39	0.6625	
0.8487	99.15	0.6545	
1.076	98.92	0.6482	
1.309	98.69	0.6426	
1.579	98.42	0.6374	
1.847	98.15	0.6323	unsaturated solutions ↑
2.118	97.88	0.6284	
2.399	97.60	0.6251	saturated solutions ↓
2.669	97.33	0.6246	
2.979	97.02	0.6244	
3.341	96.66	0.6231	
3.835	96.17	0.6219	
4.292	95.71	0.6207	
5.228	94.77	0.6162	
7.401	92.60	0.6113	

## Bromide Solutions

$C_{Ag}$	$C_{Br}$	$-E$	
0.4559	99.54	0.8036	
0.5905	99.41	0.7970	
0.7740	99.23	0.7898	
0.9587	99.04	0.7840	
1.166	98.83	0.7785	
1.423	98.58	0.7730	
1.668	98.33	0.7684	
1.868	98.13	0.7649	
2.116	97.88	0.7613	
2.355	97.65	0.7562	
2.724	97.28	0.7519	
3.142	96.86	0.7464	
3.546	96.45	0.7425	
3.898	96.10	0.7394	
4.251	95.75	0.7363	
4.602	95.40	0.7333	
4.943	95.06	0.7287	unsaturated solutions ↑
5.321	94.68	0.7243	
5.746	94.25	0.7195	saturated solutions ↓
6.163	93.84	0.7148	
6.542	93.46	0.7135	
6.961	93.04	0.7112	
7.418	92.58	0.7096	
7.919	92.08	0.7094	
9.084	90.92	0.7086	
10.72	89.28	0.7075	
12.31	87.69	0.7062	
13.81	86.19	0.7051	

Iodide Solutions

$C_{Ag}$	$C_I$	$-E$	
1.186	32.92	0.9055*	
1.683	32.76	0.8962	
1.957	32.67	0.8916	
2.225	32.58	0.8876	
2.546	32.47	0.8833	
2.866	32.37	0.8793	
3.174	32.26	0.8758	
3.486	32.16	0.8724	
3.794	32.06	0.8693	
4.097	31.95	0.8666*	
4.831	31.71	0.8607*	
5.660	31.43	0.8550*	unsaturated solutions ↑
6.451	31.17	0.8502	
6.869	31.03	0.8480	
7.428	30.85	0.8461	
7.919	30.68	0.8453	
8.489	30.49	0.8441	
9.216	30.25	0.8423	
10.05	29.97	0.8401	
10.79	29.72	0.8378	
11.68	29.43	0.8350	
12.77	29.07	0.8308	
13.80	28.72	0.8265	saturated solutions ↓

## REFERENCES

- M. Salomon and B. K. Stevenson, *J. Phys. Chem.*, **77**, 3002 (1973); **78**, 1817 (1974).
- K. P. Anderson and R. L. Snow, *J. Chem. Educ.*, **44**, 756 (1967).
- J. N. Butler, *Anal. Chem.*, **39**, 1799 (1967).
- L. G. Sillén, *Acta Chem. Scand.*, **16**, 159 (1962).

- C. W. Davies, "Ion Association," Butterworths, London (1962).
- P. S. Albright, *J. Am. Chem. Soc.*, **59**, 2098 (1937).
- M. R. Reynolds and C. A. Kraus, *ibid.*, **70**, 1709 (1948).
- G. S. Darbari and S. Petrucci, *J. Phys. Chem.*, **74**, 268 (1970).
- R. Alexander, A. J. Parker, J. H. Sharp, and W. E. Waghorne, *J. Am. Chem. Soc.*, **94**, 1148 (1972).
- D. C. Luehrs, R. T. Iwamoto, and J. Kleinberg, *Inorg. Chem.*, **5**, 201 (1966).
- E. L. Mackor, *Rec. Trav. Chim.*, **70**, 457 (1951).
- E. Berne and I. Leden, *Svensk Kem. Tidskr.*, **65**, 88 (1953).
- L. G. Sillén and A. E. Martell, "Stability Constants of Metal-Ion Complexes," The Chemical Society, London (1964).
- R. Alexander, E. C. F. Ko, Y. C. Mac, and A. J. Parker, *J. Am. Chem. Soc.*, **89**, 3703 (1967).
- K. P. Anderson, E. A. Butler, and E. M. Woolley, *J. Phys. Chem.*, **75**, 93 (1971).
- D. Feakins and C. M. French, *J. Chem. Soc.*, 2581 (1957).
- W. L. Marshall, *J. Phys. Chem.*, **74**, 346 (1970).
- D. Bax, C. L. de Ligny, and A. G. Remijnse, *Rec. Trav. Chim.*, **91**, 1225 (1972).
- D. H. Everett and S. E. Rasmussen, *J. Chem. Soc.*, 2812 (1954).
- M. Salomon, in "Physical Chemistry of Organic Solvent Systems," A. K. Covington and T. Dickinson, Editors, Chap. 2.2, Plenum Press, London (1973).

## Contributions of Dissolved Hydrogen to Potential and Irreversible Behavior of the Hydrogen Electrode

M. A. Fullenwider\*<sup>1</sup>*B-B Laboratory, Carlisle, Pennsylvania 17013*

## ABSTRACT

A statistical theory of hydrogen in metals is developed, and isotherms relating surface coverage to bulk hydrogen concentration in the metal are derived. It is shown that in certain circumstances of high concentration and energy, bulk hydrogen can contribute to irreversible behavior of the hydrogen electrode. Irreversible behavior can also be expected in the vicinity of a phase transformation.

In treatments of the hydrogen electrode to date, all (1) have involved the concept, logical from the thermodynamic point of view, that the substrate material affects the reactions involved only in as much as it participates in determining the fate of adsorbed intermediates, free radicals, etc., at the surface of the electrode. Irreversible effects, *e.g.*, those occurring in the presence of adsorbing cations and anions and in particular the  $-50$  mV (*vs.* RHE) rest potential of the palladium-hydrogen system (2) are also generally ascribed to surface effects such as the formation of covalent bonds with the surface in the case of adsorbing cations and anions and the diffusion to the surface of protons in the case of the palladium-hydrogen system.

It has long been known that atomic hydrogen penetrates into the bulk of many metals, and that the properties of the resulting systems vary considerably from metal to metal. Recently the effect of dissolved hydrogen on the thermodynamics of the platinum-hydrogen electrode under reversible conditions was dis-

cussed by Frumkin *et al.* (3), the conclusion being that dissolved hydrogen, even in large concentrations would have little or no effect. It is the purpose of this paper to examine these conclusions in more detail using statistical arguments. It will be shown that dissolved hydrogen has the possibility under certain circumstances of causing irreversible effects with the platinum-hydrogen electrode and with other metal-hydrogen systems, notably the palladium and iron system.

## Preliminaries

The hydrogen atom, or partially shielded proton as it is believed to exist within the bulk of a metal would obey Fermi-Dirac statistics. Thus we have for a total of  $N$  particles, the number  $n_r$  in state  $r$  of energy  $\epsilon_r$  and weight  $w_r$

$$n_r = w_r / [1 + \exp(\epsilon_r/kT)/\lambda] \quad [1]$$

where  $\lambda$ , the absolute activity, is given for a particle of chemical potential  $\mu$

$$\lambda = \exp(\mu/kT) \quad [2]$$

and determined by the condition

\* Electrochemical Society Active Member.  
<sup>1</sup> Present address: RKP Industries, Incorporated, Allentown, Pennsylvania 18103.

Key words: hydrogen electrode, irreversible behavior, hydrogen in metals, hydrogen embrittlement.

$$\sum_r n_r = N \quad [3]$$

It can be shown that for systems such as we will be treating, that is, dilute systems and systems at temperatures far elevated from zero Kelvins, we will have the condition

$$\lambda \ll \exp(\epsilon_r/kT) \quad [4]$$

Thus Eq. [1] and [3] reduce to

$$\lambda \sum_r w_r \exp(-\epsilon_r/kT) = N \quad [5]$$

and we have

$$n_r = N w_r \exp(-\epsilon_r/kT) / f(T) \quad [6]$$

where  $f(T)$  is the ordinary partition function and Eq. [6] is the distribution law of classical statistics. Therefore the systems we will be treating here may be approximated by classical statistics.

We will be dealing with a quantity  $\phi$ , the spreading pressure, defined

$$\phi = -\partial F^{\text{ads}} / \partial A \quad [7]$$

where  $F^{\text{ads}}$  is the free energy of adsorption of a species and  $A$  is the area of the surface.

$\phi$  is related to the variables we will be interested in by the relation

$$RT \Gamma_H = \partial \phi / \partial \ln a_H \quad [8]$$

where  $\Gamma_H$  is the surface coverage with hydrogen atoms in moles of H cm<sup>-2</sup> and  $a_H$  is the bulk hydrogen concentration in the metal in moles of H cm<sup>-3</sup>. Equation [8] will result in isotherms relating surface coverage to bulk hydrogen concentration. Now isotherms usually express surface coverage as a function of electrochemical potential, generally expressed as a function of concentration in a bulk electrolyte solution or potential across the interface (4). Our isotherms will contain this dependence since  $a_H$  is certainly dependent on these quantities, but the dependence will be hidden.

Most generally our model for the hydrogen electrode will be an ideal layer of hydrogen atoms on the surface of the electrode in equilibrium with a gas of protons or partially shielded protons within the bulk of the metal which will be assumed first to be very dilute and then, in another treatment, more concentrated. Equilibrium with hydrogen in aqueous solution will in general not be assumed, especially where there is the possibility of irreversibility, and it must be remembered, particularly in the application of the resulting isotherms, that they only apply in the approximation that the atomic hydrogen dissolved in the metal is in equilibrium with the layer of hydrogen atoms on the surface.

For the free energy of the ideal layer of adsorbed hydrogen atoms on the electrode surface we have from classical statistics (5)

$$F_H^{\text{ads}} = -kT \lambda_H f_H(T) + N_H kT \ln \lambda_H \quad [9]$$

where the symbols have the same definition as previously, and

$$f(T) = 2\pi m_H kT A / h^2 \quad [10]$$

the partition function for a two dimensional monatomic gas.

For the condition of equilibrium between surface and bulk hydrogen we need an expression for  $\lambda_H$  for hydrogen dissolved in the metal. This combined with Eq. [9], [10], and [7] will give us an expression for  $\phi$ , and Eq. [8] will result in the final isotherms.

To obtain an expression for  $\lambda_H$  we use the grand partition function for hydrogen in the metal which in general form is given by (6)

$$\Gamma(T, \lambda_H) = \sum_{N_H} [(\alpha N)! / N_H! (\alpha N - N_H)!] (\lambda_H f_H(T) \rho)^{N_H} \exp[-(N_H w_H + \frac{1}{2} N_H^2 w_{HH} / \alpha N) / kT] \quad [11]$$

where  $\alpha N$  is the number of interstitial sites,  $N_H$  is the number of hydrogen atoms distributed among the  $\alpha N$  sites in the metal,  $\rho$  is the nuclear spin weight,  $w_H$  is the potential energy of the protons relative to the state of infinite dispersion outside the metal, and where

$$f_H'(T) = (2\pi m_H kT)^{3/2} V / h^3 \quad [12]$$

simply the partition function of a three-dimensional monatomic gas, and  $V$  is the volume of the metal-hydrogen system.

The factor

$$\exp(-\frac{1}{2} N_H^2 w_{HH} / \alpha N kT) \quad [13]$$

deserves special attention. It is just this quantity, corresponding to interactions between the protons, which in some treatments of electrolytic solutions and the electric double layer is expanded in the cluster formalism of Mayer and Mayer (7). This does not suit our purposes here since it would be very complicated and there is not exact information available of, for example, the variation of the heat of solution with concentration, the nature of the species involved, etc., for the systems we will be discussing. What we have done instead is to, as Lacher (8), ignore the effect of the actual arrangement of the protons on the rate of increase of absorption energy and assumed that this rate is directly proportional to the number of holes filled,  $w_{HH}$  being a proportionality constant.

### Very Dilute Approximation

In this approximation we put the following requirements on Eq. [11]

$$w_{HH} = 0 \quad [14]$$

$$N_H \ll \alpha N \quad [15]$$

This gives us for the grand partition function

$$\Gamma(T, \lambda_H) = \sum_{N_H} (1/N_H!) (\lambda_H f_H'(T) \rho)^{N_H} \exp(-N_H w_H / kT) \quad [16]$$

Equation [16] is treated in the usual way to obtain the equilibrium value of  $N_H$  by taking

$$\partial \ln(\text{term of sum: } [\Gamma(T, \lambda_H)]) / \partial N_H = 0 \quad [17]$$

that is, replacing the series by its maximum term, we obtain

$$N_H = \lambda_H f_H'(T) \rho \exp(-w_H / kT) \quad [18]$$

and from Eq. [9], [10], [12], and [18] we have

$$F_H^{\text{ads}} = -kT \left[ \frac{N_H h^3 \exp(w_H kT)}{(2\pi m_H kT)^{3/2} \rho V} \right] \frac{2\pi m_H kT}{h^2} A + N_H kT \ln \left[ \frac{N_H h^3 \exp(w_H kT)}{(2\pi m_H kT)^{3/2} \rho V} \right] \quad [19]$$

and with Eq. [7] and the relation

$$A = V^{2/3} \quad [20]$$

that is taking a cubic symmetry, we get for  $\phi$

$$\phi = \frac{3}{2} N_{H, \text{surface}} kT / A - \frac{N_{H, \text{bulk}} kT h \exp(w_H / kT)}{2V \rho (2\pi m_H kT)^{1/2}} \quad [21]$$

which may be written

$$\phi = K \Gamma_H + K' a_H \exp(w_H / kT) \quad [22]$$

and from Eq. [8] we obtain the linear, first order differential equation

$$RT \Gamma_H = K a_H \partial \Gamma_H / \partial a_H + K' a_H \exp(w_H / kT) \quad [23]$$

which has the solution

$$\Gamma_H = C a_H^{2/3} - \frac{3}{2} K' a_H \exp(w_H / kT) \quad [24]$$

where  $C$  is a constant of integration. Equation [24] provides a relation between surface coverage and a small quantity of hydrogen dissolved in a metal for the case that the two are in equilibrium and the interactions between the dissolved species are negligible.

### Approximation for More Concentrated Systems

In this approximation we take Eq. [1] without any restrictions, and together with Eq. [17] we obtain the relation

$$N_H/(\alpha N - N_H) = \lambda_H f_H'(T) \rho \exp[-(w_H + N_H w_{HH}/\alpha N)/kT] \quad [25]$$

and from Eq. [9], [10], [12], and [25] we have

$$F_H^{ads} = -kT \left( \frac{N_H h^3 \exp[(w_H + N_H w_{HH}/\alpha N)/kT]}{(\alpha N - N_H) (2\pi m_H kT)^{3/2} \rho V} \right) \times \frac{2\pi m_H kT}{h^2} A + N_H kT \times \left( \ln \left[ \frac{N_H h^3 \exp(w_H + N_H w_{HH}/\alpha N)/kT}{(\alpha N - N_H) (2\pi m_H kT)^{3/2} \rho V} \right] \right) \quad [26]$$

and from Eq. [7] for  $\phi$  with Eq. [20]

$$\phi = \frac{3}{2} N_{H,surface} kT/A - \frac{N_H kT h \exp[(w_H + N_H w_{HH}/\alpha N)/kT]}{(\alpha N - N_H) 2V \rho (2\pi m_H kT)^{1/2}} \quad [27]$$

which may be written

$$\phi = K\Gamma_H + K'a_H' \exp[(w_H + N_H w_{HH}/\alpha N)/kT] \quad [28]$$

where

$$a_H' = N_H/(\alpha N - N_H) V \quad [29]$$

the reduced concentration. Again from Eq. [8] we have a relation similar to Eq. [24]

$$\Gamma_H/a_H'^{2/3} = C - \int (K'/a_H'^{2/3} K) \exp[(w_H + N_H w_{HH}/\alpha N)/kT] \times [1 + a_H' w_{HH} V/kT(1 + Va_H')^2] da_H' \quad [30]$$

where the integral may be expanded in different ways. Equation [30] extends Eq. [24] into regions where interactions between dissolved species are not negligible. It should be noted, however, that equilibrium between the adsorbed and absorbed protons is still assumed.

### Discussion

First of all the quantities  $w_H$  and  $(w_H + N_H w_{HH}/\alpha N)$  of Eq. [16]-[24] and Eq. [25]-[30], respectively, can be roughly taken as the heats of solution from the gas phase, since the experimental heats of solution are only rough estimates, values generally being for unspecified concentrations, and where there is more than one value in the literature considerable spread exists. Some values of the heat of solution are given in Table I, and it should be noted that some are endothermic and others exothermic. Strictly speaking the quantity in the equations, the protonic work function, refers to the process

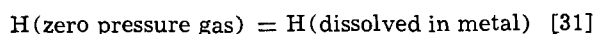
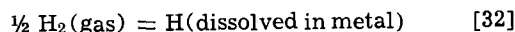


Table I. Solubilities at the reversible potential and heats of solution of hydrogen for various metals

Metal	$a_H$ (mol H cm <sup>-3</sup> )	Ref.	$\Delta H_s$ (kcal per half-mol H <sub>2</sub> )	Ref.
Pt	$1 \times 10^{-5}$	11	8.9	12
Ni	$1.4 \times 10^{-5}$	13	3.60	14
Pd	$2.7 \times 10^{-4}$	13	-9.5	15
Fe	$7.0 \times 10^{-9}$	13	7.04	16

while the values of  $\Delta H_s$  in Table I refer to the process



Secondly, there exists no correct data at the present time to test Eq. [24] and [30]. The recent paper of Breger and Gileadi (9) lists values of coverages and bulk hydrogen concentrations for the palladium-hydrogen system. However, this paper was based upon assumptions which have since been found to be erroneous (10), i.e., that of a concentration independent diffusion coefficient and an anodic stripping coverage time independent of bulk hydrogen concentration.

Equation [22] will be used first to reach some conclusions regarding the platinum-hydrogen system. Assuming a full monolayer coverage and inserting standard values for the constants we obtain the relation

$$\phi = (3 \times 10^{-9}) RT - a_H [2.5 \times 10^{-9} \exp(w_H/kT)] RT \quad [33]$$

where units for  $\phi$  might be, for example, ergs cm<sup>-2</sup>, and  $a_H$  is again moles of H cm<sup>-3</sup>. Table I lists some values of  $a_H$  at the reversible potential and heats of solution, as stated previously.  $w_H$  should be taken with the same sign as the heat of solution.

Now whenever the bulk term (second in Eq. [33]) predominates over the surface term (first in Eq. [33]) we will have irreversible behavior because this is thermodynamically impossible at the reversible potential. For platinum it can be seen that the bulk term is slightly larger than the surface term, and for other metals the surface term predominates. However, the value of  $a_H$  cited for platinum is in the presence of As<sub>2</sub>O<sub>3</sub>, a hydrogen diffusion promoter, and under normal conditions  $a_H$  would be much lower, i.e., there would be reversible behavior. Thus it is quite likely that irreversible behavior of the platinum-hydrogen electrode observed in the presence of some adsorbing cations and anions is due to their hydrogen diffusion promoting properties. Also, whereas the conclusion of Frumkin *et al.* (3) was that when there is a large quantity of bulk hydrogen present and reversibility this hydrogen has no appreciable effect, we must make the point that when there is a large quantity of bulk hydrogen present there is no reversibility.

Referring to Eq. [27] with reference to the palladium-hydrogen system we can see that the surface term will predominate except when  $N_H$  approaches  $\alpha N$ . When this happens the bulk term becomes large, and again we will have irreversible behavior. Before  $\phi$  gets too large, however, the  $\beta$  phase should start to form, and it is this that results in the -50 mV rest potential of the palladium-hydrogen system, the -50 mV corresponding to the energy increment between the  $\alpha$  and  $\beta$  phases.

We have shown how hydrogen in large concentrations dissolved within the bulk of a metal can contribute toward irreversible behavior of the hydrogen electrode. For most metals behavior of this type can usually be expected in the vicinity of a so-called phase transition. In a manner of speaking the word "phase" is inappropriate in the case of hydrogen in metals. The work of Gosar (17), for example, showed that mobile interstitials in the semiclassical approximation exist within the host lattice rather in "bands" possessing energies, band widths, and energy gaps, much the same as electrons in a lattice. This seems to explain qualitatively the fact that iron undergoes its irreversible embrittlement at such small concentrations (18), e.g.,  $10^{-7}$  moles cm<sup>-3</sup>, i.e., its first band apparently fills in this concentration range. Here the tendency for the protons to collect in regions of high tensile stress (19) acts to "pump" gaseous hydrogen into cracks and voids as the spreading pressure becomes large at their surfaces, causing embrittlement.

Manuscript submitted Aug. 22, 1973; revised manuscript received July 30, 1974.

Any discussion of this paper will appear in a Discussion Section to be published in the June 1975 JOURNAL. All discussions for the June 1975 Discussion Section should be submitted by Feb. 1, 1975.

The publication costs of this article have been assisted by B-B Laboratory.

## LIST OF SYMBOLS

$A$	surface area
$a_H$	concentration of protons
$a_H'$	reduced concentration of protons
$F_{ads}$	free energy of adsorption
$f_H(T)$	partition function of ideal two-dimensional gas of protons
$f_H'(T)$	partition function of ideal three-dimensional gas of protons
$h$	Planck's constant
$k$	Boltzmann's constant
$m_H$	proton mass
$N$	number of particles
$N_H$	number of protons
$n_r$	number of particles in state $r$
$R$	gas constant
$T$	temperature in Kelvins
$V$	volume
$w_H$	potential energy of protons in the metal with respect to infinite dispersion outside the metal, protonic work function
$w_{HH}$	a proportionality constant
$w_r$	weight of state $r$
$\alpha N$	number of interstitial sites
$\Gamma_H$	surface coverage with protons
$\Gamma(T, \lambda_H)$	grand partition function for hydrogen in the metal
$\Delta H_s$	heat of solution of hydrogen in a metal
$\epsilon_r$	energy of particles in state $r$
$\lambda$	absolute activity
$\mu$	chemical potential
$\rho$	nuclear spin weight
$\phi$	spreading pressure

## REFERENCES

1. J. O'M. Bockris and A. K. Reddy, "Modern Electrochemistry," Plenum Publishing Corp., New York (1970).
2. S. Schuldiner, G. W. Castellano, and J. P. Hoar, *J. Chem. Phys.*, **28**, 16 (1958).
3. A. Frumkin, O. Petry, and R. Marvet, *J. Electroanal. Chem.*, **12**, 504 (1966).
4. E. Gileadi, Editor, "Electrosorption," p. 3, Plenum Publishing Corp., New York (1967).
5. R. Fowler and E. A. Guggenheim, "Statistical Thermodynamics," p. 225, Cambridge University Press, New York (1965).
6. R. Fowler and E. A. Guggenheim, "Statistical Thermodynamics," p. 542, Cambridge University Press, New York (1965).
7. J. E. Mayer and M. G. Mayer, "Statistical Mechanics," Chap. 13, John Wiley and Sons, Inc., New York (1940).
8. J. R. Lacher, *Proc. Roy. Soc.*, **A161**, 525 (1937).
9. V. Breger and E. Gileadi, *Electrochim. Acta.*, **16**, (1971).
10. M. A. Fullenwider, To be published.
11. E. Gileadi, M. A. Fullenwider, and J.O'M. Bockris, *This Journal*, **113**, 926 (1966).
12. O. W. Richardson, J. Nicol, and T. Parnell, *Phil. Mag.*, **8**, 1 (1904).
13. J. O'M. Bockris, M. A. Genshaw, and M. A. Fullenwider, *Electrochim. Acta*, **15**, 47 (1970).
14. Y. Ebisuzaki, W. J. Kass, and M. O'Keefe, *J. Chem. Phys.*, **46**, 1378 (1967).
15. A. J. Maeland and T. R. P. Gibb, Jr., *J. Phys. Chem.*, **65**, 1270 (1961).
16. W. L. Bryan and B. F. Dodge, *J. Am. Inst. Chem. Engrs.*, **9**, 223 (1963).
17. P. Gosar, *Nuovo Cimento*, **31**, 781 (1964).
18. W. Beck, J. O'M. Bockris, J. McBreen, and L. Nanis, *Proc. Roy. Soc.*, **A290**, 220 (1966).
19. J. O'M. Bockris, W. Beck, M. A. Genshaw, P. K. Subramanyan, and F. S. Williams, *Acta Met.*, **19**, 1209 (1971).

## Dissolution of Mild Steel with a Rotating Ring Hemispherical Electrode

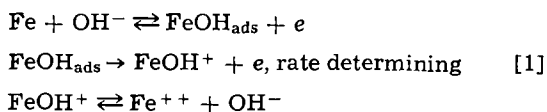
Der-Tau Chin\*

General Motors Corporation, Research Laboratories, Electrochemistry Department, Warren, Michigan 48090

## ABSTRACT

A rotating ring hemispherical electrode was used to study the active dissolution of mild steel in sulfate electrolytes. Using potentiostatic transients for the deposition of a monolayer of an iron oxide on a platinum ring electrode, the soluble  $\text{FeOH}^+$  complex ion was identified as an intermediate product during the dissolution reaction. The  $\text{FeOH}^+$  concentration was found to increase with pH of the electrolyte and to decrease with sulfate concentration. In concentrated sulfate solutions, the  $\text{FeOH}^+$  concentration also decreased with increasing dissolution current density at the mild steel hemispherical electrode. The results indicate that the dissolution reaction did not fully follow the commonly accepted Bockris or Heusler mechanism. This discrepancy is discussed with a parallel mechanism, in which sulfate ion participates in the anodic reaction.

Although numerous studies have been made of the anodic dissolution of iron and carbon steels in sulfate electrolytes, the exact mechanism of iron dissolution is still a controversial question (1-5). One of the major mechanisms as proposed by Bockris *et al.* (6) involves the following steps



Equation [1] has been supported by a number of polarization measurements (7-9). Nevertheless, the  $\text{FeOH}$  complexes in each step are still hypothetical in nature; no positive identification has been thus far reported in the literature. These complexes are also suggested in Heusler's catalysis mechanism (1). Therefore, it is of theoretical importance to determine if the principal intermediate,  $\text{FeOH}^+$  ion, is generated by iron dissolution.

Previous studies (10-11) have shown that  $\text{FeOH}^+$  ions can deposit on a platinum substrate to form a  $\gamma$ - $\text{FeOOH}$  film from sulfate solutions. On a rotating platinum ring electrode, the deposition reaction follows a mathematical model describing two-dimensional nu-

\* Electrochemical Society Active Member.

Key words: dissolution of mild steel in sulfate solution, iron oxide deposition.

cleation and growth of a monolayer of oxide on the electrode surface (12).

This evidence suggests the use of a rotating ring hemisphere for the study of iron dissolution reactions. By properly setting the potential of a platinum ring electrode within the region for the iron oxide deposition reaction, it should be possible to detect the soluble  $\text{FeOH}^+$  complex ion produced by iron dissolution at the central hemispherical electrode. The rationale for the use of a ring hemisphere combination has been discussed previously (13). Easy replacement of the central hemisphere and less change in the electrode geometry are the advantages of this combination in studying metal dissolution reactions.

Such a study has been made in this laboratory for the dissolution of mild steel in  $(\text{NH}_4)_2\text{SO}_4$  electrolytes. The methods of galvanostatic dissolution at the central hemisphere and the potentiostatic transient at the platinum ring were used for the experiments. This paper summarizes the results of the study.

### Experimental

The rotating ring hemispherical electrode used consisted of a platinum ring and a replaceable central mild steel<sup>1</sup> hemispherical electrode mounted concentrically on a Teflon support rod. The hemisphere was 0.635 cm in diameter and the dimension of the ring electrode was 0.798 cm ID  $\times$  1.003 cm OD. This arrangement had a collection efficiency of 32% as calibrated with a ferricyanide/ferrocyanide redox reaction. The details of the experimental setup have been described previously (13).

The method of galvanostatic dissolution at the central hemisphere and a potentiostatic transient at the ring were used for the study. The mild steel hemisphere was first dissolved in a test electrolyte at the steady-state conditions. To detect  $\text{FeOH}^+$  complex ions generated during the dissolution reaction, a constant potential of 0.9 V/SCE (12) was applied to the ring electrode and the ring current was recorded on a strip-chart recorder.

Two independent electrical circuits composed of two separate counterelectrodes (one for the hemisphere and the other for the ring) were used for the experiment. The constant current to the hemisphere was supplied from a Magna 4700M potentiostat, whereas the ring potential was controlled by a battery powered potentiostat which was floating with respect to ground.

For each run, the surface of the ring electrode was first polished with a 600 grit Carbimet wet grinding paper. The mild steel hemispherical electrode was then fastened to the Teflon support. The assembled ring hemisphere was cleaned with methanol and cathodically treated in 2M NaOH followed by a rinse in distilled water. The electrode was then transferred to a cell filled with the test electrolyte and was installed on a high speed rotator. At this point, a constant rotational speed was selected for the rotator and a constant current was applied to the mild steel hemisphere. The potential of the hemisphere was recorded on a strip-chart recorder. After the hemisphere potential reached a steady-state value, a constant potential of 0.9 V/SCE was applied to the ring electrode and the ring current was subsequently recorded on a Sanborn 296 recorder.

Nitrogen-saturated 0.5-2M  $(\text{NH}_4)_2\text{SO}_4$  was used as the electrolyte. The pH of these solutions was maintained at a constant value by adding proper amounts of dilute  $\text{NH}_4\text{OH}$  and  $\text{H}_2\text{SO}_4$  during the runs. All the experiments were performed at a constant temperature of  $24 \pm 1^\circ\text{C}$ .

### Results and Discussion

Figure 1 shows the recorder traces of current transients on the platinum ring when the mild steel hemispherical electrode was dissolving at a constant cur-

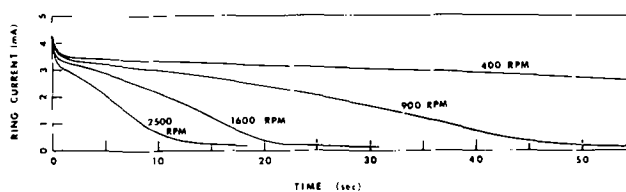


Fig. 1. Recorder traces of ring current when the central mild steel hemisphere was dissolving at a constant current density of 31 mA/cm<sup>2</sup>. The electrolyte used was pH 5, 1M  $(\text{NH}_4)_2\text{SO}_4$ .

rent density of 31 mA/cm<sup>2</sup> into pH 5, 1M  $(\text{NH}_4)_2\text{SO}_4$  electrolyte. The speed of electrode rotation for these runs varied from 400 to 2500 rpm. It is seen that the ring current jumped to a large value at the beginning of the potential step and then decreased with time. This behavior is the same as that of a previous characterization study (12) on the deposition of iron oxide from ferrous sulfate solutions.

The current jumps to a large value at zero time; this suggests that the ring picked up the dissolution product,  $\text{Fe}^{++}$  ion, and oxidized it to  $\text{Fe}^{+++}$  ion at the limiting current potential of 0.9 V/SCE. Since the amount of  $\text{Fe}^{++}$  ions transferred to the ring was limited by the rate of  $\text{Fe}^{++}$  generation at the central hemisphere, the magnitude of that current was relatively independent of the rotational speed. The sharp current peak near time zero (less than 0.5 sec from the start of the potential step) was due to establishment of a diffusion layer on the ring and is irrelevant to the results of the present study.

The dissolution intermediate,  $\text{FeOH}^+$  complex ion, is also picked up at the ring, where it was oxidized to form a monolayer of  $\gamma\text{-FeOOH}$  film (12). The current consumption for the monolayer oxide deposition reaction was very small as compared to that of the  $\text{Fe}^{++}/\text{Fe}^{+++}$  oxidation reaction; however, the oxide film reduced the active area available to the  $\text{Fe}^{++}/\text{Fe}^{+++}$  reaction, resulting in a decrease of the ring current as shown in Fig. 1. That the rate of current drop increased with the speed of rotation is in agreement with Eq. [1] that the  $\text{FeOH}^+$  complex ion dissociates in the electrolyte into ferrous and hydroxyl ions. The faster the speed of rotation, the less the time required for  $\text{FeOH}^+$  ions to travel from the central hemisphere to the ring, and hence more  $\text{FeOH}^+$  ions reached the ring undecomposed, resulting in a higher rate of the film deposition reaction. Consequently, the rate of current drop was faster at higher rotational speeds.

Figure 2 is a semilogarithmic plot of ring current vs. cube of time for three of the curves shown in Fig. 1. The exact linear relationship indicates that the oxide deposition reaction follows a model for two-dimensional nucleation and growth of a film of monolayer thickness (14)

$$I_{\text{ring}} = I_{\text{lim}} \exp\left(-\frac{\pi}{3}v^2Nt^3\right) \quad [2]$$

Here  $I_{\text{lim}}$  is the initial limiting current for the  $\text{Fe}^{++}/\text{Fe}^{+++}$  oxidation reaction at the platinum ring whose entire surface is free from oxide contamination,  $N$  is the rate of nucleation of two-dimensional centers,  $v$  is the rate of spreading of the monomolecular layer film, and  $t$  is the time. Equation [2] describes the diminishing of the current for the  $\text{Fe}^{++}/\text{Fe}^{+++}$  oxidation reaction due to the film coverage on the ring surface. The total current on the ring is actually the sum of three components. They are (i)  $\text{Fe}^{++}/\text{Fe}^{+++}$  oxidation reaction, (ii) formation of a monolayer of  $\gamma\text{-FeOOH}$  film, and (iii) other possible electrochemical processes occurring at the oxide/electrolyte interface. In the present study, the currents for the last two components were negligibly small as compared with the first component (12); thus, the ring current transient obeyed Eq. [2] as shown in Fig. 2.

<sup>1</sup> Composition of mild steel other than iron: Mn, 0.98%; S, 0.29%; C, 0.1%; P, 0.06%; Si, 0.005%.

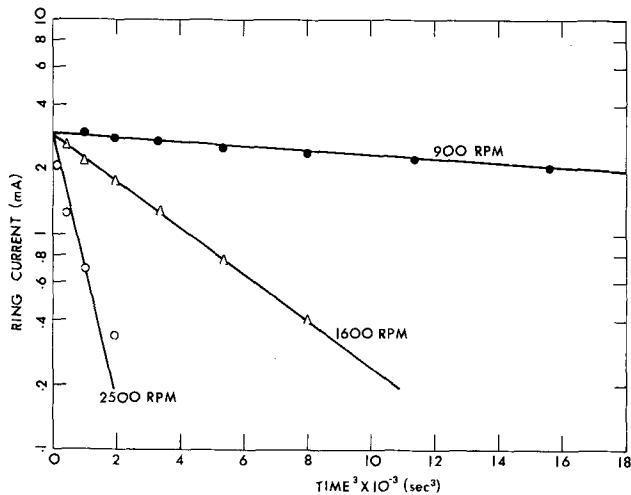


Fig. 2. Interpretation of current transients at the ring with a two-dimensional nucleation and film growth model. The data shown here were taken from a pH 5, 1M  $(\text{NH}_4)_2\text{SO}_4$  when the mild steel hemisphere was dissolving at a constant current density of 31  $\text{mA}/\text{cm}^2$ .

Equation [2] indicates that  $I_{\text{lim}}$  can be obtained by extrapolating the straight lines on the semilogarithmic plot of  $I_{\text{ring}}$  vs.  $t^3$  to the zero time. The collection efficiency for ferrous ions on the ring electrode free from oxide contamination can then be calculated by  $(2I_{\text{lim}}/I_{\text{hemisphere}}) \times 100$ , where  $I_{\text{hemisphere}}$  is the total dissolution current on the mild steel hemispherical electrode. The collection efficiency thus calculated, using the data points shown in Fig. 2, is found to be  $30 \pm 2\%$ , in close agreement with the calibrated value of 32%.

According to Eq. [2], the quantity,  $-\pi/3 v^2 N$ , is the slope of the straight lines shown in Fig. 2; the cube root of the product,  $v^2 N$ , is the composite rate constant for the over-all oxide deposition reactions. Since the  $\gamma\text{-FeOOH}$  film is formed by the oxidation of  $\text{FeOH}^+$  complex ion on the ring electrode, the magnitude of this composite rate constant should then reflect the rate of  $\text{FeOH}^+$  ions transferred to the ring, and consequently the amount of  $\text{FeOH}^+$  ions generated at the central hemisphere during the mild steel dissolution reaction. Figure 3 is a plot of the composite rate constant vs. pH of the electrolyte when the mild steel hemisphere was dissolving into 1M  $(\text{NH}_4)_2\text{SO}_4$  at a constant current density of 8  $\text{mA}/\text{cm}^2$  and at an electrode rotational speed of 1600 rpm. The effect of the dissolution current density at the central hemisphere on the composite rate constant at the ring is shown in Fig. 4 for three sulfate concentrations; in these particular runs the pH of the electrolyte was kept at 5, and the electrode rotation at 1600 rpm.

The results given in Fig. 3 and the curve for 0.5M sulfate in Fig. 4 are seen to agree with Eq. [1] in which the concentration of the dissolution intermediate,  $\text{FeOH}^+$  ion, increases with the rate of iron dissolution as well as with pH of the electrolyte. However, the curves for 1 and 2M  $(\text{NH}_4)_2\text{SO}_4$  in Fig. 4 are quite different. The horizontal relation between the composite rate constant and the dissolution current density in 1M sulfate indicates that the concentration of  $\text{FeOH}^+$  complex ion is independent of the iron dissolution rate. The curve for 2M sulfate reflects a trend contrary to Eq. [1]; it says that the rate of  $\text{FeOH}^+$  generation decreases with increasing current density at the mild steel hemispherical electrode. For a given dissolution current density, Fig. 4 further shows that the composite rate constant decreases with increasing sulfate concentration.

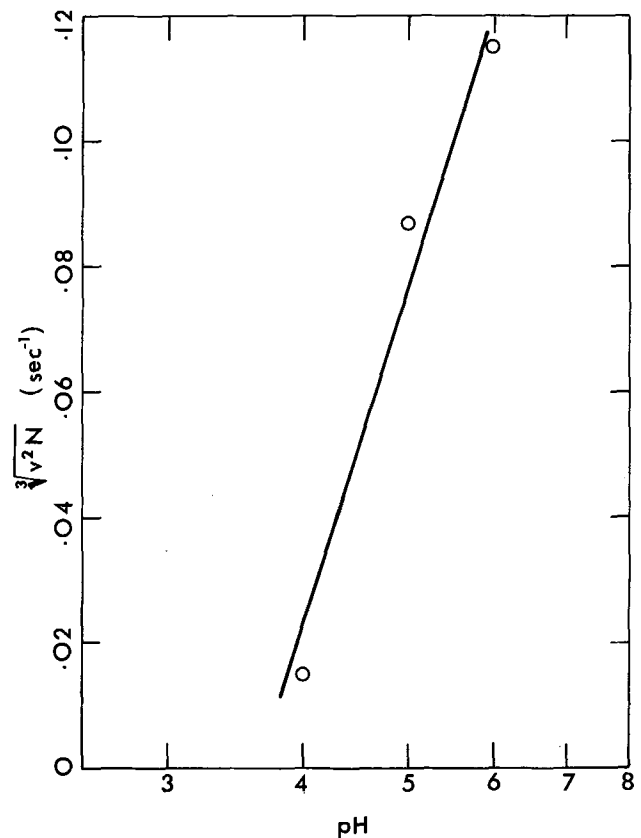


Fig. 3. Composite rate constant for the growth of the monolayer oxide on the ring vs. pH values for 1M  $(\text{NH}_4)_2\text{SO}_4$ . The current density at the mild steel hemisphere was maintained at 8  $\text{mA}/\text{cm}^2$ ; the speed of electrode rotation was 1600 rpm.

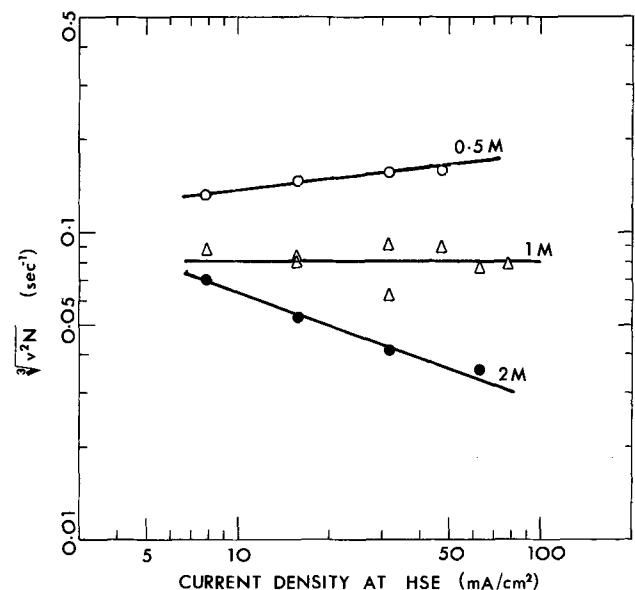


Fig. 4. Composite rate constant for the growth of the monolayer oxide on the ring vs. the dissolution current density at the mild steel hemispherical electrode for three sulfate concentrations. The pH of the electrolytes was maintained at 5; the speed of electrode rotation was 1600 rpm.

At this point, one is apt to think that this behavior is probably caused by the participation of sulfate ions in the oxide deposition reaction. That this is not true has been shown in a previous characterization study (12) of the deposition of iron oxide on a rotating platinum ring electrode from ferrous sul-

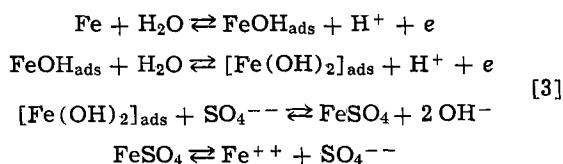
fate solutions. In that study it was found that changes in the concentration of  $(\text{NH}_4)_2\text{SO}_4$  supporting electrolyte had no effect on the composite rate constant.

One might also think that the  $\text{FeOH}^+$  collected at the ring is not a reaction intermediate, but a product formed by the hydrolysis of the final dissolution product,  $\text{Fe}^{++}$ , during the course of traveling to the ring. That this is not true can be attributed to the following two reasons:

(i) If  $\text{FeOH}^+$  is formed by the hydrolysis of ferrous ion, then the faster the rotational speed, the less would be the amount of  $\text{FeOH}^+$  formed before it reaches the ring. Consequently, for a given dissolution rate at the hemisphere, the rate of current decrease at the ring would be lower at higher rotational speeds. This contradicts the results given in Fig. 1.

(ii) The rate of film deposition reaction has been found to increase linearly with the concentration of ferrous ions in the test electrolyte (12). If the iron dissolution does not proceed through the intermediate stage of  $\text{FeOH}^+$  ion, it would then be expected that the composite rate constant at the ring would increase rapidly with increasing dissolution rate at the hemisphere. This contradicts the results shown in Fig. 4.

Thus, the present results indicate that dissolution of mild steel in sulfate electrolytes does not follow fully Eq. [1]. These results seem to support the evidence that in addition to the Bockris or the Heusler mechanism, mild steel is also dissolving via a parallel mechanism, such as the one proposed by Geana, Miligy, and Lorenz (5)



The data shown in Fig. 4 suggest that the Bockris or the Heusler mechanism probably occurs at low dissolution current densities and at low sulfate concentrations. With increasing sulfate concentration and current density, more and more sulfate ions are adsorbed on the anode and some of the iron atoms start to dissolve via the parallel mechanism. The proportion of current consumption by the parallel mechanism increases with increasing current density at high sulfate concentrations.

## Conclusions

Using the rotating ring hemisphere technique,  $\text{FeOH}^+$  complex ion has been identified as a reaction intermediate during the dissolution of mild steel in  $(\text{NH}_4)_2\text{SO}_4$  electrolyte. For a given dissolution current density, the concentration of  $\text{FeOH}^+$  ion was found to decrease with increasing sulfate concentration. The effect of the dissolution current density on the amount of  $\text{FeOH}^+$  detected varied according to sulfate concentration. In dilute sulfate, the rate of  $\text{FeOH}^+$  produced was an increasing function of dissolution current density, whereas in more concentrated  $(\text{NH}_4)_2\text{SO}_4$  it was either independent of, or a decreasing function of, the dissolution current density. The results indicate that the dissolution reaction did not fully follow the commonly accepted Bockris or Heusler mechanism. It appears that mild steel also dissolves via a parallel mechanism, in which sulfate ion participates in the dissolution reaction.

Manuscript submitted April 8, 1974; revised manuscript received June 10, 1974.

Any discussion of this paper will appear in a Discussion Section to be published in the June 1975 JOURNAL. All discussions for the June 1975 Discussion Section should be submitted by Feb. 1, 1975.

The publication costs of this article have been assisted by General Motors Corporation.

## REFERENCES

1. E. Kelly, *This Journal*, **112**, 124 (1965).
2. G. M. Florianovich, L. A. Sokolova, and Ya. M. Kolotyrlin, *Electrochim. Acta*, **12**, 879 (1967).
3. F. Hilbert, Y. Miyoshi, G. Eichkorn, and W. J. Lorenz, *This Journal*, **118**, 1919 (1971).
4. S. Barnartt, *ibid.*, **119**, 812 (1972).
5. D. Geana, A. A. El Miligy, and W. J. Lorenz, *Corrosion Sci.*, **13**, 505 (1973).
6. J. O'M. Bockris, D. Drazic, and A. R. Despic, *Electrochim. Acta*, **4**, 325 (1961).
7. J. J. Podesta and A. J. Arvia, *ibid.*, **10**, 171 (1965).
8. A. Akiyama, R. E. Patterson, and K. Nobe, *Corrosion*, **26**, 51 (1970).
9. S. Asakura and K. Nobe, *This Journal*, **118**, 13 (1971).
10. J.-L. Leibenguth and M. Cohen, *ibid.*, **119**, 987 (1972).
11. M. Ehrenfreund and J.-L. Leibenguth, *Bull. Soc. Chim. Fran.*, **7**, 2590 (1972).
12. D.-T. Chin, *This Journal*, **121**, 527 (1974).
13. D.-T. Chin, *ibid.*, **120**, 632 (1973).
14. R. D. Armstrong, D. F. Porter, and H. R. Thirsk, *J. Phys. Chem.*, **72**, 2300 (1968).



# Reflectance Changes during Formation and Reduction of Oxide Films on Gold and Platinum: Corrections for "Double-Layer Effects"

B. E. Conway, H. Angerstein-Kozłowska,\* and L. H. Laliberté<sup>1</sup>

Chemistry Department, University of Ottawa, Ottawa, Ontario, Canada

## ABSTRACT

Hysteresis between the processes of formation and reduction of thin oxide films on Au and Pt have been investigated by ellipsometric ( $\Delta$ ) and relative reflectance ( $\delta R/R$ ) measurements. The interpretation of results obtained by optical methods where thin films are in the course of formation towards a monolayer, or beyond, requires consideration of optical effects due to contributions from changing ion concentration and metal surface electron charge density in the double-layer since substantial changes of optical parameters for reflectance at Au and Pt interfaces arise with changing electrode potential. Resulting changes of  $\Delta$  and  $\delta R/R$  must therefore be corrected for continuing double-layer effects as the ad-layer is laid down or removed (in the reduction process). The theoretical basis for evaluation of double-layer optical effects is reviewed but it is proposed that, at the present time, empirical correction procedures may be preferable. Three methods are examined and an optimum procedure is recommended. The procedure is applied to the evaluation of hysteresis effects in the formation and reduction of thin oxide films at Au and Pt where evaluation of the true hysteresis effects depends in an important way on a proper correction procedure for the double-layer optical effects.

In recent papers (1-4), the state of surface oxide films on Pt (1-3) and Au (4) has been examined by electrochemical [cyclic voltammetry (3) and charging curves (1, 2)] and optical [reflectance (4) and ellipsometry (5, 6)] methods. It has been shown (3) that both after, and simultaneously with, oxygen deposition in distinguishable successive arrays [cf. similar indications from LEED work (7)], the initially chemisorbed species undergoes a rearrangement (probably place-exchange with underlying substrate metal atoms) to a more stable surface oxide phase which is reducible only at potentials less positive than those required for the initial anodic electroadsorption (8). This leads to the well-known hysteresis (8, 9) between formation and reduction of surface oxide films on most metals.

In the present paper, we compare the optical and electrochemical behavior of these surface oxide films on Pt and Au, especially with regard to evaluation of the optical behavior of the film during its reduction in relation (6, 10) to that during its formation; that is, the question to be addressed is how optical measurements can be used to provide a basis for distinction between the state of a thin oxide film in the direction of its formation and its reduction, for given extents of oxidation in the forward (anodic) and backward (cathodic) directions of charging curves or cyclic-voltammetry current-potential profiles.

Ellipsometry and electric-modulated reflectance (11) measurements which are currently of great interest in the study of surface processes (10, 12-14) and adsorption (20-24) at electrodes are especially valuable for indicating the state of oxide film formation at metals, including submonolayer films of OH discharged from water at Pt (10), Ir (10), and Au (15) and the irreversibility of surface oxide formation and reduction processes exhibiting hysteresis (10, 16).

The interpretation of optical properties of thin oxide films from ellipsometric ( $\Delta$ ) and relative reflectance ( $\delta R/R$  or  $\frac{dR}{R}/dV$ ) measurements is, however, com-

plicated, especially at Pt or Au, by the substantial dependence of ellipsometric phase-shift parameter  $\Delta$  or relative reflectance change  $\delta R/R$  on potential (and hence surface and ionic charge on the double-layer) which is observed already over the potential ranges in which no chemisorbed H- or O-species are present on Pt or Au electrode surface. We shall refer to this behavior as the "double-layer" optical effect at the metal surface.

These double-layer optical effects will continue during the surface oxidation up to a monolayer in some way related to the fraction of free metal surface available ( $1 - \theta_{\text{oxide}}$ ); in addition, and beyond a monolayer of surface oxide, some different double-layer effect will arise corresponding to the properties of the interface of that fraction of the surface which is covered by the surface oxide film.

The interpretation of  $\Delta$  or  $\delta R/R$  changes measured during film formation or reduction must therefore allow for a changing component due to the double-layer effects on  $\Delta$  and  $\delta R/R$  which maintain themselves, in some degree to be considered below, during film formation and are especially important at low coverage by the "O"-species. Corrections of this kind do not appear [cf. e.g., (5, 12, 23)] to have been made in previous work except in a preliminary presentation (6) of the present work,<sup>2</sup> so that the  $\Delta$  and  $\delta R/R$  changes actually due to oxide film formation have remained incorrectly evaluated.

This question is of particular importance if the optical condition of a surface oxide film at a given degree of oxidation,  $q_0$ , in an anodic-going potentiodynamic linear sweep (18) is to be compared with the condition at the same  $q_0$  in the cathodic sweep, thus providing indications of any intrinsic changes in the nature of the films associated with the hysteresis (8, 10, 16), commonly observed between formation and reduction of surface oxide films, with respect to electrode potential (8, 16). The double-layer corrections will be particularly important as the coverage by the electroadsorbed film changes from zero to that corresponding to a monolayer, e.g., OH on Pt and Au, with increasing anodic potential. These

<sup>2</sup> Since this paper was submitted (6), McIntyre and Peck (24) have proposed similar corrections for elucidation of the optical behavior of electroadsorbed H at Pt.

\* Electrochemical Society Active Member.  
<sup>1</sup> Present address: Pulp and Paper Research Institute, Pointe Claire, Quebec, Canada.  
Key words: oxide films, platinum, gold, ellipsometry, hysteresis in surface processes.

double-layer optical effects are experimentally more important (4, 6, 16) at Au than at Pt, since the double-layer optical effects are larger for Au than Pt.

**Basis for "double-layer" optical effects.**—The theoretical basis of the corrections for double-layer effects in optical studies of oxidation of metals depends on the extent to which electron density changes (11, 19-21) in the metal surface (ER effect) and changes of ionic concentration (22, 23) in the solution-side of the double-layer determine the double-layer effect in  $\Delta$  or  $\delta R/R$ . Work in press (13) at electrodeposited Hg indicates that the ER effect is never negligible; hence it may be expected that electrosorption of OH and O species in the initial stages of surface oxide formation will have an important effect on the electronic double-layer contribution to  $\Delta$  or  $\delta R/R$ . Such effects can arise because chemisorbed species tend to induce image charges (24) in the metal substrate or more realistically, equivalent short-range effects leading to electron density changes in the metal surface as evidenced in other work by changes of surface conductivity (34) and paramagnetic susceptibility. Related changes will be expected in the solution-side contribution to  $\Delta$  or  $\delta R/R$  since oxidation of the metal surface will change the pzc and hence the relative populations of anions and cations in the double-layer, and displace ions adsorbed, as is known (17) in the case of  $\text{SO}_4^{2-}$  or  $\text{HSO}_4^-$ . Correspondingly, when an oxide film is reduced, revealing bare metal, the double-layer contribution will again change in the course of the reduction of the film.

From the theoretical point of view, according to McIntyre and Aspnes (19), and McIntyre (21), the effect of metal surface charge,  $q_m$ , and hence potential, on the optical properties of the surface layer of a metal is determined mainly by field modulation of the free-electron contribution  $\epsilon_{3,f}$  to the dielectric constant  $\epsilon_2$  of the transition layer between bulk solution and bulk metal extending over ca 1.6 times the Thomas-Fermi screening length. Expressed in these terms, the change  $\Delta\epsilon_2$  in this transition layer by the applied field is given by

$$\Delta\epsilon_2 = -(\epsilon_{3,f} - 1) \Delta q_m / Nd \quad [1]$$

where  $N$  is the free-electron concentration in the bulk metal and  $d$  is the thickness of the transition layer,  $\Delta q_m$  the change of surface charge. Corresponding relative reflectance changes  $\frac{1}{R} \left( \frac{\delta R}{\delta q_m} \right)$  can be evaluated (24) for  $p$  and  $s$  polarization conditions, and the  $p$ -polarization behavior is dependent on both  $d$  and the rational potential,  $E$ . This treatment (24) assumes that the variation of  $\delta R/R$  with  $q_m$  or  $E$  arises mainly from modulation of free-electron effects, i.e., the ionic double-layer contributions to  $\delta R/R$  can be neglected (24), at least for the noble metals. This is a controversial point [cf. (20)] and has been discussed elsewhere (25). However, by suitable choice of angle of incidence and polarization conditions, some progress towards experimentally separating the metal electron and ionic double-layer effects can, in principle, be made (20, 24). In terms of free-electron effects,  $\delta R/R$  would be expected to be proportional to  $q_m$  and would thus scale with the differential double-layer capacitance (24). Unfortunately  $\delta R/R$  is also a complex function of charge-dependent ion accumulation in the double-layer (22, 23), solvent orientation and compression (20), and local molar refraction of ions in the double-layer.

The problems of allowing for double-layer contributions in the proper evaluation of the reflectance effects due to accumulation of a chemisorbed species are illustrated (24, 25) by the recent controversy concerning the significance of reflectance changes due to electrosorbed H at Pt where even the real relative signs of the effects are under discussion (25). Changes

of electron density in the metal surface due to binding of electrosorbed OH and O, or of H, we believe, can be a major factor in determining reflectance changes which could not be calculated *a priori* by the MA theory (19, 21). Withdrawal of electrons due to chemisorptive bonding, e.g., of H has been recognized (36).

For the purposes of the present paper, where possible differences of optical properties of thin films during their formation and reduction are to be demonstrated, it therefore seems best, because of the above

complexities, to correct the  $\frac{\delta R}{R}$  or  $\Delta$  changes (caused by electrosorption processes) for double-layer electroreflectance contributions by an empirical procedure (rather than an *a priori* calculation) based on extent of coverage of the free metal surface by the electrochemisorbed species. We outline three procedures by which this might be accomplished and propose one of them as the preferred method.

### Experimental

Full details of the experimental procedures have been given in other recent papers (6, 8, 10, 26). The following summary of conditions and methods is given here to provide a basis for the results to be discussed in this paper as examples of the correction procedures and with respect to evaluation of hysteresis in the optical behavior.

**Methods.**—Electrochemical study of the processes of oxide film formation at Au and Pt was made by the potentiodynamic method which, for pure surface reactions not involving coupled diffusion-controlled processes, gives an exact measure of: (i) the ranges of potential over which various oxidation or reduction processes occur, and hence information on reversibility; and (ii) the coulombic charges associated with resolvable processes (3, 10) in the anodic-going or cathodic-going directions of potential change. The oxidation or reduction charges can be evaluated to an accuracy equivalent to 0.02e per metal atom of the surface.

The circuit and apparatus for potentiodynamic studies was as described previously [e.g., (10)]. The various systems and precautions necessary for evaluation of oxidation/reduction charges of the above accuracy were as indicated in previous papers (3, 16, 26), especially the requirements of solution purity. All potentials were referred to an  $\text{H}_2$  electrode in the same solution. This scale is referred to as  $E_H$  in this paper.

Ellipsometric studies of the formation and reduction of very thin oxide layers were made using a Rudolph ellipsometer by the off-null intensity transient method described originally by Cahan and Brusich in Ref. (27) with modifications discussed in a later communication (28) [cf. (29)].

Relative and differential reflectance measurements were made as described previously (10). The phase-sensitive amplifier system also enabled direct measurements of a-c capacitance to be made during formation and reduction of the oxide films.

**Solutions.**—In order to achieve the required level of high purity of solutions, water subjected to 48 hr pyrocatalytic distillation (26) was employed to make up solutions. 1M aq.  $\text{H}_2\text{SO}_4$  solutions were used as electrolyte and made up in the pyro-distilled water from B.D.H. "Aristar" grade 98%  $\text{H}_2\text{SO}_4$  (the purest grade of acid available for electrochemical purposes). Experiments were conducted at  $25^\circ \pm 0.5^\circ\text{C}$ .

**Cells.**—A standard all-glass cell of the type used in our previous work was employed. The ellipsometer cell was of basically similar design except that it was provided with two optically flat windows allowing light to be reflected from the electrode at an angle of incidence of  $71^\circ$  without further refraction at the windows.

**Electrodes.**—Johnson Matthey high-purity grade Pt and Au plates ca. 1 mm in thickness were used for the optical measurements. Wires of the same grade metals were used in some of the electrochemical measurements. Surfaces of the plate electrodes were polished with a ceric oxide slurry and then thoroughly washed before use in optical experiments.

### Results and Discussion

**Methods for making "double-layer" corrections.**—The basis for possible empirical correction procedures will be considered by reference to the working diagram (Fig. 1). The curve OCAPZ represents an anodic-going profile of changing  $\Delta$  or  $\delta R/R$  while ZQCO represents the corresponding cathodic-going changes in response to anodic and cathodic linear potential sweeps in optical cyclic voltammetry (4, 10). O is the origin of charge-dependent  $\Delta$  and  $\delta R/R$  changes taken as the potential of zero-charge. The regions OCA and CO represent changes of  $\Delta$  or  $\delta R/R$  due only to "double-layer" effects while the regions APZ or ZQC represent changes of  $\Delta$  or  $\delta R/R$  when a surface film of changing coverage is being electrochemically deposited or removed (reduced) from the surface. The heavier regions, AP and QC, represent, respectively, the transition from zero coverage to a monolayer of electrosorbed species, and from monolayer to zero coverage in reduction. The curve beyond P to Z represents changes of optical properties that can arise beyond a nominal monolayer (e.g., from "PtOH" to "PtO") of, e.g., OH on Pt, as experimentally observed.

**Correction method (i).**—The simplest approach would be to subtract from the "experimental" values (curve APZ) the double-layer  $\Delta$  or  $\delta R/R$  values corresponding to the line OCA and its production to B or beyond, with values being referred to the reference line AN. Similarly, over QC, values along the line CA would be subtracted from the experimental values along QC referred to a reference line CR. The lines CR or AN simply allow the differences of  $\Delta$  or  $\delta R/R$  which arise more anodic to C or A, respectively, to be evaluated with respect to reference values at the points C or A corresponding limitingly to zero oxide coverage in the respective cathodic or anodic directions of potential change. This method is obviously not generally correct since (i) it does not allow for changing coverage by the electrosorbed species along AP or QC and (ii) in the return (cathodic) curve ZQC, when the  $\Delta$  or  $\delta R/R$  value is found experimentally to be initially constant at Pt, e.g.,

after holding<sup>3</sup> the potential at Z for  $> 120$  sec (Fig. 2), correction for the double-layer effects in  $\Delta$  or  $\delta R/R$  leads to an irrational increase of  $\Delta$  or  $\delta R/R$  as the initial part of the negative-going  $\Delta$  or  $\delta R/R$  potential profile is traversed (see below), in which range there is no increase in the extent of oxide formation or coverage after holding at Z (Fig. 2). Method (i) will therefore be rejected.

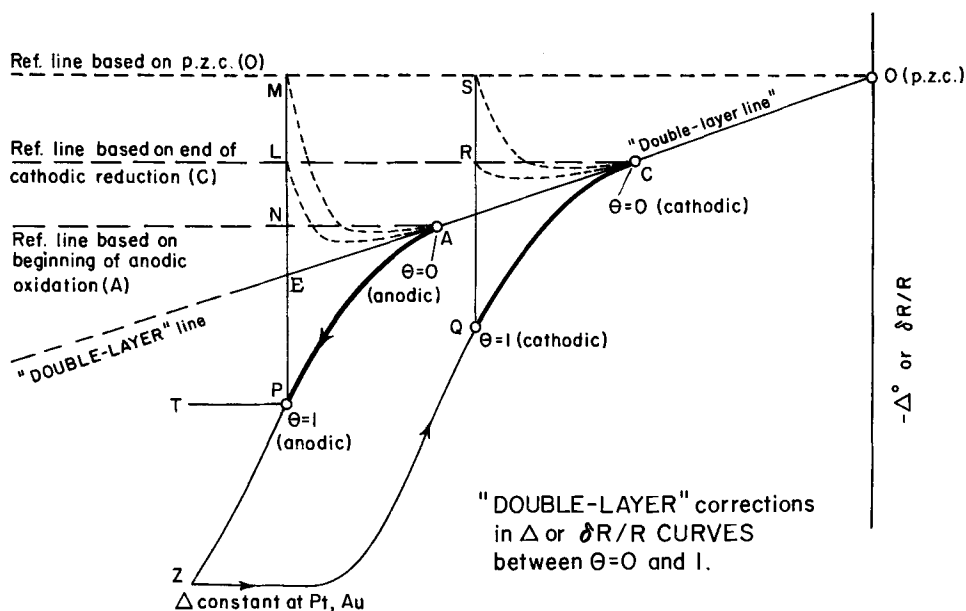
**Correction method (ii).**—Method (i) assumes that the whole of the normal double-layer change of  $\Delta$  between A and P, or between Q and C, is made as a correction to the lines AP or QC. This is obviously incorrect since along AP or QC, the coverage by "oxide" is changing. Hence, the above double-layer corrections must be diminished progressively at each potential by a factor  $1 - \theta$  for the anodic or cathodic curves. It is obviously more consistent to perform the above types of correction with respect to a common reference line CRL, applicable to both the anodic (APZ) or cathodic (ZQC) experimental lines.<sup>4</sup> Then the corrected  $\Delta$  or  $\delta R/R$  relations will correspond typically to the dashed curve AL for the anodic-going curve or RC for the cathodic-going one. A number of  $\Delta - q_0$  relations were analyzed in this manner (see below) and compared with results obtained by a (preferred) third method (iii) described below.

**Correction method (iii).**—It would appear most satisfactory to refer all corrections not only to a common reference line but one (MSO) taken up to the potential of zero charge (pzc), since finite values of  $\Delta$  due to double-layer charge effects are really relative to zero double-layer contribution to  $\Delta$  or  $\delta R/R$  at the pzc in the absence of specific adsorption. (A very small residual ionic double-layer effect may remain at the pzc due to the surface potential.) Hence, the correction on the basis of  $1 - \theta_{\text{oxide}}$  starting from A or terminating at C will follow, respectively, curves such as AM or SC, but at potentials more positive than M or S, no further change of  $\Delta$  or  $\delta R/R$  would arise from double-layer effects on this model since at these potentials  $\theta = 1$ . This method was applied to a number of the experimental  $\Delta - q_0$  relations. Both methods (ii) and (iii) assume that the metal/solution double-layer correction above " $\theta$ " = 1, becomes attenuated to zero, i.e., the presence of OH or O species eventually reduces to zero (along the line PT) the

<sup>3</sup> On a repetitive sweep at Pt or Au, the optical parameters do continue to increase over the initial part of the cathodic-going sweep at Z. This, however, is consistent with the observed continuing anodic current at the beginning of the cathodic sweep, as expected for an irreversible surface process (see p. 1600).

<sup>4</sup> That this is a valid procedure is indicated in the Appendix.

Fig. 1. Working diagram for discussion of double-layer corrections for  $\Delta$  or  $\delta R/R$  changes due to oxide film formation or reduction.



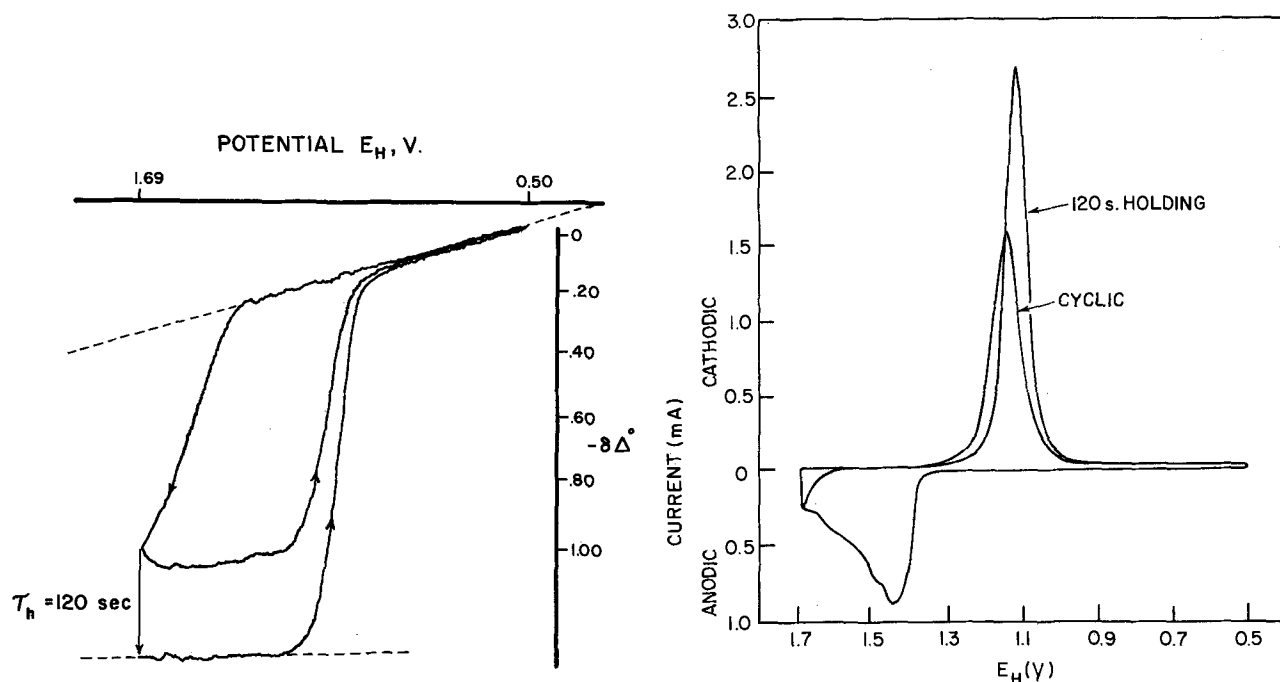


Fig. 2. (a, above left)  $\Delta$  changes as a function of potential at an Au electrode in 1M aq.  $H_2SO_4$  (25°C) in a single cyclic anodic/cathodic sweep and after holding at +1.69V  $E_H$  for 120 sec before initiation of the sweep. (b, above right) The corresponding potentiodynamic  $i$ - $V$  profiles for Au with and without holding at 1.69V for 120 sec.

normal double-layer optical effect associated with the metallic surface itself.

"Double-layer" effects at the oxide/solution interface.—In principle, the oxidized metal surface can also exhibit ER and ionic double-layer effects in  $\Delta$  and  $\delta R/R$ . In the case of Au, however, the qualitative correctness of the assumption in method (iii) that the double-layer optical effects are reduced to negligible contributions as " $\theta$ "  $\cong$  1 was indicated by observation of only very small  $\Delta$  changes in a cathodic-going potential sweep after formation of an oxide film of almost constant thickness by holding the potential constant for some time as shown in Fig. 2a. Over the potential region involved, it is seen from Fig. 2b that no significant reduction charge passes in this part of the curve, so that only double-layer effects would be involved: they are quite small ( $\sim 10\%$ ) in comparison with the effect over the potential region where the metal surface is without an oxide film. The behavior at Pt is similar (Fig. 3). The residual double-layer optical effects on the oxidized surfaces, although small, depend on the metal, so the details of the correction procedure should be chosen with reference to the metal concerned.

The significance of the small "double-layer" effect in the oxide region ( $\theta_{OH} \cong 1$ ) is also indicated by a-c modulated reflectance experiments (10) which give small but finite in-phase and zero out-of-phase differential reflectance effects at Pt and Au even at 1.4V for Pt or 1.6V for Au where almost no reversibly formed or reducible oxide can exist [cf. the cyclic voltammetry curves (3, 8)]. This residual effect must be distinguished from the resolvable region of reversible "PtOH" electrodeposition (3, 10) and reduction which can be seen in a-c modulated reflectance (10) up to ca. 0.95V.

In the case of Au (Fig. 5), the result of making further corrections for the residual double-layer effect on the oxide film itself is also shown in that figure. It is relatively small and at Pt it is even smaller. It is seen that corrections for double-layer optical effects at the oxide film interface do not change the main conclusions from Fig. 5 that hysteresis exists in the optical behavior of the oxide film itself (see below).

$\Delta$ - $q_0$  relations for anodic and cathodic-going sweeps.—Figure 4 shows the  $\Delta$ - $q_0$  relations for Pt based on corrections for double-layer contributions to  $\Delta$  made by (i) the sloping base-line method (i) assuming the double-layer  $\Delta$  change extends up to and beyond the monolayer, and (ii) by method (iii). From Fig. 4 it is evident that appreciable hysteresis exists between  $\Delta$  values for the positive-going and negative-going curves at the same degrees of oxidation  $q_0$  of the surface,<sup>5</sup> independently of the method of correction employed.

<sup>5</sup> In a given experiment, the accuracy in evaluation of  $\Delta$  is  $\pm 0.02^\circ$  and in  $q_0$ , 0.02e per metal atom. Hence the differences in the  $\Delta$ - $q_0$  lines for anodic- and cathodic-going sweeps are well outside the limits of experimental error.

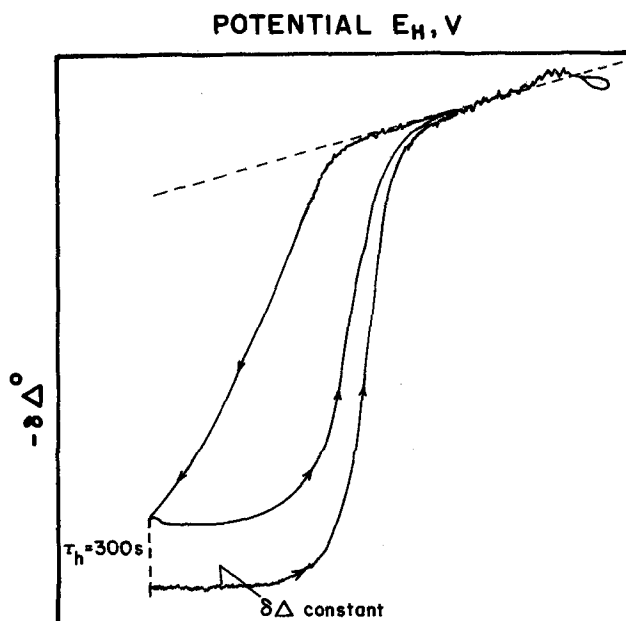
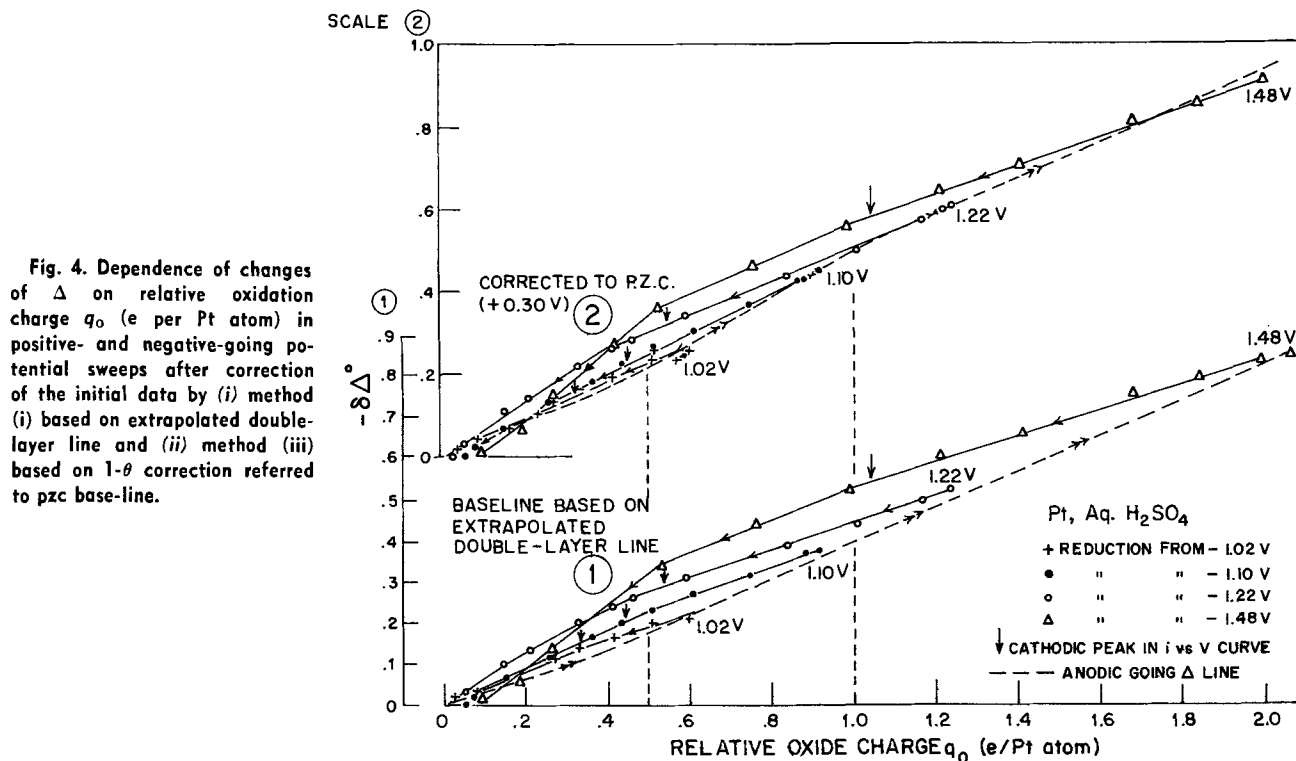


Fig. 3. As in Fig. 2a, but for Pt with 300 sec anodic holding at 1.4V  $E_H$ .

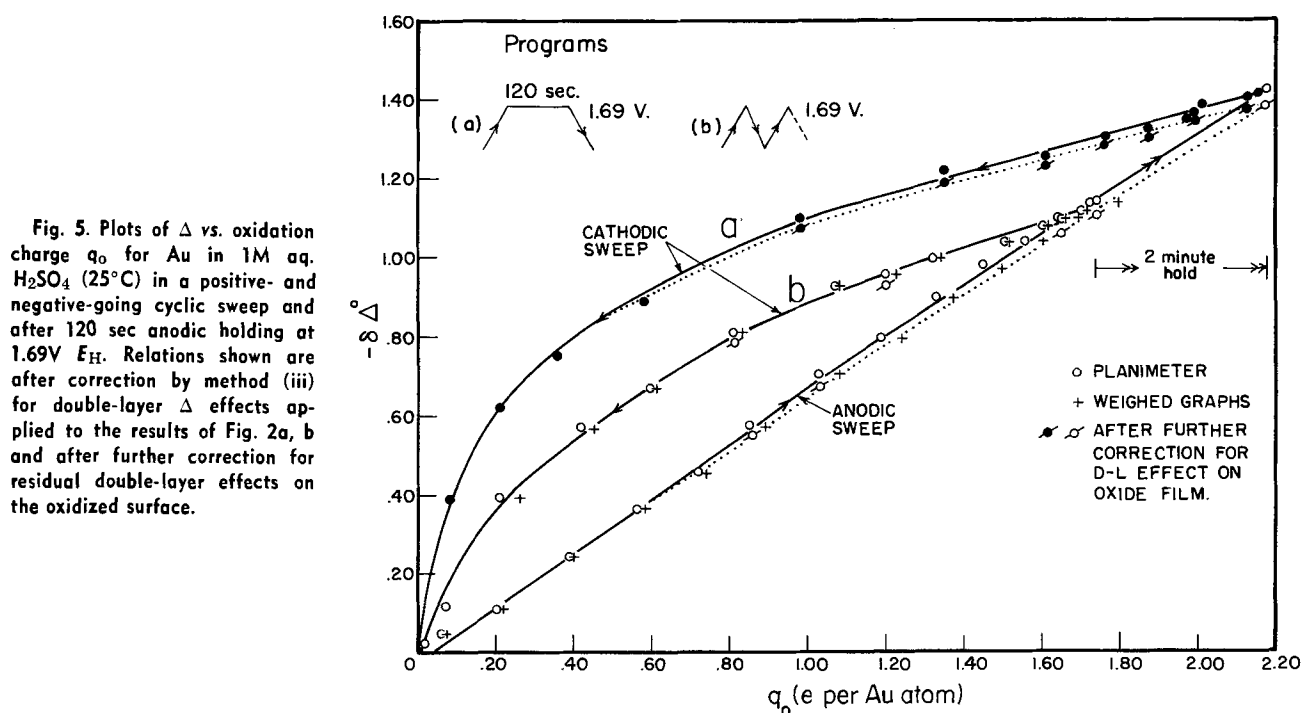


The necessity for corrections to the  $\Delta$  change based on a principle other than that the double-layer  $\Delta$  variation with potential continues into, and through, the surface oxidation region ( $>0.80V$  in the case of Pt or  $>1.375V$  in the case of Au) is clearly illustrated in Fig. 5 and 6. In these plots, the changes of  $\Delta$  in an anodic- and cathodic-going potentiodynamic sweep are compared with those for a sweep in which there has been 120 sec holding of the potential at the positive and of the sweep (see program b in Fig. 5 and  $\Delta$ -potential plot of Fig. 2a). With holding, both  $\Delta$  and the oxidation charge  $q_0$  continue to change (as expected) in the same direction as in the cyclic experiment taken to the same potential; with reversal of the sweep direction after holding,  $\Delta$  decreases, initially gradually,

(curve a, Fig. 5) and similar behavior arises in the cyclic experiment (curve b, Fig. 5); for both these cases, curves a and b, the double-layer correction has been made with respect to the pzc base-line<sup>6</sup> up to  $q_0 = \text{full coverage of OH (1e per Au atom)}$ , in proportion to  $1 - \theta_{OH}$ .

If the double-layer  $\Delta$  or  $\delta R/R$  corrections were to be made not on this basis but by assuming that the double-layer  $\Delta$  or  $\delta R/R$  effect continues with the same slope w.r.t. potential through the surface oxidation region, then a ridiculous result is obtained as shown in Fig. 6 based on the same primary experimental data (Fig. 2a, b) as those which give the curves of Fig. 5.

<sup>6</sup> Relevant pzc values have been critically reviewed and tabulated by Perkins and Anderson (35).



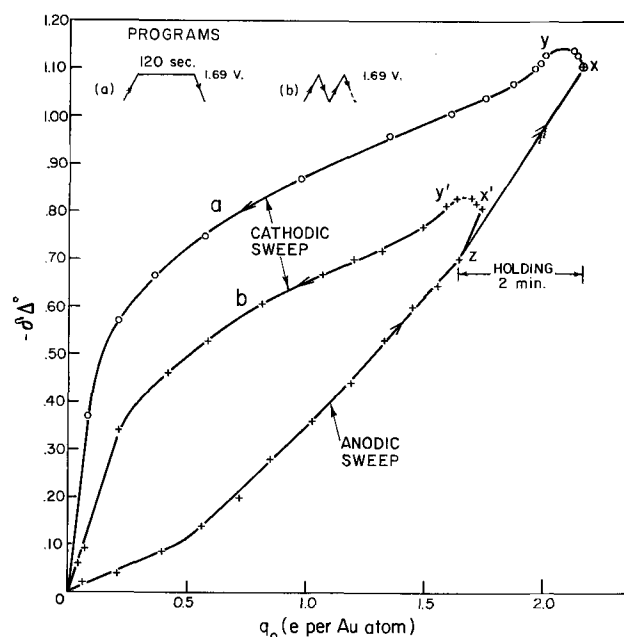


Fig. 6. Plots of  $\Delta$  vs.  $q_0$  for Au as in Fig. 5 but by the method (i) assuming double-layer  $\Delta$  line applies continuously into the oxide formation, or over the oxide reduction regions.

After the holding time of 120 sec, which is sufficient for  $q_0$  to reach a constant ( $\pm 2\%$ ) value, it is seen from Fig. 6 that  $\Delta$  apparently continues to increase on the negative-going sweep over the region  $xy$  of curve a in Fig. 6. That the double-layer optical effect for the free metal surface cannot continue with the same slope into the oxide region is also indicated indirectly by the double-layer capacity behavior studied by Rosen and Schuldiner (33).<sup>7</sup>

A similar but smaller effect arises over  $x'y'$  in curve b of Fig. 6 for the cyclic experiment, but here the behavior is complicated by the normal effect observed at Pt and Au that some oxidation of the surface continues on the initial section of the negative-going sweep after reversal of the sign of  $dV/dt$  at the end of the positive-going sweep. This is the usual behavior (3, 6) for an irreversible electrochemical surface process as we have discussed elsewhere (3) and simply means that continuing surface oxidation can occur slowly over the most positive-potential range in the negative-going side of the potential sweep. Holding at the positive potential limit allows this residual oxidation to be virtually completed before the negative going sweep is initiated (program b), so that on the subsequent initiation of that negative-going sweep only the cathodic reduction process can eventually occur, so that both  $\Delta$  and  $q_0$  must decrease, or initially remain constant and then both decrease together.

Figures 5 and 6 therefore clearly demonstrate (i) the necessity of a double-layer correction in interpretation of  $\Delta$ - (and/or  $\psi$  or  $\delta R/R$ ) measurements in oxide-film forming experiments and (ii) that this correction cannot be made simply on the basis of a linear extension of the double-layer  $\Delta$  base-line CAB (Fig. 1).

**Irreversibility and hysteresis in the optical behavior of oxide films during formation and reduction.**—The results of Fig. 5 show even more clearly than those for Pt (Fig. 4) that there is an intrinsic irreversibility in the properties of the oxide film w.r.t. quantity of oxide present on the surface in the formation direction (positive-going sweep) and in the reduction direction (negative-going sweep). This irreversibility is, however, only detectable for appreciable degrees of sur-

<sup>7</sup> A correction for double-layer effects in the H region was made by McIntyre and Peck (24) by extrapolating the ER background curve for the double-layer region into the H adsorption region but without any allowance for possible specific effects due to coverage by H.

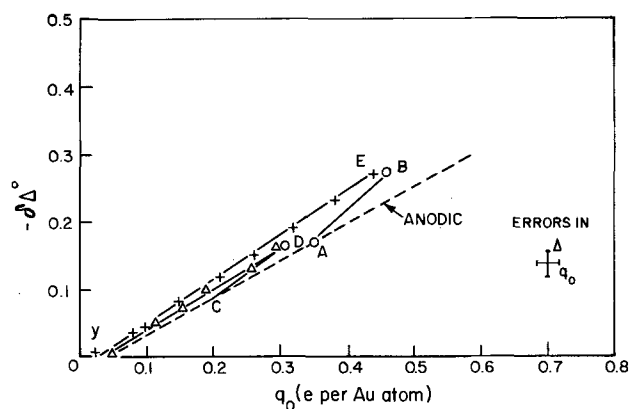


Fig. 7. Plots of  $\Delta$  vs.  $q_0$  for Au oxide formation in 1M aq.  $H_2SO_4$  and reduction up to potentials of 1.440V (+) and 1.410V ( $\Delta$ )  $E_H$  in repetitive cyclic voltammetry [ $\Delta$  values corrected w.r.t. pzc base-line by method (iii)].

face oxidation as the results of Fig. 7, for surface oxidation of Au up to ca. 0.3 and 0.45e per Au atom, show; in these cases, the (corrected)  $\Delta$ - $q_0$  lines are almost reversible in the sense that the  $\Delta$ - $q_0$  relations are almost identical for positive- and negative-going sweeps (there is, of course, still hysteresis in the  $i$ - $V$  profiles for the two directions of sweep).

The irreversibility demonstrated here, we believe, is due to a progressive rearrangement of the surface layer of OH and O electroadsorbed species<sup>8</sup> as their coverage increases, as we (3, 8) and others (12, 30) have discussed elsewhere. Thus, the state of the surface at a nominal value of  $q_0$  in the reduction sweep is evidently not identical with that in the oxidation sweep at the same  $q_0$ . This result confirms, on the basis of optical properties of the oxide films at Au and Pt, that the irreversibility in the  $i$ - $V$  profiles for anodic and cathodic-going potential sweeps is associated with a real irreversible change of properties of the film as it is laid down, i.e., an intrinsic hysteresis (3, 16, 31).

The physical origin of the optical hysteresis can be understood in the following terms: in an anodic-going sweep, an element of continuing change of  $\Delta$  will correspond to the last increment of charge passed at some typical potential  $E$  in the sweep, so the environment of the species laid down at that potential will be determined by the location of the discharged O or OH species in relation to the lattice (3) of previously existing and previously deposited oxide species. However, if the sweep continues beyond  $E$ , the relative contribution to  $\Delta$  of the species deposited at  $E$  may change because its environment changes. Especially in the case of a surface rearrangement, removal of the given particle at some potential corresponding to a state of reduction of the oxide film (measured by  $q_0$ ) will not necessarily result in the same change of  $\Delta$  as in the electrodeposition of such a particle at the same level  $q_0$  of oxidation of the surface during the anodic-going sweep. This is because the microscopic environment of particles being reduced at a given coverage corresponding to a typical level of surface oxidation  $q_0$  can be different, in the rearranged surface layer, from that at a corresponding level of surface oxidation or coverage in the anodic-going sweep. This is one of the essential features of intrinsic (as opposed to "kinetic") hysteresis in terms of domain theory (31).

The results of Fig. 5 indicate, from the course of the  $\Delta$ - $q_0$  relations, that the material first reduced in the negative-going sweep is not that which has immediately previously been laid down at the most positive potentials in the prior anodic sweep. The material electroadsorbed at the most positive potentials on the

<sup>8</sup> Optically distinguishable states of the oxidized Pt surface corresponding to "PtOH" and "PtO" degrees of oxidation were noted by Conway (13) and by McIntyre and Kolb [in Ref. (14)].

anodic sweep is, in fact, that which is reduced only at the least positive potentials in the cathodic sweep, as observed and discussed previously (8, 16). This is consistent (cf. magnetization hysteresis loops) with the observed hysteresis behavior.

The aspects of the surface oxidation processes at Pt and Au are beyond the scope of the present paper but are examined in more detail in a theoretical publication (32).

### Conclusion

It is to be concluded that significant double-layer corrections must be made not only in relating  $\Delta$  or  $\delta R/R$  to potential or film coverage at an electrode, but also in any quantitative interpretations of these optical parameters in terms of refractive index, absorption coefficient, and thickness of the film, especially in the case of development of films up to the monolayer limit.

### Acknowledgment

We are indebted to the Defence Research Board, Canada, for support of this work.

Manuscript submitted July 2, 1973; revised manuscript received June 3, 1974. This was Paper 88 presented at the Houston, Texas, Meeting of the Society, May 7-11, 1972.

Any discussion of this paper will appear in a Discussion Section to be published in the June 1975 JOURNAL. All discussions for the June 1975 Discussion Section should be submitted by Feb. 1, 1975.

The publication costs of this article have been assisted by the University of Ottawa.

### APPENDIX

#### Relation between $\Delta$ Changes Referred to Different Origins, Including the Potential of Zero-Charge

The working diagram Fig. 8 is considered. A double-layer line OCAB is again taken. Elements of anodic-going and cathodic-going curves for  $\Delta$  changes due to formation of a film are lines  $\psi$  and  $\phi$ , respectively. The coordinates of "intersection" of  $\psi$  and  $\phi$  with OCAB are  $V_2, \Delta_2$  at A,  $V_1, \Delta_1$  at C, respectively, and O, O are the coordinates of the pzc. The slopes (in supposed linear regions) of  $\psi$  and  $\phi$  are  $\bar{m}$  and  $\bar{m}$ , respectively, while the double-layer line OCAB has a slope  $m_o$ . A typical potential  $V$  is measured positively to the right.

Along  $\psi$

$$\vec{\Delta} = \Delta_2 + \bar{m}(V - V_2)$$

and along  $\phi$

$$\overleftarrow{\Delta} = \Delta_1 + \bar{m}(V - V_1)$$

Corrected for double-layer effects with a  $1 - \theta$  free metal area factor, these relations become for curve  $\psi$

$$\vec{\Delta} = \Delta_2 + \bar{m}(V - V_2) - (1 - \theta)[\Delta_2 + m_o(V - V_2)]$$

while for curve  $\phi$

$$\overleftarrow{\Delta} = \Delta_1 + \bar{m}(V - V_1) - (1 - \theta)[\Delta_1 + m_o(V - V_1)]$$

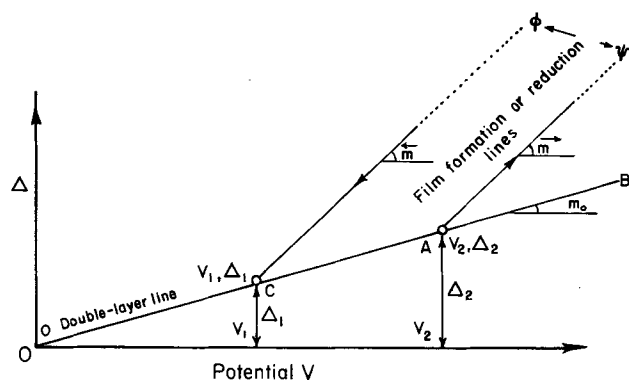


Fig. 8. Working diagram for analysis of double-layer  $\Delta$  corrections based on different base-lines.

Corrections on  $\psi$  and  $\phi$  curves are based on double-layer  $\Delta$  changes referred to zero at the pzc and the  $1 - \theta$  term is assumed to operate on the whole of the double-layer  $\Delta$  contribution referred to zero at the pzc.

Referred to an origin  $V_1, \Delta_1$  at the end of the cathodic-going curve  $\phi$  for film reduction, on line  $\psi$

$$\vec{\Delta} = \Delta_2 - \Delta_1 + m(V - V_2 + V_1)$$

$$- (1 - \theta)[\Delta_2 - \Delta_1 + m_o(V - V_2 + V_1)]$$

and

$$\overleftarrow{\Delta} = mV - (1 - \theta)m_oV$$

Then we can evaluate  $\vec{\Delta} - \overleftarrow{\Delta}$  as a function of  $V$ . For an origin O, O

$$\vec{\Delta} - \overleftarrow{\Delta} = \Delta_2 - \Delta_1 + m(V_1 - V_2)$$

$$- (1 - \theta)[\Delta_2 - \Delta_1 + m_o(V_1 - V_2)]$$

But, generally,  $\Delta_2 = \Delta_1 + m_o(V_2 - V_1)$ , therefore

$$\vec{\Delta} - \overleftarrow{\Delta} = (m_o - m)(V_2 - V_1)$$

Similarly for an origin  $\Delta_1, V_1$

$$\vec{\Delta} - \overleftarrow{\Delta} = \Delta_2 - \Delta_1 + m(V_1 - V_2)$$

$$- (1 - \theta)[\Delta_2 - \Delta_1 + m_o(V_1 - V_2)]$$

$$= (m_o - m)(V_2 - V_1)$$

Hence the difference of  $\Delta$  values in the forward and backward-going  $\Delta$ - $V$  profiles is independent of the origin chosen for representing  $\Delta$  changes.

Also, it is useful to calculate the difference of  $\Delta$  values referred to the two origins O, O and  $V_1, \Delta_1$ . We find

$$\vec{\Delta}_{V_1, \Delta_1} - \vec{\Delta}_{O, O} = \Delta_2 - \Delta_1 + m(V - V_2 + V_1)$$

$$- (1 - \theta)[\Delta_2 - \Delta_1 + m_o(V - V_2 + V_1)]$$

$$- \Delta_2 + m(V - V_2)$$

$$- (1 - \theta)[\Delta_2 + m_o(V - V_2)]$$

$$= (mV_1 - \Delta_1) - (1 - \theta)(m_oV_1 - \Delta_1)$$

and

$$\overleftarrow{\Delta}_{V_1, \Delta_1} - \overleftarrow{\Delta}_{O, O} = (m_1V_1 - \Delta_1) - (1 - \theta)[m_oV_1 - \Delta_1]$$

so that the differences of forward or backward  $\Delta$  changes expressed on different origins of the coordinate system are identical.

Thus, an individual series of corrected  $\vec{\Delta}$  or  $\overleftarrow{\Delta}$  values will depend on the choice of origin but differences  $\vec{\Delta} - \overleftarrow{\Delta}$ , or of  $\vec{\Delta}$  or  $\overleftarrow{\Delta}$  expressed on two origins, are independent of the choice of origin, as may be expected.

Hence, the experimentally indicated  $\vec{\Delta} - \overleftarrow{\Delta}$  values can be interpreted in terms of hysteresis and an irreversible change of state of the oxide between its progressive formation and progressive reduction.

### REFERENCES

1. J. W. Schultze and K. J. Vetter, *Ber. Bunsenges.*, **75**, 470 (1971).
2. K. J. Vetter and J. W. Schultze, *J. Electroanal. Chem.*, **34**, 131, 141 (1972).
3. H. Angerstein-Kozłowska, B. E. Conway, and W. B. A. Sharp, *ibid.*, **43**, 9 (1973).
4. T. Takamura, K. Takamura, W. Nippe, and E. Yeager, *This Journal*, **117**, 626 (1970).
5. M. A. Genshaw and J. O'M. Bockris, *J. Chem. Phys.*, **51**, 3149 (1969); see also *J. Electroanal. Chem.*, **8**, 406 (1964).
6. B. E. Conway, L. Laliberté, and H. Angerstein-Kozłowska, *Oxide-Electrolyte Interfaces*, R. Alwitt, Editor, p. 181, The Electrochemical Society Softbound Symposium Series, Princeton, N. J. (1973).
7. J. J. Lander, *Surface Sci.*, **1**, 125 (1964).

8. P. Stonehart, H. A. Kozłowska, and B. E. Conway, *Proc. Roy. Soc. London*, **A310**, 541 (1969).
9. K. J. Vetter and D. Berndt, *Z. Elektrochem.*, **62**, 378 (1958); see also S. B. Brummer and A. C. Makrides, *This Journal*, **111**, 1122 (1964); and H. A. Laitinen and M. S. Chao, *ibid.*, **108**, 726 (1961).
10. S. Gottesfeld and B. E. Conway, *J. Chem. Soc., Faraday Trans. I*, **69**, 1090 (1973).
11. W. N. Hansen, *Surface Sci.*, **16**, 205 (1969); see also A. Probst and W. N. Hansen, *Phys. Rev.*, **160**, 600 (1967).
12. A. K. N. Reddy, J. O'M. Bockris, and M. A. Genshaw, *J. Chem. Phys.*, **48**, 671 (1968); see also R. Greef, *ibid.*, **51**, 3148 (1969).
13. B. E. Conway, *Symp. Faraday Soc.*, **4**, 95 (1970); see also S. Gottesfeld and B. E. Conway, *Faraday Trans. I.*, In course of publication (cf. Abstract No. 104, p. 282, Electrochemical Society Extended Abstracts, Spring Meeting, Houston, Texas, May 7-11, 1972).
14. M. A. Barrett and R. Parsons, *Symp. Faraday Soc.*, **4**, 72 (1970); J. D. E. McIntyre and D. M. Kolb, *ibid.*, **4**, 99 (1970); A. Bewick and A. M. Tuxford, *ibid.*, **4**, 114 (1970).
15. B. Cahan, J. Horkans, and E. Yeager, *Symp. Faraday Soc.*, **4**, 36 (1970) [see also Ref. (4)].
16. D. Gilroy and B. E. Conway, *Can. J. Chem.*, **46**, 875 (1968); see also Ref. (31).
17. N. A. Balashova and V. E. Kazarinov, *Coll. Czech. Chem. Comm.*, **30**(12), 4148 (1965); see also N. A. Balashova and V. E. Kazarinov, *Electroanal. Chem.*, **3**, 135 (1969) and I. I. Labkorskaya, V. I. Luk'yanycheva and V. S. Bagotski, *Elektrokhimiya*, **5**, 580 (1969).
18. F. G. Will and C. A. Knorr, *Z. Elektrochem.*, **64**, 258, 270 (1960).
19. J. D. E. McIntyre and D. E. Aspnes, *Bull. Am. Phys. Soc.*, **15**, 366 (1970); *Surface Sci.*, **24**, 417 (1971); see also J. D. E. McIntyre, *Surface Sci.*, **37**, 658 (1973).
20. A. Bewick, F. A. Hawkins, and A. M. Tuxford, *Surface Sci.*, **37**, 827 (1973).
21. J. D. E. McIntyre, *Adv. Electrochem. Electrochem. Eng.*, **9**, 61 (1973); see also *Symp. Faraday Soc.*, **4**, 50, 55, 61 (1970).
22. M. Stedman, *Symp. Faraday Soc.*, **4**, 64 (1970).
23. Y.-C. Chiu and M. A. Genshaw, *J. Phys. Chem.*, **72**, 4325 (1968); see also W. Paik, M. A. Genshaw, and J. O'M. Bockris, *ibid.*, **74**, 4266 (1970).
24. J. D. E. McIntyre and W. F. Peck, Paper No. 7, Discussions of the Faraday Division, Chemical Society London, 1973, in press; see also J. D. E. McIntyre, *Surface Sci.*, **37**, 658 (1973) and Ref. (20).
25. See discussion in Ref. (24).
26. B. E. Conway, H. Angerstein-Kozłowska, W. B. A. Sharp, and E. E. Criddle, *Anal. Chem.*, **45**, 1331 (1973).
27. B. Cahan, V. Brusic, and M. A. Genshaw, *J. Appl. Optics*, **9**, 1634 (1970).
28. J. Horkans, B. Cahan, and E. Yeager, Abstract 108, p. 290, Electrochemical Society Extended Abstracts, Spring Meeting, Houston, Texas, May 7-11, 1972.
29. W. Paik and J. O'M. Bockris, *Surface Sci.*, **27**, 191 (1971).
30. N. Sato and M. Cohen, *This Journal*, **111**, 512 (1964).
31. D. H. Everett, *Trans. Faraday Soc.*, **50**, 187 (1954); **51**, 1551 (1955).
32. B. V. Tilak, B. E. Conway, and H. Angerstein-Kozłowska, *J. Electroanal. Chem.*, **48**, 1 (1973).
33. M. Rosen and S. Schuldiner, *This Journal*, **116**, 1112 (1969).
34. W. J. Anderson and W. N. Hansen, *J. Electroanal. Chem.*, **47**, 229 (1973).
35. R. S. Perkins and T. N. Anderson, *Mod. Aspects Electro-Chem.*, **5**, 203 (1969).
36. J. D. E. McIntyre and D. M. Kolb, *Symp. Faraday Soc.*, **4**, 99 (1970).

## DISCUSSION SECTION

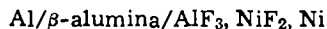


This Discussion Section includes discussion of papers appearing in the *Journal of The Electrochemical Society*, Vol. 120, No. 12; December 1973; and Vol. 121, No. 1, 2, and 4; January, February, and April 1974.

### Electromotive Force Measurements on Cells Involving Beta-Alumina Solid Electrolyte

N. S. Choudhury (pp. 1663-1667, Vol. 120, No. 12)

**A. Sterten:**<sup>1</sup> One of the cells in the paper under discussion (cell [V]) was described in the following manner



The over-all cell reaction was proposed to be



assuming the transport number of sodium ions through  $\beta$ -alumina equal to unity. However, since  $\text{AlF}_3$  and  $\beta$ -alumina are not coexistent,<sup>2,3</sup> reaction [1] above is not the correct one for cell [V] of the above-cited paper.

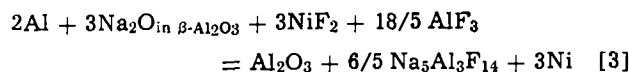
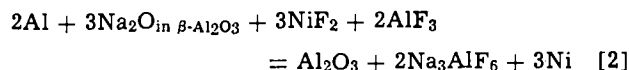
Aluminum fluoride and sodium oxide in  $\beta$ -alumina will probably react and give a thin layer of  $\text{Al}_2\text{O}_3$  and  $\text{Na}_3\text{AlF}_6$  at the interface  $\beta$ -alumina/ $\text{AlF}_3$ .  $\text{Na}_3\text{AlF}_6$  may react further with  $\text{AlF}_3$  and finally give  $\text{Na}_5\text{Al}_3\text{F}_{14}$  in the layer. From these considerations it is proposed that

<sup>1</sup> Department of Industrial Electrochemistry, The University of Trondheim, N-7034 Trondheim-NTH, Norway.

<sup>2</sup> P. A. Foster, *J. Chem. Eng. Data*, **9**, 200 (1964).

<sup>3</sup> J. Brynestad, K. Grjotheim, and J. L. Holm, *Bul. Inst. Politeh. Bucuresti*, **XXV**, 57 (1963).

one of the two following reactions is the most likely one for cell [V] of the paper being discussed

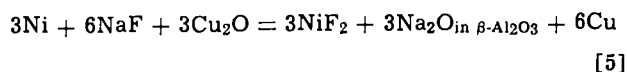


still assuming the transport number of sodium ions through the solid electrolyte equal to unity.<sup>4</sup> The experimental data given by Choudhury in the paper under discussion can be compared with available data for these two reaction schemes.

The emf for cell [V], given in Fig. 5 in the paper being discussed, seems to be well described by the following equation

$$E = 1.666 + 0.060 \times 10^{-3}T \text{ (volt)} \quad [4]$$

The emf corresponding to the following reaction



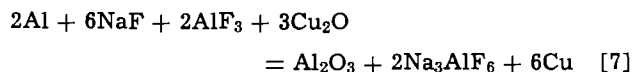
is, according to Choudhury in the above-mentioned work

$$E = 0.6465 - 0.190 \times 10^{-3}T \text{ (volt)} \quad [6]$$

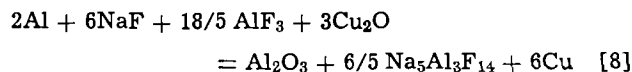
Combination of Eq. [5] with Eq. [2] gives

<sup>4</sup> E. W. Dewing, *Met. Trans.*, **1**, 2211 (1970).





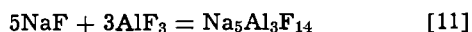
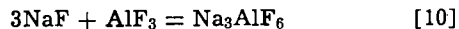
and combination of Eq. [5] and Eq. [3] gives



The corresponding emf is obtained from Eq. [4] and [6]

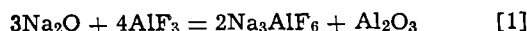
$$E = 2.3125 - 0.130 \times 10^{-3}T \text{ (volt) } (800^\circ - 900^\circ K) \quad [9]$$

The changes in standard free energy for the reactions



have been determined by Dewing.<sup>4</sup> Data for reaction [11] above are also given by Grjotheim *et al.*<sup>5</sup> These data combined with data for Cu<sub>2</sub>O<sup>6,7</sup> and α-Al<sub>2</sub>O<sub>3</sub><sup>8</sup> have been used to calculate the standard free energy change for reactions [7] and [8] above. The calculated values are given in Table I together with free energy data derived from Choudhury's experimental results in the paper under discussion as expressed by Eq. [9] above. The results in Table I indicate that reaction [2] is probably the correct over-all reaction for cell [V] of the paper being discussed. However, as there are rather large uncertainties involved in the free energy calculations for reactions [7] and [8], reaction [3] cannot be excluded as a possible over-all reaction for the above-mentioned cell [V].

**N. S. Choudhury:**<sup>9</sup> The discussion and conclusions of Sterten above are based upon the assumption that AlF<sub>3</sub> reacts with β-alumina to form a layer of Na<sub>3</sub>AlF<sub>6</sub> at the β-alumina/AlF<sub>3</sub>, NiF<sub>2</sub>, Ni interface. The equilibrium *RT* ln *a*<sub>Na<sub>2</sub>O</sub> values at 800°, 900°, and 1000°K for the reaction



are tabulated below (Table II). It is assumed that AlF<sub>3</sub>, Na<sub>3</sub>AlF<sub>6</sub>, and Al<sub>2</sub>O<sub>3</sub> are in the standard state. The second column lists computed values of *RT* ln *a*<sub>Na<sub>2</sub>O</sub> from the Δ*G*<sup>°</sup><sub>Na<sub>2</sub>O</sub>, Δ*G*<sup>°</sup><sub>Na<sub>3</sub>AlF<sub>6</sub></sub>, Δ*G*<sup>°</sup><sub>Al<sub>2</sub>O<sub>3</sub></sub>, and Δ*G*<sup>°</sup><sub>AlF<sub>3</sub></sub> values given in JANAF tables.<sup>8</sup> The third column lists *RT* ln *a*<sub>Na<sub>2</sub>O</sub> values estimated from Δ*G*<sup>°</sup><sub>Na<sub>2</sub>O</sub>, Δ*G*<sup>°</sup><sub>Na<sub>3</sub>AlF<sub>6</sub></sub>, and Δ*G*<sup>°</sup><sub>Al<sub>2</sub>O<sub>3</sub></sub> values in JANAF tables<sup>8</sup> and the more recent Δ*G*<sup>°</sup><sub>AlF<sub>3</sub></sub> values reported by Skelton and Patterson.<sup>10</sup> The *RT* ln *a*<sub>Na<sub>2</sub>O</sub> values for β-alumina-α-alumina co-

<sup>4</sup> K. Grjotheim, K. Motzfeldt, and D. Bhogeswara Rao, in "Light Metals, 1971," T. G. Edgeworth, Editor, p. 223, Proceedings of Symposium at the 100th AIME Annual Meeting, New York, 1971.

<sup>5</sup> G. G. Charette and S. N. Flengas, *This Journal*, 115, 796 (1968).  
<sup>6</sup> B. C. H. Steele and C. B. Alcock, *Trans. Met. Soc. AIME*, 233, 1359 (1965).

<sup>8</sup> JANAF Thermochemical Tables, NSRDS-NBS 37, 2nd ed. (1971).

<sup>9</sup> Present address: Materials Science Division, Argonne National Laboratory, Argonne, Illinois 60439.

<sup>10</sup> W. H. Skelton and J. W. Patterson, *J. Less-Common Metals*, 31, 47 (1973).

Table I. Standard free energy data (kcal)

T, °K	From Eq. [9]	From reaction [7]	From reaction [8]	From reaction [3]
800	-305.6	-307.1	-314.9	
900	-303.8	-306.4	-313.4	-308.0*

\* Data for reaction [11] from Grjotheim *et al.*<sup>5</sup>

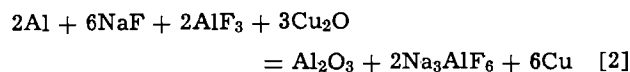
Table II.

Temperature (°K)	<i>RT</i> ln <i>a</i> <sub>Na<sub>2</sub>O</sub> <sup>9</sup> (kcal)	<i>RT</i> ln <i>a</i> <sub>Na<sub>2</sub>O</sub> <sup>10</sup> (kcal)	<i>RT</i> ln <i>a</i> <sub>Na<sub>2</sub>O</sub> for β-alumina-α-alumina co-existence ((kcal)
800	-81.76	-76.97	-78.7
900	-82.11	-75.64	-77.8
1000	-82.54	-74.17	-77.0

existence, reported in the paper under discussion, are listed in the fourth column for comparison.

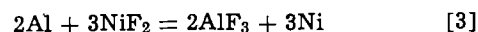
It is apparent from the above table that the formation of Na<sub>3</sub>AlF<sub>6</sub> at the β-alumina/AlF<sub>3</sub>, NiF<sub>2</sub>, Ni interface is thermodynamically possible if the data for Δ*G*<sup>°</sup><sub>AlF<sub>3</sub></sub> given in JANAF tables are used. On the other hand, if the data of Skelton and Patterson for Δ*G*<sup>°</sup><sub>AlF<sub>3</sub></sub> are used, β-alumina and AlF<sub>3</sub> should coexist without any formation of Na<sub>3</sub>AlF<sub>6</sub> at these temperatures.

In Table I above the standard free energy change for the reaction, at 800° and 900°K



are tabulated from the data reported in the literature and from the emf values reported in the paper under discussion (with the assumption that Na<sub>3</sub>AlF<sub>6</sub> did form at the β-alumina/AlF<sub>3</sub>, NiF<sub>2</sub>, Ni interface). The difference of 1.5 kcal at 800°K and 2.6 kcal at 900°K may perhaps be accounted for from the uncertainties in free energy calculations. However, these differences correspond to 11 and 18 mV, respectively, and cannot be simply accounted for from the scatter of the reported emf data.

It should be noted that the observed emf's for the cell Al/β-alumina (+α-alumina)/AlF<sub>3</sub>, NiF<sub>2</sub>, Ni agreed reasonably well with those reported by Skelton and Patterson for the cell Al, AlF<sub>3</sub>/CaF<sub>2</sub>/Ni, NiF<sub>2</sub> at above 540°C, which would correspond to the cell reaction



Thus, Sterten's assertions, that (i) the over-all cell reaction given by reaction [3] is incorrect and further that (ii) a layer of Na<sub>3</sub>AlF<sub>6</sub> formed at the β-alumina/AlF<sub>3</sub>, NiF<sub>2</sub>, Ni interface to account for Sterten's reaction schemes are inconclusive.

### Polarization Characteristics and Anodic Disintegration of Beryllium in Nonaqueous Solutions

H. Vaidyanathan, M. E. Straumanis, and W. J. James  
(pp. 7-12, Vol. 121, No. 1)

**I. Epelboin, M. Froment, and M. Garreau:**<sup>11</sup> In a recent paper<sup>12</sup> we interpreted the anomalous dissolution of beryllium (apparent valency *V*<sub>1</sub> < 2) in terms of a local inversion of the relative thermodynamic stability of Be<sup>+</sup> and Be<sup>++</sup> ions in the anodic layer. Vaidyanathan *et al.* raised some arguments to this interpretation which led them to conclude that "the assumption of the transient univalent state in postulating a mechanism for the anodic dissolution of Be is superfluous."

To draw this conclusion, the authors of the paper under discussion based their theory mainly on results obtained during very interesting studies concerning the two following fields: (i) surface studies and (ii) valency-potential relations.

Our own investigations in these two fields<sup>12-14</sup> bring us to think it necessary to make some remarks regarding the results and conclusions of Vaidyanathan, Straumanis, and James in the above-mentioned paper.

(i) *Surface studies.*—In our paper<sup>12</sup> we showed that a scanning electron microscope examination of the surface state of the anode led us to exclude any participation of a mechanical disintegration of the metal lattice ("Chunk effect") during the dissolutions that occur at high anodic potential, with an apparent valency *V*<sub>1</sub> of 1.00 ± 0.01. More recently<sup>13,14</sup> we confirmed this fact,

<sup>11</sup> Physique des Liquides et Electrochimie, Groupe de Recherches du C.N.R.S., accocié à l'Université de Paris VI, 75230 Paris, 05 Cedex, France.

<sup>12</sup> H. Aida, I. Epelboin, and M. Garreau, *This Journal*, 118, 243 (1971).

<sup>13</sup> I. Epelboin, M. Froment, M. Garreau, and H. Aida *J. Microscopie*, 15, 313 (1972).

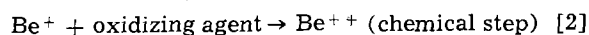
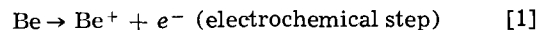
<sup>14</sup> M. Froment and M. Garreau, *Compt. Rend. Acad. Sci. Paris*, 277, 631 (1973).

which is fundamental to interpret anomalous dissolution, by determining the origin of the mechanism leading to anodic disintegration under certain experimental conditions. To this end, we first observed in transmission electron microscopy beryllium foils which were thinned electrolytically under conditions leading to  $V_i = 1.00$ . On the thin foils thus obtained, the grain boundaries and the arrangement of dislocations can clearly be seen; no trace of disintegration or oxidation could be revealed within the resolution limit of the method used for the observation (bright field or dark field observation, under an electron acceleration potential of 1 mV). The foils were subsequently subjected to very brief periods of dissolution under conditions leading to  $V_i = 1$ . After this last treatment, there appears, systematically, a heterogeneous dissolution due to the formation of beryllium oxide. The oxide was identified by electron microdiffraction on attacked areas (simultaneously, formation of very well-defined rings corresponding to the interreticular distances of hexagonal BeO with parameters,  $a = 2.698\text{\AA}$  and  $c = 4.38\text{\AA}$ , and formation of pattern points corresponding to the metal lattice).

The progression of the oxide is by no means affected by the presence of the various crystal defects (grain boundaries, dislocations). During its random progression, the oxide isolates small metal blocks which subsequently come off the electrode. The "Chunk effect" thus created can be easily identified, even before metal particles appear in the solution bulk and before its influence on the value of  $V_i$  be perceptible. Our observation technique not only constitutes a very sensitive method to reveal the existence of the "Chunk effect," but also removes all doubts on the origin of the metal particles that can be observed in the anolyte. As a matter of fact, it seems impossible to attribute such particles to a disproportionation of  $\text{Be}^+$  ions as was sometimes stated, since their presence is always related to a random formation of oxide at the metal surface; and on this particular point, we agree with Vaidyanathan *et al.* in the paper under discussion. It is to be noted that we have already been led to refute the hypothesis on a disproportionation by our first observation in scanning electron microscopy, which we performed originally not in order to check this hypothesis as was reported in the work being discussed but in order to refute it.<sup>12</sup>

This method for studying dissolution provides further information on the mechanism, according to which the metal passes into the solution, when the oxide layer shows a porous structure analogous to that formed on aluminum (3). In the case of aluminum dissolution, and under the same conditions as for beryllium ( $\text{LiClO}_4$ -ethanol solution, where  $\text{Al}^+$  reduces  $\text{ClO}_4^-$  to  $\text{Cl}^-$ <sup>12</sup>), the growth of oxide gives rise to the formation of small pockets within which lithium chloride (a salt very soluble in the electrolyte used here) is isolated from the bulk of the solution and then can crystallize. The  $\text{LiCl}$  crystallites thus formed are identified by electron microdiffraction. They are distributed randomly; their size ( $\approx 200\text{\AA}$ ) is of the same magnitude as that recently determined for the pores of amorphous aluminum oxides formed anodically.<sup>15</sup> These results, obtained at low anodic potentials, demonstrate that at such potentials an oxide layer is formed between the metal and the electrolyte. On the other hand, as soon as the anodic potential becomes sufficiently high, this porous oxide and the  $\text{LiCl}$  crystallites are no longer formed, and the "Chunk effect" no longer occurs.

This highly sensitive method permitted us to show that the experimental conditions required for obtaining anodic dissolutions without  $\text{BeO}$  oxide formation on the metal must be satisfied very accurately. And it is only under such conditions that the whole surface of the anode can undergo a dissolution process corresponding to the sequence



which leads to the critical value  $V_i = 1.00$ .

The experimental conditions leading to  $V_i = 1.00$  are drastic, not only with respect to the solution, i.e., high temperature and very low water concentrations ( $[\text{H}_2\text{O}] < 0.01\%$ ), but also with respect to the metal. Thus we observed erratic values close to 1 for  $V_i$  with metal samples having a satisfactory chemical purity but presenting mechanical elaboration defects, and this phenomenon disappears when we used single crystals in the same conditions.<sup>16</sup>

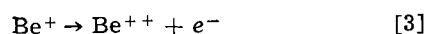
These results allow us to think that the deductions made by the authors of the paper under discussion from the fact that the "Chunk effect" still occurs when  $V_i$  is equal to 1 (0.94-1.00-0.98) are not significant for the following reasons.

First, a deviation for  $V_i$  of about 2% from unity is sufficient for the "Chunk effect" to appear unambiguously. This can explain their experimental observations in the two cases leading to  $V_i = 0.94$  and  $V_i = 0.98$ .

Secondly, even the value  $V_i = 1.00$  obtained by the authors in the work being discussed is disputable, because, with the average water concentration (0.4%) used by these authors, a partial oxidation of the anode cannot be avoided. With a similar water concentration we have indeed obtained the same sort of curve as that depicted in Fig. 1 of the paper under consideration at potentials applied to the cell ranging between 0 and 5V approximately. In agreement with the paper under discussion the value of  $V_i = 1.00$  can reasonably be considered as an upper limit of valency at high potentials when experiments are performed within this potential range. But if the curve is extended up to potentials equal to 20V, it can be seen that the value  $V_i = 1.00$  is only reached during a continuous variation of valency which passes from a value less than 1.00 to a value close to 1.04. Consequently, the value  $V_i = 1.00$  is only obtained in a purely fortuitous manner, and therefore cannot be compared to the meaningful limiting value  $V_i = 1.00$  which we described in our paper<sup>12</sup> and which corresponds to the sequence of reactions [1] and [2] above.

As to the transitory  $\text{Be}^+$  ions resulting from reaction [1], it is worth noting here that the presence of these uncommon monovalent ions in the vicinity of the anode, has been recently detected by Eckert and Forker, with the aid of the rotating ring-disk electrode.<sup>17</sup> The presence of such ions is also confirmed by the fact that  $\text{ClO}_3^-$  ions have been identified as intermediates in the reduction  $\text{ClO}_4^- \rightarrow \text{Cl}^-$  by  $\text{Be}^+$ , by Kiss *et al.* using a similar method.<sup>18</sup>

(ii) *Valency-potential relations.*—As was recalled by Vaidyanathan *et al.* in the paper under present discussion it is doubtless that  $V_i$  must tend to the limiting value  $V_i = 2$  when the anodic potential increases. With respect to this we pointed out some years ago that there must exist a more or less wide potential range which would lead to a dissolution following the sequence of reactions [1] and [2] exclusively. A minimal anodic potential is obviously necessary to create an anodic layer poor in solvent molecules within which the monovalent ion is thermodynamically more stable than the polyvalent ion; this was also confirmed by investigations we are performing on aluminum.<sup>16</sup> Once this layer formed, any subsequent increase of the potential can only facilitate the electrochemical oxidation of  $\text{Be}^+$  to the detriment of the chemical oxidation (reaction [2]) and thereby increases  $V_i$  to the value  $V_i = 2$  corresponding to the sequence



<sup>16</sup> M. Garreau *et al.*, To be published.

<sup>17</sup> J. Eckert and W. Forker, *Z. Physik. Chem. (Leipzig)*, **253**, 153 (1973).

<sup>18</sup> L. Kiss, M. L. Varsányi, and E. Dudás, *Acta Chim. Acad. Sci. Hung.*, **79**(1), 73 (1973).

<sup>15</sup> P. Neufeld and H. O. Ali, *This Journal*, **120**, 479 (1973).

The existence of a plateau in the curve  $V_1$ - $E$  is by no means incompatible with this interpretation. The presence of the plateau only seems to indicate that a new potential threshold must be overpassed so that the electrochemical oxidation of  $\text{Be}^+$  (reaction [3]) may compete with the chemical oxidation (reaction [2]). The fact that the value  $V_1 = 1.00$  was not possibly overpassed hitherto under the conditions at which the plateau appears, is due, in our opinion, to the fact that we have never succeeded in creating a sufficiently high electric field in the vicinity of the metal, despite the very high apparent anodic potentials we used ( $E > 20\text{V}$ ). The impossibility of obtaining important effective anodic potentials is due to the influence of an ohmic drop which is more important than that predicted by our first estimations.<sup>12</sup> By improving our measurement devices we possibly observed, for example, an ohmic drop close to 7V at a measured anodic potential of 8V.<sup>16</sup> The impossibility of reaching high effective anodic potentials in such solutions seems to be confirmed by the fact that, within the potential range studied, no electrochemical oxidation of either the solvent or other components of the solution has ever been observed, contrary to what happens in certain solutions used by the authors in the paper being discussed ( $\text{NaNO}_3/\text{MeOH}$  solution, for example, in which  $\text{IK}$  is anodically oxidized to  $\text{I}_2$ ).

Despite the arguments put forward by Vaidyanathan *et al.* in the paper under consideration, we believe that the points developed here, as well as those proposed recently by other investigators,<sup>17,18</sup> allow us to assert that the hypothesis on a transitory monovalent state of the metal for interpretation of the anomalous anodic dissolution of beryllium cannot actually be ruled out.

### Mutual Effect of Current Density, pH, Temperature, and Hydrodynamic Factors on Current Efficiency in the Chlorate Cell Process

M. M. Jaksic (pp. 70-77, Vol. 121, No. 1)

**H. Vogt:**<sup>19</sup> As Jaksic showed in the paper under discussion, optimum pH value to provide maximum conversion rate of hypochlorite to chlorate can be calculated from the constant  $K^*$ . While the dissociation constant of hypochloric acid,  $K_a$ , is known from experiments,  $K^*$  can only be calculated from  $K_a$  with the knowledge of activity coefficients. Based on data from several authors, Jaksic calculated<sup>20</sup>

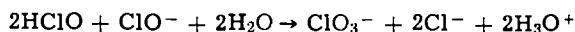
$$\frac{K^*}{K_a} = \frac{f_{\text{HClO}} \cdot a_{\text{H}_2\text{O}}}{f_{\text{ClO}^-}} \approx 1$$

But from the analysis of experimental data of Landolt and Ibl<sup>21</sup> Jaksic later concluded<sup>22</sup> that the ratio must be higher

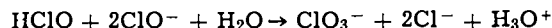
$$\frac{K^*}{K_a} \approx 10$$

In addition to Jaksic's considerations, it can be shown, that the higher value is more realistic and that the ratio is probably even higher.

Differentiating the equation for conversion rate as derived by Foerster



leads to the extreme condition  $2K^* = a_{\text{H}_3\text{O}^+}$  or  $\text{pH}_M = -\log K^* - \log 2$ . From the scheme, introduced by Flis



follows  $0.5K^* = a_{\text{H}_3\text{O}^+}$  or  $\text{pH}_M = -\log K^* - \log 0.5$ . For both the schemes, the temperature dependence of  $\text{pH}_M$  over an extended range can be derived, if one optimum pH is known at one temperature.

From Jaksic's older experiments follows  $\text{pH}_M \approx 6.0$  at  $40^\circ\text{C}$ . Values of  $K_a$  were determined by Morris and by Caramazza. They do not differ considerably and can be approximated by the simplifying equation

$$-\log K_a = \text{p}K_a = 7.744 - \frac{0.0075}{^\circ\text{C}} \cdot t$$

fitting in the range of practical application between  $25^\circ$  and  $80^\circ\text{C}$  with a deviation of  $< \pm 0.3\%$ .

For the Foerster scheme follows

$$\log \frac{K^*}{K_a} = -\text{pH}_M - \log K_a - \log 2 = 1.143$$

$$K^*/K_a = 14$$

Considering the Flis scheme to happen exclusively results in  $K^*/K_a = 56$ . Hence, these are the limits, situated in between the ratio, based on Jaksic's optimum pH.

Assuming  $f_{\text{HClO}} = 1.4 \dots 2$  and  $a_{\text{H}_2\text{O}} = 0.8$ , the activity coefficient of hypochlorite ion follows

$$f_{\text{ClO}^-} = 0.08 \dots 0.12$$

for the Foerster scheme in good agreement with Jaksic's result.

The temperature dependence of optimum pH value can be expressed as

$$\text{pH}_M = C - \frac{0.0075}{^\circ\text{C}} \cdot t$$

From Jaksic's experimental result follows  $C = 6.3$ , if one again considers the Flis scheme not to be essential. In this regard opinions are far from being unanimous. Claus, for instance, found an optimum pH value of about 7,<sup>23</sup> but more recent experiments seem to prove that  $\text{pH}_M$  is lower at about 6.3 . . . 6.5.

On the other hand, it must be postulated that one must distinguish clearly between pH in the reactor and pH at cell entrance, as Jaksic did in the paper under discussion. The optimum pH discussed here refers to a mean value in reactor.

### Mechanism of Electrocrystallization

T. Vitanov, A. Popov, and E. Budevski  
(pp. 207-212, Vol. 121, No. 2)

**K. J. Bachmann:**<sup>24</sup> A crystalline surface in thermodynamic equilibrium with an electrolyte phase, established via a reversible charge-transfer reaction  $\text{Me} = \text{Me}^{2+} + \text{ze}^-$ , contains a definite density of surface sites, e.g., steps, kink sites, adatoms, surface vacancies, and clusters thereof, which differ in their binding energy to the crystal surface. For the interfacial equilibria, crystal/vapor and crystal/melt, where the degree of surface roughening depends only on the deviation of the temperature from a critical surface roughening temperature, at which singular surfaces become thermally roughened to an extent that makes step edges indistinguishable, a detailed analysis of the distribution of surface sites has been made via Monte Carlo simulations.<sup>25</sup> Similar calculations may be applied to simulate the growth of simple crystals from the vapor phase and to some

<sup>19</sup> J. Claus, Paper 256 presented at Electrochemical Society Meeting, Boston, Mass., May 5-9, 1968.

<sup>20</sup> M. M. Jaksic, B. Z. Nikolic, I. M. Csonka, and A. B. Djordjevic, *This Journal*, 116, 684 (1969).

<sup>21</sup> N. Ibl and D. Landolt, *ibid.*, 115, 713 (1968); N. Ibl, *Chem. Ing. Techn.*, 39, 706 (1967); D. Landolt, Ph.D. Thesis, Eidgenössischen Technischen Hochschule, Zurich, Prom. Nr. 3673, Juris-Verlag, Zurich (1965).

<sup>22</sup> A. R. Despic, M. M. Jaksic, and B. Z. Nikolic, *J. Appl. Electrochem.*, 2, 337 (1972)

<sup>23</sup> J. D. Weeks, G. H. Gilmer, and H. J. Leamy, *Phys. Rev. Letters*, 31, 549 (1973); H. J. Leamy and G. H. Gilmer, *Proc. ICCG-4*, Tokyo 1974.

hypothetical situations of solution growth.<sup>26</sup> Computer simulations concerning the problem of combined nucleation and step motion have been studied by Bertocci,<sup>27</sup> who considered, also, the conditions encountered during electrocrystallization and when impurities are incorporated at steps. However, his calculations require that the step velocity and nucleation rate be known and give no information on the detailed molecular structure of the crystal/electrolyte interface. Calculations of the roughness of the crystal/electrolyte interface from first principles are very difficult since the effects of adsorption of solvent molecules and of the complicated structure of the electrical double layer are so far not accessible to a quantitative evaluation. Although one cannot derive at present the details of surface structure for a crystal/electrolyte interface, general considerations suggest a relatively high degree of surface roughening since adsorption phenomena both lower the energy and increase the entropy of a roughened surface. This may in part explain why the electrode potential is quite insensitive to surface roughening. The effect of adsorption on surface properties will be influenced by the competition of solvent and impurity adsorption, which can never be completely disregarded when working with crystal/solution interfaces.

In the paper under discussion, Vitanov *et al.* reduce the above sketched complex problem to the question of whether the exchange between crystal surface and metal ions in the electrolyte occurs predominantly via adatoms or directly from and into kink sites. The authors attempt to find an answer to this question for the Ag/Ag<sup>+</sup> electrode by comparing the exchange C.D. measured on a (100) face containing no electrochemically active steps (in the following designated as type 1 face) with the exchange C.D. measured on a (100) face containing electrochemically active steps (type 2 face), the density of which depends on the overvoltage at which these steps have been generated. They conclude from their experimental evidence, that the electrocrystallization of silver is governed by direct charge-transfer on steps.

It should be noted that the same simplified model as used by Vitanov *et al.* in the paper under consideration which assumes that the crystal/electrolyte interface is perfect except for steps with kink sites and adatoms, was utilized in the late 1950's by Gerischer,<sup>28</sup>

Bockris *et al.*,<sup>29</sup> and Lorenz.<sup>30</sup> They concluded from their internally consistent experimental work that the electrocrystallization of silver is governed by surface diffusion of adatoms. Later experiments of Bachmann and Vetter<sup>31</sup> raised some doubts in this simplified picture which is now even more challenged by the work being discussed by Vitanov *et al.* who, using the same surface model as other authors in the field,<sup>28-30</sup> suggest a different path contradicting the adatom diffusion mechanism. Clearly, the capillary growth technique developed by Budevski *et al.*<sup>32</sup> results in much more well defined crystal surfaces than used in the previous work by others, but for reasons discussed below, I have some doubts about the validity of the interpretation given in the paper under discussion.

The type 1 face behaves within  $\pm 10$  mV of the equilibrium potential of the Ag/Ag<sup>+</sup> electrode as an ideally polarizable electrode and contains, as shown by Budevski *et al.*,<sup>33</sup> no electrochemically active monoatomic steps. If such a surface is indeed free of impurities, which is difficult to assess, then after adjusting the electrode to the reversible equilibrium potential of the Ag/Ag<sup>+</sup> electrode its surface should attain the equilibrium distribution of surface sites including steps in the form of subcritical nuclei and vacancy clusters. The over-all exchange C.D.,  $i_0$ , on such a surface is then the sum over the partial exchange C.D.'s of the various surface sites. Although not specifically stated in the paper under discussion, presumably it was checked that equilibrium is, in fact, established at the time of measuring  $i_0$  and the result thus indicates that the over-all exchange C.D. on a perfect surface is much smaller than the exchange C.D. measured on surfaces of the same orientation but of nonequilibrium roughness.

Table I shows a number of literature values which were standardized for comparison to 1N Ag<sup>+</sup>-concentration assuming  $i_0(1N) \approx i_0/C^{\alpha}_{Ag^+}$ . Note that the pronounced effect of roughening expressed in the large variation of  $i_0$  does not result in large variations of the electrode potential. However, this does not indicate that all these electrodes have similar adatom concentrations since the surface activity entering into Nernst's equation becomes a complex expression when charge-transfer is understood in the statistical sense outlined above and nonequilibrium surfaces are con-

<sup>26</sup> F. F. Abraham and G. H. White, *J. Appl. Phys.*, **41**, 1841 (1970); G. H. Gilmer and P. Bennema, *ibid.*, **43**, 1347 (1972); G. H. Gilmer, H. J. Leamy, H. Reiss, and K. A. Jackson, *Proc. ICCG-4*, Tokyo 1974.

<sup>27</sup> U. Bertocci, *Surface Sci.*, **9**, 18 (1968); *ibid.*, **15**, 286 (1969); *This Journal*, **119**, 822 (1972).

<sup>28</sup> H. Gerischer and R. P. Tischer, *Z. Elektrochem.*, **61**, 1159 (1957); *ibid.*, **62**, 256 (1958).

<sup>29</sup> W. Mehli and J. O'M. Bockris, *Can. J. Chem.*, **37**, 190 (1957); A. R. Despic and J. O'M. Bockris, *J. Chem. Phys.*, **32**, 389 (1960).

<sup>30</sup> W. Lorenz, *Z. Physik. Chem. N. F.*, **17**, 136 (1958).

<sup>31</sup> K. J. Bachmann and K. J. Vetter, *ibid.*, **51**, 98 (1966).

<sup>32</sup> E. Budevski, T. Vitanov, and W. Bostanov, *Phys. Status Solidi*, **8**, 369 (1965).

<sup>33</sup> E. Budevski, W. Bostanov, T. Vitanov, Z. Stoinov, A. Kotzawa, and R. Kalschew, *ibid.*, **13**, 577 (1966).

Table I. Values of the exchange C.D. of Ag/Ag<sup>+</sup> electrodes standardized to 1N Ag<sup>+</sup> concentration in solution at room temperature

$i_0$ (A/cm <sup>2</sup> )	Electrode condition	Solution composition	Method of evaluating $i_0$	Reference
1.4-4.5*	Imperfect single crystal whisker	0.6-2.1N AgNO <sub>3</sub> solution with additions of gelatin or oleic acid	Galvanostatic single pulse technique	Footnote 34
24 ± 5**	Polycrystalline electrodes	0.001-0.1N AgClO <sub>4</sub> /~1N HClO <sub>4</sub> solutions	Galvanostatic double pulse technique	Footnote 28
6.5 ± 0.7*	(111) and (100) EDM cut electropolished or etched single crystal faces	0.1-0.5N AgClO <sub>4</sub> /1N HClO <sub>4</sub> solutions	Galvanostatic double pulse technique	Footnote 31
8.1 ± 0.8*	(100) type 1, step free single crystal face	6N AgNO <sub>3</sub> solutions	a-c technique	Paper under discussion
0.020 ± 0.001*	(100) type 2 single crystal face, step density depending on overvoltage			
0.05-0.23*		0.1N Ag(NH <sub>3</sub> ) <sub>2</sub> <sup>+</sup> + 5N NH <sub>3</sub> + 1N KNO <sub>3</sub> solution	a-c technique	Footnote 30
~1.2***	Polycrystalline microelectrode			

\* Assuming  $\alpha = 0.61$ .<sup>31</sup>

\*\*  $\alpha = 0.61$ .<sup>28</sup>

\*\*\*  $\alpha = 0.5$ .†

† W. Vielstich and H. Gerischer, *Z. Physik. Chem. N.F.*, **4**, 10 (1955); K. J. Vetter, "Elektrochemische Kinetik," p. 547, Springer-Verlag, New York, Berlin, Heidelberg (1981).

sidered. As a matter of fact, the values for the adsorption capacitance  $C_{ad}$  reported elsewhere<sup>28-31</sup> and in the paper under discussion vary as the exchange C.D.'s by orders of magnitude. If Vitanov *et al.* in the paper under discussion assume that  $C_{ad}$  is directly related to the adatom concentration, then all the different experimental results reported in the literature may be consolidated by assuming differences in roughening, including both the density of steps and adatoms. However, it is a pitfall of electrocrystallization studies that these phenomena may be explained as well by impurity adsorption and "activation" of an electrode could be simply understood as removal of dirt. Also, in my opinion, the separation of  $C_{ad}$  becomes very inaccurate when its value approaches that of the double layer capacity and the evaluation of  $C_{ad}$  on the basis of galvanostatic single pulse experiments described for the type 1 face appears to be in doubt.

It should be noted that the results of Vermilyea and Price<sup>34</sup> indicate that the exchange C.D. is not very sensitive to inhibitor adsorption. Also, there exists some experimental evidence for rearrangements on freshly prepared silver deposits<sup>35,36</sup> which indirectly support the ideas of Vitanov *et al.* in the paper under discussion as they point to the possibility that the much higher exchange C.D.'s observed by others are related to an increased step density on their electrodes and to the fact that the shift of the C.D. *vs.* overvoltage curves on low index silver surfaces immersed in a  $Ag^+$  solution toward higher overvoltages described by Bachmann and Vetter<sup>31</sup> may, at least in part, be related to rearrangements of steps and not be entirely due to diffusion controlled inhibitor adsorption as assumed there.

However, if one accepts the value of 180 A/cm<sup>2</sup> given by Vitanov *et al.* in the work under consideration as the C.D. directly at steps in a 6N  $Ag^+$  solution and compares it to the data of others (Table I), neglecting exchange with different surface sites but steps, then under the conditions of Gerischer and Tischer<sup>28</sup> and under those of Bachmann and Vetter<sup>31</sup>, about 40 and 14%, respectively, of the surface atoms would have to be step sites. This is somewhat hard to conceive, since, even when starting with a non-singular surface, at the large values of  $i_0$  observed, the surface should become rapidly faceted.<sup>37</sup>

The type 2 faces represent nonequilibrium surfaces since the step density on them was generated in a cathodic growth process at  $\epsilon < \epsilon_0$ . This is clearly stated in the above paper, since maintenance of the original nonequilibrium step density is considered by the authors as a prerequisite for being able to make their measurements. It is interesting to note that the rearrangement of a nonequilibrium step density on (111) faces, which represent the closest packed plane in the fcc lattice, is reported to be much faster than the rearrangement on (100) faces which remain unaltered for at least 30 min when the step generating cathodic current is switched off (see Footnote 1 of the paper under discussion). There exists thus an unusually strong kinetic hindrance for attaining equilibrium surface conditions on the (100) plane. Previous work<sup>31</sup> indicates that (100) faces of Ag crystals are more sensitive to inhibition by impurity adsorption than the (111) faces. The observed behavior suggests, therefore, that the (100) faces considered by Vitanov *et al.* in the work being discussed are per-

haps not perfectly clean surfaces. The inhibition of step rearrangement on (100) as compared to (111) is hard to understand when one assumes a large exchange C.D. directly on steps which eliminates the necessity of considering surface diffusion of adatoms and surface vacancies during the rearrangement process.

When a nonequilibrium step density persists on the type 2 face after switching off the generating current, then there is, in my opinion, no reason to believe that the density of all the remaining surface sites is at equilibrium level or at the same nonequilibrium level, as on type 1 face. Hence, the difference between the exchange C.D.'s of type 1 and type 2 faces does not necessarily represent the exchange C.D. directly on steps. The controversy concerning the surface diffusion of adatoms *vs.* direct charge-transfer on steps, which was introduced 50 years ago by Kohlschütter *et al.*, Brandes, and Volmer *et al.*<sup>40</sup> is thus still undecided. Instead of adhering to these early models of electrocrystallization it appears to me that one ought to acknowledge the existence of a number of surface and bulk defects in electrodeposited metals. The nature and effect upon the mechanism of electrocrystallization of these defects is presently not completely understood. The answers derived from more realistic models of electrocrystallization will be necessarily less clear cut, *i.e.*, will be of statistical meaning, but that does not decrease their value. It should be emphasized that the simplified model used by Vitanov *et al.* in the paper being discussed remains to be an interesting approximation which might be useful in some special cases, but the present evidence is insufficient to consider it as the mechanism of electrocrystallization.

**T. Vitanov, A. Popov, and E. Budevski:** The mechanism of metal deposition is doubtless a very complex process, and the main idea of the paper under discussion was to utilize the extremely simple and theoretically comprehensible behavior of electrodes representing one single crystallographic plane for the investigation of this process. The very essential point of the experiment was that a surface structure with an exactly known configuration (dislocation-free intact plane or a plane with known monoatomic step density) can be produced and reproduced relatively easily. The main experimental results of the paper are: (i) that the over-all exchange current density  $i_0$  increases linearly with step density and (ii) that the extrapolated value of  $i_0$  for zero step density is exactly that measured on a dislocation-free plane.

These two facts show that the presence of a step creates along the step new sites with a higher exchange C.D. and does not affect the remaining part of the surface. How far away from the step line the region with increased exchange C.D. extends is a question which the experiment was obviously unable to answer.

To calculate the true exchange C.D. (A/cm<sup>2</sup>) in the paper under discussion we made the simplest assumption that this range extended to the first closest atoms added to the step. It is unlikely that this assumption is very correct but it is sound as long as it is clearly understood and remembered. As we can assume every atom located on a step as an atom belonging to the crystal lattice we can call the transfer of an ion from the solution to a step a direct transfer process, *i.e.*, a transfer with simultaneous incorporation. This is why we call the exchange C.D. of these atoms the exchange C.D. of direct transfer. The calculation shows that it is by three orders of magnitude higher than the exchange C.D. of atoms on a flat surface (adatoms).

<sup>34</sup> D. A. Vermilyea and P. B. Price, *J. Chem. Phys.*, **28**, 720 (1958).

<sup>35</sup> C. Wagner, *This Journal*, **97**, 71 (1955).

<sup>36</sup> W. Jaenicke, R. P. Tinker, and H. Gerischer, *Z. Elektrochem.*, **59**, 448 (1955).

<sup>37</sup> Even higher exchange C.D.'s than that given by Gerischer and Tischer<sup>28</sup> have been observed by Frankenthal<sup>38</sup> in  $Ag^+$  solutions of extreme purity. Linear voltage sweep polarography on freshly etched  $Ag/Ag^+$  electrodes yields excellent agreement between experimental results and theory assuming pure diffusion control of the deposition process which, also, suggests an extremely high exchange C.D. on such surfaces.<sup>39</sup>

<sup>38</sup> R. P. Frankenthal, Private communication.

<sup>39</sup> K. J. Bachmann and J. K. Dohrmann, *J. Electroanal. Chem.*, **21**, 311 (1969).

<sup>40</sup> V. Kohlschütter, *Trans. Electrochem. Soc.*, **45**, 229 (1924); *Z. Elektrochem.*, **33**, 272 (1927); V. Kohlschütter and A. Toricelli, *ibid.*, **38**, 213 (1932); H. Brandes, *Z. Physik. Chem.*, **126**, 198 (1927); T. Erdey-Gruz and M. Volmer, *ibid.*, **157**, 165 (1931); M. Volmer, "Das Elektrolytische Kristallwachstum," in the series *Actualités Scientifiques et Industrielles*, Vol. 85, Hermann et Cie., Paris (1934).

Using not specially prepared solid surfaces (unknown step density) it is now quite clear that a wide range of over-all exchange C.D.'s can be measured. If we assume Bachmann's remark, in the above discussion, that the same situation and roughly the same values for the exchange current densities can be applied to the experiments of Gerischer<sup>28</sup> and Bachmann and Vetter<sup>31</sup> we can calculate back the average step distances: 7.2Å in the first case and 22Å in the second, compared with 830Å for an electrolytically grown (100) plane in our case. The misfit of the orientation in Bachmann's case is 4.5° which is not very far from what could be expected for a cut and electropolished plane. Anyway we believe that this calculation is a very vague extrapolation to extremely different conditions (AgClO<sub>4</sub> + HClO<sub>4</sub> vs. AgNO<sub>3</sub>).

The surface roughness produced by thermal motion cannot be neglected completely as we have done so far. It probably plays a major role in the process of roughening of the step edges and thus ensures a fast direct incorporation into the numerous kink sites. The two facts, however, which have been observed, namely two-dimensional nucleation on a dislocation-free plane and spiral growth mechanism on a plane with dislocations, show that the thermal surface roughening plays, in our case, a subordinate role for the process of growth and that we are really very far from that critical temperature, at which a normal mechanism of growth begins to be predominant. As a matter of fact, even propagating steps at a length of 100 mμ proved to be fairly straight.<sup>41</sup>

We are well aware of facts which show a surface contamination and adsorption. Many of them are still not so reproducible to allow theoretical speculations. But as we have not found dramatic changes in the electrochemical properties (exchange current density) changing the electrode potential in the allowed range of about 5 mV, we have no reason to use some ambiguous concepts to explain a very simple behavior of a face with a growing step on it.

Moreover, we have clearly stated that the direct transfer is a complementary process to the surface diffusion process and that in our specific case we have very good evidence for a predominance of the direct transfer mechanism. How far this can be generalized is a question which only the experiment can answer and we do not think that the title can be misleading in this respect.

### Hydrogen and Nitrogen Evolution Reactions in Acid Liquid Ammonia

M. H. Miles and C. A. Yates (pp. 230-233, Vol. 121, No. 2)

**S. Trasatti:**<sup>42</sup> In the paper under consideration, the authors have attempted to discuss the results obtained for the reaction of hydrogen evolution on various metals in liquid ammonia on the basis of correlations between  $\log i_0$  (exchange current) and  $\Phi$  (work function), and  $\log i_0$  and  $q_{ad,H}$  (heat of hydrogen adsorption), respectively, proposed by the present author<sup>43</sup> for the case of aqueous solutions. The authors of the paper under discussion state that the correlation between  $\log i_0$  and  $\Phi$  is not so linear as suggested in the previous paper,<sup>43</sup> although the reactivity scale appears to be the same as in aqueous solution. On the other hand, the authors of the above cited paper report a linear correlation between  $\log i_0$  and  $q_{ad,H}$  with a slope of 0.3 whereas Kuhn *et al.*,<sup>44</sup> as they quote, have found 0.6 for aqueous solutions.

While the reactivity scale being the same as in aqueous solutions is a very interesting fact because

it is a strong support to present views in electrocatalysis, it is the opinion of this writer that a discussion in terms of work function or heat of hydrogen adsorption is worthy of being brought into more detail than it is in the paper under discussion.

First of all, the authors of that paper state that the correlation between  $\log i_0$  and  $\Phi$  is not clearly linear. However, they rely just on six metals gathered within two orders of magnitude of  $i_0$ . If the values of  $i_0$  for the same metals in aqueous solutions are taken into consideration, a correlation between  $\log i_0$  and  $\Phi$  restricted to these metals does not appear to be better than that observable in the paper under discussion. From this point of view, it may be concluded, contrary to the authors of the paper under discussion, that the evidence for a linear correlation between  $\log i_0$  and  $\Phi$  may be considered as satisfactory.

However, various other points must be discussed before one can speak of correlation. What appears to have been overlooked by the authors of the above-mentioned paper is that there is some internal inconsistency between their experimental results and their discussion in terms of  $\Phi$  or  $q_{ad,H}$ . First of all, we notice that, apart from Ta whose behavior is puzzling, Mo, Cr, W, and Au present more or less the same  $i_0$  as in aqueous solutions, whereas Pt and Ir show lower  $i_0$  values than those in aqueous solutions by two orders of magnitude. This particular aspect does not appear to have been discussed in the paper under consideration. However, this point is particularly important. In fact, if on Pt and Ir the combination reaction is the rate determining step at 0°C as suggested by the authors in the paper being discussed, there should be evidence for some hydrogen adsorbed on the surface. The authors have not looked for and have not offered such evidence. Moreover, the rate of the combination reaction should be independent of the solvent and dependent only on the properties of the surface. From this point of view it is hardly understood why  $i_0 = 10^{-5}$  A/cm<sup>2</sup> in NH<sub>3</sub> and  $i_0 = 10^{-3}$  A/cm<sup>2</sup> in H<sub>2</sub>O. If this difference is due to partial occupation of the surface by residues of the solvent, then the rate determining step is more likely to be the ion atom reaction as suggested by Brown and Thornton,<sup>45</sup> although these authors have worked at -30°C, a temperature at which the authors of the paper under discussion admit that a shift of the rds from the combination to the ion+atom reaction may be observed. However, if the low activity of Pt is due to strong interaction of the solvent with the surface, the opinion of this writer is that this effect should also be present with the other metals inasmuch as the strength of the metal-nitrogen bond certainly increases<sup>46</sup> from Pt to Ta. In any case, an explanation must be given for the apparent low activity of Pt and Ir before any test of correlations can be attempted using the experimental results in question.

Another point which appears to have been overlooked by the authors in the paper under discussion is that in a possible correlation between  $\log i_0$  and  $\Phi$ , Au is apparently lumped with all other metals. This point is certainly worthy of more consideration. For aqueous solutions two parallel straight lines have been found<sup>43</sup> in the  $\log i_0$  vs.  $\Phi$  plot. This has been interpreted in the case of sp-metals in terms of the reaction occurring on positive and negative surfaces, respectively. Now, if Au falls in the group of transition metals in the paper under discussion, this may have a meaning in connection with the position of the potential of zero charge with respect to  $E_{rev}$  in liquid ammonia. However, in the opinion of this writer, a plot of  $\log i_0$  vs.  $\Phi$  may be misleading in this case. If the measured  $\log i_0$  for Pt and Ir are not equilibrium values, it is obvious that the position of Au turns

<sup>41</sup> W. Bostanov, R. Roussinova, and E. Budevski, *Chem. Ing. Techn.*, **45**, 179 (1973).

<sup>42</sup> Laboratory of Electrochemistry, the University, 20133 Milan, Italy.

<sup>43</sup> S. Trasatti, *J. Electroanal. Chem.*, **39**, 163 (1972).

<sup>44</sup> A. T. Kuhn, C. J. Mortimer, G. C. Bond, and J. Lindley, *ibid.*, **34**, 1 (1972).

<sup>45</sup> O. R. Brown and S. A. Thornton, *J. Chem. Soc., Faraday I*, **69**, 1568 (1973).

<sup>46</sup> S. Cerny and V. Ponec, *Catalysis Rev.*, **2**, 249 (1968).



out to be false. If the value of  $i_0$  for Pt found by Brown and Thornton<sup>45</sup> is used, a slope for the log  $i_0$  vs.  $\phi$  correlation is found very similar to that for aqueous solutions, but in this case Au, as expected, is somewhat far from the correlation for transition metals.

One more point concerns the value of the slope of the log  $i_0$  vs.  $q_{ad,H}$  plot. The authors of the paper under discussion claim a value of 0.3 for the slope, but in fact this is the value of the slope in terms of  $E(M-H)$ , the hydrogen-metal bond strength. The slope in terms of  $q_{ad,H}$  is, in reality, 0.15, in fairly good agreement with the predicted slope<sup>47</sup> of 0.18. However, this is the slope predicted for the ion+atom reaction or the discharge reaction as the rate determining step. This means that the experimental plot is possible because  $i_0$  for Pt is low. Thus, there is some internal inconsistency between the position of Pt in the log  $i_0$  vs.  $q_{ad,H}$  plot and the experimental results which suggest the combination reaction to be the rds. The authors of the paper under discussion have found a strong temperature effect for Pt and Ir. It is possible that the relative positions of the "volcano" curves for the ion+atom and the combination reactions shift with temperature. This would make a change in the mechanism for Pt and Ir understandable, in the case where the two metals would fall close to the intersection of the two curves. It would be interesting to know how  $i_0$  varies with changing temperature.

Finally, the Tafel slope shown by the authors in the paper being discussed for Pt and Ir is extended in a very narrow potential range close to  $E_{rev}$ . It would be interesting to know what the behavior is at higher overvoltages. Brown and Thornton<sup>45</sup> show that the Tafel slope region starts at some 0.2V below  $E_{rev}$ . For lower overvoltages the plot may apparently approach a lower Tafel slope. One may wonder if Fig. 6 in Brown and Thornton's paper could offer the way to understand some of the difficulties outlined above.

**M. H. Miles and C. A. Yates:** The proposed correlations suggested by Dr. Trasatti were discussed only briefly in the paper under consideration due to the limited data available for the hydrogen evolution reaction (h.e.r.) in liquid ammonia. More experimental data would be necessary to completely resolve the points under discussion, some of which remain unresolved despite the numerous studies in aqueous systems.

The correlation between log  $i_0$  and the work function,  $\phi$ , for the h.e.r. in liquid ammonia was not clearly linear due to the experimental value of  $i_0$  for Ta being very small ( $10^{-12}$  A/cm<sup>2</sup>). Of the seven metals studied, Ta has the greatest tendency to form interstitial hydrides and nitrides,<sup>48</sup> hence the electrode pretreatment evolving nitrogen and hydrogen may have produced pronounced changes in the surface properties. Omitting Ta, the correlation between log  $i_0$  and  $\phi$  is given reasonably well in acid liquid ammonia at 0°C by log  $i_0 = 4.3 \phi - 26$  which can be compared to Trasatti's relationship log  $i_0 = 6.7 \phi - 36.6$  for transition metals in aqueous solutions.<sup>43</sup>

We do not agree with Trasatti's suggestion that our value of  $i_0 = 10^{-5}$  A/cm<sup>2</sup> at 0°C on Pt and Ir in liquid ammonia should be closer to the  $i_0 = 10^{-3}$  A/cm<sup>2</sup> found in aqueous solutions at 25°C. Contrary to Trasatti's comments, the measured exchange current will be affected by the solvent even for a fast discharge and rate determining recombination mechanism. For such a mechanism the exchange current will be given by

$$i_0 = 2Fk_2 \left( \frac{k_1}{k_{-1}} \right)^2 a_{H^+}^2 e^{-2F\Delta\phi_c/RT} \quad [1]$$

where  $k_1$  and  $k_{-1}$  are rate constants for the forward and reverse reactions of the discharge step,  $k_2$  is the rate constant for the recombination step, and  $\Delta\phi_c$  is the absolute potential difference across the interface at equilibrium.<sup>49,50</sup> The solvent can influence  $k_1$ ,  $k_{-1}$ ,  $a_{H^+}$ , and even  $\Delta\phi_c$  and thus affect  $i_0$ . The close agreement between the experiments on Pt and Ir lend support to our results. Furthermore, difficulties in using the hydrogen reference electrode in liquid ammonia suggest a smaller exchange current than found for aqueous solutions. Our use of a lower temperature should also contribute to a smaller observed  $i_0$  value. Partial coverage of the Pt surface by adsorbed  $NH_x$  radicals may also be a factor as suggested by Brown and Thornton.<sup>45</sup>

By extrapolating from high overvoltages, Brown and Thornton<sup>45</sup> report  $i_0 = 2 \times 10^{-4}$  A/cm<sup>2</sup> on Pt at -30°C in liquid ammonia. From their Fig. 6, one can detect another linear Tafel region with a greater slope at lower overvoltages from which a value of  $i_0 = 1 \times 10^{-5}$  A/cm<sup>2</sup> could be extrapolated. As suggested by Parsons<sup>51</sup> and by Enyo,<sup>52</sup> increasing the overvoltage may produce a change in the reaction mechanism. The resulting dual Tafel slopes will give two different values for the exchange current, and one must then decide which  $i_0$  value should be used in the correlations suggested by Trasatti. We did detect a change in slope of our Tafel plots for Pt and Ir at higher overvoltages, but this was difficult to distinguish from effects due to the IR drop.

The Tafel slopes provide better evidence for the reaction mechanism than do the questionable log  $i_0$  vs.  $q_{ad,H}$  plot mentioned by Trasatti.<sup>43</sup> Rate determining recombination of adsorbed hydrogen is usually found under conditions of low hydrogen coverage and low overvoltages and is almost the only mechanism which gives a transfer coefficient of two.<sup>49</sup>

LeChatelier's principle predicts that the equilibrium coverage of adsorbed hydrogen atoms will increase as the temperature decreases. Hence, on Pt it is likely that some other reaction will become rate determining at lower temperatures as found in our studies. Recent investigations of the hydrogen/tritium separation factor on Pt in aqueous H<sub>2</sub>SO<sub>4</sub> solutions also indicate a change in the electrode reaction mechanism from a slow recombination step at temperatures above 10°C to a slow electrochemical desorption mechanism at lower temperatures.<sup>53</sup>

<sup>49</sup> J. O'M. Bockris and A. K. N. Reddy, "Modern Electrochemistry," Vol. 2, pp. 1238-1242, Plenum Press, New York (1970).

<sup>50</sup> S. Srinivasan, Thesis, University of Pennsylvania, Philadelphia, Pa. (1964).

<sup>51</sup> R. Parsons, *J. Chim. Phys.*, **49**, C82 (1952).

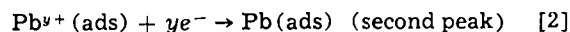
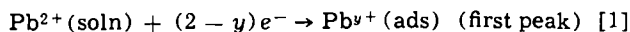
<sup>52</sup> M. Enyo, *Electrochim. Acta*, **18**, 155 (1973).

<sup>53</sup> M. E. Martins, A. J. Calandra, and A. J. Arvia, *ibid.*, **19**, 99 (1974).

### Optical and Electrochemical Studies of Underpotential Deposition of Lead on Gold Evaporated and Single-Crystal Electrodes

R. Adzic, E. Yeager, and B. D. Cahan (pp. 474-484, Vol. 121, No. 4)

**E. Schmidt and N. Wüthrich:**<sup>54</sup> In order to interpret the well-known underpotential double peak observed when Pb is deposited at polycrystalline Au electrodes, the authors of the paper under discussion considered a consecutive mechanism of adsorptive charge transfer involving the formation of a partially discharged Pb adsorbate within the voltage region of the more anodic peak, followed by reductive transformation at higher cathodic potentials



According to this model, the Pb surface concentration,  $\Gamma$ , should remain constant within the second peak,

<sup>47</sup> R. Parsons, *Trans. Faraday Soc.*, **54**, 1053 (1958).

<sup>48</sup> H. J. Goldschmidt, "Interstitial Alloys," p. 61, Butterworth and Co., London (1967).

<sup>54</sup> Institute für Anorganische, Analytische und Physikalische Chemie der Universität Bern, 3012 Bern, Switzerland.

whereas the charge/coverage stoichiometry of the undervoltage deposit should be given by

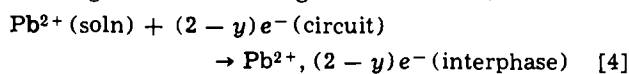
$$F d\Gamma/d\Delta q(E, \Gamma) = \begin{cases} 1/(2 - y) & \text{in the first peak} \\ 0 & \text{in the second peak} \end{cases}$$

where  $\Delta q(e, \Gamma) = q(e, \Gamma) - q_0(E)$ ,  $q$  and  $q_0$  being the (ionic) surface charges of the gold electrode in the presence of  $\text{Pb}^{2+}$  and in the lead-free supporting electrolyte, respectively.

This prediction of the model is at variance with the results of the direct determination of  $q$  and  $\Gamma$  data by means of a twin-electrode, thin layer method,<sup>55</sup> which has shown that  $\Gamma$  increases continuously with increasing  $q$  in the entire undervoltage region, the proportionality factor being equal to the nominal charge of the free  $\text{Pb}^{2+}$  ion within the limits of experimental precision

$$F d\Gamma/d\Delta q \approx 1/2 \quad \text{in } E > E_{\text{rev}} \quad [3]$$

This stoichiometry value almost certainly invalidates the mechanism proposed by Adzic *et al.* in the paper under discussion. It does, however, provide strong evidence in favor of a simple ionic adsorption process involving  $\text{Pb}^{2+}$ , whose charge contribution to the interphase is (approximately) compensated for by the electronic charge flow from the polarizing circuit, increasing the surface charge of the electrode



where  $y \approx 0$ .

Note that in all surface processes, electroneutrality of the interphase must be preserved. If there is substantial deviation from the "ideal"  $q/\Gamma$ -stoichiometry ( $|y| \gg 0$ , as in Eq. [1] and [2]), which cannot be balanced by changes of the nonspecifically adsorbed Helmholtz layer, charge compensation by specific adsorption or desorption of ionic species other than  $\text{Pb}^{2+}$  would be required. No conclusion should be drawn from stoichiometry determinations as to the actual state of charge of the Pb species adsorbed, since there is no way to decide by thermodynamic considerations whether a given amount of electronic charge delivered by the polarizing circuit is used for discharging any ionic species adsorbed, rather than being stored as free charge in the metal part of the electric double layer.

Within two orders of magnitude of the  $\text{Pb}^{2+}$  concentration, the potential dependence of the experimental  $\Gamma$  values<sup>55</sup> follows very closely a so-called pseudo-Nernstian ("metal monolayer")  $\Gamma$ - $E$ -isotherm

$$E = E^{\circ}_{\text{Pb}/\text{Pb}^{2+}} + \frac{RT}{2F} \ln[a_{\text{Pb}^{2+}}/a(\Gamma)]$$

which is thermodynamically inconsistent<sup>56</sup> with any  $q/\Gamma$  stoichiometry other than Eq. [3].

Peak multiplicity is not an exclusive feature of Pb deposition but is known from several other undervoltage deposits (Tl, Bi, Sb, Cu, Ag) on Au as well. It may easily be explained as reflecting a more or less pronounced discontinuous decrease of the free energy of desorption with increasing coverage, resulting in a steplike shape of the  $\Gamma$ - $E$  isotherm. There is evidence of a duplex layer structure of the adsorbate being built up, the second undervoltage peak corresponding to the formation of a metal layer more distant from, and therefore, less strongly bound to, the substrate.<sup>57</sup>

The existence of  $\Gamma$  values independent of  $c_{\text{Pb}^{2+}}$  at higher concentrations, as claimed by the authors in the paper being discussed, is not confirmed by thin layer experiments.

**R. Adzic,<sup>58</sup> E. Yeager, and B. D. Cahan:** Schmidt and Wüthrich propose that the sharp second voltammetry

<sup>55</sup> E. Schmidt and N. Wüthrich, *J. Electroanal. Chem.*, **34**, 377 (1972).

<sup>56</sup> E. Schmidt, *Helv.*, **52**, 1763 (1969).

<sup>57</sup> E. Schmidt and S. Stucki, *Ber. Bunsenges.*, **77**, 915 (1973).

<sup>58</sup> Present address: Institute for Chemistry, Technology and Metallurgy, Belgrade, Yugoslavia.

peak in the underpotential deposition of lead is due to a discontinuous decrease of the free energy of desorption with increasing coverage and not a phase transformation accompanied by further reduction as proposed in the paper under discussion. Their explanation for this sharp peak, however, is not compatible with our studies, which show that the sharp second peak in the voltammetry curve is not under diffusion control under conditions where the first peak is under diffusion control. This means that the sharp second peak is not associated with the further adsorption of lead, as proposed by Schmidt and Wüthrich above, but rather is caused by a surface change occurring essentially at constant surface coverage. The pronounced change in reflectivity and of the spectral dependence of the reflectance changes (Fig. 6 in the paper under discussion) attending the sharp voltammetry peak confirm that a marked change in the state of the surface has occurred. The reflectance change *vs.*  $q$  plot is linear up to 200  $\mu\text{coulombs}/\text{cm}^2$  when an abrupt change in the slope occurs (Fig. 8 in the paper under discussion). This charge density corresponds to the occurrence of the sharp second voltammetry peak. Ellipsometric measurements by Horkans *et al.*<sup>59</sup> provide evidence of a change of the layer and a shift toward more metallic properties attending this peak.

The principal argument put forth by Schmidt and Wüthrich against our explanation is that their  $\Gamma$  *vs.*  $q$  plot<sup>55</sup> should show some deviation from linearity in the vicinity of the sharp voltammetry peak and they did not observe such in their work with the twin-electrode thin layer cell. Perhaps their failure to observe such is the result of inadequate sensitivity of the method with the gold electrode and acetic acid-acetate buffered electrolyte used by Schmidt and Wüthrich.<sup>55</sup> The charge under the sharp peak in their voltammetry curves is estimated to be only  $\sim 7\%$  of the charge for saturation coverage as compared with  $\sim 30\%$  for the vapor deposited gold and  $\sim 50\%$  for the single crystal gold of (111) orientation used in our work in the paper under consideration in 1M  $\text{HClO}_4$ . The charge under the second voltammetry peak in the work of Schmidt and Wüthrich would be expected to produce only a small shift in their  $\Delta q$  *vs.*  $\Gamma$  curve by an amount not very much greater than the scatter of their points. The use of the acetic acid-acetate buffer by Schmidt and Wüthrich<sup>55</sup> also may have introduced differences because of complexing of the lead by the acetic acid,<sup>60</sup> as well as possible specific adsorption on the lead partially covered gold electrode.

According to our explanation, the charge under the second voltammetry peak is associated with a change in the effective charge of the adsorbed lead attending the phase transformation. As indicated in our paper, it is not possible to separate the faradaic charge and the nonfaradaic charge associated with the adsorption. With our explanation of the sharp voltammetry peak, the charge passed through the external circuit does not correspond directly to the change in charge of the adsorbed lead, but rather to the change in the partially compensating double layer charge. This can be seen from the following consideration. For the two-step sequence proposed in our paper under discussion (Eq. [8] and [9]), the charge through the external circuit  $\Delta q$  is the sum of the faradaic,  $\Delta q_f$ , and nonfaradaic,  $\Delta q_{\text{nf}}$ , components. Therefore

$$\Delta q_f = (2 - y)Fn; \quad \Delta q_{\text{nf}} = yFn + \Delta q_{\text{DL}} \quad [1a, b]$$

$$\Delta q = \Delta q_f + \Delta q_{\text{nf}} = 2Fn + \Delta q_{\text{DL}} \quad [2]$$

where  $n$  is the surface concentration of specifically adsorbed lead and  $\Delta q_{\text{DL}}$  is the change in the charge in the remainder of the double layer. For the sharp peak,  $n$  is essentially constant and therefore the charge under this peak must correspond to a change in  $q_{\text{DL}}$ , *i.e.*, for

<sup>59</sup> J. Horkans, B. D. Cahan, and E. Yeager, Paper 172 presented at Electrochemical Society Meeting, New York, Oct. 13-17, 1974.

<sup>60</sup> Stability Constants, p. 366, Special Publication No. 17, The Chemical Society, London, 1964.



the cathodic peak, the loss of anions in the double layer which had been compensating some of the charge of the specifically adsorbed lead as the lead layer takes on metallic properties.

We disagree with Schmidt and Wüthrich's statement that the extraordinarily narrow voltammetry peak (as narrow as 5 mV in some of our work) can be easily explained on the basis of a more or less pronounced discontinuous decrease in the free energy of adsorption with increasing coverage. Even with a very nonideal surface with various sites of different standard free energies of adsorption, it is difficult to see how the coverage of a particular set of sites of a given standard free energy can go from a low to high value over such a narrow potential range without involving the concept of some type of phase transition as proposed in the work being discussed.

In their last comment, Schmidt and Wüthrich indicate that they did not find the  $\Gamma$  values independent of lead ion concentration at higher concentrations in their thin layer experiments. Unfortunately they do not indicate either the electrolyte or the concentration range examined. If the electrolyte was the acetic acid-acetate-perchlorate system (pH 4.7) with the lead ion concentration extending only up to  $5 \times 10^{-3}M$ , as used in their published work,<sup>55</sup> we would not expect them

to observe leveling off of the adsorption isotherms. In  $1M$   $HClO_4$ , we found leveling off to occur only above  $5 \times 10^{-4}M$  in  $1M$   $HClO_4$ . In their electrolyte, complexing of the lead ions by acetic acid would depress the  $Pb^{2+}$  ion activity and probably make it impossible to reach a sufficiently high  $Pb^{2+}$  ion activity to observe leveling off of the adsorption isotherm. Adsorption of electrolyte components such as acetic acid or acetate and complexing with metal cations may introduce substantial complications in the use of the twin-electrode thin layer technique of Schmidt and Wüthrich to study cation adsorption in view of the assumption involved in their method concerning all changes in bulk cation activity being caused by specific ionic adsorption.

The unusually large change of the reflectance of gold attending the specific adsorption of lead is caused almost entirely by the modification of the surface electronic properties of the gold. In the paper under discussion in the range of coverages where the reflectance changes are directly proportional to charge, the reflectance should be a direct indication of the lead ion surface concentration in the inner Helmholtz plane. Consequently, for specific adsorption of lead on gold, the reflectance method should be a reliable indication of the adsorption isotherm.



## The Effects of Trace Amounts of Water on the Thermal Oxidation of Silicon in Oxygen

E. A. Irene

IBM Thomas J. Watson Research Center, Yorktown Heights, New York 10598

### ABSTRACT

The significance of the addition of 25 ppm of H<sub>2</sub>O to O<sub>2</sub> has been studied for the thermal oxidation of (100), (110), and (111) oriented silicon. With 25 ppm water addition to O<sub>2</sub> a sharp increase in the over-all rate of oxidation was observed for each orientation and experimental temperature (800°, 927°, and 996°C). From data analysis in terms of a linear-parabolic oxidation law, orientation effects were found for both the linear and parabolic rate constants and for both dry O<sub>2</sub> and H<sub>2</sub>O added oxidations. The major effect of trace H<sub>2</sub>O appears to be on the parabolic rate constants. The experimentally derived kinetic constants are interpreted in terms of surface geometry for the linear rate constants and in terms of the SiO<sub>2</sub> structure for the parabolic rate constants. The large kinetic effects observed with trace amounts of H<sub>2</sub>O might be a cause for the disparity of literature results for dry thermal oxidation of silicon.

The thermal oxidation of silicon produces a silicon dioxide (SiO<sub>2</sub>) passivation film with excellent electrical properties. However, the fabrication of advanced thin film electronic devices requires a knowledge of the parameters affecting thickness control and impurity content of the thin films. To describe SiO<sub>2</sub> film growth via thermal oxidation of silicon by oxygen, a linear-parabolic model is assumed. Numerous publications confirm the adherence of the SiO<sub>2</sub> growth kinetics to the linear-parabolic model [see for example Ref. (1-3)]. The qualitative effects of water and sodium on the oxidation kinetics are also known (4). However, considerable differences exist for the reported oxidation rate constants both for studies considering impurities and for so-called clean oxidation studies.

The purpose of this study is to consider the kinetic role of trace quantities of H<sub>2</sub>O (20-30 ppm) in O<sub>2</sub> on the thermal oxidation of (111), (110), and (100) oriented single-crystal silicon.

### Experimental Procedures

**Sample preparation.**—Chem-mechanically polished silicon wafers measuring 3.2 cm in diameter and 0.025 cm thick with (111), (110), and (100) orientations supplied from three different vendors were utilized for this study. Both n- and p-type Si wafers with resistivities ranging from 0.5 to 10 ohm-cm were used. For a given orientation and under identical oxidation conditions no systematic differences in oxidation rate were found for different type or resistivity silicon in the above resistivity range.

Prior to oxidation each experimental Si wafer was cleaned according to the following schedule: (i) deionized H<sub>2</sub>O rinse until H<sub>2</sub>O resistivity is 18 mohm-cm; (ii) basic peroxide rinse at 65°C with ultrasonic agitation (NH<sub>3</sub>OH:H<sub>2</sub>O<sub>2</sub>:H<sub>2</sub>O = 1:1:5); (iii) repeat step 1; (iv) acidic peroxide rinse at 65°C with ultrasonic

agitation (HCl:H<sub>2</sub>O<sub>2</sub>:H<sub>2</sub>O = 1:1:5); (v) repeat step 1; (vi) 48% HF dip for 10-15 sec; (vii) repeat step 1; (viii) blow dry in clean N<sub>2</sub>.

Samples treated as described above were found to have an SiO<sub>2</sub> film of 10-12Å thickness. Prior to oxidation the cleaned Si wafers were placed horizontally on a fused silica paddle and inserted into the furnace in a clean N<sub>2</sub> ambient. It was found that the samples reached the experimental temperature in 7-10 min and were therefore preheated for 15 min to insure temperature stability. After this warm-up in N<sub>2</sub> the residual oxide was found to be 9-11Å. This experiment served to check the quality of the N<sub>2</sub> gas which was used for initial warm-up and final flush and to establish the initial oxide thickness (*d*<sub>0</sub>) of 10Å to be used later for data analysis.

**Oxidation furnace.**—A three-zone, resistance heated furnace with a high purity alumina liner was used for this study. The oxidation chamber was a double wall, fused silica tube. Between the outer and inner walls high purity N<sub>2</sub> was constantly flowing. The oxidation tube was suspended concentric to the alumina liner by means of fused silica wool. All fused silica components were thoroughly degreased and bathed in a mixture of HNO<sub>3</sub>, HF, and H<sub>2</sub>O and thoroughly rinsed in deionized H<sub>2</sub>O.

A level temperature zone of ±1°C for about 25 cm in length could be achieved under oxidation conditions. Typically, three silicon wafers were oxidized simultaneously. The wafer load was positioned in the center of the level zone. Temperature was continuously monitored by means of a Pt/Pt-10% Rh thermocouple encased in a fused silica well. The thermocouple well was fused to the bottom of the paddle which held the Si wafers. No positional dependence of the grown oxide thickness was found for oxidations performed in the center of the level temperature region of the oxidation furnace.

**Key words:** insulating films, orientation effects, rate constants, silicon oxidation, trace impurity.

1555

**Gas purity.**—Both the nitrogen and oxygen used in this study were supplied from boil off of liquid sources and delivered to the furnace through cleaned, leak tight, stainless steel plumbing.

Dew points were measured for the various gases by means of a Panametrics Model 1000 hygrometer with remote sensors. Each sensor was provided with calibration and dew point conversion tables. The dew point of the nitrogen gas at room temperature and 1 atm pressure was found to be  $-80^{\circ}\text{C}$  which corresponds to 0.5 ppm  $\text{H}_2\text{O}$ . The hydrocarbon content was measured by gas chromatography. A heated  $\text{Al}_2\text{O}_3$  column and flame ionization detector yielded a 0.5 ppm detectability limit based on standard gas mixtures. An average of 2 ppm of  $\text{CH}_4$  was detected in  $\text{N}_2$  gas. The purity of  $\text{N}_2$  was checked for  $\text{O}_2$  content by attempting to oxidize cleaned Si wafers at  $1000^{\circ}\text{C}$ . No oxide growth was detected in 2-3 hr runs with an  $\text{N}_2$  flow of 2 liters/min.

The dew point of  $\text{O}_2$  at room temperature was  $-72^{\circ}\text{C}$  which corresponds to about 2 ppm  $\text{H}_2\text{O}$ . Gas chromatography revealed the presence of  $\text{CH}_4$  in the amount of about 17 ppm. The  $\text{O}_2$  dew point at the oxidation furnace exit was found to be  $-54^{\circ}\text{C}$  or 20-30 ppm  $\text{H}_2\text{O}$ , and  $\text{CH}_4$  was not detected. These observations show that the methane was being combusted to  $\text{H}_2\text{O}$  and  $\text{CO}_2$  in the furnace. The analysis of  $\text{N}_2$  at the furnace exit was the same as the inlet thereby demonstrating that the double wall reaction tube is effective against the diffusion of  $\text{H}_2\text{O}$  through the furnace walls. It was found that the  $\text{CH}_4$  in the  $\text{O}_2$  could be removed by precombusting the  $\text{CH}_4$  in  $\text{O}_2$  at  $1000^{\circ}\text{C}$  and cold trapping the formed  $\text{H}_2\text{O}$  at  $-78^{\circ}\text{C}$  prior to the oxidation furnace. By either using or not using the precombustor and cold trap, it was possible to study the oxidation of Si with less than 1 ppm  $\text{H}_2\text{O}$  and with about 25 ppm  $\text{H}_2\text{O}$  in  $\text{O}_2$ .

**Film measurements.**—All  $\text{SiO}_2$  thickness measurements were made by ellipsometry. The wavelength of light used was  $5461\text{\AA}$ . Two zone data was used to determine  $\Delta$  and  $\psi$  values precisely. The real part of the refractive index of Si was taken to be 4.085 (5). The imaginary part was taken to be  $-0.028$  (6). From computer analysis of the ellipsometric data for thicker films ( $\sim 1000\text{\AA}$ ) both the film thickness and refractive index could be obtained. The average value for the refractive index was  $1.465 \pm 0.006$ . This value was used to obtain the film thicknesses for thin films (less than  $\sim 400\text{\AA}$ ). The error associated with the thickness measurement is estimated to be less than  $\pm 2\%$ .

To determine the over-all quality of the  $\text{SiO}_2$  films, capacitance-voltage ( $C-V$ ) measurements were made on oxidized (100) silicon wafers. Evaporated aluminum dots were used as electrical contacts. The  $C-V$  measurements revealed an average oxide charge level of  $< 5 \times 10^{10}$  charges/cm $^2$ . Bias temperature stressing ( $\pm 10^6$  V/cm,  $200^{\circ}\text{C}$  for 15 min, and cooling under bias) revealed an average mobile positive charge level of  $5 \times 10^{10}$  charges/cm $^2$ . Systematic trends in charge levels were not found for oxidations with and without 25 ppm  $\text{H}_2\text{O}$ ; more extensive electrical evaluation is in progress.

### Experimental Results

**Data analysis.**—Figure 1 contains plots of oxide thickness,  $d$  ( $\text{\AA}$ ), vs. oxidation time,  $t$  (min), at the three experimental temperatures,  $800^{\circ}$ ,  $927^{\circ}$ , and  $996^{\circ}\text{C}$  for (111), (110), and (100) Si orientations for  $\text{O}_2$  with (W) and without (D) 25 ppm  $\text{H}_2\text{O}$ . A total spread of 3% in thickness was found for the dry  $\text{O}_2$  data and 7% for the 25 ppm  $\text{H}_2\text{O}$  in  $\text{O}_2$  data.

Each  $d$  vs.  $t$  data set for a particular orientation, temperature, and  $\text{H}_2\text{O}$  content was fitted to a linear-parabolic equation of the form

$$t = A(d - d_0) + B(d - d_0)^2 \quad [1]$$

This equation was analyzed directly by linear least squares fit in terms of  $t/d - d_0$  vs.  $(d - d_0)$ . The

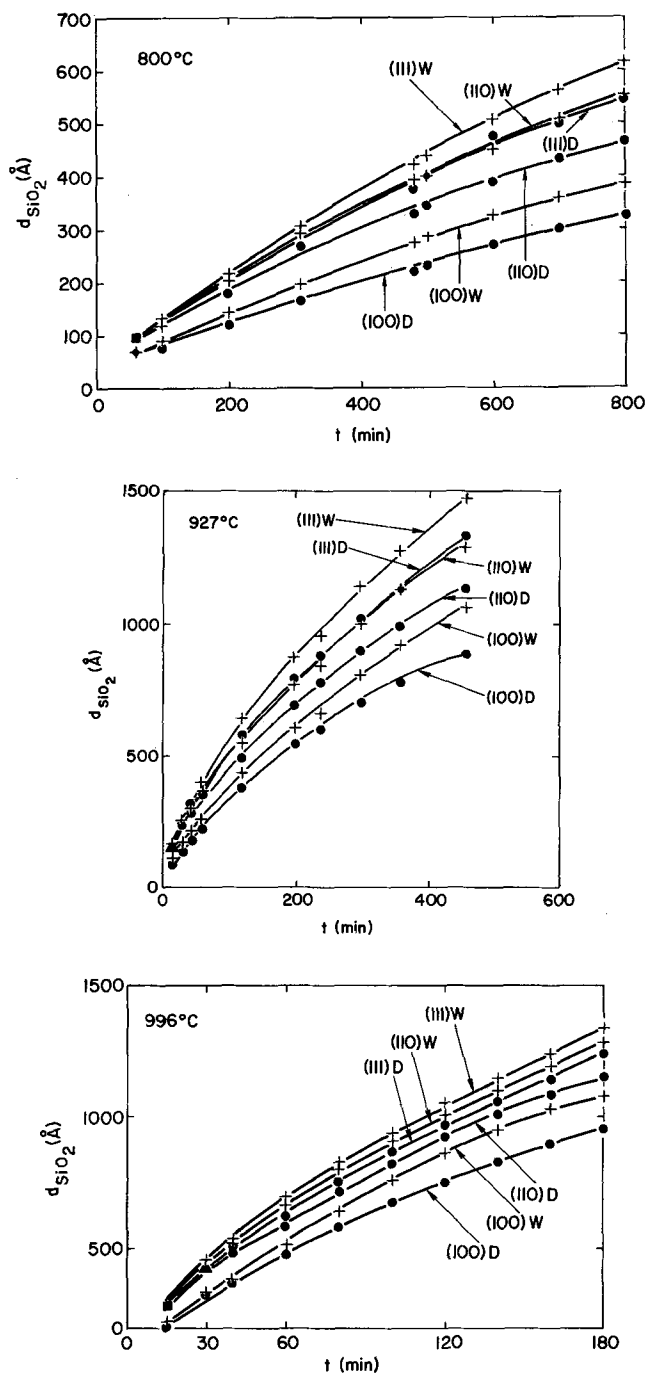


Fig. 1.  $\text{SiO}_2$  thickness,  $d$ , vs. time,  $t$ , for (100), (110), and (111) orientations for both dry  $\text{O}_2$  (D) and 25 ppm  $\text{H}_2\text{O}$  (W) in  $\text{O}_2$  at temperature (a, top)  $800^{\circ}\text{C}$ , (b, center)  $927^{\circ}\text{C}$ , and (c, bottom)  $996^{\circ}\text{C}$ . For each curve the closed circles are for dry oxygen ( $< 1$  ppm  $\text{H}_2\text{O}$ ); the crosses are for 25 ppm  $\text{H}_2\text{O}$  in oxygen. The symbols  $\diamond$ ,  $\triangle$ , and  $\blacksquare$  represent 2, 3, and 4 coincident points, respectively.

linear rate constant,  $k_{\text{LIN}}$ , is  $1/A$  ( $\text{\AA}/\text{min}$ ) and the parabolic rate constant,  $k_{\text{PAR}}$ , is  $1/B$  ( $\text{\AA}^2/\text{min}$ ). As previously mentioned  $d_0$  at  $t = 0$  was found to be  $10\text{\AA}$  and this value was used throughout the data analysis.

It was found that for the range of  $d$  and  $t$  of this study and for  $d_0 = 10\text{\AA}$  there is less than 1% difference between Eq. [1] and the more fundamentally based equation [see for example (1) and (5)]

$$t = A(d - d_0) + B(d^2 - d_0^2) \quad [2]$$

The linearization of Eq. [1] provides a numerical method to determine the extent of the logarithmic oxidation regime (1) which occurs at small oxide thicknesses. To determine the extent of the logarithmic

regime the following procedure was employed. First, for each complete data set of  $d$  vs.  $t$  from Fig. 1, a linear least squares fit in terms of  $t/d - d_0$  vs.  $(d - d_0)$  was performed. Then for each  $d$ - $t$  data set small thicknesses were sequentially dropped from the least squares analysis starting from the smallest  $d$ - $t$  value. For each linear least squares fit, the relative quality of the fit was determined from calculated standard deviation values for the fit of the data to the rate law and for the slope and intercept. The deviation values corresponding to the data fit are a relative measure of the regression line compared to the spread in the data. The standard deviations computed for the  $k_{LIN}$  and  $k_{PAR}$  values show their range. It was found that when small thickness values were sequentially eliminated from the least squares analysis the quality of the fit improved by a substantial amount ( $\sim$  a factor of 2) for the first few (2 or 3) values eliminated and then leveled off. The values of  $k_{LIN}$  and  $k_{PAR}$  reported in Table I reflect the fit where small values of thickness were dropped until the quality of the fit remained constant. In no case were more than three small thickness data points dropped from the analysis. The logarithmic regime determined in this manner shifted to greater thicknesses with temperature, and values are given in Table II.

The  $k_{LIN}$  and  $k_{PAR}$  values from Table I have been fitted to an Arrhenius relation of the form

$$k = k_0 e^{-E_a/RT} \quad [3]$$

and the resulting values of the preexponential factor,  $k_0$ , and activation energy,  $E_a$ , are listed in Table III.

Table I. Linear and parabolic rate constants for the orientations and temperatures studied for both dry ( $< 1$  ppm  $H_2O$  in  $O_2$ ) and wet ( $\sim 25$  ppm  $H_2O$  in  $O_2$ ) oxidations

Temperature (°C)	Orientation	$H_2O$ in $O_2$ (ppm)	$k_{LIN}$ (Å/min)	Standard deviation	$k_{PAR}$ (Å <sup>2</sup> /min)	Standard deviation
800	(100)	$< 1$	0.67	0.04	310	30
		$\sim 25$	0.83	0.02	430	20
	(110)	$< 1$	1.3	0.10	480	50
		$\sim 25$	1.3	0.03	800	40
	(111)	$< 1$	1.4	0.05	690	20
		$\sim 25$	1.3	0.03	1,200	60
927	(100)	$< 1$	5.3	0.20	2,700	100
		$\sim 25$	5.3	0.30	4,300	260
	(110)	$< 1$	11	0.90	3,600	150
		$\sim 25$	8.3	0.60	5,300	250
	(111)	$< 1$	8.9	0.20	5,300	110
		$\sim 25$	9.7	0.60	6,900	290
996	(100)	$< 1$	16	0.80	7,700	240
		$\sim 25$	13	1.0	12,000	690
	(110)	$< 1$	29	3.4	9,400	360
		$\sim 25$	28	0.80	12,000	210
	(111)	$< 1$	26	2.0	11,000	370
		$\sim 25$	28	0.80	13,000	230

Table II. Values of  $SiO_2$  thickness which represent the maximum thickness for the logarithmic oxidation regime

Temperature (°C)	$SiO_2$ thickness (Å)
800	100 $\pm$ 15
927	300 $\pm$ 30
996	380 $\pm$ 40

Table III. Arrhenius preexponential factors ( $k_0$ ) and activation energies ( $E_a$ ) for the linear and parabolic rate constants

Orientation	$H_2O$ in $O_2$ (ppm)	$k_{0,LIN}$ [(cm <sup>2</sup> /sec) · 10 <sup>-2</sup> ]	$E_{a,LIN}$ (eV)	$k_{0,PAR}$ [(cm <sup>2</sup> /sec) · 10 <sup>-7</sup> ]	$E_{a,PAR}$ (eV)
(100)	1	8.1	1.9	4.9	1.9
	25	0.81	1.7	18	2.0
(110)	1	13	1.9	1.8	1.8
	25	6.6	1.8	0.54	1.6
(111)	1	3.0	1.7	0.89	1.7
	25	9.9	1.9	0.13	1.5

## Discussion

From the data presented there are several trends which relate to the mechanism for the oxidation of silicon in oxygen. The more pronounced effects observed are:

1. For each orientation and at each experimental temperature the over-all rate of oxidation is increased with the addition of  $\sim 25$  ppm  $H_2O$  to oxygen.

2. The parabolic mode for silicon oxidations is thought to be due to a purely diffusion limited process (1). However, it was found in the present study that  $k_{PAR}$  values varied with Si orientation for both dry and wet oxidations at each experimental temperature.

The first effect suggests that in addition to the role of  $H_2O$  as a silicon oxidant at higher concentrations, there is a catalytic and structural effect due to trace amounts of  $H_2O$ . The catalytic effect is primarily displayed in the linear mode of oxidation while the structural effects are related to the increase of the parabolic kinetic constants with trace amounts of  $H_2O$ . The second effect, the variation of  $k_{PAR}$  with silicon orientation, appears to be related to the observation that surface states and/or positive interface charge near the Si- $SiO_2$  interface vary in the same direction with orientation as  $k_{PAR}$  values.

These observations and suggestions are treated in the light of literature results.

*Linear kinetics.*—It is seen from Table I that there is a systematic trend of the linear rate constants with Si orientation at each experimental temperature for both dry and wet oxidations. In terms of the Si orientation, this trend is summarized as follows

$$(110) \cong (111) > (100)$$

Ligenza (7) has shown that the number of Si-Si bonds is important for the consideration of the linear oxidation of Si. According to Ligenza, the number of Si-Si bonds per unit area relative to the (110) plane is as follows

$$(110) : (111) : (100) = 1 : 0.817 : 0.707$$

The  $k_{LIN}$  values of Table I agree qualitatively with the above ratios thereby confirming the importance of the silicon surface structure for linear oxidation kinetics.

The linear activation energies in Table III agree closely with a reported value for the Si-Si bond energy of 1.8 eV (8). For the (100) and (110) Si orientations the linear  $E_a$  values decrease with the addition of trace amounts of  $H_2O$  to the  $O_2$ . Coincident with this barrier lowering due to 25 ppm  $H_2O$  there is a rather sharp decrease in the linear preexponential factors. The total effect is a reduced linear rate constant for the (100) and (110) orientations at 927° and 996°C. These effects suggest a catalytic role for trace  $H_2O$  in  $O_2$ . At 800°C the trend in  $k_{LIN}$  reverses for the (100) and (110) orientations and for the (111) orientation the trends in  $k_{LIN}$ ,  $E_a$ , and  $k_{0,LIN}$  with trace  $H_2O$  are reversed as compared to the (100) and (110) orientations. An explanation of these results is not apparent within the present study but suggests that a series of competitive reactions are operative and each depends on orientation, temperature, and  $H_2O$ .

*Parabolic kinetics.*—The  $k_{PAR}$  values in Table I reveal a distinct trend with orientation for both dry and wet oxidations. This trend in  $k_{PAR}$  with Si orientation is as follows

$$(111) > (110) \cong (100)$$

This order parallels electrical measurements (9, 10) which show the amount of positive interface charge and/or surface states for the (111), (110), and (100) Si orientations. The results of Deal and Grove (1) relative to the  $O_2$  oxidation of Si demonstrate that the oxidant species is molecular. From the absence of paramagnetism in thermal oxides (14) and in light of the effects of electrical fields on the oxidation of Si (11,

12), an oxidant species is probably  $O_2^{--}$ . Therefore, in view of the above literature results and the observed parabolic nature of the oxidation data, a field enhanced diffusion mechanism for transport of oxidant through the  $SiO_2$  is proposed. Interestingly, the studies (9, 10) which show the variation of positive charge and/or surface states with Si orientation also show that the region of charge is near the Si- $SiO_2$  interface and that the charge is immobile relative to ionic alkali impurities. If the region of charge is due to unsatisfied Si bonds, then the oxidant flux and oxidation reaction would restrict the charged region to near the origin of the charges (i.e., the Si surface).

To explain the increase of  $k_{PAR}$  values with 25 ppm  $H_2O$  addition to  $O_2$ , a mechanism based on a structural alteration of  $SiO_2$  due to  $H_2O$  is proposed. It is known that  $H_2O$  attacks the bridging oxygen atoms of the  $SiO_2$  network (13, 14). The effect is a loosening of the  $SiO_2$  network thereby enhancing the diffusion of  $O_2$  (13). The  $k_{PAR,D}$  and  $k_{PAR,W}$  values of Table I show this effect of 25 ppm  $H_2O$  for the orientations and temperatures studied. Further insight is gained by considering the temperature dependence of the percentage change of the  $k_{PAR,W}$  and  $k_{PAR,D}$  values in Table IV. It is seen that for the (110) and (111) orientations the percentage change between  $k_{PAR,W}$  and  $k_{PAR,D}$  values is smaller at higher temperatures. According to Lee (15) the metastable hydroxyl content of  $SiO_2$  is a maximum at 800°C and decreases sharply with increasing temperature to 1000°C. With respect to this percentage change, the (100) orientation behaves oppositely. In addition,  $k_{O,PAR}$  and  $E_a$  values for the (110) and (111) orientations decrease with trace addition of  $H_2O$ , while again the opposite occurs for the (100) orientation. These differences in oxide growth behavior for different orientations suggest generic differences in the  $SiO_2$  film networks. For bulk amorphous materials generic differences are reported to be closely associated with the exact method of preparation (16).

### Summary

The significance of trace amounts of  $H_2O$  in  $O_2$  on the over-all rate of oxidation of Si is clearly seen in Fig. 1.

Table IV. Percentage change in  $k_{PAR}$  values with the addition of ~ 25 ppm  $H_2O$  to  $O_2$

Orientation	[ $k_{PAR,W} - k_{PAR,D}$ ]/ $k_{PAR,D} \cdot 100$		
	800°C	927°C	996°C
(100)	27	35	37
(110)	41	32	21
(111)	42	22	16

The  $SiO_2$  thickness vs. time data have been found to fit a linear-parabolic equation if a region of rapid  $SiO_2$  growth is eliminated. The linear-parabolic model allows interpretation in terms of interface and diffusion kinetics. Within the linear-parabolic model and the specific equation fitted the largest effect of trace  $H_2O$  appears to be related to the parabolic rate constants. The data analysis suggests a model based on Si surface geometry, interface charge, and what is known relative to the nature of  $H_2O$  in bulk  $SiO_2$ .

### Acknowledgment

The author gratefully acknowledges the assistance of B. Gilbert with gas chromatography measurements, Dr. W. R. Hunter for ellipsometry computer programs, Dr. R. Ghez for data fitting programs, and Drs. A. B. Fowler, R. Ghez, T. Takamori, and Y. J. van der Meulen for helpful discussions and critically reviewing this manuscript.

Manuscript submitted Feb. 28, 1974; revised manuscript received July 7, 1974.

Any discussion of this paper will appear in a Discussion Section to be published in the June 1975 JOURNAL. All discussions for the June 1975 Discussion Section should be submitted by Feb. 1, 1975.

The publications costs of this article have been assisted by the IBM Corporation.

### REFERENCES

1. B. E. Deal and A. S. Grove, *J. Appl. Phys.*, **36**, 3770 (1965).
2. A. G. Revesz, K. H. Zaininger, and R. J. Evans, *Appl. Phys. Letters*, **8**, 57 (1966).
3. T. Nakayama and F. C. Collins, *This Journal*, **113**, 706 (1965).
4. A. G. Revesz and R. J. Evans, *J. Phys. Chem. Solids*, **30**, 551 (1969).
5. Y. J. van der Meulen, *This Journal*, **119**, 530 (1972).
6. W. C. Dash and R. Newman, *Phys. Rev.*, **99**, 1151 (1955).
7. J. R. Ligenza, *J. Phys. Chem.*, **65**, 2011 (1961).
8. L. Pauling, "The Nature of the Chemical Bond," 3rd. ed., p. 85, Cornell University Press, Ithaca, New York (1960).
9. P. V. Gray and D. M. Brown, *Appl. Phys. Letters*, **8**, 31 (1966).
10. B. E. Deal, M. Sklar, A. S. Grove, and E. H. Snow, *This Journal*, **114**, 266 (1967).
11. P. J. Jorgensen, *J. Chem. Phys.*, **37**, 73 (1962).
12. T. G. Mills and F. A. Kroger, *This Journal*, **120**, 1582 (1973).
13. R. H. Doremus, *J. Phys. Chem.*, **75**, 3147 (1971).
14. R. Brückner, *J. Non-Crystalline Solids*, **5**, 177 (1971).
15. R. W. Lee, *Phys. Chem. Glasses*, **5**, 35 (1964).
16. R. Roy, *J. Non-Crystalline Solids*, **3**, 33 (1970).

# Identification of AgCl as a Surface Contaminant on Hybrid Microcircuit Capacitors Using Ion Microprobe Techniques

J. W. Guthrie

Sandia Laboratories, Albuquerque, New Mexico 87115

## ABSTRACT

An ion microprobe mass analyzer (IMMA) was used for the identification analysis of a micron-sized surface contaminant on hybrid microcircuit barium titanate capacitors with silver frit terminations. A 18.5 keV  $O_2^+$  sputtering ion beam was used to obtain characteristic positive and negative sputtered ion species for mass spectra, scanning ion micrographs, and depth profiles from clean and contaminated capacitors. The mass spectra from the contaminated capacitors contained significant peaks for  $AgOH^+$ ,  $BaCl^+$ ,  $Ag_2^+$ ,  $Ag_2OH^+$ ,  $Ag_2Cl^+$ , and  $Cl^-$  sputtered ion species. On the clean capacitors these species were detected only as low intensity peaks or not at all. Silver chloride was identified as a major contaminant by comparing AgCl calibration mass spectra with the mass spectra obtained from the clean and the contaminated capacitors. The calibration mass spectra were obtained by sputtering and analyzing AgCl deposited on Au, Mo, and Kovar substrates and AgCl deposited on the surface of a clean capacitor.

This paper describes the use of an ion microprobe mass analyzer (IMMA) (1-3) to identify AgCl as a major surface contaminant on silver frit terminations on hybrid microcircuit barium titanate capacitors. Micron-sized contamination was first revealed by scanning electron microscopy techniques. The primary problem concerned degradation of ultrasonically welded bond joints between aluminum wires ( $\sim 75 \mu m$  diameter) and the silver frit terminations on capacitors from certain production batches. It is not the purpose of this paper to discuss possible sources and/or causes of the contamination or measures taken to remove or prevent the contamination problem.

## Experimental

Figure 1 shows a  $1.9 \times 1.2 \times 0.8$  mm barium titanate capacitor and the silver frit termination areas. Besides silver, the frit contains bismuth oxide and a lead borosilicate glass. Figure 2 shows scanning electron micrographs from frit areas on clean and contaminated capacitors. The particles identified as contaminants are clearly visible.

Sputtered ion species for mass analysis were obtained by rastering a small diameter ( $< 5 \mu m$ ) probe of 18.5 keV mass-analyzed  $O_2^+$  ions of  $\sim 2 \times 10^{-9} A$  over selected rectangular sample areas (viewed optically during analysis) of  $\sim 340 \times 275 \mu m$  in size. The estimated sputtering rate for these conditions was  $< 0.1 A/sec$ . Both positive and negative sputtered sample ions were detected and recorded in mass spectra. The vacuum in the ion microprobe was  $\sim 4 \times 10^{-7}$  Torr during the sputtering process.

## Results and Discussion

Figures 3 and 4 show the spectra obtained by mass analyzing the sputtered negative ions from the frit area of a clean and a contaminated capacitor. The more intense signals for chloride ions from the contaminated sample were an indication (4) that a chlorine compound was involved.

Figures 5 and 6 show the spectra obtained by mass analyzing the sputtered positive ions. The time for each mass scan was about 10 min, during which it is estimated that less than 100Å of sample material were removed. Figure 6 (same intensity scale as Fig. 5) shows an increase in intensity for all the species observed in Fig. 5, but more important are the high-intensity silver and barium species detected for the contaminated

Key words: surface contamination, microcircuits, ion microprobe, secondary ion mass spectrometry, ion sputtering, depth profiles, scanning ion micrographs.

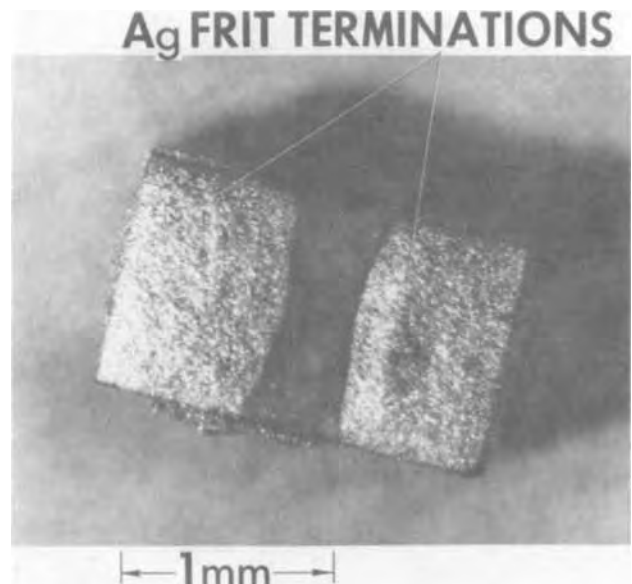


Fig. 1. Barium titanate capacitor

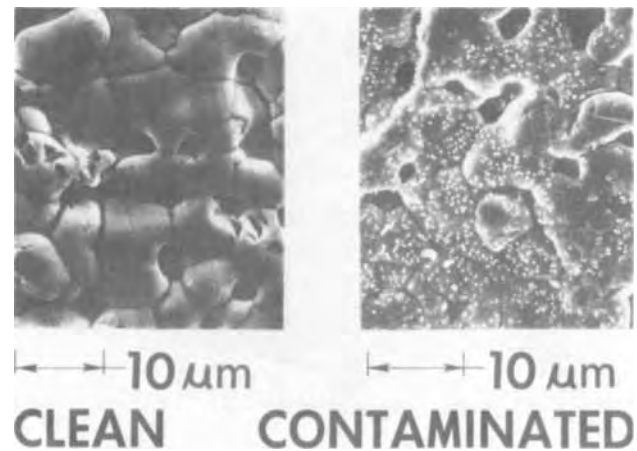


Fig. 2. Scanning electron micrographs of clean and contaminated silver frit areas.

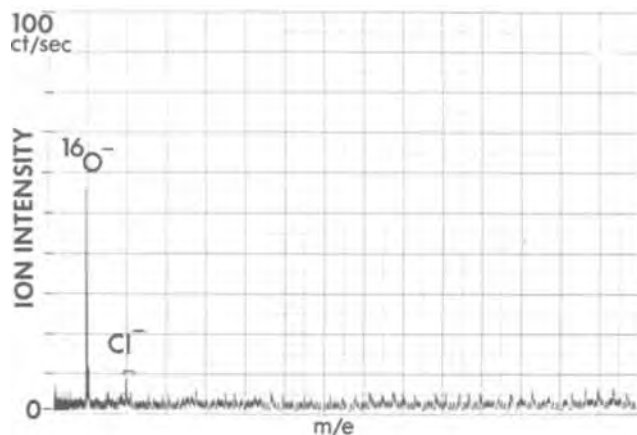


Fig. 3. Sputtered negative ion spectrum, clean capacitor

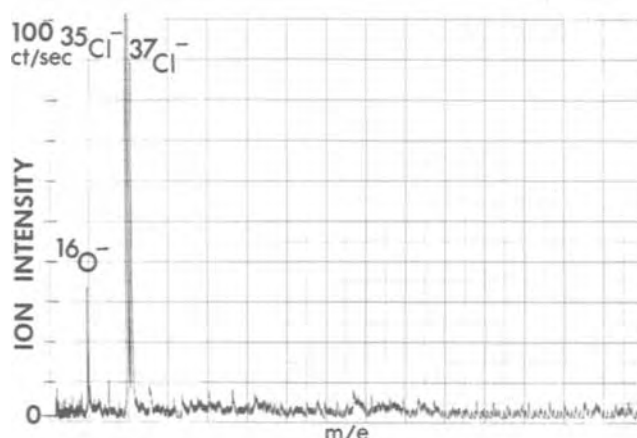


Fig. 4. Sputtered negative ion spectrum, contaminated capacitor

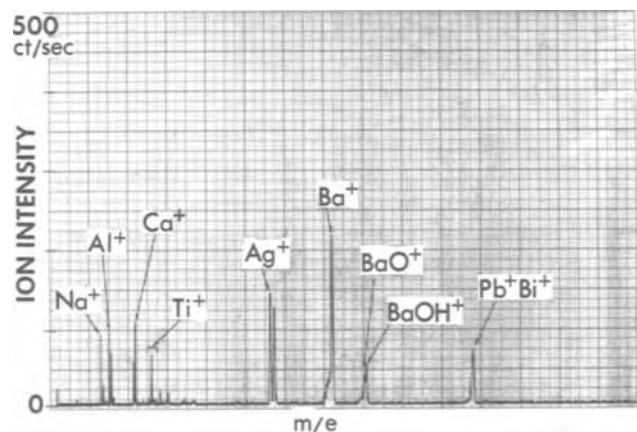


Fig. 5. Sputtered positive ion spectrum, clean capacitor

sample. These species were detected at low intensities ( $\text{Ag}^+$ ) or not at all ( $\text{AgOH}^+$ ,  $\text{AgCl}^+$ ,  $\text{BaCl}^+$ ,  $\text{Ag}_2^+$ ,  $\text{Ag}_2\text{OH}^+$ , and  $\text{Ag}_2\text{Cl}^+$ ) in the spectrum from the clean sample. The  $\text{BaCl}^+$ ,  $\text{AgCl}^+$ , and  $\text{Ag}_2\text{Cl}^+$  present further evidence that the contamination is a result of some reaction between a chlorine-containing substance and the capacitor material as opposed to an added contamination (e.g., barium chloride and silver chloride particulate matter). Because of the greater intensity and number of the silver-related sputtered species compared to the barium-related species, the identification effort was concentrated on silver compounds (actually silver chloride). By using isotopic abundance values for the two silver and the two chlorine isotopes,

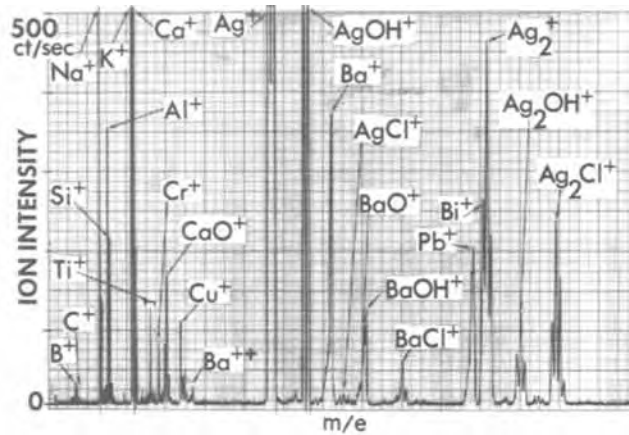
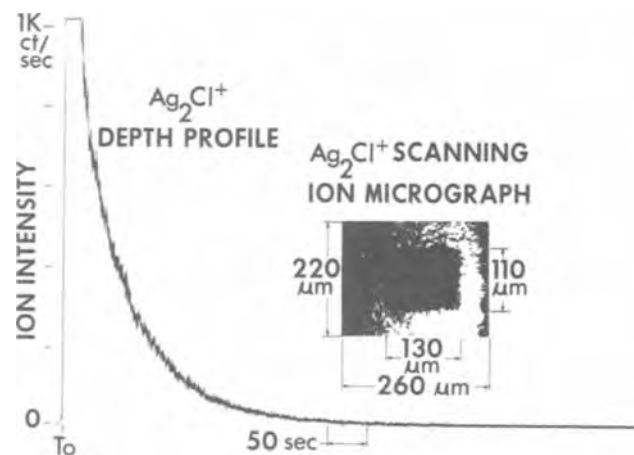


Fig. 6. Sputtered positive ion spectrum, contaminated capacitor

a near perfect match was obtained for the calculated relative intensities of the four possible  $\text{Ag}_2\text{Cl}^+$  species and the four  $\text{Ag}_2\text{Cl}^+$  peaks recorded in Fig. 6. This result implies a correct assignment of  $\text{Ag}_2\text{Cl}^+$  for these peaks.

Figure 7 shows a depth profile and a scanning ion micrograph using the most intense peak (combination of  $^{107}\text{Ag}^{107}\text{Ag}^{37}\text{Cl}^+$  and  $^{107}\text{Ag}^{109}\text{Ag}^{35}\text{Cl}^+$ ) in the  $\text{Ag}_2\text{Cl}^+$  spectrum. The depth profile was obtained by recording the intensity of the selected mass analyzed sputtered ion species as a function of time, thus depth. The scanning ion micrograph (3) was made by using the detected intensity of the selected  $\text{Ag}_2\text{Cl}^+$  sputtered ion species to modulate the intensity of a cathode-ray tube (CRT) whose electron beam was rastered in synchronism with the rastered ion probe sputtering beam, thus producing a two-dimensional distribution map for the sample species responsible for the  $\text{Ag}_2\text{Cl}^+$  sputtered species. The micrograph was made by photographing the CRT screen. The lateral resolution is limited by the size of the sputtered beam, which in this case was  $< 5 \mu\text{m}$  in diameter. The sequence of events for Fig. 7 were as follows: First, after selecting a raster size of  $130 \times 110 \mu\text{m}$ , the depth profile shown was made for about 750 sec in a previously unsputtered area. Second, immediately thereafter the raster size was increased to  $260 \times 220 \mu\text{m}$  and the raster conditions changed from 30 rasters/sec at 500 lines/raster to 1 raster/10 sec at 250 lines/raster (conditions for acceptable micrographs) which then allowed the area sputtered for the depth profile to be compared to the surrounding sample area using the contrast resulting from the intensity of the selected sputtered ion species. As seen in Fig. 7, and as expected, the micrograph shows a signal ( $\text{Ag}_2\text{Cl}^+$  yielding material) de-

Fig. 7.  $\text{Ag}_2\text{Cl}^+$  depth profile and scanning ion micrograph



pletion in the area used to make the depth profile. However, for the sputtering time used for the depth profile (750 sec) and an estimated sputtering rate range of 1-10 Å/sec it is possible that a depth less than the contamination particle size ( $\sim 1-10 \mu\text{m}$ ) was sputtered away. An attempt was made to locate the area of sputtering with a scanning electron microscope (SEM) to determine the degree of particle removal. The sputtered area could not be located, due in part to the original surface roughness and to the lack of contrast in the SEM (less than that provided by the scanning ion micrograph), and also due perhaps to incomplete removal of contamination particles.

Identification of the contaminant as silver chloride was verified by sputter analyzing deposits of AgCl on various substrates. Several substrates were chosen to avoid possible interferences from substrate ion species with the silver species spectra and to observe any unique characteristics. The deposits were prepared by evaporation of  $\sim 0.05$  mliter of a solution of AgCl (5 mg/mliter) in  $\text{NH}_4\text{OH}$ . Figure 8 shows the positive sputtered ion spectrum from AgCl deposited on a Kovar substrate. The same sputtering conditions used for previous mass scans were duplicated. Besides the expected surface contaminant indicators ( $\text{Na}^+$ ,  $\text{Al}^+$ ,  $\text{K}^+$ , and  $\text{Ca}^+$ ) and Kovar components ( $\text{Fe}^+$ ,  $\text{Co}^+$ , and  $\text{Ni}^+$ ) the silver species which were detected on the contaminated capacitor are evident, even though the relative intensities are different. Figure 9 shows the spectrum from AgCl deposited on a gold substrate, which was not clean as evidenced by several calcium sputtered ion species ( $\text{Ca}^+$ ,  $\text{CaO}^+$ ,  $\text{CaOH}^+$ , and  $\text{CaCl}^+$ ). Again the silver species of interest are de-

tected.  $\text{AuOH}^+$  has the same nominal mass as  $^{107}\text{Ag}^{107}\text{Ag}^+$  and thus interferes with the  $\text{Ag}_2^+$  spectrum. Figure 10 shows the spectrum from the AgCl deposited on a molybdenum substrate. Here the AgCl deposit formed in a molybdenum oxide matrix (seen optically) apparently as a result of the solubility of surface  $\text{MoO}_3$  in  $\text{NH}_4\text{OH}$ . The presence of a molybdenum oxide is confirmed by the presence of  $\text{MoO}^+$  in the spectrum. Again the silver species of interest are evident. Note the increased intensities of the  $\text{AgOH}^+$  and  $\text{Ag}_2\text{OH}^+$  species, due in part to the oxide matrix. In each case the  $\text{Ag}_2\text{Cl}^+$  species were more intense than the  $\text{AgCl}^+$  species, which was the same as observed in the spectrum from the contaminated capacitor.

There was a question about the relationship between the oxygen beam used for sputtering and the observed silver- and oxygen-containing sputtered species  $\text{AgOH}^+$  and  $\text{Ag}_2\text{OH}^+$ . That is, was the  $\text{O}_2^+$  sputtering beam "manufacturing" these species? Some evidence was obtained from the spectra taken from a spot of silver paint (Fansteel, Inc. Silpaint, 68% silver, thermosetting) used to mount ion microprobe samples. The spectrum indicated only  $\text{Ag}^+$  ions, even at depths where the oxygen implanted by the sputtering ion beam was encountered at its maximum concentration (5-7). Therefore, the observed species in question ( $\text{AgOH}^+$  and  $\text{Ag}_2\text{OH}^+$ ) must be a result of the silver compounds on the sample or an enhancement (3) due to the matrix as in the previously discussed molybdenum oxide case. Because the material on the calibration samples (and the contaminated capacitors) probably contains other materials besides AgCl, the relationship between the  $\text{AgOH}^+$  and  $\text{Ag}_2\text{OH}^+$  species and a pure AgCl deposit is not known from the experiments made. The use of a  $\text{N}_2^+$  beam for sputtering might have helped clarify the results obtained (8), but the  $\text{N}_2^+$  beam was not conveniently available during the experiments.

Another possible test with the solution of AgCl in  $\text{NH}_4\text{OH}$  was, of course, to use the silver frit area of a clean capacitor as a substrate. Figure 11 shows the spectrum from the AgCl deposited on a clean capacitor. Again the silver species of interest are detected, but again not with exactly the same relative intensities as obtained from the contaminated capacitor. No attempts were made to obtain negative sputtered ion spectra for the AgCl deposits. Table I lists relative intensities of the silver species of interest normalized to the  $\text{Ag}_2\text{Cl}^+$  species. The data in Table I were not taken from the figures used in this paper, but instead were taken from spectra where the peak height maxima were recorded by proper selection of counting rate attenuators.

### Conclusions

Silver chloride was found to be a major contaminant on the silver frit areas of contaminated barium titanate

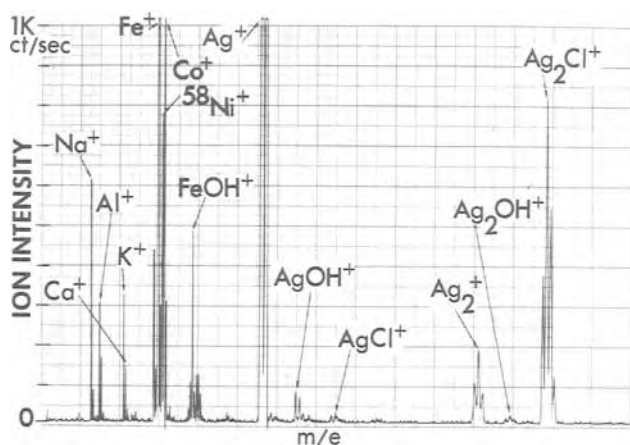


Fig. 8. Sputtered positive ion spectrum of AgCl deposited on Kovar.

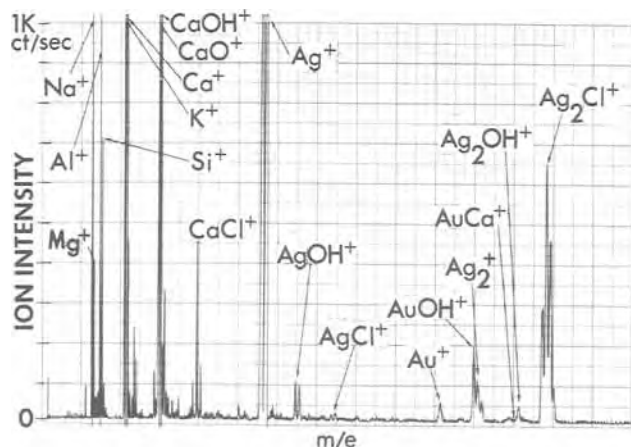


Fig. 9. Sputtered positive ion spectrum of AgCl deposited on gold.

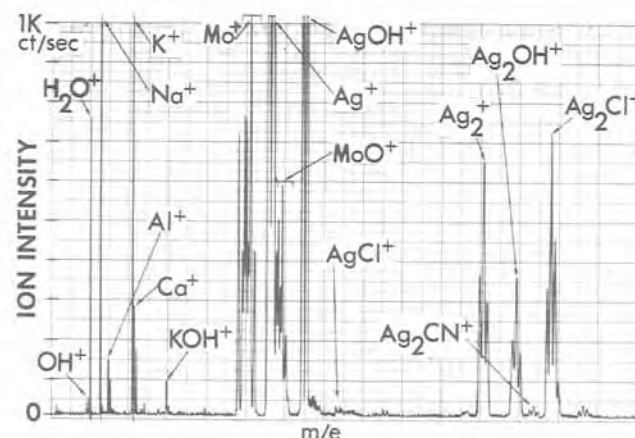


Fig. 10. Sputtered positive ion spectrum of AgCl deposited on molybdenum.



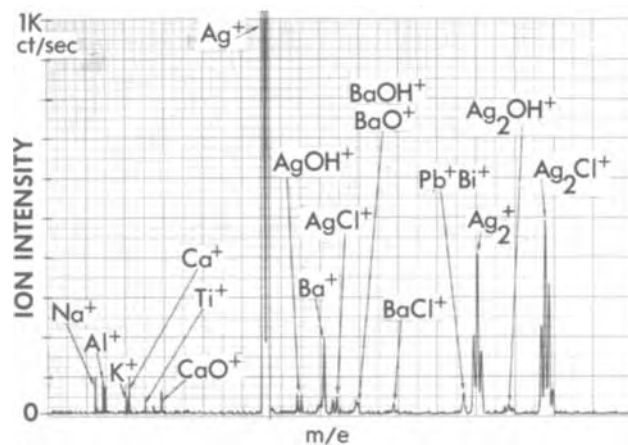


Fig. 11. Sputtered positive ion spectrum of AgCl deposited on a clean capacitor.

capacitors examined with the ion microprobe. Barium chloride was also identified as a contaminant. The  $\text{AgOH}^+$  and  $\text{Ag}_2\text{OH}^+$  species indicate the possible presence of other silver compound contaminants. Comparisons of mass spectra from contaminated capacitors with mass spectra from AgCl deposited on various substrates definitely identified the contaminant as one containing AgCl. It was determined (9) after the ion microprobe analysis that adequate bonding of aluminum wires to the silver frit terminations could be obtained after ultrasonically cleaning the capacitor (with frits) in a 50%  $\text{NH}_4\text{OH}$ -50%  $\text{H}_2\text{O}$  solution followed by an 800°C firing for 30 min in 0.2 Torr of argon. This process removes the contamination particles (SEM) and chlorine (Auger analysis), but the source of the particles or the mechanism of their formation remains a problem.

#### Acknowledgments

The author wishes to thank G. R. Fahrback for his assistance in obtaining the sample spectra with the

Table I. Relative intensities of sputtered positive silver ion species

	AgCl deposited on				
	Kovar	Au	Mo	Clean capacitor	Contaminated capacitor
$\text{Ag}^+$	8	6	9	34	Max of peak not recorded
$\text{AgOH}^+$	0.1	0.2	4	0.1	0.9
$\text{Ag}_2^+$	0.2	0.3	0.5	0.7	1.5
$\text{Ag}_2\text{OH}^+$	0.02	0.02	0.2	0.1	0.7
$\text{Ag}_2\text{Cl}^+$	1.0	1.0	1.0	1.0	1.0

IMMA, B. T. Kenna and R. G. Dosch for their preparation and analysis of the AgCl solution, and C. J. Miglionico for the SEM micrographs of the capacitors. This work was supported by the United States Atomic Energy Commission.

Manuscript submitted March 20, 1974; revised manuscript received July 8, 1974.

Any discussion of this paper will appear in a Discussion Section to be published in the June 1975 JOURNAL. All discussions for the June 1975 Discussion Section should be submitted by Feb. 1, 1975.

The publications costs of this article have been assisted by Sandia Laboratories.

#### REFERENCES

- H. Liebl, *J. Appl. Phys.*, **38**, 5277 (1967).
- T. A. Whatley, C. B. Slack, and E. Davidson, Sixth Internat. Conf. X-Ray Optics and Microanalysis, Osaka, Japan, September 1971.
- J. A. McHugh and J. F. Stevens, *Anal. Chem.*, **44**, 2187 (1972).
- H. W. Werner and H. A. M. DeGrefte, *Surface Sci.*, **35**, 458 (1973).
- F. Schulz, K. Wittmaack, and J. Maul, *Radiation Effects*, **18**, 211 (1973).
- R. K. Lewis, J. M. Morabito, and J. C. C. Tsai, *Appl. Phys. Letters*, **23**, 260 (1973).
- G. Carter, J. N. Baruah, and W. A. Grant, *Radiation Effects*, **16**, 107 (1972).
- J. W. Guthrie, *J. Less Common Metals*, **30**, 317 (1973).
- J. L. Jellison, Sandia Laboratories, Private communication.

## Poly(Styrene Sulfone)—A Sensitive Ion-Millable Positive Electron Beam Resist

M. J. Bowden and L. F. Thompson

Bell Laboratories, Murray Hill, New Jersey 07974

#### ABSTRACT

Poly(styrene sulfone) is a 2:1 copolymer of styrene to sulfur dioxide which degrades under high energy irradiation. It has a sensitivity of  $1 \times 10^{-5}$  coulomb  $\text{cm}^{-2}$  when exposed to 5 kV electrons. The resist is thermally stable to 250°C and is an excellent ion milling mask with a milling rate of 0.5 nm  $\text{sec}^{-1}$ . It also serves as an etching mask for buffered HF. Polystyrene sulfone does not vapor develop.

Following pattern delineation in a polymer resist film, it is necessary to reproduce the developed pattern in an insulating or conducting thin film. This is frequently done by wet-etching processes, e.g., buffered HF to etch  $\text{SiO}_2$ , which result in marked undercutting of the resist with attendant loss in resolution. This problem can be eliminated by ion milling which has the additional advantage of being a dry process. Recently developed techniques for producing fine grat-

ings (spacing  $\sim 200$  nm) demand ion milling procedures in order to realize such high resolution.

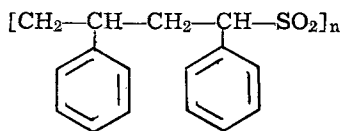
It has been found that positive electron resists, in particular, the poly(olefin sulfones), do not behave as good ion milling masks, i.e., the rate of removal of the polymer film is too high relative to the rate of removal of exposed substrate (1). On the contrary, negative resists do not suffer this limitation. In the case of the poly(olefin sulfones) it is known that chain scission is accompanied by extensive depropagation (2, 3) of the radical chain end; hence when chain scissions are in-

Key words: electron resist, polysulfones, degradation.

duced during bombardment by the high-energy ion beam the rate of removal of the resist film will be greatly enhanced. Materials which tend to depolymerize will therefore not behave as good ion milling masks. This applies to poly(methyl methacrylate) (PMMA) which, apart from the poly(olefin sulfones), is the only significant positive resist. The temperature of the substrate can rise quite significantly during the ion milling process and, at elevated temperature, PMMA depolymerizes readily (4). The rate of ion milling of PMMA was found to be  $1.2 \text{ nm sec}^{-1}$  and therefore a substantial resist thickness is required, e.g.,  $0.5 \mu$  film for  $0.3 \mu$  Au substrate (5), for successful operation. The process also requires effective heat conduction to maintain the substrate below  $100^\circ\text{C}$ .

Unlike the poly(olefin sulfones) which are strictly alternating copolymers of  $\text{SO}_2$  with the respective olefin, poly(styrene sulfone) may be synthesized with compositions ranging from a 1:1 copolymer through to homopolystyrene. Under bulk polymerization conditions in excess  $\text{SO}_2$ , the mole ratio of styrene to  $\text{SO}_2$  is reported to be 2:1 (6).

The structure of this polysulfone has been shown to be (7)



Hence cleavage of the C-S bond will result in a styryl radical with another styrene molecule in the penultimate position. Such a radical should therefore behave as a polystyrene radical and should not tend to depropagate under ion milling conditions, i.e., poly(styrene sulfone) should have a low ion milling rate.

### Experimental

**Preparation.**—Poly(styrene sulfone) (PSS) was prepared by copolymerization of styrene with sulfur dioxide. Thirty milliliters of freshly distilled styrene (Eastman Kodak) and 0.1g azobisisobutyronitrile were mixed together and the solution degassed on a high-vacuum line. Fifty milliliters of sulfur dioxide (Matheson) were condensed in the reaction flask which was then sealed under vacuum. Polymerization was carried out in a constant temperature bath at  $50^\circ\text{C}$  for 48 hr. The polymer was purified by precipitation from dioxane solution (twice) into methanol and dried at  $40^\circ\text{C}$  under vacuum for 48 hr.

Microanalysis yielded the following results corresponding to a 2/1 copolymer of styrene and sulfur dioxide; found: C = 69.7%, H = 6.0%, S = 12.2%; calculated: C = 70.5%, H = 5.9%, S = 11.8%.

The molecular weight determined by dilute solution viscometry was  $2.7 \times 10^5$ . Viscosity parameters are listed elsewhere (8).

**Exposure and development.**—The polymer was dissolved in methoxy ethyl acetate (Kodak photoresist thinner) and films  $\sim 300 \text{ nm}$  thick were spun on  $\text{SiO}_2/\text{Si}$  and  $\text{Au}/\text{Cr}/\text{Si}$  substrates using techniques described previously (3). Prior to exposure the films were baked at  $200^\circ\text{C}$  in vacuo for 30 min.

The films were exposed using a programmed electron beam from a Cambridge Mark II scanning electron microscope equipped with a 1500 line flying-spot scanner.

Sensitivity was determined in the manner previously described (3). The exposed films were developed using a 60% dioxane/40% isopropanol mixture and postbaked at  $200^\circ\text{C}$  for 30 min in vacuo. The substrates were etched in buffered HF.

Ion milling rates were determined by exposing a 300 nm film to the ion beam for different times and measuring the depth of remaining film by first gilding the sample and then measuring the film depth using polarization interferometry. An average rate of  $0.5 \text{ nm sec}^{-1}$  was obtained.

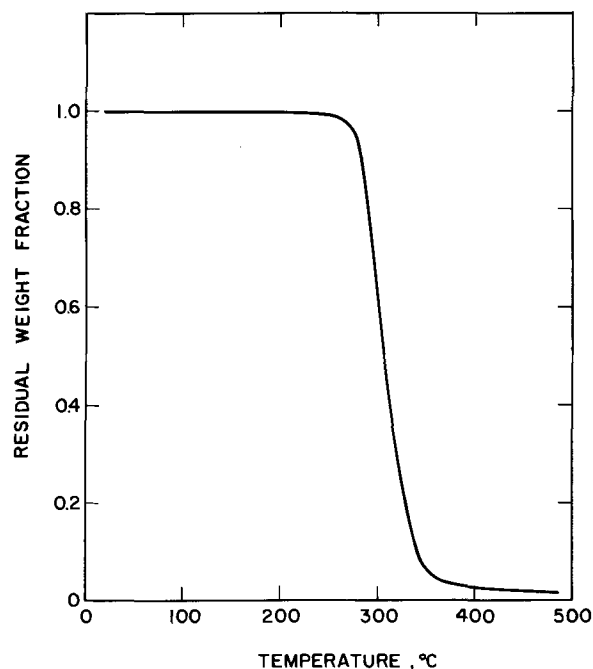


Fig. 1. TGA thermogram of PSS; atmosphere,  $\text{N}_2$ ; heating rate,  $5^\circ\text{C}/\text{min}$ .

### Results and Discussion

**Thermal stability.**—A TGA thermogram of PSS is shown in Fig. 1. The analysis was carried out in  $\text{N}_2$  at  $5^\circ \text{ min}^{-1}$  heating rate. The temperature at which degradation commences is over  $100^\circ\text{C}$  greater than for the corresponding poly(olefin sulfones) which makes the resist suitable in applications where thermal stability is required. An identical thermogram was obtained when the TGA run was conducted in an oxygen atmosphere. The glass transition temperature,  $T_g$ , was determined by DSC and was found to lie in the region  $180^\circ\text{--}200^\circ\text{C}$ . Thus,  $200^\circ\text{C}$  appears to be the best temperature for pre- and postbaking since this is above the  $T_g$  (baking above the  $T_g$  is considered necessary to relieve strain in the film) yet well below the decomposition temperature.

**Sensitivity.**—PSS underwent rapid chain scission when exposed to a beam of high-energy electrons. Molecular weight distributions well removed from the initial distribution could be produced at doses of  $1 \times 10^5 \text{ coulomb cm}^{-2}$ . The resist did not vapor develop, i.e., there was no apparent loss of material during irradiation. This value of sensitivity is an order of magnitude less than that shown by the poly(olefin sulfones) and undoubtedly stems from the presence of the benzene group in the side chain. It is well known that aromatic compounds show relatively high resistance to radiation (9), e.g., homopolystyrene is one of the most radiation resistant of long chain polymers; although it crosslinks, the energy required for crosslinking is nearly 100 times greater than in most linear polymers such as polyethylene. There is evidence to show that this "protective effect" of the benzene ring can extend to neighboring groups in the chain, e.g., Alexander and Charlesby (10) demonstrated that for copolymers of styrene and isobutylene, the extent of degradation which the isobutylene units in the polymer suffer under irradiation is greatly reduced by the presence of neighboring styrene units.

PSS showed development characteristics similar to those of the poly(olefin sulfones), in that gamma (contrast) was extremely sharp. The 60% dioxane/40% isopropanol developing solution did not attack the unexposed parts of the PSS film and the sensitivity of  $1 \times 10^{-5} \text{ coulomb cm}^{-2}$  may be compared with  $5 \times 10^{-5} \text{ coulomb cm}^{-2}$  for PMMA under similar developing conditions. As is well known, the sensitivity of the lat-

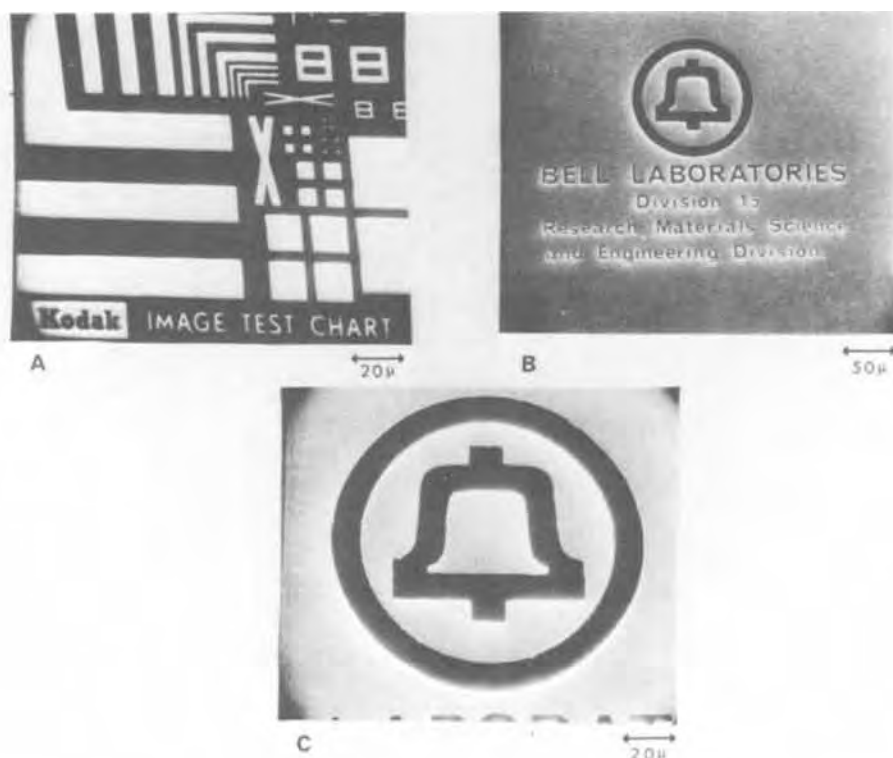


Fig. 2. Test patterns chemically etched in  $\text{SiO}_2$  through PSS mask.

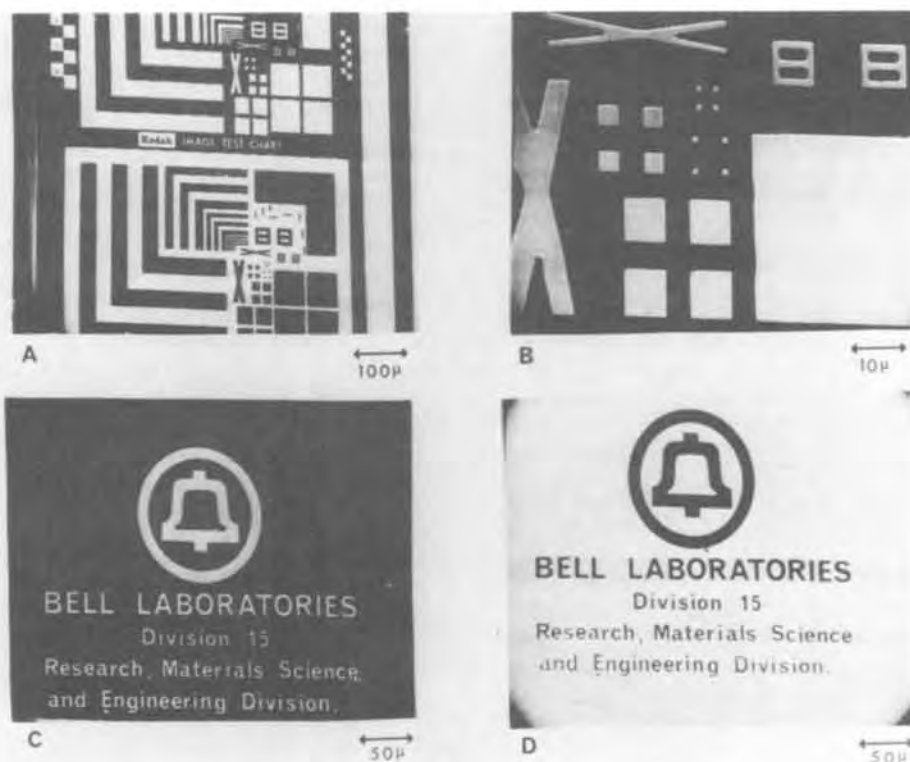


Fig. 3. Test patterns ion milled in Au through PSS mask.

ter may be enhanced by "force-developing" (using developing solutions which also attack the unexposed parts of the film but at a slower rate compared with the exposed areas) (11). Similarly, PSS may be "force-developed" resulting in sensitivities into the  $10^{-6}$  range.

**Wet-etching characteristics.**—PSS was an excellent etching mask against buffered HF (for etching  $\text{SiO}_2$ ). Figure 2 shows some typical patterns written using the flying spot scanner. The patterns are etched in  $\text{SiO}_2$ . These patterns were all written at magnification  $\geq 200$ .

The reason for this is due to the high contrast of this resist which usually resulted in the production of gratings when writing patterns at a magnification less than 200.

**Ion milling characteristics.**—PSS was an excellent ion milling mask. The ion milling rate ( $0.5 \text{ nm sec}^{-1}$ ) is low and may be compared with rates for typical negative resists; e.g., poly(glycidyl methacrylate co ethyl acrylate), a sensitive high contrast negative resist, has an ion milling rate of  $0.4\text{--}0.5 \text{ nm sec}^{-1}$ . Figure 3 shows some test patterns ion milled in Au. It was

found that the resist actually crosslinked during the ion milling process, presumably due to crosslinking of the polystyrene units in the chain. We therefore envisage the initial reaction as one of cleavage of the C-S bonds with the probable release of SO<sub>2</sub>. Since polystyrene crosslinks under ionizing radiation, the residual polystyrene units in the chain will crosslink at high enough dose. Thus even during initial exposure to high-energy electrons, we would predict that PSS would behave as a negative resist given a high enough dose. Undoubtedly the crosslinking reaction which takes place during ion milling serves to reduce the ion milling rate.

As a result of crosslinking, the removal of residual polymer requires the use of an oxidizing ambient similar to that required for negative resists. This was conveniently accomplished using a dichromate-sulfuric acid cleaning solution.

### Conclusions

Poly(styrene sulfone) has been shown to be a sensitive positive resist suitable for ion milling application. It is an order of magnitude less sensitive than the poly(olefin sulfones); this essentially limits the former to specialty applications where speed is not important. It is superior to other ion millable positive resists, notably PMMA, with respect to sensitivity and ion milling rate.

### Acknowledgments

The authors would like to thank E. G. Spencer and P. V. Lenzo for ion milling PSS and PMMA samples.

They also thank M. Y. Hellman for the viscosity measurement on PSS.

Manuscript submitted April 26, 1974; revised manuscript received July 5, 1974.

Any discussion of this paper will appear in a Discussion Section to be published in the June 1975 JOURNAL. All discussions for the June 1975 Discussion Section should be submitted by Feb. 1, 1975.

The publication costs of this article have been assisted by Bell Laboratories.

### REFERENCES

1. E. G. Spencer and P. V. Lenzo, Private communication.
2. J. R. Brown and J. H. O'Donnell, *Macromolecules*, **5**, 109 (1971).
3. M. J. Bowden and L. F. Thompson, *J. Appl. Polymer Sci.*, **17**, 3211 (1973).
4. N. Grassie and H. W. Melville, *Proc. Roy. Soc., Ser. A*, **199**, 1 (1949).
5. R. B. Radaker, Private communication.
6. M. Matsuda, M. Fino, T. Hirayama, and T. Miyashita, *Macromolecules*, **5**, 240 (1972).
7. W. G. Barb, *Proc. Roy. Soc.*, **A212**, 66 (1952).
8. R. Endo, T. Manago, and M. Takeda, *Bull. Chem. Soc. Japan*, **39**, 733 (1966).
9. A. Charlesby, "Atomic Radiation and Polymers," p. 295, Pergamon, Oxford (1960).
10. P. Alexander and A. Charlesby, *Proc. Roy. Soc.*, **A230**, 136 (1955).
11. M. Hatzakis, Am. Chem. Soc., Division Org. Coatings and Plastics, Chem. preprints, **33** (1), 358 (1973).

## A Survey of a Group of Phosphors, Based on Hexagonal Aluminate and Gallate Host Lattices

J. M. P. J. Verstegen

N. V. Philips' Gloeilampenfabrieken, Light Division, Eindhoven, The Netherlands

### ABSTRACT

A group of photoluminescent materials, which may have great influence on future fluorescent lamp development, is surveyed. The materials are based on hexagonal aluminates and gallates which are structurally related to the magnetoplumbites and  $\beta$ -alumina. When activated with Mn<sup>2+</sup>, Eu<sup>2+</sup>, Tl<sup>+</sup>, Ce<sup>3+</sup>, and Tb<sup>3+</sup>, or combinations of these ions, they are phosphors, some of them having a high efficiency and good temperature dependence.

### Crystallography of the Host Lattices

The cubic spinel MgAl<sub>2</sub>O<sub>4</sub> has a gallate and a ferrite counterpart: MgGa<sub>2</sub>O<sub>4</sub> and MgFe<sub>2</sub>O<sub>4</sub>. Structurally related are the mineral magnetoplumbite, PbFe<sub>12</sub>O<sub>19</sub>, and the ferrite, BaFe<sub>12</sub>O<sub>19</sub>, both hexagonal with the space group P6<sub>3</sub>/mmc. They consist of spinel-like blocks, separated by intermediate layers of deviating structure, containing the large cation. The spinel-like blocks in the magnetoplumbites offer, apart from the tetrahedral and octahedral sites, also pentahedral sites to the Fe<sup>3+</sup> ion. The aluminate counterparts of magnetoplumbite are BaAl<sub>12</sub>O<sub>19</sub>, SrAl<sub>12</sub>O<sub>19</sub>, and CaAl<sub>12</sub>O<sub>19</sub>. The intermediate layer may also contain large trivalent cations. We reported LaMgAl<sub>11</sub>O<sub>19</sub> and CeMgAl<sub>11</sub>O<sub>19</sub> to be isomorphous with SrAl<sub>12</sub>O<sub>19</sub> (1) and recently described a number of isostructural gallates, such as LaMgGa<sub>11</sub>O<sub>19</sub> and SrGa<sub>12</sub>O<sub>19</sub> (2). The same analogy between aluminates and gallates as in magnetoplumbites was found in the closely related  $\beta$ -alumina struc-

ture. Lattice parameters of a number of new gallates are summarized in Table I.

A large number of hexagonal ferrites has been described in the literature (3-5). Their structures are magnetoplumbite-like, but they differ in the arrangement of spinel blocks and intermediate layers. Their lattice parameter *a*, 5.8Å, is basically that of magneto-

Table I. Lattice parameters and probable space groups of various new gallates

Lattice	<i>a</i> (Å)	<i>c</i> (Å)	<i>a/c</i>	Probable space group
SrGa <sub>12</sub> O <sub>19</sub> *	5.796 ± 0.004	22.84 ± 0.02	0.2538	P6 <sub>3</sub> /mmc
BaGa <sub>12</sub> O <sub>19</sub> *	5.850 ± 0.005	23.77 ± 0.02	0.2461	P6 <sub>3</sub> /mmc (?)
LaMgGa <sub>11</sub> O <sub>19</sub> *	5.799 ± 0.003	22.71 ± 0.01	0.2553	P6 <sub>3</sub> /mmc
KGa <sub>11</sub> O <sub>17</sub> **	5.863 ± 0.306	23.57 ± 0.03	0.2487	P6 <sub>3</sub> /mmc
RbGa <sub>11</sub> O <sub>17</sub> **	5.817 ± 0.009	23.60 ± 0.03	0.2465	P6 <sub>3</sub> /mmc

\* Magnetoplumbite.  
\*\*  $\beta$ -alumina.

Key words: new lamp phosphors, aluminate and gallate host lattices, hexagonal aluminates, rare earth-activated aluminates.

plumbite, but their *c* parameter (22–23 Å in magnetoplumbite) may reach values up to 1600 Å (6). Some of the simpler compounds are designated by letters: W = BaFe<sub>2</sub><sup>II</sup>Fe<sub>16</sub><sup>III</sup>O<sub>27</sub>, Y = Ba<sub>2</sub>Fe<sub>2</sub><sup>II</sup>Fe<sub>12</sub><sup>III</sup>O<sub>22</sub>, X = Ba<sub>2</sub>Fe<sub>2</sub><sup>II</sup>Fe<sub>28</sub><sup>III</sup>O<sub>46</sub>, and Z = Ba<sub>3</sub>Fe<sub>2</sub><sup>II</sup>Fe<sub>24</sub><sup>III</sup>O<sub>41</sub> (3). The existence of Al and Ga analogues of BaFe<sub>12</sub>O<sub>19</sub>, suggested that also W, Y, X, and Z each had gallate and aluminate counterparts. So we tried to prepare the compounds W, Y, X, and Z, using MgO instead of FeO and Al<sub>2</sub>O<sub>3</sub> or Ga<sub>2</sub>O<sub>3</sub> instead of Fe<sub>2</sub>O<sub>3</sub>. X-ray diffraction showed that the phases obtained were hexagonal. No indications were found for the presence of phases analogous to the corresponding hexagonal ferrites. Apparently large quantities of MgAl<sub>2</sub>O<sub>4</sub> can be taken up by the magnetoplumbite. As is shown below, the introduction of Mg<sup>2+</sup> ions strongly influences the Eu<sup>2+</sup> luminescence.

### Experimental

A number of experimental techniques was developed to synthesize the phosphors. In many of them F<sup>-</sup> was used to decrease the reaction temperature and to stimulate grain growth.

A phosphor of the composition (Ba<sub>0.86</sub>Eu<sub>0.14</sub>)-Mg<sub>2</sub>Al<sub>16</sub>O<sub>27</sub> was obtained by firing an intimate mixture of BaCO<sub>3</sub>, Eu<sub>2</sub>O<sub>3</sub>, MgF<sub>2</sub>, and Al<sub>2</sub>O<sub>3</sub> first 2 hr at 1200°C in a stream of N<sub>2</sub> with 2% H<sub>2</sub> and afterward several times at 1200°C in a stream of N<sub>2</sub>, H<sub>2</sub>, and H<sub>2</sub>O, in order to remove the fluoride. Only part of the magnesium may be added as a fluoride and also AlF<sub>3</sub> may be used, depending on the grain size required.

Ce<sub>0.67</sub>Tb<sub>0.33</sub>MgAl<sub>11</sub>O<sub>19</sub> can be prepared by various methods: CeO<sub>2</sub>, Tb<sub>4</sub>O<sub>7</sub>, MgO, and Al<sub>2</sub>O<sub>3</sub> are ball-milled together in water for 4–6 hr. The wet oxide mixture is dried, fired twice for 1 hr at a temperature between 1550° and 1650°C in air, and cooled down in N<sub>2</sub>. Lower firing temperatures are possible when, at the same time, the number of firings is increased. Another method is based on precipitation of the hydroxides. After drying and prefiring at 700°C two firings at 1500°–1550°C are sufficient.

(Sr<sub>0.95</sub>Ce<sub>0.05</sub>)(Mg<sub>0.05</sub>Al<sub>11.95</sub>)O<sub>19</sub> can be fired in air at 1500°C and cooled down in N<sub>2</sub>, but a firing in slightly reducing atmosphere proved superior.

Sr(Ga<sub>11.997</sub>Mn<sub>0.003</sub>)O<sub>18.9985</sub> is fired twice for 2 hr at 1400°C in air and afterward in N<sub>2</sub>/H<sub>2</sub> mixtures at 1200°C. The phosphor quality is highly sensitive toward the oxygen pressure during the last firing.

K(Ga<sub>10.995</sub>Mn<sub>0.005</sub>)O<sub>16.9975</sub> is prepared in the same way, except that an excess of 100% K<sub>2</sub>CO<sub>3</sub> is applied for better reaction. The excess is washed out afterward.

(K<sub>0.9</sub>Tl<sub>0.1</sub>)Al<sub>11</sub>O<sub>17</sub> is prepared as follows: the unactivated KAl<sub>11</sub>O<sub>17</sub> is prepared with an excess K<sub>2</sub>CO<sub>3</sub>, which is washed out. The fired product is brought into contact with a melt of TlNO<sub>3</sub> and KNO<sub>3</sub>. In the melt exchange of K<sup>+</sup> for Tl<sup>+</sup> takes place. The final Tl<sup>+</sup> concentration in the phosphor can be regulated by the Tl<sup>+</sup>/K<sup>+</sup> ratio in the melt.

### Luminescence

**Mn<sup>2+</sup>-activated gallates.**—The spinel MgGa<sub>2</sub>O<sub>4</sub>:Mn<sup>2+</sup> is an efficient green emitting phosphor under ultraviolet excitation (7). The magnetoplumbite, as well as the β-alumina structure, contains spinel-like blocks, so incorporation of Mn<sup>2+</sup> therein might produce similar emission. We already reported efficient green emission of Mn<sup>2+</sup> in SrGa<sub>12</sub>O<sub>19</sub> and LaMgGa<sub>11</sub>O<sub>19</sub> (2). The luminescence of Mn<sup>2+</sup> in KGa<sub>11</sub>O<sub>17</sub> and in the higher hexagonal gallates is about as efficient as that in MgGa<sub>2</sub>O<sub>4</sub> and SrGa<sub>12</sub>O<sub>19</sub>. The spectral energy distribution of the Mn<sup>2+</sup> emission in MgGa<sub>2</sub>O<sub>4</sub>, SrGa<sub>12</sub>O<sub>19</sub>, and KGa<sub>11</sub>O<sub>17</sub> is shown in Fig. 1.

In Ref. [2] we presented evidence that Mn<sup>2+</sup> occupies a tetrahedral site. In addition we showed that efficient energy transfer from the lattice to the Mn<sup>2+</sup> ion takes place. Indeed, there is good overlap of the host lattice emission band and the Mn<sup>2+</sup> excitation lines. However, the nature of the luminescent center

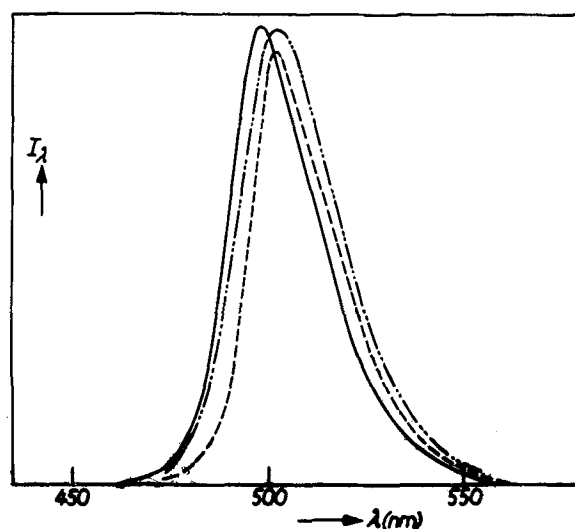


Fig. 1. Spectral energy distribution of KGa<sub>11</sub>O<sub>17</sub> (solid curve), SrGa<sub>12</sub>O<sub>19</sub> (dashed curve), and MgGa<sub>2</sub>O<sub>4</sub> (-.-.- curve) activated with Mn<sup>2+</sup>.  $I_{\lambda}$  gives the radiant power per constant wavelength interval in arbitrary units. Excitation with 254 nm radiation.

in the gallate host lattices is not known (2). Obviously the energy transfer takes place in the spinel block. The low Mn<sup>2+</sup> concentration (0.3%) required for quenching the host lattice emission, indicates that the transfer process is very efficient. It is surprising that the quantum efficiency of the Mn<sup>2+</sup> emission in BaGa<sub>12</sub>O<sub>19</sub> is so much lower than that of the Mn<sup>2+</sup> emission in SrGa<sub>12</sub>O<sub>19</sub> and LaMgGa<sub>11</sub>O<sub>19</sub> (Table II). At the moment we are unable to offer an explanation. Probably there is a connection with the crystallographic differences between BaGa<sub>12</sub>O<sub>19</sub> and BaAl<sub>12</sub>O<sub>19</sub> on the one hand and SrGa<sub>12</sub>O<sub>19</sub> and SrAl<sub>12</sub>O<sub>19</sub> on the other hand (8).

**Eu<sup>2+</sup>-activated aluminates.**—Blasse and Brill described efficient luminescence of Eu<sup>2+</sup> in BaAl<sub>12</sub>O<sub>19</sub> and SrAl<sub>12</sub>O<sub>19</sub> (9). We extended their work to more complicated aluminate compositions and found a shift of the emission toward longer wavelengths and an increase in the quantum efficiency upon addition of Mg<sup>2+</sup> or Zn<sup>2+</sup>.

The hexagonal aluminates with the composition W, Y, X, and Z (with Mg and Zn replacing Fe<sup>II</sup> and Al replacing Fe<sup>III</sup> and the large cation is either Ba or Sr) luminesce efficiently in the blue or the green, when activated with Eu<sup>2+</sup>. For further optimization we rather arbitrarily selected a phosphor of the composition (Ba,Eu)Mg<sub>2</sub>Al<sub>16</sub>O<sub>27</sub>, analogous to the W-ferrite, and a second one, (Sr<sub>5</sub>Eu<sub>0.5</sub>)Mg<sub>6</sub>Al<sub>35</sub>O<sub>94</sub>. The x-ray diagram of (Ba,Eu)Mg<sub>2</sub>Al<sub>16</sub>O<sub>27</sub> showed reflections of α-Al<sub>2</sub>O<sub>3</sub> and MgAl<sub>2</sub>O<sub>4</sub> with intensities depending on

Table II. Data on luminescent materials, based on hexagonal aluminate and gallate host lattices

Phosphor composition	$\lambda_{\max}$ of the emission (nm)	q.e. (%)
SrGa <sub>11.997</sub> Mn <sub>0.003</sub> O <sub>18.9985</sub>	500	65
LaMg <sub>0.995</sub> Mn <sub>0.005</sub> Ga <sub>11</sub> O <sub>19</sub>	505	55
BaGa <sub>11.995</sub> Mn <sub>0.005</sub> O <sub>19.9975</sub>	505	15
KGa <sub>10.995</sub> Mn <sub>0.005</sub> O <sub>16.9975</sub>	500	70
RbGa <sub>10.995</sub> Mn <sub>0.005</sub> O <sub>16.9975</sub>	500	65
(Ba <sub>0.86</sub> Eu <sub>0.14</sub> )Mg <sub>2</sub> Al <sub>16</sub> O <sub>27</sub>	450	100
(Sr <sub>5</sub> Eu <sub>0.5</sub> )Mg <sub>6</sub> Al <sub>35</sub> O <sub>94</sub>	465	100
(Ba <sub>0.86</sub> Eu <sub>0.14</sub> )(Mg <sub>2-y</sub> Mn <sub>y</sub> )Al <sub>16</sub> O <sub>27</sub>	450, 515	80–100*
K <sub>0.9</sub> Tl <sub>0.1</sub> Al <sub>11</sub> O <sub>17</sub>	385	60
Rb <sub>0.9</sub> Tl <sub>0.1</sub> Al <sub>11</sub> O <sub>17</sub>	385	60
(Na <sub>0.4</sub> Ba <sub>0.3</sub> Tl <sub>0.1</sub> )(Al <sub>10.7</sub> Mn <sub>0.3</sub> )O <sub>17</sub>	510	60
(Sr <sub>0.95</sub> Ce <sub>0.05</sub> )(Mg <sub>0.05</sub> Al <sub>11.95</sub> )O <sub>19</sub>	305	70
(La <sub>0.9</sub> Ce <sub>0.1</sub> )MgAl <sub>11</sub> O <sub>19</sub>	330	70
CeMgAl <sub>11</sub> O <sub>19</sub>	370	65
(Ce <sub>0.67</sub> Tb <sub>0.33</sub> )MgAl <sub>11</sub> O <sub>19</sub>	545	80

\* Depending on the amount of Mn<sup>2+</sup> present.

the flux used. No analysis has been done to check the amounts of the optically inert phases. The x-ray diagrams can best be indexed on a hexagonal cell with  $a = 5.619 \pm 0.005 \text{ \AA}$  and  $c = 22.06 \pm 0.03 \text{ \AA}$ . The x-ray diagram of  $(\text{Sr}_5\text{Eu}_{0.5})\text{Mg}_6\text{Al}_{55}\text{O}_{94}$  may contain reflections of  $\text{SrAl}_2\text{O}_4$ . The presence of that phase leads to a slight broadening of the emission band toward the green. For the magnetoplumbite phase the lattice parameters of  $a = 5.616 \pm 0.009 \text{ \AA}$  and  $c = 22.38 \pm 0.07 \text{ \AA}$  were calculated.  $(\text{Ba},\text{Eu})\text{Mg}_2\text{Al}_{16}\text{O}_{27}$  emits at 450 nm with a quantum efficiency under 254 nm excitation of approximately 100%.  $(\text{Sr},\text{Eu})_{5.5}\text{Mg}_6\text{Al}_{55}\text{O}_{94}$  emits at 465 nm with the same quantum efficiency. Figure 2 shows the emission spectra of  $(\text{Ba}_{0.86}\text{Eu}_{0.14})\text{Mg}_2\text{Al}_{16}\text{O}_{27}$  and  $(\text{Sr}_5\text{Eu}_{0.5})\text{Mg}_6\text{Al}_{55}\text{O}_{94}$  together with their excitation and diffuse reflection spectra. Both phosphors can be applied in an 80 lumens/W "deluxe" fluorescent lamp, to be discussed in a separate paper (10).

*Eu<sup>2+</sup>-sensitized Mn<sup>2+</sup> emission in magnetoplumbite-like aluminates.*—Kröger (11) described cathodoluminescence of  $\text{Mn}^{2+}$  in  $\text{MgAl}_2\text{O}_4$  and  $\text{SrAl}_2\text{O}_4$ . The emission is green and of the same type as that in the corresponding gallates, except for a small shift toward longer wavelengths. Obviously  $\text{Mn}^{2+}$  is incorporated on a tetrahedral site in the spinel lattice and a similar site in the spinel block of  $\text{SrAl}_2\text{O}_4$ . A comparison of the excitation lines of  $\text{Mn}^{2+}$  in the hexagonal aluminates, such as  $\text{BaMg}_2\text{Al}_{16}\text{O}_{27}$ , with those of  $\text{Mn}^{2+}$  in the gallates, supports this (Fig. 3). We found that photoluminescence of  $\text{Mn}^{2+}$  in the aluminates can be sensitized by  $\text{Eu}^{2+}$  ions. This sensitization is rather inefficient in  $\text{BaAl}_{12}\text{O}_{19}:\text{Eu},\text{Mn}$ , moderately efficient in

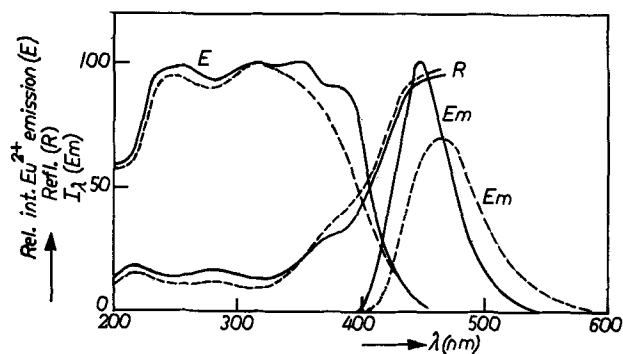


Fig. 2. Spectral energy distribution ( $E_m$ ), relative excitation spectra ( $E$ ), and diffuse reflection spectra ( $R$ ) of  $\text{BaMg}_2\text{Al}_{16}\text{O}_{27}$  (solid curves) and  $\text{Sr}_{5.5}\text{Mg}_6\text{Al}_{55}\text{O}_{94}$  (dashed curves) activated with  $\text{Eu}^{2+}$ .  $I_\lambda$  gives the radiant power per constant wavelength interval in arbitrary units. Excitation with 254 nm radiation.

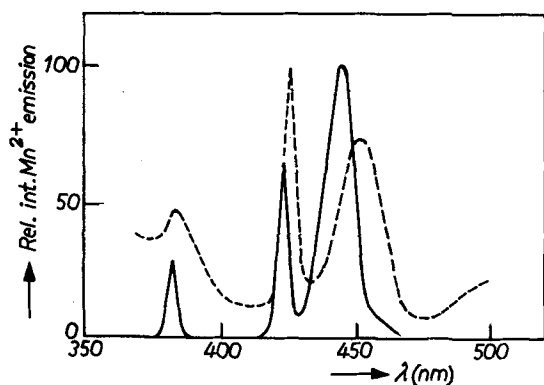


Fig. 3. Relative excitation spectra of  $\text{Mn}^{2+}$  emission in  $\text{BaMg}_2\text{Al}_{16}\text{O}_{27}:\text{Mn}^{2+}$  (dashed curve) and  $\text{SrGa}_{12}\text{O}_{19}:\text{Mn}^{2+}$  (solid curve).

$\text{Sr}_{5.5}\text{Mg}_6\text{Al}_{55}\text{O}_{94}:\text{Eu},\text{Mn}$ , but very efficient in  $\text{BaMg}_2\text{Al}_{16}\text{O}_{27}:\text{Eu},\text{Mn}$ . The  $\text{Mn}^{2+}$  emission is essentially that in  $\text{MgAl}_2\text{O}_4$  and  $\text{SrAl}_2\text{O}_4$  under excitation with cathode rays. A detailed analysis of the  $\text{Eu}^{2+} \rightarrow \text{Mn}^{2+}$  energy transfer is impossible, due to uncertainty of the precise structure of the aluminates. The amount of  $\text{Mn}^{2+}$  required to quench the  $\text{Eu}^{2+}$  emission is approximately 100 times as high as in the gallates, indicating a different energy transfer process. Since the shortest possible distance between  $\text{Eu}^{2+}$  in the intermediate layer and  $\text{Mn}^{2+}$  on a tetrahedral site is of the order of 6 Å, a dipole-multipole energy transfer seems the most likely process. The interaction takes place between the intermediate layer and the spinel block.

Figure 4 shows the emission spectrum of  $\text{BaMg}_2\text{Al}_{16}\text{O}_{27}:\text{Eu},\text{Mn}$  for various  $\text{Eu}^{2+}/\text{Mn}^{2+}$  ratios. A phosphor of the composition  $(\text{Ba}_{0.85}\text{Eu}_{0.15})(\text{Mg}_{1.4}\text{Mn}_{0.6})\text{Al}_{16}\text{O}_{27}$  emits mainly in the green.

*Tl<sup>+</sup> and Tl<sup>+</sup>,Mn<sup>2+</sup> activation of  $\text{KAl}_{11}\text{O}_{17}$  and  $\text{RbAl}_{11}\text{O}_{17}$ .*— $\text{KAl}_{11}\text{O}_{17}$  and  $\text{RbAl}_{11}\text{O}_{17}$  are excellent host lattices for  $\text{Tl}^+$  emission.  $\text{Tl}^+$  replaces  $\text{K}^+$  and  $\text{Rb}^+$  in the intermediate layer and emits in the long wavelength ultraviolet with a quantum efficiency approximately 60%. The emission overlaps reasonably well the  $\text{Mn}^{2+}$  excitation lines in  $\beta$ -alumina, which have the same shape as in magnetoplumbite. There is efficient energy transfer from  $\text{Tl}^+$  to  $\text{Mn}^{2+}$  (12). The energy transfer is from the intermediate layer to a tetrahedrally surrounded  $\text{Mn}^{2+}$  in the spinel-block. Introduction of  $\text{Mn}^{2+}$  instead of  $\text{Al}^{3+}$  is compensated for by replacement of  $\text{K}^+$  by  $\text{Ba}^{2+}$ . X-ray data show that the  $\beta$ -alumina structure during this operation is retained. In  $\beta$ -alumina the minimum distance between sensitizer and activator ion is as short as  $\sim 2.5 \text{ \AA}$ .

Figure 5 shows the ultraviolet emission of  $\text{KAl}_{11}\text{O}_{17}$  and  $\text{RbAl}_{11}\text{O}_{17}:\text{Tl}^+$  and the green emission of a phosphor of the composition  $(\text{Na}_{0.6}\text{Ba}_{0.3}\text{Tl}_{0.1})(\text{Mn}_{0.3}\text{Al}_{10.7})\text{O}_{17}$ , together with the excitation and diffuse reflection spectrum of the latter.

*Ce<sup>3+</sup>-activated magnetoplumbites (1).*—Not only  $\text{Eu}^{2+}$  but also  $\text{Ce}^{3+}$  activation turns the magnetoplumbite into efficient phosphors.  $\text{SrAl}_{12}\text{O}_{19}:\text{Ce}^{3+}$  and  $\text{CaAl}_{12}\text{O}_{19}:\text{Ce}^{3+}$  are more efficient phosphors than  $\text{BaAl}_{12}\text{O}_{19}:\text{Ce}^{3+}$ . The best phosphors are obtained by double substitution  $\text{Sr}^{2+} \rightarrow \text{Ce}^{3+}$ ;  $\text{Al}^{3+} \rightarrow \text{Mg}^{2+}$ .

Figure 6 shows the emission spectrum of  $(\text{Sr}_{0.95}\text{Ce}_{0.05})\text{Mg}_{0.95}\text{Al}_{11.95}\text{O}_{19}$  together with the excitation and diffuse reflection spectrum. A similar phosphor is  $\text{LaMgAl}_{11}\text{O}_{19}:\text{Ce}^{3+}$  with an emission occurring at longer wavelengths. Complete substitution of La by

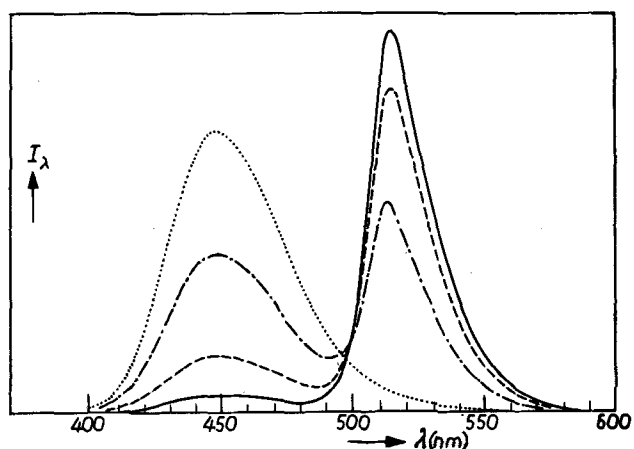


Fig. 4. Spectral energy distribution of  $\text{BaMg}_2\text{Al}_{16}\text{O}_{27}$ , activated with  $\text{Eu}^{2+}$  and  $\text{Mn}^{2+}$  in various quantities: 0.1  $\text{Eu}^{2+}$  (dotted curve); 0.1  $\text{Eu}^{2+}$ , 0.1  $\text{Mn}^{2+}$  (— curve); 0.1  $\text{Eu}^{2+}$ , 0.23  $\text{Mn}^{2+}$  (dashed curve); 0.2  $\text{Eu}^{2+}$ , 0.6  $\text{Mn}^{2+}$  (solid curve).  $I_\lambda$  gives the radiant power per constant wavelength interval in arbitrary units. Excitation with 254 nm radiation.

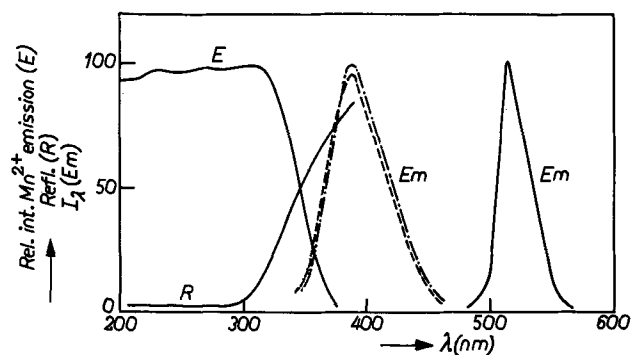


Fig. 5. Spectral energy distribution (Em) of the  $Tl^+$  emission in  $KAl_{11}O_{17}$  (dashed curve) and  $RbAl_{11}O_{17}$  (-.- curve). Spectral energy distribution (Em), relative excitation spectrum (E), and diffuse reflection spectrum (R) of the  $Mn^{2+}$  emission in  $(Na_{0.6}Ba_{0.3}Tl_{0.1})(Al_{10.7}Mn_{0.3})O_{17}$  (solid curves).  $I_\lambda$  gives the radiant power per constant wavelength interval in arbitrary units. Excitation with 254 nm radiation.

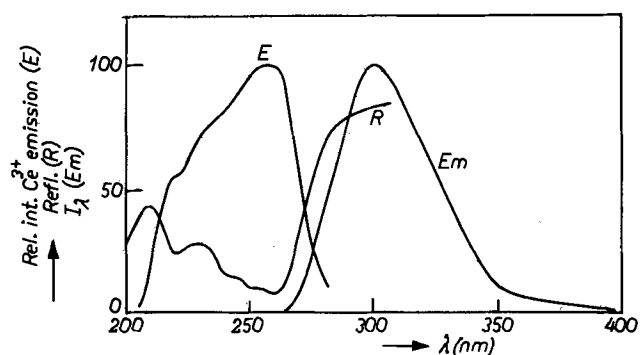


Fig. 6. Spectral energy distribution (Em), relative excitation spectrum (E), and diffuse reflection spectrum (R) of  $Sr_{0.95}Ce_{0.05}Mg_{0.05}Al_{11.95}O_{19}$ .  $I_\lambda$  gives the radiant power per constant wavelength interval in arbitrary units. Excitation with 254 nm radiation.

Fig. 7. Relative excitation spectrum (E) and diffuse reflection spectrum (R) of  $(Ce_{0.67}Tb_{0.33})MgAl_{11}O_{19}$ . Inserted are the excitation spectrum for direct excitation in the  $Tb^{3+}$  ion, 20 times amplified (Ex20) and the  $Ce^{3+}$  emission in  $CeMgAl_{11}O_{19}$  (Em).

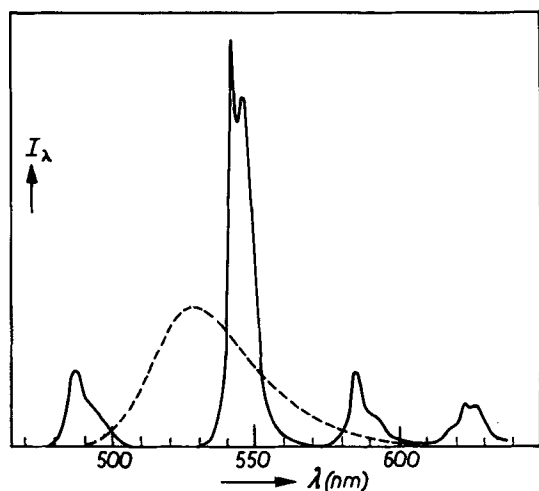
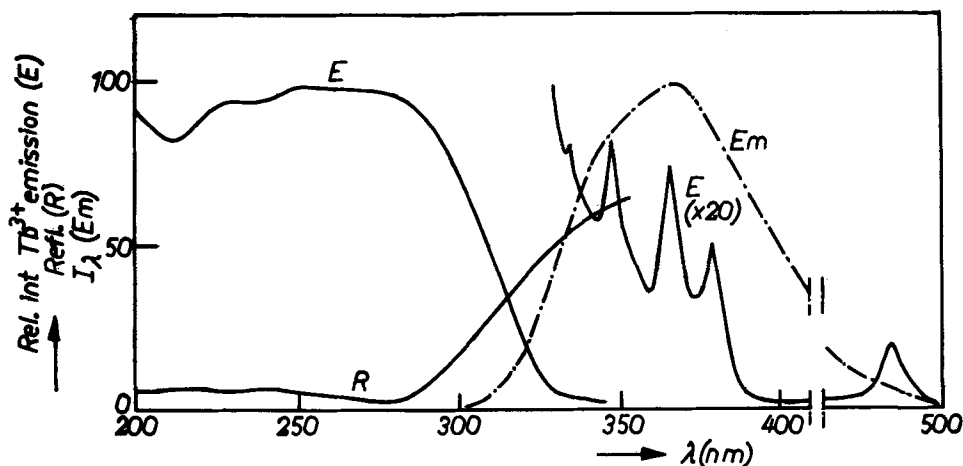


Fig. 8. Spectral energy distribution of  $(Ce_{0.67}Tb_{0.33})MgAl_{11}O_{19}$  (solid curve) compared to that of NBS green zinc silicate (dashed curve).  $I_\lambda$  gives the radiant power per constant wavelength interval in arbitrary units. Excitation with 254 nm radiation.

Ce leads to a new compound,  $CeMgAl_{11}O_{19}$ , with  $a = 5.605\text{\AA}$  and  $c = 21.97\text{\AA}$ , as described previously (1). The phosphor emits at 370 nm with a relatively high efficiency, indicating that  $Ce^{3+} \rightarrow Ce^{3+}$  transfer is unimportant. A possible explanation for this phenomenon is found in the relatively long  $Ce^{3+}-Ce^{3+}$

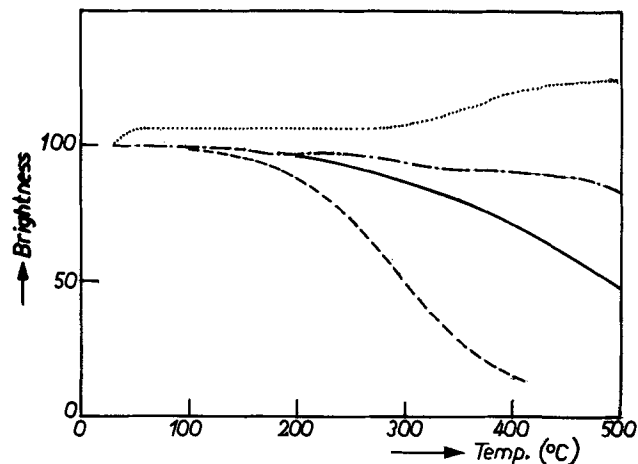


Fig. 9. Brightness vs. temperature in  $^{\circ}C$  for  $(Ba_{0.8}Eu_{0.2})(Mg_{1.6}Mn_{0.4})Al_{18}O_{27}$  (solid curve),  $(Sr_{0.95}Ce_{0.05})(Mg_{0.05}Al_{11.95})O_{19}$  (dotted curve),  $(Ce_{0.67}Tb_{0.33})MgAl_{11}O_{19}$  (-.- curve), and  $(Sr_5Eu_{0.5})Mg_6Al_{55}O_{94}$  (dashed curve).

distance (5.6Å) and the poor overlap of the  $Ce^{3+}$  excitation and emission bands (Fig. 7) (1).  $(Sr_{0.95}Ce_{0.05})(Mg_{0.05}Al_{11.95})O_{19}$  is an excellent erythral phosphor with a quantum efficiency of approximately 70%.

*Tb<sup>3+</sup> activation of  $CeMgAl_{11}O_{19}$  (1).*—Upon activation with  $Tb^{3+}$ ,  $CeMgAl_{11}O_{19}$  turns into a green phosphor

with a quantum efficiency of approximately 80%. The optimum phosphor has the composition  $(\text{Ce}_{0.67}\text{Tb}_{0.33})\text{-MgAl}_{11}\text{O}_{19}$ . Comparison of the excitation spectra of the  $\text{Ce}^{3+}$  and the  $\text{Tb}^{3+}$  emission, as well as variation in the  $\text{Tb}^{3+}$  concentration, show that  $\text{Ce}^{3+}$  acts as a sensitizer and that the excitation energy is transferred to  $\text{Tb}^{3+}$ . Figure 7 shows the excitation and diffuse reflection spectrum of  $(\text{Ce}_{0.67}\text{Tb}_{0.33})\text{MgAl}_{11}\text{O}_{19}$ . The  $\text{Ce}^{3+}$  emission efficiently overlaps 4f excitation lines of  $\text{Tb}^{3+}$  which have been inserted in the figure. The emission of  $(\text{Ce}_{0.67}\text{Tb}_{0.33})\text{MgAl}_{11}\text{O}_{19}$ , compared to NBS zinc silicate, is shown in Fig. 8.  $\text{Ce}^{3+}$  as well as  $\text{Tb}^{3+}$  are accommodated in the intermediate layer. Energy transfer from  $\text{Ce}^{3+}$  to  $\text{Tb}^{3+}$  takes place within that layer, the  $\text{Ce}^{3+}\text{-Tb}^{3+}$  distance being 5.6Å. The distance between the layers is 11Å. Energy transfer occurs mainly via electric dipole-quadrupole interactions (1). The transfer probability for that process is inversely proportional to  $R^8$ , so that energy transfer from one layer to the other is negligible. Optimum  $\text{Tb}^{3+}$  luminescence was obtained at a  $\text{Ce}^{3+}/\text{Tb}^{3+}$  ratio  $\approx 2$ . In that case the  $\text{Ce}^{3+}$  emission is very weak. Calculations on the energy transfer from  $\text{Ce}^{3+}$  to  $\text{Tb}^{3+}$  supported the experimentally found  $\text{Ce}^{3+}/\text{Tb}^{3+}$  ratio (13). The composition  $(\text{Ce}_{0.67}\text{Tb}_{0.33})\text{MgAl}_{11}\text{O}_{19}$  suggests a superstructure but neutron diffraction experiments did not reveal the appropriate reflections (13).

The luminescent materials, discussed in this paper, are summarized in Table II.

*Temperature dependence.*—Figure 9 shows the influence of temperature on the brightness of some of the phosphors. In particular the  $\text{Ce}^{3+}$ -activated and the  $\text{Ce}^{3+}$ -sensitized,  $\text{Tb}^{3+}$ -activated magnetoplumbites show high efficiency at elevated temperatures.

#### Acknowledgment

The results presented above were obtained in the course of a two-year research and development pro-

gram. I gratefully acknowledge the skillful assistance of Messrs. J. G. Verlijsdonk, E. P. J. de Meester, W. H. M. M. v. d. Spijker, J. G. Verriet, C. W. A. Schetters, and J. J. N. v.d. Wielen. Most of the measurements were performed by Mr. C. Bakker.

Manuscript submitted April 1, 1974; revised manuscript received ca. June 19, 1974. This was Paper 98 presented at the San Francisco, California, Meeting of the Society, May 12-17, 1974.

Any discussion of this paper will appear in a Discussion Section to be published in the June 1975 JOURNAL. All discussions for the June 1975 Discussion Section should be submitted by Feb. 1, 1975.

The publication costs of this article have been assisted by N. V. Philips' Gloeilampenfabrieken.

#### REFERENCES

1. J. M. P. J. Verstegen, J. L. Sommerdijk, and J. G. Verriet, *J. Luminescence*, **6**, 425 (1973).
2. J. M. P. J. Verstegen, *J. Solid State Chem.*, **7**, 468 (1973).
3. P. B. Braun, *Philips Res. Rept.*, **12**, 491 (1957).
4. J. A. Kohn and D. W. Eckart, *J. Appl. Phys.*, **35**, 968 (1964).
5. D. W. Eckart and J. A. Kohn, *Z. Krist.*, **125**, 130 (1967).
6. J. v. Landuyt, S. Amelinckx, J. A. Kohn, and D. W. Eckart, *Mater. Res. Bull.*, **8**, 339 (1973).
7. J. J. Brown, *This Journal*, **114**, 245 (1967).
8. J. M. P. J. Verstegen and A. L. N. Stevels, To be published.
9. G. Blasse and A. Bril, *Philips Res. Rept.*, **23**, 201 (1968).
10. J. M. P. J. Verstegen, D. Radielović, and L. E. Vrenken, *This Journal*, **121**, 1627 (1974).
11. F. A. Kröger, "Some Aspects of the Luminescence of Solids," Elsevier, New York (1948).
12. J. M. P. J. Verstegen and J. L. Sommerdijk, To be published in *J. Luminescence*.
13. J. L. Sommerdijk and J. M. P. J. Verstegen, To be published.

## A New Generation of "Deluxe" Fluorescent Lamps, Combining an Efficacy of 80 Lumens/W or More with a Color Rendering Index of Approximately 85

J. M. P. J. Verstegen, D. Radielović, and L. E. Vrenken

N. V. Philips' Gloeilampenfabrieken, Light Division, Eindhoven, The Netherlands

#### ABSTRACT

It has been shown previously that color-rendering capability and luminous efficacy of fluorescent lamps depend on the spectral composition of the emitted light. Three spectral regions appear to be of special interest, the blue at 450 nm, the green at 540 nm, and the orange-red at 610 nm. Among the hexagonal aluminates blue-emitting  $(\text{Ba,Eu})\text{Mg}_2\text{Al}_{16}\text{O}_{27}$  and green-emitting  $(\text{Ce,Tb})\text{MgAl}_{11}\text{O}_{19}$ , together with orange-red-emitting  $(\text{Y,Eu})_2\text{O}_3$  are particularly suited in a new generation "deluxe" fluorescent lamps. Lamps with a color temperature  $>2350^\circ\text{K}$  can be made. The efficacy of the lamps ranks from approximately 82 lm/W at  $3000^\circ\text{K}$  to 80 lm/W at  $6000^\circ\text{K}$ . The color-rendering index  $R_a$  is 81-85. A small increase of  $R_a$  is achieved when  $\text{Mn}^{2+}$  is incorporated in  $(\text{Ba,Eu})\text{Mg}_2\text{Al}_{16}\text{O}_{27}$ , giving rise to an additional green emission at 515 nm. The new blend is compared to other blends and further prospects in fluorescent lamp developments are outlined.

Various papers have been published on the optimum emission spectra of light sources. Koedam and Opstelten (1) showed that a color rendering index (CRI) (2)  $R_a \approx 80$  can be achieved by a proper choice of the

Key words: fluorescent lamps, high efficacy "deluxe" fluorescent lamps, new generation fluorescent lamps.

wavelengths and intensity ratios of three spectral bands, each having a width of only 5 nm. Although the position of the bands in the spectrum is critical, a small shift of one of them can be compensated for by shifts in the same direction of the other two: the bands are interdependent.



Not only color-rendering capability but also luminous efficacy depends on the spectral composition of the emitted light as was shown by Koedam and Opstelten (1) and Thornton (3). The Koedam-Opstelten principle, described above, can be applied to fluorescent lamps. Koedam, Opstelten, and Radielović (4) stated that good color-rendering capability and high efficacy are combined when the three phosphor blend contains a red component with a narrow emission band at 615 nm. Further calculations by Opstelten (5) also showed that a decrease of the width of the blue emission band favors high efficacy, though the effect is less dramatic than for the red one. Relatively broad band green phosphors come up to the requirements (5).

Haft and Thornton (6) published data on experimental lamps based on the Koedam-Opstelten principle. They applied blue-emitting strontium chloroapatite activated with divalent europium, green-emitting zinc silicate activated with manganese, and orange-red emitting yttrium oxide, activated with trivalent europium. For a 40W cool white fluorescent lamp they reported 3100 lumens and a CRI of 83.

Opstelten, Radielović, and Wanmaker (7) evaluated a number of phosphors, most of them, unfortunately, being unsuited for lamp application. However, their work strongly supported the use of divalent europium, trivalent terbium, and trivalent europium as the most suitable activators. This result confirms the pattern outlined above: trivalent europium phosphors show line emission in the red or orange-red. The emission of divalent europium is, compared with blue halophosphate, narrow, although the band is much broader than the line emission of trivalent europium. The  $Tb^{3+}$ -activated phosphors with line emission at 545 nm behave as relatively broad band green phosphors, due to their subsidiary emission near 490 and 590 nm. The four transitions  $^5D_4 \rightarrow ^7F_J$  in the  $Tb^{3+}$  ion can be combined to a Gaussian emission band centered at 545 nm and with a width at half intensity of 80 nm (5).  $Tb^{3+}$ -activated phosphors conform very well to the three-spectral-color criterion which allows an increase of the width of the green band with hardly any loss in luminous efficacy.

The aim of the present paper is to show how the hexagonal aluminate phosphors, presented before (8), behave in lamps according to the Koedam-Opstelten principle. We compare the results with some other blends without being exhaustive. However, computer calculations show that the aluminate phosphors together with  $(Y, Eu)_2O_3$  constitute a blend which in the region of color temperatures  $\geq 2350^\circ K$  is unsurpassed as far as lamp efficacy is concerned (9). We compare the new blend to results of current halophosphate lamps. A more detailed treatment of the lamp including a discussion of phosphor costs, maintenance, etc. will be presented elsewhere (10).

### Selection of Phosphors

As stated above, the phosphor emission bands are interdependent. The choice of one phosphor fixes, to a certain extent, the position of the other two. Except for requirements such as a high quantum efficiency and a good lamp performance, it is necessary that the three phosphors match each other. Opstelten *et al.* (7) pointed out that a narrow band green phosphor should be located at 560–570 nm and a broad band one at 525–560 nm, depending on the type of fluorescent lamp involved.

An important step forward was made by the innovation and development of the efficient and excellently performing phosphor  $(Ce_{0.67}Tb_{0.33})MgAl_{11}O_{19}$  (8, 11). In the course of our work we were able to increase the quantum efficiency of the phosphor from 65% (11) to 80% (8). In Table I we compare  $(Ce_{0.67}Tb_{0.33})MgAl_{11}O_{19}$  to  $ZnSiO_4:Mn^{2+}$ , both green-emitting phosphors.

The following conclusions may be drawn from the comparison: (a) the maintenance of the aluminate is better, (b) the quantum efficiency of the aluminate is

Table I. Properties of  $(Ce_{0.67}Tb_{0.33})MgAl_{11}O_{19}$  and  $ZnSiO_4:Mn^{2+}$  in 40W fluorescent lamps

Phosphor	Quantum eff. (%)	Refl. 254 nm (%)	Chromaticity coordinates (x/y)	Efficacy (lumens/W) in 40W lamps	
				100 hr	2500 hr
$(Ce_{0.67}Tb_{0.33})MgAl_{11}O_{19}$	80	8	0.295/0.579	108	102
$ZnSiO_4:Mn^{2+}$	75	15	0.246/0.622	94	89

higher, and (c) the value of  $y/\eta$ , where  $y$  is the  $y$  chromaticity coordinate and  $\eta$  is the luminous efficacy, is smaller for the  $Tb^{3+}$  phosphor than for green zinc silicate, indicating that the three phosphor blends containing the first one will exhibit higher efficacy.

Calculations showed that the emission of  $(Ce_{0.67}Tb_{0.33})MgAl_{11}O_{19}$  at 545 nm should be matched by an orange-red emitting phosphor. Nothing is to be gained in CRI when the red emission is shifted to wavelengths longer than about 615 nm, but, at the same time, the efficacy of the lamp decreases. This was confirmed by experimental lamps with  $(Y, Eu)_2O_3$ , emitting at 611 nm and  $(Y, Eu)_2O_2S$ , emitting at 627 nm as the red component of a cool white phosphor blend.  $(Y, Eu)_2O_2S$  is suitable, in particular when the color rendering of deep red has to be improved, but the phosphor should be combined with a green-yellow one, emitting at 560–565 nm. The best match for  $(Ce, Tb)MgAl_{11}O_{19}$  is therefore orange-red emitting  $(Y, Eu)_2O_3$ . A shift of the orange-red emission line toward shorter wavelengths [the amount of  $(Ce, Tb)MgAl_{11}O_{19}$  in the blend at the same time decreasing] increases the lamp efficacy, the  $R_a$  values soon dropping below 80. However, no efficient line emitting phosphor at a wavelength of  $\approx 600$  nm is known. The properties of  $(Y, Eu)_2O_3$  are given in Table II.

Calculations showed that a narrow band blue phosphor, peaking at 450 nm, is required for maximum luminous efficacy of the lamp. Two effects are noteworthy: (a) a shift of the blue emission toward longer wavelengths (or a shift of the chromaticity coordinates in the C.I.E. chromaticity diagram to higher  $y$  values) tends to decrease the luminous efficacy but to increase the CRI, and (b) a decrease of the width of the blue emission band tends to increase the luminous efficacy but to decrease the CRI.

The relevant aluminate blue phosphors are  $(Ba_{0.86}Eu_{0.14})Mg_2Al_{16}O_{27}$  with an emission peaking at 450 nm and  $(Sr_5Eu_{0.5})Mg_6Al_{55}O_{104}$ , emitting at 465 nm (8). Incorporation of  $Mn^{2+}$  in both lattices gives rise to a second emission at 515 nm (8). This second emission leaves the  $x$  chromaticity coordinate of the phosphors virtually unaffected but the  $y$  coordinate increases drastically when the ratio  $Mn^{2+}/Eu^{2+}$  increases. In particular the  $Eu^{2+}$ -activated Ba compound is an excellent blue component for the new generation "deluxe" fluorescent lamps.

The trends mentioned under (a) will be illustrated with blue and blue-green aluminate phosphors, that under (b) with a comparison of  $(Ba, Eu)Mg_2Al_{16}O_{27}$  to another blue phosphor,  $(Sr, Eu)$  chloroapatite (6). Both emit at 450 nm but the width at half intensity of aluminate blue is 50 nm against that of 30 nm of  $(Sr, Eu)$  chloroapatite. Our experiments on  $(Sr, Eu)$  chloroapatite showed that a quantum efficiency of 85% was within reach, 15% lower than that of the aluminates. However, one would expect the narrower emission band and the lower reflection for 254 nm radiation (see Table III) to make up for this as far as lamp effi-

Table II. Properties of  $(Y, Eu)_2O_3$  in 40W fluorescent lamps

Phosphor	Quantum eff. (%)	Refl. 254 nm (%)	Chromaticity coordinates (x/y)	Efficacy (lumens/W) in 40W lamps	
				100 hr	2500 hr
$(Y, Eu)_2O_3$	100	10	0.597/0.331	85	57

Table III. Properties of some blue phosphors in 40W fluorescent lamps

Phosphor composition	Quantum eff. (%)	Ref. 254 nm (%)	Chromaticity coordinates (x/y)	Efficacy (lumens/W) in 40W lamps	
				100 hr	2500 hr
$(\text{Ba}_{0.9}\text{Eu}_{0.1})\text{Mg}_2\text{Al}_{16}\text{O}_{27}$	100	10	0.151/0.066	24	22
$(\text{Ba}_{0.9}\text{Eu}_{0.1})(\text{Mg}_{1.9}\text{Mn}_{0.1})\text{Al}_{16}\text{O}_{27}$	100	16	0.148/0.225	50	43
$(\text{Sr}_x\text{Eu}_{0.5})\text{Mg}_6\text{Al}_{35}\text{O}_{94}$	100	8	0.149/0.181	45	Poor
$(\text{Sr}_{x.68}\text{Eu}_{0.07})(\text{FO})_3\text{Cl}$	85	3	0.159/0.038	12	9.5

efficacy is concerned. We will give a detailed comparison in the section on phosphor blends. Conventional blue phosphors such as blue halophosphate,  $\text{Sn}^{2+}$ -activated  $\text{Sr}_2\text{P}_2\text{O}_7$  and  $\text{MgWO}_4$  with widths at half intensity of approximately 120 nm do not conform to the Koedam-Opstelten principle. The efficacy of lamps containing these phosphors is at least 10 lumens/W lower.

Table III gives some properties of blue-emitting phosphors. A few conclusions to be drawn from Table III are: (a) the behavior of  $(\text{Sr},\text{Eu})_{5.5}\text{Mg}_6\text{Al}_{35}\text{O}_{94}$  in lamps is poor, and (b) the maintenance of  $(\text{Sr},\text{Eu})$  chloroapatite is a bit worse than that of the Ba aluminate blue. That the luminous efficacy  $\eta$  of the latter is twice as high is mainly due to the lower y coordinate of the  $(\text{Sr},\text{Eu})$  chloroapatite. The value of  $y/\eta$  of the aluminate blue is only approximately 15% lower, in agreement with its higher quantum efficiency.

**Selection of Blends**

Figure 1 shows the C.I.E. chromaticity diagram. The Planckian locus (BBL) as well as the chromaticity coordinates R of  $(\text{Y},\text{Eu})_2\text{O}_3$ , G of  $(\text{Ce},\text{Tb})\text{MgAl}_{11}\text{O}_{19}$ , and B of  $(\text{Ba},\text{Eu})\text{Mg}_2\text{Al}_{16}\text{O}_{27}$  have been inserted. The line GR intersects the Planckian locus at a point corresponding to a color temperature of approximately 2350°K. Up to now, fluorescent lamps of low color temperature and good color rendering capability had to be made using a blue absorbing layer in order to

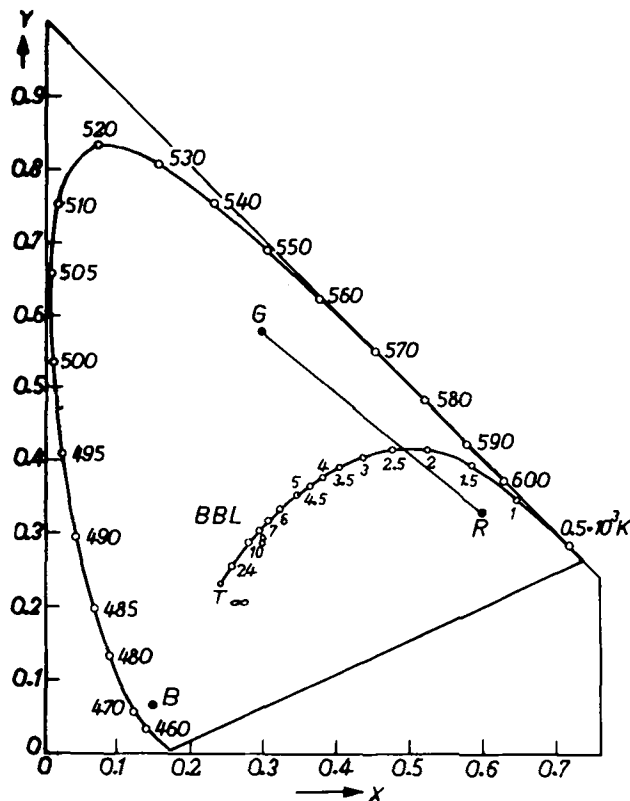


Fig. 1. C.I.E. chromaticity diagram with chromaticity coordinates R of  $(\text{Y},\text{Eu})_2\text{O}_3$ , G of  $(\text{Ce},\text{Tb})\text{MgAl}_{11}\text{O}_{19}$ , and B of  $(\text{Ba},\text{Eu})\text{Mg}_2\text{Al}_{16}\text{O}_{27}$  and with the Planckian locus (BBL).

Table IV. Efficacy at 100 hr and CRI ( $R_a$ ) of 4000°K fluorescent lamps with two different blue phosphors in the blend

Blue phosphor in 4000°K blend	Efficacy (lumens/W) 100 hr	CRI ( $R_a$ )
$(\text{Sr},\text{Eu})_{5.5}\text{Mg}_6\text{Al}_{35}\text{O}_{94}$	78.5	90
$(\text{Ba},\text{Eu})\text{Mg}_2\text{Al}_{16}\text{O}_{27}$	81.0	85

suppress the blue and violet mercury lines at 405, 408, and 436 nm. In the new lamps the mercury lines add their contribution to the emission spectrum.

The effect of the shift of the blue emission toward longer wavelengths in a 4000°K fluorescent lamp is shown by comparison of  $(\text{Sr},\text{Eu})_{5.5}\text{Mg}_6\text{Al}_{35}\text{O}_{94}$ , emitting at 465 nm, with  $(\text{Ba},\text{Eu})\text{Mg}_2\text{Al}_{16}\text{O}_{27}$  emitting at 450 nm. The green component,  $(\text{Ce},\text{Tb})\text{MgAl}_{11}\text{O}_{19}$ , and the red one,  $(\text{Y},\text{Eu})_2\text{O}_3$ , remain the same, although their amounts in the blend change. Table IV gives the results of experimental lamps with the two blue phosphors in the blend.

The effect of an increasing y value of the blue component in a 4000°K phosphor blend is suitably demonstrated with phosphors based on the general formula  $(\text{Ba}_{0.9}\text{Eu}_{0.1})(\text{Mg}_{2-x}\text{Mn}_x)\text{Al}_{16}\text{O}_{27}$ . The green component,  $(\text{Ce},\text{Tb})\text{MgAl}_{11}\text{O}_{19}$ , and the red component,  $(\text{Y},\text{Eu})_2\text{O}_3$ , remain the same. Figure 2 shows an enlarged part of the C.I.E. chromaticity diagram. The chromaticity coordinates of the  $\text{Eu}^{2+}$ -sensitized,  $\text{Mn}^{2+}$ -activated aluminates are found on the line PQ, Q corresponding to a phosphor  $(\text{Ba}_{0.9}\text{Eu}_{0.1})(\text{Mg}_{1.7}\text{Mn}_{0.3})\text{Al}_{16}\text{O}_{27}$ . Going from B to Q the lamp efficacy drops. The CRI increases in the region BP but decreases going from P

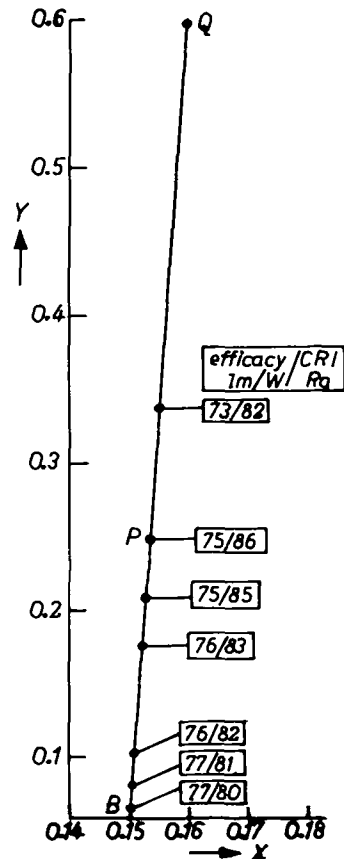


Fig. 2. Enlarged part of the C.I.E. chromaticity diagram with the chromaticity coordinates B of  $(\text{Ba}_{0.9}\text{Eu}_{0.1})\text{Mg}_2\text{Al}_{16}\text{O}_{27}$ , P of  $(\text{Ba}_{0.9}\text{Eu}_{0.1})(\text{Mg}_{1.9}\text{Mn}_{0.1})\text{Al}_{16}\text{O}_{27}$ , and Q of  $(\text{Ba}_{0.9}\text{Eu}_{0.1})(\text{Mg}_{1.7}\text{Mn}_{0.3})\text{Al}_{16}\text{O}_{27}$ . At various points of the line BQ the calculated luminous efficacy and the CRI ( $R_a$ ) are given for cool white blends of  $(\text{Ce},\text{Tb})\text{MgAl}_{11}\text{O}_{19}$ ,  $(\text{Y},\text{Eu})_2\text{O}_3$ , and  $(\text{Ba}_{0.9}\text{Eu}_{0.1})(\text{Mg}_{2-x}\text{Mn}_x)\text{Al}_{16}\text{O}_{27}$ .

Table V. Efficacy at 100 hr and CRI ( $R_a$ ) of 4000°K fluorescent lamps with  $(Ba_{0.9}Eu_{0.1})(Mg_{2-x}Mn_x)Al_{16}O_{27}$  as the blue phosphor

$x$	Efficacy (lumens/W) 100 hr	CRI ( $R_a$ )
0	81.0	85
0.05	79.5	87
0.1	78.5	88

Table VI. Efficacy at 100 hr and CRI ( $R_a$ ) of 4000°K fluorescent lamps with (Sr,Eu) chlorapatite and  $(Ba,Eu)Mg_2Al_{16}O_{27}$  as the blue phosphor

Blue phosphor	Efficacy (lumens/W) 100 hr	CRI ( $R_a$ )
$(Ba,Eu)Mg_2Al_{16}O_{27}$	81.0	85
(Sr,Eu) chlorapatite	80.0	81

to Q. P is the chromaticity coordinate of the phosphor  $(Ba_{0.9}Eu_{0.1})(Mg_{1.9}Mn_{0.1})Al_{16}O_{27}$ . At various points along the line BQ calculated values of the lamp efficacy in lumens/watt and of the CRI ( $R_a$ ) are given. Experimental lamps confirmed this trend. The results are given in Table V.

We consider an  $R_a$  of 85 as high enough for normal lighting and therefore decided to refrain from a further increase of  $R_a$  at the cost of the lamp efficacy. The effect of a decrease of the width of the blue emission band is demonstrated when lamps with (Sr, Eu) chlorapatite and  $(Ba, Eu)Mg_2Al_{16}O_{27}$  are compared. In both cases  $(Ce,Tb)MgAl_{11}O_{19}$  is the green and  $(Y, Eu)_2O_3$  the red component. The results are shown in Table VI and demonstrate that the lower quantum efficiency of (Sr, Eu) chlorapatite is compensated for by its narrower emission band: there is hardly any difference in lamp efficacy. However, color rendering capability drops rather sharply.

### Lamp Results

Many lamps at various color temperatures have been made by now, using the blend containing blue  $(Ba, Eu)Mg_2Al_{16}O_{27}$ , green  $(Ce, Tb)MgAl_{11}O_{19}$ , and red  $(Y, Eu)_2O_3$ . Measurements of luminous efficacy, color rendering indices, and maintenance show unambiguously that a new generation of "deluxe" lamps has been developed with a unique combination of properties. Table VII shows data of experimental 40W lamps of four different color temperatures and when lamps with equal CRI are compared, that the efficacy increases by 50%. Figure 3 shows the emission spectrum of a 40W fluorescent lamp of 4000°K coated with a blend of blue and green aluminate and  $(Y, Eu)_2O_3$ . The maintenance of the new lamp is comparable to that of the halophosphate lamp and we expect to be able to improve on that (10).

### Further Prospects in Fluorescent Lamp Development

The increased luminous efficacy of our "deluxe" fluorescent lamp, resulting from the phosphor research described in a previous paper (8), is welcome in these

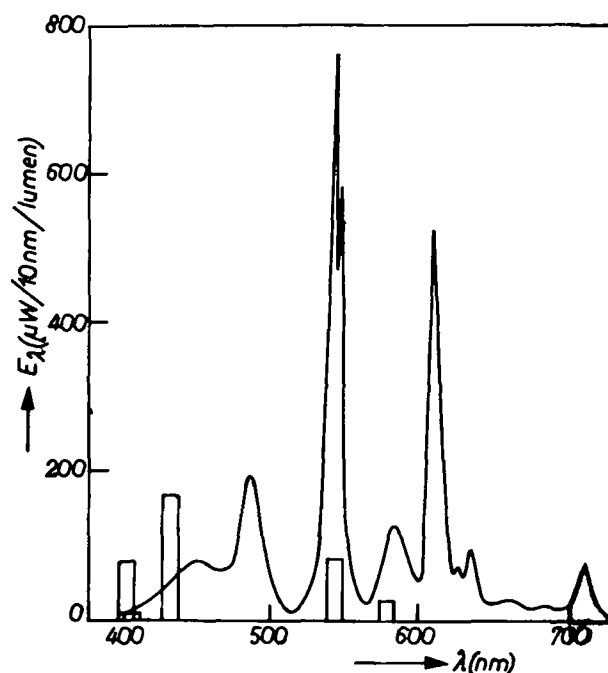


Fig. 3. Emission spectrum of a 40W fluorescent lamp of 4000°K, coated with a blend of  $(Ba,Eu)Mg_2Al_{16}O_{27}$ ,  $(Ce,Tb)Al_{11}O_{19}$ , and  $(Y,Eu)_2O_3$ .

times of energy crisis. In a separate paper we will present calculations which show that the new generation "deluxe" lamp is profitable in "deluxe" lighting installations, even though the cost of the lamp is considerably higher (10). Whether the aluminate/ $(Y, Eu)_2O_3$  blend will render the halophosphates obsolete depends on our progress in reducing the lamp price. Some possibilities to do so are outlined elsewhere (10). The high efficacy of the new "deluxe" lamp is partly due to the high quantum efficiency of the phosphors and partly to the localization of their emission close to the three wavelengths 450, 540, and 610 nm (6). Although we do not imply that the phosphor blend presented above is the ultimate one for "deluxe" fluorescent lamps of the Koedam-Opstelten principle, we believe that a dramatic increase in the efficacy of fluorescent lamps is only possible when the three-spectral-color criterion is left for the two-spectral-color one. When phosphors could be obtained with a  $Q$  (= quantum efficiency  $\times$  absolute absorption of 254 nm radiation) of 1.0 and when 22W of ultraviolet radiation (254 and 185 nm) is available for excitation, a cool white and warm white 40W fluorescent lamp with an efficacy of  $\approx 130$  lumens/W could be obtained. Such a lamp would emit in two narrow lines at 445-450 nm and 570-580 nm in agreement with Ivey's earlier results (12). The three-phosphor blend presented in this paper has a  $Q \approx 0.8$ . Table VIII shows the calculated efficacy of lamps according to the two-spectral-color criterion with  $Q = 1.0$  and 0.8. The spectral energy distribution of the 3000°K lamp is

Table VII. Efficacy in lumens/watt at 100 hr and CRI of new generation "deluxe" fluorescent 40W lamps, compared to 40W lamps of the present standard and "deluxe" range

Correlated color temp (*K)	New generation "deluxe" lamps			Present range							
	Our code	Eff. 100 hr	CRI ( $R_a$ )	Standard			"Deluxe"				
				Our code	I.E.S. code	Eff. 100 hr	CRI ( $R_a$ )	Our code	I.E.S. code	Eff. 100 hr	CRI ( $R_a$ )
2500-2700 (comfort "deluxe")	82	81.0	83	—	—	—	—	27	—	44.0	95
3000 (warm white)	83	82.0	84	29	WW	80.0	83	32	WWX	53.0	82
4000 (cool white)	84	81.0	85	33	CW	80.0	87	34	CWX	55.0	85
6000-6500 (daylight)	86	80.0	81	54	D	86.0	79	55	—	50.0	95

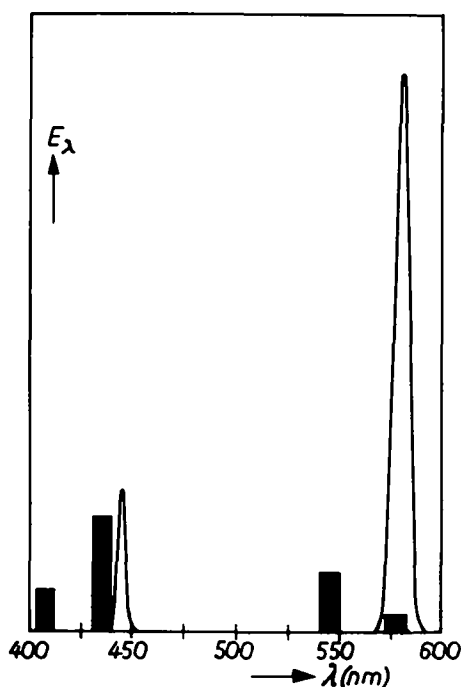


Fig. 4. Calculated emission spectrum of a 3000°K fluorescent lamp with 130 lumens/W.

given in Fig. 4. The high efficacy lamps of Table VIII show a disastrously poor color rendering capability and will only find application in outdoor lighting installations. Nevertheless, much effort is being made to find phosphors which emit in the required regions.

Manuscript submitted April 1, 1974; revised manuscript received June 19, 1974. This was Paper 98 presented at the San Francisco, California, Meeting of the Society, May 12-17, 1974.

Table VIII. Calculated efficacy of 40W fluorescent lamps with emission in two Gaussian lines

Lamp color and chromaticity coordinates	1st emission band		2nd emission band		Efficacy lumens/W in 40W lamps*	
	Peak wave-length (nm)	Width (nm)	Peak wave-length (nm)	Width (nm)	Q = 1.0**	Q = 0.8
Cool white (0.377/0.381)	445	4.8	574	7.8	131	105
Warm white (0.441/0.404)	445	4.8	580	7.9	134	107
Daylight (0.314/0.343)	450	4.8	568	7.6	121	97

\* Based on 22W of ultraviolet radiation (254 and 185 nm) available for excitation.

\*\* Q = quantum efficiency × absolute absorption of 254 nm radiation.

Any discussion of this paper will appear in a Discussion Section to be published in the June 1975 JOURNAL. All discussions for the June 1975 Discussion Section should be submitted by Feb. 1, 1975.

The publication costs of this article have been assisted by N. V. Philips' Gloeilampenfabrieken.

#### REFERENCES

1. M. Koedam and J. J. Opstelten, *Lighting Research Technol.*, **3**, 205 (1971).
2. C.I.E. Publication No. 13 (1965).
3. W. A. Thornton, *J. Opt. Soc. Am.*, **61**, 1155 (1971).
4. M. Koedam, J. J. Opstelten, and D. Radielović, *J. I.E.S.*, (July 1972) (see Discussion).
5. J. J. Opstelten, Private communication.
6. H. H. Haft and W. A. Thornton, *J. I.E.S.* (Oct. 1972).
7. J. J. Opstelten, D. Radielović, and W. L. Wanmaker, *This Journal*, **120**, 1400 (1973).
8. J. M. P. J. Verstegen, *ibid.*, **121**, 1623 (1974).
9. D. Radielović, Unpublished results.
10. J. M. P. J. Verstegen, D. Radielović, and L. E. Vrenken, *J. I.E.S.*, To be published.
11. J. M. P. J. Verstegen, J. L. Sommerdijk, and J. G. Verriet, *J. Luminescence*, **6**, 425 (1973).
12. H. F. Ivey, *J. Opt. Soc. Am.*, **53**, 1185 (1963).

## The Luminescence of $Tb^{3+}$ in Borates of the Composition $X_2Z(BO_3)_2$ ( $X = Ba, Sr, Ca$ ; $Z = Ca, Mg$ )

J. M. P. J. Verstegen

N. V. Philips' Gloeilampenfabrieken, Light Division, Eindhoven, The Netherlands

#### ABSTRACT

Four new borates of the formula  $X_2Z(BO_3)_2$ , with  $X = Ba, Sr, Ca$ , and  $Z = Ca, Mg$ , are described.  $Ca_2Mg(BO_3)_2$  is tetragonal, and  $Ba_2Mg(BO_3)_2$  is hexagonal and isomorphous with the mineral buetschliite.  $Ba_2Ca(BO_3)_2$  and  $Sr_2Mg(BO_3)_2$  are related to buetschliite but their diffraction patterns point to a crystallographic system of lower symmetry. All four borates are good host lattices for  $Tb^{3+}$  luminescence. The maximum quantum efficiencies are approximately 75% and are strongly influenced by the method of charge compensation used. The emission spectrum shows the usual  $^5D_4 \rightarrow ^7F_J$  transitions, with  $J = 6, 5, 4$ , and  $3$ , that with  $J = 5$  being the strongest. The temperature dependence of the emission is good.

Efficient luminescence of  $Tb^{3+}$  is known (1). Excitation of the luminescence may occur in four different ways: (a) in the 4f-4f absorption lines of the rare earth ion; this does not result in a high luminescence output due to the low absorption strength of these transitions; (b) in the broad absorption band of  $Tb^{3+}$  in the short-wave ultraviolet region; this band corresponds to 4f-5d

transitions (2); (c) in a sensitizer ion, followed by energy transfer to  $Tb^{3+}$ , as is found in  $(Ce,Tb)MgAl_{11}O_{19}$  (3); sensitization of  $Tb^{3+}$  emission by  $Sn^{2+}$  and  $Cu^+$  has been described previously (4); and (d) in the host lattice, followed by energy transfer to  $Tb^{3+}$  (5); phosphors such as  $SrWO_4:Tb^{3+}$  (6) belong to this type.

Luminescence of  $Tb^{3+}$  in borates was previously described by Wanmaker and Bril (7), and by Wanmaker, Bril, and Ter Vrugt (8). In general the emission spec-

Key words: luminescence of  $Tb^{3+}$ , new borates, luminescence of  $Tb^{3+}$  in borates.

Table I. Values of  $d$  and  $I/I_0$  of the borates  $\text{Ba}_2\text{Ca}(\text{BO}_3)_2$  and  $\text{Sr}_2\text{Mg}(\text{BO}_3)_2$  activated with  $\text{Tb}^{3+}$

$\text{Ba}_{1-x}\text{K}_{0.1}\text{Tb}_{0.1}\text{Ca}(\text{BO}_3)_2$ $d, \text{Å}$	$I/I_0$	$\text{Sr}_{1-x}\text{Na}_{0.1}\text{Tb}_{0.1}\text{Mg}(\text{BO}_3)_2$ $d, \text{Å}$	$I/I_0$
5.8	9	5.2	5
4.56	19	5.4	4
4.16	91	4.35	9
3.46	38	3.95	16
3.38	75	3.89	53
2.89	33	3.68	7
2.80	100	3.00	43
2.76	88	2.68	36
2.72	45	2.64	19
2.48	13	2.60	100
2.38	14	2.57	25
2.32	20	2.35	10
2.27	36	2.24	12
		2.16	49
		2.05	14
		1.98	13
		1.94	30
		1.84	21
		1.82	7
		1.78	7

trum of  $\text{Tb}^{3+}$  consists of the  $^5\text{D}_4 \rightarrow ^7\text{F}_J$  ( $J = 3, 4, 5, 6$ ) transitions, in which  $J = 5$  dominates, giving rise to a more or less saturated green emission.

### Experimental

We used luminescent grade  $\text{CaCO}_3$ ,  $\text{SrCO}_3$ ,  $\text{BaCO}_3$ ,  $\text{H}_3\text{BO}_3$ , and  $\text{MgO}$ .  $\text{Tb}_4\text{O}_7$  was obtained from the Michigan Chemical Corporation.  $\text{Na}_2\text{CO}_3$  and  $\text{K}_2\text{CO}_3$  by Merck were used.

The best results were obtained after prefiring for 1 hr at  $600^\circ\text{C}$  and 2 hr at  $900^\circ\text{C}$ , but a single firing at  $900^\circ\text{C}$  for 1 hr proved sufficient to obtain 95% of the maximum brightness of the phosphors. A slightly reducing atmosphere was used to convert Tb to the trivalent state. The optical measurements have been described before (9).

### Results

**Structure of the host lattices.**—Borates and carbonates are often structurally isomorphous.  $\text{LaBO}_3$  has, e.g., the  $\text{CaCO}_3$ -aragonite type structure and  $\text{GdBO}_3$  the  $\text{CaCO}_3$ -vaterite type structure (10). Isomorphism is also found in more complicated compounds, such as  $\text{YAl}_3\text{B}_4\text{O}_{12}$  and the mineral huntite  $\text{CaMg}_3(\text{CO}_3)_4$  (11-13). Many carbonate minerals of the composition  $\text{A}_2\text{B}(\text{CO}_3)_2$  exist, in which  $\text{A} = \text{K}$  or  $\text{Na}$ , and  $\text{B} = \text{Ca}$  or  $\text{Mg}$ , such as buetschliite (ASTM File No. 21-980), fairchildite (ASTM File No. 21-1287), whereas a compound  $\text{Na}_2\text{Ca}(\text{CO}_3)_2$  is also listed under No. 2-970. We found a number of new borates.  $\text{Ca}_2\text{Mg}(\text{BO}_3)_2$  was isomorphous with  $\text{Na}_2\text{Ca}(\text{CO}_3)_2$  and tetragonal with  $a = 5.14\text{Å}$  and  $c = 4.41\text{Å}$ .  $\text{Ba}_2\text{Mg}(\text{BO}_3)_2$  was isomorphous with the hexagonal buetschliite with  $a = 5.38\text{Å}$  and  $c = 19.21\text{Å}$ .

The diffraction patterns of  $\text{Ba}_2\text{Ca}(\text{BO}_3)_2$  and  $\text{Sr}_2\text{Mg}(\text{BO}_3)_2$  point to similar structures but some new reflections appear, possibly due to a different distribution of the cations over their sites. We were unable to index the diffraction patterns. Values of  $d$  and  $I/I_0$  are given in Table I.

**$\text{Tb}^{3+}$  luminescence.**—Figure 1 shows the excitation and diffuse reflection curves of the compounds  $\text{X}_2\text{Z}(\text{BO}_3)_2$  activated with  $\text{Tb}^{3+}$ . The broad strong absorption bands correspond to  $4f \rightarrow 5d$  transitions in the  $\text{Tb}^{3+}$  ion. Though at least the three compounds with  $\text{X} = \text{Sr}$ ,  $\text{Ba}$  have related structures, the excitation spectra differ markedly, due to the fact that the  $5d$  level is strongly influenced by the crystal field (14).

The emission spectra of  $\text{Tb}^{3+}$  in  $\text{Ba}_2\text{Mg}(\text{BO}_3)_2$  and  $\text{Ba}_2\text{Ca}(\text{BO}_3)_2$  are shown in Fig. 2 and 3. We observe the usual transitions  $^5\text{D}_4 \rightarrow ^7\text{F}_J$ , with  $J = 6, 5, 4$ , and 3. The transition  $^5\text{D}_4 \rightarrow ^7\text{F}_5$  is the stronger one. Splitting of the levels is much the same in both host lattices, indicating that the  $4f$  levels are only slightly affected by minor changes of the crystal field. Comparison of the emission curves with that of  $\text{Tb}^{3+}$  in the magnetoplumbite  $\text{CeMgAl}_{11}\text{O}_{19}$  (3) shows marked differences.

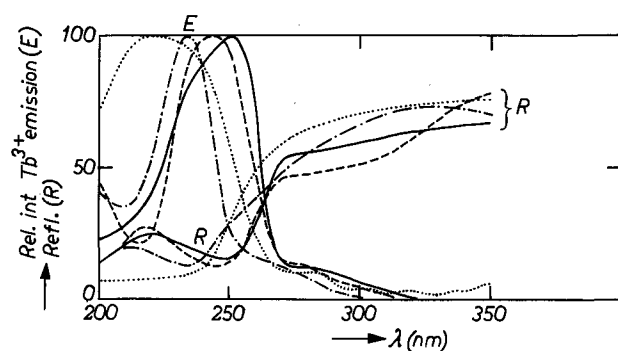


Fig. 1. Excitation (E) and diffuse reflection (R) spectra of  $\text{Tb}^{3+}$  luminescence in  $\text{Ba}_2\text{Mg}(\text{BO}_3)_2$  (full curves),  $\text{Ba}_2\text{Ca}(\text{BO}_3)_2$  (dashed curves),  $\text{Sr}_2\text{Mg}(\text{BO}_3)_2$  (dashed-dotted curves), and  $\text{Ca}_2\text{Mg}(\text{BO}_3)_2$  (dotted curves). Charge compensation with  $\text{K}^+$ .

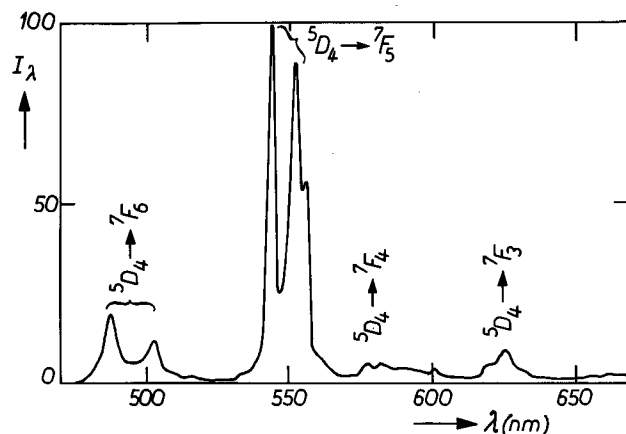


Fig. 2. Spectral energy distribution of the emission of  $\text{Tb}^{3+}$  in  $\text{K}^+$ -compensated  $\text{Ba}_2\text{Mg}(\text{BO}_3)_2$ . The relevant transitions are indicated.  $I_\lambda$  gives the radiant power per constant wavelength interval in arbitrary units. Mainly 254 nm radiation.

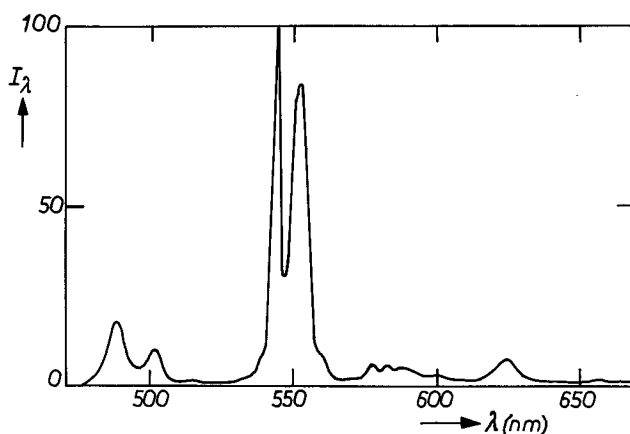


Fig. 3. Spectral energy distribution of the emission of  $\text{Tb}^{3+}$  in  $\text{K}^+$ -compensated  $\text{Ba}_2\text{Ca}(\text{BO}_3)_2$ .  $I_\lambda$  gives the radiant power per constant wavelength interval in arbitrary units. Mainly 254 nm radiation.

At least three explanations are possible: (i) the site symmetry in the borates is lower than that in the magnetoplumbites,  $\text{D}_{3h}$ , (ii) in the borates  $\text{Tb}^{3+}$  is incorporated at various sites, and (iii) the crystal forces acting on the  $\text{Tb}^{3+}$  ion are larger in the borates than in the magnetoplumbite. The latter point requires some explanation. In magnetoplumbites the  $2d$  activator site is surrounded by 12 oxygen ions at relatively long distances ( $\sim 3\text{Å}$ ). Therefore the crystal forces, acting

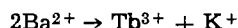
Table II. Quantum efficiencies at the maximum excitation wavelength of various borates with the composition X<sub>2</sub>Z(BO<sub>3</sub>)<sub>2</sub>, activated with Tb<sup>3+</sup>. The quantum efficiencies of Ba<sub>2</sub>Mg(BO<sub>3</sub>)<sub>2</sub>:Tb<sup>3+</sup> with various ways of charge compensation and various activator concentrations, with 254 nm radiation

Composition	Quantum efficiencies, %
Ba <sub>1.8</sub> K <sub>0.1</sub> Tb <sub>0.1</sub> Mg(BO <sub>3</sub> ) <sub>2</sub>	70
Sr <sub>1.8</sub> Na <sub>0.1</sub> Tb <sub>0.1</sub> Mg(BO <sub>3</sub> ) <sub>2</sub>	70
Ca <sub>1.8</sub> Na <sub>0.1</sub> Tb <sub>0.1</sub> Mg(BO <sub>3</sub> ) <sub>2</sub>	70
Ba <sub>1.8</sub> K <sub>0.1</sub> Tb <sub>0.1</sub> Ca(BO <sub>3</sub> ) <sub>2</sub>	75
Ba <sub>1.8</sub> K <sub>0.1</sub> Tb <sub>0.1</sub> Mg(BO <sub>3</sub> ) <sub>2</sub>	70
Ba <sub>1.8</sub> Na <sub>0.1</sub> Tb <sub>0.1</sub> Mg(BO <sub>3</sub> ) <sub>2</sub>	65
Ba <sub>1.7</sub> Tb <sub>0.1</sub> Mg(BO <sub>3</sub> ) <sub>2</sub>	35
Ba <sub>1.7</sub> Tb <sub>0.1</sub> Mg <sub>0.9</sub> Li <sub>0.1</sub> (BO <sub>3</sub> ) <sub>2</sub>	60
Ba <sub>1.8</sub> K <sub>0.07</sub> Tb <sub>0.07</sub> Mg(BO <sub>3</sub> ) <sub>2</sub>	65
Ba <sub>1.8</sub> K <sub>0.10</sub> Tb <sub>0.10</sub> Mg(BO <sub>3</sub> ) <sub>2</sub>	70
Ba <sub>1.78</sub> K <sub>0.12</sub> Tb <sub>0.12</sub> Mg(BO <sub>3</sub> ) <sub>2</sub>	75
Ba <sub>1.70</sub> K <sub>0.15</sub> Tb <sub>0.15</sub> Mg(BO <sub>3</sub> ) <sub>2</sub>	70
Ba <sub>1.80</sub> K <sub>0.20</sub> Tb <sub>0.20</sub> Mg(BO <sub>3</sub> ) <sub>2</sub>	70

on the 2d site, are relatively weak. This is strikingly illustrated by the emission behavior of the Eu<sup>2+</sup>-activated magnetoplumbite SrAl<sub>12</sub>O<sub>19</sub>, which, at 77°K, shows 4f-4f line emission (15): obviously the crystal field is so weak that the lowest excited 4f<sup>6</sup>5d state lies at higher energy than the <sup>6</sup>P<sub>7/2</sub> level. This is rather exceptional in oxidic lattices.

Borates, nitrates, and carbonates usually crystallize with calcite- or vaterite-like structures, depending on the size of the cation (16). The cations are surrounded by six or nine oxygen ions, respectively. More complicated carbonates do not deviate very much from this pattern. Dolomite, CaMg(CO<sub>3</sub>)<sub>2</sub>, has essentially the calcite and alstonite, BaCa(CO<sub>3</sub>)<sub>2</sub>, the aragonite arrangement (17). In calcite and vaterite the cation-oxygen distance is small, 2.1-2.5Å. The crystal field, acting on the cation in these structures as well as in our borates, will therefore be considerable.

**Charge compensation.**—We observed striking influence of charge compensation. The substitution



leads to the phosphor with the highest quantum efficiency, its quantum efficiency being twice as high as that of the noncompensated material. Other ways of charge compensation proved less effective (Table II). The maximum quantum efficiency is reached with an activator content of about 6% of Ba present (0.12 atom Tb per mole of the compound) and is 70-80% at the optimum excitation wavelength. However, only Ba<sub>2</sub>Mg(BO<sub>3</sub>)<sub>2</sub> and Ba<sub>2</sub>Ca(BO<sub>3</sub>)<sub>2</sub> respond favorably to the 254 nm radiation of the mercury discharge. The results are summarized in Table II.

The temperature dependence of Ba<sub>1.8</sub>K<sub>0.1</sub>Tb<sub>0.1</sub>Mg(BO<sub>3</sub>)<sub>2</sub> is shown in Fig. 4. At elevated temperature the efficiency is still high, as is usually found for luminescence from 4f levels.

#### Acknowledgment

The author is indebted to Messrs. W. H. M. M. v. d. Spijker and J. G. Verlijsdonk for preparation of the

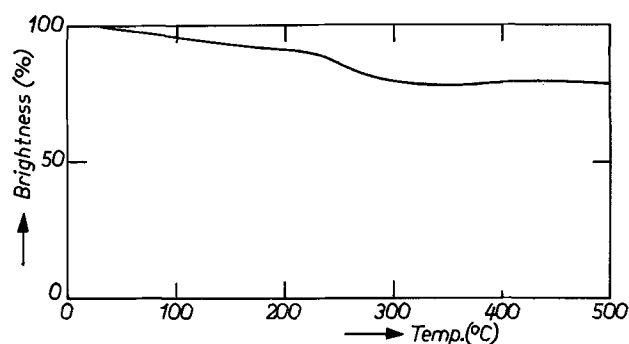


Fig. 4. Temperature dependence of the brightness of the Tb<sup>3+</sup> emission in K<sup>+</sup>-compensated Ba<sub>2</sub>Mg(BO<sub>3</sub>)<sub>2</sub>.

samples. Mr. C. Bakker performed most of the measurements.

Manuscript submitted April 8, 1974; revised manuscript received July 5, 1974.

Any discussion of this paper will appear in a Discussion Section to be published in the June 1975 JOURNAL. All discussions for the June 1975 Discussion Section should be submitted by Feb. 1, 1975.

The publication costs of this article have been assisted by N. V. Philips' Gloeilampenfabrieken.

#### REFERENCES

1. See, e.g., G. Blasse and A. Bril, *Philips Res. Rept.*, **22**, 481 (1967).
2. C. K. Jörgensen, R. Pappalardo, and E. Rittershaus, *Z. Naturforsch.*, **20a**, 54 (1965).
3. J. M. P. J. Verstegen, J. L. Sommerdijk, and J. G. Verriet, *J. Luminescence*, **6**, 425 (1973).
4. W. L. Wanmaker, A. Bril, and J. W. ter Vrugt, *Appl. Phys. Letters*, **8**, (10), 260 (1966).
5. G. Blasse and A. Bril, *J. Chem. Phys.*, **45**, 2350 (1966).
6. German Patent Application, 2,024,408.
7. W. L. Wanmaker and A. Bril, *Philips Res. Rept.*, **19**, 479 (1964).
8. W. L. Wanmaker, A. Bril, and J. W. ter Vrugt, *This Journal*, **112**, 1147 (1965).
9. A. Bril and W. L. Wanmaker, *ibid.*, **111**, 1363 (1964).
10. E. M. Levin, R. S. Roth, and J. B. Martin, *Am. Mineralogist*, **46**, 1030 (1961).
11. A. A. Ballman, *ibid.*, **47**, 1380 (1962).
12. A. D. Mills, *Inorg. Chem.*, **1**, 960 (1962).
13. D. L. Graf and W. F. Bradley, *Acta Cryst.*, **15**, 238 (1962).
14. G. Blasse and A. Bril, *Philips Tech. Rev.*, **31**, (10), 314 (1970).
15. J. M. P. J. Verstegen, J. L. Sommerdijk, and A. Bril, To be published in *J. Luminescence*.
16. A. F. Wells, "Structural Inorganic Chemistry," IInd ed., p. 81 (1962).
17. R. W. G. Wyckoff, "Crystal Structures," IInd ed., Vol. 2, p. 361.

# Calculation of the Liquidus Isotherms and Component Activities in the Ga-As-Si and Ga-P-Si Ternary Systems

A. S. Jordan\* and M. E. Weiner\*<sup>1</sup>

Bell Laboratories, Murray Hill, New Jersey 07974

## ABSTRACT

Liquidus isotherms and thermodynamic activities have been calculated for the Ga-As-Si and Ga-P-Si ternary systems. The calculations are based on the assumption that the activities of the components in the liquid phase can be represented with sufficient accuracy by the ternary regular solution model. A least square analysis of the liquidus data for Si-doped GaAs yields the three ternary interchange energies (i.c.e.'s). These are then used to construct the liquidus isotherms for Si-doped GaAs, Ga- and As-doped Si, and the ternary eutectic valley, all of which are in excellent agreement with the experimental results over a wide temperature and composition range. The ternary Ga-As and Ga-Si i.c.e.'s are in very good accord with the i.c.e.'s derived from the binary data but a similar test for the Si-As i.c.e. shows a less satisfactory agreement. As the Ga-P-Si system has not yet been investigated, the calculations presented here are based solely on binary data and they need experimental confirmation. The implications of these results to crystal growth and the limitations of the regular solution model in the vicinity of the compound composition SiAs are also discussed.

Silicon is one of the most important dopants encountered in the compound semiconductors GaAs and GaP. For example, efficient GaAs infrared light-emitting diodes (LED's) have been fabricated by taking advantage of the amphoteric nature of Si doping (1), while an alloy of Au and Si is used for establishing ohmic contact to GaP LED's (2). However, in contrast to its demonstrated usefulness, the major role of Si in these compounds is that of an unintentional contaminant arising from the frequent use of fused silica crystal growing apparatus. In particular, the electrical properties of melt-grown boules of GaAs have been analyzed by assuming that Si is the dominant residual impurity (3).

Efforts toward a thermochemical understanding of Si contamination have been initiated by Cochran and Foster (4), who discussed the conditions under which liquid Ga reacts with silica. Recently, Si contamination in open flow silica systems for the epitaxial growth of GaAs and GaP has been treated by Weiner (5). Furthermore, DiLorenzo has succeeded in growing very high mobility (6) GaAs in an AsCl<sub>3</sub>-Ga-H<sub>2</sub> vapor growth system by minimizing Si contamination via the careful adjustment of gas stream chemistry (7). Thermodynamic calculations have shown that the activity of Si in the growing crystalline phase,  $a_{Si}^s$ , is related inversely to the partial pressure of HCl (or AsCl<sub>3</sub>) (7, 8). Although much of the work on Si contamination has been concerned with GaAs, GaP is expected to behave similarly with respect to unintentional Si incorporation. Indeed, work on the water vapor synthesis of GaP has indicated that Si is the dominant residual impurity (9). In addition to isolated Si acceptors and donors, Si-O complexes are also thought to be incorporated in GaP (10) and GaAs (11). These deep centers lead to doping and annealing anomalies in GaAs and to nonradiative recombination in n-type GaP.

To achieve a more complete understanding of Si incorporation in GaAs and GaP, it is necessary to obtain information concerning the thermodynamic properties of the Ga-As-Si and Ga-P-Si ternary systems. It is the objective of this paper to present systematic calculations of liquidus isotherms and component activities for both systems. The major assumption re-

quired in performing these calculations is that the activities of the liquid phase are satisfactorily described by the regular solution model (12), which has been previously applied successfully to the ternary phase diagrams of III-V compounds (13-14).

In the present work, first the adequacy of the regular solution model for Si-based systems is tested by a comparison of the ternary interchange energies (i.c.e.'s) (12) derived by a least square analysis of the liquidus data for Si-doped GaAs (no ternary data exist for Si-doped GaP), and the i.c.e.'s obtained from the liquidus of the three bounding binary systems. Second, the ternary liquidus isotherms are calculated over a wide temperature range for both the primary (Si-doped GaAs or GaP) and secondary (Ga- and As- or P-doped Si) solid phases. Third, the intersection of these phase fields as a function of temperature, i.e., the ternary eutectic valley, for the Ga-As-Si and Ga-P-Si systems is given. Fourth, the thermodynamic self-consistency of the present treatment is demonstrated by a comparison of the experimental and calculated eutectic valleys for the Ga-As-Si system. Fifth, the thermodynamic activities for Si, Ga and As, or P in the liquid phase and Si in the solid phase are presented along the liquidus isotherms for the primary solid. Finally, the implications of the calculations for crystal growth and the limitations of the regular solution model in the vicinity of the compound SiAs are discussed.

## Calculation of the Interchange Energies

In a previous paper (15) a general equation [Ref. (15), Eq. [11] has been derived for the liquidus surface of a doped binary compound (with doping levels less than 10<sup>20</sup> cm<sup>-3</sup>) in equilibrium with a regular ternary liquid solution. Applying this equation to the Ga-As-Si system, it follows that

$$2(\Delta H_f - T\Delta S_f) + RT \ln 4x_{Ga}^l x_{As}^l \\ = \alpha_{Ga-As}[0.5 - x_{As}^l(1 - x_{Ga}^l) - x_{Ga}^l(1 - x_{As}^l)] \\ + \alpha_{Ga-Si}x_{Si}^l(2x_{Ga}^l - 1) + \alpha_{Si-As}x_{Si}^l(2x_{As}^l - 1) \quad [1]$$

where  $\Delta S_f$  (8.3 eu g-atom<sup>-1</sup>) and  $\Delta H_f$  (12,540 cal g-atom<sup>-1</sup>) are the entropy and heat of fusion of GaAs (14), the  $x^l$ 's are the atom fractions of the components in the liquid solution, and the  $\alpha$ 's are the ternary i.c.e.'s. A similar equation also holds for the Ga-P-Si system.

\* Electrochemical Society Active Member.

<sup>1</sup> Present address: University of Guadalajara Medical School, Guadalajara, Mexico.

Key words: compound semiconductors, crystal growth, doping, phase equilibria.

Table I. Interchange energies

	a (cal)	b (cal °K <sup>-1</sup> )
Ga-As	4,810	-8.72
Ga-Si	2,480	—
Si-As	21,120	-16.40
Ga-P*	5,080	-5.75
Si-P*	-46,580	27.13

Heats and entropies of fusion			
	$\Delta H_f$ (cal g-atom <sup>-1</sup> )	$\Delta S_f$ (eu g-atom <sup>-1</sup> )	$T_f$ (°K)
GaAs	12,540	8.30	1511
GaP	13,820	7.95	1738
SiAs	8,340	6.15	1356
Si	12,000	7.12	1658
As	5,600	5.14	1090

\* From analysis of binary data.

Based on previous studies of the contributing binary systems the temperature dependences of  $\alpha_{\text{Ga-As}}$  (16) and  $\alpha_{\text{Si-As}}$  (17) are satisfactorily described by relationships of the form

$$\alpha_{\text{Ga-As}} = a_{\text{Ga-As}} + b_{\text{Ga-As}}T \quad [2]$$

and

$$\alpha_{\text{Si-As}} = a_{\text{Si-As}} + b_{\text{Si-As}}T \quad [3]$$

while  $\alpha_{\text{Ga-Si}}$  (17) is taken to be a constant at all temperatures. Substituting Eq. [2] and [3] into Eq. [1] the resulting equation at any liquidus temperature is linear in five unknown parameters which define the i.c.e.'s. Hence, the method of linear least squares permits the evaluation of the "best" values of the ternary i.c.e.'s from experimental data. In the calculations, the multi-dimensional linear least square computational technique of Businger and Golub (18) is applied via Eq. [1] to the 18 ternary liquidus points of Panish (19)<sup>2</sup> and Panish and Sumski (20) for the primary phase field of Si-doped GaAs and to the 14 binary liquidus points of Koster and Thoma (21) and Hall (22) for the Ga-As system. The i.c.e.'s thus obtained are listed in Table I and plotted as a function of temperature in Fig. 1 and 2.

To test the precision of fitting the liquidus data by Eq. [1] using the tabulated ternary i.c.e.'s, a comparison of the calculated liquidus temperature,  $T_c$ , with the experimental liquidus temperature,  $T_m$ , at known compositions (input data) is required. Employing the standard error of estimate defined by  $\sqrt{\sum(T_c - T_m)^2/n}$ , where  $n$  is the number of data points, as the index of precision, we find that the standard error is 2.4°, 5.1°,

<sup>2</sup>A + 10°C correction has been applied to the tabulated liquidus data of Panish (19), as recommended by Panish and Sumski (20), to take into account the effect of supercooling.

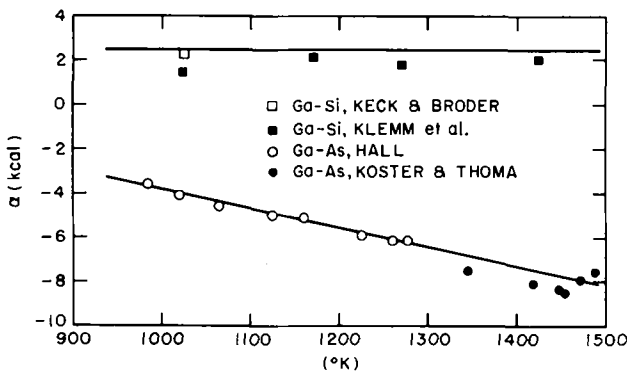


Fig. 1. Interchange energy vs. absolute temperature for the Ga-Si and Ga-As systems. The straight lines are based on the least square analysis of the ternary data.

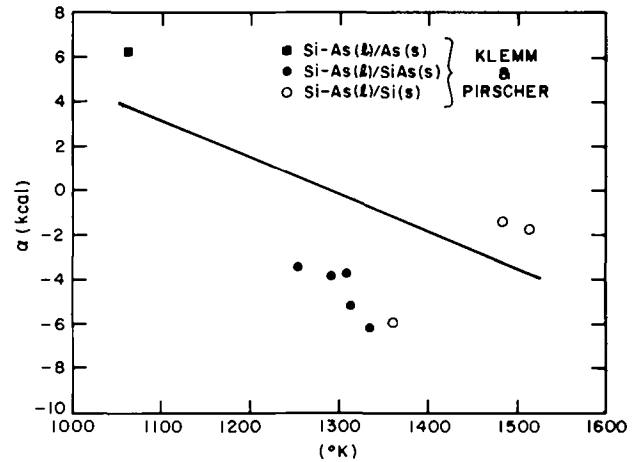


Fig. 2. Interchange energy vs. absolute temperature for the Si-As system. The straight line is based on the least square analysis of the ternary data.

and 4.2°K for the binary, ternary, and combined binary and ternary points, respectively. Thus the calculated liquidus surface and the experimental data for the equilibrium of the primary solid phase are in excellent agreement, probably well within the experimental error.

Nonetheless, a realistic description of the liquidus surface in terms of the least square parameters defining the i.c.e.'s is an incomplete test for showing the applicability of the regular solution model to a given ternary system. The validity of the model can be demonstrated if the thermodynamic properties of the liquid solution, including the variation of the component partial pressures along the liquidus isotherms are satisfactorily predicted. In previous work, applying the regular solution model to the Ga-As-Zn system (14), good agreement was found between the calculated and experimental partial pressure isotherms over a wide temperature range. Unfortunately, no partial pressure data exist for the Ga-As-Si system. Consequently, other thermodynamic techniques must be invoked to check the consistency of the present treatment.

Since there are liquidus data for the three bordering binary regular solutions, i.c.e.'s can be readily calculated. In the case of the Ga-As system,  $\alpha_{\text{Ga-As}}$  is obtained by applying Vieland's equation (23) (identical with Eq. [1] if  $x_{\text{Si}} = 0$ ) to the data of Hall (22) and Koster and Thoma (21). The resulting discrete values of  $\alpha_{\text{GaAs}}$  are plotted as a function of temperature in Fig. 1.

The values of  $\alpha_{\text{Ga-Si}}$  or  $\alpha_{\text{Si-As}}$  are derived from the solubility data for Ga- (24, 25) or As-doped (26) Si using the equation (17)

$$\alpha_{\text{Ga-Si}} \text{ (OR } \alpha_{\text{Si-As}}) = \frac{T\Delta S_f - \Delta H_f - RT \ln x_{\text{Si}}^{\text{lSi}}}{(1 - x_{\text{Si}}^{\text{lSi}})^2} \quad [4]$$

The accepted values of  $\Delta H_f$  and the melting point of Si are 12,000 cal g-atom<sup>-1</sup> and 1685°K (24), respectively, yielding  $\Delta S_f = 7.122$  eu g-atom<sup>-1</sup>. Although the Si-As system is rather complex (26), some additional values of  $\alpha_{\text{Si-As}}$  can be evaluated from the liquidus data for SiAs(s) and As(s), employing Vieland's equation (23) and one similar to Eq. [4], respectively. The required  $\Delta H_f$  for As(s) (5600 cal g-atom<sup>-1</sup>) is based on the work of Horiba (28) which in combination with the melting point of As (1090°K) (29) leads to 5.15 eu g-atom<sup>-1</sup> for  $\Delta S_f$ . For SiAs(s),  $\Delta S_f$  is estimated from the sum of the elemental entropies of fusion (30) to be 6.15 eu g-atom<sup>-1</sup> giving  $\Delta H_f = 8340$  cal g-atom<sup>-1</sup> (the melting point of SiAs is 1356°K).

The discrete values of  $\alpha_{\text{Ga-Si}}$  and  $\alpha_{\text{Si-As}}$ , derived from the binary liquidus data, are shown in Fig. 1 and 2, re-



spectively. It is immediately obvious from Fig. 1 and 2 that the least square lines of the ternary i.c.e.'s provide a very good description of the binary results for the Ga-As and Ga-Si systems. However, in the case of the complex Si-As system (Fig. 2), the total binary  $\alpha_{\text{Si-As}}$  data [from equilibria with Si(s), SiAs(s), and As(s)] scatter more widely about the ternary least square line, representing less adequate agreement.

Unfortunately, no ternary data are available for the Ga-P-Si system. However, as a result of the reasonable over-all agreement achieved between the ternary and binary i.c.e.'s for the Ga-As-Si system, the calculation of the Ga-P-Si phase diagram, using the binary i.c.e.'s appears to be justified. Clearly  $\alpha_{\text{Ga-Si}}$  is the same for both systems, while  $\alpha_{\text{Ga-P}}$  and  $\alpha_{\text{Si-P}}$  can be evaluated from the liquidus data for GaP (22, 31) and for P-doped Si (32) using Vieland's equation (23) and one similar to Eq. [4], respectively. As in previous work,  $\Delta S_f$  for GaP is taken as 7.95 eu g-atom<sup>-1</sup> (14) which yields  $\Delta H_f = 13,920$  cal g-atom<sup>-1</sup> [the melting point of GaP is 1738°K (16)]. In Fig. 3 discrete values of  $\alpha_{\text{Si-P}}$  and  $\alpha_{\text{Ga-P}}$  are presented together with the least square lines of the binary data. Numerical values of the  $\alpha$ 's are listed in Table I.

### Calculations of the Liquidus Isotherms and Eutectic Valleys

The liquidus isotherms for the primary solid phase GaAs or GaP can be readily evaluated from Eq. [1] and the i.c.e.'s listed in Table I.<sup>3</sup> At a constant temperature Eq. [1] is an implicit transcendental equation in the variables  $x_{\text{Ga}}$  and  $x_{\text{Si}}$  ( $x_{\text{As}}$  or  $x_{\text{P}} = 1 - x_{\text{Ga}} - x_{\text{Si}}$ ). A convenient procedure for finding  $x_{\text{Ga}}$  as a function of  $x_{\text{Si}}$  at a set temperature is Schonbrun's iterative technique (33) for nonlinear equations based on Newton's method, previously applied to the liquidus surfaces of the Ga-As-Zn and Ga-P-Zn systems (14). The initial values of  $x_{\text{Ga}}$  at  $x_{\text{Si}} = 0$ , required to perform these calculations, were interpolated from the Ga-As or Ga-P binary data. To assure convergence,  $x_{\text{Ga}}$  and  $x_{\text{As}}$  (or  $x_{\text{P}}$ ) along the Ga- and As- (or P-) rich branches of the liquidus isotherms, respectively, were separately evaluated by incrementing  $x_{\text{Si}}$  from zero to a value very near the maximum in the liquidus isotherms for both branches.

<sup>3</sup> It should be reiterated that the liquidus surface of the Ga-As-Si system is calculated from the ternary i.c.e.'s, while that of the Ga-P-Si system is from the binary i.c.e.'s.

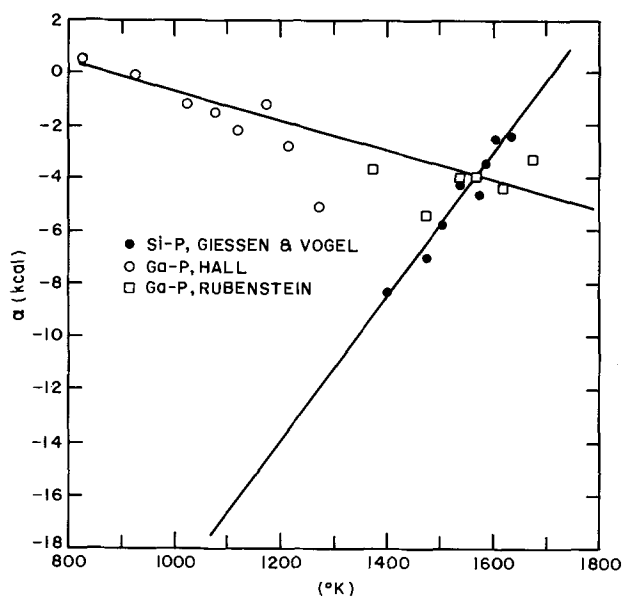


Fig. 3. Interchange energy vs. absolute temperature for the Si-P and Ga-P systems. The straight lines are from the least square analysis of the binary data.

In addition to the calculation of the primary phase fields the relatively low solid solubility of Ga, As, and P in Si (34) facilitates the determination of the liquidus isotherms for the secondary solid phases of Ga- and As- or P-doped Si. Previously, a general thermodynamic equation has been given for an elemental semiconductor doped with two solutes in equilibrium with a ternary liquid solution (15). Introducing ternary regular solution activities into this general equation yields

$$\Delta H_f - T\Delta S_f + RT \ln x_{\text{Si}}^2 = -\alpha_{\text{Ga-As}}(x_{\text{Ga}})^2 + (\alpha_{\text{Si-As}} - \alpha_{\text{Ga-Si}} + \alpha_{\text{Ga-As}})(1 - x_{\text{Si}})x_{\text{Ga}} - \alpha_{\text{Si-As}}(1 - x_{\text{Si}})^2 \quad [5]$$

where  $\Delta H_f$  and  $\Delta S_f$  are for Si. Note that for  $x_{\text{Ga}} = 0$  or  $x_{\text{As}} = 0$ , Eq. [5] reduces to Eq. [4].

At a constant temperature Eq. [5] is quadratic in  $x_{\text{Ga}}$ . Thus at any temperature the liquidus isotherm of the secondary solid phase was obtained by incrementing  $x_{\text{Si}}$  and solving the quadratic equation for  $x_{\text{Ga}}$ .

The liquidus isotherms representing the equilibria of the primary solid phase (Si-doped GaAs) and of the secondary solid phase (Ga- and As-doped Si) with Ga-As-Si ternary melts are shown in Fig. 4 on a standard equilateral composition triangle. Similar liquidus isotherms for the Ga-P-Si system are presented in Fig. 6. For the Ga-As-Si system complete isotherms are shown at 1400°, 1300°, 1200°, and 1127°C. At 1127°C the primary and secondary phase fields are tangential; below that temperature the fields intersect at a point corresponding to the three-phase equilibria of GaAs, Si, and liquid. Thus, on the Ga-rich side between 1100° and 700°C and on the As-rich side at 1100°C, the isotherms are truncated at the three-phase points which lie on the ternary eutectic valley (dashed line). On the As-rich side, the available experimental data (19) dictate the termination of the valley by the ternary eutectic point (~1031°C) arising from the coprecipitation of SiAs, while the 1000° and 900°C liquidus isotherms of Si-doped GaAs are cut at the approximate compositions where SiAs and SiAs<sub>2</sub> appear, respectively (19).

The calculated liquidus isotherms in Fig. 4 are complemented by the ternary data of Panish (19) and Panish and Sumski (20). It should be pointed out that these are not the tabulated experimental points used in the computations but values interpolated in 100°C intervals from empirical pseudobinary liquidus curves.

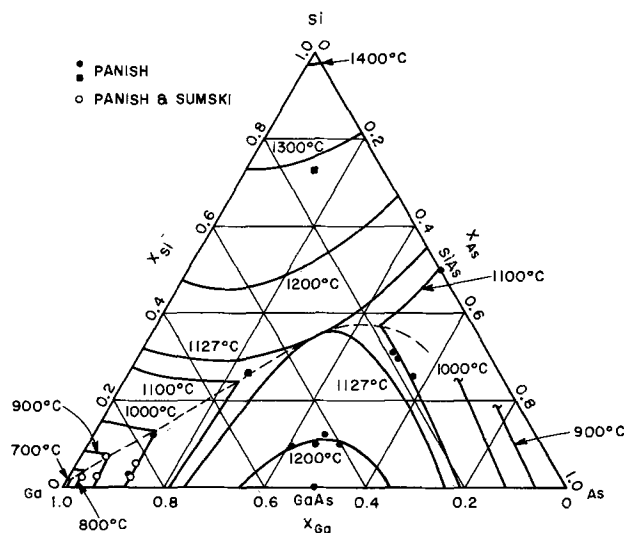


Fig. 4. Liquidus isotherms for the ternary Ga-As-Si liquid solution in equilibrium with Si-doped GaAs and Ga- and As-doped Si. The data (■) at 1100° and 1300° correspond to equilibrium with Si. The dashed line is the ternary eutectic valley.

Reinforcing the conclusions of the error analysis in the previous section, the calculated isotherms provide a very good representation of the liquidus data for Si-doped GaAs and even for Ga- and As-doped Si.

An additional check on the thermodynamic validity of the present treatment can be obtained by a comparison of the calculated and experimental eutectic valleys in the Ga-As-Si system. In Fig. 5 the eutectic valley is replotted in the form of  $\log x_{\text{Si}}^{\text{l}}$  and  $\log x_{\text{Ga}}^{\text{l}}$  vs. reciprocal temperature. Superimposed in Fig. 5 is the experimental eutectic valley derived from published works (19, 20). It should be noted that the eutectic temperatures had been measured and the corresponding eutectic compositions were interpolated from the pseudobinary liquidus data. The agreement between experimental and calculated valleys over the entire composition range investigated is rather striking.

Along the ternary eutectic valley,  $a_{\text{Si}}^{\text{s}} = 1$ ; hence the knowledge of  $x_{\text{Si}}^{\text{l}}$  and  $\Delta H_{\text{f}}$  and  $\Delta S_{\text{f}}$  for Si (27) permit the evaluation of  $\gamma_{\text{Si}}^{\text{l}}$  (activity coefficient for Si). As seen in Fig. 5 the experimental and calculated values of  $\gamma_{\text{Si}}^{\text{l}}$  are in excellent agreement.

For the Ga-P-Si system complete liquidus isotherms are given between 1400° and 1100°C in 100°C intervals (Fig. 6). At 1097°C the secondary and primary phase fields are tangential, while below that temperature the three-phase equilibria of GaP, Si, and liquid take place. On the Ga-rich side, the ternary eutectic valley is shown (dashed line) from 1097° to 800°C together with the three-phase points which terminate the isotherms drawn in 100°C intervals. The valley is replotted in Fig. 7 as a function of reciprocal temperature. The P-rich sides of the isotherms are not shown below 1100°C because of the complex phase relationships in the Si-P system resulting from compound formation and the high pressure of phosphorus (31).

#### Calculation of the Component Activities

It has been demonstrated in previous sections that the application of the regular solution model to the Ga-As-Si system provides an excellent description of the ternary liquidus surface, leads to an over-all consistency with the binary liquidus data, and predicts the ternary eutectic valley and the accompanying  $\gamma_{\text{Si}}^{\text{l}}$  in good agreement with experimental results. Consequently, a calculation of the component activities prevailing along the liquidus isotherms is warranted. The ternary regular solution activities for the Ga-As-Si

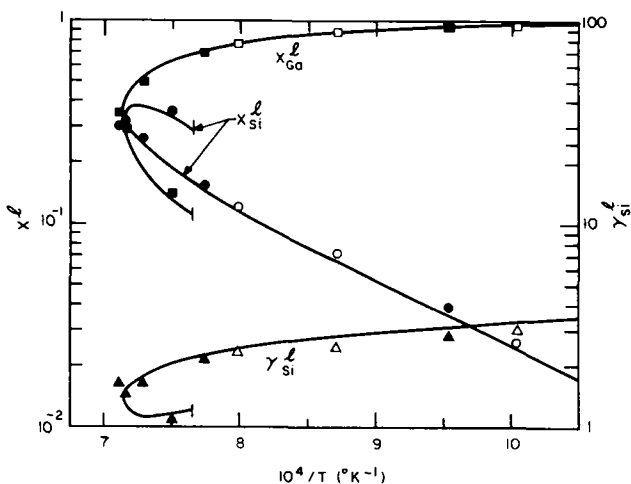


Fig. 5. The ternary eutectic valley of the Ga-As-Si system. The curves were calculated. The composition of the liquid solution (in atom fraction units) and the activity coefficient of Si are shown as a function of reciprocal temperature. The symbols  $\square$  and  $\circ$  represent values of  $x_{\text{Ga}}^{\text{l}}$  and  $x_{\text{Si}}^{\text{l}}$  from Panish and Sumski, while  $\blacksquare$  and  $\bullet$  are values of  $x_{\text{Ga}}^{\text{l}}$  and  $x_{\text{Si}}^{\text{l}}$  from Panish. The data for  $\gamma_{\text{Si}}^{\text{l}}$  denoted by  $\triangle$  and  $\blacktriangle$  are derived from  $x_{\text{Si}}^{\text{l}}$   $\circ$  and  $\bullet$ , respectively.

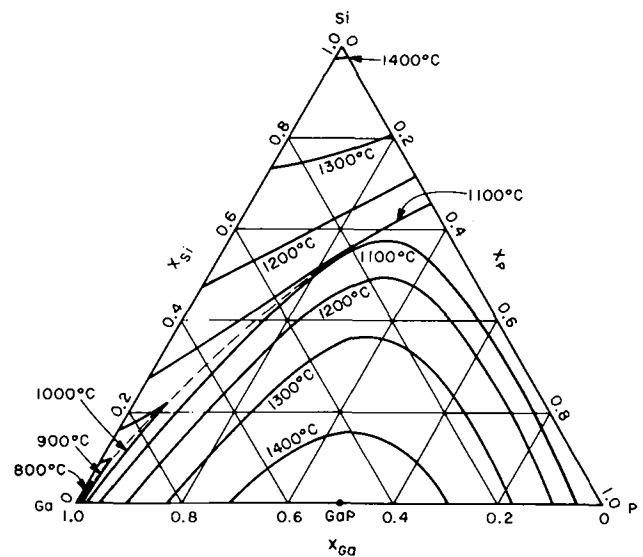


Fig. 6. Liquidus isotherms for the ternary Ga-P-Si liquid solution in equilibrium with Si-doped GaP and Ga- and P-doped Si. The dashed line is the ternary eutectic valley.

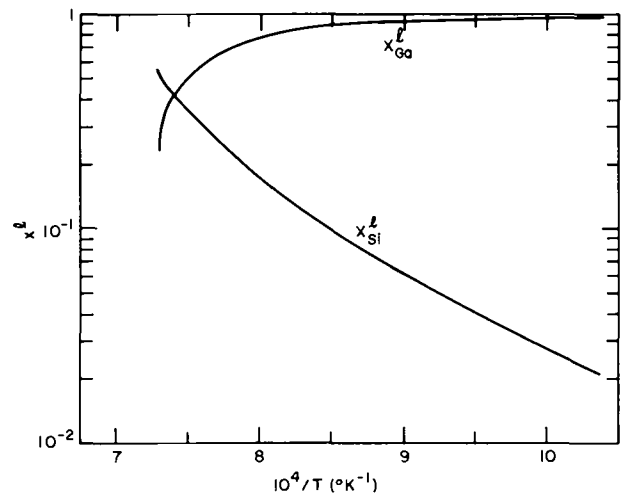


Fig. 7. The calculated ternary eutectic valley for the Ga-P-Si system. The composition of the liquid solution (in atom fraction units) is plotted vs. reciprocal temperature.

system are given by (35)

$$a_{\text{Si}}^{\text{l}} = x_{\text{Si}}^{\text{l}} \exp \left[ \frac{1}{RT} (\alpha_{\text{Ga-Si}} x_{\text{Ga}}^{\text{l}2} + \alpha_{\text{Si-As}} x_{\text{As}}^{\text{l}2} + x_{\text{Ga}}^{\text{l}} x_{\text{As}}^{\text{l}} \times (\alpha_{\text{Ga-Si}} + \alpha_{\text{Si-As}} - \alpha_{\text{Ga-As}})) \right] \quad [6a]$$

$$a_{\text{Ga}}^{\text{l}} = x_{\text{Ga}}^{\text{l}} \exp \left[ \frac{1}{RT} (\alpha_{\text{Ga-Si}} x_{\text{Si}}^{\text{l}2} + \alpha_{\text{Ga-As}} x_{\text{As}}^{\text{l}2} + x_{\text{As}}^{\text{l}} x_{\text{Si}}^{\text{l}} \times (\alpha_{\text{Ga-Si}} + \alpha_{\text{Ga-As}} - \alpha_{\text{Si-As}})) \right] \quad [6b]$$

and

$$a_{\text{As}}^{\text{l}} = x_{\text{As}}^{\text{l}} \exp \left[ \frac{1}{RT} (\alpha_{\text{Ga-As}} x_{\text{Ga}}^{\text{l}2} + \alpha_{\text{Si-As}} x_{\text{Si}}^{\text{l}2} + x_{\text{Ga}}^{\text{l}} x_{\text{Si}}^{\text{l}} \times (\alpha_{\text{Ga-As}} + \alpha_{\text{Si-As}} - \alpha_{\text{Ga-Si}})) \right] \quad [6c]$$

Where  $a_i^{\text{l}}$  is the activity of the subscripted component. A set of equations similar to Eq. [6] also holds for the Ga-P-Si system.

At any composition along a liquidus isotherm the activities for the components of the liquid phase in

equilibrium with the primary solid phase can be readily calculated from Eq. [1], Eq. [6a-c], and the i.c.e.'s listed in Table I. The important activity function for silicon dissolved in GaAs,  $a_{\text{Si}}^{\text{l}}$  is obtained from the relationship

$$a_{\text{Si}}^{\text{l}} = a_{\text{Si}}^{\text{s}} \exp \left[ \frac{1}{RT} (\mu_{\text{Si}}^{\text{l}} - \mu_{\text{Si}}^{\text{s}}) \right] \quad [7]$$

where  $\mu_{\text{Si}}^{\text{l}}$  and  $\mu_{\text{Si}}^{\text{s}}$  are the standard chemical potentials for the supercooled liquid and solid phases, respectively, derivable from published heat capacity and heat of fusion data (27).

In Fig. 8  $a_{\text{Si}}^{\text{s}}$  and  $a_{\text{Si}}^{\text{l}}$  are plotted as functions of  $x_{\text{Si}}^{\text{l}}$  along the 800°, 1000°, and 1200°C liquidus isotherms of Si-doped GaAs. A complete isotherm is shown at 1200°C, while at lower temperatures the activities are for the Ga-rich branches and are terminated at the three-phase points (solid dots). In Fig. 9 and 10,  $a_{\text{Ga}}^{\text{l}}$  and  $a_{\text{As}}^{\text{l}}$  are presented as a function of  $x_{\text{As}}^{\text{l}}$  and  $x_{\text{Ga}}^{\text{l}}$ ,

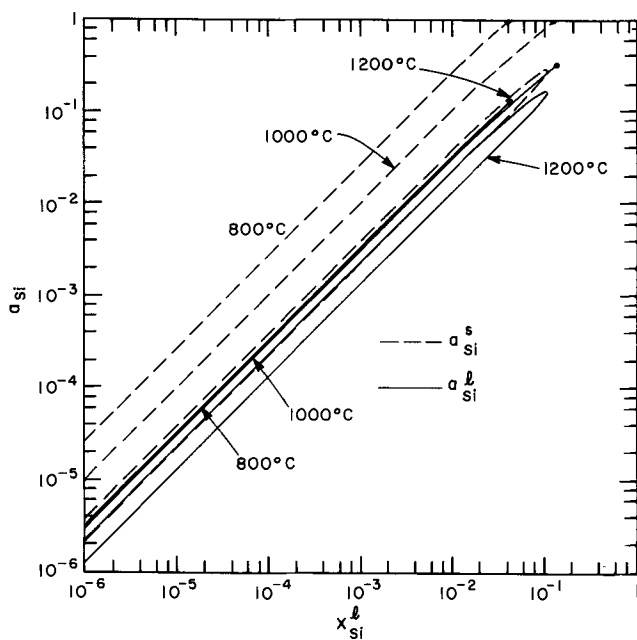


Fig. 8. The activity of Si in the liquid and the corresponding activity of Si dissolved in GaAs along the 800°, 1000°, and 1200°C liquidus isotherms for Si-doped GaAs. Only the Ga-rich isotherms are shown at 800° and 1000°C, and they are terminated at the three-phase points (solid dots).

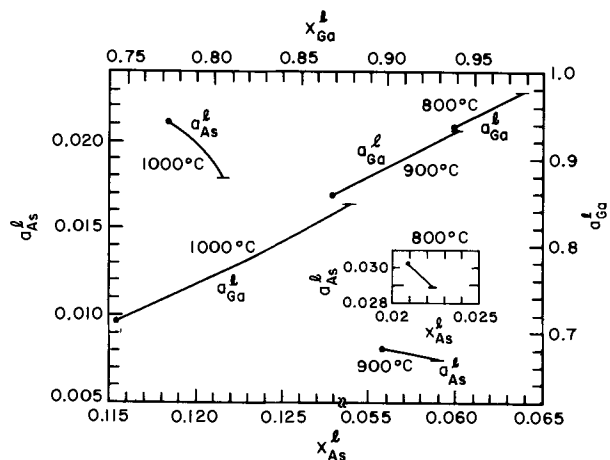


Fig. 9. Ga and As activities vs.  $x_{\text{Ga}}^{\text{l}}$  and  $x_{\text{As}}^{\text{l}}$ , respectively, along the 800°, 900°, and 1000°C liquidus isotherms for Si-doped GaAs. The Ga-rich segments are shown from the binary limits (horizontal bars) to the three-phase points (solid dots).

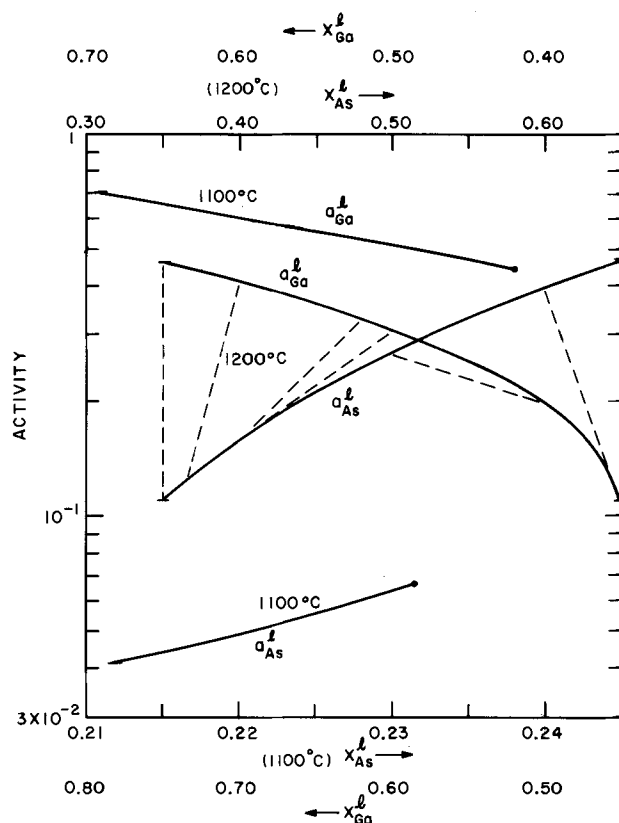


Fig. 10. Ga and As activities vs.  $x_{\text{Ga}}^{\text{l}}$  and  $x_{\text{As}}^{\text{l}}$ , respectively, along the 1100° and 1200°C liquidus isotherms for Si-doped GaAs. At 1100°C only the Ga-rich segments are shown which terminate at the three-phase points (solid dots). The horizontal bars are drawn at the binary limiting values of the activities. At 1200°C dashed lines connect activity and liquidus information along the liquidus isotherm (see text).

respectively, from 800° to 1200°C in 100°C intervals. Between 800° and 1100°C only the Ga-rich segments of the activity isotherms are given and they are ended at the three-phase points. The dashed lines drawn in Fig. 10 at 1200°C demonstrate that the compositions along a liquidus isotherm can be combined with the activities on a single plot. At  $x_{\text{Ga}}^{\text{l}} = 0.6, 0.5,$  and  $0.4$ , the  $a_{\text{Ga}}^{\text{l}}$  line is connected to the  $a_{\text{As}}^{\text{l}}$  line at a value of  $x_{\text{As}}^{\text{l}}$  given by the liquidus isotherm of Fig. 4. A like construction for the  $a_{\text{As}}^{\text{l}}$  line is given at  $x_{\text{As}}^{\text{l}} = 0.4, 0.5,$  and  $0.6$ .

In Fig. 11,  $a_{\text{Si}}^{\text{l}}$  and  $a_{\text{Si}}^{\text{s}}$  are shown as functions of  $x_{\text{Si}}^{\text{l}}$  along the 800°, 1000°, 1200°, and 1400°C liquidus isotherms for Si-doped GaP. At 800° and 1000°C only the Ga-rich branches of the activity isotherms are presented which terminate at the three-phase points. In Fig. 12, 13, and 14  $a_{\text{Ga}}^{\text{l}}$  and  $a_{\text{P}}^{\text{l}}$  are plotted as functions of  $x_{\text{Ga}}^{\text{l}}$  and  $x_{\text{P}}^{\text{l}}$ , respectively, from 800° to 1400°C in 100° intervals. Full isotherms are given at 1200°, 1300°, and 1400°C, while at lower temperatures the Ga-rich segments of the curves are truncated at the three-phase points.

## Discussion

**Implications of the ternary phase diagrams for heteroepitaxy.**—Both the Ga-As-Si and Ga-P-Si ternary systems have the property that the eutectic valley along which Si and GaAs or GaP coexist extends to the high temperatures commonly used in the preparation of these compounds. This suggests the possibility of the technologically important heteroepitaxy of GaAs and GaP on Si. One of the major techniques of epitaxial growth is liquid-phase epitaxy (LPE). In practice, first a saturated solution of GaAs or GaP in Ga is formed; then the solution is brought into contact with a substrate. If the substrate is Si, we may analyze the

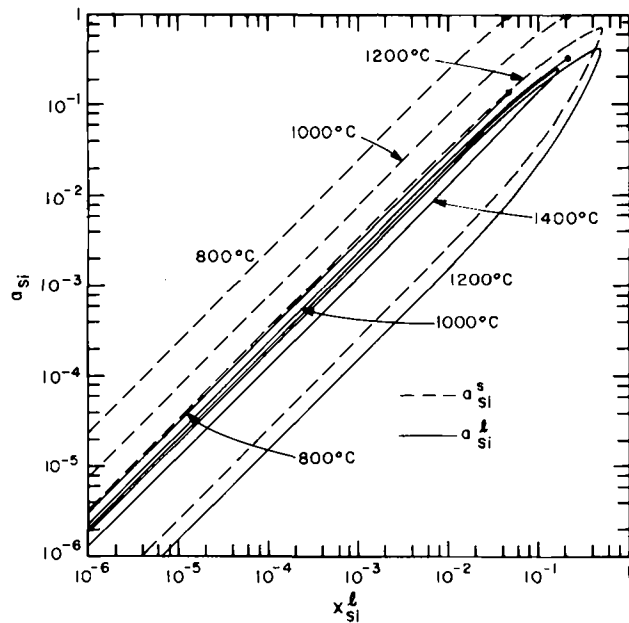


Fig. 11. The activity of Si in the liquid and the corresponding activity of Si dissolved in GaP along the 800°, 1000°, 1200°, and 1400°C liquidus isotherms for Si-doped GaP. Only the Ga-rich isotherms are shown at 800° and 1000°C, and they are terminated at the three-phase points (solid dots.)

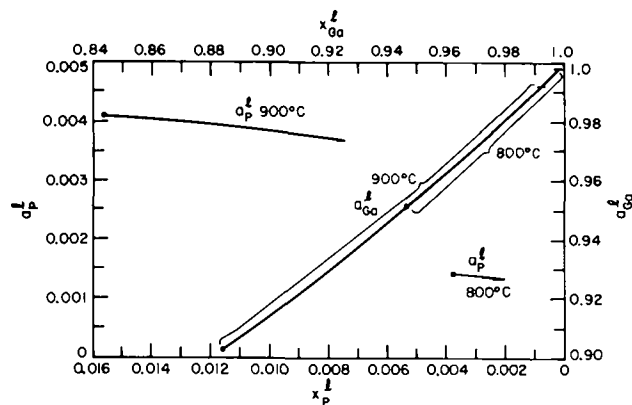


Fig. 12. Ga and P activities vs.  $x_{Ga}^l$  and  $x_P^l$ , respectively, along the 800° and 900°C liquidus isotherms for Si-doped GaP. The Ga-rich segments are shown from the binary limits (horizontal bars) to the three-phase points (solid dots).

progress of the phase reactions with reference to Fig. 4 and 6.

As long as there is no precipitation in the ternary system the ratio of Ga/As or Ga/P in the solutions remains constant. Thus at any temperature the reaction proceeds along a line extending from the Ga-rich binary saturation point to the apex of the composition triangle ( $x_{Si} = 1$ ). It can be seen in both systems at 1000°C that this line enters a single-phase liquid region, implying the dissolution of the Si-seed, until the isotherm for the secondary solid phase (Si) is reached. Upon cooling, Si will precipitate until the temperature is reached at which this line intersects the eutectic valley.

In order to deposit GaAs or GaP on Si it is required that the line described above immediately enter a two-phase liquid + GaAs or GaP region. According to Fig. 4 and 6, this appears possible below 900°C in the case of GaAs but not at any reasonable temperature for GaP. It is interesting to note that Rosztochy and Stein (36) were unable to precipitate GaP on Si from a Ga-rich

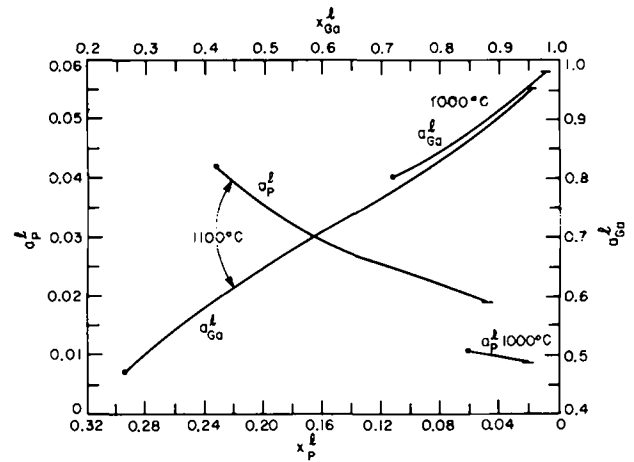


Fig. 13. Ga and P activities vs.  $x_{Ga}^l$  and  $x_P^l$ , respectively, along the 1000° and 1100°C liquidus isotherms for Si-doped GaP. The Ga-rich segments are shown from the binary limits (horizontal bars) to the three-phase points at 1000°C and its vicinity at 1100°C.

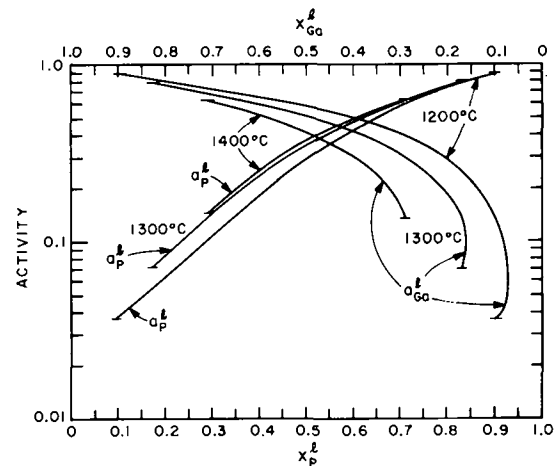


Fig. 14. Ga and P activities vs.  $x_{Ga}^l$  and  $x_P^l$ , respectively, along the 1200°, 1300°, and 1400°C liquidus isotherms for Si-doped GaP. The horizontal bars are drawn at the binary limiting values of the activities.

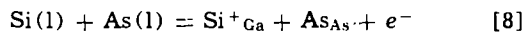
solution. However, they could achieve heteroepitaxy by using Pb or Sn as a solvent.

*Some features of the activity diagrams.*—Not unexpectedly, moving from the Ga-rich to the As- or P-rich regions of the liquidus isotherms,  $a_{Ga}$  and  $a_{As}$  or  $a_P$  decrease and increase, respectively (Fig. 9, 10, 12, 13, and 14). Appropriate combinations of  $a_{As}$  and  $a_P$  with thermodynamic data for the vapor pressure of pure liquid As (28) and P (27) yield the partial pressures of these components along the liquidus isotherms.

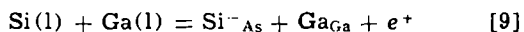
It is important to note that according to Fig. 8 and 11,  $a_{Si}^s$  for both systems is higher along the Ga-rich liquidus branch than along the As- or P-rich one. Hence, if the activity coefficient for Si dissolved in GaAs does not vary drastically with composition, vapor grown GaAs or GaP has a lower Si solubility ( $a_{Si}^s$  values enclosed by the branches) than crystals prepared by LPE ( $a_{Si}^s$  values along the Ga-rich liquidus isotherm).

Generally, the activities in the liquid phase are required in testing incorporation models. For example, for an amphoteric dopant such as Si, the analysis of solubility data as a function of temperature and doping level is quite complex because both Si acceptors ( $Si^{-As}$ ) and Si donors ( $Si^{+Ga}$ ) exist in the lattice.

However, based on the over-all incorporation reaction for the two species (11) viz.



and



it can be seen that the concentrations of  $\text{Si}^+_{\text{Ga}}$  and  $\text{Si}^-_{\text{As}}$  depend on the products  $a_{\text{SiAs}}$  and  $a_{\text{SiGa}}$ , respectively. Obviously, the knowledge of the activities facilitates the separation of experimental solubilities into donor and acceptor contributions.

*The limitations of the regular solution model.*—It has been demonstrated in previous sections that the regular solution model provides an excellent description of the measured ternary liquidus data for the Ga-As-Si system. That the ideal solution model is inadequate to treat this system can be best illustrated with reference to the eutectic valley. According to Eq. [7], for an ideal liquid solution the equation of the eutectic valley is given by ( $\gamma^1_{\text{Si}} = 1$ ,  $a^0_{\text{Si}} = 1$ )

$$x^{\text{lid}}_{\text{Si}} = \exp \left[ \frac{1}{RT} (\mu^{\text{os}}_{\text{Si}} - \mu^{\text{ol}}_{\text{Si}}) \right] \quad [10]$$

The results of sample calculations based on Eq. [10] in comparison with the data from Fig. 5 indicate that at 800° and 1100°C Eq. [10] overestimates the concentration of Si ( $x^{\text{lid}}_{\text{Si}}$ ) at the eutectic valley by about a factor of 2.7 and 1.7, respectively.

However, as there exist no ternary liquidus data for  $x^{\text{As}} > 0.6$  (19), the predictions of the regular solution model may be inaccurate in the As-rich region. One clue pointing in this direction has already been mentioned in relation to the wide scatter of the binary  $\alpha_{\text{Si-As}}$  data about the ternary least square line (Fig. 2). Examining the binary data in detail, we find a minimum near the melting point of the compound SiAs. Note that a higher estimate for the  $\Delta S_f$  of SiAs would decrease the  $\alpha_{\text{Si-As}}$  values (full circles in Fig. 2), resulting in a steeper minimum. Clearly, according to regular solution theory, any i.c.e. such as  $\alpha_{\text{Si-As}}$  measures the difference in nearest neighbor pairwise interaction energies between unlike and like bonds [ $\epsilon_{\text{Si-As}} = \omega_{\text{Si-As}} - 0.5 (\omega_{\text{Si-Si}} + \omega_{\text{As-As}})$ ] and should be the same for a binary, ternary, or even multicomponent system. Hence, if the Ga-As-Si system at all compositions and temperatures were behaving as a perfectly regular solution then the binary  $\alpha_{\text{Si-As}}$  values would not show a minimum and would exhibit a much closer agreement with the ternary least square line, as is the case for  $\alpha_{\text{Ga-As}}$  and  $\alpha_{\text{Si-Ga}}$ .

At this time, we can only speculate about the cause of the apparent minimum in the binary  $\alpha_{\text{Si-As}}$ . In previous work on regular associated solutions (RAS) such a minimum in a  $\alpha$  vs. composition (or temperature) curve in the Zn-Te and Cd-Te system has been interpreted in terms of the association of the atoms into ZnTe and CdTe molecules in the liquid phase (37). It is possible that the liquid phase of the Si-As system similarly consists of Si and As atoms and SiAs molecules. Unfortunately, a simple extension of the RAS theory to the ternary Ga-As-Si system was not successful because the transition from an RAS near the Si-As side to a completely dissociated ternary regular solution with the increasing addition of Ga is not rapid enough if the degree of dissociation is not a function of composition itself. Thus a good description of the Si-As binary can only be achieved at the expense of the ternary liquidus and eutectic valley data. Nevertheless, it seems qualitatively clear that the reason the ternary least square line provides no more than an approximate description of the total binary data is related to the progressive straightening out of the initially steep  $\alpha_{\text{Si-As}}$  curve as the solution becomes dissociated with increasing  $x^{\text{Ga}}$ .

It is possible that the Ga-As-Ge and Ga-As-Sn systems behave similarly to the Ga-As-Si system.

Recent studies show that the slope of the ternary least square lines of  $\alpha_{\text{Ge-As}}$  (38)  $\alpha_{\text{Sn-As}}$  (39) is of the same sign as of the ternary  $\alpha_{\text{Si-As}}$ . Moreover, the sign of the slope for  $\alpha_{\text{Si-As}}$  and  $\alpha_{\text{Ge-As}}$  are both the opposite of the slope of the line connecting the few binary  $\alpha_{\text{Si-As}}$  and  $\alpha_{\text{Ge-As}}$  data points for Si(s) and Ge(s) in equilibrium with their binary melts (17) (open circles in Fig. 2).

A comparison of the liquidus surface constructed from the ternary least square i.c.e.'s and the binary i.c.e.'s is instructive. To show the effect of  $\alpha_{\text{Si-As}}$  on the ternary liquidus boundary, we selected the line going through the three data points for Si(s) (open circles in Fig. 2), thus ignoring the equilibria for SiAs(s) and As(s). Performing the calculations it is found that the standard error of estimate between the calculated and experimental ternary liquidus points is 19.1°K which should be compared with 5.1°K, obtained by the use of the ternary i.c.e.'s. The recomputed surface also possesses a ternary eutectic valley which intersects the liquidus isotherms at larger values of  $x^{\text{Si}}$ . For example, at 1000°C, the eutectic valley is at  $x^{\text{Si}} = 0.251$  which should be compared with 0.135 resulting from the ternary i.c.e.'s. Obviously, the ternary least square calculation provides a superior description of the experimental data. However, even the calculation employing the binary i.c.e.'s would offer a useful guide to the phase relations in the Ga-As-Si system.

In view of the above discussion, the Ga-P-Si ternary liquidus surface which was calculated solely from the binary i.c.e.'s needs experimental confirmation. Certainly, it is not expected to depart more from the actual liquidus surface than is indicated for the Ga-As-Si system when the binary i.c.e.'s were used. To be sure, the fact that the slope of the  $\alpha_{\text{Si-P}}$  line (Fig. 3) is opposite that of the ternary least square line of  $\alpha_{\text{Si-As}}$  (Fig. 2) is puzzling. However, the eight discrete  $\alpha_{\text{Si-P}}$  values seem to be reliable for they are located close to the least square line over a 200°K temperature range.

Conceivably, one should not trust one's intuition in expecting completely parallel bonding behavior of P and As in liquid solutions. Indeed, there are well-known differences between the chemistry of P and As. For instance, the prevalent oxide of As and P is trivalent ( $\text{As}_2\text{O}_3$ ) and pentavalent ( $\text{P}_2\text{O}_5$ ), respectively. Moreover, many binary phase diagrams of As and P (40), including the Si-As (26) and Si-P (32) systems, are not homologous.

In conclusion, the regular solution treatment provides a consistent analytical representation of phase equilibria in the Ga-As-Si system, in excellent agreement with experimental results over almost the entire liquidus surface. More sophisticated models which possibly involve association are needed to improve the calculation in the vicinity of the Si-As binary. In the absence of experimental data for the Ga-P-Si ternary system, the predictions presented here may only give approximate although valuable phase relations. Thus for this system, as well as for any other system, the regular solution theory should be accepted with caution and retested against fresh experimental evidence.

### Acknowledgments

We express our gratitude to D. L. Rode and R. H. Saul for their critical reading of the manuscript.

Manuscript submitted Feb. 28, 1974; revised manuscript received July 5, 1974.

Any discussion of this paper will appear in a Discussion Section to be published in the June 1975 JOURNAL. All discussions for the June 1975 Discussion Section should be submitted by Feb. 1, 1975.

The publication costs of this article have been assisted by Bell Laboratories.

\* It should be noted that the binary and ternary least square lines for  $\alpha_{\text{Si-Ga}}$  and  $\alpha_{\text{Ge-As}}$  are nearly the same (see Fig. 1).

## REFERENCES

1. I. Ladany, *J. Appl. Phys.*, **42**, 654 (1971).
2. A. A. Bergh and R. J. Strain, in "Ohmic Contacts to Semiconductors," B. Schwartz, Editor, pp. 115-127, The Electrochemical Society Softbound Symposium Series, New York (1969).
3. J. F. Woods and N. G. Ainslie, *J. Appl. Phys.*, **34**, 1469 (1963).
4. C. N. Cochran and L. M. Foster, *This Journal*, **109**, 144 (1962).
5. M. E. Weiner, *ibid.*, **119**, 496 (1972).
6. J. V. DiLorenzo and G. E. Moore, Jr., *ibid.*, **118**, 1823 (1971).
7. J. V. DiLorenzo and A. E. Machala, *ibid.*, **118**, 1516 (1971).
8. P. Rai-Choudhury, *J. Cryst. Growth*, **11**, 113 (1971).
9. C. J. Frosch, C. D. Thurmond, H. G. White, and J. A. May, *Trans. Met. Soc. AIME*, **239**, 365 (1967).
10. R. Z. Bachrach, O. G. Lorimor, L. R. Dawson, and K. B. Wolfstirn, *J. Appl. Phys.*, **43**, 5098 (1972).
11. M. E. Weiner and A. S. Jordan, *ibid.*, **43**, 1767 (1972).
12. E. A. Guggenheim, "Mixtures," Oxford University Press, London (1952).
13. M. B. Panish and M. Ilegems, in "Progress in Solid State Chemistry," H. Reiss and J. O. McCaldin, Editors, Pergamon Press, New York (1972).
14. A. S. Jordan, *Met. Trans.*, **2**, 1965 (1971).
15. A. S. Jordan, *ibid.*, **2**, 1959 (1971).
16. C. D. Thurmond, *J. Phys. Chem. Solids*, **26**, 785 (1965).
17. C. D. Thurmond and M. Kowalchik, *Bell System Tech. J.*, **39**, 169 (1960).
18. P. Businger and G. H. Golub, *Numerische Mathematik*, **7**, 259 (1965).
19. M. B. Panish, *This Journal*, **113**, 1226 (1966).
20. M. B. Panish and S. Sumski, *J. Appl. Phys.*, **41**, 3195 (1970).
21. W. Koster and B. Thomas, *Z. Metallk.*, **46**, 291 (1955).
22. R. N. Hall, *This Journal*, **110**, 385 (1963).
23. L. J. Vieland, *Acta. Met.*, **11**, 137 (1963).
24. W. Klemm, L. Klemm, E. Hohman, H. Volk, E. Orlamunder, and H. A. Klein, *Z. Anorg. Allgem. Chem.*, **256**, 239 (1948).
25. P. H. Keck and J. Broder, *Phys. Rev.*, **90**, 521 (1953).
26. W. Klemm and P. Pirscher, *Z. Anorg. Allgem. Chem.*, **247**, 211 (1941).
27. JANAF Interim Thermochemical Tables, Dow Chemical Company.
28. S. Horiba, *Z. Phys. Chem.*, **106**, 295 (1923).
29. D. R. Stull and G. C. Sinke "Thermodynamic Properties of the Elements," Advances in Chemistry Series, No. 18, American Chemical Society, Washington, D.C. (1956).
30. O. Kubaschewski, E. LL. Evans, and C. B. Alcock, "Metallurgical Thermochemistry," 4th Ed., Pergamon Press Ltd. (1967).
31. M. Rubenstein, Abstract 65, Vol. 11, p. 129, Electrochemical Society, Extended Abstracts of the Electronics Division, Spring Meeting, Los Angeles, California, May 6-10, 1962.
32. B. Giessen and R. Vogel, *Z. Metallk.*, **50**, 274 (1959).
33. S. S. Schonbrum, Private communication.
34. F. A. Trumbore, *Bell System Tech. J.*, **39**, 205 (1960).
35. I. Prigogine and R. Defay, "Chemical Thermodynamics," Longmans, Green and Company, Ltd., London (1954).
36. F. E. Rosztochy and W. W. Stein, *This Journal*, **119**, 1119 (1972).
37. A. S. Jordan, *Met. Trans.*, **1**, 239 (1970).
38. M. B. Panish, *J. Appl. Phys.*, **44**, 2676 (1973).
39. M. B. Panish, *ibid.*, **44**, 2659 (1973).
40. See, for example, M. Hansen, "Constitution of Binary Alloys," McGraw Hill, New York (1958), and supplementary volumes edited by R. P. Elliott (1965) and F. A. Shunk (1969).

# Heteroepitaxial InAs Grown on GaAs from Triethylindium and Arsine

## I. Growth Characterization

B. Jayant Baliga and Sorab K. Ghandhi

Electrophysics and Electronic Engineering Division, Rensselaer Polytechnic Institute, Troy, New York 12181

### ABSTRACT

Single-crystal films of InAs have been grown on semi-insulating GaAs substrates by the decomposition of triethylindium and arsine over a temperature range of 550°-650°C. The growth is mass-transport limited above 575°C and kinetically controlled below 575°C. Films of more than 0.5  $\mu\text{m}$  have specular surfaces. Optimum growth conditions occur at a substrate temperature of 600°C, a flow of 2 mliters/min arsine (pure), and 2.5 liters/min hydrogen flow through the TEI bubbler.

The growth of epitaxial layers of III-V compounds using organometallic compounds as sources of the group III element and hydrides as sources of the group V element, was first reported by Manasevit and co-workers (1-3). Since then, other workers (4-6) have extensively studied the growth of GaAs by this technique, but have not investigated the growth of InAs. Although the feasibility of the epitaxial growth of InAs from triethylindium and arsine was demonstrated by Manasevit and Simpson (3), their investigations were mainly directed toward the growth and characterization of  $\text{Ga}_{1-x}\text{In}_x\text{As}$  alloys with  $x \approx 0.5$ . In this paper, we wish to report on the characterization of the growth of InAs epitaxial films. The electrical properties of these layers are reported in the companion paper (7).

### Experimental Conditions

**Apparatus.**—The epitaxial growth was carried out in a 50 mm ID quartz tube, 45 cm long, containing a molybdenum susceptor coated with  $\text{SiO}_2$ . The sus-

**Key words:** heteroepitaxy, chemical vapor deposition, organometallic compounds, indium arsenide, gallium arsenide.

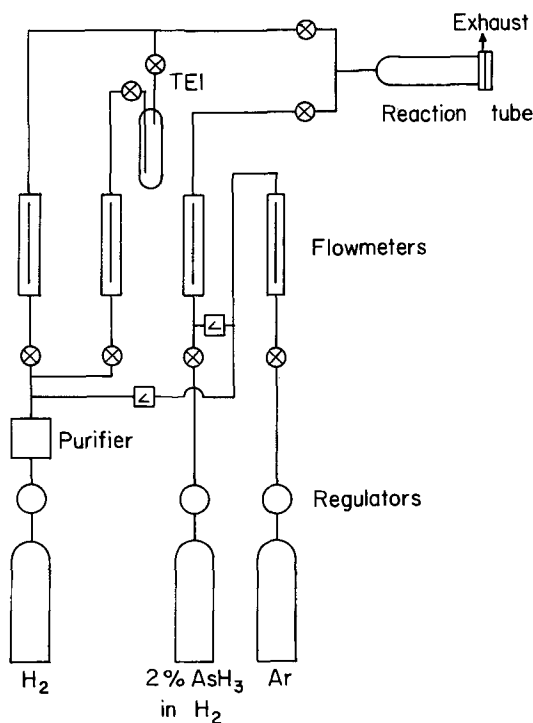


Fig. 1. Schematic of InAs epitaxial reactor

ceptor was heated by infrared radiation from a set of eight, 500W quartz-halogen lamps. This greatly simplified temperature measurement and allowed the use of a closed-loop temperature control. The temperature of the single hot zone was monitored by a platinum/platinum-rhodium thermocouple, enclosed in a quartz sheath and inserted into the molybdenum susceptor. A horizontal reactor system was used to simplify loading and cleaning operations. However, substrates were placed perpendicular to the gas flow to facilitate uniform growth over the entire surface.

Vapors of triethylindium<sup>1</sup> (TEI) were transported to the substrate by bubbling hydrogen through the liquid maintained at room temperature (25°C). Arsine gas,<sup>2</sup>

<sup>1</sup> Alfa Products Division, Beverly, Massachusetts 01915.

<sup>2</sup> Matheson Gas Products, East Rutherford, New Jersey, 07073.

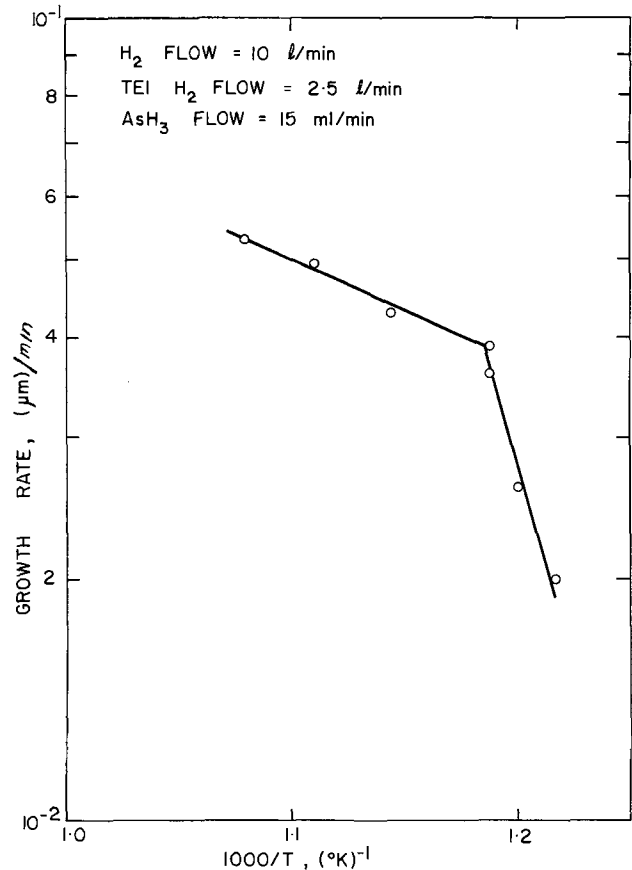


Fig. 2. Effect of substrate temperature on growth rate

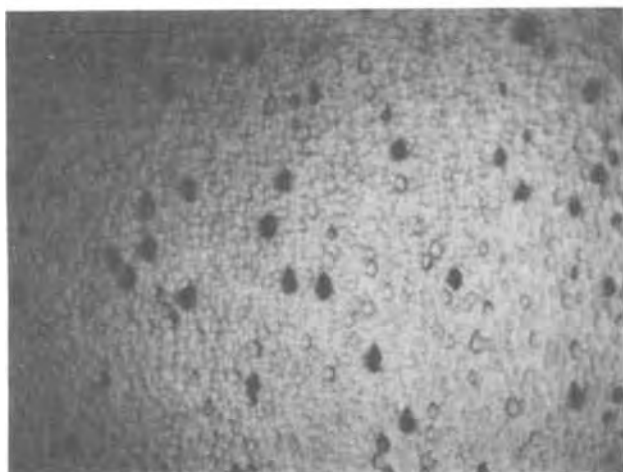


Fig. 3. Inclusions in InAs layer grown at 650°C. Layer thickness 2  $\mu\text{m}$ .

diluted to 2% in hydrogen was mixed with the TEI vapors just before entering the quartz tube. Due to the reaction between the TEI and arsine at room temperature, they were not premixed before entry to the hot zone. In addition, a separate source of ultra high purity hydrogen was used, at a flow rate of 10 liters/min in all the experiments. This carrier gas flow served to transport the reactants down the quartz tube and to minimize the formation of reaction products upstream of the susceptor. Stainless steel tubing was used throughout, in order to reduce system contamination. A schematic of the apparatus is shown in Fig. 1.

**Substrate.**—Epitaxial growth was carried out on (100) oriented chromium doped semi-insulating GaAs substrates, to facilitate subsequent electrical evaluation. The substrates were obtained commercially with one face polished.<sup>3</sup> No further attempts were made to polish the wafers. Before epitaxy, however, the substrates were thoroughly cleaned in methanol<sup>4</sup> and checked under an optical microscope to ensure the absence of dust particles.

**Procedure.**—Substrates were heated up to 500°C in hydrogen, at which point arsine was introduced into the reaction tube to suppress the sublimation of arsenic from the GaAs substrates. Arsine flows greater than 0.5 mliter/min (pure) were sufficient to prevent this dissociation from occurring up to a substrate temperature of 750°C. After stabilizing the arsine flow for 2 min, the substrate temperature was raised to the growth temperature and maintained for an additional 2 min before the introduction of TEI. Typical flow rates used were 2-15 mliters/min arsine gas (pure), and 1-2.5 liters/min hydrogen flow through the TEI bubbler. Typical growth rates under these conditions were 0.05-0.07  $\mu\text{m}/\text{min}$ .

**Growth rate determination.**—Angle lapping and staining techniques were initially used to measure the thickness of the epitaxial layers. However, etching of the surface by the staining and plating solutions, and the presence of large depletion layer widths at the interface resulted in considerable error in determining layer thickness. Consequently, this technique was abandoned in favor of a gravimetric determination of epitaxial layer thickness. Early in the growth studies, it was determined that no loss in weight of the substrate GaAs took place in the presence of arsine flows greater than 0.5 mliter/min (pure) up to a substrate temperature of 750°C. Since the TEI-arsine reaction does not contain any etchant species, the increase in

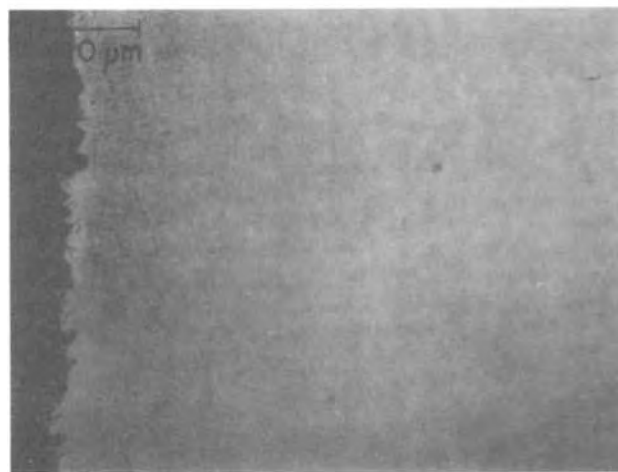
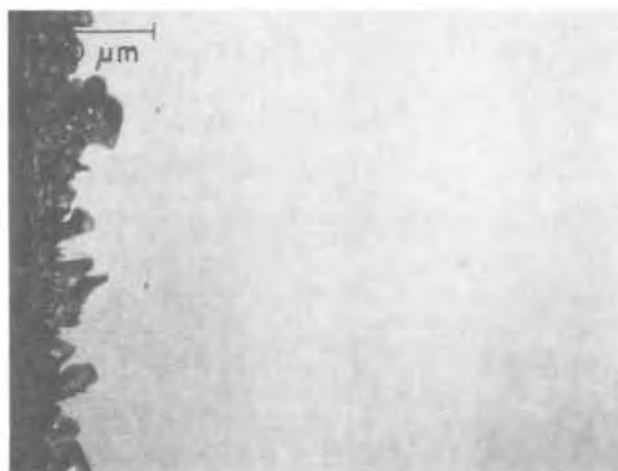


Fig. 4. Effect of substrate temperature on surface quality. (a, top) 650°C, thickness 0.53  $\mu\text{m}$ ; (b, center) 600°C, thickness 0.43  $\mu\text{m}$ ; (c, bottom) 540°C, thickness 0.57  $\mu\text{m}$ .

mass of the substrate after epitaxy could be directly used to determine the thickness of the epitaxial layers.

### Experimental Results

**Temperature.**—The effect of temperature on growth rate was determined using a flow of 2.5 liters/min of hydrogen through the TEI bubbler and a flow of 15 mliters/min of arsine (pure). Under these conditions, the growth was approximately mass-transport limited at temperatures above 575°C and kinetically controlled below this temperature, as shown in Fig. 2. The activation energy of the reaction was measured as 2.3 eV/

<sup>3</sup> Electronic Materials Corporation, Pasadena, California 91107.

<sup>4</sup> Substitution of methanol with more sophisticated cleaning solutions and procedures did not produce any significant change in the growth rate or surface quality of the epitaxial films.



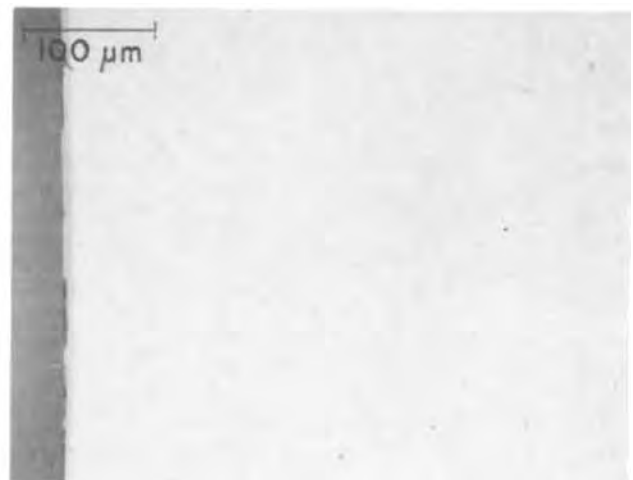
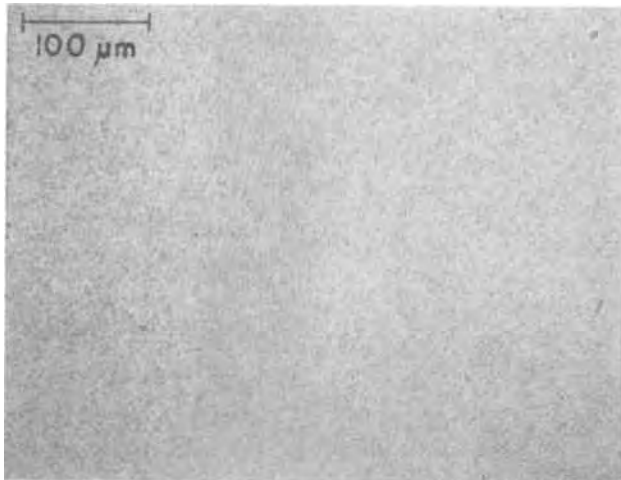
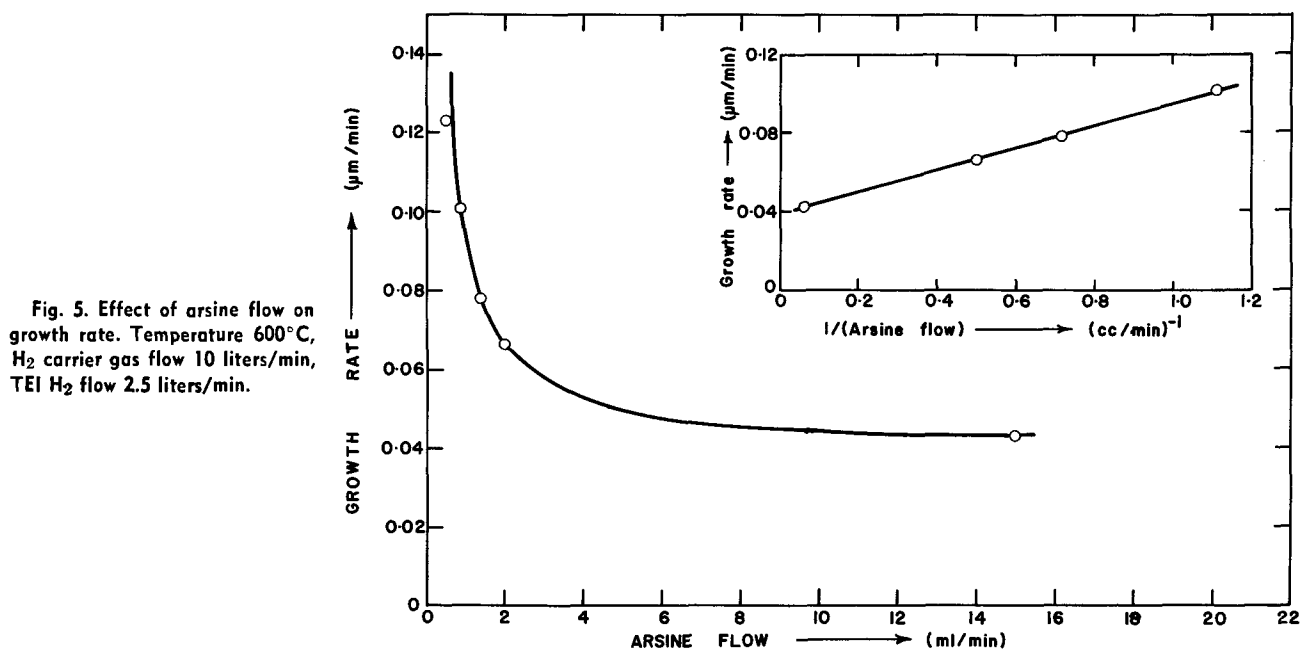


Fig. 6. Effect of arsine flow on surface quality. (a, left) 0.9 ml/min, thickness 1.2 μm; (b, right) 1.4 ml/min, thickness 0.80 μm; (c, bottom right) 2 ml/min, thickness 0.65 μm.

molecule. Below 550°C, polycrystalline layers were obtained with growth rates exceeding 0.05 μm/min.

Optical examination of the epitaxial layers showed that best surfaces were obtained at 600°C. At both higher, as well as lower, temperatures the surface quality deteriorated with the appearance of small

black inclusions as shown in Fig. 3. The surface also changed to a poorly reflecting gray color from the bright-shiny appearance obtained at 600°C. Photomicrographs of typical surfaces are shown in Fig. 4.

*Arsine flow.*—The arsine flow was found to have a strong effect on the growth rate and on the surface

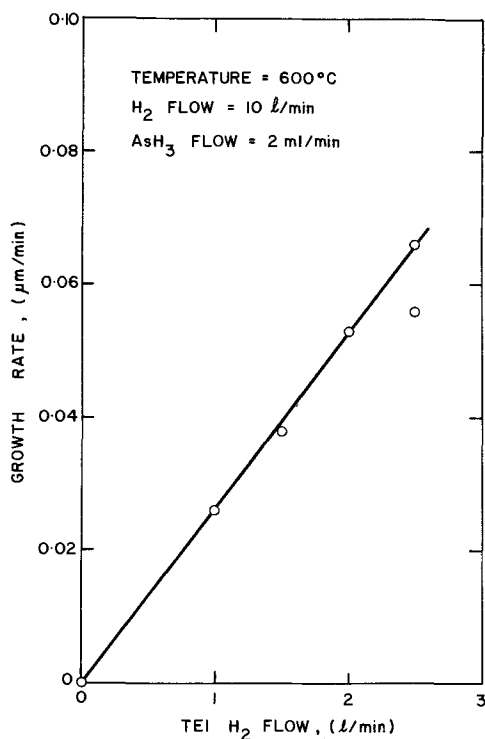


Fig. 7. Effect of increasing hydrogen flow through TEI bubbler on growth rate.

quality of the layers. Figure 5 shows the variation of growth rate with arsine flow, when the hydrogen flow through the TEI bubbler was 2.5 liters/min and the substrate temperature was 600°C. The growth rate decreased rapidly with increasing arsine flow. Retardation (8) of the heterogeneous reaction by the adsorption of arsine on the surface was verified by the linear variation of growth rate with reciprocal arsine flow, as shown in the inset of Fig. 5.

Good specular surfaces were obtained for arsine flows (pure) ranging from 1.4 to 15 mliters/min. However, a marked degradation in surface quality was observed for arsine flows less than 1.4 mliters/min (pure). Photomicrographs of typical surfaces are shown in Fig. 6.

**TEI flow.**—Figure 7 shows the growth rate of the epitaxial films as a function of hydrogen gas flow through the TEI bubbler for a substrate temperature of 600°C and an arsine flow (pure) of 2 mliters/min. This data has not been presented using an equivalent flow of TEI because of the unknown vapor pressure of this metalorganic compound at room temperature. Note, however, the use of high flow rates necessitated by its low vapor pressure (estimated to be less than 0.1 mm of Hg at 25°C). The growth rate is seen to be linear with gas flow through the bubbler, indicating an absence of saturation in the transported TEI over this flow range.

An improvement was observed in the surface quality of the epitaxial layers with increasing gas flow through the TEI bubbler, as shown in Fig. 8. Since the arsine flow used in these experiments was sufficient to produce specular surfaces over the entire range of hydrogen flow through the TEI bubbler, we conclude that the improvement in surface quality is primarily due to increasing film thickness. This is to be expected, in view of the large mismatch between the lattice parameters of the GaAs substrate and the InAs epitaxial film. The effects of strain induced by this mismatch decrease as each atomic layer is grown, resulting in a consequent improvement of surface quality with film thickness.

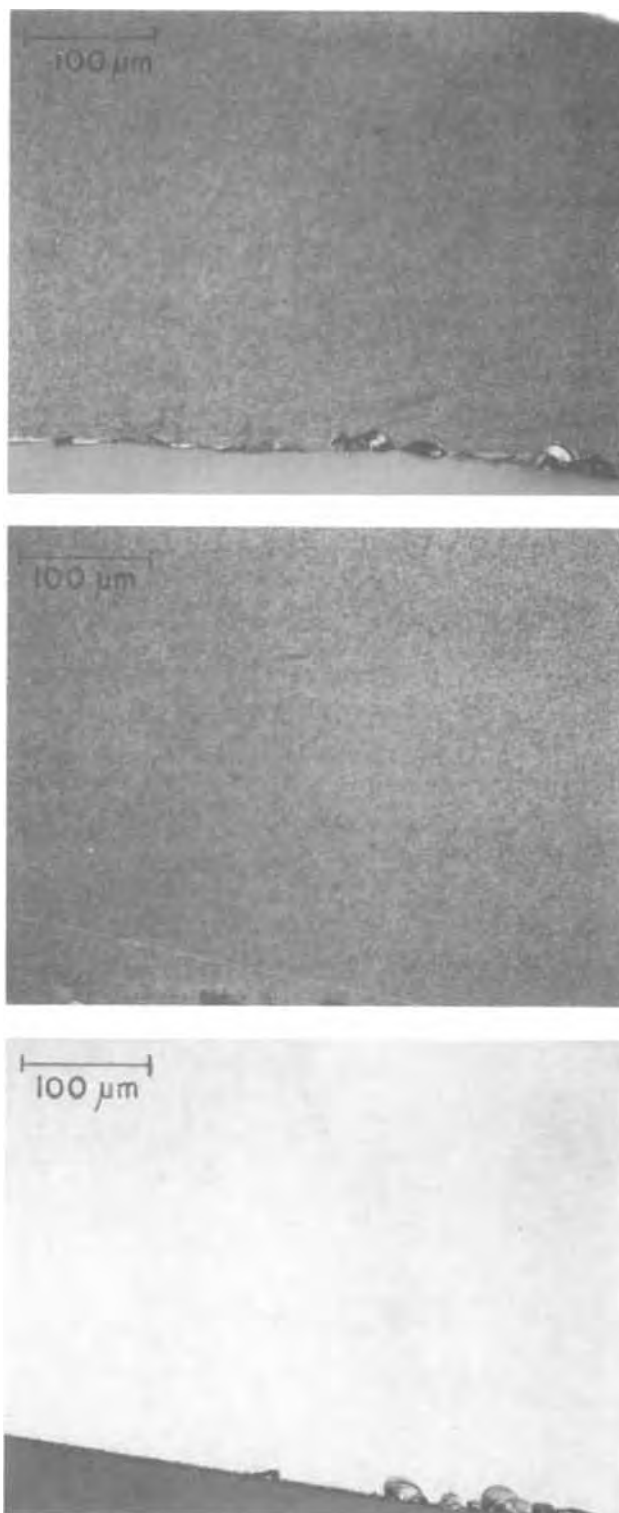


Fig. 8. Effect of increasing film thickness on surface quality. (a, top) Thickness 0.26 μm, 1.0 liter/min H<sub>2</sub> flow in TEI; (b, center) thickness 0.38 μm, 1.5 liters/min H<sub>2</sub> flow in TEI; (c, bottom) thickness 0.53 μm, 2.0 liters/min H<sub>2</sub> flow in TEI. AsH<sub>3</sub> flow in all cases was 2 mliters/min.

### Conclusions

Heteroepitaxial InAs films with specular surfaces can be grown on GaAs substrates using the reaction between triethylindium and arsine. The growth is mass-transport limited above 575°C and kinetically controlled below 575°C, with an activation energy of 2.3 eV/molecule under our experimental conditions. Polycrystalline layers are obtained below 550°C. Lay-

ers of less than 0.5  $\mu\text{m}$  have poor surfaces due to the large mismatch in lattice constants between InAs and GaAs, but become specular at large thicknesses. Best surfaces are obtained at a substrate temperature of 600°C, a flow of 2 mliters/min arsine (pure), and 2.5 liters/min hydrogen flow through the TEI bubbler. Since the reaction is mass-transport limited at the optimum growth conditions, good control over the growth rate can be obtained without stringent requirements on the substrate temperature. Furthermore, the growth rate can be varied over a wide range by adjusting the gas flows in the system.

#### Acknowledgment

This work was supported by Grant No. GK-31332 from the National Science Foundation. The authors are indebted to Dr. H. Minden for his critical review, and to Ms. R. Rafun for assistance in manuscript preparation.

Manuscript submitted Jan. 30, 1974; revised manuscript received June 28, 1974.

Any discussion of this paper will appear in a Discussion Section to be published in the June 1975 JOURNAL. All discussions for the June 1975 Discussion Section should be submitted by Feb. 1, 1975.

The publication costs of this article have been assisted by Rensselaer Polytechnic Institute.

#### REFERENCES

1. H. M. Manasevit and W. I. Simpson, *This Journal*, **116**, 1925 (1969).
2. H. M. Manasevit, *ibid.*, **118**, 647 (1971).
3. H. M. Manasevit and W. I. Simpson, *ibid.*, **120**, 135 (1973).
4. P. Rai-Choudhury, *ibid.*, **116**, 1745 (1969).
5. K. Lindeke, W. Sack, and J. J. Nickl, *ibid.*, **117**, 1316 (1970).
6. P. Smith, Ph.D. Thesis, Rensselaer Polytechnic Institute, Troy, New York (1973).
7. B. J. Baliga and S. K. Ghandi, *This Journal*, **121**, 1646 (1974).
8. S. Glasstone, "Textbook of Physical Chemistry," Second Edition, Fifteenth Printing, pp. 642-643, Van Nostrand Co., New York (1965).

## Heteroepitaxial InAs Grown on GaAs from Triethylindium and Arsine

### II. Electrical Properties

B. Jayant Baliga and Sorab K. Ghandi

*Electrophysics and Electronic Engineering Division, Rensselaer Polytechnic Institute, Troy, New York 12181*

#### ABSTRACT

Heteroepitaxial films of InAs on GaAs substrates, grown by the decomposition of triethylindium and arsine, have been characterized. Films with mobilities of up to 10,000  $\text{cm}^2/\text{V}\text{-sec}$  have been obtained. The mobility remains approximately constant with decreasing thickness up to an epitaxial layer thickness of 1  $\mu\text{m}$ . A theory is presented for the variation in defect density in epitaxial layers as a function of the growth temperature and layer thickness. The carrier concentration of the InAs layers decreases exponentially with increasing substrate temperature and decreases inversely with increasing layer thickness, in accordance with this theory.

In the preceding paper (1), the growth characteristics of InAs films made by reacting triethylindium (TEI) and arsine were described. InAs films were first grown by this technique by Manasevit and Simpson (2) on sapphire and GaAs substrates. Films of 0.5-1.1  $\mu\text{m}$  in thickness were reported to have carrier concentrations of greater than  $10^{17} \text{cm}^{-3}$  and mobilities ranging from 6700 to 11,200  $\text{cm}^2/\text{V}\text{-sec}$ . No details of the variation of the electrical properties of these layers with growth parameters were reported for these films. In this paper, we wish to describe the electrical properties of InAs layers grown on GaAs substrates, under the growth conditions described in the companion paper (1).

#### Experimental Conditions

Epitaxy was performed on (100) oriented, chromium-doped semi-insulating GaAs wafers to facilitate electrical characterization. The films were grown over a temperature range of 550°-650°C with typical gas flow rates of 15 mliters/min arsine and 2.5 liters/min hydrogen flow through the TEI bubbler. Typical growth rate under these conditions was 0.05  $\mu\text{m}/\text{min}$ . Details of the growth characteristics are described in the companion paper (1).

The mobility and carrier concentration of these films were measured by using conventional bridge samples in a Hall effect apparatus. The bridge samples were obtained by coating the epitaxial layer with silicon dioxide at 400°C using the oxidation of silane, followed by conventional photolithographic delineation of the oxide. The oxide was then used as a mask for etching the epitaxial layer in Caro's etch (1:1:1 =  $\text{H}_2\text{O}_4$ :30%  $\text{H}_2\text{O}_2$ : $\text{H}_2\text{O}$ ). Ohmic contacts were made to the arms by using silver conducting paint, applied at room temperature.

#### Mobility

The lattice constants of GaAs and InAs are 5.654 and 6.058Å, respectively, resulting in a lattice mismatch of more than 7%. This large mismatch is accommodated during epitaxy by the generation of defects in the InAs layer. The electrical properties of the epitaxial layers are expected to be dominated by the presence of these defects.<sup>1</sup> Since the defect density is expected to vary within the epitaxial layer, the mobility and carrier concentration are expected to be functions of layer thickness. The interpretation of Hall measurements must be made with due consideration to this variation (3).

<sup>1</sup> The mean free path of carriers in InAs is much smaller than the thickness of the thinnest films considered in this work. Therefore, we do not expect surface scattering effects to be important in our films.

The conductivity voltage can be shown to be proportional to

$$\left[ \int_0^d n\mu dz \right]^{-1}$$

where  $n$  and  $\mu$  are the carrier concentration and mobility of a layer of thickness  $dz$  at thickness  $z$ , and  $d$  is the total layer thickness. The Hall voltage is proportional to the ratio of

$$\left[ \int_0^d n\mu^2 dz \right] \text{ to } \left[ \int_0^d n\mu dz \right]^2$$

To determine the mobility in the layers as a function of thickness, plots of

$$\int_0^d n\mu dz \text{ and } \int_0^d n\mu^2 dz$$

were made *vs.*  $d$  for a  $7.2 \mu\text{m}$  layer which was successively etched down. The slopes of these curves were used to calculate  $\mu$  *vs.*  $d$ . The calculated mobility varied between 10,000 and 12,000  $\text{cm}^2/\text{V}\cdot\text{sec}$ . Therefore, we conclude that the mobility in the layers was essentially constant between 1 and  $7.2 \mu\text{m}$ . This result indicates that polar optical scattering is dominant in layers greater than  $1 \mu\text{m}$  in thickness. The defect density is expected to be large at the GaAs-InAs interface, and lower mobilities are expected for layers much thinner than  $1 \mu\text{m}$ . The mobility of a large number of different epitaxial samples is shown in Fig. 1. These films have been grouped according to their thickness in order to show the strong influence of this parameter on mobility. The carrier concentration is averaged over the layer thickness.

Mobilities of 20,000  $\text{cm}^2/\text{V}\cdot\text{sec}$  have been reported for heteroepitaxial InAs on GaAs substrates, grown by using the chloride transport of indium, and either arsine (4) or arsenic trichloride (5, 6) as a source of arsenic. These layers had thicknesses on the order of  $50 \mu\text{m}$ . Lower values of 10,000  $\text{cm}^2/\text{V}\cdot\text{sec}$ , with comparable carrier concentration and thickness, have been obtained by Allen and Mehal (7), using the chloride transport of indium with arsine as the source of arsenic.

The mobility of our  $7 \mu\text{m}$  (thick) epitaxial layer is comparable to that reported by the above authors. However, comparison of the mobility of our thin epitaxial layers with those grown by the above-mentioned techniques is not possible because of the lack of available information on thin epitaxial layers grown by the above techniques. Godinho and Brunnshweiler (8) have reported on the mobility of thin InAs films on GaAs substrates, produced by vacuum evaporation. They find a similar variation in mobility with decreasing thickness.

### Carrier Concentration

Figure 2 shows the variation of carrier concentration with growth temperature for a number of films of InAs, keeping the other growth parameters constant. This behavior is significantly different from that observed during the growth of GaAs epitaxial layers on GaAs substrates, where it is usually found that the carrier concentration increases with increasing substrate temperature, because of doping from the gas phase (9). We believe that the doping concentration *vs.* growth temperature dependence of our films can be explained by considering the point defects in the layers as the primary source of the carrier concentration.

*Theory.*—Since the InAs epitaxial layers are grown on GaAs substrates, a large density of point defects is present at the interface between the film and the substrate. This defect density is given by  $4(a_{\text{GaAs}}^{-2} - a_{\text{InAs}}^{-2}) = 1.61 \times 10^{14} \text{ cm}^{-2}$  for the (100) surface, if an abrupt interface between GaAs and InAs is assumed (10). Additional defects can arise from thermal cycling, due to the difference in lattice expansion coefficients. Since the substrate orientation is (100), equal numbers of defects can be expected to occur at the indium and the arsenic sites. However, because of the large hole to electron effective mass ratio, the donor defect level will be shallower than the acceptor level, leading to a net n-type doping of the epitaxial layers. All the InAs layers, grown in the absence of intentional doping, were indeed found to be n-type as expected from the above argument.

The variation in defect density with temperature and film thickness can be theoretically calculated using a simple atomic layer growth model. In this model, it is

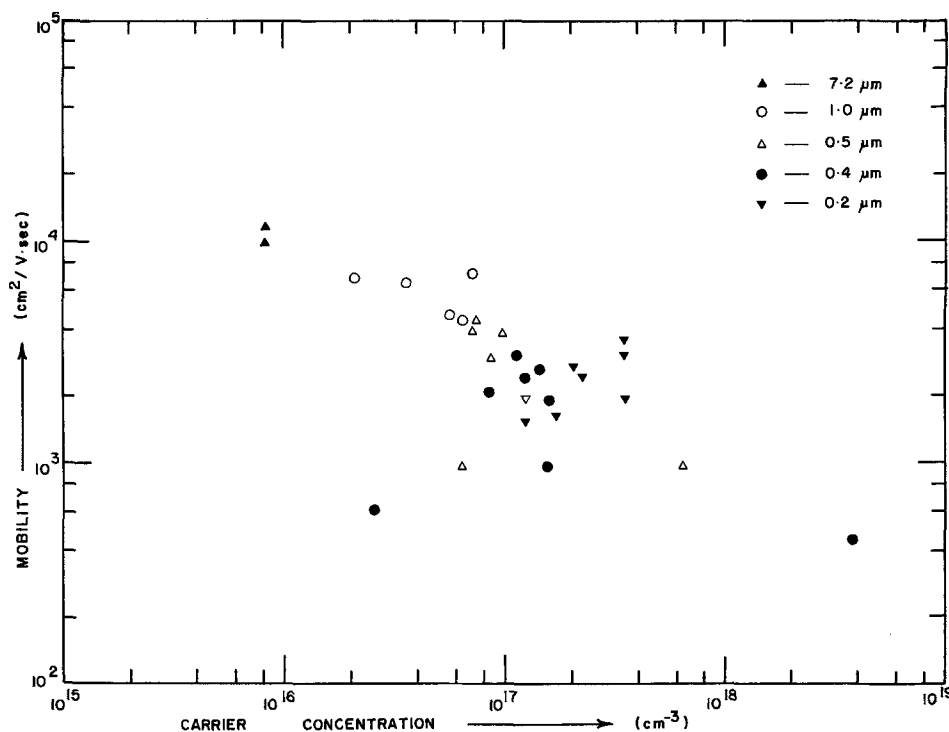


Fig. 1. Mobility vs. carrier concentration of InAs epitaxial layers.

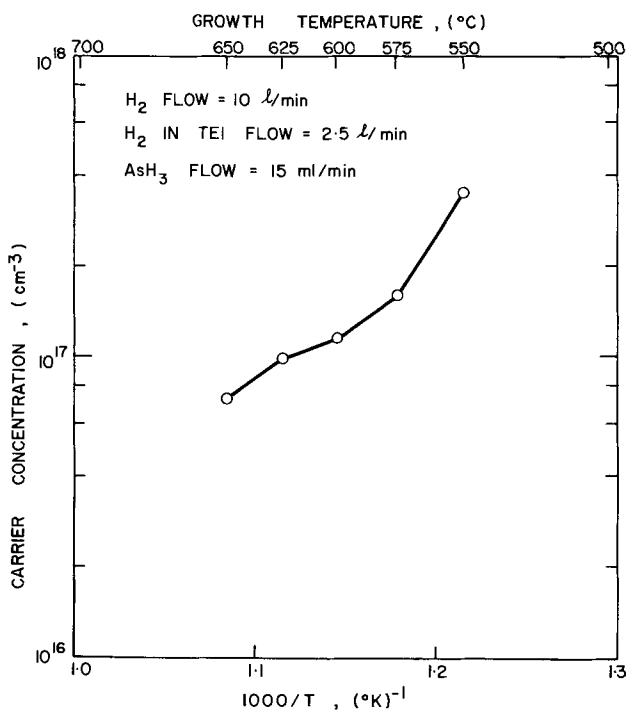


Fig. 2. Effect of substrate temperature on carrier concentration

assumed that  $g$  defects per unit area are present at the substrate layer interface. During epitaxial growth, annihilation of defects takes place by the encounter between atoms from the gas phase and lattice voids on the growing surface. The probability of such encounters is proportional to the concentration of voids in the lattice and the mobility of gas atoms on the epitaxial surface.

The concentration of defects in each growing monolayer is, therefore, proportional to their concentration in the previous monolayer. Thus, the addition of each atomic monolayer to the epitaxial film will reduce the defect density by a constant fraction  $q$ . The defect density in the first monolayer is thus  $g(1-q) = gp$ , in the second monolayer  $gp^2$ , in the third monolayer  $gp^3$ , etc., until there is a defect density of  $gp^m$  in the  $m$ th monolayer. The thickness of the epitaxial layer, composed of  $m$  monolayers, is  $ma$ , where  $a$  is the lattice constant of the growing film. The average volume concentration of defects in the epitaxial layer is thus given by

$$n_D = \frac{1}{ma} \sum_{r=1}^m gp^r \quad [1]$$

$$= \frac{g}{ma} \frac{(1-p^m)}{(1-p)} \quad [2]$$

since  $p < 1$ . For epitaxial layers of even a few thousand angstroms in thickness,  $m$  becomes very large. Hence

$$n_D \approx \frac{g}{(1-p)} \cdot \frac{1}{ma} = \frac{g}{q} \cdot \frac{1}{d} \quad [3]$$

where  $d$  is the layer thickness.

The quantity  $q$ , the probability of annihilation of defects due to the addition of each monolayer, is proportional to the surface mobility of atoms arriving from the gas phase. In general, this surface mobility follows an Arrhenius law,  $\exp(-W/kT)$ , where  $W$  is on the order of 0.5 eV/molecule (11). Therefore

$$n_D \propto \frac{e^{W/kT}}{d} \quad [4]$$

In other words, the defect density of thin epitaxial

layers should vary inversely with the thickness of the layer and decrease exponentially with increasing growth temperature. Decrease in defect density with epitaxial layer thickness is expected to occur in both homoepitaxial growth, where defects at the interface may arise from the presence of defects in the substrate and from contaminants on the substrate surface, and in heteroepitaxial growth, where defects at the interface arise primarily from lattice mismatch. Such behavior has been reported for homoepitaxial GaAs films by Williams (12) and for heteroepitaxial films by Takahashi *et al.* (13). In both cases, although a large number of defects were observed at the epi-substrate interface, a decrease in defect density was reported with increasing epitaxial film thickness, as evidenced by a corresponding decrease in etch pit density. This type of behavior is expected to occur in all epitaxial films. If the defects are active and give rise to energy levels which lie in the bandgap of the epilayer, a variation in carrier concentration according to Eq. [4] is also expected to occur in these epitaxial layers.

An exponential decrease in the product of the carrier concentration and the thickness of the epitaxial layers was observed in the case of our InAs layers, as shown in Fig. 3. Here, the data of Fig. 2 is replotted after accounting for the thickness of the layers. From this data,  $W$  is approximately 0.4 eV/molecule. These results show that the carrier concentration is due to the presence of defects produced by the large lattice mismatch and is not sensitive to the growth rate.

It was shown earlier that the mobility of the InAs layers was essentially constant in the range of thicknesses used in this study. Using a constant  $\mu$  we can obtain

$$\left[ \int_0^d ndz \right]$$

from the measured Hall and conductivity voltages. Therefore, the measurements yield average values of the carrier concentration as a function of the layer thickness and can be directly compared with the results predicted by the theory. Figure 4 shows the measured average carrier concentration as a function of thickness for a 7.2  $\mu\text{m}$  layer (grown at 600°C), which

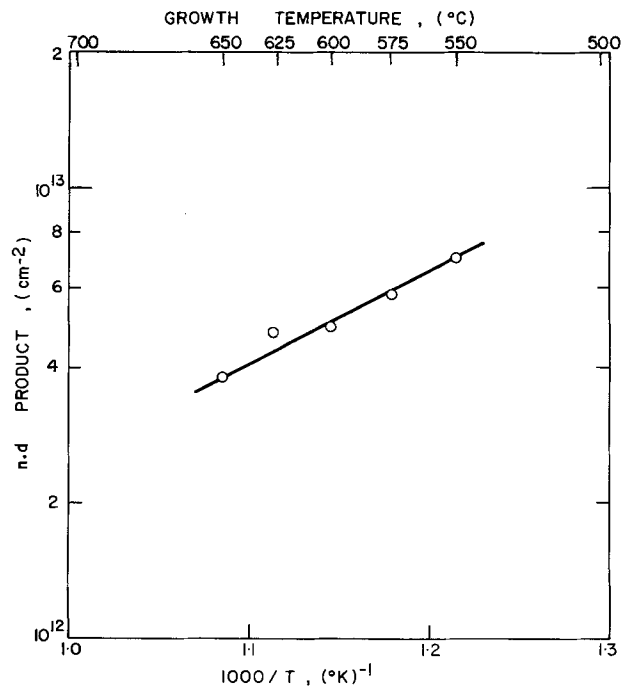


Fig. 3. Product of carrier concentration and thickness of epitaxial layers vs. substrate temperature.

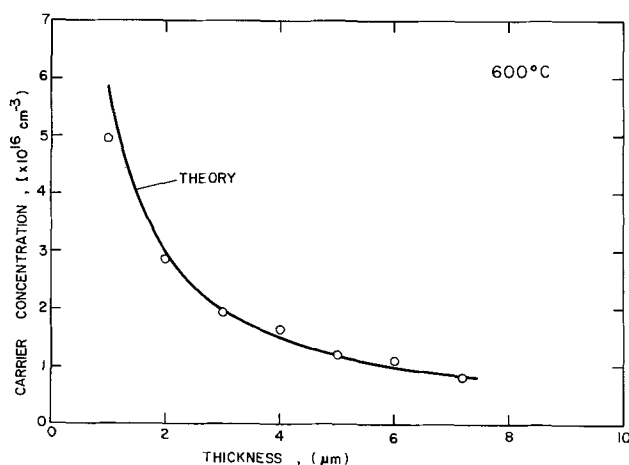


Fig. 4. Carrier concentration vs. thickness for 7  $\mu\text{m}$  InAs layer which has been successively etched down.

was successively etched down, together with the theoretical curve based on an  $n \cdot d$  product of  $4.9 \times 10^{12} \text{ cm}^{-2}$  as obtained from Fig. 3. Excellent agreement between theory and data is observed. Further confirmation was obtained by plotting the carrier concentration of layers, grown under the widely varying growth conditions of Table I, as a function of thickness. Figure 5 shows the results for films grown at 600°C with hydrogen flow through the TEI bubbler ranging from 1 to 2.5 liters/min, and arsine flows ranging from 0.9 to 15 mliters/min. The theoretical curve is again based on an  $n \cdot d$  product of  $4.9 \times 10^{12} \text{ cm}^{-2}$  obtained from Fig. 3. These results show that the carrier concentration of layers of InAs grown in this study is due to the presence of defects in the epitaxial layer and not due to doping from impurities in the source material.

No data are available on the carrier concentration vs. thickness of thin InAs layers grown on GaAs substrates by other techniques. The carrier concentration of thin getter-evaporated InAs films on glass substrates has been reported by Howson and Malina (14), and decreased inversely with film thickness in agreement with our theory. The  $n \cdot d$  product, calculated from a fit to their data, was on the order of  $10^{14}$  per  $\text{cm}^2$ . This large value is probably caused by the low growth temperatures (200°-500°C) and the amorphous substrates used for their depositions.

From the above, it is seen that the  $n \cdot d$  product of epitaxial layers is determined by two important factors: the defect density at the interface,  $g$ , and the surface mobility of the gas atoms during growth. These factors are dependent on the temperature of the reaction, the type of reactants used, and the type of surface treatment prior to epitaxial growth. The  $n \cdot d$  product of epitaxial layers could, therefore, be used as a figure of merit for the technique used to grow the layers. A small  $n \cdot d$  product would be indicative of low defect densities at the epi-substrate interface and/or a fast fall off in defect density with increasing epitaxial layer thickness, indicating a superior method for epitaxial growth. This method, of course, would be valid only for those semiconductors in which defects are ac-

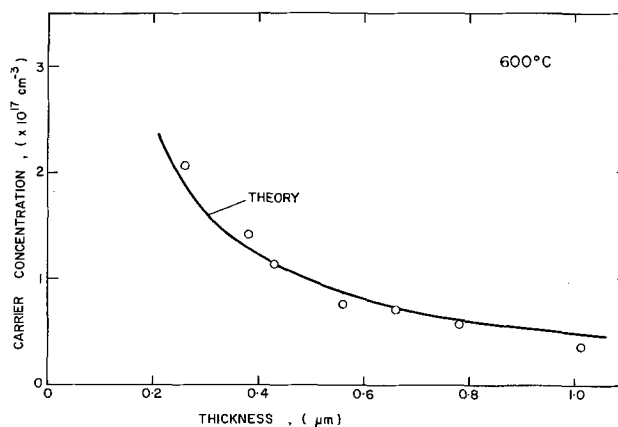


Fig. 5. Carrier concentration vs. thickness for InAs layers grown at 600°C under a wide range of TEI and arsine flows.

tive and produce unequal carrier densities in the conduction and valence bands. This is indeed the case for the majority of III-V and mixed III-V compounds.

### Conclusions

Heteroepitaxial InAs layers on GaAs substrates can be produced using triethylindium and arsine with electrical properties comparable to those obtained by vacuum evaporation and chloride transport techniques. The carrier concentration of these films is dominated by the presence of defects created at the interface between the film and the substrate by the large difference in lattice constants.

A theory has been developed for the variation in defect density with epitaxial layer thickness and substrate temperature for general heteroepitaxial growth. The carrier concentration of the InAs layers varies inversely with layer thickness and decreases exponentially with increasing substrate temperature, in agreement with this theory. It is suggested that the  $n \cdot d$  product of heteroepitaxial layers be used as a figure of merit for the epitaxial growth technique, a smaller  $n \cdot d$  product indicating a superior technique. This technique can also be used to establish the minimum thickness of interface layer which must be grown before good quality material is achieved and should have considerable technological importance in electro-optic and other heteroepitaxial systems.

### Acknowledgment

This work was supported by Grant No. GK-31332 from the National Science Foundation. The authors are indebted to Dr. H. Minden for his critical review, Dr. J. M. Borrego for assistance with the Hall analysis, and Ms. R. Rafun for assistance in manuscript preparation.

Manuscript submitted Jan. 30, 1974; revised manuscript received June 28, 1974.

Any discussion of this paper will appear in a Discussion Section to be published in the June 1975 JOURNAL. All discussions for the June 1975 Discussion Section should be submitted by Feb. 1, 1975.

The publication costs of this article have been assisted by Rensselaer Polytechnic Institute.

### REFERENCES

1. B. J. Baliga and S. K. Ghandhi, *This Journal*, **121**, 1642 (1974).
2. H. M. Manasevit and W. I. Simpson, *ibid.*, **120**, 135 (1973).
3. R. L. Petritz, *Phys. Rev.*, **110**, 1254 (1958).
4. J. J. Tietjen, H. P. Maruska, and R. B. Clough, *This Journal*, **116**, 492 (1969).
5. G. R. Cronin, R. W. Conrand, and S. R. Borrello, *ibid.*, **113**, 1336 (1966).
6. J. P. McCarthy, *Solid State Electron.*, **10**, 649 (1967).

Table I. Data on InAs layers grown at 600°C

Sample	TEI H <sub>2</sub> (liters/ min)	AsH <sub>3</sub> (mliters/ min)	d (μm)	n (cm <sup>-3</sup> )	n · d (cm <sup>-2</sup> )
JC-111	2.5	15.0	0.43	$1.14 \times 10^{17}$	$4.90 \times 10^{12}$
JC-114	2.5	0.9	1.01	$3.60 \times 10^{16}$	$3.64 \times 10^{12}$
JC-115	2.5	2.0	0.66	$7.08 \times 10^{16}$	$4.66 \times 10^{12}$
JC-116	2.5	1.4	0.78	$5.76 \times 10^{16}$	$4.49 \times 10^{12}$
JC-204	1.5	2.0	0.38	$1.42 \times 10^{17}$	$5.40 \times 10^{12}$
JC-206	2.5	2.0	0.56	$7.60 \times 10^{16}$	$4.25 \times 10^{12}$
JC-208	1.0	2.0	0.26	$2.07 \times 10^{17}$	$5.40 \times 10^{12}$

7. H. A. Allen and E. W. Mehal, *This Journal*, **117**, 1081 (1970).
8. N. Godinho and A. Brunnschweiler, *Solid State Electron.*, **13**, 47 (1970).
9. J. V. Dilorenzo, *J. Cryst. Growth*, **17**, 189 (1972).
10. A. G. Milnes and D. L. Feucht, "Heterojunctions and Metal-Semiconductor Junctions," Academic Press, New York (1972).
11. H. F. Matore, "Defect Electronics in Semiconductors," Wiley-Interscience, New York (1971).
12. F. V. Williams, 1966 Symp. on GaAs, Paper 5, 27 (1967).
13. K. Takahashi, T. Moriizumi, and S. Shirose, *This Journal*, **118**, 1639 (1971).
14. R. P. Howson and V. Malina, "Proceedings of the International Conference on the Physics and Chemistry of Semiconductor Heterojunctions and Laser Structures," Vol. III, 141 (1970).

## Asymmetric Cracking in III-V Compounds

G. H. Olsen, M. S. Abrahams, and T. J. Zamerowski

*RCA Laboratories, Princeton, New Jersey 08540*

### ABSTRACT

Experimental evidence for unidirectional cracking in III-V compounds is presented. The crack direction is shown to be a function of the sign of the applied stress and follows the asymmetry of the zinc blende structures. The critical stress for cracking in InGaP/GaAs in tension was found to be  $E/660$  ( $\sim 4.5 \times 10^9$  dynes/cm<sup>2</sup>). Cracks in InGaP and GaAsP grown on GaAs substrates are related to the zinc blende asymmetry with the aid of Sirtl's etch. A fracture mechanism which introduces asymmetric dislocations into the Cottrell fracture mechanism is advanced. Asymmetries in elastic bending and "cross-hatch" patterns are discussed. The question of "glide" vs. "shuffle" dislocations is also considered.

Asymmetry in zinc blende structures has recently been discussed by Abrahams *et al.* (1). These authors demonstrate the general asymmetries found in zinc blende structures (as compared to the diamond structure) and go on to show how these considerations predict the existence of like-sign asymmetric dislocations along  $\langle 110 \rangle$  directions. They then present experimental evidence which demonstrates that misfit dislocations in graded InGaP and GaAsP structures do indeed exhibit asymmetry in that their configurations along one  $[011]$  direction are different than those along the perpendicular  $[0\bar{1}1]$  direction. These asymmetric configurations are in turn used to justify previous assertions (2,3) of differing dislocation velocities between group III ( $\alpha$ ) and group V ( $\beta$ ) dislocations. The purpose of this paper is to present evidence for asymmetric fracture in several III-V vapor phase epitaxy (VPE) crystals and to show how this phenomenon may be explained by a fracture mechanism which involves asymmetric dislocations. Some related phenomena will also be discussed.

### Experimental

Single-crystal alloys of InGaP and GaAsP were deposited via chemical vapor deposition on (100) GaAs substrates by well-known techniques (4,5). Growth temperatures were typically  $\sim 700^\circ\text{C}$ . No compositional grading was employed during the growth of these alloys. The alloy composition was determined by photoluminescence (6) and in some cases by x-ray diffraction. Etch procedures have been described elsewhere (7,8).

### Asymmetry in Zinc Blende Structures

The asymmetry between  $\langle 011 \rangle$  and  $\langle 0\bar{1}1 \rangle$  type directions in zinc blende is a well-known property which may easily be demonstrated in GaAs with the aid of Sirtl's etch (7,8). Strictly speaking, two  $\langle 011 \rangle$  directions in zinc blende cannot be called "asymmetric" since by definition of the zinc blende structure, they are not symmetrically equivalent. However, since the cracking phenomena along these two directions is asymmetric, the term "asymmetry" will be used here to denote the asymmetric cracking. Figure 1(a) shows

a (100) polished wafer of GaAs etched in the Sirtl solution (8) for 3 min. The unequal sides of the rectangular etch figures (which are "hillocks" as opposed to pits) lies parallel to  $[011]$  and  $[0\bar{1}1]$  directions and may be used to distinguish the two directions in the (100) plane. This behavior contrasts with Sirtl etch figures on (100) Si, which are square (8), and demonstrates the nonequivalence of  $\langle 011 \rangle$  and  $\langle 0\bar{1}1 \rangle$  type directions lying in a  $\{100\}$  plane. The Sirtl etch figures on GaAs have not yet been related to a defect structure, although they have been related to dislocations in Si. A startling difference may be observed on the opposite  $(\bar{1}00)$  face of the GaAs wafer [Fig. 1(b)]. It is seen that the rectangular etch figures on  $(\bar{1}00)$  are rotated by  $90^\circ$  with respect to those on (100). However, this rotation is entirely consistent with the  $90^\circ$  rotation of symmetry which is observed in zinc blende structures when changing from one sublattice to another or when a  $180^\circ$  rotation is performed about an  $\langle 011 \rangle$  direction (see Fig. 2). It is evident then that one side of the etch figure (*e.g.*, the long or short side) may be associated with an  $\langle 011 \rangle$  direction of particular symmetry. The asymmetry of this direction is evidenced not by the atoms lying in the direction, but by the positions of the nearest neighbor atoms. The following discussion, which describes how directions in zinc blende structures may be uniquely referenced, will clarify this point.

Let the two sublattices be labeled A and B (see Fig. 2). Any atom in a  $\{111\}$  plane contains four bonds to its opposite species. However, only one of these bonds is normal to the given  $\{111\}$  plane. This bond direction is conventionally used as a vector to identify the plane. Inspection shows that parallel A and B planes have identification vectors which are antiparallel. Thus, if a unit cell is chosen with B atoms at its corners, then the  $\{111\}_B$  planes may be referred to as  $(\bar{1}\bar{1}\bar{1})$ ,  $(1\bar{1}\bar{1})$ ,  $(\bar{1}\bar{1}1)$ , and  $(\bar{1}11)$  while the  $\{111\}_A$  planes will be the corresponding negatives. Therefore, if an A or B  $\{111\}$  plane can be distinguished, all other crystallographic directions may be derived.

The nature of the Sirtl etch figures is not well understood, although much work has been devoted to this

Key words: Sirtl etch, misfit, cross-hatch, asymmetric dislocation.

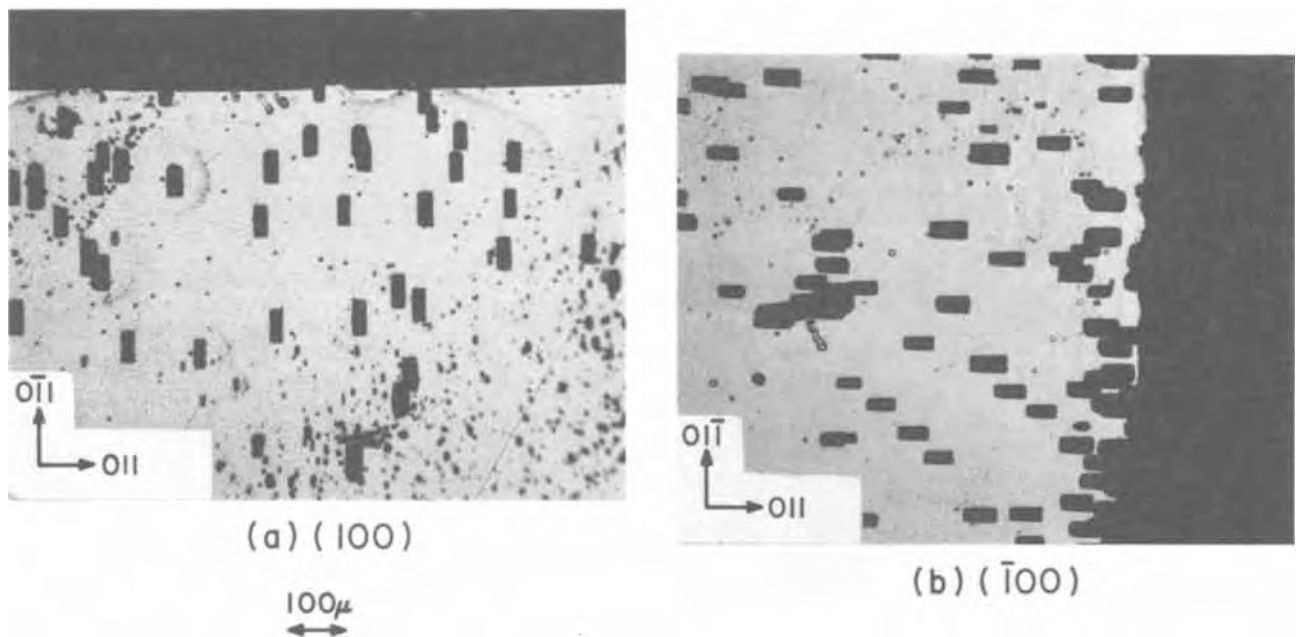


Fig. 1. Sirtl etch figures on both sides of a (100) GaAs substrate. The axis of rotation between (a) and (b) is  $[011]$ .

problem. Figure 3 shows SEM photographs of a Sirtl-etched (100) GaAs wafer. Although the geometries of the etch figures were found to vary considerably, the length/width ratio was found to be relatively constant ( $\sim 2.3$ ). Nevertheless, the work of Tarui *et al.* (8) on GaAs shows that the angle between  $\langle 111 \rangle_{As}$  directions and the  $\langle 100 \rangle$  direction in  $\langle 011 \rangle$  planes is  $54^\circ 44'$  along the short axis of the Sirtl etch figure and  $125^\circ 16'$  along the long axis. Therefore, Sirtl etching of GaAs provides a means for the unique determination of crystallographic directions as well as a differentiation of  $\langle 011 \rangle$  and  $\langle 0\bar{1}\bar{1} \rangle$  type directions.

#### Cracking in InGaP and GaAsP on GaAs

The growth of InGaP/GaAs will be considered first. One advantage of this system is that a lattice-matched condition can be approached by the direct deposition of  $\sim \text{In}_{0.49}\text{Ga}_{0.51}\text{P}/\text{GaAs}$ . The alloy can then be graded (if desired) to a different composition in order to achieve desired electrical and/or optical properties. An exact lattice match can occur only at one temperature since the thermal expansion coefficients of the two materials are different (9). If a lattice match occurs at  $700^\circ\text{C}$  ( $\sim 49.5\%$  In), then a compressive strain of  $\sim 0.09\%$  will exist in the InGaP at room temperature. However, if a room-temperature lattice match is to be achieved, a tensile stress of  $\sim 0.09\%$  must be incurred at the growth temperature. (From a mechanical point of view, the high-temperature match is to be preferred since slip is less likely to occur at lower temperatures.) A plot of strain in the InGaP layer *vs.* In composition is shown in Fig. 4 for the two temperatures.

During the preparation of such structures, unidirectional striations were sometimes observed on the composite crystal as seen in Fig. 5. Close examination revealed that these striations were cracks which extended along a single  $\langle 011 \rangle$ -type direction and that they only appeared in structures where a critical misfit between the InGaP and GaAs had been exceeded. Structures in which the InGaP was strained in tension by the GaAs substrate ( $a_{\text{InGaP}} < a_{\text{GaAs}}$ ) appeared to exhibit cracks when the misfit exceeded  $\sim 0.15\%$ , whereas those in compression ( $a_{\text{InGaP}} > a_{\text{GaAs}}$ ) were rarely observed to crack, even with misfits as large as  $0.4\%$ . These figures may vary somewhat with growth temperature, thickness, etc., but it was invariably true that InGaP layers in tension cracked at smaller misfits than those in compression. The crack direction was

referenced to GaAs by angle lapping the composite wafer and Sirtl etching the exposed GaAs. Figure 6(a) shows an InGaP layer which was put in tension by the GaAs substrate. Figure 6(b) shows a rare example of an InGaP layer which cracked in compression. Note that the tension cracks are parallel to the long axis of the Sirtl etch figures while the compressed layer has cracks perpendicular to the figures. These figures serve as a clear illustration that fracture in InGaP is asymmetric and follows the polarity of the zinc blende lattice. Further evidence of this type may be seen in Fig. 7 which shows the (100) and  $\bar{1}00$  surfaces of an InGaP layer placed in tension by a GaAs substrate where growth has occurred on both sides. The crack direction is seen to rotate  $90^\circ$  with the zinc blende polarity as do the Sirtl etch pits in Fig. 2.

Similar behavior was observed in GaAsP. Abrupt deposits of GaAsP on GaAs result in structures which exhibit unidirectional cracks (due to tensile stresses) which lie parallel to the long axis of Sirtl etch pits on the substrate. However, cracking was not observed in samples subjected to compressive stresses (GaAsP/GaP).

It must be emphasized that the above results apply only to abrupt depositions. In most cases it was found that cracking could be eliminated by grading the alloy composition. In systems which have large misfits ( $\sim 1\%$  or more) cracking is often not observed because of poor crystal growth.

#### Fracture Mechanism

Cottrell (10) has suggested a fracture mechanism whereby dislocations on intersecting slip planes combine to form sessile dislocations whose missing half planes may be viewed as microcracks. Repeated slip of this type can cause the microcracks to grow and complete fracture to eventually occur. Abrahams and Ekstrom (11) have extended this model to zinc blende structures in order to explain cleavage along  $\{011\}$  planes. These models may be used to explain asymmetric cracking in III-V compounds by invoking asymmetry of the dislocations involved in the microcrack formation.

Figure 8 shows two orthogonal  $\{011\}$  planes of an InGaP layer which has been strained in tension by the GaAs substrate. It has been shown (1) that a large fraction of the misfit strain in InGaP [as in GaAsP (14)] is relieved by  $60^\circ$  like-sign dislocations, which



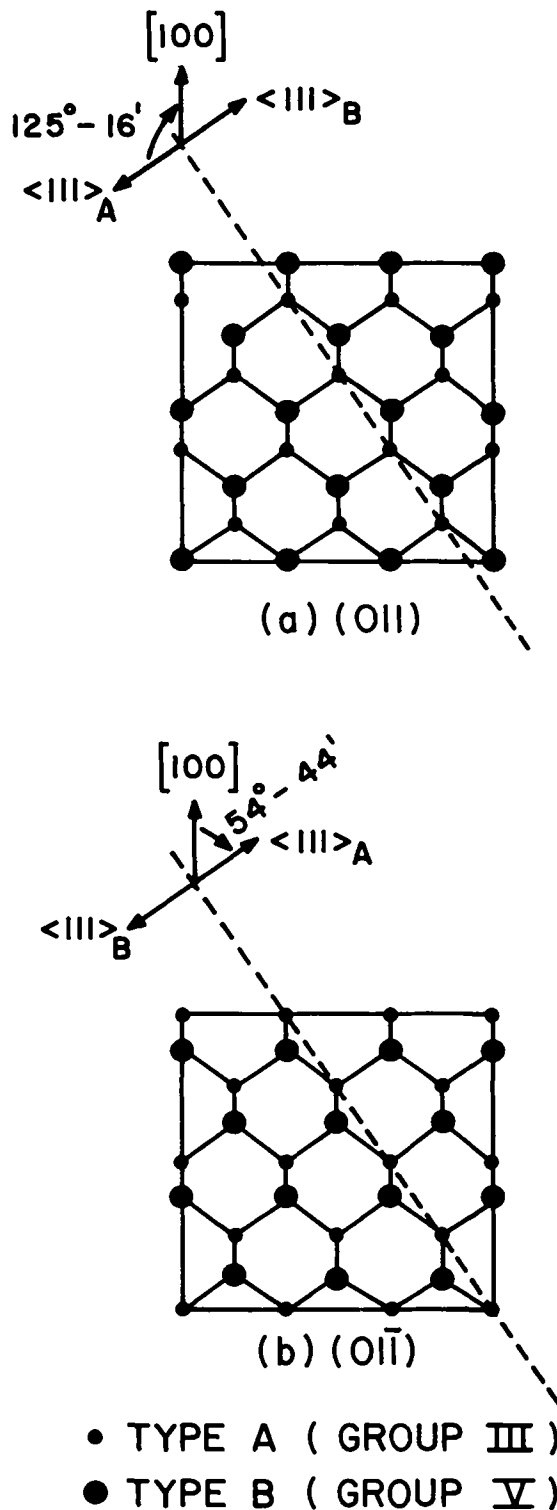


Fig. 2. A projection of two perpendicular  $\{011\}$  planes which shows the interchange of atomic species in zinc blende structures upon a  $90^\circ$  rotation.

are mobile and can bend in and out of the misfit plane during crystal growth. These dislocations are thought of as sources of glissile dislocations which eventually combine and lock up as in the above fracture mechanism. Since extensive dislocation motion is required, climb does not appear to be a likely mechanism for this process. Because the misfit is tensile, the signs of the dislocation (*i.e.*, location of extra half-plane) must be as shown in the figures. Thus, if the dislocations in Fig. 8(a) are of the  $\alpha$ -type (lying on  $\{111\}_A$  planes), then the dislocations in Fig. 8(b) must be of the  $\beta$ -type

(lying on  $\{111\}_B$  planes) by virtue of the zinc blende symmetry. Since the mobilities of these two types of dislocations are not expected to be equal (1,2), it follows that one set will move at lower stress levels than the other, and thus give rise to fracture which appears only along the one direction. As with other crack mechanisms (12), compression would tend to keep the microcracks from opening up (as they do in tension) and thereby inhibit complete fracture. The operation of this mechanism depends on the configuration of the misfit dislocation. With abrupt deposits, many dislocations would be generated over a small volume after the critical thickness (13) had been exceeded. The probability for dislocation pileup would be much greater here than with graded structures where the dislocations would be spread out over a larger volume (14). Furthermore, due to the gradual relief of strain, the local misfit stress in a graded layer would never approach that in an abrupt layer (for the same total strain).

### Discussion

The proposed model is consistent with the experimental results and appears to be the most likely mechanism for asymmetric fracture. It is also supported by the observations of Abrahams *et al.* (1) who showed that misfit dislocations in InGaP and GaAsP have different densities along the  $[011]$  and  $[0\bar{1}1]$  directions in (100) growths. Substrate orientation was also considered as a possible cause for the unidirectional cracks. Vapor-phase epitaxy is typically performed on substrates that are misoriented by  $3^\circ$ - $5^\circ$  from a major crystallographic axis. In the present work, (100) GaAs wafers, which were misoriented about  $\langle 011 \rangle$  directions, were used as substrates. The applied misfit strains were therefore not contained in the (100) plane, but in a plane slightly inclined to it. [This effect has been demonstrated (15) in Ge/GaAs where the epitaxial strain was shown to vary with deviations from a  $\langle 111 \rangle$  growth axis.] Following the method of Wayman (16), the resolved shear stress on a  $\{111\} \langle 110 \rangle$  slip system due to such an applied stress may be calculated using matrix methods with a computer. The results are shown in Fig. 9 for misorientation about an  $[011]$  axis. It can be seen that the resolved shear stress ( $\tau$ ) on a slip system of a crystal misoriented by only  $3^\circ$  can differ by as much as 10% from those in a crystal with no misorientation. Thus, it is conceivable that differences caused by misorientation could cause preferential slip on a particular slip plane. However, the results described in the section on cracking in InGaP and GaAsP on GaAs were found to be independent of substrate orientation, *i.e.*  $+3^\circ$ ,  $0^\circ$ , and  $-3^\circ$  misorientation about a single axis all yielded identical results. Hence, substrate orientation was ruled out as a cause of asymmetric cracking.

One interesting application of these results was the estimation of the critical yield stress in InGaP placed in tension by a GaAs substrate. Figure 10 shows a composite photograph of such a crystal which contained a compositional gradient along the wafer—not along the growth axis. The region about the zero strain condition is essentially featureless. As the strain increases, a "cross-hatch" pattern (17) becomes evident. Further strain leads to a more pronounced cross-hatch and finally to cracking at  $\sim 0.15\%$  strain. (Misfit strain was obtained from compositional determinations, together with Fig. 4). This value was found to be reproducible (it was also observed in several similar wafers) and leads to a critical tensile stress of  $\sim E/666$  ( $\sim 4.5 \times 10^9$  dynes/cm<sup>2</sup>). This in turn leads to a critical resolved shear stress on the  $\{111\} \langle 110 \rangle$  slip system of  $\sim G/770$  ( $\sim 1.5 \times 10^9$  dynes/cm<sup>2</sup>;  $E$  = Young's modulus and  $G$  = Shear modulus). Such stress levels should be able to support slip at the growth temperature of  $700^\circ\text{C}$ . The onset of cracking appeared to be less critical in GaAsP than InGaP and no threshold stress levels could be ascertained. This result is consistent with that of Abrahams *et al.* (1), who found the asymmetry of the

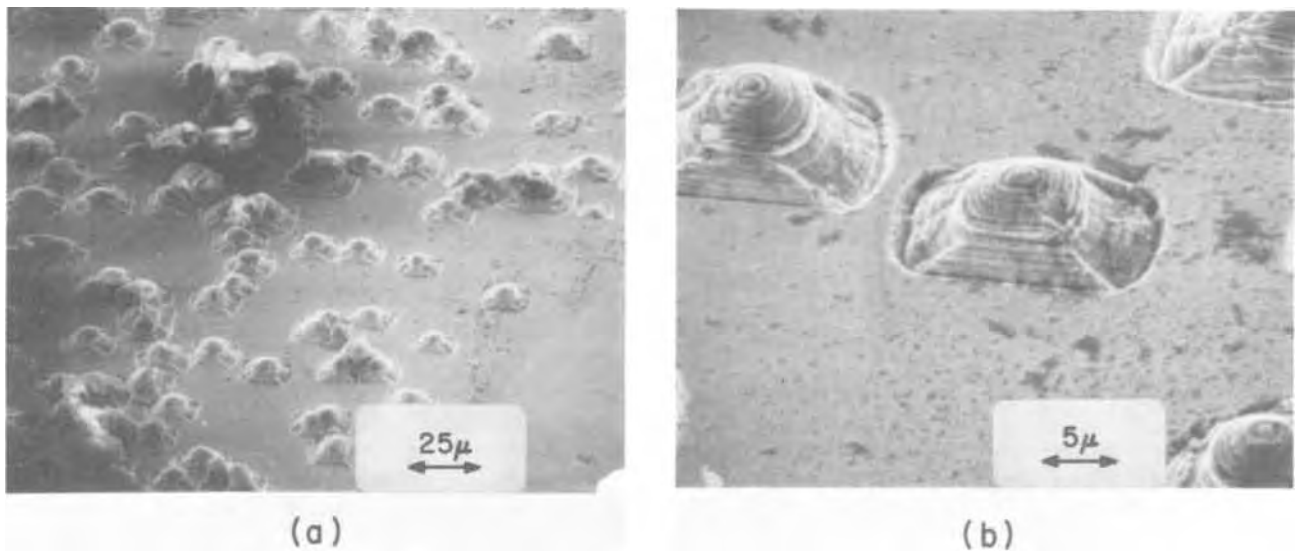


Fig. 3. Scanning electron microscope pictures of Sirtl etch figures on a (100) GaAs substrate.

dislocation arrays to be more pronounced in InGaP than GaAsP. It also suggests that the amount of asymmetry depends on the alloy constituents.

The question of whether the  $\alpha$ - or  $\beta$ -type dislocations (see Fig. 11) have higher mobilities cannot be answered without stating whether these dislocations exist as a "glide" or "shuffle" set (18). This problem has been discussed recently and apparently is still an open question. The atomic configurations about these types of dislocations are illustrated in Fig. 11. If the shuffle set is assumed in the case of InGaP and GaAsP in tension, then consideration of the section on asymmetry in zinc blende structures, together with Fig. 6

and 11, will show that in order for misfit dislocations to contribute to the crack mechanism, they must lie on  $\{111\}_B$  planes. Thus, the more mobile dislocations in both InGaP and GaAsP would be of the  $\beta$ -type. This may be seen in Fig. 11(d) if the InGaP (under tension) is assumed to be below the dislocation and the GaAs (containing the extra half plane) on top. [Interestingly, the  $\alpha$ -type dislocations were claimed to have higher mobilities in InSb when the shuffle set was assumed (2)]. For samples under compression, the Burgers vector of the dislocation would be reversed and the crack direction would have to rotate  $90^\circ$  in order to maintain the same type of dislocation.

Assuming the shuffle dislocation to be dominant, Erofeeva and Osip'yan (20) have recently shown that the  $\alpha$ -type dislocations have higher mobilities in InSb and GaAs. This, together with the above results, may indicate that a "size-effect" governs dislocation mobilities since P atoms are smaller than Sb and As atoms. However, all such discussion is mere speculation until the question of whether the "shuffle" or "glide" dislocations predominate in III-V compounds is settled.

Another manifestation of this phenomenon is asymmetric bending. Nagai (21) has demonstrated asymmetric bending about  $[011]$  and  $[0\bar{1}\bar{1}]$  directions in InGaAs and GaAsP grown on (100) GaAs substrates and has shown that if growth occurs on both sides of the wafer, a "saddle-like" curvature is observed, i.e., convex about one  $\langle 011 \rangle$ -type direction but concave about the other. Similar observations have been made during the present work and are entirely consistent with the concept of asymmetric slip. Although the misfit strain is applied equally along the two directions, slip would occur more easily about one of these directions (as in the crack mechanism) and thus less bending (due to elastic strain) would take place about this axis as compared to the other. Furthermore, the zinc blende symmetry demands that these axes interchange on the opposite side of the substrate and therefore explains the concave vs. convex bending. Nagai also presents data which indicate that the bending in  $\text{In}_{1-x}\text{Ga}_x\text{As}/\text{GaAs}$ , although asymmetric, shows no systematic variation with composition between  $x = 0$  and  $x = 1$ . This suggests that only a critical amount of strain can be accommodated by elastic bending before plastic deformation occurs. In fact, if Nagai's data are averaged, a crude calculation (17) can be made to find the stress along the  $[011]$  and  $[0\bar{1}\bar{1}]$  directions. The results are  $\epsilon \sim 6 \times 10^{-4}$  vs.  $\epsilon \sim 3 \times 10^{-3}$ . The higher value is reasonably close to the critical value found in InGaP, considering the simplifications involved.

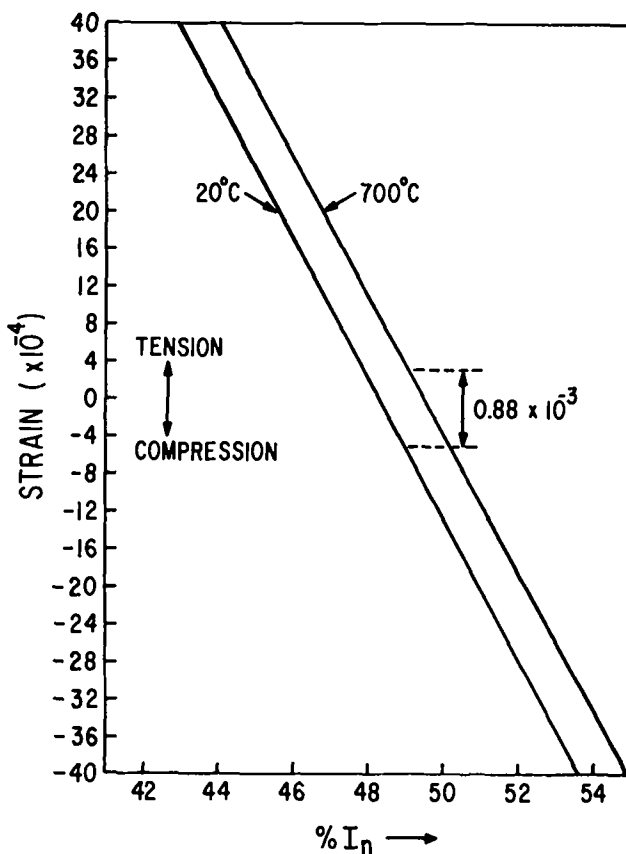


Fig. 4. Strain present in InGaP grown on GaAs due to thermal expansion effects as a function of In composition and temperature.

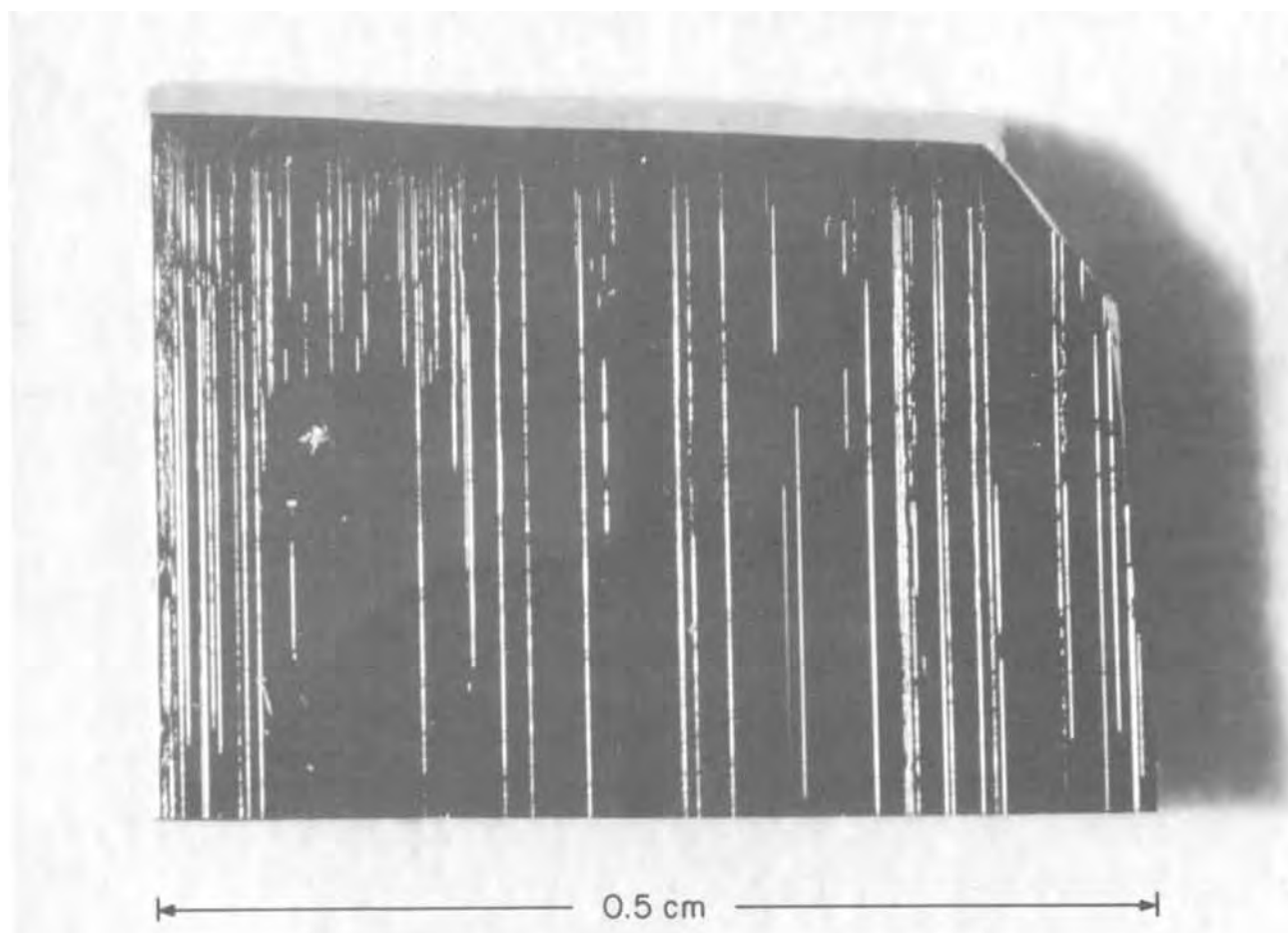


Fig. 5. Unidirectional cracks in InGaP grown on a (100) GaAs substrate. The InGaP is under tension.

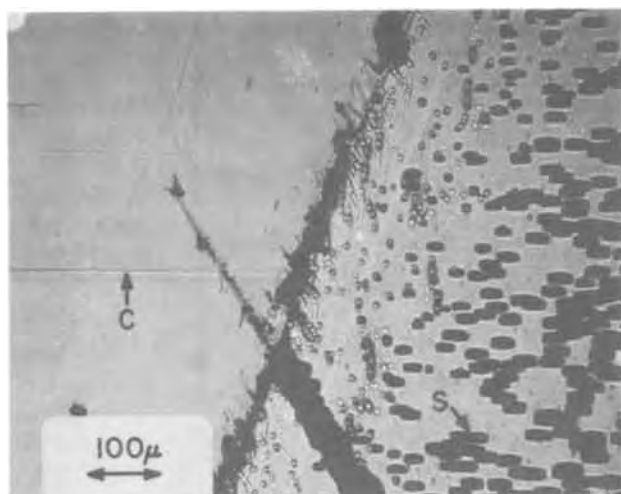


Fig. 6. InGaP/GaAs wafers which have been angle-lapped ( $\sim 3^\circ$ ) to expose the GaAs substrate which exhibits rectangular etch figures (S) due to Sirtl etching. The InGaP portion exhibits cracks (c) due to (a) tension and (b) compression.

Finally, a few remarks will be made about the so-called "cross-hatch" patterns (17). These patterns have been associated with misfit dislocations in epitaxial layers which contain regions of graded alloy composition (17). However, "cross-hatching" may also be observed in abrupt (nongraded) deposits as is seen in Fig. 10 for InGaP/GaAs. Here, an asymmetry in the pattern is to be noted. The  $[011]$  set of lines runs

fairly straight, while the  $[0\bar{1}1]$  set is not as closely spaced and more irregular. This is to be compared with the asymmetric dislocation configurations of Abrahams *et al.* (1). Although the precise origin of this pattern is not clear, the following facts have been obtained: (i) The patterns can be removed by mechanical polishing. Therefore, they are surface defects. (ii) Dislocation etches enhance the original cross-hatch pattern.

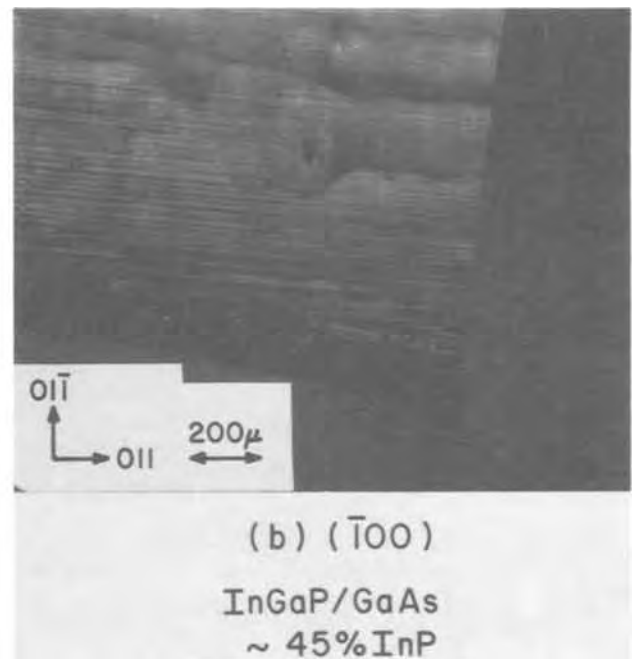
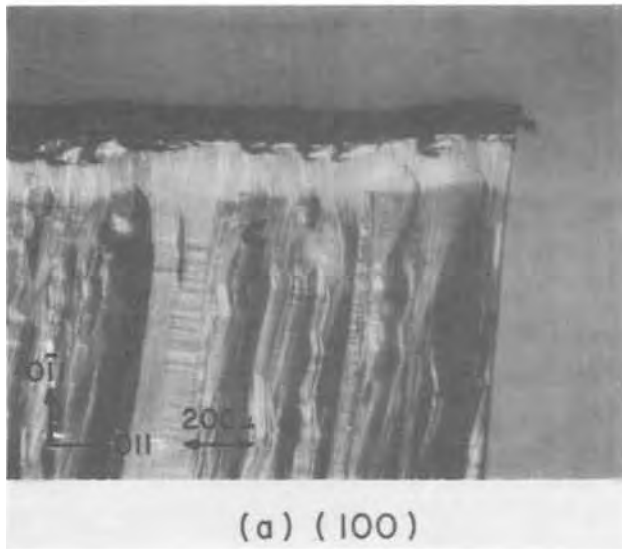


Fig. 7. Identical regions of an InGaP layer (under tension) grown on both sides of a GaAs substrate. The axis of rotation between (a) and (b) is [011].

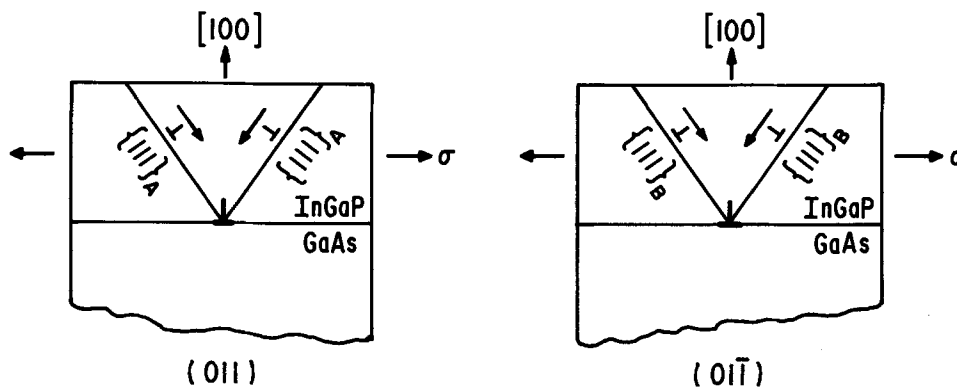


Fig. 8. Dislocation motion on perpendicular {011} planes in an InGaP layer placed in tension by a GaAs substrate. Dislocations intersect and combine as shown to form microcracks which eventually open up to form unidirectional cracks as in Fig. 5. The two gliding dislocations are 60° types with Burgers vectors pointing into and out of the plane of the figure. The bottom sessile dislocation would have a Burgers vector which lies in the (100) plane.

Therefore, there is a definite association between each line in the cross-hatch pattern and a dislocation.

Kishino *et al.* (17) concluded that the cross-hatch patterns observed in GaAsP/GaAs were caused by growth rate variations due to impurity concentration differences at dislocations in the compositionally graded region or to the screw components of these same dislocations. We suggest that the cross-hatch pattern is initially caused by accelerated crystal growth about misfit dislocations and that once initiated, these "growth perturbations" will continue to propagate with growth as will any defect (such as a scratch or pit) on a crystal surface. This effect implies the existence of some type of defect along the boundaries of the pattern such as impurity segregation or point defects. This would be consistent with the observations and propositions of Kishino *et al.* (17).

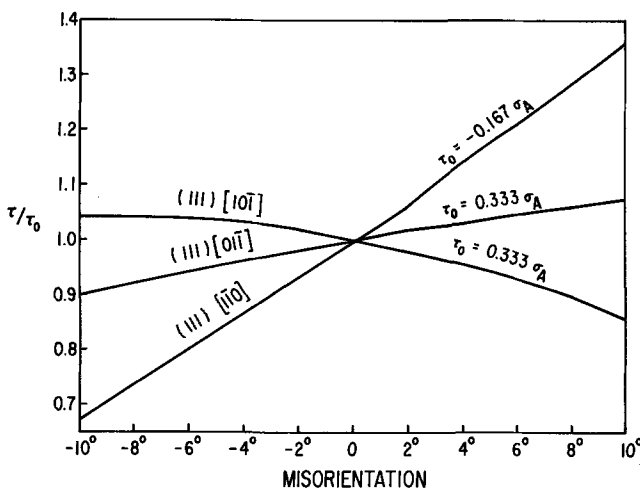


Fig. 9. The effect of substrate misorientation [from exact (100)] about the [011] direction upon resolved shear stress ( $\tau$ ) in the indicated (111)  $\langle 011 \rangle$  slip systems. The applied misfit stress in the substrate plane is  $\sigma_A$  and  $\tau_0$  is the resolved shear stress when  $\sigma_A$  is applied in the exact (100) plane.

**Acknowledgments**

The authors wish to express their appreciation to C. J. Nuese and J. J. Gannon for photoluminescence measurements and advice. Discussions with J. Blanc, D. Richman, and C. J. Buicocchi are also gratefully acknowledged.

Manuscript submitted March 21, 1974; revised manuscript received July 2, 1974.

Any discussion of this paper will appear in a Discussion Section to be published in the June 1975 JOURNAL.

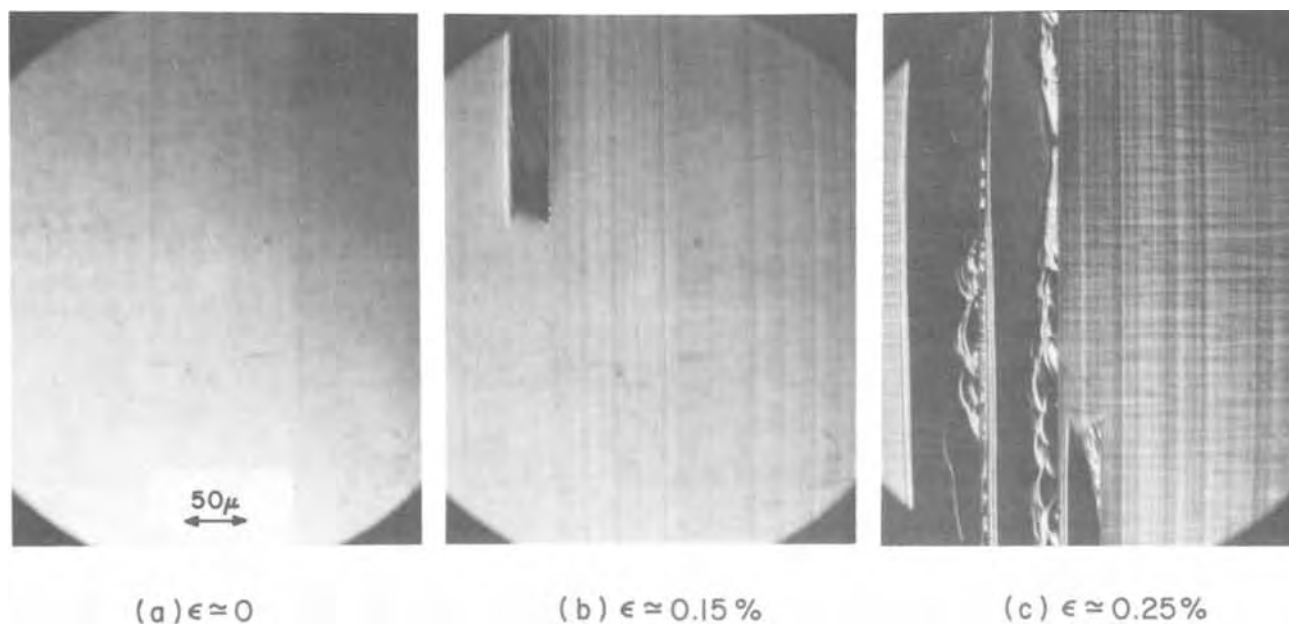


Fig. 10. Interference micrographs of a (100) InGaP/GaAs surface for various tensile strains in the InGaP. Note the asymmetries in the cracks and "cross-hatch" patterns which are parallel to  $\langle 011 \rangle$  directions.

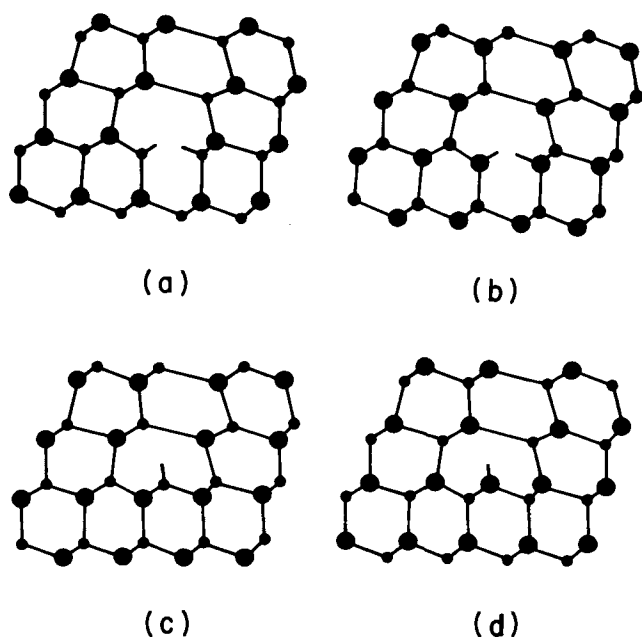


Fig. 11. Atomic configurations in an  $\{011\}$  plane about  $60^\circ$  dislocations in zinc blende structures. An  $\alpha$ -dislocation in the "glide" configuration is illustrated in (a) with the  $\beta$ -dislocation in "glide" configuration in (b).  $\alpha$ - and  $\beta$ -dislocations in "shuffle" configuration are illustrated in (c) and (d), respectively. Atom conventions are as in Fig. 2. The  $\{111\}$  planes corresponding to the  $\alpha$ - or  $\beta$ -type dislocation are horizontal.

All discussions for the June 1975 Discussion Section should be submitted by Feb. 1, 1975.

The publication costs of this article have been assisted by the RCA Corporation.

#### REFERENCES

1. M. S. Abrahams, J. Blanc, and C. J. Buicchi, *Appl. Phys. Letters*, **21**, 185 (1972).
2. R. L. Bell and A. F. W. Willoughby, *J. Mater. Sci.*, **1**, 219 (1966).
3. E. Peissker, P. Haasen, and H. Alexander, *Phil. Mag.*, **7**, 1279 (1962).
4. J. J. Tietjen and J. A. Amick, *This Journal*, **113**, 724 (1966).
5. C. J. Nuese, A. G. Sigai, R. E. Enstrom, M. S. Abrahams, J. J. Gannon, and T. J. Zamerowski, *ibid.*, **120**, 947, 956 (1973).
6. G. B. Stringfellow, *J. Appl. Phys.*, **43**, 3455 (1972).
7. E. Sirtl and A. Adler, *Z. Metallk.*, **52**, 529 (1961).
8. Y. Tarui, Y. Komiyu, and Y. Harada, *This Journal*, **118**, 118 (1971).
9. I. Kudman and R. Paff, *J. Appl. Phys.*, **43**, 3760 (1972).
10. A. H. Cottrell, *Trans. AIME*, **212**, 192 (1958).
11. M. S. Abrahams and L. Ekstrom, *Acta Met.*, **8**, 654 (1960).
12. R. E. Reed-Hill, "Physical Metallurgy Principles," p. 546, Van Nostrand Co., New York (1964).
13. J. H. van der Merwe, *J. Appl. Phys.*, **34**, 123 (1963).
14. M. S. Abrahams, L. R. Weisberg, C. J. Buicchi, and J. Blanc, *J. Mater. Sci.*, **4**, 223 (1969).
15. T. B. Light, M. Berkenblit, and A. Reisman, Abstract 113, p. 272 Electrochemical Society Extended Abstracts, Spring Meeting, Washington, D.C., May 9-13, 1971.
16. C. M. Wayman, "Introduction to the Crystallography of Martensitic Transformations," p. 33, The Macmillan Co., New York (1964).
17. S. Kishino, M. Ogirima, and K. Kurata, *This Journal*, **119**, 617 (1972).
18. J. P. Hirth and J. Lothe, "Theory of Dislocations," McGraw-Hill Book Co., New York (1968).
19. R. Meingast and H. Alexander, *Phys. Status Solidi (a)*, **17**, 229 (1973).
20. S. A. Erofeeva and Yu. A. Osi'yan, *Sov. Phys.-Solid State*, **15**, 538 (1973).
21. H. Nagai, *J. Appl. Phys.*, **43**, 4254 (1972).

# A Scanning Electron Microscope Study of $\text{In}_{1-x}\text{Ga}_x\text{P}$

V. A. Voronin,<sup>\*1</sup> W. D. Stewart, Jr.,<sup>2</sup> G. W. Marshall, and J. B. Wagner, Jr.<sup>\*</sup>

Department of Materials Science and Materials Research Center, Northwestern University, Evanston, Illinois 60201

and H. M. Macksey and N. Holonyak, Jr.<sup>\*</sup>

Department of Electrical Engineering and Materials Research Laboratory,  
University of Illinois, Urbana, Illinois 61801

## ABSTRACT

The SEM has been used to study the crystal perfection and chemical homogeneity of  $\text{In}_{1-x}\text{Ga}_x\text{P}$  crystals. Secondary electron micrographs were used to study the surface topography and microstructure away from and at inhomogeneities. Chemical and crystallographic data were obtained using the x-ray wavelength dispersive and energy dispersive analyzers and selected area channeling patterns. The channeling patterns showed that In and Ga can be substituted directly into a common (column III) sublattice without gross distortion of the lattice and without generation of unacceptable levels of structural defects. The crystals were chemically homogeneous (less than 2% maximum) except at or near inclusions.

The light-emitting properties of the  $\text{In}_{1-x}\text{Ga}_x\text{P}$  crystal system, which is very promising for LED applications, are dependent on the crystalline perfection of the lattice. There are few reported studies of the crystalline perfection (lack of bulk lattice distortion) of these materials. These materials are sometimes adversely affected by the presence of inclusions (e.g., indium) introduced during crystal growth. The very small samples used in photoexcitation experiments (1, 2) may be taken from inclusion-free regions, but for junction device applications this is not possible. The environment of the inclusions was studied and the defect sites related to these inclusions were characterized in terms of their microstructure and the attendant chemical composition and crystallographic changes relative to the bulk material.

The crystals were studied using a JEOL JSM-U3 and Cambridge Stereoscan S-4 scanning electron microscope (SEM). The SEM is a versatile electron probe which can provide various forms of information through the signals generated by the action of the scanning electron beam. These signals include back-scattered electrons, secondary electrons, characteristic x-rays, or light emission. In the present study three operational modes were correlated to obtain an integrated view of the crystals and the defect sites therein. Secondary electron micrographs were used to study the surface topography and microstructure of the defect sites. The characteristic x-rays generated by the electron beam were used to evaluate chemical composition and homogeneity near the defect sites. Information on the orientation of the samples and the deterioration of crystallinity near the sites was obtained using selected area electron channeling patterns (SACP's).

## Experimental

**Samples.**—The  $\text{In}_{1-x}\text{Ga}_x\text{P}$  crystals were grown by a modified Bridgman method and varied in composition from  $x = 0.95$  to  $x = 0.34$  as shown in Table I. The  $\text{In}_{1-x}\text{Ga}_x\text{P}$  is grown at constant temperature from an indium solution that is fed with source InP and GaP held at a temperature  $10^\circ$ – $20^\circ\text{C}$  higher than that of the growth site. The constant temperature synthesis reduces crystal composition inhomogeneities and consequent defects. The high quality of this  $\text{In}_{1-x}\text{Ga}_x\text{P}$  in the inclusion-free regions is demonstrated by the fact that most of the direct bandgap samples can be made to lase when photoexcited (1, 2).

\* Electrochemical Society Active Member.

<sup>1</sup> Present address: Department of Electrical Engineering, The Lvov Polytechnic Institute, Lvov, U.S.S.R.

<sup>2</sup> Present address: Illinois Bureau of Identification, Joliet, Illinois 60432.

Key words: channeling patterns, microprobe.

In the present study, slices from the grown ingots were mechanically polished and then chemically etched. This preparation removes any inclusions at the surface and leaves behind a characteristic defect site which was investigated with the SEM.

**Secondary electron micrographs.**—The operating principles of the SEM are well known (3). A focused electron beam or probe is scanned across the specimen in a square raster in synchronization with a second beam on a CRT. The secondary operating mode consists of the collection of the secondary emitted electrons at each point of the scan. These electrons provide the signal used to modulate the brightness of the CRT. Thus a point by point image is built up on the CRT which corresponds to the secondary electron emission at each specimen point. Other signals generated by the action of the beam can be displayed in a similar fashion.

**X-ray microanalysis.**—The characteristic x-rays excited by the electron beam were used to study the compositional variations in the samples. Compositional variations for In, Ga, and P were obtained near the defect sites and across grain boundaries. The methods used involved the use of the SEM equipped with both energy dispersive (EDX) and wavelength dispersive (WDX) x-ray spectrometers.

X-ray scans across the grain boundaries and defect sites utilized the EDX analyzer. The x-ray scans were obtained with a 25 kV electron beam and a probe current of  $2 \times 10^{-9}\text{A}$ , resulting in a  $0.2 \mu\text{m}$  beam diameter (4). Two methods were used for the x-ray scans. Initially the beam was held stationary and the sample moved at the rate of  $20 \mu\text{m}/\text{min}$ . In the second method the sample was fixed and the beam moved across the sample at a speed dependent on magnification and scan time. This resulted in an effective scan rate of  $1 \mu\text{m}/\text{sec}$  around the defect sites.

**Selected area electron channeling patterns.**—Crystallographic information on the bulk specimens was obtained from electron channeling patterns (ECP's) taken in the SEM. The information that can be obtained by this technique includes orientation, lattice

Table I.  $\text{In}_{1-x}\text{Ga}_x\text{P}$

Sample	$x$ (Ga)	$1 - x$ (In)
236	0.34	0.66
150	0.75	0.25
204	0.83	0.17
299	0.95	0.05

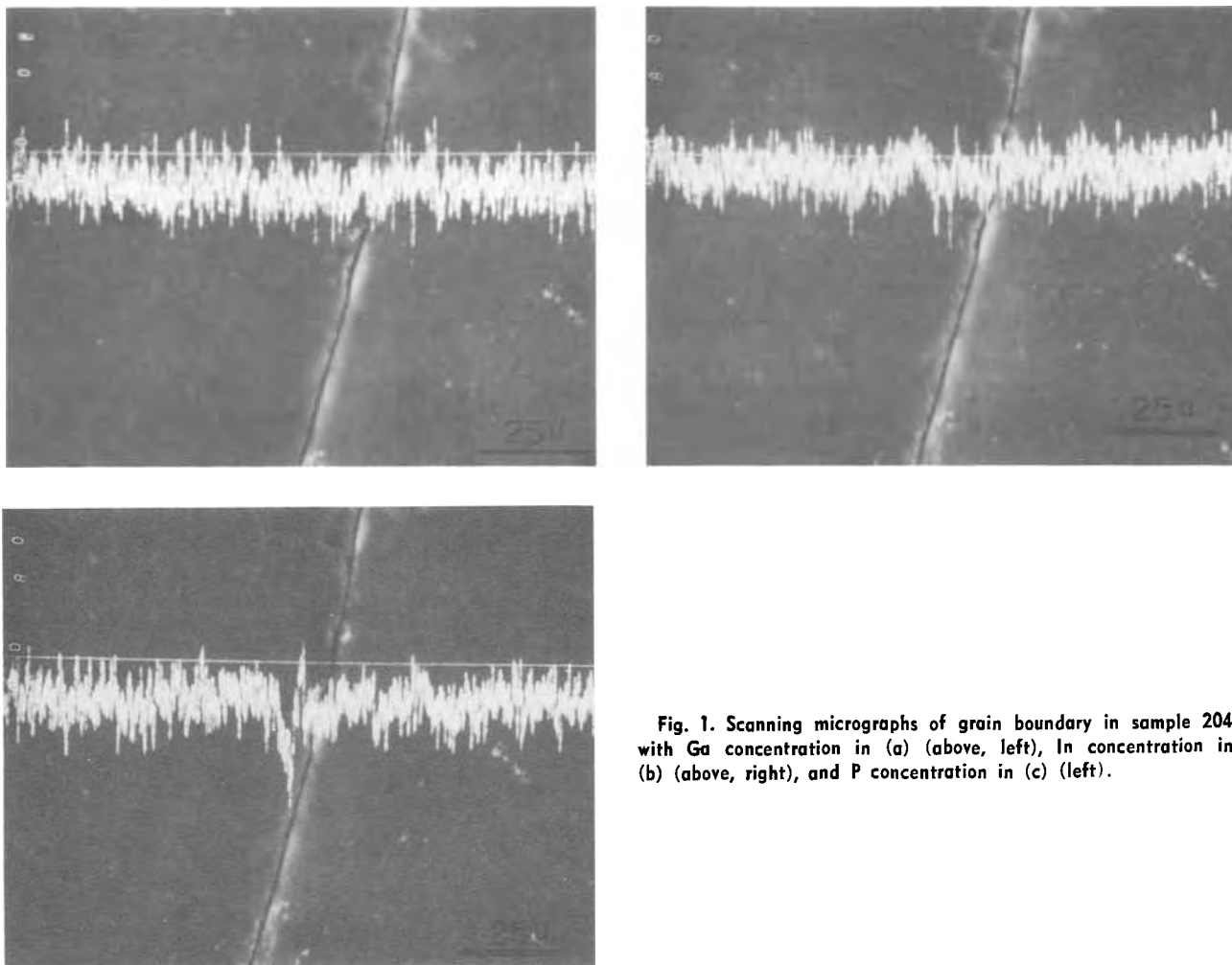


Fig. 1. Scanning micrographs of grain boundary in sample 204 with Ga concentration in (a) (above, left), In concentration in (b) (above, right), and P concentration in (c) (left).

parameters, and qualitative evaluation of the crystalline perfection of the sample (5).

Recently the ECP techniques have been refined to the point where this information can be obtained from selected areas of less than  $10\ \mu\text{m}$  diameter (6). The SAC pattern arises because of an angular dependence of electron reflection and absorption. The basic features of the contrast in ECP's has been interpreted by Hirsch and Humphries (7) in terms of the anomalous absorption effects in the dynamical theory of electron diffraction (8).

The SACP is obtained by holding the beam at a selected spot on the sample while the incident angle of the beam is rocked through a large solid angle. This leads to the formation of pronounced bands and lines at the Bragg angles of the specimen. The ECP's resemble the geometry of Kikuchi patterns and can be indexed by analogous methods. This technique was applied to determine the orientation of the  $\text{In}_{1-x}\text{Ga}_x\text{P}$  samples and to evaluate the influence of the defect sites on local crystalline perfection. The qualitative evaluation of the surface perfection is possible because the ECP's are sensitive to the perfection in the top  $100\text{\AA}$  of the specimen and any lattice distortion degrades the pattern quality.

### Results and Discussion

**Crystal uniformity.**—X-ray scans across the large grained samples and electron channeling patterns of the individual crystals revealed the local uniformity of the In-Ga composition and the freedom from lattice stretch-compression. Figure 1 shows the small fluctuations in the concentration of the indium and gallium exhibited by the bulk material as well as the negligible effect on the concentration of the boundary. The phos-

phorus scan does show a concentration variation within  $10\ \mu$  of the boundary of one grain. However, as shown in Fig. 2, not all boundaries affect the local phosphorus concentration. The average phosphorus concentration in all three grains depicted in Fig. 2 is the same, although there was a slight variation (approximately 2% maximum) within a given subgrain.

The pronounced bands and lines of the selected area channeling pattern of Fig. 3, which was taken in a defect-free area of sample 236, and the sharpness of the

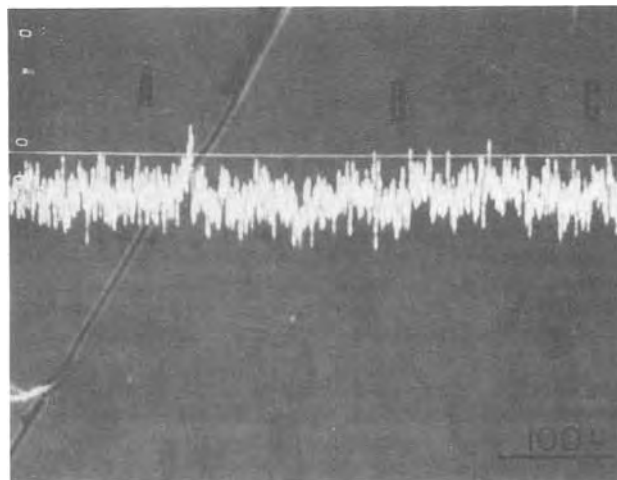


Fig. 2. Scanning micrograph with P concentration across grain boundaries in sample 150.



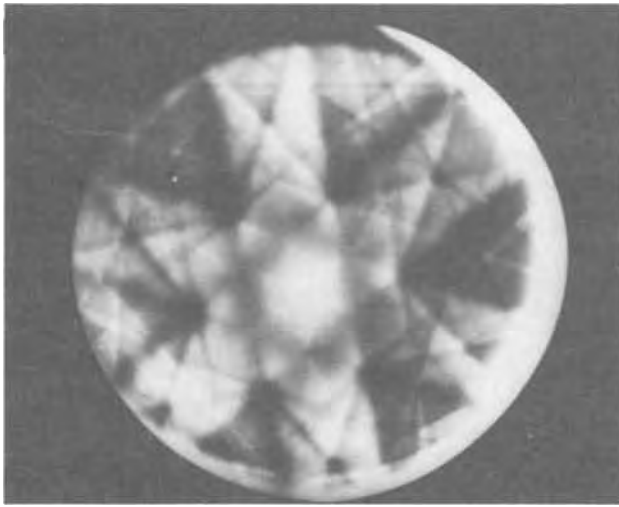


Fig. 3. Selected area channeling pattern showing typical (111) pole on sample 236. To obtain the orientation, the specimen was tilted until the (111) pole came into view.

lower part of the electron channeling pattern of Fig. 4, which represents the area away from the defects, shown in Fig. 5, confirms the presence of distortion-free areas of the crystals. The local uniformity is also demonstrated by the fact that the  $\text{In}_{1-x}\text{Ga}_x\text{P}$  crystals will lase all the way to the green (1).

**Defect site microstructures.**—The inclusions are loosely bound second phase particles (*e.g.*, indium) resulting from local inhomogeneities during crystal growth. In all samples observed the inclusions at the surface were removed during the surface preparation

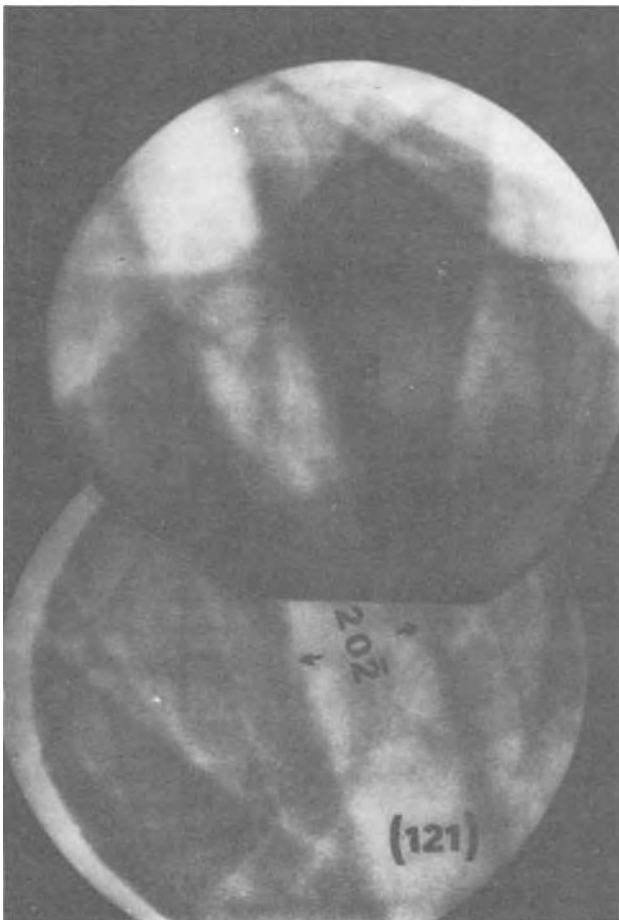


Fig. 4. Composite SACP showing the orientation of sample 236

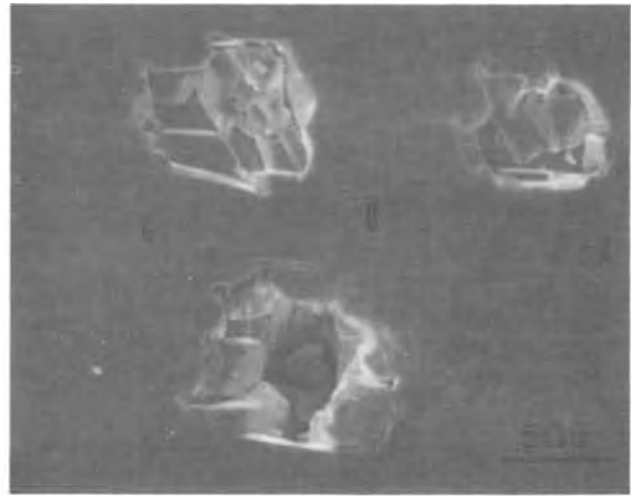


Fig. 5. Cluster of defect sites in sample 236 selected for analysis

leaving a characteristic defect site of trapezoidal shape. Figure 6 shows such a defect site which penetrated completely through sample 299. However, most defects penetrated only part of the way as shown in Fig. 7 from sample 236. At the bottom of the trapezoidal pit, bulk matrix material can be seen.

**Defect sites, composition and crystallographic effects.**—The influence of the defects on local compositional variations and crystalline perfection were evaluated using characteristic x-ray line scans and selected area ECP's. Figure 5 shows a cluster of three defect sites in sample 236 selected for this analysis.

The orientation of the surface normal can be determined by locating a low index crystallographic pole at the intersection of the bands of the channeling pattern. The SACP of Fig. 3 shows the (111) orientation obtained by tilting sample 236 through a large angle. The orientations of the area near the sites in Fig. 5 were determined from Fig. 4. This figure is a composite of two SACP's containing the (121) pole. The orientation corresponding to the point marked B in Fig. 5 is shown in Fig. 4 (also marked B). From measurements on the ECP's it was determined that the surface normal lies at an angle of  $6.8^\circ$  to the (121) pole along the  $(20\bar{2})$  band.

Comparing the ECP with the defects of Fig. 5 shows that some of the edges of the defect site must be nearly along  $(1\bar{1}1)$ . This suggests that the straight edges of

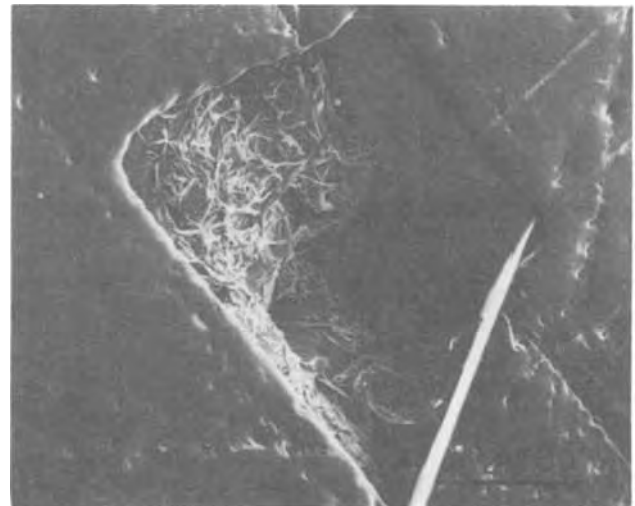


Fig. 6. Typical trapezoidal-shaped defect site in sample 299. The site penetrated completely through the specimen.



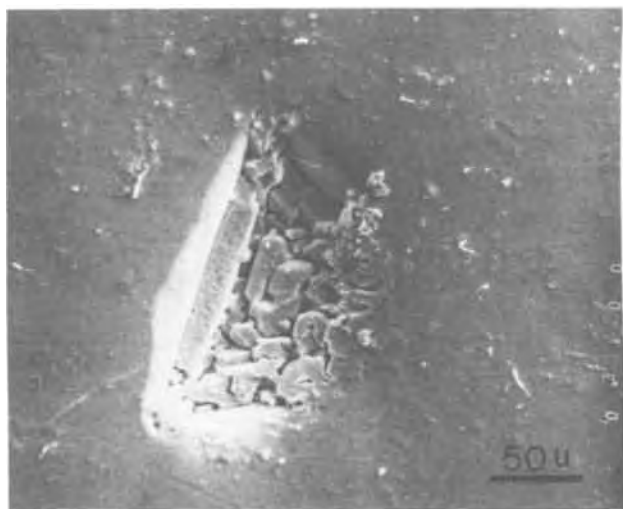


Fig. 7. Typical trapezoidal defect site in sample 236. Matrix material is seen at the bottom of the pit.

the defect sites may have resulted from a fixed crystallographic relationship between the matrix and the defects. However, the information obtained as yet is insufficient to establish the definite existence of this relationship.

X-ray scans of In, Ga, and P across the defect sites of Fig. 5, shown in Fig. 8-10, reveal deviations from stoichiometry near the defects. In particular, the P concentration in Fig. 10 changes by as much as 10% around the defect sites. The In and Ga concentrations appear to mirror each other near the defect sites with the In concentration following the P concentration profile. The deviation from stoichiometry for the indium and gallium is less than for the phosphorus, but the approximate 5% variation of the indium is higher than that encountered in the bulk material. The lower concentration of gallium and the resulting lower count rate causes the observed gallium fluctuation to fall within the counting error limits.

The influence of the defect sites on local crystalline perfection can be seen by comparing the SACPs taken near the defects with the ECP shown in Fig. 4. Figures 11-13 are the SACPs obtained from areas approximately 10  $\mu\text{m}$  in diameter at the sites marked A, B, and C, respectively, in Fig. 5. The degradation in the patterns near the defect sites is clear from the lines

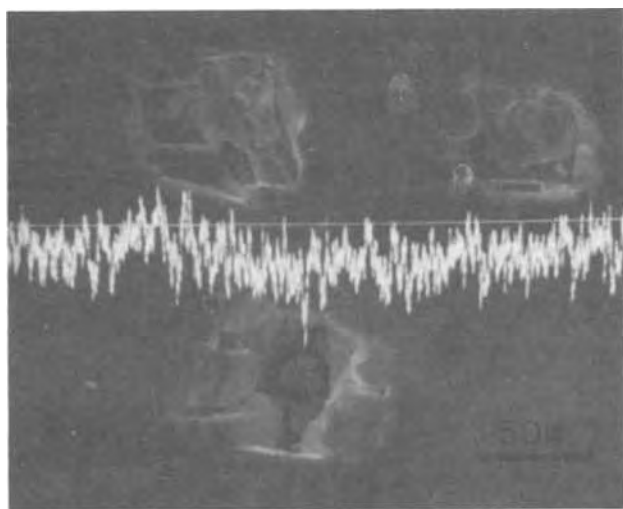


Fig. 8. Micrograph with superimposed In concentration scan from the same area of sample 236 as Fig. 3. Scan is made between the defect sites.

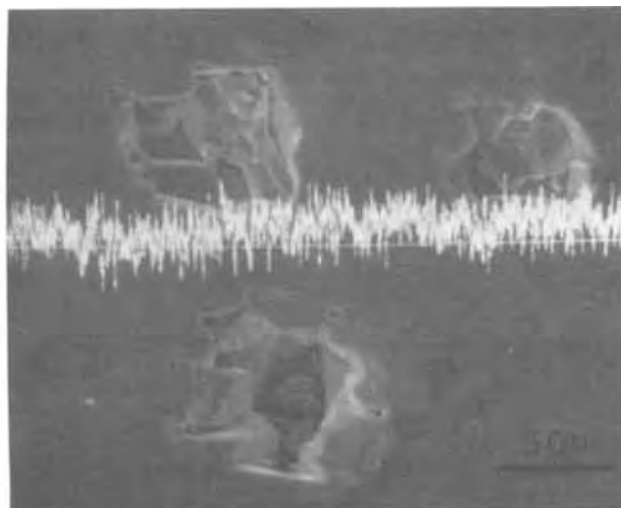


Fig. 9. Micrograph with superimposed Ga concentration scan from the same area of sample 236 as Fig. 3.

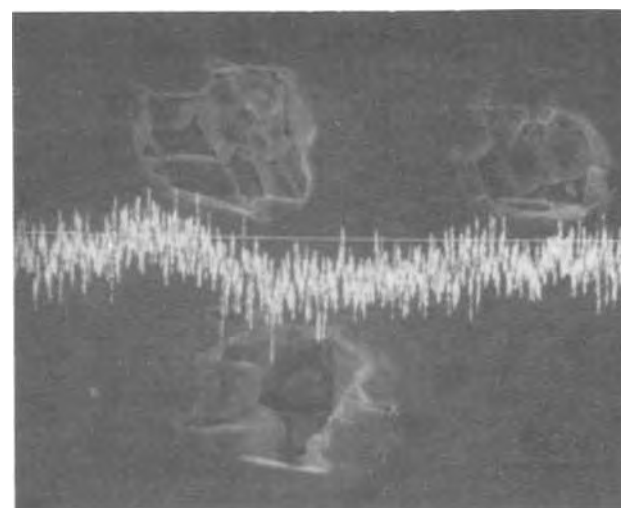


Fig. 10. Micrograph with superimposed P concentration scan from the same area of sample 236 as Fig. 3.

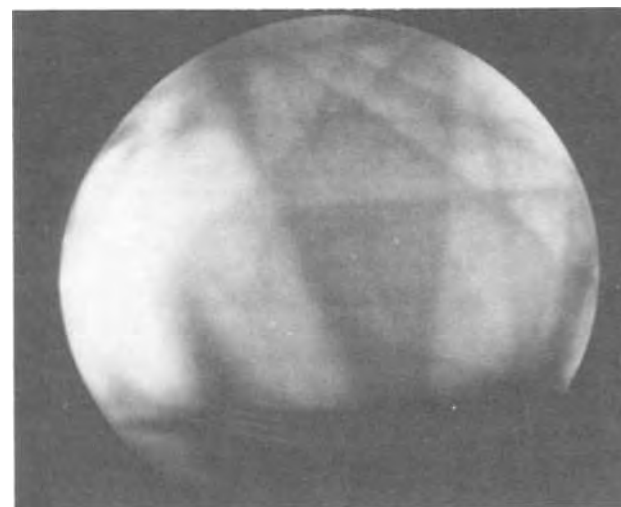


Fig. 11. SACP at inclusion A in Fig. 3

which are washed out of the patterns. Note that the (202) band is clearly apparent in all the ECP's. This

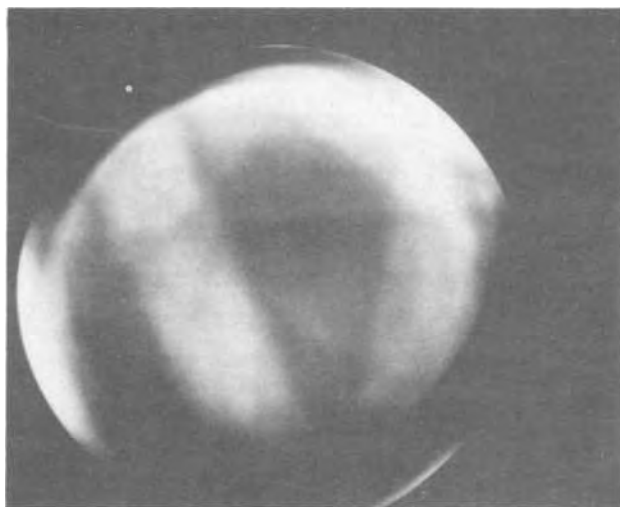


Fig. 12. SACP at inclusion site B in Fig. 3



Fig. 13. SACP at inclusion site C in Fig. 3

indicates that the defect sites introduce local damage but do not cause any orientation change in the sample.

### Conclusions

1. In and/or Ga can be substituted directly over a wide composition range into a common group III sub-

lattice so as to yield a continuous series of  $\text{In}_{1-x}\text{Ga}_x\text{P}$  crystals without changing crystal structure or severely distorting the structure.

2. Although these crystals contained large inclusions (or defect sites after surface treatment), crystal growth defects have only a limited effect on the surrounding crystal in terms of lattice distortion as determined by ECP's.

3. The localized chemical inhomogeneities caused by the defects did not significantly affect the LED qualities of the crystals.

4. Electron channeling patterns have been shown to be a valuable aid in characterizing the crystal perfection of ternary systems, in particular the LED systems.

### Acknowledgment

This work was supported in part by the Advanced Research Projects Agency under Contracts HC 15-67-C-0021, National Science Foundation Grants GH33634 and GH33771, and a grant from the Design and Development Center of Northwestern University. The authors gratefully acknowledge the technical assistance of Bernard Breton, of Kent Cambridge Scientific Inc., and John Jacoby.

Manuscript submitted May 31, 1973; revised manuscript received May 6, 1974. This was Paper 317RNP presented at the Chicago, Illinois, Meeting of the Society, May 13-18, 1973.

Any discussion of this paper will appear in a Discussion Section to be published in the June 1975 JOURNAL. All discussions for the June 1975 Discussion Section should be submitted by Feb. 1, 1975.

*The publication costs of this article have been assisted by Northwestern University.*

### REFERENCES

1. H. M. Macksey, N. Holonyak, Jr., R. D. Dupuis, J. C. Campbell, and G. W. Zack, *J. Appl. Phys.*, **44**, 1333 (1973).
2. D. R. Scifres, H. M. Macksey, N. Holonyak, Jr., and R. D. Dupuis, *ibid.*, **43**, 1019 (1972).
3. G. R. Booker in "Mod. Diff. and Imaging Techniques in Materials Science," S. Amelinckx, R. Gevers, G. Ramaut, and J. Van Landuyt, Editors, p. 553, North-Holland Publishing Co., Amsterdam (1970).
4. JEOLCO Inst., Private communication (1972).
5. G. R. Booker, in "Mod. Diff. and Imaging Techniques in Materials Science," S. Amelinckx, R. Gevers, G. Ramaut, and J. Van Landuyt, Editors, p. 613, North-Holland Publishing Co., Amsterdam (1970).
6. C. G. Van Essen and E. M. Schulson, *J. Mater. Sci.*, **4**, 336 (1969).
7. P. B. Hirsch and C. J. Humphries, in "Scanning Electron Microscopy/1970," p. 449, IITRI, Chicago, Ill. (1970).
8. P. B. Hirsch, A. Howie, R. B. Nicholson, D. W. Pashley, and M. J. Whelan, "Electron Microscopy of Thin Crystals," Plenum Press, New York (1965).

# A Lattice Parameter Criterion for Miscibility Gaps in the III-V and II-VI Pseudobinary Solid Solutions

L. M. Foster\*

IBM Thomas J. Watson Research Center, Yorktown Heights, New York 10598

## ABSTRACT

A smooth relationship is obtained when the excess free energy of mixing parameter,  $B^s$ , is plotted against the relative difference in the lattice parameters of the two components of a number of miscible III-V pseudobinary semiconductor alloys. Extrapolation of this plot to values of the size disparity in systems for which experimental phase diagram information is lacking gives estimates of  $B^s$  sufficiently large to predict miscibility gaps in the AlSb-AlAs, InSb-InP, GaSb-GaP, and AlSb-AlP systems, when the thermodynamic criterion for phase separation,  $B^s > 2RT_c$ , is employed. A cutoff point for miscibility across the entire phase diagram appears to occur at a relative lattice parameter difference of about 7.5%, the value for GaSb-GaAs. This same relative difference is found to divide miscible from immiscible II-VI zinc blende alloys as well.

In earlier studies various experimental and theoretical aspects of the phase relationships in the III-V compound semiconductor pseudobinary alloys were investigated (1-4). One of the principal concerns was the limit of miscibility in the solid phase, since this restricts the compositions that are potentially useful for device applications.

The compound semiconductor systems present onerous experimental problems in the determination of phase boundaries. Many of the systems are high melting and in most instances melting is accompanied by high dissociation pressures, so containment is difficult when the usual techniques for phase diagram determination, such as differential thermal analysis, are attempted. In view of these problems it would be desirable to develop a criterion for miscibility that is based on some easily measured property of the compounds, so as to obviate the difficult experimental determination of each system.

A miscibility gap will appear in a phase diagram if the chemical potential of a component is the same in two different compositions of the phase. The chemical potential changes in forming alloys are obtained from the free energies of mixing of the phases which, for the liquid and solid in a binary system, are

$$\Delta F^{M(l)} = RT[(1-x^l)\ln(1-x^l) + x^l \ln x^l] + B^l(1-x^l)x^l \quad [1]$$

and

$$\Delta F^{M(s)} = RT[(1-x^s)\ln(1-x^s) + x^s \ln x^s] + (1-x^s)L_1[(T/T_1) - 1] + x^s L_2[(T/T_2) - 1] + B^s(1-x^s)x^s \quad [2]$$

where  $x^l$  and  $x^s$  are the mole fractions of the second component. The terms which contain the heats of fusion,  $L_1$  and  $L_2$ , are the free energies of fusion apportioned between the two components. The last term in relations [1] and [2] is the excess free energy of mixing of the phase and accounts for the departure of the system from ideal behavior.<sup>1</sup>

A miscibility gap occurs when the positive excess free energy of mixing becomes sufficient, compared

with the negative free energy of mixing, for the  $\Delta F^M$  vs. composition curve to go through a local maximum. This results in a range of compositions where a single-phase solid solution is unstable with respect to two immiscible solid solution phases on either side.

If the excess free energy of mixing,  $Bx(1-x)$ , is a maximum near  $x = (1-x) = 0.5$ , as will be the case if  $B$  does not vary greatly across the phase diagram, it can be shown that there will be a miscibility gap when  $B > 2RT_c$ , where  $T_c$  is the critical temperature for phase separation (5). In the present application,  $T_c$  is taken to be the solidus temperature at  $x^s = 0.5$ , since, as will be seen,  $B^s$  is evaluated only along the solidus boundary. Thus, when  $B^s = 2RT_c$ , the miscibility gap extends up to the solidus boundary and continuous solid solution formation across the entire phase diagram is not possible at any temperature.

If, on the other hand,  $B^s < 2RT_c$  at the solidus boundary, this does not preclude the existence of a miscibility gap at some lower temperature. No predictions concerning this possibility can be made without knowledge of the temperature dependence of  $B^s$ . This aspect is not considered in the present study.

If both the liquidus and solidus boundaries of a binary diagram are known, the  $B$  parameters, and hence the excess free energies, can be calculated by equating the expressions for the chemical potential of a component derived from Eq. [1] and [2] for the condition of the liquid and solid phases in equilibrium at constant temperature. In an earlier paper in this series (1),  $B^l$  and  $B^s$  were expressed in a form amenable to computer solution.

It has been established experimentally that a single-phase solid solution exists across the entire phase diagram of many of the III-V compound semiconductor alloys (6). Exceptions appear to be the III-(Sb,P) alloys, although these have not been investigated fully. Other exceptions might be expected among alloys of the higher melting aluminum compounds about which little is known. Also, there are conflicting reports about miscibility in GaSb-GaAs alloys, depending on the method employed to determine the phase diagram.

It is shown here that for the miscible systems where there are sufficient data for the calculation to be made, there is a smooth relationship between relative size difference of the two components of an alloy and the excess free energy of mixing. This relationship can be used to predict which of the remaining systems should be miscible and which should exhibit miscibility gaps. These predictions are confirmed by experiment, where information is available, which has shown that the alloys in which miscibility gaps have either been

\* Electrochemical Society Active Member.

Key words: compound semiconductors, phase diagrams, thermodynamics.

<sup>1</sup> The designation of the parameter as  $B$  in this and earlier papers by the author (1-4) is consistent with the usage of Scatchard *et al.* [*J. Am. Chem. Soc.*, 57, 1809 (1935)] and is intended to be noncommittal as to the makeup of the excess free energy. This symbol was chosen over  $\Omega$ , which was originally intended to imply enthalpic interactions in liquid solutions, or  $\alpha$  which in metallurgical literature is frequently  $\alpha = \ln \gamma_1 / (1 - x_1)^2$  [L. S. Darken and R. W. Gurry, "Physical Chemistry of Metals," McGraw-Hill Book Co., New York (1935)] whereas in chemical literature it is usually  $\alpha = RT \ln \gamma_1 / (1 - x_1)^2$ .

demonstrated or suspected all have rather substantial size differences between their components.

From the limited information on the II-VI alloys with the zinc blende structure it appears that the same relationship between size difference and miscibility applies to those materials as well.

### Procedure and Results

For only six systems are there sufficient reliable phase diagram data for  $B^s$  to be evaluated. These are GaAs-AlAs, GaAs-GaP, InSb-GaSb, InAs-GaAs, InP-GaP, and GaSb-GaAs. Liquidus data are available for only the last four. To enable the calculation to be made for GaAs-AlAs and GaAs-GaP, the assumption was made that  $B^l = 0$ . Justification for this assumption was given in Ref. (3) and (4).

Table I gives the relative lattice parameter differences for the 18 III-V pseudobinary alloy systems. The excess free energy parameter,  $B^s$ , at  $x^s = 1 - x^s = 0.5$  for the six systems for which calculations were made, and the literature reference for each value, are also given. There are somewhat different values for some of these systems in the literature (6, 7) resulting from different ways of drawing phase boundaries through the data, from different methods of averaging data, or from use of different assumptions in the calculations. The choices made here reflect a bias on the part of the author for his own experimental data.

In Fig. 1,  $B^s$  for the six alloys is plotted against  $(\Delta a_0/\bar{a}_0)100$ , the relative difference in lattice parameter between the two end members of each alloy expressed in per cent of their average lattice parameter,  $\bar{a}_0$ .

A striking feature of Fig. 1 is the steep ascent of the curve at relative lattice parameter differences greater than about 7%. Reasonable extrapolation of the curve to higher values of  $(\Delta a_0/\bar{a}_0)100$  would give very large values of  $B^s$ . For example, at about an 8% lattice mismatch, corresponding to AlSb-AlAs (the next alloy after GaSb-GaAs),  $B^s$  would be of the order of 8,000-10,000 cal, rising thereafter to extremely large values. As will be shown below, these large values of  $B^s$  are incompatible with complete miscibility in both the liquid and solid across the phase diagram. The implication is, of course, that systems with relative lattice parameter differences between the two components of greater than about 7.5-8% have miscibility gaps in the solid. As seen in Table I, there are four systems, AlSb-AlAs, InSb-InP, GaSb-GaP, and AlSb-AlP clearly outside that range, and a fifth, GaSb-GaAs, with a difference of 7.52% just within the lower end of the range.

A large value of  $B^s$  by itself does not require that there be phase separation, which occurs only if  $B^s$  exceeds  $2RT_c$ . Although  $T_c$ , the solidus temperature at  $x = 0.5$ , is not known for the last four systems of Table I, the average of the melting points of the end members of each alloy will be the maximum value and can be used as a very rough estimate. With these

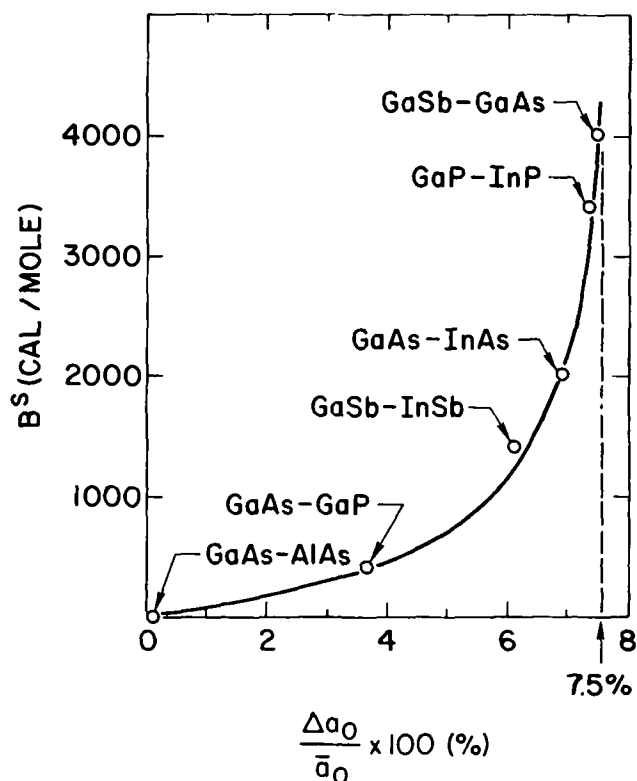


Fig. 1. Excess free energy parameter,  $B^s$ , as a function of the relative difference in lattice parameter between the two components of III-V alloys [ $\bar{a}_0 = (a_1 + a_2)/2$ ].

estimates for  $T_c$ ,  $2RT_c$  for each of the four alloys in question is for AlSb-AlAs, 6700 cal; for InSb-InP, 4200 cal; for GaSb-GaP, 5500 cal; and for AlSb-AlP, 7000 cal. Any reasonable extrapolation of the curve of Fig. 1 gives  $B^s$  for the four alloys greatly in excess of these values.

We will now examine the situation for the GaSb-GaAs system which, as shown in Fig. 1, has a value of  $B^s$  on the rapidly ascending part of the curve. It was shown in Ref. (2) that for this system  $B^s = 4000 \approx 2RT_c$ , if the calculation is made as though the solid were a continuous solid solution and the solidus were smooth throughout the composition range near the center of the diagram where there are no data [see Fig. 1 or Ref. (2)]. Thus, there should be a miscibility gap extending just to the solidus. It will be useful now to see if this is borne out by experimental observations.

Muller and Richards (8) used a flash evaporation technique to deposit very thin III-V alloy films onto cold substrates, then examined the deposits for miscibility by x-ray diffraction. Several compositions of each of nine III-V alloys, including GaSb-GaAs, were prepared (all systems except those containing aluminum compounds). Complete miscibility was observed in all except GaSb-GaP and InSb-InP. Speculating that all of the III-(Sb,P) alloys would have miscibility gaps because of the large size difference between Sb and P, they predicted that AlSb-AlP would be a third exception.

Clough and Tietjen (9) prepared GaSb-GaAs samples by vapor phase epitaxy and examined them by x-ray diffraction. They reported continuous solid solution formation across the entire phase diagram. No data were reported between  $x_{\text{GaAs}} = 0.38$  and 0.69, however.

Recently, Gratton and Woolley (10) reported results on directionally frozen GaSb-GaAs alloys that were examined by x-ray diffraction and x-ray fluorescence techniques. They found a miscibility gap of maximum range  $0.38 < x_{\text{GaAs}} < 0.69$ , corresponding to a peritectic reaction.

Table I. Lattice parameters and excess free energy parameters for the III-V alloy systems

System a b	Lattice parameter, $a_0$ a b	$(\Delta a_0/\bar{a}_0)100$ (%)	$B^s$ ( $x \times 0.5$ ) (calories)	Ref. for $B^s$	
GaAs-AlAs	5.653	5.662	0.16	0	3
GaP-AlP	5.451	5.462	0.20		
GaSb-AlSb	6.095	6.135	0.65		
InAs-InP	6.058	5.869	3.17		
AlAs-AlP	5.862	5.462	3.60		
GaAs-GaP	5.853	5.451	3.64	368	4
InSb-AlSb	6.479	6.135	5.45		
InSb-GaSb	6.479	6.095	6.11	1450	1
InSb-InAs	5.479	6.058	6.72		
InAs-AlAs	6.058	5.662	6.76		
InAs-GaAs	6.058	5.653	6.92	2000	1
InP-AlP	5.869	5.462	7.18		
InP-GaP	5.869	5.451	7.39	3400	1
GaSb-GaAs	6.095	5.653	7.52	4000	2
AlSb-AlAs	6.135	5.662	8.02		
InSb-InP	6.479	5.869	9.88		
GaSb-GaP	6.095	5.451	11.15		
AlSb-AlP	6.135	5.462	11.61		

The results of these three investigations are not necessarily discordant. The flash-evaporated samples of Muller and Richards might not have been equilibrated because of the low deposition temperature, and a immiscibility range in the middle of the diagram might have been missed by Clough and Tietjen through failure to prepare a sample there.

The experiments cited above for GaSb-GaAs serve to illustrate the difficulty in determining a phase boundary near the limit of miscibility and lead to the conclusion that GaSb-GaAs is indeed a borderline case between miscible and immiscible alloys, consistent with the relative size difference between the two components.

#### Application to II-VI Alloys

Since the II-VI compounds are isoelectronic with the III-V's and most of them have the zinc blende structure, at least in some temperature range, it might be expected that the relation between relative lattice parameter difference and miscibility that was observed for the III-V alloys might apply to the II-VI alloys as well. Table II gives the relative difference in the lattice parameter for the possible pseudobinary alloy combinations. The CdSe-CdS system is included even though the room temperature stable structure for CdSe and CdS and their mutual alloys appears to be wurtzite. The alloys are divided into two groups depending on whether or not miscibility has been demonstrated experimentally over the entire phase diagram (11).

It is seen in Table II that the relative lattice parameter difference of about 7.5% that was found to separate miscible from immiscible alloys in the III-V systems also separates the II-VI alloys into similar groupings.

#### Discussion and Conclusions

It has been shown that there is a smooth relationship between the excess free energy of mixing of the solid phase of a number of III-V pseudobinary systems and the size disparity between the two components of the alloys, as expressed by the relative difference in their cubic lattice parameters.

Extrapolation of the plot of the excess free energy parameter,  $B^s$ , vs. the size difference,  $(\Delta a_0/a_0) 100$ , to values of the latter corresponding to the four alloys, AlSb-AlAs, InSb-InP, GaSb-GaP, and AlSb-AlP, gives approximate values of  $B^s$  in excess of  $2RT_c$ , where  $T_c$  is the estimated solidus temperature at  $x = 0.5$ . Thus, a miscibility gap near the center of the diagram that intersects the solidus boundary is predicted for these alloys. A relative lattice parameter difference of about 7.5% appears to separate the miscible from immiscible III-V alloy systems.

From the limited information available for the phase diagrams of the II-VI compounds, it appears that the same relative size difference also separates those systems into groups of miscible and immiscible alloys, and thus is a characteristic of the zinc blende structure rather than of a particular class of compounds.

Restriction of mutual solubility in binary alloys as the result of size differences between the two com-

ponents is of course well known. Hume-Rothery proposed an empirical "size effect" rule for metal alloys to the effect that solid solution formation will be severely limited if the atomic radii of the components differ by more than 15% (12). That rule cannot be applied directly to mixtures of compounds, partly because of the difficulty in defining the compound radii. There is a 13% difference in the tetrahedral radii of Ga and In, for example. Since these occupy sites on the same sublattice in the zinc blende structure, it might be expected that their size difference would be the principal factor in determining the excess free energy of mixing in their pseudobinary alloys where there is a common group V element. This would imply that the degree of nonideality in InSb-GaSb, InAs-GaAs, and InP-GaP systems, as expressed by the parameter  $B^s$ , might be similar. As seen in Fig. 1 however, this is not the case, and only when the "size" of the components is expressed as their lattice parameter is there a correlation with the excess free energy.

Size can enter into calculation of alloy stability in various ways. Phillips and Van Vechten (13) showed that from spectroscopic theory the heat of formation of III-V compounds could be estimated from fundamental properties of the materials, including the lattice constant, the ionicity, and a quantity obtainable from the band gaps. From the observation that in alloys the bandgap does not vary strictly linearly with composition, Van Vechten (14) showed that the spectroscopic theory of the heat of formation could be extended to the alloys and the range of stability [i.e., the compositions where  $\Delta H < T\Delta S(\text{random})$ ] of a number of them was estimated.

Using a similar procedure for calculation of the solid and employing Hildebrand's solubility parameters (15) and electronegativities of the constituent elements for calculation of the liquid, Stringfellow (7) calculated the liquidus and solidus boundaries of the III-V alloys, but the agreement with experimentally determined phase boundaries was poor in a number of cases.

One might expect that a size difference between the two components of a binary alloy would be manifest principally as lattice strain, and there is a great deal of background to support this in metal alloy systems (16). The simplest calculation of strain energy did not give good agreement with experiment in the case of several III-V pseudobinary alloys, however (1). Moreover, the concept of lattice strain becomes vague for the virtual lattice model of semiconductors where all atoms are on lattice points and all III-V bond lengths are identical (i.e., in InP-GaP, for example, In-P and Ga-P distances are the same).

A problem in understanding the nature of the excess free energy of mixing in the III-V alloys, and therefore the role that size difference might play, is the difficulty in identifying separately the contributions of excess enthalpy and entropy. As pointed out by Panish and Ilegems (6), the gross features of the phase diagrams are principally determined by the separation in melting points of the two components and their entropies of fusion. The contribution from the excess free energy, which near the center of the phase diagram is only approximately one fourth of the interaction parameter in magnitude, is relatively small in most instances. In view of the considerable scatter in the literature data for some systems, therefore, systematic trends that might suggest the makeup of the excess free energy are difficult to establish and depend strongly on the choice of data. We found that for the systems shown in Fig. 1, the quantity  $B^s/RT$  was approximately constant, when  $T$  was the temperature along the solidus boundary (2). This is in contrast to the findings of Panish and Ilegems that most of the III-V alloys could be described fairly well by a constant  $B^s$  (their  $\alpha^s$ ) (6). If  $B^s/RT \approx \text{constant}$ , the excess free energy would come largely from an excess entropy. If  $B^s \approx \text{constant}$ , it would be largely en-

Table II. Lattice parameters for the II-VI alloy systems

System a b	Zinc blende lattice parameter, $a_0$ a b	$(\Delta a_0/a_0) 100$ (%)
Miscible systems		
CdSe-CdS	6.07 5.820	4.20
ZnSe-ZnS	5.669 5.409	4.69
CdTe-ZnTe	6.481 6.104	5.99
CdTe-CdSe	6.481 6.07	6.55
CdSe-ZnSe	6.07 5.669	6.83
CdS-ZnS	5.820 5.409	7.32
ZnTe-ZnSe	6.104 5.669	7.39
Systems with miscibility gaps		
CdTe-CdS	6.481 5.820	10.75
ZnTe-ZnS	6.104 5.409	12.07

thalpy. These differences probably cannot be resolved until much better experimental data are obtained.

Manuscript submitted July 17, 1973; revised manuscript received May 8, 1974.

Any discussion of this paper will appear in a Discussion Section to be published in the June 1975 JOURNAL. All discussions for the June 1975 Discussion Section should be submitted by Feb. 1, 1975.

The publication costs of this article have been assisted by the IBM Corporation.

**Note added in proof:** After this paper was submitted, a note by Stringfellow appeared [*J. Phys. Chem. Solids*, **34**, 1749 (1973)] in which it was shown that reasonable agreement with published values of the solid interaction parameters of the III-V pseudobinary alloys could be obtained if the parameter is identified with an enthalpy of mixing that is the difference between the heat of atomization of the alloy (at  $x = 0.5$ ) and the sum of heats of atomization of the pure components. These quantities in turn were assumed from the relation  $\Delta H^{\text{at}} = K a_0^{-2.5}$ , and thus a dependence of the interaction parameter on lattice constant was demonstrated.

#### REFERENCES

1. L. M. Foster and J. F. Woods, *This Journal*, **118**, 1175 (1971).
2. L. M. Foster and J. F. Woods, *ibid.*, **119**, 504 (1972).
3. L. M. Foster, J. E. Scardefield, and J. F. Woods, *ibid.*, **119**, 765 (1972).
4. L. M. Foster, J. E. Scardefield, and J. F. Woods, *ibid.*, **119**, 1426 (1972).
5. G. N. Lewis and M. Randall, "Thermodynamics," 2nd ed., Chap. 21, McGraw-Hill Book Co., New York (1961).
6. M. B. Panish and M. Ilegems, in "Progress in Solid State Chemistry," H. Reiss and J. O. McCaldin, Editors, Pergamon Press, Elmsford, N. Y. (1972).
7. G. B. Stringfellow, *J. Phys. Chem. Solids*, **33**, 665 (1972).
8. E. I. Muller and J. L. Richards, *J. Appl. Phys.*, **35**, 1233 (1964).
9. R. B. Clough and J. J. Tietjen, *Trans. Met. Soc. AIME*, **245**, 583 (1969).
10. M. F. Graton and J. C. Woolley, *J. Electronic Mat.*, **2**, 455 (1973).
11. M. R. Lorenz, "Physics and Chemistry of II-VI Compounds," M. Aven and J. S. Prener, Editors, Chap. 2, American Elsevier Publishing Co., New York (1966).
12. W. Hume-Rothery, "The Structure of Metals and Alloys," Institute of Metals, London (1936).
13. J. C. Phillips and J. A. Van Vechten, *Phys. Rev.*, **B2**, 2147 (1970).
14. J. A. Van Vechten, in "Proc. of the 10th Int. Conf. on Phys. of Semicond.," S. P. Keller, J. C. Hensel, and F. Stern, Editors, U.S. Atomic Energy Commission (1970).
15. J. H. Hildebrand and R. L. Scott, "The Solubility of Non-electrolytes," Dover Publications, New York (1964).
16. For example, L. S. Darken and R. W. Gurry, "Physical Chemistry of Metals," McGraw-Hill Book Co., New York (1953).

## Technical Notes



### Anodic Oxidation of Gallium Phosphide in Aqueous Hydrogen Peroxide

F. Ermanis and B. Schwartz\*

Bell Laboratories, Murray Hill, New Jersey 07974

The feasibility of growing a native oxide by anodic methods on gallium phosphide in a 30% aqueous solution of hydrogen peroxide was demonstrated recently by Schwartz and Sundburg (1); they established an apparent upper voltage limit of about 200V for obtaining uniformly thick oxide films. The present note provides additional data relating oxide thickness to the forming voltage. The effects of varying the pH of the solution and the etching characteristics of the formed oxide in aqueous HCl and NH<sub>4</sub>OH are also described.

#### Experimental Procedure

The anodic oxidations of GaP were carried out using 30% H<sub>2</sub>O<sub>2</sub> as the electrolyte, in the quartz beaker system described previously (1). The pH of the electrolyte was decreased or increased by the addition of H<sub>3</sub>PO<sub>4</sub> or NH<sub>4</sub>OH, respectively. The samples were (111)-oriented, n-type slices, selenium or tellurium doped in the concentration range 10<sup>17</sup>-10<sup>18</sup> cm<sup>-3</sup>. All samples were polished with a 0.075% bromine-in-methanol solution on a Pan-W polishing cloth (2). The experiments were performed using a constant voltage source. During the

anodization most of the samples were completely immersed in the bath while being held in self-anodizing aluminum tweezers (3). With few exceptions, the oxidized slices were routinely bake-dried in a nitrogen-purged oven as described earlier (1). Oxide film thickness and index of refraction were determined subsequent to growth on a Rudolph ellipsometer with a He-Ne laser light source at 6328Å.

#### Results and Discussion

**Effects of solution pH.**—The thickness and uniformity of the anodically grown films were found to depend not only on the applied voltage but also quite strongly on the pH of the solution; Fig. 1 shows the variation of oxide thickness with pH, for films grown at 100V for 5 min. The shape of the curve is similar to that presented by Logan *et al.* (4) in their work on the anodization of GaAs; there is a minimum near pH = 3.6, and an increase on both sides reaching maxima near pH = 2 and pH = 6. Over the entire range 2.5 ≤ pH ≤ 7.5, the thickness of the oxide films was nonuniform; it was only near pH = 2 that films of uniform thickness could be grown. In addition to nonuniformity, between pH = 3.5 and 5, pitted surfaces of GaP were produced.

\* Electrochemical Society Active Member.

Key words: compound semiconductors, native oxides, anodization.

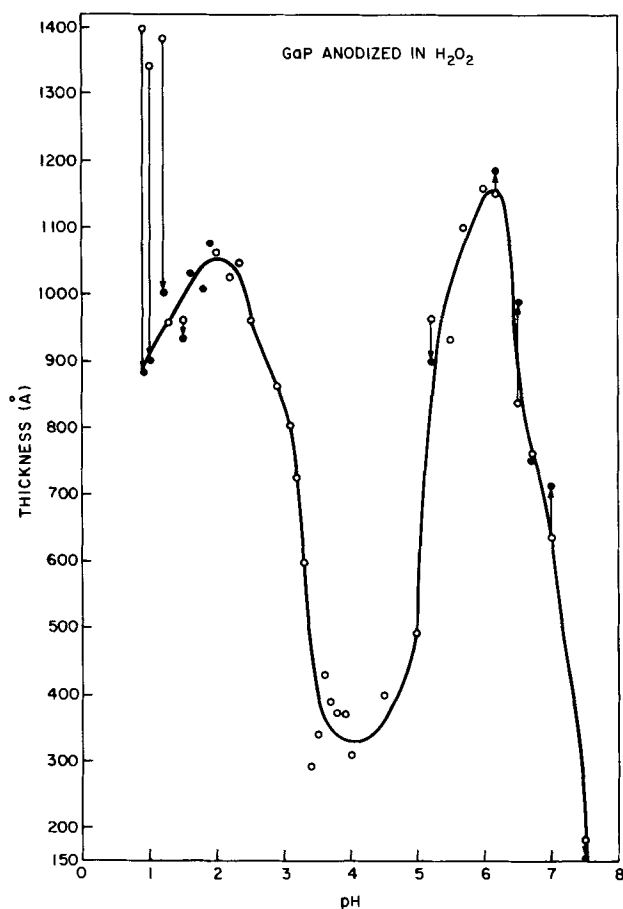


Fig. 1. Thickness of the anodically grown (100V, 5 min) oxide on GaP as a function of the pH of the  $H_2O_2$  solution.  $\circ$  = as grown;  $\bullet$  = baked at  $250^\circ C$ . Uniform oxides were grown only in the pH region of 1.5-2.5.

Oxides grown in the pH range between 1.5 and 2.5 showed insignificant (less than 5%) decrease in thickness upon being baked at  $250^\circ C$  for 2 hr. The same baking cycle, however, caused a drastic 25-35% decrease in thickness for samples anodized at a  $pH \leq 1.3$ . Oxides grown at a  $pH \geq 5$  were so nonuniform, that the effects of baking on these samples could not be determined. Films grown in basic solution (i.e.,  $pH > 7.0$ ) were always nonuniform, due to the fact that the  $NH_4OH$  is a fast acting etchant for the oxides and partly dissolves them during the time interval between the turning off of the bias and the blot-drying of the sample.

**Oxide thickness as a function of voltage and time.**— In general, the anodization behavior followed the pattern established earlier (1, 4); application of a constant voltage resulted in a fast initial growth rate followed by a slowdown of the growth process as the increasing thickness of the oxide raised the resistance of the circuit and decreased the current flow. In 2 min, about 80% and in 5 min about 90% of the ultimate thickness obtainable in a half hour was achieved. Oxides grown in 2 min, however, were not always uniform in thickness. As a routine, therefore, all oxidations were of 3-6 min duration.

A plot of oxide thickness vs. applied voltage (Fig. 2) reveals some scatter in the data for which there may be several reasons. First, the oxidation time was not identical for all samples. Secondly, a range of pH (2.0-2.5) and not a constant pH was used for the oxidizing solutions. Thirdly the carrier concentration in the material varied and was known only to within an order of magnitude ( $10^{17}$ - $10^{18}$   $cm^{-3}$ ). It is known that for a given time of oxidation and a given pH, the more

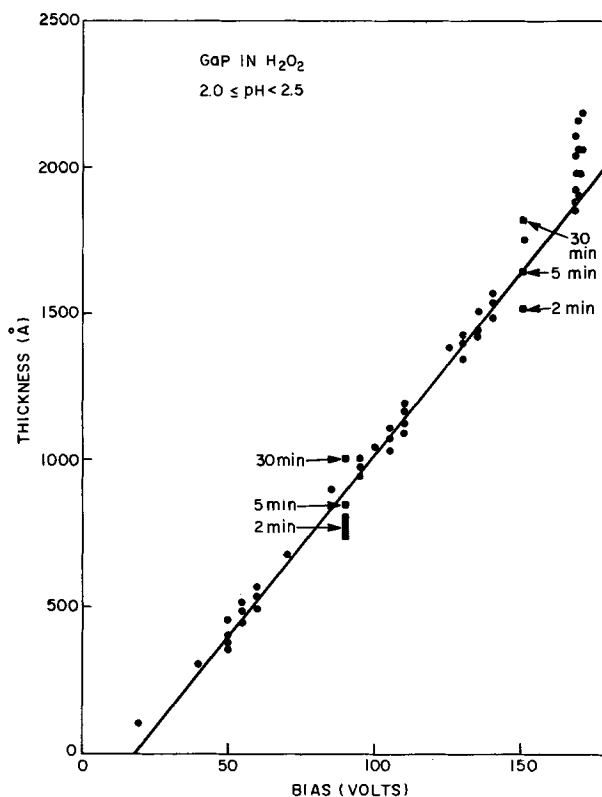


Fig. 2. Thickness of the anodically grown oxide on GaP as a function of the applied constant voltage. The time of reaction is variable, between 3 and 6 min, except for the samples anodized at 90 and 150V, where the data points are plotted after anodization of 2, 5, and 30 min. Except for the 90V anodization, all samples were baked at  $200^\circ C$ .

heavily doped material will develop a thicker oxide than the less heavily doped samples (5). Nevertheless, an approximately linear thickness-voltage relationship can be deduced with a slope of approximately 12 Å/V assuming an average growth time of 5 min.

The voltage above which smooth oxides could not be grown was found to be 170V. Since oxides grown in the range between 160 and 170V were not always uniform, 160V must be considered a safe upper voltage for reliable oxide growth.

The refractive index, which is determined concurrently with thickness from ellipsometric measurements, varied from 1.49 to 1.65 and appears to be a function of the oxide thickness (i.e., forming voltage) as shown in Fig. 3. It could not be determined from the available data, however, whether the index of re-

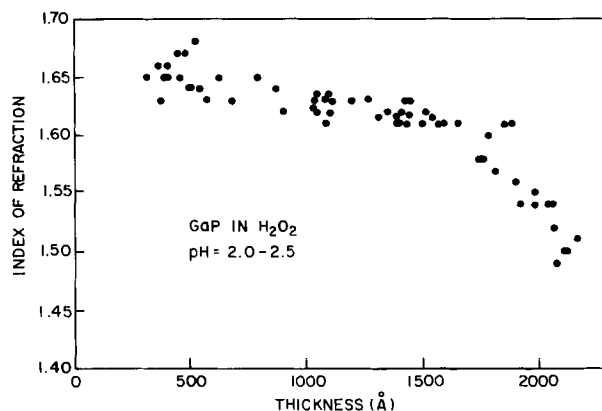


Fig. 3. Ellipsometrically determined index of refraction of anodically grown GaP oxide as a function of oxide thickness (i.e., applied bias).



fraction decreases over the entire film as the film thickens above about 1500Å, or whether a layered oxide structure with a variety of indices was present.

**Etching.**—It had been found in earlier work (1) that the native GaP-oxide is attacked by most mineral acids and common bases. In the present study two of these, HCl and NH<sub>4</sub>OH, were evaluated somewhat more closely. Samples with oxides ranging in thickness from 400 to 2000Å were dipped into several dilutions of the reagents and the disappearance of the oxide was observed visually and the time recorded. The average etch rates obtained in this manner are illustrated in Fig. 4. It is quite obvious that HCl removes the oxide much more slowly than NH<sub>4</sub>OH. Sample surfaces which had been etched in HCl also showed that acid etching left stains, and some areas, such as those near the oxidant-air boundary of the few partly immersed samples, were almost untouched. These surfaces could be markedly improved by a subsequent dip in NH<sub>4</sub>OH; in most cases not only was the surface residue "cleaned up" but a relatively constant average etch rate by the NH<sub>4</sub>OH was exhibited over a wide range of dilution.

The nonlinear etching characteristics of both etchants were also revealed by the use of a stepwise etching technique which involved a 5 or 10 sec etch followed by a measurement of the remaining thickness. Owing to an obvious in-depth chemical nonuniformity of the film, the etch rate was found to be dependent on the film thickness. The behavior of a 3/1:HCl/water solution under the above stated conditions for 4 samples with original film thicknesses of 600, 1000, 1500, and 2150Å demonstrated that the initial etch rate of the surface of the oxide is higher (30-100 Å/sec) than the

rate (5-20 Å/sec) found after a fraction of the film has been removed. The initial etch rate increases also with increasing original thickness of the oxide at an apparent linear rate of 0.05 Å/sec per angstrom. On the other hand, ammonium hydroxide exhibits the opposite behavior: a 9/1:water/NH<sub>4</sub>OH solution in 5 sec steps showed an initial etch rate of 30-50 Å/sec, which increased to about 200 Å/sec at the oxide-substrate interface. Thus, if for some purpose a partial removal of an oxide film is necessary, the application of the average etch rate to calculate the fraction of the film to be removed might lead to erroneous results.

### Summary

The main findings of this work may be summarized as follows:

1. Anodic oxidation of GaP in 30% aqueous solution of H<sub>2</sub>O<sub>2</sub> can be reproducibly performed within the pH range  $1.5 \leq \text{pH} \leq 2.5$ , obtained by adding H<sub>3</sub>PO<sub>4</sub> to the H<sub>2</sub>O<sub>2</sub>.
2. A maximum safe voltage for uniform oxide growth is 160V and the oxide thickness vs. applied bias curve has a slope of approximately 12 Å/V.
3. The index of refraction, as determined by ellipsometry, of oxide films up to 1500Å thick is  $1.65 \pm 0.05$ .
4. NH<sub>4</sub>OH, in concentrated form, as well as diluted to 1 part in 300 parts water, is a more efficient etchant of the anodic oxide than is HCl. Its action is nonlinear; the oxide at the surface is dissolved more slowly than that near the substrate-oxide interface. On the average, the etching rate is about 60 Å/sec. In contrast, the etching of the oxide in HCl proceeds faster at the surface of the oxide than near the substrate-oxide interface.

Manuscript submitted Feb. 19, 1974; revised manuscript received July 23, 1974.

Any discussion of this paper will appear in a Discussion Section to be published in the June 1975 JOURNAL. All discussions for the June 1975 Discussion Section should be submitted by Feb. 1, 1975.

The publication costs of this article have been assisted by Bell Laboratories.

### REFERENCES

1. B. Schwartz and W. J. Sundburg, *This Journal*, **120**, 576 (1973).
2. M. V. Sullivan and G. A. Kolb, *ibid.*, **110**, 585 (1973).
3. S. M. Spitzer, B. Schwartz, and G. D. Weigle, Paper 70 presented at Electrochemical Society Meeting, San Francisco, California, May 12-17, 1974.
4. R. A. Logan, B. Schwartz, and W. J. Sundburg, *This Journal*, **120**, 1385 (1973).
5. B. Schwartz and F. Ermanis, *ibid.*, **211**, 206C (1974).

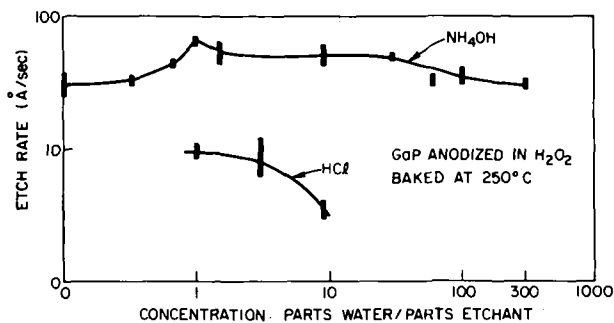


Fig. 4. Oxide etch rate vs. concentration of HCl or NH<sub>4</sub>OH. The rate was determined by timing the removal of oxides 500-2000Å thick which had been baked at 250°C.

## U.V. Imaging with Nematic Chlorostilbenes

W. E. Haas,\* K. F. Nelson, J. E. Adams, and G. A. Dir

Research Laboratories, Xerox Corporation, Webster, New York 14580

Imaging processes based on the interaction between u.v. radiation and liquid crystals have been the subject of several studies. The first reference is contained in a report by Jones *et al.* (1) which merely states that u.v.-sensitive liquid crystals exist and could be used in imaging. Haas *et al.* (2) showed that cholesteric mixtures containing cholesteryl iodide or bromide change their reflection colors in response to u.v. irradiation due to irreversible photochemical reactions, whose products shift the helical pitch and, consequently, the reflection colors of the cholesteric mixtures. Sackmann

(3) described an imaging process based on the *cis*→*trans* conversion of nonmesomorphic azobenzene. Mixtures of cholesteryl chloride and nonanoate were added to azobenzene and the cholesteric reflection colors were altered by irradiation of the samples with 313 nm light. Irradiation at this wavelength causes the *trans*→*cis* conversion of the azobenzene, which results in a pitch change of the cholesteric mixture. Another imaging process was described by Goldberg and Ferguson (4). Their approach is similar to Sackmann's, but instead of the nonmesomorphic azobenzenes they utilized the *cis*→*trans* isomerization of cholesteryl p-phenylazophenyl carbonate, which is a liquid crystal, to produce color changes.

\* Electrochemical Society Active Member.

Key words: nematics, ultraviolet, imaging, liquid crystals, stilbenes.



The imaging process described here is not based on color changes, but on the optical differences between the liquid crystalline and isotropic states. Thermotropic liquid crystals do not scatter light if heated above the isotropic transition temperature and appear dark between crossed polars due to the absence of birefringence. Below the isotropic transition point they usually scatter light and are birefringent. Between crossed polarizers the samples appear bright except in cases of special alignment. In the imaging process the isotropic transition temperature is locally lowered through u.v. irradiation at 300 nm. If the isotropic point is depressed to the observation temperature, the exposed regions appear dark between crossed polarizers, and the unexposed areas appear bright. The process is thus positive to negative. Without polarizers the contrast is weak, relying solely on the optical difference between scattering and nonscattering areas.

The nematic liquid crystals used in the experiments were *trans*-4-butyl- $\alpha$ -chloro-4'-ethoxystilbene (BCES) and *trans*-4-octyl- $\alpha$ -chloro-4'-ethoxystilbene (OCES) (5) and also mixtures between these nematics and cholesteryl oleyl carbonate (COC). The reasons for using mixtures of stilbenes and COC were twofold. First, the isotropic transition temperature of mixtures between BCES or OCES and COC is lower than the transition temperature of pure nematic stilbenes. Therefore, smaller energy levels of irradiation are required to depress the isotropic transition point to or below room temperature. Second, the scattering of the cholesteric mixtures, that is, mixtures containing cholesteryl oleyl carbonate, is more intense than the scattering of stilbenes. The contrast without polarizers is therefore increased. The mixtures had the optical characteristics of cholesterics and were obtained by heating the two components jointly above the isotropic transition temperature.

The images are only visible in a limited temperature range whose span depends on the u.v. energy absorbed per unit volume. For example, if a mixture prior to irradiation has an isotropic transition temperature of 40°C and this temperature is imagewise lowered to 20°C, observation of the image is only possible in the temperature interval 20°-40°C. Above 40°C the whole sample is isotropic and below 20°C the sample is completely birefringent. Images obtained with positive and negative inputs are shown in Fig. 1 and 2, respectively. The dark regions are isotropic and the bright regions are liquid crystalline (cholesteric focal-conic texture). The liquid crystal, BCES with 20% by weight COC, was sandwiched between two quartz slides and contact-exposed through a photographic negative. The imaged slides were then placed on the stage of a Leitz polarizing microscope and photographed between crossed polarizers.



Fig. 1. Image obtained by contact exposure through photographic negative.

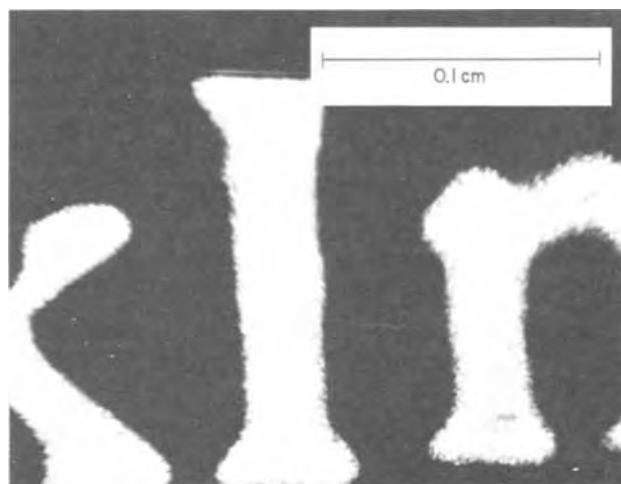


Fig. 2. Image obtained by contact exposure through photographic positive.

The changes in isotropic transition temperature of nematic stilbenes and mixtures with COC were measured as a function of irradiation. Since the absorption coefficient of stilbenes is very high in the u.v. ( $\epsilon = 28,000$  at 305 nm) (5), measurements were made on films 0.38-0.50 $\mu$  thick.

The films were prepared by deposition from petroleum ether solutions and the thickness estimated from the interference color. Quartz slides proved to be unsuitable substrates for very thin films. Due to surface tension effects the films showed a tendency to break up shortly after deposition. The problem was circumvented by the use of 0.5 mil Tedlar<sup>1</sup> films as substrates. Tedlar has a suitable absorption spectrum for measurements at 3000Å. Samples were irradiated with a filtered xenon-Hg source equipped with quartz optics. The u.v. filter used had a half width of 120Å. The light levels were measured with an United Detector Technology Incorporated light metering system. The transition temperatures were measured on a Leitz polarizing microscope equipped with a Mettler temperature control-hot stage unit.

The results obtained for BCES and OCES are shown in Fig. 3 where the nematic isotropic transition temperatures  $T_{n-i}$  are plotted vs. absorbed energy. Measurements of the cholesteric-isotropic transition temperature  $T_{c-i}$  vs. absorbed energy are shown for two compositions in Fig. 4.

The liquid crystals, BCES, OCES, and COC, were used in the experiments as received from the sup-

<sup>1</sup> Trade name for du Pont PVF films.

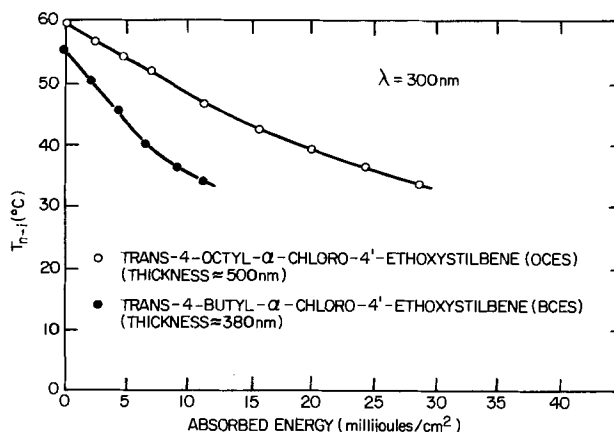


Fig. 3. Nematic-isotropic transition temperature vs. absorbed u.v. energy.

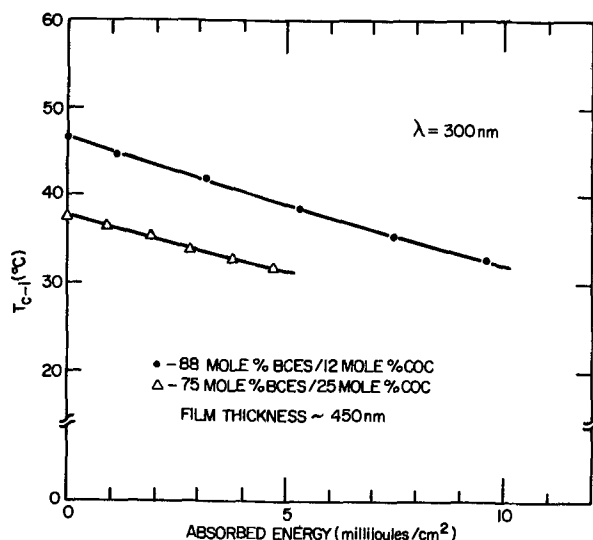


Fig. 4. Cholesteric-isotropic transition temperature vs. absorbed u.v. energy.

pliers.<sup>2</sup> Purification was deemed unnecessary because it was initially established that the isotropic transition temperatures were in good agreement with literature values, which is an indication of high purity. Further evidence for sample purity is the high resistivity of the stilbenes, which was of the order of  $10^{11}$  ohm-cm. The effect is tentatively attributed to a *trans*→*cis* conversion of the stilbenes in which the u.v.-generated *cis*-stilbene acts as an impurity which depresses the liquid crystal-isotropic transition temperature. The role of impurities in the depression of liquid crystal-isotropic transition points is well known (6) and evidence to support the assumption that a *trans*→*cis* conversion takes place is given in Fig. 5, which shows a comparison of the u.v. absorption spectrum of BCES before and after irradiation with the known spectra of nonmesomorphic *trans*- and *cis*- $\alpha$ -chloro-4-methylstilbenes (7).

#### Acknowledgment

The authors would like to acknowledge Dr. F. D. Saeva of the Xerox Research Laboratories for helpful discussions.

Manuscript submitted June 5, 1974; revised manuscript received Aug. 29, 1974. This was Paper 138 pre-

<sup>2</sup> BCES and OCES from Aldrich Chemical Company and COC from Eastman Kodak Company.

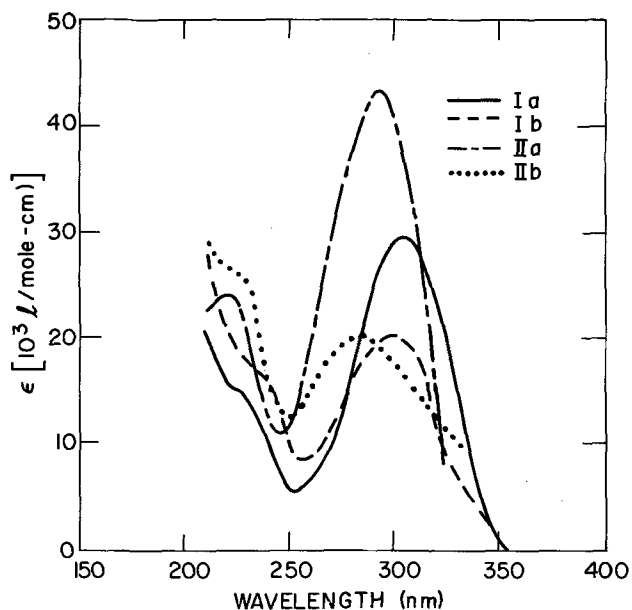


Fig. 5. U.V. spectra of BCES before and after irradiation (Ia and Ib) and spectra of *trans* and *cis*- $\alpha$ -chloro-4-methylstilbene (IIa and IIb) [after McDonald and Schwab, Ref. (7)].

presented at the San Francisco, California, Meeting of the Society, May 12-17, 1974.

Any discussion of this paper will appear in a Discussion Section to be published in the June 1975 JOURNAL. All discussions for the June 1975 Discussion Section should be submitted by Feb. 1, 1975.

The publication costs of this article have been assisted by the Xerox Corporation.

#### REFERENCES

1. C. H. Jones, J. L. Ferguson, J. A. Asars, I. Liberman, W. J. Harper, N. N. Goldberg, and W. C. Divens, RADC Report, TR54-274, Dec. 1965.
2. W. Haas, J. Adams, and J. Wysocki, *Mol. Cryst. Liquid Cryst.*, **7**, 371 (1969).
3. E. Sackmann, *J. Am. Chem. Soc.*, **93**, 7088 (1971).
4. N. N. Goldberg and J. F. Ferguson, U.S. Pat. 3,720,658 (March 1973).
5. W. R. Young, A. Aviram, and R. J. Cox, *Angew. Chem. (Int. Edit.)*, **10**, 410 (1971).
6. R. Walter, *Chem. Ber.*, **58B**, 2303 (1925).
7. R. N. McDonald and P. A. Schwab, *J. Am. Chem. Soc.*, **85**, 4004 (1963).

## Solubility Rate of Poly-(Methyl Methacrylate), PMMA, Electron-Resist

James S. Greeneich

Electronics Department, General Motors Research Laboratories,  
General Motors Technical Center, Warren, Michigan 48090

Poly-(methyl methacrylate), PMMA, is a widely used positive electron-beam resist (1). The resist sensitivity is an important property in determining its usefulness in semiconductor device fabrication. For a typical solvent developer, 1:3 methyl isobutyl ketone: isopropyl alcohol, the reported sensitivity, experimentally determined as the minimum charge per unit area to develop an area pattern, is in the range  $5 \times 10^{-5}$

Key words: electron resist, poly-(methyl methacrylate), electron-beam lithography, developer solubility rate, contrast function.

to  $5 \times 10^{-4}$  coulombs/cm<sup>2</sup>. The spread in reported sensitivities is primarily attributed to varying exposure conditions, such as incident energy, film thickness, substrate, geometry of irradiated pattern (2), and developer temperature. A more fundamental quantity for expressing resist sensitivity is in terms of the absorbed energy density,  $\epsilon$  (3). For degrading polymer resists with a large original number average molecular weight,  $\bar{M}_n$ , this description is adequate; however, for certain values of  $\bar{M}_n$ , the most meaningful quantity is the num-

ber average fragmented molecular weight,  $\bar{M}_f$ , given by (4)

$$\bar{M}_f = \frac{\bar{M}_n}{1 + \frac{g e \bar{M}_n}{\rho A_0}} \quad [1]$$

where  $\rho$  is the resist density,  $A_0$  is Avogadro's number, and  $g$  is an efficiency factor relating the susceptibility of the polymer to electron beam degradation.

Hatzakis and Broers report (5) an improved sensitivity for PMMA by using a developer system based on methyl isobutyl ketone, MIBK. For this developer system, Ting (6) reports the solubility rate for a single molecular weight as a function of an effective charge,  $\alpha Q$ , where  $Q$  is the incident charge per unit area and  $\alpha$  is the normalized depth-dose function (7)

$$\alpha(f) = 0.74 + 4.7f - 8.9f^2 + 3.5f^3 \quad [2]$$

where  $f$  is the depth,  $z$ , normalized to the Grun range,  $R_G$  (7).

For an area exposure the absorbed energy density at a depth  $z$  in the resist is found from

$$e = \frac{Q}{q} \frac{E_0}{R_G} \alpha(f) \quad [3]$$

where  $q$  is the electronic charge, and  $E_0$  is the incident energy. For thin resist films and large incident energies,  $\alpha(f)$  is nearly constant and the absorbed energy density is a weak function of penetration depth. Furthermore, according to Eq. [1], the fragmented molecular weight is nearly constant.

We report on the solubility rate of PMMA in room temperature (23°C) MIBK for various original number average molecular weights. We establish an empirical relationship between the solubility rate and the fragment molecular weight. Using this relationship and Eq. [1], we define a contrast function,  $\Gamma$ , and determine the influence of  $\bar{M}_n$  on  $\Gamma$ .

### Experimental Procedure

Silicon wafers spin-coated with  $\sim 3000\text{\AA}$  of PMMA and baked at 160°C for longer than 90 min, received various doses of 20 keV electron-beam radiation deposited over typical areas of  $10^{-3} \text{ cm}^2$ . An exposed sample was developed in MIBK and periodically the thickness determined by the interference color of the partially developed areas. Ellipsometer measurements determined the refractive index to be  $1.48 \pm 0.02$ . Ellipsometer measurements on the solubility in MIBK of nonirradiated samples established the accuracy to be better than  $\pm 150\text{\AA}$ .

Various original molecular weight materials were investigated. The values of  $\bar{M}_n$  as determined by gel permeation chromatography were between  $10^4$  and  $2 \times 10^5$ . The molecular weight distributions of these samples were nearly identical with the ratio of the weight average molecular weight to  $\bar{M}_n$  of  $\sim 3$ ; no attempt was made to alter the PMMA distribution. The resist solution was prepared by dissolving the polymer in trichlorethylene.

### Results

A typical result, Fig. 1, shows the thickness remaining vs. developer time for the indicated absorbed energy densities calculated from Eq. [3]. The linear relationship for all but very small doses is indicative of uniform energy absorption. The nonlinear behavior at very small doses for short developer times is consistent with ellipsometer measurements on high molecular weight samples receiving no electron dose.

The solubility rate,  $R$ , for a given polymer-developer system is given by the slope of the thickness-time curve. Using Eq. [1] we show  $R$  vs.  $\bar{M}_f$  in Fig. 2 for several original values of  $\bar{M}_n$ . We establish that the solubility rate of the degraded polymer in MIBK at a given temperature is only a function of the fragmented

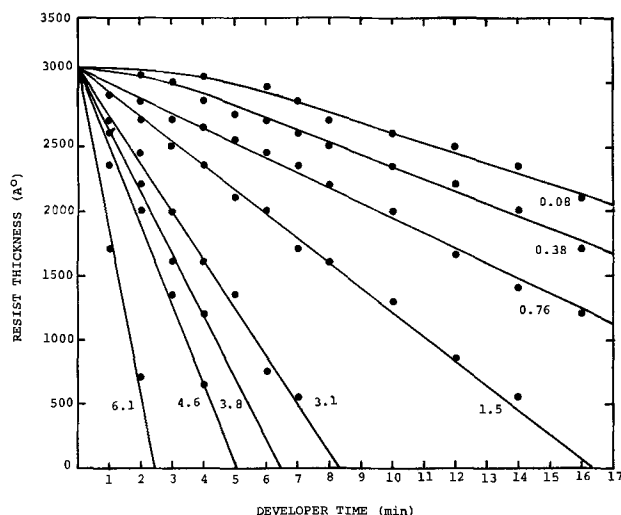


Fig. 1. PMMA resist thickness vs. MIBK development time for indicated absorbed energy densities given in units of  $10^{21} \text{ eV/cm}^2$ .

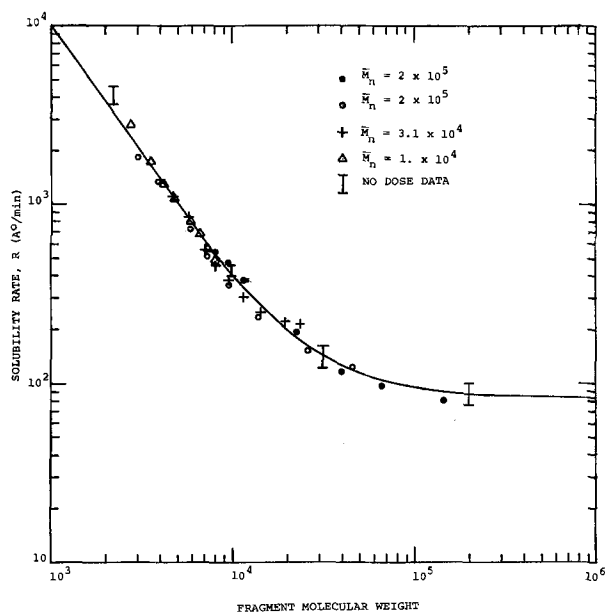


Fig. 2. Solubility rate vs. fragmented molecular weight for PMMA in MIBK at 23°C. Data from various initial molecular weight polymers is shown.

molecular weight. The no dose data shown in Fig. 2 are also consistent with the solubility rate curve. The solid curve in Fig. 2 is given by the relationship

$$R = R_0 + \frac{\beta}{\bar{M}_f^n} \quad [4]$$

where in this case  $R_0 = 84\text{\AA}/\text{min}$ ,  $\beta$  is the proportionality constant  $3.14 \times 10^8 \frac{\text{\AA}}{\text{min}} \left( \frac{\text{gm}}{\text{mole}} \right)^{1.5}$  and  $n = 1.5$ .

The solubility rate is a strong function of the developer solvent and its temperature; however, the general form of the relationship given by Eq. [4] is found to hold in the cases investigated thus far. We are investigating other temperatures and additional solvent developers, including mixtures of MIBK and isopropyl alcohol. The form of the solubility rate also holds for these mixtures and temperatures; these results will be reported later.

For a given solvent developer, the relative solubility of the irradiated region compared to the nonirradiated region determines the contrast of the developed pattern

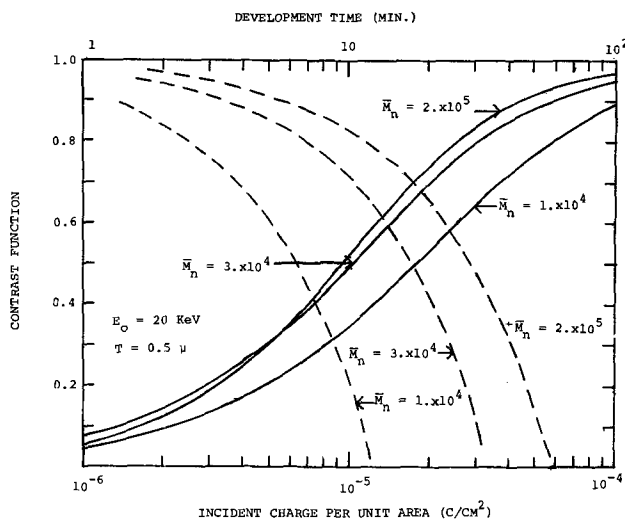


Fig. 3. The contrast function (solid lines) is plotted vs. incident charge per unit area for 5000Å of resist subjected to 20 keV electrons and developed in MIBK. The required development time (dashed lines) for a given  $\Gamma$  is found using the upper, time, axis.

and hence its suitability in device processing. The contrast,  $\Gamma$ , is determined by  $R$  which is a strong function of the incident electron dose. For a film of thickness  $T$ , original molecular weight  $\bar{M}_n$ ,  $\Gamma$  is found as

$$\Gamma = 1 - \left( R_0 + \frac{\beta}{\bar{M}_n^n} \right) \frac{1}{T} \int_0^T \frac{dz}{R_0 + \frac{\beta}{\bar{M}_f^n}} \quad [5]$$

where the dependence of  $\bar{M}_f$  on  $z$  is found from Eq. [1], [2], and [3]. In Fig. 3 we show  $\Gamma$  vs.  $Q$  for three values of  $\bar{M}_n$  for the developer system used. The initial

energy is 20 keV and  $T = 0.5\mu$ . The dotted lines in Fig. 3 show the required development time as a function of  $\Gamma$  for the given exposure condition. To obtain a high contrast exposure for a given  $Q$ , a high molecular weight polymer is preferred at the expense of longer development times than for lower molecular weight polymers.

**Acknowledgments**

The author would like to thank M. C. Steele for helpful discussions of this material, E. R. Cprek for use of the SEM, R. A. Ottovani for several samples of PMMA, A. M. Wims for molecular weight analysis of the PMMA, and B. J. Vannoy for substrate preparation.

Manuscript submitted April 8, 1974; revised manuscript received June 24, 1974.

Any discussion of this paper will appear in a Discussion Section to be published in the June 1975 JOURNAL. All discussions for the June 1975 Discussion Section should be submitted by Feb. 1, 1975.

The publication costs of this article have been assisted by the General Motors Company.

**REFERENCES**

1. M. Hatzakis, *This Journal*, **116**, 1033 (1969).
2. J. S. Greeneich and T. Van Duzer, *J. Vacuum Sci. Technol.*, **10**, 1056 (1973).
3. J. S. Greeneich and T. Van Duzer, *IEEE Trans. Electron Devices*, To be published.
4. J. S. Greeneich, Unpublished Ph.D. dissertation, University of California, Berkeley, California (1973).
5. M. Hatzakis and A. N. Broers, in "Record of 10th Symposium on Electron, Ion, and Laser Beam Technology," L. Marton, Editor, pp. 107-114, San Francisco Press, San Francisco (1969).
6. C. H. Ting, in "Record of 11th Symposium on Electron, Ion, and Laser Beam Technology," R. F. M. Thornley, Editor, pp. 337-344, San Francisco Press, San Francisco (1971).
7. T. E. Everhart and P. H. Hoff, *J. Appl. Phys.*, **42**, 5837 (1971).

## Analysis of Zone Melting Processes

E. Y. Wang

Electrical Engineering Department, Wayne State University, Detroit, Michigan 48202

For different pertinent boundary conditions Pfann (1) has derived equations which describe the impurity distribution along a crystal after passage of one molten zone. In this note, starting from the conservation of total number of impurity atoms, a general and expedient method of deriving those well-known analytic results is presented.

**General Formula**

As shown in Fig. 1, the molten zone,  $l$ , is passed from left to right. The impurity concentration in the molten zone is designated  $C_l$ , that in the melting solid  $C_{ms}$ , and that in the solidified solid  $C_{fs}$ . It is assumed that  $C_l$  is homogeneous in the molten zone, that the impurity diffusion is negligible, and that no evaporation of impurity occurs during the melting. From the conservation of impurity atoms,  $N$ , one has

$$\int_0^x C_{fs}(x') A(x') dx' + C_l(x) \int_x^{x+l(x)} A(x') dx' + \int_{x+l}^L C_{ms}(x') A(x') dx' = N \quad [1]$$

Key words: zone melting, crystal growing, zone leveling.

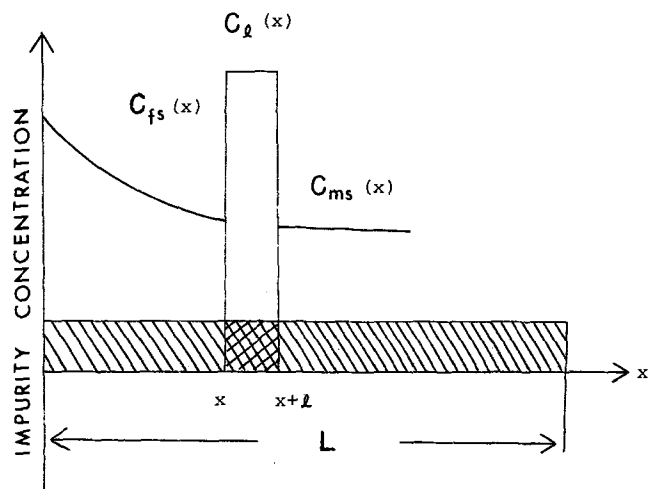


Fig. 1. Schematic representation of zone melting

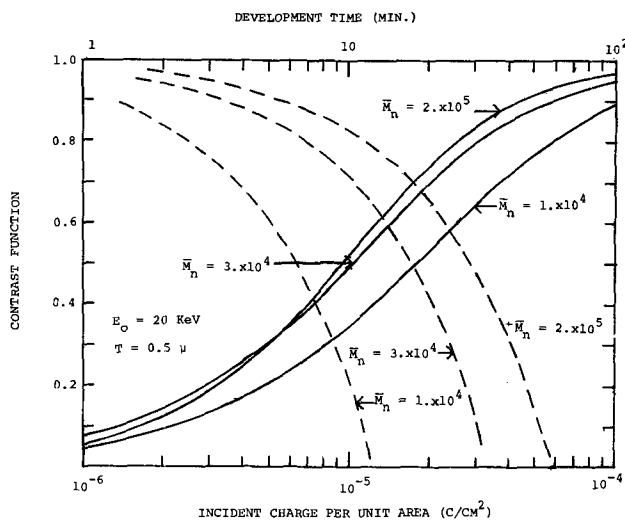


Fig. 3. The contrast function (solid lines) is plotted vs. incident charge per unit area for 5000Å of resist subjected to 20 keV electrons and developed in MIBK. The required development time (dashed lines) for a given  $\Gamma$  is found using the upper, time, axis.

and hence its suitability in device processing. The contrast,  $\Gamma$ , is determined by  $R$  which is a strong function of the incident electron dose. For a film of thickness  $T$ , original molecular weight  $\bar{M}_n$ ,  $\Gamma$  is found as

$$\Gamma = 1 - \left( R_0 + \frac{\beta}{\bar{M}_n^n} \right) \frac{1}{T} \int_0^T \frac{dz}{R_0 + \frac{\beta}{\bar{M}_f^n}} \quad [5]$$

where the dependence of  $\bar{M}_f$  on  $z$  is found from Eq. [1], [2], and [3]. In Fig. 3 we show  $\Gamma$  vs.  $Q$  for three values of  $\bar{M}_n$  for the developer system used. The initial

energy is 20 keV and  $T = 0.5\mu$ . The dotted lines in Fig. 3 show the required development time as a function of  $\Gamma$  for the given exposure condition. To obtain a high contrast exposure for a given  $Q$ , a high molecular weight polymer is preferred at the expense of longer development times than for lower molecular weight polymers.

**Acknowledgments**

The author would like to thank M. C. Steele for helpful discussions of this material, E. R. Cprek for use of the SEM, R. A. Ottovani for several samples of PMMA, A. M. Wims for molecular weight analysis of the PMMA, and B. J. Vannoy for substrate preparation.

Manuscript submitted April 8, 1974; revised manuscript received June 24, 1974.

Any discussion of this paper will appear in a Discussion Section to be published in the June 1975 JOURNAL. All discussions for the June 1975 Discussion Section should be submitted by Feb. 1, 1975.

The publication costs of this article have been assisted by the General Motors Company.

**REFERENCES**

1. M. Hatzakis, *This Journal*, **116**, 1033 (1969).
2. J. S. Greeneich and T. Van Duzer, *J. Vacuum Sci. Technol.*, **10**, 1056 (1973).
3. J. S. Greeneich and T. Van Duzer, *IEEE Trans. Electron Devices*, To be published.
4. J. S. Greeneich, Unpublished Ph.D. dissertation, University of California, Berkeley, California (1973).
5. M. Hatzakis and A. N. Broers, in "Record of 10th Symposium on Electron, Ion, and Laser Beam Technology," L. Marton, Editor, pp. 107-114, San Francisco Press, San Francisco (1969).
6. C. H. Ting, in "Record of 11th Symposium on Electron, Ion, and Laser Beam Technology," R. F. M. Thornley, Editor, pp. 337-344, San Francisco Press, San Francisco (1971).
7. T. E. Everhart and P. H. Hoff, *J. Appl. Phys.*, **42**, 5837 (1971).

## Analysis of Zone Melting Processes

E. Y. Wang

*Electrical Engineering Department, Wayne State University, Detroit, Michigan 48202*

For different pertinent boundary conditions Pfann (1) has derived equations which describe the impurity distribution along a crystal after passage of one molten zone. In this note, starting from the conservation of total number of impurity atoms, a general and expedient method of deriving those well-known analytic results is presented.

**General Formula**

As shown in Fig. 1, the molten zone,  $l$ , is passed from left to right. The impurity concentration in the molten zone is designated  $C_l$ , that in the melting solid  $C_{ms}$ , and that in the solidified solid  $C_{fs}$ . It is assumed that  $C_l$  is homogeneous in the molten zone, that the impurity diffusion is negligible, and that no evaporation of impurity occurs during the melting. From the conservation of impurity atoms,  $N$ , one has

$$\int_0^x C_{fs}(x') A(x') dx' + C_l(x) \int_x^{x+l(x)} A(x') dx' + \int_{x+l}^L C_{ms}(x') A(x') dx' = N \quad [1]$$

Key words: zone melting, crystal growing, zone leveling.

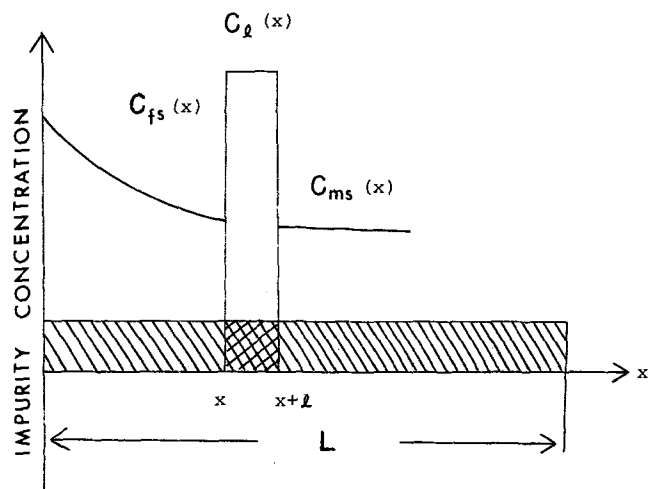


Fig. 1. Schematic representation of zone melting

where  $A(x)$  is the cross-section area of the crystal. Differentiating Eq. [1] with respect to  $x$  yields

$$C_{fs}(x)A(x) + \left[ \int_x^{x+l(x)} A(x') dx' \right] \frac{dC_1(x)}{dx} + C_1(x)A(x+l) \left( 1 + \frac{dl}{dx} \right) - A(x)C_1(x) - C_{ms}(x+l)A(x+l) \left( 1 + \frac{dl}{dx} \right) = 0 \quad [2]$$

where  $C_1(x)$  is considered as a function of  $x$  related to the location of the molten zone along a crystal, but  $C_1(x)$  is constant in the molten zone, and  $A, l$ , are treated as functions of  $x$

By the definition of the distribution coefficient  $C_{fs}(x)/C_1(x) \equiv k$ , Eq. [2] can be written

$$\left[ \int_x^{x+l(x)} A(x') dx' \right] \frac{dC_{fs}(x)}{dx} + C_{fs}(x) \left[ A(x+l) \left( 1 - \frac{dl}{dx} \right) - A(x)(1-k) \right] - kA(x+l) \left( 1 + \frac{dl}{dx} \right) C_{ms}(x+l) = 0 \quad [3]$$

Both Pfann's zone leveling conditions and impurity distributions of a single pass, multipass, and steady state can be readily obtained from Eq. [3]. The former will be presented first.

### Zone Leveling Conditions

For an initially pure rod and an addition of impurity in the first molten zone,  $C_{ms}(x+l)$  usually is several orders of magnitude smaller than  $C_{fs}(x)$ . Equation [3] can be reduced to

$$\left[ \int_x^{x+l(x)} A(x') dx' \right] \frac{dC_{fs}(x)}{dx} = A(x)(1-k) - A(x+l) \left( 1 + \frac{dl}{dx} \right) C_{fs}(x) \quad [4]$$

The zone-leveling condition along a crystal requires that

$$C_{fs}(x) = \text{constant, or } \frac{dC_{fs}(x)}{dx} = 0$$

Equation [4] can be further reduced to

$$A(x)(1-k) - A(x+l) \left( 1 + \frac{dl}{dx} \right) = 0$$

or

$$\frac{dl}{dx} = \frac{A(x)}{A(x+l)} (1-k) - 1 \quad [5]$$

Case I: If  $A(x) = \text{const}$ ,  $l(x) \neq \text{const}$ . Equation [5] gives

$$\frac{dl}{dx} = -k, \text{ or } l = l_0 - kx \quad [6]$$

Equation [6] is the condition for a uniform impurity distribution along the crystal if one varies the zone

length and retains a constant cross-section area.  $l_0$  is the initial molten zone length.

Case II: If  $l(x) = \text{const}$ ,  $A(x) \neq \text{const}$ . Eq. [5] gives

$$A(x)(1-k) = A(x+l)$$

or

$$\frac{A(x+l) - A(x)}{l} = \frac{kA(x)}{l} \quad [7]$$

Equation [7] gives an exact  $A(x) = A_0(1-k)^{x/l}$ , which is identical with Pfann's solution  $A(x) = A_0 e^{x/D}$ ,

$$\text{where } D = \frac{l}{\log_e(1-k)}.$$

For small  $l$

$$\frac{A(x+l) - A(x)}{l} \approx \frac{dA(x)}{dx} = \frac{kA(x)}{l}$$

which yields

$$A(x) = A_0 \exp\left(-k \frac{x}{l}\right) \quad [8]$$

where  $A_0$  is the initial cross-section area. Equation [8] gives the variation of cross-section area necessary to maintain a uniform impurity distribution along a crystal.

### Impurity Distribution

Now consider the impurity distribution along a crystal for the conditions  $A(x) = \text{const}$  and  $l(x) = \text{const}$ . Equation [3] becomes

$$\frac{dC_{fs}(x)}{dx} + \frac{k}{l} C_{fs}(x) - \frac{k}{l} C_{ms}(x+l) = 0 \quad [9]$$

which is exactly the same equation derived by Read (1) and Reiss (2). Lord (3) also used Eq. [9] to compute the impurity distribution for various passes by replacing  $C_{ms}(x+l)$  for  $C_{fs}(x+l)$  in preceding pass. Steady state, or ultimate impurity distribution, can easily be obtained by letting  $C_{fs}(x+l) = C_{ms}(x+l)$  and substituting into Eq. [9]. The solution of Eq. [9] is then  $C_{fs}(x) = Ae^{Bx}$  where  $A, B$  are constants obtainable from  $k = \frac{Bl}{e^{Bl} - 1}$  and  $A = \frac{NB}{e^{Bl} - 1}$ . The solution again is identical with Pfann's ultimate distribution (4).

Manuscript received April 5, 1974.

Any discussion of this paper will appear in a Discussion Section to be published in the June 1975 JOURNAL. All discussions for the June 1975 Discussion Section should be submitted by Feb. 1, 1975.

The publication costs of this article have been assisted by Wayne State University.

### REFERENCES

1. W. G. Pfann, *Trans. AIME*, **194**, 747 (1952).
2. H. Reiss, *ibid.*, **200**, 1053 (1954).
3. N. W. Lord, *ibid.*, **197**, 1531 (1953).
4. W. G. Pfann, "Zone Melting," p. 42, John Wiley & Sons, New York (1966).

## Synthesis and Properties of ZnGeN<sub>2</sub>

William L. Larson, H. Paul Maruska,\*<sup>1</sup> and David A. Stevenson\*

Department of Materials Science and Engineering, Stanford University, Stanford, California 94305

The search for new semiconductor materials with optimum properties for specific applications has led to the synthesis and characterization of new ternary compound semiconductors. One class of ternary compounds is a pseudobinary solid solution, such as the III-V compounds Ga<sub>x</sub>In<sub>1-x</sub>As or GaAs<sub>x</sub>P<sub>1-x</sub>. Another class of ternary compounds, much less extensively studied, is a solid solution formed from the isoelectronic replacement of one element in a binary compound by two different elements, such as a II-IV-V<sub>2</sub> analogue of a III-V compound (1). In addition to a great variety of combinations for the latter class of compound, there is the possibility of significant alteration in the electrical properties by variation of the ratio of the II to IV element. The present note describes the synthesis and properties of ZnGeN<sub>2</sub>, which is the II-IV-V<sub>2</sub> analogue of the III-V compound GaN.

The compound ZnGeN<sub>2</sub> has been prepared by the reaction of Zn with Ge<sub>3</sub>N<sub>4</sub> and by the reaction of ammonia with Zn<sub>2</sub>GeO<sub>4</sub> (2). In these preparative techniques, there is the possibility of incorporating a significant amount of oxygen in the final product. (The GeN<sub>4</sub> in the first synthetic scheme is prepared by the reaction of GeO<sub>2</sub> with NH<sub>3</sub>.) A recent study of the stability of ZnGeN<sub>2</sub> established that the compound may be synthesized from the metal chlorides in atmospheres of partially dissociated ammonia (3). In the present study, layers of ZnGeN<sub>2</sub> were grown in an open flow vapor growth system, similar to that used for GaN (4). An HCl-N<sub>2</sub> gas mixture (4.93 × 10<sup>-4</sup> moles HCl/minute plus 2.57 × 10<sup>-2</sup> moles N<sub>2</sub>/minute carrier gas) was successively flowed over elemental zinc (59 grade) and Ge (69 grade) at respective temperatures of ~550° and ~950°C, and the resulting vapor was mixed with an NH<sub>3</sub>-N<sub>2</sub> atmosphere (2.69 × 10<sup>-2</sup> moles NH<sub>3</sub>/minute with 2.25 × 10<sup>-2</sup> moles N<sub>2</sub>/minute carrier gas) in the reaction chamber where deposition occurred. Deposition was made on sapphire substrates with (0001) and (11̄02) orientations and a growth temperature of 850°C; (higher temperatures resulted in the deposition of zinc-doped elemental germanium). Deposition rates were typically 1 μ/hour and the final samples were yellow polycrystalline materials approximately 1-2 μ in thickness. A scanning electron micrograph of the surface revealed small particle sizes of the order of 0.1-0.5 μ (Fig. 1).

The crystal structure and the lattice parameters, measured using a Debye-Scherrer powder pattern technique, indicated a wurtzite structure with  $a = 3.193\text{\AA}$  and  $c = 5.187\text{\AA}$  at room temperature. There was a small amount of line broadening observed, presumably caused by slight distortion of the lattice resulting from the mismatch between the sapphire substrate and the ZnGeN<sub>2</sub> film. These x-ray results may be contrasted with those of Maunaye and Lang (2), who reported that ZnGeN<sub>2</sub> is monoclinic, with  $a = c = 3.167\text{\AA}$ ,  $b = 5.194\text{\AA}$  and  $\beta = 118^\circ 53'$ . It should be

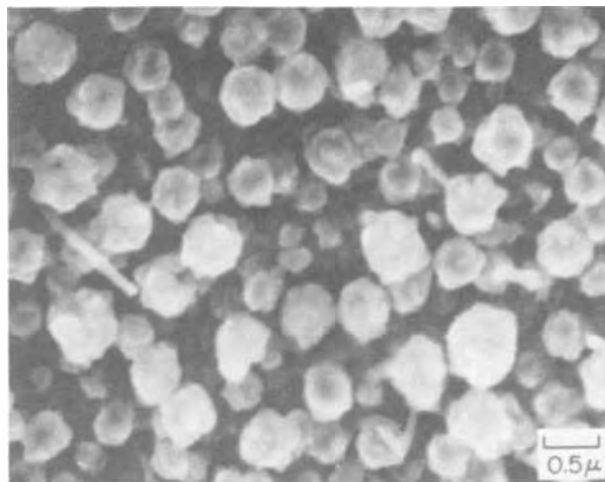


Fig. 1. Scanning electron micrograph of a layer of deposited ZnGeN<sub>2</sub>.

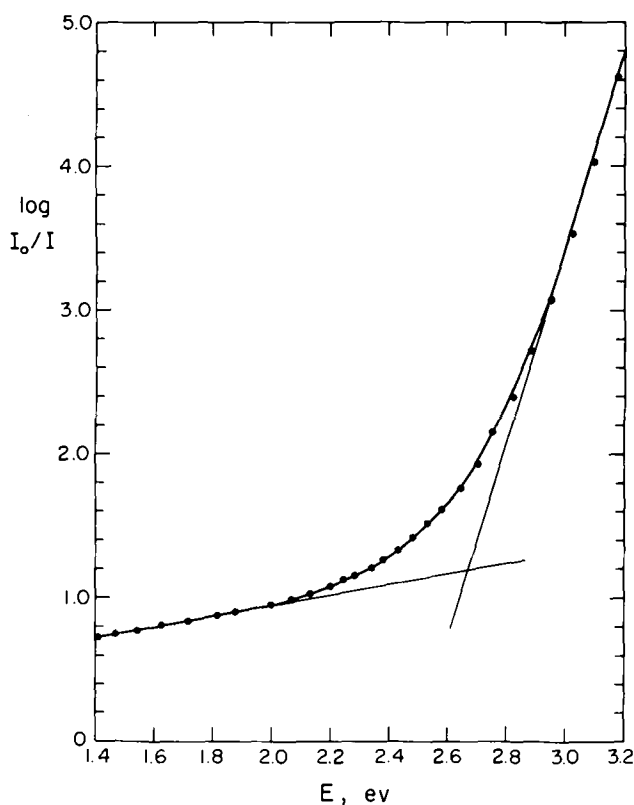


Fig. 2. Optical absorption vs. energy for ZnGeN<sub>2</sub>

\* Electrochemical Society Active Member.

<sup>1</sup> Present address: RCA Laboratories, Princeton, New Jersey 08540.

Key words: ternary compound, chemical vapor deposition, crystal structure, bandgap, carrier concentration.

noted that their results differ from a wurtzite structure only by a discrepancy of  $1^{\circ}7'$  in the angle  $\beta$ , hence one might describe their structure as slightly distorted wurtzite. This distortion might be caused by the incorporation of residual oxygen impurity, since the reactants were oxides. The structure and lattice parameters are almost identical to the isoelectronic III-V compound, GaN (wurtzite structure with  $a = 3.189\text{\AA}$  and  $c = 5.185\text{\AA}$ ).

The resistivity and Hall coefficient of the  $\text{ZnGeN}_2$  films were measured using a six contact method. Pure  $\text{ZnGeN}_2$  was always n-type with electron concentrations of  $10^{18}$ - $10^{19}\text{ cm}^{-3}$  and resistivities between 0.3 and 0.4 ohm-cm at room temperature. As might be expected for polycrystalline samples, room temperature mobilities were low, ranging from 0.5 to 5  $\text{cm}^2/\text{V}\cdot\text{sec}$ . Hall constants and resistivities measured vs. temperature were found to be constant throughout the temperature range from  $100^{\circ}$  to  $300^{\circ}\text{K}$ . Optical absorption measurements of polished  $\text{ZnGeN}_2$  samples, displayed in Fig. 2, indicate a bandgap of approximately 2.67 eV. In this particular sample, the absorption coefficient

at 3.2 eV is approximately  $58,000\text{ cm}^{-1}$ . The similarity between  $\text{ZnGeN}_2$  and the analogous III-V compound GaN is noteworthy, particularly the crystal structure and the high carrier density.

Manuscript submitted May 6, 1974; revised manuscript received July 26, 1974.

Any discussion of this paper will appear in a Discussion Section to be published in the June 1975 JOURNAL. All discussions for the June 1975 Discussion Section should be submitted by Feb. 1, 1975.

The publication costs of this article have been assisted by Stanford University.

#### REFERENCES

1. A. S. Borshchevskii, N. A. Goryunova, F. P. Kesamanly, and D. N. Nasledov, *Phys. Status Solidi*, **21**, 9 (1967).
2. M. Maunaye and J. Lang, *Mater. Res. Bull.*, **5**, 793 (1970).
3. A. M. Zikov, F. F. Grekov, and D. M. Demidov, *Zh. Prikl. Khim.*, **44**, 1700 (1971).
4. H. P. Maruska, W. C. Rhines, and D. A. Stevenson, *Mater. Res. Bull.*, **7**, 777 (1972).

## Confirmation of Existence of Phase Transitions in InSe by Specific Heat Measurement and X-Ray Analysis

Kazuaki Imai, Minoru Sato, and Yutaka Abe

Department of Nuclear Engineering, Hokkaido University, Sapporo 060, Japan

Indium monoselenide has been known as one of the layered semiconductors and several investigations have been reported concerning the electronic (1) and optical (2) properties of this material. However, experimental results are widely scattered, and it seems very difficult to find consistent results among the various investigators. We have supposed that the above inconsistency is, at least partly, due to certain inhomogeneity of the crystal which is introduced inherently during the crystal growth by Bridgman or Czochralski method.

In this short note, we report the existence of several, well-defined temperatures of phase transitions in indium selenide and the experimental result of annealing in the specimens of quenched phase.

#### Differential Thermal Analysis (DTA) and Specific Heat Measurement (SHM)

The DTA and SHM have been carried out with the following types of specimens:

1. Stoichiometric amounts of indium (99.999%) and selenium (99.999%) were enclosed in a quartz holder in vacuum of  $10^{-5}$  Torr. After direct fusion, the compound was cooled down slowly to room temperature. Hereafter, we shall refer to these specimens as A.

2. A large ingot of indium selenide was prepared by the Bridgman method. The specimens were carefully cut out of the ingot by wire sawing machine. We shall refer to these specimens as B in what follows. It was confirmed by x-ray fluorescence analysis that our specimens had the composition of  $\text{In}_{1.00}\text{Se}_{0.99}$ .

The DTA was performed with  $\alpha\text{-Al}_2\text{O}_3$  as the standard sample and the heating rate was about  $1^{\circ}\text{C}/\text{min}$ . The typical experimental result is shown in Fig. 1. Here we can clearly observe that there are four definite endothermic peaks between room temperature and  $700^{\circ}\text{C}$ . The SHM was carried out with apparatus similar to the one for DTA. In our method, the time

for the unit temperature increase (which is proportional to the specific heat under the test) was measured. As shown in Fig. 2, the peaks which correspond to the ones in the DTA were observed. The DTA has a tendency that the measured temperatures are shifted to the side of higher temperature compared with the results from the SHM. We prefer the results of SHM in designating the characteristic temperature. The above experimental results are reproducible, and the temperatures of the peaks are found to be in good agreement among the various specimens of types A and B. The sharpness of the above endothermic peaks indicates that these peaks are due to finite phase transitions rather than to the recovery of defects in the crystal. The observed transition temperatures are  $156^{\circ} \pm$

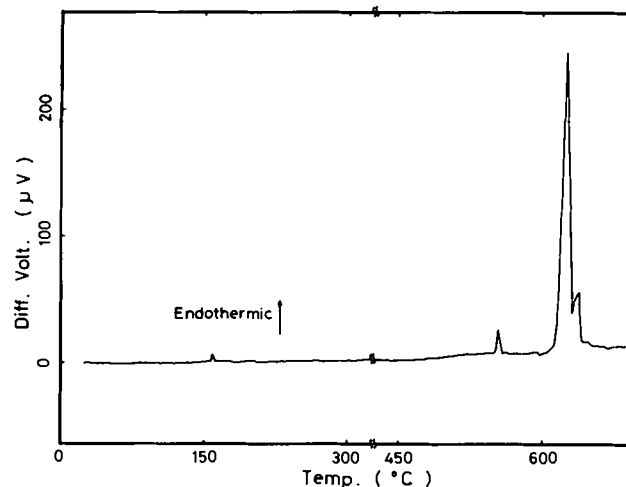


Fig. 1. A typical result of DTA. The longitudinal axis is differential thermal voltage of chromel-alumel thermocouple from the standard sample. The weight of the specimen is about 1.3g.

Key words. compound semiconductor, semiconductor materials, layered semiconductors, crystal structures, crystal structures and phase changes.



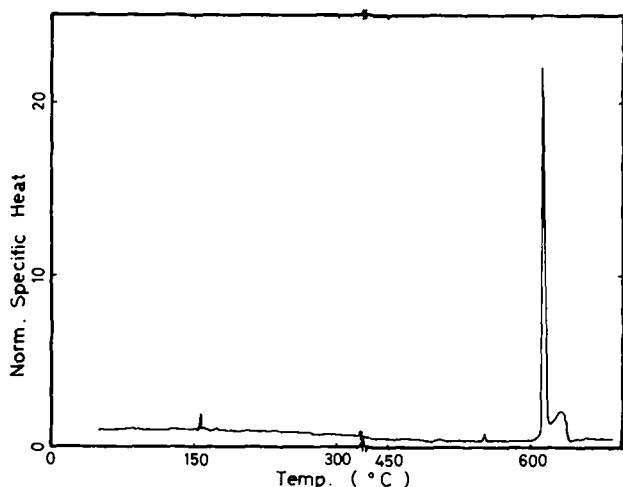


Fig. 2. A typical result of SHM. The longitudinal axis is the specific heat which is normalized at room temperature. The weight of the specimen is 14.4785g, quartz holder is 5.0042g, and the internal heater is about 60 mW.

2°,  $554^\circ \pm 3^\circ$ ,  $614^\circ \pm 3^\circ$ , and  $636^\circ \pm 3^\circ\text{C}$ , respectively. The melting point is  $614^\circ \pm 3^\circ\text{C}$ , and this value is lower than the one previously reported (3).

#### Annealing Effect

In order to find the experimental criteria for getting the single crystal of InSe of homogeneous phase, we have investigated the effect of annealing by x-ray analysis. The annealing of specimens was performed at  $480^\circ\text{C}$  for 70 hr in vacuum of  $10^{-5}$  Torr. The variation of x-ray Laue pattern by the above anneal is shown in Fig. 3. The specimens in this experiment are of type B in the previous section and cleaved surface parallel to c-plane were used. As far as we have observed the annealed specimens by high resolution optical microscope we have found no indications of local

excess of indium or selenium during the annealing process. As seen from Fig. 3(a), the Laue pattern of the as-grown specimen has diffused spots and the spot itself has fine structure. However, the pattern seems to have sixfold symmetry. After the annealing, the Laue spots become focused and have threefold symmetry as distinctly observed in Fig. 3 (b).

For specimens of type A we have investigated the annealing effect by the Debye-Scherrer photograph. However, with the obtained profile we cannot confirm the hexagonal crystal structure of  $D_{6h}^4$  which was previously reported (4).

#### Concluding Remarks

We have shown experimentally the existence of the definite phase transitions in stoichiometric indium-selenium system between room temperature and  $700^\circ\text{C}$ . We have also shown the characteristic variation of Laue pattern in the specimens of quenched phase. These results throw light on the physical origin of widely scattered experimental results of the electronic and optical properties in InSe. We conjecture that similar situations are likely to occur in other layered semiconductors such as GaSe and GaS. To clarify the conditions for getting the perfectly monophase crystals, further quantitative investigations of SHM are in progress.

#### Acknowledgment

The authors would like to thank Professors M. Kaneko and K. Hikichi of Department of Polymer Science, for the provision of experimental facilities and for their valuable suggestions on the method of the present measurements.

Manuscript submitted June 7, 1974; revised manuscript received Aug. 20, 1974.

Any discussion of this paper will appear in a Discussion Section to be published in the June 1975 JOURNAL. All discussions for the June 1975 Discussion Section should be submitted by Feb. 1, 1975.

The publication costs of this article have been assisted by Hokkaido University.

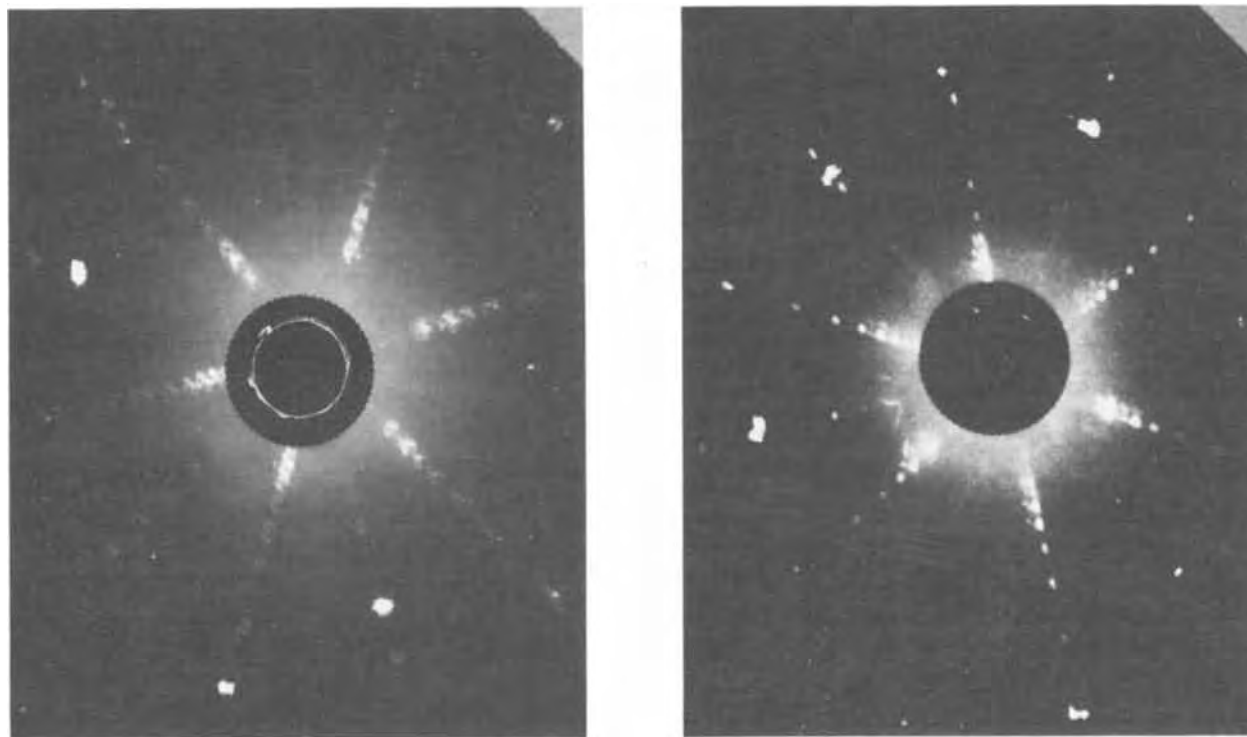


Fig. 3. Laue pattern of the as-grown specimen (a, left) and the annealed specimen (b, right)

## REFERENCES

1. R. W. Damon and R. W. Redington, *Phys. Rev.*, **96**, 1498 (1956).
2. M. Yu. Sakhnovskii, V. B. Timofeev, and A. S. Yakimova, *Soviet Phys.-Semicond.*, **2**, 168 (1968).
3. F. A. Shunk, "Constitution of Binary Alloys," Second supplement, p. 450, McGraw-Hill Book Co., New York (1969).
4. S. A. Semiletov, *Soviet Phys.-Cryst.*, **3**, 292 (1958).

## DISCUSSION

---

## SECTION



This Discussion Section includes discussion of papers appearing in the *Journal of The Electrochemical Society*, Vol. 121, No. 1, 2, 4, and 5; January, February, April, and May 1974.

### The Temperature and Compositional Dependence of the Electrical Conductivity of Nonstoichiometric $\text{CeO}_{2-x}$

R. N. Blumenthal and R. L. Hofmaier (pp. 126-131, Vol. 121, No. 1)

**B. Claudel:**<sup>1</sup> In the afore-mentioned paper, the authors report that they find a low temperature conductivity  $\sigma$  for  $\text{CeO}_{2-x}$  which can be expressed as

$$\sigma = \sigma_0 \exp\left(-\frac{Q}{kT}\right)$$

where  $Q$ , independent of  $x$  is found equal to  $0.61 \pm 0.03$  eV. We had previously reported<sup>2</sup> the same value for the activation energy of the electrical conductivity of a ceria powder put under a nitrogen atmosphere at temperatures below  $400^\circ\text{C}$ . Although our experiments were certainly carried out under cruder conditions than those of Blumenthal and Hofmaier, this agreement seems remarkable. In connection with the interpretation given by these authors in the paper under discussion to the occurrence of a two phase domain, it is worth noting that our samples were prepared by a low temperature process [calcination of  $(\text{NH}_4)_2\text{Ce}(\text{NO}_3)_8$  at  $450^\circ\text{C}$ ] which could hardly yield solid phases in thermal equilibrium, and that we were unable to detect any other phase than  $\text{CeO}_2$ , either by x-ray or by electron diffraction.

### Comments on the Article "On the Theory of Thermal Quenching of Luminescence"

by H. Payen de la Garanderie and D. Curie

R. Pappalardo (pp. 312-313, Vol. 121, No. 2)

**H. Payen de la Garanderie**<sup>3</sup> and **D. Curie:**<sup>4</sup> Quite recently the paper under discussion which criticizes one of our papers<sup>5</sup> was published.

First, confusion must be carefully avoided between: (i) the radiative transition probability per unit time interval, which is denoted by  $I_r$  in our paper,<sup>5</sup> and (ii) the light efficiency,  $\eta$ , of the material, which is commonly referred to by the expression

$$\eta = \frac{I_r}{I_r + I_{nr}}$$

$I_{nr}$  is, in the same way as for  $I_r$ , the probability of non-radiative transitions per unit time interval.

<sup>1</sup>Institute for Research on Catalysis, F-69626 Villeurbanne, France.

<sup>2</sup>M. Breyse, M. Guenin, B. Claudel, H. Latreille, and J. Veron, *J. Catalysis*, **27**, 275 (1972).

<sup>3</sup>Laboratoire de Luminescence, Université de Poitiers, France.

<sup>4</sup>Laboratoire de Luminescence, Université de Paris VI, France.

<sup>5</sup>H. Payen de la Garanderie and D. Curie, in "Luminescence of Organic and Inorganic Materials," Kallmann and Spruch, Editors, p. 334, John Wiley and Sons, Inc., New York (1962).

Of course, in the thermal quenching temperature region  $I_{nr}$  increases vs. temperature much faster than  $I_r$  does, and therefore this increase of  $I_r$  does not mean that "the fluorescence intensity can be enhanced by temperature increases," as is stated in the paper under discussion.

However, some enhancement effects have been reported in some cases, but they are generally ascribed to additional mechanisms, for instance to displacements in the peak positions of the absorption spectra.

A second point is the following one. We considered the case of a monochromatic excitation occurring in a large band emitting and absorbing phosphor. Then the following set of equations was used

$$\frac{dn_j}{dt} = An_{j-1} - (A + E)n_j + En_{j+1} - pn_j = 0 \quad [1]$$

(The notations are described in both the paper under discussion and in our article,<sup>5</sup>  $n_j$  refers to the population of vibrational level  $j$ .) But this equation must be modified for the vibrational level which is reached by excitation; let us call  $j_0$  this level

$$\frac{dn_{j_0}}{dt} = An_{j_0-1} - (A + E)n_{j_0} + En_{j_0+1} - pn_{j_0} + q = 0$$

where  $q$  is the pumping intensity. A similar modification occurs for the level corresponding to the crossing point of the excited state and fundamental state configurational curves. For other levels, Eq. [1] remains unchanged. The complete set of equations used is, of course, described in a more detailed fashion in our paper.<sup>5</sup>

On the other hand, Pappalardo in the paper under discussion considers indeed the case when pumping occurs by means of a large band excitation and thus leads to the whole set of vibrational levels. In such a case all sets of Eq [1] for the populations of the vibrational levels must be changed in the way described above

$$\frac{dn_j}{dt} = An_{j-1} - (A + E)n_j + En_{j+1} - pn_j + q = 0 \quad [2]$$

If one assumes, as Pappalardo did in the above mentioned work, the case of an approximate Boltzmann distribution to be valid, then Eq. [2] has for equilibrium

$$pn_j = q$$

and

$$I_r = p \sum n_j = \text{the total pumping intensity } \Sigma q$$

in agreement with expression [3] of the paper under discussion.  $\Sigma q$  here must be performed upon any vibrational levels of the center that are reached by excitation.

The reader will notice, however, that the "pump intensity"  $q$  in the work being discussed means actually the sum of populations  $\sum n_j$ , i.e., an expression which is proportional to the pumping intensity, but not the pumping intensity itself, for if this were the case, Eq.

[2] and [3] of the paper under discussion would not be dimensionally correct.

**R. Pappalardo:** In Payen de la Garanderie's and Curie's comments above about my criticism of their article<sup>5</sup> in the paper under discussion, they point out in particular that the dimensions of  $q$  in Eq. [2] and [3] of my paper are not correct. In these equations I have used  $q$  as a pump-energy term (proportional to the total number of exciting transitions). Since  $q$  is used in their work as a pump-power term (proportional to the rate of exciting transitions) their criticism is justified.

My basic objections to the article in question,<sup>5</sup> which I stated in the paper being discussed, are not clearly refuted. Since some of the remarks in that paper seem to have been misinterpreted, I shall briefly summarize my previous observations. Quotation marks are used for statements contained in the article by Payen de la Garanderie and Curie.<sup>5</sup>

My criticism was basically aimed at such statements as:<sup>5</sup> "But usually  $I_r$  is considered to be a constant term, while here  $I_r$  increases with increasing temperature," and also " $I_r$  increases because the effective number of states leading to a light transition increases with temperature." I have pointed out that this conclusion is incorrect, even within the context of quasi-monochromatic excitation<sup>5</sup> because of inconsistencies in the mathematical derivation.

The "radiatively emitted light intensity  $I_r$ " is expressed<sup>5</sup> in approximate form as a product of three factors: the constant  $p$  (the "light-emitting transition rate"); the population  $n_0$  of the lowest vibrational level in the excited electronic state; and the factor  $[1 - \exp(-h\nu_e/kT)]^{-1}$ . My objection is to Payen de la Garanderie's and Curie's implicit assumption<sup>5</sup> that the factor containing the exponential is the only temperature dependent quantity. Actually, with the increase in temperature the increase in the  $[1 - \exp(-h\nu_e/kT)]^{-1}$  factor will be compensated by a decrease in  $n_0$ , so that the over-all value of  $I_r$  will not increase with temperature. This was already discussed in my paper under present consideration. This conclusion can also be proved as follows. When the equilibrium rate Eq. [I] and [II] of Payen de la Garanderie's and Curie's paper<sup>5</sup> are summed together the resulting expression is

$$q = sn_{j_1} + \sum' p n_j \quad [1]$$

where the prime indicates that the summation is carried out over the vibrational levels up to, and including, the vibrational level  $j_1$  from which radiationless decay takes place with rate  $s$ . This is a mathematical formulation of the obvious result that in the particular physical model under discussion, the excitation (expressed via  $q$ ) will be dissipated as radiative emission from all the vibrational levels of the excited state up to  $j_1$ , and as radiationless transitions from the latter vibrational level. (Incidentally, since equilibrium conditions have been assumed, it is irrelevant which vibrational level is excited, as long as it is below the  $j_1$  level.)

Since the rate  $p$ ,  $s$ , and  $q$  are assumed to be constant and temperature independent in the particular model under discussion, and since  $n_{j_1}$  increases monotonically with temperature, the radiative intensity term  $I_r = \sum' p n_j$  can only decrease when the temperature increases, in agreement with physical intuition.

## Effect of Dielectric Insert on Surface Charge Density of Electrets

K. Ikezaki, I. Fujita, K. Wada, and J. Nakamura  
(pp. 591-593, Vol. 121, No. 4)

**B. Gross:**<sup>6,7</sup> K. Ikezaki, I. Fujita, K. Wada, and J. Nakamura describe in the paper under discussion the process of generation of homocharge as follows: "According to the theory of Perlman and Reedyk,<sup>8</sup> applying a voltage between electrodes increases the polarization of the inserted glass disk and the field in the air gap. Eventually, this field will exceed the breakdown strength of the air in the gap and the spray discharge will occur. The homocharge deposition of this spray discharge reduces the field in the gap to a value below breakdown and the discharge is quenched . . ." I wish to point out that this theory is contained in a series of papers which I have published since 1944.<sup>9-12</sup> To quote from a paper published in 1949:<sup>10</sup> "With increasing polarization of the dielectric, the field . . . in the interface rises to high values. Finally the interface breaks down and a considerable amount of charge is rushed from the electrode to the surface of the dielectric. This charge has a polarity which is contrary to that of the original charge of the dielectric; it neutralizes part of the latter and thus reduces the field in the interface below sparking threshold." As indicated in a previous comment,<sup>11</sup> the detailed theory of the effect, involving the Paschen curve, has also been developed at an early stage.<sup>12</sup> It has been confirmed by later authors.<sup>13, 14</sup>

## Anomalous Boron Diffusion in Silicon from Planar Boron Nitride Sources

J. Stach and A. Turley (pp. 722-724, Vol. 121, No. 5)

**D. M. Brown:**<sup>15</sup> The anomalous boron diffusion effects reported in the paper under discussion by Messrs. Stach and Turley ("Deeper penetration in the high concentration area suggests a concentration dependent diffusivity giving enhanced diffusion at high concentrations; however, the concentration gradient near the surface indicates that the diffusivity probably reaches a maximum value and then begins to decrease with higher concentrations.") indicate probable confirmation of previously published data on this phenomenon.<sup>16</sup> Figures 5 and 6 of this earlier work<sup>16</sup> show that the boron diffusivity does indeed increase until the concentration reaches about  $3 \times 10^{20}/\text{cm}^3$  whereupon it peaks and then rapidly decreases by a factor of three or four for concentrations above this. Possible causes of this effect were also discussed. Similar results were also observed by L. F. Cordes.<sup>17</sup> The similarity between these boron diffusion results and those observed for arsenic diffusions have also been previously presented in detail and comparatively discussed.<sup>18</sup>

Stach's and Turley's preliminary conclusions, on the anomalous diffusion of boron in the paper under discussion were correct and consistent with the earlier work cited here.<sup>16-18</sup>

<sup>6</sup> Instituto de Física e Química de São Carlos, Universidade de São Paulo, 13560 São Carlos, Estado de São Paulo, Brazil.

<sup>7</sup> Present address: Sternwartestrasse 55, A-1180 Vienna, Austria.

<sup>8</sup> M. M. Perlman and C. W. Reedyk, *This Journal*, 115, 45 (1968).

<sup>9</sup> B. Gross, *Phys. Rev.*, 60, 26 (1944).

<sup>10</sup> B. Gross, *J. Chem. Phys.*, 17, 886 (1949).

<sup>11</sup> B. Gross, *This Journal*, 116, 824 (1969).

<sup>12</sup> B. Gross, *Brit. J. Appl. Phys.*, 1, 259 (1950).

<sup>13</sup> R. A. Draughn and A. Catlin, *This Journal*, 115, 391 (1968).

<sup>14</sup> J. Roos, *J. Appl. Phys.*, 40, 3135 (1969).

<sup>15</sup> General Electric Company, Corporate Research and Development, Schenectady, New York 12301.

<sup>16</sup> D. M. Brown and P. R. Kennicott, *This Journal*, 118, 293 (1971).

<sup>17</sup> L. F. Cordes, Private communication on unpublished data.

<sup>18</sup> D. M. Brown, M. Garfinkel, M. Ghezzi, E. A. Taft, A. Tenney, and J. Wong, *J. Crystal Growth*, 17, 276 (1972).



## Report of the Electrolytic Industries for the Year 1973<sup>1</sup>

J. Parker\*

*Electrode Corporation, Chardon, Ohio 44024*

and R. S. Karpiuk\*

*The Dow Chemical Company, Midland, Michigan 48640*

### Chlorine—Caustic Soda

**I. Production.**—U.S. production of chlorine reached a record level of 10,421,115 tons in 1973, an increase of 6.2% over 1972 and of 11.4% over 1971. Canadian production was 1,006,473 tons, up 9.1% from the preceding year (1).

Production rates in the U.S. were very high throughout the year of 1973, averaging 95.9% of capacity (2). In the last two months of 1973, production was 99.1% of capacity, and a record production was established in December at 29,710 tons per day (1, 2). In Canada, for 1973, production averaged 92.6% of capacity.

The year saw the start-up of expanded or modernized chlorine facilities at six locations in the U.S., while two plants were shut down. In Canada, there was one expansion, plus two shutdowns. Total capacity increased in both countries, but the increase was less than 1% in the U.S. and about 6.5% in Canada (1-3).

Both chlorine and caustic were in short supply throughout 1973, and it is expected that the shortage will continue to exist throughout most of 1974. However, at the beginning of 1975, chlorine capacity should begin to overtake consumption (4).

The combination of short supply and skyrocketing energy costs forced the prices upward for both chlorine and caustic. During the first half of 1973, chlorine prices went up about \$5/ton, finally rising from discount levels to its long posted \$75/ton, in tank car quantities. The second half brought some boosts to \$80-81/ton. Caustic's 1972 move to list prices, meanwhile, was all but completed; the price at year's end was about \$76/ton for 50% solution (4, 5).

No relief from price increases for chlorine and caustic appears in the offing for 1974 because of the continuing shortage and increasing power costs.

The Chlorine Institute estimates that by January 1, 1975, expansions underway will boost U.S. capacity from the present 30,000 to about 35,000 tons/day, an increase of about 16.7% (1,4). Of this increase, about 2000 tons will come on-stream during the first three-quarters of 1974, and the remaining capacity the last quarter of that year. Diaphragm cell plants in the size ranges of 800-1200 tons/day will contribute about 4000 of the 5000 ton capacity. The remaining tonnage will come from the Kellogg nonelectrolytic HCl oxidation process, Kel Chlor (600 tons/day), from by-product chlorine from magnesium production (200 tons/day),

and from small increases from expansion of existing diaphragm and mercury cell facilities (4, 9).

In 1973, 71.8% of U.S. chlorine production was from diaphragm cells and 24.6% from mercury cells; miscellaneous production from all other sources accounted for 3.6% (9).

The market breakdown for chlorine remains about the same as in the past (4):

Vinyl chloride monomer (VCM)	20%
Chlorinated organic solvents	25%
Other chlorinated organics	20%
Chlorinated inorganics	10%
Pulp and paper	10%
Water and waste treatment	5%
Miscellaneous	10%

As noted above, VCM is the largest single product user of chlorine, and much of the growth in chlorine is dependent on the growth rate of this product. With the exception of 1971-1972, the VCM chlorine demand increased at the rate of 12-15%/year over the last decade. In 1974, the growth rate is expected to be 10-15% if VCM makers can get enough ethylene, the co-ingredient with chlorine, and build new facilities (4). Also an unknown factor is the O.S.H.A. standard with regard to VCM concentration in air. If the maximum allowable concentration is fixed at 1 ppm in air, which most plants presently feel they would be unable to meet, this regulation would have serious implications on chlorine production.

The demand for chlorine in the chlorinated organics area will be largely dictated by the availability of hydrocarbons.

The chlorine shortage was reported to be affecting municipal drinking water supplies. Legislation is being considered by Congress to assure adequate supplies. Chlorine suppliers, such as Dow Chemical and Diamond Shamrock, say they can meet any municipal needs and that legislation is not required (6-8).

The biggest threat seen to meeting production goals is inadequate electrical power. In 1973, power interruptions were more frequent and more severe than ever before. Plants in the Northwest were affected most, with the Northeast close behind (4).

Caustic is in continuing short supply because of the high demand by the paper, glass, and aluminum industries. Generally, even with the expansion of the natural soda ash facilities, chlor-alkali producers do not expect any excess caustic for several years (4).

All chlorine producers, whether using mercury or diaphragm cells, are facing government regulations in water and air pollution and also in the areas of working conditions at both Federal and State levels. It has been predicted that the net effect of these regulations will be to increase plant costs by 2-5%; how-

<sup>1</sup> This report is sponsored by the Industrial Electrolytic Division of The Electrochemical Society. While it is primarily a summary of production and developments in the chlor-alkali industry, reports of other electrolytic industries are included.

The material presented herein has been gathered from many sources as noted in the References, and does not necessarily represent the opinions of the authors.

\* Electrochemical Society Active Member.

## II. Current changes in chlorine operations (4, 9)

Company and location	Type of cell	Total capacity, tons/day	Completion date
<b>A. Production Started</b>			
BASF Wyandotte Geismar, La.	Added Hooker H-2 cells	—	September 1973
Linden Chlorine Products Linden, N.J.	Krebs cells	—	December 1973
Dow Chemical of Canada Sarnia, Ontario	Dow diaphragm cells	1000	September 1973
The Dow Chemical Co. Pittsburg, Calif.	Cell replacement	—	July 1973
The Dow Chemical Co. Midland, Mich.	Modernization	—	1st Quarter 1973
FMC Corp. South Charleston, W. Va.	Conversion to DSA®	—	November 1973
Pennwalt Corp. Portland, Ore.	Diamond DS-43, modernization	330	January 1973
<b>B. Plant Shutdowns Scheduled</b>			
Olin Corp. Pisgah Forest, N.C.	Sorensen (mercury cell)	—	July 1973
Canadian Industries, Ltd. Hamilton, Ontario	ICI (mercury cell)	—	July 1973
Dow Chemical of Canada Sarnia, Ontario	Dow (mercury cell)	700	July 1973
Dow Chemical of Canada Thunder Bay, Ontario	Dow (mercury cell)	—	September 1973
Oregon Metallurgical Co. Albany, Ore.	Alcan—magnesium	—	—
BASF Wyandotte Geismar, La.	Uhde mercury cells	150	December 1974
Hooker Chemical Corp. Niagara Falls, N.Y.	Gibbs and Hooker S cells	—	1973-1974
Weyerhaeuser Co. Longview, Wash.	de Nora mercury cell	265	1st Quarter 1975
Pennwalt Corp. Tacoma, Wash.	Gibbs diaphragm	—	When new facility is completed

## III. New or expanded plants planned or under construction (4, 9)

Plant and location	Type of cell	Capacity, tons/day	Completion date
Olin Corp. McIntosh, Ala.	Olin E-8	—	2nd Quarter 1974
Pennwalt Corp. Calvert City, Ky.	Conversion to DSA®	—	1st Quarter 1974
PPG Industries Lake Charles, La.	Glanor V bipolar	1500	Not announced
Kaiser Aluminum Chemical Gramercy, La.	Conversion of S3B and S3C to DSA®	—	Middle 1974
Sobin Chlor-Alkali, Inc. Orrington, Maine	Additional de Nora cells	—	3rd Quarter 1974
Hooker Chemical Corp. Niagara Falls, N.Y.	Phase I, convert Hooker cells to DSA®	—	1974
	Phase II, new Hooker cells	—	
Hooker Sobin Corp. Niagara Falls, N.Y.	Conversion to DSA®	—	3rd Quarter 1974
Olin Corp. Charleston, Tenn.	Conversion to Marstolin anodes	—	3rd Quarter 1974
Shell Chemical Co. Deer Park, Texas	Modest expansion, Olin E812	—	
The Dow Chemical Co. Freeport, Texas	Convert to DSA® and 50% ex- with Hooker diaphragm	375	2nd Quarter 1974
Aluminum Co. of America Port Comfort, Texas	Dow diaphragm	1000	2nd-4th Quarter 1974
Hercules, Inc. Hopewell, Va.	Conversion to DSA®	—	4th Quarter 1974
Allied Chemical Corp. Moundsville, W. Va.	Conversion to DSA®	—	2nd Quarter 1974
PPG Industries, Inc. New Martinsville, W. Va.	Modest expansion	—	4th Quarter 1974
Georgia Pacific Corp. Flaquemine, La.	Conversion to DSA®	—	4th Quarter 1974
Hooker Chemical Co. Taft, La.	Hooker H-4	800	4th Quarter 1974
E. I. du Pont de Nemours Corpus Christi, Texas	Kel Chlor process	400	1st Quarter 1974
Diamond Shamrock Corp. Deer Park, Texas	Diamond MDC-55 diaphragm	1000	2nd Quarter 1976
NL Industries, Inc. Rawley, Utah	Diamond MDC-29 diaphragm	1200	4th Quarter 1974
Weyerhaeuser Co. Longview, Wash.	Bayer (magnesium)	220	3rd/4th Quarter 1974
Pennwalt Corp. Tacoma, Wash.	Diamond MDC-29 diaphragm	385	1st Quarter 1975
Dow Chemical of Canada Ft. Saskatchewan, Alberta	PPG bipolar diaphragm	—	3rd Quarter 1975
Canadian Occidental Petrol. N. Vancouver, B.C.	Dow diaphragm	50% expansion	1st Quarter 1974
Canadian Industries, Ltd. Becancour, P.Q.	Conversion to DSA®	10% expansion	3rd Quarter 1974
BASF Wyandotte Wyandotte, Mich.	Hooker H-2A diaphragm	385	1st Quarter 1974
	Conversion Hooker S-3 to DSA®	—	4th Quarter 1974

ever, there should be some inherited benefits from these legislated environmental controls (27).

**IV. Developments.—A. Metal anodes.**—The installation of metal anodes has continued at an increasing tempo during the year. Over 10,000 tons of chlorine is now produced each day on metal anodes in North

America. Known contracts indicate that half the total industry will be operating with metal anodes by the end of 1974.

The rate of conversion in North America is similar to that worldwide. All new plants are using coated titanium anodes, and new designs of cells are reaching

the market to optimize the characteristics of the metal anodes. Three new designs of diaphragm cells are now operating at high loads with metal anode components.

The Marstolin Electrolytic Systems have announced their ability to supply metal anodes, thus joining the Electrode Corporation, which has now produced over 250,000 anodes as suppliers (11, 12).

Conversion of chlorate cells to titanium-based anodes has been continued and new designs of cells are being finalized which will use systems to take full advantage of the titanium-based anode characteristics. A variety of hypochlorite cells is now available using brine or seawater to produce low strength hypochlorite on site. Several precious metal coatings on titanium are used in these systems.

Metalwinning cells with titanium-based anodes are being developed for various hydrometallurgical processes. Expanded research and development efforts to produce titanium-based anodes with the performance that will justify the economics involved are being continued (13).

**B. New chlorine process developments.**—E. I. du Pont de Nemours introduced the first new diaphragm material which is being used in commercial development work. The material called Nafion is made from sulfonated polyperfluoroethylene. Ionics offers a sodium hypochlorite cell using the material, and others have this or a very similar material under evaluation (14, 15).

Apart from a complete substitute, polymers such as Halar are being researched as a possible binder in an asbestos diaphragm to prolong operational life (15).

The first large nonelectrolytic plant to produce chlorine from hydrochloric acid using the Kel Chlor process is scheduled for start-up in early 1974. The reference is to du Pont's 600 ton/day plant at Corpus Christi, Texas (15, 16).

The NL Industries, Inc. magnesium plant at Rawley, Utah, is designed to produce 220 tons chlorine/day as a by-product (17).

Ionics, Engelhard Industries, Pacific Engineering, de Nora, and Diamond Shamrock offer cells with coated metal anodes for on-site generation of sodium hypochlorite, which is used in water purification, waste treatment, and paper bleaching, particularly where gaseous chlorine handling may present a problem (14, 18, 26).

Asahi Glass will use Friedrich Uhde GmbH electrolytic process to recover chlorine from effluent hydrochloric acid from a refrigerant plant. Capacity will be 37,200 tons chlorine/year. A number of electrolysis plants that process effluent HCl from toluene diisocyanate plants are in operation, but this is the first application to a refrigerant plant (19, 20).

The first oceangoing liquid chlorine tanker is now being built by Friedrich Uhde GmbH for Spain's Energear Industries Arogonesas S.A. The vessel will hold 1000 tons and is to be in operation next spring (21).

Dow Chemical USA has phased out its last caustic soda flake unit at Freeport, Texas. All anhydrous caustic soda flake units (Freeport, Texas; Midland, Michigan; and Pittsburg, California) have been converted to the caustic bead form (23).

**C. Mercury cells.**—No new mercury cell plants were built in 1973; however, there was some modernization of a few existing plants. In the U.S. one plant was shut down while in Canada two plants were shut down in 1973 (1, 9).

Though much of the public furor has abated over mercury cells, companies hesitate investing money for existing and, particularly, for new plants since they have no way of knowing the eventual standards for mercury emissions. In the foreseeable future, all new capacity will probably come from diaphragm cells (17, 22).

U.S. chlorine plants have made great strides in cutting down mercury emissions. According to the Chlorine Institute surveys, mercury discharges have been reduced 95% since February 1971. An Institute

spokesman estimates that the cost of this clean-up effort and process tightening has been about one-tenth the original cost of the chlorine plants (22).

The Japanese chlorine producers are, by government decree, to have 65% of their mercury cell plants converted to diaphragm cells by September 1975 (22). The diaphragm cell technology is almost totally furnished by U.S. firms, such as Hooker Chemical, PPG Industries, and Diamond Shamrock.

Yet there are areas in the world where mercury cell installations are being made and apparently will continue to be made, for instance, South America, Africa, Asia, and parts of Europe (24).

U.S. consumption of mercury during 1973 was estimated at 54,550 flasks, slightly higher than 1972. Mercury for the production of chlorine-caustic required 12,780 flasks or an increase of about 11%.

U.S. mercury production in 1972 was 1968 flasks. At year's end there were seven producing mines in the U.S.

The average New York price of mercury during 1973 was \$286/flask compared to \$218 in 1972 and \$295 in 1971. Early in 1973, the average quarterly price of mercury was \$300; a low of \$269 was established in the second quarter of the year, and gradually the price increased so that the last quarter average was \$294. In 1973, GSA sold 2583 flasks of mercury compared to 512 flasks for 1972.

Imports of mercury during 1973 amounted to 46,076 flasks compared to 30,000 flasks for 1972. Imports were from Canada (37.8%), Algeria (25.7%), Spain (15.8%), and Yugoslavia (8%) (25).

#### Other Alkalis and Electrolytic Processes

**Caustic potash.**—Caustic potash production in 1973 was 188,454 short tons as 88-92% liquid; this represents an increase of 6.5% over 1972 but is still 5% lower than 1971 production (33).

While production of caustic potash increased during 1973, domestic production of marketable natural potassium chloride, sulfate, magnesium sulfate, and manure salts decreased 2.4% to 2.6 million tons of K<sub>2</sub>O equivalent, but increased 2.9% in value (28). The government of Saskatchewan continued prorating of production during 1973, allowing production to increase to 70% of rated capacity (29). The Canadian potash producers posted price increases of \$0.03-0.04/unit of K<sub>2</sub>O effective November 1, 1973 (30).

Diamond Shamrock expanded its potassium carbonate facilities at Muscle Shoals, Alabama, to 36,000 tons/year. Production is scheduled to be expanded to 54,000 tons during 1974 (32).

Government price controls held the price of caustic potash at the list price level established in early 1973. Price of 45% liquid caustic potash in bulk shipments was \$4.25/cwt and \$7.00/cwt for 50% liquid caustic potash from West Coast terminals (34).

Price controls were scheduled for removal on April 30, 1974.

**Soda ash.**—Soda ash was in short supply during 1973 in spite of a 22% increase in production of natural soda ash from the trona beds of Wyoming (35). There was a drop, however, in the production of synthetic (Solvay) soda ash caused by stricter controls over pollution of waterways by the soda ash plants. For the first time in history, over half of the soda ash production came from natural sources, and also for the first time there was importation of soda ash. Exports of soda ash decreased by one-third in view of the rising domestic demand. The unit value of soda ash rose about 7% during the year. Production of soda ash is now running at about 4.4 million tons/year sodium oxide equivalent. Trona-based capacity is now about 4.5 million tons/year and total soda ash capacity is about 8.5 million tons/year (36).

Four suppliers of natural soda ash have announced sizable increases in their installed capacity over the next 2 years and a fifth company has announced its intention to open a new soda ash mine and processing

plant (35). Texasgulf, Inc. has awarded contracts for the construction of a \$75 million soda ash mine and processing plant at Granger, Wyoming, with completion expected in 1976. The capacity of the plant is 1 million tons/year soda ash (37). The only foreseen problems in the future soda ash picture are a lack of processing fuel, a shortage of skilled labor, and possibly insufficient railroad shipping capacity.

Although soda ash mines are being expanded, PPG shut down its 600,000 tons/year Solvay process plant at Barberton, Ohio, at the end of March because of environmental problems (38).

Soda ash capacity in India will double in the next five years. The new units will be based on the modified Solvay process which produce ammonium chloride as a by-product. It is expected that the by-product will be used in fertilizers (39).

BASF Wyandotte raised soda ash prices in late 1973, subject to approval by the Cost of Living Council. The prices were up \$2.50/ton to \$38 for bulk; up \$5/ton to \$54.50 for bags, carload, and truckload lots. The company says the increases recover only part of its higher costs under Phase IV guidelines (40). This announcement was followed by similar increases by Food Machinery Corporation and by Stauffer Chemical Company (41).

Soda ash supplies are tight worldwide, and will remain this way for about 2 years when additional production is scheduled to be on-stream. The price of soda ash is expected to increase, unless the economy falls well short of its anticipated performance in 1974 and 1975 (36).

The threat of discontinuation of the depletion allowance for trona mines by the Treasury Department is being countered by the introduction of an amendment which would guarantee continuation of depletion allowances (42).

**Sodium chlorate.**—Preliminary data from the U.S. Department of Commerce indicates that U.S. production of sodium chlorate in 1973 was 198,300 tons, an increase of about 9.6% from 1972 production of 182,500 tons (43).

Sodium chlorate production facilities in the U.S. and their 1973 listed capacities are as follows (46, 50).

Company	Capacity (tons/year)
Brunswick Chemical Co. Brunswick, Ga.	7,000
Georgia-Pacific Corp. Bellingham, Wash.	3,500
Hooker Chemical Corp. Columbus, Miss.	62,500
Hooker Chemical Corp. Niagara Falls, N.Y.	15,500
Hooker Chemical Corp. Taft, La.	20,000
Huron Chemicals Co. Butler, Ala.	4,000
Huron Chemicals Co. Riegelwood, N.C.	7,000
Kerr-McGee Hamilton, Miss.	32,500
Kerr-McGee Henderson, Nev.	30,000
Pacific Engineering & Production Co. Henderson, Nev.	6,000
Penn-Olin Corp. Calvert City, Ky.	31,000
Pennwalt Corp. Portland, Ore.	16,500
<b>Total</b>	<b>235,500</b>

Erco Industries Ltd. of Canada is expanding its chlorate facility (9000 tons/year) in Vancouver. The technology, from Krebs and Cie., Paris, includes NC-12 electrolytic cells, equipped with metal anodes and natural electrolyte circulation (44).

The Dow Chemical Company may change the product mix at its proposed Dallesport, Washington, plant on the Columbia River. The unit was designed as a \$20 million project to produce magnesium with chlorine as a by-product. Word now is that sodium chlorate used by the pulping industry as a bleach may be the primary product (45).

Hooker Chemical brought on-stream in July a 20,000 ton/year sodium chlorate facility at Taft, Louisiana. The plant is being further expanded to 45,000 tons/year with additional electrolytic cells (46).

Erco Industries is to expand its sodium chlorate plant at Buckingham, Quebec, by 5000 tons/year to 38,000 tons/year. The new cell line is expected to be completed in the third quarter of 1974 (47).

PPG Industries, Inc. of Pittsburgh has purchased a license (U.S. and Canada) for KemaNord's bi-metal electrode for the production of sodium chlorate. The electrode assembly is presently used in KemaNord's 25,000 ton/year plant at Stockviksverken, Sweden (48).

Because of Government price controls, the list price for pulp and paper grade sodium chlorate remained at \$135/ton throughout 1973 (49). Price controls were scheduled for removal April 1974.

**Sodium.**—The American production of sodium in 1973 by three producers totaled 176,903 short tons, an increase of 10.5% from the 160,054 tons in 1972 (51). The demand was fairly uniform throughout 1973, although the production did slacken slightly during the last quarter of the year.

As over 80% of the sodium produced goes into tetraethyl and tetramethyl lead manufacture, the production of sodium is tied very closely with the demand for gasoline. The current regulations of the Environmental Protection Agency require a reduction in the average lead content of gasoline to 2.00 g/gal in 1975, 1.70 g/gal by 1976, 1.5 g/gal by 1977, and 1.25 g/gal by 1978. Thus, the regulations will have a direct effect on sodium production over the next four years.

Ethyl Corporation has filed a suit to block the standards for the lead content in gasoline set by EPA (52). Ethyl contends that EPA did not meet legal requirements of the Clean Air Act by failing to prove that lead emissions from automobiles are a health hazard. There was also considerable opposition to the reduction of lead from gasoline by the oil companies, citing the increased refinery cost to meet the federal standards and the 10-20% increase in consumption of gasoline due to the reduction in lead (53). The lower miles per gallon for unleaded gasoline has been estimated to be equivalent to dumping 1 million barrels of crude per day (54).

It has been estimated by a consulting firm that \$4370 million will have to be expended for refinery modifications by the oil industry by 1980 to produce gasolines which meet federal standards (53). In contrast, EPA estimates that \$250 million in capital investment must be spent on existing refineries to comply with the new regulations (54).

**Aluminum.**—A new record for the U.S. aluminum industry was established this year with production of primary metal at about 4,529,117 short tons. This represents an increase of about 10.5% over last year's production (55). Record production was made even though an electric power shortage prevented the aluminum industry in the Pacific Northwest from reaching its full production potential (56).

There was an 18% increase over last year in domestic consumption of aluminum and a severe aluminum supply deficit was averted by sales of about 800,000 tons of aluminum by the Government (56). It is predicted that primary aluminum producers will be operating at 100% of their capacity in 1975 and 1976 (57).

Under price controls, the domestic price for primary aluminum from large producers remained at 0.25/lb throughout most of 1973. On December 6, the Phase IV base price for aluminum was increased to \$0.29/lb and some of the domestic producing companies raised their price to that level. Prices on the major world markets approached \$0.275/lb in midyear and by December were reportedly in the \$0.30-0.45 range (56).

Easing of the power shortage in the Northwest at year's end and high demand for aluminum had re-



sulted in decisions by Anaconda, Kaiser Aluminum & Chemical Company, Intalco, Reynolds Aluminum, Alcoa, and Martin Marietta Aluminum to restart and/or increase production capacity of existing potlines (59).

Anaconda Aluminum in Sebree, Kentucky, and Columbia Falls, Montana, and Alcoa at Massena, New York, and Rockdale, Texas, also installed new potlines, or reactivated or increased capacity during 1973 (58).

Aluminum Company of America, Alcoa, broke ground late in 1973 for a plant at Palestine, Texas. The plant, expected to be operational in 1975, will test a new type of electrolytic process for obtaining aluminum metal. Alcoa expects to receive sixteen U.S. patents for the process, which is expected to cut environmental pollution dangers as well as electrical power needs. In this process, the aluminum-containing raw material is combined with chlorine in a reactor to form anhydrous aluminum chloride. The aluminum chloride is then electrolytically reduced in a molten electrolyte of controlled oxide content to molten aluminum and chlorine. The chlorine is then available for recycle. Indications thus far are that this process will require 30% less electric power than the 6.5 kW-hr/lb needed by the most efficient Hall process cells. In addition, there will be no fluoride in the process, so fluoride emission control will not be necessary, and the process apparently will work on a variety of aluminum-bearing minerals, such as alunite, kaolin, and anorthosite. Initial capacity for the plant will be 15,000 tons/year, to be expanded to 30,000 tons/year with eventual expansion planned to be to 300,000 tons/year (60).

A joint venture by three companies, National Steel Corporation of Pittsburgh, Southwire Company of Carrollton, Georgia, and Earth Sciences, Inc. of Golden, Colorado, to test the feasibility of extracting aluminum from domestic alunite is underway. The three companies are planning to use a technique developed in the USSR because of a bauxite shortage there; the plant will cost \$1 million and will process 12 tons/day of alunite into 1-2 tons/day of alumina. The long range goal is a commercial plant to feed a 180,000 tons/year aluminum plant. The plant will be constructed at Cedar City, Utah (61, 62).

Applied Aluminum Research of New Orleans, Louisiana, announced a new process for obtaining aluminum from clay material. The process involves chlorinating the clay, then reducing the mixture of metal chlorides (including aluminum chloride, titanium chloride, silicon chloride, etc.) with molten manganese to form aluminum, manganese chloride, and metal chlorides. The manganese chloride is then oxidized with oxygen to give chlorine, for recycle, and manganese dioxide, which is smelted to recover the manganese for recycle. The group is now putting up a 1 ton/week pilot plant at New Orleans, and is trying to raise \$25 million through a London firm for a 100 ton/day plant to be built in Europe. The method uses much less power than the Bayer-Hall process, and the company, headed by the inventor of the process, Charles Toth, claims prices will be as low as \$0.10/lb (63, 64).

Recycling is the aim of Combustion Power, Inc. of Menlo Park, California, as they have developed a method which may make recovery of aluminum more practical. The method, mainly for separating aluminum can stock from other solid wastes, begins with an air classification and conventional magnet system, which remove paper and ferrous materials, respectively. Then the remaining shredded scrap is moved into the field of a new "magnet." This induces eddy currents in the aluminum scrap which interacts with the producing field to repel the scrap off the belt (65).

American Metal Climax announced in early August that it was going ahead with plans for construction of a two-potline 160,000 tons/year aluminum plant near Warrenton, Oregon. The company expected to meet

strong opposition from shrimp and tourist industries, but said they planned to limit fluoride emissions to 1.5 lb/ton of aluminum, presently the lowest in the industry. By the end of October, however, it was apparent that the plant was in trouble. Oregon Governor Tom McCall withdrew support for the project, citing the energy crisis and pointing to the 240 MW contract Amax holds with the Bonneville Power Administration for the plant. Because the contract already exists, however, the State has turned to the Department of Environmental Quality, which may recommend that fluoride emissions must be no more than 1 lb/ton which industry says is technologically infeasible (66, 67).

Consolidated Aluminum Corporation of USA, owned 60% by Swiss Aluminum, Ltd., Zurich, and 40% by Phelps-Dodge Corporation, New York, has purchased the aluminum business of Olin Corporation of Hannibal, Ohio, a 600,000 ton/year alumina plant at Burnside, Louisiana, and seven other mill and fabricating plants. The transaction does not include Olin holding in the Friguia bauxite plant in the Republic of Guinea (68).

Alcoa is in the process of expanding the aluminum smelting plant at Massena, New York, from 135,000 tons/year to 190,000 tons/year. Also announced by Alcoa were plans for construction of an aluminum reduction plant in Valleyfield, Quebec. The power will be supplied by Hydro-Quebec, and initial production is expected to be 60,000 tons/year. Target date for both projects is 1976 (69).

Meanwhile, Georgia still is looking for a way to profit from its kaolin deposits, considered to be the largest in the world. The Senate passed a resolution that would give \$250,000 to the first person or company to produce either alumina or aluminum chloride from the deposits. Now the bill must go to the State House. The resolution also states that the plant must produce a minimum of 300,000 tons in its first year (70).

**Magnesium**—While U.S. magnesium production rose only 1.3% to 122,431 tons in 1973, shipments increased 23.5% to 137,277 tons from 111,185 tons in 1972. About 29% of last year's shipments were to the export market. In 1973, the U.S. exported 39,585 tons of magnesium and only imported 3,282 tons (71, 72). NL Industries, Inc. produced a small quantity of magnesium at its 45,000 ton/year primary magnesium plant located on the shore of the Great Salt Lake in Utah (73). Since the plant experienced considerable difficulties during the year, its contribution to total U.S. production was less than expected. The electrolytic magnesium plant of the American Magnesium Company in Snyder, Texas, remained closed during the year. However, the plant was expected to resume production during the first quarter of 1974 (74), although problems may cause slippage to the second quarter. The installation has a capacity of 10,000 tons/year of magnesium.

U.S. secondary production was around 15,000 tons, exports 36,600 tons, and consumption of primary magnesium 126,000 tons in 1973.

Magnesium metal was in tight supply in the U.S.A. Demands were also high worldwide. Dow Chemical U.S.A. processed stockpile metal (6,000,000 lb) at its Freeport, Texas, plant (75). Dow recently disclosed that it has purchased an additional 21,420 tons of magnesium from GSA to be transferred monthly through 1974 and 1975 (76). NL Industries also purchased 10,000 tons of magnesium from the GSA stockpile to fill its substantial in-house requirements and possibly some outside orders (77).

Higher magnesium prices will take effect on January 1, 1974, when the Dow price will be from 38.25 to 42¢/lb for 99.8% pig, and from 33.75 to 42¢/lb for AZ91B die cast alloy, f.o.b. Freeport, Texas. Higher energy costs were given as the reason for the increase (78).

Alcoa announced a 40,000 ton/year magnesium and silicon plant at Addy, Washington. Construction was



slated for early 1974 with a completion date in 1976, at a cost of \$50 million (79). After conducting a feasibility study of producing magnesium, silicon, and ferrosilicon from dolomitic limestone and quartzite deposits in the Addy area in November 1970, Alcoa signed contracts with the Bonneville Power Administration for power to become available in October 1974. The plant, now called Northwest Alloys, Inc. (80), as a subsidiary of Alcoa, will use the Magnetherm Process (licensed by France's Pechinney Ugine Kuhlmann), the only plant in the U.S.A. to use this process (81).

Environmentalists are seeking to prevent the construction of the Alcoa plant by forcing cancellation of its power contract with Bonneville Power Administration (82).

Norsk Hydro will build a 50,000 ton/year magnesium plant in Mongstad, north of Bergen, Norway. The plant should be operational by 1980 (83).

Considerable optimism has prevailed in the industry, and a new era of growth has been predicted (84). Factors which brighten the outlook are: (i) the automobile industry's intensified quest for lighter weight components; (ii) improved hot chamber casting techniques; (iii) improvement in the competitive cost relationship with aluminum and zinc; (iv) prospects for new sources of supply; and (v) the new developments in fluxless melting (84).

A new market is the use of magnesium as a sulfur-sequestering agent in the production of special grades of steel. Steel desulfurized with magnesium has better strength and formability properties (81).

A growth rate of 7-8%/year has been forecasted, a rate which would bring 1980 demand to some 500,000 tons/year worldwide (85).

**Manganese.**—Strong demand for manganese in steel, which was not met by any increase in mine production of manganese, created a tight supply situation in 1973. Steel production was at a record in 1973 and accounted for 95% of manganese consumption (96).

As in 1972, there was no actual production of manganese ore, nodules, or concentrates, with a concentration of 35% or more manganese in the U.S. in 1973 (88).

General imports of manganese ore were down 1.2% from the level of 1972 to 1,600,000 short tons. Major suppliers of the ore were Brazil and Gabon. Imports of ferromanganese, on the other hand, were up 12% from last year to 384,000 short tons. As in the previous year, the major suppliers of the ferromanganese were the Republic of South Africa and France (87, 88, 96).

Domestic consumption of manganese ore was down 6%, from the 1972 level of 2,050,000 to 1,922,000 short tons, although consumption of alloy and metal increased substantially (88).

Manganese ore, alloys, and metal were sold by the General Service Administration (GSA) from its stockpile (96).

Prices for metallurgical manganese ore containing 48% manganese, minimum, increased 85%, from 58 to 61¢ nominal per long ton unit in 1972, when a drop occurred, to \$1.05-1.15/long ton unit by the end of December 1973 (86, 87).

A bill was signed by President Nixon continuing the suspension of import duties on manganese ore from favored nations. The bill will be in effect for three more years until June 30, 1976 (88).

The Electrolytic Manganese plant belonging to Delta Manganese in Nelspruit, Republic of South Africa, will begin production in the second quarter of 1974. The firm, a subsidiary of Delta Metal Company, Ltd., London, expects 14,500 tons/year immediately, with a capacity of 16,000 tons/year to be reached within 2 years (95).

Delta Manganese also concluded, earlier in 1973, an agreement with Foote Mineral, in which Foote will be the U.S. and Mexican distributor for electrolytic manganese chip and other related products (94).

The processing of manganese nodules is now considered to be no problem by most major organizations involved in the study of deep ocean mining. Summa Corporation, an affiliate of Hughes Tool Company, has a large 324 ft long barge, resembling a floating dry dock, which will be sunk to the ocean floor at a suitable site to collect manganese nodules and pass them through a pipe to the surface ship.

Tests of the much publicized continuous bucket line system of nodule recovery developed by the Japanese were reported to have experienced difficulties under conditions of rough ocean floor topography and rapidly changing currents.

Kennecott Copper of New York has joined with four other international firms in a \$50 million joint venture to research the mining of manganese nodules from the floor of the ocean. Kennecott's interest is basically in the copper-nickel values of the nodules. Kennecott's partners are mostly interested in the manganese content of the nodules (91-93, 96).

Kerr-McGee Chemical announced an expansion of its Henderson, Nevada, manganese dioxide electrolytic plant with a proposed completion date of early 1975. The expansion will increase capacity an additional 260% from 3,300 to 12,000 tons/year (90).

Mitsui Denman (Ireland), newly created part of Mitsui Mining and Smelting (Japan), will build a 12,000 ton/year electrolytic manganese dioxide plant in County Cork, Ireland. The plant will be designed and built by Lummus Company, and will cost \$15 million (89).

**Beryllium.**—The over-all American consumption of beryllium ores appeared to be slightly higher in 1973 than in 1972 (97). The increase resulted from a larger demand for alloy products. Domestic production of beryllium ore increased, although there were no reports of beryl production from any state. Imports of beryl, however, decreased to an estimated 1700 tons valued at \$510,000. Imports were principally from Brazil, the Republic of South Africa, and Argentina.

Brush-Wellman uses bertrandite and beryl ores for the production of beryllium. The pure metal is then shipped to Delta, Utah, or Elmore, Ohio, for refining. The other American producer, Kawecki Berylco Industries, has plants at Hazelton and Reading, Pennsylvania, and only uses beryl ore.

One of the two companies processing beryl has put its equipment on standby basis and will have the imported beryl it purchases toll processed.

Beryllium is used as the metal, as an alloying agent, and as an oxide. Major uses for the metal are for aerospace applications, utilizing its light weight and high strength and rigidity, and for nuclear applications where its low thermal-neutron absorption and high neutron scatter cross section are required. About three-fifths of the beryllium is used as a beryllium-copper alloy, in which it imparts qualities of strength and resistance to fatigue and corrosion that are superior to those of copper. Beryllium copper molds are used to give plastic furniture the appearance of a woodgrain surface.

Beryllium consumption was 47% in nuclear reactors and aerospace applications, 29% as an alloy in electrical equipment, 13% in electronic components, and 10% in other applications. About 1% of the beryllium was used as the oxide.

At midyear Government stockpile inventories contained 17,988 short tons of beryl (11% BeO equivalent), 7,387 tons of beryllium-copper master alloy (approximately 4% Be), and 229 tons of beryllium metal. Since the stockpile objectives for both beryl and the master alloy were set at zero, the full inventory of both items is surplus. The stockpile objective for beryllium metal is 88 short tons, leaving 141 tons surplus.

At the end of 1973, the price of beryl ore ranged from \$30 to \$35 per stu. In the U.S., beryllium-copper 25 alloy was quoted at \$3.54/lb, cast ingot at \$2.39/lb, and the master alloy at \$56/lb. Beryllium rod was priced at \$102.83/lb during June 1973 (98).

**Chromium.**—In 1973, the U.S. continued to rely on imports and purchases from Government stockpiles of excess material for its chromium requirements. Domestic consumption of chromite was 1.4 million tons, 23% higher than in 1972. Increases were registered by all three consuming categories: metallurgical consumption was up 26%; the refractory industry increased by 16%; the chemical industry increased by 7% (99).

Imports for consumption of chromite followed the same trend as in 1972; namely, they were less than consumption as industry drew from its own stocks and previously sold Government stockpiles. Imports for ferrochromium were expected to reach a level of 150,000 gross tons, up 6% from last year's total of 141,000 gross tons. Major sources were the Republic of South Africa, Southern Rhodesia, Japan, and Finland.

Late in December, Union Carbide announced price hikes effective on January 1, 1974. Electrolytic chrome is \$1.53/lb, vacuum grade is \$1.60 f.o.b. Marietta, Ohio, and 9% carbon chrome is unchanged at \$1.50/lb (100).

Foote Mineral shut down its Steubenville, Ohio, plant at the end of 1973, while pollution regulations forced Ohio Ferro-Alloys to drop its chrome alloy production. The future of ferrochrome production in the U.S. is dependent upon the E.P.A.'s final decision on its proposed standards for ferroalloy plants as well as the availability of ore and the ability to compete with low cost South African and Rhodesian material (102).

In December of 1973, the Senate passed a bill to repeal the "Byrd Amendment" of 1971. This "Amendment" has ended U.S. observance of the U.N. sponsored embargo of Rhodesia due to that nation's racial policies. Next, the new bill will go to the House, where its future is uncertain. Support for this bill will probably be due in part to the "energy crisis," in view of black Africa's economic boycott of Rhodesia. Proponents feel that taking a stand against Rhodesia will help U.S. negotiations for Nigerian oil. In any event, the drop in imports from Rhodesia makes the matter less critical (100, 101).

**Titanium.**—Outstanding features of the titanium market during the year were increased production of titanium sponge, continued strong demand for pigment, and rising prices for ores and concentrates (103).

Production of titanium sponge in the U.S. increased by more than 40% during the year. Much of this increase was due to production under contract with GSA for the national stockpile; deducting quantities produced for this account, the increase in production was more modest. Consumption of sponge and scrap was about 19,250 and 10,000 tons, respectively. Production of ingot was about 28,000 tons, a 39% increase over that of 1972. Imports of sponge for consumption were about 6700 tons, a 64% increase. Of this quantity, 59% came from Japan, 28% from the USSR, and 13% from the United Kingdom.

Only RMI (Reactive Metals) and TMCA currently produce sponge in the U.S., at Ashtabula, Ohio, and Henderson, Nevada, and only RMI sells its material on the market. Oregon Metallurgical has a partially completed sponge facility at Albany, Oregon, which is not in operation. Both TMCA and RMI are currently supplying GSA with some 14 million pounds of sponge combined in a 2 year upgrading program implemented in early 1972. GSA has recently sliced its titanium stockpile objective to zero from the old 33,500 ton level, and the Government apparently hopes to eventually sell off its present holdings as part of its new accelerated disposals. Japan's two major producers, Osaka Titanium and Toho Titanium, are the principal suppliers of imported sponge, while the United Kingdom's Imperial Metals Industries also ships some material to the U.S. The USSR, which uses a magnesium reduction method in its production, has been moving increasingly large quantities to the U.S., renewing the old debate over titanium dumping (104).

Howmet Corporation and The Dow Chemical Company were jointly engaged in developing a continuous electrolytic process for making titanium metal at a pilot plant in Whitehall, Michigan. Howmet says the process should have several advantages over the present widely used processes such as a 40% energy reduction and fewer pollution control problems (105).

Dow has considerable experience in titanium, and was in fact the first commercial domestic producer, at that time using the Kroll process for its production. Dow later teamed up with Crucible Steel, now Colt Industries, in a partnership to examine the potential of producing sponge, but the two companies later decided to drop the venture (104).

Higher labor, power, and rutile costs, among others, have forced domestic sponge prices upward. The prices for Japanese sponge were reported as \$1.34-1.37/lb for contract material and \$1.46-1.50 on a spot basis. RMI, which sells some sponge, has boosted its U.S. quote from \$1.32 to a \$1.42-1.45 range (104).

Field erection of big titanium or titanium-clad vessels will be possible by a suitable welding technique developed by Wyatt (Houston), a division of U.S. Industries. Previously, clean-room conditions were needed for fabricating titanium. Consequently, vessels had to be shop built in one piece and shipped to the construction site, limiting the size of equipment. The new welding technique was demonstrated at an Olin plant in Augusta, Georgia, where two sections of a 15 ft diameter, 20,000 gal solid titanium tank were welded together successfully (106).

According to a survey by the Bureau of Mineral Resources, Australia's titanium ore deposits may be exhausted in less than 30 years. The country presently supplies 90% of the world's rutile and 20% of its ilmenite (107).

The U.S. patent covering the alloy Ti-6Al-4, which accounts for 80% of all titanium used by defense contractors, expired in July 1973.

Mine production of titanium minerals was about 850,000 short tons, an increase of 14% over the 1972 figure. Titanium Enterprises, at Green Cove Springs, Florida, had its first full year of production, and the American Smelting and Refining Company mine in Ocean County, New Jersey, began production at the end of June. Both mines shipped their product to titanium pigment plants.

Imports of ilmenite increased to about 70,000 tons, while imports of slag remained about constant at 295,000 tons. Imports of rutile, including synthetic rutile, increased to 212,000 tons, up slightly from the previous year.

In April the stockpile objective for rutile was reduced to zero. Thereafter, during the last half of the year, the General Services Administration (GSA) sold 13,756 tons from the Defense Production Act stockpile.

The price of rutile increased from \$175 to \$210/short ton in May and the rutile released by GSA commanded prices up to \$226/ton. Ilmenite prices increased from \$22-24/long ton to \$32 in August, and the price of Sorel slag increased from \$53 to \$61/long ton in August. The declared valuation of imported synthetic rutile ranged from \$90 to \$100/short ton. A bill, H. R. 9246, to suspend the tariff on synthetic rutile through 1976, was before Congress during the year, but no final action was taken.

In response to continued strong demand, production of titanium pigment reached 770,000 tons, a 12% increase over 1972 levels, in spite of a few short-lived strikes and some brief period of mechanical difficulty. Production at the New Johnsonville, Tennessee, plant of E. I. du Pont de Nemours and Company, passed the 200,000 ton/year mark by year's end; however, that company's plans for construction of a 100,000 ton/year plant near Brunswick, Georgia, were being restudied.

Imports of pigment were about 67,000 tons during the year, 22% less than in 1972. Heavy demand for pigment in Western and Central Europe and in Japan reduced the quantity available for export, and higher

priced markets elsewhere reduced the quantity coming to the U.S. Domestic prices for various grades of pigment held generally at or below 30¢/lb during the year (103).

An Ashtabula, Ohio, plant will be the world's first user of an Australian rutile process. The Sherwin-Williams Company facility, due ready for start-up late next year, will use an ilmenite-to-rutile process developed by Rutile and Zircon Mines (Newcastle), Ltd., which up to now has performed only in pilot plant units. Ultimate capacity and cost of the facility will be 50,000 tons/year and \$2 million, respectively (108).

Process details are unavailable. Sherwin-Williams discloses merely that the technology dovetails well with the company's manufacture of titanium dioxide from rutile via the chloride process (108)

Worldwide, the increased demand for titanium ores and titanium pigment was encouraging geological investigations in Uruguay, Mauretania, and Liberia; mine development in the Republic of South Africa and Sierra Leone; expansion of mine production in Sri Lanka, Australia, and Norway; pilot plant investigations into synthetic rutile in Australia, where a currently producing plant is also being expanded; and planning, construction, or expansion of pigment plants in Mexico, Spain, Poland, Yugoslavia, Finland, West Germany, and India. Activities of environmentally concerned groups were, however, acting as a brake on the industry in Italy, France, and on the Australian east coast (103).

**Lithium.**—Domestic production of spodumene and lithium carbonate was the largest ever reported according to the Bureau of Mines (111). Domestic and international consumption of lithium products was also at record high levels; the three leading consumers were the U.S., Europe, and Japan (111).

It is probable that domestic lithium production has been extended to its maximum and further increases may require installation of additional capacity.

Actual production figures were not available for 1973, but world consumption was estimated at 49,500,000 lb of  $\text{Li}_2\text{CO}_3$  equivalent which represents a 33% increase in the last year.

During 1973, Foote Mineral increased capacity by tapping additional wells and adding more evaporation pond acreage. Foote Mineral also put on-stream the first commercial plant to chemically remove iron from spodumene ore (112).

Lithium Corporation of America expanded its operation at Bessemer City, North Carolina, during 1973 and is essentially self-sufficient in lithium raw material (112).

International producers of lithium compounds include Russia, Germany, France, and Japan, although little information is available on production (112).

Work is being continued on the development of lithium batteries for use in the electric transportation industry. Both ESB and Argonne National Laboratories are developing systems for their commercial production (113).

Foote Mineral announced a 12 million lb/year lithium carbonate plant to be built at Kings Mountain, North Carolina; production is scheduled to begin in early 1976 (109).

Lithium prices were raised in December 1973 by both U.S. producers to between 55 and 56¢/lb for bulk lithium carbonate. Foote Mineral and Lithium Corporation of America also raised lithium metal ingot prices from \$8.18 to \$8.53/lb (110). Anhydrous lithium chloride was \$0.94/lb; anhydrous lithium bromide was \$1.70/lb (111).

**Copper.**—On a refined copper basis, the U.S. experienced reduced production, net exports, near record high consumption, and a drawdown of industrial stocks (114). A shortage of available copper relative to demand developed in the first quarter and became a critical supply problem for some users. Salient factors causing the imbalance included: a surge in world de-

mand; disruptions to production in Chile, Canada, and Belgium; some curtailment in domestic output to meet air quality standards, as required by the Environmental Protection Agency; transport problems in Canada and Zambia; the fuel shortage; and the effect of U.S. price controls coupled with a rapid escalation of world prices. Several of the supply disruptions were resolved, but the continuing high demand and depleted inventories left supplies tight at year's end. The national copper stockpile objective was reduced to zero in March, making available 252,000 tons of surplus copper pending congressional authorization.

Mine production was 1.73 million tons, a 3% increase and approximately equal to the record high of 1970. Principal copper producing states were Arizona with 54% of the total, Utah (15%), New Mexico (12%), Montana (8%), Nevada (5%), and Michigan (4%).

Smelters, despite some curtailment of operations to meet air quality standards, increased output 2% to an indicated 1.73 million tons from primary materials, a record high quantity for the second successive year. Refinery production from primary materials was projected to decline 2% from the 1972 record high to 1.83 million tons. Production of refined copper from secondary materials was 465,000 tons, compared with 423,000 tons in 1972.

Consumption of refined copper advanced 6% to 2.40 million tons. This increase reflected the greater activity in the general economy for most of the year and was approximately equal to the record high consumption of 1966.

Stocks of refined copper at primary producers were drawn down from 57,000 tons at the start of the year to 28,600 tons at the end of October. Stocks of copper at brass plants and wire mills were reduced from 77,200 tons at the start of the year to 61,400 tons by the end of June, increased to 95,100 tons during July, and then declined to 49,000 tons by the end of October.

Imports of refined copper were 201,500 tons, a 14% increase from the preceding year and equal to 1971 imports. Imports of blister were indicated to be 154,000 tons compared with 157,400 tons in 1972. Public Law 93-77 suspended the 0.8¢/lb duty on copper from July 1, 1973 to June 30, 1974, reinstating the suspension that had been in effect from 1966 to June 30, 1972.

Exports of refined copper increased 3.5% to 189,400 tons, the largest quantity since 1970. There was a 27% increase in exports of copper-base scrap (alloyed and unalloyed) to 109,000 tons. Scrap exports were particularly large during June, July, and August following the domestic price ceilings imposed in early June and the escalation of foreign copper prices. Copper-base scrap was exempted from price controls, effective August 6, and there was a significant reduction in exports following this action.

Domestic copper price quotations were increased by 9.5¢/lb in three steps during the first quarter of 1973 to a quoted price of 60-60.25¢/lb. Price controls prohibited any price increase between early June and December 6, after which most quotes were increased by approximately 8¢ to a range of 68.15-69.25¢/lb. Prices on the London Metal Exchange increased from an average 50.7¢/lb equivalent for January to \$1.029 for November, and were \$0.906 in mid-December.

World refined copper output rose 3% to 6,550,000 tons in 1973, while consumption rose 8% to 8,542,000 tons, according to preliminary figures from the World Bureau of Metals Statistics. World mine production was up 6% to 7,463,000 tons from 1972 (115, 116).

Zambia, Zaire, Chile, and Peru produced a total of 2.16 million tons, a rise of 3% over 1972 and 36% of the total for the Western world. Canadian mines produced 783,000 tons in 1973, up 10%.

Refined copper production in Japan rose 17% to 945,000 tons in 1973. Consumption of refined copper in Japan was a remarkable 1,199,000 tons in 1973, a 26% increase over 1972. Western European consumption rose 7% last year.

Cominco Ltd. and Sherritt Gordon Mines Ltd., both of Canada, are planning a pilot plant (\$10 million) on their new copper recovery process (S-C process) at Fort Saskatchewan, Alberta. The program is funded by both firms and the Canadian Government. The pilot unit initially will be operated on copper sulfide concentrates from Sherritt-Gordon mines at Fox and Ruton in Manitoba. The process is applicable to low-grade and complex ores; it produces a high purity copper, elemental sulfur, and recovers precious metals in addition to zinc and molybdenum (117).

Cyprus Mines will establish a new open pit copper mine at a site midway between Benson and Wilcox, Arizona, where it operated a 200 ton/day copper-zinc mine and concentrator until the high-grade ore body was exhausted and the plant dismantled in 1960. Reserves stand at 14.7 million tons of oxidized copper ore averaging 0.5% copper, of which 1.4 million tons/year will be mined and 5000 tons/year of 99.9% cathode copper produced by a process of leaching and electro-winning. The cost of the project, scheduled to go into production in the first quarter of 1975, will be \$6 million (118).

Cyprus Mines has delayed the start-up of its demonstration plant just outside of Tucson, Arizona, which is to use the new Cymet process for recovering copper. Delays in equipment delivery have postponed the opening until sometime in the second quarter of 1974 (118).

The military government of Peru formally took over the operations of Cerro de Pasco on January 1, 1974. Cerro is confident that Peru will pay prompt compensation for the book value of the operation. The expropriation does not apply to other Cerro holdings in Peru (119).

A massive copper find 250 miles southwest of Mexico City in the State of Michoacan is attracting the interest of two of the world's largest mining corporations, Hudson Bay Mining and Smelting Company, Ltd., Manitoba, Canada, and Anglo American Corporation of Canada, Ltd., Toronto. A representative of the Patino Society N.V. of The Hague, Netherlands, which owns the field, reveals that Patino has agreed to sell its interest to the two other companies. Details on the negotiations and possible future development have not yet been revealed (120).

A major copper smelting complex has been put into operation near Dzhezkazgan, in the Soviet central Asian Republic of Kazakhstan. Copper reserves in the area, which have traditionally been the largest in the USSR, are shallow lying and lend themselves to low cost, open-pit mining (120).

Poland's Heavy Industry Ministry is working on plans for a Western-financed, multimillion-dollar project that could make the country a leading world copper producer by the early 1980's. Major new copper deposits were discovered in 1957 in Lower Silesia near Wroclaw. Two mines, one in Lubin and the other in Polkowice, have been in operation since 1969. The new mine and smelter, which are expected to be built by 1982, could, according to Western experts, put Polish copper production at well over 200,000 tons/year (121).

Texasgulf Inc. is planning to increase copper mining and concentrates production at Kidd Creek Mines, Timmins, Canada. Capacity will increase from the present 3.6 million to 5 million tons/year (122).

Peru plans to increase copper production capacity from the present 215,000 to 560,000 tons/year in 1976 and 1 million tons/year in 1980, according to the Minister of Power and Mines. Projects that will be commissioned this year are: 150,000 tons/year copper at Ilo and 75,000 tons/year at Zajamarquilla (123).

A recent in-depth report on copper (124) listed the Free World copper producers. Plants under construction are the Phelps Dodge plant at Tyrone, New Mexico (100,000 tons), the Hindustan copper plant at Khetri, India (34,200 tons), the Black Sea copper

plant at Samsun, Korea (44,100 tons), and the AMMI plant at Ausso-Corno, Italy (66,200 tons).

The same article described the environmental confrontation in the copper industry with government requirements. The regulations for new plants will be even stricter than those of existing plants. The copper industry commitment to the prevention of air pollution has increased annually. During 1972, the industry spent 22% of the capital expenditures on the problem. The copper companies have until 1975 to comply with the primary air standards, unless technology is not available.

In the report, the state-of-the-art of copper extraction, particularly smelting, is reviewed. The new technology, its uses, and its reasons for use, such as improved emissions control and improved economics, are also reported. Newer Mitsubishi, WORCRA, and Noranda smelting processes, and the Cymet and the Arbiter hydrometallurgical processes are described. Other processes, still in various stages of development, are also briefly outlined. The cleaning up of sulfur dioxide by a number of routes in various stages of development is also reviewed (124).

An ion exchange and solvent extraction method was developed for extracting copper, cobalt, nickel, and zinc by Bayer in association with Duisburger Kupferhutte, a copper smelter owned by other hydrometallurgical operations. In the process, the metals (except manganese) are taken up by Bayer's ion-exchange resin, Lewatit TP 207. Acid treatment then frees the metals, which can be separated. The big plus for its method, Bayer claims, is that the acid is reduced to only 12% of its original volume, making it adaptable to leach solutions with high manganese content (125).

A new approach to chemically treating sulfide ores to obtain metal will get its first large-scale commercial test in a \$22 million plant that Anaconda is building in Anaconda, Montana. It will produce 36,000 tons/year of copper (126, 127).

All copper companies have investigated hydrometallurgical methods in which the metal is leached from the ore with a solvent, then recovered from the solution in a relatively pure form. The big advantage is that there are no smelters, fumes, dust, or sulfur dioxide pollution problems. Moreover, much of the solids-handling equipment can be replaced by simpler liquid-handling techniques. However, corrosion problems have been formidable, and producers have had trouble applying the technique to sulfide ores.

Anaconda's method, called the Arbiter process, begins with ammonia leaching of copper concentrate milled from sulfide ores. The leaching is carried out in a series of low-temperature and low-pressure vats. The copper in the leach solution is then separated by ion exchange and recovered by electrolysis.

The basic technique also has been piloted on nickel and other nonferrous metal ores with good results.

Anaconda says it is also doing engineering work on combining the leaching and certain other stages of the Arbiter process with conventional smelter design. The work could help control sulfur dioxide emissions from smelters that are now in operation. By late December, the construction was 50% complete and engineering 80% complete (128).

The copper market for 1974 has been predicted to be tight in early 1974, since copper output increases are not likely until the second or third quarter (129).

Consumers have been living hand-to-mouth. The stockpile release of 170,000 tons to U.S. consumers will help achieve a finer balance between supply and demand. The 1974 prospects of a 300,000 ton increase in Free World primary production capacity may not be realized because of the energy crisis. Economic growth, and consequently copper consumption, will be slowed by energy limitations. Despite a slow down in the economy, there will be inflation at home and abroad, and inflation spells higher prices. Decontrol of copper

in April 1974, should this occur when wage-price controls end, may see a producer price increase to above 70¢/lb to compensate for increased production costs (129).

**Nickel.**—A balance was finally reached throughout the world in the latter part of 1973 between nickel supply and demand. This balance was due to a cut-back of mine production in Canada and New Caledonia, as well as a greatly increased demand in the U.S., Western Europe, and Japan. The part played by the U.S. in this was significant, as consumption was 196,000 tons during the year, a 19% increase from the 165,000 tons consumed in 1972. Production in the U.S. in 1973 was approximately equivalent to that of the last 5 years. The main American producer was Hanna Mining, with 17,000 tons of nickel (130).

World trade in nickel was marked by the changing supply base. Imports of Russian nickel for consumption in the U.S. increased more than tenfold compared to 1972; imports from the Dominican Republic increased almost fivefold; and Southern Rhodesian producers supplied more than 6,000,000 lb of nickel to the U.S. markets. A new trade channel was opened as Canadian nickel was sold to the People's Republic of China (130).

The price of pure nickel was stable throughout the year of 1973. International Nickel Company (INCO) raised the price of nickel pellets and electrolytic nickel from \$1.53 to \$1.62/lb, which went into effect on January 4, 1974. Falconbridge Nickel Mines followed suit and hiked prices 9¢/lb for the pure metal (131).

The price of ferronickel, which accounted for the major part of the U.S. consumption, was raised by several companies. On July 9, Société Le Nickel increased its price 6-7¢/lb and Falconbridge increased its prices by 11¢ for the same product. Hanna Nickel Mining Company raised its prices from \$1.38 to \$1.53/lb following exemption by the Cost of Living Council from price controls, effective January 15, 1974. INCO raised the price on nickel in oxide sinters 90 and 75 to \$1.43, and \$1.40, respectively, an increase of 3¢. The price was effective July 20, 1973 (130, 131).

According to INCO, the most technologically advanced nickel refinery was opened late in 1973 at its \$140 million plant at Copper Cliff, Ontario. This facility will be the only one in North America to produce nickel pellets, at a rate of 100 million lb/year. The plant will also make 25 million lb/year of nickel and nickel-iron powders. By-products are expected to be electrolytic copper, cobalt carbonate, and precious metal concentrates. The plant is the first to use top-blown rotary converters in nonferrous metallurgy and employs the INCO Pressure Carbonate process (132, 133).

Major nickel exploration projects were in progress in Australia, the South Pacific Islands, the Philippine Islands, and Indonesia. Exploration throughout Canada and in the Duluth gabbro of northern Minnesota was undiminished (130).

In New Caledonia, exploration activities at the Penamark nickel prospect have been effectively completed. Joint research by Penarroya and Amax at the site continues as they try to find a way to extract nickel, cobalt, chrome, and iron from the ore. One Amax spokesman remarked that the \$400 million venture could probably be a reality by 1980. The ore contains 400 million tons of 1.4% nickel (134).

Amax Nickel Refining's plant in Plaquemine Parish, Louisiana, should go into operation in the second quarter of 1974. Amax will import nickel ore from Africa and refine it to 80 million lb/year of usable nickel (135).

A significant part of the nickel supply in the U.S. came from nickel scrap. The consumption of nickel scrap in November 1973 was 738,711 lb (131).

**Zinc.**—The continuing rise in the demand for zinc in 1973 created a short supply situation compelling record imports of metal, a large release of stockpiled

zinc, and record levels for the prices of domestic and foreign zinc in the U.S. (136).

Mine production in 1973 was approximately 485,000 tons, 1% higher than that of 1972. Eighteen states reported mine production, one more than in 1972. Nine states showed increases and nine registered decreases. New York moved up to first place, Missouri's by-product zinc recovery from mines of the lead-belt was second, Tennessee was third, Colorado was fourth, and Idaho fifth. In Tennessee, production was lost from the Flat Gap mine that closed near the end of 1972 and the Young and Coy mines which were shut down early in 1973. The Young mine was reopened in October and construction began at its new concentrator to replace the present Mascot mill. New Jersey Zinc Company's New Elmo mine at Carthage in central Tennessee is scheduled to begin operations soon (136).

Smelter production of slab zinc from ore was 500,000 tons, a decline of 133,000 tons from that of last year. AMAX Lead and Zinc Company discontinued zinc production at the horizontal retort smelter at Blackwell, Oklahoma; however, the roasting facilities will continue to operate until May or June 1974. Rehabilitation of the AMAX Zinc Company electrolytic plant (closed by the American Zinc Company in mid-1971) was completed. The National Zinc Company obtained permission from the State of Oklahoma to continue operating the Bartlesville horizontal retort plant. The Texas Air Control Board, on July 26, 1973, rescinded a previous notice for the Amarillo horizontal retort smelter to be in compliance with air quality standards or close by December 31, 1973, and issued a variance permitting the smelter to continue operating until May 30, 1975. Construction plans for two more electrolytic zinc plants were announced during the year: the American Smelting and Refining Company reported plans for erection of a plant at Stephensport, Kentucky, with an annual capacity of 180,000 tons; and the New Jersey Zinc Company is considering construction of one along with a zinc oxide plant near Clarksville, Tennessee. With a favorable labor picture, large deposits of zinc ore in the area, and the availability of low-cost TVA power, the final decision depends on relaxation of price control on zinc (137).

Park City Ventures, jointly owned by Anaconda Company (60%) and American Smelting and Refining Company (40%), is in the process of completing a development program at its Ontario Mine in Park City, Utah, where a production of 5000 tons/week of ore is expected. By early 1975, mining and processing operations will produce 43,000 tons/year of zinc concentrate, 25,000 tons/year of lead concentrate, and 1.2 million oz/year of silver (138).

The \$30 million expansion of the zinc plant at Canadian Electrolytic Zinc in Valleyfield, Quebec, is expected to be completed at the end of 1975 (139).

General imports of zinc in ores and concentrates declined 22% to approximately 200,000 tons, the lowest since 1940; the major sources continued to supply less. Receipts from Canada were down 4% and those from Mexico, Honduras, Peru, and Ireland were substantially lower than last year. Imports for consumption of zinc in ores and concentrates decreased 5% from those in 1972 to 165,000 tons. General imports and imports for consumption of slab zinc were practically the same at 590,000 tons with increases over last year of 14% and 15%, respectively. Canada accounted for approximately 60% of the slab zinc imports, Japan 8%, Belgium-Luxembourg 7%, Australia 7%, and Zaire 4%.

Consumption of slab zinc increased 6% to a record high of over 1.5 million tons. The quantities used for all major categories increased: galvanizing was up 6% from 1972; brass and bronze, 5%; zinc base alloy, 8%; and zinc oxide, 20%. The minor uses declined: rolled zinc was off 12%; and other uses including zinc dust, wet batteries, desilverizing lead, and light metal alloys declined 6%.

The General Services Administration (GSA) continued to release zinc from the national stockpile as authorized by Public Law 92-283. Effective July 1, 1973, GSA increased the quarterly quota to 25,000 tons/quarter (including 5000 tons Special High Grade) and permitted the participating producers to draw more zinc from the stockpile. GSA sales of Government stockpiled zinc in 1973 amounted to approximately 285,000 tons. Sales from the set-aside program totaled 62,477 tons, and 223,000 tons were sold to the participating domestic primary producers who remelted 149,400 tons and shipped 73,600 tons directly to customers. The balance of 40,000 tons will be released in the first quarter of 1974. In early April the stockpile objective for zinc was reduced from 560,000 to 202,700 tons creating an additional surplus of 357,300 tons. New legislation authorizing disposal of this quantity was signed by the President on December 31, 1973.

The lead and zinc flexible-tariff bill and the bill to suspend the duty on imports of zinc concentrates were reintroduced in Congress in March. Each incorporates a significant change from the previous bills. The new flexible-tariff bill permits a larger quantity of zinc metal to enter the U.S. before the higher duties become effective, and the duty suspension bill on zinc concentrates is for 2 years instead of 1 year. At year's end, both bills were in the House Ways and Means Committee. Another bill, also in the House Ways and Means Committee, proposed suspension of the duty on imports of slab zinc (140).

Texasgulf and Canada Development Corporation have patched up their differences, with the CDC now controlling about 30% of Texasgulf stock.

Mitsubishi has cut production of zinc by more than 20% and of lead by some 12% during December, probably due to the energy crisis.

Early in the year, prices advanced from a range of 18-18.5¢/lb to 20.25-21¢/lb where they were frozen June 13 by Presidential order. The ceiling prices prevailed until December 6, 1973, when the Cost of Living Council abolished the control on zinc. One company raised its price to 32¢/lb and the others quoted prices between 28 and 30¢/lb. The European producer price for zinc quoted at 18.5¢/lb (U.S. equivalent) in January rose after five increases to 32.5¢/lb at year's end. The London Metal Exchange price for zinc was 17.5¢/lb at the beginning of the year, 31.5¢ at the end of June, and advanced to a high of 99¢ on December 4, 1973, then declined to 60¢/lb at the end of the year.

### Electrical Energy

**U.S. power generation.**—The following tables give a preliminary summary of the production and consumption of electrical energy for the twelve-month period January through December, 1973 (141, 142).

#### Production of Electrical Energy in 1973 (Billion-kW-hr)

	1972	1973	% Change
<b>Production by electric utilities</b>			
Coal-fired plants	770.6	843.6	9.5
Gas-fired plants	375.7	337.5	-10.2
Oil-fired plants	272.5	314.7	15.5
Nuclear plants	54.0	81.3	50.5
Total fuel burning	1472.8	1577.1	7.1
Hydroelectric plants	272.7	277.6	1.8
Total	1745.5	1854.7	6.3
Private industry, self-generated	106.1	106.1	0
Total U.S. power generated	1851.6	1960.8	5.9

#### Installed Generating Capacity\* (Millions-kW)

	1972	1973
<b>Public owned</b>		
Steam	46.6	51.0
Hydro	37.3	39.6
Nuclear**	0.9	2.4
Total	84.8	93.0
<b>Investor owned</b>		
Steam	281.1	301.5
Hydro	19.3	21.9
Nuclear**	14.4	19.3
Total	314.8	342.7
Total electric utility industry capacity	399.6	435.7

\* Not including privately owned capacity.

\*\* Nuclear plants having about 4000 MW capacity received operating licenses but were not placed into operation. This capacity not included in the above figures.

#### Electric Utility Fuel Consumption in 1973

Fuel	1972	1973	% Change
Coal, million tons	351.0	386.6	10.1
Gas, billion cu ft	3,978.7	3,754.2	-5.6
Oil, million barrels	493.9	565.5	14.5
Coal and coal equivalent, million tons	646.3	723.7	12.0

#### Total Electric Utility Sales to Ultimate Consumers in 1973 (Billions-kW-hr)

Consumer	1972	1973	% Change
Residential	511.4	554.2	8.4
Commercial	361.8	396.9	9.7
Industrial	639.5	687.2	7.5
Other	64.9	64.9	—
Total	1577.6	1703.2	8.0

The year 1973 was marked with intensive concern by all sectors of society with all forms of energy. The growing demands of the U.S. and recent foreign political actions have brought national awareness of the reality of the energy crisis.

Project Independence was launched by President Nixon with the objective of meeting U.S. energy needs without depending on foreign resources by 1980 (143). He also asked for consideration by the Congress for the formation of an Energy Research and Development Administration. Initial funding of the increased energy Research and Development Program called for \$1.0 billion in the 1974 fiscal year, followed by a 5 year \$10 billion program. Dixie Lee Ray, Chairman of the Atomic Energy Commission (AEC), presented the details of the urgent proposed programs toward the end of the year. William E. Simon was named the new energy advisor and head of the Federal Energy Office (144).

With electrochemical plants and other high energy-consuming industries operating at near capacities, power sporadically became in short supply in localized areas.

Late in the year, the sudden Arab oil embargo became a reality, intensifying the energy shortage. Although knowledgeable people and agencies proclaimed the coming fuel shortage for a decade, the embargo rudely awakened the complacent that the U.S. cannot indefinitely rely on foreign sources of fuel to meet the increasing domestic demands.



The Arab oil embargo created a national crisis as well as a sudden shift from apparent abundance to an immediate scarcity. However, the crossover point of foreign and domestic supply and increasing domestic demand was fast approaching, and the scarcity would inevitably arrive. The embargo only hastened the day of scarcity and made us aware that dependence on foreign oil would be exceedingly dangerous to the U.S. economy and our national defense obligations.

To achieve minimal dependence on imported oil in the immediate future, it is necessary to encourage the development of four major areas: provide stronger incentives for bringing new domestic natural gas and oil to the market, accelerate the drilling of the Outer Continental Shelf for oil and gas, increase the use of coal, including the conversion of coal to gas and the opening of new mines, and increase the construction of nuclear power plants. The development of other forms of energy, such as shale oil deposits, geothermal power, and solar energy, is not expected to have any perceptible impact on energy production within the next decade.

The significance of the huge resources of American coal is reported by the National Petroleum Council on coal availability. This review of the U.S. energy outlook concludes that domestic coal reserves can make a major contribution to the nation's future energy demands (145).

The conventional domestic demand for coal is expected to increase at an annual growth rate of 3.5%, or 863 million tons in 1985. Exports were predicted to grow by 4.5% annually, or up to 138 million tons in 1985. The big unknown in coal demand over the next decade is that required for production of gaseous and synthetic fuels.

Total coal reserves are estimated by the U.S. Geological Survey to be a 3.2 trillion tons, with 2 trillion tons potentially recoverable. The Bureau of Mines has converted a ton of coal into two barrels of low sulfur, low ash oil. At this rate, the recoverable coal in the U.S. is equivalent to 4 trillion barrels of oil, or 10 times the known worldwide oil reserves.

The survey concludes much remains to be done if this potential is to be reached. Mining technology must be improved to offset the severe impact of the Coal Mine Health and Safety Act of 1969 on production capacity. New mine workers and mining engineers must be developed to produce the increased production. Technology must be developed to permit use of high-sulfur coal in power generation without air pollution. Expanded and reliable transportation must be constructed, including railroads, river systems, and coal handling (145).

The construction of the trans-Alaskan pipeline to move crude oil from the Northern Slope was delayed by a lawsuit based on the width of the right-of-way, initiated by environmentalists (146). However, legislative action was taken to amend the law to permit the pipeline to be built (147).

**New developments.**—In new technology, nickel-plated aluminum conductor has been produced at half the cost of copper with easy connectability of the conductor. The nickel thickness ranges from 0.1–10 $\mu$ . For telecommunication applications, copper-clad aluminum conductor is produced by means of hydrostatic extrusion (148).

The possibility of manufacturing methanol offshore in the North Sea has been proposed. Previous studies have centered on land-based plants in the Middle East. The conversion of natural gas to methanol simplifies the ocean shipping of fuel, but with an energy loss (149).

According to the U.S. Bureau of Mines, methane from coal mines, obtained by hydraulic fracturing of the coal bed to release more gas and by drilling horizontal drainage holes through the coal bed, could double U.S. gas reserves. The Bureau of Mines estimates 260 trillion cu ft of methane, about equal to U.S. proved natural gas reserves, lie in coal beds

between strip mining depth and 3000 ft. In conducted experiments, methane from coal beds was produced as fast as from commercial gas wells (150).

The U.S. and USSR have agreed to exchange ideas on magnetohydrodynamics (MHD) as a means of energy conversion. The Soviets already have a 25 MW pilot plant in Moscow, whereas U.S. research on MHD is at a less advanced stage. However, the Soviets have run into technical problems, and both countries agreed that an exchange of data will be mutually beneficial (149).

The feasibility of piping coal in oil is being studied by Shelpac Research and Development, Ltd., for Interprovincial Pipe Line Company of Canada. Using an existing pipeline to minimize capital costs, the slurry would contain up to 35% coal. The coal would be separated in Eastern Canada by the refiners and the oil left with the low-sulfur Alberta subbituminous coal would be used as fuel by the power companies (151).

A limestone process for removing sulfur dioxide from stack gases will be getting a full-scale tryout at the Detroit Edison 170 MW Saint Clair generating station in the spring of 1974. The trial follows a successful 1 MW pilot plant test of the process (145).

A new process for combining the sulfur from coal is the intimate mixing of the coal fines with lime before firing. The lime ties up the sulfur as sulfate with up to 95% sulfur removal. Further tests with pulverized coal are planned (152).

The Tymponic Corporation, developers of a device employing ultrasonic emulsification of fuel oil with up to 25% water, has demonstrated the reduction of fuel oil consumption in boilers by more than 20% (153).

Interest in the so-called hydrogen economy, advocated by proponents of clean fuel and those concerned with energy beyond the year 2000, has been accelerating with increasing shortages of fossil fuel. Hydrogen, derived from water by one of several methods, is proposed to supplant all fossil fuels. Basically, a remotely sited nuclear reactor (fission or fusion) supplies the energy to form oxygen and hydrogen from water. The hydrogen, acting as an energy carrier, can be pumped through pipelines either as a compressed gas or a liquid to a populous center, where the hydrogen is burned with oxygen or air in a steam generating plant, or piped to homes and burned catalytically, or to a fuel cell to provide electrical energy (154).

The hydrogen energy system was the topic of two national meetings in 1973, at the American Chemical Society meeting in Boston in the spring and at the annual Intersociety Energy Conversion Engineering Conference in San Diego in the fall. Conferences in 1974 were slated for Houston in January, Miami in March, and at the Fall Meeting of The Electrochemical Society in New York.

**Nuclear power.**—Fourteen nuclear power plants received operating licenses during 1973, thereby boosting the nuclear generating capacity by more than 70% to 25,670 MW. The Atomic Industrial Forum listed 42 U.S. nuclear units as operable, 56 under construction, an additional 101 under firm order, and 14 others covered by options or letters of intent. By the end of 1973, nuclear facilities had 7% of the total U.S. generating capacity. It has been predicted that by 1980, 1985, and 1990 the nuclear-based energy sources for electrical utilities will be 20, 35, and 44%, respectively. Of the power plants under construction, 18 may get their operating licenses in 1974 (155).

During 1973, the fuel costs for San Diego Gas and Electric Company were estimated at \$0.763/million BTU on fuel oil compared with \$0.163/million BTU on nuclear fuel. These costs do not consider the 50% plus increase in price of petroleum products in the last 2 months of 1973 (155). The operating performances of nuclear vs. nonnuclear plants were compared by Commonwealth Edison Company (Chicago) from data on their fossil-fueled and nuclear-

fueled plants (68 and 32%). The latest 12 month figures for average plant capacity availability were 82.6% for nuclear and 79% for fossil plants (155).

The Atomic Energy Commission announced a new reduced rate of \$36/unit of separation for uranium enriching services. The total uranium enrichment revenues from the nuclear power industry in U.S.A. and abroad have exceeded a billion dollars (156).

Kerr-McGee signed a \$150 million contract with a group of utilities to supply nuclear fuel for electrical power plants (157).

The National Petroleum Council urged stepped-up uranium exploration to be prepared to supply the fuel for the U.S. nuclear energy generating capacity of 240,000-450,000 MW by 1985. It is estimated that 8-10 years will be required for exploration to find the 400,000-700,000 tons of  $U_3O_8$  that will be needed (150).

Westinghouse has increased its activity in supplying nuclear fuel in Europe by a formation of a new company with Belgian interests. Previously, Westinghouse formed Euro Fuel with French participation to supply fuel for light water reactors, as well as fuel production in Italy and West Germany (158). Bechtel, Union Carbide, and Westinghouse have proposed joint study with Japan's Enrichment Survey Committee to determine the feasibility of building a U.S.-Japanese uranium enrichment plant (159).

KMS Industries, Inc., Ann Arbor, Michigan, sponsored by Texas Gas Transmission Corporation, will carry out laboratory and theoretical work on producing hydrogen and combustion fuels by KMS nuclear fusion techniques (1969).

A European effort in controlled nuclear fusion research, named Joint European Tokamak (JET), has been proposed to start in 1976. This program will continue the joint efforts in nuclear fusion after the present 5 year research program terminates (170).

Hydrogen fuel from water by a nuclear route is being sought by Gulf General Atomic Company, sponsored by Southern California Edison and Northeast Utilities, Gulf General's high temperature reactor technology may provide a method of obtaining hydrogen fuel. In the process, heat and catalytic chemicals split water at a temperature of 1500°-1800°F (160).

A new company, Nuclear Power Products Company, a joint venture of Gulf Atomic Company and Foster Wheeler, will make steam generator equipment for high temperature, gas-cooled reactor (HTGR) nuclear power plant systems (161).

The closing of 20 nuclear power plants is the aim of environmentalists led by Ralph Nader and the Friends of the Earth. At issue is the safety of the emergency core cooling system. Failure of this system could lead to vertical melting of a plant and widespread radiation damage (162). A moratorium on nuclear plants in California was urged by environmentalists, who are planning to put an initiative to that effect on the November 1974 ballot (1968). Environmentalists were active in many hearings on nuclear power plants throughout the U.S. and have been successful in delaying the issuance of construction and start-up permits.

The Atomic Energy Commission is sponsoring development of geothermal energy, with a goal of 20,000 MW by the year 2000 (163). The only dry steam unit in commercial operation is the 400 MW plant at The Geysers in northern California. Hot water fields are estimated to be 10-20 times as abundant as dry steam fields. The high concentration of dissolved solids in the water presents processing and corrosion problems. Field trials of using hot rocks, which are close to the surface, as a geothermal energy source are under way. It has been estimated that hot rock fields could provide 10 times the power of dry steam and hot water fields combined. The total power generation potential of geothermal sources has been es-

timated at about 400,000 MW by the year 2000 (164).

One of the stronger incentives to bring natural gas to the market is an increase in price. The Federal Power Commission has generally approved applications at prices above ceilings in effect at the beginning of the year. For instance, the price of gas coming from offshore Louisiana wells was raised to \$0.45/1000 cu ft, compared to an earlier ceiling of \$0.26 (a 73% increase) (165).

Significant increases in electricity costs, especially from utilities dependent on Mideast oil, are projected for 1974. Power charge increases from 5-26% have been requested by New England and mid-Atlantic area power companies, hardest hit by the Arab embargo and new oil price schedules (166).

The Bonneville Power Administration which serves the Pacific Northwest will hike the price of power 20-30% beginning in December 1974. The 25% boost in rates charged aluminum producers would amount to less than 2% of the 1973 price of aluminum. Other electroprocess industries would be affected to a lesser degree (167).

Manuscript received July 17, 1974. This report was presented at the Industrial Electrolytic Division Luncheon at the San Francisco, California, Meeting of the Society, May 12-17, 1974.

Any discussion of this paper will appear in a Discussion Section to be published in the June 1975 JOURNAL. All discussions for the June 1975 Discussion Section should be submitted by Feb. 1, 1975.

#### REFERENCES

1. Chlorine Institute News Release, Feb. 13, 1974.
2. Chlorine Statistical Report—United States, Dec. 1973.
3. Chlorine Statistical Report—Canada, Dec. 1973.
4. *Chemical Engineering*, pp. 80-82, Feb. 18, 1974.
5. *Chemical Week*, p. 23 June 13, 1973.
6. *Ibid.*, p. 25, March 6, 1974.
7. *Chemical and Engineering News*, p. 4, July 30, 1973.
8. *Chemical Week*, Market Newsletter, p. 6, February 4, 1974.
9. North American Chlor-Alkali Industry Plants and Production Data Book, Jan. 1974.
10. *Chemical Week*, p. 84, Feb. 18, 1974.
11. *European Chemical News*, p. 12, Dec. 7, 1973.
12. *Chemical Week*, Technology Newsletter, p. 46, Nov. 28, 1973.
13. Stuart Holden, Electrode Corporation.
14. *Chemical Week*, p. 32, Oct. 31, 1973.
15. *Chemical Engineering*, p. 34, Feb. 18, 1974.
16. *Chemical Week*, p. 23, Feb. 14, 1973.
17. *Chemical Engineering*, pp. 84-86, Aug. 20, 1973.
18. *Business Week*, May 19, 1973.
19. *Chemical Week*, p. 76, Nov. 7, 1973.
20. *European Chemical News*, p. 18, Nov. 2, 1973.
21. *Chemical Week*, April 14, 1973.
22. *Ibid.*, p. 4, Aug. 1, 1973.
23. *Electrochemical Progress*, p. 10, Nov. 1973.
24. *Chemical Engineering Progress*, p. 61, March 1974.
25. Mineral Industry Surveys, U.S. Dept. of the Interior, Bureau of Mines, "Mercury in the Fourth Quarter 1973."
26. *European Chemical News*, p. 11, Dec. 7, 1973.
27. J. A. Sales, Monsanto Enviro-Chem System, "New Chlorine Plant Design As affected By Recent Regulations."
28. Mineral Industries Survey, U.S. Department of Interior, Bureau of Mines, Annual Preliminary, "Potash in 1973."
29. *Chemical and Engineering News*, Feb. 4, 1974.
30. *Chemical Week*, Oct. 24, 1973.
31. *Ibid.*, Sept. 26, 1973.
32. *Ibid.*, July 4, 1973.
33. Inorganic Chemicals, Current Industrial Reports, 1973.
34. *Chemical Marketing Reporter*, Feb. 25, 1974.
35. Mineral Industry Surveys, U.S. Department of the Interior, Bureau of Mines, Washington, D. C.,



- Annual Preliminary, "Sodium Compounds in 1973."
36. *Chemical Week*, p. 23, Dec. 19, 1973.
  37. *Electrochemical Progress*, p. 9, Oct. 1973.
  38. *Chemical Week*, March 14, 1973.
  39. *European Chemical News*, p. 18, Dec. 14, 1973.
  40. *Chemical Week*, p. 29, Dec. 19, 1973.
  41. *Ibid.*, p. 33, Jan. 9, 1974.
  42. *Ibid.*, p. 10, Jan. 2, 1974.
  43. Inorganic Chemicals, U.S. Dept. of Commerce, January-December, 1973.
  44. *Electrochemical Progress*, p. 10, Dec. 1973.
  45. *Chemical Week*, Oct. 31, 1973.
  46. *Electrochemical Progress*, p. 9, 10, Nov. 1973.
  47. *European Chemical News*, p. 11, Jan. 4, 1974.
  48. *Electrochemical Progress*, p. 4, Dec. 1973.
  49. *Chemical Marketing Reporter*, Feb. 25, 1974.
  50. *Ibid.*, p. 9, Dec. 25, 1972.
  51. Inorganic Chemicals for 1972, U.S. Dept. of Commerce, December 1973.
  52. *Chemical Week*, p. 51, Dec. 12, 1973.
  53. *Chemical Engineering*, pp. 68-70, March 19, 1973.
  54. *Metals Week*, p. 2, Dec. 3, 1973.
  55. Mineral Industry Survey, U.S. Department of the Interior, Bureau of Mines, Aluminum Monthly, "Aluminum Industry in December 1973."
  56. Mineral Industry Survey, U.S. Department of the Interior, Bureau of Mines, Annual Preliminary, "Aluminum and Bauxite in 1973."
  57. *Chemical and Engineering News*, p. 12, April 30, 1973.
  58. *Chemical Week*, May 2, 1973.
  59. *Metals Sourcebook*, p. 2, Jan. 28, 1974.
  60. *Chemical Week*, June 6, 1973.
  61. *Ibid.*, June 13, 1973.
  62. *Ibid.*, July 4, 1973.
  63. *Chemical Engineering*, July 23, 1973.
  64. *Electrochemical Progress*, Sept. 1973.
  65. *Chemical Engineering*, Feb. 4, 1974.
  66. *Chemical Week*, Aug. 8, 1973.
  67. *Ibid.*, Oct. 31, 1973.
  68. *Electrochemical Progress*, Oct. 1973.
  69. *Ibid.*, Nov. 1973.
  70. *Chemical Week*, Feb. 6, 1974.
  71. *Metals Week*, p. 7, March 18, 1973.
  72. Mineral Industry Surveys, U.S. Department of Interior, Bureau of Mines, Annual Preliminary, "Magnesium and Magnesium Compounds in 1973."
  73. *Metals Sourcebook*, II (2), 4 (1974).
  74. *Metals Week*, p. 10, May 14, 1973.
  75. *Electrochemical Progress*, p. 6, Oct. 1973.
  76. *Metals Week*, p. 7, Jan. 7, 1974.
  77. *Chemical Week*, p. 21, June 21, 1973.
  78. *Metals Week*, p. 7, Dec. 24, 1973.
  79. *Chemical Week*, p. 7, Jan. 24, 1973.
  80. *Electrochemical Progress*, p. 11, Nov. 1973.
  81. *Chemical Engineering*, Vol. 80, No. 19, Aug. 20, 1973.
  82. *Chemical Week*, p. 14, Jan. 2, 1973.
  83. *Metals Week*, p. 7, Jan. 21, 1974.
  84. *Ibid.*, p. 9, May 14, 1973.
  85. *Chemical Weeks*, p. 24, Jan. 17, 1973.
  86. Report of the Electrolytic Industries for 1972.
  87. Mineral Industry Surveys, U.S. Dept. of the Interior, Bureau of Mines, Manganese, December 1973.
  88. Mineral Industry Surveys, U.S. Dept. of the Interior, Bureau of Mines, Manganese, Annual Preliminary, 1973.
  89. *Chemical and Engineering News*, Dec. 24, 1973.
  90. *Chemical Week*, Dec. 19, 1973.
  91. *Metals Week*, Jan. 24, 1974.
  92. *Chemical and Engineering News*, Feb. 11, 1973.
  93. *Chemical Week*, Feb. 6, 1974.
  94. *Ibid.*, May 30, 1973.
  95. *Metals Sourcebook*, Feb. 11, 1974.
  96. *Engineering and Mining Journal*, p. 81, March 1974.
  97. Mineral Industry Surveys, U.S. Dept. of the Interior, Bureau of Mines, Annual Preliminary, "Beryllium in 1973."
  98. *Metals Week*, Jan. 7, 1974.
  99. Metal Industry Surveys, Chromium in 1973.
  100. *Metals Week*, Dec. 24, 1973.
  101. *Chemical Week*, Jan. 2, 1974.
  102. *Engineering and Mining Journal*, pp. 154-156, March 1974.
  103. Mineral Industry Surveys, U.S. Dept. of the Interior, Bureau of Mines, Washington, D. C., Annual Preliminary, "Titanium in 1973."
  104. *Metals Week*, p. 7, May 7, 1973.
  105. *Ibid.*, p. 10, May 14, 1973.
  106. *Chemical Week*, p. 35, Jan. 17, 1973.
  107. *Electrochemical Progress*, p. 5, Nov. 1973.
  108. *Chemical Engineering*, p. 64, March 19, 1973.
  109. *Chemical and Engineering News*, March 4, 1974.
  110. *Metals Week*, Dec. 31, 1973.
  111. Mineral Industries Survey, U.S. Dept. of the Interior, Bureau of Mines, Annual Preliminary, "Lithium in 1973."
  112. *Engineering and Mining Journal*, March 1973.
  113. Barry Profeta, ESB.
  114. Mineral Industries Survey, U.S. Dept. of the Interior, Bureau of Mines, Annual Preliminary "Copper in 1973."
  115. *Metals Week*, p. 3, Jan. 14, 1974.
  116. *American Metal Market*, Jan. 15, 1974.
  117. *Electrochemical Progress*, p. 13, Dec. 1973.
  118. *Metals Sourcebook*, II (2), 3 (Jan. 28, 1974).
  119. *Metals Week*, Jan. 7, 1974.
  120. *Chemical Engineering*, p. 68, March 19, 1973.
  121. *Ibid.*, p. 65, Oct. 15, 1973.
  122. *Electrochemical Progress*, p. 7, Nov. 1973.
  123. *Ibid.*, p. 6, Oct. 1973.
  124. *Chemical Engineering*, April 16, 1973.
  125. *Chemical Week*, p. 36, Dec. 5, 1973.
  126. *Chemical Week*, Jan. 24, 1973.
  127. *Chemical and Engineering News*, p. 12, Jan. 15, 1973.
  128. *Metals Week*, p. 11, Dec. 17, 1973.
  129. *Ibid.*, p. 2, Jan. 14, 1974.
  130. Mineral Industry Surveys, U.S. Dept. of the Interior, Bureau of Mines, Annual Preliminary, "Nickel in 1973."
  131. Mineral Industry Surveys, U.S. Dept. of the Interior, Bureau of Mines, "Nickel in November 1973."
  132. *Chemical Engineering*, Nov. 12, 1973.
  133. *Electrochemical Progress*, Dec. 1973.
  134. *Metals Sourcebook*, Jan. 28, 1974.
  135. *Chemical Week*, April 4, 1973.
  136. Mineral Industry Surveys, U.S. Dept. of the Interior, Bureau of Mines, Annual Preliminary, "Zinc in 1973."
  137. *Metals Week*, Dec. 1973.
  138. *Electrochemical Progress*, p. 6, Oct. 1973.
  139. *Chemical Week*, Jan. 17, 1973.
  140. *Metals Week*, p. 2, Dec. 17, 1973.
  141. *Electrical World*, pp. 50-55, March 15, 1974.
  142. Edison Electric Institute, March 18, 1974.
  143. *Chemical and Engineering News*, Nov. 19, 1973.
  144. *Ibid.*, Dec. 10, 1973.
  145. *Ibid.*, Nov. 12, 1973.
  146. *Chemical Week*, p. 10, March 7, 1973.
  147. *Ibid.*, p. 18, April 11, 1973.
  148. *Electrochemical Progress*, p. 5, Dec. 1973.
  149. *Chemical Engineering*, Vol. 80, No. 18, p. 35, Aug. 6, 1973.
  150. *Chemical Week*, p. 40, Sept. 19, 1973.
  151. *Ibid.*, p. 31, May 2, 1973.
  152. *Chemical and Engineering News*, p. 25, Dec. 24, 1973.
  153. *Ibid.*, p. 24, Dec. 24, 1973.
  154. *Chemical Engineering*, Vol. 79, No. 29, pp. 24-26, Dec. 25, 1972; *This Journal*, 120, 295C (1973).
  155. *Chemical Week*, p. 11, Jan. 16, 1974.
  156. *Electrochemical Progress*, p. 6, Oct. 1973.
  157. *Chemical Week*, p. 15, Nov. 21, 1973.
  158. *Chemical and Engineering News*, p. 7, Sept. 17, 1973.
  159. *Chemical Week*, p. 27, May 16, 1973.
  160. *Chemical and Engineering News*, Nov. 5, 1973.
  161. *Chemical Week*, p. 35, Jan. 17, 1973.
  162. *Ibid.*, p. 55, June 6, 1973.
  163. *Ibid.*, p. 39, Dec. 19, 1973.
  164. *Ibid.*, p. 37, Dec. 19, 1973.
  165. *Ibid.*, p. 22, June 6, 1973.
  166. *Ibid.*, p. 9, Nov. 7, 1973.
  167. *Ibid.*, p. 13, Dec. 19, 1973.
  168. *Chemical and Engineering News*, May 7, 1973.
  169. *Ibid.*, p. 14, Oct. 15, 1973.
  170. *Ibid.*, p. 12, Oct. 22, 1973.